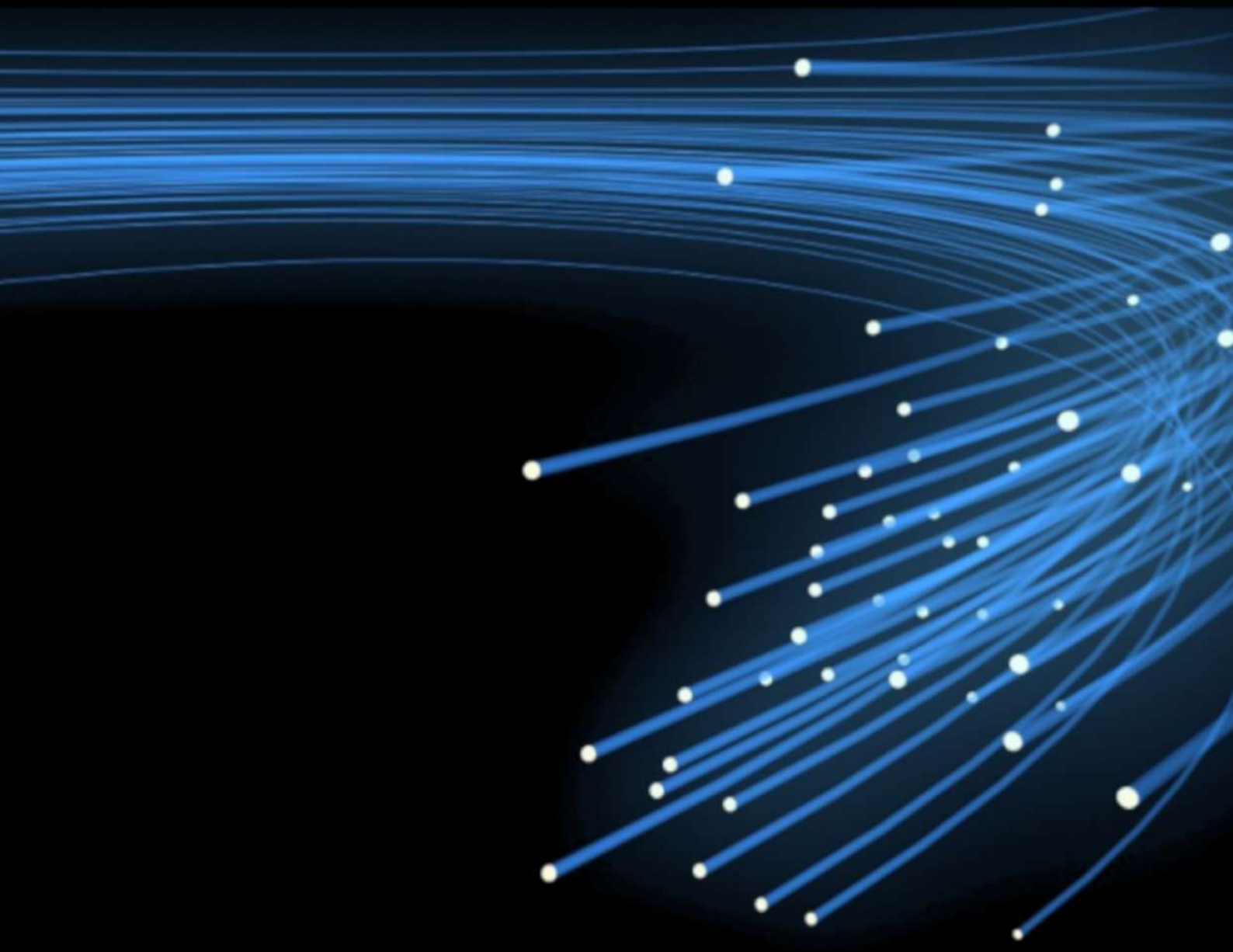
META 2019 Lisbon - Portugal

The 10th International Conference on Metamaterials, Photonic Crystals and Plasmonics



Proceedings

ISSN 2429-1390

metaconferences.org

META 2019 Lisbon - Portugal

The 10th International Conference on Metamaterials, Photonic Crystals and Plasmonics

Proceedings

July 23 – 26, 2019
Lisbon - Portugal

metaconferences.org


UNIVERSITÉ PARIS SUD
TÉCNICO LISBOA
Santander Universidades
AEM JOURNAL .ORG
NANOPHOTONICS
photonics
an Open Access Journal by MDPI
YSL 安扬激光
université PARIS-SACLAY
Photon Design.
BRUKER
LIGHT TEC
see the nanoworld
nea spec
RAITH
NANOFABRICATION
isotropic

META 2019 Lisbon - Portugal

The 10th International Conference on Metamaterials, Photonic Crystals and Plasmonics

Please share your comments, photos & videos !



www.facebook.com/metaconference



@metaconference

Edited by

Said Zouhdi | Paris-Sud University, France
Antonio Topa | Instituto Superior Técnico, Portugal

CONTENTS

ABOUT META 5

META 2019 ORGANIZATION 6

SPONSORS AND SUPPORTERS 8

PLENARY SPEAKERS 9

KEYNOTE SPEAKERS 12

CONFERENCE TUTORIALS 14

META 2019 VENUE 16

GUIDELINES FOR PRESENTERS 22

TABLE OF CONTENTS 22

ABOUT META

The International Conference on Metamaterials, Photonic Crystals and Plasmonics (META) features every year the latest developments in the area of Nanophotonics, Metamaterials and related topics.

The conference program consists of plenary lectures, keynote talks, special sessions of invited talks, general sessions and high-profile poster sessions that typically cover a broad range of exciting physics, such as metamaterials and negative index materials, metatronics and graphene metamaterials, plasmonics and nanophotonics, plasmon-enhanced photovoltaics, photonic and plasmonic crystals and cavities, materials for photonics (Graphene, MoS2, WS2, etc), quantum photonics, nanobiophotonics, structured light, near-field optics and nano-optics, transformational electromagnetics and cloaking, acoustic metamaterials, optomechanics, nanofabrication technologies, etc.

The origin of the conference dates back to 2002 as a NATO Advanced Research Workshop at a time when many of the current topical research areas began to emerge from the field of complex electromagnetic materials.

Following a now well-established tradition META takes place every year in unique locations around the world.

Year	Organizers	Venue
2019	Antonio Topa, Said Zouhdi	Instituto Superior Técnico
2018	Said Zouhdi	Western Mediteranean Cruise
2017	Junsuk Rho, Hakjoo Lee, Said Zouhdi	Incheon, Korea
2016	Manuel Nieto-Vesperinas, Said Zouhdi	Torremolinos, Spain
2015	Vinod Menon, Said Zouhdi	New York, USA
2014	Nikolay Zheludev, Jing Hua Teng, Said Zouhdi	Singapore
2013	Hamid M. K. Al-Naimiy, Said Zouhdi	Sharjah-Dubai, United Arab Emirates
2012	Xavier Begaud, Said Zouhdi	Paris, France
2010	Hadia Elhennawy, Said Zouhdi	Cairo, Egypt
2008	Alexey Vinogradov, Said Zouhdi	Marrakesh, Morocco
2002	Said Zouhdi	Marrakesh, Morocco

META 2019 ORGANIZATION



Said Zouhdi, General Chair
Paris–Sud University, France



Antonio Topa, General Co-Chair
Instituto Superior Técnico, Portugal

LOCAL ORGANIZING COMMITTEE

David Fernandes, Portugal
Sylvain Lannebère, Portugal
Haffsaa Latiou, Portugal
Tiago Morgado, Portugal
Filipa Prudencio, Portugal
Solange Silva, Portugal
Mario Silveirinha, Portugal
Zakaria Zouhdi, France

INTERNATIONAL ADVISORY COMMITTEE

Harry Atwater, USA
Federico Capasso, USA
Nader Engheta, USA
Teruya Ishihara, Japan
Tatsuo Itoh, USA
Yuri Kivshar, Australia
Graeme W. Milton, USA
Manuel Nieto-Vesperinas, Spain
Susumu Noda, Japan
Franco Nori, Japan & USA
Masaya Notomi, Japan
Yahya Rahmat-Samii, USA
Vladimir Shalaev, USA
David R. Smith, USA
Martin Wegener, Germany
Xiang Zhang, USA
Nikolay Zheludev, UK

TECHNICAL PROGRAM COMMITTEE

Pierre-Michel Adam, France
Ishwar Aggarwal, USA
Javier Aizpurua, Spain
Xavier Begaud, France
Mohamed Bakr, Canada
Svetlana V. Boriskina, USA
Alberto Bramati, France
Kurt Busch, Germany
Rafael Caldeirinha, Portugal
Nuno Borges Carvalho, Portugal
Che Ting Chan, Hong Kong
Debashis Chanda, USA
Pai-Yen Chen, USA
Johan Christensen, Spain
Naresh Das, USA
Alfredo De Rossi, France
Mohamed Farhat, Saudi Arabia
Michael A. Fiddy, USA
Monika Fleischer, Germany
Wolfgang Fritzsche, Germany
Francisco Garcia-Vidal, Spain
Alexander Govorov, USA
Ortwin Hess, United Kingdom
Joachim Krenn, Austria
Laura M. Lechuga, Spain
Howard (Ho Wai) Lee, USA
Jensen Li, Hong Kong
Jichun Li, USA
Haitao Liu, China
Anatole Lupu, France
Stanislav Maslovski, Portugal
Bumki Min, Korea
Fernando Moreno, Spain
Teri Odom, USA
Namkyoo Park, Korea
Dorota Pawlak, Poland
Min Qiu, China
Jun Suk Rho, Korea
Kazuaki Sakoda, Japan
Luca Sapienza, UK
Mario Silveirinha, Portugal
Mohamed Swillam, Egypt
Takuo Tanaka, Japan
Giorgos P. Tsironis, Greece
Augustine Urbas, USA
Hong Wei, China
Joel K. W. Yang, Singapore
Anatoly V Zayats, UK
Lei Zhou, China

SPECIAL SESSIONS ORGANIZERS

Benfeng Bai, China
Henri Benisty, France
Jamal Berakdar, Germany
Mohamed B. Larosi, Spain
Shah Nawaz Burokur, France
Debashis Chanda, USA
Pai-Yen Chen, USA
Pedro David Garcia, Spain
Artur Davoyan, USA

Alexandre Dmitriev, Sweden
Ramy El-Ganainy, USA
Mohamed Farhat, Saudi Arabia
Braulio Garcia-Camara, Spain
Patrice Genevet, France
Jonathan Gratus, UK
Jean-Philippe Groby, France
Stephen Hanham, UK
Eugene Kamenetskii, Israel
Alina Karabchevsky, Israel
Paul Kinsler, UK
Sylvain Lannebère, Portugal
Stéphane Lanteri, France
Daniel Lanzillotti-Kimura, France
Qiang Li, China
Yang Li, China
Anatole Lupu, France
Nicolo Maccaferri, Luxembourg
Martin McCall, UK
Konstantinos Makris, Greece
Khaled Mnaymneh, Canada
Tiago A. Morgado, Portugal
Miguel Navarro-Cia, UK
Taiichi Otsuji, Japan
Sahin Ozdemir, USA
Dorota Pawlak, Poland
Andrea Perucchi, Italy
Virginie Ponsinet, France
Badreddine Ratni, France
Ilya Razdolski, The Netherlands
Luca Razzari, Canada
Vicente Romero Garcia, France
Almas Sadreev, Russia
Dondu Sahin, UK
Khaled N. Salama, Saudi Arabia
David Schmool, France
Vasily Temnov, France
Frederic Teppe , France
Andrea Toma, taly
Paolo Vavassori, Spain
Ricardo Vergaz, Spain
Jian Wang , China
Hong Wei, China
Yuanmu Yang, China
Jianjia Yi, China
Kuang Zhang, China

SPECIAL SYMPOSIA ORGANIZERS



Alexander Govorov
USA



Eugene Kamenetskii
Israel



Hakjoo Lee
Korea



Howard Lee
Korea



Xing Yi Ling
Singapore



Andrey Miroshnichenko
Australia



Namkyoo Park
Korea



Jerome Plain
France



Junsuk Rho
Korea



Din Ping Tsai
Taiwan



Tetsuya Ueda
Japan

SPONSORS AND SUPPORTERS

META 2019 gratefully acknowledges the support of these institutions and companies for their contribution to the success of this conference.

SUPPORTERS

SILVER SPONSORS

Photon Design
www.photond.com

Bruker
www.bruker.com

Light Tec
www.lighttec.fr

Neaspec
www.neaspec.com

Raith Nanofabrication
www.raith.com

Isotropic Systems
www.isotropicsystems.com

PLENARY SPEAKERS



Jeremy J. Baumberg

University of Cambridge, UK

Extreme nanophotonics : How to confine light below a cubic nanometre

Jeremy J. Baumberg FRS, directs a UK Nano-Photonics Centre at the University of Cambridge and has extensive experience in developing optical materials structured on the nano-scale that can be assembled in large volume. He is also Director of the Cambridge Nano Doctoral Training Centre, a key UK site for training PhD students in interdisciplinary Nano research. Strong experience with Hitachi, IBM, his own spin-offs Mesophotonics and Base4, as well as strong industrial engagement give him a unique position to combine academic insight with industry application in a two-way flow. With over 20000 citations, he is a leading innovator in Nano. This has led to awards of the IoP Faraday gold Medal (2017), Royal Society Rumford Medal (2014), IoP Young Medal (2013), Royal Society Mullard Prize (2005), the IoP Charles Vernon Boys Medal (2000) and the IoP Mott Lectureship (2005). He frequently talks on NanoScience to the media, and is a strategic advisor on NanoTechnology to the UK Research Councils. He is a Fellow of the Royal Society, the Optical Society of America, and the Institute of Physics. His recent popular science book “The Secret Life of Science : How Science Really Works and Why it Matters” is just published by PUP, see np.phy.cam.ac.uk.



Alexandra Boltasseva

Purdue University, USA

Transdimensional Materials for Nanophotonics : From 2D to 3D

Alexandra Boltasseva is a Professor at the School of Electrical & Computer Engineering at Purdue University. She received her PhD in electrical engineering at Technical University of Denmark, DTU in 2004. Boltasseva specializes in nanophotonics, nanofabrication, optical materials, plasmonics and metamaterials. She is 2018 Blavatnik National Award for Young Scientists Finalist and received the 2013 IEEE Photonics Society Young Investigator Award, 2013 Materials Research Society (MRS) Outstanding Young Investigator Award, the MIT Technology Review Top Young Innovator (TR35), the Young Researcher Award in Advanced Optical Technologies from the University of Erlangen-Nuremberg, Germany, and the Young Elite-Researcher Award from the Danish Council for Independent Research. She is a Fellow of the Optical Society of America (OSA) and Fellow of SPIE. She served on MRS Board of Directors and is Editor-in-Chief for OSA’s Optical Materials Express.



Federico Capasso

Harvard University, USA

Metaoptics in the visible

Federico Capasso is the Robert Wallace Professor of Applied Physics at Harvard University, which he joined in 2003 after 27 years at Bell Labs where he was Member of Technical Staff, Department Head and Vice President for Physical Research. He is visiting professor at NTU with both the School of Physical and Mathematical Sciences and Electrical and Electronic Engineering. His research has focused on nanoscale science and technology encompassing a broad range of topics. He pioneered band-structure engineering of semiconductor nanostructures and devices, invented and first demonstrated the quantum cascade laser and investigated QED forces including the first measurement of a repulsive Casimir force. His most recent contributions are new plasmonic devices and flat optics based on metasurfaces. He is a member of the National Academy of Sciences, the National Academy of Engineering, the American Academy of Arts and Sciences. His awards include the King Faisal Prize, the IEEE Edison Medal, the SPIE Gold Medal, the American Physical Society Arthur Schawlow Prize in Laser Science, the Jan Czochralski Award for lifetime achievements in Materials Science, the IEEE Sarnoff Award in Electronics, the Materials Research Society Medal, the Wetherill Medal of the Franklin Institute, the Rank Prize in Optoelectronics, the Optical Society Wood Prize, the Berthold Leibinger Future Prize, the Julius Springer Prize in Applied Physics, the European Physical Society Quantum Electronics Prize.



Nader Engheta

University of Pennsylvania, USA

Analog processing with metastructures

Nader Engheta is the H. Nedwill Ramsey Professor at the University of Pennsylvania in Philadelphia, with affiliations in the Departments of Electrical and Systems Engineering, Materials Science and Engineering, Physics and Astronomy, and Bioengineering. He received his B.S. degree from the University of Tehran, and his M.S and Ph.D. degrees from Caltech. His current research activities span a broad range of areas including nanophotonics, metamaterials, nano-scale optics, graphene optics, optical metatronics, imaging and sensing inspired by eyes of animal species, optical nanoengineering, microwave and optical devices, and physics and engineering of fields and waves He has received several awards for his research including the 2017 William Streifer Scientific Achievement Award from the IEEE Photonics Society, the 2015 Gold Medal from SPIE, the 2015 Fellow of US National Academy of Inventors (NAI), the 2015 National Security Science and Engineering Faculty Fellow (NSSEFF) Award (also known as Vannevar Bush Faculty Fellow Award) from US Department of Defense, the 2015 IEEE Antennas and Propagation Society Distinguished Achievement Award, the 2015 Wheatstone Lecture in King's College London, the 2014 Balthasar van der Pol Gold Medal from the International Union of Radio Science (URSI), the 2013 Inaugural SINA Award in Engineering, the 2012 IEEE Electromagnetics Award, 2006 Scientific American Magazine 50 Leaders in Science and Technology, the Guggenheim Fellowship, and the IEEE Third Millennium Medal. He is a Fellow of seven international scientific and technical societies, i.e., IEEE, URSI, OSA, APS, MRS, SPIE, and American Association for the Advancement of Science (AAAS). He has received the honorary doctoral degrees from the Aalto University in Finland in 2016 and from the University of Stuttgart, Germany in 2016.



Sir John Brian Pendry

Imperial College London, UK

Singular plasmonic surfaces and their properties

Sir John B. Pendry is an English theoretical physicist educated at Downing College, Cambridge, UK, graduating with a Master of Arts degree in Natural Sciences and a PhD in 1969. He is a professor of theoretical solid - state physics at Imperial College London where he was Head of the Department of Physics (1998 – 2001) and Principal of the Faculty of Physical Sciences (2001 – 2002). John Pendry has made seminal contributions to surface science, disordered systems and photonics. His most famous work has introduced a new class of materials, metamaterials, whose electromagnetic properties depend on their internal structure rather than their chemical constitution. He discovered that a perfect lens manufactured from negatively refracting material would circumvent Abbe's diffraction limit to spatial resolution, which has stood for more than a century. His most recent innovation of transformation optics gives the metamaterial specifications required torearrange electromagnetic field configurations at will, by representing the field distortions as a warping of the space in which they exist. In its simplest form the theory shows how we can direct field lines around a given obstacle and thus provide a cloak of invisibility. John Pendry's outstanding contributions have been awarded by many prizes, among which the Dirac Prize(1996), the Knight Bachelor (2004), the Royal Medal (2006), the Isaac Newton Medal (2013) and the Kavli Prize (2014).



Eli Yablonovitch

UC Berkeley, USA

Optical Antenna Physics : Spontaneous Emission Faster than Stimulated Emission

Eli Yablonovitch introduced the idea that strained semiconductor lasers could have superior performance due to reduced valence band (hole) effective mass. With almost every human interaction with the internet, optical telecommunication occurs by strained semiconductor lasers. He is regarded as a Father of the Photonic BandGap concept, and he coined the term "Photonic Crystal". The geometrical structure of the first experimentally realized Photonic bandgap, is sometimes called "Yablonovite".

Prof. Yablonovitch is elected as a Member of the National Academy of Engineering, the National Academy of Sciences, the American Academy of Arts & Sciences, and is a Foreign Member of the Royal Society of London. He has been awarded the Buckley Prize of the American Physical Society, the Isaac Newton Medal of the UK Institute of Physics, the Rank Prize (UK), the Harvey Prize (Israel), the IEEE Photonics Award, the IET Mountbatten Medal (UK), the Julius Springer Prize (Germany), the R.W. Wood Prize, the W. Streifer Scientific Achievement Award, and the Adolf Lomb Medal.

Eli Yablonovitch is the Director of the NSF Center for Energy Efficient Electronics Science (E3S), a multi-University Center headquartered at Berkeley. He received his Ph.D. degree in Applied Physics from Harvard University in 1972. He worked for two years at Bell Telephone Laboratories, and then became a professor of Applied Physics at Harvard. In 1979 he joined Exxon to do research on photovoltaic solar energy. Then in 1984, he joined Bell Communications Research, where he was a Distinguished Member of Staff, and also Director of Solid-State Physics Research. In 1992 he joined the University of California, Los Angeles, where he was the Northrop-Grumman Chair Professor of Electrical Engineering. Then in 2007 he became Professor of Electrical Engineering and Computer Sciences at UC Berkeley, where he holds the James & Katherine Lau Chair in Engineering.

KEYNOTE SPEAKERS



Konstantin Bliokh

Theoretical Quantum Physics Laboratory - Riken, Japan

Topological non-Hermitian origin of surface Maxwell waves



Mark Brongersma

Stanford University, USA

Metasurfaces for Augmented and Virtual Reality



Sven Burger

Zuse Institute Berlin, Germany

Computing resonances in nano-photonic devices using Riesz-projection methods



Giulio Cerullo

Politecnico di Milano, Italy

Tracking ultrafast light-heat conversion in plasmonic nano-assemblies



Manfred Fiebig

ETH Zurich, Switzerland

On the Search for Toroidal Order in Magnetic Materials



Jean-Jacques Greffet

Institut d'Optique Graduate School, France

Electrical generation of surface plasmons with resonant nanoantennas



Thomas Krauss

University of York, UK

Metasurfaces for sensing and imaging



Stefan Maier

LMU Munich, Germany

Plasmonic hot electrons for nanoscale self-assembly and imaging



Sahin K. Ozdemir

The Pennsylvania State University, USA

Non-Hermiticity in Optics and Optomechanics



Nam-gyu Park

Sungkyunkwan University, Korea

Organic-inorganic Lead Halide Perovskite for High Efficiency Energy Conversion



Junsuk Rho

POSTECH, Korea

Artificial chirality evolution in micro-/nano-scale 3D metamaterials



Vladimir Shalaev

Purdue University, USA

Plasmonic Metamaterials Meet Quantum



David R. Smith

Duke University, USA

Optical Field Enhancement in the Nano-Patch Antenna for Lasing, Nonlinear Optics, and Other Nanophotonic Applications



Marin Soljacic

MIT, USA

Neural Networks in Nanophotonics



Jelena Vuckovic

Stanford University, USA

Optimized quantum photonics



Rachel Won

Nature Photonics, UK

Publishing in Nature journals



Nikolay Zheludev

University of Southampton, UK & NTU, Singapore

Optical imaging and metrology with nanoscale resolution

CONFERENCE TUTORIALS

META 2019 features several technical tutorials instructed by world-leading experts on various topics of interest to the META community. Tutorials are intended to provide a high quality learning experience to conference attendees. The tutorials address an audience with a varied range of interests and backgrounds : beginners, students, researchers, lecturers and representatives of companies, governments and funding agencies who wish to learn new concepts and technologies.
The tutorials are part of the conference technical program, and are free of charge for the conference attendees.

ORGANIZER



Prof. Ishwar Aggarwal, UNC Charlotte, USA

Tutorials & Instructors



Prof. Nader Engheta

University of Pennsylvania, USA

Tuesday 23rd July
11:40 - 12:40 — Auditorium I

Near-Zero-Index Metamaterials

In this tutorial, I will present an overview of some of the fundamental principles and unique features of wave interaction with structures with effective refractive index near zero, which include epsilon-near-zero (ENZ), mu-near-zero (MNZ), epsilon-and-mu-near-zero (EMNZ) and Dirac-cone photonic media. I will then discuss some of the applications of near-zero-index metamaterials in photonics and microwave technologies. Possible future directions of research in this field will also be forecasted.



Prof. Federico Capasso

Harvard University, USA

Wednesday 24th July
10:50 - 11:50 — Auditorium I

Flat optics

This tutorial focuses on how metasurfaces enable the redesign of optical components into novel thin and planar diffractive optical elements, that overcome the limitations of Fresnel and refractive optics, promising a major reduction in footprint and system complexity as well as the introduction of new optical functions. The planarity of flat optics will lead to the unification of semiconductor manufacturing and lens making, where the planar technology to manufacture computer chips will be adapted to produce CMOS-compatible metasurface-based optical components, ranging from metalenses to novel multifunctional phase plates.



Prof. Eli Yablonovitch

UC Berkeley, USA

Wednesday 24th July
14:00 - 15:00 — Auditorium II

The Electromagnetic Spectra of Ordinary Objects

There is an aspect of Electromagnetics that has been somewhat overlooked. Common everyday objects can act as electromagnetic resonators. Indeed ordinary objects have a series of resonant frequencies extending from radio waves up to optical frequencies. These resonant modes can be modeled as LC circuits. Thus every object that we encounter is an LC resonator. Since LC circuits support ac currents, and since ac currents imply electron acceleration, they inherently radiate into the far-field. Therefore ordinary objects that we come across, in our daily lives, can act as electromagnetic antennas. This means that ordinary object have a Q-factor and a radiation Q-factor for each resonant mode.The lowest frequency resonance is especially characteristic of the object geometry, but there is an entire spectrum of higher frequencies to work with, a spectral fingerprint for everyday objects. Many of the properties that have been attributed to plasmonic resonances are actually universal, and they arise already in ordinary electromagnetics.In communications technology, the antenna application is the most important. The antennas in cellphones, carried by almost everyone on the planet, are examples of multi-frequency resonant objects, enabling wireless connectivity.



Dr. Rachel Won

Nature Photonics, UK

Thursday 25th July
11:00 - 12:00 — Auditorium II

Writing and submitting your papers : Dos and Don'ts

In this tutorial, Rachel will talk you through the detailed information and guidelines on scientific paper preparation and submission. Guidelines and tips for writing an abstract and a paper will be provided. Submission, editorial and peer-review processes will be discussed. At the end of the tutorial, you will walk away knowing how to write an informative cover letter, an outstanding abstract and a comprehensive scientific paper. You will also get to know where to submit your papers to, what editors seek, how your papers are reviewed and how to make an appeal.



Prof. Michael Fiddy

DARPA, USA

Thursday 25th July
14:00 - 15:00 — Auditorium I

DARPA's interests in metamaterials

Almost twenty years ago, some of the earliest research into metamaterials and their applications was funded by DARPA. The field has grown enormously since, and DARPA still supports fundamental research into improving our understanding and modeling of these engineered materials. This talk will provide the background and context for research of current interests. These include the study of new material properties, including bianisotropy and nonlinearity, advancing flat optics, and developing nonreciprocal and tunable components, all of which may impact imaging and remote sensing capabilities.

META 2019 VENUE

META 2019 will be held at the Congress Center of **Instituto Superior Técnico (IST)**, situated at the Civil Engineering Building. All talks are scheduled for the Congress Centre of IST **except for the Plenary talks** which will be held in **Culturgest**, an independent conference center located 500m away from IST (see map).



Instituto Superior Técnico - Congress Center
Civil Engineering Building (Pavilhão de Civil)
Av. Rovisco Pais 1
1049-001, Lisbon

Website : https ://tecnico.ulisboa.pt/en/

Culturgest
Rua Arco do Cego 77
1000-300
Lisbon

Website : https ://www.culturgest.pt/en/

GETTING TO VENUE



Taxi

The quickest way to get from Lisbon Airport (LIS) to Instituto Superior Técnico is to taxi which costs 7€ - 9€ and takes 10mn.

Metro

Being close to the Lisbon city centre, IST is easily reached by metro (metro station **"Alameda"** - Red and Green lines ; metro sation **"Saldanha"** - Red and Yellow lines), from any location in town, including the airport (metro station **"Aeroporto"**- Red line).

Bus

The bus routes cover all Lisbon and extend to its outskirts. The tickets can be pre-paid, at the counters of Carris, the surface transportation operator for Lisbon, or bought aboard the bus, electric cars or funiculars. For IST hop off on one of the following bus stops :

- ☐ Av. Manuel da Maia
- ☐ Av. Rovisco Pais
- ☐ Arco do Cego

GENERAL INFORMATION

Registration

Registered participants may pick up their conference material at the registration desk which will be located :

• Monday, July 22 (15 :00-18 :00) : IST Civil Engineering Building
• Tuesday, July 23 (08 :00 - 10 :45) : **Culturgest**, in the foyer next to the Main Auditorium

• Tuesday, July 23 (10 :45 - 18 :00) : IST Civil Engineering Building
• Wednesday, July 24 (08 :30-18 :00) : IST Civil Engineering Building
• Thursday, July 25 (08 :30-17 :00) : IST Civil Engineering Building
• Friday, July 26 (08 :30-11 :00) : IST Civil Engineering Building

Plenary Lectures

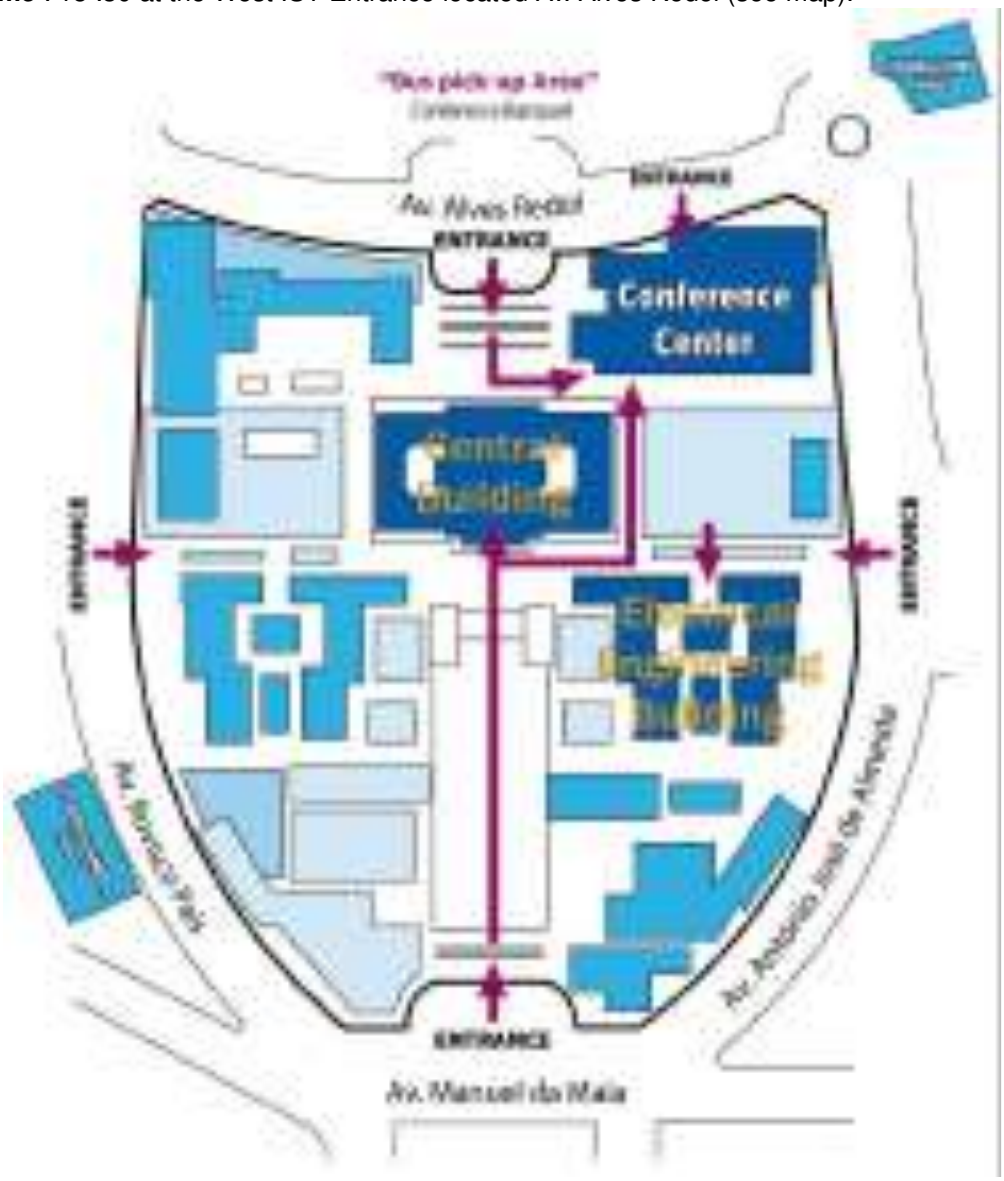
Plenary Lectures will be held at the Main Auditorium of **Culturgest**, located 500m away from Instituto Superior Técnico Congress Center :
• Tuesday, July 23 (08 :45-10 :45)
• Thursday, July 25 (08 :30-10 :15)

Banquet

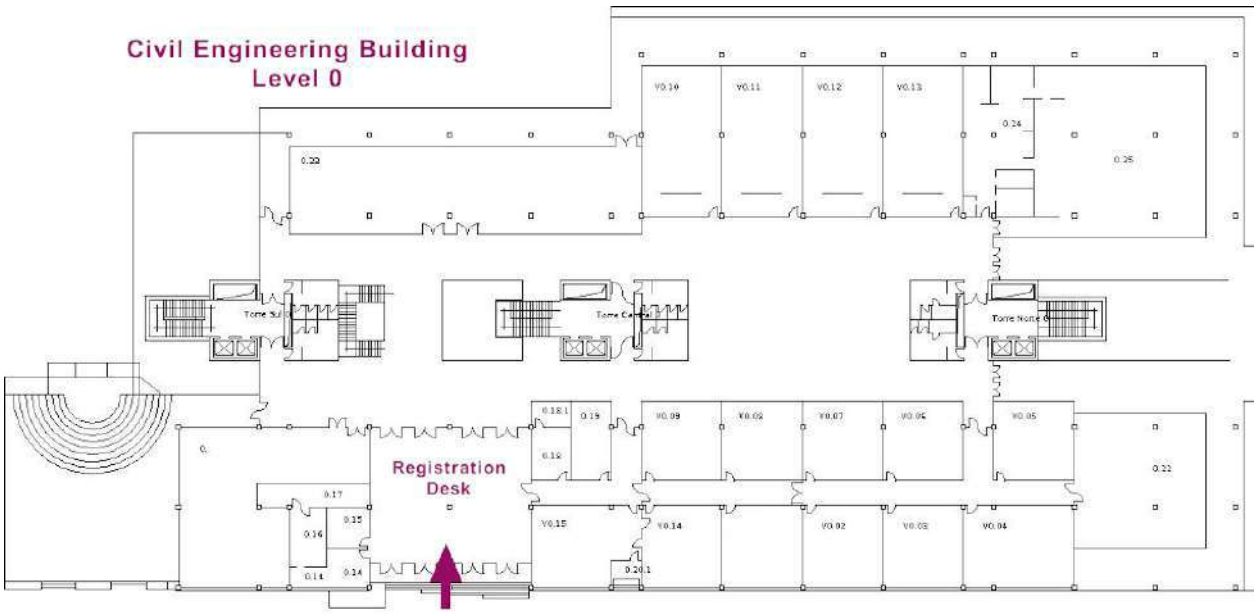
Venue : KAIS Restaurant, Cais da Viscondessa, R. da Cintura – Santos, 1200-109 Lisboa, Portugal.
Schedule : Thursday, July 25 at 20 :00.

Free Shuttle bus service will be provided between the Instituto Superior Técnico Congress Center and the KAIS Restaurant.

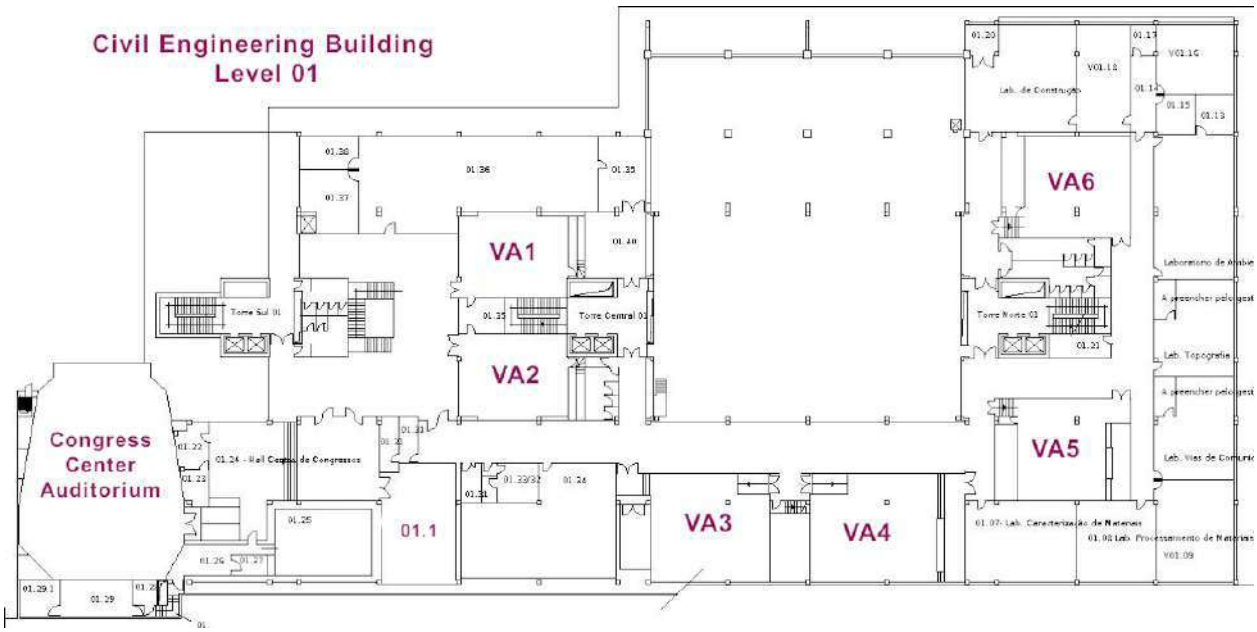
Pick-up time : 18 :30 at the West IST Entrance located Av. Alves Redol (see map).



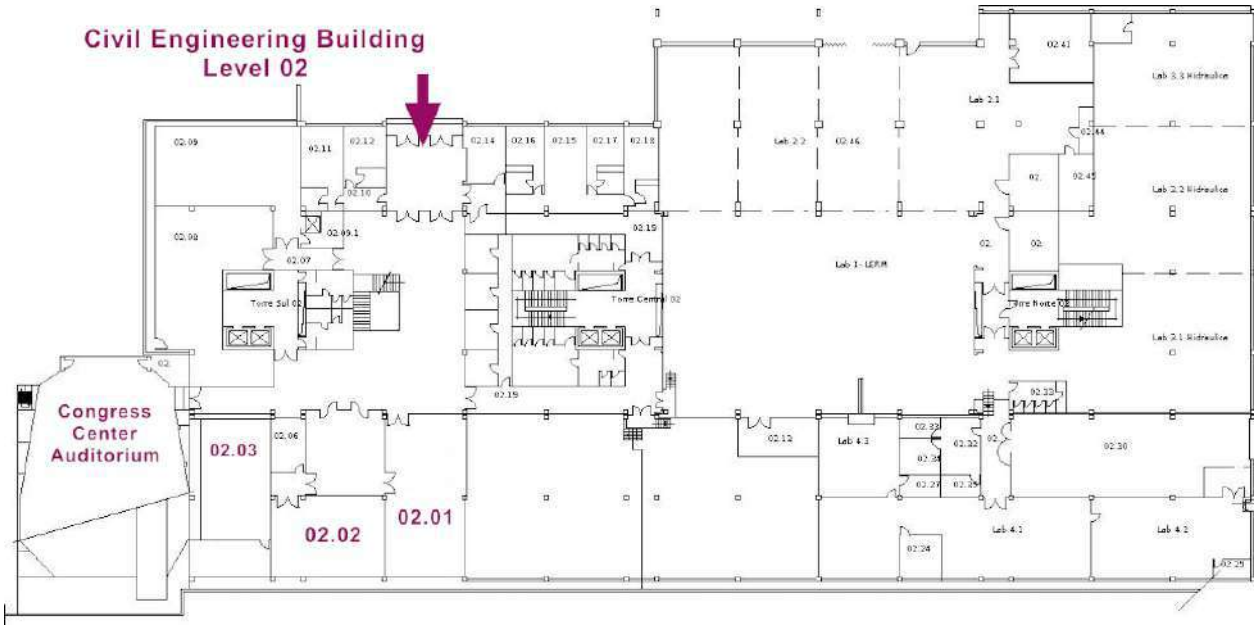
IST CONGRESS CENTER FLOOR PLANS



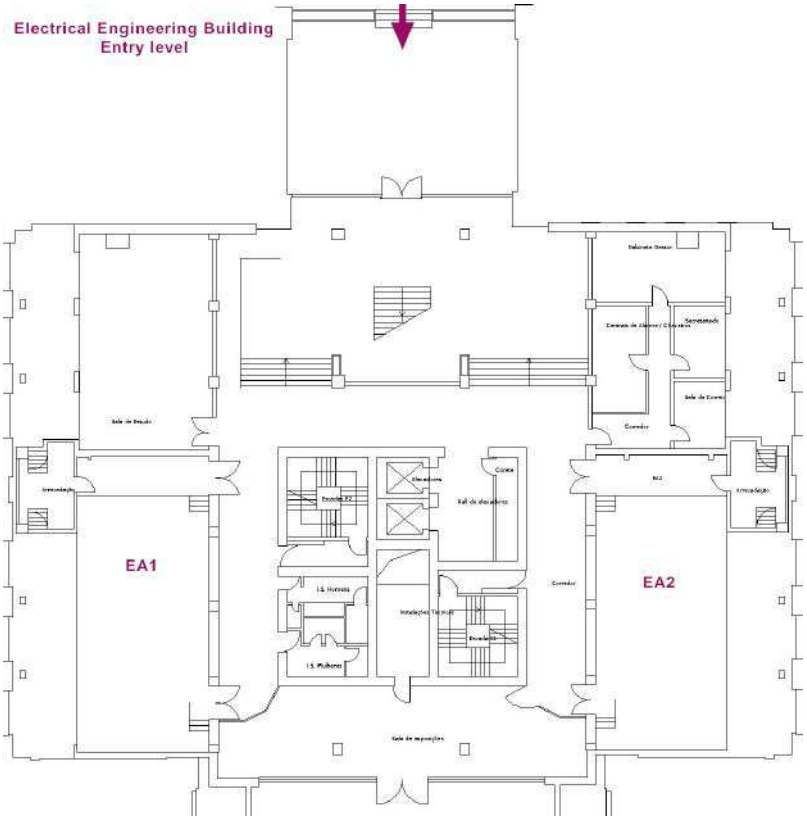
Civil Engineering Building - Level 0



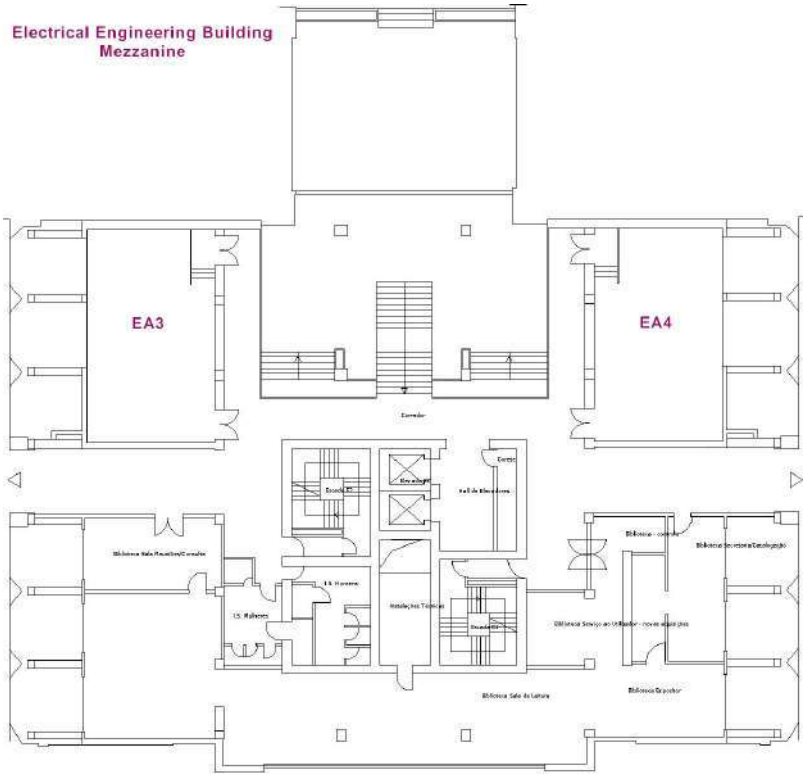
Civil Engineering Building - Level 01



Civil Engineering Building - Level 02



Electrical Engineering Building - Entry level



Electrical Engineering Building - Mezzanine

WI-FI INSTRUCTIONS

Wi-Fi instructions for **META 2019** participants :

1. Browse available wireless networks and select as SSID "tecnico-guest" ;
2. Set IP to automatic (DHCP). This is usually the default setting, so you may probably skip this step ;
3. Open your browser and try to access any external website. You will be automatically redirected to the page **https ://wifi.ist.utl.pt/index_auth.php**. Follow the link 'Web based login' at the top of the page concerning short-time, conference and meetings accounts. Enter the following username/password when requested ;

   Username : **META2019**
   Password : **jwvr2f**

4. After step 3 you may freely browse and access the Internet. You may need to repeat the above steps if you close your browser or if the connection times out.

GUIDELINES FOR PRESENTERS

ORAL PRESENTATIONS

Each session room is equipped with a stationary computer connected to a LCD projector. Presenters must load their presentation files in advance onto the session computer. Technician personnel will be available to assist you.

Scheduled time slots for oral presentations are 15 mn for regular, 20 mn for invited presentations, 30 mn for keynote talks and 35 mn for plenary talks, including questions and discussions. Presenters are required to report to their session room and to their session Chair at least 15 minutes prior to the start of their session.

The session chair must be present in the session room at least 15 minutes before the start of the session and must strictly observe the starting time and time limit of each paper.

POSTER PRESENTATIONS

Presenters are requested to stand by their posters during their session. One poster board, A0 size (118.9 x 84.1 cm), in portrait orientation, will be available for each poster (there are no specific templates for posters). Pins or thumbtacks are provided to mount your posters on the board. All presenters are required to mount their papers 30mn before the session and remove them at the end of their sessions. Posters must prepared using the standard META poster template (available on the conference website).

TABLE OF CONTENTS

Plenary Lectures

Metasurface Polarization Optics (pp. 83)
Federico Capasso,

Optical Antenna Physics: Spontaneous Emission Faster than Stimulated Emission (pp. 84)
Eli Yablonovitch, Ming Wu, Seth Fortuna,

Extreme nanophotonics: How to confine light below a cubic nanometre (pp. 85)
Jeremy J. Baumberg,

Singular plasmonic surfaces and their properties (pp. 86)
J. B. Pendry,

Transdimensional Materials for Nanophotonics: From 2D to 3D (pp. 87)
Alexandra Boltasseva,

Analog processing with metastructures (pp. 89)
Nader Engheta,

Keynote Lectures

Artificial Chirality Evloution in Micro-/Nano-scale 3D Plasmonic Metamaterials (pp. 91)
Junsuk Rho,

Computing resonances in nano-photonic devices using Riesz-projection-based methods (pp. 92)
Sven Burger, Felix Binkowski, Lin Zschiedrich,

Utilizing plasmonic hot electrons for bridging top-down and bottom-up nanofabrication and for sub-wavelength absorption imaging (pp. 94)
Stefan Maier,

Publishing in Nature journals (pp. 95)
Rachel Won,

Optical imaging and metrology with nanoscale resolution (pp. 96)
Nikolay I. Zheludev,

Electrical generation of surface plasmons with resonant nanoantennas (pp. 97)
C. Zhang, J. P. Hugonin, A. L. Coutrot, C. Sauvan, F. Marquier, J. J. Greffet,

Optical Field Enhancement in the Nano-Patch Antenna for Lasing, Nonlinear Optics, and Other Nanophotonic Applications (pp. 99)
David R. Smith, Patrick Bowen,

Organic-inorganic Lead Halide Perovskite for High Efficiency Energy Conversion (pp. 101)
Nam-Gyu Park,

Tracking ultrafast light-heat conversion in plasmonic nanoassemblies (pp. 102)
Andrea Mazzanti, Zhijie Yang, Marie-Paule Pileni, Giuseppe Della Valle, Giulio Cerullo,

On the Search for Toroidal Order in Magnetic Materials (pp. 104)
Manfred Fiebig,

Topological non-Hermitian origin of surface Maxwell and acoustic waves (pp. 106)
Konstantin Bliokh,

Can plasmonics help outpace quantum decoherence? (pp. 107)
Simeon I. Bogdanov, Alexandra Boltasseva, Vladimir M. Shalaev,

Neural Networks in Nanophotonics (pp. 108)
Marin Soljacic,

Metasurfaces for sensing and imaging (pp. 109)
D. Conteduca, I. Barth, J. Juan-Colas, Steve Johnson, E. R Martins, Thomas F. Krauss,

Non-Hermiticity in Optics and Optomechanics (pp. 110)
Sahin K. Ozdemir,

Optimized quantum photonics (pp. 111)
Jelena Vuckovic,

Hybrid Photonic and Plasmonic Materials for Sensing, Energy conversion and Imaging Applications

Adsorption Site Recognition in Single Molecule Junction (pp. 113)
Manabu Kiguchi,

Hybrid Plasmonic Nanomaterials for Uranyl Detection (pp. 115)
Hoa Phan, Amanda J. Haes,

Plasmonic Hot-Carrier-Mediated Solar Energy Conversion and Tunable Photochemical Reactions (pp. 117)
Yu Zhang, Tammie Nelson, Sergei Tretiak, Hua Guo, ChiYung Yam, George Schatz,

Multistructured metallic substrate: a promising SERS platform for detecting trace molecules (pp. 119)
Mathieu Edely, Nicolas Delorme, Guy Louarn, Ludovic Douillard, Jean-Francois Bardeau,

Materials for Photonics Beyond Noble Metals (pp. 121)
Marina S. Leite,

Plasmonic hot electron nano-emitters by on-chip ablation for femtosecond on-chip electronics (pp. 123)
Alexander Holleitner,

First Observation of Optical Activity in Hyper-Rayleigh Scattering (pp. 124)
Ventsislav K. Valev,

Near and far-field optical properties of non-noble metal nanoparticles deposited on nanopatterned dielectric surfaces (pp. 125)
Sophie Camelio, David Babonneau, FrÃ©dÃ©ric Pailloux, Alexandre Fafin, GrÃ©gory Abadias, Panos Patsalas,

Complex materials created by warped spaces for energy harvesting, bio-imaging, and broadband light control at the nanoscale (pp. 127)
Andrea Fratalocchi,

Tunable Shape-controlled Plasmonic Nanoparticles Superlattices for Surface-enhanced Raman Scattering Applications (pp. 129)
Xing Yi Ling,

Interface Design for Visible-Light Induced Photochemical Reactions Promoted by Refractory Transition Metal Nitride Nanoparticles Incorporated into TiO2 Matrix (pp. 130)
Olga A. Baturina, Albert Epshteyn, Gregory T. T Forcherio, Alexander Govorov, Asher C. Leff, Andrew Purdy, Blake Sympkins,

Structural Alteration of Genomic DNA upon Interaction with Silver Nanoparticles (pp. 132)
Luca Guerrini,

Energy Transfer in Donor-acceptor Quantum Dots Simultaneous Mediated by Double Plasmon Modes of Gold Nanorod (pp. 134)
Hanjie Zhang, Deren Yang, Dongsheng Li,

Refractory plasmonic nanocavities for chemistry at high temperatures (pp. 136)
Alberto Naldoni, Zhaxylyk A. Kudyshev, Luca Mascaretti, Stepan Kment, Alexandra Boltasseva, Vladimir M. Shalaev, Patrik Schmuki, Radek Zboril,

Comparison of the optical magnetism of Au dodecahedral clusters and plasmonic raspberries produced by bottom up approach (pp. 138)
Laurent Lermusiaux, Veronique Many, Alexandre Baron, Romain Dezert, Etienne Duguet, Virginie Ponsinet, Serge Ravaine, Philippe Richetti, Philippe Barois, Mona Treguer-Delapierre,

Surface-enhanced resonant Raman scattering and surface-enhanced fluorescence spectra of a strong coupling system between plasmon and molecular exciton (pp. 140)
Tamitake Itoh,

Photoluminescence from emitters on periodic diffractive arrays of plasmonic and non-plasmonic nanocylinders (pp. 142)
Shunsuke Murai, Kazuki Noguchi, Katsuhisa Tanaka,

Nanoplasmonics for Terahertz Light (pp. 144)
Luca Razzari,

Opto-mechanical control of the plasmonic heat generation towards the realization of smart biochips (pp. 145)
Roberto Caputo, Giovanna Palermo, Giuseppe Emanuele Lio, Antonio De Luca,

Synthesis of AgCl Nanoparticles and Their Plasmonic Replicas as Photocatalysts and SERS Probes (pp. 147)
Han-Hung Ryu, Jang Ho Joo, Jae-Seung Lee,

In Situ Surface-Enhanced Raman Spectroscopic Study of Chemical Reactions on Bifunctional Nanoparticles (pp. 149)
Wei Xie,

Nanoscale Imaging and Control of Chiral Plasmons (pp. 151)
Hiromi Okamoto,

Photochemical properties of organic dye molecules under vibrational strong coupling regimes (pp. 153)
Kosei Ueno,

Optical properties of plasmonic spiked particles as a function of their size and shape (pp. 155)
Ramon A. Alvarez-Puebla,

Circularly Polarized Luminescence for Handedness Determination in Chiral Lanthanide Phosphate Nanocrystals (pp. 156)
Uri Hananel, Eitam Vinegrad, Assaf Ben-Moshe, Ori Cheshnovsky, Gil Markovich,

Synthesis of highly brilliant SERS-encoded core-satellite nanostructures (pp. 158)

Nicolas Pazos-Perez, Ramon Alvarez Puebla,

Keeping an eye on the eye through plasmonics (pp. 160)
Andrea Lopez-Marino, Ana Sousa-Castillo, Enrique Carbo-Argibay, Francisco Otero-Espinar, Ramon A. Alvarez-Puebla, Moises Perez-Lorenzo, Miguel A. Correa-Duarte,

Manipulation of Strong Light-Matter Interactions in Two-Dimensional Transition-Metal Dichagenides Coupled with Nanophotonic Structures (pp. 162)
Huanjun Chen, Hao Wang, Jinxiu Wen,

Plasmonic Hot Holes: Fundamentals and Devices (pp. 164)
Giulia Tagliabue, Joseph S. DuChene, Harry A. Atwater,

Spaser assisted coherent generation of nuclei vibrations in Raman active molecules (pp. 165)
Evgeny Andrianov, Vladislav Shishkov, Alexander Pukhov, Alexey Vinogradov, Alexander Lisyansky,

FRET in Hybrid Nanostructures: General Dimensionality Classes, Assembly Effects and Unique Cases (pp. 167)
Pedro Ludwig Hernandez Martinez, Hilmi Volkan Demir,

Probing optical chirality in the near-field of achiral nanostructures (pp. 169)
Andreas Horrer, Yinping Zhang, Thinhinane Aoudjit, Jeremie Beal, Jerome Plain, Renaud Bachelot, Davy Gerard,

Electrochemical Tuning of Plasmoinc Surface Lattice Resonance (pp. 171)
Hiro Minamimoto, Kei Murakoshi,

Plasmonic biosensing with silver nanowires (pp. 173)
Karolina Sulowska, Ewa Rozniecka, Joanna Niedziolka-Jonsson, Sebastian Mackowski,

Quantum dot-cavity QED: Acoustic phonon-induced dephasing of polaritons (pp. 175)
Egor Muljarov, Amy Morreau,

Tailoring electric and magnetic dipole emissions by high-refractive index dielectric nanostructures (pp. 176)
Peter R. Wiecha, Clement Majorel, Christian Girard, Arnaud Arbouet, Bruno Masenelli, Olivier Boisron, Aurelie Lecestre, Guilhem Larrieu, Aurelien Cuche, Vincent Paillard,

Plasmonics-Nanofluidics Hydrid Metamaterials for Ultrasensitive Infrared Spectroscopy and Studies of Water Confined in Nanospaces (pp. 178)
Thu H. H. Le, Akihiro Morita, Kazuma Mawatari, Takehiko Kitamori, Takuo Tanaka,

Optical Circular Dichroism Expressed by Self-Assembled Plasmonic Materials for Molecular Sensing Applications (pp. 180)
Alessandro Belardini, Grigore Leahu, Emilija Petronijevic, Marco Centini, Roberto Li Voti, Tiziana Cesca, Giovanni Mattei, Teemu Hakkarainen, Ventsislav K. Valev, Mircea Guina, Concita Sibilia,

Two-Photon Excitation of Biomolecules using Mid-infrared Surface-Plasmon Polaritons confined on Metasurfaces (pp. 182)
Iram T. Awan, Manoel M. P. Miranda Messias, Otavio Brito Silva, Euclydes Marega Junior,

Hot electron generation in plasmonic nanostructures - thermal vs. non-thermal effects (pp. 184)
Y. Sivan, Y. Dubi,

Revisiting Plasmonic Photocatalysts Based on Titanium Nitride Nanoparticles (pp. 186)
Diane Rawach, Peipei Liu, Peikui Wang, Jerome Claverie,

From nonlinear plasmonics to entangled photon pair generation in hybrid nanostructures (pp. 188)
Nicolas Chauvet, Maeliss Ethis de Corny, Guillaume Laurent, Eric Dujardin, AurÃ©lien Drezet, Serge Huant, Gilles Nogues, Guillaume Bachelier,

Improving the Applicability of Hybrid Plasmonic Nanoparticles by Studying and Tailoring Interfaces (pp. 190)
Kholud Dardir, Hao Wang, Ted V. Tsoulos, Supriya Atta, Sakshi Sardar, Laura Fabris,

Plasmonic Metamaterials for Sensing Applications (pp. 192)
Pan Wang, Alexey Krasavin, Mazhar Nasir, Wayne Dickson, Anatoly Zayats,

Folding a 2D material into a W-shape periodic nano-structure: the case of a gold nano-layer and the consequences on its plasmonic and photonic properties (pp. 194)
Laurent Arnaud, Shijian Yang, Soukaina Es Saidi, Aurelien Bruyant, serguei Kostcheev, Abdelhamid Hmima, Yassine Hadjar, Sylvain Blaize, Demetrio Macias, Remi Vincent,

Ultrafast Nanophotonics and Quantum Optics in Nano-bio Assemblies, Colloidal Nanostructures, and Metamaterials (pp. 196)
Gary Wiederrecht,

Polariton chemistry: thinking inside the (photon) box (pp. 198)
Joel Yuen-Zhou,

Plasmon Modulated Silicon Photodetectors based on Photothermoelectric Effect (pp. 200)
Weikang Liu, Wenqiang Wang, Zhiqiang Guan, Hongxing Xu,

Plasmon-enhanced fluorescence of EGFP immobilized on optically thin perforated Al films (pp. 202)
Vladimir E. Bochenkov, Artyom A. Astafiev, Alexander M. Shakhov, Vadim A. Timoshenko,

Plasmonics in complex geometries: Modal optical properties and coupling with nanoscale emitters (pp. 204)
Pierre-Michel Adam,

Broadband Mid-Infrared Absorber Using Gosper Curve (pp. 206)
Jihua Zou, Peng Yu, Alexander Govorov, Jiang Wu, Zhiming Wang,

Plasmonic Aluminum Nanohole Arrays for ITO-Free Ultraviolet Photodetectors with Improved Response Stability and Tunability (pp. 208)
Monica Esopi, Qiuming Yu,

Nanostructuring of functional polymers for the directed assembly of nano-objects and the integration of hybrid nanosources (pp. 210)
Safi Jradi, Ali Issa, Hongshi Chen, Xiaolun Xu, Aurelie Broussier, Dandan Ge, Christophe Couteau, Sylvain Blaize, Renaud Bachelot,

Understanding Hot Electron Generation in Plasmonic Nanocrystals and Delineating New Research Avenues (pp. 212)
Lucas Vazquez Besteiro, Tianji Liu, Zhiming Wang, Alexander O. Govorov,

Metamaterial Absorber-empowered Light-harvesting Devices (pp. 214)
Peng Yu, Zhiming Wang, Alexander Govorov,

Plasmonics with refractory TiN (pp. 216)
Arrigo Calzolari, Alessandra Catellani,

Nonlinear Chiral Response of Planar Plasmonic-Photonics Hybrid Metasurfaces (pp. 218)

Feng Wang, Hayk Harutyunyan,

Anisotropic metal nanostructures (pp. 219)
Yurii K. Gun'ko, Valerie Gerard, Daniel K. Kehoe,

Wafer-scale gold nanocube arrays for tuneable absorption and refractive-index sensing (pp. 221)
Shaolong Wu, Liang Li, Liujing Li, Zhongyuan Zhou, Su Shen, Xiaofeng Li,

Super-hydrophobic Surface-enhanced Raman Scattering platform (pp. 223)
In Yee Phang,

Generation, thermalization and extraction of hot carriers in metallic nanoparticles (pp. 224)
Johannes Lischner,

VIS-UV resonance Raman scattering study of chemical enhancement mechanism in surface enhanced Raman spectroscopy (SERS) (pp. 226)
Jayeong Kim, Tomke Glier, Benjamin Grimm-Lebsanft, Soren Buchenau, Melissa Teubner, Florian Biebl, Nam-Jung Kim, Heehun Kim, Gyu-Chul Yi, Michael Rubhausen, Seokhyun Yoon,

Finite-difference time-domain (FDTD) simulation for optimization of non-metal based Surface enhanced Raman spectroscopy (SERS) (pp. 228)
Eunji Ko, Jayeong Kim, Heehun Kim, Gyu-Chul Yi, Seokhyun Yoon,

Cooperative emission by quantum plasmonic superradiance (pp. 230)
Hugo Varguet, Stephane Guerin, Hans Rudolf Jauslin, GÃ©rard Colas des Francs,

Shaping and measuring temperature at the microscale for biological applications (pp. 232)
Chang Liu, Pascal Berto, ClÃ©mence Gentner, Minh-Chau Nguyen, Ivan Flores, Robert Kuszelewicz, Marc Guillon, Gilles Tessier,

Phase transition of methylammonium lead halide perovskite (MAPbX3) single crystals studied by Raman scattering spectroscopy (pp. 234)
Trang Thi Thu Nguyen, Yejin Kim, Hye Ri Jung, William Jo, Won Seok Woo, Chang Won Ahn, Shinuk Cho, Ill Won Kim Kim, Maryam Bari, Zuo Guang, Seokhyun Yoon,

Entanglement in Hybrid Quantum Dot/Plasmonic Systems (pp. 236)
Matthew Otten, Stephen K. Gray, German Kolmakov,

Laser photopatterning of metal oxide functional micro-nano-structures from precursor solutions (pp. 238)
C. C. Yeh, S. Y. Yu, P. Y. Chang, B. Leuschel, D. Berling, A. Spangenberg, H. W. Zan, Olivier Soppera,

New trends in nanophotonics and advanced materials

Impact of plasmonic bowtie nanoantennas and nanocavities on the dynamics of nearby nanoemitters (pp. 241)
Victor Pacheco-Pena, Ruben Alves, Miguel Navarro-Cia,

On-chip fabricated non-transfer plasmonic nanolaser (pp. 243)
Ya-Lun Ho, J. Kenji Clark, A. Syazwan Kamal, Jean-Jacques Delaunay,

Hybrid plasmonic nanostructures based on controlled deposition of MoS2 flakes on plasmonic nanostructures (pp. 245)
Dario Mosconi, Ermanno Miele, Andrea Jacassi, Giorgia Giovannini, Nicolo Maccaferri, Denis Garoli,

Fast Optoelectronic Modulation of Surface Plasmons Polaritons at Degenerate Semiconductor Intefraces (pp. 247)

Dentcho A. Genov,

Intuitive Semi-analytical Model of Channel Plasmon Polaritons in Subwavelength Plasmonic Trench Waveguide (pp. 249)
Haitao Liu, Junda Zhu, Tong Zhu, Hongwei Jia, Ying Zhong,

Vertical Lasing from InP Nanowire with Cat's Eye Antenna (pp. 252)
Fangfang Ren, Wei-Zong Xu, Jiandong Ye, Yi Yang, Hark Hoe Tan, Chennupati Jagadish,

Quantum Plasmons and Plasmon-Emitter Interactions at the Nanoscale (pp. 254)
Paulo AndrÃ© Dias Goncalves, Thomas Christensen, Nicholas Rivera, Antti-Pekka Jauho, Marin Soljacic, N. Asger Mortensen,

Novel deep-learning-based techniques for design and optimization of photonic metastructures (pp. 256)
Yashar Kiarashinejad, Sajjad Abdollahramezani, Mohammadreza Zandehshahvar, Omid Hemmatyar, Ali Adibi,

Active Tunable Photonic Topological insulator (pp. 257)
Xiaoyong Hu, Yutian Ao, Xinxiang Niu, You Wu,

Optical switching of the Second Harmonic Generation in AlGaAs nanoantennas (pp. 258)
Michele Celebrano, Eva A. A. Pogna, Lavinia Ghirardini, Francesco Rusconi, Paolo Biagioni, Andrea Mazzanti, Giuseppe Della Valle, Lamberto Duo, Luca Carletti, Davide Rocco, Carlo Gigli, Giuseppe Marino, Giuseppe Leo, Costantino De Angelis, Giulio Cerullo, Marco Finazzi,

Spatiotemporal Manipulation of Optical Fields enabled by Metasurfaces (pp. 260)
Amit Agrawal, Wenqi Zhu, Cheng Zhang, Lu Chen, Shawn Divitt, Henri Lezec,

Current-Driven Plasmonic Instability in Graphene Metasurfaces for Terahertz Applications (pp. 262)
Stephane A. Boubanga-Tombet, Deepika Yadav, Akira Satou, Wojciech Knap, Vyacheslav V. Popov, Taiichi Otsuji,

Self-assembled Nano-rings of Plasmonic Nanoparticles (pp. 264)
Anna M. Ritcey, Denis Boudreau, Marie-Pier CotÃ©,

Nanoplasmonics in Embedded CMOS Electronics: Future mm-scale Complex Nano-optical Sensory Systems (pp. 266)
Kaushik Sengupta,

Novel Photonic Architectures by Nanoimprinting Unconventional Materials (pp. 268)
Agustin Mihi,

Photocontrollable dynamic chirality in plasmonic nanoassemblies (pp. 269)
Rongyao Wang, Wenjing Zhao, W. Zhang, X. Wu, X. D. Zhang,

Photon drag of Bose-Einstein condensates (pp. 270)
M. V. Boev, A. E. Miroshnichenko, V. M. Kovalev, I. G. Savenko,

Broadband extraordinary transmission and focusing of sound with flat thin meta-lens (pp. 272)
Shanjun Liang, Yong Li, Qian Cheng, Jie Zhu,

Active Polaritonic Metasurfaces (pp. 274)
Clementine Symonds, Kevin Chevrier, Jean-Michel Benoit, Semion Saikin, Joel Yuen-Zhou, Joel Bellessa,

(Chiro)-optical properties of chiral inorganic-plasmonic nanocomposites (pp. 276)
Thierry Verbiest, Ward Brullot, Tom Swusten,

Block copolymer based self-assembled metamaterials and metasurfaces at optical frequencies (pp. 278)
Alberto Alvarez-Fernandez, Cian Cummins, Guillaume Fleury, Xuan Wang, Morten Kildemo, Alexandre Baron, Virginie Ponsinet,

Topological Photonic Metamaterials with Honeycomb Structure (pp. 280)
Xiao Hu,

Sharp Fano resonance and active response changes in 4D-printed photonic structures (pp. 282)
Soo-Chan An, Eunsongyi Lee, Chang-Hyun Lee, Hoon Yeub Jeong, Taek-Sun Kwon, Jeong-Hae Lee, Young Chul Jun,

Mid Infrared Metasurfaces (pp. 284)
Yoshiaki Nishijima, Naoki To, Takuhiro Kumagai,

Electrically Tunable Mirror Arrays for Spatial Modulation of Terahertz Radiation over a Wide Frequency Range (pp. 286)
Jan Kappa, Dominik Sokoluk, Steffen Klingel, Corey Shemelya, Egbert Oesterschulze, Marco Rahm,

Propagation and spectral sorting of single photons in high-index dielectric nanowires (pp. 288)
Melodie Humbert, Peter R. Wiecha, Gerard Colas des Francs, Aurelie Lecestre, Guilhem Larrieu, Christian Girard, Vincent Paillard, Aurelien Cuche,

Manipulating Electric or Magnetic Spontaneous Emission in the Near-Field of Silicon Nanoantennas (pp. 290)
Mathieu Mivelle, Dorian Bouchet, Yannick De Wilde, Valentina Krachmalnicoff, Maria Sanz-Paz, Niek F. van Hulst, Maria F. Garcia-Parajo, Nicolas Bonod, Sebastien Bidault,

Surface plasmon-driven ultrafast dynamics of hot electrons (pp. 292)
Ilya Razdolski, Alexander L. Chekhov, Alexander I. Stognij, Andrzej Stupakiewicz,

Silicon Particle Synthesis and 2D Assembly (pp. 294)
Glenna L. Drisko, Benoit Miller, Maria Letizia De Marco, Alyxandra N. Thiessen, Jonathan G. C. Veinot, Alex Baron, Philippe Barois, Virginie Ponsinet,

Hybridization between Parallel and Orthogonal Surface Lattice Resonances (pp. 296)
Shao-Ding Liu, Peng Yue, Shi Zhang, Mingshan Wang, Hongwei Dai, Yiqin Chen, Zhong-Quan Nie, Yanxia Cui, Jun-Bo Han, Huigao Duan,

Invisible Dielectric Cylinders at Optical Frequency (pp. 298)
Kotaro Kajikawa, Yusuke Kobayashi,

Photonic Integrated Nanojet (pp. 300)
Ali Belarouci, Michele Calvo, Oleksii Hudz, Pedro Rojo Romeo, Regis Orobtchouk,

Cooperative emission mediated by energy transfer to plasmonic antenna (pp. 302)
Tigran V. Shahbazyan,

Advances in Sub-Wavelength Nanophotonic Devices (pp. 304)
Jian Wang,

Chirowaveguides: a balance between circular and linear birefringences (pp. 306)
Alban Gassenq, Leo Colliard, Amina Bensalah-Ledoux, Bruno Baguenard, Laure Guy, Stephan Guy,

Ultrafast Light-Induced Magnetism in Plasmonic Nanoparticles (pp. 308)
Oscar Hsu-Cheng Cheng, Dong Hee Son, Matthew Sheldon,

Saturable photoexcited carrier refraction in graphene-covered on-chip waveguides (pp. 310)
David Castello-Lurbe, Jurgen Van Erps, Mulham Khoder, Iwona Pasternak, Aleksandra Krajewska, Tymoteusz Ciuk, Wlodek Strupinski, JinLuo Cheng, Hugo Thienpont, Nathalie Vermeulen,

Surface Acoustic Wave generation of guided Modes in Phononic Nanobeams (pp. 312)
Alexander Korovin, Yan Pennec, Matteo Stocchi, Davide Mencarelli, Luca Pierantoni, Tapani Makkonen, Jouni Ahopelto, Bahram Djafari Rouhani,

Enhancing Light Absorption with a Complex Environment: What Are the Limits of the Playground? (pp. 314)
Emilie Sakat, Leo Wojszvzyk, Jean-Jacques Greffet, Jean-Paul Hugonin, Christophe Sauvan,

Fabrication of Plasmonic Supercrystals for Microfluidic Sensing (pp. 316)
Daniel Garcia-Lojo, Sergio Gomez-Grana, Jorge Perez-Juste, Isabel Pastoriza-Santos,

Manipulation of nanoparticles using hyperbolic metasurfaces (pp. 318)
Nayan Kumar Paul, J. Sebastian Gomez Diaz,

Development of a wave machine to model phononic crystals and elastic metamaterials (pp. 320)
Motonobu Tomoda, Masahiro Ino, Osamu Matsuda, Oliver B. Wright ,

BIC-inspired nonradiating states under structured light illumination (pp. 322)
Lei Xu, Lujun Huang, Mohsen Rahmani, Khosro Zangeneh Kamali, Rocio Camacho-Morales, Matt Wolley, Dragomir Neshev, Andrey E. Miroshnichenko,

A Graphene-Integrated Topological Insulator: Electrical Control of Terahertz Plasmon Polartions (pp. 324)
Chihun In, Beom Kim, Hyunyong Choi,

On-chip quantum photonic sources based on silicon waveguide (pp. 326)
Lantian Feng, Ming Zhang, Yang Chen, Zhiyuan Zhou, Hao Wu, Ming Li, Guoping Guo, Guangcan Guo, Daoxin Dai, Xifeng Ren,

Hyperbolic meta-antennas: a new way to manipulate absorption and scattering of light towards bio-medical applications (pp. 328)
Nicolo Maccaferri, Yingqi Zhao, Marzia Iarossi, Tommi Isoniemi, Daniel Darvill, Antonietta Parracino, Giuseppe Strangi, Francesco De Angelis,

Arbitrary Tuning of the Isotopic Hydrogen Evolution Reactions (pp. 329)
Hiro Minamimoto, Ryo Osaka, Kei Murakoshi,

Super-Periodic Liquid Crystal Metasurfaces (pp. 331)
Maxim V. Gorkunov, Alexey V. Kondratov, Irina V. Kasyanova, Vladimir V. Artemov, Alena V. Mamonova, Alexander A. Ezhov, Serguei P. Palto,

Photo-physical properties of intramolecular charge transfer emissions controlled by hyperbolic metamaterials (pp. 333)
Kwang Jin Lee, Yeon Ui Lee, Frederic Fages, Jean-Charles Ribierre, Jeong Weon Wu, Anthony D'Aelo,

Elastic Mode Converter based on Supersymmetric Ladders (pp. 335)
Choonlae Cho, Sunkyu Yu, Namkyoo Park,

Optomechanical Kerker effect for trembling resonant particles (pp. 337)
Alexander V. Poshakinskiy, Alexander N. Poddubny,

Deciphering, Characterization and Nanocontrol of Single Quantum Dots for Single Photon Emission and Near-field Imaging

(pp. 339)
Xuewen Chen,

Key Issues in the Rational Design of Plasmonic Nanoparticles for Second Harmonic Generation (pp. 340)
Pierre-Francois Brevet,

Optical slot Yagi-Uda antennas (pp. 342)
Yeonsang Park, Jineun Kim, Young-Geun Roh, Q-Han Park,

Flexible metasurfaces in the visible range for imaging and biophotonic applications (pp. 344)
Andrea Di Falco,

Heterogeneous Integrated Nanomaterials for Attojoule Optoelectronics and Neuromorphic Information Processing (pp. 346)
Jonathan K. George, Mario Miscuglio, Rubab Amin, Zhizhen Ma, Volker J. Sorger,

Minimal Designs of Lorentz Non-reciprocal Metasurfaces and Diatomic Resonator Arrays (pp. 348)
Wenyan Wang, Wang Tat Yau, K. F. Lee, Jin Wang, Kin Hung Fung,

Optical Pump - Terahertz Probe Spectroscopy of Semiconductor Nanostructures (pp. 350)
Hynek Nemec, Petr Kuzel,

Mid IR Dirac-cone dispersion relation materialized in SOI photonic crystal slabs (pp. 352)
Yuanzhao Yao, Naoki Ikeda, Takashi Kuroda, Takaaki Mano, Hiromi Koyama, Yoshimasa Sugimoto, Kazuaki Sakoda,

Subwavelength polarization optics using helical travelling-wave nanoantennas (pp. 354)
Mengjia Wang, Roland Salut, Huihui Lu, Miguel Angel Suarez, Nicolas Martin, Thierry Grosjean,

Plasmonic mode conversion and second harmonic imaging of tilted plasmonic nanocones (pp. 356)
Christoph Dreser, Dominik A. Gollmer, Godofredo Bautista, Xiaorun Zang, Dieter P. Kern, Martti Kauranen, Monika Fleischer,

Bismuth-based Metasurfaces for Nanophotonics from the Ultraviolet to the Far Infrared (pp. 358)
Johann Toudert, Rosalia Serna,

Recovering molecular orientation using single molecule SERS in plasmonic nano-gaps (pp. 360)
Jean-Sebastien Bouillard, Addison Marshall, Francesco Viscomi, John Proctor, Matthew Roberts, Johannes Gierschner, Ali Adawi,

Water-processable cellulose-based sacrificial layers for advanced nanofabrication (pp. 362)
Camilla Dore, Juan Luis Garcia Pomar, Johann Osmond, Agustin Mihi,

Destabilization of polariton condensates due to acousto-optic interactions (pp. 364)
Alexey Yulin, Valery K. Kozin, Anton V. Nalitov, Ivan A. Shelykh,

Femtosecond laser pulse modification of gold nanorods to provide identical optical response (pp. 366)
Guillermo Gonzalez-Rubio, Pablo Diaz-Nunez, Antonio Rivera, Alejandro Prada, Gloria Tardajos, Jesus Gonzalez-Izquierdo, Luis Banares, Pablo Llombart, Luis G. Macdowell, Mauricio Alcolea Palafox, Luis M. Liz-Marzan, Ovidio Pena-Rodriguez, Andres Guerrero Martinez,

Pathways for Ultrafast All-optical Magnetic Recording in Garnets (pp. 368)
Andrzej Stupakiewicz,

Using femtosecond laser pulses to control the assembly and welding of plasmonic nanostructures (pp. 370)

Ovidio Pena-Rodriguez, Guillermo Gonzalez-Rubio, Pablo Diaz-Nunez, Antonio Rivera, Luis Banares, Luis M. Liz-Marzan, Andres Guerrero-Martinez,

Multiphysics simulations of active meta-surfaces (pp. 372)
Dmitry N. Chigrin,

Negative-index metamaterials made by low-cost approaches (pp. 373)
Mayte Gomez-Castano, Juan Luis Garcia-Pomar, Renaud Vallee, Agustin Mihi, Serge Ravaine,

Use of novel metamaterials for magnetic resonance imaging (pp. 375)
Carlo Rizza, Marco Fantasia, Elia Palange, Marcello Alecci, Angelo Galante,

Mapping electron emission and multiphoton absorption in plasmonic nanoantenna arrays (pp. 377)
Kamonpan Chumpol, Kenan Elibol, Xia Zhang, Richard Hobbs,

Excitation of near-field resonances in system of two coupled small particles by fast electrons (pp. 379)
Daria Sergeeva, A. A. Tishchenko,

Plasmonic nanocavities: New understanding on the correlation of near- and far-field spectra and their impact on strong coupling dynamics (pp. 381)
Angela Demetriadou, Kalun Bedingfield, Antonios Kotsampaseris,

Coupled oscillator ensembles with loss and gain: a graph approach of PT symmetry (pp. 383)
Henri Benisty, Vincent Brac de la Perriere, Abderrahim Ramdane, Anatole Lupu,

Optical Helmholtz resonators (pp. 385)
Patrick Bouchon, Paul Chevalier, Riad HaÃ¯dar,

Metasurface Photodetectors for Directional Image Sensing (pp. 387)
Leonard Kogos, Yunzhe Li, Jianing Liu, Yuyu Li, Lei Tian, Roberto Paiella,

Control of Ge(Si) Quantum Dot Emission by Mie Resonances in Silicon Nanodisks (pp. 389)
Viktoriia Rutckaia, Dominik Schulze, Vadim Talalaev, Frank Heyroth, Mihail Petrov, Mikhail Shaleev, Alexey Novikov, Joerg Schilling,

Photonic phase transitions in dielectric structures (pp. 391)
Mikhail V. Rybin,

Plasmon-enhancement in nanostructured shells for single particle protein assays and photodynamic therapy (pp. 393)
Christophe Silien, Grace Brennan, Daragh Rice, Matthew Gleeson, Rabah Mouras, Tewfik Soulimane, Syed A. M. Tofail,

Single hybrid plasmonic structures for efficient photon pair production at the nanoscale (pp. 395)
Nicolas Chauvet, Maeliss Ethis de Corny, Guillaume Laurent, AurÃ©lien Drezet, Gilles Nogues, GÃ©raldine Dantelle, Thierry Gacoin, Atsushi Uchida, Hirokazu Hori, Serge Huant, Guillaume Bachelier, Makoto Naruse,

Translational invariant structured mirrors for beam-shaping (pp. 397)
Ramon Herrero Simon, Pei-Yu Wang, Yu-Chieh Cheng, Muriel Botey, Kestutis Staliunas,

Periodic metasurface structures processed with spatially shaped femtosecond laser: Fundamentals and Applications (pp. 399)
Xiaowei Li,

Revealing Light-Matter Interactions at the Nanoscale using Single-Molecule Super-Resolution Microscopy (pp. 400)

Nathan Kimmitt, Zachary Hallenbeck, Evan Kalinowsky, Andrew Dibiasio, Esther Wertz,

Hybrid plasmonic to plasmonic only transition and photonic only mode supported by semiconductor near metal (pp. 402)
Ning Liu,

III-V Semiconductor Nanowires for Optoelectronic Applications (pp. 404)
Ziyuan Li, Hark Hoe Tan, Chennupati Jagadish, Lan Fu,

Plasmonic transition metal nitride and carbide for photocatalytic and photothermal applications (pp. 406)
Satish L. Shinde, Satoshi Ishii, Manpreet Kaur, Thang Duy Dao, Tadaaki Nagao,

Nonlinear Light Generation from Si Nanoplasmonic Waveguides (pp. 408)
Abdulhakem Elezzabi, Curtis Firby, Shawn Sederberg,

Thin and Multifunctional Metasurfaces for Display Applications (pp. 410)
Jonghwa Shin, Hyowook Kim, Min Sung Heo, Arthur Baucour, Nayeong Kim,

Direct and Inverse Magneto-Optics of Structured All-Dielectric Iron-Garnet Films (pp. 411)
Andrey Kalish, Andrey Voronov, Daria Ignatyeva, Mikhail Kozhaev, Miguel Levy, Dolendra Karki, Vladimir Belotelov,

Bifacial metasurfaces and their applications (pp. 413)
Byoungho Lee, Jangwoon Sung, Gun-Yeal Lee,

Engineering the Refractive Index and Phase of Optical Metamaterials (pp. 415)
Zi Jing Wong,

Index-Tunable Terahertz Metadevices Based on Double-Layered Closed-Ring Resonator Arrays (pp. 417)
Tatsunosuke Matsui,

Nano-opto-electro-mechanical systems for optical switching and sensing (pp. 419)
Andrea Fiore, Tianran Liu, Francesco Pagliano, Rene van Veldhoven, Vadim Pogoretskii, Yuqing Jiao,

Quantum control of bosonic modes with superconducting circuits (pp. 421)
Liang Jiang,

Large-parameter-space optimization of photonic crystal structures (pp. 423)
Vincenzo Savona,

Dielectric nanostructures to enhance the efficiency of solar cells (pp. 424)
Braulio Garcia-Camara, Eduardo Lopez-Fraguas, Mahmoud H. Elshorbagy, Ricardo Vergaz,

Metasurfaces Enabled by Locally Tailoring Disorder in Phase-Change Materials (pp. 426)
Martin Hafermann, Philipp Schoppe, Jura Rensberg, Carsten Ronning,

Can optical forces be used to measure the polarization state of light inside a birefringent waveguide? (pp. 427)
Vincent Ginis, Lulu Liu, Alan She, Federico Capasso,

Long-range FRET-mediated exciton diffusion in cesium lead halide perovskite nanostructures (pp. 429)
Monica Lorenzon, Anna Loiudice, Edward S. Barnard, Nicholas J. Borys, Matthew J. Jurow, Min Ji Hong, Yi-Hsien Lu, Igor Rajzbaum, Edward K. Wong, Miquel Salmeron, Yi Liu, Stefano Cabrini, Stephen Whitelam, Raffaella Buonsanti, Adam M. Schwartzberg, Erika Penzo, Alexander Weber-Bargioni,

Dielectric-based Hyperbolic Metamaterials and Nano-Optical Cavity (pp. 430)

Junichi Takahara, Jun Sagara,

Nanocrystal Optoelectronics (pp. 432)
Hilmi Volkan Demir,

Novel Phenomena in Optical Manipulation due to Magnetic-Field Induced Resonant States (pp. 433)
S. Edelstein, R. M. Abraham Ekeroth, P. A. Serena, J. J. Saenz, A. Garcia-Martin, Manuel I. Marques,

Direct Integration of Scalable Quantum Sources into Pre-Fabricated Integrated Optics (pp. 434)
Khaled Mnaymneh, Dan Dalacu, David B. Northeast, Joseph McKee, John Weber, Sofiane Haffouz, Jean Lapointe, Philip P. Poole, Geof C. Aers, Robin L. Williams,

Self-assembled composite metamaterials for hydrogen sensing (pp. 436)
Mazhar Ejaz Nasir, Wayne Dickson, Anatoly Zayats,

Light Scattering from Solid-State Quantum Emitters: Beyond the Atomic Picture (pp. 438)
Alistair J. Brash, Jake Iles-Smith, Catherine L. Phillips, Dara P. S. McCutcheon, Jesper Mork, Maurice S. Skolnick, A. Mark Fox, Ahsan Nazir,

Flexible control of silicon Bragg grating filters enabled by sub-wavelength and modal engineering (pp. 440)
Dorian Oser, Xavier Le Roux, Florent Mazeas, Diego Perez-Galacho, Daniel Benedikovic, Elena Duran-Valdeiglesias, Vladyslav Vakarin, Olivier Alibart, Pavel Cheben, Sebastien Tanzilli, Laurent Labonte, Delphine Marris-Morini, Eric Cassan, Laurent Vivien, Carlos Alonso-Ramos,

Optical manipulation of exciton polaritons in semiconductor microcavity structures: from transitional to rotational motion (pp. 443)
Yong-Hoon Cho,

Plasmonic near-field probing with sub-nm sensitivity using photoelectrons (pp. 445)
Peter Dombi,

Photonic topological edge states in a zig-zag chain composed of split ring resonators (pp. 447)
Yuto Moritake,

Nanophotonic Technology and Applications (pp. 449)
Yeshaiahu Fainman,

Strong Light-Matter Interaction in Lithography-free Metamaterial Perfect Absorbers: Energy conversion, color filtering, and sensing applications (pp. 451)
Ekmel Ozbay, Amir Ghobadi, Hodjat Hajian, Bayram Butun,

Synthetic Weyl points in plasmonic-dielectric crystals (pp. 453)
Z. Z. Liu, Q. Zhang, Jun Jun Xiao,

Magnon Kerr Effect in a Cavity QED System (pp. 455)
Tiefu Li,

Field-Resolved Detection of the Temporal Response of a Mid-Infrared Plasmonic Antenna (pp. 456)
Marco P. Fischer, Kevin Gallacher, Jacopo Frigerio, Giovanni Pellegrini, Niccolo Maccaferri, Giovanni Isella, Alfred Leitenstorfer, Douglas J. Paul, Paolo Biagioni, Daniele Brida,

Control of Emission Photon Statistics from a Single Colloidal Quantum Dot Using Plasmonic Nanostructures (pp. 458)
Sadahiro Masuo,

Colossal infrared and terahertz magneto-optical activity in graphene/hBN heterostructures (pp. 460)
Ievgeniia O. Nedoliuk, Sheng Hu, Andre K. Geim, Alexey B. Kuzmenko,

Angular momentum of light induces chiral mass transport (pp. 461)
Takashige Omatsu,

Design and Experiments of Planar Metamaterial Luneburg Lens on SOI (pp. 463)
Hamdam Nikkhah, Trevor J. Hall,

Polarization Engineering via in-Plane Rotation of Uniaxial Bilayers (pp. 465)
Constantinos Valagiannopoulos,

Enabling Plasmonic Metasurfaces by Laser Processing (pp. 467)
Alberto Pique, Ray C.Y. Auyeung, Heungsoo Kim, Kristin M. Charipar, Jake Fontana, Nicholas A. Charipar,

Fully CMOS compatible high-Q photonic crystal nanocavity devices and their applications (pp. 469)
Takasumi Tanabe, Nurul Ashikin Binti Daud, Hajime Kumazaki, Shengji Jin,

Modulating Propagating Surface Plasmons on Silver Nanowires (pp. 471)
Qiang Li, Li Chen, Hongxing Xu, Zhaowei Liu, Hong Wei,

Laser induced nanostructuring of plasmonic composite films for color image multiplexing (pp. 472)
Nipun Sharma, Marie Vangheluwe, Matthieu Bugnet, Alice Vermeulin, Nathalie Destouches,

Acousto-plasmonics: from acoustic metasurfaces to chirality in coherent phonon generation experiments (pp. 474)
Kevin O'Brien, Jun Rho, Haim Suchowski, Xiang Zhang, Alba Jimenez, Antonio Garcia-Martin, Daniel Lanzillotti Kimura,

Non-invasive Bio-imager Based on Frequency-tunable Terahertz Plasmonics (pp. 476)
Yukio Kawano,

Superconducting thin films and nanowires for mid-infrared single photon detection (pp. 478)
Dmitry Morozov, Gregor Taylor, Archan Banerjee, Kleanthis Erotokritou, Umberto Nasti, Shigehito Miki, Hirotaka Terai, Robert H. Hadfield,

sp3 Defects of Single Walled Carbon Nanotubes: Photonic and Electronic Integration (pp. 480)
Han Htoon,

Graded metasurface for elastic energy harvesting (pp. 481)
Jacopo Maria De Ponti, Andrea Colombi, Richard Craster, Raffaele Ardito, Francesco Braghin, Alberto Corigliano,

Multipole Decomposition of Bound States in the Continuum in Dielectric Metasurfaces (pp. 482)
Zarina Sadrieva, Kristina Frizyuk, Mihail Petrov, Yuri Kivshar, Andrey Bogdanov,

Direct Imaging of Isofrequency Contours of Strongly Localized Guided Modes in Planar Photonic Structures (pp. 484)
Anton K. Samusev,

Metasurfaces for Optical Antireflection and Bandpass Filters (pp. 485)
Hou-Tong Chen, Chun-Chieh Chang, Beibei Zeng, Li Huang,

Optimal Design of Rectennas for IR Energy Harvesting (pp. 487)
Ahmed Elsharabasy, Mohamed Bakr, M. Jamal Deen,

Aggregation Enhanced Two-photon Photoluminescence of Plasmonic Metal Nanoparticles and Their Biomedical

Applications (pp. 488)
Peiyan Yuan, Zhenping Guan, Cuifeng Jiang, Monalisa Garai, Qing-Hua Xu,

Spontaneous emission near photonic Weyl points (pp. 490)
Inaki Garcia-Elcano, Alejandro Gonzalez-Tudela, Jorge Bravo-Abad,

Advances in novel composite materials obtained by crystal growth (pp. 492)
D. A. Pawlak, P. Paszke, R. Nowaczynski, K. Szlachetko, P. Piotrowski, M. Tomczyk, K. Sadecka, A. Materna, B. Surma, A. Belardini, J. Toudert, C. Sibilia,

All-optical charging and charge transport in quantum dots (pp. 493)
Nika Akopian,

Gold nanorod bending and splitting with light: A new route towards functional plasmonic surfaces (pp. 494)
Theobald Lohmuller,

Recent advances in subwavelength metamaterial silicon photonics (pp. 495)
Pavel Cheben, Carlos Alonso-Ramos, Robert Halir, Jens Schmid, Jiri Ctyroky, Daniel Benedikovic, Alejandro Ortega-Monux, Alejandro Sanchez-Postigo, David Gonzalez-Andrade, Gonzalo WanguÌˆemert-Perez, Inigo Molina-Fernandez, Aitor Velasco, Alaine Herrero-Bermello, Jose Manuel Luque-Gonzalez, Daniel Pereira-Martin, Jean Lapointe, Siegfried Janz, Dan Xia Xu, Daniele Melati, Yuri Grinberg, Shurui Wang, Martin Vachon, Mohsen KamandarDezfouli, Ross Cheriton, Vladyslav Vakarin, Milan Dado, Dorian Oser, Florent Mazeas, Diego D. PÃ©rez-Galacho, Xavier Le Roux, Elena Duran-Valdeiglesias, Laurent LabontÃ©, Sebastien Tanzilli, Eric Cassan, Delphine Marris-Morini, Laurent Vivien,

Far-field sub-diffraction imaging with wire array metamaterials (pp. 497)
Alessio Stefani, Simon Fleming, Boris Kuhlmey,

DNA Self-Assembled Plasmonic Nanoantennas (pp. 499)
Mauricio Pilo-Pais,

Recent advances in phase-change materials for high-speed optoelectronics (pp. 501)
Imad Agha,

Plasmonic Monitoring of Lithium Metal Evolution in Nanobatteries (pp. 503)
Yan Jin, Jia Zhu, Lin Zhou,

3D Porous Silicon Gradient Refractive Index Micro-Optics and Waveguides (pp. 505)
Paul V. Braun,

Local Symmetries in Wave Mechanics: From Fundamentals to First Applications (pp. 507)
Peter Schmelcher,

Integrated frequency combs for the on-chip generation of optical quantum states (pp. 508)
Stefania Sciara, Michael Kues, Christian Reimer, Piotr Roztocki, Benjamin Wetzel, Brent E. Little, Sai T. Chu, David J. Moss, Lucia Caspani, Roberto Morandotti,

Diamond nano-optomechanical devices (pp. 510)
Paul Barclay,

Balancing the photo-budget in far-field optical imaging for enhanced lateral resolution (pp. 511)
Wyatt Adams, Chito Kendrick, Christopher Middlebrook, Durdu Guney,

Correlated Photon pairs at 2 microns: Generation, Characterisation, and Detection (pp. 513)

Shashi Prabhakar, Taylor Shields, Gregor G. Taylor, Dmitry Morozov, Michael Kues, Corin Gawith, Lucia Caspani, Robert H. Hadfield, Matteo Clerici,

All-optical signal processing with hybrid III-V-on-silicon chip (pp. 515)
LÃ©a Constans, Dorian Sanchez, Sylvain CombriÃ©, Fabrice Raineri, Alfredo De Rossi,

Generation of on-chip D-dimensional entangled cluster states and their characterization via optimal entanglement witnesses (pp. 517)
Lucia Caspani, Stefania Sciara, Christian Reimer, Piotr Roztocki, Mehedi Islam, Luis Romero CortÃ©s, Yanbing Zhang, Bennet Fischer, SÃ©bastien Loranger, Raman Kashyap, Alfonso Cino, Sai T. Chu, Brent E. Little, David J. Moss, William J. Munro, JosÃ© AzaÃ±a, Michael Kues, Roberto Morandotti,

Multifunctional plasmon-enhanced nanoscopy for nanoscale control of chemical reactions (pp. 519)
Taka-aki Yano,

Comparison of Plasmonic Response of Semiconductor Nanostructures with Spherical Symmetry and Their Prospect for Terahertz Applications (pp. 520)
Thomas T. Y. Wong, Tao Shen, Zhijing Hu, Yanlin Li, Zi Wang,

Light-Trapping Transparent Electrodes For Photodetection and Photovoltaics (pp. 524)
Mengdi Sun, Pieter G. Kik,

Dirac-like photonic structures: from pseudospin to topology (pp. 526)
Zhigang Chen,

Shaping of light in non-Hermitian disordered media (pp. 527)
Konstantinos Makris, Andre Brandstotter, Stefan Rotter,

Advanced passive and active metasurfaces

Extreme Nonlinear Optics in Epsilon-Near-Zero Meta-Films (pp. 530)
Yuanmu Yang,

Metasurface for artificial neural computing (pp. 532)
Zongfu Yu,

Revealing the Near-Field Dynamics in Chiral Metasurfaces: Interactions of Spatially Displaced Surface Plasmon vortices (pp. 533)
Chen-Bin Huang,

Integrated single photon sources with colloidal semiconductor nanocrystals (pp. 535)
Alberto Bramati,

Super-cell Geometric Phase Metasurface for Multispectral Imaging (pp. 536)
Bo Qiang, Jie Deng, Xiao Siong Tang, Soo Seng Ang, Jing Hua Teng, Qi Jie Deng, Qian Wang,

Alternative Plasmonic Materials for SERS and Metasurface Applications: Aluminum and Titanium Nitride (pp. 538)
Shangjr Gwo,

Selectively reconfigurable molecularization of terahertz meta-atoms (pp. 540)
Hyunseung Jung, Hyunwoo Jo, Wonwoo Lee, Moon Sung Kang, Hojin Lee,

Recent Advances in Mid-Infrared Graphene Plasmonics: Metasurface for Complex Amplitude Modulation and Compact

Waveguide Switch (pp. 542)
Sangjun Han, Seyoon Kim, Sergey Menabde, Victor Brar, Harry Atwater, Min Seok Jang,

Electrically-pumped Vertical Cavity Metasurface-Emitting Lasers for directional lasing emissions (pp. 543)
Yiyang Xie, Peinan Ni, Gauthier Briere, Qiuhua Wang, Zhuangzhuang Zhao, Chen Xu, Qiang Kan, Hongda Chen, Patrice Genevet,

Light sailing to interstellar space and nearby stars (pp. 545)
Artur R. Davoyan,

Dielectric passive metasurface and active tunable nonlinear metasurface (pp. 547)
Junxiao Zhou, Haoliang Qian, Zhaowei Liu,

Enhancing Chiral Light-Matter Interactions by Metamaterials (pp. 549)
Yongmin Liu,

Microfluidic Sensing and Dynamic Tuning with Huygens Metasurfaces (pp. 551)
Adam J. Ollanik, Isaac O. Oguntoye, George Z. Hartfield, Brittany Simone, Yaping Ji, Matthew D. Escarra,

van der Waals Metasurfaces and Transdimensional Photonic Lattices (pp. 553)
Viktoriia Babicheva,

Chalcogenide Glasses: Potential for Passive and Active Dielectric Metasurface Applications (pp. 555)
Jesse A. Frantz, Robel Y. Bekele, Jason D. Myers, Anthony Clabeau, Vinh Q. Nguyen, Yun Xu, Jingbo Sun, Mikhail Shalaev, Wiktor Walasik, Apra Pandey, Alexander Tsukernik, Natalia M. Litchinitser, Jasbinder S. Sanghera,

Optical elements based on engineered subwavelength dielectric structures (pp. 557)
Adrei Faraon,

Topological protection in spin and valley Hall metasurfaces (pp. 558)
Matthias Saba, Stefan Wong, Sang Soon Oh, Ortwin Hess,

Highly-Confined Surface Phonon Polaritons in Semiconductor Metamaterial Interfaces (pp. 560)
Alexander M. Dubrovkin, Bo Qiang, Nikolay I. Zheludev, Qijie Wang,

Chirality, magnetism, and magnetoelectricity: Separate phenomena and joint effects in metamaterial structures

Collective polarization-dependent plasmon routing by means of spin-locking metasurface (pp. 563)
Matan Revah, Andre Yaroshevsky, Yuri Gorodetski,

Enhancing Circular Dichroism and Chiral Sorting with Chiral Surface Waves (pp. 567)
Marco Finazzi, Giovanni Pellegrini, Michele Celebrano, Lamberto Duo, Paolo Biagioni,

Theoretical Design of Two-Dimensional Magnetoelectric Materials (pp. 569)
Shuai Dong,

Enantio-separation of chiral molecules adsorbed on a magnetic nanostructure with perpendicular anisotropy (pp. 571)
Koyel Banerjee-Ghosh, Oren Ben Dor, Francesco Tassinari, Eyal Capua, Shira Yochelis, Amir Capua, See-Hun Yang, Stuart Stephen Papworth Parkin, Soumyajit Sarkar, Leeor Kronik, Ron Naaman, Yossi Paltiel, Lech Tomasz Baczewski,

Spin-Polarized Plasmonics (pp. 573)
Vladimir Drachev, Hari Bhatta, Ali Aliev,

Magnetoelectric structures and magnetoelectric fields (pp. 575)
Eugene Kamenetskii,

Plasmon assisted improvement of figure of merit of magneto-optical Kerr effect and magnetic anisotropy in Au/Co/Au multilayered nanorectangular array structures (pp. 577)
Takuo Tanaka,

Tunable ferromagnetic resonance in coupled trilayers with crossed perpendicular and in-plane magnetic anisotropies (pp. 579)
Daniel Marko, Fernando Valdes-Bango Garcia, Carlos Quiros Fernandez, Aurelio Hierro-Rodriguez, Maria Velez Fraga, Jose Ignacio Martin Carbajo, Jose Maria Maestro Alameda, David Schmool, Luis Manuel Alvarez-Prado,

Chirality and Optical Spin-orbit Coupling in Topological Photonic Crystals (pp. 581)
Nikhil Parappurath, Filippo Alpeggiani, L.(Kobus) Kuipers, Ewold Verhagen,

A surface plasmon platform for angle-resolved chiral sensing (pp. 583)
Lykourgos Bougas, Sotiris Droulias,

Terahertz metamaterials: accessing nonlinear spin and phonon dynamics (pp. 585)
Stefano Bonetti,

Dynamical chiral metasurfaces: mechanical based modulation and polarimetry (pp. 587)
Alessandro Pitanti,

Structural chirality combined with optical activity (aka magneto-electricity) (pp. 589)
Martin McCall,

Controlling the plasmon resonance of an Au/Ni hybrid nanostructures using external magnetic field or temperature (pp. 591)
Silvere Schuermans, Thomas Maurer, Alexander Govorov, Jerome Plain,

Nonlocal effects in piezoelectromagnetic metamaterials (pp. 593)
Anatolii Konovalenko, Felipe Perez-Rodriguez,

Electromagnetic Sink Based on a Nonreciprocal Metasurface Cavity (pp. 595)
Mojtaba Dehmollaian, Guillaume Lavigne, Christophe Caloz,

Simple Spintronics and Superconducting Spintronics, Based on the Chiral Induced Spin Selectivity (CISS) Effect (pp. 597)
Yossi Paltiel,

Topological Magnonic Materials and Devices (pp. 598)
Xiangrong Wang,

Chirality and Anti-ferromagnetism in Artificial Micro-/Nano-Structures (pp. 599)
Kun Huang,

Generation and Propagation of Surface-Plasmon Polaritons at Lossy Interfaces (pp. 601)
Nafiseh Sang-Nourpour, Saeid Asgarnezhad-Zorgabad, Barry C. Sanders,

Optical response of magnetoelectric materials with spin-induced chirality and polarity (pp. 603)
Youtarou Takahashi,

Photonic properties of multiferroic layered metasurfaces (pp. 604)

Ramaz Khomeriki, Levan Chotorlishvili, Jamal Berakdar,

Engineering the Optical Magnetoelectric Effect in Crystals on the Sub-Unit-Cell Scale (pp. 605)
Istvan Kezsmarki, Sandor Bordacs,

Electromagnetic Responses and Non-reciprocal Phenomena of Metamaterials with Chirality and Magnetism (pp. 607)
Kei Sawada, Satoshi Tomita, Hiroyuki Kurosawa, Tetsuya Ueda,

Microwave-Active Dynamics of Magnetic Skyrmions under Application of a Tilted Magnetic Field (pp. 609)
Masahito Mochizuki, Tatsuya Koide, Masahito Ikka, Akihito Takeuchi,

Spin waves in thin films and magnonic crystals with Dzyaloshinskii-Moriya interactions (pp. 611)
Rodolfo Gallardo, David CortÃ©s-Ortuno, Roberto Troncoso, Pedro Landeros,

Chiral Metastructures and Bio-Assemblies: Plasmonic, Thermal and Hot-Electron Effects (pp. 612)
Alexander Govorov, Larousse Khosravi Khorashad, Lucas V. Besteiro,

Tailoring the Chiral Response of Achiral Nanostructures Using Structured Light (pp. 614)
Peter Banzer,

Theory of chiral transport in chiral crystals (pp. 615)
Shuichi Murakami,

Stability and dynamics of skyrmions in multiferroic transition metal halides (pp. 616)
Maxim Mostovoy, Alessio Pozzi,

Magnetic and chemical steering of chiral light at the nanoscale (pp. 618)
Alexandre Dmitriev,

Circular Dichroism and Spontaneous Chiral Symmetry Breaking in Rotational Particles (pp. 619)
Deng Pan, Hongxing Xu, Javier Garcia de Abajo,

Metamaterials and Photonic Crystals for THz Science and Technology

Gate-controlled Optical Properties in Graphene Based Metasurfaces (pp. 622)
Teun-Teun Kim, Hyeon-Don Kim, Hyunjun Kim, Sang Soon Oh, Bumki Min, Shuang Zhang,

High Performance Spintronic Terahertz Emitter Enabled by Metal- Dielectric Photonic Crystal and Metamaterials (pp. 624)
Zheng Feng, Dacheng Wang, Haifeng Ding, Jianwang Cai, Wei Tan,

Photonic Crystal Waveguide Technologies for Terahertz Applications (pp. 626)
Masayuki Fujita,

Photonic Crystal Resonators as Liquid Sensing Platforms in the Terahertz Band (pp. 628)
Stephen M. Hanham, Clare Watts, Munir M. Ahmad, William J. Otter, Stepan Lucyszyn, Norbert Klein,

Singular graphene metasurfaces for broadband absorption (pp. 630)
Paloma Arroyo Huidobro, Emanuele Galffi, J. B. Pendry,

Terahertz Spoof Surface Plasmon Polaritons: Modelling, Design, and Experimental Characterization (pp. 632)
Mehmet Unlu,

THz Metasurfaces for Spatial Beam Modulation and Chemical Identification (pp. 634)
Polina Stefanova, Rhiannon Lees, Andreas K. Klein, Michael D. Cooke, Andrew J. Gallant, Claudio Balocco,

High-Performance Metamaterial-Inspired Quasi-Optical Instrumentation for THz Range (pp. 636)
Sergei A. Kuznetsov, Victor N. Fedorinin, Andrey V. Arzhannikov, Alexander N. Gentselev, Pavel A. Lazorskiy, Nazar A. Nikolaev,

All-dielectric metasurfaces for terahertz science and technology (pp. 638)
Willie J. Padilla, Kebin Fan,

Recent progress in the development of efficient semiconductor based THz sources (pp. 640)
Edik Rafailov, A. Gorodetsky, T. Gric, N. Bazieva,

Exploiting the Vacuum State in Materials with Plasmonic-to-Dielectric State Transition in Terahertz Gratings and Metasurfaces (pp. 642)
Andriy E. Serebryannikov, Akhlesh Lakhtakia, Guy A. E. Vandenbosch,

Graphene based terahertz optoelectronics (pp. 644)
Coskun Kocabas,

Chirality, magnetism, and magnetoelectricity: Separate phenomena and joint effects in metamaterial structures

Chiral (excitation of) spin waves in ferromagnetic films and spheres (pp. 646)
Tao Yu, Sanchar Sharma, Yaroslav Blanter, Gerrit Bauer,

Spin waves and electromagnetic waves in photonic-magnonic crystals (pp. 647)
Jaroslaw W. Klos, Igor L. Lyubchanskii, Yuliya S. S. Dadoenkova, Maciej Krawczyk, Nataliya N. Dadoenkova,

Toroidal Resonances and Reconfigurable Chiral Responses in Kirigami Metamaterials (pp. 649)
Liqiao Jing, Zuojia Wang, Bin Zheng, Hongsheng Chen,

Cavity optomagnonics with magnetic quasi-vortices (pp. 651)
Alto Osada,

3D near-field circular dichroism measured by optical force (pp. 653)
Masayuki Hoshina, Nobuhiko Yokoshi, Hajime Ishihara,

Chirality Generation in Discrete Silicon Nanostructures (pp. 655)
Xin Zhao, Bjoern Reinhard,

Generalization of the Optical Chirality to Arbitrary Media (pp. 657)
J. Enrique Vazquez-Lozano, Alejandro Martinez,

Chiral terahertz wave emission from the Weyl semimetal TaAs (pp. 659)
Y. Gao, Y. Qin, Y. P. Liu, Y. L. Su, S. Kaushik, E. J. Philip, X. Chen, Z. Li, H. Weng, D. E. Kharzeev, M. K. Liu, Jingbo Qi,

Photonic Orbital Angular Momentum Transfer and Magnetic Skyrmion Rotation (pp. 661)
Wenrui Yang, Huanhuan Yang, Yunshan Cao, Peng Yan,

Chiral quantum photonics (pp. 663)
Nir Rotenberg,

Chiral electric transport effects in topological solitons (pp. 664)
Fabian Lux, Jonathan Kipp, Matthias Redies, Jan-Philipp Hanke, Frank Freimuth, Stefan Blugel, Yuriy Mokrousov,

Switchable topological spin textures at a coherent oxide interface (pp. 665)
Kathrin Doerr, Martin Koch, Lukas Bergmann, Sujit Das, Stefano Agrestini, Igor Maznichenko, Nicolas Gauquelin, Diana Rata,

Magnetoelectricity of Micromagnetic Structures and Chirality (pp. 667)
Alexander Pyatakov, Daria Kulikova, Elena Nikolaeva, Tatiana Kosykh, Alexey Kaminskiy, Wei Ren, Athinarayanan Sundaresan, Anatoly Zvezdin,

Theory for Ultrafast Control of Spin Current and Spin Textures with AC Fields (pp. 669)
Masahiro Sato,

Chiral Optomagnonics with Polarized Light in Magnetic Insulators (pp. 670)
Igor Proskurin, Alexander S. Ovchinnikov, Jun-Ichiro Kishine, Robert L. Stamps,

Manifestation of the spatial Kramers-Kroning relations in plasmonic chiral metasurface (pp. 672)
Leeju Singh, Shmuel Sternklar, Yuri Gorodetski,

Electromagnetic responses, dynamics, and superconductivity emerging from multipole order (pp. 674)
Hikaru Watanabe, Atsuo Shitade, Akito Daido, Jun Ishizuka, Youichi Yanase,

Biomacromolecular Charge Chirality Detected Using Chiral Plasmonic Nanostructures (pp. 676)
Marion Rodier, Maryam Hajji, Malcolm Kadodwala,

Skyrmions, Antiskyrmions and Bobbers: Novel particles in chiral magnets (pp. 677)
Markus Hoffmann, Bernd Zimmermann, Gideon Muller, Christof Melcher, Nikolai Kiselev, Filipp Rybakov, Aleksandr Borisov, Fengshan Zheng, Andras Kovacs, Rafal E. Dunin-Barkowski, Stefan Bluegel,

Ultrafast Magnetic Recording with Terahertz Light (pp. 679)
I. Radu, M. Shalaby, M. Hennecke, D. Engel, C. von Korff Schmising, A. Tsukamoto, C. P. Hauri, S. Eisebitt,

Spatio-Temporal Conductivity Modulation: A Pathway Towards CMOS Compatible, Low Loss, Magnetic-Free Non-Reciprocity (pp. 681)
Aravind Nagulu, Negar Reiskarimian, Tolga Dinc, Harish Krishnaswamy,

Topology in photonic crystals, metamaterials, and metasurfaces: physics and design

Topological valley transport on the surface of biaxial hyperbolic metamaterials (pp. 684)
Ruo-Yang Zhang, Che Ting Chan,

Observations of Polarization Vortices in Momentum Space (pp. 686)
Yiwen Zhang, Ang Chen, Wenzhe Liu, Chia Wei Hsu, Bo Wang, Fang Guan, Xiaohan Liu, Lei Shi, Ling Lu, Jian Zi,

Optimal distance above ENZ-materials for fluorescence inhibition: Insight from a perturbative analysis of the surface Green function (pp. 687)
Claudio Silvestre Castro, Eugenio Rafael Mendez, Alexandre Vial, Gilles Lerondel, Aurelien Bruyant, Remi Vincent,

Inverse design and demonstration of on-chip ultracompact multimode silicon photonic devices (pp. 689)
Weijie Chang, Xinshu Ren, Longhui Lu, Minming Zhang,

Design of Photonic Topological Insulators Using Density Based Topology Optimization (pp. 691)
Rasmus E. Christiansen, Fengwen Wang, Ole Sigmund, Soren Stobbe,

Optically Tunable Epsilon-Near-Zero Metamaterials (pp. 693)
Surya Ayyagari, Alireza R. Rashed, Humeyra Caglayan,

Experimental demonstration of topological photonic states based on composite left/right-handed coupled ring resonators (pp. 695)
Zhi-Wei Guo, Yong Sun, Haitao Jiang, Hong Chen,

Topological edge modes in dielectric kagome photonic crystals (pp. 697)
Stephan Wong, Matthias Saba, Ortwin Hess, Sang Soon Oh,

Approaching the fundamental limits of heat transfer at the nanoscale: the surprisingly limited role of inverse design (pp. 699)
Prashanth Venkataram, Sean Molesky, Weiliang Jin, Alejandro Rodriguez,

Topology Optimization of Photonic Crystals and Large-area Metasurfaces (pp. 700)
Zin Lin, Steven G. Johnson,

Optimal metasurfaces: Theory and inverse design (pp. 701)
Owen Miller,

Modelling, simulation and optimization of metasurfaces

Designing nanophotonic structures using conditional-deep convolutional generative adversarial network (pp. 706)
Sunae So, Junsuk Rho,

Generalized Brewster conditions and bound states in the continuum in metal and all-dielectric metasurfaces through a coupled electric/magnetic dipole model (pp. 708)
Diego R. Abujetas, Juan J. Saenz, Jose A. J. Sanchez-Gil,

Optimized 3D metasurface for maximum light deflection at visible range (pp. 710)
Mahmoud M. R. Elsawy, Stephane Lanteri, Regis Duvigneau, Peinan Ni, Gauthier Briere, Patrice Genevet,

Numerical dipoles method for light scattering by disordered metasurfaces (pp. 712)
Maxime Bertrand, Alexis Devilez, Jean-Paul Hugonin, Philippe Lalanne, Kevin Vynck,

Designer hyperbolic nanostructures for thermo-plasmonic bio-medical applications using finite element and finite difference time domain methods (pp. 714)
Nicolo Maccaferri,

Perfect Penetrable Cloaking Using Arbitrary-Shape Bianisotropic Metasurfaces (pp. 715)
Mojtaba Dehmollaian, Christophe Caloz,

Effective transmission conditions for an array of locally resonant inclusions (pp. 717)
Kim Pham, Agnes Maurel, Jean-Jacques Marigo,

Biosensor chip based on VCSELs and gold grating (pp. 719)
YiYang Xie, Chen Xu, Qiang Kan, Beijv Huang, Hongda Chen,

Beam Steering Chip based on VCSEL (pp. 721)
Guanzhong Pan, Chen Xu, Weiling Guo, Baolu Guan, Beijv Huang, Hongda Chen,

Modelling of Nonlinear Metasurfaces: Second-Harmonic Generation and Kerr Effect (pp. 723)
Karim Achouri, Olivier J. F. Martin,

Different Photonic Structures via Inverse-Design Algorithm (pp. 725)
Done Yilmaz, Mediha Tutgun, Ahmet M. Alpkilic, Yusuf A. Yilmaz, Hamza Kurt,

Inverse Design and Optimization along Machine Learning for Metasurfaces (pp. 727)
Samad Jafar-Zanjani, Hossein Mosallaei,

Multiple scattering by complex objects: revisiting the methods of fictitious sources (pp. 729)
Anthony Gourdin, Patrice Genevet, Didier Felbacq,

Global Topology Optimization Networks (GLOnets) for Metasurface Design (pp. 731)
Jonathan A. Fan,

Metasurface-based Light Sources, Modulators, and Detectors

Dielectric metasurfaces for holography, color printing and crypto-display (pp. 733)
Junsuk Rho,

Dynamic Formation of Ultra-Small Images via Metasurfaces (pp. 734)
Khosro Zangeneh Kamali, Lei Xu, Jonathan Ward, Kai Wang, Guixin Li, Andrey E. Miroshnichenko, Dragomir Neshev, Mohsen Rahmani,

Metasurface Based Arbitrary Polarization Control and Its Applications (pp. 736)
Xianzhong Chen, Chunmei Zhang, Yuttana Intaravanne,

Dielectric Metasurfaces for Ultrathin Half Waveplates (pp. 738)
Yuttana Intaravanne, Xianzhong Chen,

Tunable and Reconfigurable Mid-Infrared Metasurfaces (pp. 740)
Clayton Fowler, Sensong An, Mikhail Y. Shalaginov, Yifei Zhang, Bowen Zheng, Hong Tang, Hang Li, Tian Gu, Juejun Hu, Hualiang Zhang,

High-dimensional vectorial metasurface holography (pp. 742)
Lingling Huang, Ruizhe Zhao, Basudeb Sain, Qunshuo Wei, Chengchun Tang, Xiaowei Li, Thomas Weiss, Yongtian Wang, Thomas Zentgraf,

Terahertz Photonic Devices Employing Graphene-based Hybrid Metasurfaces (pp. 744)
Peter Qiang Liu,

Nanophotonic Enhancement of Light Out-Coupling for Deep-UV LEDs (pp. 745)
Phillip Manley, Martin Hammerschmidt, Sven Burger, Christiane Becker,

Electric-Field-Induced Second Harmonic Generation from Organic Polymer (pp. 747)
Shumei Chen, King Fai Li, Guixin Li, Kok Wai Cheah, Shuang Zhang,

Transmissive metasurface lens for a mid-wavelength infrared detectors and focal plane arrays (pp. 749)
Alexander Soibel, Shuyan Zhang, Sam Keo, Dan Wilson, Sir Rafol, Alan She, David Z. Ting, Federico Capasso, Sarath D. Gunapala,

High-performance, All-dielectric Metasurfaces in the Ultraviolet Regime (pp. 751)
Cheng Zhang, Shawn Divitt, Qingbin Fan, Wenqi Zhu, Amit Agrawal, Ting Xu, Henri J. Lezec,

Gate-tunable Conducting Oxide Epsilon-near-zero Metasurfaces with Active Nonlinear and Quantum Responses (pp. 752)
Aleksei Anopchenko, Subhajit Bej, Sudip Gurung, Khant Minn, Jingyi Yang, Howard (Ho Wai) Lee,

Metasurface Light Sources and Modulators Based on Kerker Effects (pp. 753)
Austin Howes, Zhihua Zhu, Wenyi Wang, Joshua R. Nolen, Ivan I. Kravchenko, Richard Haglund, Joshua Caldell, Jason Valentine,

High-efficiency coupling and reshaping of surface plasmon with metasurfaces (pp. 755)
Xiaoer Li, Zhuo Wang, Shaohua Dong, Sixiong Yi, Yizhen Chen, Huijie Guo, Fuxin Guan, Qiong He, Lei Zhou, Shulin Sun,

Structural Color for Displays and Imaging

Electrically tunable multicolored filter based on plasmonic nanoscale phase retarder and liquid crystals (pp. 757)
Luc Driencourt, Dimitrios Kazazis, Yasin Ekinci, Francois Federspiel, Richard Frantz, Rolando Ferrini, Benjamin Gallinet,

Hybrid Plasmonic and Electrochromic Displays (pp. 759)
Magnus Jonsson,

Optimizing electrochromism for plasmonic electronic paper: Inorganic vs organic (pp. 760)
Marika Gugole, Oliver Olsson, Jose Montero Amenedo, Kunli Xiong, Gunnar A. Niklasson, Andreas Dahlin,

Nano-structured optical surfaces based on ultrathin materials for displays and sensing (pp. 762)
Bruno Paulillo, Rinu Maniyara, Juan Rombaut, Kavitha Kalavoor Gopalan, Nestor Bareza, Valerio Pruneri,

Tunable All-dielectric Metasurface for Color Printing (pp. 763)
Jianfeng Zang, Xin Liu, Zhao Huang,

High-Density Data Storage with Plasmonic Color Metapixels (pp. 765)
Alexander V. Kildishev, Maowen Song, Di Wang, Zhaxylyk A. Kudyshev, Honglin Yu, Alexandra Boltasseva, Vladimir M. Shalaev,

Light manipulation by natural photonic structures in diatom microalgae (pp. 766)
Johannes Goessling, Martin Lopez Garcia,

Dual-color plasmonic filters (pp. 768)
E. Heydari, J. Sperling, S. Neale, Alasdair W. Clark,

Tunable spherical colloidal photonic pigments with non-iridescent structural color (pp. 769)
Laurinda R. P. Areias, JosÃ© Paulo S. Farinha,

High purity reflective structural colors using bilayer hybrid absorbers and investigation of solution process via electrodeposition of thin-films (pp. 771)
L. Jay Guo, Saurabh Acharya, Zhengmei Yang, Chengang Ji,

Skin-like Full-Color Angle Independent Plasmonic Reflective Displays (pp. 773)
Pablo Manuel Cencillo Abad, Debashis Chanda,

Acoustic Metamaterials in the audible frequency range

Using mean flow to make a broadband acoustic diode (pp. 775)
Vassos Achilleos, Yves AurÃ©gan, Vincent Pagneux,

Perfect absorption using sparse arrays of Helmholtz resonators (pp. 777)
Jean-Francois Mercier, Agnes Maurel, Kim Pham,

Effective transmission conditions across a resonant bubbly metascreen (pp. 779)
Kim Pham, Jean-Francois Mercier, Daniel Fuster, Agnes Maurel, Jean-Jacques Marigo,

Sound absorbing metafluid inspired by cereal straws (pp. 781)
Weichun Huang, Logan Schwan, Vicente Romero-Garcia, Jean-Michel Genevaux, Jean-Philippe Groby,

Scattering by arrays of open ended resonators (pp. 783)
Agnes Maurel, Jean-Francois Mercier, Kim Pham,

Deep Sub-wavelength Materials for Controlling Sound Diffusion: Experimental Validation of Metadiffusers (pp. 785)
E. Ballestero, N. Jimenez, J.-P. Groby, S. Dance, V. Romero-Garcia,

Stealth Acoustic Materials for Scattering Cancellation (pp. 787)
V. Romero-Garcia, N. Lamothe, G. Theocharis, O. Richoux, L. M. Garcia-Rafï¬•,

Sound Transmission Loss through a Phononic Crystal Panel: Prediction and Validation (pp. 789)
Bart Van Damme, Armin Zemp, Sepide Ahsani, Lucas Van Belle, Claus Claeys, Elke Deckers,

On the use of plate-type metamaterial to experimentally highlight a hiding zone in Density Near Zero acoustic metamaterial (pp. 791)
Matthieu Mallejac, Aurelien Merkel, Jose Sanchez Dehesa, Johan Christensen, Vincent Tournat, Vicent Romero-Garcia, Jean-Philippe Groby,

Unidirectional zero sonic reflection in passive Partity-Time symmetric Willis media (pp. 793)
Aurelien Merkel, Vicent Romero-Garcia, Jean-Philippe Groby, Jensen Li, Johan Christensen,

Acoustic cloaking and self-cloaking inside ducts using liners (pp. 795)
Maaz Farooqui, Yves Auregan, Vincent Pagneux,

Experimental observation of topological edge waves in a two-dimensional Su-Schrieffer-Heeger acoustic network (pp. 797)
Liyang Zheng, Vassos Achilleos, Olivier Richoux, Georgios Theocharis, Vincent Pagneux,

Acoustic antennas based on the topological insulators (pp. 800)
Zhiwang Zhang, Ye Tian, Ying Cheng, Xiaojun Liu, Johan Christensen,

Effective Decay Coefficient of Low Frequency Sound in Phononic Crystals with Viscous Background (pp. 802)
Martin Ibarias, Jesus Arriaga, Arkadii Krokhin,

Acoustic demultiplexer based on Fano and induced transparency resonances in slender tubes (pp. 804)
Abdelkader Mouadili, El Houssaine El Boudouti, Bahram Djafari-Rouhani,

A bottom-up approach towards metamaterials and plasmonics

Spherically Confined Self-Assembly of Molecular Bottlebrushes - A Facile Route to Hierarchical Photonic Pigments (pp. 813)
Richard Mark Parker, Dong-Po Song, Tianheng H. H Zhao, Giulia Guidetti, Silvia Vignolini,

Nanoparticle clusters as building blocks for bottom-up metasurfaces (pp. 815)
Alexandre Baron, Romain Dezert, Rajam Elancheliyan, Olivier Mondain-Monval, Philippe Barois, Philippe Richetti,

DNA-Based Self-Assembly of Plasmonic Nanoantennas (pp. 817)
Sebastien Bidault,

Self-Assembled Plasmon-Upconversion Nanoclusters for Cancer Theranostics (pp. 819)
Wounjhang Park,

Correlated disordered nanostructures embedded in flexible film (pp. 821)
Frederic Hamouda, Gil Cardoso, Saber Hammami, Beatrice Dagens,

Ligand-free synthesis of gold nanoparticles incorporated within oriented cylindrical block copolymer filmsÂ : towards optical metamaterials (pp. 823)
Florian Aubrit, Fabienne Testard, Aurelie Paquirissamy, Frederic Gobeaux, Xuan Wang, Frederic Nallet, Philippe Fontaine, Virginie Ponsinet, Patrick Guenoun,

Second-harmonic generation from metal oxide metasurfaces and photonic crystals (pp. 825)
Flavia Timpu, Viola Valentina Vogler-Neuling, Rachel Grange,

Leaky Mode Engineering for Spectral Light Conversion Enhancement on Silicon Photonic Crystal Slabs (pp. 827)
Doguscan Ahiboz, Phillip Manley, Christiane Becker,

Silicon Particles with Optical Magnetic and Electric Mie Scattering: from the Synthesis to the Assembly of a Metamaterial (pp. 829)
Maria L. De Marco, Taizhi Jiang, Jie Fang, Benoit Miller, Brian Korgel, Yuebing Zheng, Philippe Barois, Glenna L. Drisko, Cyril Aymonier,

Photonic crystal phosphors: materials meet structures for efficient color conversion (pp. 831)
Tae-Yun Lee, Jongho Lee, Yeonsang Park, Kyung-Sang Cho, Kyungtaek Min, Heonsu Jeon,

Cooperative Energy Transfer Controls the Spontaneous Emission Rate Beyond Field Enhancement Limits (pp. 833)
Mohamed ElKabbash, Tigran V. Shahbazyan, Jesse Berezovsky, Francesco De Angelis, Giuseppe Strangi,

Metasurfaces atop Self-Assembled Metamaterials (pp. 835)
Ullrich Steiner,

Synthesis and characterization of plasmonic nanostructures

Plasmonic Horizon in Noble Metal Nanosponges (pp. 837)
Thomas A. Klar,

Liquid Crystalline Metasurfaces for Spin Control of Light (pp. 838)
Yanjun Liu, Zhen Yin, Yue Shi, Ruiheng Peng, Guixin Li, Dan Luo,

Au nanorods based core@shell SERS tags with incorporated Raman reporters (pp. 839)
Vitaly Khanadeev, Boris Khlebtsov, Snezhana Kushneruk, Nikolai Khlebtsov,

Recent advances in the bottom-up approach to artificial optical magnetism (pp. 841)
Philippe Barois, Alexandre Baron, Romain Dezert, Etienne Duguet, Rajam Elancheliyan, Veronique Many, Olivier Mondain-Monval, Virginie Ponsinet, Serge Ravaine, Philippe Richetti, Mona Treguer-Delapierre,

Laser implantation of plasmonic nanoparticles into glass (pp. 843)
Jurgen Ihlemann, Jorg Meinertz, Maximilian Heinz, Manfred Dubiel,

Plasmonic nanoparticles synthesized by laser ablation and their antibacterial activity (pp. 845)

M. Fernandez-Arias, M. Boutinguiza, J. del Val, A. Riveiro, R. Comesana, F. Lusquinos, Juan Pou,

Bottom-up fabrication for ultradense, ultraclean plasmonic ensembles (pp. 847)
Francesco Bisio, Michele Magnozzi, Marzia Ferrera, Remo Proietti Zaccaria, Alessandro Alabastri, Maurizio Canepa,

Plasmonic nanoparticles for molecular detection (pp. 849)
David Zopf, Angelina Pittner, Cornelia Arnold, Stephan Kastner, Andre Dathe, Matthias Thiele, Jacqueline Jatschka, Thomas Schneider, Ondrej Stranik, Andrea Csaki, Wolfgang Fritzsche,

Anisotropic noble metal nanoparticles coated by SiO2 and ZrO2 nanolayer for SHINERS environmental analysis (pp. 851)
Jan Krajczewski, Andrzej Kudelski,

Synthesis, characterization and application of novel bifunctional magneto - plasmonic nanocomposites (pp. 853)
Jan Krajczewski, Karol Kolataj, Andrzej Kudelski,

Light management in solar cells

Subwavelength High Refractive Index Dielectric structures for photovoltaic applications (pp. 856)
Angela Inmaculada Barreda, AmÃ©lie Litman, Francisco Gonzalez, Pablo Albella, Jean-Michel Geffrin, Fernando Moreno,

Nanophotonic enhanced perovskite-silicon solar cell devices (pp. 858)
Christiane Becker, Phillip Manley, Klaus Jager, David Eisenhauer, Johannes Sutter, Steve Albrecht, Kaibo Zheng, Tonu Pullerits, Sven Burger,

Nanostructuring photovoltaic cells: How to push some limits. (pp. 860)
Mahmoud Elshorbagy, Alexander Cuadrado, Javier Alda,

Complex epsilon-near-zero materials enhances light absorption in ultra-thin solar cells (pp. 862)
Marcella Bonifazi, Valerio Mazzone, Andrea Fratalocchi,

Correlation between Light Absorption and External Quantum Efficiency of Metamaterial Perfect Absorber Solar Cell (pp. 864)
Wakana Kubo,

Ultrathin Semiconductor Superabsorbers from the Visible to the Near Infrared (pp. 866)
Pau Molet Bachs, Juan Luis Garcia Pomar, Cristiano Matricardi, Miquel Garriga, Maria Isabel Alonso, Agustin Mihi,

Next generation solar cells and photodetectors with III-V nanowires (pp. 868)
Anna Fontcuberta i Morral,

Total internal reflection using nano-gratings for enhancing the optical response of perovskite solar cells (pp. 870)
Eduardo Lopez-Fraguas, Braulio Garcia-Camara, Ricardo Vergaz,

Novel perforated all-dielectric metamaterials (pp. 872)
Alexey A. Basharin,

Some insights on the light management in halide perovskite solar cells and optoelectronic devices (pp. 873)
Ivan Mora-Sero,

Nanophotonic tools for exploring low-energy excitations in nanomaterials

Probing Plasmons, Phonons, and Phase-Change Materials with Synchrotron Infrared Nanospectroscopy (pp. 876)
Hans A. Bechtel, Omar Khatib, Stephanie N. Gilbert Corder, Mengkun Liu, Markus B. Raschke, Michael C. Martin, G. Lawrence

Carr,

Between photonics and electronics: is THz the promised land of graphene technologies? (pp. 878)
Alessandro Tredicucci,

Extraordinarily transparent compact metallic metamaterials (pp. 879)
Vincenzo Giannini,

Nonlinear THz response of graphene plasmonic structures (pp. 881)
Stephan Winnerl, M. Mehdi Jadidi, Matt Chin, Angelika Seidl, Harald Schneider, Manfred Helm, H. Dennis Drew, Thomas E. Murphey, Martin Mittendorff,

In-plane anisotropic and ultra-low-loss polaritons in a natural van der Waals crystal (pp. 883)
Javier Taboada Gutierrez, Weiliang Ma, Pablo Alonso Gonzalez, Shaojuan Li, Alexey Nikitin, Jian Yuan, Javier Martin Sanchez, Iban Amenabar, Peining Li, Saul Velez, Christopher Tollan, Zhigao Dai, Yupeng Zhang, Sharath Sriram, Kourosh Kalantar-Zadeh, Shuit-Tong Lee, Rainer Hillenbrand, Qiaoliang Bao,

Highly anisotropic phonon polaritons in natural biaxial hyperbolic van der Waals alpha-MoO3 (pp. 885)
Zebo Zheng, Huanjun Chen,

Non Linear Single-Particle and Plasmonic Terahertz Properties of 3D Topological Insulators (pp. 887)
Paola Di Pietro, Federica Piccirilli, N. Adhlakha, Andrea Perucchi, Stefano Lupi,

Photonic Crystals for Nano-Light in Twisted Bilayer Graphene (pp. 889)
D. N. Basov,

Imaging ultrafast dynamics on the nanoscale with terahertz scanning tunneling microscopy (pp. 890)
Frank Hegmann,

Plasmonics and Nanophotonics Based on 2D Materials: Graphene and Beyond

Surface plasmon-polaritons in deformed graphene layer (pp. 892)
Maksim Usik, Igor Bychkov, Olga Kharitonova, Vladimir Shavrov, Dmitry Kuzmin,

Second harmonic generation in graphene-based hyperbolic metasurface (pp. 894)
Olga Kharitonova, Igor Bychkov, Maksim Usik, Vladimir Shavrov, Dmitry Kuzmin,

Graphene Plasmonic Slot Photodetector on Silicon-on-insulator with High Responsivity (pp. 896)
Zhizhen Ma, Mario Miscuglio, Volker J. Sorger,

Novel guided wave configurations with nanostructures for emerging applications

Photonic nanojet generated by dielectric multi-material microstructures. (pp. 899)
Oksana Shramkova, Laurent Blonde, Valter Drazic, Bobin Varghese, Valerie Allie,

Topological Phase Transitions in Guiding Photonic Systems (pp. 901)
Zhaxylyk A. Kudyshev, Vladimir M. Shalaev, Alexandra Boltasseva, Alexander V. Kildishev,

Light Propagation in Synthetic Photonic Lattices in the Presence of Disorder (pp. 903)
Stanislav Derevyanko,

Towards an integrated quantum photonics platform on GaAs (pp. 905)

L. Dusanowksi, Christof. P. Dietrich, Andrea Fiore, Mark Thompson, Martin Kamp, Sven Hofling,

Biosensing using Metamaterials and Plasmonics

Holey metal films for sensing applications - Impact of nonlocality on extraordinary optical transmission (pp. 907)
Christin David, Johan Christensen,

Tunable SiC Metasurface for Mid-infrared Biochemical Detection (pp. 909)
Zhao Huang, Xin Liu, Jianfeng Zang,

Engineered Lab-On-Fiber SERS Optrodes based on Nanosphere Lithography (pp. 911)
Giuseppe Quero, Gianluigi Zito, Stefano Manago, Francesco Galeotti, Marco Pisco, Anna Chiara De Luca, Andrea Cusano,

Photonics for space systems and propulsion

Metal Oxide Meta-optical Solar Reflector for Space Applications (pp. 914)
Kai Sun, Wei Xiao, Yudong Wang, Mirko Simeoni, Alessandro Urbani, Sandro Mengali, Fausto Lucantonio, Marco Ivagnes, Maksim Zalkovskij, Brian Bilenberg, C. H. de Groot, Otto L. Muskens,

Reflectivity control devices for solar sail actuation (pp. 916)
Jeremy Munday,

Relative and Absolute Phase Control of Lasers (pp. 918)
Firooz Aflatouni,

Passively Actuated Thermal Coating for Radiative Controlled Homeostasis (pp. 920)
Philip W. C. Hon, Ahmed Morsy, Virginia D. Wheeler, Michael Barako, Vladan Jankovic, Michelle Povinelli, Luke A. Sweatlock,

Optical rectification and resonant absorption in active nonlinear metasurfaces (pp. 922)
Richard Osgood, M. Kang, K-B. Kim, Y. Ait-El-Aoud, S. Dinneen, S. Kooi, G. Fernandes, J. M. Xu,

Simulating the Dynamic Structural Stability of Ultrathin Lightsails (pp. 925)
Michael D. Kelzenberg, Harry A. Atwater,

Exotic Meta-media - Spatial, Non-local and Other Novel Responses

Sensitivity of layered structures in critical conditions (pp. 928)
Agnes Maurel, Kim Pham, Jean-Francois Mercier,

Simultaneous amplification and attenuation of plane waves and surface waves possible using nanoengineered materials (pp. 930)
Tom Mackay, Akhlesh Lakhtakia,

Nonlocal homogenisation of centro-symmetric optical metamaterials (pp. 932)
Karim Mnasri, Fatima Z. Goft¬•, Michael Plum, Carsten Rockstuhl,

Challenging the foundations of electromagnetism: the excitation fields D and H (pp. 934)
Jonathan Gratus, Paul Kinsler, Martin W. McCall,

Electron Spill-Out Effects on Strong Light-Matter Coupling in Plasmonic Systems (pp. 936)
Radoslaw Jurga, Khalid Muhammad, Fabio Della Sala, Cristian Ciraci,

Spatial dispersion and local field effects in metamaterials (pp. 938)
Alexey Tishchenko,

Electromagnetic clocks at the rim of metamaterial black holes (pp. 940)
Sophie Viaene, Vincent Ginis, Jan Danckaert, Ortwin Hess, Philippe Tassin,

Electromagnetic Wave generation and Amplification mediated via Artificial Materials. (pp. 942)
Rebecca Seviour, Simon Foulkes,

Omnidirectional impedance match and its applications based on effective nonlocal media (pp. 944)
Jie Luo, Yun Lai,

Modeling large scale metamaterials for elastic waves control (pp. 946)
Bogdan Ungureanu, StÃ©phane BrulÃ©, Younes Achaoui, Stefan Enoch, Richard Craster, SÃ©bastien Guenneau,

Exotic symmetry-induced effects in photonic and phononic systems (pp. 948)
Mehul Makwana, Richard Craster, SÃ©bastien Guenneau, Kun Tang, Patrick Sebbah, Gregory Chaplain, Kin Ian Lo,

Structured and topological photonic fields

Visible vector beams using dielectric metasurfaces (pp. 951)
Antonio Ambrosio, Yao-Wei Huang, Noah Rubin, Federico Capasso,

Optical spin and orbital angular momentum effects in multiple Laguerre-Gaussian beams (pp. 953)
Mohamed Babiker, K. Koksal, V. E. Lembessis, J. Yuan,

Microwave magnetoelectric photonics based on magnetic-dipolar-mode resonators (pp. 954)
Eugene Kamenetskii, A. Davidov,

Optical helicity gratings (pp. 956)
Koen Corstiaan van Kruining, Robert Peter Cameron, Jorg Bernhard Gotte,

Skyrmion structure in vector beams (pp. 958)
Sijia Gao, Joerg B. Goette, Fiona Speirits, Neal Radwell, Sonja Franke-Arnold, Stephen M. Barnett,

Charge and spin dynamics driven by topological photonic fields (pp. 960)
Jonas Watzel, Jamal Berakdar,

Interaction of an Archimedean spiral structure with twisted light (pp. 962)
Richard M. Kerber, Jamie M. Fitzgerald, Xiaofei Xiao, Stefan A. Maier, Vincenzo Giannini, Doris E. Reiter, Sang Soon Oh,

Controlling Internal Quantum States of Subwavelength Systems with Optical Vortices (pp. 964)
Andrei Afanasev, Maria Solyanik-Gorgone,

Nonreciprocal and Topological Photonics

Experimental realization of valley-Hall photonic topological insulators with dual-band kink states (pp. 967)
Qiaolu Chen, Li Zhang, Mengjia He, Yihao Yang, Huaping Wang, Hongsheng Chen,

Experimental Discovery of Photonic Nodal Chains (pp. 968)
Rongjuan Liu, Qinghui Yan, Zhongbo Yan, Boyuan Liu, Hongsheng Chen, Zhong Wang, Ling Lu,

Theory of Chiral Edge State Lasing in a 2D Topological System (pp. 970)

Matteo Secli, Massimo Capone, Iacopo Carusotto,

Nonreciprocity, Isolation and Time-reversal Symmetry in Nonlinear Devices (pp. 972)
David E. Fernandes, Mario G. Silveirinha,

Photonic analogues of the Haldane and Kane-Mele Models (pp. 974)
Sylvain Lannebere, Mario G. Silveirinha,

One-way surface plasmons in drift-current biased graphene (pp. 976)
Tiago Morgado, Mario Silveirinha,

Synthetic gauge fields and tilted Dirac cones in photonic honeycomb lattices (pp. 978)
Omar Jamadi, Marijana Milicevic, Elena Rozas, Grazia Salerno, Tomoki Ozawa, Iacopo Carusotto, Gilles Montambaux, Luc Le Gratiet, Abdelmounaim Harouri, Isabelle Sagnes, Aristide Lemaitre, Jacqueline Bloch, Alberto Amo,

Protected Edge Modes in Metasurface Junctions (pp. 980)
Enrica Martini, Mario G. Silveirinha, Stefano Maci,

First Principles Calculation of Topological Invariants by Means of the Photonic Green's Function (pp. 982)
Filipa Prudencio, Mario Silveirinha,

Nanophononics and nanomechanics

Synthetic magnetic fields for on-chip phonons through nano-optomechanical interactions (pp. 985)
John Mathew, Javier del Pino, Ewold Verhagen,

Dispersive Measurements of Flux-Qubit States: Energy-Level Splitting and Beyond (pp. 987)
Jeong Ryeol Choi,

Picosecond acoustics of vanadium dioxide (pp. 989)
Iaroslav Mogunov, Anatolii Fedianin, Felix Fernandez, Sergiy Lysenko, Anthony Kent, Alexey Scherbakov, Alexandra Kalashnikova, Andrey Akimov,

Controlling the vibrational quality factors of an individual supported nano-object by tuning its morphology (pp. 991)
Aurelien Crut, Fabio Medeghini, Romain Rouxel, Marco Gandolfi, Francesco Rossella, Paolo Maioli, Fabrice Vallee, Francesco Banfi, Natalia Del Fatti,

Following heat transport in 2D materials using ultrafast techniques (pp. 993)
KlaasJan Tielrooij, Niels Hesp, Alexander Block, Matz Liebel, AloÃ¯s Arrighi, Marianna Sledzinska, Sergio O. Valenzuela, Clivia Sotomayor Torres, Frank Koppens, Niek van Hulst,

Anisotropic Thermal Magnetoresistance in Radiative Heat Transfer (pp. 994)
Antonio Garcia-Martin,

Optomechanical coupling in the Anderson-localization regime (pp. 995)
Guillermo Arregui Bravo, Norberto D. Lanzillotti Kimura, Clivia M. Sotomayor-Torres, Pedro D. Garcia,

Modulation of the THz Emission by a Quantum Cascade Laser using Coherent Acoustic Phonon Pulses (pp. 996)
Anthony J. Kent, Aniela Dunn, Caroline Poyser, Andrey Akimov, Paul Dean, A. Giles Davies, Aleksandar Demic, Dragan Indjin, Lianhe Li, Edmund Linfield, Alexander Valavanis, John Cunningham,

First principles calculation of the real-time dynamics of inter-valley electron-phonon coupling after photoexcitation (pp. 998)

Philip Murphy Armando, Eamonn Murray, Ivana Savic, Mariano Trigo, David Reis, Stephen Fahy,

Study of the resonant modes of hypersonic acoustic cavities by an ultrafast pump-probe technique (pp. 999)
Camille Lagoin, Daniel Garcia-Sanchez, Paola Atkinson, Bernard Perrin,

Dynamics of nanomechanical pillar resonators (pp. 1001)
Juliane Doster, Simon Honl, Heribert Lorenz, Philipp Paulitschke, Eva M. Weig,

Mechanical Synchronization of Optomechanical Oscillators (pp. 1002)
Daniel Navarro Urrios, Martin F. Colombano, Guillermo Arregui, Nestor E. Capuj, Alessandro Pitanti, Jeremie Maire, Simone Zanotto, Amadeu Griol, Alejandro Martinez, Clivia M. Sotomayor-Torres,

Stochastic and vibrational resonance with a driven electro-mechanical resonator (pp. 1004)
Guilhem Madiot, Franck Correia, Avishek Chowdhury, Sylvain Barbay, Marcel Clerc, Remy Braive,

Electromagnetically-optomechanically induced transparency in atom-photon-phonon system (pp. 1006)
He Hao, Juanjuan Ren, Fan Zhang, Ying Gu,

Ultrafast microscopy of the acoustic eigenmodes of a single nanoparticle (pp. 1008)
Yannick Guillet, Allaoua Abbas, Serge Ravaine, Bertrand Audoin,

Optomechanics with hybrid carbon nanotube resonators (pp. 1009)
Alexandros Georges Tavernarakis, Alexandros Stavrinadis, Alex Nowak, Ioanis Tsioutsios, Adrian Bachtold, Pierre Verlot,

A self-assembled array of microspheres for radiative cooling (pp. 1011)
Juliana Jaramillo, G. L. Whitworth , J. A. Pariente, P. D. Garcia, C. Lopez, C. M. Sotomayor-Torres,

Topological states of acoustic phonons in semiconductor nanocavities (pp. 1013)
Martin Esmann, Fabrice Roland Lamberti, Guillermo Arregui, Omar Ortiz, Clivia M. Sotomayor-Torres, Ivan Favero, Olivia Mauguin, Bernard Perrin, Olivier Krebs, LoÃ¯c Lanco, Pascale Senellart, Carmen Gomez-Carbonell, Pedro David Garcia, Aristide Lemaitre, Norberto Daniel Lanzillotti-Kimura,

Ultrafast THz coherent excitation of optical and acoustic phonon modes in topological insulators (pp. 1014)
Vincent JuvÃ©, Artem Levchuk, Matteusz Weis, Brice Arnaud, Gwenaelle Vaudel, Bartosz Wilk, Jacek Szade, Pascal Ruello,

Pulsed Two-Dimensional Atomic Crystal Cavity Optomechanics (pp. 1016)
Yuhao Xu, Wen Chen, Shunping Zhang, Hongxing Xu,

Brillouin scattering in nanofibers (pp. 1018)
Jean-Charles Beugnot,

Engineering and measuring thermal transport in nanowires (pp. 1019)
Marta De Luca, Milo Y. Swinkels, Claudia Fasolato, Daniel Vakulov, Erik P. A. M. Bakkers, Xavier Cartoixa, Riccardo Rurali, Ilaria Zardo,

Magnon-Phonon Coupling in Lateral Ferromagnetic Nanogratings (pp. 1020)
Alexey V. Scherbakov, Felix Godejohann, Serhii Kukhtaruk, Dmitro Yaremkevych, Achim Nadzeyka, Andrew Rushforth, Dmitri Yakovlev, Andrey Akimov, Manfred Bayer,

Two Level Systems at the surface of crystalline Nano-OptoMechanics (pp. 1022)
Mehdi Hamoumi, ChÃ©rif Belacel, Pierre Allain, William Hease, Aristide Lemaitre, Giuseppe Leo, Ivan Favero,

Surface waves beat phonons in polar ultra-thin films (pp. 1023)

Sebastian Volz,

Phonon Engineered Detectors and Refrigerators (pp. 1024)
Mika Prunnila,

Non-Hermitian Complex Systems: Photonics, Plasmonics and Metamaterials

Non-Hermiticity in optical microcavities (pp. 1026)
Jan Wiersig, Julius Kullig,

Coherent perfect absorber and laser for nonlinear waves (pp. 1028)
Vladimir Konotop, Herwig Ott, Dmitry Zezyulin,

Proposal for a New Topological Laser (pp. 1030)
Xiao-Chen Sun, Xiao Hu,

Coherent perfect absorption in disordered media: experimental realization of the random anti-laser (pp. 1032)
Kevin Pichler, Matthias Kuhmayer, Julian Bohm, Andre Brandstotter, Philipp Ambichl, Ulrich Kuhl, Stefan Rotter,

Encircling an exceptional point in waveguide structures and electrical circuits (pp. 1034)
Youngsun Choi, Jae Woong Yoon, Choloong Hahn, Pierre Berini, Jong Kyun Hong, Yeonghwa Ryu, Seok Ho Song,

Photonic topological insulator in synthetic dimensions (pp. 1035)
Eran Lustig, Steffen Weimann, Yonatan Plotnik, Yaakov Lumer, Miguel Bandres, Alexander Szameit, Mordechai Segev,

Exceptional-point parity-time symmetry based sensors: limitations due to fluctuations and noise (pp. 1037)
Christos Tserkezis, Christian Wolff, N. Asger Mortensen,

Optical Amplifications at Non-Hermitian singularities (pp. 1039)
Q. Zhong, Sahin Ozdemir, Alexander Eisfeld, Anja Metelmann, Ramy El-Ganainy,

Controlling photonic systems via topological anomalies (pp. 1041)
Henning Schomerus,

PT symmetry in a Double Quantum Dot circuit-QED set-up (pp. 1043)
Manas Shreekanth Kulkarni, Archak Purkayastha, Yogesh Joglekar,

Demonstration of a two-dimensional PT-symmetric crystal: Bulk dynamics, topology and edge states (pp. 1045)
Lukas Maczewsky, Mark Kremer, Tobias Biesenthal, Matthias Heinrich, Ronny Thomale, Alexander Szameit, Lukas Maczewsky,

Coherent absorption in non-Hermitian multilayers: when the weak controls the strong (pp. 1047)
Simone Zanotto, Giuseppe Carlo La Rocca, Alessandro Tredicucci,

PT-symmetric quantum optics (pp. 1049)
Friederike Ulla Johanna Klauck, Lucas Teuber, Marco Ornigotti, Matthias Heinrich, Stefan Scheel, Alexander Szameit,

Synthetic Dimensions, PT-Symmetry and Nonlinearity in Photonic Mesh Lattices (pp. 1051)
Andre Luiz Marques Muniz, Martin Wimmer, Arstan Bisianov, Roberto Morandotti, Ulf Peschel,

Chiral metamaterials with PT symmetry and beyond (pp. 1053)
Sotiris Droulias, Ioannis Katsantonis, Maria Kafesaki, Costas M. Soukoulis, Eleftherios N. Economou,

Port swithing and replication in cyclic non-Hermitian arrays (pp. 1055)
Blas M. Rodriguez-Lara, Benjamin Jaramillo Avila,

Quantum criticality and nonequilibrium phases: topology in non-Hermitian physics (pp. 1057)
Yuto Ashida, Shunsuke Furukawa, Masahito Ueda,

Quasi-Normal-Mode Approach for Dissipative Systems - Classical and Quantum Regime (pp. 1059)
Kurt Busch,

Bloch-oscillations in a lattice with passive PT-symmetry (pp. 1060)
Eva-Maria Graefe, Bradley Longstaff,

Intensity fluctuations and mode correlations in strongly coupled nanolasers (pp. 1061)
A. M. Yacomotti, M. Marconi, A. Pan, F. Raineri, A. El Amili, J. A. Levenson, Yeshaiahu Fainman,

Nonreciprocity, Chirality and PT-Symmetry in Photonics and Functional Materials (pp. 1063)
Avadh Saxena,

Thermal-photonics for information and energy applications

Hybrid Plasmonics for Solar Energy Harvesting Through Radiative Heating (pp. 1065)
Mina Shiran Chaharsoughi, Dan Zhao, Daniel Tordera, Simone Fabiano, Xavier Crispin, Magnus P. Jonsson,

Near-infrared selective thermal emitter for thermo-photovoltaic energy conversion system (pp. 1066)
Takashi Asano, Masahiro Suemitsu, Susumu Noda,

Near field based energy applications - thermophotovoltaics and photonic refrigeration by controlling the chemical potential of photons (pp. 1068)
Linxiao Zhu, Anthony Fiorino, Dakotah Thompson, Rohith Mittapally, Edgar Meyhofer, Pramod Reddy,

Resonant laser processing for fabrication of nanobiophotonic devices (pp. 1069)
Xiaolong Zhu, Airidas Zukauskas, Andreas Raimund Stilling-Andersen, Anders Kristensen,

Nanoscale Surface Thermal Hotspots of Vertical Antenna Arrays Activated by Mid-infrared Quantum Cascade Lasers (pp. 1071)
Andrea Mancini, Valeria Giliberti, Alessandro Alabastri, Eugenio Calandrini, Francesco De Angelis, Denis Garoli, Michele Ortolani,

Tunable Infrared Perfect Absorption in Bismuth-based Nanostructures for Thermal Photonics (pp. 1073)
Rosalia Serna, Johann Toudert,

Temperature dependent Mie resonances and spectral characteristics of semiconductor nanoparticles and their composites (pp. 1075)
Vaibhav Thakore, Janika Tang, Kevin Conley, Tapio Ala-Nissila, Mikko Karttunen,

Narrowband Photothermal Converters for Infrared Sensors (pp. 1077)
Tadaaki Nagao, Anh Tung Doan, Thang Duy Dao, Satoshi Ishii, Hai Dang Ngo,

Photothermal epoxy curing with plasmonic nanoparticles: From modeling to experiments (pp. 1079)
Alessandro Alabastri, Adam Roberts, Jian Yang, Matthew Reish, Naomi Halas, Peter Nordlander, Henry Everitt,

Thermo-plasmonics on vanadium oxide and silicon-based infrared sensor platforms (pp. 1081)
Xu Fang,

Thermal emission engineering with confined plasmons in semiconductors (pp. 1082)
Angela Vasanelli, S. Huppert, Y. Todorov, D. Gacemi, Carlo Sirtori,

Dynamic and spatial multilevel control over emissivity with phase transition material (pp. 1083)
Qiang Li,

Porous Thermochromic Nano-composite for Smart Window Systems (pp. 1084)
Man Xu, Charlotte Jansen, Pascal Buskens,

Mid-IR emission at high modulation rates with incandescent metasurfaces (pp. 1086)
Jean Jacques Greffet, Leo Wojszvzyk, Anne-Lise Coutrot, Mondher Besbes, Jean-Paul Hugonin, Benjamin Vest,

Parity-Time and related symmetries in Photonics, Plasmonics, Acoustics

Chiral symmetry in non-Hermitian systems: product rule and Clifford algebra (pp. 1088)
Li Ge,

Short Pulse Propagation in Quasi-PT-Symmetric Structure (pp. 1090)
Dmitri Tsvetkov, Vladimir Bushuev, Vladimir Konotop, Boris Mantsyzov,

Odd-PT-symmetric couplers (pp. 1092)
Vladimir Konotop, Dmitry Zezyulin,

Coupled resonances with dynamic modulation for selective wavelength conversion (pp. 1094)
Galaad Altares Menendez, Bjorn Maes,

Non-Hermitian transformations with optical metasurfaces (pp. 1096)
Andrey A. Sukhorukov,

Anisotropic exceptional points of arbitrary order (pp. 1098)
Yi-Xin Xiao, Zhao-Qing Zhang, Zhi Hong Hang, Che Ting Chan,

Topological protection and quantum noise in nonlinear photonic systems (pp. 1100)
Henning Schomerus,

Nonlinear scattering by PT-symmetric layered periodic structures with gain and loss saturation effects (pp. 1102)
Oksana Shramkova, Giorgos Tsironis,

Regularization of broad-area lasers by non-Hermitian potentials (pp. 1104)
Muriel Botey, Waqas Wasser Ahmed, Judith Medina, Ramon Herrero, Ying Wu, Kestutis Staliunas,

Active parity-time symmetric and exceptional point structures (pp. 1106)
Choloong Hahn, Youngsun Choi, Jae Woong Yoon, Seok Ho Song, Pierre Berini,

Nonreciprocal Passive Acoustic Structures with Broken PT-Symmetry (pp. 1107)
Arkadii Krokhin, Yurii Zubov, Jyotsna Dhillon, Andrey Bozhko, Ezekiel Walker, Arup Neogi,

Active Electroacoustic Resonators and their Application to Non-Hermitian Acoustics (pp. 1109)
Romain Fleury,

Chiral-reversing vortex radiation at the exceptional point of a plasmonic nanocavity (pp. 1110)
Renmin Ma, Xing-Yuan Wang, Hua-Zhou Chen, Suo Wang, Li Ge, Shuang Zhang,

Electrically injected DFB laser based on the Parity-Time symmetry concept (pp. 1111)
Vincent Brac de la Perriere, Quentin Gaimard, Henri Benisty, Abderrahim Ramdane, Anatole Lupu,

Metamaterials/Metasurfaces in Dirac/Kane Plasmons

Controlling the THz Dirac plasmon in Bi2Se3 Topological Insulator at the TeraFERMI beamline (pp. 1114)
Paola Di Pietro, Andrea Perucchi, Nidhi Adhlakha, Federica Piccirilli, Seangshik Oh, Alessandra Di Gaspare, Stefano Lupi,

Ratchet and magneto-ratchet phenomena excited by THz radiation in semiconductor nanostructures and graphene with lateral superlattices (pp. 1115)
Sergey Ganichev,

Massless Dirac fermions in III-V semiconductor quantum wells (pp. 1117)
Sergey S. Krishtopenko, Wilfried Desrat, Christophe Consejo, Sandra Ruffenach, Benoit Jouault, Wojciech Knap, Fernando Gonzalez-Posada, Guilhem Boissier, Eric TourniÃ©, FrÃ©dÃ©ric Teppe,

Far and Mid IR lasers based on Dirac heterostructures HgTe/CdHgTe (pp. 1119)
Sergey Morozov,

Graphene based field-effect transistors as tunable plasmonic interferometers for terahertz radiation detection (pp. 1121)
G. E. Fedorov, D. Svintsov, D. Bandurin, I. Gayduchenko, G. Goltsman,

Quantum phenomena with collective excitations in confined systems (pp. 1122)
Angela Vasanelli, S. Huppert, Y. Todorov, D. Gacemi, Carlo Sirtori,

Emergent optoelectronic functionality in low dimensional non-centrosymmetric semiconductors (pp. 1123)
Yijin Zhang, Toshiya Ideue, Masaru Onga, Feng Qin, Ryuji Suzuki, Alla Zak, Reshef Tenne, Jurgen Smet, Yoshihiro Iwasa,

Towards High Efficiency Detectors and Sources for Field-Ready Quantum Nanophotonics

Limits to the delity of on-demand single photon sources using quantum dot-cavity systems (pp. 1126)
Stephen Hughes,

Generating and routing single photons in GaAs nanophotonic circuits (pp. 1128)
Leonardo Midolo,

Engineering Photon-pair Sources for Integrated Quantum Technologies (pp. 1129)
Gary Sinclair, Will McCutcheon, Imad Faruque, Imad Faruque, John G. Rarity,

Metrology for single-photon detectors and sources (pp. 1131)
Angela Gamouras,

High efficiency entangled photon sources and single photon detectors based-on semiconductor nanowires (pp. 1132)
Michael E. Reimer, Arash Ahmadi, Mohd Zeeshan, Simon Daley, Nachiket Sherlekar, Bradley van Kasteren, Burak Tekcan, Sandra J. Gibson, Andreas Fognini, Klaus Jons, Val Zwiller, Dan Dalacu, Philip J. Poole,

Impact of ultrasmall capacitance for OE/EO conversions using photonic crystals (pp. 1133)
Masaya Notomi, Kengo Nozaki, Shinji Matsuo, Akihiko Shinya,

Plasmonics: Fundamentals and Application

Tailoring Induced Plasmonic Circular Dichroism in Hybrid Nanostructures with Different Geometric Configurations (pp. 1136)
Wei Zhang,

Strong coupling between plasmonic meta-atoms and plasmonic surface bloch waves (pp. 1138)
Chun-Yuan Wang, Yungang Sang, Xinyue Yang, Soniya S. Raja, Haozhi Li, Yufeng Ding, Shuoyan Sun, Chang-Wei Cheng, Hyeyoung Ahn, Chih-Kang Shih, Shangjr Gwo, Jinwei Shi,

Chiral Weak and Strong Photon-Emitter Coupling in Coupled Photonic Structures (pp. 1140)
Fan Zhang, Juanjuan Ren, Lingxiao Shan, Xueke Duan, Yan Li, Tiancai Zhang, Qihuang Gong, Ying Gu,

Optical and spectroscopic properties of large scale and flexible plasmonic metasurfaces by colloidal self-asssembly (pp. 1142)
Tobias A. F. Konig,

Extraordinary Transmission and Polarization Control of Cavity Modes in Thue-Morse Gold Nanocavities (pp. 1145)
Antonio De Luca, Rakesh Dhama, Vincenzo Caligiuri, Lucia Petti, Alireza R. Rashed, Massimo Rippa, Raffaella Lento, Roberto Termine, Humeyra Caglayan,

Optically Thin Plasmonic Nanohole Metasurfaces: Fano Interferences and Strong Coupling (pp. 1147)
Evan S. H. Kang, Magnus P. Jonsson,

Plasmon Enhancement of Luminescence Upconversion (pp. 1148)
Wounjhang Park,

Emission spectra of plasmon-exciton hybrid systems: A simple model (pp. 1150)
Xiaoguang Li,

Optical Diversity of Metal Nanoparticles Modified by Stilbene Compounds: Plasmon Coupling, Raman Resonance Enhancement and Fluorescence Quenching (pp. 1152)
Elena Solovyeva, Alexey Smirnov, Olga Odintsova, Vlad Deev,

Tuning phase matching conditions in second harmonic generation via the excitation of higher order plasmonic mode in waveguides (pp. 1154)
Ning Liu, Brian Corbett,

Quasicrystal Photonic Metasurfaces for Radiation Control of Second Harmonic Generation (pp. 1156)
Yutao Tang, Junhong Deng, King Fai Li, Mingke Jin, Jack Ng, Guixin Li,

Energy of plasmonic photocatalytic sites (pp. 1158)
Emiliano Cortes,

Continuously tuning the coupling strength of bow-tie nanoantennas by strain variation (pp. 1159)
Florian Laible, Dominik A. Gollmer, Simon Dickreuter, Dieter P. Kern, Monika Fleischer,

Out-of-equilibrium dynamics of silver: saturated nonlinear response (pp. 1161)
Andrea Marini, Alessandro Ciattoni, Claudio Conti,

Single-molecule sensing mediated by localized plasmon resonances (pp. 1163)
Peter Zijlstra, Rachel Armstrong, Michael Beuwer, Matej Horacek, Yuyang Wang,

Collective effects on periodic arrays of plasmonic nanostructures (pp. 1164)
Alejandro Manjavacas,

The role of the thermo-optic nonlinearity of metals in plasmonic-assisted photocatalysis (pp. 1165)
Ieng Wai Un, Yonatan Dubi, Y. Sivan,

Backward groove-regulated light wave resonance inside a subwavelength metallic slit (pp. 1166)
Jian-Shiung Hong, Kuan-Ren Chen,

Confining plasmon-exciton interaction in individual nanocavity (pp. 1168)
Jiawei Sun, Huatian Hu, Di Zheng, Daxiao Zhang, Shunping Zhang, Hongxing Xu,

Plasmoemission: Nonlinear Electron Emission from Surface Plasmon Polaritons (pp. 1170)
Frank J. Meyer zu Heringdorf, Daniel Podbiel, Philip Kahl, Pascal Dreher, David Janoschka,

Emission Pathways for Electrons in Surface Plasmon Enhanced Photoemission (pp. 1172)
David Janoschka, Pascal Dreher, Timothy J. Davis, Frank J. Meyer zu Heringdorf,

Silicon Photonic Integrated Circuits

Hybrid on silicon photonics for light amplification and Fano-enhanced electro-optical modulation at telecom wavelengths (pp. 1175)
Jianhao Zhang, John Ronn, Xavier Le Roux, Carlos Alonso-Ramos, Mathias Berciano, Delphine Marris-Morini, Sailing He, Zhipei Sun, Laurent Vivien, Eric Cassan,

Scaling of monolayer 2D photonic crystal surface emitting lasers for 3D integrated photonics (pp. 1177)
Weidong Zhou, Xiaochen Ge ,

Power Efficient Thermal Optical Tunable Grating Coupler Based on Silicon Photonic Platform (pp. 1178)
Lifeng Chen,

Lithium Niobate Michelson Interferometer Modulator on Silicon-On-Insulator Platform (pp. 1180)
Xinlun Cai,

Plasmonics in Silicon Photonics for Microwave Photonics (pp. 1182)
Yannick Salamin, Wolfgang Heni, Ping Ma, Yuriy Fedoryshyn, Benedikt Baeuerle, Arne Josten, Christian Haffner, Michael Baumann, Bojun Cheng, Tatsuhiko Watanabe, Maurizio Burla, Alexandros Emboras, Delwin L. Elder, Larry R. Dalton, Juerg Leuthold,

Heterogeneously integrated membrane III-V/Si photonic devices (pp. 1184)
Tatsurou Hiraki, Takuma Aihara, Koji Takeda, Takuro Fujii, Hidetaka Nishi, Takaaki Kakitsuka, Tai Tsuchizawa, Hiroshi Fukuda, Shinji Matsuo,

Silicon Integrated Quantum Photonics (pp. 1186)
Yunhong Ding, Davide Bacco, Karsten Rottwitt, Mark Thompson, Jianwei Wang, Leif Katsuo Oxenlowe,

Application opportunities for Field-Programmable Photonic Integrated Circuits (pp. 1188)
Daniel Perez Lopez, Prometheus DasMahapatra, Jose Capmany,

Laser Processing of Amorphous Semiconductors on Planar Substrates for Photonic and Optoelectronic Applications (pp. 1190)
Ozan Aktas, Yohann Franz, Antoine Runge, Stuart MacFarquhar, Swe Zin Oo, Vinita Mittal, Antulio Tarazona, Harold Chong, Sakellaris Mailis, Anna Peacock,

Microresonator Soliton frequency combs (pp. 1192)
Tobias J. Kippenberg,

Fano resonances in optics and microwaves: Physics and application

Tunable Fano resonances in the radiative decay rate of a dipole emitter near a graphene-coated nanowire (pp. 1194)
Tiago J. Arruda, Romain Bachelard, John Weiner, Philippe W. Courteille,

Fano Resonances in Dimer Nanoantennas: Switching and Directionality Effects (pp. 1197)
Angela Inmaculada Barreda, Hassan Saleh, AmÃ©lie Litman, Francisco Gonzalez, Jean-Michel Geffrin, Fernando Moreno,

Trapped light states in spatially dispersive plasmonic nanostructures (pp. 1199)
Solange Vieira da Silva, Tiago AndrÃ© Morgado, Mario Goncalo Goncalo Silveirinha,

Silent enhancement of SERS signal without increasing the hot spot intensity (pp. 1201)
Mehmet Emre Tasgin,

Coupled-wave model of bound states in the continuum in diffraction gratings and integrated diffractive structures (pp. 1203)
Dmitry A. Bykov, Evgeni A. Bezus, Leonid L. L. Doskolovich,

The passive and active controls of Fano resonances in metasurfaces (pp. 1205)
Shuo Du, Zhe Liu, Junjie Li , Changzhi Gu,

Interference of Multipolar Lattice Resonances in Plasmonic Crystal Excited by Structured Light (pp. 1207)
Keiji Sasaki, Hiroki Kitajima, Kyosuke Sakai,

Highly-efficient nonlinear image tuning through magnetic dipole quasi-BIC ultra-thin resonators (pp. 1209)
Lei Xu, Khosro Zangeneh Kamali, Lujun Huang, Mohsen Rahmani, Alexander Smirnov, Rocio Camacho-Morales, Yixuan Ma, Guoquan Zhang, Matt Wolley, Dragomir Neshev, Andrey E. Miroshnichenko,

High-Q modes in a single dielectric nonspherical nanocavity (pp. 1211)
Lujun Huang, Lei Xu, Mohsen Rahmani, Dragomir Neshev, Andrey Miroshnichenko,

Spin-Polarized Directive Coupling of Light and Near-Field Amplification at the Bound States in the Continuum of a Transparent Photonic Crystal (pp. 1213)
Gianluigi Zito, Silvia Romano, Stefano Manago, Stefano Cabrini, Giuseppe Calaï¬•ore, Anna Chiara De Luca, Erika Penzo, Vito Mocella,

Superchirality, circular dichroism bands and singular value resonances of a minimal dielectric metasurface (pp. 1215)
Simone Zanotto,

Hybrid plasmonic-dielectric resonant waveguide grating for diffraction with high color purity (pp. 1217)
Giorgio Quaranta, Olivier J. F. Martin, Benjamin Gallinet,

Acoustic topological Fano resonances (pp. 1219)
Farzad Zangeneh Nejad, Romain Fleury,

Coupling regimes in a complex of two rods: from core-shell particle to dimer (pp. 1221)
Alexey A. Dmitriev, Mikhail V. Rybin,

Fano resonances and exceptional points in waveguides and quantum conductors (pp. 1223)
Alexander Gorbatsevich, Nikolay Shubin, Vladimir Kapaev, Alexander Friman,

Bound States in the Continuum in Hybrid Photonic-Plasmonic Structures (pp. 1225)
Shaimaa Azzam, Vladimir Shalaev, Alexandra Boltasseva, Alexander Kildishev,

Multiple Fano Feature due to Optical Bound States in the Continuum (pp. 1227)
Dmitrii N. Maksimov, Evgeny N. Bulgakov,

Multipolar properties of bound states in the continuum supported in all-dielectric metasurfaces (pp. 1228)
Yi Xu,

Asymmetric to symmetric line-shape transition of guided-mode resonance enabled by cross-polarization filtering (pp. 1230)
Jiaxin Lu, Jicheng Jin, Xuefan Yin, Chao Peng,

Light-Matter Interaction in Antenna-based Infrared Nanocavities (pp. 1232)
Andrea Toma,

Theory of Fano Resonances in the electromagnetic scattering from two-dimensional bodies. (pp. 1233)
Carlo Forestiere, Giovanni Gravina, Giovanni Miano, Mariano Pascale, Roberto Tricarico,

Bound states and resonances in lattice models (pp. 1235)
Ya Yan Lu,

Reaching dark mode condition in a system of gain-loss assisted coupled resonators (pp. 1237)
Anatole Lupu, Vasily Klimov, Henri Benisty, Alexander Uskov, Abderrahim Ramdane,

Rigorous modal analysis of photonic micro and nanoresonators (pp. 1239)
Philippe Lalanne, Wei Yan,

Magnetic interactions and transport properties of parallel coupled magnetic molecules in presence of spin-orbit interactions (pp. 1242)
Seif Alwan, Jonas Fransson,

Disordered metamaterials: Strong interactions, subradiance and field localization (pp. 1244)
Stewart D. Jenkins, Nikitas Papasimakis, Salvatore Savo, Nikolay I. Zheludev, Janne Ruostekoski,

Photonic crystal structures treated by the resonant state expansion (pp. 1246)
Sam Neale, Egor Muljarov,

Interaction between dielectric particles enhances the Q-factor (pp. 1247)
Evgeny Bulgakov, Konstantin Pichugin, Almas Sadreev,

Magneto-plasmonics

Ultra-wideband graphene circulators for THz region (pp. 1258)
Victor Dmitriev, Samara Leandro Matos da Silva, Wagner Castro,

Plasmon-induced inverse Faraday Effect and switchable routers and modulators in magneto-plasmonic structures (pp. 1260)
Joachim Herrmann, Song-Jin Im, Ji-Song Pae, Kum-Song Ho, Yong-Ha Han,

Second Harmonic Generation in Hyperbolic Magneto-Plasmonic Metasurfaces (pp. 1262)
Dmitry Kuzmin, Igor Bychkov, Vladimir Shavrov, Vasily Temnov,

Enhancement of Faraday rotation of iron thin layers on periodic array of Al nanocylinders (pp. 1264)
Taisuke Atsumi, Shunsuke Murai, Katsuhisa Tanaka,

Versatile Tb18Co72 magnetoplasmonic nanooptical antennas (pp. 1266)

Richard Matthew Rowan-Robinson, Jerome Hurst, Agne Ciuciulkaite, Ioan-Augustin Chioar, Matteo Pancaldi, Paolo Vavassori, Peter M. Oppeneer, Alexander Dmitriev, Vassilios Kapaklis,

Transverse magnetic routing of light emission in hybrid plasmonic semiconductor structures (pp. 1268)
Lars Klompmaker, Felix Spitzer, Alexander N. Poddubny, Ilya A. Akimov, Leonid V. Litvin, Ralf Jede, Grzegorz Karczewski, Maciej Wiater, Tomasz Wojtowicz, Dmitri R. Yakovlev, Manfred Bayer,

Nonlinear and parametric magneto-elastic dynamics in ferromagnetic nanostructures (pp. 1270)
Vladimir Vlasov, Anton Golov, Alexandr Alekhin, Alexey Lomonosov, Leonid Kotov, Dmitry Kuzmin, Igor Bychkov, Vasily Temnov,

Optical isolators based on magnetoplasmonic subwavelength gratings (pp. 1272)
Sevag Abadian, Beatrice Dagens, Vy Yam, Giovanni Magno,

THz graphene four-port circulators with elliptic resonators (pp. 1274)
Victor Dmitriev, Gabriel Barros, Thiago Oliveira, Wagner Castro,

Magnetoplasmonic Modulators for Integrated Optics (pp. 1276)
Curtis Firby, Abdulhakem Elezzabi,

Layer-selective All-Optical Magnetization Switching in Plasmonic Magnetic Heterostructure (pp. 1278)
Daria Ignatyeva, Carl Davies, Daria Sylgacheva, Arata Tsukamoto, Hiroki Yoshikawa, Pavel Kapralov, Andrey Kirilyuk, Vladimir Belotelov, Alexei Kimel,

Faraday Rotation Enhancement in Graphene Metasurfaces (pp. 1280)
Jean-Marie Poumirol, M. Tamagnone, T. M. Slipchenko, L. Martin-Moreno, J. R. Mosig, Alexey B. Kuzmenko,

Ultrafast Magnetization Dynamics of CoFeB-based multilayer thin films with perpendicular anisotropy (pp. 1281)
Ana S. Silva, Simao P. Sa, Sergiy Bunyayev, Gleb Kakazei, Miguel Canhota, Miguel Miranda, Carlos Garcia, Inigo J. Sola, Helder Crespo, David Navas,

Nonreciprocal magnetoplasmonic gratings (pp. 1283)
Rafael Cichelero, Mikko Kataja, Gervasi Herranz,

Naturally Hyperbolic and Chirality Too: The Optics of Antiferromagnets (pp. 1285)
Robert Stamps, Rair Macedo, Igor Proskurin,

Nanoscale Localization of sub-Terahertz Spin Dynamics in Au/Garnet Magnetoplasmonic Crystals (pp. 1287)
Alexander L. Chekhov, Alexander I. Stognij, Takuya Satoh, Tatiana V. Murzina, Ilya Razdolski, Andrzej Stupakiewicz,

Revealing the Coupling Mechanism of Plasmonic and Magneto-Optically Induced Near-Fields in Bi:YIG/Au nanostructures (pp. 1289)
Spiridon D. Pappas, Philipp Lang, Evangelos Papaioannou,

The Transverse Magneto-Optical Kerr Effect in Two-Dimensional Magnetoplasmonic Periodic and Quasicrystalline structures (pp. 1291)
Andrey Kalish, Roman Komarov, Mikhail Kozhaev, Achanta Venu Gopal, Aman Agrawal, Vladimir Belotelov,

Metasurfaces and 2D Metamaterials in microwave region

Experimental Realization of Tunable Microwave Coherent Perfect Absorber in Graphene-based Sandwich Structure (pp. 1294)
Jin Zhang, Weiren Zhu,

Size influence of checkerboard-like wideband metamaterial absorbers (pp. 1296)
Andre Barka, Xavier Begaud, Anne-Claire Lepage, Stefan Varault, Michel Soiron, Olivier Rance,

Dynamically controlling focal point position with reconfigurable metasurface (pp. 1298)
Badreddine Ratni, Zhuochao Wang, Kuang Zhang, Xumin Ding, Andre de Lustrac, Shah Nawaz Burokur,

Metasurface Surface-Wave Dispersion Analysis and Synthesis Technique (pp. 1300)
Karim Achouri, Olivier J. F. Martin,

Abnormal Refractions with Independent-Polarizations Enabled by Transmissive-Type Metasurface in Microwave Region (pp. 1302)
Kuang Zhang, Yueyi Yuan, Xumin Ding, Badreddine Ratni, Shah Nawaz Burokur, Qun Wu,

Active Metasurfaces and Waveguiding with Photoexcited Graphene (pp. 1304)
Yuancheng Fan, Fuli Zhang, C. T. Chan,

Holographically-modulated metasurface leaky-wave antennas for multiple near-field focused spots manipulation (pp. 1306)
JosÃ© Luis Gomez-Tornero, Miguel Poveda Garcia,

Advanced passive and active metasurfaces

Optical Metasurfaces for Designing Planar Cassegrain-Schwarzschild Objective (pp. 1309)
Xuan Liu, Junhong Deng, King Fai Li, Yutao Tang, Mingke Jin, Jing Zhou, Xing Cheng, Wei Liu, Guixin Li,

Ultralow-power thermo-optical switching in graphene metasurfaces (pp. 1311)
Joel Douglas Cox,

Design of Meta-reflector by Deep Learning (pp. 1313)
Wei Xiao, Peter R. Wiecha, Kai Sun, C. H. de Groot, Otto L. Muskens,

Vortex generation by graphene and near-zero index thin films (pp. 1315)
Alessandro Ciattoni, Andrea Marini,

Hiding a QR code in a Vector Light Beam (pp. 1317)
Chunmei Zhang, Yuttana Intaravanne, Wei Wang, Xianzhong Chen,

Applying computer graphics techniques to optical metasurfaces: Broadband reflective metasurfaces for the visualisation of 3D effects (pp. 1319)
Diane J. Roth, Alexander E. Minovich, Guixin Li, Anatoly V. Zayats,

Plasmonic open systems: theory and applications (pp. 1321)
Shiyi Xiao, Jing Lin, Meng Qiu, Xiyue Zhang, Huijie Guo, Lei Zhou,

Metasurface and Epsilon-near-zero Resonances on Optical Fiber (pp. 1323)
Jingyi Yang, Indra Ghimire, Khant Minn, Aleksei Anopchenko, Sudip Gurung, Ho Wai Howard Lee,

Dynamic metamaterials

Bose-Einstein condensation and K-point lasing in a plasmonic lattice (pp. 1326)
Jani-Petri Martikainen, Antti Moilanen, Rui Guo, Aaro Vakevainen, Marek Necada, Konstantinos S. Daskalakis, Heikki T. Rekola, Aleksi Julku, Paivi Torma,

Functional all-dielectric nanophotonic: from colloidal syntesis to transition metal dichalcogenides nanoantennas (pp. 1327)

Ruggero Verre, Nils Odebo-Lank, Denis Baranov, Timur Shegai, Mikael Kall,

Magnetic field modulation of plasmon properties (pp. 1329)
Gaspar Armelles, Alfonso Cebollada, Fernando Garcia, Raquel Alvaro, Maria Ujue Gonzalez, Luca Bergamini, Nerea Zabala, Javier Aizpurua,

Geometric Frustration in Arrays of Au Nanoelements (pp. 1330)
Ana Conde-Rubio, Arantxa Fraile Rodriguez, Francesc PÃ©rez-Murano, AndrÃ© Espinha, Agustin Mihi, Xavier Batlle, Amilcar Labarta,

Light modulating and detecting in on-chip plasmonic-graphene hybrid platforms (pp. 1332)
Sanshui Xiao, Hao Hu, Michael Galili, Asger Mortensen, Leif Katsuo Oxenloewe, Yunhong Ding,

Nanoporous metamaterials as novel electrodes for enhanced in-vitro electrophysiology and toxicology (pp. 1334)
Michele Dipalo, Giovanni Melle, Laura Lovato, Andrea Jacassi, Francesca Santoro, Valeria Caprettini, Andrea Schirato, Alessandro Alabastri, Denis Garoli, Giulia Bruno, Francesco Tantussi, Francesco De Angelis,

Advances in Nanomechanical Metamaterials (pp. 1336)
Eric Plum, Dimitrios Papas, Jun-Yu Ou, Artemios Karvounis, Kevin F. MacDonald, Nikolay I. Zheludev,

Epsilon-Near-Zero Resonant Tunneling Modes in Metal/Insulator/Metal nanocavities (pp. 1338)
Vincenzo Caligiuri, Milan Palei, Giulia Biffi, Sergey Artyukhin, Liberato Manna, Roman Krahne,

Ultrafast Laser-Induced Control of Interface-Induced Magnetic Anisotropy in Ferromagnetic Thin Films (pp. 1341)
Alexandra Kalashnikova,

Spiral metamaterials for terahertz magnetic ï¬•eld enhancement (pp. 1343)
Matteo Pancaldi, Debanjan Polley, Nanna Zhou Hagstrom, Matthias Hudl, Paolo Vavassori, Sergei Urazhdin, Clemens von Korff Schmising, Stefan Eisebitt, Stefano Bonetti,

Reprogrammable Nano-Optical Computing Using Metatronic Circuits (pp. 1345)
Mario Miscuglio, Joseph Crandall, Shuai Sun, Zhizhen Ma, Engin Kayraklioglu, Jeffery Anderson, Yousra Alkabani, Tarek A. El-Ghazawi, Volker J. Sorger,

Magnetic Metamaterials (pp. 1346)
Vassilios Kapaklis,

Localization of light in magnetophotonic structures for ultrafast magnetism (pp. 1347)
Vladimir I. Belotelov, Alexander Chernov, Mikhail Kozhaev, Daria Ignatyeva, Miguel Levy, Alexander Shaposhnikov, Vladimir Berzhansky,

Control of Hot-Electron Dynamics: From Ballistic Collection to Ultrafast Hot-Hole Removal (pp. 1349)
Giulia Tagliabue, Joseph S. DuChene, Ravishankar Sundararaman, Harry A. Atwater,

Self-assembled magnetic nanoparticles on plasmonic nanoantennas (pp. 1350)
G. Petrucci, O. Lysenko, E. Fantechi, C. Sangregorio, A. Dmitriev, Francesco Pineider,

Tunable and nonlinear metamaterials for circular polarization control (pp. 1352)
Kuniaki Konishi,

Towards optically adjustable and rewriteable metasurfaces enabled by phase-change materials (pp. 1354)
Andreas Hessler, Ann-Katrin Michel, Sebastian Meyer, Julian Pries, Yuan Yu, Thomas Kalix, Martin Lewin, Julian Hanss, Angela de Rose, Tobias Mass, Matthias Wuttig, Dmitry N. Chigrin, Thomas Taubner,

Exploiting the polarization of nanoparticles near surfaces: position sensing, recoil optical forces, and full angular spectrum engineering (pp. 1356)
Lei Wei, Jack J. Kingsley-Smith, Michela F. Picardi, Anatoly V. Zayats, Francisco J. Rodriguez-Fortuno,

Lighting up magneto-optics to its limit with dark plasmons (pp. 1358)
Mario Zapata-Herrera, Alberto Lopez-Ortega, Nicolo Maccaferri, Matteo Pancaldi, Mikel Garcia, Paolo Vavassori,

Ultrafast dynamics at fs-laser-excited magnetic meta-surfaces (pp. 1360)
Alexandr Alekhin, Vasily Temnov,

Single-shot all-optical switching in GdFeCo alloys using pulses of varying photon energies and durations (pp. 1362)
Carl Davies, Thom Janssen, Johan Mentink, Arata Tsukamoto, Alexey V. Kimel, Lex van der Meer, Andrzej Stupakiewicz, Andrei Kirilyuk,

Electrochemical plasmonics for dynamic control of optical properties of self-assembling metamaterials (pp. 1364)
J. B. Edel, Alexei A. Koryshev, A. R. Kucernak, Y. Ma, Y. Montelongo, D. Sikdar, M. Urbakh, L. Velleman, C. Zagar,

Atomically-thin tunable zone plate lens (pp. 1366)
Jorik van de Groep, Jung-Hwan Song, Umberto Celano, Mark L. Brongersma,

Beyond plasmonic functional materials: the challenge of magnetoplasmonics towards single molecule detection (pp. 1367)
Maria Grazia Manera, Adriano Colombelli, Maura Cesaria, Antonietta Taurino, Roberto Rella,

Enhanced Magneto-Optical Activity of noble metal nanostructures (pp. 1369)
Adriano Colombelli, Maria Grazia Manera, Daniela Lospinoso, Antonietta Taurino, Roberto Rella,

Designed electron temperature environments for the control of all-optical switching (pp. 1371)
Luke H. Nicholls, Tomasz Stefaniuk, Mazhar E. Nasir, Francisco J. Rodriguez-Fortuno, Gregory A. Wurtz, Anatoly V. Zayats,

Playing with temperature at the nanoscale (pp. 1373)
Remo Proietti Zaccaria, Tianlong Guo, Joao Cunha, Alessandro Alabastri,

Active Terahertz Superconducting Metamaterial-Based Modulator (pp. 1374)
Jingbo Wu, Chun Li, Caihong Zhang, Biaobing Jin,

Thermomechanical behavior of a multistable phase-change/dielectric bimaterial cantilever in response to radiative heat flux (pp. 1376)
Marta Reina, Riccardo Messina, Philippe Ben-Abdallah,

Coupled resonances of Surface Plasmon Polaritons and Localized Surface Plasmons in Ferromagnetic Nanoparticle Arrays (pp. 1378)
Francisco Freire-Fernandez, Mikko Kataja, Sebastiaan van Dijken,

Transformation optics concept and applications

Designing devices for sub-wavelength imaging using a transformation-optics approach (pp. 1381)
Mircea Giloan, Robert Gutt, Gavril Saplacan,

Extended two dimensional transformation optics for reflection suppression (pp. 1383)
Hossein Eskandari, Oscar Quevedo-Teruel, Amir Reza Attari, Mohammad Saeed Majedi,

Space Transformation Based Recombinable Lens for Generating Multi-mode OAM Radio Beams (pp. 1385)
Jianjia Yi, Xueqi Cao, Zhihao Jiang, Rui Feng, Badreddine Ratni, AndrÃ© de Lustrac, Shah Nawaz Burokur,

Electromagnetic wave shaping, wire media, and transformation optics (pp. 1387)
Paul Kinsler, Jonathan Gratus, Taylor Boyd,

Applications of semiconductor-based and conformal Metasurfaces (pp. 1389)
P. Ni, A. De Luna Bugallo, Yi-Yang Xie, H. Ren, G. Briere, S. Chenot, S. Vezian, V. Brandli, B. Damilano, J. Y. Duboz, M. Iwanaga, Patrice Genevet,

Transformation optics with invisible loss and gain (pp. 1391)
Yun Lai, Jie Luo,

Biophotonics

Numerical Design of BioResonator with Filtering Effect (pp. 1393)
Niloufar Raeis-Hosseini, C. Papvassiliou,

New materials for photonics (Graphene, MoS2, WS2, etc)

Synthesis and Plasmon Responses of Sodium Tungsten Bronze Nanoparticles (pp. 1396)
Levi Tegg, Dylan Cuskelly, Vicki J. Keast,

Optoelectronic Mixers Based on Graphene Photodetectors (pp. 1398)
Chuantong Cheng, Beiju Huang, Huan Zhang, Hengjie Zhang, Hongda Chen,

Hybrid graphene-antenna structure for terahertz detection (pp. 1400)
KlaasJan Tielrooij, Sebastian Castilla, Bernat TerrÃ©s, Marta Autore, Leonardo Viti, Alexey Nikitin, Miriam Vitiello, Rainer Hillenbrand, Frank Koppens,

Plasmonic TiOxNy based micro-structured films obtained by ammonolysis photopatternable TiO2 sol-gel film (pp. 1402)
Maria Alejandra Usuga, Crespo-Monteiro Nicolas, Vocanson Francis, Koussi Erika, Jamon Damien, Verrier Isabelle, Langlet Michel, Jourlin Yves,

Near-field nano-imaging of buried microcavity for enhancement of WS2 monolayer exciton photoluminescence (pp. 1404)
Oliver Mey, Franziska Wall, Lorenz Maximilian Schneider, Darius Gunder, Frederik Walla, Amin Soltani, Hartmut G. Roskos, Ni Yao, Peng Qing, Wei Fang, Arash Rahimi-Iman,

Organic materials for plasmonics: nanoscale light-confinement using J-aggregates (pp. 1406)
Samuel Holder, Martin Lopez-Garcia, Ruth Oulton, Sara Nunez-Sanchez,

Organic excitonic core-shell nanoparticles with plasmon-like response: Towards fully plastic metamaterials (pp. 1408)
Sara Nunez-Sanchez, C. Estevez-Varela, I. Pastoriza-Santos ,

Hybrid plasmon-magnon polariton modes in graphene-antiferromagnet heterostructures (pp. 1410)
Yuliy Bludov, Jose Gomes, Gil Farias, Joaquin Fernandez-Rossier, Mikhail Vasilevskiy, Nuno Peres,

Electrically Controllable Directional Coupler Based on Dielectric Loaded Graphene Plasmon Waveguide (pp. 1412)
Wei Xu, Hanyu Wang, Chao Li, Jianfa Zhang, Chucai Guo, Ken Liu, Xiaodong Yuan, Zhihong Zhu, Shiqiao Qin,

Electrically Tunable Graphene Polarization Controlling (pp. 1414)
Chao Li, Hanyu Wang, Wei Xu, Jianfa Zhang, Chucai Guo, Ken Liu, Xiaodong Yuan, Zhihong Zhu, Shiqiao Qin,

Graphene-based Perfect Absorption in the Near Infrared (pp. 1416)
Hanyu Wang, Wei Xu, Chao Li, Jianfa Zhang, Chucai Guo, Ken Liu, Xiaodong Yuan, Zhihong Zhu, Shiqiao Qin,

Optical antennas and plasmonics-based devices

Multiband Antennas for Si-based Terahertz Detectors (pp. 1419)
Ke Wang, Fangfang Ren, Yi Yang, Ping Han, Xiaoli Ji,

Real-Time In-Situ Optical Tracking of Oxygen Vacancy Migration in Memristors (pp. 1421)
Giuliana Di Martino, Dean Kos, Weiwei Li, Bonan Zhu, Xuejing Wang, Haiyan Wang, Angela Demetriadou, Judith Driscoll, Jeremy Baumberg,

High Q-factor coupled Fabry-Perot plasmonic nanoresonator (pp. 1423)
Baptiste Fix, Julien Jaeck, Patrick Bouchon, Nathalie Bardou, Sebastien Heron, Benjamin Vest, Riad HaÃ¯dar,

Antenna-Controlled Photon Antibunching from Individual Carbon Nanotubes as Quasi-1D systems (pp. 1425)
Lucas Lange, Frank Schafer, Alexander Biewald, Richard Ciesielski, Achim Hartschuh,

Self-Assembled Plasmonic DNA Origami Nanoantennas for Diagnostic Applications (pp. 1427)
Florian Steiner, Carolin Vietz, Sarah Ochmann, Kateryna Trofymchuk, Viktorija Glembockyte, Cindy Close, Hakan Inan, Lennart Grabenhorst, Florian Selbach, Guillermo Acuna, Birka Lalkens, Philip Tinnefeld,

Hexagonal Arrays of Gold Nanodot Dipole Nanoantennas Fabricated by Displacement Talbot Lithography (pp. 1429)
Jon Pugh, Pierre Chausse, Andrei Sarua, Philip Shields, Martin James Cryan,

Photoluminescence Enhancement by Hybrid plasmonic Nanodisks Arrays (pp. 1431)
Alireza Rahimi Rashed, Mohsin Habib, Nekhel Das, Humeyra Caglayan,

A 10 um x 10 um Longwave Infrared Imaging Pixel Based on Split Ring Resonators (pp. 1433)
Mohammed R. AlShareef, Mohamed Ramy Abdel-Rahman,

Photothermal and photoelectric nanophotonics

Thermal behavior and managament of thermophotovoltaic cells (pp. 1437)
Etienne Blandre, Rodolphe Vaillon, Jeremie Drevillon,

Solar Thermal Characterisation of Micro Patterned Solar Absorbers (pp. 1439)
Hanyu Cen, Sara Nunez Sanchez, Neil Fox, Martin Cryan,

Plasmon-enhanced photovoltaics, photocatalysis, and solar fuels

Optical properties of self-assembled, thin-walled nanotube TiO2 arrays (pp. 1442)
Christin David,

Plasmon enhancement of energy transfer from single up-converting nanocrystals to P3HT (pp. 1444)
Justyna Grzelak, Aneta Prymaczek, Maciej Cwierzona, Marcin Nyk, Dawid Piatkowski, Sebastian Mackowski,

Designed Au-TiO2 Nanoreactors for Photocatalytic Transformations in Living Cells (pp. 1446)
Ana Sousa-Castillo, Miguel Comesana-Hermo, Moises Perez-Lorenzo, Miguel A. Correa-Duarte,

Plasmonics and nano-optics

Angle-insensitive mid-IR spectrum filter using slit nanoresonator structure (pp. 1449)
Evan M. Smith, Ivan Avrutsky, Shiva Vangala, Justin W. Cleary, Josh R. Hendrickson,

Coupling of Gap Plasmon and Lattice Plasmon Resonances in Metal-Dielectric-Metal Gratings (pp. 1451)

Ricky Gibson, Joshua R. Hendrickson, Shivashankar Vangala, Dennis E. Walker,

EIT-like Effect Induced by Hybrid State of Tamm and Localized Plasmon-Polaritons in the region of Infrared (pp. 1453)
Fusheng Deng, Lijuan Dong, Yanhong Liu, Lixiang Liu, Yunlong Shi,

Plasmon-assisted terahertz detection in graphene transistors (pp. 1455)
Dmitry Svintsov, Denis Bandurin, Igor Gayduchenko, Maxim Moskotin, Andre Geim, Georgy Fedorov,

Quantum Mechanical Effects on Nanofocusing Limits of Metal-Insulator-Metal Plasmonic Waveguides (pp. 1457)
Daniel Rimoli Assumpcao, Hyuck Choo,

Photon-plasmon coupling in microtubular optoplasmonic cavities (pp. 1459)
Yin Yin, Jiawei Wang, Libo Ma, Oliver G. Schmidt,

Nonlocality and singular metasurfaces (pp. 1461)
Fan Yang, Yao-Ting Wang, Paloma Arroyo Huidobro, John B. Pendry,

Characterization of surface plasmon-polariton resonances at solvent-metal interfaces using Fano approximation (pp. 1463)
Dmitry V. Nesterenko, Roman Pavelkin, Shinji Hayashi, Victor Soifer,

Generation of the Robust and Low Loss Diffration-free Bloch Surface Wave (pp. 1465)
Ruxue Wang, Douguo Zhang, Aimin Wu,

Nonlocal optical processes mediated by surface plasmon polaritons (pp. 1467)
Dawid Piatkowski, Aneta Prymaczek, Maciej Cwierzona, Justyna Grzelak, Dorota Kowalska, Marcin Nyk, Sebastian Mackowski,

Metal-enhanced up-conversion luminescence tuned by optically controlled orientation of dipoles (pp. 1469)
Maciej Cwierzona, Aneta Prymaczek, Justyna Grzelak, Marcin Nyk, Sebastian Mackowski, Dawid Piatkowski,

Propagation of surface plasmon polaritons in silver nanowires placed on graphene (pp. 1471)
Aneta Prymaczek, Maciej Cwierzona, Justyna Grzelak, Dorota Kowalska, Marcin Nyk, Sebastian Mackowski, Dawid Piatkowski,

Rock-salt CdZnO for IR plasmonics (pp. 1473)
Julen Tamayo-Arriola, Eduardo Martinez Castellano, Adelaida Huerta-Barbera, Miguel Montes Bajo, Elias Munoz, Vicente Munoz-Sanjose, Adrian Hierro,

Double-interface surface plasmon modes in CdZnO thin films and their hybridization with phonons (pp. 1475)
Eduardo Martinez Castellano, Julen Tamayo-Arriola, Miguel Montes Bajo, Adelaida Huerta-Barbera, Elias Munoz, Vicente Munoz-Sanjose, Adrian Hierro,

Direct Demonstration of Biexciton Quantum Yield Enhancement in an Individual Quantum Dot Coupled with Gold Nanoparticles in a Thin-film Hybrid Material (pp. 1477)
Victor Krivenkov, Pavel Samokhvalov, Ana Sanchez-Iglesias, Marek Grzelczak, Igor Nabiev, Yury Rakovich,

Ultrafast response of a plasmonic distributed feedback laser in large-signal modulation regime (pp. 1479)
Nikita Nefedkin, Alexander Zyablovsky, Evgeny Andrianov, Alexander Pukhov, Alexey Vinogradov,

Superradiant molecular aggregates on dielectric surfaces interacting with plasmonic structures (pp. 1481)
Alexander Eisfeld,

Propagation of Strongly Hybridized Plasmonic Modes: Theory and Applications (pp. 1482)

Ivan A. Pshenichnyuk, Sergey S. Kosolobov, Andrei I. Maimistov, Vladimir P. Drachev,

Near-field phase imaging using phase-shifting digital holography (pp. 1484)
Petr Dvorak, Michal Kvapil, Petr Bouchal, Zoltan Edes, Tomas Samoril, Michal Horak, Martin Hrton, Filip Ligmajer, Vlastimil Krapek, Tomas Sikola,

Babinet's Principle for Solid and Hollow Plasmonic Antennas (pp. 1486)
Michal Horak, Vlastimil Krapek, Martin Hrton, Andrea Konecna, Filip Ligmajer, Michael Stoger-Pollach, Tomas Sikola,

An Atomistic Approach for Hybrid Plasmonic Systems (pp. 1488)
Giulia Giannone, Fabio Della Sala, Stefania D'Agostino,

Slender-body theory for localized-surface-plasmon resonance (pp. 1490)
Matias Ruiz, Ory Schnitzer,

From Classical to Quantum Interactions in Molecular Plasmonics (pp. 1492)
Giulia Giannone, Fabio Della Sala, Stefania D'Agostino,

Angular momentum transfer from a swift electron to a small nanoparticle (pp. 1494)
Jose A. Castellanos-Reyes, Alejandro Reyes-Coronado,

Fundamentals of linear momentum transfer from swift electrons to nanoparticles (pp. 1496)
Alejandro Reyes-Coronado, Jesus Castrejon-Figueroa, Jose angel Castellanos-Reyes,

Pure toroidal dipole excitation in dielectric nanoparticles (pp. 1498)
Reza Masoudian Saadabad, Marcus Cai, Lei Xu, Andrey E. Miroshnichenko,

Synthesis and Plasmonic Properties of Au Double Nanorings Supported by Pd Cyclic Nanosheets (pp. 1500)
Yukie Yokota, Takumi Takatsuki, Tsuyoshi Tokita, Yushi Yabuki, Kazuo Watanabe,

Efficient Resonance of Double Active Silicon Nanowires (pp. 1502)
Shengqiong Chen, Lina Shi, Jiebin Niu, Changqing Xie,

Chemistry of remotely separated species hybridized by strong light-matter coupling (pp. 1504)
Matthew Du, Raphael F. Ribeiro, Luis A. Martinez Martinez, Zixuan Hu, Vinod M. Menon, Joel Yuen-Zhou,

Plasmonic Properties of Silver Amalgam Nano- and Microparticles (pp. 1506)
Lukas Kejik, Filip Ligmajer, Michal Horak, Ales Danhel, Miroslav Fojta, Tomas Sikola,

Coupling a single carbon-nanotube to a plasmonic hotpots-patch antenna. (pp. 1508)
Clement Beaufils, Nicolas Izard, Didier Felbacq, Guillaume Cassabois, Emmanuel Rousseau,

Unidirectional Optical Nanoantenna Design by Bayesian Optimization (pp. 1510)
F. F. Qin, D. S. Zhang, Jun Jun Xiao,

Wavelength-dependent surface plasmon polariton propagation in long silver nanowire waveguide (pp. 1512)
Dorota Buczynska, Michal Cwik, Ewa Rozniecka, Sebastian Mackowski, Joanna Niedziolka-Jonsson,

Metamaterial flat lens with properties independent of light polarization (pp. 1514)
Alexander Agashkov, Nadezhda Ivanova, Nikolay Kazak, Vladimir Agabekov,

Spontaneous Formation of Cold Welded Plasmonic Nanostructures at the Air Water Interface for Intense Raman Scattering (pp. 1516)

Andrea Marino Lopez, Maria Blanco Formoso, Leonardo N. Furini, Ana Sousa Castillo, Ecem Tiryaki, MoisÃ©s PÃ©rez Lorenzo, Martin Testa Anta, Veronica Salgueirino, Miguel A. Correa Duarte,

Double-sided, omnidirectional and broadband absorber in visible regime using moth-eye nanostructures covered by non-noble metal (pp. 1518)
Su Shen, Yun Zhou, Yanhua Liu, Shaolong Wu,

Ultra-Narrowband and Full-Angle Refractive Index Sensor Based on a Planar Multilayer Structure (pp. 1520)
Linling Qin, Shaolong Wu, Cheng Zhang, Xiaofeng Li,

Self-Similar Nanostructured Waveguides for Efficient and Direction Sensitive Plasmon Propagation (pp. 1522)
Mario Miscuglio, Davide Spirito, Philip Schaefer, Roman Krahne,

Multi-polarized Nano-antenna for Surface Enhanced Raman Spectrescopy Application (pp. 1524)
Monir Morshed, Ahasanul Haque, Lei Xu, Andrey Miroshnichenko, Haroldo Hattori,

Self-beating during pulsed light transmitting through a plasmonic slit (pp. 1526)
Kuan-Ren Chen, Jian-Shiung Hong, Alex E. Chen,

Bridging Classical and Quantum Plasmons via an FDTD-TDDFT Hybrid Model (pp. 1528)
Jianwei You, Nicolae Coriolan Panoiu,

Controlling the polarization of surface phonon polaritons (pp. 1530)
Michael A. Meeker, Eric M. Jackson, Chase T. Ellis, Zhizhen Ma, Mario Miscuglio, Marko J. Tadjer, Sarah Brittman, Janice E. Boercker, Nii-Okaitey Tetteh, Volker J. Sorger, Joseph G. Tischler,

Glass microspheres doped with Ag nanoparticles and CdTe quantum dots: towards a plasmonic microlaser (pp. 1532)
Piotr Piotrowski, Rafal Nowaczynski, Barbara H. Surma, Dorota A. Pawlak,

Off-axis digital holography for cathodoluminescence microscopy (pp. 1533)
Nick Schilder, Femius Koenderink, Albert Polman,

Metamaterials-based probing weak quantum absorber in coupled three-resonator system with guided wave surface plasmons: sensing or all-optical switching? (pp. 1535)
Alina Karabchevsky, Adir Hazan,

Biomechanical sensor based on gold plasmonic nanorods for mechanotransduction investigation (pp. 1537)
Maria Salbini, Tiziana Stomeo, Cristian Ciraci, Roberto Fiammengo, Vincenzo Mangini, Marco Leoncini, A. Toma, Filippo Pisano, Ferruccio Pisanello, Tiziano Verri, David Smith, Massimo De Vittorio,

A Deep Sub-wavelength Scale Surface Plasmon Polariton Travel Wave Amplifier with Multiple Quantum Wells (pp. 1541)
Ruijian Rao, Shuwen Chen, Bing Chen,

Scattering by Core-Shell Semiconductor Microinclusions for Plasmonically Enhanced Near-IR Applications (pp. 1545)
Fahime Sadat Seyedheydari, Kevin Conley, Tapio Ala-Nissila,

Gain Mediated Surface Plasmon Polariton Propagation in the Near-Infrared (pp. 1551)
Preksha Tiwari, Svenja Mauthe, Noelia Vico Trivino, Markus Scherrer, Chang-Won Lee, Kirsten Moselund,

Ultimate Material Selection Methodology for Ultra-Broadband M-I-M Metamaterial Absorber (pp. 1554)
Imre Ozbay,

Photogenerated Excitons of Cesium Lead Bromide Perovskite Quantum dots through ligand Passivation (pp. 1555)

Sunjoong Park, Hyunjin Cho, Wonseok Choi, Hongjoo Shin, Duk Young Jeon,

Rapid and Highly efficient annealing process for photoluminescence efficiency improvement of quantum dots using intence pulse light (pp. 1556)
Chulhee Lee, Taeyoung Song, Duk Young Jeon,

Tunable Infrared Energy Transfer through Surface Phonon Polaritons (pp. 1557)
Mohsen Janipour, Matthias Hensen, Walter Pfeiffer,

Quantum and topological photonics

Unidirectional edge states in two dimensional plasmonic arrays (pp. 1559)
Matthew Proctor, Stefan A. Maier, Richard V. Craster, Paloma Arroyo Huidobro,

Dynamics of entanglement for quantum emitters near MoS2 nanodisks (pp. 1561)
Nikolaos Iliopoulos, Vasilios Karanikolas, Dionisios Stefanatos, Emmanuel Paspalakis,

Long-lived Event Horizon Induced by Topological Phase Transition (pp. 1563)
Meng Kang, Huaqing Huang, Shunping Zhang, Hongxing Xu, Feng Liu,

Bifurcations of topological edge states in non-linear quantum walks: originating from unique features to Floquet non-linear systems (pp. 1565)
Ken Mochizuki, Norio Kawakami, Hideaki Obuse,

Correlation between bands structure and quantum magneto-transport in In0.53Ga0.47As/InP type I superlattice for short-infrared detection (pp. 1566)
Merieme Benaadad, Abdelhakim Nafidi, Samir Melkoud, Nassima Benchtaber, Es-saÃ¯d Es-Salhi, Fatiha Chibane, Mustapha Massaq,

Super-resolution imaging

Superresolution Stimulated Raman Microscopy (pp. 1574)
Sergey Kharintsev, Anton Kharitonov, Aleksander Alekseev, Sergei Kazarian,

Haze removal method based on decomposition (pp. 1576)
Xifang Zhu, Ruxi Xiang, Feng Wu, Qingquan Xu, Ye Lu,

Haze Removal based on New Estimation of the Atmospheric Light (pp. 1578)
Ruxi Xiang, Xifang Zhu, Feng Wu, Qingquan Xu, Ye Lu,

Ultrafast and nonlinear phenomena

Nonlinear Optical Bleaching of a Monolayer of Au Plasmonic Coupled Nanoparticles and Percolation-like Films with Nanoslits (pp. 1581)
Vladimir Kaydashev, Piero Ferrari, Pavel Timoshenko, Mikhail Shestakov, Ewald Janssens, Peter Lievens, Evgeni Kaidashev,

Acoustic and seismic metamaterials

Multiple Weyl and Double-Weyl Points in Elastic Chiral Lattices (pp. 1584)
Yao-Ting Wang, Ya-Wen Tsai,

Phononic Crystals with Archimedean-Like Tiling's: Transmission, Band Structure and Transformation of Sound (pp.

1585)
Zafer Ozer,

Elastic Wave Control in Double-Zero-Index Elastic Metamaterials (pp. 1586)
Bing Li, Zheng Li, Johan Christensen, K. T. Tan,

Band Gap and Wave Propagation on Liquid Crystal Based Sonic Metamaterials (pp. 1588)
Selami Palaz,

Band Structure and Transmission in Multiferroic based Sierpinski Carpet Phononic Crystal (pp. 1589)
Selami Palaz, Zafer Ozer, Amirullah M. Mamedov, Ekmel Ozbay,

Nonviscous damping effects on the wave dispersion and dissipation of locally resonant acoustic metamaterials (pp. 1590)
Taufeeq Abbasi, Hui Zheng,

Asymmetric Wave Transmission in Dissipative Acoustic Metamaterials (pp. 1592)
Sagr Alamri, Bing Li, K. T. Tan,

Acoustic Metamaterial Lenses for 40kHz Ultrasound Fabricated with Consumer 3D-printers (pp. 1594)
James Hardwick, Jordi Prat-Camps, Sriram Subramanian,

Sn2P2X2 (X=S, Se) as novel materials for phononic crystals (pp. 1596)
Selami Palaz, Zafer Ozer, Sevket Simsek, Husnu Koc, Amirullah Mamedov, Ekmel Ozbay,

Negative phase velocity sound propagation in 1D hyperbolic phononic metamaterials (pp. 1597)
Yurii Zubov, Arkadii Krokhin, Bahram Djafari-Rouhani,

Negative In-plane Elastic Moduli of Metallic Lattices: Experimental Investigations (pp. 1599)
Sondipon Adhikari, Alex Shaw, Tanmoy Mukhopadhyay, Nick Lavery,

Chiral and bianisotropic materials

High-efficiency asymmetric transmisson in terahertz metamaterials (pp. 1602)
J. H. Shi, Tingting Lv, Guohua Dong, Zheng Zhu, Yuxiang Li, Chunying Guan,

The roles of superchirality, optical chirality dissipation and interference in biomolecular detection with chiral plasmonic structures (pp. 1604)
Cameron Gilroy, Shun Hashiyada, Kensaku Endo, Affar Shahid Karimullah, Laurence Barron, Horomi Okamoto, Yoshihiko Togawa, Malcolm Kadodwala,

Metamaterial-based devices

All dielectric frequency-division multiplexing wave plate metasurface (pp. 1607)
Shuo Du, Zhe Liu, Junjie Li , Changzhi Gu,

Polarization-sensitive coherent absorption in metamaterials (pp. 1609)
Yuxiang Li, Bowen Li, Jintong Shi, Wenjin Lv, Chunying Guan, Jinhui Shi,

Control of IR emissivity with metasurface structures (pp. 1611)
Roxana Tomescu, Mihai Kusko, Dana Cristea, Laura Mihai, Ramona Calinoiu, Cristian Kusko, Catalin Parvulescu,

Detection of organic molecules using asymmetric plasmonic nanostructures (pp. 1613)
Ili Farhana Mohamad Ali Nasri, Graham Sharp, Richard De La Rue, Nigel Johnson, Marc Sorel, Caroline Gauchotte-Lindsay,

Wave Propagation in Mechanical Metamaterial Configurations with Piezoelectric Vibration Energy Harvestors (pp. 1615)
Jatin Patrick, Sondipon Adhikari,

Tunable high-birefringence metamaterial nanoparticles dispersed in water (pp. 1617)
Ying Tang, Seungkyu Ha, Thomas Begou, Julien Lumeau, Nynke Dekker, Aurele Joseph Louis Adam, Paul Urbach,

Monolithic high contrast gratings - highly reflective mirrors for VCSELs (pp. 1619)
Magdalena Marciniak, Artur Broda, Marcin Gebski, Jan Muszalski, Maciej Dems, Michal Wasiak, James A. Lott, Tomasz Czyszanowski,

Frequency Shift of Light in Highly Dispersive Time-Varying Metasurfaces (pp. 1621)
Jagang Park, Hyukjoon Cho, Hyun Sung Park, Bumki Min,

Quantification of Resonance Scaling for Open Subwavelength-Resonator Based Structures (pp. 1623)
Andriy E. Serebryannikov, Guy A. E. Vandenbosch, Ekmel Ozbay,

Dual-Band Wireless Power Transmission Using Coupled Metamaterial Resonators for Wireless Sensor Networks (pp. 1625)
Safiullah Khan, Thomas F. Eibert,

Broadband Metamaterial Absorbers: Gold and Tungsten Boride (pp. 1627)
Ahasanul Haque, Monir Morshed, Ziyuan Li, Li Li, Kaushal Vora, Lei Xu, Lan Fu, Andrey Miroshnichenko, Haroldo Hattori,

Metasurfaces based coils for MRI (pp. 1629)
Alena Shchelokova, Alexey Slobozhanyuk, Stanislav Glybovski, Irina Melchakova, Pavel Belov,

Interference phenomena and pulse propagation in a plasmonic wide-ridge metal-dielectric waveguide (pp. 1631)
Georgiy Yankovskii, Vladimir Kornienko, Alexey Shaimanov Shaimanov, Anton Ignatov, Alexander Merzlikin, Alexander Baryshev,

Miniature Spectroscopes with Metasurfaced Transmitted Color Filters Integrated on a Photodiode Array (pp. 1633)
Yoshiaki Kanamori, Daisuke Ema, Kazuhiro Hane,

Wideband Absorbing Nonlinear Optical Metamaterials Using Coupled Epsilon-Near-Zero Mode (pp. 1635)
Jinnan Chen, Evan M. Smith, Justin Cleary, Chandriker Dass, Amber Reed, Shiva Vangala, Joshua R. Hendrickson, Junpeng Guo,

Metamaterials and negative index materials

Programmable Electromagnetic Properties of Microwire Metacomposites (pp. 1638)
Azim Uddin, Faxiang Qin,

Dielectric metamaterials with epsilon-near-zero regime (pp. 1640)
Ekaterina E. Maslova, Mikhail V. Rybin,

Anti-crossing of counter propagating modes within the Brillouin Zone (pp. 1642)
Milo Baraclough, William Leslie Barnes, Ian Richard Hooper,

Synthetic Biological Approaches for the Fabrication of Optical Metamaterials (pp. 1644)
Simon Butler, Rebecca Seviour,

Complex Band Structure and Dispersion Relation of Acoustic Waves in Piezoelectric Based Topological Phononic Crystals (pp. 1647)

Selami Palaz, Zafer Ozer, Sevket Simsek, Husnu Koc, Amirullah Mamedov, Ekmel Ozbay,

Split Ring Resonator Loaded Double Opposite E-shaped Left-Handed Metamaterial for Modern Electronic Communications (pp. 1648)
Ahmed Mahfuz Tamim, Mohammad Rashed Iqbal Faruque, Mohammad Tariqul Islam,

Much Ado About Nothing: Applying a Metamaterial Model with Negative Energy to Address the Vacuum Catastrophe (pp. 1650)
Thomas Paul Weldon, Kathryn Leigh Smith,

Near Perfect Absorption in Epsilon Near Zero Thin Films (pp. 1652)
Stephen A. O'Brien, Frank Bello, Lisanne Peters, Niall McEvoy, David McCloskey, John Donegan,

Blueshift in graphene-based hyperbolic metamaterials as a tunable narrowband reflection modulators (pp. 1654)
Alessandro Pianelli, Rafal Kowerdziej, Marek Olifierczuk, Karol Sielezin, Michal Dudek, Janusz Parka,

Utilization of Cross-Metamaterial Nano-Antenna to Expand the Light Absorption in the Active Layers of Organic Thin Films (pp. 1656)
Yadgar Ibrahim Abdulkarim, Lianwen Deng , Fahmi F. Muhammad, Muharrem Karaaslan, Shengxiang Huang,

Conception of Circular Microstrip Patch Antenna Based on SINRD Substrate for WI-FI Application (pp. 1663)
Korchi Narimane, Rachid Oussaid,

Optical and Nonlinear-Optical Properties of Gold Nanorods' Based Hyperbolic Metamaterials (pp. 1669)
Irina A. Kolmychek, Aleksander R. Pomozov, Vladimir B. Novikov, Aleksei P. Leontiev, Kirill S. Napolskii, Tatiana V. Murzina,

Optical properties of planar metal-dieletric layered films: from coupled Fabry-PeÌ•rot resonators to hyperbolic metamaterials (pp. 1673)
Manuel Goncalves, Hayk Minassian, Armen Melikyan, Othmar Marti,

Metasurfaces and flat optics, FSS, HIS,

Touching-dimer metagratings with high asymmetric diffraction in the full visible range (pp. 1681)
Tan Shi, Yujie Wang, Zi-Lan Deng, Shumin Xiao, Xiangping Li,

Focusing and Ultra-high Resolution by Integrated Metalens (pp. 1683)
Juntao Li, Qian Sun, Yuhao Ren, Haowen Liang,

Comparison of the negative energy flow in linearly and circularly polarized beams focused with metalens (pp. 1685)
Victor Kotlyar, Anton Nalimov, Sergey Stafeev,

Spiral metalens for tight focusing of azimuthally polarized optical vortex (pp. 1687)
Anton Nalimov, Sergey Stafeev, Liam O'Faolain, Victor Kotlyar,

Design and Manufacturing of Bitmap-type Microwave Absorber Metasurface (pp. 1689)
Ye-Pil Kwon, Eun-Chae Jeon, Tae-Jin Je, Je-Ryung Lee, Seunghwan Moon, Myungjoon Kim, Joonkyo Jung, Jonghwa Shin, Doo-Sun Choi,

Singular Polaritonic Metasurfaces: Graphene and Beyond (pp. 1691)
Emanuele Galiffi, Paloma Arroyo Huidobro, John Brian Pendry,

Ultrafast modulation in a THz graphene-based flat absorber through negative photoconductivity (pp. 1693)
Anna Tasolamprou, Anastasios Koulouklidis, Christina Daskalaki, Charalampos Mavidis, George Kananakis, George

Deligeorgis, Zacharias Viskadourakis, Polina Kuzhir, Stelios Tzortzakis, Eleftherios Economou, Maria Kafesaki, Costas Soukoulis,

Reconfigurable coding metamaterial (pp. 1695)
Eistiak Ahamed, Mohammad Rashed Iqbal Faruque, Mohd Fais Bin Mansor,

Computational Spectral Imaging with Metasurface-based, Pixel-scale Color Splitters (pp. 1697)
Masashi Miyata, Mitsumasa Nakajima, Toshikazu Hashimoto,

High-efficiency anomalous refraction in terahertz metamaterial (pp. 1699)
Chunying Guan, Ruiqiang Zhao, Rongyu Liu, Zheng Zhu, Yuxiang Li, Jinhui Shi,

Efficiency improvement in wireless power transfer system using artificial magnetic conductors (pp. 1701)
Lijuan Dong, Fusheng Deng, Yanhong Liu, Lixiang Liu, Yunlong Shi,

Coding Huygens' Metasurface for Microwave Holography (pp. 1703)
Chunsheng Guan, Xumin Ding, Kuang Zhang, Badreddine Ratni, Shah Nawaz Burokur, Ming Jin, Qun Wu,

Broadband flattened parabolic reflector antenna based on metasurface (pp. 1708)
Vivien Taverny, Badreddine Ratni, Shah Nawaz Burokur,

Mitigating Chromatic Dispersion with Hybrid Optical Metasurfaces (pp. 1710)
Rajath Ravindra Sawant, Purva Bhumkar, Alexander Y. Zhu, Peinan Ni, Federico Capasso, Patrice Genevet,

Metasurface-based ultra-lightweight high-gain flat parabolic reflectarray for microwave beam collimation/focusing (pp. 1712)
Sinhara Rishi Malinda Silva, Abdur Rahman, Wilton Kort-Kamp, Diego Dalvit, Hou-Tong Chen, Abul Azad,

Incidence angle-dependence in image reconstruction crosstalk of broadband birefringent c-Si Metasurfaces (pp. 1714)
Augusto Martins, Juntao Li, Achiles Fontana Mota, Yin Wang, Luiz Goncalves Neto, Ben-Hur Viana Borges, Emiliano Rezende Martins,

High-Resolution Quantitative Phase Imaging of Plasmonic Metasurfaces (pp. 1716)
Petr Bouchal, Petr Dvorak, Jiri Babocky, Zdenek Bouchal, Filip Ligmajer, Lukas Kejik, Martin Hrton, Vlastimil Krapek, Alexander Fassbender, Stefan Linden, Radim Chmelik, Tomas Sikola,

Reflective metamirror grating for far field spatial filterin (pp. 1718)
Pei-Yu Wang, Yu-Chieh Cheng, Ramon Herrero, Muriel Botey, Kestutis Staliunas,

Reaching the Abbe-Sine condition with curved conformal metasurfaces. (pp. 1720)
Sandeep Yadav Golla, Patrice Genevet,

Simulation study of metasurfaces for hemp concrete hydration monitoring (pp. 1722)
Mehdi Ferhat, Badreddine Ratni, Fares Bennai, Franck Daout, Kamilia Abahri, Eric Vourc'h,

Random interleaved meta-surface for controllable C-Points (pp. 1724)
Enliang Wang, Jiebin Niu, Lina Shi, Changqing Xie,

Resonant Lattice Kerker Effect in Metasurfaces of Titanium Dioxide Nanocubes (pp. 1726)
Longjie Li, Lina Shi, Changqing Xie,

Invisible metasurfaces based on high-order Kerker and anapole effects (pp. 1728)
Hadi Shamkhi, Kseniia Baryshnikova, Andrey Sayanskiy, Pavel Terekhov, Egor Gurvitz, Adria Canos Valero, Alina

Karabchevsky, Polina Kapitanova, Andrey Evlyukhin, Pavel Belov, Yuri Kivshar, Alexander Shalin,

A dual-to-single mode metasurface absorber using phase transition of vanadium dioxide (pp. 1730)
Ayman Negm, Mohamed Bakr, Matiar Howlader, Shirook Ali,

Hybrid achromats with metasurfaces for IR imaging (pp. 1732)
Philippe Lalanne,

Polarization and diffraction engineering of nonlinear dielectric metasurfaces (pp. 1734)
C. Gigli, G. Marino, S. Suffit, G. Patriarche, G. Beaudoin, K. Pantzas, I. Sagnes, I. Favero, G. Leo,

Effect of Ballistic Electrons on the Optical Response of Hyperbolic Metamaterials (pp. 1736)
Guilherme Migliato Marega, Achiles Fontana Mota, Ben-Hur Viana Borges, Euclydes Marega Junior,

Quantum metamaterials

Quantum electronic magneto-transport in GaAs/AlxGa1-xAs superlattice at high magnetic fields and low temperature for near-infrared detection (pp. 1742)
Rachid Ben Koujan, Abdelhakim Nafidi, Merieme Benaadad, Samir Melkoud, Driss Barkissy, Nassima Benchtaber, Abderrazak Boutramine,

Thermal metamaterials

Infrared metasurfaces for polarization control of thermal emission (pp. 1750)
Sergey A. Dyakov, Nikolay A. Gippius, Sergei G. G. Tikhodeev,

Background-independent thermal camouflage evolved from fin heat sink (pp. 1752)
Xiayao Peng, Jinlin Song, Run Hu, Xiaobing Luo,

Generalized Two-Temperature Fitting Algorithm for Ultrashort Laser Heating of Metal Films. (pp. 1754)
Paul Bresson, Jean-Francois Bryche, Julien Moreau, Mondher Besbes, Paul-Ludovic Karsenti, Denis Moreau, Paul Charette, Michael Canva,

Laser and cavities

Monolithic Graphene single-mode Vertical-cavity Surface-emitting Lasers (pp. 1757)
Baolu Guan, Weiling Guo, Yiyang Xie, Chen Xu,

Metasurface lasers based on resonant dark states (pp. 1759)
Sotiris Droulias, Thomas Koschny, Costas M. Soukoulis,

Rabi splitting of broadband emission of strongly coupled organic dye excitons in tunable optical microcavity (pp. 1761)
Dmitriy Dovzhenko, Konstantin Mochalov, Ivan Vaskan, Irina Kryukova, Yury Rakovich, Igor Nabiev,

Electrically-injected vertical-cavity surface-emitting lasers incorporating monolithic high contrast gratings (pp. 1763)
Marcin Gebski, James A. Lott, Tomasz Czyszanowski,

Optimal design of Quantum-Cascade Vertical-Cavity Surface-Emitting Laser (pp. 1765)
Sandra K. Grzempa, Wlodzimierz Nakwaski, Tomasz Czyszanowski,

Mode cooperation in plasmonic lasers (pp. 1767)
Alexander A. Zyablovsky, Nikita Nefedkin, Evgeny Andrianov, Alexander Pukhov, Alexey Vinogravov,

Strong coupling and low, room temperature threshold in nanolasers using optical nanopatch antennas: an analytical and computational study (pp. 1769)
Patrick Bowen, Xander Deputy, Roberto Zecca, David R. Smith,

Spatio-temporal simulation of defect mode laser in 2D groove metal array inside MIM Structure (pp. 1771)
Seong-Han Kim, Chul-Sik Kee,

Photonic crystals

Pseudo Jahn Teller effect: Application to Time Crystals (pp. 1774)
Zafer Ozer, Amirullah M. Mamedov, Ekmel Ozbay,

Angle-Independent Structural Colors for Personal Thermal Management (pp. 1775)
Zhijie Zhu, Xiang-Yun Du, Chang Liu, Qing Li, Su Chen,

Coalescence-controlled large-scale colloidal films towards robust structural colors (pp. 1777)
Su Chen, Zhijie Zhu, Xiang-Yun Du, Chang Liu, Qing Li,

Versatile Functionalized Photonic Crystals and Their Self-Assembly Applications through Chip Microfluidic Technology (pp. 1779)
Chang Liu, Xiang-Yun Du, Zhijie Zhu, Qing Li, Su Chen,

Photonic crystal bead 2D code patterns based on microfluidic 3D printing (pp. 1781)
Xiang-Yun Du, Zhijie Zhu, Chang Liu, Qing Li, Su Chen,

Near-field focusing devices (pp. 1783)
Yu Chieh Cheng, Kestutis Staliunas,

Classification of deformed photonic Dirac cones (pp. 1785)
Jungmin Kim, Sunkyu Yu, Namkyoo Park,

Wavefront manipulation based of the excitation of bound states in dielectric photonic crystals and bilayer metasurfaces (pp. 1787)
Anna Tasolamprou, Maria Kafesaki, Thomas Koschny, Costas Soukoulis,

Hybrid External Cavity Laser based on Silicon Nitride 1D Photonic Crystals Cavities for dWDM applications (pp. 1789)
Simone Iadanza, Alessio Tedesco, Giuseppe Giannino, Marco Grande, Liam O'Faolain,

Emerging applications

Broadband photoacoustic microscopy based on surface plasmon resonance sensing (pp. 1793)
Changjun Min,

Bloch surface wave based sensor utilizing a multilayer interference filter (pp. 1795)
Michal Gryga, Dalibor Ciprian, Petr Hlubina,

Micro/Nano fabrication and characterization techniques

Titanium nitride nanowires fabricated by oblique deposition for hyperbolic metamaterials (pp. 1799)
Kenichi Yatsugi, Kazutaka Nishikawa,

High Photoelectrochemical Activity of CuInS2 Quantum Dots/In2S3/ZnO Nanowire Arrays Electrode (pp. 1801)
Yu-Kuei Hsu, Hao-Hsuan Chang,

Scattering-type scanning near-field optical microscopy and spectroscopy for real space observation of various polaritons (pp. 1803)
Philip Schafer, Adrian Cernescu, Sergiu Amarie, Andreas Huber,

Nanostructuring of Graphene Membranes with Focused Ion Beams: Towards 2D Metamaterials (pp. 1805)
Ivan Shorubalko,

Large area fabrication of complex periodic nanostructures by 'Double Displacement Talbot Lithography': Fundamentals and applications (pp. 1807)
Pierre Chausse, Andrei Sarua, Jon Pugh, Pierre-Marie Coulon, Martin Cryan, Philip Shields,

Freestanding metallic mesh for transparent electromagnetic interference shielding (pp. 1809)
YanHua Liu, Su Shen,

FIB based Sketch & Peel with various Ion Species for Fast and Precise Patterning of Large Structures (pp. 1811)
Achim Nadzeyka, Michael Kahl, Huigao Duan, Yiqin Chen, Kaixi Bi,

Direct-Write Electron-Beam Lithography (pp. 1813)
Soroosh Daqiqeh Rezaei, Jinfa Ho, Tao Wang, Seeram Ramakrishna, Joel K. W. Yang,

Modeling and computational techniques

Invariant-Based Dynamics Towards Optimal Adiabatic Qubit-Information Detection with Superconducting Qubit Resonators (pp. 1818)
Jeong Ryeol Choi,

Inverse Design of THz Filter based on Self-Complementary Metasurfaces and Deep Neural Network (pp. 1820)
Celso Martines Leite, Kyung-Bin Lee, Hyo-Jeong Kim, Pyeung-Hwi Choi, Muhammad Tayyab Nouman, Jae-Hyung Jang,

Multiobjective Optimization-aided Metamaterial Synthesis (pp. 1822)
Ronald Paul Jenkins, Sawyer Duane Campbell, Pingjuan L. Werner, Douglas H. Werner,

A Circuit Model for the Spoof Surface Plasmon Polariton Waveguides for the Terahertz Band (pp. 1824)
Gulay Ozsahin, Muhammed Abdullah Unutmaz, Mehmet Unlu,

Effective Approach for Design and Simulation of Metalens Structures (pp. 1826)
Chenglin Xu, Matt Novak, Dan Herrmann, Li-Ce Hu, Evan Heller, Mayank Bahl,

Plenary Lectures

Metasurface Polarization Optics

Federico Capasso

John A. Paulson School of Engineering and Applied Sciences

Harvard University, Cambridge MA 02139

Abstract

The basic elements of polarization optics are polarizers and phase retarders (waveplates). Retarders most commonly take the form of bulk bi/uniaxial crystals whose birefringent properties allow for polarization conversion. These plates are, however, difficult to fabricate and process and are challenging to integrate. For example, current polarimeters use multiple optical components in sequence for polarization analysis and therefore often become bulky and expensive. The elements comprising a metasurface may possess tailored structural birefringence, making metasurface based flat optics a fascinating platform for new polarization optics to circumvent the above problems[1]. A new class of phase plates has emerged from our research in this area[2] along with major advances in polarimetry and polarization imaging, with greatly reduced complexity and increased functionality compared to existing technology.[3,4]

References

1. Federico Capasso, *Nanophotonics* **7**, 953 (2018)
2. J. P. Balthasar Mueller, Noah A. Rubin, Robert C. Devlin, Benedikt Groever, and Federico Capasso *Physical Review Letters* **118**, 113901 (2017)
3. J.P. Balthasar Mueller, Kristjan Leosson, and Federico Capasso, *Optica* 3, 42 (2016)
4. Noah A. Rubin, Aun Zaidi, Michael Juhl, Ruo Ping Li, J.P. Balthasar Mueller, Robert C. Devlin, Kristján Leósson, and Federico Capasso, Optics Express 26, 21455 (2018)

Optical Antenna Physics: Spontaneous Emission Faster than Stimulated Emission

Eli Yablonovitch, Ming Wu, & Seth Fortuna

Electrical Engineering & Computer Sciences Dept.,
University of California, Berkeley
Berkeley California, 94720 USA
*corresponding author, E-mail: eliy@eecs.berkeley.edu

Abstract

An optical antenna, like a radio antenna, can concentrate electromagnetic energy within a volume <<< 1 cubic wavelength. That same concentration factor applies to quantum zero-point electromagnetic energy. Intense pump radiation makes Stimulated Emission very fast. Likewise highly concentrated zero-point electromagnetic energy can make Spontaneous Emission very fast.

The question arises: Can zero-point electromagnetic energy be more intense than the strongest real pump fields? Real pump intensity in a laser is limited by various optical nonlinearities including saturation, hole-burning, gain-medium-damage, etc. Therefore optical antennas have a real opportunity to be faster than stimulated emission, but the Ohmic skin effect losses in the metals are a limitation.

We will describe the correct optical antenna conditions for making Spontaneous-faster-than-Stimulated emission, and we will review the improvements in our electrically pumped antenna Light Emitting Diodes.

Extreme nanophotonics: How to confine light below a cubic nanometre

Jeremy J Baumberg[1]

[1] NanoPhotonics Centre, Cavendish Laboratory, University of Cambridge, UK
*corresponding author, E-mail: jjb12@cam.ac.uk

Abstract

Coupling between coinage metal 'plasmonic' nano-components generates strongly red-shifted optical resonances combined with intense local light amplification on the nanoscale. I will show how we now create ultralow volume plasmonic cavities trapping light to the atom scale <1nm^3, and are routinely able to watch individual molecules and bonds vibrating. Using DNA origami we couple 1-4 dye molecules together optomechanically, and produce strong-light matter coupling that changes their quantum emission properties. We also watch redox chemistry in real time, watching single electrons shuttle in and out of single molecules, as well as 2D materials confined in the same gap. Prospective applications range from (bio)molecular sensing to fundamental science. I particularly focus on applications to nanomachinery actuation by light.

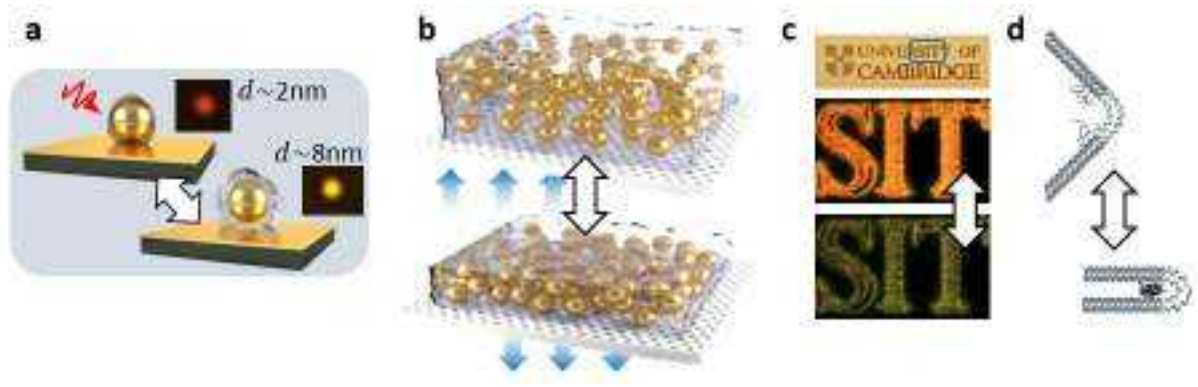


Fig. 1 Reversible nanoactuating systems under light, (a) ANT-on-mirror, (b) active metamaterial, (c) electro-plasmonic pixels, and (d) DNA origami nanomachines.

These concepts, which can be scaled up using bottom-up directed assembly, open up many new possibilities for applications of plasmonics and nano-optics.

Singular plasmonic surfaces and their properties

J.B. Pendry[1]

[1] The Blackett Laboratory, Imperial College London, London SW7 2AZ, UK

E-mail: j.pendry@imperial.ac.uk

Abstract

Plasmonic surfaces derive their properties from their structure. This is especially true when a singularity of some sort is present such as two touching spheres, or a sharp edge. Both these instances and many more give rise to intense concentrations of energy near the singularity. Singularities can be removed using transformation optics to relate properties of the singular structure to those of another structure in a higher dimensional space. The singularity can be regarded as a ‘compacted’, or ‘hidden’ dimension.

Transdimensional Materials for Nanophotonics: From 2D to 3D

Alexandra Boltasseva

School of Electrical & Computer Engineering and Birck Nanotechnology Center, Purdue University, 1205 West State St., West Lafayette, IN 47907, USA
*corresponding author, E-mail: aeb@purdue.edu

Abstract

The field of nanophotonics has recently seen a surge of new materials to address the need for tunable and durable nanophotonic components. In this talk, emerging photonic materials such as transparent conducting oxides, transition metal nitrides (TMNs), transdimensional (ultra-thin) materials (TDMs) and MXenes for photonic devices will be discussed. TDMs and MXenes are promising platforms for achieving actively switchable and tailorable metasurfaces, while TMNs are ideal for robust refractory plasmonic devices. Our recent progress on merging topology optimization with artificial intelligence assisted algorithms for designing photonic metasurfaces will also be covered.

1. Introduction

Due to their exceptional plasmonic properties, noble metals such as, gold and silver, have been the materials of choice for the demonstration of various plasmonic and nanophotonic phenomena. However, noble metals' softness, lack of tunability, and low melting point, along with challenges in thin film fabrication, have prevented the realization of practical plasmonic devices requiring tailorable optical properties and durable metallic nanostructures. In response to these pressing requirements, investigations into new plasmonic materials that meet the need for tunable and robust nanophotonic devices have increased.

It has recently been predicted that as film thicknesses of plasmonic materials approaching the two dimensional (2D) regime can enable unusually strong tailorability of the optical properties. Transitioning from bulk, three dimensional (3D) structures to their 2D counterparts has uncovered truly new physics unattainable with 3D systems. However, the materials optical properties' evolution in the transitional regime between 3D and 2D is still underexplored. The optical and electronic properties of these transdimensional materials (TDMs) which have thicknesses of only a few atomic layers are expected to show unprecedented tailorability, including strong dependences on the film thickness, composition, strain, and surface termination [1]. TDMs are also predicted to show extreme sensitivity to external optical and electrical perturbations [2]. TDMs and 2D materials may enable a variety of promising designs and demonstrations of miniaturized, tunable optical devices, owing to their extraordinary light confinement, tailorability of the optical properties and dynamic tunability.

In addition to tunable plasmonic devices, achieving durable metallic components for harsh environment applications has remained a challenge. Transition metal nitrides, such as titanium nitride (TiN), have emerged as a promising metallic material platform for nanophotonic devices operating at elevated temperatures for energy conversion, harsh environment sensors, and heat-assisted applications due to their refractory nature and remarkable plasmonic properties.

Alongside the development of new tunable and refractory metallic materials for plasmonic metasurfaces, novel approaches, such as topology optimization, have emerged as a successful method for the systematic design of photonic structures. Recently, it has been demonstrated that inverse design problems applied to metasurface and photonic crystal reconstruction can be efficiently solved using topology optimization techniques to obtain significantly improved performance in comparison with those obtained with direct optimization [3]. Combining topology optimization with new material development provides a synergistic approach for designing novel plasmonic metasurfaces.

2. New Materials for Tunable Plasmonics

The optical responses of atomically thin plasmonic films can be engineered by precise control of their structural and compositional parameters. This unique tailorability establishes TDMs as an attractive material for the design of tailorable and dynamically switchable metasurfaces. Due to their epitaxial growth on lattice matched substrates, TiN is an ideal material to investigate the tailorable properties of plasmonic films with thicknesses of just a few monolayers. The optical and electrical properties of smooth, epitaxial, ultra-thin TiN ranging from 2 to 10 nm have been characterized by ellipsometry and Hall measurements [4]. Although the metallicity decreases in smaller thicknesses, the thinnest film (2 nm) still retains a carrier density of 10^{22} cm^{-3} and is plasmonic properties at visible wavelengths (Figure 1). The role of quantum confinement, oxidation, and strain is explored through first principles density functional (DFT) calculations [5]. Gate dependent Hall measurements on a 1 nm film also reveals extreme tunability of the carrier concentration (up to 8.5%).

MXenes, a class of 2D nanomaterials formed of transition metal carbides and carbon nitrides, are yet anotherpromising material platform for tailorable plasmonic metamaterials. They have the general chemical form

$M_{n+1}X_nT_x$, where 'M' is a transitional metal, 'X' is either C or N, and 'T' represents a surface functional group (O, -OH or -F) and are chemically synthesized from a corresponding layered ternary carbides or nitrides phase known as MAX ($M_{n+1}AX_n$) phases [5]. Until now, MXenes have been widely explored in a variety of applications, such as electromagnetic shielding and SERS. However, investigations of MXenes in the context of nanophotonics and plasmonics have been limited leading to this current exploration of MXenes as building blocks for plasmonic and metamaterial devices. We have demonstrated an MXene based broadband plasmonic absorber and a dynamically tunable random laser (Figure 2).

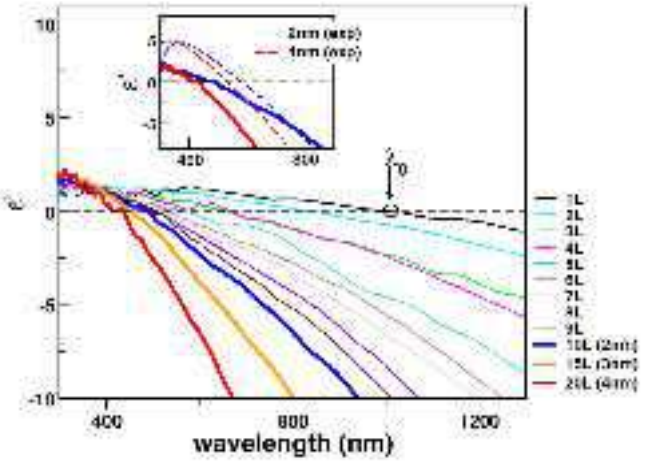


Figure 1: Ab initio calculations for 1 to 20 monolayers of TiN. The inset compares experimental results for 10 and 20 monolayers with theoretical results.

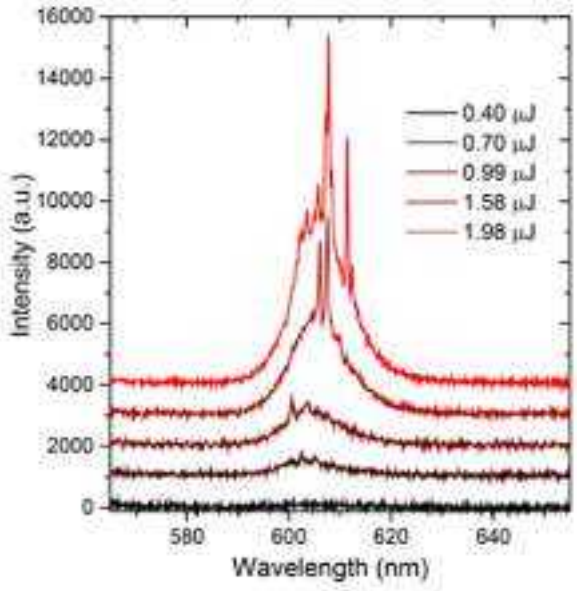


Figure 2: Emission spectra of random laser consisting of monolayer $Ti_3C_2T_x$ nanoflakes and R101 molecules recorded under various pump energies

3. Artificial Intelligence Assisted Photonics

Compared to other inverse-design approaches that require extreme computation power to undertake a comprehensive search within a large parameter space, topology optimization can expand the design space while improving the computational efficiency. We will discuss our studies on implementing deep-learning assisted topology optimization for advanced metasurface design development, focusing on highly efficient thermal emitter/absorber development for thermal-photovoltaics applications. We applied a topology optimization method to determine highly efficient metasurface designs with a non-trivial topology for efficient spectral reshaping of black-body radiation.

4. Conclusions

Ultrathin TiN and MXenes have been explored in the realm of tunable nanophotonics and plasmonics. As the material class and their synthesis techniques continue to mature, applicability in optics along with device performances are also expected to improve further. We have also coupled deep-learning-based techniques with the topology optimization of thermal emitters for TPV applications. The emerging classes of plasmonic materials in conjunction with machine learning assisted design optimization provide exciting opportunities for realizing novel metasurfaces with unprecedented functionalities.

Acknowledgements

This work is financially supported by ONR MURI Grant N00014–13–0649 (random lasing), AFOSR MURI Grant FA9550-14-1-0389 (MXenes) and AFOSR grant FA9550-18-1-0002 (transdimensional materials).

References

[1] A. Manjavacas and F. J. G. de Abajo, "Tunable plasmons in atomically thin gold nanodisks," *Nature Commuications*, 5, 3548 (2014).

[2] I. V. Bondarev and V. M. Shalaev, "Universal features of the optical properties of ultrathin plasmonic films," *Optical Materials Express*, 7(1), 3731–3740 (2017)

[3] D. Sell, et.al., Large-Angle, Multifunctional Metagratings Based on Freeform Multimode Geometries, *Nano Letters*, 17(6) (2017)

[4] D. Shah, H. Reddy, N. Kinsey, V. M. Shalaev, and A. Boltasseva, "Optical Properties of Plasmonic Ultrathin TiN Films," *Advanced Optical Materials*, 5(13) 1700065 (2017).

[5] D. Shah, A. Catellani, H. Reddy, N. Kinsey, V. M. Shalaev, A. Boltasseva, and A. Calzolari, "Controlling the Plasmonic Properties of Ultrathin TiN Films at the Atomic Level," *ACS Photonics,* 5(6) 2816-2824 (2018).

Analog processing with metastructures

Nader Engheta[1]

[1] University of Pennsylvania, 200 South 33rd street, Philadelphia, PA 19104, USA
*corresponding author, E-mail: engheta@ee.upenn.edu

Abstract

In my group we have been developing metamaterials that perform analog computation with waves. In particular, we have designed and tested metastructures that solve integral equations as waves go through them. We have been working on two different platforms for such analog processing: (1) Inhomogeneous metamaterials, and (2) Collections of Mach-Zehnder interferometers (MZIs). In this talk, I will present some of our results and will discuss several relevant research directions currently being explored in my group.

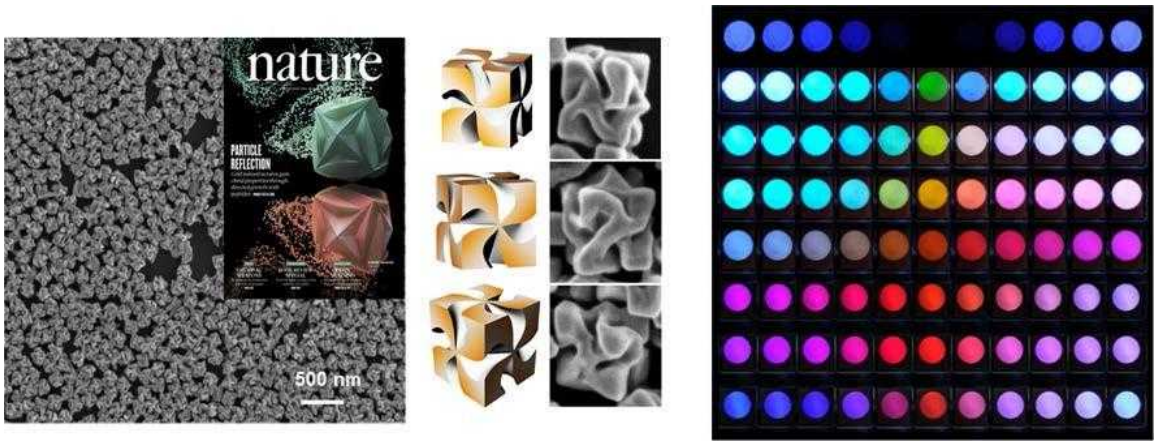
Keynote Lectures

Artificial Chirality Evloution in Micro-/Nano-scale 3D Plasmonic Metamaterials

Junsuk Rho[1,2]

1. *Department of Mechanical Engineering, Pohang University of Science and Technology (POSTECH), Pohang 37673, Korea*
2. *Department of Chemical Engineering, Pohang University of Science and Technology (POSTECH), Pohang 37673, Korea*

Plasmonic chiral metamaterials has attracted significant attention at it provides a new route to intriguing optical properties such as negative refractive index, light polarization filters, and phase modulation. However, the fabrication regarding with limited resolution in conventional synthesis and complexity of asymmetric synthesis pose a major hindrance for further development. In this study, a new class of three dimensional chiral plasmonic nanostructures was successfully fabricated using molecular shape modifiers and crystallographic control of nanoparticle. Previously, we developed three-dimensional chiral metamaterials based on photolithography overlay and electron-beam lithography overlay for terahertz and near-infrared, respectively. We found scaling down them further to visible frequency is extremely difficult. As an alternative solution, we discovered a novel system that characteristic of molecule is transformed into distinctive gold nanoparticle shape. On the basis of this system, chirality transfer between molecular modifier and gold surface allow us to achieve numerous chiral morphologies of gold nanoparticle, named plasmonic helicoids. Particularly, enantiospecific interaction of molecule and high index plane plays pivotal role to provide asymmetric structuring process on the gold surface, forming distinct chiral morphology in single nanoparticle level. One of the representative shapes of helicoid structure showed gammadion-like structure, consisting of four highly curved arms of increasing width, in all six faces of cubic geometry. The unprecedented chiral morphology of plasmonic helicoid has remarkable optical activity (dissymmetry factor ~ 0.2 at 622 nm) even in a randomly dispersed solution, substantiated by direct visualization of macroscopic color transformation. Changes in molecular recognition and growth parameter led to different morphological evolution, and structural alterations provided a straightforward means of tailoring optical response, such as optical activity, handedness, and resonance wavelength. Also, our aqueous phase synthesis is readily scalable without losing exquisite chiral structure at nanoscale. In these aspects, our approach, chirality evolution in single nanoparticle, provides a truly new paradigm and valuable insight for chiral metamaterial fabrication. Such unique fabrication technique will provide the opportunity to achieve the significant step making metamaterials from science to technology.



References

[1] H. Lee et al., "Amino-acid- and peptide-directed synthesis of chiral plasmonic gold nanoparticles," Nature **556**, 360-365 (2018).
[2] G. Yoon et al., "Fabrication of three-dimensional suspended, interlayered and hierarchical nanostructures by accuracy-improved electron beam lithography overlay," Sci. Rep. **7**, 6668 (2017).
[3] S. Zhang et al., "Photo-induced handedness switching in terahertz chiral meta-molecules," Nat. Commun. **3**, 942 (2012).

Computing resonances in nano-photonic devices using Riesz-projection-based methods

Sven Burger[1,2], **Felix Binkowski**[1], **Lin Zschiedrich**[2]

[1]Zuse Institute Berlin, Takustr. 7, 14195 Berlin, Germany
[2]JCMwave GmbH, Bolivarallee 22, 14050 Berlin, Germany

Abstract

Nano-optics and quantum optics setups and devices typically rely on optical structures incorporating resonance effects. Advanced modeling and simulation methods are essential for an effective design of the experimental setups and for the interpretation of the physical results. In this contribution, we review simulation techniques for computing optical resonances. In particular, we point out Riesz-projection-based methods for computing the interaction of light emitters with resonance modes and for computing eigensolutions in dispersive systems.

1. Riesz projection expansion for computing coupling to light emitters

Nano-optical resonators have been demonstrated in various material systems [1, 2], including plasmonic [3] and dielectric structures [4]. Placing point-like sources in the vicinity of such nanoresonators or antennas enables exploration of new regimes of light-matter interaction. For quantifying the interaction, Maxwell's equations can be solved directly to obtain solutions for the electromagnetic field. For a deeper insight into physical properties, an expansion using the eigenmodes of the systems, so-called quasi-normal modes (QNMs), can be used [5, 6]. The situation is depicted schematically in Figure 1. As indicated, the total electromagnetic field caused by any light source can be decomposed to resonance modes of the structure and to nonresonant components.

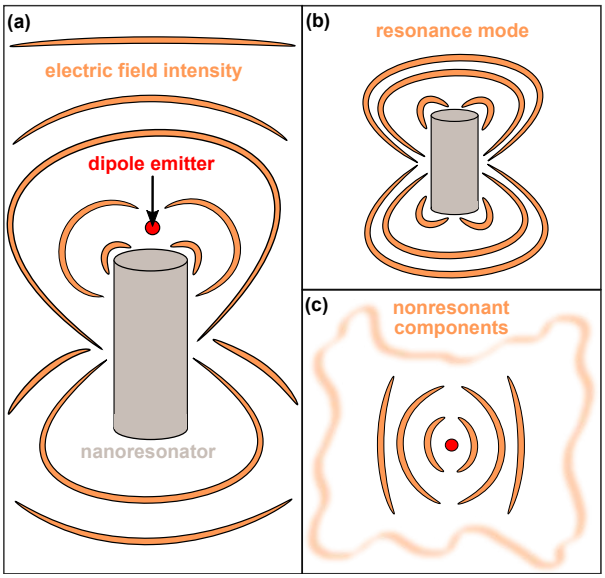


Figure 1: Schematic decomposition of the electromagnetic field caused by a dipole emitter in the vicinity of a nanoresonator. (a) Total electromagnetic field. (b) A resonance mode of the nanoresonator. (c) Nonresonant components of the electromagnetic field. This part includes also the singularity resulting from the dipole source. Reprinted figure with permission from [8], copyright (2018) by the American Physical Society.

However, Riesz projections (RPs), well-known in spectral theory [7], are based on contour integration and provide a powerful means to analyze the spectrum of partial differential operators. RPs can be used to compute QNMs, the coupling of emitters to QNMs, and the coupling to a nonresonant background in an elegant way. Recently, we have presented a theory and a numerical implementation for modeling dispersive light-matter interaction based on RPs [8]. This approach has also been used in an investigation of emitters placed in the small gap between a plas-

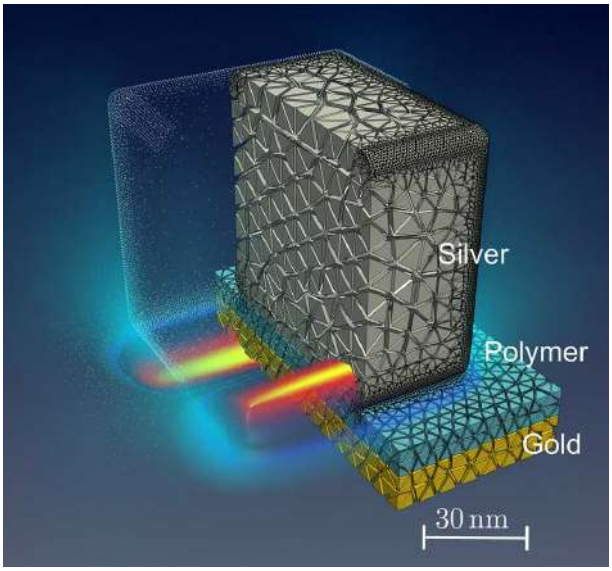


Figure 2: Visualization of the geometry, the finite-element mesh and the electromagnetic field distribution of a plasmonic nanoantenna investigated numerically in a recent benchmark [12].

monic nanoantenna and a metal surface [9]. In particular, it was studied under which conditions the strong coupling regime can be reached in such systems.

2. Riesz-projection-based method for computing photonic resonances

In a recent benchmark, a RP-based method for the computation of photonic resonances [10], as well as a specific auxiliary field approach [11], have been compared with other methods for approaching this simulation task [12]. We have used a finite-element based implementation (JCMsuite). Figure 2 shows a visualization of one of the benchmark problems: a silver cube with rounded corners placed on a thin polymer spacer above a gold substrate. An optical resonance with a strongly localized field in the polymer spacer material is also shown. Experimentally, such setups have been used to demonstrate large enhancements of light emission from optical sources placed in the spacer layer. In the benchmark, a general agreement of the results from most of the methods was demonstrated. The RP-based algorithm was shown to belong to the group of methods exhibiting high performance regarding accuracy and convergence for the computation of the eigenfrequency, quality factor, and mode volume of the resonance mode.

Acknowledgement

This project has received funding from the DFG Cluster of Excellence MATH+ (projects OT9, AA4-6). This work is partially funded through the project 17FUN01 "BeCOMe" within the Programme EMPIR. The EMPIR initiative is co-founded by the European Union's Horizon 2020 research and innovation program and the EMPIR Participating Countries. This project has received funding from the European Union's Horizon 2020 research and innovation programme under the Marie Sklodowska-Curie grant agreement No 675745 (MSCA-ITN-EID NOLOSS).

References

[1] K. J. Vahala, "Optical microcavities," *Nature* 424, 839 (2003).

[2] P. Bharadwaj, B. Deutsch, and L. Novotny, "Optical Antennas," *Adv. Opt. Photon.* 1, 438 (2009).

[3] V. Giannini, A. I. Fernández-Domínguez, S. C. Heck, and S. A. Maier, "Plasmonic Nanoantennas: Fundamentals and Their Use in Controlling the Radiative Properties of Nanoemitters," *Chem. Rev.* 111, 3888 (2011).

[4] A. I. Kuznetsov, A. E. Miroshnichenko, M. L. Brongersma, Y. S. Kivshar, and B. Luk'yanchuk, "Optically resonant dielectric nanostructures," *Science* 354, aag2472 (2016).

[5] M. Zworski, "Resonances in physics and geometry," *Notices Amer. Math. Soc.* 46, 319 (1999).

[6] P. Lalanne, W. Yan, K. Vynck, C. Sauvan, and J.-P. Hugonin, "Light interaction with photonic and plasmonic resonances," *Laser Photonics Rev.* 12, 1700113 (2018).

[7] P. Hislop and I. Sigal, *Introduction to spectral theory. With applications to Schrödinger operators.* Springer, New York (1996).

[8] L. Zschiedrich, F. Binkowski, N. Nikolay, O. Benson, G. Kewes, and S. Burger, "Riesz-projection-based theory of light-matter interaction in dispersive nanoresonators," *Phys. Rev. A* 98, 043806 (2018).

[9] G. Kewes, F. Binkowski, S. Burger, L. Zschiedrich, and O. Benson, "Heuristic modeling of strong coupling in plasmonic resonators," *ACS Photonics* 5, 4089 (2018).

[10] F. Binkowski, L. Zschiedrich, and S. Burger, "A riesz-projection-based method for nonlinear eigenvalue problems," arXiv:1811.11624 (2018).

[11] F. Binkowski, L. Zschiedrich, and S. Burger, "An auxiliary field approach for computing optical resonances in dispersive media," *J. Eur. Opt. Soc.-Rapid*, in production (2019).

[12] P. Lalanne, W. Yan, A. Gras, C. Sauvan, J.-P. Hugonin, M. Besbes, G. Demesy, M. D. Truong, B. Gralak, F. Zolla, A. Nicolet, F. Binkowski, L. Zschiedrich, S. Burger, J. Zimmerling, R. Remis, P. Urbach, H. T. Liu, and T. Weiss, "Quasinormal mode solvers for resonators with dispersive materials," arXiv:1811.11751 (2018).

Utilizing plasmonic hot electrons for bridging top-down and bottom-up nanofabrication and for sub-wavelength absorption imaging

Stefan A Maier[1]

[1]Chair in Hybrid Nanosystems, Nanoinstitute Munich, Faculty of Physics, Ludwig-Maximilians-Universität München, 80539 München, Germany
* E-mail: Stefan.Maier@physik.uni-muenchen.de

Abstract

We demonstrate a novel approach towards the combination of top-down and bottom-up nanofabrication, based on controlled modification of the surface functionalization of plasmonic nanoantennas facilitated by hot electron bond cleaving.

Results

Plasmon decay in sub-wavelength metallic nanostructures leads to the generation of energetic, "hot" electrons, which can catalyze chemical reactions at the nanoparticle's surface. Here we demonstrate two exciting applications of this phenomenon.

Firstly, we show how top-down nanofabrication of Au nanostructures ("nanoantennas") can be combined with bottom-up self-assembly of colloidal units, thereby generating hybrid structures that bridge both fabrication methodologies [1]. This is achieved via controlled cleaving of thiol bonds on molecularly functionalized nanoantennas, allowing for refunctionalization with a second molecular unit (see picture) that links to the colloidal system of choice. Exploiting polarization and wavelength degrees of freedom hence enables to assemble the colloidal units to selected parts of the nanoantenna.

Secondly, we demonstrate how the thiol-bond cleaving can be utilized to map absorption sites in complex metallic nanostructures, utilizing fluorescence-based super-resoluation localization microscopy on DNA-functionalized Au nanoantennas [2]. Spatially localized decay of hot electrons leads to thiol-bond cleaving only where optical absorption has occurred, allowing for spatial identification of absorption sites via monitoring changes in fluorescence.

These two examples demonstrate avenues to exploit plasmonic hot electrons beyond catalysis and Schottky-based photodetection. In particular, the combination of top-down and bottom-up nanofabrication facilitated by this approach should allow new approaches towards metasurface creation combining both nanoantennas and colloidal particles.

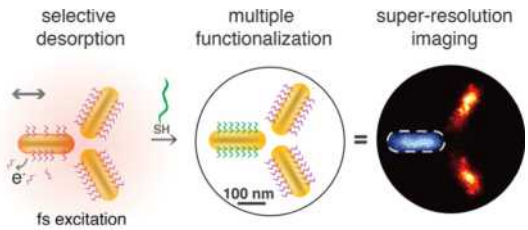


Figure 1. Thiol-bond cleaving via plasmonic hot electrons allows selective modification of nanoantenna surface functionalization

References

[1] Simoncelli, S., Li, Y., Cortés, E., & Maier, S.A., ACS Nano 12, 2184 (2018)

[2] Simoncelli, S., Li, Y., Cortés, E., & Maier, S.A., Nano Letters 18, 3400 (2018)

Publishing in *Nature* journals

Rachel Won

Nature Photonics, Nature Publishing Group,
The MacMillan Campus, 4 Crinan Street, London N1 9XW, United Kingdom.
E-mail: r.won@nature.com

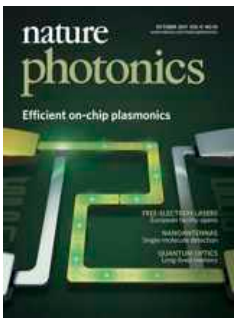
Abstract

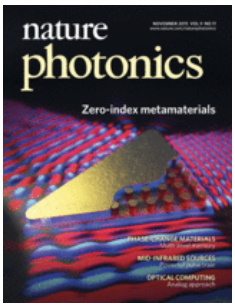
This talk introduces you to all the existing and new journals in the family of *Nature*, and covers the detailed information and guidelines on scientific manuscript preparation and submission.

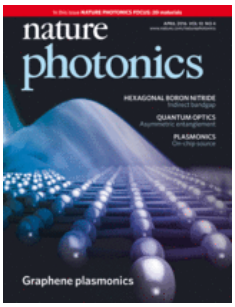
1. Introduction

Launched in January 2007, *Nature Photonics* is a monthly journal dedicated to optics and photonics that publishes top-quality, peer-reviewed research in all areas of light generation, manipulation and detection. Coverage extends from research into the fundamental properties of light and how it interacts with matter through to the latest designs of photonic devices and emerging applications that exploit photons. Both fundamental optical physics and applied photonics technologies, such as nonlinear optics, ultrafast photonics, quantum optics, plasmonics, metamaterials, nanophotonics, imaging, optical communications, optical storage, photovoltaics and optical communications, are covered. For more information: **https://www.nature.com/nphoton.**

This talk, although with an emphasis on *Nature Photonics*, will introduce you to all the existing and new *Nature* journals, and cover the detailed information and guidelines on scientific manuscript preparation and submission. Also presented is an overview on the editorial and peer-review processes in all *Nature* journals. You will get to know what editors seek, how to write a good cover letter and a good scientific paper, the peer review process that your paper goes through and how to make an appeal. More importantly, you will find out how you can contribute to the journals apart from publishing your research.







Optical imaging and metrology with nanoscale resolution

Nikolay I. Zheludev

University of Southampton UK and Nanyang Technological University, Singapore

*corresponding author, E-mail: niz@orc.soton.ac.uk

Abstract

We introduce a new free space label free imaging paradigm and metrology technique that exploit optical singularities in super-oscillatory optical fields. Imaging resolution beyond λ/100 and displacement metrology with resolving power of λ/800 have been demonstrated.

Electrical generation of surface plasmons with resonant nanoantennas

C. Zhang[1*], J.P. Hugonin[1], A.L. Coutrot, C. Sauvan[1], F. Marquier[2], J.J. Greffet[1]

1. Laboratoire Charles Fabry, Institut d'Optique Graduate School, CNRS, Université Paris-Saclay, 91127 Palaiseau, France
2. Laboratoire Aimé Cotton, Ecole Normale Supérieure de Paris-Saclay, CNRS, Université Paris-Saclay, 91405 Orsay, France

*corresponding author, E-mail: jean-jacques.greffet@institutoptique.fr

Abstract

We report the design, fabrication and characterization of antennas to emit surface plasmons by inelastic tunneling. The antenna controls the emission spectrum and enhance the emission efficiency by four orders of magnitude. We measure an emitted optical power of 10pW, four orders of magnitude larger than the power emitted by a scanning tunnelling tip. We introduce a theoretical model of the antenna in good agreement with the results.

1. Introduction

Surface plasmon polaritons are mixed electronic and electromagnetic modes propagating along the interface between a metal and a dielectric. The corresponding electromagnetic field can be confined to nanometer scale and has a decay time on the order of 10 fs so that a new generation of devices can be designed. An important limitation of surface plasmon is that in most cases, they are optically excited by a diffraction limited beam. In order to fully benefit from the field confinement, it is necessary to generate surface plasmon polaritons in the near field with a subwavelength device. This can be done using electronic inelastic tunneling through a tunnel junction.

Light emission by electrons tunneling inelastically through a planar tunnel junction was discovered by Lambe and McCarthy[1]. This process is rather inefficient with a typical efficiency on the order of one photon per a million electrons. Furthermore, light emission by inelastic tunneling (LEIT) has important advantages. Firstly, LEIT is intrinsically fast[2]. The fundamental limit is given by the tunneling time which is on the order of eV/h where e is the electron charge, V the applied voltage on the order of 1V and h is Planck's constant yielding a time limit on the order of 4 fs. Secondly, LEIT can be a highly localized source. The source current density can be confined in a nanoantenna or in a metallic tip enabling electromagnetic excitation localized at the nanometer scale. Both photon and plasmon emission has been reported using scanning tunneling microscope tips[3,4]. More recently, surface plasmon emission has been reported with metallic nanostructures[5]. Hence, antenna surface plasmon emission by inelastic tunneling (ASPEIT) appears to be a suitable candidate for ultrafast and highly localized plasmon emission.

However, a number of issues need to be addressed before ASPEIT can become a practical source. It is required to control the emission spectrum, the angular emission pattern and to increase significantly the emission efficiency. In order to tackle these issues, resonant nanoantennas can be used. Photon emission in the visible by electrically driven optical antennas has been reported demonstrating a spectral control of the emission[6] and also a directional control[7]. So far, surface plasmon emission by inelastic tunneling has received comparably less attention. It was proposed[8] to use antennas to engineer the plasmon mode in order to increase the efficiency and to control the emission spectrum.

2. Results

Here, we report the design, fabrication and characterization of nanopatch antennas to emit surface plasmons, schematically shown in Fig. 1(a). The electrical excitation of propagating SPP (PSPP) can be launched along an air/Al interface, shown in Fig. 1(b). We design the antennas in order to control the emission frequency and we observe a narrow emission spectrum with an enhancement of the electron to plasmon conversion efficiency over three orders of magnitude.

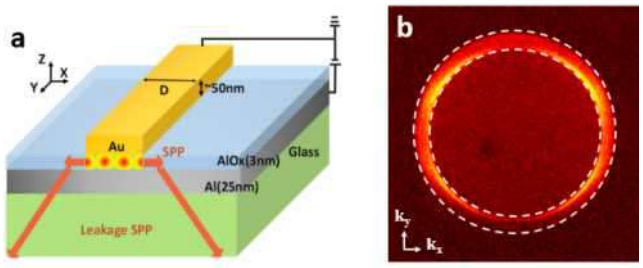


Figure 1: (a) Schematic of the ASPEIT device consisting of an Au nanopatch antenna on an Al film with 3nm of AlOx layer in between. (b) Electroluminescence angular far-field distribution through the substrate. The inner dashed circle corresponds to $k=\omega/c$, and the outer dashed circle corresponds to $k=1.3k_0$; the yellow bright ring indicates the plasmon wave vector at the air/Al interface.

References

[1] Lambe, J. and S.L. McCarthy, "Light Emission from Inelastic Electron Tunneling", *Phys. Rev. Lett.* **37,** 923 (1976)

[2] Février, P. and J. Gabelli, ″ Tunneling time probed by quantum shot noise ", *Nature Communications*, **9**, 4940 (2018)

[3] Bharadwaj, P., A. Bouhelier, and L. Novotny, " Electrical excitation of surface plasmons ", *Phys. Rev. Lett*., **106**, 226802 (2011)

[4] Berndt, R., et al., "Photon emission at molecular resolution induced by a scanning tunneling microscope ", *Science,* **262**, 1425 (1993)

[5] Du, W., et al., " Highly efficient on-chip direct electronic–plasmonic transducers", *Nature Photonics*, **11**, 623 (2017)

[6] Kern, J., et al., " Electrically driven optical antennas", *Nature Photonics*, **9**,582 (2015)

[7] Gurunarayanan, S.P., et al., " Electrically driven unidirectional optical nanoantennas", *Nano Letters*, **17**, 7433 (2017)

[8] Bigourdan, F.,et al.," Nanoantenna for Electrical Generation of Surface Plasmon Polaritons", *Phys. Rev. Lett*. **116**, 106803 (2016)

Optical Field Enhancement in the Nano-Patch Antenna for Lasing, Nonlinear Optics, and Other Nanophotonic Applications

David R. Smith[1,*], Patrick Bowen[1]

[1]Center for Metamaterials and Integrated Plasmonics and Department of Electrical and Computer Engineering, Duke University, Durham, North Carolina, USA
*corresponding author, E-mail: drsmith@ee.duke.edu

Abstract

The optical nanopatch antenna consists of a metal, planar nanoparticle spaced nanometers from a metal film. For symmetric nanoparticles (e.g., cubes or disks), semi-analytic expressions can be obtained for all relevant optical scattering properties, useful for describing such phenomena as perfect absorption, bistability, enhanced fluorescence and lasing. These analytical expressions enable the nanopatch system to be rapidly optimized for a wide variety of nanophotonic applications. We review the nanopatch antenna and discuss its role as a novel photonic device.

1. Introduction

The nanopatch geometry is illustrated in Fig. 1, which shows a periodic array of nanopatch antennas deposited on a thin insulating layer above a metallic film. As is well-known in plasmonics, two closely spaced, coupled nanoparticles (a *dimer*) will support a plasmon resonance in which the optical field between the nanoparticles can be enhanced by two orders of magnitude or more. This same enhancement can be achieved by a nanoparticle interacting with its electromagnetic image formed in a nearby conducting layer.

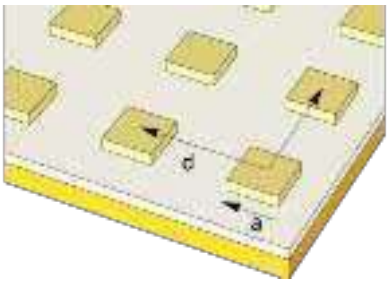


Figure 1: Illustration of an array of nanopatch antennas, in this case metal nanoparticles with square cross-section deposited on an insulating layer a distance h above a metal film.

While the enhancement associated with a dimer and that between a nanoparticle and its image are similar, the ease of fabrication associated with the nanopatch geometry makes it a nearly ideal platform to study enhancement effects. With planar deposition techniques, the insulating layer can be precisely controlled to sub-nanometer dimensions, enabling the effective gap between nanoparticle and image to be carefully varied and optimized. In addition, by using colloidal methods to deposit the nanoparticles, time-consuming lithography can be avoided, and large surface areas patterned.

The nanoscale region between the nanoparticle and film where the fields are enhanced can be understood as a leaky cavity with moderate quality (Q-) factor (usually on the order of 10-30). While the Q-factor is quite low, the very small effective cavity volume makes the Q/V ratio large in comparison with other nano- and micro-cavity formats. This Q/V parameter is important for many quantum optical phenomena, including enhanced fluorescence and lasing, so that despite the low Q (arising from both radiative and resistive losses), plasmon nanocavities can be used to potentially achieve the strong coupling needed in many quantum optical devices.

2. Modeling the Nanopatch

The region between the planar nanoparticle and metal film of a nanopatch effectively behaves as a resonant cavity, with cavity modes closely resembling those corresponding to two planar electric conductors bounded by magnetic conducting walls. These modes can be found by solving a standard boundary value problem, including the plasmonic responses of the nanoparticle and metal film. The total field within the nanocavity region can then be expressed as an expansion over the cavity modes, $\mathbf{E}_\mu(\mathbf{r})$, or [1]

$$\mathbf{E}(\omega, \mathbf{r}) = \sum_\mu e_\mu(\omega)\mathbf{E}_\mu(\mathbf{r}). \quad (1)$$

Here, the cavity modes are lossless, which requires assuming the metal is lossless and that the boundary around the insulating region is terminated in a perfect magnetic conductor. Radiative and resistive losses are then taken into account via a perturbation approach. The coupling coefficients, $e_\mu(\omega)$, depend on the form of the excitation field and can be determined using coupled mode theory. For a plane wave incident on the nanopatch, the magnetic field incident on the surface of the gap between nanoparticle and film can be viewed as an effective electric current density source $\mathbf{K}_e = \hat{n} \times \mathbf{H}_{inc}$ that drives the cavity modes. The coupling coefficients can then be derived as

$$e_\mu(\omega) = -\frac{i\omega}{\omega_\mu^2-\omega^2-i\omega_\mu^2/Q_\mu}\cdot\frac{\int \mathbf{K}_e\cdot\mathbf{E}_\mu^* dS}{\int \varepsilon_0|\mathbf{E}_\mu|^2} \quad (2)$$

where the mode-dependent Q-factor, Q_μ, can be determined using a perturbative approach.

The fields scattered from the patch result from effective magnetic currents excited on the gap surface. If the total electric field at the gap surface is known, then approximately $\mathbf{K}_m = (1-r_{\mathrm{TM}})\mathbf{E}\times\hat{n}$. From these effective surface currents, an effective dipole moment can be found from $i\omega\mu_0\mathbf{m} = \int_{gap}\mathbf{K}_m dS$, from which an effective polarizability is obtained:

$$\alpha_\mu = \frac{4hc^2(1-r_{\mathrm{TM}})^2}{\omega_\mu^2-\omega^2-i\omega_\mu/Q_\mu} \quad \mu \text{ odd}. \quad (3)$$

While Eq. 3 is simplified for an individual nanoparticle much smaller than the wavelength, the general form provides the basis for obtaining accurate analytical expressions for a wide variety of potential metasurface applications.

3. Examples

Once having obtained the complete scattering solution for a single nanopatch, the properties of arrays of nanopatches—or nanopatch metasurfaces—can be readily determined [2]. The closed form expressions that emerge for a variety of nanopatch surface applications provide key insights that guide design and allow performance metrics to be predicted. Two examples are summarized below.

3.1. Reflectance of a Nanopatch Array

The reflectance from a nanopatch array can be determined by summing over the contributions from radiating effective magnetic dipoles at each nanopatch location. Near the fundamental resonance of the nanopatch, the reflectivity can be readily obtained as

$$r = r_{\mathrm{TM}} + \frac{i4h(c^2/d^2)(1-r_{\mathrm{TM}})^2}{\omega^2-\omega_\mu^2+i\omega_\mu/Q_\mu}, \quad (4)$$

where normal incidence is assumed (so that $r_{\mathrm{TM}}\approx -1$). The radiative Q-factor can be calculated as

$$Q_r = \frac{kd^2}{2h|1-r_{\mathrm{TM}}|^2}. \quad (5)$$

As a simple application, the above formulas can be used to design a nanopatch perfect absorbing surface. When the nanopatches are driven near their resonance, Eq. 4 reduces to

$$r = r_{\mathrm{TM}} + \frac{(1-r_{\mathrm{TM}})^2}{|1-r_{\mathrm{TM}}|^2}\frac{2Q_\Omega}{Q_r+Q_\Omega}, \quad (6)$$

where we have used $Q_\mu^{-1} = Q_r^{-1} + Q_\Omega^{-1}$. Assuming the metal film has a reflectance close to $r_{\mathrm{TM}} = -1$, Eq. 6 shows that perfect absorption occurs when the Ohmic losses are equal to the radiative losses. Using this condition, nanopatch surfaces with near zero reflectance can be designed.

3.2. Bistability in a Nonlinear Nanopatch Array

If the gap region between the nanoparticle and film has a nonlinear polarizability, we can define a nonlinear current density of the form $\mathbf{J}_{nl} = i\omega\mathbf{P}_{nl}$, which then appears as an additional volume source term in Eq. 2. Assuming the nanopatch has width a, the total current density then has the form

$$\mathbf{J} = i\omega\mathbf{P}_{nl} + 2(\mathbf{H}_{inc}\times\hat{n})[\delta(x)+\delta(x+a)]. \quad (7)$$

Inserting the above current density into Eq. 2 leads to

$$e_\mu(\omega) = \frac{\omega^2}{\int\varepsilon_0|\mathbf{E}_\mu|^2}\frac{\int \mathbf{P}_{nl}\cdot\mathbf{E}_\mu^* - i8\omega H_0/(\varepsilon_0 d\tilde{E})}{\omega_\mu^2-\omega^2-i\omega_\mu^2/Q_\mu}. \quad (8)$$

Assuming a $\chi^{(3)}$ nonlinearity, we have

$$\mathbf{P}_{nl}(\mathbf{r}) \approx \frac{3\varepsilon_0\chi^{(3)}}{4}e_\mu|e_\mu|^2\mathbf{E}_\mu(\mathbf{r})|\mathbf{E}_\mu(\mathbf{r})|^2. \quad (9)$$

Since the electric field of the fundamental mode in the gap has the form $\mathbf{E}_\mu = \tilde{E}\cos(\mu\pi x/d)\,\hat{z}$, the above equations can be combined to yield the nonlinear equation

$$x_\mu\left[\omega_\mu^2 - i\omega_\mu^2/Q_\mu - \omega^2\left(1+\phi|x_\mu|^2\right)\right] = -8\omega^2 Z_0 H_0/(kd). \quad (10)$$

where $x_\mu = e_\mu\tilde{E}$, $\phi = 9\chi^{(3)}/16$, and Z_0 is the impedance of free space.

For a given excitation, the roots of Eq. 10 can be found and thus the effective polarizabilities of each nanopatch. Summing over these scattering dipoles yields a nonlinear reflectivity that exhibits bistability.

4. Conclusion

We have summarized the dipole approach to analyzing nanopatch metasurfaces, in which the polarizability of each nanopatch is computed using coupled mode theory. The accuracy of this basic approach can be improved by including additional effects, such as interactions among the nanopatches (coupled dipoles) as well as coupling of the nanopatches to surface plasmons. In addition, the expansion of Eq. 2 can be made in quasi-normal modes, which capture the Ohmic losses in a more natural and appropriate manner. The quasi-normal mode expansion is of particular relevance for predicting quantum optical phenomena, such as lasing and strong coupling, where obtaining accurate accounting of losses is crucial. Coupled-mode theory combined with coupled dipoles provides a foundation for functional metasurface design, particularly relevant for the co-design of tailored reflectance combined with enhancement effects.

Acknowledgements

This work was supported by the Air Force Office of Scientific Research (FA9550-18-1-0187).

References

[1] P. T. Bowen, D. R. Smith, Coupled-mode theory for film-coupled plasmonic nanocubes, *Phys. Rev. B* 90: 195402, 2014.

[2] P. T. Bowen, A. Baron, D. R. Smith, Theory of patch-antenna metamaterial perfect absorbers, *Phys. Rev. A* 93: 063849, 2016.

Organic-inorganic Lead Halide Perovskite for High Efficiency Energy Conversion

Nam-Gyu Park*

School of Chemical Engineering, Sungkyunkwan University, Suwon 16419, Korea

*corresponding author, E-mail: npark@skku.edu

Abstract

Since the first report on the high efficiency, stable solid-state perovskite solar cell (PSC) in 2012 by our group[1], following seed work on perovskite-sensitized liquid junction solar cells in 2011 [2], PSC demonstrated its power conversion efficiency (PCE) over 24% as of March, 2019. According to Web of Science, publications on PSC have been increased exponentially since 2012 and total number of publications reaches over 12,000, which is indicative of a paradigm shift in photovoltaics. Although small area cell exhibited superb efficiency surpassing the performance of thin film technologies, scale-up technology is required toward commercialization. In addition, further higher efficiency toward Shockley–Queisser limit of 31% based on bandgap of 1.6 eV is required in parallel. In this talk, the advent of solid state PSC is briefly introduced, which is followed by progress of PSC in terms of materials and devices. Issues in PSC such as current-voltage hysteresis, control of recombination and stability are also discussed based on doping approach, interface modification using post-treatment and additive engineering [3-6]. For scaling up, large-area coating technologies on perovskite cluster embedded coating solution and D-bar coating process are discussed [7]. Bi-facial stamping method was developed for not only scale-up technique but also interface modification and low-temperature phase stabilization [8]. Commercially available perovskite powders were developed using precipitate method at ambient condition. With our perovskite powder, power conversion efficiency over 22% was reproducibly achieved. Recent advancements using organic-inorganic lead halide perovskites in X-ray imaging [9] and light emitting diode [10] are introduced.

Acknowledgements

This work was supported by the National Research Foundation of Korea (NRF) grants funded by the Ministry of Science, ICT Future Planning (MSIP) of Korea under contracts NRF-2012M3A6A7054861 and NRF-2014M3A6A7060583 (Global Frontier R&D Program on Center for Multiscale Energy System), NRF-2016M3D1A1027663 and NRF-2016M3D1A1027664 (Future Materials Discovery Program) and NRF-2015M1A2A2053004 (Climate Change Management Program).

References

[1] H.-S. Kim, C.-R. Lee, J.-H. Im, K.-B. Lee, T. Moehl, A. Marchioro, S.-J. Moon, R. Humphry- Baker, J.-H. Yum, J. E. Moser, M. Gratzel, N.-G. Park, Lead iodide perovskite sensitized all-solid-state submicron thin film mesoscopic solar cell with efficiency exceeding 9%, *Scientific Reports*, 2, 591 (2012)

[2] J.-H. Im, C.-R. Lee, J.-W. Lee, S.-W. Park, N.-G. Park, 6.5% efficient perovskite quantum-dot-sensitized solar cell, *Nanoscale*, 3, 4088 (2011)

[3] J.-H. Im, I.-H. Jang, N. Pellet, M. Gratzel., N.-G. Park, Growth of $CH_3NH_3PbI_3$ cuboids with controlled size for high-efficiency perovskite solar cells, *Nature Nanotechnology*, 9, 927-932 (2014)

[4] N. Ahn , D.-Y. Son , I.-H. Jang, S. M. Kang, M. Choi, N.-G. Park, Highly Reproducible Perovskite Solar Cells with Average Efficiency of 18.3% and Best Efficiency of 19.7% Fabricated via Lewis Base Adduct of Lead(II) Iodide, *J. Am. Chem. Soc*., 137, 8696–8699 (2015)

[5] J.-W. Lee, H.-S. Kim, N.-G. Park, Lewis Acid–Base Adduct Approach for High Efficiency Perovskite Solar Cells, *Acc. Chem. Res*., 49, 311–319 (2016)

[6] D.-Y. Son, J.-W. Lee, Y. J. Choi, I.-H. Jang, S. Lee, P. J. Yoo, H. Shin, N. Ahn, M. Choi, D. Kim, N.-G. Park, Self-formed grain boundary healing layer for highly efficient CH3NH3PbI3 perovskite solar cells, *Nature Energy*, 1, 1-8, (2016)

[7] D.-Y Jeong et al., Perovskite Cluster-Contained Solution for Scalable D-bar Coating Toward High Throughput Perovskite Solar Cells. *ACS Energy Lett*., accepted.

[8] Y. Zhang, S.-G. Kim, D. Lee, H. Shin, N.-G. Park. Bi-facial Stamping for High Efficiency Perovskite Solar Cells. *Energy & Environ. Sci*. 12, 308-321 (2019)

[9] Y. C. Kim, K. H. Kim, D.-Y. Son, D.-N. Jeong, J.-Y. Seo, Y. S. Choi, I. T. Han, S. Y. Lee, N.-G. Park, Printable organometallic perovskite enables large-area, low-dose X-ray imaging, *Nature,* 550, 87-91 (2017)

[10] J.-W. Lee, Y. J. Choi, J.-M. Yang, S. Ham, S. K. Jeon, J. Y. Lee, Y.-H. Song, E. K. Ji, D.-H. Yoon, S. Seo, H. Shin, G. S. Han, H. S. Jung, D. Kim, N.-G. Park, In-Situ Formed Type I Nanocrystalline Perovskite Film for Highly Efficient Light-Emitting Diode, *ACS Nano*, 11, 3311-3319 (2017)

Tracking ultrafast light-heat conversion in plasmonic nano-assemblies

Andrea Mazzanti[1], Zhijie Yang[2], Marie-Paule Pileni[3], Giuseppe Della Valle[1]and Giulio Cerullo[1*]

[1]Dipartimento di Fisica, Politecnico di Milano, Piazza L. da Vinci 32, I-20133 Milano (IT)
[2]Université Paris Diderot, Sorbonne Paris Cité, ITODYS, UMR 7086 CNRS, 15 Rue J-A de Baïf, 75205 Paris, Cedex 13 (FR).
[3]CEA/IRAMIS, CEA Saclay F-91191 Gif-sur-Yvette (FR).
*corresponding author, E-mail: giulio.cerullo@polimi.it

Abstract

We investigate the photothermal properties of water-soluble hybrid organic-inorganic Au nanocrystal assemblies, comprising plasmonic nanocrystals embedded in a matrix of organic ligands, via a combination of ultrafast optical spectroscopy and semi-classical numerical modeling. We observe a complex transient optical response, with picosecond electron-phonon equilibration followed by heat release to the matrix on the 100-ps timescale. Our results indicate that assemblies operate as efficient nanoheaters exploiting the high absorption from the individual nanocrystals, enabled by the dilution of the inorganic phase.

1. Introduction

The last decade has witnessed an explosive growth of interest for the photothermal properties of nanostructures, both for fundamental and applied aspects [1]. Examples are photothermal therapy for cancer, in which light, following irradiation of nanocrystals, is converted to cytotoxic heat in order to selectively kill cancer cells and minimize the invasive injury to normal tissues [2, 3], as well as novel solar photodevices for water vapour generation [4] and direct light-driven desalination [5]. Particularly interesting in this respect are nanocrystal assemblies, as the interaction between nanocrystals and the heat transfer though molecular linkers can, in principle, strongly change their thermal properties and, subsequently, the dynamics of the photo-thermal energy conversion. Recently, some of the authors synthesized hybrid organic-inorganic nanoassemblies that are stable in water, paving the way to real-world *in vivo* applications [6]. These structures consist of hydrophobic inorganic nanocrystals that self-assemble in fcc structures thanks to the presence of hydrophilic organic materials.

Here we study the specific heat release properties of hundred-nm size Au clustered structures, ferrite (Fe_3O_4) supraparticles and Au/ferrite eggs, i.e. $(Fe_3O_4)Au_{13}$ assemblies trapped in ferrite colloidosomes. With the Au clustered structure we find that the hierarchical nanostructuring translates into a hierarchical mechanism for the energy flow that starts with the absorption of light in the metal phase, thanks to plasmonic resonances occurring at the individual nanocrystal level, and leads to the heating of the matrix ligands. The latter process, which we reveal by optical means thanks to thermo-optical effect, turns out to be comparatively fast because of the homogeneous distribution of the individual nanocrystals heaters in the assembly enabled by their periodic arrangement. A similar behavior is observed in Fe_3O_4 supraparticles and $(Fe_3O_4)Au_{13}$ nanoeggs on the same time scale. This indicates that the light-heat conversion in these kind of nanomaterials is governed by a universal mechanism that relies on the intrinsic hybrid composition of the assembly involving optically-active inorganic nanocrystals and a matrix of organic ligands with relatively high heat capacity, embedded in a water environment [7].

2. Results and discussion

We studied clustered structures of Au nanocrystals with r = 2.75 nm radius coated with 1-octadecane-thiol, forming spherical assemblies with 160±50 nm diameter. The samples were excited by 100-fs pulses at 400 nm and probed by broadband white-light pulses covering the visible and the near-infrared (NIR) range. Figure 1A and 1B show differential transmission (ΔT/T) spectra, recorded as a function of probe wavelength and delay, in the visible and NIR, respectively. On the initial time scale of ten picoseconds, the transient signal resembles the typical ΔT/T map recorded for plasmonic nanoparticles. Cross sections at early time delays (black and red traces in the bottom panels of Figs. 1A-1B) show the characteristic transient spectra of isolated nanocrystals which are dominated by shift and broadening of the plasmonic resonances. These spectra exhibit a decay constant of few ps, that is the timescale of electron-phonon scattering in noble metals. On longer times scales, surprisingly, the ΔT/T of Au clustered structures exhibits very distinct features: instead of a monotonic decrease over time, we observe the build-up of a positive signal which is red-shifted by about 100 nm (blue and magenta traces in the bottom panels of Figs. 1A and 1B) as compared to the early spectra.

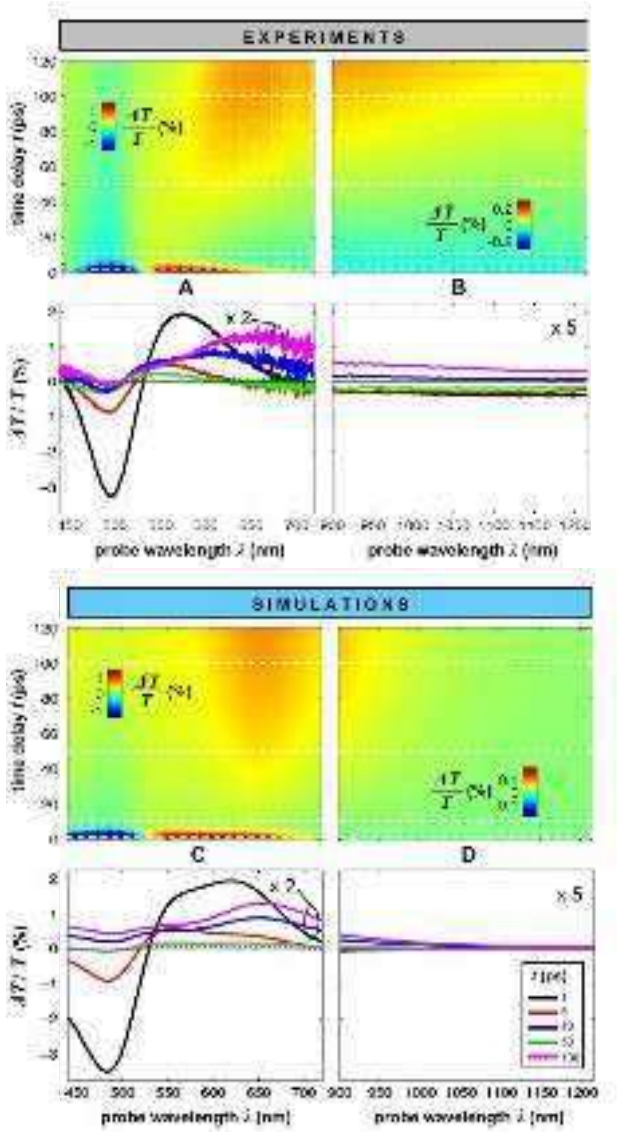


Figure 1: Measured (A)-(B) and simulated (C)-(D) ΔT/T maps and cross-sections at selected time delays for the water dispersed Au clustered structures. The dotted curve in (C)-(D) is the result of a simulation which neglects account thermo-optical effect in the organic matrix.

To understand the unexpected transient optical response on the 100-ps timescale, we developed a model to simulate the optical experiments. The model combines finite element method (FEM) electromagnetic simulations of the optical response of the supracrystal to a semi-classical four-temperature model to describe the non-equilibrium optical response. The model considers the energy density of the out-of-equilibrium electrons in the metal nanocrystals, the temperature of thermalized electrons in the metal, the temperature of the metal lattice and the temperature of the organic subsystem embedding the nanocrystals. Using a negative thermooptic coefficient of the organic matrix, the model reproduces the experimental results very accurately (see panels C and D of Fig. 1).

According to our model, the delayed build-up of the ΔT/T signal on the few hundred ps time scale is the signature of the final step in the light-heat conversion process, that ultimately results in the heating of the matrix of organic ligands. As such, this dynamical feature in the transient optical response is expected to be an intrinsic property of any hybrid assembly of hydrophobic nanocrystals, regardless the peculiar nature (i.e. plasmonic or not) of their building blocks, as observed in our experiments on non-plasmonic structures [7].

3. Conclusions

We have investigated the photothermal properties of water-soluble nanocrystal assemblies via a combination of ultrafast optical spectroscopy and semi-classical numerical modeling. Their hybrid composition at the nanoscale, comprising plasmonic (Au) nanocrystals embedded in a matrix of organic ligands, results in a complex transient optical response. Broadband pump-probe experiments in the visible and near infrared has allowed us track the whole chain of photothermal energy flow: (i) light absorption by the individual nanocrystals and subsequent excitation of out of equilibrium carriers; (ii) electron-phonon equilibration occurring in a few picoseconds; (iii) heat release to the matrix.

2D finite element method electromagnetic simulations of the composite nanostructure and multi-temperature modeling of the energy flow dynamics enable us to identify the mechanisms presiding over the light-heat conversion in this novel kind of nanomaterials. Our results indicate that hybrid (organic-inorganic) nanocrystal assemblies can operate as efficient nanoheaters by exploiting the high absorption from the individual nanocrystals, enabled by the dilution of the inorganic phase, that is followed by a relatively fast heating of the embedding organic matrix, occurring on the 100-ps timescale.

References

[1] A.O. Govorov, H.H. Richardson, Generating heat with metal nanoparticles, *Nanotoday* 2: 30–38, 2007.

[2] J.H. Park *et al.*, Cooperative nanomaterial system to sensitize, target, and treat tumors, *PNAS* 107:981–986, 2010.

[3] R. Huschka, O. Neumann, A. Barhoumi, N.J. Halas, (2010) Visualizing light-triggered release of molecules inside living cells. *Nano Lett.* 10:4117–4122, 2010.

[4] O. Neumann *et al.*, Compact solar autoclave based on steam generation using broadband light-harvesting nanoparticles, *PNAS* 110:11677–11681, 2013.

[5] P.D. Dongare *et al.*, Nanophotonics-enabled solar membrane distillation for off-grid water purification, *PNAS* 114:6936–6941, 2017.

[6] N. Yang, C. Deeb, J.L. Pelouard, N. Felidj, M.P. Pileni, Water-dispersed hydrophobic au nanocrystal assemblies with a plasmon fingerprint, *ACS Nano* 11:7797–7806, 2017.

[7] A. Mazzanti *et al.*, Light-Heat Conversion: Tracking Photothermal Energy Flow in Highly Diversified Water-Dispersed Hydrophobic Nanocrystal Assemblies, *PNAS* in press, 2019.

On the Search for Toroidal Order in Magnetic Materials

Manfred Fiebig[1]

[1]Department of Materials, ETH Zurich, Vladimir-Prelog-Weg 4, 8049 Zurich, Switzerland
*corresponding author, E-mail: Manfred.fiebig@mat.ethz.ch

Abstract

Spontaneous long-range order of magnetic vortices is discussed as possible fourth form of primary ferroic order, called ferrotoroidicity. We define the underlying magneto-toroidal moment and discuss manifestations of the hallmark properties of ferroic order in magneto-toroidal materials: domains that are described by the orientation of an associated phase-transition-driving order parameter and that are switchable by a conjugate field. It turns out that "magneto-toroidal metamaterials" are ideal for elucidating the nature of the ferrotoroidic order and its conjugate toroidal field.

1. Magneto-toroidal moment and order

Although ferromagnetism is known to be of enormous importance, the exploitation of materials with a compensated (for example, antiferromagnetic) arrangement of long-range ordered magnetic moments is still in its infancy. Antiferromagnetism is more robust against external perturbations, exhibits ultrafast responses of the spin system and is key to phenomena such as exchange bias. However, there is no conjugate field for the manipulation of antiferromagnetic order, hindering both its observation and direct manipulation.

An interesting alternative to antiferromagnetism is a state with spontaneous long-range order of magnetic vortices called *toroidal moments* [1]. The toroidal moment is shown and defined in Fig. 1c as vortex-like head-to-tail arrangement of magnetic moments. The toroidal moment vector is given by

$$\mathbf{t}_i = \Sigma_i \, \mathbf{r}_i \times \mathbf{m}_i \,, \qquad (1)$$

where **r** is the vector pointing from the center of the unit cell to the magnetic moment **m**, and i sums over all the magnetic moments in the unit cell. Spontaneous uniform long-range alignment of these toroidal moments yields a macroscopic *toroidization* $\mathbf{T} = V^{-1} \Sigma_n \, \mathbf{t}_n$, where n sums over all the unit cells contained in the volume V. Here, **T** can be regarded as order parameter of a so-called ferrotoroidic state. Such ferrotoroidic order is discussed as complement to ferromagnetism, ferroelectricity and ferroelasticity as fourth type of a primary ferroic state.

The potential of ferrotoroidic materials is twofold. On the one hand, they represent a magnetically ordered state with compensated magnetization, yet, in contrast to antiferromagnetism, associated to an alternative field, the toroidization, that may be used to probe and switch domains despite their zero magnetization. On the other hand, the ferrotoroidic state involves a breaking of spatial and temporal inversion symmetries, which inherently allows the linear magnetoelectric effect: an electric field inducing a proportional magnetization and a magnetic field inducing an electric polarization.

2. Ferrotoroidicity as primary ferroic order

The existence of ferrotoroidic state has been discussed for many decades [2]. In order to establish it as genuine ferroic state, a variety of criteria have to be fulfilled [3]. A state can be called ferroic if it is reached by a non-disruptive phase transition involving a reduction of point symmetry. The phase transition is accompanied by the formation of domains where the domain states are distinguished by the respective orientation of the corresponding order parameter. A conjugate field acts on the orientation of the order parameter and can thus switch the domains in a hysteretic fashion. There has to ba a macroscopic property diverging at the ferroic phase transition. Finally, in order to describe a proper manifestation of ferroic order, the order parameter needs to drive the phase transition instead of just following another phase-transition-driving order parameter in which case the ferroic state would be called improper.

2.1. Verified ferroic properties

Over the years, most of these criteria have been verified for the toroidal order in magnetic materials. A reduction of magnetic symmetry with the formation and hysteretic switching of domains was observed by optical second harmonic generation [3, 4]. A divergence of the magnetoelectric susceptibility at the phase transition has been detected [5] and indications for proper ferrotoroidic order have been identified by Landau theory and magnetoelectric susceptibility measurements [6].

2.2. The open issue of the toroidal field

A crucial, intensely debated point is the conjugate toroidal field. This is a field violating spatial and temporal inversion symmetry just as the ferrotoroidic order parameter does. Its

existence is yet unclear – there is no "toroidal field generator". Up to now, access to the ferrotoroidic domains and the two-fold breaking of inversion symmetry are almost always realized by the simultaneous application of static, orthogonal magnetic and electric fields [1]. Application of *two* fields would render the ferrotoroidic state a *secondary* ferroic state. Alternatively, it may be argued that the two fields are merely *coupling* to the actual, sole toroidal field, which would retain the notion of a primary ferroic state.

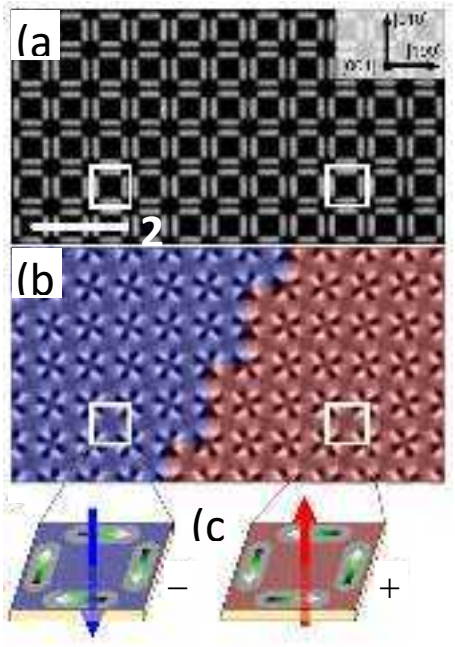


Figure 1: (a) Atomic force microscopy image of an artificial magneto-toroidal crystal built from permalloy nanomagnets on a silicon substrate. Unit cells comprising four nanomagnets are highlighted by the white boxes. (b) Corresponding magnetic force microscopy image revealing an as-grown toroidal domain structure with a domain boundary separating states of opposite toroidization. (c) The handedness of the arrangement of the magnetic moments in the unit cell determines the toroidal moment as –t or +t.

3. Magneto-toroidal metamaterials

A way out of this dilemma is to upscale the magneto-toroidal order to length scales that can be probed more easily and directly than phenomena on the atomic-unit-cell level [7]. For this purpose, we created an artificial crystal consisting of mesoscopic planar nanomagnets. We designed this "magneto-toroidal metamaterial" to possess a magneto-toroidally ordered ground state as shown in Fig. 1b that we probe locally by scanning with a magnetic tip. Furthermore, by scanning the array with the magnetic tip in a suitable way, we can generate an effective toroidal poling field that we use to pole the toroidization of our nano-magnetic array locally, writing regions with the toroidization +T or –T as shown in Fig. 2. In this process, the magnetic tip catalyses the generation of the effective toroidal field, but it does not exert a poling field in itself. Thus, the experiment allows us, for the first time, to generate a toroidal field directly and apply it to set the toroidization of a sample.

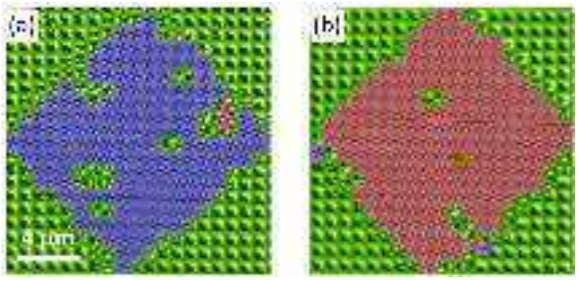


Figure 2: Magnetic force microscopy images of two regions of an artificial magneto-toroidal crystal to which toroidal poling fields of opposite signs in (a) and (b) were applied. Colour codes as in Fig. 1.

4. Outlook

Our experiment on magneto-toroidal metamaterials brings us a significant step closer to consolidating the magneto-toroidal order as fourth form of primary feroic order. Furthermore, the possibility to write specified regions with a uniform toroidization of defined orientation into a magnetic nano-array is the key to engineering unusual optical properties such as nonreciprocal directional dichroism up to unidirectional light propagation in the visible range.

Acknowledgements

M. F. thanks the coauthors of Ref. 7 and acknowledges support by the ETH Research Grant "ETH-28 14-1".

References

[1] N. A. Spaldin, M. Fiebig, M. Mostovoy, The Toroidal Moment in Condensed-Matter Physics and its Relation to the Magnetoelectric Effect, *J. Phys.: Condensed Matter* 20: 434203, 2008.

[2] V. K. Wadhawan, *Introduction to Ferroic Materials*, Gordon & Breach, Amsterdam, 2000.

[3] B. B. van Aken, J. P. Rivera, H. Schmid, M. Fiebig, Observation of ferrotoroidic domains, *Nature* 449: 702–705, 2007.

[4] A. S. Zimmermann, D. Meier, M. Fiebig, Ferroic nature of magnetic toroidal order, *Nat. Comms.* 5: 4796, 2014.

[5] D. Sannikov, Ferrotoroidic phase transition in boracites, *Ferroelectrics* 219: 177–181,1998.

[6] P. Tolédano, M. Ackermann, L. Bohatý, P. Becker, T. Lorenz, N. Leo, M. Fiebig, Primary ferrotoroidicity in antiferromagnets, *Phys. Rev. B* 92: 094431, 2015.

[7] J. Lehmann, C. Donnelly, P. M. Derlet, L. J. Heyderman, M. Fiebig, Poling of an artificial magneto-toroidal crystal, *Nat. Nano* 14: 141–144, 2019.

Topological non-Hermitian origin of surface Maxwell and acoustic waves

Konstantin Bliokh

Theoretical Quantum Physics Laboratory - Riken, Japan
*corresponding author, E-mail: k.bliokh@gmail.com

Abstract

More than 60 years ago it was shown that interfaces between isotropic homogeneous optical media (including dielectrics, metals, negative-index materials) can support surface electromagnetic waves, which now play crucial roles in plasmonics, metamaterials, and nano-photonics. I will show that such surface Maxwell waves have a topological origin explained by the bulk-boundary correspondence. Importantly, the topological classification is determined by the photon helicity operator within the Weyl-like representation of Maxwell equations, which is generically non-Hermitian even in lossless optical media. The corresponding topological invariant, which determines the number of surface modes, is a Z4 number (or a pair of Z2 numbers) describing the winding of the complex helicity spectrum across the interface. I will also provide similar considerations and topological explanation of the surface acoustic wave that appears at interfaces between positive- and negative-density acoustic media. Instead of helicity, its properties are described by the effective non-Hermitian four-momentum operator within the Klein-Gordon representation of sound waves, which provides a single Z2 bulk index. Our theory provides a new twist and insights for several areas of wave physics: Maxwell electromagnetism, topological quantum states, non-Hermitian wave physics, and metamaterials.

Can plasmonics help outpace quantum decoherence?

Simeon I. Bogdanov[1,2], Alexandra Boltasseva[1,2] and Vladimir M. Shalaev[1,2]

School of Electrical & Computer Engineering, Birck Nanotechnology Center
& Purdue Quantum Science and Engineering Institute
Purdue University, West Lafayette, Indiana 47907, USA

*corresponding author, E-mail: shalaev@purdue.edu

Abstract

Photons are the primary candidates for implementing quantum networks, i.e. systems capable of distributing entanglement and transmit quantum information. Photonic modes must be coupled to matter in order to produce single photons or make them interact. However, naturally the interaction between light and matter is relatively weak, which is one of the reasons why most present photonic quantum technologies suffer from low bit rates. A targeted and strong enhancement of light-matter interaction based on plasmonic nanostructures has a potential to transform the way quantum photonic systems operate. It relies on speeding up processes beyond the rates of dephasing, rather than on achieving long coherence times in matter. We discuss our recent and planned work aimed at outpacing decoherence in quantum optical devices using nanoscale plasmonic metamaterials. We also outline future directions in the development of a platform for high-speed integrated quantum photonics and the application of machine-learning techniques for quantum optical measurements.

Neural Networks in Nanophotonics

Marin Soljacic[1]

[1] MIT, Department of Physics, 77 Massachusetts Avenue , Cambridge, MA 02139, USA
*corresponding author, E-mail: soljacic@mit.edu

Abstract

The recent deep-learning revolution offers many exciting opportunities in photonics, both to help with photonics research, but also for photonics to advance deep-learning. Some of our recent work on these topics will be presented.

Metasurfaces for sensing and imaging

D Conteduca[1], I. Barth[1], J. Juan-Colas[2], Steve Johnson[2], E.R Martins[3] and Thomas F Krauss[1]*

[1]Department of Physics, University of York, York, YO10 5DD, UK
[2]Department of Electronic Engineering, University of York, York, YO10 5DD, UK
[3]School of Engineering São Carlos, University of São Paolo, São Carlos, Brazil

*corresponding author, E-mail: thomas.krauss@york.ac.uk

Abstract

Recent developments in metasurfaces, including the phenomenon of bound states in the continuum (BIC) have injected a new dynamics into the paradigm of guided mode resonances for sensing and imaging applications. We will discuss and compare the various geometries, both dielectric and plasmonic, introduce our silicon nanohole approach and demonstrate its superiority in terms of surface sensitivity, which is a key metric for label-free optical sensors yet one that is rarely discussed.

Non-Hermiticity in Optics and Optomechanics

Sahin K. Ozdemir

Department of Engineering Science and Mechanics & Materials Research Institute,
The Pennsylvania State University, University Park, PA, 16802, USA

In recent years, there has been a tremendous progress in the theory and experimental implementations of the concepts rooted in non-Hermitian physics. This progress has led to a host of new intriguing results in the physics of light–matter interactions with promising potential applications. One of the most notable property of non-Hermitian systems is the emergence of non-Hermitian degeneracies known as exceptional points (EPs) where complex eigenvalues and the corresponding eigenstates of the system coalesce. The presence of an EP affects the system significantly, leading to nontrivial physics with interesting features. In this talk, after briefly reviewing the related physics and the applications that have been developed in the past few years, I will present the progress in our experimental and theoretical studies towards a better understanding of optical processes and optomechanical interactions at EPs for realizing photonic and phononic devices with novel functionalities. I will also present a brief perspective on the developments and discuss possible future research directions that can benefit from the notion of non-Hermitian engineering.
S.K.O. is supported by ARO Grant No. W911NF-18-1-0043, AFOSR Award No. FA9550-18-1-0235, National Science Foundation (NSF) Award No. ECCS 1807485.

Optimized quantum photonics

Jelena Vuckovic

Ginzton Lab, Spilker Building, Stanford University, Stanford, CA 94305-4088, USA
E-mail: jela@stanford.edu

Abstract

We present our recent progress on developing high quality qubits based on color centers in diamond and silicon carbide, combined with powerful optimized photonic structures providing efficient optical interfaces and interconnects. Our inverse design approach offers a powerful tool to implement classical and quantum photonic circuits with superior properties, including robustness to errors in fabrication and temperature, compact footprints, novel functionalities, and high efficiencies.

nic and Plasmonic Materials for Sensing, Energy conversion and Imagi

Adsorption Site Recognition in Single Molecule Junction

Satoshi Kaneko and Manabu Kiguchi

Department of Chemistry, School of Science, Tokyo Institute of Technology, Tokyo, Japan
*corresponding author, E-mail: kiguti@chem.titech.ac.jp

Abstract

We report on a new methodology for identifying the connectivity of a single molecule junction through the combination of surface enhanced Raman scattering and current-voltage response, with the density functional theory simulations. This new methodology discriminates three different atomistic connectivity for the benzenedithiol and aminobenzenethiol in the junctions, and uncovers the transition between different connectivity, which had never been detected. Using this methodology we reveal the changes in the atomistic connectivity as a function of applied voltage and time.

1. Introduction

Single-molecule circuits, in which individual molecules are wired into the circuit and act as the active electronic components, represent the ultimate limit to the miniaturization of electronic devices. Although conceptually simple, this goal has proven elusive. Up until then, charge transport properties of a variety of individual molecules have been investigated using the scanning probe miscopy and break junction techniques. Pioneering studies have demonstrated that unambiguous connection of a single-molecule to electrodes is difficult to confirm and achieve, as shown by large disparities in conductivities reported for identical molecules or similar molecules. On the single-molecule scale, conducting properties are strongly dependent on the atomistic connectivity of individual molecules to the external electrodes. The direct link between the connectivity and the device performance of the junction including the conductivity is very poorly revealed due to numerous experimental challenges. Thus, it is essential to achieve a detailed understanding and elucidation of the single-molecule connectivity at the molecule-electrode interfaces [1-4].

2. Experimental

Single molecule junctions were prepared using MCBJ, which offers high electrode stability and fine-tuning of the electrode spacing. This control is realized by bending a flexible substrate in a three-point bending geometry (Fig. 1). The free standing Au nano bridge (see scanning electron microscopy (SEM) image in Fig. 1) was fabricated on the bending phosphor bronze substrate with the electron beam lithography. Molecules were deposited on the unbroken Au nano bridge using self-assembly from 1mM ABT or BDT ethanol solution. On bending the substrate, the junction was stretched until it broke. The two sides of the broken Au nano bridge then acted as electrodes, the separation of which could be adjusted with picometer resolution using a piezo element. The electric current was monitored under the bias voltage application, Raman spectra from the junction was simultaneously measured with a Raman spectrometer using excitation wave length of 785 nm.

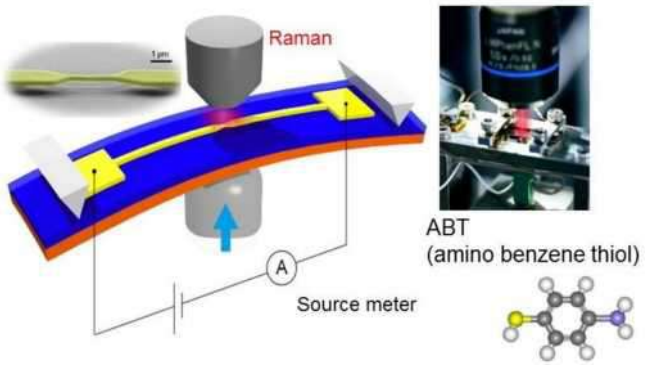


Figure 1: Scheme of a molecular junction under the Raman setup. Near-infrared excitation laser (λ_{ex} = 785 nm) is focused by a lens on the molecular junction fabricated on the phosphor bronze substrate. The molecular junction is prepared by bending the Au nano bridge that is covered with molecules.

3. Results and Discussion

The SERS spectra observed in the single molecule junction regime show two distinct Raman bands, which are assigned to a C-S stretching mode (~1060 cm^{-1}, ν_{7a}, and a C-C stretching mode (~1560 cm^{-1}, ν_{8a}). The appearance of Raman modes characteristic of ABT indicates the presence of ABT molecule in the gap. Dimerization reactions have been reported for ABT molecules on Au nano particles. However, the absence of 1380cm^{-1} and 1430cm^{-1} peaks corresponding to the ABT dimer indicates that dimerization reaction does not take place at the junction in the present experimental condition.

Figure 2 shows the two dimensional mapping for ABT of the metal-molecule electronic coupling Γ and the Raman shift of the ν_{8a} mode for the SERS active samples i.e. samples for which the ν_8 mode displays over 10 counts per second. The value of Γ is obtained from fits to *I-V* curves. In the mapping, we can clearly observe two intense regions corresponding to H and M states for both BDT and ABT. For ABT, the M region extends around ν=1582 cm^{-1}, Γ≈ 0.064 eV, and the H state extends around ν=1580 cm^{-1}, Γ≈ 0.14 eV. The ν_{8a} for the conductive H state is lower than for the M state. For comparison, we plot the statistical distribution of Γ and ν. Each distribution can be fitted by two Gaussian functions with different positions of the peaks, indicating the existence of two states with different Γ or ν. However, the two states overlap, and their boundary is not clear. These two states which cannot be separated by either electric coupling or Raman shift alone, can be well distinguished in the combined analysis of SERS and *I-V* curves.

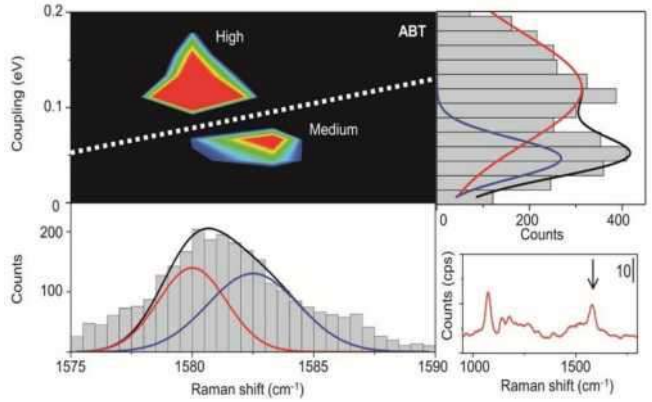


Figure 2: Two dimensional Γ-Raman shift (ν :ν_{8a} mode) histogram of ABT single molecule junctions constructed from 3792 samples. The bias voltage is 0.1V during the SERS measurement. Two regions (high and medium) with large number of counts are separated by the white dashed line. The M region extends around ν=1582 cm^{-1}, Γ≈0.064 eV, and the H state extends around ν=1580 cm^{-1}, Γ≈0.14 eV. One dimensional Γ and ν histograms are shown to the right and under the 2D histogram. Red and blue lines represent the distributions of H and M states, respectively. While distributions of H and M states overlap in the 1D histogram, both states are clearly distinguishable in the 2D Γ-ν histogram.

We calculated the metal-molecule electronic coupling Γ and the Raman shift of the ν_{8a} mode by the theoretical calculation. The good match between calculation and experiment in both conductance, resonance broadening, and frequency trends suggests that the conducting state probed experimentally is the one described in the simulations. Based on these results, we conclude that the H, M and L conductance states relate to bridge, hollow and atop binding sites, respectively.

Having resolved the characterization of molecular adsorption geometry underlying the junction electrical characteristics through simultaneous SERS and *I-V* characteristics and DFT simulations, we now address the dynamical fluctuations between these sites. We can see the transition from the hollow to bridge, and other way round, through changes in Γ and ν. Here, it is noted that some transitions cannot be detected by electrical or vibrational measurements alone.

Next, we address fluctuations in molecular adsorption site induced by the application of a bias voltage to the single molecule junction. As the bias is increased, the intensity of the bridge region decreases, and hollow regions become intense, indicating an increase in bridge to hollow site transitions.

4. Conclusions

We have demonstrated an adsorption site recognition technique based on an analysis combining SERS and measurements, with the aid of density functional theory calculations. This new methodology distinguishes multiple molecular adsorption sites, and uncovers the origin of conductance fluctuations, which had never been detected experimentally up to now. In the case of ABT and BDT single molecule junctions, electrical conductance can vary by up to a factor 100, a situation that hampers the development of clear, reproducible conductance signatures. The present study unambiguously monitors the changes in molecular adsorption geometry for the first time and demonstrates their significant role on junction conductance fluctuations. Using this new methodology we further monitored the changes in the population of adsorption sites as a function of time and applied voltage.

Acknowledgements.

This work was performed with Dr. Satoshi Kaneko, Mr. Sho Suzuki, Dr. Shintaro Fujii (Tokyo Institute of Technology), Mr. Enrique Montes, Prof. Héctor Vázquez (Academy of Sciences of the Czech Republic).

References

[1] Y. Isshiki, S. Fujii, T. Nishino, M. Kiguchi, ***J. Am. Chem. Soc.,*** 140, 3760−3767 (2018).

[2] Fujii, S. Marqués-González, J. Shin, H. Shinokubo, T. Masuda, T. Nishino, N. P. Arasu, H. Vázquez, M. Kiguchi, ***Nat. Comm***. 8, 15984 (2017).

[3] S. Kaneko, D. Murai, S. M. González, H. Nakamura, Y. Komoto, S. Fujii, T. Nishino, K. Ikeda, K. Tsukagoshi, M. Kiguchi*, ***J. Am. Chem. Soc.*** *138*, 1294–1300 (2016).

[4] S. Fujii, M. Ziatdinov, S. Higashibayashi, H. Sakurai, M. Kiguchi, ***J. Am. Chem. Soc***. 138, 12142-12149 (2016).

Hybrid Plasmonic Nanomaterials for Uranyl Detection

Hoa T. Phan[1] and Amanda J. Haes[1,*]

[1]Department of Chemistry, University of Iowa, Iowa City, Iowa USA
*corresponding author, E-mail: amanda-haes@uiowa.edu

Abstract

Reproducible detection of uranyl, an important biological and environmental contaminant, from complex matrices by surface-enhanced Raman scattering (SERS) is successfully achieved using hybrid plasmonic nanoparticles. Traditionally, non-specific binding of interfering species limits detects of molecules such as uranyl. Herein, this is overcome using materials design and rigorous sample analysis workflow design. Synergistic approaches for uranyl isolation and SERS detection is promising for real-world sample detection and eliminates the need of radioactive tracers and extensive sample pretreatment steps.

1. Introduction

Uranium, a radioactive material with a long half-life, accumulates in the environment in its oxidative form uranyl, which can contaminate soil and water [1]. Importantly, uranyl forms complexes with anions and cations thereby influencing solubility, toxicity, and fate of these heavy metal species. Furthermore, uranyl speciation varies with pH. The resulting complex speciation complicates detection and/or requires significant sample pretreatment. As such, methods that are capable of identifying trace uranyl species in complex samples are needed.

Herein, hybrid plasmonic nanomaterials (Figure 1) and experimental workflow implementation will be used to establish a rigorous protocol for uranyl detection [2,3]. Namely, localized surface plasmon resonance spectroscopy (LSPR), Raman spectroscopy [4], and surface enhanced Raman scattering (SERS) [5,6] serve as label-free and near real-time methods for identifying uranium species in complex aqueous solutions.

2. Experimental Approaches

A straight-forward protocol for spectral analysis will be shown using Raman spectroscopy and aqueous uranium samples. Raman excitation wavelength, pH, and coordinating ions are systematically varied. The spectral analysis results are rigorously validated using uranyl speciation models. Next, plasmonic nanomaterials are used to enhance the Raman signals for trace detection of low (and high) abundant species. Finally, an approach that promotes the reproducible detection of uranyl using SERS will be shown. All in all, the developed protocol provides an accurate and routine analysis of Raman spectra for uranyl species identification and relative abundance elucidation. These advances are expected to provide a straight-forward approach for uranium species identified using hybrid plasmonic nanomaterials.

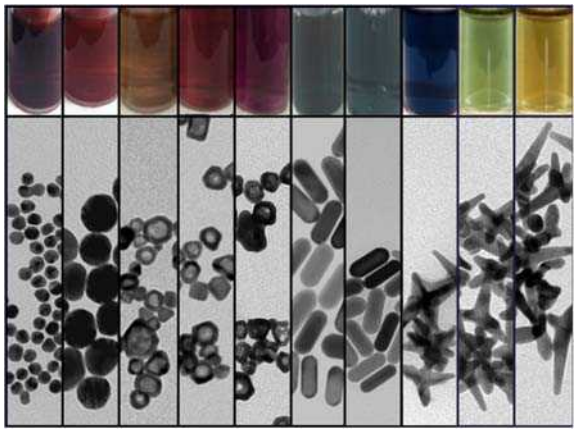


Figure 1: Hybrid plasmonic nanostructures with tunable sizes, shapes and compositions are shown. Photographs and TEM images (width of each image = 50 nm) are shown. These are Au nanospheres (diameter = 12, 30 nm), Ag@Au nanospheres with 8 nm silver spheres coated with 4, 8, and 12 nm gold shells, Au nanorods with aspect ratios 3 and 5, and gold nanostars with branch lengths of 10, 15, and 20 nm.

3. Results and Discussion

Plasmonic nanomaterials offer many advantages over traditional methodologies in applications ranging from catalysis, sensing, and imaging. Despite these strengths, challenges arise including for both direct and indirect SERS detection of uranyl include nanoparticle stability, SERS spectral complexity, and variations in SERS intensities and vibrational frequencies. All of these challenges depend on intra- and intermolecular interactions at the plasmonic metal interface as well as the plasmonic nanomaterial stability in complex matrices.

Uranyl, unfortunately, exhibits poor affinity to traditional SERS substrates. Methods to promote molecule-metal interactions often lead to nanoparticle instability. Herein, gold nanostars and gold coated silver nanospheres are used. Implications of nanoparticle architecture are investigated for maximizing SERS responses and detectability of uranyl. Nanoparticle architecture and surface potential drive these interactions.

To promote detectability in complex matrices, both polymer and silica surface chemistries will be evaluated to initially "screen" unwanted interfering species for adsorbing to the metal surface while also permitted the adsorption and detection of uranyl for SERS detection.

Finally, solution conditions are used to identify key features that rationally promote uranyl-surface interactions without compromising the physical stability of the nanostructures. Solution composition induces changes in nanoparticle architecture and/or adsorption processes, yet systematic responses are observed. As a result, we expect these studies will broaden the scope of SERS and plasmonic-based assays as small molecules with weak affinity to metal nanostructures will be more readily detected.

4. Conclusions

While uranyl is a difficult molecule to detect in complex matrices, hybrid nanomaterial design and carefully designed experimental approaches facilitate detectability in a reproducible manner. By using polymers and silica hybrid materials, influences from interfering species are minimized and solution impacts reduced. Future advances in further reducing detection limits and integrating these materials with rapid sampling platforms have the potential to lead to a revolutionary sensor for heavy metal detection.

Acknowledgements

Research reported in this publication was supported by the National Institute of Environmental Health Sciences of the National Institutes of Health under award number R01ES027145 and the National Science Founda-tion, (CHE-1707859).

References

[1] G. Lu, A.J. Haes, T.Z. Forbes, Detection and identification of solids, surfaces, and solutions of uranium using vibrational spectroscopy, *Coordination Chemistry Reviews* 374: 314−344, 2018.

[2] H.T. Phan, A.J. Haes, Impacts of pH and intermolecular interactions of surface-enhanced Raman scattering of chemical enhancements, *Journal of Physical Chemistry C*, 122, 14846-14856, 2018.

[3] G. Lu, B.K. Shrestha, A.J. Haes, Importance of tilt angles of adsorbed aromatic molecules on nanoparticle rattle SERS substrates, *Journal of Physical Chemistry C,* 120, 20759-20767, 2016.

[4] G. Lu, T.Z. Forbes, A.J. Haes, Evaluating best practices in Raman spectral analysis for uranium speciation and relative abundance in aqueous solution, *Analytical Chemistry,* 88, 773-780, 2016.

[5] G. Lu, T.Z. Forbes, A.J. Haes, SERS detection of uranyl using functionalized gold nanostars promoted by nanoparticle shape and size, *Analyst,* 141, 5137-5143, 2016.

[6] G. Lu, A.J. Johns, B. Neupane, H.T. Phan, D.M. Cwiertny, T.Z. Forbes, A.J. Haes, Matrix-independent surface-enhanced Raman scattering detection of uranyl using electrospun amidoximated polyacrylonitrile mats and gold nanostars, *Analytical Chemistry*, 90, 6766-5772, 2018.

Plasmonic Hot-Carrier-Mediated Solar Energy Conversion and Tunable Photochemical Reactions

Yu Zhang[1*], Tammie Nelson[1], Sergei Tretiak[1,2], Hua Guo[3], ChiYung Yam[4], and George C. Schatz[5]

[1]Physics and Chemistry of Materials, Theoretical Division, Los Alamos National Laboratory, Los Alamos, NM, US
[2] Center for Integrated Nano-Technology, Los Alamos National Laboratory, Los Alamos, NM, US
[3]Department of Chemistry and Chemical Biology, University of New-Mexico, Albuquerque, NM, USA
[4]Beijing Computational Science Research Center, Beijing, China
[5]Department of Chemistry, Northwestern University, Evanston, IL, USA
*corresponding author, E-mail: zhy@lanl.gov

Abstract

A new design for hot-carrier solar cells is discussed in which a conventional semiconductor heterojunction is attached to a plasmonic medium. Our theoretical model indicates the opportunities and limitations of employing plamsonic hot-carriers for solar energy conversion. In addition, applications of plasmonic hot-carriers in photochemistry will also be introduced. The atomistic-scale mechanisms of tunable photochemistry via plasmonic hot-carriers will be discussed.

1. Introduction

Surface plasmon polaritons (SPPs) and localized surface plasmon resonances (LSPRs) are collective oscillations of electrons in conductors excited by electromagnetic modes. Surface plasmons results in concentration of light in the near-field around the particle interfaces, which enables efficient spatial control of charge and energy fluxes in a variety of applications. However, surface plasmons suffer from significant dissipation, with most of the plasmon's energy loss due to Landau damping leading to hot electron-hole (e-h) pairs. Several recent efforts have proposed the possible extraction of these energetic carriers before dissipation takes place, which has simulated the application of hot carriers to several branches of applied physics, chemistry, and materials and energy sciences [1].

2. Plasmonic hot-carriers for solar energy conversion

In this work, we explore the opportunities and limitations for making plasmonic solar cells, here considering a design for hot-carrier solar cells in which a conventional semiconductor heterojunction is attached to a plasmonic medium such as arrays of gold nanoparticles. The underlying mechanisms and fundamental limitations of this cell are studied using a nonequilibrium Green's function method [2]. The numerical results indicate that this cell can significantly improve the absorption of solar radiation with energy lower than the gap (Fig. 1b) without reducing open-circuit voltage, as photons can be absorbed to produce mobile carriers in the semiconductor as long as they have energy larger than the Schottky barrier rather than above the bandgap. However, a significant fraction of the hot-carriers have energies below the Schottky barrier, which makes the cell suffer low internal quantum efficiency (Fig. 1d). Moreover, quantum efficiency is also limited by hot-carrier relaxation and metal-semiconductor coupling. The connection of these results to recent experiments is described, showing why plasmonic solar cells can have less than 1% efficiency.

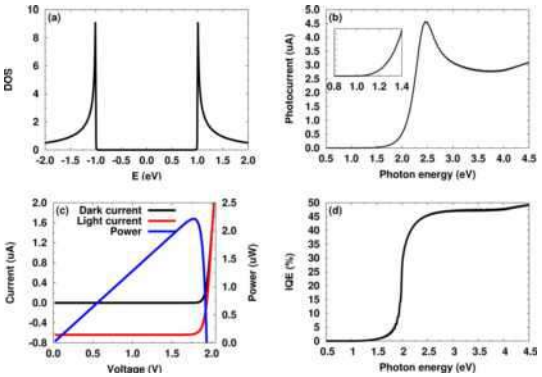


Figure 1: (a) Density of states (DOS) of the system. The gap is exactly 2 eV. (b) Photocurrent of the plasmonic hot-carrier solar cells. An SPP-induced resonant absorption is observed, at which point a pronounced photocurrent is generated. (c) Current-voltage characteristics and (d) Internal quantum efficiency (IQE) of the solar cells. The IQE is much smaller than that of a conventional solar cell.

3. Plasmonic hot-carrier-mediated tunable photochemistry

Even though our recent theoretical studies have shown that extracting hot carriers for solar energy conversion suffers from fundamental limitations [2], the opportunities for using plasmonic hot-carrier extraction to drive photochemistry are less-well known. In this work, we demonstrate the principles of plasmonic enhancement and control of chemical reactions by considering the photoinduced dissociation

of an adsorbed molecule on a plasmonic nanoparticle and plasmonic dimer [3]. Non-adiabatic molecular dynamics were performed to model the bond dynamics of H_2 adsorbed on the surface of metallic nanoparticle (NP) with the NP treated in the Jellium approximation.

We start by examining the electronic structure of H_2 adsorbed on the NP. The bonding and anti-bonding (AB) state of the H_2 are 8.05 eV below and 1.48 eV above the Fermi energy. Because of the gap between the bonding and AB states of H_2, 9.53 eV, is much larger than the energy of a visible light quantum, no chemical reaction can be induced in the visible regime. However, in the coupled system, the AB state is only 1.48 eV above the Fermi level. Numerical simulations confirm that the hot-electrons generated in the metallic NP can indeed transfer to the AB state of H_2 and drive the H_2 dissociation.

In practical applications, an assembly of NPs is usually employed allowing for the formation of dimers and other aggregates that have more significant optical properties [4]. Thus, it is natural to consider if the stronger field-enhancement can facilitate H_2 dissociation. Consequently, we calculated H_2 dissociation in the plasmonic dimer for different geometrical configurations. As an example, we consider the H_2 molecule placed between the NPs shown in Figure 2(a). D is fixed at 1.59 Åand d is taken as a variable. The time evolution of H-H bond lengths for different d is plotted in Figure 2(b-e). When $d = D = 1.59$ Å, the H_2 is placed precisely in the center of the plasmonic dimer, with the stronger field-enhancement compared to larger values of d. However, no matter what the excitation energy is, the H-H bond never breaks as shown by the green curves in Figure 2. Our simulations further demonstrate that tuning the d can affect the dynamics significantly. As shown in Figure 2, the H_2 starts to dissociate for some excitation frequencies when d reaches 5.82 Å. An even larger distance d more strongly favors dissociation of the H-H bond. These results demonstrate that chemical reaction can either be suppressed or enhanced by the plasmonic dimer depending on the relative position of the molecule between the dimer. Thus, hot-carrier mediated dissociation can be tuned by controlling the location of the molecule in the gap. We have further examined the charge dynamics of the H_2 molecule in the dimer. Overall we see that hot-carriers transferred from one NP to the H_2 will undergo another charge transfer to the other NP before H_2 dissociation can develop when $d = 1.59$ Å. With increasing d, the charge loss from the H_2 molecule to the right NP is suppressed. At a certain distance, the charge accumulation on H_2 can be large enough to induce bond dissociation.

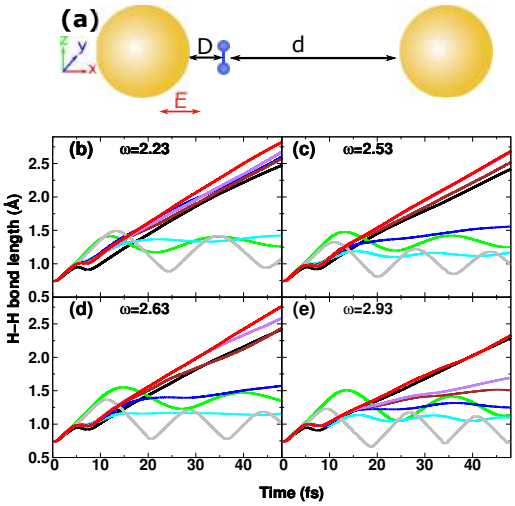


Figure 2: Bond dynamics of H_2 in plasmonic dimer with different distance. H_2 dissociation in a dimer of two 1.9 nm NP with different distances (for D=1.59 Å): Monomer (black); d=1.59 Å(green); d=3.70 Å(cyan); d=5.82 Å(blue), d=7.94 Å(brown); d=10.05 Å(purple); d=12.17 Å(red); and D=d=5.82 Å(gray). Photochemical reaction for $d = 1.59$ Å is significantly suppressed. Tuning the distance d can affect the dynamics of H_2 in the plasmonic dimer.

4. Conclusions

In summary, we have demonstrated the opportunities and limitations of extracting hot-carriers for solar energy conversion. In addition, we have performed TDDFT and NAMD calculations which enable us to directly look at the dynamic process of H_2 dissociation on the surface of a metallic NP. Our results illustrate the mechanism of plasmon-induced H_2 dissociation at the atomic scale and identify how hot-carriers can be transferred from a NP to the adsorbed molecule to drive photochemistry. Our results also demonstrate that the photochemistry can be tunable in the case of a plasmonic dimer.

Acknowledgement

This work was supported by the U.S. Department of Energy through the Los Alamos National Laboratory (LANL). LANL is operated by Triad National Security, LLC, for the National Nuclear Security Administration of the U.S. Department of Energy (Contract No. 89233218NCA000001).

References

[1] M. Brongersma, N. J. Halas. P. Nordlander, Plasmon-Induced Hot Carrier Science and Technology. *Nat. Nano.*. 2015, 10, 25-34.

[2] Y. Zhang, C. Y. Yam, G. C. Schatz, Fundamental Limitations to Plasmonic Hot-Carrier Solar Cells. *J. Phys. Chem. Lett.* 2016, 7, 1852-1858.

[3] Y. Zhang, T. Nelson, S. Tretiak, H. Guo, G. C. Schatz, Plasmonic Hot-Carrier-Mediated Tunable Photochemical Reactions. *ACS Nano*. 2018, 12, 8415-8422.

[4] W. Zhu, R. Esteban, A. G. Borisov, J. J. Baumberg, P. Nordlander, H. J. Lezec, J. Aizpurua, K. B. Crozier, Quantum Mechanical Effects in Plasmonic Structures with Sub-nanometer Gaps. *Nat. Commun*. 2016, 7, 11495.

Multistructured metallic substrate: a promising SERS platform for detecting trace molecules

Mathieu Edely[1], Nicolas Delorme[1], Guy Louarn[2], Ludovic Douillard[3], Jean-François Bardeau[1]

[1]Institut des Molécules et Matériaux du Mans - UMR CNRS 6283- PRES LUNAM
Le Mans Université, Avenue Olivier Messiaen, F-72085 Le Mans Cedex 9, France
[2]Institut des Matériaux Jean Rouxel, Université de Nantes, BP 32229, F-44322 Nantes, France
[3]Nanophotonics Laboratory, Service de Physique de l'État Condensé, IRAMIS, CEA,
UMR CNRS 3680 F-91191 Gif-sur-Yvette Cedex, France

*corresponding author, E-mail: Jean-Francois.Bardeau@univ-lemans.fr

Abstract

An efficient methodology based on scanning probe lithography technique to design complex metallic nanostructures on rigid or flexible substrates will be presented. Our results show that this methodology opens up new possibilities of applications for which an individual control of the height, shape, and periodicity of each printed nano(micro)structure is necessary. As the ability to control the 3D arrangement of gold nanostructures is of prior interest for plasmonics and surface-enhanced optical techniques we explored the potential of the substrate for biosensing and in particular for SERS measurements.

1. Introduction

Today, it remains difficult to detect, identify and quantify different analytes in complex mixtures and it is even more challenging if the pollutants are highly diluted. Among various analytical techniques, surface-enhanced Raman scattering (SERS) is among the most promising methods in detecting trace molecules due to its high molecular specificity (i.e., differentiation via molecular fingerprint characteristics) and high sensitivity thanks to the strong local field enhancements (« hot spots ») that can exist (under certain conditions) in the near-field region of nanostructured metallic surfaces.

2. Results

Recently we developed a new methodology for elaborating nanostructured metal supports based on soft lithography using an atomic force microscope as a tool of nanostructuration [1]. This original and patented [2] method allows on the same substrate to design different 3D architectures at the nanoscale (Figure 1). The discriminating advantage with respect to commercial substrates is the control and reproducibility of the patterns characterized by specific localized surface plasmon resonances which facilitates multi-wavelength analyses.

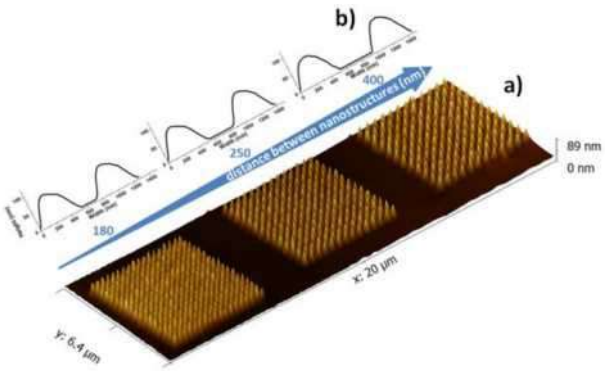


Figure 1: a) 3D AFM image of arrays of periodic gold nanostructures. b) The height profiles exhibit the different distances between the nanostructures.

Photoemission electron microscopy (PEEM) constitutes an alternative tool to investigate the optical near field at the nanometer scale. Indeed, Douillard et al. [3-5] show a direct evidence of the link between a localized surface plasmon excitation of metal nanoparticles and its electron emission counterpart as measured by PEEM. When the incident photons are resonant with the surface plasmon frequency the local field enhancement leads to an increase of the photoemission yield.
Therefore, by collecting the photo-emitted electrons on the nanostructured gold pattern under illumination, PEEM allowed to reveal the distribution of the near-optical field at nanoscale in the visible and near-infrared ranges (400–900 nm) (Figure 2). The samples were illuminated by a femtosecond pulsed laser (Ti:sapphire ultrafast oscillator Chameleon Ultra II, Coherent Inc., repetition rate 80 MHz, hyperbolic-secant-squared pulse, pulse width 140 ± 20 fs). In PEEM-imaging mode, the measured brightness in a given

image area is proportional to the electron emission flux from this area. The spectral dependency observed in PEEM_intensiy was confirmed by calculating (using COMSOL Multiphysics) the local field enhancement of patterned arrays for different distances between nanostructures.

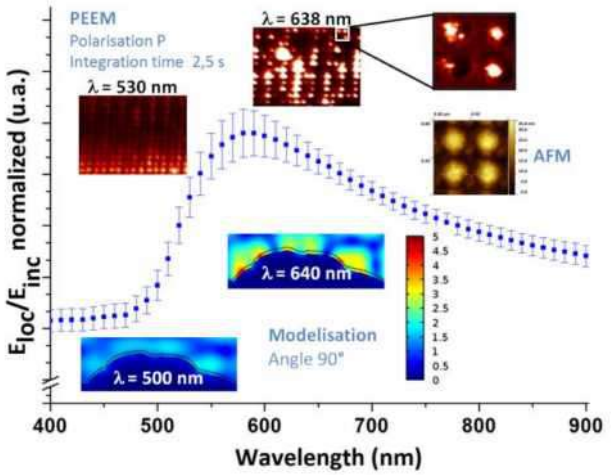


Figure 2: Calculated local field enhancement factor for a nanostructure as function of wavelength and experimental two-dimensional photoemission electron intensity maps (top)

Then, we showed that by tuning the geometrical parameters of the arrays at nanoscale we can modulate the SERS efficiently (Figure 3). This work was carried out on nanostructures with the same shape and the same size but with three different distances between them. A 785 nm excitation line was used to measure Raman spectra after immersion of the substrate in a 10^{-6} M solution of thiophenol.

The experimental phenomenon was confirmed by calculating the local field enhancement of arrays for different distances between nanostructures. The simulation made from a nanostructured profile, extracted from AFM images, shows the enhancement of the local field between gold nanoparticles and the effect of distance between structures.

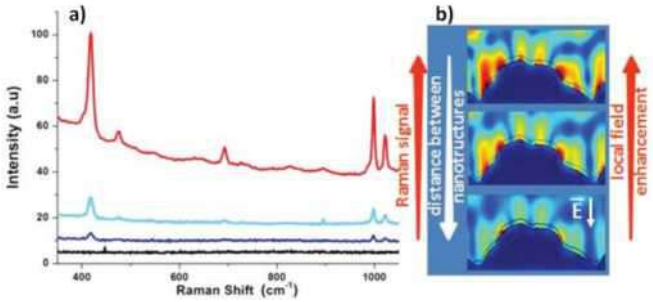


Figure 3: a) Raman spectra of thiophenol recorded on three different nanostructures and smooth surface (black spectrum). b) Calculated local field enhancement as a function of spacing between nanostructures.

Works are in progress to detect and identify pesticides commonly found in water and emerging pollutants and we are focusing in particular on verifying the reproducibility, linearity and limit of detection of diluted multi-component solutions.

References

[1] M. Edely, N. Delorme, D. Siniscalco, and J.-F. Bardeau, Alternative Strategy Based on Scanning Probe Lithography for Patterning Complex Metallic Nanostrutures on Rigid or Flexible Substrates, *Advanced Materials Technologies, 1800134-1800141, 2018*

[2] FR Patent deposit n° 1461880, December 2014

[3] L. Douillard, F. Charra, Z Korczak, R. Bachelot, S. Kostcheev, G. Lerondel, P.-M. Adam, P. Royer, Short range plasmon resonators probed by photoemission electron microscopy, *Nano Lett. 8, 935-940, 2008*

[4] L. Douillard, F. Charra, High-resolution mapping of plasmonic modes: photoemission and scanning tunnelling luminescence microscopies, *J. Phys. D: Applied Physics 44, 464002, 2011*

[5] C. Hrelescu, T. K. Sau, A. L. Rogach, F. Jäckel, G. Laurent, L. Douillard, F. Charra, Selective Excitation of Individual Plasmonic Hotspots at the Tips of Single Gold Nanostars, *Nano Lett. 11, 402–407, 2011*

Materials for Photonics Beyond Noble Metals

Marina S. Leite[1]

[1]Department of Materials Science and Engineering, Institute for Research in Electronics and Applied Physics, University of Maryland, College Park, USA
*corresponding author, E-mail: mleite@umd.edu

Abstract

In this talk I will present how metallic materials beyond coinage metals have enabled us achieve materials with *on demand* optical responses ranging from the Vis to NIR. First, I will discuss the opportunities for developing optical components using metallic materials beyond noble metals for energy harvesting and superabsorption applications. Second, I will demonstrate a novel platform for transient, dynamic photonics based uniquely on earth-abundant materials: Mg and MgO.

1. Introduction

To date, different classes of materials have been explored for photonic applications, including metals, ceramics, intermetallics, semiconductors, and metallic alloys. Depending on the desired wavelength range of operation one of the abovementioned systems might be more suitable than others. There is still a pressing need for finding a material that with tailored optical response in the UV-NIR range of the electromagnetic spectrum. Despite all the work accomplished to date using noble metals, their pre-determined permittivities and lack of CMOS compatibility currently limit their use in photonic devices.

2. Results and Discussion

2.1. Metal Alloys

We demonstrate how alloyed metals (Ag, Au, Cu, Al) enable optical materials with responses not achievable by its pure counterparts and, therefore, with superior performance. First, we build a library of their permittivity by mapping ε as a function of chemical composition for a series of thin films formed by the binary combination of Ag, Au, Cu and Al. We combine transmission and reflection measurements using a B-spline model to resolve both ε_1 and ε_2 [1]. To corroborate the ε_1 measurements we compare the obtained values with SPP experiments using the Krechtmann configuration, and find an excellent agreement between the two independent methods.

For the Ag-Au model system, we resolve the alloys' *d* intraband electronic transitions by calculating their band structure through DFT. Our calculations are combined with XPS measurements of the valence band spectra and with transmission measurements of the Ag_xAu_{1-x} thin films [2]. We identify the individual contribution of each metal, Ag and Au, to the band structure of the alloys, never resolved before.

Concerning alloyed nanostructures, we developed a scalable approach to obtain fully alloyed AgAu nanoparticles. For that, we expand the thin film deposition + annealing method, which provdes a platform for lithography-free nanoscale building blocks. We characterize the optical repsonse of these nanostructures by spectrally dependent near-field scanning optical microscopy (NSOM) – see Figure 1. We spatially resolve the 'hot-spots' of these nanoparticles: for $Ag_{0.5}Au_{0.5}$ we find a subtantial local field enhancement at 600 nm, just underneath the nanostrcutures. Our expeirmental results are in ver good agreement with 3D full-field simulations [2].

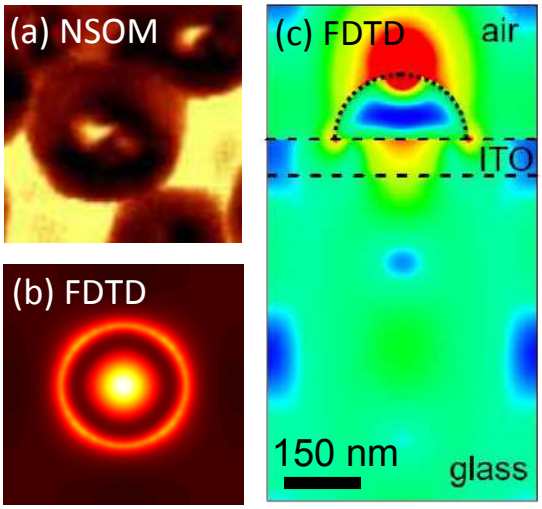


Figure 1: (a) NSOM measurement and (b) FDTD calculation for $Ag_{0.5}Au_{0.5}$ nanoparticle at 600 nm. (c) Field profile for the same nanoparticle showing 'hot spots' at 600 nm.

While Ag and Au represent an ideal model system to investigate the effect of alloying on the material's optical

response, these noble metals are not CMOS-compatible and are high cost. Thus, we overcome these contrains by exploring the combination of earth0abundament metals, such as Al and Cu. In particular, this combination is excellent for superabsorption. We numerically demnstrate the superior performance of thin film AlCu as the metallic layer of planar superabsorbers [4]. AlCu outperforms other metals commonly used in photonics, e.g. Ag, Au, and Cr. Si/AlCu shows >99% omnidirectional absorption across the Vis and NIR, as presented in Figure 2. The tunability of the high absorption peak primarily depends on the thickness of the semiconductor film. We validate our calculations by fabricating and testing this potentially CMOS–compatible system.

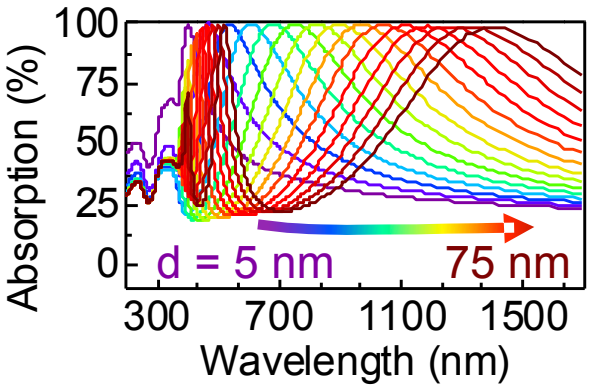


Figure 2: Near-unity (> 99%) absorption for (*d* nm) Si / 100 nm AlCu lithography-free, thin film superabsorber.

2.2. Earth-Abundant Metals

Reconfigurable photonic devices that can change in functionality can transform the design of next-generation optical devices such as modulators, sensors, and signal processors. We present the notion of transient photonic devices based on Mg, where we demonstrate color pixels formed by Mg/MgO/Mg thin films. Vivid colors ranging from blue to burgundy is obtained by varying the thickness of the dielectric spacer. The pixels vanish in hue in less than 10 minutes due to the dissolution of both Mg and MgO in water, at room temperature and neutral pH, as shown in Figure 3 [5]. We will also present transient devices based on Mg nanostructures.

3. Conclusions

In summary, metal alloys have recently emerged as an alternative material for photonics due to its tailored, *on demand* optical properties. We demonstrated that permittivity values not achievable by noble metals can be obtained by the binary mixture of Au, Ag, Cu, and Al.

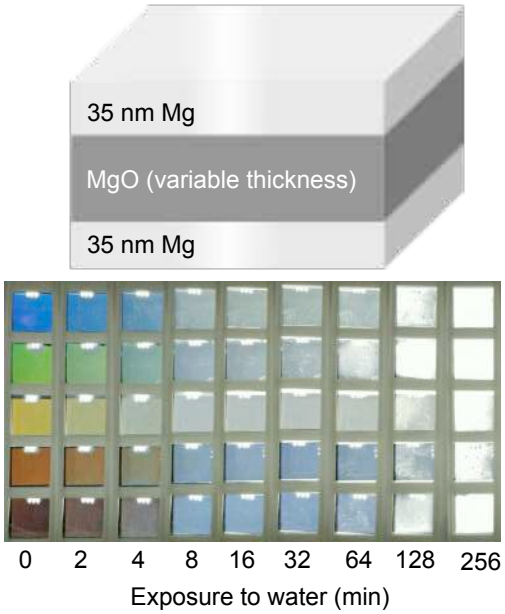


Figure 3: (Top) Schematic of MIM structure for color pixels. (Bottom) Photographs of color pixels as a function of etching time in water, showing transiency.

Moreover, we have shown the near-unity (> 99%) absorption of thin-film formed Si/AlCu stacks. To elucidate how the optical behavior of the metal alloys differs from the linear combination of their pure counterparts we calculate their band structure by DFT, and identify the individual contribution of each metal.

Acknowledgements

The author acknowledges the financial support from the National Science Foundation Grants No. 16-09414 (DMR) and HRD1008117 (ADVANCE program).

References

[1] C. Gong, M. S. Leite. Noble Metal Alloys for Plasmonics, *ACS Photonics* 3: 507, 2016.

[3] C. Gong, et al., Near-Field Optical Properties of Fully Alloyed Noble Metal Nanoparticles, *Advanced Optical Materials* 5, 1600568: 2017.

[2] C. Gong, et al., Band Structure Engineering by Alloying for Photonics, *Advanced Optical Materials 6*, 1800218: 2018.

[4] M. R. Dias, et al., Lithography-free, Ominidirectional, CMOS-compatible AlCu Alloys for Thin-Film Superabsorbers, *Advanced Optical Materials* 6: 1700830, 2018.

[5] T. G. Farinha et al., Magnesium for Transient Photonics, *ACS Photonics* 6: online, 2019. DOI: 10.1021/acsphotonics.8b01299

Plasmonic hot electron nano-emitters by on-chip ablation for femtosecond on-chip electronics

Alexander Holleitner[1,2,*]

[1]Walter Schottky Institut and Physics Department, TU Munich, Germany
[2]Munich Center for Quantum Science and Technology (MCQST), Schellingstr. 4, D-80799 München
*corresponding author, E-mail: holleitner@wsi.tum.de

Abstract

We demonstrate that prestructured metal nanogaps can be shaped on-chip to below 10 nm by femtosecond laser ablation (Figure 1 and [1]). We explore the plasmonic properties and the nonlinear photocurrent characteristics of such formed tunnel junctions. The photocurrent can be tuned from multiphoton absorption toward the laser-induced strong-field tunneling regime in the nanogaps, and gives rise to a field emission of ballistic hot electrons propagating across the nanoscale junctions. We demonstrate that a unipolar current of hot electrons is achieved by designing the plasmonic enhancement factors in the junctions to be asymmetric, which allows ultrafast electronics on the nanometer scale.

We particularly demonstrate that femtosecond optical pulses in the near-infrared (NIR) applied to such nanogaps can drive electronic circuits with a bandwidth of up to 10 THz [2]. The corresponding THz transients propagate on-chip in stripline circuits on a macroscopic, millimeter scale [3]. We discuss the effective diffraction index and attenuation of coplanar stripline circuits with microscale lateral dimensions on various substrates including sapphire, GaN, silica glass, and diamond grown by chemical vapor deposition. We show how to include dielectric, radiative and ohmic losses to describe the pulse propagation in the striplines to allow femtosecond on-chip electronics with frequency components up to 10 THz [4].

Moreover, we apply a similar THz time-domain spectroscopy to detect the electron dynamics in nanoscale materials [5]. In particular, we access the ballistic time-of-flight of photogenerated charge carriers in carbon nanotubes, as well as non-equilibrium thermo-electric currents, ultrafast lifetime limited currents, and non-radiative energy transfer processes in 2D materials [5-9].

Our results combine the advantages of ultrafast femtosecond optics with on-chip plasmonics to enable ultrafast nanoscale electronics on the way toward femtosecond electronics in waferscale circuits.

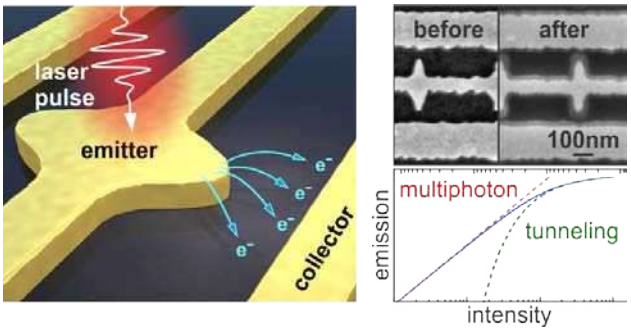


Figure 1: Asymmetric plasmonic nano-emitters enhance the electric field of an ultrafast laser pulse such that hot electrons tunnel from the emitter to the collector. Right top: the junctions are formed by a combination of nanofabrication (before) and laser-ablation (after) with an overall sub-10nm gap-distance. Right bottom: the emission of hot electrons is guided by a multiphoton-absorption and driven tunneling processes. Reprinted with permission from [1]. Copyright (2019) American Chemical Society.

Acknowledgements

We thank R. Kienberger, J. Finley, K. Müller, P. Zimmermann, A. Hötger, H. Fernandez, P. Zechmann, A. Nolinder, M. Wörle for a very fruitful collaboration. The work is funded by the Deutsche Forschungsgemeinschaft (DFG, German Research Foundation) under Germany´s Excellence Strategy – EXC 2089/1 – 390776260 and EXC-2111 – 390814868.

References

[1] P. Zimmermann, et al. Nano Lett. 19: 1172, 2019.
[2] C. Karnetzky, et al., Nature Comm. 9: 2471, 2018.
[3] C. Kastl, et al. IEEE JSTQE 23: 8700305. 2017.
[4] N. Fernández, et al. submitted 2019.
[5] P. Seifert, et al. Nano Lett. 17: 973, 2017.
[6] P. Seifert, et al. Nature Comm. 9: 331, 2018.
[7] E. Parzinger, et al. Nature 2D 1: 40, 2017.
[8] C. Karnetzky, et al. Phys. Rev. B 95: 1611405 (R) 2017.
[9] A. Brenneis, et al. Nature Nano. 10: 135–139, 2015.

First Observation of Optical Activity in Hyper-Rayleigh Scattering

Ventsislav Valev[1]

[1] Centre for Photonics and Photonic Materials and Centre for Nanoscience and Nanotechnology, University of Bath, Bath, United Kingdom
*corresponding author, E-mail: v.k.valev@bath.ac.uk

Abstract

We report the first experimental observation of a chiroptical effect that was predicted 40 years ago [1,2].

1. Introduction

Chiral nano/metamaterials and surfaces enable striking photonic properties, such as negative refractive index and superchiral light, driving promising applications in novel optical components, nanorobotics, and enhanced chiral molecular interactions with light [3]. In characterizing chirality, although nonlinear chiroptical techniques are typically much more sensitive than their linear optical counterparts, separating true chirality from anisotropy is a major challenge [4,5].

Optical Second Harmonic Generation (SHG) is a nonlinear optical effect whereby two photons at the fundamental frequency of light are converted into a single photon at the double frequency. Like all nonlinear optical effects, SHG scales as a power law of the fundamental electromagnetic field, which makes it very sensitive to near-field enhancements. However, among the nonlinear effects, SHG holds a special place; because it is the first term in the nonlinear optical expansion, it is often the largest nonlinear optical effect. Moreover, contrary to third harmonic generation for instance, SHG is forbidden in centrosymmetric materials (within the dipole approximation). As a consequence, SHG is exquisitely sensitive to symmetry breaking, such as the one caused by chirality.

2. Results

Here, we report the first observation of optical activity in second harmonic hyper-Rayleigh scattering (HRS). We demonstrate the effect in a 3D isotropic suspension of Ag nanohelices in water, see Fig. 1. The effect is 5 orders of magnitude stronger than linear optical activity and is well-pronounced above the multiphoton luminescence background.

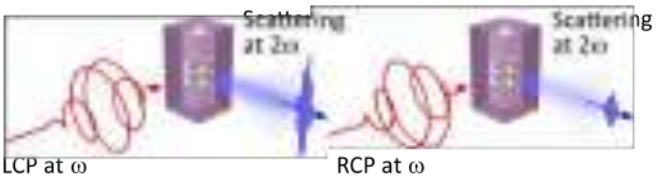


Figure 1: Schematic diagram of the HRS OA effect upon illumination with left circularly polarized (LCP) and right circularly polarized light (RCP).

3. Conclusions

Because of its sensitivity, isotropic environment, and straightforward experimental geometry, HRS optical activity constitutes a fundamental experimental breakthrough in chiral photonics, for media including nano/metamaterials and chemical molecules.

Acknowledgements

VKV acknowledges support from the Royal Society through the University Research Fellowships.

References

[1] J. T. Collins, K. R. Rusimova, D. C. Hooper, H.-H. Jeong, L. Ohnoutek, F. Pradaux-Caggiano, T. Verbiest, D. R. Carbery, P. Fischer, V. K. Valev, *Phys. Rev. X 9*: 011024, 2019.

[2] D. L. Andrews, T. Thirunamachandran, *J. Chem. Phys.* 70: 1027, 1979.

[3] J. T. Collins, C. Kuppe, D. C. Hooper, C. Sibilia, M. Centini, V. K. Valev, *Adv. Opt. Mater. 5*: 1700182, 2017.

[4] D. C. Hooper, A. G. Mark, C. Kuppe, J. T. Collins, P. Fischer, V. K. Valev, *Adv. Mater. 29*: 1605110, 2017.

J. T. Collins, D. C. Hooper, A. G. Mark, C. Kuppe, V. K. Valev, *ACS Nano* 12: 5445–5451, 2018.

Near and far-field optical properties of non-noble metal nanoparticles deposited on nanopatterned dielectric surfaces

Sophie Camelio[1*], David Babonneau[1], Frédéric Pailloux[1], Alexandre Fafin[1], Gregory Abadias[1] and Panos Patsalas[2]

[1]Institut Pprime, CNRS-Université de Poitiers, Poitiers, France
[2] Department of Physics, Aristotle University of Thessaloniki, Thessaloniki, Greece
*corresponding author, E-mail: sophie.camelio@univ-poitiers.fr

Abstract

Periodic nanoripple patterns produced by ion-beam sputtering of dielectric surfaces (Si_3N_4 or Al_2O_3) are used as templates to elaborate self-aligned nanoparticles and nanowires arrays by deposition at glancing-angle of aluminum and refractory conducting nitrides (TiN, ZrN). From experimental and numerical investigations of their far-field and near-field optical properties, we will show that these alternative materials for plasmonics devices exhibit original dichroic properties.

1. Introduction

For the beginnings of plasmonics, most of the studies were focused on gold and silver nanoparticles because of their favorable bulk dielectric properties in the visible and near infrared (NIR) spectral range. However, gold and silver suffer from limitations such as low abundance on Earth, high cost, optical losses in the ultraviolet (UV) range due to interband transitions, as well as poor processing compatibility with silicon nanofabrication techniques and thermal instabilities. Hence, alternative plasmonic materials have received ever-growing attention these last years [1,2]. Among the most commonly suggested materials, aluminum [3] and transition metal nitride [4,5] nanostructures are currently at the focus of numerous studies and are suggested as a promising alternative for light absorption and near-field enhancement from UV (Al) to the visible and NIR (TiN, ZrN). However, until now, technical challenges make it difficult to achieve the production of such nanostructures over large areas with controlled morphology and composition. In this work, we present a two-step process for the formation of self-assembled non-noble metal nanostructures with substantial dichroic substantial plasmonic response. It is based on exploiting the shadowing effects during the glancing angle deposition (GLAD) of metallic species on pre-patterned rippled substrate.

2. Results

The first step of the elaboration process is the patterning of a dielectric buffer layer (silicon nitride or alumina films) by ion erosion with a collimated 1 keV Xe+-ion beam at oblique incidence to form periodic ripples [6,7] (Fig.1).
The second step is the GLAD of Al, or TiN or ZrN on the rippled surface that enables the growth of self-assembled and well-aligned nanostructures along the ripples. For the GLAD two versions of sputter-deposition are used: ion beam sputtering for Al and magnetron sputtering for TiN and ZrN. For some samples, after deposition of the metal and prior to exposure to the atmosphere, the nanostructures are covered with a dielectric capping-layer. The nanostructures are deposited onto flat silicon and NaCl single crystal for structural characterizations with Atomic Force Microscopy (AFM) and Transmission Electron Microscopy (TEM) respectively, and onto fused silica substrate for absorbance measurements.

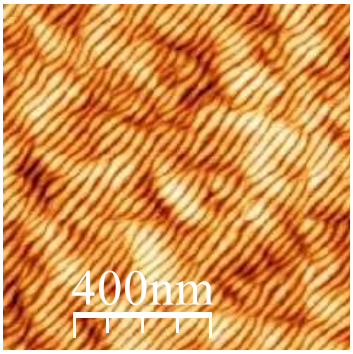


Figure 1: AFM topographic image of amorphous Al_2O_3 thin film deposited on Si after 1 keV Xe+-ion exposure

We will show that the elaboration process used with the pair (Al, Si_3N_4) leads to the formation of flat aluminum nanoparticles array with a core@shell Al@AlN structure (Figure 2a). The nanostructure exhibits surface plasmon resonances whose spectral positions depend on the polarization of the electric field with respect to the particles chains, as revealed by absorbance measurements (Figure 2b). Near-field calculations, performed using finite-difference time domain method, highlight the overlap

between the surface plasmon resonance of the nanoparticles and the interband transitions of aluminum.

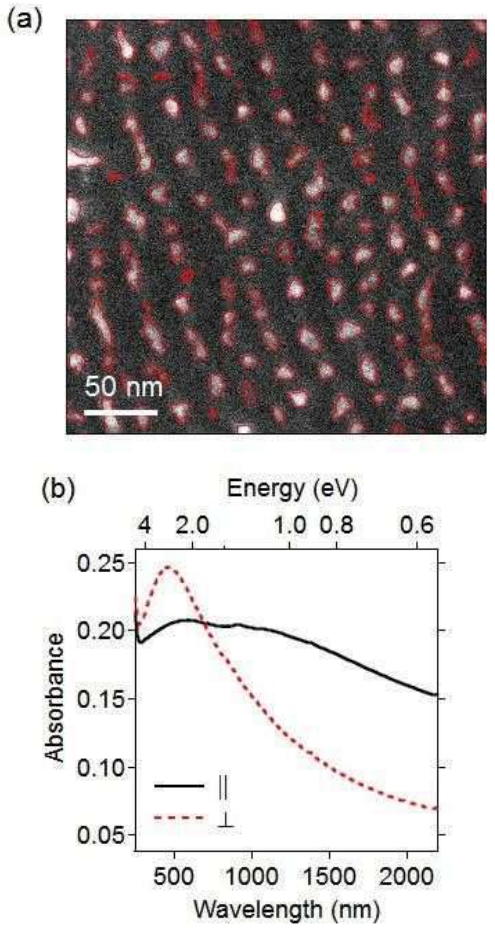


Figure 2 : (a) Energy Filtered Transmission electron microscopy (EF-TEM) and (b) absorption spectra of Al nanoparticles embedded in silicon nitride

ZrN and TiN nanostructures on rippled alumina surface in the form of nanowires arrays also exhibit polarization dependent absorbance spectra. As shown in Figure 3, the spectral position of transverse resonance of ZrN nanostructure takes place in the UV range and can be shifted in the visible region by covering the nanowires with a silicon nitride film (Figure 3).

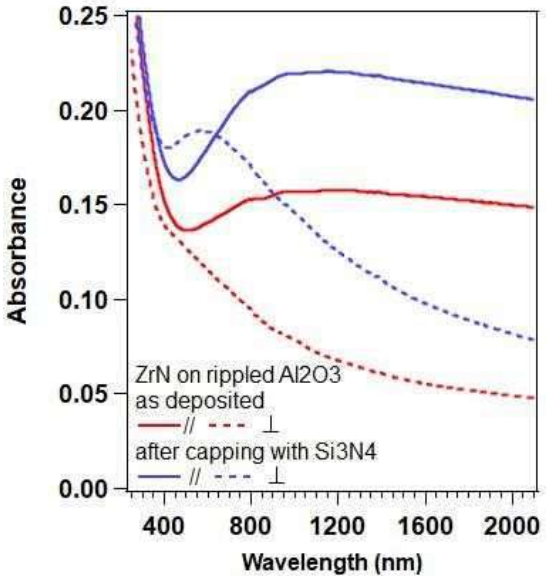


Figure 3: Absorbance spectra of ZrN nanowires on rippled alumina buffer layer deposited onto fused silica substrate, as deposited (red) and after capping with a silicon nitride thin film (blue).

Acknowledgements

Part of this work has been carried out within the Région Nouvelle-Aquitaine IMATOP project funded by the European Regional Development Fund (FEDER).

References

[1] P. West, S. Ishii, G. Naik, N. Emani, V. Shalaev, A.Boltasseva, Searching for better plasmonic materials, *Laser Photon. Rev*., 4, 795-808, 2010.

[2] A. Lalisse, G. Tessier, J. Plain, G. Baffou, Quantifying the Efficiency of Plasmonic Materials for Near-Field Enhancement and Photothermal Conversion, *J. Phys. Chem. C*, 119, 25518-25528, 2015.

[3] D. Gérard, S. K. Gray, Aluminium plasmonics, J. *Phys. D-Appl. Phys*., 48, 184001, 2015.

[4] U. Guler, V. M. Shalaev, A. Boltasseva, Nanoparticle plasmonics: going practical with transition metal nitrides, *Mater. Today*, 2015, 18, 227-237.

[5] P. Patsalas, N. Kalfagiannis, S. Kassavetis, Optical Properties and Plasmonic Performance of Titanium Nitride, *Materials* 8, 3128-3154, 2015.

[6] D. Babonneau, S. Camelio, E. Vandenhecke, S. Rousselet, M. Garel, F. Pailloux, Quantitative analysis of nanoripple and nanoparticle patterns by grazing incidence small-angle x-ray scattering 3D mapping, *Phys. Rev. B* 85, 235415/1-11, 2012.

[7] D. Babonneau, E. Vandenhecke, S. Camelio, Formation of nanoripples on amorphous alumina thin films during low-energy ion-beam sputtering: Experiments and simulations, *Phys. Rev. B*, 95, 085412, 2017.

Complex materials created by warped spaces for energy harvesting, bio-imaging, and broadband light control at the nanoscale

A. Fratalocchi[1]

[1]Faculty of Electrical Engineering Applied Mathematics and Computational Science, King Abdullah University of Science and Technology, Thuwal 23955-6900, Saudi Arabia
*corresponding author, E-mail: andrea.fratalocchi@kaust.edu.sa

Abstract

In this invited talk, I will review our recent results on complex photonics materials created by warped spaces with application in energy harvesting, structural coloration, bio-imaging and broadband light control in nanoscale structures.

1. Introduction

Traditionally, photonics materials are assembled by carefully engineering dispersive properties of semiconductors, dielectrics or metallic structures. Recently, we demonstrated that it is possible to engineer materials with arbitrary complex responses by using suitably defined geometrical defamations and space warping. These structures opened new important applications in a variety of areas, ranging from energy harvesting to bio imaging.

In Energy harvesting, photocatalytic conversion of solar energy to chemical fuels or feedstock is considered as an attractive strategy to solve the increasing demand of renewable energy sources. Typically, in a solar-conversion-system, semiconductors serve as photoactive materials, which capture, absorb and then transfer photo-excited electrons to catalytic sites to enable proton reduction reaction [1-3]. Direct photo-excitation of metal has emerged in recent years as a new promising strategy applied in photochemistry. Plasmonics is capable to provide the ultimate spatial and temporal manipulation over light and photo-derived chemical reactions, with help of an exquisitely designed metallic nanostructure network can efficiently enclose electromagnetic irradiation within a nanometric region. Surface plasmons, that charge-density oscillation, consequently are excited at the metallic surface and decay by photons reemission or through the creation of energetic electrons and holes. These photo-excited energetic carriers can be leveraged to trigger efficient photo-derived fuels and chemicals production, such as hydrogen evolution [4].

In this talk, I will illustrate a new efficient Photocatalysis in a material based on 3D multi-scale epsilon-near-zero (ENZ) nanostructures created by tree-like warped metallic geometries. This structure [5] achieves a hydrogen production rate of 9.5-μmol $h^{-1}cm^{-2}$ that exceeds, by a factor of 3.2 that of the best previously reported plasmonic-based photocatalysts for the dissociation of H_2 with 50 h stable operation.

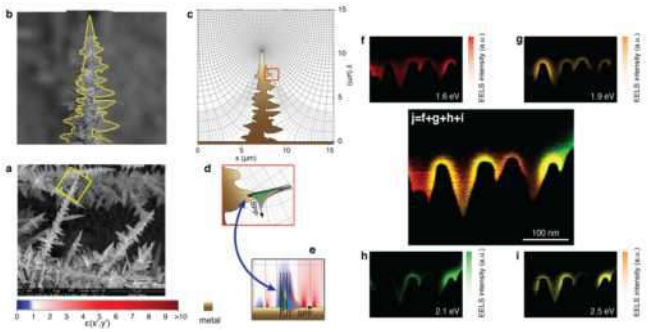


Figure 1: General idea, sample fabrication and EELS demonstration. (a)-(b) SEM images of metallic needle shape structures. (c) Equivalent structures of panel b, calculated by applying transformation optics. (d) Zoomed a local area of panel c, and shows the corresponding broadband squeezing of light in the points of positive curvatures of the material, where equivalent ENZ region exist in panel e. (e) Optical properties of the complex ENZ structure, showing the motion of SPP wave excited by incident light. (f)-(i) EELS plasmon mapping at various input energy of nanoscale features of the ENZ materials. (j) Overlap of EELE signals to illustrate the broadband ENZ effect.

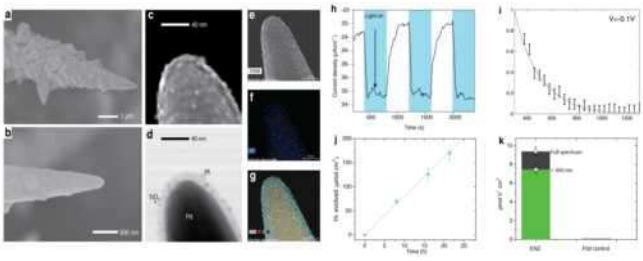


Figure 2: ENZ photocatalyst assembly and hydrogen generation performance. (a)-(g) The SEM and TEM image of ENZ Photocatalysis device, and the element mapping. (h) Current-time trace at -0.1V reversible hydrogen electrode potential. (i)

Photoelectrochemical external quantum efficiency spectra characterization. (j) Amount of H_2 evolved at different times. (k) Comparison of H_2 generation rates for full-spectrum illumination with a control sample.

Other applications that will be discussed are structural coloration [6], new membranes for Surface Enhanced Raman Spectroscopy (SERS) [7], and new materials that allow to control broadband light from dielectric structures with only 10 nm thickness.

References

[1] J. Liu, Y. Liu, N. Liu, Y. Han, X. Zhang, H. Huang, Y. Lifshitz, S. Lee, J. Zhang, Z. Kang, Water splitting Metal-free efficient photocatalyst for stable visible water splitting via a two-electron pathway, *Science*, *347*, 970, 2015.

[2] M. L. Brongersma, N. J. Halas, P. Nordlander, Plasmon-induced hot carrier science and technology, *Nat. Nanotechnol. 10*, 25, 2015.

[3] C. Clavero, Plamon-induced hot-electron generation at nanoparticle/metal-oxide interfaces for photovoltaic and Photocatalytic devices, *Nat. Photonics***,** *8*, 95, 2014.

[4] S. Mubeen, J. Lee, N. Singh, S. Kramer, G. D. Stucky, M. Moskovits, An autonomous photosynthetic device in which all charge carriers derive from surface plasmons,*Nat. Nanotechnol.*, *8*, 247, 2013

[5] Y. Tian, F. P. García de Arquer, C.-T. Dinh, G. Favraud, M. Bonifazi, J. Li, M. Liu, X. Zhang, X. Zheng, Md. G. Kibria, S. Hoogland, D. Sinton, E. H. Sargent, A. Fratalocchi, Enhanced Solar-to-Hydrogen Generation with Broadband Epsilon-Near-Zero Nanostructured Photocatalysts. *Adv. Mater.* 2017, 29, 1701165

[6] H. Galinsky *et al.*, Scalable, ultra-resistant structural colors based on network metamaterials, *Light: Science & Applications* **6**, page e16233 (2017).

[7] M. Peng *et al.*, Broadband single molecule SERS detection designed by warped optical spaces, Nature Communications, 9, 5428 (2108).

Tunable Shape-controlled Plasmonic Nanoparticles Superlattices for Surface-enhanced Raman Scattering Applications

Xing Yi Ling

Chemistry and Biological Chemistry Division, School of Physical and Mathematical Sciences, Nanyang Technological University, Singapore 637371

*corresponding author, E-mail: xyling@ntu.edu.sg

Abstract

A major challenge in nanoparticle self-assembly is programming the large-area organization of a single type of anisotropic nanoparticle into distinct superlattices with tunable packing efficiencies. In this talk, I will discuss how nanoscale surface chemistry is used to direct the self-assembly of shape-controlled silver nanoparticles into three distinct two-dimensional plasmonic superlattices at a liquid/liquid interface. Systematically tuning the surface chemistry of the silver nanoparticles leads to a continuous superlattice structural evolution, from close-packed to progressively open structures. Notably, silver octahedra standing on vertices arranged in a square lattice is observed using hydrophobic particles. The structure-to-function characterization reveals that the nanoparticle assembly with the least packing density generates plasmonic 'hotstrips', leading to nearly 10-fold more efficient surface-enhanced Raman scattering compared with the other more densely packed configurations.

Interface Design for Visible-Light Induced Photochemical Reactions Promoted by Refractory Transition Metal Nitride Nanoparticles Incorporated into TiO_2 Matrix

Olga A. Baturina[1,*], Albert Epshteyn[1], Gregory T. Forcherio[2], Alexander Govorov[3,*], Asher C. Leff[2,4], Andrew Purdy[1], and Blake Sympkins[1]

[1]Chemistry Division, US Naval Research Laboratory, Washington DC, USA
[2]Sensors & Electron Devices Directorate, US Army Research Laboratory, Adelphi MD, United States
[3]Department of Physics and Astronomy, Ohio University, Athens OH, USA
[4]General Technical Services, Adelphi MD, USA

Abstract

Plasmonic nanoparticle (NP)-semiconductor interface plays crucial role in photocatalysis, in particular for separation of photo-generated carriers. Here, we explore two strategies to improve charge separation at the refractory transition metal nitride NP/TiO_2 interface: creating a Schottky barrier between the NP and TiO_2 by decorating the TiN core with a gold shell and application of an electric field at a ZrN NP/TiO_2 interface. Photoelectrochemical methanol oxidation is used to probe both interfaces under visible excitation. Computational analysis supports experimental observations.

1. Introduction

Refractory transition metal nitrides (RTMNs) such as TiN and ZrN are an emerging class of materials that have potential for harvesting energy of visible light for photocatalysis [1]. TiN and ZrN NPs can absorb efficiently at 450-1200 nm wavelenghtes, covering most of the solar spectrum. Their broad localized surface plasmon resonance (LSPR) indicates damped plasmons; this in contrast to conventional plasmonic materials, such as Au, Ag, Cu and Al [2]. Photo-excited carriers in TiN and ZrN can be generated both by intraband and interband transitions. Because plasmonic resonances of TiN and ZrN NP are weak and red-shifted compared to those of Au and Ag, RTMN NPs present a good platform to explore photocatalytic rections driven by plasmonic carriers generated by interband transitions. Previous research has shown that interband transitions in TiN NPs play a major role in phooelectrochemical (PE) methanol (CH_3OH) oxidation at the interface between TiN and semiconducting TiO_2 support [3]. Here, we extend our analysis to the ZrN/TiO_2 photocatalyst that offer advantages over TiN/TiO_2 due to higher rates of hot carriers generation by ZrN vs TiN NPs [2]. An important feature of the TiN/TiO_2 interface is an absence of an electronic barrier between the plasmonic NP and a semiconductor support, which leads to a poor separation of photo-generated carriers. This issue can be addressed either by utilizing (1) a Schottky barrier by decorating the TiN core with a shell of a strongly plasmonic material (such as Au) or (2) a potential bias. Both strategies will be discussed in the presentation.

2. Experimental

2.1. Synthesis and characterization

ZrN NPs were synthesized by ammonolysis of $Zr(NMe_2)_4$, and all manipulations were done in a drybox under Ar or on a vacuum line. Clean $Zr(NMe_2)_4$ was prepared following a protocol from the literature [4]. A portion of the $Zr(NMe_2)_4$ (1.28 g, 4.78 mmol) was dissolved in heptane in a reaction bulb and 21.6 mmol NH_3 was condensed into the bulb at 77K. The mixture was stirred at room temperature for one day and then at 80 °C for another day. Solids were isolated by filtration. The solid was loaded into an alumina boat, inserted into a furnace, and heated under NH_3 flow first at 250 °C for 15 min, and then at 900 °C for 2.5 h. It was then cooled under N_2 flow once temperature dropped to 500 °C. A mostly black powder was isolated. Crystallite size was 11 nm, as determined by XRD.

TiN@Au core-shell NPs were synthesized by (1) wet chemistry methods, and (2) hot-electron assisted photodeposition [5]. The wet chemistry method involved *in situ* generation of an oleilamine – Au (I) complex in heptane, followed by the addition of 20 nm TiN NPs (US Nano Research) and brief sonication. Then the vial was placed on a shaker table and allowed to gently agitate over 7 days. The hot-electron-assisted photodeposition method utilized 550 nm long-pass filtered broadband irradiation of TiN NPs to generate plasmonic hot electrons in the presence of Au (III) complex at a 1:5 ratio. CH_3OH was used as a sacrificial reagent to complete the oxidation half reaction.

Following the synthesis of ZrN and TiN@Au NPs, they were incorporated into P25 TiO_2 matrix by mixing the NPs and TiO_2 powders in 50:50 (v/v) H_2O: ethanol mixture overnight. The ZrN/TiO_2, TiN@Au/TiO_2 and bare TiO_2 films for PE experiments were prepared as described elsewhere [3]. Experiments were conducted in a three-

electrode PE cell. The photocatalysts films deposited on FTO-coated glass substrates served as working electrodes, while Pt foil and Ag/AgCl in 3 M NaCl (BioLogic, Inc) were used as counter and reference electrodes, respectively.

2.2. Theoretical modelling

For this project, we performed both electromagnetic and quantum calculations. Using COMSOL and DDA, we computed both free-standing and embedded TiN and ZrN NPs. Simulations of NPs (TiN and ZrN) in solution agree with the solution experiments. The NPs embedded into the TiO_2 matrix show red shifted LSPRs due to the dielectric screening effect, as expected. Along with the classical electromagnetic calculations, we computed the rates of generation of over-barriers hot electrons using a quantum formalism [6]. Our classical and quantum calculations were used to interpret and understand the optical and PE data from experiments.

3. Results and Discussion

Figure 1 shows experimental extinction spectra of aqueous suspensions of TiN and ZrN NPs. The absorption maximum

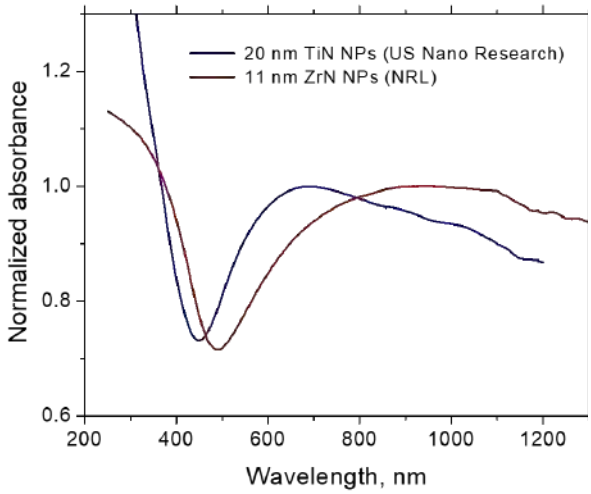


Figure 1. Normalized absorbance of 20 nm TiN and 11 nm ZrN NPs.

of ZrN NPs is broader than that of TiN NPs and shifted to the IR region. An increase in absorption below 500 nm is due to interband transitions in TiN and ZrN NPs.

Figure 2 demonstrates how the interaction between the TiN/TiO_2 photocatalyst and visible light can be utilized for PE CH_3OH oxidation. Two important points come across when comparing incident photon to electron efficiencies (IPCEs) for CH_3OH oxidation on TiN/TiO_2 vs TiO_2. First, potential need to be applied in order to initiate CH_3OH photooxidation at the TiN/TiO_2 interface since it forms Ohmic junction. Second, increase in IPCE, observed for TiN/TiO_2 photocatalyst at wavelengths below 650 nm in Fig. 2, correlates with enhancement in optical absorption due to interband transitions in TiN NPs in Fig. 1. This correlation points towards participations of highly reactive holes generated by interband transitions in TiN NPs in CH_3OH oxidation.

IPCE vs wavelength curves depicted in Fig.2 will be used as a baseline for comparison of ZrN/TiO_2 and $TiN@Au/TiO_2$ to TiN/TiO_2 material.

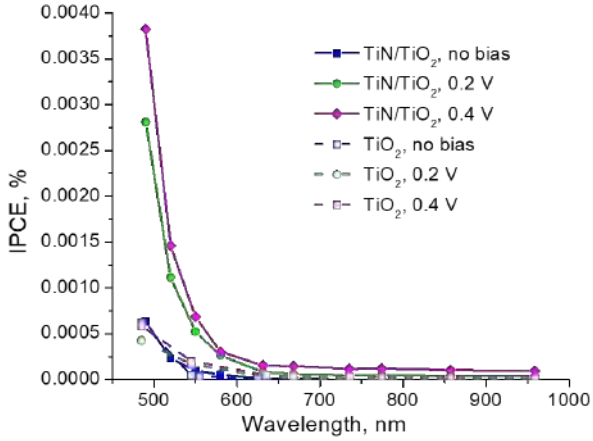


Figure 2.IPCE vs wavelength for TiN/TiO_2 and TiO_2 photocatalysts at potentials equal to open circuit potential, 0.2 and 0.4 V, in aqueous solution of 0.5 M CH_3OH+0.1 M NaOH

4. Conclusions

We have developed novel approaches for synthesis of ZrN and TiN@Au NPs. ZrN NPs establish broader LSPR compared to that of TiN NPs, which makes them more efficient light absorber under the solar illumination and, therefore, holds promise for photocatalytic application. We demonstrate that the efficiency of photocatalytic reactions can be controlled by intelligent interface design.

Acknowledgements

AE, AP, BS, and OAB are grateful to ONR for financial support of this program. GTF acknowledges financial support from USARL Cooperative Agreement award W911NF-17-2-0057.

References

[1] A. Naldoni, U. Guler, Z.X. Wang, M. Marelli, F. Malara, X.G. Meng, L.V. Besteiro, A.O. Govorov, A.V. Kildishev, A. Boltasseva, V.M. Shalaev, Advanced Optical Materials, 5 (2017).

[2] T. Liu, L.V. Besteiro, Z. Wang, A.O. Govorov, Faraday Discussions, (2018) Ahead of Print.

[3] O.A. Baturina, A. Epshteyn, B. Simpkins, N. Bhattarai, T.H. Brintlinger, Journal of the Electrochemical Sociaty, (2019).

[4] M.H. Chisholm, C.E. Hammond, J.C. Huffman, Polyhedron, 7 (1988) 2515.

[5] G.T. Forcherio, D.R. Baker, J. Boltersdorf, A.C. Leff, J.P. McClure, K.N. Grew, C.A. Lundgren, Journal of Physical Chemistry C, 122 (2018) 28901.

[6] G.V. Hartland, L.V. Besteiro, P. Johns, A.O. Govorov, Acs Energy Letters, 2 (2017) 1641.

Structural Alteration of Genomic DNA upon Interaction with Silver Nanoparticles

Luca Guerrini

Departamento de Quimica Fisica e Inorganica, EMaS, Universitat Rovira i Virgili,
Carrer de Marcel$l´ı Domingo s/n, 43007 Tarragona, Spain. E-mail: luca.guerrini@urv.cat

Abstract

The cooperative binding of cationic nanoparticles and duplex nucleic acids can alter the structural properties of the double-helix leading to strand separation. Still, the exact determinants and underlying mechanisms leading to such perturbation remain unclear. Here, we highlights new fundamental insights in this process by tackling the role of key variables, mainly surface charge and size/geometrical arrangement of DNA/nanoparticle clusters.

Introduction

The combination of DNA and nanoparticles has been generating a wealth of research in the field of bionanotechnology resulting in very diverse applications in areas such as biomedicine, sensing, and bioelectronics,[1, 2] These applications mostly exploit chemically modified oligonucleotides to impart unique biochemical properties to the nanomaterials. On the other hand, the understanding of the interaction of native DNA in its duplex form and nanoparticles has been far less explored, and often contradictory findings are found in the literature. This is most likely associated with the complex variability of the physicochemical properties of the metal-liquid interface that largely define the DNA/nanoparticle binding and the resulting impact on the biomolecular structure.

Surface-enhanced Raman scattering (SERS) spectroscopy profits from the localized-surface plasmon resonances (LSPR) generated by plasmonic nanoparticles to provide highly intensified Raman fingerprinting of molecules located in close proximity to the metallic surface (mainly, Ag or Au). Thus, SERS has the potential to be used as a highly sensitive and informative analytical technique for interrogating the union of genetic materials with plasmonic nanoparticles (NPs).[3, 4]

Nanoparticle surface charge plays a central role in determining the DNA/NPs interaction. In this regard, within the frame of SERS, it has been shown that negatively-charged nanoparticles show a limited affinity towards double-stranded DNA duplexes (dsDNA) as the surface binding typically requires direct interaction with nucleobases which, in the double-helix, are sterically hindered.[5] Cationic nanoparticles activate, on the other hand, an adhesion route via purely electrostatic binding of the readily accessible phosphate groups. Notably, spermine-coated positively-charged silver nanoparticles (AgSp) has been successfully used as an efficient plasmonic substrate for the acquisition of highly reproducible and intense SERS spectra of DNA duplexes, which translated into multiple applications such as the detection of single-base mismatches and nucleobase lesions,[6, 7] quantification of base composition,[8] differentiation of tumour-related point mutations in K-Ras genes,[9] and, more recently, Trau and coworkers combined this SERS approach with RNA pre-amplification kits to generate target amplicons for prostate cancer (PCa) risk stratification.[10] Herein, we discuss the application of SERS to investigate the structural alteration of DNA duplexes resulting from the electrostatic binding with cationic silver nanoparticles of different ζ potential.

Discussion

AgSp nanoparticles of ca. 22 nm size and ζ potential tuned in the +20 to +40 range were exposed to both short (21 base pairs) and genomic (calf thymus) DNA duplexes ($dsDNA_{21}$ and ctDNA, respectively). Regardless of the DNA size, intense and well-defined SERS spectra of short and genomic DNAs are obtained, revealing a progressive reshaping of the spectral profile for decreasing colloidal ζ potential and nanoparticle concentration (Fig. 1A). These spectral changes are associated with an increasing extent of base unstacking and unpairing. Among others, we highlight the spectral shifts cytosine+thymine (C/T) ring breathing mode at ca. 785 cm^{-1} which is informative of a larger degree of duplex separation. Both surface-charge (correlated with the ζ potential) and DNA/NP ratio (which affects the relative distribution of different particle clusters) play key roles in the alteration of the double-helix structure. Monitoring the spectral shifts of the C/T ring breathing at different DNA/NP ratios (fixed ζ potential) reveals minimal structural perturbation at intermediate ratios (Fig. 1B) when particle clustering is maximized. Accordingly, molecular dynamic simulations of model DNA-clusters suggest that size and geometrical architecture of particle clusters contribute at determining the extent of structural stress underwent by the duplex at the gap.[3] Specifically, larger aggregates appear to minimize the structural stress of the interparticle duplexes by favoring a more compact conformation. Subsequently, we fixed the DNA/NP at the

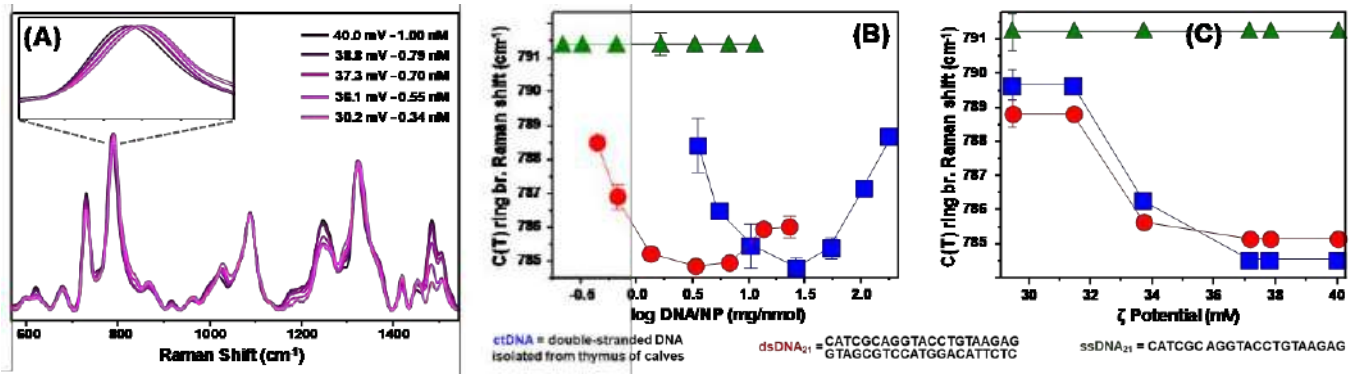


Figure 1. (A) SERS spectra of ctDNA (7.96 µg/mL) in AgSp colloids with different ζ potential (mV) and particle concentration (nM). (B) Frequency shift of C/T ring breathing band in AgSp (+40mV) for different DNA/NP ratios (logarithmic scale, mg/mol). (C) Frequency shift of C/T ring breathing band for constant DNA/NP ratio and variable ζ potential.

value providing minimal duplex perturbation and progressively varied the ζ potential of the colloids (Fig. 1C). In this case, both short and genomic DNA display a sudden red-shift of the C/T peak position at ζ potential below ca. 32-34 mV. This transition may be associated with the drop in concentration of spermine surface molecules under a critical level below which the reduction of anchoring points for DNA adhesion forces the adsorbed duplexes to significantly alter their local structure to efficiently bind a second nanoparticle.

Conclusions

This study provides new fundamental insights into the interaction of DNA duplexes and cationic nanoparticles. In particular, the key roles of both surface charge and cluster geometrical features on defining the integrity of the double-helix structure upon cooperative binding with nanoparticles have been demonstrated.

Acknowledgements

LG acknowledges Spanish Ministerio de Economia y Competitividad (CTQ2017-88648R, CTQ2014-59808R and RYC-2016-20331), the Generalitat de Catalunya (2017SGR883 and AGAUR 2015-DI-015), the Universitat Rovira i Virgili (2017PFR-URV-B2-02), and the Universitat Rovira i Virgili and Banco Santander (2017EXIT-08).

References

[1] A. Samanta, A. I.-L. Medintz, Nanoparticles and DNA - a powerful and growing functional combination in bionanotechnology. *Nanoscale* 8: 9037-9095, 2016.

[2] P.D.-Howes, S. Rana, M.-M. Stevens, Plasmonic nanomaterials for biodiagnostics. *Chem. Soc. Rev.* 43: 3835-3853, 2014.

[3] P. Gisbert-Quilis, M. Masetti, J. Morla-Folch, J.M. Fitzgerald, N. Pazos-Perez, E. Garcia-Rico, V. Giannini, R.A. Alvarez-Puebla, L. Guerrini, The Structure of Short and Genomic DNA at the Interparticle Junctions of Cationic Nanoparticles. *Adv. Mater. Interfaces* 4: 1700724, 2017.

[4] A. Torres-Nunez, K. Faulds, D. Graham, R.A. Alvarez-Puebla, L. Guerrini, Silver colloids as plasmonic substrates for direct label-free surface-enhanced Raman scattering analysis of DNA, *Analyst* 141: 5170-5180, 2017.

[5] E. Garcia-Rico, R.A. Alvarez-Puebla, L. Guerrini, Direct surface-enhanced Raman scattering (SERS) spectroscopy of nucleic acids: from fundamental studies to real-life applications, *Chem. Soc. Rev.* 47: 4909-4923, 2018.

[6] L. Guerrini, Ž. Krpetić, D. van Lierop, R.A. Alvarez-Puebla, D. Graham, Direct Surface-Enhanced Raman Scattering Analysis of DNA Duplexes, *Angew. Chem.-Int. Edit.* 54: 1144-1148, 2015.

[7] J. Morla-Folch, H.-n. Xie, P. Gisbert-Quilis, S. Gómez-de Pedro, N. Pazos-Perez, R.A. Alvarez-Puebla, L. Guerrini, Ultrasensitive Direct Quantification of Nucleobase Modifications in DNA by Surface-Enhanced Raman Scattering: The Case of Cytosine, *Angew. Chem.-Int. Edit.* 54: 13650-13654, 2015.

[8] J. Morla-Folch, R.A. Alvarez-Puebla, L. Guerrini, Direct Quantification of DNA Base Composition by Surface-Enhanced Raman Scattering Spectroscopy, *J. Phys. Chem. Lett.* 7: 3037-3041, 2016.

[9] J. Morla-Folch, P. Gisbert-Quilis, M. Masetti, E. Garcia-Rico, R.A. Alvarez-Puebla, L. Guerrini, Conformational SERS Classification of K-Ras Point Mutations for Cancer Diagnostics, *Angew. Chem.-Int. Edit.* 56: 2381-238, 2017.

[10] K.-M. Koo, J. Wang, R.-S. Richards, A. Farrell, J.-W. Yaxley, H. Samaratunga, P.-E. Teloken, M.J. Roberts, G.D. Coughlin, M.-F. Lavin, P.-N. Mainwaring, Y. Wang, R.-A. Gardiner, M. Trau, Design and Clinical Verification of Surface-Enhanced Raman Spectroscopy Diagnostic Technology for Individual Cancer Risk Prediction, *ACS Nano* 12: 8362-8371 (2018).

Energy Transfer in Donor-acceptor Quantum Dots Simultaneous Mediated by Double Plasmon Modes of Gold Nanorod

Hanjie Zhang, Deren Yang, Dongsheng Li*

State Key Laboratory of Silicon Materials and Department of Materials Science and Engineering, Zhejiang University, Hangzhou 310027, P.R. China
*Corresponding author: Dongsheng Li, email: mselds@zju.edu.cn;

Abstract

In this paper, the gold nano-rod (GNR) with silica shell and quantum dots (QDs) adsorbed on the silica surface, i.e. the GNR@SiO2@QD hybrid structures were constructed to investigate the energy transfer between quantum dots. Two plasmon peaks of gold nano-rod are coupled with the emission peaks of donor and acceptor respectively, in fluorescent resonance energy transfer (FRET). The energy transfer efficiency from donor to acceptor is 35.34%, and the fluorescence intensity of acceptor is increased by 2 times.

1. Introduction

Localized surface plasmon has been widely used to enhance fluorescence, increase light absorption efficiency, enhance Raman scattering, and improve FRET efficiency[1, 2]. The FRET has a wide range of applications in the field of biosensors, such as ion detection[3], biomolecular conformations and so on. In addition, FRET has recently demonstrated potential applications in optoelectronic switches, light capture and LEDs[4,5]. When the local surface plasmon (LSP) couple with the FRET system, the energy transfer distance and efficiency can be improved effectively. Many metal nano-particles were used to study the LSP-coupled FRET, such as nano-sphere, nano-rods, nano-platelets and so on. To date, few articles utilize two plasmon peaks of GNR simultaneously. Therefore, it is expected to improve the energy transfer performance that two kinds of local surface plasmon resonance peaks couple with the luminescence peaks of donor and acceptor simultaneously.

In this paper, the transversal surface plasmon resonance (TSPR) peak and longitudinal surface plasmon resonance (LSPR) peak of the GNR couple with the donor and acceptor luminescence peak respectively. And the fluorescence intensity of the quantum dots increased by 15 times. In the meanwhile, the fluorescence enhancement increased from 1.3 times to 2 times. Time-resolved spectroscopy also proved this phenomenon, and the calculated energy transfer efficiency reached 35.34%.

2. Experimental section

GNR was prepared via modified seed growth method [6]. The new prepared GNR was centrifuged three times, and dissolved in a CTAB solution with a proper concentration. After standing at room temperature for more than 2 hours. The pH of the solution was adjusted to 10-11, using a 0.1 M NaOH aqueous solution. Then, adding appropriate tetraethylorthosilicate (TEOS) to the solution.12 hours later, the GNR would be coated with silica, and this structure was called GNR@SiO_2. The GNR@SiO_2 particles were first centrifuged twice with ethanol, and then centrifuged twice with toluene. Finally these particles were dispersed into 2 mL toluene. 100 μL 1 vol% 3-aminopropyltriethoxysilane (APTES) was added to the solution dropwisely. After stirring for 12 hours, solution was centrifuged twice with toluene and tetrahydrofuran (THF) twice, the solution was dissolved in 2 mL of THF. Then 1-100 μL of aliphatic-amine modified QDs solution was added to the solution. After stirring for 12 hours. The structure GNR@ SiO_2@QD was completed.The morphology of the particles was carried on transmission electron microscope (TEM, Philips CM200). The extinction spectra of nano-rods were measured by using UV-vis-NIR spectrophotometer (U4100, Hitachi). The photoluminescence and time-resolved photoluminescence were characterized by a multichannel photon counting system (Edinburg Photonics, Livingston, UK).

3. Results and Discussion

Fig.1 is the TEM image of GNR@SiO_2 and GNR@ SiO_2@QD. It illustrates that the gold bar is coated with silica evenly as shown in Fig.1a. The thickness of silica is around 17 nm. After APTES treatment, silica surface has amino groups. In the meanwhile, surface of the QDs are absorbed by fatty amine ligand, so the QDs could adsorb on the surface of GNR@SiO_2, via ligand exchange. The Fig.1b shows the structure GNR@ SiO_2@QD. The small black dots around GNR@SiO_2 are QDs. The Fig.1c is the HRTEM image of GNR@SiO_2@QD. The lattice of QDs can be seen from this image.

Fluorescence of quantum dots coupled to two different local surface plasmon resonance of GNRs simultaneously was shown in Fig.2.The brown dotted line is the extinction curve of GNR. The peaks of TSPR (536nm) and LSPR (605nm) overlap with QDs, whose fluorescence peaks are 525nm (QD525) and 605nm (QD605), respectively. The green short line is the fluorescence spectrum of QD525 (donor), and the

fluorescence spectrum of GNR@QD525+ QD605 is pink solid line. Compared GNR@QD525+QD605 and GNR@ QD605. The fluorescence intensity of acceptor (QD605) is increased by 2 times. By adjusting the extinction peaks of quantum rods and the emission peaks of quantum dots, the coupling area between the peaks of quantum dots and gold rods is greatly improved. When the LSPR peak and TSPR peak couple with QD525 and QD605 respectively, the donor can deliver more energy to the acceptor. This makes the fluorescence enhancement of the acceptor more obvious.

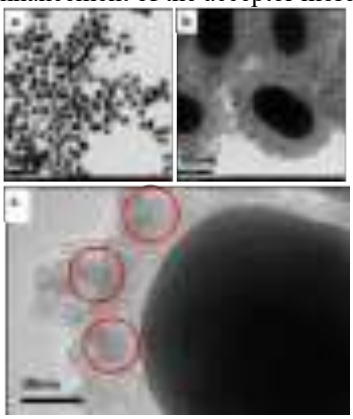


Fig. 1. Structure change during particle preparation (a, GNR@SiO_2 particles; b, GNR@SiO_2@QD particles; c, the HRTEM of GNR@SiO_2 @QD)

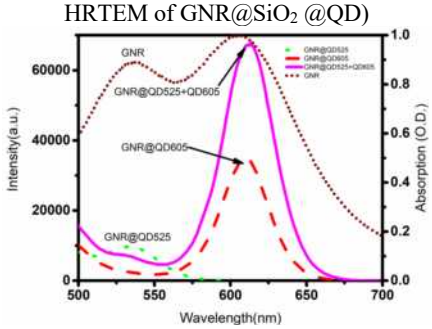


Fig. 2. Fluorescence spectra of quantum dots coupled to two different local surface plasmon resonance of GNRs simultaneously.

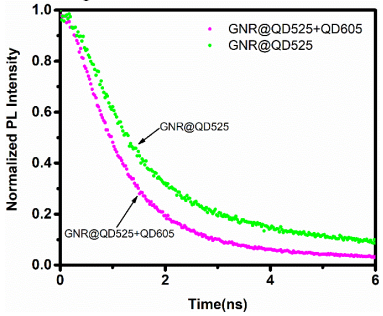


Fig. 3. The lifetime of donors in GNR@QD525+QD605 and GNR@QD525.

Fig.3 shows that when the FRET occurs, the lifetime of the donor is significantly reduced from 2.15 ns to 1.39 ns. The energy transfer efficiency is 35.34%. Fig.4. is the photoluminescence and time-resolved photoluminescence of QD adsorbed on silica spheres and without the GNRs. The QD605 means the silica spheres adsorb QD605 only. However, the QD525+QD605 stands for the silica spheres adsorb QD525 and QD605 simultaneously. Comparing the fluorescence intensity of GNR@QD605 (in Fig.2) and QD605 (in Fig.4), the fluorescence intensity of acceptor increases 8% under the effect of the surface plasmon. In the right figure, the lifetime of the donor decreases from the 4.26ns to 2.36ns, which proves the occurrence of the energy transfer phenomenon.

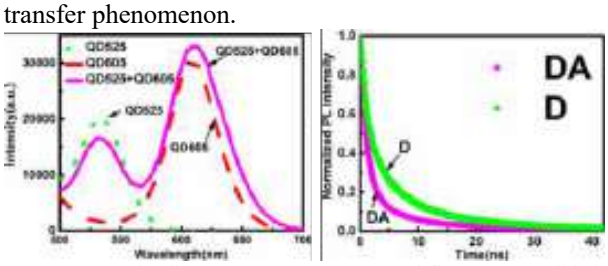


Fig. 4. The fluorescence spectrum and fluorescence lifetime of control group.

4. Conclusions

In conclusion, GNR@SiO2@QD hybrid structures were constructed. When the two kinds of surface plasmon are coupled to two quantum dots with different fluorescence wavelengths, the energy transfer efficiency increases to 35.34% and the fluorescence intensity of acceptor increases 2 times. Taking into account the significant enhancement of energy transfer phenomenon, this structure has a guiding role in the design of energy transfer structures, and is expected to improve the efficiency of light harvesting and LED devices.

Acknowledgements

This work was supported by National Natural Science Foundation of China (Nos. 61874095 and 61721005).

References

[1] M.Zhao, L.Shao, H.Chen.and J.Wang, Plasmon-Controlled Förster Resonance Energy Transfer, The *Journal of Physical Chemistry C*, 116:8287-8296, 2012.

[2] H.Sugimoto, T.Chen, R.Wang, M.Fujii.and B.Reinhard, Plasmon-Enhanced Emission Rate of Silicon Nanocrystals in Gold Nanorod Composites, *ACS Photonics*, 2015, 2(9):150804114306005.

[3] E.Goldman, I.Medintz, J.Whitley, A.Hayhurst, A.Clapp, H.Uyeda, J.Deschamps, M.Lassman and H.Mattoussi, A Hybrid Quantum Dot−Antibody Fragment Fluorescence Resonance Energy Transfer-Based TNT Sensor, *JACS*, 127:6744-6751, 2005.

[4] S.Akhavan, M.Akgul, P.Hernandez-Martinez,.and H.Demir, Plasmon-Enhanced Energy Transfer in Photosensitive Nanocrystal Device, *ACS Nano*, 11(6):5430-5439, 2017.

[5] K. C. E. K. Tae-Ho Kim, Full-colour quantum dot displays fabricated by transfer printing, *Nature Photonics*, 3(5):176-182, 2011.

[6] X.Ye, C.Zheng, J.Chen, Y.Gao and C.Murray, Using Binary Surfactant Mixtures to Simultaneously Improve the Dimensional Tunability and Monodispersity in the Seeded Growth of Gold Nanorods, *Nano Letters*, 13: 765-771, 2013.

Refractory plasmonic nanocavities for chemistry at high temperatures

Alberto Naldoni[1*], Zhaxylyk A. Kudyshev[2], Luca Mascaretti[1], Štěpán Kment[1], Alexandra Boltasseva[2], Vladimir M. Shalaev[2], Patrik Schmuki[1,3], Radek Zbořil[1]

[1] Regional Centre of Advanced Technologies and Materials, Faculty of Science, Palacký University, Šlechtitelů 27, 78371 Olomouc, Czech Republic

[2] School of Electrical and Computer Engineering and Birck Nanotechnology Center, Purdue University, West Lafayette, IN 47907, USA

[3] Department of Materials Science and Engineering, University of Erlangen-Nuremberg, Martensstrasse 7, D-91058 Erlangen, Germany

*corresponding author, E-mail: alberto.naldoni@upol.cz

Abstract

Plasmonic metamaterials provide sub-wavelength light concentration and consequent localized heating, which holds great potential in the development of solar–thermal technologies. Here, I will present our recent efforts to fabricate large-scale refractory metamaterial films made by cylindrical plasmonic cavities of titanium nitride (TiN) and their use in various thermoplasmonic applications such as decomposition of molecules, synthesis of metal nanoparticles, conformal deposition of inorganic thin films, and steam generation.

1. Introduction

The use of nanostructures sustaining surface plasmons to control heat at the nanoscale, known as thermoplasmonics [1], has recently emerged as a subfield of plasmonics and holds great promises in several solar energy conversion applications including solar-thermophotovoltaics [2,3], fabrication of nanostructures [4], heterogeneous catalysis [5,6], optical trapping [7,8], and steam generation [9–11].

These demonstrations have been limited to nanostructures made of noble metals, which, despite showing outstanding optical properties for plasmonic applications, raise major issues related to their high cost and poor chemical and thermal stability.

In contrast, refractory TiN exhibits high chemical resistance to harsh environments, optical properties similar to Au and it can be utilized as plasmonic material in the visible and near-infrared regions [12–14]. Combining refractory material properties with broad plasmonic resonances, TiN offer a unique solution to material-related limitations in solar-thermal applications, where high temperature durability and/or chemical stability are needed.

Here we present our recent results on sub-wavelength plasmonic TiN nanocavities and their corresponding local heating properties. A new fabrication strategy to achieve broadband plasmonic absorbers will be outlined, while the solar-to-heat conversion efficiency along with examples of large-scale solar-thermal applications in chemistry will be discussed in detail.

2. Results and discussion

We start fabricating TiO_2 nanocavities assembled in hexagonal lattice geometry through anodization of a titanium foil. After nitridation in ammonia atmosphere, TiO_2 is completely converted to TiN nanocavities with diameter of 80 nm, length of 150 nm, wall thickness of about 20 nm, and period of 100 nm.

The resulting TiN nanocavity films show near unity light absorption in the visible and near-infrared wavelength ranges as shown in Figure 1.

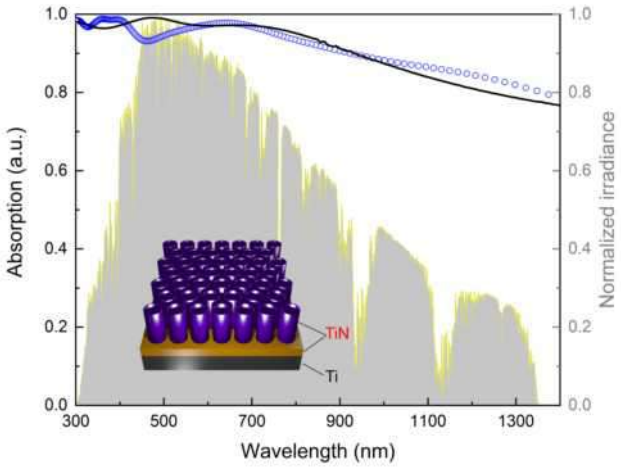


Figure 1: Experimental (black line) and simulated (empty blue dots) absorption spectra of TiN nanocavities, along with the normalized irradiance of the AM 1.5G solar spectrum (grey shaded area). The inset shows a schematic representation of the film stack composed by a Ti foil substrate, a TiN thermal layer, and TiN nanocavities.

In this talk, the results on experimental and simulated optical properties will be discussed and it will be shown that

both cavity modes and plasmonic resonances are supported inside the nanocavities. As a result, the plasmonic TiN nanocavity metamaterials are capable of generating intense local heating upon solar illumination. The opto-thermal properties and solar-to-heat conversion efficiency of our thermoplasmonic films will be analyzed, providing possible metamaterial designs to improve the performance of plasmonic TiN nanocavities.
Finally, some examples of utilization of large-scale thermoplasmonic TiN films will be illustrated, including decomposition of metal-organic complexes, conformal deposition of ultrathin films, and steam generation.

3. Conclusions

Our results demonstrate the possibility of fabricating large scale refractory plasmonic metamaterials made by plasmonic TiN nanocavities through a simple and scalable strategy. These films provide efficient solar–to–heat energy conversion producing temperatures above 600 ºC under moderate concentrated solar power and can be conveniently utilized as nanofurnaces or nanoreactors to drive chemical processes with attolitre scale precision.

Acknowledgements

Authors acknowledge the support by the Operational Programme Research, Development and Education - European Regional Development Fund, project no. CZ.02.1.01/0.0/0.0/15_003/0000416 of the Ministry of Education, Youth and Sports of the Czech Republic.

References

[1] G. Baffou, R. Quidant, Thermo-plasmonics : using metallic nanostructures as nano-sources of heat. *Laser & Photonics Reviews* 17: 1–17, 2012.

[2] A. Lenert, D. M. Bierman, Y. Nam, W. R. Chan, I. Celanović, M. Soljačić, E. N. Wang, A nanophotonic solar thermophotovoltaic device. *Nature Nanotech.* 9: 126–130, 2014.

[3] W. Li, U. Guler, N. Kinsey, G. V. Naik, A. Boltasseva, J. Guan, V. M. Shalaev, A. V. Kildishev, Refractory plasmonics with titanium nitride: broadband metamaterial absorber. *Adv. Mater.* 26: 7959–7965, 2014.

[4] D. A. Boyd, L. Greengard, M. Brongersma, M. Y. El-Naggar, D. G. Goodwin, Plasmon-assisted chemical vapor deposition. *Nano Lett.* 6: 2592–2597, 2006.

[5] J. R. Adleman, D. A. Boyd, D. G. Goodwin, D. Psaltis, Heterogenous catalysis mediated by plasmon heating. *Nano Lett.* 9: 4417–4423 (2009).

[6] L. Zhou, D. F. Swearer, C. Zhang, H. Robatjazi, H. Zhao, L. Henderson, L. Dong, P. Christopher, E. A. Carter, P. Nordlander, N. J. Halas, Quantifying hot carrier and thermal contributions in plasmonic photocatalysis. *Science* 362: 69–72 (2018).

[7] J. C. Ndukaife, A. V. Kildishev, A. G. Agwu Nnanna, V. M. Shalaev, S. T. Wereley, A. Boltasseva, Long-range and rapid transport of individual nano-objects by a hybrid electrothermoplasmonic nanotweezer. *Nature Nanotech.* 11: 53–59, 2015.

[8] M. L. Juan, M. Righini, R. Quidant, Plasmon nano-optical tweezers. *Nature Photonics* 5: 349–356, 2011.

[9] O.Neumann, A. S. Urban, J. Day, S. Lal, P. Nordlander, N. J. Halas, Solar Vapor Generation Enabled by Nanoparticles. *ACS Nano* 7: 42–49, 2013.

[10] L. Zhou, Y. Tan, J. Wang, W. Xu, Y. Yuan, W. Cai, S. Zhu, J. Zhu, 3D self-assembly of aluminium nanoparticles for plasmon-enhanced solar desalination. *Nature Photonics* 10: 393–398, 2016.

[11] L. Zhou, Y. Tan, D. Ji, B. Zhu, P. Zhang, J. Xu, Q. Gan, Z. Yu, J. Zhu, Self-Assembly of Highly Efficient , Broadband Plasmonic Absorbers for Solar Steam Generation. *Science Advances* 2, e1501227, 2016.

[12] P. R. West, S. Ishii, G. V. Naik, N. K. Emani, V. M. Shalaev, A. Boltasseva, Searching for better plasmonic materials *Laser & Photonics Reviews* 4: 795–808 (2010).

[13] G. V. Naik, V. M. Shalaev, A. Boltasseva, Alternative plasmonic materials: beyond gold and silver. *Adv. Mater.* 25: 3264–3294 (2013).

[14] U. Guler, A. Boltasseva, V. M. Shalaev, Refractory plasmonics. *Science* 344: (6181), 263–264 (2014).

Comparison of the optical magnetism of Au dodecahedral clusters and plasmonic raspberries produced by bottom up approach

Laurent Lermusiaux[1], Véronique Many[1], Alexandre Baron[2], Romain Dezert[2], Etienne Duguet[1], Virginie Ponsinet[2], Serge Ravaine[2], Philippe Richetti[2], Philippe Barois[2] and Mona Treguer-Delapierre[1]

[1] Institut de Chimie de la Matière Condensée de Bordeaux, CNRS-Université de Bordeaux, UMR5026, 33600 Pessac, France
[2] Centre de Recherche Paul Pascal, CNRS-Université de Bordeaux, UMR5031, 33600 Pessac, France
*corresponding author, E-mail: treguer@icmcb-bordeaux.cnrs.fr

Abstract

The generation in artificial composites of a magnetic response to light comparable in magnitude with the natural electric response, may offer an invaluable control parameter for a fine steering of light at the nanoscale. In many experimental realizations however, the magnetic response of artificial meta-atoms is too weak so that there is a need for new designs with increased magnetic polarizability. Numerical simulations show that geometrical plasmonic nanostructures based on the ideal model of Platonic solids are excellent candidates for the production of strong optical magnetism in the visible range. Inspired by this model, we have recently developed a bottom-up approach to synthesize plasmonic nano-clusters made of a precise number of gold or silver patches around a central silica core. In this talk, we will compare the optical magnetic response of clusters made of twelve gold or silver patches located at the center of the faces of a dodecahedron and the one of disordered plasmonic clusters ("plasmonic raspberries") of the same size. We will demonstrate that the regular organization of the satellites around the core is more efficient than a random distribution for the generation of a circular current mode. Controlling the uniform separation of the satellites in the regular distribution warrants a better control of the collective electromagnetic coupling which determines the strength of the circular plasmonic currents generating the magnetization.

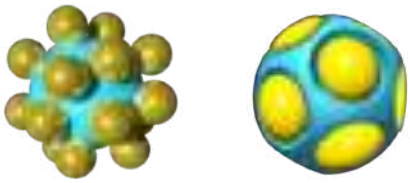


Figure 1 – Sketch of the plasmonic raspberries (random distribution of the satellites around a dielectric core) and the gold dodecapod clusters (12 satellites symmetrically arranged around the dielectric core made of silica).

Introduction

Metamaterials are ensembles of nanoresonators that exhibit unsual optical properties that are otherwise attainable with natural materials. The first metamaterial was realized by Smith et al. in 1999[1] who produced a composite medium that had simultaneously negative electric permittivity and magnetic permeability, which constitutes a negative index material. Such a material has only been thought of purely theorically by Veselago in 1968 and many profound physical implications had been predicted such as the reversal of the Cherenkov radiation.[2] Since then, the metamaterials concept has been used to produce extraordinary devices ranging from invisibility cloaks to hyperlenses that enable imaging beyond the diffraction limit.[3,4] Today, metamaterials have moved beyond electromagnetic waves and now includes acoustic, mechanical, thermal and seismic waves. When optics are concerned, most metamaterials produced thus far have been fabricated using top-down lithographic approaches which severely limits the total amount of nanoresonators that can be build. As a result, the total surface area that metamaterials typically cover rarely exceeds 100 μm^2. The bottom-up approach offers a serious alternative to tackle this hurdle, because it allows considering the nanoresonators and the metamaterial separately, in a way that we may refer to as hierarchical self-assembly.[5] Indeed, nanochemistry tackles the problem of synthesizing complex nanoparticles with desired dispersions of the electric and magnetic polarizabities, while soft matter self-assembly focuses on producing materials made of large volumes of these meta-atoms. Recently, we have proved that we could produced via bottom-up approach a bulk magnetic material exhibiting non-natural values of the magnetic permeability.[6] In this material, the resonators consist of a set of plasmonic nanoparticles evenly, but randomly distributed around a dielectric core nanoparticle (plasmonic raspberries). The ratio of the magnetic to electric dipole scattering cross-section of a single raspberry is about 1/3 and the magnetic permeability of the assembled bulk metamaterial ranges from 0.8 to 1.45 μ_0 units.[6]

In order to increase the magnetic response of the

metamaterial, we investigate in this work novel morphologies guided by numerical simulations. We show experimentally that a significant increase of the magnetic dipole can be obtained by a well-controlled geometrical organization of twelve plasmonic satellites onto the dielectric core.[7]

Results

The highly symmetrical clusters were prepared by a multistep synthetic process from dodecahedral-dimpled silica particles. The details of the synthesis have been recently published.[7] Figure 2 shows typical micrographs of the nano-objects produced in high yield, at the gram scale. The twelve gold satellites are symmetrically arranged around a silica core of 100 nm.

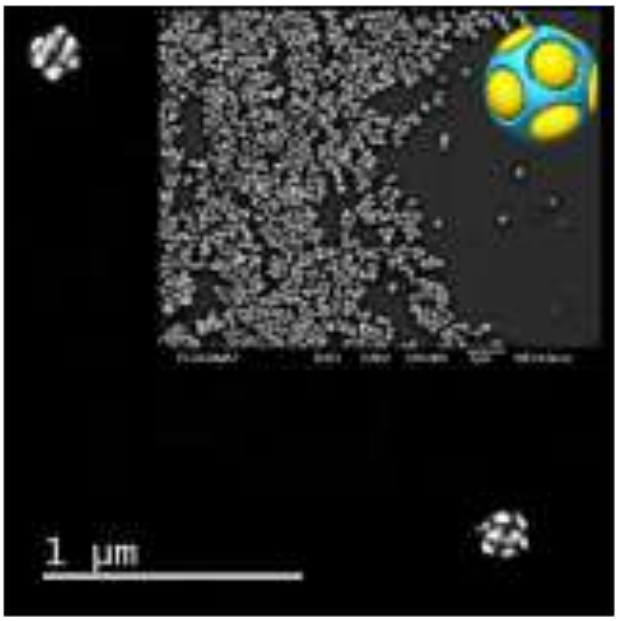


Figure 2: SEM micrographs of gold dodecapod clusters produced by a bottom up approach.

The optical response of the golden dodecapods has been measured by a polarization-resolved static light scattering. The ratio of the magnetic to electric scattering is increased by a factor >3 when compared to plasmonic raspberries of the same size with the same amount of gold. These overall results validate the superiority of the dodecapod structure over the distorted distribution of a large number of satellites in the raspberry model. Changing the composition of the satellites toward silver-gold ones allowed to reduce the optical losses and strongly enhances the magnetic response. These new clusters are good candidates for the fabrication of Huyghens' sources in which the electric and magnetic scattering display equal strength.

Conclusions

The bottom-up approach can be used to elaborate highly regular plasmonic clusters. The regular organization of the satellites around the core is more efficient than a random distribution for the generation of circular current mode. This observation is fully consistent with the initial inspiring models of resonant LC Inductor-capacitor nanocircuits.[8,9] The bottom-up approach enables cost-effective, large-scale production of such magnetic resonators, hence opening the way to the fabrication of 2D and 3D magnetic metamaterials.[10]

Acknowledgements

This work was supported by the LabEx AMADEus (ANR-10-LABX-42) and IdEx Bordeaux (ANR-10-IDEX-03-02), i.e. the Investissements d'Avenir programme of the French government managed by the Agence Nationale de la Recherche.

References

[1] D. Schmitt *et al*., "Composite medium with simultaneously negative permeability and permittivity" *Physical review letters*, 84, 4186 (2000).

[2] V. Veselago *et al*., "Metamaterial electromagnetic cloack at microwave frequencies", *Soviet Physics uspekhi*, 314, 977 (1968).

[3] D. Schuring *et al*., "Metamaterial electromagnetic cloak at microwave frequencies", *Science*, 314, 977 (2006).

[4] Z. Liu *et al*., "Far-field optical hyperlens magnifying sub-diffraction limited objects", *Science*, 315, 1686 (2007).

[5] A. Baron *et al*., "Self-assembled optical metamaterials", *Optics and Laser Technology*, 82, 94 (2016).

[6] S. Gomez-Graña *et al*., "Hierarchical self-assembly of a bulk metamaterial enables isotropic magnetic permeability at optical frequencies", *Mater. Horiz*. **3**, 596 (2016).

[7] V. Many *et al*.,"High optical magnetism of dodecahedral plasmonic meta-atoms". *Nanophotonics*, 2018. DOI: 10.1515/nanoph-2018-0175.

[8] C.R. Simovski *et al*., "Model of isotropic resonant magnetism in the visible range based on core-shell clusters". Phys. Rev B **79**, 045111 (2009).

[9] C. Rockstuhl *et al*., "Design of an Artificial Three-Dimensional Composite Metamaterial with Magnetic Resonances in the Visible Range of the Electromagnetic Spectrum". Phys. Rev. Lett. **99**, 017401 (2007).

[10] R. Dezert *et al*. "Isotropic Huygens dipoles and multipoles with colloidal particles". Phys Rev B **96**, 180201(R) (2017).

Surface-enhanced resonant Raman scattering and surface-enhanced fluorescence spectra of a strong coupling system between plasmon and molecular exciton

Tamitake Itoh[1]

[1] Health Research Institute, National Institute of Advanced Industrial Science and Technology (AIST), Takamatsu, Japan
*corresponding author, E-mail: tamitake-itou@aist.go.jp

Abstract

Surface-enhanced resonant Raman scattering (SERRS) and surface enhanced fluorescence (SEF) from single silver nanoparticle dimers under strong coupling regimes are investigated. Enhancement and quenching factors are derived from the Purcell factors, which are estimated by coupling energies obtained from the spectral changes in plasmon resonance based on a coupling oscillator model. The reproduced SERRS spectral changes are consistent with the experimental ones. The calculated SEF spectral changes reproduce the experimental ones by assuming transitions from ultra-fast SEF to conventional SEF.

1. Introduction

Thanks to the discovery of single-molecule (SM) detection of SERRS by single plasmonic nanoparticle (NP) systems like NP dimer, the electromagnetic (EM) coupling between plasmon resonance and molecular exciton has been investigated to clarify SM SERRS. Such single plasmonic NP systems enables us direct observation of relationships between plasmon resonance and SERRS. The observations have shown that the EM coupling in a field confined by plasmon within several cubic nanometers at junctions of NP dimers, called "hotspots", facilitates such large enhancement [1]. SERRS hotspots have also revealed unique phenomena, e.g., strong coupling, in which the rates of EM coupling are larger than the dephasing rates of both plasmon resonance and molecular exciton resonance [2], ultra-fast SEF, in which the SEF rates exceed the molecular vibrational decay rates, resulting in emission from vibrationally excited states in the electronically excited state [3]. Various interesting hotspots have also developed to examine such unique phenomena e.g. Ref. 4.

The present EM model should assume strong coupling. Furthermore, the model should also include not only the quenching of fluorescence but also the quenching of resonant Raman scattering by higher-order plasmons. Such improvement in the EM model and experimental examination might enable us to gain deeper insights from experiments.

We develop a coupling oscillator model to treat the strong coupling between a plasmon and a molecular exciton, including its phonon replicas for representing the multi-level system of a molecule. By considering both enhancement and quenching factors due to the higher-order Purcell factors derived from the coupling energies, spectral changes in SERRS is successfully reproduced. In the case of SEF, we can successfully reproduce the spectral changes by assuming the transition from ultra-fast SEF to conventional one.

2. Experimental

The average diameter of the silver NPs was estimated to be 40 nm. The final concentrations of the R6G solutions and NP dispersion were 6.34×10^{-9} M and 5.5×10^{-11} M, respectively. These mixed solutions were left for 30 min so that the R6G molecules could be adsorbed onto the NPs and the NPs could aggregate for SERRS activation. After the sample solution (50 μL) was dropped onto a slide glass plate, the drop was sandwiched by a glass plate to immobilize it on the plate. The plate was then set on the stage of an inverted optical microscope. The spectroscopic setup for detecting SERRS and SEF and the plasmon resonance spectra have been presented elsewhere [2].

3. Discussion

The model for evaluating the strong coupling system is developed by modifying a coupled oscillator model [2]. The model uses a Franck–Condon mechanism to yield phonon replicas of the exciton line. Thus, the coupled oscillator is composed of an oscillator representing a plasmon and multiple oscillators representing a molecular exciton and its phonon replicas. From the coupled oscillators one can derive scattering cross-section of the system. We evaluated the temporal spectral changes in plasmon resonance during the loss of SERRS activity using the scattering cross-section spectra. The plasmon resonance spectra exhibit blue shifts by 100–200 meV simultaneously with the disappearing SERRS activity. The origin of SERRS is EM coupling between a plasmon and a molecular exciton. Thus, the simultaneous blue shifts are due to the loss of the coupling energy. Figures 1(a) and 1(b) show the temporal changes in the experimental plasmon resonance spectra and the calculated ones, respectively. The blue shift and

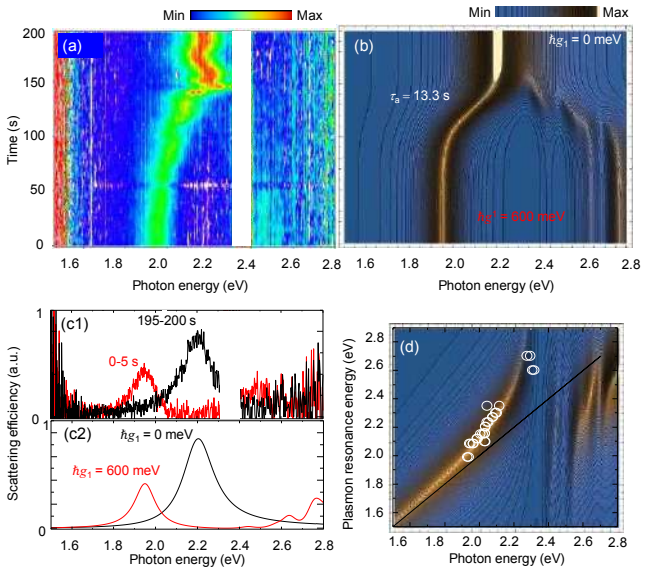


Figure 1: (a) Changes in plasmon resonance spectra during the SERRS disappearance. (b) Calculated changes with decreasing coupling energy. (c1) Experimental plasmon resonance spectra of dimer before (red curve) and after (black curve) the loss of SERRS activity. (c2) Calculated plasmon resonance spectra with decreasing coupling energy from 600 meV (red curve) to 0 meV (black curve). (d) Anti-crossing properties of strong coupling with coupling energy of 400 meV.

complicated spectral change in the blue region are reproduced in the calculation. Figures 1(c1) and 1(c2) show the experimental spectra before and after the loss of SERRS activity and the calculated spectra by reducing from 600 to 0 meV, respectively. Figure 1(d) shows the anti-crossing behavior calculated with coupling energy of 400 meV and the plots of the reproduced plasmon resonance peaks by assuming coupling energy of 400 meV. The positions of all the plots are consistent with the anti-crossing behavior, indicating that the observed spectral changes can be explained by the decreasing coupling energy.

Here, we derive the enhancement and quenching factors for SERRS and SEF from the estimated coupling energy. In the derivation, we phenomenologically apply the Purcell factor,

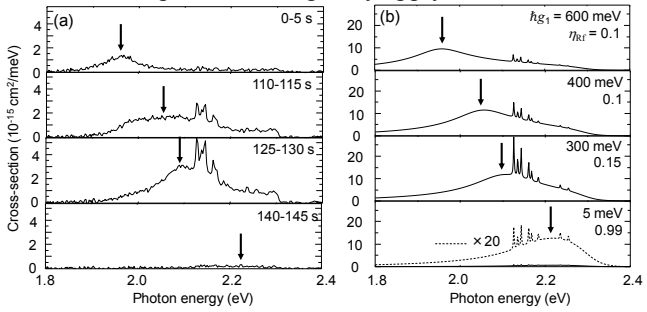


FIG. 2 (a) Changes in SERRS and SEF during the disappearance process. (b) Calculated changes in p SERRS and SEF with decreasing coupling energy and increasing quantum efficiency of SEF.

which originally assumes a weak coupling condition [5]. Figures 2(a) show the temporal changes in the experimental SERRS with SEF spectra of the dimer [6]. The envelopes of the SEF spectra show clearly slow blue shifts; then, SEF finally disappears with rapid blue shifts. We try to reproduce the spectral changes in SERRS with SEF as a function of the coupling energy. Figure 2(b) shows the calculated SERRS and SEF spectra assuming transitions from ultra-fast SEF to conventional SEF with decreasing EM coupling energy [6]. These SERRS and SEF spectra are well reproduced in the experimental results in Fig. 2(a).

4. Conclusions

We analyzed SERRS and SEF under strong coupling conditions. The analysis involved the following: (1) evaluation of coupling energies using a coupled oscillator model, (2) derivation of mode volumes from the energies, (3) estimation of enhancement and quenching factors using the Purcell factors based on the volumes, and (4) reproduction of SERRS and SEF spectra using these factors. The derived factors reproduced the experimental SERRS and SEF spectra by considering ultra-fast SEF.

Acknowledgements

This work was supported by JSPS KAKENHI Grant-in-Aid for Scientific Research (C) Number 18K04988.

References

[1] T. Itoh, M. Iga, H. Tamaru, K. Yoshida, V. Biju, and M. Ishikawa, Quantitative evaluation of blinking in surface enhanced resonance Raman scattering and fluorescence by electromagnetic mechanism, *J. Chem. Phys.* 136: 024703, 2012.

[2] T. Itoh, Y. S Yamamoto, H. Tamaru, V. Biju, S. Wakida, and Y. Ozaki, Single-molecular surface-enhanced resonance Raman scattering as a quantitative probe of local electromagnetic field: The case of strong coupling between plasmonic and excitonic resonance, *Phys. Rev. B* 89:195436, 2014.

[3] T. Itoh, Y. S. Yamamoto, H. Tamaru, V. Biju, N. Murase, and Y. Ozaki, Excitation laser energy dependence of surface-enhanced fluorescence showing plasmon-induced ultrafast electronic dynamics in dye molecules, *Phys. Rev. B* 87: 235408, 2013.

[4] T. Itoh, Y. S. Yamamoto, Y. Kitahama, J. Balachandran, One-dimensional plasmonic hotspots located between silver nanowire dimers evaluated by surface-enhanced resonance Raman scattering, *Phys. Rev. B* 95: 115441, 2017.

[5] T. Itoh, Y. S. Yamamoto, and Y. Ozaki, Plasmon-enhanced spectroscopy of absorption and spontaneous emissions explained using cavity quantum optics, *Chem. Soc. Rev.* 46: 3904, 2017.

[6] T. Itoh and Y. S. Yamamoto, Reproduction of surface-enhanced resonant Raman scattering and fluorescence spectra of a strong coupling system composed of a single silver nanoparticle dimer and a few dye molecules, *J. Chem. Phys*. 149: 244701, 2018.

Photoluminescence from emitters on periodic diffractive arrays of plasmonic and non-plasmonic nanocylinders

Shunsuke Murai[1*], Kazuki Noguchi[1], Katsuhisa Tanaka[1],

[1]Department of Material Chemistry, Graduate School of Engineering, Kyoto University, Katsura, Nishikyo-ku, Kyoto, 606-8510, Japan

*corresponding author, E-mail: murai@dipole7.kuic.kyoto-u.ac.jp

Abstract

We fabricated periodic diffractive arrays of Al, Ag and Si nanocylinders with the identical design and compared their photoluminescence (PL) outcoupling abilities. We deposited a polymer layer containing rhodamine 6G molecules and observed enhanced PLs from the layers on the arrays. The optical transmission with varied incident angle revealed the excitation the hybrid modes of diffraction and localized surface plasmon resonance in Al and Ag arrays and diffraction and Mie resonance in the Si array. The PL enhancements in the three arrays, which came from outcoupling, were explainable by the spectral and spatial profiles of the hybrid modes.

1. Introduction

An array of nanoclyinders can modulate photoluminescence (PL) of emitters via simultaneous excitation of local resonances and light diffractions. Regarding the local resonance, localized surface plasmon resonance (LSPP) has been commonly applied[1 , 2], while Mie resonance can be also a candidate. In recent years, there is a trend to change the material for nanophotonics including metamaterials and metasurfaces, from metal to high-refractive-index dielectrics in order to avoid large absorption losses of metal and deactivation of luminescent center due to energy transfer to metal. However, experimental comparison of PL enhancement between plasmonic and non-plasmonic nanocylinder arrays has hardly been verified. In this study, we compared the PL enhancement of the dye molecules by Al, Ag, and Si nanocylinder arrays. As an emitter we selected rhodamine 6G (R6G), which shows a high quantum yield, and designed the array to have a triangle lattice with a periodicity of 460 nm to show a resonance at the emission wavelength of the emitter.

2. Experimental section

2.1. Sample Fabrication

Al nanocylinders arranged in a triangle lattice with a periodicity of 460 nm were fabricated using nanoimprint lithography in combination with reactive ion etching (RIE), as described elsewhere[3]. Ag nanocylinder arrays were fabricated using nanoimprint lithography in combination with an electron cyclotron resonance Ar ion milling. Si nanocylinder arrays were fabricated by the combination of nanoimprint lithography and Si deep etching. The same mold was used so that the designs of the Al, Ag and Si arrays were identical to each other.

A film of polymethylmethacrylate (PMMA) containing 0.8 wt% R6G was spin-coated on the array. The thickness of the film was estimated with a surface stylus profiler (KLA Tencor) to be ca. 600 nm.

2.2. Optical Characterization

Zeroth-order optical transmission spectra were measured as a function of the angle of incidence θ_{in}. For the measurement, the sample was placed on a rotation stage and white light from a halogen lamp was incident from the backside (substrate side). The zeroth-order optical transmission spectra were obtained by normalizing the transmission of the incident light through the sample to that through the glass substrate.

PL measurements were performed by illuminating the samples with a laser diode (excitation wavelength λ = 460 nm) at θ_{in} = 5° from the backside. The PL was measured from the opposite side as a function of the angle from the surface normal θ_{em} by a fiber-coupled spectrometer (USB4000, Ocean Optics) mounted on a computer-controlled rotation stage, which could be rotated around the excitation spot.

3. Results and Discussion

Figure 1 compares the optical transmissions of the Al, Ag, and Si nanocylinder arrays with PMMA + R6G layer on the top. At θ_{in} = 0 º, A dip appears at λ = 650 nm for the Al nanocylinder array due to LSPPs hybridized to the in-plane diffraction. Angular dispersion of the hybrid mode is largely modulated by the in-plane diffraction, i.e., Rayleigh anomaly, which is represented by dotted lines. Excitation of the hybrid mode is also obvious in the spectra for Ag nanocylinder array (Fig. 1(b)). Because of the less density of free carrier compared to Al, the hybridized mode is slightly redshifted for the Ag case. The transmittance of Si nanocylinder array is much higher and the resonance is sharper compared to those of Al and Ag nanocylinder arrays. The resonances follow the Rayleigh anomaly, indicating the

hybridization between Mie resonance and in-plane diffraction.

Figure 2 compares PL enhancement, defined as PL intensity normalized to that from the PMMA with R6G layer on the flat silica substrate. PL enhancement follows the Rayleigh anomaly, indicating the enhancement comes from outcoupling, i.e., the PL generated inside the layer is scattered out into a direction predefined by the lattice pattern and periodicity. Because of the resonance of the LSPPs of Ag is redshifted with respect to that of Al, the PL enhancement occurs at longer wavelengths regions. The PL enhancement for the Si nanocylinder array is much sharper and directional, reflecting a shaper resonance in transmittance.

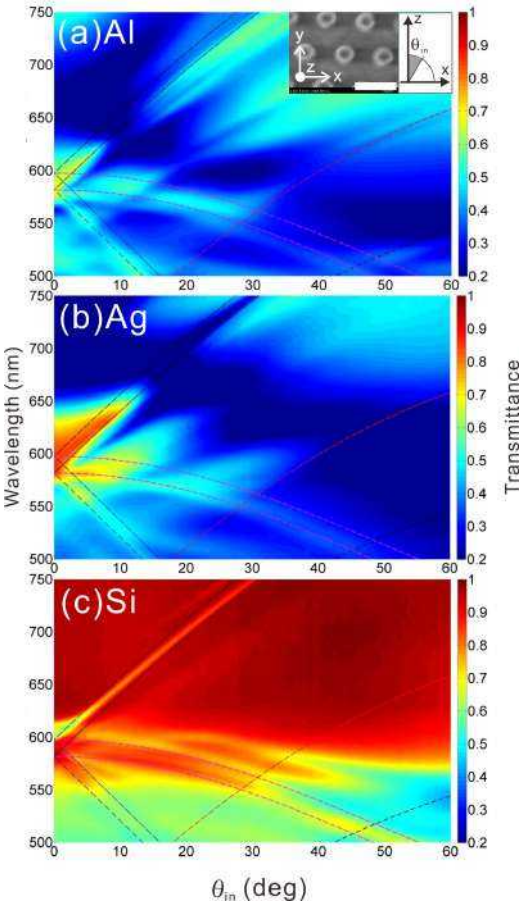


Figure 1: Optical transmittance of the PMMA layer containing R6G on the (a) Al, (b) Ag, and (c) Si nanocylinder arrays. The insets show top-view SEM images of the arrays with the coordination axes used in this study (scale bar: 500 nm), and the experimental configuration: θ_{in} is varied to provide momentum in the x-direction.

4. Conclusions

We experimentally compared the PL enhancements of the Al, Ag and Si nanocylinder arrays where the light diffraction could be simultaneously excited with LSPP or Mie resonance. PL enhancement occurred in all the arrays; however, it was more directive for the Si nanocylinder array and more omni-directional for the Al and Ag nanocylinder arrays. Outcoupling was the main mechanism of the directional increase of PL intensity for all the nanocylinder arrays.

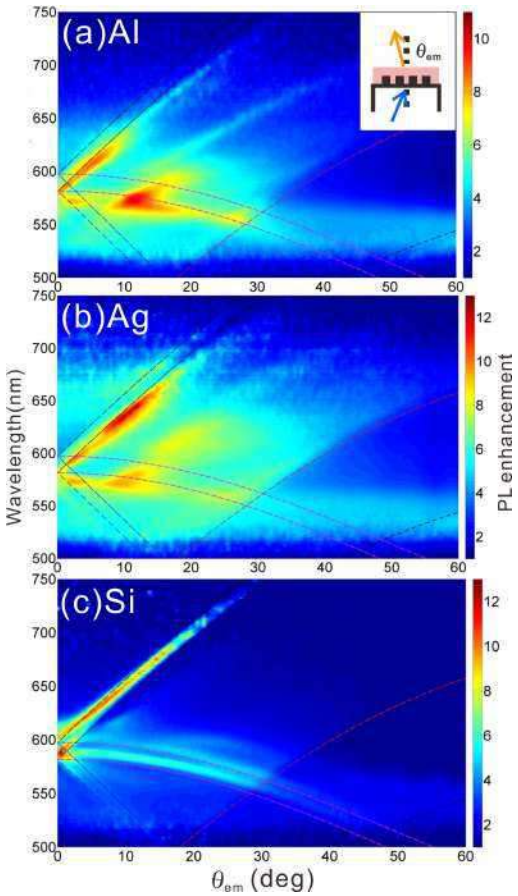


Figure 2: PL enhancement, defined as the PL intensity of the sample normalized to that of the reference polymer layer without nanocylinder arrays, plotted as a function of the wavelength and angle of emission (θ_{em}) with respect to the surface normal for the (a) Al, (b) Ag, and (c) Si nanocylinder arrays. The inset is a sketch of the experiment.

Acknowledgements

The samples were prepared at Nanotechnology Hub (Kyoto U.), Nanofabrication Platform (NIMS), and CINTS (Tohoku U.). Financial support from MEXT (No. 16H04217), JST (PRESTO, No. JPMJPR131B, Nanotech CUPAL), Iketani Science and Technology foundation, and the Asahi Glass Foundation are acknowledged.

References

[1] G. Lozano *et al.*, Plasmonics for solid-state lighting: enhanced excitation and directional emission of highly efficient light sources, *Light-Sci Appl*, **2** (2013).

[2] S. Murai *et al.*, Directional Outcoupling of Photoluminescence from Eu (III)-Complex Thin Films by Plasmonic Array, *APL Photonics*, **2** (2017) 026104.

[3] Y. Kawachiya *et al.*, Collective plasmonic modes excited in Al nanocylinder arrays in the UV spectral region, *Opt Express*, **26** (2018) 5970-5982.

Nanoplasmonics for Terahertz Light

Luca Razzari

INRS Énergie, Matériaux et Télécommunications, 1650 Blvd Lionel Boulet, J3X 1S2 Varennes (Québec), Canada.

E-mail: razzari@emt.inrs.ca

Abstract: I will give a brief overview of our group activities on the use of plasmonic nanostructures to enhance terahertz radiation matter interaction.

Terahertz (THz) radiation has vast potentialities in characterizing specific features of various elementary excitations, such as phonons, excitons, and magnons. However, its long wavelength (300 μm at 1 THz) severely hinders its interaction with nano-objects, which has limited traditional far-field THz studies to macroscopic ensembles of nano-compounds. To overcome such limitation, during the last years we have explored the use of gold plasmonic nanostructures resonating in the THz frequency range [1,2]. These "antennas" can significantly enhance the THz electric field by confining it on a scale ~ 1000 times smaller than the wavelength. Using properly designed nanocavities made by antennas coupled end-to-end, we have demonstrated nanoantenna-enhanced THz spectroscopy [3], a technique that allowed retrieving the phonon spectral signature of a single layer of semiconductor quantum dots.

We have also shown that the phonon response of selected nanomaterials can be drastically modified inside such plasmonic nanocavities, without the need of any THz illumination, just exploiting the phonon strong coupling with the cavity "vacuum electric field" [4]. Such phonon response modification could open new avenues for altering the energy dissipation mechanism in nanosystems, towards the improvement of nanodevice performance.

In this talk, I will summarize the above results and also show how advanced nanoplasmonic architectures can be exploited in combination with intense THz sources for exploring strong-field physics phenomena in this frequency range.

References

[1] L. Razzari et al., Extremely large extinction efficiency and field enhancement in terahertz resonant dipole nanoantennas, *Opt. Express* 19: 26088, 2011.

[2] L. Razzari et al., Terahertz Dipole Nanoantenna Arrays: Resonance Characteristics, *Plasmonics* 8: 133, 2013.

[3] A. Toma et al., Squeezing Terahertz Light into Nanovolumes: Nanoantenna Enhanced Terahertz Spectroscopy (NETS) of Semiconductor Quantum Dots, *Nano Lett.* 15: 386, 2015.

[4] X. Jin et al., Reshaping the Phonon Energy Landscape of Nanocrystals Inside a Terahertz Plasmonic Nanocavity, *Nat. Commun.* 9: 763, 2018.

Opto-mechanical control of the plasmonic heat generation towards the realization of smart biochips

Roberto Caputo, Giovanna Palermo, Giuseppe E. Lio and Antonio De Luca

[1]Department of Physics and CNR Nanotec, University of Calabria, 87036 Rende (CS), Italy

*corresponding author, E-mail: roberto.caputo@unical.it

1. Abstract

In this contribution, we show how it is possible to rigorously predict strain-related phenomena in case of plasmonic systems made of arrangements of metallic nanoparticles immobilized on a flexible elastomeric tape. This insight allows the study of the thermal response of the system and of the heat photogenerated at the nanoscale. Results evidence how the opto-mechanical control of the system depends on external parameters like incident light polarization, nanoparticle inter-distance, and distribution arrangement.

2. Introduction

A noticeable research interest is addressed to materials and methods to control the nanoscale response of resonant nanostructures. The potential for applications in tunable and reconfigurable devices is relevant. Typical approaches promote the interplay between external macroscale stimuli (mechanic, thermal, acoustic, electric, and chemical) and plasmonic systems to achieve nanoscale effects [1,2]. An interesting case is to consider mechanical strains applied to a flexible substrate to induce plasmonic coupling between neighboring Au nanoparticles [3,4]. Experiments performed by our group have already demonstrated the validity of the approach [5,6]. One of the basic tests of materials in mechanics is a tension test, in which a strip or cylinder of the material, with a given length and cross-sectional area, is anchored at one end and subject to an axial load. In elastic regime, a tensile strain in one direction contributes a compressive strain in the other direction, just as stretching a rubber band to make it longer in one direction makes it thinner in the other directions. However, acquiring the information about the amount of local deformation of the involved material is more challenging. This insight can be quite useful if an ensemble of plasmonic subentities (Au nanoparticles) is immobilized on the surface of a flexible material and it is intented to compute the plasmonic response of the single nanoparticle as a result of the interaction with neighboring ones during light excitation. It is worth noting that the load applied at the extremities of the sample is not distributed uniformly along its volume so that the calculation of the overall plasmonic response of the system results quite complicated. Recently, we have considered this problem by exploiting the functionalities of a finite element method (FEM) simulation tool (COMSOL Multiphysics) which offers the possibility to compute the plasmonic response of the sample versus the applied strain and polarization direction of the exciting light. This enables the design and test of an extremely wide variety of possible geometries [7].

3. Discussion

The flexible substrate considered in experiments and numerical simulations is polydimethylsiloxane (PDMS) while the simplest geometry of AuNPs immobilized on its surface is a square one with 5 x 5 NPs (NP radius r = 20 nm) periodically distributed with relative distance 3r = 60 nm (center-to-center) in both *x* and *y* directions. This inter-particle separation has been chosen to be larger than the limit distance after which the particle-particle coupling can be considered negligible.

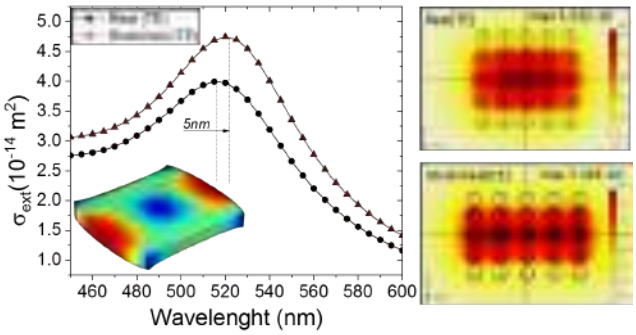


Figure 1. (left) Numerical cross-section extinction curves of a square geometry of AuNPs when the substrate supporting them is at rest or stretched of few percents (19%). In the inset, the sketch of simulated sample is reported indicating the distribution of the tensile stress along the sample area when identical loads are applied on its extremities; (right) thermal maps of the same sample respectively at rest (up) and under tensile stress (down) indicating the maximum temperature calculated on the sample surface.

In Figure 1, the extinction cross-section curves are reported, calculated for this geometry at rest and under tensile stress, in case of an exciting light with electric field oriented perpendicular to the tensile direction. Obtained results evidence a noticeable red-shift (about 5nm) of the localized plasmon resonance (LPR) wavelength deriving from the approaching of particles along the direction perpendicular to the stretching that gives rise to plasmonic coupling.
This coupling has a direct consequence on the thermal response of the particles cluster [8-10] that has been calculated with the same simulation and reported in the inset of Figure 1. Indeed, the thermal maps of the sample at rest and under stretching show a noticeable difference in terms of photogenerated heat ($\Delta T=1.77*10^{-10}$°C).
The AuNPs belonging to the second considered ensemble are distributed in a radial, centro-symmetric, fashion as represented in the inset of Figure 2. Extinction cross-section curves and thermal maps of this particles configuration are reported in the same figure.

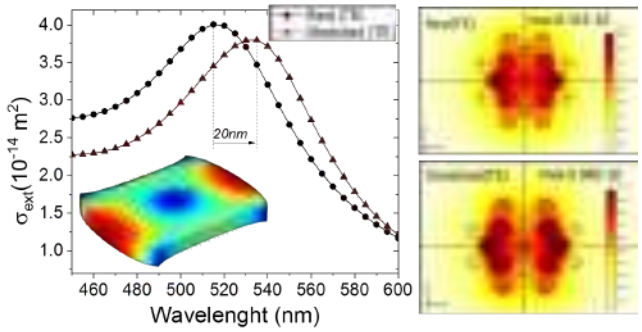


Figure 2. (left) Numerical cross-section extinction curves of a radial geometry of AuNPs when the substrate supporting them is at rest or stretched of few percents (19%). In the inset, the sketch of the simulated sample is reported indicating the distribution of the tensile stress along the sample area when identical loads are applied on its extremities; (right) thermal maps of the same sample respectively at rest (up) and under tensile stress (down) indicating the maximum temperature calculated on the sample surface.

In this case, upon tensile stress, the different particles distribution undergoes a sensitive overall displacement resulting in the formation of strongly coupled "chains" of particles. This is confirmed by the much larger redshift of the LPR wavelength (about 20nm). The calculated thermal behavior shows in this case an absolute maximum temperature value that is slightly smaller than the one observed in case of the square geometry. However, the photoheated area is now more confined suggesting a possible utilization of this geometry for precision temperature-dependent applications. Indeed, a suitable design of the particle configuration can be beneficial for realizing specific thermo-plasmonic functionalities. In more detail, a large area distribution of particles could eventually realize the presence of specific hot-spots with gradients of temperature able to drive complex multi-stage biological reactions.

4. Conclusions

In this communication, we have numerically investigated the plasmonic behavior of different AuNPs arrangements under an externally applied tensile stress. Upon excitation with linearly polarized light, the first geometry (square) reveals a strain-dependent plasmonic field enhancement that is mainly due to the AuNP coupling. This results in an increase of the extinction cross section amplitude with respect to the rest condition. This amplitude value can be changed by acting on the stretching percentage value. The thermal response of the plasmonic system is noticeable and reproduces the symmetry of the particles configuration. As an alternative to the square geometry, a radial one has been proposed showing a larger red-shift of the extinction cross-section curve under stretching with respect to the rest case. In terms of thermal response, there is a consistent advantage with respect to the square geometry for the possibility to concentrate the photogenerated heat in a smaller area. This result opens the way towards implementation of this concept to smart bio-chips where the efficiency of a biological reaction can be finely controlled through utilization of mechanical actions.

5. Acknowledgements

The research leading to these results has received support and funding from the CNR User Facility 'Materials and processes BEYOND the NANO scale', Beyond 'Nano, Pole of Cosenza, cod. PONa3-00362.

6. References

[1] L. De Sio, R. Caputo, U. Cataldi and C. Umeton, J. Mater. Chem. 21, 18967–18970, 2011.
[2] L. De Sio, A. Cunningham, V. Verrina, C.M. Tone C, R. Caputo, T. Bürgi and C. Umeton, Nanoscale 4, 7619–7623, 2012.
[3] C. Burel, A. Alsayed, L. Malassis, C.B. Murray, B. Donnio, B. and R. Dreyfus, Small, 13 39, 2017.
[4] M. Böhm, T. Uhlig, S. Derenko and L.M. Eng, Optical Materials Express, 7(6), 1882-1897, 2017.
[5] T. Maurer, J. Marae-Djouda, U. Cataldi, A. Gontier, G. Montay, Y. Madi, B. Panicaud, D. Macias, P.-M. Adam, G. Lévêque, T. Bürgi and R. Caputo, Front. Mat. Sci. 9, 170, 2015.
[6] U. Cataldi, R. Caputo, Y. Kurylyak, G. Klein, M. Chekini, C. Umeton and T. Bürgi, J. Mater. Chem. C, 2, 7927, 2014.
[7] G.E. Lio, G. Palermo, R. Caputo, & A. De Luca, Journal of Applied Physics, 125(8), 082533, 2019.
[8] G. Palermo, U. Cataldi, A. Condello, R. Caputo, T. Bürgi, C. Umeton & A. De Luca, Nanoscale, 10(35), 16556-16561, 2018.
[9] A.O. Govorov and H. Richardson, Nano Today 2, 30–38, 2007.
[10] A.O. Govorov, W. Zhang, T. Skeini, H. Richardson, J. Lee and N.A. Kotov, Nanoscale Res. Lett. 1, 84–90, 2006.

Synthesis of AgCl Nanoparticles and Their Plasmonic Replicas as Photocatalysts and SERS Probes

Han-Jung Ryu[1], Jang Ho Joo[1], and Jae-Seung Lee[1*]

[1]Department of Materials Science and Engineering, Korea University, Seoul, Korea
*corresponding author, E-mail: jslee79@korea.ac.kr

Abstract

We reported a rapid one-pot room-temperature aqueous synthesis of highly monodisperse sub-100-nm AgCl nanomaterials with various shapes and sizes. We successfully reduced the size of the AgCl nanomaterials which were replicated into metallic nanomesh structures that were small enough (~100 nm) to show intense surface-plasmon-absorption bands. The complex comprising semiconducting AgCl/metallic nanomesh replica exhibited excellent plasmonic photocatalysis properties for the complete removal of Cr(IV), and intense surface-enhanced Raman scattering (SERS) properties in a single-particle enhancing the electromagnetic field.

1. Introduction

The template-assisted growth method is one of the powerful, universal, and efficient strategies to synthesize noble metal nanostructures, because the shape and size of the nanostructures can be easily regulated by controlling the structural properties of the templates. Therefore, the morphology control of the templates and their replication into the metallic structures without deformation are the key factors to accurately design and synthesize the nanostructures with various shapes and sizes. AgCl nanomaterials are emerging as intact templates that are not associated with the galvanic replacement because they cannot be oxidized by the aforementioned replica precursors. Moreover, AgCl is one of the most promising materials for electrochemical and photocatalytic applications owing to their physicochemical properties. In particular, nano-sized AgCl is typically used in combination with Ag for outstanding photocatalysis under visible-light irradiation. However, AgCl nanostructures have been rarely used as building blocks or templates for synthesis, specifically compared to their metallic analog, AgNCs. This limited use of AgCl is attributed to insufficient studies to control the AgCl morphologies. In this work, we present a strategy for synthesizing sub-100-nm monodisperse AgCl nanostructures with elaborate controls of their shapes and sizes in aqueous media. Furthermore, we successfully synthesized replicated metallic nanostructures based on AgCl nanomaterials as templates and completely regulated the morphological properties of the final structures through the chemical control of AgCl nanotemplates and their surfaces. The detailed synthetic mechanism was investigated.

2. Results and Discussion

2.1. Synthesis of AgCl nanocubes

We successfully and easily controlled the size of AgCl nanocubes (AgClNCs) by changing the mole ratio of $AgNO_3$ to $HAuCl_4$ (Figure 1). When the mole ratio was 11:1 ($AgNO_3$:$HAuCl_4$), the synthesized AgClNCs had sharp edges whose length was 210 nm on average (Figure 1a). As

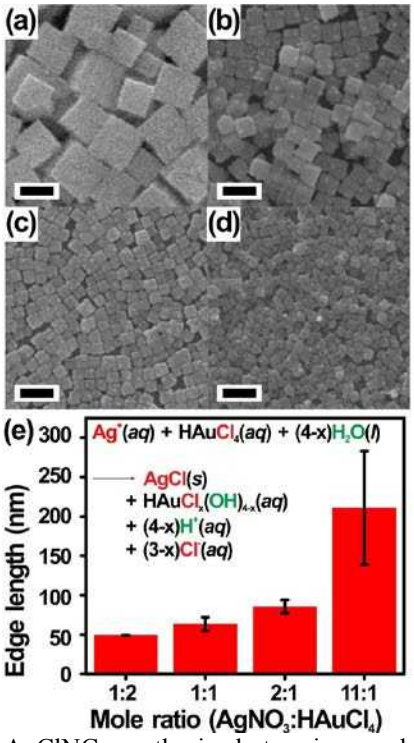


Figure 1. AgClNCs synthesized at various mole ratios of $AgNO_3$ to $HAuCl_4$. $AgNO_3$:$HAuCl_4$ = (a) 11:1 (b) 2:1 (c) 1:1 and (d) 1:2 (scale bars 200 nm). Small bumps were often generated on the surface of the AgClNCs during the observation using SEM, because of the reduction of AgCl into Ag by the electron beam. (e) Comparison of the edge length of AgClNCs. The proposed reaction mechanism for the synthesis of AgClNCs is notated above the bars.

the mole ratio changed to 2:1, the highly monodisperse smaller AgClNCs with an edge length of 100 nm were obtained (Figure 1b). When the mole ratio further changed to 1:1, AgClNCs with a much smaller edge length (~80 nm) were observed (Figure 1c). Finally, the truncated and tiny AgClNCs (50 nm in size) were prepared at the mole ratio of 1:2 (Figure 1d). As the mole ratio of Ag^+ to Cl^- decreased, the edge length of the products also decreased with narrower size distributions (Figure 1e). To the best of our knowledge, this work is the first demonstration of systematic size control of AgClNCs in aqueous media at room temperature. The results were similar to those previously obtained in organic media at much higher temperatures (>100 °C).

2.2. Metallic replica nanomesh structures

The mesh structures in the panels of Au/Ag cubic meshes (AuAgCMs) and Au/Ag spherical meshes (AuAgSMs) were further investigated in detail using the elemental mapping technique. In Figure 2, the distribution of the gold almost overlapped with that of the silver, indicating both metals were evenly distributed in the AuAgCMs and AuAgSMs.

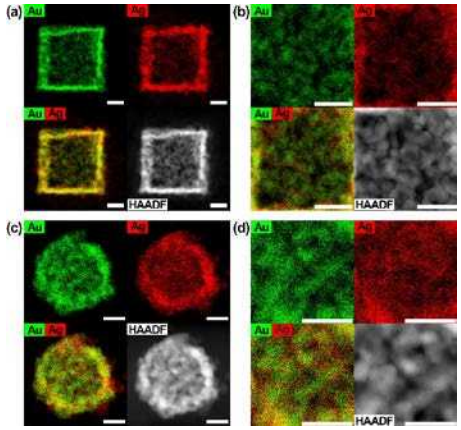


Figure 2. ((a) and (c)) EDS elemental mapping images and scanning TEM (STEM) images of the AuAgCMs and the AuAgSMs, respectively. ((b) and (d)) Highly magnified EDS and STEM images of the AuAgCMs and the AuAgSMs, respectively. Au is shown in green and Ag in red (scale bars 25 nm). The atomic ratio of Au to Ag is 5.5 to 4.5 according to the EDS analysis.

2.3. Photocatalysis and SERS

Owing to the absorption properties of the metallic mesh structures in the visible and near-infrared ranges, and the hot electrons generated by the absorbed energy in AgClNCs, AgCl@AuAgCMs and AgCl@AuAgSMs were expected to exhibit photocatalytic activities. Therefore, we examined their photocatalytic performance for the reduction of Cr^{6+} under visible-light irradiation using a metal-halide lamp (Figure 3a). Potassium dichromate was used as a source of Cr^{6+}, whose reduction progress was monitored by measuring the absorbance at 350 nm. We also obtained the single-nanoparticle SERS spectra of 1,4-benzenedimethanethiol (BDMT) that was absorbed by the individually dispersed AuAgCMs and AuNPs on a glass

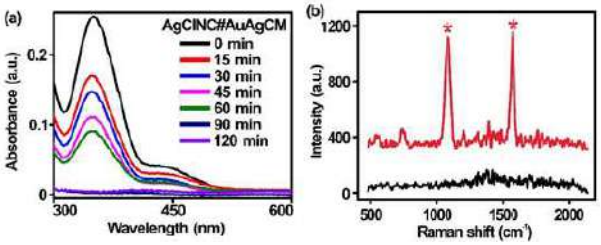


Figure 3. (a) UV-vis spectra obtained by monitoring the reduction of Cr^{6+} to Cr^{3+}, which was photocatalyzed by AgCl@AuAgCMs. (b) SERS spectrum of 1,4-benzenedimethanethiol (BDMT)-coated AuAgCM (red) and 100-nm AuNP (black).

substrate (Figure 3b). As expected, two distinctive Raman bands of BDMT were observed at 1080 and 1572 cm^{-1} when individual AuAgCM was used as single-particle SERS substrate. On the other hand, the dispersed AuNPs nearly did not enhance any SERS signals of BDMT.

3. Conclusions

Silver halide (AgX) nanocubes have provided only specific facets in their metallic replication, mainly resulting in nanoframes. In this study, we carefully investigated the surface chemistry of AgCl and successfully overcame this limitation, demonstrating that not only faceted AgCl nanocubes but also almost facetless AgCl nanospheres could be the nanotemplates for their mesh-structured bimetallic replicas. The detailed synthetic mechanism has been thoroughly investigated, too. Moreover, unlike previous monometallic nanoframes, these metallic nanomeshes showed a high potential to enhance the SERS properties as single-nanoparticle substrates. Importantly, other mineral nanocrystals than AgX, such as faceted Ag_3PO_4 nanocubes, were successfully replicated.

Acknowledgements

This work was supported by the NRF funded by the Korean government, MSIP (NRF2015M3A9D7031015, NRF-2018R1A1A1A05079384 and NRF-2016R1A5A1010148).

References

[1] J. H. Joo, B. -H. Kim, J. -S. Lee, Synthesis of Gold Nanoparticle-Embedded Silver Cubic Mesh Nanostructures Using AgCl Nanocubes for Plasmonic Photocatalysis, *Small* 13: 1701751, 2017.

[2] X. Wang, J. Feng, Y. Bai, Q. Zhang, Y. Yin, Synthesis, Properties, and Applications of Hollow Micro-/Nanostructures, *Chem. Rev.* 116:10983-11060, 2016.

[3] X. J. Sun, J. Kim, K. D. Gilroy, J. Y. Liu, T. A. F. Konig, D. Qin, Gold-Based Cubic Nanoboxes with Well-Defined Openings at the Corners and Ultrathin Walls Less Than Two Nanometers Thick, *ACS Nano* 10: 8019-8025, 2016.

In Situ Surface-Enhanced Raman Spectroscopic Study of Chemical Reactions on Bifunctional Nanoparticles

Wei Xie

Key Lab of Advanced Energy Materials Chemistry (Ministry of Education), Renewable Energy Conversion and Storage Center, College of Chemistry, Nankai University, Tianjin, China
*corresponding author, E-mail: wei.xie@nankai.edu.cn

Abstract

Characterization of reactions catalyzed by nanoparticles (NPs) is challenging because the chemical transformation occurs only at the catalytic interfaces, where the many different components are difficult to separate and purify. Therefore, surface-selective analytical methods are required to monitor the reactions directly on the NP surface. Here, we show the use of surface-enhanced Raman spectroscopy (SERS) for in situ monitoring of catalytic reactions on bifunctional NPs.

1. Introduction

Surface-enhanced Raman spectroscopy (SERS) is very surface-selective and has high sensitivity plus chemical specificity which fulfills the requirements for in situ monitoring of molecular transformations in heterogeneous catalysis.[1] However, catalytically active materials such as Pt, Pd, Ni and small Au NPs do not provide sufficient plasmonic activity for the required SERS enhancement. On the other hand, conventional SERS substrates such as large Au or Ag NPs are not catalytically active. Bifunctional nanostructures that combine both plasmonic and catalytic activity can enhance the Raman signal of chemical species involved in the catalytic reactions.

Au-Pt-Au core-shell nanoraspberries with both high Pt surface area and high plasmonic activity represent an example of bifunctional hybrid NPs for combined catalysis/SERS monitoring.[2] Reactions catalyzed by Pt can be monitored by SERS due to the plasmonic Au protuberances grown on the Pt surface. Alternatively, the small catalytically active NP satellites can be self-assembled onto a large plasmonically active core to form a plasmonic superstructure; in this case the chemical species on the catalyst surface experiences a sufficient SERS enhancement due to the plasmonic coupling between the small satellites and the large core.[3]

By using SERS, we characterized reactions catalyzed by different metals and found a couple of interesting interfacial chemical processes. For example, reduction in aqueous sodium borohydride solution is usually driven by H2, and the real hydride reduction occurs only in very basic solutions.[4] Another example is the hot-electron reduction on Ag NPs promoted by photodissociation of silver halides, which enables six-electron reduction without using conventional chemical reducers such as hydride and H_2.[5,6] Recently, we studied C-C bond-forming reactions catalyzed by Pd and Ni NPs, respectively. According to the findings enabled by in situ SERS, the catalytic activity of the catalysts in the corresponding reactions was significantly improved.

2. Results and Discussion

To synthesize Au-Pd core-satellite superstructures with a SERS-active Au core inside and many small Pd NPs on the surface of the Au core. The 80 nm Au cores are first encapsulated in an ultrathin silica shell and then functionalized with thiol groups. Then 5 nm Pd satellites are added and anchor onto the core via strong metal-sulfur interaction. X-ray photoelectron spectra indicate the formation of Pd-S bond in the super-structures. The ~1.5 nm inert silica shell between the core and the satellites ensures the required SERS enhancement on the satellite surfaces and more importantly, isolates the Au core from direct contact with the reactants.

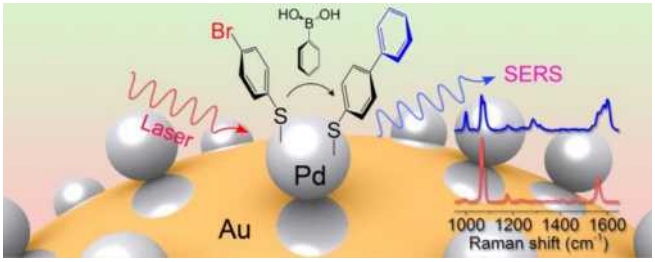


Figure 1: In situ SERS monitoring of Suzuki-Miyaura cross-coupling reaction between aryl bromides and phenylboronic acids.

We use the Suzuki-Miyaura C-C cross-coupling reaction as our model reaction for in situ SERS monitoring (Figure 1). Although this prominent reaction is extensively used in C-C bond-forming chemistry, in the presence of Pd NPs, it is not clear whether the coupling reaction is catalyzed heterogeneously (by solid-state Pd metal) or homogeneously (by leached Pd species in solution). Via in situ SERS detection, solid evidence of heterogeneously catalytic Suzuki coupling has been found on the Pd nanoparticle surface. In contrast, the soluble Pd leaching out from the particle surface cannot catalyze the reaction, indicating that the direct contact between organohalide molecules and metallic Pd surface is prerequisite for the C-C cross-coupling. This finding highlights a key factor, in addition to the particle size, component and surface morphology (atomic defects), for rational design of nanoparticle catalysts: the increased molecule-metal contact will facilitate the C-C cross-coupling. As expected, the catalytic activity of Pd nanoparticles has been significantly enhanced when there is a proper electric attraction between the organohalide and the metal surface.

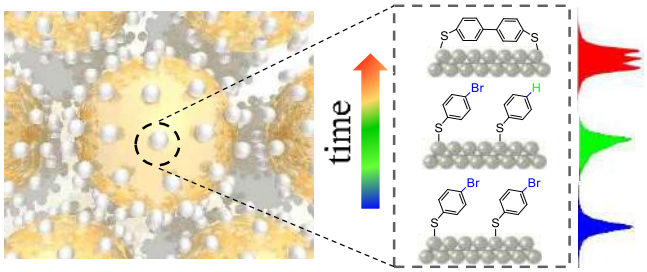


Figure 2: In situ SERS monitoring of C-C bond formation proceeding via photo-induced aromatic C-H bond arylation on Ni NPs.

In another example, the C-C bond-forming on cheap Ni NP catalysts is studied by in situ SERS monitoring. Formation of 4,4'-biphenyldithiol (4,4'-BPDT) from 4-bromothiophenol (4-BTP) is used as the model reaction. This reaction, which was thought to be an Ullmann-type self-coupling reaction, is found to be a cross-coupling reaction proceeding via photo-induced aromatic C-H bond arylation on Ni NPs (Figure 2). According to this finding, the yield of the reaction is significantly improved by using a mixed monolayer of 4-BTP and thiophenol (TP) instead of the 4-BTP monolayer reactant. In order to show the general applicability of this photocatalytic C-H arylation, “real” C-C bond-forming reactions without using thiolated reactants are performed. More than 10 biphenyl products are successfully synthesized at room temperature using the new mechanism discovered by in situ SERS.

3. Conclusions

We monitor chemical reaction on metal NPs that are originally not SERS-active by using bifunctional nanostructure substrates. The surface-selective SERS directly focuses on the molecular conversions at the catalytic interfaces and enables many interesting findings which are very important for understanding the reaction mechanisms. These results show that SERS is a powerful technique for interfacial chemistry and can be utilized as a useful tool for the broad chemistry community.

Acknowledgements

We acknowledge the financial support from the National Natural Science Foundation of China (21775074, 51601098 & 21861132016), the Natural Science Foundation of Tianjin (17JCQNJC05400), and the National Key R&D Program (2017YFA0206702 & 2016YFB0901502).

References

[1] W. Xie, S. Schlücker, Rationally designed multifunctional plasmonic nanostructures for surface-enhanced Raman spectroscopy: a review, *Rep. Prog. Phys.* 77: 116502, 2014.

[2] W. Xie, C. Herrmann, K. Kömper, M. Haase, S. Schlücker, Synthesis of bifunctional Au/Pt/Au core/shell nanoraspberries for in situ SERS monitoring of platinum-catalyzed reactions, *J. Am. Chem. Soc.* 133: 19302−19305, 2011.

[3] W. Xie, B. Walkenfort, S. Schlücker, Label-free SERS monitoring of chemical reactions catalyzed by small gold nanoparticles using 3D plasmonic superstructures, *J. Am. Chem. Soc.* 135: 1657−1660, 2013.

[4] W. Xie, R. Grzeschik, S. Schlücker, Metal nanoparticle-catalyzed reduction using borohydride in aqueous media: a kinetic analysis of the surface reaction by microfluidic SERS, *Angew. Chemie. Int. Ed.* 55: 13729−13733, 2016.

[5] W. Xie, S. Schlücker, Hot electron-induced reduction of small molecules on photorecyling metal surfaces, *Nat. Commun.* 6: 7570, 2015.

[6] E. Cortes, W. Xie, J. Cambiasso, A. S. Jermyn, R. Sundararaman, P. Narang, S. Schlücker, S. A. Maier, Plasmonic hot electron transport drives nano-localized chemistry, *Nat. Commun.* 8: 14880, 2017.

Nanoscale Imaging and Control of Chiral Plasmons

Hiromi Okamoto

Institute for Molecular Science, National Institutes of Natural Sciences, Okazaki, Japan
*corresponding author, E-mail: aho@ims.ac.jp

Abstract

Novel near-field optical imaging methods were developed to visualize local optical activity and circularly polarized fields in the vicinities of metal nanostructures. We found not only chiral but also achiral gold nanostructures gave strong optical activity. Based on the result, we propose a method to generate highly circularly polarized local field with controllable handedness using an achiral nanostructure. We also found that chiral plasmon induces highly circularly polarized luminescence from achiral fluorescent molecules that interact with it.

1. Introduction

Chirality is a broad concept that characterizes structures of systems in almost all hierarchy of materials in natural sciences. Molecular chirality is sometimes essential in biological functions. In nanomaterials sciences, it is of fundamental importance to investigate internal structures (geometrical distributions) of chiral optical responses in nanomaterials, to design chiral characteristics of the materials and their functions. We developed a few types of near-field optical activity imaging methods that allow us to visualize local optical activity structures of nanomaterials: (i) Near-field CD imaging, where circularly polarized light (far-field) is incident on the sample and near-field scattering intensity in the vicinity of the sample is detected through the aperture near-field probe (in some cases, near-field circularly polarized illumination and far-field optical response detection was adopted). (ii) Near-field polarimetry imaging, where linearly polarized near-field radiation is incident on the sample through the aperture probe and the polarization state (ellipticity and azimuth angle) of the scattered light (far-field) is detected as the signal for imaging. These methods were applied to observe chiral plasmonic fields for two-dimensional gold nanostructures fabricated with electron beam lithography lift-off technique, and we found that chiral plasmons yield very strong local optical activity even for achiral nanostructures. Based on the results obtained with these methods, we proposed a simple method to generate highly circularly polarized local fields with an achiral nanostructure, with controllable handedness of the field. We also demonstrate that the locally highly chiral fields arising from plasmon resonances induce highly circularly polarized luminescence from achiral fluorescent molecules conjugated with the chiral plasmons.

2. Results and Discussion

2.1. Near-filed optical activity imaging

We observed near-field optical activity images of two-dimensional chiral gold nanostructures. We found that the amplitudes of local CD signals were as large as 100 times the macroscopic CD signals of the same samples, for two-dimensional chiral ("S"-shaped) gold nanostructures [1]. Furthermore, even highly symmetric achiral structures, such as rectangles that never gave CD signals macroscopically, gave locally very strong CD signals [2,3]. In this case, average of the signal over the nanostructure yielded roughly null CD intensity. Figure 1 shows an ellipticity image of gold nano-rectangle obtained with near-field polarimetry imaging, which approximately corresponds to a CD image [4]. We also found that the observed spatial structure of the chiral field is qualitatively well reproduced by a simple dipolar excitation model. This result shows that any structure can have (local) chiral interaction with optical fields.

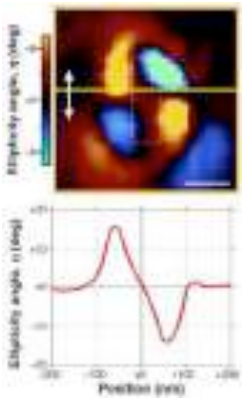


Figure 1: Top: Near-field ellipticity image (at 800 nm) of a gold rectangle [4]. Bottom: Line profile along the horizontal line indicated in the left panel. η=±45° for circularly polarized light.

2.2. Generation of controllable circularly polarized local fields with an achiral nanostructure

As an extension of the optical imaging study, we have shown that controllable local circularly polarized field can be generated by a combination of linearly polarized light and a gold nanorod (an achiral structure) [5]. When the polarization direction of the incident light is oblique to the nanorod axis, it was found that highly circularly polarized local field can be generated, and the handedness of the circular polarization and the ellipticity can be controlled by adjusting the oblique direction and angle of the incident polarization. The results obtained here provide basic principle to get highly chiral and switchable local optical fields, which may give us a chance to pioneer analytical applications of chiral optical fields and novel optical devices.

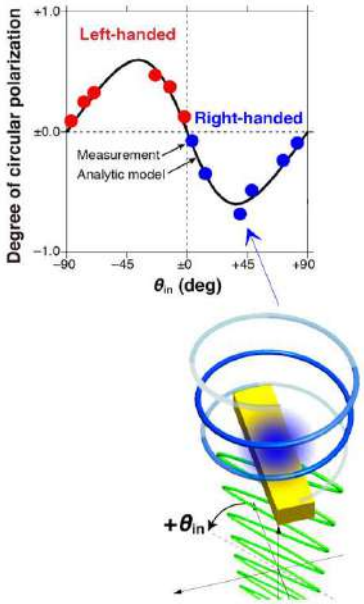


Figure 2: Generation of highly circularly polarized local field with gold nanorod and linearly polarized light [5]. Degree of circular polarization (±1 for circularly polarized light) at the position above the center of the rod depends on the incident poarization angle, and the exceeds 0.5 around $\theta_{in} \sim 45°$.

2.3. Highly circularly polarized luminescence from molecules conjugated with chiral nanostructures

We also demonstrate here that interaction between fluorescent molecules and chiral plasmons yield highly circularly polarized luminescence [6]. We used organic dyes as fluorescent emitters with luminescence enhanced by its near-field interaction with the chiral plasmons excited on a two-dimensional chiral metal nanostructure. The photoluminescence enhancement dissymmetry spectra showed maximum amplitudes in the wavelength region, which correspond approximately to the wavelength providing maximal circular dichroism of the plasmonic nanostructures. The dissymmetry factor of the luminescence exceeded g>0.1 (as compared to those of the most of circularly-polarized emitters with chiral molecular structures, g~0.001). We discuss the physics behind the circularly polarized luminescence from such hybrid dye-doped chiral nanostructures with the aid of an electromagnetic model analysis. We found that the (two-dimensional) chiral structure of the resonant plasmon mode is the origin of the highly circular polarized luminescence.

3. Conclusions

By observation of local chiral field structures, we found that local optical activity of nanomaterials show some unique and valuable features compared to macroscopic one, which gives highly enhanced chiral natures of optical characteristics through near-field interactions. It may provide some useful applications in optical devices, chemical analysis, bioimaging, and so forth.

Acknowledgements

Contributions of Drs. Shun Hashiyada, Tetsuya Narushima, Khai Q. Le, and Yoshio Nishiyama (IMS) is acknowledged. This research was supported by Grants-in-Aid for Scientific Research (KAKENHI) (JP15K13683, JP15H02161, JP16H06505) and by Core-to-Core Program from JSPS, and by the Photon Frontier Network Program of MEXT.

References

[1] T. Narushima, H. Okamoto, Strong nanoscale optical activity localized in two-dimensional chiral metal nanostructures, *J. Phys. Chem. C* 117: 23964-23969, 2013.

[2] S. Hashiyada, T. Narushima, H. Okamoto, Local optical activity in achiral two-dimensional gold nanostructures, *J. Phys. Chem. C* 118: 22229-22233, 2014.

[3] Y. Nishiyama, H. Okamoto, Near-field nonlinear CD imaging of single gold nanostructures, *J. Phys. Chem. C* 120: 28157-28162, 2016.

[4] S. Hashiyada, T. Narushima, H. Okamoto, Imaging chirality of optical fields near achiral metal nanostructures excited with linearly polarized light, *ACS Photon.* 5: 1486-1492, 2018.

[5] S. Hashiyada, T. Narushima, H. Okamoto, Active control of chiral optical near fields on a single metal nanorod, *ACS Photon.*, in press. (doi: 10.1021/acsphotonics.8b01500)

[6] K. Q. Le, S. Hashiyada, M. Kondo, H. Okamoto, Circularly polarized photoluminescence from achiral dye molecules induced by plasmonic two-dimensional chiral nanostructures, *J. Phys. Chem. C* 122: 24924–24932, 2018.

Photochemical properties of organic dye molecules under vibrational strong coupling regimes

Kosei Ueno[1]

[1]Research Institute for Electronic Science, Hokkaido University, Sapporo, Japan
*corresponding author, E-mail: k-ueno@es.hokudai.ac.jp

Abstract

The photochemical properties of dye molecules under vibrational strong coupling regimes have been studied by using plasmonic and microcavity structures which confines infrared light strongly. Fluorescence lifetime apparently shortened with increasing of the electromagnetic field intensity of the optical modes, which implies the decreasing of non-radiative rate constant in the energy relaxation process accompanying with the acceleration of vibrational relaxation due to vibrational strong coupling.

1. Introduction

Strong coupling has received considerable attention because molecular electronic states can be modulated by quantum mechanical interactions with optical modes such as microcavity, plasmon, and so on [1, 2]. If the electronic state is modulated by the strong coupling, it is expected to change the reactivity of molecules, so that it can work like a catalyst for promoting chemical reactions. On this basis, we have explored strong coupling between localized surface plasmon resonance (LSPR) and molecular excitonic states by using J-aggregate of molecules having relatively larger dipole moment [3, 4]. Ebbesen and co-workers recently demonstrated the strong coupling between microcavity and molecular vibrational modes in the infrared wavelength range and a possibility of modulating chemical reaction activities by the strong coupling [5, 6]. If the chemical reaction activity is changed by the vibrational strong coupling, it means that the transition state of molecule is influenced. Therefore, we study on the vibrational strong coupling and its influence on the electronic state of molecules under vibrational strong coupling. In the present study, we explored fluorescence properties of dye molecules in infrared plasmon−cavity strong coupling systems by several spectroscopic techniques.

2. Experimental

We constructed a modal strong coupling system in the infrared wavelength region utilizing LSPR and Fabry-Pérot cavity modes showing strong near-field enhancement in the wide wavelength range. The strategy for fabricating the strong coupling system is analogous to our modal strong coupling system in the visible wavelength range [7]. Only the resonant wavelength of plasmonic structures and Fabry-Pérot cavity mode were tuned to the infrared wavelength region by changing the structural size and shape of gold (Au) nanostructures and the thickness of titanium dioxide (TiO_2). Au-film with a thickness of 100 nm is deposited on the quarts glass (SiO_2) by sputtering, and subsequently TiO_2 film with a thickness of 450 nm is deposited on the Au-film/SiO_2 substrate by an atomic layer deposition (ALD) system. Au nanochains (AuNCs) which shows a dipole resonance band in infrared wavelength region were fabricated by electron beam lithography and lift-off processes on the TiO_2/Au-film cavity [8, 9]. Al_2O_3 with a thickness of 2 nm was additionally deposited on the AuNCs/TiO_2/Au-film substrate to improve the electromagnetic interaction between LSPR and Fabry-Pérot cavity modes as well as not to directly contact between Au surface and fluorescence dye molecules for suppressing the fluorescence quenching. Fluorescence dye molecules of Eosin Y were adsorbed to the surface of the modal strong coupling system. Fluorescence spectra and decay curves were measured by spectrometer and time-correlated single photon counting. Absorption spectrum of the modal strong coupling system was obtained by measuring transmission (T) and reflection (R) spectra by Fourier-transform infrared (FT-IR) spectrometer and represented as 1-T-R spectrum.

3. Results and Discussions

A schematic illustration of the modal strong coupling system with fluorescence dye molecules on the surface is shown in Figure 1. Absorption spectra of the TiO_2/Au-film cavity substrate and AuNCs/TiO_2/Au-film structure are shown in Figure 2. As a reference, the broken line in Figure 2 shows a reflection spectrum of AuNCs on a TiO_2/SiO_2 substrate, whose TiO_2 thickness is 100 nm. The length of AuNC is set at 516 nm, which is corresponding to four chains

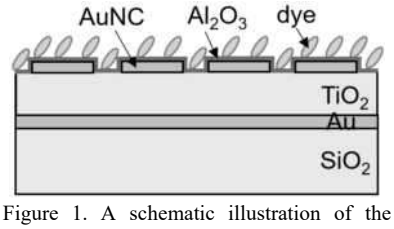


Figure 1. A schematic illustration of the cross-section of the infrared modal strong coupling system with fluorescence dye molecules on the surface.

diagonally aligned Au nanoblocks (100 × 100 × 30 nm^3). From the absorption spectrum of the TiO_2/Au-film substrate, it can be found that the fundamental Fabry−Pérot cavity mode is located around 2400cm^{-1} when TiO_2 thickness is 450 nm. On the other hand, the LSPR band of AuNCs is closely to the cavity mode, the spectrum is modulated and the spectrum is divided into two peaks like a modal strong coupling system in the visible wavelength range due to the formation of hybrid modes [7]. When the LSPR band completely overlaps with the cavity mode by increasing the length of AuNCs from 750 nm to 2380 nm, the absorption in the wavenumber range of 2000−4000cm^{-1} (2.5−5 μm as a wavelength) is dramatically increased. In the wavenumber rage of 2000−4000cm^{-1}, OH stretching vibrational mode of the dye molecule is overlapped with the plasmon−cavity hybrid modes. Interaction between OH stretching vibrational mode and plasmon−cavity hybrid modes is expected. It is noteworthy that the high-order cavity mode exists also in the visible wavelength range. Therefore, Purcell effect cannot be ignored, which can be confirmed by the modulation of fluorescence spectrum and extremely fast fluorescence lifetime. Importantly, fluorescence lifetime changed with changing of the absorption in infrared wavelength range due to the degree of detuning between plasmon and cavity modes. There is a possibility that vibrational strong coupling affects the vibrational relaxation by OH group.

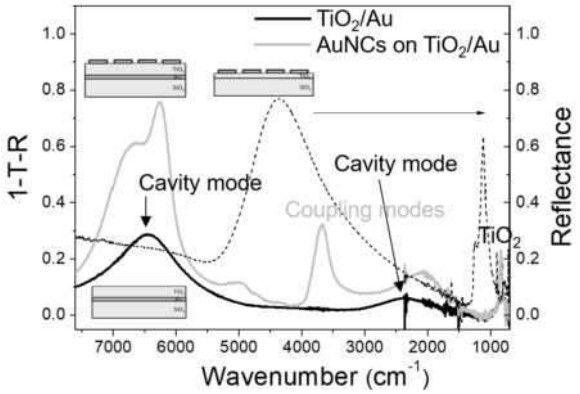


Figure 2. Absorption spectra of the TiO_2/Au-film cavity substrate and AuNCs/TiO_2/Au-film structure. The broken line shows a reflection spectrum of AuNCs on TiO_2/SiO_2 substrate whose TiO_2 thickness is 100 nm.

4. Conclusions

We investigated the photochemical properties of dye molecules in the infrared plasmon−cavity strong coupling system, which is composed of Au nanochains/TiO_2/Au-film structure. When the localized surface plasmon band of Au nanochains is closely to the Fabry-Pérot cavity mode of TiO_2/Au-film, the spectrum is modulated due to the formation of hybrid modes, and the absorption in the infrared wavelength region increased with decreasing the degree of detuning between plasmon and cavity modes. When OH stretching vibrational mode of the dye molecule is overlapped with the plasmon−cavity hybrid modes, fluorescence lifetime apparently changed. We speculate that vibrational strong coupling affects the vibrational relaxation by OH group.

Acknowledgements

The author acknowledges Prof. Hiroaki Misawa in Research Institute for Electronic Science, Hokkaido University for fruitful discussions. The author also acknowledges financial supports from JSPS-KAKENHI (Nos. JP17H05245, JP17H05459, and JP18H05205), Nanotechnology Platform of MEXT (Hokkaido University), and Dynamic Alliance for Open Innovation Bridging Human, Environment and Materials (Five-Star Alliance) of MEXT.

References

[1] A. Salomon, C. Genet, T. W. Ebbesen, Molecule-light complex: dynamics of hybrid molecule-surface plasmon states, *Angew. Chem. Int. Ed.* 48: 8748−8751, 2009.

[2] J. A. Hutchison, T. Schwartz, C. Genet, E. Devaux, T. W. Ebbesen, Modifying chemical landscapes by coupling to vacuum fields, *Angew. Chem. Int. Ed.* 51: 1592−1596, 2012.

[3] Y.-W. Hao, H.-Y. Wang, Y. Jiang, Q.-D. Chen, K. Ueno, W.-Q. Wang, H. Misawa, H.-B. Sun, Hybrid-state dynamics of gold nanorods/dye J-aggregates under strong coupling, *Angew. Chem. Int. Ed.* 50: 7824−7828, 2011.

[4] J. Li, K. Ueno, H. Uehara, J. Guo, T. Oshikiri, H. Misawa, Dual strong couplings between TPPS J-aggregates and aluminum plasmonic states, *J. Phys. Chem. Lett.* 7: 2786−2791, 2016.

[5] A. Shalabney, J. George, J. Hutchison, G. Pupillo, C. Genet, T. W. Ebbesen, Coherent coupling of molecular resonators with a microcavity mode, *Nat. Commun.* 6: 5981 (2015).

[6] A. Thomas, J. George, A. Shalabney, M. Dryzhakov, S. J. Varma, J. Moran, T. Chervy, X. Zhong, E. Devaux, C. Genet, J. A. Hutchison, T. W. Ebbesen, Ground-state chemical reactivity under vibrational coupling to the vacuum electromagnetic field., *Angew. Chem. Int. Ed.* 55: 11462−11455, 2016.

[7] X. Shi, K. Ueno, T. Oshikiri, Q. Sun, K. Sasaki, H. Misawa, Enhanced water splitting under modal strong coupling conditions, *Nat. Nanotechnol.* 13: 953−9958, 2018.

[8] K. Ueno, S. Juodkazis, V. Mizeikis, D. Ohnishi, K. Sasaki, H. Misawa, Surface-enhanced terahertz spectroscopy using gold rod structures resonant with terahertz waves, *Opt. Express* 15: 16527−16539, 2015.

[9] K. Ueno, Q. Sun, M. Mino, T. Itoh, T. Oshikiri, H. Misawa, Surface plasmon optical antennae in the infrared region with high resonant efficiency and frequency selectivity, *Opt. Express* 24: 17728−17737, 2016.

Optical properties of plasmonic spiked particles as a function of their size and shape

Ramon A. Alvarez-Puebla

ICREA, Passeig Lluís Companys 23, 08010 Barcelona, Spain

Departamento de Quimica Fisica e Inorganica; Universitat Rovira i Virgili, Edifici N5, Carrer de Marcel•lí Domingo s/n, 43007 Tarragona, Spain.

The anisotropy in the particle geometry determines the field distribution of the plasmon modes in the nanostructure [1]. Upon excitation with light of the appropriate energy, these structures can sustain large electromagnetic fields at ends (nanorods) [2], vertices (triangles) [3], or tip apexes (nanostars) [4], Such field localization can be readily exploited for SERS and thus, for the fabrication of ultrasensitive devices. The intrinsic optical properties of nanostars were theoretically demonstrated by Nordlander and co-workers [5], indicating that the plasmon modes of a nanostar result from the hybridization of the individual plasmons of the core and the tips. The core would serve as a nanoscale antenna, dramatically increasing the excitation cross-section and the electromagnetic field enhancements of the tip plasmons. Recently, the efficiency of gold nanostars for SERS was as well experimentally evidenced [6-7].

Here we discuss the advantages of using different spiked particles for photonic and sensing applications including distant excitation, direct sensing and bioimaging through the use of encoded particles.

References

[1] R. Alvarez-Puebla, L. M. Liz-Marzan, F. J. Garcia de Abajo, J. Chem. Phys. Lett. 2010, 1, 2428-2434.

[2] G. W. Bryant, F. J. Garcia de Abajo, J. Aizpurua, Nano Lett. 2008, 8, 631-636.

[3] J. Nelayah, M. Kociak, O. Stephan, F. J. Garcia de Abajo, T. M., L. Henrard, D. Taverna, I. Pastoriza-Santos, L. M. Liz-Marzan, C. Colliex, Nature. Phys. 2007, 3, 348-353.

[4] L. Rodriguez-Lorenzo, R. A. Alvarez-Puebla, I. Pastoriza-Santos, S. Mazzucco, O. Stephan, M. Kociak, L. M. Liz-Marzan, F. J. Garcia de Abajo, J. Am. Chem. Soc. 2009, 131, 4616-4618.

[5] F. Hao, C. L. Nehl, J. H. Hafner, P. Nordlander, Nano Lett. 2007, 7, 729-732.

[6] L. Rodriguez-Lorenzo, R. A. Alvarez-Puebla, F. J. Garcia de Abajo, L. M. Liz-Marzan, J. Chem. Phys. C 2010, 114, 7336-7340.

[7] L. Rodríguez-Lorenzo, R. de la Rica, R. Alvarez-Puebla, L.M. Liz-Marzán, M.M. Stevens Nature Mater. 2012, 11, 604-607; 2018, 17, 205–207

[8] J. Morla-Folch, L. Guerrini, N. Pazos-Perez, R. Arenal, R.A. Alvarez-Puebla Synthesis and optical properties of homogeneous nanoshurikens ACS Photonics 2014, 1, 1237–1244

[9] M Sivis, N Pazos-Perez, R Yu, R.A. Alvarez-Puebla, F de Abajo, C Ropers Continuous-Wave Multiphoton Photoemission from Plasmonic Nanostars Communications Physics 2018, 1, Art 13 (1-6 pp)

[10] N. Pazos-Perez, Ramon Alvarez-Puebla Plasmon Tunability of Gold Nanostars at the Tip Apexes ACS Omega 2018, 3, 17173−17179

Circularly Polarized Luminescence for Handedness Determination in Chiral Lanthanide Phosphate Nanocrystals

Uri Hananel, Eitam Vinegrad, Assaf Ben-Moshe, Ori Cheshnovsky, Gil Markovich*

School of Chemistry, Tel Aviv University, Tel Aviv 6997801, Israel
*corresponding author, E-mail: gilmar@post.tau.ac.il

Abstract

The handedness of chiral $TbPO_4$ nanocrystals can be controlled by preparing the nanocrystals in the presence of certain natural chiral acids, such as tartaric acid. We use circularly polarized luminescence measurements to follow the handedness and enantiomeric purity of the produced nanocrystals. Using single particle circularly polarized luminescence microscopy we proved that we obtain enantiomerically pure terbium phosphate nanocrystals when prepared with tartaric acid molecules.

We have previously demonstrated on enantioselective synthesis of α-HgS [1], and Te, Se nanocrystals [2] using thiolated chiral ligands (cysteine, penicillamine, glutathione). Those nanocrystal ensembles exhibited strong circular dichroism, indicating that they were produced with significant enantiomeric excess. However, there was no experimental method to determine how large was this enantiomeric excess.

We have recently turned to another chiral crystal system: lanthanide phosphate hydrates (Rhabdophanes, $LnPO_4 \cdot H_20$). We synthesized Eu^{3+} doped $TbPO_4.H_2O$ nanocrystals, which correspond to a chiral space group ($P3_121$), in the presence of chiral ligands, such as tartaric acid. The nanocrystals were rod-shaped, about 0.5-1 μm long, and ~20-40 nm wide.

We have changed the enantiomeric excess of the tartaric acid used in the synthesis of the lanthanide phosphate nanocrystals and observed the change in the magnitude of the circular polarization in the emission lines of the Eu^{3+} ions. As shown in Figure 1, we have obtained an unusual behavior of the dependence of the circularly polarized luminescence dissymmetry factor

$$g_{lum} = 2\frac{I_L - I_R}{I_L + I_R}$$

on the enantiomeric excess of the tartaric acid molecules. I_L is the emission intensity of the left-handed circular polarization component, and I_R the right handed circularly polarized emission. A saturation of the g_{lum} values at about h~0.4 indicates that already at that stage the formed nanocrystals are enantiomerically pure. This saturation phenomenon enabled us to normalize the relation between g_{lum} and the enantiomeric excess of the formed nanorods (NRee), as seen in the inset of Figure 1.

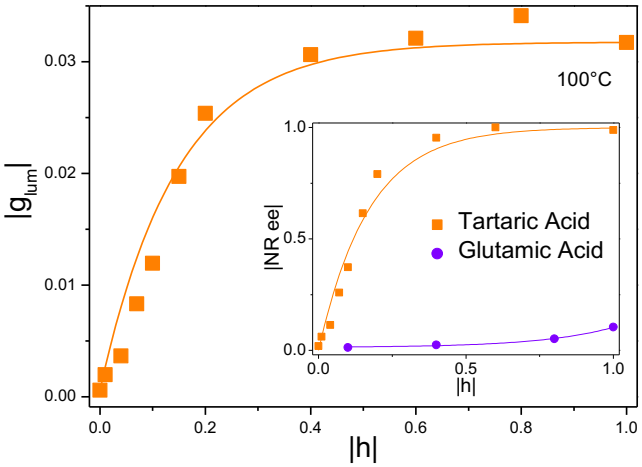


Figure 1: Nanocrystal dissymmetry as a function of the enantiomeric excess of the tartaric acid ($h=x_L-x_R$, where x_L, x_R are the mole fractions of the left- and right-handed tartaric acid). The g_{lum} was measured at 699 nm emission line for the nanocrystals synthesized with different h values. Both g_{lum} and h are shown in absolute value for simplicity. The inset compares the behavior of the tartaric acid-based synthesis to that of a glutamic acid-based one, where both are normalized by the saturation value of g_{lum} observed for the TA-based synthesis. All syntheses in this figure were performed at 100°C. The solid lines are added as guides to the eye.

It can also be seen in Fig. 1 that glutamic acid is much less effective in directing the nanocrystal handedness.

In order to prove that the saturation of the tartaric acid curve in Fig. 1 is indeed due to achievement of full enantiomeric purity of the nanocrystals we have performed single particle circularly polarized luminescence microscopy measurements [3]. Using a sophisticated spectral analysis to overcome the noise in the single particle circularly polarized emission spectra which involved a machine

learning algorithm, we have basically proven that indeed the samples prepared with pure L- or R-tartaric acid contained almost pure left- or right-handed crystals (with the exception of one particle out of ~140 particles sampled).

Acknowledgements

This research was supported by The Israel Science Foundation grant no. 507/14.

References

[1] A. Ben-Moshe, A. O. Govorov, G. Markovich, Enantioselective synthesis of intrinsically chiral mercury sulfide nanocrystals, *Angew. Chem. Int. Ed.* 52: 1275-1279, 2012.

[2] A. Ben-Moshe, S. Grayer Wolf, M. Bar Sadan, L. Houben, Z. Fan, A. O. Govorov, G. Markovich, Enantioselective control of lattice and shape chirality in inorganic nanostructures using chiral biomolecules, *Nature Comm.* 5: 4302, 2014.

[3] E. Vinegrad, U. Hananel, G. Markovich, O. Cheshnovsky, Determination of handedness in a single chiral nanocrystal via circularly polarized luminescence, *ACS Nano* 13: 601–608, 2019.

Synthesis of highly brilliant SERS-encoded core-satellite nanostructures

Nicolas Pazos-Perez[1,*], and Ramon Alvarez-Puebla[1,2]

[1]Department of Physical Chemistry and Inorganic and EMaS, Universitat Rovira i Virgili, Spain
[2]Institució Catalana de Recerca i Estudis Avançats (ICREA), Spain
*corresponding author, E-mail: nicolas.pazos@urv.cat

Abstract

In this work, we report a novel method to produce complex core-satellites SERS encoded nanoparticles (SEPs). Single codified NPs are produced in an easy and fast one-pot approach which, are further use as building blocks to produce the core–satellite SEPs. The presented protocol is very versatile allowing SERS codification with a wide variety of Raman active molecules and the use of different materials and shapes. Moreover, the core–satellite are designed to exhibit minimal interparticle distances (<2–3 nm) with maximum satellite loading, while positioning the encoding agents at the gaps. Thus, achieving a very high optical efficiency. In addition to such versatility, these fabrication methods are simple, cheap, scalable and robust, yielding stable SPEs in high yields.

1. Introduction

Nowadays, the use of SERS encoded nanoparticles (SEPs) is becoming a powerful method to solve analytical problems in complex media such as biological fluids,[1-5] due to their high-throughput screening, multiplexing capabilities, and large surface area for bioconjugation.[6,7] In general, SEPs are made using a plasmonic core, responsible for the generation of the electric field necessary for the Raman amplification; a SERS encoding agent, responsible for the unique vibrational fingerprint of the encoded particle; and a protective layer which allows the attachment of biorecognition elements meanwhile preventing SEPs degradation.[8,9] In this work, we propose an easy and fast approach to produce SEPs. This procedure allows the SERS codification of particles with a wide variety of Raman active molecules (more than 31 different encoded particles were produced). However, although SEPs composed of single plasmonic particles are desirable because of their homogeneous SERS signals.[8] Their efficiency is limited because they cannot form electromagnetic hot spots. Thus, hindering their applicability to other more demanding applications in which acquisition time or spatial resolution are of paramount importance. To solve this problem, we present a synthetic approach to produce SERS encoded core-satellites structures with maximum particle loading and minimal interparticle gaps (< 2-3 nm). Besides improving the SERS efficiency and keeping intensity homogeneity of the signals, these structures also keep the appropriate size ca. 100 nm for biological applications.[10] The presented encoded core-satellites structures can be produced with cores of different materials (Au and Ag) and different shapes following the same protocol.

2. Results and discussion

2.1. Synthesis of SERS encoded building blocks

The successful production of SEPs, requires the simultaneous control of different experimental parameters which can be divided in four main different steps: 1) synthesis of plasmonic NPs; 2) mercaptoundecanoic acid (MUA) functionalization; 3) SERS codification; and 4) silica coating. Fig. 1 shows a schematic representation of the process.

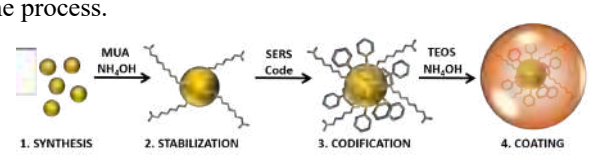


Figure 1: Schematic representation of the process.

Due to the low stability of colloidal solutions upon functionalization with SERS active molecules, a pre-stabilization step is required. Therefore, a molecule that binds covalently to the gold surface while providing particle stability (steric and electrostatic repulsion due to a long aliphatic chain and a terminal carboxylic group) was chosen. It is important that the selected molecule presents a negligible Raman cross-section to avoid undesired SERS signals. Therefore, MUA was used in a first step to functionalize the NPs.[8,10,11] Another crucial issue is that MUA should be added in an adequate proportion to avoid the formation of a compact monolayer that could passivate the metallic surface, preventing the retention of the SERS codes, and with extreme care to avoid heterogeneous adsorption of the molecule by some of the colloids in the solution. Thus, after the NPs synthesis, MUA was rapidly added under vigorous stirring at basic pH to functionalize the plasmonic nanoparticles with 0.8 MUA molecules nm^{-2}, the minimal amount required to provide colloidal stability to the NPs.[9,10] After that, the SERS code can be added

without inducing NPs aggregation. Finally, to ensure the SEPs stability for long periods and generate a readably external surface for further functionalization, the nanoparticles were encapsulated in a silica matrix using the well-known Stöber method.[12,13,14] Fig. 2 shows representative example of the produced NPs.

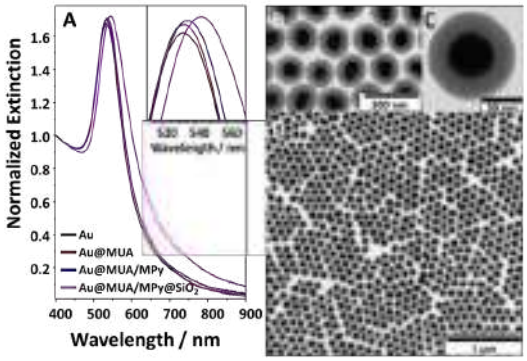


Figure 2: Extinction spectra of Au particles after each step of the presented protocol. (B–D) Representative TEM images at different magnifications of the produced SEPs.

2.2. Synthesis of Core-Satellites SEPs

The assembling strategy for the fabrication of silica-coated SERS-encoded core–satellites is described in the following: plasmonic nanoparticles were first codified using the previously described MUA-mediated protocol[8,10] without the silica coating to use them as cores. Next, the negatively charged SEPs were wrapped with a single layer of positively charged branched polyethyleneimine (PEI) to yield the corresponding positively charged NPs. These NPs were subsequently exposed to a large excess of negatively charged small Au NPs which, via electrostatic interactions, are attached to the positive particles yielding the plasmonic assemblies. Finally, silica encapsulation was performed using a modification of the Stöber method directly on the mixture containing the core–satellites assemblies and the residual unbound satellites. In this specific synthetic approach, the silica coating allows the efficient separation of the light satellites from the clustered particles via post-centrifugation cycling with no risks of perturbing the aggregation state of the assemblies. Fig. 3 shows three different representative encoded core-satellite structures with cores of different materials (Au and Ag) and different shapes (spheres, rods, and stars).



Figure 3: Core-satellites structures with different core shapes, spheres, rods, and stars.

2.3. Optical enhancing properties

To test the optical enhancing properties of the materials produced and their usability for single particle detection, diluted solutions of the colloidal preparations were spin-coated on silicon slides to reach concentrations below one particle per μm^2. The obtained results reveal that all the core-satellite materials yielded strong SERS signals for all lasers lines used (532, 633 and 785 nm) in the single particle regime. However, in the case of individual silver and gold nanoparticles, more concentrated films were required to provide a measurable signal, specifically, 18 and 5 particles per μm^2 were required for gold and silver cores, respectively. In fact, the enhancement factors for the core-satellites are 4 orders of magnitude higher than those of the individual gold or silver SEPs.

3. Conclusions

In summary, we have developed an innovative and easy approach to produce SERS encoded nanoparticles which allows the use of a wide variety of Raman active molecules. This versatile strategy relies in the use of plasmonic NPs that are first stabilized with MUA for the further codification process. This approach allows for the further use of these nanoparticles as building blocks to produce core-satellites encoded structures. The obtained structures are highly brilliant SERS tags that allows for single particle detection.

References

[1] L. Guerrini, R. A. Alvarez-Puebla, N. Pazos-Perez, N. Materials 2018, 11, 1154.

[2] R. A. Alvarez-Puebla, N. Pazos-Perez, L. Guerrini, Applied Materials Today 2018, 13, 1-14.

[3] Wu, T.-J. et al. Nanotechnologies in Preventive and Regenerative Medicine 2018, 1-92 (Elsevier).

[4] N. Pazos-Perez, et al. Scientific Reports 2016, 6, 29014.

[5] C. Catala, et al. Advanced Materials Technologies 2016, 1, 1600163.

[6] A. Doerr, Nature Methods 2007, 4, 381.

[7] H. Fenniri, R. A. Alvarez-Puebla, Nature Chemical Biology 2007, 3, 247.

[8] B. Mir-Simon, I. Reche-Perez, L. Guerrini, N. Pazos-Perez, R. A. Alvarez-Puebla, Chemistry of Materials 2015, 27, 950-958.

[9] R. Jiang, B. Li, C. Fang, J. Wang, Advanced Materials 2014, 26, 5274-5309.

[10] N. Pazos-Perez, J. M. Fitzgerald, V. Giannini, L. Guerrini, R. A. Alvarez-Puebla, Nanoscale Advances 2019, 1, 122-131.

[11] P. J. G. Goulet, N. P. W. Pieczonka, R. F. Aroca, Analytical Chemistry 2003, 75, 1918-1923.

[12] W. Stöber, A. Fink, E. Bohn, Journal of Colloid and Interface Science 1968, 26, 62-69.

Keeping an eye on the eye through plasmonics

Andrea López-Mariño[a], Ana Sousa-Castillo[a], Enrique Carbó-Argibay [b], Francisco Otero-Espinar[c], Ramon A. Alvarez-Puebla[d,e,*], Moisés Pérez-Lorenzo[a,*], Miguel A. Correa-Duarte[a,*]

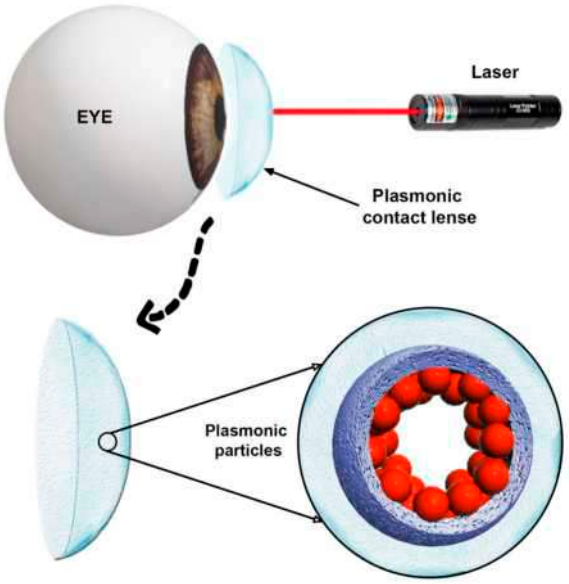
[a] *Department of Physical Chemistry, Biomedical Research Center (CINBIO), Southern Galicia Institute of Health Research (IISGS), and Biomedical Research Networking Center for Mental Health (CIBERSAM), Universidade de Vigo, 36310 Vigo, Spain*
[b] *International Iberian Nanotechnology Laboratory (INL), Av. Mestre José Veiga s/n, 4715-330 Braga, Portugal*
[c] *Department of Pharmacy and Pharmaceutical Technology, and Industrial Pharmacy Institute, Faculty of Pharmacy, Universidade de Santiago de Compostela, Santiago de Compostela, 15782, Spain*
[d] *Department of Physical Chemistry and EMaS, Universitat Rovira i Virgili, 43007 Tarragona, Spain*
[e] *ICREA, Passeig de Lluís Companys 23, 08010 Barcelona, Spain*

Abstract

The synthesis of a hydrogel-based soft contact lens featuring laser shielding capabilities is reported. These light-protective properties are accomplished through the integration of gold-based plasmonic nanoresonators into the lens polymer network, which provides the hydrogel with a high optical density while preserving visible light transmittance. The implementation of these hybrid materials shows great potential in the eye care setting in terms of applications. Along these lines, the ability of the Au nanocomposites to act as efficient light concentrators renders this approach a cost-effective alternative to other less absorbing formulations which may also be toxic or degradable upon light irradiation. Furthermore, the use of these hybrid lenses would provide the wearer with an all day long protection and a minimal obstruction to perform common tasks in those scenarios where high powered light sources are operated.

Introduction

In the past few years, nanoscience has emerged as a source of innovative solutions to eye-related diseases and conditions.[1–3] In this line, the implementation of nanomaterials in the ophthalmologic field has propelled a vast array of applications including sensing,[4–6] imaging,[7–9] and ocular drug delivery.[10–12] Among these operational uses, electromagnetic shielding is also of great interest since, as known, excessive light exposure is a potential cause of ocular disorders such as cataracts or retinal damage.[13–15] In this context, high powered lasers constitute a major concern among the sources of artificial lighting given their widespread use in many industries as well as research, education, medicine and military.[16] For that reason, the current market of safety eyewear offers a wide range of products including spectacles, goggles and wrap-around glasses.[17] These accessories are aimed at protecting the human eye from laser irradiation by filtering specific (or a narrow range of) wavelengths depending on which applications they are intended for. This is usually accomplished through glass filters where heavy metal ions or colloidal particles are introduced. Polymer-based substrates (typically polycarbonates) can also be exploited to this end. In this case, this is achieved by the impregnation of the polymer with different dyes during the molding process, which enables the mimicking of the absorptive properties of glass laser filters.



Scheme 1. Illustration depicting the architecture of the plasmonic Au-based silica-shelled nanocapsules and their integration in a soft contact lens as an electromagnetic shielding component

Additionally, lamination of different glasses or hybrid combinations of glass and polymer substrates may be also employed in order to manufacture products offering protection against multiple wavelengths. However, despite the vast range of eyewear products available in the market,

no much efforts have been made from the field of nanoscience aiming at developing novel and more efficient strategies for the electromagnetic shielding in the eye care setting.[18] This lack of interest contrasts with the great progress made in the last years on the field of plasmonics, which has provided many technological opportunities due to the unprecedented ability of metallic nanostructures to concentrate light into deep-subwavelength volumes.[19]

The present work reports the fabrication of a hybrid soft contact lens featuring the integration of gold-based plasmonic silica-shelled nanocapsules (Scheme 1). Through this synthetic approach, the growth of the Au nanoparticles immobilized into these architectures can be chemically controlled thereby, allowing for a precise manipulation of the absorptive properties of the metal across the visible and infrared spectrum. In the end, this high degree of control enables the modulation of the optical behavior of the lens and thus, its exploitation as an electromagnetic shield.

Acknowledgements

This work was funded by MINECO-Spain (CTM2014-58481-R, CTM2017-84050-R, and CTQ2017-88648-R), Xunta de Galicia (Centro Singular de Investigación de Galicia, Acc. 2016–2019 and EM2014/035), Generalitat de Catalunya (2017SGR883), URV (2017PFR-URV-B2-02), URV and Banco Santander (2017EXIT-08), and European Union (ERDF).

References

[1] M.A. Kamaleddin, Nano-ophthalmology: Applications and considerations, Nanomedicine. 13 (2017) 1459–1472.

[2] Y. Diebold, M. Calonge, Applications of nanoparticles in ophthalmology, Prog. Retin. Eye Res. 29 (2010) 596–609.

[3] M.A. Zarbin, C. Montemagno, J.F. Leary, R. Ritch, Nanotechnology in ophthalmology, Can. J. Ophthalmol. 45 (2010) 457–476.

[4] J. Park, J. Kim, S.-Y. Kim, W.H. Cheong, J. Jang, Y.-G. Park, K. Na, Y.-T. Kim, J.H. Heo, C.Y. Lee, J.H. Lee, F. Bien, J.-U. Park, Soft, smart contact lenses with integrations of wireless circuits, glucose sensors, and displays, Sci. Adv. 4 (2018).

[5] J. Kim, M. Kim, M.-S. Lee, K. Kim, S. Ji, Y.-T. Kim, J. Park, K. Na, K.-H. Bae, H. Kyun Kim, F. Bien, C. Young Lee, J.-U. Park, Wearable smart sensor systems integrated on soft contact lenses for wireless ocular diagnostics, Nat. Commun. 8 (2017) 14997.

[6] N.M. Farandos, A.K. Yetisen, M.J. Monteiro, C.R. Lowe, S.H. Yun, Contact Lens Sensors in Ocular Diagnostics, Adv. Healthc. Mater. 4 (2014) 792–810.

[7] A. Nair, P. Thevenot, W. Hu, L. Tang, Nanotechnology in the treatment and detection of intraocular cancers, J. Biomed. Nanotechnol. 4 (2008) 410–418.

[8] R.A. Schachar, W. Chen, B.K. Woo, B.K. Pierscionek, X. Zhang, L. Ma, Diffusion of nanoparticles into the capsule and cortex of a crystalline lens, Nanotechnology. 19 (2008).

[9] D.L. Holligan, G.T. Gillies, J.P. Dailey, Magnetic guidance of ferrofluidic nanoparticles in an in vitro model of intraocular retinal repair, Nanotechnology. 14 (2003) 661–666.

[10] U.B. Kompella, A.C. Amrite, R. Pacha Ravi, S.A. Durazo, Nanomedicines for back of the eye drug delivery, gene delivery, and imaging, Prog. Retin. Eye Res. 36 (2013) 172–198.

[11] H.-Y. Zhou, J.-L. Hao, S. Wang, Y. Zheng, W.-S. Zhang, Nanoparticles in the ocular drug delivery, Int. J. Ophthalmol. 6 (2013) 390–396.

[12] S.K. Sahoo, F. Dilnawaz, S. Krishnakumar, Nanotechnology in ocular drug delivery, Drug Discov. Today. 13 (2008) 144–151.

[13] P.G. Söderberg, N. Talebizadeh, Z. Yu, K. Galichanin, Does infrared or ultraviolet light damage the lens?, Eye. 30 (2016) 241.

[14] J.J. Hunter, J.I.W. Morgan, W.H. Merigan, D.H. Sliney, J.R. Sparrow, D.R. Williams, The susceptibility of the retina to photochemical damage from visible light, Prog. Retin. Eye Res. 31 (2012) 28–42.

[15] P.N. Youssef, N. Sheibani, D.M. Albert, Retinal light toxicity, Eye. 25 (2011) 1–14.

[16] Y. Barkana, M. Belkin, Laser Eye Injuries, Surv. Ophthalmol. 44 (2000) 459–478.

[17] H.A. Jones-Bey, Laser safety takes on the real world, Laser Focus World. 41 (2005) 52–54.

[18] S. Lee, I. Jo, S. Kang, B. Jang, J. Moon, J.B. Park, S. Lee, S. Rho, Y. Kim, B.H. Hong, Smart Contact Lenses with Graphene Coating for Electromagnetic Interference Shielding and Dehydration Protection, ACS Nano. 11 (2017) 5318–5324.

[19] J.A. Schuller, E.S. Barnard, W. Cai, Y.C. Jun, J.S. White, M.L. Brongersma, Plasmonics for extreme light concentration and manipulation, Nat. Mater. 9 (2010) 193–204.

Manipulation of Strong Light–Matter Interactions in Two-Dimensional Transition-Metal Dichagenides Coupled with Nanophotonic Structures

Huanjun Chen[1,*], Hao Wang[2], Jinxiu Wen[2]

[1]State Key Laboratory of Optoelectronic Materials and Technologies, Guangdong Province Key Laboratory of Display Material and Technology, and School of Electronic and Information Technology, Sun Yat-sen University, Guangzhou 510275, China
[2]School of Physics, Sun Yat-sen University, Guangzhou 510275, China
[*]corresponding author: chenhj8@mail.sysu.edu.cn

Abstract

Strong light–matter interactions in two-dimensional transition-metal dichagenides (TMDCs) coupled with nanophotonic structures can have great potential in future high-performance nanophotonic and quantum devices which operate at room temperature. I will introduce our recent progresses on manipulation of this type of strong interactions using semiconductor as well as plasmonic nanostructures.

1. Introduction

Due to their intriguing optical and electrical responses, TMDCs with atomic thicknesses have attracted much attention in recent years, both from fundamental and application aspects.[1] In particular, if the TMDCs are placed within an optical cavity, the coupling between the 2D excitons and cavity modes can lead to exotic photonic behaviors, such as Rabi splitting, Fano resonances, enhanced absorption and photoluminescence, and lasing. These processes are very important for nanophotonics devices and have attracted much attention in the past decade. From an application point of view, it is required that the strong interactions between the TMDCs and optical cavity can occur at room temperature and active control on such interactions is also strongly desired. The large exciton binding energies (0.3−0.9 eV), strong exciton transition dipole moments, and excitonic characteristics that are amenable to external stimulus in the TMDCs can well tackle these challenges.[1,2]

In this talk I will introduce our recent works on manipulation of the coupling between the TMDCs with the plasmonic and dielectric nanocavities. Depending on the coupling strength and the cavity used, strong coupling phenomena, with a large Rabi splitting upto ~ 100 meV, and Fano-type resonances were observed at room temperature. The active control on these coupling processes were achieved using temperature scanning, electrostatic gating, as well as electrochemical approach.

2. Results and discussions

2.1. Manipulation of strong coupling between plasmonic nanorods and 2D excitons in monolayer WS_2

By integrating the individual gold nanorods with the 2D WS_2 and WSe_2, we achieve strong coupling at room-temperature, where a Rabi splitting energy can reach upto 106 meV. In addition, the strong coupling can be tailored by applying temperature scanning, electrostatic gating, and proton doping to the hybrid nanostructure. In particular, the modulation depth of the electric approach can be upto 17% (Fig. 1).[3,4]

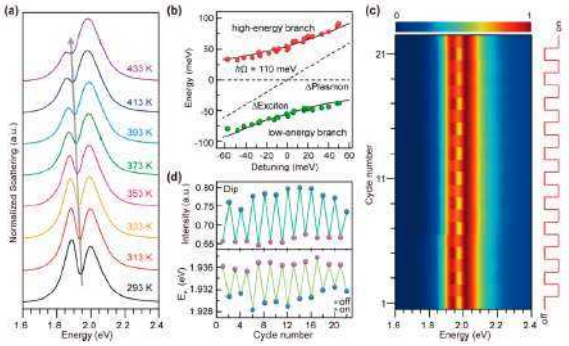


Fig. 1. Manipulation of the strong coupling in individual plasmonic nanorod coupled with monolayer WS_2.[3]

2.2. Manipulation of resonance coupling between Si nanospheres and 2D excitons in monolayer WS_2

High-refractive-index dielectric nanostructures are another type of nanocavities capable of confining the free-space light into nanoscale volumes.[5] We showed that resonance coupling could occur between the magnetic dipole mode of the Si nanosphere and two-dimensional excitons in monolayer WS_2 (ML-WS_2). For a silicon nanosphere coated with a ML-WS2, a distinct mode splitting and anticrossing behavior with a splitting energy of 43 meV can be observed, which can be attributed to the coherent energy transfer between the magnetic dipole resonance and exciton transition. However, if a silicon nanosphere is deposited onto a flat ML-WS_2 flake, the resonance coupling is manifested by a Fano interference effect.[6] In particular, such a Fano lineshape can be actively tailored by temperature scanning.

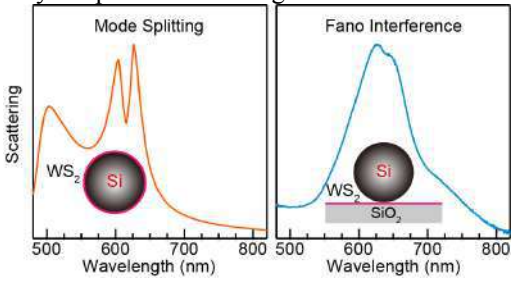


Fig. 2. Resonance coupling between an individual silicon nanosphere and ML-WS_2.

3. Conclusions

In summary, I have reviewed our recent studies on manipulation of strong light–matter interactions between 2D excitons in monolayer WS_2 and nanophotonic structures. These results can not only further our understanding on light–matter interactions at the nanoscale, but also benefit the design of nanophotonic devices rely on 2D materials.

Acknowledgements

This work was financially supported by the National Natural Science Foundation of China (Grant Nos. 51290271, 11474364), the National Key Basic Research Program of China (Grant Nos. 2013CB933601), the Guangdong Natural Science Funds for Distinguished Young Scholars (Grant No. 2014A030306017), the Guangdong Special Support Program (201428004), and the Fundamental Research Funds for the Central Universities (17lgzd05).

References

[1] Q. H. Wang, K. Kalantar-Zadeh, A. Kis, J. N. Coleman, M. S. Strano, Electronics and optoelectronics of two-dimensional transition metal dichalcogenides. *Nat. Nanotechnol.* 7: 699−712, 2012.

[2] H. Zeng, J. Dai, W. Yao, D. Xiao, X. D. Cui, Valley polarization in MoS_2 monolayers by optical pumping. *Nat. Nanotechnol.* 7: 490−493, 2012.

[3] J. X. Wen, H. Wang, W. L. Wang, Z. X. Deng, C. Zhuang, Y. Zhang, F. Liu, J. C. She, J. Chen, H. J. Chen, S. Z. Deng, N. S. Xu, Room-temperature strong light−matter interaction with active control in single plasmonic nanorod coupled with two-dimensional atomic crystals. *Nano Lett.* 17: 4689–4697, 2017.

[4] J. X. Wen, H. Wang, H. J. Chen, S. Z. Deng, N. S. Xu, Room-temperature strong coupling between dipolar plasmon resonance in single gold nanorod and two-dimensional excitons in monolayer WSe_2. *Chin. Phys. B* 27: 096101, 2018.

[5] A. B. Evlyukhin, S. M. Novikov, U. Zywietz, R. L. Eriksen, C. Reinhardt, S. I. Bozhevolnyi, B. N. Chichkov, Demonstration of magnetic dipole resonances of dielectric nanospheres in the visible region. *Nano Lett.* 12: 3749–3755, 2012.

[6] H. Wang, J. X. Wen, W. L. Wang, N. S. Xu, P. Liu, J. H. Yan, H. J. Chen, S. Z. Deng, Resonance coupling in heterostructures composed of silicon nanosphere and monolayer WS_2: a magnetic-dipole-mediated energy transfer process. *ACS Nano* DOI: 10.1021/acsnano.8b07826, 2019.

Plasmonic Hot Holes: Fundamentals and Devices

Giulia Tagliabue[1,2,3,*], Joseph S. DuChene[1,2], Harry A. Atwater[1,2,3]

[1]Thomas J. Watson Laboratory of Applied Physics, California Institute of Technology, Pasadena, CA 91125 United States.
[2]Joint Center for Artificial Photosynthesis, California Institute of Technology, Pasadena, CA 91125 United States.
[3]Laboratory of Nanoscience for Energy Technologies, EPFL, 1015 Lausanne, Switzerland.

*corresponding author, E-mail: giulia.tagliabue@epfl.ch

Abstract

Highly-absorbing, plasmonic-metal nanostructures offer a promising route to bandgap-less ultra-fast photodetectors and broadband solar photocatalysts, due to their tunable absorption characteristics and ability to generate hot carriers[1-3]. For this reason, fundamental knowledge of hot-carrier energy distributions as well as their dynamics and associated lifetimes are necessary to adequately harness these energetic, non-equilibrium carriers. To date, experimental studies of hot carrier devices have focused almost entirely on the exploitation of hot electrons to produce a photocurrent or initiate a chemical reaction. Furthermore, numerous efforts have been devoted to understanding the temporal evolution of hot electrons within photo-excited metal nanostructures and various metal-semiconductor assemblies[4-6]. In contrast, there have been very few realizations of hot-hole based plasmonic devices and the dynamics of hot holes in metal nanostructures have remained largely unknown, despite the favorable energetics of hot holes predicted by ab-initio calculations[7].

Here, we report the construction, optoelectronic and photoelectrochemical characterization of plasmon-driven photodiodes and photocathodes based on a metal/p-type gallium nitride (p-GaN) heterostructure that operate within the visible regime via hot-hole injection. First, we report a photoelectrochemical platform for improving the selectivity of solar-to-fuel energy conversion via plasmonic hot-carriers[8]. Next, through solid-state measurements we elucidate the fundamental role played by the metal band structure in determining device performance[9]. Lastly, we use ultrafast transient absorption spectroscopy to show that plasmon-induced hot-hole injection from gold (Au) nanoparticles into the valence band of p-GaN occurs on a similar timescale as previous observations of hot-electron injection. Furthermore, we show that the thermalization process of hot-electrons is significantly affected by hot-hole collection by the p-GaN support[10]. Taken together, our studies substantially advance the understanding of hot-hole transfer in metal-semiconductor heterostructures and demonstrate new opportunities for expanding the scope of hot-carrier optoelectronics beyond hot-electron-based devices.

References

[1] Brongersma, M. L.; Halas, N. J.; Nordlander, P. Plasmon-induced hot carrier science and technology. Nat. Nanotechnol. 10, 25-34 (2015).

[2] Christopher, P.; Moskovits, M. Hot charge carrier transmission from plasmonic nanostructures. Annu. Rev. Phys. Chem. 68, 379-398 (2017).

[3] Linic, S.; Aslam, U.; Boerigter, C.; Morabito, M. Photo-chemical transformations on plasmonic metal nanoparticles. Nat. Mater. 14, 567-576 (2015).

[4] Link, S.; El-Sayed, M. A. Spectral properties and relaxation dynamics of surface plasmon electronic oscillations in gold and silver nanodots and nanorods. J. Phys. Chem. B 103, 8410-8426 (1999).

[5] Hartland, G. V. Optical studies of dynamics in noble metal nanostructures. Chem. Rev. 111, 3858-3887 (2011).

[6] Harutyunyan, H.; Martinson, A. B. F.; Rosenmann, D.; Khorashad, L. K.; Besteiro, L. V.; Govorov, A. O.; Wiederrecht, G. P. Anomalous ultrafast dynamics of hot plasmonic electrons in nanostructures with hot spots. Nat Nano, 10, (9), 2015

[7] Brown, A. M.; Sundararaman, R.; Narang, P.; Goddard III, W. A.; Atwater, H. A. Nonradiative plasmon decay and hot carrier dynamics: effects of phonons, surfaces, and geometry. ACS Nano 10, 957-966 (2016).

[8] JS DuChene, G Tagliabue, AJ Welch, WH Cheng, HA Atwater, Hot Hole Collection and Photoelectrochemical CO2 Reduction with Plasmonic Au/p-GaN Photocathodes, *Nano letters* 18 (4), 2545-2550

[9] G Tagliabue, AS Jermyn, R Sundararaman, AJ Welch, JS DuChene, R Pala, AR Davoyan, P Narang, H A Atwater, Quantifying the role of surface plasmon excitation and hot carrier transport in plasmonic devices, *Nature Communications* 9 (1), 3394

[10] G. Tagliabue, JS. DuChene, M. Abdellah, A. Habib, Y.Hattori, K.Zheng, SE Canton, DJ Gosztola, W.H Cheng, R. Sundararaman, J Sá, HA Atwater, Ultrafast Studies of Hot-Hole Dynamics in Au/p-GaN Heterostructures, *arXiv preprint arXiv*:1810.04238

Spaser assisted coherent generation of nuclei vibrations in Raman active molecules

Vladislav Yu. Shishkov[1,2,3], Evgeny S. Andrianov[1,2,*], Alexander A. Pukhov[1,2,3], Alexey P. Vinogradov[1,2,3], and Alexander A. Lisyansky[4,5]

[1]Dukhov Research Institute of Automatics (VNIIA), 22 Sushchevskaya, Moskow 127055, Russia
[2]Moscow Institute of Physics and Technology, 9 Institutskiy per., Dolgoprudny 141700, Moscow reg., Russia
[3]Institute for Theoretical and Applied Electromagnetics, 13 Izhorskaya, Moscow 125412, Russia
[4]Department of Physics, Queens College of the City University of New York, Flushing, New York 11367, USA
[5]The Graduate Center of the City University of New York, New York, New York 10016, USA
*corresponding author, E-mail: andrianov.es@mipt.ru

Abstract

We consider excitation of the plasmonic nanoparticle interacting with Raman active molecules by the external coherent field. We show that there is a threshold value of external field amplitude above which coherent generation both of surface plasmons and nuclei vibrations in the molecules arises. We find that the coherent generation of surface plasmons is always followed by the coherent generation of nuclei vibration in the Raman active molecules.

1. Introduction

The discovery of lasers gave a new impetus to the development of the Raman spectroscopy. The new phenomena such as stimulated Raman scattering, coherent (anti-)Stokes Raman scattering were discovered [1, 2]. The stimulated Raman scattering occurs when the Raman active molecules are illuminated by two coherent electromagnetic waves: a weak signal wave and a high pump one [1]. In the case when the pump frequency is greater than the signal frequency, and the frequency difference of the incident waves is close to the frequency of nuclei vibration of the molecule, the wave with signal frequency is amplified. If the Raman active molecules are placed in a resonator, then the role of a signal wave can be played by the resonator mode. In this case, when the system is illuminated with a coherent wave with high amplitude, the electric field inside resonator will exhibit self-oscillations. This device is called Raman laser.

In 2003, Bergman and Stockman introduced the spaser (Surface Plasmon Amplification by Stimulated Emission of Radiation), a quantum amplifier of surface plasmons by stimulated emission of radiation [3]. The spaser includes two parts: gain medium, that amplifies the electromagnetic field, and resonator, that provides the positive feedback. Principles of spaser operation are analogous to those for a laser with the role of photons played by surface plasmons localized at a metal surface. The main feature of the spaser is the strong subwavelength field localization that emerges due to the nature of the surface plasmons.

In this work, we consider the case of Raman laser when the role of the resonator mode is played by the plasmon resonance of a metal nanoparticle. We show that the nuclei vibrations can be coherently generated by self-oscillations of surface plasmons.

2. Results and Discussion

We consider Raman active molecules with the frequency of electronic transition ω_{el} placed in the vicinity of plasmonic nanoparticle with the frequency of dipole plasmonic resonance ω_{pl}. Excitation of such a system is produced by external coherent wave with frequency ω_{ex}. This coherent wave interacts with dipole moment of plasmonic nanoparticle. In turn, its near field excites the electron subsystem of the molecule through the dipole-dipole interaction. Nuclei vibrations of the molecules with eigenfrequency ω_{v} arise as a response to oscillation of molecule electronic subsystem. We assume that the condition $\omega_{\mathrm{ex}} \simeq \omega_{\mathrm{pl}} + \omega_{\mathrm{v}} \ll \omega_{\mathrm{el}}$ is fulfilled. After second quantization procedure, the Hamiltonian of the system takes the form

$$\hat{H} = \hbar\omega_{\mathrm{pl}}\hat{a}^{\dagger}\hat{a} + \hbar\Omega\left(\hat{a}^{\dagger}\exp\left(-i\omega_{\mathrm{ex}}t\right) + \hat{a}\exp\left(i\omega_{\mathrm{ex}}t\right)\right) + \hbar\omega_{\mathrm{el}}\hat{\sigma}^{\dagger}\hat{\sigma} + \hbar\Omega_{\mathrm{R}}\left(\hat{a}^{\dagger}\hat{\sigma} + \hat{\sigma}^{\dagger}\hat{a}\right) + \hbar\omega_{\mathrm{v}}\hat{b}^{\dagger}\hat{b} + \hbar g\left(\hat{b}^{\dagger} + \hat{b}\right)\hat{\sigma}^{+}\hat{\sigma} \quad (1)$$

Here, $\hat{a}$, $\hat{\sigma}$, and $\hat{b}$ are plasmon annihilation operators, lowering operator of electronic subsystem of a molecule, and annihilation operator of nuclei vibrations, respectively. Ω, Ω_{R} and g are interaction constants between external filed and plasmonic nanoparticle dipole moment, between nanoparticle dipole moment and dipole moment of molecule electronic transition, and between molecule electronic subsystem and nuclei vibrations of molecule, respectively.

Using Heisenberg equation for the amplitudes of plasmon oscillations $\hat{a}$, electronic subsystem oscillations $\hat{\sigma}$ and nuclei vibrations $\hat{b}$, we obtain the following system of equa-

tions

$$\frac{d\hat{a}}{dt} = -\left(i\omega_{\rm pl} + \gamma_{\rm pl}\right)\hat{a} - \frac{1}{2}i\Omega_{\rm R}\hat{\sigma} - \frac{1}{2}i\Omega e^{-i\omega t} \quad (2)$$

$$\frac{d\hat{\sigma}}{dt} = -\left(i\omega_{\rm el} + \gamma_{\rm el}\right)\hat{\sigma} - ig\hat{\sigma}\left(\hat{b}^{\dagger} + \hat{b}\right) + \quad (3)$$

$$+\frac{1}{2}i\Omega_{\rm R}\left(2\hat{\sigma}^{\dagger}\hat{\sigma} - 1\right)\hat{a}$$

$$\frac{d\hat{b}}{dt} = -\left(i\omega_{\rm v} + \gamma_{\rm v}\right)\hat{b} - ig\hat{\sigma}^{\dagger}\hat{\sigma} \quad (4)$$

Numerical simulations of Eqs. (2) – (4) show that there is a threshold value of external field amplitude above which self-oscillations of both electric field of surface plasmons and nuclei vibrations arise. Coherent self-oscillations of surface plasmons in the considered system are analogous to surface plasmon self-oscillations in spaser proposed by Bergman and Stockman in [3]. Coherent oscillations of electric field of surface plasmons induced coherent vibrations of nuclei. The greatest number of nuclei vibration quanta is observed when the decay rate of nuclei vibrations is much smaller than the one of surface plasmon which usually takes place in most experiments.

3. Conclusions

In this work we propose spaser assisted coherent generation of nuclei vibrations in Raman active molecules. The Raman active molecules play the role of gain medium and coherent light source is used as a pump. It is shown that the coherent generation of surface plasmons is always followed by the coherent generation of nuclei vibration in the Raman active molecules. This provides the potential application in the vibrational spectroscopy as well as access the optically driven chemistry [4].

References

[1] R.W. Boyd, *Nonlinear Optics*, Academic Press, 2007.

[2] J.-X. Cheng, X.S. Xie, *Coherent Raman Scattering Microscopy*, CRC Press, 2007.

[3] D. J. Bergman, M. I. Stockman, Surface Plasmon Amplification by Stimulated Emission of Radiation: Quantum Generation of Coherent Surface Plasmons in Nanosystems, *Phys. Rev. Lett.* 90: 027402, 2003.

[4] A. Lombardi, et. al., Pulsed Molecular Optomechanics in Plasmonic Nanocavities: From Nonlinear Vibrational Instabilities to Bond-Breaking, *Phys. Rev. X* 8: 011016, 2018.

FRET in Hybrid Nanostructures: General Dimensionality Classes, Assembly Effects and Unique Cases

Pedro Ludwig Hernandez-Martinez[1] and Hilmi Volkan Demir[1,2]

[1]*LUMINOUS!* Centre of Excellence for Semiconductor Lighting and Display,
School of Electrical and Electronic Engineering and School of Physical and Mathematical Sciences,
Nanyang Technological University, 639798, Singapore
[2]Department of Electrical and Electronics Engineering, Department of Physics,
UNAM−National Nanotechnology Research Center, and Institute of Materials Science and Nanotechnology,
Bilkent University, Ankara 06800, Turkey
*corresponding author, E-mail: pedro@ntu.edu.sg, HVDEMIR@ntu.edu.sg

Abstract

We present a unified picture for Foerster resonance energy transfer in hybrid nanostructures with mixed dimensionality and in assembly arrays. In addition to general classes of FRET, we will also discuss peculiar examples of FRET processes including the exciton migration from quantum well to an energy gradient structure and near unity energy transfer from Nanoplatelets to a monolayer of MoS2. The general effects of dimensionality and assembly, along with peculiar examples, show the richness of FRET phenomena.

1. Introduction

Today nanotechnology offers means to assemble and study hybrid nanostructures compose of metal and semiconductor materials. Each element of the nanostructure contributes to the overall structure with their distinctive properties resulting from quantum confinement and interactions between them, enhancing optical properties for the structure. The Förster resonance energy transfer (FRET) is an important mechanism for strong coupling between elements, based on the Dipole Coulomb interaction, where the exciton flows from the donor (D) to the acceptor (A) (D →A). Excitons play an important role in optical devices such as solar cell, lasers, photodetectors, and LEDs. Thus, understanding FRET in these nanostructures is crucial for high efficiency light generation and harvesting.

2. Discussion

We obtained the Förster resonance energy transfer (FRET) rates in the long distance asymptotic behaviour in the dipole approximation for all possible combinations with mixed dimensionality [1,2]. The FRET rate were calculated using the expression:

$$\gamma_{trans} = \frac{2}{\hbar}\mathrm{Im}\left[\int dV\left(\frac{\varepsilon_A(\omega)}{4\pi}\right)\mathbf{E}_{in}(\mathbf{r})\cdot\mathbf{E}_{in}^{*}(\mathbf{r})\right] \qquad (1)$$

where the integration is over the acceptor geometry, $\varepsilon_A(\omega)$ is the dielectric function of the acceptor, and $E_{in}(\mathbf{r})$ is the effective electric field created by an exciton at the donor side.

Table 1 shows the functional distance dependency for the FRET: (1) when the acceptor is an NP, FRET is proportional to d^{-6}; (2) when the acceptor is an NW or 1D array structure, FRET is proportional to d^{-5}; (3) when the acceptor is a QW or a 2D array, FRET is proportional to d^{-4}, and when the acceptor is bulk or a 3D array, FRET is proportional to d^{-3}. It is worth mentioning that the effective dielectric constant depends only on the donor's geometry its confinement effect is summary in table 2.

To illustrate the effect acceptor confinement on FRET rate, we discuss peculiar examples for FRET processes. For instance, the exciton migration from a quantum well (QW) to an energy gradient structure consisting of layer-by-layer assembled quantum dot (QD) bilayer [3]. The energy gradient of these QDs provides a substantial increase in the exciton transfer efficiency with respect to the bilayer of a single type of QDs. These results suggest that the energy difference between the QD layers significantly boosts the QW-QD exciton transfer rate compared to the mono-dispersed case. Another example is the near unity energy transfer between CdSe/CdS core/crown Nanoplatelets (NPLs) to a monolayer of MoS_2 [4]. This systematic study suggested that the FRET rate decay as d^{-2}, where d is the distance between the donor NPL and the acceptor MoS_2 2D structure. We found that the strong field screening and the dipole electric field delocalization play a major role in modifying the energy transfer kinetics from d^{-4} to d^{-2} (Fig. 1).

Table 1: Generic distance dependency for the FRET rates, with equivalent cases of arrayed nanostructures in term of d dependence (Reprinted from Ref [2]).

Generic Distance Dependence	FRET Donor (D) → Acceptor (A)
$\gamma \propto \frac{1}{d^6}$	$X \rightarrow$
$\gamma \propto \frac{1}{d^5}$	$X \rightarrow \equiv X \rightarrow$
$\gamma \propto \frac{1}{d^4}$	$X \rightarrow \equiv X \rightarrow \equiv X \rightarrow$
$\gamma \propto \frac{1}{d^3}$	$X \rightarrow \equiv X \rightarrow \equiv X \rightarrow$
$X =$	

d: distance between D and A. ≡ : equivalent.

Table 2: Effective Dielectric Constant as a function of geometry (Reprinted from Ref [1]).

Exciton Orientation	NP	NW	QW
X	$\varepsilon_{eff} = \frac{\varepsilon_{NP} + 2\varepsilon_0}{3}$	$\varepsilon_{eff} = \frac{\varepsilon_{NW} + \varepsilon_0}{2}$	$\varepsilon_{eff} = \varepsilon_0$
Y	$\varepsilon_{eff} = \frac{\varepsilon_{NP} + 2\varepsilon_0}{3}$	$\varepsilon_{eff} = \frac{\varepsilon_{NW} + \varepsilon_0}{2}$	$\varepsilon_{eff} = \varepsilon_0$
Z	$\varepsilon_{eff} = \frac{\varepsilon_{NP} + 2\varepsilon_0}{3}$	$\varepsilon_{eff} = \frac{\varepsilon_{NW} + \varepsilon_0}{2}$	$\varepsilon_{eff} = \varepsilon_0$

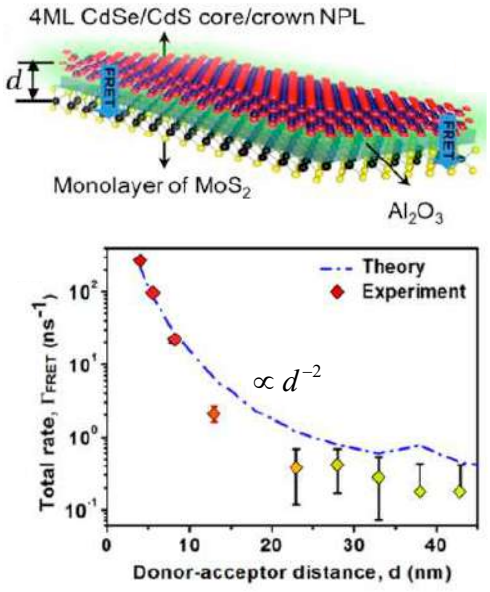


Figure 1: Top: Illustration of the hybrid assembled films of NPLs−Al_2O_3−MoS_2 (donor−spacer−acceptor) system. Bottom: Total FRET rate as a function of the Al_2O_3 thin-film thickness (separation thickness). The blue dot-dashed line is the COMSOL electromagnetic numerical simulation behaviour of the system (Reprinted from Ref [4]).

3. Conclusion

In summary, we present a complete picture and unified understanding FRET in hybrid nanostructures with mixed dimensionality and in assembled nanostructures arrays. We obtain the analytical expressions for the energy transfer rate in the long distance approximation. Our findings show that the acceptor quantum confinement dimension sets the generic NRET distance dependence and the donor geometry dimension modifies the effective dielectric function. This generic distance dependence can be remodified by arraying (stacking) the nanostructures. Therefore, the functional distance dependency of the NRET rate is determined by the quantum confinement as well as array stacking dimensionality of the acceptor.

References

[1] P.-L. Hernández-Martínez, A.-O. Govorov, and H.-V. Demir, Förster-type Nonradiative Energy Transfer for Assemblies of Arrayed Nanostructures: Confinement Dimension vs. Stacking Dimension, *J. Phys. Chem. C*, Vol. 118, No. 9, 4951–4958, 2014.

[2] P.-L. Hernández-Martínez, A.-O. Govorov, and H.-V. Demir, Generalized Theory of Förster-type Nonradiative Energy Transfer in Nanostructures with Mixed Dimensionality, *J. Phys. Chem. C*, Vol 117, No 19, 10203−10212, 2013.

[3] S. Nizamoglu, P.-L. Hernández-Martínez, E. Mutlugun, D.-U. Karatay, and H.-V. Demir, Excitonic Enhancement of Nonradiative Energy Transfer from a Quantum Well in the Optical Near Field of Energy Gradient Quantum Dots, *Appl. Phys. Lett.*, 100, 241109, 2012.

[4] N. Taghipour, P. L. Hernández-Martínez, A. Ozden, M. Olutas , D. Dede, K. Gungor, O. Erdem, N. K. Perkgoz, H. V. Demir, "Near-Unity efficiency energy transfer from colloidal quantum wells of CdSe/CdS nanoplatelets to a monolayer of MoS2", *ACS Nano*, 12, 8547, 2018

Probing optical chirality in the near-field of achiral nanostructures

Andreas Horrer[1], Yinping Zhang[1], Thinhinane Aoudjit[1], Jérémie Béal[1], Jérôme Plain[1], Renaud Bachelot[1], and Davy Gérard[1,*]

[1] Light, Nanomaterials, Nanotechnologies (L2n), Institut Charles Delaunay, CNRS, Université de Technologie de Troyes, Troyes, France
*corresponding author, E-mail: davy.gerard@utt.fr

Abstract

We study the optical properties of plasmonic oligomers with trigonal symmetry. Albeit achiral, such structures exhibit a near-field response that depends upon the handedness of the exciting light (i.e., left- or right-circular polarization). This effect stems from near-field interference between the modes sustained by the structure. Then, we experimentally demonstrate this effect by imprinting the local optical chirality into a photosensitive polymer.

1. Introduction

A structure is said to be chiral if it cannot be superimposed with its mirror image. Chirality leads to a number of fascinating effects, especially when light interacts with chiral objects. For instance, a chiral molecule exhibits different absorption coefficients under left- (LCP) and right-circular polarization (RCP), an effect known as circular dichroism. With the advent of nanotechnology, a variety of artificial nanostructures (metamaterials) have been designed to exhibit artificial chirality [1]. Such nanostructures can even exhibit a *local* chirality of higher magnitude than the chirality of a circularly polarized plane wave. This super-chirality could be used, for instance, to enhance opto-chiral interactions for molecular detection with enantioselectivity [2].
Interestingly, chiral-related optical effects can be observed in the near-field of achiral nanostructures. For instance, structures like nanorods [3] or V-shaped metallic nanostructures [4] do not shown any circular dichroism (no far-field chirality) but do exhibit different near-field responses under LCP and RCP excitation. The effect stems from a near-field interference effect between the modes sustained by the nanostructure. In this Communication, we use a photosensitive azobenzene-containing polymer (PAP) to probe the near-field chirality with nanoscale resolution. We show that handedness-dependent effects can happen in symmetric plasmonic oligomers.

2. Near-field chirality in symmetric plasmonic oligomers

The structure under investigation consists of three gold nanodisks arranged as an equilateral triangle (Fig. 1a). The structure is symmetric and, at first sight, does not seem to exhibit any chiral effect. Its scattering spectra computed for LCP and RCP excitation are identical: as expected, the far-field optical properties of the plasmonic oligomer do not depend upon the handedness of the impinging light. However, the picture is different in the near-field of the oligomer. Figures 1b and c show that the electric field intensity computed in the near-field is different for LCP and RCP. Whereas the intensity distribution inside the gap is identical for both polarization, outside the oligomer the near-field intensity appears "twisted", the sense of twist depending upon the handedness of the excitation.
To understand this phenomenon, it is necessary to use a rigorous representation of the plasmonic modes sustained by the oligomer. From the trigonal symmetry, group theory allows to retrieve the symmetry adapted coordinates (SACs). Each field distribution can then be projected onto the SACs [5]. For a specific wavelength, the phase difference between the excited modes reaches 90°. Once added to the ±90° phase-shift between the two linear components of circular polarization, this leads to handedness-dependent field distribution around the oligomer.

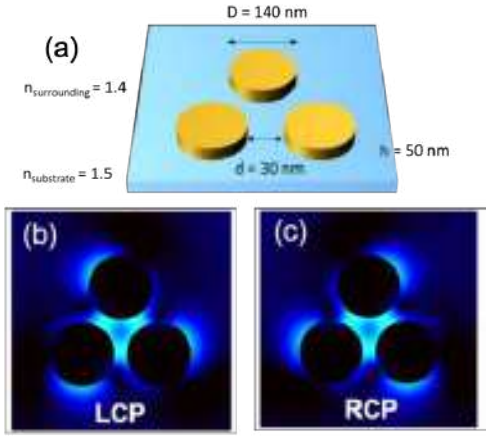


Figure 1: (a) Schematic of the structure: three gold nanodisks (diameter 140 nm), separated by a 30 nm gap and arranged into a triangle. (b) FDTD calculation of the near-field intensity inside the oligomer at λ=780 nm, for LCP excitation. (c) Same, for RCP excitation.

3. Experiment

This effect has been experimentally verified using an original approach based on a photosensitive azobenzene-containing polymer (PAP). The PAP consists of an azobenzene derivative (disperse red 1) grafted to a polymer backbone (PMMA). Under illumination, the azobenzene molecule undergoes *trans-cis-trans* isomerization cycles, leading to a "worm-like" movement and a global displacement of matter. The subsequent topographical changes can be mapped using atomic force microscopy (AFM), giving an insight of the field distribution inside the nanostructure [6]. We recently showed that the PAP could be excited using 2-photon excitation in the near-infrared, evidencing hot spots inside plasmonic gap antennas [7].

The plasmonic oligomer has been fabricated using electron-beam lithography. Then, it has been covered with a thin layer (45 nm) of PAP and exposed to circularly-polarized light at λ=790 nm. After illumination, the topography of the structure was imaged using AFM. Results of this procedure are shown in Figure 2a and b, for LCP and RCP excitation, respectively. A clear difference is observed between the two images, demonstrating handedness-dependence. The topographical maps also closely resemble to the field intensity maps of Figure 2b-c.

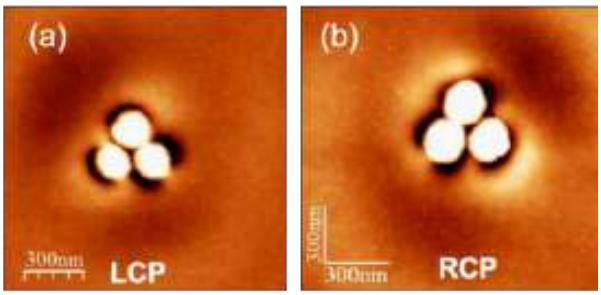


Figure 2: (a) Atomic force microscopy image of the PAP-covered plasmonic oligomer after illumination by LCP light. (b) Same, for RCP excitation.

4. Conclusions

We showed that a symmetric nanostructure, here a plasmonic oligomer with trigonal symmetry, can produce near-field intensity distributions that depend upon the handedness of the impinging light. This effect has been demonstrated experimentally using a photosensitive polymer, allowing us to imprint the chiral near-field into the polymer. Interestingly, after its interaction with light the initially achiral nanostructure is turned into a chiral nanostructure.

Acknowledgements

This research has been funded by the French National Research Agency (ANR) under grant 2D-CHIRAL (ANR-17-CE24-0039-01).

References

[1] J.T Collins, C. Kuppe, D.C. Hopper, C. Sibilia, M. Centini and V.K. Valev, Chirality and chiroptical effects in metal nanostructures: fundamentals and current trends, *Adv. Opt. Mater.* 5:1700182, 2017.

[2] Y. Tang & A.E. Cohen, A. Enhanced enantioselectivity in excitation of chiral molecules by superchiral light. *Science*, 332:333–336, 2011.

[3] M. Schäferling, X. Yin, H. Giessen, Formation of chiral fields in a symmetric environment. *Opt. Express* 20:26326–26336, 2012.

[4] S. Zu, T. Han, M. Jiang, F. Lin, X. Zhu, Z. Fang, Deep-Subwavelength Resolving and Manipulating of Hidden Chirality in Achiral Nanostructures. *ACS Nano*, 12:3908–3916, 2018.

[5] J. Alegret, T. Rindzevicius, T. Pakizeh, Y. Alaverdyan, L. Gunnarsson, M. Käll, Plasmonic Properties of Silver Trimers with Trigonal Symmetry Fabricated by Electron-Beam Lithography, *J. Phys. Chem. C*, 112:14313–14317, 2008.

[6] J. Plain, G.P. Wiederrecht, S.K. Gray, P. Royer, R. Bachelot, Multiscale Optical Imaging of Complex Fields Based on the Use of Azobenzene Nanomotors, *J. Phys. Chem. Lett.* 4:2124–2132, 2013.

[7] Y. Zhang, G. Demesy, M. Haggui, D. Gérard, J. Béal, S. Dodson, et al. Nanoscale Switching of Near-Infrared Hot Spots in Plasmonic Oligomers Probed by Two-Photon Absorption in Photopolymers. *ACS Photon.* 5:918–928, 2018.

Electrochemical Tuning of Plasmoinc Surface Lattice Resonance

Hiro Minamimoto and Kei Murakoshi*

Department of Chemistry, Faculty of Science, Hokkaido University
Sapporo, Hokkaido 060-0810, Japan.
*corresponding author, E-mail: kei@sci.hokudai.ac.jp

Abstract

Plasmonic properties of the surface lattice resonance (SLR) mode of the Au lattice structure were controlled by electrochemical potential. The energy and the lifetime of SLR are determined by the periodicity, diameter, and height of Au lattice structures. The structural factors were optimized through metal dissolution. Varying the density of electrons in metals also resulted in the change of SLR. In situ observation of the optical properties of Au lattice structures by electrochemical dark-field scattering microscopy proves the fine-tuning of the plasmonic SLR properties as the changes in the resonance energy and the spectral width. The present method successfully controlled the structure by controlled surface dissolution of the Au lattice structure at a rate of a few nanometers per minute to prepare the lattice structures showing a spectral width of 0.145 eV with a resonance maximum of 1.74 eV (714 nm). Characteristics of the strong coupling states using the structure with dye molecules were also evaluated.

1. Introduction

Precise tuning of plasmonic properties is an important target for the realization of effective plasmonic devices [1-3]. Generally it has been recognized that the tuning requires the controllability in an atomic scale. Even the top down methods, including electron beam lithography, control of the metal structures in the size scale is difficult especially at room temperature. We have developed the methods for the electrochemical structural control of metals in that size range for the tuning of plasmonic properties. [4, 5] As an important properties of the plasmonic properties, it is known that the dephasing of the coherent oscillation is induced by electronic/vibrational excitation, radiation damping. For nanostructures with diameters larger than a few tens nm, radiation damping is predominant. To discuss the lifetime of the plasmonic excited state, evaluation of the linewidth, which is defined as the full width at half maximum (FWHM), is effective because the linewidth depends on nonradiative and radiative damping of the plasmon modes.

The values of plasmon lifetimes are 2–10 fs. The control of the lifetime could be characterized by the change in FWHM. Recently, two-dimensionally arranged metal nanoparticles have received much attention because of the advantage on the control of plasmon lifetimes. In a two-dimensional (2D) square grating of metal nanoparticles (lattice structure), the scattered light from one particle is absorbed by neighboring nanoparticles to excite the plasmon, resulting in a transformation from radiative to evanescent. By this suppression of radiative loss, strongly coupled nanoparticles in the lattice structures show the surface lattice resonance (SLR) mode with an extremely narrow linewidth (<0.15 eV). The lifetime of the excited state for the SLR mode reaches τ_{SLR} = ~200 fs, which is ten times longer than that for LSPR (τ_{LSPR} = ~10 fs). Thus the structural control of 2D lattice may provide the plasmonic field with superior lifetime.

2. Experiment

The Au lattice structures were prepared on indium tin oxide (ITO) substrates by the electron beam lithography method. The details of the sample preparation procedure are given in our previous report. [*] The lattice spacing (a), diameter (D), and height (h) of each particle in the lattice structure were varied to tune the lattice plasmon modes. The prepared structures were analyzed by scanning electron microscopy (SEM, JSM-6700FT, JEOL Ltd.) and atomic force microscopy (AFM, Nanoscope-IIIa, Digital Instruments). The electrochemical measurements were performed with a three-electrode system. The working, counter, and reference electrodes were a lattice-supported ITO substrate, a Pt plate, and a Ag/AgCl electrode, respectively. The electrolyte solution was 0.1 M NaClO4. For electrochemical dissolution, 10 mM KBr was added to the electrolyte solution. Before the electrochemical measurements, UV/ozone cleaning of the substrate was performed to remove the organic compounds on the surface. The electrochemical extinction and dark-field scattering measurements were performed in situ with an inverted microscope (IX-71, OLYMPUS Co.) equipped with a 100 W halogen lamp, a dark field condenser, and a 60×/0.7 numerical aperture objective lens. All of the spectra and images were obtained with a spectrometer (IsoPlane SCT-320, Princeton Instruments) and a charge-coupled device detector (PIXIS 100BR EX-M, SCIENTIFIC). For the

preparation of the substrates showing strong coupling states, controlled amounts of cyanine dye molecules S0366 were deposited on the lattice structures.

3. Discussion

The maximum resonance wavelength shifts from 693 to 730 nm with increasing *a* with *D* = 140 nm and *h* = 100 nm. his intense peak can be assigned to the SLR mode because of far-field coupling in the 2D nanoparticle. The electrochemically controlled metal dissolution reaction was introduced to tune the lattice plasmon modes via fine structural control of a single disk unit. The extinction spectra during electrochemical potential polarization of the Au lattice structure (*a* = 400 nm, *D* = 140 nm, and *h* = 100 nm) at the potential 0.8 V for 600 s in 0.1 M NaClO4 containing 10 mM KBr. The significant change in the extinction spectrum indicates decreases in the extinction intensities for both SLR and LSPR. The correlation between the structural factors (*a, D*, and *h*) and the lattice plasmon modes was investigated focusing on the resonance wavelength and FWHM of the spectra. The extinction spectra of Au lattice structures with a = 300–460 nm a showed a linear relationship between the blue shift and the *a* value. Additionally, the FWHM values of respective structures showed similar behavior as the wavelength shift of a linear relationship between the FWHM and *a*. At the electrochemical dissolution, the FWHM decreases from an initial value of 0.165 eV to a minimum of 0.145 eV after polarization for 120 s, and it then increases to above 2.0 eV. At the FWHM minimum, the SLR resonance maximum is 714 nm (1.74 eV) [6]. This characteristic change in the FWHM suggests that that the lifetime of the excited SLR mode can be precisely tuned by decreasing *D* and *h* at a rate of a few nanometers per minute. This decrease in the FWHM could originate from the changes in the LSPR and lattice spacing, leading to a confined light field for long lifetime. It should be emphasized that the absolute minimum FWHM value achieved in the present system is comparable with those in previous studies. Real-time observation of the FWHM associated with controlled surface dissolution is important to obtain a lattice structure with tailored plasmonic properties for an extended lifetime. The structures with narrower FWHM provided the strong coupling states of plasmons and dye excitons at the deposition of dyes. Consequently, the present method can produce a confined light field with a relatively long lifetime excited state tuned to the target energy of the plasmon.

4. Conclusions

We have succeeded in tuning both the resonance wavelength and FWHM for the SLR mode by electrochemical potential control. By changing the electrochemical potential, the resonance wavelength can be tuned with precision below a few nanometers, which cannot be achieved by structural control techniques. The fine tuning the FWHM was also achieved by the control of the electrochemical metal dissolution to have a minimum spectral width of 0.145 eV at a resonance maximum of 714 nm (1.74 eV). This result indicates the possibility of application of the method to control plasmonic light confinement in the lattice structure, especially for the preparation of the strong coupling states.

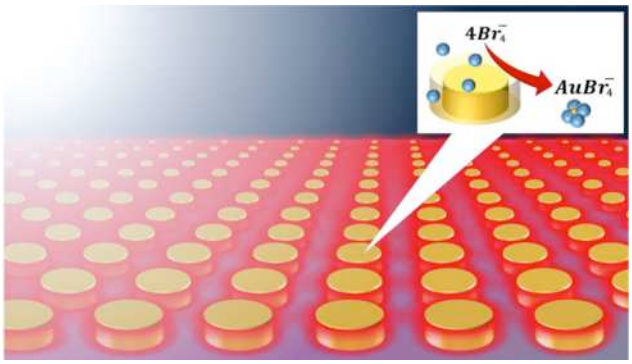


Figure: Schematic presentation of electrochemical tuning of SLR mode in nanoscale [6].

Acknowledgements

The present work was partially supported by Grants-in-Aid for Scientific Research (No. 16K17848), from the Ministry of Education, Culture, Sports, Science, and Technology of Japan, especially that of Scientific Research on Innovative Areas “Nano-Material Optical-Manipulation” (16H06506).

References

[1] H. Minamimoto, S. Oikawa, X. Li, and K. Murakoshi, "Plasmonic Field Focused to Molecular Size", *ChemNanoMat* **3**, 843-856 (2017).

[2] F. Kato, H. Minamimoto, F. Nagasawa, Y. S. Yamamoto, T. Itoh, and K. Murakoshi, "Active Tuning of Strong Coupling States between Dye Excitons and Localized Surface Plasmons via Electrochemical Potential Control", *ACS Photonics* **5**, 788-796 (2018).

[3] H. Minamimoto, F. Kato, F. Nagasawa, M. Takase, and K. Murakoshi, "Electrochemical Control of Strong Coupling States between Localized Surface Plasmons and Molecule Excitons for Raman Enhancement", *Faraday Discuss*. **205**, 261-269 (2017).

[4] S. Oikawa, H. Minamimoto, and K. Murakoshi, "Reversible Electrochemical Tuning of Optical Property of Single Au Nano-bridged Structure via Electrochemical Under Potential Deposition", *Chem. Lett.* **46**, 1148-1150 (2017).

[5] S. Oikawa, H. Minamimoto, X. Li, and K. Murakoshi, "Nanoscale control of plasmon-active metal nanodimer structures via electrochemical metal dissolution reaction", *Nanotechnology* **29**, 045702 (2018).

[6] H. Minamimoto, S. Oikawa, T. Hayashi, A. Shibazaki, X. Li, and K. Murakoshi, "Electrochemical Fine Tuning of Plasmonic Property for Au Lattice Structures", *J. Phys. Chem. C* **122**, 14162-14167 (2018).

Plasmonic biosensing with silver nanowires

Karolina Sulowska[1], Ewa Różniecka[2], Joanna Niedziółka-Jönsson[2], Sebastian Maćkowski[1,3]

[1] Institute of Optoelectronic, Nicolaus Copernicus University, Torun, Poland
[2] Institute of Physical Chemistry, Polish Academy of Sciences, Warszawa, Poland
[3] Baltic Institute of Technology, Gdynia, Poland
*corresponding author, E-mail: sulowska@fizyka.umk.pl

Abstract

Silver nanowires are applied as a sensor for natural photoactive protein complexes. The surface of silver nanowires is modified in a selective way to detect specific fluorescent protein using wide-field fluorescence imaging, a fast technique, which gives information about sample morphology. In this work we studied and compared three methods of sensor design: mixing in solution, nanowires on glass substrate and in PDMS microchannels. Advantages and limitations of every approach are described and analyzed.

1. Introduction

Detection of biological substances, such as viruses, proteins, molecules, is important in many aspects of life. Research efforts are aimed at developing faster and more sensitive ways of searching substances. Another aspect of modern detection chips concerns also simplicity of an approach.

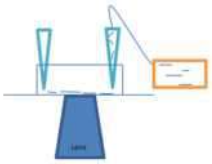
Silver nanowires (AgNWs) are highly advantageous as functional nanostructures in sensing design [1]. These structures are synthesized by wet chemistry and are very stable in water solution. They feature diameters around 100 nm and lengths around 50 μm, thus can be imaged using optical microscopy. Moreover, since they have the plasmon resonance around 400 nm, the AgNWs can be used for enhancing fluorescence of emitters. In order to facilitate such coupling, the surfaces should be chemically modified to enable specific conjugation with the analyte.

2. Materials and Methods

Our sensor was tested for detecting photoactive proteins. First, Peridinin-Chlorophyll-Protein (PCP), equipped with streptavidin linker. PCP complex isolated from algae *Amphidinium carterae* and with a size of 4 nm, was used. The size of PCP is much less than the diameter of AgNWs. The absorption spectrum of PCP overlaps with the extinction spectrum of AgNWs. Second, we used green fluorescent protein (GFP) equipped with His-tag linker. GFP has similar size as PCP, although the different linker may lead to changes in attachment dynamics.

All the results were obtained using wide-field fluorescence imaging. This technique gives information about both the morphology and the fluorescence dynamics within the sample. For detection was used EMCCD camera, which allows to collect movies of fluorescence intensity.

The first type of our sensor is based on detecting photosynthetic molecules in a PDMS microchannel. In this approach biotynylated AgNWs are introduced into the channel through injection by a pump. Glass substrates are modified with streptavidin, facilitating attachment of AgNWs and simultaneous repulsion of PCP. The AgNWs are arranged along this same direction. Upon injecting protein solution into the channel we observe real-time attachment of PCP to AgNWs. The readout contrast is substantially improved after removal of unbound PCP.



The second strategy concerns the experiment in solution. We modify AgNWs surface and disperse them in water. In next step PCP solution was added. After few minutes AgNWs conjugated with PCP were deposited on a glass coverslip.



The last type of experiment is based on real-time fluorescence detection, where functionalized AgNWs are deposited on a glass surface in advance. Using transmission mode of a microscope we search for separated AgNWs. Then in a fluorescence mode, acquisition of kinetics is initiated, shortly before a droplet containing photosynthetic complexes is deposited on the surface with AgNWs.



3. Discussion

In all cases we observed connection of PCP to silver nanowires. For high concentration of PCP the surface coverage of AgNWs is uniform and homogenous. At the same time we also quantify the enhancement of fluorescence of PCP attached to AgNWs.

Typical results obtained for our sensor are showed on Figure 1. First in a transmission mode we locate separated AgNWs and indicate their positions (Fig. 1A). Next fluorescence intensity of PCP complexes is measured, and usually the fluorescence pattern reflects the positions of AgNWs seen in the trnsmission mode (Fig. B).

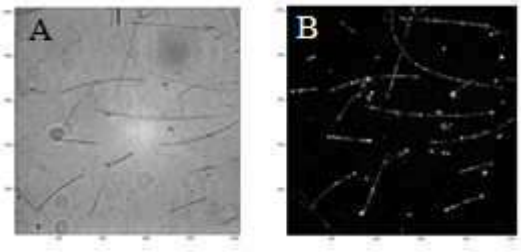


Figure 1. A Transmission picture showing the AgNWs, B Fluorescence map of single PCP attached to surfaces of AgNWs.

In the experiment involving microchannels the whole process takes place in solution so detected molecules can be placed in the buffer. The most important advantage of this scheme is that the positions of AgNWs are known and every AgNW is at the same angle defined by the flow through the microchannel. Additionally, the AgNWs are attached to the glass surface. Using microchannels and the approach studied in this work, allows for using less sensitive imaging detectors in the experiments.

In the experiment carried out in solution we can catch all of the detected molecules in the sample. The effective surface of the AgNW sensor is bigger because PCP and AgNWs are swimming around in the solution. The detection also takes place in the buffer environment. Time which is needed for conjugation can be rather short (typically within minutes), but the molecules have to be attached to AgNWs.

Last but not least, the real-time imaging experiment is the fastest approach as the results can be seen directly during the kinetic acquisition. Sensitivity of this approach is determined – among others – by the number of AgNWs on the surface.

4. Conclusions

Functionalization of silver nanowires is simple, fast and cheap. Emitters need just a few seconds to find the AgNWs and efficiently conjugate with them. For highly concentrated solution of PCP in real-time we can see that all of the complexes are attached to the AgNWs. Plasmonic enhancement of fluorescence substantially improves the signal-to-noise ratio seen in the fluorescence images, enabling thus easier detection. Silver nanowires, as building blocks of sensor chip offer big potential in designing sensing platforms for commercial applications.

Acknowledgements

Research was partially financed by the National Science Centre (Poland) within the OPUS grant 2016/21/B/ST3/02276, project 3/DOT/2016 funded by the City of Gdynia, Poland and Project nr POWR.03.05.00-00-Z302/17 "Universitas Copernicana Thoruniensis In Futuro" (2018-2022) co-financed from the European Social Fund – the Operational Programme Knowledge Education Development. Module 5. Interdisciplinary PhD School "Academia Copernicana".

References

[1] M. Szalkowski, K. Sulowska J. Grzelak, J. Niedziółka-Jönsson, E. Roźniecka, D. Kowalska, S. Maćkowski, Wide-field fluorescence microscopy of real-time bioconjugation sensing, *Sensors* 18 290, 2018.

[2] S. Mackowski, Hybrid nanostructures for efficient light harvesting, *J Phys Condens.* Matter, 22 193102, 2010.

[3] J. Grzelak, K. Sulowska, A. Lesniewski, E. Rozniecka, M. Janczuk-Richter, L. Richter, M. Los, M. Jönsson-Niedziółka, S. Maćkowski, J. Niedziółka-Jönsson, Capturing fluorescing viruses with silver nanowires, *Sens. Actuator B-Chem.* 273 ,689-695, 2018.

Quantum dot-cavity QED: Acoustic phonon-induced dephasing of polaritons

Egor A. Muljarov and Amy Morreau

School of Physics and Astronomy, Cardiff University, Cardiff CF24 3AA, United Kingdom

Phonon-induced optical decoherence in semiconductor quantum dots is a well-studied phenomenon which has been successfully explained within an exactly solvable independent boson model. This model picks up the major effect of a non-Markovian pure dephasing of a quantum dot exciton coupled to bulk acoustic phonons. In the case of a quantum dot embedded within an optical microcavity, this model does not work on its own as the exciton also interacts with an optical mode in the microcavity. Various approaches to this problem have been suggested in the literature, ranging from Born-Markov approximations to non-equilibrium Green's function techniques. However, to the best of our knowledge no exact solution to this problem has been found so far.

In this talk, we present an exact solution to the problem of the phonon-induced dephasing in a quantum dot-microcavity system, alongside simple analytic approximations [1]. Central to our approach is a Trotter decomposition of the full system Hamiltonian into two exactly solvable parts: a phonon-free Jaynes-Cummings model and a cavity-free independent boson model, thus taking into account the effects of the exciton-photon and exciton-phonon coupling on equal footing. Our approach is valid in a wide range of the exciton-phonon and exciton-cavity coupling parameters, covering regimes of weak, intermediate and strong coupling.

The obtained exact solution allowed us not only to confirm and rigorously prove results already known in the literature, such as temperature dependent renormalization of the vacuum Rabi splitting, but also to predict new important physical phenomena which have not been observed so far, such as phonon-assisted transitions between polariton states in the cavity and dephasing in the very strong coupling regime, in which the polaron and polariton timescales become comparable. We show that in this regime, the optical decoherence is determined by acoustic phonon-induced transitions between different polariton states of the quantum dot-cavity system and the polariton line broadening is well described by Fermi's golden rule.

[1] A. Morreau and E. A. Muljarov, arXiv:1807.10977 (2018).

Tailoring electric and magnetic dipole emissions by high-refractive index dielectric nanostructures

Peter R. Wiecha[1], Clément Majorel[1], Christian Girard[1], Arnaud Arbouet[3], Bruno Masenelli[2], Olivier Boisron[3], Aurélie Lecestre[4], Guilhem Larrieu[4], Aurélien Cuche[1], and Vincent Paillard[1*]

[1]CNRS-CEMES, University of Toulouse, Toulouse, France
[2]INL, University of Lyon, INSA Lyon, CNRS, Villeurbanne, France
[3]ILM, University of Lyon, CNRS, Villeurbanne, France
[4]CNRS-LAAS, University of Toulouse, Toulouse, France
*corresponding author, E-mail: vincent.paillard@cemes.fr

Abstract

Silicon nanostructures, providing well-separated electric and magnetic hot spots, are covered by thin films doped by Europium ions supporting both electric and magnetic dipole transitions. Photoluminescence mappings, obtained by raster scanning a laser beam at saturation over the sample, exhibit very distinct features corresponding either to the electric or magnetic dipole transition. They are interestingly comparable to the corresponding radiative electric or magnetic local density of optical states, calculated using the Green dyadic method.

1. Introduction

High-index dielectric nanostructures allow to manipulate optical Mie resonances through the material (*e.g.* silicon (Si), n $\approx$ 4), and the object size and shape. It has been shown that they offer the same ability to manipulate, concentrate or redirect visible light as plasmonic nanostructures made of of noble metals, but with several key advantages such as much weaker absorption losses than in metals for wavelengths longer than the direct band gap (near UV to near IR for Si), and access to semiconductor (CMOS) technology for nanostructure fabrication.[1, 2] Furthermore, high-index dielectric nanostructures support both strong electric and magnetic resonances, giving the unique opportunity to separate and redistribute in the near-field the energy of the magnetic and electric parts of the electromagnetic field, inextricably connected in the far-field.[1] Rare-earth ions such as Europium (Eu^{3+}) supporting electric (ED) and magnetic (MD) dipole transition of similar strength at close wavelengths, when positioned in the near-field of subwavelength Si nanostructures (Si-NS), can be used as probes of the relative electric and magnetic local density of optical states (LDOS).[2] Such results were usually obtained using a scanning near field optical microscope (SNOM) with emitters localized at the apex of the SNOM tip.[3] We propose an approach using a far-field optical set-up, allowing fast scanning, high signal-to-noise ratio and good spatial resolution, which is able to show spatially well-separated electric and magnetic dipole emission of an Eu^{3+}-doped thin film deposited on top of isolated Si nanostructures.[4]

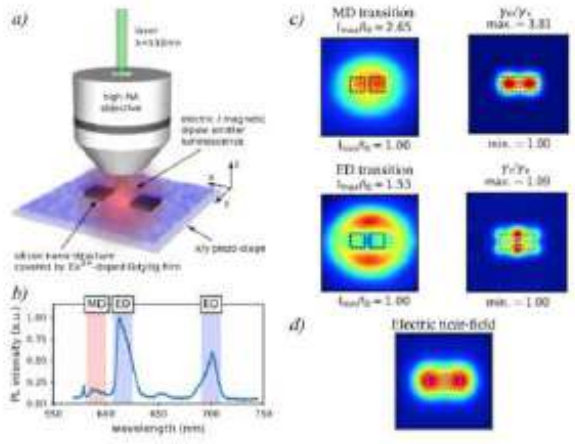


Figure 1: a) Scheme of the experimenal set-up; b) PL spectrum showing the ED and MD transitions; c) Normalized experimental PL maps of the MD and ED transitions (left column) and normalized simulated decay rate maps (right column); d) average electric near-field intensity as function of laser spot position (FWHM = 300 nm)

2. Results and discussion

Si-NS are obtained by electron lithography on a Silicon-On-Insulator substrate (SOI). They are then covered by a 30-nm thick film of Eu^{3+}-doped Gd_2O_3 nanoclusters, obtained by Low Energy Cluster Beam deposition. Photoluminescence (PL) mappings are obtained by raster scanning the sample under a laser beam (λ = 532 nm) focused through a 0.9 NA microscope objective. A PL spectrum (see Fig.1) is acquired in each point, so that emission intensities corresponding to either the MD ($\lambda \approx$ 590 nm) or ED ($\lambda \approx$ 610 nm) transition are simultaneously recorded.

The signal of each contribution is normalized to its corresponding background intensity recorded far from the nanostructure. The laser power density is set to excite

the emitters close to saturation, so that PL maps should be driven by radiative LDOS at the emission wavelength rather than by near-field intensity distribution at the excitation wavelength.

Looking at Figure 1, it is obvious that MD and ED PL mappings are totally different. For a Si dimer (two elements of 300x300x90 nm^3 (LxWxH), gap = 100 nm), there is a clear contrast with a maximum of MD emission above the Si elements, while the maximum of ED emission is located around each Si-NS. First, it seems that this contrast is not due to the electric near-field intensity distribution (Fig.1d). The decay rate γ_m (γ_e, respectively) of MD (resp. ED) transitions, proportional to the magnetic (resp. electric) LDOS, are calculated using the Green Dyadic Method (GDM), γ_m being described in terms of mixed electric-magnetic field susceptibilities. [4, 5]

The maps of the decay rates are obtained by raster scanning a magnetic or electric dipole at 30 nm above the nanostructure to stay close to the experimental system. The total LDOS is obtained by summing two in-plane dipoles (the emission of an out-of-plane dipole is mostly in-plane, thus not detected by the microscope objective). We then compare the PL maps to the corresponding decay rates (convoluted with a Gaussian profile to model the finite size of the laser spot), assuming that radiative and total LDOS are the same due to negligible optical absorption of Si nanoantennas at the MD and ED emission wavelengths. The comparison between experimental PL maps and simulated radiative decay rates show a striking qualitative agreement, exhibiting unambiguously a separation of electric and magnetic LDOS above and around the Si-NS. The intensity ratios are also in good agreement.

3. Conclusions

In conclusion, we have shown that the ED an MD transition dynamics of quantum emitters such as rare-earth ions can be tailored when positioned in the vicinity of high-index dielectric nanostructures. There is also a qualitative agreement between far field PL maps and electric and magnetic LDOS. It should be interesting to design specific resonant Si-NS to control independently MD and ED radiation patterns and magnetic and electric Purcell effects.

Acknowledgement

We acknowledge support from Agence Nationale de la Recherche (ANR-455 10-LABX-0037-NEXT, ANR-11-IDEX-0002-02), supercomputing facility center CALMIP (P12167) and nanotechnology platform (RENATECH).

References

[1] A. Kuznetsov *et al*, Optically resonant dielectric nanostructures, *Science* **354**, 846 (2016).

[2] D. G. Baranov *et al*, Modifying magnetic dipole spontaneous emission with nanophotonic structures, *Laser and Photonics Review* **11**, 1600268 (2017).

[3] M. Sanz-Paz *et al*, Enhancing Magnetic Light Emission with All-Dielectric Optical Nanoantennas, *Nano Lett.* **18**, 3481 (2018).

[4] P. R. Wiecha *et al*, Enhancement of electric and magnetic dipole transition of rare-earth-doped thin films tailored by high-index dielectric nanostructures, *Appl. Opt.* **58**, 1682 (2019).

[5] P. R. Wiecha *et al*, Decay rate of magnetic dipoles near nonmagnetic nanostructures, *Phys. Rev. B* **97**, 085411 (2018).

Plasmonics-Nanofluidics Hydrid Metamaterials for Ultrasensitive Infrared Spectroscopy and Studies of Water Confined in Nanospaces

Thu H. H. Le[1, 2], Akihiro Morita[3], Kazuma Mawatari[2], Takehiko Kitamori[2], Takuo Tanaka[1]

[1]Department of Applied Chemistry, Graduate School of Engineering, The University of Tokyo, Japan
[2]Innovation Photon Manipulation Research Team, RIKEN Center for Advanced Photonics, Japan
[3]Department of Chemistry, Graduate School of Science, Tohoku University, Japan
*corresponding author, E-mail: thu.le@riken.jp

Abstract

This study reports a metamaterial consisting of a nanofluidic channel sandwiched between plasmonic resonators and a metal film. This configuration enables a controllable delivery of molecules into the most enhanced field arising from the quadrupole mode of the structure, forming a strong plasmon–molecular coupled system. It offers an ultrasensitive IR spectroscopic platform for identification and quantitative detection of molecules. Morover, the precise handling of molecules in a well-controlled nanogap allows us to stydy the molecular structures and physical properties of molecules confined in nanospaces.

1. Introduction

IR absorption spectroscopy is one of the most powerful biochemical analysis tools, as it extracts essential information of chemical bonds and molecular structures in a label-free fashion. It is especially useful in tracing subtle changes of the conformational structures in response to surrounding environment or probing the kinetics of chemical events. Recently, surface-enhanced and plasmonic metamaterials-based IR spectroscopies have emerged as promising approaches to improve the sensitivity, owning to the localized enhanced electromagnetic field ("hot-spots") in plasmonic materials. It is of significance to control the spatial overlapping of molecules and hot-spots, yet it is a long-standing challenge, since it involves the handling of molecules in nanoscale spaces. Here we proposed and demonstrated a structure that significantly enhance the resonant coupling of molecules and plasmonic structures by combining molecules and plasmonic resonators in a heterogeneous configuration. It is composed of plasmonic resonators and a metal film sandwiched by a nanofluidic channel.[1] The fluidic channel enables a controllable and effective delivery of molecules into the most enhanced electromagnetic field of the resonance arising from the interference between the top resonators and bottom metal mirror, which is known as "MIM absorber" structure. It is thus expected to perform as an ultrasensitive IR spectroscopic platform for molecular detection. Notably, the manipulation of molecules in 10–100 nm spaces also allows us to characterize the molecular structures and physical properties of molecules confined in nanospaces, which is crucial to understanding the chemical processes in biological or nanomaterial systems.

2. Results and Discussion

2.1. Principle and fabrication

The structure comprises of a metal mirror and a batch of periodic nano square-disks separated by a nanofluidic channel of several tens of nanometers in depth, as described in Fig. 1(a). The numerical calculation of the corresponding system carried out by the finite-element method (FEM) reveals that there is a strong resonant mode that exhibits the intrinsic property of trapping the plasmonic energy inside the gap between two metal layers (Fig. 1(b)) (*i.e.*, quadrupole mode). When molecules are introduced into the channel, vibrational modes of molecules can strongly couple with this plasmon modes, resulting in a large change in the far-field spectral response of the system, and signals of molecules are apparently amplified. The nano square-disk arrays and the metal mirror were fabricated on two separate SiO_2 substrates prepared with fluidic channels in advanced, and the two substrates were bonded at room temperature to form a sealed fluidic device. The nanogap *g* between two structures is well-controlled at nanometer precision in fabrication. The optical responses were measured at normal incident angle by using an FT-IR spectrometer equipped with a microscope.

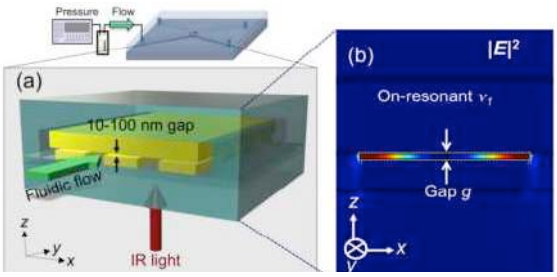


Figure 1. (a) Concept and (b) Calculated field distribution in plasmonics-nanofluidics hydrid metamaterial

2.2. Ultrasensitive IR spectroscopy

To demonstrate the performance of our device in detecting and tracing the quantities of molecules, we used octadecane ($C_{18}H_{38}$) dissolved in CCl_4 as target molecules. The device was purposely designed to exhibit the resonance at 2800–3000 cm^{-1} that covers the C–H vibrational bands of $C_{18}H_{38}$ molecules. Fig. 2(a) shows the reflectance spectra of a channel filled with CCl_4 and $C_{18}H_{38}/CCl_4$ solution respectively. It unveils three C–H vibrational modes including the asymmetric, symmetric stretching of $-CH_2$, and asymmetric stretching of $-CH_3$ as distinct peaks in the broad reflectance dip of the quadrupole mode. The precise control of molecules inside the nanogap also allowed us to quantitatively determine the molecules with prominent reproducibility, as shown in the calibration curve in Fig. 2(b). The LOD estimated from the calibration curve shows an improvement of more than two orders of magnitudes, compared to reported metamaterials-based IR spectroscopies.

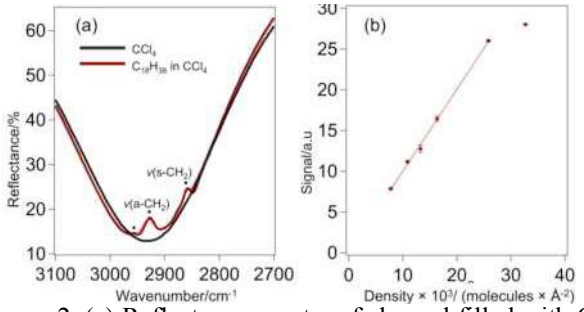


Figure 2. (a) Reflectance spectra of channel filled with CCl_4 and $C_{18}H_{38}/CCl_4$ solution, and (b) Calibration curve of $C_{18}H_{38}$

2.3. Characterization of nanoconfined water

2.3.1. Molecular structures by IR spectroscopy

The spatial distribution of the enhanced electric field indicates that the vibrational modes of the molecules confined in the nanogap can be selectively detected. Exploiting this characteristic, we have successfully measured the infrared absorption characteristic and elucidated the molecular structures of water confined in a 10-100 nm gap. The reflectance spectra when the filling liquid in a 10 nm gap is changed from D_2O to H_2O in Fig. 3(a) exhibits the asymmetric Fano line-shape, which is typical for the coupled systems. The drastic change of reflectance from less than 10% to more than 70% in the presence of water indicates the detection of water confined in 10 nm gap with a pronounced sensitivity, even it is equivalent to merely 30 layers of water molecules. The absorption spectrum of confined water is fitted from the coupled spectrum using the temporal coupled model theory, and the absorption spectrum of the confined water is retrieved from the fitting (Fig. 3(b)). The modes of wavenumber lower than 3200 cm^{-1} can be attributed to the so-called "network water" (NW), which corresponds to the strongly H-bonded water molecules. The component with wavenumber in the range of 3300-3550 cm^{-1} can be assigned to the "liquid water" (LW) representing the bulk water. The higher wavenumber higher than 3550 cm^{-1} can be assigned to interfacial water (IW) molecules with a small number of H-bonds. Our result reveals a high ratio of NW of water confined in ~10 nm, compared to the bulk one. Our method is also able to distinguish the subtle differences in the molecular structures, revealing the scaling behavior of confined water in 10-100 nm size regime.[2]

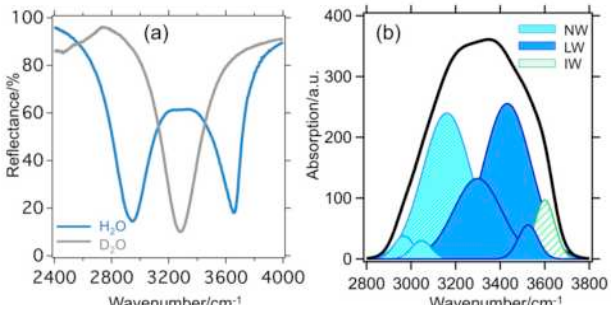


Figure 3. (a) Reflectance spectra of 10 nm gap filled with D_2O and H_2O, and (b) Retrieved absorption spectrum of water confined in 10 nm gap

2.3.2. Measurement of refractive index

The aforementioned quadrupole mode also carries information on the dielectric property of the molecules in the nanogap. It is applied to determine the refractive index (RI) of nanoconfined water. The device was designed to exhibit the resonance at 5000-6000cm^{-1}, which is "off-resonant" with vibrational modes of water and common organic solvents. Water and various organic solvents were introduced into the device, and the resonant wavelengths of the corresponding plasmon modes were measured and plotted against the published RI values of the corresponding solvents. The result unveils that the resonant peaks of confined water is significantly deviated and blue-shifted from the linear relationship. This result indicates that water confined 10 nm exhibits smaller RI with respect to bulk water. This property is in consistence with the molecular structures revealing the presence of a strongly H-bonded water under nanoconfinement. We also succeeded in determining for the first time the RI value of water confined in 10-100 nm gap.

3. Conclusions

A plasmonics–nanofluidics hybrid metamaterial that enables the handling of molecules at the nanoscale hot-spots of the electromagnetic field was demonstrated. It offered a platform for IR absorption spectroscopy that is not only superior in sensitivity but also able to address some critical issues in molecular detection. It also offers powerful method for *in-situ* study of nanoconfined molecules and chemical reactions, that gives us a fundamental insight into the nanoconfinement effects.

References

[1] T. H. H. Le, T. Tanaka, Plasmonics–Nanofluidics Hybrid Metamaterial: An Ultrasensitive Platform for Infrared Absorption Spectroscopy and Quantitative Measurement of Molecules, *ACS Nano* 11: 9780−9788, 2017.

[2] T. H. H. Le, A. Morita, K. Mawatari, T. Kitamori, T. Tanaka, Metamaterials-Enhanced Infrared Spectroscopic Study of Nanoconfined Molecules, *ACS Photon* 5: 3179−3188, 2018.

Optical Circular Dichroism Expressed by Self-Assembled Plasmonic Materials for Molecular Sensing Applications

Alessandro Belardini[1,*], Grigore Leahu[1], Emilija Petronijevic[1], Marco Centini[1], Roberto Li Voti[1], Tiziana Cesca[2], Giovanni Mattei[2], Teemu Hakkarainen[3], Ventsislav K. Valev[4], Mircea Guina[3] and Concita Sibilia[1]

[1]SBAI Department, Sapienza University of Rome, 00161 Rome, Italy
[2]Università di Padova, Dipartimento di Fisica e Astronomina, Padova, Italy
[3]Optoelectronics Research Centre, Tampere University of Technology, 33720 Tampere, Finland
[4]Department of Physics, University of Bath, Bath, BA2 7AY, United Kingdom.
*corresponding author, E-mail: alessandro.belardini@uniroma1.it

Abstract

The detection of biomolecules can be boosted by coupling them with field enhancing substrates such as plasmonic nanoantennas or photonics crystals. Many natural occurring molecules are chiral, thus detecting schemes have to discriminate from two opposite enantiomers. This can be obtained by suitable chiral substrate nanopatternig. Among different fabrication methods the self-assembly approach can lead to low cost, large area metasurfaces with desired functionalities. Here we present the optical circular dichroic behavior of some of these structures and possible applications.

1. Introduction

By proper design of basic elements, it is possible to realize metasurfaces that allow manipulation of the electromagnetic field in order to achieve desired functionalities [1]. Besides the top-down direct realization, through e-beam lithography, which gives precise and perfectly calculable results, bottom-up approaches techniques have also evolved allowing interesting reliable results with less effort for large scale metasurfaces. For example it is possible to obtain anomalous refraction [2], second harmonic generation (SHG) enhancement [3], chiral light polarization manipulation [4]. Here we present an overview of self-assembled metasurfaces that lead to an effective optical chiral response [5], that can be used as substrate for molecular recognition and enantiomer selectivity [6].

2. Nanostructured materials

2.1. Metal nano-antennas on polystyrene spheres

The self-assembled metasurface is composed by polystyrene spheres partially covered by few nanometers of metal (Cr, Ag, Au).
The spheres (starting diameter of 530 nm), deposited on a glass substrate are self-organized in a hexagonal lattice. The diameter of the spheres are then reduced by selective etching up to 450nm and partially coated by 50 nm metal evaporated by an glancing angle of 45°. The 2-D periodical arrangement of the spheres can be seen in the fig.1.

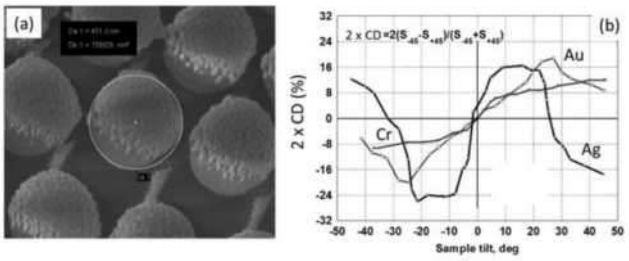


Figure 1: (a) SEM image of the realized metasurface. (b) circular dichroism as a function of incidence angle for different metals (Cr, Ag, Au).

In this case we directly measured the selective absorption of circular polarized light of different handedness by using the photoacoustic absorption (PA) technique [7]. Extrinsic chiral behavior is evidence by the circular dichroism (CD) measured as a function of the incidence angle of light (fig.1).
Once the polystyrene spheres were removed, the substrate show an asymmetric nanopatterned metallic hole array that shows intrinsic chiral behavior and that can be used as ideal substrate for molecular sensing.

2.2. GaAs nanowires with asymmetric gold capping

Another metasurface consists of GaAs nanowires 5 microns long fabricated on Si substrate by a self-catalyzed approach (Fig.2). The wires are partially covered by gold that was evaporated at glancing angle [8].
On these sample we performed different measurements: photoacoustic (PA) measurements and nonlinear

measurements via second harmonic generation circular dichroism (CD-SHG).

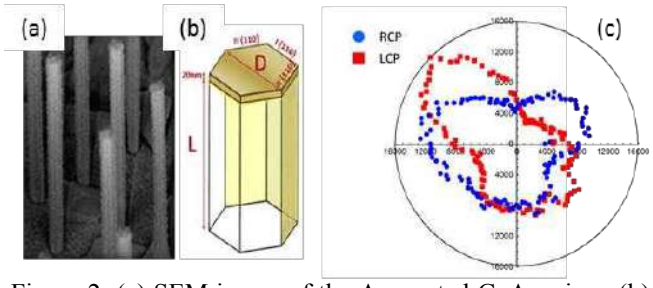


Figure 2: (a) SEM image of the Au-coated GaAs wires; (b) scheme of the NWs structures with gold; (c) SHG-CD measurements.

The measurements where performed with different incident angles and polarization states of the light, in order to put in evidence the extrinsic chiral response of the samples.

3. Discussion

All samples here discussed show peculiar optical chiral properties due the coupling of light with the asymmetric geometrical features of metallic nanoantennas. Indded, the geometrical arrangement of the metal clusters with high field confinement induced by metallic edges produces symmetry breaking and chiral response.

4. Conclusions

The potentiality of the self-assembled approach in the fabrication of low-cost nanostructured materials for photonics applications are here demonstrated and illustrated in some real cases. Different optical techniques, such as photacoustic absorption or nonlinear second harmonic circular dichroism are used in order to put into evidence the effective chiral behavior of such metamaterials, which can be utilized in different potential applications, such as selective molecular recognition.

References

[1] J. B. Pendry, A. J. Holden, D. J. Robbins, and W. J. Stewart, IEEE Trans. Microwave Theory Tech. 47, 2075 (1999)

[2] A. Belardini, F. Pannone, G. Leahu, M.C. Larciprete, M. Centini, C. Sibilia, C. Martella, M.C. Giordano, D. Chiappe, F. Buatier de Mongeot, J. Europ. Opt. Soc. Rap. Public. 7, 12051 (2012).

[3] A. Belardini, M. C. Larciprete, M. Centini, E. Fazio, C. Sibilia, M. Bertolotti, A. Toma, D. Chiappe, F. Buatier de Mongeot, Opt. Express 17, 3603 (2009).

[4] A. Belardini, Benedetti, A., Centini, M., Leahu, G., Mura, F., Sennato, S., Sibilia, C., Robbiano, V., Giordano, M. C., Martella, C., Comoretto, D. and de Mongeot, F. B. Advanced Optical Materials 2, 208–213 (2014).

[5] A. Belardini, M. C. Larciprete, M. Centini, E. Fazio, C. Sibilia, D. Chiappe, C. Martella, A. Toma, M. Giordano, and F. Buatier de Mongeot, Phys. Rev. Lett. 107, 257401 (2011).

[6] Emilija Petronijevic, Marco Centini, Alessandro Belardini, Grigore Leahu, Teemu Hakkarainen, and Concita Sibilia, "Chiral near-field manipulation in Au-GaAs hybrid hexagonal nanowires," Opt. Express 25, 14148-14157 (2017).

[7] E. Petronijević, G. Leahu, R. Li Voti, A. Belardini, C. Scian, N. Michieli, T. Cesca, G. Mattei, C. Sibilia. ‘Photo-acoustic detection of chirality in metal-polystyrene metasurfaces’. Applied Physics Letters 114, 053101 (2019).

[8] G. Leahu, E. Petronijevic, A. Belardini, M. Centini, C. Sibilia, T. Hakkarainen, E. Koivusalo, M. Rizzo Piton, S. Suomalainen, and M. Guina, Adv. Optical Mater. 2017, 1601063 (2017).

Two-Photon Excitation of Biomolecules using Mid-infrared Surface-Plasmon Polaritons confined on Metasurfaces

Iram T. Awan, Manoel M. P. Miranda, Otavio B. Silva and Euclydes Marega Jr.*

Instituto de Fisica de Sao Carlos
Universidade de Sao Paulo, CP 369, Sao Carlos 13560-970, SP, Brazil
*corresponding author, E-mail: euclydes@ifsc.usp.br

Abstract

We explored the potential of using metasurfaces to excite and detect photoluminescence from biomolecules, in particular double-strained DNA (ds-DNA). The excitation of the genetic material placed over a metasurface can be mediated by surface plasmon polaritons (SPPs), that became responsible to excite the ds-DNA aqueous solution. In our case, two photon excitation (TPE) at $800nm$ was used to excited the molecule close by the metasurface generating spectral images recorded in the region of $400nm$ to $700nm$. The DNA fluorescence intensity in the presence of nanostructure came out orders of magnitude as that obtained in the region without the nanostructure. The interaction between SPPs and DNA molecules happened to increase the optical activity (emission rate) of the molecules. The plasmonic fields generated by the nanostructures decreased the emission life time of the molecules and increased their fluorescence, which only happened in case of TPE.

1. Introduction

Two-photon fluorescence excitation is a very powerful method for enhancing the sensitivity and resolution in far-field light microscopy of biomolecules. To achieve the ideal conditions an intense light source must be focused to increase the density of photons per unit volume and per unit time becomes high enough for two photons to be absorbed into the same molecule. In our case the intense laser field was used to generates SPPs on a metasurface which consist in an array of concentric $50nm$ tick rings. The generated confined plasmons can enhanced the fluorescence [1] and is being applied in the last decades in many research areas in particular for bio-sensing. The transfer of energy between photoactive molecules and metal surfaces is an ultrafast process (in the order of pico-seconds) and only can be effective if the molecule is closed to the metal surface ($< 60nm$). The local electromagnetic field due to SPPs, enhance the fluorescence of photoexcited molecules to several orders of magnitude because SPPs can interact with the macromolecules that are in the vicinity of the surface, up to distances of around $300nm$, which is the extension of the evanescent field. In this paper we used the plasmonic properties of a nanostructure to enhance the fluorescence signal of intrinsic DNA, whose week fluorescence intensity [2], makes it challenging to develop fluorescence-based DNA biosensors and devices [3, 4, 5]. No functionalization of a surface is needed to the excitation and detection. The goal of this work was towards making DNA a more viable material to be efficiently useful in photonic devices, such as photonic biosensors and was also to study the effects of two photons excitation.

2. Experimental Methods and Results

For the study of the interaction of plasmon-polaritons with ds-DNA molecules, concentric metallic nanostructures (CMN) were designed on a $200nm$ thick Silver film which was deposited on a Borofloat 33- Schott glass (refractive index around 1.45 in the study region of 450 to 850nm). The fabrication of nanostructures took place by using the ion beam lithography technique with a FEI Quanta 3D 200i microscope. The nanostructures were formed in to concentric arrangements of circular slits with circumferential diameter d, up to $20\mu m$, width of $50nm$ for each circular slit and the separation between each two (that is, the periodicity) of $400nm$. This geometric clear shows the SPPs by using polarized laser fields (see Figure 1). The excitation and detection was performed using a Zeiss DSM 700 confocal optical microscopy. The ds-DNA in aqueous solution ($230\mu g/l$) was dropped over the surface covering complete the nanostructure. The result shown on Figure 2 shows SEM of the CMN and horizontal and vertical polarized dark field images of extraordinary optical transmission. The transmitted spectra shows a transmission peak around $850nm$, close to the laser excitation. The results shown on Figure 2 represents spectral images obtained with laser field set at $800nm$. For the image with the aqueous solution of DNA (c) an increase of signal in the region of $450nm$ to $500nm$ is observed due to the emission of low energy states of the molecule. For images (a) and (b) we observe the luminescence from the generation of electronic excitation in the silver film. The increase in the emission signal detected in the nanostructure region can be observed by the decrease in the total lifetime of the radiative process. Figure 3 shows a Fluorescence Lifetime Images (FLIM), with laser excitation at $800nm$. The image of Figure 3 (c) and the time spectrum observed in (d) shows clear that the mean lifetime for molecules close by the nanostructure is of the order of $250ps$, whereas for molecules away from the metal surface this is on the order of $2ns$.

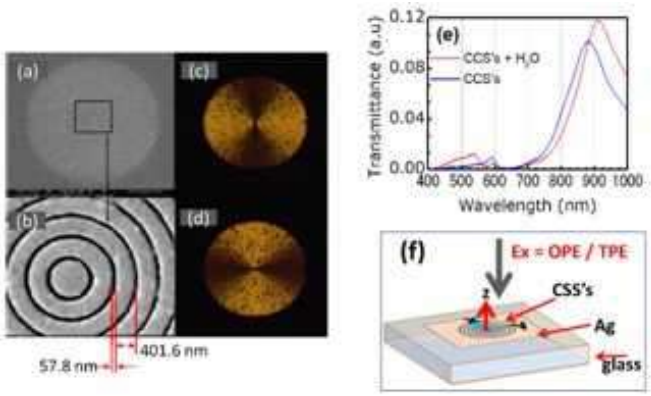


Figure 1: (a) and (b) are the scanning electron microscopy images of the nanostruture. (c) and (d) shows the horizontal and vertical polarized dark field images of extraordinary optical transmission obtained through the nanostructure. (e) is the simulation spectrum of the EOT obtained through the CMN, without and with water over the surface. (f) is the schematic representation of the assembly detection for the experiment, where Ex is the excitation source.

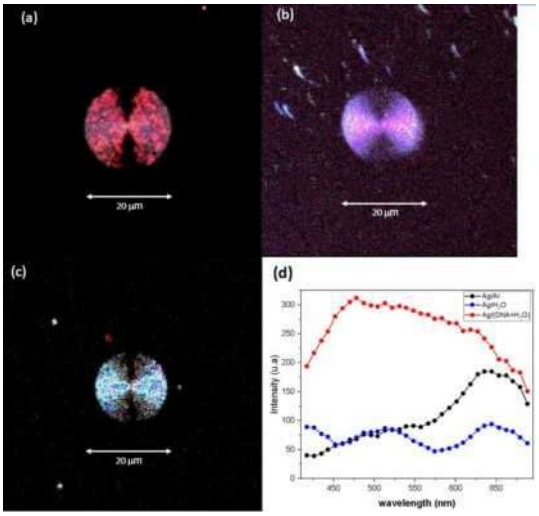


Figure 2: Spectral images of the CMN with three different interfaces exposed to TPE excitation($800nm$). (d) Spectral decomposition of the images of the plasmonic CMNs (a),(b) and (c).

3. Conclusions

The use of two-photon spectroscopy though plasmonic nanostructures shows to be feasible for the detection of biomolecules, especially ds-DNA in aqueous solution, without the use of biomarkers. All optical process of excitation and detection occurs through the mediation of SPPs.

Acknowledgement

Acknowledgements to The Sao Paulo Research (FAPESP)

Foundation under the grant 2013/07276-1.

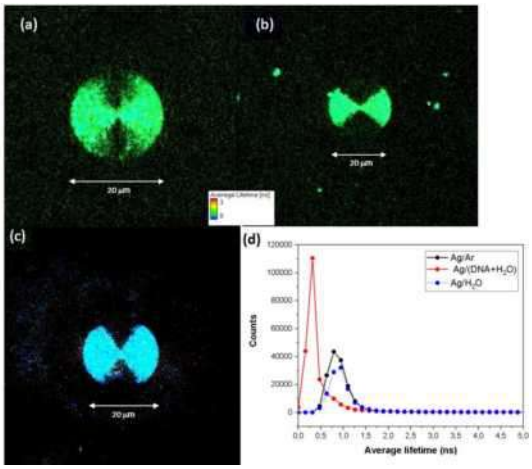


Figure 3: Average lifetime image (FLIM) in the region of the plasmonic structure. (a) for the Silver/air interface. (b) for the Silver/ H_2O interface. (c) for the Silver/($dsDNA + H_2O$) interface. (d) Average lifetime spectra of the FLIM images (a), (b) and (c) in the spectral range of $450nm$ to $500nm$.

References

[1] T. Ming, H. Chen, R. Jiang, Q. Li, and J. Wang, Plasmon-controlled fluorescence: Beyond the intensity enhancement, J. Phys. Chem. Lett., vol. 3, no. 2, pp. 191202, 2012.

[2] I. Vay, T. Gustavsson, F. A. Miannay, T. Douki, and D. Markovitsi, Fluorescence of natural DNA: From the femtosecond to the nanosecond time scales, J. Am. Chem. Soc., vol. 132, no. 34, pp. 1183411835, 2010.

[3] J. Malicka, I. Gryczynski, and J. R. Lakowicz, Enhanced Emission of Highly Labeled DNA Oligomers near Silver Metallic Surfaces, vol. 75, no. 17, pp. 44084414, 2003.

[4] M. Barozzi et al., Optical Fiber Sensors for Label-Free DNA Detection, J. Light. Technol., vol. 35, no. 16, pp. 34613472, 2017.

[5] J. R. Lakowicz, B. Shen, Z. Gryczynski, S. DAuria, and I. Gryczynski, Intrinsic fluorescence from DNA can be enhanced by metallic particles, Biochem. Biophys. Res. Commun., vol. 286, no. 5, pp. 875879, 2001.

[6] Y. Chen, K. Munechika, and D. S. Ginger, Dependence of luorescence intensity on the spectral overlap between fluorophores and plasmon resonant single silver nanoparticles, Nano Lett., vol. 7, no. 3, pp. 690696, 2007.

"Hot" electron generation in plasmonic nanostructures – thermal vs. non-thermal effects

Yonatan Sivan[1], Yonatan Dubi[2]

[1]Unit of Electro-optic Engineering, Ben-Gurion University, Israel, [2] Department of Chemistry, Ben-Gurion University, Israel,

*corresponding author, E-mail: sivanyon@bgu.ac.il

Abstract

We present a self-consistent theory of the steady-state electron distribution in metals under continuous-wave illumination which treats both thermal and non-thermal effects. We show that reported faster chemical reactions likely originate from pure heating.

The possibility to use high energy (aka "hot") electrons in illuminated plasmonic nanostructures for applications such as photo-catalysis, sensing, up-conversion attracts a lot of interest recently. A complete theoretical model of this problem should account for the non-equilibrium nature of the electron distribution, but also for the possibility of both the electrons and the underlying lattice to heat up. Furthermore, the theory should take into account that technologically important applications such as photo-catalysis are performed under continuous wave (CW) illumination, driving the electron distribution into a non-equilibrium *steady-state*.

Surprisingly, to date, there is no comprehensive theoretical approach that takes all these elements into account. Typically, the *transient* electron dynamics are studied [1], focusing on an accurate description of the material properties, e.g., metal band structure and relaxation rates; some studies also accounted, to some extent, for the electron temperature and permittivity dynamics. However, it is not a-priory clear what can be learned from the transient case about the *steady-state* case. On the other hand, the few pioneering studies of the steady-state non-equilibrium (e.g., the most recent and comprehensive [2]) accounted for the electron distribution in great detail, but did not adjust the electron temperature, and ignored the heating of the phonons.

Here, we develop a coupled Boltzmann-heat equations formulation for calculating the electron distribution in plasmonic nanostructures under continuous wave illumination, taking into account non-equilibrium and thermal effects on the same footing. This is done by ensuring a total energy balance and basic thermodynamics. This allows us to determine self-consistently and uniquely the increase in electron and lattice temperatures above ambient conditions although the system is inherently away from thermal equilibrium. In particular, we show that the electron and lattice temperatures are nearly identical, providing, to our knowledge, the first ever justification for the use of classical single temperature models.

Our results also provide the first ever quantitative prediction of the high energy nonthermal electron densities, and show that close the Fermi level, the non-equilibrium is dominated by holes (rather than by electrons, as it usually claimed)! Most importantly, we find that most absorbed power causes heating, and only an extremely small fraction actually leads to high energy electron generation.

Finally, we develop a simple model for the catalytic enhancement for chemical reactions based on illuminated metal nanoparticles. It shows that the faster chemical reactions reported in many previous papers are extremely unlikely to originate from the high energy non-thermal electrons. Instead, the faster reactions very likely originate from a purely thermal effect.

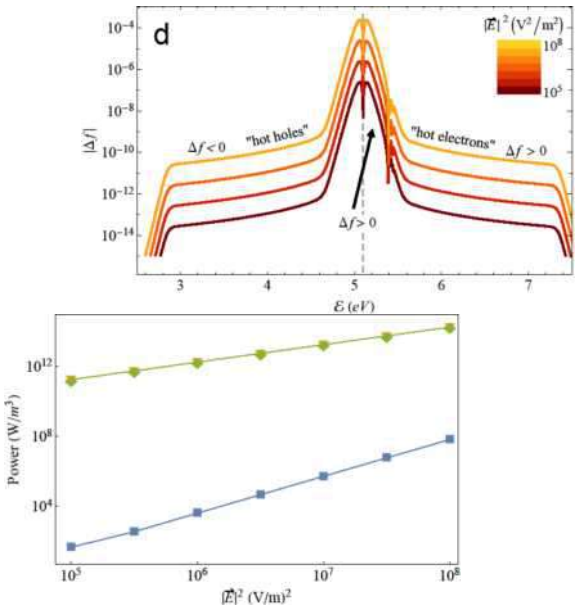


Fig. 1 (Left) Deviation from the equilibrium distribution at the ambient electron temperature as a function of electron energy for various incoming field levels; the system is an Ag

nanoparticle illuminated at resonance. The dashed vertical line represents the Fermi energy. (Right) Power densities going into the thermal electron and lattice systems (green diamonds and orange triangles, respectively; indistinguishable), compared with the power going to the non-thermal electrons (blue squares), all as a function of local field. The power fraction that flows into the thermal channels is substantially larger than that going into generating non-thermal electrons.

References

[1] J. P. Grua, et al., Phys. Rev. B 68, 035424 (2003); L. D. Pietanza et al., Eur. Phys. J. D 45, 369-389 (2007); J. R. M. Saavedra et al., ACS Photonics 3, 1637-1646 (2016).

[2] L. V. Besteiro et al., ACS Photonics 4, 2759-2781 (2017).

Revisiting Plasmonic Photocatalysts Based on Titanium Nitride Nanoparticles

Diane Rawach[1], Peipei Liu[1], Peikui Wang[1], Jerome Claverie[1]

[1]Université de Sherbrooke, Dept of Chemistry, Sherbrooke, Canada
*corresponding author, E-mail: jerome.claverie@usherbrooke.ca

Abstract

The use of plasmonic nanoparticles has been limited to noble metal NPs such as Au, Ag because they exhibit strong resonances in the visible region but have poor chemical and thermal stability and are costly. An alternative is the use of transition metals such as TiN NPs which exhibit strong resonances in the red, high mechanical strength, durability, thermal and chemical stability. We have combined the TiO_2 nanobelts coated with TiN_x NPs to achieve an enhanced photodegradation photocatalyst. Photodegradation of organic pollutants are performed on TiO_2 decorated with TiN_x NPs to study their photocatalytic efficiency.

1. Introduction

The rapid increase of environmental water pollution has seriously affected human health and the entire ecosystem [1-3]. Consequently, a green, cost-efficient method for removing the dissolved organic compounds (dye) from waste water is desired. Heterogeneous photocatalytic degradation technologies are one of the most promising method to purify the dye contaminated water [1]. The degradation efficiency depends on the type of photocatalyst. The plasmonic photocatalyst has been highly investigated to enhance the photocatalytic ability because of localized surface plasmon resonance (LSPR) effect which leads to the expansion of light absorption and enhance charge separation [4-5].

Titanium nitride nanoparticles (TiNx NPs) are hard materials with gold-like optical properties and significant plasmonic performance, allowing them to expand light absorption to visible and near-infrared light region [6-7]. In comparison with noble metals, TiNx NPs also possesses superior performance such as high temperature durability, chemical stability, low cost, which has great potentials for various environmental application [6]. Recently, the plasmonic enhancement of photocatalysts based on TiN has been reported [7-8]. Naldoni et al. have found TiN NPs injected into TiO2 nanowires show superior performance for water splitting [7]. Edwin et al. show TiN/TiO2 nanoparticle composites with plasmonic enhancement for H_2 evolution [8]. Therefore, the TiN-based photocatalyst is still of great interest for dye photodegradation.

TiO_2 nanobelts have unique one-dimensional (1D) structure and high crystallinity [9]. 1D favors the transport of electrons with high speed along the axial direction [9]. High crystallinity can decrease the recombination of electrons and holes because of low defects [9]. However, TiO_2 nanobelts with wide band gap is only active in UV light, which severely limits its photoactivity under solar irradiation. The decoration of TiO_2 NBs by plasmonic materials is one of most effective method to improve its properties. Here, the plasmonic $TiNx$ NPs is combined with TiO_2 NBs, by a facile method through impregnation for photocatalytic degradation purposes.

2. Experimental Section

2.1. TiO_2 Nanobelt Synthesis

The TiO2 NBs were prepared by a hydrothermal method. P25 (0.8 g) was added into a concentrated NaOH aqueous solution (10 M, 180mL) in a Teflon-lined stainless-steel autoclave which was subjected to 200°C for 24 h. The resulting white fluffy product was collected and abundantly washed with deionized water and 0.1 M HCl until the pH of the washing solution was less than 7. The as-washed samples were then calcinated at 600℃ for 3h30.

2.2. TiN_x/TiO_2 preparation

The TiN_x/TiO_2 was prepared using the impregnation method. The TiN solution was added to the TiO_2 NBs in water and the pH was adjusted to pH=3 with HCl solution (0.1M). The mixture was washed thoroughly with water a few times and finally with EtOH. The as-washed mixture was then dried at 80°C for 12hrs.

2.3. Characterization

SEM images of the TiO_2 nanobelts decorated with titanium nitride nanoparticles (20 nm) were taken using a Hitachi S-4700 Field Emission SEM. Transmission electron microscopy (TEM) and high-resolution transmission electron microscopy (HRTEM) analyses were taken using a Jeol JEM-2100F. The AFM images were taken using a Bruker/Veeco Icon dimension 3100 with scan assyst.

2.4. Photodegradation

The photodegradation tests were done using the photochemical reactor Rayonnet RPR-200 equipped with sixteen lamps of a wavelength of 253.7 nm and a power of 12.5 mW/cm^2. Typically, 40 mg of the photocatalyst were dispersed in 40 mL of 40 mg/L methylene blue (MB). This solution was put under stirring in darkness for 1h. The solution was irradiated at room temperature by UV light.

3. Results and Discussion

3.1. Morphology

The morphology of the TiN_x/TiO_2 nanobelts were characterized using different microscopy techniques as seen in figure 1. All three microscopy techniques show very well the nanobelt morphology: very long (>1µm) and very thin (a few nm). In figure 1 B) it is possible to see that the titanium nitride NPs are dispersed uniformly on the TiO_2 nanobelts.



Figure 1. A) SEM B) TEM C) AFM images of TiN_x spherical NPs (20nm)/TiO_2 nanobelts.

3.2. Phase structure

The phase structure of the TiN_x/TiO_2 nanobelts was measured using XRD as seen in figure 2. The XRD pattern clearly indicates that the TiO_2 obtained is pure anatase. However, for the TiN_x/TiO_2 NBs, it was not possible to detect the titanium nitride nanoparticles due to the low quantity used (0.1 wt% of TiN NPs). Moreover, as seen in figure 3, the HRTEM-EDS clearly shows the presence of the titanium nitride nanoparticles adsorbed on the TiO_2 nanobelts.

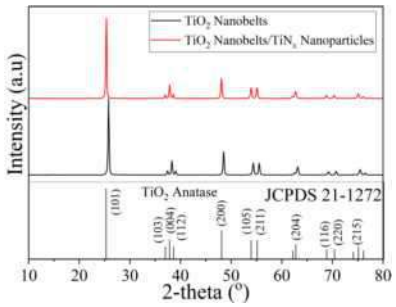


Figure 2. XRD of TiO_2 NBs and TiO_2 NBs decorated with titanium nitride nanoparticles (20nm).



Figure 3. HRTEM-EDS of TiO_2 NBs decorated with titanium nitride nanoparticles (20nm).

3.3. Performance

The preliminary performance of the TiN_x/TiO_2 nanobelts was measured by performing the photodegradation of an organic dye (in our case MB and MO). As seen in figure 4, the photodegradation efficiency of MB and MO by TiN_x/TiO_2 nanobelts photocatalyst was 97.2% and 86.3% in an hour respectively which shows high photocatalytic activity.

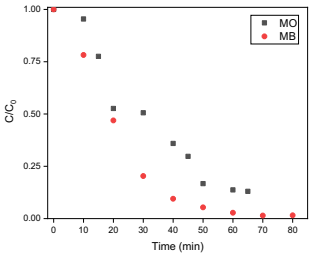


Figure 4. Photodegradation of MB and MO by TiN_x/TiO_2 nanobelts as the photocatalyst.

4. Conclusion and Perspective

TiN_x NPs as an alternative plasmonic material is being actively investigated. The TEM and SEM images show that the TiN*x* NPs were roughly dispersed onto TiO_2 NBs. It also shows that the length of TiO_2 NBs and the size of TiN_x NPs is 1µm and 20nm respectively. The TiN*x* phase could hardly be detected by XRD due to its low content. However, through the HRTEM-EDX analyses, the TiN_x phase was confirmed. The preliminary photodegradation of MB and MO by the TiN_x/TiO_2 photocatalyst shows promising results with the TiO_2 NBs. The performance of the TiN_x/TiO_2 photocatalyst will be thoroughly investigated by PEC tests, H_2 evolution and compared with other photocatalysts.

References

[1] Ind. Eng. Chem. Res. 2019, 58, 2099−2112

[2] J. Phys. Chem. Lett. 2018, 9, 5962−5969

[3] ACS Appl. Mater. Interfaces 2016, 8, 1903−1912

[4] J. Mater. Chem. C, 2017,5, 1008-1021

[5] J. Mater. Sci. Technol. 34, 969–975 (2018)

[6] Lalisse, A., Tessier, G., Plain, J. & Baffou, G. Plasmonic efficiencies of nanoparticles made of metal nitrides (TiN, ZrN) compared with gold. Sci. Rep. (2016)

[7] Adv. Opt. Mater. 5, 1–11 (2017)

[8] J. Phys. Chem. C 2019, 123, 3740−3749

[9] Adv. Mater. 2015, 27, 2557–2582

From nonlinear plasmonics to entangled photon pair generation in hybrid nanostructures

Nicolas Chauvet[1], Maeliss Ethis de Corny[1], Guillaume Laurent[1], Eric Dujardin[2], Aurélien Drezet[1], Serge Huant[1], Gilles Nogues[1], Guillaume Bachelier[1*],

[1]Institut Néel - CNRS, Université Grenoble Alpes, Grenoble, France
[2]CEMES, Toulouse, France

Abstract

Nanoscale second harmonic generation (SHG) and photon pair generation is quantitatively investigated in hybrid nonlinear/plasmonic antennas by coupling quantum and numerical approaches. We demonstrate that the origin of SHG in plasmonic nanostructures are often not coming from the usually invoked local surface nonlinearity and that measurable photon pair production are reachable at the single nanostructure level.

1. Introduction

Although nonlinear photonics addresses many applications in the field of quantum optics, the realization of devices at the nanoscale raises major challenges. Reducing the size of a medium to a few tens of nanometers dramatically drops its optical nonlinear response. Among the different strategies that can be adopted to compensate that loss of efficiency, we chose to enhance the local fields with plasmonic nanoantennas. Such structure response depends on their shape, the presence of substrate, but also the tight focusing generally used, so that an in-depth investigation requires efficient numerical tools.
If simulations relying on a classical description are sufficient for up conversion processes, such as second harmonic generation (SHG), a quantum approach is required for the investigation of entangled photon pair production via spontaneous parametric down conversion (SPDC), where quantum fluctuations play a major role. In this context, we have developed for the first time simulation tools mixing quantum formalisms and numerical approaches solving Maxwell's equations for investigating hybrid nanostructures. This allows a quantitative evaluation of the photons pair production yield in realistic experimental configurations.

2. Methods

Realistic experimental features such as laser specifications (polarization, wavelength and beam profile), excitation and collection optical path (through a high NA objective and several medium interfaces) are implemented analytically. The induced currents in the sample (at the excitation and the emission wavelengths) are computed numerically with a finite element method following classical equations [1]. This approach has been validated by quantitative comparison with experimental data obtained by SHG in plasmonic nanoantennas.

In a second step, both up- and down-conversion processes were described through a quantum formalism based on measure theory. The former (SHG) was used to validate the overall approach, by comparing with the classical results discussed above, while the latter (SPDC) opens completely new horizons for investigating quantum optics at the nanoscale [2]. This quantum approach requires the knowledge of the near-field distribution of the pump beam as well as the Green functions relating any point in the nanostructure to the two or four photon detectors, depending on the configuration (polarization resolved measurements as well as second order photon correlation investigation). Both are accessible using the numerical tools developed previously so that the absolute number of correlated photon pairs can be evaluated. Transmission efficiency through an experimental setup can also be included to match realistic constraints as close as possible. This is of fundamental importance as the actual correlation rate drastically drops down with increased losses.

3. Discussion

Using classical numerical simulations, we investigate the origin of the second harmonic signals in different nanostructures as arising from local surface or non-local bulk contributions depending on the metal (aluminum or gold) and its crystallinity. Through a quantitative comparison with experiments, we show that, most of the time, the source usually considered in the literature is not the dominant one and can even be overpassed by largely disregarded contributions.

With our quantum simulations, we demonstrate, for the first time, that photon pair creation is achievable in plasmonic nanostructures holding a nonlinear nanocrystal, under realistic experimental configurations [2]. We show how plasmonic resonances tailor the SPCD spectral response and replace the phase-matching condition at the nanoscale. Optimized photon pair production rates are obtained by

tuning the antenna morphology for a given excitation and emission wavelength, yielding doubly resonant nanostructures. Huge (hundred- to thousand-fold) SPDC enhancement factors are reached by matching the nonlinear nanocrystal size with the near-field spatial distribution. As a consequence, a trade-off must be found between large enhancements and large emission rates, as the latter are intrinsically driven by the squared crystal volume. This work paves the way for investigating entangled photon pair generation at the nanoscale for an ultimate integration of quantum information and cryptography devices.

4. Conclusions

Thanks to numerical simulations accounting for all experimental features (presence of substrate, large numerical apertures, etc.), we have quantitatively inferred the origin of second harmonic generation in plasmonic nanostructures and demonstrated that the generally invoked mechanism is not the dominant one in the studied gold nanostructures. Extending these simulations to the quantum regime, we have shown that photon pair production is achievable provided that a nonlinear nanocrystal is inserted into the gap between plasmonic antennas. Although the net photon pair generation rate is still modest, this is a first proof of principle holding promise for future improvement.

Acknowledgements

The authors acknowledge the financial support from the Agence Nationale de la Recherche, France, through the TWIN project (Grant No. ANR-14-CE26-0001-01-TWIN), the Université Grenoble Alpes, France, for the Chaire IUA award to G.B and the Ph.D. grant to N.C. from the Laboratoire d'excellence LANEF in Grenoble (ANR-10-LABX-51-01).

References

[1] M. Ethis de Corny, N. Chauvet, G. Laurent, M. Jeannin, L. Olgeirsson, A. Drezet, S. Huant, G. Dantelle, G. Nogues, G. Bachelier, Wave-Mixing Origin and Optimization in Single and Compact Aluminum Nanoantennas, *ACS Photonics* 3: 1840-1846, 2016.

[2] G. Laurent, N. Chauvet, G. Nogues, A. Drezet, G. Bachelier, Photon-pair production at the nanoscale with hybrid nonlinear/plasmonic antennas, *arXiv* 2018.

Improving the Applicability of Hybrid Plasmonic Nanoparticles by Studying and Tailoring Interfaces

Kholud Dardir[1], Hao Wang[2], Ted V. Tsoulos[2,3], Supriya Atta[1,4], Sakshi Sardar[5], and Laura Fabris[2,*]

[1]Department of Chemistry and Chemical Biology, Rutgers University, Piscataway, USA
[2]Department of Materials Science and Engineering, Rutgers University, Piscataway, USA
[3] Current Address: Department of Mechanical Engineering, École Polytechnique Fédérale de Lausanne, Lausanne, Switzerland
[4] Current Address: Department of Biomedical Engineering, Rutgers University, Piscataway, USA
[5]Department of Electrical and Computer Engineering, Rutgers University, Piscataway, USA
*corresponding author, E-mail: lfabris@soe.rutgers.edu

Abstract

Hybrid plasmonic nanoparticles, designed to encompass dielectric or semiconducting coatings, whether of biological nature or not, are fundamental components in sensing platforms or photocatalytic substrates. While the overall properties of the nanomaterial define its performance, we argue that it is in general the interface between the metal and the surrounding medium that plays the most important role. Herein, we will discuss how studying and *ad hoc* tailoring interfaces can lead to achieving excellence in performance. We will discuss applications in both photocatalysis and surface enhanced Raman spectroscopy (SERS)-based sensing, demonstrating that only accurate assessment of the interfacial properties can push the boundaries and lead to unexpected results.

1. Introduction

Gold nanostars (NS) have recently emerged as powerful nanostructures for surface enhanced Raman scattering (SERS) [1-3], MRI imaging [4], and hot electron-driven phtocatalysis [5]. In particular, numerical simulations and photocatalytic experiments have shown that, in nanostars placed in close proximity to TiO_2, the location of the hot spots at the tip of the spike enables the localization of hot electrons at the metal-semiconductor interface, facilitating hot electron injection into the latter [6]. In biomedical applications, in particular those leveraging the gold nanoparticle both as field enhancer and as platform for oligonucleotide loading, proper bioconjugation schemes and surface coatings are necessary for sensitive, selective, and accurate detection of the biological targets. In both instances, careful design and control of the nanoparticle surface properties is mandatory. Herein, we discuss how the rational design and the careful synthesis of the gold-TiO_2 interface leads to efficient injection of hot electrons generated at the tips of the nanostar into the thin semiconductor layer and how the presence of a perfectly realized interface leads to hydrogen production from water with yields that are seven times higher than those measured in systems with non-ideal interfaces. From the biological standpoint, we will show how the careful surface functionalization of gold nanostars with RNA strands and polymer shells allows for efficient cellular uptake, endosomal escape, and recognition of mutations in influenza A (IAV) RNA strands. Furthermore, we will report how the presence of a protein corona on the nanoparticles can affect their ability to recognize their viral targets, but not to the extent of completely cancelling their responsiveness to it.

2. Hot Electron Photocatalysis

Surfactant free gold nanostars were synthesized following traditional solution-based methods [7]. Because these nanoparticles have shown to be sensitive to high temperature and undergo restructuring at the tips, traditional protocols for crystallization of amorphous titania, which are carried out at least at 200°C, could not be followed. Therefore, we developed a new low temperature protocol leveraging titanium isopropoxide (TTIP) as the TiO_2 precursor and running for 2 days in isopropanol at 70°C. While one could expect that carrying out the reaction at slightly higher temperature would have allowed us to reduce its length, this approach was not feasible due to the sensitivity of the nanostars to temperatures in excess of 80°C. The reaction time proved also to be a sensitive knob to tune the semiconductor shell thickness, allowing us to limit it to 4 nm, which is thin enough to enable effective hot electron transfer to the surrounding water environment. Furthermore, our protocol led to the epitaxial growth of TiO_2 onto gold, further facilitating electron transfer owing to an unstrained interface. The overall lack of impurities at the metal-semiconductor interface further removed obstacles and freed-up the electron path. Finally, the synthesis produced an ideal mix of rutile and anatase in the thin titania shell, which has been hypothesized as ideal for band alignment with the water reduction reaction. Photocatalytic conversion experiments were carried out employing broad band illumination (200-1500+ nm) of a Xe-arc lamp. Using methanol as the sacrificial solvent for hole capture, we observed that the core-shell nanostars with the ideal interface produced at least 7-times more molecular

hydrogen compared to the case in which the shell thickness was higher, the interface was not epitaxial, or the shell was not crystalline. Furthermore, comparison with published literature on similar systems, led us to calculate improved H_2 yields in excess of four-fold. Control experiments carried out on TiO_2-coated gold nanorods confirmed the need of realizing an ideal interface for efficient hot electron-based photocatalysis [8]. Because gold nanorods are synthesized employing cetyltrimethylammonium bromide (CTAB) as shape inducing surfactant, and because the micelle it forms is sensitive to alcohols, we needed to carry out the reaction in water. We could have employed protocols reported in the literature in which polymer shells are introduced to replace CTAB, but those would have introduced steric hindrance against electron transfer. Because TTIP is very reactive in water, we introduced acetic acid to slow down its kinetics. Nonetheless, the synthesis was not as effective as what observed in nanostars, producing only partial titania coating on the nanorods. Even so, our approach led to yields of hydrogen higher than reported in the literature, suggesting once more the importance of unhindered interfaces in hot electron-based photocatalysis.

3. Detection of Viral RNA

The influenza A virus (IAV) is a segmented RNA virus whose high rate of mutation affects our ability to design and develop vaccines with broad spectrum effectiveness over long-time scales. This issue is similarly encountered for other RNA viruses, such as HIV, dengue, Ebola, etc. When IAV replicates, the high degree of mutations produced leads to the generation of highly defective genomes, some of which lacking the majority of the genes. It has been hypothesized that these products, called defective interfering particles (DIPs), could be important allies against the virus, as their presence has been associated to reduced pathogenicity. We demonstrate here that gold nanostars and surface enhanced Raman spectroscopy (SERS) can be employed to study viral mutations in intact cells at the single cell level. This single-cell approach could be interesting to understand viral superspreaders and associate viral evolution dynamics to environmental conditions and interactions. We synthesized gold nanostars using a known surfactant free protocol [7] and functionalized them with an RNA beacon carrying a fluorophore at the 3' terminus. Fluorophores are known to have good Raman cross sections as well and can be useful for dual modality imaging. The proximity of the dye to the nanostar surface, achieved upon hybridization with the targeted strand, yields intense SERS signals unique to the fluorophore. The signal intensity is the highest in the presence of the perfectly complementary target, and linearly decreases with the number of mismatches. Importantly, no signal is observed when a random target is introduced, as expected. To achieve these results and render them quantitative, it was necessary to carefully understand the metal-RNA interactions, model the distance dependence of the E-field enhancement, and ensure that proteins in the surrounding medium, forming a thick shell on the nanostar, also known as protein corona, would not affect the performance of the sensor. To assess this hypothesis, we spiked cell lysates with target RNA and determined that while the signal was slightly reduced, the sensitivity and selectivity were not affected. Studies in individual intact cells further proved the validity of the assay. However, to avoid retention in the endosomes upon uptake, we needed to further engineer the surface with a polymer coating layer enabling endosomal escape. This functionalization step proved to lead to increased retention in the cytosol with minimal loss of signal intensity. Similar results were observed when studying the effect of protein corona using fluorescence as the transduction mechanism. Overall, these results are promising and suggest that hybrid plasmonic nanoparticles could be relevant sensing platforms for the SERS-based detection of intracellular events.

4. Conclusions

Hybrid nanostructures based on the use of gold nanostars have shown promising applicability in studies involving electric field enhancements and hot electrons. In both cases, the need to carefully design, engineer, and realize a perfect metal-nonmetal interface is mandatory to optimize performance and achieve expected or transformative results, especially if quantification is needed.

References

[1] Y. W. Wang, S. Kang, A. Khan, P. Q. Bao, J. T. Liu. Biomed. Opt. Express **6**, 3714 (2015).

[2] A.-I. Henry, B. Sharma, M. F. Cardinal, D. Kurouski, R. P. Van Duyne. Anal. Chem. **88**, 6638 (2016).

[3] L. Fabris. J. Optics **17**, 114002 (2015).

[4] M. W. Rotz, K. S. B. Culver, G. Parigi, K. W. MacRenaris, C. Luchinat, T. W. Odom, T. J. Meade. ACS Nano **9**, 3385 (2015).

[5] S. Atta, A. M. Pennington, F. E. Celik, L. Fabris. *Chem* **4**, 2140 (2018).

[6] A. Sousa-Castillo, M. Comesaa-Hermo, B. Rodrguez-Gonzlez, M. Prez-Lorenzo, Z. Wang, X.-T. Kong, A. O. Govorov, M. A. Correa-Duarte. J. Phys. Chem. C **120**, 11690 (2016).

[7] A. S. D. S. Indrasekara, S. Meyers, S. Shubeita, L. C. Feldman, T. Gustafsson, L. Fabris. *Nanoscale* **6**, 8891 (2014).

[8] S. Atta, F. E. Celik, L. Fabris. *Faraday Discuss*. DOI: 10.1039/ C8FD00152A (2018).

Plasmonic Metamaterials for Sensing Applications

Pan Wang[1,2,*], Alexey V. Krasavin[1], Mazhar E. Nasir[1], Wayne Dickson[1], and Anatoly V. Zayats[1]

[1]King's College London, Strand, London WC2R 2LS, UK
[2]State Key Laboratory of Modern Optical Instrumentation, College of Optical Science and Engineering, Zhejiang University, Hangzhou 310027, China
*corresponding author, E-mail: pan.wang@kcl.ac.uk

Abstract

In this talk, we will overview the sensing applications of plasmonic metamaterials including Au nanorod arrays and metal-dielectric multishells.

1. Introduction

Surface plasmons are the collective oscillations of electron gas at a metal-dielectric interface, which have the ability to concentrate light on subwavelength scales, produce high local-field intensities and generate energetic hot electrons. Benefiting from the high sensitivity of plasmonic modes to changes in the local dielectric environment, surface plasmons are very promising for optical sensing applications. In this talk, we will overview the sensing applications of plasmonic metamaterials including Au nanorod arrays and metal-dielectric multishells.

2. Results

Firstly, we will discuss the enhanced sensitivity (more than 30,000 nm per refractive-index unit) of Au nanorod array to refractive-index variations of the medium between the rods for (bio)chemical[1] and ultrasound[2] sensing, benefiting from a substantial overlap between the probing field and the analytes incorporated between the nanorods and a strong plasmon-mediated energy confinement inside the porous nanorod layer, as shown in Fig. 1a.

Secondly, we will discuss the extension of sensing capabilities of the nanorod metamaterials by functionalization, for example, high-sensitivity optical hydrogen gas sensing by coating the surface of Au nanorods with a thin layer of palladium[3], as shown in Fig. 1b.

Thirdly, we will introduce an extremely compact and versatile sensing platform based on plasmonic tunnel junction array constructed on a nanorod metamaterial[4], as shown in Fig. 1c. During the tunnelling process, inelastic electron tunnelling excites plasmonic modes in the nanorod metamaterial, while elastic electron tunnelling produces energetic hot electrons in the nanorod tips. The hot electrons are harvested to activate chemical reactions in the tunnel junctions with analytes, while the radiative decay of plasmons which can be observed as a light emission from the metamaterial is used for the high-sensitivity detection of the highly-confined reactions.

Finally, we will show hyperbolic metaparticles based on metal-dielectric multishells (Fig. 1d)[5], which are promising for applications such as sensing and plasmon-enhanced spectroscopy.

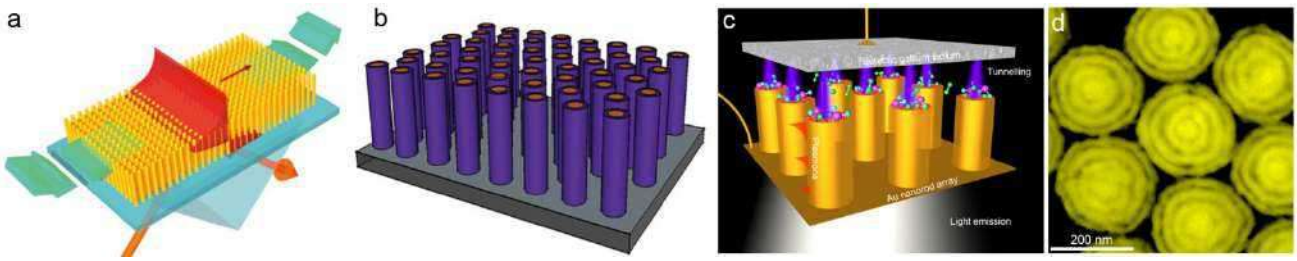


Fig. 1. (a) Schematic of the nanorod metamaterial for (bio)chemical sensing. (b) Schematic of nanorod metamaterial for hydrogen sensing based on an Au/Pd nanorod array. (c) Plasmonic tunnel junction based sensing platform. (d) TEM image of gold-silica multishells.

3. Conclusions

In conclusion, plasmonic metamaterials including Au nanorod arrays and metal-dielectric multishells are promising platforms for high-sensitivity sensing applications.

Acknowledgements

This work has been funded in part by the Engineering and Physical Sciences Research Council (UK) and the European Research Council iPLASMM project (321268). A.V.Z. acknowledges support from the Royal Society and the Wolfson Foundation.

References

[1] A. V. Kabashin et al., Plasmonic nanorod metamaterials for biosensing, *Nat. Mater.* **8**, 867–871 (2009).

[2] V. V. Yakovlev et al., Ultrasensitive non-resonant detection of ultrasound with plasmonic metamaterials, *Adv. Mater.* 25, 2351–2356 (2013).

[3] M. E. Nasir, W. Dickson, G. A. Wurtz, W. P. Wardley, A. V. Zayats, Hydrogen detected by the naked eye: optical hydrogen gas sensors based on core/shell plasmonic nanorod metamaterial, *Adv. Mater.* **26**, 3532–3537 (2014).

[4] P. Wang, A. V. Krasavin, M. E. Nasir, W. Dickson, A. V. Zayats, Reactive tunnel junctions in electrically driven plasmonic nanorod metamaterials, *Nat. Nanotechnol.* **13**, 159–164 (2018).

[5] P. Wang, A. V. Krasavin, F. N. Viscomi, A. M. Adawi, J. -S. G. Bouillard, L. Zhang, D. J. Roth, L. M. Tong, A. V. Zayats, Metaparticles: dressing nano-objects with a hyperbolic coating, *Laser Photon. Rev.* **12**, 1800179 (2018).

Folding a 2D material into a W-shape periodic nano-structure: the case of a gold nano-layer and the consequences on its plasmonic and photonic properties

Laurent Arnaud[1], Shijian Wang[1], Soukhaina Es Saidi[1], Aurelien Bruyant[1], Serguei Kostcheev[1], Abdelhamid Hmima[1], Yassine Hadjar[1], Sylvain Blaize[1], Demetrio Macias[1], Remi Vincent*[1]

[1]Institut Charles Delaunay, Equipe Lumiere Nanomateriaux Nanotechnologies (ICD - L2N), CNRS UMR 6279, Universite de Technologie de Troyes, 12 rue Marie Curie CS 42060, 10004 Troyes Cedex, France
*corresponding author, E-mail: remi.vincent@utt.fr

Abstract

Our experiments and simulations show notable effects in the photonic and plasmonic properties when transitioning from a single flat gold layer to a periodically folded layer. In particular the coupling of surface plasmon polaritons to free-space propagating waves becomes possible through the refraction orders, some localized resonances along the segments created by the folding are observed and result in an increased absorption, wedge/corner resonances with a strongly localized enhanced electric field are also observed.

1. Introduction

We managed to fabricate and study theoreticaly gold nanostructure with a shape of a periodic W. These structures are interesting for possible applications such as control of the LDOS, application to sensors and control of SPP. And we were also interested in the more fundamental aspect of the study of the transition between a single layer and a folded W-shape gold layer, since this is a way to structurate a 2D material.

2. Sample fabrication and measurement

The first part of the sample fabrication consists in fabrication of a silicon matrix in which the metallic structure will be later deposited. The grating structure is projected onto a silicon nitride (Si_3N_4) mask layer above the silicon substrate. Reactive-ion etching (RIE) is used to create the grooves and because of the silicon anisotropy, the etching rate is not the same along the different crystal axes. At the beginning of the etching process, trapezoidal grooves appear; And with a precisely matched etching time, the trapezoidal grooves change into triangle grooves. Figure (1) shows an example of such a silicon matrix. After the silicon ould is finished, metal is deposited on the surface. Template stripping is used to do metal lift-off, and metal is easy to remove due to the bad adhesion between metal layer and Si surface.

The resulting metallic structure on its polymer substrate was then put in an optical bench to measure its transmission in the visible range (400-900nm), for various angles of incidence and both linear polarizations.

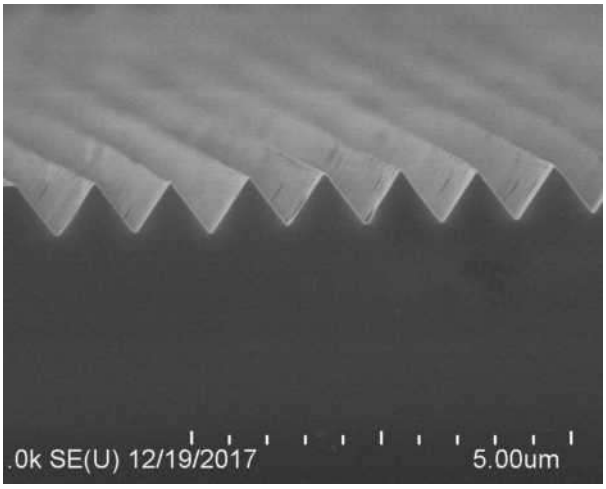


Figure 1: One of the silicon matrices used for the moulding of the gold nanostructure.

3. Theoretical study

The gold W-structures are characterized by complex spectra that only rigorous electromagnetic numerical methods are able to fully describe acurately. However we were interested in understanding the underlaying phenomena that distinguish these folded structures from a single flat gold layer. For this study we used the differential method for gratings [1],[2] and Chandezon [3] method as theoretical tools to explore further the properties that are more difficult to acces experimentally, such as the near field and for extensive parametric studies. And we were able to distinguish at least 3 of different types. First the periodic nature of the structure create diffraction orders which play a fundamental role in the patterning of the spectra and also importantly, allow the coupling of SPP even for free space propagative waves (Fig.2). Another interesting phenomena is the presence of localized plasmon resonances along the segments created by the folding (Fig.3)). Lastly, a sharp field resonance can occur at the edges of the structure. A very localised enhancement of the electric field can be obtained, up to a factor x20 in the case corresponding to one of our sample of 400nm period and a folding angle of 54.7.

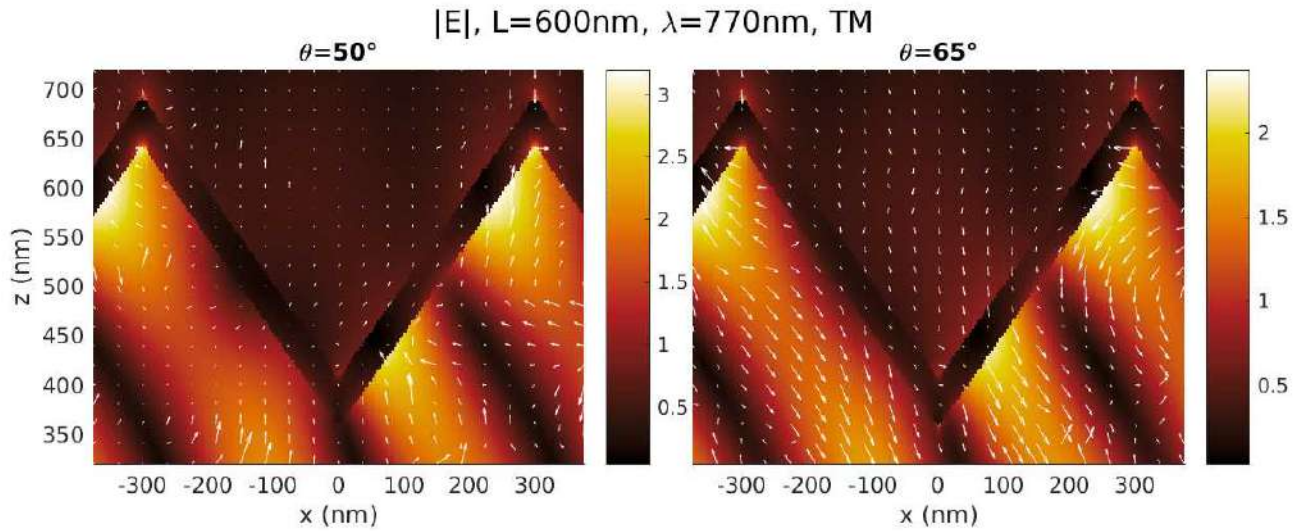


Figure 3: Local field map of a gold W-structure with a 600nm period and 50nm height, for a wavelength of 770nm corresponding to a 2nd order segment resonnance. Notice that the phenomena which corresponds to the propagation of a surface plasmon along one segment of the W, depends little on the angle of incidence.

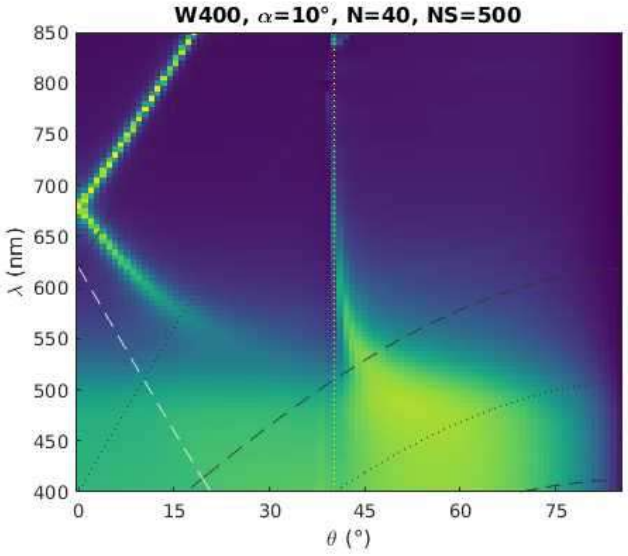


Figure 2: Absorption map as a function of the incidence angle and wavelength in the case of a slightly folded gold layer slightly with an angle of 10 degrees from the flat surface. The surface plasmon polariton coupling with (-1) and (+1) orders is clearly visible in the upper left corner, where increased absorption above the limit of (-1) (dark dashed line) and (+1) (white dashed line) orders. A similar signature as the plasmon in Kretschmann configuration for a single layer also appears on the right side of the vertical yellow line representing the total internal reflection limit.

4. Conclusion

Now that our fabrication method is validated and we have some theoretical elements of understanding regarding the transition from a flat layer to a periodically folded structure, we would like to explore other original 2D materials such as graphene.

Acknowledgement

This work has been supported by the Region Grand-Est and EIPHI Graduate School (contract "ANR-17-EURE-0002").

References

[1] M. Neviere and E. Popov, *Light Propagation in Periodic Media: Differential Theory and Design*, Marcel Dekker publisher, 2003.

[2] E. Popov and M. Neviere, Grating theory: new equations in Fourier space leading to fast converging results for TM polarization, *J. Opt. Soc. Am. A* 17(10), 17731784, 2000.

[3] L. Li, J. Chandezon, G. Granet, and J. P. Plumey, Rigorous and efficient grating-analysis method made easy for optical engineers, *Appl. Opt.* 38, 304313, 1999.

Ultrafast Nanophotonics and Quantum Optics in Nano-bio Assemblies, Colloidal Nanostructures, and Metamaterials

Gary P. Wiederrecht[1]

[1]Center for Nanoscale Materials, Argonne National Laboratory, Lemont, Illinois 60437, USA
*corresponding author, E-mail: wiederrecht@anl.gov

Abstract

We describe the ultrafast dynamics and quantum optic behavior of three different light-activated hybrid nanostructures. These include colloidal semiconductor nanoplatelets, chromophore-doped peptide bio-assemblies, and plasmonic gap-mode metamaterials. Ultrafast transient absorption and photoluminescence studies, as well as single photon correlation studies, are described. Insight into the design considerations for cooperative nanoassemblies for efficient light-activated structures is given.

1. Introduction

Light-matter coupling in excitonic or plasmonic nanostructures has produced phenomena of interest for nanophotonics applications, including the realization of single photon emitters for quantum optics and the generation of energetic carriers in plasmonic metamaterials for enhanced light harvesting or ultrafast nonlinear optics. A detailed understanding of the ultrafast processes produced in these nanostructures following photoexcitation is important for realizing and improving the efficiency of a desired nanophotonic application. In this talk I will first describe recent efforts to produce high quality single photon emitters using colloidal CdSe/CdS semiconductor core/shell nanoplatelets.[1,2] Interestingly, these structures show size dependent biexciton production with a quantum yield that can approach unity under ideal conditions. The emission of correlated photons is of interest for the possibility of producing entangled photon pairs from a single nanostructure for quantum information science applications. We explore the necessary parameters to produce efficient biexciton production, and also how to improve polarized, directional emission from the nanostructures. These properties are ultimately important for coupling the emission to photonic networks. In the second part of the talk, I describe our efforts to design chromophore-doped peptide nanoassemblies for long range, one dimensional exciton transport.[3] In the third part of the talk, I describe our work in generating a large number of hot electrons following ultrafast photoexcitation of nanostructured gap-plasmon metamaterials.[4,5] In this work, efforts to alter the size, shape, composition, and gap-plasmon spacing to improve hot carrier production are described. As a result of greater hot carrier production and improved signal to noise, we are further able to spectroscopically characterize the decay pathways for energetic plasmonic electrons. Evidence for anisotropic decay of nonthermal electrons is presented. I conclude by introducing some of the new user science capabilities at the Center for Nanoscale Materials, particularly for quantum optics and quantum information science.

2. Light-activated nanoscale structures

Below are some of the examples of light activated hybrid nanostructures used in these studies.

2.1. Colloidal semiconductor nanoplatelets

A new class of semiconductor quantum materials, nanoplatelets is studied for quantum optical behavior, using photon correlation optical spectroscopic methods. Semiconductor nanoplatelets are nanostructures with quantum confinement in the thickness direction. Compared to conventional semiconductor quantum dots, the lateral sizes of the nanoplatelets can be tuned from medium confinement to weak confinement. This tuning indicates that the excitonic properties of the nanoplatelets can also be adjusted. Using single particle spectroscopy, we show that with the increase of the nanoplatelet lateral sizes, the radiative decay rate, which is proportional to the oscillator strength of the nanoplatelets, first increases and then flattens out, whereas electric dipole approximation predicates a monotonic increase.[1,2] This deviation can be explained by the strong exciton-phonon coupling in the nanoplatelets at room temperature, which limits the coherent size of the excitons to a value that is smaller than the nanoplatelets lateral sizes. We also show that with the increase of the nanoplatelet lateral sizes, the photon correlation statistics, which are measures of the single photon and biexciton emission probabilities, also increase. This finding indicates that nanoplatelets with large lateral sizes accommodate more biexcitons.

2.2. Exciton transport in bio-assemblies

Light harvesting proteins are the primary light capturing entities in photosynthesis. Motivated by nature's ability to orient and control molecular coupling in photosynthesis, we have designed peptides to not only self-assemble into 1D

nanofibers, but also coordinate a light activated chromophore, zinc porphyrin. We report an in depth study of the photophysical properties of our bioinspired light harvesting material.[3] By varying the amount of porphyrin added to the assembly, we showed the formation of an excimer complex that increased as concentration increased. Time resolved photoluminescence studies clearly show that the exciton hopping distance along the 1D nanofiber was short (~3.5 nm) when the porphyrin concentration was high. The hopping distance increased as we decreased the amount of porphyrin (~60 nm). Our investigation revealed that the excimer functioned as an energy trap, and was more likely to form in high concentrations of porphyrin, thereby reducing the exciton propagation.

2.3. Energetic carriers in plasmonic metamaterials

The creation of energetic electrons through plasmon excitation of nanostructures before thermalization has been proposed for a wide number of applications in optical energy conversion and ultrafast nanophotonics. However, the use of "nonthermal" electrons is primarily limited by both a low generation efficiency and their ultrafast decay. We report experimental and theoretical results on the use of broadband plasmonic nanopatch metasurfaces comprising a gold substrate coupled to gold or silver nanoparticles that produce large concentrations of hot electrons, which we measure using transient absorption spectroscopy.[4,5] We find evidence for three subpopulations of nonthermal carriers which we propose arise from anisotropic electron-electron scattering within sp-bands near the Fermi surface. The bimetallic character of the metasurface strongly impacts the physics, with dissipation occurring primarily in the gold whereas the quantum process of hot electron generation takes place in both components. Our calculations show that the choice of geometry and materials is crucial for producing strong ultrafast nonthermal electron components. Theoretical efforts to directly extract hot carrier populations from transient absorption spectra are also described.[6]

3. Conclusions

We described the unusual nanophotonic and quantum optical behavior of three different hybrid nanostructures. A broad range of synthetic or fabrication approaches are used, including colloidal synthesis, biomimetic peptide assembly, and top-down fabrication approaches are used. Predictions and guidelines for improving the efficiency of light-activated nanostructures are given.

Acknowledgements

Use of the Center for Nanoscale Materials, an Office of Science user facility, was supported by the U.S. Department of Energy, Office of Science, Office of Basic Energy Sciences, under Contract No. DE-AC02-06CH11357.

References

[1] X. Ma, B. T. Diroll, W. Cho, I. Fedin, R. D. Schaller, D. V. Talapin, G. P. Wiederrecht, Size-dependent biexciton quantum yields and carrier dynamics of quasi-two-dimensional core/shell nanoplatelets, *ACS Nano* 11: 9119, 2017.

[2] X. Ma, B. T. Diroll, W. Cho, I. Fedin, R. D. Schaller, D. V. Talapin, G. P. Wiederrecht, Anisotropic photoluminescence from isotropic optical transition dipoles in semiconductor nanoplatelets, *Nano Lett*. 18: 4647, 2018.

[3] L. A. Solomon, M. E. Sykes, Y. A. Wu, R. D. Schaller, G. P. Wiederrecht, and H. C. Fry, Tailorable exciton transport in doped peptide-amphiphile assemblies, *ACS Nano* 11: 9112, 2017.

[4] M. E. Sykes, J. W. Stewart, G. M. Akselrod, X.-T. Kong, Z. Wang, D. J. Gosztola, A. B. F. Martinson, D. Rosenmann, M. H. Mikkelsen, A. O. Govorov, G. P. Wiederrecht, Enhanced generation and anisotropic Coulomb scattering of hot electrons in an ultra-broadband plasmonic nanopatch metasurface, *Nature Comm*. 8: 986, 2017.

[5] H. Harutyunyan, A. B. F. Martinson, D. Rosenmann, L. K. Khorashad, L. V. Besteiro, A. O. Govorov, G. P. Wiederrecht, Anomalous ultrafast dynamics of hot plasmonic electrons in nanostructures with hot spots, *Nat. Nanotech*. 10: 770, 2015.

[6] T. Heilpern, M. Manjare, A. O. Govorov, G. P. Wiederrecht, S. K. Gray, H. Harutyunyan, Determination of hot carrier energy distributions from inversion of ultrafast pump-probe reflectivity measurements, *Nature Comm*. 9: 1853, 2018.

Polariton chemistry: thinking inside the (photon) box

Joel Yuen-Zhou[1]

[1]Department of Chemistry and Biochemistry, University of California San Diego, La Jolla, CA 92093

Abstract

In this talk, I will showcase recent theoretical and computational studies that my group has carried out in terms of controlling the physicochemical properties and processes of molecular ensembles that undergo strong light-matter coupling with confined electromagnetic modes in the mid-IR range. Examples include enhancement of thermally-activated ground-state chemical reactions, design of exotic optical nonlinearities, and remote control of chemical reactions.

1. Introduction

The usual suspect of cavity quantum electrodynamics (CQED) is a "photon box" containing pristine atomic and molecular systems with highly controllable degrees of freedom, to be manipulated for quantum information purposes. In contrast, in recent years, there has been a big effort to sacrifice the simplicity of these well-defined quantum optical systems and import the CQED toolbox into the context of complex molecular materials with the idea of endowing the resulting hybrid light-matter systems with drastically different physicochemical properties and phenomena than the bare molecular counterparts [1, 2].

In this talk, I will focus on systems like the one depicted in Fig. 1, which can be described by a single mid-infrared (IR) cavity mode which can couple to $N \approx 10^6 - 10^{10}$ molecules, each supporting a high-frequency vibrational mode (other studies involving UV-visible molecular excitations will be briefly mentioned). The low energy excitations of this problem are given by the Tavis-Cummings (TC) model. At light matter resonance ($\omega_{ph} = \omega_{exc}$), the cavity mode chooses a totally symmetric linear combination of molecular excitations (the "bright" state) $|B\rangle$ with which to pair, forming hybrid light-matter modes $|\pm\rangle = \frac{1}{\sqrt{2}}(|B\rangle \mp |ph\rangle)$ called upper and lower polaritons (UP, LP), whose energies at resonance are given by $\omega_\pm = \omega_{ph} \pm 2\sqrt{N}g$, where g is the single molecule light-matter coupling. Note that when $\sqrt{N}g \gg \kappa, \Gamma$ (the photonic and molecular linewidths), the polariton states are separated in energy by a large Rabi splitting $\Omega = 2\sqrt{N}g$, signaling the onset of (collective) strong light-matter coupling. However, it is important to emphasize that this superradiant enhancement of coupling comes at the expense of having a macroscopic reservoir of $N-1$ "dark" (subradiant) states ($\{|D_i\rangle\}$, $i = 1, \cdots, N-1$) that are parked at the bare molecular energy $\hbar\omega_{exc}$ and do not mix with light [3].

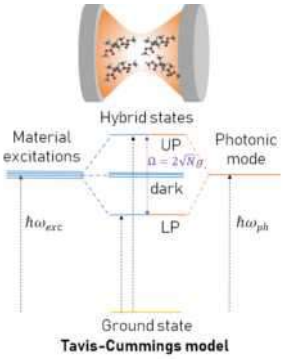


Figure 1: Collective strong light-matter coupling regime. (Figure adapted from [3]).

2. Enhancement of thermally-activated reactions via vibrational polaritons

Recently, it has been experimentally shown that kinetics of thermally-activated reactions can be enhanced or suppressed by formation of vibrational polaritons between high-frequency molecular vibrations and optical cavities [4]. From the explanation above, it is not obvious that this strategy should work at all given that, at thermal equilibrium, most excitations are dark and not polaritonic. However, in recent work[5], we have theoretically shown, using a Marcus-Jortner electron transfer model [6, 7], that a judicious arrangement of polaritonic channels can lead to smaller activation energies that can outcompete the entropy associated with the dark reservoir (see Fig. 2). We believe that this mechanism is universal and might be able to explain the experiments described above.

3. Exotic vibrational polariton optical nonlinearities

In recent work together with our experimental colleagues[8], we have shown that optical nonlinearities vibrational polaritons exhibit anomalies with respect to their bare molecular counterparts. At fixed pump and probe fluences as well as fixed molecular concentrations, the cavity with twice the longitudinal length shows a weaker nonlinearity than the original one. This result can be interpreted as follows: Since the cavity length sets the polariton wavefunction lengthscale, the longer cavity features a smaller *density* of anharmonic transitions to be probed. This is an usual situation that does not occur

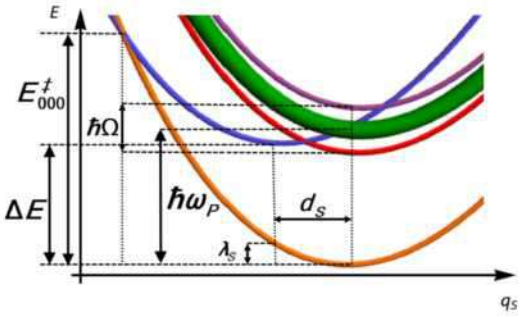


Figure 2: A generalization of Marcus-Jortner electron transfer theory that potentially explains the observed control of thermally-activated chemical reactions via vibrational polaritons. (Figure adapted from [5]).

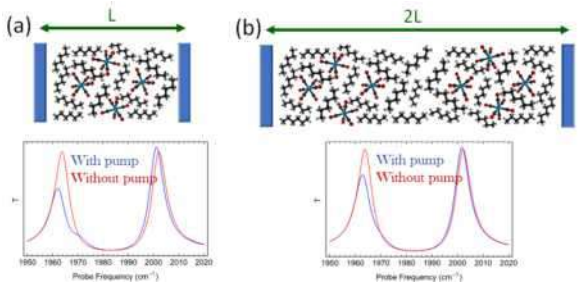


Figure 3: Linear (red) and nonlinear (blue) optical probe transmission through a vibrational polariton sample. At fixed molecular concentration, the optical nonlinearity of the sample is reduced by ˜50% when the size of the sample is doubled. (Figure adapted from [8]).

with regular molecular samples, and crucially inherits essential physics from both matter (anharmonicities) and light (delocalization).

4. Remote control of chemistry

Harnessing our recent understanding of polariton nonlinearities, we have recently developed the concept of remote control of chemical reactions[9] mediated by optical microcavities: the idea is that pumping molecules in one cavity can affect the chemical reactivity of molecules in another one. This idea opens doors to spatially nonlocal concepts in control of chemical reactivity.

References

[1] T. W. Ebbesen, "Hybrid light-matter states in a molecular and material science perspective," *Acc. Chem. Res.*, vol. 49, no. 11, pp. 2403–2412, Nov. 2016.

[2] R. F. Ribeiro, L. A. MartÃnez-MartÃnez, M. Du, J. Campos-Gonzalez-Angulo, and J. Yuen-Zhou, "Polariton chemistry: controlling molecular dynamics with optical cavities," *Chem. Sci.*, vol. 9, pp. 6325–6339, 2018.

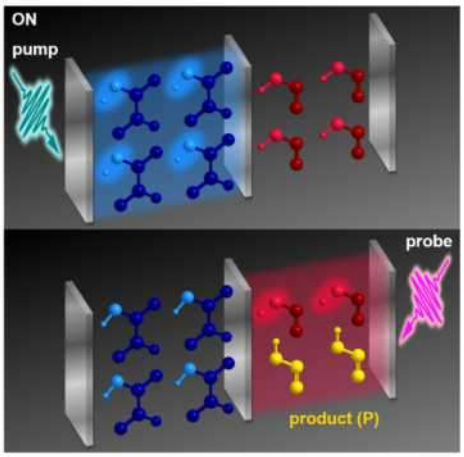


Figure 4: Optical pumping of the vibrations of a "remote catalyst" in one cavity activates the cis-trans HONO isomerization in another cavity (Figure adapted from [9]).

[3] J. Yuen-Zhou and V. M. Menon, "Polariton chemistry: thinking inside the (photon) box," *Proc. Nat. Acad. Sci.*, no. in press, 2018.

[4] A. Thomas, L. Lethuillier-Karl, K. Nagarajan, R. M. A. Vergauwe, J. George, T. Chervy, A. Shalabney, E. Devaux, C. Genet, J. Moran, and T. W. Ebbesen, "Tilting a ground-state reactivity landscape by vibrational strong coupling," *Science*, vol. 363, no. 6427, p. 615, Feb. 2019.

[5] J. A. Campos-Gonzalez-Angulo, R. F. Ribeiro, and J. Yuen-Zhou, "Resonant enhancement of thermally-activated reactions via vibrational polaritons," *arXiV*, Feb. 2019.

[6] R. A. Marcus, "Chemical and electrochemical electron-transfer theory," *Annu. Rev. Phys. Chem.*, vol. 15, no. 1, pp. 155–196, Feb. 1964.

[7] J. Jortner, "Temperature dependent activation energy for electron transfer between biological molecules," *J. Chem. Phys.*, vol. 64, no. 12, pp. 4860–4867, Feb. 1975.

[8] B. Xiang, R. F. Ribeiro, Y. Li, A. D. Dunkelberger, B. B. Simpkins, J. Yuen-Zhou, and W. Xiong, "Manipulating optical nonlinearities of molecular polaritons by delocalization," *arXiv preprint arXiv:1901.05526*, 2019.

[9] M. Du, R. F. Ribeiro, and J. Yuen-Zhou, "Remote control of chemistry in optical cavities," *Chem, in press*, 2018.

Plasmon Modulated Silicon Photodetectors based on Photothermoelectric Effect

Weikang Liu[1], Wenqiang Wang[1], Zhiqiang Guan[1*], and Hongxing Xu[1,2*]

[1] School of Physics and Technology, Center for Nanoscience and Nanotechnology, and Key Laboratory of Artificial Micro- and Nano-structures of Ministry of Education, Wuhan University, Wuhan 430072, China.
[2] The Institute for Advanced Studies, Wuhan University, Wuhan 430072, China
*corresponding author, E-mail: zhiqiang.guan@whu.edu.cn, hxxu@whu.edu.cn

Abstract

High integration density, high responsivity, and multifunctional Silicon photodetectors are the long term goals in the field of light detection. The photothermoelectric (PTE) effect provides a promising way towards the requirement above. Here we report a plasmon modulated silicon nanostripe PTE detector with an open-circuit photovoltage responsivity ~82 mV/μW. The gold subwavelength nanogratings provide enhanced optical absorption and polarization and wavelength sensitivity. This plasmon enhanced silicon PTE effect would pave the way for high integration, CMOS compatible light harvesting devices.

1. Introduction

Light induced temperature gradient can drive the consequent photocarriers diffusion process, thus produce a detectable photoelectric signal, which is named as the photothermoelectric (PTE) effect. The PTE effect have been reported in carbon nanotubes[1,2], semiconductor nanowires[3], graphene[4,5] and two dimensional metal dichalcogenide materials[6,7]. For further applications, it will be useful to combine plasmon structure with PTE device, such as silicon nanostructures, which have much potential both in optoelectronics and thermoelectric devices. Though the silicon PTE photodetectors is reported in ref[8], further reducing the silicon structure to the nanometer scale and utilizing surface plasmons to enhance the silicon nanostructure photoresponsivity still need to be explored towards high integration density, high sensitivity and low cost silicon photodetectors.

Here we report a plasmon modulated silicon PTE photodetector, which combines the gold subwavelength slit gratings with silicon nanostripes. An open-circuit photovoltage responsivity of as high as ~82 mV/μW was achieved with a 633 nm laser illuminating the nanograting region. This originates from the large Seebeck coefficient of the silicon nanofilm and the plasmon enhanced optical absorption (~10 fold) in the silicon film. The polarization and wavelength sensitivity of the photoresponse due to the plasmon resonance were demonstrated. The reversed sign of the Seebeck coefficient of silicon due to the Cr/Si contact was discovered and explained by the charge injection from the Cr adhesion layer.

2. Results and discussion

Figure 1a shows the false color SEM image of the device. An enlarged SEM image of the plasmonic nanograting is in the inset. Our device is composed of Si nanostripes and a Au grating with a 350 nm period and 25 nm slit width. For utilizing the PTE effect in silicon nanofilms experimentally, we need to carefully design the electrode/silicon contact to minimize the PV effects. This was achieved by forming an Ohmic contact instead of a Schottky contact. The Ohmic contact was achieved by using 5 nm thick Cr as an inter-layer between Au and Si and was confirmed by the measured current-voltage measurement. The Ohmic contact is due to the energy matching between the fermi energy of Cr and the lightly doped p-type Si. The measured conductance verified a boron doping level of 1.52×10^{12} /cm^3.

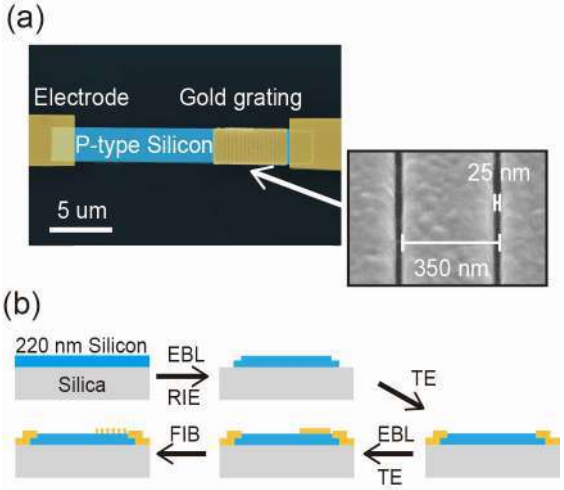


Figure 1: (a) False colour SEM image of the prepared sample. The inset shows the detailed grating structure with a 350 nm period and 25 nm slit width. (b) Fabrication process of the device. In the cross-section of the final sample, close to the right end, a gold nanograting is integrated on the silicon nanostripe.

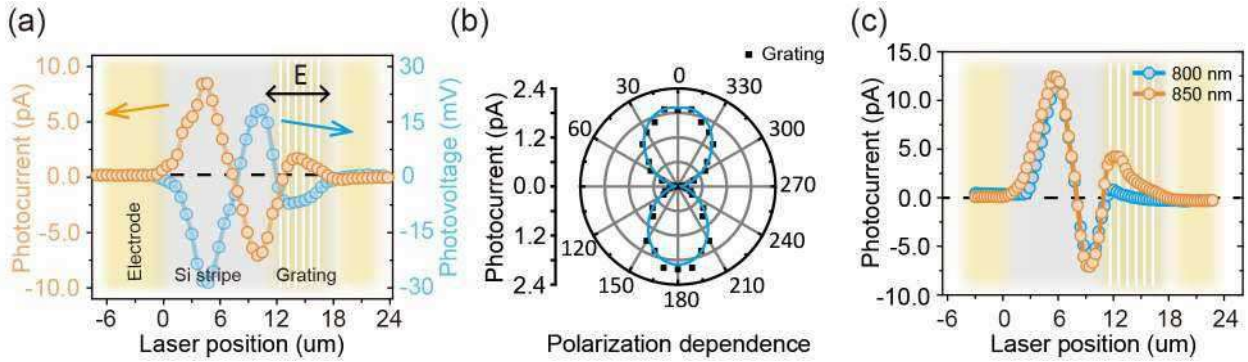


Figure 2. (a) Spatially resolved photocurrent and photovoltage along the Si nanostripe with on-resonance grating excitation. The polarization of the incident laser is perpendicular to the grating slits. (Laser wavelength 633 nm, power 0.09μW) (b) The Photocurrent in the grating region exhibits a $\cos^2\alpha$ angular dependence as a function of the polarization angle α of the incident light. (c) Spatially resolved photocurrent with 800 nm and 850 nm incident laser light.

The Seebeck effect, $\Delta V = -S\nabla T$ ($J = -\sigma S\nabla T$), predicts that when the laser illuminates the "left" ("right") sides, the voltage of left side should be lower (higher) than that on the right side, leading to a negative (positive) photovoltage or positive (negative) photocurrent detected by the sourcemeter. The measured spatially resolved short-circuit photocurrent and open-circuit photovoltage are plotted in the Figure 2a, with incident 633 nm laser light polarized perpendicular to the grating slits (p-polarization). The laser power was 0.09 μW. A distinct photocurrent occurred for laser illuminating on the nanograting region under p-polarization, compared with the photocurrent response under s-polarization. The polarization dependence of the short-circuit photocurrent exhibit a $\cos^2\alpha$ angular dependence and verified the contributions by SPPs excitation, as seen in Figure 2b. α is the incident polarization angle with 0 degree corresponding to p-polarization. The photocurrent polarizability $p = 0.95$, revealed a sensitive photoresponse to the polarization of the incident laser. We studied the wavelength dependence of the short-circuit photocurrent by the tunable laser wavelength from a supercontinuum laser. The spatially resolved short-circuit photocurrent for 800 nm and 850 nm wavelengths show a distinct photocurrent response in the grating region, as seen in Figure 2c. The photocurrent under the 850 nm wavelength laser is ~ 10 times higher than the photocurrent under the 800 nm wavelength laser.

Although the gold gratings offered a plasmon enhanced optical absorption in the silicon film, the maximum photocurrent response in the grating region was only ~40% of the maximum photocurrent in the silicon stripe region under 850 nm wavelength. In addition, the sign of the photocurrent was reversed compared with the silicon located nearby. The reversed sign of the photocurrent means that the Seebeck coefficient turns to a negative value and is different to the original positive value of the Seebeck coefficient in p-type silicon. The influence of Cr/Au coating on the Seebeck coefficient of Si is explained by the work function. The adhesion layer material Cr has Fermi energy $E_f = -4.5\ eV$ and is slightly smaller than the Fermi level for the weakly p-doped Si $E_f = -4.74\ eV$. Therefore, Cr has doped the Si film with electrons and turned the lightly doped p-type Si into intrinsic n-type. This implicates a careful design of the contact barrier and the doping level is important for optimized PTE photodetection. With further efforts to explore the plasmon enhanced silicon PTE effects in the infrared region and achieving higher integration density, the plasmon enhanced Si nanostructures are promising for silicon based multifunctional on-chip subwavelength photodetection.

References

[1] M. Barkelid, V. Zwiller. Photocurrent generation in semiconducting and metallic carbon nanotubes. Nature Photonics, 8(1): 47-51, 2014.

[2] T. Deborde, L. Aspitarte, T. Sharf, et al. Photothermoelectric Effect in Suspended Semiconducting Carbon Nanotubes. Acs Nano, 8(1): 216-221, 2014.

[3] S. Limpert, A. Burke, I. J. Chen, et al. Bipolar Photothermoelectric Effect Across Energy Filters in Single Nanowires. Nano Letters, 17(7): 4055-4060, 2017.

[4] X. D. Xu, N. M. Gabor, J. S. Alden, et al. Photo-Thermoelectric Effect at a Graphene Interface Junction. Nano Letters, 10(2): 562-566, 2010.

[5]N. M. Gabor, J. C. W. Song, Q. Ma, et al. Hot Carrier-Assisted Intrinsic Photoresponse in Graphene. Science, 334(6056): 648-652, 2011.

[6] D. J. Groenendijk, M. Buscema, G. A. Steele, et al. Photovoltaic and Photothermoelectric Effect in a Double-Gated WSe2 Device. Nano Letters, 14(10): 5846-5852, 2014.

[7]Y. Zhang, H. Lu, L. Wang, et al. Photothermoelectric and photovoltaic effects both present in MoS2. Scientific Reports, 5: 7938, 2015.

[8] Y. Lai, C. Tsai, C. Chang, et al. Photothermoelectric Effects in Nanoporous Silicon. advanced materials, 28(13): 2644-2648, 2016.

Plasmon-enhanced fluorescence of EGFP immobilized on optically thin perforated Al films

Vladimir E. Bochenkov[1*], Artyom A. Astafiev[1,2], Alexander M. Shakhov[1], and Vadim A. Timoshenko[1]

[1]Chemistry department, Lomonosov Moscow State University, Moscow, Russia
[2]Semenov Institute of Chemical Physics of RAS, Moscow, Russia
*corresponding author, E-mail: boch@kinet.chem.msu.ru

Abstract

Hybrid bionanomaterial comprised of Enhanced Green Fluorescent Protein covalently bound to 20 nm thick perforated Al film has been created. The short-ordered arrays of nanoholes with diameter in range 65–120 nm have been fabricated using sparse colloidal lithography. By changing the diameter of the nanoholes, the plasmon-polariton frequency has been tuned across the spectrum. The strongest plasmon-enhanced fluorescence has been observed for the systems with 120 nm nanoholes, reaching the 2.75 enhancement factor.

1. Introduction

Single-molecule imaging is a fast-growing area of research, which offers unique experimental tools for studying various microscopic processes with high sensitivity and unprecedented resolution. In this technique, spatially isolated fluorescent molecules conjugated to biomolecules of interest serve as point light sources. The position of each dye molecule can be determined with nanometer precision by fitting the diffraction-limited emission profile. Despite lower brightness and stability compared to many organic dyes, fluorescent proteins (FPs) are widely used as tags for labeling proteins *in vivo*, since they can be genetically encoded with high specificity inside the cell. Therefore, it is important to improve the brightness and the lifetime of normally dim FPs. One of the promising approaches is to utilize the plasmon-enhanced fluorescence by placing the FP near the surface of a plasmonic nanostructure. However, it is not a straightforward task. At short distances between the fluorophore and metal the non-radiative energy transfer prevails, thus one has to carefully design the spacer and immobilization route. Additionally, FPs are more sensitive to the environment and can denature when adsorbed on the surface. In this work we demonstrate the successful immobilization of EGFP on surface-oxidized perforated Al thin films and the observation of plasmon-enhanced fluorescence in this hybrid system.

2. Experiment

2.1. Nanofabrication

Hybrid Al–Enhanced Green Fluorescent Protein (EGFP) bionanosystems have been constructed using the following strategy. First, aluminum nanostructures have been fabricated using sparse colloidal lithography approach, described in detail elsewhere [1]. Samples with average diameter of nanoholes of 60, 80 and 120 nm have been obtained.

The protein binding step has been carried using the (3-Glycidyloxypropyl)trimethoxysilane (GLYMO) as an anchor. Covalent binding of EGFP has been achieved via the reaction of GLYMO epoxy-groups with one of the protein's surface amine groups. For each sample, a 20 μL droplet of 0.25 M EGFP solution in phosphate buffered saline (PBS) has been placed on top of the GLYMO-modified surface and covered by a microscope slide to prevent water evaporation. After 20 min, the sample has been rinsed by PBS to remove the unbound protein molecules and studied.

2.2. Spectroscopy

Extinction (1-T) spectra of the perforated Al films have been recorded in range of 300–700 nm using UV-vis-NIR spectrometer (Jasco V-770). Spectra have been registered in two-beam mode using a clean glass slide as a reference. Fluorescence emission spectra have been registered using a custom built optical setup. Femtosecond laser pulses with a 80 MHz repetition rate, 950 nm central wavelength, and energy up to 25 nJ were generated by a Titanium-Sapphire oscillator (Tsunami, Spectra-Physics). Frequency-doubled pulses at 475 nm were focused on the sample's bottom surface. Fluorescence was filtered with 500 nm long-pass filter and coupled to an Acton SP300i monochromator and then to a PI-MAX 2 CCD camera (Princeton Instruments), which recorded fluorescence emission spectra.

3. Results and discussion

Nanohole arrays, fabricated using sparse colloidal lithography, are characterized by short-range order (SRO), while the long-range order in such systems is absent [1]. Optical properties of SRO nanohole arrays are defined by a combination of two contributions: the surface plasmon polari-

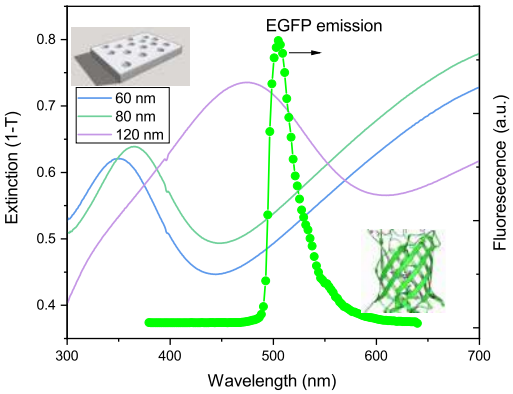


Figure 1: Extinction spectra of perforated Al films (solid lines) and the EGFP emission spectrum (green circles + green line). The insets illustrate the perforated Al film and the molecular structure of EFGP.

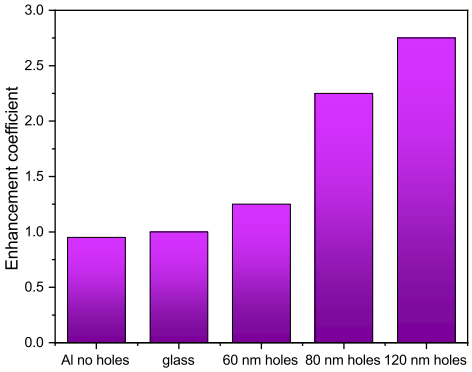


Figure 2: Fluorescence enhancement coefficient of EGFP, immobilized on various surfaces.

tons (SPPs) between the holes, and the localized surface plasmon resonance (LSPR) in the holes. The former manifests itself as an extinction maximum (peak), while the latter — as an extinction minimum (dip) in the spectra [2, 3]. By increasing the diameter of nanospheres used for fabrication, the diameter of the holes and the distance between them are gradually increased, thus allowing one to tune the plasmonic resonances to longer wavelength. The extinction spectra of perforated Al films fabricated in this work clearly demonstrate such behavior, as depicted in Fig. 2. The fluorescence emission spectrum of EGFP is presented in the same graph for comparison.

Fluorescence emission spectra have been normalized by the intensity of EGFP immobilized on glass surface (without Al layer). Additionally, to take into account the extinction of light by metal reflection and absorption, the spectra are divided by the transmission at the excitation wavelength (475 nm). The resulting fluorescence intensity at EFGP emission maximum (510 nm) are presented in Fig. 2. One can see that the fluorescence intensities on glass and on Al film without nanoholes are almost the same, which suggests that 1) the amount ot EGFP molecules immobilized on glass and on Al are close, and that 2) there is no significant fluorescence quenching by Al in these conditions. Introducing plasmon resonances by adding nanoholes to Al films leads to stronger fluorescence, which reaches factor 2.75 for the 120 nm holes.

4. Conclusions

We have created a hybrid nanobiosystem based on Al short-ordered nanohole arrays and the covalently attached fluorescent protein molecules EGFP. The natural oxide layer on Al surface serves as an efficient spacer between the metal and the protein's chromophore, allowing to decrease the non-radiative energy transfer. The observed fluorescence intensity has increased by the factor of 2.75 compared to the protein, immobilized on a glass surface. The advantage of the proposed approach is in relative simplicity of the immobilization procedure as well as in its low cost.

References

[1] J. Prikulis, P. Hanarp, L. Olofsson, D. Sutherland, and M. Käll, "Optical spectroscopy of nanometric holes in thin gold films," *Nano Letters*, vol. 4, no. 6, pp. 1003–1007, 2004.

[2] T. Sannomiya, O. Scholder, K. Jefimovs, C. Hafner, and A. B. Dahlin, "Investigation of plasmon resonances in metal films with nanohole arrays for biosensing applications," *Small*, vol. 7, no. 12, pp. 1653–1663, 2011.

[3] T. M. Schmidt, V. E. Bochenkov, J. D. A. Espinoza, E. C. P. Smits, A. M. Muzafarov, Y. N. Kononevich, and D. S. Sutherland, "Plasmonic fluorescence enhancement of DBMBF2 monomers and DBMBF2–toluene exciplexes using Al-hole arrays," *The Journal of Physical Chemistry C*, vol. 118, no. 4, pp. 2138–2145, 2014.

Acknowledgement

Part of this work has been carried out using the cleanroom facilities of Aarhus University (Denmark), VEB is grateful to Duncan S. Sutherland for support. Authors thank A. Mishin and A. Bogdanov (Shemyakin-Ovchinnikov Institute of Bioorganic Chemistry RAS, Moscow) for the provided solution of EGFP. The work has been funded by Russian Science Foundation grant number 17-13-01276.

Plasmonics in complex geometries:

Modal optical properties and coupling with nanoscale emitters

Pierre-Michel Adam[1]

[1]Light, nanomaterials, nanotechnologies (L2n), Université de Technologie de Troyes,
12 Rue Marie Curie, CS42060, 10004 Troyes Cedex, France
*corresponding author: adam@utt.fr

Abstract

Plasmonics deals with the properties and the control of localized and delocalized surface plasmons at the subwavelength scale. It has highly potential applications for nanoscale ultrafast photonics and for ultrasensitive sensors. Two types of resonances exist, Surface Plasmons Polaritons (SPP) and Localized Surface Plasmons (LSP). Understanding the coupling properties between quantum emitters and surface plasmons resonances and/or nanonantennas is a key step towards realistic applications in the near future. We will present in this paper our latest experimental and theoretical results on the optical properties of different plasmonic systems exhibiting complex resonant modes and applications for the sensitive detection of molecules Surface Enhanced Spectroscopies, such as Surface Enhanced Raman Spectroscopy (SERS) and Surface Enhanced Fluorescence (SEF).

Main

Plasmonics is a now well-established field finding numerous applications in pharmacology, biology, optoelectronics and metamaterials among others. Two types of resonances exist, Surface Plasmons Polaritons (SPP) and Localized Surface Plasmons (LSP). SPPs are delocalized waves, which can be launched either on thin metallic films or on nanoscale waveguides [1]. LSPs are confined modes at the subwavelength scale, which are localized in metallic nanoparticles. Electric dipolar modes are the simplest modes observed, whose resonance wavelength depend on the size and shape of the nanoparticles (Fig.1) [2]. They also depend on their environment, such as the presence of a substrate, and on the mutual interactions between nanoparticles, both in near-field and in far-field. These optical properties are extensively used in Localized Surface Plasmon Resonance sensing. The incident field spatial distribution, through its amplitude, phase and polarization variations, can excite more complex modes of nanoparticles, multipolar modes, such as electric quadrupoles or magnetic dipoles, but also hybrid modes, which result from the coupling of two or more modes. All these modes can be observed in extinction spectroscopy for ensembles of nanoparticles, or in scattering and photoluminescence spectroscopies for single nanoparticles [3-5]. Even more complicated plasmonic systems, such as metal-insulator-metal nanostructures, can sustain both LSPs and SPPs and other modes whose intense field is confined in the gap between the two metals [6].

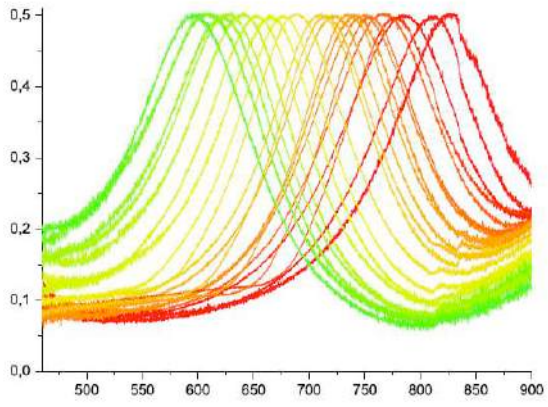


Figure 1: Normalized extinction of arrays of gold ellipsoidal nanoparticles [2]

For the sensitive detection of molecules or nanocrystals, organic or inorganic, Surface Enhanced Spectroscopies, such as Surface Enhanced Raman Spectroscopy (SERS) and Surface Enhanced Fluorescence (SEF), are widespread and the most used for applications. Both these enhanced spectroscopies rely on local field enhancements in the near vicinity of resonant metallic nanoparticles when one or several Surface Plasmon oscillations are driven for a specific optical wavelength. Double enhancement can be obtained if surface plasmons resonances coincide with both excitation/emission wavelengths for fluorescence or with both excitation/scattering wavelengths for Raman scattering.

SERS can achieve a high sensitivity, detecting traces of a species, even reaching single molecule detection. Such sensitivity is obtained with specific systems of plasmonic nanoparticles, especially when two or more metallic nanoparticles are coupled through their optical near-fields, resulting in huge enhancements usually ranging from 4 up to 10 orders of magnitude [7]. Even if most SERS studies have been made on organic molecules, it has also been recently showed that significant enhancement can be observed on semiconductor nanocrystals [8]. In order to detect few amounts of inorganic nanocrystals or organic molecules specific large-scale plasmonic systems have been developed, which incorporates monometallic or bimetallic nanoparticles on substrates, separated by small gaps [9-10].

Less enhancement of the spectroscopic signal is obtained with SEF. In SEF one has to take into account the quantum yield modifications in the presence of the metallic nanoparticles. Quantum yield can be enhanced or even reduced, although always resulting in a decrease of the excited level lifetime. In the former case double resonance enhancement can be achieved while leading in the latter case to a competition between local field excitation enhancement and quantum yield reduction. In that case the possibility of quenched fluorescence from the emitters can be observed but the effect is also dependent on the distance between the emitter and the metallic nanoparticle. Double resonant enhancement of the fluorescence of single photosystems has recently been observed with large-scale plasmonic platforms both at room and low temperatures [11]. More complex systems of emitters, mixing organic photochromic molecules and inorganic quantum dots, have also been studied where the organic absorbing species can induce a switch from quenching to enhancement of the nanocrystals luminescence [12].

References

[1] F. Tang, P.-M. Adam, and S. Boutami**,** *Optics Express,* 24 (19), 21244-21255, 2016.

[2] J. Grand, P.-M. Adam, A.-S. Grimault, A. Vial, M. Lamy De La Chapelle, J.-L. Bijeon, S. Kostcheev, P. Royer, *Plasmonics* 1 (2-4), 135-140

[3] A. Movsesyan, A.-L. Baudrion, P.-M. Adam, *Optics Express* 26 (5), 6439-6445, 2018

[4] A. Movsesyan, A.-L. Baudrion, P.-M. Adam, *The Journal of Physical Chemistry C* 122 (41), 23651-23658

[5] J. Wang, E. Gürdal, A. Horneber, S. Dickreuter, S. Kostcheev, A.J. Meixner, M. Fleischer, P.-M. Adam, D. Zhang, *Nanoscale* 10 (17), 8240-8245

[6] R. Nicolas, G. Lévêque, J. Marae-Djouda, G. Montay, Y. Madi, J. Plain, Z. Herro, M. Kazan, P.-M. Adam, T. Maurer, *Scientific Reports* 09/2015; 5:14419

[7] J. Grand, M. Lamy de La Chapelle, J.-L. Bijeon, P.-M. Adam, A. Vial, P. Royer, *Physical Review B* 72 (3), 033407

[8] A. Rumyantseva, S. Kostcheev, P.-M. Adam, S.V. Gaponenko, S.V. Vaschenko, O. S. Kulakovich, A. A. Ramanenka, D. V. Guzatov, D. Korbutyak, V. Dzhagan, A. Stroyuk, V. Shvalagin, *ACS nano* 7 (4), 3420-3426

[9] M.Y. Khaywah, S. Jradi, G. Louarn, Y. Lacroute, J. Toufaily, T. Hamieh, P.-M. Adam, *The Journal of Physical Chemistry C* 119 (46), 26091-26100

[10] A. Muravitskaya, A. Rumyantseva, S. Kostcheev, V. Dzhagan, O. Stroyuk and P.-M. Adam, *Optics Express*, 24 (2), A168-A173, 2016

[11] S. Ashraf, A. Konrad, H. Lokstein, M. Skandary, M. Metzger, J.M. Djouda, T. Maurer, P.-M. Adam, A. J. Meixner, and M. Brecht, *Nanoscale,* 9(12), 2017

[12] G. Lamri, A. Movsesyan, E. Figueiras, J.B. Nieder, J. Aubard, P.-M. Adam, C. Couteau, N. Felidj, A.-L. Baudrion, *Nanoscale* 11 (1), 258-265

Broadband Mid-Infrared Absorber Using Gosper Curve

Jihua Zou[1], Peng Yu[1], Alexander Govorov[1], Jiang Wu[1], and Zhiming Wang[1]
[1]Institute of Fundamental and Frontier Science, University of Electronic Science and Technology of China, Chengdu, China
*corresponding author, E-mail: jiangwu@uestc.edu.cn

Abstract

Designing broadband metamaterial perfect absorbers is challenging due to the intrinsically narrow bandwidth of surface plasmon resonances. Here, we designed an ultra-broadband metamaterial absorber by using space filling Gosper curve. The optimized design shows an average absorption up to 95.78% from 2.64 to 9.79 μm across the entire mid-infrared region. Meanwhile, the absorber shows a great insensitivity to polarization and the angle of light incidence. The broadband perfect absorption can be attributed to the defined Gosper curve with different segments that support electric resonances at different wavelengths. This work provides a new concept for the design of broadband absorbers and sheds light on practical applications, such as broadband infrared photodetection and biomedical sensing.

1. Introduction

Metamaterials have intriguing electromagnetic response with tailored permittivity and permeability that are not available in naturally occurring materials, promising for perfect lenses, holographic display and invisible cloaking. Metamaterial absorbers (MMAs) demonstrated a variety of applications at different frequencies,[1] such as thermal imaging,[2-5] thermal emitters, [2],[6] solar photovoltaics, [7-9] plasmonic sensors[10], and single photon source. [11] MMAs can be divided into two types−narrow band and broadband.[1] Narrow band MMAs have been demonstrated extensively, such as single-band[1],[4],[12-13], dual-band, [6],[14-16] triple-band,[17-18] and multi-band.[19-21] However, achieving broadband MMAs at a higher frequency—still remains a challenge, due to the intrinsically narrow bandwidth of localized surface plasmon resonances (LSPRs) or surface plasmon polaritons (SPPs) generated on metallic structure.[1] Gao et al. proposed a MMP with binary-pattern which demonstrated absorption over 95% from 3 to 3.9 μm. However, achieving perfect absorption in the entire mid-infrared (MIR) region, 3-8 μm, has so far remained as a challenging task.

Here, based on the space-filling Gosper curve, we propose a broadband MIR MMAs that demonstrates a nearly-perfect absorption covering the entire MIR—over 95% absorption spanning from 2.6 to 9.8 μm. Simulation shows an angle-independent absorption greater than 90% over 60° range under either transverse electric (TE) or transverse magnetic (TM) polarization. Our device may have applications on surface-enhanced infrared spectroscopy—infrared vibrations of molecules located in these fields can be boosted by orders of magnitude and permitting a spectroscopic characterization with unprecedented sensitivity.

2. Simulation

2.1. Method

The finite-difference time-domain (FDTD) and Finite Element Method (FEM) were employed to simulate the MMAs. Lumerical and COMSOL Multiphysics were used, respectively. In the z direction, we used perfectly matched layers (PML) boundary conditions to eliminate the boundary scattering. A single unit of the MMAs is simulated with periodic boundary in the x and y directions. A single unit of the space-filling Gosper curve is shown in Fig. 1.

2.2. Figures



Figure 1. The diagram of absorber structure.

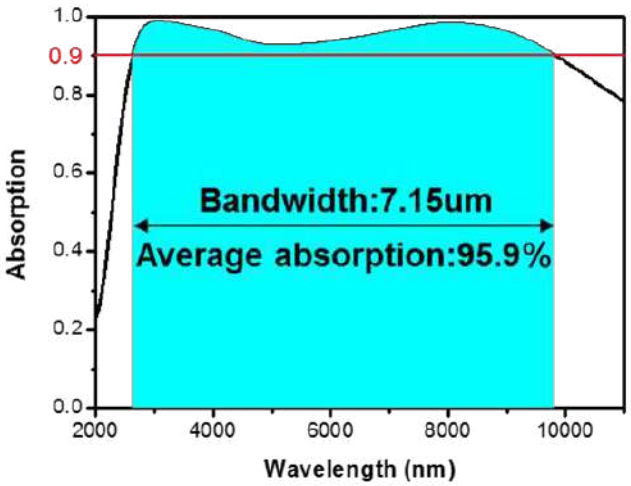


Figure 2. The absorption spectrum of the absorber.

3. Results and Discussion

We simulated first three stages in the construction of a fractal array based on Peano-Gosper space-filling curve as shown in Fig. 1. Polymide, a dielectric superstrate is used to tailor the impedance match to free space in order to minimize reflection and maximize absorption in the MIR region. Platinum (Pt) is used to replace conventional gold resonator to extend the bandwidth of MMAs. The proposed MMA exhibits a nearly perfect absorption with an average absorbance of 95.78% and 90% absorption bandwidth over 7.15μm from 2.64 to 9.79μm, as shown in Fig. 2. Meanwhile, the MMA is insensitive to the incident angle. Especially for TM mode, 90% absorption bandwidth still maintains as high as 3.53μm at the incident angle of 60°, the average absorptivity is 97.64% from 2.87 to 6.40μm. The broadband MIR perfect absorption can be attributed to the defined Gosper curve with different segments that support multipole resonances at different wavelengths. Interestingly, the electric resonances dominants in the MMA while its conventional counterparts have electric and magnetic resonances.

4. Conclusion

In this paper, we reported an ultra-broadband based on space filling Gosper curve and it demonstrates the highest bandwidth in the near-mid infrared region with nearly perfect absorption among their single layer counterparts. This work provides a new concept for the design broadband MMA and paves the way for its practical application, such as infrared imaging, broadband photodetection and biomedical sensing, etc.

References

[1] P. Yu, L. V. Besteiro, Y. Huang, J. Wu, L. Fu, H. H. Tan, C. Jagadish, G. P. Wiederrecht, A. O. Govorov, and Z. Wang, "Broadband Metamaterial Absorbers," Advanced Optical Materials 7, 1800995 (2019).

[2] M. Diem, T. Koschny, and C. M. Soukoulis, "Wide-angle perfect absorber/thermal emitter in the terahertz regime," Physical Review B 79 (2009).

[3] N. I. Landy, C. M. Bingham, T. Tyler, N. Jokerst, D. R. Smith, and W. J. Padilla, "Design, theory, and measurement of a polarization-insensitive absorber for terahertz imaging," Physical Review B 79(2009).

[4] X. Liu, T. Starr, A. F. Starr, and W. J. Padilla, "Infrared Spatial and Frequency Selective Metamaterial with Near-Unity Absorbance," Physical Review Letters 104, 207403 (2010).

[5] A. Tittl, A.-K. U. Michel, M. Schäferling, X. Yin, B. Gholipour, L. Cui, M. Wuttig, T. Taubner, F. Neubrech, and H. Giessen, "A Switchable Mid-Infrared Plasmonic Perfect Absorber with Multispectral Thermal Imaging Capability," Advanced Materials 27, 4597-4603 (2015).

[6] X. Liu, T. Tyler, T. Starr, A. F. Starr, N. M. Jokerst, and W. J. Padilla, "Taming the Blackbody with Infrared Metamaterials as Selective Thermal Emitters," Physical Review Letters 107, 045901 (2011).

[7] T. V. Teperik, F. J. García de Abajo, A. G. Borisov, M. Abdelsalam, P. N. Bartlett, Y. Sugawara, and J. J. Baumberg, "Omnidirectional absorption in nanostructured metal surfaces," Nature Photonics 2, 299-301 (2008).

[8] N. Liu, M. Mesch, T. Weiss, M. Hentschel, and H. Giessen, "Infrared Perfect Absorber and Its Application As Plasmonic Sensor," Nano Letters 10, 2342-2348 (2010).

[9] Y. Kawaguchi, T. Tsukahara, M. Motozawa, Experimental and numerical investigations of turbulent drag reduction phenomena by additives, Proc. ASCHT09, Jeju, Korea, pp. 23−32, 2009.

[10] Z. H. Jiang, S. Yun, F. Toor, D. H. Werner, and T. S. Mayer, "Conformal Dual-Band Near-Perfectly Absorbing Mid-Infrared Metamaterial Coating," ACS Nano 5, 4641-4647 (2011).

[11] W. Wang, X. Yang, T. S. Luk, and J. Gao, "Enhanced quantum dots spontaneous emission with metamaterial perfect absorbers," Applied Physics Letters 114, 021103 (2019)

[12] P. Yu, L. V. Besteiro, J. Wu, Y. Huang, Y. Wang, A. O. Govorov, and Z. Wang, "Metamaterial perfect absorber with unabated size-independent absorption," Opt Express 26, 20471-20480 (2018).

[13] D. Shrekenhamer, W.-C. Chen, and W. J. Padilla, "Liquid Crystal Tunable Metamaterial Absorber," Physical Review Letters 110, 177403 (2013).

[14] Z. H. Jiang, S. Yun, F. Toor, D. H. Werner, and T. S. Mayer, "Conformal Dual-Band Near-Perfectly Absorbing Mid-Infrared Metamaterial Coating," ACS Nano 5, 4641-4647 (2011).

[15] K. Chen, R. Adato, and H. Altug, "Dual-Band Perfect Absorber for Multispectral Plasmon-Enhanced Infrared Spectroscopy," ACS Nano 6, 7998-8006 (2012).

[16] P. Yu, J. Wu, E. Ashalley, A. Govorov, and Z. Wang, "Dual-band absorber for multispectral plasmon-enhanced infrared photodetection," Journal of Physics D: Applied Physics 49, 365101 (2016).

[17] X. Shen, T. J. Cui, J. Zhao, H. F. Ma, W. X. Jiang, and H. Li, "Polarization-independent wide-angle triple-band metamaterial absorber," Opt. Express 19, 9401-9407 (2011).

[18] X. Shen, Y. Yang, Y. Zang, J. Gu, J. Han, W. Zhang, and T. Jun Cui, "Triple-band terahertz metamaterial absorber: Design, experiment, and physical interpretation," Applied Physics Letters 101, 154102 (2012).

[19] J. W. Park, P. V. Tuong, J. Y. Rhee, K. W. Kim, W. H. Jang, E. H. Choi, L. Y. Chen, and Y. Lee, "Multi-band metamaterial absorber based on the arrangement of donut-type resonators," Opt Express 21, 9691-9702 (2013).

[20] B. X. Wang, X. Zhai, G. Z. Wang, W. Q. Huang, and L. L. Wang, "Design of a Four-Band and Polarization-Insensitive Terahertz Metamaterial Absorber," IEEE Photonics Journal 7, 1-8 (2015).

[21] X.-Y. Peng, B. Wang, S. Lai, D. H. Zhang, and J.-H. Teng, "Ultrathin multi-band planar metamaterial absorber based on standing wave resonances," Opt. Express 20, 27756-27765 (2012).

Plasmonic Aluminum Nanohole Arrays for ITO-Free Ultraviolet Photodetectors with Improved Response Stability and Tunability

Monica Esopi and Qiuming Yu*

Department of Chemical Engineering, University of Washington, Seattle, WA, USA
*corresponding author, E-mail: qyu@uw.edu

Abstract

Incorporating plasmonic nanostructures into photodetectors provides an avenue for enhancing photoresponse strength, selectivity and tunability. Here, aluminum nanohole arrays (Al-NHAs) were incorporated as transparent electrodes into ultraviolet photodetectors. The optimal gap/pitch were determined to be 175/200 nm by 3-dimensional finite-difference time-domain (3D-FDTD) simulations. Devices incorporating these Al-NHAs had comparable photoresponse, under reverse biases, compared to ITO-based control devices. Under forward biases, improved, spectrally distinct photoresponse was obtained by the Al-NHA-based devices, enabling a new bias-dependent response tunability.

1. Introduction

Nanostructured films incorporated into optoelectronic devices, including photodetectors, have attracted attention for their ability to support surface plasmon polaritons (SPPs), which can enhance optical absorbance, internal electric field, and ultimately device performance[1, 2]. Metal films can also serve as a transparent device electrode, making them a cost-effective, flexible, high-performance alternative to the commonly used indium tin oxide (ITO), which is expensive and brittle[3]. Photodetectors, particularly those that are selective to ultraviolet (UV) light, are important in a variety of applications including environmental monitoring, imaging, and flame and missile detection[4, 5]. Despite this applicability, extension of plasmonic enhancements to UV-selective devices has been relatively slow. Although oxide formation on the surface can cause a redshift in its plasmonic properties, Al provides an abundant, low-cost option for supporting SPPs in the UV spectral range due to its carrier concentration and dielectric function[6-8].

In this work, Al nanohole arrays (Al-NHA) were designed using 3-dimensional finite-difference time-domain (3D-FDTD) simulations and employed as transparent electrodes in conventional UV photodetectors. These photodetectors utilize organic active materials, which provide a low-cost, flexible alternative to inorganic materials. The active layer consists of the UV-absorbing polymer poly(9,9-dioctylfluorene-alt-bithiophene) (F8T2) and the electron acceptor phenyl-C_{71}-butyric acid methyl ester ($PC_{71}BM$) blended in a 100:4 weight ratio. The hole and electron transport layers were Poly(3,4-ethylenedioxythiophene) :poly(styrene sulfonate) (PEDOT:PSS) and LiF respectively. The substitution of Al-NHA for ITO as a transparent conducting electrode resulted in similar photoresponse under reverse bias, improved response under forward bias, and new bias-dependent response tunability.

2. Discussion

2.1. Evaluating Al-NHAs with 3D-FDTD Simulations

To design the Al-NHA electrodes, a broad range of gap/pitch combinations were tested in 3D-FDTD simulations. The full device structure was glass/ITO or Al-NHA/PEDOT:PSS/F8T2:$PC_{71}BM$/LiF/Al, and is shown in Fig. 1a with an Al-NHA electrode. The simulated active layer absorbance was used to distinguish between different nanopattern geometries and determine that, considering fabrication constraints, a hexagonal NHA with a gap/pitch of 175/200 nm was optimal. The internal electric field distribution calculated for a simulated device on an optimal Al-NHA is shown in Fig. 1b, and corresponds to an x-y point at the edge of a nanohole. The field is mapped in the z direction at various wavelengths of incident light, which are plotted on the x axis. The electric field distribution for an ITO-based device is shown in Fig. 1c for comparison, illustrating the enhancement provided to the simulated, particularly in the lower portion of the device, upon incorporation of the Al-NHA electrode.

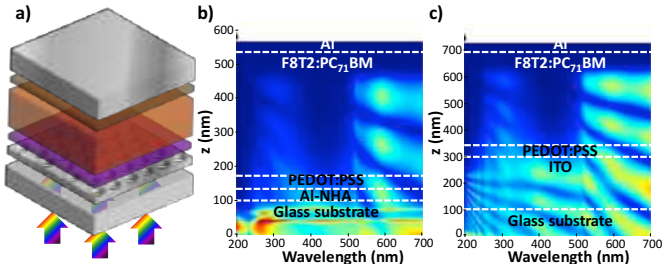


Figure 1: (a) device schematic, (b) simulated electric field distribution for an Al-NHA-based device, and (c) simulated electric field distribution for an ITO-based device.

2.2. Incorporating Al-NHA Electrodes into Devices

Devices with a structure of glass/ITO or Al-NHA/PEDOT:PSS/F8T2:$PC_{71}BM$/LiF/Al were fabricated and evaluated experimentally. A nanosphere lithography process, beginning with a monolayer of nanospheres, illustrated in Fig. 2a, followed by etching, Al deposition and chemical liftoff, was used to produce the Al-NHAs, an SEM of which is shown in Fig. 2a. Devices were evaluated based

on their photoresponse strength, speed, UV-selectivity and tunability under both reverse and forward biases. The specific detectivity (D*) encompasses many of these criteria, so it was calculated and is shown in Fig. 2b-c.

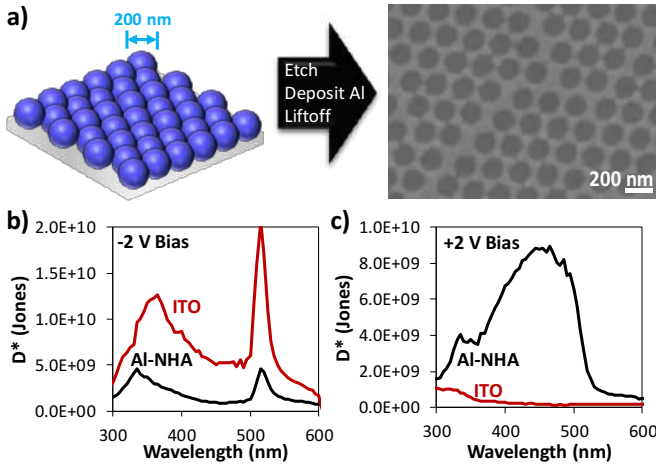


Figure 2: (a) Illustration of nanosphere lithography fabrication and SEM image of resulting Al-NHA. (b-c) D* spectra for ITO- and Al-NHA-based devices under applied biases of (b) -2 V and (c) +2 V.

Under reverse biases (Fig. 2b), both ITO- and Al-NHA-based devices produce photoresponse spectra with two peaks, around 360 and 510 nm, which correspond to the edges of the F8T2 absorption spectra. Light with these wavelengths is absorbed weakly, so it penetrates the active layer and is absorbed in the top portion, engaging a photomultiplicative response mechanism based on holes injected from the top electrode, which has been previously reported for the ITO-based devices[9]. The Al-NHA electrodes have lower transmittance than ITO, yielding a lower photoresponse, but the noise in Al-NHA-based devices is also lower than ITO-based-devices, so the D* values are comparable. Thus, an ITO-free device is obtained without diminishing the reverse-bias photoresponse.

Al-NHA-based devices exhibit a spectrally distinct, broad photoresponse under forward biases (Fig. 2c), unlike the ITO-based devices, whose behavior is unstable under forward biases because they rely on hole injection from the top electrode, which is more difficult under forward bias. The electrode symmetry of the Al-NHA-based devices enables them to produce photoresponse from photons within the F8T2 absorption peak, which are absorbed strongly in the lower portion of the active layer and result in photogenerated holes being collected at the top electrode. This mechanism produces a spectrally distinct, stable photoresponse, enabling the Al-NHA-based devices to improve upon the photoresponse of ITO-based devices under forward bias, and to unlock a response tunability based on the bias applied during testing.

3. Conclusions

In this work, Al-NHA electrodes were designed by 3D-FDTD simulations and incorporated into conventional, organic ultraviolet photodetectors. The hexagonal NHA had a gap and pitch of 175 and 200 nm, respectively, and was successfully fabricated by nanosphere lithography. Upon incorporation into devices, the reverse-bias photoresponse was maintained at a comparable level due to the low noise levels in the Al-NHA-based devices. Additionally, under forward biases, the photoresponse was improved compared to the ITO-based control devices, and a new bias-dependent tunability was enabled. To further investigate the mechanisms of this photoresponse, devices based on planar Al electrodes and hole-only devices based on ITO, planar Al, and Al-NHA electrodes were also fabricated and tested, to isolate the impact of the NHA from the impact of the electrode material and the impact of external and internal biases. These devices provide an example of ITO-free devices utilizing cost-effective materials resulting in UV photodetectors with improved photoresponse strength, stability, selectivity and tunability.

Acknowledgements

This work was supported by the Defense Threat Reduction Agency (HDTRA1-15-1-0021). Part of this work was conducted at the Washington Nanofabrication Facility/ Molecular Analysis Facility, a National Nanotechnology Coordinated Infrastructure (NNCI) site at the University of Washington (UW), which is supported in part by funds from the National Science Foundation (awards NNCI-1542101, 1337840 and 0335765), the National Institutes of Health, the Molecular Engineering & Sciences Institute, the Clean Energy Institute (CEI), the Washington Research Foundation, the M. J. Murdock Charitable Trust, Altatech, ClassOne Technology, GCE Market, Google and SPTS. Some of the work was carried out in the UW Department of Chemistry's Photonics Research Center. MRE acknowledges a fellowship from the CEI.

References

[1] M.L. Brongersma Plasmonic Photodetectors, Photovoltaics, and Hot-Electron Devices, *Proc. IEEE* 104*:* 2349-61, 2016

[2] P. Berini Surface plasmon photodetectors and their applications, *Laser Photonics Rev.* 8: 197-220, 2014

[3] B.J. Richardson, L. Zhu, Q.M. Yu Design and development of plasmonic nanostructured electrodes for ITO-free organic photovoltaic cells on rigid and highly flexible substrates, *Nanotechnology* 28 *2017*

[4] P. Bhattacharya *Semiconductor Optoelectronic Devices*: Prentice Hall, 1996

[5] S.O. Kasap S O 2006 *Principles of Electronic Materials and Devices,* McGraw-Hill, New York, 2006/

[6] M.W. Knight, N.S. King, L.F. Liu, H.O. Everitt, P. Nordlander, N.J. Halas, Aluminum for Plasmonics *ACS Nano* 8: 834-40, 2014

[7] A. Boltasseva, H.A. Atwater, Low-Loss Plasmonic Metamaterials *Science* 331: 290, 2011

[8] A.Y. Zhu, A.I. Kuznetsov, B. Luk'yanchuk, N. Engheta, P. Genevet, Traditional and emerging materials for optical metasurfaces *Nanophotonics* 6: 452-71, 2017

[9] M.R. Esopi, M Calcagno, Q.M. Yu, Organic Ultraviolet Photodetectors Exhibiting Photomultiplication, Low Dark Current, and High Stability *Adv. Mater. Technol.* 2: 9, 2017

Nanostructuring of functional polymers for the directed assembly of nano-objects and the integration of hybrid nanosources

Safi Jradi[1,*], Ali Issa[1], Hongshi Chen[1], Xiaolun Xu[1], Aurélie Broussier[1], Dandan Ge[1], Christophe Couteau[1], Sylvain Blaize[1], and Renaud Bachelot[1]

[1] Light, nanomaterials, nanotechnologies (L2n), Technological University of Troyes, France.

*corresponding author, E-mail: safi.jradi@utt.fr

Abstract

In this work, we show a general strategy of directed assembly of nano-objects. This assembly concerns a wide range of colloidal nanoparticles including Gold, Silver, Iron Oxide, Fluorescent polystyrene and CdSe/ZnS Quantum Dots. We show the possibility to integrate nano-emitters into plasmonic nano-antennas (gold nanocubes, nano-wires), optical waveguides and optical fiber tips with a spatially controlled manner.

The integration of efficient single photons in on-chip optical circuits is one of the main challenges in quantum optics. In this context, we developed a new approach of integrating nano-emitters. This approach is based on the use of a specific home-made functional photopolymer to make nano-lithography followed by colloidal deposition in order to trap single nanoparticles with a highly selective manner. This "nano-patch" of polymer can be integrated at the extremity of plasmonic nano-antennas either by 2-photon polymerization or by near-field plasmon induced photopolymerization.

First, the multidimensional directed assembly of gold, silver, iron oxide and polystyrene nano-spheres is demonstrated. In particular, 50 nm gold nano-spheres are assembled into 1D, 2D and 3D (Figure 1).

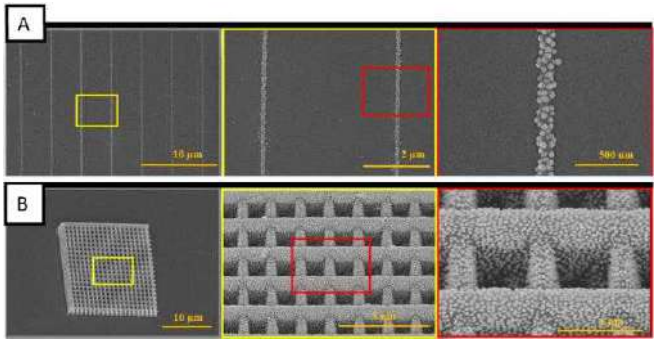


Figure 1: SEM images of gold nanoparticles assembled on continuous lines (A) and 3D woodpile microstructures (B).

This directed assembly results in the formation of monolayer of NPs with tunable coverage rate depending on the immersion time and concentration of functionalizing molecules. Thus, tuning the intensity of the plasmonic resonance band and the coupling between nano-spheres within 3D microstructures is demonstrated. The potential application of the obtained 3D microstructures in sensing and as metamaterials is illustrated.

To make it possible the integration of the functionalized polymer with sub-100 nm resolution, the photopolymer is optimized in order to chemically confine the polymerization volume (Figure 2).

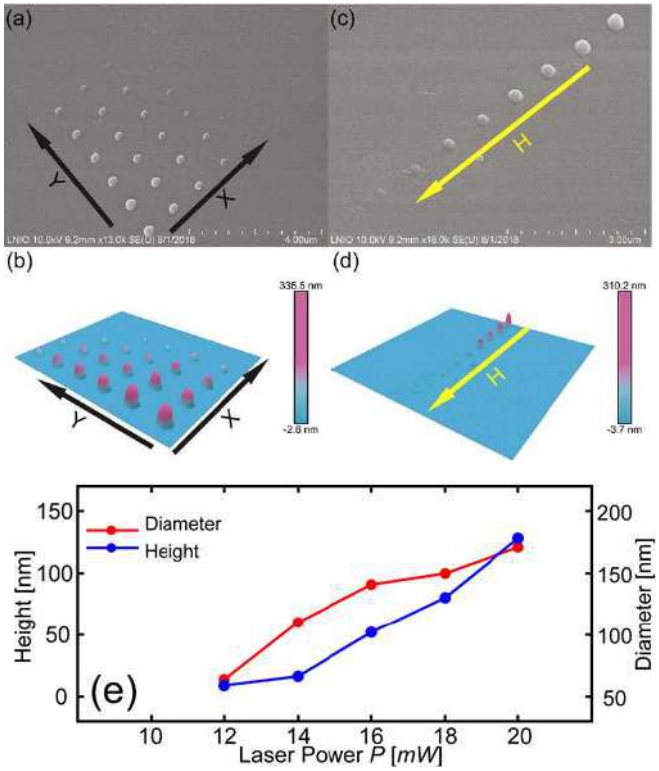


Figure 2: Polymer nano-pillars (PNPs) fabricated by two photon polymerization under various conditions: (a,b) decreased laser power and decreased exposure time, following Y and X respectively. (c,d) Adjusting the laser

focal plane. (e) Diameter and height of the PNPs as a function of the laser power.

Using this approach, single fluorescent polystyrene nanospheres (PSNS) and few quantum dots are selectively trapped by the polymer nano-pillars (PNPs) (Figure a). The same approach is used in order to fabricate new active nano-probes for scanning near field optical microscopy by trapping single fluorescent PSNS at the extremity of PNP, itself integrated at the extremity of an optical fiber (Figure 3-d and Figure 3-e).

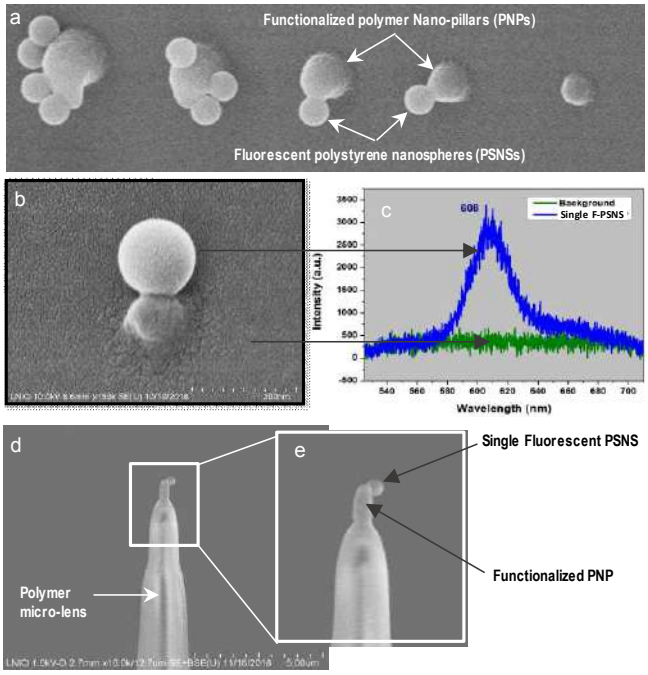


Figure 3: Examples illustrating the potential of our approach for the deterministic positioning of nano-emitters. (a) SEM image showing fluorescent polystyrene nanospheres (PSNSs) attracted by functionalized polymer nano-pillars (PNPs). The PNPs are done by two-photon polymerization at different laser powers. (b) Single Fluorescent PSNS trapped by a one PNP of 150 nm-diameter. (c) Fluorescence spectrum from the single PSNS shown in b. (d) SEM image showing single fluorescent PSNS attached at a PNP fabricated by one photon polymerization on the top of a polymer micro-lens. The polymer micro-lens is fabricated by one photon polymerization at the extremity of an optical fiber. (e) Zoom on d.

Experiments are under progress in order to realize 10 nm-polymer patchs by near-field plasmon-induced polymerization and make it possible the integration of single photon sources in the gap of plasmonic nano-antennas.

Acknowledgements

Financial support of "Fonds Européen de Développement Régional" (Projet Nano-Assemblage 3D), the "Conseil Régional Grand Est", EUR EIPHI Recherche (Projet Nano-intégration), ANR (projet Active Nanophot), NanoMat (www.nanomat.eu) by the "Ministère de l'enseignement supérieur et de la recherche" is acknowledged.

Understanding Hot Electron Generation in Plasmonic Nanocrystals and Delineating New Research Avenues

Lucas V. Besteiro[1,2], Tianji Liu[1,3], Zhiming Wang[1,*], and Alexander O. Govorov[1,3,*]

[1]Institute of Fundamental and Frontier Sciences, University of Electronic Science and Technology of China, Chengdu, Sichuan, China
[2]Institut National de la Recherche Scientifique – Énergie, Materiaux Télécommunications, Varennes, Québec, Canada
[3]Department of Physics and Astronomy, Ohio University, Athens, Ohio, USA
*corresponding author, E-mail: zhmwang@gmail.com, govorov@ohio.edu

Abstract

Plasmonic hot electrons can carry up to the full energy of the photons impinging in a nanostructure, allowing them to be emitted or injected into adjacent media. They can be used to induce secondary processes relevant in, e.g. photodetection and energy conversion processes. We present work intended to further our fundamental knowledge on hot electron excitation dynamics, provide guidelines to improve their generation efficiency and highlight new research avenues for their study.

1. Introduction

Plasmonic resonances couple strongly with light and provide great local field enhancement, so that plasmon-supporting structures have become rich scientific tools for research in Nanophotonics, [1] proving useful in a variety of technological applications. Among them, the capability of plasmonic nanocrystals and metastructures to harvest light's energy and convert into other forms of power is particularly promising, as this can be used for purposes ranging from photovoltaics to photodetection. [2,3]

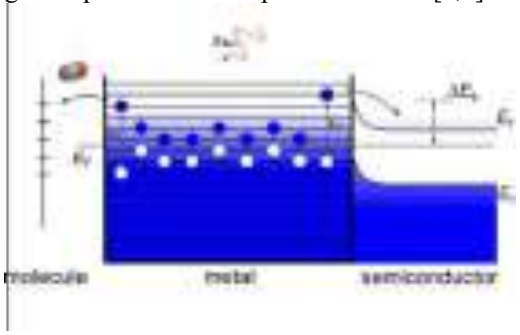


Figure 1: Diagram of a plasmonic excitation in a metal nanostructure. Hot electrons are generated at the surfaces due to the change of electronic momentum through electron-surface scattering, and can be injected into adjacent materials to contribute to photocurrents or chemical reaction rates. [5].

The generation of energetic (hot) electrons is one of the different physical mechanism by which plasmonic systems can operate this process, as these carriers can be injected into neighboring systems to contribute to the output of other photoconversion processes in the device, as depicted in Fig. 1. [4,5]

On the other hand, hot electrons typically make a small percentage of the total excited electrons in a plasmonic system, with the majority being low-energy carriers. Therefore, to take full advantage of their scientific and technological promise, we should fully understand the mechanisms underlying their fast excitation and decay, and seek ways to increase their overall energy contribution to secondary processes.

2. Model

We describe the process of generation of single-particle excited states in a plasmonic materials through the equation of motion for the density of electronic states, perturbed by an external driving field, and study its linear regime. [4-6] This model can be formulated such that it can be connected with classical methods to obtain the plasmonic response of large nanoparticles, allowing the study of hot electron generation in relatively large nanoparticles, complex geometries or systems with interacting structures. [5] Such a computational approach opens up the possibility of studying the relevance of hot spots in the generation of hot electrons, [7] and how to take advantage of them to create more efficient systems utilizing hot electrons for, e.g. photocatalysis. [5,8,9]

Importantly, this model offers a picture for the energy distribution of populated excited states in a plasmonic nanostructure that is different to the traditional one found in the literature (Fig. 2), which becomes relevant both when studying the ultrafast response of the system under short excitations [7] and when predicting the rates of hot electron generation under continuous wave excitation. [3-6,8,9]

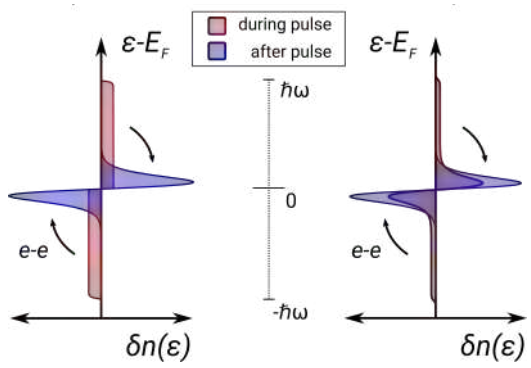


Figure 2: Contrast between a commonly used model describing the excitation of hot and warm carriers in a two-step process (left) and the picture offered by our model, with an initial excitation step that includes Drude-like low energy and hot carriers simultaneously. [4]

3. Alternative materials

The most commonly studied materials in plasmonics are noble metals, due to their sharp and strong resonances around the visible and near IR spectrum. We have theoretically explored the potential of different plasmonic materials in the context of photocatalytic applications, contrasting non-interacting nanoparticles with metamaterial structures, and materials with sharp and broad resonances, finding that materials such as TiN and ZrN can offer good hot electron generation efficiencies at cheaper prices than strongly-plasmonic materials such as Ag and Au. [8]

4. Chiral photocatalysts: circular polarization-sensitive photochemistry

The field of chiral photocatalysis focuses on creating differential reaction rates for chiral enantiomers at the molecular level. We propose a different approach, setting the differential chiral response at the scale of the plasmonic nanoparticles. Due to their large interaction cross sections and strongly chiral geometries, plasmonic complexes can show circular dichroic signals orders of magnitude larger than those of molecules, and can be used to create functional setups showing chiral plasmonic nanoparticle growth, polarization-sensitive photochemistry, and chiral recognition or separation. [9]

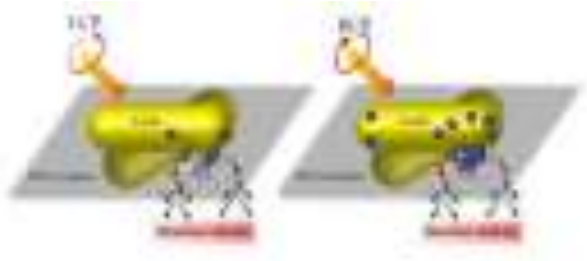


Figure 3: Diagram of the fundamental working principle of circular polarization-sensitive photochemistry. A chiral plasmonic complex will couple more strongly with the appropriately polarized CPL, increasing the rate of hot electron generation, and in turn increasing the reaction rates at its surface. [9]

5. Conclusions

Research on the generation of hot electrons has already produced useful applications and insights on their ultrafast generation. Our work elaborates on its fundamental understanding, develops useful design techniques to improve hot electron-based device efficiency and sketches different novel research directions.

Acknowledgements

L.V.B. was supported by China Postdoctoral Science Foundation (2017M622992). Z.W. was supported by National Basic Research Program of China (project 2013CB933301) and National Natural Science Foundation of China (project 51272038). A.O.G. is Chang Jiang (Yangtze River) Chair Professors of the Government of China.

References

[1] S.A. Maier, *Plasmonics: fundamentals and applications*, Springer, New York, 2007.

[2] Y.H. Jang, Y.J. Jang, S. Kim, L.N. Quan, K. Chung, D.H. Kim, Plasmonic Solar Cells: From Rational Designs to Mechanism Overview, *Chem. Rev.* 116: 14982-15034 (2016).

[3] W. Li, Z.J. Coppens, L.V. Besteiro, W. Wang, A.O. Govorov, J. Valentine, Circularly Polarized Light Detection with Hot Electrons in Chiral Plasmonic Metamaterials, *Nat. Commun.* 6: 8379 (2015).

[4] G.V. Hartland, L.V. Besteiro, P. Johns, A.O. Govorov, What's so Hot about Electrons in Metal Nanoparticles? *ACS Energy Letters* 2: 1641-1653 (2017).

[5] L.V. Besteiro, X.-T. Kong, Z. Wang, G.V. Hartland, A.O. Govorov, Understanding Hot-Electron Generation and Plasmon Relaxation in Metal Nanocrystals: Quantum and Classical Mechanisms, *ACS Photonics* 4: 2759-2781 (2017).

[6] A.O. Govorov, H. Zhang, Y.K. Gun'ko, Theory of Photoinjection of Hot Plasmonic Carriers from Metal Nanostructures into Semiconductors and Surface Molecules, *J. Phys. Chem. C* 117: 16616-16631 (2013).

[7] H. Harutyunyan et al., Anomalous Ultrafast Dynamics of Hot Plasmonic Electrons in Nanostructures with Hot Spots, *Nat. Nanotech.* 10: 770-774 (2015).

[8] T. Liu, L.V. Besteiro, Z. Wang, A.O. Wang, Generation of Hot Electrons in Nanostructures Incorporating Conventional and Unconventional Plasmonic Materials, *Faraday Discussions*, DOI: 10.1039/C8FD00145F (2018).

[9] T. Liu, L.V. Besteiro, T. Liedl, M.A. Correa-Duarte, Z. Wang, A.O. Govorov, Chiral Plasmonic Nanocrystals for Generation of Hot Electrons: Towards Polarization-Sensitive Photochemistry, *Nano Letters* 19: 1395-1407 (2019).

Metamaterial Absorber-empowered Light-harvesting Devices

Peng Yu[1], Zhiming Wang[1], and Alexander O. Govorov[1,2,*]

[1]Institute of Fundamental and Frontier Science, University of Electronic Science and Technology of China, Chengdu 610054, China
[2]Department of Physics and Astronomy, Ohio University, Athens, OH 45701, USA
*corresponding author, E-mail: govorov@ohio.edu

Abstract

Absorption of light is critical to light-trapping devices such as photovoltaics, biosensors, photodetectors, etc. Naturally occurring materials have weak absorption, while perfect absorbers based on metamaterials are developed to solve the weak light absorption of light-harvesting devices. This presentation will provide an overview of metamaterial absorber enhanced light harvesting devices and our recent research progress on metamaterial absorbers.

1. Introduction

Naturally occurring material-based absorbers are unsatisfactory for many modern photonics and optoelectronic applications due to their large impedance mismatch ($z = \sqrt{\mu / \varepsilon}$) between the material and free space. Artificial metamaterial absorbers (MAs) have opened a new door for light-harvesting devices operating from optical regimes to microwave—deliberately engineered resonators can collectively serve as a metasurface, creating impedance matching to free space with an effective electric and magnetic response. The structure is typically composed of three layers: a continuous metallic ground layer to block the light transmission, a dielectric spacer layer and periodically arranged metallic resonators. After a seminal demonstration by W. Padilla et al., this concept has been extended to other frequencies, researches on the fundamental investigation and a variety of applications are mushroomed.[1] MAs with single-band, dual-band, triple-band and more are experimentally and theoretically demonstrated. Also, according to their bandwidth, they are divided into two types—narrow and broad bandwidth. Achieving a narrow and broadband for special applications is a challenge. MA with a narrow absorption is desired for applications such as refractive index sensing, biomolecular sensing, strain sensing, coloration of imaging, data storage, and so on. On the other hand, broadband absorption is critical for applications such as photovoltaics, bolometry, photodetection, stealth technology, mechanical manipulation, etc. However, a typical line width of surface plasmon polaritons (SPPs) or localized surface plasmon is several tens of nanometers. Therefore, achieving ultra-narrow and broadband MAs is one important research direction in the field of MAs. Based on the MAs, many light-harvesting devices are demonstrated with satisfactory performance, such as sensors, solar thermophotovoltaics, imaging devices, photodetectors, infrared emitters, optomechanical converters, and single photon sources.

2. Recent progress and main results

2.1. Metamaterial perfect absorber with unabated size-independent absorption

The top resonators in MAs are critical for tuning resonant frequency, bandwidth, and maximum absorption—one can define their material, shape, and size. The maximum absorption is usually decreased as the size of the resonator changes, due to the high sensitivity of impedance matching with the medium. We experimentally demonstrated an MA using a metal square inscribed with a hollow square (MSIHS) with unabated absorption robust to resonator's size changes, as shown in figure 1(a).[2] The maximum absorption maintains above 98% as the size changes from 600 to 1500 nm in the mid-infrared region, in accordance with simulated absorption of ~100%. We adopted the equivalent circuit theory to explain the unabated absorption. The structure is less sensitive to size change while its square counterpart only shows maximum absorption at size=800 nm, as shown in figure 1(b)-(d).

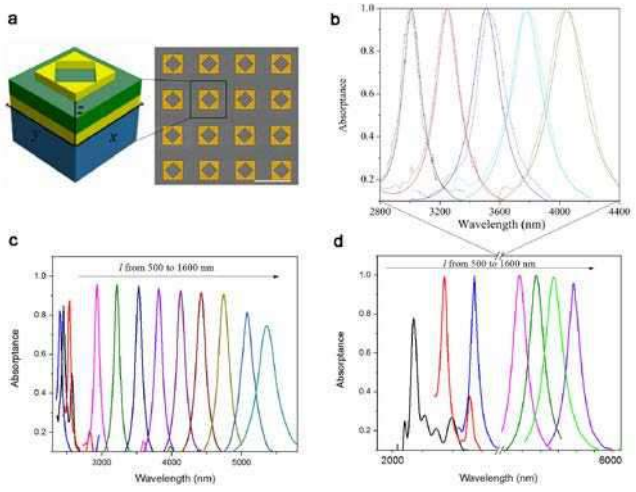


Figure 1: (a) Geometry of the MA structure; (b) Simulated (solid lines) and experimental (dashed lines) absorption of MAs with different values of *l* (left to right: 800, 900, 1000, 1100, 1200 nm); Simulated absorption spectra of MSIHS (c) and square resonator (d) with *l* changes from 500 to 1600 nm (Δ=100 nm).

2.2. Metamaterial Absorber for Photodetection

In a metal-dielectric interface, a Schottky barrier is formed. If a hot electron has enough energy, it can transport to the junction interface and then be injected into the conduction band of the semiconductor. Therefore, the photodetection bandwidth is determined by Schottky barrier height rather than the bandgap of semiconductor, as shown in figure 2.[3]

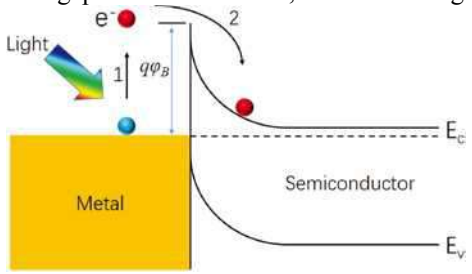


Figure 2: Energy band schematic for hot electrons transport.

We simulated a dual-band absorber, potential for multispectral plasmon-enhanced infrared photodetection, as shown in figure 3.[4] The dual-band MA is based on two gold nanorings. Two perfect peaks can be readily tailored in 3-5 μm and 8-14 μm via changing the geometric parameter of the MA.

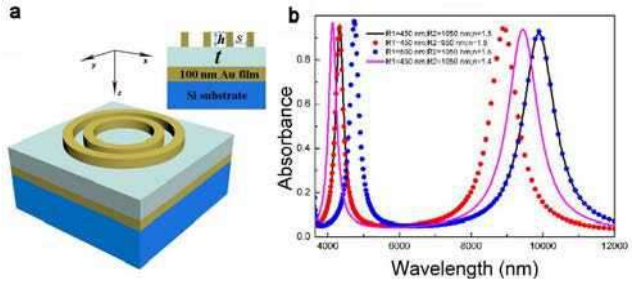


Figure 3: (a) Schematic illustration of the dual-band MAs; (b) Absorption spectra of MAs in 3-5 μm and 8-14 μm.

2.3. Ultra-broadband MA Using Space-filling Gosper Curve

By integrating different-sized or shaped geometries into a unit cell, multiple resonances can be merged into a broadband resonance; the second method is staking different dielectrics and metals as an individual bilayer and then merge resonances into a broadband one or leverage slow-light mode of the MAs; the third method is introducing lumped elements into the MAs to reduce their Q-factor in GHz region; finally, due to the localized surface plasmon resonances of metallic nanoparticles in nanocomposite, the metal-dielectric nanocomposite system can offer impedance matching of the medium to free space.
We designed an unconventional MAs by using a space-filling Gosper curve. The MA has an average absorption of 95.78% from 2.64 to 9.79 μm (bandwidth 7.15μm) across the mid-infrared region, as shown in figure 4. According to our knowledge, this is the broadest MAs among their single layer counterparts.

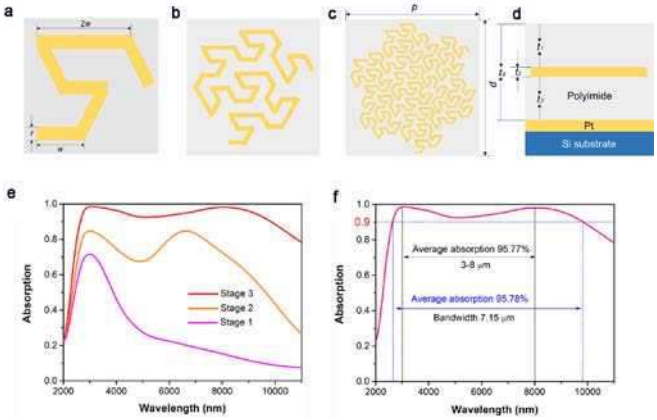


Figure 4: Broadband MA based on a space-filling Gosper curve. (a) stage 1;(b) stage 2; (c) stage 3; (d) cross-section view of the MA; (e) absorption spectra of stage 1-3; (f) detailed absorption and bandwidth of stage 3 MA.

3. Conclusions

Although MA opens an avenue for light-harvesting devices, there are still some challenges to overcome, including achieving ultra-narrow and broadband absorption, addressing the parasitic loss of metal, developing more devices via trapping light and convert it into physical effects such as force, electric, acoustics, and heat.[5-6] If these problems are addressed, the MAs will renew light-harvesting devices for industrial application.

References

[1] N. I. Landy, S. Sajuyigbe, J. J. Mock, D. R. Smith, and W. J. Padilla, "Perfect Metamaterial Absorber," Physical Review Letters **100**, 207402 (2008).

[2] P. Yu, L. V. Besteiro, J. Wu, Y. Huang, Y. Wang, A. O. Govorov, and Z. Wang, "Metamaterial perfect absorber with unabated size-independent absorption," Opt. Express **26**, 20471-20480 (2018).

[3] P. Yu, L. V. Besteiro, Y. Huang, J. Wu, L. Fu, H. H. Tan, C. Jagadish, G. P. Wiederrecht, A. O. Govorov, and Z. Wang, "Broadband Metamaterial Absorbers," Advanced Optical Materials **7**, 1800995 (2019).

[4] P. Yu, J. Wu, E. Ashalley, A. Govorov, and Z. Wang, "Dual-band absorber for multispectral plasmon-enhanced infrared photodetection," Journal of Physics D: Applied Physics **49**, 365101 (2016).

[5] X.-T. Kong, L. Khosravi Khorashad, Z. Wang, and A. O. Govorov, "Photothermal Circular Dichroism Induced by Plasmon Resonances in Chiral Metamaterial Absorbers and Bolometers," Nano Letters 18, 2001-2008 (2018).

[6] H. Zhu, F. Yi, and E. Cubukcu, "Plasmonic metamaterial absorber for broadband manipulation of mechanical resonances," Nature Photonics 10, 709 (2016).

Plasmonics with refractory TiN

Arrigo Calzolari[1*] and Alessandra Catellani[1]

[1] CNR-NANO Institute of Nanoscience, S3 Center, I-41125 Modena Italy
*corresponding author, E-mail: arrigo.calzolari@nano.cnr.it

Abstract

Using simulations from first principles we study the optoelectronic and plasmonic properties of Titanium Nitride, a refractory compound that has been proposed as a feasible route to substitute gold in harsh environment applications. The microscopic origin of the plasmon resonances and their dispersions are discussed on the basis of the analysis of the electronic structure and of the interplay between collective and single-particle excitations. The effects of nanostructuring and the formation TiN/dielectric interfaces are also deeply investigated.

Introduction

The development of plasmonic and metamaterial devices requires the research of high-performance materials alternative to standard noble metals. Recently refractory Titanium Nitride has been proposed as a valid alternative to gold, [1] even for application in harsh and high-temperature environments. Indeed, being refractory this compound exhibits extraordinary mechanical stability over a large range of temperatures (~2000°C) and pressures (~3.5 Mbar), well above the melting point of standard noble metals (~800°C). This material is furthermore resistant to corrosion and compatible with silicon technology. TiN has optical and plasmonic properties (color, electron density, plasmon frequency) very similar to gold and has been exploited for the realization of waveguides, broadband absorbers, local heaters, and hyperbolic metamaterials in connection with selected dielectric media (e.g., MgO, AlN, sapphire, etc.).

Even though the fundamental mechanical and optoelectronic properties of TiN have been largely studied so far from experimental and theoretical points of view, very little is known about its plasmonic behavior. Here, we present a fully first principles investigation, based on time-dependent density functional theory (TDDFT), of the plasmon properties of stoichiometric titanium nitride [2]. The microscopic origin of plasmonic excitations are analyzed in terms of the fundamental collective and/or radiative exctations of TiN electronic structure. From the simulation of energy-loss spectra at different momentum transfer, we derive the TiN plasmon dispersion relations that are directly accessible by experimental measurements.

We also investigated the optoelectronic characteristics of the compound in relation to the crystal phase transition, experimentally observed at very high pressure or in the case of ultrathin TiN films [3]. Finally, we furthermore analyze different interfaces between TiN and conventional semiconductors in order to describe TiN surface-plasmon polaritons for the realization of waveguides [2] or the growth of hyperbolic metamaterials for photonics [4]. The similarities and the differences with other noble metals, in particular with gold, are thoroughly discussed.

Results and discussion

We investigate the plasmon dispersion relations of TiN bulk in the different range of the electromagnetic spectrum (0-30 eV). In agreement with experimental results, TiN exibits a low-energy plasmonic resonance in the visible range at E_p=2.5 eV. The microscopic origin of this plasmonic excitation is analyzed in terms of the fundamental collective and/or radiative excitation of TiN electronic structure: TiN is not a purely free-electron metals, but a partially lossy materials where absorption processes take place over a large section of the electromagnetic spectrum.

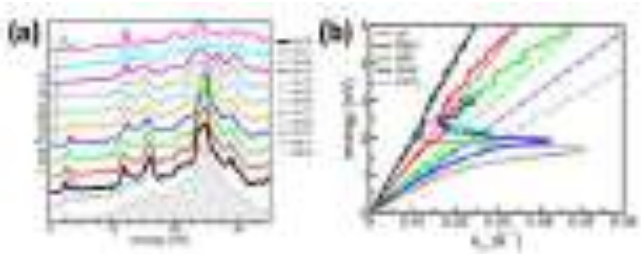


Fig. 1 (a) Simulated loss function for TiN bulk at increased transferred momentum |q| in units of 2π/a0. Dot- dashed line follows the low-energy single-particle (el-h) contribution at increasing |q|. Two sets of experimental EELS spectra (gray curves) are superimposed for comparison. (b) SPP dispersion relations at TiN/dielectric interfaces. Dashed lines are the dispersion relations for light in the corresponding dielectrics. Image adapted from Ref. [2].

The overall plasmonic properties result from a complex balance between intraband and interband transitions that act as screening term of the global electron gas. From the simulation of energy loss spectra at different momentum transfer we derivate also the plasmon dispersion of TiN (Figure 1a). We demonstrate the retention of TiN optical

proper ties against the applied pressure and we prove a universal scaling law that relates the bulk modulus and the plasmonic properties of TiN.The dissipative contributions to TiN surfaces have also a critical effect on the stability and the spatial properties of surface-plasmon polaritons (SPP) [2] at the TIN/dielectric interfaces as well as on the overall optical response of metamaterial TiN/dielectric heterostructures [4].

The simulated dispersion relations of Fig. 1b show an increase of the stability of SPP at TiN/dielectric interfaces, as the dielectric constant is increased. Air is not able to stabilize a SPP at the TiN surface, and the TiN/air interface is not suitable for realistic applications. However, as dielectric constant of non-metal part is increased, the SPP can be progressively stabilized, giving rise to oscillating waves that propagate along the metal surface, with a wavevector sensitively larger than light (i.e. non-radiative mode). MgO and nitride compounds (AlN and GaN) in particular seem the best choices for the generation of SPP in TiN, in agreement with the recent experimental studies of these interfaces.

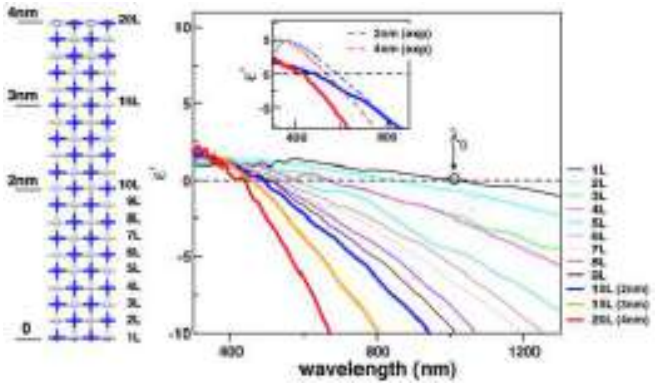


Fig. 1 (a) Side view of 1−10, 15, and 20 layer thick TiN(100) slabs used in the simulations. (b) Real part of the dielectric function as a function of the number of layers NL. Inset shows the comparison between theoretical (thick straight lines) and experimental (thin dashed lines) for 2 (blue) and 4 nm (red) films, respectively. Image adapted from Ref. [3].

Finally, by combining first-principles theoretical calculations and experimental optical and structural characterization techniques, we study the plasmonic properties of ultrathin TiN films (2-10 nm) at an atomistic level for the realization of ultrathin metasurfaces with plasmonic nonlinear properties [3]. Our results indicate a remarkably persistent metallic character of ultrathin TiN films and a progressive red shift of the plasmon energy as the thickness of the film is reduced, which is consistent with recent experimental studies (Fig. 2). Surface oxidation and substrate strain are also investigated to explain the deviation of the optical properties from the ideal case.

Conclusions

Our ab initio results confirm that at standard conditions TiN exhibits plasmonic properties in the visible regime, very close to gold, in agreement with experimental data. In contrast with malleable noble metals, the hardness of refractory ceramics allows for the exploitation of plasmonic properties also at high temperature and under pressure, conditions where standard plasmonic materials cannot be used. We also study on the plasmonic behavior of ultrathin (down to a few atomic layers) TiN films to determine the role of thickness, surface oxidation and interface strain on TiN optical properties. The observed plasmonic properties, in combination with the confinement effects, make TiN ultrathin films a promising material for the realization of plasmonic metasurfaces with enhanced nonlinearities and electrical tunability.

References

[1] G. V. Naik, V. M. Shalaev, and A. Boltasseva, “Alternative plasmonic materials: beyond gold and silver,” Adv. Mater. 25: 3264–3294, 2013.

[2] A. Catellani, A. Calzolari, Plasmonic properties of refractory titanium nitride, *Phys. Rev. B* 95: 115145, 2017.

[3] D. Shah, A. Catellani, H. Reddy, N. Kinsey, V. M Shalaev, A. Boltasseva, A. Calzolari Controlling the plasmonic properties of ultrathin TiN films at the atomic level, *ACS Photonics*: 2816-2824, 2018.

[4] A. Catellani, A. Calzolari, Tailoring the plasmonic properties of ultrathin TiN films at metal-dielectric interfaces, Opt. Mater. Exp. 9:1459-1468, 2019.

Nonlinear Chiral Response of Planar Plasmonic-Photonics Hybrid Metasurfaces

Feng Wang[1] and Hayk Harutyunyan[1,*]

[1]Department of Physics, Emory University, Atlanta, GA 30322, USA
*corresponding author, E-mail: hayk.harutyunyan@emory.edu

Abstract

Planar structures that can exhibit chiral response are highly desirable because of their facile fabrication, however fundamental challenges arising from the 2-dimensional nature of these systems prevent the generation of strong chiro-optical effects. In this work, giant enhancement of the handedness-dependent optical response in planar metallic nanostructures is shown by exploring the hybridization of plasmonic-photonic modes in a chiral metasurface.

1. Introduction

The advent of nanotechnology have made it possible to engineer sophisticated chiral platforms at the nanoscale [1, 2]. Importantly, such sample preparations require complex nanofabrication processes due to the 3-dimenasional (3D) nature of chiral materials. Over the past two decades various approaches have been implemented including fabrication of nano-helices and layer-by-layer deposition of chiral materials. 2-dimensional (2D) fabrication, on the other hand, represents a more facile sample preparation method since materials can be simply fabricated in a single step, e.g. after lithographic patterning of the substrate. However, strictly 2D objects with rotational symmetry do not possess chiral properties because the sense of twist is reversed when light propagation is reversed. This leads to a diminished chiral response for planar plasmonic samples and metamaterials. Indeed, the experimental observation of spin-dependent optical effects for right circularly polarized (RCP) and left circularly polarized (LCP) light in planar samples have been attributed to such 3D effects as the presence of the substrate and off-normal illumination conditions. Here, we demonstrate an alternative approach to enhance the chiral optical effects in planar plasmonic systems by coupling them to photonic modes of a dielectric waveguide.

2. Results and Discussion

The hybrid modes of the plasmonic-photonic metasurface exhibit some unique properties that enable not only a strong enhancement of Third Harmonic Generation (THG) but also the observation of giant spin-dependent nonlinear chiral response, Figure 1. The metasurface is based on a straightforward planar lithography process and a standard nanophotonic platform, Silicon-on-Insulator (SOI) wafer, which makes its fabrication accessible for any potential applications. By tuning the periodicity of the plasmonic arrays and geometric parameters of the chiral unit cell facilitates full control of the spin-dependent optical response.

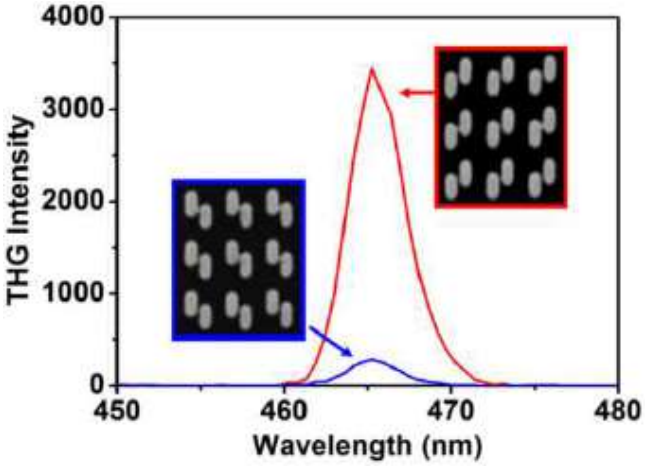


Figure 1: Chirality-dependent response of third harmonic generation in nonlinear hybrid metasurface.

Our demonstration opens up a novel approach for enhancing the chiral optical properties in metamaterials and nanostructures by coupling them to judiciously engineered photonic modes of the substrate. We believe that our results will pave the way for better fundamental understanding of planar chirality and spin-dependent optical response at the nanoscale.

References

[1] J. T. Collins, C. Kuppe, D. C. Hooper, C. Sibilia, M. Centini, V. K. Valev, Adv. Opt. Mater. 2017, 5, 1700182.

M. Hentschel, M. Schäferling, X. Duan, H. Giessen, N. Liu, Sci. Adv. 2017, 3, e1602735

Anisotropic metal nanostructures

Yurii K. Gun'ko*[1,2], Valerie Gerard[1], Daniel K. Kehoe[1]

[1]School of Chemistry, University of Dublin, Trinity College, Dublin 2, Ireland
[2] BEACON, Bioeconomy Research Centre, University College Dublin, Dublin 4, Ireland
*corresponding author, E-mail: igounko@tcd.ie

Abstract

Metal nanoparticles are very interesting and important nanomaterials with unique properties and a number of applications. The main goal of our work is to develop new anisotropic metal nanomaterials and explore their properties and potential uses. We have prepared a range of homo- and bi-metallic noble metal based anisotropic nanomaterials with a complex morphology. The materials have been characterized by various instrumental techniques and their biological behavior and catalytic activities in selected reactions have been tested. We believe that new nanomaterials developed in this work will find various applications in biomedical research, photonics and energy science.

1. Introduction

The optical properties of metal nanoparticles are highly dependent on their size and shape and as a result anisotropic plasmonic nanostructures have attracted much attention in recent years. These nanomaterials have been widely investigated due to their unique optical and electronic properties enabling important potential applications including biological sensing, catalysis, drug delivery energy harvesting and optoelectronics amongst others [1-5]. The main attraction of metal nanostructures resides in the surface plasmon resonance (SPR) phenomenon, which can be tuned both in wavelength and intensity by varying the size, shape and composition of metal nanoparticles. That collective oscillation of electrons creates a strong enhancement of the electromagnetic field in the vicinity of the nanoparticles upon photo-excitation. This in turn is the basis for many applications. It has been successfully employed to enhance Raman signals in Surface Enhanced Raman Spectroscopy (SERS). Raman spectroscopy is a characterisation technique based on the inelastic scattering of photons by certain molecules. The photon sets the material into vibration and is scattered with a different frequency, or energy, and that shift is measured. SERS arises from the presence of metal nanoparticles on the substrate. The SPR-induced enhancement of the electromagnetic field in the vicinity of the surface strongly enhances the vibrational modes. A charge-transfer complex may also be formed between the surface and the analyte molecule, with electronic transitions in the visible range. It should be noted that the SERS effect does not occur on smooth surfaces, but only on rough, nanoparticulate ones. Although initially developed with spherical nanoparticles, SERS has been proven to be influenced by the particle size and shape [1-3]. Furthermore, there is a growing interest for gold nanoparticles in the fields of drug delivery and biological imaging. They are indeed a biologically inert material which also provides opportunities for functionalization as well as plasmonic imaging [4]. They can also be triggered by an external stimulus to release their cargo or produce heat [5]. The main aim of our work is the synthesis of a variety of anisotropic metal nanostructures and the investigation of their properties for potential biomedical and catalytic applications.

2. Results and Discussion

A variety of anisotropic nanostructured materials were produced based on the reduction of silver and gold salts, in a rapid synthesis at room temperature. TEM images of some examples of our anisotropic plasmonic nanostructures are shown in Fig. 1 below.

Silver nanoprisms were successfully synthesised and coated with a protective layer of gold according to published procedure [6]. As-synthesised silver nanoprisms were also used as templates to form gold nanorings. This was achieved by depositing a layer of gold at the edges of silver nanoprisms and subsequently etching away the remaining silver. It resulted in the formation of closed shapes from triangles to circles, best described as toroidal polyhedra. In common parlance, a ring designates a band-like object with a vacant centre, usually of circular shape. By extension, the closed triangles may be viewed as degenerated rings with nanometric dimensions. For simplicity, such materials are referred to as nanorings.

Addition of a large amount of gold and ascorbic acid in excess to initial silver nanoprisms resulted the formation of a hollow triangular nanostructure which was designated as nanobox. The postulated growth mechanism for these nanoboxes is through the galvanic replacement of silver by gold despite the presence of excess ascorbic acid. After the initial oxidation, Ag^+ ions are believed to be co-reduced with $HAuCl_4$ by ascorbic acid and to form an alloy at the Au/Ag interface that reforms the particle shape while leaving a hollow space in the middle.

Then the deposition of gold onto silver nanowires was achieved through galvanic replacement using a solution of chloroauric acid which was added to the nanowires resulting in gold/silver nanotubes.

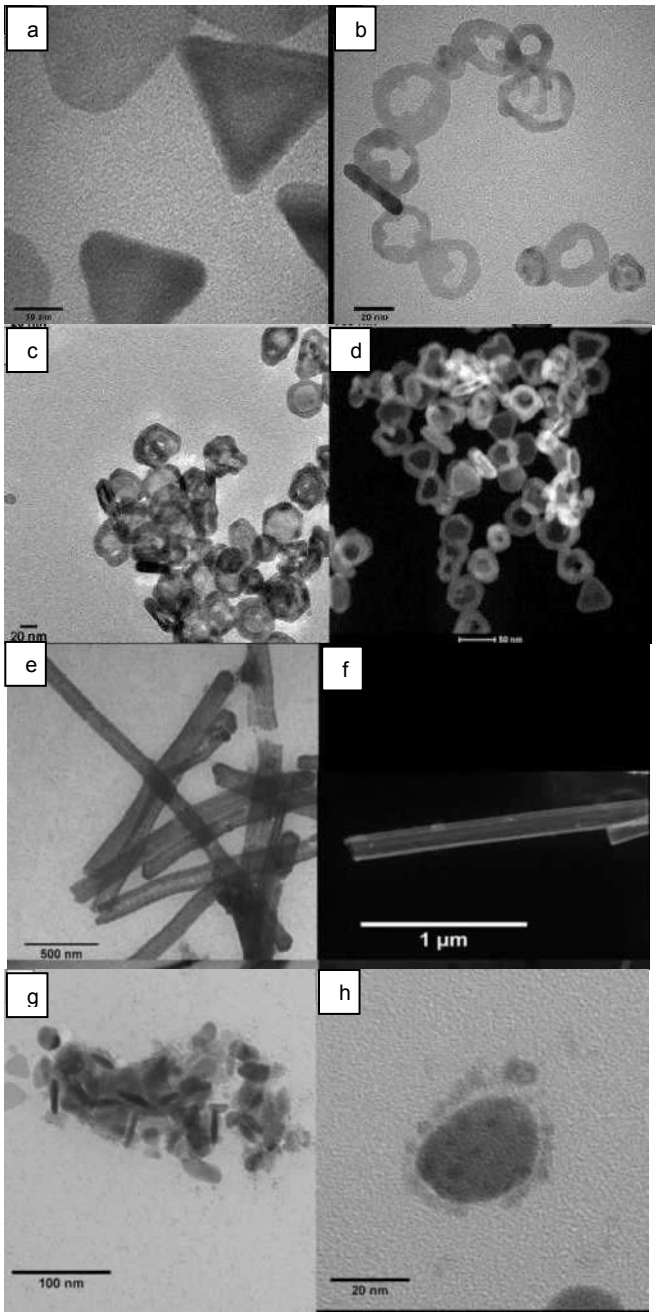


Figure 1: TEM images of (a) gold-coated silver nanoprisms; (b) gold nanorings; (c), (d) gold-silver nanoboxes; (e), (f) gold-coated silver nanotubes; and (g), (h) quantum dot-gelatin-silver nanoprisms hetero-nanostructures.

The coating of silver nanoprisms with gelatin was performed in order to improve their biocompatibility and provide a platform for functionalisation. After that CdTe quantum dots (QDs) were incorporated into the gelatin shell of the coated nanoprisms resulting in new QD-gelatin-silver nanoprisms hetero-nanostructures.

We have also developed new tunable synthesis of water soluble ultrathin AuAg nanowires. These nanowires were produced via a new two step approach involving the formation of nanowire templates during an aging period and the subsequent formation of thicker nanowires by a solvent driven fusion and wetting following a dilution step. By using temperature control the protocol was further optimised, reducing the poly-dispersity of the products and shortening the reaction time. These 1D ultrathin AuAg nanomaterials exhibit remarkable catalytic performance for the electro oxidation of ethylene glycol. Then we have developed ligand induced chiral modification of these 1D ultrathin materials using a ligand exchange method.

Finally, we have developed and investigated novel plasmonic-excitonic nanowire-quantum dot hybrid structures in which the quantum dots form a helical self-assembly around the metal nanowires.

3. Conclusions

We have prepared a range of anisotropic gold and silver nanostructures and investigated the influence of a number of parameters on their final shape and size. Deposition of gold on silver templates and galvanic replacement reactions led to the formation of hollow nanostructures. Precise control over the ratio of gold to silver allowed us to selectively retain or remove the initial silver nanoparticle. Gelatin was used to prepare a series of nano-composites with CdTe QDs and silver nanoprisms which have been characterised in terms of their cellular behaviour and structural features. We believe that new nanomaterials developed in this work will find applications in biomedical research, photonics and energy science.

Acknowledgements

Acknowledgements belong here. The authors would like to acknowledge the Science Foundation of Ireland (Grant SFI 12/IA/1300), and BEACON, Bioeconomy Research Centre (SFI 16/RC/3889) for supporting this work.

References

[1] S. E. J. Bell, N. M. S. Sirimuthu, Quantitative surface-enhanced Raman spectroscopy, *Chem. Soc. Rev.*, 37: 1012-1024, 2008.

[2] A.O. Govorov, Y.K. Gun'ko, J.M. Slocik, V.A. Gerard, Z. Fan, R.R. Naik, Chiral nanoparticle assemblies: circular dichroism, plasmonic interactions, and exciton effects, *J. Mater. Chem*., 21: 16806-16818, 2011.

[3] A. Ben-Moshe, B.M. Maoz, A.O. Govorov, G. Markovich, Chirality and chiroptical effects in inorganic nanocrystal systems with plasmon and exciton resonances, *Chem. Soc. Rev.*, 42: 7028-7041, 2013.

[4] L. A. Austin, B. Kang, C.-W. Yen, M. A. El-Sayed, Plasmonic Imaging of Human Oral Cancer Cell Communities During Programmed Cell Death by Nuclear Targeting Silver Nanoparticles, *J. Amer. Chem. Soc.,* 133: 17594-17597, 2011.

[5] J. H. Park, G. von Maltzahn, L. L. Ong, A. Centrone, T. A. Hatton, E. Ruoslahti, S. N. Bhatia, M. J. Sailor, Cooperative Nanoparticles for Tumor Detection and Photothermally Triggered Drug Delivery, *Adv. Mater.*, 22: 880-885, 2010.

[6] D. Aherne, M. Gara, J. M. Kelly, Y.K. Gun'ko, From Ag nanoprisms to triangular AuAg nanoboxes. *Adv. Func. Mater*. 2010, 20, 1329-1338.

Wafer-scale gold nanocube arrays for tuneable absorption and refractive-index sensing

Shaolong Wu[1*], Liang Li[1], Liujing Li[1], Zhongyuan Zhou[1], Su Shen[1], and Xiaofeng Li[1]

[1] School of Optoelectronic Science and Engineering, Soochow University, Suzhou 215006, China.
*corresponding author, E-mail: shaolong_wu@suda.edu.cn

Abstract

Here, we have cost-efficiently prepared the large-area Au nanocube arrays (NCAs) only with the help of electrostatic force interacting. This method provides a flexible way for obtaining the controlled Au NCAs with various fill fractions and sizes, leading to a significant and tuneable light absorbance from visible to near-infrared spectrum. Besides, the as-prepared Au NCAs used as a prototype refractive-index (RI) sensor perform excellent stability and a sensitivity over 560 nm per RI unit.

1. Introduction

Over the last one to two decades, nanoscale particles, especially metallic nanostructures, have attracted extreme attention for exploiting new applications due to the novel properties strongly distinguished from the bulk counterparts. In particular, two-dimensional (2D) arrays of the metallic nanoparticles have been applied to a wide range of fields, involving biosensors, solar cells, photodetectors, nonlinear optics, and surface-enhanced Raman scattering (SERS). In these systems, precisely controlling the intervals between neighbouring elements in nanoscale is the key point for the specific applications. Currently, much more endeavours have been devoted to the synthesis of a wide range of nanoparticles in various shapes, sizes, and materials; nevertheless, less attention has been paid for the fabrication of large-area nanoparticle arrays with a reduced-cost method.

The patterned template, made from these techniques such as electron beam lithography, focused ion beam, and double-exposure interferometry, are the most common approaches to prepare 2D arrays of nanostructures. These methods usually involve a top-down nanofabrication technology integrated with evaporation deposition and lift-off processes. Nevertheless, direct etching and nanolithography methods are resisted by the high cost of experimental instruments and the scalability to large area. In addition, evaporation deposition technology has its limitation on roughness and choice of target materials.

Here, low-cost realization of the Au nanocube arrays (NCAs), via directly assembling the as-synthesized colloidal Au NCs atop of a polyelectrolyte (PE) spacer without any lithographic process, is reported. When these Au NCAs are coupled to a metallic film, the optical resonance inside the gap can excited and manipulated from visible to near-infrared spectrum by varying the Au NC size as well as the spacer thickness, leading to a narrow-band tuneable absorbance. Furthermore, a prototype refractive-index sensor based on the prepared Au NCAs is demonstrated to be with a considerable sensitivity and excellent stability.

2. Results and Discussion

Fig. 1a illustrates the diagrammatic drawing of the Au NCAs atop an Au film with a spacer. Fig. 1b shows the top-view SEM image of the prepared Au NCAs with fill fraction (*ff*) of ~12.4%. High-resolution SEM image of the as-synthesized Au nanocube powder centrifuged from colloidal solution is also given in the set of Fig. 1b, from which one can see that the nanocubes are relatively uniform in size and shape. The measured reflectance spectrum of the prepared Au NCAs is plotted in Fig. 1c, and an obvious and narrow-band reflection dip is observed.

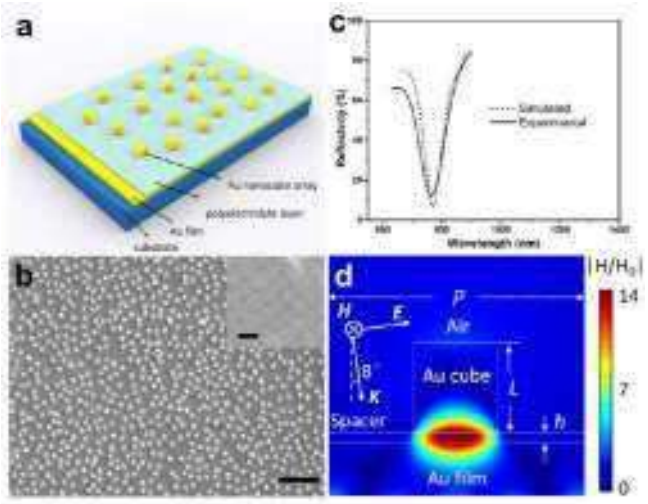


Figure 1: Experimental and simulated result of Au nanocube arrays (NCAs). (a) Schematic of the disordered Au NCAs assembled atop an Au film with a polyelectrolyte spacer. (b) SEM image of the prepared NCA with a surface fill fraction of 12.4%, an edge length of 85 nm and a spacer of 8 nm. The scale bar is 1 μm. Inset is the high magnification SEM image of nanocubes and the scale bar is 100 nm. (c) Measured reflection spectra (solid line) of the prepared disordered Au NCAs coupled with Au film, with a comparison of the simulated ordered one (dotted line). (d) Cross profiles of the normalized magnetic field of the simulation cell at wavelength of 770 nm.

To reveal the underlying reason for the reflection dip, we performed the optical simulation and examined the

electric/magnetic field profiles. The Au NCAs are simplified to be periodically arranged in the simulation, and the main structure parameters of the simulated unit are indicated in Fig. 1d. One can see that the two reflection dips are nearly overlapped, implying the cause for the observed reflection dip can be explained by the optical simulation. Fig. 1d shows that the normalized magnetic field ($|H/H_0|$) is intensively confined inside the gap, while there is no electromagnetic coupling between the neighbouring nanocubes, that is, the optical resonance inside the gap (named as plasmonic gap mode) is excited and the in-plane coupling mode is not excited at the present conditions.

Furthermore, we demonstrated the superiority of the Au NCAs relative to the Au nanorod and nanosphere arrays, and observed that there is no obvious refection dip for the two references [1]. The tuneable absorption is realized by varying the spacer thickness and the edge length of Au nanocubes. It should be noted that when the *ff* increases, the reflection dip does not shift, but the value of the reflection dip gradually decreases.

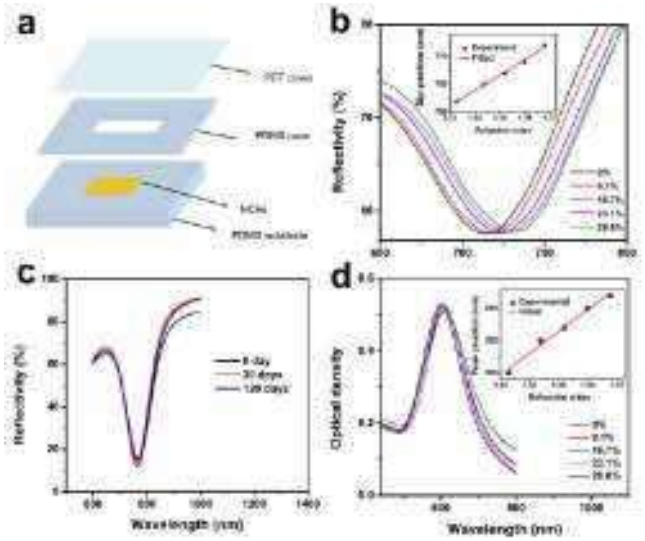


Figure 2: (a) Schematic configuration of a prototype device base on the Au NCAs for the bulk solution sensing. (b) Measured reflection spectra of the prepared sensor measured in the solution of different glucose concentrations. (c) Reflectance spectra of the prepared sensor repeatedly measured for three times. (d) The sensing performance of the Au NCs dispersed in an aqueous solution with different glucose concentrations as a comparison.

Finally, we fabricated a prototype device for refractive index sensing based on the above-mentioned Au NCAs. The working principle of the sensor is the optical resonance dependent on the background-material refractive index (n_0). As shown in Fig. 2a, when the PDMS cave is filled with various solutions, the pre-loaded Au NCAs would be surrounded by different n_0. Here we discretely used aqueous solutions of glucose in different concentration (i.e., 0, 9.1%, 16.7%, 23.1% and 28.6%), the corresponding refractive indices were 1.3328, 1.3437, 1.3519, 1.3597 and 1.3676, respectively. When the Au NCAs with L = 85 nm, h = 8 nm and *ff* = 5.5% are employed, we observed a red shift in the reflection dip as the glucose concentration increases (as shown in Fig. 2b), similar to previous refractive-index sensor [2]. The fitted linear relationship is shown in the inset of Fig. 6b, and a sensitivity (S) of 560 nm/RIU is calculated.

To assess the stability of the Au NCAs based sensor, the reflectance spectra of one device was repeatedly tested after being preserved for 0 day, 30 days and 120 days, separately. Fig. 2c show that all the dip positions and values are nearly the same, implying that the device possess excellent stability and repeatability. As a comparison, the sensing performance from the colloidal Au NC solution with varying glucose concentrations is also evaluated via optical density spectrum (as shown in Fig. 2d). One can see the peak wavelength of the OD spectrum shows a slight redshift as n_0 increases. A much smaller S (341 nm/RIU) for colloidal Au NC solution confirms the advanced performance for the Au NCAs-based sensor.

3. Conclusions

We have facilely fabricated Au nanocube arrays and investigated its potential application for refractive index sensing due to the strong optical resonance between the upper Au nanocube arrays and the lower Au film. The gap-mode resonance can be tailored by controlling the cube sizes and the gap thicknesses according to the reflectance dip change. The surface fill fraction can also be tuned by controlling the nanocube solution concentration. Long-term stability and repeatability for the optical response can be achievable. The refraction index sensing experiments show that the sensitivity can be up to 560 nm/RIU. This work gives a cost-efficient route to prepare the large-area Au nanocube arrays and point out a potential application.

Acknowledgements

This work is supported by National Natural Science Foundation of China (61575133, 61675142, 61875143), China Postdoctoral Science Foundation (2017M611898, 2018T110549), Natural Science Foundation of the Jiangsu Higher Education Institutions of China (17KJA480004), Natural Science Foundation of Jiangsu Province (BK20181169, BK20180042).

References

[1] L. Qin, S. Wu, J.-H. Deng, L. Li, X. Li, Tunable light absorbance by exciting the plasmonic gap mode for refractive index sensing, *Opt. Lett.* 43: 1427–1430, 2018.

[2] W. C. Shih, G. M. Santos, F. Zhao, O. Zenasni, M. M. P. Arnob, *Nano Lett.* Simultaneous Chemical and Refractive Index Sensing in the 1–2.5 μm Near-Infrared Wavelength Range on Nanoporous Gold Disks, 16: 4641–4647, 2016.

Super-hydrophobic Surface-enhanced Raman Scattering platform

In Yee Phang

Institute of Materials Research and Engineering, Agency for Science, Technology and Research (A*STAR), 2 Fusionopolis Way, Innovis, #08-03, Singapore 138634.

E-mail: phangiy@imre.a-star.edu.sg

In this seminar, I will present our team's effort in fabricating a stable super-hydrophobic surface-enhanced Raman Scattering (SH-SERS) platform for trace molecular sensing [1-2]. The design strategy of our SH-SERS focuses on integrates the intense electromagnetic field confinement generated by highly crystalline Ag nanocubes or nanowires with a superhydrophobic surface capable of analyte concentration to lower the molecular detection limit. These single crystalline Ag nanocubes or nanowires are assembled using the Langmuir-Blodgett technique to create surface roughness followed by chemical functionalization with perfluoro-decanethiol. The resulting substrate has an advancing contact angle of >150° and an analyte concentrating factor of 10-100 fold for water and 8-fold for toluene, as compared to a hydrophilic surface. Our protocol is a general method that provides a simple, cost-effective approach to develop a stable and uniform superhydrophobic SERS platform for trace molecular sensing.

Reference

[1] H.K. Lee, Y.H. Lee, Q. Zhang, I. Y. Phang, J. M. R. Tan, Y. Cui, X. Y. Ling. *ACS Appl. Mater. Interfaces* **2013**, *5*, 11409.

[2] X. Li, H. K. Lee, I. Y. Phang, C. K. Lee, X. Y. Ling. *Anal. Chem.* **2014**, 86, 10437.

Generation, thermalization and extraction of hot carriers in metallic nanoparticles

Johannes Lischner

Department of Materials,
Imperial College London, London, United Kingdom
*corresponding author, E-mail: j.lischner@imperial.ac.uk

Abstract

Plasmon-induced hot carriers in metallic nanostructures have attracted significant attention as they can be harnessed for applications in sensing, photovoltaics and photocatalysis. To study hot carrier properties, I have developed a material-specific approach that combines quantum-mechanical calculations of large nanoparticles with a classical electrodynamic treatment of localized surface plasmon excitations. I have used this approach to study hot-carrier generation in both mono-metallic nanoparticles and also in bi-metallic core-shell nanoparticles. Combining this approach with the Boltzmann equation and Marcus theory of electron transfer allows me to capture also the thermalization of hot carriers and their extraction.

1. Introduction

There has been significant interest in energetic or "hot" carriers generated from the decay of localized surface plasmons in metallic nanostructures. Potential applications of such systems involve sensing, optoelectronics, photovoltaics and also photocatalysis. Recently, there has been an active debate about the physico-chemical origin of the photocatalytic activity of metallic nanostructures. Specifically, the question is whether hot carriers are relevant to nanoplasmonic photocatalysis or if experimental observations can be explained by the local heating of the nanoparticle leading to enhanced rates of chemical reactions according to the Arrhenius law.

2. Methods

In this section, we describe the techniques used to model hot carrier generation in metallic nanoparticles as well as hot carrier extraction and thermalization.

To calculate the rate of hot carrier generation in an illuminated nanoparticle, we employ Fermi's golden rule. To calculate the electron-plasmon coupling constant, we use the plasmon potential from the quasistatic approximation and electron wavefunctions from a spherical well model of the nanoparticle, where the depth of the well is adjusted to reproduce the experimentally measured workfunction of the material. Finally, we obtain transition linewidths by adding the quasparticle linewidths of electrons and holes involved in the transition which include contributions from electron-electron and electron-phonon interactions [1]. To model core-shell nanoparticles, a spherical two-step potential is solved where the energy difference between the potential steps is given by the experimentally measured contact potential between the two metals [2].

To study the photocatalytic activity of nanoplasmonic systems, we focus on water splitting. The total number of photocatalytically active electrons is obtain by calculating the number of hot electrons with energies larger than the redox potential of the hydrogen evolution reaction. Similarly, photocatalytically active holes must have an energy lower than the oxygen evolution reaction.

To study the thermalization and extraction of hot carriers, we solve Boltzmann's equation. We include scattering terms that capture the effects of electron-electron and electron-phonon interactions. We assume a continuous wave illumination. We also include the extraction of hot carrier due to redox reactions at the surface of the nanoparticle. Electron transfer is described using Marcus theory.

2.1. Results

Figure 1 shows the total rate of plasmon-induced hot carriers that are photocatalytically active for water splitting. Results are shown for different materials and different dielectric environments. We find that hot holes are predominantly produced by transition-metal nanoparticles, such Ag and Au. In contract, alkali and alkaline-earth nanoparticles exhibit the best performance in producing hot electrons for the hydrogen evolution reaction.

Figure 2 compare the performance of various bimetallic core-shell nanoparticles for water splitting. We find that core-shell systems perform better than mono-metallic systems, which are the diagonal elements. In particular, core-shell nanoparticles with thin transition-metal shells and alkali metal core exhibit the best performance.

3. Conclusions

We have developed a new material-specific approach to study the generation, thermalization and extraction of hot carrier in nanoplasmonic materials. In particular, we have studied the performance of mono-metallic and bi-metallic core-shell nanoparticles for water splitting and have discovered novel material combinations as promising photocatalysts.

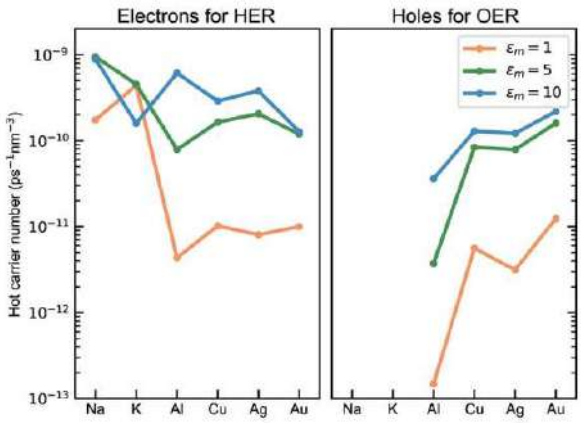


Figure 1: Total number of plasmon-induced hot electrons and hole in different mono-metallic nanoparticles that can trigger the hydrogen evolution reaction (HER) and oxygen evolution reaction (OER), respectively. Results are shown for different dielectric environments.

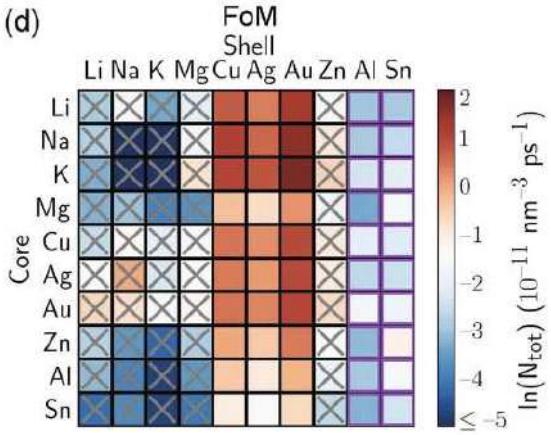


Figure 2: Comparison of different bi-metallic core-shell nanoparticles for water splitting. The figure of merit (FOM) is given by the lower of the hot electron and hot hole generation rates. Crosses denote systems which are not stable in aqueous environments and purple frames indicate systems where the formation of an oxide layer is expected.

Acknowledgement

I gratefully acknowledge the contributions of my students

Stefano Dal Forno, Lara Roman Castellanos and Luigi Ranno.

References

[1] S. Dal Forno, L. Ranno, J. Lischner, Material, Size, and Environment Dependence of Plasmon-Induced Hot Carriers in Metallic Nanoparticles, *J. Phys. Chem. C* 122: 8517–8527, 2018.

[2] L. Ranno, S. Dal Forno, J. Lischner, Computational design of bimetallic core-shell nanoparticles for hot-carrier photocatalysis *npj Computational Materials* 4:31, 2018.

VIS-UV resonance Raman scattering study of chemical enhancement mechanism in surface enhanced Raman spectroscopy (SERS)

Jayeong Kim[1], Tomke E. Glier[2], Benjamin Grimm-Lebsanft[2], Sören Buchenau[2], Melissa Teubner[2], Florian Biebl[2], Nam-Jung Kim[3], Heehun Kim[3], Gyu-Chul Yi[3], Michael Rübhausen[2], and Seokhyun Yoon[1].

[1]Department of Physics, Ewha Womans University, Seoul, Korea
[2]Institut für Nanostrukturforschung, Center for Free Electron Laser Science (CFEL), Universität Hamburg, Germany
[3] Department of Physics and Astronomy, Seoul National University, Seoul, Korea
*corresponding author, E-mail: syoon@ewha.ac.kr

Abstract

Surface enhanced Raman scattering (SERS) for amplification of Raman signals has been studied for several decades [1-3]. Nevertheless, a mechanism of chemical enhancement, one of the mechanisms of SERS, is not yet completely understood [4-7]. We investigated the chemical contribution of the SERS effect of 4-Mpy molecules deposited on ZnO nanostructure by resonance Raman scattering with incident photon energy ranging from 1.7 eV to 5.7 eV. Through this study, we provide theoretical and experimental means to study chemical enhancement mechanism for SERS.

1. Introduction

SERS is a tool that amplifies small Raman signals [4-9]. In particular, many studies have been made as a very attractive tool in that signals from single molecules can be detected. SERS has two major mechanisms. One is the electromagnetic mechanism originated from surface plasmon resonance. This occurs when the energy of excitation laser matches the surface plasmon energy of a metal substrates and is most strong at hot spots between metal substrates, leading to a very large enhancement factor up to 10^{12} [8]. The other is the charge transfer enhancement, also called chemical enhancement, which is associated with charge transfer between the molecule and the substrate [9-12]. Although there have been a lot of studies on SERS, the chemical mechanism has yet to be completely clarified. This study suggests theoretical and experimental methods to study the mechanism of chemical enhancement of SERS in depth. We have used semiconductor substrates in order to exclude the contribution from surface plasmon resonance as Raman enhancement mechanism.

2. Results

Figure 1 shows Raman spectra of 4-MPY molecules adsorbed on ZnO nanostructure as a function of excitation energy. The range of excitation energies is from 1.96eV to 5.64eV, which contains both the transition energy between the highest occupied molecular orbital (HOMO) of the molecule and the conduction band (CB) of the ZnO (in UV range) and the transition energy between the valence band (VB) of the ZnO and the lowest unoccupied molecular orbital (LUMO) of the molecule (in visible range).

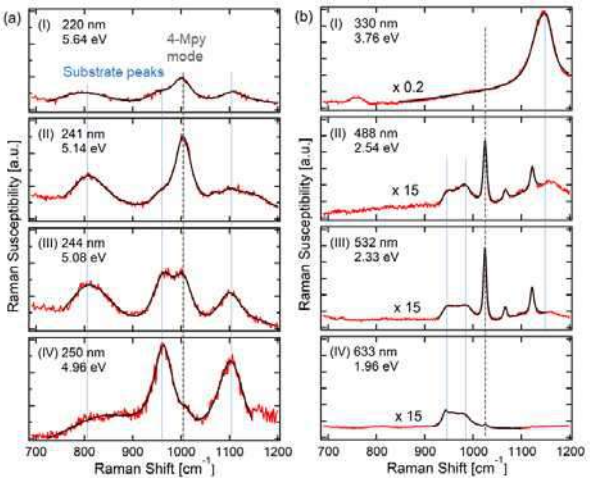


Figure 1: (a) Raman spectra of a monolayer of 4-Mpy deposited on nanostructured ZnO rod arrays for four exemplarily laser energies in the deep UV range between 5.64 eV (220 nm) and 4.96 eV (250 nm). (b) Raman spectra of a monolayer of 4-Mpy deposited on ZnO rod arrays for excitation energies covering from mid UV to visible spectral range.

Figure 1 also shows that the ring-breathing mode of molecules near 1000 cm^{-1} is greatly increased at 5.14 eV excitation, starting from 4.96 eV. In the visible range, the signal gradually increases from 2.54 eV to 2.33 eV. However, the signal is not observable at 3.76 eV and at 1.96 eV. We observed that the Raman intensities of 4-Mpy peaks at 5.14 eV in the UV region is about 20 times

larger than that in the visible region, due to resonance transition of HOMO to LUMO of 4-MPY molecule itself.

3. Discussion

We also calculated the Raman susceptibility profile by using the four-photon Green's function [13] in the resonant Raman scattering process, which showed a good agreement with our experimental results as shown in Fig 2 (a). As expected, we observe two major resonances that visually convert from molecular HOMO to CB and from semiconductor VB to molecular LUMO in UV. Each arrow in Fig. 2 (a) is the result of each charge transfer transition in the same color in Fig. 2 (b). Surprisingly, the UV resonance consists of two contributions. These two are ~400 meV apart from each other as shown in Fig. 2 (a). Considering the energy difference shown in Fig. 2 (b), we could see that the charge transfer from 4-Mpy HOMO to the excitonic state of ZnO exhibits a very strong Raman signal.

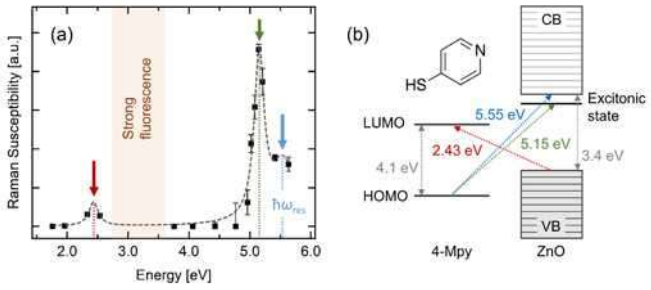


Figure 2: (a) SERS Raman susceptibility (Intensity of the Raman response of a 4-Mpy monolayer on ZnO rods) of the mode at 1000 cm^{-1} as a function of excitation energy. (b) Pictorial model of the investigated system, outlining the observed resonances in (a) due to the indicated optical transitions.

4. Conclusions

We studied the chemical SERS effect of 4-Mpy adsorbed on semiconducting ZnO rods by resonant Raman spectroscopy in the ultraviolet and visible spectral region. We describe the observed resonance using a model based on a four-photon Green's function calculation. In addition to the two resonances of 5.15 eV and 5.55 eV in UV, one resonance is observed at about 2.43 eV. The strongest resonance is found at 5.15 eV ultraviolet radiation and is the result of transitioning to an exciton-related state below the ZnO CB.

Our findings suggest that consideration of every possible charge transfer route should be needed for studying chemical enhancement of SERS and from the consideration deeper understanding of enhancement mechanism can be attained.

Acknowledgements

This work is supported by Basic Science Research Program (NRF-2016R1D1A1B01009032, NRF - 2018R1A6A1A03025340) through the National Research Foundation of Korea (NRF).

References

[1] Stiles, P. L., Dieringer, J. A., Shah, N. C., and Van Duyne, R. P. Surface-Enhanced Raman Spectroscopy. *Annu. Rev. Anal. Chem*. 1:601-626, 2008.

[2] Nie, S. Probing Single Molecules and Single Nanoparticles by Surface-Enhanced Raman Scattering. *Science.* 275: 1102–1106, 1997.

[3] Kneipp, K., Wang, Y., Kneipp, H., Perelman, L. T., Itzkan, I., Dasari, R. R., and Feld, M. S. Single Molecule Detection Using Surface-Enhanced Raman Scattering (SERS). *Phys. Rev. Lett.* 78: 1667–1670, 1997.

[4] Tian, Z.-Q., and Ren, B. Adsorption and reaction at electrochemical interfaces as probed by surface-enhanced Raman spectroscopy. *Annu. Rev. Phys. Chem.* 55: 197–229, 2004.

[5] Zhang, B., Wang, H., Lu, L., Ai, K., Zhang, G., and Cheng, X. Large-Area Silver-Coated Silicon Nanowire Arrays for Molecular Sensing Using Surface-Enhanced Raman Spectroscopy. *Adv. Funct. Mater*. 18: 2348–2355, 2008.

[6] Chan, S., Kwon, S., Koo, T.-W., Lee, L. P., and Berlin, A. A. Surface-Enhanced Raman Scattering of Small Molecules from Silver-Coated Silicon Nanopores. *Adv. Mater*. 15: 1595–1598, 2003.

[7] Wang, X. T., Shi, W. S., She, G. W., Mu, L. X., and Lee, S. T. (2010). High-performance surface-enhanced Raman scattering sensors based on Ag nanoparticles-coated Si nanowire arrays for quantitative detection of pesticides. *Appl. Phys. Lett*. 96: 053104, 2010.

[8] David, C., Guillot, N., Shen, H., Toury, T., and Chapelle, M. L. de la. SERS detection of biomolecules using lithographed nanoparticles towards a reproducible SERS biosensor. *Nanotechnology*. 21: 475501, 2010.

[9] Wang, X., Shi, W., She, G., and Mu, L. Surface-Enhanced Raman Scattering (SERS) on transition metal and semiconductor nanostructures. *Phys. Chem. Chem. Phys*. 14: 5891-5901, 2012.

[10] Alessandri, I., and Lombardi, J. R. Enhanced Raman Scattering with Dielectrics. Chem. Rev. 116: 14921-14981, 2016.

[11] Shin, H. Y., Shim, E. L., Choi, Y. J., Park, J. H., and Yoon, S. Giant enhancement of the Raman response due to one-dimensional ZnO nanostructures. Nanoscale 6: 14622-14626, 2014.

[12] Kim, N. J., Kim, J., Park, J. B., Kim, H., Yi, G. C., and Yoon, S. (2019). Direct observation of quantum tunnelling charge transfers between molecules and semiconductors for SERS. Nanoscale 1: 45-49, 2019.

[13] Kawabata, A. Green Function Theory of Raman Scattering. J. Phys. Soc. Jpn, 30: 68–85, 1971.

Finite-difference time-domain (FDTD) simulation for optimization of non-metal based Surface enhanced Raman spectroscopy (SERS)

Eunji Ko[1], Jayeong Kim[1],
Heehun Kim[2], Gyu-Chul Yi[2], Seokhyun Yoon[1,*]

[1]Department of Physics, Ewha Womans University, Seoul 03760, Korea
[2]Department of Physics and Astronomy, Institute of Applied Physics, and Research Institute of Advanced Materials (RIAM), Seoul National University, Seoul 08826, Korea
*Seokhyun Yoon, E-mail: syoon@ewha.ac.kr

Abstract

We focus on less studied effect in SERS of chemical enhancement responsible for selective enhancement of Raman response of different analyte molecules adsorbed on same substrate materials. We incorporate finite-difference time domain (FDTD) simulations to discuss how the design of structures attributes to electric field and absorption of non-metallic SERS system which does not involve surface plasmonic resonance. Comparing to our experimental results, we suggest optimization conditions for chemical enhancement in SERS without involving surface plasmon resonance.

1. Introduction

There have been large number of theoretical and experimental studies of Surface enhanced Raman spectroscopy (SERS) over several decades for its huge enhancement. Huge enhancement factors of up to over 10^{10} is explained to be mainly due to surface plasmon resonance between substrate materials and incident laser light. However, chemical enhancement, another of the SERS mechanisms, has not yet been described for its obvious mechanism. Chemical enhancement can be very fascinating and highly available in that it plays a role in selectively enhancing the Raman reaction of different analyte molecules adsorbed on the same substrate material. In this study, We discussed the mechanism of this chemical enhancement. We incorporate finite-difference time domain (FDTD) simulations to calculate electric field intensity and absorption profile on the surface while varying design of models. As a result, we can exclude the electric effect generated by the structure from the experimental results so that we can solely study the chemical enhancement mechanism. In a previous study, we found that the shape of the semiconductor substrate structure affects the enhancement factor.[1] Furthermore, in this study, we suggest optimization conditions for the chemical enhancement of SERS without including surface plasmon resonance by comparing FDTD simulation results to our experimental results.

2. Discussion

2.1. Simulation of substrate structure effect

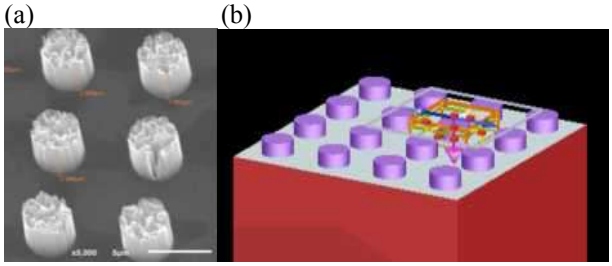
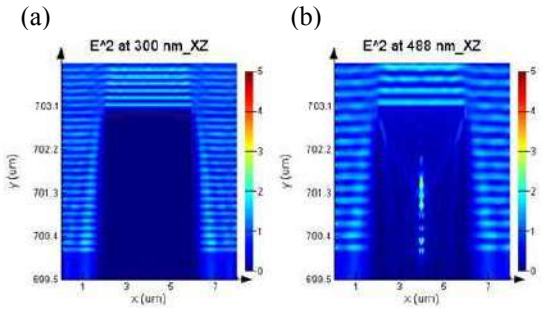


Figure 1: (a) Optical image of ZnO rods. (b) model of structure (a) in FDTD simulation.

First, to investigate the electric field effect of the substrate structure before the molecule was adsorbed, we built the model similar to the actual structure we used for experiments in the FDTD simulation program as shown in Figure 1. Figure 1-(a) shows optical image of the actual structure of ZnO rods on the substrate and Figure 1-(b) is the the model we made in the FDTD simulation program to calculate the electric field distribution and the absorption. We set the frequency-domain field monitors above the rod, on the surface of the substrate and also in the rod to record electric field and the power passing through the monitors. The laser beam in the actual experiments was considered to be a plane wave source in this simulation.



(c) (d)

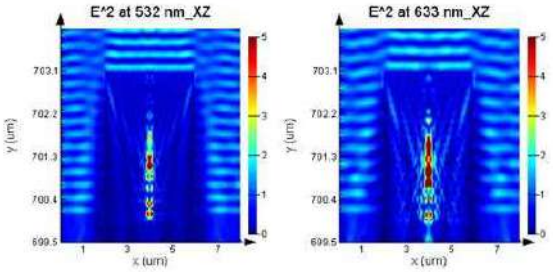
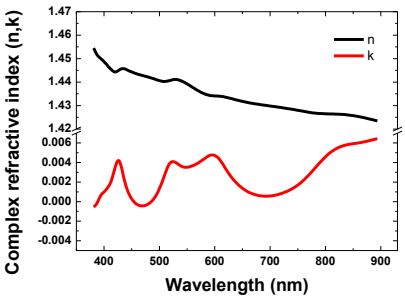


Figure 2: The electric field intensity distribution of four different wavelength source by FDTD simulation (a) at 300 nm (b) at 488 nm (c) at 532 nm (d) at 633 nm

The results of this FDTD simulation are shown in Figure 2. Figure 2 shows the electric field intensity distribution of four different wavelength source. The most concern in chemical SERS experiments at various wavelengths is the overlap of SERS effects due to penetration depth and reflection at each wavelength. However, as the result of simulation, although the electric field intensity inside the rod seems to be larger at longer wavelength sources, the electric field intensity outside the rod has little difference depending on the wavelength of source. This result excludes the possibility that it is the wavelength that makes the difference in enhancement of Raman signal. In other words, although the reflection by the substrate occurs more intensely in longer wavelength because of its longer penetration depth, the reflection is only confined to the rods and doesn't affect Raman signal.

2.2 Simulation of molecularly adsorbed ZnO rods

(a)



(b)

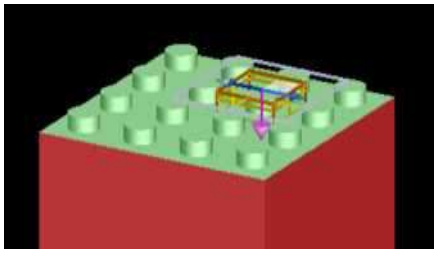


Figure 3: (a) Measured complex refractive index of 4-MPY by ellipsometry (b) Model of adsorbed 4-MPY molecules on ZnO rod substrate in FDTD simulation

The chemical enhancement effect was observed when 4-MPY molecules were adsorbed on ZnO rod substrate which the combination has been widely used in chemical enhancement experiments. [2,3] However, the FDTD simulation of adsorbed 4-MPY molecules on a substrate had not been conducted before, therefore, we measured the refractive index of 4-MPY using ellipsometry so that we can calculate FDTD simulation. As a result, we could obtain a complex reflective index of the 4-MPY molecule as shown in Figure 3-(a). Figure 3-(b) shows the model of adsorbed 4-MPY molecules on ZnO rod substrate in FDTD simulation. The molecules on the substrate were considered to be thin film. By running FDTD simulation, we could find what kind of combination of a structure and molecule can enhance the SERS signal effectively.

3. Conclusions

We calculated the absorption and electric field profile using finite-difference time domain (FDTD) simulation and compared to our experimental data. The results of the simulation indicate that the reflection by the substrate is only confined to the rods and it is not the reflection that enhances the raman signal, hence, we were able to effectively eliminate the electric effects of wavelength and substrate structure when analyzing chemical SERS experiments which use various wavelengths.

Furthermore, we measured complex refractive index of 4-MPY molecules by ellipsometry to obtain FDTD simulation results for molecule-adsorbed ZnO rod substrates. Our study would be very interesting in that we measured the refractive index of 4-MPY molecules for the first time, which are widely used in chemical SERS experiments, and applied to the FDTD simulation to suggest optimized models for larger enhancement.

References

[1] Shin, Hae-Young, et al. "Giant enhancement of the Raman response due to one-dimensional ZnO nanostructures." *Nanoscale* 6.24 (2014): 14622-14626.

[2] Kim, Nam-Jung, et al. "Direct observation of quantum tunnelling charge transfers between molecules and semiconductors for SERS." *Nanoscale* 11.1 (2019): 45-49.

[3] Wang, Yanfei, et al. "Direct observation of surface‐enhanced Raman scattering in ZnO nanocrystals." Journal of Raman Spectroscopy: An International Journal for Original Work in all Aspects of Raman Spectroscopy, Including Higher Order Processes, and also Brillouin and Rayleigh Scattering 40.8 (2009): 1072-1077.

Cooperative emission by quantum plasmonic superradiance

Hugo Varguet, Stéphane Guérin, Hans Rudolf Jauslin, and Gérard Colas des Francs

Laboratoire Interdisciplinaire Carnot de Bourgogne (ICB),
UMR 6303 CNRS, Université Bourgogne Franche-Comté,
9 Avenue Savary, BP 47870, 21078 Dijon Cedex, France
*corresponding author, E-mail: gerard.colas-des-francs@u-bourgogne.fr

Abstract

We investigate the correlated emission from an assembly of emitters coupled to a plasmonic particle, in a quantized model. We observe burst of emission but demonstrate that modal destructive interferences can inhibit the cooperative behaviour.

1. Introduction

Superradiance refer to the collective emission from N emitters gathered in a subwavelength volume. In such configuration, their emission is coupled to the same electromagnetic mode so that fast decay rate (proportionnal to the number of emitter; $\Gamma_N = N\Gamma_1$) and bright emission (proportionnal to N^2) occur. It originates from spontaneous phase-locking of the atomic dipoles through an electromagnetic mode and is very similar to the building of cooperative emission in a laser amplifier [1]. Using a classical approach, it has been proposed to realize plasmon analogous of superradiant states by coupling an ensemble of emitters to a metal nanoparticle to further increase the brightness and miniaturization of the collective nanosource [2, 3]. In this work, we discuss the properties of plasmonics superradiant and subradiant states (Dicke plasmonic states) with particular attention devoted to describe the construction of the cooperative behaviour, a fully quantum characteristic of superradiance [4].

2. Discussion

Figure 1a) represents the dynamics of correlated emission for 6 radial emitters coupled to a silver nanoparticle and its comparison with two limits cases: ideal superradiance and incoherent emission. Ideal superradiance is obtained when all the emitters are located at the same position. We observe a short burst of emission, on a timescale $\tau_N \simeq \tau_1/N$, characteristics of superradiance collective emission (blue curves). On the opposite, independent emitters emission gives the well-known Purcell enhanced spontaneous emission with an exponential decay (red curves). In case of homogeneous repartition of azimutal emitters around the MNP, we still observe the burst of emission since the LSP symmetry leads to identical coupling of the emitters. In case of radial emitters (Fig. 1b), the cooperative process is degraded because of the coupling to high-order modes. The

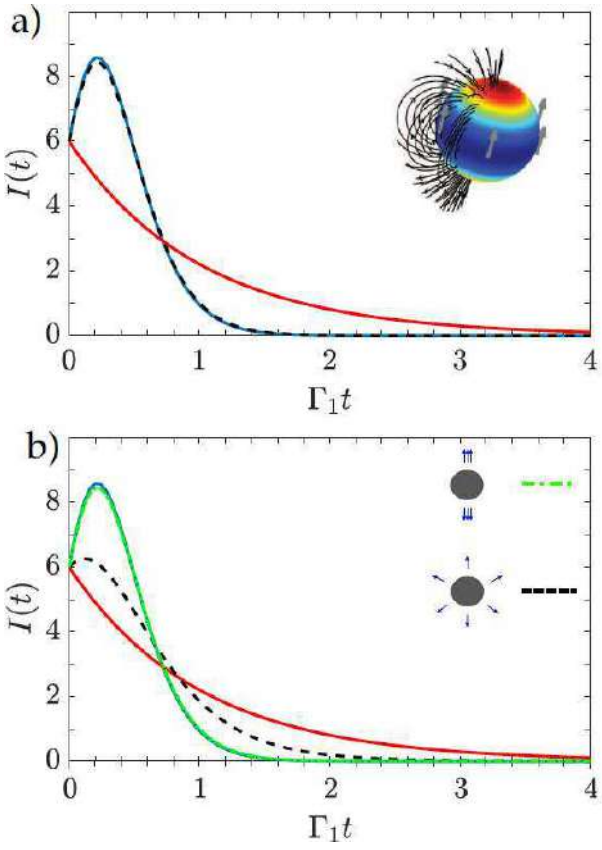


Figure 1: Collective rate for 6 emitters coupled to a 16 nm silver nanoparticle. a) azimuthal orientation. b) radial orientation. Blue curves corresponds to ideal superradiance with the emitters located at the same position. Red curves present the incoherent emission. Green and black curves refer to the configuration schemed on the graph (emitters on the MNP poles or homogeneously distributed). The emission wavelength is resonant with the dipolar mode LSP_1 ($\omega_0 = \omega_1 = 2.789$ eV) and the separation distance between the mitterand the MNP is $h = 20$ nm.

apparent quantum yield of the collective emission, defined as the ratio between the far-field scattering and the total superradiance emission, is about 15% for 30 nm silver MNP.

3. Conclusions

We derive a quantum approach for plasmonic superradiance and discuss the dynamics of cooperative emission. The system follows the plasmonic Dicke ladder and strong correlations build up between the emitters, LSP mediated, so that superradiance can be Purcell enhanced. However, superradiance blockade occurs at small distances. We emphasize that the origin of superradiance degradation at short distances is different from the mechanism of fluorescence quenching. Superradiance cooperativity is jeopardized because of modal destructive interferences whereas fluorescence quenching originates from an increase of the non radiative rate. We expect that plasmonic superradiance could be experimentally investigated on metallo-dielectric nanohybrids [5, 6, 7, 8]. This constitutes ultrafast and extremelly bright optical nanosources of strong interest for integrated nano-optics platforms.

Acknowledgement

This work is supported by the French program Investissements d'Avenir, through the project ISITE-BFC IQUINS (contract ANR-15-IDEX-03) and EUR-EIPHI contract (17-EURE-0002). This work is part of the european COST action MP1403 Nanoscale Quantum Optics.

References

[1] M. Gross and S. Haroche, "Superradiance: An essay on the theory of collective spontaneous emission," *Physics Reports*, vol. 93, pp. 301–396, 1982.

[2] V. Pustovit and T. Shahbazyan, "Cooperative emission of light by an ensemble of dipoles near a metal nanoparticle:the plasmonic dicke effect," *Physical Review Letters*, vol. 102, p. 077401, 2009.

[3] P. Fauché, S. Kosionis, and P. Lalanne, "Collective scattering in hybrid nanostructures with many atomic oscillatorscoupled to an electromagnetic resonance," *Physical Review B*, vol. 95, p. 195418, 2017.

[4] H. Varguet, S. Guérin, H. Jauslin, and G. Colas des Francs, "Cooperative emission by quantum plasmonic superradiance," *arxiv*, vol. 1810.11315, 2018.

[5] M. A. Noginov, G. Zhu, A. M. Belgrave, R. Bakker, V. M. Shalaev, E. E. Narimanov, S. Stout, E. Herz, T. Suteewong, and U. Wiesner, "Demonstration of a spaser-based nanolaser," *Nature*, vol. 460, pp. 1110–1112, 2009.

[6] X. Zhou, J. Wenger, F. Viscomi, L. L. Cunff, J. Béal, S. Kochtcheev, X. Yang, G. Wiederrecht, G. Colas des Francs, A. S. Bisht, S. Jradi, R. Caputo, H. V. Demir, R. Schaller, J. Plain, A. Vial, X. Sun, and R. Bachelot, "Two-color single hybrid plasmonic nano-emitters with real time switchable dominant emission wavelength," *Nano Letters*, vol. 15, pp. 7458–7466, 2015.

[7] B. Ji, E. Giovanelli, B. Habert, P. Spinicelli, M. Nasilowski, X. Xu, N. Lequeux, J.-P. Hugonin, F. Marquier, J. Greffet, and B. Dubertret, "Non-blinking quantum dot with a plasmonic nanoshell resonator," *Nature Nanotechnology*, vol. 10, pp. 170–175, 2015.

[8] P. Fauché, "Plasmonic superradiance in metallo-dielectric nanohybrids," Ph.D. dissertation, Université de Bordeaux, 2017.

Shaping and measuring temperature at the microscale for biological applications

Chang Liu[1], Pascal Berto[1,2], Clémence Gentner[1], Minh-Chau Nguyen[1], Iván Flores[2], Robert Kuszelewicz[1], Marc Guillon[2], Gilles Tessier*[1,2]

[1] Sorbonne Université, CNRS, INSERM, Institut de la Vision, 17 Rue Moreau, 75012 Paris, France.
[2] Neurophotonics Laboratory, UMR 8250 CNRS, Université Paris Descartes, 45 rue des Saints-Pères, 75006 Paris, France.
*corresponding author, E-mail: gilles.tessier@sorbonne-universite.fr

Abstract

Using a spatial light modulator, a pre-calculated heat source distribution is projected on a plasmonic nanoparticle carpet to produce a fast, reconfigurable and accurate temperature distribution in an arbitrarily-shaped 2D region. The temperature maps induced by the thermoplasmonic effect are deduced from images obtained using two types of wavefront sensors, a shearing interferometer and a thin-diffuser-based imaging approach.

1. Introduction

Temperature is often a critical factor, in physics as well as biology. Most existing techniques (e.g. ovens, incubators…) only provide global temperature control and incur strong inertia. Thermoplasmonic heating can give access to fast, local and contactless optical temperature control. However, tailoring temperature at the micro-scale is not straightforward since heat diffusion alters temperature patterns. In this study, we propose and demonstrate an accurate and reconfigurable microscale temperature shaping technique by precisely tailoring the illumination intensity that is sent on the sample. A homogeneous array of absorbing plasmonic nanoparticles is used to efficiently convert light into heat through thermoplasmonic effects.

2. Light and heat structuration

The method consists in (i) calculating the distribution of heat sources, also named Heat Source Density (HSD), which pre-compensates heat diffusion effects [1] so as to produce the desired temperature distribution, and (ii) using a Spatial Light Modulator (SLM) and a Gerschberg-Saxton calculation of the appropriate phase pattern in order to shape the illumination and reproduce this HSD in the nanoparticle plane. After heat diffusion, the tailored heat source distribution produces the desired microscale temperature pattern, as illustrated in Fig.1.

The resulting temperature distribution is measured using wavefront-sensing-based temperature imaging microscopy [2,3] using a shearing imaging interferometer.

Beyond this interferometer, we will present a wavefront imaging technique based on the use of a simple thin diffuser in order to measure speckle changes using the memory effect. We will show how this type of cost-efficient wavefront sensing system can be used to derive temperature distributions, particularly in the context of thermoplasmonic effects.

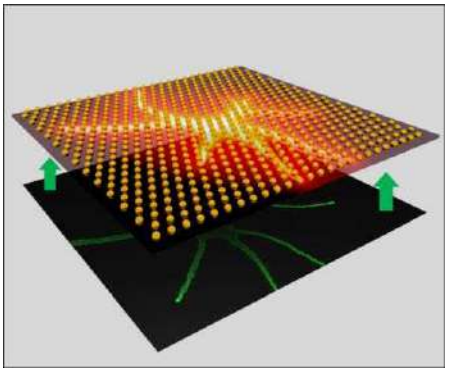


Figure 1: Schematic representation of the Spatial Light Modulator-based projection of an optical pattern calculated to pre-compensate heat diffusion. After photothermal conversion by a gold nanoparticle array, heat diffusion induces the desired 2D temperature distribution.

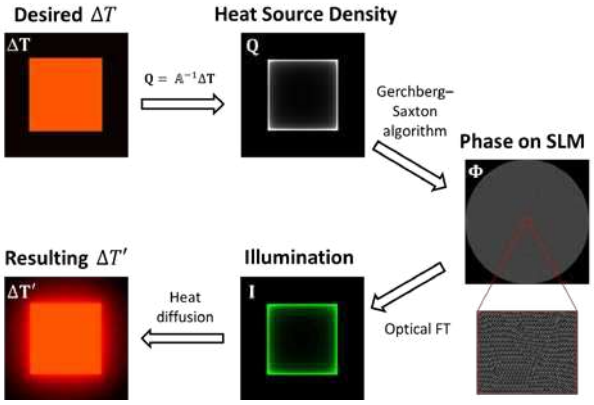


Figure 2: Reconfigurable temperature- shaping workflow (calculated images). ΔT is the targeted temperature increase distribution; Q is the associated HSD distribution; **Φ** is the corresponding phase distribution in the Fourier plane of the illumination pattern; I is the light intensity distribution in the

sample plane; $\Delta T'$ is the resulting temperature increase distribution.

Fast (sub-ms) thermalisation is possible when addressing microscale domains, and we demonstrate accurate, and reconfigurable temperature patterns over arbitrarily-shaped regions. In the context of cell biology, we present a methodology combining fluorescence imaging with reconfigurable temperature shaping to thermally target a given population of cells or organelles of interest, opening new strategies to locally study their response to thermal activation [4].
Finally, we will illustrate applications of microscale heat shaping, using resistors with optimized shapes, in order to engineer thermal landscapes and manipulate the phase of light. Various adjustable optical functions including lenses, phase pistons, axicons or Zernike polynomial-type phase shaping can be generated by calculating the appropriate heat source density and the corresponding resistor design. Using this electro-thermo-optical approach, we will show that a broad range of optical elements can be reproduced and electrically controlled, opening a broad range of imaging applications.

Acknowledgements

This work was partially funded by the Agence Nationale pour la Recherche, ANR BoroGaN and ANR Neocastip projects.

References

[1] G. Baffou, E. B. Ureña, P. Berto, S. Monneret, R. Quidant, and H. Rigneault, "Deterministic temperature shaping using plasmonic nanoparticle assemblies," Nanoscale 6, 8984–8989 (2014).
[2] G. Baffou, P. Bon, J. Savatier, J. Polleux, M. Zhu, M. Merlin, H. Rigneault, and S. Monneret, "Thermal imaging of nanostructures by quantitative optical phase analysis," ACS Nano 6, 2452–2458 (2012).
[3] P. Berto, E. B. Ureña, P. Bon, R. Quidant, H. Rigneault, and G. Baffou, "Quantitative absorption spectroscopy of nano-objects," Phys. Rev. B - Condens. Matter Mater. Phys. 86, 1–5 (2012).
[4] C.Liu, G.Tessier, S.I. Flores Esparza, M.Guillon, P. Berto. "Reconfigurable Temperature Control at the Microscale by Light Shaping", ACS Photonics 6 (2), 422 (2019) DOI: 10.1021/acsphotonics.8b01354
[5] Berto, P., Rigneault, H. & Guillon, M. Opt. Lett. 42, (2017).

Phase transition of methylammonium lead halide perovskite ($MAPbX_3$) single crystals studied by Raman scattering spectroscopy

Trang Thi Thu Nguyen[1], Yejin Kim[1], Hye Ri Jung[1], William Jo[1], Won Seok Woo[2], Chang Won Ahn[2], Shinuk Cho[2], Ill Won Kim[2], and Maryam Bari[3], Zuo-Guang[3] and Seokhyun Yoon[1*]

[1]Department of Physics, Ewha Womans University, Seoul 03760, Korea

[2]Department of Physics and Energy Harvest-Storage Research Center, University of Ulsan, Ulsan 44919, Korea

[3]Department of Chemistry, Simon Fraser University, Burnaby, Canada

*syoon@ewha.ac.kr

Abstract

For decades, many studies have been conducted to improve the efficiency of photovoltaic devices. In this study, we focused on structural properties, especially phase transition behavior as a results of temperature changes in methylammonium lead halide perovskite ($CH_3NH_3PbX_3$, X-I, Br, and Cl) to understand fundamental properties in these materials. The properties of perovskite materials on halogen elements, and Raman scattering can show that the contribution to the structural phase transition from each atomic/molecular vibration varies from compound to compound.

1. Introduction

Inorganic-organic hybrid lead halide perovskites have been getting huge attention because of its various merits; low cost to make, earth abundant, tunable bandgap etc. In addition, the efficiency of solar cells made of these materials is quite high (~23%), which promotes more studies towards next generation photovoltaic devices. However, perovskite thin films are unstable in ambient conditions, especially under UV illumination or presence of water vapor so in order to minimize stability issues, we used single crystal samples in this study of fundamental properties. The perovskite materials exhibit different properties upon the halogen elements (chlorine, bromine and iodine), so the temperature at which phase transition occurs changes with different compounds. For example, $CH_3NH_3PbBr_3$ exhibits a structural phase transition from a cubic to a tetragonal structure at ~236K and $CH_3NH_3PbCl_3$ shows the similar phase transition at ~179K. To understand the basic properties leading to photovoltaic mechanism of $CH_3NH_3PbX_3$, first we focused on phase transition behavior of materials. Raman scattering spectroscopy observes small changes in phonon spectrum that reflect microscopic environments and configurations, so it is useful as a research mean and a sensitive monitoring tool to study structural changes that lead to understand fundamental properties of materials.

2. Results

There are 2 groups of vibration modes in $MAPbX_3$; external vibration mode of inorganic (PbX_3) anion, internal vibration mode of MA (CH_3NH_3) cation. The internal vibration modes of MA cation range from 400-3300cm^{-1}.

2.1. $CH_3NH_3PbBr_3$,

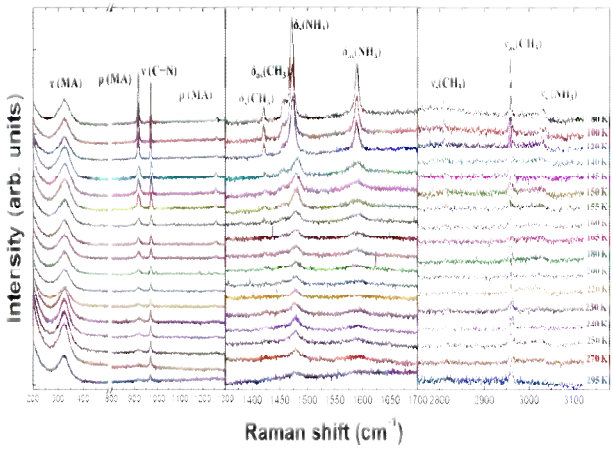


Figure 1: Temperature dependent Raman spectra of $CH_3NH_3PbBr_3$ single crystal from 80 K to RT. The spectra range from 300 cm^{-1} to 3100 cm^{-1}.

$CH_3NH_3PbBr_3$ has 3 phases: cubic, tetragonal (I, II), and orthorhombic depending on temperature. $CH_3NH_3PbBr_3$ exists as cubic phase at RT then upon cooling down, at 236.6K, a phase transition from cubic to tetragonal I phase occurs. If temperature goes down further to 154.5K, another phase transition occurs and the structure of the material changes from tetragonal I to tetragonal II phase that are not clearly different but show different space groups. The space group of tetragonal I phase is *I4/mcm* and that of tetragonal

II phase is *P4/mcm*. At 145K, another phase transition from tetragonal II to orthorhombic phase occurs. As can be seen clearly in our results, some peaks show an abrupt change at ~140K in frequency and/or intensity.

2.2. $CH_3NH_3PbCl_3$

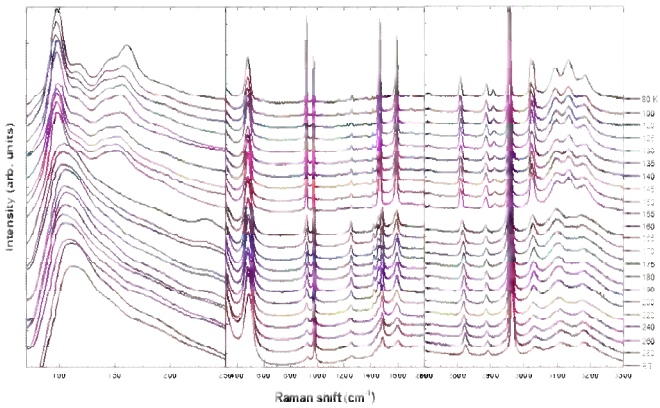


Figure 2: Temperature dependent Raman spectra of $CH_3NH_3PbCl_3$ single crystal from 80 K to RT. The spectra range from 100 cm^{-1} to 3300 cm^{-1}.

$CH_3NH_3PbCl_3$ also has 3 phases: cubic, tetragonal, orthorhombic depending on temperature. In case of chloride, space group of tetragonal phase is *P4/mcm* and the window of phase transition temperatures is narrow: The phase transition from cubic to tetragonal phase is done at 178.8K and the subsequent phase transition from tetragonal to orthorhombic phase occurs at 172.9K. In $CH_3NH_3PbCl_3$, more changes are observed shown especially at high frequency than Bromine. There are two peaks at 3150 cm^{-1} and near 2900 cm^{-1} appearing in orthorhombic phase, and they abruptly change around 160K.

3. Discussion

Comparing $CH_3NH_3PbBr_3$ and $CH_3NH_3PbCl_3$, both materials show abrupt change in each phonon spectra. Each change is associated with phase transition from tetragonal to orthorhombic phase at their respective temperatures, ~140 K for bromides and ~160 K for chlorides. Though the two materials exhibit qualitatively similar changes with respect to temperature change, there are differences that reflect differences in microscopic environment, especially in MA configuration.

4. Conclusions

MA perovskites are known to possess different phases with respect to temperatures. They also show phase transition behavior accordingly. For understanding structural characteristics, study of various phases and relation between them is essential. However, thin film perovskite is unstable at ambient conditions. We used single crystalline samples to study structural properties and did not find any stability issues. By measuring temperature dependence in Raman spectra, it was observed that the contributions to the phase transition from each atom/molecule vibration were qualitatively different. We also show that Raman scattering spectroscopy is a very effective mean to monitor different phases by observing abrupt and/or gradual changes in phonon spectra that sensitively reflect microscopic environmental changes..

Acknowledgements

This work is supported by Basic Science Research Program (NRF-2016R1D1A1B01009032, NRF - 32018R1A6A1A03025340) through the National Research Foundation of Korea (NRF).

References

[1] R. G. Niemann, et al., Halogen Effects on Ordering and Bonding of $CH_3NH_3^+$ in $CH_3NH_3PbX_3$(X = Cl, Br, I) Hybrid Perovskites, *J. Phys. Chem. C* 120, pp. 2509-2519, 2016.

[2] R. Yadav, et al., Dielectric and Raman investigations of structural phase transitions in $(C_2H_5NH_3)_2CdCl_4$, *Phys. Chem. Phys.* 17, pp. 12207-12214, 2015.

[3] Yin, et al., Hydrogen-Bonding Evolution during the Polymorphic Transformations in $CH_3NH_3PbBr_3$, *Chem. Mater.* 29, pp. 5974-5981, 2017.

[4] Aurelien M. A. Leguy, *et al.,* Dynamic disorder, phonon lifetimes, and the assignment of modes to the vibrational spectra of methylammonium lead halide perovskites, *Phys.Chem.Chem.Phys*. 18, pp. 27051‑27066, 2016

Entanglement in Hybrid Quantum Dot/Plasmonic Systems

Matthew Otten,[1] Stephen K. Gray[1*] and G. V. Kolmakov[2]

[1]Center for Nanoscale Materials, Argonne National Laboratory, Argonne, Illinois 60439, U.S. A.
[2]New York City College of Technology, the City College of New York, Brooklyn, New York 11201, U.S.A.
[*]corresponding author, E-mail: gray@anl.gov

Abstract

Cavity quantum electrodynamics calculations are used to elucidate how quantum dots can become entangled in hybrid systems composed of quantum dots and plasmonic resonators. By coupling the quantum dots to photonic cavities it is further shown how measurement of the two-photon correlation function can be used to verify the entanglement.

1. Introduction

There is much interest and research activity in quantum computing, quantum communication and quantum sensing, collectively known as quantum information science (QIS). Entanglement between or among systems is a highly quantum mechanical state that cannot be written as a separable product of component states and is a key component of a lot of QIS protocols. For example, entanglement can improve the sensitivity of measurements beyond what can be achieved classically [1].

A number of simple models and calculations, e.g., Refs. [2-5] have suggested that quantum dots, taken to be simple two-level systems, interacting with plasmonic structures (waveguides, nanoparticles and cavities) can become entangled due to their coupling through the plasmonic structure. One can imagine laser excitation or driving of one of the quantum dots in a two quantum dot/plasmonic system, and the second quantum dot becoming excited and exchanging energy with the first quantum dot via their mutual coupling with the plasmonic system. A significant degree of entanglement, as characterized by concurrence, also can result [6]. An important question to address is how one could experimentally verify entanglement in such systems. One measure, proposed by Dumitrescu and Lawrie [5], is to measure photon coincidences associated with the emission from the quantum dots, with these coincidences exhibiting features characteristic of anti-bunching (a dip in the steady-state, same-time two-photon correlation function or $g^{(2)}$). In this contribution a different, time-dependent approach is suggested that leads to $g^{(2)}$ exhibiting maxima when the quantum dots are entangled [7].

2. Results and Discussion

We consider the system depicted in Figure 1, which is composed of two quantum dots, each placed or interacting with a photonic cavity and a plasmonic nanoparticle.

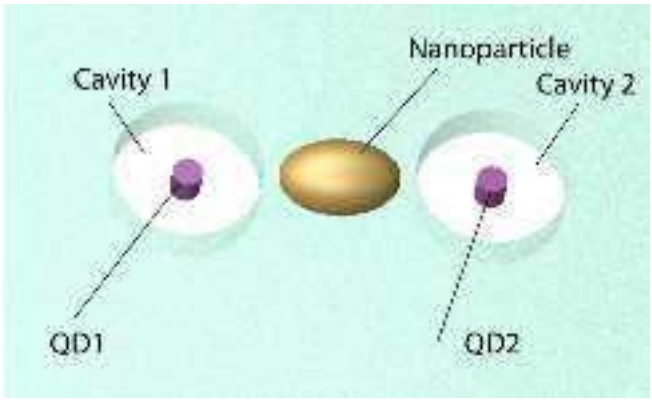


Figure 1: Schematic diagram of the proposed system for verifying quantum dot entanglement.

We imagine that the photonic cavities are connected to detectors in the fashion of a Hanbury Brown Twiss experiment [8]. In addition, we imagine a femtosecond pulse exciting quantum dot 1 (QD1), which leads to the second quantum dot (QD2) becoming entangled with QD1. Our cavity quantum electrodynamics calculations of this system yield results such as those depicted in Figure 2. In this figure we plot the concurrence associated with entanglement of the two quantum dots (left-hand axis) as well as $g^{(2)}$ (right-hand axis). As time evolves after the initial excitation the concurrence oscillates from small or zero values to moderately large values (a concurrence of 1 is maximal entanglement), and the two-photon correlation function is seen to exhibit significant spikes whenever the concurrence is close to or reaches a maximum.

This remarkable correlation between concurrence and two-photon correlation function, as well as the periodic oscillations in time, can be understood in terms of the entanglement passing between the two quantum dots and the two photonic cavities. The overall entanglement (sum of entanglement of the cavities and the quantum dots) remains

a constant. An analytical model can also be constructed to show this behavior [7].

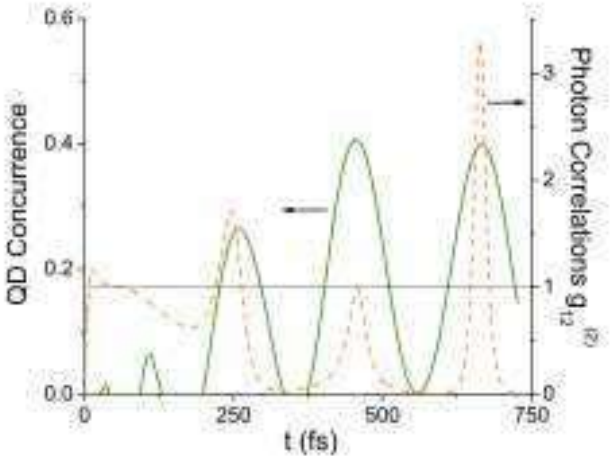


Figure 2: Strong correlations are exhibited between the concurrence of QD1 and QD2 (a measure of entanglement) and photon coincidences associated with photon emission from the photonic cavities.

Acknowledgements

This work was performed, in part, at the Center for Nanoscale Materials, a U.S. Department of Energy Office of Science User Facility, and supported by the U.S. Department of Energy, Office of Science, under Contract No. DE-AC02-06CH11357.

.

References

[1] C. L. Degen, F. Reinhard, P. Cappellaro, Quantum Sensing, *Rev. Mod. Phys.* 89: 035002, 2017.

[2] D. Martin-Cano et al., Dissipation-Driven Generation of Two-Qubit Entanglement Mediated by Plasmonic Waveguides, *Phys. Rev. B* 106:020501, 2011.

[3] M. Otten et al., Origin and Optimization of Entanglement in Plasmonically Coupled Quantum Dots, *Phys. Rev. A* 94:022312, 2016.

[4] M. Hensen, T. Heilpern, S. K. Gray, W. Pfeiffer, Strong Coupling and Entanglement in a Nanoantenna-Enhanced Plasmonic Cavity, *ACS Photonics* 5:240-248, 2018.

[5] E. Dumitrescu, B. Lawrie, Antibunching Dynamics of Plasmonically Mediated Entanglement Generation, *Phys. Rev. A* 96: 053826, 2017.

[6] W. K. Wootters, Entanglement of Formation of Arbitrary State of Two Qubits, *Phys. Rev. Lett.* 80:2245-2248, 1998.

[7] M. Otten, S. K. Gray, G. V. Kolmakov, Optical Detection and Storage of Entanglement in Plamsonically Coupled Quantum-Dot Qubits, *Phys. Rev. A* 99:032339, 2019.

[8] Y. Yamamoto and A. Imamoglu, *Mesoscopic Quantum Optics*, Wiley, New York, 1999.

Laser photopatterning of metal oxide functional micro-nano-structures from precursor solutions.

C. C. Yeh,[1,2,3] S. Y. Yu, [1,2,3] P. Y. Chang, [1,2,3] B. Leuschel, [1,2] D. Berling, [1,2] A. Spangenberg, [1,2] H. W. Zan, [1,2,3] O. Soppera [1,2,*]

[1] Université de Haute-Alsace, CNRS, IS2M UMR 7361, Mulhouse, France
[2] Université de Strasbourg, France
[3] Department of Photonics, College of Electrical and Computer Engineering, National Chiao Tung University, Hsinchu, Taiwan 30010, Republic of China
*corresponding author, E-mail: Olivier.soppera@uha.fr

The transparency and tunable electrical, optical, and magnetic properties of metal oxide thin films make them very attractive for many applications in electro-optical devices. However, the integration of such materials at the micro or nanoscale is still challenging. In recent years, solution processing combined with direct-patterning techniques such as micro-/nanomolding, inkjet printing, e-jet printing, e-beam writing, and photopatterning has drawn much attention because of the inexpensive and simple fabrication process that avoids using capital-intensive vacuum deposition systems and chemical etching. [1]

We present here our latest results on the laser direct writing of metal oxide micro and nanostructures. The key step is to develop photosensitive metal-oxo precursors solutions that can be patterned with high resolution. Stable solution of metal-oxo clusters were prepared by reaction between metal alkoxide precursors (Zn, Ti, Zr) and ligands (mostly carboxylic acids). These solutions were doped to tune the electrical or magnetic properties (In, Al, Co) and thin films were prepared by spin-coating.

Photocrosslinking was studied by spectroscopy (FTIR, Raman), spectroscopic ellipsometry with irradiation wavelength in the deep-UV range (193 nm and 266 nm). It was demonstrated that the Deep-UV irradiation is very efficient to induce the elimination of the organic molecules complexing the metal and then provoke crosslinking by condensation reaction.[2]

These materials were evaluated for photopatterning with resolution between 50 nm to several hundreds of microns.[3, 4] Furthermore, practical applications are demonstrated in thin-film transistors and biochemical sensors on a wide range of substrates. We show in particular application of these metal oxide nanostructures as gas sensors and for magnetic properties. [5]

Since direct-patterning techniques enable low-cost fabrication of nanoscale metal oxide structures, these methods are expected to accelerate the development of nanoscale devices and systems based on metal oxide components in important application fields such as flexible electronics, the Internet of Things (IoT), and human health monitoring. [6]

References

[1] C. C. Yeh, H. W. Zan, O. Soppera, Adv Mater 2018, 1800923

[2] C. C. Yeh, H. C. Liu, M. Y. Chuang, J. Denzer, D. Berling, H. W. Zan, O. Soppera, Adv Mater Interfaces 2016, 3.

[3] B. Leuschel, A. Gwiazda, W. Heni, F. Diot, S. Y. Yu, C. Bidaud, L. Vonna, A. Ponche, H. Haidara, O. Soppera, Sci Rep 2018, 8.

[4] C. C. Yeh, H. C. Liu, W. Heni, D. Berling, H. W. Zan, O. Soppera, J Mater Chem C 2017, 5, 2611.

[5] C. C. Yeh, S. Colis, P. Fioux, H. W. Zan, D. Berling, O. Soppera, Adv Mater Interfaces 2017, 4.

[6] S.-Y. Yu, G. Schrodj, K. Mougin, J. Dentzer, J.-P. Malval, H.-W. Zan, O. Soppera, A. Spangenberg, Advanced Materials 2018, 0, 1805093.

New trends in nanophotonics and advanced materials

Impact of plasmonic bowtie nanoantennas and nanocavities on the dynamics of nearby nanoemitters

Víctor Pacheco-Peña[1], Rúben Alves[2], and Miguel Navarro-Cía[2]

[1]School of Engineering, Newcastle University, Merz Court, Newcastle Upon Tyne NE1 7RU, UK
[2]School of Physics and Astronomy, University of Birmingham, Birmingham, Edgbaston B15 2TT, UK
*corresponding author, E-mail: m.navarro-cia@bham.ac.uk

Abstract

Metallic nanoparticles exert a strong influence on the electrodynamics and mechanical dynamics of nanoemitters in their vicinity. Transformation optics can provide analytical descriptions and physical insight on these scenarios. As a case of study, we discuss the use of conformal transformation to understand the nonradiative Purcell enhancement and the optical forces experienced by nanoemitters nearby bowtie nanocavities and nanoantennas.

1. Introduction

Recent advances in nanofabrication has made it possible to fabricate nanostructures with a wide range of topologies [1]. This flexibility in attainable topologies opens endless possibilities, but at the same time makes the optimization of designs more challenging. Full-wave simulations can assist in the design process, but they have two main disadvantages compared to analytical solutions: computational burden that can potentially be unaffordable and limited physical insight.

Among the limited number of existing analytical techniques suitable for nanoplasmonics, transformation optics [2] is becoming the norm given its rigor and accuracy, which have made it possible to have analytical electromagnetic descriptions of crescent-shaped [3], cylindrical sector [4], bowtie [5] and tripod nanoantennas [6], as well as ring-disk [7] and crescent-shaped nanocavities [8]. This success should not come as a surprise though since conformal transformation was already used successfully in microwave engineering to provide analytical description of planar transmission lines [9].

Inspired by [2]-[8],[10] we investigate analytically and numerically the Purcell enhancement and the optical forces experienced by a nanoemitter (modelled as a point dipole) inside a 20 nm inner diameter bowtie nanocavity [11] and we also unveil hidden symmetries in bowtie nanocavities and 20 nm outer diamter nanoantennas.

2. Conformal mapping

Given the subwavelength diameter of the plasmonic structures under study, we assume a quasi-static problem. In this case, the electric and magnetic fields are decoupled and the former can be described by an electrostatic potential satisfying Laplace's equation.

By applying the conformal transformation $z = \ln(z'/a)$, the bowtie topologies shown on the left-hand side of Fig. 1 can be transformed into the geometries shown on the right-hand side of Fig. 1. Here $z = x + iy$ and $z' = x' + iy'$ correspond to the spatial coordinates in the transformed and original frames, respectively, and a is the distance between the nanoemitter and the coordinate origin. Notice that the nanocavity in panel (c) and the nanoantenna in panel (e) have mirror symmetric transformed spaces (see Fig. 1(d,f)).

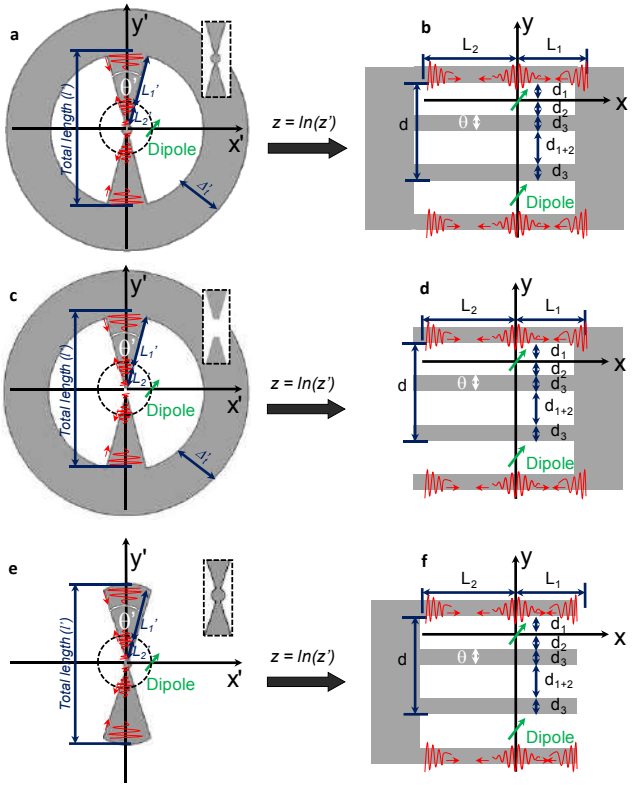


Figure 1: (a, c, e) bowtie nanocavities and nanoantenna. (b, d, f) electromagnetic equivalent transformed scenario that is analytically solvable.

The transformed space preserved the physics all the original space. Hence, the potential and power dissipation in

the transformed space, $P_{\text{abs}}^{(x,y)}$, are the same as those of the original space. Given the simplicity of the transformed space,

$$P_{\text{nr}} = P_{\text{abs}}^{(x',y')} = P_{\text{abs}}^{(x,y)} = -\frac{1}{2}\omega \text{Im}\{\vec{p}^* \vec{E}_1^s(x,y)\} =$$

$$= -\frac{1}{2}\omega \text{Im}\{p_x^* E_{1x}^s(x,y) + p_y^* E_{1y}^s(x,y)\}, \quad (1)$$

where P_{nr} is the nonradiative power emission by the dipole source, $\vec{p}^*$ is the dipole moment of the nanoemitter, $\omega = 2\pi c/\lambda_0$ is the angular frequency at the operation wavelength λ_0 and c is the velocity of light in vacuum. Additionally, the nonradiative Purcell enhancement spectra is given by $P_{\text{nr}}(\omega)/P_0(\omega)$, where $P_0(\omega)$ is the power radiated by the dipole in free space. From the potential one can compute the electric field and then the optical force using the Maxwell stress tensor.

3. Results and Discussion

The nonradiative Purcell enhancement for a horizontally- and vertically-polarized dipole nearby the different geometries described in Fig. 1 is shown in Fig. 2. One can see the strong influence that the center of the nanostructure plays. Full-wave simulations (Comsol Multiphysics®) of the original space (Fig. 1(a, c, e))) agree very well with the analytical calculations (Fig. 1(b, d, f)).

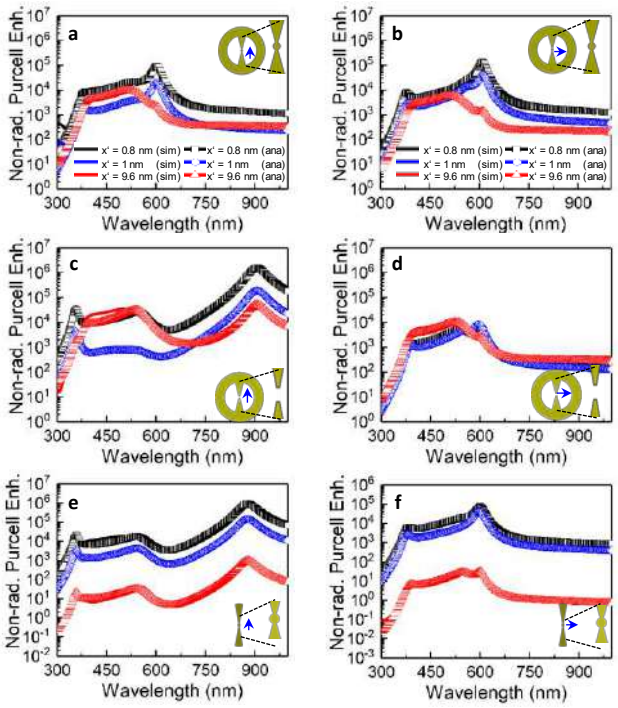


Figure 2: Numerical (solid lines) and analytical (symbols) results of the nonradiative Purcell enhancement under vertical (first column) and horizontal (second column) polarization of the dipole placed at different positions along the *x'*-axis. (a, b) bowtie nanocavity with connected metal arms; (c, d) bowtie nanocavitiy with disconnected metal arms; (e, f) bowtie nanoantenna with connected arms.

4. Conclusions

Conformal transmission is utilized to understand the physics in nanoplasmonic scenarios involving a nanoemitter and bowtie-shaped plasmonic nanostructures. The underlying mechanisms are easily unveiled by inspection of the transformed space. Also, within the transformed space a hidden symmetry between the bowtie nanocavity with disconnected metal arms and the bowtie nanoantenna with connected arms is clearly shown.

Acknowledgements

V.P.-P. is supported by the Newcastle University (Newcastle University Research Fellow). R.A. is supported by the University of Birmingham (PhD studentship). M. N.-C. is supported by the University of Birmingham (Birmingham Fellowship).

References

[1] V. Giannini, A. I. Fernández-Domínguez, S. C. Heck, S. A. Maier, Plasmonic nanoantennas: fundamentals and their use in controlling the radiative properties of nanoemitters, *Chem. Rev.* 111: 3888–3912, 2011.

[2] A. Aubry and J. B. Pendry, *Active Plasmonics and Tunable Plasmonic Metamaterials*, John Wiley & Sons, Hoboken, NJ, US, 2013, ch. 4, pp. 105–152.

[3] Y. Luo, D. Y. Lei, S. A. Maier and J. B. Pendry, Broadband Light Harvesting Nanostructures Robust to Edge Bluntness, *Phys. Rev. Lett.* 108: 023901, 2012.

[4] Y. Luo, J. B. Pendry and A. Aubry, Surface Plasmons and Singularities, *Nano Lett.* 10: 4186-4191, 2010.

[5] V. Pacheco-Peña, M. Beruete, A. I. Fernández-Domínguez, Y. Luo and M. Navarro-Cía, Description of Bow-Tie Nanoantennas Excited by Localized Emitters Using Conformal Transformation, *ACS Photonics* 3: 1223-1232, 2016.

[6] V. Pacheco-Peña, A. I. Fernández-Domínguez, Y. Luo, M. Beruete and M. Navarro-Cía, Aluminum Nanotripods for Light - Matter Coupling Robust to Nanoemitter Orientation, *Laser Photonics Rev.* 11: 170051, 2017.

[7] M. Kraft, Y. Luo and J. B. Pendry, Transformation Optics: A Time- and Frequency-Domain Analysis of Electron-Energy Loss Spectroscopy, *Nano Lett.* 16: 5156-5162, 2016.

[8] J. B. Pendry, A. I. Fernández-Domínguez, Y. Luo and R. Zhao, Capturing photons with transformation optics, *Nat. Phys.* 9: 518-522, 2013.

[9] R. E. Collin, *Field Theory of Guided Waves*, IEEE Press-Wiley, New York, 1990.

[10] M. Navarro-Cía, and S. A. Maier, Broad-Band Near-Infrared Plasmonic Nanoantennas for Higher Harmonic Generation, *ACS Nano* 6:3537-3544, 2012.

[11] V. Pacheco-Peña, and M. Navarro-Cía, Understanding quantum emitters in plasmonic nanocavities with conformal transformation: Purcell enhancement and forces, *Nanoscale* 10: 13607, 2018.

On-chip fabricated non-transfer plasmonic nanolaser

Ya-Lun Ho[1], J. Kenji Clark[1], A. Syazwan A. Kamal[1], Jean-Jacques Delaunay[1]

[1]School of Engineering, The University of Tokyo, Tokyo, Japan
*corresponding author, E-mail: jean@mech.t.u-tokyo.ac.jp

Abstract

We demonstrate a monolithically fabricated plasmonic-waveguide nanolaser. This is the first report showing a non-transfer plasmonic-waveguide nanolaser with a structure size (not only the mode size) in the sub-wavelength regime. A plasmonic waveguided mode capable of sustaining lasing is carefully designed so that top-down fabrication techniques can be used (no need of nanostructure transfer) to simultaneous fabricate the nanolasers together with waveguides for an optical circuit. Moreover, the design supports a lasing mode with a large effective area and confines the absorption of the pump light to the area in which the plasmonic-waveguide mode is most intense, reducing the lasing threshold. Lasing up to room temperature with a low threshold intensity of 0.20 mJ/cm^2 is demonstrated.

1. Introduction

Due to the strong demand for photonic computing, on-chip optical communication, medical imaging, and biosensing at the nanoscale, interest in nanolasers has grown dramatically in recent years. Plasmonic lasers are promising as nanoscale laser sources [1] and have been widely studied using semiconductor nanowires on metal surfaces synthesized by bottom-up techniques [2,3]. However, these nanowire plasmonic lasers require transfer and positioning after fabrication, making their use in practical on-chip devices difficult.

Here, we propose a plasmonic structure, as shown in Figure 1, consisting of ZnO cavities with Al top layers directly grown on a sapphire substrate [4]. The ZnO cavities are directly fabricated on the sapphire wafer using pulsed laser deposition for ZnO, ion beam sputtering for Al, and top-down fabrication techniques such as electron-beam lithography and reactive ion etching. Due to the use of top-down techniques, the dimensions, positions, and alignment of nanolaser cavities can be controlled without transfer and manipulation processes. As a result, the nanolaser device was fabricated on the sapphire wafer coated with Al/ZnO without the need for transfer of nanostructures, which is needed for other reported nanostructures-on-a-film devices.

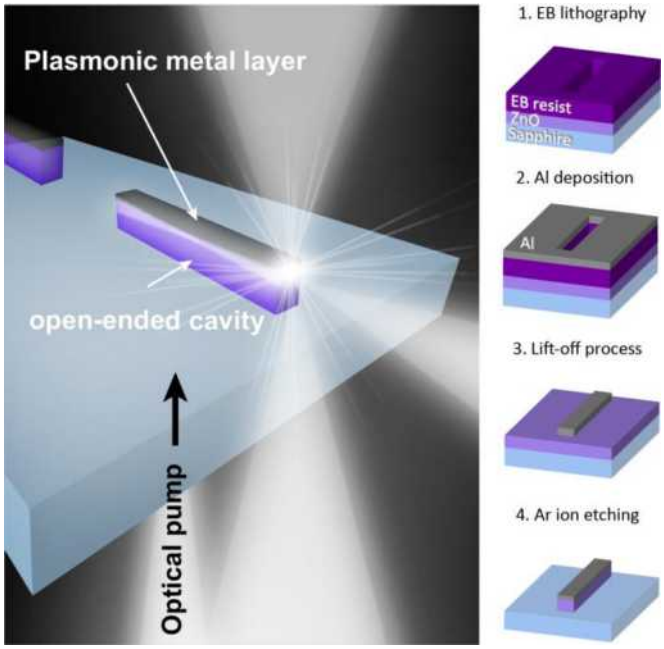


Figure 1: (left) Illustration of the on-chip fabricated ZnO/Al plasmonic nanolasers. ZnO open-ended cavities with Al top layers are directly grown and fabricated on a sapphire substrate. (right) Fabrication process of the plasmonic nanolaser.

2. Results and discussion

Figure 2 shows a comparison between the electric field enhancement achieved by the proposed Al/ZnO plasmonic cavity and the conventional nanowire-on-a-film structure. For the Al/ZnO plasmonic structure, the electric field enhancement is calculated for the wavelength λ = 372 nm and the absorption distribution for the wavelength λ = 343 nm (the structure is pumped from the bottom through the sapphire substrate). For comparison purposes, the electric field enhancement of the fundamental plasmonic mode in the ZnO nanowire laser sitting on the Al surface at wavelength λ = 372 nm and the absorption distribution at wavelength λ = 343 nm (pump light from the top of the structure) are also shown. It is noted that the mode distribution and the absorption have good overlap in the

case of the on-chip plasmonic cavity nanolaser. In contrast, the nanowire laser cavity exhibits a mismatch between its strong field enhancement near the bottom of the cavity and its absorption maxima near the edge of the cavity bottom and close to the center of the cavity. This mismatch suggests inefficient exciton-plasmon coupling for the nanowire-on-a-film structure.

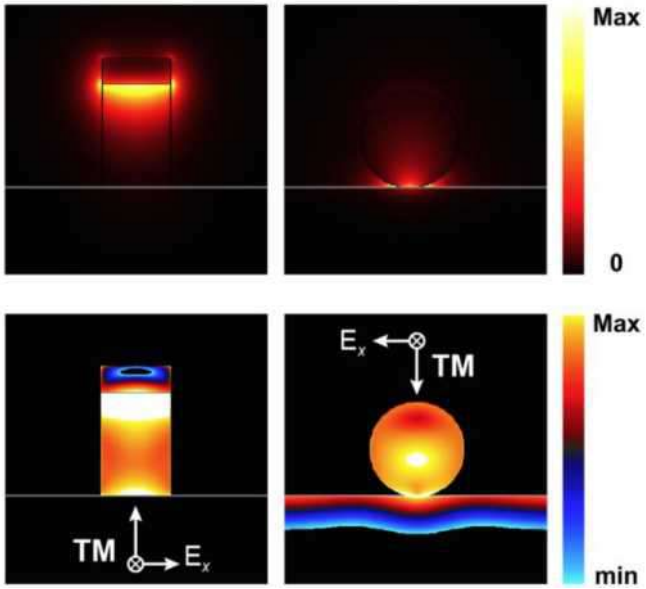


Figure 2: (top) Comparison between simulated distributions of the electric field and absorption for (left) the Al/ZnO cavity on a sapphire substrate and (right) the ZnO nanowire on an Al surface. (bottom) Absorption of the pump light in both structures. Note that the absorption for the Al/ZnO cavity structure is obtained for the light pump coming from the bottom of the structure through the sapphire substrate.

The variation in the emission intensity with the pump energy density for the fabricated plasmonic nanolaser is shown in Figure 3 as a log-log plot. When the pump energy density reaches 0.09 mJ/cm^2, the emission intensity increases nonlinearly. The nonlinear region ranges from 0.09 to 0.12 mJ/cm^2 and represents the threshold region between spontaneous emission and lasing. The bandwidth of the emission decreases drastically in the nonlinear region confirming the lasing of the structure. It was also found that the emitted light was polarized along the cavity axis as expected for a plasmonic mode. Finally lasing was observed at 330 K confirming the possibility for this structure to sustain lasing at room temperature.

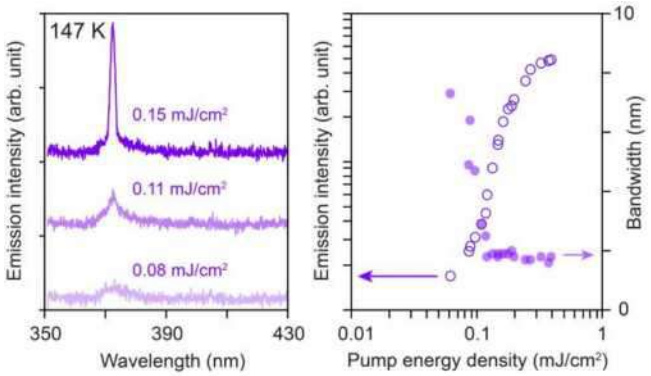


Figure 3: (left) Emission spectra at 147 K of the fabricated ZnO/Al plasmonic cavity with a width of 100 nm. (right) Emission intensity versus pump energy together with the emission bandwidth.

3. Conclusions

We demonstrate a monolithically fabricated ZnO/Al plasmonic-waveguide nanolaser compatible with the fabrication requirements of on-chip circuits. The nanolaser is designed with a plasmonic metal layer on the top of the laser cavity only, providing highly efficient energy transfer between photons, excitons, and plasmons, and achieving lasing in the ultraviolet region up to 330 K with a low threshold intensity. This work demonstrates the realization of a plasmonic-waveguide nanolaser without the need for transfer and positioning steps, which is the key for on-chip integration of nanophotonic devices.

Acknowledgments

This work was supported through Japan Society for the Promotion of Science (JSPS) KAKENHI Grant Numbers (17H03229, 17K18867, 18K13799).

References

[1] D. J. Bergman, M. I. Stockman, Surface plasmon amplification by stimulated emission of radiation: quantum generation of coherent surface plasmons in nanosystems, *Phys. Rev. Lett.* 90: 027402, 2003.

[2] R. M. Ma, R. F. Oulton, V. J. Sorger, X. Zhang, Plasmon lasers: coherent light source at molecular scales, *Laser Photon. Rev.* 7: 1, 2013.

[3] P. Berini, I. De Leon, Surface plasmon–polariton amplifiers and lasers, *Nat. Photon.* 6: 16, 2012.

[4] Y.-L Ho, J. K. Clark, A. Syazwan A. Kamal, J.-J. Delaunay, On-chip monolithically fabricated plasmonic-waveguide nanolaser, *Nano Letters* 18: 7769–7776, 2018.

Hybrid plasmonic nanostructures based on controlled deposition of MoS_2 flakes on plasmonic nanostructures

Dario Mosconi[1], Ermanno Miele[2], Andrea Jacassi[2], Giorgia Giovannini[2], Nicolò Maccaferri[2,4], and Denis Garoli[2*]

[1]Dipartimento di Chimica, Università degli Studi di Padova, Via Marzolo 1, 35132 Padova, Italy
[2]Istituto Italiano di Tecnologia, Via Morego 16, 16136 Genova, Italy
[3]Physics and Materials Science Research Unit, University of Luxembourg, 165, avenue de la Faïencerie, L-1511, Luxembourg
*corresponding author, E-mail: denis.garoli@iit.it

Abstract

We report on easy and robust strategies for the versatile integration 2D material flakes on plasmonic nanoholes by means of site selective deposition of MoS_2. The methods can be applied both to simple metallic flat nanostructures and to complex 3D metallic structures comprising nanoholes. The deposition methods allow the decoration of large ordered arrays of plasmonic structures with single or few layers of MoS2.

1. Introduction

In the last decade, intensive research efforts have been devoted to the investigation of two-dimensional (2D) materials, such as graphene and various transition metal chalcogenides (TMDCs).[1–2] Molybdenum disulfide (MoS_2) is a typical representative of TMDCs materials family, which consists of S-Mo-S layers bonded by van der Waals interaction. MoS_2 offers a powerful platform for applications in nanophotonics and optoelectronics due to its remarkable optical properties. In fact, MoS_2 behaves like a semiconductor with direct band gap electronic structure, notable flexibility, and tunable optical emission.[3] An extensive interest from researchers raised in the last years to explore potential physical phenomena, especially on light−matter interaction, such as multiexciton photoluminescence (PL), interlayer exciton coupling, strong coupling and valley polarization effect.[4] Great efforts have been devoted to realize the active control of MoS_2 by utilizing photonic cavity modes and metallic surface plasmons.[5] However, most designed structures must be fabricated precisely with the structure geometries and the coupling distance, which limits the development of active-controlled optoelectronic devices in the future. Moreover, one of the main limitation of MoS_2 application in photonics and plasmonics is related to the challenging alignment between nanostructures and the 2D material. New approached for easy and controlled integration of 2D materials with metallic or semiconductor nanostructures can now represent a significant help in the cited field of research. We have recently proposed and demonstrated the possibility to control the deposition of single layer MoS_2 flakes on metallic nanostructures by means of chemical conjugation and electrophoretic process.[6,7] Here we illustrate a direct comparison between the two methods. As we will show, both the procedure are reliable and allow high yield controlled deposition in both flat nanostructures and 3D elements.

2. Materials and Methods

2.1. Exfoliation of MoS_2

In a glove-box (water < 1 ppm, O_2 < 10 ppm), $LiBH_4$ (0.109 g, 5 mmol) and MoS_2 (0.320 g, 2 mmol) were grounded in a mortar and subsequently transferred in a Schlenk-tube, which then was brought outside of the glove-box and connected to a Schlenk-line. This mixture was heated in a sand bath at 330°C for 4 days under nitrogen. Afterwards, the Schlenk-tube was brought again inside the dry-box, where it was newly grounded with additional $LiBH_4$ (0.109 g, 5 mmol). The sample was subsequently heated for 3 days at 330°C under nitrogen. The intercalation product was added in a single shot in 270 ml of degassed water and the resulting suspension was bath-sonicated for 1 h to facilitate the exfoliation. In order to remove the LiOH produced, the suspension was equally divided into six centrifugation tubes (45 ml/tube) and centrifuged at 10000 rpm (23478*g*) for 20 min for three times, replacing the supernatant with clean solvent.

2.2. Fabrication of plasmonic nanostructures

The fabrication of the metallic nanoholes follows simple and robust procedures for the 2D and 3D geometry. In both cases the substrate was a Si_3N_4 membrane (100 nm thick) prepared on a Silicon chip. [8-10].

2.3. Electrophoretic deposition

The electrophoretic method has been already proposed for MoS_2 nanosheet deposition for several applications, here, with respect to the previous reported cases, the substrate where the flakes are deposited is not used as electrode. On the contrary, in order to obtain a controlled deposition only over our nanostructures, the substrate is placed in the middle of a fluidic chamber where two Pt electrodes are present. In particular, the nanoholes present in the substrate allow the flow of ions though them and at the same time they

represent an obstacle for the MoS_2 flakes that are there forced to stop and deposit.

2.4. Chemical conjugation deposition

The method used for the deposition is based on the conjugation between a gold (or another noble metal) surface and a dithiol-terminated organic chain as well as the same conjugation between the MoS_2 flake and the dangling –SH group of the same molecule. In particular, to perform a controlled deposition of MoS_2 over metallic holes, we used a 1,12-dodecanedithiol molecule as a linker between the gold surface and local –S vacancies in MoS_2 flakes.

3. Results and discussion

Micrographs of the deposited MoS_2 flakes on flat and 3D plasmonic nanoholes are shown in Fig. 1. In left panels examples of different samples deposited by means of chemical conjugation are reported. In the right panels similar depositions performed by means of electrophoretic process are reported.

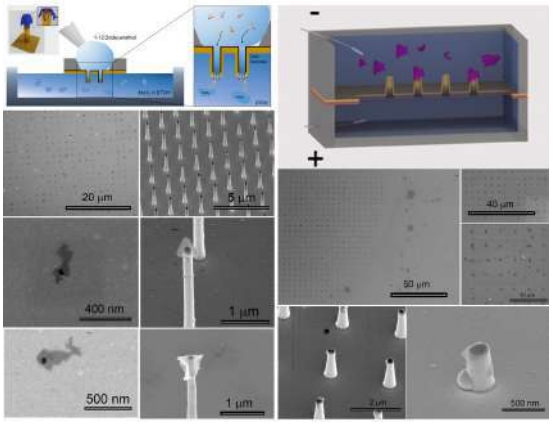


Figure 1: SEM micrographs of the prepared MoS_2 hybrid structures.

To verify the deposition of MoS_2 flakes and to compare the two processes, we performed Raman spectroscopy on our samples at wavelength of excitation of 532 nm.

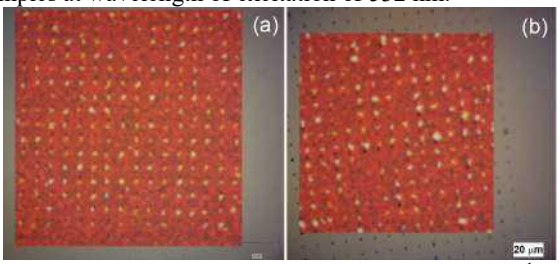


Figure 2 – Raman map integrated between 400 and 410 cm^{-1} (A_{1g} mode). (a) Sample deposited by means of thiol conjugation (b) Sample deposited by means of electrophoretic force.

4. Conclusions

In conclusion, we presented methods for hybrid plasmonic 2D material structure preparation. The fabrication procedure allows to obtain ordered structures over large array using a low-cost procedure and without the use of complex lithographic processes. This strategy can be applied to not only MoS2 but also to other 2D materials.
We believe that such an approach can be interesting for the realization of new hybrid devices for use in several applications, including photoluminescence, strong coupling and valley-polarization studies. With respect to previously reported hybrid plasmonic nanostructures, our scheme significantly reduces the complexity of fabrication, leading to a more robust and low-cost approach for the integration of 2D materials with plasmonic nanopores.

References

[1] A. K. Geim, K. S. Novoselov, "The rise of graphene," Nat. Mater. 6, 183–191 (2007).

[2] Q. H. Wang, K. Kalantar-Zadeh, A. Kis, J. Coleman & M. S. Strano, "Electronics and optoelectronics of two-dimensional transition metal dichalcogenides," Nat. Nanotechnol. 7, 699–712 (2012).

[3] A. K. Geim & I. V. Grigorieva "Van der Waals heterostructures," Nature 499, 419–425 (2013).

[4] Y. J. Chen, et al "Valley-polarized exciton-polaritons in a monolayer semiconductor," Nat. Photonics 11, 431–435 (2017).

[5] S. Butun, et al. "Enhanced Light Emission from Large-Area Monolayer MoS2 Using Plasmonic Nanodisc Arrays," Nano Lett. 15, 2700–2704 (2015).

[6] D. Garoli "Hybrid Plasmonic Nanostructures base on controlled integration of MoS2 flakes on metallic nanoholes," Nanoscale, DOI: 10.1039/c8nr05026k (2018).

[7] D. Mosconi, etl a. "Controlled integration of MoS2 flakes on metallic nanopores by means of electrophoretic deposition," arXiv: 1808.02672 (2018).

[8] D. Garoli, et al. "Beaming of Helical Light from Plasmonic Vortices via Adiabatically Tapered Nanotip," Nano Lett. 16, 6636–6643 (2016).

[9] D. Garoliet al. "Boosting infrared energy transfer in 3D nanoporous gold antennas," Nanoscale 9, 915–922 (2017).

[10] D. Garoli & G. Della Giustina, "Directly patternable high refractive index ferroelectric sol-gel resist," Mater. Chem. Phys. 164, 63–70 (2015).

Fast Optoelectronic Modulation of Surface Plasmons Polaritons at Degenerate Semiconductor Interfaces

D. A. Genov[1], R. K. Vinnakota[1] , Z. Dong[2], A. F. Briggs[2], L. Nordin[2], S. R. Bank[2], and D. Wasserman[2]

1 Department of Physics, Louisiana Tech University, Ruston, LA 71272 USA
2 Department of Electrical and Computer Engineering, University of Texas Austin, Austin, TX 78758, USA
*Corresponding author: dgenov@latech.edu

In this talk we present an optoelectronic switch for functional plasmonic circuits based on active control of Surface Plasmon Polaritons (SPPs) at degenerate pn++ - junction interfaces. Self-consistent multi-physics simulations of the electromagnetic, thermal and IV characteristics of the device have been performed. The lattice matched Indium Gallium Arsenide ($In_{0.53}Ga_{0.47}As$) is identified as the best semiconductor material for the practical implementation of the optoelectronic switch providing high optical confinement, reduced system size and fast operation. The optimal device is shown to be capable of providing SPP signal modulation surpassing -20dB and switching rates up to 50GHz, thus potentially providing a new pathway toward bridging the gap between electronic and photonic devices. Experimental validation of the device performance and specifically it potential for strong bias modulation is presented.

Photonics and in particular plasmonics has been recognized as a key technology for fast data communication and computing[1-3]. Here we propose a fast optoelectronic switch termed Surface Plasmon Polariton Diode (SPPD)[3], shown in Fig. 1a. The device consists of a degenerate pn++ - junction with an active drift-diffusion region formed between two control electrodes. Under forward bias minority carriers (electrons) are injected in the *p*- doped layer and for applied voltage higher than a critical value $V > V_c$ the *p*- layer acquires a metal like characteristics impeding the propagation of the SPP across the active region and establishing the OFF state of the device. A steady-state SPP signal modulation higher than -20dB is predicted, and responsivities in excess of $-1000\ \text{dB}\cdot\text{V}^{-1}$for Si and $-500\ \text{dB}\cdot\text{V}^{-1}$ are expected for applied bias close to a critical values $V_c = 1.14V$ for Si and $V_c = 0.81V$ for $In_{0.53}Ga_{0.47}As$. The fast response of the devices under step type of input voltage is studied, see Fig. 1b. The numerical results show a well-defined distinction between the OFF and ON response times, with the former being substantially faster. This distinction can be attributed to the drastically different physical processes that are involved, with the OFF times governed by the electric field facilitated injection of minority carriers while the ON times are set by charge diffusion. Consistently, a faster response is observed for the $In_{0.53}Ga_{0.47}As$ device. Moreover, the modulation rates are revealed to dependent on the acceptor doping, with higher doping's leading to faster signal modulation with 3dB data rates in excess of 50Gbit/s for $In_{0.53}Ga_{0.47}As$ and up to 10Gbit/s for Si.

A proof of concept experimental study has been performed to assess the main switching mechanism behind the SPPD operation. A degenerate p-n^{++} junctions are grown epitaxially on InP and fabricated by spin-doping on Si-on-insulator (SOI) wafers, see Fig. 1c. The devices are characterize both electrically and optically as a function of applied forward bias (Fig. 1c), with the measured change in reflectivity compared to the theory, see Fig. 1d. Our simulations match our experimental data with excellent agreement, and indicate the potential of the presented device architectures for integration into an actual SPPD.

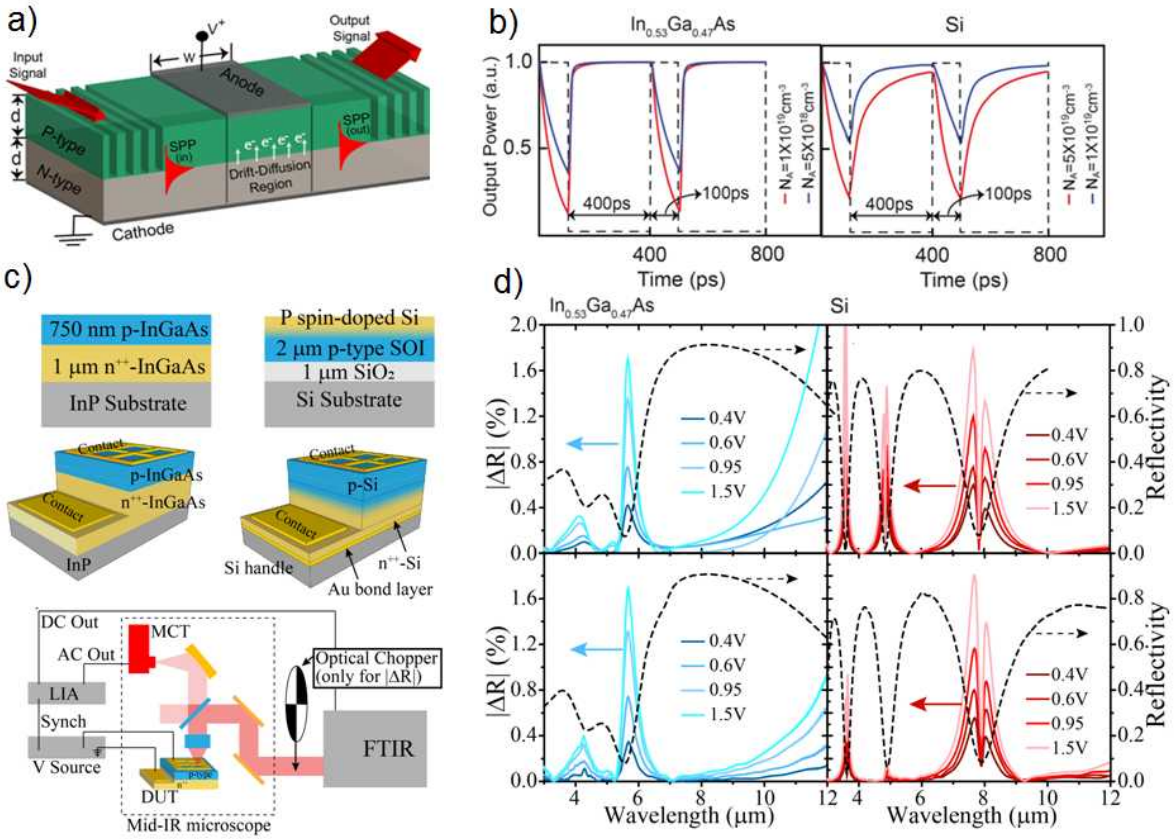


Figure 1. (a) Basic schematic of a Surface Plasmon Polarition Diode (SPPD). (b) Simulated SPPD signal modulation under step-type of input voltage (dashed line) with magnitude 1.3V for Si and 0.9V for $In_{0.53}Ga_{0.47}As$ devices. (c) Manufactured devices and experimental set up. (d) Constant voltage reflection responsivity curves simulated (top) and experimentally obtained (bottom).

References

1. R. Zia, J. A. Schuller, A. Chandran, and M. L. Brongersma, "Plasmonics: the next chip-scale technology," *Mater. Today*, vol. 9, no. 7–8, pp. 20–27 (2006).

2. E. Ozbay, "Plasmonics: merging photonics and electronics at nanoscale dimensions," *Science*, vol. 311, no. 5758, pp. 189–93 (2006).

3. R. K. Vinnakota, and D. A. Genov, "Active Control of Charge Density Waves at degenerate Semiconductor Interfaces", *Scientific Reports*, vol.7, pp. 10778 (2017).

Intuitive Semi-analytical Model of Channel Plasmon Polaritons in Subwavelength Plasmonic Trench Waveguide

Haitao Liu[1,*], Junda Zhu[1,2], Tong Zhu[1], Hongwei Jia[1], Ying Zhong[3]

[1]Tianjin Key Laboratory of Optoelectronic Sensor and Sensing Network Technology, Institute of Modern Optics, College of Electronic Information and Optical Engineering, Nankai University, Tianjin 300350, China
[2]MOE Key Laboratory of Weak Light Nonlinear Photonics, TEDA Institute of Applied Physics and School of Physics, Nankai University, Tianjin 300457, China
[3]State Key Laboratory of Precision Measurement Technology and Instruments, Tianjin University, Tianjin 300072, China
*corresponding author, E-mail: liuht@nankai.edu.cn

Abstract

An intuitive semi-analytical model is proposed to describe the channel plasmon polaritons (CPPs) guided by a subwavelength rectangular groove cut into a metal substrate. The model is built up by considering an intuitive multiple scattering process of gap surface plasmons (GSPs) bouncing between the mouth and the bottom of the groove. The evolution of the CPPs from guided, quasi-guided to evanescent modes with the increase of wavelength is explained with the model.

1. Introduction

CPPs supported by plasmonic channel waveguides (such as a metallic V-groove or rectangular trench) can simultaneously realize a strong confinement of field and a low propagation loss, and have important applications such as plasmonic nanocircuit components [1], quantum plasmonics [2], and nanolaser [3]. To analyze the channel waveguides, full-wave numerical methods such as the finite-difference time-domain method and the finite element method have been used. However, these numerical methods are lack of intuitive physical pictures on the formation of the CPP, and could be time consuming due to the discretization of the total space. Besides the numerical methods, the effective index method (EIM) [4,5] has been widely used to model channel waveguides. However, the EIM turns to be less accurate as the frequency approaches the cut off and cannot provide the field distribution of CPPs [5]. The mode-matching method is able to provide analytical expressions for the mode fields and to determine the mode dispersion numerically [6].

In this talk, we introduce an intuitive semi-analytical model for the CPP supported by a rectangular trench waveguide [7]. The model can comprehensively reproduce all the features of the CPP including the dispersion relation, the electromagnetic field, and the critical parameters for identifying the guided, quasi-guided and evanescent CPP modes. With the model, the two-dimensional (2D) field distribution of the CPP in the waveguide transverse section can be reproduced with the 1D field distribution of the GSP, which decreases the computational amount compared to the full-wave numerical methods.

2. Results and discussion

As sketched in Fig. 1(a), the considered waveguide is formed by a rectangular air groove (with depth h and width w) cut into a gold substrate. To achieve a strong confinement of field, we consider a subwavelength groove ($w<0.5\lambda$, λ being the wavelength). In the model, by only considering the fundamental propagative GSP mode supported by the metal-insulator-metal (MIM) structure and neglecting all other higher-order evanescent GSP modes, a set of coupled-GSP equations can be written,

$$a = bur_a, \tag{1a}$$

$$b = aur_m, \tag{1b}$$

where a and b are the unknown complex coefficients of the up-going and down-going GSPs [Fig. 1(b)], r_a and r_m are the reflection coefficients of the GSP at the mouth and the bottom of the groove, respectively [Figs. 1(c) and 1(d)], and $u=\exp(ik_zh)$ is the z-direction phase shift factor of the GSP travelling over one groove depth h. Equation (1a) can be understood intuitively in view that the down-going GSP (with coefficient a) should result from the reflection of the up-going GSP (with coefficient b and phase shift factor u) at the groove mouth. Equation (1b) can be understood in a similar way. The CPP modes are the nonzero solutions of Eq. (1) and thus satisfy a resultant eigenequation $u^2r_ar_m=1$, which can be rewritten as

$$k_z = \frac{2m\pi - \arg(r_a r_m)}{2h} + i\frac{\ln|r_a r_m|}{2h}, \tag{2}$$

where m is an integer corresponding to different orders of CPPs. With Eq. (2) and $k_y^2 + k_z^2 = k_{\mathrm{GSP}}^2$, one can solve the dispersion relation $k_y=k_y(\lambda)$ of the CPP modes for a given λ, where k_y, k_z and k_{GSP} are the y-direction, z-direction and total GSP propagation constants, respectively. The electromagnetic field of the CPPs can then be obtained with

the use of the GSP field in the groove and of the transmitted fields $\Psi_{t,a}$ and $\Psi_{t,m}$ out of the groove for an incident GSP with unitary coefficient [Figs. 1(c) and (d)].

As shown in Figs. 2 and 3, the model can accurately reproduce both the dispersion relation and the electromagnetic field of the CPPs obtained with the full-wave aperiodic Fourier modal method (a-FMM). Figure 2 shows that with the increase of the wavelength λ, the CPP evolves from the guided mode first, then the quasi-guided mode [$\mathrm{Re}(k_y)<k_0$], and finally to the evanescent mode [$\mathrm{Re}(k_z)>\mathrm{Re}(k_{GSP})$]. The exceptional case is the fundamental CPP mode (m=0) which is always a guided mode. With the model, the critical wavelengths λ_g and λ_q among the guided, quasi-guided and evanescent CPPs can be derived to be $\frac{2\pi}{\lambda_g} \approx \frac{(2m+1)\pi}{2h\sqrt{n_{GSP}^2-1}}$ and $\frac{2\pi}{\lambda_q} \approx \frac{(2m+1)\pi}{2hn_{GSP}}$ with $n_{GSP}= k_{GSP}/k_0$.

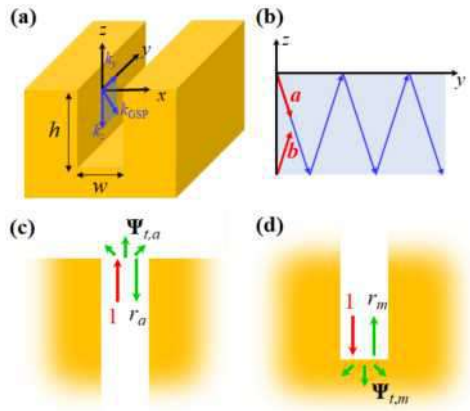


Figure 1: Definition of quantities used in the model.

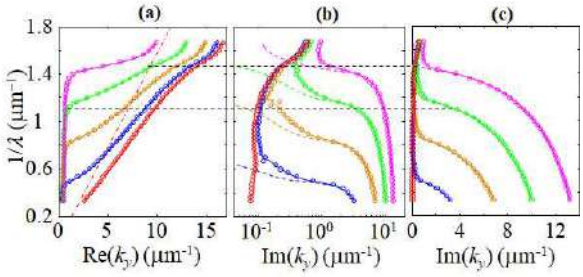


Figure 2: Dispersion relation of $\mathrm{Re}(k_y)$ and $\mathrm{Im}(k_y)$ as a function of $1/\lambda$ for the considered trench waveguide. The results are obtained with the model (solid and dashed curves for the lossy and lossless metal, respectively) and with the full-wave a-FMM (circles, for the lossy metal) for groove width w=50nm and depth h=1μm and for different orders of CPPs (m=0,1,2,… from bottom to top). The red dash-dotted line in (a) denotes the dispersion relation $k_y=k_0=2\pi/\lambda$ of light in air. (b) takes a logarithmic scale of $\mathrm{Im}(k_y)$ to show the slight increase of $\mathrm{Im}(k_y)$ from the guided CPPs to the quasi-guided CPPs. The critical wavelengths λ_g and λ_q for distinguishing the guided, quasi-guided and evanescent CPP (of order m=3) are marked with the two horizontal black dashed lines.

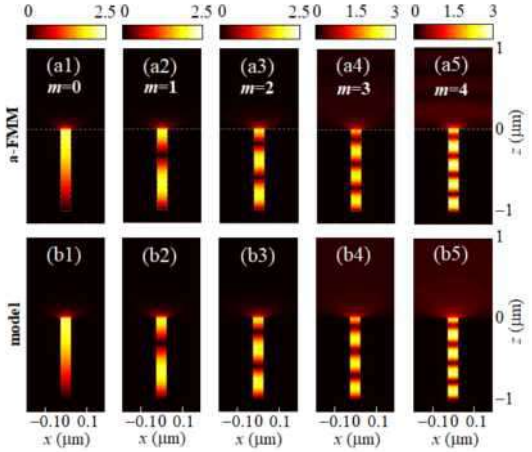


Figure 3: Modulus $|E_x|$ of the x-component of the electric field (the dominant electric field component in the groove) for the first five orders of CPPs (m=0,…,4). The results are obtained with the full-wave a-FMM (a1)-(a5) and the model (b1)-(b5) for h=1μm and λ=0.75μm.

Acknowledgements

National Natural Science Foundation of China (NSFC) (61775105, 11504270), 111 Project (B16027), Engineering Research Center of Thin Film Photo-electronics Technology of Ministry of Education, and International Cooperation Base for New PV Technology.

References

[1] S.I. Bozhevolnyi, V.S. Volkov, E. Devaux, J.Y. Laluet, T.W. Ebbesen, Channel plasmon subwavelength waveguide components including interferometers and ring resonators, *Nature* 440: 508-511, 2006.

[2] A. Gonzalez-Tudela, D. Martin-Cano, E. Moreno, L. Martin-Moreno, C. Tejedor, F.J. Garcia-Vidal, Entanglement of two qubits mediated by one-dimensional plasmonic waveguides, *Phys. Rev. Lett.* 106: 020501, 2011.

[3] E. Bermudez-Urena, G. Tutuncuoglu, J. Cuerda, C.L.C. Smith, J. Bravo-Abad, S.I. Bozhevolnyi, A.F.I. Morral, F.J. Garcia-Vidal, R. Quidant, Plasmonic waveguide-integrated nanowire laser, *Nano Lett.* 17: 747-754, 2017.

[4] S.I. Bozhevolnyi, Effective-index modeling of channel plasmon polaritons, *Opt. Express* 14: 9467-9476, 2006.

[5] S.I. Bozhevolnyi, J. Jung, Scaling for gap plasmon based waveguides, *Opt. Express* 16: 2676-2684, 2008.

[6] H.T. Jia, K. Yasumoto, K. Yoshitomi, Analysis of rectangular-groove waveguides using the Fourier-transform technique, *Microw. Opt. Technol. Lett.* 41: 388-392, 2004.

[7] J. Zhu, T. Zhu, H. Jia, Y. Zhong, H. Liu, Intuitive analysis of subwavelength plasmonic trench waveguide, *J. Lightwave Technol.*, DOI: 10.1109/JLT.2019.2893015

Vertical Lasing from InP Nanowire with Cat's Eye Antenna

Fang-Fang Ren[1], Wei-Zong Xu[1], Jiandong Ye[1], Yi Yang[1], Hark Hoe Tan[2], and Chennupati Jagadish[2]

[1]School of Electronic Science and Engineering, Nanjing University, Nanjing, China
[2]Department of Electronic Materials Engineering, Research School of Physics and Engineering, The Australian National University, Canberra, Australia
*corresponding author, E-mail: ffren@nju.edu.cn

Abstract

Cat's eye antennas have been designed and fabricated to modify the emission efficiency and profile of InP nanowire lasers. Narrower emission angle, higher polarization degree, increased internal quantum efficiency and lower lasing threshold were achieved from the antenna-coupled system, in comparison to bare nanowire lasers.

1. Introduction

Semiconductor nanowires have undergone a significant expansion and became a highly active research area within the nanoscience community. As one of the most promising applications, nanowire lasers provide both gain medium and photonic cavity, but still suffer from high threshold and poor directionality. In this work, InP nanowire lasers are demonstrated by integrating with Cat's eye (CE) antenna, aiming at tailoring and enhancing the emission properties, including focused far-field distribution, enhanced polarization degree, increased internal quantum efficiency (IQE), and reduced lasing threshold [1].

2. Modeling and design

2.1. Guided modes in InP nanowires

The nanowire geometry, including diameter w and length L, was optimized to support guided optical modes at the wavelengths of 750 and 870 nm, these being the near-band emissions of InP nanowires at low (~7 K, LT) and room temperature (RT), respectively. RT-lasing would be observed from nanowire lasers with w = 600 nm, L = 7.5 μm. While for the case of w = 290 nm and L = 900 nm, the required minimum threshold gain for lasing is calculated to be 2400 cm^{-1}, which indicates that lasing action would be hard to be obtained at RT or even LT.

2.2. Design of the CE antennas

The design of the CE antenna was divided into two steps. First, the inner circular grating, located at a distance s from the antenna center, was designed to form an enhanced Q-factor metal resonant cavity for the nanowire guided modes. The second step was then to optimize the periodical circular grating of the antenna to guarantee efficient surface plasmon (SP) coupling resonance and also function as a lens, focusing the emission. The parameters of grating period, p = 650 nm, metallic concentric grating width b = 200 nm and depth d = 300 nm, split-gap width g = 200 nm, and inner circular grating distance, s = 900 nm, are finally chosen for the nanowire with a diameter w =290 nm and a length L = 900 nm by considering SP excitation, maximum E intensity at the focal point, minimal footprint of the device, as well as the feasibility in fabrication. Similarly, p = 650 nm, b = 200 nm, d = 600 nm, g = 700 nm and s = 800 nm are chosen for the case of nanowire with w = 600 nm and L = 7.5 μm.

3. Nanowire growth and device fabrication

The InP nanowires were grown on (111)A InP substrates by selective area epitaxy (SAE). Fabrication for Sample A (Fig. 1a) with w = 290 nm and L = 900 nm began by first transferring InP nanowires from growth substrate onto quartz substrate. Then a layer of 300 nm-thick SiO_2 was deposited by plasma enhanced chemical vapor deposition, followed by a 30 nm Al deposition via e-beam evaporation. The antenna design was then imported by intaglio printing into the SiO_2/Al structure around the InP nanowire with depth of ~330 nm. Finally, another 1 μm-thick Al layer was deposited to form the CE antenna. Two additional reference samples (B and C) were also fabricated. Sample B was consisted of an InP nanowire laying horizontally on a bare quartz substrate, whilst Sample C was formed by an InP nanowire coated with a 1 μm-thick Al film on a 300-nm thick un-patterned SiO_2 cladding layer. The fabrication process of Sample D (Fig. 1d) with larger nanowire (w = 600 nm and L = 7.5 μm) embedded in CE antenna was similar with Sample A. For comparison purposes, Sample E was also fabricated by a bare InP nanowire laser (w = 600 nm, L = 7.5 μm) placed on Al substrate.

4. Results

4.1. Focused far-field distribution

The far-field angular distribution of the emitted light from Samples A and C was characterized when a pumping fluence of 0.8 mJ/cm^2 was utilized at RT (Fig. 1b,c). When compared to Sample C, the far-field distribution of Sample

A shows a narrower emission angle which indicates that the integrated CE antenna strongly governs the propagation direction of the nanowire emission. For Samples D and E, lasing can be obtained at RT. As shown in Fig. 1e,f, interference patterns were observed in the far-field intensity distribution of both Samples D and E at a pumping fluence of 12.8 mJ/cm^2. The comparison of the far field patterns further confirms that the InP nanowire laser with CE antenna exhibits a much improved vertical emission directionality above the threshold.

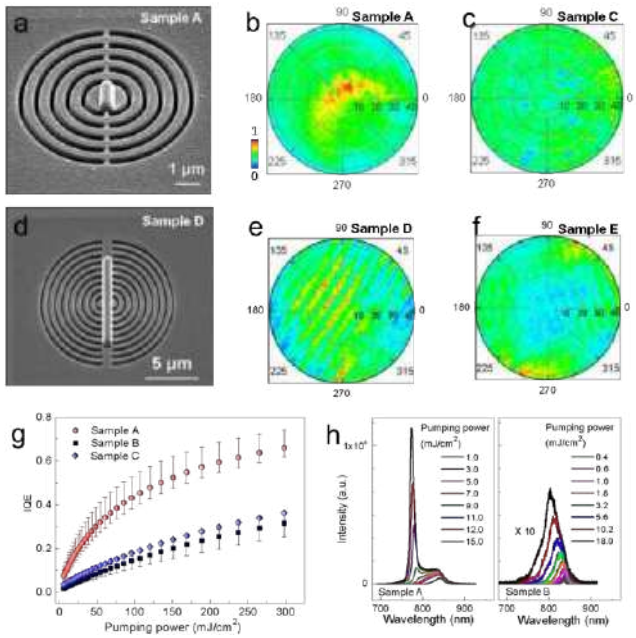


Figure 1: (a,d) SEM images of the fabricated Samples A and D before Al deposition. (b,c) Directionality characterization of light emission from Samples A and C below threshold at RT. (e,f) Directionality characterization of lasing from Samples D and E above threshold at RT. (g) Statistical results of IQE as a function of pumping power for Samples A-C at RT. (h) Lasing characterization from nanowire Samples A and B at LT.

4.2. Enhanced polarization degree

As measured, a degree of polarization (DOP) of 0.7 is obtained at 870 nm from Sample A, which is higher than the value of 0.5 from Sample B. To exclude the influence arising from reflections at the Al layer, we have also measured the polarization-dependent emission spectrum from Sample C. As a result, no distinct DOP enhancement can be observed from Sample C as compared to Sample B. It is therefore concluded that the improved DOP of Sample A is a direct result of the polarization sensitivity of the integrated split-gap CE antenna due to the cylindrical symmetry breaking.

4.3. Increased internal quantum efficiency (IQE)

The RT IQE (Fig. 1g) was measured and extracted from the variation in the integrated photoluminescence (PL) intensity as a function of excitation power density and based on rate-equations analyses. Clear improvement in IQE was obtained from Sample A, as compared to Samples B and C, which further verifies the distinct localization of optical energy densities in the nanowire.

4.4. Lasing characterization

Figure 1h shows the micro-PL spectra obtained from Samples A and B by optically pumping a pulsed laser (λ = 522 nm) at LT under different pumping fluences from 1.0 to 18.0 mJ/cm^2. At low pumping fluences, a single broad peak around 840 nm appears in both samples. With increasing fluence up to 18.0 mJ/cm^2, the PL intensity increases almost linearly but lasing is not observed from Sample B. On the other hand, for Sample A, upon exceeding a lasing threshold of only 5.8 mJ/cm^2, an additional peak emerges at 775 nm showing a dramatic increase of output intensity and a sudden linewidth narrowing. The observed spectral clamping indicates transition from spontaneous to amplified spontaneous emission and finally reaching lasing.

5. Conclusions

CE antenna has been designed to modify the emission characteristics of InP nanowires. The emission efficiency and profile were largely improved in following aspects: enhanced narrower emission angle, higher polarization degree, enhanced internal quantum efficiency, and reduced lasing threshold. It provides a promising solution to achieve high-performance nanoscopic light sources and other integrated nanophotonics applications.

Acknowledgements

The authors acknowledge the Australian Research Council, the National Natural Science Foundation of China (No. 91850112), and the Natural Science Foundation of Jiangsu Province, China (No. BK20161401) for financial support, and the Australian National Fabrication Facility for access to facilities.

References

[1] W.-Z. Xu, F.-F. Ren, D. Jevtics, A. Hurtado, L. Li, Q. Gao, J. D. Ye, F. Wang, B. Guilhabert, L. Fu, H. Lu, R. Zhang, H. H. Tan, M. D. Dawson, and C. Jagadish, Vertically emitting indium phosphide nanowire lasers," Nano Lett. 18: 3414−3420, 2018.

Quantum Plasmons and Plasmon–Emitter Interactions at the Nanoscale

P. A. D. Gonçalves[1,2,3,4,*], T. Christensen[1], N. Rivera[1], A.-P. Jauho[3,5], M. Soljačić[1], and N. A. Mortensen[2,3,6]

[1]Department of Physics, Massachusetts Institute of Technology, Cambridge, MA 02139, USA
[2]Center for Nano Optics, University of Southern Denmark, Campusvej 55, 5230 Odense M, Denmark
[3]Center for Nanostructured Graphene, Technical University of Denmark, 2800 Kgs. Lyngby, Denmark
[4]Department of Photonics Engineering, Technical University of Denmark, 2800 Kgs. Lyngby, Denmark
[5]Department of Physics, Technical University of Denmark, 2800 Kgs. Lyngby, Denmark
[6]Danish Institute for Advanced Study, University of Southern Denmark, Campusvej 55, 5230 Odense M, Denmark
*corresponding author, E-mail: padgo@fotonik.dtu.dk

Abstract

We present a theory for quantum nanoplasmonics that incorporates nonlocality and quantum effects like electronic spill-out and surface-enabled Landau damping, while also including retardation. Focusing on the planar and sphere geometries, we derive analytical expressions for the nonclassical scattering coefficients, from which the optical response of the systems can be unambiguously determined. We compute the systems' plasmonic excitations and investigate the role of quantum surface corrections to plasmon–emitter interactions, e.g., Purcell enhancement, dipole-forbidden transitions rates, and plasmon-mediated energy transfer.

1. Introduction

In this work, we provide a theoretical framework that remedies the shortcoming of classical electrodynamics in the mesoscopic regime, and, crucially, whose validity spans the intermediate regime where both quantum and classical effects coexist.

2. Results and Discussion

We develop a theory which rigorously accounts for quantum nonlocal effects in quantum nanoplasmonics, specifically, nonlocality, electronic spill-out, and surface-assisted electron-hole pair generation (known as Landau damping).

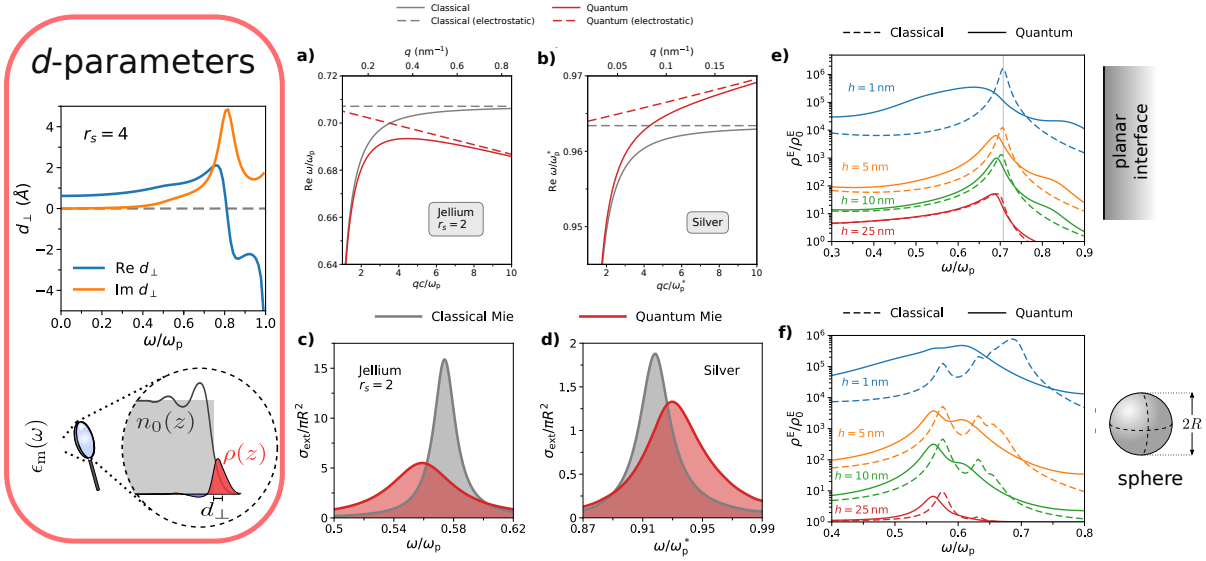


Figure 1: Illustration of the d-parameters obtained from TDDFT for a $r_s = 4$ jellium, together with an artistic impression of the quantum mechanical spill-out of the induced charge density in response to an external potential. a–b) Classical and quantum plasmon dispersion diagrams for a half-space, in the case of a a) simple metal and b) silver. c-d) Classical and quantum extinction cross-sections for a c) jellium and d) silver sphere. Classical and quantum Purcell enhancement experienced by a dipole emitter at different emitter–metal separations: e) planar interface; f) $R = 5\,\mathrm{nm}$ jellium sphere.

In particular, we further develop and extend the formalism of Feibelman's d-parameters [1–3], and derive analytical expressions for the nonclassical scattering coefficients—$\{r^{\text{TM}}, r^{\text{TE}}\}$ and $\{a_l^{\text{TM}}, b_l^{\text{TE}}\}$, for the planar interface and for metal spheres, respectively—with TDDFT-level accuracy to leading-order. Using these nonclassical scattering coefficients, we unambiguously determine the far- and near-field optical responses of the considered plasmonic structures. Our approach allows a simultaneous account of both quantum mechanical phenomena and retardation effects. Our calculations show that the simultaneous treatment of quantum effects and retardation is indeed essential for an accurate description of plasmons and plasmon-enabled phenomena in systems located in the blurred "classical–quantum boundary". In good agreement with experiments [1, 4], we predict nonclassical redshifts (blueshifts) of the plasmon resonances in simple (noble) metals accompanied by nonclassical damping, the latter being consequence of surface-enabled plasmon decay into electron-hole pairs. Moreover, we further investigate the impact of the above-mentioned quantum surface corrections in the context of plasmon–emitter interactions, where we find that these effects impose bounds to the enhancement of the electromagnetic local density of states (LDOS), modify dipole-forbidden transitions (namely, electric multipolar and two-photon processes), as well as plasmon-mediated energy transfer between two emitter.

3. Conclusions

In summary, our theoretical framework provides a comprehensive account of both plasmons and plasmon–emitter interactions at the nanoscale, that is, in the regime of quantum nanoplasmonics. Therefore, we show that our theory constitutes a simple, rigorous, and unified platform to incorporate quantum effects in nanoplasmonics.

Acknowledgement

N. A. M. is a VILLUM Investigator supported by VILLUM FONDEN (grant No. 16498) and Independent Research Fund Denmark (grant No. 7079-00043B). Center for Nano Optics is financially supported by the University of Southern Denmark (SDU 2020 funding). The Center for Nanostructured Graphene is sponsored by the Danish National Research Foundation (Project No. DNRF103).

References

[1] A. Liebsch, *Electronic Excitations at Metal Surfaces*, Springer (1997)

[2] P. J. Feibelman, Surface Electromagnetic Fields, *Prog. Surf. Sci.* **12**, 287–407 (1982).

[3] T. Christensen, W. Yan, A.-P. Jauho, M. Soljačić, and N. A. Mortensen, Quantum Corrections in Nanoplasmonics: Shape, Scale, and Material, *Phys. Rev. Lett.* **118**, 157402 (2017).

[4] S. Raza, S. Kadkhodazadeh, T. Christensen, M. Di Vece, M. Wubs, N. A. Mortensen, and N. Stenger, Multipole plasmons and their disappearance in few-nanometre silver nanoparticles, *Nat. Commun.* **6**, 8788 (2015).

Novel deep-learning-based techniques for design and optimization of photonic metastructures

Yashar Kiarashinejad, Sajjad Abollahramezani, Mohammadreza Zandehshahvar, Omid Hemmatyar, and Ali Adibi

School of Electrical and Computer Engineering
Georgia Institute of Technology
Atlanta, GA 30332-0250
Phone: (404) 385-2738
Fax: (404) 894-4641
Email: adibi@ece.gatech.edu

ABSTRACT
A computationally efficient new approach based on deep-learning techniques for analysis, design, and optimization of electromagnetic nanostructures will be presented. Using the strong correlation among features of an electromagnetic design problem, deep-learning techniques are employed to considerably reduce the dimensionality of the problem and thus, the computation complexity, without imposing considerable error. This approach reduces the computational complexity in both solving the forward problem (or analysis) and inverse problem (i.e., design) by orders of magnitude compared to conventional approaches. In addition, it provides analytic formulations that, despite their complexity, can be used to obtain intuitive understanding of the physics and dynamics of electromagnetic wave interaction with nanostructures with minimal computation requirements. In addition to explaining the fundamental properties of this approach, its application to designing a series of photonic metastructures, especially a new class of on-demand reconfigurable optical metasurfaces will be discussed and compared with more conventional design approaches.

KEYWORDS
neural networks, dimensionality reduction, metasurface, nanophotonic design, phase-change materials, manifold learning, autoencoder, deep learning

Active Tunable Photonic Topological insulator

Xiaoyong Hu[1]*, Yutian Ao[1], Xianxiang Niu[1], You Wu[1]

[1] Department of Physics, Peking University, Beijing 100871, China
*corresponding author, E-mail: xiaouonghu@pku.edu.cn

Abstract

We realized active tunable photonic topological states in photonic crystal topological insulators based on the thermo-optic effect and electro-optic effect. This may provide a useful way for the practical applications of photonic topological insulators in integrated optical devices.

1. Introduction

Photonic crystal topological insulators play an essential way in the realization of novel integrated photonic devices, because of their unique properties of controlling propagation states of photons. The topological protection properties are very important for the device fabrication. However, active control of the topological state is also a basis for the realization of device function. Therefore, the contradiction between the topological protection and active control has limited the applications of photonic crystal topological insulators.

2. Results and discussion

We realized active tunable photonic topological states in photonic crystal topological insulators based on the thermo-optic effect and electro-optic effect. We firstly realized an one-dimension photonic crystal topological insulator in the optical communication range thermo-optic effect. A one-dimensional silicon dioxide/vanadium dioxide photonic crystal heterostructure etched in a silicon waveguide, sandwiched between two gold films, was fabricated using electron-beam lithography etching. A photonic topological edge state centered at 1550 nm was obtained. The topological state could be switched on or off based on insulator-to-metal transition of VO_2. we also realized an electro-optic tunable two-dimensional photonic crystal topological insulator made of TiO_2 and $BaTiO_3$. The refractive of $BaTiO_3$ could be adjusted by using an external applied voltage. Then the band inversion was achieved and the resonant frequency and propagation direction of the topological state changed.

References

[1] You Wu, Xiaoyong Hu, Qihuang Gong, Reconfigurable topological states in valley photonic crystals, *Physical Review Materials* 2: 122201(R), 2018.

[2] Yutian Ao, Xiaoyong Hu, Chong Li, Yilong You, Qihuang Gong, Topological properties of coupled resonator array based on accurate band structure, *Physical Review Materials* 2: 105201(R), 2018.

[3] Chong Li, Xiaoyong Hu, Wei Gao, Yutian Ao, Saisai Chu, Hong Yang, Qihuang Gong, Thermo-optical tunable ultracompact chip-integrated 1D photonic topological insulator, Advanced Optical Materials 6: 1701071, 2018.

Optical switching of the Second Harmonic Generation in AlGaAs nanoantennas

Michele Celebrano[1],* Eva A. A. Pogna[1], Lavinia Ghirardini[1], Francesco Rusconi[1], Paolo Biagioni[1], Andrea Mazzanti[1], Giuseppe Della Valle[1], Lamberto Duò[1], Luca Carletti[2], Davide Rocco[2], Carlo Gigli[3], Giuseppe Marino[3], Giuseppe Leo[3], Costantino De Angelis[2], Giulio Cerullo[1], Marco Finazzi[1]

[1] Department of Physics, Politecnico di Milano, Piazza Leonardo Da Vinci 32, 20133 Milano, Italy
[2] Department of Information Engineering, University of Brescia, Via Branze 38, 25123 Brescia, Italy
[3] Matériaux et Phénomènes Quantiques, Université Paris Diderot - Sorbonne Paris Cité, 10 rue A. Domon et L. Duquet, 75013 Paris, France
*Corresponding author: michele.celebrano@polimi.it

Abstract

We demonstrate efficient optical switching of the second harmonic generation (SHG) in AlGaAs nanoantennas. We observe more than 50% enhancement/suppression of the SHG excited at telecom wavelength, when simultaneously illuminating with a control beam at an energy above the material bandgap. By means of pump-probe experiments, where the control beam serves as pump, we addressed the temporal evolution of this process revealing ultrafast build-up times (< 300 fs) and slower recovery times above 10 ps.

1. Introduction

Metal-less nanophotonics has recently raised an increasing interest because the optical response of high-permittivity dielectric nanoparticles exhibits negligible dissipative losses and strong magnetic multipole resonances in the visible and near-IR [1–3]. Semiconductors such as GaAs are extensively studied and employed in photonics due to their pronounced second order nonlinear properties [4]. In this context, we have recently devised [5] and realized [6] a nanophotonic platform characterized by an unprecedented second harmonic generation (SHG) conversion efficiency. This is an all-dielectric platform composed of 400nm-high AlGaAs nanopillars suspended on a low-refractive-index AlOx substrate fabricated from an aluminum-rich (100) GaAs wafer [6]. The result is an array of nanopillars on an aluminum-oxide (AlOx) substrate. We report SHG conversion efficiency higher than 10^{-5} when individual nanoantennas are illuminated with femtosecond pulses (150 fs pulses, 80 MHz repetition rate, 1554 nm wavelength) with an intensity of about 1.6 GW/cm^2, in excellent agreement with our simulation [5-8]. Such a remarkable efficiency is achieved thanks to the exploitation of magnetic and electric resonances emerging at coincidence with both the illumination and the SHG wavelength, which are characterized by sizeable quality factors due to the relatively low refractive index of the substrate. The choice of the fundamental wavelength and, consequently, of the SHG (about 777 nm) wavelength, both set below the energy of the material bandgap, allows minimizing the two-photon absorption of the pump and the re-absorption of SHG.

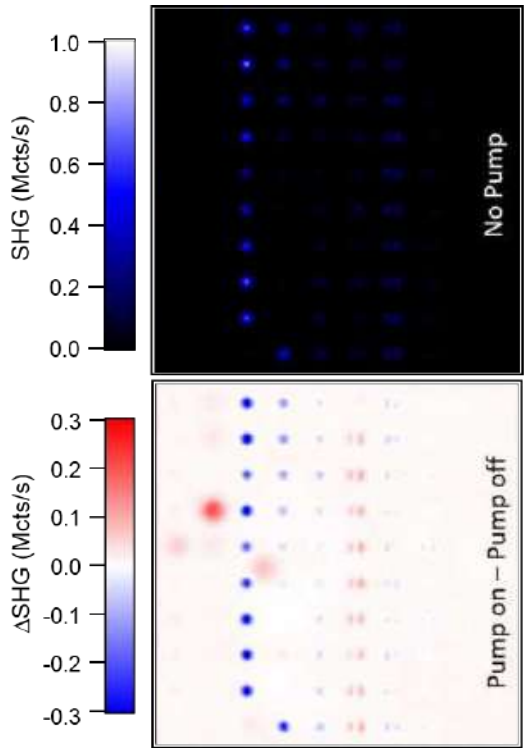


Figure 1. a) SHG intensity map obtained illuminating individual nanopillars at 1554 nm. Each column presents a replica of identical nanopillars, while in each row the pillar radius spans from 200 nm to 240 nm. b) Differential SHG map obtained by subtracting the SHG intensity map with CW control beam off from the one with control beam on. The nanopillars distance is 3 μm and the image size is 18 x 18 μm. The CW control beam is set at 100 μW.

2. Results & Discussion

Here, we study the behavior of the SHG signal excited at 1550 nm, when the nanoantennas are concurrently illuminated with a low-power (below 300 μW average power) control beam with energy above the bandgap (either 405 or 510 nm wavelength, i.e. about 3.2 or 2.5 eV). Figure 1 shows the comparison between a SHG intensity map and a SHG differential map (ΔSHG) acquired on an array of nanopillars with variable radius (along the horizontal axis), from 200 to 240 nm. The ΔSHG map is the difference between the SHG map obtained under simultaneous irradiation with a continuous wave (CW) control laser at 405 nm and the SHG map retrieved with the control laser is off (Figure 1b). In this way, we observe a variation in the SHG yield of the nanoantennas up to 60% with 300 μW power impinging on the nanoantenna. More importantly, depending on the nanoantenna radius, we observe that, while the SHG from the smaller nanopillar (r = 205 nm) is *decreased*, larger nanopillars (i.e. 220-nm-radius nanopillar) show a SHG yield *enhancement* when the control beam is on. A similar behavior is observed when the control wavelength is set at 532 nm (here not shown), while no sizeable ΔSHG has been measured using a control laser photon energy below the bandgap of the material (λ = 980 nm laser wavelength, not shown here).

We also investigated the ultrafast modulation of the SHG in a pump-probe experiment, where an ultrashort control pulse at λ = 510 nm (above material bandgap) acts as the pump, while the probe is a time-delayed pulse at λ = 1550 nm generating the SHG. In this way, we could study the SHG dynamics when the pillars are brought out of equilibrium and a transient plasma is photoinjected in the dielectric. Time-traces of the SHG as a function of the pump-probe delay are shown in Figure 2. We measured an ultrafast SHG quenching (< 0.5 ps) and a slower (10 to 100 ps) recovery times, which strongly depend on the nanopillars, hence on the resonances involved.

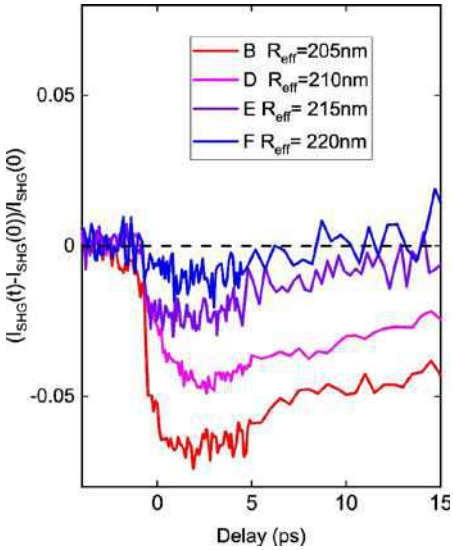


Figure 2. Time traces of SHG yield from different pillars using an ultrafast (Δt < 100 fs) pump beam at 510 nm (above bandgap). The timetraces refer to the pillars whose behavior was already assessed in the CW pump measurements.

3. Conclusions

We report efficient (more than 50%) modulation of the SHG yield in all-dielectric $Al_{0.18}Ga_{0.82}As$-on-AlOx nanodisks when an additional control beam with energy set above the material bandgap is concurrently illuminating the nanodisks. Pump-probe experiments employing an ultrashort control beam with energy above the material bandgap as pump indicate also the possibility to achieve an ultrafast modulation of the SHG (hundreds of fs) in these nanostructures with recovery times above 10 ps. Our results allow gaining further insight in the photophysics of the nonlinear emission in AlGaAs-on-insulator all-dielectric platforms and pave the way to the realization of nanoscale devices for all-optical data storage and quantum information processing.

Acknowledgements

G.L. acknowledges SATT IdF-Innov, ANR "Science and Engineering of Advanced Materials" (SEAM) Labex, and MULTIPLY EU Co-fund program for financial support. The work was partially supported by the Erasmus Mundus NANOPHI Project.

References

[1] A. I. Kuznetsov, A. E. Miroshnichenko, Y. H. Fu, J. Zhang, and B. Lukyanchuk, "Magnetic light," Sci. Rep. 2, 1–6 (2012).

[2] A. B. Evlyukhin, S. M. Novikov, U. Zywietz, R. L. Eriksen, C. Reinhardt, S. I. Bozhevolnyi, and B. N. Chichkov, "Demonstration of magnetic dipole resonances of dielectric nanospheres in the visible region," *Nano Lett.* **12**, 3749–3755 (2012).

[3] S. Person, M. Jain, Z. Lapin, J. J. Sáenz, G. Wicks, and L. Novotny, "Demonstration of zero optical backscattering from single nanoparticles," *Nano Lett.* **13**, 1806–1809 (2013).

[4] S. Bergfeld and W. Daum, Phys. Rev. Lett. **90**, 036801 (2003).

[5] L. Carletti, A. Locatelli, O. Stepanenko, G. Leo, and C. De Angelis, "Enhanced second-harmonic generation from magnetic resonance in AlGaAs nanoantennas," *Opt. Expr.* **23**, 26544–26550 (2015).

[6] V. F. Gili, L. Carletti, A. Locatelli, D. Rocco, M. Finazzi, L. Ghirardini, I. Favero, C. Gomez, A. Lemaître, M. Celebrano, C. De Angelis, and G. Leo, "Monolithic AlGaAs second-harmonic nanoantennas," *Opt. Expr.* **24**, 15965-15971 (2016).

[7] L. Ghirardini, L. Carletti, V. Gili, G. Pellegrini, L. Duò, M. Finazzi, D. Rocco, A. Locatelli, C. De Angelis, I. Favero, M. Ravaro, G. Leo, A. Lemaître, and M. Celebrano, *Opt. Lett.* **42**, 559-562 (2017).

[8] L. Carletti, D. Rocco, A. Locatelli, C. De Angelis, V. F. Gili, M. Ravaro, I. Favero, G. Leo, M. Finazzi, L. Ghirardini, M. Celebrano, G. Marino, A. V. Zayats, "Controlling second-harmonic generation at the nanoscale with monolithic AlGaAs-on-AlOx antennas", *Nanotechnology* **28**, 114005 (2017).

Spatiotemporal Manipulation of Optical Fields enabled by Metasurfaces

A. Agrawal[1,2], W. Zhu[1,2], C. Zhang[1,2], L. Chen[1,2], S. Divitt[1,2] and H. J. Lezec[1]

[1]National Institute of Standards and Technology, Gaithersburg, MD 20899
[2]Maryland Nanocenter, University of Maryland, College Park, MD 20742
*corresponding author, E-mail: amit.agrawal@nist.gov

Abstract

We demonstrate the versatility of dielectric metasurfaces to (*i*) shape the temporal evolution of ultrafast optical pulses, and (*ii*) discuss their applications towards creating integrated photonic interfaces with quantum systems.

1. Introduction

Over the last decade, flat optical elements composed of an array of deep-subwavelength dielectric or metallic nanostructures of nanoscale thicknesses – referred to as metasurfaces – have revolutionized the field of optics and nanophotonics [1-2]. Because of their ability to impart an arbitrary phase, polarization or amplitude modulation to an optical wavefront as well as perform multiple optical transformations simultaneously on the incoming light, they promise to replace the traditional bulk optics in applications requiring compactness, integration and/or multiplexing. The primary focus of research in this area has been on applications requiring arbitrarily manipulation of light in the spatial domain such as high numerical aperture focusing or generation of novel polarization states.

2. Metasurface enabled spatio-temporal beam shaping

2.1. Ultrafast pulse shaping

In this talk, we discuss the ability of metasurfaces to arbitrarily shape instead the temporal evolution of ultrafast optical pulses. This requires independent control over the amplitude, phase and/or polarization of the spectral lines covering the entire bandwidth of an optical pulse. We achieve this by designing a metasurface to operate on the spectral components of an ultrafast pulse that are separated spatially using a Fourier transform setup (Fig. 1). By designing metasurface elements to act as individual half wave plates, and combining it with an integrated broadband polarizer – we demonstrate the ability to shape <10 fsec pulses with a spectral resolution of approx. 140 GHz.

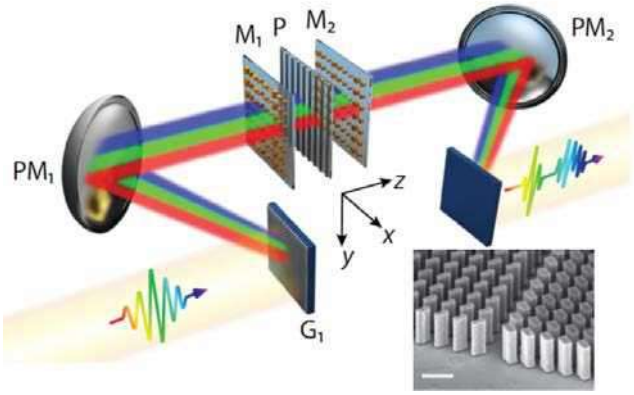


Figure 1: Metasurface-enabled Fourier-transform optical pulse shaper embedding one or more metasurfaces and a polarizer. Inset shows the SEM image of a typical metasurface composed of Si rectangular pillars on a fused-silica substrate. Scale bar represents 500 μm.

As an example requiring simultaneous and independent control over the spectral amplitude and phase, we demonstrate the ability to split an optical pulse into two time separated replicas (Fig. 2). Other examples such as dispersion compensation to arbitrarily higher orders including mechanical approaches towards dynamic control will be presented. We discuss the advantages of the metasurface approach to pulse shaping over the more traditional use of spatial light modulators to do the same. Finally, ongoing work on extending the spectral resolution of the system to sub GHz range enabling control of individual frequency comb lines from an ultrafast oscillator for applications in optical arbitrary waveform generation will be presented.

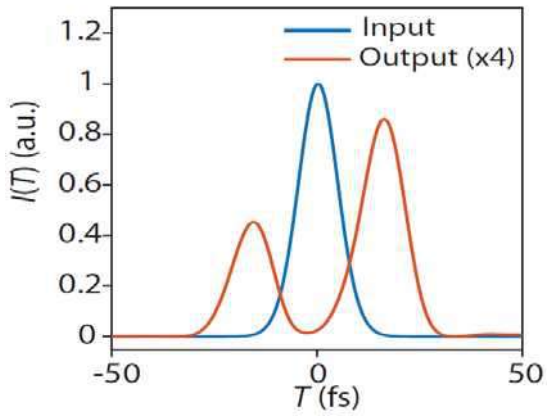


Figure 2: Metasurface enabled pulse shaping requiring simultaneous control of both spectral amplitude and phase. An input Gaussian pulse of length 10 fsec is shown to split into two time separated replicas separated by 30 fsec.

2.2. Metasurface enabled integrated photonic interfaces to quantum systems

In the second part of the talk, we will demonstrate the versatility of spatial shaping metasurfaces to be directly integrated on integrated photonic chips for their applications as an interface to quantum or biological systems (Fig. 3). Through spatial multiplexing of metasurfaces integrated with grating out-couplers directly on a nanophotonic chip, we show the ability to create arbitrary optical fields in the far-field that may enable applications such as optical trapping, biosensing or LIDAR.

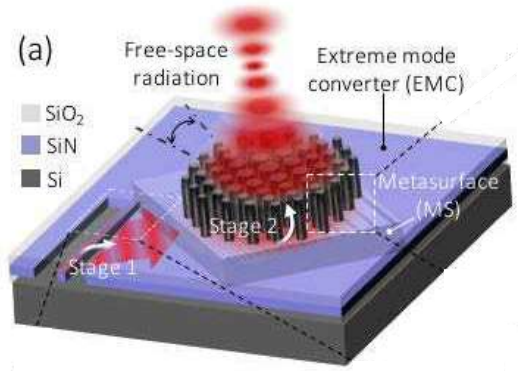


Figure 3: Metasurface-integrated photonic platform to create arbitrary spatial field off an integrated nanophotonic chip.

3. Conclusions

In conclusion, we show the versatility of dielectric metasurfaces as replacement for traditional spatial light modulators both for temporal and spatial domain shaping of optical fields. The ability to directly integrate them, monolithically in a CMOS platform, with photonic chips will enable novel applications in the areas of biosensing and quantum optics.

Acknowledgements

A.A., W. Z., C. Z., L. C. and S. D. acknowledge support under the Cooperative Research Agreement between the University of Maryland and the National Institute of Standards and Technology Physical Measurement Laboratory, Award#70NANB14H209, through the University of Maryland.

References

[1] A. Arbabi, Y. Horie, M. Bagheri, and A. Faraon, Dielectric metasurfaces for complete control of phase and polarization with subwavelength spatial resolution and high transmission, *Nat. Nanotech.* 10: 937–943, 2015.

[2] M. Khorasaninejad, W. T. Chen, R. C. Devlin, J. Oh, A. Y. Zhu, and F. Capasso, Metalenses at visible wavelengths: Diffraction-limited focusing and subwavelength resolution imaging, *Science* 352: 1190–1194, 2016.

Current-Driven Plasmonic Instability in Graphene Metasurfaces for Terahertz Applications

Stephane Boubanga-Tombet[1], Deepika Yadav[1], Akira Satou[1], Wojciech Knap[2,3], Vyacheslav V. Popov[4], and Taiichi Otsuji[1]

[1]Research Institute of Electrical Communication, Tohoku University, Sendai, Japan
[2] Int'l Research Laboratory CENTERA, Institute of High Pressure Physics, Polish Academy of Sciences, Warsaw, Poland
[3]Laboratory Charles Coulomb, University of Montpellier and CNRS, Montpellier, France
[4] Kotelnikov Institute of Radio Engineering and Electronics (Saratov Branch), Russian Academy of Sciences, Saratov, Russia
*corresponding author, E-mail: otsuji@riec.tohoku.ac.jp

Abstract

We explore current-driven plasmon dynamics including perfect transparency and light amplification in monolayer graphene metasurfaces. Current-induced complete suppression of the graphene absorption is experimentally observed in a broad frequency range followed by a giant amplification (up to ~ 9 % gain) of an incoming terahertz radiation at room temperature.

1. Introduction

The generation and amplification of electromagnetic waves by plasmonic instabilities in conventional two-dimensional (2D) electron systems (2DESs) have been actively investigated since 1980 [1]. However, after about forty years, we are still a long way from the realization of efficient emitters and amplifiers based on those plasmonic instability-driven mechanisms. The intensity of radiation reported experimentally so far is weak, the plasmon resonances too broad and not tunable enough to be promising for device applications [2]. The rise of graphene and its extremely strong light-plasmon coupling and superior carrier transport properties [3] make this work worth to be revisited. We investigate dc current driven plasmonic instabilities in high mobility graphene meta-materials that combine the advantage of an efficient tunable absorber, emitter and amplifier at room temperature (RT).

2. Device structure and physics

Plasmon modes in our devices are excited in monolayer graphene on hexagonal boron nitride (hBN) with a periodic dual-grating gate structure [4] positioned above the graphene sheets. The grating gate modulates the incoming electromagnetic wave and defines the plasmonic wave vectors. The samples are fabricated as field effect transistors (Fig. 1) with structures featuring an interdigitated asymmetric-dual-grating-gate (ADGG) [5]. The plasmonic cavities are formed below the gates electrodes and designed with symmetric or asymmetric boundaries and electron mobilities around 50.000 cm^2/Vs at RT.

ADGG-bias-dependent electron density modulation causes spatial complementary modulation of the plasmon and drift velocities. This may cause Doppler-shift (DS) type, transit-time-modulation (TTM) type, Cherenkov (CK) type, and/or plasmonic boom (PB) type instabilities under asymmetric cavity boundaries [6][8]. When the instability-driven gain surpasses the Drude loss, the system yields the net gain, resulting in plasmon self oscillation at the resonant frequencies. The ADGG works as a broadband antenna that can convert the non-radiative plasma oscillations to radiative THz waves. This, in turn, enables spontaneous THz emission of radiation as well as coherent light amplification to the incident THz waves.

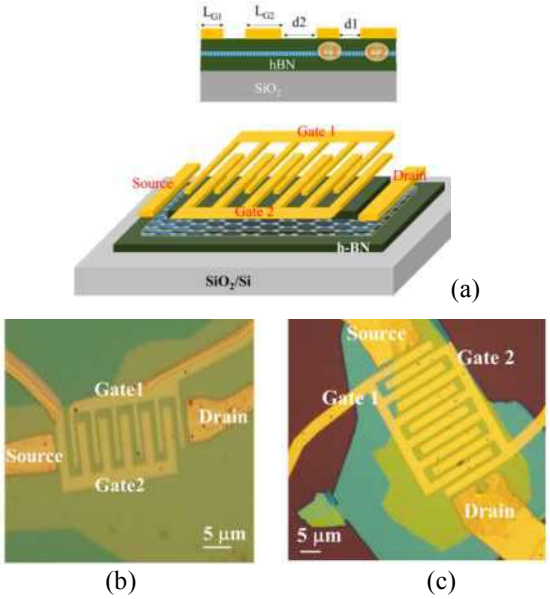


Figure 1: hBN/graphene/hBN FET with a DGG. (a) Bird's view schematic, (b) top view of an ADGG type sample, and (c) top view of a SDGG type sample.

3. Experimental results and discussion

We examined three samples: two ADGG type (ADGG1 (Fig. 1(b)) and ADGG2) and one symmetric DGG type (SDGG) alignment (Fig. 1(c)). With the applied gate

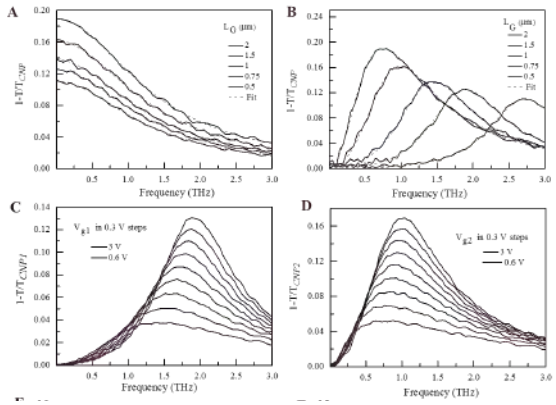
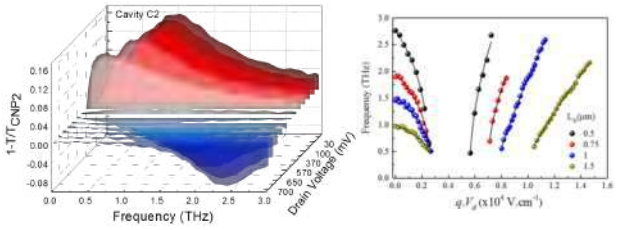


Figure 2: Measured extinction spectra at V_d = 0 V to the radiations with polarization parallel to the SDGG (a), perpendicular to the SDGG (b), ADGG-C1 (c), and ADGG-C2 (d).

voltages V_{g1} and V_{g2} each device supports the formation of two different plasmonic cavities (types C1 and C2) below the fingers of Gate 1 and Gate 2 in the DGG device structure (top part of Fig. 1). Terahertz (THz) time-domain spectroscopy (THz-TDS) was employed to measure the changes in the THz pulses transmitted through the graphene plasmonic cavities of type C1 (C2) when sweeping V_{g1} (V_{g2}) and keeping the voltage on the other gate electrode constant at the charge neutral point (CNP) $V_{g2} = V_{CNP2}$ ($V_{g1} = V_{CNP1}$). The source-to-drain voltage (V_d) dependent measurements were also conducted at a constant V_g. The transmission coefficient at a given V_g and V_d is referred to as T while T_{CNP} is the transmission coefficient at $V_g = V_{CNP}$. The measured extinction spectra ($1-T/T_{CNP}$) at V_d = 0 V exhibited similar tendencies of polarization-sensitive resonant absorptions among the three samples (Fig. 2).



(a) (b)

Figure 3: Drain bias dependent extinction spectra of the graphene metamaterial. (a) Spectra measured in cavities C2 of device ADGG1 for fixed $V_{g2} - V_{CNP2}$ = 3 V and $V_{g1} = V_{CNP1}$ when varying V_d. (b) Drain bias dependent resonance frequencies, gain and phase spectra. Scaling laws of the measured graphene plasmon resonance frequency in the three devices as a function of characteristic field intensity qV_d and fits to data shown as solid lines, where q is the plasmon wave vector, $q = 2\pi/L_g$, and L_g is the gate length of one finger of the GG.

When V_d increases, the absorption peaks weakened with red shifting, only ADGG samples approaching perfect transparency over the measured entire frequency range (at V_d = 370 mV for C2 of ADGG1). Further increase in V_d for only ADGG samples gives rise to negative absorption peak, i.e. resonant amplification, appears in the extinction spectra with a noticeable blue shift, reaching the maximal gain (9%), which is far beyond the interband-transition-limited quantum efficiency (2.3%) (Fig. 3(a)). The measured frequency dependence of the extinction peaks perfectly traces the theory with sharp gain thresholds [7] (Fig. 3(b)). Considering the extracted plasmon and drift velocity relations, a mixture of DS and TTM instabilities may cause such phenomena.

4. Conclusions

We explored current-driven plasmon dynamics in monolayer graphene active metamaterials. Frequency tunable THz light amplification up to 9% gain at RT by current-driven plasmon instabilities produced in an ADGG-GFET structure has been successfully demonstrated.

Acknowledgements

We thank Dr. Dmitry Svintsov, Dr. Akira Satou, Pr. Michel Dyakonov, Pr. Victor Ryzhii and Pr. Michael S. Shur for helpful discussions. This work was supported by JSPS KAKENHI (#18H05331 and #16H06361), Japan.

References

[1] D. Tsui, E. Gornik, R. Logan, Far infrared emission from plasma oscillations of Si inversion layers. *Solid State Comm.* 35: 875–877, 1980.

[2] A. El Fatimy, N. Dyakonova, Y. Meziani, T. Otsuji, W. Knap, S. Vandenbrouk, K. Madjour, D. Theron, C. Gaquiere, M. Poisson, S. Delage, P. Prystawko, C. Skier- biszewsk, AlGaN/GaN high electron mobility transistors as a voltage-tunable room temperature terahertz sources. *J. Appl. Phys.* 107: 024504, 2010.

[3] L. Ju, B. Geng, J. Horng, C. Girit, M. Martin, Z. Hao, H. A. Bechtel, X. Liang, A. Zettl, Y. R. Shen, F. Wang, Graphene plasmonics for tunable terahertz metamaterials. *Nature Nanotechnol.* 6: 630–634, 2011.

[4] T. Otsuji, M. Hanabe, T. Nishimura and E. Sano, A grating-bicoupled plasma-wave photomixer with resonant-cavity enhanced structure, *Opt. Exp.* 14: 4815-4825, 2006.

[5] V. Popov, D. Fateev, T. Otsuji, Y. Meziani, D. Coquillat, W. Knap, Plasmonic terahertz detection by a double-grating-gate field-effect transistor structure with an asymmetric unit cell. *Appl. Phys. Lett.* 99: 243504, 2011.

[6] Y. Koseki, V. Ryzhii, T. Otsuji, V. V. Popov, and A. Satou, Giant plasmon instability in dual-grating-gate graphene field-effect transistor, *Phys. Rev. B* 93: 245408, 2016.

[7] S.A. Mikhailov, Plasma instability and amplification of electromagnetic waves in low-dimensional electron systems, *Phys. Rev. B* 58: 1517-1532, 1998.

[8] G. Aizin, J. Mikalopas, M. Shur, Current-driven plasmonic boom instability in three- dimensional gated periodic ballistic nanostructures. *Phys. Rev. B* 93: 195315, 2016.

Self-Assembled Nano-Rings of Gold Nanoparticles

Anna M. Ritcey[1,2,3], Denis Boudreau[1,3] and Marie-Pier Côté[1,2,3]

[1]Department of Chemistry, Université Laval, Québec, Canada
[2]Centre de recherche sur les matériaux avancés (CERMA)
[3]Centre d'optique, photonique et laser (COPL)
*corresponding author, E-mail: Anna.Ritcey@chm.ulaval.ca

Abstract

In order to exploit the plasmonic properties of metal nanoparticles in actual applications convenient methods must be developed for the production of ordered assemblies covering macroscopic surface areas. Our work addresses this goal through the directed assembly of metal nanoparticles within periodic block copolymer templates. This self-assembly method allows for the preparation of unique arrangements, such as nano-rings and hybrid core-satellite structures. The optical properties of these individual nanostructures are characterised by combining hyperspectral imaging and scanning electron microscopy.

1. Introduction

Metal nanoparticles can interact with light in a unique way, offering exciting new possibilities for both fundamental science and the design of novel optical materials. This interaction is dominated by the collective excitation of free electrons, known as the surface plasmon. Plasmon excitation is in fact the most efficient process by which light can interact with matter, conferring to metal nanostructures the unique ability to concentrate and manipulate light at dimensions well below the diffraction limit. Because of these new capabilities, the field of plasmonics has grown rapidly, being identified [1] as a potential pervasive technology capable of achieving unprecedented optical functionalities.

Nanoparticle assemblies, as opposed to single particles, offer multiple advantages for the fabrication of plasmonic devices. Excitation of the surface plasmon leads to local electromagnetic field enhancement that is at the basis of surface enhanced spectroscopies. In the case of assemblies, strong interparticle interactions can increase this field enhancement by up to several orders of magnitude as compared to that of isolated particles. Furthermore, interparticle coupling provides a way to tune the plasmon frequency through the characteristic redshift associated with particle aggregation. Of particular relevance to sensing applications, is the observation that the plasmon frequency of coupled modes shows a stronger response to local refractive index changes than does that of single particles [2,3].

2. Objective and Experimental Approach

When spread at the air-water interface, amphiphilic block copolymers self-assemble into a periodic array of surface micelles, such as those illustrated in Figure 1, composed of circular hydrophobic domains surrounded by coronas of hydrophilic segments [4].

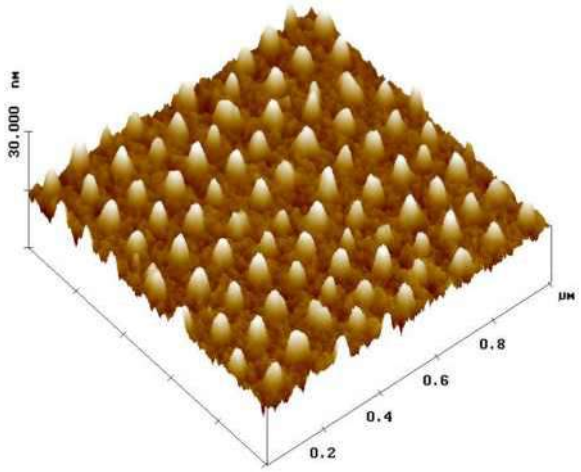


Figure 1: AFM image of surface micelles formed by poly(styrene)-b-poly(methyl methacrylate). The sample was prepared by self-assembly at the air-water interface followed by transfer to glass substrates.

We have prepared composite films by co-spreading thiol-capped gold nanoparticles with poly(styrene)-b-poly(2-vinylpyridine) (PS-b-P2VP) and found that particle size, capping ligand length, and particle loading all have an impact on the precise spatial distribution of the particles within the block copolymer template [5]. Of particular interest is the formation of ring assemblies resulting from the spontaneous relegation of the nanoparticles to the periphery of the circular hydrophobic domains [6].

Although the self-assembled rings exhibit significant plasmon coupling, the extinction spectra recorded for ensembles of nanostructures are very broad [7]. This can be attributed to variations in the details of particle organisation from one ring to another. To address this heterogeneity, we have combined scanning electron microscopy with hyperspectral imaging to characterise the plasmonic properties of individual structures.

3. Results and Conclusions

In order to image individual nanostructures with dark field hyperspectral microscopy the structures must be separated at distances greater than the diffraction limit. The addition of P2VP homopolymer to the PS-b-P2VP matrix results in a loss of periodic order and an increase in the distance of separation between the hydrophobic domains and, consequently between the metal nanoparticle rings that surround them. This is illustrated in Figure 2.

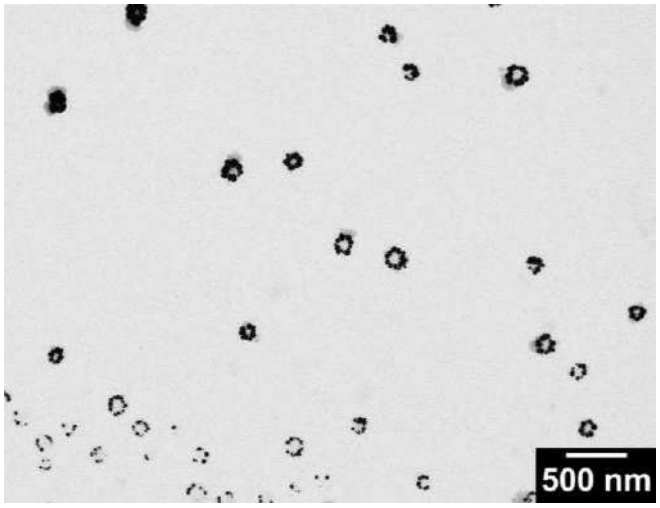


Figure 2: TEM image of gold particle nano-rings formed around surface micelles of PS-b-P2VP with the addition of P2VP homopolymer. The sample was prepared by spreading at the air-water interface followed by transfer to carbon-coated microscope grids.

Using dark field hyperspectral microscopy, plasmonic scattering spectra were recorded from individual rings such as those shown in Figure 2. Through the use of marked substrates, the corresponding structures were imaged by scanning electron microscopy. Typically, scattering spectra exhibit more than one resonance, as shown for the example provided in Figure 3. Furthermore, the spectral features recorded from individual structures are much narrower than those of ensemble measurements. As anticipated, significant structure-to-structure variation is observed and the plasmonic spectral signature is very sensitive to structural details. These results clearly indicate the importance of coupled modes. Further investigation will be required to assign specific resonances to specific modes.

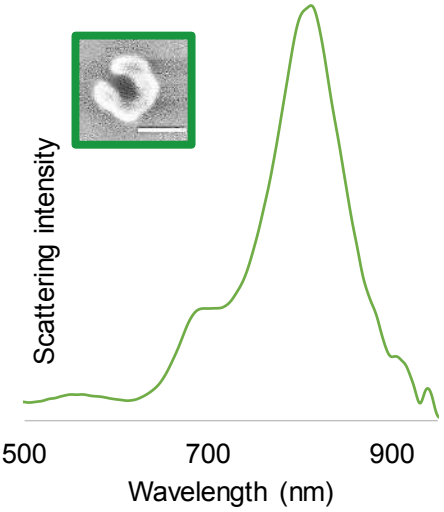


Figure 3: SEM image and corresponding plasmon scattering spectrum of a single gold nanostructure.

Acknowledgements

The authors would like to acknowledge the financial support of le Fonds de recherche du Québec – Nature et technologies (FRQNT) and the National Sciences and Engineering Research Council of Canada (NSERC). Hyperspectral imaging was performed in the laboratory of E. Ringe (Rice U.) by J. Richard-Daniel.

References

[1] "Plasmonics for extreme light concentration and manipulation", JA Schuller, ES Barnard, W Cai, YC Jun, J S White and M L Brongersma, *Nature Materials* **2010**, *9*,193.

[2] "Highly Sensitive Plasmonic Optical Sensors Based on Gold Core-Satellite Nanostructures Immobilized on Glass Substrates", K Ode et al., *ACS Appl. Mater. Interfaces* **2016**, *8*, 20522−20526.

[3] "Optimizing the Refractive Index Sensitivity of Plasmonically Coupled Gold Nanoparticles", E Martinsson, B Sepulveda, P Chen, A Elfwing, B Liedberg, D Aili, *Plasmonics*, **2014,** *9*,773.

[4] "Aggregation Behaviors of a Polystyrene-b-poly(methyl methacrylate) Diblock Copolymer at the Air/Water Interface", Y Seo, JH Im, JS Lee, JH Kim,. *Macromolecules* **2001**, *34*, 4842.

[5] "Controlled 2D organization of gold nanoparticles in block copolymer monolayers", SS Lamarre, C Lemay, C Labrecque and AM Ritcey, *Langmuir*, **2013**, *29(34)*, 10891.

[6] "Plasmonic nanorings obtained by the self-assembly of metallic nanoparticles and block copolymers", J-F Lemineur, S Schuermans, J M-Djouda, T Maurer, AM Ritcey *J. Phys. Chem. C*, **2016**, *120* (16),8883.

[7] "Controlled growth of gold nanoparticles pre-organized in Langmuir-Blodgett monolayers", J-F Lemineur and AM Ritcey, *Langmuir*, **2016**, *32 (46)*, 12056.

Nanoplasmonics in Embedded CMOS Electronics: Future mm-scale Complex Nano-optical Sensory Systems

Kaushik Sengupta[1]

[1] Department of Electrical Engineering, Princeton University, NJ 08544.

Abstract

Here we demonstrate for the first time massively parallelizable nanoplasmonic structures exploiting the sub-wavelength lithography of embedded copper-based interconnect layers in an industry standard CMOS process with 65-nm feature size. We show this in the context of a fully integrated, fluorescence based CMOS bio-molecular sensor array with integrated angle and scattering insensitive nanoplasmonic filters. The nano-optics and the all the readout analog and digital electronics are all co-designed and co-integrated in a single 2 mm^2 CMOS chip with absolutely 'no change' approach to the CMOS foundry processes.

1. Introduction: Why CMOS and Nano-optic co-integration matters?

The ability to integrate multi-functional, complex and robust nanoplasmonic structures operating in the visible and near-IR domain, with embedded electronics in the same substrate can allow a new class of intelligent, connected, ultra-miniaturized and low power nano-optical systems on chip. This is particularly true for CMOS-based foundry platforms that allows complex systems with high levels of integration in a single chip at low cost, high yield, small form factor and with low power dissipation.

In this paper, we show how the lowest metal layers in modern day CMOS processes that typically carry electronic information within the chip can be exploited to realize massively paralliezable and robust nano-photonic structures. With Moore's law in scaling, as transistors have reached 20-nm in dimensions, the embedded copper-based electronic interconnects have also reached deep sub-wavelength regime in the visible and near-IR. Understandably copper nanostructures can be more lossy compared to gold. However, the critical point to note is that the co-integration and co-design of the optics and the electronics in the same substrate potentially with billions of transistors opens up a new design space and system capabilities. This is expected to be well beyond the traditional partitioned design approach that locally optimizes at a component level. An analogy can be drawn with modern-day wireless connectivity that relies on highly sophisticated and integrated radio-frequency integrated circuit (RFIC) technology in CMOS. The components realized in silicon RFICs are not the most efficient. However, collectively, with the integrated signal processing, digital control and high levels of integration, the approach has revolutionized our use of the RF spectrum. The nano-optic and CMOS co-integration can viewed as an enabling technology for the next generation of sensing and imaging systems.

2. CMOS Nano-optical System: Electronic and Photonic Co-design

In this paper, we demonstrate this approach in the context of a fully integrated, optics-free, 96-sensor multiplexed CMOS fluorescence biosensor array. This has been extremely challenging for nucleic acid and protein assays, since detection of fluorescence emission from tagged trace bio-molecules can be typically 70-80 dB lower than the excitation signal. Processing of such levels of signal typically requires a series of optical components including multiple filter sets, lenses, collimators, and photo-multiplier tubes that can be large, complex, bulky and expensive. Prior efforts in miniaturizing these systems have focuses on the same components in tighter packaging systems.

We achieve this with integrated nanofilters realized with lowest metal layers in a 65-nm CMOS process. The scattering and angle-insensitive nature of the filter eliminates all optical components and allows us to incorporate the entire biosensor interface, sensor array and the optics into a 2 mm^2 chip and the packaged system into a volume small enough to fit inside a pill(Fig. 1a). In spite of this, the system demonstrates sensitivities of 100 fM for DNA and 5 pm for proteins, comparable to, if not better than commercial reader and ELISA systems. This is achieved through co-design of the electronic and photonic front-ends where 50 dB of rejection is achieved optically, and 27 dB is achieved electronically allowing us to reach sensitivity of fluorescence detection that is 77 dB below the excitation (Fig. 1a).

3. Nano-waveguide based Filters

The nano-waveguide based filters are realized with four metal layers inside the CMOS chip with 100 nm width and 130 nm spacing. The filter sheet spreads over the entire 2 mm^2 chip. As shown in Fig. 1, when the excitation field (405 nm) is incident on the fluorescence tags on the chip surface, the tags act as optical nano-antennas and they emit randomly polarized fluorescence signal in a complex radiation pattern. Therefore, by removing all the collimating elements in a classical fluorescence set up to allow for true miniaturization, the filters need to be robust against all an-

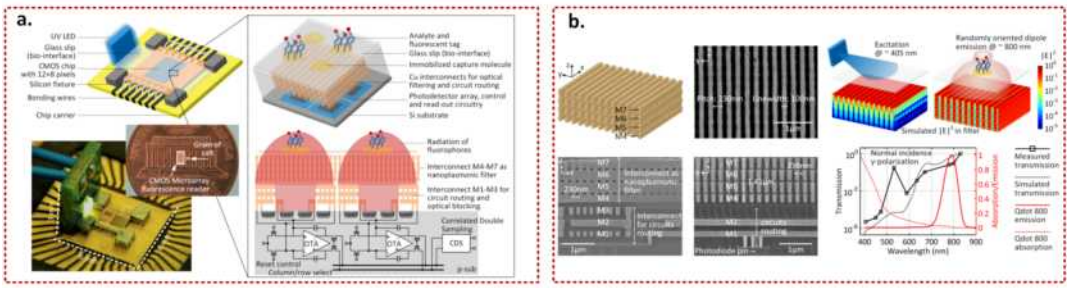


Figure 1: **a.** A 96-sensor, multiplexed, optics-free CMOS chip with a disposable bio-interface, occupying 0.1 cc of volume. **b.** Integrated nanoplasmonic filters and simulated and measured performance [2, 3].

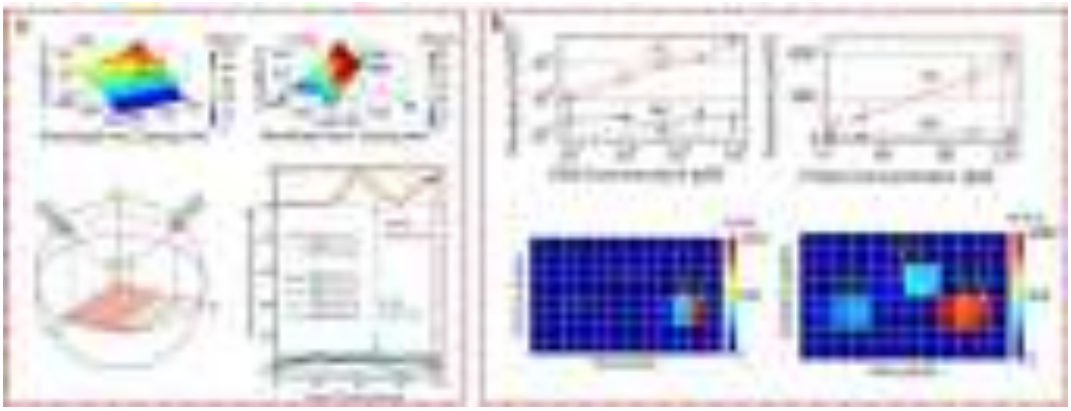


Figure 2: **a.** Nano-waveguide filter design and measured angle-insensitiveness eliminating the need for collimation and lenses.**b.** Measured DNA and protein sensitivity in sandwich assay and multiplexing ability in a hybridization assay [2, 3].

gles of incidence in a highly scattered background. The incidence excites multiple modes in the vertical waveguides, and the fundamental propagating mode (TM0) or the coupled surface plasmonic polariton mode constitutes the lowest losses. The filter operates by exploiting the differential absorption losses of the SPP modes between the excitation and the incident wavelengths, and the design of the sub-wavelength spacing suppresses the higher modes even more strongly between 60-120 dB [2]. The non-resonant nature of the filter is key towards the angle-insensitive nature of the filtering allowing it to operate in presence of uncollimated and scattering environment. This is illustrated in the measurement result in Fig 2a.

4. CMOS Nano-optic Biosensor Array

Under the plasmonic filter sheet, we implement a highly multiplexed 96-sensor photodetector array, low-noise read out circuitry and digital control all integrated in the same chip. The ability to detect 96 different bio-molecules simultaneously over the same chip is key for robust diagnostics and better statistics, reducing false positive sad false negatives. A packaged LED and a disposable bio-interface over the chip with printed capture probes (for proteins and DNAs) (Fig. 1a) allows the entire system to have a volume less than 0.1 cc, small enough to fit inside a pill. In spite of the miniaturization, this demonstrates measured sensitivities of 100 fM for DNAs and 5 pM for proteins, the latter being comparable with the gold standard ELISA systems. To the best of our knowledge, this is the first demonstration of a multiplexed, fully integrated and optics-free florescence system in a CMOS chip with integrated nanoplasmonic filers [1]. More importantly, it demonstrates the feasibility of utilizing the co-design space to allow scalable and complex sub-wavelength optical field and electronic integration for future mm-scale nano-optical systems.

References

[1] L. Hong, H. Li, H. Yang and K. Sengupta, "Fully Integrated Fluorescence Biosensors On-Chip Employing Multi-Functional Nanoplasmonic Optical Structures in CMOS," *in IEEE J.Solid-State Circuits*, vol. 52, no. 9, pp. 2388-2406, Sept. 2017.

[2] L.Hong, H.Li, H.Yang and K.Sengupta, "Nanoplasmonics and electronics co-integration in CMOS enabling a pill-sized multiplexed fluorescence microarray system," *Biomed. Opt. Exp.*, vol. 9, no. 11, pp. 5735-5758 (2018).

[3] L.Hong, H.Li, H.Yang and K.Sengupta, "Integrated Angle-Insensitive Nanoplasmonic Filters for Ultra-miniaturized Fluorescence Microarray in a 65 nm Digital CMOS Process," *ACS Photon.*, vol. 5, no. 11, pp 43124322 (2018).

Novel Photonic Architectures by Nanoimprinting Unconventional Materials

Camilla Dore, Cristiano Matricardi , Juan Luís García-Pomar, Pau Molet, André Espinha and Agustín Mihi*

[1]Institut de Ciència de Materials de Barcelona (ICMAB-CSIC), Campus de la UAB, 08193 Bellaterra, Spain
*corresponding author, E-mail: amihi@icmab.es

Abstract

Nanostructured dielectric and metallic photonic architectures can concentrate the electric field through resonances, increase the light optical path by strong diffraction and exhibit many other interesting optical phenomena that cannot be achieved with traditional lenses and mirrors. The use of these structures within actual devices will be most beneficial for enhanced light absorption in thin solar cells, photodetectors and to develop new sensors and light emitters. However, emerging optoelectronic devices rely on large area and low cost fabrication routes such as roll to roll or solution processing, to cut manufacturing costs and increase the production throughput. If the exciting properties exhibited photonic structures are to be implemented in these devices then, they too have to be processed in a similar fashion as the devices they intend to improve.

In this presentation, I will show how we use soft nanoimprinting lithography to mold unconventional materials such as polymers, cellulose or metal colloids to produce a variety of photonic architectures exhibiting exciting optical properties with tremendous applications as inexpensive disposable photonic components and sensors.

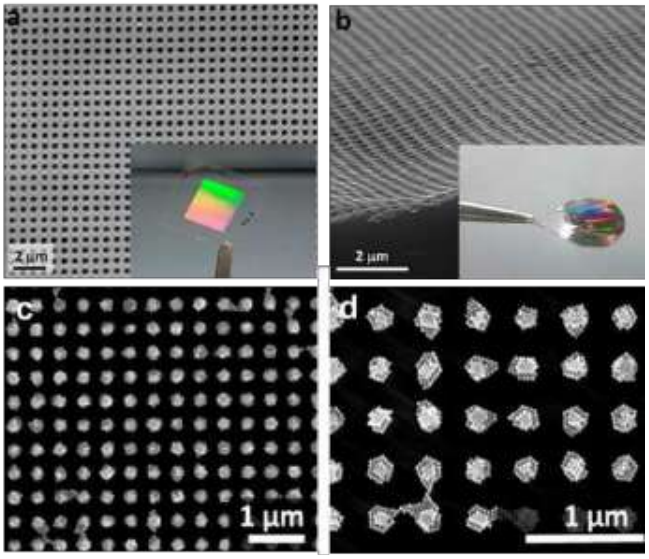


Figure 1: Cellulose based Photonic (a) and Plasmonic (b) architectures fabricated via nanoimprint lithography. Plasmonic crystal arrays formed with 50nm Au nanoparticles (c and d).

By nanostructuring these unconventional materials, we combine the complex optical properties of the nanostructure with the properties of the original materials: biodegradability (cellulose), electrical transport (conductive polymers) and sensing (Au colloids).

In particular, to the extraordinary properties of the cellulose, we incorporate enhanced photonic functionality by shaping it into photonic and plasmonic crystal structures via nanoimprinting lithography (Fig 1a,b), the most promising method for mass-produced nanostructures. [1] This combination opens up new venues in the field of cellulose based photonic architectures, offering a smart opportunity for the ecofriendly production of color in packaging systems or in photonic papers, anti-counterfeiting technology, washable and edible detectors or labels for the food industry. In addition, I will demonstrate further uses of the cellulose derivatives as water processable and environmentally friendly nanoimprinting resists. I will demonstrate the patterning of silicon wafers and the fabrication of metal nanoparticles with the aid of cellulose and water as only chemicals. [2]
To conclude, I will demonstrate how gold colloids can be assembled into hierarchical plasmonic crystals(Fig 1c,d), allowing the interplay of the optical response of the colloid with that of the plasmonic lattice. [3]

Acknowledgements

We thank the Spanish Ministry of Economy and Competitiveness (MINECO) for its support through Grant MAT2016-79053-P. and the auspices of the Spanish Severo Ochoa Centre of Excellence programme (grant SEV-2015-0496). This project has received funding from the European Research Council (ERC ENLIGHTMENT grant agreement No 637116).

References

[1] A. Espinha et al., Cellulose-based biodegradable and multifunctional photonic architectures, *Nature photonics* **12**, 343, **2018**.

[2] C. Dore et al., Water-processable cellulose-based resist for green nanofabrication, *Nanoscale 10 (37)* 17884, **2018**.

[3] C. Matricardi et al. Ultrathin Semiconductor Superabsorbers from the Visible to the Near-Infrared, *ACS Nano*. 12 (8), 8531, **2018.**

Photocontrollable dynamic chirality in plasmonic nanoassemblies

R.Y. Wang[1*], W. J. Zhao[1], W. Zhang[1], X. Wu[2], and X. D. Zhang[1]

[1]School of Physics, Beijing Institute of Technology, 100081 Beijing, China

[2] CAS Key Laboratory of Standardization and Measurement for Nanotechnology, CAS Center for Excellence in Nanoscience, National Center for Nanoscience and Technology, 100190 Beijing, China

[*]corresponding author: wangry@bit.edu.cn

Abstract- Reversible photocontrol of dynamic chirality in self-assembly systems is of great importance in exploitations of artificial nanomachines for scientific and industrious applications[1-4]. In this talk, we present a new method to achieve controllable chiral switching and selection in plasmonic nanoassemblies. We show here how light enables the switching between opposite chiral states of plasmonic dimers, and how can the light polarization and frequency be regulated to achieve a selectable chirality amplification in the grown plasmonic nanoassemblies.

REFERENCES

1. Szymański, W., Beierle, J. M., Kistemaker, H. A. V., Velema, W. A. & Feringa, B. L. "Reversible photocontrol of biological systems by the incorporation of molecular photoswitches," Chem. Rev. 113, 6114–6178, 2013.
2. Kuzyk, A., Yang, Y., Duan, X., Stoll, S., Govorov, A. O., Sugiyama, H., Endo, M., Liu, N. "A light-driven three-dimensional plasmonic nanosystem that translates molecular motion into reversible chiroptical function," Nat. Commun. 7, 10591, 2016.
3. Homaeigohar, S. and Elbahri, M. "Switchable Plasmonic Nanocomposites," Adv. Opt. Mater. 7, 1801101, 2019.
4. Hentschel, M., Schäferling, M., Duan, X., Giessen, H. & Liu, N. "Chiral plasmonics," Sci. Adv. 3, e1602735, 2017.

Photon drag of Bose-Einstein condensates

M. V. Boev[1,2], **A. E. Miroshnichenko**[3], **V. M. Kovalev**[1,2], **and I. G. Savenko**[1,4,5]

[1]Novosibirsk State Technical University, Novosibirsk 630073, Russia
[2]Institute of Semiconductor Physics, Novosibirsk 630090, Russia
[3]University of New South Wales, Canberra ACT 2600, Australia
[4]Center for Theoretical Physics of Complex Systems, Institute for Basic Science, Daejeon 34051, Korea
[5]Basic Science Program, Korea University of Science and Technology (UST), Daejeon 34113, Korea
ivan.savenko@pcs.ibs.re.kr

Abstract— We report on the photon drag effect of Bose-Einstein condensates. We develop a microscopic theory of this effect, which occurs in a general system containing Bose–Einstein-condensed particles, possessing an internal structure of quantum states. Analyzing the response of the system to an external electromagnetic field, we find that the drag results in a flux of particles constituting both the condensate and the excited states. We show that in the presence of the condensed phase, the response of the system acquires step-like behavior as a function of the electromagnetic field frequency with the elementary step determined by the internal energy structure of the particles.

1. INTRODUCTION

Light acting on atoms, molecules and other particles might result in a momentum transfer between light and matter particles [1]. This phenomenon is called the radiation pressure. In condensed matter, light pressure results in a current of charge carriers and it is called the Photon Drag Effect (PDE). Charge carriers, such as free electrons and holes, can absorb radiation by means of interaction with an electromagnetic field (EMF), and they move in a direction of the wave vector of light. PDE has been studied in semiconductors [2], dielectrics [3], metals [4], and other systems.

In classical description, the PDE current reads $\mathbf{j}(\omega) \sim \mathbf{k}\alpha(\omega)I$, where $\mathbf{k}$ is the photon wave vector, $I = cE^2/8\pi$ is the intensity of the electromagnetic wave and $\alpha(\omega)$ is the absorption coefficient of light by the charge carriers. Evidently, the frequency dependence of the drag current is determined by the spectrum of the absorption coefficient. In the majority of cases, this dependence is monotonous or resonant if the frequency of the EMF ω is close to the energy of quantum transitions in the system. However, there are exceptions.

2. THEORY

We study the radiation pressure phenomenon in a system of bosons, containing particles in the BEC state [5, 6]. The spectrum of a single boson with an eigenfunction $|\eta, \mathbf{p}\rangle$ reads $\varepsilon_\eta(\mathbf{p}) = \varepsilon(\mathbf{p}) + \Delta_\eta$, where $\varepsilon(\mathbf{p}) = \mathbf{p}^2/2M$ is a kinetic energy of the particle center-of-mass motion, and Δ_η is the energy spectrum of the internal motion. Here index η stands for the full set of quantum numbers, characterizing the internal spectrum of the particle and the value $\eta = 0$ refers to the ground state of the internal spectrum of Bose particles.

The electric field of light depends on the center-of-mass coordinate $\mathbf{r}$ only, $\mathbf{E}(x) = \mathbf{E}_0 e^{\mathrm{i}\mathbf{kr}-\mathrm{i}\omega t} + \mathbf{E}_0^* e^{-\mathrm{i}\mathbf{kr}+\mathrm{i}\omega t}$, and the light–matter coupling can be described by the matrix elements $\mathbf{d}_{21}\cdot\mathbf{E}$. Here the indices 1, 2 stand for the ground and excited quantum states of the internal particle motion, $|1\rangle \equiv |\eta = 0\rangle$ and $|2\rangle \equiv |\eta \neq 0\rangle$. Then $\mathbf{d}_{12} = \langle 1|\mathbf{d}|2\rangle$ is a matrix element of the dipole moment operator of the particle. The system response to a pressure of the external EMF is a current of particles which is determined by the light absorption coefficient. The BEC–EMF interaction Hamiltonian reads $H_I = \mathbf{d}_{21}\cdot\mathbf{E}_0 \sum_{\mathbf{p}} c^\dagger_{\eta,\mathbf{p}+\mathbf{k}}(t) a_{\mathbf{k}}(t) c_{0,\mathbf{p}}(t) + \text{h.c.}$, where $c_{\eta,\mathbf{p}}(t) = c_{\eta,\mathbf{p}}(0)\exp(-\mathrm{i}\varepsilon_\eta(\mathbf{p})t)$ and $a_{\mathbf{k}}(t) = a_{\mathbf{k}}(0)\exp(-\mathrm{i}\omega t)$ are the annihilation operators for the Bose particle and EMF photon, respectively. The theoretical description of BEC is based on the Bogoliubov theory of a weakly interacting Bose gas [**?**]. To describe the dynamics of the BEC, we will use the Gross-Pitaevskii equation. Then low-energy excitations of the BEC represent Bogoliubov quasiparticles (bogolons) with the dispersion $\omega_{\mathbf{p}} = \sqrt{\varepsilon_{\mathbf{p}}(\varepsilon_{\mathbf{p}} + 2gn_c)} = sp\sqrt{1 + (p\xi)^2}$, where $s = \sqrt{gn_c/M}$, $\xi = 1/(2Ms)$ are the sound velocity and the healing length, g is interparticle interaction strength, n_c is density of particles in the

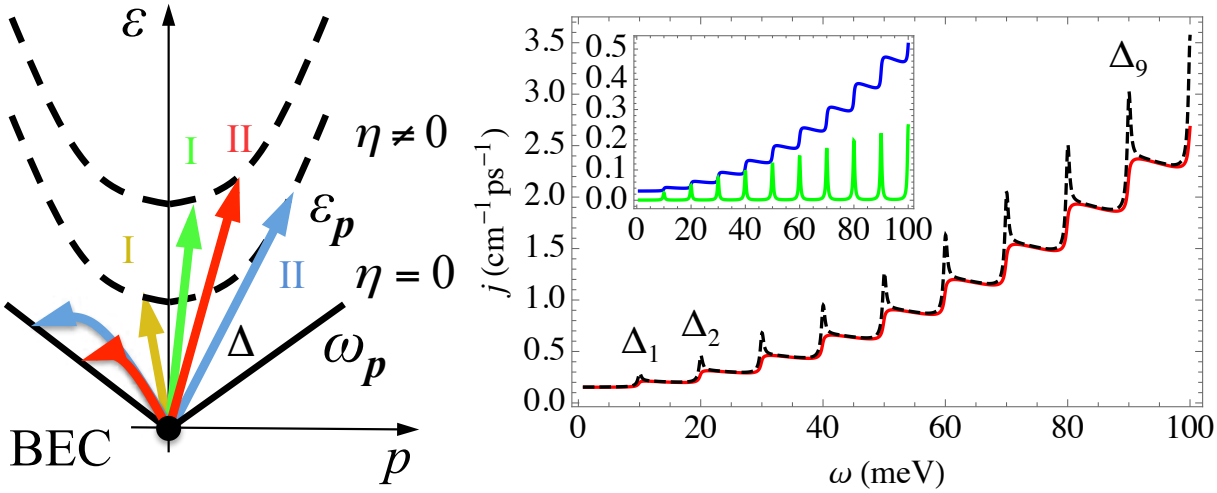


Figure 1: (left panel) Excitation spectrum of the internal degrees of freedom of the boson during absorption of a quantum of EMF. (Right panel) Spectrum of the total current density $j_c = j_{c1} + j_{c2}$ (main plot). Two components of the current j_{c1} (green curve) and j_{c2} (blue curve).

BEC. In a long-wavelength limit $\xi p \ll 1$ (that is equivalent to $\varepsilon_{\mathbf{p}} \ll gn_c$) the dispersion law of the bogolons becomes linear, $\omega_{\mathbf{p}} = sp$. We will consider $T = 0$ thus disregarding the processes of thermal excitation of bogolons. Further we present $c_{0,\mathbf{p}}$ in the form [**?**] $c_{0,\mathbf{p}}(t) = c_{0,0}\delta(\mathbf{p}) + u_{\mathbf{p}} b_{\mathbf{p}}(t) + v_{\mathbf{p}} b^{\dagger}_{-\mathbf{p}}(t)$, where $c_{0,0}$ describes the particles in the BEC state with zero momentum and $|c_{0,0}|^2 = n_c$. Here $u_{\mathbf{p}}$ and $v_{\mathbf{p}}$ are the Bogoliubov transformation coefficients and $b_{\mathbf{p}}(t) = b_{\mathbf{p}}(0)\exp(-\mathrm{i}\omega_{\mathbf{p}} t)$ are Bogoliubov excitation operators. Summing up, we come up with several principal quantum channels of the EMF absorption.

3. RESULTS

The first term of current describes a transition of a Bose particle from the BEC to an excited state $\eta \neq 0$ with the energy conservation law $\omega = \varepsilon_{\mathbf{k}} + \Delta_\eta \approx \Delta_\eta$, see Fig. 1 transitions I. Beside these, there exists another type of transitions described by the second and third terms of the current density. They can be referred to as the *Belyaev processes* and happen when the light absorption is accompanied by not only excitation of the particle but also the emission or absorption of a Bogoliubov excitations of the condensate, see Fig. 1 transitions II. Such processes result in the step-like behavior of the BEC response (right panel). Therefore taking into account the internal structure of the particles leads to the "quantization" of the response of the system to the external light pressure in a 2D condensate.

ACKNOWLEDGMENT

The authors would like to thank A. Chaplik, M. Entin and D. Gangardt for fruitful discussions. We have been supported by the Institute for Basic Science in Korea (Project No. IBS-R024-D1), the University of New South Wales Scientia Fellowship, and the Russian Science Foundation (Project No. 17-12-01039).

REFERENCES

1. A. F. Gibson, M. F. Kimmitt, and A. C. Walker, Appl. Phys. Lett. **17**, 75 (1970).
2. C. Rodrigues-Costa and O. A. C. Nunes, Phys. Rev. B **46**, 15046 (1992).
3. R. Loudon, S. M. Barnett, and C. Baxter, Phys. Rev. A **71**, 063802 (2005).
4. J. E. Goff and W. L. Schaich, Phys. Rev. B **61**, 10471 (2000).
5. V. M. Kovalev, A. E. Miroshnichenko, I. G. Savenko, Phys. Rev. B **98**, 165405 (2018).
6. V. M. Kovalev, M. V. Boev, I. G. Savenko, Phys. Rev. B **98**, 041304(R) (2018).

Broadband extraordinary transmission and focusing of sound with flat thin meta-lens

Shanjun Liang[1], Yong Li[2], Qian Cheng[2], Jie Zhu[1]
[1]Department of Mechanical Engineering, The Hong Kong Polytechnic University, Hong Kong SAR, China
[2]Institute of Acoustics, Tongji University, Shanghai 200092, China

*corresponding author, E-mail: jiezhu@polyu.edu.hk

Abstract

We report a broadband metalens that can realize wavefront modulation with high energy efficiency. Based on the impedance-matched gradient material, we theoretically and experimentally study a gradient index helical-structured metamaterial that can modulate sound wavefront with near perfect transmission over a broad bandwidth. A thin flat metalens is constructed to demonstrate sound focusing with the extraordinary transmission for more than 1/3 octave band. It is anticipated that this engineered material may be used in ultrasonography, ultrasound surgery, and DNA fragmentation.

1. Introduction

Acoustic metasurfaces developed rapidly in recent decades, enriching the acoustic wave control technology, offering abundant unique wavefront modulation functionalities in different application scenarios. There are two reasons limiting their bandwidth and performance. First, many approaches utilize cavity-resonance-based structures to generate phase delay, which only works ideally near the resonant frequencies. Secondly, for those who resort to coiling up space to obtain the high effective refractive index, accompanied by impedance mismatching with host media and Fabry–Pérot resonances that lead to a dramatical decrease of transmission coefficients. To extend the working frequency range, for reflected wave modulation, corrugated surface and circular-holed cube have been adopted. For the transmitted wave control, metamaterials with varying geometrical shape were introduced being an ideal model as it can decrease the reflection with a better impedance matching behavior, while the high index region is restricted by the viscous or structural loss because of the structural complexity. Moreover, many approaches are in primary stage, and more experimental investigation is needed. Notably, by compressing space by using helicoid surface, a dispersion-free metamaterial[1] has been developed with higher space utilization rate compared with previous designs. Former works attempted to make an impedance-matched layer by using gradient pitch distribution and sound devices with diverse functionalities[2-4]. A systematic investigation as well is experimental study is highly desirable to evaluate the effect of viscous and thermal loss and demonstrate the broadband sound wavefront modulation with high energy transitive ratio.

In this work, we introduce linearly distributed pitch to helical-structured metamaterials, matching the impedance of air with small helicity density at both ends. A transfer-matrix-based model is established to describe its behavior in frequency domain. To verify the performance practically, a flat meta-lens has been constructed to realized broadband focusing, showing excellent experimental results[5].

2. Design of elements

Different from the former approaches, we developed a helicoid structure with gradient pitch distribution. A theoretical model of the inhomogeneous medium has been conducted to calculate the phase and transmission spectra of the element.

The unit element of the proposed helical structure has the largest pitch at both ends and the smallest pitch in the middle, symmetric about the middle point. The effective acoustic parameters of such a gradient structure are no longer uniformly distributed but instead decided by the on-site pitch value. The effective impedance, dynamic density and refractive index of an element are in the same variation trend that is against the pitch change. From the end to the middle point along the Y-axis, they all increase gradually with decreasing pitch value and a tighter arrangement of the blades.



Figure 1: Photo of the newly designed gradient helicoid metamaterials. (manufactured by 3-D printing)

Because of the distribution of the acoustic parameter can be expressed analytically. The wave propagation equation can be used to establish the theoretical model of the elements, as well as paves the way to design reversely based on the model. For the host media, we use the one-dimensional monochromatic wave equation, while for the effective media, with inhomogeneous properties, the governing equation can be

$$\frac{\mathrm{d}^2 p_1(y)}{\mathrm{d}y^2}+\left(\frac{\omega}{c}n_{eff}(y)\right)^2 p_1(y)-\left(\frac{\mathrm{d}\ln\rho_{eff}(y)}{\mathrm{d}y}\right)\frac{\mathrm{d}}{\mathrm{d}y}p_1(y)=0 \qquad (1)$$

By using the analytical solution of the host media and the inhomogeneous effective model layers, a transfer matrix description can be built to predict the frequency response.

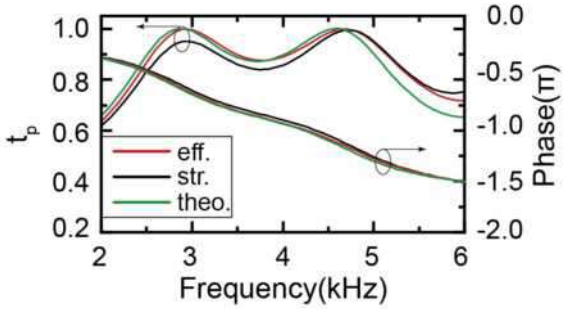


Figure 2: Transmission and phase spectra of an element

Calculated by using different methods, the results' good agreement indicates the rationality of the theoretical method. The high transmission coefficient and gentle phase shift over spectra allow the elements to work together to generate unchanged lead-and-lag of phase in wide frequency regime. Hence a broadband meta-lens can be achieved.

3. Experimental results

3.1. Measured effective index

The experimental results verify the slight dispersion of an element. The imaginary part – the attenuation coefficient— is near to zero and keeps flat during the calculated frequency range. Hence the gradient-pitched helical structure can be described by a lossless model reasonably.

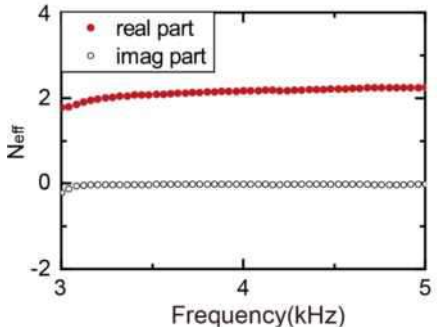


Figure 3: Experimentally tested the complex refractive index of a single element (same one as Figure 2)

3.2. A broadband focal lens

We design a focal lens based on

$$\varphi(x)=\frac{2\pi f}{c}\left(\sqrt{x^2+F^2}-F\right) \quad (2)$$

where φ denotes the phase delay at any specific location x, f is the operating frequency, c is the sound speed in the air (343.2 ms^{-1}), and F is the focal length. In the design procedure, we use 4000 as the target frequency. in a wide frequency range, which is tested from 3500Hz to 4500Hz, about 1/3 octave.

4. Conclusions

In this study, we theoretically and experimentally investigated the acoustic characteristic of the graded helicoid metamaterial and constructed a broadband focal lens with the studied element cell. The lossy property of the element has been evaluated in the experiment, and the broadband performance of the lens has been measured. The theory work paves the way of inverse design of metasurfaces while the experimental work studied the properties of such kind of metamaterial, providing valuable references for research and engineering.

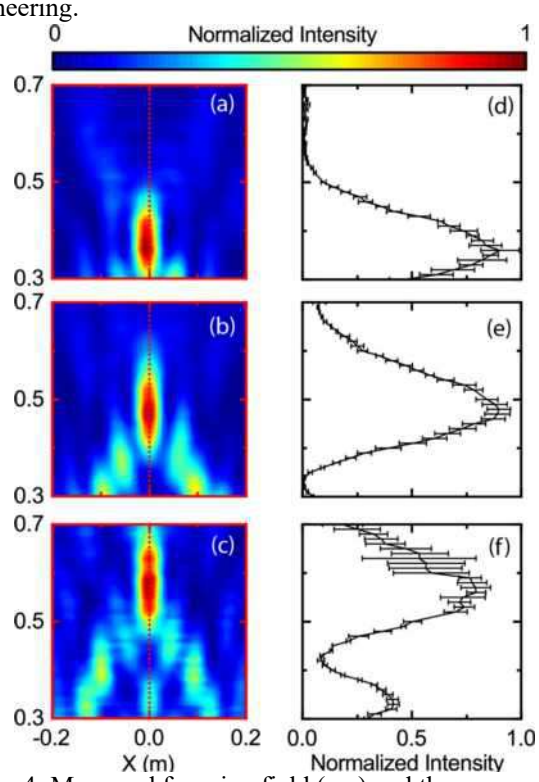


Figure 4: Measured focusing field (a-c) and the cross-section distribution of sound intensity (d-f) realized by the meta-lens.

Acknowledgements

The work was supported by the Early Career Scheme (ECS) of Hong Kong RGC [grant number 25208115]

References

[1] X. Zhu, K. Li, P. Zhang, J. Zhu, J. Zhang, C. Tian, S. Liu, Implementation of dispersion-free slow acoustic wave propagation and phase engineering with helical-structured metamaterials, *Nature Communication,* 7 (2016) 11731.

[2] K. Li, B. Liang, J. Yang, J. Yang, J.-c. Cheng, Acoustic broadband metacouplers, *Applied Physics Letters*, 110 (2017) 203504.

[3] Y. Ding, E.C. Statharas, K. Yao, M. Hong, A broadband acoustic metamaterial with impedance matching layer of gradient index, *Applied Physics Letters*, 110 (2017) 241903.

[4] L. Kun, L. Bin, Y. Jing, Y. Jun, C. Jian-Chun, Broadband transmission-type coding metamaterial for wavefront manipulation for airborne sound, A*pplied Physics Express*, 11 (2018) 077301.

[5] S. Liang, T. Liu, F. Chen, J. Zhu, Theoretical and experimental study of gradient-helicoid metamaterial, *Journal of Sound and Vibration*, 442 (2019) 482-496.

Active Polaritonic Metasurfaces

Clementine Symonds[1], Kevin Chevrier[1], Jean-Michel Benoit[1], Semion Saikin[2], Joel Yuen-Zhou[3], and Joel Bellessa[1]

[1]Univ Lyon, Université Claude Bernard Lyon 1, CNRS, Institut Lumière Matière, F-69622, LYON, France
[2] Department of Chemistry and Chemical Biology, Harvard University, Cambridge, MA 02138, USA
[3] Department of Chemistry and Biochemistry, University of California San Diego, La Jolla, CA, USA
*corresponding author, E-mail: clementine.symonds@univ-lyon1.fr

Abstract

We propose a new type of metasurface, which builds on the extended coherent states associated to plasmon/exciton polaritons. For this purpose, periodic stripes of organic dye are deposited on a continuous silver film. With a structuration exceeding the polaritonic wavelength by more than one order of magnitude, we demonstrate anisotropy generation in transition energies and emission patterns. These findings pave the way towards a novel type of artificial materials which require micro- instead of nano-structuration.

1. Introduction

The strong-coupling phenomenon that occurs when light-matter interaction prevails over damping leads to remarkable changes in the optical properties of matter, modifying both the spectrum [1] and dynamics of excitations [2]. When a large number of emitters is involved, a coherent coupling of the emitters through the electromagnetic mode occurs [3, 4]. In metal semiconductors systems, the strongly-coupled state (polariton) arising between molecules and a propagating plasmon has an extension ranging from a few [4, 5] to several tens of microns [6]. Polariton states have previously been tailored by confining either their electromagnetic [7,8] or excitonic parts [9]. Here, we will show that by patterning the emitters at the micron scale, it is possible to generate a new type of metasurface that builds on the polariton extended coherence.

2. Results

The sample consists of stripes of active dye, periodically deposited (period p) on a continuous silver film. The inactive stripes have been created in a homogeneous cyanine dye film (TDBC, 17 nm thick with a sharp absorption peak at 2.1 eV) by photobleaching the dye molecules using local UV-irradiation. The UV-irradiated material has the same optical index as the cyanine dye film, except around 2.1 eV where the Lorentzian peak related to the sharp absorption is eliminated. On the sample thus coexist regions where the material is non-absorbing (forbidding the strong coupling regime), and regions with strong material absorption (Fig. 1a).

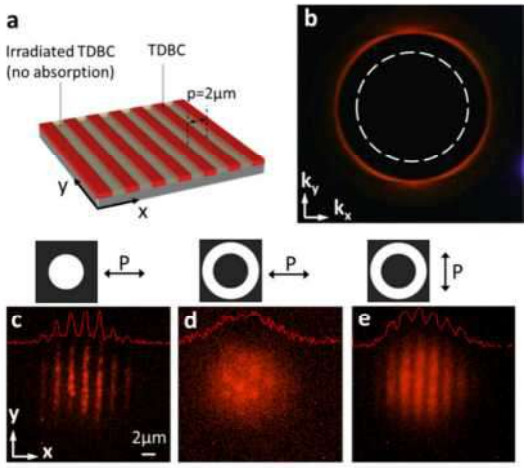


Figure 1: a. Sketch of the sample b. Fourier image of the emission. The dotted line indicates the position of the beam-blocks inserted in the Fourier plane for the direct emission images. c-e. Direct images of the emission by keeping only (c) the central part of the Fourier plane (incoherent states); (d, e) the outer part of the Fourier plane (polaritonic states.

In order to first analyze the impact of a micron-size structuration on the polaritonic state, the spatial distribution of the emission for a p=2µm stripe array is presented Fig. 1. To separate the contributions of uncoupled TDBC states from those associated with polaritonic states, Fourier-space filtering is performed using a circular or ring-shaped mask (Fig. 1b). Figure 1c shows the emission in the recorded direct space by conserving only the small wave vectors associated with the incoherent states. In this configuration, the dye stripes appear distinctly, and no emission is recorded in the irradiated areas. When only large wave vectors, associated with polaritons, are conserved, the emission behavior is radically different. For a horizontal polarization (along x), that is to say when considering only

the wave vectors associated with a propagation perpendicular to the lines, a uniform emission is obtained (Fig. 1d). In the case of propagation parallel to the lines, the emission takes place only on the dye stripes (Fig. 1e). This experiment highlights the formation of a coherent state: the patterning having a characteristic size smaller than the extent of the polaritonic state, the structured system behaves like a homogeneous effective medium for a propagation perpendicular to the lines, and as the sum of two distinct modes for propagation parallel to the lines.

This effect is also confirmed by reflectometry measurements obtained on a sample with a 5 µm stripe period. For a propagation direction along the lines (Fig. 2a), the dispersion relation simultaneously reveals a surface plasmon and a polariton. The Rabi splitting in this case is about 160 meV. However, for propagation perpendicular to the lines, only the polariton exists (Fig. 2b), with a Rabi splitting of the order of 100 meV. This reduction in the Rabi splitting is close to the factor $\sqrt{2}$ expected for a filling factor ½. This difference in behavior as a function of the direction of propagation is summarized in Figure 2c, reconstructed from the dispersions relations recorded for different orientations of the sample. In the energy range corresponding to dye absorption (2.1 eV nm), the surface plasmon mode is present only for directions of propagation contained in a cone of ± 20 ° around the y axis (along the stripes). For higher angles, the plasmon disappears, and no mode remains in this energy range since it corresponds to the exclusion band of the polariton. Our approach thus allows the generation of anisotropic dispersions relations in a given energy band, the system remaining isotropic outside this band.

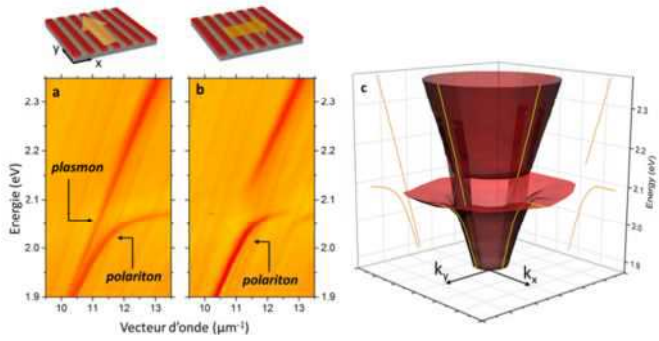


Figure 2: Dispersion relations in reflection for a sample with p=5µm, associated with propagation: a. parallel to the stripes and b. perpendicular to the stripes. c. Reflection dips energies as a function of the orientation of the propagation with respect to the lines, measured between 0 and 360 °.

In this talk, simulation results as well as a study of the period effect on the metasurface behavior will in addition be discussed. Finally, we will also show that by changing the stripes filling factor it is possible to generate anisotropic polaritonic emission.

3. Conclusions

In conclusion, we have shown that the properties of molecules strongly coupled to surface plasmons can be drastically modified by structuring the sample on distances which are large compared to wavelengths. The modified material band structure can find applications in polarization controlled sources, as well as in topological photonics based on anisotropic dispersions and Dirac cones [10] or exceptional points [9]. The active polaritonic metasurfaces we propose are not restricted to plasmonic modes nor organic dyes alone, but can be extended to a large variety of structures in strong coupling such as cavity polaritons which have similar extended coherence lengths [11]

References

[1] C. Weisbuch, M. Nishioka, A. Ishikawa, and Y. Arakawa, *Phys. Rev. Lett*. 69, 3314, 1992.

[2] T.B. Norris, J.-K. Rhee, C.-Y. Sung, Y. Arakawa, M. Nishioka, and C. Weisbuch. *Phys. Rev. B* 50, 14663, 1994

[3] V.M. Agranovich, M. Litinskaia, and D. Lidzey, *Phys. Rev. B* 67, 085311, 2003.

[4] S. Aberra Guebrou, C. Symonds, E. Homeyer, J. C. Plenet, Yu. N. Gartstein, V. M. Agranovich, and J. Bellessa, *Phys. Rev. Lett.* 108, 066401, 2012.

[5] L. Shi, T. Hakala, H. Rekola, J.-P. Martikainen, R. Moerland, and P. Törmä, *Phys. Rev. Lett.* 112, 153002, 2014.

[6] K. Chevrier, J.-M. Benoit, C. Symonds, J. Paparone, J. Laverdant, and J. Bellessa, *ACS Photon*. 5, 80, 2018.

[7] D. Bajoni, P. Senellart, E. Wertz, I. Sagnes, A. Miard, A. Lemaître, and J. Bloch, *Phys. Rev. Lett.* 100, 047401, 2008.

[8] A. Benz, S. Campione, S. Liu, I. Montaño, J.F. Klem, A. Allerman, J.R. Wendt, M.B. Sinclair, F. Capolino, and I. Brener, *Nature Commun.* 4, 2882, 2013.

[9] W. Gao, X. Li, M. Bamba, and J. Kono, *Nature Photon.*12, 362, 2018.

[10] J. Yuen-Zhou, S.K. Saikin, T. Zhu, M.C. Onbasli, C.A. Ross, V. Bulovic, and M.A. Baldo, *Nat. Commun*. 7, 11783, 2016.

[11] A. Shalabney, J. George, J. Hutchison, G. Pupillo, C. Genet, and T. W. Ebbesen, *Nature Commun.* 6, 5981, 2015.

(Chiro)-optical properties of chiral inorganic-plasmonic nanocomposites

Thierry Verbiest[1*], Ward Brullot[1], Tom Swusten[1],

[1]University of Leuven, Department of Chemistry, Belgium
*corresponding author, E-mail: Thierry.verbiest@fys.kuleuven.be

Abstract

We will discuss the chiro-optical properties of chiral self-assembled nanostructures that are composed of superparamagnetic iron oxide and plasmonic nanoparticles.

1. Introduction

We recently developed a self-assembly method to prepare multi-layered materials composed of inorganic and metallic nanoparticles coupled together by organic molecules [1]. Due to their hybrid character they exhibit peculiar optical properties. For example, multi-layered structures composed of plasmonic gold nanoparticles and superparamagnetic nanoparticles exhibit unusually strong magneto-optical effects, asymmetric optical transmission and optical activity effects [2,3]. Instead of using self-assembly, these structures can also be prepared via spray coating techniques, making it possible to prepare them on a larger scale [4].
Here we will investigate the chiro-optical properties of chiral self-assembled nanostructures.

2. Results and discussion

2.1. Preparation of self-assembled nanostructures

The self-assembled nanostructures were prepared according to a procedure described by Brullot *et al.*[1]. In brief, gold nanoparticles prepared via the well-known Turkovich method are deposited onto a glass slide that was coated with APTMS by soaking the glass slide in a dispersion of gold nanoparticles. After rinsing with water and methanol, the glass slide covered with gold nanoparticles is immersed into a dispersion of APTMS coated iron oxide nanoparticles. After rinsing with solvent, we now have a double layer of gold and iron oxide nanoparticles that are covalently bonded together by the APTMS linker. By repeating this procedure, several of these nanoparticle double layers can be deposited onto the glass slide. Note that via this procedure, nanoparticle layers are deposited on both sides of the glass. For our experiments we always mechanically removed one side of the coating. These nanocomposites can be made chiral by immersing them into a solution of D- or L-proline.

2.2. Optical rotation experiments

Optical rotation experiments were done using a home-made experimental set-up. Light from a semiconductor laser (785 nm) is send through a polarizer and focused onto the sample perpendicular to the substrate. After the sample, the light is splitted into an s- and p-polarized component via a Wollaston prism and send to two photo diodes. The whole system is aligned in such a way that in the absence of optical rotation, the intensities on the two photodiodes are equal. Hence, any optical rotation in the sample will result in an imbalance in light intensity on the photodiodes from which the optical rotation can be calculated.
For our first experiments we used a sample composed of alternating layers of gold nanoparticles and iron oxide nanoparticles with 9 nanolayers in total and impregnated with L-proline. The optical rotation was found to be +0.0024°. For samples impregnated with D-proline the optical rotation -0.0044°. We realize that the optical rotation for D- and L-enantiomer should only differ in sign, not magnitude. However, we found that impregnating the samples is not always reproducible, since it depends on a variety of parameters. Nevertheless, the difference in sign for both enantiomers is clearly present. While these optical rotations may seem very small we have to consider the fact that the thickness of the samples is only 40 nm. Hence per mm, this amounts to an optical rotation of 111°/mm, much higher than what is typically observed in concentrated solutions of proline. Probably, this high optical rotation is due to plasmonic effects.
Even more peculiar was the following observation: the optical rotation was found to be different when the sample was illuminated from the front or from the back. For front side illumination the optical rotation for the L-proline sample was 0.0024°, while for back side illumination the optical rotation was -0.0055°, a difference of 0.0079°. For the D-proline sample, front side illumination resulted in 0.0044°, while back side illumination yielded -0.0018°. In principle anisotropy or a heterogeneous sample could account for such observation, but polarized UV/Vis spectroscopy clearly indicates that the sample is perfectly in-plane isotropic and optical microscopy reveals no heterogeneities. We currently do not have a solid explanation for this behavior, but interestingly, a similar phenomenon was observed by Zheludev *et al.* in a chiral crystal and the effect was called nonreciprocal natural optical rotation. The authors attributed the effect to the presence of a nonvanishing symmetric part of the nonlocality tensor.

3. Conclusions

We have observed extremely strong optical rotation in chiral self-assembled nanostructures composed of plasmonic gold nanoparticles and iron oxide nanoparticles. Furthermore, the optical rotation was found to be asymmetric in the sense that forward and backward propagation of light through the sample yields a different optical rotation.

References

[1] W. Brullot, R. Strobbe, M. Bynens, M. Bloemen, P.J. Demeyer, W. Vanderlinden, S. De Feyter, V.K. Valev, T. Verbiest, Layer-by-layer synthesis and tunable optical properties of hybrid magnetic-plasmonic nanocomposites using short bifunctional molecular linkers, *Materials Letters* 118: 99−102, 2014.

[2] W. Brullot, T. Swusten, T. Verbiest, Broadband Nonreciprocal Quadrupolarization-Induced Asymmetric Transmission (Q-AT) in Plasmonic Nanoparticle Aggregates, *Advanced Materials* 27: art.nr. adma.201405409, 2015.

[3] W. Brullot, M.K. Vanbel, T. Swusten, T. Verbiest, resolving enantiomers using the optical angular momentum of twisted light, *Science Advances* 2: e1501349, 2016.

[4] J. Stryckers, T. Swusten, W. Brullot, J. D'Haen, T. Verbiest, W. Deferme, Ultrasonic spray coating as a fast alternative technique for the deposition of hybrid magnetic-plasmonic nanocomposites, *Advanced Engineering Materials* 20: art nr 1800681, 2018.

[5] P.J. Bennett, S. Dhanjam, Yu. P. Svirko, N.I. Zheludev, nonreciprocity of natural rotatory power, *Optics Letters* 21: 1955-1957, 1996

Block copolymer based self-assembled metamaterials and metasurfaces at optical frequencies

Alberto Alvarez-Fernandez[1,2], Cian Cummins[1,2], Guillaume Fleury[2], Xuan Wang[1], Morten Kildemo[3], Alexandre Baron[1], and Virginie Ponsinet[1*]

[1]Univ. Bordeaux, CNRS, Centre de Recherche Paul Pascal (CRPP), UMR 5031, 33600 Pessac, France
[2]Laboratoire de Chimie des Polymères Organiques (LCPO), CNRS UMR 5629, ENSCPB, Univ. Bordeaux, 33600 Pessac, France
[3]Physics Department, NTNU, Høgskoleringen 1, Trondheim 7491, Norway
*corresponding author, E-mail: ponsinet@crpp-bordeaux.cnrs.fr

Abstract

Self-assembled diblock copolymers were used as templates to produce well-defined gold nanostructures in 3D or 2D, with so degree of order. Resulting structures were shown to present specific and tunable optical resonant properties, and include hyperbolic metamaterials and high-index metasurfaces.

1. Introduction

Optically resonant nanostructures provide unprecedented capacities to manipulate light at a sub-wavelength scale. Their applications span the whole range of optical functions (filters, modulators, polarizers, absorbers, etc) while being accessible at sub-wavelength dimensions with the benefit of enabling miniaturized devices. In spite of tremendous recent progress in the nanofabrication methodologies, such nanostructures usually require complex fabrication processes via *top-down* approaches of low scalability. To circumvolve these technological issues, *bottom-up* approaches including colloidal assembly, micellar-induced assembly, or self-assembly of diblock copolymers (dBCPs) have been successfully introduced as alternative methodologies since they give access to various 3D or 2D metal, dielectric or metal/dielectric nanostructures. In particular, the selective hybridization of dBCP thin films with metallic species is known as a fabrication methodology for visible range metamaterials [1-4]. Indeed, dBCPs self-assemble into nanomaterials with well-defined morphology. They are macromolecules made of two molecular chains of distinct chemical nature linked together, called the blocks, and present solid state spontaneous organizations with long-range order and tunable characteristic sizes, ranging typically from a few nanometers to a few hundred nanometers. The accessible morphologies include hexagonally packed cylinders and lamellae. Here, we report on the use of dBCPs presenting a lamellar morphology to produce two types of plasmonic structures. The first one is a uniaxial 3D multilayer stack, in which we show that the optical anisotropy allows reaching hyperbolic permittivities. The second is a 2D nanostructure, in which out-of-plane lamellae lead to an azimuthally isotropic resonant thin film reaching high refractive index.

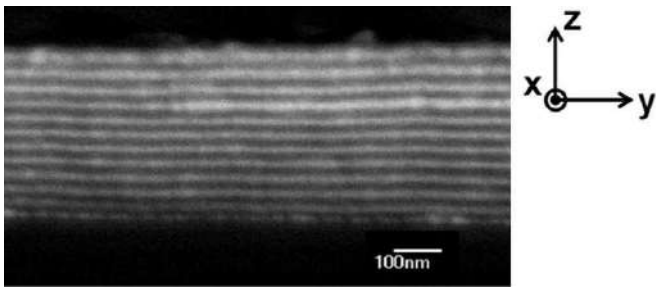


Figure 1: Backscattering scanning electron microscopy side-view image (SEM) of a 370nm-thick film of alternating layers of PS (appearing black) and Au nanoparticles:P2VP nanocomposite (NC, appearing white). The trihedral indicates the ordinary ((x,y) or //) and extraordinary (z) directions.

2. 3D plasmonic lamellar nanomaterials

2.1. Fabrication

Here, we use a lamellar poly(styrene)-*block*-poly(2-vinylpyridine) (PS-*b*-P2VP) copolymer with both blocks of molar mass 25 kg/mol, which spontaneously develops a multilayered structurally uniaxial thin film of alternate PS and P2VP layers with a period of 37 nm in the bulk. We use a process combining spin-coating of a polymer solution on a selective surface and thermal annealing, which produces a flat and homogeneous film with a parallel alignment of the organized structures, throughout the thickness of the film between 200 and 700 nm. This ordered structure spans an area as large as the spin-coating process can produce (we use 15 x 15 mm^2 wafers). In order to induce dielectric permittivity contrast depending on the probed direction, we dope one of the polymer phase with metallic nanoparticles of radius 5 nm. For this, we use an impregnation methodology, in which a previously ordered and aligned copolymer nanostructure is selectively swollen with a gold precursor solution. After action of a reducing agent, Au nanoparticles form selectively within the P2VP layers, thus producing alternate stacks of pure PS layers, and composite

layers of gold nanoparticles and P2VP (see Fig. 1). We can increase and control the volume fraction of nanoparticles in the composite layers, by repeating the impregnation process and we can then follow the structural and optical evolution of the material.

2.2. Optical properties

We determine by spectroscopic ellipsometry that the dielectric functions $\varepsilon_{//}$ and ε_z both present a resonance at the wavelength $\lambda \sim 580$ nm, close to the plasmon resonance of the gold nanoparticles. This resonance amplitude for ε_z, is limited and varies only little while the resonance of $\varepsilon_{//}$ is stronger and its amplitude significantly increases with the gold loading, reaching a regime of negative values for gold volume fractions beyond 30%. These results demonstrate the capacity of our bottom-up self-assembled multilamellar stack to respond as a hyperbolic effective medium in a given region of the visible spectrum ($520 < \lambda < 560$ nm). In the hyperbolic region, the dispersion relation allows propagative modes for large values of $|k_x|$, potentially providing super-resolution.

3. 2D plasmonic fingerprint nanostructures

3.1. Fabrication

A thin (~40 nm) film of a lamellar PS-*b*-P2VP dBCP, with Mn_{PS} = 102.0 kg/mol and Mn_{P2VP} = 97.0 kg/mol, was directly deposited by spin-coating onto a silicon wafer, chemically modified by a polystyrene-*stat*-poly(methyl methacrylate) copolymer ($f_{PS} = 0.63$) to promote the out-of-plane alignment of the dBCP. The films were then impregnated with a gold precursor solution, and exposed to a reactive ion etching (RIE) O_2 plasma, in order to remove the BCP template and reduce the gold salts. The as-cast copolymer films, as well as the resulting gold decorated surfaces, present a lamellar morphology (of period 64 nm), (see Fig. 2). Interestingly, there is no defined azimuthal orientation, leading to characteristic fingerprint patterns. The shape of the produced gold nanostructures was tuned by varying the metal content within the P2VP lamellae, using different impregnation durations. This resulted in different gold nanofeature shapes from well-defined Au dots to rodlike particles of increasing aspect ratio.

3.2. Optical properties

The evolution of the measured ellipsometric angles φ and Δ as a function of the photon energy reveals a clear resonance feature in the region near 540 nm, which is attributed to the LSPR of the Au NPs templated from the P2VP domains. The effective refractive index of the thin film was extracted from the spectroscopic ellipsometry measurements, using a Maxwell-Garnett effective medium approximation with either spherical or ellipsoidal inclusions. High-refractive index surfaces (up to 3.2) with relatively low extinction coefficient (1.4) are obtained with the film of high aspect ratio particles. Finally, the precise control on the shape, structure and volume fraction obtained with the fabrication process, along with the effect of the localized surface plasmon, allows modulating the optical response while keeping a low gold content and little plasmonic coupling effects.

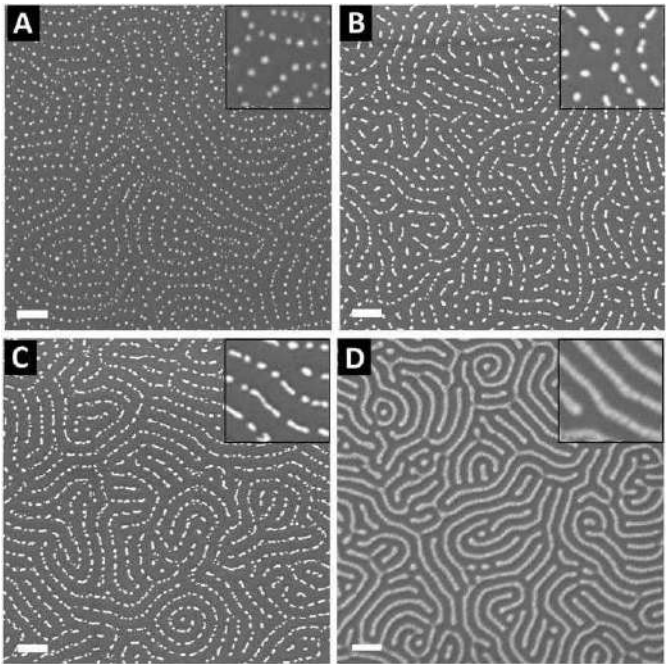


Figure 2: Top-view SEM images of discreet gold nanoparticles arrays formed on a silicon substrate using a PS-b-P2VP BCP template by immersion in a gold precursor solution for different times and a subsequent O_2 RIE treatment. (A) 1 h, (B) 48 h and (C) 120 h. (D) SEM image of continuous gold lines formed on a silicon substrate after 120 h of immersion in the gold precursor solution and a subsequent Ar plasma treatment. Scale bars = 100 nm.

4. Conclusions

Self-assembled diblock copolymers can be used as templates to produce well-defined plasmonic nanostructures in 3D or 2D, with specific and tunable optical resonant properties.

Acknowledgements

This work was supported by the China Scholarship Council; by an Aurora Hubert Curien Partnership, funded by the Norges Forskningsraad (NFR) and by the French ministers des Affaires étrangères et du Développement international (MAEDI) and de l'Education nationale l'Enseignement supérieur et de la Recherche (MENESR); and by the LabEx AMADEus (ANR-10-LABX-42) and IdEx Bordeaux (ANR-10-IDEX-03-02), i.e. the Investissements d'Avenir programme of the French government managed by the Agence Nationale de la Recherche.

References

[1] S. Salvatore, et al, *Adv. Mater.*, 25:2713, 2013.

[2] J. Toudert, X. Wang, et al, *ACS Photon.*, 2:1443, 2015.

[3] X. Wang, et al, *Opt. Laser Technol.*, 88:85, 2017.

[4] A. Alvarez-Fernandez, et al, *Nanoscale Adv,* 1:849, 2019.

Topological Photonic Metamaterials with Honeycomb Structure

Xiao HU

International Center for Materials Nanoarchitectonics (WPI-MANA)
National Institute for Materials Science (NIMS), Tsukuba, Japan
*corresponding author, E-mail: Hu.Xiao@nims.go.jp

Abstract

We propose a generic way to create topological metamaterials. The strategy of our approach is of two steps: (1) create the Dirac-type linear dispersion with the honeycomb lattice, which may be called artificial graphene, and (2) open a band gap and carry out band engineering based on real-space manipulations. Our work shows that fascinating topological functionality can be created using the advanced nanotechnology.

1. Introduction

A couple of years ago, we proposed theoretically that topological electromagnetic transportations can be realized in honeycomb-type photonic crystals of dielectric cylinders [1]. Recently, the proof-of-concept experiment has been carried successfully in microwave regime using Al_2O_3 [2]. The strategy of our approach is of two steps: (1) create the Dirac-type linear photonic dispersion with the honeycomb photonic crystal, which may be called artificial graphene, and (2) open a frequency gap and carry out band engineering based on real-space manipulations.

Crystalline symmetries play the crucial roles since the Dirac-type dispersions in honeycomb lattice are guaranteed by the C_{6v} symmetry with respect to the center of hexagonal unit cell, and the C_3 symmetry with respect to individual sites. Breaking the C_3 symmetry opens a gap accompanied by the lifting of degeneracy between the p and d bands.

We reveal that there are always two conjugating ways in breaking the C_3 symmetry where the p and d bands are inverted in the order of frequency (or energy), which induces the nontrivial topology.

2. New topological metamaterials

Along this line, we have designed a couple of new topological metamaterials of honeycomb structure.

2.1. Topological LC circuit

We design a topological LC circuit with $L_1 > L_0$ as shown schematically in Figure 1, where the C_3 symmetry is broken by the texture in inductance. The design has been realized successfully in microstrips, a typical transmission line [3].

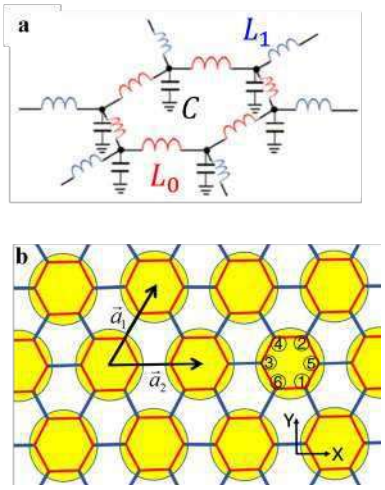


Figure 1: Topological LC circuit with capacitors on the sites and inductors between nearest neighboring sites of honeycomb lattice. (a) hexagonal unit cell and (b) the honeycomb structure shown in the way of triangular lattice of hexagonal unit cells.

2.2. Topological photonic crystal of dielectric cuboids

As another example, we propose to achieve topological electromagnetic propagations by using honeycomb lattice of dielectric cuboids, where the C_3 symmetry is broken by the shape of cuboids [4]. A transition between trivial and topological photonic states is achieved by merely rotating the cuboids around their centers.

3. Conclusions

We propose a generic way to create honeycomb-type topological metamaterials. Our approach is based on the Dirac-type linear dispersion, where the C_{6v} symmetry with respect to the center of hexagonal unit cell, and the C_3 symmetry with respect to individual sites are crucially important. We have revealed that there are always two conjugating ways to break the C_3 symmetry, which lifts the degeneracy of the p and d orbitals and invert them in the order of frequency or energy, and thus induces the nontrivial topology with time-reversal symmetry. Our approach requires only local real-space manipulations, without resorting to spin-orbit coupling, and other special materials. Therefore, our approach is applicable to both

bosonic and fermionic systems, as well as all physical waves. Our work bridges the brand-new topology physics and the advanced nanotechnology.

Acknowledgements

This work is supported by JSPS KAKENHI (No. 17H02913) and JST CREST (No. JPMJCR18T4).

References

[1] L.-H. Wu and X. Hu: Phys. Rev. Lett. 114, 223901 (2015).
[2] Y.-T. Yang, Y.-F. Xu, T. Xu, H.-X. Wang, J.-H. Jiang, X. Hu and Z.-H. Hang: Phys. Rev. Lett. 120, 217401 (2018)
[3] Y. Li, Y. Sun, W.-W. Zhu, Z.-W. Guo, J. Jiang, T. Kariyado, H. Chen and X. Hu: Nat. Commun. 9, 4598 (2018).
[4] X.-X. Wang and X. Hu: in preparation for submission.

Sharp Fano resonance and active response changes in 4D-printed photonic structures

Soo-Chan An[1], Eunsongyi Lee[1], Chang-Hyun Lee[2], Hoon Yeub Jeong[1], Taek-Sun Kwon[2], Jeong-Hae Lee[2], and Young Chul Jun[1*]

[1]*School of Materials Science and Engineering, Ulsan National Institute of Science and Technology (UNIST), Ulsan 44919, Korea*

[2]*School of Electronic and Electrical Engineering, Hongik University, Seoul 04066, Republic of Korea*

[*]corresponding author: ycjun@unist.ac.kr

Abstract

Fano-resonant structures that exhibit sharp spectral resonances are demonstrated employing shape memory polymers. When heated above the glass-transition temperature, disordered lattices are transformed into an ordered lattice, resulting in a drastic change in photonic response. This could be useful for long-distance environmental monitoring.

1. Introduction

Four-dimensional (4D) printing combines smart materials with 3D printing and can thus realize a complex geometry of smart materials with fine details [1, 2]. Therefore, it is a very interesting route for various stimuli-responsive structures with highly enhanced functionalities. 4D-printed structures are also called 'programmable matter', because their response can be programmed into materials by structural and compositional design. However, 4D printing studies have thus far been limited to relatively simple demonstrations. No active or reconfigurable photonic structures with remarkable spectral responses have been reported. Here, we demonstrate 4D printing of shape memory polymers to realize stimuli-responsive, Fano-resonant lattice structures. The optimized lattice structure can exhibit sharp Fano resonances in the microwave region. Deformed lattices can be transformed to the original, ordered lattice upon heating, resulting in a drastic change in the spectrum. This stimuli-responsive action occurs as a result of material properties and thus does not require an electric power supply. It can therefore be used in very creative applications, such as long-distance environmental monitoring via microwave detection. With various smart materials, 4D printing could enable a unique platform for active, reconfigurable photonics. Our work suggests that abundant new opportunities exist for exploration.

2. Results and Discussion

An SMP beam array was fabricated by fused deposition modeling (FDM) 3D printing. After thermomechanical programming, the SMP lattice was randomized. This disordered lattice does not show a sharp spectral resonance. Later, when it was heated again, the lattice returned to its permanent, ordered structure (Figure 1a). A sharp Fano resonance then appeared and we obtained a drastic change in the microwave spectrum (Figure 1b-d). In our dielectric lattice structure, sharp Fano resonances occur because of guided resonances in the periodic, dielectric beams, which interfere with a slowly varying, background Fabry–Perot resonance. Upon heating, the sharp spectral change occurs because the Fano resonance in the ordered lattice structure is induced by a collective, coherent mode distributed over the whole lattice, not by localized resonances in individual beams. Figure 1 below summarizes our sample and microwave measurement results.

In conclusion, 4D printing of shape memory polymers that enable a drastic change in photonic response is demonstrated. Shape-memory-polymer lattices are designed, implemented (by 3D printing), and characterized. The sharp Fano resonance and spectral collapse are measured and analyzed. The effect of the degree of disorder on the Fano resonance is investigated.

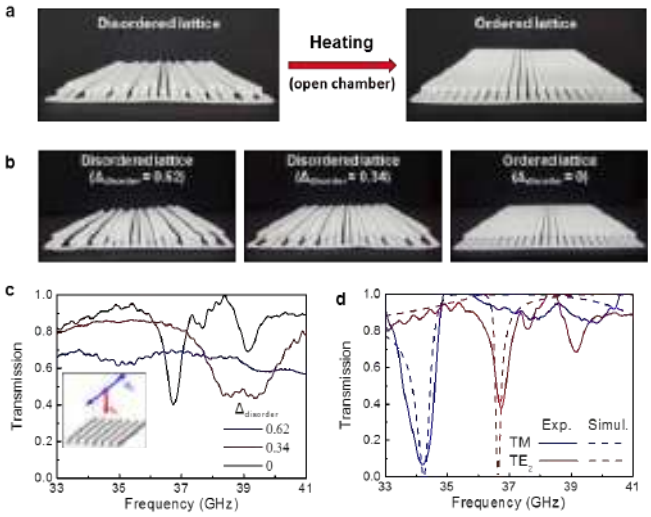


Figure 1: Sample and Microwave measurement results

References

[1] F. Momeni, S. M.M. Hassani.N, X. Liu, J. Ni, A review of 4D printing, *Materials and Design*, 122, 42 (2017).

[2] J. Lee, H.-C. Kim, J.-W. Choi, I. H. Lee, A Review on 3D Printed Smart Devices for 4D Printing. *Int. J. Precis. Eng. Manuf.-Green Tech.* 4, 373-383 (2017).

Mid Infrared Metasurfaces

Yoshiaki Nishijima[1], Naoki To[1], and Takuhiro Kumagai[1]

[1]Faculty of Engineering, Yokohama National University
*corresponding author, E-mail: nishijima-yoshiaki-sp@ynu.ac.jp

Abstract

Mid infrared wavelength is unique to detect the molecular vibration mode. Especially absorption type of frequency selective meta surface can be used for thermal light source, detector and sensing material. Here we demonstrate the recent advances of plasmonic meta surfaces in mid infrared wavelength region. The experimentally measured optical properties were compared with simulations by Finitedifference time-domain calculations. Also, we demonstrate applications of these structures for the plasmonic IR-light sources and detectors.

1. Introduction

Plasmonic metasurface become essential material to control optical transmission, reflection and absorption. One of the popular trends in plasmonics and metamaterials are mid infrared applications. Recent progress in mid infrared metasurface are broad band light absorber for energy harvester, thermal light emitter/absorber and so on [1–4]. The simple configuration of the metal-insulator-metal(MIM) are easy to design and to make by a well-established semiconductor nanofabrication processes or self assembly of nano particles. We focused on PPA structures as the photo-thermal light emitter and detector in mid-infrared (IR) wavelengths for constructing plasmonic non-dispersive infrared (NDIR) gas sensors. The Kirchhoffs law of the thermal radiation defines the absorption and emission efficiencies being equal to each other.

In mid infrared wavelength region, metasurface can be fabricated with well established technology, such as reduction projection photolithography and electron beam lithography techniques, still it requires expensive semiconductor equipment. Therefore the requirement of lithography free plasmonic absorber is enhanced. Here, I will present the methodology for realizing real perfect absorption with plasmonic metasurface, and FabryPero type of metasurfaces and their thermal radiation properties, hydrogen sensing applications.

2. Experiments

Sub-micrometer structure dimensions are required for the MIM structures functional at the IR wavelength range. Therefore, EB lithography with low resolution, high trough put mode or the reduction projection photo lithography is suitable for the mass production of devices. 200 nm Au film was deposited on top of Si substrate, which both side was polished mirror grade. After lithography process (EB or stepper), development and metal deposition, a lift-off was perfromed in an organic solvent to obtain final plasmonic metasurface structures. Lithography free metasurface has been obtained with EB deposition of metal and insulator layers.

Optical reflection spectroscopy has been performed with the combination of the FT-IR (FT-IR 4200, JASCO CO.) and microscope unit (IRT-1000). As a reference for the reflectance spectra, a Au mirror with the 98reflectance has been used. For the thermal radiation spectroscopy, specially modified FT-IR system was implemented. The light from the outside was coupled into the FT-IR setup from an optical side port. The light passed through the interferometer and directed to the HgCdTe (MCT) detector. Samples were contacted to the ceramic heaters on a Al plate with ceramic glue.

3. Results and discussions

Figure 1 shows reflection spectra of plasmonic metasurfaces. Exhaustive FDTD simulation predicts over 90% absorption in various points. In the experimental aspect, resonance wavelength is well agreed with FDTD, but absorption value is not completely suit with FDTD. However controlling the thickness of insulator layer and nanodisks, diameter of nanodisks, distance between two nanodisks (periodicity), we have realeze 95% absorption.

Figure 2 shows reflection and emission spectra of Fabry Pero metasurface. Absorption peaks have appeared around 1.5, 2.5, 7 μm. These peaks comes from multiple reflection in Fabry Pero resonance. In FDTD simulation well agreed with sharp shorter wavelength peaks. However, around 7 μm has not reproducible by FDTD. In the emission spectra, we have observed this broad band emission spectra. According to the Kirchhoff's emission law, only real absorption mode can be realize photo-thermal energy conversion. Detail analysis of this mode is now under consideration, but we have successfully realized near perfect absorption and emission in the mid infrared wavelength region.

4. Conclusions

In this study, we have demonstrated the optical absorption properties of various kinds of plasmonic and label free absorbers in mid-IR wavelengths. Still further improvement is needed to realize real perfect absorber in mid infrared wavelength region. Mid infrared plasmonics and metasur-

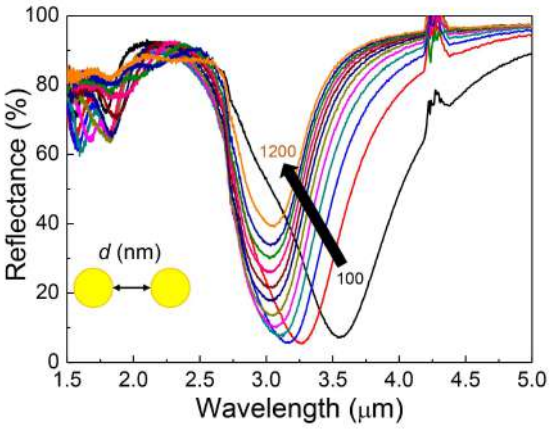


Figure 1: Reflection spectra of plasmonic metasurface with 60 nm of insulator thickness, 50 nm of metal nanostructure thickness and 800 nm of diameter, with 100 to 1200 nm of distance between two disks.

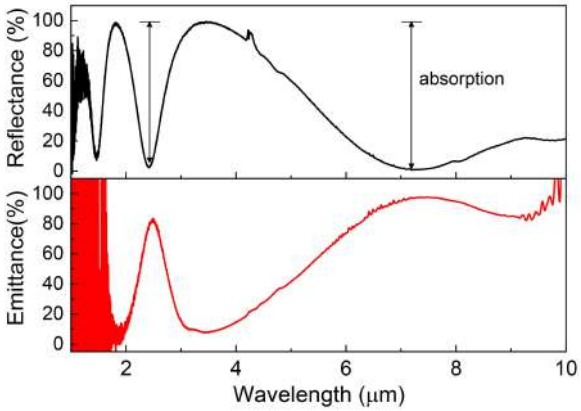


Figure 2: Reflection and emission spectra of Fabry Pero metasurfaces.

faces are interesting field for application of sensing and energy harvesting.

Acknowledgement

Authors are grateful for Tokyo Ohka Kogyo Co. Ltd for their support of reduction exposure lithography to produce NDA and MHA PPAs. YN is thank to Dr. H. T. Miyazaki, National institute for materials science (NIMS), Wako Japan for his kind advise for thermal radiation measurements.

References

[1] Y. Nishijima, Y. Adachi, L. Rosa, and S. Juodkazis, Augmented sensitivity of an IR-absorption gas sensor employing a metal hole array, *Opt. Mat. Express* 3: 968976, 2013.

[2] Y. Nishijima, S. Suda, G. Seniutinas, A. Balcytis, and S. Juodkazis Plasmonic sensor: towards parts-perbillion level sensitivity, *Sens. Mater*. 29: 12531258, 2017.

[3] H. T. Miyazaki, T. Kasaya, M. Iwanaga, B. Choi, Y. Sugimoto, K. Sakoda, Dual-band infrared metasurface thermal emitter for CO2 sensing. *Appl. Phys. Lett.* 105: 121107-1, 2014.

[4] Y. Nishijima A. Balcytis S. Naganuma G. Seniutinas S. Juodkazis, Tailoring Metal and Insulator Contributions in Plasmonic Perfect Absorber Metasurfaces *ACS Applied Nano Materials*, 1, 3557-3564, 2018.

Electrically Tunable Mirror Arrays for Spatial Modulation of Terahertz Radiation over a Wide Frequency Range

Jan Kappa[1], Dominik Sokoluk[1], Steffen Klingel[2], Corey Shemelya[1], Egbert Oesterschulze[2], and Marco Rahm[1]

[1]Department of Electrical and Computer Engineering, Research Center OPTIMAS, Technische Universität Kaiserslautern, Kaiserslautern, Germany
[2]Department of Experimental Physics, Physics and Technology of Nanostructures, Nano Structuring Center, Technische Universität Kaiserslautern, Kaiserslautern, Germany
*corresponding author, E-mail: marco.rahm@eit.uni-kl.de

Abstract

We demonstrate spatial modulation of terahertz waves in a frequency range from 0.97 THz to 2.28 THz by means of an electrically tunable multi-mirror grating. The terahertz spatial light modulator (THz-SLM) consists of 768 actuatable mirrors with each a length of 220 µm and a width of 100 µm. Within the investigated frequency bandwidth, the modulation contrast exceeds 50% with a maximum modulation contrast of 87% at a frequency of 1.38 THz. The THz-SLM can be used to generate almost arbitrary spatial pixel sizes by changing the grouping of the mirrors that are collectively addressed as a pixel. The mirrors are fabricated as a chrome-copper-chrome multilayer material. Due to intrinsic stress in the structure, the mirrors incline to an upstanding position at an angle of 35°. By application of a bias voltage of 35 V, the mirrors can be individually addressed and be pulled down to a ground electrode on the substrate. In addition, hysteretic switching enables spatial light modulation at arbitrary pixel modulation patterns without the necessity to electrically address each individual mirror in the array.

1. Introduction

Terahertz radiation attracts the interest of scientists and industrial developers due to its favorable property of penetrating through most dielectrics without significant attenuation. Furthermore, terahertz pulses with a multi-THz spectral bandwidth can be generated and measured in amplitude and phase. Merging these assets renders terahertz technology an ideal candidate for non-invasive spectroscopy that is urgently needed for quality control and security technology. However, terahertz systems suffer from two major drawbacks. First, imaging terahertz spectroscopes are sophisticated measurement instruments that cannot be fabricated at low cost. Second, terahertz imagers only enable monitoring at low data acquisition rates. The latter especially carries weight when amplitude and phase and thus the whole spectrum is measured for each image pixel. A possible method for faster terahertz imaging is the coded aperture technique, in which a variety of projections of a scene are imaged onto a single-pixel detector [1]. The scene is then reconstructed by either fast direct matrix inversion [2] or compressive computation [3,4]. In contrast to multi-pixel cameras that usually only record the pulse amplitude, the single-pixel detector can be a commercial terahertz antenna that measures amplitude and phase and thus the whole frequency spectrum of the pulse. Yet, coded aperture imaging requires THz-SLMs for the encoding of the spatial projection masks. Among a great variety of different approaches for the realization of THz-SLMs, reconfigurable metamaterials have proven to achieve fast dynamic spatial modulation, but only for limited spectral working range [5-10].

Here, we report the fabrication of a THz-SLM that allows spatial terahertz light modulation over a frequency bandwidth of more than 1 THz. The THz-SLM is based on an electrically tunable grating that consists of actuatable mirrors. The THz-SLM can be used to modulate the projection masks for coded aperture imaging without sacrificing the spectral bandwidth in the measurement process.

2. Results and Discussion

Figure 1 shows a photograph of the fabricated THz-SLM. The THz-SLM is mounted on a circuit board that contains the contact pads for applying the bias voltage patterns to the multi-mirror array. Without biasing, the mirrors of a pixel are inclined at an angle of 35° and form a grating that diffracts incident terahertz radiation away from the position of the single-pixel terahertz detector. The detected terahertz electric field is therefore minimal, when no bias voltage is applied. For a bias voltage of 35 V, the mirrors of a pixel are pulled down to the ground electrode and lie flat on the substrate. In this position, the mirrors of a pixel reflect the incident radiation directly into the direction of the position of the detector and the detected terahertz field is maximal.

In the experiment, we investigated the spectral dependence

of the achievable modulation contrast of the THz-SLM by simultaneously switching all pixels between the flat and inclined mirror position. Figure 2 depicts the plot of the modulation contrast vs. frequency. We observed that the modulation contrast exceeds a value of 0.5 for frequencies between 0.97 THz and 2.28 THz, corresponding to a frequency working range of about 1.3 THz. As shown in a great number of publications, a modulation contrast of 0.5 is sufficient for application of the THz-SLM in a terahertz coded aperture imager. Due to the wide spectral working range, the THz-SLM is not only suited for reconstruction of intensity images in a coded aperture imager, but also for spatially resolved terahertz spectroscopy [11].

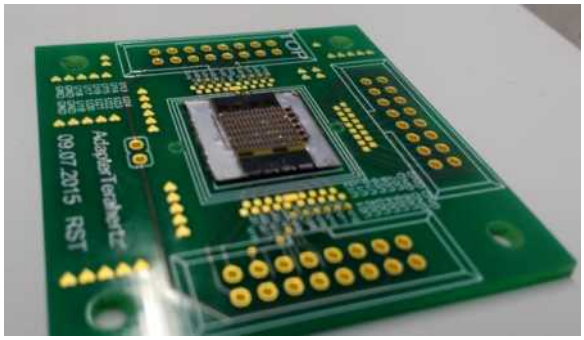


Figure 1: Fabricated THz-SLM on a chip with contact pads for application of a bias voltage. The modulator concept relies on active tuning of an electrically reconfigurable grating.

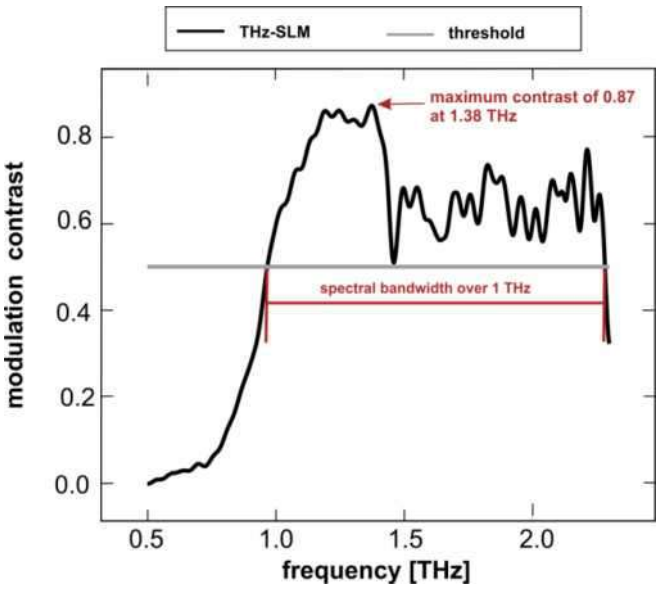


Figure 2: Dependence of the modulation contrast on the frequency. The modulation contrast exceeds 50% over a spectral frequency range of more than 1 THz with a maximum modulation contrast of 87% at 1.38 THz.

3. Conclusions

We experimentally demonstrated spatial terahertz wave modulation with a modulation contrast exceeding a value of 0.5 over a frequency working range from 0.97 THz to 2.28 THz. Due to its wide working range, the terahertz spatial light modulator is very well suited for spatially resolved terahertz spectroscopy based on the coded aperture imaging method.

Acknowledgements

The authors thank the Nano Structuring Center (NSC) at the Technische Universität Kaiserslautern for the technical support.

References

[1] Kannegulla, A.; Jiang, Z.; Rahman, S. M.; Shams, M. I. B.; Fay, P.; Xing, H. G.; Cheng, L. J.; Liu, L. IEEE Transactions on Terahertz Science and Technology 2014, 4, 321.

[2] Augustin, S.; Frohmann, S.; Jung, P.; Hübers, H.-W. Scientific Reports 2018, 8, 4886.

[3] Chan, W. L.; Charan, K.; Takhar, D.; Kelly, K. F.; Baraniuk, R. G.; Mittleman, D. M. Applied Physics Letters 2008, 93, 121105.

[4] Watts, C. M.; Shrekenhamer, D.; Montoya, J.; Lipworth, G.; Hunt, J.; Sleasman, T.; Krishna, S.; Smith, D. R.; Padilla, W. J. Nature Photon 2014, 8, 605–609.

[5] Chan, W. L.; Chen, H.-T.; Taylor, A. J.; Brener, I.; Cich, M. J.; Mittleman, D. M. Applied Physics Letters 2009, 94, 213511.

[6] Shrekenhamer, D.; Chen, W.-C.; Padilla, W. J. Physical Review Letters 2013, 110, 177403.

[7] Shrekenhamer, D.; Montoya, J.; Krishna, S.; Padilla, W.J.; Advanced Optical Materials 2013, 1, 905–909.

[8] Liu, M.; Susli, M.; Silva, D.; Putrino, G.; Kala, H.; Fan, S.; Cole, M.; Faraone, L.; Wallace, V. P.; Padilla, W. J.; Powell, D. A.; Shadrivov, I. V.; Martyniuk, M. Microsystems and Nanoengineering 2017, 3, 17033.

[9] Rout, S.; Sonkusale, S. R. APL Photonics 2016, 1, 086102.

[10] Hu, F.; Xu, N.; Wang, W.; Wang, Y.; Zhang, W.; Han, J.; Zhang, W. Journal of Micromechanics and Microengineering 2016, 26, 025006.

[11] Kappa, J.; Sokoluk, D.; Klingel, S.; Shemelya, C.; Oesterschulze, E.; Rahm, M. Scientific Reports 2019, 9, 2597.

Propagation and spectral sorting of single photons in high-index dielectric nanowires

Mélodie Humbert[1,2], Peter R. Wiecha[1], Gérard Colas des Francs[3], Aurélie Lecestre[4], Guilhem Larrieu[4], Christian Girard[1], Vincent Paillard[1], and Aurélien Cuche[1]

[1]CEMES-CNRS, Université de Toulouse, CNRS, UPS, Toulouse, France
[2]LPCNO, Université de Toulouse, CNRS, INSA, UPS, 135 Avenue de Rangueil, 31077 Toulouse, France
[3]ICB, UMR 6303 CNRS, Université Bourgogne-Franche Comté, Dijon, France
[4]LAAS-CNRS, Université de Toulouse, CNRS, INP, Toulouse, France
*corresponding author, E-mail: aurelien.cuche@cemes.fr

Abstract

We show both experimentally and theoretically that dielectric nanowires (Si-NW) are an efficient platform to transfer visible light from quantum emitters. We first study the effect of high index dielectric nanowires on the spontaneous emission of the emitters positioned in their vicinity. Then, we demonstrate that the 1D propagation of light can be efficiently controlled by the geometry of the wire. These emitter-nanowire hybrid structures might be good candidates as building blocks for the design of complex optical nanodevice architectures working in the single photon regime.

1. Introduction

For a couple of decades, nanoscale optics has mainly been driven by plasmonics since noble metal nanostructures sustain strong resonances that can be used to enhance, confine, propagate or redirect visible light. Such properties have led to numerous actual or potential applications in integrated optics, sensors, nonlinear optics, field-enhanced spectroscopies, or photovoltaics. Recently, an alternative to plasmonics emerged with high refractive index dielectric nanostructures, which offer the same range of applications as plasmonics by manipulating waveguide and Mie optical resonances instead of plasmonic ones [1].
These resonances can be efficiently tuned by modifying the size, shape, and material of those nanostructures (e.g. silicon, optical index n≈4). Furthermore, high index dielectric nanostructures offer several advantages when compared to their metallic counterparts: absorption losses are far weaker for wavelengths greater than the direct band gap, access to semiconductor (CMOS) technology for nanostructure fabrication, and presence of intrinsic strong electric and magnetic resonances [2,3].

In the context of quantum nanophotonics, which aims to combine the confinement and propagation of light at the nanoscale along with quantum properties of light, their appealing properties make Si nanostructures an interesting platform to investigate classical to quantum optics transition in coplanar devices.

2. Discussion

First, we discuss the effect of high index dielectric nanowires on the spontaneous emission of quantum emitters placed in their optical near field. The local density of photonic states (LDOS), therefore the emission rate of punctual emitters, are driven by the presence of the nanostructure. With time-resolved photoluminescence acquisitions, we show that the photodynamics of the quantum emitters are modified in the vicinity of Si wires. The experimental data are systematically compared to decay rate and LDOS maps computed with the Green Dyadic Method (GDM).

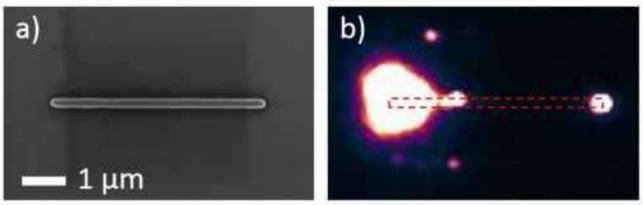


Figure 1: (a) SEM image of a silicon wire (cross-section: 200 nm). (b) Corresponding photoluminescence map recorded in the image plane which reveals the propagation of single photons in the Si-NW.

In a second stage, we show that visible photons emitted by a single emitter coupled at one extremity of Si nanowires is guided efficiently by the waveguide modes up to the second extremity, located several micrometers away. By performing image plane acquisitions (as illustrated in Figure 1) on a set of emitter-wire hybrid structures, we observed in good agreement with numerical experiments that the geometrical parameters of the wires plays an important role in the efficiency of the transfer.

Acknowledgements

This work was supported by Programme Investissements d Avenir under the program ANR-11-IDEX-0002-02, reference ANR-10-LABX-0037-NEXT, by LAAS-CNRS micro and nanotechnologies platform member of the French Renatech network, by the Région Midi-Pyrénées and by the computing facility center CALMIP of the University of Toulouse under grants P12167 and P1107.

References

[1] H. Kallel, A. Arbouet, G. Benassayag, A. Chehaidar, A. Poti, B. Salem, T. Baron, V. Paillard, Tunable enhancement of light absorption and scattering in Si1xGex nanowires, P*hys. Rev. B* 12: 085318, 2012.

[2] P.R. Wiecha, A. Cuche, A. Arbouet, C. Girard, G. Colas des Francs, A. Lecestre, G. Larrieu, F. Fournel, V. Larrey, T. Baron, V. Paillard, Strongly directional scattering from dielectric nanowires, *ACS Photonics* 4: 2036–2046, 2017.

[3] P.R. Wiecha, C. Majorel, C. Girard, A. Arbouet, B. Masenelli, O. Boisron, A. Lecestre, G. Larrieu, V. Paillard, A. Cuche, Enhancement of electric and magnetic dipole transition of rare-earth doped thin films tailored by high-index dielectric nanostructures, *App. Opt.*, 58: 1682-1690, 2019.

Manipulating Electric or Magnetic Spontaneous Emission in the Near-Field of Silicon Nanoantennas

Mathieu Mivelle[1,2,3], Dorian Bouchet[1], Yannick De Wilde[1], Valentina Krachmalnicoff[1], Maria Sanz-Paz[2], Niek F. van Hulst[2], Maria F. Garcia-Parajo[2], Nicolas Bonod[4], and Sébastien Bidault[1]*

[1]Institut Langevin, ESPCI Paris, CNRS, PSL University, Paris, France
[2]ICFO-Institut de Ciencies Fotoniques, The Barcelona Institute of Science and Technology, Castelldefels, Barcelona, Spain
[3]Institut des NanoSciences de Paris, Sorbonne Université, CNRS, Paris, France
[4]Institut Fresnel, Aix Marseille Univ, CNRS, Centrale Marseille, Marseille, France
*corresponding author, E-mail: sebastien.bidault@espci.fr

Abstract

High-index dielectrics such as silicon are an exciting alternative to plasmonic materials for the design of optical nanoantennas with low ohmic losses. We review our recent results on the use of Si-based nanoscale resonators to manipulate magnetic and electric spontaneous emission processes.

Results and discussion

Thanks to their enhanced and confined optical near-fields, broadband subwavelength resonators have the ability to enhance the spontaneous emission rate and brightness of solid-state emitters at room temperature. Over the last few years, high-index dielectrics have emerged as an alternative platform to plasmonic materials in order to design optical resonators with low ohmic losses (Figure 1-a) [1]. In particular, we recently demonstrated experimentally that silicon-based nanoantennas can enhance or inhibit spontaneous emission from fluorescent molecules [2]; but also enhance specifically magnetic decay processes from rare-earth based emitters [3]. In practice, the interaction between silicon nanoantennas and solid-state emitters is controlled using scanning probe microscopy, either by grafting fluorescent emitters or milling a nanoscale resonator (using a focused ion beam) at the tip of a tapered optical fiber.

By coupling a 100 nm fluorescent sphere to silicon nanodisks, we observe that matching the antenna resonance to the fluorescence emission wavelength leads to enhanced decay rates at short distances; while, for an out-of-resonance antenna, the fluorescence lifetime is locally increased (Figure 1-b). Furthermore, these experiments highlight the ability of silicon antennas to increase far-field collection efficiencies, in agreement with numerical simulations.

To study the enhancement of magnetic spontaneous emission processes, we couple oxide nanoparticles doped with trivalent europium cations to cylindrical silicon antennas. By monitoring the relative intensities of the electric and magnetic transitions of europium while scanning the nanoparticle in the vicinity of the nanoantenna, we demonstrate strong nanoscale modulations of the local densities of magnetic or electric optical states, allowing a local enhancement of magnetic emission over its electric counterpart (Figure 1-c).

These results demonstrate the potential of silicon antennas for the manipulation of solid-state emitters at the nanoscale and at room temperature.

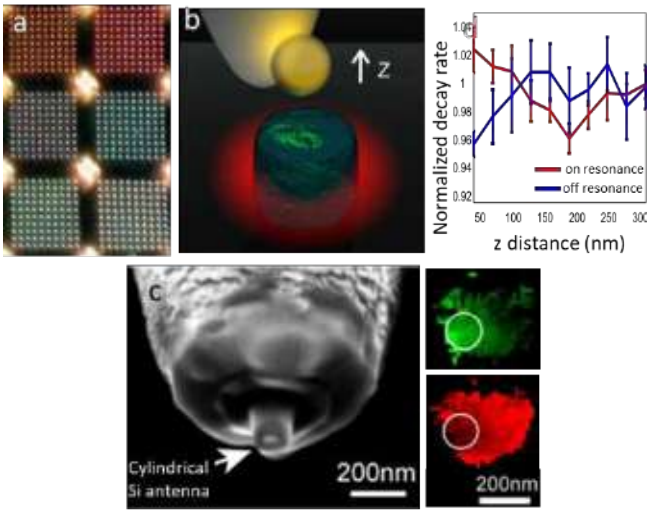


Figure1: (a) Darkfield image of single Si nanoantenna arrays with resonances spanning the entire visible range. (b) Spontaneous decay rate of a fluorescent nanosphere as a function of its distance from a silicon nanodisk: principle of the experiment using scanning probe microscopy (left) and results for antennas that are "on resonance" or "off resonance" with the emission of the nanosphere (right) [2]. (c) Cylindrical silicon antenna used to enhance spontaneous magnetic emission: (left) SEM image of the nanoresonator milled by FIB at the end of an optical fiber and (right) measured magnetic (top) and electric (bottom) LDOS recorded while scanning the resonator in the near-field of a Eu^{3+} doped nanoparticle [3].

References

[1] R. Regmi, J. Berthelot, P. M. Winkler, M. Mivelle, J. Proust, F. Bedu, I. Ozerov, T. Begou, J. Lumeau, H. Rigneault, M. F. García-Parajó, S. Bidault, J. Wenger, and N. Bonod, All-Dielectric Silicon Nanogap Antennas To Enhance the Fluorescence of Single Molecules, *Nano Lett.* 16, 5143, 2016

[2] D. Bouchet, M. Mivelle, J. Proust, B. Gallas, I. Ozerov, M. F. Garcia-Parajo, A. Gulinatti, I. Rech, Y. De Wilde, N. Bonod, V. Krachmalnicoff, and S. Bidault, Enhancement and Inhibition of Spontaneous Photon Emission by Resonant Silicon Nanoantennas, *Phys. Rev. Applied* 6, 064016, 2016

[3] M. Sanz-Paz, C. Ernandes, J. U. Esparza, G. W. Burr, N. F. van Hulst, A. Maitre, L. Aigouy, T. Gacoin, N. Bonod, M. F. Garcia-Parajo, S. Bidault, and M. Mivelle, Enhancing Magnetic Light Emission with All-Dielectric Optical Nanoantennas, *Nano Lett.* 18, 3481, 2018

Surface plasmon-driven ultrafast dynamics of hot electrons

Ilya Razdolski[1,2*], Alexander L. Chekhov[3], Alexander I. Stognij[4], Andrzej Stupakiewicz[5]

[1]Fritz Haber Institute of the Max Planck Society, 14195 Berlin, Germany
[2]Radboud University, 6525 AJ Nijmegen, The Netherlands
[3]Department of Physics, Moscow State University, 119991 Moscow, Russia
[4]Scientific-Practical Materials Research Center of the NASB, 220072 Minsk, Belarus
[5]Faculty of Physics, University of Bialystok, 15-245 Bialystok, Poland
*corresponding author, E-mail: ilyar@science.ru.nl

Abstract

We analyze ultrafast hot electron dynamics in the time domain upon optical excitation of propagating surface plasmon-polaritons in metal-dielectric heterostructures. Considering both local and non-local hot electron relaxation on equal footing, we develop a kinetic model elucidating the role of surface plasmon-polaritons in an apparent slowdown of electron transport. We show how the time-transmissivity data can be employed for the direct measurement of surface plasmon lifetimes at arbitrary corrugated interfaces with unknown losses.

1. Introduction

Ultrafast dynamics of electronic excitations is of growing fundamental interest in modern physics. Femtosecond electron dynamics after an ultrashort optical excitation cannot be accurately described within the thermal equilibrium models. Instead, non-equilibrium electron distributions should be considered on the timescale of a few hundred of femtoseconds [1-2]. Small penetration depth of the optical field in metals ensures inhomogeneous excitation profile and the in-depth transport of hot laser-excited electrons in the ballistic regime [3-4]. Interestingly, the SPP lifetime in plasmonic metals usually resides on a similar timescale, enabling an interplay of these excitations with the relaxation of hot electrons. It is thus intriguing that the role surface plasmon-polariton (SPP) excitations in the hot electron dynamics has not yet been clearly identified.

2. Results

Femtosecond laser excitation of a metal results in the generation of hot electrons above the Fermi level. The population of these non-thermal electrons evolves by means of ballistic transport and electron-electron scattering, constituting non-local and local relaxation, respectively. We employed 40 fs-long laser pulses for studying transient transmittance of a periodically corrugated Au/Co-doped yttrium iron garnet (YIG:Co) magneto-plasmonic crystal (period 800 nm, gap width 100 nm, Au thickness 50 nm). The Au grating enables phase-matched free-space excitation of propagative SPPs at the metal-dielectric interface. In the time-resolved experiments, the pump (fluence 1 mJ/cm2) angle of incidence and wavelength were tuned in the near-IR spectral range around the SPP resonance at the Au/garnet interface at about 1300 nm and 24 degrees of incidence. The weak probe pulses at 800 nm monitored the transient transmittance variations. The experimental data were fitted with a bi-exponential function, allowing to extract the characteristic relaxation timescales at each pump wavelength and incidence angle. We found the local relaxation rate of hot electrons on the order of 1.5 ps, whereas the non-local (fast) relaxation demonstrated a consistent retardation at the SPP resonance (from 50 to 200 fs) in both experimental approaches. No spectral variations of these timescales were detected on a continuous Au film.

To explain this behavior, we employ rate equation for the non-thermal electron population and incorporate the SPP dynamics into the source term. This approach is further corroborated by the excellent agreement of the retardation of the hot electron dynamics and the SPP lifetime estimated from the linewidth of the resonance (~150 fs). Furthermore, this value is very close to the half of the SPP lifetime on a continuous Au/garnet interface (310 fs), as expected if the radiative losses are added up to the intrinsic (Joule) ones. We thus conclude that the hot electrons can be employed for measurements of the SPP lifetimes at interfaces with arbitrary losses. Allowing for external engineering of their losses, SPPs can be envisioned as flexible photonic tools for the spintronic functionality, as well as other applications of the hot electron science and technology.

Acknowledgements

The authors thank A. Melnikov and A. Kirilyuk for valuable comments.

References

[1] R. H. M. Groeneveld, R. Sprik, and A. Lagendijk, Effect of a non-thermal electron distribution on the electron-phonon energy relaxation process in noble metals, *Phys.Rev. B* **45**, 5079 (1992).

[2] C.-K. Sun, F. Vallee, L. H. Acioli, E. P. Ippen, and J. G. Fujimoto, Femtosecond-tunable measurement of electron thermalization in gold, *Phys. Rev. B* **50**, 15337 (1994).

[3] S. D. Brorson, J.G. Fujimoto, E.P. Ippen, Femtosecond Electronic Heat-Transport Dynamics in Thin Gold Films, *Phys. Rev. Lett.* **59**, 1962 (1987).

[4] A. Melnikov, I. Razdolski, T. O. Wehling, E. T. Papaioannou, V. Roddatis, P. Fumagalli, O. Aktsipetrov, A. I. Lichtenstein, and U. Bovensiepen, Ultrafast Transport of Laser-Excited Spin-Polarized Carriers in Au/Fe/MgO[001], *Phys. Rev. Lett*. **107**, 076601 (2011).

Silicon Particle Synthesis and 2D Assembly

Glenna L. Drisko[1*], Benoit Miller[1], Maria Letizia De Marco[1], Alyxandra N. Thiessen[2], Jonathan G. C. Veinot[2], Alex Baron[3], Philippe Barois[3], Virginie Ponsinet[3]

[1] Institut de Chimie de la Matière Condensée de Bordeaux-CNRS, 87 Avenue du Dr Albert Schweitzer, 33608, Pessac, France
[2] Department of Chemistry, University of Alberta, Edmonton, Alberta, Canada, T6G2G2
[3] Centre de Recherche Paul Pascal-CNRS, 115 Avenue du Dr Albert Schweitzer, 33600 Pessac, France
*corresponding author, E-mail: glenna.drisko@icmcb.cnrs.fr

Abstract

Spherical, crystalline silicon particles, smaller than the wavelength of incident light, demonstrate intense dipolar electric and magnetic resonances. A new bottom-up route has been developed allowing us to produce mass quantities of these meta-atoms. Thanks to their large diameter (80-115 nm), high degree of crystallinity, purity and the absence of pores, both electric and magnetic Mie resonance has been measured using static light scattering. The scattering properties of these particles have been additionally characterized by single particle dark field scattering. The silicon particles were organized on 2D substrates via dip-coating with the aim of manufacturing metasurfaces.

1. Introduction

All-dielectric optical metamaterials and metasurfaces have attracted interest in recent years due to the short-comings of plasmonic metamaterials [1,2]. Plasmonic resonators often possess weak magnetic scattering, which cannot compensate for the strong losses due to friction between electrons during plasmonic resonance. Among all-dielectric metamaterials, silicon is the favourite candidate as it supports intense Mie resonances at optical frequencies, has low losses and will be easily interfaced with existing silicon electronics technologies [3]. In silicon, the magnetic dipole scattering is the most intense resonance mode and occurs slightly red-shifted compared to the electric dipole scattering. To exhibit Mie scattering at visible frequencies, silicon particles should have a particle diameter between 75 and 200 nm, they should be non-porous, pure in composition and crystalline [3]. Zywietz *et al.* experimentally showed the interest in silicon particles as meta-atoms, by laser printing particles with controlled diameters and degrees of crystallinity one by one [4]. Thus chemists are now given the challenge of producing these resonant particles via bottom-up methods capable of producing sufficient quantities of particles to assemble a material. Silicon is a particularly difficult material for synthetic chemists as silicon precursors are highly reactive, often dangerously so, and silicon quickly oxidizes to silica. Silica possesses a low refractive index, and thus must be avoided. We explored a modification of the synthesis published by A. Thiessen *et al.* [5] in order to produce Si particles with larger diameter, possessing visible magnetic and electric scattering. We then have begun assembling these silicon particles on 2D substrates to produce all-dielectric metamaterails.

2. Experimental

Silicon nanoparticles were prepared via a modification of an established and widely embraced synthetic route involving the thermally-induced disproportionation of hydrogen silsesquioxane (HSQ) to produce bulk quantities of silicon particles having Mie resonance [5]. Silicon nanoparticle size was tuned via controlling the thermal processing conditions of HSQ. Silicon meta-atoms between 80 and 115 nm have been prepared. The resulting SiNPs were liberated from the oxide matrix via alcoholic HF etching. Silicon nanoparticles were evaluated for crystallinity and purity using X-ray diffraction, X-ray photoelectron spectroscopy, TEM, SEM, SAED, EDX, and FTIR spectroscopy.

Dip-coating experiments were performed on an ACEdip 2.0 dip-coater obtained from SolGelWay. The withdrawal speed and the chamber temperature were controlled using the software ACEdip 2.0 SOLGELWAY. Boron-doped prime CZ silicon wafers with (100) orientation were obtained from Sil'tronix. The wafers were cleaned, rinsed with absolute ethanol and wiped dry with a Kimwipe paper, before use as the substrate for silicon nanoparticle self-assembly.

3. Results and discussion

In this work, we produced Si meta-atoms via the thermal decomposition of HSQ. This method produces spherical, dense, crystalline silicon particles that have Mie scattering resonances in the visible spectrum (Figure 1). The particles were characterized for optical magnetism using single particle dark field microscopy and static light scattering. These are among the best silicon meta-atoms produced via bottom-up chemistry to date.

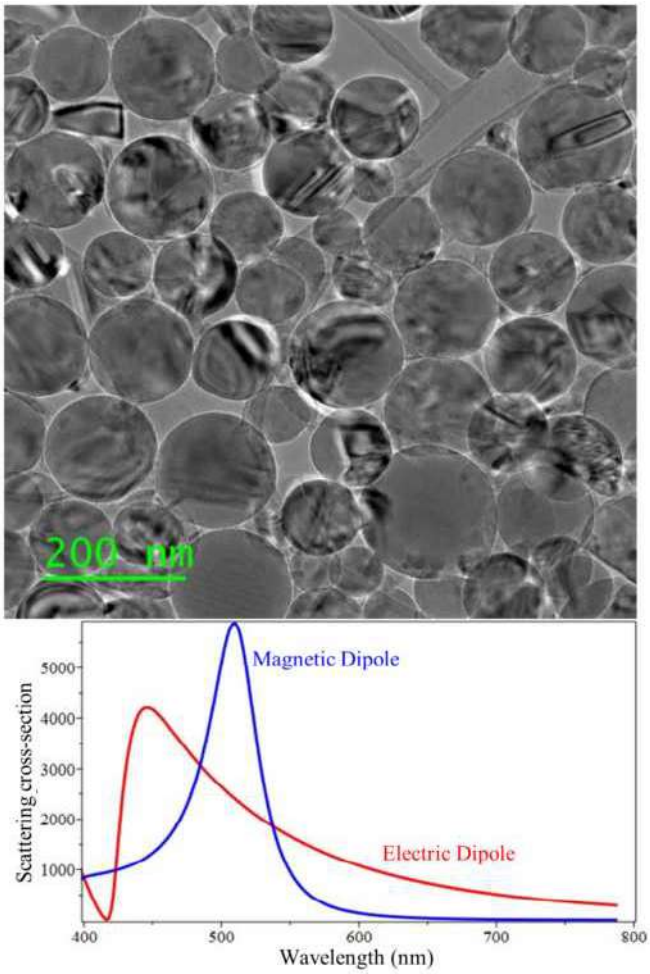


Figure 1: (Top) TEM image of crystalline, non-porous silicon nanoparticles. (Bottom) Theoretical simulation of the Mie resonance for the particles shown above. The experimental results were accurately predicted.

The silicon nanoparticles were then suspended and dip-coated onto silicon wafers. Critical to a good deposition is a stable colloidal solution. Thus solvent properties were studied to obtain a dispersion with several hours of shelf-life. Although this was sufficient for film processing, the particles were then sterically stabilized to further increase the colloidal stability and decrease particle aggregation. Films were then created, maximizing the degree of compactness via changing the evaporation conditions and the deposition rate. Stick-slip deposition lines were observed at withdrawal rates equal to or slower than 25 μm/s (Figure 2). Continuous films were obtainable by tuning the processing conditions. These films are currently being characterized using ellipsometry.

4. Conclusions

Si particles can be produced on the gram scale using HSQ as a silicon precursor. The silicon particles released from the oxide matrix are stable in air, even after several months of storage, attesting to their density. Due to the optimum parameters of these beads, Mie scattering resonance was

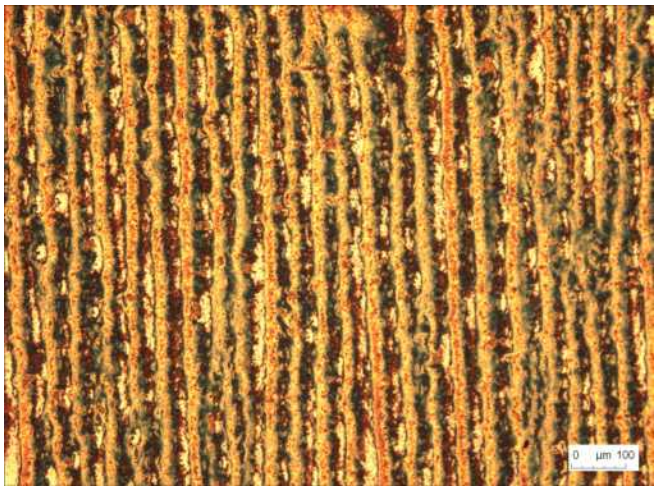


Figure 2: Optical microscopy image of a thin film of silicon particles deposited at 50 °C and 25 μm/s. The bands represent "stick" zones arising from the stick-slip phenomenon.

observed via static light scattering measurements of dilute suspensions of silicon particles. These particles were then deposited onto 2D substrates using dip-coating. Dip-coating is an effective technique for silicon nanoparticle deposition, giving rise to tightly packed films of controllable thickness. These materials are unique to date, prompting us to study these films using ellipsometry in order to extract μ_{eff} and ε_{eff}. In the future, complex clusters will be explored in order to spectrallyoverlap the magnetic and electric scattering properties [6].

References

[1] P. Moitra, B. A. Slovick, W. Li, I. I. Kravchencko, D. P. Briggs, S. Krishnamurthy, Large scale all-dielectric metamaterial perfect reflector, *ACS Photonics* 2: 692-698, 2015.

[2] I. Staude, J. Schilling, Metamaterials inspired silicon nanophotonics, *Nat. Photon.* 11: 274-284, 2017

[3] M. L. De Marco, S. Semlali, B. A. Korgel, P. Barois, G. L. Drisko, C. Aymonier, Silicon based optical metamaterials: Focus on the current synthesis challenges, *Angew. Chem. Int. Ed.,* 57: 4478-4498, 2018.

[4] U. Zywietz, A. B. Evlyukhin, C. Reinhardt, B. N. Chichkov, Laser printing of silicon nanoparticles with resonant optical electric and magnetic responses, *Nat. Commun.*, 5: 3402-3409, 2014.

[5] A. N. Thiessen, M. Ha, R. W. Hooper, H. Yu, A. O. Oliynyk, J. G. C. Veinot, Silicon nanoparticles: Are they crystalline from the core to the surface?, *Chem. Mater.*, 31, 678–688, 2019.

[6] R. Dezert, P. Richetti, A. Baron, Isotropic Huygens sources made of clusters of nanoparticles for metasurfaces appliations, *J. Phys.: Conf. Ser.*, 1092, 012022, 2018.

Hybridization between Parallel and Orthogonal Surface Lattice Resonances

Shao-Ding Liu,[1,*] Peng Yue,[1] Shi Zhang,[2] Mingshan Wang,[3] Hongwei Dai,[3] Yiqin Chen,[2] Zhong-Quan Nie,[1] Yanxia Cui,[1] Jun-Bo Han,[3,*] and Huigao Duan[2,*]

[1] Key Lab of Advanced Transducers and Intelligent Control System of Ministry of Education, and Department of Physics and Optoelectronics, Taiyuan University of Technology, Taiyuan 030024, P. R. China.

[2] State Key laboratory of Advanced Design and Manufacturing for Vehicle Body, College of Mechanical and Vehicle Engineering, Hunan University, Changsha 410082, P. R. China.

[3] Wuhan National High Magnetic Field Center, Huazhong University of Science and Technology, Wuhan 430074, P. R. China.

*corresponding author, E-mail: liushaoding@tyut.edu.cn (S. D. L.), duanhg@hnu.edu.cn (H. D.) and junbo.han@mail.hust.edu.cn (J. B. H.)

Abstract

Multiple surface lattice resonances generated under normal incidence suppress radiative losses effectively around several spectral positions, and it is important to develop reliable methods to generate multiple surface lattice resonances. In this work, we propose an approach to excite multiple surface lattice resonances with rationally designed plasmonic molecule arrays. It is demonstrated that owning to the formation of various hybridized localized surface plasmon resonances (LSPRs) with a plasmonic trimer, multiple surface lattice resonances can be excited with plasmonic trimer arrays caused by the hybridization between parallel and orthogonal surface lattice resonances.

1. Introduction

Compared with that of a single surface lattice resonance, metallic nanoparticles arrays that support multiple single surface lattice resonances suppress radiative losses around several spectral positions simultaneously. Therefore, multiple single surface lattice resonances are promising for multi-wavelength related applications. It is shown that multiple surface lattice resonances are excited in plasmonic nanoparticle superlattices caused by the coupling between single patch surface lattice resonances and Bragg modes [1]. Similar as the plasmon hybridization theory, hybridization of individual lattice resonances results in the formation of multiple surface lattice resonances in overlapped nanoparticle arrays with multi-particle unit cell [2]. Not long ago, the realization of multi-modal nanolasing and lasing at *K* points has been demonstrated with multiple surface lattice resonances [3, 4]. In this study, we show that the symmetry of single oligomer clusters plays an important role for the collective responses of plasmonic molecule arrays. We experimentally and theoretically demonstrated that multiple surface lattice resonances can be generated with plasmonic oligomer cluster arrays.

2. LSPRs with single trimers

Depending on the structural symmetry, the collective optical responses of single plasmonic molecules are constructed from linear combinations of the plasmon modes of individual nanoparticles. Therefore, the optical responses of a plasmonic molecule such as the gold nanodisk trimer can be strongly modified by manipulating the structural symmetry [5]. When the trimer symmetry is lowered to C_{2v} point group [6], the symmetry breaking lifts the degeneracy of the resonances, where the E′ modes of a symmetric trimer evolve into four non-degenerate A_1 and B_2 resonances. Besides that, the ring-like dipole arrangement of the dark A_2' mode for the D_{3h} trimer is perturbed by the symmetry breaking, and the resonance evolves into another bright B_2 mode for the C_{2v} trimer.

3. Hybridization between parallel and orthogonal surface latter resonances

Since plasmonic trimers possess various LSPRs, and the spatial arrangements of the equivalent dipoles for individual resonances are different with each other, it is expected that the coupling between these LSPRs and RAs may occur simultaneously for plasmonic molecule arrays, which makes it possible to generate multiple surface lattice resonances.

To that end, a series of C_{2v} gold trimer arrays with different lattice spacing along the *x*-axis have been fabricated (the middle panels of Figure 1). A home-built optical setup was used to measure the transmission spectra, where the NA of the incident beam is reduced to about 0.03. In this way, the diffraction coupling between the unit cells and the excitation of SLRs can be observed in the transmission spectra due to the near-normal incidence. The left and right panels of Figure 1 show the measured and calculated transmission spectra under *x*-polarized incidence, respectively. When the lattice spacing P_x = 650 nm, the hybridization between the parallel and orthogonal surface lattice resonances leads to the formation of two hybridized collective resonances.

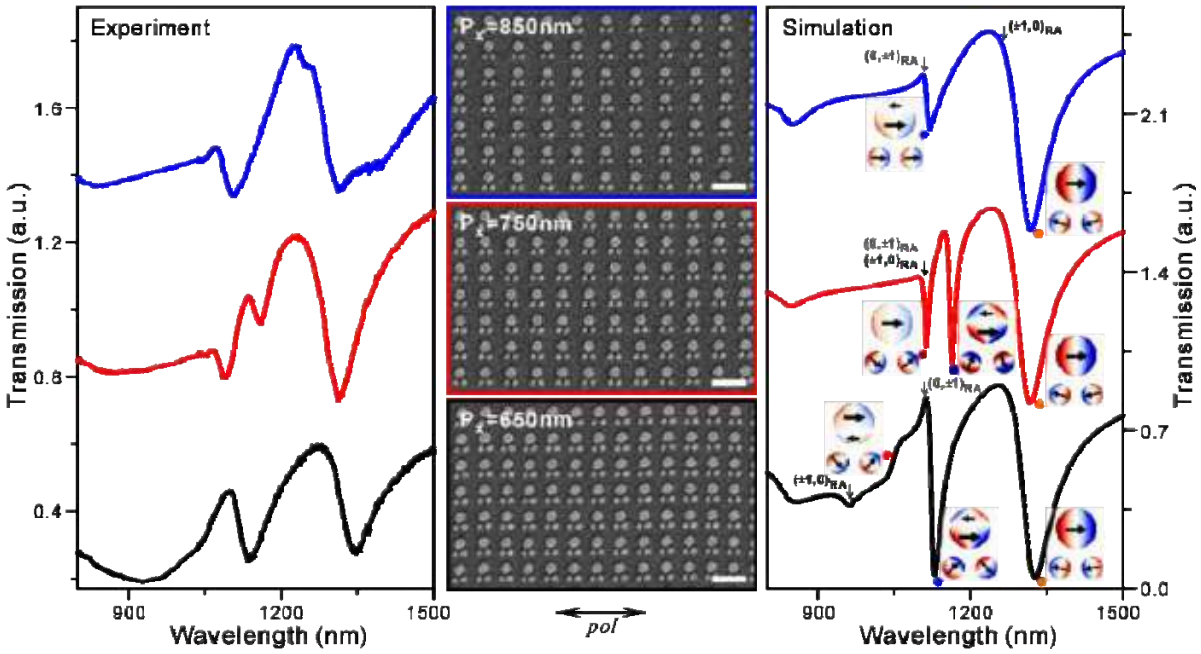


Figure 1: Realization of the hybridization between parallel and orthogonal surface lattice resonances with plasmonic trimer arrays by adjusting the lattice spacing along the *x*-axis.

4. Conclusions

In conclusion, we propose and demonstrate that plasmonic molecule arrays are promising platforms to generate multiple surface lattice resonances under normal incidence. Depending on the plasmon hybridization and the structural symmetry, plasmonic molecules such as the trimer possess various localized plasmon resonances belonging to different irreducible representations. The coupling between these LSPRs and RAs occurs for plasmonic molecule arrays by manipulating the lattice spacing, which leads to the formation of multiple surface lattice resonances. It is interesting to find that in addition to the conventional orthogonal surface lattice resonances, a spectral feature related to the excitation of the parallel surface lattice resonance is observed in the transmission spectra, which is attributed to the formation of equivalent dipoles perpendicular to the incident polarization. What's more important is the plasmon hybridization theory reveals that the collective resonances of plasmonic molecules are non-orthogonal with each other. Therefore, even though the parallel surface lattice resonance is very weak, the resonance coupling between the parallel and orthogonal surface lattice resonances occurs when the two kinds of surface lattice resonances are approaching to each other, and a pronounced anti-crossing behavior is observed in the energy diagram, thereby forming two new eigenmodes that possess the characteristics of both parallel and orthogonal RAs.

Acknowledgements

S.D.L. acknowledges the financial support by NSFC (11874276 and 11574228), the Natural Science Foundation of Shanxi Province (201601D021005), and the San Jin Scholars Program of Shanxi Province. H.D. acknowledges the support by NSFC (11574078, 51722503). J.B.H. acknowledges the Fundamental Research Funds for the Central Universities (2018KFYXKJC011) and the magneto-optical facilities at Wuhan National High Magnetic Field Center.

References

[1] Wang, D.; Yang, A.; Hryn, A. J.; Schatz, G. C.; Odom, T. W. Superlattice Plasmons in Hierarchical Au Nanoparticle Arrays. *ACS Photonics* 2015, 2, 1789-1794.

[2] Baur, S.; Sanders, S.; Manjavacas, A. Hybridization of Lattice Resonances. *ACS Nano* 2018, 12, 1618-1629.

[3] Wang, D.; Yang, A.; Wang, W.; Hua, Y.; Schaller, R. D.; Schatz, G. C.; Odom, T. W. Band-edge engineering for controlled multi-modal nanolasing in plasmonic superlattices. *Nature Nanotech.* 2017, 12, 889-894.

[4] Guo, R.; Necada, M.; Hakala, T. K.; Vakevainen, A. I.; Torma, P. Lasing at K points of a honeycomb plasmonic lattice. *Phys. Rev. Lett.* 2019, 122, 013901.

[5] Prodan, E.; Radloff, G.; Halas, N. J.; Nordlander, P. A Hybridization Model for the Plasmon Response of Complex Nanostructures. *Science* 2003, 302, 419-422.

[6] Chuntonov, L.; Haran, G. Trimeric Plasmonic Molecules: The Role of Symmetry. *Nano Lett.* 2011, 11, 2440-2445.

Invisible Dielectric Cylinders at Optical Frequency

Kotaro Kajikawa, Yusuke Kobayashi

Department of Electrical and Electronic Engineering, School of Engineering,
Tokyo Institute of Technology, 4259 Nagatsuta, Midori-ku, Yokohama 226-8502, Japan

Abstract

Reported here is invisible circular cylinders at optical frequency, with no coating, on the basis of analytical and numerical calculations . We can realize this, using a dielectric cylinder with its refractive index ranging from 2.7 to 3.8. According to our FDTD calculations, the invisibility stems from cancellation of the dipoles generated in the cylinder.

1. Introduction

Optical cloaking is one of the methods to be an object invisible. In most cases, the object becomes invisible by wrapping with a cloaking medium. There are two major mechanisms for cloaking: one the cancellation of the polarizations arising in the object and in the cloaking medium[1], the other the detouring of light in the cloaking medium having designed distribution of refractive index[2, 3]. Although many studies on the cloaking have been reported, no reports have appeared on an invisible object at optical frequency. In this paper, we report invisible circular cylinders with no cloaking, at optical frequency, on the basis of analytical and numerical calculations.

2. Results and discussion

We investigated optical parameters for invisibility of a cylinder, with a radius r and a refractive index m at an optical wavelength λ. Analytical calculations on the basis of the Mie theory were carried out to find the invisible condition. Figure 1(a) shows a contour plot of scattering efficiency $Q_{\rm sca}$, as a function of the size parameter $\alpha = 2\pi r/\lambda$ and the refractive index m, for TE polarization, defined as a polarization perpendicular to the axis of the cylinder. As expected, the scattering efficiency is low at $m \sim 1$ and at a small size parameter. There are a few regions of low scattering efficiency other than those. In the region pointed out with a red arrow, there are points with the lowest scattering efficiency $Q_{\rm sca} \sim 0.08$, where the refractive index ranges from 2.7 to 3.6. The natural materials with these indexes are exemplified by Si, GaAs and AlAs. Therefore, we can realize the invisible cylinder with these materials, experimetnally.

Figure 1(b) shows a contour plot of scattering efficiency $Q_{\rm sca}$ for TM polarization, defined as a polarization along the axis of the cylinder. Although there are some regions of low scattering efficiency, the lowest efficiency is not very low, $Q_{\rm sca} \sim 0.4$. Figure 1(c) shows the scattering efficiency of a sphere. The profile is similar to that of the cylinder

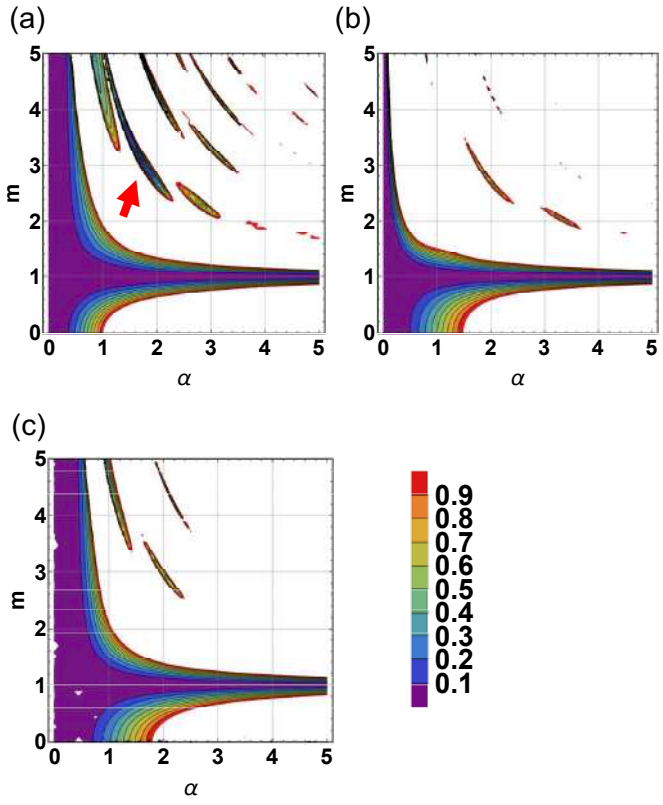


Figure 1: Contour plots of $Q_{\rm sca}$, as a function of the size parameter, α and the refractive index m for (a) a cylinder for TE polarization (b) a cylinder for TM polarization, and (c) a sphere.

for TM polarization, indicating that there exists no condition of the low scattering efficiency at optical frequencies. Thus, we conclude the invisibility can be made only for a cylinder with high refractive index, on the illumination of TE polarization.

FDTD calculations were made to clarify the mechanism of the invisibility. At the low scattering condition, the wavefront was scarcely distorted by the invisible cylinder. The calculated field distribution in the cylinder is symmetric, indicating that the radiation is canceled in the cylinder.

3. Conclusions

We reported invisible circular cylinders with no coating, at optical frequency, on the basis of analytical and numerical

calculations. This condition can be achieved using a dielectric cylinder with the refractive index of the dielectric cylinder ranges from 2.7 to 3.8. This can be realized with natural materials, such as Si, GaAs and AlAs. According to the calculations based on FDTD, the invisibility stems from cancellation of the dipoles generated in the cylinder.

References

[1] A. Alù, N. Engheta, Electromagnetic cloaking by layered structure of homogeneous isotropic materials, *Phys. Rev. E* 72: 316623, 2005.

[2] J. B. Pendry, D. Schurig, and D. R. Smith, Controlling Electromagnetic Fields, *Science* 312: 1780–1782, 2006.

[3] U. Leonhardt, Optical Conformal Mapping, *Science* 312: 1777–1780, 2006.

Photonic Integrated Nanojet

Ali Belarouci[1,*], Michele Calvo[2], Oleksii Hudz[1], Pedro Rojo Romeo[1], Régis Orobtchouk[2]

[1]Lyon Institute of Nanotechnologies, CNRS UMR 5270, Ecole Centrale de Lyon, Université de Lyon, 36 Avenue Guy de Collongue, 69134 Ecully cedex, France
[2]Lyon Institute of Nanotechnologies, CNRS UMR 5270, INSA de Lyon, Université de Lyon, 7 Avenue Jean Capelle, 69621 Villeurbanne cedex, France
*corresponding author, E-mail: ali.belarouci@ec-lyon.fr

Abstract

We report the direct experimental observation of photonic nanojets created by single Si_xN_y microdisks illuminated by a waveguide. High intensity sub-wavelength spots and low divergence nanojets are observed at a wavelength of 1550nm. Light scattered from the disk is observed by imaging from above. The electromagnetic distributions inside and outside the microdisk are calculated by using finite-difference-time-domain method and compared to the experimental image.

1. Introduction

The effect of enhanced and subwavelength focus of visible light by dielectric microspheres and microcylinders has been recently the subject of several papers [1-4]. These investigations predict, under specific conditions, the existence of a subdiffracted-waist beam that emerges from the structure with high intensity and low divergence. This beam, inaccessible with a classical Gaussian laser beam focused by a high numerical aperture objective, has been named photonic nanojet (PNJ) [4]. However, much of the experimental work has been focused on PNJs from dielectric spheres and cylinders. The use of a planar disk based configuration offers many advantages. The disks size and shape and position can be easily controlled to high precision in a lithography microfabrication process. We report the direct experimental observation of photonic nanojets created by single SixNy microdisks illuminated by a waveguide. Microdisks with diameters of 5μm have been fabricated and incident wavelengths of 1550nm has been used. By simply imaging the disks from the top, many of the properties of light scattering have been confirmed.

2. Device fabrication

A 900nm layer of non-stoichiometric – low index Si_xN_y was deposited on a 2 µm layer of thermally grown SiO2 on a Si wafer. The 2 µm thick low refractive index oxide layer acts as an optical spacer between the Si_xN_y guiding layer and the Si base wafer. The microdisks and waveguides were then patterned using a 30 kV FEI- ebeam lithography system under a PMMA/MMA bilayer positive tone resist. A 100nm thick chromium hard mask is then deposited followed by a lift-off process. The sample was etched using an RIE with a mixture of SF6 and CHF3 gases to reveal patterns with smooth sidewalls. Finally, a wet etching process step was used to remove the remaining chromium from the surface.

3. Experiment

Samples were characterized with a linearly polarized tunable laser set to the desired wavelength (1550 nm) and light was injected by buttcoupling into the waveguide. The waveguide has been designed to produce a nearly plane wave excitation of the disk. The scattered light is observed from above using a long working distance, flat field corrected, 100x microscope objective with an NA of 0.7 (Mitutoyo). The objective is infinity corrected, thus a tube lens of focal length 200mm is used to form the primary image directly on the CCD. The result is a gray-scale pixel image of the scattered light distribution as shown in Figure 1.

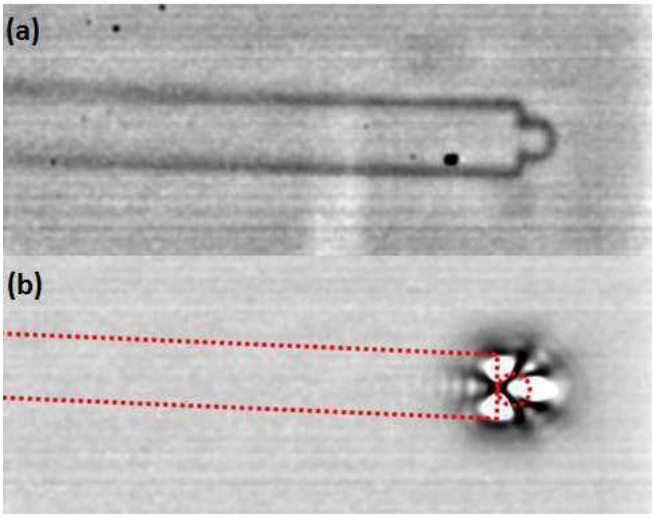


Figure 1: (a) Optical image of waveguide coupled microdisk. (b) Scattering distribution from a 5µm microdisk illuminated at 1550nm.

4. Conclusions

We proposed and demonstrated a new plateform for the integration of photonic nanojet on a chip. The scattering properties of a microdisk have been fully investigated and revealed a localized PNJ generated at the shadow-side surface of the SiN based microdisk illuminated by the waveguide.

References

[1] L. E. Helseth and T. M. Fischer, "*Cooperative microlenses*," Opt. Express **12**, 3428-3435 (2004).

[2] M. Mosbacher, H. J. Munzer, J. Zimmermann, J. Solis, J. Boneberg, and P. Leiderer, "*Optical field enhancement effects in laser-assisted particle removal*," Appl. Phys. A **72**, 41-44 (2001).

[3] D. A. Fletcher, K. E. Goodson, and G. S. Kino, "*Focusing in microlenses close to a wavelength in diameter*," Opt. Letters **26**, 399-401 (2001).

[4] Z. Chen, A. Taflove, and V. Backman, "*Photonic nanojet enhancement of backscattering of light by nanoparticles: a potential novel visible-light ultramicroscopy technique*," Opt. Express **12**, 1214-1220 (2004).

Cooperative emission mediated by energy transfer to plasmonic antenna

Tigran V. Shahbazyan
Department of Physics, Jackson State University, Jackson, MS 39217 USA
E-mail: shahbazyan@jsums.edu

Abstract

We describe a new cooperative mechanism of spontaneous emission by an ensemble of quantum emitters near a plasmonic nanostructure based on cooperative energy transfer to plasmonic antenna from collective states formed due to plasmonic correlations.

1. Introduction

Spontaneous decay of a quantum emitter (QE), such as dye molecule or semiconductor quantum dot, placed near a metal nanostructure supporting surface plasmons in the same spectral range can be greatly enhanced due to new efficient energy transfer (ET) channel from the QE to resonant plasmon mode. The enhancement of spontaneous emission (SE) rate is characterized by the Purcell factor [1] $F_p = 6\pi Q\omega^3/c^3V$, where Q is the plasmon mode quality factor and V is the mode volume characterizing field localization (ω and c are the frequency and speed of light). If the system size is not too small, a considerable part of transferred energy is radiated away by the plasmonic antenna, resulting in strong enhancement of radiated power spectrum observed, e.g., in plasmon-enhanced fluorescence experiments [2,3], while the rest of transferred energy is dissipated mainly through the Ohmic losses in metal. Note, however, that the plasmon local density of states (LDOS), which characterizes ET rate, is limited by nonlocal effects in the electron optical response near the metal surface.

At the same time, SE by an ensemble of QEs can be greatly accelerated through electromagnetic correlations between QEs. A prominent example of cooperative emission is Dicke superradiance [4] of QEs interacting with a common radiation field, which leads to emergence of collective states radiating at a rate proportional to the full ensemble size (even if only a few QEs are excited). In the presence of plasmonic structure, superradiance is modified: while the QEs' correlations are enhanced due to resonant Mie scattering, thus reducing the negative impact of direct dipole interactions, the Ohmic losses in the metal suppress correlations for QEs located too close to the metal surface [5]. Observation of plasmon-enhanced superradiance remains a challenge as it hinges on delicate interplay between QEs' direct interactions, plasmon-enhanced radiative coupling, and metal losses.

2. Results and discussion

On the other hand, strong absorption by a plasmonic nanostructure gives rise to another collective effect – *cooperative energy transfer* (CET) from an ensemble of QEs to resonant plasmon mode [6]. Namely, if the emission frequencies of N excited QEs lie within the plasmon spectral band, the plasmonic correlations between QEs lead to emergence of a collective state that transfers its energy at a rate $\gamma_{et}^c = \sum_i \gamma_{et}^i$, where γ_{et}^i are individual QE-plasmon ET rates determined by the plasmon LDOS at the QE positions (see Fig. 1). If radiation efficiency of a plasmonic antenna is sufficiently high, this energy is radiated away at the same rate γ_{et} it is being received from the QE ensemble. Importantly, CET mechanism is insensitive to natural variations of QE frequencies due to, e.g., direct dipole interactions or, in the case of QDs, their size variations, if QEs' frequencies stay within plasmon's broad spectral band. Furthermore, the power spectrum retains the plasmon resonance lineshape and, therefore, is also largely independent of QEs frequency variations within the ensemble.

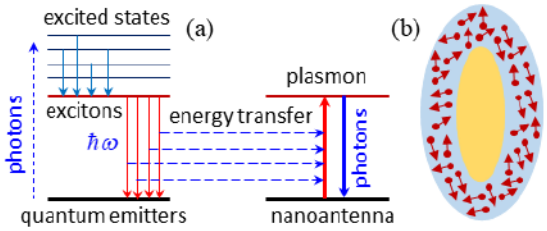


Figure 1. (a) Schematics of CET from incoherently excited QEs to a plasmonic antenna. (b) Schematics of core-shell plasmonic nanoparticle with QE distributed within the dielectric shell surrounding the metal core.

Here we present a theory of cooperative spontaneous emission by an ensemble of QEs coupled to a plasmonic resonator mediated by CET mechanism. For an ensemble of N excited QEs coupled to plasmonic resonator, we pinpoint the collective state that saturates the ensemble ET rate to the plasmon mode and derive cooperative Purcell factor as the sum of individual factors, $F_p^c = \sum_i F_p^i$ (see Fig. 2a). The power spectrum enhancement factor for cooperative emission has the form $M_c = F_p^c\eta$, where η is the antenna radiation efficiency (see Fig. 2b). For comparable individual ET rates, e.g., if QEs are confined within a plasmonic cavity, the CET

rate scales with the ensemble size. In contrast, if QEs are distributed outside the metal structure, the local fields that determine the individual ET rates rapidly decrease as the distance to metal surface increases, so that the remote QEs are not coupled to the plasmon mode. In this case, if QEs are uniformly distributed in an extended region that saturates the plasmon mode volume, the cooperative Purcell factor is independent of local fields and is determined solely by the system parameters measured in experiment [7].

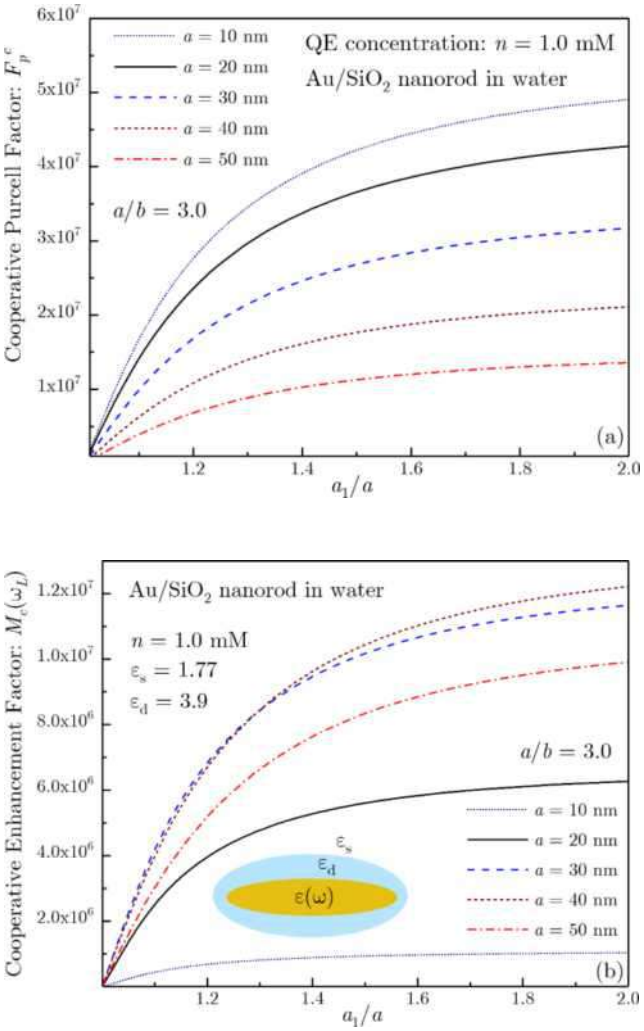


Fig. 2. Numerical calculations of SE from an ensemble of QEs uniformly distributed at concentration n within dielectric shell of a core-shell nanorod, modeled by two confocal spheroids with semi-major and semi-minor axes (a,b) and (a_1,b_2). (a) Cooperative Purcell factor is shown with increasing QE region at different nanorod overall sizes. (b) Same for enhancement factor of radiated power spectrum.

This work was supported in part by NSF grants DMR-1610427, DMR-1826886, and HRD-1547754.

References

[1] E. M. Purcell. "Spontaneous emission probabilities at radio frequencies". Phys. Rev. 69, 681 (1946).

[2] P. Anger, P. Bharadwaj, and L. Novotny. "Enhancement and Quenching of Single-Molecule Fluorescence". Phys. Rev. Lett. 96, 113002 (2006).

[3] S. Kuhn, U. Hakanson, L. Rogobete, and V. Sandoghdar. "Enhancement of Single-Molecule Fluorescence Using a Gold Nanoparticle as an Optical Nanoantenna". Phys. Rev. Lett. 97, 017402 (2006).

[4] R. H. Dicke. "Coherence in Spontaneous Radiation Processes". Phys. Rev. 93, 99 (1954).

[5] V. N. Pustovit and T. V. Shahbazyan. "Cooperative emission of light by an ensemble of dipoles near a metal nanoparticle: the plasmonic Dicke effect". Phys. Rev. Lett. 102, 077401 (2009).

[6] T. V. Shahbazyan. "Local density of states for nanoplasmonics". Phys. Rev. Lett. 117, 207401 (2016).

[7] T. V. Shahbazyan, "Spontaneous emission mediated by cooperative energy transfer to a plasmonic antenna", arXiv:1806.01508

Advances in Sub-Wavelength Nanophotonic Devices

(Invited Talk)

Jian Wang*

Wuhan National Laboratory for Optoelectronics, School of Optical and Electronic Information, Huazhong University of Science and Technology, Wuhan 430074, Hubei, China. *Corresponding author, E-mail: jwang@hust.edu.cn

Abstract

In this talk, we review our recent progress in sub-wavelength nanophotonic deivces and their wide applications. We discuss a variety of sub-wavelength structures on different platforms (silicon, metal, fiber): 1) microring resonator and photonic crystal nanocavity for linear and nonlinear optical signal processing; 2) slot, hybrid plasmonic slot and sub-wavelength slot waveguides for on-chip optical interconnects; 3) surface grating structures, plasmonic and dielectric metasurfaces for spatial light manipulation. The demonstrations show impressive performance in diverse implementations of sub-wavelength nanophotonic devices.

1. Introduction

Analogous to the importance of electronic integrated circuits, Photonic integrated circuits are the trend of optoelectronic devices. Photonic integration can be implemented on different platforms such as silicon, metal and fiber. In particular, silicon photonics is one of the most promising photonic integration platforms owing to its high-index contrast, small footprint, low power consumption, and availability of complementary metal-oxide- semiconductor (CMOS) fabrication technology for low-cost mass production [1]. Very recently, the emerging opportunity to design and fabricate photonic integrated devices at the sub-wavelength scale, enabling wide applications with favorable performance, has attracted increasing interest [2]. Remarkably, most of the sub-wavelength nanophotonic devices can still be fabricated using the similar fabrication techniques to conventional photonic integrated devices, such as electron-beam lithography (EBL) followed by induced coupled plasma (ICP) etching, focused ion beam (FIB), etc. Figure 1 shows typical sub-wavelength nanophotonic devices on different platforms (silicon, metal, fiber) fabricated in our lab, including microring resonator, photonic crystal nanocavity, slot waveguide, hybrid plasmonic slot waveguide, sub-wavelength slot waveguide, grating coupler, tilted grating, surface hologram, plasmonic metasurface on metal, dielectric metasurface on silicon, and metasurface on fiber facet. In this talk, we review recent advances in these sub-wavelength nanophotonic devices and their diverse applications.

2. Microring resonator and photonic crystal nanocavity for optical signal processing

Using nonlinear four-wave mixing (FWM) in fabricated silicon waveguides, we demonstrate chip-scale wavelength conversion of orthogonal frequency division multiplexing m-ary quadrature amplitude modulation (OFDM m-QAM) signals [3], regeneration of 4-ary pulse amplitude modulation (PAM-4) signals [4], and chip-scale high-base optical computing (quaternary/octal/decimal addition/subtraction) [5]. Using enhanced nonlinearity in grapheme-assisted microring resonator, we demonstrate efficient wavelength conversion of advanced modulation signals [6]. Using enhanced resonance in photonic crystal nanocavity, we demonstrate linear and nonlinear microwave photonic signal processing functions [7].

3. Slot, hybrid plasmonic slot and sub-wavelength slot waveguides for on-chip optical interconnects

Using reduced nonlinearity in slot waveguide and tight mode confinement in hybrid plasmonic slot waveguide, we demonstrate chip-scale data transmission with advanced multi-carrier multi-level modulation signals. Ultrahigh-bandwidth low-penalty 1.8-Tbit/s (161 WDM 11.2-Gbit/s OFDM 16-QAM) data transmission is demonstrated in the experiment [8, 9], showing great potential of on-chip optical interconnects. Additionally, we also propose and demonstrate sub-wavelength grating slot (SWGS) waveguide on silicon platform. The SWGS waveguide combines the advantages of sub-wavelength grating (SWG) and slot waveguide, showing greatly reduced nonlinearity compared to the slot waveguide by pushing mode out of the silicon region [10]. Moreover, we also propose, fabricate and demonstrate SWGS microring resonator for athermal and sensing applications with impressive performance.

4. Surface grating structures, plasmonic and dielectric metasurfaces for spatial light manipulation

The conventional surface grating structure is widely used for fiber-chip-fiber vertical coupling. The modified surface grating structure can be also applied to other emerging applications. We design, fabricate and demonstrate an on-chip optical vortex lattice emitter consisting of three parallel waveguides with etched tilted gratings [11]. The tilted gratings facilitate flexible light emission in a wide range of directions, enabling the generation of an optical vortex lattice above the silicon chip. The optical vortex is also known as orbital angular momentum (OAM) mode having helical phase front. We propose and demonstrate chip-scale generation and synthesization of ultrabroadband optical vortices (OAM modes) on silicon platform [12]. By introducing a sub-wavelength holographic fork grating on top of a silicon waveguide, the in-plane guided mode is converted to the free-space OAM mode. Inputs from both sides of the waveguide enable the synthesization of OAM modes. The chip-scale ultrabroadband OAM generator and synthesizer may find potential applications in multidimensional optical communications and quantum key distribution. Moreover, we propose and demonstrate

plasmonic metasurfaces on metal and fiber facet and dielectric metasurface on silicon for flexible spatial light manipulation [13-16]. The obtained results show impressive performance of metasurface structures.

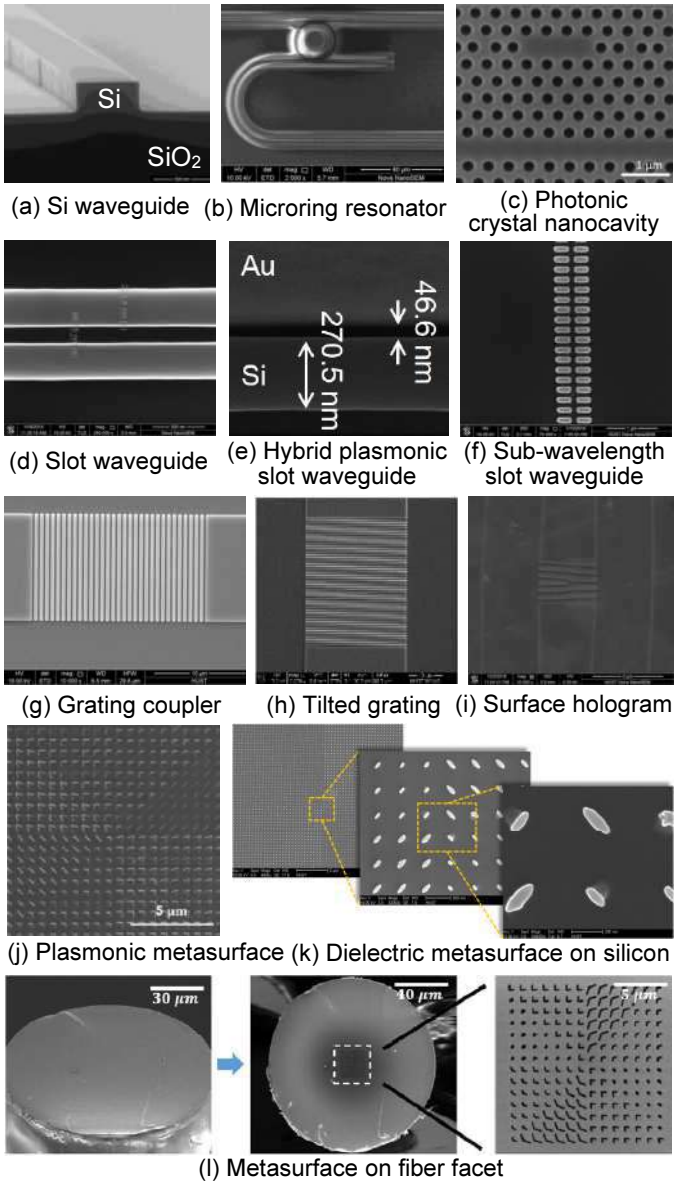


Figure 1: Measured scanning electron microscope (SEM) images of the fabricated typical sub-wavelength nanophotonic devices. (a) Si waveguide (building block of other devices); (b) microring resonator ; (c) photonic crystal nanocavity ; (d) slot waveguide ; (e) hybrid plasmonic slot waveguide ; (f) sub-wavelength slot waveguide ; (g) grating coupler ; (h) tilted grating ; (i) surface hologram ; (j) plasmonic metasurface ; (k) dielectric metasurface ; (l) metasurface on fiber facet.

5. Conclusions

We give an overview of recent advances in sub-wavelength nanophotonic devices (microring resonator, photonic crystal nanocavity, slot waveguide, hybrid plasmonic slot waveguide, sub-wavelength slot waveguide, grating coupler, tilted grating, surface hologram, metasurface) on different platforms (silicon, metal, fiber) and their wide applications (linear and nonlinear optical signal processing, on-chip optical interconnects, spatial light manipulation). The demonstrations show great significance in developing sub-wavelength nanophotonic devices.

Acknowledgements

National Natural Science Foundation of China (NSFC) (11774116, 11574001, 61761130082); Royal Society-Newton Advanced Fellowship, Natural Science Foundation of Hubei Province of China (2018CFA048); Program for HUST Academic Frontier Youth Team (2016QYTD05).

References

[1] J. Wang, Y. Long, On-chip silicon photonic signaling and processing: a review, *Sci. Bull.* 63: 1267–1310 (2018).

[2] P. Cheben, R. Halir, J. H. Schmid, H. A. Atwater, D. R. Smith, Subwavelength integrated photonics, *Nature* 560: 565–572, 2018.

[3] C. Li, C. Gui, X. Xiao, Q. Yang, S. Yu, J. Wang, On-chip all-optical wavelength conversion of multicarrier, multilevel modulation (OFDM m-QAM) signals using a silicon waveguide, *Opt. Lett.* 39: 4583–4586 (2014).

[4] Y. Long, A. Wang, L. Zhou, J. Wang, "All-optical wavelength conversion and signal regeneration of PAM-4 signal using a silicon waveguide, *Opt. Express* 24: 7158–7167 (2016).

[5] Y. Long, C. Gui, A. Wang, X. Hu, L. Zhu, L. Zhou, J. Wang, All-optical three-input simultaneous multicasted quaternary addition/subtraction using non-degenerate FWM in a silicon waveguide and 20 Gibt/s QPSK signal, *Proc. OFC2016*, paper Th2A.6 (2016).

[6] Y. Long, Y. Wang, X. Hu, M. Ji, L. Shen, A. Wang, J. Wang, Channel-selective wavelength conversion of quadrature amplitude modulation signal using a graphene-assisted silicon microring resonator, *Opt. Lett.* 42: 799–802 (2017).

[7] Y. Long, Y. Zhang, X. Zhang, J. Xia, J. Dong, J. Wang, Linear and nonlinear microwave responses of a microwave photonic filter based on a photonic crystal microcavity, *J. Appl. Phys.* 121: 233102 (2017).

[8] C. Gui, C. Li, Q. Yang, J. Wang, Demonstration of terabit-scale data transmission in silicon vertical slot waveguides, *Opt. Express* 23: 9736–9745 (2015).

[9] J. Du, J. Wang, Design and fabrication of hybrid SPP waveguides for ultrahigh-bandwidth low-penalty terabit-scale data transmission, *Opt. Express* 25: 30124–30134 (2017).

[10] Z. Ruan, L. Shen, S. Zheng, J. Wang, Subwavelength grating slot (SWGS) waveguide on silicon platform, *Opt. Express* 25: 18250–18264 (2017).

[11] J. Du, J. Wang, Chip-scale optical vortex lattice generator on silicon platform, *Opt. Lett.* 42: 5054–5057 (2017).

[12] N. Zhou, S. Zheng, X. Cao, S. Gao, S. Li, M. He, X. Cai, J. Wang, Generating and synthesizing ultrabroadband twisted light using a compact silicon chip, *Opt. Lett.* 43: 3140–3143 (2018).

[13] Y. Zhao, J. Du, J. Zhang, L. Shen, J. Wang, Generating structured light with phase helix and intensity helix using reflection-enhanced plasmonic metasurface at 2 μm, *Appl. Phys. Lett.* 112: 171103 (2018).

[14] J. Du, J. Wang, Dielectric metasurfaces enabling twisted light generation/detection/(de)multiplexing for data information transfer, *Opt. Express* 26: 13183–13194 (2018).

[15] Y. Zhao, J. Zhang, J. Du, J. Wang, Meta-facet fiber for twisting ultra-broadband light with high phase purity, *Appl. Phys. Lett.* 113: 061103 (2018).

[16] J. Wang, Metasurfaces enabling structured light manipulation: advances and perspectives, *Chin. Opt. Lett.* 16: 050006 (2018).

Chirowaveguides: a balance between circular and linear birefringences

Alban Gassenq[1], Léo Colliard[1], Amina Bensalah-Ledoux[1], Bruno Baguenard[1], Laure Guy[2] and Stéphan Guy[1 1*]

[1] Univ. Lyon, Université Claude Bernard Lyon 1, CNRS, UMR 5306, Institut Lumière Matière, F-69622, Lyon, France
[2] Univ. Lyon, ENS Lyon, CNRS, Université Claude Bernard Lyon 1, UMR 5182, Laboratoire de Chimie, F69342, Lyon, France
*corresponding author, E-mail: stephan.guy@univ-lyon1.fr

Abstract

We have demonstrated that planar chirowaveguides made of chiral hybrid material can propagate circularly polarized light. These chirowaveguides require symmetric structure with low refractive index mismatch. We show that chiral propagation behavior is the result from the balance between circular and modal birefringence. Based on coupled mode theory, we numerically simulate the performance of rib chiro-waveguide in air and show that circular polarization can be obtained by tailoring the dimensions of the waveguide.

1. Introduction

The transverse polarizations propagating in integrated photonic devices are the two well known linear TE and TM polarizations. As a consequence, any set-up requiring other polarizations, especially the circular polarization (chiral sensing, 3D-display, quantum optics...), can not take the full advantage of integrated optics. However, chiral materials, via the optical rotation, can overcome the geometrical properties of the waveguides to produce new states of polarization for the guided light as stated by Engheta in the last 80's[1].

We have recently demonstrated the proof of concept of the simple fabrication of chirowaveguides allowing the propagation of any polarization from elliptical to nearly circular, along a few centimeters with losses lower than 1dB/cm[2]. These results have been obtained for waveguides made of a new chiral Ormosil (Organically Modified Silica) based on binaphthyl organic molecules bonded to a silica network.

The best results (i.e. quasi circularly polarized modes) are obtained for symmetric waveguide (core layer sandwiched between two identical layers) with low refractive index contrast $\sim 10^{-3}$. This requirement is a serious limitation to the use of planar chirowaveguides in the area of chiral sensing. Indeed, evanescent wave sensing implies highly non symmetric waveguide[3].

In this work, we will numerically show how channel waveguides can be optimized to achieve circular polarization even with air top cladding. In the first part, we introduce the two relevant parameters describing the chirowaveguides: the circular birefringence (CB) and the modal birefringence ΔN_m. A simple equation from the coupled mode theory can then be used to quantify the polarization propagation in chirowaveguides[4, 5]. Our results on planar chirowaveguides are presented in the first section with respect to the relevant birefringences CB and ΔN_m showing a qualitative good agreement with the coupled mode theory. In the last part, we numerically simulate the performance of raised strip chirowaveguides in term of polarization eccentricity (ratio of the main axes of the polarization ellipse).

2. Theoretical considerations

The transition from an *achiral* waveguide (linearly polarized modes) to a *chirowaveguide* with circularly polarized (CP) modes requires special conditions. Indeed, chirowaveguides are devices combining both the isotropic circular birefringence (CB) coming from the core chiral material characterized by its optical rotation OR=$\frac{CB}{2k_0}$ and the modal linear birefringence (ΔN_m) which denotes the difference between the effective indices of TE and TM modes.The eigenpolarizations in chirowaveguides result from the competition between these two birefringences.

Different theoretical approaches can be used to quantitatively study chirowaveguides. Here, we will use the simple coupled mode theory to explain the general trend of our chirowaveguides. In this framework, ΔN_m is calculated for the chirowaveguide structure but without chiralty (OR=CB=0). The effect of the chirality is described as a weak cross coupling between the two TE/TM modes of the achiral structure leading to two new eigenmodes of eccentricity e_c given by[5]:

$$e_{c\pm} = \frac{\mathrm{CB}}{\Delta N_m \pm \sqrt{\mathrm{CB}^2 + \Delta N_m^2}} \qquad (1)$$

3. Planar chirowaveguides results

We have made different series of planar chirowaveguides and characterized the mode polarization for monomode waveguides[2]. The evolution of the first mode eccentricity e_{c0} versus CB can be estimated by changing the work-

ing wavelength. Indeed, the different layers being made by nearly the same material[2], the refractive index contrast does not change significantly compared to the CB. e_{c0} increases with CB as shown in Fig. 1-left. The coupling theory –green curve–, assuming a constant $\Delta N_m = 4.5\ 10^{-6}$, fits quite well the results.

By tailoring the refractive indices and the core thickness of the devices different ΔN_m are obtained. The corresponding e_{c0} are drawn in Fig. 1-right for a given CB($\lambda = 633nm$). e_{c0} requires ΔN_m in the same order of CB to reach significant values. Again, there is a good qualitative agreement with the simple mode coupling theory.

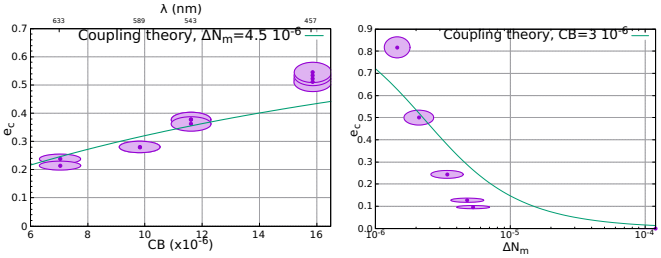


Figure 1: Measured polarization eccentricities and corresponding polarization ellipses in planar chirowaveguides. Left: Measurements on a given waveguide Right: $\lambda = 633$nm, CB=3 10^{-6} planar waveguides with different parameters leading to different ΔN_m.

4. Channel chirowaveguides

Results on planar chirowaveguides, as well as Eq.1 show that polarization's eccentricity can be increased either by increasing the CB or by lowering ΔN_m. The last point can be engineered in channel waveguides by playing on the geometry of the channels to achieve phase matching.Here, we use EMpy (version 1.3.0) to find ΔN_m of the two first modes[6]. As an exemple, we present the e_{c0} of rib waveguides of width w, rib wall height h and outer slab depth $d = 1.5\mu$m (inset of Fig. 2). The refractive indices are chosen to match our materials. In Fig. 2, the polarization's eccentricity of the first mode is shown against w and h. It clearly shows an optimum rib geometry ($w = 2.8\mu$m, $h = 1.9\mu$m) for which circularly polarized waves can propagate.

5. Conclusions

Propagating light with significant polarization's eccentricities in chirowaveguides requires to reduce the modal birefringence at values lower than the circular birefringence. It can be done in planar waveguides by designing symmetric waveguide with small ($\leq 10^{-3}$) refractive index mismatch. The use of channel waveguides can help to develop chirowaveguides because they offer another degree of liberty to engineer the modal birefringence. By playing on the dimensions of the channel, quasi-degenerated waveguide can be achieved allowing the chirality to dominate even for high

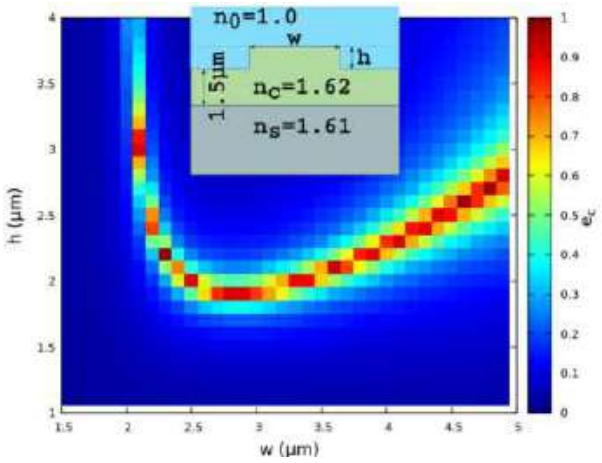


Figure 2: Calculated eccentricity via perturbation theory. OR=2/mm. $\lambda = 640$nm.

refractive index contrast.

Acknowledgement

This work is supported by the ANR Grant 2018 CAPTOR.

References

[1] N. Engheta and P. Pelet, "Modes in chirowaveguides," *Opt. Lett.*, vol. 14(11), pp. 593–595, 1989.

[2] S. Guy, B. Baguenard, A. B.-L. D. Hadiouche, and L. Guy, "Full polarization control of optical planar waveguides with chiral material," *ACS Photonics*, vol. 4, no. 11, pp. 2916–2922, 2017.

[3] P. Kozma, F. Kehl, E. Ehrentreich-Forster, C. Stamm, and F. F. Bier, "Integrated planar optical waveguide interferometer biosensors: A comparative review," *Bios. and Bioelec.*, vol. 58, pp. 287–307, 2014.

[4] P. Pelet and N. Engheta, "Coupled-mode theory for chirowaveguides," *J. Appl. Phys.*, vol. 67(6), pp. 2742–5, 1990.

[5] A. Yariv and J. F. Lotspeich, "Coupled-mode analysis of light propagation in optically active crystals," *J. Opt. Soc. Am., JOSA*, vol. 72, no. 2, pp. 273–277, Feb 1982.

[6] L. Bolla, "Empy [computer software]," 2017. [Online]. Available: https://github.com/lbolla/EMpy/

Ultrafast Light-Induced Magnetism in Plasmonic Nanoparticles

Oscar Hsu-Cheng Cheng[1], Dong Hee Son[1,2,] Matthew Sheldon[1,3]*

[1]Department of Chemistry, Texas A&M University, TX, USA
[2]Center for Nanomedicine, Institute for Basic Science, Seoul, Republic of Korea
[3]Department of Material Science & Engineering, Texas A&M University, TX, USA
*corresponding author, E-mail: sheldonm@tamu.edu

Abstract

Strategies for ultrafast optical control of magnetism have been a topic of intense research for several decades because of the potential impact in technologies such as magnetic memory1,2, spintronics3, and quantum computation, as well as the opportunities for non-linear optical control and modulation4 in applications such as optical isolation and non-reciprocity.5 Here we report the first experimental quantification of optically induced magnetization in plasmonic Au nanoparticles due to the inverse Faraday effect (IFE). The induced magnetic moment in nanoparticles is found to be ~1,000x larger than that observed in bulk Au, and ~20x larger than the magnetic moment from optimized magnetic nanoparticle colloids such as magnetite6. Furthermore, the magnetization and demagnetization kinetics are instantaneous within the sub-picosecond time resolution of our study.

1. Introduction

This The IFE is an opto-magnetic phenomenon that manifests as an induced magnetization, that is parallel or anti-parallel with the axis of circularly polarized excitation based on the helicity of the radiation (Fig. 1b)[1]. The IFE has been studied extensively in materials with large Verdet constants, such as $Tb_2Ti_2O_7$ and $Ta_3Ga_5O_{12}$ for application in optically-written magnetic hard drives[2,3]. Notably, strong resonant field concentration from plasmonic metasurfaces interfaced with these materials can further enhance sub-wavelength magnetization[4]. Circularly polarized femtosecond laser pulses can also be used to non-thermally align electron spins in magnetic materials via the IFE[5]. However, there has been limited research studying magnetization that occurs within non-magnetic plasmonic metals due to the IFE, without other magnetic structures, despite compelling theoretical studies that suggest plasmonic nanomaterials may out-perform more conventional magnetic materials in terms of induced magnetic field strength, spatial confinement, ultrafast time response, and other technologically relevant optoelectronic behavior[6-9]. Several studies have also reported anomalously large Verdet constant in plasmonic colloids, further suggesting strong enhancement of the IFE may also be possible[10,11].

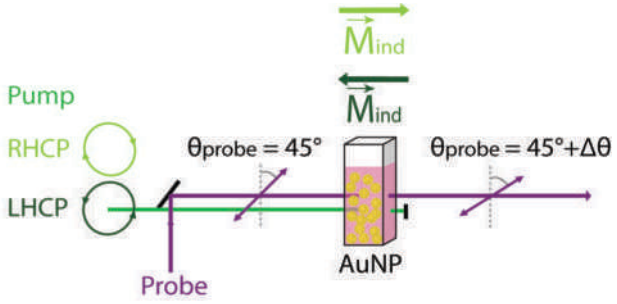


Figure 1: Schematic illustration of the the inverse Faraday effect (IFE) in Au nanoparticle colloids (AuNP). The inverse Faraday effect is the induced magnetization of a medium during circularly polarized excitation (green line). The direction of induced magnetization depends on the helicity of the light. In our experiments the optical rotation of a probe beam (purple line) indicates the induced magnetization.

2. Results

The maximum induced optical rotation as a function of peak pump intensity is plotted in Fig. 2. The optical rotation shows a linear dependence. These observations provide further confirmation that the optical rotation of the probe beam is due to the optically-induced magnetic field. The effective induced magnetic field of the AuNP during excitation can be estimated by the induced optical rotation angle in the pump-probe experiments (Fig. 2). This value can be thought of as the strength of an externally applied magnetic field that would be required to induce the same optical rotation in the pump-probe measurement. The value of can be further analyzed to determine the magnetic moment of each Au nanoparticle by applying the following relation

We observe up to 0.032 T at a peak pump intensity of 4.9 x 10^{13} W/m^2. If we consider that the individual Au nanoparticles act as small bar magnets with rotation and diffusion that is much slower than the pulse duration, the of the ensemble corresponds to an induced magnetic moment per particle of 2.5 x 10^7 μ_B or 8.0 x 10^{-1} μ_B per Au atom, where μ_B is Bohr magneton. This induced magnetic moment is approximately one order of magnitude larger than the magnetic moment in other magnetic nanoparticles such as magnetite or $CoFe_2O_4$ colloidal nanoparticles[12,13].

Further, the induced magnetic moment per Au atom in bulk Au films due to the IFE at the same incident power density and wavelength is reported to be 3.9 x 10^{-4} μ_B, verifying the extraordinary >1,000-fold plasmonic enhancement of the optically induced magnetization measured here[8,14].

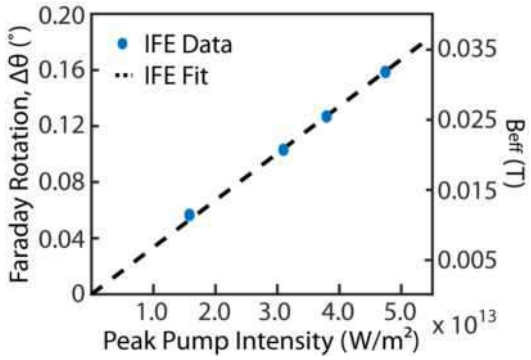


Figure 2: Dependence of Optical Rotation on Pump Intensity and Corresponding Effective Magnetic Field. Optical rotation as a function of peak pump intensity. The fit shows a linear trend.

3. Conclusions

In summary, we report the first experimental observation of optically-induced magnetization in Au nanoparticles due to the IFE. By controlling the relative polarization difference between the pump and probe beams in an ultrafast time-resolved study, the contribution of the IFE and OKE was clearly distinguished. Our experiments measured optical rotation indicative of magnetization that is parallel or anti-parallel with a pump beam depending on the helicity of the excitation. Additionally, we observe optically induced magnetization that is ~1,000 times larger than in bulk Au. We anticipate these results may be of great interest in the photonics community for application in ultrafast optical control of magnetic properties, and for all-optical methods of optical isolation that do not require externally applied magnetic fields.

Acknowledgements

The authors acknowledge the technical support of Dr. D. Rossi. This work is funded in part by the Gordon and Betty Moore Foundation through Grant GBMF6882. M.S. also acknowledges support from the Welch Foundation (A-1886). D.H.S. appreciates the support from the Institute for Basic Science (IBS-R026-D1).

References

1 van der Ziel, J. P., Pershan, P. S. & Malmstrom, L. D. Optically-Induced Magnetization Resulting from the Inverse Faraday Effect. *Physical Review Letters* **15**, 190-193, doi:10.1103/PhysRevLett.15.190 (1965).

2 Mikhaylovskiy, R. V., Hendry, E. & Kruglyak, V. V. Ultrafast inverse Faraday effect in a paramagnetic terbium gallium garnet crystal. *Physical Review B* **86**, doi:10.1103/PhysRevB.86.100405 (2012).

3 Raja, M. Y. A., Allen, D. & Sisk, W. Room - temperature inverse Faraday effect in terbium gallium garnet. *Applied Physics Letters* **67**, 2123-2125, doi:10.1063/1.114740 (1995).

4 Belotelov, V. I., Bezus, E. A., Doskolovich, L. L., Kalish, A. N. & Zvezdin, A. K. Inverse Faraday effect in plasmonic heterostructures. *Journal of Physics: Conference Series* **200**, doi:10.1088/1742-6596/200/9/092003 (2010).

5 Kimel, A. V. *et al.* Ultrafast non-thermal control of magnetization by instantaneous photomagnetic pulses. *Nature* **435**, 655-657, doi:10.1038/nature03564 (2005).

6 Hertel, R. Theory of the inverse Faraday effect in metals. *Journal of Magnetism and Magnetic Materials* **303**, L1-L4, doi:10.1016/j.jmmm.2005.10.225 (2006).

7 Singh, N. D., Moocarme, M., Edelstein, B., Punnoose, N. & Vuong, L. T. Anomalously-large photo-induced magnetic response of metallic nanocolloids in aqueous solution using a solar simulator. *Opt. Express* **20**, 19214-19225, doi:10.1364/OE.20.019214 (2012).

8 Nadarajah, A. & Sheldon, M. T. Optoelectronic phenomena in gold metal nanostructures due to the inverse Faraday effect. *Opt Express* **25**, 12753-12764, doi:10.1364/OE.25.012753 (2017).

9 Hurst, J., Oppeneer, P. M., Manfredi, G. & Hervieux, P.-A. Magnetic moment generation in small gold nanoparticles via the plasmonic inverse Faraday effect. *Physical Review B* **98**, 134439, doi:10.1103/PhysRevB.98.134439 (2018).

10 Gu, Y. & Kornev, K. G. Plasmon enhanced direct and inverse Faraday effects in non-magnetic nanocomposites. *J. Opt. Soc. Am. B* **27**, 2165-2173, doi:10.1364/JOSAB.27.002165 (2010).

11 Prashant K. Jain, Y. X., Ronald Walsworth, Adam E. Cohen. Surface Plasmon Resonance Enhanced Magneto-Optics (SuPREMO)- Faraday Rotation Enhancement in Gold-Coated Iron Oxide Nanocrystals.pdf. *Nano Letters* **9** (2009).

12 Sievers, S. *et al.* Quantitative measurement of the magnetic moment of individual magnetic nanoparticles by magnetic force microscopy. *Small* **8**, 2675-2679, doi:10.1002/smll.201200420 (2012).

13 Stein, C. R., Bezerra, M. T. S., Holanda, G. H. A., André-Filho, J. & Morais, P. C. Structural and magnetic properties of cobalt ferrite nanoparticles synthesized by co-precipitation at increasing temperatures. *AIP Advances* **8**, doi:10.1063/1.5006321 (2018).

14 Kruglyak, V. V. *et al.* Ultrafast third-order optical nonlinearity of noble and transition metal thin films. *Journal of Optics A: Pure and Applied Optics* **7**, S235-S240, doi:10.1088/1464-4258/7/2/031 (2005).

Saturable photoexcited carrier refraction in graphene-covered on-chip waveguides

David Castelló-Lurbe[1,2*], Jürgen Van Erps[1], Mulham Khoder[1], Iwona Pasternak[3,4], Aleksandra Krajewska[3], Tymoteusz Ciuk[3], Wlodek Strupinski[4], JinLuo Cheng[5], Hugo Thienpont[1], and Nathalie Vermeulen[1]

[1]Brussels Photonics, Dept. of Applied Physics and Photonics, Vrije Universiteit Brussel, Brussel, Belgium
[2]Institut Universitari de Ciències dels Materials, Universitat de València, Paterna, Spain
[3]Institute of Electronic Materials Technology, Warsaw, Poland
[4]Faculty of Physics, Warsaw University of Technology, Warsaw, Poland
[5]The Guo China-US Photonics Laboratory, Chinese Academy of Sciences, Changchun, China
*corresponding author, E-mail: dcastell@b-phot.org

Abstract

Based on a novel analysis of pulse spectral broadening experiments in graphene-covered silicon nitride waveguides, we show that, contrarily to a long-standing belief, self-phase modulation in such waveguides does not rely on the Kerr effect. The unconventional spectral broadening behavior observed in our experiments is successfully explained by means of the saturable refraction of free carriers produced by one-photon absorption in graphene.

1. Introduction

Along the lines of further miniaturization of nonlinear-photonics technologies, different research groups have succeeded in increasing the nonlinear response of on-chip devices covering them with graphene, a single atomic layer of carbon atoms, which can notably reduce the device length demands for nonlinear applications [1, 2]. Despite being a one-atom-thick layer, graphene shows an extremely large third-order nonlinearity [3], which can still enhance the nonlinear performance of a device. The potential of graphene for nonlinear optics motivated *ab-initio* calculations of the third-order nonlinearities of this 2D material within a perturbation theory frame [4]. However, the Kerr nonlinear response led to a divergent result for photon energies allowing one-photon absorption (1PA) [4]. Moreover, recently we experimentally demonstrated a negative graphene's nonlinearity through pulse spectral broadening experiments in graphene-covered silicon waveguides [2]. These results called for further investigations about the underlying mechanism of pulse spectral broadening in graphene-cladded waveguides.

In this work, we show exponentially growing spectral broadening in graphene-covered silicon nitride waveguides that cannot be explained through the Kerr effect and thus provide evidence of the different nature of this nonlinear response of graphene. Subsequently, we demonstrate that spectral broadening observed in our experiments can be still attributed to a self-phase modulation (SPM) process. Finally, based on a nonperturbative theory that accounts for the pulse chirp generated through saturable photoexcited carrier refraction (SPCR), we explain the most important features of our experiments [6].

2. Results

We investigate how the width of the spectrum of picosecond pulses —quantified by means of the spectral variance μ_2— evolves along different graphene lengths on silicon nitride waveguides fabricated in a multi-project wafer run of the LioniX foundry [see Fig. 1(a)]. According to Kerr-based SPM, the broadening factor $\mu_2^{\text{out}}/\mu_2^{\text{in}}$ should increase until a distance around α^{-1}, α being the linear loss coefficient, where the broadening factor should level off. Transmission measurements indicated that this length was around $220\,\mu$m. Contrarily, our experiments showed an exponential-like growth of the broadening factor beyond this distance [see Fig. 1(b)].

These results demanded a careful revision of the nonlinear response of our waveguides. On the one hand, we conceived an experiment to test whether the pulse spectral broadening still relied on a SPM process. In [2], we developed a method to control the sign of the pulse chirp. Here this approach allowed us to observe a significant dependence of the broadening factor on the input pulse chirp, which clearly pointed out a SPM mechanism. At the same time, these results also indicated a negative nonlinearity, in agreement with our previous work [2]. On the other hand, inspired by [5] —where the negative nonlinearity produced by the refraction of free carriers induced by two-photon absorption in silicon waveguides was modeled— we proposed the following phenomenological theory to describe the chirp, and hence μ_2, induced by the saturable refraction of free carriers excited through 1PA in graphene [6]:

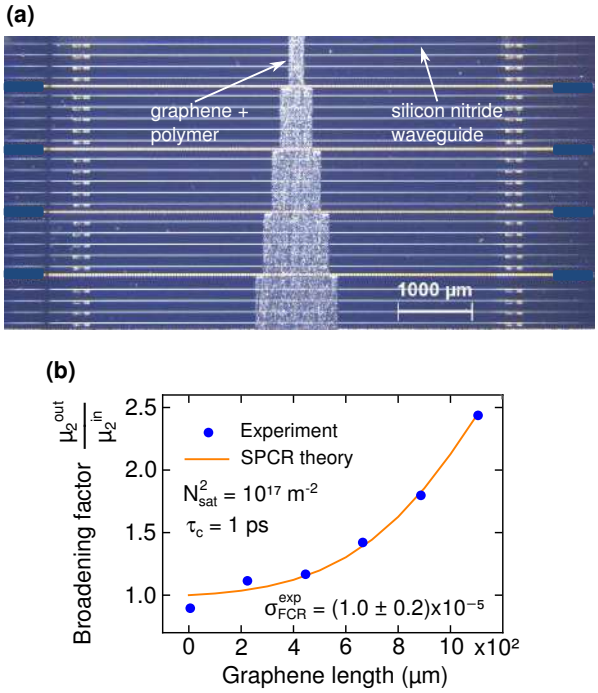


Figure 1: (a) Microscope image of our waveguides covered by different sections of graphene (with polymer on top); (b) Experimental (blue points) and theoretical (orange solid line) broadening factor as a function of graphene length at 2.7 W incoupled peak power.

$$\partial_z A = -\frac{\alpha}{2} A - i\sigma_{\mathrm{FCR}} N_c A \tag{1}$$

$$\partial_t N_c = \frac{\alpha}{\hbar\omega_0}(1 - \frac{N_c}{N_{\mathrm{sat}}})|A|^2 - \frac{N_c}{\tau_c} \tag{2}$$

where A is the complex envelope of the pulse; N_c stands for the (one-dimensional) carrier density in graphene; ω_0 denotes the mean frequency of the pulse; N_{sat} and τ_c correspond to the saturation carrier density and carrier lifetime measured in previous works; and we introduced σ_{FCR} as the free-carrier-refraction efficiency. It is worth noting that this modeling allows tackling nonperturbative regimes and that the relatively low values of N_{sat} and τ_c make a difference in SPCR compared to the free-carrier refraction in other materials such as silicon [5].

In contrast to the theory of Kerr-based SPM, our SPCR theory does explain why most of the spectral broadening is produced after α^{-1} in graphene-covered silicon nitride waveguides. The dominant refractive-index modulation in graphene is induced by the free carrier density generated through 1PA, instead of the light pulse itself. Since the carrier density is almost constant over the pulse due to the saturation at distances shorter than α^{-1}, no significant chirping is produced. Nevertheless, at longer distances, the carrier density is not saturated any longer, thus giving rise to spectral broadening.

3. Conclusions

We have demonstrated that SPCR is responsible for pulse spectral broadening in graphene-cladded waveguides. Our novel SPCR theory explains both quantitatively and qualitatively the experimental data reported here. These insights constitute a key step towards the optimal use of graphene-covered on-chip waveguides for nonlinear applications.

Acknowledgement

This work was supported by the ERC-FP7/2007-2013 grant 336940, the EU-FET GRAPHENICS project 618086, the EU-FP7 Graphene Flagship 604391, the Hercules-stichting grant UABR/007/09, the Research Foundation Flanders (FWO) under Grants GA00213N and G0F6218N (EOS-convention 30467715), the VUB-OZR, BELSPO-IAP, and Methusalem. The LioniX foundry and Cathleen De Tandt from VUB-ETRO are acknowledged for the photonic chip fabrication and postprocessing. D.C.L. is grateful for funding from Subprograma Atracció de Talent – Contractes Postdoctorals de la Universitat de València.

References

[1] T. Gu, N. Petrone, *et al.*, Regenerative oscillation and four-wave mixing in graphene optoelectronics, *Nat. Photon.* 6: 554–559, 2012.

[2] N. Vermeulen, D. Castelló-Lurbe, *et al.*, Negative Kerr nonlinearity of graphene as seen via chirped-pulse-pumped self-phase modulation, *Phys. Rev. Appl.* 6: 044006, 2016.

[3] E. Hendry, P. J. Hale, *et al.*, Coherent nonlinear optical response of graphene, *Phys. Rev. Lett.* 105: 097401, 2010.

[4] J. L. Cheng, N. Vermeulen, and J. E. Sipe, Third order optical nonlinearity of graphene, *New J. Phys.* 16: 053014, 2014.

[5] Q. Lin, O. J. Painter, and G. P. Agrawal, Nonlinear optical phenomena in silicon waveguides: Modeling and applications, *Opt. Express* 15: 16604–16644, 2007.

[6] N. Vermeulen†, D. Castelló-Lurbe†, *et al.*, Graphene's nonlinear-optical physics revealed through exponentially growing self-phase modulation, *Nat. Commun.* 9: 2675, 2018. (†These authors contributed equally.)

Surface Acoustic Wave generation of guided Modes in Phononic Nanobeams

A. Korovin[1], Y.Pennec[1], M. Stocchi[2,3], D. Mencarelli[2,4], L. Pierantoni[2,4], T. Makkonen[5], J. Ahopelto[5] and B. Djafari Rouhani[1,*]

[1]IEMN, UMR CNRS 8520, University of Lille, 59652 Villeneuve d'Ascq, France
[2]Department of Information Engineering, Marche Polytechnic University, Ancona, Italy
[3]IHP Innovation for High Performance, Franckfurt (Oder) 15236 Germany",
[4]Laboratori Nazionali di Frascati (LNF), Istituto Nazionale di Fisica Nucleare (INFN), Frascati, Roma, Italy
[5]VTT Technical Research Centre of Finland Ltd, Finland
*corresponding author, E-mail: Bahram.djafari-rouhani@univ-lille.fr

Abstract

We investigate theoretically the conversion of surface acoustic waves generated on a substrate by means of interdigital transducers to the guided modes of a phononic nanobeam. An efficiency of -23 dB is demonstrated. We study the interaction of these converted modes with a structured phononic crystal nanobeam containing a cavity and evaluate the transmission through localized cavity modes. We also discuss the optomechanic interaction of the phononic cavity with an external optical waveguide and the emission of phonons into the nanobeam.

There is a growing interest in the development of new structures and devices using phonons for the purpose of carrying and processing the information [1,2]. Among these, the study of cavity optomechanics (OM) and their potential applications from sensing to quantum information has known a great deal of attention during the last decade [3]. Currently, the design of new phononic circuits, based on the coupling between several OM cavities connected through waveguides, for the purpose of generation and detection of coherent phonons is of high interest. In parallel, some works have been devoted to the excitations of phonons in an OM cavity by means of Surface Acoustic Wave (SAW) generated on a piezoelectric substrate in front of the phononic/photonic crystal [4,5].
In this paper, we demonstrate the conversion of SAW generated on a substrate by means of interdigital transducers (IDT) into the guided modes of a phononic nanobeam (NB). Then, we study the interaction of these converted modes with a nanobeam phononic crystal containing a cavity and evaluate the transmission properties of the structure. Finally, we discuss the OM interaction of the cavity with an external optical waveguide and the emission of phonons into the NB.

A schematic presentation of the device is presented in Fig. 1. The SAWs are generated on a Si substrate supporting a three-layer structures consisting of a SiO2 layer, a thin 220nm Si layer and a piezoelectric AlN layer over which the Al interdigital transducers (IDT) are deposited. The substrate is connected to a Si nanobeam of 220 nm thickness where the guided modes should be generated. The geometrical parameters of the structure are optimized in order to generate SAW at 2 GHz sufficiently confined in the Si layer. Then, the focusing of SAW by means of radially curved-shaped IDT's and the utilization of a taper at the entrance of the NB allow a conversion efficiency of -23 dB into the guided modes of the NB. We show in Fig. 2 the excitation of the acoustic modes inside the NB together with its decomposition into the eigenmodes of the NB, namely a longitudinal mode (1) and a flexural mode (4) in the geometry of our design. The conversion efficiency is calculated as the ratio between the time-averaged Poynting vector integrated over the section of NB and the apparent electric power consumption.

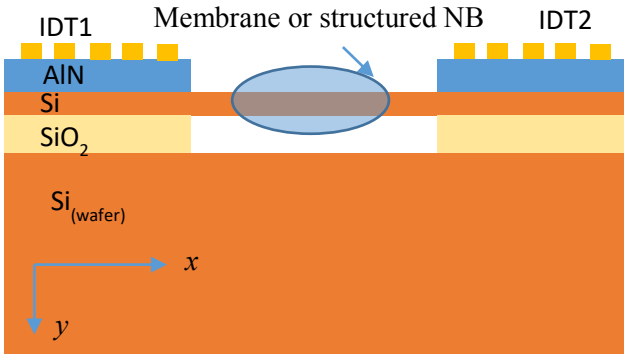


Figure 1: Schematic representation of a prototype device for the phonon generation and detection by electrical means using IDT on a piezoelectric AlN film deposited on the Si membrane. The surface acoustic wave generated by the IDT propagates through the Si-membrane or through the nanobeam (where optomechanical effects can occur) and can be detected by another IDT system.

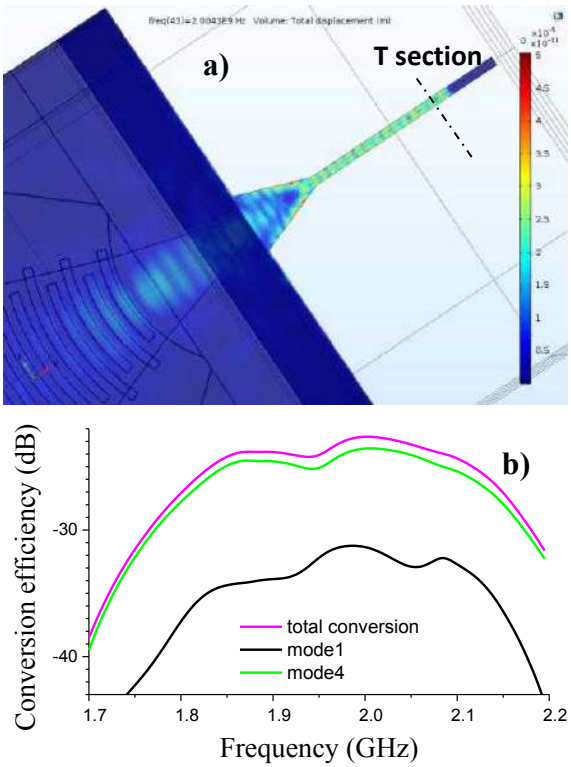


Figure 2: (a) The spatial distribution of the displacement field in Silicon at 2 GHz in the system of curved IDT consisting of 7 fingers with geometrical parameters: L_{IDT} = 2.21 µm, h_{AlN} = 250 nm, h_{Si} = 220 nm. (b) Spectrum of the x-component of the Poynting vector averaged over T plane (the end of straight NB before PML region in the full piezoelectric simulation).

In a second step, we calculate the scattering by these converted modes, considered as an incident wave, with a structured phononic crystal NB. The latter [6-8] is a one-dimensional crystal constituted by a periodic array of stubs and holes as shown in Fig. 3a. As demonstrated in our earlier works, the stubs and holes are respectively favorable to open phononic and photonic band gaps and therefore provides us with a structure suitable for OM applications working in the telecom optical range and GHz acoustic frequencies. In this crystal, a cavity supporting both localized phonons and photons with high quality factors is created [7]. The transmission of the above incident wave with such a structure gives rise to the acoustic transmission spectrum shown in Fig. 3b where one can recognize the localized modes inside the cavity. Possibly, such transmitted acoustic waves can be detected by a second substrate (see Fig. 1) where they can generate a SAW. Finally, we discuss the interaction between the OM cavity described above with an external optical waveguide with the aim of generating cavity phonons and their emission into the NB.

In conclusion, this work presents the design of an electromechanical device for an efficient conversion of SAW into the guided modes of a NB. Then, the interaction of these modes with a structured phononic crystal and the

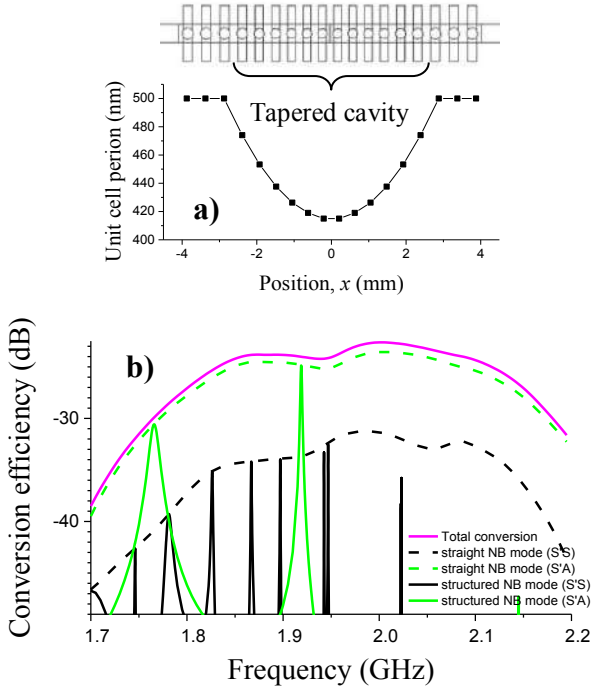


Figure 3: (a) Schematic presentation of distributed defect in quasi-periodic structured NB system. (b) Spectrum of the SAW conversion efficiency for two NB modes which are symmetrical with respect to the vertical mid-plane (S')

transmission properties through an OM cavity are investigated

Acknowledgements

This work was supported by the European Commission H2020 project PHENOMEN, under Grant Agreement No. 713450

References

[1] Kejie Fang, Matthew H. Matheny, Xingsheng Luan and Oskar Painter, *Nature photonics* **10**, 489, 2016.

[2] J. Maire , G. Arregui, N.E. Capuj, M.F. Colombano, A. Griol, A. Martinez, C.M. Sotomayor-Torres and D. Navarro-Urrios, *APL Photonics* **3** 126102, 2018.

[3] M. Aspelmeyer, T.J. Kippenberg and F. Marquardt, *Rev. Mod. Phys.* **86** 1391, 2014.

[4] D.A. Fuhrmann, S.M. Thon, H. Kim, D. Bouwmeester, P.M. Petroff, A. Wixforth and H. Krenner, *Nature Photonics* **5** 605, 2011.

[5] K.C. Balram, M. Davanco, J. Dong Song and K. Srinivasan, *Nature Photonics* **10** 346, 2016.

[6] B. Djafari Rouhani, S. El-Jallal and Y. Pennec, *Comptes Rendus Physique* **17**, 555 (2016).

[7] M. Oudich, S. El-Jallal, Y. Pennec, B. Djafari-Rouhani, J. Gomis-Bresco, D. Navarro-Urrios, C.M. Sotomayor Torres, A. Martinez and A. Makhoute, 2014 *Phys. Rev. B* **89** 245122, 2014.

[8] J. Gomis-Bresco, D. Navarro-Urrios, M. Oudich, S. El-Jallal, A. Griol, D. Puerto, E. Chavez, Y. Pennec, B. Djafari-Rouhani, F. Alzina, A. Martínez and C.M. Sotomayor Torres, *Nature Communications* **5** 4452, 2014

Enhancing Light Absorption with a Complex Environment: What Are the Limits of the Playground?

Emilie Sakat, Léo Wojszvzyk, Jean-Jacques Greffet, Jean-Paul Hugonin, and Christophe Sauvan*

[1]Laboratoire Charles Fabry, Institut d'Optique Graduate School, CNRS, Université Paris Saclay, 91127 Palaiseau, France
*corresponding author, E-mail: Christophe.sauvan@institutoptique.fr

Abstract

We have studied light absorption by a subwavelength particle in a complex environment. We have derived an upper bound for the absorption, which is valid for any environment and any illumination. The upper bound allows decoupling the choice of the environment from the one of the absorber. It provides a meaningful figure of merit to compare the ability of different systems to enhance absorption. In the scalar approximation, the relevant physical parameter is the ratio between the field enhancement and the local density of states. Consequently, a plasmonic structure supporting hot spots is not necessarily a good choice to enhance absorption. Furthermore, we have applied our theoretical results beyond the scalar approximation and the case of plane-wave illumination.

Light absorption and emission are two fundamental processes of light-matter interaction. Absorption converts electromagnetic energy carried by photons to internal energy of matter carried by electrons or phonons. Controlling the absorption in small volumes is a major issue for a vast array of applications, such as photovoltaics [1,2], sensing by surface-enhanced infrared absorption (SEIRA) [3], photothermal cancer therapy [4], thermoplasmonics and thermal emission [5,6].

Absorption inside subwavelength objects is in general weak but different strategies can be used to circumvent this limitation. First, the absorber properties can be engineered. Many works have been dedicated to the optimization of the absorption by a single nanoparticle. For an absorber in a homogeneous medium, the physical bounds of the problem are known; they are driven by the multipolar character of the particle [7-10]. The maximum absorption cross-section of a molecule or a nanoparticle that can be assimilated to an electric dipole is $3\lambda^2/(8\pi n^2)$, with λ the wavelength and n the surrounding refractive index [7,10]. This upper bound can only be reached if the absorber polarizability α matches a precise value. Subwavelength particles that go beyond the dipolar approximation offer additional degrees of freedom and are governed by different physical bounds [8-10]. Absorption by an ensemble of particles in a homogeneous medium is yet another related problem with a different upper limit [11].

Plunging the absorber in a complex medium or modifying the illumination offers a myriad of possibilities to further tailor the absorption [6,12,13]. In this work, we consider the general problem of a subwavelength absorber in a complex environment. We focus on the absorption inside the absorber and do not discuss dissipation in the surroundings, if any. To fully exploit the control possibilities offered by the environment, it is crucial to know the relevant figures of merit. The absorption density is proportional to the local electric-field intensity $|\mathbf{E}(\mathbf{r})|^2$, which results from both the environment *and* the absorber. It is highly desirable to decouple both contributions to provide figures of merit that are intrinsic to the environment. Only then can we properly compare the ability of different structures to modify absorption.

Let us draw a parallel with spontaneous emission, which also depends on the environment. Emission is enhanced by a factor that is proportional to the photonic local density of states (LDOS). For an emitter coupled to a resonant system, the emission enhancement has an upper bound, the Purcell factor, which is intrinsic to the resonator and independent of the emitter. The upper bound is reached if emitter and resonator fulfill a few matching conditions – spectral, spatial and in polarization.

The link between the absorption and the environment properties is more complex than the proportionality relation between emission and LDOS. Within the Born approximation, the absorption is simply proportional to the field enhancement provided by the environment. Hence, hot spots are often thought to lead to large absorption enhancements. But if the presence of the absorber significantly affects the local field, the situation is much more complex. It has been recently shown that both the field enhancement and the LDOS play an intricate role in the absorption [12]. However, no clear upper bound – kind of Purcell factor analogue – has been derived for the general problem of an absorber in a complex environment.

Antenna theory provides a solution in one specific case. For an antenna receiving a signal incident from the direction (θ,ϕ), the maximum absorption cross-section of the load is $G(\theta,\phi)\lambda^2/(4\pi n^2)$, with G the antenna gain [14]. The system reaches the upper bound if the load is impedance-matched with the antenna. The gain is defined for an emitting antenna as the fraction of the total power that is radiated in the direction (θ,ϕ) and can be written as $G(\theta,\phi) = \eta_r D(\theta,\phi)$, with D the directivity and η_r the radiative efficiency [14]. Unfortunately, the $G(\theta,\phi)\lambda^2/(4\pi n^2)$ limit only applies to plane-wave illumination and to antennas that can be reduced to a scalar problem. *For structures in which the vectorial nature of the electromagnetic field cannot be neglected, the problem remains open.* Moreover, the antenna point of view highlights the radiative efficiency and the directivity, whereas other derivations underline the field enhancement and the LDOS [12]. It is thus essential to generalize existing results, while enlightening the link between them.

We have derived a general upper bound for the power dissipated in a subwavelength absorber surrounded by a complex environment. The upper bound is independent of the absorber; it entirely depends on the environment and the illumination. Thus, it provides a relevant figure of merit for comparing the ability of different systems to enhance absorption. This novel figure of merit is a complex vectorial interplay between two fundamental properties of the environment, the field enhancement and the Green tensor. We show under which assumptions the LDOS and the directivity are (or are not) relevant parameters. We also discuss under which conditions the system can reach the upper bound.

We have applied the theory to a few emblematic examples of nanophotonics: a plasmonic dimer nano-resonator, dielectric nanoantennas, and a silicon-on-insulator (SOI) ridge waveguide. In particular, we evidence that a plasmonic system providing extremely large field enhancements is not necessarily an optimal choice to increase absorption.

References

[1] H. A. Atwater and A. Polman, *Nature Mater.* 9: 205, 2010.

[2] K. Vynck, M. Burresi, F. Riboli and D. S. Wiersma, *Nature Mater.* 11: 1017, 2012.

[3] F. Neubrech, C. Huck, K. Weber, A. Pucci and H. Giessen, *Chem. Rev.* 117: 5110, 2017.

[4] L. R. Hirsch, R. J. Stafford, J. Bankson, S. R. Sershen, B. Rivera, R. Price, J. D. Hazle, N. J. Halas and J. L. West, *Proc. Natl. Acad. Sci. USA* 100: 13549, 2003.

[5] G. Baffou and R. Quidant, *Laser Photonics Rev.* 7: 171, 2013.

[6] E. Sakat, L. Wojszvzyk, J. P. Hugonin, M. Besbes, C. Sauvan and J. J. Greffet, *Optica* 5: 175, 2018.

[7] S. Tretyakov, *Plasmonics* 9: 935944, 2014.

[8] R. Fleury, J. Soric and A. Alù, *Phys. Rev. B* 89: 045122, 2014.

[9] O. D. Miller, C. W. Hsu, M. T. H. Reid, W. Qiu, B. G. DeLacy, J. D. Joannopoulos, M. Soljacic and S. G. Johnson, *Phys. Rev. Lett.* 112: 123903, 2014.

[10] V. Grigoriev, N. Bonod, J. Wenger and B. Stout, *ACS Photonics* 2: 263, 2015.

[11] J. P. Hugonin, M. Besbes and P. Ben-Abdallah, *Phys. Rev. B* 91: 180202, 2015.

[12] E. Castanie, R. Vincent, R. Pierrat and R. Carminati, *International Journal of Optics* 2012: 452047, 2012.

[13] A. Sentenac, P. C. Chaumet and G. Leuchs, *Opt. Lett.* 38: 818, 2013.

[14] C. A. Balanis, *Antenna theory: Analysis and design*, 2nd edition (J. Wiley and Sons, New York, 1997).

Fabrication of Plasmonic Supercrystals for Microfluidic Sensing

Daniel García-Lojo[1], Sergio Gómez-Graña[1], Jorge Pérez-Juste[1] and I. Pastoriza-Santos[1*]

[1]Department of Physcical Chemistry and Biomedical Research Center (CINBIO), University of Vigo, 36310 Vigo, Spain
*corresponding author, E-mail: pastoriza@uvigo.es

Abstract

Microfluidic technology allows to operate on liquids within microscale channels as well as to fabricate microfluidic devices for lab-on-a-chip applications. Nowadays a wide range of materials can be used for manufacturing of microfluidic devices which makes possible to design chips with specific features such as optical properties, size/morphology, chemical properties, biological compatibility, etc. Poly(dimethylsiloxane) (PDMS) is one of the most popular materials in microfluidics since it is a cheap polymer with high biocompatibility, optical transparency, ease handle for chip fabrication, etc.
Recently we have demonstrated that PDMS-based microfluidic channels can be also used for the fabrication of plasmonic supercrystals through self-assembly of uniform Au octahedrons inside their microchannels through the pervaporation of the solvent (Figure 1A-B).[1] Furthermore, the microfluidic approach enables the fabrication of uniform assemblies of any dimension or morphology. The resulting plasmonic devices could be used for the detection of analytes, even without affinity for gold nanoparticles.
Surface-enhanced Raman spectroscopy, SERS, is an advanced analytical technique that can be used for the ultrasensible detection of analytes since it offers orders of magnitude increases in Raman signals. It occurs at the surface of a plasmon surface mainly due to the presence of strong electromagnetic fields generated after the plasmon excitation. Moreover, this effect could be more intense in the case of hierarchical nanoparticles assemblies due to an antenna effect as demonstrated by recent simulations.[2]

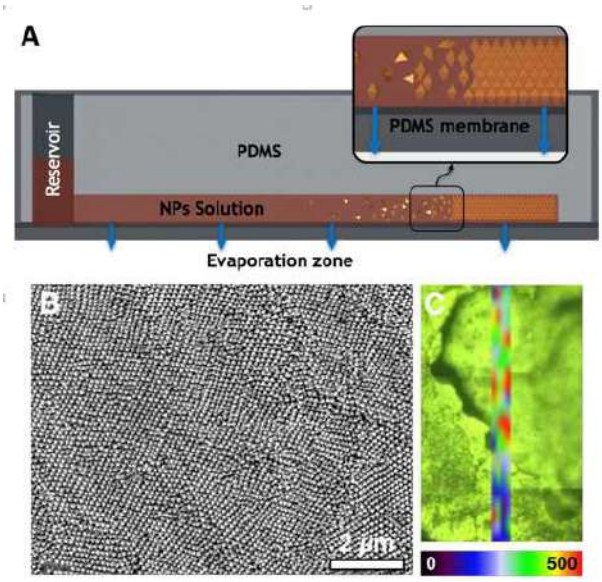


Figure 1: (A) Schematic illustration of the evaporation-based microfluidic cell used for controlled assembly of Au nanoparticles. (B) SEM images of the hierarchical nanoparticles assembly (C) SERS mapping of the channel in the presence of 100 fM of Malachite Green.

While the plasmonic substrates made by drop-casting show poor uniformity that limits their potential plasmonic applications, the microfluidic approach gives rise to platforms with highly uniform and intense SERS activity (being both key parameter to achieve quantitative analysis and low detection limits (LOD). Herein we will show the fabrication and characterization of plasmonic platforms fabricated using Au octahedra synthesized through a wet chemical method. Besides, the sensing capabilities of the platforms will be analyzed by investigating the SERS efficiency using different Raman active analytes. For instance, experiment performed with Malachite Green showed a great LOD, lower than 100fM, which is several orders of magnitude lower than those found in the literature.

References

[1] S. Gómez-Graña, C. Fernández-López, L. Polavarapu, J.-B. Salmon, J. Leng, I. Pastoriza-Santos, J Pérez-Juste, Gold Nanooctahedra with Tunable Size and Microfluidic-Induced 3D Assembly for Highly Uniform SERS-Active Supercrystals, *Chem. Mater.* 27: 8310-8317, 2015.

[2] D. Solís, J. M. Taboada, F. Obelleiro*, L. M. Liz-Marzán, F. J. García de Abajo, Toward Ultimate Nanoplasmonics Modeling, *ACS Nano* 8: 7559−7570, 2014.

Manipulation of nanoparticles using hyperbolic metasurfaces

N. K. Paul and J. S. Gomez-Diaz*

Department of Electrical and Computer Engineering, University of California Davis,
One Shields Avenue, Kemper Hall 2039, Davis, CA 95616, USA

*corresponding author, E-mail: jsgomez@ucdavis.edu

Abstract

Electromagnetic waves can exert optical forces on microscopic or nanoscopic objects via scattering or absorption due to the momentum transfer. Such responses have opened a new paradigm of confining and trapping small objects and molecules [1] and have been exploited for numerous applications in bioengineering, physical science and chemistry [2]. Recent reports have suggested using surface plasmon polaritons (SPPs), waves that can be confined well beyond the diffraction limit, as promising candidates to enhance the optical forces induced on nanoparticles [3]. Specifically, illuminating a dipolar particle located above a planar plasmonic substrate (such as gold or silver) induces optical forces that compensate the momentum of the directional SPPs excited during the scattering process [4,5]. We note that relation between the induced lateral forces and the wavenumber of the plasmon is not linear, but exponential. As a result, maximum optical forces induced on particles over isotropic surface appears at the intrinsic plasmonic resonance of the material, where the wavenumber of the excited plasmons is larger. In a related context, hyperbolic metasurfaces (HMTSs), structures able to exhibit dielectric or metallic behavior as a function of electric field polarization, have recently been attracted significant attention thanks to their exciting electromagnetic properties [6]. In particular, these surfaces boost the local density of states, support ultra-confined SPPs with ideally infinite momentum (bounded in practice by loss and nonlocal mechanisms), and enable a large set of near-field functionalities.

Here, we merge the photonic spin Hall effect of light with the large local density of states and extremely confined SPPs supported by HMTSs to manipulate Rayleigh particles located nearby with plane waves. By adequately illuminating the particle, it can acquire out-of-plane polarization spin and excite unidirectional surface plasmons over the metasurface during the scattering process. The lateral recoil force experienced by the particle is dramatically enhanced, several orders of magnitude compared to forces on particle over standard surfaces, due to the very large momentum carried out by the hyperbolic modes. To investigate such optical forces, we have developed an anisotropic Green's function formalism within the dipole approximation, and we have validated our results using full-wave numerical simulations from COMSOL Multiphysics. Our theoretical analysis

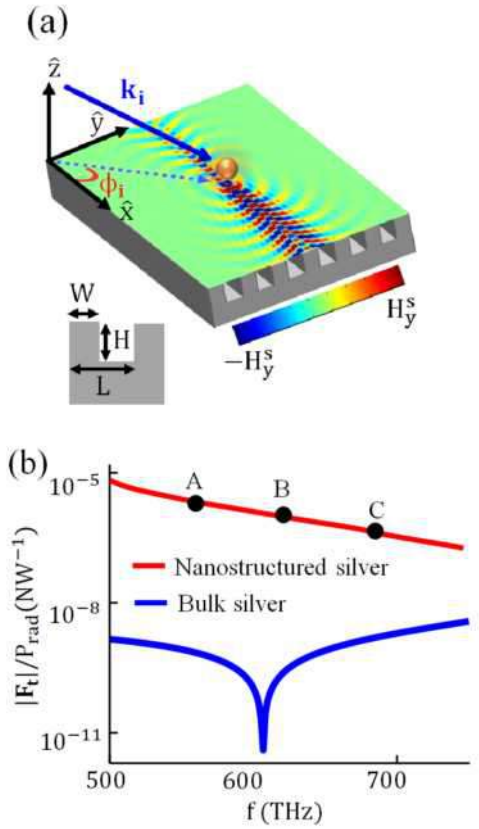


Figure 1: Lateral optical forces on a Rayleigh particle, with radius of 15nm and a relative permittivity of 3, located 25 nm above the nanostructured silver surface. Results have been obtained with COMSOL Multiphysics. (a) 3D schematic, showing an incident TM plane wave coming from $\theta_i = 35^0$ (elevation angle with respect to $\hat{z}$-axis) and $\phi_i = 25^0$. Superimposed field plot illustrates the y-component of the magnetic field excited on the structure at 612 THz due to the scattering process. (b) Strength of lateral optical forces induced on the particle versus frequency normalized with respect to the power radiated by the dipole when polarized in the absence of the metasurface. Results are plotted versus frequency assuming that the particle is located over a hyperbolic metasurface based of silver (red line) and over pristine silver (blue line). The metasurface dimensions are W = 120nm H = 80nm and L = 180nm.

reveals that the strength of the induced lateral forces primarily depends on two mechanisms: (i) the helicity of the particle polarizability, which measures the ability of the scattering process to excite unidirectional surface plasmons through the photonic spin-Hall effect; (ii) the confinement of the supported surface plasmons. As an example, we have analyzed a HMTSs composed of a subwavelength periodic silver grating operating in visible frequencies [7]. Such a visible frequency HMTS induces 2-4 orders of magnitude enhanced lateral forces than those found above pristine silver over a large frequency band. Importantly, the broadband nature of these configurations makes them very resilient against fabrication tolerances. The potential applications of such HMTSs are not limited to optical manipulations or force measurement technologies but can also be exploited to trap and characterize particles, biological cells and molecules. For instance, in the presence of a normally incident Gaussian beam, a dipolar particle located above such a plasmonic configuration experiences a set of lateral forces due to the interplay between the incoming wave, dipole's own retarded field and the surface waves. Such forces exhibit odd symmetric behavior as a function of the dipole's spatial position around the incoming beam axis, yielding to introducing optical trapping or anti-trapping mechanisms [8]. Our numerical analysis reveal that different sized dipolar particles located above HMTSs experience stable optical trapping over a large frequency band with strong resiliency against the beam focus. Besides, the induced trap stiffness and trap depth are significantly stronger (orders of magnitude) than those found above pristine plasmonic materials near their intrinsic plasmon resonance frequency. We envision that our proposed configuration may pave the way to the next generation nano-optical plasmonic tweezers opening unprecedented applications in physics, chemistry and bioengineering.

Acknowledgements

This work is supported by the National Science Foundation with Grant. No. ECCS-1808400 and a CAREER Grant No. ECCS-1749177.

References

[1] A. Ashkin, Acceleration and trapping of particles by radiation pressure, *Phys. Rev. Lett.* 24: 156−159, 1970.

[2] O. M. Maragò, P. H. Jones, P. G. Gucciardi, G. Volpe, and A. C. Ferrari, Optical trapping and manipulation of nanostructures, *Nat. Nanotechnol.* 8: 807-819, 2013.

[3] M. L. Juan, M. Righini, and R. Quidant, Plasmon nano-optical tweezers *Nat. Photonics* 5: 349, 2011.

[4] M. I. Petrov, S. V. Sukhov, A. A. Bogdanov, A. S. Shalin, and A. Dogariu, Surface plasmon polariton assisted optical pulling force, *Laser Photon. Rev.* 10: 116-122, 2016.

[5] F. J. Rodríguez-Fortuño, N. Engheta, A. Martinez, and A. V. Zayats, Lateral forces on circularly polarizable particles near a Surface, *Nat. Commun.* 6: 8799, 2015.

[6] J. S. Gomez-Diaz, and A. Alù, Flatland optics with hyperbolic metasurfaces, *ACS Photonics* 3: 2211-2224, 2016.

[7] A.A. High, R. C. Devlin, A. Dibos, M. Polking, D. S. Wild, J. Perczel, N. P. De Leon, M. D. Lukin, and H. Park, Visible-frequency hyperbolic metasurface, *Nature* 522: 192−196, 2015.

[8] A. Ivinskaya, M. I. Petrov, A. A. Bogdanov, I. Shishkin, P. Ginzburg, and A. Shalin, Plasmon-assisted optical trapping and anti-trapping, Light Sci. Appl. 6: e16258 (2017).

Development of a wave machine to model phononic crystals and elastic metamaterials

Motonobu Tomoda*, Masahiro Ino, Osamu Matsuda, and Oliver B. Wright

Division of Applied Physics, Graduate School of Engineering, Hokkaido University, Sapporo, Japan
*corresponding author, E-mail: mtomoda@eng.hokudai.ac.jp

Abstract

To demonstrate and understand wave motion in phononic crystals, i.e acoustic periodic structures, and elastic metamaterials, i.e. structures with local vibrational resonances, we develop an instructive instrument to visualize one-dimensional torsional waves based on a Shive wave machine. Phononic crystals are made by adding extra masses in a spatially periodic fashion, and elastic metamaterials are made by adding blade springs. The frequencies of band gaps agree well with theories based on torsional vibrations, analogous to those based on mass-spring models.

1. Introduction

Techniques for blocking waves in specific frequency ranges are widely applied to filters and isolators. Two main methods for blocking waves by static structures exist. One way is by the use of spatial periodicity, such as in the case of photonic crystals in optics or phononic crystals in acoustics. At the atomic level, crystals exhibit both phononic and electronic band gaps arising from spatial periodicity. Another way of blocking waves is by the use of local oscillators. Examples are electromagnetic, acoustic and elastic metamaterials. At the atomic level, polaritons are one example. To bring out the basic physics of such phenomena in an educational way, recent experiments have demonstrated the properties of elastic metamaterials by the use of mechanical structures of human dimensions [1-3], but their detailed motion is not immediately visually accessible.

The Shive wave machine, as shown in Figs. 1 and 2, was developed 50 years ago [4], and has been widely used to demonstrate wave phenomena [5]. It consist of a periodic one-dimensional array of torsionally-coupled rods suspending on wires, along which passes a torsional wave. Shive wave machines realise a conveniently low wave speed, in the sub-m/s range, with easily visible amplitude. Various wave phenomena such as reflection, transmission, and standing waves etc. can be viewed.

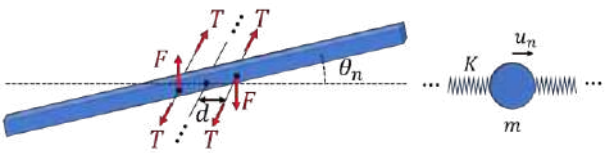


Fig. 1 The correspondence between a Shive wave machine and a mass spring model.

Shive wave machines are characterized by the moment of inertia of each rod I and the torsional spring constant $\kappa = 2Td^2/a$, where T is tension of the two wires that provide the torsional coupling, d is the distance from the center of the rods to the two wires, and a is the lattice constant. The equation of motion of the n-th unit cell in the wave machine is governed by (see Fig. 1)

$$I\frac{d^2\theta_n}{dt^2} = \kappa(\theta_{n+1} + \theta_{n-1} - 2\theta_n), \quad (1)$$

where θ is the torsion angle. On the other hand, the equation of motion of the n-th unit cell in a conventional one-dimensional mass-spring model is governed by (see Fig. 1)

$$m\frac{d^2u_n}{dt^2} = K(u_{n+1} + u_{n-1} - 2u_n), \quad (2)$$

where u is the displacement, m is the mass and K is the spring constant. One can appreciate exact correspondence.

By the use of a unit cell with two different moments of inertia, it is possible to mimic the behavior of a phononic crystal. By the use of rods with two blade springs attached to both ends, it is possible to mimic the behavior of an elastic metamaterial. To our knowledge these have not previously been constructed in the form of a Shive wave machine. In this study, we demonstrate the physics of phononic crystals and elastic metamaterials on a Shive wave machine. By tracking the displacements of each rod and taking the spatiotemporal Fourier transform, we demonstrate how one can obtain the dispersion relations governing the wave propagation.

2. Developed instruments

Figure 2 shows a photograph of the wave machine. Approximately 100 acrylic rods of dimension $320 \times 6 \times 6$ mm^3 are mounted on an axial central steel wire, and the two

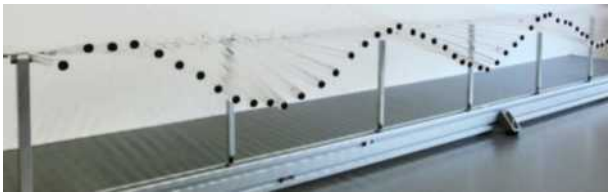


Fig. 2 View of the basic wave machine, About 100 unit cells are constructed with acrylic rods and threaded wires. A travelling wave is clearly visible.



Fig. 3 A movie frame recorded in a dark room. Fluorescent makers on the rod ends are illuminated. The rectangles show automatic identification by the image tracking system.

polyethylene wires that provide torsional coupling are also arranged to pass through the rods. Pipe-shaped spacers of length 10 mm are used, providing a unit cell of length 16 mm. We arrange for the speed of the travelling wave to be ~100 mm/s, and the wave amplitude to be ~30 mm. Black and fluorescent makers are put on each rod end for enhanced visibility. For systematic measurements, we measure the torsional displacement of each rod by means of a visual tracking system that can capture the displacement of the rod ends in real time.

A phononic crystal can be constructed by incorporating a spatially periodic variation in the moment of inertia of the rods by the addition of extra masses (4.5 g). The moment of inertia with and without the masses are $I_1 = 1.05 \times 10^{-4}$ kg m^2 and $I_2 = 3.13 \times 10^{-4}$ kg m^2, respectively as measured by pendulum experiments.

A elastic metamaterial is constructed by adding thin polystyrene blades of dimensions $180 \times 6.3 \times 0.5$ mm^3 (1.9 g with fixing nuts and screws) and resonance frequency 3.5 Hz.

3. Results

To monitor the frequency response, we record constant-frequency waves generated with a motor-and-crank. Figure 4 shows constant-frequency frames from a movie of the phononic crystal at certain frequencies. In the case when the unit cell consists of four rods as in Fig. 4, four branches exist in the dispersion relation. The measured frequency of every band edge and band gap as well as the wave velocity in the limit of low frequency agree with the dispersion relation calculated from a one-dimensional mass-spring model analogy. Figure 5 shows constant-frequency frames from a movie of the elastic metamaterial at certain frequencies. The torsional wave propagates from a non-metamaterial zone to a metamaterial zone. The measured first resonance frequency of the blade springs attached to the rods is 3.5 Hz, as expected. Waves can propagate in the metamaterial zone at frequencies sufficiently below and above resonance. Damping is evident at frequencies approaching the resonance, and the waves only penetrate to distances of around one or two rods on resonance, as shown as Fig. 5(b). On resonance, the extremities of the rods and blade springs vibrate with opposite phase.

Conclusions

In conclusion, we have demonstated that it is possible to model the behavior of a torsional phononic crystal and an elastic metamaterial with a Shive wave machine. This gives a dramatic visual demonstration of the physics involved, ideal for educational purposes. In future, we will attempt to realise time-modulated phononic crystals and time-modulated elastic metamaterials on a Shive wave machine.

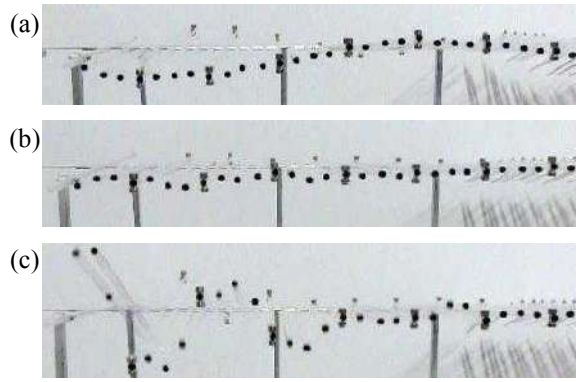


Fig. 4 Frames of constant frequency movies in torsional phononic crystals (a) in acoustic phonon branch at 1 Hz, (b) in the band gap at 2.7 Hz, (c) in the first optical phonon branch at 4.7 Hz. To form the phononic crystal, the moment of inertia of the rods is spatially modulated by the addition of masses every 4 rods. The wave is generated with a motor and crank from the left hand side.

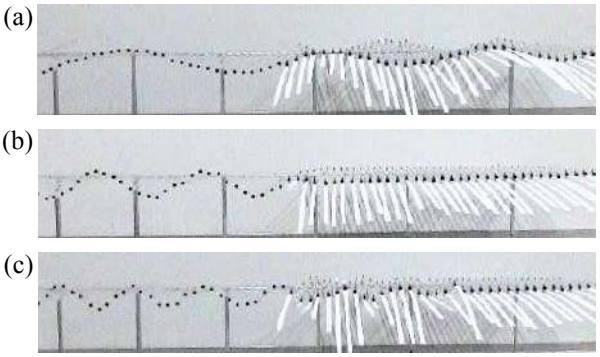


Fig. 5 Frames of constant frequency movies in which the wave propagates from a non-metamaterial zone (left) to a metamaterial zone (right) (a) below the resonance, at 1.5 Hz, (b) in the band gap at 3.5 Hz (i.e. the resonance of the blade springs), and (c) above the resonance, at 5 Hz. To form the elastic metamaterial, the blade springs are added at the ends of the rods.

References

[1] G. Ma and P. Sheng, Acoustic metamaterials: From local resonances to broad horizons, *Science Advances* 2: e1501595-1-16, 2016.

[2] Y. Wu, M. Yang, P. Sheng, Perspective: Acoustic metamaterials in transition, *Journal of Applied Physics* 123: 090901-1-7, 2018.

[3] K. Bertoldi, V. Vitelli, J. Christensen and M. van Hecke, Flexible mechanical metamaterials, *Nature Reviews* 2: 17066-1-11, 2017.

[4] J. N. Shive, *Similarities in Wave Behavior,* Williams & Wilkins Co. Series, Baltimore, Md., 1961.

[5] K. D. Skeldon, J.E. Milne, A. I. Grant, and D. A. Palmer, Making Waves: A Classroom Torsional Wave Machine (Part I and II), *The Physics Teacher* 36: 392-398, 466-472, 1998.

BIC-inspired nonradiating states under structured light illumination

Lei Xu[1*], Lujun Huang[1], Mohsen Rahmani[2], Khosro Zangeneh Kamali[2], Rocio Camacho-Morales[2], Matt Wolley[1], Dragomir Neshev[2], and Andrey E. Miroshnichenko[1]

[1]School of Engineering and Information Technology, University of New South Wales, Canberra ACT 2600, Australia
[2]Nonlinear Physics Centre, The Australian National University, Canberra ACT 2601, Australia
*corresponding author, E-mail: lei.xu@unsw.edu.au

Abstract

We propose a novel approach to confine light into isolated silicon nanodisk with high-quality (Q) factor electric dipole (ED) or magnetic dipole (MD) states with suppressed scattering inspired by the mechanism of the symmetry-protected bound state in the continuum (BIC). We demonstrate the efficient optical excitation of such states under structured beam illumination, which is not possible for the conventional symmetry-protected BICs in the periodic system. Owing to the strong near-field enhancement, such quasi-BIC state opens a novel opportunity for boosting nonlinear optical processes.

1. Introduction

Control of the light at the nanoscale has been a vibrant field of research for many years due to the various applications including photonic metadevices, high-performance data processing, optical computing, etc. High-index dielectric nanostructures have emerged as a promising tool to enhance light-matter interactions due to its ability to efficiently manipulate light based on the control over both optically induced electric and magnetic Mie-type resonances, offering great potential for applications in nanophotonics and nonlinear optics [1, 2, 3, 4].

BICs, being originally predicted by von Neumann and Wigner in 1929 [5], which represent localised states with energies embedded in the continuous spectrum of radiating waves, has been extensively studied in different fields including acoustics, microwaves and nanophotonics [6]. In a periodic system, when the coupling of particular resonance to the radiation modes is forbidden by symmetry mismatch, a symmetry-protected BIC will form. BICs provide a promising tool for light localisation with high Q and enhancing light-matter interactions.

In this work, inspired by symmetry-protected BIC mechanism in the periodic system, we propose a novel approach to design high Q nonradiating states, i.e., quasi-BIC MD and quasi-BIC ED state in isolated silicon nanodisk by surrounding PEC/PMC-based nanocuboids. These PEC/PMC-based components can be formed through designed metasurfaces, photonic crystal slabs, metals or superconductors, etc. Importantly, such states can be directly excited using structured beam illumination, leading to a robust near-field enhancement which can significantly boost optical processes involving light-matter interactions, such as third-harmonic generation (THG) process in silicon.

2. Results and Discussion

Based on image dipole model, the excited circularly displacement electric currents from MD and the circular displacement magnetic currents from ED in periodic system can be transformed to the corresponding induced electric or magnetic currents from a single resonator surrounded by perfect electric conductor (PEC) or perfect magnetic conductor (PMC) materials [4] (Figure 1a-c). Here, focusing on the fundamental Mie resonance ED and MD, we employ this approach to obtain high Q quasi-BIC ED and MD states in isolated silicon disks by surrounding PEC/PMC-based cuboids at all four sides. We focus the working wavelength λ_0 around 1556nm, and the thickness of our silicon disk and PEC/PMC cubodis to be 400nm. The gap between the aSi nanodisk and adjacent PEC/PMC-based structures are 100 nm, which can be easily fabricated experimentally. With the introduction of the PEC-based nanocuboids surrounding aSi nanodisk, a quasi-periodic boundary condition is formed around the nanodisk, leading to the formation of high Q MD state with $Q \approx 1341$ which can be directly linked to the symmetry-protected BIC with MD nature at Γ point of a TE band structure from a periodic array of Si disk. Importantly, owing to mode matching of this state with the azimuthally-polarised beam, it can be directly excited under AP beam illumination, while the scattering can be well suppressed due to the quasi-periodic boundary condition which limits the outgoing radiation channels (Figure 1d), resulting in a strong near-field enhancement (Figure 2e-f). Similarly, a quasi-BIC ED state ($Q \approx 2206$) with suppressed scattering is formed when the Si disk is surrounded by PMC-based nanocuboids at all four sides and can be efficiently excited under a radially-polarised pump illumination (see Figure. 1g). Interestingly, significant field enhancement is obtained inside the Si disk from this ED state, which is different from the conventional ED resonator where the electric field is mainly confined near the edge of the nanoresonators. This feature can further open the way for utilizing ED enhancing light-matter interactions in dielectric nanoparticles.

Such high Q states manifest strong electric energy con-

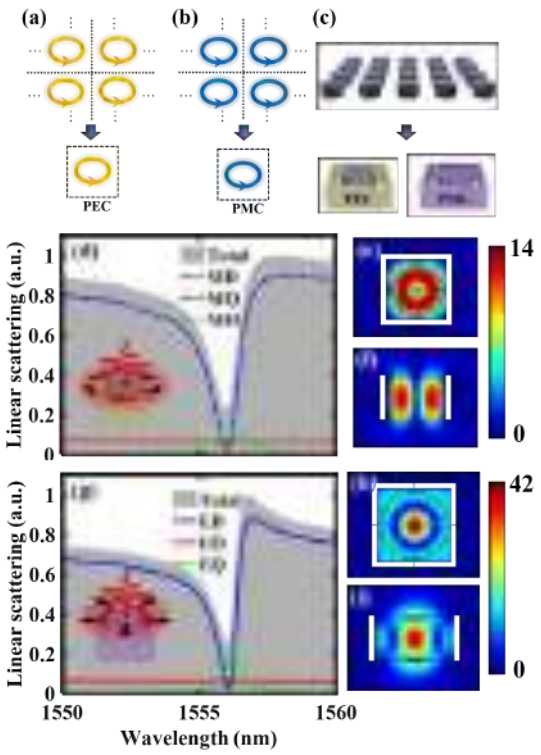


Figure 1: (a-c) Schematic illustration of the transformation of electric and magnetic currents from periodic system to a single resonator surrounded by PEC or PMC material. (d-f) Calculated multipolar structure and electric near-field distributions for silicon disk surrounde by PEC nanoboid under AP beam illumination. (g-i) Calculated multipolar structure and electric near-field distributions for silicon disk surrounde by PMC nanoboid under RP beam illumination.

centration inside the Si disk, leading to a giant THG emission as shown in table 1. We further estimate the conversion efficiency using the collected total THG emission power normalized by the pump power incident on the disk area [7]. The predicted conversion efficiency significantly exceeds that from conventional Si MD or ED resonators under structured pump illumination. Specifically, under AP or RP beam illumination with peak pump intensity $I_0 = 1.0\,\mathrm{GW/cm^2}$, we have observed record-high THG efficiency of 6×10^{-3} for quasi-BIC MD resonator and 0.8 for quasi-BIC ED resonator, which corresponds to more than 300-fold and 2×10^6-fold enhancements from conventional Si MD, ED resonators, respectively.

3. Conclusions

In summary, we have demonstrated high-quality nonradiating MD and ED states formed in isolated Si disk with surrounding PEC/PMC nanocuboid at all four sides inspired by the mechanism of symmetry-protected BIC. Such states can be efficiently and directly excited under structured beam illumination due to the mode overlapping and manifest strong near-field enhancement leading to a giant THG emission from Si disks. Our results show the great potential of dielectric nanostructures for nanophotonics applications including strong coupling, quantum photons generation, and the robust structured beam steering at the nanoscale.

Table 1: THG efficiency comparison between quasi-BIC MD/ED states (excited in Si disks with surrounding PEC/PMC nanocuboids under structured pump illumination) and conventional MD/ED states (excited in Si disks under structured pump illumination).

Quasi-BIC ED resonator	MD resonator	Enhancement
6.8×10^{-3}	2.2×10^{-5}	300 fold
Quasi-BIC ED resonator	ED resonator	Enhancement
0.8	3.5×10^{-7}	2×10^6 fold

Acknowledgement

The authors acknowledge the funding support provided by the Australian Research Council (ARC) and UNSW Scientia Fellowship program.

References

[1] A. I. Kuznetsov, A. E. Miroshnichenko, M. L. Brongersma, et al, Optically resonant dielectric nanostructures, *Science* 354, aag2472, 2016.

[2] R. Camacho-Morales, M. Rahmani, S. Kruk, et al, Nonlinear Generation of Vector Beams From AlGaAs Nanoantennas, *Nano Lett.* 16, 71917197, 2016.

[3] M. Rahmani, L. Xu, A. E. Miroshnichenko, et al, Reversible Thermal Tun-ing of All-Dielectric Metasurfaces, *Adv. Funct. Mater.* 1700580, 1700580 2017.

[4] L. Xu, M. Rahmani, K. Zangeneh Kamali, et al, Boosting third-harmonic generation by a mirror-enhanced anapole resonator, *Light. Sci. Appl.* 7, 44 2018.

[5] J. von Neuman and E. Wigner, Uber merkwrdige diskrete Eigenwerte. Uber das Verhalten von Eigenwerten bei adiabatischen Prozessen, *Physikalische Zeitschrift* 30, 467470 1929.

[6] C. W. Hsu, B. Zhen, A. D. Stone, J. D. Joannopoulos, and M. Soljačić, Bound states in the continuum, *Nat. Rev. Mater.* 1, 16048, 2016.

[7] L. Carletti, A. Locatelli, O. Stepanenko, G. Leo, and C. De Angelis, Enhanced second-harmonic generation from magnetic resonance in AlGaAs nanoantennas, *Opt. Express* 23, 26544, 2015.

A Graphene-Integrated Topological Insulator: Electrical Control of Terahertz Plasmon Polartions

Chihun In[1], Beom Kim[1], and Hyunyong Choi[1*]

[1]School of Electrical and Electronic Engineering, Yonsei University, Seoul 03722, South Korea
*corresponding author, E-mail: hychoi@yonsei.ac.kr

Abstract

Collective oscillations of massless particles in two-dimensional (2D) Dirac materials offer an innovative route toward controlling low-energy quasiparticle resonances. Here, we report the experimental realization of electrically tunable 2D Dirac plasmon polaritons using a topological insulator (TI) in a proximity contact with gate-controlled graphene. In our integrated TI–graphene devices, the 2D Dirac plasmons in micro-patterned TI generate constant plasmon momenta at terahertz (THz) frequency, while the proximity-integrated graphene controls the TI Dirac plasmon polariton resonances.

1. Introduction

The Coulomb interaction between free carriers and collective charge oscillations is of particular interest in the field of plasmonics. Metal-based surface plasmon polaritons are essentially based on interface charge characteristics between a dielectric and a metal, or a combination of the two. For the active control of the surface plasmon polaritons, either isolated [1], stacked [2], or metamaterial-integrated graphene [3] is a promising for steering the resonances of plasmon toward far-infrared ranges. Coupling graphene plasmons with incident photons, however, is often hampered by inactive electronic states across the physical boundary, which significantly reduces the plasmon polariton lifetime and alters the corresponding dispersion [4]. In turn, the 2D Dirac surfaces of the topological insulator (TI) are protected by time-reversal symmetry, which leads to robust electrical transport against non-magnetic scatterers because of the π Berry phase during the scattering event [5]. Hence, the plasmon momentum on the TI surface is immune to weak disorders on the sample boundary, which contrasts TI plasmons from the metal or graphene cases. In this respect, it is important to exploit the surface plasmon characters of the TI Dirac surface in the light–matter interactions.

2. Experimental results

In this work, we explore the electric control of 2D Dirac plasmon polariton resonances using vertically integrated Bi_2Se_3 TI and graphene heterostructures. The far-field coherent THz radiation excites the 2D surface Dirac plasmons associated with two distinct 2D Dirac layers. We experimentally show that the electrostatic gating on our heterostructure mainly changes the graphene carrier density; hence, we can minimize the effect of bulk carrier excitation.

Figure 1a is the schematic illustration of our experimental scheme, where a single-layer CVD-grown graphene (G) is transferred onto the Bi_2Se_3 TI microribbon structures. The thickness of Bi_2Se_3 TI is 30 quintuple layers (QL) (1 QL ≈ 1 nm). As reported in prior studies, the periodic micro-patterns of Bi_2Se_3 TI produce an in-plane plasmon momentum when coupled to the incident THz radiation [6,7]. A proximity contact of graphene onto the Bi_2Se_3 TI was realized by carefully eliminating any insulating barrier, e.g., natural oxide barrier. A gate voltage V_g is applied through ionic double-layer configuration in graphene to electrically control the graphene carrier density. The fabricated TI–graphene heterostructure is shown in Fig. 1b, where the Bi_2Se_3 TI was grown on a series of buffer layers consisting of 8 QL In_2Se_3 and 8 QL $(In_{0.5}Bi_{0.5})_2Se_3$ to reduce the defect sites compared to the nominally grown Bi_2Se_3. The microscopic image shows that the width of Bi_2Se_3 microribbon is W = 20 mm with a periodicity of $2W$, which corresponds to the plasmon momentum $q = \pi / W \sim 1{,}570$ cm^{-1}.

Figures 2 c–f show the experimental confirmation of the electrical control of the surface plasmon polariton. The gate-dependent THz extinction spectra $E(v)$ are shown in Fig. 2c. The plasmon momentum q is produced when the incident THz electric field is perpendicular to the microribbon ($\mathbf{E}_\perp$). The sharp resonance at ~2 THz indicates the Bi_2Se_3 optical phonon, which weakly interferes with the quasi-continuous plasmons. Such phonon-plasmon interference can be simply understood by a well-established Fano model [7,8], from which we can extract the bare plasmon spectra. The corresponding fit (solid) and plasmon spectra (dashed) are plotted in the same panel of Fig. 2c. Each panel displays data with a relative change in gate voltage, i.e., $\Delta V = V_g - V_{CNP}$, where V_{CNP} is the gate voltage at the graphene charge-neutral-point (CNP). The spectra at ΔV = 0 V represent the intrinsic Bi_2Se_3 plasmon polaritons, whereas those at $|\Delta V| > 0$ V involve the extrinsic contribution from graphene carriers. Note that the Bi_2Se_3 plasmon spectra are clearly blue-shifted with increasing $|\Delta V|$. On the other hand, the THz electric field parallel to

the microribbon ($\mathbf{E}_{\parallel}$) yields no gate-dependent shift, showing featureless Drude responses.

In Fig. 2d, we compare the gate-dependent plasmon frequency v_p (obtained from the data in Fig. 2c) with the density-dependent 2D Dirac plasmon model. An excellent agreement was seen. From the curve, we obtain the topological surface state (TSS) and two-dimensional electron gas (2DEG) chemical potential of $\mu^{TSS} \sim 200$ meV and $\mu^{2DEG} \sim 50$ meV, respectively, which corresponds to the carrier density of $n^{TSS} = 2 \times 10^{12}$ cm^{-2} and $n^{2DEG} = 3\times10^{12}$ cm^{-2}. Figure 2e shows the square-root dependence of v_p on the graphene carrier density n^G. This anomalous density dependence of 2D Dirac plasmons is valid when n^G is sufficiently small compared to n^{TSS} and n^{2DEG} [7,8]. Here, we emphasize that although the change in n^G is small within our ΔV range, the 2D Dirac plasmon can be modulated up to ~50%. This is primarily due to the anomalous density dependence. In Fig. 2f, we examine the gate-dependent plasmon width Γ. Because there exists no noticeable dependence of Γ on n^G, we experimentally exclude the contribution of bulk Bi_2Se_3 population to the plasmon resonance shifts. The broader plasmon width ($\mathbf{E}_{\perp}$) than the Drude width ($\mathbf{E}_{\parallel}$) indicates additional inhomogeneous broadening from the TSS and 2DEG.

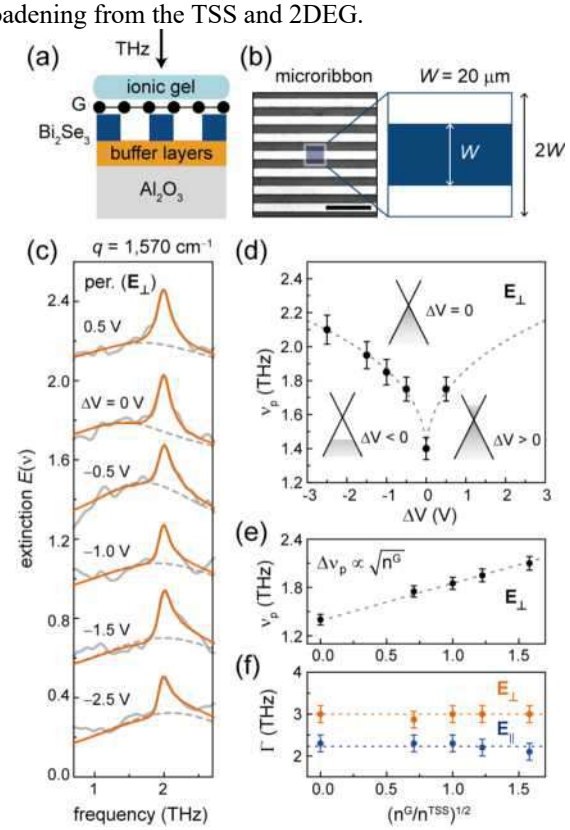


Figure 1: (a) The vertical cross-sectional view of the heterostructure. (b) The microscopic image of Bi_2Se_3 microribbon with width $W = 20$ μm. The scale bar is 100 μm. (c) THz extinction spectra $E(v)$ are plotted at different gate voltage. THz electric field polarization is perpendicular to the Bi_2Se_3 microribbon direction. Grey solid lines are the experimental results. Orange solid lines are the Fano fits to the data. Bare plasmon-extinction spectra are extracted from the fits (grey dashed lines). The experiments were performed at cryogenic temperature $T = 77$ K. (d) Plasmon frequency v_p is plotted as a function of ΔV (solid dots). Inset illustrates the graphene doping with different ΔV. The density-dependent v_p model is plotted on the same panel (grey dashed line). (e) v_p is plotted as a function of $(n^G/n^{TSS})^{1/2}$. (f) Scattering rates Γ for plasmon ($\mathbf{E}_{\perp}$, orange dots) and Drude response ($\mathbf{E}_{\parallel}$, blue dots) are shown, both of which are independent of ΔV. The horizontal dashed lines are a visual guide.

3. Conclusions

In summary, we demonstrated that all 2D Dirac heterostructures consisting of graphene and TI control coherent plasmon polariton oscillations. The 2D Dirac plasmon resonances are modulated through electrically gated graphene, which is in a proximity contact with TI. Our work is different from conventional metallic plasmons or graphene-integrated dipole resonances in that the screening effect on plasmons is weak. The coherent coupling of gate-controlled graphene with TI is manifested by an unconventional blue shift of Bi_2Se_3 TI plasmon polariton resonances, which otherwise would exhibit a red shift due to strong Coulomb screening. Our integrated device may provide a new opportunity for exploring Dirac quasiparticle physics in low-energy optical modulators with low power consumption in compact heterostructures.

Acknowledgements

C.I., B.K., and H.C. were supported by the National Research Foundation of Korea (NRF) through the government of Korea (MSIP) (Grant No. NRF-2018R1A2A1A05079060, NRF-2016R1A4A1012929) and Institute for Basic Science (IBS), Korea, under the Project Code (IBS-R014-G1-2016-a00). C.I. was supported by NRF through MSIP (Grant No. NRF-2015H1A2A1034809).

References

[1] L. Ju *el al*., Graphene plasmonics for tunable terahertz metamaterials, *Nature Nanotechnology* 6: 630-634, 2011.

[2] H. Yan *et al*., Tunable infrared plasmonic devices using graphene/insulator stacks, *Nature Nanotechnology* 7: 330-334, 2012.

[3] S. H. Lee *et al*., Switching terahertz waves with gate-controlled active graphene metamaterials, *Nature Materials* 11: 936-941, 2012.

[4] H. Yan *et al*., Damping pathways of mid-intrared plasmons in graphene nanostructures, *Nature Photonics* 7: 394-399, 2013.

[5] P. Di Pietro *et al*., Observation of Dirac plasmons in a topological insulator, *Nature Nanotechnology* 8: 556-560, 2013.

[6] S. Sim *et al*., Ultra-high modulation depth exceeding 2,400% in optically controlled topological surface plasmons, *Nature Communications* 6: 8814, 2015.

[7] C. In *et al*., Control over electron-phonon interaction by Dirac plasmon engineering in the Bi_2Se_3 topological insulator, *Nano Letters* 18: 734-739, 2018.

On-chip quantum photonic sources based on silicon waveguide

Lantian Feng[1,2], Ming Zhang[3], Yang Chen[1,2], Zhiyuan Zhou[1,2], Hao Wu[3], Ming Li[3], Guoping Guo[1,2], Guangcan Guo[1,2], Daoxin Dai[3] and Xifeng Ren[1,2,*]

[1] Key Laboratory of Quantum Information, CAS, University of Science and Technology of China, Hefei, Anhui 230026, China.
[2]Synergetic Innovation Center of Quantum Information & Quantum Physics, University of Science and Technology of China, Hefei, Anhui 230026, China
[3]State Key Laboratory for Modern Optical Instrumentation, Centre for Optical and Electromagnetic Research, Zhejiang Provincial Key Laboratory for Sensing Technologies, College of Optical Science and Engineering, Zhejiang University, Zijingang Campus, Hangzhou 310058, China.
*corresponding author, E-mail: renxf@ustc.edu.cn

Abstract

Integrated quantum photonics has attracted intensive attention due to the compactness, scalability, and stability. An on-chip photonic quantum source, especially an on-chip entangled photon source, is a basic device for realizing quantum photonic integrated circuits (QPICs) [1]. Here, I will introduce our recent works on on-chip quantum photonic sources based on silicon waveguide.

1. Introduction

Quantum photon pair sources are not only critical to advancing our fundamental understanding of quantum mechanics, but also play a key role in many applications for quantum technologies. Compared with free-space ones, integrated photon pair sources have attracted much attention owing to their compactness, scalability, and stability. For example, path or polarization entangled photon pairs were demonstrated by using the nonlinear processes in a single-mode waveguide or in a micro-ring cavity. Multi-photon quantum sources are critical resources for quantum communication, computation, simulation, and metrology. Great efforts have been made for the realization of high-quality, bright, and scalable multi-photon quantum states to enable a practical and powerful implementation of quantum technologies. Since it is difficult to achieve a nonlinear process directly coupling multiple photons together due to the weak nonlinear susceptibilities of those common optical materials, traditionally multi-photon quantum sources are generated by multiplexing several bi-photon sources and performing post-selections. As the efficiency of the multiplexing process decreases exponentially with the number of entangled photons, it is essential to achieve bright bi-photon sources with high-fidelity and increase the coupling efficiency wherever possible9. In comparison with free-space optics, integrated photonics has been recognized as a promising platform for realizing quantum photon-pair sources and compatible with chip-based processes of quantum manipulation and detection. The strong mode-confinement in optical waveguides and filed-enhancement in high-Q optical cavities can greatly enhance the nonlinear optical interactions, so that it is possible to achieve on-chip multi-photon quantum sources.

Here, I will introduce three works on on-chip quantum photonic sources based on silicon waveguide: 1. On-chip transverse-mode entangled photon pair source [2]; 2. Generation of multi-photon quantum states on silicon [3]; 3. Frequency-degenerate multi-photon entangled state generation with silicon [4].

2. On-chip transverse-mode entangled photon pair source

Integrated entangled photon pair source is an essential resource for both fundamental investigations and practical applications of quantum information science. Currently there have been several types of entanglement, among which the transverse-mode entanglement is becoming attractive because of its unique advantages. Here, we report an on-chip transverse-mode entangled photon pair source via the spontaneous four-wave mixing processes in a multimode silicon waveguide. Transverse-mode photon pairs are verified over multiple frequency channels within a bandwidth of ~2THz, and a maximally entangled Bell state is also produced with a net fidelity of 0.96. Our entangled photon pair source is the key element for quantum photonics based on transverse-mode, and also has the possibility to extend to higher-dimensional Hilbert space. Furthermore, the transverse-mode entanglement can be converted coherently to path and polarization entanglement, which paves the way to realizing highly complex quantum photonic circuits with multiple degrees of freedom.

3. Generation of multi-photon quantum states on silicon

Multi-photon quantum states play a critical role in emerging quantum technologies, and greatly improves our fundamental understanding of the quantum world. Integrated photonics is well recognized as an attractive technology offering great promise for the generation of photonic quantum states with high brightness, tunability, stability and scalability. Here, we demonstrate the generation of multi-photon quantum states by using a single silicon nanophotonic waveguide. The detected four-photon rate reaches 0.34 Hz even with a low pump power of 600 μW. This multi-photon quantum state is also qualified with multi-photon quantum interference as well as quantum state tomography. For the generated four-photon states, the quantum interference visibilities are above 95% and the fidelity is 0.78±0.02. Furthermore, such a multi-photon quantum source is fully compatible with on-chip processes of quantum manipulation as well as quantum detection, which is helpful for the realization of large-scale quantum photonic integrated circuits(QPICs) and also shows great potential for the research in the area of multi-photon quantum science.

4. Frequency-degenerate multi-photon entangled state generation with silicon

Integrated photonics is an attractive platform for generating photonic quantum states with high brightness, high stability and scalability. The photonic quantum states generated so far using integrated circuits have shown important practical applications in a range of quantum technologies. However, the schemes used produce photons at different frequencies and therefore the photons are distinguishable, which limits their further use in many quantum information applications. Here, we prepare frequency-degenerate multi-photon quantum states with a silicon nanophotonic waveguide. Two-photon and four-photon polarization entangled states are generated with the help of a Sagnac interferometer. The states are analyzed using quantum interference and state tomography techniques. As an example, we show that the generated quantum states can be used to achieve phase super-resolution. Our work shows the possibility of using integrated waveguides to prepare indistinguishable multi-photon entangled states and realizing quantum algorithms in a compact on-chip setting.

Acknowledgements

This work was supported by the National Key R \& D Program (No. 2016YFA0301700), the National Natural Science Foundation of China (NSFC) (Nos. 61590932, 11774333, 61725503, 61431166001), the Strategic Priority Research Program of the Chinese Academy of Sciences (No. XDB24030601), Anhui Initiative in Quantum Information Technologies (No. AHY130300), the Fundamental Research Funds for the Central Universities.

References

[1] Caspani, L. *et al*. Integrated sources of photon quantum states based on nonlinear optics. *Light Sci. Appl*. **6,** e17100 (2017).

[2] LT Feng, M Zhang, X Xiong, Y Chen, H Wu, M Li, GP Guo, GC Guo, DX Dai and XF Ren, On-chip transverse-mode entangled photon pair source, npj Quantum Information 5 (1), 2 (2019).

[3] Ming Zhang, Lan-Tian Feng, Zhi-Yuan Zhou, Yang Chen, Hao Wu, Ming Li, Guo-Ping Guo, Guang-Can Guo, Dao-Xin Dai, Xi-Feng Ren, Generation of multiphoton entangled quantum states with a single silicon nanowire, arXiv preprint arXiv:1803.01641

[4] Lan-Tian Feng, Yang Chen, Zhi-Yuan Zhou, Ming Zhang, Ming Li, Dao-Xin Dai, Hong-Liang Ren, Guo-Ping Guo, Guang-Can Guo, Mark Tame, Xi-Feng Ren, Frequency-degenerate multi-photon entangled state generation with silicon, arXiv preprint arXiv:1812.02368

Hyperbolic meta-antennas: a new way to manipulate absorption and scattering of light towards bio-medical applications

Nicolò Maccaferri[1,2*], Yingqi Zhao1, Marzia Iarossi[1,3], Tommi Isoniemi[1], Daniel Darvill[1], Antonietta Parracino[1], Giuseppe Strangi[4,5], and Francesco De Angelis[1*]

[1]Istituto Italiano di Tecnologia, Via Morego 30, 16163, Genova, Italy
[2]Physics and Materials Science Research Unit, Université du Luxembourg, 165, avenue de la Faïencerie, L-1511, Luxembourg
[3]Department of Informatics, Bioengineering, Robotics and Systems Engineering (DIBRIS), Università degli Studi di Genova, Via Balbi 5, 16126 Genova, Italy
[4]Department of Physics, Case Western Reserve University, 10600 Euclid Avenue, Cleveland, Ohio 44106, USA
[5]CNR-NANOTEC Istituto di Nanotecnologia and Department of Physics, University of Calabria, 87036, Italy

*corresponding author, E-mail: nicolo.maccaferri@uni.lu; francesco.deangelis@iit.it

Abstract

Besides its fundamental importance, manipulation of light at the nanoscale is of great interest for the prospect of real-life applications, such as energy harvesting and photovoltaics, wave-guiding and lasing, optoelectronics, biochemistry and medicine. Novel optical designs and architectures that modify the optical power flow through plasmonic nanostructures represent another crucial step towards a nanoscale manipulation of light-matter interactions. In this framework hyperbolic metamaterials (HMMs) have received great attention due to their unusual properties at optical frequencies that are rarely or never observed in nature [1].
Here, we report about unconventional optical properties of metal-dielectric meta-antennas supporting type II hyperbolic dispersion, which enable almost pure and spectrally separated absorption and scattering channels in the visible/near-infrared spectral range [2]. We demonstrate that the physical mechanism responsible for the control of scattering and absorption lies in the different nature of the plasmonic modes excited within the hyperbolic meta-antennas. We also show that scattering is the dominating electromagnetic decay channel, when an electric super-radiant dipolar mode is induced in the system, whereas strong light absorption occurs when a magnetic sub-radiant dipole is excited. Importantly, both modes can be excited directly by coupling with far-field radiation, thereby making the proposed architecture suitable for practical applications. In this framework, we demonstrate also that HMM meta-antennas could find promising applications in photo-thermal therapy. Our findings open the pathway towards novel routes for exploiting light to energy conversion channels beyond what is offered by current plasmon-based architectures, possibly enabling applications including thermal emission manipulation, thermoplasmonics-based theragnostic nano-devices, novel nano-antenna designs and plasmon-enabled enhanced molecular spectroscopy.

References

[1] A. Poddubny, I. Iorsh, P. Belov, Y. Kivshar, Hyperbolic metamaterials, *Nat. Photon.* 7: 958-967, 2013.
[2] N. Maccaferri, Y. Zhao, T. Isoniemi, M. Iarossi, A. Parracino, G. Strangi, F. De Angelis, Hyperbolic Meta-Antennas Enable Full Control of Scattering and Absorption of Light, *Nano Lett.* 10.1021/acs.nanolett.8b04841, 2019.

Arbitrary Tuning of the Isotopic Hydrogen Evolution Reactions

Hiro Minamimoto*, Ryo Osaka, and Kei Murakoshi

Department of Chemistry, Faculty of Science, Hokkaido University
Sapporo, Hokkaido 060-0810, Japan.
*corresponding author, E-mail: minamimoto@sci.hokudai.ac.jp

Abstract

The hydrogen evolution reaction in the mixed solution of H_2O and D_2O has been investigated on the nano-structured electrodes using the electrochemical mass (EC-mass) spectroscopy system. By the establishment of the EC-mass system, we have successfully discussed about the isotopic selectivity of the hydrogen evolution reaction at the specific nano-structures electrodes. We have demonstrated the specific factor for the precise control of the isotopic selectivity on the hydrogen evolution reactions. The present results prove the importance of in-situ mass spectroscopic measurement for the investigation to establish the arbitrary control of the isotopic hydrogen evolution reactions.

1. Introduction

For the sustainable society, the hydrogen evolution reaction (HER) is one of the most important electrochemical reactions [1]. Although the HER process seems to be a simple two-electron reduction, the actual molecular behavior on the electrode surface is quite complicated. As the well-known process of the HER process, three molecular processes, such as the adsorption, chemical recombination, and electrochemical recombination steps occur simultaneously at the electrode surface [2]. There are various efforts to control the effective HER process, but the arbitrary control of the isotopic selectivity is still a challenging issue in that field. According to the previous reports, it has been reported that the ratio of the generated isotopic molecules, which are generally described as the separation factor (S_D), is sensitively dependent on the HER conditions, such as the mixed ratio of H_2O and D_2O, the solution temperature, over potential or the metal species. From the electrochemical point of view, it can be said that the arbitrary tuning of the reaction selectivity is quite important not only for optimization of HER efficiency but also development of the novel industrial techniques for the D_2O/H_2O condensation.

Up to date, various both experimental and theoretical attempts have been carried out to clarify the specific factor for the control of the selectivity on the isotopic reaction. As the interesting fact, the selectivity of the isotopic reaction is also affected not only by metal species but also the morphology or the configuration of the electrode surface. In this study, we have established the EC-mass system to observe the reaction products originated from the advanced materials of the Ag nano-structured electrodes. In present results, it is interesting that the curious reaction selectivity tuning was observed only in the case for specific Ag nano-structures. Through the *in-situ* analyses, mechanistic studies of the structure morphological effect on the isotopic reaction selectivity became possible [3]. The present findings would provide important aspects for future methods to control the reaction selectivity of the isotopic HER.

2. Experiment

The electrochemical HER measurements have been carried out using a handmade three-electrode electrochemical cell. The working electrodes were Ag (99.99%), electrochemically roughened Ag, or the well-defined Ag nano-structures supported on the glassy carbon electrode. The Ag nano-structures (Ag-NSL) were prepared by the nano-sphere lithography method as described in the previous report [1]. The counter and reference electrodes were Pt plate and Ag/AgCl, respectively. The supporting electrolyte was 0.5 M Na_2SO_4. The mixed electrolyte solution was prepared by the diluting H_2O (0.991 g, 0.99 mol) to D_2O (9.91 g, 9.01 mol), leading to 90wt% D_2O.

The real-time observations of the reaction product generations were conducted with a quadrupole mass spectrometer, Q-mass (Qulee-HGM, 202, ULVAC Co., Japan) attached to the handmade electrochemical cell. The generated gases are immediately flowed to the mass spectrometer via the capillary immersed into the electrolyte solutions. For avoiding the insertion of the solution into the system, the capillary was coated with the porous Teflon membrane with the pore size of 10 μm. All measurements have been performed under the ambient temperature.

3. Discussion

Figure a shows *in-situ* mass spectra obtained with the polarization at −2.0 V to the Ag and roughened Ag electrodes. Basically, the main products of electrochemical isotopic HER from the D_2O rich solution is HD (m = 3) due to the much faster reaction kinetics of H adsorption to the metal surface. However, it is interesting that we have successfully found that the amount of the generated H_2 (m =

2) at roughed Ag was larger than that at smooth while the ion currents of HD and D_2 (m = 4) at roughened Ag were comparable to those at smooth one. This means that the characteristics to the selective improvement of H_2 generation at roughened Ag were observed. It must be strongly emphasized that the effect of AgCl or Cl ions originated from the electrochemical surface roughening process on the isotopic selectivity can be ignored in the present case. This is because that the residual AgCl or adsorbed Cl anions can be completely reduced and removed at more negative region than −0.9 V. From these, improvement of H_2 generation would imply the possibility that selective acceleration of the reaction processes for only H_2 generation process at the structured electrodes. Therefore, we could conclude the acceleration of the electrochemical desorption reaction at the surface of the roughened Ag electrode appeared. This would be due to the surface or the environmental change at the surface during HER or the appearance of the reaction active site by the electrochemical roughening process.

As the next step, we have prepared the well-defined Ag-nano structured on the carbon electrode using the template method. By this method, the well-defined small Ag triangle structures were deposited on the entirely surface of the carbon electrode. With this electrode, the real time observation of the isotopic products was obtained under the same electrochemical condition as the case in Fig. Very surprisingly, the reaction amounts of H_2 drastically improved and exceeded that of HD. And also the S_D value achieved above 20. To the best of our knowledge, this is the first report about the extremely high S_D value on the Ag electrode. It should be stressed that this interesting isotopic selectivity only appeared in the case for the specific size of the Ag triangle structure. We think that this size dependence would imply the deeply relationship between the S_D value and the plasmon energy which is deeply correlated with the size and morphology of the Ag.

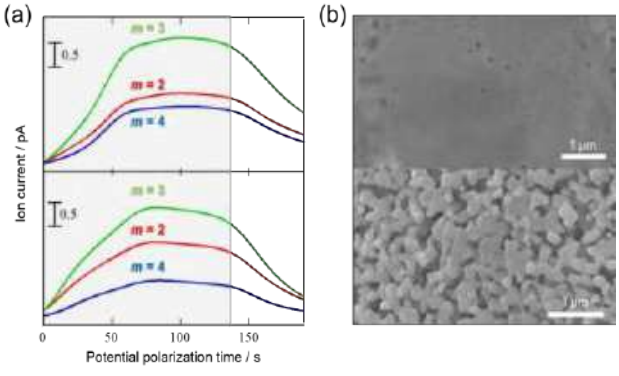


Figure: (a) Electrochemical mass spectra obtained with (upper) smooth and (bottom) roughened Ag electrodes in the mixed solution of H_2O and D_2O. The electrode potential was set to −2.0 V. (b) SEM images of (upper) smooth and (bottom) roughened Ag surface [3].

4. Conclusions

The *in-situ* electrochemical mass spectral measurement system has successfully been established. By using this system, the detail structural morphological effect on the isotopic selectivity has been discussed based on the real time detection of generated reaction products. As the important facts demonstrated in the present investigations, the Ag with the specific nano-structured electrode shows the high selectivity of H_2 generation. This could be originated from the selective acceleration of the H_2 generation at the advanced Ag nano-structures. We now believe that the real time observation of the isotopic reaction products would provide us quite new fact against the various isotopic electrochemical reactions as demonstrated in present paper.

Acknowledgements

The present work was partially supported by Grants-in-Aid for Scientific Research (No. 16K17848), from the Ministry of Education, Culture, Sports, Science, and Technology of Japan, especially that of Scientific Research on Innovative Areas “Nano-Material Optical-Manipulation” (16H06506).

References

[1] Y. Yonezawa, H. Minamimoto, F. Nagasawa, M. Takase, S. Yasuda, K. Murakoshi, In-Situ Electrochemical Surface-Enhanced Raman Scattering Observation of Molecules Accelerating the Hydrogen Evolution Reaction. *J. Electroanal. Chem*. 800, pp. 7–12, 2017.

[2] . J. O’M. Bockris, Recent Developments in the Study of Hydrogen Overpotential, *Chem. Rev*. 43, pp. 525–577, 1948.

[3] H. Minamimoto, R. Osaka, K. Murakoshi, In-situ Observation of Isotopic Hydrogen Evolution Reactions using Electrochemical Mass Spectroscopy to Evaluate Surface Morphological Effect, *Electrochimi. Acta*, just accepted.

Super-Periodic Liquid Crystal Metasurfaces

Maxim V. Gorkunov*[1], Alexey V. Kondratov[1], Irina V. Kasyanova[1], Vladimir V. Artemov[1], Alena V. Mamonova[1], Alexander A. Ezhov[1,2] and Serguei P. Palto[1]

[1] Shubnikov Institute of Crystallography, FSRC "Crystallography and Photonics", Russian Academy of Sciences, 119333 Moscow, Russia
[2] Faculty of Physics, Lomonosov Moscow State University, 119991 Moscow, Russia
*corresponding author, E-mail: gorkunov@crys.ras.ru

Abstract

We study liquid crystal metasurfaces self-assembling on polymer layers patterned by focused ion beam, which are capable of strong visible light diffraction with millisecond-fast electro-optical control. To improve the efficiency of diffraction into a particular channel, we propose super-periodic metasurface designs generated by a multi-parametric optimization algorithm. While such selective diffraction at small angles is achievable with super-periodic structuring of a single substrate of a liquid crystal cell, obtaining it for larger angles requires consistent structuring of both substrates.

1. Introduction

Metasurfaces – ultrathin two dimensional analogues of metamaterials – allow for precise optimization of their versatile functional optical properties [1]. Hybrid metasurfaces combining planar metal and semiconductor nanostructures with soft matter can be switched by weak electric signals [2] and laser irradiation [3] Liquid crystal (LC) metasurfaces, proposed recently [4], combine the soft matter flexibility with exceptional optical quality as they self-assemble from transparent nematic LC under appropriate external conditions upon specially patterned polymer layers.

In this contribution, we analyse the performance of LC metasurfaces as diffractive optical elements and focus on their designs optimal for the blazed grating performance. We analyse the experimental data available for metasurfaces assembled on periodical stripe patterns and show that, unlike most colour filters, the metasurfaces possess distinct colouring not related to a selective light absorption but rather to a diffractive light energy redistribution. However, in simple periodic LC metasurfaces, several diffraction channels appear simultaneously. In order to achieve a dominant diffraction into a single particular channel, more complex designs are necessary. We develop a numerical model of LC metasurfaces assembling upon complex aligning patterns and use it for multi-parametric optimization of the diffraction efficiency. We analyse the feasible diffraction efficiency and conclude on limitations imposed by the continuous medium nature of LCs.

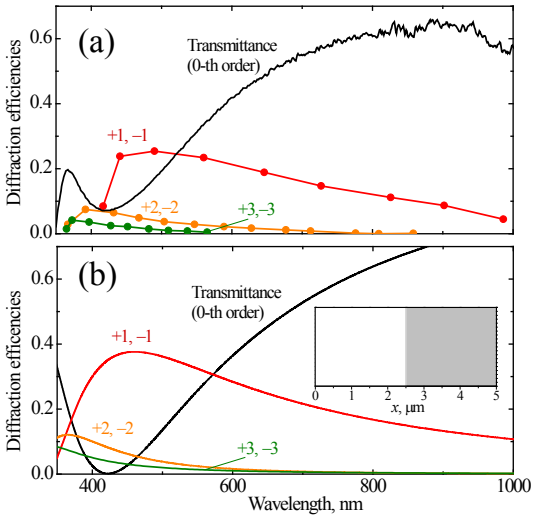


Figure 1: Measured (a) and calculated (b) diffraction efficiencies of 5 μm periodic metasurface in 3 μm thick LC-cell. The inset in (b) shows the unit cell of periodic stripe pattern imprinted on one substrate (light grey colour represents FIB-processed area).

2. Periodic LC metasurfaces

As previously [4], glass substrates covered with 10 nm thin rubbed polyimide (PI) layer are patterned with focused ion beam (FIB) in FEI Scios dual-beam electron microscope. Periodic stripes with a 0.5 duty factor and a period from 1 to 8 μm are imprinted on areas of 0.5×0.5 mm^2 each. The LC cells are assembled by stacking the patterned substrates with chromolane coated non-patterned substrates and filling a few micrometer wide gaps with Merck E7 nematic LC.

Efficiencies of light diffraction in transmission geometry are measured using Horiba Jobin-Yvon UVISEL 2 ellipsometer combined with Ocean Optics USB4000 fibre spectrometer. The data confirm that the lacking transmitted energy is redistributed among a few first strong diffraction orders, see Fig. 1(a).

Neglecting certain peculiarities of the LC elastic anisotropy, we develop a model allowing to calculate the diffraction efficiencies for arbitrary periodic boundary values taken by the LC director polar angle on the sub-

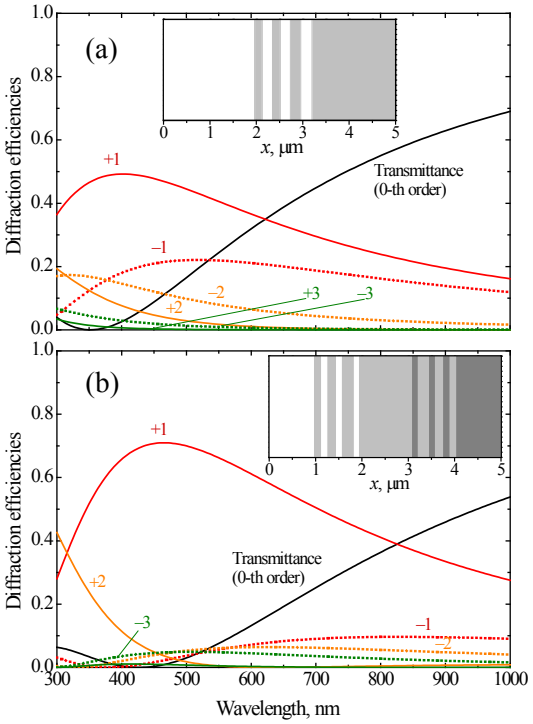


Figure 2: Diffraction efficiencies of 5 μm periodic LC metasurfaces self-assembled in 4 μm thick LC-cells upon one patterned substrate (a) and between two patterned substrates (b) with maximized +1 order diffraction at 500 nm wavelength. The insets show the unit cells of super-periodic patterns: (a) – to be imprinted on one substrate and (b) – to be imprinted on both substrates. Light and dark grey stripes represent FIB-processed areas on different substrates.

strates [4]. Assuming that the LC director is aligned in-plane along the PI rubbing direction everywhere except the areas irradiated by FIB, where it is aligned normally to the substrate, we are able to adequately reproduce the main optical characteristics of LC-metasurfaces assembled on periodic stripe patterns, see Fig. 1.

3. Super-periodic designs

The established connection between the patterns imprinted in PI by FIB and the optical characteristics of LC-metasurfaces enables their multi-parametric numerical optimization. As example, we focus on enhancing the +1 order diffraction at a 500 nm wavelength with the pattern periodicity and LC-cell thickness kept fixed. We employ MATLAB fminsearch routine with the patterned stripe boundaries being varied. For different initial patterns consisting of different number of stripes, the procedure yields same optimal patterns, i.e., the problem has a single global solution. For larger periods, the optimal patterns consist of more stripes, while for smaller periods less stripes are sufficient and excessive ones tend to merge.

Generally, all obtained optimal patterns are similar: they induce a planar adjacent LC alignment on one side of the unit cell and its vertical alignment on the other side, while finer stripes in between provide a gradual transition. Note that the director field in the LC bulk is smoother than at the substrates due to the LC elasticity.

The feasible diffraction efficiency is strongly determined by the metasurface period. For example, optimizing a 10 μm periodic pattern on one substrate allows achieving a 63% efficiency of the +1 diffraction order. For a 5 μm periodic pattern, only a 49% efficiency is possible, see Fig. 2(a). Note that larger periods yield smaller diffraction angles: the 10 μm and 5 μm periodic patterns deflect light by 2.9^o and 5.7^o respectively. The diffraction can be noticeably enhanced by consistent super-periodic patterning of both LC-cell substrates: as illustrated by Fig. 2(b), such 5 μm periodic metasurface provides up to 71% diffraction efficiency with other channels noticeably suppressed.

4. Conclusions

While LC-metasurfaces assembled upon substrates with periodic patterning produce remarkably strong diffraction, the outgoing light energy is evenly distributed between a few first diffraction channels. To concentrate the outgoing light in a particular direction, more sophisticated super-periodic designs are necessary. Further enhancement can be achieved by consistent super-periodic patterning of both LC-cell substrates. The latter design is optimal for LC-metasurface-based tunable blazed gratings and lenses.

Acknowledgement

The research is supported by the Russian Science Foundation (project 18-12-00361). The equipment of Shared Research Center of FSRC "Crystallography and Photonics" RAS supported by the Ministry of Education and Science of the Russian Federation is used.

References

[1] S. B. Glybovski, S. A. Tretyakov, P. A. Belov, Y. S. Kivshar, and C. R. Simovski, "Metasurfaces: From microwaves to visible," *Physics Reports*, vol. 634, pp. 1–72, may 2016.

[2] M. Gorkunov, I. Kasyanova, V. Artemov, M. Barnik, A. Geivandov, and S. Palto, "Fast surface-plasmon-mediated electro-optics of a liquid crystal on a metal grating," *Physical Review Applied*, vol. 8, no. 5, p. 054051, nov 2017.

[3] S. Palto, Y. Draginda, V. Artemov, and M. Gorkunov, "Optical control of plasmonic grating transmission by photoinduced anisotropy," *Journal of Optics*, vol. 19, no. 7, p. 074001, jun 2017.

[4] I. V. Kasyanova, M. V. Gorkunov, V. V. Artemov, A. R. Geivandov, A. V. Mamonova, and S. P. Palto, "Liquid crystal metasurfaces on micropatterned polymer substrates," *Optics Express*, vol. 26, no. 16, p. 20258, jul 2018.

Photo-physical properties of intramolecular charge transfer emissions controlled by hyperbolic metamaterials

Kwang Jin Lee[1], Yeon Ui Lee[1], Frédéric Fages[2], Jean-Charles Ribierre[3] Jeong Weon Wu[1*], and Anthony D'Aléo[2,4]

[1]Department of Physics, Ewha Womans University, Seoul 03760, South Korea
[2]Aix Marseille Univ, CNRS, CINaM UMR 7325, Campus de Luminy, Case 913, 13288 Marseille, France
[3]OPERA, Kyushu University, Fukuoka, Japan
[4]2BFUEL, UMI, CNRS 2002, Seoul, Korea
[5]Center for Quantum Nanoscience, Institute for Basic Science, Seoul, Korea
*corresponding author, E-mail: jwwu@ewha.ac.kr

Abstract

Noting that emission in organic molecules is from either π-π^* or intramolecular charge-transfer (ICT) states, we address here how hyperbolic metamaterial (HMM)modifies ICT emission spectral features by comparing them with a spectral shift dependent on the local polarity of the medium. The 7.0 nm blue shift is observed in ICT emission from 4-dicyanomethylene-2-methyl-6-(p-dimethylaminostyryl)-4H-pyran dispersed into a polymer matrix prepared on HMM multilayered structure, while no spectral shift is observed in π-π^* emission from perylene diimide.

1. Introduction

Photophysical properties of ICT emitters in solution are characterized by a strong dependence on the local solvent polarity. In particular, solvatochromism arises from local reorganization of solute and solvent dipoles to minimize the total energy. Similarly, solvatochromic shift can take place in organic thin-films, depending on the local polarity of the light-emitting medium, and the ICT character of the emitter. Here, we demonstrate that ICT dyes doped in polymer thin films deposited on HMM multilayered structure exhibit a blue-shifted emission due to the nonlocal changes in dielectric permittivity and refractive index. In addition, their fluorescence radiative and nonradiative decay rates and their PLQYs are found to undergo significant changes due to HMM. Lippert-Mataga formalism turns out to be very useful to distinguish and describe local and nonlocal effects of the dielectric permittivity and refractive index in evidencing the appearance of spectral changes in ICT emission.

2. Local and nonlocal effects on spectral shift

In order to compare the local effect of the medium polarity and the nonlocal effect of the HMM substrate in giving rise to a spectral shift of the emission, we compare steady-state photophysical properties of two sets of samples, DCM :PMMA films with 2 and 5 wt % on 0p (fused silica) as well as DCM :PMMA films with 2 wt % on $0p$ and $4p$ HMM substrates. Figure 1 displays the normalized steady-state photoluminescence (SSPL) spectra of two sets of samples. Figure 1c shows a red shift of 9.4 nm (35 meV) when the concentration of DCM is increased from 2 wt % to 5 wt % in the first set of samples. This is attributed to the increased local medium polarity, resulting from the increased local dielectric permittivity when increasing the concentration of polar DCM dye in the PMMA host. In contrast, the blue shift of 6.0 nm (23 meV) in the emission from 2 wt % DCM :PMMA on $4p$ HMM structure (Figure 1d) compared to that on $0p$ in the second set of samples indicates that the HMM structure produces a modulation of the ICT excited state and ground state. This is related to changes of the nonlocal dielectric permittivity and refractive index in the vicinity of ICT emitter when HMM substrate is present.

3. Local and nonlocal effects on fluorescence life-time

Time-resolved photoluminescence (TRPL) was carried out to examine the influence of the Purcell factor on ICT emission. To identify how spectral shift and spontaneous decay rate are related with local medium polarity and nonlocal HMM effects, TRPL spectra of two films of 5 wt % DCM :PMMA on 0p and 2 wt % DCM :PMMA on $4p$ HMM substrate are then compared with those of 2 wt % DCM :PMMA on $0p$.

As shown in Figure 2 a), while there are differences in the weight of monomer and dimer contributions to red-shift in 5 wt % DCM :PMMA on $0p$ and blue shift in 2 wt % DCM :PMMA on $4p$ HMM substrate in TRPL spectra, an increased spontaneous emission rate is strikingly pronounced in 2 wt % DCM :PMMA on $4p$ HMM substrate. Figure 2 b) shows the integrated PL spectra along with time axis. Upon time gating the emission (after about 4.2 ns for $0p$ and 3.6 ns for $4p$), the spectrum of the long-lived species corresponding to dimer can be recorded, which allows to deconvolute the spectrum of short-lived species corresponding to monomer from the SSPL spectrum. SSPL spectrum for 2 wt % DCM :PMMA on $4p$ (5 wt % DCM :PMMA

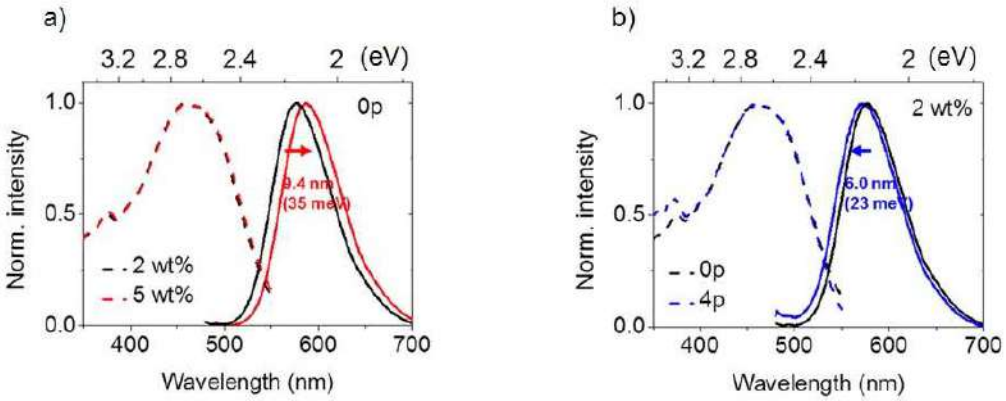


FIGURE 1 – Spectral shift of the ICT emission. (a) Steady-state photoluminescence (SSPL) spectra (excited at 470 nm) of DCM :PMMA film with 2 wt % (black curve) and 5 wt % (red curve) on $0p$ (fused silica) (b) SSPL spectra of DCM :PMMA film with 2 wt % in the absence ($0p$, black curve) and presence of $4p$ (blue curve) HMM substrate.

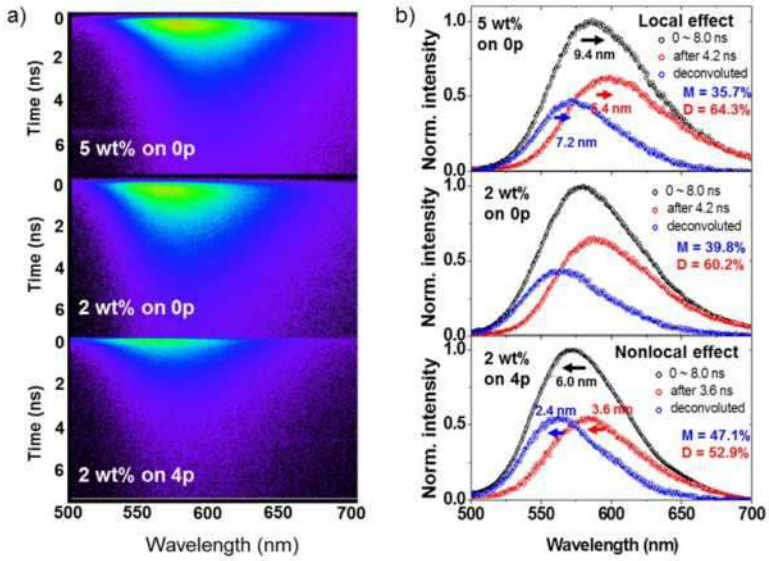


FIGURE 2 – Spectral and temporal behavior of ICT emission from DCM blends. (a) Streak camera images of DCM :PMMA film with 2 and 5 wt % on $0p$ and 2 wt % on $4p$ substrates (excited at 470 nm). (b) Integrated photoluminescence spectra for the entire time range (black), the dimer (red) emission integrated from 4.2 ns to the end, and the monomer (blue) emission obtained by the deconvolution of the entire PL spectra with the dimer spectra

on $0p$) shows a blue shift (red shift) of 2.4 nm (7.2 nm) for monomer and 3.6 nm (5.4 nm) for dimer compared to those for 2 wt % DCM :PMMA on $0p$. This indicates that the spectral shifts of both monomer and dimer result from local medium polarity in 5 wt % DCM :PMMA on $0p$ and from nonlocal HMM effect in 2 wt % DCM :PMMA on $4p$ HMM.

4. Conclusions

It is shown that HMM alters both dielectric permittivity and refractive index of environment of ICT emitter, though via very different mechanisms. Image dipole interaction of charge transfer state present in multilayered HMM structure is accounted for by nonlocal dielectric permittivity, while the Purcell factor enhancement from HD of HMM allows to introduce nonlocal refractive index. [1]

References

[1] Kwang Jin Lee, Yeon Ui Lee, Frdric Fages , Jean-Charles Ribierre, Jeong Weon Wu, and Anthony DAlo, Blue-Shifting Intramolecular Charge Transfer Emission by Nonlocal Effect of Hyperbolic Metamaterials, *Nano Letters* 18 : 1476–1482, 2018.

Elastic Mode Converter based on Supersymmetric Ladders

Choonlae Cho, Sunkyu Yu, and Namkyoo Park

Department of Electrical and Computer Engineering, Seoul National University, Seoul, Korea
*corresponding author, E-mail: nkpark@snu.ac.kr

Abstract

We propose an elastic mode converter for the control of multi- mode and polarization elastic waves. As an elastic analogy of supersymmetric (SUSY) optical transformation, we establish elastic effective potentials and verify quasi-isospectrality in between original and its SUSY partner potentials. Elastic mode filtering is then achieved by using an elastic SUSY ladder, with the concept of the polarization-selective elastic mode filtering.

1. Introduction

The theory of Supersymmetry in particle physics has extended its boundary to quantum mechanics and optics. Using the Helmholtz's equation of the optical system which resembles the time-independent Schrödinger equation, the optical SUSY transformation has achieved significant progress: in terms of the fundamental interest on finding isospectral potential set [1], as well as practical applications: modal multiplexer [2] with the experimental realization [3] based on the global phase-matching condition, disordered optical potentials with perfect bandgap [4], and random wave switching for binary and fuzzy logics [5].

In this work, we apply the SUSY transformation to polarization-dependent elastic potentials [6], in order to develop the SUSY elastic mode converter which systematically filters the multimode elastic waves. For this, we impose the quantum-classical analogy on elastic systems, to derive the Schrödinger-like elastic Hamiltonian equations. By adopting SUSY formalism into the elastic Hamiltonian, mode filtering in the elastic SUSY mode converter is demonstrated in the SUSY ladders. The polarization-diversity elastic potentials each for the longitudinal and shear wave mode, which allows the polarization selective elastic wave manipulation, will also be discussed.

2. Results

2.1. Elastic SUSY transformation

SUSY transformation relates original potential and its partner, similar to the creation-annihilation operation in quantum mechanics. In SUSY formalism, the original Hamiltonian operator $H^{(0)}$ is decomposed into Hermitian adjoint pair, by Cholesky decomposition: $H^{(0)} - E_0^{(0)} = A^{(0)\dagger}A^{(0)}$, where $A^{(0)} = -d/dx + W$ and $A^{(0)} = d/dx + W$ are Hermitian adjoint pair operators, $E_0^{(0)}$ is ground state eigenvalue, and W is the superpotential which satisfies the Riccati equation $W^2 - dW/dx = V^{(0)} - E_0^{(0)}$. The SUSY Hamiltonian $H^{(S)}$ and SUSY partner potential $V^{(S)}$ are then defined by $H^{(S)} = A^{(0)}A^{(0)\dagger} + E_0^{(0)}$, $V^{(S)} = V^{(0)} + 2dW/dx$, respectively. A particular solution of the superpotential W is given by logarithmic derivatives of ground-state eigenmode, $W_0 = -d(\log \psi_0^{(0)})/dx$, where $\psi_0^{(0)}$ is the ground state eigenvector. It is well known that the SUSY Hamiltonian which is constructed by the above superpotential W_0 conserves all the eigenvalues of original one except the ground state: *i.e.* ground state annihilation. More explicitly, the intertwining relation $A^{(0)}H^{(0)}\psi_n^{(0)} = H^{(S)}(A\psi_n)$ is satisfied; the SUSY partner eigenvalues and corresponding eigenfunctions are given by $E_{n-1}^{(S)} = E_n^{(0)}$ and $\psi_{n-1}^{(S)} = A\psi_n^{(0)}$ where n is non-negative integer.

To apply the SUSY formalism, we first develop quantum-classical analogy to the elastic wave system. Equations of motion in inhomogeneous elastic media can be written as [6]

$$\rho\frac{\partial^2\mathbf{u}}{\partial t^2} = (\lambda+\mu)\nabla(\nabla\cdot\mathbf{u}) + \mu\nabla^2\mathbf{u} + \nabla\lambda\,(\nabla\cdot\mathbf{u}) + \nabla\mu\times(\nabla\times\mathbf{u}) + 2(\nabla\mu\cdot\nabla)\mathbf{u}\,, \qquad (1)$$

where ρ is medium density, λ and μ are Lamé 's first and second parameters. Focusing on the case of one-dimensional (1D) material variations along x-axis, Schrödinger-like formulation of the wave equation can be re-written as the eigenvalue equation $H\psi_n = E_n\psi_n$, where $H = -d^2/dx^2 + V(x)$ is the system Hamiltonian, $V(x)$ is a effective potential, ψ_n and $E_n = -k_n^2$ are the eigenfunction and corresponding eigenvalue, respectively, and k_n is the spatial frequency. In the paraxial approximation, the elastic potential is then described by a set of polarization dependent effective potentials $V_{L,S}(x) = -\omega^2 n_{L,S}^2(x)$, where ω is the angular frequency and n_L and n_S are refractive indices of longitudinal and shear elastic wave, respectively.

2.2. SUSY ladders for mode selectivity

From the Schrödinger-like formulation of elastic waves, we then establish the concept of elastic SUSY transformations, for the construction of *quasi*-isospectral potentials. For arbitrary elastic potentials shown in Fig.1, we obtain the ground-state-annihilated SUSY partner potentials which satisfy the quasi-isospectrality. Each polarization-dependent SUSY *ladder* can then be constructed by assembling SUSY partner *potentials*. In these SUSY ladders, evanescent mode coupling between adjacent waveguides in the weak coupling regime achieves the perfect power transfer by the global phase matching condition of SUSY partner potentials.

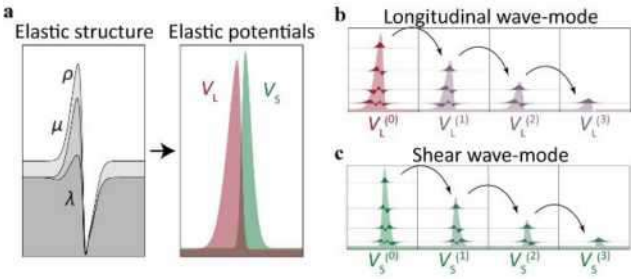


Figure 1: (a) Elastic potentials of the Schrödinger-like elastic wave equations. (b,c) Elastic SUSY partner potentials from original potentials $V^{(0)}$ for longitudinal (b) and shear (c) waves.

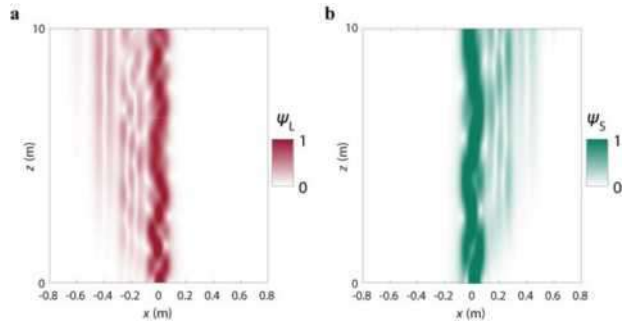


Figure 2: Polarization dependent mode selective elastic wave-mode separation in SUSY ladder. (a) The longitudinal wave-modes are coupled to the left side, and (b) the shear wave-mode are coupled into the right side. Single polarized multimodal waves are then separated, based on SUSY mode filtering.

By arranging two polarization dependent SUSY ladders of which the mode annihilation directions are opposite, an elastic SUSY mode converter can then be constructed, which offers the complete modal filtering; not only for spatial modes but also for polarization modes. Figure 2 shows the operation of SUSY-based polarization-dependent mode-selective filter, for the input of arbitrary spatial- and polarization- mode at the center.

3. Conclusions

In summary, we proposed and achieved an elastic SUSY mode converter, by establishing isospectral elastic potentials via the quantum-classical analogy of the elastic wave equation. With the peculiarity in the elastic wave, i.e., the polarization mixing between longitudinal and transversal waves, polarization diversity SUSY ladders are proposed in order to achieve mode conversion both in spatial- and polarization- domain. Our elastic Hamiltonian and SUSY transformation enables the tailoring of the modal spectra, which differs from conventional dispersion modulation methods, opening up the possibility of constructing polarization and mode number selective devices.

Acknowledgments

This work was supported by the National Research Foundation of Korea (NRF) through the Global Frontier Program (GFP) NRF-2014M3A6B3063708 and the Basic Science Research Program 2016R1A6A3A04009723.

References

[1] F. Cooper, A. Khare, and U. Sukhatme, Supersymmetry and quantum mechanics, *Physics Reports* **251**, 267-385 (1995).

[2] M.-A. Miri, M. Heinrich, R. El-Ganainy, and D.N. Christodoulides, Supersymmetric optical structures, *Phys. Rev. Lett.* **110**, 233902 (2013).

[3] M. Heinrich, M.-A. Miri, S. Stützer, R. El-Ganainy, S. Nolte, A. Szameit, and D.N. Christodoulides, Supersymmetric mode converters, *Nat. Commun.* **5**, 3698 (2014).

[4] S. Yu, X. Piao, and N. Park, Bloch-like waves in random-walk potentials based on supersymmetry, *Nat. Commun.* **6**, 8269 (2015).

[5] S. Yu, X. Piao, and N. Park, Controlling Random Waves with Digital Building Blocks Based on Supersymmetry, *Phys. Rev. Applied* **8**, 054010 (2017).

[6] F.C. Karal Jr. and J.B. Keller, Elastic wave propagation in homogeneous and inhomogeneous media, *J. Acoust. Soc. Am.* **31**, 694 (1959).

Optomechanical Kerker effect for trembling resonant particles

Alexander Poshakinskiy* **and Alexander Poddubny**

Ioffe Institute, St. Petersburg, Russia
*corresponding author, E-mail: poshakinskiy@mail.ioffe.ru

Abstract

We propose an optomechanical Kerker effect, where the tunable directional inelastic scattering is achieved for a small particle that trembles in space. We show that the motion of the electric dipole leads to appearance of a magnetic dipole. The interference of the electric and magnetic dipole radiation patterns is governed by the frequency dependence of the particle permittivity. For a resonant particle, the light is scattered preferably forward at resonance and backward away from it.

1. Introduction

The control of the scattered light direction is essential for optical circuits. However, small particles usually scatter light symmetrically, in particular, forward and backward scattered waves have equal intensities. The asymmetry can be induced if the scatterer moves. Then, the Doppler effect leads to a difference between the incident and scattered light frequencies, that is maximal for the wave scattered backward and vanishes for that scattered forward [1]. Still, the asymmetry of the emission intensity pattern remains small unless the particle velocity becomes comparable to that of light. Another way to achieve strong scattering directionality was proposed by M. Kerker [2]. It can be realized for scatterers that have both electric dipole (ED) and magnetic dipole (MD) susceptibilities. Since the electric fields corresponding to ED and MD have opposite spatial parity, their interference enables directional forward or backward scattering. The implementation of the Kerker effect requires magnetic response of the same strength as the electric one. At optical frequencies, that is challenging due to the vanishing magnetic susceptibility. A possible solution is to exploit electric and magnetic Mie resonances in high-refractive-index dielectric nanoparticles [3]. However, Kerker effect for the particles smaller than the wavelength in the medium is still unfeasible.

2. Optomechanical multipole conversion

We put forward an optomechanical Kerker effect, where strong tunable directionality is achieved for light scattered by a small particle without any magnetic response that trembles in space. The concept is sketched in Fig. 1(a). The incident wave at frequency ω excites oscillating electric dipole polarization. Trembling of the electric dipole in space with the amplitude $\boldsymbol{u}$ and frequency Ω induces the loop electric current $\boldsymbol{j}$ with non-zero magnetic momentum $\boldsymbol{m}$ as well as the electric quadrupole (EQ) momentum at the shifted frequencies $\omega \pm \Omega$. Interference of ED and MD+EQ contributions results in unidirectional scattering as shown in Fig. 1(b).

To describe light scattering by trembling objects, we developed a novel theoretical framework that incorporates the effect of the resonant dispersion of the moving medium [4]. We found that the electric dipole $\boldsymbol{d}$, quadrupole $\boldsymbol{Q}$, and magnetic dipole $\boldsymbol{m}$ induced in the vibrating particle at anti-Stokes frequency $\omega' = \omega + \Omega$ are given by

$$\begin{aligned} \boldsymbol{d} &= \alpha(\omega')\tfrac{\mathrm{i}\omega}{c}(\boldsymbol{n}_0 \cdot \boldsymbol{u})\boldsymbol{E}_0\,, \\ \boldsymbol{Q} &= \alpha(\omega)[3\boldsymbol{E}_0 \otimes \boldsymbol{u} + 3\boldsymbol{u} \otimes \boldsymbol{E}_0 - 2\boldsymbol{I}(\boldsymbol{u} \cdot \boldsymbol{E}_0)], \\ \boldsymbol{m} &= \alpha(\omega)\tfrac{\mathrm{i}\omega}{2c}[\boldsymbol{E}_0 \times \boldsymbol{u}]\,, \end{aligned} \tag{1}$$

where $\boldsymbol{E}$ and $\boldsymbol{n}_0$ are the electric field and propagation direction of the incident wave, $\alpha(\omega)$ is frequency-dependent particle polarizability, $\boldsymbol{I}$ is the identity matrix, and we supposed $\Omega \ll \omega$. Note that the induced ED is proportional to the polarizability at the scattered light frequency $\alpha(\omega')$, while EQ and MD are determined by $\alpha(\omega)$. Therefore, the frequency dependence of the polarizability can be exploited to tune $\boldsymbol{d}$, $\boldsymbol{m}$, and $\boldsymbol{Q}$ to the Kerker condition.

Figures 2(a)–(e) show the radiation pattern of the light scattered on the particle trembling along the light propagation direction, $\boldsymbol{u} \parallel \boldsymbol{n}_0$. Panel (a) shows the case when $\alpha(\omega') \gg \alpha(\omega)$ and the radiation pattern is a determined by the ED contribution. Panel (b) shows the contribu-

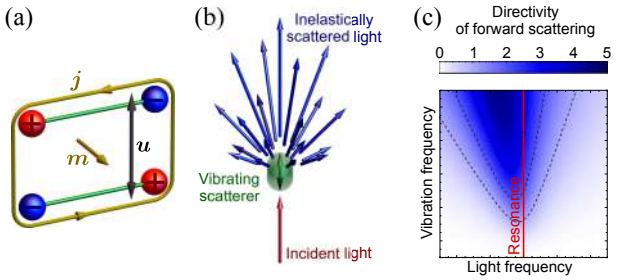


Figure 1: (a) A sketch of the motion-induced multipole conversion. Trembling of an oscillating dipole in the space $\boldsymbol{u}$ leads to appearance of an electric quadrupole and a current curl. The latter yields a magnetic dipole $\boldsymbol{m}$. (b) A sketch of the directional inelastic light scattering on a trembling particle. (c) Forward directivity of the light scattered by a trembling resonant particle depending on the incident light frequency and trembling frequency.

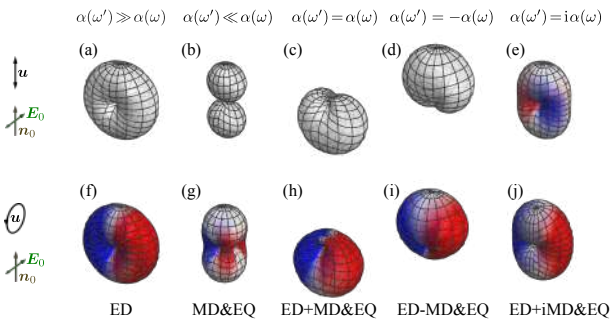


Figure 2: The scattering pattern with the degree of circular polarization marked by red and blue colors. Light is incident from the bottom and linearly polarized. Rows correspond to different trembling directions indicated on the left. Columns correspond to different relations between particle polarizabilities at the frequencies of incident and scattered light, $\alpha(\omega)$ and $\alpha(\omega')$, indicated in the top.

tions of MD and EQ that dominate in the opposite case $\alpha(\omega') \ll \alpha(\omega)$. If the particle polarizabilities at initial and final frequencies are comparable, scattering intensity is a superposition of the patterns Fig. 2(a) and Fig. 2(b) with the coefficients $\alpha(\omega')$ and $\alpha(\omega)$, respectively. Figures 2(c) and (d) show the two limiting cases when $\alpha(\omega') = \pm\alpha(\omega)$ and the interference of ED, MD, and EQ radiation patterns leads to the complete suppression of forward or backward inelastic scattering.

The asymmetry of the light scattering pattern can be quantified by the directivity D, which is the ratio of the scattering intensity in the direction of interest and the total scattering intensity. Figure 1(c) shows by color the forward directivity for the case when particle polarizability has a resonance. In the vicinity of the resonance, the polarizabilities $\alpha(\omega)$ and $\alpha(\omega')$ can differ strongly. That leads to the strong forward directivity that can reach 5.25. The directivity of the optomechanical Kerker effect surpasses the limiting value of 3 for the classical Kerker effect, because the EQ contribution is additionally involved [3]. Away from the resonance, polarizabilities $\alpha(\omega)$ and $\alpha(\omega')$ are close, so forward scattering vanishes while backscattering is enhanced.

3. Optomechanical spin Hall effect

Due to the interference of the ED and MD emission patterns, the light with opposite circular polarization can be scattered in different directions, which is termed as an optical spin Hall effect [5]. It results in the emergence of the scattered light circular polarization under linearly polarized excitation. We put forward an optomechanical spin Hall effect, i.e., inelastic polarization-dependent directional scattering on a trembling particle.

There are two origins of the effect. The first is the phase difference between the particle polarizabilities at the initial and scattered light frequencies, that can be achieved in the vicinity of a resonance. For such case, the scattered light circular polarization degree is shown by color on the scattering pattern Fig. 2(e), where $\alpha(\omega)$ and $\alpha(\omega')$ are chosen to have $\pi/2$ phase difference. The other possibility is to consider light scattering on a particle trembling around a circular trajectory. Then, as shown in Figs. 2(f)–(i), the light scattered to the left and to the right with respect to the particle motion plane will have opposite circular polarization. If both mechanisms are present, the scattering intensity pattern and the circular polarization pattern turn to be strongly asymmetric, see Fig. 2(j).

4. Conclusions

The optomechanical Kerker and spin Hall effects with trembling-induced magnetic response open a pathway to engineer chiral optomechanical coupling at nanoscale, expanding the chiral quantum optics to the optomechanical domain. Our results can be instructive for the design of nonreciprocal topological circuits, where the disorder-robust propagation of light and sound is ensured by the time modulation of optical and mechanical properties [6]. The proposed effects can be implemented in quantum dots and transitional metal dichalcogenide monolayers featuring exciton resonance, cold atomic gases, atomic nuclei probed by Mössbauer γ-ray spectroscopy, or superconducting resonators for radio-frequency electromagnetic field.

Acknowledgement

This work was supported by the RFBR project No. 18-32-00486, the Foundation "Basis," and the Russian President Grants No. MD-5791.2018 and No. MK-599.2019.2.

References

[1] C. V. Raman, The Doppler effect in the molecular scattering of radiation, *Nature* 103: 165, 1919.

[2] M. Kerker, D.-S. Wang, C.L. Giles, Electromagnetic scattering by magnetic spheres, *J. Opt. Soc. Am.* 73: 765, 1983.

[3] W. Liu, Y.S. Kivshar, Generalized Kerker effects in nanophotonics and meta-optics, *Opt. Express* 26: 13085, 2018.

[4] A.V. Poshakinskiy, A.N. Poddubny, Optomechanical Kerker Effect, *Phys. Rev. X* 9: 011008, 2019.

[5] K.Y. Bliokh, F.J. Rodríguez-Fortuño, F. Nori, A.V. Zayats, Spin-orbit interactions of light, *Nat. Photon.* 9: 796, 2015.

[6] A.V. Poshakinskiy, A. N. Poddubny, Phonoritonic crystals with a synthetic magnetic field for an acoustic diode, *Phys. Rev. Lett.* 118: 156801, 2017.

Deciphering, Characterization and Nanocontrol of Single Quantum Dots for Single Photon Emission and Near-field Imaging

Xuewen Chen

School of Physics, Huazhong University of Science and Technology, Wuhan, 430074, China,
*corresponding author, E-mail: xuewen_chen@hust.edu.cn

Abstract

Absorption and emission of matter comprise the majority of optical phenomena in our world. Among various kinds of nanoscopic optical emitters, colloidal quantum dots (QDs) have gained great attention due to intense broad-band absorption, tunable narrow-band emission, solution processibility, and compatibility with photonic structures [1]. The ultimate success of the applications crucially relies on the absorption or/and emission properties of QDs at single-dot level. In comparison to a single-molecular emitter, density of states of a QD is usually very large and a QD in the charged states can be quite stable. Consequently, upon photo- or electrical-excitation, a QD is often found in multi-carrier states. Despite impressive progress in chemical synthesis of non-blinking QDs for the past years, charging, blinking, multiexciton generation and emission still generally occur under relatively intense optical excitation, electric bias or imbalanced current injection. In this presentation, we show in-situ deciphering the charging status, and precisely assessing the absorption cross section, and determining the absolute emission quantum yield of mono-exciton and biexciton states for neutral, positively-charged, and negatively-charged single core/shell CdSe/CdS QD [2]. We uncover very different photon statistics of the three charge states in single QD and unambiguously identify their charge sign together with the information of their photoluminescence decay dynamics. In addition, we report on nano-controlled coupling of one colloidal quantum dot to a dielectric nanotip for single-mode outcoupling of the single photons [3]. We demonstrate three-dimensional manipulation of the QD towards precise integration of nanophotonic structures and near-field imaging.

Acknowledgements

We acknowledge financial support from the National Natural Science Foundation of China (grant 11874166, 11604109)

References

[1] A.P. Alivisatos, Science 271, 933-937 (1996).

[2] W. Xu, X. Hou, Y. Meng, R. Meng, Z. Wang, H. Qin, X. Peng, X.-W. Chen, Nano Letters 17, 7487−7493 (2017)

[3] Z. Wang, W. Xu, X. Hou, J. Dong, Z Tian, H. Qin, X. Peng, X.-W. Chen. Manuscript in preparation (2019).

Key Issues in the Rational Design of Plasmonic Nanoparticles for Second Harmonic Generation

Pierre-François Brevet[1]*

[1]Institut Lumière Matière, UMR CNRS 5306 and University Claude Bernard Lyon 1, University of Lyon, Villeurbanne, France
*corresponding author, E-mail: pfbrevt@univ-lyon1.fr

Abstract

Second Harmonic Generation from plasmonic nanoparticles requires a delicate balance between material size, shape or morphology for the best performances according to the laser excitation conditions. We investigate all these issues in a first step using available experimental data and then present further avenues to explore using hybrid dielectric – metallic nanoparticles.

1. Introduction

Second harmonic Generation (SHG) is an ideal method to investigate metallic nanoparticles dispersed as liquid suspensions in the absence of any supporting substrate [1]. SHG is indeed a nonlinear optical phenomenon where symmetry is critical in determining these properties. This process entails the conversion of two photons at a fundamental frequency into one photon at the sum frequency. Involving three photons simultaneously, it obeys strict symmetry rules, in particular the requirement of a non centrosymmetric material medium to mediate the conversion [2]. Hence, substrates supporting nanoparticles naturally break the inherent symmetry of nanoparticles. The removal of the substrates using liquid suspension fully alleviates the problem. Over the recent years, metallic nanoparticles of different sizes and shapes have been investigated thoroughly, especially those with a centrosymmetric shape like nanospheres, nanorods or nanocubes [3]. Understanding the origin of the response in such system is indeed of utmost importance, as it is not expected at first glance that large SHG intensities can be obtained. Besides, an in-depth understanding of the origin of the response may lead to new paradigms for application, as we have shown for sensing [4]. In this work, we first review the problem of size and shape in the design of plasmonic nanoparticles for SHG before proposing new routes in the second part to engineer efficient nanoparticles.

2. Size effects

In designing metallic nanoparticles for SHG, the most simple route is to start with nanospheres of gold or silver and investigate how the SHG intensity scales with the nanoparticle diameter. This operation is achieved using the standard Second Harmonic Scattering (SHS) technique, also known as Hyper Rayleigh Scattering (HRS) [5], where the nanoparticles are monodispersed in an aqueous suspension as a result from their synthesis. The latter is realized directly in solution by the mere reduction of the corresponding metallic salt with a reducing agent [6].

The SHS intensity I collected from a suspension of metallic nanoparticles is given by :

$$I = G\left\langle N_S\beta_S^2 + N_{NP}\beta_{NP}^2 \right\rangle I_0^2 \qquad (1)$$

where I_0 is the fundamental intensity, N_S and N_{NP} the respective concentrations of the solvent molecules and the nanoparticles and β_S and β_{NP} the respective first hyperpolarizabilities of the solvent molecules and the nanoparticles. In Equation (1), G is a general constant and the brackets stand for an orientational average due to the liquid suspension isotropy. Interestingly, the solvent contribution that is known by other means serves as a ruler to provide absolute values of the quantity $<\beta_{NP}^2>$. Using this method, the hyperpolarizability of silver and gold nanosphere particles have been measured and reported [7].

In-depth analysis of these data has been rationalized in terms of an extended version of Mie theory where the frequency conversion is also taken into account. Other methods like finite element method (FEM) and surface integral equation (SIE) have also been used [8, 9]. It appears that the scaling of the hyperpolarizability with the ratio a/λ between the nanoparticle radius a and the fundamental wavelength λ is a power law with exponent three as soon as the electrostatic approximation breaks down. At small sizes, the SHS signal is sensitive to the exact shape of the nanoparticles and in particular their deviation from that of a perfect sphere. The hyperpolarizability scaling in this domain is quadratic with the ratio a/λ□□□□□□□□□□□□□□□□□□□□with gold nanospherical particles, the change of scaling exponent appears around 50 nm diameter nanoparticles [7].

Beside the hyperpolarizability absolute value measurement, it is also of interest to understand the nature of the SHS response from metallic nanoparticles in order to use these

features and properties in potential applications. A polarization analysis of the SHS intensity for vertically polarized output as a function for the input polarization angle has yielded the data reported on Figure 1 for 150 nm diameter gold nanoparticles aqueous suspension.

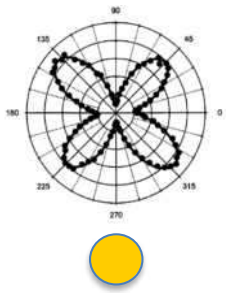


Figure 1 : Polar plot of the Second Harmonic Scattering intensity polarized perpendicularly to the plane of scattering recorded for an aqueous suspension of 150 nm gold nanospheres.

This feature clearly show that an input polarization angle for the fundamental beam at 45° instead of a vertical or horizontal polarization is much more favorable to yield the largest intensity as the response exhibit a strong quadrupolar nature. This feature has been used in devising a new method for sensing [4].

3. Shape effects

Chemical synthesis of metallic nanoparticles has been developed as well to produce other shapes than just spheres. Hence, metallic nanoparticles with shapes of rods, triangles, cubes, … have been investigated as well. When designing plasmonic nanostructures, it is well known that introducing roughness induces electromagnetic confinements and enhancements. Hence, nanoparticles with tips like nanocubes with their corners present local regions of enhanced SHG response, as it has been shown with FEM or SIE methods [9].

Investigation has been performed on nanocubes for instance albeit in the regime where the scaling of the hyperpolarizability is that with the third power of the a/λ ratio. In this size regime, the hyperpolarizability has been shown to be dominated by retardation and therefore avolume scaling. As a result, the role of the nanocube corners is not prominent despite the localized field enhancements.

4. Conclusions and Perspectives

We have discussed two key parameters for the design of plasmonic nanoparticles with the best performance for SHG. It is interesting to note that other parameters are also important, for instance the nature of the metal used. With the size and the shape of the nanoparticles as well as their environment, this will in particular allow for a precise determination of the resonance location, another way to enhance the electromagnetic fields and therefore the performances.

Nevertheless, we pursue other routes where the introduction of hybrid morphologies and hybrid material structures can provide new benefit. In particular, systems where a non centrosymmetric nanocrystals is inserted in a plasmonic nanoshell opens interesting perspectives in this context.

Acknowledgements

The author acknowledges support from the French National Research Agency under contract 2017-CE24-RACINE.

References

[1] J. Butet, P.F. Brevet, O.J.F. Martin, Optical Second Harmonic Generation in Plasmonic Nanostructures: From Fundamental Principles to Advanced Applications, *ACS Nano,* 9 (2015) 10545

[2] R.W Boyd, Nonlinear Optics, Academic Press, New York, 1984

[3] J. Nappa, I. Russier-Antoine, E. Benichou, Ch. Jonin, P. F. Brevet, Second-harmonic light generation from small gold metallic particles: From the dipolar to the quadrupolar response, *J. Chem. Phys.*, 125 (2006) 184712

[4] J. Butet, I. Russier-Antoine, Ch. Jonin, N. Lascoux, E. Benichou, P.F. Brevet Sensing with Multipolar Second Harmonic Generation from Spherical Metallic Nanoparticles, *Nano Lett.,* 12 (2012) 1697

[5] K. Clays, A. Persoons, Hyper Rayleigh Scattering in Solution, Phys. Rev. Lett., 66 (1991) 2980

[6] P.C. ray, Size and Shape Dependent Second Order Nonlinear Optical Properties of Nanomaterials and Their Application in Biological and Chemical Sensing, Chem. Rev., 110 (2010) 5335

[7] I. Russier-Antoine, E. Benichou, G. Bachelier, Ch. Jonin, P.F. Brevet Multipolar Contributions of the Second Harmonic Generation from Silver and Gold Nanoparticles, *J. Phys. Chem. C*, 111 (2007) 9044

[8] G. Bachelier, I. Russier-Antoine, E. Benichou, Ch. Jonin, P.F. Brevet, Multipolar Second Harmonic Generation in Noble Metal Nanoparticles*, J. Opt. Soc. Am. B*, 25 (2008) 955

[9] I. Russier-Antoine, H.J. Lee, A.W. Wark, J. Butet, E. Benichou, Ch. Jonin, O.J.F. Martin, P.F. Brevet, Second Harmonic Scattering from Silver Nanocubes, *J. Phys. Chem. C*, 122 (2018) 17447

Optical Slot Yagi-Uda Antennas

Yeonsang Park[1]*, Jineun Kim[1], Young-Geun Roh[1], Q-Han Park[2]

[1]Imaging Device Lab, Samsung Advanced Institute of Technology, Suwon, Korea
[2]Department of Physics, Korea University, Seoul, Korea
*corresponding author, E-mail: yeonsang.park@samsung.com

Abstract

We present the design of optical slot Yagi-Uda antennas and demonstrate the directional radiation from optical slot Yagi-Uda antennas. By calculating the phase between a feed slot and an auxiliary groove, we can find out parameters where the groove works as a good reflector and fabricate optical slot Yagi-Uda antennas with a good directivity. Through coupling with the optimized optical slot Yagi-Uda antenna, random light from quantum dot light emitting diodes can be directed towards a specific direction well.

1. Introduction

Since the first report in 2005, an optical antenna has been widely studied because of its various physical properties and functionalities [1-4]. Similar to the radio frequency antenna, the optical antenna can transfer electromagnetic energy from one point to another and pick up energy from propagating EM wave at the wavelength of interest efficiently. In 2014, we presented an optical slot antenna made of a metallic nanoslot [5,6]. We experimentally proved that a metallic nanoslot works as a slot antenna in visible region and it can control the direction of radiation like an optical rod Yagi-Uda antenna by adding the auxiliary element of groove. Compared to the optical rod antenna, an optical slot antenna is easier to be combined with light sources because a precise alignment with antennas and emitters is not necessary in fabrication. This means that radiation from light source devices such as LEDs can be coupled with an optical slot Yagi-Uda antenna easily and its direction can be controlled in micro-scale.

2. Design of optical slot Yagi-Uda antennas

Figure 1(a) shows the schematics of our slot-type Yagi-Uda antennas. It is made of a feed slot and an auxiliary groove. Because the resonance wavelength of a slot is dependent on its length [7], we should investigate an optimal antenna length resonant with 614 nm, the wavelength of our interest. By measuring the transmission spectra of slots with various lengths, we obtained the resonance relation of $\lambda\ (nm) = 1.66\ l\ (nm) + 314.14$ (where λ is a resonance wavelength and l is an antenna length) and chose 180 nm as a slot length.

The phase difference between a feed slot and an auxiliary groove provides us a guide line in designing slot Yagi-Uda antennas. Since it is well-known that an optical slot antenna has linear-polarization perpendicular to its length (x-axis in Fig. 1), the y- and z-components of E-field are very weak [5]. Therefore, we can calculate the phase from the Ex-field in structure. Figure 1(b) shows the calculated phase difference while changing the groove length (L) from 100 nm to 400 nm by 50 nm and the distance between a slot and a groove (D) from 100 nm to 300 nm by 50 nm. At the condition of $\pi/2$ phase difference, which is shown as the red line in the contour map, we can see that far-field patterns show a directional radiation well.

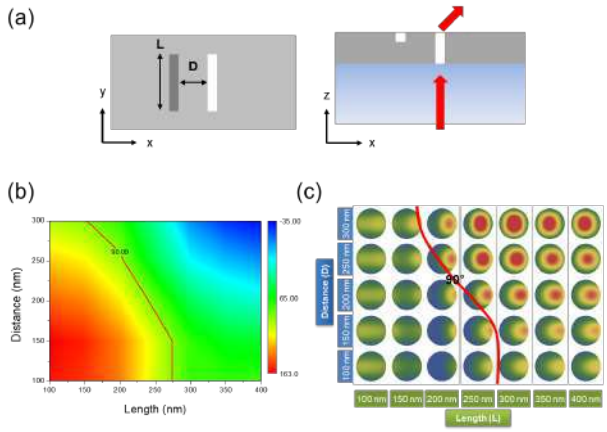


Figure 1: (a) Schematics of a feed slot and an auxiliary groove (b) Calculated phase difference between a slot and a groove (c) Calculated far-field patterns while changing L and D.

3. Experimental results

To make sure the feasibility of our design in use of the phase difference, we have measured far-field patterns with various samples with the groove length (L) changed from 100 nm to 240 nm. Figure 2 shows the measured far-field patterns in each sample. While measuring far-field patterns, we have fixed the distance D between a slot and a groove as 120 nm in order to show the role of a groove clearly. We could see that experimental results are very coincident with the calculated phase map. As L gets increased, the groove

changes from a director, which directs toward where a groove is located, to a good reflector, which reflects radiation from a feed slot. In case of sample with L of 240 nm, we could see that far-field pattern shows a good directivity.

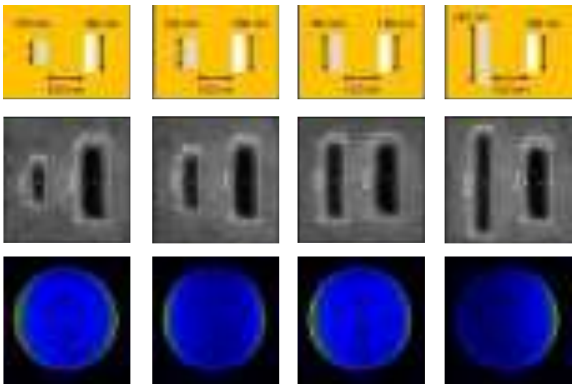


Figure 2: Far-field patterns obtained in samples with the fixed D of 120 nm and various groove lengths.

Using the above structure with L of 240 nm and D of 120 nm, we controlled the direction of emission from colloidal quantum dot light emitting diodes (CQD-LEDs) [8,9]. On the electrode of LEDs, we have fabricated an optical slot Yagi-Uda antenna made of a slot and a groove as shown in Fig. 3(a). The LEDs have operated well in supplying voltage and showed electroluminescence as shown in Fig 3(b). When only a slot was fabricated on the electrode of LEDs, we could have obtained bidirectional far-field pattern shown in Fig. 3(c). On the contrary, when a slot and a groove, which is an optical slot Yagi-Uda antenna, were fabricated, directional far-field pattern could be measured as like Fig. 3(d).

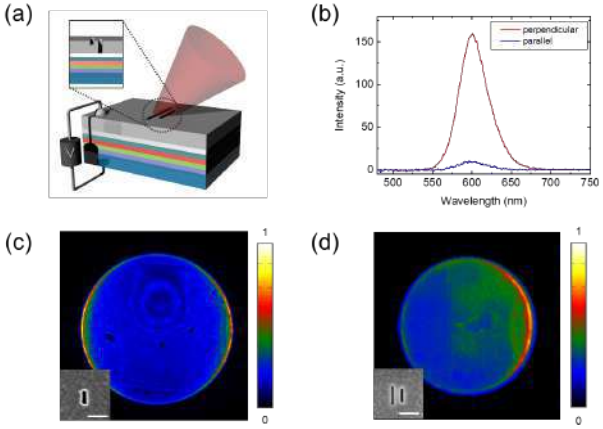


Figure 3: (a) Schematics of LEDs with a slot antenna fabricated on the electrode of LEDs. (b) Measured electroluminescence from LEDs. (c) Bidirectional far-field pattern obtained in LEDs with a slot antenna. (d) Directional far-field pattern obtained in LEDs with an optical slot Yagi-Uda antenna.

4. Conclusions

In conclusion, we presented the design of an optical slot Yagi-Uda antenna and that our design is well-coincident with experimental results by measuring far-field patterns with various samples. Additionally, we showed that random light sources can be well-coupled with optical slot Yagi-Uda antennas and its direction can be controlled. We expect that an optical slot Yagi-Uda antenna will be a promising device in the application of 3D display panel, holography, and nanoscale integrated photonic chips for the future.

References

[1] P. Mühlschlegel, H.-J. Eisler, O. J. F. Martin, B. Hecht, D. W. Pohl, Resonant optical antennas. *Science* 308:1607-1609, 2005.

[2] L. Novotny, N. van Hulst, Antennas for light. *Nat. Photon.* 5:83-90, 2011.

[3] A. G. Curto *et al*. Unidirectional emission of a quantum dot coupled to a nanoantenna. *Science* 329:930-933, 2010.

[4] T. Kosako, Y. Kadoya, H. F. Hofmann, Directional control of light by a nano-optical Yagi-Uda antenna. *Nat. Photon.* 4:312-315, 2010.

[5] J. Kim *et al*. Babinet-inverted optical Yagi–Uda antenna for unidirectional radiation to Free Space. *Nano Letters* 14:3072-3078, 2014.

[6] J. Kim *et al.* Directional radiation of Babinet-inverted optical nanoantenna integrated with plasmonic waveguide. *Scientific Reports* 5:11832, 2015

[7] J. Dorfmuller *et al.* Plasmonic nanowire antennas: experiment, simulation, and theory. *Nano Letters* 10:3596-3603, 2010.

[8] K.-S. Cho *et al.* High-performance crosslinked colloidal quantum-dot light-emitting diodes. *Nat. Photon.* 3:341-345, 2009.

[9] Y. Park *et al.* Metasurface electrode light emitting diodes with planar light control, *Scientific Reports*, 7:14753, 2017

Flexible metasurfaces in the visible range for imaging and biophotonic applications

Andrea Di Falco

School of Physics and Astronomy, University of St Andrews, North Haugh, St Andrews, KY16 9SS UK
E-mail: adf10@st-andrews.ac.uk

Abstract

We present our recent results on biophotonic applications of flexible photonic metasurfaces in the visible range, including sensing and imaging in microfluidic environments.

1. Introduction

Flexible metasurfaces retain all the potentials of standard metasurfaces while introducing a variety of unique practical features respect to their rigid counterparts [1-4]. For example their fabrication can be scaled up using techniques typical of printed electronic, like roll to roll manufacturing; they can be conformed to target with irregular shapes [5,6], thus relieving the fabrication requirement and/or to transfer a complex photonic response to otherwise dull materials or objects; they can be easily tuned post-fabrication in different ways, thus offering an additional degree of freedom to design advanced photonic behaviors.

Here, after briefly reviewing a possible fabrication pathway, we present our recent results on holographic imaging and sensing applications, and discuss the potential of flexible metasurface for microfluidic based biophotonic applications.

2. Fabrication

Fig. 1 a)-d) shows the typical fabrication procedure for the flexible metasurface [1]. a) A polymer of choice (blue layer) is spun on rigid carrier precoated with a sacrificial lift off layer (red layer). The specific polymer can be chosen to control the thickness of the membranes (typical values go from few tens of nanometers to a few microns) and other physical parameters, like the elasticity or the bio-compatibility. A representative example is SU8, a commercially available (Microchem) epoxy based negative resist. In this case the sacrificial layer is also commercially available. In step b) the shape of the membrane is defined lithographically. The form factor is arbitrary and the total area can go from a few square microns to several square cm. Step c) is the definition of meta-atoms, which can be completed using e-beam lithography of metallic or dielectric materials, either with a lift-off or etch-back technique (see also panel e), which shows a scanning electron microscope picture of a typical sample. Step d) is the definition of handles for the all-optical manipulation of the defined metasurfaces in microfluidic environments. It is an optional feature, which can be completed e.g. using the same polymer used for the membrane, with an additional lithographic step. Panel f) shows a completed membrane released in a microfluidic chip. The individual square

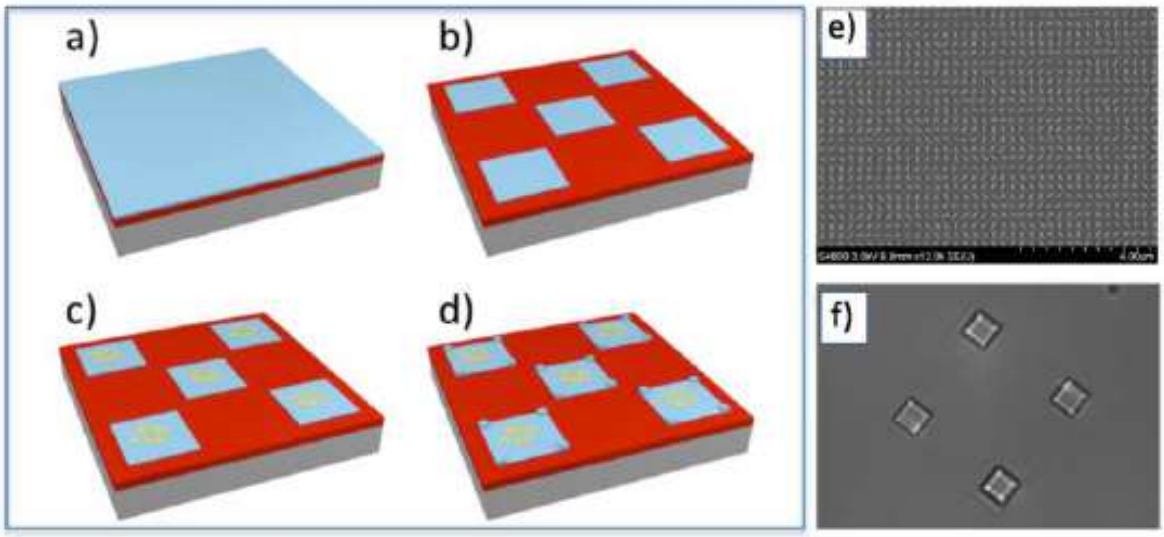


Figure 1 Fabrication protocol: a) the membrane polymer is spun on a sacrificial layer (red); b) the individual membranes are defined; c) the metallic meta-atoms are defined; d) if required, polymeric handles are added, before lift off. e) Example of meta-atoms patterned on flexible metasurfaces. f) Microscope image of a metasrufaces in a microfluidic chip.

handles have side equal to 1μm.

3. Results and Discussion

Following the body of work available in literature in holographic metasurfaces, we designed conformable flexible holographic MSs, using a common three layers configuration [7]. Here we show that the shape of the substrate can be considered as an independent degree of freedom to encode the image information, so that an intelligible image can be obtained only if the substrate has a specific, predesigned topology [8].

As second example, we show that flexible metasurfaces can be used as efficient sensors for Surface Enhanced Raman Scattering (SERS). The key advantage of this approach is that a microscopic solid target of interest can be coated with a conformable SERS substrate, rather than resting unevenly on a rigid and flat surface. Here we discuss how this approach can be used for SERS imaging of extended objects.

Finally, we discuss how flexible holographic metasurfaces and SERS enabled metasurfaces can be scaled to convenient sizes and used in a microfluidic environment, where they can be optically manipulated to interact with specimens of interest. In this context, we will discuss the optomechanical properties of the trapped membranes.
This approach has the unique advantage of bringing the full potential and versatility of metasurfaces in terms of light control at the interface with cell and single molecules biology.

4. Conclusions

In this communication we will show our recent achievement in the fields of photonic metasurfaces and discussed critically our preliminary results in their suitability for biophotonic applications.

Acknowledgements

We acknowledge support from EPSRC (EP/M000869/1 and EP/L017008/1). This project has received funding from the European Research Council (ERC) under the European Unions Horizon 2020 research and innovation programme (grant agreement No. 819346).

References

1. A. Di Falco, M. Ploschner, and T. F. Krauss, Flexible metamaterials at visible wavelengths, *New J. Phys.* 12: 113006, 2010.
2. A. Di Falco, Y. Zhao, and A. Alú, Optical metasurfaces with robust angular response on flexible substrates, *Appl. Phys. Lett.* 99: 163110, 2011.
3. P. Reader-Harris, P. and A. Di Falco, Nanoplasmonic Filters for Hollow Core Photonic Crystal Fibers, *ACS Photonics* 1: 985-989, 2014.
4. S. Song, X. Ma, M. Pu, X. Li, K. Liu, P. Gao, Z. Zhao, Y. Wang, C. Wang, X. Luo, Actively tunable structural color rendering with tensile substrate, *Advanced Optical Materials* 5: 1600829 (2017).
5. J. Burch, D. Wen, X. Chen, and A. Di Falco, Conformable Holographic Metasurfaces. *Sci. Rep.* 7: 501–7 (2017).
6. S. M. Kamali, A. Arbabi, E. Arbabi, Y. Horie, A. Faraon, Decoupling optical function and geometrical form using conformal flexible dielectric metasurfaces, *Nature Comm.* 7: 11618 (2016).
7. G. Zheng, H. Mühlenbernd, M. Kenney, G. Li, T. Zentgraf, S. Zhang, Metasurface holograms reaching 80% efficiency, *Nat. Nanotechnol.* 10: 308−312, 2015.
8. J. Burch and A. Di Falco, Surface Topology Specific Metasurface Holograms, *ACS Photonics* 5: 1762–1766 (2018).

Heterogeneous Integrated Nanomaterials for Attojoule Optoelectronics and Neuromorphic Information Processing

Jonathan K. George[1], Mario Miscuglio[1], Rubab Amin[1], Zhizhen Ma[1], and Volker J. Sorger[1,*]

[1] Department of Electrical and Computer Engineering, The George Washington University, 800 22nd St NW, Washington, DC 20052, USA

*corresponding author, E-mail: sorger@gwu.edu

Abstract

Photonic technologies are at the forefront of the ongoing 4th industrial revolution of digitalization supporting applications such as virtual reality, autonomous vehicles, and electronic warfare. The development of integrated photonics in recent years enabled functional devices and circuits through miniaturization. However, fundamental challenges such as the weak light-matter integration have limited silicon and III-V-based devices to millimeter-scale footprints demanding about a million photons-per-bit. Overcoming these challenges, in the first part of this talk we will show how nanoscale photonics together with heterogeneous integration of emerging materials into foundry-based photonic chips leads to the exciting topic of attojoule optoelectronics.

Here we will discuss our recent devices (**Fig. 1**) demonstrating 100aJ/bit modulators [1], graphene photodetectors [2], and exotic epsilon-near-zero modes [3] empowering record-efficient phase shifters [4] for applications in data-communication, LiDAR, and photonic neural networks (NN) [5,6].

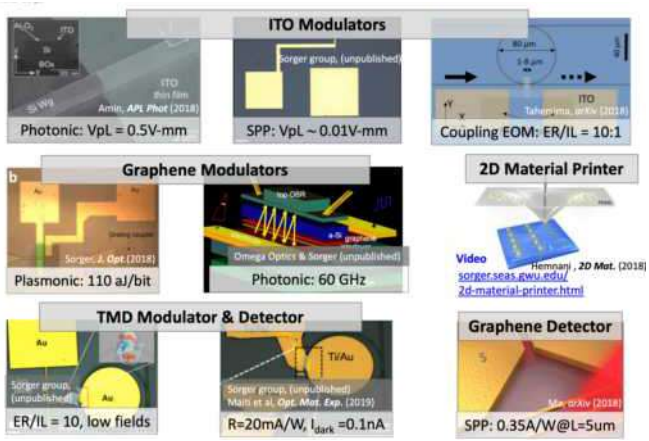


Figure 1. *Overview of recent opto-electronics devices by the Sorger group towards achieving attojoule-per-bit efficiency. All devices use heterogeneous integration of emerging materials into silicon photonics.*

We further show that underlying mathematical function of a multiply-accumulate (MAC) of NN's can be realized photonically; here the nonlinear activation function (threshold) can be achieved through electro-optic modulators [7]. We will discuss power efficiencies and scaling laws of photonic NN's and show that just 10aC (or 60 electronic carriers) are required if a MAC/J efficiency of 10^18 is to be achieved (i.e. the goal of the NSF/SRC E2CDA program) [8] (**Fig. 2**).

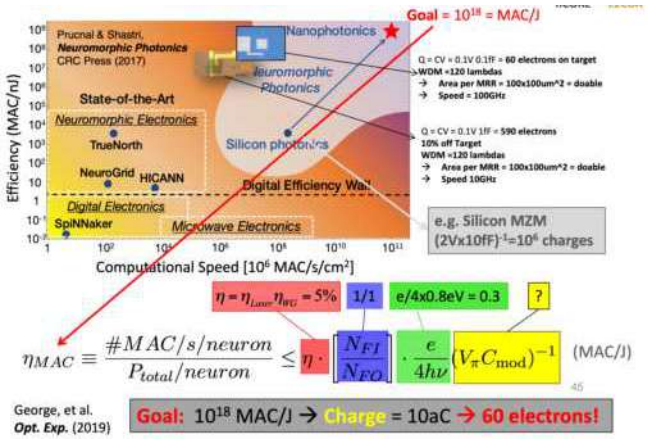


Figure 2. *Overview of recent opto-electronics devices by the Sorger group towards achieving attojoule-per-bit efficiency. All devices use heterogeneous integration of emerging materials into silicon photonics.*

With Moore's law and Dennard scaling now being limited by fundamental physics, optical information processing has reemerged for special-purpose compute systems such as NNs or RF-signal & image filtering. Here unique opportunities exist, for example, given by signal parallelism (e.g. multiplexing) or avoidance of capacitive wire loading, thus opening prospects for distributed non-van Neumann architectures.

In the second part of this talk, we will share our latest examples of photonic chip-based processors to include a) a feed-forward fully-connected NN [6] (**Fig. 3**), b) a convolutional NN processor where convolutions are expressed as multiplications in the Fourier domain (4f) enabling 1 PMAC/s throughputs at nanosecond-short delays for real-time processing with applications in automated target recognition and ranging, c) mirror symmetry perception via coincidence detection of spiking neurons using the leaky-integrate-and-fire protocol [9], and an all-optical photonic neural network [10].

While the former uses silicon and III-V photonics to realize a two-dimensional mapping of photonic connectivity of neurons, the 4f system is a three-dimensional realization of photonic neurons. Using this system, we show demonstrations in edge-detection. Using the system recurrently, however, one can perform convolutional filtering such as image classification through DeepLearning.

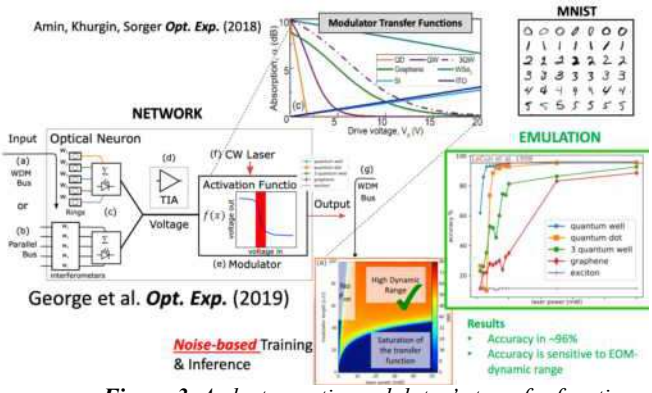


Figure 3. *A electro-optic modulator's transfer function can be used to provide nonlinear activation (thresholding) in photonic neurons (here perceptron model). Training a 2-layer NN with 100 nodes each including noise (shot noise from the photodetector), we find a decent accuracy of 96% in inference for the MNIST data set of handwritten digits* [7].

In summary, integrated (nano)photonics connects the worlds of electronics and optics, thus enabling new classes of a) attojoule optoelectronics, and b) neuromorphic circuits by employing the distinctive properties of light for parallel processing and order $O(1)$ operations.

References

1. V. J. Sorger, R. Amin, J. B. Khurgin, Z. Ma, S. Khan, "Scaling Vectors for Atto-Joule per Bit Modulators" ***Journal Optics***, 20, 014012 (2018).
2. Z. Ma, K. Kikunage, H. Wang, S. Sun, R. Amin, M. Tahersima, M. Miscuglio, H. Dalir, V. J. Sorger, "Compact Graphene Plasmonic Slot Photodetector on Silicon-on-insulator with High Responsivity", ***arXiv***, 1812:00894 (2018).
3. Y. Gui, M. Miscuglio, Z. Ma, M. T. Tahersima, S. Sun, R. Amin, H. Dalir, and V. J. Sorger, "Towards integrated metatronics: a holistic approach on precise optical and electrical properties of Indium Tin Oxide," ***arXiv***:1811.08344 (2018).
4. R. Amin, R. Maiti, C. Carfano, Z. Ma, M.H. Tahersima, Y. Lilach, D. Ratnayake, H. Dalir, V.J. Sorger, "0.52 V-mm ITO-based Mach-Zehnder Modulator in Silicon Photonics" ***APL Photonics***, 3,12 (2018).
5. Y. Shen, N. C. Harris, S. Skirlo, M. Prabhu, T. Baehr-Jones, M. Hochberg, X. Sun, S. Zhao, H. Larochelle, D. Englund, and M. Soljačić, "Deep learning with coherent nanophotonic circuits," ***Nature Photonics*** **11**, 441–446 (2017).
6. A. N. Tait, T. F. de Lima, E. Zhou, A. X. Wu, M. A. Nahmias, B. J. Shastri, and P. R. Prucnal, "Neuromorphic photonic networks using silicon photonic weight banks," ***Scientific Reports*** **7**, 7430 (2017).
7. J. K. George, A. Mehrabian, R. Armin, J. Meng, T. Ferreira De Lima, A. N. Tait, B. Shastri, P. Prucnal, T. El-Ghazawi, V. J. Sorger, "Noise and Nonlinearity of Electro-optic Activation Functions in Neuromorphic Compute Systems" ***Optics Express*** 27, 4 (2019).
8. V.S. is supported by the National Science Foundation (1740262) and Semiconductor Research Corporation (SRC) (nCORE, E2CDA).
9. J. K. George, C. Soci, V. J. Sorger, "Identifying Mirror Symmetry with Delay in Spiking Neural Networks" ***arXiv***: 1709.02684 (2017).
10. M. Miscuglio, A. Mehrabian, Z. Hu, S.I. Azzam, J.K. George, A.V. Kildishev, M. Pelton, V.J. Sorger, "All-optical Nonlinear Activation Function for Photonic Neural Networks" ***Optical Material Express*** 8(12), 3851-3863 (2018).

Minimal Designs of Lorentz Non-reciprocal Metasurfaces and "Diatomic" Resonator Arrays

Wenyan Wang, Wang Tat Yau, K. F. Lee, Jin Wang, and Kin Hung Fung*

Department of Applied Physics, The Hong Kong Polytechnic University, Hong Kong, China
*corresponding author, E-mail: kin-hung.fung@polyu.edu.hk

Abstract

Compared to reciprocal systems, the designs of Lorentz non-reciprocal metasurfaces and metamaterials require extra complexity associated with many broken symmetries. We provide minimal designs of Lorentz non-reciprocal metasurface and arrays made of simple dimer unit cells. We find that a coupled dipole-monopole theory (with 2x2 matrix) is enough for describing the one-way metasurface.

1. Introduction

Unconventional phenomena could emerge in metamaterials using the internal structural properties of the artificial unit cells. Recently, designs of complex structures made of Lorentz non-reciprocal materials have introduced many new directions to create unusual photonic devices such as isolators, one-way waveguides, and non-reciprocal antennas. Analytical modeling of these complex systems is not trivial and many designs such as topological photonic crystals are bulky. We aim at reducing the thicknesses and sizes of the non-reciprocal metasurfaces and devices while maintaining the simplicity of the structures.

2. Methodology

We use coupled dipole-monopole theory to design a "diatomic" metamolecules consisting of two cylinders with at least one of the cylinders made of gyromagnetic/gyroelectric materials. The functional performance of the metasurface design is also verified numerically using the commercial software COMSOL. Finally, we have used an effective medium theory to describe the metasurface design.

The analytical results are based on coupled dipole-monopole theory, which expands the fields of each cylinders using multiple expansion up to dipoles. The coupled dipole-monopole equations are written as a 2x2 matrix equation in the form as shown below:

$$\left[\begin{pmatrix} -b_{YIG}^{-1} & 0 \\ 0 & -b_{di}^{0} \end{pmatrix}^{-1} - \begin{pmatrix} L_0 & \xi_1 \\ \xi_1 & L_0 \end{pmatrix}\right]\begin{pmatrix} a_{YIG}^{-1} \\ a_{di}^{0} \end{pmatrix} = \begin{pmatrix} a^{-1} \\ a^{0} \end{pmatrix}, \quad (1)$$

where a rotating magnetic dipole (m = -1) is coupled to a monopole (m = 0) through long-range dynamic coupling.

3. Results

The schematic of our design is shown in Figure 1(a). The associated numerical and analytical results for the difference in transmittance ($\Delta T = T_1 - T_2$) between forward and backward incident waves are shown in Fig. 1(b). Simulated field patterns at one of the peak-dip pair is shown in Fig. 1(c).

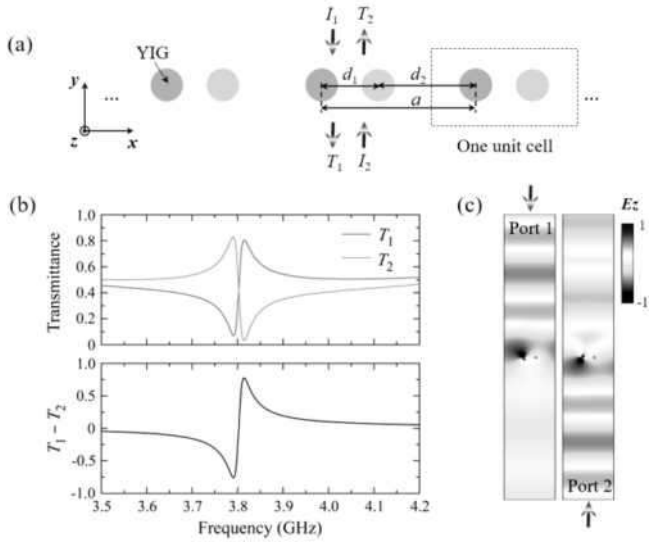


Figure 1: (a) Schematic of Lorentz non-reciprocal "diatomic" metasurface. (b) Transmission difference between forward and backward incident waves. (c) Simulation field patterns for the same case as in (b).

4. Conclusions

We provide a minimal dimer design of Lorentz non-reciprocal metasurface. Such a simple design supports strong asymmetric transmission properties when the incident wave direction is reversed. The results also show an anomalous anti-resonance-like feature in transmittance,

which is associated with Fano resonance effect. Our 2x2 matrix model accurately predicts such an interesting feature.

Acknowledgements

The authors would like to acknowledge the funding support from the Hong Kong Research Grant Council thought the General Research Fund (15301917) and the Area of Excellence Scheme (AoE/P-02/12).

Optical Pump – Terahertz Probe Spectroscopy of Semiconductor Nanostructures

Hynek Němec* **and Petr Kužel**

Institute of Physics, Czech Academy of Sciences, Czech Republic
*corresponding author, E-mail: nemec@fzu.cz

Abstract

Charge transport in semiconductor nanostructures can be studied in non-contact way and with sub-picosecond time resolution using optical pump – terahertz probe spectroscopy. Interpretation of the measurements requires a careful description of photonic effects governing the propagation of the optical excitation beam, modelling of the terahertz conductivity of confined charges and consideration of the depolarization field effects. All these issues will be addressed in this paper.

1. Introduction

High-frequency conductivity carries information about the charge transport at short distances. In particular, terahertz frequencies (10^{11} – 10^{13} Hz) probe the transport on nanometer length scales, while they are insensitive to defects acting on the transport on longer distances. Further benefits of the time-resolved terahertz spectroscopy are the non-contact nature of measurements and the sub-picosecond time resolution.

We will examine in detail the processes which have a fundamental impact on the interaction of the probing terahertz radiation with a nanostructure:

- Absorption of the excitation beam generates an initial inhomogeneous distribution of charge carrier density.
- Terahertz radiation inside nanoparticles is screened by depolarization fields induced due to the inherent heterogeneity of investigated structures.
- Charge confinement strongly influences the conduction response function of charges in individual nanoparticles.

Accounting for all these effects permits determination of the mechanism and parameters of the charge transport in the nanoparticles. Such information is important e.g. for the development of photo-voltaic or opto-electronic devices based on semiconductor nanoparticles.

2. Theory

2.1. Propagation of the optical excitation beam

For nanoparticle sizes much smaller than the excitation wavelength, the nanostructured sample can be regarded as an effective medium. The typically small contrast of optical permittivities of nanoparticles and surrounding environment ensures that common effective-medium models like Maxwell-Garnett or Bruggeman are good approximations for effective absorption.

If the nanoparticle size becomes comparable with the wavelength, photonic effects including wave-guiding and interferences become important (Fig. 1). For example, the effective absorption may be resonantly enhanced in an array of regular nanowires (see the peak at 750 nm in Fig. 1*c*) [1].

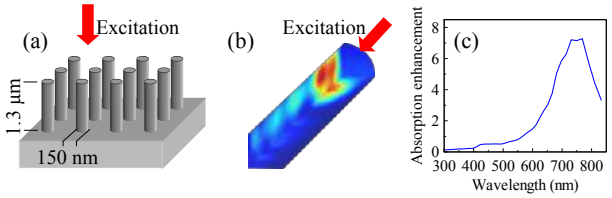


Figure 1: (a) Array of InP nanowires. (b) Distribution of the initial carrier density (=absorbed optical energy) inside a single nanowire upon excitation at 610 nm. (c) Enhancement factor of the effective absorption $\alpha_{eff}/(s\cdot\alpha_{InP})$ (effective absorption α_{eff} compared to the intrinsic absorption α_{InP} of bulk InP taking into account the filling factor s of InP in the nanostructure).

2.2. Depolarization fields

The macroscopic (measured) response is determined by the conductive response of components as well as by their morphology and spatial distribution. In a vast majority of structures, the effective photo-conductivity $\Delta\sigma$ simplifies to

$$\Delta\sigma = V\Delta\sigma_{loc} + \frac{B\Delta\sigma_{loc}}{1 + iD\Delta\sigma_{loc}/(\omega\varepsilon_0)}, \qquad (1)$$

where $\Delta\sigma_{loc}$ is the microscopic photo-conductivity of the nanostructure (response to the local field), and V, B, and D are constants determined by the morphology of the nanostructure [2]. In percolated structures, $B \ll V$, therefore the macroscopic (effective) conductivity is simply proportional to the microscopic one. However, in non-percolated structures, V is equal to 0 and the B-term dominates. In particular, a plasmonic resonance appears at frequencies where the denominator in (1) is small. Variation of $\Delta\sigma_{loc}$ by changing the excitation density allows a clear

distinguishing between percolated and non-percolated structures.

2.3. Terahertz response of confined charges

For semi-classical systems, the mobility of charges can be efficiently calculated using the Kubo formula

$$\mu(f) = \text{Fourier transform of}\left[\frac{1}{k_B T}\langle v(t)v(0)\rangle\right], \qquad (2)$$

where the velocity autocorrelation $\langle v(t)v(0)\rangle$ is obtained using Monte-Carlo simulations [3]. The spectra of confined non-degenerate electron gas exhibit a broad resonance (Fig. 2). Its peak frequency follows the reciprocal round-trip time in the nanoparticle $v_{\text{therm}}/(2d)$, where d is the size of the nanoparticles and $v_{\text{therm}} = \sqrt{3k_B T/m}$ is the mean thermal velocity.

A quantum-mechanical formalism is needed for smaller nanoparticles and/or low temperatures where discrete energy transitions are no longer smeared by thermal fluctuations or by scattering (as e.g. for the 32 nm-size nanoparticles in Fig. 2). Although conceptually based on Kubo-Greenwood formula, quantum mechanical calculations in relaxation time approximation have to consider the restoring diffusion current of scattered charges, which emerges as a consequence of broken translational symmetry [4].

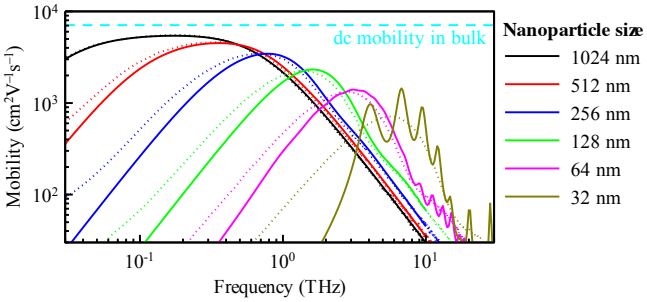


Figure 2: Comparison of quantum-mechanical calculations (solid lines, [4]) and semi-classical Monte-Carlo calculations (dotted lines, [3]) for GaAs nanocubes with various sizes at room temperature. These calculations match perfectly for the micron-sized nanocubes. Discrete quantum transitions become prominent for nanoparticle sizes below 64 nm.

3. Discussion

In Fig. 3 we show an example of transient conductivity spectra of an array of InP nanowires (in a geometry as in Fig. 1) prepared by metal organic vapor phase epitaxy (diameter of 150 nm, length of 1.3 μm). The imaginary part of conductivity is negative and its magnitude dominates over the real part: this indicates a strong influence of carrier confinement, far from the Drude response of free charges. The conductivity saturates with increasing excitation fluence according to Eq. (1), thus confirming the non-percolated nature of the structure.

When combining all the processes discussed in Section 2, we are left with just two adjustable parameters: carrier scattering time τ_s, and quantum yield of generated charges ξ. A global fit of all the data in Fig. 3 yields $\tau_s \geq 150$ fs (mobility exceeding 3000 $\text{cm}^2\text{V}^{-1}\text{s}^{-1}$), and $\xi = 65\%$. The former value shows an excellent quality of the nanowires (the mobility is close to the bulk value of 5400 $\text{cm}^2\text{V}^{-1}\text{s}^{-1}$), while the yield indicates that a significant part of the excitation photons generates immobile (trapped) carriers.

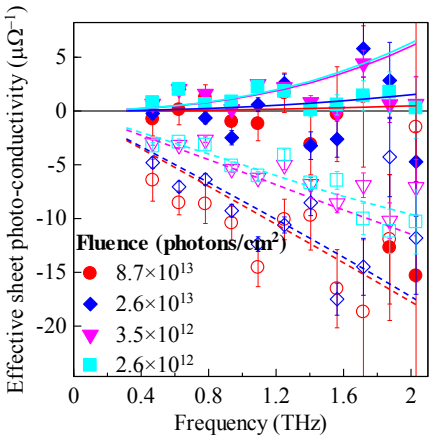


Figure 3: Transient effective sheet conductivity of an array of InP nanowires photo-excited at 610 nm. Symbols: measurements, lines: calculations. Closed symbols/solid lines: real part, open symbols/dashed lines: imaginary part (after [1]).

4. Conclusions

Time-resolved terahertz spectroscopy allows non-contact measurement of conductivity with sub-picosecond time resolution. A careful description of processes governing the interaction of the terahertz beam with the photo-excited nanostructure made it possible to determine the charge transport mechanism and its parameters.

Acknowledgements

Czech Science Foundation (project 17-03662S)
Operational Program Research, Development and Education financed by European Structural and Investment Funds and the Czech Ministry of Education, Youth and Sports (SOLID21—CZ.02.1.01/0.0/0.0/16_019/0000760).

References

[1] C. S. Ponseca, Jr., H. Němec, J. Wallentin, N. Anttu, J. P. Beech, A. Iqbal, M. Borgström, M.-E. Pistol, L. Samuelson, and A. Yartsev, Phys. Rev. B **90**, 085405 (2014).

[2] H. Němec, V. Zajac, I. Rychetský, D. Fattakhova-Rohlfing, B. Mandlmeier, T. Bein, Z. Mics, and P. Kužel, IEEE T. THz. Science Technol. **3**, 302 (2013).

[3] H. Němec, P. Kužel, and V. Sundström, Phys. Rev. B **79**, 115309 (2009).

[4] T. Ostatnický, V. Pushkarev, H. Němec, and P. Kužel, Phys. Rev. B **97**, 085426 (2018).

Mid IR Dirac-cone dispersion relation materialized in SOI photonic crystal slabs

Yuanzhao Yao[1], Naoki Ikeda[2], Takashi Kuroda[1], Takaaki Mano[1], Hiromi Koyama[1], Yoshimasa Sugimoto[2], Kazuaki Sakoda1

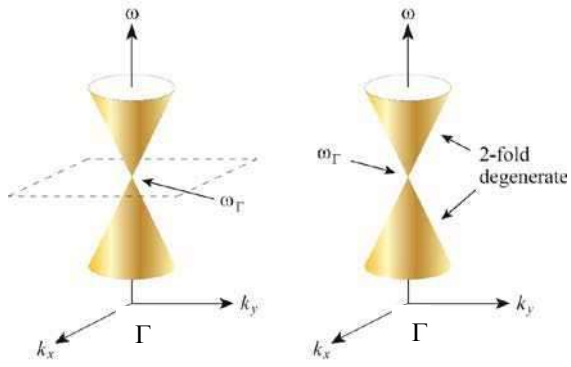
[1] Research Center for Functional Materials, National Institute for Materials Science, Tsukuba, Japan
[2] Research Network and Facility Services Division, National Institute for Materials Science, Tsukuba, Japan
*corresponding author, E-mail: sakoda.kazuaki@nims.go.jp

Abstract

We materialized the isotropic Dirac-cone dispersion relation in the mid infrared range by electron beam lithography of SOI (silicon-on-insulator) wafers. The dispersion relation was examined by the angle-resolved reflection spectra, which showed a good agreement with numerical calculation and the selection rule derived from the symmetry of Dirac-cone modes.

1. Introduction

The linear dispersion relation on the Γ point of the first Brillouin zone in periodic structures was first materialized in microwave frequencies [1-3], which is known as the CRLH (composite right/left handed) transmission line. Later, the theory was extended to more general cases and higher dimensions by the tight-binding approximation [4,5] and the k-p perturbation theory [6,7]. For highly symmetric periodic structures, we can materialize the isotropic linear dispersion, which is called Dirac cone (Fig. 1). Because the Dirac cone dispersion relation is purely a consequence of the accidental degeneracy of two eigenmodes with certain combinations of their spatial symmetries, we can expect the formation of the Dirac cone dispersion in other wave systems like phonons [6] and electrons [8] as well. Because the effective refractive index is vanishing at the Dirac point frequency, ω_Γ (See Fig. 1), we can expect curious phenomena and their applications like tunneling through sharp bends and cloaking [9].



Dirac cone Double Dirac cone

Fig. 1 Isotropic linear dispersion relation on the Γ point of the first Brillouin zone materialized by the accidental degeneracy of two eigenmodes with certain combinations of spatial symmetries. Left: Dirac cone with a quadratic dispersion surface (dotted line). Right: Doubly degenerate Dirac cone.

When the constituent eigenmodes of the Dirac cone have a finite lifetime due to diffraction loss, etc., the linear dispersion is distorted and the group velocity calculated from the slope of the dispersion curve exceeds the speed of light [10,11]. The amount of the distortion is governed by the quality factor of the Dirac-cone mode. To check and examine the linearity of the Dirac cone dispersion relation, we fabricated photonic crystal (PhC) slabs in the mid infrared range by electron beam lithography of SOI wafers. In this presentation, we report on their design, fabrication, characterization, selection rule for angle-resolved reflection, and dispersion relation.

2. Sample fabrication

We fabricated PhC slabs in SOI wafers with a 400 nm-thick top Si layer. Figure 2 shows their photo and SEM images. The PhC slabs consisted of a square array of circular air cylinders with a typical depth of 210 nm. The radius of the air cylinder ranged from 440 to 620 nm. The lattice constant of the PhC was 2.27 μm. These structural parameters were designed by the calculation of the dispersion relation by the finite element method with the perfectly-matched-layer (PML) absorbing boundary condition.

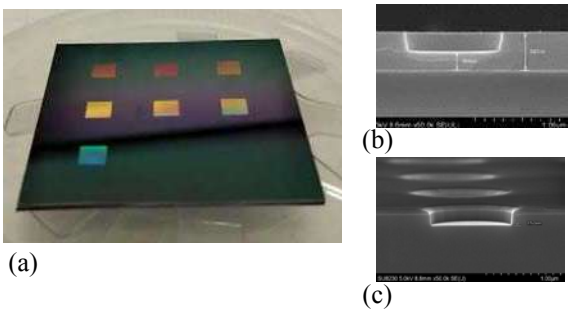


Fig. 2 (a) Photo and (b), (c) SEM images of PhC slabs fabricated in the SOI wafer.

3. Angle-resolved reflection

We examined the dispersion relation by measuring the angle-resolved reflection spectra of the specimens. To obtain a sufficiently high angle resolution, we fabricated a home-made optical system in the sample chamber of a commercial FT-IR spectrometer (Fig. 3). The optical system materialized a non-focused and polarized incident beam onto the specimen at small incident angles. The angle resolution was estimated at 0.3 deg.

Figure 4 shows the spectra measured for a specimen whose dispersion was closest to the Dirac cone dispersion, which have several peculiar features. (1) Two linear dispersions due to the Dirac cone cross each other around 2630 cm^{-1}. (2) In addition to the Dirac cone, there is a flat band (quadratic dispersion surface) as predicted by the k-p perturbation theory. (3) All modes including a nearby A_1-symmetric mode show their own selection rules with respect to the tilt direction and polarization of the incident beam. In addition, A_1-symmetric mode is inactive to an incident beam from the normal direction, so that its reflection peak disappears at an incident angle of 0 deg. These features also agree well with the dispersion relation calculated by the finite element method, which is shown in Fig. 5.

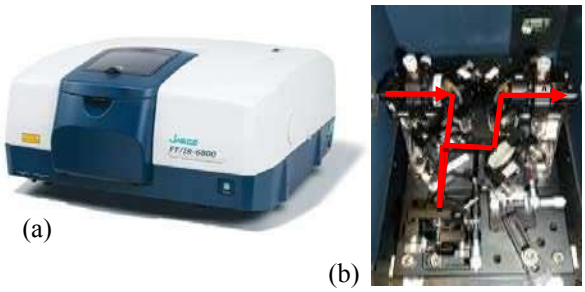


Fig. 3 (a) IR Spectrometer (JASCO FT/IR-6800) and (b) the home-made optics fabricated in the sample chamber.

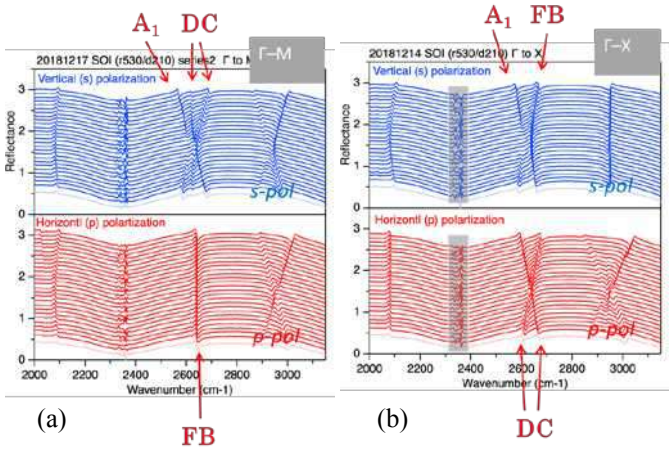


Fig. 4 Angle-resolved reflection spectra for an incident beam tilted to (a) the Γ-to M direction and (b) the Γ-to X direction. The upper and lower panels are for the s and p polarizations, respectively. DC, FB, and A_1 denote the reflection peaks of the Dirac cone, the flat band, and an A_1-symmetric mode. The spectra were measured for the incident angle of -1 to 1 deg.

4. Conclusions

We successfully fabricated PhC slabs by electron beam lithography of SOI wafers that materialized the Dirac cone dispersion relation in the mid infrared range, which was confirmed by the angle-resolved reflection spectra measured by the home-made optics that attained a high angle resolution of 0.3 deg. The observed spectra agreed quite well with the dispersion relation calculated by the finite element method and the selection rules due to the spatial symmetry of eigenmodes. The Dirac cone dispersion thus materialized may find applications such as cloaking and beam shaping.

Acknowledgements

This work was supported by Innovative Science and Technology Initiative for Security, ATLA, Japan.

References

[1] A. Sanada, C. Caloz, T. Itoh, IEEE Microw. Wireless Compon. Lett. **14**, 68 (2004).

[2] C. Caloz, A. Sanada, T. Itoh, IEEE Trans. Microw. Theory Tech. **52**, 980 (2004).

[3] A. Sanada, C. Caloz, T. Itoh, IEEE Trans. Microw. Theory Tech. **52**, 1252 (2004).

[4] K. Sakoda, H. Zhou, Opt. Express **18**, 27371 (2010).

[5] K. Sakoda, Opt. Express **20**, 3898 (2012); ibid. **20**, 9925 (2012).

[6] J. Mei et al., Phys. Rev. B **86**, 035141 (2012).

[7] K. Sakoda, Opt. Express **20**, 25181 (2012).

[8] Y. Yao, K. Sakoda, J. Phys. Soc. Jpn. **85**, 065002 (2016).

[9] X. Huang et al., Nature Mater. **10**, 582 (2011).

[10] K. Sakoda, H. Takeda, 10th Int. Symp. Modern Opt. Appl., 68 (2015).

[11] B. Zhen et al., Nature **525**, 354 (2015).

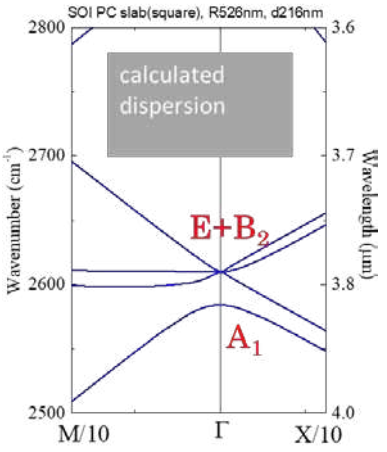


Fig. 5 The dispersion relation of the PhC slab specimen calculated by the finite element method with the PML absorbing boundary condition. M/10 denotes that the horizontal axis is magnified by 10 times.

Subwavelength polarization optics using helical travelling-wave nanoantennas

Mengia Wang[1], Roland Salut[2], Huihui Lu[2], Miguel Angel Suarez[1], Nicolas Martin[1], and Thierry Grosjean[1]

[1]FEMTO-ST Institute, UMR 6174 CNRS - University Bourgogne Franche-Comte, Besancon, France
[2]Guangdong Provincial Key Laboratory of Optical Fiber Sensing and Communications, Department of Optoelectronic Engineering, Jinan University, Guangzhou 510632, China
*Corresponding author, E-mail: thierry.grosjean@univ-fcomte.fr

Abstract

We present and demonstrate the concept of a helical travelling-wave nanoantenna (HTN) consisting of a tiny gold-coated helix end-fired with a rectangular aperture nanoantenna. The resulting non-resonant nano-antenna produces a background-free directional light beam of tunable polarization and intensity by swirling surface plasmons and taking advantage of optical spin-orbit interaction. Taken as individual or coupled nanostructures, HTNs lead to subwavelength polarization optics which provide new degrees of freedom in light polarization control.

1. Introduction

A wide variety of optical applications and techniques demand control of light polarization. Manipulation of light polarization has recently experienced extraordinary advances with the emergence of plasmonics, leading to the concepts of polarization meta-optics [1-4]. However, all the structures developed so far rely on collective optical effects on arrays of nanostructures. They are therefore restricted to areas much larger than the wavelength of light, which limits design strategies in polarization control. Tailoring light with individual subwavelength devices would overcome limits but it remains a challenge [5,6].

On the basis of spin-orbit interaction of light [7], we have generated a helical travelling-wave nanoantenna to produce directional light beam of tunable polarization through a swirling plasmonic effect. Our optical nanoantenna differs from existing helical plasmonic structures [1,8] by its non-resonant nature, thus extending the concept of helical travelling-wave antenna to optics [9]. Four closely packed HTNs are shown to locally convert an incoming light beam into four beams of tunable polarizations and intensities. Moreover, by coupling HTNs of opposite handedness, we demonstrated a subwavelength waveplate-like structure providing a degree of freedom in polarization control that is forbidden with usual polarization optics and metamaterials.

2. Results and discussion

The HTN consists of a narrow gold-coated wire wound up in a screw-like shape forming a tiny helix (Fig. 1a). The gold-coated wire sustains a cutoff-free axially symmetric surface plasmon (SP), known as the TM_0 mode. It is locally excited with the dipolar mode of a rectangular aperture nanoantenna that perforates a 100 nm thick gold layer right at the helix pedestal. An incident wave on the back of the aperture is transmitted as a subdiffraction guided SP, which is non-radiatively converted into the wire mode of the helix. The nanoscale wire mode is non-resonantly converted into the helix-guided mode spreading over the overall structure cross-section and propagating along the helix axis. In the course of propagation, the helix-guided mode acquires OAM oriented along the helix axis (0z).

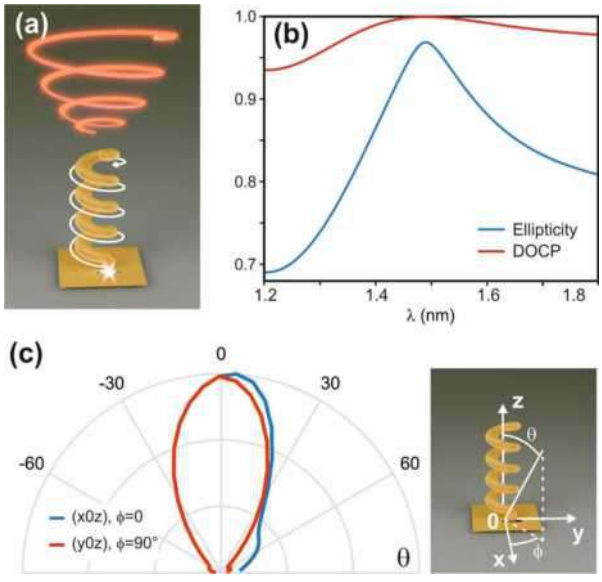


Figure 1: (a) Schematics of the HTN and its operation principle. (b) Spectra of the ellipticity factor and DOCP of the HTN output beam. They reveal the tunable polarization properties of the nanoantenna. (c) Radiation pattern of the HTN in the polar angle θ measured in two orthogonal

longitudinal planes (x0z) and (y0z) defined in the figure inset.

When circular polarization is generated by a HTN, a vortex guided mode (of charge ±1 depending on the helix handedness) is released as freely propagating waves carrying SAM of ±1 per photon (in ħ units). A HTN designed to operate as a circular polarizer at λ=1.5 µm has been predicted to radiate light with a polarization ellipticity and a degree of circular polarization peaking at 0.97 and 0.999, respectively (Fig. 1b). The polarization can be tuned either by tuning the operation wavelength or by modifying the geometrical parameters of the helix. The waveguiding properties of the plasmonic helix allows for producing directional beam: our nanoantenna of λ/3 lateral size produces an emission pattern whose full width at half-maximum approaches 55° (Fig. 1(c)).

The antennas were fabricated by combining focused-ion-beam-induced deposition, metal coating and focused ion beam milling. Fig. 2(a) shows a scanning electron micrograph of a resulting structure. The HTNs were back-illuminated with polarized light from a tunable laser at telecommunication wavelengths, the nanoantenna output beams were measured and their polarization states were analysed with a rotating linear polarizer. The observed polarization properties (Fig. 2b) agree well with the theoretical model, with an ellipticity factor peaking at 0.97.

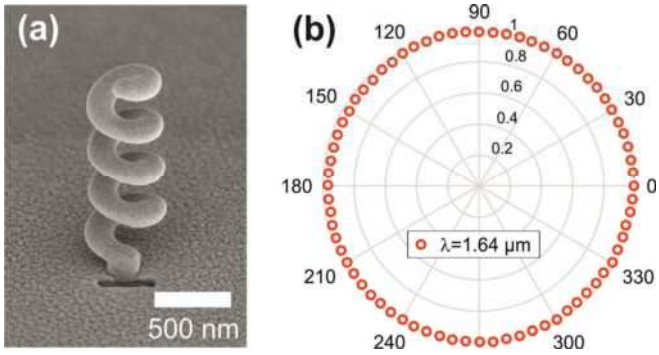


Figure 2: (a) Scanning electron micrograph of a fabricated HTN. (b) Experimental polarization diagram of the HTN at λ = 1.64 µm.

First, we showed that HTNs arranged at will on a surface locally convert an incoming light beam into an arbitrary distribution of directional beams of tunable polarizations and intensities. Different polarization states are here imparted to the output beams in a controllable and tunable way. Second, by near-field coupling four HTNs of opposite handedness, we obtained a subwavelength waveplate-like structure providing a degree of freedom in polarization control that is forbidden with ordinary polarization optics and current metamaterials (i.e., devices utilizing or artificially reproducing birefringence and dichroism).

3. Conclusions

Relying on spin-orbit interaction of light, HTNs lead to ultracompact, versatile and robust individual components for manipulating light polarization on the subwavelength scale. They provide functionalities in light polarization control that have never previously been demonstrated. Taken as individual or coupled nanostructures, such nanoantennas may pave the way towards highly integrated polarization-encoded optics, particularly for the generation and control of spin-encoded photon qubits in quantum information and opto-spintronics. More generally, our results lay a solid basis for subwavelength polarization optics, thus opening new perspectives in photonic information processing, polarimetry, miniaturized displays, optomagnetic data storage, microscopy, sensing and communications, etc.

Acknowledgements

This work is supported by the Labex ACTION program (contract ANR-11-LABX-01-01), the EIPHI Graduate School (contract ANR-17-EURE-0002), the Region "`Bourgogne Franche-Comte"', the French Agency of Research (contract ANR-18-CE42-0016), and by the French RENATECH network and its FEMTO-ST technological facility.

References

[1] Gansel, J. K. et al. Gold helix photonic metamaterial as broadband circular polarizer. Science **235**, 1513 (2009).

[2] Yu, N. et al. A broadband, background-free quarter-wave plate based on plasmonic metasurfaces. Nano Lett. **12**, 6328 (2012).

[3] Zhao, Y., Belkin, M. and Alù, A. Twisted optical metamaterials for planarized ultrathin broadband circular polarizers. Nat. Commun. **3**, 870 (2012).

[4] Ding, F., Wang, Z., He, S., Shalaev, V. M. and Kildishev, A. V. Broadband high-efficiency half-wave plate: a supercell-based plasmonic metasurface approach. ACS Nano **9**, 4111 (2015).

[5] Eismann, J. S., Neugebauer, M. and Banzer, P. Exciting a chiral dipole moment in an achiral nanostructure. Optica **5**, 954 (2018).

[6] O'connor, D., Ginzburg, 275 P., Rodrıguez-Fortuno, F., Wurtz, G. and Zayats, A. Spin–orbit coupling in surface plasmon scattering by nanostructures. Nat. Commun. **5**, 5327 (2014).

[7] Bliokh, K., Rodriguez-Fortuno, F., Nori, F. and Zayats, A. Spin-orbit interactions of light. Nat. Photon. **9**, 796 (2015).

[8] Schäferling, M., Yin, X., Engheta, N. and Giessen, H. Helical plasmonic nanostructures as prototypical chiral near-field sources. ACS Photon. **1**, 530 (2014).

[9] Kraus, J. D., Marhefka, R. J. and Khan, A. S. Antennas and wave propagation (Tata McGraw-Hill Education, 2006).

Plasmonic mode conversion and second harmonic imaging of tilted plasmonic nanocones

Christoph Dreser[1,2], Dominik A. Gollmer[1,2], Godofredo Bautista[3], Xiaorun Zang[3], Dieter P. Kern[1,2], Martti Kauranen[3], and Monika Fleischer[1,2]

[1]Institute for Applied Physics, Eberhard Karls University of Tübingen, Germany
[2]Center for Light-Matter Interaction, Sensors and Analytics LISA+, Eberhard Karls University of Tübingen, Germany
[3]Laboratory of Photonics, Tampere University, P.O. Box 692, FI-33014 Tampere, Finland
*corresponding author, E-mail: monika.fleischer@uni-tuebingen.de

Abstract

Plasmonic nanocones offer strong, highly localized near-fields at the cone apex that can be utilized for applications in microscopy and sensing. However, the tip mode can only be excited by electric field components parallel to the cone axis. To enable the excitation of the tip mode under vertical illumination, tilted cones are fabricated. Their linear optical properties are investigated and simulated, and their nonlinear optical properties are illustrated by second harmonic imaging.

1. Introduction

Near-field enhancement and confinement of the electric field of electromagnetic waves are promising features in plasmonics and nano-photonics. Therefore specially designed optical antennas are needed, which have broad applications, for example in surface-enhanced Raman spectroscopy or single molecule detection [1,2]. Nanocones are well-suited for such applications as they can easily be fabricated and have a very sharp tip with a radius smaller than 10 nm [3]. For an efficient plasmon excitation along the vertical axis the electric field vector of the exciting external electromagnetic wave should have a significant component parallel to the vertical axis [4]. This is only the case for certain laser modes or the illumination of the cones from the side. Therefore the excitation of many cone tips at once under vertical incidence is not possible. If the electric field is oriented perpendicular to the cone axis, no excitation of the tip will take place [3]. But for many potential applications it would be beneficial if the electric field of the light was enhanced at the tips of many cones simultaneously.
It was recently shown that this difficulty can be circum-vented by breaking the symmetry of the nanocone. In one case, wing protrusions were added on one side of the cone bases, leading to a conversion of the in-plane excitation of plasmons in the winged base to an excitation of tip plasmons through the asymmetric geometry [5]. This approach was further pursued through the investigation of randomly distributed tilted nanopillars, whose axes were forming defined angles with the substrate plane [6,7].

2. Discussion

In the present work we introduce two strategies for the fabrication of gold nanocones with a pre-defined tilt of the cone axis [8]. In the first process, circular oxide nanodiscs are prepared as hard masks on top of a gold film by electron beam lithography and a lift-off. The masks are subsequently transferred into the gold layer by argon ion milling, where the substrate is tilted relative to the ion beam by the amount of the tilting angle. In the second process, electron beam lithography is performed under an angle, such that the resulting nanoholes in the resist are tilted relative to the substrate. Afterwards, metal is evaporated under the same tilting angle, leading to tilted nanocones remaining on the surface after the lift-off. Examples of a symmetric vertical vs. an asymmetric tilted nanocone are shown in Figure 1.

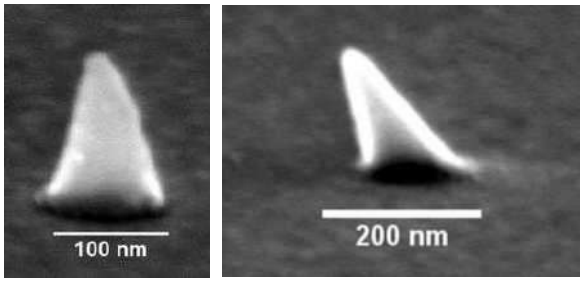


Figure 1: (left) vertical gold nanocone, tilting angle 0°; (right) tilted gold nanocone.

The asymmetric geometry supports the transformation of a transversal (parallel to the substrate) electric far-field to a longitudinal (perpendicular to the substrate) plasmonic excitation. Extinction spectra obtained by transmission spectroscopy and corresponding simulations will be shown, in which cones with a variety of tilting angles are illuminated under a variety of illumination angles, thus systematically changing the ratio of the electric field components oriented parallel vs. perpendicular to the respective cone axes. Furthermore second harmonic generation microscopy of tilted cones will be shown. The cones are scanned through tightly focused radially or

azimuthally polarized cylindrical vector beams (CVBs), and for each relative position between the cone and focus center the second harmonic intensity generated by the interaction is recorded. The expected simulated results are shown in Figure 2 and will be discussed in comparison with the corresponding experiments [8].

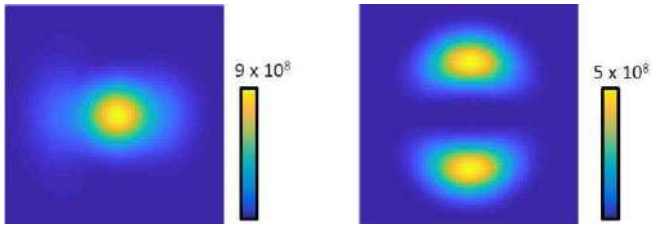


Figure 2: Simulated second harmonic imaging patterns of (left) a tilted nanocone scanned through the focus of a radially polarized CVB, and (right) a tilted nanocone scanned through the focus of an azimuthally polarized CVB.

3. Conclusions

Two processes for the nanofabrication of tilted gold nanocones with defined tip displacements are presented. Under vertical illumination, plasmon resonances are excited in the base plane of the nanocones, as is also observed for symmetrical nanocones. In contrast to symmetrical cones, the symmetry breaking leads to a conversion of the base mode into a tip mode, such that an enhanced near-field can be observed at the tip apex even under vertical illumination. These findings are confirmed by the nonlinear optical properties observed in second harmonic imaging of the nanocones gained by scanning through radially and azimuthally polarized focused cylindrical vector beams.

Acknowledgements

Financial support by the European Cooperation in Science and Technology through COST Action MP1302 Nanospectroscopy (STSM), the Landesgraduierten-förderung Baden-Württemberg, and the Academy of Finland (287651 and Flagship of Photonics Research and Innovation) is gratefully acknowledged.

References

[1] A. M. Kern, D. Zhang, M. Brecht, A. I. Chizhik, A. V. Failla, F. Wackenhut, A. J. Meixner, Chemical Society Reviews 43, 1263-1286 (2014).

[2] D. Nie, S. R. Emory, Science 275, 1102-1106 (1997).

[3] M. Fleischer, C. Stanciu, F. Stade, J. Stadler, K. Braun, A. Heeren, M. Häffner, D. P. Kern, A. J. Meixner, Applied Physics Letters 93, 111114-111114 (2008).

[4] C. Schäfer, D. A. Gollmer, A. Horrer, J. Fulmes, A. Weber-Bargioni, S. Cabrini, P. J. Schuck, D. P. Kern, M. Fleischer, Nanoscale 5, 7861-7866 (2013).

[5] M. J. Huttunen, K. Lindfors, D. Andriano, J. Mäkitalo, G. Bautista, M. Lippitz and M. Kauranen, Optics Letters, 2014, 39, 3686-3689.

[6] R. Verre, M. Svedendahl, N. O. Länk, Z. J. Yang, G. Zengin, T. J. Antosiewicz and M. Käll, Nano Letters, 2015, 16, 98-104.

[7] K.-Y. Yang, R. Verre, J. Butet, C. Yan, T. J. Antosiewicz, M. Kall and O. J. F. Martin, Nano Letters, 2017, 17, 5258-5263.

[8] C. Dreser, D. A. Gollmer, G. Bautista, X. Zang, D. P. Kern, M. Kauranen, M. Fleischer, accepted for publication in Nanoscale (2019).

Bismuth-based Metasurfaces for Nanophotonics from the Ultraviolet to the Far Infrared

Johann Toudert[1], and Rosalía Serna[1]

[1]Laser Processing Group, Instituto de Óptica, IO-CSIC, Madrid, Spain
*corresponding authors, E-mails: johann.toudert@gmail.com; rosalia.serna@csic.es

Abstract

Bi-based nanostructures show outstanding optical properties making them ideal building blocks for the fabrication of metasurfaces with tunable response over a broad spectral region, from the ultraviolet to the far infrared. We will report the design, fabrication, and relevant optical properties of Bi-based metasurfaces. We will show how their optical absorption, reflection and phase can be tuned using planar optical cavity designs. The impact of the proposed optical structures for applications in several areas of nanophotonics will be discussed.

1. Introduction

Bismuth-based nanostructures (consisting of bismuth, Bi, or one of its chalcogenides, $Bi_{1-x}Sb_xTe$, $Bi_{1-x}Sb_xSe$ or $Bi_{1-x}Sb_xTe_{1-y}Se_y$) are promising candidates for applications in nanophotonics in a broad range from the ultraviolet to the far infrared.[1-4] The peculiar electronic structure of Bi and its chalcogenides is characterized by giant near-infrared optical transitions that make their dielectric permittivity values turn negative in the ultraviolet-visible, and their refractive index values turn giant in the mid-to-far infrared.[1] These remarkable features make Bi-based nanostructures prone to display epsilon-near-zero and interband plasmonic properties in the ultraviolet-visible range,[2,3] and to enable a markedly-subwavelength dielectric confinement in the mid-to-far infrared range.[1,4] This opens the way to a broad range of applications in areas such as photocatalysis, color generation, optical data encryption, switchable plasmonics and photonics, thermal photonics.

Getting the best from Bi-based nanostructures for such applications will undoubtedly require using them as the building blocks of metasurfaces in which their individual responses will be coupled or hybridized to enable enhanced optical effects. In this presentation, we will report the design, fabrication, and optical response of different types of Bi-based metasurfaces showing tunable optical properties (absorption, reflection, phase) in the ultraviolet-visible and mid-to-far infrared and discuss their potential for nanophotonic applications.

2. Results

2.1. Optical properties of Bi and its chalcogenides: bulk and nanostructures

Only very recently the bulk optical properties of Bi and its chalcogenides have been characterized accurately.[2,4] Bi presents a negative dielectric permittivity ($\varepsilon_1 < 0$) in the ultraviolet-visible, with an epsilon-near-zero response in the ultraviolet, and a giant refractive index ($n \sim 10$) and small extinction coefficient ($k \sim 1$) from the mid to the far infrared.[4] The optical properties of Bi chalcogenides, while sharing common features with those of pure Bi, can be additionally tailored by compositional tuning.[2] In this work we will discuss the role of electronic and optical confinement on the optical properties of nanostructures of Bi and its chalcogenides.

2.2. Bi-based metasurfaces for ultraviolet-visible nanophotonics

Two approaches to achieve Bi-based metasurfaces with tunable optical properties in the ultraviolet-visible will be considered. First, we will focus on metasurface designs combining the interband plasmonic resonances of 3d-confined Bi nanostructures (such as nanospheres or nanospheroids) with the photonic modes of a planar optical cavity. Such hybridization enables tuning in a flexible way the optical absorption in the nanostructures, and to achieve optical darkness and phase singularities.[5] Second, we will consider metasurface designs where an ultrathin Bi film is integrated into a planar optical cavity and evaluate their optical absorption properties.[6]

2.3. Bi-based metasurfaces for mid-to-far infrared nanophotonics

We will show how to achieve resonant perfect absorption in Bi-based metasurfaces, at a wavelength tunable in the whole mid-to-far infrared from 3 μm to 20 μm. Perfect absorption can be targeted by harnessing the lossy Mie dielectric resonances of 3d-confined Bi nanostructures, or by integrating a very thin Bi film into a planar optical cavity. We will focus on this second approach, and demonstrate the perfect absorption of infrared light in a sub - λ/100 Bi nanofilm. The absorption wavelength is tunable by simply

varying film thicknesses. The remarkable simplicity, tunability and compactness of the proposed perfect absorber design is enabled by an extraordinary fractal optical interference mechanism that operates thanks to the already mentioned giant infrared refractive index and small extinction coefficient of Bi.[7]

3. Discussion

Bismuth-based metasurfaces in view of their outstanding optical properties are suitable for a wide range of nanophotonic applications. In particular:

- The tunable ultraviolet-visible optical absorption and small thickness of Bi-based metasurfaces is promising for photocatalysis and color generation. Optical darkness and phase singularities are interesting for optical data encryption.

- Achieving a tunable resonant perfect absorption of light in the mid-to-far infrared is appealing for thermal photonics.

- Bi is a phase-change material, with a significant optical contrast between its solid and liquid phase.[8] This property is appealing for applications in switchable plasmonics and photonics.

4. Conclusions

The outstanding optical properties of Bi and its chalcogenides make Bi-based nanostructures excellent building blocks for metasurfaces with tunable response over a broad spectral range from the ultraviolet to the far infrared. This tunability is enabled by optical phenomena that do not take place in standalone nanostructures but occur when the nanostructures are part of a metasurface, such as hybrid interband plasmonic-photonic modes or fractal optical interference. Such optical phenomena and the tunability they imply are relevant for applications including photocatalysis, color generation and optical data encryption, switchable plasmonics and photonics, and thermal photonics.

Acknowledgements

This work was partially funded by the Spanish Ministry for Economy and Competitiveness through the project MINECO/FEDER TEC2015-69916-C2-1-R.

References

[1] J. Toudert, R. Serna, Interband transitions in semi-metals, semiconductors and topological insulators: a new driving force for plasmonics and nanophotonics [Invited], *Opt. Mater. Express* 7, 2299, 2017.

[2] D. Piccinotti, B. Gholipour, J. Yao, K.F. MacDonald, B.E. Hayden, N.I. Zheludev, Stoichiometric engineering of chalcogenide semiconductor alloys for nanophotonic applications, *Adv. Mater.* 1807083, 2019.

[3] J. Toudert, R. Serna, M. Jiménez de Castro, Exploring the optical potential of nano-bismuth: tunable surface plasmon resonances in the near ultraviolet-to-near infrared range, *J. Phys. Chem. C* 116, 20530-20539, 2012.

[4] J. Toudert, R. Serna, I. Camps, J. Wojcik, P. Mascher, E. Rebollar, T.A. Ezquerra, Unveiling the far infrared-to-ultraviolet optical properties of bismuth for applications in plasmonics and nanophotonics, *J. Phys. Chem. C* 121, 3511-3521, 2017.

[5] G. Baraldi, M. García Pardo, J. Gonzalo, R. Serna, J. Toudert, Self-assembled nanostructured photonic-plasmonic metasurfaces for high-resolution optical thermometry, *Adv. Mater. Interfaces* 5, 1800241, 2018.

[6] A. Ghobadi, H. Hajian, B. Butun, E. Ozbay, Strong light-matter interaction in lithography-free planar metamaterial perfect absorbers, *ACS Photonics* 5, 4203-4221, 2018.

[7] J. Toudert, R. Serna, M. García Pardo, N. Ramos, R.J. Peláez, B. Maté, Mid-to-far infrared tunable perfect absorption by a sub-λ/100 nanofilm in a fractal phasor resonant cavity, *Opt. Express* 26, 34043, 2018.

[8] M. Jiménez de Castro, F. Cabello, J. Toudert, R. Serna, E. Haro-Poniatowski, *Appl. Phys. Lett.* 105, 113102, 2015.

Recovering molecular orientation using single molecule SERS in plasmonic nano-gaps

Jean-Sebastien Bouillard*[1,5], Addison Marshall[1], Francesco Viscomi[1], John Proctor[1,2], Matthew Roberts[3], Johannes Gierschner[4], Ali Adawi*[1,5]

[1]Department of Physics and Mathematics, University of Hull, Cottingham Road, Hull, HU6 7RX, UK
[2]Materials and Physics Research Group, School of Computing, Science and Engineering, University of Salford, Manchester M5 4WT, UK
[3]Cambridge Display Technology Limited, Company number 02672530, Unit 12, Cardinal Park, Cardinal Way, Godmanchester, PE29 2XG, UK
[4]Madrid Institute for Advanced Studies - IMDEA Nanoscience, Calle Faraday 9, Ciudad Universitaria de Can-toblanco, 28049 Madrid, Spain
[5]Nano[3] Research grouping, G. W. Gray Centre for Advanced Materials, University of Hull, Cottingham Road, Hull, HU6 7RX, UK
*corresponding authors, E-mail: j.bouillard@hull.ac.uk and a.adawi@hull.ac.uk

Abstract

Determining the molecular orientation at the single molecule level is of key importance for a wide range of applications ranging from molecular electronic devices to biomedical applications. In a first instance, plasmonic nano-gaps formed between a spherical nanoparticles and a metallic film were optimized for single molecule Surface Enhanced Raman Scattering (SERS) spectroscopy. Finite Difference Time Domain (FDTD) simulations were performed to complement the experimental measurements, highlighting the complex interplay between the excitation enhancement and the emission enhancement of the system as a function of particle size.

Using the optimized geometry, single molecule SERS was performed on both a small molecule, rhodamine 6G and single chains of the PF-based conjugated co-polymer, F8-PFB. The anisotropy of the field enhancement in the nano-gap was used in conjunction with Density Functional Theory (DFT) to recover the orientation of the single molecule of each analyte, rhodamine 6G and F8-PFB, within the plasmonic nano-gap.

1. Introduction

Plasmonic technology, referring to the study of specific surface electromagnetic waves resulting from the coupling of photons and collective electron oscillations in metals, has seen a rapidly increasing interest over the past two decades. Combining key advantages directly linked to their nature, such as high field confinement, strong field enhancement, with polarisation and spectral selectivity, plasmonic systems promise many applications encompassing bio- and chemical sensing, signal manipulation and guiding on subwavelength

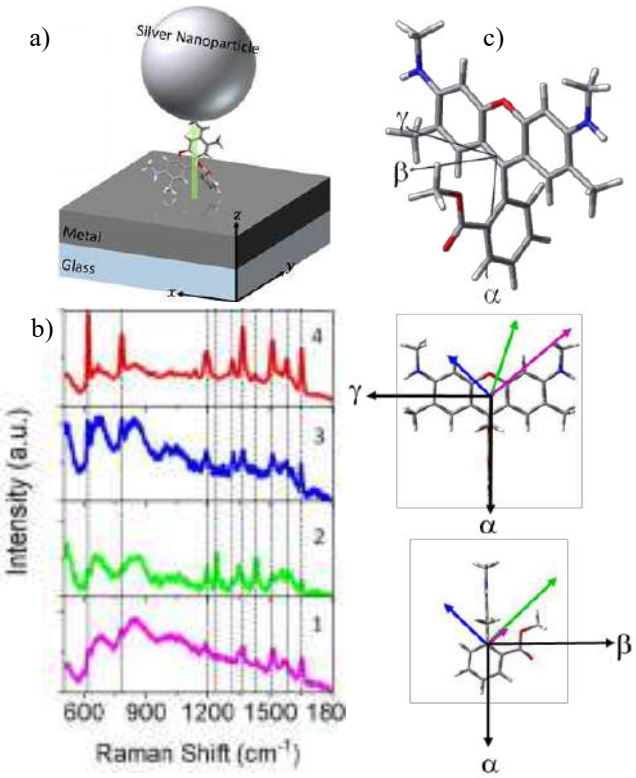


Figure 1: Recovering the molecular orientation in plasmonic nano-gaps. a) Schematics of sample geometry. b) Single molecule SERS spectra showing different peaks with different enhancements. c) 3D molecular structure and orientation of single molecule inside nano-gap [1]

scales, and extend to include photonic devices with enhanced performances, such as photodetectors, solar cells and light emitting diodes.

By bringing metallic nanostructures in close proximity to one another it is possible to generate highly confined regions of electromagnetic field arising from the hybridization of plasmon modes. The so-called nanoparticle on a mirror (NPoM) geometry, formed between a nanoparticle and a metallic film, allows for the simple fabrication of plasmonic nano-gaps giving rise to strong field enhancement and confinement that can be used to enhance light matter interactions. Here we present the use of NPoM systems for single molecule SERS, allowing to recover the molecular orientation.

2. Experimental procedure

Plasmonic nano-gaps were fabricated by coupling an extended silver film with spherical silver nanoparticles with a dielectric spacer containing the analyte molecules. A 100 nm thick silver film was thermally evaporated on top of a glass substrate. In the case of rhodamine 6G, a 5 nm spacer layer was spin coated from a 1 mg mL^{-1} solution of a Zeonex polymer matrix in chloroform doped with the molecular dye rhodamine 6G in concentrations ranging from 5×10^{-5} M to 2×10^{-7} M.

For the chain of F8:PFB, the polymer itself (M_w = 355 kDa and 0.95:0.05 F8:PFB) was dissolved in toluene at concentrations ranging between 2.8×10^{-5} M to 2.8×10^{-10} M ([2] and [3]) and deposited via spin coating was spin coated at different concentrations onto the silver film. The conjugated polymer F8-PFB.

3. Discussion

The effect of near-field enhancement and photon scattering efficiency to the far-field on the SERS signal have been investigated theoretically and experimentally as a function of the plasmonic particle size. Concentration dependent SERS measurements highlight the single molecule sensitivity of the optimized nano-gap geometry.

Using the optimized geometry, single molecule SERS is performed on both a small molecule, rhodamine 6G [1] and a single chain of the PF-based conjugated co-polymer, F8-PFB. It was observed that, in the single molecule regime, the same molecular species yielded different SERS spectra from nano-gap to nano-gap. This is linked to the well-defined field enhancement direction in the nano-gaps which preferentially enhances the Raman modes with a tensor component along the field enhancement. In the case of many molecules, this anisotropy is usually averaged out by the random orientation of each molecule. However, in the case of a single molecule, the anisotropy results in a different enhancement of the various Raman modes, leading to a SERS spectrum which is dependent on the molecular orientation.

Using this anisotropy of the field enhancement in the nano-gap, in conjunction with a DFT analysis of the Rama tensor for each Raman mode, it is possible to recover the orientation of the single molecule within the plasmonic nano-gap.

Conclusion

In this work we demonstrated the capability of the simple nanoparticle on a mirror nano-gap geometry to reach single molecule SERS levels. By correlating the single molecule SERS spectra, which reflect the single molecule orientation with respect to the anisotropic field enhancement within plasmonic nano-gaps, with the Raman mode tensors calculated by DFT, we were able to recover the orientation of single molecule inside the nano-gap. We showed this approach to work on both small molecules (rhodamine 6G) and longer polymer chains (F8-PFB). By correlating with Density Functional Theory (DFT) calculations, it was used to determine the orientation of the molecule.

References

[1] A. R. L. Marshall, J. Stokes, F. N. Viscomi, J. E. Proctor, J. Gierschner, J.-S. G. Bouillard, A. M. Adawi, "Determining Molecular Orientation via Single Molecule SERS in a Plasmonic Nano-gap", *Nanoscale* **9**, 44, pp. 17415-17421 (2017)

[2] G. E. Khalil, A. M. Adawi, A. M. Fox, A. Iraqi, D. G. Lidzey, "Single Molecule Spectroscopy of Red- and Green-Emitting Fluorene-Based Copolymers", *J. Chem. Phys.* **130B,** 4, pp. 2–9 (2009)

[3] K. Kneipp, Y. Wang, H. Kneipp, L. T. Perelman, I. Itzkan, R. R. Dasari, M. S. Feld, "Single Molecule Detection Using Surface-Enhanced Raman Scattering (SERS)", *Phys. Rev. Lett.* **78**, 9, pp. 1667–1670 (1997)

Water-processable cellulose-based sacrificial layers for advanced nanofabrication

Camilla Dore[1], Juan Luis García Pomar[1], Johann Osmond[2], Agustin Mihi[1]*

[1]Institut de Ciència de Materials de Barcelona (ICMAB-CSIC), Campus de la UAB, 08193 Bellaterra, Catalonia, Spain
[2]ICFO-The Institute of Photonic Sciences, Av. Carl Friedrich Gauss, 3, 08860 Castelldefels, Barcelona
*corresponding author, E-mail: amihi@icmab.es

Abstract

Cellulose is the most abundant polymer on Earth and for centuries has had a wide technological impact in areas such as textile, packaging or knowledge storage. It is low cost and biodegradable, and possesses excellent mechanical characteristics that have raised the interest of many engineering fields. The versatility of cellulose has recently opened new venues [1] in advanced materials in electronics, energy and biomedical applications. In this work, we combine hydroxypropyl cellulose (HPC), a water soluble and biodegradable cellulose derivate, with nanoimprinting lithography (NIL), the most promising method for mass-produced inexpensive nanostructures over large areas and with a very low density of defects.

Particularly, I will show all-green advanced nanofabrication processes, achievable when using the cellulose derivative as water soluble sacrificial layer [2].

Using HPC as NIL resist we are able to pattern silicon wafers or fabricate metallic nanoparticle arrays in a straight forward process that requires only water as solvent. Furthermore, HPC can be alternatively stacked with traditional resists such as Poly(methyl methacrylate), where one of the two materials can be selectively removed by developing in orthogonal solvents. This capability becomes even more interesting by including nanoimprinted layers in the stack, leading to the encapsulation of arrays of air features in the resist.

HPC solutions in water can be also processed in order to obtain thick free standing membranes that can be used as support layer for transfer printing of nanostructured metal electrodes. The cellulose membranes in fact serves as actual adhesive, allowing us to pick and place thin metallic film from patterned silicon substrate to active devices, obtaining simultaneously the metallic contact and the encapsulation layer.

Furthermore, if necessary, the HPC layer can be eventually dissolved in water, leaving only metallic pattern printed on a target substrate. Interestingly, by simply reiterating this process it is possible to fabricate novel 3D structures made of stacked nanopatterned metallic films that present intense plasmonic resonances and exotic optical properties.

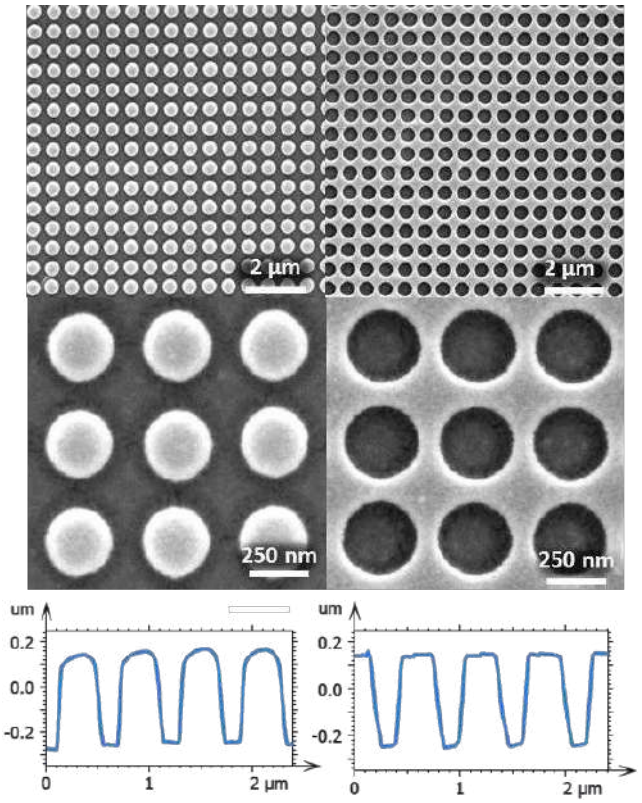


Figure 1: SEM images and AFM analysis of holes and pillar arrays with aspect ratio grater than one imprinted in HPC by soft lithography..

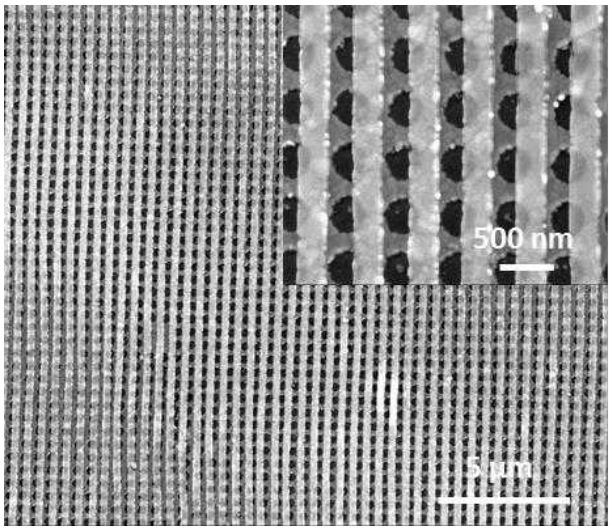


Figure 2: SEM images of multilayer patterned metal electrode obtained by transfer print technique using HPC membranes as sacrificial support.

References

[1] A. Espinha, C. Dore, C. Matricardi, M. I. Alonso, A. R. Goñi and A. Mihi, *Hydroxypropyl cellulose photonic architectures by soft nanoimprinting lithography*, Nature Photonics 12, 343–348 (2018)

[2] C. Dore, J. Osmond and A. Mihi, A water-processable cellulose-based resist for advanced nanofabrication , Nanoscale (2018)

Destabilization of polariton condensates due to acousto-optic interactions

Alexey V. Yulin[1]*, Valery K. Kozin[1,2], Anton V. Nalitov[1,2], and Ivan A. Shelykh[1,2]

[1]ITMO University, Kronverkskiy prospekt 49, Saint Petersburg 197101, Russia
[2]Science Institute, University of Iceland, Dunhagi 3, IS-107, Reykjavik, Iceland
*corresponding author, E-mail: a.v.yulin@corp.ifmo.ru

Abstract

We analyse the dynamics of the exciton-polaritons interacting with sound waves propagating in the system. The polaritons are excited by coherent optical pump. The stationary polariton states are found and their stability is examined by solving the corresponding spectral problem and by direct numerical simulations. It is found that the interaction with the acoustic waves can destabilize the polariton condensates. The nonlinear stage of the instability is studied by numerical simulations. A simple theory describing the stationary hybrid acousto-polariton states are developed.

1. Introduction

Complex many-body interactions play an important role in the dynamics of condensed matter systems. One of the very interesting phenomena intensively studied in recent years is Bose-Einstein condensation of the polaritons in semiconductor microcavities [1]. The temperature of the condensation is extraordinary high because of the very low mass and strong mutual interactions of the hybrid light-matter excitations appearing in the strong coupling regime between the excitons and phonons. It was demonstrated that the spectrum of the elementary excitation in such systems is of Bogolubov kind and thus the coherent polariton states demonstrate the effect of superfluidity [2, 3]. The coupling of the polaritons to other quasi particles makes the behaviour of the systems even more complicated. For example, the polariton-electron interaction can lead to polariton lasing [4] and to the transition to a superconducting regime [5]. Another important example is the interaction between polariton and phonons [6]. In has been reported that this interactions give rise to such phenomena as the formation of hybrid exciton-acoustopolaritons [7], polariton Bloch oscillations [8] and the condensation of the polaritons in the periodic potential produced by the standing acoustic waves [9, 10].

The present paper is devoted to the resonant interactions between the polaritons and the phonons in one-dimensional cavity excited by a laser beam. To describe the mutual dynamics of the polaritons and the acoustic waves we adopt the model reported in [7, 11] which in dimensionless units can be written in the form

$$\partial_t \Psi = \left[i\delta + \frac{i}{2}\partial_x^2 - igU - i\alpha|\Psi|^2 - \gamma \right] \Psi + Pe^{i\kappa x}, \quad (1)$$

$$\partial_t^2 U + \Gamma U - \partial_x^2 U = g\partial_x^2 |\Psi|^2. \quad (2)$$

The complex field Ψ is the order parameter function describing the polariton condensate, the real field U describes the acoustic wave, δ is the detuning of the pump from the cavity resonance, κ characterises the phase gradient of the pump, γ and Γ account for the losses in the polariton and the phonon systems, P is the amplitude of the external coherent pump, g is the parameter describing the strength of polariton-phonon interaction, α is the coefficient accounting for nonlinear polariton-polariton interaction. Let us remark that the polaritons are described under the assumption that the upper polariton branch does not contribute to the polariton dynamics and the lower polariton branch can be approximated by a parabola. We assume that the geometry is annular and thus the boundary conditions are periodic.

2. The results

It is easy to see that the system in question has a solution with zero acoustic component $U = 0$. The polariton component Ψ_0 is spatially uniform and its amplitude is defined by the amplitude of the pump. For the absolute value of Ψ_0 it is easy to obtain $|P| = \sqrt{(\delta + \alpha|\Psi_0|^2)^2 + \gamma^2}|\Psi_0|$. The polariton state can be bistable, for the repelling polariton-polariton interaction the upper branch of the bifurcation diagram is stable, the intermediate is unstable and the stability of the lower branch depends on the value of the losses in the system. Our goal is to study how the stability is affected by the interaction with phonons. To analyse the problem we will look for a solution in the form $\Psi = \Psi_0 + \psi$ where ψ is a small correction. The equations for ψ and U are then linear with the coefficients independent on the space and time. Looking for a solution in the form of plane waves we obtain the dispersion relation for the frequency ω and the wave vector of the linear excittaions

$$\left(\omega + \sqrt{k^2 - \frac{\Gamma}{4} + \frac{i\Gamma}{2}}\right)\left(\omega - \sqrt{k^2 - \frac{\Gamma}{4} + \frac{i\Gamma}{2}}\right) = \frac{(\omega - \kappa k + D + i\gamma)\,(\omega - \kappa k - D + i\gamma)}{= g^2|\Psi_0|^2 k^2 (k^2 - 2(\mu + \alpha|\Psi_0|^2)),} \quad (3)$$

where $D = \sqrt{(\mu + 3\alpha|\Psi_0|^2 - \frac{k^2}{2})(\mu + \alpha|\Psi_0|^2 - \frac{k^2}{2})}$ and $\mu = \delta - \frac{\kappa^2}{2}$.

For arbitrary set of parameters the solutions of the dispersive equation (3) can be found only numerically. However assuming that the polariton-phonon interaction constant g is small the equation can be solved by perturbation

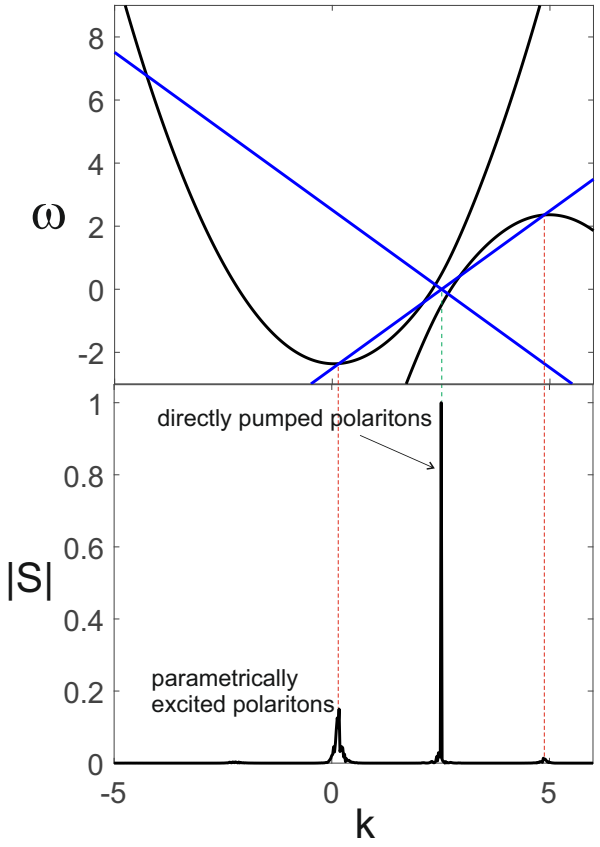


Figure 1: The graphical solution of the polariton-phonon resonance condition (a) and the spatial spectrum of the polariton filed (b) obtained from direct numerical simulations. The parametars are $P = 0.1233$, $\gamma = 0.02$, $\Gamma = 0.01$, $\alpha = -1$, $g = 0.075$, $\delta = 3.7$ and $\kappa = 2.512$

method. The interaction is the strongest in the vicinity of the resonances where the phase matching condition is met. The perturbation anaylsys show that some of the resonances lead to the splitting of the dispersion characteristics but the other resonances produce instability,

The instabilities predicted by the spectral analysis have been checked against direct numerical simulations. The comparison has shown that the analytical predictions fit the observed spectra very well, see Fig. 1. The more complex nonlinear regimes were studied by extensive numerical simulations but the lack of space does not allow to discuss them in this summary.

3. Conclusion

It was shown that the interaction between the polaritons and the phonons can results in the instability leading to the emission of the phonons and to the down conversion of the frequency of the polaritons. The process can be cascaded which causes a complex, possibly chaotic behaviour of the hybrid acousto-polariton state. A simpler quasi monochromatics mixed states can be effectively analysed by perturbation theory. The discovered effect can be used for the generation of coherent phonons (phonon laser) and possibly for multi-frequency polariton lasers.

Acknowledgement

AVY acknowledges support from the Government of the Russian Federation (Grant 074-U01) through the ITMO University early career fellowship.

References

[1] J. Kasprzak, M. Richard, S. Kundermann, A. Baas, P. Jeambrun, J.M.J. Keeling, F.M. Marchetti, M.H. Szymanska, R. Andre, J.L. Staehli, V. Savona, P.B. Littlewood, B. Deveaud, and Le Si Dang, *Nature* 443, 409, 2006.

[2] S.V. Patankar,A. Amo, D. Sanvitto, F.P. Laussy, D. Ballarini, E. del Valle, M.D. Martin, A. Lematre, J. Bloch, D.N. Krizhanovskii, M.S. Skolnick, C. Tejedor and L. Vina, *Nature*, 457, 291, 2009.

[3] A. Amo, J. Lefrere, S. Pigeon, C. Adrados, C. Ciuti, I. Carusotto, R. Houdre, E. Giacobino, A. Bramati, *Nature Physics*, 5, 805, 2009.

[4] G. Malpuech, A. Kavokin, A. Di Carlo, and J.J. Baumberg, *Phys. Rev. B*, 65, 153310, 2002.

[5] F.P. Laussy, A.V. Kavokin, and Ivan A. Shelykh, *Phys. Rev. Lett.*, 104, 106402, 2010.

[6] N.D. Lanzillotti-Kimura, A. Fainstein, A. Huynh, B. Perrin, B. Jusserand, A. Miard, and A. Lemaitre, *Phys. Rev. Lett.*, 99, 217405, 2007.

[7] D.V. Vishnevsky, D.D. Solnyshkov, G. Malpuech, N.A. Gippius, and I.A. Shelykh *Phys. Rev. B*, 84, 035312, 2011.

[8] H. Flayac, D.D. Solnyshkov, and G. Malpuech, *Phys. Rev. B*, 83, 045412, 2011.

[9] E.A. Cerda-Mendez, D.N. Krizhanovskii, M. Wouters, R. Bradley, K. Biermann, K. Guda, R. Hey, P.V. Santos, D. Sarkar, and M.S. Skolnick, *Phys. Rev. Lett.*, 105, 116402, 2010.

[10] E.A. Cerda-Mndez, D.N. Krizhanovskii, K. Biermann, R. Hey, M.S. Skolnick and P.V. Santos, *New J. Phys.*, 14, 07501, 2012.

[11] A.L. Ivanov, P.B. Littlewood *Phys. Rev. Lett.* 87, 13, 2001.

Femtosecond laser pulse modification of gold nanorods to provide identical optical response

Guillermo González-Rubio[1,2], Pablo Díaz-Núñez[3], Antonio Rivera[3*], Alejandro Prada[3], Gloria Tardajos[1], Jesús González-Izquierdo[4], Luis Bañares[1,4], Pablo Llombart[1], Luis G. Macdowell[1], Mauricio Alcolea Palafox[1], Luis M. Liz-Marzán[2,5,6*], Ovidio Peña-Rodríguez[3*], Andrés Guerrero-Martínez[1]

[1]Departamento de Química Física I, Universidad Complutense de Madrid, Avda. Complutense s/n, 28040 Madrid, Spain
[2]Bionanoplasmonics Laboratory, CICbiomaGUNE, Paseo de Miramón 182, 20014 Donostia – San Sebastián, Spain
[3]Instituto de Fusión Nuclear, Universidad Politécnica de Madrid, José Gutiérrez Abascal 2, E-28006 Madrid, Spain
[4]Centro de Láseres Ultrarápidos, Universidad Complutense de Madrid, Avda. Complutense s/n, 28040 Madrid, Spain
[5]Ciber de Bioingeniería, Biomateriales y Nanomedicina, Ciber-BBN, 20014 Donostia – San Sebastián, Spain.
[6]Ikerbasque, Basque Foundation for Science, 48013 Bilbao, Spain
*corresponding author, E-mail: antonio.rivera@upm.es

Abstract

In this presentation we show how to achieve an extreme control over the energy deposited in plasmonic systems with femtosecond laser pulses to induce predictable changes in temperature and in turn, in the morphology of gold nanoparticles. We demonstrate that there exists a laser fluence window that combined with the appropriate concentration of the organic surfactant hexadecyltrimethylammonium (CTAB) leads to a gentle multishot modification of the nanorods to a stable situation at which the nanorod aspect ratio is the same for all the nanorods. The result is an ensemble of optically identical nanorods with unprecedented properties.

1. Introduction

The interaction between electromagnetic radiation and the conduction electrons of metals leads to a collective oscillation of these electrons in resonance with the incoming radiation [1]. This effect is known as localized surface plasmon resonance (LSPR) when it is spatially confined in a metal nanostructure (or a nanocavity). The LSPR can concentrate a huge amount of electromagnetic energy in nanometric volumes, offering the maximum possible spatial and temporal control over light [2]. LSPRs decay through re-emission of a photon, creating very energetic electrons and holes (hot carrier emission) and by collisional processes that lead to plasmon decoherence and subsequent carrier thermalization [3]. Equilibration with the atomic lattice takes place by energy transfer through electron-phonon mechanisms, which in addition to balance of the hot carrier emission can lead to a dramatic temperature increase in a nanometric volume within an otherwise cold medium. This released heat is detrimental for most plasmonic devices, but recent studies indicate that it can be used to catalyze chemical reactions [4] or modify structures at the nanometer scale [5-7].

We show in this presentation that irradiation of gold nanorod colloids with a femtosecond laser can be tuned to induce controlled nanorod reshaping, yielding colloids with unprecedentedly narrow localized surface plasmon resonance bands [7]. The process relies on a regime characterized by a gentle multi-shot reduction of the aspect ratio, whereas the rod shape and volume are barely affected. Successful reshaping can only occur within a narrow heat dissipation rate window, i.e. low cooling rates lead to drastic morphological changes and fast cooling has nearly no effect. Hence, a delicate balance must be achieved between irradiation fluence and surface density of the surfactant. This perfection process is appealing because it provides a simple, fast, reproducible and scalable route toward gold nanorods with an optical response of exceptional quality, near the theoretical limit.

2. Methods

We irradiated gold nanorods (Figure 1) with the LSPR at 800 nm with 50 fs laser pulses provided by a Ti:sapphire laser. The repetition rate was 1 kHz and the laser fluence varied from 3.2 to 5.1 J/m^2. The nanorod dispersion had a concentration of 1 nM and was synthesized by the seeded growth method. The CTAB concentration was varied around the the critical micelle concentration (cmc) of CTAB (1 mM). Transmission optical measurements were carried out during the measurements thanks to an in-situ characterization set up (Figure 1).

We carried out sophisticated computational simulations to understand the results. (i) Optical simulation with a FDTD method to determine the energy absorbed per nanorod as a function of the laser fluence and nanorod orientation. (ii) Molecular dynamics (MD) ignoring the CTAB molecules and the surrounding aqueous medium. The temperature in this case was fixed to simulate the energy absorbed by the nanoparticle and the subsequent evolution to the medium was included with a Langevin term using different

characteristic decay times. The MD results helped to understand the morphological modifications of a nanoparticle. (iii) A Monte Carlo code to take into account the fact that the nanorods in dispersion are randomly oriented with the laser polarization. With the Monte Carlo we could understand the effect of the irradiation on the nanorod ensemble, as well as, its optical response.

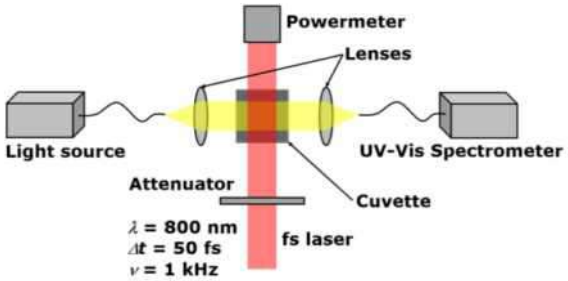


Figure 1: Schematic representation of the in-situ optical transmission setup to carry out fs-laser irradiation of the colloidal nanorod dispersion and in-situ characterization.

3. Results and discussion

Figure 2, schematically shows the effect of irradiation of a nanorod with a fs-laser pulse. The LSPR leads to a severe energy localization in the nanorod. If the fluence is high enough the temperature can exceed the melting point. Even below this point morphological changes towards a stable sphere take place. If on the other hand a gentle irradiation is carried out in (Figure 3). The fluence is low and heat dissipation is slow (time constant ~350 ps), thus, morphological changes towards the sphere occur. As the aspect ratio changes the LSPR absorption is reduced. Below certain aspect ratio, absorption does not lead to any further change. Since the modification takes place in such a gentle way, all the nanorods change their aspect ratio to the same value, resulting in a dispersion with an absorption spectrum equal to that of a single nanorod. High fluence irradiation leads to direct transformation to sphere. In addition, an important fraction of the absorbed energy can be transformed in electron emission to the surrounding medium (up to 25% in our experiments).

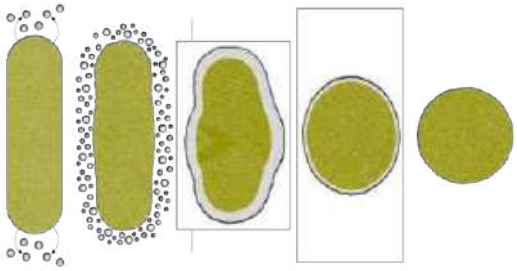


Figure 2. Schematically. Plasmon excitation by means of an intense laser pulse. The nanorod reaches thermal equilibrium and dissipates heat to the medium changing its morphology and becoming a sphere (stable shape) at high irradiation fluences. (Adapted from [7]).

4. Conclusions

It was shown how to modify in a controlled way the aspect ratio of an ensemble of nanorods in water, in such a way that all of them become optically identical. It is remarkable that laser fluences as low as 3 J/m2 lead to deposited energies of the order of 0.3 eV/atom. Around 25% of the absorbed energy is lost by hot carrier injection and the nanorod reaches temperatures near the melting point of Au. As a result, the irradiation leads to a fast heating and carrier injection into the surrounding medium.

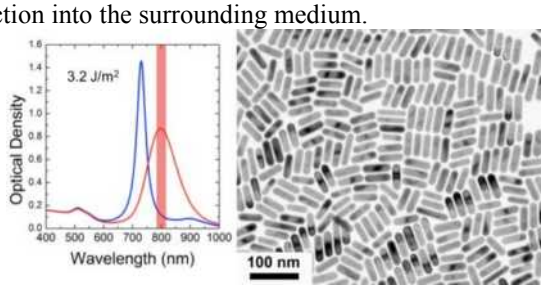


Figure 3. Optical density of a nanorod dispersion before and after fs-laser irradiation. TEM image of the irradiated nanorods showing with the same aspect ratio.

Acknowledgements

Spanish MINECO (CTQ2012-37404-C02-01, MAT2013-46101-R, MAT2014-59678-R, ENE2015-70300-C3-3-R and CTQ2015-65033-P), EUROfusion Consortium (AWP15-ENR-01/CEA-02), Madrid Regional Government (S2013/MIT-2775 and S2013/MIT-2807) and European Research Council (ERC Advanced Grant Number 267867, Plasmaquo). A.G.-M. and G.G.-R., acknowledge Ramón y Cajal and FPI Fellowships from MINECO. P. D.-N. acknowledges a Fellowship from Madrid Regional Government. Computer resources were provided by CESVIMA (Universidad Politécnica de Madrid) and facilities at Center for Ultrafast Lasers and National Center of Microscopy (Universidad Complutense de Madrid).

References

[1] Maier, S. A. *Plasmonics: Fundamentals and Applications*, 1st ed.; Springer, 2007.

[2] Schuller, J. A.; Barnard, E. S.; Cai, W.; Jun, Y. C.; White, J. S.; Brongersma, M. L. *Nat. Mater.* 2010, *9* (3), 193–204.

[3] Hartland, G. V.; Besteiro, L. V.; Johns, P.; Govorov, A. O. *ACS Energy Lett.* 2017, *2* (7), 1641–1653.

[4] Kim, M.; Lin, M.; Son, J.; Xu, H.; Nam, J.-M., *Adv. Opt. Mater.* 2017, *5* (15), 1700004.

[5] Herrmann, L. O.; Valev, V. K.; Tserkezis, C.; Barnard, J. S.; Kasera, S.; Scherman, O. A.; Aizpurua, J.; Baumberg, J. J. Threading Plasmonic *Nat. Commun.* 2014, *5*, 4568.

[6] González-Rubio, G.; González-Izquierdo, J.; Bañares, L.; Tardajos, G.; Rivera, A.; Altantzis, T.; Bals, S.; Peña-Rodríguez, O.; Guerrero-Martínez, A.; Liz-Marzan, L. M. *Nano Lett.* 2015, *15* (12), 8282–8288.

González-Rubio, G.; Díaz-Núñez, P.; Rivera, A.; Prada, A.; Tardajos, G.; González-Izquierdo, J.; Bañares, L.; Llombart, P.; Macdowell, L. G.; Palafox, M. A.; Liz-Marzán, L. M.; Peña-Rodríguez, O.; Guerrero-Martínez, *Science* 2017, *358* (6363), 640–644.

Pathways for Ultrafast All-optical Magnetic Recording in Garnets

A. Stupakiewicz

Faculty of Physics, University of Bialystok, Poland
*corresponding author, E-mail: and@uwb.edu.pl

Abstract

Nonthermal ultrafast photo-magnetic recording in iron garnet films with femtosecond laser single and multi-pulses was demonstrated. Mechanism of recording is based on a multiple resonant pumping of localized *d*-electron transitions in a garnet. The information transferred from light to spins can be encoded not only in polarization state, but also in the wavelength and the intensity of the recording beams.

1. Introduction

In the recent years finding an electronic transition a subtle excitation of which can launch dramatic changes of electric, optical or magnetic properties of media is one of the long-standing dreams in the field of photo-induced phase transitions [1,2]. Therefore the discovery of the magnetization switching only by a femtosecond laser pulse [3] triggered intense discussions about mechanisms responsible for these laser-induced changes. Research concerning phenomena such as the inverse Faraday effect and ultrafast demagnetization shows exciting possibilities of sub-picosecond optical control over spins and applications in magnetic memory devices [1,4]. In this study we focus on an Co-substituted yttrium-iron garnet (YIG:Co) with nonthermal induced photo-magnetic effect. We demonstrated in such garnet at room temperature a large angle of the magnetization precession through excitation by linearly polarized femtosecond laser pulses via the photo-induced magnetic anisotropy [5]. Recent our discovery revealed a possibility of fastest magnetic recording with a single ultrafast laser pulse in YIG:Co without relying on heat [6]. This result raised question about the optimal wavelength, the polarization and the intensity of light, for such a recording.

Here we report the pathways for spectral and polarization selectivity of ultrafast photo-magnetic recording. The all-optical magnetic recording under both single pulse and multiple-pulse sequences can be achieved at room temperature, in near-infrared spectral ranges with light polarized either along <110> or <100> crystallographic axes of the garnet. The experimental results indicate that the excitations responsible for the coupling of light to spins are *d*-electron transitions in octahedral and tetrahedral Co-sublattices, respectively.

2. Experimental details

Samples of composition $Y_2CaFe_{3.9}Co_{0.1}GeO_{12}$ were grown by liquid phase epitaxy on (001) plane-oriented paramagnetic gadolinium gallium garnet substrate [7]. Saturation magnetization at room temperature was 7 Gs and the Neel temperature was T_N=445 K. Dopant Co^{2+} and Co^{3+} ions were located in both tetrahedral and octahedral sites. Fig. 1. shows the crystallographic sublattices in the sample. Photo-induced magnetic anisotropy in such garnets was attributed to transitions between Co ions in nonequivalent sites [7], driven by linear polarization of femtosecond laser pulses [5].

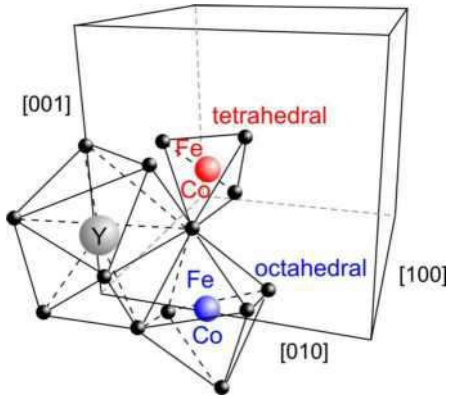


Figure 1: Schematics of the unit cell of the Co-doped garnet crystal structure.

Measurements were performed by means of magneto-optical microscope using Faraday geometry at room temperature without external magnetic field. The magnetic contrast in polarizing microscope comes from the fact that magnetic domains with different out-of-plane magnetization component will result in different angles of the Faraday rotation. The garnet film was excited with one or and multiple pulses. The duration of each pulse was about 50 fs and pulse-to-pulse separation was varied. The wavelength of the pump pulses was tuned within the range between 900 nm and 1600 nm. The images of magnetic domains were taken before and after the pump excitation. Taking the difference between the images we deduced photo-induced effects on the magnetization in the garnet. All

measurements were done in zero applied magnetic field and at room temperature.

3. Results and discussion

The recording was observed for single pump and multiple-pulse excitation with pulse-to-pulse separation time in the range from 1 ms to 20 ms. The spectral tuning of laser-induced magnetization switching by selective pumping of octahedral or tetrahedral Co-sublattices in a garnet was demonstrated. The switching properties are vastly different, related to the crystal site hosting the excited Co ions. Changing the pump wavelength near 1140 nm and 1300 nm and linear polarization of pump pulses along [110] and [100] directions, resonantly excites the single optical transitions in Co ions (see Fig. 2). As these ions are the source of the strong magnetic anisotropy in garnet, this represents a coherent and ultrafast manipulation of the spin-orbit interaction by femtosecond pulses. Moreover, the limited number of absorbed photons in garnet film contributes to the modification of anisotropy, underlining the remarkable efficiency of the photo-magnetic switching.

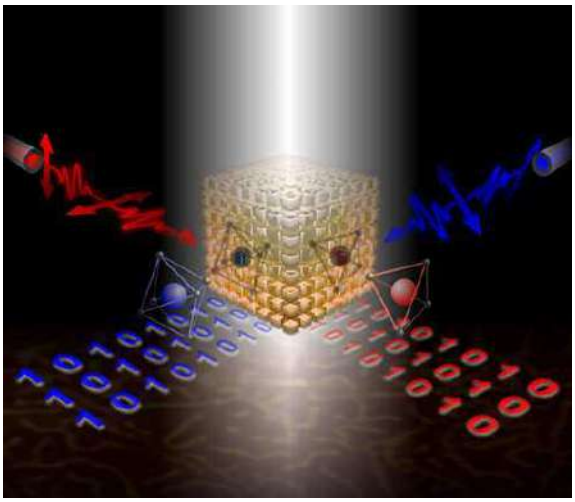


Figure 2: Pathways for ultrafast all-optical recording.

4. Conclusions

The photo-magnetic effect is a general phenomenon in numerous dielectrics. However, by using ultrashort laser pulses and precisely tuning to optical resonances we vastly enhance the effective light-induced field amplitude. This novel understanding highlights the principles for the engineering of materials for the cold all-optical recording.

Acknowledgements

This work was supported by the project TEAM/2017-4/40 of the Foundation for Polish Science co-financed by the EU within the ERDFund. The author would like to acknowledge the contributions of K. Szerenos for measurements. The author are grateful to A. Kimel, A. Kirilyuk, A. Zvezdin for fruitful discussions.

References

[1] A. Kirilyuk, A.V. Kimel, and T. Rasing, Ultrafast optical manipulation of magnetic order, *Rev. Mod. Phys.* 82: 2731 (2010).

[2] L. Stojchevska, I. Vaskivskyi, T. Mertelj, P. Kusar, D. Svetin, S. Brazovskii, D. Mihailovic, Ultrafast Switching to a Stable Hidden Quantum State in an Electronic Crystal, *Science* 344: 177–180 (2014).

[3] C. D. Stanciu, F. Hansteen, A. V. Kimel, A. Kirilyuk, A. Tsukamoto, A. Itoh, T. Rasing, All-optical magnetic recording with circularly polarized light, *Phys. Rev. Lett***.** 99: 047601 (2007).

[4] C-H. Lambert, S. Mangin, B. Varaprasad, Y. K. Takahashi, M. Hehn, M. Cinchetti, G. Malinowski, K. Hono, Y. Fainman, M. Aeschlimann, E. E. Fullerton, All-optical control of ferromagnetic thin films and nanostructures, *Science* 345: 1337 (2014).

[5] F. Atoneche, A. M. Kalashnikova, A. V. Kimel, A. Stupakiewicz, A. Maziewski, A. Kirilyuk, and Th. Rasing, Large ultrafast photoinduced magnetic anisotropy in a cobalt-substituted yttrium iron garnet, *Phys. Rev. B* 81: 214440 (2010).

[6] A. Stupakiewicz, A. Szerenos, D. Afanasiev, A. Kirilyuk, A. V. Kimel, Ultrafast nonthermal photo-magnetic recording in a transparent medium, *Nature* 542: 71 (2017).

[7] A. Stupakiewicz, A. Maziewski, I. Davidenko, V. Zablotskii, Light-induced magnetic anisotropy in Co-doped garnet films, *Phys. Rev. B* 64: 644405 (2001).

Using femtosecond laser pulses to control the assembly and welding of plasmonic nanostructures

Ovidio Peña-Rodríguez,[1,2,*] Guillermo González-Rubio,[3,4] Pablo Díaz-Núñez,[1] Antonio Rivera,[1,2] Luis Bañares,[3,5] Luis M. Liz-Marzán[4,6,7] and Andrés Guerrero-Martínez[2]

[1] Instituto de Fusión Nuclear, Universidad Politécnica de Madrid, Spain
[2] Departamento de Ingeniería Energética, ETSII, Universidad Politécnica de Madrid, Spain
[3] Departamento de Química Física I, Universidad Complutense de Madrid, Spain
[4] Bionanoplasmonics Laboratory, CIC biomaGUNE, San Sebastián, Spain
[5] Centro de Láseres Ultrarápidos, Universidad Complutense de Madrid, Spain
[6] Ciber de Bioingeniería, Biomateriales y Nanomedicina, San Sebastián, Spain
[7] Ikerbasque, Basque Foundation for Science, 48013 Bilbao, Spain
*corresponding author, E-mail: ovidio.pena@upm.es

Abstract

We describe a light-controlled synthetic procedure to fabricate selected plasmonic oligomers. Directed assembly of gold nanorods using dithiolated molecular linkers allows the controlled tip-to-tip assembly. With the aid of fs laser pulses, this process can be tuned to increase the temperature at the interparticle gaps to either destroy the organic ligands or melt particle tips and weld the particles together, offering a new pathway toward fabrication of novel complex nanoparticles with a plasmonic response not attainable by other methods.

1. Introduction

Gold nanoparticles have unique optical properties, which originate from the interaction of light with free conduction electrons. This phenomenon is known as localized surface plasmon resonance (LSPR) [1], and has a lot of potential for applications in sensing [2], photovoltaics and photocatalysis [3], as well as in waveguides and metamaterials [4], to cite just a few examples. Many of such applications are based on the collective optical properties of nanoparticles in close proximity of each other [5]. When the distance between two particles is sufficiently short, new hybridized plasmon modes appear through LSPR coupling [6], in such a way that the intensity of the resulting interaction is controlled by the interparticle distance [7]. For tip-to-tip NR assemblies of gold nanorods (NRs), the longitudinal mode registers a significant red-shift and an increase of the effective polarizability, with respect to the single rod, as the distance is reduced [8]. Moreover, the the near field enhancement at the interparticle gap depends directly on the distance between the nanocrystals, being greater as the gap gets smaller [5].

The strong interaction of light, particularly laser pulses, with plasmonic nanoparticles can result in irreversible morphological changes of the nanocrystals [1]. Ultrashort fs irradiation can induce melting of nanoparticles, whereas ns pulses produce both photothermal melting as well as fragmentation [9]. All these effects have been ascribed to the relaxation dynamics of the localized surface plasmon electron oscillations in resonance with the laser wavelength. In the case of irradiation with a fs laser, a thermal equilibration process takes place after irradiation, whereas for the ns laser the electrons continue absorbing photons when the nanocrystal lattice is still "hot", ultimately resulting in nanoparticle fragmentation [9]. In this work, we exploit not only the melting capability of fs lasers, but also the possibility of using lower fluence fs laser irradiation to control the assembly of plasmonic nanostructures.

2. Results and discussion

Optimized dithiol concentrations were used to control, both initiation and polymerization rates [10]. Termination of the reaction was achieved by blocking the free thiols of the linker by means of a "click" thiol-maleimide reaction [11]. The redshift of the longitudinal LSPR band resulting from tip-to-tip rod assembly was monitored to follow the polymerization process. Initiation occurs along with a decrease of the LSPR band intensity at 600 nm, and formation of a new intense band centered at ca. 700 nm, likely due to the longitudinal LSPR of dimers. After 8 minutes, the LSPR bands corresponding to single rods and rod dimers showed similar intensities, while after 10 minutes the reaction was stopped, when the LSPR of trimers at ca. 800 nm reached an analogous intensity.

Then we performed fs laser irradiation during rod polymerization, acquiring in situ the extinction spectra (Figure 1a-c). The relative concentration of the main species was determined by fitting the experimental spectra with those calculated using FDTD [10]. Possible configurations for the rod oligomers are rather large, far more than can be simulated, which introduces an error in the concentrations predicted by the model. We assume that the nanorods are

preferentially bonded by the tips, according to TEM analysis [10], which considerably reduces the possible number of configurations. The angle between rods does not change the position of the LSPR but only its intensity [12]. Moreover, we considered the spectra for the main species (single rod, dimers and trimers), whereas all larger-chain oligomers were approximated by a Gaussian curve. In spite of its simplicity, the model is able to yield reasonable results for the relative concentrations of the main species.

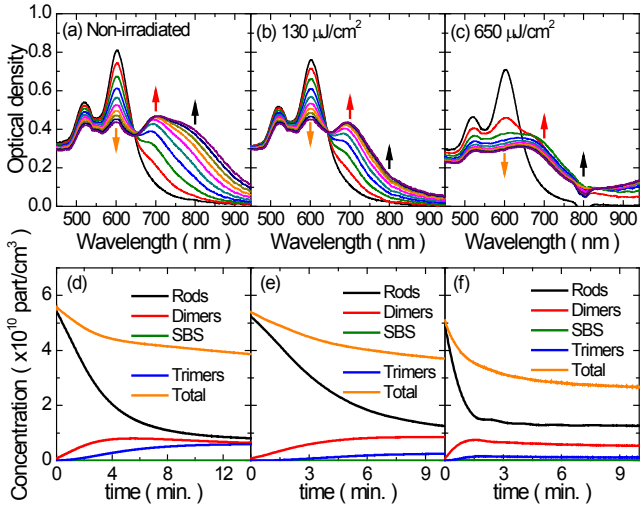


Figure 5. Evolution of AuNRs-polymerization for different irradiation conditions. (a-c) Extinction spectra at 20 s intervals for 10 min: (a) without laser irradiation, (b) 130 μJ/cm^2 per pulse at 1 kHz, and (c) 650 μJ/cm^2 per pulse at 1 kHz. Arrows point to the spectral region at the LSPR maxima for the monomer (orange), dimer (red) and trimer (black). Concentration of side-by-side (SBS, green lines) dimers yielded by the fit is very close to zero. (d-f) Concentration of single rod, dimers and trimers obtained from the fits for (d) no laser, and pulse fluences of (e) 130 μJ/cm^2 and (f) 650 μJ/cm^2.

Concentration of the main species as a function of time are shown in Figure 1d-f for the non-irradiated reaction, as well as those for medium and large fluences. The rate of rod assembly is slightly decreased by laser irradiation with respect to the non-irradiated polymerization, which is apparent for a fluence of 130 μJ/cm^2. This suggests that fs irradiation not only affects trimers but also a small fraction of dimers, due to the natural polydispersity of gold nanorods in aspect ratio, resulting in an increase of monomer concentration at early reaction stages. Our model predicts an inversion of the concentrations of dimers and trimers due to fs irradiation (Figure 1d,e), in good agreement with the proportion of oligomers determined by TEM [10]. We also found a significant increase of the rate at which monomers vanish at the early stages of reaction at the fluence of 650 μJ/cm^2, suggesting that an alternative reaction pathway based on the activation of chemical reactants by light [13] takes place for larger fluences. When the reactions stops, there is still a significant remaining concentration of monomers (~10^{10} particles/cm^3) because the reaction rate stagnates from this point onwards. This is probably due to the polydispersity of gold nanorods, from which dimers with large aspect ratios are affected by the laser pulses, increasing the population of non-reactive monomers.

3. Conclusions

We have devised a light-controlled synthetic procedure where selective inhibition of the formation of gold nanorod trimers is attained by exciting the longitudinal localized surface plasmon resonance with 800 nm femtosecond laser pulses, allowing efficient trapping of the dimers by hot spot mediated photothermal decomposition of the interparticle molecular linkers. Laser irradiation at higher energies produces near-field enhancement at the interparticle gaps, which is large enough to melt particle tips, offering a new pathway toward tip-to-tip welding of gold nanorod oligomers. Optical and electron microscopy characterization indicates that plasmonic oligomers can be selectively trapped and welded, which has been analyzed in terms of a model that predicts with reasonable accuracy the relative concentrations of the main plasmonic species. Although we have only illustrated the use of laser irradiation for controlling the assembly kinetics of nanorods and spherical particles, this technique can be generalized to a variety of shapes, limited only by the wavelength of available fs lasers.

References

1. S. Link and M. A. El-Sayed, Annu. Rev. Phys. Chem. **54**, 331 (2003).
2. K. A. Willets and R. P. Van Duyne, Annu. Rev. Phys. Chem. **58**, 267 (2007).
3. Z. Liu, W. Hou, P. Pavaskar, M. Aykol, and S. B. Cronin, Nano Lett. **11**, 1111 (2011).
4. D. K. Gramotnev and S. I. Bozhevolnyi, Nat. Photonics **4**, 83 (2010).
5. V. Myroshnychenko, J. Rodríguez-Fernández, I. Pastoriza-Santos, A. M. Funston, C. Novo, P. Mulvaney, L. M. Liz-Marzán, and F. J. García de Abajo, Chem. Soc. Rev. **37**, 1792 (2008).
6. P. Nordlander, C. Oubre, E. Prodan, K. Li, and M. I. Stockman, Nano Lett. **4**, 899 (2004).
7. I. Romero, J. Aizpurua, G. W. Bryant, and F. J. García De Abajo, Opt. Express **14**, 9988 (2006).
8. P. K. Jain, W. Huang, and M. A. El-Sayed, Nano Lett. **7**, 2080 (2007).
9. S. Link and M. A. El-Sayed, J. Phys. Chem. B **103**, 8410 (1999).
10. G. González-Rubio, J. González-Izquierdo, L. Bañares, G. Tardajos, A. Rivera, T. Altantzis, S. Bals, O. Peña-Rodríguez, A. Guerrero-Martínez, and L. M. Liz-Marzan, Nano Lett. **15**, 8282 (2015).
11. B. H. Northrop, S. H. Frayne, and U. Choudhary, Polym. Chem. **6**, 3415 (2015).
12. J. Wu, X. Lu, Q. Zhu, J. Zhao, Q. Shen, L. Zhan, and W. Ni, Nano-Micro Lett. **6**, 372 (2014).
13. R. Klajn, K. J. M. Bishop, and B. A. Grzybowski, Proc. Natl. Acad. Sci. **104**, 10305 (2007).

Multiphysics simulations of active meta-surfaces

D. N. Chigrin[1, 2*]

[1]DWI - Leibniz Institute for Interactive Materials, Aachen, Germany

[2]Institute of Physics (IA), RWTH Aachen University, Aachen, Germany

[*]corresponding author: chigrin@dwi.rwth-aachen.de

Phase-change materials (PCMs) provide excellent opportunities to alter electromagnetic response of artificial materials facilitating design of active and reconfigurable meta-surfaces. PCMs possess a high contrast of electromagnetic response between amorphous and crystalline phases accompanied by low optical losses. The phase transition can be triggered using thermal annealing on a hot plate or employing electrical or optical pulses. These allow active altering of both entire meta-surface as well as its individual unit cells enabling an efficient post-production tuning and reconfigurability. Theoretical description and design of PCM based reconfigurable meta-surfaces require a careful analysis of rich multiphysical phenomena associated with the phase transition at nano-scale in inhomogeneous environment. These involves self-consistent treatment of phase-transition, electromagnetic and thermal models. Here some aspects of multiphysics modelling of PCM based meta-surfaces are discussed. Different phase transition models are self-consistently coupled to full wave electromagnetic and heat transfer solvers. Developed methods are used to design active meta-surfaces. An importance of multiphysics modelling is demonstrated.

Negative-index metamaterials made by low-cost approaches

Mayte Gomez-Castano[1,2*], Juan Luis Garcia-Pomar[2], Renaud Vallee[1], Agustin Mihi[2] and Serge Ravaine[1]

[1]Research Center Paul Pascal, CNRS, UMR 5031, University of Bordeaux, 33600 Pessac, France
[2]Institute of Materials Science of Barcelona, CSIC, Bellaterra, Spain
*corresponding author, E-mail: mtgomez@icmab.es

Abstract

Despite the exciting electromagnetic properties metamaterials exhibit, their implementation in nowadays technology is limited by the expensive and low-throughput used procedures. In this communication, we present new low-cost and up-scalable routes for the fabrication of double fishnet metamaterials, based on the combination of colloidal lithography, nanoimprinting lithography and electrodeposition. The proper design of our architectures enables the tuning of the effective refractive index from positive to negative and zero values.

1. Introduction

Metamaterials have attracted a great deal of attention over the past years because of the exotic electromagnetic phenomena that they can present, such as negative refraction. A widely studied geometry to achieve such negative refractive index is the fishnet design, which consists of a 2D array of dielectric holes penetrating a multilayered stack of metallic and dielectric films. However, the production of such metamaterials is hampered by the commonly used top-down techniques, which involve rather costly processes [1]. As alternative, we have developed new cost-effective routes for the fabrication of centimeter-sized negative-index metamaterials. Our approaches rely on the combination of low-cost patterning techniques such as colloidal lithography and nanoimprinting lithography with metallic electrodeposition [2].

2. Results and discussion

The proposed designs are based on hexagonally and squared ordered arrays of dielectric beads or pillars produced by colloidal or nanoimprinting lithography, respectively. These periodic structures serve as templates for alternatively infiltrate metallic layers of gold and sacrificial nickel through the structure by electrodeposition. A selective chemical etching removes the nickel parts and leads to a multilayered structure of gold films separated by an air gap and perforated by a 2D dielectric array (Figure 1).

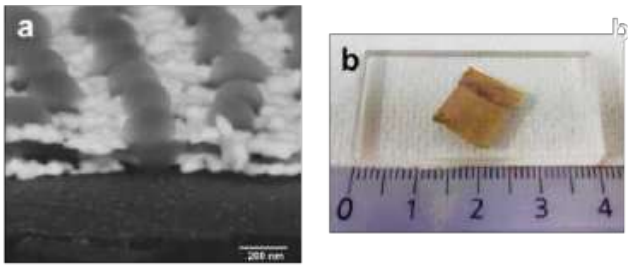


Figure 1: (a) SEM image and (b) macroscopic view of the fishnet metamaterial.

The obtained structures exhibit extinction resonances in the near-infrared that are tunable as a function of the different features of our structures, such the pitch of the array, the size of the dielectric elements or the separation between the gold layers. The good agreement between the optical measurements and FDTD simulations attests the success of our fabrication process.
The effective optical properties, retrieved from the calculations by the homogeneization method [3], demonstrate that we are experimentally able to tailor the refractive index from positive to negative and zero values by the proper choice of the geometrical parameters of our structures (Figure 2).

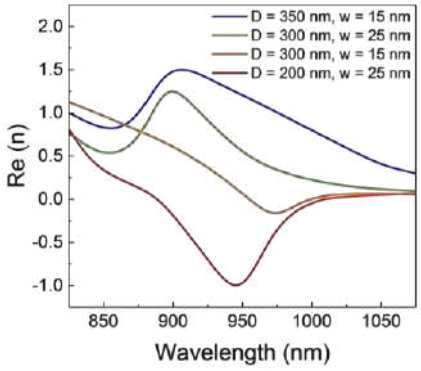


Figure 2: Real part of the effective refractive indices extracted from the calculations.

3. Conclusions

This work presents an effective route for the low-cost and large-scale implementation of fishnet metamaterials. The performed simulations confirm the quality of our structures and demonstrate the feasibility of these new approaches to produce negative-index metamaterials over a broad electromagnetic band.

Acknowledgements

This work was supported by the French National Research Agency (ANR) as part of the Initiative for Excellence Bordeaux program and the Spanish Ministry of Economy, Industry and Competitiveness (MINECO). This project received funding from the European Research Council (ERC) under the European Union's Horizon 2020.

References

[1] G. Yoon, I. Kim and J. Rho, Challenges in fabrication towards realization of practical metamaterials, *Microelectron. Eng.*, 163, 7-20, 2016.

[2] M. Gomez-Castano, H. Zheng, J. L. Garcia-Pomar, R. Vallee, A. Mihi and S. Ravaine, Tunable index metamaterials made by bottom-up approaches, *Nanoscale Adv.*, advance article, 2019.

[3] D. R. Smith, D. C. Vier, T. Koschny and C. M. Soukoulis, *Phys. Rev. E*, 71, 036617, 2005.

Use of novel metamaterials for magnetic resonance imaging

Carlo Rizza[1], Marco Fantasia[2], Elia Palange[3], Marcello Alecci[1,2,4], Angelo Galante[1,2,4]

[1]CNR-SPIN, Via Vetoio 1, I-67100 L'Aquila, Italy
[2]MESVA, University of L'Aquila, Via Vetoio 1, I-67100 L'Aquila, Italy
[3]DIIIE, University of L'Aquila, Via G. Gronchi 18, I-67100 L'Aquila, Italy
[4]LNGS (INFN), Assergi, I-67100 L'Aquila, Italy
*corresponding author, E-mail: carlo.rizza@aquila.infn.it

Abstract

We propose a novel metamaterial-based device inserted in a magnetic resonance imaging (MRI) setup in order to enhance the MRI efficiency. More precisely, we show that a negative magnetic permeability metamaterial, coupled to a standard radio-frequency surface coil, allows to boost the magnetic resonance imaging signal to noise ratio with respect to the standard setup. We believe that the proposed setup holds great potential in MRI applications.

1. Introduction

Magnetic resonance imaging is a cornerstone technique for diagnostic medicine, biology and neuro-science since it shows different advantages (e.g. this imaging method is noninvasive and does not use ionizing radiation), so that significant research efforts have been expended for achieving high-performance MRI setups. In the last decade, several research groups have introduced metamaterials concepts for designed high efficiency MRI scanners [**?**, **?**, **?**, **?**, **?**]. In particular, Freire *et al.* [**?**] investigated a $Re(\mu_m) = -1$ metamaterial (i.e. a metamaterial where the real part of the magnetic permeability is -1) integrated with a standard surface radio-frequency (RF) coil to improve MRI efficiency. In Freire's configuration, the metamaterial acts as "a poor-man's superlens" [**?**] able to suitable refocus the RF magnetic field, such as to enhance both MRI signal and signal-to-noise ratio. It is very surprising that a $Re(\mu_m) = -1$ metamaterial can also support the excitation of magnetic surface plasmons [**?**, **?**], showing relevant characteristics, such as a resonant nature, a strong enhancement and a highly confinement of the local electromagnetic field.

Here, we consider a $Re(\mu_m) = -1$ metamaterial slab as depicted in Fig.1 where the metamaterial lying between the RF surface coil and the sample. We prove that, in this configuration, the metamaterial can support magnetic surface plasmons and their excitations can boost the MRI signal-to-noise ratio (SNR) with respect to the standard setup. In the case considered by Freire *et al.*, the $Re(\mu_m) = -1$ slab is located between the coil and the sample and it has the ability to duplicate the electromagnetic field configuration present on the RF coil plane to another plane inside the sample. In our configuration, we exploit the fact that a localized plasmons can be excited near the metamaterial surface. As a consequence, the proposed configuration has the advantages to introduce no limitations to the sample-coil relative position since the metamaterial slab is located in a region usually free in many MRI setups.

2. Numerical simulations

We perform full-wave simulations using the RF COMSOL axis-symmetric package [**?**] where we simulate the configuration displayed in Fig.1. We set the radiation frequency $\nu = 63.866$ MHz, $l_m = 5.7$ cm, $l_s = 20$ cm, $d_m = d_s = 0$ cm, the sample relative permittivity $\epsilon_s = 90 + i197$ (corresponding to a conductivity of $\sigma = 0.69$ S/m) and the metamaterial relative permittivity $\epsilon_m = 1$. The RF surface coil is modeled with negligible thinckness along the z-axis and by a surface current density having only an azimuthal component, viz., $J_\phi = K_\phi \delta(z)$, where $K_\phi(\rho) = K_0 \rho \exp\left[-(\rho - \rho_0)^2/w^2\right]$ ($\rho_0 = 2$ cm, $w = 2$ mm, K_0 is a constant whose value is fixed to obtain unitary current and $\delta(\cdot)$ is the Dirac delta function). From simulations, we obtain the RF electric and magnetic fields and the system dissipated power and, applying the principle of reciprocity, the receiving RF coil signal-to-noise ratio (SNR). In Fig.2, we report the spatial distribution of the normalized signal-to-noise ratio $SNR^{(n)}$ (viz., $SNR^{(n)} = SNR_m/SNR_v$ where SNR_m, SNR_v are the values calculated with and without metamaterial slab, respectively), where the real part of the metamaterial permeability is $Re(\mu_m) = -1$. In Fig.2(a), we consider the situation where $Im(\mu_m) = 0.1$ and we get both a significant enhancement of the magnetic field and a spatial modulation of the SNR due to the excitations of a surface plasmon at the metamaterial interface. On the other hand, in this situation, the metamaterial and sample losses are quite high and they reduce the setup performance ($SNR^{(n)} < 1$). In Fig.2(b) and (c), we consider the situation very close to the surface plasmon resonance condition $\mu_m = -1$ [(b)$Im(\mu_m) = 10^{-3}$, (c) $Im(\mu_m) = 10^{-2}$] and hence we obtain a significant enhancement of RF coil SNR.

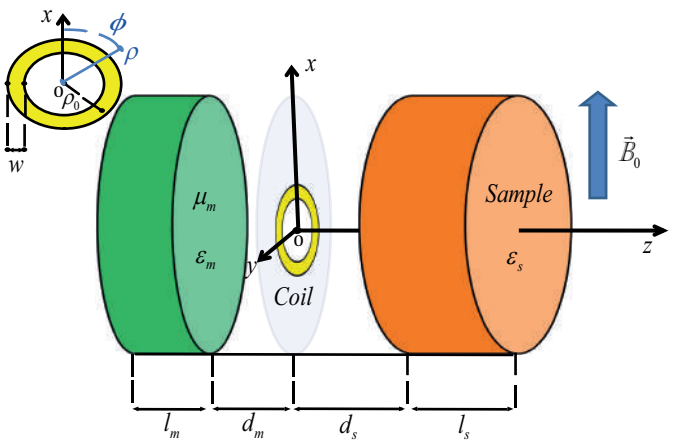


Figure 1: Sketch of the considered setup. A standard surface radio-frequency (RF) coil (with radius ρ_0 and radial width w) at $z = 0$ is positioned between the metamaterial slab (with thickness l_m, and relative permittivity ϵ_m and permeability μ_m) and the sample (with thickness l_s, and relative permittivity ϵ_s). Here, $\vec{\mathbb{B}}_0$ is the applied static magnetic field and d_m (d_s) is the distance between the metamaterial (the sample) and the RF coil.

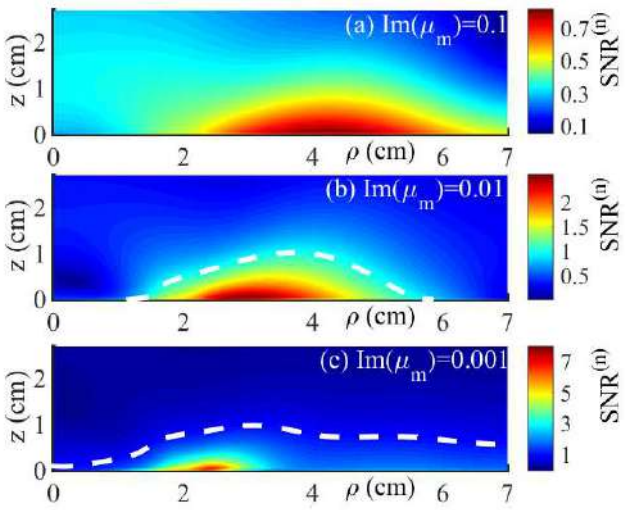


Figure 2: $SNR^{(n)}$ maps setting $\phi = \pi/2$ and $Re(\mu_m) = -1$ with $Im(\mu_m) = 0.1$ (panel a), $Im(\mu_m) = 10^{-2}$ (panel b), $Im(\mu_m) = 10^{-3}$ (panel c). Dashed white lines are $SNR^{(n)} = 1$ contour lines.

3. Conclusions

In conclusion, we suggest that a negative permeability metamaterial embedded into a MRI setup can increase the performances of a RF coil in an MRI experiment. A $Re(\mu_m) = -1$ metamaterial is able to support magnetic localized surface plasmons around its surface and we exploit this resonance phenomenon to improve the MRI efficiency.

Acknowledgement

CR thanks the US Army International Technology Center Atlantic for financial support (Grant No. W911NF-14-1-0315). This work has partially been supported by the CNR-SPIN seed project No. B52F17001370005 and CNR-SPIN Nano-Agents project.

References

[1] M. C. K. Wiltshire, J. B. Pendry, I. R. Young, D. J. Larkman, D. J. Gilderdale, J. V. Hajnal, Science **291**, 849 (2001).

[2] M. J. Freire, R. Marques, and L. Jelinek, Appl. Phys. Lett. **93**, 231108 (2008).

[3] A. V. Shchelokova, A. P. Slobozhanyuk, I. V. Melchakova, S. B. Glybovski, A. G. Webb, Y. S. Kivshar, and P. A. Belov, Phys. Rev. Appl. **9**, 014020 (2018).

[4] R. Schmidt, A. Slobozhanyuk, P. Belov and A. Webb, Scientific Report **7**, 1678 (2017).

[5] A. P. Slobozhanyuk, A. N. Poddubny, A. J. E. Raaijmakers, C. A. T. van den Berg , A. V. Kozachenko , I. A. Dubrovina, I. V. Melchakova, Y. S. Kivshar, and P. A. Belov, Adv. Mater. **28**, 1832 (2016).

[6] J. B. Pendry, Phys. Rev. Lett. **85**, 3966 (2000).

[7] S. Zhang, W. Fan, B. K. Minhas, A. Frauenglass, K. J. Malloy, and S. R. J. Brueck, Phys. Rev. Lett. **94**, 037402 (2005).

[8] J. N. Gollub, D. R. Smith, D. C. Vier, T. Perram, and J. J. Mock Phys. Rev. B **71**, 195402 (2005).

[9] COMSOL Group, COMSOL Multiphysics.

Mapping electron emission and multiphoton absorption in plasmonic nanoantenna arrays

Kamonpan Chumpol[1], Kenan Elibol[1], Xia Zhang[1], Richard G. Hobbs[1*]

[1]School of Chemistry, Centre for Research on Adaptive Nanostructures and Nanodevices (CRANN) and Advanced Materials and Bio-Engineering Research Centre (AMBER), Trinity College Dublin, Dublin 2, Ireland
*corresponding author, E-mail: hobbsr@tcd.ie

Abstract

Understanding plasmon-driven electron emission and energy transfer on the nanometer length scale is critical to controlling light-matter interactions at nanoscale dimensions. In photoresist and electron-beam resist materials, electron emission and energy transfer lead to chemical transformations. In this work, we use such chemical transformations in two different high-resolution electron-beam lithography resists to map local electron emission and energy transfer with nanometer resolution from plasmonic nanoantennas by exciting both localized surface plasmon resonances and lattice resonances within the antenna arrays.

Results and discussion

Measurement and control of hot carriers produced via surface-plasmon decay may enable routes to guide photochemical reactions,[1]–[4] drive local heating on the nanoscale,[5]–[7] and harvest energy from light.[2] Direct observation of the spatial extent of hot-carrier-mediated chemical processes in materials at the surface of plasmonic nanoparticles will be key to engineering plasmonic nanoantennas for hot-carrier driven reactions. Moreover, identifying and differentiating between different electronic processes within individual plasmonic nanoparticles will allow for greater control of reaction pathways on the surface of these nanoparticles. In this work, we will build on our recent report that took advantage of two common electron-beam lithography resists poly(methyl methacrylate) (PMMA) and hydrogen silsesquioxane (HSQ), to image electron emission from plasmonic gold nanoantennas excited by femtosecond laser pulses at resonant frequencies.[8] Here, we extend this approach to arrays of aluminium nanoantennas excited by continuous-wave (CW) lasers.

We have previously characterized electron emission from plasmonic nanoantennas illuminated by intense femtosecond pulses of near-infrared light. In these recent studies, we have observed signatures of optical-field-dependent emission that are consistent with an emission mechanism based on strong-field tunneling.[9], [10] Moreover, we observed that the distribution of lithographic activity in PMMA thin films on arrays of plasmonic nanoantennas illuminated by intense (~10 GW cm^{-2} peak intensity) femtosecond laser pulses, followed the simulated near-field intensity distribution of the nanoantennas. The estimated electron dose received by PMMA in the near-field is comparable to that used in previous reports for low-energy electron-beam lithography using a scanning probe,[11] while also being in agreement with simulated electron emission yields calculated using a model based on strong-field tunneling emission. Investigations using HSQ as an imaging layer showed that HSQ cross-links forming silicon dioxide at the centre of nanorod antennas where resistive losses are strongest. Hot electrons produced at the centre of nanorods were proposed to drive cross-linking of HSQ at the metal surface.

In our most recent work, we have imaged PMMA exposure in the near-field of aluminium nanoantenna arrays illuminated by CW visible lasers (~0.1 MW cm^{-2} peak intensity). We have observed localized exposure of PMMA in nanometer-scale hotspots and investigated the effects of nanoantenna geometry as well as lattice resonances controlled by nanoantenna spacing within arrays. The exposed regions of PMMA may provide a route to produce strongly coupled nanoantenna systems for use as single-photon sources as well as plasmon-enhanced photocatalysts by enabling controlled deposition of quantum systems (molecules, quantum dots) within plasmonic hotspots.

Acknowledgements

R.G.H. acknowledges support from the Royal Society-Science Foundation Ireland University Research Fellowship through grants 17/RS-EA/3466 and 15/RS-URF/3306.

References

[1] S. Linic, U. Aslam, C. Boerigter, and M. Morabito, "Photochemical transformations on plasmonic metal nanoparticles," *Nat. Mater.*, vol. 14, pp. 567–576, 2015.

[2] S. Linic, P. Christopher, and D. B. Ingram, "Plasmonic-metal nanostructures for efficient conversion of solar to chemical energy," *Nat.*

Mater., vol. 10, pp. 911–921, 2011.

[3] S. Mukherjee, F. Libisch, N. Large, O. Neumann, L. V Brown, J. Cheng, J. B. Lassiter, E. A. Carter, P. Nordlander, and N. J. Halas, "Hot Electrons do the Impossible: Plasmon-Induced Dissociation of H2 on Au," *Nano Lett.*, vol. 13, pp. 240–247, 2013.

[4] C. Clavero, "Plasmon-induced hot-electron generation at nanoparticle/metal-oxide interfaces for photovoltaic and photocatalytic devices," *Nat. Photonics*, vol. 8, pp. 95–103, 2014.

[5] S. Lal, S. E. Clare, and N. J. Halas, "Nanoshell-enabled photothermal cancer therapy: Impending clinical impact," *Acc. Chem. Res.*, vol. 41, pp. 1842–1851, 2008.

[6] D. Zhu, M. Bosman, and J. K. W. Yang, "A circuit model for plasmonic resonators," *Opt. Express*, vol. 22, pp. 9809–9819, 2014.

[7] G. Baffou, C. Girard, and R. Quidant, "Mapping heat origin in plasmonic structures," *Phys. Rev. Lett.*, vol. 104, p. 136805, 2010.

[8] R. G. Hobbs, W. P. Putnam, A. Fallahi, Y. Yang, F. X. Kartner, and K. K. Berggren, "Mapping Photoemission and Hot-Electron Emission from Plasmonic Nanoantennas," *Nano Lett.*, vol. 17, pp. 6069–6076, 2017.

[9] R. G. Hobbs, Y. Yang, A. Fallahi, P. D. Keathley, E. De Leo, W. S. Graves, and K. K. Berggren, "High-Yield, Ultrafast, Surface Plasmon-Enhanced , Au Nanorod Optical Field Electron Emitter Arrays," *ACS Nano*, vol. 8, pp. 11474–11482, 2014.

[10] W. P. Putnam, R. G. Hobbs, P. D. Keathley, K. K. Berggren, and F. X. Kärtner, "Optical-field-controlled photoemission from plasmonic nanoparticles," *Nat. Phys.*, vol. 13, pp. 335–337, 2017.

[11] M. A. McCord and R. F. W. Pease, "Lift-off metallization using poly(methyl methacrylate) exposed with a scanning tunneling microscope," *J. Vac. Sci. Technol. B*, vol. 6, pp. 293–296, 1988.

Excitation of near-field resonances in system of two coupled small particles by fast electrons

D.Yu. Sergeeva[1,2], A.A. Tishchenko[1,2]

[1]National Research Nuclear University "MEPhI", Russia
[2]National Research Center "Kurchatov Institute", Russia
*corresponding author, E-mail: dysergeyeva@mephi.ru

Abstract

The first-principles theory of the radiation generated by an electron passing near the system of coupled particles is constructed. Proceeding from microscopic approach and performing the consistent calculations such characteristics as polarizability of the metastructure (the system of many particles) were expressed through the characteristics of a single particle. The obtained results demonstrate essential step towards the further rigorous analysis of the radiation processes in the systems with interaction and collective effects like plasmons, surface plasmon-polaritons, local field effects.

1. Introduction

A charged particle moving near an inhomogeneous target produces different kinds of radiation like diffraction radiation, Cherenkov diffraction radiation, Smith-Purcell radiation. All these are caused not by the scattering of the moving charge in the media, but arise due to the exciting the dynamically changed currents in the material of target [1]. Usually, the calculation of the characteristics of polarization radiation is based on the phenomenological theoretical treatment [2-5], while the microscopic calculations remained undeveloped.

On the other hand, during the last two decades the number of articles dedicated to different processes like radiation, surface waves and localized plasmons generated by moving electrons from metamaterials, local field effects [6-9], including giant enhanced surface phenomena [9, 10], new applications and ways of realization of Smith-Purcell effect from metasurfaces is getting increased.

In such problems it is possible to consider the macroscopically large single particles (nano-, micro-particles, etc) as initial objects, and to construct the theory based on the exact description of the systems consisting of such objects [10-12]. This consideration still needs taking into account the properties of single elements and effects caused by their interaction [6-9,13].

While all these effects in the case of a single particle as a target could be solve, the finding solution for the system of many interacting particles is not trivial. However, proceeding from microscopic approach and performing the consistent calculations it becomes possible to express the characteristic of the metastructure as a whole (the system of many particles) through the properties of a single particle. The latter is the main goal of this report.

2. Field of radiation from coupled particles

Let us consider the generation of radiation while the electron with the charge e passes uniformly and rectilinearly near a system of two small particles, see Figure 1. The impact-parameter is h.

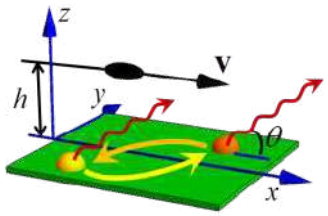


Figure 1: Passing electron (black) generates radiation from two coupled small particles. The particles may be different, which is marked by their different colours.

The interacting spherical particles are of different sizes r_α, r_β, and polarizabilities $\alpha(\omega)$, $\beta(\omega)$. The form is unimportant in the long-wave approximation $r_{\alpha,\beta} << \lambda$, which is supposed to be fulfilled. The positions of the particles are defined by $\mathbf{R}_a$ and $\mathbf{R}_b$, the distance between particles is $R = |\mathbf{R}_a - \mathbf{R}_b|$.

Calculating the field of radiation from two interacting particles and comparing it with the result for one single particle it becomes possible to find the property of the metastructure (for example, polarizability) as a function of characteristics of it selements.

The calculation is performed in terms of local field approach [6, 11-13]. The short schema is given below. Proceeding from Maxwell's equations we found the field of radiation at far distances through the current density $j'_s(\mathbf{k},\omega)$ in form:

$$E_i^{rad}(\mathbf{r},\omega) = i(2\pi)^3 \omega^{-1}\left(k^2\delta_{is} - k_i k_s\right) j'_s(\mathbf{k},\omega) e^{ikr}/r, \quad (1)$$

where $\mathbf{k} = \mathbf{n}\omega/c$, and $\mathbf{j}'(\mathbf{k},\omega) = \mathbf{j}_a(\mathbf{k},\omega) + \mathbf{j}_b(\mathbf{k},\omega)$.

Within the dipole approximation $\mathbf{j}_{a,b}(\mathbf{k},\omega)$ are defined by the dipole moments:

$$\begin{aligned}\mathbf{d}_a(\mathbf{R}_a,\omega)&=\alpha(\omega)\left[\mathbf{E}^0(\mathbf{R}_a,\omega)+\mathbf{E}_b(\mathbf{R}_a,\omega)\right],\\ \mathbf{d}_b(\mathbf{R}_b,\omega)&=\beta(\omega)\left[\mathbf{E}^0(\mathbf{R}_b,\omega)+\mathbf{E}_a(\mathbf{R}_b,\omega)\right],\end{aligned} \quad (2)$$

where $\mathbf{E}^0(\mathbf{R}_a,\omega)$ is the electron's Coulomb field acting in points $\mathbf{R}_a$ or $\mathbf{R}_b$. The field $\mathbf{E}_{a,b}(\mathbf{R}_{b,a},\omega)$ is the field produced by one particle and acting on another one, it is the exact solution of Maxwell's equations.

After some calculations one can obtain the field of radiation:

$$\begin{aligned}E_i^{rad}(\mathbf{r},\omega)&=\frac{e^{ikr}}{r}\left(k^2\delta_{is}-k_ik_s\right)\times\\ \times\Big\{&\alpha(\omega)e^{-i\mathbf{k}\mathbf{R}_a}\left(E_s^0(\mathbf{R}_a,\omega)+E_s^{(1)}(\mathbf{R}_a,\omega)\right)+\\ &+\beta(\omega)e^{-i\mathbf{k}\mathbf{R}_b}\left(E_s^0(\mathbf{R}_b,\omega)+E_s^{(2)}(\mathbf{R}_b,\omega)\right)\Big\}.\end{aligned} \quad (3)$$

where notation is entered:

$$\begin{aligned}E_s^{(1)}(\mathbf{R}_a,\omega)&=-e^{iRk}\beta(\omega)V^{-1}t_{sj}^{(1)}E_j^0(\mathbf{R}_b,\omega)+\\ &+\beta(\omega)e^{2iRk}\alpha(\omega)V^{-1}t_{sj}^{(2)}E_j^0(\mathbf{R}_a,\omega),\\ E_s^{(2)}(\mathbf{R}_b,\omega)&=-e^{iRk}\alpha(\omega)V^{-1}t_{sj}^{(1)}E_j^0(\mathbf{R}_a,\omega)+\\ &+\alpha(\omega)e^{2iRk}\beta(\omega)V^{-1}t_{sj}^{(2)}E_j^0(\mathbf{R}_b,\omega),\end{aligned} \quad (4)$$

$$\begin{aligned}t_{sj}^{(1)}&=B\delta_{sj}-\left(\alpha(\omega)\beta(\omega)e^{2iRk}AB(A+B)+A\right)\frac{R_sR_j}{WR^2},\\ t_{sj}^{(2)}&=B^2\delta_{sk}-A(A+2B)W^{-1}R^{-2}R_sR_k.\end{aligned} \quad (5)$$

and also

$$\begin{aligned}V&=1-\alpha(\omega)\beta(\omega)e^{2iRk}B^2,\\ W&=\alpha(\omega)\beta(\omega)e^{2iRk}(A+B)^2-1,\\ A&=\frac{k^2R^2+3ikR-3}{R^3},\ B=-\frac{k^2R^2+ikR-1}{R^3}.\end{aligned} \quad (6)$$

Equation (3) describes the total radiation field from two coupled particles, excited by the field of external sources. Note the solution has been obtained in the most general form without suggestion about any concrete form of the field $\mathbf{E}_0$ (providing the correctness of the dipole approximation).

3. Conclusions

We report the theory of radiation for the fundamental problem: the system of two interacting particles excited by the field of passing an electron. The resulting field of radiation differs from the mere sum of the radiation fields from two particles, while the basic equations are linear.

The property of the metastructure as a whole was found as a function of characteristics of its elements. Despite the fact that the analytical solution was found for the case of only two interacting particles, the approach demonstrates the possibility of expansion and generalization the result. In addition, even in the most fundamental problems of physics, like the laws of conservation for system consisting of many objects, all the interactions are considered via two-body interactions, between all possible couples. For that reason, the exact theory describing analytically the effects of interaction between two particles can be of primary importance for further rigorous analysis of the radiation processes when it comes to the systems with strong interaction and collective effects, like plasmons, surface plasmon-polaritons, local field effects, including giant surface enhanced phenomena, etc.

Acknowledgements

This research was supported by the Russian Foundation for Basic Research (RFBR), grant № 18-32-00662.

References

[1] A.P. Potylitsyn, M.I. Ryazanov, M.N. Strikhanov, A.A. Tishchenko, *Diffraction Radiation from Relativistic Particles*, Springer, Berlin, 2011.

[2] Y. Song, J. Du, N. Jiang, L. Liu, X. Hu, Efficient terahertz and infrared Smith–Purcell radiation from metal-slot metasurfaces, *Opt. Letters* 43, p. 3858, 2018.

[3] F.J. García de Abajo, Optical Excitations in Electron Microscopy, *Rev. Mod. Phys*. 82, p. 209, 2010.

[4] M. Kozák, *et al.,* Optical gating and streaking of free electrons with sub-optical cycle precision, *Nature Communications* 8, p. 14342, 2017.

[5] W. Liu, Coherent and tunable light radiation from nanoscale surface plasmons array via an exotic Smith–Purcell effect, *Opt. Letters* 40, p. 4579, 2015.

[6] M.I. Ryazanov, M.N. Strikhanov, A.A. Tishchenko, Local field effect in diffraction radiation from a periodical system of dielectric spheres, *Nucl. Instr. and Meth. B* 266, p. 3811, 2008.

[7] P.-N. Li, H.-H. Tsao, J.-S. Huang, C.-B. Huang, Subwavelength localization of near fields in coupled metallic spheres for single-emitter polarization analysis, *Opt. Leters* 36, p. 2339, 2011.

[8] F. Schertz, *et al.,* Near Field of Strongly Coupled Plasmons: Uncovering Dark Modes, *Nano Lett.* 12, p. 1885, 2012.

[9] X. Ye, H. Liu, Y. Qiao, aX. Chen, Enhancement of surface plasmon polariton excitation via feedback-based wavefront shaping, *Opt. Letters* 43, p. 6021, 2018.

[10] E. Rahimi, H. Xu, B.-C. Choi, R. Gordon, Lorentz Nanoplasmonics for Nonlinear Generation, *Nano Lett.* 18, p. 8030, 2018.

[11] D.Yu. Sergeeva, A.A. Tishchenko, M.N. Strikhanov, Microscopic theory of Smith-Purcell radiation from 2D photonic crystal, *NIM B* 402, p. 206, 2017.

[12] D.Yu. Sergeeva, A.A. Tishchenko, A.S. Aryshev, M.N. Strikhanov, Smith-Purcell radiation from concave dotted gratings, *JINST* 13, p. C02045, 2018.

[13] M.I. Ryazanov, A.A. Tishchenko, Clausius-Mossotti-Type relation for planar monolayers, *JETP* 103, p. 539, 2006.

Plasmonic nanocavities: New understanding on the correlation of near- and far-field spectra and their impact on strong coupling dynamics

Angela Demetriadou, Kalun Bedingfield, Antonios Kotsampaseris

School of Physics and Astronomy, University of Birmingham, Egbaston, Birmingham, B15 2TT, United Kingdom
*corresponding author, E-mail: a.demetriadou@bham.ac.uk

Abstract

Plasmonic nano-cavities are the ideal photonic environment to realize light-matter strong-coupling at room temperature. However, they support multiple types of modes, each with a large bandwidth, that can interfere both constructively and destructively. We demonstrate that the interference between such modes leads to a very complex photonic system, with different near-field and far-field spectra, which ultimately change our understanding and interpretation of the strong-coupling dynamics measured experimentally in the far-field.

1. Introduction

Plasmonic nanocavities are formed by gaps of just few nanometres between two nano-metallic structures. Such small plasmonic gaps allow the extreme enhancement and confinement of light in mode volumes of only few cubic nanometers. The extreme light confinement has lead to very interesting phenomena, such as single molecule strong coupling at room temperature [1] and the observation of sub single-molecule spectroscopic behaviour [2].

When two metallic structures are brought close together, the plasmons from each structure become tightly coupled to each other, such that higher order modes in nanocavities loose their non-radiative behaviour and acquire a radiative component [3]. This behaviour suppresses the quenching regime for nanoplasmonics [3], which is the main mechanism that allows for strong coupling of a single molecule at room temperatures. We have also shown that other types of dark modes are excited in plasmonic nanocavities, and in fact have a significant impact on the strong coupling dynamics of a quantum emitter with a plasmonic nanocavity [4].

In this paper, we present a theoretical study on how different plasmonic modes in a nanocavity interfere both destructively and constructively to create a photonic system that is not reciprocal any-more. To create a plasmonic nanocavity we consider a spherical nanoparticle assembled on a flat metal surface (Nanoparticle on mirror - NPoM), with the two structures separated by a distance of $1\,nm$. Spherical nanoparticles though are never perfectly spherical structures, but actually quite faceted. From experimental measurements [5], it has been shown that faceted nanoparticles assemble with their facet parallel to the metal mirror, creating a "waveguide"-like cavity.

2. Near- and Far-field spectra in nanocavities

In figure 1 (left), numerical calculations of the scattering efficiency for faceted NPoM nanocavities is shown. One can observe that for perfectly spherical nanoparticles, the lowest order mode radiates more efficiently than higher order modes. This behaviour correlates well with the near-field spectra (figure 1(right)), where the field enhancement is primarily due to the lowest order mode.

However for very faceted NPoM, (i.e. facets $\sim 40\,nm$), the near-field and far-field spectra are not corelated any more. One can see that the second order mode radiates to the far-field more efficiently than the near-field enhancement due to the same plasmonic mode. For even more faceted NPoM, the third and fourth order modes radiate efficiently to the far-field, while the near-field enhancement takes similar values for each plasmonic mode in the system. This behaviour breaks reciprocity for the nanophotonic system.

3. Discussion

In this paper, we derive an analytical description that decomposes the normal modes in such plasmonic nanocavities. We find that bright modes interference destructively in the near-field, but constructively in the far-field, contributing to some of the discrepancies between the near- and far-field spectra. However, reciprocity breaks primarily due to the dark modes in plasmonic nanocavities that are excited more efficiently for more faceted NPoM. In addition, such dark plasmons spectrally shift as the facet size grows, as previously reported [6]. Also, we break the parity symmetry for the "waveguide"-like nanocavity by considering a facet nanoparticle assembled with its edge on the mirror. Such asymmetric systems have an even more significant impact on the near-field and far-field correlation of plasmonic nanocavities.

Finally, we take the non-reciprocal behaviour of plasmonic nanocavities in the strong coupling regime, by placing a quantum emitter in the nanocavity. The Rabi oscillations of the system reveal that the quantum emitter is coupled to multiple modes simultaneously but with different coupling strengths. However, the far-field spectra show a more simplified picture for the interaction compared to the near-field dynamics.

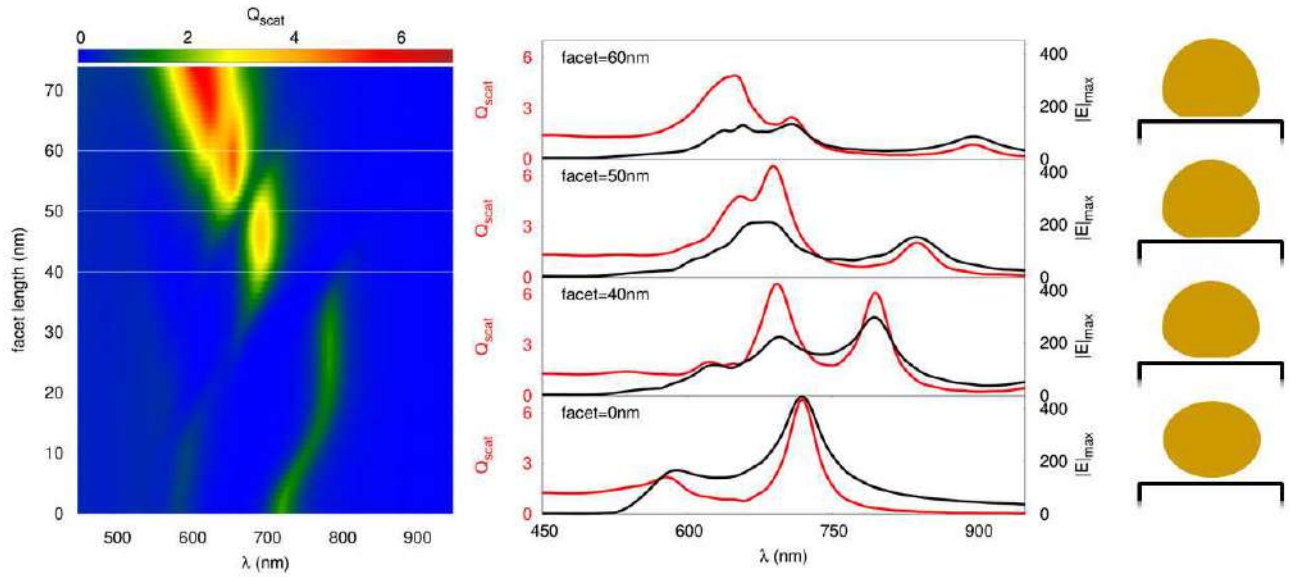


Figure 1: The scattering efficiency of the Nanoparticle on Mirror (NPoM) nanocavity, as the facet size increases (left). The relationship between the near-field and far-field spectra for various faceted NPoM configurations (right).

4. Conclusions

In conclusion, we show that the geometry of a plasmonic nanocavity dominates the reciprocity of the photonic system and as a consequence the spatio-temporal dynamics of a plasmon-exciton.

Acknowledgement

We gratefully acknowledge financial support from the Royal Society International Exchanges grant IE151097 and the Royal Society University Research fellowship URF/R1/180097.

References

[1] R. Chikkaraddy, B. de Nijs, S.J. Barrow, O.A. Scherman, E. Rosta, A. Demetriadou, P. Fox, O. Hess and J.J. Baumberg, "Single-molecule strong coupling at room temperature in plasmonic nanocavities," *Nature* 535: 127, 2016.

[2] F. Benz, M.K. Schmidt, A. Dreismann, R. Chikkaraddy, Y. Zhang, A. Demetriadou, C. Carnegie, H. Ohadi, B. de Nijs, R. Esteban, J. Aizpurua and J.J. Baumberg, "", *Science* 354: 726-729, 2016

[3] N. Kongsuwan, A. Demetriadou, R. Chikkaraddy, F. Benz, V.A. Turek, U.F. Keyser, J.J. Baumberg, and O. Hess, "Suppressed Quenching and Strong-Coupling of Purcell-Enhanced Single-Molecule Emission in Plasmonic Nanocavities," *ACS Photonics* 5: 186-191, 2017 .

[4] A. Demetriadou, J.M. Hamm, Y. Luo, J.B. Pendry, J.J. Baumberg and O. Hess, "Spatio-temporal dynamics and control of strong coupling in plasmonic nanocavities," *ACS Photonics* 4: 2410-2418, 2017.

[5] J. Mertens, A. Demetriadou, R. W. Bowman, F. Benz, M.E. Kleemann, C. Tserkezis, Y. Shi, H. Y. Yang, O. Hess, J. Aizpurua, and J. J. Baumberg, "Tracking Optical Welding through Groove Modes in Plasmonic Nanocavities," *Nano Letters* 16: 5605-5611, 2016.

[6] C. Tserkezis, R. Esteban, D. O. Sigle, J. Mertens, L. O. Herrmann, J. J. Baumberg, and J. Aizpurua, "Hybridization of plasmonic antenna and cavity modes: Extreme optics of nanoparticle-on-mirror nanogaps," *Physical Review A* 92: 053811, 2015.

Coupled oscillator ensembles with loss and gain: a graph approach of PT symmetry

Henri Benisty[1], Vincent Brac de la Perrière[2], Abderrahim Ramdane[2], Anatole Lupu[2]

[1] Laboratoire Charles Fabry de l'Institut d'Optique, CNRS, Univ. Paris Saclay, Palaiseau, France
[2] Centre de Nanosciences et de Nanotechnologies, CNRS, Univ. Paris-Sud, Université Paris-Saclay, Palaiseau, France
*corresponding author, E-mail: henri.benisty@institutoptique.fr

Abstract

We present a approach aimed at generalizing Parity-Time symmetry to mesoscopic ensembles of coupled oscillators with gain and loss, with inspiration from graph-theoretic tools. We globally minimize the imaginary part of the eigenvalues for small gain/loss and describe how couplings adopt some topologies. We also discuss recent results on distributed-feedback laser diodes operating at 1550 nm and having both real and imaginary index modulation. We notably study their resistance to optical feedback.

1. Introduction

The introduction of Parity-time symmetry concepts in optics has prompted numerous re-examinations of optical devices, notably integrated optics devices: waveguide couplers, lasers, multimode waveguides [1,2], etc.

Parity-time symmetry in optics is well-known to be interesting with either "transversal" gain/loss modulation (coupling between adjacent elements), or "longitudinal" gain/loss modulation (e.g. periodic). The first case lends itself to a generalization, e.g. in multimode devices, or in a bunch of coupled fibers. It is the first topic on which we shall report in Sec.2.

We will next report in Sec.3 on our recent results on distributed-feedback laser diodes operating at 1550 nm and having both real and imaginary index modulation, these latter being respectively obtained by (i) ridge shape modulation and (ii) metallic wire elements that periodically modulate the losses. We notably study their resistance to optical feedback, a topic of great importance for high-coherence lasers, and highly desirable in the optical telecommunication realm.

2. Graph PT symmetry for small mesoscopic ensembles

In our main contribution, we will examine a set of "gainy" and "lossy" oscillators connected by a random graph with some constraints such as constant coupling constants for simplicity. The situation could arise for instance in a bunch of a few tens of fibers that couple to each other evanescently, half of them having gain and the other half losses (Fig.1, the drawing in the top is for a example of an ensemble with 5+5 oscillators). The question then arises of making the system "maximally PT-symmetric-like": we attempt to reduce the imaginary part of the eigenvalue |Im(λ)| as much as possible by reconfiguring the graph edges (the connections). We do this for a small finite gain where we estimate that the exceptional point is almost never already reached.

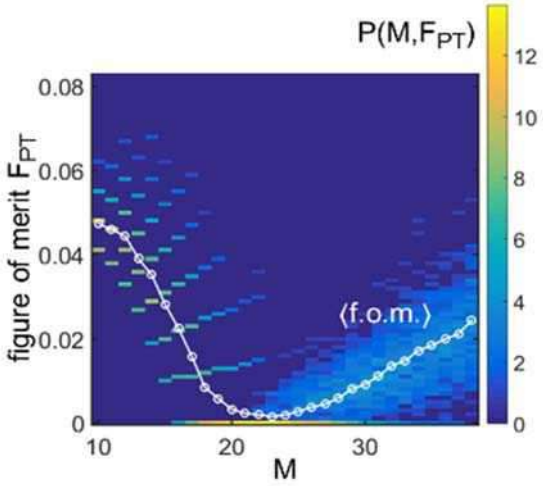


Fig.1: Top inset : Gain and loss (5+5) elements and a set of M=11 coupling between them. Main colormap and plot : attained minimum of <|Im(λ)|> , the figure of merit generalizing PT symmetry for various M in the case of a 16+16 elements in a graph, the color being the frequency in the histogram of statitistical results of miminization. The white dots and lines are the average figure of merit < f.o.m.>.

In the simulation of Fig.1, we obtain for instance the statistical histogram of the dependence of the minimum of -<|Im(λ)|> on the number M of edges after optimization from a random start for a fixed number of 16+16 gain+loss units in Fig.1. We show the distribution for 200 random starts and 36,000 iteration steps consisting of single-edge changes towards a minimal <|Im(λ)|>. We will discuss the possible implications of such considerations in optics and possibly beyond.

We believe that such systems are also of interest in the broader framework of non-equilibrium thermodynamics, when units must collaborate to channel energy flux (solar, biological,…) by optimizing their organization in a complex system. These are century-old topics, started notably with the

work of Alfred Lotka in 1922 on the way living systems maximize the use of energy (or not). Recent work by C. Goupil et al. [3] recently outlined how to revisit basic thermodynamic rules such as Carnot efficiency theorem, when dynamic has a finite rate and some kind of "impedance" prevents the attainment of the ideal efficiency, a frame much closer to real life engines. There is some analogy with our coupling that manages energy flow between gain elements and loss elements, and within each category as well. More generally, the issue of how a dynamical association of gain and loss elements behaves can have profound echoes in other areas, at least this is our firm belief that we will partly try to convey.

3. Laser diodes with complex coupling

In this second part of our contribution, we will discuss laser diodes operating with PT-symmetric Bragg gratings, in other words "PT-DFB laser diodes", which are a sub-class of the more general "complex coupled" laser diodes, whereby the Bragg coupling coefficients have a real and an imaginary part. The real part comes, in our case, from the width modulation of the ridge and the imaginary part from the loss modulation of periodic metal stripes. Gain is continuous and comes from electrical injection, and overall, such diodes compare well with DFB laser diodes with index only or gain only coupling (i.e. periodic modulation). Experimental realizations of such diodes might solve some long-standing issues such as feedback immunity of coherence in DFB laser diodes. To this end, we will start by revisiting the threshold discrimination criteria in the PT-symmetric context, taking into account both the grating phase and the facet phase, using Coupled Mode theory. An example of threshold gain studies for variable facet position is given in Fig.2. We will explain and extend it

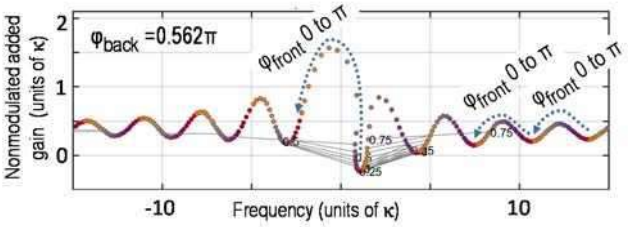


Fig. 2: Threshold g_{th} discrimination study for variable facet phases. The gain threshold of all possibly lasing modes are tracked vs. Thephase of the front facet, a phase of π bringing, far from the Braggfrequency, one mode to the frequency of the next mode at 0 phase. The situation close and across the stopband can be much more complex.

Acknowledgements

This work is supported by French ANR within the PARTISYMO project.

References

[1] A. Lupu, V. V. Konotop, and H. Benisty, "Optimal PT-symmetric switch features exceptional point," Scientific Reports **7**, 13299 (2016).

[2] H. Benisty, A. Lupu, and A. Degiron, "Transverse periodic PT symmetry for modal demultiplexing in optical waveguides," Phys. Rev. A, **91**, 053825 (2015).

[3] C. Goupil, H. Ouerdane, E. Herbert, G. Benenti, Y. DAngelo, and Ph. Lecoeur, \Closed-loop approach to thermodynamics", Phys. Rev. E, **94**, 032136 (2016).

Optical Helmholtz resonators

Patrick Bouchon[1], Paul Chevalier[1], and Riad Hadar[1,2]

[1] DOTA, ONERA, Universit Paris-Saclay, F-91123 Palaiseau, France
[2] DOTA, ONERA, Universit Paris-Saclay, F-91123 Palaiseau, France
*corresponding author, E-mail: patrick.bouchon@onera.fr

Abstract

Optical nanoantennas are studied to manipulate light and enhance light matter interactions. Here, we experimentally demonstrate the optical Hemholtz resonance in a metallic slit-box structure, which is predicted to be harmonic and to enhance the electric field intensity by several orders of magnitude. It is fabricated thanks to a two steps electron beam lithography, between which the box was filled with benzocyclobutene (BCB).

1. Introduction

Designing nanoantenna that could strongly and efficiently concentrate incident light into deep subwavelength volumes is a key issue to locally enhance the electric field and thus produce strong light-matter interactions. Many existing designs are inspired by structures widely used in the radiofrequency domain such as bowtie or Yagi-Uda antennas. Here, we rather use an analogy between acoustics and electromagnetism wave equations, in order to adapt the acoustic Helmholtz resonator to optics. This resonator, made of a slit-box structure, behave as a LC circuit. The deep subwavelength slit acts as a capacitance, which concentrates the electric field at resonance, leading to huge enhancement in a hot volume. Here, we present a way to fabricate this nanoantenna, and experimentally demonstrate the optical Helmholtz resonance.

2. the Optical Helmholtz Resonator

2.1. Properties

This structure is made of a tiny slit above a larger cavity (see Fig. 1(a)), and exhibits several appealing features: total absorption at resonance, absence of harmonic resonance, giant field intensity enhancement in the whole slit volume, angular independence of the Helmholtz resonance [1, 3].

The key properties of the Helmholtz resonance are:

(i) A giant field enhancement, typically two orders of magnitude higher than expected with gap plasmons resonances.

(ii) A single resonance behavior with no harmonics.

(iii) No influence of the permittivity of the material filling the cavity on the resonance wavelength.

(iv) The resonance wavelength λ_r depends on the square root of all four geometrical parameters according to the following formula:

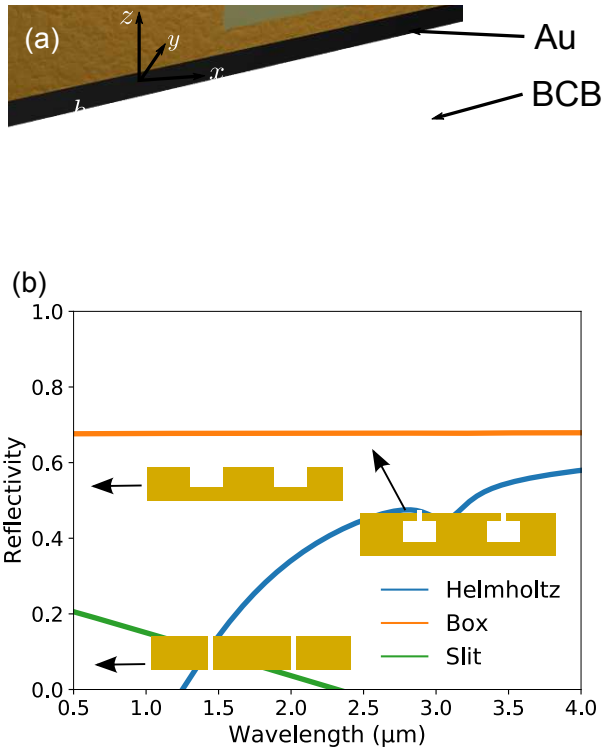


Figure 1: (a) General schematic of the optical Helmholtz resonator, made of a box and a slit in metal, both infinite along the y direction. (b) Computed reflectivity spectrum of the Helmholtz resonator array (period $d = 450\,\mathrm{nm}$) made of a slit (width $w_s = 52\,\mathrm{nm}$, height $h_s = 37\,\mathrm{nm}$) and a box (width $w_b = 400\,\mathrm{nm}$, height $h_b = 77\,\mathrm{nm}$), compared with the reflectivity spectra of the array of slits (height $4h_s$, width w_s, orange curve) and boxes (height h_b, width w_b,green curve). The impinging light is normally incident and TM-polarized.

$$\lambda_r \propto 2\pi\sqrt{\varepsilon_s \frac{h_b w_b h_s}{w_s}}, \tag{1}$$

where ε_s is the permittivity of the material filling the slit.

2.2. Comparison to other resonances

The computed absorption spectrum, for a transverse magnetic (TM) polarized and normally incident light, is plot-

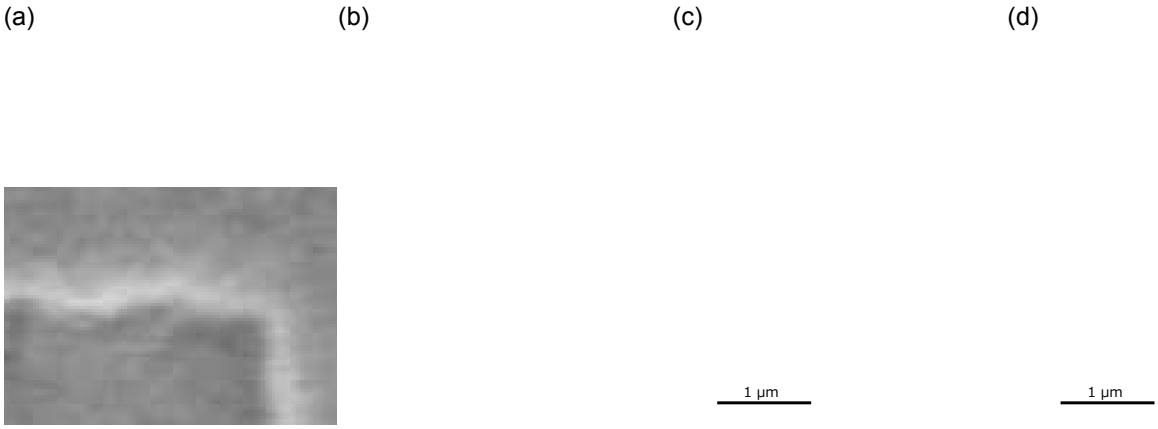


Figure 2: Fabrication steps for a periodic grating of optical Helmholtz resonators with the corresponding top view SEM image: (a) Gold trenches are created by the lift-off of $80\,\mathrm{nm}$ of gold after a first e-beam lithography ($d = 3\,\mu\mathrm{m}$).(b) A dielectric (BCB) is spin coated on the surface and etched by RIE to reach the gold surface ($d = 3\,\mu\mathrm{m}$). (c) A two layer lithography process is performed using PMMA and HSQ ($d = 1.5\,\mu\mathrm{m}$). (d) Gold is lifted-off resulting in the fabrication of the optical Helmholtz resonator ($d = 1.5\,\mu\mathrm{m}$). The narrow slits in the gold surface above the BCB-filled cavity, which is barely distinguishable.

ted in Fig. 1(b) for a given geometry ($w_\mathrm{b} = 400\,\mathrm{nm}$, $h_\mathrm{b} = 77\,\mathrm{nm}$, $w_\mathrm{s} = 52\,\mathrm{nm}$, $h_\mathrm{s} = 37\,\mathrm{nm}$, $d = 450\,\mathrm{nm}$). At $\lambda = 2.53\,\mu\mathrm{m}$, 36 % of the light is absorbed due to the Helmholtz resonance. Other resonances appear at lower wavelengths between $500\,\mathrm{nm}$ and $700\,\mathrm{nm}$. The small peak at $\lambda = 3.4\,\mu\mathrm{m}$ is due to a vibrational absorption of BCB that is enhanced by the Helmholtz resonator. For the sake of comparison, the absorption spectra are also plotted under the same illumination conditions for an array of slits (height $4h_\mathrm{s}$, width w_s) and for an array of cavity filled with BCB (width w_b, height h_b) that also exhibit resonant absorption, but at lower wavelengths.

2.3. Fabrication

Due to its complex architecture and its deeply subwavelength dimensions, the fabrication of the Helmholtz resonator is a rather complex challenge. We have developed a process in two parts, the first consists in fabricating the cavity, which is subsequently filled with benzocyclobutene (BCB), a planarizing dielectric, as shown in Fig. 1(a) to reduce the complexity of fabrication by avoiding freestanding parts. A first step of e-beam lithography is performed to define the cavity on top of the gold layer. $80\,\mathrm{nm}$ of gold are evaporated onto the sample and lifted-off (see Fig. 2(a)) to fabricate trenches of height $80\,\mathrm{nm}$ and width $400\,\mathrm{nm}$. Benzocyclobutene (BCB) is spin coated on the sample and baked, then a reactive ion etching (RIE) plasma is done so that the surface of the BCB reaches the gold surface while keeping the cavity filled with dielectric (see Fig. 2(b)). On top of theses trenches, a bi-layer resist stack (PMMA-HSQ) is used to define the slit with a fine resolution. The second level is aligned on the lower level with alignment markers positioned during the first step of lithography and detected by the e-beam pattern generator. The accuracy of this alignment on the sample size is about $50\,\mathrm{nm}$, and a slight shift of the slit in regard to the cavity can be seen on the SEM images (see Fig. 2(c-d)). Near and mid infrared with a Fourier transform infrared spectrometer confirms the presence of the Helmholtz resonance at $\lambda_r = 2.84\,\mu\mathrm{m}$.

3. Conclusion

A process involving a two-steps e-beam lithography was used to fabricate optical Helmholtz resonators. It was used to experimentally demonstrate the optical Helmholtz resonance thanks to measurements in the near and mid-infrared. This resonators produces high field intensity enhancement that can be used to enhance SEIRA.

Acknowledgement

We acknowledge financial support from the ONERA through the MOLIERE project and from the Agence Nationale de la Recherche (ANR) (ANR-16-CE39-0007)

References

[1] P. Chevalier, P. Bouchon, R. Hadar, and F. Pardo, Optical Helmholtz resonators, *Appl. Phys. Lett.* 105: 071110, 2014

[2] P. Chevalier, P. Bouchon, E. Sakat, J.L. Pelouard, F. Pardo, and R. Hadar, Extraordinary transmission in optical Helmholtz resonators, *Opt. Lett.* 40: 2735, 2015

[3] P. Chevalier, P. Bouchon, J.J Greffet, J.L. Pelouard, R. Hadar, and F. Pardo, Giant field enhancement in electromagnetic Helmholtz nanoantenna, *Phys. Rev. B* 90: 195412, 2014

[4] P. Chevalier, P. Bouchon, et al., Experimental demonstration of the optical Helmholtz resonance, *Appl. Phys. Lett.* 112, 171110 (2018)

Metasurface Photodetectors for Directional Image Sensing

**Leonard Kogos, Yunzhe Li, Jianing Liu,
Yuyu Li, Lei Tian, and Roberto Paiella***

Department of Electrical and Computer Engineering and Photonics Center, Boston University, Boston, USA
*corresponding author, E-mail: rpaiella@bu.edu

Abstract

We report the development of photodetectors integrated with plasmonic metasurfaces that only allow for the detection of light incident along a single, geometrically tunable direction (within a small distribution of angles). These devices are promising for the realization of ultrasmall lensless cameras providing the distinctive imaging capabilities of compound eyes.

1. Introduction

Typical photodetectors measure light intensity isotropically, with only a weak dependence on incident direction dictated by the Fresnel formulas for transmission across the device surface. Here we demonstrate a new family of directional image sensors that only detect light incident along a small, geometrically tunable distribution of angles, whereas light incident along all other directions is reflected. This behavior is produced by coating the photosensitive active layer with a specially designed plasmonic metasurface that acts as a directional filter. The resulting devices are functionally equivalent to the individual elements (ommatidia) of the compound eyes of common invertebrates such as insects and crustaceans, while at the same time featuring a planar lensless architecture. Therefore, they provide a promising new approach to harness the distinct attributes of the compound-eye vision modality (including extreme size miniaturization, wide-angle fields of view, and high acuity to motion [1]), in a flat package that is fully compatible with existing CCD/CMOS image sensor arrays.

In this paper, we will describe the design, fabrication, and characterization of a set of infrared devices providing directional photodetection peaked at different angles, based on simple metal-semiconductor-metal (MSM) Ge photoconductors. Furthermore, we will present the results of computational-imaging simulations showing that high-quality images of relatively complex objects can be reconstructed using flat ultrasmall arrays of these devices.

2. Results and discussion

2.1. Metasurface design

The directional image sensors developed in this work are illustrated schematically in Fig. 1. The device active material (a Ge photoconductor) is coated with a metal film supporting a periodic array of metallic nanoparticles (NPs). The metal film is sufficiently thick (~ 100 nm) to block any externally incident light from propagating directly into the underlying active layer. Therefore, photodetection in this geometry can only take place through an indirect process where light incident along the desired direction is first diffracted by the NP array into surface plasmon polaritons (SPPs) – i.e., guided optical waves propagating on the top surface of the metal film. A small number of suitably positioned subwavelength slits in the metal film are then used to scatter these SPPs into radiation propagating predominantly into the absorbing active layer [2], and as a result a photocurrent signal is produced. Light incident along any other direction is instead either immediately reflected back by the metasurface, or diffracted into SPPs propagating towards a "reflector region" (shown on the right side of Fig. 1), where the SPPs are then scattered into the air above.

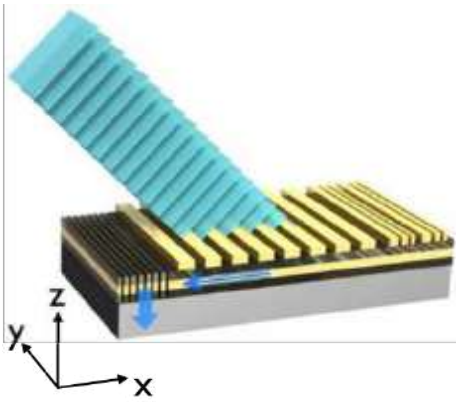


Figure 1: Schematic illustration of the directional photodetectors developed in this work.

The metasurfaces just described were designed via FTDT electromagnetic simulations. Representative results are shown in Fig. 2, where we plot the calculated *p*-polarized power transmission coefficient through the metal film into the absorbing substrate as a function of the polar angle of incidence θ (on the *x*-*z* plane of Fig. 1). Each trace corresponds to a different design with different array period. As shown in the figure, these devices can provide tunable directional photodetection with a wide tuning range for the angle of peak detection θ_p of over ±75° and relatively

narrow angular resolution. The peak transmission is in the range of 30-45 % for all devices. In contrast, the *s*-polarized transmission is negligible small for all incident directions. This intrinsic polarization dependence could be exploited to enable polarization vision. Alternatively, polarization independent operation can be obtained with more complex metasurface designs, involving two-dimensional NP arrays and orthogonally oriented slits.

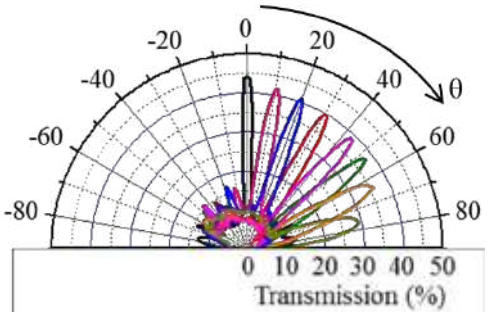


Figure 2: Calculated power transmission coefficient through several metasurfaces for *p* polarized light versus angle of incidence θ on the *x*-*z* plane.

2.2. Experimental results

Several devices were fabricated based on simple MSM Ge photoconductors, with the metasurface patterned in the region in between two metal contacts deposited on the top surface of a Ge substrate. Figure 3 shows a scanning electron microscopy (SEM) image of a representative sample. Angle-resolved photocurrent measurements under near-infrared monochromatic illumination show highly directional response in good agreement with simulations. To illustrate, in Fig. 4 we plot the measured photocurrent of a device designed for peak detection at $\theta_p \approx 30°$, as a function of polar illumination angles. The full 3D response maps of these devices (versus both polar and azimuthal angles of incidence) are also being measured.

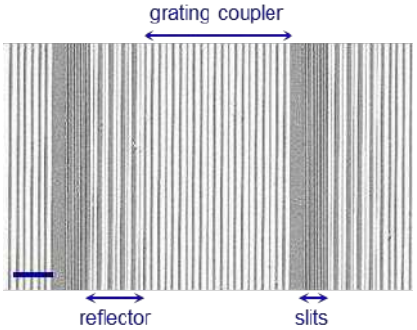


Figure 3: Top-view SEM image of an experimental sample. The scale bar is 5 μm.

2.3. Imaging applications

The angle-sensitive photodetectors just described may be employed for the development of ultrasmall lensless cameras providing the distinctive imaging capabilities of compound eyes, in the form of planar arrays where each pixel selectively detects light incident at a different combination of polar and azimuthal angles. The ability of such arrays to reconstruct relatively complex images is currently being validated with computational imaging simulations. Importantly, these simulations also indicate that the resulting images can have substantially higher resolution compared to the single-pixel angular selectivity, if devices with appropriate overlaps in their angular responses are combined.

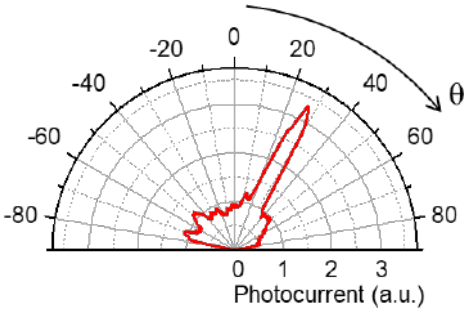


Figure 4: Measured angular dependence of the photocurrent of a device designed for peak response at $\theta_p = 30°$. The illumination wavelength is 1.55 μm.

3. Conclusions

We have developed a new class of photodetectors that are uniquely sensitive to the direction of propagation of the incident light. The devices presented in this work are based on metallic NP arrays on Ge photoconductors, but can be extended to other materials systems and photodetector technologies. Their key operating principle (i.e., the integration of a photosensitive active layer with a metasurface to selectively control the properties of the detected light) is also quite general and can be applied to other device functionalities, such as polarization vision and direct wavefront sensing.

Acknowledgements

This work was partly supported by the National Science Foundation under Grant ECCS-1711156. The FDTD simulations were performed using the Shared Computing Cluster facility at Boston University.

References

[1] M. F. Land, D. E. Nilsson, *Animal Eyes*, Oxford University Press, Oxford, 2002.

[2] F. López-Tejeira, S. G. Rodrigo, L. Martín-Moreno, F. J. García-Vidal, E. Devaux, T. W. Ebbesen, J. R. Krenn, I. P. Radko, S. I. Bozhevolnyi, M. U. González, J. C. Weeber, A. Dereux, Efficient unidirectional nanoslit couplers for surface plasmons, *Nature Phys.* 3: 324-328, 2007.

Control of Ge(Si) Quantum Dot Emission by Mie Resonances in Silicon Nanodisks

Viktoriia Rutckaia[1*], Dominik Schulze[2], Vadim Talalaev[1], Frank Heyroth[3], Mihail Petrov[4], Mikhail Shaleev[5], Alexey Novikov[5], and Joerg Schilling[1]

[1]Centre for Innovation Competence SiLi-nano®, Martin-Luther-University Halle-Wittenberg, Halle (Saale), Germany
[2]Institute of Physics, Martin-Luther-University Halle-Wittenberg, Halle (Saale), Germany
[3]Interdisciplinary center of material science, Martin-Luther-University Halle-Wittenberg, Halle (Saale), Germany
[4]Department of Nanophotonics and Metamaterials, ITMO University, St. Petersburg, Russia
[5]Institute for Physics of Microstructures of the Russian Academy of Sciences (IPM RAS), Nizhniy Novgorod, Russia
*corresponding author, E-mail: viktoriia.rutckaia@physik.uni-halle.de

Abstract

In this work, we describe an active photonic system based on Ge(Si) quantum dots (QDs) embedded into silicon nanodisks. We show experimentally the enhancement of the photoluminescent signal from quantum dots coupled to Mie modes of the nanodisks. Using numerical modeling, we identify the coupling mechanism, which allows for engineering the resonant Mie modes through the interaction of several nanodisks. As the example, we look at linear chains consisting of several silicon nanodisks placed next to each other. We demonstrate the resonance-mediated change of photon spontaneous emission rate in the considered systems (Purcell effect) by investigating emission lifetimes obtained from time-resolved photoluminescence measurements .

1. Introduction

Control of the light at the nanoscale can be achieved in optical nanoantennas through the resonant coupling of the quantum source emission to localized modes. Plasmonic nanostructures allow a strong field enhancement and high spatial localization of the resonant modes. However, metallic systems have high optical losses that can quench spontaneous emission limiting their potential applications. Recently, the resonant all-dielectric photonic nanostructures based on high refractive index materials showed a wide range of applications in nanophotonics and optics [**?**]. The interaction of quantum emitters with all-dielectric systems have been actively studied theoretically in the recent years. Nevertheless, there were only a few experimental realizations demonstrating the interaction of quantum sources with all-dielectric structures[**?**, **?**]. The incorporation of quantum emitters into silicon nanoresonators would path a way towards applications in active silicon nanophotonics. For that, we propose all-dielectric systems based on silicon nanodisks with self-assembled Ge(Si) QDs, showing a broad emission in the 1200-1600 nm range at room temperature [**?**]. These Ge(Si) QDs have already demonstrated their suitability for optoelectronic applications in photonic crystal cavities, LEDs, and NIR photodetectors[**?**].

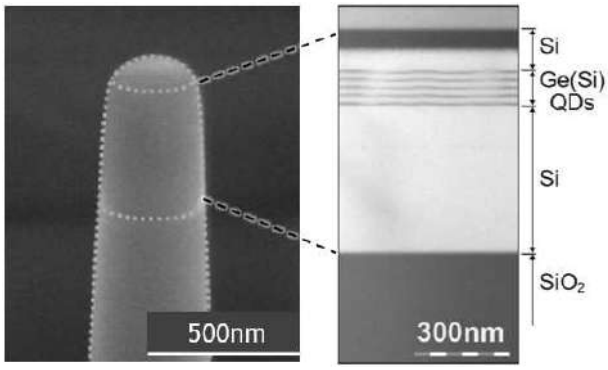


Figure 1: SEM and TEM images of a fabricated Si nanodisk that contains 5 layers of Ge(si) QDs.

2. Results and discussion

Mie resonances of small dielectric Mie-resonators can be used to enhance the luminescence of embedded Ge(Si) quantum dot emitters in the telecom range via the Purcell effect. To investigate this experimentally, we fabricated several cylindrical silicon disks with varying diameter in the range of 300-640 nm containing MBE-grown Ge(Si) quantum dots (Figure **??**). The emission spectra revealed an enhanced emission intensity at the spectral position of the Mie resonances and a characteristic red shift of the emission maxima with increasing resonator size in the wavelength range 1200-1600 nm (Figure **??**). This corresponded very well with finite element simulations determining the resonantly enhanced mode field within the Mie-resonators. To test, if the observed luminescence increase is caused by an increase in radiative emission rate (Purcell factor) or just caused by a redirection of emission in the far field, time-resolved photoluminescence measurements were performed. The observed decrease of emission lifetime at the Mie resonances revealed a clear impact of Purcell-enhancement. However, due to the low Q-factors of the single disk resonances, only moderate Purcell factors up to about 1.4 compared to the unstructured substrate were obtained. This is in agreement with numerical calculations

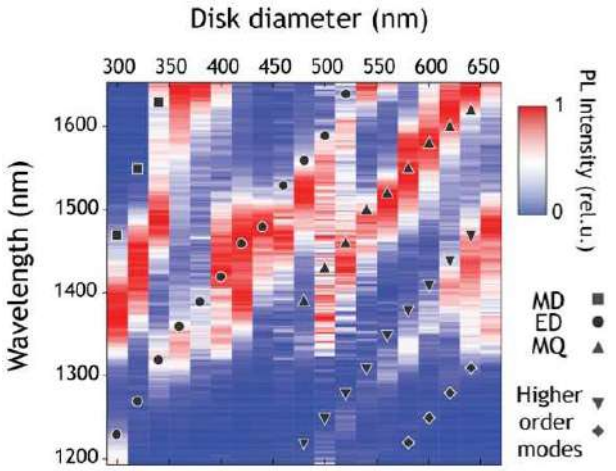


Figure 2: PL map of disks with various diameter. Symbols represent simulated spectral positions of Mie-modes.

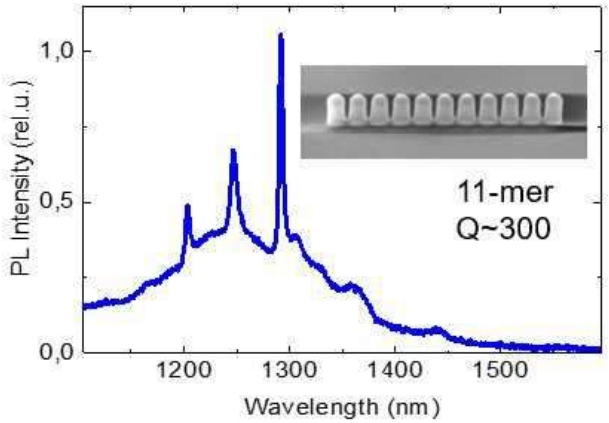


Figure 3: PL spectrum of an 11-disk chain exhibits several high-Q peaks corresponding to hybridized modes.

considering a dipole source inside the Mie-resonator and integrating the overall radiated intensity. To increase the Purcell factor further, collective Mie-resonances of trimers and periodic chains of dielectric nanoresonators are investigated leading to higher Q-factor resonances. An up to 10-fold intensity enhancement could already be achieved due to a partial cancellation of radiative losses in the far field of the collective Mie-resonators. A systematic investigation of the luminescence response from resonator chains with increasing number of individual resonators confirms the coupling of the emission to the collective resonances. Time-resolved photoluminescence measurements are used to experimentally determine the Purcell factors, and the experimental data are compared with finite element and finite difference time domain simulations.

3. Conclusions

In this work, we demonstrated that Ge(Si) QDs embedded in Si nanodisks can be effectively coupled to the Mie resonances of the nanodisk, which was observed as a strong modification of the PL spectra of QDs. The numerical analysis of the dipole emission resulted in a good correspondence to the experimental results. The emission pattern and intensity can be significantly changed by engineering dipole modes in nanodisk structures consisting of several nanodisks. Here, an up to 10-fold emission enhancement and Q-factors as high as 300 were achieved by exciting hybrid modes inside linear chains with various length (3-11 disks). The suppression of the dipole emission increases the quality factor of the resonant modes and paves a way towards a stronger Purcell effect for emitters inside silicon Mie resonators. The results reported in this paper open a way for efficient nanoscale light sources based on resonant structures supporting Mie modes.

Acknowledgement

V.R. and J.S. thank the Federal Ministry for Education and Research (Bundesministerium fr Bildung und Forschung, Project N. 03Z2HN12) for their financial support within the Centre for Innovation Competence SiLi-Nano®. We acknowledge Bodo Fuhrmann and Sven Schlenker for the help in the sample fabrication. In addition, we acknowledge Peter Werner from the Max-Planck Institute of Microstructure Physics for the use of the JEOL JEM 4010 microscope. M.P. acknowledges support from Academy of Finland (Grant 310753), Ministry of Education and Science of the Russian Federation (Minobrnauka) (2.2267.2017/4.6) and the Russian Foundation for Basic Research (16-32-60167, 16-02-00684). A.N. and M.S. acknowledge Russian Foundation for Basic Research (15-02-05272).

References

[1] Yu. Kivshar, All-dielectric meta-optics and non-linear nanophotonics, *National Science Review* 5(2), Pages 144158, 2018.

[2] I. Staude, V. Khardikov, N. Fofang, S. Liu, M. Decker, D. Neshev, T.S. Luk, I. Brener, and Yu. Kivshar, Shaping Photoluminescence Spectra with Magnetoelectric Resonances in All-Dielectric Nanoparticles *ACS Photonics*, 2(2), 172-177, 2015.

[3] S.T. Ha, Y.H. Fu, N.K. Emani, Z. Pan, R.M. Bakker, R. Paniagua-Domnguez, A. Kuznetsov, Directional lasing in resonant semiconductor nanoantenna arrays, *Nature Nanotechnology*, 13, 10421047, 2018.

[4] D.J. Lockwood, J.-M. Baribeau, B.V. Kamenev, E.-K. Lee, L. Tsybeskov, Structural and optical properties of three-dimensional $Si_{1x}Ge_x$/Si nanostructures, *Semiconductor Science and Technology*, 23(6), 2008.

[5] K.L. Wang, J.L. Liu, G. Jin, Self-assembled Ge quantum dots on Si and their applications, *Journal of Crystal Growth* 237239(3), 1892-1897, 2002.

Photonic phase transitions in dielectric structures

Mikhail V. Rybin[1,2]

[1]Department of Physics and Engineering, ITMO University, St Petersburg 197101, Russia
[2]Ioffe Institute, St Petersburg 194021, Russia
E-mail: m.rybin@mail.ioffe.ru

Abstract

Dielectric metamaterials are promising low-loss platform for applications in photonics. In contrast to photonic crystals metamaterials allow a description with effective material parameters. The transition from photonic crystal to metamaterials is found to be accompanied with an abrupt change in electromagnetic field patterns which is typical behavior of phase transitions. Here we review the recent progress in photonic phase transitions between these two classes of artificial structures.

1. Introduction

The advances in adaptation of many concepts borrowed from condensed matter physics to the case of electromagnetic wave propagation have made a great impact on modern photonics. Recently, the concept of photonic phase transitions was introduced to describe how a photonic crystal becomes a metamaterial with a gradual change of the structure parameters [1].This problem is fascinating by itself as an academic study and has an importance for designing the dielectric metamaterials for applications in optical devices.

Let us remind some aspects of conventional thermodynamic transitions. Among other types of phase transitions we consider those related to an appearance of some property, such as metal-to-dielectric transitions due to the opening of bandgap between the valence and conduction bands. In the dielectric phase there exists a frequency interval (limited by the photon energy below the bandgap width) for the material to be transparent. However, at a certain frequency both phase are opaque, while at other ones they both transparent. Thus, we have to distinguish two terms *phase* and *regime*. Regime means the conditions for the effect to be observed, e.g., the frequency range. For example, silicon being a typical semiconductor recently becomes one of the most important dielectric materials for photonics. In other words, for measurements of electric conductivity, silicon is in a semiconductor regime and the same silicon is in a dielectric regime for an interaction with a high frequency electromagnetic field. We use the term *phase* to emphasis a potential ability to obtain some properties under certain conditions.

Now we turn to the photonic phase transitions related to photonic crystals and metamaterials [1]. The main property of photonic crystals is Bragg resonances owing to a coherent interference of wave scattering on the periodic structure. Thus, at Bragg frequencies the electromagnetic waves propagate though the structure under the condition of strong spatial dispersion. In contrast, a metamaterial operates because of a local resonance supported by each structural element and the effects of spatial dispersion are weak despite the resonant conditions. We notice that the Bragg wavelength obeying the law $\lambda_{\mathrm{Bragg}} \propto \cos\theta$ limits this resonance at the low-frequency edge, however the high-frequency limit is tends to infinity. Thus, above the lowest Bragg frequency the electromagnetic waves propagate under the condition of strong spatial dispersion and in general case the metamaterial regime is not possible. The metamaterial regime occurs when the local resonance of structure elements is lower than the lowest Bragg resonance and a corresponding photonic band diagram contain a polariton-type feature [2]. Therefore, the appearance of the polariton-type feature in the band diagram makes it possible to define the metamaterial phase.

2. Study of photonic phase transitions

The first systematic study of photonic phase transitions was reported in paper [1], which considers high-dielectric index structures of cylindrical rods arranged in a square lattice. A comparison between scattering on a single dielectric rod, a photonic band diagram and a transmission of a 10 layer sample reveals that the structures become a metamaterial with artificial magnetic response when the fundamental dipole Mie resonance in a single rod opens a lowest bandgap in the structure. An analysis of bandgap map as a function of the rod permittivity reveals that the appearance of the polariton-type feature corresponds to the Mie-gap splitting below the Bragg gap.

The way how a periodic structure acquires the metamaterial properties is an important problem of modern photonics. Although the appearance of the polariton-type feature in band diagram is a binary criterion of metamaterial phase, the intuition supposes that a gradual change in structural parameters leads to incremental growth of a metamaterial quality. However, simulations of electromagnetic field pattern in periodic structures uncover the abrupt modifications of the pattern are coincided to the appearance of the polariton-type feature in band diagrams [3]. This result justifies the usage of phase transition terminology when we consider the appearance of metamaterial properties in di-

electric structures.

Since the demonstration of structures with resonant effective magnetic permittivity μ was a mile stone in a study of artificial media, the researches on the dielectric metamaterials were focused to the systems with magnetic response, while the dielectric metamaterials with electric response were not reported. The reason is in a stronger optical mode coupling between the neighbor rods for the case of electric dipoles than their magnetic counterpart. Recently dielectric metamaterials with resonant electric response were presented [4]. These metamaterials have sparse structures, i.e., the lattice spacing is about ten times the rod radius. However it requires the higher values of dielectric index. In particular, the dielectric metamaterials with magnetic response are possible for $\varepsilon > 20$ at $r \approx 0.3a$ [1], while the electric metamaterials exist for $\varepsilon > 28$ at $r \approx 0.1a$ [4].

In order to minimize metamaterial rod permittivity one can consider a hexagonal lattice that has the biggest Brillouin zone, and therefore the condition for the Mie resonance splitting off is weaker. We notice that the structures with a hexagonal lattice possess a near-boundary phase that corresponds to a pair of states per frequency and a strong spatial dispersion condition of wave propagation though the structure. However a hexagonal lattice minimizes the rod permittivity to $\varepsilon \approx 22$ in the case of electric metamaterials [5].

The phase criterion described above is based on the analysis of the second dispersion branch. The metamaterial phase requires high-index materials, which usually have a strong frequency dependence of complex permittivity. However photonic band diagrams do not allow distinguishing the first and the second branches of structures, which constituents have complex permittivity [6]. The behavior of complex branches in the bandgap range makes it possible to introduce another criterion of metamaterial phase based on a crossing or an anti-crossing dependence [3]. These two criteria were found to give the same results for the lossless structure. Recently, the crossing/anti-crossing criterion makes it possible to build photonic phase diagram of silicon-based metamaterials with magnetic response [3]. The predicted metamaterials consisting of silicon nanorods operate at the visible range since the semiconductor permittivity grows when the wavelength becomes shorter.

The existence of dielectric metamaterials was verified in microwave measurements [1]. The experimental sample was the array of 5 by 10 plastic tubes filled with distilled water ($\varepsilon = 50$ - 80) and fixed by an adjustable frame. Transmission spectra in dependence on the square lattice spacing exhibit that at a certain value the transmission dip related to the dipole Mie mode becomes the lowest gap of the structure in agreement with the numerical simulations.

3. Outlook and perspectives

We have reviewed recent advantages of photonic phase transitions, which is a new topic in metamaterial research. For example, disorder-induced phase transitions in metasurfaces were reported recently [7]. Among a great application potential in designing dielectric metamaterial devices, this topic defines a number of basic problems. In particular, the abrupt change in the photonic subsystem during the phase transition is expected to be accompanied with the peculiarities in energy. We anticipate a study of photonic phase transitions from photonic crystal gratings to flat metasurfaces. The experimental confirmation of a bulk dielectric metamaterial in visible or near infrared range is a challenging but desirable task.

Acknowledgement

I thank M. Limonov and Y. Kivshar for fruitful discussions. This work was supported from the Ministry of Education and Science of the Russian Federation (3.1500.2017/4.6).

References

[1] Rybin M.V. et al., Phase diagram for the transition from photonic crystals to dielectric metamaterials, *Nature Commun.* 6: 2015.

[2] Kaina N., Lemoult F., Fink M., Lerosey G., Negative refractive index and acoustic superlens from multiple scattering in single negative metamaterials, *Nature* 77: 77–81, 2015.

[3] Li S. V., Kivshar Y. S., and Rybin M. V., Towards silicon-based metamaterials, *ACS Photonics*, 5: 4751-4757, 2018.

[4] Maslova E.E., Limonov M.F., Rybin M.V., Dielectric metamaterials with electric response, *Opt. Lett.* 43: 5516–5519, 2018.

[5] Maslova E.E., Limonov M.F., Rybin M.V., Transition "photonic crystal–metamaterial with electric response" in dielectric structures, *JETP Letters* 109: 348–353, 2019.

[6] Rybin, M. F. and M. F. Limonov, Inverse dispersion method for calculation of complex photonic band diagram and PT symmetry, *Phys. Rev. B*, 93:165132, 2016.

[7] Rahimzadegan A. et al., Disorder-induced phase transitions in the transmission of dielectric metasurfaces, *Phys. Rev. Lett.*, 122:015702, 2019.

Plasmon-enhancement in nanostructured shells for single particle protein assays and photodynamic therapy

Christophe Silien[1,2,*], Grace Brennan[1,2], Daragh Rice[1,2], Matthew Gleeson[1,2]
Rabah Mouras[1,2], Tewfik Soulimane[1,2], and Syed A.M. Tofail[1,2]

[1]School of Natural Sciences, University of Limerick, Ireland
[2]Bernal Institute, University of Limerick, Ireland
*corresponding author, E-mail: Christophe.Silien@ul.ie

Abstract

The ability to grow plasmonic shells on micro- and nanoparticles by electroless plating leads to the creation of novel and easily deployable heterogeneous materials for detection of biomolecules and medical therapy with high sensitivity and low irradiation needs. The overall quality, optical performances, and stability of the shells are important to address and can be controlled by rational design of the shell structures. Here, Ag and Au nanostructured shells are discussed in the context of magneto-plasmonics and attomolar multiplex protein assays.

1. Introduction

When involving targeted operation with light, multifunctional micro- and nanoparticles can rely on plasmons so that efficient diagnosis and therapy materials can be rationally designed. We explore two practical cases of Ag and Au shells in the context of single particle attomolar sensitive protein assay and magneto-plasmonics for photodynamic therapy.

Current best practices for diagnostics are time consuming and laborious, and plasmonic substrates can revolutionize this industry. Aiming to detect and quantify samples of mixed antigens, we have developed multi-shell microparticles including plasmonic Ag shells enhancing both the Raman and fluorescence in dual multiplex assays. Sandwich immunoassays in this way afford attomolar detection, and are here oriented towards the targeting of a unique panel of antigens for pancreatic cancer.

Because, for plasmonic nanomaterials, incident resonant light results in local heat dissipation [1], photodynamic therapy is possible. It is hypothesized that when the plasmon shell cores are magnetic, the plasmon absorption can be controlled by magnetic self-assembly and tuned towards near-infrared wavelengths where tissue scattering and absorption are minimum, in the so-called "biological windows" between ~700 and ~2000 nm [2].

2. Magnetic-tuned Au plasmon in photodynamic therapy

Through magnetic dipole-dipole interactions, superparamagnetic nanoparticles form chain-like structures when an external static magnetic field is applied. Upon removal of the field, the nanoparticles dissociate into a colloidal solution. These superparamagnetic nanoparticles can be used for tunable plasmonic coupling, see Figure 1.

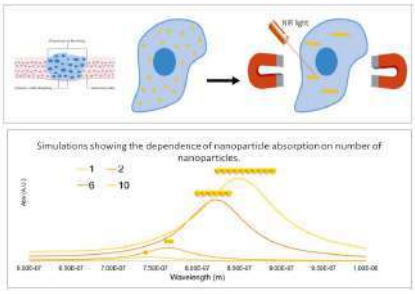


Figure 1: (top panel) Intercellular assembly of magnetic-plasmonic nanoparticles. (bottom panel) Simulations of nano-chain assembly plasmonic activity using COMSOL Multiphysics®. The simulations predict redshift into the NIR and increase of the plasmon absorption.

Iron oxide/gold core/shell nanoparticles were synthesized and were shown to be both magnetically responsive and plasmon active. The synthesis schematic can be followed in Figure 2. To assess the thermo-plasmonic activity, infrared thermography was used after embedding the assembled particles in chitosan hydrogel. A clear increase in laser-induced heating was observed with respect to the control, see Figure 2.

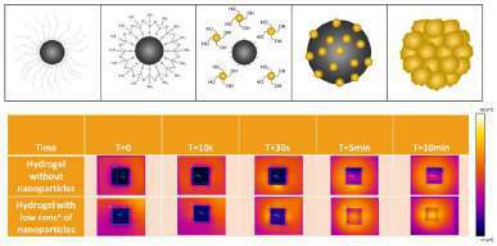


Figure 2: (top panel) Synthesis steps for magnetic-plasmonic nanostructures. Further functionalisation is possible for better tumour targeting (PEGylation/targeting moieties [3]). (bottom panel) IR thermography of magnetic-plasmonic

nanoparticles embedded in chitosan hydrogel, compared to the control (irradiated @ 753nm).

3. Nanoporous silica templated Ag shells

Ag nanoparticle shells were grown from $AgNO_3$ in ethanolic solutions, at the surface of SiO_2 nanoporous microspheres/beads via direct electroless plating, utilizing a novel reducing agent in aminopropyltriethoxy silane (APTES) [4]. The nanoporous silica surface drives the formation of dense nanoparticles films with excellent optical enhancement and excellent reproducibility, with circa 11% variation in signal when measuring 10 individual microparticles. The Ag shells structures can be seen from SEM and TEM micrographs in Figure 3.

APTES also develops inter-particle SiO_2 allowing for the direct growth of SiO_2 shells by further addition of a silica precursor and pH adjustment, using for example the Stober chemistry [5]. The system further facilitates the formation of immunoassay substrates as SiO_2 can be readily functionalized with various surface chemistries.

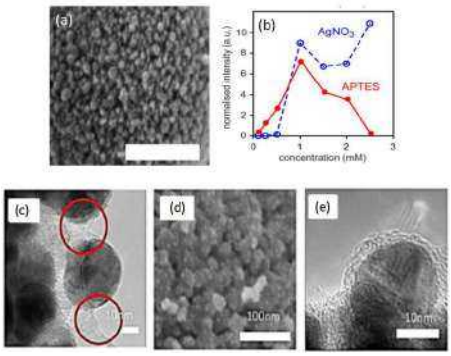


Figure 3: (a) FE-SEM image of as-grown Ag nanoparticle on nanoporous silica cores. (b) SERS intensity at 1452 cm^{-1} on single beads after self-assembly of amino-thiophenol revealing that equal amount of $AgNO_3$ and APTES supports most optically efficient films. (c) HR-TEM images revealing the embedding of the individual Ag particles within silica. (d) FE-SEM image following SiO_2 shell formation. (e) HR-TEM image of the silica covered Ag nanoparticle.

4. Lab-on-a-bead multiplex assay

For assays, the Ag/SiO_2 beads were functionalized with unique Raman reporter molecules and the SiO_2 shells were grafted with amine surface groups to immobilize monoclonal antibodies. The overall structure allows forming supports for dual sandwich immunoassay at the level of each single beads, whereby the Raman markers afford identification, and secondary fluorescent-tagged antibody offer quantification.

The surface grafted antibodies were chosen to be specific for three novel pancreatic cancer antigens, TSP-2, CEACAM1 and TIMP-1, all were easily detected utilizing Raman spectroscopy. Plotting of the fluorescence intensity against antigen concentration also shows that this system is capable of near attomolar detection from the measurement of single particles.

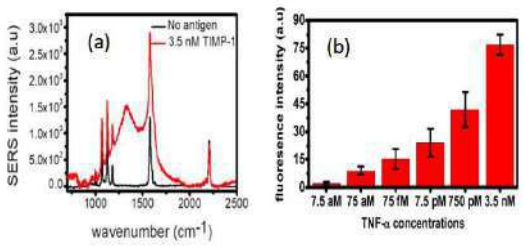


Figure 4: (a) SERS/fluorescence spectra on a single particle after formation of immunoassay (black: no antigen is present; red antigen present). (c) Fluorescence intensity with respect to antigen concentration, showing attomolar sensitivity.

5. Conclusions

Through the use of direct colloid chemistry, highly controlled Ag nanoparticle films form on silica cores, with excellent reproducibility and spectral enhancement. These are ideal immunoassay substrates and were shown to give excellent SERS as well as fluorescence for attomolar sensitive detection from single particle measurements.

When grown on a magnetic core, Au shells are both superparamagnetic and plasmonic, and form chain like structures in the presence of an external magnetic field. Infrared thermography confirmed the additional heat generation in hydrogels containing magnetoplasmonic nanoparticles in comparison to blank hydrogel, paving the way towards targeted photodynamic therapy.

Acknowledgements

The research leading to these results has received funding from Science Foundation Ireland's Career Development Award program (13CDA2221). The research was also supported by the Science Foundation Ireland (SFI) centre CÚRAM and the European Regional Development Fund (Grant Number 13/RC/2073).

References

[1] L. Pezzi et al., "Photo-thermal study of a layer of randomly distributed gold nanoparticles: from nano-localization to macro-scale effects," J. Phys. D. Appl. Phys., vol. 50, no. 43, p. 435302, Nov. 2017.

[2] S. Zhu, B. C. Yung, S. Chandra, G. Niu, A. L. Antaris, and X. Chen, "Near-Infrared-II (NIR-II) Bioimaging via Off-Peak NIR-I Fluorescence Emission," Theranostics, vol. 8, no. 15, pp. 4141–4151, 2018.

[3] S. D. Steichen, M. Caldorera-Moore, and N. A. Peppas, "A review of current nanoparticle and targeting moieties for the delivery of cancer therapeutics," 2012.

[4] Rice, D., et al., APTES Duality and Nanopore Seed Regulation in Homogeneous and Nanoscale-Controlled Reduction of Ag Shell on SiO2 Microparticle for Quantifiable Single Particle SERS. ACS Omega, 2018. **3**(10): p. 13028-13035.

[5] Stöber, W., Fink, A. and Bohn, E., 1968. Controlled growth of monodisperse silica spheres in the micron size range. Journal of colloid and interface science, 26(1), pp.62-69.

Single hybrid plasmonic structures for efficient photon pair production at the nanoscale

Nicolas Chauvet[1,2*], Maëliss Ethis de Corny[1], Guillaume Laurent[1], Aurélien Drezet[1], Gilles Nogues[1], Géraldine Dantelle[1], Thierry Gacoin[3], Atsushi Uchida[4], Hirokazu Hori[5], Serge Huant[1], Guillaume Bachelier[1], Makoto Naruse[2]

[1]Institut Néel - CNRS, Université Grenoble Alpes, Grenoble, France
[2]The University of Tokyo, Tokyo, Japan
[3]Laboratoire Charles Fabry, Palaiseau, France
[4]Saitama University, Saitama, Japan
[5]University of Yamanashi, Yamanashi, Japan
*corresponding author, E-mail: nicolaschauvet2004@gmail.com

Abstract

Efficiency of single hybrid plasmonic nanostructures are discussed for SHG and SPDC. After successful fabrication, results show good agreement between experiments and FEM simulations, indicating field enhancement effect as the main factor for increased efficiency. SPDC simulations at the nanoscale predict measurable pair rate for structures already optimized for SHG. Finally, use of entangled photon pairs as a resource for decision-making applications is shown as advantageous over classical photonic states.

1. Introduction

Combining the optical nonlinear efficiency of dielectric media with the electromagnetic field enhancement of double resonant plasmonic nanostructures [1] is a promising way toward nanosized nonlinear photonic devices, with potential applications in integrated and quantum optics. However, previous studies on nanostructure arrays [2] have neither yet shown significant nonlinear efficiency increase, nor if the slight increase comes from the field enhancement inside the dielectric medium or from the plasmonic structures themselves influenced by their dielectric surrounding.

The goal of our work is to obtain single hybrid nanostructures which optimize the efficiency of Second Harmonic Generation (SHG) and/or Spontaneous Parametric Down Conversion (SPDC) inside a nonlinear nanocrystal by using plasmonic nanoantennas.

2. Efficient nonlinear optics at the nanoscale

2.1. Tools and methods

This project requires several kinds of nonlinear optical experiments to be conducted at a single nanoparticle level, while being able to detect weak signals with different wavelengths. To this end, we have realized a versatile setup able to easily switch from one experiment to another while keeping the sample at the same spot, thus reducing experimental variability. The setup is also fully computer controlled, with an autonomous optimization algorithm to run experiments in the most reproducible way.

The numerical simulation part is based on a Finite Element Method to estimate the nonlinear intensity generated by a single nanoparticle in a quantitative way, so as to compare and discriminate between different origins of nonlinear signal [3].

Finally, a rigorous nanofabrication protocol based on electronic lithography and precise realignment has been elaborated. This enables one to optimize each nanostructure according to the crystalline orientation of each nanocrystal experimentally determined beforehand.

2.2. Results

Obtained hybrid nanostructures with gold or aluminum antennas and KTP crystals are pictured on figure 1 with SEM imaging. For each of them, a replica of the bare plasmonic antennas is fabricated nearby to directly compare their efficiency.

After fabrication, SHG measurements let us compare the efficiency between the bare crystal (before), the bare antennas and the hybrid. Efficiency is significantly higher for hybrid structures compared to each isolated component as for the case of figure 1, reaching SHG enhancement of up to 3 orders of magnitude compared with nonlinear nanocrystal, and up to 2 orders of magnitude compared with bare aluminum or gold antennas.

Simulations are in agreement with such enhancement factors, and indicate the main origin of nonlinear efficiency is attributed to the crystal and not the antennas.

2.3. SPDC predictions at the nanoscale

Our team has developed a theoretical model for SPDC at the nanoscale [4], enabling one to quantitatively evaluate the produced photon pair rate for any given configuration. Simulations show that optimizing a hybrid nanostructure in SHG makes it optimized in SPDC as well, confirming the increase of nonlinear efficiency within the nanocrystal thanks to field enhancement effect.

Quantitative evaluations have been made in realistic experimental conditions. Adding plasmonic antennas to a nanocrystal raises nonlinear efficiency by several orders of magnitude, to the point it becomes theoretically measurable. Noise estimate from experimental attempts on

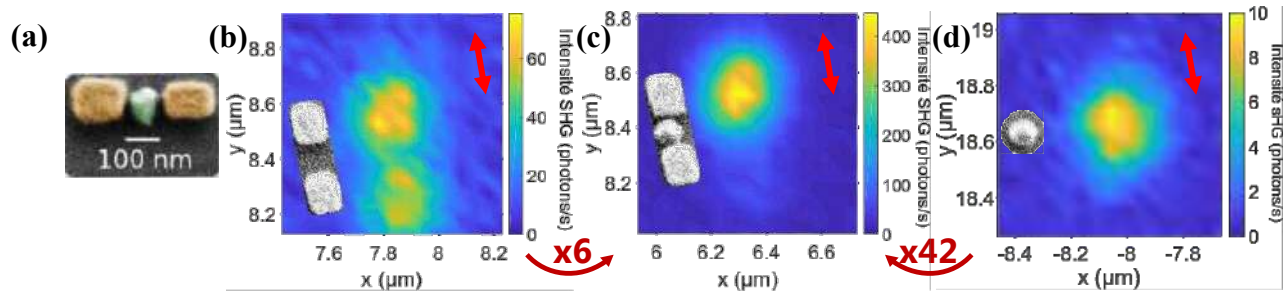


Figure 1: (a) Scanning Electron Microscopy (SEM) image of an Au-KTP-Au hybrid nanostructure (fake colors), (b) SHG excitation cartography of bare gold antennas, (c) of hybrid structure and (d) of bare KTP crystal at 850 nm excitation wavelength, 100 µW of average power and excitation polarization along the red arrow axis. Ratios are indicated.

bare KTP is below the theoretical expected optical signal, opening the way to SPDC detection from a single nanostructure for the first time.

3. Entangled photon pairs for decision making

Macroscopic sources of SPDC are commonly used for frequency conversion, as well as entangled photon pair production in quantum optics experiments. The relative simplicity of production, modification and transmission of such quantum photonic states has also attracted interest from the artificial intelligence community to study the potential advantage of quantum information processing over binary information in this respect.

Recent works on single-photon-based decision making [5] have triggered new discussions on the advantages of using entangled photons as a resource for situations like the Competitive Multi-Armed Bandit problem, a typical competitive decision-making situation related to resource allocation between isolated, individual decision makers in an uncertain environment. Such configuration raises new questions with respect to the single decision maker, such as fairness, maximum common income or protection from greedy actions of a player against another.

The 2-arms bandit problem has been experimentally implemented, using a well-known design [6] enabling one to produce either single photons, correlated photon pairs or entangled photon pairs using the polarization of light as a quantum state basis. Higher common benefits and equality for entangled photons, as well as near-zero conflict of decision, are demonstrated for entangled photons whereas correlated photon pairs only show similar performances for a restricted set of initial conditions. With entangled photons, greedy actions are shown to be counterproductive with respect to both common and individual reward: in this situation, a given player can never get more benefits than the other whatever its decision. On the other hand, both common and individual benefits can be optimized by autonomous polarization alignment schemes, thus providing error correction protocol without any communication between players.

4. Conclusions

Hybrid plasmonic nanostructures have been fabricated and demonstrated as optimized for SHG with both gold and aluminum as plasmonic material. Field enhancement is shown to be the main cause of efficiency increase, in agreement with predictions for SPDC. Finally, entangled photon pairs from a macroscopic source are shown to be of interest for social decision-making situations.

Acknowledgements

The authors acknowledge the financial support from the Agence Nationale de la Recherche, France, through the TWIN project (Grant No. ANR-14-CE26-0001-01-TWIN, ANR-13-BS10-0007-PlaCoRe), the Université Grenoble Alpes, France, for the Chaire IUA award to G. Bachelier and the Ph.D. grant to N. Chauvet from the Laboratoire d'excellence LANEF in Grenoble (ANR-10-LABX-51-01). This work was supported in part by CREST project (JPMJCR17N2) funded by the Japan Science and Technology Agency, the Core-to-Core Program A. Advanced Research Networks and the Grants-in-Aid for Scientific Research (JP17H01277 and JP16H03878) funded by the Japan Society for the Promotion of Science.

References

[1] M. Celebrano, X. Wu, M. Baselli, S. Grossmann, P. Biagioni, A. Locatelli, C. De Angelis, G. Cerullo, R. Osellame, B. Hecht, L. Duò, F. Ciccacci, M. Finazzi, Mode matching in multiresonant plasmonic nanoantennas for enhanced second harmonic generation, *Nature nanotechnology* 10: 412−417, 2015.

[2] H. Linnenbank, Y. Grynko, J. Förstner, S. Linden, Second harmonic generation spectroscopy on hybrid plasmonic/dielectric nanoantennas, *Light: Science and Applications* 5: e16013, 2016.

[3] M. Ethis de Corny, N. Chauvet, G. Laurent, M. Jeannin, L. Olgeirsson, A. Drezet, S. Huant, G. Dantelle, G. Nogues, G. Bachelier, Wave-Mixing Origin and Optimization in Single and Compact Aluminum Nanoantennas, *ACS Photonics* 3: 1840-1846, 2016.

[4] G. Laurent, N. Chauvet, G. Nogues, A. Drezet, G. Bachelier, Photon-pair production at the nanoscale with hybrid nonlinear/plasmonic antennas, *arXiv* 2018.

[5] M. Naruse, M. Berthel, A. Drezet, S. Huant, M. Aono, H. Hori, S.-J. Kim, Single-photon decision maker, *Scientific Reports* 5: 13253, 2015.

A. Fedrizzi, T. Herbst, A. Poppe, T. Jennewein, A. Zeilinger, A wavelength-tunable fiber-coupled source of narrowband entangled photons, *Optics Express* 15: 15377, 2007.

Translational invariant structured mirrors for beam-shaping

R. Herrero[1], P-Y. Wang[2], Y-C. Cheng[2], M. Botey[1] and K. Staliunas[1,3]

[1] Departament de Física, Universitat Politècnica de Catalunya (UPC), Barcelona, Catalonia
[32] University, Taipei, Taiwan
[3]3Institució Catalana de Recerca i Estudis Avançats (ICREA), Barcelona, Catalonia
*corresponding author, E-mail: ramon.herrero@upc.edu

Abstract

We propose beam-shaping and light filtering in reflection based on translational invariant structured mirrors. These meta-mirrors are composed by a thin structured layer with a transverse modulation of the refractive index in the micron scale and positioned in front of a metallic flat mirror. The strong transverse spectrum modification allows spatial filtering and beam-shaping of the reflected beam. The study points toward new possible type of filtering devices without alignment needs due to its translational invariance.

1. Introduction

Angular filtering and beam-shaping are commonly used in many applications to obtain suitable beams from a large variety of radiation sources. The enhancement of the spatial characteristics of the radiation becomes critical for active systems as lasers where the maximal radiation brightness is linked to a single transverse mode emission. Moreover, conventional filtering methods use large sized and external gratings that strongly diminish the robustness of lasers and in particular of micro-lasers. Therefore, the spatial filtering is especially a huge problem in Broad Area Semiconductor (BAS) lasers, Vertical Cavity Surface Emitting Lasers (VCSELs) and microchip lasers, where external filtering arrangements are not convenient.

Beam-shaping and spatial filtering methods based on Photonic Crystals (PhCs) have been proposed as an alternative method for micro-lasers [1]. It has been numerically demonstrated for BAS amplifiers in a single path configuration but also in intracavity arrangement for lasers [2]. Such filters involve simultaneous transverse and longitudinal refractive index periodicities, demanding 2D and 3D spatial photonic structures, an important challenge for current technologies. A satisfactory solution is the replacement of a cavity mirror by a structured meta-surface with filtering and beam-shaping properties.

2. Model

The present paper considers a flat meta-mirror for this purpose. It is based on a thin grating, i.e. a structured layer with a transverse modulation of the refractive index in the micron scale and positioned at a distance of some wavelengths from a metallic mirror. The created transverse structured cavity strongly modifies the transverse spectrum of reflected beams allowing spatial filtering and beam-shaping. The obtained translational invariant meta-mirror would not need supplementary alignments, would neither decrease the micro-laser robustness and becomes more suitable for fabrication purposes. The fabrication of such structures, with wavelength scale size and sufficient index contrast have been experimentally demonstrated by laser writing technologies in organic and nonorganic materials [3].

The analytic approximation considers the meta-mirror as a structured layer composed by equispaced rectangular elements in front of the flat totally reflecting mirror creating a transverse modulated Fabry-Perot cavity, see Fig.1.a. The structured layer is considered as a pair of shifted diffraction gratings and each rectangular element introduces Mie resonances in the system in addition to the ones associated to the cavity.

We consider the incident wave with wavenumber vector k_0 incident angle α with respect the surface normal direction and corresponding wavevector $\vec{k} = (k_x, k_z) = k_0(\sin\alpha, \cos\alpha)$. The grating with transverse period a and wavenumber $q_x = 2\pi / a$ diffracts the entering light in components corresponding to the diffraction orders. We consider the field expansion into the zero- and first diffraction orders with transverse wavenumbers $k_x \pm q_x$ which field amplitudes are written in the vector form $\vec{A} = (A_{-1}, A_0, A_1)$. The reflection matrix of the whole structured mirror as a function of the incident angle is

$$\hat{R}_{\mathrm{Ref}}(k_x) = \left[\hat{R} + \hat{T}\hat{P}\left(1 + \hat{R}\hat{P}\right)^{-1}\hat{T} \right], \qquad (1)$$

where the complex matrices correspond to reflection $\hat{R}$ and transmission $\hat{T}$ of the structured layer and propagation between the structured layer and mirror $\hat{P}$.

We scan the incident angle of the plane wave to obtain the reflection coefficient profile, arising filtering and beam-shaping properties for certain parameter sets (Fig.1.b). The reflection profiles are associated to diffraction associated to the grating, resonances of the structured cavity and Mie resonances of the structured layer elements.

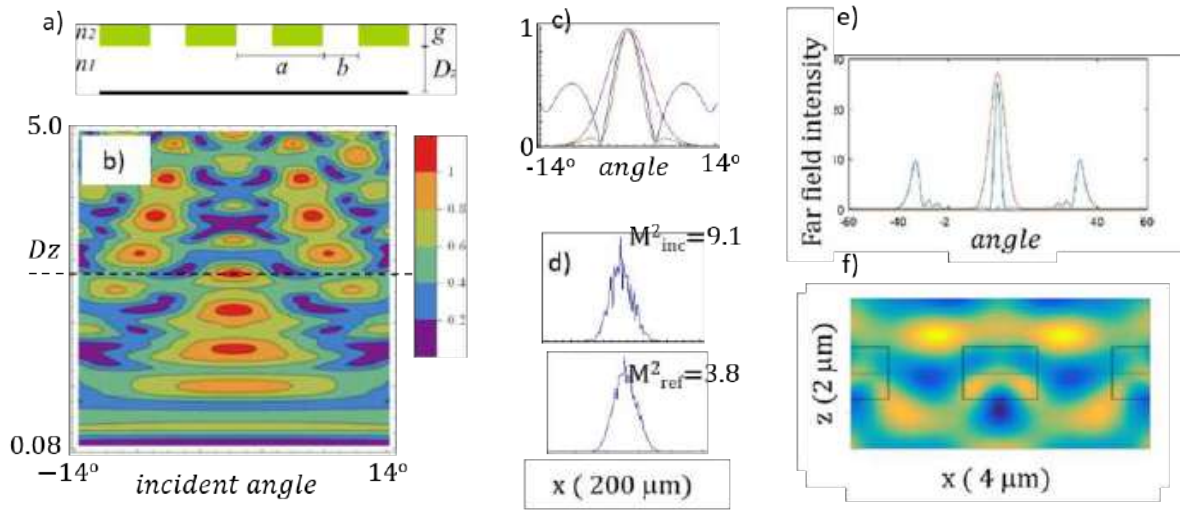


Fig. 1 (a) Scheme of the structured mirror. (b) Reflection coefficient R as a function of the incident angle and distance between the structured layer and mirror (Dz), the rest of the parameters are g=0.7μm, a=2μm, b=1μm, n1=1, n2=1.68, and incident wavelength λ=1μm. (c) Reflection coefficient profile (blue), spectrum of an incident Gaussian beam (red) and reflected spectrum (green) for Dz=3μm. (d) Incident noisy beam with high M^2 and reflected beam with a strongly improved beam quality factor. (e) Far field intensity obtained by FDTD integration with the same parameter set and (f) field intensity distribution between the rectangular elements and mirror for the corresponding spatial mode.

A possible application is the generation of hypergaussian and top-hat beams from Gaussian beams by the simple reflection in selected structures. Filtering and noise reduction in light beams is available from narrow reflection spectra, see Fig.1c, obtaining a decrease of the beam quality factor M^2 in a factor 2 due to the reduced angular spectrum in reflection (see Fig.1.d).

The reflection spectra given by the model is in good agreement with the far field intensity obtained from full FDTD simulations with proper beam widths, obtaining similar profiles of first diffraction orders (compare the central part of Fig.1.e. with Fig.1.c).

The reported study uncovers rich possibilities for these new structured mirrors allowing to model beam spectra by simple reflection. We expect the proposed meta-mirrors for applications in micro-lasers and other devices where classical filtering mechanisms are not possible.

References

[1] E. Colak, A.O. Cakmak, A.E. Serebryannikov, E. Ozbay, J. Appl. Phys. 108, 113106, 2010

[2] R. Herrero, M. Botey, M. Radziunas, and K. Staliunas, Opt. Lett. 37, 5253, 2012

[3] S. Kumar, R. Herrero, M. Botey, and K. Staliunas, Opt. Lett. 39, 5598, 2014

[4] L. Maigyte, T. Gertus, M. Peckus, J. Trull, C. Cojocaru, V. Sirutkaitis, K. Staliunas, Phys. Rev. A. 82, 043819, 2010.

Periodic metasurface structures processed with spatially shaped femtosecond laser: Fundamentals and Applications

Xiaowei Li

Beijing Institute of Technology, Beijing, China
*corresponding author, E-mail: lixiaowei@bit.edu.cn

Abstract

We propose a mask-free approach of femtosecond laser nonablative processing to fabricate extremely long-range uniform periodic metasurface structures. A cylindrically focused femtosecond laser efficiently produce large-area periodic modified-stripes, then, the modified-stripes act as fine etch stops to generate desirable structures on sample surfaces during the subsequent chemical-etching process. The diffraction efficiency of the incident light could be flexibly tuned. This morphology-controllable periodic surface structures may facilitate application prospects in broad fields, such as optical communications, optical sensors, etc.

Revealing Light-Matter Interactions at the Nanoscale using Single-Molecule Super-Resolution Microscopy

Nathan Kimmitt[1], Zachary Hallenbeck[1], Evan Kalinowsky[1,2], Andrew Dibiasio[1] and Esther Wertz[1,*]

[1]Department of Physics, Applied Physics and Astronomy, Rensselaer Polytechnic Institute, Troy, NY, USA
[2]Department of Physics, Massachusetts College of Liberal Arts, North Adams, MA, USA
*corresponding author, E-mail: wertze@rpi.edu

Abstract

We use super-resolution imaging to unravel the coupling of light to a bowtie antenna and investigate single-molecule trapping dynamics.

1. Introduction

Metal nanoparticles (NPs) sustain a collective oscillation of their free electrons, called a localized surface plasmon resonance (LSPR), when excited by an electromagnetic wave. When this incident wave is resonant with the LSPR frequency, the field intensity is strongly increased in the near field of the NP [1]. Plasmonics thus provides a unique tool for the manipulation and confinement of light well beyond the diffraction limit. These plasmonic systems have a broad range of applications, from biology [2] and sensing [3], to nonlinear optics [4] and as antennas transmitting and receiving light signals at the nanoscale [5].

Bowtie nano-antennas (BNAs) are small dimers composed of two equilateral triangles with a nano-gap, which have been shown to be very effective for optical manipulation. Indeed, while conventional optical tweezers have the ability to trap and manipulate particles on the micron-scale, the plasmon resonances in BNAs can be used to induce forces on a scale well below the diffraction limit of light. The field enhancement and confinement drastically amplifies optical gradient forces, allowing for trapping and manipulation of these nanoparticles in a sub-diffraction-limited volume [7]. However, many difficulties remain in experimentally detecting and measuring the trapping dynamics in real and their dependence on shape, size, and enhanced field properties of the localized electromagnetic modes due to the limitations of optical microscopy. Single-molecule fluorescence (SMF) imaging is a powerful technique to optically study structures beyond the diffraction limit by localizing isolated fluorophores and fitting the emission profile to the microscope point-spread function [6].

In this work, we use SMF in combination with plasmonic

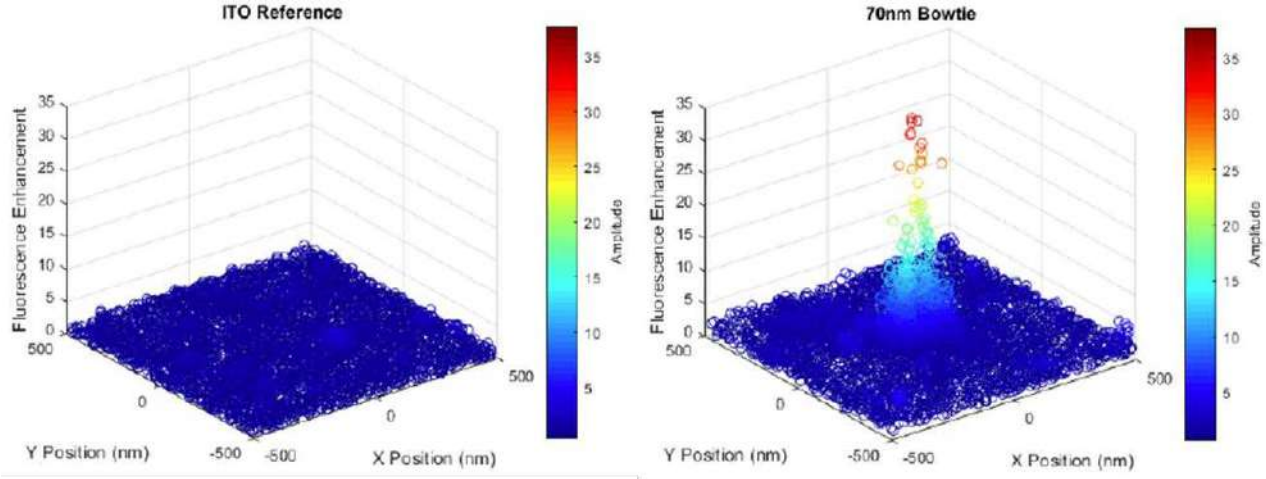


Figure 1: Super-resolution maps of Cy5 molecules (a) on an ITO reference sample, and (b) near 80 nm bowties. The x- and y-positions correspond to the relative fit coordinates, and the z-axis gives the intensity enhancement of the fit molecule. In the reference case, the dye molecules adsorb homogenously on the sample surface and the distribution of intensities is quite narrow. On the other hand, when the dye emission wavelength is resonant with the LSPR, the BNA acts as a very efficient antenna, and a strong fluorescence enhancement is observed.

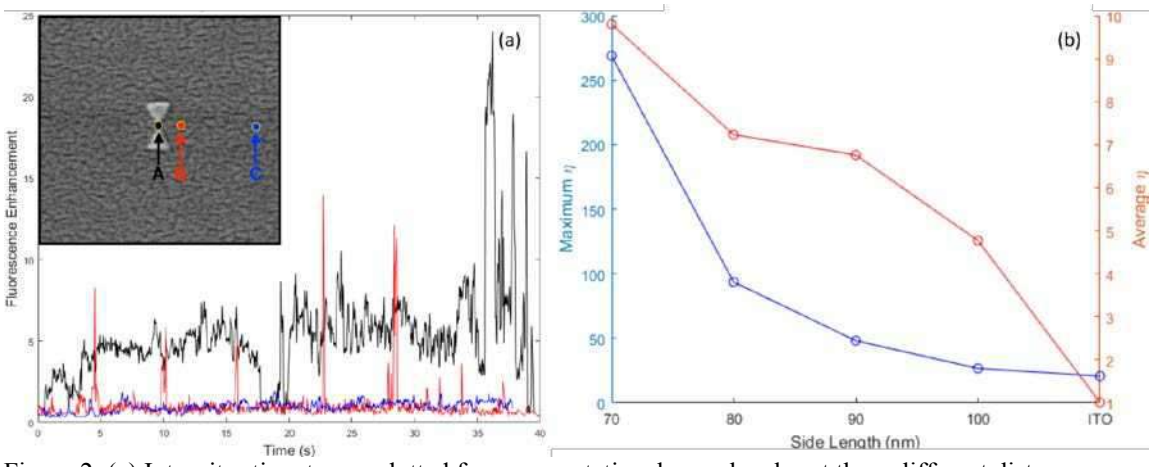


Figure 2: (a) Intensity−time traces plotted for representative dye molecules at three different distances from the BNA nano-gap, as indicated in the inset. As the distance from the BNA increases, the fluorescence enhancement and molecule "on" time decreases. (b) Trapping efficiency for differing BNA side lengths. Even for largest detuning, a fivefold trapping efficiency enhancement is observed compared to the reference case.

optical trapping to experimentally investigate the plasmon-fluorophore coupling at the nanoscale.

2. Results and Discussion

SMF measurements of Cy5 in a water solution were made using the random absorption of molecules onto the surface. Dye molecules in a water solution diffuse too fast to be detectable. When one of these molecules adsorbs stochastically to the surface of the sample, it is immobilized long enough to be imaged at which point the intensity distribution of the dye is fit to a 2D Gaussian. The emission location of a single molecule is then determined by the fit, and the localization precision increases with the number of collected photons, thus allowing precisions at the nanometer scale for the brightest points. By observing the adsorption and desorption process over thousands of frames, a map of all single-molecule intensities over the entire sample surface can be made (Figure 1). For the ITO reference sample (no BNAs), a homogenous spatial distribution of dye molecule positions can be seen, with no fluorescence enhancement. However, when the dye molecules couple to BNAs a large fluorescence enhancement can be seen, illustrating the efficiency of these bowties as nano-antennas.

By tracking the molecules over time, we can further probe the dynamics of the system. We define a trapping efficiency function η, which takes into account the average intensity enhancement, and track length (Figure 2). For the ITO reference values, the average of η over all tracks is 1. It reaches a maximum when the dye emission has the best overlapp with the BNA LSPR (70 nm side-length BNAs), then monotonically decreases as the detuning between dye and LSPR increases.

BNAs thus provide a useful balance between enhancement and losses for single-molecule fluorescence applications. This plasmon-coupled emission has the potential to improve the resolution of single-molecule imaging by increasing the quantum yield and photostability of fluorescent probes, while significant reductions in emission decay times result in high-emission-rates with emitters that can be controlibly coupled to the antennas.

3. Conclusions

By using the random motion of single dye molecules in solution to stochastically scan the surface, and by assessing emission intensity, wavelength, and density of emitters as a function of position and time, we gain new insight into the properties of plasmonic systems and observe the plasmonic optical trapping dynamics in real time.

References

[1] S. A Maier, *.Plasmonics: Fundamentals and Applications*, Springer, 2007.

[2] Righini, M., *et al.*, Nano-optical Trapping of Rayleigh Particles and Escherichia coli Bacteria with Resonant Optical Antennas, *Nano Lett.* 9, 3387−3391, 2009.

[3] K. A. Willets, R. P. Van Duyne, Localized Surface Plasmon Resonance Spectroscopy and Sensing. *Annu. Rev. Phys. Chem.* 58, 267−297, 2007.

[4] M. Kauranen, A. V. Zayats, Nonlinear plasmonics. *Nat. Phot.* 6, 737, 2012.

[5] V. Giannini, A. I. Fernández-Domínguez, S. C. Heck, S. A. Maier, Plasmonic Nanoantennas: Fundamentals and Their Use in Controlling the Radiative Properties of Nanoemitters, *Chem. Rev.* 111, 3888−3912, 2011.

[6] E. A. Wertz, B. P. Isaacoff, J. D. Flynn, and J. S. Biteen.Single-Molecule Super-Resolution Microscopy Reveals How Light Couples to a Plasmonic Nanoantenna on the Nanometer Scale, *Nano Lett.* 15, 2662−2670, 2015.

[7] M. L. Juan, M. Righini, R. Quidant, Plasmon nano-optical tweezers, *Nat. Phot.*5, 349–356, 2011.

'Hybrid plasmonic' to 'plasmonic only' transition and 'photonic only' mode supported by semiconductor near metal

Ning Liu[1*]

[1] Department of Physics and Bernal Institute, University of Limerick, Co. Limerick, Ireland
*corresponding author, E-mail: ning.liu@ul.ie

Abstract

Optical modes supported by dielectric-semiconductor-insulator-metal 4-layered structure have gained increasing popularity in recent years due to their applications in nanoscale waveguides and lasers. In this communication, the author is going to discuss different optical modes that co-exist in this configuration, their physical origins and their applications in nanophotonics.

Among all optical modes that are supported by the dielectric-semiconductor-insulator-metal 4-layered configuration, the author studied in detail the fundamental TM and TE modes. The fundamental TM mode has demonstrated significant advantages over pure photonic modes, which are supported by similar structures without metal, to realize resonant cavities at sub-diffraction limited volumes [1]. It is still under debate in literature, however, how to understand this fundamental TM mode and if the hybridization picture is an accurate description to this mode. Using a model system of insulator-semiconductor-insulator-metal planar structure, the author is able to show analytically and also through variational methods that a transition from 'hybrid plasmonic' mode to 'plasmonic only' mode exists in this fundamental TM mode at a given configuration as the frequency of the mode increases [2].

The author recently discussed the fundamental TE mode that co-exists in this 4-layered structure [3]. The dispersion relation of this TE mode closely resembles that of the TE photonic mode supported by a dielectric-semiconductor-insulator 3-layered structure. Because no TE mode can exist at a single insulator-metal interface, this TE mode can be called a 'photonic only' mode. This TE mode can also be regarded as the superposition of TE photonic mode in the 3 layered structure and its mirror mode due to metal response [2, 3].

Once the semiconductor layer is no longer with infinite lateral span, resonant cavities can be formed (Fig. 1(a)). In most cases, the resonant cavity modes with TE characteristics have poor quality factors due to their lack of mode confinement. Nevertheless, as the length scale of the nanocavity decreases to near the diffraction limit ~ λ/2, only resonant electric dipole and magnetic dipole modes are supported by these semiconductor nano-patches. In this case, when the magnetic dipole mode is perpendicular to the metal substrate, its mirror dipole is in the opposite direction to its original one (Fig. 1(b)) and the total magnetic dipole moment decreases due to the metal response. As a result, the radiation loss of this magnetic dipole mode, even though based on TE 'photonic only' mode, is substantially smaller than that of the electric dipole mode, which is based on the TM plasmonic mode [3]. The author therefore calls this magnetic dipole mode near metal as a 'dark' magnetic dipole. Low loss photonic cavities at extremely small dimensions (down to 110 nm × 210 nm × 210 nm) via 'dark' magnetic dipole mode is predicted [3]. These subwavelength cavities show great promises to be used in the future high density integrated plasmonic applications.

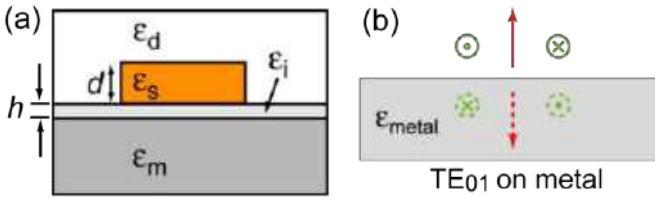


Figure 1: (a) Diagram of side view of a truncated cylindrical semiconductor disk near metal. (b) diagram showing the metal response creating an opposing electric field, and therefore a magnetic dipole in the opposite direction.

Acknowledgements

N. L. acknowledge the support by Science Foundation Ireland Career Development Award 17/CDA/4733.

References

[1] R.-M Ma, R. F. Oulton, Applications of nanolasers, *Nature Nano.* 14: 12−22, 2019.

[2] N. Liu, Analytical and approximation approach to solve 'hybrid plasmonic' – 'plasmonic only' transition of TM_0 mode in dielectric-semiconductor-insulator-metal multi-layers (to be submitted) 2019.

[3] N. Liu, C. Silien, G. Sun, B. Corbett, Low loss photonic nanocavity via dark magnetic dipole resonant mode near metal, *Sci. Rep*. 8:17054, 2018.

III-V Semiconductor Nanowires for Optoelectronic Applications

Ziyuan Li[1], Hark Hoe Tan[1], Chennupati Jagadish[1], and Lan Fu[1]

[1]Department of Electronic Materials Engineering, Research School of Physics and Engineering,
The Australian National University, Canberra, ACT2601, Australia
*corresponding author, E-mail: ziyuan.li@anu.edu.au, lan.fu@anu.edu.au

Abstract

III-V semiconductor nanowires have been extensively studied for optoelectronic device applications such as lasers, photodetectors, solar cells and light-emitting diodes owing to their small footprint, unique morphology and physical properties, as well as high flexibility to form heterostructures on lattice mismatched substrates such as Si. Here we review our work on the growth and fabrication of III-V semiconductor nanowire materials for solar cell and photodetector applications.

1. Introduction

In the 21st century, there is an increasing demand globally for high performance optoelectronic devices due to their wide range of potential applications. For example, solar cell devices convert the solar energy, a renewable and sustainable resource, into electricity [1]. Photodetectors and cameras working in a broad wavelength range have been applied in manufacturing inspection/measurement systems, scientific instrumentation (e.g. IR spectroscopy), astronomy, search and rescue, surveillance, free space optical communications, missile tracking, and night vision. One-dimensional nanostructures such as III-V semiconductor nanowires (NWs) have tunable absorption and emission properties as optical antennae due to their highly anisotropic morphology and large refractive index [1]. Their development may lead to high-performance, multi-functional, compact but low-cost devices outperforming current planar structure-based optoelectronic technologies. In this talk, we will present our work on binary InP nanowire based solar cells and ternary GaAsSb nanowire based infrared photodetectors.

2. Experimental

In this work, the III-V semiconductor nanowires were synthesized using metalorganic chemical vapor deposition (MOCVD) technique. The axial junction InP nanowires were grown by selective-area epitaxy (SAE) technique on a SiO_2-masked p^+-doped (111)A InP substrate [2-3], while the GaAsSb nanowires were grown by metal-catalyzed vapor-liquid-solid (VLS) technique on a GaAs (111)B substrate with 40 nm Au colloids as seed particles [4]. To fabricate single horizontal nanowire based optoelectronic devices, the single nanowires were first mechanically transferred to a thermally oxidized p^+-Si substrate with a 300-nm SiO_2 layer. Ti/Au (10/220 nm) contacts were defined by electron beam lithography (EBL) patterning and deposited on each side of nanowires using electron beam evaporation followed by a lift-off process [1-4].

3. Optoelectronic applications

3.1. Axial junction InP single nanowire solar cells

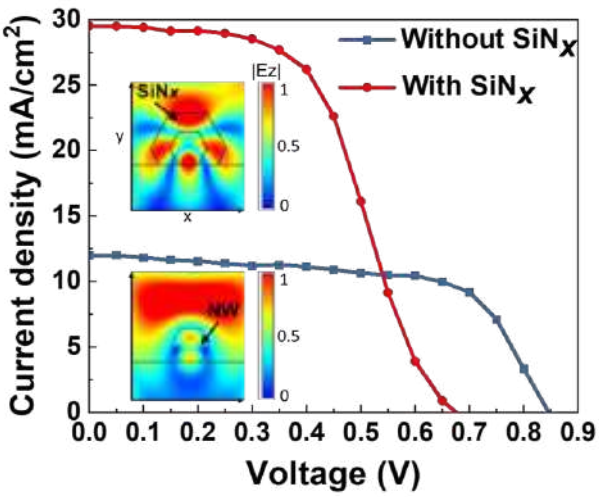


Figure 1: *I-V* curves under 1 Sun @ AM1.5G illumination for the p-i-n nanowire solar cells without (blue curve) and with (red curve) SiN_x coating layer [2]. The inset shows TE mode electric field distribution of the devices simulated by COMSOL under 680 nm light illumination, respectively.

For solar cell applications, in comparison with other III-V nanowires, InP nanowires have the advantages of the most suitable bandgap, low surface recombination velocity and excellent mobility [2,3]. We demonstrated axial p-i-n junction InP single horizontal nanowire solar cells (growth starts with p-segment) whose efficiency could reach up to 6.5% [2]. Furthermore, we changed the bottom up growth sequence of the nanowires with n-segment first and then i- and p-segments, obtaining solar cells with an enhanced efficiency up to 7.73% due to the reduced p-type dopant (Zn) diffusion [3]. By further coating the nanowire devices with a conformal SiN_x dielectric layer of 100 nm, the solar cell efficiency can be significantly enhanced due to an

optical antenna effect from SiN_x coating [2]. Figure 1 shows the typical *I-V* curves under 1 Sun@AM1.5G illumination from the best single p-i-n nanowire solar cells without and with SiN_x coating layer, respectively. The electric field distribution of the devices under 680 nm light illumination and TE mode simulated by COMSOL are presented in the inset, respectively, indicating the enhanced optical antenna effect and thus doubled light absorption introduced by the dielectric coating, leading to remarkably improved peak efficiency of the solar cells to 10.5% [2].

3.2. GaAsSb single nanowire infrared photodetectors

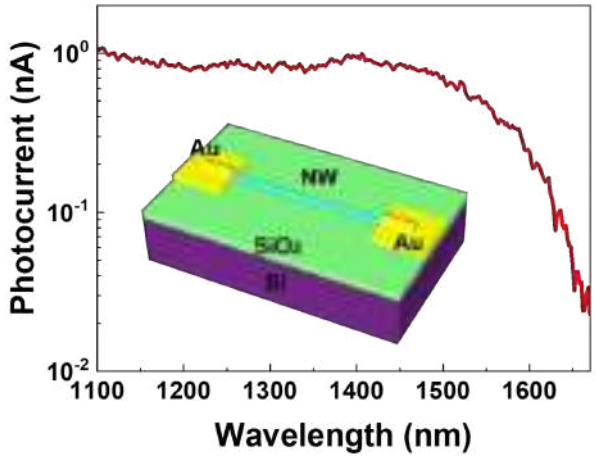


Figure 2: Photocurrent spectral response of the single horizontal $GaAs_{0.56}Sb_{0.44}$ nanowire photodetector at 0.15 V under the room temperature [4]. The inset shows the schematic of the device.

III-V semiconductor nanowires (NWs) have also been widely used as photodetectors. In particular, ternary $GaAs_{1-x}Sb_x$ NWs offer wide tunable bandgaps (from 870 (GaAs) to 1700 nm (GaSb)) with associated flexibility in bandgap engineering for infrared photodetection [4]. We demonstrated a room temperature single horizontal $GaAs_{0.56}Sb_{0.44}$ nanowire based photodetector as shown in Figure 2, obtaining high responsivity (2.37 and 1.44 A/W) and detectivity (1.08×10^9 and 6.55×10^8 cm$\sqrt{Hz}$/W) under a very low bias voltage of 0.15 V at the telecommunication wavelengths of 1.3 and 1.55 μm, respectively [4]. The performance could be further improved by *in-situ* passivation such as adding an InP shell on the GaAsSb core nanowires. The results indicate that the nanowires are promising candidates for applications in future nanoscale integrated optical telecommunication/sensing systems.

4. Future work

To further enhance the nanowire based optoelectronic devices, we propose that plasmonic or metamaterial structures could help enhancing as well as engineering nanowires' light absorption and thus to realize high-performance and more functionalities. On the other hand, low-dimensional quantum structures such as quantum wells or dots are also potential candidates to be integrated into nanowires to extend the detection wavelength to mid- to long-wavelength infrared range.

5. Conclusions

In conclusion, axial junction InP nanowires were grown by SAE technique and successfully fabricated as solar cells, showing higher efficiency by various approaches, such as changing the bottom up growth sequence of the device structure or coating a SiN_x layer on the nanowires to enable the optical antenna effect. We also demonstrated room temperature $GaAs_{0.56}Sb_{0.44}$ single nanowire infrared photodetectors grown by VLS technique, showing broadband infrared photoreponse and potential in telecommunication applications.

Acknowledgements

The authors would like to thank the Australian Research Council (ARC) for the financial support and the Australian National Fabrication Facility (ANFF) ACT node for the fabrication facility support.

References

[1] Z.Y. Li, H.H. Tan, C. Jagadish, L. Fu, III-V Semiconductor Single Nanowire Solar Cells: A Review, *Adv. Mat. Tech.* 1800005: 1-12, 2018.

[2] Z. Zhong, Z.Y. Li, Q. Gao, Z. Li, K. Peng, L. Li, S. Mokkapati, K. Vora, J. Wu, G. Zhang, Z. Wang, L. Fu, H.H. Tan, C. Jagadish, Efficiency enhancement of axial junction InP single nanowire solar cells by dielectric coating, *Nano Energy* 28: 106-114, 2016.

[3] Z.Y. Li, I. Yang, L. Li, Q. Gao, J.S. Chong, Z. Li, M.N. Lockrey, H.H. Tan, C. Jagadish, L. Fu, Reducing Zn diffusion in single axial junction InP nanowire solar cells for improved performance, *Prog. Nat. Sci.-Mater.* 28: 178-182, 2018

[4] Z.Y. Li, X. Yuang, L. Fu, K. Peng, F. Wang, X. Fu, P. Caroff, T.P. White, H.H. Tan, C. Jagadish, Room temperature GaAsSb single nanowire infrared photodetectors, *Nanotechnology* 26: 445202, 2015.

Plasmonic transition metal nitride and carbide for photocatalytic and photothermal applications

S. L. Shinde[1], S. Ishii[1], M. Kaur[1,2], T. D. Dao[1], and T. Nagao[1,2*]

[1]National Institute for Materials Science, 1-1 Namiki, Tsukuba, Ibaraki 305-0044, Japan
[2]Hokkaido University, Kita-ku, Sapporo 060-0808, Japan
*corresponding author, E-mail: NAGAO.Tadaaki@nims.go.jp

Abstract

Optical excitation of hot carriers in metals can be injected into adjacent semiconductors to collect sub-bandgap photons. In the present work, we experimentally demonstrate that transition metal nitrides and carbides can act as metals and generate hot electrons by optical illumination similar to metals. Since transition metal nitrides and carbides have broad absorption in the visible spectrum with tunable plasmon resonances, they have the potential to be used for photocatalytic, photovoltaic, and photothermal applications to harvest solar energy.

1. Introduction

Photons which go through non-radiative decay processes excite hot carriers and a number of novel applications with photo- or plasmon- induced hot carriers have been studied in the past decade. Recently it has been shown that highly conductive ceramics can be alternative materials of noble metals. In the search for alternative plasmonic materials, transition metal nitrides have been one of the most studied materials in the past few years [1,2]. This is due to their chemical stability, cost effectiveness, and ease of fabrication. Most importantly, transition metal nitrides are one of the few classes of non-metallic materials with plasmon resonances in the visible range.

As transition metal nitrides and transition metal carbides are categorized as cermets, the band structures of both classes of materials are metallic, implying that carbides can also be used in plasmon enhanced photoelectric and photothermal conversions. Owing to their large intrinsic absorption in the visible and NIR range, transition metal carbides have intrinsically high photothermal effects. Among them titanium nitride (TiN), titanium carbide (TiC), tantalum carbide (TaC) are such materials which become plasmonic in the optical range. Previous studies have shown that nitride/carbide seems to be best suited for applications related to photo-absorption and photothermal effects. To further explore the possibility of nitride/carbide for photo-absorption related applications, here we present our recent results on nano-structured of nitride/carbide for photocatalytic, photoelectric, and photothermal applications.

2. Discussion

We synthesized a composite of metal-free carbon nitride–carbon dots (C_3N_4–C dots) and plasmonic TiN NPs to improve the photoelectrochemical water-splitting performance under simulated solar radiation (Fig. 1(a and b)) [3]. Hot-electron injection from plasmonic TiN NPs to C_3N_4 played a role in photocatalysis, whereas C dots acted as catalysts for the decomposition of H_2O_2 to O_2. By incorporating the TiN NPs and C dots, a six-fold improvement in the catalytic performance of C_3N_4 was observed (Fig. 1(c)). This two-step approach overcame the low optical absorption, limited spectral utilization, and charge recombination losses and presented an effective way to improve the photocatalytic activity.

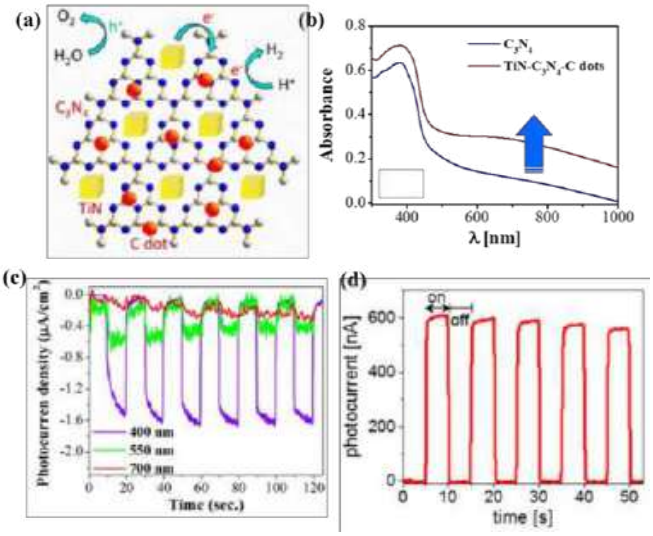


Figure 1: (a) Schematic structure of TiN-C_3N_4-C dots composite, (b and c) absorptance and visible photoresponse of TiN-C_3N_4-C dots composite. (d) Photocurrent from TiN-oxide-TiN trilayers upon 700 nm light irradiation.

In the photoelectric application, a metal-insulator-metal structure was fabricated using TiN thin films instead of metals. Upon visible light illumination to the sample, photocurrent were observed as shown in Fig. 1(d). The photon energies were smaller than the bandgap of the insulator, hence the photo-excited electrons were generated

not at the insulator film but at the TiN film [4]. Another example is a TiN/Ge sub-bandgap photodetector shown in Fig. 2(a). The TiN and Ge films were sputtered on Si/SiO_2 substrate by DC-magnetron sputtering. The Ge and TiN films show broad absorption in visible-near infrared (Vis-NIR) region. For Ge with top TiN, the generation of photocurrent by NIR light illumination is confirmed up to 2600 nm, well exceeding the absorption limit of Ge (Fig. 2(b)). Figs. 2(c) and 2(d) show the time-dependent photocurrent response of TiN/Ge samples with Ni and Au contacts without bias at different excitation wavelengths. The photocurrent observed for the wavelengths which have smaller photon energies than the bandgap of Ge, the hot carriers were excited at the TiN film. The photocurrent of TiN/Ge with Ni contact is nearly twice than that with Au contact. Thus, fabricating TiN plasmonic nanostructures will inevitably increase hot carrier excitation from TiN by improving the optical absorption and hence performance of TiN/Ge photodetector.

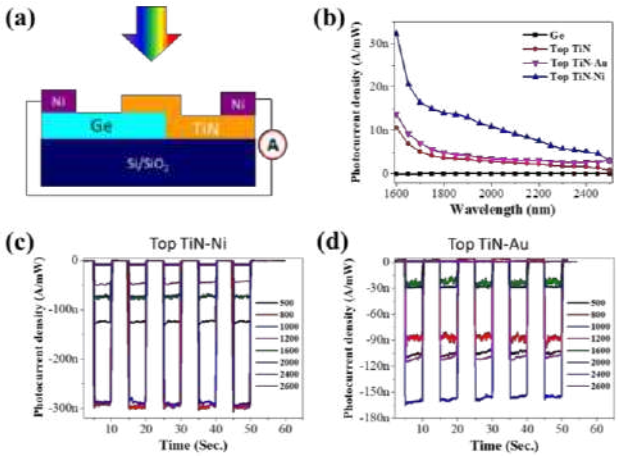


Figure 2: (a) Schematic structure of TiN/Ge sub-bandgap photodetector, (b) Photocurrent density of Ge and top TiN with Au and Ni contacts at zero bias. Time-dependent photoresponse of Ge and Top TiN with Ni and Au contacts at different excitation wavelengths.

To explore carbide for photovoltaic application, a TiC/ZnO/TiC trilayer was fabricated, and the photoresponse of the sample was observed up to 1000 nm, as shown in Fig. 3(a) [2]. Since the bandgap of ZnO is ≈3.2 eV (≈390 nm), the measured photoresponse was attributed to the optically excited hot electrons in the TiC layer. However, more investigation on plasmonic properties of TiC needed. Compared to TiC, the tantalum carbide (TaC) can have a strong plasmon resonance in the visible to NIR range. Thus, TaC nanostructures are candidates for use in plasmon enhanced hot carrier generation.

The plasmon enhanced photothermal conversion of transition metal carbides has found applications in chemical reactions. A nanocomposite catalyst (Co@TaC) consisting of cobalt (Co) NPs and TaC NPs has been shown to produce hydrogen and carbon monoxide from carbon dioxide and methane (i.e., carbon dioxide reforming), as shown in Figure 3(b) [5]. The nanocomposite was free from precious metals and was heated by both a heater and a Xe lamp, where the TaC acted as a light-to-heat transducer. This work demonstrates that plasmonic nanomaterials comprising catalytic late-d-metals and early-d-metal carbides and/or nitrides are promising materials toward efficient solar-to-chemical energy conversions.

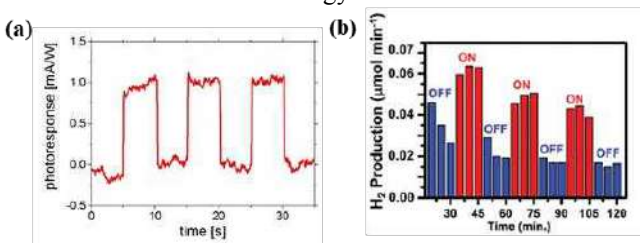


Figure 3: a) Time dependent photocurrent measured at a wavelength of 1000 nm for the TiC/ZnO/TiC structure. b) Production of hydrogen over Co@TaC by flowing methane and carbon dioxide gases at 600 °C. The red and blue bars correspond to hydrogen production in light and darkness, respectively.

3. Conclusions

We have demonstrated that transition metal nitrides and carbides can be used for plasmonic photoelectric and photothermal conversions by the excitation of hot carriers. Since those non-metallic materials can be less expensive and can have higher conversion efficiencies than noble metals, research on non-metallic materials for plasmonic photoelectric and photothermal conversions will be an exciting field that will lead to practical applications.

Acknowledgements

This work is partially supported by the JSPS KAKENHI (15K17447, 16K17496, and 17H04801) and CREST (JPMJCR13C3).

References

[1] S. Ishii, S. L Shinde and T. Nagao, Nonmetallic materials for plasmonic hot carrier excitation, *Adv. Opt. Mater.* 7: 1800603, 2019.

[2] S. Ishii, S. L Shinde and T. Nagao, Photocurrent generation with transition metal nitrides and transition metal carbides, *Proc. ICTON*, Bucharest, Romania, 2018, pp. 1-2, 2018.

[3] S. L. Shinde, S. Ishii, T. D. dao, R. P. Sugavaneshwar, T. Takei, K. K. Nanda and T. Nagao, Enhanced Solar Light Absorption and photoelectrochemical conversion using TiN nanoparticle-incorporated C_3N_4-C dot sheets, *ACS Appl. Mater. Interfaces* 10: 2460-2468, 2018.

[4] S. Ishii, S. L. Shinde, W. Jevasuwan, N. Fukata, T. Nagao, Hot electron excitation from titanium nitride using visible light, *ACS Photonics* 3: 1552-1557, 2016.

[5] O. Anjaneyulu, K. Takeda, S. Ishii, S. Ueda, T. Nagao, P. Xiaobo, T. Fujita, M. Miyauchi, H. Abe, Light-promoted conversion of greenhouse gases over plasmonic metal–carbide nanocomposite catalysts, *Mater. Chem. Front.* 2: 580-584, 2018.

Nonlinear Light Generation from Si Nanoplasmonic Waveguides

Abdulhakem Elezzabi*[1], Curtis Firby[1], and Shawn Sederberg[1]

[1]Ultrafast Optics and Nanophotonics Laboratory, Department of Electrical and Computer Engineering, University of Alberta, Edmonton, Alberta, T6G 1H9, Canada
*corresponding author, E-mail: elezzabi@ece.ualberta.ca

Abstract

Silicon-based nanoplasmonic waveguides are key in integrated chip-scale nanoplasmonic circuitry. In this work, we demonstrate a Si-nanoplasmonic waveguide platform to examine nonlinear light emission processes, such as third harmonic generation, second harmonic generation, white light emission, as well as photogenerated carrier ultrafast streaking and carrier amplification. We envision these structures to be vital components in integrated nanoplasmonic CMOS nanoplasmonic devices.

1. Introduction

As a critical material for electronics, Si has also become the foundation for integrated optical systems, and it merges electronics, photonics, and nanoplasmonics on a single platform. The potential of Si as a functional nonlinear optical material has incited many nonlinear frequency conversion studies. The well-established growth and processing techniques of silicon (Si), along with its transparency at telecommunication wavelengths (1260nm-1675nm) and a high nonlinear refractive index, have made silicon-on-insulator (SOI) nanophotonic waveguides a top contender for chip-scale optical circuitry [1]. However, to date, light emission from silicon is most practically accessible through nonlinear optical wave mixing due to the indirect bandgap of the material. Although silicon is a material that absorbs visible light, third-harmonic generation driven by infrared signals can be used to generate visible light in silicon structures.

In this work, we present the current state-of-the-art physics and applications of Si-based nanoplasmonic waveguides pertaining to strong nonlinear light interaction within the Si core of a Si-loaded nanoplasmonic waveguide. In particular, we present coherent light-emitting mechanisms and incoherent broadband light generation. Furthermore, we also show that the strong light-induced nanoplasmonic field streaks and amplifies the electronic charge within the Si layer. We envisage that the coherent generation in silicon-based nanoplasmonic waveguides could provide a platform for integrated, broadband visible light sources and entangled photons on future hybrid electronic-silicon photonic chips.

2. Results and Discussion

Nanofabrication processes are developed to integrate Si photonic waveguides and Si-based nanoplasmonic waveguides. First, passive propagation and nonlinear interactions are investigated in silicon-on-insulator photonic waveguides to provide a detailed understanding of nonlinear interactions present in silicon at λ= 1550nm and the relevant timescales of the interactions.

Figure 1 illustrates the Si-loaded nanoplasmonic waveguide fabricated on a SOI wafer.

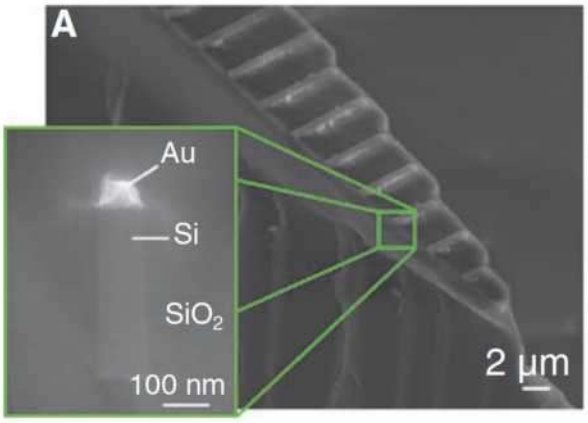


Figure 1: Scanning electron micrograph of Si-loaded nanoplasmonic waveguides integrated onto a deeply-etched characterization beam.

Extensive investigations into third-harmonic and second harmonic generation in silicon nanoplasmonic waveguides are performed. When nonlinear light generation and ultrafast modulation are then applied to sub-wavelength silicon-based nanoplasmonic waveguides, we measure third-harmonic light generation with conversion efficiencies greater than 7×10^{-5} in a nanoplasmonic waveguide having a footprint of only $0.40\mu m^2$. Furthermore, we demonstrate that the strong nanoplasmonic field at the metal-Si interface can result

in ponderomotive acceleration of the two-photon absorption-generated free-carriers in the Si layer. We show that such electrons can be accelerated to energies exceeding the threshold for impact ionization.

Measurements of the emitted light intensity reveal that the highly confined nanoplasmonic field drives an electron avalanche, and white light emission resulting from the avalanche is observed to scale exponentially with the input power.

3. Conclusions

These results demonstrate the feasibility for conversion of near-IR radiation to visible radiation with technologically significant efficiencies, enabling nanoscale Si-based visible light sources on a chip.

Acknowledgements

This work was funded by the Natural Sciences and Engineering Research Council of Canada.

Thin and Multifunctional Metasurfaces for Display Applications

Jonghwa Shin[1*], Hyowook Kim[1], Min Sung Heo[1], Arthur Baucour[1], and Nayeong Kim[1]

[1]Department of Materials Science and Engineering, KAIST, Daejeon, Korea
*corresponding author, E-mail: qubit@kaist.ac.kr

Abstract

Modern information display panels are composed of many optical films with different functions. The trend in the industry has been reducing both the number and thickness of these films. While there have been many proposals so far to replace these films with plasmonic structures or metasurfaces, their optical performance is less than ideal, often below that of current technology. Here, design principles of optical metasurfaces for display applications are investigated and examples with promising optical performances are provided.

1. Introduction

Information displays, from those in smart phones, tablets, and computers to those in television sets and head-up displays, have become integral part of modern society. With ever-increasing demand for mobility or higher aesthetics, the display panels are becoming thinner and lighter at a fast rate: commercial panels from only five years ago already look very thick and bulky by today's standards. Now even foldable products are in the market and the trend is expected to continue for foreseeable future.

One of the biggest challenges in the field is the number and thickness of required optical films or layers. Both in liquid-crystal displays (LCD) and organic light-emitting diode (OLED) dipslays, there are many optical layers. Two linear polarizers are typically required for LCD's due to their working principle (voltage-controlled polarization rotation); a circular polarizer is used in OLED to reduce the reflectance of external light; a set of color filters are used to express colors; a set of compensation films or retardation films are used to improve the contrast and other properties at large viewing angles; a transparent electrode is used to route the electric signals while transmitting the optical signals.

All these optical layers were at least several tens of microns in earlier display panels. Many of the layers have been reduced in their thicknesses: for example, recent resin-type polarizers have thicknesses of a few microns rather than a few tens of microns or even a hundred of a film-type polarizer. However, due to intrinsic limitation of the anisotropy or absorption coefficient of available materials, it is becoming much harder to reduce the thickness further.

2. Metasurfaces for displays

2.1. Opportunities and challenges

The above mentioned problems with current materials are the reason why plasmonic structures or metasurfaces with artificially tailored resonances are providing interesting alternatives. Due to the large density of conduction electrons, a few nanometer or tens of nanometer-thick metallic films can already possess very strong optical response. By tailoring the shape and size of these metallic inclusions or subwavelength holes in metallic films, one can hope to achieve desired optical characteristics required for display panels. In this spirit, there have been numerous proposals to use these plasmonic structures to applications, ranging from color filters to polarizers, over the last decade. However, the optical loss coming from the non-zero imaginary part and finite magnitude of the complex permittivity of metals in the visible wavelengths are providing an enormous challenge to metal-based metasurfaces. It limits the sharpness of the resonances and can also place an upper bound for efficiency. Hence, a very careful design is needed to realize a metasurface-based optical films that possess a comparable optical performance with conventional films but have much smaller thicknesses.

2.2. New designs of metasurfaces for displays

Here we show that a systematic design approach can result in much improved performance for color filters as well as polarizers. Especially, the coupled-mode theory plays an important role in designing the spectral properties of metasurfaces. It is also shown that a multi-functional device is possible in a sub-micron-thick design.

Acknowledgements

This work is supported by Korean government (2017R1A2B2005702, 2018M3D1A1058998) and LG Display.

References

[1] H. Kim et al., Bright and vivid plasmonic color filters having dual resonance modes with proper orthogonality, *Optics Express* 26: 27403−27417, 2018.

[2] R. Kim et al., Metal Nanoparticle Array as a Tunable Refractive Index Material over Broad Visible and Infrared Wavelengths, ACS Photonics 5: 1188−1195, 2018.

Direct and Inverse Magneto-Optics of Structured All-Dielectric Iron-Garnet Films

Andrey Kalish[1,2*], Andrey Voronov[1,2], Daria Ignatyeva[1,2], Mikhail Kozhaev[2,3], Miguel Levy[4], Dolendra Karki[4], and Vladimir Belotelov[1,2]

[1]Faculty of Physics, Lomonosov Moscow State University, Moscow, Russia
[2]Russian Quantum Center, Moscow, Russia
[3]Prokhorov General Physics Institute of the Russian Academy of Sciences, Moscow, Russia
[4]Michigan Technological University, Houghton, MI, USA
*corresponding author, E-mail: kalish@physics.msu.ru

Abstract

The use of all-dielectric materials instead of plasmonic ones to enhance magneto-optical effects allows one to avoid significant energy losses that are present in metals. In this paper, we perform experimental research of the transverse magneto-optical Kerr effect and the inverse Faraday effect in 1D dielectric magnetic structures. Experimental results demonstrate a significant enhancement of magneto-optical effects, as well as high transparency and high Q-factor of the obtained resonances, which opens up broad opportunities for applications.

1. Introduction

The transverse magneto-optical Kerr effect (TMOKE) is promising for light modulation since it allows laser beam intensity control via external magnetic field that could be switched at GHz frequencies. Magnetoplasmonic crystals were shown to provide resonant enhancement of the TMOKE at the excitation of surface plasmon polaritons, as their propagation constant is sensitive to structure magnetization [1]. However, plasmonic structures have high absorption due to the presence of metal layers. Nowadays there is a growing interest to another type of structures with significantly higher quality factor – hybrid metal-dielectric and all-dielectric structures – which possess lower absorption and could be used for efficient light localization and control. Instead of surface plasmon polaritons, waveguide or Mie modes could be excited to increase the light-matter interaction in these structures. We concentrate our attention on all-dielectric gratings where guided modes with narrow resonances are known to be excited [2].

Excitation of the waveguide modes is responsible for enhancement of the magneto-optical effects with simultaneous increase of the resonance Q-factors demonstrated experimentally in Kretschmann configuration in smooth magnetic films [3]. At the same time, numerical simulations show that the use of all-dielectric magnetic gratings leads to a significant increase of magneto-optical effects [4]. On the other hand, inverse magneto-optical effects can be enhanced as well due to local field concentration.

We present an experimental study of both the TMOKE and the inverse Faraday effect in 1D all-dielectric gratings etched in ferromagnetic iron-garnet film and show that magneto-optical effects experience multifold increase due to the excitation of the waveguide modes.

2. Waveguide modes in all-dielectric iron-garnet gratings

To enhance the magneto-optical effects, we use a 1D all-dielectric grating made of bismuth-substituted iron garnet film perforated with ion beam etching deposited on gadolinium gallium garnet substrate. The width of the air gap of our grating is 200 nm, and the period of the grating is 400 nm. The height of the grating is 225 nm, and the smooth iron-garnet sublayer of 75-nm thickness is left below the grating.

In such a grating, the waveguide modes propagating perpendicular to the slits are excited under the following excitation condition:

$$k_{inc}\sin\theta + mG = \pm\beta_0, \qquad (1)$$

where $k_{inc} = \frac{2\pi}{\lambda}$ is the propagation constant of the incident light, λ is the wavelength in free space, m is the diffraction order (an integer number), G is the reciprocal lattice vector value, $\beta_0 = \frac{2\pi}{\lambda} n_{eff}$ is the propagation constant of the waveguide mode, n_{eff} is the effective refractive index of the mode. Light is incident from the air.

3. The TMOKE in all-dielectric iron-garnet gratings

When a waveguide mode is excited, the propagation constant β acquires a linear on gyration coefficient $\Delta\beta$, which is dependent on the direction of magnetization [1]:

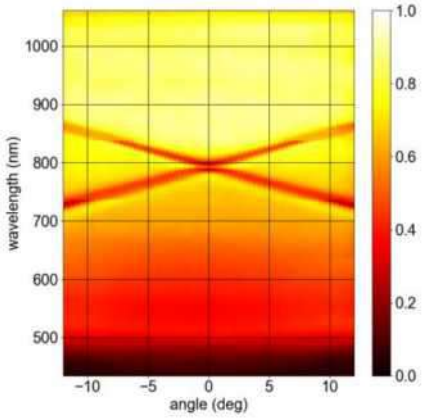
$$\beta = \beta_0 + \Delta\beta(\mathbf{M}). \qquad (2)$$

As a consequence, the TMOKE arises, which is determined by the relative change in the intensity of the reflected or transmitted light at the magnetization reversal. Usually, the TMOKE is observed in absorbing media with oblique incidence of light polarized in the plane of incidence (*p*-polarization) and is characterized by the parameter δ:

$$\delta = \frac{I(+M) - I(-M)}{I(+M) + I(-M)}, \quad (3)$$

where $I(+M)$ and $I(-M)$ is the intensity of the transmitted light in the magnetized in two opposite directions. It is worth noting that the TMOKE is usually measured for reflected light, but in the case of transparent structures, the effect can also be investigated in transmitted light.

a



b

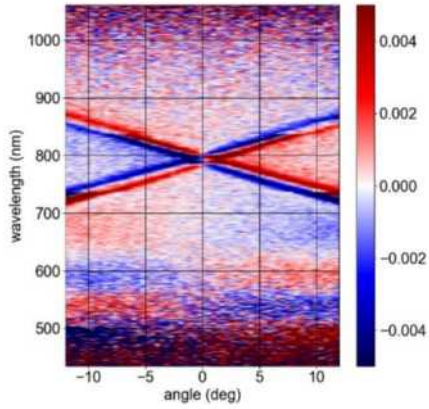


Figure 1: Transmittance (a) and the TMOKE (b) spectra.

Experimental results presented in Fig. 1 show a significant enhancement of the TMOKE in all-dielectric structures up to δ=0.5% with simultaneously high transmittance T=50%. For a comparison, the smooth iron-garnet film of the same width provides the TMOKE of about δ=0.004%. At the same time, the TMOKE resonances in grating structures also have high Q-factor and a width of about 5 nm, which is a significant advantage over plasmonic structures.

4. The inverse Faraday effect

The excitation of waveguide modes leads to a significant enhancement of the local field in the iron-garnet layer. This is favorable for the increase of the inverse Faraday effect, as its value is proportional to the local electric field: $\mathbf{H}_{IFE} \propto [\mathbf{E} \times \mathbf{E}^*]$. The experimental results demonstrate the presence of the resonance in the inverse Faraday effect, related to the waveguide mode excitation (Fig. 2).

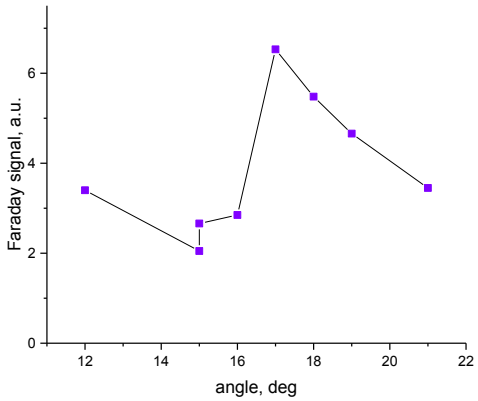


Figure 2: The angular spectrum of the inverse Faraday effect.

5. Conclusions

The TMOKE and the inverse Faraday effect in all-dielectric 1D-periodic structures of iron-garnet was investigated. The multifold enhancement of magneto-optical effects in such structures was confirmed experimentally. The optical and magneto-optical resonances in 1D gratings are characterized by the high transmittance and high Q-factors making 1D iron-garnet gratings promising for various applications.

Acknowledgements

This work was supported by the RSF grant No. 18-72-00233.

References

[1] O.V. Borovkova, H. Hashim, M.A. Kozhaev, S.A. Dagesyan, A. Chakravarty, M. Levy, V.I. Belotelov, TMOKE as efficient tool for the magneto-optic analysis of ultra-thin magnetic films, *Appl. Phys. Lett.* 112: 063101, 2018.

[2] S.S. Wang, R. Magnusson, Design of waveguide-grating filters with symmetrical line shapes and low sidebands, *Optics Letters* 19: 919−921, 1994.

[3] D.O. Ignatyeva, P.O. Kapralov, G.A. Knyazev, S.K. Sekatskii, G. Dietler, M. Nur-E-Alam, M. Vasiliev, K. Alameh, V.I. Belotelov, High-Q surface modes in photonic crystal/iron garnet film heterostructures for sensor applications, *JETP Lett.* 104: 679−684, 2016.

[4] I.S. Maksymov, J. Hutomo, M. Kostylev, Transverse magneto-optical Kerr effect in subwavelength dielectric gratings, *Optics Express* 22: 8720−8725, 2014.

Bifacial metasurfaces and their applications

Byoungho Lee*, Jangwoon Sung, Gun-Yeal Lee

Inter-University Semiconductor Research Center and School of Electrical and Computer Engineering, Seoul National University, Gwanak-Gu Gwanakro 1, Seoul 08826, Korea
*corresponding author, E-mail: byoungho@snu.ac.kr

Abstract

Metasurfaces, which are periodic or semi-periodic arrangement of artificially made nanostructures, have attracted enormous attention thanks to its unprecedented ability to control the electromagnetic properties of light. In this invited talk, general introduction of metasurface will be presented with their principles and applications. Furthermore, a full-space control, which indicates simultaneous phase modulation of transmission and reflection space, will be discussed with its theoretical and experimental demonstration.

1. Introduction

Metasurfaces composed of planar distribution of subwavelength-scale structure have been studied by various research groups due to their superb capacity for modulation of light properties, such as optical phase, amplitude, polarization, spectral resonance, etc [1-3]. Especially, phase modulation via metasurface have been considered to show outstanding performance because unwanted diffraction order can be suppressed unlike conventional spatial light modulators. This is also because the application of Pancharatnam-Berry (PB) phase method is intuitive: the phase shifts exactly twice the in-plane rotation angle of each scatterers. This properties are well understood by many research groups and applied in various optic devices such as augmented reality device [4], complex-amplitude modulation [5], achromatic optical lens operating in various frequency ranges [6]. However, most of the metasurface devices handle or design only one space, i.e. transmission or reflection spaces, only to discard the remnant space undesigned.

Recently, thanks to widespread attention of metamaterials in nanophotonics, which are manmade materials for the implementation of desired effects, the scattering radiation pattern including multipolar phase effects are utilized for various optical or physical applications [7]. Kerker effect is a typical example, which is zero backward scattering under the condition that electric permittivity and magnetic permeability are equal to each other. Thanks to the development of nanofabrication, control of magnetic permeability becomes possible in optical frequency regime, and this leads to Huygens' metasurface by overlapping electric and magnetic dipole mode with equal values [8]. In addition, the control of multipolar coefficients has been studied for various purposes in nanophotonics, such as magnetic mirror [9], diffraction control [10], polarization control devices [11].

In this invited talk, several metasurfaces for unprecedented light manipulation will be presented. Firstly, we will outline the physical instruments and examples of metasurfaces. Particularly, the generalized Kerker effect will be discussed and metasurfaces providing phase modulation will be introduced with their applications. Then, we will introduce bifacial metasurface that can control the phase value of transmission and reflection simultaneously, in visible region [12]. The physical analysis and experimental demonstration will be explained, and this shows the independent phase modulation at both spaces is successfully realized.

2. Results and Discussion

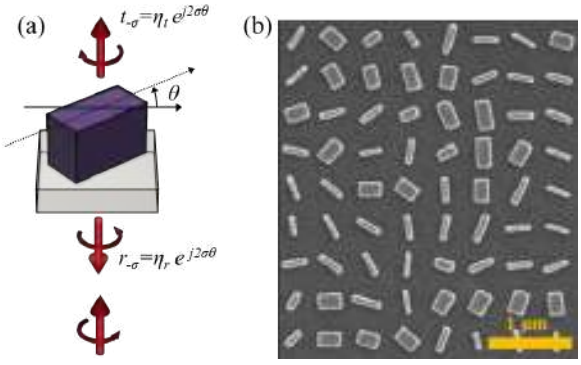


Figure 1: Bifacial metasurface (a) Operational mechanism of the bifacial metasurface. Unit cell is composed of the amorphous silicon, which operates by circularly polarized light. (b) SEM image of the fabricated bifacial metasurface.

Fig. 1 shows the schematic and morphology of the bifacial metasurface. Fig. 1a represents the general concept of the bifacial metasurface. Bifacial metasurface operates on the circularly polarized transmission and reflection, which are cross-polarized components that are influenced by PB phase, at target wavelength of 660 nm. In principle, the geometric size of each meta-atom determines the phase difference between transmission and reflection spaces, and PB phase is exploited to cover the whole phase values of both spaces. As a physical background, the phase difference can be explained by interference of multipolar components. Since

multipolar components has their own phase parity with respect to forward and backward scattering, and by fine-tuning of the nanostructures' size, it is possible to control the portion of excited multipole modes, which is to modulate phase difference. Fig. 1b shows the SEM image of the fabricated sample, and this shows that the geometric sizes and in-plane rotation angles are spatially varying parameters for desired design method.

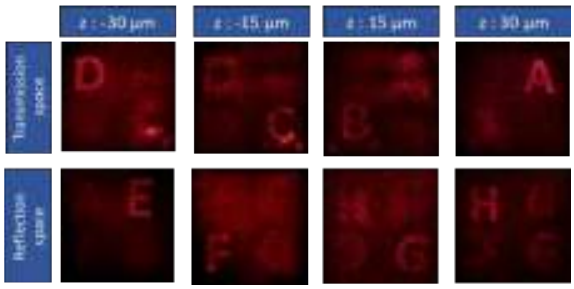


Figure 2: Experimentally captured holographic images from bifacial metasurfaces. Upper four images are captured from transmission space, and lower four images are from reflection space.

Fig. 2 shows the holographic images captured while varying z-plane from -30 μm to 30 μm. Hologram images were measured from optical microscope setup with beam splitter to capture image from reflection space. It is noteworthy that the distinctive hologram images are generated from same image plane, although the focused z-plane is same at both cases. The hologram conversion efficiency is calculated from numerical simulation, which is up to 9.85% and 16.8% for reflection and transmission space, respectively.

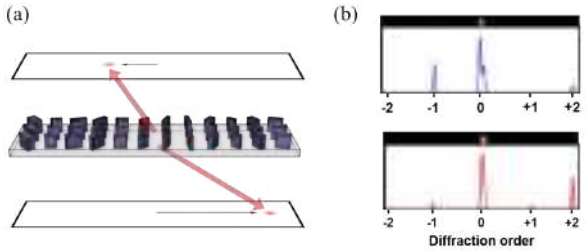


Figure 3: Experimentally captured beam deflection sample from bifacial metasurfaces. (a) Schematic illustration of asymmetric beam steering. (b) Upper graph shows image captured from transmission, and lower from reflection space.

Fig. 3 shows the second example of bifacial metasurface: Unlike conventional metasurface beam deflection, presented sample in Fig. 3a can detour light beam with distinctive deflection angles in transmission and reflection beam. When CP light is incident onto this sample, deflection angles are determined as 7.903° and -15.96° for transmission and reflection space, respectively [2]. The images captured by CCD camera is shown in Fig. 3b, showing extinction ratio of 6.33 and 6.81 dB, respectively.

3. Conclusion

In this invited talk, several metasurfaces which show hologram and unprecedented manipulation of light properties are discussed. We present physical mechanisms and conceptual illustration of the recent metasurfaces as well. Then we introduced bifacial metasurface, which is a new platform for full-space light control that can be applicable in future optic devices. Finally, we will discuss our perspective on this area.

Acknowledgements

This research was supported by Basic Science Research Program through the National Research Foundation of Korea(NRF) funded by the Ministry of Science and ICT (2017R1A2B2006676).

References

[1] N. Meinzer, W. L. Barnes, I. R. Hooper, Plasmonic meta-atoms and metasurfaces, *Nat. Photon.* 8:889-898, 2014.

[2] N. Yu, F. Capasso, Flat optics with designer metasurfaces, *Nat. Mater.* 13:139-150, 2014.

[3] A. I. Kuznetsov, A. E. Miroshnichenko, M. L. Brongersma, Y. S. Kivshar, B. Luk'yanchuk, Optically resonant dielectric nanostrucutres, *Science* 354:aag2472, 2016.

[4] G.-Y. Lee, J.-Y. Hong, S. Hwang, S. Moon, H. Kang, S. Jeon, H. Kim, J.-H. Jeong, B. Lee, Metasurface eyepiece for augmented reality, *Nat. Commun.* 9:4562, 2018.

[5] G.-Y. Lee, G. Yoon, S.-Y. Lee, H. Yun, J. Cho, K. Lee, H. Kim, J. Rho, B. Lee, Complete amplitude and phase control of light using broadband holographic metasurfaces, *Nanoscale* 10:4237-4245, 2018.

[6] W. T. Chen, A. Y. Zhu, V. Sanjeev, M. Khorasaninejad, Z. Shi, E. Lee, F. Capasso, A broadband achromatic metalens for focusing and imaging in the visible, *Nat. nanotech.* 13:220-226, 2018.

[7] W. Liu, Y. S. Kivshar, Multipolar Interference Effects in Nanophotonics, *Philos. Trans. R. Soc. A.* 375:20160317, 2017.

[8] M. Decker, I. Saude, M. Falkner, J. Dominguez, D. N. Neshev, I. Brener, T. Pertsch, Y. S. Kivshar, High-Efficiency dielectric Huygens' surfaces, *Adv. Opt. Mater.* 3:813-820, 2015.

[9] W. Liu, Generalized magnetic mirrors, *Phys. Rev. Lett.* 119:123902, 2017.

[10] W. Liu, A. E. Miroshnichenko, Beam Steering with dielectric metalattices, *ACS Photonics* 5:1733-1741, 2018.

[11] S. Kruk, B. Hopkins, I. I. Kravchenko, A. Miroshnichenko, D. V. Neshev, Y. S. Kivshar, Broadband highly efficient dielectric metadevices for polarization control, *APL Photonics* 1:030801, 2016.

[12] J. Sung, G.-Y. Lee, C. Choi, J. Hong, B. Lee, Single-layer bifacial metasurface: Full-space visible light control, *Adv. Opt. Mater.* doi:10.1002/adom.201801748.

Engineering the Refractive Index and Phase of Optical Metamaterials

Zi Jing Wong

Department of Aerospace Engineering, Texas A&M University, College Station, USA
E-mail: zijing@tamu.edu

Abstract

Subwavelength structuring of materials can lead to exotic material properties and device functionalities. Using nanostructures, we engineered the real and imaginary part of refractive index and the phase distribution to create optical metamaterials with extraordinary properties and performances.

1. Introduction

For centuries, the extent of light control and optical functionality has been bounded by the limited range of natural materials' refractive index. This limit is finally broken with the advent of metamaterials which utilize artificially-engineered subwavelength nanostructures to create new material properties. Similarly, the restricted performance of optical materials based on periodic nanostructures has been substantially improved with the use of spatially-varying subwavelength nanostructures. The in-plane symmetry breaking has led to many novel ultrathin optical devices. Here we discuss our experimental efforts in engineering both the real and imaginary part of refractive index as well as the spatial phase distribution to realize new optical phenomena and functionalities.

2. Experiments

2.1. Engineering real part of refractive index

Negative refractive index metamaterials (NIMs) and zero refractive index metamaterials (ZIMs) have shown many extraordinary light behaviors, such as negative refraction, superresolution imaging, electromagnetic tunneling, gigantic optical nonlinearity, photon doping, etc. However, these metamaterials suffer significant optical loss, particularly at visible wavelengths. We showed that by using low beam current focused ion beam patterning through a nanomembrane, low-loss bulk optical metamaterials can be realized in both the near infrared and visible wavelengths [1,2]. More than 40% transmission is achieved even for a 20-layer metal-dielectric metamaterial. We also utilized the low-loss negative phase property at 780 nm to probe the existence of hyper-complex quantum theories in a single-photon quantum optics setup (Figure 1) [2]. The results show that the metamaterial phase commutes with other phases with high precision, placing a new limit on the prediction of hyper-complex quantum theories.

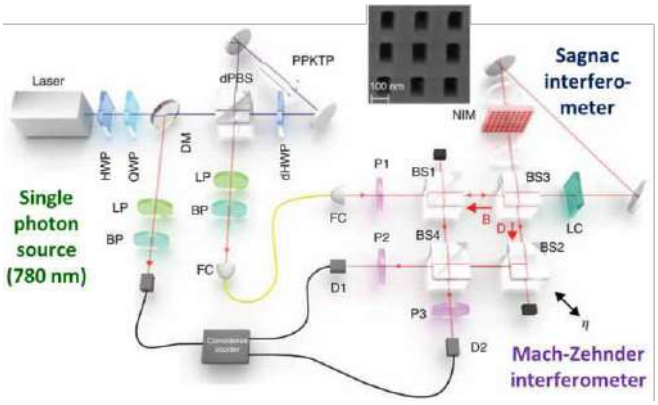


Figure 1: The use of a NIM in a single-photon optical setup to provide the negative phase to probe the fundamental quaternion quantum theory at 780 nm visible wavelength.

2.2. Engineering imaginary part of refractive index

Material loss is usually undesired in optoelectronics, as it leads to heating and power dissipation. To compensate the loss, material gain is often used, which gives birth to amplifiers and lasers. By judiciously designing both material gain and loss using parity-time (PT) symmetry, a new path for optical mode and emission control can be attained. For instance, a PT-symmetric microring cavity with the unique feature of single-mode lasing can be realized [3]. Here we reveal a novel PT-symmetric structure which supports both lasing and coherent perfect absorption (CPA) modes at the same frequency within a single device (Figures 2 and 3) [4]. This enables strong modulation from coherent amplification to coherent absorption and paves the way for a compact on-chip multifunctional optical device.

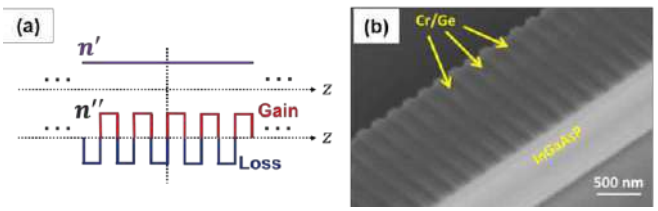


Figure 2: (a) Effective real and imaginary refractive index of the designed PT-symmetric structures and (b) its experimental realization.

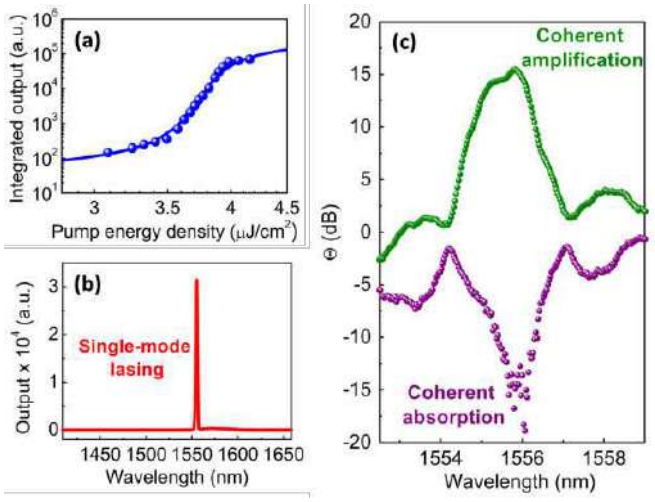


Figure 3: (a) Measured light-light curve when only the pump is on. (b) Lasing spectrum when the pump is at 4.2 μJ/cm^2. (c) At the lasing threshold of 3.6 μJ/cm2, coherent amplification and coherent absorption are experimentally observed at the same wavelength of 1555.8 nm, which give rise to about 30 dB modulation. Θ is the total output coefficient of the CPA-laser device.

2.3. Engineering subwavelength phase distribution

Metamaterial-based optical cloaks have thus far used volumetric distribution of the material properties to gradually bend light and thereby obscure the cloaked region. Hence, they are bulky and hard to scale up to macroscopic sizes. In addition, typical carpet cloaks introduce unnecessary phase shifts in the reflected light, making the cloaks detectable. Here we demonstrate an ultrathin metasurface cloak working at visible wavelengths using the concept of reflection phase manipulation (Figure 4) [5]. The skin cloak comprises a metasurface with distributed phase shifts rerouting light and rendering the object invisible. Our conformal cloak conceals a three-dimensional arbitrarily-shaped object by complete restoration of not only the wavefront, but also the phase of the reflected light. In contrast to bulky cloaks with volumetric index variation, our device is only 80 nanometer (about one-ninth of the wavelength) thick and potentially scalable to hide macroscopic objects. We believe the ultrathin image manipulation capability demonstrated here can lead to practical applications in flexible optoelectronics, 3D display and military technologies.

3. Conclusion

Using subwavelength nanostructures, exotic real and imaginary part of refractive index, and spatially-varying phase distribution can be engineered. These give rise to novel optical properties and many unconventional optical behaviors. Future integration of metamaterials with soft materials and quantum materials will potentially lead to exciting applications in smart optoelectronics, high-speed optical communications and quantum computing.

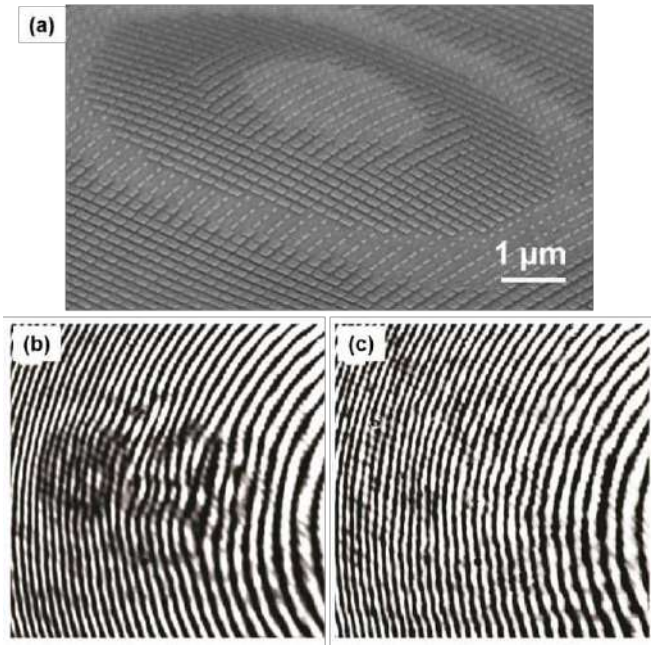


Figure 4: (a) An SEM image of the object onto which a metasurface skin cloak has been fabricated. (b) When the cloak is off, the interference fringes are distorted on the 3D object. (c) When the cloak is on, the interference fringes realign themselves, rendering the object invisible in both the wavefront and phase.

Acknowledgements

This work was primarily funded by the Director, Office of Science, Office of Basic Energy Sciences, Materials Sciences and Engineering Division of the US Department of Energy within the Metamaterials Program (KC12XZ). The author would also like to thank the T3: Texas A&M Triads for Transformation program for the funding support.

References

[1] H. Suchowski, K. O'Brien, Z. J. Wong, A. Salandrino, X. Yin, X. Zhang, Phase mismatch-free nonlinear propagation in optical zero-index materials, *Science* 342: 1223-1226, 2013.

[2] L. M. Procopio, L. A. Rozema, Z. J. Wong, D. R. Hamel, K. O'Brien, X. Zhang, B. Dakić, P. Walther, Single-photon test of hyper-complex quantum theories using a metamaterial, *Nature Communications* 8: 15044, 2017.

[3] L. Feng, Z. J. Wong, R.-M. Ma, Y. Wang, and X. Zhang, Single-mode laser by parity-time symmetry breaking, *Science* 346: 972-975, 2014.

[4] Z. J. Wong, Y.-L. Xu, J. Kim, K. O'Brien, Y. Wang, L. Feng, X. Zhang, Lasing and anti-lasing in a single cavity, *Nature Photonics* 10: 796-801, 2016.

[5] X. Ni, Z. J. Wong, M. Mrejen, Y. Wang, X. Zhang, An ultra-thin invisibility skin cloak for visible light, *Science* 349: 1310-1314, 2015.

Index-Tunable Terahertz Metadevices Based on Double-Layered Closed-Ring Resonator Arrays

Tatsunosuke Matsui[1]

[1]Department of Electrical and Electronic Engineering, Graduate School of Engineering, Mie University, Japan
*corresponding author, E-mail: matsui@elec.mie-u.ac.jp

Abstract

We demonstrate index-tunable metamaterials and metadevices working in the terahertz (THz) frequency range based on double-layered closed-ring resonator (CRR) arrays. The double-layered CRR arrays have a narrow-band transmission peak which shows negative refractive index even in normal incidence. We show that the effective refractive index can be widely tuned by slightly shifting relative position of the arrays. We also demonstrate that THz beam steering can be realized by utilizing the double-layered CRR arrays arranged in a wedge-shaped prism.

1. Introduction

In recent years, numerous studies have been carried out to develop novel types of metamaterials and metadevices [1]. In typical metamaterials, working frequencies are usually restricted only in a narrow range due to their resonant characteristics. Therefore, numerous attempts have been made to add tunability to develop active metadevices. Slightly shifting relative position of layered metamaterials is one of approaches taken to develop such active metadevices [2–6]. Here we demonstrate our recent results on index-tunable terahertz (THz) metamaterials and devices based on double-layered closed-ring resonator (CRR) arrays [7, 8]. The THz response of double-layered CRR arrays was first reported by Gu *et al*., in which negative refractive index was demonstrated even in normal incidence [9]. Here we show that the resonant characteristics [7] and the effective refractive indices [8] of double-layered CRR arrays can be tuned by slightly shifting relative position of the arrays. We also show that index-tuning capability can be utilized to make beam steering devices.

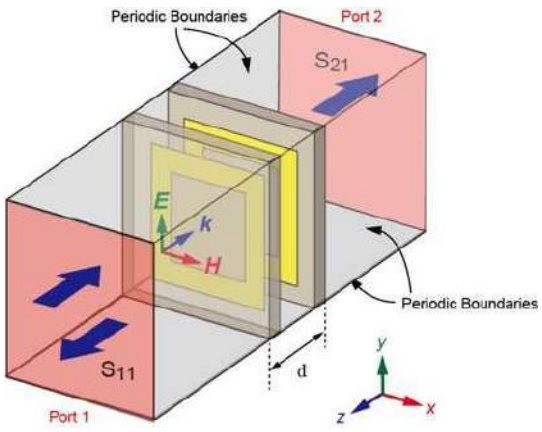


Figure 1: Schematic diagram of the unit cell of a double-layered CRR arrays in a periodic boundary conditions.

2. Numerical simulation

In this study, modeling of the devices and analysis of their THz responses were performed using 3D EM field analysis software, CST Microwave Studio (Computer Simulation Technology Inc.).

In Fig. 1, the unit cell of a double-layered CRR arrays is schematically shown. We assume that periodic arrays of CRR made of aluminum are placed on quartz substrate and the periodic boundary conditions are applied in x and y directions. The linearly polarized EM plane wave is incident from normal (z) direction and complex scattering parameters are evaluated. The impedance and the effective refractive indices were retrieved from the analyzed complex scattering coefficients.

We have further simulated negative refraction and beam steering characteristics of EM waves by arranging double-layered CRR arrays in a wedge-shaped prism.

3. Results and discussion

In double-layered CRR arrays, the resonant modes between the two sides of the paired CRRs and the near field coupling between adjacent CRRs on the same substrate can be excited and show negative refractive indices at their resonant frequency. These resonant modes can be approximately modeled by a composite LC-resonance circuit [7, 9]. The effective values of capacitance and inductance of such an LC circuit is quite sensitive to the geometrical parameters of the CRR array. Therefore, slight displacement of relative position of CRR arrays mainly alter effective capacitance and thus our operative principle is possible. Figure 2 summarize real (n_r) and imaginary (n_i) part of the retrieved effective refractive indices, respectively, for each relative displacement Δx. It can be seen that the effective refractive indices can be widely tuned by slightly shifting relative position of the arrays.

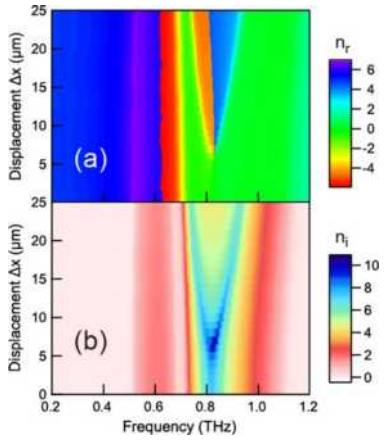


Figure 2: Summary of relative displacement Δx dependence of the (a) real and (b) imaginary part of the effective refractive indices.

At around 0.70 THz, double-layered CRR arrays show relatively low reflection loss and negative refractive index. Therefore, we arranged double-layered CRR arrays in a wedge-shaped prism and simulated negative refraction and beam steering characteristics of EM waves at around this resonant frequency. Figure 3 summarize negative refraction behaviors of THz EM waves from double-layered CRR arrays arranged in a wedge-shaped prism for different relative displacement Δx. It can be seen that THz EM wave is negatively refracted and the angles of refraction can be changed by slightly shifting relative position of the arrays, which implies that THz beam steering devices can be fabricated by our index-tuning principles.

4. Conclusions

In this study, we have numerically analyzed THz responses of the double-layered CRR arrays and we show that effective refractive indices can be widely tuned by slightly shifting relative position of the arrays. We have also demonstrated THz beam steering devices can be developed by utilizing index-tunable metamaterials.

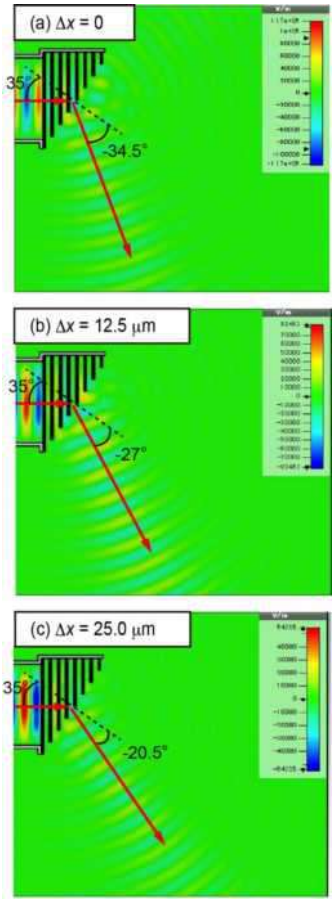


Figure 3: Summary of negative refraction behaviors of THz EM waves from double-layered CRR arrays arranged in a wedge-shaped prism for relative displacement Δx of (a) zero (b) 12.5 μm, and (c) 25.0 μm.

Acknowledgements

This project was partly supported by the Strategic Information and Communications R&D Promotion Programme (SCOPE) from the Ministry of Internal Affairs and Communications of Japan.

References

[1] N. I. Zheludev, Y. S. Kivshar, From metamaterials to metadevices, *Nature Materials* 11: 917–924, 2012.

[2] M. Lapine, D. Powell, M. Gorkunov, I. Shadrivov, R. Marqués, Y. Kivshar, Structural tunability in metamaterials, *Appl. Phys. Lett.* 95: 084105–1–3, 2009.

[3] D. A. Powell, K. Hannam, I. V. Shadrivov, Y. S. Kivshar, Near-field interaction of twisted split-ring resonators, *Phys. Rev. B* 83: 235420–1–6, 2011.

[4] M. Liu, Y. Sun, D. A. Powell, I. V. Shadrivov, M. Lapine, R. C. McPhedran, Y. S. Kivshar, Nonlinear response via intrinsic rotation in metamaterials, *Phys. Rev. B* 87: 235126–1–6, 2013.

[5] T. Matsui, M. Liu, D. A. Powell, I. V. Shadrivov, Y. S. Kivshar, Electromagnetic tuning of resonant transmission in magnetoelastic metamaterials, *Appl. Phys. Lett*. 104: 161117–1–4, 2014.

[6] T. Matsui, Y. Inose, D. A. Powell, I. V. Shadrivov, Electroactive Tuning of Double-Layered Metamaterials Based on π-Conjugated Polymer Actuators, *Adv. Opt. Mater*. 4: 135–140, 2016.

[7] T. Matsui, S. Asano, H. Mori, Terahertz Active Metamaterials Based on Stacked Closed-Ring Resonator Arrays, *IEEJ Trans. Sens. Micromach.* 137: 371–378, 2017 (in Japanese).

[8] Y. Watanabe, T. Matsui, Index-tunable terahertz metamaterials based on double-layered closed-ring resonator arrays, *J. Photon. for Energy* 8: 032211, 2018.

[9] J. Gu, J. Han, X. Lu, R. Singh, Z. Tian, Q. Xing, W. Zhang, A close-ring pair terahertz metamaterial resonating at normal incidence, *Opt. Express* 17: 20307–20312, 2009.

Nano-opto-electro-mechanical systems for optical switching and sensing

Andrea Fiore[1*], Tianran Liu[1], Francesco Pagliano[1,2], René van Veldhoven[1], Vadim Pogoretskii[1], and Yuqing Jiao[1]

[1]Institute for Photonic Integration, Eindhoven University of Technology, Eindhoven, The Netherlands
[2]nanoPHAB, Eindhoven, The Netherlands
*corresponding author, E-mail: a.fiore@tue.nl

Abstract

We report integrated nano-opto-electromechanical systems consisting of coupled InP waveguides on a silicon platform. Due to the tight optical confinement, large phase shifts are obtained over short propagation lengths, enabling efficient switching at low voltages in a small footprint. Due to their large response to nanomechanical displacements, they can also be applied as integrated displacement and force sensors.

1. Introduction

The mechanical reconfiguration of a photonic structure can result in strong changes in the propagation constant of a guided mode or in the resonant frequency of a confined mode, which enables optical switching in an integrated circuit and tuning of filters and lasers, among others. This concept, borrowed from micro-opto-electro-mechanical systems, is now being implemented in nanophotonic structures, resulting in nano-opto-electro-mechanical systems (NOEMS) [1], where nm-scale displacements of a moving part produce sizable changes in the device response. A practical challenge however is the implementation of advanced NOEMS within integration platforms where other functionalities such as light amplification and detection can be realized. In this paper we describe NOEMS based on vertically-coupled nanophotonic InP waveguides on a silicon wafer, a platform suitable for the integration of lasers and detectors.

2. Device structure

Figure 1 (a) shows an electron microscope image of an optical switch based on InP NOEMS. It is 2x2 switch based on Mach-Zehnder Interferometer (MZI). Two 50/50 Multi-Mode Interferometers (MMIs) split light into two branches and then recombine it. Electromechanically actuated phase modulators are implemented in both branches (Figure 1 (b)). The InP waveguides are defined by patterning a InP/InGaAsP/InP layer bonded on top of a silicon layer using silicon nitride, BCB and silica. Grating couplers, ridge waveguides and MMIs are defined in the bottom InP layer only, while the phase modulator consists of a double-membrane InP/air/InP waveguide obtained by selective etching of the InGaAsP sacrificial layer. 60μm-long tapers ensure efficient coupling from the mode of the bottom waveguide to the supermode of the double-membrane waveguide. The two InP membranes are oppositely doped to form a p-i-n junction, where the application of a reverse bias results in an electrostatic force on the top suspended membrane. At zero applied bias the vertical gap spacing between the membranes is 200 nm, and light exits through the cross port after interference. When a bias is applied, the distance between the membranes and thereby the effective index of the mode changes, leading to a phase change. The light is switched to the through port when the phase difference reaches π. The total length of the actuated part, including tapers, is 140 μm.

3. Results

Switching from the cross to the through port is obtained with a voltage as low as 4.4V and provides an extinction ratio above 15dB within a 34 nm bandwidth in the C-band. The device also serves as a very efficient optical phase modulator, being able to modify the optical phase by more than 4π with only 6.5V voltage in a 140μm-long waveguide. As compared to other MEMS switch structures, mostly involving switching voltages of tens of V [2], the low switching voltage of our device facilitates the electrical driving. Besides its application as a compact, low-voltage and low-power optical switch, the device can also function as an integrated optical sensor of displacement and force, as a nm-scale displacement of the top membrane results in a measurable transmission change.

4. Conclusions

An integrated optical switch based on nanomechanical InP waveguides on silicon is demonstrated. Strong optical confinement and efficient actuation based on vertical p-i-n junctions enable a small footprint and a low switching voltage. As lasers, detectors and passive circuit elements can be realised in the same InP-on-Si membrane technology [3], this approach can lead to the integration of nanomechanical switches and sensors in photonic integrated circuits.

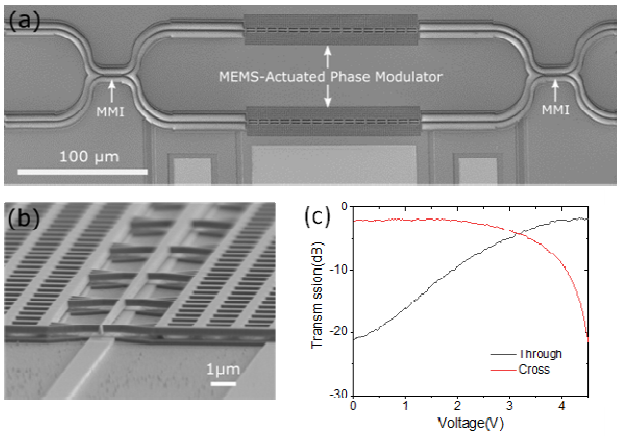


Figure 1: (a) Scanning electron microscope (SEM) image of a 2x2 switch. (b) Zoomed-in SEM image of the nanomechanical phase modulator. (c) Measured transmission of the switch as a function of voltage bias at 1530nm.

Acknowledgements

This work was partially supported by the Gravitation program "Research Center for Integrated Nanophotonics".

References

[1] L. Midolo, A. Schliesser and A. Fiore, Nano-opto-electro-mechanical systems, *Nature Nanotechnology* 13: 11-18, 2018.

[2] S. Han, T.J. Seok, N. Quack, B.W. Yoo, and M.C. Wu: Large-scale silicon photonic switches with movable directional couplers, *Optica*, 2: 370-375, 2015.

[3] J. J. G. M. v. d. Tol, Y. Jiao, L. Shen, A. Millan-Mejia, V. Pogoretskii, J. P. v. Engelen, and M. K. Smit, Indium Phosphide Integrated Photonics in Membranes, *IEEE Journal of Selected Topics in Quantum Electronics* 24: 6100809, 2018.

Quantum control of bosonic modes with superconducting circuits

Liang Jiang[1]

[1]Departments of Applied Physics and Physics, Yale University, New Haven, CT, U.S.A.
[2]Yale Quantum Institute, Yale University, New Haven, CT, U.S.A.
*corresponding author, E-mail: liang.jiang@yale.edu

Abstract

Bosonic modes are widely used for quantum communication and information processing. Recent developments in superconducting circuits enable us to control bosonic microwave cavity modes and implement arbitrary operations allowed by quantum mechanics -- in particular, quantum error correction against excitation losses. We investigate universal control of a single bosonic code with superconducting circuits, including unitary control, driven-dissipative control, holonomic dissipative control and quantum feedback control.

1. Introduction

Quantum computation holds the promise of solving certain problems much faster than any known classical computers, such as the larger integer factorization and simulation of quantum many-body problems. To build a real quantum computer, the physical platform should work in the quantum regime with long coherence time, fast quantum operations and good scalability, which are seemingly insurmountable obstacles for current technologies. The promising strategies to overcome such obstacles are quantum error correction (QEC) and fault-tolerant quantum computation, where the coherence time of the quantum memories can be extended and the quantum operations fault-tolerant to some low-probabilistic errors below a certain threshold.

The physical platform we consider is circuit quantum electrodynamics (QED), which is an analog of cavity QED using superconducting circuits. Cavity QED engineers the environment of the atoms by placing them in a cavity that supports only discrete bosonic modes of the electromagnetic field. Circuit QED uses superconducting qubits (such as transmon qubits) as artificial atoms coupled to microwave resonators. A key advantage of circuit QED is that it is trivial to obtain extremely strong coupling between the superconducting qubits and the cavity. For quantum computation using circuit QED, a storage cavity resonator with long coherence time as a harmonic oscillator can encode the quantum information, while the transmon qubits can act as an ancilla and the Josephson junctions coupled to a readout cavity as the reservoir to aid universal control of the storage cavity.

2. Key Results

We investigate the universal control of a harmonic oscillator with the aid of an ancilla qubit dispersively coupled to it. Quantum control of the harmonic oscillator can be achieved in the coupled qubit-oscillator system with qubit as an ancilla. Many theoretical and experimental works were devoted to preparing arbitrary oscillator states assisted by an ancilla qubit with Jaynes-Cummings (JC) coupling. However, it is more challenging to universal control of the oscillator, which usually needs a multi-level ancilla, slow adiabatic evolutions or a large number of control operations. In superconducting circuits, the transmon qubit (as an ancilla) and the cavity resonator (as a harmonic oscillator) can be tuned to be largely off-resonant with the off-resonance much larger than their JC coupling strength, resulting in a strongly dispersive model [1],

$$H = \omega_T |e\rangle\langle e| + \omega_C a^\dagger a - \chi a^\dagger a |e\rangle\langle e|$$

where ω_T and ω_C are the ancilla qubit transition frequency and the oscillator frequency, respectively, a is the annihilation operator of the oscillator excitation, χ is the dispersive coupling strength, and $|e\rangle$ denotes the excited state of the ancilla.

We may understand the dispersive Hamiltonian in two different ways with different applications [Fig. 1(a) (upper panel)]. On the one hand, the oscillator frequency has a shift dependent on the ancilla state, which leads to changes in the amplitude and phase of photons reflected from or transmitted through the cavity and therefore enables a QND measurement on the ancilla state. On the other hand, the ancilla transition frequency has a shift proportional to the oscillator photon number that is much larger than the cavity line width and atomic line width in the strongly dispersive regime, which splits the qubit spectrum into a series of separately resolved peaks representing the distribution of photon numbers within the driven cavity and hence can be used as a photon number detector. Moreover, for quantum control of the cavity, such a dispersive coupling regime in circuit QED makes it possible to selectively address the ancilla if and only if the cavity state has a specific photon number, hence providing new opportunities for universal control of the oscillator.

Recently, we have theoretically proposed [2] and experimentally demonstrated [3,4] the selective number-dependent arbitrary phase (SNAP) gate of the cavity mode,

$$R[\vec{\phi}] = \sum_{n=0}^{\infty} e^{i\phi_n} |n\rangle\langle n|,$$

where $\vec{\phi} = \{\phi_n\}_{n=0,1,2,\cdots}$ and the geometric phase ϕ_n is associated with the photon number state $|n\rangle$. Together with the displacement operation of the cavity mode

$$D[\varepsilon] = e^{\varepsilon a^\dagger - \varepsilon^* a},$$

SNAP gate enables universal control of the cavity mode. We have proved the existence and constructed the composite

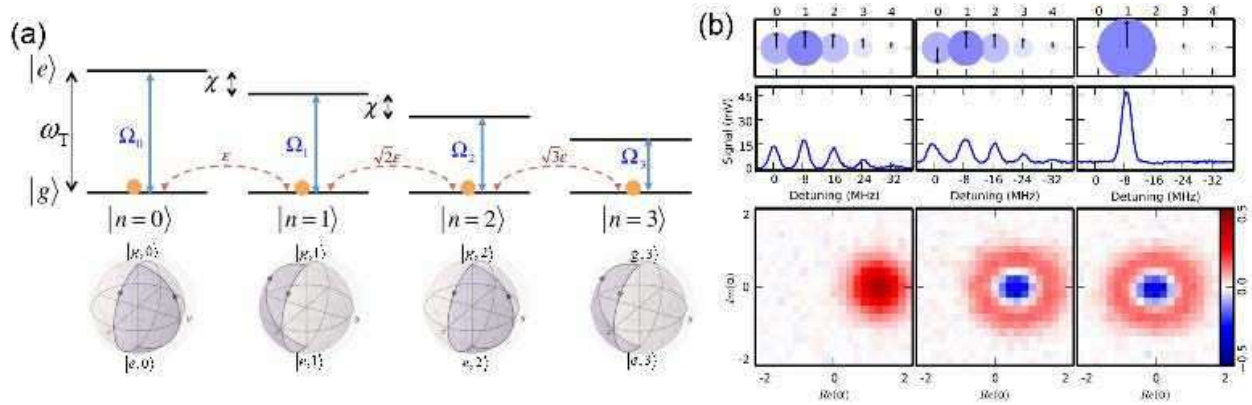


Fig. 1 Universal control of a harmonic oscillator by SNAP gates and displacement operations. (a) Schematic of universal control of the qubit-oscillator system. The SNAP gate (blue solid arrows) can simultaneously accumulate different Berry phases $\{\varphi_n\}$ to states $\{|g,n\rangle\}$. Here we adopt the rotating frame so that the states $\{|g,n\rangle\}$ have the same energy. (b) Phasor representation, qubit spectrum, and Wigner function after each of the steps in the Fock-state creation experiment. In the phasor representation, the arrow corresponds to the complex amplitude c_n of the initial cavity state $|\psi\rangle = \sum_n c_n |n\rangle$ and the area of the circle is proportional to $|c_n|^2$. The qubit spectrum refers to the qubit transition frequency dependent on the number of photons in the cavity.

sequences of $D[\varepsilon]$ and $R[\vec{\phi}]$ (e.g., $\cdots D_5 R_4 D_3 R_2 D_1$ pulse sequences with tunable parameters $\varepsilon_1, \varepsilon_3, \varepsilon_5, \cdots$ and $\vec{\phi}_2, \vec{\phi}_4, \cdots$) to convert the cavity ground state $|0\rangle$ to an arbitrary target state $|\psi\rangle = \sum_{n=0}^{n_{max}} c_n |n\rangle$. For example, we can now deterministically prepare single microwave photon inside the cavity, which can be used as a deterministic single microwave photon source. Moreover, our protocol can provide a deterministic source that can generate arbitrary microwave photon states. Besides prepare arbitrary photon states, using composite sequences can achieve an arbitrary unitary rotation $U = \sum_{i,j=0}^{n_{max}} U_{i,j} |i\rangle\langle j|$ that acts non-trivially in the subspace spanned by $\{|0\rangle, \cdots, |n_{max}\rangle\}$. This enables us to universally control a d-level system associated with the lowest d-levels of the cavity mode.

Then we further investigate the extension from the universal unitary control to arbitrary quantum channel construction (CPTP maps) for the oscillator by quantum non-demolition (QND) readout of the ancilla and quantum feedback control [5]. After that, we show that reservoir engineering can be another promising strategy to realize universal quantum computation in some unitarily evolving subspace of the oscillator [6,7]. Finally, we can use the quantum control schemes to entangle different bosonic modes for universal quantum computation [8,9].

3. Conclusions

We have shown that universal control of the oscillator can be achieved with the aid of an ancilla qubit. The SNAP gates of a harmonic oscillator (cavity resonator) can be implemented by indirect control of a dispersively coupled ancilla (transmon qubit), and the SNAP gates combined with displacement operation are sufficient for universal control. We may even construct arbitrary quantum channels for the oscillator by QND readout of the ancilla and quantum feedback control. However, it is still an open problem to find the optimal control of the qubit oscillator system with minimized expenditure of energy and resources.

Acknowledgements

We acknowledge support from the ARL-CDQI (W911NF-15-2-0067, W911NF-18-2-0237), ARO (W911NF-18-1-0020, W911NF-18-1-0212), ARO MURI (W911NF-16-1-0349), AFOSR MURI (FA9550-14-1-0052, FA9550-15-1-0015), DOE (DE-SC0019406), NSF (EFMA-1640959), and the Packard Foundation (2013-39273).

References

[1] D. I. Schuster *et al.*, Nature **445**, 515 (2007).
[2] S. Krastanov, V. V. Albert, C. Shen, C.-L. Zou, R. W. Heeres, B. Vlastakis, R. J. Schoelkopf, and L. Jiang, Phys. Rev. A **92**, 040303 (2015).
[3] R. W. Heeres, P. Reinhold, N. Ofek, L. Frunzio, L. Jiang, M. H. Devoret, and R. J. Schoelkopf, Nature Communications **8**, 94, 94 (2017).
[4] R. W. Heeres, B. Vlastakis, E. Holland, S. Krastanov, V. V. Albert, L. Frunzio, L. Jiang, and R. J. Schoelkopf, Phys. Rev. Lett. **115**, 137002 (2015).
[5] C. Shen, K. Noh, V. V. Albert, S. Krastanov, M. H. Devoret, R. J. Schoelkopf, S. M. Girvin, and L. Jiang, Physical Review B **95**, 134501 (2017).
[6] M. Mirrahimi, Z. Leghtas, V. V. Albert, S. Touzard, R. Schoelkopf, L. Jiang, and M. Devoret, New Journal of Physics **16**, 045014 (2014).
[7] V. V. Albert *et al.*, Phys. Rev. Lett. **116**, 140502 (2016).
[8] K. S. Chou *et al.*, Nature **561**, 368 (2018).
[9] Y. Y. Gao, B. J. Lester, K. Chou, L. Frunzio, M. H. Devoret, L. Jiang, S. Girvin, and R. J. Schoelkopf, arXiv:1806.07401 (2018).

Large-parameter-space optimization of photonic crystal structures

V. Savona

Institute of Physics, École Polytechnique Fédérale de Lausanne (EPFL), CH-1015 Lausanne, Switzerland

vincenzo.savona@epfl.ch

Recently, considerable progress has been made in the optimization of various figures of merit of photonic crystal (PhC) cavities and waveguides [1–5], leading to record performance in terms of quality factors in various materials [6,7], broad band slow light [8], second and third harmonic generation [9,10]. Here, by combining large scale numerical simulations to a hybrid stochastic-global optimization strategy, we demonstrate that there is still considerable room for further improvement of these figures of merit when increasing the size of the parameter space. In particular, we optimize a silicon-on-air L3 PhC cavity to a quality factor $Q > 80 \times 10^6$. While this result may have limited impact on applications, as disorder in the current state of the art in fabrication sets a statistical upper bound of roughly $Q \sim 4 \times 10^6$, we show that the same optimization strategy leads to unprecedented results for buried Si/SiO_2 PhC cavities, where we demonstrate a theoretical Q-factor in the 10 million range. We also optimize a buried Si/SiO_2 nanobeam cavity to an unloaded quality factor $Q \sim 6 \times 10^6$ with a nanobeam length much shorter than existing optimized structures. These results set the new state of the art for the PhC cavities under study. The present optimization approach opens the way to a new class of optimized PhC designs for monolithic structures or for structures made of low-index-contrast materials, such as AlN, GaN or silicon nitride, holding great promise for enhanced optical nonlinearity, sensing, and solid-state quantum optics.

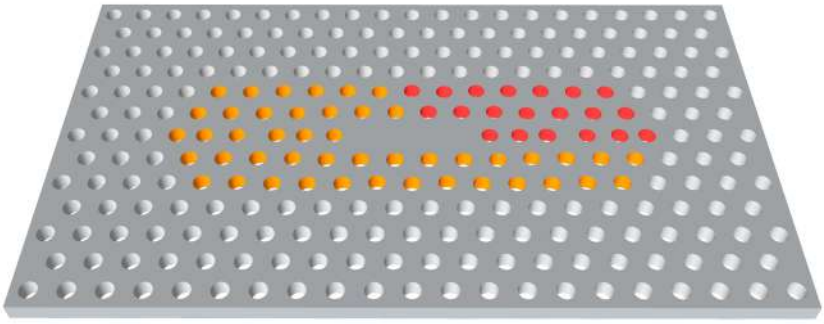


Fig. 1. Scheme of a L3 cavity where the highlighted holes are allowed to vary in position and size. Preserving the two mirror symmetries, only the parameters of the 20 red holes are independently varied, resulting in 53 independent parameters.

References

1. Y. Akahane et al., *Nature*, **425**, 944-947, 2003.
2. M. Minkov et al., *Sci. Rep.*, **4**, 5124, 2014.
3. M. Minkov et al., *Optica*. **2**, 631, 2015.
4. M. Minkov et al., *Appl. Phys. Lett.*, **111**, 131104, 2017.
5. T. Asano et al., *Opt. Express*, **25**, 1769, 2017.
6. Y. Lai et al., *Appl. Phys. Lett.*, **104**, 241101, 2014.
7. N. V. Triviño et al., *Appl. Phys. Lett.*, **105**, 231119, 2014.
8. Y. Lai et al., *Sci. Rep.*, **8**, 14811, 2018.
9. M. S. Mohamed et al., *APL Photon.*, **2**, 031301, 2017.
10. U. P. Dharanipathy et al., *Appl. Phys. Lett.*, **105**, 101101, 2014.

Dielectric nanostructures to enhance the efficiency of solar cells

Braulio Garcia-Camara[1], Eduardo Lopez-Fraguas[1], Mahmoud H. Elshorbagy[1], Ricardo Vergaz[1]

[1] Group of Displays and Photonic Applications (GDAF-UC3M), Department of Electronic Technology, Carlos III University of Madrid, Leganes, Madrid, Spain
*corresponding author, E-mail: brgarcia@ing.uc3m.es

Abstract

The recent results on multilayer solar cells and perovskite solar cells may revolve the photovoltaics field, but they still require light control strategies to optimize their performance. Dielectric nanostructures have the ability to efficiently control light at the nanoscale by directing or confining it. This has an enormous interest in several fields, and in particular in solar cells. This contribution pretends to summarize the latest results in this key topic in the fields of nanophotonic and energy harvesting.

1. Introduction

Photovoltaics is currently considered one of the most promising renewable energy sources. For this reason, scientific efforts are nowadays focused on the enhancement and improvement of the solar cells performance. This is a multidisciplinary work involving material engineering, electrical and electronic engineering, as well as photonics.

In the last years, encouraging materials like perovskites [1], or brilliant complex devices as multilayer solar cells are producing great expectations to achieve very high efficient solar cells, even larger than the Shockely-Quessier limit [2]. However, both options require further efforts in order to optimize their optical and electrical performance. On one side, convenient materials for the electron and hole transport layers are required, while on the other side an efficient light management inside the solar cells is critical.

While the use of plasmonic nanoparticles was introduced several years ago for improving the light confinement in solar cells [3,4], the recent advances in the dielectric nanostructures is awakening the interest on them to direct and also confine light into the active layers [5,6].

2. Methodology

The control of light in a solar cell can be achieved in several parts of the device. While some strategies considered the nanostructuration of the front and/or rear electrodes, other works have been considering the insertion of nanostructures in the intermediate or even in the active layers [8, 9]. All these strategies will be considered and analyzed.

3. Discussion

In this contribution, we will discuss about the latest results in the use of the dielectric nanostructures to improve the light management inside solar cells, including our latest results on this topic as well. With this analysis, we want to show the importance and the promising future of these techniques, helping on the improvement of the solar cells performance.

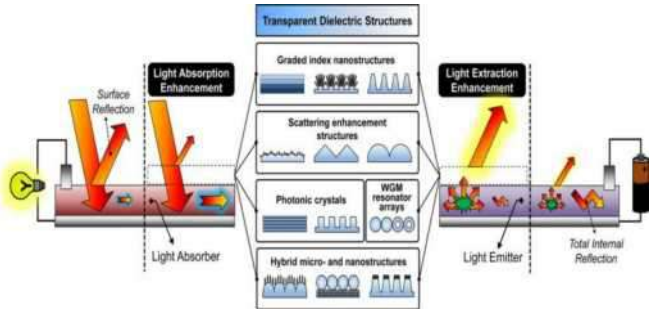


Figure 1: Different strategies for improving solar cells operation by using dielectric nanostructures. From [8].

Acknowledgements

This work was supported by the Spanish Ministerio de Economía y Competitividad TEC2016-77242-C3-1-R Grant (AEI/FEDER, UE funds) and Comunidad de Madrid SINFOTON-CM Research Program (S2013/MIT-2790). ELF wants to express his gratitude to the Ministerio de Educación y Formación Profesional for his doctoral grant (FPU research fellowship Ref. FPU17/00612).

References

[1] Q. Lin, A. Armin, R.C.R. Nagiri, P.L. Burn, P. Meredith. Electro-optics of perovskite solar cells. *Nat. Photon*. 9: 106-112, 2015.

[2] W. Shockley, H.J. Queisser. Detailed Balance Limit of Efficiency of p-n Junction Solar Cells. *J. Appl. Phys*. 32: 510-519, 1961.

[3] H.A. Atwater, A. Polman. Plasmonics for improved photovoltaic devices. *Nat*. *Mater*. 9: 205-2013 (2010).
[4] F. Enrichi, A. Quandt, G.C. Righini. Plasmonic enhanced solar cells: Summary of possible strategies and recent results. *Renew Sust Energ Rev*. 83: 2433-2439, 2018.
[5] M. C. Beard, J.M. Luther, A.J. Nozik. The promise and challenge of nanostructured solar cells. *Nat*. *Nanotechnol*. 9: 951–954 , 2014.
[6] M.L. Brongersma, Y. Cui, S. Fan. Light management for photovoltaics using high-index nanostructures. *Nat*. *Mater*. 13: 451-460, 2014.
[7] J. Yin, H.Qu, J. Cao, H. Tai, J. Li, N. Zheng. Light absorption enhancement by embedding submicron scattering TiO2 nanoparticles in perovskite solar cells. *RSC Adv*. 6: 24596-24602, 2016.
[8] G. Kang, J. Yoo, J. Ahn, K. Kim. Transparent dielectric nanostructures for efficient light management in optoelectronic applications. *Nano Today* 10: 22-47, 2015.
[9] D.-L. Wang, H.-J. Cui, G.-J. Hou, Z.-G.Zhu, Q.-B. Yan, G. Su. Highly efficient light management for perovskite solar cells. *Sci*. *Rep*. 6: 18922, 2016.

Metasurfaces Enabled by Locally Tailoring Disorder in Phase-Change Materials

Martin Hafermann[1], Philipp Schöppe[1], Jura Rensberg[1], Carsten Ronning[1]

[1] Institute of Solid State Physics, University of Jena, 07743 Jena, Germany

Abstract

Active optical metasurfaces with dynamic switchable, tunable, and reconfigurable optical functionalities are an emerging field in photonics and optoelectronics. Especially, chalcogenide-based phase-change materials, such as $Ge_2Sb_2Te_5$ (GST), can be fast and repeatedly switched by external stimuli between crystalline and amorphous states, typically accompanied by a tremendous difference of the electronic and photonic properties. Here, we demonstrate that focused ion beam-induced disorder in highly confined regions can transform phase-change materials in active optical metasurfaces by locally adjusting the phase [1]. A careful control of the amount of disorder can locally tailor the effective refractive index in GST films on the nanometer scale, which is highly promising for multilevel switching applications. In contrast to direct laser writing, focused ion beam irradiation enables the fabrication of subwavelength-scaled, planar, nonvolatile, and reconfigurable optical metasurfaces, with pattern sizes clearly below the diffraction limit of common laser light sources.

Acknowledgements

This work was financed by the Deutsche Forschungs-gemeinschaft (DFG) through Grant Ro1198/21-1.

References

[1] M. Hafermann, P. Schöppe, J. Rensberg, C. Ronning, *ACS Photonics* 5: 5103-5109, 2018.

Can optical forces be used to measure the polarization state of light inside a birefringent waveguide?

Vincent Ginis[1,2*], Lulu Liu[1], Alan She[1], and Federico Capasso[1]

[1] Harvard John A. Paulson School of Engineering and Applied Sciences,
Harvard University, 29 Oxford Street, Cambridge, MA 02138
[2] Vrije Universiteit Brussel, Pleinlaan 2, 1050 Brussel, Belgium
*corresponding author, E-mail: ginis@seas.harvard.edu

Abstract

We investigate whether optical forces acting on Mie particles in the vicinity of a birefringent waveguide can be used to reconstruct the polarization state of light inside that waveguide and we identify an interesting parameter regime in which an unambiguous retrieval is possible. This result is utilizing the fact that the lateral Belinfante momentum strongly depends on the helicity of the confined light.

1. Mie resonances and Optical forces

We investigate whether the displacement of a microparticle on top of a waveguide, caused by the near-field optical forces, can be used to retrieve the polarization of light inside that waveguide [1]. We start by evaluating the different forces acting on a particle that is positioned on top of—or at a fixed height above—a waveguide. In general, three optical force components act on a particle, held in the evanescent field of a birefringent waveguide: one acting in each direction (x, y, z). The most important force is the gradient force (F_z). This force attracts the particle towards the region of largest intensity [2]. For very small particles, this is the strongest force. The second component (F_x) pushes the particle along the direction of propagation of the guided modes [3]. The final component (F_y) is proportional to the spin density of the field. In the case of a dipolar, Rayleigh particle, these components can be calculated analytically, for larger particles, one needs to calculate several terms of the Mie series [4, 5, 6, 7]. The complete geometry is visualized in Fig. 1A.

2. A non-invasive measurement of the polarization of light in optical networks

The polarization of light is used to encode information in optical networks [8]. This increases the need for efficient techniques that allow for sensitive probing of the polarization state [9, 10]. An optical probe, with versatility comparable to the microwave probes, would be extremely beneficial to the development of photonic chips. Such a probe would allow for a direct, local measurement of the polarization, thus reducing design iterations and streamlining fabrication.

3. Results

It is known that the lateral force (F_y), which ultimately exists because of a transfer of the Belinfante momentum from the evanescent field to the particle, depends on the helicity of light. This suggests that this force can be used as a proxy for light's helicity. To confirm this idea, we calculate the lateral Belinfante force as a function of the polarization space (Poincaré sphere) and as a function of the electromagnetic properties of the Mie particles (radius, refractive index). In Fig. 1 we visualize the two-dimensional mapping of the Poincaré sphere on a rectangular grid (Fig. 1B-C) and subsequently show the lateral force acitng on a Silicon microparticle with radius $a = 300\ \mathrm{nm}$ on this grid (Fig. 1D). Here, we show that the lateral force acting on microparticles in the evanescent field of a waveguide strongly depends on the size of the particle. Moreover, it is intriguing to see that the maximum and the minimum of the lateral force do not coincide with the north and south poles of the Poincaré sphere. Instead, we find that the maxima are shifted along the great circle of the sphere. This shift depends on the size and refractive index of the particle. The physical origin of this resonant effect relies in the phase difference between scattered TE and TM components of light.

This effect can be used to retrieve the polarization state of light inside waveguides. Indeed, the displacement of a particle on top of a waveguide is found by balancing the lateral force, shown in Fig. 1D with the restoring gradient force that tries to keep the particle at the position of highest intensity. By comparing this displacement of a large Mie particle with the displacement of a smaller one, it is possible to retrieve the polarization state of the light inside the waveguide. This is visualized in Fig. 1F.

4. Conclusions

In addition to the celebrated examples of actuation, sorting, and spectroscopy, our work explores a new application of lateral forces, enabling the development of a local, minimally invasive probe of the polarization state inside waveguide.

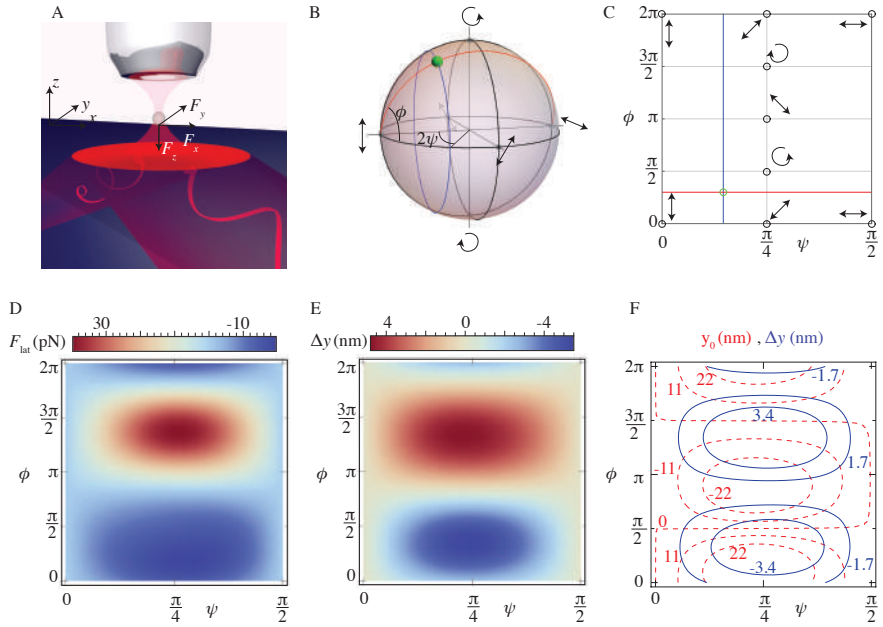


Figure 1: (A) Schematic desciption of the forces acting on a particle in the evanescent field of a waveguide. The guided mode that generates the evanescent wave can have any polarization state represented by the green dot on the Poincaré sphere in (B). (B) and (C) together illustrate the mapping from the Poincaré sphere onto a rectangular grid. (D) and (E) show the helicity-dependent lateral force on a 300 nm radius silicon particle on top of a birefringent waveguide and the corresponding displacements. (F) The overlap of several contour lines of y_0 and Δy. Because of the relative displacement of these contour lines in the ϕ direction, we generally find only two intersections per set of two measurements.

Acknowledgement

We acknowledge the support of NSF GFRP grant number

DGE1144152 and the Research Foundation Flanders grant number 12O9115N.

References

[1] Vincent Ginis, Lulu Liu, Alan She, and Federico Capasso. Using the belinfante momentum to retrieve the polarization state of light inside waveguides. Submitted.

[2] Lulu Liu, Simon Kheifets, Vincent Ginis, and Federico Capasso. Subfemtonewton Force Spectroscopy at the Thermal Limit in Liquids. *Physical Review Letters*, 116(22):228001, 2016.

[3] Lulu Liu, Simon Kheifets, Vincent Ginis, Andrea Di Donato and Federico Capasso. Elliptical orbits of microspheres in an evanescent field. *Proceedings of the National Academy of Sciences*, 114(42):11087–11091, 2017.

[4] Silvia Albaladejo, Manuel I Marqués, Marine Laroche, and Juan José Sáenz. Scattering forces from the curl of the spin angular momentum of a light field. *Physical review letters*, 102(11):113602, 2009.

[5] Konstantin Y Bliokh, Aleksandr Y Bekshaev, and Franco Nori. Extraordinary momentum and spin in evanescent waves. *Nature Communications*, 5:14, 2013.

[6] M Antognozzi, C R Bermingham, R L Harniman, S Simpson, J Senior, R Hayward, H Hoerber, M R Dennis, A Y Bekshaev, K Y Bliokh, and F Nori. Direct measurements of the extraordinary optical momentum and transverse spin-dependent force using a nano-cantilever. *Nature Physics*, 12(8):731–735, 2016.

[7] Lulu Liu, Andrea Di Donato, Vincent Ginis, Simon Kheifets, Arman Amirzhan, and Federico Capasso. Three-dimensional measurement of the helicity-dependent forces on a Mie particle. *Physical review letters*, 120(22):223901, 2018.

[8] Robert W Tkach. Scaling optical communications for the next decade and beyond. *Bell Labs Technical Journal*, 14(4):3–9, 2010.

[9] Dandan Wen, Fuyong Yue, Santosh Kumar, Yong Ma, Ming Chen, Ximing Ren, Peter E Kremer, Brian D Gerardot, Mohammad R Taghizadeh, Gerald S Buller, et al. Metasurface for characterization of the polarization state of light. *Optics express*, 23(8):10272–10281, 2015.

[10] Anders Pors, Michael G Nielsen, and Sergey I Bozhevolnyi. Plasmonic metagratings for simultaneous determination of stokes parameters. *Optica*, 2(8):716–723, 2015.

Long-range FRET-mediated exciton diffusion in cesium lead halide perovskite nanostructures

Monica Lorenzon[a,b], Anna Loiudice[c], Edward S. Barnard[a], Nicholas J. Borys[a], Matthew J. Jurow[a, b], Min Ji Hong[a], Yi-Hsien Lu[a,b], Igor Rajzbaum, Edward K. Wong[a], Miquel Salmeron[b], Yi Liu[a,b], Stefano Cabrini[a], Stephen Whitelam[a], Raffaella Buonsanti[c], Adam M. Schwartzberg[a]*, Erika Penzo[a]*, Alexander Weber-Bargioni[a]*

[a] *The Molecular Foundry, Lawrence Berkeley National Laboratory, Berkeley, CA, USA*
[b] *Materials Sciences Division, Lawrence Berkeley National Laboratory, Berkeley, CA, USA*
[c] *Department of Chemical Sciences and Engineering, École Polytechnique Fédérale de Lausanne (EPFL), Sion, Switzerland*

* Corresponding authors: epenzo@lbl.gov, amschwartzberg@lbl.gov, afweber-bargioni@lbl.gov

Colloidal inorganic perovskite nanocrystals (PNCs) are solution-processable functional materials whose emission can be easily tuned via both size and composition.[1] Their exciting optical properties such as the large absorption cross-section and high photoluminescence quantum yield (PLQY) make them ideal candidates for a broad range of photonics and optoelectronics applications.[2] In this work, we present an overview of the exceptionally efficient exciton transport mediated by Förster Resonant Energy Transfer (FRET) in perovskite systems of increasing dimensionality. With a specifically designated optical setup, we directly measure the spatial extent of exciton hopping in a controlled two-dimensional assembly of 0D PNCs, which provides a flat energy landscape with minimal geometric disorder.[3] Steady-state and time-resolved PL microscopy, together with physical modeling of exciton transport, shows an exciton diffusion length of 200 nm and diffusivity as high as 0.5 cm^2/s, which greatly exceed the values reported for FRET-mediated exciton diffusion in chalcogen-based quantum dot solids, and, importantly, matches the optical absorption depth. We further explore the exciton diffusion paradigm in 1D perovskite nanowires and 2D nanosheets, where we image the diffusion across the whole system, with diffusion lengths larger than 1μm. In addition to the exciton diffusion mapping, a significant portion of this work has been dedicated to the optimization of the substrate and the sample passivation. Specifically, we show that with a thermal-based atomic layer deposition process we are able to apply a ~3nm-thick transparent ceramic coating (aluminum oxide) which ensure optical stability over a four month period, thus overcoming the instability issue which often hinders the actual integration of perovskite materials in optoelectronics devices. Our investigation therefore provides the foundation for employing FRET-mediated exciton diffusion in nanostructured perovskites, while also demonstrating practical guidelines to use these bright emitters in optoelectronic devices beyond proof of principle.

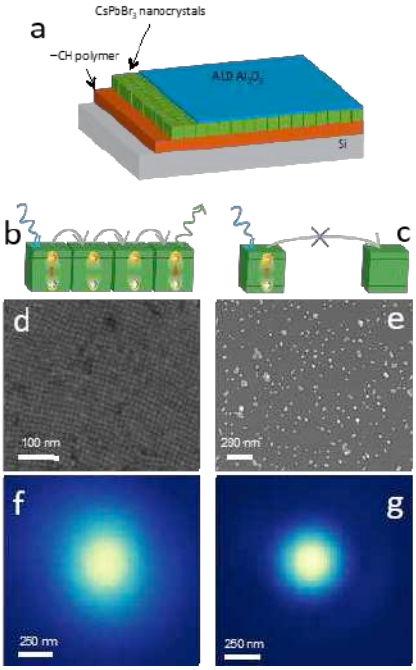


Fig. 1: (a) Schematics of the sample architecture. (b) Efficient and (c) inhibited FRET mediated exciton diffusion depending on the inter PNC distance. SEM micrograph of (d) a closed packed and (e) spease monolayer of PNCs. PL intensity profiles emitted by the (f) close-packed and (g) sparse PNC monolayer

References

[1] L. Protesescu, S. Yakunin, M. I. Bodnarchuk, F. Krieg, R. Caputo, C. H. Hendon, R. X. Yang, A. Walsh and M. V. Kovalenko, Nano Lett. **15**, 6 (2015).

[2] M. V. Kovalenko, L. Protesescu and M. I. Bodnarchuk, Science, **358**, 6364 (2017).

[3] G. M. Akselrod, P. B. Deotare, N. J. Thompson, J. Lee, W. A. Tisdale, M. A. Baldo, V. M. Menon and V. Bulović, Nat. Commun. **5**, 3646 (2014).

Dielectric-based Hyperbolic Metamaterials and Nano-Optical Cavity

Junichi Takahara*[1,2] and Jun Sagara[1]

[1]Graduate School of Engineering, Osaka University, Osaka, Japan
[2]Photonics Center, School of Engineering, Osaka University, Osaka, Japan
*corresponding author, E-mail: takahara@ap.eng.osaka-u.ac.jp

Abstract

We study theoretically dielectric-based TiO_2/SiO_2 Hyperbolic Metamaterial (HMM) at mid-infrared region with high transparency in visible. We report unique resonant properties of a HMM resonator and specific field distribution due to its hyperbolic dispersion relation. We also report an active metasurface which is switchable between HMM and Mie resonator.

1. Introduction

Hyperbolic metamaterial (HMM) is a structure in which substances of positive and negative permittivity are periodically stacked, and novel optical functions are expected by making the equi-frequency surface of hyperboloid in wavenumber(k)-space. HMMs extremely modify the shape of dispersion relation of light because their unconventional open isofrequency surface in k-space permits enlargement of k without limitation [1]. Such isofrequency surface induces the divergence of density of state, resulting in enhancing light-matter interactions. Although similar enlargement of k without limitation can be obtained in negative dielectric (ND) optical waveguide (i.e. plasmonic waveguide), propagation modes are not bulk (3D) waves, but surface (2D) waves [2,3]. Hence, HMMs show a great promise in nanophotonics for the miniaturization of bulk optical components such as optical waveguides or optical cavities.

There are some theoretical proposals in an nano-optical waveguide based on HMMs [4,5]. Anomalous resonant properties are observed experimentally in HMM cavity [6]. However, since conventional HMMs utilize metals, large losses hide interesting properties of HMMs. To solve the problem, HMM utilizing dielectric is promising. Since phonons have Reststrahlen band where the real part of the permittivity is negative with smaller imaginary part than metals, resulting in achieving lower loss HMMs.

In this paper, we report TiO_2/SiO_2 multilayered HMM and describe the resonant properties of its optical cavity.

2. Dielectric-based HMMs

Figure 1 shows a schematic view of a rectangular HMM optical cavity with the cross section of W_y x W_x, where the length of the cavity is infinite. Optical axis of the HMM is taken in x-direction.

Figure 2(a) shows permittivity spectra of TiO_2 and SiO_2 in mid-infrared region, where ND is observed at λ_0=8-9μm and λ_0>12.5μm. This is caused by Reststrahlen band between TO and LO phonon. Figure 2(b) shows effective permittivity spectra of infinite TiO_2/SiO_2 multilayered system (W_x=W_y=infinite). The multilayered system becomes type II HMM at λ_0=8-9μm (the gray area in Fig. 2(b)).

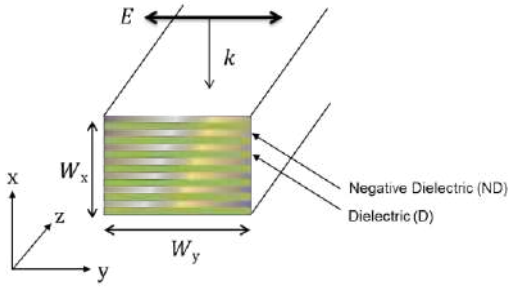


Figure 1: A schematic view of a rectangular HMM optical cavity with the width of Wy and the height of Wx. The length of the cavity is infinite. Linearly y-polarized light is incident along the x-axis.

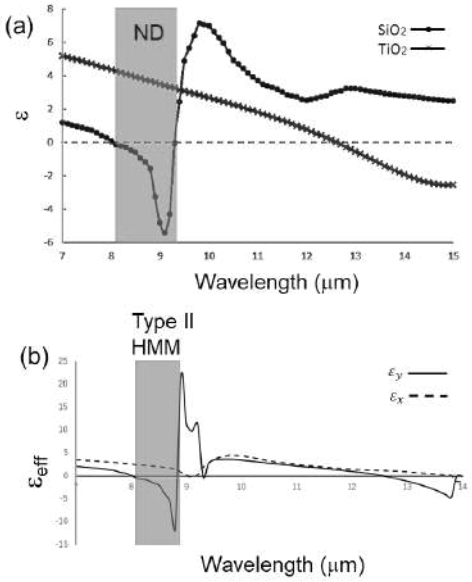


Figure 2: Permittivity dispersion spectra: (a) bulk permittivity of TiO_2 and SiO_2 , (b) effective permittivity ε_x and ε_y of TiO_2/SiO_2 multilayered HMM.

4. HMM optical cavity

To investigate unique resonant property of HMM cavity, we performed FDTS (Finite-Difference Time Domain) simulation using the above effective permittivity in the configuration as shown in Fig. 1. Linearly polarized pulsed light was irradiated along the x-axis as an incident light and resonant conditions were investigated from an absorption spectral map with respect to the cavity size.

Figure 3 shows the calculated electric field distribution inside a TiO_2/SiO_2 HMM resonator (W_x=50nm and W_y=90nm) at the resonance of λ_0=8.58μm. X-shaped resonant mode is observed clearly thanks to the lower loss permittivity beside the phonon resonance [1,7]. Such mode profile is attributed to the hyperbolic dispersion relation in k-space of HMMs. We will discuss the mechanism of the resonant pattern and the application to nano-optical cavity.

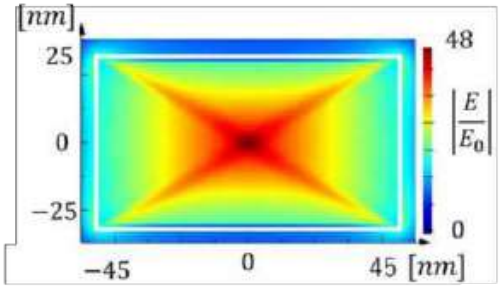


Figure 3: Electric field distribution at 8.58μm inside TiO_2/SiO_2 HMM cavity with W_x=50nm and W_y=90nm.

Acknowledgements

This work was supported in part by JSPS KAKENHI Grant Number 17K19077 and JSPS Core-to-Core program.

References

[1] A. Poddubny I. Iorsh, P. Belov, Y. Kivshar, Hyperbolic metamaterials, *Nature Photon*. 7, 958, 2013.
[2] J. Takahara, S. Yamagishi, H. Taki, A. Morimoto and T. Kobayashi, Guiding of a one-dimensional optical beam with nanometer diameter, *Opt*. *Lett*., 22, 475, 1997.
[3] M. S. Tame, K. R. McEnery, Ş. K. Özdemir, J. Lee, S. A. Maier, and M. S. Kim, Quantum plasmonics, *Nat*. *Phys*. 9(6), 329, 2013.
[4] S. Ishii, M.Y. Shalaginov, V.E. Babicheva, A. Boltasseva and A.V. Kildishev, Plasmonic waveguides cladded by hyperbolic metamaterials, *Opt*. *Lett*. 39, 4663, 2014.
[5] M. Higuchi and J. Takahara, Plasmonic interpretation of bulk propagating waves in hyperbolic metamaterial optical waveguides, *Opt*. *Express* 26(2), 1918, 2018.
[6] X. Yang, J. Yao, J. Rho, X. Yin, and X. Zhang, Experimental realization of three-dimensional indefinite cavities at the nanoscale with anomalous scaling law, *Nature Photon*. 6(7), 450, 2012.
[7] A.V. Chshelokova, P.V. Kapitanova, A.N. Poddubny, D.S. Filonov, A.P. Slobozhanyuk, Y.S. Kivshar, and P.A. Belov, Hyperbolic transmission-line metamaterials, *J*. *Appl*. *Phys*. 112, 073116, 2012.

Nanocrystal Optoelectronics

Hilmi Volkan Demir

NTU LUMINOUS! Singapore and Bilkent University UNAM Turkey

Solution-processed semiconductor nanocrystals have been attracting increasingly greater interest in photonics including spectrally pure color conversion and enrichment in quality lighting and display backlighting [1,2]. These nanocrystals span different types and structures of semiconductors in the forms of colloidal quantum dots and rods to a more recently developing class of colloidal quantum wells. In this talk, we will introduce the emergent field of nanocrystal optoelectronics using solution-processed quantum dots and wells. In particular, we will present a new concept of all-colloidal lasers developed by incorporating nanocrystal emitters as the optical gain media, intimately integrated into fully colloidal cavities [3]. In the talk, we will then focus on our most recent work on the latest rising star of tightly-confined atomically flat nanocrystals, the quasi-2D colloidal quantum wells (CQWs), also popularly nick-named 'nanoplatelets'. Latterly we have discovered that the CQWs uniquely enable record high optical gain coefficients among all colloids [4]. In addition, we will show the controlled stacking and assemblies of these nanoplatelets, which provides us with the ability to tune and master their excitonic properties, and present the first accounts of doping them for high-flux solar concentration and precise wavefunction-engineered magnetic properties [5]. Given their current accelerating progress, these solution-processed quantum materials hold great promise to challenge their epitaxial thin-film counterparts in semiconductor optoelectronics in the near future.

[1] NANO TODAY 6, 632 (2011)
[2] NANO LETTERS 12, 3986 (2012), NANO LETTERS 13, 3065 (2013) and ACS NANO 8, 8224 (2014)
[3] ADVANCED MATERIALS 27, 2741 (2015) and ACS NANO 8, 6599 (2014)
[4] NANO LETTERS 19, 277 (2019)
[5] ACS NANO 12, 8547 (2018); ADVANCED FUNCTIONAL MATERIALS 26, 2891 (2016); NANO LETTERS 18, 2047 (2018) and ADVANCED MATERIALS 29, 1700821 (2017)

Novel Phenomena in Optical Manipulation due to Magnetic-Field-Induced Resonant States

S. Edelstein[1], R. M. Abraham Ekeroth[2;3], P. A. Serena[1], J. J. Sáenz[4;5], A. García-Martín[3], and M. I. Marqués[6*]

[1]Instituto de Ciencia de Materiales de Madrid (ICMM-CSIC), Campus de Cantoblanco, 28049 Madrid, Spain
[2]Instituto de Física Arroyo Seco, U. Nacional del Centro de la Provincia de Buenos Aires, Pinto 399, 7000 Tandil, Argentina
[3]Instituto de Micro y Nanotecnología IMN-CNM, CSIC, CEI UAM+CSIC, Isaac Newton 8, Tres Cantos, Madrid 28760, Spain
[4]Donostia International Physics Center (DIPC), Paseo Manuel Lardizabal 4, 20018 Donostia-San Sebastian, Spain
[5]IKERBASQUE, Basque Foundation for Science, Bilbao 48013, Spain
[6]Departamento de Física de Materiales, Condensed Matter Physics Center (IFIMAC) and Instituto Nicolás Cabrera, Universidad Autónoma de Madrid, Madrid 28049, Spain
*corresponding author, E-mail: manuel.marques@uam.es

Abstract

We study the effect of optical forces [1] and torques on a spherical isotropic magneto-optical (MO) nanoparticle [2]. The force on the direction of the applied external magnetic field has two contributions: A first conservative component coming from the "Zeeman" coupling between the light spin density and the external magnetic field through the imaginary part of the MO polarizability, and a second component coming from the direct transfer of the helicity of the electromagnetic field to the particle through the real part of the MO polarizability. The torque also has two contributions: The usual one coming from the spin of the light field and another one depending only on the modulus of the electromagnetic field.

We explicitly show examples where these new contributions lead to: (i) An optical torque on an isotropic, spherical particle using a linearly polarized plane wave, (ii) the formation of a conservative optical lattice with non-interfering incoming fields and (iii) radiation pressure using electromagnetic fields with zero average value of the Poynting vector.

References

[1] S. Albaladejo, M. I. Marqués, M. Laroche and J. J. Sáenz, Phys. Rev. Lett. 102, 113602 (2009).

[2] V. V. Temnov, G. Armelles, U. Woggon, D. Guzatov, A. Cebollada, A. García-Martín, J. M. García-Martíın, T. Thomay, A. Leitenstorfer, and R. Bratschitsch Nat. Photonics 4, 107 (2010).

Direct Integration of Scalable Quantum Sources into Pre-Fabricated Integrated Optics

Khaled Mnaymneh[1*], Dan Dalacu[1], David B. Northeast[1], Joseph McKee[1], John Weber[1], Sofiane Haffouz[1], Jean Lapointe[1], Philip P. Poole[1], Geof C. Aers[1], and Robin L. Williams[1]

[1]National Research Council, Ottawa, Canada
*corresponding author, E-mail: khaled.mnaymneh@nrc-cnrc.gc.ca

Abstract

We present a monolithic integration technique for the direct integration of single quantum sources into pre-fabricated photonic circuitry. Using a SEM-based nanomanipulator, we preselect, transfer and place epitaxially grown tapered InP nanowires embedded with a single InAs quantum dot on top of or beside pre-fabricated optical waveguides. Because the nanowires are tapered, the optical mode of the nanowire can evanescently couple into the nearby waveguide. The coupling is also bidirectional allowing the optical pumping of the dot to be done by the waveguide as well.

1. Introduction

On-chip demonstrations of photonic integrated circuits for quantum information processing have almost exclusively relied on off-chip sources of quantum light. Our presentation describes a significant technological advance towards overcoming this drawback by integrating a highly-robust, single photon light source with high brightness and near-unity efficiency. We show deterministic integration of single quantum emitters within on-chip photonic circuitry with coupling efficiencies of 74% and single-photon purities of 97%. We demonstrate, for the first time, how the taper geometry of a semiconductor nanowire, with an embedded emitter, can be used to optimize the evanescent coupling between emitter and photonic circuitry. Importantly, the proposed technique allows for the use of pre-fabricated photonic integrated circuitry, as shown in Fig 1a., so that emitters can be added after the integrated optics circuitry is fabricated, facilitating experiments where complex photonic circuits are required, such as boson sampling, optical quantum computing and quantum metrology. The coupling strategy we demonstrate is bidirectional, so that excitation of the emitter can be done through the coupled waveguide itself, removing any need for the free-space optics that is normally used for optical excitation and opening the way for real-world, quantum 'plug and play' systems.

2. Numerical Results

We have shown, using numerical simulations, Fig. 1b, that the coupling efficiency using our evanescent coupling technique can approach 100% (Fig 1c). In order for integrated quantum schemes to be practical, on-chip quantum light extraction efficiency is paramount [1]. In this talk, we show a physically demonstrated efficiency of 74%, already beyond the theoretical limit of 36% found for buried nanowire sources.

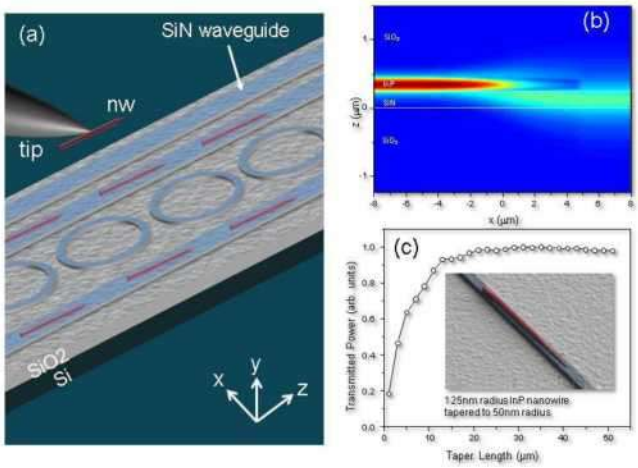


Figure 1: (a) Cartoon showing placed quantum sources on a pre-fabricated photonic circuit. (b) Numerical simulation of the evanescent coupling between a placed nanowire and a silicon nitride waveguide. (c) Numerical results of coupling efficiency versus taper length. Inset shows a placed nanowire on a silicon nitride waveguide.

3. Scalability

Our technique increases the scalability of solid state quantum sources integrated into photonic circuitry many fold. Removing the need for alignment marks and introducing the capability to use pre-fabricated photonic circuitry reduces the number of fabrication steps needed to realize complex photonic devices for quantum information applications such as in boson sampling and quantum simulation. With companies like IME [2] now providing pre-fabricated chips ready for integrated quantum optics, our technique provides a method to deterministically place large numbers of nanowire sources in strategic locations on such pre-fabricated circuitry. This point has been emphasized in the talk and additional details of the nanomanipulator

transfer process will be shown talk where 2 videos of the transfer process itself will be shown.

4. Experimental Results

Figure 2 shows the resolution-limited spectrum of the ground state emission of the embedded quantum dot collected at the facet of the waveguide at the chip edge.

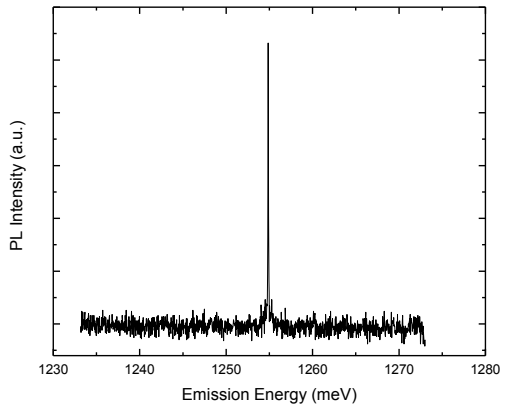


Figure 2: Resolution limited peak of ground state emission of embedded quantum dot collected from chip edge.

Figure 3a shows the placed nanowire on a silicon nitride waveguide with the associated power spectrum shown in Figure 3b. Other complexes can be seen as the power is increased. It is important then to filter these energies when the source is operated at saturation. Saturation is required when a high single-photon repetition rate is desired. Figure 3c shows the experimental setup for optical pumping and collection into fiber as well as performing a fiber based Hanbury-Brown Twiss measurement.

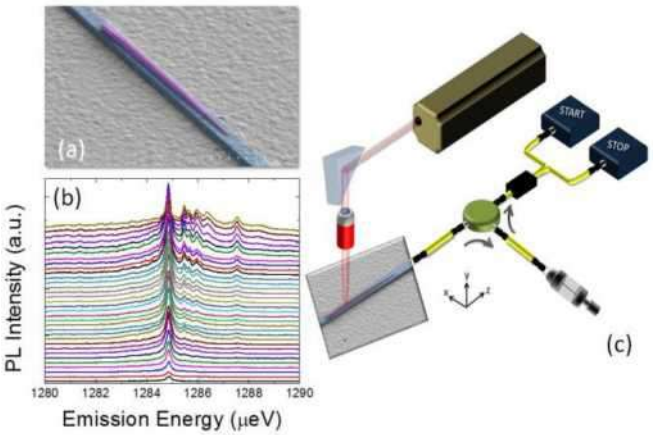


Figure 3: (a) Placed nanowire. (b) Power spectrum of collected emission. (c) Experimental setup of Hanbury-Brown Twiss measurement.

Single photon statistics where demonstrated using CW and pulsed excitation, as shown in figure 4, respectively. When the detector response is deconvolved from the CW data, a multiphoton probability at zero delay was found to be 2%, showing that the single photon emission of sources integrated with waveguides is not effected.

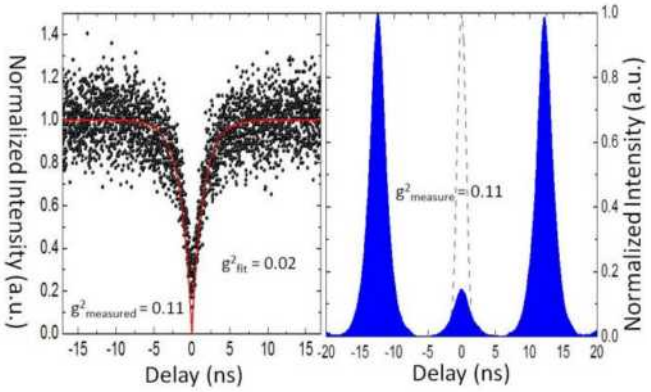


Figure 4: CW and pulsed excitation of the single-photon measurements.

5. Conclusions

Solid state single photon sources can be monolithically integrated into pre-fabricated photonic circuitry using a SEM-based nanomanipulator, which essentially transforms conventional photonic circuitry into quantum photonic circuitry. The work presented moves the field of integrated quantum sources significantly closer to field-ready quantum technologies

Acknowledgements

We acknowledge the Canadian Space Agency in this work.

References

[1] J. L. O'Brien, A. Furusawa and J. Vučković, Photonic quantum technologies, Nat. Photon. 3, 687 (2009)

[2] X. Qiang, X. Zhou, J. Wang, C. M. Wilkes, T. Loke, S. O'Gara, L. King, G. Marshall, R. Santagati, T. C, Ralph, J. B. Wang, J. L. O'Brien, M. G. Thompson and J. C. F . Matthews, Nature Photonics 12, 534 (2018)

[3] M-C. Tien, J. F. Bauters, J. R. Heck, D. J. Blumenthal and J. E. Bowers, Opt. Express 18, 23562 (2010)

Self-assembled composite metamaterials for hydrogen sensing

Mazhar E. Nasir, Wayne Dickson and Anatoly V. Zayats
Department of Physics and London Centre for Nanotechnology, King's College London, Strand, London WC2R 2LS, UK
**corresponding author: mazhar.nasir@kcl.ac.uk*

Abstract:

Hyperbolic metamaterials are playing a key role in the design of integrated deep-subwavelength biochemical sensors, nonlinear nanophotonic devices and magneto-optical applications. Here, we report composite metamaterials, Au-Core/Pd-Shell arrays, over cm^2 areas using an inexpensive and industrial-friendly self-organization technique. In reflection and transmission typically more than 30% change has been observed with 2% H_2 concentration (2% Vol. Hydrogen mixed with 98% Vol[1]. Nitrogen), these changes are visible to the naked eye with conventional illumination of the sensing substrate.

Introduction:

Hydrogen (H_2) is considered to be one of the most promising clean energy carriers for use in fuel cells and combustion engines. It is extensively used in scientific research and industry, especially in glass and steel manufacturing, refining petroleum products, and in the chemical industry in general.[2-4]In standard conditions, hydrogen is a highly combustible colourless and odourless gas, extremely flammable in ambient atmospheric conditions at concentrations exceeding 4% in volume.[5] The resonant wavelengths in self-assembled Au nanorod metamaterials modified by interaction between the nanorods, can be tuned throughout the visible and into the infra-red spectral range.[6] These resonances are very sensitive to the surrounding medium.[7, 8] The metamaterials developed here sensitive to the presence of hydrogen, are based on hybrid Au-core/Pd-shell (Fig. 1a) nanorods Palladium is used as the transducer in many hydrogen sensing technologies first because Pd-hydride formation is reversible and thermodynamically stable under ambient conditions and second because it leads to changes of both DC electrical conductivity and optical properties upon exposure to hydrogen due to both electronic and structural modifications.[9]

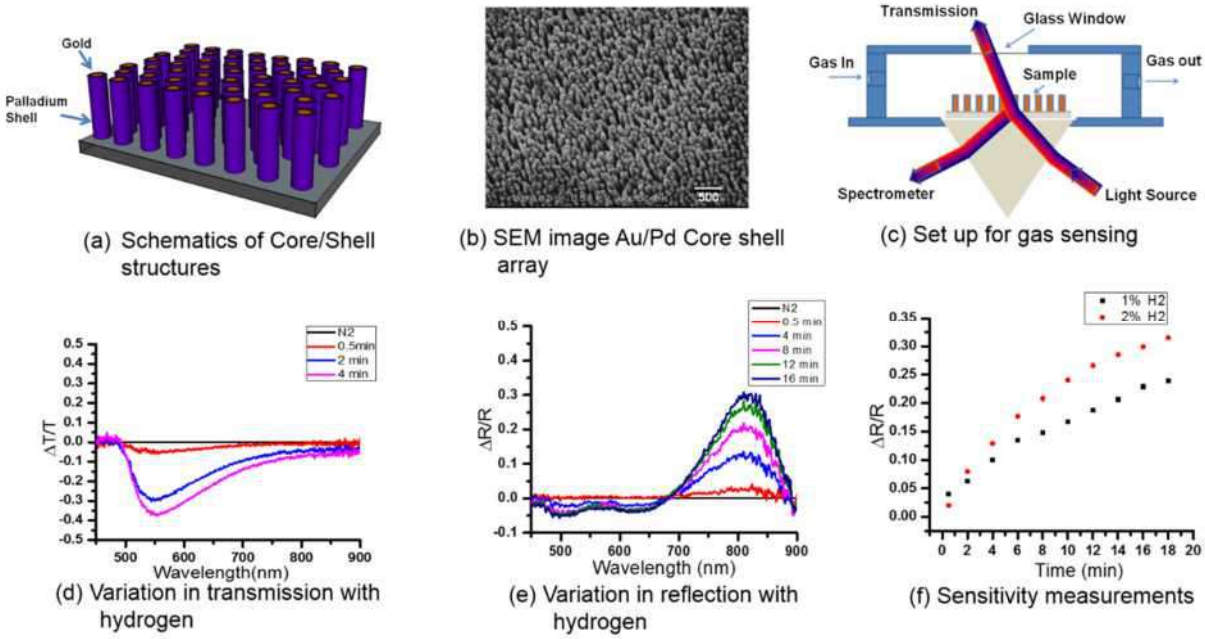


Figure 1: (a) Schematic of core/shell structures. (b) SEM image of Au/Pd-core/shell arrays. (c) Schematic of gas sensing set up. (d, e) Variation in transmission and reflection spectra on exposure to 2% hydrogen in nitrogen. (f) Variation in reflection with different hydrogen concentration.

Variations in the refractive index can therefore be detected optically with very high sensitivity by the incorporation of H_2 in the Pd based plasmonic metamaterial. In most cases carbon monoxide (CO) is produced as by product during hydrogenation. Therefore effects of CO on these composite metamaterials are also investigated.

Experimental Section:

Metamaterials based on ordered Au-core/Pd-shell, electrochemically grown into perfectly ordered nanoporous alumina membranes, having large domain areas (~square microns) obtained by employing two-step anodization. The pore geometry and spacing can be controlled over a wide range with nanoscale precision by a choice of anodization conditions and chemical post processing. Gold and palladium electrodeposition was performed with a three electrode system.

Discussion:

SEM cross-section of the sample is shown in Fig. 1b and schematic of gas sensing set up is shown in Fig. 1c. When the designed metamaterial is exposed to hydrogen, the extinction changes by almost 40% (Fig. 2d) which, although not quantitative, is clearly noticeable to the naked eye as a change in the brightness of light transmitted by the metamaterial. As soon as hydrogen gas is introduced to the flow cell, the transmission of the Au/Pd core/shell metamaterial starts to change at an initial rate of about 0.1% per second. Within the first 60 s, the change in transmission exceeds 5%, then increases substantially with time at a rate of 0.2%/s reaching 38% at saturation. Similarly, the response of the sensor in the reflection geometry (Fig. 1e) demonstrates an almost 40% change in reflection at wavelengths corresponding to a TM-polarized, leaky mode. The high sensitivity of this optical sensor to changes in hydrogen concentration results from a combination of both the change of the plasmonic properties of individual core-shell nanorods and the modification of inter-rod coupling in the metamaterial due to the thickness change of the palladium shell. Both result in the variation of the effective permittivity of the metamaterial. The structural changes result from a chemical reaction between Pd and H_2 forming palladium hydride (Pd-H). Reflectivity dependence on time with time for different concentrations of hydrogen is shown in Fig 1f. Initial investigations showed no interaction between Au/Pd core-shell metamaterials and CO at room temperature

Conclusions:

We have designed a plasmonic metamaterial sensor for the optical detection of hydrogen gas. More than a 30% change in both the reflection and transmission from the metamaterial layer is observed when exposed to 2% hydrogen mixed with nitrogen gas. It provides extremely strong modification of the transmission and reflection of light as a result of the presence of hydrogen gas and can be easily seen by naked eye. Plasmonic nanorod metamaterials present a versatile platform also for development of oxygen and other gas sensors.[10]

References:

1. M. E. Nasir, W. Dickson, G. A. Wurtz, W. P. Wardley and A. V. Zayats, *Adv. Mater.* **26** (21), 3532 (2014).
2. F. Rumiche, H. Wang, W. Hu, J. Indacochea and M. Wang, *"Sens. Actuators, B "* **134** (2), 869-877 (2008).
3. K. T. Kim, J. Sim and S. M. Cho, *IEEE Sens. J.* **6** (3), 509-513 (2006).
4. J.-S. Noh, H. Kim, B. S. Kim, E. Lee, H. H. Cho and W. Lee, *J. Mater. Chem.* **21** (40), 15935-15939 (2011).
5. P. Fedtke, M. Wienecke, M.-C. Bunescu, M. Pietrzak, K. Deistung and E. Borchardt, *"Sens. Actuators, B "* **100** (1-2), 151-157 (2004).
6. M. Nasir, S. Peruch, N. Vasilantonakis, W. Wardley, W. Dickson, G. Wurtz and A. Zayats, *Appl. Phys. Lett.* **107** (12), 121110 (2015).
7. V. V. Yakovlev, W. Dickson, A. Murphy, J. McPhillips, R. J. Pollard, V. A. Podolskiy and A. V. Zayats, *Adv Mater* **25** (16), 2351 (2013).
8. N. Vasilantonakis, G. Wurtz, V. Podolskiy and A. Zayats, *Opt. Express* **23** (11), 14329-14343 (2015).
9. T. Shegai, P. Johansson, C. Langhammer and M. Käll, *Nano Lett.* **12** (5), 2464-2469 (2012).
10. P. Wang, A. V. Krasavin, M. E. Nasir, W. Dickson and A. V. Zayats, *Nat. Nanotechnol.* **13** (2), 159 (2018).

Light Scattering from Solid-State Quantum Emitters: Beyond the Atomic Picture

Alistair J. Brash[1,*], Jake Iles-Smith[1,2], Catherine L. Phillips[1], Dara P. S. McCutcheon[3], Jesper Mørk[4], Maurice S. Skolnick[1], A. Mark Fox[1] and Ahsan Nazir[2]

[1]Department of Physics and Astronomy, University of Sheffield, Sheffield, S3 7RH, United Kingdom
[2]School of Physics and Astronomy, The University of Manchester, Oxford Road, Manchester M13 9PL, UK
[3]Quantum Engineering Technology Labs, H. H. Wills Physics Laboratory and Department of Electrical and Electronic Engineering, University of Bristol, Bristol BS8 1FD, UK
[4]Department of Photonics Engineering, DTU Fotonik, Technical University of Denmark, Building 343, 2800 Kongens Lyngby, Denmark
*corresponding author, E-mail: a.brash@sheffield.ac.uk

Abstract

The coherent scattering of light by a single quantum emitter is fundamental to quantum optics. Unlike atomic systems, solid-state emitters couple strongly to their host lattice via phonons. Through both theory and experiment we develop an intuitive model of coherent scattering for the case of a solid-state emitter coupled to a nano-cavity. The phonon coupling leads to a sideband that is completely insensitive to excitation conditions, a major deviation from the atomic model of scattering.

1. Introduction

Scattering of light by a single quantum emitter is one of the fundamental building-blocks of quantum optics. First observed in atomic systems, and more recently studied extensively in self-assembled quantum dots (QDs), coherent scattering is attractive as the scattered light retains the coherence of the laser rather than the emitter, giving a means to generate photons whose coherence exceeds the conventional radiative limit whilst still exhibiting anti-bunching on the timescale of the emitter lifetime. Exploiting this behavior by scattering light from a single quantum emitter gives rise to a number of exciting possibilities for quantum technologies such as the generation of single photons with arbitrary waveforms, non-linearities at the single photon level, and the construction of entangled states between photonic or spin degrees of freedom.

Solid-state emitters (SSEs), particularly self-assembled QDs are an attractive system with which to realise such schemes owing to their high brightness, excellent coherence properties and ease of integration with nano-photonic structures. However, in contrast to their atomic counter-parts, working in the solid-state introduces coupling to vibrational modes of the host material, leading to the emergence of a phonon sideband band (PSB) in the emission spectrum [1]. This is attributed to a rapid change in lattice configuration of the host material during an exciton recombination event, leading to the simultaneous emission or absorption of longitudinal acoustic (LA) phonons with the emission of a photon. Therefore, to obtain perfectly indistinguishable photons the PSB must be filtered out, naturally reducing the efficiency of the device, even when using an optical cavity to Purcell enhance emission into the zero phonon line (ZPL) [1].

It is perhaps natural then to presume that phonon coupling may be eliminated by operating in the coherent scattering regime: weak driving leads to vanishing excited state population and therefore no change in charge configuration, suggesting that one may adopt an atom-like picture where the coherent fraction tends towards unity for excitation far below saturation. Recent theoretical work has indicated that this is not the case, predicting that a sideband will persist even for vanishingly weak resonant driving [2]. Here, we experimentally verify this hypothesis and develop a comprehensive model that reproduces experimental results by incorporating cavity effects and off-resonant driving. The results demonstrate that the fraction of light emitted into the PSB is insensitive to the excitation conditions. We interpret this observation using an intuitive picture that attributes the PSB to transitions within the phonon-dressed ground state manifold during a scattering event, implying that any optical spectral features will have an associated PSB.

2. Characterizing the Phonon Coupling

The device studied comprises a single self-assembled InGaAs QD which is coupled (in the weak regime) to a single mode of an H1 photonic crystal cavity, resulting in a large Purcell enhancement of 43 [3]. In order to experimentally resolve the time dynamics of the phonon environment, and consequently characterize the electron-phonon interaction, we make a high time resolution measurement of the first order correlation function ($g^{(1)}(\tau)$) of the emission. The sample is held in a liquid helium bath cryostat at T = 4.4 K and resonantly excited below saturation ($S = 0.25$) where coherent scattering is expected to dominate the emission. The result is presented in Fig. 1(a) with the dynamics relating to

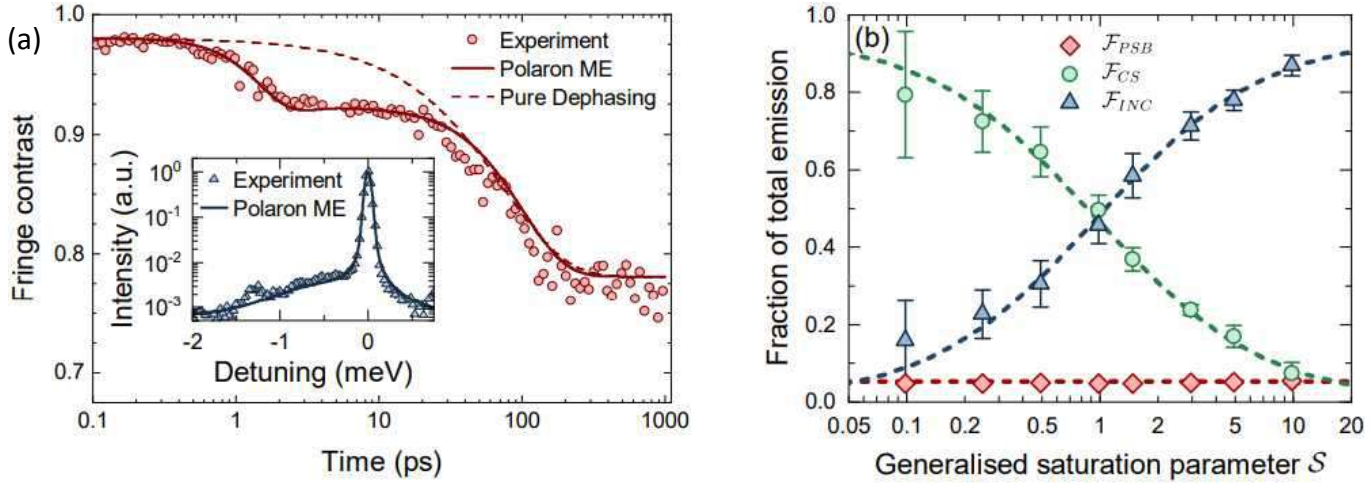


Figure 1: (a) First order correlation function ($g^{(1)}(\tau)$) of the QD emission: red circles - experimental measurements; solid red line - polaron ME; dashed line – a simple pure dephasing model that does not capture the phonon dynamics. The phonon parameters α and ν_c are extracted by fitting the short-time data whilst all other parameters are independently experimentally determined. *Inset:* Spectrum under identical conditions: blue triangles - experimental data; solid line - polaron model with same parameters as the main figure. (b) Evolution of the fractional ($\mathcal{F}$) contributions to the resonant scattering spectrum with increasing **Ω**: red diamonds – phonon sideband; green circles - coherent scattering and blue triangles - incoherent resonance fluorescence. Dashed lines are the prediction of the polaron ME model using the same parameters as (a).

emission into the PSB occurring in the first few picoseconds. By fitting this region with a Polaron master equation (ME) model we extract an electron-phonon coupling strength α = 0.0447 ps^2 and cut-off frequency ν_c = 1.28 ps^{-1}.

In the second phase of the dynamics starting at around τ = 20 ps, radiative decay associated with incoherent resonance fluorescence occurs on the timescale of the coherence time (T_2). Noticeably, despite the large Purcell enhancement, this timescale is still an order of magnitude slower than phonon dynamics. In a crude pure dephasing model increasing the Purcell factor suppresses phonon interactions, the separation of timescales observed here shows that this is not the case. Thus, a pure dephasing model (dashed line) cannot accurately describe the phonon coupling. To check the accuracy of the extracted parameters we independently measure the spectrum under identical conditions (inset to Fig. 1(a)), a theoretical spectrum derived by Fourier transforming the model $g^{(1)}(\tau)$ shows excellent agreement.

3. Phonon Sidebands in Coherent Scattering

To investigate to what extent the PSB persists in the coherent scattering regime, we measure the resonance fluorescence spectrum as a function of saturation (S) by varying the strength of the resonant driving. Fig. 1(b) shows the resulting evolution of the components of the resonant scattering spectrum. The polaron model produces a curve for the coherent fraction (green dashed line) that qualitatively exhibits a similar shape to atomic behaviour. However, when considering additionally the PSB fraction $\mathcal{F}_{PSB}$, a surprising result emerges in agreement with recent theoretical predictions [2]. The fraction of the emission in the PSB (red diamonds in Fig. 1(b)) is constant and independent of **Ω**, and thus the fraction of light scattered coherently from the emitter

This result can be explained by considering that the phonon coupling dresses both the ground and excited states of the transition. Whilst most of the light scatters directly from the "bare" transition as in an atomic system, it is also possible for the scattering event to end in one of the phonon continuum states of the ground state manifold, reducing/increasing the energy of the scattered photon, and leading to the emergence of a phonon sideband. By convention, these inelastic events are classified according to the energy of the scattered photon: Stokes/Anti-Stokes scattering correspond respectively to the emission of a lower/higher energy photon accompanied by the emission/absorption of an LA phonon. At the low bath temperatures here, the probability of phonon emission ≫ absorption, resulting in the characteristic asymmetry of the PSB. The branching ratio between the phonon-mediated inelastic scattering events and elastic (Rayleigh) scattering is determined solely by the square of the Franck-Condon factor (B^2). As such, whilst coherent scattering is often cited as a means to avoid emitter dephasing, it has no influence on the phonon sideband. Additional experiments with the laser detuned from the emitter show that all optical features have an associated sideband and that phonon interactions strongly influence the coherent/incoherent ratio away from resonance.

4. Conclusions

We have demonstrated that irrespective of excitation conditions, a fixed fraction (B^2) of the emission of a solid-state emitter is always emitted through a phonon sideband, even in the presence of a large Purcell factor. Our results stress that appropriate modeling of phonon coupling is essential and could be applied to optimize processes such as spin-photon entanglement for solid-state emitters.

References

[1] J. Iles-Smith et al. Nature Photonics **11**, 521 (2017)

[2] J. Iles-Smith et al. Phys. Rev. B **65** 195313 (2017)

[3] F. Liu, A.J. Brash et al. Nature Nano. **13**, 835 (2018)

Flexible control of silicon Bragg grating filters enabled by sub-wavelength and modal engineering

D. Oser[1], X. Le Roux[1], F. Mazeas[2], D. Pérez-Galacho[3], D. Benedikovic[1], E. Durán-Valdeiglesias[1], V. Vakarin[1], O. Alibart[2], P. Cheben[4], S. Tanzilli[2], L. Labonté[2], D. Marris-Morini[1], E. Cassan[1], L. Vivien[1], and C. Alonso-Ramos[1]

[1]Centre de Nanosciences et de Nanotechnologies, CNRS, Orsay, 91405 Orsay cedex, France.
[2] Université Côte d'Azur, CNRS, Institut de Physique de Nice, Parc Valrose, 06108 Nice Cedex 2, France
[3] ITEAM research institute, Universitat Politècnica de València, Camino de Vera s/n, 46022, Valencia, Spain
[4] National Research Council, Ottawa, K1A 0R6, Canada
*corresponding author, E-mail: carlos.ramos@u-psud.fr

Abstract

Bragg filters stand as a key building blocks of the silicon-on-insulator photonics platform. However, achieving narrowband Bragg filters with large rejection is challenging due to fabrication constraints and imperfections. Here, we present our recent results in de development high-performance Bragg filters based on subwavelength and modal engineering. We experimentally show flexible control over the width and depth of the Bragg resonance. These results pave the way towards high-performance on-chip wavelength filters.

1. Introduction

Driven by the impressive technology development in the recent years, silicon photonics is expanding its frontiers towards new applications beyond Datacom. These include, among others, chemical and biological sensing, radio-over-fiber and quantum cryptography. In this context, nanostructured photonic metamaterials have opened new prospects for controlling and manipulating light in planar waveguide circuits. By periodically patterning silicon with a pitch sufficiently small to suppress diffraction effects, subwavelength engineered structures open new degrees of freedom to control light propagation in silicon photonic circuits with unprecedented flexibility. Since the early demonstrations of a silicon wire waveguide with subwavelength grating (SWG) metamaterial core [1], metamaterial SWG waveguides have garnered a great research interest, enabling the demonstration of various devices with record performance, including fiber-chip couplers, ultra-wideband power splitters and mode converters, to name a few [2]. Here, we present our recent results on the implementation of high-performance wavelength filters in silicon, based on subwavelength engineering.

Bragg filters are a fundamental building block in the silicon photonics technology. However, yielding narrowband Bragg filters with large rejection levels is challenging due to fabrication constraints and imperfections. Here, we present high-performance Bragg filters that harness SWG, modal and symmetry engineering to overcome this bandwidth-rejection trade-off. We experimentally show flexible control over the width and depth of the Bragg resonance, unlocking new tools for the implementation of notch filters with arbitrary bandwidth and rejection level.

2. Silicon Bragg grating filters based on sub-wavelength and modal engineering

A Bragg filter is a periodic structure that rejects light power at a specific wavelength range. From coupled-mode theory [3], the bandwidth is determined by

$$\Delta\lambda = \frac{\lambda_0^2}{\pi\, n_g}\sqrt{\kappa^2 + \frac{\pi^2}{L^2}} \qquad (1)$$

while the rejection level can be calculated as

$$\mathrm{R} = \tanh^2(\kappa L) \qquad (2)$$

where κ is the coupling coefficient (coupling rate between the forward and the backward propagating modes), L is the filter length, and n_g is the group index. From these equations it follows that that filter bandwidth and rejection level are governed by the index modulation and the grating length L.

Achieving narrowband filtering requires weak index modulations, being the minimum achievable bandwidth determined by the weakest index modulation that can be effectively implemented. Therefore, due to the high refractive index difference between silicon and silica cladding, conventional SOI Bragg filters require 10 nm or even weaker corrugations to yield narrowband operation. This approach complicates device fabrication and seriously compromises the repeatability and yield of the devices.

A particularly promising approach to reduce the filter bandwidth keeping relaxed minimum feature size constraints is subwavelength engineering of the Bragg period [4-6]. In subwavelength engineered Bragg filters, the Bragg period is divided in two subwavelength sub-periods that implement the narrow and wide parts of the conventional geometry. By engineering the modal confinement and effective waveguide

index, this configuration allows weak index modulations with comparatively large corrugations, thereby relaxing constraints in minimum feature size.

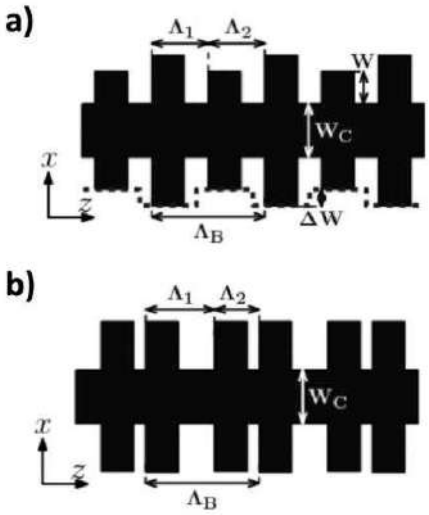


Figure 1: Schematic representation of subwavelength-engineered Bragg gratings based on: a) two width corrugation, and b) longitudinally shifted corrugation.

In this work, we theoretically and experimentally compare the performance of conventional Bragg filters with different subwavelength engineering filters. We show that by combining subwavelength engineering and asymmetric corrugation, we can implement remarkably narrowband filters, yet keeping minimum feature sizes compatible with large-volume fabrication processes.

Figure 1 schematically shows two examples of subwavelength-engineered Bragg filters. The double-width corrugation Bragg filter, depicted in Fig. 1a, implements the index modulation by the difference in width between the two subwavelength periods. On the other hand, the subwavelength filter shown in Fig. 1b, relies on a relative longitudinal shift of the tooth in one of the sub-periods to implement the index modulation.

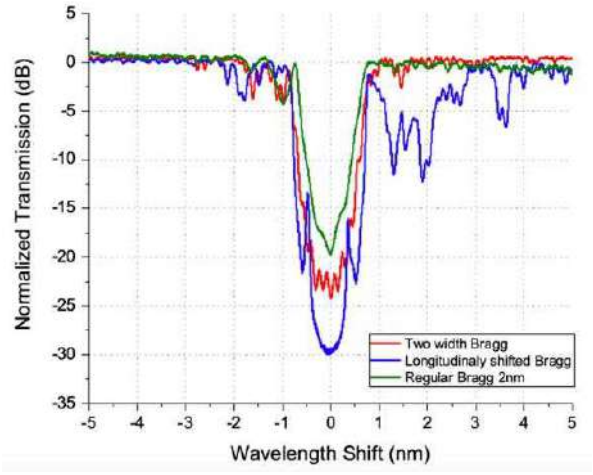


Figure 2: Measured spectra of Bragg grating filters with 500 µm length, implementing conventional and subwavelength engineered corrugations.

As an illustrative example, Fig 2 shows the measured spectra for narrowband Bragg filters based on the conventional corrugation approach, and subwavelength engineering strategy. Note that the conventional Bragg grating requires a 2 nm wide corrugation to yield similar bandwidth as that in subwavelength engineered filters, that have corrugation widths larger than 100 nm.

3. Conclusions

In conclusion, we have experimentally demonstrated that subwavelength engineering of modal confinement in Bragg gratings provides a great flexibility for the implementation of high-performance SOI Bragg filters. In this presentation we will show different results illustrating how by proper geometry design we can implement different filter responses ranging from ultra-narrowband, with a few-hundred pm bandwidth, to ultra-deep operation, with rejection levels of ~50 dB. This approach opens a new path for the realization of high-performance, tailorable Bragg filters for the SOI platform.

Acknowledgements

This work has been partially funded by the Agence Nationale de la Recherche (ANR-SITQOM-15-CE24-0005, ANR-MIRSPEC-17-CE09-0041) and the H2020 European Research Council (ERC) (ERC POPSTAR 647342). The fabrication of the device was performed at the Plateforme de Micro-Nano-Technologie/C2N, which is partially funded by the Conseil Général de l'Essonne. This work was partly supported by the French RENATECH network.

References

[1] P. Cheben, D.-X. Xu, S. Janz, A. Densmore, Subwavelength waveguide grating for mode conversion and light coupling in integrated optics, *Opt. Express* 14: 4695-4702, 2006.

[2] P. Cheben, R. Halir, J. H. Schmid, H. A. Atwater, D. R. Smith, Subwavelength integrated photonics, *Nature* 560: 565-572, 2018.

[3] D. C. Flanders, H. Kogelnik, R. V. Schmidt, C. V. Shank, Grating filters for thin-film optical waveguides, *Appl. Phys. Lett.* 24: 194–196, 1974.

[4] J. Wang, I. Glesk, and L. R. Chen, Subwavelength grating Bragg grating filters in silicon-on-insulator, *Electron. Lett.* 51: 712-714, 2015.

[5] D. Oser, D. Pérez-Galacho, C. Alonso-Ramos, X. Le Roux, S. Tanzilli, L. Vivien, L. Labonté, E. Cassan, Subwavelength engineering and asymmetry: two efficient tools for sub-nanometer-bandwidth silicon Bragg filters, *Opt. Lett.* 43: 3208-3211, 2018.

[6] P. Cheben, J. Ctyroky, J. H Schmid, S. Wang, J. Lapointe, J G. Wangüemert-Pérez, I. Molina-Fernández, A. Ortega-Moñux, R. Halir, D. Melati, D. Xu, S. Janz,

M. Dado, Bragg filter bandwidth engineering in subwavelength grating metamaterial waveguides, *Opt. Lett.* 44: 1043-1046, 2019.

Optical manipulation of exciton polaritons in semiconductor microcavity structures: from transitional to rotational motion

Yong-Hoon Cho*

Department of Physics and KI for the NanoCentury,
Korea Advanced Institute of Science and Technology, Daejeon 34141, Republic of Korea
*corresponding author, E-mail: yhc@kaist.ac.kr

Abstract

We present the intriguing physical phenomena including generation of quantum vortex and ballistic transport via the optical manipulation of exciton polariton condensate. Exciton polaritons generated in two-dimensional microcavity based on arsenide semiconductor system are exploited for the generation of quantum vortex via directly transferring orbital angular momentum of optical pump to polariton quantum fluid. Nitride semiconductor based one-dimensional exciton polariton shows ballistic transport of exciton polariton condensate at room temperature through the gradient control of exciton reservoir.

1. Introduction

Excitons in low-dimensional semiconductor have attracted a lot of attention due to their rich and unique optical properties and their versatile photonic and quantum photonic applications. Especially, the control of light-matter interaction between photons in microcavity and excitons in low dimensional structure is of great interest for cavity quantum electrodynamics studies and quantum information science. Advanced semiconductor technology can allows entering hybrid nature of exciton cavity polaritons (polaritons), which comply with Bose-Einstein statistics, in the regime of strong light-matter coupling between excitons and cavity photons.[1,2] Photonic components provide the ultrafast velocity of polaritons due to low effective mass, while the excitonic components are responsible for interaction with the environment and polaritons. A crucial benefit of the polariton system is potential energy engineering with real-time controllability via optical manipulation through the excitonic component. Here, we present the intriguing physical phenomena including generation of quantum vortex,[3] large Rabi splitting energy,[4] and ballistic transport via the optical control of polariton condensate. Exciton polaritons formed in distributed Bragg reflector based on arsenide semiconductor system are used for the creation of quantum vortex through direct transfer of orbital angular momentum (OAM) of non-resonant optical pump to polariton quantum fluid. Toward room temperature application, one-dimensional polaritons based on nitride semiconductor system are exploited for ballistic transport of polariton condensate due to their pure potential properties.

2. Results and Discussion

Starting from two-dimensional polaritons based on arsenide semiconductor system, optical manipulation of quantized OAM can probe characteristics of basic topological object and can be utilized for quantum technology such as information processing and sensing for fundamental physics. In this study, we can directly transfer OAM of optical pump to polariton quantum fluid.[3] In experiment, the quantized vortices were generated from polaritonic potential and flow induced by transferred optical OAM in out-of-equilibrium polariton condensate above threshold density. Quantized rotation of this collective polaritons could be maintained robustly without large dependence on size and shape of optical pump in polariton related interactions.

For achieving room temperature polariton, nitride semiconductor system is one of suitable candidates due to strong oscillator strength and large exciton binding energy. Nevertheless, fabrication of two-dimensional microcavity for high-quality distributed Bragg reflectors based on nitride semiconductor system is challenging due to low refractive index contrast and large lattice mismatch between AlN and GaN in contrast to arsenide semiconductor system. We present robust one-dimensional, room-temperature polariton system based on nitride semiconductor microrod structures.[4] A hexagonal wire structure can spontaneously generate high-qualified whispering gallery modes without complicated fabrications. High quality excitons are formed because of dislocation bending to bottom part and absence of internal field on *m*-plane quantum wells for stronger oscillator strength. Therefore, we obtained one-dimensional polaritons from strong coupling between three-dimensional (bulk GaN) or two-dimensional (InGaN quantum well) excitons and crystallographically defined one-dimensional whispering gallery photons. First, we observe unprecedentedly large Rabi splitting in GaN/InGaN core-shell wires. This giant large Rabi splitting result from large spatial overlap between photons and excitons from high quality, non-polar quantum wells. Second, exploiting pure potential property of bulk GaN wire, we demonstrate single mode one-dimensional polariton condensate with ballistic transport. We optically manipulate the ballistic propagation of the condensate along the wire axis by gradient control of polariton potential via exciton reservoir.

3. Conclusions

We optically manipulate the fundamental physical phenomena including quantum vortex and ballistic transport based on the exciton-polariton condensates in semiconductor microcavities. Two-dimensional polaritons systems are exploited for the generation of quantum vortex via directly transferring orbital angular momentum of optical pump to polariton quantum fluid. One-dimensional room temperature polariton shows ballistic transport of exciton polariton condensate through the gradient control of exciton reservoir. These results can suggest versatile potential applications such as all optical control of topological charge in quantum simulator and all optical devices using exciton-polariton quantum fluid system.

References

[1] J. Kasprzak, M. Richard, S. Kundermann, A. Baas, P. Jeambrun, J. M. J. Keeling, F. M. Marchetti, M. H. Szymańska, R. André, J. L. Staehli, V. Savona, P. B. Littlewood, B. Deveaud, and Le Si Dang, Bose–Einstein condensation of exciton polaritons. *Nature* 443: 409, 2006.

[2] H. Deng, H. Haug, and Y. Yamamoto, Condensation of semiconductor microcavity exciton polaritons. *Science* 298: 199, 2010.

[3] M.-S. Kwon, B. Y. Oh, S.-H. Gong, J.-H. Kim, H. K. Kang, S. Kang, J. D. Song, H. Choi, and Y.-H. Cho, Direct transfer of light's orbital angular momentum onto a nonresonantly excited polariton superfluid, *Phys. Rev. Lett.* 122: 045302, 2019.

[4] S. H. Gong, S. M. Ko, M. H. Jang, and Y.-H. Cho, Giant Rabi splitting of whispering gallery polaritons in GaN/InGaN core-shell wire, *Nano Lett.* 15: 4517, 2015.

Plasmonic near-field probing with sub-nm sensitivity using photoelectrons

Péter Dombi[1,2,*]

[1]Wigner Research Centre for Physics, 1121 Budapest, Hungary
[2]ELI-ALPS Research Institute, 6728 Szeged, Hungary
*E-mail: dombi.peter@wigner.mta.hu

Abstract

Probing nanooptical near-fields is a major challenge in plasmonics. Photoemission from metal nanostructures induced by femtosecond laser pulses proved to be highly sensitive tools for plasmonic near-field probing. I will show how this technique can provide sub-nm sensitivity. First applications in the investigation of plasmon-plasmon coupling are also demonstrated. In addition, time-resolved measurements of plasmonic near-field dynamics with unprecedented resolution were also performed, the results of which will be presented.

1. Introduction

Plasmonic enhancement of optical near-fields at nanostructures ensures the nanoscale localization of the energy of light. Although this phenomenon allowed pioneering applications in spectroscopy, photovoltaics and sensorics, the measurement of the maximum achievable nanoplasmonic field enhancement for a particular sample is still a challenging problem. Here, we present a method for nanoplasmonic near-field measurement with the help of photoemitted electrons induced by femtosecond laser pulses, and demonstrate its capabilities by studying plasmon-plasmon coupling on nanostructured silver films.

2. Near-field probing with ultrafast photoemission

Our field enhancement measurement method is based on the observation that if photoelectrons are emitted at a favorable phase of the electric field, after roughly a half optical cycle they can return to the metal surface and elastically rescatter there [2], boosting their kinetic energy (Q_{max}) until up to 10 times the ponderomotive energy according to

$$Q_{max} = 10.01\, e^2\lambda^2 E_{loc,max}^2 / (16\pi^2 mc^2) + 0.54W. \quad (1)$$

Here e and m are the electron charge and mass, respectively, λ is the laser wavelength, E_{loc} is the local electromagnetic field, c is the speed of light and W is the work function of the metal. Thus, by measuring the highest electron kinetic energy for a given plasmonic structure, the maximum hot-spot field enhancement can be extracted, since electron spectral cutoff regions are composed of rescattered electrons that are directly sensitive to nanooptical field maxima.

In our experimental scheme, ultrashort laser pulses excite propagating or localized plasmons, of which plasmonic near fields induce photoemission of electrons into vacuum surrounding the sample. Photoelectron spectra are then measured with a time-of-flight spectrometer [1,2], see also in Fig. 1 (a). Since the highest photoelectron energies originate from nanometric rescattering of the electrons from

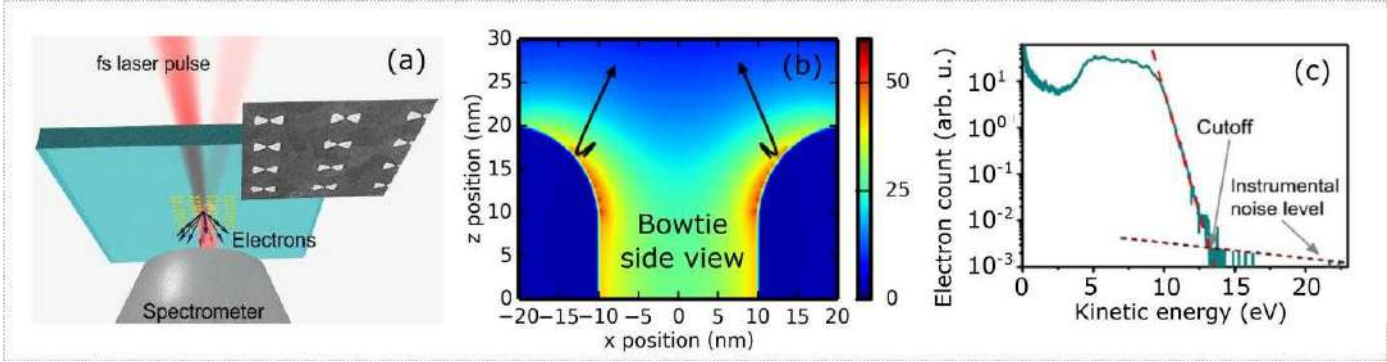


Fig.1. (a) Scheme of the experimental setup for nanoplasmonic near-field measurement with photoelectrons (black arrows). The femtosecond laser pulse and the entrance to the time-of-flight electron spectrometer are indicated. (b) Field distribution map of the bowtie structure with black arrows indicating the trajectories of rescattered electrons. These electrons gain the highest kinetic energy, therefore they contribute the spectral cutoff. (c) Photoelectron spectrum with the spectral cutoff point indicated from which field enhancement is extracted.

the metal surface [2], nanoscale near-fields can be deduced by analyzing the cutoffs (highest electron energies) of the electron spectra (Fig. 1).

The method is experimentally demonstrated on different model systems involving nanoparticles exhibiting localized plasmons and thin films with controlled surface roughness hosting propagating surface plasmons [1]. We acquired time-of-flight electron spectra for different laser intensities for each sample type by collecting the photoemitted electrons according to the geometry in Fig. 1.(a). For each sample, the validity of equation (1) is clearly shown. Field enhancement factors extracted with the procedure described above are also verified with finite difference time-domain simulations without using fitting parameters [1].

3. Plasmon-plasmon coupling

As a first application of this measurement tool, plasmon-plasmon coupling phenomenon and its effect on field enhancement was studied on nanostructured Ag thin films supporting not only propagating plasmons, but also localized plasmon oscillations in different surface grains [3,4]. In our experimental concept, ultrashort laser pulses excite propagating plasmons in Kretschmann geometry, while localized plasmons are excited on the surface grains via the coupling of propagating and localized surface plasmons [4]. Measurement and analysis of the energy spectra of photoelectrons generated by plasmonic near fields yielded maximum plasmonic field enhancement values ×21, ×23 and ×31 for surfaces exhibiting 0.8, 1.6 and 4.5 nm average roughness values, respectively.

These measurement results showed that there is a non-trivial relationship between the experimental field enhancement values and the surface roughness of the samples. To analyze this relationship, we performed numerical simulation of the plasmon excitation and plasmon-plasmon coupling processes. Simulation results of the individual rough surfaces not only support the measured field enhancement values, but also revealed the contributions from propagating and localized plasmons. By analyzing the field amplitude along the surface normal taken at the hottest spots of each grain, two decay lengths were clearly visible: one sharp component corresponding to localized plasmons with a few nm 1/e decay length and a shallow decay with ~600 nm length corresponding to propagating plasmons [4]. Interestingly, it was also shown, that the propagating plasmon component accounts for some 60 % of the field enhancement.

4. Conclusions

With our method, field enhancement values for different samples (supporting localized and/or propagating plasmons) can be measured within <1 nm distance from the plasmonic surface. The demonstrated method, combined with more sophisticated electron imaging techniques can be extended for full characterization of nanoplasmonic near-fields promising nanometer lateral resolution in the near future. As a first application of this method we probed field enhancement attributed to plasmon-plasmon coupling. Ultrasensitive near-field probing revealed maximum field enhancement factors between 20 and 31 for silver surfaces with controlled roughness. Simulation results corresponded well to measured maximum field enhancement values and this way, the field enhancement contribution provided by the localization of propagating plasmons on surface grains could be clearly identified, amounting to ~50% of the total field enhancement at samples where strong plasmon-plasmon coupling is realized.

These experiments open a pathway not only toward the investigation of plasmon coupling processes, but also toward better exploitation of these phenomena in real-world environments and engineering of plasmonic samples with experimental field enhancement feedback.

Acknowledgements

We acknowledge the National Research, Development and Innovation Office of Hungary (projects VEKOP-2.3.2-16-2017-00015 and 2018-1.2.1-NKP-2018-00012). This research was supported by a FET Open Grant of the European Union („PETACom") and the Max Planck Society with a Partner Group Grant.

References

[1] P. Rácz *et al.:* Measurement of Nanoplasmonic Field Enhancement with Ultrafast Photoemission, *Nano Lett.* **17**, 1181-1186 (2017).

[2] P. Dombi *et al.:* Ultrafast Strong-Field Photoemission from Plasmonic Nanoparticles, *Nano Lett.* **13**, 674-678 (2013).

[3] P. Dombi *et al.:* Observation of few-cycle, strong-field phenomena in surface plasmon fields, *Opt. Express* 18, 24206-24212 (2010).

[4] J. Budai et al.: Plasmon-plasmon coupling probed by ultrafast strong-field photoemission with <7A sensitivity, *Nanoscale* **10**, 16261 (2018).

Photonic topological edge states in a zig-zag chain composed of split ring resonators

Yuto Moritake[1, 2, *]

[1]Department of Physics, Tokyo Institute of Technology, Tokyo, Japan
[2]JST, PRESTO, Tokyo, Japan
*corresponding author, E-mail: moritake@phys.titech.ac.jp

Abstract

Recently, Topological photonics has attracted significant attentions form optics community stimulated by discovery of topological phases of matter. One of the interesting photonic systems mimicking SSH model, which is a fundamental system exhibiting topological nature, is a zig-zag chain. In this study, the zig-zag chains composed of split ring resonators (SRRs) were numerically investigated. The photonic topological edge states (PTESs) in the zig-zag chain was observed at the same resonant wavelength as the single SRR. In the PTESs, Electromagnetic fields concentrate at the edge SRR of the zig-zag chain. Introducing SRRs into the zig-zag chain results in polarization and wavelength selective PTESs due to asymmetry of SRRs. Moreover, PTES of the quadrupole mode was also demonstrated. The zig-zag chain is a great platform to demonstrate PTESs with exotic optical properties. By applying various kinds of meta-atoms, new type of topological edge state would be able to realized.

1. Introduction

Recently, stimulated by discovery of topological phases of matter, research fields utilizing topological nature of systems has attracted a lot of attention. In photonics, many photonic systems exhibiting topological phenomena have been proposed and demonstrated using photonic crystals [1], metamaterials [2], coupled waveguides [3], and coupled resonators [4], leading to emergence of "topological photonics." Topological photonic systems show exiotic optical properties such as such as robustness against disorder, spin-locked non-dissipative propagation, adiabatic pumping and so on, which can be understood by analogies with topological insulators [5].

In contrast to material science, controlling interactions in system is relatively easy so that photonic system is a great platform to examine topological phenomena predicted by theories. For example, SSH (Su-Schrieffer–Heeger) model, which is fundamental system exhibiting topological properties, is experimentally demonstrated in many photonic systems [4,6-8]. One of the interesting systems mimicking SSH model is a one-dimensional zig-zag chain [9]. In a zig-zag chain, manipulation of dipole-dipole interactions results in a photonic topological edge state (PTES) depending on incident polarization.

In this presentation, I will present my recent numerical studies on PTESs in zig-zag chain composed of split-ring-resonators (SRRs). Applying SRRs realizes the PTESs with novel optical properties including wavelength selectivity, PTES of higher order mode at PTESs were achieved.

2. Structure and simulated model

Figure 1 shows a zigzag chain composed of SRRs. The SRRs is constituted of gold and thickness is 10 nm. The width and split angle are 20 nm and 30 degree, respectively. The SRRs are aligned along zig-zag line with gap of 10 nm. The zigzag chain is placed periodically with period of 500 nm on a SiO2 substrate.

Simulations were carried out using FEM. Input wave is illuminated normal to the surface along z-axis. Polarization is along x- or y-axes. Periodic boundary condition is used. The dielectric constant of gold from Ref. [10] is used and the refractive index of substrate is set to 1.46.

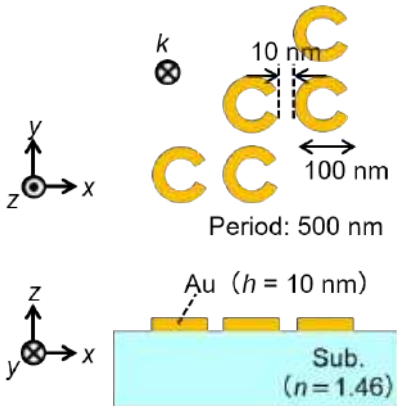


Figure 1: A schematic of a zig-zag chain composed of SRRs.

3. Simulated results and discussion

Transmission spectra for x- and y- polarization are presented in Fig. 2(a) and 2(b), respectively. Blue, green, and red line correspond to results for single SRRs, 4-SRRs

chain, and 5-SRRs chain, respectively. In the case of x-polarization, single SRR shows dipole resonance at around 1033 nm, as shown in Fig. 3(a). Transmission for 5-SRRs shows two resonant dips at 1033 nm and 1115 nm. The resonance at around 1033 nm, which is the same as resonance of single SRRs, corresponds to PTES (Figs. 3(b) and 3(c)). The resonance at around 1115 nm is dimer mode, which is also observed in the case of 4-SRRs chain (Fig. 2(a)). On the other hand, the lowest mode (dipole mode) is observed at 1993 nm (Fig. 3(d)). Although PTES should be observed for this mode, edge mode and dimer mode are overlapped and mixed due to weak interactions among SRRs and broad resonance band (Figs. 3(e) and 3(f)). The resonance at 830 nm is PTES of a higher mode (quadrupole mode) as shown in Figs. 3(h) and 3(i). The resonant wavelengths of PTESs for x- and y-polarization are different, meaning polarization and wavelength selective PTESs can be achieved in the proposed zig-zag chain.

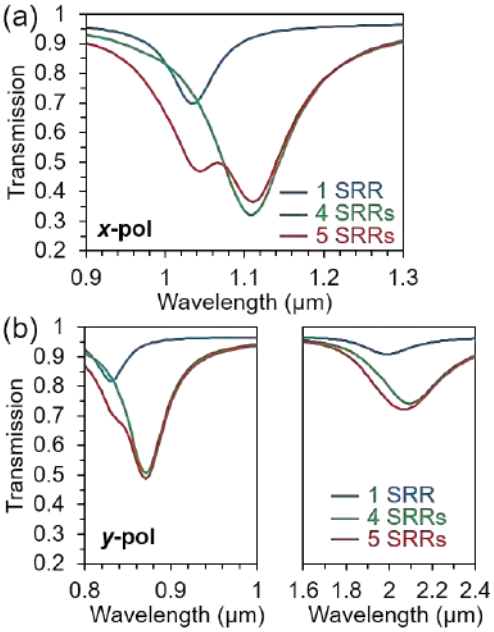


Figure 2: Transmission spectra of the zig-zag chain composed of SRRs. (a) x-pol. (b) y-pol. Blue, green, and red lines correspond to results for single SRR, 4-SRRs chain, and 5-SRRs chain, respectively.

4. Conclusions

The zig-zag chains mimicking SSH model were numerically investigated. The PTESs in the zig-zag chain was observed at the same resonant wavelength as the case of single elements. Electromagnetic fields concentrate at the edge site of the zig-zag chain. Introducing SRRs into the zig-zag chain results in polarization and wavelength selective PTESs due to asymmetry of SRRs. Moreover, PTES of the quadrupole mode was also demonstrated in addition to the PTESs of the lowest dipole mode. The zig-zag chain is a great platform to demonstrate PTES with exotic optical properties like as demonstrated in this study. By applying various kinds of meta-atoms developed so far, new type of topological edge state would be able to realized.

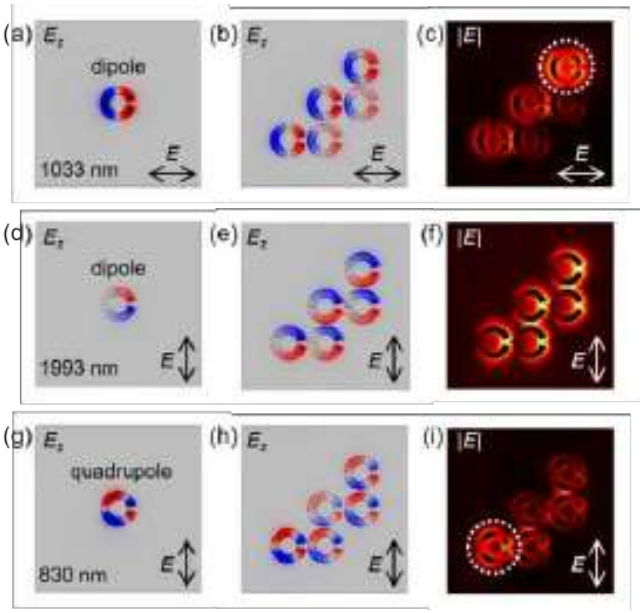


Figure 4: Electric field distributions for (a-c) 1033 nm (x-pol), (d-f) 1993 nm (y-pol), (g-i) 830 nm (y-pol). Z-component of electric field (a,b,d,e,g,h). Electric field intensity (c,f,i).

Acknowledgements

This work is partially supported by Grant-in-Aid Young Scientist (B), No. 17K14128 from JSPS, Japan, and by Japan prize foundation, and by JST, PRESTO Grant Number JPMJPR19L9, Japan.

References

[1] L. H. Wu and X. Hu, Scheme for Achieving a Topological Photonic Crystal by Using Dielectric Material, Phys. Rev. Lett. 114, 223901 (2015).

[2] A. B. Khanikaev *et al.*, Photonic topological insulators, Nat. Matter. 12, 233 (2013).

[3] Y. E. Kraus *et al.*, Topological States and Adiabatic Pumping in Qasicrystals, Phys. Rev. Lett. 109, 106402 (2012).

[4] M. Parto et al., Edge-Mode Lasing in 1D Topological Active Arrays, Phys. Rev. Lett. 120, 113901 (2018).

[5] L. Lu *et al.*, Topological Photonics, Nat. Photon. 8 821 (2014).

[6] A. B.-Redondo *et al.*, Topological Optical Waveguiding in Silicon and the Transition between Topological and Trivial Defect States, Phys. Rev. Lett. 116, 163901 (2016).

[7] C. W. Ling et al., Opt. Exp. 23(3) 2021 (2015).

[8] J. Jiang *et al.*, Experimental demonstration of the robust edge states in a split-ring-resonator chain, Opt. Exp. 26(10), 12891 (2018).

[9] A. Poddubny *et al.*, Topological Majorana States in Zigzag Chains of Plasmonic Nanoparticles, ACS Photon. 1, 101 (2014).

[10] P. B. Johnson and R. W. Christy, Optical Constants of the Noble Metals, Phys. Rev. B 6, 4370 (1972).

Nanophotonic Technology and Applications

Yeshaiahu (Shaya) Fainman

Department of Electrical and Computer Engineering
University of California San Diego
La Jolla, CA, 92093-0407
USA
fainman@ece.ucsd.edu

Abstract

Dense photonic integration requires miniaturization of materials, devices and subsystems, including passive components (e.g., engineered composite metamaterials, filters, etc.), active components (e.g., modulators and nonlinear wave mixers) and integrated circuits (Fourier transform spectrometer, programmable phase modulator of free space modes, etc.).

1. Introduction

The current optical technology is costly, bulky, fragile in their alignment, and difficult to integrate with electronic systems, both in terms of the fabrication process and in terms of delivery and retrieval of massive volumes of data that the optical elements can process. Our most recent work emphasizes the construction of optical subsystems directly on-chip, with the same lithographic tools as the surrounding electronics. This has been made possible by the advances in lithographic tools, which can now create features significantly smaller than the optical wavelength and is predicted to reach as fine as 11 nm by 2020. Arranged in a regular pattern, subwavelength features act as a metamaterial whose optical properties are controlled by the density and geometry of the pattern and its constituents [1-7]. Such future systems, further require the discovery of new technologies that can operate not only at ultrafast rates (<1 ps), but also at extremely low energies, and with low levels of insertion loss. Additionally, future technologies will need to be highly compact, as well as resilient to temperature change. Moreover, the device designs should provide scalability with respect to the operating wavelength, and the optical carrier should be allowed to range in a broad spectral range to support the necessary aggregate information bandwidth. As specific examples of our most recent work, we present nanoscale engineered second order nonlinearities in silicon

The integration of photonic systems requires miniaturization of the optical components, similar to the effort that has led to the extensive miniaturization in electronics. For applications involving a photonics layer between different components on the same chip, the photonic components must be comparable in size to the electronic components, and minimally interfere with each other when densely packed. By taking advantage of advances in lithographic tools predicted to reach features as fine as 11 nm by 2020, it is possible to arrange deeply subwavelength features in a patterned material composition to act as a metamaterial with space variant polarizability [1-8]. The future systems on a chip, further require the discovery of new technologies that can operate not only at ultrafast rates (<1 ps), but also at extremely low energies, and with low levels of insertion loss. Additionally, future technologies will need to be highly compact, as well as resilient to temperature change. Moreover, the device designs should provide scalability with respect to the operating wavelength, and the optical carrier should be allowed to range in a broad spectral range to support the necessary aggregate information bandwidth. As specific examples of our most recent work towards these goals, we discuss nonlinear optical devices [9, 10], chip-scale integrated Fourier Transform Spectrometer [11] and programmable phase modulation of free-space modes at GHz rates [12].

2. Second-order nonlinearity in silicon-rich-nitride films

We will present experimental results on second-harmonic generation in non-stoichiometric, silicon-rich nitride films. The as deposited film presents a second-order nonlinear coefficient, or $\chi^{(2)}$, as high as 8 pm/V. This value can be widely tuned using the electric field induced second harmonic effect, and a maximum value of 22.7 pm/V was achieved with this technique. We further will illustrate that the second-order nonlinear coefficient exhibited by these films can be highly dispersive in nature and require further study and analysis to evaluate their viability for in-waveguide applications at telecommunication wavelengths [9, 10].

3. Fourier transform spectrometers in silicon photonics

Miniaturized integrated spectrometers will have unprecedented impact on applications ranging from unmanned aerial vehicles to mobile phones, and silicon

photonics promises to deliver compact, cost-effective devices. Mirroring its ubiquitous free-space counterpart, a silicon photonics-based Fourier transform spectrometer (Si-FTS) can bring broadband operation and fine resolution to the chip scale. Here we will present the modeling and experimental demonstration of a thermally tuned Si-FTS accounting for dispersion, thermo-optic non-linearity, and thermal expansion. We show how these effects modify the relation between the spectrum and interferogram of a light source and we develop a quantitative correction procedure through calibration with a tunable laser. We retrieve a broadband spectrum (7 THz around 193.4 THz with 0.38-THz resolution consuming 2.5W per heater) and demonstrate the Si-FTS resilience to fabrication variations—a major advantage for largescale manufacturing. Providing design flexibility and robustness, the Si-FTS is poised to become a fundamental building block for on-chip spectroscopy [11].

4. Programmable phase modulation of free-space wavefronts at gigahertz rates

Space-variant control of optical wavefronts is important for many applications in photonics, such as the generation of structured light beams, and is achieved with spatial light modulators. Commercial devices, at present, are based on liquid-crystal and digital micromirror technologies and are typically limited to kilohertz switching speeds. To realize significantly higher operating speeds, new technologies and approaches are necessary. Here we demonstrate two-dimensional control of free-space optical fields at a wavelength of 1,550 nm at a 1 GHz modulation speed using a programmable plasmonic phase modulator based on near-field interactions between surface plasmons and materials with an electrooptic response. High $\chi^{(2)}$ and $\chi^{(3)}$ dielectric thin films of either aluminium nitride or silicon-rich silicon nitride are used as an active modulation layer in a surface plasmon resonance configuration to realize programmable space-variant control of optical wavefronts in a 4 × 4 pixel array at high speed [12].

Acknowledgements

This work was supported by the Defense Advanced Research Projects Agency (DARPA), DARPA NLM, DARPA MOABB, the Office of Naval Research (ONR) Multidisciplinary University Research Initiative (MURI), the National Science Foundation (NSF) grants DMR-1707641, CBET-1704085, ECCS-1405234, ECCS-1644647, CCF-1640227 and ECCS-1507146, the NSF ERC CIAN, the Semiconductor Research Corporation (SRC), the NSF's NNCI San Diego Nanotechnology Infrastructure (SDNI), the Chip-Scale Photonics Testing Facility (CSPTF), Nano3, the Army Research Office (ARO) and the Cymer Corporation.

References

[1] I. Richter, P. C. Sun, F. Xu and Y. Fainman, "Design considerations of form birefringent microstructures," Appl. Opt., Vol. 34, 2421-2429, 1995.

[2] R. Tyan, P. C. Sun, A. Scherer and Y. Fainman, "Polarizing beam splitter based on the anosotropic spectral reflectivity characteristic of form-birefringent multilayer grating,´Opt. Lett., Vol. 21, 761-763, 1996

[3] W. Nakagawa, P. C. Sun, C. H. Chen, and Y. Fainman, "Wide field of view narrow band spectral filter base on photonic crystal nanocavities," Opt. Lett., Vol. 27, pp.191-193, 2002

[4] U. Levy, C. H. Tsai, L. Pang and Y. Fainman, "Engineering space-variant inhomogeneous media for polarization control," Opt. Lett., Vol. 29, 1718-1720, 2004

[5] R. Rokitski, KA. Tetz, Y. Fainman, "Propagation of femtosecond surface plasmon polariton pulses on the surface of a nanostructured metallic film: Space-time complex amplitude characterization," Phys. Rev. Lett., Vol. 95, No.17, 177401/1-4, 2005.

[6] K. Ikeda, R.E. Saperstein, N. Alic, and Y. Fainman, "Thermal and Kerr nonlinear properties of plasma-deposited silicon nitride/silicon dioxide waveguides." Optics Express, Vol. 16, pp. 12987-12994, August 18, 2008.

[7] D.T.H. Tan, K. Ikeda and Y. Fainman, "Coupled chirped vertical gratings for on-chip group velocity dispersion engineering," Appl. Phys. Lett., Vol. 95, 141109-11, 2009

[8] D.T. H. Tan, P. C. Sun,Y. Fainman, "Monolithic nonlinear pulse compressor on a silicon chip," Nature Communications, Vol. 1, 1-6, 2010

[9] M. W. Puckett, R. Sharma, H-H. Lin, M-H. Yang, F. Vallini, and Y. Fainman, "Observation of second-harmonic generation in silicon nitride waveguides through bulk nonlinearities," Optics Express 24, 16923-16933 (2016)

[10] H-H. Lin, R. Sharma, A. Friedman, B. M. Cromey, F. Vallini, M. W. Puckett, K. Kieu, Y. Fainman, "On observation of dispersion in tunable second-order nonlinearities of silicon-rich nitride thin films," APL, in press, 2019 (arXiv.org > physics > arXiv:1808.07587)

[11] M. Souza, A. Grieco, N. Frateschi, Y. Fainman, "Fourier transform spectrometer on silicon with thermo-optic non-linearity and dispersion correction," NATURE COMMUNICATIONS Volume: 9 Article Number: 665 Published: FEB 14 2018

[12] A. Smolyaninov, A. El Amili, F. Vallini, S. Pappert, Y. Fainman, "Programmable plasmonic phase modulation of free-space wavefronts at gigahertz rates," Nature Photonics, 11 February 2019, https://doi.org/10.1038/s41566-019-0360-3

Strong Light−Matter Interaction in Lithography-free Metamaterial Perfect Absorbers: Energy conversion, color filtering, and sensing applications

Ekmel Ozbay[1, 2, 3, 4, *], Amir Ghobadi[1, 2, *], Hodjat Hajian[1], Bayram Butun[1]
[1]*NANOTAM-Nanotechnology Research Center, Bilkent University, 06800 Ankara, Turkey*
[2]*Department of Electrical and Electronics Engineering, Bilkent University, 06800 Ankara, Turkey*
[3]*Department of Physics, Bilkent University, 06800 Ankara, Turkey*
[4]*UNAM-Institute of Materials Science and Nanotechnology, Bilkent University, Ankara, Turkey*
** Corresponding authors: ozbay@bilkent.edu.tr*

Abstract: In this paper, we will summarize our latest studies on the use of metamaterial designs for energy conversion, filtering, and sensing applications using lithography-free light perfect absorbers

OCIS codes: 000.0000, 999.9999. [8-pt. type] For codes, see http://www.osapublishing.org/submit/ocis/

1. Summary

Strong interference in metal-lossy interface could provide the condition to obtain perfect light absorption. This phenomenon offers the opportunity to use planar lithography-free multilayer designs for ultrathin optoelectronic applications. These multilayer resonant absorbers have been realized in different material types including metals, semiconductors, and polar materials. A recent perspective with our group reviews strong light-matter interaction in lithography-free planar perfect absorbers[1]. It was shown, upon choice of proper material and configuration this absorbing behavior can be realized in almost all parts of EM spectrum. Although the common materials for design of multilayer absorber metasurfaces are metals, this strong interference can be also found in semiconductors in the photon energies above their optical band gap. Moreover, phonon and polar materials have been the subject of many absorber designs specifically in mid and far infrared regimes. Figure. 1 shows the right choice of materials that can be utilized for light perfect absorption in different portions of EM spectrum. Upon constructing the proper geometry, we could realize perfect light absorption in planar designs.

Initial studies of our group members on this field was mainly focused on realization of perfect absorption in metal based designs. The common cavity design that has been frequently used for perfect absorbers is based on metal-insulator-metal (MIM) design. However, our theoretical findings based on transfer matric method (TMM) revealed substantial potential in the case of metal-insulator-metal-insulator (MIMI) cavity absorbers[1]. Taking these findings into consideration, we applied different modifications to improve light absorption in MIMI cavities while keeping the overall fabrication route lithography. The use of multi-thickness surface texture[2], disordered plasmonic nano holes[3], and the optimum choice of back reflector metal[4] were examples of these ideas. However, the absorption bandwidth of these designs is limited due to inherent permittivity response of metals. The real permittivity part of most of metals becomes negative as we go toward longer wavelengths however the ideal model predict the desired permittivity to be positive. However, Bismuth (Bi) shows an extraordinary response where it is greatly matched into ideal model data. Our recent results demonstrate a near unity absorption from 500 nm to ~3000 nm using simple MIMI cavity which is far beyond any bandwidth reported for MIMI cavities[5]. Further, in another direction to make lithography free ultrabroadband absorber, we utilized densely packed dielectric nanowires as excellent trapping scaffold. We experimentally proved an absorption above 97% in an ultrabroad range using a thin Pt layer[6]. Besides this studies, we also studied the strong light-matter interaction in phononic materials. We showed that far-infrared surface plasmon polaritons of a single-layer graphene can be tailored using plasmon-phonon hybridization in graphene-LiF heterostructures[7]. We also designed a nearly perfect resonant absorption and coherent thermal emission by hexagonal boron nitride (hBN)-based photonic crystals[8].

Long with metal structures, it is possible to design semiconductor based metasurfaces to spectrally control their response. Our recent findings show that the use of metal-insulator-semiconductor (MIS) cavity could tune the absorption response of photodetector design. Employing 3 nm thick Si layer on top of Al-Al_2O_3 cavity leads to strong light absorption in ultraviolet (UV) region and no photo response in visible spectrum. Thus, by his way, visible blind UV photodetector was realized in a couple of nm thick semiconductor layer. The use of titanium dioxide (TiO_2) instead of Si could lead to solar blind system which we use it as gas sensor.

Combination of these metal and semiconductor based metamaterials was later found as excellent strategy to obtain color filters in the reflection mode. Generation of red-green-blue (RGB) colors using planar fabry-perot (FP) designs is commonly possible in the transmission mode of a MIM cavity. However, due to inherent loss of metal layers the efficiency of this filtering is below 0.6. We showed that series connection of MIM and MIS cavities which leads to a MIMIS multilayer design can create RGB colors in reflection mode by higher efficiency value[9]. The amplitude of RGB colors were found to be as high as 0.7 in this design. Later, we constructed a MIMSI design to create these RGB colors in efficiencies as large as 0.95.

Finally, in or recent study, we fabricated a colorimetric MS cavity to act as a refractive index sensor. This sensor was made using a innovative technique based on oblique angle deposition. Using this technique, we were able to make Au-Ge nanostructure resonating in visible range. Upon coating this cavity by different materials with different refractive index, the resonance frequency shifts toward longer wavelengths and consequently the color changes. From color change, we can predict the refractive index of the agent. Considering the large scale compatible and polarization insensitive nature of this design, this could be a promising for sensing of bio agents using naked eye.

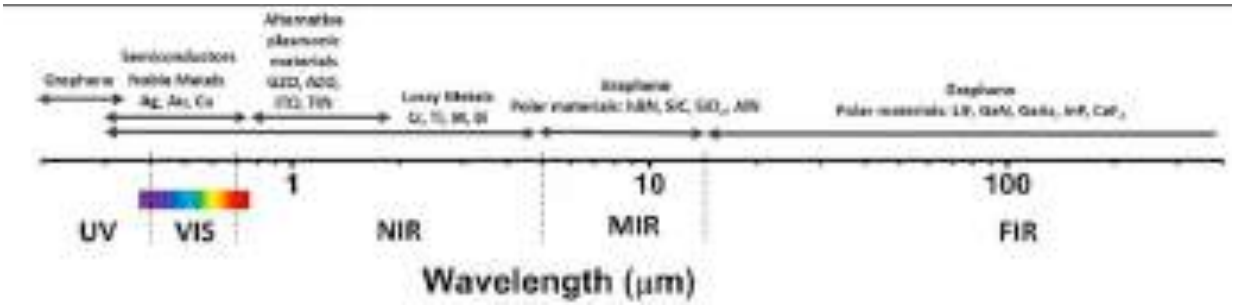


Figure 1. A graph summarizing the proper choice of materials to realize light perfect absorption in a sub-wavelength, lithography-free, planar, multilayer design.

2. References

[1] A. Ghobadi, H. Hajian, B. Butun, and E. Ozbay, "Strong Light − Matter Interaction in Lithography-free Planar Metamaterial Perfect Absorbers," ACS Photonics, vol. 5, pp. 4203–4221, 2018.

[2] A. Ghobadi, S. A. Dereshgi, H. Hajian, B. Bozok, and B. Butun, "Ultra-broadband , wide angle absorber utilizing metal insulator multilayers stack with a multi- thickness metal surface texture," Sci. Rep., vol. 7, p. 4755, 2017.

[3] A. Ghobadi, H. Hajian, S. A. Dereshgi, B. Bozok, B. Butun, and E. Ozbay, "Disordered Nanohole Patterns in Metal-Insulator Multilayer for Ultra-broadband Light Absorption: Atomic Layer Deposition for Lithography Free Highly repeatable Large Scale Multilayer Growth," Sci. Rep., vol. 7, p. 15079, 2017.

[4] S. Abedini Dereshgi, A. Ghobadi, H. Hajian, B. Butun, and E. Ozbay, "Ultra-Broadband, Lithography-Free, and Large-Scale Compatible Perfect Absorbers: The Optimum Choice of Metal layers in Metal-Insulator Multilayer Stacks," Sci. Rep., vol. 7, no. 1, p. 14872, 2017.

[5] A. Ghobadi, H. Hajian, B. Butun, and G. Turhan-sayan, "Extremely broadband ultrathin metal-insulator- metal-insulator based perfect near infrared absorber using highly lossy Bismuth metal," Submitt. to Nanophotonics, 2018.

[6] A. Ghobadi et al., "97 percent light absorption in an ultrabroadband frequency range utilizing an ultrathin metal layer: randomly oriented, densely packed dielectric nanowires as an excellent light trapping scaffold," Nanoscale, vol. 9, no. 43, pp. 16652–16660, 2017.

[7] H. Hajian et al., "Tailoring far-infrared surface plasmon polaritons of a single-layer graphene using plasmon-phonon hybridization in graphene-LiF heterostructures," Sci. Rep., vol. 8, no. 1, p. 13209, 2018.

[8] H. Hajian, A. Ghobadi, B. Butun, and E. Ozbay, "Nearly perfect resonant absorption and coherent thermal emission by hBN-based photonic crystals," Opt. Express, vol. 25, no. 25, 2017.

[9] A. Ghobadi, H. Hajian, M. C. Soydan, B. Butun, and E. Ozbay, "Lithography-Free Planar Band-Pass Reflective Color Filter Using Series Connection of Cavities," Just Accept. Sci. Reports, 2018.

Synthetic Weyl points in plasmonic-dielectric crystals

Z. Z. Liu[1,2] Q. Zhang, and J. J. Xiao[1,2,*],

[1]Shenzhen Engineering Laboratory of Aerospace Detection and Imaging, Harbin Institute of Technology (Shenzhen), Shenzhen, China
[2]College of Electronic and Information Engineering, Harbin Institute of Technology (Shenzhen), Shenzhen, China

*corresponding author, E-mail: eiexiao@hitsz.edu.cn

Abstract

Weyl points, where three-dimensional linearly dispersive bands cross, give rise to many intriguing phenomena including topologically protected surface states and chiral anomaly. The section Chern number defined on two-dimensional momentum space is changed as the normal momentum component pass through a WP. We show that a geometrical dimension can also induce a phase transition in 1D plasmonic-dielectric crystals, where a Dirac point emerges. The surface states can be engineered by such synthetic Weyl point concept and observed in lower dimensional systems. We expect similar results be found in 2D as well.

1. Introduction

In analogy to the two-dimensional (2D) system Dirac Point, three-dimensional (3D) linearly dispersive bands were also discovered, referred to as "Weyl points" (WPs) which also manifest topologically protected phenomena. Apart from the electronic topological insulators, their classical wave counterparts have attracted a lot of attention, such as photonics, acoustic, and plasmonic systems. The characteristic Fermi arc surface states have been theoretically predicted and experimentally observed. Many intriguing phenomena are revealed by the presence of such topologically protected WP which represents a source or sink of the Berry curvature in the momentum space.

Time-reversal symmetry requires a WP at an arbitrary momentum k to have the same charge as its companion point $-k$, while inversion symmetry requires them to have the opposite charge. Then it can be concluded the existence of WPs in a system with both inversion and time-reversal symmetry are prohibited. Such nodal points can exist in various systems with broken PT symmetry. In addition to the geometric dimensions, synthetic dimensions can be combined to form higher dimensional synthetic space [1]. Hence, 1D or 2D structures are easier to explore WP physics with the aid of synthetic dimension.

It has been verified that the existence of interface states are guaranteed by the bulk-edge correspondence, i.e., the difference of the bulk topological invariants across the interface [2]. For the case of 1D inversion symmetric systems, the difference can be featured by the Zak phase below the common gap. Whereas the topological invariants for inversion-symmetry broken systems are no longer the Zak phase, which cannot be quantized as 0 or π. Recall the aforementioned inversion-symmetry broken property of WP, the concept of WP acts as a powerful tool to explore the topological properties of such 1D crystal with broken inversion symmetry.

2. Synthetic WP in 1D crystals

Multilayered plasmonic-dielectric crystals (PDC) with broken inversion symmetry are taken to illustrate the design and explore the synthetic WP. In addition to the 1D Bloch wave number q, two more intrinsic structural parameters fill up the 3D space wherein a synthetic WPs are constructed. The introduction of the synthetic space provides new possibilities for manipulating more internal degrees of freedom, which are of significant importance for potential applications.

Figure 1(a) shows the considered 1D crystal, whose dispersion relation for transverse magnetic modes reads [3]

$$\begin{aligned}\frac{4\cos(q\Lambda)}{\Xi} &= 4-(\tau_{24}+\frac{1}{\tau_{24}}+\tau_{21}\tau_{34}+\frac{1}{\tau_{21}\tau_{34}})\tan\kappa_2\tan\kappa_4 \\ &+(\tau_{24}+\frac{1}{\tau_{24}}-\tau_{21}\tau_{34}-\frac{1}{\tau_{21}\tau_{34}})\frac{\tan\kappa_2\tan\kappa_4\cos(\kappa_1-\kappa_3)}{\cos(\kappa_1+\kappa_3)} \\ &-2(\tau_{21}+\tau_{32})\tan\kappa_2\tan(\kappa_1+\kappa_3) \\ &-2(\tau_{14}+\tau_{43})\tan\kappa_4\tan(\kappa_1+\kappa_3),\end{aligned} \quad (1)$$

where $\Xi=\cos\kappa_2\cos\kappa_4\cos(\kappa_1+\kappa_3)$, $\kappa_m=k_m d_m$ $\tau_{mn}=\varepsilon_m k_n/\varepsilon_n k_m$, $k_m=\sqrt{k_0^2\varepsilon_m-k_y^2}$, $\Lambda=d_1+d_2+d_3+d_4$.

Figures 1(b) and 1(c) illustrate the evolution of dispersion relation and two distinct cases of emergence of the linear crossing with fine-tuned parameters for fixed wavelength $\lambda=1650$ nm. Obviously, the close and re-opening of the band gap are closely related to the geometrical parameter d_0, and imply the topological feature of the bands. In this case, the topological invariants for inversion-symmetry broken systems are no longer the Zak phase, which cannot be quantized as 0 or π.

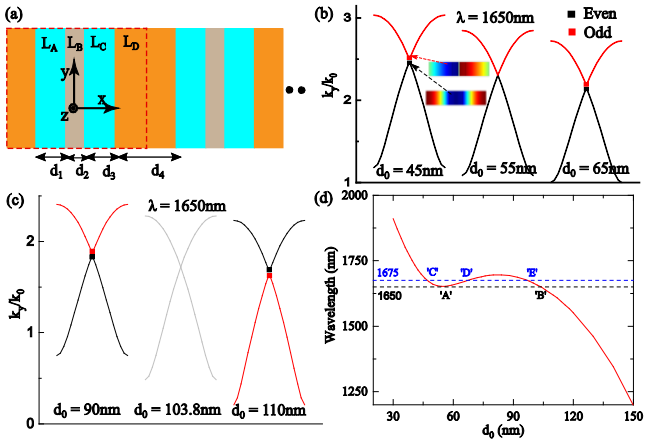


Figure 1: (a) Schematic diagram of the multilayered lattices composed of four alternating stacks. (b) and (c), respectively, illustrate the evolution of the band structure (k_y versus q) for the inversion-symmetric PDC ($d_1 = d_3 = d_0$) as d_0 pass through 55 nm and 103.8 nm. Here, the wavelength is fixed as $\lambda = 1650$ nm and the insets in (b) are the fields distribution at the center of BZ, i.e., $q = 0$. (d) The trajectory of DPs as a function of d_0. Two dashed lines (for wavelength 1650 nm and 1675 nm) cross the curves with different nodal points, labeled as 'A'-'E'.

In the notion of Weyl points, the topological surface states can be determined by breaking the space inversion symmetry. For the generic configurations in Fig. 1(a), the inversion-symmetry of this crystal is broken with unequal d_1 and d_3. Then we employ these two spatial parameters to simulate the second and the third dimensions for the 3D synthetic space.

A general Hamiltonian to describe WP dispersions reads $H_{eff} = E_0\sigma_0 + \mathbf{v}_0 \cdot \mathbf{k}\sigma_0 + \sum_{i=1}^{3} \mathbf{v}_i \cdot \mathbf{k}\sigma_i$, where $\mathbf{k} = (k_x, k_y, k_z)$ is the wave vector in reciprocal space, and (σ_0, σ_i) are the identity matrix and Pauli matrices, respectively [2]. Extended to synthetic space of this structure, the new space becomes $\mathbf{k} = \mathbf{k}_e = (\Delta d_1, \Delta d_3, \Delta q)$, with $\Delta d_1 = (d_1 - d_0)/0.5\Lambda$, $\Delta d_3 = (d_3 - d_0)/0.5\Lambda$, and $\Delta q = q\Lambda/\pi$. When extended to synthetic space, the surface states are topologically protected. Figures 2(b)-2(d) clearly sketch the key properties of the interface states: (1) its dispersion starts at the bulk bands and terminates at the boundary of parameter space, (2) the connection to bulk band I or II switches as k_y crosses the WP, and (3) the number of interface states is always unity in accord to the bulk-edge correspondence. The interface state dispersion terminates at the first (I) or second (II) bulk bands, depending on the cover medium being air or silver. This represents a hallmark of the topological protected interface states.

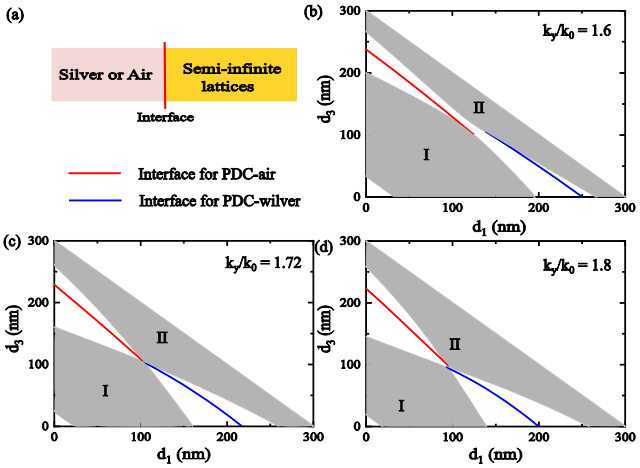


Figure 2: (a) The schematic structure of the interface formed by a homogeneous medium and the designed 1D PDC. The projected bulk band structure (gray regions, labeled as "I" and "II") and interface trajectories in the parameter space d_1-d_3 for (b) $k_y = 1.6k_0$, (c) $k_y = 1.72k_0$, (d) $k_y = 1.8k_0$. The structure for semi-infinite lattices connected with air (silver) is marked as PDC-air (PDC-silver). Then, the red (blue) line corresponds to the trajectory of the interface states for PDC-air (PDC-silver).

3. Conclusions

Synthetic 3D space serves as a promising platform to mimic Weyl point in 1D or 2D plasmonic-dielectric crystals, with the aid of bands linear crossing in inversion-symmetry systems. The use of synthetic space enriches the internal degree of freedom and enables new possibilities for manipulating the topologically protected interface states between bulk crystals and ambient homogenous medium (including plasmonic and dielectric).

Acknowledgements

This work was supported by the Shenzhen Municipal Science and Technology Plan (Grant No. JCYJ20170811154119292), NSF of Guangdong Province (Grant No. 2015A030313748), and the China Postdoctoral Science Foundation (Grant No. 2018M630356).

References

[1] L. Yuan, Q. Lin, M. Xiao, and S. Fan, Synthetic dimension in photonics, *Optica* 5: 1396, 2018.

[2] X. Wan, A. M. Turner, A. Vishwanath, and S. Y. Savrasov, Topological semimetal and Fermi-arc surface states in the electronic structure of pyrochlore iridates, *Phys. Rev. B* 83: 205101, 2011.

[3] Z. Z. Liu, Q. Zhang, F. F. Qin, D. Zhang, X. Liu, and J. J. Xiao, Surface states ensured by a synthetic Weyl point in one-dimensional plasmonic dielectric crystals with broken inversion symmetry, *Phys. Rev. B* 99: 085441, 2019.

Magnon Kerr Effect in a Cavity QED System

Tiefu Li
Tsinghua University, China

Abstract— We experimentally demonstrate magnon Kerr effect in a cavity quantum electrodynamics (QED) system, where magnons in a small yttrium iron garnet (YIG) sphere are strongly but dispersively coupled to the photons in a three-dimensional cavity. The Kerr term comes from the magnetocrystalline anisotropy of the YIG sphere. When the YIG sphere is pumped to generate considerable magnons, the Kerr effect yields a perceptible shift of the cavity central frequency and more appreciable shifts of the magnon modes. We derive an analytical relation between the magnon frequency shift and the drive power for the uniformly magnetized YIG sphere and find that it agrees very well with the experimental results of the Kittel mode. Our study paves the way to explore nonlinear effects in the cavity QED system with magnons. The nonlinear properties may be utilized in the hybrid quantum information processing system.

Field-Resolved Detection of the Temporal Response of a Mid-Infrared Plasmonic Antenna

Marco P. Fischer[1], Kevin Gallacher[2], Jacopo Frigerio[3], Giovanni Pellegrini[4], Niccolò Maccaferri[5], Giovanni Isella[3], Alfred Leitenstorfer[1], Douglas J. Paul[2], Paolo Biagioni[4], and Daniele Brida[1,5*],

[1]Department of Physics and Center for Applied Photonics, University of Konstanz, D-78457 Konstanz, Germany
[2]School of Engineering, University of Glasgow, Rankine Building, Oakfield Avenue, Glasgow, G12 8LT, UK
[3]L-NESS, Dipartimento di Fisica del Politecnico di Milano, Via Anzani 42, 22100 Como, Italy
[4]Dipartimento di Fisica, Politecnico di Milano, Piazza Leonardo da Vinci 32, 20133 Milano, Italy
[5]Physics and Materials Science Research Unit, Université du Luxembourg, L-1511 Luxembourg, Luxembourg
*corresponding author, E-mail: daniele.brida@uni.lu

Abstract

We performed electro-optic sampling of the pulses re-emitted by a heavily-doped germanium antenna resonant in the mid-infrared. This field-resolved measurement allows observing the time domain response of a single plasmonic structure in amplitude and phase.

1. Introduction

Plasmonic nanoantennas receive broad attention in the nanophotonics field owing to the large field enhancement on sub-diffraction limited volumes that allows various applications ranging from nearfield microscopy to sensitive material detection and to the observation of higher order optical nonlinearities. Traditional studies are performed in the visible and near-infrared spectral range generally on metallic (gold) subwavelength structures.

While classic intensity detection allows to study the spectral resonance behavior, the underlying temporal dynamics within the antenna stay hidden. Nonlinear femtosecond spectroscopy in combination of field simulations can be employed to gain insight into these dynamics [1]. With the development of the new material class of heavily doped semiconductors [2], the research expands into the mid-infrared spectral frequency range [3] with new interesting perspectives.

.

2. Results

We present, for the first time, full time- and field-resolved experimental studies of the response of resonant plasmonic antennas. Our approach relies on femtosecond multi-THz time-domain spectroscopy (TDS) in combination with high-resolution confocal microscopy (Fig. 1(a)).

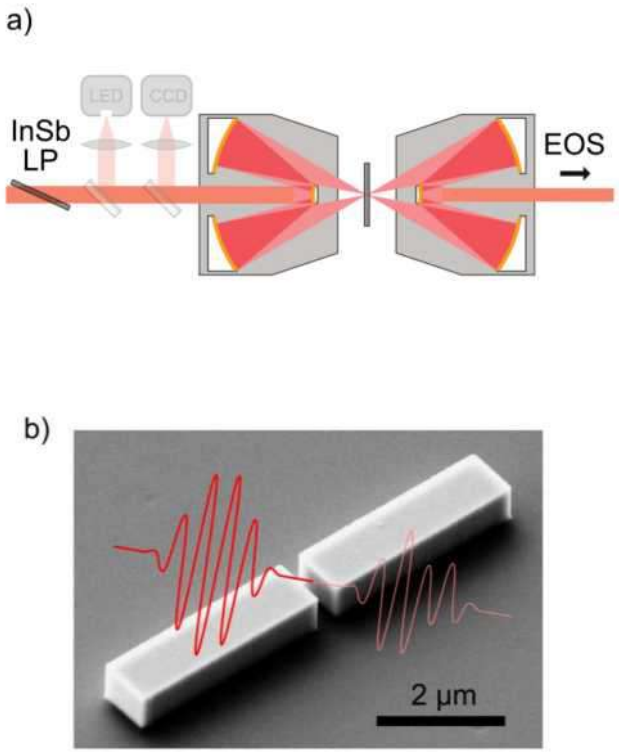


Figure 1: (a) confocal imaging setup employed to study single germanium nanoantennas. InSb LP is a low pass filter and a white light LED and a CCD camera are employed for alignment of the confocal microscope. The mid-IR pulses transmitted through the sample are characterized by electro-optical sampling (EOS) in presence and in absence of a resonant antenna. (b) Micrograph of a germanium antenna with the sketch of the pulsed illumination and the effect of the resonance on the transmitted mid-IR transient

Heavily doped germanium antenna structures (see Fig. 1 (b)) with resonance in the mid-IR are fabricated via electron beam lithography from epitaxial films on silicon substrate. The corresponding plasma frequency of 31 THz is located well inside the mid-infrared spectral range [2]. All studied double rod antennas feature a structure thickness and width of 1 µm at a gap width of 300 nm while the arm length and thus the aspect ratio and resonance frequency are varied.

Isolated double rod antennas are targeted in a confocal microscope based on two Cassegrain-geometry all-reflective objectives. To probe the antenna response, broadband phase-stable femtosecond pulses in the mid-IR (or multi-THz) frequency range are generated via phase-matched difference frequency generation in GaSe bulk crystals by a system driven by a femtosecond Yb:KGW laser [4]. At a bandwidth of 10.7 THz, the pulse duration equals 58 fs (see Fig. 2 (a,c) blue curves).

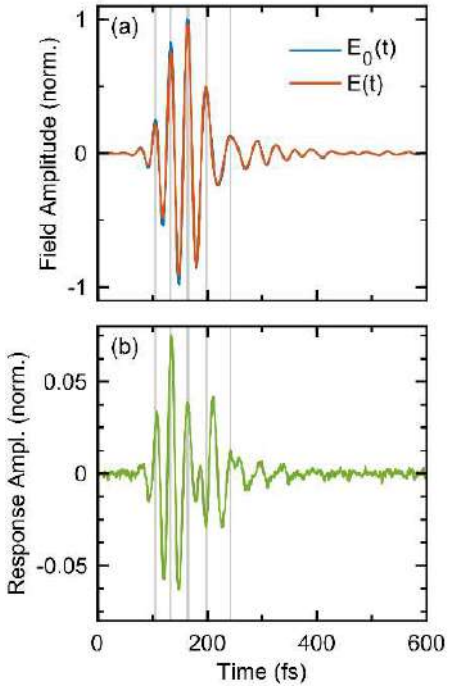


Figure 1: Multi-THz TDS on a heavily doped Ge double rod antenna with arm lengths of 5.5 µm: (a) normalized EOS field transient after interaction with the antenna structure (red) in comparison to the unobstructed probe pulse (blue); (b) time-resolved antenna response field amplitude.

The antenna response is detected in transmission geometry via sensitive electro-optic sampling in GaSe (thickness 80 µm). As EOS gating pulses, a broadband white light supercontinuum is generated in bulk YAG crystal and compressed to sub-15 fs durations. To avoid phase fluctuations within the acquisition time, transients are recorded in fast-scan at an acquisition rate of 5 Hz using a piezo delay scanner. Low-noise detection is accomplished by employing a boxcar amplifier on a shot-to-shot basis in combination with optimized ellipsometry balanced detection scheme. The presented data is averaged from 1250 recorded transients each.

Figure 2(a) and 2(c) show the mid-IR field transient and the intensity spectrum of the pulses after propagation through the silicon substrate without the antenna structures (blue curves). In direct comparison, the temporal field trace and intensity spectrum after interaction with a Ge double rod antenna of arm length 5.5 µm in the microscope focal area is plotted as red curves. The difference between the two measurements in the time domain (Fig. 2 (b)) leads to extraction of the antenna response in amplitude and phase (Fig 2 (d)). The time-domain and frequency-domain response of the individual antennas is reproduced by finite-difference time-domain simulations, which analyze their response. A pulse with the same central frequency and bandwidth as in the experimental conditions is injected into the simulation volume and the transmitted pulse after interaction with the antennas is recorded to calculate the differential response both in the time-domain and, by Fourier transformation, in the frequency domain (amplitude and phase).

3. Conclusions

In conclusion, we introduce a new experimental strategy to investigate the resonance of plasmonic nanostructures that is capable of accessing the full temporal structure in amplitude and phase. This capability offers unique opportunities for the study of fundamental aspects in plasmonic excitations and is particularly appealing in a frequency range that is ideally suited for sensing application in the fingerprint region of molecular vibrations.

References

[1] T. Hanke, et al., “Tailoring spatiotemporal light confinement in single plasmonic nanoantennas,” Nano Lett. 12, 992–6, 2012.

[2] J. Frigerio, et al. “Tunability of the dielectric function of heavily doped germanium thin films for mid-infrared plasmonics,” Phys. Rev. B 94, 85202, 2016.

[3] L. Baldassarre, et al., “Mid-infrared Plasmon-Enhanced Spectroscopy with Germanium Antennas on Silicon Substrates,” Nano Lett. 15, 7225–7231, 2015.

[4] A. Grupp, et al. “Broadly tunable ultrafast pump-probe system operating at multi-kHz repetition rate,” J. Opt. 20, 14005, 2018.

Control of Emission Photon Statistics from a Single Colloidal Quantum Dot Using Plasmonic Nanostructures

Sadahiro Masuo[1]

[1]Depaetment of Applied Chemistry for Environment, Kwansei Gakuin University, Hyogo, Japan
*corresponding author, E-mail: masuo@kwansei.ac.jp

Abstract

One of the important emission behavior of semiconductor nanocrystal quantum dots (QDs) is the emission photon statistics, i.e., single-photon and multiphoton emission. Generally, the emission photon statistics of the QDs are governed by the multiexciton dynamics based on the quantum confinement depending on the size, shape, and atomic composition of QDs themselves. In this work, we demonstrated that the emission photon statistics from a single QD could be controlled by the interaction with the plasmonic nanostructures.

1. Introduction

Colloidal nanocrystal quantum dots (QDs) are a unique class of tunable, dispersible fluorophores that are of great interest for applications in a wide range of opto-electronic devices. An important and interesting exciton dynamics is the simultaneous existence of multiple excitons (MX) in a single QD. By utilizing the MX, the efficiency of the optoelectronic devices can be considerably increased. Furthermore, the cascade emission from MX, i.e., multiphoton emission from triexciton (TX) and biexciton (BX) states, is valued for its production of correlated photon pairs (also called entangled photons) to realize quantum information and communication technologies. However, when MX are generated in a single QD, they can decay by nonradiative Auger recombination (AR), i.e., the MX are reduced to a single exciton (SX) by AR and are wastefully consumed. AR also causes the emission blinking behavior that is known as Auger ionization. Therefore, suppression of AR has been extensively studied for efficient use of the excitons. On the other hand, AR facilitates single-photon emission for the single QD, i.e., photon antibunching in the QD emission, because the surviving SX can emit a single photon even when MX are produced in a QD. The single-photon emission is also an important and interesting optical property of the single QD for quantum information and communication technologies. Therefore, it is very important to control the MX dynamics and subsequent emission photon statistics for applications employing QDs.

We previously reported that the emission photon statistics, i.e., multiphoton emission and a single-photon emission from a single QD, can be modified through interactions of the QD with plasmonic nanostructures [1-8]. Recently, a similar enhancement of multiphoton emission was reported using several QDs-plasmonic nanostructures systems. Two possibilities have been discussed to describe the mechanism behind these increases in the BX emission. One mechanism involves the enhancement of the BX emission rate by the plasmonic nanostructure, which is similar to our previous results. Another is the quenching of SX emission by the plasmonic nanostructure, i.e., a decrease in the QY of SX emission rather than an actual increase in the QY of BX emission. Thus, the interplay of QDs and plasmonic nanostructures, particularly the influence of the nanostructures on the MX dynamics of the QD, is not fully understood. To understand the interaction between single QDs and plasmonic nanostructures, one would have to directly observe changes in the emission behavior of a single QD that accompany the interaction with a plasmonic nanostructure. To achieve this direct observation, we used two atomic force microscopy (AFM) techniques.

2. Results and discussion

2.1. AFM manipulation of a gold nanocube (AuCube)[5]

Monodispersed AuCube of a well-defined size and shape was used in this work. The size of the AuCube was estimated as 87±2.4 nm. The localized surface plasmon resonance (LSPR) band of the AuCube overlaps with both the absorption and emission spectra of the QD. This indicates that both excitation and relaxation processes of the QD can be enhanced with the AuCube by with choice of excitation wavelength. It is well known that the fluorophore-metallic nanostructure interaction strongly depends on the spectral overlap and the distance between a fluorophore and a metallic nanostructure. When the absorption of the fluorophore overlaps with the LSPR band, the excitation rate of the fluorophore can be augmented by the electric field of the LSPR generated by the excitation light. Similarly, when the fluorescence spectrum of the fluorophore overlaps with the LSPR band, this relaxation process can be enhanced. Under our experimental conditions, the LSPR could not be efficiently generated by the excitation laser (405 nm). Therefore, the enhancement of the relaxation process was considered. The advantage of the well-defined AuCube is that there is little variation of the LSPR band in each AuCube; hence, we can simply consider the mechanism of the QD-metallic nanostructure interaction.

The emission behavior of the single QD accompanying the above AFM manipulation of the AuCube is summarized in Fig. 1. Before moving the AuCube near the QD, in the

photon correlation histogram shown in Fig. 1d, the contribution of the center peak at a delay time of 0 ns was lower than the other peaks. The $g^{(2)}(0)$ values were calculated to be 0.14, indicating that the individual QD exhibited single-photon emission, i.e., photon antibunching. This emission behavior is characteristic of the single QD itself and was dramatically changed by interacting with the AuCube. The emission behavior of the single QD in proximity of the AuCube is shown in Fig. 1b, e, and h. The maximum emission count of the single QD increased. In the photon correlation histogram, the contribution of the center peak increased dramatically, and the $g^{(2)}(0)$ values increased to 0.97. This result indicates that the efficiency of the BX emission from the single QD was 6.9 times higher than that of the single QD before approaching the AuCube. The emision behavior of the single QD after the AuCube was pushed away is shown in Fig.1c, f, and i. It is clear that the emission intensity, photon antibunching behavior, and decay curve were returned to those detected from the QD before the approach of the AuCube. The importance of the above results is that the change in the emission behavior was directly observed by manipulating the distance between an AuCube and a single QD.

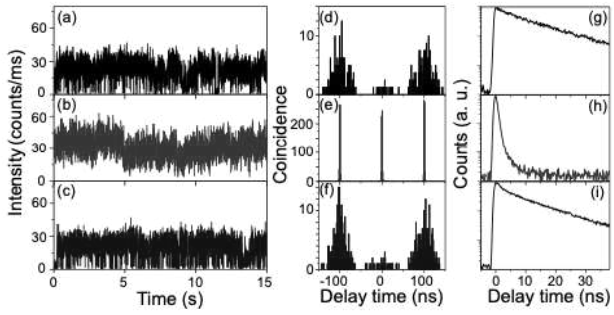


Figure 1: Time traces of emission intensity (a-c), photon correlation histograms (d-f), and fluorescence decay curves (g-i) detected from a single QD before (a, d, g) and after (b, e, h) the approach of AuCube, and after the AuCube was pushed away (c, f, i).

2.2. Approach of a silver-coated AFM tip (AgTip)[6]

In this work, the enhancement of multiphoton emission from a QD interacting with a plasmonic nanostructure was investigated using a silver-coated atomic force microscopy tip (AgTip) as the plasmonic nanostructure. Using the AgTip, which exhibited a well-defined localized surface plasmon (LSP) resonance band, we controlled the spectral overlap and the distance between the single QD and the AgTip. The emission behavior of the single QD when approaching the AgTip at the nanometer scale was measured using off-resonance (405 nm) and resonance (465 nm) excitation of the LSP.

We directly observed the conversion of the single-photon emission from a single QD to multiphoton emission with reduction of the emission lifetime at both excitation wavelengths as the QD-AgTip distance decreased, whereas a decrease and increase in the emission intensity were observed at 405 nm and 465 nm excitation, respectively. By combining theoretical analysis and the numerical simulation of the AgTip, we deduced that the enhancement of the multiphoton emission was caused by the quenching of the single-exciton state due to the energy transfer from the QD to the AgTip and that the emission intensity was increased by enhancement of the excitation rate due to the electric field of the LSP on the AgTip. These results provide evidence that the photon statistics and the photon flux from the single QD can be manipulated by the plasmonic nanostructure through control of the spectral overlap and the distance.

Acknowledgements

We thank Prof. T. Teranishi and Prof. R. Sato at Kyoto University for providing the AuCube, Prof. H. Fujiwara and Prof. K. Sasaki at Hokkaido University for the scattering spectrum measurement of the AgTip, and also thank Prof. N. Tamai and Dr. L. Wang at Kwansei Gakuin University for the numerical simulation of the AgTip.

References

[1] S. Masuo, H. Naiki, S. Machida, A. Itaya, Photon Statistics in Enhanced Fluorescence from a Single CdSe/ZnS Quantum Dot in the Vicinity of Silver Nanoparticles, *Appl. Phys. Lett*., 95: 193106, 2009.

[2] H. Naiki, S. Masuo, S. Machida, A. Itaya, Single-Photon Emission Behavior of Isolated CdSe/ZnS Quantum Dots Interacting with the Localized Surface Plasmon Resonance of Silver Nanoparticles, *J. Phys. Chem. C*, 115: 23299-23304, 2011.

[3] S. Masuo, T. Tanaka, S. Machida, A. Itaya, Photon Antibunching in Enhanced Photoluminescence of a Single CdSe/ZnS Nanocrystal by Silver Nanostructures, *J. Photochem. Photobio. A*, 237: 24-30, 2012.

[4] H. Naiki, A. Masuhara, S. Masuo, T. Onodera, H. Kasai, and H. Oikawa, Highly Controlled Plasmonic Emission Enhancement from Metal-Semiconductor Quantum Dot Complex Nanostructures, *J. Phys. Chem. C*, 117: 2455-2459, 2013.

[5] S. Masuo, K. Kanetaka, R. Sato, T. Teranishi, Direct Observation of Multiphoton Emission Enhancement from a Single Quantum Dot Using AFM Manipulation of a Cubic Gold Nanoparticle, *ACS Photonics*, 3: 109-116, 2016.

[6] H. Takata, H. Naiki, L. Wang, H. Fujiwara, K. Sasaki, N. Tamai, and S. Masuo, Detailed Observation of Multiphoton Emission Enhancement from a Single Colloidal Quantum Dot Using a Silver-Coated AFM Tip, *Nano Lett*., 16: 5770-5778, 2016.

[7] H. Naiki, H. Oikawa, S. Masuo, Modification of Emission Photon Statistics from Single Quantum Dots Using Metal/SiO_2 Core/Shell Nanostructures, *Photochem. Photobio. Sci*., 16: 489-498, 2017.

[8] H. Naiki, T. Uedao, L. Wang, N. Tamai, S. Masuo, Multiphoton Emission Enhancement from a Single Colloidal Quantum Dot Using SiO_2-Coated Silver Nanoparticles, *ACS Omega*, 2: 728-737, 2017.

Colossal infrared and terahertz magneto-optical activity in graphene/hBN heterostructures

Ievgeniia O. Nedoliuk[1], Sheng Hu[2,3], Andre K. Geim[2,3], and Alexey B. Kuzmenko[1*]

[1]Department of Quantum Matter Physics, University of Geneva, CH-1211 Geneva 4, Switzerland
[2]School of Physics & Astronomy, University of Manchester, Manchester M13 9PL, United Kingdom
[3]National Graphene Institute, University of Manchester, Manchester M13 9PL, United Kingdom
*corresponding author, E-mail: Alexey.Kuzmenko@unige.ch

The large spacing between the Landau levels (LLs) in graphene is expected to produce a strong optical intensity of the inter-LL transitions [1, 2, 3, 4]. However, so far the reported magneto-infrared spectra revealed only a weak magnetic increase of the absorption [2, 5, 6, 7], in a complete disagreement with theory. A probable origin of the small intensity of the LL transitions is a high concentration of defects in large-area graphene used so far in these experiments.

In order to address this issue, we developed a new magneto-infrared microscopy setup allowing us to obtain circular polarization-resolved magneto-absorption spectra on small exfoliated samples down to the diffraction limit [8]. Through this, we measure magneto-optical circular polarization resolved spectra on high-mobility graphene encapsulated in hexagonal boron nitride (hBN) in magnetic fields up to 4.2 T [8, 9]. We find a series of extremely sharp and intense interband LL transitions in the mid-infrared range. The quality factor of the LL peaks reaches 20-50, which is much higher than what has been previously reported in graphene deposited on other substrates. The maximum electromagnetic absorption in weakly doped graphene of almost 36% is observed, which approaches the fundamental absorption limit of 50% for a thin film illuminated from one side. At the same time the off-resonance absorption can be magnetically tuned below 1%, due to the depletion of the density of states in the quantum Hall regime, which is much lower than the universal absorption of 2.3% [10, 11].

When graphene is doped, we observe intraband LL transitions in the far-infrared/THz range. Interestingly, a strong absorption ($> 30\%$) at about 3 THz is seen already at 1 T, which is a field intensity attainable with a permanent magnet. Another effect of doping is a full magnetic circular dichroism of some inter- and intraband LL transitions due to the polarization dependent Pauli blocking. In this regime we see the absorption of circular polarized light close to 50% on the transition the between the zeroth and the first LLs. Additionally, the resonant Faraday rotation of more than 0.15 radian in the mid-IR ranges is seen, which surpasses our previous observation in epitaxial graphene [6].

Overall, our results demonstrate a new potential of magnetic tuning in graphene-based long-wavelength optoelectronics and plasmonics. Using the colossal magneto-optical activity of graphene is also highly promising for constructing new magnetically controlled and non-reciprocal metamaterials.

This research was supported by the EU Graphene Flagship and by the Swiss National Science Foundation.

References

[1] N.H. Shon, , T. Ando, Quantum Transport in Two-Dimensional Graphite System, *J. Phys. Soc. Jpn.* **67**, 2421-2429 (1998).

[2] M.L. Sadowski *et al.,* Landau Level Spectroscopy of Ultrathin Graphite Layers, *Phys. Rev. Lett.* **97**, 266405 (2006).

[3] V.P. Gusynin, , S.G. Sharapov, J.P. Carbotte, Magneto-optical conductivity in graphene, *J. Phys. Condens. Matter* **19**, 026222 (2007).

[4] D.S.L. Abergel, V.I. Falko, Optical and magneto-optical far-infrared properties of bilayer graphene, *Phys. Rev. B* **75**, 155430 (2007).

[5] M. Orlita, *et al.,* Approaching the Dirac Point in High-Mobility Multilayer Epitaxial Graphene *Phys. Rev. Lett.* **101**, 267601 (2008).

[6] I. Crassee, *et al.,* Giant Faraday rotation in single- and multilayer graphene, *Nature Physics* **7**, 48-51 (2011).

[7] Z.-G. Chen *et al.,* Observation of an intrinsic bandgap and Landau level renormalization in graphene/boron-nitride heterostructures. *Nature Communications* **5**, 4461 (2014).

[8] I.O. Nedoliuk, PhD thesis (2018).

[9] I.O. Nedoliuk *et al.,* submitted.

[10] R.R. Nair., *et al.,* Fine Structure Constant Defines Visual Transparency of Graphene. *Science* **320**, 1308 (2008).

[11] A.B. Kuzmenko, E. van Heumen, F. Carbone, D. van der Marel, Universal Optical Conductance of Graphite. *Phys. Rev. Lett.* **100**, 117401 (2008). 108, 047401 (2012).

Angular momentum of light induces chiral mass transport

Takashige Omatsu[1,2]

[1]Graduate School of Engineering, Chiba University, Japan
[2]Molecular Chirality Research Center, Chiba University, Japan
*corresponding author, E-mail: omatsu@faculty.chiba-u.jp

Abstract

We discovered that irradiation with light possessing orbital angular momentum owing to its phase singularity, i.e. an optical vortex, twists a variety of materials, including metal, silicon, polymer, and even liquid-phase resin to form various helically structured materials. In this presentation, we report on the unique helical structures created via the interaction between the orbital angular momentum of light and matter. Such light-induced helical structured materials will potentially provide us to develop metamaterials for ultra-sensitive detection and reactions for chiral chemical composites.

1. Introduction

Helical light field, i.e. light field possessing orbital angular momentum (OAM) associated from its helical wavefront [1,2] and spin angular momentum (SAM) owing to a helical electric field, has been intensely investigated in a variety of research fields, such as optical manipulations, telecommunications, quantum optics, and micro-fabrications.

In recent years, we discovered that helical light field enables the orbital motion of the irradiated materials, such as metals, polymers, and even liquid-phase resin, to establish chiral structures on a nano- or micro-scale [3-6]. Such chiral structures fabricated by the optical vortex illumination will have a potential to develop chiral metamaterials for highly sensitive detection and reaction of chiral chemical composites.

For instance, surface relief on azo-polymers is formed through mass transport of azo-polymers owing to an optical gradient force, anisotropic photo-fluidity, and trans-cis photoisomerization [7-9], and thus, it mostly reflects a nonuniform intensity profile of the illuminated light. An optical vortex with OAM twists azo-polymers to shape a single-arm chiral surface relief with the aid of the spin angular momentum associated with the circular polarization [10,11]. Also, it is worth noting that chiral surface relief can be created simply by illuminating circularly polarized light via SAM-OAM coupling [12]. Such helical surface reliefs further enable the generation of nearfield OAM light on a sub-wavelength scale, leading to a further nanoscale mass-transport of azo-polymers (Figure 1) [13].

Interestingly, self-focusing of the incident beam occur upon initiating polymerization due to a permanent refractive index change of the resin, resulting in the formation of a laser-induced self-written fiber. The OAM light creates a helical fiber, manifesting helical trajectories of the optical vortex solitons.

In this presentation, we introduce such unique chiral structures formed by illumination of helical light field.

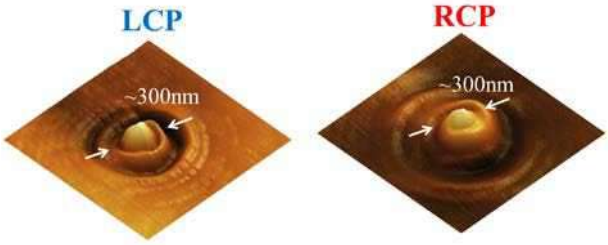


Figure 1: Chiral nanoscale surface relief on an azo-polymer film.

Acknowledgements

The authors acknowledge support from the Japan Society for the Promotion of Science (JSPS) KAKENHI Grants (JP 16H06507; JP 17K19070; JP 18H03884).

References

[1] L. Allen, M. W. Beijersbergen, R. J. C. Spreeuw, J. P. Woerdman, *Phys. Rev. A* 45, 8185 (1992).
[2] M. Padgett, R. Bowman, *Nat. Photonics* 5(6), 343–348 (2011).
[3] F. Takahashi, K. Miyamoto, H. Hidai, K. Yamane, R. Morita, T. Omatsu, *Sci. Rep.* 6, 21738 (2016).
[4] K. Toyoda, K. Miyamoto, N. Aoki, R. Morita, T. Omatsu, *Nano Lett.* 12, 3645−3649 (2012).

[5] K. Toyoda, F. Takahashi, S. Takizawa, Y. Tokizane, K. Miyamoto, R. Morita, T. Omatsu, *Phys. Rev. Lett.* 110, 143603/1-5 (2013).
[6] J. Lee, Y. Arita, S. Toyoshima, K. Miyamoto, P. Panagiotopoulos, E. M. Wright, K. Dholakia, T. Omatsu, *ACS Photonics* 5(10) 4156-4163 (2018).
[7] N. K. Viswanathan, D. Y. Kim, S. B. J. Williams, W. Liu, L. Li, L. Samuelson, J. Kumar, S. K. Tripathy, *J. Mater. Chem.* 9(9), 1941–1955 (1999).
[8] D. Y. Kim, S. K. Tripathy, L. Li, J. Kumar, *Appl. Phys. Lett.* 66(10), 1166–1168 (1995).
[9] P. Rochon, E. Batalla, A. Natansohn, *Appl. Phys. Lett.* 66(2), 136–138 (1995).
[10] M. Watabe, G. Juman, K. Miyamoto, T. Omatsu, *Sci. Rep.* 4, 4281 (2014).
[11] D. Barada, G. Juman, I. Yoshida, K. Miyamoto, S. Kawata, S. Ohno, T. Omatsu, *Appl. Phys. Lett.* 108, 051108 (2016).
[12] K. Masuda, S. Nakano, D. Barada, M. Kumakura, K. Miyamoto, T. Omatsu, *Opt. Express* 25(11), 12499-12507 (2017).
[13] K. Masuda, R. Shinozaki, Y. Kinezuka, J. Lee, S. Ohno, S. Hashiyada, H. Okamoto, D. Sakai, K. Harada, K. Miyamoto, T. Omatsu, *Opt. Express*, 26(17), 22197-22207 (2018).

Design and Experiments of Planar Metamaterial Lüneburg Lens on SOI

Hamdam Nikkhah[1,2], Trevor J. Hall[1]

[1] Centre for Research in Photonics at the University of Ottawa, School of Electrical Engineering & Computer Science, Advanced Research Centre, Ottawa, ON K1N 6N5, Canada
[2] Now with Lumentum, Ottawa, Canada

*corresponding author, E-mail: Trevor.Hall@uottawa.ca

Abstract

A 2D Lüneburg lens may be formed by patterning a planar slab waveguide with a subwavelength grating structure using a silicon photonics integration platform with the advantage of small footprint. Confocal telescopes employing 15 μm diameter lenses were fabricated using a 300 nm silicon on insulator integration platform. The experimentally measured loss of the fabricated structures was found to be 0.726 dB per lens which is close to the value of 0.517 dB predicted by FDTD simulations.

1. Introduction

3D optical systems and components are regularly bulky and vulnerable to environmental perturbations, sensitive to alignment tolerances, and unsuited to volume manufacture. These issues may be addressed by omitting one dimension and implementing components in a planar slab waveguide of a silicon integration platform with the advantage of a small footprint. The Lüneburg graded index lens may be implemented in a photonic integrated circuit to provide a Fourier transform on a chip for a complex optical interconnection system [1, 2]. It may be built on a planar slab waveguide with solid core, such as silicon, with air as the upper cladding and silica as substrate which together form an asymmetric 1D slab waveguide. The light is confined in the direction normal to the plane but the wave-vector of the fundamental mode can be pointed in any direction in a 2D free-space within the plane [1]. The effective index of the fundamental mode is lower than the refractive index of the core and higher than the substrate for the light to be confined in the core of the waveguide. To construct a structure such as a lens, the effective index of the mode needs to be varied; decreasing radially from the centre of the lens to its rim. The core and cladding materials and their thickness must be selected carefully for a specified operating vacuum wavelength. A major issue arises as the thickness of the slab waveguide must be varied to fulfill the specified graded refractive index profile which requires multiple steps of etching that would add complexity and high cost to the fabrication process.

In this work, the effective refractive index of the Lüneburg lens is engineered by nano-structuring the core layer of an SOI slab waveguide to form a waveguide with a metamaterial core. This offers the simplicity of single etch step in the fabrication process. The process used an SOI wafer with a 300 nm silicon core thickness layer with cylindrical inclusions of air in a silicon slab waveguide. The inclusions may be placed on a regular sub-wavelength lattice and the diameter of cylinders varied according to the local effective index required [2].

2. Simulations

The prediction of the dependence of the local effective index on the hole diameter in a local unit cell was done by a homogenization method [2]. The confocal telescope lens system in which two Lüneburg lenses are placed side-by-side with their rims touching on axis was defined to obtain the insertion loss that may arise from the approximation of a continuous graded index material by a graded metamaterial. In this way, the input to the lens through a single mode access waveguide may be considered as a point source at the rim of the lens. The first lens transforms the point source at its input rim to a plane wave at its output rim and the second lens then transforms the plane wave at its input rim to a point source at its output rim.

In this design, each lens diameter is 15 μm with the effective index varying from 1.925 at the rim to 2.722 in the centre. A single mode ridge waveguide is used to launch the light in and couple light out of the telescope system.

Figure 1 shows the confocal telescope Lüneburg lens system that was built and simulated in FDTD. The predicted insertion loss on each lens was obtained as -0.517 dB with the assumption that the waveguide-lens insertion loss is small.

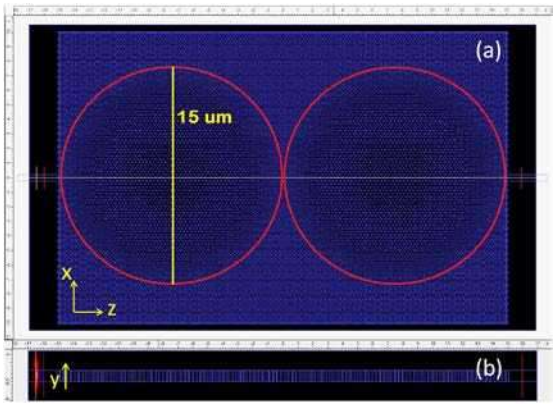


Figure 1: Top view of a confocal telescope Lüneburg lens system contains the two lenses with diameter of 15 µm are placed side-by-side.

3. Experimental results

The confocal telescope structure was fabricated and tested. Figure 2 shows an SEM of the fabricated structure on SOI.

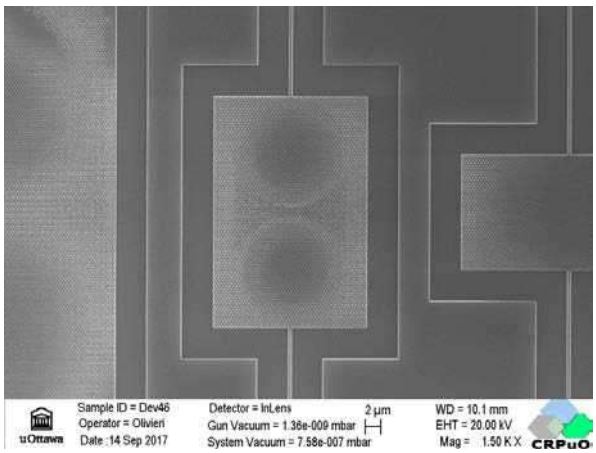


Figure 2: SEM of telescope composed of two lenses each with the diameter of 15 µm

The loss per lens without any other considerations of other losses was measured as 0.726 dB per lens which is close to the prediction of the simulation presented in previous section.

The loss of each interface between lens and access waveguide was 3.965 dB. This loss may be reduced by adiabatic lateral taper and/or adiabatic effective index transition between the conventional waveguide and the metamaterial slab waveguide of the lens.

4. Conclusions

The metamaterial structure can offer simplicity in fabrication process in addition to the smaller footprint structures. Metamaterial Lüneburg lens may be built on a slab waveguide with single step etch process. The simulation on a confocal telescope system of two side by side Lüneburg predicted an insertion loss of -0.517 dB on each lens. The experimental result of a fabricated structure was obtained the insertion loss of 0.726 dB per lens which is close to the prediction of the simulation.

Acknowledgements

This work was performed and completed when Dr. Hamdam Nikkhah was with the University of Ottawa prior joining Lumentum. The authors are grateful to CMC Microsystems for supporting the fabrication of the silicon photonic integrated circuit. Dr. Trevor Hall is grateful to the University of Ottawa for the support provided by a University Research Chair.

References

[1] H. Nikkhah, *Optical Switch on a Chip: The Talbot Effect, Lüneburg Lenses & Metamaterials*, MSc. Thesis, Université d'Ottawa/University of Ottawa, Canada, August 2013.

[2] H. Nikkhah, T. J. Hall, *Metamaterial Lüneburg lens for Fourier optics on-a-chip*, Proc. SPIE 8988, Integrated Optics: Devices, Materials, and Technologies XVIII, 89880J-89880J, 2014

Polarization Engineering via in-Plane Rotation of Uniaxial Bilayers

Constantinos Valagiannopoulos[1*]

[1]Department of Physics, Nazarbayev University, Astana, Kazakhstan
*corresponding author, E-mail: konstantinos.valagiannopoulos@nu.edu.kz

Abstract

Engineering the polarization of the transmitted electromagnetic signals within a small fraction of the operational wavelength is an objective with numerous applications. The necessary anisotropy for this objective can be emulated in various ways but the simplest one is with multiple opaque rods stacked on a transparent background. It is shown that the polarization conversion ratio is kept small in the presence of realistic losses; however, we propose a pair of identical multilayers suitably tilted in-plane to overcome that bottleneck.

1. Introduction

Polarization of photonic beams constitutes a continuous variable and thus can be used as an reliable information container; therefore, changing it within a thin volume of space is critical for the operation of various devices based on the diversity of wave polarization [1]. A mandatory requirement to accomplish any polarization conversion is the effective anisotropy of the employed media which admits the coupling between different directions of the electric fields. Such a property is usually realized with use of arrays of small particles such as elliptical posts [2] or chiral resonators [3] with suitable polarizabilities. Alternatively, complete polarization control is achieved as a topologically protected effect [4] or at two-dimensional materials with built-in anisotropy like black phosphorus [5].

In this work, which is based on our prequel study [6], where all the technical details are thoroughly explained, we consider the simplest possible structure suitable for polarization engineering: multilayers of plasmonic rectangular rods stacked in a transparent background. It is shown that if losses are ignored, perfect polarization twist is possible via a single cluster of parallel layers with a specific optically small thickness. Such a flawless outcome is based on the huge asymmetry between the developed modes into the cluster, combined with a 45°-tilted axis. However, the performance gets much poorer when realistic losses are considered being always present in plasmonic media. For this reason, we are introducing a bilayer configuration comprising a pair of these clusters rotated by different angles by keeping the overall thickness small. Therefore, an additional set of waves are excited and that mode interplay "opens" a window for the incident beam to pass with totally different polarization characteristics. By sweeping a large part of the parametric space, we conclude to several optimal designs which have been proven extremely robust with respect to fabrication defects, frequency mismatch and incidence obliqueness. We believe that our study will inspire further theoretical and experimental investigations towards the direction of polarization engineering with help from simple structures.

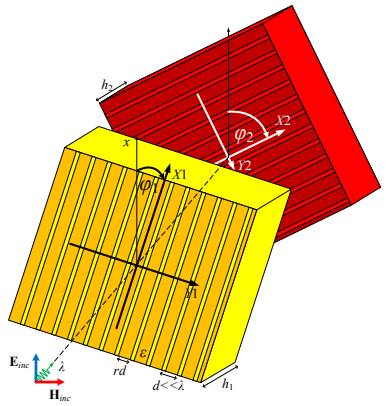


Figure 1: The physical configuration of the regarded structure: a bilayer comprising slabs of the same uniaxial medium suitably rotated to achieve perfect polarization conversion.

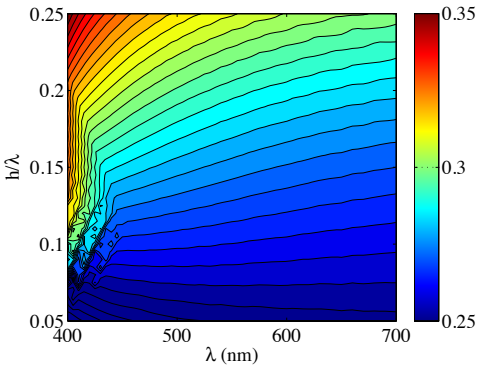
2. One Slab

The physical configuration of the analyzed structure is depicted in Fig. 1, where two uniaxial layers of identical texture possess thicknesses h_1 and h_2; the utilized Cartesian coordinate system (x, y, z) is also defined. Each one is comprised of free-standing multilayers (d-periodic) of opaque medium with relative permittivity ε and duty cycle $0 < r < 1$, which are in-plane rotated by angle φ_1 and φ_2 respectively. In a single slab of thickness h with tilt of optical axis φ, two waves are developed with propagation constants:

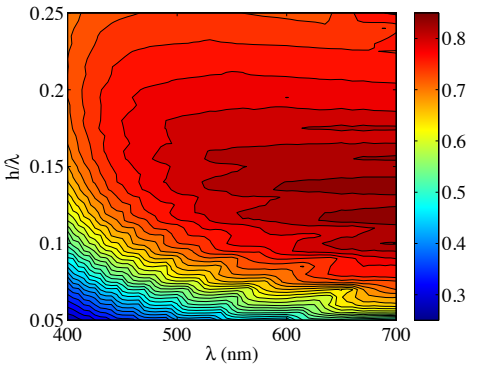
$$k_{\rm I,II} = k_0 \sqrt{\frac{(\varepsilon_X + \varepsilon_Y) \pm \sqrt{(\varepsilon_X - \varepsilon_Y)^2}}{2}}, \qquad (1)$$

where $\varepsilon_X = \frac{\varepsilon}{(1-r)\varepsilon + r}$ and $\varepsilon_Y = r\varepsilon + (1-r)$ are the homogenized effective-medium permittivities (for $d \ll \lambda$) and $k_0 = 2\pi/\lambda$ the free-space wavenumber. The matching conditions are these of the Fabry-Perot resonator: $\sin(k_{\rm I} h) = \sin(k_{\rm II} h) = 0$; however, flawless polarization conversion

is possible only for $\varphi = 45^\circ$ and, most importantly, for huge contrast between the developed modes: $k_{\rm I} \gg |k_{\rm II}|$. The later condition is only feasible once the effective permittivity ε_Y blows up, namely for a lossless metal $\varepsilon = -\frac{r}{1-r} < 0$. Once the losses (being inevitable to any plasmonic medium) are present, the performance in polarization shift gets severely deteriorated.



(a)



(b)

Figure 2: Maximal polarization conversion as function of the operational wavelength λ and optical thickness h/λ for: (a) a single uniaxial slab by sweeping tilts φ and duty cycles r, (b) the bilayer of Fig. 1 by sweeping (φ_1, φ_2) and r for $h_1 = h_2 = h/2$. Free-standing silver rods are employed [6].

3. Pair of Slabs

What if we keep using the same materials having identical level of losses $\mathrm{Im}[\varepsilon]$ and, by slightly modifying the structure, we achieve a substantial improvement in polarization conversion at the same overall thickness? Indeed, by considering the axes tilts (φ_1, φ_2) and plasmonic portion r (for $h_1 = h_2 = h/2$) as basic design parameters, we report structures, employing actual plasmonic media with realistic losses, with very efficient polarization swifts.

In Figs 2, we show the highest degree of polarization conversion that can be achieved at a specific operational wavelength λ with a metasurface of specific thickness h. In Fig. 2(a), we optimize a single uniaxial slab with respect to direction φ and duty cycle r; on the contrary, in Fig. 2(b), we show the response of the best performing device of Fig. 1 by sweeping (φ_1, φ_2) and r, under the assumption of $h_1 = h_2 = h/2$. As plasmonic material, we use silver with well-known dispersion $\varepsilon = \varepsilon(\lambda)$ as in [6]. One can clearly notice that for the first configuration (one slab, Fig. 2(a)), the maximal possible polarization shift is less than 35%; however, by simply cutting the same structure in two and properly tilting the formed layers (pair of slabs, Fig. 2(b)), the polarization conversion reaches 90% for a rather extensive range of working λ. Further results regarding the operation of the same setup across alternative bands and the immunity of the proposed bilayers with respect to various defects and errors, will be presented.

4. Conclusions

Perfect polarization transformation through metasurfaces is a challenging goal with significant scientific and funding interest. We propose a simple configuration which, in spite of the presence of the realistic losses, gives almost flawless polarization twists with huge robustness in its performance.

Acknowledgement

This work has been supported by Nazarbayev University Small Grant No. 090118FD5349. Funding from MES RK state-targeted program BR05236454 is also acknowledged.

References

[1] J. Lin, J. P. B. Mueller, Q. Wang, G. Yuan, N. Antoniou, X.-C. Yuan, and F. Capasso, Polarization-Controlled Tunable Directional Coupling of Surface Plasmon Polaritons, *Science* 12: 331–334, 2013.

[2] A. Arbabi, Y. Horie, M. Bagheri, and A. Faraon, Dielectric metasurfaces for complete control of phase and polarization with subwavelength spatial resolution and high transmission, *Nature Nanotechnology* 10: 937–943, 2015.

[3] T. Niemi, A. O. Karilainen, and S. A. Tretyakov, Synthesis of Polarization Transformers, *IEEE Transactions on Antennas and Propagation* 61: 3102–3111, 2013.

[4] Y. Guo, M. Xiao, and S. Fan, Topologically Protected Complete Polarization Conversion, *Physical Review Letters* 119: 167401, 2017.

[5] C. A. Valagiannopoulos, M. Mattheakis, S. N. Shirodkar, and E. Kaxiras, Manipulating polarized light with a planar slab of black phosphorus, *Journal of Physics Communications* 1: 045003, 2017.

[6] A. Sarsen and C. Valagiannopoulos, Robust polarization twist by pairs of multilayers with tilted optical axes, *Physical Review B* 99: 115304, 2019.

Enabling Plasmonic Metasurfaces by Laser Processing

Alberto Piqué*, Raymond C.Y. Auyeung, Heungsoo Kim, Kristin M. Charipar, Jake Fontana[2], and Nicholas A. Charipar

Materials Science & Technology Division, Code 6360, U.S. Naval Research Laboratory, Washington, DC 20375, USA
[2]Center for Biomolecular Science & Engineering, Code 6907, U.S. Naval Research Laboratory, Washington, DC 20375, USA
*corresponding author, E-mail: pique@nrl.navy.mil

Abstract

This work aims to study the influence of material growth and laser processing conditions on the plasmonic behavior of various types of laser-patterned thin films, from metal-oxides such as ITO and vanadium dioxide (VO_2) to monolayers of hexagonally packed ligand capped gold nano-spheres. Here, direct laser interference patterning or DLIP enables the patterning of these films into plasmonic metasurfaces suitable for flat optics. In addition, the plasmonic assisted ultrafast optically induced nonlinear switching of VO_2 patterned structures will also be discussed.

1. Introduction

Ultrathin surfaces that interact strongly with electromagnetic radiation on length scales far below their free-space wavelength are commonly referred to as metasurfaces. These surfaces stand in stark contrast to traditional optical components that require interaction scales comparable to the wavelength of light. While these ultrathin metasurfaces could enable flat optical components and high field concentration, there is an inherent difficulty associated with their fabrication. Optical metasurfaces have traditionally relied upon electron beam lithography to produce the required feature size and spatial gradients. Identifying alternatives to electron beam lithography for the patterning of widely dissimilar types of thin film materials ranging from metal oxides to self-assembled monolayers is very important in order to be able to investigate their plasmonic behavior. This work will discuss one such alternative based on direct laser interference patterning or DLIP, as a way to efficiently generate plasmonic gratings and other types of metasurfaces with potential uses for flat optics applications. DLIP is used to pattern single- or multilayer films containing plasmonic materials such as metal oxides (ITO or VO_2) or self-assembled monolayers of gold nanoparticles.

2. Background

Typically, the patterning of metasurfaces is performed by conventional photolithography and subsequent wet/dry etching techniques. These multistep processes can degrade the plasmonic materials being processed and they are not compatible with self-assembled monolayers since they require the application and removal of photoresists. Alternative patterning techniques are required in order to process dissimilar materials such as metal-oxides and monolayers of gold nanoparticles.

2.1. Materials

Conventional metals with high carrier concentrations, such as gold and silver, are typically used in plasmonic and metamaterial devices since their associated plasma frequencies are in the visible and near ultraviolet (UV) ranges. However, these metals exhibit large absorption losses across the near infrared (NIR), which degrade and limit their use for any practical applications in the NIR. For applications in this portion of the spectrum, certain semiconducting metal oxides known as transparent conducting oxides (TCOs), such as Sn-doped In_2O_3 (ITO) must be considered. Unlike metals, the electrical transport properties of TCOs can be adjusted easily by doping, thus making their optical properties tunable as well [1].

A different class of metal oxides opens the possibility of active tunability and switching of the plasmonic behavior. This class of semiconducting metal oxides which exhibit a temperature dependent metal-insulator transition (MIT) are commonly referred to as phase change materials. Among MIT materials, VO_2 is the most studied given that it can be processed into thin films form with a reduced MIT near room temperature, making VO_2 films very attractive for active devices such as optical switches, photoconductive emitters, and modulators. To this end, we have shown how VO_2 growth conditions can affect not only the transition temperature and switching magnitude but also the switching speed. In particular, the influence of strain and the use of near lattice matched substrates and buffer layers to modify the intrinsic VO_2 film properties has been demonstrated [2]. Furthermore, the phase transition dynamics of strained and relaxed VO_2 films have been compared together with analysis of the electrical conductivity of VO_2. In strained VO_2 films, the electrical conductivity can be modulated by a factor of one hundred in less than 500 fs [3]. Based on these properties, we selected ITO and VO_2 as the types of metal-oxides for studying their behavior once patterned into metasurfaces.

Large scale plasmonic metasurfaces can be made by directed self-assembly [4]. The molecular control offered by directed self-assembly enables sub-nanometer control of the separation between individual gold nano-spheres. These narrow gaps enable extreme field enhancement and as such are sensitive to the properties of their surrounding environment. In this way, these metasurfaces can serve to probe the refractive index of their environment. Because the direct self-assembly of these plasmonic metasurfaces rely on surface tension during the assembly process, it can be difficult to spatially pattern these films due to the complex wetting behavior of patterned photoresist layers. Fortunately, DLIP provides a clean and efficient means to pattern plasmonic gratings out of these self-assembled monolayers.

2.2. Direct Laser Interference Machining (DLIP)

The DLIP technique is a derivative of laser interference lithography or LIL, both of which rely on the interference of two or more laser beams to form periodic structures on a surface. By using higher intensity laser sources, DLIP is able to use the standing wave pattern existing at the intersection of two or more laser beams to remove material by ablation and generate periodic patterns with a defined long-range order on the scale of typical microstructures given by the interference periodicity [5].

3. Results and Discussion

Thin films ranging of various thickness (25-150 nm for ITO and 25-100 nm for VO_2) were deposited via PLD. For the gold self-assembled monolayers, the films were prepared by directed self-assembly [4]. The films were patterned via DLIP into regular gratings with ~300 nm wide film lines spaced ~600 nm from center-to-center, see Figure (1). Similar patterns were achieved with DLIP on the VO_2 and the gold nanoparticle films. The optical properties of each of the resulting films was determined via spectroscopic ellipsometry. The effective index of the films after patterning via DLIP into a given metasurface was determined assuming an anisotropic layer of the appropriate thickness for each material.

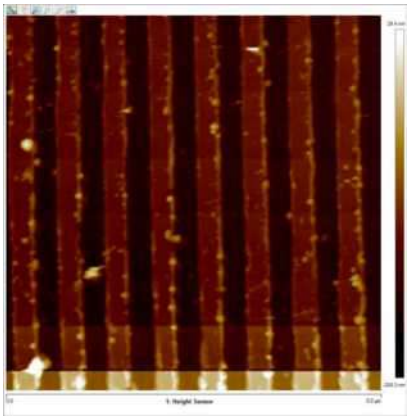


Figure 1: Atomic force micrograph of an ITO film processed via DLIP

When illuminated, the DLIP patterned surfaces exhibited classical diffraction along with the spectral dispersion modified by the metasurface as expected. Finally, multilayer test structures were fabricated to characterize the effect of the plasmonic metasurface on the optical switching properties of VO_2. The three-layer test structures consisted of a titanium nitride ground plane, a VO_2 spacer, and a gold thin film capping layer. In this configuration, the gold thin film served as the metasurface for the entire stack after it was patterned into a periodic grating.

4. Summary

We have shown how DLIP can be used to generate various metasurfaces comprising of different thin film materials including ITO, VO_2 and self-assembled gold nanoparticles, without negatively impacting their plasmonic properties. The behavior of each of these plasmonic metasurfaces will be compared and their response will be analyzed under this work.

Acknowledgements

This work was funded by the Office of Naval Research (ONR) through the Naval Research Laboratory Basic Research Program

References

[1] H. Kim, M. Osofsky, S.M. Prokes, O.J. Glembocki, and A. Piqué, "Optimization of Al-doped ZnO films for low loss plasmonic materials at telecommunication wavelengths," Appl. Phys. Lett., 102 (17), 171103, 2013.

[2] E. Breckenfeld, H. Kim, K. Burgess, N.A. Charipar, S.-F. Cheng, R. Stroud, and A. Piqué, "Strain effects in epitaxial VO2 thin films on columnar buffer-layer TiO_2/Al_2O_3 virtual substrates," ACS Appl. Mat. & Interfaces 9 (2), 1577-1584, 2016.

[3] R.J. Suess, N.S. Bingham, K.M. Charipar, H. Kim, S.A. Mathews, A. Piqué, and N.A. Charipar, "Ultrafast Phase Transition Dynamics in Strained Vanadium Dioxide Films," Advanced Materials Interfaces, 4 (22), p. 1700810, 2017.

[4] D. Doyle, N. Charipar, C. Argyropoulos, S.A. Trammell, R. Nita, J. Naciri, A. Piqué, J.B. Herzog, J. Fontana, "Tunable Subnanometer Gap Plasmonic Metasurfaces," ACS Photonics 5 (3), 1012-1018 (2018)

[5] A.F. Lasagni, C. Gachot, K.E. Trinh, M. Hans, A. Rosenkranz, T. Roch, S. Eckhardt, T. Kunze, , M. Bieda, D. Günther, , V. Lang, & F. Mücklich, "Direct Laser Interference Patterning, 20 Years of Development: From the Basics to Industrial Applications," SPIE Proc. 10092, 109211, 2017.

Fully CMOS compatible high-*Q* photonic crystal nanocavity devices and their applications

Takasumi Tanabe*, Nurul Ashikin Binti Daud, Hajime Kumazaki, and Shengji Jin,

Department of Electronics and Electrical Engineering, School of Science and Technology, Keio University, Yokohama, Japan
*corresponding author, E-mail: takasumi@elec.keio.ac.jp

Abstract

Although it has been claimed that silicon photonic crystal nanocavity devices are compatible with complementary metal-oxide semiconductors, it remains a challenge to make the structure and the fabrication fully compatible. We demonstrate a photolithographically fabricated photonic crystal nanocavity device that has a high quality factor even when clad with silicon dioxide. These characteristics make it possible to integrate this device with other silicon photonic devices.

1. Introduction

Silicon (Si) photonics is considered a promising candidate as a key technology with which to develop optical interconnects due to the mature state of nanofabrication, together with the unique characteristics of Si, namely a high refractive index and a low absorption loss at telecom wavelengths. Today, researchers are working towards accomplishing complementary metal-oxide-semiconductor (CMOS) compatible fabrication. On the other hand, Si photonic crystal (PhC) has been attracting a lot of attention since it enables us to use even smaller devices because it can realize high-*Q* nanocavities with a small mode volume [1]. The use of high-*Q* nanocavities will facilitate various functional operations at a very low power [2].

Hence, the integration of a Si PhC with Si photonics will allow us to expand the functionality of Si photonic systems. Although it is often claimed that existing Si PhC devices are compatible with CMOS and Si photonics, several challenges need to be met before complete integration is achieved.

2. CMOS compatible high-*Q* PhC nanocavity

The key device throughout this study is a CMOS compatible high-*Q* PhC nanocavity fabricated on a silicon chip [3]. The meaning of CMOS compatibility includes both fabrication and structure. Fabrication is undertaken using a photolithographic process that will allow integration with other silicon photonic devices and also allow future mass producibility. The device structure is clad with SiO_2; this is different from previous structures, which required an air-bridge process. Higher stability is achieved thanks to the clad structure.

Now we can use a silicon photonics foundry process, which allows us to conduct a study without having our own expensive nanofabrication facilities.

The fabricated device is shown in Fig .1(a). The SiO_2 cladding is removed simply to facilitate observation with a scanning electron microscope (SEM). A waveguide-width modulated line defect cavity [4] is designed to obtain a high *Q*. The theoretical *Q* is 8.1×10^5, where a *Q* of 2.2×10^5 is obtained from the transmittance spectrum in Fig 1(b) [3]. We confirmed that the light is indeed localized in the cavity, by observing the light field from the top of the slab as shown in Fig. 1(c).

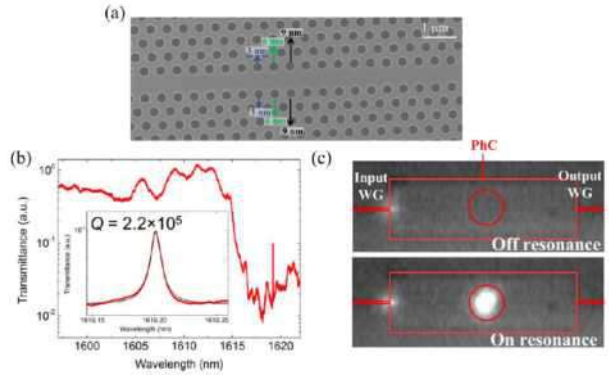


Fig. 1: (a) SEM image of the PhC nanocavity. (b) Transmission spectrum of the structure. The inset is an enlarged view of the peak transmission. It shows that cavity resonance occurred at a wavelength of 1619.20 nm. *Q* is 2.2×10^5. (c) Image of on and off resonance from the IR camera. With on resonance, the light is localized at the cavity.

The use of a standard Si photonics foundry allows us to integrate the photonic components with electrical heaters and *p-i-n* junctions, which will enable us to fabricate various active devices.

3. DeMUX filter

Figure 2(a) shows a fabricated eight-channel DeMUX filter [5]. PhC nanocavities are placed along the bus waveguide to drop light at different wavelengths from the input bus waveguide. Since the device is composed of small PhC nanocavities, its footprint is extremely small. The resonance of the cavity can be controlled with integrated heaters.

By carefully optimizing the structure we obtained the transmittance spectra shown in Fig. 2(b), where the power penalty was about -5.5 dB.

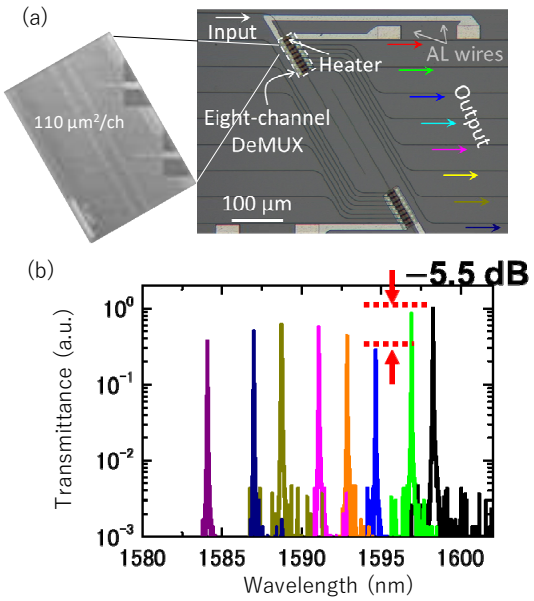


Fig. 2: (a) Fabricated PhC nanocavity based DeMUX filter, which is an eight-channel device integrated with heaters. (b) The transmittance spectrum of the device.

4. Electro-optic modulator

When a PhC nanocavity is integrated with a pin junction, it can be used as an electro-optic modulator when carriers are injected into the *pin* structure [6, 7]. Figure 3 shows the experimental setup that we used to realize electro-optic modulation with a PhC nanocavity. The result is shown in Fig. 3(b) where a 0.5 GHz modulation is demonstrated. Although the speed is not high, it is based on the carrier-plasma dispersion effect, and so it can cover GHz frequencies.

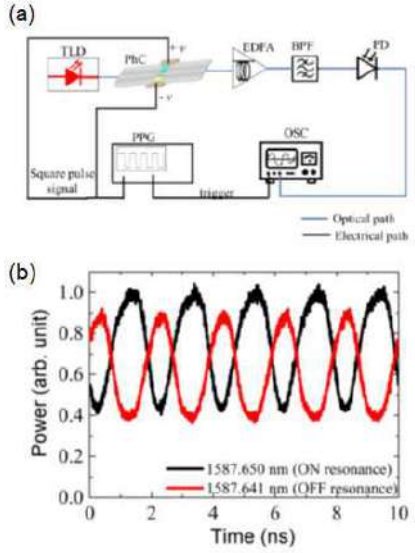


Fig. 3: (a) Block diagram of the experimental setup. A square pulse wave is applied and the output is recorded with an oscilloscope. (b) Modulated optical signal when a 0.5-GHz modulation frequency is applied. The black and red lines represent ON and OFF modulation when the input wavelength is set at the resonance and detuned -0.01 nm away from the resonance, respectively

5. Photo-receiver

A pin integrated photonic crystal nanocavity can also be used as a photo-receiver [8, 9]. Although Si is transparent at telecom wavelengths, photo-carriers can be generated due to two-photon absorption (TPA) because the light confinement of a PhC nanocavity is very strong. The TPA coefficient is usually too small to allow this phenomenon to be used for photo-receiver operation, but this is not the case when we use a high-Q PhC nanocavity. The device can outperform others in terms of minimum detectable power, because it has a monolithic silicon structure, which allows us to obtain a small dark current.

Figure 4(a) shows the responsivity of the device, where a sensitivity of 13.4 mA/W is obtained in a linear regime and a minimum detectable power at about the μW level is demonstrated. Figure 4(b) shows the recorded signal when we apply an optical signal modulated with pseudo random bit sequence. Since the PhC operates as an optical WDM filter, we can selectively detect a single wavelength (channel).

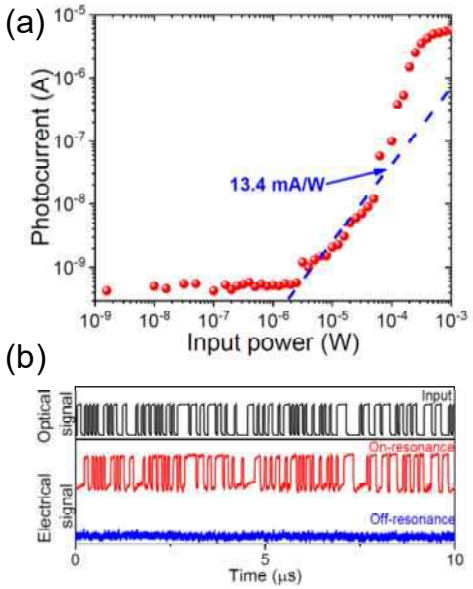


Fig. 4: (a) Responsivity of all-Si PhC nanocavity pin receiver at a telecom wavelength. (b) Photoreceiver operation when a random pulse sequence is input into the device.

References

[1] T. Tanabe, *et al.*, Nature Photon. **1**, 49 (2007).

[2] K. Nozaki, *et al.*, Nature Photon. **4**, 477 (2010).

[3] Y. Ooka, *et al.*, Sci. Rep. **5**, 11312 (2015).

[4] E. Kuramochi, *et al.*, Appl. Phys. Lett. **88**, 041112 (2006).

[5] Y. Ooka, *et al.*, Opt. Express, **25**, 1521 (2017).

[6] T. Tanabe, *et al.*, Opt. Express 17, 22505 (2009).

[7] N. A. B. Daud, *et al.*, IEICE Trans. Electron. **E100-C**, 670 (2017).

[8] T. Tanabe, *et al.*, Appl. Phys. Lett. **96**, 101103 (2010).

[9] N. A. B. Daud and T. Tanabe, AIP Adv. **8**, 105224 (2018).

Modulating Propagating Surface Plasmons on Silver Nanowires

Qiang Li[1,2], Li Chen[3], Hongxing Xu[4], Zhaowei Liu[3], and Hong Wei[1,*]

[1]Institute of Physics, Chinese Academy of Sciences, Beijing 100190, China
[2]School of Information and Optoelectronic Science and Engineering, South China Normal University, Guangzhou 510006, China
[3]Materials Science and Engineering, University of California, San Diego, La Jolla, California 92093, United States
[4]School of Physics and Technology, and Institute for Advanced Studies, Wuhan University, Wuhan 430072, China
*corresponding author, E-mail: weihong@iphy.ac.cn

Abstract

Due to the photothermal property of silver nanowire, the local temperature is increased under the excitation of a control laser beam, which results in the increase or decrease of the intensity of the transmitted surface plasmons on the nanowire generated by a probe laser beam. The amplitude of the photothermal modulation depth is found to be strongly dependent on the focal positions, polarizations, and power of the control beam.

Plasmonic devices have received much attention in recent years due to their ability to confine light beyond the diffraction limit. Manipulating the propagation of surface plasmons (SPs) is of great importance for developing integrated nanophotonic devices. Metal nanowires (NWs) with the size of cross section well below the diffraction limit are highly-compact nanowaveguides for long distance propagation of SPs. The metal NW can be regarded as a Fabry-Pérot resonator with the propagating SPs partly reflected back and forth between the two NW terminals. The fundamental properties of the propagating SPs on metal NWs and some SPs signal processing functionalities in metal NW networks have been studied [1, 2]. The propagating SPs on metal NWs have also been used to control the photoluminescence of single quantum emitters, due to their nanoscale field confinement and microscale propagation length [3].

The active control of propagating SPs is a crucial step toward the realization of highly integrated nanophotonic circuits. This talk will present our study on modulating the propagating SPs on a silver NW using the photothermal property of the NW. Due to the Fabry-Pérot resonances of the SPs on the NW, the intensity of the transmitted SPs generated by a probe laser beam can increase or decrease under the excitation of a control laser beam. We systematically investigated the dependence of the modulation depth on the focal positions, polarizations, and power of the control beam. Both numerical simulation and theoretical analysis were performed, which agree well with the experimental results and provide basic understanding about the photothermal response of propagating SPs.

Acknowledgements

This work was supported by Ministry of Science and Technology of China (Grant 2015CB932400), National Natural Science Foundation of China (Grants 11422436, 11774413, 11674256, and 11704133), the Prominent Young Scientist Program and the "Strategic Priority Research Program (B)" (Grant XDB07030100) of Chinese Academy of Sciences, the New Star of Science and Technology Program of Beijing Municipal Science and Technology Commission, and the Foundation for Distinguished Young Talents in Higher Education of Guangdong (Grant 2016KQNCX031).

References

[1] H. Wei, D. Pan, S.P. Zhang, Z.P. Li, Q. Li, N. Liu, W.H. Wang, H.X. Xu, Plasmon Waveguiding in Nanowires, *Chem. Rev.* 118: 2882-2926, 2018

[2] L. Gao, L. Chen, H. Wei, H.X. Xu, Lithographically Fabricated Gold Nanowire Waveguides for Plasmonic Routers and Logic Gates, *Nanoscale* 10: 11923-11929, 2018

[3] Q. Li, D. Pan, H. Wei, H.X. Xu, Plasmon-Assisted Selective and Super-Resolving Excitation of Individual Quantum Emitters on a Metal Nanowire, *Nano Lett.* 18: 2009-2015, 2018

Laser induced nanostructuring of plasmonic composite films for color image multiplexing

Nipun Sharma[1], Marie Vangheluwe[2], Mathieu Bugnet[3], Alice Vermeulin[2], Nathalie Destouches[1]

[1]Univ Lyon, UJM-Saint-Etienne, CNRS, Institut d Optique Graduate School, Laboratoire Hubert Curien UMR 5516, F-42023 Saint-Etienne, France
[2]HID Global CID, 92150 Suresnes, France
[3]Univ Lyon, INSA Lyon, Univ Claude Bernard Lyon 1, MATEIS UMR CNRS 5510, F-69621 Villeurbanne, France
*corresponding author, E-mail: nathalie.destouches@univ-st-etienne.fr

Abstract

Plasmonic and interferometric colors are of great interest for their vibrancy, stability over time and their potential dichroic properties. Here, we present a laser-based technology that allows controlling the colors of plasmonic nanocomposite films and to print multiplexed images observable under white light independently in reflection, transmission or diffraction. Two approaches described here, leads either to hide diffractive images in a homogeneous reflective area or to encode three different images selectively displayed in reflection or polarized transmission on the same area.

1. Introduction

Hiding several images in a single printing, which appear selectively under different angles of observation, is of great interest for applications to security, data storage or design. Several techniques have been developed based on holography [1], moiré methods [2], multiple laser image (MLI) systems [3] or on the use of dichroic plasmonic colors [4-5]. A technology combining plasmonic nanocomposite films and laser scanning is presented here. It provides a simple implementation for printing multiplexed images with high flexibility and a micrometric spatial resolution. It is based on the shaping by ultra-short laser pulses of metallic Ag nanoparticles within thin TiO_2 films and the triggering of self-organization mechanisms that lead to very regular periodic patterns controlled at the sub-wavelength scale. Here, we present the main physico-chemical mechanisms that contribute to the shaping of plasmonic films at the nanometer scale and we show how such a laser technology allows engineering plasmonic colors and reinventing image multiplexing.

2. Experimental section

The initial films in which colors are produced by laser processing are mesoporous films of amorphous TiO_2 synthesized by a sol-gel process and coated on transparent flexible substrates. Their porosity is filled with metallic silver precursors by soaking the film in a silver salt solution. Small Ag nanoparticles are created inside the film volume prior to laser irradiations to create absorbers of visible light. A focused femtosecond (200 fs) laser at 515 nm wavelength scanning the sample surface is used to initiate the growth, reshaping and organization of nanoparticles within the film. The irradiation parameters are far below the damage threshold of the film and substrate. The formed nanostructures and their colors differ depending on the scanning speed, laser power, polarization, focusing, repetition rate or density of the drawn lines [6].

3. Results and Discussion

3.1. Laser-driven plasmonic gratings for multiple images hiding

The laser parameters can be tuned to trigger the formation of self-organized gratings on the film surface, which result from the excitation of transient surface plasmon polaritons during the pulse duration. These self-organized surface gratings have a period very close to the laser wavelength (495 ± 15 nm) and their orientation is perpendicular to the laser polarization, whatever the scanning direction [6]. This control of the grating orientation is used to encode grey-level images that can be observed in diffraction. Such a methodology is used to print three interlaced images, whose 256 grey-levels are converted into 256 grating orientations ranging over 15° and starting for each image at 0°, 60° and 120° respectively. The printed area displays successively the three different pictures shown in Figure 1 when observed in diffraction and, when rotating the sample in its plane with an azimuthal angle varying from 0° to 120°. The negative images are obtained at angles 15°, 75°, and 135°, respectively, and the color of the diffracted images can be changed by varying the angle of observation in the incidence plane. The low grating period actually ensures a high angular dispersion, and well-separated colors. Moreover, all images being printed with the same fluence, scanning speed, spacing between laser lines, and repetition rate (only the polarization angle being tuned), the sample appears fully homogeneous in reflection and transmission, thus

hiding the three images. This technology can be implemented on glass as well as on flexible polycarbonate substrates [7].

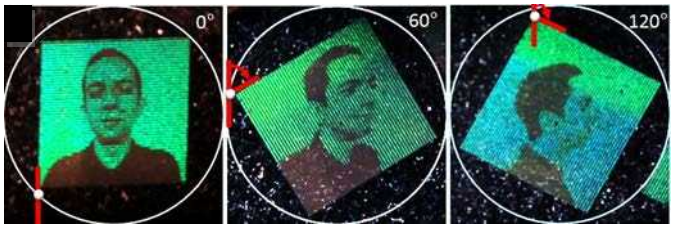


Figure 1: Photographs of a sample recorded in a diffraction configuration for three different azimuthal angles obtained by rotating the sample in its plane. The three different images appear at 0°, 60° and 120°, respectively.

3.2. Laser-driven plasmonic color management for image multiplexing

Such laser process can also result in the generation of micrometer size plasmonic nanostructured areas where the film birefringence and dichroism can be controlled at will, to produce unprecedented color gamuts that satisfy conditions for three-fold image multiplexing in three selected modes of observation under white light: reflection under non-polarized light and transmission between polarizers for two different polarization angles. The conditions that the color gamuts in the three modes must fulfil to produce three-fold image multiplexing are explained, followed by how such conditions can be satisfied with laser-controlled plasmonic colors. Three-fold image multiplexing (Figure 2) is shown using different color combinations [4]. Such laser processing is also applied to print dual multiplexed color images, for which more colors can be used. This methodology could be implemented with other technologies like electron beam lithography with a larger freedom on the choice of colors, along with a higher spatial resolution. Laser technologies however hold advantage for being more suitable for rapid and contactless printing on large surfaces.



Figure 2: Photographs of multiplexed images obtained with a single printing on a single layer. Each pixel of the printed encoded image contains three different colors, each of them being displayed in one of the modes. A large number of well-suited nanostructures allows getting all possible combinations of colors in the three modes and displaying three independent images. The first image is observed in reflection, the next two ones in transmission between two polarizers, while the sample is rotated in its plane.

4. Conclusion

Here a scanning laser technique is presented, that allows printing plasmonic colors on large areas. The singular optical properties of these colors and their ability to vary in different manners depending on the mode of observation and illumination in which they are observed allows printing interlaced diffractive images or multiplexed images that can be observed independently in reflection and transmission.

Acknowledgements

The authors acknowledge the Region Auvergne Rhone-Alpes, ANR project MIXUP (ANR-18-CE39-0010) and LABEX MANUTECH-SISE (ANR-10-LABX-0075) of Université de Lyon, within the program Investissements d'Avenir (ANR-11-IDEX-0007). The authors are grateful to F. Vocanson from the Laboratory Hubert Curien for elaborating the TiO_2 films.

References

[1] W. T. Chen, K. Y. Yang, C. M. Wang, Y. W. Huang, G. Sun, I. Da Chiang, C. Y. Liao, W. L. Hsu, H. T. Lin, S. Sun, L. Zhou, A. Q. Liu and D. P. Tsai, Nano Lett., 2014, 14, 225–230S.V. Patankar, *Numerical Heat Transfer and Fluid Flow*, Hemisphere Publishers, New York, 1980.

[2] S. M. Chosson and R. D. Hersch, ACM Trans. Graph, 2014, 34, 1–11.

[3] M. Li, Y. Meuret, R. Geelen, J. Jung, M. Vervaeke, H. Thienpont and F. Duerr, Appl. Opt., 2015, 54, 6162–6171.

[4] E. Heydari, J. R. Sperling, S. L. Neale and A. W. Clark, Adv. Funct. Mater., 2017, 27, 1–6

[5] X. M. Goh, Y. Zheng, S. J. Tan, L. Zhang, K. Kumar, C. W. Qiu and J. K. W. Yang, *Nat. Commun.*, 2014, **5**, 5361

[6] Z. Liu, J. Siegel, M. Garcia-Lechuga, T. Epicier, Y. Lefkir, S. Reynaud, M. Bugnet, F. Vocanson, J. Solis, G. Vitrant and N. Destouches, *ACS Nano*, 2017, **11**, 5031–5040

[7] N. Sharma, M. Vangheluwe, F. Vocanson, A. Cazier, M. Bugnet, S. Reynaud, A. Vermeulin, N. Destouches, Mater. Horizons, DOI: 10.1039/C9MH00017H (2019)

Acousto-plasmonics: from acoustic metasurfaces to chirality in coherent phonon generation experiments

K. O'Brien[1], J. Rho[1], H. Suchowski[1], X. Zhang[1], A. L. Jimenez[2], A. Garcia-Martin[2], and N. D. Lanzillotti-Kimura[3]

[1]Nanoscale Science and Engineering Center, 3112 Etcheverry Hall, University of California, Berkeley, California, USA
[2]IMN-Instituto de Micro y Nanotecnología (CNM-CSIC), Isaac Newton 8, PTM, E-28760 Tres Cantos, Madrid, Spain
[3]Centre de Nanosciences et de Nanotechnologies (C2N), CNRS, Univ. Paris-Sud, Univ. Paris-Saclay, 91120 Palaiseau, France
*corresponding author, E-mail: daniel.kimura@c2n.upsaclay.fr

Abstract

We propose the integration of plasmonics concepts into the field of nanophononics using metallic nanoresonators as coherent phonon generators and detectors. Picosecond ultrasonics tools give direct access to the study of phonon propagation both in the time and frequency domains, and to the spatial distribution of strain in nanostructures.

1. Introduction

The development of micro- and nanofabrication techniques enabled the study of nanostructures where it is possible to engineer the acoustic phonon dynamics –acoustic waves with nanometric wavelengths and frequencies in the GHz-THz range). In these structures it is also possible to engineer the plasmonic properties and control both the dynamics and the interactions between the photonic and phononic fields. Picosecond ultrasonics tools gave direct access to the study of phonon propagation both in the time and frequency domains, and to the spatial distribution of strain in nanostructures.[1-2]

2. Acousto-plasmonic engineering

We propose the integration of plasmonics concepts into the field of nanophononics using metallic nanoantennas as coherent phonon generators and detectors. The polarization-dependent optical resonances and the phononic modes of metallic nanostructures are determined by their geometry –size and shape– and material properties -index of refraction and sound velocity, respectively–. We show how an array of metallic optical nanoantennas optimized to work at visible wavelengths can be tailored to generate and detect acoustic phonons of variable frequencies in the GHz range, and how the interactions of these modes with plasmons can be put in evidence. We also discuss how the selection of the geometrical parameters of the crosses enables the design and engineering of optimized hypersound sources, with tailored and tunable spectra. We find that the detected phonon spectrum changes significantly when the polarization of the probe light is rotated 90 degrees. This ability to distinguish in the far field the response from local regions of nanostructures is a powerful metrology tool. The presented results expand the toolbox for the design of novel nanophononic systems and the development of opto-acoustically functionalized surfaces.

The possibility to create and manipulate nanostructured materials encouraged the exploration of new strategies to control the electromagnetic properties. Among the most intriguing nanostructures are those that respond is a different way to helical polarization, i.e. exhibit chirality. These structures have been used to boost the signal of an enantiomer over the other to be able to enhance detection. [3-7] Very recently, it has been put forward that planar chiral nanostructure can also present similar extinction properties, but in one enantiomer it would come from absorption, whereas in the other from scattering.[6]

Here we present a simple structure based on crossed bars exhibiting the same property, in a definite spectral range. Due to selective absorption and scattering, the plasmonic modes excited in the bars will depend on light handedness. The coherent generation of acoustic phonons using pulsed lasers strongly relies on how efficiently light is absorbed and scattered by a structure. The proposed structure opens the way to enhanced and selective coherent phonon excitation and detection. [8].

References

[1] K. O'Brien, N.D. Lanzillotti-Kimura, J. Rho, H. Suchowski, X. Yin, X. Zhang, Ultrafast acousto-plasmonic control and sensing in complex nanostructures, *Nature communications* 5: 4042, 2014.

[2] N.D. Lanzillotti-Kimura, K.P. O'Brien, J. Rho, H. Suchowski, X. Yin, X. Zhang, Polarization-controlled coherent phonon generation in acoustoplasmonic metasurfaces, *Phys. Rev. B* 97: 245403, 2018

[3] N. Liu, et al., Stereomaterials, *Nat. Photon.* 3: 157, 2009

[4] Z. Fan and A. Govorov, Plasmonic circular dichroism of chiral metal nanoparticle assemblies, *Nano Lett.* 10: 2580, 2010

[5] A. Guerrero-Martínez et al., From individual to collective chirality in metal nanoparticles, *Nano Today* 6: 381, 2011

[6] V.K. Valev et al., Chirality and Chiroptical Effects in Plasmonic Nanostructures: Fundamentals, Recent Progress, and Outlook, *Adv. Mater.* 25: 2517, 2013

[7] G. Armelles, et al., Interaction effects between magnetic and chiral building blocks: a new route for tunable magneto-chiral plasmonic structures, *ACS Photonics* 2: 1272, 2015

[8] B. Hopkins, et al., Circular dichroism induced by Fano resonances in planar chiral oligomers, *Laser Photonics Rev.* 10: 137, 2016

Non-invasive Bio-imager Based on Frequency-tunable Terahertz Plasmonics

Yukio Kawano[1*]

[1]Laboratory for Future Interdisciplinary Research of Science and Technology, Tokyo Institute of Technology, Tokyo, Japan
*corresponding author, E-mail: kawano@pe.titech.ac.jp

Abstract

We report on a frequency-tunable non-circular plasmonic structure for multi-frequency terahertz (THz) analysis on a sub-wavelength scale. In spite of much interest in plasmon-based THz technologies, a main shortcoming of conventional devices is that they exhibit poor frequency-tunability in fixed structures. We here demonstrated that the frequency of THz plasmonic resonance is tunable according to the angle of polarization of the incident THz wave, which enhanced the flexibility in near-field THz applications. Biological and medical applications with this method are presented.

1. Introduction

Recently, applications of plasmon-based technologies have been attracting much attention because of their plasmon-mediated ability to strongly confine an electromagnetic wave [1-4], which enables highly sensitive evanescent-field detection and analysis. Such studies on a scale beyond the diffraction limit have been in strong demand, especially in research fields such as nano-materials characterization, chemical spectroscopy, and biological and medical analysis. Interest in medical applications is growing particularly rapidly, further pushing such demand. However, resonant frequency tuning in plasmonic devices has not been fully established, which limits the availability and flexibility of plasmon-based sub-wavelength applications.

Here we report on a continuously frequency-tunable plasmonic structure in THz region and its application to a non-invasive bio-imager [5,6]. By developing a non-circular shaped structure with a subwavelength aperture surrounded by continuously varied, concentric plasmonic grooves, we demonstrated that the resonant frequency of the plasmon-mediated THz concentration becomes freely tunable, which largely enhances its usefulness for evanescent-field THz sensing and analysis.

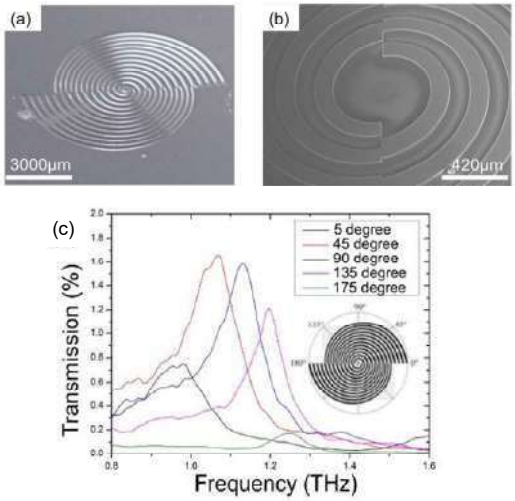


Figure 1: (a) Photograph of the frequency-tunable non-circular plasmonic structure. (b) Magnified image of (a). (c) Transmission spectra for (a) with different polarization direction of the incident THz wave.

2. Results

Figure 1 displays our frequency-tunable plasmonic structure. One of the key features of this device is its non-circular shaped design. Due to its smoothly varied grooves, the

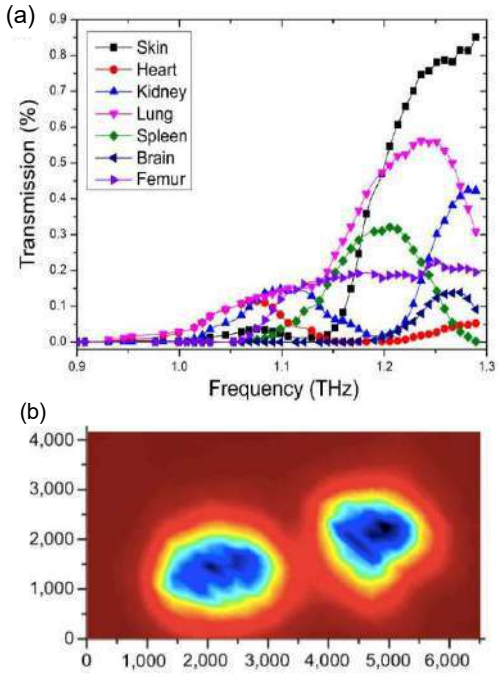


Figure 2: (a) THz spectroscopy of sections of mice organ tissues, taken by rotaging the non-circular plasmonic device in Fig. 1(a). (b) THz imaging of the mouse-tail transverse sections using the device in Fig. 1(a).

groove period continuously changes by simply changing the rotation of the non-circular plasmonic structure relative to the diameter direction. This design results in continuously frequency-tunable characteristics in a much convenient manner. The device also increases the electric field intensity at the subwavelength aperture, thus significantly amplifying the transmission.

In order to utilize this device for observations and analysis of biological tissues, we measured THz transmission spectra for several mouse organs (Fig. 2(a)). We successfully observed distinct biological-tissue-dependent THz spectra through the interaction between the frequency-tunable plasmons and bio-samples. We further performed THz mapping of mouse tails (Fig. 2(b)). The obtained image showed that hair (yellow and red), skin (light blue), and bone (dark blue) were clearly distinguished.

3. Conclusions

The above advantages demonstrate that our frequency-tunable non-circular plasmonic metasurface with rotational symmetry breaking can increase the availability of evanescent-field THz detection with much more convenient and simple operation. This is promising for practical applications in future THz medical devices for daily heath monitoring and intraoperative mapping. Our structure can be modified to fit most frequency ranges for surface plasmons by changing the diameter and depth of the non-circular shaped grooves, and therefore can be utilized in wide-band, frequency-selective applications including microwave, infrared, and visible light.

Acknowledgements

This work was supported in part by the JST-Mirai Program, the Matching Planner Program, and the Center of Innovation Program from the Japan Science and Technology Agency, JSPS KAKENHI Grant Numbers JP16J09937, JP17K19026, JP17H02730, JP16H00798, JP16H00906 and JP18H03766 from the Japan Society for the Promotion of Science, the Murata Science Foundation, and Support for Tokyo Tech Advanced Researchers (STAR). We acknowledge technical support from the Semiconductor and MEMS Processing Center of Tokyo Institute of Technology.

References

[1] R. Stanley, “Plasmonics in the mid-infrared”, Nature Photonics, Vol. 6, 409–411, 2012.

[2] S. Maier, “Plasmonics: Fundamentals and Applications”, Springer, 2007.

[3] K. Ishihara, G. hatakoshi, T. Ikari, H. Minamide, H. Ito, and K. Ohashi, “Terahertz Wave Enhanced Transmission through a Single Subwavelength Aperture with Periodic Surface Structures”, Jpn. J. Appl. Phys. Vol. 44, 1005, 2005.

[4] T. Iguchi, T. Sugaya, and Y. Kawano, “Silicon-immersed terahertz plasmonic structures”, Appl. Phys. Lett. Vol. 110, 151105, 2017.

[5] X. Deng, S. Oda, and Y. Kawano, “Frequency Selective, High Transmission Spiral Terahertz Plasmonic Antennas”, Journal of Modeling and Simulation of Antennas and Propagation, Vol. 2, 1–6, 2016.

[6] X. Deng, L. Li, M. Enomoto, and Y. Kawano, “Continuously Frequency-Tuneable Plasmonic Structures for Terahertz Bio-sensing and Spectroscopy”, Scientific Reports, Vol. 9, 3498-1-9, 2019.

Superconducting thin films and nanowires for mid-infrared single photon detection.

Dmitry Morozov[1], Gregor Taylor[1], Archan Banerjee[1], Kleanthis Erotokritou[1], Umberto Nasti[1], Shigehito Miki[2,3], Hirotaka Terai[2], and Robert H. Hadfield[1]

[1]School of Engineering, University of Glasgow, Glasgow, UK
[2]Advanced ICT Research Institute, National Institute of Information and Communications Technology, Kobe, Japan
[3]Graduate School of Engineering Faculty of Engineering, Kobe University, Kobe, Japan
*corresponding author, E-mail: Dmitry.Morozov@glasgow.ac.uk

Abstract

Superconducting nanowire single-photon detectors (SNSPDs) are typically made from an ultra-thin superconducting film (with thickness of 4 to 10 nm) patterned into a ~50 – 200 nm wide nanowire. An example of such nanowire in a form of a meander is shown on Figure 1(a). The detection mechanism is based on creation of the normal resistive domain across the superconducting current carrying nanowire upon absorption of the photon as shown on Figure 1(b). In turn, normal domain across the nanowire causes the voltage pulse in the readout circuit to appear (Figure 1(c, d)). Sometimes, fluctuations without photon absorption cause the formation of a normal domain; these events are dark counts [1]. SNSPDs are capable of counting photons from ultraviolet (UV) to mid-infrared (mid-IR) and offering unparalleled performance at telecom wavelength in comparison to other available photon counting technologies [2, 3]. At wavelengths of 1310 and 1550 nm detection efficiency (QE) as high as 94% can be achieved [4, 5], with low dark count rate (DCR) of < 100Hz, sub 3ps timing jitter [6] and close to GHz count rate [7]. Furthermore, superconducting nanowires can be integrated into optical waveguide circuits [8] and are compatible with optical nano-antennas [9]. Extension of SNSPD operation into mid-IR (2 – 10 μm) will open new avenues in photonics and quantum communication including mid-IR single-photon laser ranging (LIDAR), free space communication and characterization of mid-IR photon pair sources. Commonly SNSPDs are made with NbN films with transition temperature of 7-10 K. Such detectors have a peak performance at telecom wavelength but their performance sharply decreases at wavelengths longer than 2 μm. Fabrication of ultra-narrow 30 nm wide nanowires increases performance of NbN SNSPDs in the mid-IR [10] but pushes the boundary of robust planar fabrication capability. Another pathway to improve mid-IR performance is a usage of superconducting materials with smaller energy gap as this property helps to create more quasiparticles per absorbed photon.

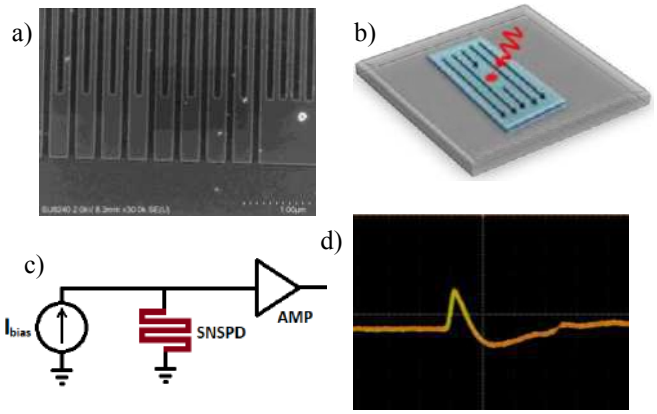


Figure 1: a) Scanning electron microscopy image of SNSPD device; b) schematic illustration of photon absorption by a current carrying superconducting nanowire: c) bias and readout circuit; d) voltage pulse registered at the output of an amplifier.

Here we report on the comprehensive study of superconducting materials and SNSPD devices for mid-IR. We report on thin sputtered films of NbTiN, TiN, NbN, MoSi and on TiN films grown by atomic layer deposition (ALD). We report on electrical transport and superconducting properties such as sheet resistance (R_s), critical temperature (T_c) and critical current (I_c) at low temperatures. Optical properties of the films were tested at room temperature with spectroscopic ellipsometry [11]. The wavelength dependence of refractive index and extinction coefficient of the ALD TiN films is shown on Figure 2. Using thin TiN and MoSi films we have fabricated a range of nanowires with various widths up to 400 nm and tested their low temperature electrical and optical performance.

For characterization of detectors in mid-IR (wavelength 2 – 4.2 μm) we have built a test setup based on pulsed picosecond optical parametric oscillator (OPO). We have designed, fabricated and tested SNSPD devices for mid-IR using NbTiN films. At wavelength of 2.3 μm these detectors have QE~1.5% and FWHM timing jitter of 280 ps. A pair of NbTiN detectors was used to characterize a photon pair source at 2.08 μm [12] and to demonstrate laser ranging at 2.3 μm [13]. The detection efficiency of our detectors can be further improved by engineering an optical cavity to enhance in-band photon absorption probability [14]. These initial results with TiN, MoSi and NbTiN films show that development of high performance mid-IR SNSPDs for photonic applications is within reach.

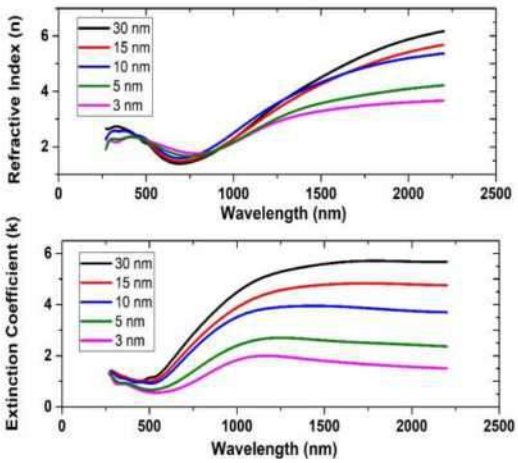


Figure 2: Refractive index and Extinction coefficient of ALD grown TiN films.

Acknowledgements

The authors acknowledge support through QuantIC, the UK Quantum technology Hub in Quantum Enhanced Imaging (EPSRC grant EP/M01326X/1). RHH acknowledges a European Research Council Consolidator Grant (IRIS 648604). Fabrication of the devices was carried out at the James Watt Nanofabrication Centre (JWNC) at the University of Glasgow.

References

[1] G. Goltsman *et al*, Appl. Phys. Lett.: 79, 705, 2001
[2] R. H. Hadfield, Nature Photonics: 3, 696, 2009
[3] C.M. Natarajan *et al*, Supercond. Sci. Technol.: 25, 063001, 2012
[4] K. Smirnov *et al*, Supercond. Sci. Technol.: 31, 035011, 2018
[5] F. Marsili *et al*, Nat. Photon.: 7, 210–4, 2013
[6] B. A. Korzh *et al*, arXiv:1804.06839
[7] A. Korneev *et al*, Microelectronic Engineering: 69, 274, 2003
[8] J. Li *et al*, Opt. Express: 24(13), 13931, 2016
[9] R. M. Heath e*t al*, Nano Lett.: 15(2), 819, 2015
[10] F. Marsili et al, Nano Letters: 12(9), 4799, 2012
[11] A. Banerjee *et al*, Optical Materials Express: 8, 2072, 2018
[12] S. Prabhakar *et al*, CLEO-2019 (accepted contribution)
[13] G. Taylor *et al*, CLEO-2019 (accepted contribution)
[14] K. Erotokritou *et al*, Supercond. Sci. Technol.: 31 125012, 2018

Defects of Single Walled Carbon Nanotubes: Photonic and Electronic Integration

Han Htoon

[1]Center for Integrated Nanotechnologies, Materials Physics and Application Division, Los Alamos National Laboratory, Los Alamos, New Mexico, 87545, United States

Single walled carbon nanotubes with covalently functionalized sp^3 defects have been rapidly emerging as a new class of transformational optical materials. Particularly, recent demonstration of room temperature, 1.55 μm single photon generation establish these covalent defects of SWCNTs as promising fundamental building blocks for defect driven quantum information technologies such as quantum key distribution. Defects also provide a significant boost in photoluminescence quantum yield (from <1% to ~28%) and emission stability, making envisioned applications of SWCNTs in optoelectronics, sensing, and imaging technologies more feasible. The key to full exploitation of these technological potential lie in the ability to integrate these SWCNTs with defect into plasmonic/photonic cavities for enhancement of light matter interaction and into nano-electronic devices for electrical stimulation. Here in this talk I will report recent progresses we made together with our collaborators toward achieving this critical photonic and electronic integration. We have successfully integrated the SWCNTs with sp^3 defects into 2D slab photonic crystals[1] and metallo-dielectric antenna arrays.[2] In case of coupling with 2D photonic crystal, we were able to demonstrate room temperature single photon generation with 3meV linewidth defined by the cavity quality factor and 50 fold enhancement in emission.[1] We achieved narrowest low temperature emission linewidth of 35 μeV by coupling the defects with metallo-dielectric antennas.[2] We were also successful in fabricating single SWCNT field effect transistors using dielectrophoresis and attained electroluminescence from the sp^3 defects.

1. Ishii, A.; He, X.; Hartmann, N. F.; Machiya, H.; Htoon, H.; Doorn, S. K.; Kato, Y. K. Enhanced Single-Photon Emission from Carbon-Nanotube Dopant States Coupled to Silicon Microcavities. ***Nano Lett. 18***, 3873-3878 (2018).
2. Shayan, K.; He, X.; Luo, Y.; Rabut, C.; Li, X.; Hartmann, N.F.; Blackburn, J.L.; Doorn, S.K.; Htoon, H.; Strauf, S.; "Suppression of Pump-Induced Exciton Dephasing in Sidewall-Functionalized Single-Walled Carbon Nanotubes", ***Nanoscale 10***, 12631 (2018).

Graded metasurface for elastic energy harvesting

Jacopo Maria De Ponti1[1], Andrea Colombi [2]*, Richard Craster[1], Raffaele Ardito[3], Francesco Braghin[4], Alberto Corigliano[3]

[1]Dept of Mathematics, Imperial College London, United Kingdom
[2]Dept of Civil, Geomatic and Environmental Engineering, ETH, Zurich, Switzerland
[3]Dept of Civil and Environmental engineering, Politecnico di Milano, Italy
[4]Department of Mechanics, Politecnico di Milano, Italy
*Corresponding author, E-mail: andree.colombi@gmail.com

Abstract

Metamaterial designs combining graded arrays of resonators and elastic wave excitation allows a precise control of the propagation of mechanical waves in solid media. In this study metamaterial's broadband control capacities are used to design an innovative piezoelectric energy harvester.

1. Introduction

Recent years have witnessed an increasing popularity of metamaterial concepts, based on the so-called local resonance phenomenon, to control the propagation of electromagnetic, acoustics and elastic waves in artificially engineered media. While the momentum initially focused on the subwavelength bandgaps generated by the resonance, the research has delivered new forms of control, encompassing tailored graded designs to obtain spatially varying refraction index, wide bandgaps and mode conversion [1]. In the field of photonics and acoustic this transition has already taken place and new graded design allows a tailored control of the propagation of light, micro-waves and sound.
Elastic waves, are characterized by different compressional and shear wave speeds resulting in mode conversions at the interfaces. On the one hand this makes elastic metamaterials complex to model and the use of computational elastodynamics technique mandatory, on the other hand it offers new control possibilities not achievable in the electromagnetic or acoustic case [2,3].

2. Results

Starting from the seminal work on the resonant metawedge that supports both conversion and broadband reflection [2], we have restricted the problem to the case of a plate with graded rod-like resonators. This configuration has the twofold advantage of focusing the energy exactly on one resonator depending on the type of grading used, its slope and spatial extension. Each rod-like resonator has been complemented with a piezoelectric cantilever beam located at the top, also graded, to match the rod resonance strongly amplifying the motion (Fig. 1). This result in a doubly graded pattern that fosters harvesting over a broad spectrum of frequencies and hence a constant energy production when more rods are equipped with tip harvesters.
After an introduction of the control capacity of graded elastic metasurface, the talk will present the numerical optimization of the focusing capacity and the results from an experiment with this device in the kHz range.

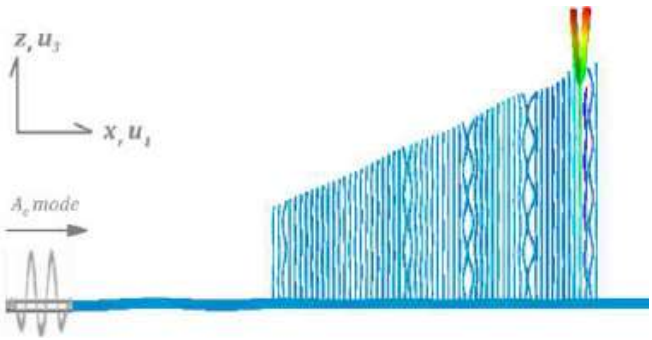


Figure 1: The elastic metasurface is made of a plate and an array of resonators of increasing height. A piezoelectric beam is inserted at the tip of the rod where the waves are concentrated.

References

[1] Colombi, A. Resonant metalenses for flexural waves. J. Acoust. Soc. Am. 140, EL423 (2016).
[2] A. Colombi, D. Colquitt, P. Roux, S. Guenneau, and R.V.Craster. A seismic metamaterial: The resonant metawedge. *Sci. Rep.,* 6:27717, (2016).
[3] E A Skelton, R V Craster, A Colombi, and D J Colquitt. The multi-physics metawedge: graded arrays on fluid-loaded elastic plates and the mechanical analogues of rainbow trapping and mode conversion. *New Journal of Physics*, 20(5):053017, 2018.

Multipole Decomposition of Bound States in the Continuum in Dielectric Metasurfaces

Zarina Sadrieva[1], Kristina Frizyuk[1], Mihail Petrov[1], Yuri Kivshar[1,2], and Andrey Bogdanov[1*]

[1]ITMO University, St. Petersburg 197101, Russia
[2]Nonlinear Physics Center, Australian National University, Canberra ACT 2601, Australia
*corresponding author, E-mail: a.bogdanov@metalab.ifmo.ru

Abstract

We suggest a novel approach to explain the physics of bound photonic states embedded into the radiation continuum. We study dielectric metasurfaces composed of planar periodic arrays of Mie-resonant nanoparticles ("meta-atoms") which support both symmetry protected and accidental bound states in the continuum, and employ the multipole decomposition approach to reveal the physical mechanism of the formation of such nonradiating states in terms of multipolar modes generated by isolated meta-atoms.

1. Introduction

The quest for compact photonic systems with high quality factor (Q factor) modes led to the rapid development of optical bound states in the continuum (BICs). BICs are nonradiating states, characterized by the resonant frequencies embedded to the continuum spectrum of radiating modes of the surrounding space [1, 2]. The BICs first appeared as a mathematical curiosity in quantum mechanics [3]. The discovery of BICs in optics immediately attracted broad attention due to high potential in applications in communications, lasing, filtering, and sensing.

Despite the number of existing approaches to understand the nature of BICs, there is still a room for further development of the theory. During the previous few years the electromagnetic multipole theory has been extensively developed as a natural tool of nanophotonics dealing with the lowest (fundamental) resonances of the system. The main advantage of the multipole decomposition method (MDM) is that it provides a representation of an arbitrary field distribution as a superposition of the fields created by a set of multipoles [4].

In this work, we extend the MDM approach for explaining both symmetry protected and accidental BICs. We provide a theory of BICs origin in terms of MDM for a general case of any periodic structure and develop an analytical method, which determines the contribution of the vector spherical harmonics to the far field [5].

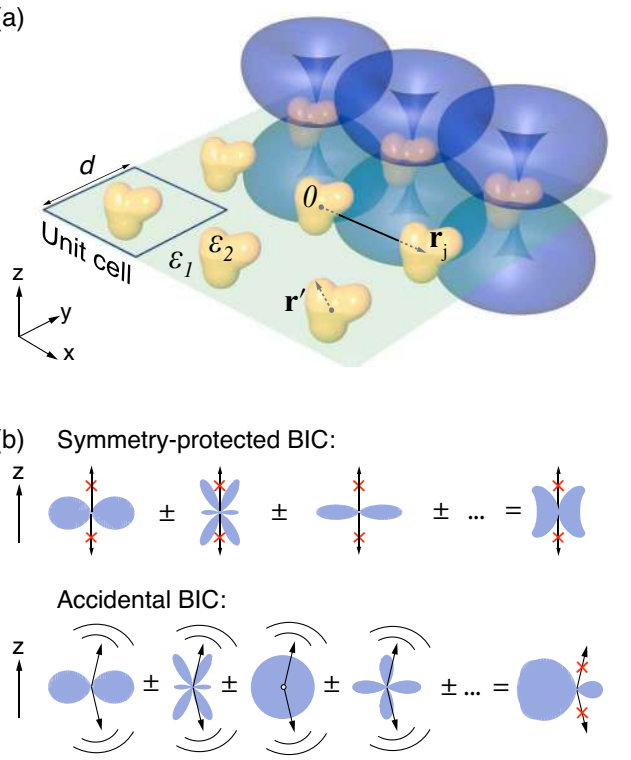


Figure 1: (a) Metasurface with square unit cell composed of dielectric meta-atoms. (b) The upper and lower panels show the formation mechanism of symmetry protected (at-Γ) and accidental (off-Γ) BIC as an interference of multipole moment of the unit cell.

2. Results

For the frequencies below the diffraction limit, the far-field of any metasurface (see Fig. 1) can be expressed as

$$\mathbf{E}(\mathbf{r}) = \frac{E_0 V_b}{2\pi k_1 k_{1z}} e^{i\mathbf{k}_1\mathbf{r}} \sum_\alpha \tilde{A}_\alpha \mathbf{Y}_\alpha \left(\frac{\mathbf{k}_1}{k_1}\right). \qquad (1)$$

Here $k_{1z} = \pm\sqrt{k_1^2 - k_{||}^2}$, $k_1 = \sqrt{\varepsilon_1}\frac{\omega}{c}$, V_b is the volume of the first Brillouin zone. The spherical vector functions $\mathbf{Y}_\alpha(\mathbf{n})$ depend on the spherical coordinates of a unity vector $\mathbf{n}$ and α is a set of indices encoding the multipoles [6]. $\tilde{A}_\alpha$ are the coefficients of the multipolar decomposition.

Equation (1) provides the correspondence between the radiation pattern of a single unit cell and the far-field properties of the whole infinite array allowing for interpreting the BIC in terms of MDM. In strong contrast to a single nanoparticle, where each multipole contributes to the far field, in case of a subdiffractive array there might be direction, where non of the multipole gives any contribution, or alternatively the non-zero contribution of different terms may eventually sum up to zero. The formulated alternative gives a sharp distinction between the symmetry protected and accidental BIC.

The Γ-point BIC corresponds to the absence of the far-field radiation in the direction along the z-axis. Due to the structure of VSH, it appears that a number of multipoles do not radiate in the vertical direction along the z-axis. If the field inside a single unit cell consists only of such multipoles, there will be no total radiation in z-direction. This simple fact is illustrated in the upper panel in Fig. 1(b). Noticing that only $\mathbf{Y}_\alpha$ functions with orbital angular momentum $m = 1$ are non-zero in parallel to the z-axis direction, we can conclude that at the Γ-point in the subdiffractive array all the modes which do not contain the harmonics with $m = 1$ are symmetry-protected BICs. This fundamental conclusion lies in the basis of recent experimental demonstration of lasing with BIC in a 2D subdiffractive array of nanoparticles. The particular operational mode consisted of vertical dipoles oriented along the z-axis, thus, not contributing into the only open channel. There exist an approach that the eigenmodes at the Γ-point can radiate in the normal direction z if their fields are odd under C_2^z rotations, and do not have any other rotational symmetry of C_n^z-type. In terms of multipole moments, this follows from the fact that at the Γ-point any radiative mode should contain multipoles with $m = 1$. On the other hand, in virtue of the symmetry, the even modes have zero radiation losses, i.e. infinite radiation quality factor, which are known as symmetry-protected BICs.

Let us now turn to the case of accidental BIC description. In general case, coefficients $\tilde{A}$ are complex numbers. They define the amplitudes and phase delay between the multipoles. However, in accordance with [7], if the structure has time reversal and inversion symmetry, the eigenmodes must satisfy the condition $\mathbf{E}(\mathbf{r}) = \mathbf{E}^*(-\mathbf{r})$. It results in a fact that every term of the sum in Eq. (1) is purely real, and all multipoles are in-phase or anti-phase. All coefficients depend on k-vector and structure's parameters and in a case of the off-Γ BICs this sum turns to zero. In other words, for the particular $\mathbf{k}_1$ all vector harmonics add up to zero in the direction of $\mathbf{k}_1$, analogously to the anti-Kerker effect, because they are already in phase and only amplitudes are modulated while k-vector is changed [Fig. 1(b), lower panel].

3. Conclusions

We have demonstrated that symmetry-protected bound states in the continuum in dielectric metasurfaces at the frequencies below the diffraction limit are associated with the multipole moments of the elementary meta-atoms which do not radiate in the transverse direction. Similarly, we have revealed that the accidental bound state in the continuum corresponding to an off-Γ point in the reciprocal space are formed due to destructive interference of the multipole fields in the far-zone. We believe that our results will provide a new way for designing high-quality resonant photonic systems based on the physics of bound states in the continuum.

Acknowledgement

This work was supported by the Russian Science Foundation (18-72-10140). The authors acknowledge useful discussions with I. D. Avdeev. Y. K. acknowledges a support from the Strategic Fund of the Australian National University. Z. S. and A. B. acknowledge support from the Foundation for the Advancement of Theoretical Physics and Mathematics "BASIS" (Russia).

References

[1] C. W. Hsu, B. Zhen, A. D. Stone, J. D. Joannopoulos, and M. Soljačić, "Bound states in the continuum," *Nat. Rev. Mater.*, vol. 1, no. 9, p. 16048, 2016.

[2] K. Koshelev, A. Bogdanov, and Y. Kivshar, "Meta-optics and bound states in the continuum," *Sci. Bull.*, 2018.

[3] J. V. Neumann and E. P. Wigner, "Uber merkwurdige diskrete Eigenwerte," *Phys. Z.*, no. 30, pp. 465–467, 1929.

[4] S. S. Kruk, R. Camacho-Morales, L. Xu, M. Rahmani, D. Smirnova, L. Wang, H. H. Tan, C. Jagadish, D. N. Neshev, and Y. S. Kivshar, "Nonlinear optical magnetism revealed by second-harmonic generation in nanoantennas," *Nano Lett.*, vol. 17, no. 6, pp. 3914–3918, 2017.

[5] Z. Sadrieva, K. Frizyuk, M. Petrov, Y. Kivshar, and A. Bogdanov, "Multipolar origin of bound states in the continuum," *arXiv preprint arXiv:1903.00309*, 2019.

[6] K. Frizyuk, "Second harmonic generation in dielectric nanoparticles with different symmetries," *arXiv preprint arXiv:1812.02988*, 2018.

[7] C. W. Hsu, B. Zhen, J. Lee, S.-L. Chua, S. G. Johnson, J. D. Joannopoulos, and M. Soljačić, "Observation of trapped light within the radiation continuum," *Nature*, vol. 499, p. 188, 2013.

Direct Imaging of Isofrequency Contours of Strongly Localized Guided Modes in Planar Photonic Structures

Anton Samusev

Department of Nanophotonics and Metamaterials,
ITMO University, St. Petersburg, Russia
*corresponding author, E-mail: a.samusev@metalab.ifmo.ru

Abstract

In this work, we investigate all-dielectric metasurfaces and based on the silicon on insulator platform for manipulating strongly localized evanescent waves in the visible and near-infrared spectral ranges. For an anisotropic metasurface, we use the Fourier modal method to demonstrate that it supports both hyperbolic-like and elliptic dispersion regimes. We implement a back focal plane microscope combined with a high refractive index solid immersion lens to directly image the isofrequency contours of the guided modes (surface waves). Reconstruction of 2D dispersion law unambiguously reveals the transition between different regimes of in-plane propagation of the electromagnetic waves.

1. Introduction

Surface waves (SWs) on metasurfaces attract special interest. SWs are propagating electromagnetic states localized perpendicular to the interface and do not radiate into the far-field. These properties make them very promising for applications in modern optoelectronic and all-optical on-chip signal delivery. In straightforward analogy with metamaterials used for the control over bulk waves, metasurfaces form a flexible platform for manipulating surface waves and guided modes.

2. Results and discussion

Modern optoelectronics is based on planar photonic structures, which include periodic ones such as photonic crystal waveguides or metasurfaces. The key characteristic of these structures is the spatial and temporal spectrum of their eigenmodes. Experimental studies of guided and surface modes in planar systems are especially challenging since their dispersion curves reside below the light line. In this work, we implement a back focal plane (BFP) microscope combined with a high refractive index solid immersion lens (ZnSe hemispherical prism) to directly visualize the isofrequency contours of guided modes supported by arbitrary metasurfaces. The numerical aperture of such a setup may reach exceptional values of 2.25 and even higher. The radiation losses, coupling regime and efficiency can be precisely tuned by varying of prism-to-sample air gap [1]. We study an all-dielectric metasurface for manipulating guided modes in the optical spectral range. Using to Fourier modal method we optimize the metasurface design to demonstrate both hyperbolic-like and elliptic dispersion at different frequencies. Reconstruction of the full dispersion surface from experimental data unambiguously reveals the transition between different dispersion regimes [2]. Finally, recent progress of our group in the experimental studies of exciton-polaritons in hybrid 2D systems based on transition metal dichalcogenide (TMD) monolayers coupled to all-dielectric metasurfaces will be highlighted.

3. Conclusions

We have studied dispersion properties of optical SWs supported by a strongly anisotropic all-dielectric metasurface. The nanostructured array composed of closely-packed silicon bars on a silica buffer layer was designed to support hyperbolic-like and elliptic dispersion regimes. In the experiment, the IFCs of SWs were visualized by means of back focal plane microscopy.

The use of a hemispherical solid immersion lens allowed to drastically enhance the numerical aperture of the system and gain access to strongly localized states. Using FDTD simulations, we illustrated multiple dispersion regimes depending on the wavelength and polarization of the incident wave. Finally, joining the whole set of the experimental data we have the full dispersion $\omega(k_x, k_y)$ of surface waves propagating along the metasurface in all directions.

Acknowledgement

This work was supported by the Ministry of Education and Science of the Russian Federation (No.3.8891.2017/8.9, 3.1668.2017/4.6).

References

[1] D.V. Permyakov, et al., Visualization of isofrequency contours of strongly localized waveguide modes in planar dielectric structures, *JETP Letters* 107.1: 10–14, 2018.

[2] D.A. Pidgaiko, et al., Direct imaging of isofrequency contours of guided modes in extremely anisotropic all-dielectric metasurface, *ACS Photonics*, 6, 2: 510-515, 2019.

Metasurfaces for Optical Antireflection and Bandpass Filters

Hou-Tong Chen[1,*], Chun-Chieh Chang[1], Beibei Zeng[1], and Li Huang[2]

[1]Center for Integrated Nanotechnologies, Los Alamos National Laboratory, Los Alamos, New Mexico, USA
[2]Physics Department, Harbin Institute Technology, Harbin, Heilongjiang, China
*corresponding author, E-mail: chenht@lanl.gov

Abstract

We experimentally demonstrate bilayer metasurfaces for optical antireflection. The metasurfaces consist of a square array of silicon pillars with self-aligned top gold resonators and complementary bottom gold slots, enabling near-zero reflection and simultaneously close-to-unity transmission at designed operational frequencies in the terahertz and mid-infrared spectral regions. We further demonstrate THz bandpass filters based on stacked bilayer metasurfaces, allowing fairly narrow, fast roll-off, and high-transmission bandpass performance, with an extremely clean background outside the passband.

1. Introduction

Optical antireflection has been critical for a wide range of applications from reducing losses to avoiding adverse effects in optical systems and optoelectronic devices. Based on the principle of interference, quarter-wave antireflection coating is the oldest, yet still simplest and widely used, approach to realize narrowband antireflection by introducing a dielectric film with a matched refractive index and a quarter-wave thickness. Broadband antireflection coatings can be accomplished using multilayer dielectric thin films with appropriately arranged refractive index and thickness profiles. However, in the mid- and far-infrared wavelength regions, it becomes a challenge to identify low-loss dielectric materials with the required refractive indices and, at the same time, suitable for cost-effective, high-quality film coating with increasing thicknesses.

The development of metasurfaces [1] – two-dimensional equivalent of metamaterials – has enabled the unprecedented control of the amplitude, phase, and polarization states of reflection and transmission using an array of ultrathin subwavelength metal/dielectric resonators. It has also been shown that few-layer metasurfaces – a stack of metasurfaces separated by dielectric spacers of subwavelength thicknesses – can not only dramatically enhance the performance but also create new functionalities beyond the constituent metasurface layers. Here we demonstrate narrowband, dual- and broadband optical antireflection using simple bilayer metallic metasurfaces in the terahertz (THz) and mid-infrared (mid-IR) spectral ranges. These metasurfaces consist of a square array of silicon pillars with self-aligned top gold resonators and complementary bottom gold slots, enabling near-zero reflection and simultaneously close-to-unity transmission at designed operational frequencies [2]. We further demonstrate narrowband THz bandpass filtering by cascading multiple bilayer antireflection metasurface structures. We show that, by simply stacking multiple identical bilayer metasurfaces, the transmission passband of the resulting filters significantly narrows as compared to that of a single bilayer metasurface, while maintaining 50% peak transmission power intensity in the passband with an extremely clean background (i.e., zero transmission) in the stop band [3].

2. Results

Figure 1 shows the scanning electron microscopy (SEM) images of the antireflection metasurface structures consisting of a square array of silicon pillars directly created on top of a high-resistivity silicon substrate by photolithography/e-beam lithography and reactive ion etching (RIE), where the top and bottom surfaces, but not the sidewall of the silicon pillars, were then coated with thin Ti/Au films (10 nm/200 nm thick for THz and 1 nm/30 nm thick for mid-IR), illustrated by the unit cell false color SEM images in Figure 1(a) and (b).

In Figure 2(a), we plot the experimentally measured reflection and transmission spectra for the THz metasurface structure shown in Figure 1(a) with diameter d vary-

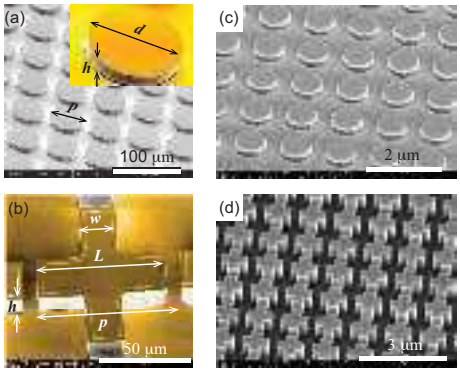


Figure 1: Scanning electron microscopy (SEM) images of the fabricated bilayer metasurfaces for antireflection. (a) Narrowband and (b) dual and broadband operating at THz frequencies. (c) Narrowband and (d) broadband operating at mid-IR frequencies.

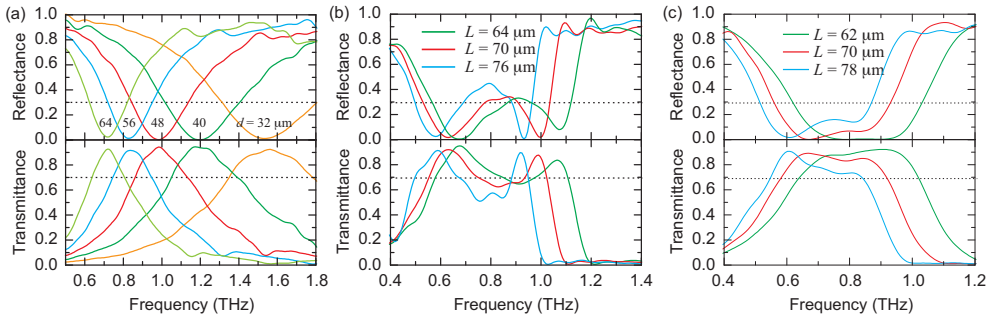


Figure 2: Experimentally measured reflection and transmission spectra for (a) single band, (b) dual band, and (c) broadband THz antireflection metasurfaces.

ing from 32 to 64 μm, period $p = 1.2 \times d$, but height fixed $h = 8$ μm, demonstrating a dramatic reduction of Fresnel reflection and significant enhancement of transmission at frequencies depending on the cylinder diameter. For the sample with a designed cylinder diameter $d = 48$ μm, the measured reflectance is $R = 0.19\%$, and the transmittance reaches $T = 94.3\%$ at 0.983 THz. For the samples with other cylinder diameters, the measured reflectance is $R < 2.5\%$ and the transmittance is $T > 91\%$ at their respective operational frequencies spanning from 0.72 to 1.53 THz.

In Figure 2(b) and (c) we plot the measured reflection and transmission spectra for the dual and broadband THz antireflection metasurface structures shown in Figure 1(b), where $w = 20$ μm and $h = 20$ μm while L varies from 64 μm to 76 μm, and $p = 1.1 \times L$ for dual band operation, and $w = 15$ μm and $h = 37$ μm while L varies from 62 μm to 78 μm, and $p = 1.1 \times L$ for broadband operation. For the dual-band THz metasurface with $L = 76$ μm, we achieve low reflection and high transmission at two frequencies, $\omega_1/2\pi = 0.587$ THz with $R_1 = 2.43\%$, $T_1 = 91.3\%$ and $\omega_2/2\pi = 0.932$ THz with $R_2 = 0.56\%$, $T_2 = 89.3\%$. The best broadband antireflection performance occurs when $L = 62$ μm, achieving small reflectance $R < 3\%$ in a frequency range between 0.719 and 0.953 THz, a bandwidth of 234 GHz (or a fractional bandwidth of 28%). The corresponding experimental transmittance is $T > 87\%$ in this frequency range, with the highest transmittance $T_{max} = 92\%$ at near 0.9 THz. It is worthwhile pointing out that, in the frequency range between 0.748 and 0.932 THz (a fractional bandwidth of 22%), the experimentally measured reflectance is $R < 1\%$, attractive for many applications where eliminating the undesirable reflection over a broad bandwidth is critical. Similar results were observed for the metasurface structures operating in the mid-IR frequency range, with results not shown here.

Although the quality factor of a single metasurface is relatively low ($\sim$2), taking advantage of the high transmission, we have further demonstrated high-performance THz bandpass filters by simply stacking multiple identical bilayer antireflection metasurfaces, achieving a reasonably high transmission in a very narrow passband, and a fast roll-off to an extremely clean background in the stop band. By stacking 4 double-side metasurfaces we narrowed the bandwidth by a factor of 3, with transmittance about 50% (results not shown here). Compared to conventional THz bandpass filters using suspended metal mesh structures or subwavelength metal hole-arrays, the demonstrated narrowband THz bandpass filters are easy to fabricate and mechanically robust and are potentially suitable for a wide variety of applications in the THz frequency region.

3. Conclusions

By using metal/dielectric/metal bilayer metasurfaces we experimentally demonstrate low-loss optical antireflection in the terahertz and mid-infrared spectral regions. We further demonstrate THz bandpass filters based on stacked bilayer metasurfaces, allowing fairly narrow, fast roll-off, and high-transmission bandpass performance, with an extremely clean background outside the passband.

Acknowledgement

The authors acknowledge the partial financial support from Los Alamos National Laboratory LDRD program. This work was performed, in part, at the Center for Integrated Nanotechnologies, a U.S. Department of Energy, Office of Basic Energy Sciences, Nanoscale Science Research Center, operated jointly by Los Alamos and Sandia National Laboratories.

References

[1] H.-T. Chen, A. J. Taylor, and N. Yu, A review of metasurfaces: Physics and applications, Rep. Prog. Phys. 79, 076401 (2016).

[2] L. Huang, C.-C. Chang, B. Zeng, J. Nogan, S.-N. Luo, A. J. Taylor, A. K. Azad, and H.-T. Chen, Bilayer metasurfaces for dual and broadband optical antireflection, ACS Photon. 4, 2111 (2017).

[3] C.-C. Chang, L. Huang, J. Nogan, and H.-T. Chen, Narrowband terahertz bandpass filters employing stacked bilayer metasurface antireflection structures, APL Photon. 3, 051602 (2018).

Optimal Design of Rectennas for IR Energy Harvesting

A. Y. Elsharabasy*, M. H. Bakr, and M. Jamal Deen
Department of Electrical and Computer Engineering, McMaster University, ON, Canada
*corresponding author: elsharay@mcmaster.ca

Abstract

In this work, we present a novel approach to design efficient rectennas for the infrared (IR) energy harvesting applications. The rectenna is composed mainly of a rectifying element, i.e. diode, and an antenna. In the IR regime, the ultra-high frequency ac signal captured by the antenna terminals has to be efficiently transformed into a useful dc signal. Owing to the ultra-fast quantum tunneling as a conduction mechanism, metal-insulator-metal (MIM) diode represents the best candidate to operate at these IR ranges. The impedance matching between the antenna and the diode, the diode nonlinearity, and the capacitance effect on the device's cutoff frequency represent challenges to achieve an efficient rectenna. An optimization algorithm is carried out to improve the rectenna's performance taking into consideration the aforementioned challenges.

1. Introduction

The infrared (IR) radiations coming from sun or that emitted from earth surface represent untapped energy sources that have been attractive for many research groups [1]. The current photovoltaics technology is still struggling to utilize the full IR portion of solar irradiance. At these terahertz frequencies corresponding to the 1-10 μm wavelength range, silicon and conventional semiconductors are not suitable to support electron conduction with these insufficient photon energies [2].

A direct approach can be used to harvest high frequency ac signal is by using rectennas. A rectenna is an antenna where its terminals are connected to a rectifying diode. Since the rectenna concept was proposed in 1972 [3], the idea has been implemented many times in different configurations [4-7]. After the antenna captures the high frequency ac signal form the surrounding radiations, the diode rectifies this signal and produces a dc current.

The diode at IR frequencies has to possess a short transit time in the range of few femtoseconds. Metal-insulator-metal (MIM) diodes are the best fit to perform at these ultra-high frequencies due to their ultra-fast quantum tunneling mechanism [8]. MIM diode's performance is controlled by its materials' properties and geometry. Trade-offs between diode's resistance and responsivity and resistance and capacitance lead to unexpected degradation of the device performance. Careful considerations should be drawn to select the appropriate materials to improve the efficiency.

The antenna configuration is desired to efficiently match the diode's impedance. Additionally, polarization-insensitive design will boost the rectenna's overall performance [9].

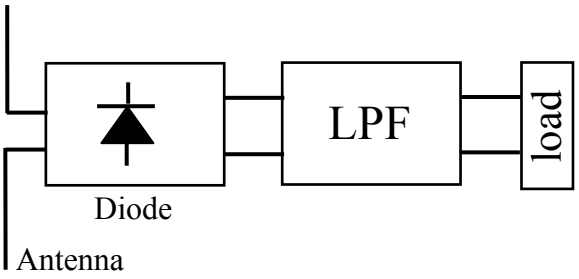


Figure 1: Block diagram of rectenna

The selection of the antenna dimensions and correspondingly the resonance frequency can manipulate the unwanted effects exhibited by the diode. In this work, attention is drawn to each element of the rectenna to achieve a considerably acceptable overall performance.

References

[1] J. F. Escobedo *et al.*, "Ratios of UV, PAR and NIR components to global solar radiation measured at Botucatu site in Brazil," *Renew. Energy*, vol. 36, no. 1, pp. 169–178, 2011.

[2] A. J. McEvoy *et al.*, *Solar cells: materials, manufacture and operation*. Academic Press, 2012.

[3] R. L. Bailey, "A proposed new concept for a solar-energy converter," J. Eng. Power, vol. 94, pp. 73–77, 1972.

[4] S. Grover, S. Joshi, and G. Moddel, "Quantum theory of operation for rectenna solar cells," *J. Phys. D. Appl. Phys.*, vol. 46, no. 13, p. 135106, 2013.

[5] M. Bareiß *et al.*, "Rectennas revisited," *IEEE Trans. Nanotechnol.*, vol. 12, no. 6, pp. 1144–1150, 2013.

[6] S. Krishnan *et al.*, "Thin film metal-insulator-metal junction for millimeter wave detection," *Procedia Chem.*, vol. 1, no. 1, pp. 409–412, 2009.

[7] P. Maraghechi *et al.*, "Enhanced rectifying response from metal-insulator-insulator-metal junctions," *Appl. Phys. Lett.*, vol. 99, no. 25, pp. 1–4, 2011.

[8] D. Vasileska and S. M. Goodnick, *Nano-Electronic Devices Semiclassical and Quantum Transport Modeling*, Springer, New York, 2011.

[9] A. Y. Elsharabasy *et al.*, "Double Hot-Spot Dual-Polarization Chand-Bali Nanoantenna for NIR Detection Applications," *2018 Photonics North (PN)*, 2018.

Aggregation Enhanced Two-photon Photoluminescence of Plasmonic Metal Nanoparticles and Their Biomedical Applications

Peiyan Yuan, Zhenping Guan, Cuifeng Jiang, Monalisa Garai, and Qing-Hua Xu[1*]

[1]Department of Chemistry, National University of Singapore, Singapore 117543
*corresponding author, E-mail: chmxqh@nus.edu.sg

Abstract

Noble metal nanoparticles were found to display significantly enhanced two-photon photoluminescence upon aggregate formation, which has been studied in the colloid solutions and on the single particle level. This phenomenon has been utilized to develop various schemes for two-photon excitation based biomedical applications.

1. Introduction

Noble metal nanoparticles (NPs) have found wide range of applications in optoelectronic and biomedical fields owing to their unique optical properties. Resonant interactions of noble metal NPs with light will result in collective oscillation of conduction band electrons, which has been known as localized surface Plasmon resonance (SPR). Plasmon coupling interactions between adjacent NPs in aggregated nanostructures will result in dramatically enhanced local electric-field in the gap region, which have been known to result in giant enhancement in various linear and nonlinear optical responses such as surface-enhanced Raman scattering, fluorescence, second harmonic generation, and two-photon photoluminescence (2PPL) [1].

Two-photon photoluminescence (2PPL) is light emission from materials that are excited by simultaneous absorption of two photons. Due to its nonlinear nature, 2PPL is highly sensitive to the incident light intensity. Very minor change in the local environment can make significant difference in 2PPL responses of metal NPs. 2PPL responses therefore can serve as sensitive probe signals to study local electric-field amplification in plasmonic nanostructures. Furthermore, two-photon excitation possesses unique advantages such as 3-dimensionally confined excitation at the focal volume and deep penetration into biological tissues of near-infrared light, 2PPL has lots of potential biological applications.

Noble metals, such as Au and Ag are generally considered as nonfluorescent due to their low quantum yield. Spherical metal NPs generally display relatively weak 2PPL. Our group recently found that 2PPL of metal NPs became significantly enhanced in the aggregated nanostructures [2-7]. Up to 800 times enhancement in the colloid solution [3] and several orders of magnitude on the single particle level [6] have been achieved. The phenomenon of aggregation enhanced 2PPL of metal NPs has been further utilized to develop various schemes for two-photon excitation based applications such as sensing, imaging and phototherapy [3, 7].

2. Results and Discussion

2.1. Observation of Aggregation Enhanced 2PPL in different systems.

Aggregation enhanced 2PPL of metal NPs were accidentally found when we studied interactions between noble metal NPs and conjugated polymers. Ag and Au NPs were found to exhibit extraordinary quenching effects on the fluorescence of cationic poly(fluorinephenylene). On the other hand, cationic conjugated polymers induce the aggregate formation of metal NPs. 2PPL of Ag and Au NPs were significantly enhanced upon addition of conjugated polymers, by a factor of 51-times and 9-times compared to the isolated nanoparticles for Ag and Au, respectively. [2]

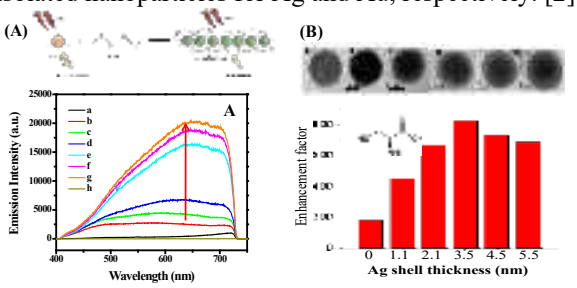


Fig. 1: (A) 2PPL of conjugated polymer induced aggregation of metal NPs (A) and cysteamine induced aggregation of Au@Ag NPs(B)

This aggregation enhanced 2PPL were subsequently demonstrated to be universal for Plasmonic metal NPs. 2PPL enhancement was observed in Au and Ag NPs of different sizes. A maximum 2PPL enhancement factor of up to 840-fold was obtained for Au@Ag core shell NPs with ~3.5 nm Ag nanoshells when a small molecule, cysteamine, was utilized to induced the aggregation of Ag@Ag NPs [3]. Plasmon coupling interactions between metal NPs in the aggregated nanostructures were believed responsible for the observed aggregation enhanced 2PPL. DNA tuned Au NP assemblies with well controlled separation distances from 2.0 to 12.2 nm were further prepared to investigate plasmon coupling strength and particle size effects on 2PPL enhancement [4]. 2PPL intensities of these DNA coupled nano-assemblies were found to increase rapidly as the separation distance decreases. The largest 2PPL enhancement factors of 115 and 265 were achieved at the

shortest available separation distance of 2.0 nm for 21 and 41 nm Au NPs-dsDNA assemblies, respectively [4].

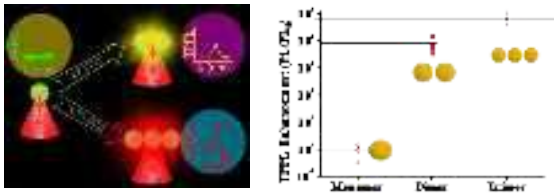


Fig. 2. 2PPL of different single Au nanoparticle clusters.

2.2. Studies of Aggregation Enhanced 2PPL on the single particle Level

2PPL of aggregated metal NPs are expected to be strongly dependent on the morphology of nanostructures. To under the underlying mechanism and explore the optimum enhancement, 2PPL of coupled metal nanostructures have been studied on the single particle level. Single particle study on the 2PPL enhancement of coupled Au NPs revealed that the 2PPL signal increases from monomer to trimer, and the average enhancement was found to be ~7.8×10^3 and ~7.0×10^4 for a dimer and trimer respectively, as compared to that of individual Au NPs [5]. 2PPL of trimers strongly depends on the coupling angle. The trimer with coupling angle of 180° was found to display the largest 2PPL intensity, which decreases rapidly as the coupling angle decreases. Single particle studies on 2PPL of different dimers also indicate that their 2PPL are strongly dependent on their morphology and relative orientations [6].

2.3. Application of Aggregation Enhanced 2PPL in Sensing, Imaging and Phototherapy.

As many chemically and biologically important species can cause aggregation of metal NPs. This phenomenon can be utilized to develop various schemes for two-photon excitation based biomedical applications. 2PPL-based sensing uses metal NPs themselves as the probe and does not require any probe molecules like Raman tags for SERS. One can monitor 2PPL intensity versus concentration of the analyte for label free quantitative detection.

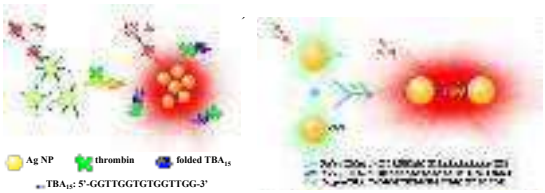


Fig. 3: Scheme for detection of Thromobin (A) and DNA (B)

Various bio-sensing schemes have been developed. For example, label-free 2PPL-based assay for sensing thrombin in serum have been developed by using Ag NPs and a thrombin binding aptamer (TBA) [7]. TBA adsorbs on the surface of Ag NPs and helps to stabilize them, whereas, the addition of thrombin selectively binds to TBA and leads to formation of aggregates. The detection limit of the method was found to be 3.1 pM in buffer solution, which was two orders of magnitude better than the detection limit obtained from the change in UV-Vis extinction spectra. Similarly, DNA induced coupling of Au NPs and 2PPL enhancement have been further utilized to develop a two-photon sensing scheme for detection of DNA sequences [4]. This 2PPL based method displayed high sensitivity with a limit of detection of 2.9 pM and excellent selectivity against ssDNA with mismatched bases. A single mismatch can be easily differentiated at room temperature. Taking the unique advantages of two-photon excitation, this method could be potentially further extended to DNA detection inside cells or even in vivo.

3. Conclusions

2PPL of metal NPs were found significantly enhanced in the aggregated nanostructures: up to 800-fold enhancement in the colloid solution and several orders of magnitude on the single particle level**.** This phenomenon have been further utilized to develop various two-photon excitation based applications with high sensitivity and selectivity, with potential for in-vivo biomedical applications.

Acknowledgements

We thank the financial support from Ministry of Education, Singapore and the Defense Science and Technology Agency of Singapore.

References

[1] L. Polavarapu, Jorge Pérez-Juste, Q.-H. Xu, L.M. Liz-Marzán, "Optical Sensing of Biological, Chemical and Ionic Species Through Aggregation of Plasmonic Nanoparticles", *J. Mater. Chem. C* 2: 7460-7476, 2014.

[2] Z.P. Guan, L. Polavarapu, Q.-H. Xu, Enhanced two-photon emission in coupled metal nanoparticles induced by conjugated polymers, *Langmuir*, 26:18020-18023, 2010.

[3] P Yuan, R Ma, N Gao, M Garai, Q.-H Xu, Plasmon coupling-enhanced two-photon photoluminescence of Au@Ag core–shell nanoparticles and applications in the nuclease assay", *Nanoscale* 7:10233-10239, 2015.

[4] P.Y. Yuan, R.Z. Ma, Z.P. Guan, N.Y. Gao, and Q.-H. Xu, Tuning two-photon photoluminescence of gold nanoparticle aggregates with DNA and its application as turn-on photoluminescence probe for DNA sequence detection, *ACS Appl. Mater. Interf.* **2014**, 6(15), 13149-13156.

[5] Z.P. Guan, N.Y. Gao, F. Han, Q.-H. Xu, Huge enhancement in two-photon photoluminescence of Au nanoparticle clusters revealed by single particle spectroscopy, *J. Am. Chem. Soc. 135*: 7272-7277, 2013.

[6] M. Garai, N. Gao, Q.-H. Xu, Single particle spectroscopic studies on two-photon photoluminescence of coupled Au nanorod dimers, *J. Phys. Chem. C* 122: 23102-23110, 2018.

[7] C.F. Jiang, T.T. Zhao, S. Li, N.Y. Gao, Q.-H. Xu, Highly sensitive two-photon sensing of thrombin in serum using aptamers and silver nanoparticles, *ACS Appl. Mater. Interf.* 5: 10853–10857, 2013.

Spontaneous emission near photonic Weyl points

Iñaki García-Elcano[1], Alejandro González-Tudela[2], and Jorge Bravo-Abad[1*]

[1]Departamento de Física Teórica de la Materia Condensada and Condensed Matter Physics Center (IFIMAC), Universidad Autónoma de Madrid, E-28049 Madrid, Spain
[2] Instituto de Física Fundamental IFF-CSIC, Calle Serrano 113b, Madrid 28006, Spain
* corresponding author, E-mail: jorge.bravo@uam.es

Abstract

We investigate the quantum electrodynamics of a quantum emitter coupled to a Weyl-point photonic lattice. We find that, despite the smoothness of the density of states near photonic Weyl points, fractional decay is observed when the transition of the quantum emitter is tuned to the frequency of a Weyl point. In addition, we show the emergence in the system of a light-matter bound state exhibiting tunable power-law localization, a feature with no counterpart in any other quantum optical scenario.

1. Introduction

The recent advent of new concepts and experimental techniques in nanophotonics has enabled unprecedented opportunities to tailor the emission properties of quantum emitters (QEs) through modifications of their environment [2, 3]. Of particular interest in this context are periodic structures with band-gaps [4].

In parallel, last decade has witnessed a spectacular progress in the application to physics of concepts originated in topology [5]. In this context, Weyl physics is playing a prominent role. The recent observation of Weyl excitations in photonic systems [6] has boosted the interest in this class of systems as highly controllable platforms to explore non-trivial topological properties.

In this work, we investigate the quantum electrodynamics of photonic Weyl points. By using a fully non-perturbative approach based on the resolvent operator method, we analyze the decay dynamics of a quantum emitter coupled to a Weyl-like photonic reservoir. We find unique characteristics such as fractional decay in the presence of a smooth density of states and the emergence of a light-matter bound state featuring tunable power-law localization [7].

2. Analyzed system

Figure 1(a) renders a schematic view of the considered system. It consists of a quantum emitter of transition frequency ω_e interacting with a periodic cubic lattice of localized photonic modes. The modes are coupled among them following the first-neighbor hopping pattern displayed in Fig. 1(a), which leads to a two-sublattice structure (A/B sublattice, shown in blue/red in Fig. 1(a)). We also assume that the

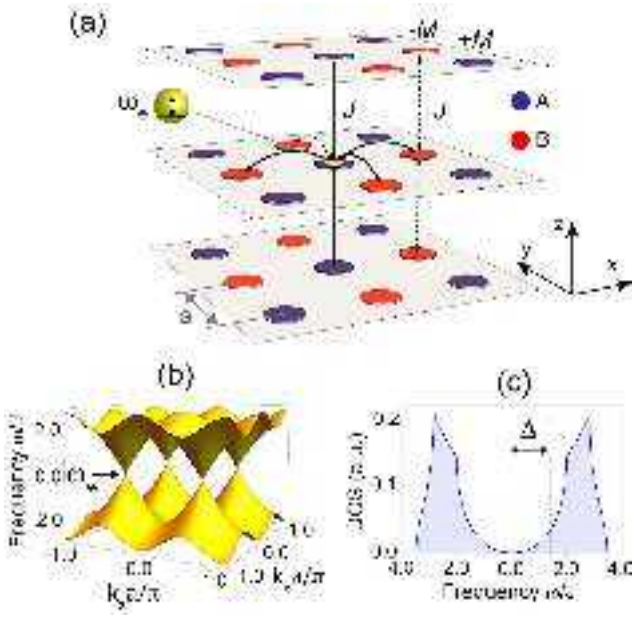


Figure 1: (a) Schematics of the analyzed system: a quantum emitter coupled to a Weyl-point photonic lattice. (b) Dispersion relation of the lattice shown in Panel (a), as calculated for M=0 and k_y=0. (c) Calculated density of states associated to the lattice shown in Panel (a). Δ denotes the detuning of the quantum emitter emission frequency with respect to the Weyl frequency.

system features a tunable sublattice frequency offset M, so the frequencies of the bosonic modes in sites A and B are $\omega_A = \omega_W + M$ and $\omega_B = \omega_W - M$, respectively. Figure 1(b) shows the corresponding dispersion relation, $\omega(\mathbf{k})$, as a function of $\{k_x, k_z\}$, calculated for $k_y = 0$ and $M = 0$. As observed, four frequency-isolated single linear degeneracies (Weyl points) emerge at $\{k_x, k_z\} = \{\pm\pi/2, \pm\pi/2\}$. Figure 1(c) displays the corresponding density of states (DOS), which shows the expected quadratic dependence in the vicinity of the Weyl points frequency.

3. Main results

We first analyze the upper level population of the QE ($|C_e(t)|^2$), obtained from the resolvent operator technique [7]. Figure 2(a) summarizes the results for several

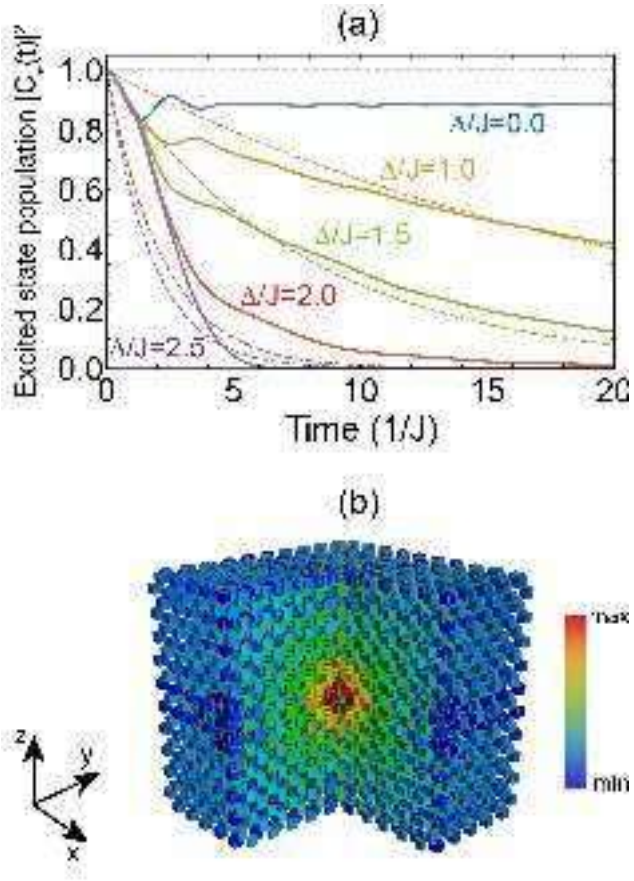


Figure 2: (a) Dynamics of the quantum emitter's excited state population, $|C_e(t)|^2$, calculated for M=0 and different values of Δ. Solid lines correspond to a non-perturbative approach (resolvent operator method). Dashed lines display the results of a perturbative approach (Fermi's Golden rule). In both cases, a light-matter interaction strength of $g = 0.5J$ is assumed. (b) Real space distribution of the photonic probability amplitudes corresponding to the light-matter bound state emerging in the system at long-times for $\Delta = 0$.

representative values of the detuning, Δ, of the quantum emitter emission frequency with respect to the Weyl frequency (solid lines). For comparison, the predictions from a perturbative approach (Fermi's Golden rule) are also included (dashed lines). As observed, for all considered values of Δ the perturbative approach fails to reproduce the corresponding non-perturbative results. This discrepancy is most remarkable for $\Delta = 0$. In that case, the DOS and its first derivative are smooth near ω_e, from which the predictions of Fermi's Golden rule (no decay of the QE) would be expected to hold. Instead, our results show that after an initial decay, followed by a set of oscillations, $|C_e(t)|^2$ settles down to a value smaller than 1. This *fractional decay* can be interpreted as the signature of a light-matter bound state [7].

The emergence of this light-matter bound state can be further demonstrated by investigating the real space distribution of the photonic part of the system's wavefunction for $\Delta = 0$ and long times (i.e., the bound state wavefunction). Figure 2(b) shows a three-dimensional visualization of the corresponding photonic probability amplitude for a $20 \times 20 \times 20$ lattice (the QE emitter is located at the center of the figure). As shown, the probability amplitude is indeed localized around the QE, which fully confirms the presence of a light-matter bound state in the analyzed system.

To quantitatively characterize the real space distribution of the obtained bound state, we analyzed the dependence with the distance from the emitter, d, of the above mentioned probability amplitude. For illustrationn, we discuss here the dependence along the z-axis. For the case of no offset between sublattices, $M = 0$, we found that a power-law $1/d^2$ matches well the numerical results. Remarkably, we also found that the variation of the sublattice frequency offset M actually enables *tuning* the exponent of the observed power-law decay. For $M/J = 2$, we obtained that the bound state decays with a power-law $1/d^3$. For intermediate values in-between $M = 0$ and $M/J = 2$, we observe a broad variety of different decay behaviors. For instance, for the case of $M/J = 1$, we obtained that both $1/d^2$ and $1/d^3$ power-law decays coexist in the same system.

This tunability is enabled by the fact that the sublattice frequency off-set can change the system band-structure without opening a band-gap for $|M| < 2J$, which in turn is because a Weyl point is only annihilated when it meets another one with opposite chirality. To our knowledge, this bound-state power-law tunability has not been reported before in any other structured photonic reservoir.

References

[1] E. M. Purcell, Spontaneous Emission Probabilities at Radio Frequencies, *Phys. Rev.* 69: 681, 1946.

[2] P. Lodahl, S. Mahmoodian, and S. Stobbe, Interfacing single photons and single quantum dots with photonic nanostructures, *Rev. Mod. Phys.* 87: 347–400, 2015.

[3] D. E. Chang, J. S. Douglas, A. González-Tudela, C.-L. Hung, and H. J. Kimble, Quantum matter built from nanoscopic lattices of atoms and photons, *Rev. Mod. Phys.* 90: 031002, 2018.

[4] S. John and J. Wang, Quantum electrodynamics near a photonic band gap: Photon bound states and dressed atoms, *Phys. Rev. Lett.* 64: 2418, 1990.

[5] M. Z. Hasan and C. L. Kane Topological insulators, *Rev. Mod. Phys.* 82: 3045–3067, 2010.

[6] L. Lu, Z. Wang, D. Ye, L. Ran, L. Fu, J. D. Joannopoulos, and M. Soljać, Experimental observation of Weyl points, *Science* 349: 622 (2015).

[7] I. García-Elcano, A. González-Tudela, and J. Bravo-Abad, Quantum electrodynamics near photonic Weyl points, *Arxiv:1903.07513*, 2019.

Advances in novel composite materials obtained by crystal growth

D. A. Pawlak,[1] P. Paszke,[2] R. Nowaczyński,[2] K. Szlachetko,[2] P. Piotrowski,[2] M. Tomczyk,[2] K. Sadecka,[1] A. Materna,[1] B. Surma,[1] A. Belardini,[3] J. Toudert,[4] C. Sibilia,[3]

[1]Institute of Electronic Materials Technology, ul. Wolczynska 133, 01-919 Warsaw, Poland, Dorota.Pawlak@itme.edu.pl
[2]Dept. of Chemistry, University of Warsaw, ul. Pasteura 1, 02-093 Warsaw, Poland
[3]Dipartimento di Scienze di Base ed Applicate per l'Ingegneria, Sapienza Università di Roma, Via A. Scarpa 16, Rome 00161, Italy
[4]Laser Processing Group, Instituto de Óptica, CSIC, C/Serrano 121, 28006 Madrid, Spain

We will demonstrate how to utilize the crystal growth methods for manufacturing of novel composite materials for various applications and especially photonics (metamaterials, plasmonic materials [1-7]), and energy conversion [8-9]. We will focus on two novel bottom-up manufacturing methods: (i) method based on directionally-grown self-organized eutectic structures [1, 5-9]; and (ii) NanoParticles Direct Doping method (NPDD) [2-4] based on directional solidification of dielectric matrices doped with various nanoparticles. In both of these methods we can easily use all available resonant phenomena to develop materials with unusual electromagnetic properties. Eutectic composites are simultaneously monolithic and multiphase materials forming self-organized micro/nanostructures, which enable: (i) the use of various component materials including oxides, semiconductors, metals, (ii) the generation of a gallery of geometrical motifs and (iii) control of the size of the structuring, often from the micro- to nanoregimes. On the other hand, the novel method of NanoParticles Direct Doping enables doping of dielectric matrices with various nanoparticles (varying chemical composition, size and shape) and with the possibility of co-doping with other chemical agents as eg. optically active rare earth ions or quantum dots.

Acknowledgments: This work was supported by Foundation for Polish Science under TEAM project, as well as previously by the National Science Centre under MAESTRO and HARMONIA projects.

References:

[1] D. A. Pawlak, et al. **Adv. Funct. Mat. (2010) 20, 1116.**
[2] M. Gajc, et al. **Adv. Funct. Mat. (2013) 23, 3443.**
[3] R. Nowaczynski, et al. **PPSC (2019) 36,1800124.**
[4] M. Gajc, et al. **Sci. Rep. (2018) 8,13425.**
[5] K. Sadecka, et al. **Adv. Opt. Mat. (2015) 3, 381.**
[6] K. Sadecka, et al. **Opt. Express (2015) 23, 19098.**
[7] V. Myroshnychenko, **Opt. Express (2012) 20, 10879.**
[8] K. Wysmulek, et al. **Appl. Catalysis B: Environ. (2017) 206, 538.**
[9] K. Kolodziejak, et al. **J. Catalysis (2017) 352, 93.**

All-optical charging and charge transport in quantum dots

Nika Akopain

DTU Fotonik, Technical University of Denmark, 2800 Kongens Lyngby, Denmark
E-mail: nikaak@fotonik.dtu.dk

Abstract

Semiconductor quantum dots are one of the best on-demand sources of single and entangled photons to date, simultaneously merging the highest brightness and indistinguishability of the emitted photons. They are, therefore, among the strongest candidates for practical *single-qubit* quantum photonic devices. However, to exploit the full advantage of quantum physics, *multi-qubit* photonic devices are absolutely necessary. Here we propose, for the first time, an experimentally feasible *multi-qubit* photonic device, and a method for *individual charging* of multiple quantum dots and *coherent charge transport* between them.

1. Summary

The spin- or location-states of isolated charges in optically-active quantum dots are one of the promising candidates for fundamental building blocks in quantum science and technology. Many practical applications would comprise of multiple coupled quantum dots, each of which must be individually chargeable. However, the most advanced demonstrations are currently limited to devices with only a single dot, and individual charging and charge transport has neither been demonstrated nor proposed for a scalable array of optically active quantum dots.

In this talk I will present a device where we propose and numerically demonstrate a method for controlled charging of multiple quantum dots and coherent charge transport between the dots [1]. We show that charging and charge transport can be implemented in a realistic structure with fidelities greater than 99.9% in a few μs. Our scheme is based on all-optical resonant manipulation of charges in a 1-dimensional array of quantum dots formed by a type-II band alignment. Such structures can be practically realized using, for example, crystal-phase quantum dots in nanowires [2], and are feasible in view of recent advances in controlling the crystal phases in nanowires during growth [3].

Our work opens new practical avenues for realizations of advanced quantum photonic devices such as, for instance, a solid-state quantum register with a photonic interface.

References

[1] Hastrup, J., Leandro, L. & Akopian, N. All-optical Charging and Charge Transport in Quantum Dots. *Submitted* (2019).

[2] Akopian, N., Patriarche, G., Liu, L., Harmand, J.-C. & Zwiller, V. Crystal phase quantum dots. *Nano Lett.* **10**, 1198–1201 (2010).

[3] Harmand, J.-C. *et al.* Atomic Step Flow on a Nanofacet. *Phys. Rev. Lett.* **121**, 166101 (2018).

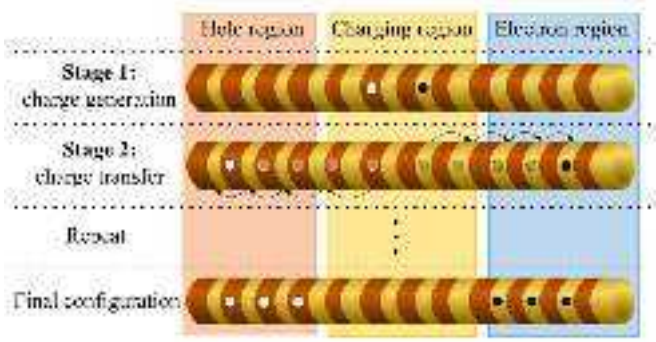


Figure 1: All-optical charge initialization concept in an array of quantum dots.

Gold nanorod bending and splitting with light: A new route towards functional plasmonic surfaces

Theobald Lohmüller[1,2]

[1]Photonics and Optoelectronics Group, Nano-Institute Munich, Department of Physics, LMU München, Königinstrasse 10, Munich, 80799, Germany
[2]Nanosystems Initiative Munich (NIM) and Center for NanoScience (CeNS), Schellingstraße 4, 80539 Munich, Germany
*E-mail: t.lohmueller@lmu.de

SUMMARY

Plasmonic "*V*-shaped" nanoantennas and nanorods are building blocks for the rational design of flat metamaterials and optical devices. Yet, the fabrication and structural patterning of such small antennas is not a simple task. E-beam lithography is widely used, but shows limitations when it comes to fabricating very small structures with high crystallinity and purity.

Optical printing of plasmonic particles represents an alternative to standard lithography approaches. In recent years, the use of optical forces has emerged as a straightforward way to pattern spherical gold or silver nanoparticles with a high localization precision and lateral resolution [1]. For nanorods, it has even been shown that not only the patterning, but also the controlled alignment of individual rods can be obtained by using polarized laser light [2].

Optical printing has been achieved for a variety of nanoparticles. Indeed, many particle shapes and compositions are nowadays accessible by synthetic chemistry. The synthesis of *V*-shaped plasmonic particles, however, remains a challenge. In this presentation, I will demonstrate on the possibility of re-shaping and patterning plasmonic nanoantennas with light as an intriguing alternative to conventional nanofabrication.

First, I will discuss how laser manipulation and heating of individual gold nanorods can be applied to controllably re-shape and bend them in solution. Secondly, I will present how the optical force, which emerges during the bending process, can be utilized to simultaneously pattern these bent particles onto an underlying substrate. Finally, I will show that adjusting the laser conditions not only allows to control the bending angle and the alignment of the bent nanoantennas, but also to optically split a single nanorod into two spherical nanoparticles of equal size. Scanning electron microscopy and transmission electron microscopy imaging reveals that the particles are separated at distances of less than ~2 nm with the smallest gaps being in the sub-nanometer regime. Such dimer nanoantennas obtained by optical nanorod splitting thus display a very strong field confinement in the gap region, which is advantageous for sensing and spectroscopy applications such as surface enhanced Raman spectroscopy (SERS).

[1] A. Urban, S. Carretero-Palacios, A.A. Lutich, T. Lohmüller, J. Feldmann, F. Jäckel, Optical trapping and manipulation of plasmonic nanoparticles: fundamentals, applications and perspectives, *Nanoscale* 6 (9), 4458-4474 (2014).

[2] J. Do, M. Fedoruk, F. Jäckel,, J. Feldman, Two-Color Laser Printing of Individual Gold Nanorods, *Nano Letters*, 13 (9), 4164-4168 (2013).

[3] A. Babynina, M. Fedoruk, P. Kühler, A. Meledin, M. Döblinger, T. Lohmueller, Bending Gold Nanorods with Light, *Nano Letters*, 16 (10), 6485-6490 (2016).

Recent advances in subwavelength metamaterial silicon photonics

P. Cheben[1,*] C. Alonso-Ramos[2], R. Halir[3], J.H. Schmid[1], J. Čtyroký[4], D. Benedikovic[2], A. Ortega-Moñux[3], A. Sánchez-Postigo[3], D. González-Andrade[5], J. G. Wangüemert-Pérez[3], I. Molina-Fernández[3], A. V. Velasco[5], A. Herrero-Bermello[5], J. M. Luque-González[3], D. Pereira-Martín[3], J. Lapointe[1], S. Janz[1], D.-X. Xu[1], D. Melati[1], Y. Grinberg[1], S. Wang[1], M. Vachon[1], M. Kamandar Dezfouli[1], R. Cheriton[1], V. Vakarin[2], M. Dado[6], D. Oser[2], F. Mazeas[7], D. Pérez-Galacho[8], X. Le Roux[2], E. Durán-Valdeiglesias[2], L. Labonte[7], S. Tanzilli[7], E. Cassan[2], D. Marris-Morini[2], and L. Vivien[2]

[1]National Research Council Canada, Ottawa, K1A 0R6, Canada
[2]Centre for Nanoscience and Nanotechnology (C2N), CNRS, Univ. Paris-Sud, Univ. Paris-Saclay, 91120 Palaiseau, France
[3]Departamento de Ingeniería de Comunicaciones, ETSI Telecomunicación, Universidad de Málaga, 29010 Málaga, Spain
[4]Institute of Photonics and Electronics, CAS, Chaberská 57, 182 51 Prague, Czech Republic
[5]Grupo de Dinámica No-lineal y Fibras Ópticas, Instituto de Óptica Daza de Valdés, CSIC, 28006 Madrid Spain
[6]University of Žilina, Faculty of ElectricalEngineering, Univerzitná 1, 01026 Žilina, Slovakia
[7]Université Côte d'Azur, CNRS, Institut de Physique de Nice, Parc Valrose, 06108 Nice Cedex 2, France
[8]ITEAM research institute, Universitat Politècnica de València, Camino de Vera s/n, 46022, Valencia, Spain
*E-mail: Pavel.Cheben@nrc-cnrc.gc.ca

Abstract

Subwavelength grating metamaterial waveguide structures are becoming established as important building blocks for silicon photonic integrated circuits. The novel optical properties found in these structures and ability to control their optical responses with unprecedented accuracy are opening new prospects for controlling flow of light in nanophotonic waveguides circuits. In this invited talk we will present an overview of our recent advances in this exciting field, including silicon-based subwavelength structures for highly efficient fiber-chip couplers, ultra-broadband waveguide devices, Bragg filters with high spectral sensitivity and nanophotonic waveguides with engineered anisotropy.

1. Introduction

Metamaterial photonics has seen tremendous progress, particularly in nanostructured engineered materials: metamaterials, metallic and dielectric subwavelength structures and subwavelength engineered waveguides. The novel optical properties found in these structures, along with the capability, through advanced fabrication techniques, to control their optical responses with unprecedented accuracy, has opened new prospects for controlling and manipulating light in planar waveguide circuits. Since the early demonstrations of a silicon wire waveguide with a subwavelength grating (SWG) metamaterial core [1-5], metamaterial SWG waveguides have attracted a strong research interest in academia and industry because of their unique potential to control light propagation in planar waveguides [6,7]. The SWG metamaterial waveguides have been adopted by industry for fiber-chip coupling [8] and subwavelength engineered structures in general [6,7] are likely to become key building blocks for the next generation of integrated photonic circuits. In this invited talk we will present a brief overview of our recent advances in this field.

2. Fiber-chip couplers

SWG metamaterial fiber-chip edge couplers, first demonstrated at the NRC Canada [1,5], are becoming the state-of-the-art solution for silicon photonics allowing coupling loss of -0.32 dB and negligible polarization dependence [9]. Barwicz et al. at IBM showed an SWG metamaterial coupler, optimized to interface cleaved SMF-28 fibers, for the O-, S-, and C- communication bands [8]. Surface grating couplers (SGCs) utilize a diffraction grating to couple the light between planar waveguides and optical fibers, allowing wafer-scale testing and relaxed alignment tolerances. We demonstrated the first apodized surface grating couplers hybridized with subwavelength gratings [10], and a record sub-decibel efficiency of -0.7 dB for a single etch process [11]. An alternative way to achieve high-efficiency grating couplers is to increase the intrinsic directionality of the grating by using the blazing effect in an L-shaped geometry. This concept has also been implemented for 193 nm deep-UV lithography, yielding an efficiency of -2.7 dB [12]. A significant practical drawback of grating couplers is their limited spectral bandwidth (~35nm at 1dB). We have proposed a new design concept for highly-efficient and ultra-broadband operation, using the zeroth diffraction order in a prism-assisted configuration, which results in an unprecedented efficiency-bandwidth product: a coupling efficiency of -0.41 dB and a 1 dB bandwidth of 126 nm [13].

3. Dispersion engineered devices

We have leveraged the inherent anisotropy and dispersion of a sub-wavelength structured photonic metamaterial to demonstrate ultra-broadband integrated beam splitting [14-

15]. The reported device [15] achieves high performance over an unprecedented 500 nm design bandwidth exceeding all optical communication bands combined. The broadband performance is achieved by taking advantage of the SWG anisotropy to attain a wavelength independent Talbot imaging distance.

Spectral filtering is an important functionality in integrated optics. However, the high index contrast of SOI makes it difficult to obtain the weak grating coupling coefficients required for narrow bandwidth Bragg gratings. Recently, SWG corrugated waveguides have been used to yield flexible design of the Bragg rejection and bandwidth [16]. We have demonstrated that integrated Bragg gratings with narrow rejection bandwidths on the order of ~100 pm can be designed using a conventional SWG waveguide core optically loaded with lateral silicon segments [17].

4. Conclusions

These recent advances open exciting prospects for development of a plethora of advanced silicon photonic devices, building upon the fundamental principle of subwavelength grating metamaterial waveguide engineering [7,18].

References

[1] P. Cheben, D.-X. Xu, S. Janz, A. Densmore, Subwavelength waveguide grating for mode conversion and light coupling in integrated optics, *Opt. Express* 14: 4695-4702, 2006.

[2] J. H. Schmid, P. Cheben, S. Janz, J. Lapointe, E. Post, D.-X. Xu, Gradient-index antireflective subwavelength structures for planar waveguide facets, *Opt. Lett.* 32: 1794-1796, 2007.

[3] P. J. Bock, P. Cheben, J. H. Schmid, J. Lapointe, A. Delâge, S. Janz, G. C. Aers, D.-X. Xu, A. Densmore, T. J. Hall, Subwavelength grating periodic structures in silicon-on-insulator: a new type of microphotonic waveguide, *Opt. Express* 18: 20251-20262, 2010.

[4] U. Levy, M. Abashin, K. Ikeda, A. Krishnamoorthy, J. Cunningham, Y. Fainman, Inhomogenous, Dielectric metamaterials with space-variant polarizability, *Phys. Rev. Lett.* 98: 243901-1-243901-4, 2007.

[5] P. Cheben, P. J. Bock, J. H. Schmid, J. Lapointe, S. Janz, D.-X. Xu, A. Densmore, A. Delâge, B. Lamontagne, T. J. Hall, Refractive index engineering with subwavelength gratings for efficient microphotonic couplers and planar waveguide multiplexers, *Opt. Lett.* 35: 2526-2528, 2010.

[6] R. Halir, P. Bock, P. Cheben, A. Ortega-Moñux, C. Alonso-Ramos, J. H. Schmid, J. Lapointe, D.-X. Xu, J. G. Wangüemert-Pérez, I. Molina-Fernández, S. Janz, Waveguide sub-wavelength structures: principles and applications, *Laser Photonics Rev.* 9: 25-49, 2014.

[7] P. Cheben, R. Halir, J. H. Schmid, H. A. Atwater, D. R. Smith, Subwavelength integrated photonics, *Nature* 560: 565-572, 2018.

[8] T. Barwicz, N. Boyer, A. Janta-Polczynski, J. F. Morissette, Y. Thibodeau, L. Patry, T. W. Lichoulas, E. L. Kimbrell, S. Martel, S. Kamlapurkar, S. Engelmann, A metamaterial converter centered at 1490 nm for interfacing standard fibers to nanophotonic waveguides, in Optical Fiber Communication Conference M2I.3 (OSA, 2016).

[9] P. Cheben, J. H. Schmid, S. Wang, D.-X. Xu, M. Vachon, S. Janz, J. Lapointe, Y. Painchaud, M.-J. Picard, Broadband polarization independent nanophotonic coupler for silicon waveguides with ultra-high efficiency, *Opt. Express* 23: 22553-22563, 2015.

[10] R. Halir, P. Cheben, J. H. Schmid, R. Ma, D. Bedard, S. Janz, D.-X. Xu, A. Densmore, J. Lapointe, I Molina-Fernández, Continuously apodized fiber-to-chip surface grating coupler with refractive index engineered subwavelength structure, *Opt. Lett.* 35: 3243-3245, 2010.

[11] D. Benedikovic, P. Cheben, J. H. Schmid, D.-X. Xu, B. Lamontagne, S. Wang, J. Lapointe, R. Halir, A. Ortega-Moñux, S. Janz, M. Dado, Subwavelength index engineered surface grating coupler with sub-decibel efficiency for 220-nm silicon-on-insulator waveguides, *Opt. Express* 23: 22628-22635, 2015.

[12] D. Benedikovic, C. Alonso-Ramos, D. Pérez-Galacho, S. Guerber, V. Vakarin, G. Marcaud, X. Le Roux, E. Cassan, D. Marris-Morini, P. Cheben, F. Boeuf, C. Baudot, L. Vivien, L-shaped fiber-chip grating couplers with high-directionality and low-reflectivity fabricated with deep-UV lithography, *Opt. Lett.* 42: 3439-3442, 2017.

[13] A. Sánchez-Postigo, J. G. Wangüemert-Pérez, J. M. Luque-González, I. Molina-Fernández, P. Cheben, C. Alonso-Ramos, R. Halir, J. H. Schmid, A. Ortega-Moñux, Broadband fiber-chip zero-order surface grating coupler with 0.4 dB efficiency, *Opt. Lett.* 41, 3013-3016, 2016.

[14] A. Maese-Novo, R. Halir, S. Romero-García, D. Pérez-Galacho, L. Zavargo-Peche, A. Ortega-Moñux, I. Molina-Fernández, J. G. Wangüemert-Pérez, P. Cheben, Wavelength independent multimode interference coupler, *Opt. Express* 21: 7033-7040, 2013.

[15] R. Halir et al., Ultra-broadband nanophotonic beamsplitter using an anisotropic sub-wavelength metamaterial, *Laser Photonics Rev.* 10: 1039-1046, 2016.

[16] D. Oser, D. Pérez-Galacho, C. Alonso-Ramos, X. Le Roux, S. Tanzilli, L. Vivien, L. Labonté, E. Cassan, Subwavelength engineering and asymmetry: two efficient tools for sub-nanometer-bandwidth silicon Bragg filters, *Opt. Lett.* 43: 3208-3211, 2018.

[17] P. Cheben et al., Bragg filter bandwidth engineering in subwavelength grating metamaterial waveguides, *Opt. Lett.* 44: 1043-1046, 2019.

[18] R. Halir et al., Subwavelength-grating metamaterial structures for silicon photonic devices," doi: 10.1109/jproc.2018.2851614, Proceedings of the IEEE, 2018.

Far-field sub-diffraction imaging with wire array metamaterials

Alessio Stefani[1,2,*], Simon C. Fleming[1], and Boris T. Kuhlmey[1]

[1]Institute of Photonics and Optical Science (IPOS), School of Physics, The University of Sydney, NSW 2006, Australia
[2]DTU Fotonik, Department of Photonics Engineering, Technical University of Denmark, 2800, Kgs. Lyngby, Denmark
*corresponding author, E-mail: alessio.stefani@sydney.edu.au

Abstract

Fiber drawing is used to realize extended and scalable metamaterials. Such metamaterials are used for light guidance and sub-resolution imaging. In this paper, the application of fiber drawn wire array metamaterials for far field imaging is reported. The scalability of the process allows fabrication of structures sized for frequencies between the THz and the IR.

1. Introduction

The ability to co-process different materials at the same time in a thermal process opens up the possibility of realizing metamaterials in large sizes and volumes. In particular, we have exploited the fiber drawing technique combined with the Taylor wire method to realize large volume metal-dielectric structures [1]. The structures produced are invariant in one direction and therefore lead to wire array and slotted cylinders array metamaterials. Such metamaterials are used for guiding radiation in hollow structures [1-3] and to realize hyperlenses for sub-resolution imaging [4-7]. The nature of the fiber drawing process allows us to easily scale the structures with features from hundreds of microns to hundreds of nanometers, allowing operation from the THz to the IR [8]. Moreover, by carefully choosing the dielectric, we are able to fabricate deformable structures allowing tunability of the metamaterial properties [9].

One of the most attractive applications of hyperbolic metamaterials is the ability to support sub-diffraction imaging [10-11]. The use of hyperbolic metamaterials for sub-diffraction imaging has been demonstrated in the microwave [12-14], terahertz [4, 15], infrared [16], and visible spectrum [17].

We present the use of wire array hyperlenses for imaging applications in the far field. Two configurations are used for reconstructing images: reflection and transmission. As imaging devices we use a 8X magnification hyperlens in the THz and show imaging to $1/13^{th}$ of the wavelength. By cascading hyperlenses we demonstrate that this limit can be pushed further. We also show proof of principle of the scalability of the fabrication process to realize imaging in the Mid-IR with low magnification hyperlenses.

Acknowledgements

This work was supported by the Marie Sklodowska-Curie grant of the European Union's Horizon 2020 research and innovation programme (708860). The work was supported in part by Australian Research Council (ARC) Discovery Projects DP140104116 and DP170103537. This work was performed in part at the Optofab node of the Australian National Fabrication Facility (ANFF), using NCIRS and NSW State Government funding.

References

[1] S. Atakaramians, A. Stefani, H. Li, Md. S. Habib, J. G. Hayashi, A. Tuniz, X. Tang, J. Anthony, R. Lwin, A. Argyros, S. C. Fleming, B. T. Kuhlmey., "Fiber-Drawn Metamaterial for THz Waveguiding and Imaging," J. Infrared, Millimeter, Terahertz Waves, vol. 38, no. 9, pp. 1162–1178, 2017.

[2] X. Tang, B. T. Kuhlmey, A. Stefani, A. Tuniz, S. C. Fleming, and A. Argyros, "Electromagnetic Wave Propagation Through Air-Core Waveguide with Metamaterial Cladding," J. Light. Technol., vol. 34, no. 22, pp. 5317–5324, 2016.

[3] H. Li, S. Atakaramians, R. Lwin, X. Tang, Z. Yu, A. Argyros, B. T. Kuhlmey, "Flexible single-mode hollow-core terahertz fiber with metamaterial cladding," Optica, vol. 3, no. 9, pp. 941–947, 2016.

[4] A. Tuniz, K. J. Kaltenecker, B. M. Fischer, M. Walther, S. C. Fleming, A. Argyros, B. T. Kuhlmey, "Metamaterial fibres for subdiffraction imaging and focusing at terahertz frequencies over optically long distances," Nat. Commun., vol. 4, pp. 2706, 2013.

[5] J. G. Hayashi, R. Lwin, A. Argyros, S. Fleming, B. T. Kuhlmey, A. Stefani, "Extreme sub-diffraction focusing of THz radiation with magnifying metamaterial hyperlenses," The 3rd Australia New Zealand Conference on Optics and Photonics (ANZCOP), Paper 37, 2017.

[6] Md. S. Habib, A. Stefani, S. Atakaramians, S. C. Fleming, A. Argyros, B. T. Kuhlmey, "A prism based magnifying hyperlens with broad-band imaging," Appl. Phys. Lett., vol. 110, no. 10, pp. 101106, 2017.

[7] Md. S. Habib, “Sub-diffraction Imaging with Wire Array Metamaterial Fibres: Novel Geometries and Mitigation of Artefacts,” PhD thesis, The University of Sydney, http://hdl.handle.net/2123/18702.

[8] J. G. Hayashi, “Wire array Infrared Metamaterial Fibers: Fabrication and Applications” PhD thesis, The University of Sydney, http://hdl.handle.net/2123/17790.

[9] S. Fleming, A. Stefani, X. Tang, A. Argyros, D. Kemsley, J. Cordi, R. Lwin, “Tunable metamaterials fabricated by fiber drawing,” J. Opt. Soc. Am. B, vol. 34, no. 7, p. D81, 2017.

[10] L. Ferrari, C. H. Wu, D. Lepage, X. Zhang, and Z. W. Liu, "Hyperbolic metamaterials and their applications," *Progress in Quantum Electronics,* vol. 40, pp. 1-40, Mar 2015.

[11] C. R. Simovski, P. A. Belov, A. V. Atrashchenko, and Y. S. Kivshar, "Wire Metamaterials: Physics and Applications," *Advanced Materials,* vol. 24, pp. 4229-4248, Aug 16 2012.

[12] P. A. Belov, G. K. Palikaras, Y. Zhao, A. Rahman, C. R. Simovski, Y. Hao, *et al.*, "Experimental demonstration of multiwire endoscopes capable of manipulating near-fields with subwavelength resolution," *Applied Physics Letters,* vol. 97, Nov 8 2010.

[13] X. Radu, A. Lapeyronnie, and C. Craeye, "Numerical and experimental analysis of a wire medium collimator for magnetic resonance imaging," *Electromagnetics,* vol. 28, pp. 531-543, 2008.

[14] Y. Zhao, G. Palikaras, P. A. Belov, R. F. Dubrovka, C. R. Simovski, Y. Hao, *et al.*, "Magnification of subwavelength field distributions using a tapered array of metallic wires with planar interfaces and an embedded dielectric phase compensator," *New Journal of Physics,* vol. 12, Oct 29 2010.

[15] M. G. Silveirinha, P. A. Belov, and C. R. Simovski, "Ultimate limit of resolution of subwavelength imaging devices formed by metallic rods," *Optics Letters,* vol. 33, pp. 1726-1728, Aug 1 2008.

[16] M. G. Silveirinha, P. A. Belov, and C. R. Simovski, "Subwavelength imaging at infrared frequencies using an array of metallic nanorods," *Physical Review B,* vol. 75, Jan 2007.

[17] B. D. F. Casse, W. T. Lu, Y. J. Huang, E. Gultepe, L. Menon, and S. Sridhar, "Super-resolution imaging using a three-dimensional metamaterials nanolens," *Applied Physics Letters,* vol. 96, Jan 11 2010.

DNA Self-Assembled Plasmonic Nanoantennas

Mauricio Pilo-Pais

[1]Department of Physics, University of Fribourg, Fribourg, Switzerland
*corresponding author, E-mail: Mauricio.pilopais@unifr.ch

Abstract

DNA can be used as a tool to rationally assemble metallic nanoparticles (NPs) and single photon emitters (e.g. organic fluorophores and quantum dots) with a defined arrangement, nanometer spacing, and tunable plasmon resonance. These structures can be tailored to have unique optical properties. In this talk, I will discuss our assembly strategies to use DNA as a self-assembly tool to fabricate optical antennas that include a variety of hybrid nanocomponents such as a single QD positioned between two metallic NPs.

1. Introduction

DNA is a great tool to position optically active components with both, high accuracy and in a large parallel manner. DNA self-assembly has already been exploited to obtain custom-tuned hot spots for surface enhanced Raman and fluorescence spectroscopies [1], and to produce small mode volumes able to promote strong-coupling between plasmons and molecular excitons [2]. Recently, we have developed a facile approach to assemble plasmonic antennas that consist of two metallic nanoparticles (40 nm) with an individual colloidal quantum dot (e.g. CdSeS/ZnS) positioned at the hot spot.

2. Results

Using DNA complementarity, an individual QD is positioned at exactly the center between two metallic NPs [3]. The design approach of the QD-NP antennas is shown on Figure 1, and it is based on DNA complementarity, stoichiometry, and steric hindrance principles. The structures possess a small gap (~ 5 nm) which is desired to achieve high Purcell factors and plasmonic enhancement, since no intermediate molecules are used other than short DNA strands. The fluorescence emission from antennas assembled with spherical gold particles displays an increased in fluorescence up to ~30-fold, compared to quantum dots without antenna. Fluorescence lifetime measurements on the antennas show the lifetimes of the analyzed traces to be highly suppressed compared to individual QDs. The values obtained, following a deconvolution analysis, exhibit a mean lifetime of 0.065 ns, which are greatly below reported values of similar QDs [4] and as one would expect from Purcell enhancement due to the nearby AuNPs.

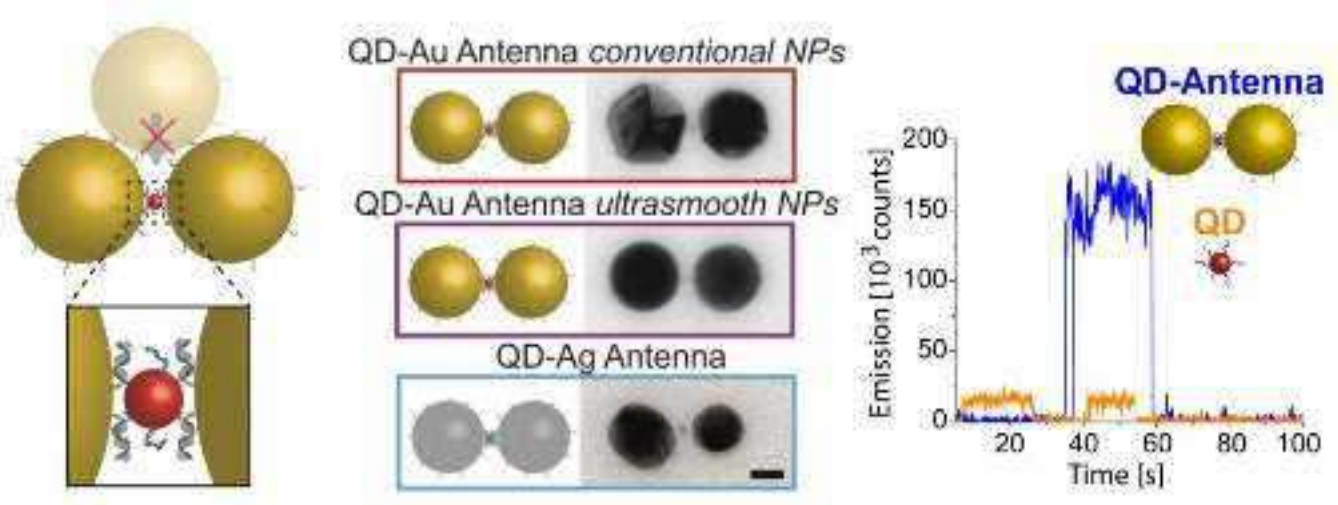


Figure 1: Example of DNA self-assembled nanoantenna. Here, an individual QD is positioned exactly between two metallic NPs. The large molar excess of the larger species and their disproportionate size difference prevents more than two NPs to be attached to an individual QD. The antennas display enhanced fluorescence in respect with individual QDs.

3. Conclusions

DNA is a pre-programmable material capable to self-assemble optical antennas. As an example, a simple strategy to build plasmonic antennas with a single QD located at the center of the gap with high yields using DNA-mediated self-assembly is presented. The functionality of these antennas is demonstrated by measuring the fluorescence enhancement of QDs up to ~30-fold as well as increased radiative rate. The fine tuning of this fabrication technique, which is based on steric hindrance and controlled stoichiometry of the species, permits the fulfillment of two important requirements: 1) a small gap combined with 2) a single QE at the center of a plasmonic cavity. This simple self-assembly approach is not only scalable (trillions of QD–antennas are produced in a few simple steps) but can be extended to any other plasmonic material and/or QE functionalized with DNA. Furthermore, these structures can be deposited and measured on different substrates.

References

[1] M. Pilo-Pais, G. P. Acuna, P. Tinnefeld, T. Liedl, *MRS Bull.*, 42: 936, 2017.

[2] E.-M. Roller, C. Argyropoulos, A. Högele, T. Liedl, M. Pilo-Pais, *Nano Lett.,* 16: 5962, 2016.

[3] F. Nicoli, T. Zhang, K. Hübner, B. Jin, F. Selbach, G. Acuna, C. Argyropoulos, T. Liedl, and M. Pilo-Pais. *Small*, 1804418, 2019.

[4] W. Qin, R. A. Shah, P. Guyot-Sionnest, *ACS Nano*, 6: 912, 2012.

Recent advances in phase-change materials for high-speed optoelectronics

Imad Agha[1,2,*]

[1]Department of Physics, University of Dayton, Dayton OH 45469, USA
[32]Department of Electro-Optics and Photonics, University of Dayton, Dayton OH 45469,
*corresponding author, E-mail: iagha1@udayton.edu

Abstract

By doping Ge2Sb2Te5 phase change material with different metals, we produce material with improved electrical properties while simultaneously maintaining the optical contrast necessary for light modulation and switching. On the other hand, by nanopatterning the material into nanorod metamaterials, we can change its thermal response by orders of magntidude, paving the way towards ultrahigh-speed materials for reconfigurable photonic applications.

1. Introduction

Spatial light modulation is a critical component of modern free-space optical devices for communications [1] and beam steering, LIDAR [2], and others. Currently, most of the work relies on Liquid Crystal on-Silicon (LCoS) or micromechanical adaptive mirrors (MEMS) for achieving the necessary control of light. These two techniques, while viable, generally rely on non-scalable fabrication techniques and suffer from limited reconfiguration speeds due to the nature of the underlying mechanism of light control. Phase-change materials (PCMs), such as germanium-antimony-tellurium (GST) offer an alternate path for high-speed light modulation [3]. PCMs generally alter their optical constants via an electronic, optical, or thermal stimulus (even though ultimately the change is due to a thermal effect), leading to a phase transition between a low-index amorphous state (index = 4.0) and a high-index crystalline state (index = 5.5). For spatial light modulators, the core idea (Fig. 1) is to implement an electrically actuated device where the refractive index of each individual pixels can be independently addressed as to affect a 0-π phase control on the incoming wavefront. Unfortunately, due to the high-impedance nature of the amorphous state coupled with the high contact resistance with metallic electrodes, electrical actuation a) is relatively slow and b) cannot rely on off-the-shelf radio-frequency (RF) components due to the incompatibility with standard 50Ω termination. Moreover, the slow nature of the thermal response requires new techniques for improving the speed of PCMs. In this work, we show a path both towards RF-compaible devides as well as towards high-speed PCM-based components.

2. Doping of GST

It is possible through doping the underlying GST thin film with various metals, to simultaneously improve electrical properties of GST while maintaining the necessary optical contrast for efficient light modulation devices [4]. The idea is similar to the standard doping methods for silicon that reduce its resistivity by orders of magnitude by generating excess holes or electrons in the material. We choose tungsten (W) as the alloy material since a) we expect a transition metal to improve the conductivity and consequently reduce the resistance, b) it can be used as an effective electrode for actuating the pixels, and c) it has a close atomic radius to tellurium and can act as a substitutional active dopant. GST thin films are fabricated via magnetron sputtering with an independent cathode for co-sputtering tungsten into the film allowing for independent control over the percentage of tungsten introduced into the GST alloy. Once the W-doped GST film is deposited with varying doping percentages (2 to 18% [4], the electrical resistivity is measured using a four point probe technique as a function of temperature/ phase (amorphous vs crystalline). Figure 1 shows that for pure GST, phase transition (near 160 oC) is coupled with a large drop in resistivity, while, as tungsten is introduced, the electrical contrast between the two states is decreased, leading to a relatively low resistance value both in the amorphous and crystalline states of GST, as desired. The inset in Fig. 1 shows that even at the highest tungsten concentration, there is a strong transmission, indicating relatively low losses.

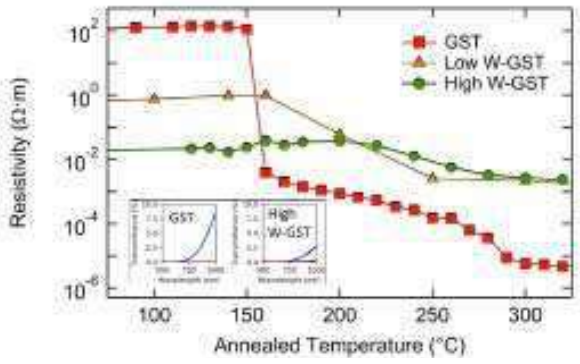


Fig 1: Resistivity of W-doped GST-based PCM, showing a sharp decrease (reaching a point where both states offer the same resistance). Inset shows the transmission properties of both doped/undoped material.

3. Nanopatterning of GST-based PCMs

While doping improves the electronic properties of the material, improving the speed requires a manipulation of the thermal properties of the material itself. This can be done by exploiting the scaling laws that govern thermal heating and dissipation: By imploying a metamaterial approach, through which GST is grown into a nanorod geometry (Fig 2), the material can potentially absorb and dissipate heat a lot faster than the bulk thin film, due to the increased surface-to-volume ratio. In our experiments, we produce GST-nanorods via glancing-angle deposition, and employ conformal coating methods to provide both a high-dissipative thermal bath as well as structural stability to the nanorods.

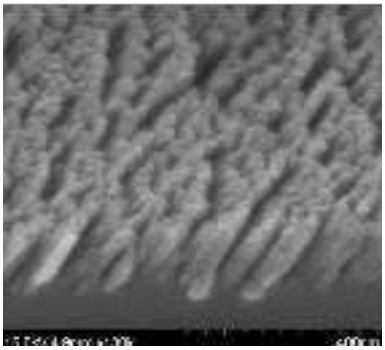


Fig 2: GST-based nanorods grown via self-assembly

4 Single-pulse time dynamics and novel structures

In this set of experiments, we characterize the temporal dynamics and quantity of crystallization of Ge2Sb2Te5 (GST) utilizing a pump-probe technique. The amount of change in the material can be determined by the reflectivity measurement from the probe laser and the temporal dynamics can be gleaned from the resulting graph. In our results we see multiple levels of reflectivity indicating partial change of the GST. After a number of pulses (dictated by the power of each pulse), the reflectivity levels off indicating that the GST is fully changed up to the penetration depth of the laser. From the shape of the graph the cooling times as well as information about the mechanisms of the change can be inferred. This uique, single-pulse setup that operates in the low aborption regime allows us not only to better understand the temporal dynamics of GST-based PCMs, but also to create novel structures for light modulation (e.g. phase plates) with point-by-point phase control, as well as electronic strucutres (variable resistors) that can be implemented into a circuit post-fabrication (Fig. 3).

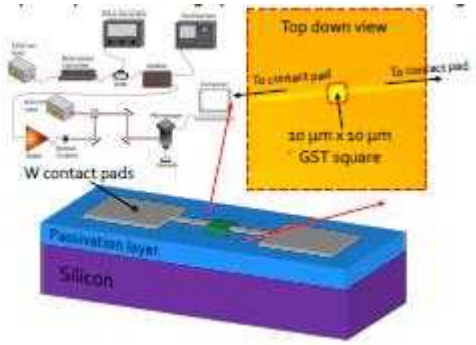


Fig 3: Variable resistor created via optical excition of GST-PCMs between two tungsten electrodes

Acknowledgements

This work was supported by the National Science Foundation, the Dayton Area Graduate Studies Initiative, and the University of Dayton STEM Catalyst program.

References

[1] F. Feng, I. H. White, and T. D.Wilkinson, "Free space communications with beam steering a two-electrode tapered laser diode using liquid-crystal slm," J. Lightw. Technol. 31, 2001–2007 (2013).

[2] B. Smith, B. Hellman, A. Gin, A. Espinoza, and Y. Takashima, "Single chip lidar with discrete beam Steering by digital micromirror device," Opt. Express 25, 14732–14745 (2017).

[3] H.-S. P.Wong, S. Raoux, S. Kim, J. Liang, J. P. Reifenberg, B. Rajendran, M. Asheghi, and K. E. Goodson, "Phase change memory," Proceedings of the IEEE 98, 2201–2227 (2010).

[4] P. Guo, J. A. Burrow, G. A. Sevison, A. Sood, M. Asheghi, J. R. Hendrickson, K. E. Goodson, I. Agha, and A. Sarangan, "Improving the performance of ge2sb2te5 materials via nickel doping: Towards rf-compatible phase-change devices," Appl. Phys. Lett. 113, 171903 (2018).

Plasmonic Monitoring of Lithium Metal Evolution in Nanobatteries

Yan Jin, Jia Zhu* and Lin Zhou*

[1]National Laboratory of Solid State Microstructures, College of Engineering and Applied Sciences, School of Physics, Key Laboratory of Intelligent Optical Sensing and Manipulation, and Collaborative Innovation Center of Advanced Microstructures, Nanjing University, Nanjing 210093, P. R. China.
[2]School of Electrical and Computer Engineering, Georgia Institute of Technology, Atlanta, GA 30332, USA.
*corresponding author, E-mail: linzhou@nju.edu.cn, jiazhu@nju.edu.cn

Abstract

The development of plasmonics has led to significant advancement in sensitive chemical and biological sensing and surface enhanced spectroscopies, which is urgent for real-time electrochemical detection in batteries. Alkali metals featured by ideal free electron gas models, have long been regarded as promising plasmonic materials but seldom been explored due to their high chemical reactivity. Here, we demonstrate our recent progresses in lithium metal plasmonics and in operando monitoring of lithium metal evolution during battery cycling.

1. Introduction

Plasmonics arising from collective oscillations of the free electron gas density, has been widely used for non-destructive, real-time and sensitive chemical and biological detection (1, 2). Alkali metals such as lithium and sodium with free electron gas behavior have long been theoretically predicted as promising plasmonic materials (3) but have seldom been explored, primarily due to their high chemical reactivity (4). The lithium metal battery, which features the highest specific capacity (3860 mAh g^{-1}) is regarded as the most promising candidate for next-generation energy storage devices (5). However, dendrite formation leads to limited cycle life and safety hazard, which calls for fundamental understanding, real-time monitoring and control of the electrochemical evolution of reactive lithium metals (6).

2. Plasmonic monitoring

Fig. 1 shows the plasmonic monitoring platform of lithium metal evolution by electrochemical reactions. There are two kinds of lithium morphology evolution, including lithium particle and lithium dendrite. We establish the relationship between the lithium metal morphology and optical spectrum by numerical calculations. For the normal lithium morphology (upper panel in Fig. 1B), there are at least two types of optical modes, the localized surface plasmon (LSP) related to the isolated lithium particles as well as Wood's anomaly (WA) related to the periodic geometry. As depicted in Fig. 1C, the referenced reflectance spectrum of the Ag pattern (black solid line) shows a high intensity with unnoticeable plasmonic modes from 400 nm to 1600 nm. WA modes of Ag pattern is theoretically determined by the formula $\lambda_{WA} = 2\pi n_d/G_{mn}$ (7). Note that the pronounced asymmetric profiles at ~ 800 nm and 1200 nm can be ascribed to the hybridizations of the LSP and WA, with amplified LSP observed around $WA_{1,0}$ ~ 1230 nm and $WA_{1,1}$ ~ 710 nm. In contrast, the optical evolution of the abnormal dendrite formation is quite different (lower panel of Fig. 1*C*). The broadband anti-reflection (flat spectra) can be observed with drastically attenuated reflectance (< 10%), which stems from plasmonic light trapping by light scattering and coupling (8). This distinct difference of optical modes (instead of mere variation of intensity) between periodically controllable normal-lithium particles and random dendrites forms the basis of plasmonic monitoring of the morphological evolution of lithium metal during electrochemical cycling.

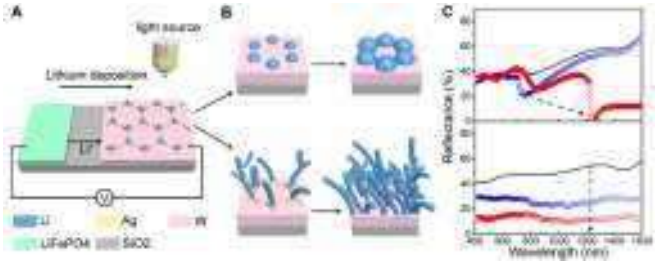


Figure 1: In operando plasmonic monitoring of lithium morphological evolution in battery. (A) Schematic of planar battery device and in operando reflectance spectra measurement. (B) Two pathways of lithium morphological evolution. (C) Simulated reflectance spectra.

To further demonstrate the relationship between the optical spectra and lithium morphology, we measured the reflectance spectra during the lithium deposition process (Fig. 2). Two representative electrical currents (I = 0.03 mA and 1mA) were applied to induce the two different evolution pathways: lithium particle growth and lithium dendrite formation, respectively. For the case I =0.03 mA, the in operando reflection spectra were measured as shown in Fig. 2A. At the initial time of deposition (t = 0 s), the measured spectrum was flat from 400 nm to 1600 nm (relative reflectance ~ 60%). During the process of electrochemical lithium deposition, the overall intensity of reflectance decreases gradually, and a clear dip at ~ 800 nm was developed at t = 8 min. In addition, further deposition resulted in an additional dip at ~ 1200 nm emerging at t = 18 min, which agrees with the tendency of the numerical model. The reflectance at 1225 nm in Fig. 2A was extracted and is plotted versus time after normalization in Fig. 2C, which demonstrates the relatively slow and gentle evolution

process during lithium particle growth. To further identify the ordered morphology of the lithium particles, we removed the current, disassembled the planar cell once the plasmonic modes (800 nm, 1200 nm) were identified, and examined the morphology under SEM, as illustrated in Fig. 2E and G, respectively. It is confirmed that lithium tends to nucleate as discrete nanoparticles on silver triangles and that the average size is ~ 190 nm and 370 nm, as suggested in Fig. 1B. Similar in operando optical measurements of lithium dendrite formation were performed with I = 1 mA. The measured reflectance spectrum remains flat in the range of 400 - 1600 nm. In addition, the reflectance decreased drastically to ~ 10% at t = 5 s and remained stable (~ 5%) after t = 45 s (Fig. 2B). To study the drastic transition, in operando spectra in a narrower wavelength range (1100 - 1300 nm) were measured. Compared with that of ordered particles, the evolution of normalized reflectance at 1225 nm of lithium dendrites over time is plotted in Fig. 2D, which indicates the rapid dendrite growth process and is notably different from Fig. 2B. The SEM images of the evolved dendrites at t = 5 s and 85 s are presented in Fig. 2F and H, respectively, resembling the main features predicted in Fig. 1. To further address the necessity of periodic Ag pattern as electrodes, we performed the same in-situ reflection measurements during lithium deposition with two substrates without periodic Ag pattern (bare W and random Ag/W substrate). Because of the random deposition-sites dominated features, both cases possess almost flat spectra and similar intensity evolution profiles for both normal and abnormal lithium states, making them difficult for fast identification during operando monitoring.

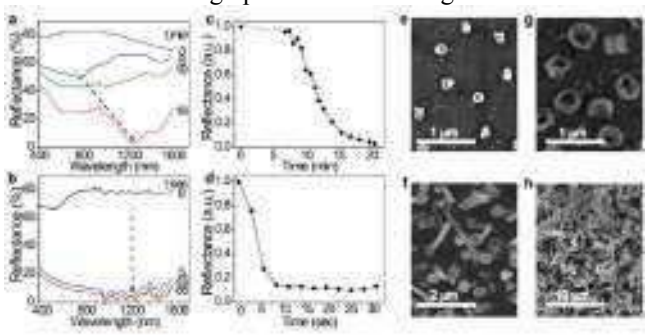


Figure 2: In operando characterization of different pathways of lithium evolution. (A, B) In operando optical reflectance monitoring of the two representative lithium evolution pathways over time during electrochemical lithium deposition: (A) growth of patterned lithium hemispheres and (B) formation of random dendrites. (C, D) Evolution of normalized reflectance at the wavelength of 1225 nm. (E, G) Typical SEM images of lithium morphologies indicating the two essential plasmonic modes λp observed at (E) λp ~ 800 nm and (G) λp ~ 1200 nm. (F, H) SEM images of lithium dendrite morphology at the beginning and end of lithium deposition, respectively.

3. Conclusions

The relationships between the evolving morphologies of lithium metal and in operando optical spectra are established both numerically and experimentally: ordered growth of lithium particles shows clear size-dependent reflective dips due to hybrid surface plasmon resonances, while the formation of undesirable disordered lithium dendrites exhibits a flat spectroscopic profile with pure suppression in reflection intensity. Under the in operando plasmonic monitoring enabled by the microscopic morphology of metal, the differences of lithium evolutionary behaviors with different electrolytes can be conveniently identified without destruction. At the intersection of energy storage and plasmonics, it is expected that the ability to actively control and in operando plasmonically monitor electrochemical evolution of lithium metal can provide a promising platform for investigating lithium metal behavior during electrochemical cycling under various working conditions.

Acknowledgements

This work is jointly supported by the National Key Research and Development Program of China (No. 2017YFA0205700) and the State Key Program for Basic Research of China (No. 2015CB659300), National Natural Science Foundation of China (Nos. 11621091, 11574143, 61735008, 11874211, 21805132), and the Fundamental Research Funds for the Central Universities (Nos. 021314380135, 021314380128).

References

[1] Stewart ME, et al. (2008) Nanostructured plasmonic sensors. Chem Rev 108(2):494-521.

[2] Liu N, Hentschel M, Weiss T, Alivisatos AP, & Giessen H (2011) Three-Dimensional Plasmon Rulers. Science 332(6036):1407-1410.

[3] Naik GV, Shalaev VM, & Boltasseva A (2013) Alternative Plasmonic Materials: Beyond Gold and Silver. Adv Mater 25(24):3264-3294.

[4] 18. Boltasseva A & Atwater HA (2011) Low-Loss Plasmonic Metamaterials. Science 331(6015):290-291.

[5] Lin DC, Liu YY, & Cui Y (2017) Reviving the lithium metal anode for high-energy batteries. Nat Nanotechnol 12(3):194-206.

[6] Jin Y, et al. (2018) In operando Plasmonic Monitoring of electrochemical evolution of Lithium Metal. 115(44); 11168-11173

[7] Baptiste Auguié and William L. Barnes (2008) Collective Resonances in Gold Nanoparticle Arrays. Phys. Rev. Lett.101(14):14392.

[8] Zhou L, Yu XQ, & Zhu J (2014) Metal-Core/Semiconductor-Shell Nanocones for Broadband Solar Absorption Enhancement. Nano Lett 14(2):1093-1098.

3D Porous Silicon Gradient Refractive Index Micro-Optics and Waveguides

Paul V. Braun[1*]

[1]University of Illinois at Urbana-Champaign
*corresponding author, E-mail: pbraun@illinois.edu

Abstract

Via electrochemical etching of silicon, various nanophotonic elements, including flat lenses, photonic nanojet generators, Bragg mirrors, polarization sensitive optical splitters and structures with nearly arbitrary refractive index distributions were formed. The conversion from silicon to silica and titania enabled the optics to operate in the visible with minimal loss, something particularly important for visible light applications. A detailed model was developed which enabled tight control over optical properties based only on the electrochemical etch conditions.

1. Introduction

Porous silicon (PSi) exhibits structural birefringence originating from its geometrically anisotropic internal mesostructure.[1–5] Other examples of structurally birefringent optical materials composed of asymmetric subwavelength structures include porous alumina membranes, porous glass fibers, porous glasses, and doped glasses.[6–10] In PSi, it has been shown that the magnitude of the birefringence can be engineered across a broad range by controlling the etching conditions, and is larger than is found in any intrinsically birefringent crystal.[1,3–5] In this work, we use PSi's tunable optical anisotropy and other patterning approaches to engineer novel birefringent gradient refractive index (GRIN) micro-optics where lensing behavior is governed by the material's refractive index-dependent birefringence profiles. This builds off our previous work where we reported that square PSi GRIN posts bifurcate an illuminating beam into two focal regions when light is polarized along PSi's optic axis (TE illumination), and converge an orthogonally polarized illuminating beam (TM illumination) into a single focal region.[10].

2. Results

We suggest that a versatile approach to 3D GRIN elements is to use a defined Si topography to serve as the starting point for the lateral etch required to form a GRIN profile. Now, a time-varying current density generates the GRIN along the PSi etch pathway that initiates at all unmasked Si/electrolyte interfaces (Figure 1a). Our process begins with a p+-type Si wafer doped to form a shallow (~100 nm) n-type surface. Photolithography, followed by deep reactive ion etching, generates an array of microscale elements (e.g., square micro-columns (SMCs)) with less than 10 nm roughness sidewalls across the wafer (Figure 1b). Electrochemical etching (Figure 1a) simultaneously converts all of the elements to PSi in a few minutes. The n-type cap restricts PSi formation to the sidewalls, resulting in an etch path and GRIN profile that runs inward from and perpendicular to each of the SMC sidewalls (Figure 1c). Changes in the current density, whether discrete or continuous, provide nearly arbitrary and highly reproducible control over the refractive index and porosity of PSi (Figure 1d).

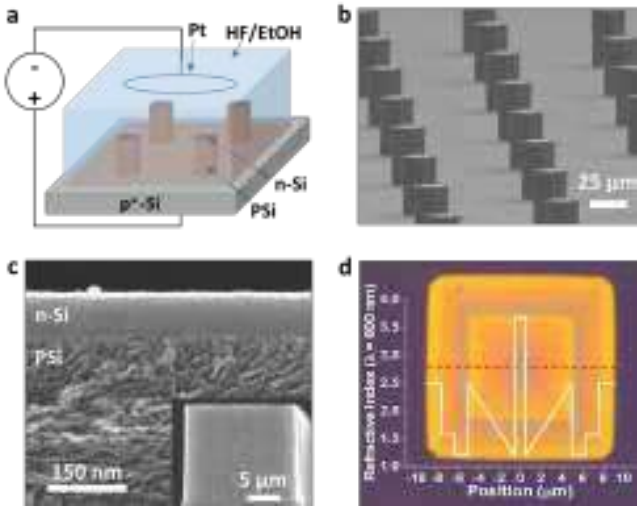


Figure 1. Shape-defined electrochemical etching of PSi for GRIN micro-optics. (a) Schematic outlining the process by which p-type Si SMCs with n-type caps undergo shape-defined electrochemical etching to endow them with nanoscale porosity that defines the local refractive index. (b) SEM image of a section of an array of Si SMCs subjected to shape-defined PSi formation. (c) SEM cross-section of an etched feature showing how PSi formation proceeds beneath the n-type cap. (Inset) SEM cross-section of a fully porous ridge, showing that shape-defined etching can proceed through the Si microstructures. (d) Reflection-

mode optical micrograph from the top of an ~18 μm PSi SMC with an arbitrary GRIN that can be observed through the structure's n-type Si cap. The GRIN profile along the dashed red line is superimposed on top of the optical image.

3. Discussion

Using PSi as a host, we fabricate a range of optical elements including waveguides, lenses, compound lenses, and polarization sensitive beam splitters. As just one example, starting from shaped silicon features on a waver, we use the shape-defined electrochemical formation of PSi to form polarization splitters and an element which possesses a linear GRIN that is capable of focusing TM light to a diffraction-limited line, while TE light is directed to two high-intensity regions in roughly the same plane as, but laterally displaced to either side of, the TM focus. The optical physics of these structures is readily predictable, while the flexibility of the fabrication process lends itself to scaling to dimensions on the order of 100 – 200 μm if appropriate measures are taken to promote uniformity (e.g., electrolyte stirring and etching breaks) of the electrochemical etch.

4. Conclusions

The optical response of PSi-based GRIN elements is controlled by engineering its refractive index and birefringence profile. PSi's programmable optical properties were incorporated into the design of polarization independent and dependent optics that perform a range of functions based on the magnitude of the birefringence profile. The results shown in this work point to the possibility of designing novel GRIN optics from PSi.

Acknowledgements

This work was supported by the U.S. Department of Energy "Light-Material Interactions in Energy Conversion" Energy Frontier Research Center under grant DE-SC0001293, and the U.S. Department of Energy "Photonics at Thermodynamic Limits" Energy Frontier Research Center under grant DE-SC0019140, and the University of Illinois at Urbana-Champaign.

References

[1] M. Fujii and J. Diener, in *Handb. Porous Silicon*, edited by L. Canham (Springer International Publishing, Cham, 2014), pp. 245–253.

[2] V. Y. Timoshenko, L. A. Osminkina, A. I. Efimova, L. A. Golovan, P. K. Kashkarov, D. Kovalev, N. Künzner, E. Gross, J. Diener, and F. Koch, Phys. Rev. B **67**, (2003).

[3] O. G. Sarbey, E. K. Frolova, R. D. Fedorovich, and D. B. Danko, Phys. Solid State **42**, 1240 (2000).

[4] K. Hakshur and S. Ruschin, Appl. Phys. Lett. **104**, 051909 (2014).

[5] L. A. Golovan', P. K. Kashkarov, and V. Y. Timoshenko, Crystallogr. Rep. **52**, 672 (2007).

[6] A. A. Lutich, M. B. Danailov, S. Volchek, V. A. Yakovtseva, V. A. Sokol, and S. V. Gaponenko, Appl. Phys. B **84**, 327 (2006).

[7] D. A. G. Bruggeman, Ann. Phys. **416**, 636 (1935).

[8] F. Genereux, S. W. Leonard, H. M. van Driel, A. Birner, and U. Gösele, Phys. Rev. B **63**, (2001).

[9] M. Born and E. Wolf, *Principles of Optics: Electromagnetic Theory of Propagation, Interference and Diffraction of Light*, 7th expanded ed (Cambridge University Press, Cambridge ; New York, 1999).

[10] N. A. Krueger, A. L. Holsteen, S.-K. Kang, C. R. Ocier, W. Zhou, G. Mensing, J. A. Rogers, M. L. Brongersma, and P. V. Braun, Nano Lett. **16**, 7402 (2016).

Local Symmetries in Wave Mechanics: From Fundamentals to First Applications

Peter Schmelcher

Zentrum für Optische Quantentechnologien, Universität Hamburg
Luruper Chaussee 149, 22761 Hamburg, Germany
Hamburg Centre for Ultrafast Imaging, Universität Hamburg
Luruper Chaussee 149, 22761 Hamburg, Germany,

Abstract

The concept of local symmetries which hold only in spatially limited domains is developed. Decomposing space into domains where different local symmetries hold a novel layer of complexity is derived. This way the parity and Bloch theorems are generalized to the case of broken global symmetry [1]. Local inversion or translation symmetries are shown to yield invariant currents that characterize wave propagation. These currents map the wave function from an arbitrary spatial domain to any symmetry-related domain. Nonvanishing values of the invariant currents provide a systematic pathway to the breaking of discrete global symmetries [1]. Some examples of applications are provided. A classification of perfectly transmitting resonances in completely locally symmetric scattering setups [2] allows for the design of the scattering behaviour in these non-periodic setups. The emergence and control of flatbands in corresponding discrete quasi 1D setups based on local symmetries are discussed [3]. Local symmetries also allow for the real space design of edge states in aperiodic chains [4]. A generalization to interacting many-body systems is outlined [5].

References

[1] P.A. Kalozoumis, C. Morfonios, F.K. Diakonos and P. Schmelcher, Phys. Rev. Lett. 113, 050403 (2014)

[2] P.A. Kalozoumis, C. Morfonios, N. Palaiodimopoulos, F.K. Diakonos and P. Schmelcher, Physical Review A 88, 033857 (2013)

[3] M. Roentgen, C. Morfonios and P. Schmelcher, Physical Review B 97, 035161 (2018)

[4] M. Roentgen, C. Morfonios, R. Wang, L. dal Negro and P. Schmelcher, arXive 1807.06812

[5] P. Schmelcher, S. Kroenke and F.K. Diakonos, Journal of Chemical Physics 146, 044116 (2017)

Integrated frequency combs for the on-chip generation of optical quantum states

Stefania Sciara[1,2], Michael Kues[3,4], Christian Reimer[1,5], Piotr Roztocki[1], Benjamin Wetzel[1,6], Brent E. Little[7], Sai T. Chu[8], David J. Moss[9], Lucia Caspani[10], and Roberto Morandotti[1,11,12*]

[1] Institut National de la Recherche Scientifique (INRS-EMT), Varennes, Canada
[2] Department of Energy, University of Palermo, Palermo, Italy
[3]School of Engineering, University of Glasgow, Glasgow, Scotland
[4]Hannover Center for Optical Technologies (HOT), Leibniz University Hannover, Hannover, Germany
[5]School of Engineering and Applied Sciences, Harvard University, Cambridge, USA
[6]Department of Physics and Astronomy, University of Sussex, Brighton, England
[7] Chinese Academy of Science, Xi'an, China
[8]Department of Physics and Material Science, City University of Hong Kong, Hong Kong, China
[9]Centre for Micro Photonics, Swinburne University of Technology, Hawthorn, Australia
[10]Institute of Photonics, Department of Physics, University of Strathclyde, Glasgow, Scotland
[11]University of Electronic Science and Technology of China, Chengdu, China
[12]ITMO University, St Petersburg, Russia
*corresponding author, E-mail: morandotti@emt.inrs.ca

Abstract

We make use of integrated frequency combs to generate on-chip heralded single photons, cross-polarized photon pairs, as well as two- and multiphoton time-bin entangled states and high-dimensional frequency entangled states.

1. Introduction

Sources of entangled photon-pairs are key building blocks towards applications in quantum information processing [1], quantum communications [2], as well as imaging and sensing with resolutions exceeding the classical limit [3]. The realization of, e.g. polarization, time- and frequency-bin entangled photon-pairs has been demonstrated using spontaneous parametric down-conversion (SPDC) in nonlinear second-order media, as well as spontaneous four-wave mixing (SFWM) in third-order nonlinear media. Specifically, nonlinear (third-order) interactions in on-chip microring resonators have been exploited to achieve classical frequency combs, mode-lock lasers, signal processing, etc [4-6]. Integrated photonics can also find applications for quantum state generation in compact, scalable and efficient devices, required for future optical quantum circuits. In contrast to waveguides, microring resonators with narrow resonances and high Q-factors, offer an improvement in photon-pair generation efficiency, as well as a narrow photon-pair bandwidth, making them compatible with quantum optical devices [7,8]. Most importantly, in contrast to non-resonant waveguides, where individual photon-pairs, featuring one signal/idler frequency pair, are generally created, resonant nonlinear cavities (e.g., microring resonators) enable the generation of correlated photon-pairs on multiple signal/idler frequency channels [9], due to their periodic and equidistant resonance structure.

Here, we investigate different approaches to generate optical quantum states by means of integrated frequency combs. These include the realization of multiplexed heralded single-photons [9] and cross-polarized photon-pairs on a photonic chip [10], as well as the first on-chip generation of two- and multi-photon time-bin entangled states [11], and, finally, the first realization of high-dimensional frequency-entangled photon pairs on-chip and their coherent control [12].

2. Methods and Results

The quantum frequency combs were realized by using a 4-port integrated microring resonator with a 200 GHz free spectral range (FSR), fabricated in a CMOS-compatible high refractive index silica glass [13] and excited with a pulsed mode-locked fiber laser. The high field enhancement and nonlinearity of the resonator allowed generating photon-pairs through SFWM on several frequency channels (corresponding to the ring resonances) symmetrically located with respect to the pump frequency [9]. Depending on the targeted application, different excitation schemes were used. If the pump spectral bandwidth was chosen to be larger than the resonator bandwidth, the laser was spectrally-filtered to excite either a single or multiple resonances. The coupling into the resonator then further spectrally filtered the pump to perfectly match its bandwidth. This configuration enabled the generation of pure single frequency-mode photons [11]. Coincidence detections were used to characterize the photon coincidence statistics as well as their temporal duration. The (heralded) second-order coherence of the emitted photons were measured by using a Hanbury Brown and Twiss setup. In order to create time-bin entangled photons, an unbalanced, fiber-based phase-stabilized Michelson interferometer generating double

pulses was used before the chip. If the pump power was then set to generate no more than one photon-pair per double pulse on average, the photon-pairs were created in a coherent superposition of two discrete time-bins, thus forming an entangled state [11]. To verify entanglement through quantum interference measurement, we added interferometers having a path length difference matched to the first interferometer (see Figure 1). Using coincidence detection, this setup enabled to measure quantum interference and perform full quantum state tomography, which characterize the entangled photon-pairs and multi-photon states. In order to generate high dimensional entangled states, we excited a single resonance of the resonator with a spectrally-filtered mode-locked laser [12]. Due to the broad phase-matching condition, the generated photon pairs cover multiple resonances. Furthermore, the photons are intrinsically created as a high-dimensional superposition of resonance frequency mode states, and are entangled due to SFWM energy conservation. The frequency-entangled photon pairs were coherently controlled via fiber-based electro-optic modulation techniques allowing to perform quantum state tomography and quantum interference measurements [12].

By simultaneously exciting two orthogonal-polarization mode resonances, we introduced a new type of SFWM to the toolbox of integrated photonics [10]. In particular, we demonstrated the first realization of type-II SFWM that allows to directly generate orthogonally-polarized photon-pairs on a chip [10]. We measured photon coincidences, and also drive the system to optical parametric oscillation, generating orthogonally-polarized beams.

Using double pulse excitation, we demonstrated time-bin entangled photon-pairs over the entire frequency comb spectrum [11]. We measured the violation of a Bell-like inequality through quantum interference [14] reaching a visibility of 82.4% which is higher than the 71% threshold. Performing quantum state tomography [15], we confirmed qubit entanglement with 94% fidelity, enabling the implementation of quantum information processing protocols. We repeated tomography measurements after 40 km of fiber propagation, and confirmed that the quantum states are well preserved during propagation (a 64% fidelity). This opens up possible implementations in quantum communications applications.

Finally, we achieved the generation of high-dimensional frequency-entangled photon pairs with up to 10 dimension per photon [12]. We validated the dimensionality of the generated states using the Schmidt number, while their entanglement was validated via quantum interference measurements that showed Bell inequalities violation for dimensionality D=2,3, and 4, as well as via quantum state tomography for the same dimensionalities that provided high fidelities (exceeding 80%) [12].

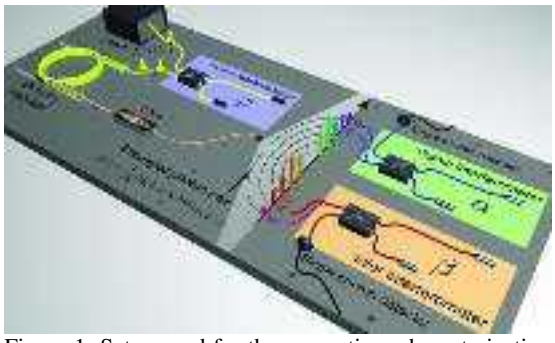


Figure 1: Setup used for the generation, characterization and detection of two- and multiphoton entangled states [11].

3. Conclusion

We demonstrate the realization of different optical quantum states by means of integrated optical frequency comb sources. Our results indicate the strong potential to use on-chip frequency combs to generate both heralded single photons, two and multi-photon time-bin entangled states, as well as high-dimensional frequency-entangled photon pairs.

References

[1] P. Walther et al., Experimental one-way quantum computing, *Nature* 434, 169 (2005)

[2] H. J. Kimble, The quantum internet, *Nature* 453, 1023 (2008)

[3] M. Kolobov, The spatial behavior of nonclassical light, *Rev. Mod. Phys.* 71, 1539 (1999).

[4] A. Pasquazi et al., Micro-combs: a novel generation of optical sources, *Physics Reports* 729, 1-82 (2018).

[5] M. Kues et al., Passively mode-locked laser with an ultra-narrow spectral width, *Nature Photon.* 11, 159-162 (2017)

[6] M. Ferrera et al., On-chip CMOS –compatible all-optical integrator, *Nature Commun.* 1, 29 (2010)

[7] L. Caspani et al., Integrated sources of photon quantum states based on nonlinear optics, *Light Sci. Appl.* 6, e17100 (2017)

[8] M. Kues et al., Quantum optical microcombs, *Nature Photonics* 13, 170-179 (2019)

[9] C. Reimer et al., Integrated frequency comb source of heralded single photons, *Opt. Express* 22, 1023 (2014)

[10] C. Reimer et al., Cross-polarized photon-pair generation and bi-chromatically pumped optical parametric oscillation on a chip, *Nature Commun.* 6, 8236 (2015)

[11] C. Reimer et al., Generation of multiphoton entangled quantum states by means of integrated frequency combs, *Science* 351, 1176 (2016)

[12] M. Kues et al., On-chip generation of high-dimensional entangled quantum states and their coherent control, *Nature* 546, no. 7660, pp. 622– 305 (2017).

[13] D. J. Moss et al., New CMOS-compatible platforms based on silicon nitride and Hydex for nonlinear optics, *Nature Photon.* 7, 597 (2013)

[14] J. F. Clauser et al., Proposed experiment to test local hidden-variable theories, *Phys. Rev. Lett.* 23, 880 (1969)

[15] D.F.V. James et al., Measurement of qubits, *Phys. Rev. A.* 64, 052312 (2001)

Diamond nano-optomechanical devices

Paul Barclay[1]

[1]Department of Physics and Astronomy, University of Calgary, Canada
*corresponding author, E-mail: pbarclay@ucalgary.ca

Abstract

Using a novel quasi-isotropic etching process we have created a range of diamond optomechanical devices. These include high-Q microdisk resonators operating in the sideband resolved regime that can be used for optical information processing applications such as pulse storage, wavelength conversion, and multi-colour optical interference.

1. Introduction

Nanoscale cavity optomechanical devices enhance the interaction between co-localized optical cavity modes and nanomechanical resonances. For sufficiently strong optical confinement and field strengths, and appropriate nanophotonic device design, it is possible to realize large optomechanical coupling rates between light and the mechanical motion of the resonator in these devices. When combined with low optical and mechanical loss rates, coherent optical control of mechanical motion can be realized, enabling fundamental studies and new technologies ranging from quantum information processing to sensing.

2. Diamond optomechanics

Realizing optomechanical devices from diamond is of particular interest owing to its exceptional material properties together with its ability to host high quality spin qubits. Diamond optomechanical devices have low optical and mechanical dissipation and can support high optical intensity thanks to the material's large electronic bandgap, and correspondingly low multi-photon absorption at telecommunication wavelengths. This latter point allows diamond optical cavities to support large numbers of photons before their optical properties degrade, a major benefit for many optomechanics applications.

Until recently, realizing diamond optical devices have been an outstanding challenge. We have invented a new fabrication process that solves this problem and have used it to create a variety of diamond devices, including microdisk cavities [1,2] and nanobeam waveguides [3]. In our most recent work [4], we have harnessed the high optomechanical performance of these devices for several optical information processing applications. In this talk we will show data demonstrating coherent transfer of a pulse of light to the mechanical motion of a diamond microdisk cavity optomechanical device. This pulse storage scheme allows microsecond long optical delays that are optically tunable, as well as wideband wavelength conversion in which the pulse is readout at a wavelength 40 nm detuned from the input pulse. We will also present a novel form of multicolor interferometer, where the optomechanical device mediates interference between widely separated wavelengths of light, allowing construction of a two colour optical switch.

References

[1] M. Mitchell, B. Khanaliloo, D. Lake, T. Masuda, J. P. Hadden, P. E. Barclay, "Single crystal diamond low-dissipation cavity optomechanics," Optica 3, 963 - 970 (2016)

[2] B. Khanaliloo, M. Mitchell, A. C. Hryciw, P. E. Barclay, "High-Q/V monolithic diamond microdisks fabricated with quasi-isotropic etching," Nano Letters 15 5131-5136 (2015)

[3] B. Khanaliloo, H. Jayakumar, A. C. Hryciw, D. Lake, H. Kaviani, P. E. Barclay, Single crystal diamond nanobeam waveguide optomechanics, Physical Review X 5, 041051 (2015)

[4] M. Mitchell, D. P. Lake, P. E. Barclay, Optomechanically amplified wavelength conversion in diamond microcavities, submitted (2018), open access preprint: arxiv:1902.07763 [optics]

Balancing the photo-budget in far-field optical imaging for enhanced lateral resolution

Wyatt Adams, Chito Kendrick, Christopher T. Middlebrook, and Durdu Ö. Güney*

Department of Electrical and Computer Engineering, Michigan Technological University, Houghton, MI, USA
*corresponding author, E-mail: dguney@mtu.edu

Abstract

Owing to the semiclassical process of photodetection, the resolution of optical imaging systems is often limited by shot noise. Here we present a theory to improve the shot noise limit in incoherent imaging and experimentally show its validity with a low numerical aperture system. The same principles can also improve the performance of near-field sub-diffraction-limited imaging via hyperbolic metamaterials.

1. Introduction

While the diffraction limit is often identified as the barrier to image resolution in the far-field, optical systems can also be limited by the statistics of detecting photons. Since photodetection can be modeled as a Poisson impulse process [1], it is shown in this summary (and independently in other recent works [2, 3]) that the shot noise variance in the Fourier spectrum of an image is given by the total number of expected photons in the image. It follows that decreasing the number of photons decreases the variance, but it will also decrease the signal proportionally.

To achieve an improvement in resolution, we show that the image "photo-budget" can be better balanced by preferentially transferring the high spatial frequency photons to the image, and then deconvolving the resulting image to eliminate the induced low spatial frequency blurring. The result is improved lateral resolution.

2. Theory

The process of incoherent optical imaging is readily modeled by a two-dimensional convolution operation

$$I(\mathbf{r}) = H(\mathbf{r}) * O(\mathbf{r}), \tag{1}$$

where $I(\mathbf{r})$, $O(\mathbf{r}) \in \mathbb{R}_{\geq 0}$ are photon flux densities (photons/$s \cdot m^2$) and $H(\mathbf{r}) \in \mathbb{R}_{\geq 0}$ is the point spread function (PSF) of the optical system. At the detector, an array of rectangular pixels of size Δx by Δy collect the photons contained in the continuous signal $I(\mathbf{r})$, giving a discrete output signal at pixel p

$$\begin{aligned}\bar{I}_p &= \eta T \int_{A_p} I(\mathbf{r}) d^2\mathbf{r} \\ &= \eta T \int_{y_p-\Delta y/2}^{y_p+\Delta y/2} \int_{x_p-\Delta x/2}^{x_p+\Delta x/2} I(x,y) dx dy,\end{aligned} \tag{2}$$

where η is the pixel efficiency, T is the exposure time, and $(x_p, y_p) = \mathbf{r}_p$ is the center location of pixel p.

Since the pixels absorb light in discrete packets (photons), the signal will have a Poissonian probability mass function. Also, there is noise added by the electronics reading out the signal. Therefore, the observed signal at pixel p becomes

$$I_p = \bar{I}_p + N_{p,\gamma} + N_{p,e}, \tag{3}$$

where $N_{p,\gamma}$ is the photon (shot) noise and $N_{p,e}$ is an electronic noise term independent of the input light signal. In many cases, $\mathrm{Var}(N_{p,\gamma}) \gg \mathrm{Var}(N_{p,e})$ and we can neglect the third term. We can find the variance of the photon noise in the Fourier domain by

$$\begin{aligned}\mathrm{Var}(\tilde{N}_{q,\gamma}) &= \mathrm{Var}\left(\sum_p N_{p,\gamma} e^{-i2\pi \mathbf{k}_q \cdot \mathbf{r}_p}\right) \\ &= \sum_p \mathrm{Var}(N_{p,\gamma}) |e^{-i2\pi \mathbf{k}_q \cdot \mathbf{r}_p}|^2 \\ &= \sum_p \bar{I}_p = n_\gamma,\end{aligned} \tag{4}$$

where $\mathbf{k}_q$ is the location of pixel q in the Fourier space corresponding to $\{\mathbf{r}_p\}$, and n_γ is the total number of expected photons in the entire image. From this simple result, it becomes apparent that reducing the number of photons in the image will reduce the noise level distributed throughout the Fourier space.

Consider a $4f$ system with a Fourier plane pupil function such as in Figure 1(b) described by

$$\tilde{P}_q = \begin{cases} 1 & \text{if } k_- \leq |\mathbf{k}_q| \leq k_+ \\ 0 & \text{otherwise,} \end{cases} \tag{5}$$

where $k_0 = 1/\lambda_0$, λ_0 is the free space center wavelength, $k = 2\mathrm{NA}k_0$, NA is the numerical aperture, and $k_- < k_+ \leq k$. For an incoherent imaging system, the optical transfer function (OTF) $\tilde{H}_q$ obeys

$$\tilde{H}_q = \sum_\kappa \tilde{P}_\kappa \tilde{P}^*_{\kappa - q} = \tilde{P}_q \star \tilde{P}_q, \tag{6}$$

with $\star$ denoting the autocorrelation. The spectral SNR for an image formed by the $4f$ system then becomes

$$\mathrm{SNR}_q = \frac{|\bar{\tilde{I}}_q|}{\sqrt{n_\gamma}} = \frac{\left|\left[\tilde{P}_q \star \tilde{P}_q\right] \tilde{O}_q\right|}{\sqrt{n_\gamma}}. \tag{7}$$

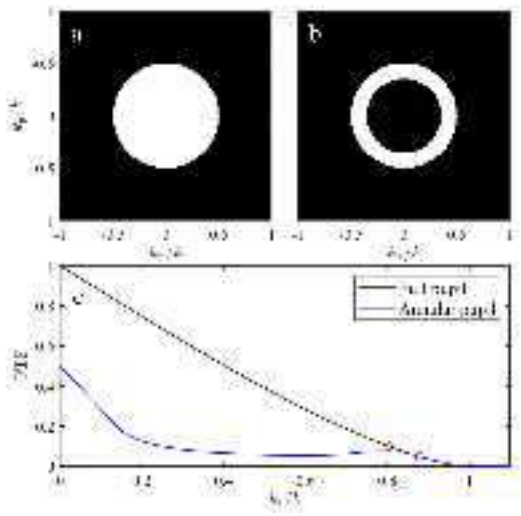


Figure 1: (a) Open and (b) annular pupil functions. (c) OTFs of the pupils in (a) and (b). The dashed lines show 10% noise levels corresponding to each OTF, and the red circles indicate the corresponding noise resolution limits. The annular pupil resolution limit exceeds that of the open pupil.

From Equation (7), the argument can clearly be made that $\tilde{P}_q$ gives us control over the SNR_q by way of both the numerator and denominator. In Figure 1(c), it can be seen that the noise resolution limit for the annular pupil is greater than that of the open pupil.

3. Results

We performed an experiment in which a USAF-1951 resolution target (Thorlabs R1DS1N) is illuminated with an incoherent light source (Thorlabs LIU525B) and imaged by a $4f$ system consisting of two achromatic-doublet lenses (Space Optics Research Labs) and a custom printed pupil transparency in the Fourier plane. The images were collected with an inexpensive CMOS camera (Thorlabs DCC1645C) and post-processed in MATLAB. Figure 2 shows the collected images with two different pupil transparencies. In (a), the pupil is a 10mm diameter opening, while (b) is the image with annular pupil with obstruction diameter $10\mathrm{mm}/\sqrt{2}$.

In Figure 2(a), it can be seen that the line visibility in element 4 is poor, and disappears completely in element 5. However, in (b) the lines remain qualitatively visible until element 6. The image quality is further improved by Richardson-Lucy deconvolution in part (d), where the blurring introduced in the lower spatial freqencies are partially corrected.

4. Conclusion

We presented a theory for pushing the lateral resolution of optical imaging systems beyond the shot noise limit. The theory was experimentally implemented using a $4f$ system with a pupil transparency in the Fourier plane, showing improved resolution when the Fourier plane pupil preferentially transfers spatial frequencies near the diffraction limit, compared to an open pupil of the same numerical aperture. This idea is a far-field extension of our previous works in near-field superresolution imaging with hyperbolic metamaterials [4, 5].

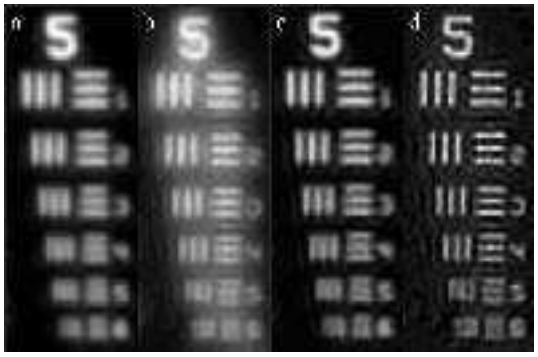


Figure 2: Images of a USAF-1951 resolution target with $T = 20$ms (brightness is scaled to max value in each image) resolution with (a) open pupil (Figure 1(a)) and (b) annular pupil (Figure 1(b)) with $k_- = k/2\sqrt{2}$ and $k_+ = k/2$. (c) and (d) are the images in (a) and (b) respectively after deconvolution. Deconvolution was performed with PSFs constructed from Equation 6 and MATLAB's built-in Richardson-Lucy algorithm (20 iterations).

Acknowledgement

This work was supported by Office of Naval Research (award N00014-15-1-2684).

References

[1] J.W. Goodman, *Statistical Optics*, Wiley, New York, pp. 466–468, 2000.

[2] E.A. Ingerman, R.A. London, R. Heintzmann, M.G.L. Gustafsson, Signal, noise, and resolution in linear and nonlinear structured-illumination microscopy, *J. Microsc.* vol. 273, no. 1, pp. 3-25, 2019.

[3] J. Becker, R. Förster, R. Heintzmann, Better than a lens - A novel concept to break the SNR-limit, given by Fermat's principle, arXiv:1811.08267 [physics.optics], 2018.

[4] W. Adams, A. Ghoshroy, D.Ö. Güney, Plasmonic superlens imaging enhanced by incoherent active convolved illumination, *ACS Photonics* vol. 5, no. 4, pp. 1294-1302, 2018.

[5] A. Ghoshroy, W. Adams, X. Zhang, D.Ö. Güney, Hyperbolic Metamaterial as a Tunable Near-Field Spatial Filter to Implement Active Plasmon-Injection Loss Compensation, *Phys. Rev. Appl.* vol. 10, no. 2, 024018, 2018.

Correlated Photon pairs at 2 microns: Generation, Characterisation, and Detection

Shashi Prabhakar[1], Taylor Shields[1], Gregor G. Taylor[1], Dmitry Morozov[1], Michael Kues[1,2], Corin Gawith[3], Lucia Caspani[4] Robert H. Hadfield[1] and Matteo Clerici[1]

[1]School of Engineering, University of Glasgow, Glasgow, G12 8QQ, UK
[2]Hannover Center for Optical Technologies (HOT), Leibniz University Hannover, Hannover, Germany
[3]Covesion Ltd. & Optoelectronics Research Centre, University of Southampton, Southampton, SO17 1BJ, UK
[4]Institute of Photonics, Department of Physics, University of Strathclyde, Glasgow G1 1RD, UK
*corresponding author, E-mail: matteo.clerici@glasgow.ac.uk

Abstract

We report the generation and characterization of non-classical photon states in the 2-micron spectral region, paving the way to low-loss free-space and guided wave quantum communication in the 2-micron window.

1. Introduction

The spectral region just above 2 μm is attractive for several applications, spanning from sensing to communication. Due to the difficulty in source and detector development, the 2 μm technology lags behind that in the telecom region.

Daylight quantum communication has been recently demonstrated at telecom wavelengths [1] and could be further enhanced by moving to a region with a lower solar background. Roughly between 2 and 2.5 μm the atmosphere is transparent, and the solar background is nearly half of that at telecom wavelengths. This makes it extremely relevant for free-space communications and becomes crucial for satellite-to-ground, and satellite-to-satellite quantum-secured communications [1], [2].

The 2 μm region is also relevant for classical guided wave communications, as it may give new breadth to fiber-based links avoiding bandwidth saturation. Efforts to develop low-losses and large bandwidth fibers in this spectral region have already produced remarkable results, e.g., in the form of photonic bandgap fibers [3]. Similarly, from an integrated optics viewpoint, silicon germanium waveguides have recently shown to reach 10 Gb/s [4], [5].

Stimulated by the situation detailed above, we have investigated the generation of non-classical photon states at 2.080 μm and we report the characterization of a correlated photon pair source.

We have characterized the photon pair source quality in terms of the coincidence to accidental ratio (CAR) and also demonstrated the photon pair indistinguishability with a Hong-Ou-Mandel (HOM) measurement.

2. The experiment

We generated photon pairs from spontaneous parametric down-conversion of a 1040 nm pulsed laser radiation delivered by a Chromacity Spark 1040 Ytterbium laser system. The mode-locked laser had a repetition rate of 80 MHz, a pulse duration of 120 fs and a maximum average power of 3 W. The nonlinear process was excited in a periodically poled MgO doped lithium niobate crystal specially designed for the experiment and realized by Covesion Ltd. The chosen crystal had a 31.24 μm poling period and was operated in a Type-0 configuration. The crystal was temperature-controlled with a 0.1°C accuracy and operated at 39.5°C so that the phase matching is optimal for collinear generation of the 2.080 μm photon pairs. Signal and idler photons were separated with a D-shaped mirror in the spatial far-field of the emission and then coupled into single-mode SM2000 fibers by achromatic collimators. The experimental set up is sketched in Fig.1.

To remove the residual pump field, two filters were used. The first is a long-pass filter, with a cut-off at 1450 nm and the second is an antireflection coated 1 mm thick germanium window, which has a high rejection for radiation at a

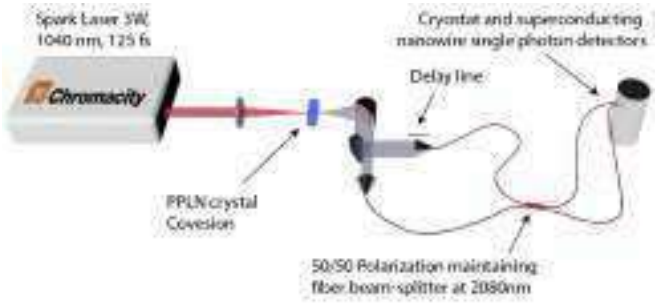


Figure 1: Experimental setup for the Hong-Ou-Mandel interference measurement. The coincidence measurements were performed connecting the fibers directly to the detector without a fiber beam splitter.

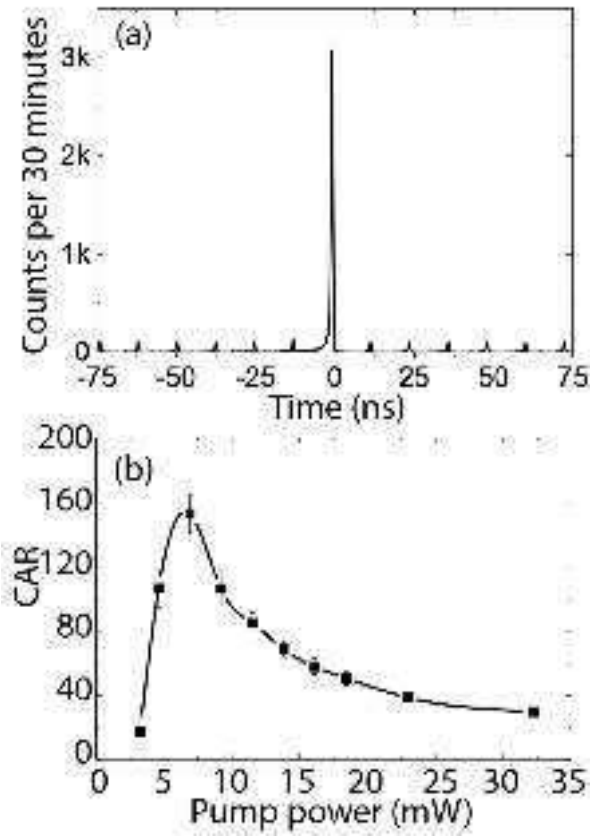


Figure 2 (a) Coincidence counts for a 30 minutes long measurement. (b) Coincidence-to-accidental ratio (CAR) as a function of average pump power. The curve is a guide for the eye.

wavelength shorter than 1.850 μm. In addition, bandpass filters centered at the degenerate wavelength with 50 nm or 10 nm bandwidth were employed to select the portion of the generated spectrum relevant to the experiment.

We first characterized the photon pair generation efficiency and the losses of the components in the experiment, observing an efficiency of up to $\eta = 10^{-10}$ in a regime where ~50 photon pairs were generated each laser pulse. To perform the characterization of properties of photon pairs we employed superconducting nanowire single-photon detectors (SNSPD), with a recorded quantum efficiency of $\sim 10^{-2}$. The overall losses from generation to the detectors was estimated to approx. 12 dB (excluding detection efficiency). The coincidences were recorded using a time-to-digital converter (HydraHarp 400). An example of a histogram of the coincidences obtained from a 30 minutes long measurement is shown in Fig 2 (a).

3. Discussion

The coincidence histogram shown in Fig. 2(a) is characterized by a peak in the coincidence counts for zero delay, which means signal and idler photons were created in a time-correlated fashion. Peaks with less counts can be noticed at larger delays, which correspond to coincidences between unrelated laser pulses, and which are therefore defined as accidentals. To quantify the photon pair production rate, we determined the coincidence to accidental ratio (CAR). We measured the CAR as a function of increasing pump power (corresponding to increasing single-photon counts per channel) as shown in Fig. 2 (b). The maximum CAR is achieved for a pump power of 6 mW. The CAR could be further increase with better detector quantum efficiencies and lower losses.

Finally, we observed the interference of photon pairs in a HOM scheme, with visibility of >72% (without background correction), thus demonstrating the indistinguishability of the two photons.

4. Conclusions

In conclusion, we demonstrated the generation and detection of 2.080 μm photon pairs with a maximum CAR of ~160 in the photon-starved regime. With the improvement of the detector technology at longer wavelengths, down-conversion systems based on MgO:PPLN driven by mW-level Ytterbium lasers can become a practical source of correlated and entangled photon pairs. These sources will be ideal for daylight free-space quantum key distribution in a spectral region with high atmospheric transparency and low solar background. The experimental setup for measuring the photon interference giving rise to the Hong-Ou-Mandel effect is shown in Fig. 1.

Acknowledgments

The authors acknowledge the support from EPSRC/Innovate UK (EP/R043299/1). M.C. acknowledges the support of UKRI (innovation fellowship EP/S001573/1). M.K. acknowledges support from BMBF Quantum Futur programm. The authors acknowledge the support of Chromacity Ltd and Covesion Ltd.

References

[1] S. K. Liao *et al.*, "Satellite-Relayed Intercontinental Quantum Network," *Phys. Rev. Lett.*, vol. 120, no. 3, p. 30501, 2018.

[2] H. Kaushal and G. Kaddoum, "Optical Communication in Space: Challenges and Mitigation Techniques," *IEEE Commun. Surv. Tutorials*, vol. 19, no. 1, pp. 57–96, 2017.

[3] M. N. Petrovich *et al.*, "Demonstration of amplified data transmission at 2 μm in a low-loss wide bandwidth hollow core photonic bandgap fiber," *Opt. Express*, vol. 21, no. 23, p. 28559, Nov. 2013.

[4] M. Lamy *et al.*, "High speed optical transmission at 2 μm in subwavelength waveguides made of various materials," in *Advanced Photonics 2018 (BGPP, IPR, NP, NOMA, Sensors, Networks, SPPCom, SOF)*, 2018, vol. 1, p. ITu4I.6.

[5] M. Lamy *et al.*, "Ten gigabit per second optical transmissions at 1.98 μm in centimetre-long SiGe waveguides," *Electron. Lett.*, vol. 53, no. 17, pp. 1213–1214, Aug. 2017.

All-optical signal processing with hybrid III-V-on-silicon chip

Léa Constans[1,2], Dorian Sanchez[2], Sylvain Combrié[1], Fabrice Raineri[2], Alfredo de Rossi[1*]

[1] Thales Research and Technology, Palaiseau, France
[2] Center of Nanosciences and Nanotechnologies, CNRS, Univ. Paris-Sud, Université Paris-Saclay, Palaiseau, France
*corresponding author, e-mail: alfredo.derossi@thalesgroup.com

Abstract

We discuss the properties of ultrafast nonlinear hybrid devices on a silicon-photonic platform. Nanoscale resonators made of III-V alloys are used as all-optical gates. As an example we have considered this technology for on-chip optical sampling of signals up to 40 GHz. Due to their ultrafast dynamics, high non-linearity and low footprint, these nanoswitches can easily be combined to build complex photonic circuits, e.g. for advanced photonic computing.

1. Introduction

Due to light-matter interaction, light is a mean to perform a variety of measurements and physical characterizations in numerous fields, leading to breakthroughs in domains like sensing, communication and defense over the last decades. In particular it is possible to use the properties of light to perform calculations and signal processing, by using as an example optical correlation [1], or more recently for deep learning via optical neural networks [2].

As it comes to signal processing, photonics is a key component for high-rate operation for it provides low-time-jitter sources [3], overcoming electronic analog-to-digital converters (ADCs) bottleneck [4]. Indeed, a low time jitter improves both the speed and resolution, enabling to implement high performance ADCs. This has first led to photonic-assisted ADCs where e.g. a low-time-jitter optical pulse train (the clock) is modulated by an RF input (signal to be sampled) before being digitized [4]. Some integrated systems in silicon photonics were demonstrated [4,5].

Now, to exploit the properties of light even further, high performance ADC can also be performed through all-optical sampling, with both optical clock and optical input analog signal. These all-optical switches, or all-optical gates (AOGs), would allow to process optical signals without optical-to-electrical (O/E) conversion before sampling, while benefiting from high performance photonic clocks. The main types of AOGs are shown in the graph Fig. 1, where they are compared according to the figure of merit 'speed vs. energy'. It can be seen that photonic crystals (PhC) are highly suitable to maximize this figure of merit, using for example PhC Fano cavity to maximize the transmission contrast [6].

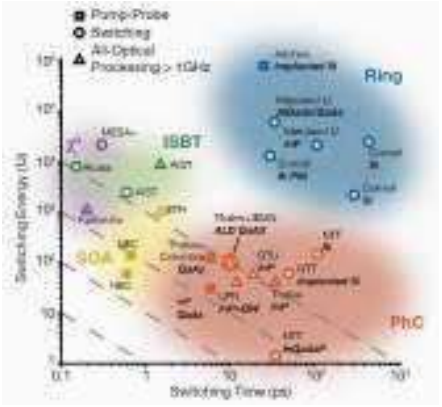


Figure 1: Comparison of AOGs

During my presentation, I will present our nonlinear AOGs using III-V PhC cavities on silicon, and show some possible all-optical signal processing applications such as all-optical sampling and neuromorphic computing.

2. All-optical gate using III-V-on-silicon photonic crystal nanocavities

2.1. All-optical gate based on a resonator

The working principle of an AOG based on a resonator works as illustrated in Fig. 2.

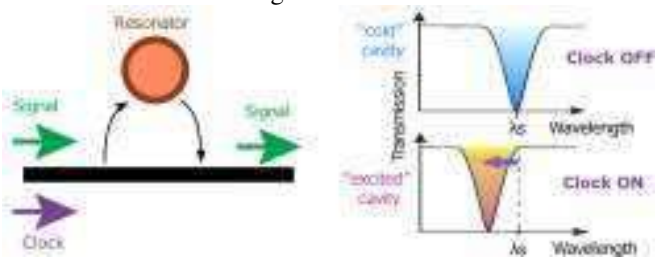


Figure 2: Working principle of an AOG based on a resonator

The system consists of a semiconductor optical resonator next to a waveguide, which carries the signal to be sampled as well as the clock. The resonator is designed so that the wavelength of the signal λ_s corresponds to a resonant mode of the cavity. The sampling function is obtained as follows: the resonant-enhanced absorption of a clock pulse by the cavity excites free carriers, which induce a spectral shift of the resonances of the cavity towards the blue, leading to an increased transmission of the signal.

2.2. Use of III-V-on-silicon PhC nanocavities

As optical cavity we chose to use III-V PhC nanocavities, whose high quality factor and small modal volume lead to high field enhancement and thus strong nonlinearity. Moreover, using III-V alloys allows to benefit from a wide variety of materials in order to tune the interesting properties such as the absorption, the carriers dynamics, and the nonlinearity [7,8]. III-V materials are also integrable in silicon photonics due to numerous wafer-bonding techniques.

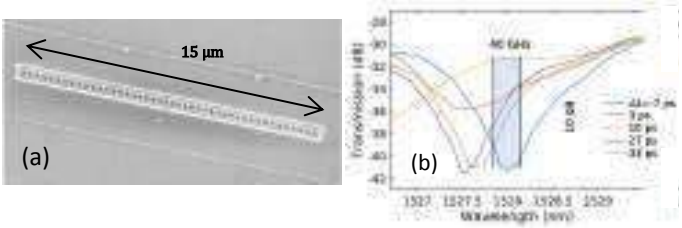


Figure 3: (a) SEM pictures of fabricated InP nanobeams on silicon (b) Estimation of the transmission contrast by pump-probe measurements

For our work we designed and fabricated InP 1D cavities called nanobeams which are shown in Fig. 3(a), with surface InGaAs quantum wells to accelerate the carriers dynamics. More details will be given about the design and fabrication process during the presentation. The nonlinear dynamics can be characterized by pump-probe measurements from which we determine the spectral shift of the probed resonance, and the recovery time of the nonlinear effect. As shown in Fig. 3(b), this measurement allows to estimate the dynamic contrast of the gate, which is the transmission contrast between 1- and 0-samples, here 10 dB.

3. All-optical processing applications

3.1. All-optical sampling

The AOGs we fabricated (shown in Fig. 3(a)) were designed to perform all-optical sampling, whose general principle is recalled in Fig. 4. We assessed the sampling capacity of the AOG by sampling and reconstructing a known optical analog signal, as it will be explained in more details in the presentation. By comparing the sampled signal and the ideal input signal, we derive the signal-to-noise ratio (SNR) and the corresponding Effective Number of Bits (ENOB). With our InP nanobeams we achieved the all-optical sampling of an optical signal modulated at nearly 40 GHz at a 2 GS/s sampling rate, with a SNR of 15 dB (i.e. 2.4 ENOB), with a power budget of 1mW [9].
These results are preliminary, the performance will be improved with the future integration of the photonic sampling circuit, in particular in order to increase the sampling rate via time interleaving, about which I will show some dedicated photonic circuits, being studied at present.

3.2. Neuromorphic photonic computing

To follow the massive data increase of the recent years, new computing paradigms have to be introduced, such as non-Von-Neumann architectures to overcome the processor-memory bottleneck. Amongst others, optical deep learning circuits mimicking the brain have been implemented using artificial neural networks [2]. Such all-optical implementations need a nonlinear activation function, e.g. the function of the Fano AOG in [6], and we believe that our integrated nonlinear III-V PhC-based AOGs are also completely suitable to fulfill this function, and that they can easily be integrated and inserted in a silicon photonic neuromorphic circuit.

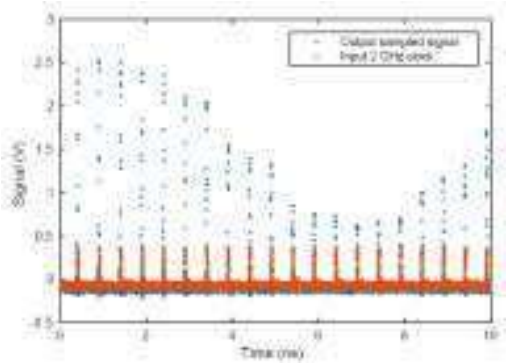


Figure 4: (Oscilloscope trace after O/E conversion) Example of all-optical signal processing with an AOG: all-optical sampling. A continuous optical sinusoidal signal has been sampled by an AOG driven by an optical clock (**red**), we obtain the sampled signal in **blue**.

4. Conclusion

We have demonstrated and presented integrable energy-efficient AOGs based on III-V-on-silicon nanophotonics by using small-footprint PhC cavities, through which all-optical sampling was performed. More generally, these optical gates are relevant for scalable integrated architectures combining both linear and nonlinear features, benefiting from their low footprint and femtoJoule operation energy.

Acknowledgements

This work was supported by the French Directorate General of Armaments (DGA) under the ASTRID project ETHAN and by the European H2020 project Fun-COMP.

References

[1] Rajbenbach et al., OSA Trends in Optics and Photonics 170, 1998.

[2] Y. Shen et al., *Nat. Phot.* 11, 441, 2017.

[3] R. Bouchand et al., *IEEE Photonics Techn. Letters* 29, 1403–1406, 2017.

[4] A. Khilo et al., *Opt. Exp.* 20, p.12, 2012.

[5] H. Gevorgyan et al., *Opt. Exp.* 24, 2016.

[6] Bekele et al., *Opt. Exp.* 26, 2018.

[7] M. Boroditsky et al., *J. Appl. Phys.* 87, 2000.

[8] B. R. Bennett et al., *IEEE J. Quantum Electron.* 26, 1990.

[9] L. Constans et al., OSA Advanced Photonics, Paper IM3B.4., 2018.

Generation of on-chip D-dimensional entangled cluster states and their characterization via optimal entanglement witnesses

Lucia Caspani[1], Stefania Sciara[2,3], Christian Reimer[2,4], Piotr Roztocki[2], Mehedi Islam[2], and Luis Romero Cortés[2], Yanbing Zhang[2], Bennet Fischer[2], Sébastien Loranger[5], Raman Kashyap[5,6], Alfonso Cino[3], Sai T. Chu[7], Brent E. Little[8], David J. Moss[9], William J. Munro[10,11], José Azaña[2], Michael Kues[2,12], and Roberto Morandotti[2,13,14]

[1]Institute of Photonics, Department of Physics, University of Strathclyde, Glasgow G1 1RD, UK
[2]Institut National de la Recherche Scientifique (INRS-EMT), 1650 Blvd. Lionel-Boulet, Varennes, J3X 1S2, Canada
[3]Department of Energy, Information Engineering and Mathematical Models, University of Palermo, Palermo, Italy
[4]John A. Paulson School of Engineering and Applied Sciences, Harvard University, Cambridge, 02138, USA
[5]Engineering Physics Department, Polytechnique Montreal, 2900 Blvd. Édouard-Montpetit, Montreal H3T 1J4, Canada
[6]Electrical Engineering Department, Polytechnique Montreal, 2900 Blvd. Édouard-Montpetit, Montreal H3T 1J4, Canada
[7]Department of Physics and Material Science, City University of Hong Kong, Tat Chee Avenue, Hong Kong, China
[8]State Key Laboratory of Transient Optics, Xi'an Institute of Optics and Precision Mechanics, Chinese Academy of Science, Xi'an, China
[9]Centre for Micro Photonics, Swinburne University of Technology, Hawthorn, Victoria 3122, Australia
[10]NTT Basic Research Laboratories and NTT Research Center for Theoretical Quantum Physics, NTT Corporation, Kanagawa, Japan
[11]National Institute of Informatics, Tokyo, Japan
[12]Hannover Center for Optical Technologies (HOT), Leibniz University Hannover, Hannover, Germany
[13]Institute of Fundamental and Frontier Sciences, University of Electronic Science and Technology of China, Chengdu 610054, China
[14]ITMO University, St Petersburg, Russia

*corresponding author, E-mail: lucia.caspani@strath.ac.uk

Abstract

We report the on-chip generation of hyper-entangled states in the time-frequency domain and their transformation in high-dimensional cluster states via deterministic controlled phase gates. We characterized these states developing a universal technique for deriving "experimentally friendly" entanglement witness operators.

1. Introduction

Polarization-entangled photon pairs have been the work-horse for quantum optical experiments for many years. More recently, however, there has been a growing interest in the generation of more complex quantum states of light. These ranged from states with increased dimensionality, both in the continuous and discrete variable regimes (for e.g. increasing the amount of information carried by a single photon), to the increased number of parties (multiphoton states), to a combination of both. Among these complex states, cluster states [1] have gained particular attention as they represent a universal resource for a type of measurement-based quantum computation, i.e. one-way quantum computing [2]. Cluster states are multipartite entangled states characterized by maximal connectedness (any two parties of the system can be projected into a maximally entangled state through measurements on the remaining parties), as well as by the highest persistency of entanglement (compared to other entangled systems, they require a maximal number of projection measurements to fully destroy entanglement in the system). While discrete two-level (i.e. qubit) cluster states have been realized so far, increasing the number of particles to boost the computational resource comes at the price of significantly reduced coherence time and detection rates, as well as increased sensitivity to noise, thus restricting the realization of discrete cluster states to a record of eight qubits [3]. Increasing the dimensionality of the states (from qubit of qu*d*it) by entangling the parties over high-dimensional variables, rather than increasing the number of particles, has the potential to address several limitations of qubit cluster states. First, the quantum resource can be increased without modifying the number of particles; second, d-level quantum states enable the implementation of highly efficient computational protocols; and third, higher dimensions reduce the noise sensitivity of the cluster states. However, so far, the realization of discrete cluster states (i.e. using discrete variables) have been restricted to two-dimensional states. Here we demonstrate the realization of d-level cluster states and we perform d-level one-way quantum processing operations [4].

Similarly to the difficulty of generating discrete d-level quantum states, their characterization also presents some challenges. Indeed, with increasing dimensionality and number of parties the experimental measurements necessary to fully characterize these states increase exponentially. We

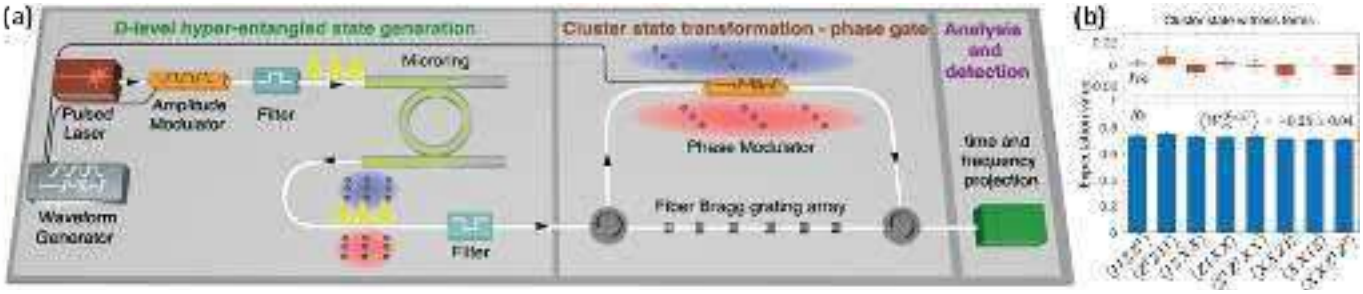


Figure 1. (a) Layout of the experimental setup for the generation of frequency-time hyperentangled states (left) and their transformation in clusters states (center), prior to detection (right). (b) Individual measured values of the stabilizers that contribute to the total entanglement witness operator, confirming (negative expectation value) the achievement of a four-partite three-level cluster state. Adapted from [4].

therefore developed a compact and universal method for deriving customized entanglement witness operators given different realistic experimental restrictions. By reducing the operator selectivity, it is possible to largely reduce the measurements necessary for identifying a specific entangled state [5].

2. Results

In order to achieve a high-dimensional cluster state without increasing the number of photons we exploit hyperentanglement, i.e. the simultaneous entanglement over independent degrees of freedom. We consider the spontaneous four-wave mixing process occurring in a nonlinear microring resonator pumped by multiple pulses (three in this case) for generating the entangled photons (Fig. 1). The resonance structure of the microcavity allows to achieve frequency-bin entanglement, while the multiple pump pulses generate time-bin entanglement. Provided the pulse repetition rate is much lower than the cavity free spectral range, i.e. the time-frequency product is much larger than 1, time and frequency can be considered as independent despite being non-commuting observables. This allowed us to access the individual state terms and thus transforming a high-dimensional hyper-entangled state (3-dimensional in both time and frequency) in a three-level four-partite cluster state, via a specifically-developed deterministic phase gate. A fiber Bragg grating array, placed in a self-referenced and phase-stable loop configuration, generated a frequency-to-time mapping where the state terms could be individually accessed with a phase modulator (see Figure 1a). By choosing the appropriate phase pattern, the bi-separable hyper-entangled state was transformed into a three-level four-partite cluster state.

In order to characterize the obtained high-dimensional cluster state we exploit the stabilizer formalism [6,7] to derive an experimentally-friendly witness operator for N-partite d-level cluster states that consists of only two measurement settings. Specifically, of the all stabilizers necessary to describe the ideal entanglement witness, we only considered the ones that can be measured with two measurement settings, while we substitute the difficult to measure stabilizers with their maximum eigenvalue. This results in a less selective witness operator, yet easier to measure. Through projection measurements in the time/frequency framework [8,9], we measured a witness expectation value $-0.28\pm0.04<0$ (Fig. 1b), thus confirming the realization of genuine four-partite cluster state. We furthermore found that the prepared state can tolerate up to 37.5% incoherent noise, in comparison to a qubit cluster state which can only endure 33%.

3. Conclusions

We have shown the generation and processing of high-dimensional cluster states, exploiting integrated photonic chips and optical fiber communication components. We also developed a novel universal technique for deriving experimentally-optimized witness operator for complex entangled states. Our work provides an important step towards achieving powerful and noise-tolerant quantum computation in a scalable and mass-producible platform.

References

[1] H. J. Briegel and R. Raussendorf, "Persistent Entanglement in Arrays of Interacting Particles", *Phys. Rev. Lett.* **86**, 910 (2001).

[2] R. Raussendorf and H. J. Briegel, "A one-way quantum computer", *Phys. Rev. Lett.* **86**, 5188 (2001).

[3] X.-C. Yao et al., "Experimental demonstration of topological error correction", *Nature* 482, 489 (2012).

[4] C. Reimer et al., "High-dimensional one-way quantum processing implemented on d-level cluster states", *Nature Phys.* **15**, 148 (2019).

[5] S. Sciara et al., "Universal N-partite d-level pure-state entanglement witness based on realistic measurement settings", *Phys. Rev. Lett.* **122**, 120501 (2019).

[6] G. Toth and O. Guhne, "Entanglement detection in the stabilizer formalism", *Phys. Rev. A* **72**, 022340 (2005).

[7] D.L. Zhou, et al. "Quantum computing based on d-level cluster states", *Phys. Rev. A* **68**, 062303 (2003).

[8] C. Reimer, et al. "Generation of multiphoton entangled quantum states by means of integrated frequency combs", *Science* **351**, 1176 (2016).

[9] M. Kues, et al. "On-chip generation of high-dimensional entangled quantum states and their coherent control", *Nature* **546**, 622 (2017).

Multifunctional plasmon-enhanced nanoscopy for nanoscale control of chemical reactions

Taka-aki Yano[1,2,3]

[1] School of Materials and Chemical Technology, Tokyo Institute of Technology, Yokohama, Japan
[2]RIKEN, Saitama, Japan
[3]Institute of Post-LED Photonics, Tokushima University, Tokushima, Japan
E-mail: yano@echem.titech.ac.jp

Abstract

We have developed multifunctional plasmon-enhanced nanoscopy for molecular control and analysis. A plasmonic probe tip is utilized not only to enhance Raman scattering from sample molecules but also to apply pressure and voltage to them, enabling us to locally initiate chemical reactions in the vicinity of the plasmonic tip. Combination of plasmon-enhanced nanoscopy with the local external stimuli has now opened up a new way to control molecular properties and functions on a nanometer scale.

Main text

Tip-enhanced Raman scattering (TERS) microscopy has been regarded as a promissing application of plasmonics for nano-imaging and nano-analysis with a nanoscale spatial resolution far beyond the diffraction limit of light. A sharp metallic probe tip plays important roles in plasmonically enhancing Raman scattering from sample molecules in the vicinity of tip. However, TERS microscopy has been still limited to passive measurement of intrinsic molecular properties and functions. Recently, we have proposed to utilize the plasmonic tip to locally apply various kinds of external stimuli such as pressure and voltage to sample molecules through the tip apex (Fig. 1), enabling us to actively modulate the intrinsic molecular properties at the nanometer scale. The dynamic change in physicochemical properties can be spectroscopically probed by detecting tip-enhanced Raman scattering in response to the external stimuli.

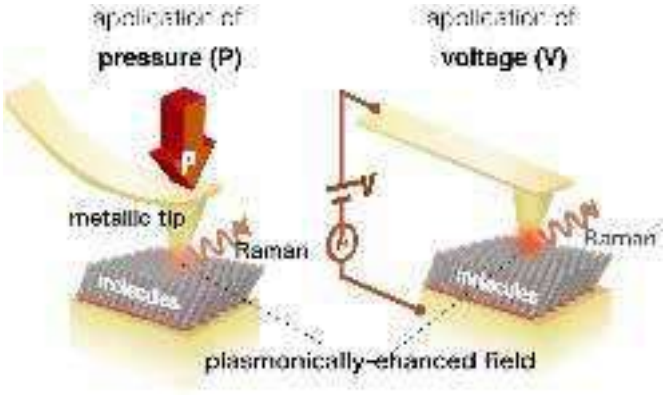


Figure 1: Multifunctional plasmon-enhanced nanoscopy in combination with the external stimuli.

When the plasmonic tip is controlled by an atomic force microscope in TERS measurement, the tip is utilized to locally apply pressure onto molecules under the tip. The tip-applied pressure has enabled to induce local deformation of molecular structures, which is detected by tip-enhanced Raman spectral changes. In this study, we demonstrated pressure-induced molecular isomerization in-situ observed through TERS spectral change. TERS spectra were measured on self-assembled monolayer (SAM) of cysteamine conformers while applying uniaxial pressure to them through the plasmonic tip with the nanometric apex. As the tip-applied pressure increased, the Raman band of the trans conformers exhibited decreasing of the intensity while Raman intensity of the gauche conformers increased. This result indicates the conformational change from the trans to the gauche conformers in the close vicinity of the tip-apex. We also utilized the plasmonic tip to apply DC voltage to sample molecules under the tip, enabling us to locally induce electrochemical reactions by regulating the tip-applied DC voltage. The details of the experiments will be discussed in our presentation.

Comparison of Plasmonic Response of Semiconductor Nanostructures with Spherical Symmetry and Their Prospect for Terahertz Applications

Thomas Wong[1], Tao Shen[2], Zhijing Hu[3], Yanlin Li[1], and Zi Wang[1]

[1]Department of Electrical and Computer Engineering, Illinois Institute of Technology, Chicago, Illinois, USA
[2]College of Information Engineering and Automation, Kunming University of Science and Technology, Kunming, Yunnan, China
[3]Keysight Technologies, Inc., Thousand Oaks, California, USA

Abstract

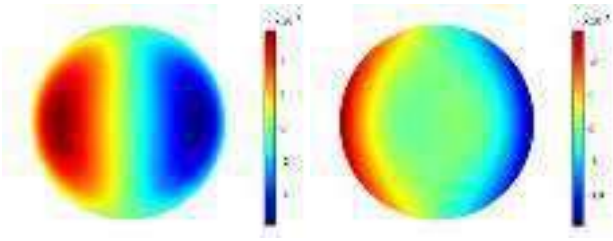
Electric polarization in three types of spherical semiconductor nanoparticles are compared: bare particle, semiconductor core with dielectric shell, and its dual. Physical insight is drawn from the dipole moments and the equivalent circuits. Their possible role as impetus for development of components in terahertz frequency range is explored.

1. Introduction

With a bulk plasma frequency in the terahertz frequency range, extrinsic semiconductors can be expected to find applications in that part of the electromagnetic spectrum [1][2]. Surface plasmon resonance in metallic nanoparticles has led to a variety of applications including sensor, field trapping, filter, polarizer, and waveguides. Spherical nanoparticles are of fundamental interest due to its high symmetry and availability in a large range in size. Much attention has been given to metallic nanoparticles. The semiconductor nanoparticle has been less studied. Although it has weaker polarizability than the metallic nanoparticle, it possesses the provision for varying the charge concentration by doping or otherwise, enabling the plasmon frequency to be adjusted over a substantial range. The presence of an insulating shell on a semiconductor nanoparticle is expected to influence the polarization in terms of the amplitude in the dipole moment and the surface plasmon resonance frequency. Insight can be obtained by comparing the polarization in a bare semiconductor nanoparticle to that of a core-shell structure with a semiconductor core enclaved in a dielectric shell. At the same time, a dielectric core within a semiconductor shell, which is the dual of the core-shell particle mentioned above, can provide a contrast to the comparison, providing additional insight to how plasmonic interactions are mediated in spherical nanostructures. In this paper, the polarization response obtained from electromagnetic simulation on these three nanostructures with spherical symmetry are presented, along their possible role in the realization of devices and circuit elements in the terahertz frequency range.

2. Charge Transport and Polarization

Owing to a lower carrier concentration than that of a metallic nanoparticle, field penetration into a semiconductor nanoparticle is more pronounced so that space charge effect is more significant. To provide a realistic account of charge distribution in the nanoparticle, a transport formulation needs to be employed to describe the dynamics of the charge carriers [3]. By coupling the equation for the electric field to the Boltzmann's equation, the carrier screening effect is revealed from the interior field within the nanoparticle. Figure 1 shows the real (left) and imaginary (right) parts of the charge density in a semiconductor nanoparticle doped at 10^{18} cm^{-3} and placed in an electric field close to its bulk plasma frequency. It can be seen that the charge is confined to a layer close to the surface. As a result, the electric field does not penetrate deep into the interior of the nanoparticle.



(a) (b)

Figure 1: Net charge in a semiconductor particle placed in an electric field near the bulk plasma frequency. Results are obtained by electromagnetic simulation. In this particular example, radius of particle $a = 50$ nm, doping level $N_e = 10^{18}$ cm^{-3}, relative permittivity $\varepsilon_r = 10$, electron effective mass $m^* = 0.25m_o$ and momentum relaxation time $\tau_n = 2\times10^{-13}$ s.
(a) Real part (C/cm^3), (b) Imaginary part (C/cm^3).

From the charge distribution, the induced dipole moment can be obtained. It displays a dispersion in the real part and an absorption peak at the surface plasmon resonance frequency [3]. To gain insight to the process of polarization and to facilitate the analysis of interactions in a cluster of nanoparticles, an equivalent circuit has been developed. The dipole moment calculated from the equivalent circuit give good agreement with the results obtained from electromagnetic simulation [4]. As seen in Figure 2, the circuit has a capacitor $\tilde{C}_l$ that dominates the low frequency response, accounting for the screening effect of the space charge. In the high frequency limit, where the electrons cannot respond rapidly to the varying field, the polarization in the particle comes mainly from the lattice, and is represented by the two capacitors series, $\tilde{C}_l$ and $\tilde{C}_h$. At

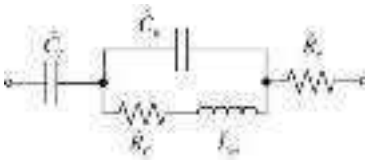


Figure 2: Equivalent circuit of a semiconductor nanoparticle obtained from consideration of the induced dipole moment.

intermediate frequencies, the dynamics of the mobile electrons contribute to the polarization process and the surface plasmon resonance is revealed. The resonance frequency is determined jointly by the inductor, the resistor, and the capacitors. The resistor on the right, R_r, is the radiation resistance, which accounts for the energy loss resulting from an oscillating dipole in open space.

Most nanoparticles acquire an oxide layer on their surfaces when exposed to air. At times, an insulating shell is deliberately coated outside to modify its characteristics [5-12], leading to a core-shell structure, as shown in Figure 3.

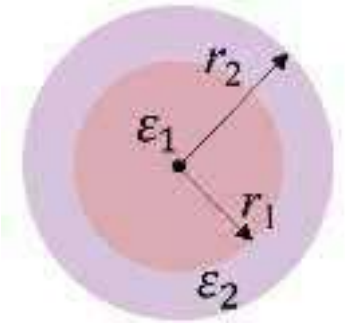


Figure 3: A nanoparticle with a core-shell structure.

The presence of an insulating layer on the surface will lead to a redshift in the surface plasmon frequency while the dipole moment is increased, as a result of the enhancement of the local field while the layer itself is polarized [13].

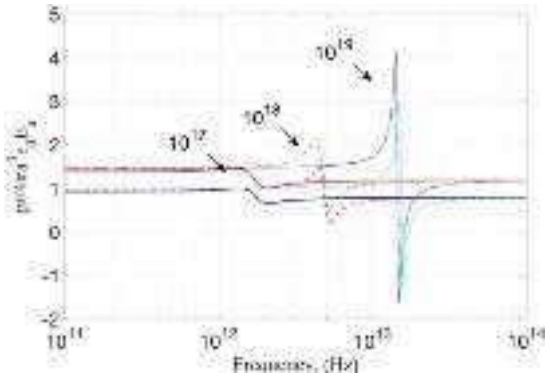


Figure 4 (a)

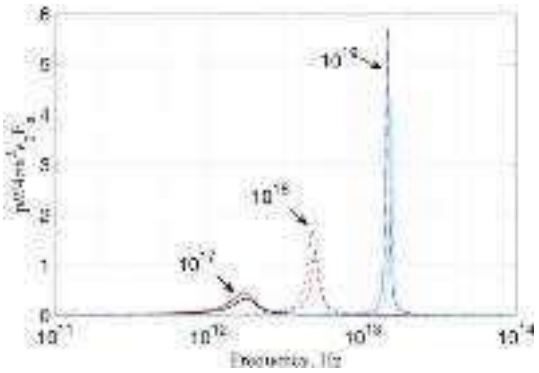


Figure 4 (b)

Figure 4: Induced dipole moment of core-shell and unclad semiconductor nanoparticles with different doping levels (a) real part, (b) imaginary part. Curves for core-shell particles have larger amplitude.

Figure 4 shows the induced dipole moment on core-shell semiconductor nanoparticles with different dopings in the cores. For these calculations the core has a radius of 50 nm. The thickness of the dielectric shell is 5 nm and its relative permittivity is 3.9. Response of the bare nanoparticles with corresponding dopings are included for comparison. They have a smaller amplitude and a plasmon resonance frequency higher than that of the corresponding core-shell nanoparticle. The insulating shell leads to an added capacitor in the equivalent circuit [13], as shown in Figure 5. For simplicity, the radiation resistance is suppressed in the figure.

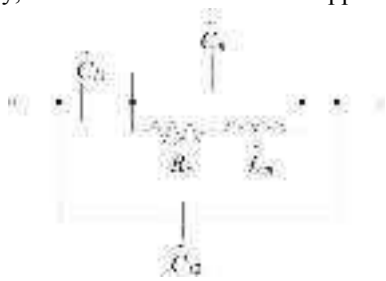


Figure 5: Equivalent circuit of a core-shell semiconductor nanoparticle.

Above the plasmon resonance frequency, the inertia effect of the mobile charges gives rise to a negative contribution to the real part of the dipole moment. When the carrier concentration is sufficiently high, such as the case at doping of 10^{19} cm^{-3} in Figure 4, the real part of the dipole moment can become negative immediately above the plasmon frequency. This negative dipole moment can be exploited to provide inductive reactance in circuit elements. However, the negative dipole moment is not of same magnitude as the positive side below the resonance, owing to the polarization of the lattice which makes a positive contribution that offsets the negative value resulting from the dynamics of the mobile charge carriers. In any case, this is a situation for generating inductive reactance without relying on magnetic material.

The nanoparticle in this frequency range may be viewed as a meta-material.

If the roles of the semiconductor and dielectric are interchanged in the above shown core-shell structure, a nanoparticle with a semiconductor shell enclaving a dielectric core is obtained. Under the action of a dynamic electric field, the charge carriers are set to motion in the shell, following a circular path that contributes to the inductive reactance. This effect is readily evidenced by reviewing the dipole moment of the semiconductor nanoparticle shown in Figure 6. Of particular interest is the blue shift in the surface plasmon resonance and a larger polarization response. The negative value in the real part of the dipole moment above the surface plasmon resonance frequency is more pronounced in this case compared to the previous one. Hence this structure is preferred for providing inductive reactance above the surface plasmon resonance frequency.

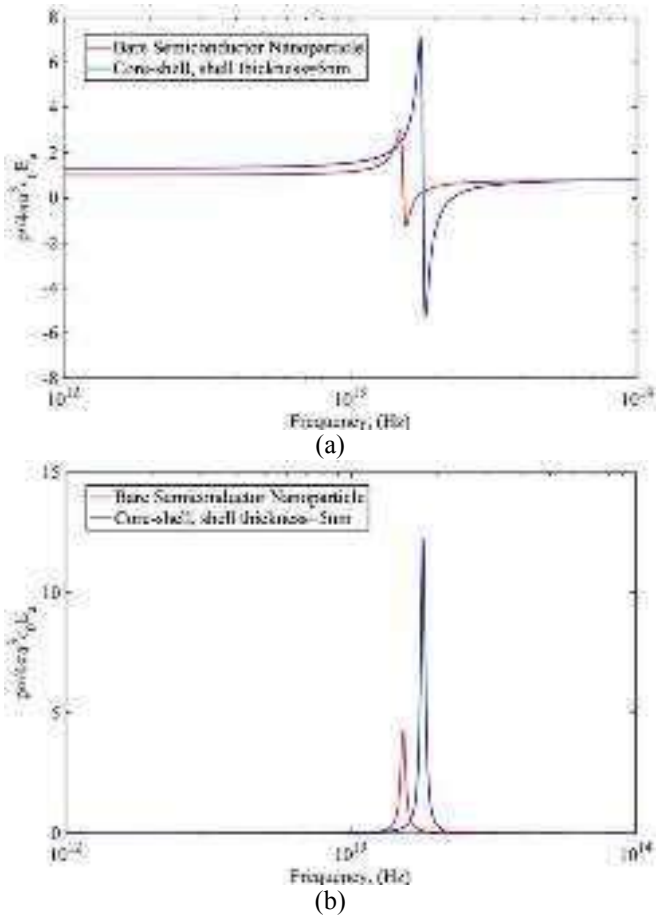


Figure 6. Induced dipole moment of a nanoparticle with a dielectric core enclaved by a semiconductor shell at 10^{19} cm^{-3} nominal carrier concentration (top) real part, (bottom) imaginary part. The radius of the dielectric core is 45 nm. The thickness of the semiconductor shell is 5 nm. Response of the bare semiconductor nanoparticle of similar size as the core is included for comparison.

3. Conclusion

Semiconductor nanoparticles exhibit plasmonic resonance in the terahertz frequency range which can be employed for functional applications. Transport-based analysis and simulation for the nanoparticle can account for the space-charge effects in the particles, leading to the construction of equivalent circuits to facilitate the design of nanoparticles and their derivatives. The polarizations in a bare spherical semiconductor nanoparticle and those of core-shell structures are compared. The presence of a dielectric shell on a semiconductor core results in polarization enhancement and a redshift in the surface plasmon frequency. On the other hand, a dielectric core inside a semiconductor shell shows a blueshift in the surface plasmon frequency. The real part of the dipole moment above the surface plasmon resonance of the latter core-shell nanoparticle acquires a negative value that is considerably larger than that of its dual. It can serve as impetus for providing inductive reactance as an entity in sensors and in circuit applications.

References

[1] N. Yu, Q.J. Wang, M.A Kats, J.A. Fan, F. Capasso, S.P. Khanna, L. Li, A.G. Davies and E.H. Linfield, "Terahertz plasmonics," *Electron. Lett.* vol. 46, no. 26, pp. s52–s57, 2010.

[2] S. Lo and T. Murphy, "Terahertz surface plasmon propagation in nanoporous silicon layers," *Appl. Phys. Lett.*, vol. 96, p. 201104, 2010.

[3] T. Shen, M. Yan, T. Wong, "Charge polarization and current distribution in a conductive particle in the Rayleigh region," *IEEE Trans. Antennas Propag.*, vol. 61, pp. 4229-4238, 2013.

[4] T. Shen, Z. Hu and T. Wong: "Transport-based equivalent circuit for semiconductor nanoparticle in terahertz frequency range", *Electron. Lett*., vol. 49, pp. 52-54, Jan. 2013.

[5] M. Grzelczak, B. Rodríguez-González, J. Pérez-Juste, and L. M. Liz-Marzán: "Quasi-Epitaxial growth of Ni nanoshells on Au nanorods", *Adv. Mater.*, vol. 19, pp. 2262–2266, Aug. 2007.

[6] A. E. Schlather, A. Manjavacas, A. Lauchner, V. S. Marangoni, C. J. DeSantis, P. Nordlander, and N. J. Halas: "Hot hole gphotoelectrochemistry on Au@SiO2@Au nanoparticles", *J. Phys. Chem. Lett.*, vol. 8, pp. 2060−2067, Apr. 2017.

[7] C. P. Byers, H. Zhang, D. F. Swearer, M. Yorulmaz, B. S. Hoener, D. Huang, A. Hoggard, W. Chang, P. Mulvaney, E. Ringe, N. J. Halas, P. Nordlander, S. Link, C. F. Landes: "From tunable core-shell nanoparticles to plasmonic drawbridges: Active control of nanoparticle optical properties", *Sci. Adv.*, vol. 1, No.11, Dec. 2015.

[8] Y. Zhang, A. Manjavacas, N. J. Hogan, L. Zhou, C. Ayala-Orozco, L. Dong, J. K. Day, P. Nordlander, and N. J. Halas, "Toward surface plasmon-enhanced optical parametric amplification (SPOPA) with engineered

nanoparticles: a nanoscale tunable infrared source", *Nano Lett.*, vol. 16, pp. 3373−3378, Apr. 2016.

[9] R. G. Chaudhuri and S. Paria: "Core/Shell nanoparticles: classes, properties, synthesis mechanisms, characterization, and applications", *Chem. Rev.*, vol. 112, pp. 2373-2433, Dec. 2011.

[10] B. Shahmoradi, M. Negahdary, and A. Maleki: "Hydrothermal synthesis of surface-modified, manganese-doped TiO2 nanoparticles for photodegradation of methylene blue", *Environ. Eng. Sci.*, vol. 29, pp. 1032-1037, Nov. 2012.

[11] H. P. Shivaraju, C. P. Sajan, T. Rungnapa, V. Kumar, C. Ranganathaiah and K. Byrappa: "Photocatalytic treatment of organic pollutants in textile effluent using hydrothermally prepared photocatalytic composite", *J. Mater. Res. Innov.*, vol. 14, pp. 80-86, Jul. 2013.

[12] A. Maleki and B. Shahmoradi: "Solar degradation of direct blue 71 using surface modified iron doped ZnO hybrid nanomaterials", *J. Water Sci. Tech.*, vol. 65, pp. 1923-1928, Jan. 2012.

[13] Y. Li, Z. Hu, and T. Wong, "Polarization enhancement and resonance tuning inferred from theoretical consideration and numerical simulation for a semiconductor nanoparticle with a dielectric shell," *IEEE Trans. Nanotechnology*, vol. 17, pp. 1029-1035, 2018.

Light-Trapping Transparent Electrodes For Photodetection and Photovoltaics

Mengdi Sun and Pieter G. Kik[1]

[1]CREOL, The College of Optics and Photonics, Orlando, FL, USA
*corresponding author: kik@creol.ucf.edu

Abstract

Shadowing losses by electrical contacts remain a pervasive challenge in a wide range of optical devices. Here we demonstrate that light-trapping electrodes consisting of arrays of metallic nanowires in a dielectric cover layer can practically eliminate all shadowing losses at surprisingly high metal coverage. This is achieved through directional reflection by the electrode surfaces toward angles beyond the critical angle. The approach is shown to allow efficient shadowing mitigation using structure sizes smaller than half the optical wavelength. The optical and electrical performance of these electrodes are shown to rival several current approaches in a compact microstructured surface.

Transparent electrodes are widely used in optoelectronic devices, such as solar cells, high speed photodetectors, imaging arrays and displays. In all such devices there is an intrinsic trade-off between optical and electrical performance, with low resistivity typically accompanied by poor optical transmission. In the case of metallic electrodes, transmission loss is predominantly caused by shadowing losses. To mitigate these losses, several approaches have previously been proposed, including encapsulated metal gratings [1-3], high-aspect-ratio metallic contacts [4, 5], periodic structures with plasmon-enhanced transmission [6-8] and patterned electrodes with textured surfaces [9-14]. Recently we proposed light-trapping electrodes using shaped surfaces [10]. In this design, arrays of metal wires with inclined surfaces are embedded in a dielectric cover layer. Under certain conditions a large fraction of light incident on the metallic wires is recovered by total internal reflection (TIR), allowing for transmission approaching 100% with a metal areal coverage well exceeding 25%.

Here we study the optical and electrical performance of silver light-trapping electrodes. Specifically the spectral performance and sheet conductivity of light-trapping electrodes containing triangular and cylindrical silver nanowires are investigated as a function of wire size. Figure 1 shows the angular scattering patterns of triangular and cylindrical silver wires embedded in silicon nitride for wire widths 200nm, 600nm, 1.2 μm and 2 μm. The wires are illuminated at normal incidence at a wavelength of 750nm using TE (top panel, electric field along the metal wire axis) and TM (bottom panel, electric field normal to the wire axis) polarization. The results have been scaled by the total power incident on the metal wire to facilitate comparison between wires with different width. These results show the key features that enable reduction of shadowing losses: any light reflected (scattered) toward angles above 30° can be recovered due to light trapping.

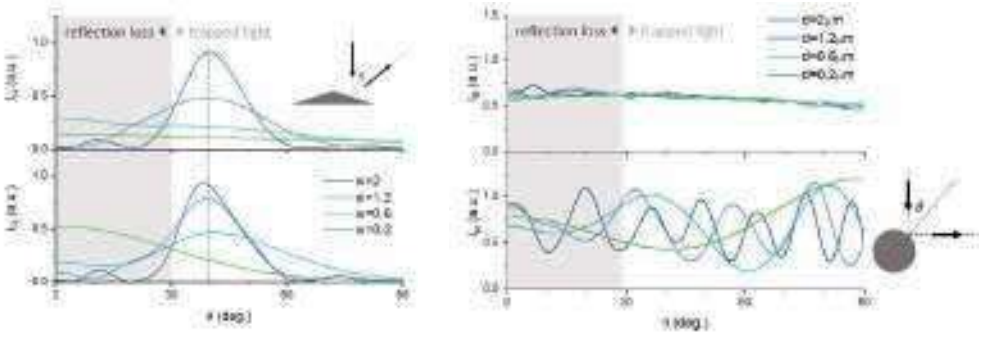


Fig. 1. Angle dependent reflected irradiance of a) triangular silver electrodes under TE illumination and b) TM illumination, c) cylindrical silver electrodes under TE illumination and d) TM illumination.

While small wire sizes are produce undesirable broad angular reflection distributions, larger triangular wires are seen to produce directional reflection with most reflected power directed toward angles above the critical angle of silicon nitride, allowing efficient light recovery. Cylindrical wires show oscillatory directional reflection resulting from the excitation of multipolar surface plasmon polariton distributions on the wires, leading to relatively inefficient light trapping at all sizes.

To evaluate the size-dependent optical performance of real-world high-conductivity light-trapping electrodes, periodic metallic wire arrays with a relatively high areal coverage of 25% were considered. The arrays are embedded in a transparent layer (n=2) and covered with an anti-reflection coating with a thickness of 133 nm and index n=1.41, producing reduced top surface reflection at the 750nm illumination wavelength. Figure 2 shows the simulated size-dependent transmitted, reflected, and absorbed power fraction of these interdigitated light-trapping electrodes with triangular (left) and cylindrical (right) electrode lines, at a fixed metal areal coverage of f=0.25, averaged over TE and TM polarization. For all electrode widths the transmitted fraction is found to significantly exceed 75%, corresponding to the maximum transmission of traditional flat electrode arrays at this metal coverage (horizontal dashed line) in the ray optics limit. This directly demonstrates the reduction of shadowing losses through recovery of the light incident on the metallic electrode lines. The light trapping efficiency increases from 35% to 80% as the electrode width increases from 200nm to 2 μm due to the increased directionality of the reflected light. Note that even small (200 nm width) triangular electrodes outperform traditional rectangular electrodes. For the largest triangular structures investigated, high optical transmittance (>97%) and low sheet resistance (<0.35 Ω/sq) are achieved simultaneously in a compact light trapping structure

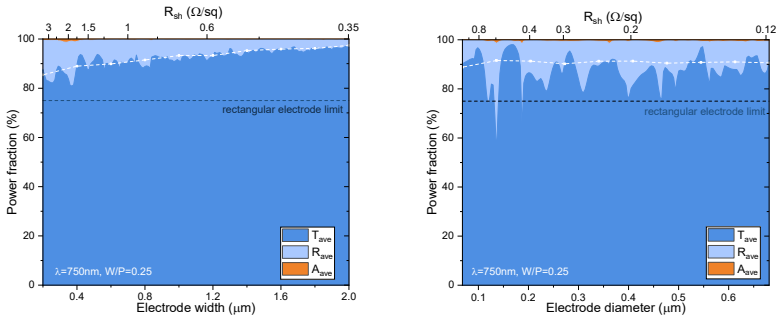


Fig. 2. Size-dependent optical and electrical performance of light-trapping electrodes consisting of triangular silver wires (left) and cylindrical silver wires (right) at 25% metal areal coverage. The white lines represent a model that ignores plasmonic grating effects.

References

1. Blakers, A.W., *Shading losses of solar - cell metal grids.* Journal of Applied Physics, 1992. **71**(10): p. 5237-5241.
2. Chen, F.H., et al., *Increasing light capture in silicon solar cells with encapsulants incorporating air prisms to reduce metallic contact losses.* Opt Express, 2016. **24**(22): p. A1419-A1430.
3. Kuang, P., et al., *Metal-nanowall grating transparent electrodes: achieving high optical transmittance at high incident angles with minimal diffraction.* Opt Express, 2013. **21**(2): p. 2393-401.
4. Saive, R. and H.A. Atwater, *Mesoscale trumps nanoscale: metallic mesoscale contact morphology for improved light trapping, optical absorption and grid conductance in silicon solar cells.* Opt Express, 2018. **26**(6): p. A275-A282.
5. Ward, J.S., et al., *High aspect ratio electrodeposited Ni/Au contacts for GaAs-based III-V concentrator solar cells.* Progress in Photovoltaics: Research and Applications, 2015. **23**(5): p. 646-653.
6. Genet, C. and T.W. Ebbesen, *Light in tiny holes.* Nature, 2007. **445**(7123): p. 39-46.
7. Lee, S.J., et al., *A monolithically integrated plasmonic infrared quantum dot camera.* Nat Commun, 2011. **2**: p. 286.
8. Martin-Moreno, L., et al., *Theory of extraordinary optical transmission through subwavelength hole arrays.* Phys Rev Lett, 2001. **86**(6): p. 1114-7.
9. Gao, T. and P.W. Leu, *The role of propagating modes in silver nanowire arrays for transparent electrodes.* Opt Express, 2013. **21 Suppl 3**: p. A419-29.
10. Kik, P.G., *Catoptric electrodes: transparent metal electrodes using shaped surfaces.* Opt Lett, 2014. **39**(17): p. 5114-7.
11. Saive, R., et al., *Silicon heterojunction solar cells with effectively transparent front contacts.* Sustainable Energy & Fuels, 2017. **1**(3): p. 593-598.
12. Saive, R., et al., *Effectively Transparent Front Contacts for Optoelectronic Devices.* Advanced Optical Materials, 2016. **4**(10): p. 1470-1474.
13. Xie, S., et al., *Enhancing the optical transmittance by using circular silver nanowire networks.* Journal of Applied Physics, 2014. **115**(19).
14. Zhao, Z., K.X. Wang, and S. Fan, *Analysis of an anti-reflecting nanowire transparent electrode for solar cells.* Journal of Applied Physics, 2017. **121**(11).

Dirac-like photonic structures: from pseudospin to topology

Zhigang Chen
The MOE Key Laboratory of Weak-Light Nonlinear Photonics, TEDA Applied Physics Institute and School of Physics, Nankai University, Tianjin 300457, China
Department of Physics and Astronomy, San Francisco State University, San Francisco,CA 94132, USA

*corresponding author, E-mail: zhigang@sfsu.edu

Abstract

Photonic lattices have provided a powerful platform to emulate Dirac physics while discovering new phenomena that would otherwise be inaccessible in natural 2D materials. In this talk, I will present some of our recent work based on Dirac-like photonic structures, including valley vortex states and degeneracy lifting via photonic higher-band excitation, valley Bloch oscillations and Zener tunneling, and unusual flatband localized states protected by real-space topology. I will then focus on discussing pseudospin-orbit angular momentum conversion and universal momentum-to-real-space mapping of topological singularities arising from the interplay of Berry phase, pseudospin, and orbital angular momentum of light.

Shaping of light in non-Hermitian disordered media

Konstantinos Makris[1*], Andre Brandstötter[2], and Stefan Rotter[2],

[1]Physics Department, University of Crete, 71003, Heraklion, Greece
[2]Institute for Theoretical Physics, Vienna University of Technology, 1040 Vienna, Austria
*corresponding author, E-mail: makris@physics.uoc.gr

Abstract

In the context of non-Hermitian photonics, we examine a unique method of controlling light inside complex media by engineering the imaginary part of the refractive index appropriately. Using this approach to shape the intensity of light in non-hermitian photonic media with gain and loss, we manage to create waves with constant intensity that make a disordered medium unidirectionally invisible or that produce a strong focus inside the disordered structure.

1. Introduction

The scattering of waves through disordered media is a paradigmatic phenomenon that has captured the interest of various communities for quite some time now [1]. While much work has been invested into understanding the statistical properties of the corresponding wave transport there has recently been a surge of interest in controlling the scattering of waves through systems for specific purposes such as detection, imaging, and efficient transmission across disordered materials [1]. Remarkable progress in these endeavors has recently been made in the optical domain, largely due to the availability of spatial light modulators and new concepts for how to apply them on turbid media. In a first generation of corresponding experiments the focus was laid on shaping the input wave front impinging on an immutable disordered sample such as to achieve a desired output, like a spatial or temporal focus behind the medium. More recent studies focused instead on controlling the medium itself, e.g., through the material fabrication process or through a spatially modulated pumping leading, e.g., to a versatile control of random and micro-cavity lasers.

Largely in parallel to these efforts on disordered media, it was recently realized that materials and devices can get entire new functionalities when adding to them a suitably arranged combination of gain and loss [2, 3]. In particular the field of PT-optics [4] has demonstrated that such an unconventional combination can lead us to counterintuitive phenomena with many novel applications (for a recent review see [4]). One of the celebrated breakthroughs in this field was the insight that PT-symmetric gain-loss gratings are unidirectionally invisible at specific frequencies-a property that has meanwhile also been realized experimentally. Transferring these concepts now to disordered materials, one could ask the question whether also a randomly assembled background medium can be engineered by just adding a tailored gain-loss distribution to it in order to control the multiple scattering. Whereas a successful strategy to answer this question would already be quite remarkable in its own right, we will go here an essential step further by demonstrating that we can generate waves in a disordered medium that are both perfectly transmitted and free of any intensity-variations throughout the entire scattering process. Since interference fringes and the intensity buildup associated with a strongly scattering medium are at the heart of disordered photonics, our new wave states touch on a very central issue in this field with potentially far-reaching consequences for the engineering of light transport.

2. Wave control in non-Hermitian media

2.1. Constant-Intensity Waves

In this framework of non-Hermitian disordered photonics, we have shown that for a general disordered medium, given by a distribution of the real part of the refractive index $n_R(x)$, a corresponding distribution of its imaginary part $n_I(x)$ can be found, such that an incoming wave will feature a constant intensity (CI-waves) throughout the entire non-uniform scattering landscape [5, 6]. In other words, we can show that adding a judiciously chosen distribution of gain and loss to a disordered medium will make waves lose all their interference fringes including perfect transmission through the disorder. Such types of waves have been experimentally realized in the context of acoustics [7], resulting in constant pressure waves in a strongly disordered medium.

2.2. Shaping light in complex disordered media

Regarding the possibility to achieve unidirectional invisibility as well as a complete control of the wave's intensity inside a complex medium (localized patterns for example), we now explore a solution strategy based on the one-dimensional Helmholtz equation that describes time-independent scattering of a linearly polarized electric field both in forward and in backward direction.

2.2.1. Non-Hermitian Invisibility

We show how one can make any disordered medium, that supports constant-intensity waves, also unidirectionally invisible [8]. In Fig.1(a-c) we can see the real (Fig.1a) and

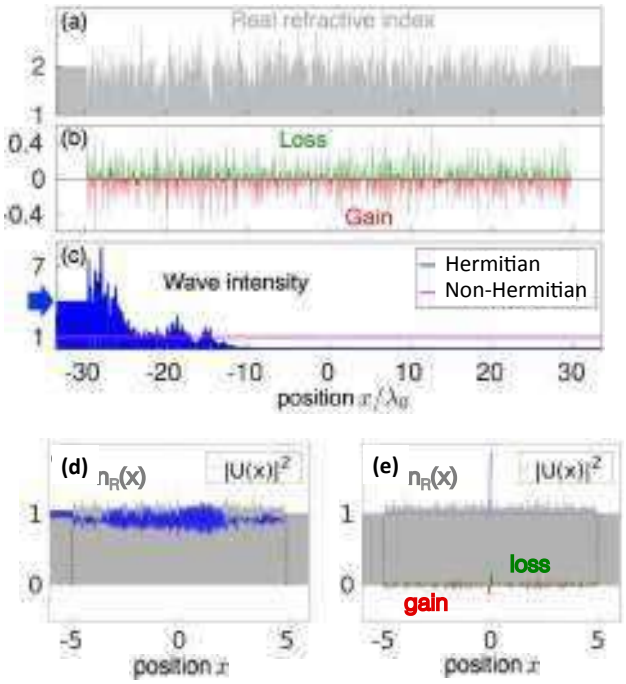


Figure 1: Scattering wave function control. (a-c) perfect transmission and unidirectional invisibility and (d,e) strongly localized intensity pattern inside a disordered medium. In both cases the medium is non-Hermitian with gain (red line) and loss (green line).

imaginary part (Fig.1b) of the complex index of refraction and in (Fig.1c) the corresponding scattered field. The intriguing features of such an approach is that only with gain one cannot achieve perfect transmission and also that by adding gain and loss the dependence on wavelength becomes relatively broad, allowing thus in principle to transmit even pulses through such a unidirectionally invisible medium.

2.2.2. *Complete control of wave's intensity*

By extending our analysis to the case of a general wave intensity pattern inside the disordered medium, we can derive the gain-loss distribution that is required for such purpose. In Fig.1(d-e) we provide an example of such a localized pattern inside a strongly scattered medium. In other words, we can find a class of non-Hermitian potentials for every form of the profile of the wave's intensity that we impose. In all cases gain and loss are absolutely necessary for the wave's intensity control.

3. Discussion

Based on these preliminary results we also apply the same methodology in two-spatial dimensions in order to fully control multiple scattering of waves and to examine the relation of our CI-waves to similar two-dimensional solutions of Bohmian photonics [9]. We start from the two-dimensional Helmholtz equation and reformulate the problem as a non-Hermitian eigenvalue problem with appropriate radiation boundary conditions. The mathematical methods that we apply to study multiple scattering in non-Hermitian environments are the volume integral methods and the recursive Green's function method.

4. Conclusions

In conclusion, we have presented recent results regarding CI-waves in non-Hermitian media. More specifically, we examined a new way to construct a family of unidirectionally invisible one-dimensional structures. By using a generalized class of non-Hermitian potentials we show how complete wave control can be achieved. Extensions to higher dimensions will also be discussed.

Acknowledgement

We acknowledge support from the European Commission under project NHQWAVE (MSCA-RISE 691209). K.G.M. is also supported by the European Union Seventh Framework Programme (FP7- REGPOT-2012-2013-1) under grant agreement 316165. A.B. is a recipient of a DOC Fellowship of the Austrian Academy of Sciences at the Institute of Theoretical Physics of the Vienna University of Technology (TU Wien). The computational results presented were partly achieved using the Vienna Scientific Cluster (VSC).

References

[1] S. Rotter and S. Gigan, *Rev. Mod. Phys.*, **89**, 015005 (2017).

[2] K. G. Makris, R. El-Ganainy, D. N. Christodoulides, and Z. H. Musslimani, *Phys. Rev. Lett.*, **100**, 103904 (2008).

[3] C. E. Rüter, K. G. Makris, R. El-Ganainy, D. N. Christodoulides, M. Segev, and D. Kip, *Nat. Phys.*, **6**, 192 (2010).

[4] R. El-Ganainy, K. G. Makris, M. Khajavikhan, Z. H. Musslimani, S. Rotter, and D. N. Christodoulides, *Nat. Phys.*, **14**, 11 (2018).

[5] K. G. Makris, Z. H. Musslimani, D. N. Christodoulides, and S. Rotter, *Nat. Comm.*, **6**, 7257 (2015).

[6] K. G. Makris, A. Brandstötter, P. Ambichl, Z. H. Musslimani, and S. Rotter, *Light Sci. Appl. 6, e17035*, (2017).

[7] E. Rivet, A. Brandstötter, K. G. Makris, H. Lissek, S. Rotter, and R. Fleury, *Nat. Phys.*, **14**, 942 (2018).

[8] A. Brandstötter, K. G. Makris, and S. Rotter, arXiv:1811.04839, *Phys. Rev. B*, to appear (2019).

[9] S. Yu, X. Piao, and N. Park, *Phys. Rev. Lett.*, **120**, 193902 (2018).

Advanced passive and active metasurfaces

Extreme Nonlinear Optics in Epsilon-Near-Zero Meta-Films

Yuanmu Yang[1]

[1]State Key Laboratory for Precision Measurement Technology and Instruments, Department of Precision Instruments, Tsinghua University, Beijing, China
*corresponding author, E-mail: ymyang@tsinghua.edu.cn

Abstract

We demonstrate extreme nonlinear optical properties leveraging epsilon-near-zero (ENZ) effect in plasmonic conductive metal oxide thin films. With the aid of high-mobility indium-doped cadmium oxide (CdO: In) as the gateway plasmonic material, we manage to construct an ultrafast all-optical switch with an absolute change in the p-polarized reflectance from 1.0 to 86.3% within 800 fs. Furthermore, we utilize the ENZ structure to achieve UV high-harmonic generation up to the 9th-order.

1. Introduction

Recently, materials that exhibit a vanishing real part of their permittivity in certain spectral ranges, commonly known as epsilon-near-zero (ENZ) materials, have been found to exhibit outstanding nonlinear optical properties[1]. For example, a giant nonlinear refractive index can be expected when the linear permittivity of the material approaches zero[2]. Here, we report on an ENZ meta-film based on a indium-doped cadmium oxide (CdO: In). Benefiting from the low material loss and a perfect absorber cavity design, we are able to modulate the absolute p-polarized reflectance of the cavity from 1% to 86% on a sub-picosecond time scale, at a wavelength of 2.08 μm[3]. We further demonstrate high-harmonic generation (HHG) based on such a platform.

2. Results and discussion

2.1. Static optical response

The CdO-based thin film perfect absorber is schematically shown in Fig. 1(a) and consists of a magnesium oxide (MgO) substrate, a 75-nm-thick doped CdO layer, and an optically thick gold capping layer. For the reflectance spectrum measurements, infrared light is incident on the CdO film from the substrate side. The CdO film is deposited on the (100) MgO substrate via sputtering, with the gold layer sequentially deposited by electron-beam evaporation. The carrier density and mobility of the CdO film are retrieved from the ellipsometry measurements to be 2.8×10^{20}cm^{-3} and 300 cm^{2}V^{-1}s^{-1}, respectively, resulting in a zero-crossing of its permittivity at 2.1 μm. Note that the carrier density is tunable by changing the In flux ratio during the material growth, allowing its corresponding ω_p to span from near-to mid-infrared frequencies. The exceedingly high electron mobility of the epitaxially grown CdO film, roughly an order of magnitude larger than conventional CMOs such as GZO and ITO, is a result from the sufficiently small substitutional lattice strain induced by In doping[4].

Reflectance spectra of the sample at incident angles ranging from 30° to 70° are obtained using an infrared spectral ellipsometer under free space excitation, and are shown in Fig. 1(b). The minimum measured reflectance of the sample is 1% at an incident angle of 50° and a wavelength of 2.08 μm.

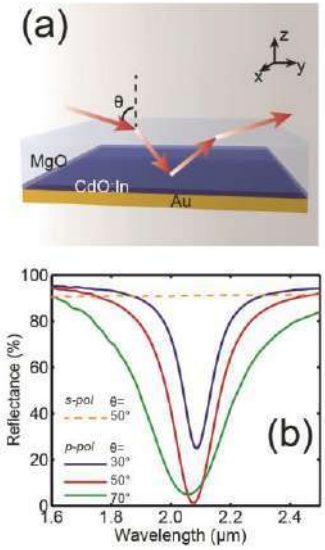


Fig. 1.(a), schematic of the CdO-based perfect absorber. (b), measured reflectance of the sample for p-polarized light at incident angles ranging from 30° to 70°, and for s-polarized light at an incident angle of 50°.

2.2. Ultrafast all-optical switching

We examine its transient response following optical excitation with pump-probe measurements. We use one beam from the idler output of an optical parametric amplifier (OPA) fed by a Ti: Sapphire amplified laser as the pump. The pump wavelength is tuned to 2.08 μm, and is p-polarized with an incident angle of 30° to allow resonant sample absorption. The probe beam is also p-polarized, but at an incident angle of 50∘ to achieve minimum reflectance at 2.08 μm, and to spatially separate from the pump beam.

The spectral bandwidth of the probe beam is large because of the ~50 fs pulse width of the OPA. Therefore, to accurately determine the change of absorption of the sample at different wavelengths after being reflected by the sample, the probe beam is sent through a monochromator prior to being detected by the photodetector. In Fig. 2(b). we present the absolute reflectance of the sample as a function of pump probe delay time, showing a transient bleaching at 2.08 μm and an induced absorption at 2.23 μm. we observe an absolute reflectance change from 1% to 86% at 2.08 μm and an absolute reflectance change from 73% to 11% at 2.23 μm.

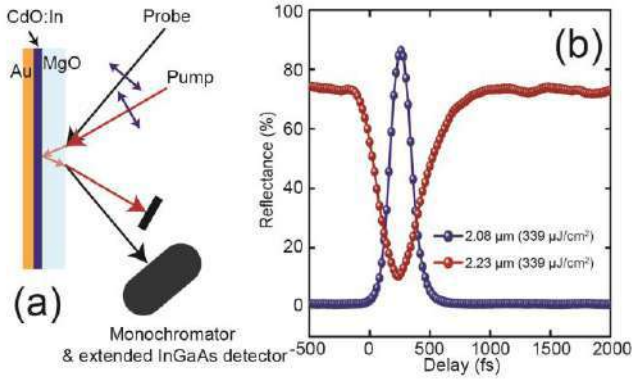


Fig. 2 (a) schematic of the pump-probe measurement setup. (b), the measurement absolute reflectance of the sample at 2.08 μm and 2.23 μm at a function of pump-probe delay time.1.(a), schematic of the CdO-based perfect absorber. (b), measured reflectance of the sample for p-polarized light at incident angles ranging from 30° to 70°, and for s-polarized light at an incident angle of 50°.

2.3. High-harmonic generation

We will also report high-harmonic generation up to the 9th order directly from the ENZ medium.

3. Conclusions

To summarize, by taking advantage of a low loss plasmonic material (CdO) with a stringently designed Berreman mode plasmonic cavity, we manage to construct a high quality factor perfect absorber for the extremely high contrast dynamic tuning of the amplitude and polarization state of infrared light at a sub-picosecond time scale. We envision many more exciting applications, including THz generation and two-photon emission with ENZ meta-films are the platform.

References

[1] N. Engheta. Pursuing Near-Zero Response. *Science* **340**, 286 (2013).

[2] M. Z. Alam, I. De Leon, and R. W. Boyd. Large optical nonlinearity of indium tin oxide in its epsilon-near-zero region. *Science* **352**, 795 (2016).

[3] Y. Yang *et al*. Femtosecond optical polarization switching using a cadmium oxide-based perfect absorber. *Nature Photonics* **11**, 390-395 (2017).

[4] E. Sachet *et al*. Dysprosium-doped cadmium oxide as a gateway material for mid-infrared plasmonics. *Nature Materials* **14**, 414-420 (2015).

Metasurface for artificial neural computing

Zongfu Yu

University of Wisconsin Madison

We show that optical waves passing through a nanophotonic medium can perform artificial neural computing. Complex information, such as an image, is encoded in the wave front of in-put light. The medium continuously transforms the wave front to realize highly sophisticated computing tasks such as image recognition. At the output, optical energy is concentrated to well defined locations, which for example can be interpreted as the identity of the object in the image. These computing media can be as small as tens of wavelengths in size and thus offer extremely high computing density. They exploit sub-wavelength linear and nonlinear scatterers to realize sophisticated input-output mapping far beyond traditional nanophotonic devices. To enable these complex neural computing, we draw inspiration from artificial neural network and use stochastic gradient decent to optimize nonlinear nanophotonic structures with structural gradient computed from adjoint state method.

Revealing the Near-Field Dynamics in Chiral Metasurfaces: Interactions of Spatially Displaced Surface Plasmon vortices

Chen-Bin Huang[1,*]

[1]Institute of Photonics Technologies, National Tsing Hua University, Hsinchu, Taiwan
*corresponding author, E-mail: robin@ee.nthu.edu.tw

Abstract

The potential to mold user-desired surface plasmon field flow with the existence of two simultaneous surface plasmon vortices with proper spatial offset is studied numerically. In the first case, a squeezed vortex with opposite rotation direction is generated between two co-rotating vortices. In the second case, a linear flow channel is formed in between two counter-rotating vortices.

1. Introduction

Surface plasmons (SPs) are near-field waves that propagate along the metal-dielectric interface as the result of collective electrons induced by external electromagnetic waves. Optical vortices are waves carrying optical angular momentum and exhibit abrupt azimuthal phase discontinuities. Recently, the ability to generate SP vortex in plasmonic chiral structures has attracted immense research attentions [1-3]. Among various nanoscopic chiral structures, Archimedean spiral with a geometric charge of 1 is a representative and noteworthy geometry in two means: (1) Such spiral can be used to convert far-field spin angular momentum of circularly-polarized light having the same sign as the geometric charge into near-field orbital angular momentum, therefore generating SP vortex with a topological charge of 2; (2) On the other hand, exciting the spiral with optical spin angular momentum having the reversed sign would end up with a strong subwavelength SP focusing field. This unique optical selectable SP field characteristic was applied to optofluidics for user-controllable microparticle trapping (using the focusing field) or rotation (using the vortex field) [4]. However, the particle controls were limited in a sense during trapping, only a single spatial trapping potential could be provided by the focusing SP field, and limited to a unidirectional rotation under the vortex field.

Here we propose geometrical design of plasmonic spirals that leads to the potential of controllable SP field flow directions. By incorporating two plasmonic Archimedean spirals with spatial offsets, two SP vortices are generated simultaneously. We numerically demonstrate unique controllability to the local SP field flows is allowed by changing the relative offsets and the topological charges of the two cortices. Our result could find immediate application in optofluidics and opens up a new path to optical manipulations.

2. Design

Our numerical analyses are performed using the three-dimensional finite-difference time-domain (FDTD) method [5]. The simulation volume is large enough to avoid nonphysical absorption of the near fields by the perfectly matched layers and an uniform mesh step ((10 nm)3) is used such that satisfactory calculation accuracy is obtained with reasonable speed and memory consumption. In our simulations, the plasmonic slits are formed by etching through a silver film of 200 nm thickness on top of a Si substrate. The optical source is a -z-propagating right-hand circularly polarized plane wave with vacuum wavelength of 570 nm, exciting the spiral at the air-Ag interface. The dielectric function of silver is modeled using Drude-Lorentz function to match the experiments [6].

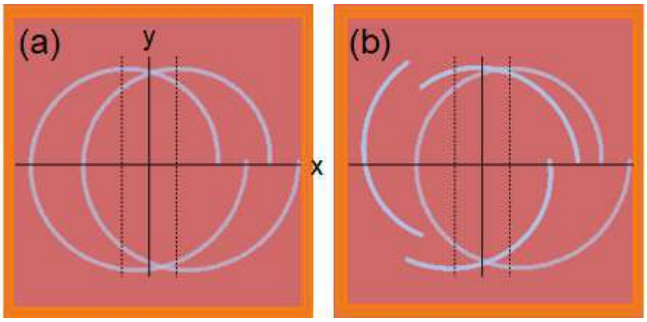


Figure 1. The two designs where two surface plasmon vortices are generated simultaneously with a spacing of 1000 nm: (a) The two vortices are having equal topological charge of 2; (b) the vortex on the left is having a topological charge of -2.

Figure 1(a) shows the geometry of our first design: two right-hand plasmonic Archimedean spirals both with geometric charge of 1 are displaced by 1000 nm in the x-direction. The intersection of the two solid black lines marks the origin in the cylindrical coordinate, while the dotted lines indicate the geometric centers of the two spirals. This design generates two SP vortices with equal topological charge of 2 under right-hand circularly polarized excitation. Figure 1(b) shows the second design: here the spiral offset to the left is replaced with a three-slit structure, equivalent to a left-hand plasmonic Archimedean spiral with a geometric charge of -

3. In this case, SP vortex with a topological charge of 2 is generated with an offset of 500 nm, while the second SP vortex with a topological charge of -2 is generated with an offset of -500 nm under right-hand circularly polarized excitation.

3. Result and discussion

Figures 2 and 3 show the time evolution of the SP fields generated by design 1 and design 2, respectively. For each design, four snap-shots are displayed. In Fig. 2, one could observe in addition to the two vortices centered respectively at x= -500 nm and 500 nm, there is a third vortex with opposite sense of rotation centered at x = 0 nm.

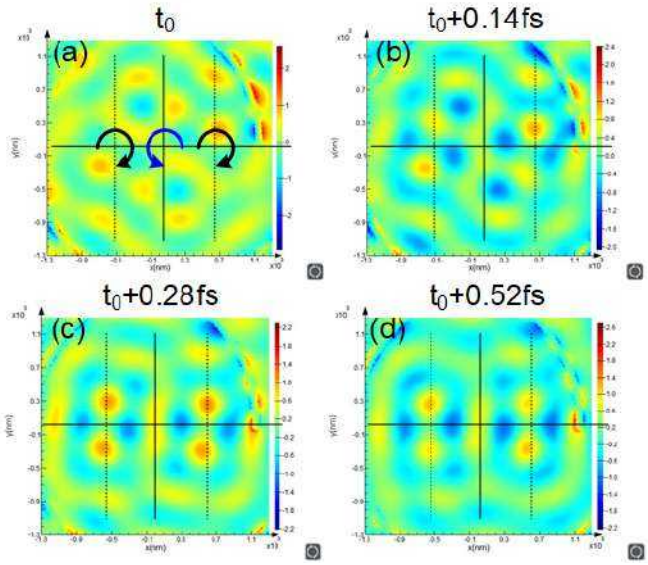


Figure 2. (a)-(d) Four snap-shots the resulting SP E_z field for design 1.

In Fig. 3, a SP field flow channel in the –y-direction is formed along x = 0 nm, which is created by the two counter-rotating SP vortices. In the presentation, movies will be used to better illustrate the effects.

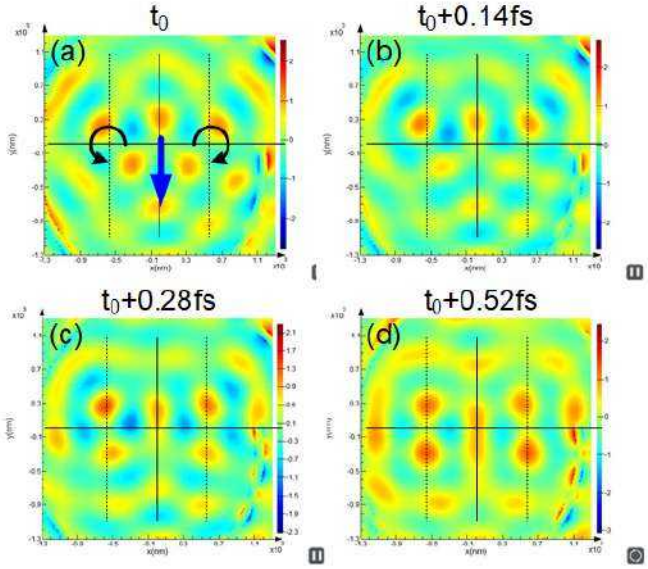


Figure 3. (a)-(d) Four snap-shots the resulting SP E_z field for design 2.

4. Conclusions

The existence of two simultaneous surface plasmon vortices with spatial offset provides opens up a path to mold user-desired field flow. We anticipate our results to find immediate application in optofluidics.

Acknowledgements

This work was supported by the Ministry of Science and Technology in Taiwan MoST under grant 106-2112-M-007-004-MY3.

References

[1] Y. Gorodetski, A. Niv, V. Kleiner, and E. Hasman, Phys. Rev. Lett. **101**, 043903 (2008).

[2] H. Kim, J. Park, S.-W. Cho, S.-Y. Lee, M. Kang, and B. Lee, Nano Lett. **10**, 529 (2010).

[3] C.-F. Chen, C.-T. Ku, Y.-H. Tai, P.-K. Wei, H.-N. Lin, and C.-B. Huang, Nano Lett. **15**, 2746 (2015).

[4] W.-Y. Tsai, J.-S. Huang, and C.-B. Huang, Nano Lett. **14**, 547 (2014).

[5] FDTD Solutions, Lumerical Solutions Inc., Vancouver, Canada. http://www.lumerical.com/

[6] E. D. Palik, Handbook of Optical Constants of Solids (Academic Press, 1985).

Integrated single photon sources with colloidal semiconductor nanocrystals

Alberto Bramati

Laboratoire Kastler Brossel, Sorbonne Universités, CNRS, ENS, Collège de France, Paris, France

Core/shell colloidal semiconductor nanocrystals are very efficient room temperature single photon emitters. In particular, in asymmetric core/shell nanoparticles (dots-in rods) with a spherical CdSe core surrounded by a rod-like CdS shell, blinking effects, multi-excitonic emission and polarization of the emitted photons can be independently controlled by tuning the shell dimensions [1]. This allows an unprecedented capability in radiative channels engineering, making dot-in-rods "state of the art" blinking-free sources of polarized single photons on-demand.

In this talk I will discuss our recent results and the different strategies we are pursuing to develop hybrid photonic devices by coupling single nanocrystals with photonic structures such as deep parabolic mirrors [2], liquid crystals [3], semiconductor nanowires [4] and tapered nanofibers. In particular the deposition of a single emitter on a nanofiber and the observation of single photon statistics through the guided mode of the fiber will be reported. Finally I will show how this hybrid system is a very promising playground for novel chiral optics experiments, including a spin-orbit coupling effect for light [5]



Figure 1: Nano-Fiber based toroidal-knot resonator.

References:

[1] F. Pisanello, G. Leménager, L. Martiradonna, L. Carbone, S. Vezzoli, P. Desfonds, P.D. Cozzoli, J.P. Hermier, E. Giacobino, R. Cingolani, M. DeVittorio & A. Bramati, *Non-blinking single photon generation with anisotropic colloidal nanocrystals : toward Room-temperature efficient colloidal quantum sources,* Advanced Materials, *25*, 1974 (2013)

[2] V. Salakhutdinov, M. Sondermann, L. Carbone, E. Giacobino, A. Bramati, G. Leuchs, *Optical trapping of nanoparticles by full solid-angle focusing* , Optica, 3, 1181 (2016)

[3] L. Pelliser, M. Manceau, C. Lethiec, D. Coursault, S. Vezzoli, G. Leménager, L. Coolen, M. DeVittorio, F. Pisanello, L. Carbone, A. Maître, A. Bramati, E. Lacaze, *Alignement of Rod-Shaped Single Photon Emitters driven by Line Defects in Liquid Crystals*, Adv. Funct. Mat. 25, 1719 (2015)

[4] W. Geng, M. Manceau, N. Rahbany, V. Sallet, M. De Vittorio, L. Carbone, Q. Glorieux, A. Bramati, C. Couteau, *Localised excitation of a single photon source by a nanowaveguide,* Scientific Reports 6, 19721 (2016)

[5] M. Joos, C. Ding, V. Loo, G. Blanquer, E. Giacobino, A. Bramati, V. Krachmalnikoff and Q. Glorieux, *Polarization Control of Linear Dipole radiation using an Optical Nanofiber,* Phys. Rev. Applied, 9, 064035 (2018)

Super-cell Geometric Phase Metasurface for Multispectral Imaging

Bo Qiang[1], Jie Deng[2], Xiao Siong Tang[2], Soo Seng Ang[2], Jing Hua Teng[2], Qi Jie Wang[1,3], Qian Wang[2*]

[1]Centre for OptoElectronics and Biophotonics, School of Electrical and Electronic Engineering & The Photonics Institute, Nanyang Technological University, Singapore, 639798
[2]Institute of Materials Research and Engineering, A*STAR, 2 Fusionopolis Way, Innovis, Singapore 138634
[3]Centre for Disruptive Photonic Technologies, School of Physical and Mathematical Sciences, Nanyang Technological University, Singapore, 637371

*corresponding author, E-mail: wangqian@imre.a-star.edu.sg

Abstract

A metasurface is designed to combine the generation of a focused beam and a vortex beam in the same imaging plane which can be used for super-resolution imaging in stimulated emission depletion (STED) microscopy. It is composed of sub-micron sized nanobar array to modulate the phase of the multi-spectral incident light locally. With this metasurface, the STED imaging system will be greatly simplified, and there is no need to align the two beams with high precision in the same optical path.

1. Introduction

Optical inspection always requires high resolution imaging technology. Stimulated emission depletion (STED) microscopy [1] is one of the technique to achieve super-resolution imaging (~ tens nm). It is a deterministic functional technique exploring the non-linear response of fluorophores to achieve the beyond diffraction limit resolution image. Basically, any object with multi-state energy level can allow for super-resolution imaging with STED microscopy, for example quantum dot [2]. Therefore, the STED microscopy is an enabling technique for semiconductor optical inspection and biological imaging applications. The current STED system is bulky and costly (~1 million US dollars). One of the biggest technical challenges in STED microscopy system is to couple two modified laser beams, one is optical vortex beam and the other is focusing beam, in the same focusing plane to excite and deplete the fluorophore at the same time. Additionally, sophisticated optical system is used to tailor the beams in two different beam shapes and align them precisely at the focal spot in the imaging plane of high NA objective lens. Therefore, a simple solution to alleviate the challenging optical alignment and the complexity of STED system is of great significance.

Metasurface, achieving functionality through nano-structuring, has becoming an enabling technique to control and manipulate light in term of amplitude, phase and polarization state [3]. Thus, the wavefront of light can be arbitrarily shaped for various application, such as beam steering, focusing imaging, and holographic display [4-6]. In this paper, a planar dielectric metasurface is used to shape and focus two beams to suppress the fluorescence for super resolution imaging. With the metasurface, the optical system will be greatly simplified, and there is no need for precise alignment of the focusing beam and the vortex beam in the system. The cost of phase microscope can be dramatically reduced, and it is possible to realize on-chip super-resolution STED imaging with this invention.

2. Experimental results

In this work, the metasurface is designed to combine the generation of a focused beam and a vortex beam in the same imaging plane. It is composed of sub-micron sized nanobar array to modulate the phase of incident light locally [7]. Four nanobars are arranged in a rectangular area and optimized for two different wavelengths. When the two-wavelength light is incident on this metasurface, some of the nanobars respond to one wavelength for light focusing, while the others respond to another wavelength for generation of vortex beam. The efficiency ratio of focused beam and vortex beam can be tuned through the optimization of nanobar parameters.

Figure 1 shows the phase distribution at the multi-spectral metasurface to form optical vortex spot with 633nm (a1) and solid focusing spot with 532nm (a2). (b1) and (b2) are simulated intensity distribution of two beams at imaging plane. Figure 1c shows the normalized cross section of the vortex beam and the focusing beam intensity distribution. The dash line is the cross talk of red beam through the focus cell and green beam through the vortex cells.

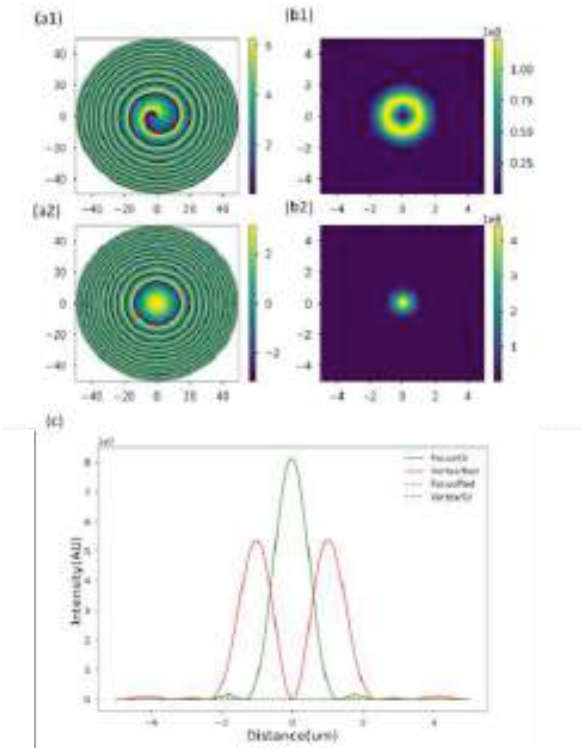


Fig. 1 (a1) and (a2) are phase distribution of vortex beam with 633nm and excitation beam with 532nm at metasurface. (b1) and (b2) are the simulation results of intensity distribution of two wavelength at imaging plane. (c) cross section of intensity distribution of two beam. Dash line is the cross talk 633nm through the green cell and 532 through the vortex cell. Green and Red solid line is the cross section of the focusing and vortex beam.

The amorphous Si with 380 nm thickness is growth on a quartz substrate by PECVD. A thin layer of ZEP photoresist is spin coated on the a-Si film. The metalens is patterned on the ZEP photoresist by electron beam lithography. After developing, the sample is dry etched to get the a-Si nano structures. Figure 2 is the scanning electron beam image of the fabricated metasurface. The green boxes indicate supercells composed of four nanobars in each of them. The smaller bar is designed to work at 532 nm, and the bigger one is for 633 nm.

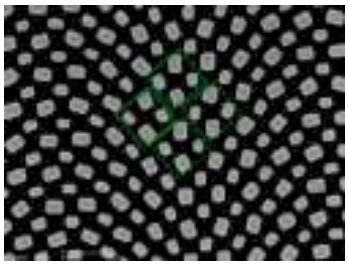


Fig. 2 The SEM photo of part of STED metalens.

Figure 3 shows the characterization of STED metasurface. When the 633nm light is normal incident into the metasurface, an optical vortex sport is generated at the focal plane. When the 532nm light is normal incident, a solid focal spot is generated at the same focal plane. With this metasurface, a simple STED imaging system can be realized on a chip.

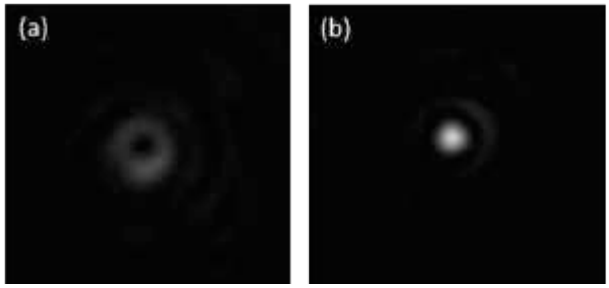


Fig. 3 The characterization result of STED lens. (a) the 633nm wavelength light is shaped to a vortex beam in the imaging plane. (b) the 532nm wavelength light is focused in the same imaging plane.

3. Conclusions

Two different sized nano-bars are specially designed to form a supercell metasurface to achieve independent geometric phase modulations for two different wavelength. The supercell metasurface can be utilized to arbitrarily control the wavefront of multi-spectral electromagnetic waves, thus enabling many functionalities. Using this approach, we demonstrate a multispectral metasurface to create a focused optical vortex doughnut-shaped spot at a longer wavelength and a solid light spot at a short wavelength at the same location in the image plane. It is especially useful for stimulation emission depletion (STED) microscope system for minimizing the area of fluorescence emission. This approach alleviates the stringent requirements for precise alignment of two wavelength focus spots in a conventional STED super-resolution imaging systems.

Acknowledgements

This study was supported by the Agency for Science, Technology and Research (A*STAR) of Singapore (Grant no.182-243-0030).

References

[1] G. Vicidomini, P. Bianchini, A. Diaspro. STED super-resolved microscopy,Nature Methods 15: 173-182, 2018

[2] T. Kaldewey, et al. Far-field nanoscopy on a semiconductor quantum dot via a rapid-adiabatic-passage-based switch, Nature Photonics 12: 68-72, 2018

[3] N.Yu, F. Capasso, Flat optics with designer metasurface. Nat. Mater. 13:139-150, 2014.

[4] Z. Zhao, et al, Multispectral optical metasurfaces enabled by achromatic phase transition, Scientific Report 5:15781, 2015.

[5] Y.-W. Huang, et al. Aluminum Plasmonic Multicolor Meta-Hologram, Nano Lett. 15:3122, 2015

[6] B. Wang, et al. Visible-Frequency Dielectric Metasurfaces for Multiwavelength Achromatic and highly Dispersive Holograms, Nano Lett. 16:5235, 2016

[7] N.Yu, et al, Light propagation with phase discontinuities: generalized laws of reflection and refraction. Science 334: 333-337, 2011.

Alternative Plasmonic Materials for SERS and Metasurface Applications: Aluminum and Titanium Nitride

Shangjr Gwo[1,2]

[1]Research Center for Applied Sciences (RCAS), Academia Sinica, Nankang, Taipei 11529, Taiwan
[2]Department of Physics, National Tsing-Hua University, Hsinchu 30013, Taiwan
*E-mail: gwo@sinica.org.tw

Abstract

Recently, we have developed epitaxial techniques to grow forming smooth, single-crystalline aluminum (Al) and titanium nitride (TiN) films on transparent sapphire substrates using molecular-beam epitaxy (MBE). In comparison to silver and gold, Al- and TiN-based plasmonics have better material stabilities and spectral responses in the ultraviolet (UV) and visible spectral regions, making them particularly suitable for UV surface-enhanced surface Raman spectroscopy (SERS), optical energy harvesting, and metasurface-based linear and nonlinear optics.

1. Introduction

The development of plasmonics and metasurface-based optical structures requires alternative, high-performance plasmonic materials, in replacement of commonly used noble metals. Ideally, plasmonic materials should have the properties of low-cost, low-loss, high chemical, mechanical, and thermal stabilities, biocompatibility, spectral tunability, as well as integrability with existing semiconductor technologies. In comparison to silver and gold, Al- and TiN-based plasmonics have better materials stabilities and spectral responses, making them particularly suitable for UV-SERS and metasurface-based linear and nonlinear optics. Here, recent experimental results from my group related to these application areas are presented.

2. Advantages of Aluminum and Titanium Nitride as Plasmonic Materisla

In comparison to gold and silver [1,2], Al is a sustainable and widely applicable plasmonic material owing to its abundance in the Earth's crust and compatibility with the complementary metal–oxide–semiconductor (CMOS) technology. In particular, Al has a superior performance in the UV region with the lowest material loss and good performance in the full visible spectral range [3,4]. Furthermore, aluminum films remain very stable under ambient conditions due to the formation of surface native oxide (alumina), acting as a passivation layer. On the other hand, TiN [5] is a refractory plasmonic material in the visible and near-infrared (IR) range, exhibiting extraordinary mechanical strength (machine-tool grade), high melting temperature (~3,000°C), high corrosion resistance, and excellent bio- and CMOS compatibilities. Interestingly, TiN is also a superconductor with transition temperature higher than the liquid helium temperature (~6 K in the case of stoichiometric TiN).

3. Experimental

In practice, high-quality Al and TiN films require an ultraclean growth environment because of their propensity to react with residue gases. Especially, titanium is an active absorbing agent or getter material, which is widely used as a sublimation pump material in ultrahigh vacuum systems. Therefore, the achievable material properties of Al and TiN films are so far limited by the growth technique. Recently, we have developed molecular-beam epitaxy (MBE) growth techniques for Al and TiN (N_2-plasma-assisted) epitaxial films, which can be used as alternative plasmonic materials to silver and gold, respectively. Additionally, to make it possible to integrate plasmonic metasurfaces with two-dimensional van der Waals materials, we have also developed the method to grow hexagonal boron nitride (h-BN) epitaxial films using plasma-assisted MBE.

In the case of TiN, the stoichiometry and carrier concentration of nonstoichiometric TiN_x films ($x < 1$) can be controlled by the nitrogen plasma flux and sample temperature during MBE growth. The lower carrier concentration in TiN_x films further allows for tunability in their plasmonic response using electric gating. Here, MBE-grown Al and TiN epitaxial films are characterized and utilized for plasmonic device applications. Experimental results, in contrast to standard noble-metal-based plasmonics, are presented.

4. Results

Recently, smooth Al and TiN epitaxial films grown on transparent *c*-plane (0001) sapphire using MBE have been demonstrated by us. The MBE-grown Al and TiN films have small plasmonic losses, enabling us to fabricate and utilize high-quality Al- and TiN-based plasmonic metasurfaces for a variety of applications (i.e., SERS substrates and linear/nonlinear metasurfaces). The surface roughness and crystal structure of MBE-grown Al and TiN films were characterized by atomic force microscopy (AFM) and X-ray diffraction (XRD). Moreover, the formation of single-crystalline close-packed rock-salt TiN structure has been

confirmed by transmission electron microscopy (TEM). We have also measured the optical dielectric function of MBE-grown Al and TiN films by using spectroscopic ellipsometry (SE). These results show that the structural and optical properties of epitaxial Al and TiN films grown by MBE are of high quality, compared to conventional Al and TiN films grown by other deposition methods (e.g., thermal deposition, sputtering, chemical vapor deposition, etc.).

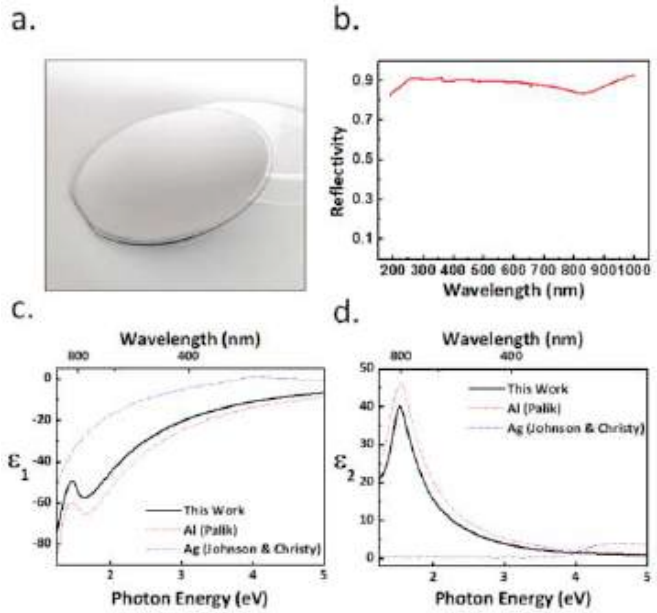


Figure 1: Optical properties of epitaxial aluminum film grown on *c*-plane sapphire substrate [4]. (a) Optical image of an aluminum epitaxial film grown on a double-side polished *c*-sapphire wafer. (b) Reflectivity spectrum of the as-grown aluminum film with a native oxide layer (~3.5 nm) shows a high reflectivity (~0.9) in a wide spectral range. The interband transition is at about 800 nm. (c) Real part of the dielectric function (ε_1) extracted from the spectroscopic ellipsometry data as a function of photon energy (black solid curve). (d) Imaginary part of the dielectric constant (ε_2). For comparison, literature data of Al (red dotted curve) and Ag (blue dotted curve) are also shown in the plots.

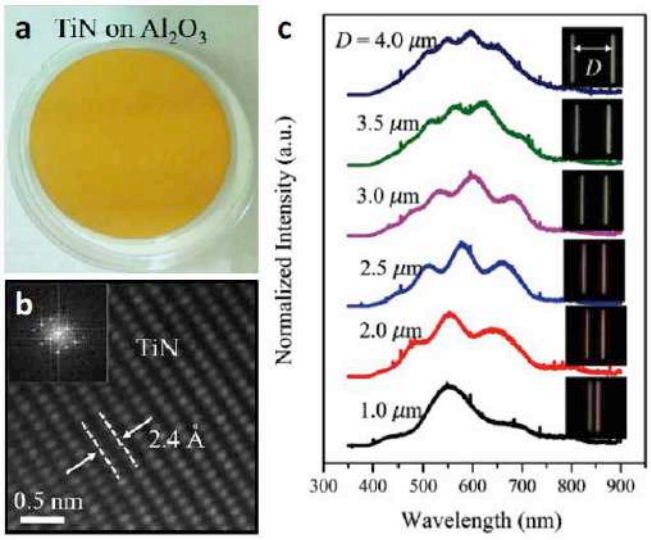


Figure 2: Epitaxial TiN film grown on *c*-plane sapphire substrate [5]. (a) Optical image of a TiN epitaxial film grown on a double-side polished *c*-sapphire wafer. (b) High-resolution TEM image of a TiN epifilm. (c) Surface plasmon polariton (SPP) interference patterns obtained from different double-nanogroove surface plasmon cavities. Corresponding dark-field optical images are shown in the insets.

5. Conclusions

According to these experimental results, epitaxial Al and TiN films represent two versatile plasmonic material platforms in the UV, full visible, and infrared spectral regions, especially for applications related to energy-harvesting and biosensing applications.

Acknowledgement

I would like to acknowledge the support from the Ministry of Science and Technology (MOST) in Taiwan (MOST 105-2112-M-007-011-MY3).

References

[1] C.-Y. Wang, H.-Y. Chen, L. Sun, W.-L. Chen, Y.-M. Chang, H. Ahn, X. Li, S. Gwo, *Nat. Commun.* **2015**, *6*, 7734.

[2] S. Gwo, H.-Y. Chen, M.-H. Lin, L. Sun, X. Li, *Chem. Soc. Rev.* **2016**, *45*, 5672–5716.

[3] F. Cheng, P.-H. Su, J. Choi, S. Gwo, X. Li, C.-K. Shih, *ACS Nano* **2016**, *10*, 9852–9860.

[4] C.-W. Cheng, Y.-J. Liao, C.-Y. Liu, B.-H. Wu, S. S. Raja, C.-Y. Wang, X. Li, C.-K. Shih, L.-J. Chen, S. Gwo, *ACS Photonics*, **2018**, 5, 2624–2630.

[5] W.-P. Guo, R. Mishra, C.-W. Cheng, B.-H. Wu, L.-J. Chen, M.-T. Lin, S. Gwo, **2019**, manuscript in preparation.

Selectively reconfigurable molecularization of terahertz meta-atoms

Hyunseung Jung[1], Hyunwoo Jo[2], Wonwoo Lee[3], Moon Sung Kang[2], and Hojin Lee[1,3*]

[1]School of Electronic Engineering, Soongsil University, Seoul, Korea
[2]Department of Chemical Engineering, Soongsil University, Seoul, Korea
[3]Department of Information Communication, Materials, and Chemistry Convergence Technology, Soongsil University, Seoul, Korea
*corresponding author, E-mail: hojinl@ssu.ac.kr

Abstract

In this study, we propose selectively reconfigurable terahertz meta-molecules by controlling the micro-patterned ion-gel gate structures to change the conductance of graphene bridges between adjacent meta-atoms. Moreover, we experimentally verify that the proposed structures can change the resonance frequency of metamaterial from 1.40, 1.10, to 0.74 THz, by changing the metamaterial unit cell from the individual atom to dimeric and tetrameric molecules, respectively.

1. Introduction

Recently, active terahertz metamaterials have received numerous attentions in realizing diverse applications by manipulating the incident terahertz waves in real-time [1]. Especially, ion-gel gated graphene terahertz modulators have provided an effective way to change the terahertz properties by applying electrical biases without any complicated optical setups [2, 3]. However, most of the active terahertz metamaterials have exhibited only simple switchable property in resonance frequency, which is hard to be utilized for multi-channel selection of terahertz waves. In this study, by controlling individual micro-patterned ion-gel gating lines on the graphene inter-connected terahertz meta-atoms, we develop a selectively reconfigurable molecularization of meta-atoms for selecting various resonance frequencies in real-time.

2. Results and Discussion

Figure 1 shows the schematic design and optical microscope images of the fabricated active meta-atom molecularization system. The proposed structure consists of metallic meta-atoms and graphene bridges for conductively controllable inter-connection between adjacent meta-atoms [3]. To control resonance frequency of the active meta-atom molecularization system, we designed micro-patterned ion-gel gating system to change the conductance of graphene bridges, individually. The mirco-patterned ion-gel array is formed on the graphene bridges in metamaterial sample by using ion-gel patterning methods as reported in [4]. Because the micro-patterned ion-gel lines were intended to select

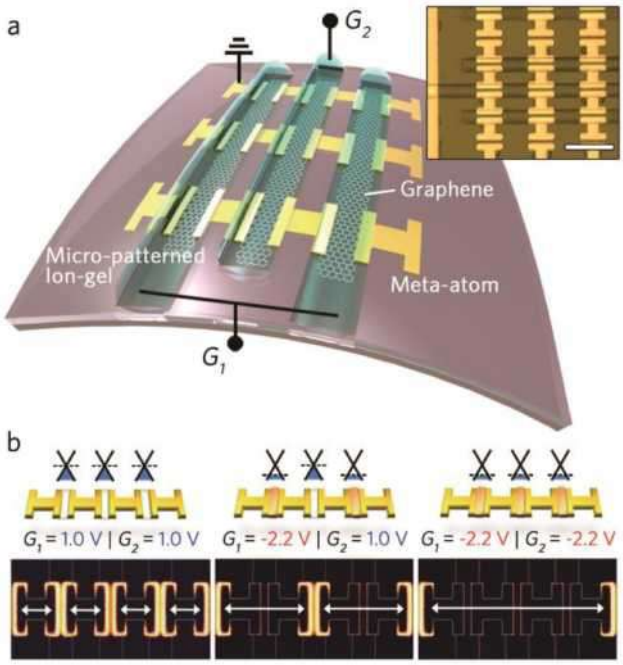


Figure 1: (a) Schematic design of the selective molecularization of terahertz meta-atoms. Inset shows an optical microscope image of the fabricated sample (scale bar: 100 μm). (b) Electric field distributions of the selective meta-atom molecularization system for the different gate bias configurations.

controllable gating lines, we applied two different gate voltages (G_1 and G_2) on the individual ion-gel lines to change the molecularization state of meta-atoms as monomeric, dimeric, and tetrameric meta-molecules. Figure 1b shows the electric field distributions of the proposed selective meta-atom molecularization system for the different gate voltage configurations. When the gate voltages are applied as $G_1 = G_2 = 1.0$ V, the inter-connected graphene bridges have low conductivity to achieve a meta-atom resonance. In contrast, when $G_1 = -2.2$ V and $G_2 = 1.0$ V, since only the graphene bridge in the middle of interconnected meta-atoms has low conductivity, the proposed molecularization system can exhibit dimeric meta-

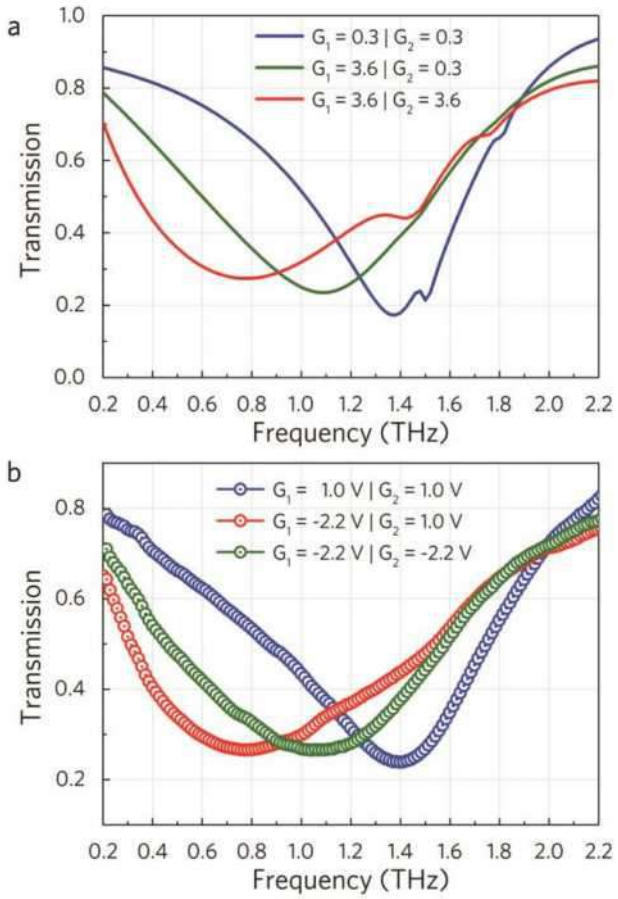


Figure 2: (a) Simulated and (b) measured transmission spectra of the selective molecularization system for the different sheet conductance of graphene lines and their corresponding gate voltage configurations.

molecule resonance. Finally, when $G_1 = G_2 = -2.2$ V, the tetrameric meta-molecule resonance occurs on the entire metamaterial sample, because four meta-atoms are conductively inter-connected to each other as shown in Figure 1b.

Figure 2a shows the simulated transmission spectra of the proposed selective meta-atom molecularization sample. By changing the gate voltage configuration as discussed above, we can confirm that the resonance frequency of monomeric, dimeric, and tetrameric meta-molecule is successfully modulated from 1.40, 1.10, to 0.74 THz, respectively. As shown in Figure 2b, the measured transmission spectra of the fabricated sample show well defined three different resonance properties, which are very similar with the simulated transmission spectra. These results clearly show that the micro-patterned ion-gel gating structure can selectively control the graphene bridges to achieve three different resonance frequencies. Therefore, we can expect that the multi-channel frequency modulators can be realized by using the proposed electrically controllable selective meta-atom molecularization systems in the terahertz regime.

3. Conclusions

In conclusion, we successfully demonstrated that the electrical reconfiguration of the terahertz meta-molecules by selectively control the conductance of graphene bridges between adjacent meta-atoms with micro-patterned ion-gel gating lines. Moreover, we found that the fabricated sample could actively change its resonance frequency in the spectral range from 0.74 to 1.40 THz with three different gate bias configurations. These intriguing active properties indicate that the proposed metamaterials can customize their resonance properties by changing the numbers of interconnected graphene bridges, which will pave the way for diverse applications including frequency tunable and switchable filters in terahertz and optical regime.

Acknowledgements

This work was supported by Samsung Research Funding Center of Samsung Electronics under Project Number SRFC-MA1601-02 and by the National Research Foundation of Korea (NRF) grant funded by the Korean government (MSIP) (NRF-2017R1A5A1015596, NRF-2017R1D1A1B03035056).

References

[1] K. Fan, W. J. Padilla, Dynamic electromagnetic metamaterials, *Mater*. *Today* 18: 39−50, 2015.

[2] Y. Wu, C. La-o-vorakiat, X. Qiu, J. Liu, P. Deorani, K. Banerjee, J. Son, Y. Chen, E. E. M. Chia, H. Yang, Graphene terahertz modulators by ionic liquid gating, *Adv*. *Mater*. 27: 1874−1879, 2015.

[3] H. Jung, J. Koo, E. Heo, B. Cho, C. In, W. Lee, H. Jo, J. H. Cho, H. Choi, M. S. Kang, H. Lee, Electrically controllable molecularization of terahertz meta-atoms, *Adv*. *Mater*. 30: 1802760, 2018.

[4] C. A. Gunawan, M. Ge, C. Zhao, Robust and versatile ionic liquid microarrays achieved by microcontact printing, *Nat*. *Commun*. 5: 3744, 2014.

Recent Advances in Mid-Infrared Graphene Plasmonics: Metasurface for Complex Amplitude Modulation and Compact Waveguide Switch

Sangjun Han[1], Seyoon Kim[1, 2], Sergey Menabde[1], Victor Brar[2], Harry Atwater[3], and Min Seok Jang[1, *]

[1]School of Electrical Engineering, Korea Advanced Institute of Science and Technology (KAIST), Korea
[2]Department of Physics, University of Wisconsin-Madison, USA
[3]Thomas J. Watson Laboratories of Applied Physics, California Institute of Technology, USA
*corresponding author, E-mail: jang.minseok@kaist.ac.kr

Abstract

Tunable plasmonic modes offered by graphene provide new opportunities to create electo-optically active devices with novel characteristics that have thus far been impossible to be realized by using conventional media. Here we introduce two recent theoretical research results in mid-IR graphene plasmonics: (1) Dynamic complex amplitude modulation in graphene-based metasurfaces and (2) modulated resonant transmission of graphene plasmons across a deep-subwavelength plasmonic waveguide gap.

Electronically Tunable Graphene Metamolecules for Complete Complex Amplitude Modulation

Metasurfaces have been shown to manipulate wavefront of light in subwavelength structures, overcoming the limitations in conventional optical systems. Although many efforts have been made to realize dynamic wavefront reconstruction in nanophotonic elements, current active metasurfaces suffer from inevitable interference between amplitude modulation and phase modulation as well as limited range in tunabilities. Here, we report dynamic complete complex amplitude modulation in metamolecules operating in the mid-infrared. The metamolecule is composed of a pair of metaatoms, and graphene plasmonic nanoresonators are utilized to incorporate electronically tunable functionalities. In the metamolecule, the two metaatoms are independently controlled to secure the two degree of freedoms required for modulating the amplitude and the phase of light, enabling 2π phase shift as well as large amplitude modulation including perfect absorption. We develop a generalized graphical model to examine the underlying requirements for complete complex amplitude modulation, offering intuitive design guidelines to maximize the tunabilities in metasurfaces. To illustrate the reconfigurable capability of our designs, we demonstrate dynamic beam steering and holographic wavefront reconstruction in a structurally identical metasurface by simply tuning the metamolecules

Modulated Resonant Transmission of Graphene Plasmons Across a λ/50 Plasmonic Waveguide Gap

We theoretically demonstrate the nontrivial transmission properties of a graphene-insulator-metal waveguide segment of deeply subwavelength scale. We show that, at mid-infrared frequencies, the graphene-covered segment allows for the resonant transmission through the graphene-plasmon modes as well as the nonresonant transmission through background modes, and that these two pathways can lead to a strong Fano interference effect. The Fano interference enables a strong modulation of the overall optical transmission with a very small change in graphene Fermi level. By engineering the waveguide junction, it is possible that the two transmission pathways perfectly cancel each other out, resulting in a zero transmittance. We theoretically demonstrate the transmission modulation from 0% to 25% at 7.5-μm wavelength by shifting the Fermi level of graphene by a mere 15 meV. In addition, the active region of the device is more than 50 times shorter than the free-space wavelength. Thus, the reported phenomenon is of great advantage to the development of on-chip plasmonic devices [1].

References

[1] Jang, M. S.[#, *], Kim, S.[#], Brar, V. W., Menabde, S. G., Atwater, H. A., "Modulated resonant transmission of graphene plasmons across a λ/50 plasmonic waveguide gap," Phys. Rev. Applied 10, 054053 (2018).

Electrically-pumped Vertical Cavity Metasurface-Emitting Lasers for directional lasing emissions

Yi-Yang Xie[1], Pei-Nan Ni[2], Gauthier Briere[2], Qiu-Hua Wang[1], Zhuang-Zhuang Zhao[1], Chen Xu[1], Qiang Kan[3], Hong-Da Chen[3], and Patrice Genevet[2,*]

[1]Key Laboratory of Optoelectronics Technology (Beijing University of Technology) Ministry of Education, Beijing 100124, China

[2] Université Côte d'Azur, CNRS, Centre de Recherche sur l'Hétéro-Epitaxie et ses Applications, Valbonne, 06560, France

[3] Institute of Semiconductor, Chinese Academy of Sciences, Beijing 100083, China

*corresponding author: *pg@crhea.cnrs.fr*

Abstract

Vertical cavity metasurface-emitting lasers (VCMELs) have been proposed and designed into back-emitting configuration. We have demonstrated that the integration with metasurface allow the effective control of the lasing emission wavefront.

1. Introduction

Vertical-cavity surface emitting laser (VCSEL) technology has been rapidly and consistently developing over the last 30 years, in particular after the demonstration of the first continuous-wave room-temperature device.[1,2] The unique features provided by this type of lasing devices such as low-power consumption, wafer-level testing, circular output beam profile, large-scale two-dimensional (2D) array have made them the most versatile laser sources for various applications including fiber optics optical communications, laser manufacturing, smart-glasses and etc.[3,4] Metasurfaces have emerged as a new class of subwavelength-carved two-dimensional optical components, offering exceptional spectral and spatial controllability over the electromagnetic waves. Their extraordinary capabilities of molding the light in a very compact and efficient ways have been demonstrated from a large variety of novel optical components including frequency selective surface (FSS), polarization converter, wavefront shaping and hologram [5-7]. In comparison with conventional optical components, their unique planar configuration and their CMOS compatible processing techniques hold great potential for monolithic integration into semiconductor optoelectronic devices.

In this work, we propose a wafer-level approach that addresses the problem of wavefront engineering without altering the VCSEL characteristics. Arrays of identical devices with varying beam deflecting properties, called vertical cavity metasurface-emitting lasers (VCMELs), can be fabricated on the same chip. The realization of array of identical emitting beam shaped lasers would find various applications, including image forming and compact laser scanning systems.

2. Discussion

As shown in Fig. 1(a) and (b), our approach consists in integrating wavefront engineering high index dielectric metasurfaces into back-emitting configuration to arbitrary control the phase of lasing beam for directional beam emissions. Centro-symmetric GaAs nanopillars of different diameters are employed as polarization insensitivity meta-atoms. The phase and amplitude of the scattered light can be controlled by adjusting the pillar radius as determined by the finite difference time domain (FDTD Lumerical) simulations, as shown reported in Fig. 1(c).

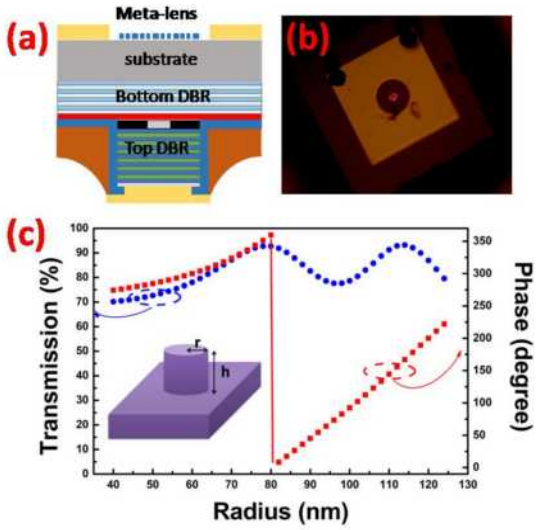


Fig.1 The Schematic (a) and photograph (b) of VCMELs, (c) The transmission and the phase of the designed GaAs nanopillars as a function of its radius at λ=980 nm, the inset represents a single nanopillar.

As a proof of concept, we design and fabricate the integrated metasurfaces for the generation of Bessel beam and dynamic beam steering applications, respectively, as shown in Fig. 2. For the generation of Bessel beam, the GaAs nanopillars need to be assembled individually to impart a conical phase profile (Fig. 2(a)). Intense field distribution along the laser axis can be clearly observed from the transverse plane intensity profiles of the VCMEL

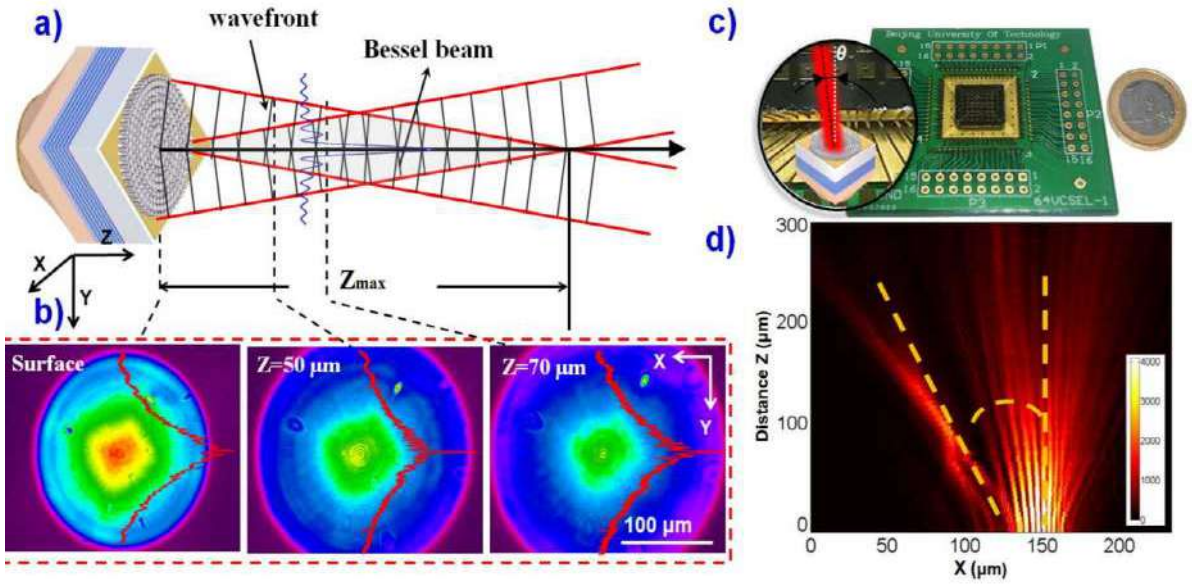


Fig. 2 The Schematic of VCMEL for Bessel beam generation (a), the measurement of the field distribution of lasing beam in the X-Y plane after transmitting through the metasurface and their corresponding Y-cut intensity profiles (b), The photograph of the array of 8x8 VCMELs with different deflection angles mounted onto a PCB board by flip-chip method, the inset shows the schematic of an individual device with deflection angle of θ.(c), the field distribution of lasing beam in the X-Z plane.(d)

emitting beam and their corresponding x-cut intensity profiles, as shown in Fig. 2(b). It can be seen that the beam size of the device with metasurface remains almost the same along the propagation direction. Furthermore, the intensity profile of the emitting beam of the VCMEL can be well fitted into Bessel function. The above facts indicate the generation of Bessel beam from this VCMEL.

Moreover, dynamic beam steering can be realized by making advantage of the two dimensional array of VCMELs. As a proof of concept, a chip of 8x8 VCMELs has been fabricated as shown in Fig. 2(c) and (d). Metasurface based beam deflector with different deflection angle has been integrated onto it, respectively. Such configuration allows each VCMEL from the same chip to individually emitting a deflected beam with a given angle to be used for the dynamic beam steering applications.

3. Conclusions

In this work, vertical cavity metasurface-emitting lasers have been proposed and designed into back-emitting configuration for directional beam emissions. We demonstrated that the wavefont of the lasing beam from the VCMELs can be controlled and arbitrarily shaped arbitrarily with properly designed metasurfaces, thus leading to compact, wafer-level collimation and wavefront shaping of laser radiation.

References

[1] F. Koyama, S. Kinoshita, K.Iga, Room Temperature CW Operation of GaAs Vertical Cavity Surface Emitting Laser, *Trans. IEICE*, E71:1089-1090 1988.

[2] K. Iga, Surface emitting laser – It's birth and generation of new optoelectronics field, *IEEE J. Sel. Topics Quantum Electron*., 6: 1201 2000.

[3] P. Moser, J.A. Lott, D. Bimberg, Energy Efficiency of Directly Modulated Oxide-Confined High Bit Rate 850-nm VCSELs for Optical Interconnects, *IEEE J. Sel. Topics Quantum Electron*., 19: 1702212 2013.

[4] A. Pruijmboom, R. Apetz, R. Conrads, C. Deppe, G. Derra, S. Gronenborn, J.S.Kolb, H. Moench, F. Ogiewa, P. Pekarski, J. Pollmann-Retsch, U. Weichmann, X. Gu, and M. Miller, Vertical-cavity surface emitting laser-diodes arrays expanding the range of high-power laser systems and applications, *Journal of Laser Applications* 28: 032005 2016.

[5] N Yu, P Genevet, MA Kats, F Aieta, JP Tetienne, F Capasso, Z Gaburro, Light propagation with phase discontinuities: generalized laws of reflection and refraction, *Science*, 334: 333-337 2011.

[6] M.Esfandyarpour, E. C.Garnett, Y. Cui, M. D.McGehee, M. L. Brongersma, Metamaterial mirrors in optoelectronic devices, *Nature nanotechnology*, 9: 542-547 2014.

[7] S. Wang, P. C. Wu, V.-C. Su, Y.-C. Lai, M.-K. Chen, H. Y. Kuo, B. H. Chen, Y. H. Chen, T.-T. Huang, J.-H. Wang, R.-M. Lin, C.-H. Kuan, T. Li, Z. Wang, S. Zhu and D. P. Tsai, A broadband achromatic metalens in the visible, *Nature Nanotechnology* 13:227–232 2018

[8] P Genevet, F Capasso, F Aieta, M Khorasaninejad, R Devlin, Recent advances in planar optics: from plasmonic to dielectric metasurfaces *Optica* 4:, 139-152 2017

[9] D. Neshev and I. Aharonovich, Optical metasurfaces: new generation building blocks for multi-functional optics, *Light: Science & Applications* 7:58 2018.

[10] P. Cheben, R. Halir, Jens H. Schmid, Harry A. Atwater and David R. Smith, Subwavelength-integrated-photonics, *Nature*, 560: 565 2018.

Light sailing to interstellar space and nearby stars

Artur R. Davoyan[1,2]

[1]Department of Mechanical and Aerospace Engineering, University of California, Los Angeles, CA
[2]Thomas J. Watson Laboratories of Applied Physics, California Institute of Technology, California, USA
*corresponding author, E-mail: davoyan@seas.ucla.edu

Abstract

In this talk we will overview our recent efforts directed at the design of light sails for interstellar missions. We will highlight our ongoing work on both solar and laser sailing with a particular emphasis on photonic materials, sail design criteria, and light-materials interaction.

1. Introduction

Past sixty years of space flight have led to fascinating discoveries within our solar system. Regular missions to inner and outer planets pave the way to new scientific discoveries informing about the solar system formation and the origins of life. Nonetheless, space travel to Neptune and beyond it into the interstellar medium presents a significant technological challenge. Hence, to date only two space probes – Voyager 1 and Voyager 2 – have crossed the boundaries of our heliosphere. It took them over 40 years of flight to reach the interstellar space. Clearly, novel breakthrough advances are needed to enable sustainable and scalable exploration of the outskirts our solar system and for interstellar flight. In this talk we will discuss conceptually new ways of spacecraft propulsion that can revolutionize the future of deep space exploration. In particular, we will show that photon propulsion may be capable of accelerating a lightweight spacecraft to unprecedented velocities beating currently achieved records. We will discuss two means of light driven propulsion, including solar sailing and laser sailing, highlighting challenges and opportunities of both of these technologies.

2. Solar sailing

Solar sails have recently emerged as a robust means of in-space spacecraft propulsion. In particular several technology demonstration missions have been launched within the past decade, with a number of missions scheduled for launch in the next couple of years, including Near Earth Asteroid Scout. Solar sails make use of sunlight radiation pressure and are propelled essentially without using any energy. Whereas sailing in the inner solar system has been demonstrated and regular missions are planned, sailing into the interstellar medium remains of a big technological challenge. It has been shown recently that with the use of solar gravity assist and high solar radiation flux in the vicinity of the sun, sails may be propelled to over 25 AU/year – unprecedented velocities outperforming any the known and demonstrated propulsion means. However, such a propulsion requires a very close approach to the sun, posing a significant problem for materials science, thermal engineering, and trajectory control. We will survey these challenges and highlight our work on identifying suitable designs that can enable future interstellar solar sail missions.

3. Laser sailing

Laser sailing has the potential to advance space travel to even higher velocities and distance. Hence, recently established Breakthrough Starshot Initiative poses an audacious goal of propelling a spacecraft to 20% of the speed of light in order to reach a potentially habitable planet in the Alpha Centauri star system in just 20 years [1]. Achieving this unprecedented speed requires engineering at the limits of current technology. In particular, project assumes that a lightweight sail with a payload will be propelled with the use radiation pressure from a high powered phased array of lasers on Earth (~10 GW/m2 of net laser intensity). The lightsail should have an area of ~10m^2 with a mass of under ~1 gram. Clearly, design of the lightsail will need to push the boundaries of materials science, photonic design and systems engineering to enable performance at these extreme conditions and constraints. We will discuss these challenges in the second part of the talk. Specifically, we will talk about photonic materials, thermal control, and highlight the issues of laser beam riding stability. We will then discuss the possible use of nanophotonics in the design of sustainable and stable Starshot lightsail. We will survey key challenges and discuss potential solutions.

4. Conclusions

We will review our efforts in the design of novel photonic materials for future photon driven in-space propulsion. We show that solar and laser sailing may disrupt the way of space exploration paving the way to conceptually new interstellar missions.

Acknowledgements

We acknowledge the support of Professor Harry Atwater and his group, as well as useful discussions with Dr. Louis Friedman and Aerospace Corp. SGL team.

References

[1] H.A. Atwater, A.R. Davoyan, O. Ilic, D. Jariwala, M.C. Scerrott, C.M. Went, W.S. Whitney, J. Wong. Material challenges for the Starshot lightsail. Nature Mat. 17: 861-867, 2018.

Dielectric passive metasurface and active tunable nonlinear metasurface

Junxiao Zhou,[1,2] Haoliang Qian,[1] Zhaowei Liu[‡ *]

[1]Department of Electrical and Computer Engineering, University of California, San Diego, 9500 Gilman Drive, La Jolla, California 92093, United States

[2]Key Laboratory for Micro-/Nano-Optoelectronic Devices of Ministry of Education, School of Physics and Electronics, Hunan University, Changsha 410082, China

* Corresponding author, E-mail: zhaowei@ucsd.edu

Abstract

Metasurface enables a new paradigm to manipulate electromagnetic wave by tailoring subwavelength artificial structures, which provides a promising method for compact, cascadable, and miniaturization elements in integrated optics. Here, we review some of our works on passive dielectric metasurfaces and Kerr nonlinear tunable metasurfaces enabled by metallic quantum wells. The mentioned metasurface may lead important applications in image processing, sensing, switching, and multifunctional photonics devices.

1. Introduction

Metasurface, two-dimensional equivalent of metamaterial, is composed of discrete subwavelength structures, which possesses the capability of full control of light properties [1, 2]. Here, we present a broadband dielectric spin Hall metasurface achieved by integrating two geometric phase metasurface into one single dynamic phase lens, which is demonstrated to control photonic spin-dependent splitting on transverse and longitudinal directions simultaneously at the whole visible range. Furthermore, we study the tunable Kerr metasurface based on quantum sized metal film with enhanced giant optical nonlinearity. By changing the incident optical power through the designed metasurface, the active functionality of the device could be achieved.

2. Passive and active metasurface

In this section, we will first introduce the broadband dielectric spin Hall metasurface, which attain the spin dependent splitting in multiple directions [3]. Then, the nonlinear tunable Kerr metasurface enabled by metallic quantum well is studied [4].

2.1. Broadband dielectric spin Hall metasurfaces

Figure 1(a) describes the schematic drawing of the spin-dependent splitting in transverse and longitudinal directions. When the photonic spin Hall metasurface (PSHM) is normally illuminated with a linearly polarized (LP) Gaussian light beam, the transmitted beam composing both left-handed circularly polarized (LCP) and right-handed circularly polarized (RCP) components are generated, respectively. The LCP and RCP beams propagate towards different directions and focused at different depths, which corresponds to the desired longitudinal spin-dependent splitting. The microscopy images of the employed PSHM is shown in Figure 1 (b)-(e). Here, the PSHM is fabricated by a laser writing method in a glass substrate, which avoids the typical high-resolution photolithography or e-beam lithography process [5]. As we can see in Figure 1(b) and (c), PSHM is embedded inside of the glass slide. The dark-field optical image (Figure 1(d)) reveals that the laser written layer has a thickness around 80 μm. The SEM image in Figure 1(e) further confirms that the laser exposure formed some self-assembled vertically aligned nanostructures at deep subwavelength scales.

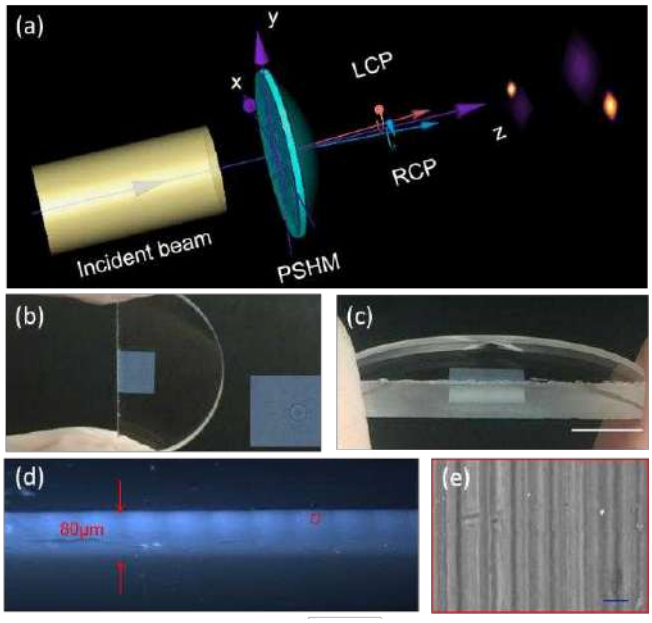


Figure 1. (a) Schematic illustration of transverse and longitudinal splitting by using a photonic spin Hall metasurface (PSHM). (b) Top-view photograph of the PSHM sample. Inset: zoomed-in view shows the center patterned area of the sample. (c) Side-view photograph of

the PSHM sample. Scale bar, 4 mm. (d) The dark field microscopy image for the cross-section of the PSHM sample reveals microscopic laser written patterns. (e) Zoomed-in SEM image of the boxed area in Figure 1(d). Scale bar is 300 nm.

2.2. Kerr metasurface enabled by metallic quantum wells

Active, tunable, and reconfigurable devices are highly desirable in modern electromagnetic and photonic systems, since they create the dynamic manipulations of the incident wave. Optical Kerr effect provides a straightforward solution for such tunable metasurface and devices. However, the Kerr effect of traditional materials is typically too low to fulfill the aforementioned task. Recently, ultrathin metal films with a giant optical Kerr nonlinear response has been demonstrated due to the quantum size effect [6]. Here, we proposed a tunable metasurface design that is employed such quantum-sized gold films. Figure 2(a) shows the basic unit of the nonlinear metasurface, consisting of 6 pairs of Au-SiO_2 multilayers (3 nm Au and 2 nm SiO_2), 50 nm MgF_2 spacer layer, and 80 nm gold layer as a back mirror. One-unit cell length is L_x=300 nm, and its width is L_y=120 nm. Figure 1(b) shows the linear permittivity $\varepsilon = \varepsilon' + i \times \varepsilon''$ for the 3 nm gold film (red lines, obtained experimentally from an identical Au-SiO2 multilayer) and bulk gold (blue lines, from Johnson and Christy) [7]. Figure 2(c)- (h) shows the performance of designed nonlinear metasurface based on proposed materials at the case of oblique incident light. When the incident light angles are 15°, 30°, and 45°, the linear far field results are shown in Figure 2(c)- (e). As we can see, the metasurface acts as a mirror with most the energy going into the specular reflection angle at the low intensity. When the incident light intensity becomes large, most reflected energy goes into diffraction orders, as shown in Figure 2(f)- (h).

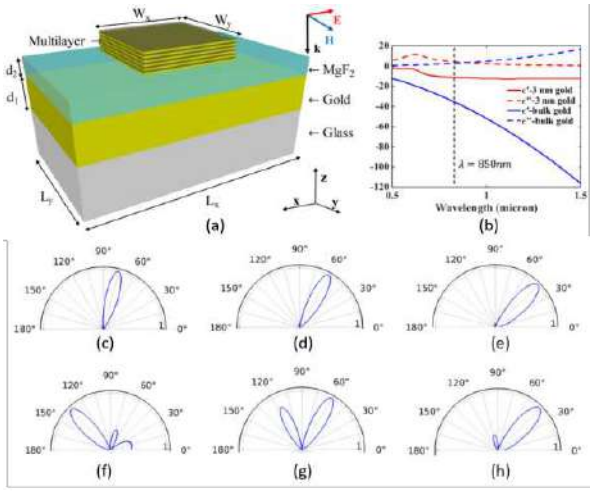


Figure 2. (a) Schematic of a building block of the nonlinear metasurface. The whole structure sits on a glass substrate, which is made of a top multilayer nanostructure and a bottom bulk gold layer separated by a spacer layer, MgF_2. (b) Permittivity (solid and dashed lines for real and imaginary parts, respectively) for 3 nm gold (red) and bulk gold (blue). (c)-(h) Simulated angular distribution of the reflected far field. The linear (I=1MW/cm^2) cases of the incident angles of 15°, 30°, and 45° are shown in (c), (d) and (e), respectively. The corresponding nonlinear (I = 1GW/cm^2) cases are shown in (f), (g) and (h), respectively.

3. Conclusions

In this work, we have introduced two types of metasurfaces, passive dielectric metasurfaces and Kerr metasurfaces enabled by metallic quantum wells. The passive dielectric metasurface have been demonstrated to achieved multiple directions splitting, which could be an integrated metasurface by combining with several single functional metasurface. For the Kerr type metasurface, by varying the optical power of the incident light through quantum sized gold film, the active functionality of the material can be achieved. At low power region, the device acts as a normal reflecting surface. It becomes a phase grating when the incident power is high enough. The mentioned metasurface indicates potential applications in image processing, switching, modulator and multifunctional photonic devices.

Acknowledgements

This research is supported by the National Science Foundation, Division of Material Research (NSF-DMR-1610538).

References

[1] N. F. Yu, F. Capasso, Flat optics with designer metasurfaces. Nat Mater 13: 139–150, 2014.

[2] A. V. Kildishev, A. Boltasseva, V. M. Shalaev. Planar photonics with metasurfaces. Science 339: 1232009 2013.

[3] J. Zhou, H. Qian, G. Hu, H. Luo, S. Wen, Z. Liu, Broadband Photonic Spin Hall Meta-Lens. ACS nano 12: 82-88, 2018.

[4] Y. Xiao, H. Qian, Z. Liu, Nonlinear Metasurface Based on Giant Optical Kerr Response of Gold Quantum Wells. ACS Photonics 5: 1654-1659, 2018.

[5] M. Beresna, M. Gecevičius, P. G. Kazansky, T. Gertus, Radially Polarized Optical Vortex Converter Created by Femtosecond Laser Nanostructuring of Glass. Appl. Phys. Lett. 98: 201101, 2011.

[6] H. Qian, Y. Xiao, Z. Liu, Giant Kerr Response of Ultrathin Gold Films from Quantum Size Effect. Nat. Commun. 7: 13153, 2016.

[7] P. B. Johnson, R.-W, Christy, Optical Constants of the Noble Metals. Phys. Rev. B 6: 4370, 1972.

Enhancing Chiral Light-Matter Interactions by Metamaterials

Yongmin Liu[1,2,*]

[1]Department of Mechanical and Industrial Engineering, Northeastern University, Boston, MA, USA
[2]Department of Electrical and Computer Engineering, Northeastern University, Boston, MA, USA
*corresponding author, E-mail: y.liu@northeastern.edu

Abstract

In this talk, I will discuss how to design novel metamaterials by symmetry analyses and deep learning to enhance chiral light-matter interactions, which promise important applications in polarimetric imaging and enantioselective sensing.

1. Introduction

Chirality refers to the structural property of an object that cannot be superposed onto its mirror image. The existence of chirality in nature is universal, ranging from molecules at the nanoscale to gastropod shells at the macroscale. Light can be chiral as well. Circularly polarized light with opposite helicity has its electric field vector rotating clockwise or counterclockwise during propagation. Chiral light-matter interactions are widely used in molecule detection, optical communication and quantum information processing. However, the chiroptical response of natural materials is inherently weak. The advent of metamaterials, which are composed of artificial meta-atoms with elaborately engineered optical properties [1], offers an elegant and effective solution to this problem. Over the past decades, a variety of metamaterials with strong intrinsic and extrinsic chiral responses have been demonstrated [2-4].

Here we show how we can design chiral metamaterials based on symmetry analyses and deep learning technique to greatly enhance chiral light-matter interactions. More specifically, we design and demonstrate the so-called chiral metamirror, which can achieve near-perfect reflection of designated circularly polarized light without reversing its handedness, yet complete absorption of the other polarization state [5-8]. It is analytically shown that the building block of such a metamirror needs to simultaneously break the n-fold rotational ($n > 2$) symmetry and mirror symmetry [7]. Such a metamaterial can be used for polarimetric imaging to extract the polarization information of light [8]. However, the guidelines based on symmetry requirements are insufficient when we want to quantitatively design a metamaterial structure given a desired chiral response or even to simply predict the trend in chiral response as the structure transforms. To overcome this limitation, we have recently applied the deep learning approach to accelerate the design of chiral metamaterials with prescribed chiroptical responses [9]. Our findings would lead to novel metadevices for circular dichroism spectroscopy, enantioselective sensing and sorting.

2. Results

To design a chiral metamirror that can selectively reflect one designed state of circular polarization, we first analyze the necessary symmetry conditions based on Jones calculus. We can readily prove that complete reflection of left circularly polarized (LCP) waves and total absorption of right circularly polarized (RCP) waves require the reflection matrix satisfying

$$\mathbf{R}=\begin{pmatrix} r_{xx} & r_{xy} \\ r_{yx} & r_{yy} \end{pmatrix}=\frac{e^{i\alpha}}{2}\begin{pmatrix} 1 & i \\ i & -1 \end{pmatrix} \qquad (1)$$

Then based on symmetry analysis, including rotational and mirror symmetries, we can derive the structural symmetry required for the chiral metamirror. In short, the general yet necessary condition to realize the chiral metamirror is simultaneous breaking of the n-fold rotational ($n>2$) and mirror symmetries [7].

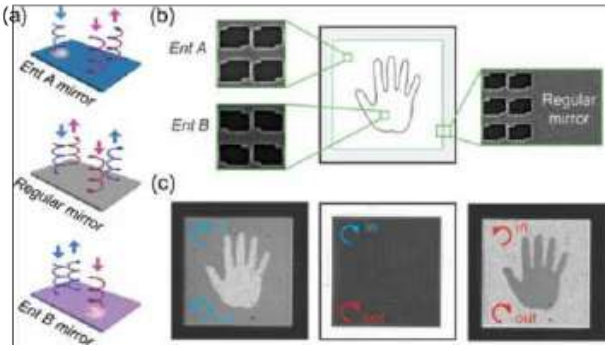


Figure 1: (a) Comparison of the reflection behavior of a chiral metamirror and a regular mellitic mirror. A chiral metamirror composed of enantiomer A (B) reflects RCP (LCP) incident light and absorbs the entire LCP (RCP) component. (b) Schematic of the fabricated hand pattern. The exterior and interior regions of the hand are formed by enantiomer A and B, respectively. (c) Microscopic images of the metamirror. The sample is illuminated by circularly polarized light, and the reflected light is recorded by a camera after it passes through a circular polarized analyzer.

In collaboration with Prof. Wenshan Cai's group, we have demonstrated a chiral metamirror consisting of a sandwich system with an asymmetric-hole array perforated film, a thin dielectric layer and an optically thick metallic back plane [8]. In contrast to a metal mirror, there are distinct features associated with the metamirror, that is, the chiral selective absorption and the circular polarization preservation, which are schematically shown in Figure 1a. These features are unambiguously identified through a comprehensive visualization of a fabricated sample, in which a hand pattern consists of the designed enantiomer B while the outside region consists of enantiomer A (Figure 1b). From Figure 1c, one can see that for LCP incident light, a bright hand against a dark surrounding area can be seen with a LCP analyzer, while the entire metamaterial pattern becomes dark when a RCP analyzer is applied. Furthermore, the imaging behavior completely inverts when a RCP wave impinges upon the sample, i.e., a dark hand stands out with a bright background with a RCP analyzer implemented. Note the reflection from the boundary of sample, which is unpatterned metallic film, always shows the opposite contrast compared to the hand pattern, because the spin state reflected from a regular metallic film is always flipped. These results comprehensively visualize the chiral-selective reflection and the circular polarization preservation properties of the chiral metamirror.

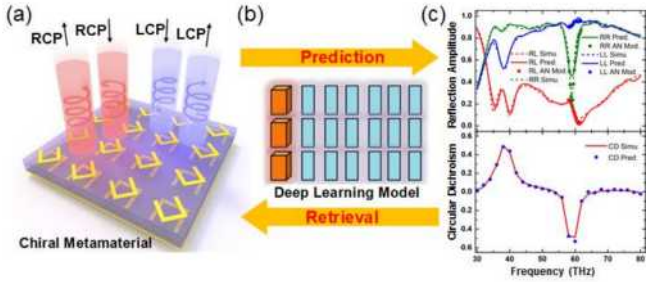


Figure 2: (a) Schematic of the designed 3D chiral metamaterial. (b) Illustration of the deep learning model to predict the optical response of chiral metamaterials and inversely design the geometry of chiral metamaterials. (c) Prediction results for the full reflection spectra (top) and circular dichroism spectra (bottom) in comparison with the ground truth.

Although the symmetry requirements provide some useful guidelines for us to design chiral metamaterials, there is no closed-loop solution to efficiently construct the specific metamaterial structures from given requirements, such as the operating wavelength and strength of chirality. This is mainly due to the nonintuitive and highly nonlinear relationship between geometric chirality and chiroptical responses. To solve this problem, we employ the deep-learning technique to automatically model and optimize three dimensional chiral metamaterials [9]. As illustrated in Figure 2a, the unit cell of the metamaterial consists of two stacked gold split ring resonators twisted at a certain angle and separated by two spacing dielectric layers with a continuous gold reflector at bottom. Depending on the geometry, including the size, separation distance and twisting angle of the SRRs, this metamaterial can function as a chiral meta-mirror enabling selective reflection of designated circularly polarized light without reversing its polarization state. We have developed a deep learning model allowing data to flow in both forward path and inverse path as illustrated in Figure 2b. The predicted results from neural networks are in very good agreement with the numerical simulation (Figure 2c), which clearly verifies that neural network can indeed model the complicated nonlinear relationship between meta-atoms and the desired spectral features.

3. Conclusions

The necessary symmetry requirements for a chiral metamirror has been obtained, and its unique optical functionality, that is, selective reflection of one circular polarization without flipping the polarization state, has been experimentally demonstrated. Furthermore, we propose a purpose-designed deep-learning model to accelerate the design of chiral metamaterials. These results open up a new way to design novel metadevices for circular dichroism spectroscopy, polarimetric imaging, enantioselective sensing, sorting and synthesis.

Acknowledgements

Y. Liu acknowledges the financial support from the Office of Naval Research (N00014-16-1-2409).

References

[1] Y. Liu and X. Zhang, "Metamaterials: a new frontier of science and technology," *Chemical Society Reviews,* vol. 40, pp. 2494-2507, 2011.

[2] V. Fedotov, P. Mladyonov, S. Prosvirnin, A. Rogacheva, Y. Chen, and N. Zheludev, "Asymmetric propagation of electromagnetic waves through a planar chiral structure," *Physical Review Letters,* vol. 97, p. 167401, 2006.

[3] J. K. Gansel, M. Thiel, M. S. Rill, M. Decker, K. Bade, V. Saile*, et al.*, "Gold helix photonic metamaterial as broadband circular polarizer," *Science,* vol. 325, pp. 1513-1515, 2009.

[4] A. Kuzyk, R. Schreiber, Z. Fan, G. Pardatscher, E.-M. Roller, A. Högele*, et al.*, "DNA-based self-assembly of chiral plasmonic nanostructures with tailored optical response," *Nature,* vol. 483, pp. 311-314, 2012.

[5] E. Plum and N. I. Zheludev, "Chiral mirrors," *Applied Physics Letters,* vol. 106, p. 221901, 2015.

[6] W. Li, Z. J. Coppens, L. V. Besteiro, W. Wang, A. O. Govorov, and J. Valentine, "Circularly polarized light detection with hot electrons in chiral plasmonic metamaterials," *Nature Communications,* vol. 6, 2015.

[7] Z. Wang, H. Jia, K. Yao, W. Cai, H. Chen, and Y. Liu, "Circular Dichroism Metamirrors with Near-Perfect Extinction," *ACS Photonics,* vol. 3, pp. 2096-2101, 2016.

[8] L. Kang, S. P. Rodrigues, M. Taghinejad, S. Lan, K.-T. Lee, Y. Liu*, et al.*, "Preserving Spin States upon Reflection: Linear and Nonlinear Responses of a Chiral Meta-Mirror," *Nano Letters,* vol. 17, pp. 7102-7109, 2017.

[9] W. Ma, F. Cheng, and Y. Liu, "Deep-Learning Enabled On-Demand Design of Chiral Metamaterials," *ACS Nano,* vol. 12, pp. 6326-6334, 2018.

Microfluidic Sensing and Dynamic Tuning with Huygens Metasurfaces

Adam J. Ollanik, Isaac O. Oguntoye, George Z. Hartfield, Brittany Simone, Yaping Ji, and Matthew D. Escarra

Department of Physics and Engineering Physics, Tulane University, New Orleans, LA, U.S.A.
*corresponding author, E-mail: escarra@tulane.edu

Abstract

Huygens metasurfaces have optical performance that is especially sensitive to perturbations in their geometry or constituent material properties. Here we take advantage of this sensitivity for both sensing and dynamic tuning applications. First, we show that silicon metasurfaces embedded in a microfluidic channel provide an affordable, customizable, and highly sensitive platform for refractive index sensing, with experimental transmittance response of 820% T/RIU. Second, we show that by using VO_2 for the antenna elements, we can create dynamically tunable metasurfaces.

1. Introduction

Huygens metasurfaces are characterized by spectrally overlapping electric and magnetic dipole resonances. These nanoantenna structures each act as a point emitter for light of resonant wavelengths, and their interactions with incoming light are highly sensitive to geometric parameters, such as antenna width, height, and spacing, and material parameters, such as antenna, substrate, and encapsulant refractive index. For a homogeneous array of these antennas, by tuning any one of these geometric or material properties by ~10%, the optical response of these antennas can be tuned from near unity transmission to near unity reflection of incident light, at a specified wavelength. This level of sensitivity can be useful in a variety of contexts, including liquid or gas-phase sensing, tunable optics, optical computing, communications, and more.

2. Refractive Index Sensing with Silicon-Based Metasurfaces

Dielectric Huygens metasurfaces provide a practical platform for very low-loss manipulation of light, with efficiency of anomalous refraction of at least 78% of incident light expected for ultraviolet, visible, and near-infrared wavelengths [1]. Such structures may also take advantage of overlapping electric and magnetic field resonances to create metasurfaces that either transmit or reflect with near unity (>99%) efficiency, with only minor differences in geometry or material properties. These CMOS compatible structures may be fabricated over large area and may be integrated with microfluidic arrays for liquid or gas-phase sensing. This sensing is accomplished by directly assessing changes in the refractive-index of the medium surrounding the antennas. While most resonance-based sensing techniques employ optical spectroscopy to measure shifts in the resonant wavelength, here we show that with Huygens metasurfaces, such a measurement may be done with a single wavelength method, providing significant cost savings by using a simple light source and photodetector.

We fabricate such a metasurface, integrate it with a microfluidic channel, and experimentally measure sensitivity of 323 nm/RIU (refractive index unit) for 1217nm light using purified water contrasted with a saline solution ($\Delta n = 0.0062$). This corresponds to a figure of merit of 5.4 (figure of merit defined as sensitivity divided by linewidth of the reflectance peak) and a single wavelength transmittance response of 820% change in transmittance per RIU. We further measure the contrast between purified water and $25*10^{-3}$ M solution of $CaCl_2$ ($\Delta n = 0.0006$), with a measured response of 880% change in transmittance per RIU. Technoeconomic analysis predicts a device costing ~$2400 with ability to measure refractive index changes on the order of $2*10^{-8}$. We are currently fabricating a hand-held, integrated, low-cost sensor prototype based on this single-wavelength metasurface sensing technique [2].

Furthermore, by utilizing off-normal anti-symmetric resonances, we computationally demonstrate a Huygens metasurface with sensitivity of 350 nm/RIU, figure of merit of 219, and single wavelength transmission response of 36,000% per RIU. This FOM exceeds that of any previously reported plasmonic or dielectric nanostructure surface-based refractive index sensor [2].

3. Dynamically Tunable VO_2 Metasurfaces

The sensitive nature of Huygens metasurfaces makes them ideal for dynamic tuning applications, where the optical performance of the metasurfaces may be tuned by an external stimulus, such as electric field, optical irradiation, or temperature change. Here we use vanadium dioxide (VO_2) as the material for these resonant nanoantennas. VO_2 is well-known for its metal-insulator phase transition at

relatively low temperature (~70°C). Our modeling shows that metasurfaces from these materials have strong optical tunability within less than 10% of the phase transition from insulator to metal. We synthesize thin VO_2 films using pulsed laser deposition and pattern these films into nanoantennas using reactive ion etching, via a chlorine-based etch, to achieve desired geometries. Experimental analysis is ongoing, and resonant tunable metasurfaces will be presented.

In order to accurately characterize the properties of dynamically tunable thin films and metasurfaces, one must measure transmission and optical phase shift as a function of external stimuli. We have developed a unique three-beam interferometry technique to perform this characterization. Our approach leads to a >92% decrease in both noise and drift of measured phase shift, achieved through constant measurement referencing with a third beam. We demonstrate this phase shift measurement capability on temperature-tuned VO_2 thin films, and we also show its effectiveness with resonant silicon-based dielectric metasurfaces. An additional method, utilizing Fourier transform processing of measurements with artificially induced periodicity, allows accurate measurement of phase shift with standard deviation of 0.067°, significantly beneath the floor of both noise and drift in our measurements. We demonstrate the effectiveness of this technique by measuring phase shift differences due to monolayer thickness variations in two-dimensional MoS_2 materials.

Finally, in pursuit of passive and active metaholograms from dielectric and phase change Huygens metasurfaces, we report on a design algorithm that takes into account the strong nearest neighbor coupling of these resonant structures. By properly extracting the phase shift of individual antennas despite the coupling to their neighbors, we may build a toolbox of phase-shifting elements that may be used for complex phase front manipulation with resonant Huygens metasurfaces.

4. Conclusions

In summary, we report on highly resonant Huygens metasurfaces from low-loss dielectric and phase change materials. The strong sensitivity of these antenna arrays to changes in material properties enables high performance in a number of important applications. Here we demonstrate their implementation in affordable and highly sensitive microfluidic refractive index measurements. We also show their potential for use in dynamically tunable metasurfaces.

Acknowledgements

This work is supported in part by the National Science Foundation (Grant No. DMR-1654765). The authors thank Diane A. Blake of the Tulane University Medical School for conversations regarding microfluidic sensor medical applications, sample preparation, and protein detection.

References

[1] A.J. Ollanik, J.A. Smith, M.J. Belue, and M.D. Escarra, "High-Efficiency All-Dielectric Huygens Metasurfaces from the Ultraviolet to the Infrared," *ACS Photonics*, Vol. **5** (4), 1351-1358 (2018). dx.doi.org/10.1021/acsphotonics.7b01368

[2] A.J. Ollanik, I.O. Oguntoye, G.Z. Hartfield, and M.D. Escarra, "Highly Sensitive, Affordable, and Adaptable Refractive Index Sensing with Silicon-Based Dielectric Metasurfaces," *Advanced Materials Technologies*, 1800567, 1-9 (2018). dx.doi.org/10.1002/admt.201800567

van der Waals Metasurfaces and Transdimensional Photonic Lattices

Viktoriia Babicheva

College of Optical Sciences, University of Arizona, Tucson, AZ, United States
E-mail: vbab.dtu@gmail.com

Abstract

Transdimensional photonics is an emerging field of science and engineering dealing with the optical properties of nanostructures in the translational regime. We consider optical nanoantennas out of hexagonal boron nitride (hBN) which is a natural material with hyperbolic dispersion in the mid-infrared spectral range. The hBN nanoantennas in the lattice support multipole electric and magnetic resonances, and such lattice possesses a 2D/3D translational nature as the optical properties are defined by nanoantenna size and shape as well as in-plane lattice arrangement.

1. Introduction

Nanostructures with excitation of phonon-polaritons have been suggested as an alternative to conventional metals supporting plasmonic resonances. Phonon-polariton excitations in strongly anisotropic van der Waals materials, such as hBN and orthorhombic molybdenum trioxide, enable propagative waves with hyperbolic dispersion and ultra-tight mode field confinement.

Antennas made of hyperbolic (meta)materials along with plasmonic and all-dielectric nanostructures can be used for designing optical resonators and scattering elements in metasurfaces [1]-[3]. We propose van der Waals metasurface that includes periodic array of hBN antennas and study different multipole resonances in the lattice (Fig. 1). Nanoantenna resonances and optical properties of the metasurfaces can be controlled by scatterers' size and shape as well as periodic arrangement of the antennas in the lattice and cross-coupling of the multipole resonances.

2. Model

In the cuboid particle with strongly reflective boundaries and dimensions a_x, a_y, and a_z, resonances occur when

$$k_i a_i = \pi n_i , \qquad (1)$$

where i = x, y, or z, and n_i are the integers. In turn, in the hyperbolic medium, the propagation wavenumber (k_x, k_y, k_z) satisfies the dispersion equation

$$\frac{k_x^2 + k_y^2}{\varepsilon_z} + \frac{k_z^2}{\varepsilon_x} = k_0^2 , \qquad (2)$$

where ε_x , ε_y, and ε_z are permittivity component of the nanoantenna material, $k_0 = 2\pi/\lambda_0$, and λ_0 is the free-space wavelength.

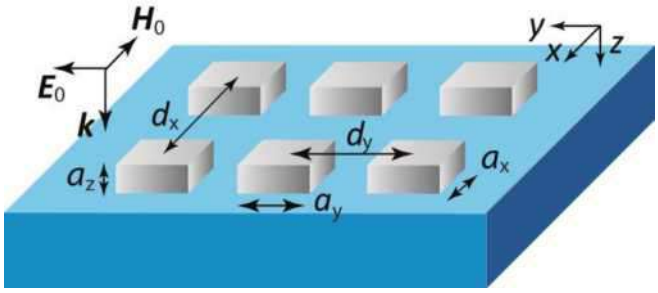


Figure 1: The transdimensional lattice of hBN nanoantennas that incorporates 3D design of the resonators, including size and shape, and 2D periodic arrangement of the nanoantennas.

Thus, from Eqs. (1)-(2), in the resonance of hyperbolic nanoantenna, the following condition is satisfied and defines conditions for nanoantenna resonances in case of material with anisotropic permittivity tensor:

$$\frac{1}{\varepsilon_z}\left(\frac{n_x}{2a_x}\right)^2 + \frac{1}{\varepsilon_z}\left(\frac{n_y}{2a_y}\right)^2 + \frac{1}{\varepsilon_x}\left(\frac{n_z}{2a_z}\right)^2 = \frac{1}{\lambda_0^2} . \qquad (3)$$

Hexagonal boron nitride nanoparticle supports electric and magnetic multipole resonances in the mid-infrared wavelength range (around 6-7 and 13 μm). Because of the hyperbolic dispersion of the medium, higher-order multipole resonances appear at the longer wavelength with respect to dipole ones. The nanoantennas support excitations of magnetic resonances because of the high-*k* wave reflection from antenna boundaries, and it brings an additional degree of freedom in designing metasurfaces with subwavelength scatterers.

3. Lattice resonances

The excitations of lattice resonances in the hBN nanoantenna array closely follow Rayleigh anomaly. Upon overlap of the nanoantenna multipole resonances, one can observe a decrease of reflection with resonant scattering

forward by the antennas in the array, which indicates that generalized Kerker condition of forward scattering is satisfied.

4. Discussion

Material or metamaterial that possesses hyperbolic dispersion supports high-*k* modes, and consequently, an effective mode index in such hyperbolic medium can be much higher than the one in high-refractive-index dielectric nanostructure or plasmonic one. The thickness of hBN nanoantennas with strong multipole resonances can be further decreased down to several hundreds of nanometers and facilitate ultra-thin optical components and metasurfaces.

Acknowledgments

This material is based upon work supported by the Air Force Office of Scientific Research under Grant No. FA9550-19-1-0032.

References

[1] V. E. Babicheva, "Directional scattering by the hyperbolic-medium antennas and silicon particles," MRS Advances 3, 1913, 2018.

[2] V. E. Babicheva, "Lattice Kerker effect in the array of hexagonal boron nitride antennas," MRS Advances 3, 2783-2788, 2018.

[3] V. E. Babicheva, "Multipole resonances and directional scattering by hyperbolic-media antennas," 2017. arxiv.org/abs/1706.07259

Chalcogenide Glasses: Potential for Passive and Active Dielectric Metasurface Applications

Jesse A. Frantz[1], Robel Y. Bekele[2], Jason D. Myers[1], Anthony Clabeau[2], Vinh Q. Nguyen[1], Yun Xu[3], Jingbo Sun[3], Mikhail Shalaev[3], Wiktor Walasik[3], Apra Pandey[4], Alexander Tsukernik[5], Natalia M. Litchinitser[3], Jasbinder S. Sanghera[1]

[1]U.S. Naval Research Laboratory, Code 5620, Washington, D.C. 20375, USA
[2]University Research Foundation, Greenbelt, MD, USA 20770, USA
[3]Department of Electrical and Computer Engineering, Duke University, Durham, NC, 2770, USA
[4]CST of America, LLC, Santa Clara, CA 95054, USA
[5]Department Toronto Nanofabrication Centre, University of Toronto, Toronto, ON M5S 3G4, Canada
*corresponding author, E-mail: jesse.frantz@nrl.navy.mil

Abstract

Chalcogenide glasses (ChGs) are of interest for use in dielectric metastructures for several reasons. They typically possess high linear refractive indices, enabling high index contrast devices; they exhibit exceptionally large optical nonlinearities, making them useful for tunable applications; and they have wide transmission windows extending from the visible through the long-wave infrared. We discuss the potential advantages of these materials in the context of dielectric metasurfaces and present recent results for both passive and active devices.

1. Introduction

ChGs are amorphous semiconductors that contain as a major constituent at least one of the "chalcogen" elements – sulfur, selenium and tellurium – covalently bonded to network formers such as As, Ge, Ga, Sb, etc. They have a number of properties that distinguish them from other glass families. Their refractive indices are typically large. For instance, the linear refractive index, n, of As_2S_3 is approximately 2.4 and that of As_2Se_3 is even higher, with n=2.8. ChGs can also have exceptionally high values for their nonlinear index of refraction n_2, with values >1000× that of silica observed [1]. This high nonlinearity makes them good candidates for both tunable metamaterials and nonlinear frequency conversion. Their low phonon energies result in wide transmission windows that, depending on composition, may extend from the visible through beyond 14 μm. Thus, they are useful for devices operating in various parts of the optical spectrum, potentially in bands not accessible with traditional glasses.

ChGs have been used for decades in bulk or fiber optic form. More recently, they have been used in thin film form for integrated optic applications [2]. Thin films of ChGs are appealing for several reasons. Many compositions can be deposited simply via thermal evaporation or sputtering, with the composition of the deposited film matching that of the source material. Some ChG materials can act as a photoresist [3], making it straightforward to directly pattern devices. Furthermore, it is possible to locally alter their properties via a photodoping procedure [4], permitting the fabrication of devices with a spatially varying nonlinearity.

Recently, the authors have shown results for nonlinear metasurface devices based on As_2S_3 thin films that control the orbital angular momentum (OAM) of a beam [3], [5]. In these devices, the OAM state of the output beam depends on the input beam intensity. In addition, they have demonstrated initial passive devices in As_2Se_3, a material that is of interest for its even higher nonlinear refractive index in comparison to that of As_2S_3 [6]. Here, we summarize ChG properties for a range of compositions, discuss results for their use in metamaterial devices, and consider their prospects for use in future devices.

2. Experiment

Bulk ChG samples were batched from purified precursors in an N_2 purged glovebox. For a given glass composition, a melt was formed by heating the precursors in a sealed quartz ampoule in a rocking furnace. The glass boule was removed, and small pieces were used as deposition materials. Thin films were deposited via thermal evaporation. The resulting films were spatially uniform with low surface roughness (typically, with root mean squared roughness <10 Å) and with compositions similar to those of the deposition materials. Images of an example ChG are shown in Fig. 1 in (a) bulk and (b) thin film form.

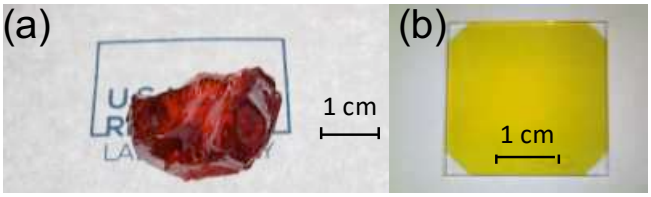


Figure 1: A sulfide ChG in (a) bulk and (b) thin film form.

Films were patterned either using traditional photolithography, with a polymer photoresist, or directly, using the ChG as a photoresist.

3. Discussion

A simple metasurface was designed using an As_2Se_3 glass film on a crystalline Si substrate. The metasurface consists of an array of holes in in the film arranged in a square grid. The metasurface is bordered on the top by air, and the hole is filled with air as well. The lattice constant, a, was fixed at 1.32 µm, and the thickness of the film, t, was fixed at 200 nm. For modeling purposes, the width of the hole was $a \times f$ where f ranged from 0.3 to 0.65, and the free space wavelength, λ_0, ranged from 1.0 to 4.0 µm. The thicknesses of the air and Si layers were both 4.0 µm. The metasurfaces were modeled using COMSOL Multiphysics. The sides of the unit cell were treated as a periodic boundary, so modeling an individual unit cell permitted the prediction of the response of an infinite array of holes.

The predicted transmittance, T, of this structure is shown in Fig. 2(a) as a function of both f and λ_0. Two distinct bands of high T, adjacent to bands of low T, are evident across all values of f, representing resonant modes of the structure. The presence of higher order modes can be observed for shorter wavelengths.

Metasurfaces based on this design were fabricated with f=0.56. In order to perform lithography, a laser direct write system was used to pattern a photoresist layer, and the As_2Se_3 was patterned via the lift-off method. T was measured as a function of λ_0 using a spectrophotometer. The results for both a metasurface and a neat film are shown in Fig. 2(b). T is corrected to account for Fresnel reflection from the back surface of the Si substrate. For the metasurface sample, a resonance is clearly visible with a decrease in T at λ_0=2.25 µm, with a higher T band on either side. A weaker resonance is evident near λ_0=1.3 µm with a less pronounced decrease in T. This resonance is partially masked by the roll off in T due to substrate absorption for shorter λ_0. While the resonances have a similar form to that predicted by the model, their magnitude and position differ slightly, with the model predicting dips near λ_0=1.5 and 2.0 µm. The differences are likely due to imperfections in lithography, which can cause a variation in feature size and rough sidewalls as well. In addition, the dispersion curve of the deposited As_2Se_3 may differ slightly from the values used for modeling.

4. Conclusions

In this work, we evaluate the potential of various ChG film materials for their use in metamaterials. The high refractive index, optical nonlinearity, and wide transmission windows of these materials make them appealing for metamaterial applications. Simple devices were patterned in an As_2Se_3 film, showing the presence of resonances similar to those predicted by modeling. Future designs will take advantage of the high nonlinearity of As_2Se_3 and other ChGs to realize tunable devices and nonlinear frequency generation.

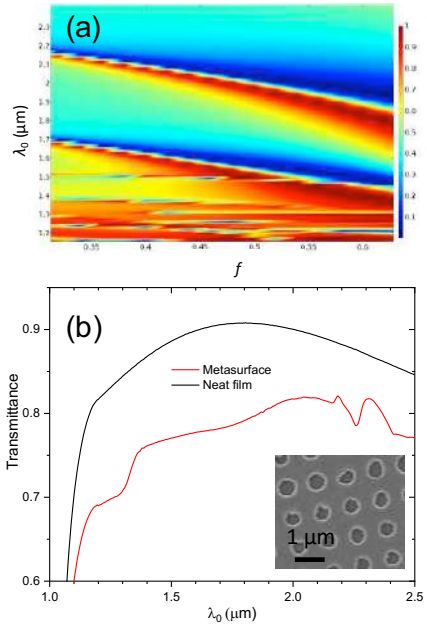


Figure 2: A metastructures in As2Se3 showing (a) modeled transmittance as a function of fill factor, f, and (b) measured transmittance as a function of λ. The inset shows an SEM image of a fabricated device.

Acknowledgements

The authors would like to thank the Office of Naval Research (ONR) for their support (grant N0001419WX01197).

References

[1] J. M. Harbold, F. O. Ilday, F. W. Wise, J. S. Sanghera, I. D. Aggarwal, B. G. Aitken, Highly nonlinear chalcogenide glasses for all-optical switching, *Proc. SPIE* 5061, pp. 143–148, 2003.

[2] B. J. Eggleton, B. Luther-Davies, K. Richardson, Chalcogenide Photonics, *Nat. Photonics* 5: 141–148, 2011.

[3] Y. Xu, J. Sun, J. Frantz, M. I. Shalaev, W. Walasik, A. Pandey, J. D. Myers, R. Y. Bekele, A. Tsukernik, J. S. Sanghera, N. M. Litchinitser, Reconfiguring structured light beams using nonlinear metasurfaces, *Opt. Express* 26: 30930–30943, 2018.

[4] T. Wagner, P. J. S. Ewen, Photo-induced dissolution effect in $Ag/As_{33}S_{67}$ multilayer structures and its potential application, *J. Non-Cryst. Solids* 266: 979–984, 2000.

[5] Y. Xu, J. Sun, J. Frantz, M. I. Shalaev, W. Walasik, A. Pandey, J. D. Myers, R. Y. Bekele, A. Tsukernik, J. S. Sanghera, N. M. Litchinitser, Nonlinear Metasurface for Structured Light with Tunable Orbital Angular Momentum, *Appl. Sci.* 9: 958, 2019.

[6] J. A. Frantz, J. D. Myers, R. Y. Bekele, A. Clabeau, V. Nguyen, C. C. McClain, N. Litchinitser, J. S. Sanghera, Arsenic selenide dielectric metasurfaces, *Proc. SPIE* 10914, pp. 109140-1-7, 2019.

Optical elements based on engineered subwavelength dielectric structures

Andrei Faraon

T.J. Watson Laboratory of Applied Physics, California Institute of Technology, Pasadena, CA, USA

*corresponding author: faraon@caltech.edu

Abstract- In this talk I give an overview of our recent work on various optical components and systems based on engineered subwavelength dielectric structures

Flat optical devices based on lithographically patterned sub-wavelength dielectric nano-structures provide precise control over optical wavefronts, and thus promise to revolutionize the field of free-space optics. I introduce our work on high contrast transmitarrays and reflectarrays composed of high index nano-posts located on top of low index substrates like silica glass or transparent polymers. After presenting their advantages and limitations, I discuss newer concepts based on three dimensional arrangements of sub-wavelength dielectric structures.

Topological protection in spin and valley Hall metasurfaces

Matthias Saba[1,2,*], Stephan Wong[1,3], Sang Soon Oh[1,3], and Ortwin Hess[1,†]

[1] The Blackett Laboratory, Department of Physics, Imperial College London, Prince Consort Road, SW7 2BB, UK
[2] Adolphe Merkle Institute, University of Fribourg, Chemin des Verdiers 4, 1700 Fribourg, CH
[3] School of Physics and Astronomy, Cardiff University, Cardiff, CF 24 3AA, UK
* corresponding author, E-mail: matthias.saba@unifr.ch
† corresponding author, E-mail: o.hess@imperial.ac.uk

Abstract

Topological protection in on-chip optical devices promises strongly improved wave-guiding, insensitive to structural imperfections and environmental fluctuations. Traditional approaches, however, suffer from practicability challenges at optical wavelengths. Periodic dielectric metasurfaces based on optical analogues of the quantum spin and valley Hall effects have recently emerged as a potential remedy, but the nature and strength of topological protection is poorly understood. We here introduce a group theoretical approach to rigorously characterize topological protection for a broad class of designs.

1. Introduction

Since Haldane and Raghu proposed an optical analogue of the integer quantum Hall effect [1] in the advent of topological photonics in 2008, the field has grown substantially. The broad interest in these entirely classical systems is mainly founded in the unique and practically relevant unidirectional edge mode propagation behaviour being insensitive to fluctuations and perturbations. While the original proposal worked as a corner stone with an experimental proof of principle following shortly after at microwave frequencies [2], the need for extremely strong static magnetic fields further up the spectrum towards near-infrared and optical frequencies deems it impractical for real-life solutions in communication and data processing technologies. A number of remedies have been proposed over the years, including emulation of the static magnetic field [3, 4], parity-time-duality symmetric spin emulation [5], and Floquet topological insulators [6].

All these approaches, however, offer limited minituarization potential, or are expensive and hard to fabricate. Approaches based on purely dielectric platforms, conceivably related to the quantum spin Hall effect (SHE) [7] or the quantum spin valley effect (VHE) [8], have recently been established as an alternative to overcome these difficulties. While these new systems do not require exotic constituent materials or strong magnetic fields, the role and nature of topological protection is ambiguous.

Topological protection has so far been characterized by the spin and valley Chern numbers, respectively. Both these quantities are, however, no topological integers and thus do not yield topological protection in the Hatsugai or Kane Mele sense [9, 10]. Associated surface states are not guaranteed in general, nor are those existent rigorously orthogonal counter-propagating modes. Here we investigate, based on group and perturbation theory [11], in which sense and under which circumstances states are protected in the bandgap, and define a rigorous topological bulk-boundary correspondence for VHE structures. Our analysis focusses on a complete list of perturbed fully $p6mm$ (17) symmetric hexagonal structures, and can be equally applied to square lattices.

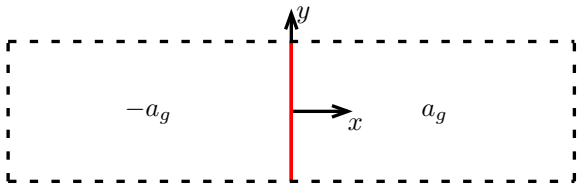


Figure 1: VHE strong protection: Two Semi-infinite half-space domains are perturbed with opposite perturbation strength a_g, separated by a (red) domain wall pointing in y direction.

2. Methodology

Using group and perturbation theory, the physical vector space of electro-magnetic fields can be reduced to a small 4-dimensional vector space close to K/K'-point degeneracies. The 4-dimensional index runs over the *irreducible representation* (irrep) of the full wallpaper group $p6mm$ with K/K'-point Bloch dispersion (outer 2D vector space) and the 2D irrep of the associated little group (inner 2D Rodrigues matrix representation) [12]. The set of group generators $\mathcal{G}$ is chosen as a 60 degrees rotation (C_6), a $y \mapsto -y$ mirror (σ), and a translation by the lattice constant a along x direction (T). The irrep can thus be defined by the mapping $\Lambda(C_6) = \sigma_1 \otimes R_6^4$, $\Lambda(\sigma) = \mathbb{1} \otimes \sigma_3$, and $\Lambda(T) = \mathrm{diag}(w^2, w) \otimes \mathbb{1}$, where σ_i are Pauli matrices, $R_6 = \left(\mathbb{1} - \sqrt{3}\imath\sigma_2\right)/2$ is the planar Rodrigues matrix of a C_6 rotation, $\mathbb{1}$ is the identity matrix, and $w := \exp\{2\pi\imath/3\}$ (see [12] for details).

Perturbing around an evaluation point where the field

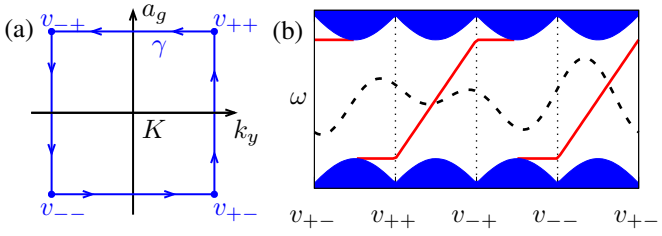


Figure 2: Topological surface states in the extended parameter space corresponding to Fig. 1. (a) The path γ encompassing the evaluation point $(a_g, k_y) = 0$ in the extended edge Brillouin zone parameter space. (b) Along γ, the signed number of crossings between the topologically protected surface bands (red lines) and an arbitrary continuous curve within the band gap (dashed line) is $\mathcal{C} = 2$.

has a dispersion at K/K' ($\boldsymbol{k} = 0$) and the geometry has the full $p6mm$ symmetry ($\boldsymbol{a}_g = 0$) yields the kernel finding problem $\sum_{g\in\mathcal{G}} [\hat{g} - \mathbb{1}]\, W_{\alpha\beta}(\boldsymbol{a}_g, \boldsymbol{k}, \omega) = 0$ that imposes selection rules on the corresponding 4×4 perturbation matrix elements $W_{\alpha\beta}$. The associated frequency shift ω can be seen as a non-linear eigenvalue which alongside the first order perturbation fields f_β, expressed as a linear combination of fields at the evaluation point, forms the eigensolution of the problem $W_{\alpha\beta}(\boldsymbol{a}_g, \boldsymbol{k}, \omega_n) f_\beta^{(n)} = 0$. This allows us to calculate the first Chern number [13] of a non-degenerate band n (or a cluster of connected bands) of a closed 2D manifold within the extended parameter space $(\boldsymbol{a}_g, \boldsymbol{k})$.

3. Topological Edge States

We enumerate the possible geometrical perturbations that break the $p6mm$ symmetry by decomposing them into space group representations. Only 3 of all possible representations lead to an opening of a band-gap and thus potentially topological edge states: The first (labeled $\Gamma 2$) opens a gap only if optical reciprocity is broken and is for example found in the Haldane model of graphene [14]. The second ($\Gamma 4$) leads to the documented VHE and two topologically strongly protected edge bands (Fig. 2), predicted by the non-trivial Chern number $\mathcal{C} = \mathrm{sgn}(a_g)$ of the corresponding closed manifold in the extended parameter space in two adjacent domains (Fig. 1). Well established extrema at the K/K' points in the bulk bandstructure thus guarantee frequency isolated edge states at moderate arbitrary structural or environmental perturbations. The third representation ($K1$) includes the known SHE with no similar rigorous topological protection to be found, but with ostensible spin Hall dispersion in the limit of infinitesimally small geometrical perturbations instead. Orthogonality of counter-propagating edge modes is only guaranteed in the limit of infinitesimal perturbations in both the VHE and the SHE cases. In conclusion, the VHE systems seem well suited to provide a simple platform for topologically protected wave-guiding in 2D as long as the associated limitations on backscattering immunity and inclination are not a major concern.

References

[1] S. Raghu and F. D. M. Haldane, "Analogs of quantum-Hall-effect edge states in photonic crystals," *Phys. Rev. A*, 78, 033834, 2008.

[2] Z. Wang, Y. Chong, J. D. Joannopoulos and M. Soljačić, "Observation of unidirectional backscattering-immune topological electromagnetic states," *Nature*, 461(7265), 772–775, 2009.

[3] M. Hafezi, E. A. Demler, M. D. Lukin and J. M. Taylor, "Robust optical delay lines with topological protection," *Nature Physics*, 7(11), 907–912, 2011.

[4] K. Fang, Z. Yu and S. Fan, "Realizing effective magnetic field for photons by controlling the phase of dynamic modulation," *Nature Photonics*, 6(11), 782–787, 2012.

[5] A. B. Khanikaev, S. H. Mousavi, W.-K. Tse, M. Kargarian, A. H. MacDonald and G. Shvets, "Photonic topological insulators," *Nature Materials*, 12(3), 233–239, 2012.

[6] M. C. Rechtsman, *et al.*, "Photonic Floquet topological insulators," *Nature*, 496(7444), 196–200, 2013.

[7] L.-H. Wu and X. Hu, "Scheme for Achieving a Topological Photonic Crystal by Using Dielectric Material," *Physical Review Letters*, 114(22), 2015.

[8] X.-D. Chen, F.-L. Zhao, M. Chen and J.-W. Dong, "Valley-contrasting physics in all-dielectric photonic crystals: Orbital angular momentum and topological propagation," *Phys. Rev. B*, 96, 020202, 2017.

[9] Y. Hatsugai, "Chern number and edge states in the integer quantum Hall effect," *Phys. Rev. Lett.*, 71, 3697–3700, 1993.

[10] C. L. Kane and E. J. Mele, "Z_2 Topological Order and the Quantum Spin Hall Effect," *Phys. Rev. Lett.*, 95, 146802, 2005.

[11] M. Saba, J. M. Hamm, J. J. Baumberg and O. Hess, "Group Theoretical Route to Deterministic Weyl Points in Chiral Photonic Lattices," *Phys. Rev. Lett.*, 119, 227401, 2017.

[12] M. Saba, S. Wong, M. Elman, S. S. Oh and O. Hess, "The Role and Nature of Topological Protection in Reciprocity Symmetric Photonic Topological Insulators,", 2018.

[13] S. Chern, "On the Curvatura Integra in a Riemannian Manifold," *Annals of Mathematics*, 46(4), 674–684, 1945.

[14] F. D. M. Haldane, "Model for a Quantum Hall Effect without Landau Levels: Condensed-Matter Realization of the "Parity Anomaly"," *Phys. Rev. Lett.*, 61, 2015–2018, 1988.

Highly-Confined Surface Phonon Polaritons in Semiconductor Metamaterial Interfaces

Alexander M. Dubrovkin[1], Bo Qiang[1,2], Nikolay I. Zheludev [1,3], and Q. J. Wang[1,2*]

[1]Centre for Disruptive Photonic Technologies, TPI, SPMS, Nanyang Technological University, Singapore
[2]Centre for OptoElectronics and Biophotonics, EEE, Nanyang Technological University, Singapore
[3]Optoelectronics Research Centre and Centre for Photonic Metamaterials, University of Southampton, UK
*E-mail: qjwang@ntu.edu.sg

Abstract

We demonstrate that owing to highly-confined surface phonon polaritonic modes, the interfaces between ultra-thin germanium layers and silicon carbide substrate can be used for building diverse mid-IR photonic elements and metamaterials with small on-chip footprints at deeply subwavelength scale. We show that the unique dispersion of the interface phononic modes enables efficient resonant tuning of the optical response by small changes in the layer thickness and composition, as well as in the operation frequency of the device.

1. Introduction

Improvements in device performance and density in photonic circuits can only be achieved with interconnects exploiting highly confined and tunable states of light. Surface phonon polaritons (SPhPs) in high-index nanometric layers on polar substrates bear potential as technology-ready platform for moving forward in this direction. The reported dispersion and scaling of the SPhP modes gives high promise for efficient tuning of the polariton wavelength by small changes in the coating thickness and operation frequency of the phononic device [1,2]. In this work, we demonstrate for the first time highly-confined SPhPs and SPhP-based metamaterials on CMOS-compatible semiconductor platform, consisted of silicon carbide substrate coated with nanometric germanium film of deeply subwavelength thickness.

2. Results

Germanium structures have been fabricated on silicon carbide substrate using electron beam lithography, followed by a few to hundred nm thick Ge layers deposition and lift-off processes. Owing to its excellent adhesion, the Ge film enables low-loss ultra-smooth interfaces, which is critical for achieving high quality factors for SPhPs resonances.

2.1. Real-space nanoimaging of nanometric mid-IR resonators on Ge-SiC interface

Using scattering-type scanning near-field microscopy (s-SNOM) we demonstrate SPhPs in germanium slabs and nano-resonators on silicon carbide, and show first observations of infrared field concentration in sheet and edge modes with optical features more than two orders of magnitude smaller than the wavelength of the free-space light. As an example, s-SNOM optical image of a square Ge resonator (500x500 nm in size), made from several-nm thick film is shown in Figure 1. We experimentally demonstrate that tuning of the resonator modes is possible by a very small adjustment of the excitation frequency, providing efficient spectral control of its optical performance. We also show tuning of the resonator modes by sub-nm oxidation of germanium, which reveals atomic-scale sensitivity of the device to molecular interactions.

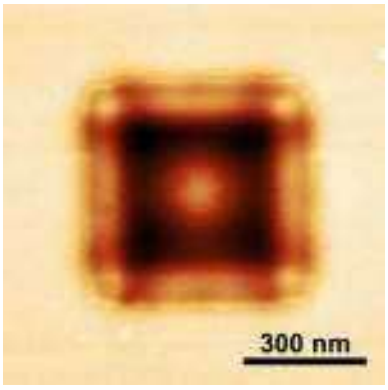


Figure 1: Near-field optical image of an ultra-thin nanometric germanium resonator on silicon carbide substrate. Excitation laser line is 924.5 cm^{-1}.

•

2.2. Infrared spectroscopy of Ge-SiC metamaterials

FTIR spectroscopy of metamaterials made of disk arrays and gratings revealed that that the Ge-SiC platform can be used for flexible building of mid-IR devices with small on-

chip footprints consisting of meta-cells with deeply subwavelength dimensions.

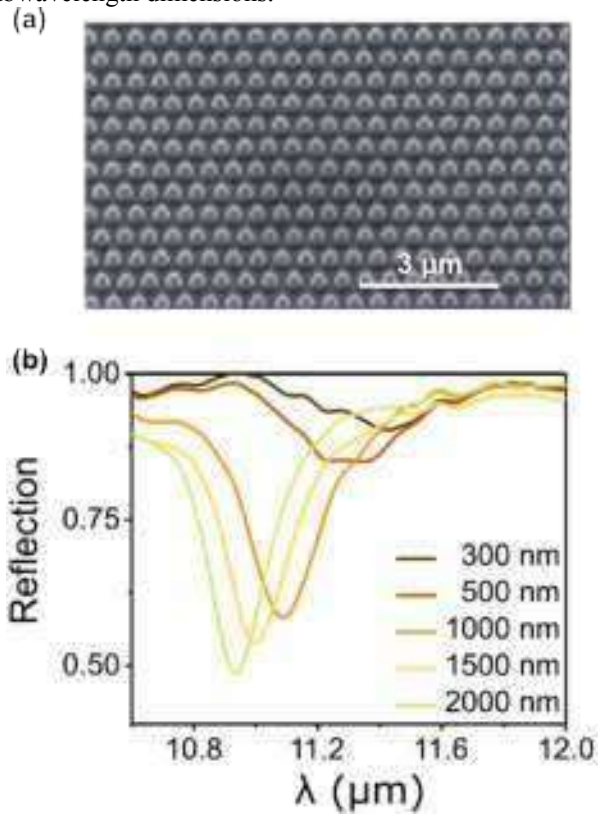


Figure 2: (a) SEM image of a metamaterial made of an array of deeply subwavelength size germanium disks on silicon carbide. (b) Dependence of metamaterial mid-IR reflection on the disk diameter.

The reflection spectrums of several disks-based metamaterials (Figure 2) show that it is possible to achieve up to ~50% absorption of far-field mid-IR radiation using a disk thickness as small as ~1% of the radiation wavelength.

We note that our fabrication procedure bypasses ion etching – the fabrication step typically used for making phonon-polariton metamaterials. The procedure eliminates the damage of the polar crystal lattice, which is beneficial for achieving high quality (Q) factor resonances. The experimentally demonstrated resonance Q-factors reach ~100 and ~200 for dipole and higher order modes in Ge-SiC gratings and ~40 in disk-array metamaterials.

We further demonstrate via experiments and simulations that the Ge-SiC grating's resonant wavelength and the field confinement can be well controlled by coupling the localized hybrid mode of the interface with the propagating SPhPs in silicon carbide. Tuning either the propagating mode or the localized hybrid mode affects the coupling, which can be controlled by the grating period or by the germanium ribbon width.

3. Conclusions

Our research would be useful in designing on-chip, low-loss and highly integrated phononic devices in the infrared part of the spectrum. By patterning a thin layer of high-index dielectric on phononic substrate, high-quality surface phonon polaritonic modes can be excited, enabling a new type of metamaterials with small unit cell dimension based on hybrid phononic-dielectric resonance. In particular, we show for the first time that nanometric interfaces between germanium and silicon carbide can support highly-confined mid-IR surface phonon polariton modes at the nanoscale. The demonstrated phononic elements features sub-micron-size footprints, supporting tunable resonances of sheet and edge modes when excited with coherent radiation with a wavelength that is up to hundred times larger than their physical dimensions. Such subwavelength resonant elements could be of interest for highly-integrated optoelectronic applications, filters and optical delay components. The concept can be potentially applied to number of technologically important semiconductor and dielectric compounds.

Acknowledgements

This research was supported by the Singapore Ministry of Education Academic Research Fund MOE2016-T3-1-006 (S), and MOE 2016-T2-1-128); Agency for Science, Technology and Research (A*STAR) (1426500050); and by the National Research Foundation Singapore program NRF-CRP18-2017-02.

References

[1] P. Li, X. Yang, T. W. W. Maß, J. Hanss, M. Lewin, A.-K. U. Michel, M. Wuttig, T. Taubner, Reversible optical switching of highly confined phonon-polaritons with an ultrathin phase-change material, *Nature Mater*. 15: 870–875, 2016.

[2] A. M. Dubrovkin, B. Qiang, H. N. S. Krishnamoorthy, N. I. Zheludev, Q. J. Wang, Ultra-confined surface phonon polaritons in molecular layers of van der Waals dielectrics, *Nature Commun*. 9: 1762, 2018.

sm, and magnetoelectricity: Separate phenomena and joint effects in me

Collective polarization-dependent plasmon routing by means of spin-locking metasurface

Matan Revah[1], **Andre Yaroshevsky**[1], **Yuri Gorodetski**[1,2]

[1]Electrical engineering and electronics department, Ariel University, Ariel, 407000, Israel
[2]Mechanical engineering and mechatronics department, Ariel University, Ariel, 407000, Israel
*corresponding author, E-mail: yurig@ariel.ac.il

Abstract

We propose a spin-locking metasurface incorporating a transverse spin of the SP wave to selectively route the near-field beams. Owing to the combination of the oblique incidence of circularly polarized light with the accurately designed momentum matching of the grating we achieve a precise directional control over the plasmonic distributions. The experimental verification of the directional launching is performed by a time-resolved leakage radiation measurements allowing one to visualize the shape and the dynamics of the excited beam.

1. Introduction

The increasing desire for nanophotonics integrated devices has led to an intensive investigation of surface waves such as surface plasmons (SP) due to their unique optical properties and compatibility with nanoelectronics [1, 2]. Different types of nanopatterned metallic surfaces have been proposed as functional metasurfaces capable of locally modulating the plasmonic wavefront phase and amplitude. Upon these, the metasurfaces providing an externally controlled near-field manipulation seem to be particularly appealing for nanophotonic devices [3]. Intrinsic polarization selectivity of the plasmonic wave makes it possible to use a plasmonic spin-orbit interaction for spin-based metasurfaces [4, 5]. Such structures exhibit different behavior when excited by right-handed or left-handed circularly polarized light (RCP/LCP). In these systems the space-variant rotation of the structure unit-cell induces a geometric Berry phase of the plasmonic wavefront which results in a spin-dependent near-field distribution [6, 7, 8]. This effect has been widely studied and various promising nanophotonic applications have been proposed [9, 10]. Nevertheless, recently it was suggested that the SPs could carry a so-called transverse spin (TS) angular momentum which resulted from the relative quarter period phase lag between the longitudinal and the transverse field components [11, 12]. This TS was shown to be locked to the wave propagation direction and it had already been demonstrated that by illuminating a single slit in a metallic surface it was possible to create a projection of the longitudinal spin (LS, circular polarization handedness) onto the TS of the SP and excite unidirectional plasmonic wave [13, 14]. In this work we present a novel type of a spin-locking metasurface based on the LS-to-TS coupling and enhanced by the accurately designed momentum matching. Our structure collectively excites an SP wavefront in a desired direction depending on the incident circular state. In contrast with other spin-based metasurfaces, here we demonstrate a periodic array of *uniform apertures with full mirror symmetry*. The spin-locking is achieved through the incident beam inclination combined with apertures periodicity which allows a flexible design and relatively simple realization.

2. Spin-locking metasurface

When the SP wave propagates on a planar metal-air interface in x direction its TS is given as

$$\mathbf{s}_{\perp} \propto \frac{Re\mathbf{k} \times Im\mathbf{k}}{(Re\mathbf{k})^2} \tag{1}$$

where $\mathbf{k} = k_{SP}\hat{\mathbf{x}} + i\kappa\hat{\mathbf{z}}$ is the the complex valued evanescent wave vector with $\kappa = \sqrt{k_{SP}^2 - k_0^2}$, $k_0 = 2\pi/\lambda_0$ is the vacuum wavenumber and k_{SP} is the in-plane plasmonic wavenumber [15]. As stated previously the transverse spin results from the rotation of the resultant of the vectorial plasmonic field, $\mathbf{E}_{SP} = E_p(\hat{\mathbf{x}} - i\chi\hat{\mathbf{z}})$ in a transverse plane and solely arises from the amplitude ratio between the longitudinal and the transverse field components χ. Accordingly, $s_{\perp}$ is locked to the SPs' propagation direction and can appear with a single handedness. This has led to suggest a scheme for spin-dependent unidirectional plasmonic excitation [14, 13] where the incidence geometry provides a considerable projection of the LS onto the TS of the plasmonic wavefront. Hereafter we refer to this effect as a "longitudinal to transverse spin (LTS) coupling" . One experimental way to achieve that was by using a single slit as a launching structure illuminated by an inclined Gaussian beam. Then, by choosing the inclination angle an optimal coupling conditions could be obtained. Here we suggest using a periodic structure of short and narrow (100 nm wide) nanoslits as a spin-locking metasurface. The system is designed to perform as follows. We bear in mind that an individual slit illuminated by a planewave at the incidence angle θ produces two plasmonic wings propagating at angle α with respect to the slit that can be derived via momentum matching condition as, $\cos\alpha = \frac{\lambda_{SP}}{\lambda_0}\sin\theta$. Instead of the single slit we now consider the array of slits placed roughly along the SP propagation direction at a distance

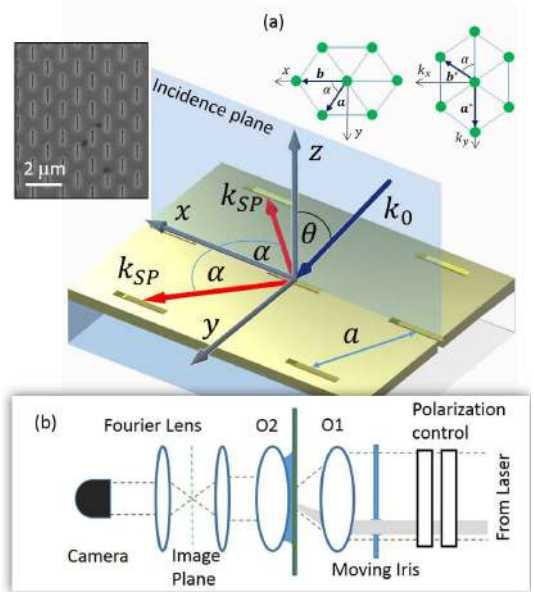


Figure 1: The metasurface physical principle. (a) The light is incident at an angle θ and couples to SPs propagating in the metasurface plane along the angle α. The periodicity of the grating is a. The inset shows the direct and the reciprocal lattice corresponding to our metasurface. (b) The Fourier imaging leakage radiation microscopy setup. The sample is illuminated by an objective with NA = 0.45 while the leakage radiation is extracted by an oil immersion objective O2 with NA = 1.25 coupled with a 100 mm tube lens. An additional lens is then used to generate a Fourier image in the camera. A movable slit controls the incidence tilt angle.

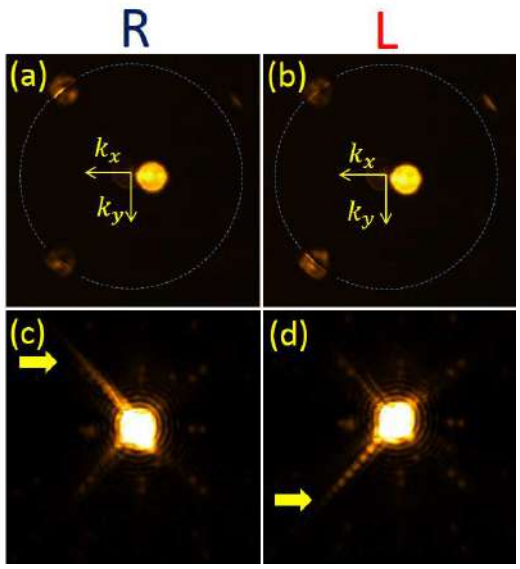


Figure 2: Spin-selective unidirectional plasmonic excitation with the grating parameters - $a = 700$ nm, $\alpha = 45°$. (a) and (b) show the k-space for right and left-handed incident polarization respectively and (c) and (d) show the real-space images for these states. The dashes circle guides the eye for the plasmonic wave-vector. Note that the coupling in the k-space is clearly seen as a bright narrow line.

providing the perfect phase matching.

These leads to a rhombic lattice of slits with a diagonal angle α (see Fig. 1). In a periodic lattice, however, the momentum matching is different from the case of a single slit and should be derived by calculating the k-space of the array, i.e. its reciprocal lattice [16]. Inset in Fig. 1 shows the geometry of our rhombic lattice represented by the pair of primitive vectors, $\mathbf{a} = a\sin\alpha\hat{\mathbf{y}} + a\cos\alpha\hat{\mathbf{x}}$, $\mathbf{b} = b\hat{\mathbf{x}}$. The corresponding primitive vectors in the k-space are then $\mathbf{a}^* = \frac{2\pi}{a\sin\alpha}\hat{\mathbf{k}}_y$ and $\mathbf{b}^* = \frac{2\pi}{2a}\left(\frac{\hat{\mathbf{k}}_x}{\cos\alpha} - \frac{\hat{\mathbf{k}}_y}{\sin\alpha}\right)$. We use these vectors to achieve the momentum matching condition for oblique incidence at angle θ:

$$\left|\mathbf{b}^* \pm \frac{2\pi}{\lambda_0}\sin\theta\hat{\mathbf{x}}\right| = \frac{2\pi}{\lambda_{SP}} \qquad (2)$$

We note that the $\pm$ sign choice depends on the desired tilting of the beam with respect to the plasmonic propagation direction. This point will be discussed later in the paper. Clearly, the higher is the illumination tilting angle the larger momentum mismatch should be compensated which requires larger initial grating period. However, the tilt in our system is limited by the NA of the objective (we used NA = 0.45). Therefore we have chosen to work with two structures: ($a = 700$nm; $\alpha = 45°$ and $a = 1200$nm; $\alpha = 67°$). These configurations are suitable for excitations with the incident angles of $\theta = -7°$ and $\theta = 7.5°$ respectively, where the negative angles correspond to the case when the tilt of the illumination is in the opposite direction to the SP propagation.

3. Experimental results

The metasurfaces were fabricated using focused ion beam (FIB) milling in a 65 nm-thick gold film that had been evaporated beforehand on top of a thin glass substrate. Our setup, shown in Fig. 1b consisted of the pulsed laser at $\lambda_0 = 785$ nm whose beam was expanded to properly fill the aperture of the microscope objective O1, illuminating the sample. The second, oil immersion objective, O2 was brought into a contact with the back (glass) side of our sample in order to produce leakage radiation which was then collected by the tube lens (100 mm) into the imaging system terminated by a camera (Pixelink, PL-B771U, MONO 27, 1280 x 1024). An additional lens was placed on a flipping mount one focal distance ahead of the camera in order to produce the Fourier image of the light distribution. Our way to manipulate the incidence angle was by moving an iris placed right in front of the illumination objective in x direction as schematically shown in Figure 1b. Additionally our setup included the possibility to make a time-resolved imaging of the plasmonic pulses by means of the heterodyne interference method described in the following sections. Figures 2 and 3 show the measured real and momen-

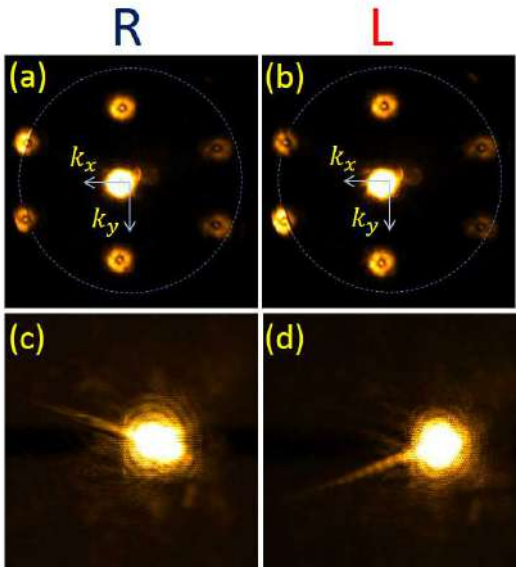


Figure 3: Spin-selective unidirectional plasmonic excitation with the grating parameters - $a = 1200$ nm, $\alpha = 67°$. (a) and (b) show the k-space for right and left-handed incident polarization respectively and (c) and (d) show the real-space images for these states.

tum space images of the two structures with the tilt chosen above and two circular polarization states. The coupling of light to SP wave is clearly seen in the Fourier images as a bright arc inside the diffraction order spot. We verify the polarization dependence of this coupling by comparing the LCP and the RCP states. Real space images follow the Fourier space and show a unidirectional excitation of the SPs by the metasurface. Moreover, by comparing Fig. 2 and 3 one recognizes that in order to excite SP beam in the positive x direction the tilt should be negative in the case of $a = 700$ nm and positive when $a = 1200$ nm.

As expected from the basic theory of the LTS projection the directionality dependence on the incident spin-state stays the same for the two cases. The projection of the incident spin onto the transverse spin vector of the SP should vary as $\sim \sin\theta\cos\alpha$, so this is clear that the effect can be more enhanced with higher tilt angles. Nevertheless even within the limitations of our simple setup the effect seems to be quite convincing.

Acknowledgement

We acknowledge the Ministry Of Science, Technology and Space of Israel.

References

[1] T. W. Ebbesen, H. J. Lezec, H. Ghaemi, T. Thio, and P. Wolff, "Extraordinary optical transmission through sub-wavelength hole arrays," *Nature*, vol. 391, no. 6668, p. 667, 1998.

[2] W. L. Barnes, A. Dereux, and T. W. Ebbesen, "Surface plasmon subwavelength optics," *Nature*, vol. 424, no. 6950, p. 824, 2003.

[3] A. V. Kildishev, A. Boltasseva, and V. M. Shalaev, "Planar photonics with metasurfaces," *Science*, vol. 339, no. 6125, p. 1232009, 2013.

[4] Y. Gorodetski, N. Shitrit, I. Bretner, V. Kleiner, and E. Hasman, "Observation of optical spin symmetry breaking in nanoapertures," *Nano Letters*, vol. 9, no. 8, pp. 3016–3019, 2009.

[5] L. Huang, X. Chen, H. Mühlenbernd, G. Li, B. Bai, Q. Tan, G. Jin, T. Zentgraf, and S. Zhang, "Dispersionless phase discontinuities for controlling light propagation," *Nano Letters*, vol. 12, no. 11, pp. 5750–5755, 2012.

[6] S. Pancharatnam, "Generalized theory of interference, and its applications," *Proceedings of the Indian Academy of Sciences - Section A*, vol. 4, no. 5, pp. 247–262, 1956.

[7] M. V. Berry, "The adiabatic phase and pancharatnam's phase for polarized light," *Journal of Modern Optics*, vol. 34, no. 11, pp. 1401–1407, 1987.

[8] K. Y. Bliokh, F. Rodríguez-Fortuño, F. Nori, and A. V. Zayats, "Spin–orbit interactions of light," *Nature Photonics*, vol. 9, no. 12, p. 796, 2015.

[9] L. Huang, X. Chen, H. Mühlenbernd, H. Zhang, S. Chen, B. Bai, Q. Tan, G. Jin, K.-W. Cheah, C.-W. Qiu, J. Li, T. Zentgraf, and S. Zhang, "Three-dimensional optical holography using a plasmonic metasurface," *Nature Communications*, vol. 4, p. 2808, 2013.

[10] Q. Jiang, J. Laverdant, C. Symonds, A. Pham, C. Leluyer, S. Guy, A. Drezet, and J. Bellessa, "Metasurface for reciprocal spin-orbit coupling of light on waveguiding structures," *Physical Review Applied*, vol. 10, no. 1, p. 014014, 2018.

[11] K. Y. Bliokh, A. Y. Bekshaev, and F. Nori, "Extraordinary momentum and spin in evanescent waves," *Nature Communications*, vol. 5, pp. 1–8, 2014. [Online]. Available: http://dx.doi.org/10.1038/ncomms4300

[12] A. Aiello, P. Banzer, M. Neugebauer, and G. Leuchs, "From transverse angular momentum to photonic wheels," *Nature Photonics*, vol. 9, no. 12, p. 789, 2015.

[13] D. O'Connor, P. Ginzburg, F. J. Rodríguez-Fortuño, G. A. Wurtz, and A. V. Zayats, "Spin-orbit coupling in surface plasmon scattering by nanostructures," *Nature Communications*, vol. 5, pp. 1–7, 2014.

[14] A. E. Miroshnichenko and Y. S. Kivshar, "Polarization traffic control for surface plasmons," *Science*, vol. 340, no. 6130, pp. 283–284, 2013.

[15] K. Y. Bliokh and F. Nori, "Transverse and longitudinal angular momenta of light," *Physics Reports*, vol. 592, pp. 1–38, 2015.

[16] R. Guo, T. K. Hakala, and P. Törmä, "Geometry dependence of surface lattice resonances in plasmonic nanoparticle arrays," *Physical Review B*, vol. 95, no. 15, p. 155423, 2017.

Enhancing Circular Dichroism and Chiral Sorting with Chiral Surface Waves

Marco Finazzi*, Giovanni Pellegrini, Michele Celebrano, Lamberto Duò, and Paolo Biagioni†,

Dipartimento di Fisica, Politecnico di Milano, Piazza Leonardo da Vinci 32, 20133 Milano, Italy
*corresponding author, E-mail: marco.finazzi@polimi.it
†corresponding author, E-mail: paolo.biagioni@polimi.it

Abstract

A platform that combines a one-dimensional photonic crystal with a birefringent surface termination is presented. The platform sustains transverse electric and transverse magnetic surface modes having the same phase velocity, which can be combined to generate chiral surface waves providing homogeneous fields of either handedness over arbitrarily large areas in a wide spectral range. The predicted circular dichroism signals and chiral sorting forces are predicted to be more than two orders of magnitude larger than in any other existing platform.

1. Introduction

Biomolecules typically do not posses reflection symmetry. Therefore, the vast majority of biochemical processes is profoundly influenced by the chiral properties of the involved chemical compounds. For this reason, trapping, separating, or - more generally - discriminating between the two different enantiomers of a chiral chemical compound is of paramount importance for biochemical and pharmaceutical applications. Circularly polarized light is one of the most relevant tools for the discrimination of enantiomers and for the determination of their configuration and conformation thanks to circular dichroism (CD) spectroscopy. Moreover, circularly polarized light can exert enantioselective optical forces on chiral molecules. However, both CD signals and optical chiral sorting forces are extremely weak, making both analysis of small amounts of chiral analytes and enantiomer separation very challenging.

Recently, novel approaches have been proposed to enhance the interaction between light and chiral matter by tailoring the optical chirality $|C|$ of the former. $|C|$ is one of the factors that determines the degree of asymmetry in the absorption rate of a chiral molecule between left and right circularly-polarized light in the dipolar approximation and is defined as [1]:

$$|C| = \frac{\epsilon_0 \omega}{2} \left| \mathrm{Im} \left(\mathbf{E}^* \cdot \mathbf{B} \right) \right| . \qquad (1)$$

Its value for circularly-polarized plane waves of unitary intensity is $|C_{\mathrm{CPL}}| = \epsilon_0 \frac{\omega}{2c}$ [1]. $|C_{\mathrm{CPL}}|$ does not represent a limitation and "superchiral" electromagnetic field solutions can be obtained [1].

In this framework, an ideal platform for the exploitation of chiral light should be able to (i) provide uniform chiral optical fields over large areas, (ii) generate optical chiralities of both handednesses upon reversing the polarization state of the incident field, and (iii) work at wavelengths ranging from the near-UV to the IR depending on the platform design, with a particular attention to the high energy range of the spectrum, below 400 nm, where most electronic molecular transitions occur. Plasmonic nanostructures have been widely proposed and employed as a viable solution for the enhancement of the optical chiral response of biomolecules [2, 3]. However, to date plasmonic platforms do not meet all the above criteria simultaneously. In particular, molecular spectroscopy in the blue and near-UV energy range is not accessible with standard Au plasmonics. Moreover, superchiral optical fields are spatially confined to the so-called plasmonic "hot spots" and large homogeneous optical chiralities are usually obtained only for chiral plasmonic nanostructures [4, 5, 6], hindering the possibility of switching the local field handedness upon reversal of the incident light polarization state. This last drawback represents a universal limitation to plasmonic chirality [6] and has motivated recent proposals to move to dielectric materials for the realization of superchiral assets [5].

Along this line, we introduce the novel concept of "chiral surface waves" originating from the coherent superposition of the TE and TM surface modes in a one-dimensional photonic crystal (1DPC) with a birefringent termination [7, 8]. The resulting platform provides chiral fields with $|C| \gg |C_{\mathrm{CPL}}|$ over arbitrarily large areas and wide spectral ranges (down to the UV regime), with CD signals and chiral sorting forces more than 2 orders of magnitude larger than those provided by alternative solutions. These findings pave the way towards on-chip surface-enhanced chiral sensing, spectroscopy, and all-optical manipulation.

2. Discussion

We devise a 1DPC supporting both transverse-electric (TE) and transverse-magnetic (TM) Bloch surface waves (BSWs). The 1DPC is terminated by an additional 1DPC with stacking period much smaller than the light wavelength. Because of the small period, we can describe this termination as a single slab with an anisotropic effective optical constant (see Fig. 1). By tuning the birefringence, we can tailor the relative phase velocities of TE and TM waves and have their dispersion relation overlap. In this

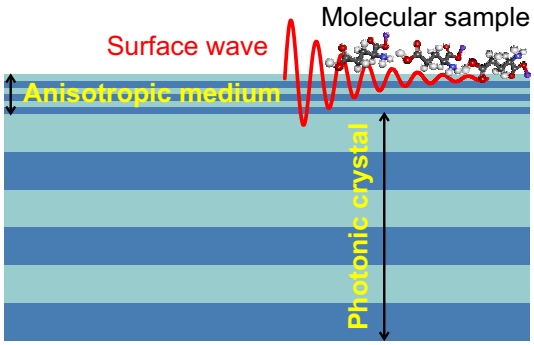


Figure 1: A sketch of the photonic crystal supporting chiral surface waves. The sample consists in chiral molecules exposed to the evanescent fiels of the surface waves. The latter are excited by illuminating the photonic crystal with elliptically polarized plane waves impinging from the bottom at the correct incidence angle.

way, TE and TM waves can be simultaneously excited with the desired phase relation to produce BSWs of any polarization state. Thanks to the field confinement at the surface ensured by the 1DPC, this configuration allows generating BSWs that provide intense, homogeneous, and switchable chiral local fields over arbitrarily large surfaces and a wide spectral range [7, 8]. The resulting optical chirality $|C|$ is predicted to be strongly enhanced with respect to $|C_{\mathrm{CPL}}|$, by more that one order of magnitude.

Because of the evanescent nature of SBWs, the chiral properties of our platfrom can be exploited by placing the sample in close proximity to the free top surface of the 1DPC termination (see Fig. 1). Chiral molecules, either in a solution flowing into a microfluidic channel or embedded into an amorphous film spin-coated on top of the 1DPC termination represent practical realization of this concept.

To evaluate the performances of the platform, we have applied a simple formalism where all the relevant chiroptical quantities are expressed in terms of the Fresnel reflection matrix for the system (1DPC platform + chiral molecules). We obtain the reflection matrix by using the transfer matrix approach together with the constitutive relations for the chiral medium. We find a strong enhancement of the optical chirality provided by the near field of the BSWs supported by our platform, resulting in CD signals [7, 8] and chiral sorting optical forces [9] that exceed by two orders of magnitude the performances of any existing alternative.

3. Conclusions

We have devised a 1DPC supporting chiral surface waves coupled with a uniform and isotropic optically active thin film deposited on its surface, operating over a broad spectral range. This platform provides chiral signal enhancements and chiral-sorting forces of more than two orders of magnitude larger than those obtained with alternative approaches.

Acknowledgement

The research leading to these results has received funding from the Italian Ministry of Education, Universities and Research (MIUR) through the PRIN 2015 program (Project No. 2015FSHNCB "Plasmon-enhanced vibrational circular dichroism").

References

[1] Y. Tang, A.E Cohen, Optical Chirality and Its Interaction with Matter, *Phys. Rev. Lett.* 104: 163901, 2010.

[2] E. Hendry, T. Carpy, J. Johnston, M. Popland, R.V. Mikhaylovskiy, A.J. Lapthorn, S.M. Kelly, L.D. Barron, N. Gadegaard, M. Kadodwala, Ultrasensitive detection and characterization of biomolecules using superchiral fields, *Nature Nanotech*. 5: 783–787, 2010.

[3] Y. Zhao, A.N. Askarpour, L. Sun, J. Shi, X. Li, A. Alù, Chirality detection of enantiomers using twisted optical metamaterials, *Nature Comm.* 8: 14180, 2017.

[4] M. Schäferling, D. Dregely, M. Hentschel, H. Giessen,. Tailoring Enhanced Optical Chirality: Design Principles for Chiral Plasmonic Nanostructures, *Phys. Rev. X* 2: 031010, 2012.

[5] A. García-Etxarri, J. Dionne, Surface-enhanced circular dichroism spectroscopy mediated by nonchiral nanoantennas, *Phys. Rev. B*, 87: 235409, 2013.

[6] M. Finazzi, P. Biagioni, M. Celebrano, L. Duò, Quasistatic limit for plasmon-enhanced optical chirality, *Phys. Rev. B*, 91: 195427, 2015.

[7] G. Pellegrini, M. Finazzi, M. Celebrano, L. Duò, P. Biagioni, Chiral surface waves for enhanced circular dichroism, *Phys. Rev. B* 95: 241402(R), 2017.

[8] G. Pellegrini, M. Finazzi, M. Celebrano, L. Duò, P. Biagioni, Surface-enhanced chiroptical spectroscopy with superchiral surface waves, *Chirality* 30: 883–889, 2018.

[9] G. Pellegrini, M. Finazzi, M. Celebrano, L. Duò, M.A.Iatì, O.M. Maragò, P. Biagioni, Superchiral Surface Waves for All-Optical Enantiomer Separation, arXiv:1803.10010 .

Theoretical Design of Two-Dimensional Magnetoelectric Materials

Shuai Dong[1,*]

[1]School of Physics, Southeast University, Nanjing, China
*corresponding author, E-mail: sdong@seu.edu.cn

Abstract

Achieving two-dimensional magnetoelectric materials should enable numerous functionalities in nanoscale devices. Until now, however, predicted two-dimensional magnetoelectric materials are very few and with coexisting yet only loosely coupled ferroelectricity and magnetism. In this talk, I will introduce several recent works on two-dimensional magnetoelectric materials done in my group.

1. Introduction

Magnetoelectric materials contain both the magnetic and electric degrees of freedom, and thus very important for scientific research as well as functional applications. In the past decades, magnetoelectric materials in the three-dimensional crystals have been extensively studied [1, 2]. Only till very recently, the experimental discoveries of two-dimensional ferromagnets and two-dimensional ferroelectrics bring us attention to the branch of two-dimensional magnetoelectric.

2. Results

In this talk, I will present our recent works on two dimensional ferroelectric materials and magnetoelectric materials.

2.1. $CrI_{3-\delta}$

CrI_3 monolayer is an experimental verified two-dimensional ferromagnetic material. Our calculation based on density functional theory found that the vacancies of iodine can create (almost) isolated and switchable electric dipoles, making $CrI_{3-\delta}$ monolayer a magnetoelectric system [3]. Such vacancies can also enhance both the local magnetization as well as the effective Curie temperature.

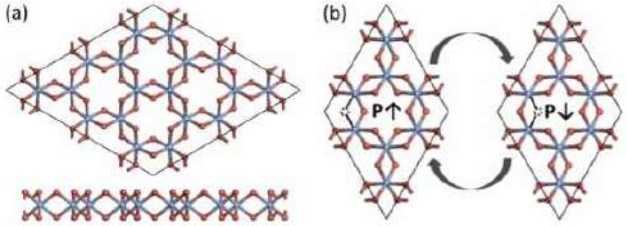


Figure 1. (a) Structure of monolayer CrI_3 from top and side views where I and Cr atoms are represented by red and blue balls. (b) Schematic diagram of CrI_3 working as an atom-thick two-dimensional material with switchable out-of-plane polarization in which the vacancy is represented by the black dotted circle.

2.2. $Hf_2VC_2F_2$

The magnetoelectric coupling in most known two-dimensional magnetoelectric materials are loose since the origins of magnetic moments and electric dipoles are independent, which is disadvantage for the cross control. To obtain the strong intrinsic magnetoelectric coupling, we have predict a member of MXene, $Hf_2VC_2F_2$, to be a type-II multiferroic material, in which the polarization is generated by the noncollinear spin order [4]. The magnetic Neel temperature, i.e. the ferroelectric Curie temperature, can be above room temperature, and more than 98% of polarization comes from the bias of electronic cloud instead of the displacements of ions.

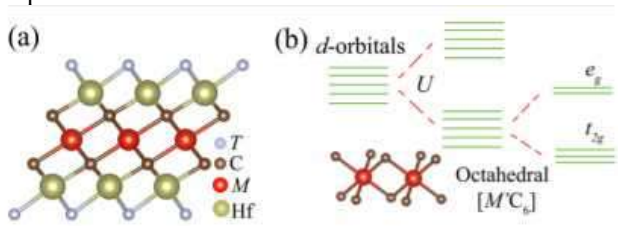


Figure 2. (a) Side views of the $Hf_2MC_2T_2$. (b) Sketch of the energy splitting of 3*d* orbitals for *M*. *M*: transition metal. *T*: anion.

2.3. CuInPS

CuInPS is an experimental verified two-dimensional ferroelectric material with out-of-plane polarization, generated by the pair of Cu-In. We found that CuInPS multilayer can show a giant negative piezoelectricity, which is very rare especially in inorganic materials. The loose vdW layer plays an important role.

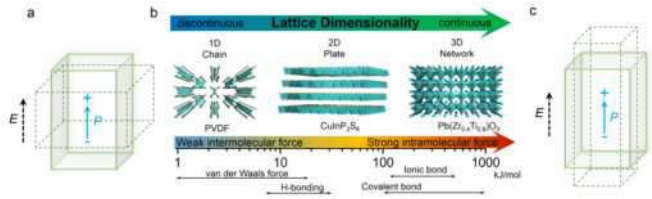


Figure 3. (a) and (c) Illustrations of negative (**a**) and positive (**c**) longitudinal piezoelectric effects, where the lattice contracts or elongates when the electric field is along the direction of the spontaneous polarization. (b) A schematic that outlines the lattice

dimensionalities of three representative ferroelectric materials: 1D PVDF, 2D $CuInP_2S_6$ (CIPS) and 3D $Pb(Zr_{0.4}Ti_{0.6})O_3$ (PZT). The bottom part shows the energy scales of the inter- and intra-molecular bonds. PVDF is known to possess negative piezoelectric coefficient as schematically shown in (**a**), while 3D ferroelectrics usually show positive piezoelectric coefficients as illustrated in (**c**).

3. Conclusions

In summary, several new two-dimensional magnetoelectric materials have been designed, predicted, and synthesized. More effects are needed to push forward the frontiers of this field.

Acknowledgements

Works were done in collaboration with Prof. Jinlang Wang, Prof. Junling Wang, and Prof. Boris Yakobson, as well as Dr. Yinghe Zhao, Dr. Junjie Zhang, and Dr. Lu You. Works were supported by National Natural Science Foundation of China (Grant Nos. 11834002 and 11674055). Most calculations were done on Tianhe II of National Supercomputer Center in Guangzhou (NSCC-GZ).

References

[1] S. Dong, J.-M. Liu, S.-W. Cheong, Z.-F. Ren, Multiferroic materials and magnetoelectric physics: symmetry, entanglement, excitation, and topology, *Adv. Phys.* 64: 519−626, 2015.

[2] S. Dong, H. J. Xiang, E. Dagotto, Magnetoelectricity in multiferroics: a theoretical perspective, *Natl. Sci. Rev.* in press, 2019.

[3] Y. H. Zhao, L. F. Lin, Q. H. Zhou, Y. H. Li, S. J. Yuan, Q. Chen, S. Dong, J. L. Wang, Surface vacancy-induced switchable electric polarization and enhanced ferromagnetism in monolayer metal trihalides, *Nano Lett.* 18: 2943-2949, 2018.

[4] J.-J. Zhang, L. F. Lin, Y. Zhang, M. H. Wu, B. Yakobson, S. Dong, Type-II multiferroic $Hf_2VC_2F_2$ MXene monolayer with high transition temperature, *J. Am. Chem. Soc.* 140: 9768-9773, 2018.

[5] L. You, Y. Zhang, S. Zhou, A. Chaturvedi, F. C. Liu, L. Chang, D. Ichinose, H. Funakubo, W. J. Hu, T. Wu, Z. Liu, S. Dong, J. L. Wang, Origin of giant negative piezoelectricity in a layered van der Waals ferroelectric, *Sci. Adv.* in press, 2019.

Enantioseparation of chiral molecules adsorbed on a magnetic nanostructure with perpendicular anisotropy

K. Banerjee-Ghosh[1], O. Ben Dor[2], F. Tassinari[1], E. Capua[1], S. Yochelis[2], A. Capua, See-Hun Yang[3], S. S. P. Parkin[3,4], S. Sarkar[5], L. Kronik[5],R. Naaman[1], Y. Paltiel[2], L. T. Baczewski[6]*

[1]Department of Chemical and Biological Physics, Weizmann Institute of Science, Rehovot, Israel.
[2]Department of Applied Physics, Hebrew University, Jerusalem, Israel.
[3]IBM Research Division, Almaden Research Center, USA.
[4]Max Planck Institute for Microstructure Physics, Halle, Germany.
[5]Department of Materials and Interfaces, Weizmann Institute of Science, Israel.
[6]Institute of Physics Polish Academy of Sciences, Warszawa, Poland.
*corresponding author, E-mail: bacze@ifpan.edu.pl

Abstract

It is shown experimentally that the interaction of chiral molecules with a perpendicularly magnetized substrate is enantiospecific. Thus, one enantiomer adsorbs preferentially when the magnetic dipole is pointing up, whereas the other adsorbs faster for the opposite magnetization alignment. The interaction is not controlled by the magnetic field but by the respective electron spin orientations. Magnetization reorientation of magnetic layer can be realized solely by adsorption of chiral molecules on its surface without presence of magnetic or electric fields.

1. Introduction

Enantioselectivity is ubiquitous in nature and many of the molecules in plants and living organisms have their properties depending on the type of enantiomer. Chiral recognition and enantiomeric selectivity, both in nature and in artificial systems, are commonly assumed to be related to a spatial effect, with the recognition process typically described by a “lock and key” type model. Accordingly, chromatography-based enantioseparation requires the chiral substrate to be adjusted so as to interact optimally with a specific enantiomer . Indeed, enantio-separation is an extremely important process in the pharmaceutical and chemical industries. The importance of chirality was only realized by scientists in the sixties of last century after a disaster with Thalidomide drug used by pregnant women which caused birth of children with malformations due to mutagenic effect of one of the enantiomers. Since then chromatography and electromigration techniques have long been the methods of choice in this field. However, despite intensive efforts, obtaining enantiomerically pure synthetic materials remains a challenge, as the cost of separation is relatively high and an extensive effort is required.

2. Results and discussion

In our earlier paper [1] we have demonstrated a new effect of magnetization switching of ferromagnetic thin film without applying a magnetic or electric field but being induced solely by adsorption of chiral molecules. In this case, about 10^{13} electrons per cm^2 are sufficient to induce magnetization reversal. The direction of the magnetization depends on the handedness of the adsorbed chiral molecules. It is commonly assumed that recognition and discrimination of chirality, both in nature and in artificial systems, depend solely on spatial effects. However, recent studies have suggested that charge redistribution in chiral molecules manifests an enantiospecific preference in electron spin orientation. Therefore it is possible that the induced spin polarization may affect enantio-recognition through exchange interactions. It is shown [2] experimentally that the interaction of chiral molecules with a perpendicularly magnetized substrate is enantiospecific. Thus, one enantiomer adsorbs preferentially when the magnetic dipole is pointing up, whereas the other adsorbs faster for the opposite alignment of the magnetization. The interaction is not controlled by the magnetic field per se, but rather by the electron spin orientations, and opens prospects for a distinct approach to enantiomeric separations.

The enantioselective interaction of chiral molecules and a magnetic substrate with perpendicular anisotropy provides a potentially generic chromatographic method for enantioseparation, which does not require a specific and costly separating column. As the observed effect depends on the electrical polarizability of the system (that is accompanied by spin polarization) and because this polarization depends on the global structure of the chiral molecule, this new method may also allow the separation of chiral molecules from a mixture of molecules, either chiral or achiral. In addition, this technique could potentially be applied for separating chiral molecules based on their secondary structure and/or for separating two secondary structures of the same chiral molecule. Clearly, the

efficiency of the method depends on the electric and spin polarization properties of the molecules. We hope that this work will motivate further exploration of the detailed mechanisms and ultimate efficiency of this approach.

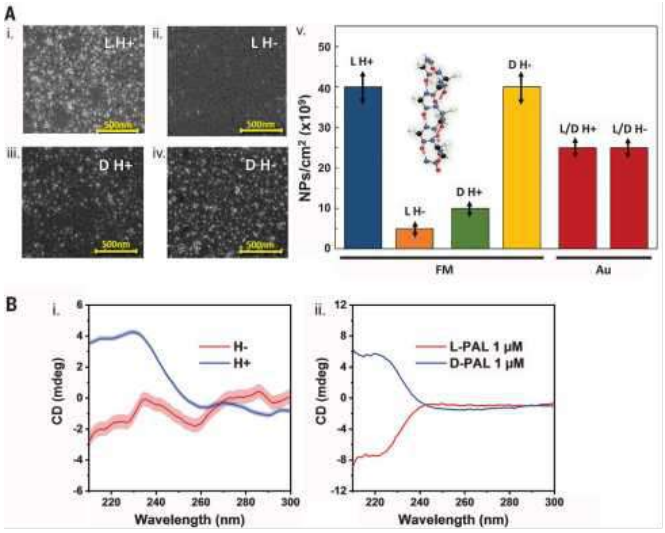


Fig. 1. Enantiospecific adsorption of a peptide. (A) Adsorption of the PAL oligopeptide [shown in inset of (v)] on FM samples (silicon with a 1.8-nm Co film and a 5-nm Au film), magnetized with the magnetic dipole pointing up (H+) or down (H–) relative to the substrate surface. SiO2 nanoparticles were attached to the adsorbed oligopeptides. Panels (i) and (ii) L-PAL and (iii) and (iv) D-PAL were adsorbed for 2 s on a substrate magnetized up or down. Panel (v) summarizes the nanoparticle adsorption densities shown in (i) to (iv), compared with the adsorption density on Au with an applied external magnetic field (red bars). Double-headed arrows represent error bars. The errors are the standard deviation among 10 measurements conducted on each of the 10 samples, hence a total of 100 measurements. (B) Panel (i) shows the enantiospecific CD spectra of PAL, obtained from exposure of a racemic PAL mixture exhibiting no CD to a substrate with magnetization pointing down (red) or up (blue). CD spectra were obtained postadsorption. After the specific adsorption of one enantiomer, the resulting CD spectra clearly indicate the presence of the opposite enantiomer. The linewidth reflects the uncertainty of the results. Panel (ii) shows the CD spectra of the pure enantiomers, provided for comparison. mdeg, millidegrees.

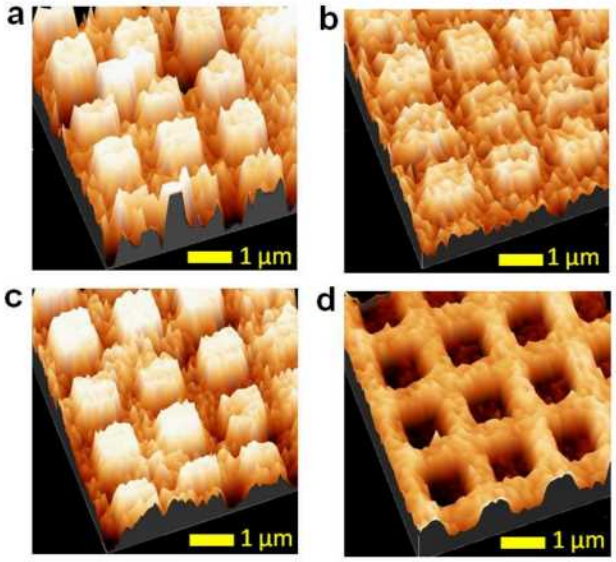


Fig.2 Topography and magnetic phase MFM images of molecular induced magnetization orientation. a, b**,** AFM topography images of SAMs of AHPA-L **(a)** and AHPA-D **(b)** adsorbed on FM Co thin layer coated with 5nm Au overlayer and their corresponding MFM magnetic phase images of AHPA-L **(c)** and AHPA-D **(d)** magnetization orientation . The change of a contrast in MFM images clearly indicates the magnetization reorientation depending on the type of enatiomer (L or D) adsorbed on magnetic nansotructure.

3. Conclusions

It was shown for the first time that magnetization reorientation of magnetic layer can be realized solely by adsorption of specific enantiomer of chiral molecules on its surface without any presence of magnetic or electric fields. A new method of enantio-separation is proposed based on the interaction of chiral molecules with a perpendicularly magnetized substrate. one enantiomer adsorbs preferentially when the magnetic dipole is pointing up, whereas the other adsorbs faster for the opposite magnetization alignment. The interaction is not controlled by the magnetic field but by the respective electron spin orientations of the ferromagnetic layer and chiral molecules.

References

[1] O. Ben Dor, S. Yochelis, A. Radko, K. Vankayala, E. Capua, A. Capua, S.-H. Yang, L. T. Baczewski, S. S. P. Parkin, R. Naaman, Y. Paltiel, Magnetization switching in ferromagnets by adsorbed chiral molecules without current or external magnetic field. Nature Commun. 8, 14567 (2017)

[2] K. Banerjee-Ghosh, O. Ben Dor, F. Tassinari, E. Capua, S. Yochelis, A. Capua, See-Hun Yang, S. S. P. Parkin, S. Sarkar, L. Kronik, L. T. Baczewski, R. Naaman, Y. Paltiel SCIENCE, Vol. 360, Issue 6395, pp. 1331-1334, (2018)

Spin-Polarized Plasmonics

Vladimir P. Drachev,[1,2] Hari Bhatta,[2] Ali Aliev[3]
1 – Skolkovo Institute of Science and Technology, Moscow, Russia
2 – University of North Texas, Denton, TX, USA
3- A. G. MacDiarmid NanoTech Institute, University of Texas at Dallas, Richardson, TX, USA
****corresponding author, E-mail v.drachev@skoltech.ru***

Abstract

Magnetic nanoparticles with a single-domain crystal structure support a plasmon resonance in the deep UV range with the quality better than gold nanoparticle plasmons. The exchange interaction of electrons splits the energy bands between spin-up electrons and spin-down electrons. These two group of electrons have very different relaxation constants providing high and low plasmon quality for two independent plasmons. The scattering without spin flip is required to keep these two plasmons independent.

1. Introduction

Two largely independent channels of conductivity with a distinct spin-dependent electron scattering rate [1] is the primary origin of giant magnetoresistance [2]. These ideas of two independent channels have been projected onto collective electron oscillations in spin-polarized nanoparticles [3]. Understanding the effect of spin polarization on plasmon oscillations of the free electrons in nanoparticles is, essentially, unexplored and crucial in many envisioned applications at the cross road of magnetism and plasmonics. Particularly, it results in a new type of plasmon, specific for spin-polarized magnetic nanoparticles.

2. Results and discussion

Our results show that Co nanoparticles with a single-domain crystal structure support an excellent plasmon resonance at about 280 nm with the quality comparable to gold nanoparticles. This type of plasmons is unusual in a way that two plasmons coexist in a particle at the same frequency and polarizations of excitation, but for electrons of opposite spin. Inter-nanoparticle interactions completely demolish plasmon quality resonance, which is the probable reason why it was not observed previously and why the results for bulk films [4] cannot be used for single domain nanoparticles evaluations. It is known that the exchange interaction of electrons splits the energy bands between spin-up (majority) electrons and spin-down (minority) electrons. We suggest that minority electrons with a partially populated d-band increase the relaxation rate of the conduction electrons and consequently reduce the plasmon resonance quality, while majority electrons with a completely filled d-band does not affect the plasmon resonance of the conduction spin-up electrons within magnetic nanoparticles [3].

Understanding the effect of spin polarization on plasmon oscillations of the free electrons is, essentially, unexplored and crucial in many envisioned applications at the cross road of magnetism and plasmonics. It was a common belief that the quality of the plasmon resonance of magnetic nanoparticles such as Co is quite low, which follows, in particular, from the experimental data for permittivity of bulk cobalt by Johnson and Christy (J&C) [4].

To address the mechanism of new type of plasmons specific for magnetic nanoparticles our work involves an advanced fabrication, dynamic light scattering, structural electron microscopy, SQUID magnetometry, and optical spectroscopy of Co nanoparticles. The main goal of the work is to explain the physical origins of the high quality plasmon resonance observed in the experiments. Note that the plasmon resonance of Co is in the ultraviolet spectral range, which is the range for bio-molecule resonances and therefore attractive for bio-medical applications.

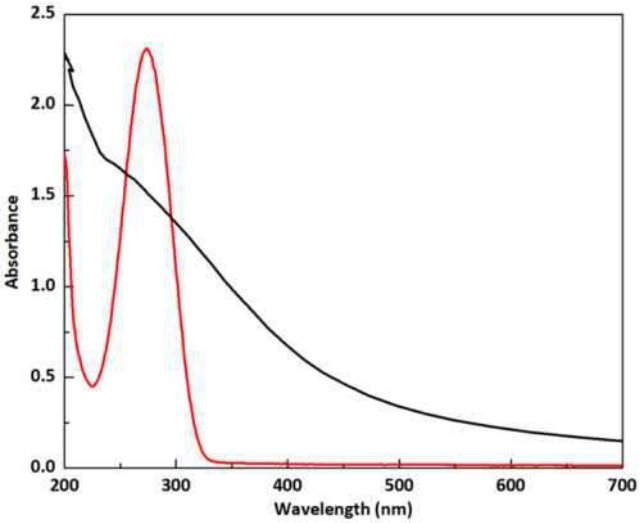


Figure 1. Absorbance of the Co NPs in hexane solution: experiment (red) and calculated (black) using J&C data [3,4].

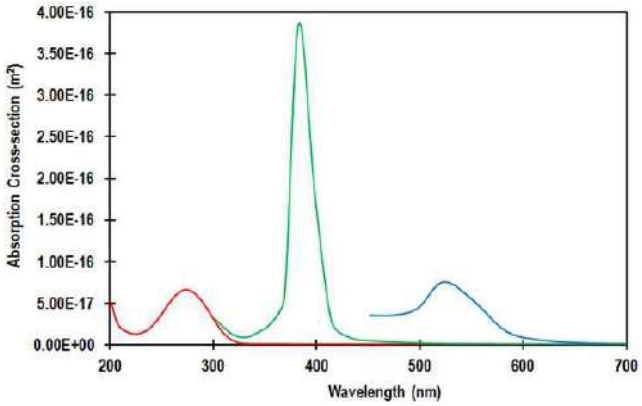
Here a concept of two independent plasmons explains the observed behavior, namely sharp plasmon in contrast to J&C based predictions and the vanishing due to mixing of these two channels. Indeed, according to simulations

performed for GMR a number of s-p electrons in Co is approximately equal for spin-up and spin-down electrons [5]. Terms majority and minority electrons and the bands splitting due to exchange interaction is relevant to d-electrons. This splitting makes difference in the density of empty states in the d-band and thus providing conditions for strongly different mean free path of the s-p electrons. The plasma frequency is related to the conduction electrons. Taking into account that the ratio between spectral width of two plasmons can be up to 20 [5], certainly there is an overlap and the sharp

Briefly, cobalt nanoparticles synthesized by high temperature reduction of cobalt salt show strong plasmon resonance at 280 nm with better quality than that of gold nanoparticles in the visible spectrum, see comparison in Fig. 2. Our experiments with Co nanoparticles clearly show a new type of plasmon excitation, which is specific for spin polarized single domain nanoparticles. Similar features we observe for Fe nanoparticles as well. This type of plasmon has unusual properties due to existence of two independent groups of electrons with opposite spins providing weak interaction so that all electron scattering processes occur without spin flip. Magnetic response of the nanoparticles enables controlled and reversible aggregation accompanied by the tailoring of optical absorption.

These statements are supported by the following arguments. An extensive collection of literature on GMR including first principle simulations proof that the materials with spin polarization of d-electrons have two independent channels of the conductivity (note, that the conductivity is mainly caused by the s-p electrons). The values of conductivity are very different for two channels. The two channels are independent only if the electron scattering goes without spin-flip. The scattering with spin flip can be initiated by the domain structure. These points, known from the Mott's seminal papers, allow explaining our experimental observations, which were possible only by following the described in [3] synthesis recipe.

Our observations include correlation of sharp plasmon resonance with magnetic properties, specifically only singe-domain superparamagnetic nanoparticles show sharp resonance. Larger nanoparticles with domain structure does not show that. The optical absorption measurements are accompanied by the transmission electron microscopy, dynamic light scattering, and magnetometry to characterize the domain structure in a single nanoparticle, aggregation state, and magnetization. The vanishing of the resonance under aggregation (induced by magnetic field with sonication and reversible) can be explained only by the electron scattering with spin flip in the presence of second magnetic particles, since the spin-flip scattering is the only difference relative to the Ag or Au nanoparticles.



Acknowledgements

This work was partially supported by the Ministry of Education and Science of the Russian Federation, project RFMEFI58117X0026.

References

[1] Mott, N. F. Electrons in transition metals. *Adv*. *Phys*. **13,** 325 (1964).

[2] Baibich, M. N.; Broto, J. M.; Fert, A.; Van Dau, N.; Petroff, F.; Etienne, P.; Creuzet, G.; Friederich, A.; Chazelas, Giant magnetoresistance of (001) Fe/(001) Cr magnetic superlattices. *Phys*. *Rev*. *Lett*. **61**, 2472 (1988).

[3] Bhata, H. L., Aliev, A. E., Drachev, V. P. New mechanism of plasmons specific for spin- polarized nanoparticles. *Scientific Reports 9, 2019 (2019)*.

[4] Johnson, P. B., and Christy, R. W. Optical Constants of Transition Metals: Ti, V, Cr, Mn, Fe, Co, Ni, and Pd. *Phys*. *Rev*. **9**, 5056 (1974).

[5] Tsymbal, E.Y.; Pettifor, D.G. *Perspectives of Giant Magnetoresistance*. in Ehrenreich, H. & Spaepen, F. (Eds): Solid state physics **,** (Academic Press, Boston), 56, pp. 213-237 (2001).

Magnetoelectric structures and magnetoelectric fields

E. O. Kamenetskii

Microwave Magnetic Laboratory, Department of Electrical and Computer Engineering,
Ben Gurion University of the Negev, Beer Sheva, Israel. E-mail: kmntsk@bgu.ac.il

Abstract

The question on relationship between magnetoelectricity and electromagnetism is a subject of a strong interest and numerous discussions in microwave and optical wave physics and material sciences. The definition of the energy and momentum of the electromagnetic (EM) field in a magnetoelectric (ME) medium is not a trivial problem. Together with certain constraints on the constitutive parameters of a medium, definite constrains on the field structure should be imposed. Visualization of the ME states require an experimental technique that is based on an effective coupling to the violation of spatial as well as temporal inversion symmetry. There should be a probe with special ME near-field structures.

1. Introduction

In a macroscopic description of the linear magnetoelectric (ME) effect, the magnetoelectric susceptibility tensor is a second rank tensor, which changes sign under space inversion and time reversal and, accordingly, is invariant under simultaneous space and time inversion. Therefore, the ME effect can occur in magnetically ordered systems where spin ordering breaks the spatial inversion symmetry. In crystalline insulators, one observes macroscopic toroidization. Toroidal moment can directly couple with the cross product between the electric field and the magnetic field. So, an energy is in a form: $W_{ME} \propto \vec{T} \cdot \left(\vec{E} \times \vec{H} \right)$. Recently, is was showed that an EM angular momentum density directly couple with magnetic moments to provide an energy: $W_{ME} \propto \vec{r} \times \left(\vec{E} \times \vec{H} \right) \cdot \vec{M}$. Also, ME materials contain a dynamic axion field $\theta(t,\vec{r})$. This gives an additional term of the Lagrangian density, $L_\theta \propto \theta \vec{E} \cdot \vec{B}$, which couples electric and magnetic fields. Pseudoscalar term $\theta \vec{E} \cdot \vec{B}$ provides ME coupling in topological insulators and antiferromagnet chromia.

2. Magnetoelectric fields

The definition if the energy and momentum of the EM field in a ME medium is not a trivial problem. If a ME material has a certain structure (with the known constitutive tensors), a certain demands on the field structure should be also imposed. We consider propagation of quasimonochromatic EM waves in ME medium. The medium is described by local material parameters: $\vec{\vec{\varepsilon}}$, $\vec{\vec{\mu}}$, $\vec{\vec{\xi}}$, $\vec{\vec{\zeta}}$. The fields are expressed as $\vec{E} = \vec{E}_m \, e^{i\left(\omega t - \vec{k}\cdot\vec{r}\right)}$ and $\vec{H} = \vec{H}_m \, e^{i\left(\omega t - \vec{k}\cdot\vec{r}\right)}$, where complex amplitudes $\vec{E}_m$ and $\vec{H}_m$ are time and space smooth-fluctuation functions. From an analysis of the Poynting theorem in a ME medium, it was shown [1] that the energy balance equation can be reduced to a form of a continuity equation $-\nabla \cdot \left\langle \vec{S} \right\rangle = \dfrac{\partial \langle W \rangle}{\partial t} + \langle P \rangle$ only at certain constraints imposed to slowly time-varying complex amplitudes: $E^*_{m_i}(t) \dfrac{\partial H_{m_j}(t)}{\partial t} = H_{m_j}(t) \dfrac{\partial E^*_{m_i}(t)}{\partial t}$. In such a case, the average energy density is expressed as

$$\langle W \rangle = \frac{1}{4} \left\{ \frac{\partial\left(\omega \varepsilon^h_{ij}\right)}{\partial \omega} E^*_i E_j + \frac{\partial\left(\omega \mu^h_{ij}\right)}{\partial \omega} H^*_i H_j + \frac{\partial\left[\omega\left(\zeta^h_{ij} + \xi^h_{ij}\right)\right]}{\partial \omega} \left(H^*_i E_j\right)^h + \frac{\partial\left[\omega\left(\zeta^{ah}_{ij} - \xi^{ah}_{ij}\right)\right]}{\partial \omega} \left(H^*_i E_j\right)^{ah} \right\},$$

where superscripts *h* and *ah* mean, respectively, "Hermitian" and "anti-Hermitian". The first two terms in the right-hand side describe the energy density of an “ordinary” dielectric/magnetic temporary-dispersive medium, whereas the last two terms are the terms that characterize the ME energy density, $\langle W_{ME} \rangle$. Evidently, the $\langle W_{ME} \rangle$ is defined by both the parameters of a medium and the structure of the field. In contradiction to the well-known from the literature fact that for the lossless wave propagation in a ME material, all the parameters $\vec{\vec{\varepsilon}}$, $\vec{\vec{\mu}}$, $\vec{\vec{\xi}}$, $\vec{\vec{\zeta}}$ should be Hermitian, we can see that the ME medium can be lossless even if there exist also anti-Hermitian parts of tensors $\vec{\vec{\xi}}$, $\vec{\vec{\zeta}}$ and a special, anti-Hermitian-part, field structure. This state can be possible due to *PT*-symmetry property of ME crystals.

In EM processes in any lossless dielectric medium, a phase shift between complex amplitudes of the electric and magnetic fields, $E_m \measuredangle H_m$, can be $0^\circ\left(180^\circ\right)$ or $\pm 90^\circ$. In a case of a lossless ME material the angle $E_m \measuredangle H_m$ can be of different degrees. Because of the presents of non-electromagnetic coupling parameter, in lossless EM structure with ME material we can observe non-Maxwellian field fluctuations – the ME fields.

3. Magnetoelectric near-field structures

When the violation of the invariances under space reflection parity and time inversion are necessary conditions for the emergence of the ME effect, the same symmetry properties should be observed for the near-fields. Visualization of the ME states require an experimental technique that is based on an effective coupling to the violation of spatial as well as temporal inversion symmetry. There should be a probe with special ME near field structures. What kind of the near fields originated from a ME sample one can observe? In the near-fields region of a subwavelength sample, we can only measure the electric *E* or the magnetic field *H* with accuracy. There is Heisenberg's uncertainty principle binding *E* and *H* of the EM wave. However, in case of a subwavelength ME sample, the near-field interactions are dominated by two types of the fields: the electric and magnetic fields.

To characterize inherent macroscopic properties of ME materials, a novel near-field microwave sensor had been proposed recently [2]. The sensor is based on a subwavelength ferrite-disk resonator with magnetic-dipolar-mode (MDM) oscillations [3]. Due to a spin-orbit interaction, at MDM resonances in a quasi-2D ferrite disk, one has nonzero product on magnetization: $\vec{m}\cdot\left(\vec{\nabla}\times\vec{m}\right)^*$. The near fields originated from a MDM resonator are characterized by the helicity factor $F = \frac{\varepsilon_0}{4}\,\mathrm{Im}\left[\vec{E}\cdot\left(\nabla\times\vec{E}\right)^*\right] = \frac{\omega\varepsilon_0\mu_0}{4}\,\mathrm{Re}\left(\vec{E}\cdot\vec{H}^*\right) \neq 0$ and power-flow vortices [4, 5]. When the direction of a bias magnetic field is changed, the sign of the helicity factor and the direction of the power-flow vortex are changed as well. The ME near-field sensor based on a MDM resonator is shown in Figs. 1, 2.

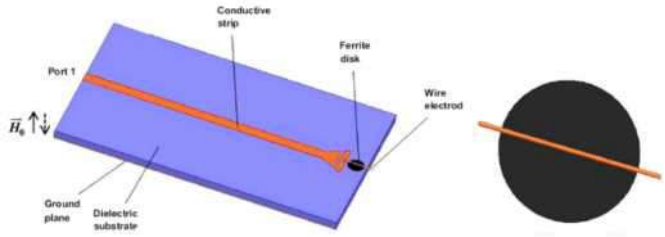


Fig. 1. A microwave probe for near-field measuring of macroscopic properties of ME materials.

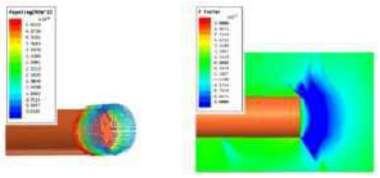


Fig. 2. The power-flow vortex and helicity factor on a butt end of a thin metallic-wire electrode.

Strong energy concentration and unique topological structures of the near fields originated from the MDM resonators allow effective measuring material parameters in microwaves, both for ordinary samples and objects with ME properties.

References

[1] E. O. Kamenetskii, "Energy balance equation for electromagnetic waves in bianisotropic media", Phys. Rev. E 54, 4359 (1996).
[2] E. O. Kamenetskii, E. Hollander, R. Joffe and R. Shavit, "Unidirectional magnetoelectric-field multiresonant tunneling", J. Opt. 17, 025601 (2015).
[3] A. G. Gurevich and G. A. Melkov, Magnetization Oscillations and Waves (CRC Press, 1996).
[4] E. O. Kamenetskii, "Vortices and chirality of magnetostatic modes in quasi-2D ferrite disc particles", J. Phys. A: Math. Theor. 40, 6539 (2007).
[5] E. O. Kamenetskii, R. Joffe, and R. Shavit, "Microwave magnetoelectric fields and their role in the matter-field interaction," Phys. Rev. E 87, 023201 (2013).

Plasmon assisted improvement of figure of merit of magneto-optical Kerr effect and magnetic anisotropy in Au/Co/Au multilayered nanorectangular array structures

Takuo Tanaka[1,2,3]

[1]Metamaterials Laboratory, RIKEN Cluster for Pioneering Research
[2] Innovative Photon Manipulation Research Team, RIKEN Center for Advanced Photonics
[3] School of Materials and Chemical Technology, Tokyo Institute of Technology

*corresponding author, E-mail: t-tanaka@riken.jp

Abstract

We experimentally demonstrated the significant improvement of the figure of merit (FOM) of the longitudinal magneto-optical Kerr effect and the increase of in-plane magnetic anisotropy in Au/Co/Au multilayered nano rectangular patch array structures. When the local-mode surface plasmons were resonantly excited in the nanostructures, its FOM becomes 3.8 times higher and the in-plane magnetic anisotropy energy density was increased about 24 % comparing to those of bare Co nano patch array.

1. Introduction

The magneto-optical (MO) effect such as Kerr effect has attracted much attention owing to its capability of manipulating the polarization state of light, in particular, with the reciprocal optical properties. The angle of polarization rotation by the MO Kerr effect (MOKE) is usually very small, around 1.0 degree, while practical MO devices need a larger polarization angle rotation. Therefore, the enhancement of the MO effect is strongly demanded. Recently, several research groups reported that a large MO effect is observed at the resonant wavelength of local-mode surface plasmons (LSPs). It is well-known that the LSP resonance creates highly localized and high intensity light field. These enhancements by the plasmon resonance are attributed to light/photon accumulation, which is so-called "field-enhancement effect", at the surface of metals. On the other hand, since the degree of the MO effect is intrinsically independent of the light intensity, the mechanism behind the plasmonic enhancement of the MO effect is different from merely the field enhancement effect.

2. Enhancement of MO Kerr effect

We designed and fabricated an Au/Co/Au multilayered nano rectangular patch array with different short axis lengths (L_s) and fixed long axis length (L_l) on indium thin oxide (ITO) coated glass substrates as shown in Figure 1 [1]. Since nano rectangular shape is geometrically anisotropic, it enables us to switch the LSP resonance on and off only by changing the polarization direction of the incident light at a certain wavelength.

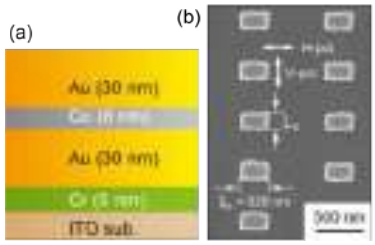


Figure 1: (a) Schematic illustration of cross-sectional structure of Au/Co/Au nanostructure. (b) its SEM image.

MO properties of fabricated structures were measured via an L-MOKE measurement system based on a polarization modulation technique. A diode laser with wavelength of 785 nm was used as a light source. Laser light was collimated and introduced at the device surface with a fixed incident angle of 14 degrees and with a fixed power of 28 mW. In the optical setup a half waveplate was introduced and by rotating it, we changed the polarization direction of incident light to switch the surface plasmon resonance on and off. An external magnetic field of 1000 Gauss, which is enough to measure the saturated values of Kerr rotation and ellipticity, was applied parallel to the long axis of the structure.

When the polarization direction of the incident light was set parallel to the short axis, we defined it as "V-pol.", and that parallels to the long axis is defined as "H-pol." as shown in Fig. 1. Under the V-pol. condition, absorption peaks were gradually shifted to longer wavelength as L_s becomes long. On the other hand, under the H-pol. illumination, no absorption peaks were observed in the visible region because the resonant wavelength of all structures were in the IR region. From these results, we verified that by changing the lengths of the rectangular patch the wavelength of the SP resonance can be tuned and polarization control enables us to switch the localized SP resonance on and off.

We evaluated the MOKE activities in fabricated Au/Co/Au nanorectangular structures. Figure 2 (a) shows the relationship between absolute value of the complex Kerr rotation ($|\Phi|$) and L_s. As shown in Fig. 2 (a), $|\Phi|$ for V-pol. ($|\Phi_{V\text{-pol.}}|$) is always larger than that for H-pol. ($|\Phi_{H\text{-pol.}}|$). While $|\Phi_{H\text{-pol.}}|$ shows an almost constant value regardless of L_s, $|\Phi_{V\text{-pol.}}|$ varies according to the L_s and becomes maximum at L_s = 200 nm, in which the LSPs are excited at the laser wavelength. Fig. 2 (b) shows the ratio of $|\Phi_{V\text{-pol.}}|$ to $|\Phi_{H\text{-pol.}}|$ ($|\Phi_{V\text{-pol.}}| / |\Phi_{H\text{-pol.}}|$) as a function of L_s. It is clear that the ratio becomes maximum at L_s = 200 nm.

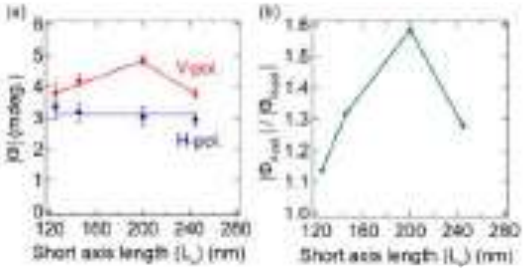


Figure 2: (a) absolute values of complex Kerr rotation in Au/Co/Au nanostructures, (b) $|\Phi_{V\text{-pol.}}| / |\Phi_{H\text{-pol.}}|$ as a function of L_s.

We evaluated the FOM that is defined as

$$FOM = \sqrt{R} \times \theta \quad (1)$$

Figure 3 show the FOM values with respect to L_s. As shown in this figure, FOM in H-pol. ($FOM_{H\text{-pol.}}$) is gradually decreased with increasing L_s. However, as similar to the MO activities, FOM in V-pol. ($FOM_{V\text{-pol.}}$) takes the maximum value at L_s = 200 nm. Moreover, at L_s = 200 nm, $FOM_{V\text{-pol.}}$ becomes about 1.8 times larger than $FOM_{H\text{-pol.}}$. This result indicates that the excitation of LSPs on Au layer improves FOM of the device. In Fig. 3, we also plotted FOMs for bare Co nanostructure.

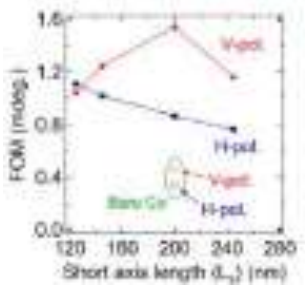


Figure 3: FOM parameters of Au/Co/Au nanostructures for V-pol. and H-pol. illuminations.

3. Plasmonic strengthen of magnetic anisotropy

Magnetic anisotropy is another essential factor for practical applications of magneto-optical devices, because it determines the thermal stability of magnetic devices.

An array of these square patch nanostructures (170 nm × 170 nm in lateral direction) consisting of Cr (5 nm) / Au (30 nm) / Co (6 nm) / Au (30 nm) were fabricated on an ITO substrate using electron beam lithography [2].

The out-of-plane magnetization curve was evaluated via a polar magneto-optical Kerr effect (P-MOKE) measurement system (BH-M800UV-HD-10, NEOARK Corp.). The plane of incidence was set parallel to the edge of the nanostructure surface. The incident angle was fixed at about 5˚. A magnetic field of ±20 k Gauss was applied perpendicular to the sample plane.

Figure 4 shows the relationship between the normalized Kerr ellipticity (η) and the external magnetic field in polar geometry (P-MOKE curve) measured with λ = 500 and 750 nm. We could found that there was a significant difference between the shape of P-MOKE curves for λ = 500 and 750 nm. To clarify this difference, we estimated the slope of the P-MOKE curve ($\Delta\eta / \Delta H$) in the range from -6 k to 6 k Gauss for λ = 500 and 750 nm to be 0.148 and 0.120 (unit: arb. unit of Kerr ellipticity / k Gauss), respectively. We evaluated the magnetic anisotropy field (H_k) in the P-MOKE curve. H_k is defined as the intersection of the fitted line of $\Delta\eta / \Delta H$ (λ = 500 nm, red dashed line; λ = 750 nm, blue dashed line) and the fitted line of the saturation Kerr ellipticity (black dashed line) in the range of -13k to -20k and 13k to 20k Gauss (Fig. 4(b)). The average magnitude of H_k in λ = 500 and 750 nm were about 7.10k and 9.03k Gauss, respectively. Reflection on some of these results made clear that H_k was drastically increased when the surface plasmons were excited in the structure (λ = 750 nm).

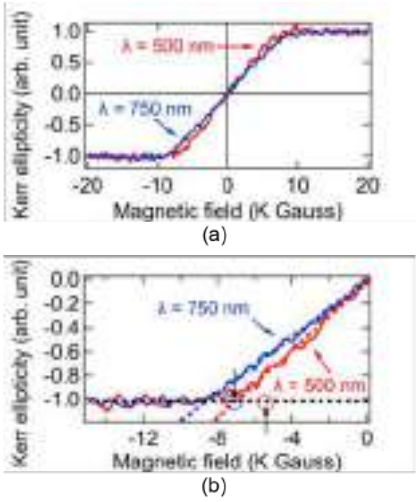


Figure 4: Magnetic field dependence of normalized Kerr ellipticity in P-MOKE curve at two different incident wavelengths (λ): 500 nm (red line) and 750 nm (blue line).

References

[1] Y. Kikuchi and T. Tanaka, *Jpn. J. Appl. Phys.* **57** 110305, 2018.

[2] Y. Kikuchi and T. Tanaka, Sci. Rep. (submitted).

Tunable ferromagnetic resonance in coupled trilayers with crossed perpendicular and in-plane magnetic anisotropies

Daniel Markó[1], Fernando Valdés-Bango García[2], Carlos Quirós Fernández[2,3]
Aurelio Hierro-Rodríguez[4], María Vélez Fraga[2,3], José Ignacio Martín Carbajo[2,3]
José María Maestro Alameda[2,3], David S. Schmool[1*], and Luis Manuel Álvarez-Prado[2,3]

[1]Groupe d'Etude de la Matière Condensée (GEMaC), UMR8635, CNRS and Université de Versailles/Saint-Quentin-en-Yvelines, Université Paris-Saclay, Versailles, France
[2]Departamento de Física, Facultad de Ciencias, Universidad de Oviedo Oviedo, Spain
[3]Centro de Investigación en Nanomateriales y Nanotecnología (CINN), CSIC-Universidad de Oviedo-Principado de Asturias, Llanera, Spain
[4]SUPA, University of Glasgow, School of Physics and Astronomy, Glasgow, UK
*corresponding author, E-mail: david.schmool@uvsq.fr

Thin films with weak perpendicular magnetic anisotropy (PMA) exhibit stripe domains which could be used to control reconfigurable magnonic devices [1, 2]. In amorphous $NdCo_x$ alloys, the Nd concentration is at the origin of the averaged PMA [3]. To further increase the versatility of PMA-based material systems, the effect of controllably coupling a 64 nm thick, hard magnetic $NdCo_x$ film with PMA to a 10 nm thick, soft magnetic $Ni_{80}Fe_{20}$ film with in-plane magnetic anisotropy (IMA) through a non-magnetic Al spacer is investigated. By varying the Co concentration ($X = 5, 7.5, 9$) in the $NdCo_x$ films, the strength of the PMA can be modified. By adjusting the Al spacer thickness T, the type of coupling between the two magnetic layers can be set to either exchange-coupled ($T < 1$ nm) or stray-field coupled ($T \geq 2.5$ nm), respectively. Using transverse magneto-optical Kerr effect and alternating gradient force magnetometry as well as ferromagnetic resonance spectroscopy, the influence of both Co concentration X and Al spacer thickness T on the static and dynamic magnetic properties, respectively, of coupled bi- and trilayers is studied. The two most striking effects of the coupling between the PMA and IMA layers can be observed in their ferromagnetic resonance spectra displayed in Fig. 1, which, compared to a single Py film, show a significant increase of the zero field resonance frequency up to 6.6 GHz and, for low bias fields applied along the hard axis, a frequency hysteresis with a maximum difference between the two field sweep directions as high as 1 GHz. The latter corresponds to a tunability of about 20% at external fields of typically less than 0.1 T. Effectively, only the FMR of the soft Py film is observed, whose magnetic properties are modified by the exchange-coupling to the hard $NdCo_x$ layer [4], resulting in an induced effective domain pattern as illustrated in Fig. 2. From the top panels (a-c) in Fig. 1, in which the results for samples with fixed Al spacer thickness are shown, it can be seen that an increase of the Co concentration X in the $NdCo_x$ films leads to a decrease of the resonance frequencies due to the reduced PMA, resulting in a gradual convergence of the frequencies within the hysteretic part of the spectra to the frequencies of the single Py film. Similarly, as depicted in the lower panels (d-f) in Fig. 1, an increase of the Al spacer thickness for a constant Co concentration leads to a decrease of the FMR frequencies and their gradual convergence towards the single Py film frequencies as a result of a weaker coupling between PMA and IMA films.

Complementary 3D micromagnetic simulations have been shown to reproduce the observed features in the FMR spectra both qualitatively and quantitatively with excellent agreement. By combining the data from magnetization reversal curves and FMR spectra with the simulated domain configuration, which is depicted in Fig. 2, an explanation for the occurrence of the frequency hysteresis along the hard axis of the coupled trilayers is given.

D. S. S. and L. M. Á.-P. acknowledge CNRS for financial support. This work is supported by Spanish MINECO under project FIS2016-76058 (AEI/FEDER, UE).

References

[1] C. Banerjee, P. Gruszecki, J. W. Klos, O. Hellwig, M. Krawczyk, and A. Barman, *Phys. Rev. B* 96, 024421 (2017).

[2] G. Csaba, Á. Papp, and W. Porod, *Phys. Lett. A* 381, 1471 – 1476 (2017).

[3] R. Cid, J. M. Alameda, S. M. Valvidares, J. C. Cezar, P. Bencok, N. B.Brookes, and J. Díaz, *Phys. Rev. B* 95, 224402 (2017).

[4] B. M. S. Teixeira, A. A. Timopheev, R. Schmidt, M. R. Soares, M. Seifert, V. Neu, and N. A. Sobolev, *J. Phys. D: Appl. Phys.* 49, 315002 (2016).

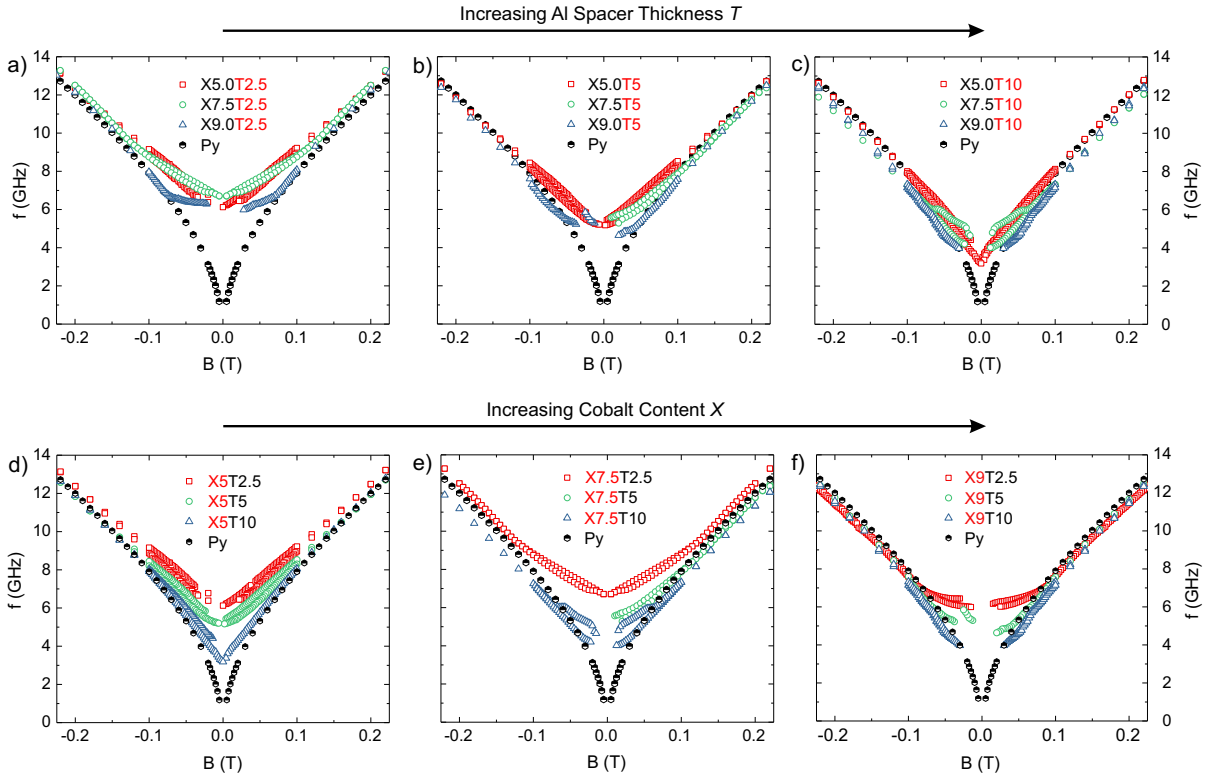


Figure 1: f vs. B dependency of the coupled trilayers for the magnetic field applied long the hard axis. In the top row (a−c), the FMR spectra of trilayers having the same Al spacer thickness (T) are compared, whereas in the bottom row (d−f), the results for trilayers with identical Co concentrations (X) are displayed. In both rows, the values for X and T increase from left to right, respectively. Within the hysteretic part of the FMR spectra, the lower frequency branch at negative fields and the higher frequency branch at positive fields can be accessed when increasing the value of the applied field. Conversely, the lower frequency branch at positive fields and the higher frequency branch at negative fields can be accessed when decreasing the value of the applied field. For comparison, the spectrum of a single 10 nm thick Py film has been added to each plot.

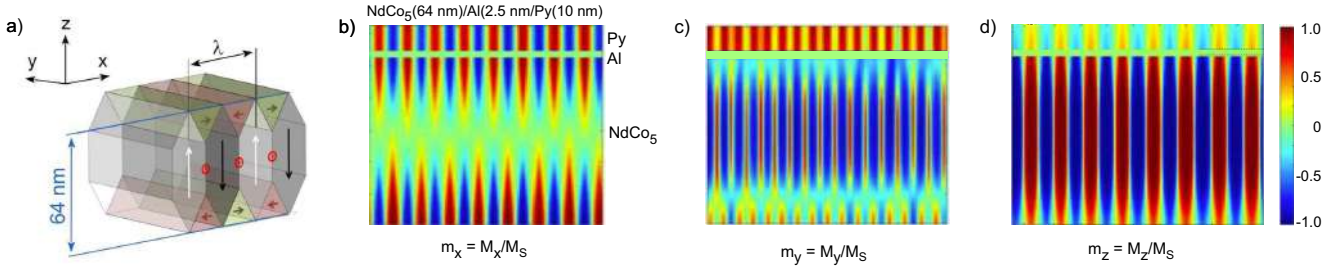


Figure 2: (a) Sketch of the domain configuration in the x-z plane of a single 64 nm thick $NdCo_5$ film. (b-d) Simulated normalized x-, y-, and z-components of the magnetization at remanence in a coupled trilayer of $NdCo_5$(64 nm)/Al(2.5 nm)/Py(10 nm) after application of a magnetic field along the y direction. The values of the individual magnetization components are coded according to the color bar on the right. The NdCo film exhibits stripe domains of periodicity λ with up/down magnetization, whose stray field generates closure domains in the Py layer.

Chirality and Optical Spin-orbit Coupling in Topological Photonic Crystals

Nikhil Parappurath[1], Filippo Alpeggiani[2], L. (Kobus) Kuipers[2], and Ewold Verhagen[1,*]

[1]Center for Nanophotonics, AMOLF, Amsterdam, The Netherlands
[2]Department of Quantum Nanoscience, Kavli Institute of Nanoscience, Delft University of Technology, Delft, The Netherlands
*corresponding author, E-mail: verhagen@amolf.nl

Abstract

We directly observe the states of topological photonic crystals at telecom wavelengths. We show that the unidirectional character of the topological edge states is directly linked to the circular polarization of the states' far fields. Using this intrinsic radiation, we measure dispersion, loss, pseudospin, and spin-spin scattering. We image spin-selective unidirectional propagation around sharp corners and junctions and characterize topological nanocavities.

1. Introduction

The concept of topology has proven immensely powerful in physics, describing new phases of matter with unique properties. There has been a recent surge in attempts to implement topological protection in the photonic domain [1], owing to the application potential of robust transport immune to scattering at disorder. A famous class of electronic topological insulators relies on the quantum spin-Hall effect (QSHE) [2], which uses spin-orbit coupling to cause spin-up and -down electrons to propagate in opposite directions in states that are protected by time-reversal symmetry. Photonic analogues of QSHE were realized using arrayed ring resonators [3, 4], and recently predicted to occur in photonic crystals with special symmetries [5, 6]. Such states were observed in the microwave domain [7, 8], and coupled to spin-polarized quantum dots [9]. Interestingly, topological photonic crystals employing QSHE offer the possibility to access their properties via far-field radiation [10].

2. Results

Here we directly observe topological photonic states at telecom wavelengths in photonic crystals in silicon-on-insulator (SOI) technology. Through angular spectroscopy and polarimetry, we retrieve the properties of the bulk states of crystals with different topological order, as well as the edge states that appear at their interfaces. We reveal that the radiation of the topological states carries a signature of their origin in photonic spin-orbit coupling, linking unidirectional propagation to circular polarization (see Fig. 1a). Through this connection, we selectively excite modes in opposite directions and map their propagation in real space.

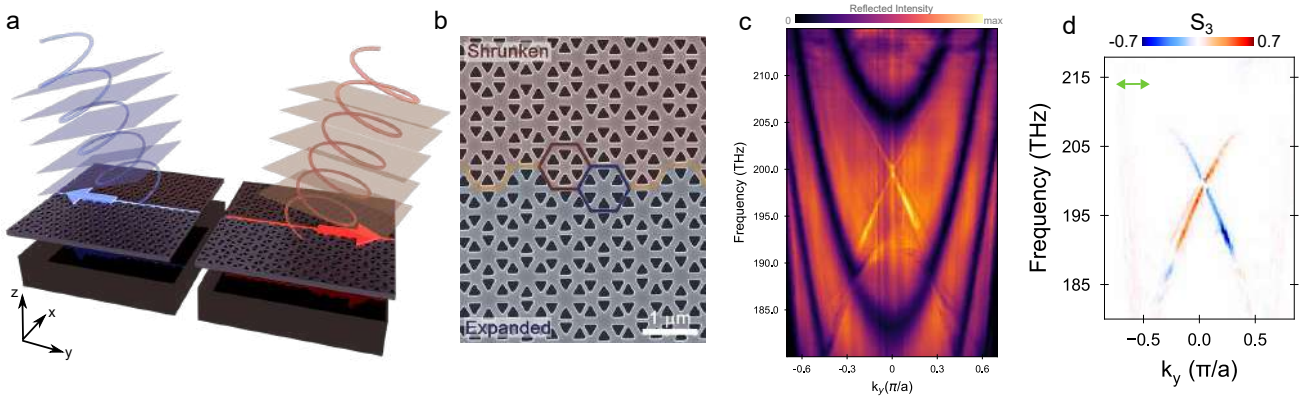


Figure 1: a. Schematic representation of spin-orbit coupling in topological photonic crystals: Chirality of the radiation field is connected to propagation direction of states at edges between photonic crystals with different topological bandstructure. b. A scanning electron micrograph of the fabricated sample, with unit cells indicated in blue and red and edge between two topologically different domains by the yellow line. e. Measured reflectometry, showing the edge state dispersion. d. Measured circular polarization intensity (normalized Stokes parameter S_3) when the edge is excited with light that is linearly polarized along y, showing that the pseudospin is encoded in S_3.

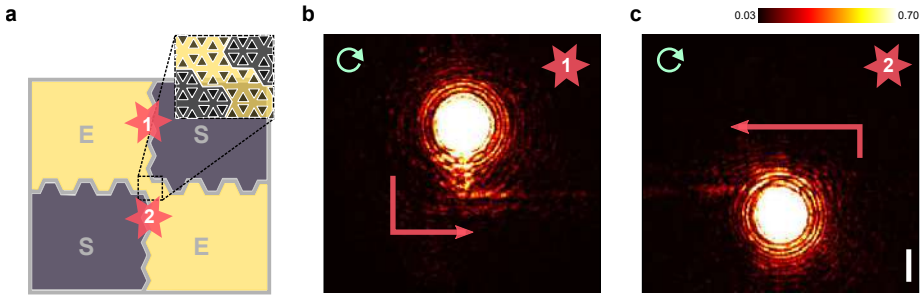


Figure 2: Real-space images of edge state propagation. a. A schematic diagram showing a junction formed by four topological edges. Inset shows a zoomed-in image of the chiral junction. Real-space images b and c show light propagation when the sample is excited by a right circularly polarized single wavelength laser at positions 1 and 2 marked in a. The images are normalized to the maximum pixel value among the two. Scalebar corresponds to 10 μm.

Figure 1b shows the employed photonic crystals, composed of hexagonal unit cells with six sites each, that are either 'shrunken' or 'expanded' to open bandgaps of different topological order at the Γ point [5, 6]. The edge between two domains supports topological edge states of differing pseudospin, protected by the C_6 symmetry of the photonic crystal lattice. We analyze these states by dispersing normal-incidence reflected intensity in both frequency and angle, to map the edge state dispersion shown in Fig. 1c. It displays the characteristic linear dispersion of the edge states, with measured group velocity $c/6$ and quality factor ~ 450.

We demonstrate that the positive and negative group velocity modes can be selectively excited with opposite circular polarization. Conversely, the states' pseudospin can be probed directly in the far field through the S_3 Stokes parameter obtained from polarimetry (Fig. 1d). Our Fourier spectroscopic measurements moreover reveal a small gap at the edge state crossing that is related to spin-spin scattering. This coupling is inherent to the symmetry breaking at the edge, and differentiates these bosonic topological states from their fermioning QSHE counterparts.

Through the far-field spin-orbit link, we selectively excite edge states in opposite directions, and image their propagation in real-space microscopy. Figure 2 shows examples of the spin-selective excitation with a focused laser beam of circular polarization, and the routing of the edge state at a sharp waveguide junction. Interestingly, we observe an absence of backscattering or forward scattering, demonstrating the topological protection of unidirectional propagation. In fact, the states closely follow the photonic crystal edge — defined by the junction's chiral structure of sub-unit cell size — even though their transverse extent is significantly larger.

The employed imaging and Fourier spectroscopy techniques establish a straightforward yet versatile path for testing and optimizing novel topological systems for a wide variety of applications in optics, including components for integrated photonic chips, quantum optical interfaces, enantiomeric sensing, and lasing at the nanoscale.

Acknowledgement

This work is part of the research programme of the Netherlands Organisation for Scientific Research (NWO).

References

[1] Ozawa, T. *et al.*, Topological Photonics, *arXiv:1802.04173*, 2018.

[2] Kane, C. L. and Mele, E. J., Quantum Spin Hall Effect in Graphene, *Phys. Rev. Lett.* 95: 226801, 2005.

[3] Hafezi, M., Mittal, S., Fan, J., Migdall, A., and Taylor, J. M., Imaging topological edge states in silicon photonics, *Nat. Photonics* 7: 1001–1005, 2013.

[4] Mittal, S. *et al.*, Topologically Robust Transport of Photons in a Synthetic Gauge Field, *Phys. Rev. Lett.* 113: 087403, 2014.

[5] Wu, L.-H., and Hu, X., Scheme for Achieving a Topological Photonic Crystal by Using Dielectric Material, *Phys. Rev. Lett.* 114: 223901, 2015.

[6] Barik, S., Miyake, H., DeGottardi, W., Waks, E., and Hafezi, M., Two-dimensionally confined topological edge states in photonic crystals, *New J. Phys.* 18: 113013, 2016.

[7] Yves, S. *et al.*, Crystalline metamaterials for topological properties at subwavelength scales, *Nat. Commun.* 8: 16023, 2017.

[8] Yang, Y. *et al.*, Visualization of a Unidirectional Electromagnetic Waveguide Using Topological Photonic Crystals Made of Dielectric Materials, *Phys. Rev. Lett.* 120, 2018.

[9] Barik, S. *et al.*, A topological quantum optics interface, *Science* 359: 666, 2018.

[10] Gorlach, M. A. *et al.*, Far-field probing of leaky topological states in all-dielectric metasurfaces, *Nat. Commun.* 9: 909, 2018.

A surface plasmon platform for angle-resolved chiral sensing

Lykourgos Bougas [1,*] **and Sotiris Droulias** [2]

[1]Institut für Physik, Johannes Gutenberg Universität-Mainz, 55128 Mainz, Germany
[2]Institute of Electronic Structure and Laser, FORTH, 71110 Heraklion, Crete, Greece
*corresponding author, E-mail: lybougas@uni-mainz.de

Abstract

Chiral sensing is crucial in probing the fundamental symmetries of the universe, study biomolecular structures, and even develop safe drugs. As chiral signals are inherently weak, different techniques have been proposed to overcome the limitations of traditionally used chiral polarimetry. We propose an angle-resolved chiral surface plasmon resonance scheme that can detect the absolute chirality (handedness and magnitude) of a chiral sample and is sensitive to both the real and imaginary part of a chiral sample's refractive index.

1. CHISPR

Chirality is a fundamental property of life with far-reaching implications among all disciplines of science. Chiral sensitive techniques have enabled the study of fundamental symmetries of the universe, determination of biomolecular structures, and development of safe and effective drugs, to name few of the most prominent applications of chiral sensing.

The polarimetric techniques of optical rotatory dispersion (ORD) and circular dichroism (CD) are among the most widely used research tools in modern science for chiral sensing. However, polarimetric measurements are typically challenging as the measured signals are small and often suppressed by large backgrounds. To overcome the limitations of traditional polarimetry in chiral sensing, different techniques have been proposed in the recent years. These techniques, which aim to enhance the chiral wave-matter interaction, can in principle be arranged into two main categories, as they rely mainly on either (a) path-length enhancement or (b) chiral-field enhancement. The first type of techniques is primarily cavity-based, for which the ORD and CD signals are enhanced by the number of cavity-passes (typically about 10^3-10^4) [1, 2]. However, cavity-enhanced techniques become inadequate in systems with losses originating from absorption and/or scattering (e.g. chiral molecules within complex matrices, thin films, liquid and/or solid systems), because losses hinder the path-length enhancement. The chiral-field-enhancement techniques rely primarily on generating probing-electromagnetic-fields with chiral densities higher than circularly polarized plane waves (see for example Refs.[3, 4]). Chiral and achiral nanophotonic systems, such as plasmonic/dielectric nanostructures and metamaterials, can generate contorted intense near-fields with high chiral densities around a resonance frequency of the nanosystem, thus amplifying the chiral-chiral interactions between them and a molecule. However, in most demonstrations, elaborate fabrication is required and the employed nanosystems have their own intrinsic chiroptical response that contributes in the total CD signal and, thus, inhibits the absolute and quantitative measurement of chirality. Moreover, to the best of our knowledge, in most nanophotonic-based chiral-sensing protocols only the case of circular dichroism is discussed and, therefore, most results are typically analyzed with respect to the imaginary part of chiral refractive index, while chiral-sensing technologies, which are routinely applied in the pharmaceutical, agricultural, and food industry, require the detection of both real and imaginary parts of the chiral refractive index.

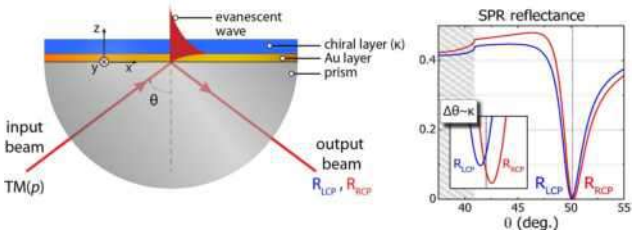


Figure 1: Chiral Surface Plasmon Resonance: A linearly TM(p) polarized beam incident on a thin gold layer placed onto a prism, excites a surface plasmon polariton (SPP) (indicated by the evanescent wave) at a particular angle, θ, which propagates along the metal-chiral-layer interface. The SPP wave is modified by the chiral environment resulting in an outgoing optical chirality flux, which can be used to infer the properties of the chiral layer by analyzing the reflected power into right- and left-circular polarized components, R_{RCP}, R_{LCP}, respectively. In particular, the effect of chirality appears as a chiral-dependent angular split ($\Delta\theta = \theta_{\mathrm{RCP}} - \theta_{\mathrm{LCP}}$) between R_{RCP} and R_{LCP}, and the magnitude and sign of $\Delta\theta$ depends on the chiral parameter κ.

Considering the importance of chiral sensing, it is vital to develop novel schemes that overcome the above-mentioned limitations of path-length enhancement and/or chiral-field enhancement techniques, but most importantly ones that allow for **absolute** chiral sensing. We propose an angle-resolved chiral surface plasmon resonance (CHISPR) scheme (Fig. 1) that can detect the absolute chirality (handedness and magnitude) of a chiral sample and is sensitive

to both the real and imaginary part of a chiral sample's refractive index, contrary to most demonstrations that employ metallic nanostructures and/or metasurfaces. We present analytical results and numerical simulations of CHISPR measurements, predicting signals in the mdeg range for chiral samples of <100 nm thickness at visible wavelengths (as a comparison, optical rotation signals from a transmission measurement of similar chiral samples with realistic chiral parameters would be at least an order of magnitude smaller [5]. We show that CHISPR is particularly suitable for chiral sensing from thin samples which are not easily measurable using alternative techniques, and that our technique has the advantage of being applicable directly on existing SPR instrumentation without the need for additional elaborate fabrication. In addition, with a CHISPR measurement scheme the whole evanescent-wave volume is sensitive to the probed chiral substance (due to the mobility of the propagating surface plasmon polaritons), contrary to schemes based on local surface plasmons, where the sign and magnitude of the chiroptical response possess a complex dependence on sample geometry.

In the outlook, we will also discuss alternative routes towards absolute chiral sensing using nanoplasmonic-based approaches.

Acknowledgement

This research was supported by European Commission Horizon 2020, Ultrachiral Project (grant no. FETOPEN-737071).

References

[1] D. Sofikitis, L. Bougas, G. E. Katsoprinakis, A. K. Spiliotis, B. Loppinet, and T. P. Rakitzis, Evanescent-wave and open-air chiral sensing via signal-reversing cavity-enhanced polarimetry, *Nature* **514**, 76 (2014).

[2] L. Bougas, D. Sofikitis, G. E. Katsoprinakis, A. K. Spiliotis, P. Tzallas, B. Loppinet, and T. P. Rakitzis, Chiral Cavity Ring Down Polarimetry: Chirality and magnetometry measurements using signal reversals, *J. Chem. Phys.* **143**, 104202 (2015).

[3] Y. Zhao, A. N. Askarpour, L. Sun, J. Shi, X. Li, and A. Alu, Chirality detection of enantiomers using twisted optical metamaterials, *Nature Comm.* **8**, 14180 (2017).

[4] E. Mohammadi , K. L. Tsakmakidis, A. N. Askarpour, P. Dehkhoda, A. Tavakoli, and H. Altug, *ACS Photonics*, **5** 2669 (2018).

[5] S. Droulias and L. Bougas, A surface plasmon platform for angle-resolved chiral sensing, *arXiv*, arXiv:1901.09609 (2019).

Terahertz metamaterials: accessing nonlinear spin and phonon dynamics

Stefano Bonetti[1,2]

[1]Department of Physics, Stockholm University, Stockholm, Sweden
[2]IDepartment of Molecular Sciences and Nanosystems, Ca Foscari University of Venice, Italy
*corresponding author, E-mail: stefano.bonetti@fysik.su.se

Abstract

In this talk, I will describe a few metamaterials design that can be used to drive large amplitude, nonlinear dynamics in condensed matter systems, focusing in particular to the spin and lattice degrees of freedom. For this scope, I will discuss different designs aimed at enhancing either the electric or the magnetic field component of terahertz radiation. The metamaterial structures have been investigated thoroughly using three-dimensional finite element simulations in both the frequency and the time domain. Preliminary results of the observation of the large amplitude dynamics induced by such metamaterials will be shown, detected using time-resolved pump-probe microscopy.

1. Introduction

The use of terahertz radiation to investigate different physical systems has been rapidly increasing in recent years. In condensed matter physics, collective excitations of the lattice and spin degrees of freedom are typically found in this frequency range, offering a natural playing field for observing terahertz dynamics. The concomitant development of commercial, intense Ti:sapphire laser systems, as well as of nonlinear crystal able to generate efficient optical rectification, has allowed researchers to have relatively easy access to terahertz electric (magnetic) fields as high as 1 MV/cm (0.3 T). Such large fields are strong enough to initiate nonlinear dynamical effects in both phonon [1] and spin [2] degrees of freedom.

However, it would be desirable to increase such fields by one or two orders of magnitude in order to fully explore the nonlinear regimes in solids. Terahertz metamaterials [3] offer a solution to this demand compatibly with the use of the same commercial laser systems, i.e. without the need of large scale facilities. In metamaterials, typically comprising of periodically arranged gold electrodes deposited on a dielectric substrate, the electric or magnetic field of the impinging radiation are concentrated in localized areas. These areas extend over as much as several square micrometers for the terahertz case, allowing for fabrication using inexpensive and reliable optical lithographic methods.

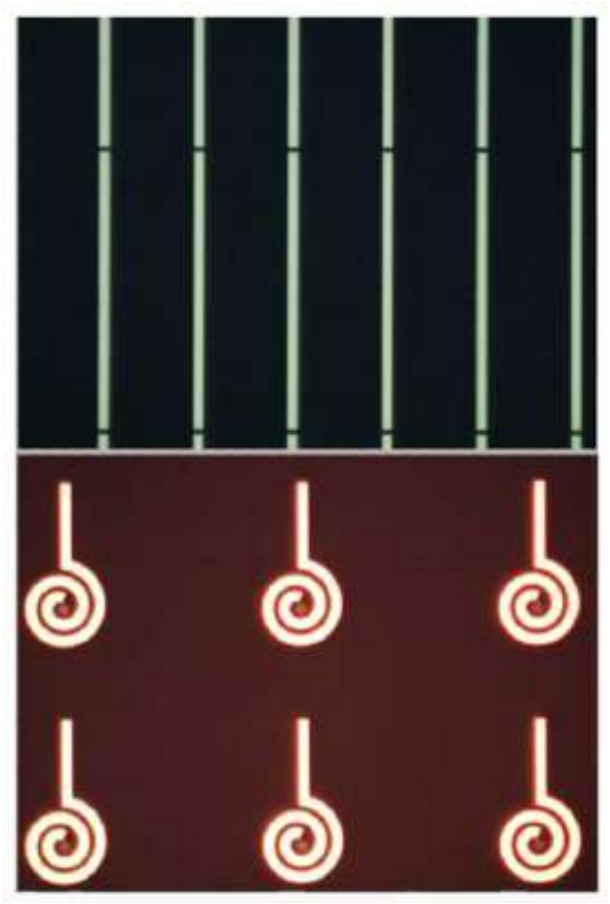


Figure 1: Top: dipolar antennas for electric field enhancement. Bottom: "lollipop" metematerials for magnetic field enhancement.

2. Discussion

In this talk, I will present the design of several metamaterials aimed at enhancing either the electric or the magnetic field of the impinging terahertz radiation. In both cases, I will illustrate finite three-dimensional element simulations detailing the spatial distribution of the electric and magnetic fields, both in the frequency and time-domain. The latter description is key to properly estimate the near-field enhancement when the impinging field is a broadband, single-cycle terahertz pulse, which is the most typical realization



Figure 2: Time-resolved terahertz pump / near-infrared probe scheme implemented. The strong terahertz radiation is generated via optical rectification of mJ infrared pulses from a parametric amplfier driven by a Ti:sapphire amplfied system. OH1 or DSTMS crystals are used for the optical rectification in the different terahertz regions. A small fraction of the Ti:sapphire radiation is used to probe the dynamics using a variable delay line (not shown here). A 100x objective collect the light transmitted through the sample and measure the magneto-optical Faraday effect.

in table-top systems.

I will also discuss experimental results showing evidence for nonlinear phonon dynamics driven by strong terahertz electric fields, that can be enhanced further in antennas structure such as the one shown in the top panel of Fig. 1. I will also discuss a novel scheme to drive highly nonlinear spin dynamics using lollipop metamaterials (showed in the bottom panel of Fig. 1, that would allow to reach the ballistic magnetization switching regime, so far only observed using terahertz radiation generated in mile-long particle accelerators, on table-top setups [4].

Finally, I will show preliminary spectroscopic measurements demonstrating the accuracy of careful 3-dimensional finite element simulations to reproduce the experimental response of the metamaterials. I will also present the preliminary data of spin dynamics driven in the near-field region of the metamaterial, and recorded using time-resolved magneto-optical microscopy with terahertz pump and near-infrared probing scheme, as shown schematically in Fig. 2.

3. Conclusions

We discussed the design of several metamaterial structures aimed at enhancing either the electric or the magnetic field of terahertz radiation in the near-field. We showed preliminary results demonstrating the optical properties of the metamaterials, as well as time-resolved microscopy data showing large amplitude, terahertz-driven dynamics in solids. We envision that the combination of metamaterials with suitable condensed matter systems will allow for investigating yet unexplored areas of strongly non-equilibrium states in materials of both fundamental and applied interest.

Acknowledgement

Stefano Bonetti gratefully acknowledges support from the European Research Council, Starting Grant Number 715542 MAGNETIC-SPEED-LIMIT and from the Knut and Alice Wallenberg foundation under the Wallenberg Academy Fellow program.

References

[1] I. Katayama et al, *Phys. Rev. Lett.* 108:097401, 2012

[2] S. Baierl et al, *Phys. Rev. Lett.* 117:197201 (2016)

[3] W. J. Padilla et al., *Phys. Rev. Lett.* 96:107401, (2006)

[4] D. Polley et al., *Journal of Physics B: Atomic Molecular and Optical Physics* 51:224001 (2018)

Dynamical chiral metasurfaces: mechanical based modulation and polarimetry

Alessandro Pitanti[1,*]

[1]NEST, CNR Istituto Nanoscienze and Scuola Normale Superiore, Piazza San Silvestro 12, 56127 Pisa, Italy
*corresponding author, E-mail: alessandro.pitanti@nano.cnr.it

Abstract

We combine the chiral properties of an all-dielectric GaAs metasurfaces operating in the near-infrared range with micro-mechanical motion. We demonstrate polarization modulation and spring-effect based light polarimetry at frequency exceeding 300 kHz.

1. Introduction

Among the amazing properties of metasurfaces, very large circular dichroism has been reported, fairly exceeding the one found in biological molecules or in classical waveplates [1]. An interesting feature would be to enhance the device properties by adding an active response to the original static tunability by-design. To this end, we show how the chiral response of a minimal, all-dielectric metasurface can be dynamically controlled by placing it in a suspended, mechanically actuable membrane. By activating its drum-like mechanical motion, we are able to achieve ~350 kHz polarization modulation; moreover, by using the thermal induced back action of light on the mechanics, we are able to deterministically infer the polarization state of light, paving the way to extremely fast polarimetry.

2. Methods

The metasurfaces consists of a suspended, patterned, 210 nm thick GaAs layer. The pattern used to obtain a chiral response consists of "L-shaped" holes. Fabrication starts from a 220nm/3µm GaAs/$Al_{0.5}Ga_{0.5}As$ heterostructure grown on a GaAs wafer, the pattern has been transferred employing an electronic resist mask (AR-P 6200) and subsequent chlorine based reactive ion etching. Details on sample fabrication and pattern geometrical parameters have been reported elsewhere [2]. The final device configuration is sketched in Fig. 1 (a); it consists of a proper metasurface, whose final pattern is reported in Fig. 1 (b), plus a GaAs substrate showing multiple Fabry-Perot resonances. The membrane vibration modifies the phase of light traveling through the device granting optomechanical coupling. In particular, we investigated the coupling between delocalized electromagnetic modes around 1550nm (see the single cell finite-element-method (FEM) simulations of Fig. 1 (c)) and the fundamental drum-like membrane motion (see the full-membrane FEM simulations of Fig. 1 (d)). The motion is activated by mounting the full chip on top of a piezo-stack.

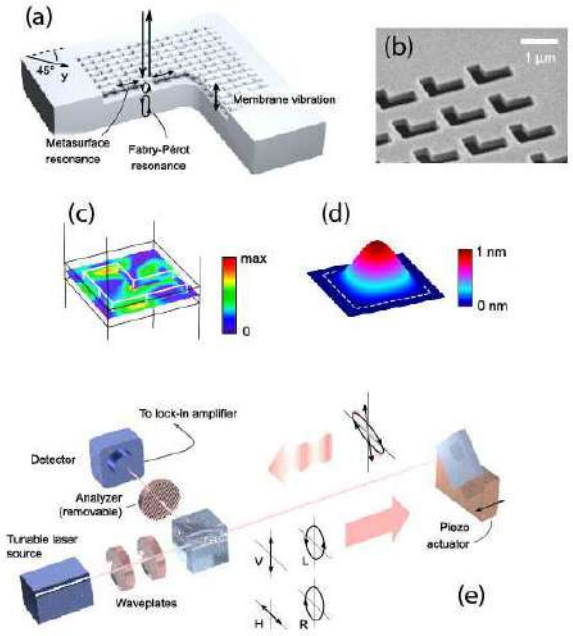


Figure 1: (a): Sketch of the device under investigation. (b): Scanning Electron Micrograph of the L-shaped pattern which defines the metasurface. (c): Simulation of the electromagnetic mode in a single cell. (d): Simulation of the whole membrane mechanical mode. (e): Sketch of the experimental setup.

The sample holder is then placed in a vacuum chamber and placed in a simple optical line as the one sketched in Fig. 1 (e). The input laser signal is shined onto the sample with an arbitrary polarization; the reflected light is then analyzed using optical waveplates and a lock-in amplifier with the piezo-drive taken as a reference.

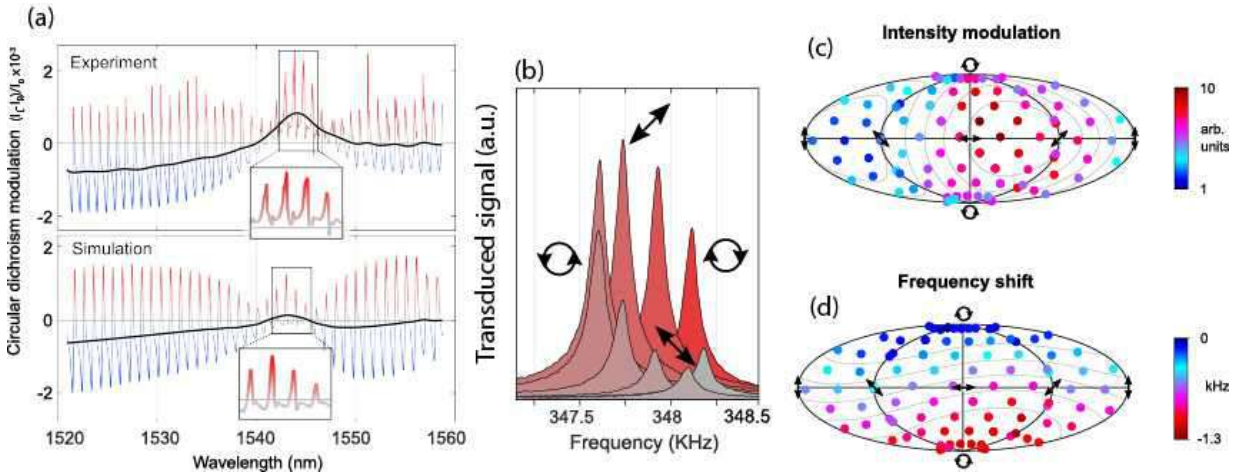


Figure 2: (a): Experiment and simulation of the circular dichroism modulation. The signal is composed by a broad metasurfaces resonance and fast-oscillating Fabry-Perot fringes coming from the substrate. (b): Polarization induced back-action. (c)-(d): full characterization of the mechanical resonance intensity and resonant frequency as a function of the input polarization.

3. Results

3.1. Polarization modulation

At first we investigated the effect of the mechanical motion on the system optical response. At atmospheric pressure, where the mechanical resonator is overdamped, a 300 kHz monochromatic bias was fed to the piezo stack and used as a phase reference for the coherent measurements. By acting on the phase of light interacting with the sample, mechanical motion affects the linear and circular dichroism of the system. As an example, the modulation of circular dichroism (defined as the normalized intensity difference of light reflected under left-circular and right-circular polarization) is reported in Fig. 2 (a) along with a simulation based on a hybrid scattering-transfer matrix formalism. A very good agreement between experiment and simulation and the use of polarization filters let us to distinguish between intensity and polarization modulation effects, finding a linear, pure polarization modulation exceeding 0.5 rad on the Poincaré sphere, mainly limited by the linearity of mechanical motion.

3.2. Optomechanical polarimetry

The back-action of light on the mechanical motion was investigated by pumping the sample chamber to a pressure linewidth as small as 0.15 kHz (Q ~ 2000). A residual heating of the membrane (few hundredths of K) which conversely shifted and modified the observed mechanical resonance. of 3e-5 mbar. absorption of light in the GaAs layer produced a small In vacuum the air damping is greatly reduced and the mechanical mode appears as a narrow peak, with Given the strong polarization sensitivity displayed by the metasurface, a small change of polarization input induced a different thermal heating and therefore a different aspect of the mechanical mode. As an example, Fig. 2 (b) reports several mechanical spectra along a meridian on the Poincaré sphere, where each one is characterized by a particular frequency shift and intensity. The full mapping of the sphere is reported in Fig. 2 (c)-(d) where it can be seen that for each polarization input it is possible to obtain a unique set of mechanical parameters, which can be used to completely identify the polarization of input light at a frequency exceeding 300 kHz.

4. Conclusion

Our device combines together the polarization modulation properties of metasurfaces together with the dynamical tuning and sensitivity of micromechanical resonators. While showing polarization modulation and light polarimetry employing the fundamental mechanical mode oscillating at 350 kHz, we foresee the possibility of producing ultra-fast modulators and polarimeters combining our device with surface acoustic waves which naturally are created on the piezoelectric, GaAs device layer.

Acknowledgements

This work was supported by the EC, FET project PHENOMEN (H2020-EU-713450).

References

[1] A. Y. Zhu et al., Giant intrinsic chiro-optical activity in planar dielectric nanostructures, *Light: Sci. App.* 7, 17158, 2018.

[2] S. Zanotto et al., Optomechanics of chiral dielectric metasurfaces, arXiv:1810.01773, 2018

Structural chirality combined with optical activity (aka magneto-electricity)

Martin McCall

Department of Physics,
Imperial College London, UK
E-mail: m.mccall@imperial.ac.uk

Abstract

We present a fully analytic solution for axial propagation along a structurally chiral dielectric medium infiltrated by an optically active medium that is chiral at the molecular level.

1. Introduction

On account of the fact that photons are circularly polarized, there is considerable focus nowadays on media that intrinsically engage the photon's chirality. There are two fundamental types such chiral media: (a) optically active media where chirality occurs at the molecular level, and is due to magneto-electric coupling, and (b) structurally chiral media where chirality occurs due to dielectric inhomogeneity and is formed by the periodic rotation of the principal axes of the dielectric tensor. Our focus here is to examine how these two aspects may be combined into a single medium.

2. Optical Activity

The most frequently used frequency domain constitutive relations for an optically active medium are the so-called Drude-Born-Fedorov (DBF) relations [1],

$$\mathbf{d} = \epsilon \mathbf{E} + i\alpha \mathbf{h}\,, \quad \mathbf{b} = -i\alpha \mathbf{E} + \mu \mathbf{h}\,. \tag{1}$$

where the usual electromagnetic fields $\mathbf{D}$, $\mathbf{B}$ and $\mathbf{H}$ have been replaced by scaled fields $\mathbf{h} = \eta_0 \mathbf{H}$, $\mathbf{b} = (\eta_0/\mu_0)\mathbf{B} = c\mathbf{B}$ and $\mathbf{d} = \epsilon_0^{-1}\mathbf{D}$, that have the same dimensions as the electric field $\mathbf{E}$. Here $\eta_0 = (\mu_0/\epsilon_0)^{1/2}$ is the free-space impedance and ϵ, μ and α are dimensionless. For harmonic fields, the Maxwell curl relations then become

$$\nabla \times \mathbf{E} = k_0 \alpha \mathbf{E} + i\mu k_0 \mathbf{h}\,, \tag{2}$$

$$\nabla \times \mathbf{h} = -ik_0 \epsilon \mathbf{E} + k_0 \alpha \mathbf{h}\,, \tag{3}$$

where $k_0 = \omega/c$. Solving these equations for a plane wave determines that the transverse electric field vector satisfies

$$\begin{pmatrix} E_x \\ E_y \end{pmatrix}_z = e^{ik_0(\epsilon\mu)^{1/2} z} \begin{pmatrix} \cos\alpha k_0 z & \sin\alpha k_0 z \\ -\sin\alpha k_0 z & \cos\alpha k_0 z \end{pmatrix} \begin{pmatrix} E_x \\ E_y \end{pmatrix}_0 \tag{4}$$

Thus, as it propagates through the medium, a linear polarization is rotated in a *left*-handed sense at a rate of αk_0 rad m^{-1}.

3. Structural Chirality

Structural chirality is characterized by a tensorial $\boldsymbol{\epsilon}$ the principal axes of which rotate periodically about the $z-$axis (see Fig. 1)

$$\tilde{\boldsymbol{\epsilon}} = \mathcal{R}^{-1} \underline{\underline{\boldsymbol{\epsilon}}} \mathcal{R}\,, \quad \mathcal{R} = \begin{pmatrix} \cos pz & -\sin pz \\ \sin pz & \cos pz \end{pmatrix}. \tag{5}$$

It turns out that by defining the transverse fields

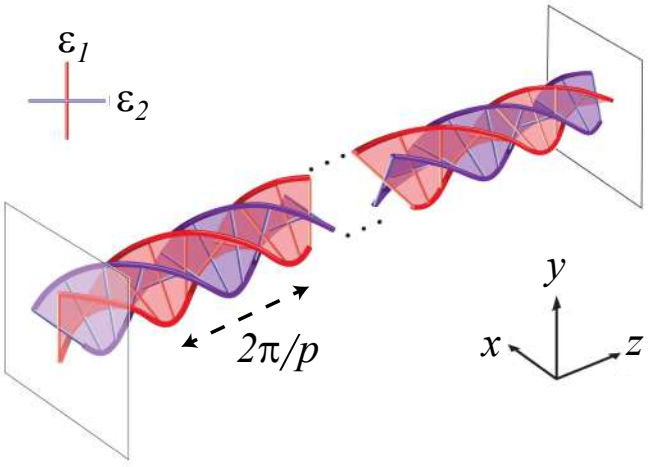


Figure 1: Structurally chiral medium as described by Eq. (5). The eigenaxes rotate about the z-axis with period $2\pi/p$.

$$\mathbf{e} = \mathcal{R}E\,, \quad \tilde{\mathbf{h}} = \mathcal{R}\mathbf{h}\,, \tag{6}$$

the Maxwell curl relations for a harmonic field propagating along the z-axis reduce to

$$\frac{d}{dz}\begin{pmatrix} \mathbf{e} \\ \tilde{\mathbf{h}} \end{pmatrix} = \begin{pmatrix} -p\mathcal{S} & i\mu k_0 \mathcal{S} \\ -ik_0 \mathcal{S} \underline{\underline{\boldsymbol{\epsilon}}} & -p\mathcal{S} \end{pmatrix} \begin{pmatrix} \mathbf{e} \\ \tilde{\mathbf{h}} \end{pmatrix}, \tag{7}$$

where $\mathcal{S} \equiv \begin{pmatrix} 0 & -1 \\ 1 & 0 \end{pmatrix}$. Since the matrix appearing on the right of Eq. (7) is independent of z, the system admits a straightforward analytic solution that can be written formally as

$$\begin{pmatrix} \mathbf{e} \\ \tilde{\mathbf{h}} \end{pmatrix}_z = \exp\begin{bmatrix} -pz\mathcal{S} & i\mu k_0 z \mathcal{S} \\ -ik_0 z \mathcal{S} \underline{\underline{\boldsymbol{\epsilon}}} & -pz\mathcal{S} \end{bmatrix} \begin{pmatrix} \mathbf{e} \\ \tilde{\mathbf{h}} \end{pmatrix}_0 \tag{8}$$

This solution has been well studied (see, for example Refs. [2] and [3]), and can be used to compute the various reflection/transmission coefficients (R_{LL}, T_{LR}, etc.) associated with axial propagation. These can be computed in the presence of interface reflections and with complex principal dielectric coefficients (i.e. gain/absorption).

4. Combining Optical Activity with Structural Chirality

Simply stated, the problem of combing optical activity with structural chirality amounts to replacing the scalar ϵ in Eq. (3) with the tensor $\tilde{\boldsymbol{\epsilon}}$ of Eq. (5). We will show that the combined system is also fully analytic. A key emergent formula is the Bragg wavelength at which co-handed reflection is maximized:

$$\lambda_0^{(Br)} = \left(\left[(\epsilon_1 + \epsilon_2)/2 \right]^{1/2} - \alpha \right) \frac{2\pi}{p}, \qquad (9)$$

Thus the effect of making the structurally chiral medium optically active is to shift the Bragg resonance from its value ($= 2\pi\bar{n}/p$) in the absence of optical activity.

Of experimental interest is the so-called g-parameter, measuring the chiral dysymmetry:

$$g_{abs} = 2\frac{A_L - A_R}{A_L + A_R} \qquad (10)$$

where $A_{L,R}$ are the absorbed fractions of incident left or right circularly polarized light, computed via

$$A_L = 1 - T_{LL} - T_{RL} - R_{LL} - R_{RL}, \qquad (11)$$
$$A_R = 1 - T_{LR} - T_{RR} - R_{LR} - R_{RR}, \qquad (12)$$

where (e.g.) T_{RL} is the transmitted fraction of *R*CP when the incident light is *L*CP. By way of illustration of the Bragg formula, Eq. (9), in Fig. 2 we compute g_{abs} both in the absence, and in the presence of optical activity.

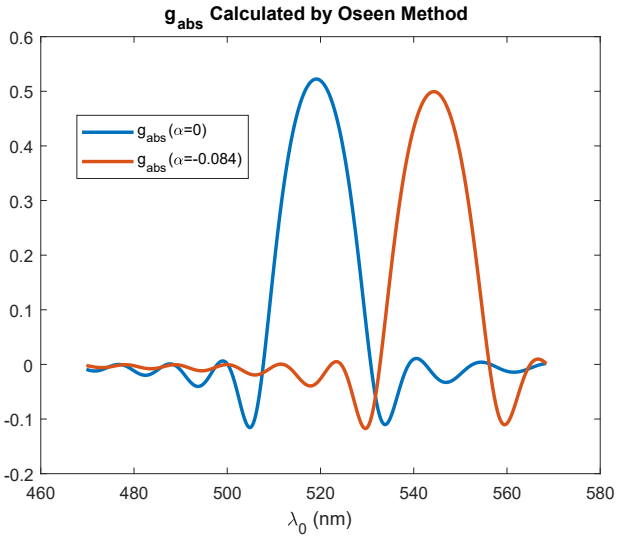


Figure 2: Calculated g_{abs}. Parameters: $\epsilon_x = 3.2 + 0.02i$, $\epsilon_y = 2.9 + 0.02i$, film thickness $d = 6\mu$m, $\alpha = -0.084$ (corresponding to 1 rad/μm at the Bragg wavelength), structural period, $2\pi/p = 300$nm.

5. Conclusions and Prospects

We have successfully combined known analytic solutions for isotropic optical activity with axial propagation along a structurally chiral medium. We will show how practical formulae emerge for the reflectivities/transmissivities, when the fully analytic solution is replaced by an approximate approach based on coupled wave theory. From the practical viewpoint we will consider the implications of our results on (a) circularly polarized luminescence in chiral dyes [4, 5, 6], (b) chiral lasers [7, 8] and (c) effects occuring when $\alpha k_0 = p$, i.e. the effects of optical activity are offset by structural chirality.

References

[1] C. Bohren, *Introduction to Complex Mediums for Optics and Electromagnetics*. SPIE, 2003, ch. 3: Isotropic Chiral Materials.

[2] A. Lakhtakia and R. Messier, *Sculptured Thin Films: Nanoengineered Morphology and Optics*. Bellingham, WA: SPIE Optical Engineering Press, 2005.

[3] M. W. McCall, "Simplified theory of axial propagation through structurally chiral media," *Journal of Optics A: Pure and Applied Optics*, vol. 11, p. 074006, 2009.

[4] E. M. Sanchez-Carnerero, F. Moreno, B. L. Maroto, A. R. Agarrabeitia, M. J. Ortiz, B. G. Vo, G. Muller, and S. d. l. Moya, "Circularly polarized luminescence by visible-light absorption in a chiral o-bodipy dye: unprecedented design of cpl organic molecules from achiral chromophores," *Journal of the American Chemical Society*, vol. 136, no. 9, pp. 3346–3349, 2014.

[5] J. R. Brandt, X. Wang, Y. Yang, A. J. Campbell, and M. J. Fuchter, "Circularly polarized phosphorescent electroluminescence with a high dissymmetry factor from pholeds based on a platinahelicene," *Journal of the American Chemical Society*, vol. 138, no. 31, pp. 9743–9746, 2016.

[6] Y. Yang, R. C. Da Costa, M. J. Fuchter, and A. J. Campbell, "Circularly polarized light detection by a chiral organic semiconductor transistor," *Nature Photonics*, vol. 7, no. 8, p. 634, 2013.

[7] R. D. M. Topf and M. W. McCall, "Modes of structurally chiral lasers," *Phys. Rev. A.*, vol. 90, p. 053824, 2014.

[8] H. Coles and S. Morris, "Liquid-crystal lasers," *Nature Photonics*, vol. 4, no. 10, p. 676, 2010.

Controlling the plasmon resonance of an Au/Ni hybrid nanostructures using external magnetic field or temperature

Silvère Schuermans[1], Thomas Maurer[1], Alexander Govorov[2], and Jérôme Plain[1]

[1]L2n/ICD, University of technology of Troyes and CNRS, France
[2] Ohio University, Department of Physics and Astronomy, Clippinger Research Labs , Athens OH 45701
*corresponding author, E-mail: jerome.plain@utt.fr

Abstract

We report on the fabrication of plasmonic hybrid Ni-Au nanoantennas. The optical properties of such nanostructure depend on the applied magnetic field and/or the temperature. Thus, we tune under control the plasmon resonance using external stimuli.

1. Introduction

Over the past two decades, metallic nanoparticles have attracted increasing interest because of their varied and complex optical properties. These properties are mainly governed by the collective oscillations of conduction electrons called "plasmons". In particular, the excitation of the latter by optical fields leads to a local exaltation of the electromagnetic field on the surface of the nanoparticle. This very intense nanosource makes it possible to envisage nanometric optical concepts by controlling, manipulating and amplifying light at this scale. In recent years, a new challenge is the control and manipulation of optical properties using an external stimulus [1,2]. In this context, we developed Ni-Au plasmonic nanoantennas which exhibit an optical response that can be modulated either by the application of an external magnetic field or by a change in temperature.

2. Results and discussion

We realized Au/Ni nanorods with different aspect ratio though a top-down approach (e-beam lithography and metal evaporation). Then, the localized surface plasmon resonances of the different nanostructures have been studied using extinction spectroscopy under an applied magnetic field or a local increase of the temperature.
In both cases, the LSPR present a clear red shift of about 10 to 20nm for an applied magnetic field (see figure 1) and up to 100nm for a local increase of the substrate temperature (see figure 2). The two process are clearly different. In the case of the magnetic field, one can understand the red-shift as a deviation of the electrons path due to the creation of a Lorentz force.

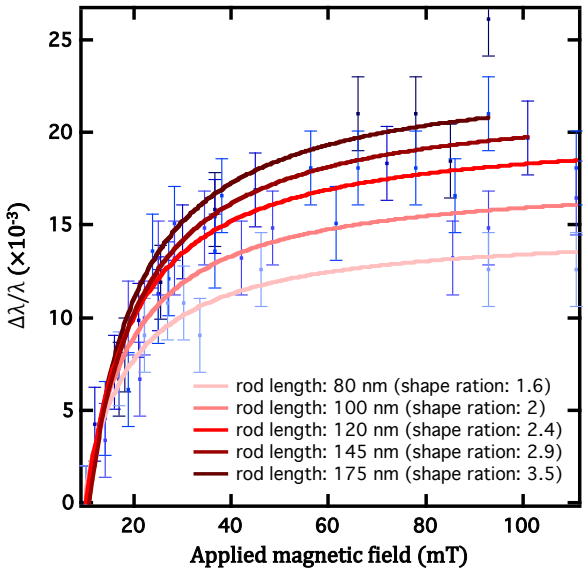


Figure 1: Relative shift of the plasmon resonance as a function of the applied magnetic field. The LSPR maximum are comprised between 600nm and 700nm.

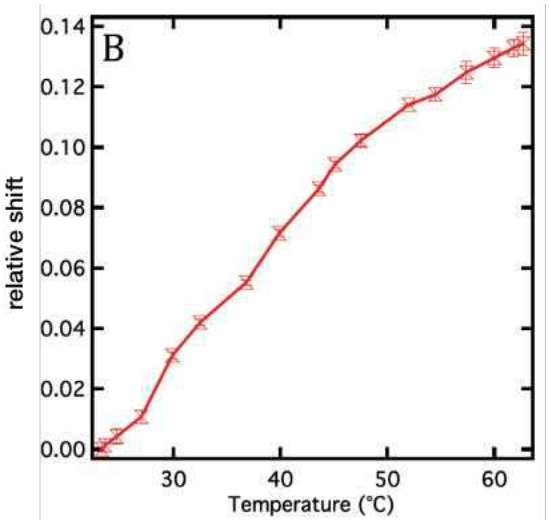


Figure 2: Relative shift of the plasmon resonance as a function of the substrate temperature for nanorods with an aspect ratio of 2.5. The LSPR is situated around 650nm.

In the case of the temperature, the LSPR-shift is directly correlated with the change of the dielectric functions of the metals.

3. Conclusions

In summary, we demonstrate the possibility to tune under control the plasmon resonance of hybrid Ni/Au nanorods though an applied magnetic field or a local control of the temperature.

Acknowledgements

This work has been supported by the EIPHI Graduate School (contract "ANR-17-EURE-0002"). Financial supports of Nano'Mat (www.nanomat.eu) by the "Ministère de l'enseignement supérieur de la recherche et de l'innovation", the " region Grand-Est", the "FEDER fund", and the "Conseil départemental de l'Aube" are acknowledged. We also acknowledge support from the CNRS and the Agence Nationale de la Recherche (ANR) under the HYNNA, TWINS, NATO and SMFluona grants.

References

[1] Berthelot J. et al. "Tuning of an Optical Dimer Nanoantenna by Electrically Controlling Its Load Impedance », *Nanoletters*, Vol. 9, No 11, 3914–3921, 2009.
[2] Zhou X. et al. "Two-Color Single Hybrid Plasmonic Nanoemitters with Real Time Switchable Dominant Emission Wavelength", *Nanoletters,* Vol.15, No 11, 7458–7466, 2015.

Nonlocal effects in piezoelectromagnetic metamaterials

Anatolii Konovalenko, Felipe Pérez-Rodríguez*

Instituto de Física, Benemérita Universidad Autónoma de Puebla, Puebla, Pue., 72570, México
*corresponding author, E-mail: fperez@ifuap.buap.mx

Abstract

A homogenization theory for calculating the nonlocal effective parameters of piezolectromagnetic crystals with any inclusion form and arbitrary Bravais lattice is proposed. The theory allows to describe the bulk photonic-phononic band structure even beyond the long wavelength limit. Applying the method of expansion into bulk modes, the theory can be used to study the propagation of coupled electromagnetic and sound waves in finite-size piezoelectromagnetic metamaterials.

1. Introduction

Homogenized photonic crystals (PC), i.e. photonic metamaterials have been studied intensively over the last three decades because of their extraordinary optical properties, which can be described by using effective parameters at wavelengths larger than the lattice constant. At present, there exist several homogenization methods, which can be applied to calculate the effective parameters of metamaterials (see, for example, [1, 2, 3] and references therein). Among them, the general homogenization theory [4], which is based on the Fourier formalism, provides explicit formulas for determining all the components of bianisotropic response tensors - the effective permittivity, permeability and crossed magneto-electric tensors for arbitrary Bravais lattice and shape of the inclusions. Besides, such a homogenization theory can also be applied at high frequencies where the bianisotropic response becomes nonlocal, i.e. the effective parameters depend on both frequency ω and Bloch wave vector $\mathbf{k}$. An important characteristic of the nonlocal homogenization approach (NHA) is associated with the fact that the effective parameters describe the photonic band structure even beyond the long wavelength limit. Nevertheless, the application of the homogenization theory [4] still requires the inversion of very large matrices and, consequently, a very long computing time. To make feasible the calculations of the effective bianisotropic-response tensors, an approach based on the form-factor division (FFDA) to get highly accurate results at any filling fraction of the inclusions and arbitrary forms of the inclusion, was proposed in Ref. [6]. As is shown there, the NHA can be complemented with the method of expansion into bulk modes (MEBM) to calculate and interpret optical spectra of finite-size regular structures.

Phononic crystals are periodic structures composed of materials with different mass density and elastic parameters. As in the case of homogenized photonic crystals, at sufficiently long wavelengths, the phononic one can be considered as a homogeneous medium, whose elastic properties are described by employing effective parameters such as the effective mass density and the effective compliance tensor. In the work [5], a very general homogenization theory for describing the propagation of sound waves in three-dimensional solid phononic crystals (SPC) was proposed. The theory is based on the Fourier formalism and provides explicit expressions for the effective mass density and compliance tensors of phononic crystals with arbitrary inclusion form and Bravais lattice. As is was shown in [5], in the quasi-static case, rectangular two-dimensional lattices of water-filled holes in an elastic host matrix behave as metasolids since they exhibit solid-like behavior with strongly anisotropic mass density in the low-frequency limit. The homogenization approach [5] was recently applied [6] to calculate the nonlocal effective parameters, namely mass density and stiffness tensor, for 3D solid phononic crystals, using the FFDA. With the calculated effective elastic parameters, the phononic band structure of the phononic crystal can be described not only in the long wavelength limit, but also beyond it. In addition, it was shown that the anisotropy in the effective dynamic mass-density, appearing at sufficiently large frequencies, is associated with the dependence of the nonlocal metasolid response on the phononic-mode polarization, form of the inclusions, and type of the periodic array.

2. Piezoelectromagnetic metamaterials

Here, we shall introduce a homogenization theory to calculate the effective parameters of periodic structures composed of both piezoelectric and piezomagnetic materials. The theory is based on the Fourier formalism and considers any inclusion shape, arbitrary Bravais lattice, and any linear coupling between electrodynamic and elastic properties of the components. Within the proposed homogenization procedure, we have derived explicit expressions for all the components of the effective response matrix given by the effective bianisotropic ($\overleftrightarrow{\epsilon}$, $\overleftrightarrow{\mu}$, $\overleftrightarrow{\gamma}$, $\overleftrightarrow{\delta}$), mass-density ($\overleftrightarrow{\rho}$), compliance ($\overleftrightarrow{S}$), piezoelectric ($\overleftrightarrow{e}$) and piezomagnetic ($\overleftrightarrow{d}$)

tensors:

$$\overline{\overline{A}}_{\text{eff}} \equiv \begin{bmatrix} \overleftrightarrow{\rho} & 0_{3\times 6} & 0_{3\times 3} & 0_{3\times 3} \\ 0_{6\times 3} & \overleftrightarrow{S} & \overleftrightarrow{S}\cdot\overleftrightarrow{e}^{T} & \overleftrightarrow{S}\cdot\overleftrightarrow{d}^{T} \\ 0_{3\times 3} & \overleftrightarrow{e}\cdot\overleftrightarrow{S} & \overleftrightarrow{\epsilon}' & \overleftrightarrow{\gamma}' \\ 0_{3\times 3} & \overleftrightarrow{d}\cdot\overleftrightarrow{S} & \overleftrightarrow{\delta}' & \overleftrightarrow{\mu}' \end{bmatrix}, \quad (1)$$

In the case when there is no coupling between the electromagnetic and elastic responses, the matrix blocks, corresponding to the bianisotropic, mass-density, and compliance tensors go over into the expressions, which were derived in the works [4, 5], respectively. The effective response of the homogenized piezoelectromagnetic crystal (piezoelectromagnetic metamaterial) is nonlocal because the components of the effective matrix depend on both the Bloch wave vector and the frequency. Using the FFDA, we have applied the nonlocal homogenization approach to specific piezoelectromagnetic crystals. In particular, their photonic-phononic band structure is described even beyond the long wavelength limit, where the nonlocal effects are well manifest. Moreover, we show how the proposed NHA for piezoelectromagnetic crystals and the MEBM can be applied to calculate and interpret optical and acoustical spectra of finite-size piezolectromagnetic metamaterials.

Acknowledgement

This work was partially supported by CONACyT, VIEP-BUAP, and PFCE.

References

[1] D.R. Smith, J.B. Pendry, Homogenization of metamaterials by field averaging (invited paper), *J. Opt. Soc. Am. B* 23: 391–403, 2006.

[2] M.G. Silveirinha, Nonlocal homogenization model for a periodic array of ϵ-negative rods, *Phys. Rev. E* 73: 046612, 2006.

[3] P. Halevi, A. Krokhin, J. Arriaga, Photonic Crystal Optics and Homogenization of 2D Periodic Composites, *Phys. Rev. Lett.* 82: 719, 1999.

[4] V. Cerdán-Ramírez, B. Zenteno-Mateo, M.P. Sampedro, M.A. Palomino-Ovando, B. Flores-Desirena, F. Pérez-Rodríguez, Anisotropy effects in homogenized magnetodielectric photonic crystals, *J. Appl. Phys.* 106: 103520, 2009.

[5] J. Flores-Méndez, F. Pérez-Rodríguez, Metasolid with anisotropic mass density, *EPL* 103: 54001, 2013.

[6] A. Konovalenko, F. Pérez-Rodríguez, Nonlocal response of tunable photonic metamaterials with semiconductor inclusions, *J. Opt. Soc. Am. B* 34: 2031–2040, 2017.

Electromagnetic Sink Based on a Nonreciprocal Metasurface Cavity

Mojtaba Dehmollaian[1*], Guillaume Lavigne[2], and Christophe Caloz[2]

[1]School of Electrical and Computer Engineering, University of Tehran, Iran
[2]Poly-Grames Research Center, Polytechnique Montréal, Montreal, Quebec, Canada
*corresponding author, E-mail: m.dehmollaian@ut.ac.ir

Abstract

This paper proposes a nonreciprocal bianisotropic metasurface cavity to absorb the electromagnetic radiation of a given illumination. Using Generalized Sheet Transition Conditions (GSTCs), it first synthesizes the bianisotropic susceptibility tensors, corresponding to specifications. Next, it employs combined Integral Equations (IEs) and GSTCs to compute the wave scattering by the cylindrical metasurface cavity. Finally, it presents results for a circular cylindrical metasurface cavity illuminated by a plane wave, which reveal that the fields inside the cavity are exactly those of a waveguide mode at its cutoff frequency and that a shadow area appears on the backside of the cavity.

1. Introduction

Metasurfaces represent a vast field of exploration for new electromagnetic concepts and applications. A recent overview of them is presented in [1].

Nonreciprocal ferrite components are costly, heavy, incompatible with integrated circuit technology, and require a cumbersome biasing magnet. Recently, there has been a number of attemps to realize magnetless nonreciprocal components [2]. For instance, Kodera and Caloz introduced in [3] a transistor load ring metamaterial mimicking ferrites at microwaves which exhibits the main properties of ferrites including Faraday rotation. Such a "metaferrite", enables novel electromagnetic effects and applications.

Confining electromagnetic energy in a small region of space is of significant importance in many areas of science and technology. Such an operation of light trapping has been presented in [5] and [4] by leveraging nonlinearity. Paper [4] suggests a mechanism to store light in an open core-shell plasmonic structure ('meta-atom') with a nonlinear optical response, where the tarpped light energy can be pumped with a plane wave excitation [5].

Here, we present the idea of electromagnetic wave trapping using a *linear* nonreciprocal metasurface cavities based on metaferrite technology. This device operates as an efficient sink for electromagnetic energy.

2. Concept

Figure 1 shows the proposed concept of a nonreciprocal linear bianisotropic metasurface cavity that absorbs and traps electromagnetic radiation from an illuminating plane wave.

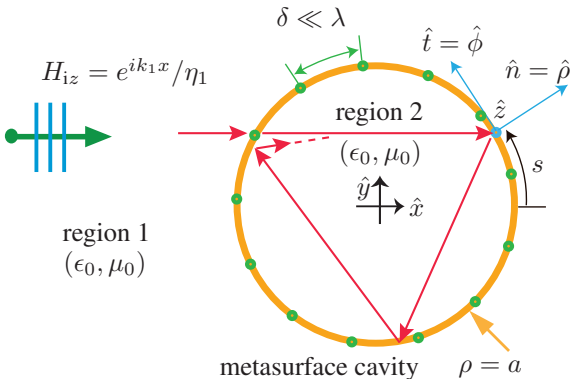


Figure 1: Nonreciprocal bianisotropic metasurface cavity that absorbs electromagnetic radiation and stores the corresponding energy. The waves perfectly penetrate into the cavity but are then trapped in it.

This is accomplished by a nonreciprocal penetrable metasurface cavity that allows full-transmission from outside to inside while fully reflecting inside energy.

The metasurface consists of subwavelength scatterers, that are separated by a distance much smaller than the wavelength. Electromagnetic rays perfectly penetrate into the metasurface cavity from outside to inside. However, the rays inside it can not get outside and are trapped inside the cavity.

2.1. Nonreciprocal Metasurface

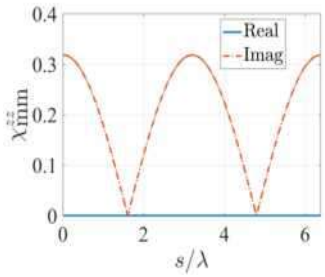
We use the Generalized Sheet Transition Conditions (GSTCs) to model metasurfaces. The harmonic ($e^{-i\omega t}$) GSTCs are [1]

$$\hat{n} \times \Delta\vec{E} = ik_0 \overline{\overline{\chi}}_{\text{me}\,\parallel} \cdot \vec{E}_{\parallel,\,\text{av}} + ik_0\eta_0 \overline{\overline{\chi}}_{\text{mm}\,\parallel} \cdot \vec{H}_{\parallel,\,\text{av}}, \quad \text{(1a)}$$

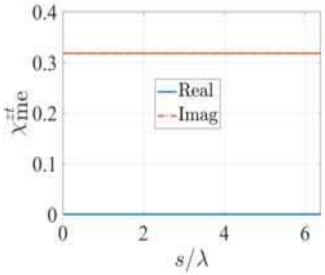
$$\hat{n} \times \Delta\vec{H} = -ik_0 \overline{\overline{\chi}}_{\text{ee}\,\parallel} \cdot \vec{E}_{\parallel,\,\text{av}}/\eta_0 - ik_0 \overline{\overline{\chi}}_{\text{em}\,\parallel} \cdot \vec{H}_{\parallel,\,\text{av}}, \quad \text{(1b)}$$

where Δ denotes the difference of the fields at both sides of the metasurface, and $\overline{\overline{\chi}}_{\text{me}}$, $\overline{\overline{\chi}}_{\text{mm}}$, $\overline{\overline{\chi}}_{\text{ee}}$ and $\overline{\overline{\chi}}_{\text{em}}$ are the electric-to-magnetic, magnetic-to-magnetic, electric-to-electric and magnetic-to-electric surface susceptibilitiy tensors, respectively, and where "av" denotes the average of the fields at both sides of the metasurface [1].

Here, we assume that the metasurface has only transverse electric and magnetic surface polarization densities.



(a)



(b)

Figure 2: Nonreciprocal bianisotropic susceptibilities (a) χ^{zz}_{mm} and (b) χ^{zt}_{me}.

For the case in Fig. 1 where the illuminating field is a TE_z plane wave only χ^{tt}_{ee}, χ^{tz}_{em}, χ^{zt}_{me}, and χ^{zz}_{mm} are excited and the other susceptibilities are hence set to zero. We use two transformations to synthesize these susceptibilities. In the 1st transformation for a fixed incidence angle we enforce full transmission from region a to region b, while in the 2nd transformation, we set zero transmission from regions b to a. We then synthesize the bianisotropic susceptibilities using the GSTCs. We further assume that the magnetic specular reflection coeffieient in the 2nd transformation is -1, then $\chi^{tt}_{\text{ee}} = 0$ and $\chi^{tz}_{\text{em}} = 0$ while χ^{zt}_{me} and χ^{zz}_{mm} are nonzero.

3. Full-Wave Illustration

We compute the scattering of waves by the cylindrical metasurface cavity using the synthesized susceptibilities of the previous section and the combined GSTCs and integral equations method presented in [6].

Corresponding results are shown in Fig. 2 and Fig. 3 for a cylinder of radius $a = X_{31}/k_0$, where $X_{31} = 6.3802$ is the first root of the Bessel function of first kind and 3rd order. Figures. 2(a) and (b) plot χ^{zz}_{mm} and χ^{zt}_{me} versus position along the metasurface cavity. Inserting these susceptibilities into the IEs provides the magnetic field shown in Fig. 3 which perfectly exhibits the field distribution of the TE_{31} mode of a circular waveguide at its cutoff frequency inside the cavity and the expected shadow area at the back of the cavity.

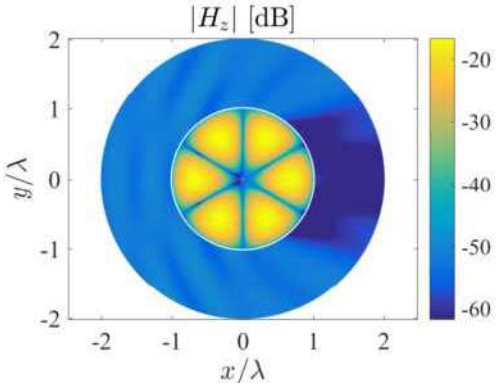


Figure 3: Magnitude of the total magnetic field inside and outside of the metasurface cavity.

4. Conclusions

We presented the concept of electromagnetic wave trapping by a linear nonreciprocal metasurface cavity. The idea is to use a nonreciprocal penetrable metasurface cavity that allows full-transmission from outside to inside while reflecting all energy from inside. This structure leverages metasurface technology to creat a device that sinks electromagnetic energy. We illustrated the concept with results for a circular-cylindrical metasurface, which revealed that the fields inside the cavity are exactly those of a circular waveguide mode and that a shadow area appears at the backside of the cavity, as expected.

References

[1] K. Achouri and C. Caloz, Design, Concepts, and Applications of Electromagnetic metasurfaces, *Nanophotonics*, vol. 7, no. 6, pp. 1095-1116, 2018.

[2] T. Kodera and C. Caloz, Unidirectional loop metamaterials (ULM) as magnetless artificial ferrimagnetic materials: principles and applications, *IEEE Antennas Wirel. Propag. Lett.*, vol. 17, no. 11, pp. 1943-1947, 2018.

[3] T. Kodera, D. L. Sounas, and C. Caloz, Artificial Faraday rotation using a ring metamaterial structure without static magnetic field, *Appl. Phys. Lett.*, vol. 99, no. 3, Jul. 2011, 031114.

[4] S. Lannebère, and M. G. Silveirinha, Optical meta-atom for localization of light with quantized energy, *Nat. Commun.*, vol. 6, no. 8766, Oct. 2015.

[5] S. Silva, T. A. Morgado, and M. G. Silveirinha, Discrete light spectrum of complex-shaped meta-atoms, *Radio Sci.*, vol. 53, no. 2, Feb. 2018.

[6] M. Dehmollaian, N. Chamanara, and C. Caloz, Wave scattering by a cylindrical metasurface cavity of arbitrary cross-section: theory and applications, *arXiv preprint arXiv:1808.09530*, 2018.

META2019 - Symposium IV: Chirality, magnetism, and magnetoelectricity: Separate phenomena and joint effects in metamaterial structures

SIMPLE SPINTRONICS AND SUPERCONDUCTING SPINTRONICS, BASED ON THE CHIRAL INDUCED SPIN SELECTIVITY (CISS) EFFECT

Yossi Paltiel

Applied Physics Department and the Center for Nano science and Nanotechnology, Hebrew University, Jerusalem 91904, Israel

With the increasing demand for miniaturization, nano-structures are likely to become the primary components of future integrated circuits. Different approaches are being pursued towards achieving efficient electronics, among which are spin electronics devices (spintronics). In principle, the application of spintronics should result in reducing the power consumption of electronic devices. A new, promising, effective approach for spintronics has emerged using spin selectivity in electron transport through chiral molecules, termed Chiral-Induced Spin Selectivity (CISS). Studying the CISS effect it was found that chiral molecules, and especially helical ones, can serve as very efficient spin filters.[1, 2]

Recently, by utilizing this effect we demonstrated a magnet less spin based magnetic memory.[3] The presented technology has the potential to overcome the limitations of other magnetic-based memory technologies to allow fabricating inexpensive, high-density universal and embedded memory-on-chip devices.[4] We have shown that the memory device can work at ambient temperatures and scaled sown to 30nm.[5,6] To further enhance efficiency, we also investigated the interface between superconducting thin films and the magnetic layers improving and simplifying superconducting spintronics devices.[7,8]

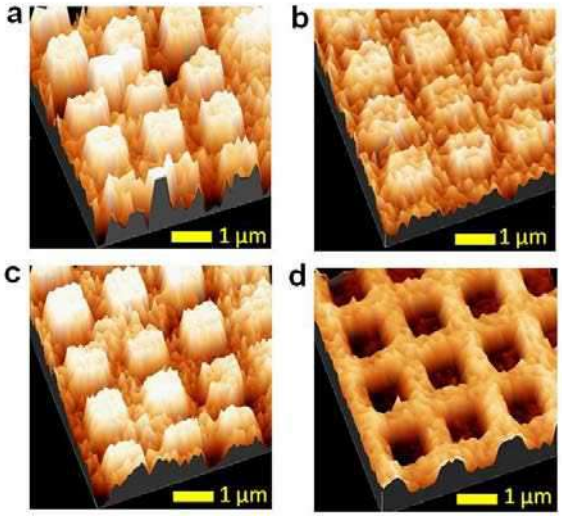


Fig. 1 | Topography and magnetic phase MFM images of a molecular induced magnetization orientation. AFM topography images of SAMs of AHPA-L **(a)** and AHPA-D **(b)** adsorbed on FM Co thin layers coated with a 5nm Au over-layer and their corresponding MFM molecular induced magnetic phase images of AHPA-L **(c)** and AHPA-D **(d)** magnetization orientation.

[1] B. Göhler,V. Hamelbeck, T.Z. Markus, M. Kettner, G.F. Hanne, Z. Vager, R. Naaman, H. Zacharias, "Spin Selectivity in Electron Transmission Through Self-Assembled Monolayers of dsDNA" *Science* **331,** 894-897 (2011).

[2] K. B. Ghosh, O. Ben Dor, F. Tassinari, E. Capua, S. Yochelis, A. Capua, S.-H. Yang, S. S. P. Parkin, S. Sarkar, L. Kronik, L. T. Baczewski, R. Naaman, and Y. Paltiel; Enantio-Specific Interaction of Chiral Molecules with Magnetic Substrates; *Science* 10.1126/science.aar4265 (2018).

[3] O. Ben Dor, S. Yochelis, S. P. Mathew, R. Naaman, and Y. Paltiel "A chiral-based magnetic memory device without a permanent magnet" *Nature Communications* **4**, 2256 Highlighted in Nature Nanotechnology: "A memory device with a twist" 7.8.2013

[4] O. Ben Dor, N. Morali, S. Yochelis and Y. Paltiel "Local Light-Induced Magnetization Using Nanodots and Chiral Molecules" *Nano Letters* **14** 6042 (2014).

[5] G. Koplovitz, D. Primc, O. Ben Dor, S. Yochelis, D. Rotem, D. Porath, and Y. Paltiel; Magnetic nano platelets based memory device operating at ambient temperatures Advanced Materials **29** 1606748 (2017).

[6] H. Al Bustami, G. Koplovitz, D. Primc, S. Yochelis, E. Capua, D. Porath, R. Naaman, and Y. Paltiel Single Nanoparticle Magnetic Sn Memristor; *Small* **14** 1801249 (2018).

[7] H. Alpern, E. Katzir, S. Yochelis, Y. Paltiel, and O. Millo, Unconventional superconductivity induced in Nb by adsorbed chiral molecules *New J. Phys*. 18 113048 (2016).

[8] T. Shapira, H. Alpern, S. Yochelis, T. K. Lee, C. C. Kaun, Y. Paltiel, G. Koren, and O. Millo; Unconventional order parameter induced by helical chiral molecules adsorbed on a metal proximity-coupled to a superconductor *Physical Review B* (2018).

e-mail: Paltiel@mail.huji.ac.il

Topological Magnonic Materials and Devices

Xiangrong Wang

Physics Department, The Hong Kong University of Science and Technology, Clear Water Bay, Kowloon, Hong Kong
and HKUST Shenzhen Research Institute, Shenzhen 518057, China

*corresponding author, E-mail: phxwan@ust.hk

Abstract

I will discuss several topological magnonic materials. The edge spin waves in these magnonic materials are robust against perturbations. Functional magnonic devices such as beamsplitter and interferometer can be made out of domain walls in a strip. It is shown that an incoming spin wave beam along one strip edge splits into two spin wave beams propagating along two opposite directions on the other strip edge after passing through a domain wall.

1. Introduction

Topological matters have attracted enormous attention in recent years because of their interesting and exotic properties. One such property is the existence of unidirectional and topologically protected surface/edge states that are robust against internal and external perturbations. The study was initially exclusive for electron systems and was believed to be a quantum phenomenon. It is now known that the topological states can exist in classical mechanics and photonics. Topological states can also exist in magnetic materials govern both by quantum mechanics at the zero temperature and by classical magnetization dynamics at finite temperatures.

2. Discussion

Magnetic materials are highly correlated spin systems that do not respect the time-reversal symmetry. The low-energy excitations of magnetic materials are spin waves whose quanta are magnons. In the ambient temperature, the magnetization dynamics of real magnetic material shall be govern by the Landau- Landau-Lifshitz-Gilbert (LLG) equation. Like electronic materials that can be topologically nontrivial, magnetic materials govern by the LLG equation can also be topologically nontrivial with topologically protected edge spin waves. Unlike the normal spin waves that are very sensitive to the system changes and geometry, these edge spin waves are robust against internal and external perturbations such as geometry changes and spin wave frequency change. Therefore, the magnetic topological matter is of fundamental interest and technologically useful in magnonics.

3. Conclusions

We will see several examples of magnonic topological materials, including pyrochlore [1] and stacked honeycomb [2] ferromagnets as Weyl magnons, as well as perpendicularly magnetized two-dimensional films with Dzyaloshinskii-Moriya and/or pseudodipolar interactions as generic magnonic insulators [3,4]. The edge spin waves in these magnonic materials are robust against perturbations. Interesting reconfigurable functional magnonic devices called beamsplitter and interferometer can be made out of domain walls in a strip. It is shown that an in-coming spin wave beam along one edge splits into two spin wave beams propagating along two opposite directions on the other edge after passing through a domain wall.

Acknowledgements

This work was supported by the National Natural Science Foundation of China (Grant No. 11774296) and the Hong Kong RGC (Grants No. 16300117 and No. 16301518).

References

[1] Ying Su, X.S. Wang, and X.R. Wang, “Magnonic Weyl semimetal and chiral anomaly in pyrochlore ferromagnets”, Phys. Rev. B 95 (22), 224403 (2017).

[2] Ying Su and X. R. Wang, “Chiral anomaly of Weyl magnons in stacked honeycomb ferromagnets", Phys. Rev. B 96, 104437 (2017).

[3] .X.S. Wang, Ying Su, and X.R. Wang, “Topologically protected unidirectional edge spin waves and beam splitter”, Phys. Rev. B 95 (1), 014435 (2017).

[4] X. S. Wang, H. W. Zhang, and X. R. Wang, “Reconfigurable topological spin wave beamsplitters and interferometers”, Phys. Rev. Appl. 9, 024029 (2018).

Chirality and Anti-ferromagnetism in Artificial Micro-/Nano-Structures

Kun Huang[1, *]

[1]Department of Optics and Optical Engineering, University of Science and Technology of China, Hefei, China
*corresponding author, E-mail: huangk17@ustc.edu.cn

Abstract

The light-matter interaction is usually dominated by the coupling between microscopic electromagnetic modes and the geometry of structures. In this talk, the roles of chiral light in enhancing the helical dichroism and exciting anti-ferromagnetic modes will be introduced. Direct detection of chiral microstructures is implemented by using sign-opposite twisted vortices. High-efficiency polarization conversion in dielectric geometric metasurfaces is also interpreted in terms of microscopic antiferromagnetic modes induced by chiral circular-polarized light.

1. Introduction

Chirality is a common feature in nature and exists in many areas such as human hands, bilateral pictures in arts. In optics, the chirality of light also plays an important role in the light-matter interaction. The optical chirality usually refers to the circularly polarized light and the optical vortex beams with sign-opposite wavefronts. The circularly polarized light has the upward and downward spins, which can be used to detect the chiral objects or artificial structures with birefringence. For example, most molecules are chiral so that their transmission under the illumination of circularly polarized (CP) light depends on the spins of incident light, which induces the so-called circular dichroism (CD). However, the CD interaction is quite weak because the scale of molecules is much smaller than the operating wavelength. Although the optical vortices have been used to detect the chirality of structures[1], it fails due to the scale mismatch between optical vortex modes and electromagnetic multiple modes supported by molecules. It indicates that the supporting modes in nanostructures or nanoobjects play the important roles in the interaction with light[2]. A strong interaction requires the nearly perfect match between microscopic modes and the probe light. It is valid in the entire nanophotonics that focus on the interaction between light and artificial nanostructures. In a dielectric nanorod, the supporting modes could be taken as a coherent superposition of different-order electromagnetic dipoles[3]. When designed properly, the nanorod could work as a nanoscale half-waveplate (HWP) to convert one spin of a CP light beam into the other, which is quite useful in metasurfaces that refer to the subwavelength-pixel diffractive optics[4]. Although it is well-known that the microscopic electromagnetic modes are important during this process, the detailed roles are still not recognized comprehensively. So, the work will focus on these two problems: 1) the strong dichroism of helical objects interacted with vortex beams; 2) the microscopic interpretation of dielectric nano-halfwaveplates by using antiferromagnetic modes.

2. Strong helical dichroism

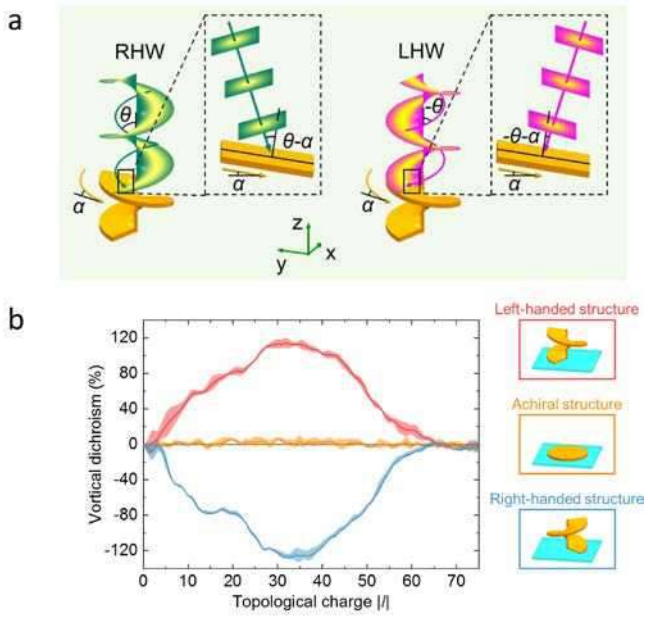


Figure 1. (a) Illustration of OAM beams with RHW (left panel) and LHW (right panel) illuminating on a chiral structure. (b) Vortical dichroism measurements of chiral microstructures.

Inspired by the scale match, we investigate the strong interaction that is induced by introducing the optical vortex beams and the artificially designed chiral micro-structures with its dimension comparable to the diameter of focused vortex beams by a high-NA objective[5]. The sketch of such an interaction is shown in Figure 1a. The Poynting vector (green and magenta arrows) screws around the beam axis. The helical angle of Poynting vector for right- (or left) handed helical wavefront and chiral structure are θ (-θ), and α, respectively. The insets in the Fig. 1 illustrate two slant plane waves illuminating on a sloped sheet by unfolding the

helical wavefront and chiral structure. Figure 1b shows our observed results, which show symmetric distribution of vertical dichroism (VD) between two chiral microstructures with opposite handedness. The grey straight line indicates VD=0 for guide-to-the-eye. The solid lines represent the mean values; shading indicates the standard deviation of a set of three measurements with the same sample. One can see that the VD is 120%, which is enhanced by 200 times compared with the previous results.

3. Anti-ferromagnetic modes in dielectric nano-HWPs

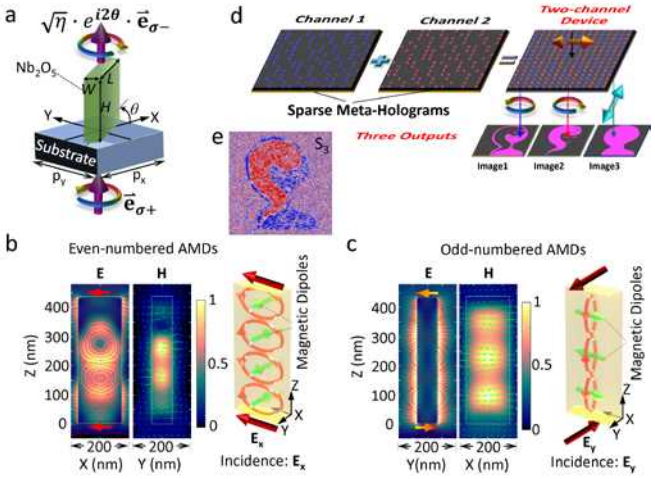


Figure 2. (a) Sketch of a cell unit with the dimension of p_x=p_y=250nm. (b-c) Antiferromagntic mode with even- and odd-numbered anti-parallel magnetic dipoles. (d) Ultra-channel holograms. (e) Vector holographic image.

Geometric dielectric metasurfaces made of spatially rotating nanorods could be used to tune the phase of transmitted light with its polarization cross to the incident one, as sketched in Fig. 2a. A detailed simulation about the induced electromagnetic modes within the nanorod is provided in Figs. 2b and 2c. For the E_x component, its induced electric fields contain four circle displacement currents with the alternative clockwise and anti-clockwise directions, which are relative to four antiparallel magnetic dipoles (AMDs) that are vertically located along the z axis. In such antiferromagnetic modes, the even circle currents orientate both electric vectors of light at the incident (bottom) and output (top) ends of the nanobrick towards the same direction (see Figure 2b). It implies that the x-component of the incident CP light is maintained after passing through nanobricks. However, for the E_y component, an antiferromagnetic mode with three AMDs is induced, so that these odd circle displacement currents make the electric vector of the transmitted light inverse to that of incident light (Figure 2b), indicating a phase delay of π. Differing from the birefringent effects in traditional HWPs and the electric dipole response in plasmonic nano-HWPs, the antiferromagnetic modes with the AMDs provide an alternative approach to investigate the dielectric nano-HWPs.

Finally, as a proof-of-concept demonstration of ultraviolet vectorial anticounterfeiting, we design and fabricate an ultra-channel meta-hologram that encodes two spin-channel sparse holograms (Fig. 2d) while generates three diffrent images with polarization features (Fig. 2e), which provides a new approach for optical encryption and security.

4. Conclusions

In summary, we have introduced the strong vortical dichroism induced by the micro-structure and optical vortices with an enhancement of around 200 times. The roles of antiferromagnetic modes in dielectric nano-halfwaveplates have also been investigated and shown that it holds the fundamental origin of polarization conversion from one circular polarization to its cross.

Acknowledgements

K. H. thanks the support from Dr. J.C. Ni, Dr. H. S. Leong, Prof. Dong Wu, Dr. Hong Liu, Dr. Jie Deng, Prof. Yanlei Hu and other collaborators involved in this work. K. H. thanks the support from CAS Poineer Hundred Talents Program， “the Fundamental Research Funds for the Central Universities” in China, and the National Natural Science Foundation of China (Grant No. 61875181 and 61705085).

References

[1].W. Löffler, D. Broer, and J. Woerdman, Circular dichroism of cholesteric polymers and the orbital angular momentum of light. *Physical Review A*, 83: 065801,2011.

[2].K. Huang, Z. Dong, S. Mei, L. Zhang, Y. Liu, H. Liu, H. Zhu, J. Teng, B. Luk'yanchuk, and J.K. Yang, Silicon multi - meta - holograms for the broadband visible light. *Laser Photonics Rev.* , 10: 500-509,2016.

[3].K. Huang, J. Deng, H.S. Leong, S.L.K. Yap, R.B. Yang, J. Teng, and H. Liu, High-Efficiency Ultra-Violet Dielectric Meta-Holograms with Antiferromagnetic Resonances. *arXiv preprint arXiv:1806.03131*,2018.

[4].L. Zhang, S. Mei, K. Huang, and C.-W. Qiu, Advances in Full Control of Electromagnetic Waves with Metasurfaces. *Adv. Opt. Mater.* , 4: 818-833,2016.

[5].J. Ni, Z. Wang, Z. Lao, Y. Hu, K. Huang, S. Ji, J. Li, Z. Huang, D. Wu, and C. Qiu, Ultra-sensitive Experimental Detection of Chiral Meso-structures by Orbital Angular Momentum of Light. *arXiv preprint arXiv:1809.02754*,2018.

Generation and Propagation of Surface-Plasmon Polaritons at Lossy Interfaces

Nafiseh Sang-Nourpour[1,2], Saeid Asgarnezhad-Zorgabad[1,3], and Barry C. Sanders[1,*]

[1]Institute for Quantum Science and Technology, University of Calgary, Calgary, Alberta, Canada
[2]Department of Mechanical Engineering, University of Alberta, Edmonton, Alberta, Canada
[3]Department of Physics, Sharif University of Technology, Tehran, Iran
*corresponding author, E-mail: sandersb@ucalgary.ca

Abstract

We study surface-plasmon polaritons (SPPs) for lossy isotropic media, with the plasmon concept applicable both to metals and to double-negative-index media, and apply this framework to generate, propagate and control linear/nonlinear SPPs. We derive SPP propagation conditions along planar and curved interfaces and study controllable propagation of SPP breathers and creation of polaritonic frequency combs at interfaces between an atomic medium and metamaterials. Our results are important for subwavelength photonic-circuit elements such as SPP phase modulators and frequency-comb generators.

1. Introduction

Linear and nonlinear SPPs [1] are valuable in miniaturized photonic circuits [2] with applications to sensing, waveguiding [3], switching and modulating [4]. SPPs arise at dielectric-metal interfaces [2], and effective SPPs arise as well at the interface between a dielectric and a double-negative-index (DNI) metamaterial; metal is a single-negative-index (SNI) medium, and a dielectric is a double-positive-index (DPI) medium. The DNI metamaterial can be regarded as being a doubly plasmonic DNI medium [5], based on interpreting the metamaterial as comprising free-moving electric and magnetic charges (monopoles) [6].

Generating and controlling linear and nonlinear SPPs is challenging due to dependence on material properties at the interfaces, including linear and nonlinear electromagnetic (EM) susceptibilities and surface roughness [7]. We address this design problem by developing a framework that accounts for lossy isotropic media, including materials and metamaterials, and use this framework to design schemes for exciting and propagating linear and nonlinear SPPs. Such capabilities could advance micro-chip detectors, high-speed SPP phase modulators and polaritonic frequency combs.

2. Model

We develop a framework for SPPs that accounts for lossy media. To controllably excite and characterize SPP propagation along these lossy interfaces/waveguides, we employ DPI, SNI and DNI media interfaces with dielectrics. Our results are specialized to the quite general case of linear, homogeneous, isotropic (LHI) media and we assume the interface is subject to a plane-wave driving laser field with uniform intensity distribution via end-fire coupling [3].

We characterize linear SPP propagation along planar and curved interfaces. To this aim, we determine necessary and sufficient conditions for SPP propagation by introducing strict bounds on the real and imaginary parts of the squared propagation coefficient to decide whether a given mode corresponds to a propagating SPP or not. These bounds on the squared propagation coefficient at planar interfaces reduce to a set of conditions on the real and imaginary parts of EM susceptibilities, which we refer to as characteristic equations.

We employ these characteristic equations to determine regions for which transverse electric (TE) and transverse magnetic (TM) SPPs propagate along the planar interface between SNI or DNI media with air. Our SPP characterization is valuable for checking application viability; e.g., our method falsifies a prediction that SPPs could propagate through the surface of a DNI medium with any values of permittivity and permeability [8]. Instead, SPP propagation can occur only for certain medium parameters [6]. Thus, SPPs cannot stably propagate in frequency regions corresponding to DNI medium (at interfaces comprising free-moving electric and magnetic charges).

To characterize SPP propagation along circular interfaces between lossy LHI media, we employ conformal transformations [9]. We build on previous techniques for characterizing or guiding SPP propagation at curved interfaces or bent waveguides [10]. Specifically, we employ conformal logarithmic mapping to map circular interfaces between two LHI media to a planar interface between two linear inhomogeneous isotropic (LII) media. We consider circular interfaces due to the simplicity of their solutions; our approach can be extended to other curvatures.

We show that the SPP dispersion equation at the curved interface is analogous to the dispersion equation at the conformally mapped LII media planar interface. To decide whether a given mode at LII media planar interfaces is a propagating SPP or not, we apply bounds on the real and imaginary parts of the complex propagation coefficient. we confirm our SPP solutions by checking the physical intuition through analyzing the field intensity and Poynting-vector properties at the interfaces. Ascertaining the viability of SPP propagation at planar and curved interfaces and checking SPPs sensitivity to materials EM susceptibili-

ties through the characteristic equations is advantageous for designing miniaturized photonic circuit elements including waveguides and sensors.

Now we proceed from a simple dielectric medium and linear optics to multi-level atoms that yield nonlinear optics. For active control of nonlinear SPPs, we recommend driving a four-level N-type atomic (4NAs) cloud [11], treated as a cold ^{87}Rb due to its considerable Kerr nonlinearity and controllable dispersion, at the DNI interface. The atomic cloud is trapped near the interface by a magneto-optical trap [12] with a thickness more than five $|5S_{1/2}, F = 2\rangle \mapsto |5P_{1/2}, F = 2\rangle$ dipole transition wavelengths. This nonlinear waveguide drive by three co-propagating fields: a pump signal, a coupling signal and a weak probe signal, all injected by end-fire coupling.

Our quantitative description of the system is obtained by solving Maxwell-Bloch equations based on a perturbative, asymptotic, multi-scale position and time expansion [13]. Our third-order truncated solution yields a nonlinear Schrödinger equation. We establish a controllable Kerr nonlinearity by sufficient field concentration and appropriate intensities and detunings for the laser fields. We investigate the Rabi-frequency dynamics for resultant nonlinear SPPs including temporal solitons [14], breathers, solitary localized nonlinear waves with a periodically oscillating amplitude and surface polaritonic rogue waves [15] as functions of laser-field intensities and detunings.

For spatial control of nonlinear SPPs, we suggest driving 4NAs on the surface of a DNI medium. These components are contained in a stable cavity and serve as a nonlinear planar waveguide. We assume Pr^{3+} dopants, as the atomic medium, in a Y_2SiO_5 transparent crystal over a thickness of several dipole transition wavelengths. The waveguide is driven by three co-propagating fields: pump, weak probe and standing wave coupling signals, all injected by end-fire coupling.

We show that the laser driving fields excite nonlinear SPPs including Akhmediev breathers, and a frequency comb, as a nonlinear wave that appears briefly at specific positions. We propose generating these nonlinear waves by coupling the probe laser to the dipole moment of the 4NA transition. Stability is arises via a low-loss SPP condition and judiciously modifying SPP nonlinearity and dispersion at the interface.

3. Conclusions

We present a framework for linear and nonlinear SPPs along lossy media interfaces to excite, propagate and control SPPs. We extend the case of SPPs at lossless metallic planar interfaces to define and derive characteristic equations for SPPs at lossy planar and curved interfaces. We then propose controllable propagation of SPP breathers and polaritonic frequency combs at atomic materials interfaces with DNI media.

References

[1] A.V. Zayats, I.S. Igor, A.M. Alexei, Nano-optics of surface plasmon polaritons, *Phys. Rep.* 408: 131314, 2005.

[2] W.L. Barnes, A. Dereux, T.W. Ebbesen, Surface plasmon subwavelength optics, *Nature* 424: 824–830, 2003.

[3] S.A. Maier, H.A. Atwater, Plasmonics: Localization and guiding of electromagnetic energy in metal/dielectric structures, *J. Appl. Phys.* 98: 0111011-10 2005.

[4] M. Kauranen and A.V. Zayats, Nonlinear plasmonics, *Nat. Photonics* 6: 737, 2012.

[5] V.M. Shalaev, Optical negative-index metamaterials, *Nat. Photonics* 1: 41–48 2007.

[6] N. Sang-Nourpour, B.R. Lavoie, R. Kheradmand, M. Rezaei, B.C. Sanders, Characterization of surface-plasmon polaritons at lossy interfaces, *J. Opt.* 19: 125004 2017.

[7] A. Nahata, R.A. Linke, T. Ishi, and K. Ohashi, Enhanced nonlinear optical conversion from a periodically nanostructured metal film, *Opt. Lett.* 28: 423–425 2003.

[8] A.A. Kamli, S.A. Moiseev, B.C. Sanders, Quantum informatics with plasmonic metamaterials, *Int. J. Quantum Inf.* 9: 263–279 2011.

[9] L. Xu, H. Chen, Conformal transformation optics, *Nat. Photonics*, 09: 15–23, 2015.

[10] M. Kadic, S. Guenneau, S. Enoch, P.A. Huidobro, L. Martín-Moreno, F. J. García-Vidal, J. Renger, R. Quidant, Transformation plasmonics, *Nanophotonics* 1: 51–64 2012.

[11] J. Sheng, X. Yang, H. Wu, M. Xiao, Modified self-kerr nonlinearity in a four-level N-type atomic system, *Phys. Rev. A* 84: 053820– 2011.

[12] C.G. Townsend, N.H. Edwards, C.J. Cooper, K.P. Zetie, C.J. Foot, A.M. Steane, P. Szriftgiser, H. Perrin, J. Dalibard, Phase-space density in the magneto-optical trap, *Phys. Rev. A* 52: 1423– 1995.

[13] S. Asgarnezhad-Zorgabad, R. Sadighi-Bonabi, B.C. Sanders, Excitation and propagation of surface polaritonic rogue waves and breathers, *Phys. Rev. A* 98: 013825 2018.

[14] S. Asgarnezhad-Zorgabad, R. Sadighi-Bonabi, C. Hang, Coupler-free surface polariton excitation and propagation with cold four-level atomic medium, *J. Opt. Soc. Am. B* 9: 1787–1795 2017.

[15] B. Kibler, J. Fatome, C. Finot, G. Millot, F. Dias, G. Genty, N. Akhmediev, J.M. Dudley, The peregrine soliton in nonlinear fibre optics, *Nat. Phys.* 6: 790–799 2010.

Optical response of magnetoelectric materials with spin-induced chirality and polarity

Youtarou Takahashi[1,2]

[1] Department of Applied Physics and Quantum Phase Electronics Center (QPEC), University of Tokyo, Tokyo, Japan
[2] RIKEN Center for Emergent Matter Science (CEMS), Saitama, Japan
*corresponding author, E-mail: youtarou-takahashi@ap.t.u-tokyo.ac.jp

Abstract

Optical effects induced by the spin-driven chirality and polarity are investigated by using the time-domain terahertz polarimetry. The resonantly enhanced nonreciprocal optical effects are observed on the electromagnon excitation, which is an electrically active collective spin excitation. The observed nonreciprocal directional dichroism, gyrotropic birefringence and natural optical activity can be viewed as the dynamical counterpart of the magnetoelectric coupling.

1. Introduction

Magnetoelectric multiferroics exhibit the strong cross-coupling between the ferroelectricity and magnetism, leading to the novel functionalities of matter. An electromagnon, which is a magnon endowed with the electric activity, is the elementary excitation inherent in magnetoelectric multiferroics. For example, the helical spin orders give rise to the spin-driven ferroelectricity and concomitant electromagnon excitation as reported in many multiferroics. A unique character of the electromagnon is the resonantly enhanced optical magnetoelectric effect; which is induced by the cross-coupling between the electric- and magnetic- transition dipoles. Consequently, the optical response of matter is determined by the sign of the propagation vector of light ($\pm k^{\omega}$), resulting in the nonreciprocal optical effect. In fact, the nonreciprocal directional dichroism, which is the k^{ω}-dependent absorption of light, has been reported on the electromagnon resonance in the various multiferroics [1].

2. Result and Discussion

We investigated the optical magnetoelectric effects and natural optical activity on the electromagnon resonance of the helimagnets by using the time-domain terahertz spectroscopy and polarimetry. The helical spin orders including proper screw and cycloidal spin structures (Fig. 1) break the space-inversion symmetry. The screw spin structure exhibits the spin-induced chirality and the left- and right-handed screw habits possess different chirality. On the electromagnon resonance, the magnetochiral effect, which leads to the nonreciprocal directional dichroism, has been observed in the magnetic field [2]. In addition, the chiral nature of proper screw order produces the enhanced natural optical activity. On the other hand, the polar nature of the cycloidal spin structure has been attracting increasing attention in recent years since it induces the spin-driven ferroelectricity. The nonreciprocal directional dichroism on the resonance of the electromagnon has been also

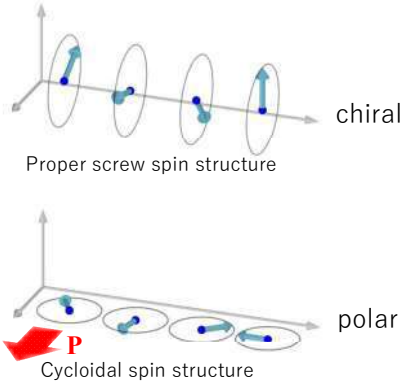


Figure 1: Proper screw spin structure with chirality (upper panel) and cycloidal spin structure with polarity (lower panel).

demonstrated on the cycloidal spin order in the magnetic field [1]. The polarity of this magnetic order gives rise to the different nonreciprocal optical effect, which is referred to as gyrotropic birefringence [3]. These helimagnets induce the versatile optical effects through the dynamical magnetoelectric coupling as well as the multiferroicity.

References

[1] Y. Takahashi, R. Shimano, Y. Kaneko, H. Murakawa and Y. Tokura, Nature Phys. 8, 121 (2012).
[2] S. Kibayashi, Y. Takahashi, S. Seki and Y. Tokura, Nat. Commun. 5:4583 (2014).
[3] T. Kurumaji, Y. Takahashi, J. Fujioka, R. Masuda, H. Shishikura, S. Ishiwata and Y. Tokura Phys. Rev. Lett. 119, 077206 (2017).

Photonic properties of multiferroic layered metasurfaces

R. Khomeriki [1,2], L. Chotorlishvili [2], and Jamal Berakdar[2*]

[1] Physics Department, Tbilisi State University, 3 Chavchavadze, 0128 Tbilisi, Georgia
[2] Institute for Physics, Martin-Luther-University Halle-Wittenberg, 06099 Halle, Germany
*corresponding author, E-mail: jamal.berakdar@physik.uni-halle.de

Abstract:.- We discuss the electromagnetic wave propagation in a multiferroic, insulating oxide-based metastructure consisting of alternating coupled layers of ferroelectric ($SrTiO_3$) and ferromagnetic ($Y_3Fe_2(FeO_4)_3$, YIG) layers. The dynamic magnetic and electric polarization responses are explicitly accounted for by self-consistent, discretized, coupled equations for the Maxwell/ferroelectric/ferromagnetic dynamics. We obtain biquadratic relation for the refractive index and work out explicitly the dependence on the ferroelectric/ferromagnetic phase of the constituent layers. Depending on the geometry and the material parameters we find frequency-dependent regimes for ordinary and negative refraction that we analyze analytically. We propagate fully numerically the electromagnetic-waves injected at the edges of the photonic structure and find for particular GHz frequencies that waves with different polarizations are characterized by different signs of the refractive index, implying new phenomena such as a positive-negative birefringent effect, and magnetically controlled light trapping and accelerations.

For materials where both the electric permittivity ϵ and the magnetic permeability μ are negative Veselago's predicted [1, 2] negative refraction which was later confirmed experimentally [3, 4]. Realization based on metallic heterostructures suffer from losses that can be avoided by using insulating multiferroics that offer also new functionalities. We study synthesized structures that exhibit simultaneously multiple orderings such as ferromagnetic, ferroelectric phases and have thus a coupled electric/magnetic response . The system is sketched in Fig.1. We setup a theory describing adequately the magnetic dynamics as well as the ferroelectric polarization and couple both self-consistently the to the Maxwell-equations [5]. We find negative refraction in ferroelectric (FE)/ferromagnetic(FM) multilayers. Experimentally, the large mismatch between conventional ferroelectric and ferromagnetic resonance frequencies might be an obstacle (e.g., $BaTiO_3$ has a resonance in THz range, while the resonance of the insulating ferromagnet, rhodium-substituted ε-$Rh_xFe_{2-x}O_3$ with largest known coercivity is $\approx$ 200GHz). However, there is a large class of synthetic materials and other oxides (such as ferroelectric $SrTiO_3$ (STO) and the insulating ferromagnet $Y_3Fe_2(FeO_4)_3$ (called YIG)) with suitable frequencies. In the pilot numerical simulations shown in Fig.1 the ferroelectric (ferromagentic) layer is 10 nm (1 μm) thick.

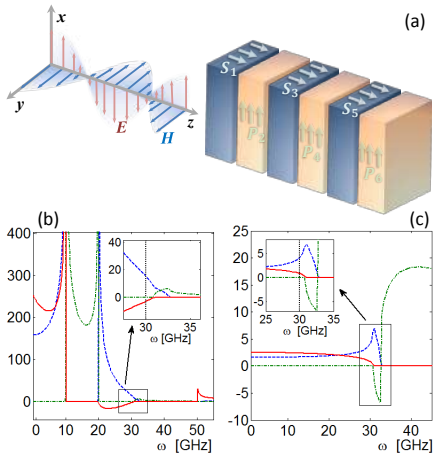


Figure 1: (a) Schematics for the photonic/ferroelectric/ferromagnetic heterostructure. The electric polarization $\mathbf{P}_j$ in the layer j is aligned along x axis. The incident light wave propagating along z axis. $\mathbf{E}$ and $\mathbf{H}$ denote the electric and magnetic field components. The magnetization $\mathbf{S}_i$ in the layer i points also along the z axis. (b) and (c) graphs show real (dashed blue curve) and imaginary (dashed-dotted green curve) parts of the refraction index n versus the mode frequency according to our biquadratic equation. Red solid curve is the z component of the time averaged dimensionless Poynting vector $\langle W_z \rangle / P_0 S_0$. Graphs (b) and (c) correspond to the negatively and positively refracting waves, respectively for the same excitation frequency 30GHz indicated by vertical dotted lines in the insets. Insets display enlarged views of the frequencies in interest.

References

[1] Veselago, V. G. *Sov. Phys. Solid State*, **1967**, 8, 2854-2856.

[2] Veselago, V. G. *Sov. Phys. Usp.* **1968**, 10, 509-514.

[3] Pendry, J.B.; Holden, A.J.; Robbins, D.J.; Stewart, W.J. *IEEE Trans. Microwave Theory Tech.* **1999** 47, 2075-2085.

[4] Smith, D.R.; Padilla, W.J.; Vier, D.C.; Nemat-Nasser, S.C.; Schultz, S. *Phys. Rev. Lett.* **2000**, 84, 4184-4187.

[5] Khomeriki, R.; Chotorlishvili, L.; Tralle, I.; Berakdar, J. *Nano letters* **2016**, 11 ,7290.

Engineering the Optical Magnetoelectric Effect in Crystals on the Sub-Unit-Cell Scale

Istvan Kezsmarki[1,*] and Sandor Bordacs[2]

[1]Center for Electronic Correlations and Magnetism, University of Augsburg, Augsburg, Germany
[2]Department of Physics, Budapest University of Technology and Economics, Budapest, Hungary
*corresponding author, E-mail: istvan.kezsmarki@physik.uni-augsburg.de

Abstract

Multiferroics permit magnetic control of the electric polarization and electric control of the magnetization. These static magnetoelectric effects are of enormous interest: The ability to read and write a magnetic state current-free by an electric voltage would provide great technological advantages. Optical magnetoelectric effects are equally interesting, because they give rise to unidirectional light propagation in multiferroic compounds. We show that static and optical magnetoelectric phenomena can be engineered in crystals on the sub-unit-cell scale, similarly to metamaterials.

1. Introduction

In conventional media light propagation is reciprocal, that is counter-propagating beams experience the same refractive index. However, reciprocity can be violated in multiferroic or more generally in magnetoelectric materials, where the refractive index depends not only on the polarization of light but also on the ±**k** direction of the propagation [1]. Such unidirectional transmission is the consequence of the dynamic or magnetoelectric effect emerging in materials with simultaneously broken time reversal and spatial inversion symmetries. This phenomenon, exclusively observed in multiferroic and magnetoelectric materials so far [2-5], may allow the development of optical diodes, transmitting unpolarized light in one, but not in the opposite, direction [5]. Recently, the emergence of such unidirectional light propagation, governed the dynamic magnetoelectric effect, has also been demonstrated in multi-antiferroics [6], i.e. in materials with coexisting purely antiferromagnetic and antiferroelectric (or antipolar) orders.

2. Optical magnetoelectric effect in the GHz-THz frequency range

In the following we show three typical examples when the optical magnetoelectric effect was observed at spin-wave excitations of non-centrosymmetric magnetic crystals.

2.1. Optical magnetoelectric effect in multiferroics

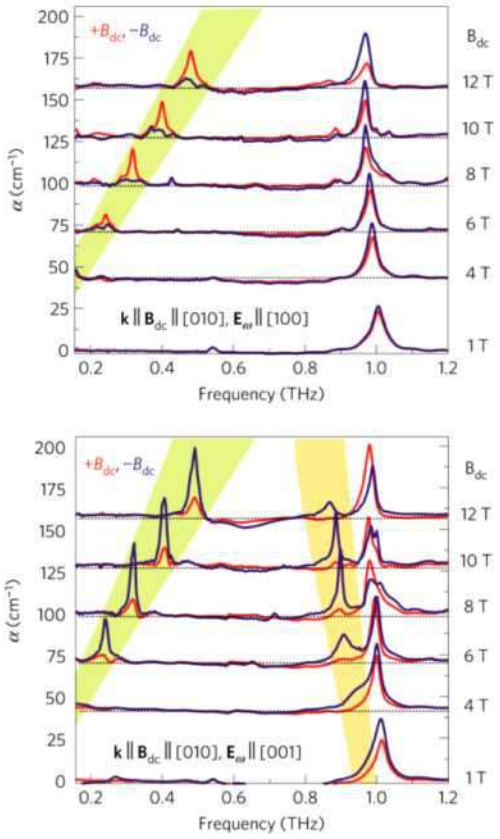


Figure 1: Optical magnetoelectric effect observed in resonance with magnon excitations in $Ba_2CoGe_2O_7$ [3]. The absorption difference found between THz beams co-propagating (red spectra) and counter-propagating (blue spectra) with the applied static magnetic field is the consequence of the magnetically induced chirality of the material.

2.2. Optical magnetoelectric effect in multi-antiferroics

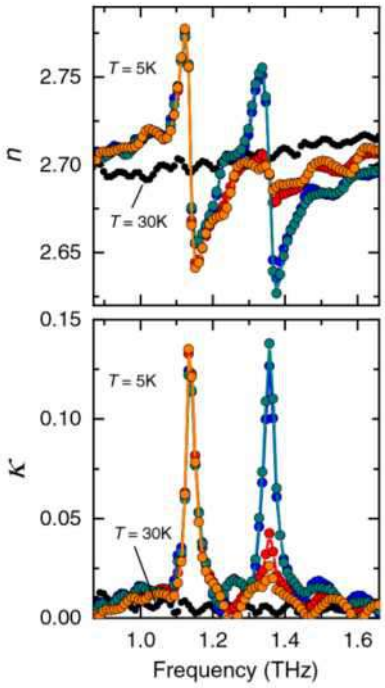


Figure 2: Optical magnetoelectric effect of magnon excitations in the antiferromagnetic state of $LiCoPO_4$ [6]. A strong difference both in the real part (n) and the imaginary part (κ) of the refractive index is found at the magnon resonance near 1.4 THz between the two antiferromagnetic domains. By different combinations of poling electric and magnetic fields either one or the other antiferromagnetic domain can be realized. The spectra obtained for one domain are displayed in orange and red, while spectra characteristic to the other domain are plotted in cyan and blue.

2.3. Optical magnetoelectric effect of skyrmion crystals

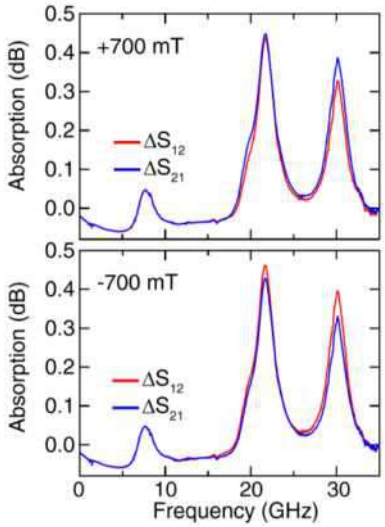


Figure 3: Microwave magnetoelectric effect observed at the collective spin modes in the Néel-type skyrmion hosting material GaV_4S_8 [7].The red and blue absorption spectra are measured for the transmission of microwaves in opposite directions.

Acknowledgements

This work has been supported by the National Research, Development and Innovation Office NKFIH Grants No. ANN 122879 and No. K 124176, by the BMENanonotechnology and Materials Science FIKP grant of EMMI (BME FIKP-NAT), by the Deutsche Forschungsgemeinschaft (DFG) via the Transregional Research Collaboration TRR 80: From Electronic Correlations to Functionality (Augsburg—Munich—Stuttgart) and via the Skyrmionics Priority Program SPP2137.

References

[1] D. Szaller, S. Bordacs, and I. Kezsmarki, Symmetry conditions for nonreciprocal light propagation in magnetic crystals, *Phys. Rev. B* 87: 014421, 2014.

[2] I. Kezsmarki *et al.*, Enhanced Directional Dichroism of Terahertz Light in Resonance with Magnetic Excitations of the Multiferroic $Ba_2CoGe_2O_7$ Oxide Compound, *Phys. Rev. Lett.* 106: 057403, 2011.

[3] S. Bordacs *et al.*, Chirality of matter shows up via spin excitations, *Nat. Phys.* 8: 734, 2012.

[4] I. Kezsmarki *et al.*, One-way transparency of four-coloured spin-wave excitations in multiferroic materials, *Nat. Commun.* 5: 3203, 2014.

[5] I. Kezsmarki *et al.*, Optical Diode Effect at Spin-Wave Excitations of the Room-Temperature Multiferroic $BiFeO_3$, *Phys. Rev. Lett.* 115: 127203, 2015.

[6] V. Kocsis *et al.*, Identification of Antiferromagnetic Domains Via the Optical Magnetoelectric Effect, Phys. Rev. Lett. 121: 057601, 2018.

[7] Y. Okamura *et al.*, Microwave Directional Dichroism Resonant with Spin Excitations in the Polar Ferromagnet GaV_4S_8, *Phys. Rev. Lett.* 122: 057202, 2019.

Electromagnetic Responses and Non-reciprocal Phenomena of Metamaterials with Chirality and Magnetism

Kei Sawada[1], Satoshi Tomita[2], Hiroyuki Kurosawa[3], and Tetsuya Ueda[4]

[1]RIKEN SPring-8 Center, Hyogo, Japan
[2]Department of Physics, Tohoku University, Sendai, Japan
[3]Advanced ICT Research Institute, National Institute of Information and Communication Technology, Kobe, Japan
[4]Department of Electrical Engineering and Electronics, Kyoto Institute of Technology, Kyoto, Japan
E-mail: sawada@spring8.or.jp

Abstract

Non-reciprocal phenomena of metamaterials are studied in a system containing both chirality and magnetism. Structural chirality and intrinsic magnetism break spatial inversion and time-reversal symmetries, respectively. Such a symmetry breaking gives a magneto-chiral effect, which is a kind of directional birefringence. We experimentally demonstrated and numerically verified that the magneto-chiral effect was enhanced in artificial metamolecules.

1. Introduction

Optical phenomena are often related to symmetry breakings. A simple and familiar example is refraction. Refraction is a change of the wavevector, and is interpreted as a result of a translational symmetry breaking. In a chiral material, a broken space-inversion symmetry splits the degeneracy of refractive indices with respect to polarization states, resulting in polarization rotation, called the natural optical activity. When light is shinned again from the other side of a medium, the rotation angle is reversed. Similar but different phenomena on polarization rotation are the magneto-optical Faraday effects in magnetic materials, in which the time-reversal symmetry is broken. The polarization angle rotates twice if light is again incident from the other side of a medium. It is interesting to ask what happens if a system breaks both spatial inversion and time-reversal symmetry. The answer is polarization-independent directional birefringence dichroism, called the magneto-chiral effect and the optical magneto-electric effect. In Fig. 1, symmetry breakings and resulting optical phenomena are schematically represented. Here we focus on the magneto-chiral effect in a microwave region, realized in artificial media possessing both structural chirality and intrinsic magnetism [1-3].

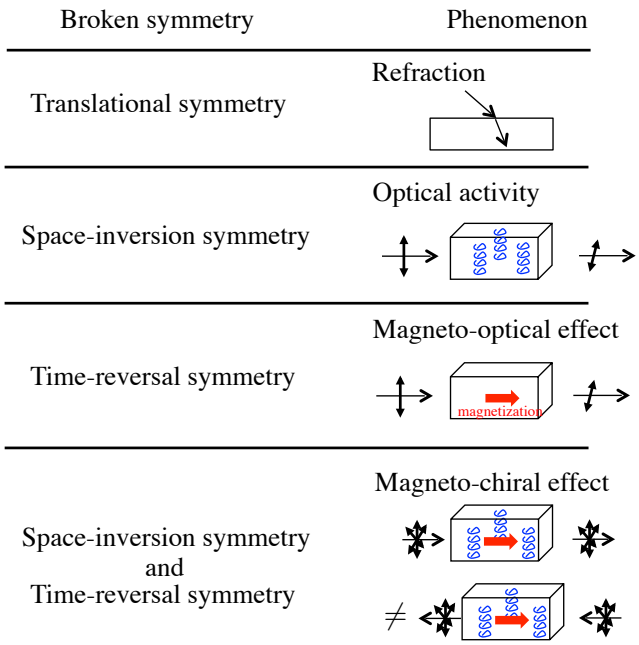


Figure 1: Symmetry breakings and optical phenomena.

2. Theoretical background

Fundamental electromagnetic responses of materials are characterized by two parameters: a dielectric constant, ε, and a magnetic permeability, μ. Electromagnetic waves feel these parameters not always independently but as their product and quotient, namely the refractive index, $n = \sqrt{\varepsilon}\sqrt{\mu}$, and the impedance, $Z = \sqrt{\mu}/\sqrt{\varepsilon}$, respectively. It is interesting that these product and quatient are regarded as fictitious interactions between electric and magnetic responses. If a system has a structural chirality and intrinsic magnetization, these expressions are not the case. Let us consider the following constitutive equations,

$$\vec{D} = \varepsilon_0 \hat{\varepsilon} \vec{E} - iY_0 \hat{\xi} \vec{B}, \quad (1)$$

$$\vec{H} = (\mu_0 \hat{\mu})^{-1} \vec{B} - iY_0 \hat{\xi} \vec{E}, \quad (2)$$

where ε_0, μ_0, and $Y_0 = \sqrt{\varepsilon_0 / \mu_0}$ are the dielectric constant, the magnetic permeability and the admittance of vacuum, respectively. The tensor, $\hat{\xi}$, relates to chirality that causes the optical activity. The magneto-optical is given by the off-diagonal components of $\hat{\varepsilon}$ or $\hat{\mu}$. In this formulation, the chirality and the magnetism do not interact each other. From the constitutive equations and Maxwell equations, we can show that the refractive indices have several terms, representing the optical activity, the magneto-optical effect. Remarkably, we obtained another term, proportional to both chiral parameter and magnetization independent of polarization states. This term represents the magneto-chiral effect caused by a fictitious interaction between the chirality and the magnetism.

3. Experimental and numerical results

To realize the magneto-chiral effect, we prepared a metamolecules as shown in Fig. 2. A helical Cu wire of 4 turns was equipped with a ferrite rod of 15 mm length. This sample was put into a waveguide. Microwave was introduced from Port 1(2), and its amplitude, S_{12} and S_{21}, were measured at Port 2(1). The external magnetic field was applied to *z*-direction. The magneto-chiral effect is a non-reciprocal phenomenon that is proportional to the difference between S_{12} and S_{21}. Figure 3 shows the pseudo color plot of $\log|\arg S_{12}-S_{21}|$ as a function of the external magnetic field and frequencies of microwaves. We found three resonances at 10.6, 13.7 and 14.5 GHz due to the chiral structure. These resonances are nothing but magneto-chiral resonances because they are linearly dependent on the ferromagnetic resonance induced by external magnetic field. In the inset of Fig. 3, the intensity of magnetization and the distribution of the surface current density at 14.5 GHz are represented. We observed simultaneous existence of the ferromagnetic and the chiral resonances, resulting in enhanced magneto-chiral responses.

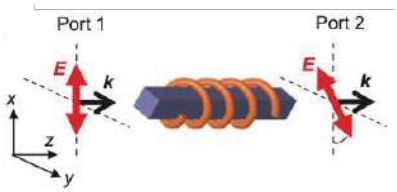


Figure 2: Magneto-chiral metamolecule composed of a ferrite rod and a helical cupper wire, and its configuration in microwave measurements.

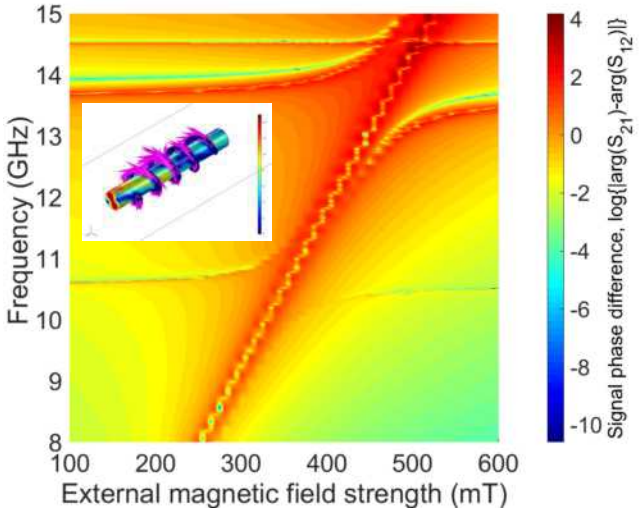


Figure 3: Pseudo color plot of amplitude difference, between S_{21}-S_{12},, as a function of frequencies and the external magnetic field. Inset: Numerical results of the surface current density (cone) and the intensity of magnetization (pseudo color).

4. Conclusions

We show a new kind of fictitious electromagnetic interactions, a magneto-chiral coupling, realized in magnetic materials together with chiral media. This effect was experimentally demonstrated in microwave regions by using an artificial metamolecule composed of helical metal and a ferrite rod. The results were verified by numerical simulations.

Acknowledgements

We are grateful to M. Hangyo and A. Sanada for fruitful discussions.

References

[1] S. Tomita, K. Sawada, A. Porokhnyuk, and T. Ueda, Direct observation of magnetochiral effects through a single metamolecule in microwave regions. *Phys. Rev. Lett.* , 113: 235501, 2014. 0.

[2] S. Tomita, H. Kurosawa, K. Sawada, and T. Ueda. Enhanced magnetochiral effects at microwave frequencies by a single metamolecule. *Phys. Rev. B*, 95: 085402, 2017.

[3] S. Tomita, H. Kurosawa, T. Ueda, and K. Sawada, Metamaterials with magnetism and chirality. *J. Phys. D*, 51: 083001, 2018, and references therein.

Microwave-Active Dynamics of Magnetic Skyrmions under Application of a Tilted Magnetic Field

Masahito Mochizuki[1*], Tatsuya Koide[2], Masahito Ikka[2], Akihito Takeuchi[2]

[1]Department of Applied Physics, Waseda University, Okubo, Shinjuku-ku, Tokyo 169-8555, Japan
[2]Department of Physics and Mathematics, Aoyama Gakuin University, Sagamihara, Kanagawa 229-8558, Japan
*corresponding author, E-mail: mochizuki@phys.aoyama.ac.jp

Abstract

Magnetic skyrmions in magnets with broken spatial inversion symmetry have rich device functions and thus have attracted a great deal of research interest. We discuss our recent theoretical studies on dynamical phenomena and functionalities of magnetic skyrmions originating from their peculiar microwave-active spin-wave modes. Excitations of the spin-wave modes under application of a tilted magnetic field give rise to microwave-driven translational motion of skyrmions and skyrmion-based microwave-DC-voltage conversions.

1. Introduction

Magnetic skyrmions have attracted a great deal of interest in the spintronics field [1, 2, 3]. In particular, their microwave-active spin-wave modes and related dynamical phenomena are an important subject [4, 5, 6]. Our theoretical studies recently uncovered intriguing microwave-induced phenomena of magnetic skyrmions in a two-dimensional system under application of a tilted magnetic field [7, 8].

2. Model and Method

A thin-plate magnet with a broken inversion symmetry is described by a classical spin model on the square lattice,

$$\begin{aligned}\mathcal{H} &= -J\sum_{i,\hat{\boldsymbol{\mu}}} \boldsymbol{m}_i \cdot \boldsymbol{m}_{i+\hat{\boldsymbol{\mu}}} - \boldsymbol{H}_{\rm ex}\cdot\sum_i \boldsymbol{m}_i \\ &\quad -\sum_{i,\hat{\boldsymbol{\mu}}} \boldsymbol{D}_\mu \cdot (\boldsymbol{m}_i \times \boldsymbol{m}_{i+\hat{\boldsymbol{\mu}}}) \end{aligned} \quad (1)$$

where $\hat{\boldsymbol{\mu}}$=$\hat{\boldsymbol{x}}$, $\hat{\boldsymbol{y}}$, and $\boldsymbol{m}_i$ is the normalized magnetization vector on the ith site. The first and the second terms denote the ferromagnetic-exchange interactions and the Zeeman interactions, respectively. The third term depicts the DM interaction where the DM vectors $\boldsymbol{D}_\mu$ determine the skyrmion type, i.e., the Bloch type and the Neel type [Fig. 1(a) and (b)]. To investigate the microwave-driven dynamics, coupling between magnetizations and the microwave electromagnetic fields should be taken into account as well. The skyrmions confined in a two-dimensional system generally have a circular symmetry when the $\boldsymbol{H}_{\rm ex}$ field is perpendicular to the plane. On the other hand, when the $\boldsymbol{H}_{\rm ex}$ field is tilted [Fig. 1(c)], their circular symmetry becomes to be broken, and the magnetization distribution has a disproportionate weight slanted from the center [Fig. 1(d)]. The microwave-driven magnetization dynamics are simulated by numerically solving the Landau-Lifshitz-Gilbert equation.

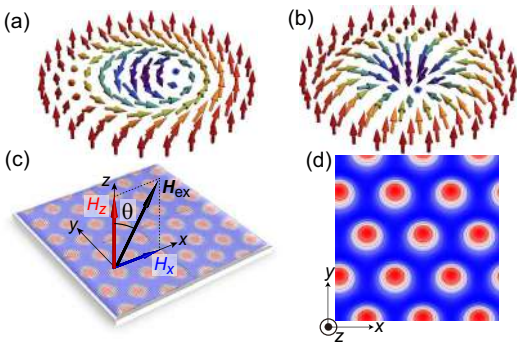


Figure 1: (a) Bloch-type skyrmion. (b) Neel-type skyrmion. (c) Thin-plate specimen of a skyrmion-hosting magnet under a tilted magnetic field $\boldsymbol{H}_{\rm ex}$ where θ is the tilting angle. (c) Bloch-type skyrmion crystal under a tilted magnetic field with $\theta = 30°$.

3. Microwave-induced phenomena

It was theoretically revealed that hexagonally packed skyrmions in a skyrmion crystal exhibit peculiar spin-wave modes at microwave frequencies [4, 5], in which the skyrmions uniformly rotate in a counterclockwise (CCW) or clockwise (CW) fashion (the rotation modes) [Fig. 2(a)] or uniformly expand and shrink in an oscillatory manner (the breathing mode) [Fig. 2(b)]. When the $\boldsymbol{H}_{\rm ex}$ field is perpendicular, both the CCW and CW rotation modes are excited only by an in-plane polarized microwave $\boldsymbol{H}^\omega \| x, y$, whereas the breathing mode is excited only by an out-of-plane polarized microwave $\boldsymbol{H}^\omega \| z$. In contrast, both the in-plane and out-of-plane polarized microwaves can excite all these spin-wave modes when the $\boldsymbol{H}_{\rm ex}$ field is tilted as seen in Fig. 2(c) and (d).

It was theoretically demonstrated that continuous excitation of the skyrmion spin-wave modes under a tilted $\boldsymbol{H}_{\rm ex}$ field induces a translational motion of skyrmion crystal [Fig. 3(a)]. Detailed investigations on the frequency de-

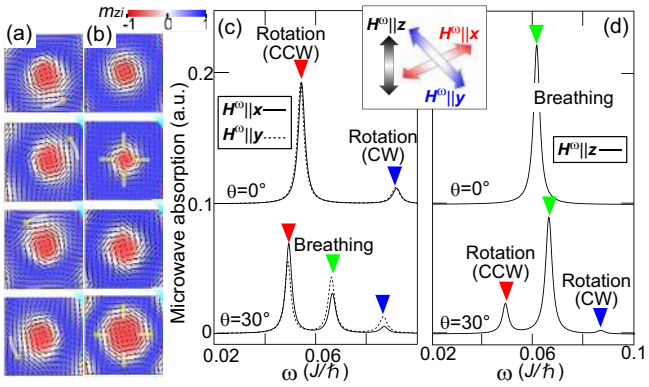


Figure 2: (a), (b) Microwave-active spin-wave modes of skyrmion crystal, i.e., the counterclockwise (CCW) rotation mode (a) and the breathing mode (b). (c), (d) Microwave absorption spectra of skyrmion crystal under perpendicular (θ=0°) and tilted (θ=30°) magnetic fields $\boldsymbol{H}_{\rm ex}$ for the in-plane microwave polarization $\boldsymbol{H}^{\omega}\|\boldsymbol{x},\boldsymbol{y}$ (c) and the out-of-plane microwave polarization $\boldsymbol{H}^{\omega}\|\boldsymbol{z}$ (d).

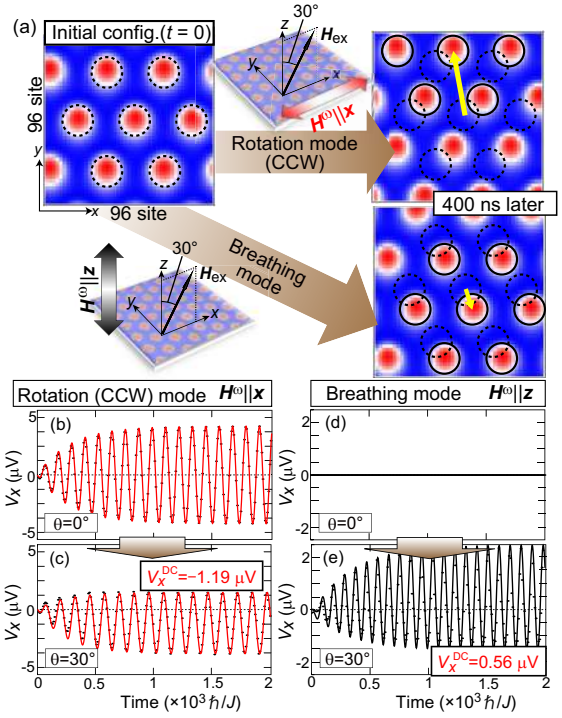


Figure 3: (a) Translational motion of skyrmion crystal driven by the continuous spin-wave excitation through microwave application under a tilted magnetic field. (b), (c) Time profiles of the spin-driven electric voltage induced by the CCW rotation mode excited by the in-plane microwave field $\boldsymbol{H}^{\omega}\|\boldsymbol{x}$ under perpendicular (b) and tilted (θ=30°) (c) magnetic fields. The oscillating electric voltage has a zero average in (b) but has a finite DC component in (c). (d), (e) Those induced by the breathing mode excited by the out-of-plane microwave field $\boldsymbol{H}^{\omega}\|\boldsymbol{z}$.

pendence of the motion elucidated that the drift velocity has maxima at eigenfrequencies of the spin-wave modes, which indicates that the resonant excitation of the spin waves drives the fast skyrmion motion. It was also proved that the velocity and direction of this translational motion vary depending on the mode and the microwave polarization.

It was also theoretically demonstrated that temporally oscillating spin motive force and spin voltage with a large DC component are generated by exciting the skyrmion spin-wave modes under a tilted magnetic field [Fig. 3(b)-(e)]. The DC component and the AC amplitude of the oscillating electric voltage show significant enhancement when the frequency of applied microwave is tuned at eigenfrequencies of the skyrmion spin-wave modes. It was also revealed that the sign of the DC voltage varies depending on the microwave polarization and the mode. This finding enables efficient conversion of microwaves to DC electric voltage using skyrmion-hosting magnets.

4. Conclusions

Continuous excitations of the skyrmion spin-wave modes under application of a tilted magnetic field give rise to intriguing microwave-induced dynamical phenomena. These phenomena are of great interest from the viewpoints of both fundamental science and technical application, which require further studies in the future.

References

[1] N. Nagaosa, Y. Tokura, Topological properties and dynamics of magnetic skyrmions, *Nat. Nanotech.* 8: 899 (2013).

[2] A. Fert, V. Cros, J. Sampaio, Skyrmions on the track, *Nat. Nanotech.* 8: 152 (2013).

[3] S. Seki, M. Mochizuki, *Skyrmions in Magnetic Materials* Springer, Berlin, 2015.

[4] M. Mochizuki, S. Seki, Dynamical magnetoelectric phenomena of multiferroic skyrmions, *J. Phys.: Cond. Mat.* 27: 503001 (2015).

[5] M. Mochizuki, Spin-Wave Modes and Their Intense Excitation Effects in Skyrmion Crystals, *Phys. Rev. Lett.* 108: 017601 (2012).

[6] M. Mochizuki, S. Seki, Magnetoelectric resonances and predicted microwave diode effect of the skyrmion crystal in a multiferroic chiral-lattice magnet, *Phys. Rev. B* 87: 134403 (2013).

[7] M. Ikka, A.Takeuchi, M.Mochizuki, Resonance modes and microwave-driven translational motion of a skyrmion crystal under an inclined magnetic field, *Phys. Rev. B* 98: 184428 (2018).

[8] A. Takeuchi, M. Mochizuki, Selective activation of an isolated magnetic skyrmion in a ferromagnet with microwave electric fields, *Appl. Phys. Lett.* 113: 072404 (2018).

Spin waves in thin films and magnonic crystals with Dzyaloshinskii-Moriya interactions

Rodolfo Gallardo[a,b], David Cortés-Ortuño[c], Roberto Troncoso[d], Pedro Landeros[a,b]

[a] Departamento de Física, Universidad Técnica Federico Santa María, Valparaíso, Chile
[b] Center for the Development of Nanoscience and Nanotechnology (CEDENNA), Santiago, Chile
[c] Faculty of Engineering and Physical Sciences, University of Southampton, Southampton, United Kingdom
[d] Center for Quantum Spintronics, Department of Physics, Norwegian University of Science and Technology, Trondheim, Norway

The influence of the Dzyaloshinskii-Moriya interaction (DMI) on the behavior of spin waves in ultra-thin ferromagnetic films and chiral magnonic crystals is reviewed [1]. During the last decade, it has been shown, both theoretically and experimentally, that this anisotropic exchange interaction produces non-reciprocal features on the spin-wave spectrum of a magnetic system, a phenomenon that occurs both for bulk [2-3] and interfacial Dzyaloshinskii-Moriya coupling [4-6]. More recently, the concept of a chiral magnonic crystal has been introduced [7], where the interfacial Dzyaloshinskii-Moriya interaction is periodic. The effect of this periodicity includes additional features such as flat bands, indirect gaps, and an unusual spin-wave evolution, with standing waves showing finite phase velocities in the zones where the DMI is nonzero. These results have been obtained with micromagnetic simulations and using a theoretical approach based on the plane-wave method. These chiral magnonic crystals with periodic DMI, which may be attained for instance by covering a thin ferromagnetic film with an array of heavy-metal wires [7], host interesting physical properties, encouraging future experimental studies to prove and evidence these phenomena.

---

[1] R. A. Gallardo, D. Cortés-Ortuño, R. E. Troncoso, and P. Landeros, To be published on: Three-dimensional Magnonics: Layered, micro- and nano-structures, Ed. by G. Gubbiotti, arXiv:1903.04288 (2019).

[2] Y. Iguchi, S. Uemura, K. Ueno, and Y. Onose, Phys. Rev. B **92** (2015), 184419.

[3] S. Seki, Y. Okamura, K. Kondou, K. Shibata, M. Kubota, R. Takagi, F. Kagawa, M. Kawasaki, G. Tatara, Y. Otani, and Y. Tokura, Phys. Rev. B **93** (2016), 235131.

[4] K. Di, V. L. Zhang, H. S. Lim, S. C. Ng, M. H. Kuok, J. Yu, J. Yoon, X. Qiu, and H. Yang, Phys. Rev. Lett. **114** (2015), 047201.

[5] J. Cho, N.-H. Kim, S. Lee, J.-S. Kim, R. Lavrijsen, A. Solignac, Y. Yin, D.-S. Han, N. J. J. van Hoof, H. J. M. Swagten, B. Koopmans, and C.-Y. You, Nat. Commun. **6** (2015), 7635.

[6] M. Belmeguenai, J.-P. Adam, Y. Roussigné, S. Eimer, T. Devolder, J.-V. Kim, S. M. Cherif, A. Stashkevich, and A. Thiaville, Phys. Rev. B **91** (2015), 180405.

[7] R. A. Gallardo, D. Cortés-Ortuño, T. Schneider, A. Roldán-Molina, F. Ma, R. E. Troncoso, K. Lenz, H. Fangohr, J. Lindner, and P. Landeros, Phys. Rev. Lett. **122** (2019), 067204.

Chiral Metastructures and Bio-Assemblies: Plasmonic, Thermal and Hot-Electron Effects

Alexander Govorov[1,2], Larousse Khosravi Khorashad[2], Lucas V. Besteiro[1,3]

[1]Institute of Fundamental and Frontier Science (IFFS), University of Electronic Science and Technology of China (UESTC), Sichuan, P.R. China
[2]Department of Physics, Ohio University, Athens, OH, 45701; govorov@ohio.edu
[3]Institut National de la Recherche Scientifique – Énergie, Materiaux Télécommunications, Varennes, Québec, Canada

Metamaterials and bio-assembled colloidal complexes incorporating metal and semiconductor nanocrystals exhibit strong optical absorption associated with exciton and plasmon resonances. When a system includes chiral molecules, the Coulomb and electromagnetic interactions between excitons and plasmons are able to alter and enhance natural circular dichroism (CD) of chiral molecular dipoles [1,2]. Especially strong enhancement factors for the molecular CD signals can be achieved using plasmonic hot spots [3,4,5]. Strong CD signals can also appear in purely plasmonic systems with a chiral geometry and a strong particle-particle interaction [6,7,8].

In our theoretical approach, we model electromagnetic interactions between chiral and achiral building blocks using both classical and quantum formalisms. The theory predicts several novel mechanisms to transfer and induce circular dichroism in the visible wavelength region using plasmonic and excitonic nanostructures. The CD mechanisms described in our studies come from: the plasmon-molecule Coulomb interaction [2], plasmonic hot-spot enhancement [3,4,5], a long-range electromagnetic interaction in micron-scale nanostructures with a chiral geometry, plasmonic and excitonic resonances in nanocrystals with chiral shapes [9,10], and strong plasmon-plasmon interactions in helical and other chiral assemblies [6,7,8]. In planar metamaterial absorbers, chiral responses and circular dichroism can be observed using the hot-electron injection mechanism and the photo-thermal effect [11,12,13]. Finally, chiral plasmonic nanocrystals enable a new direction of research at the nanoscale - chiral plasmonic photochemistry [14]. Potential applications of the chiral nanostructures are in bio-sensors, optical materials and asymmetric chemistry.

References

[1] X.T. Kong, L.V. Besteiro, Z. Wang, A.O. Govorov, Advanced Materials, DOI: 10.1002/adma.201801790 (2018).
[2] A. O. Govorov, F. Zhiyuan, P. Hernandez, J. M. Slocik, and R. R. Naik, Nano Letters, 10, 1374 (2010).
[3] H. Zhang and A.O. Govorov, Phys. Rev. B 87, 075410 (2013).
[4] M. Layani, A. Ben Moshe, M. Varenik, O. Regev, H. Zhang, A. Govorov, G. Markovich, J. Phys. Chem. C, 117, 22240 (2013).
[5] L. M. Kneer, E.-M. Roller, L. V. Besteiro, R. Schreiber, A. O. Govorov, and T. Liedl, ACS Nano, 12 (9), 9110-9115 (2018).
[6] Z. Fan, A.O. Govorov, Nano Letters, 10, 2580 (2010).
[7] A. Kuzyk, R. Schreiber, Z. Fan, G. Pardatscher, E.-M. Roller, A. Högele, F.C. Simmel, A. O. Govorov, T. Liedl, Nature, 483, 311 (2012).
[8] A.Kuzyk, R. Schreiber, H. Zhang, A.O. Govorov, T. Liedl, and Na Liu, Nature Materials, 13, 862 (2014).
[9] Z. Fan and A. O. Govorov, Nano Lett. 12, 3283–3289 (2012).
[10] A. Ben-Moshe, S. G. Wolf, M. Bar Sadan, L. Houben, Z. Fan, A. O. Govorov, G. Markovich, Nature Communications 5, 4302 (2014).
[11] W. Li, Z. J. Coppens, L.V. Besteiro, W. Wang, A.O. Govorov, J. Valentine, Nature Communications 6, 8379 (2015).
[12] X.-T. Kong, L. Khosravi Khorashad, Z. Wang, A. O. Govorov, Nano Letters 18 (3), 2001–2008 (2018).
[13] C. Jack, A. S. Karimullah, R. Tullius, L. Khosravi Khorashad, M. Rodier, B. Fitzpatrick, L. D. Barron, N. Gadegaard, A. Lapthorn, V. M. Rotello, G. Cooke, A.O. Govorov, M. Kadodwala, Spatial Control of Chemical Processes on Nanostructures

through Nano-Localized Water Heating, Nature Communications, 7, 10946 (2016).
[14] T. Liu, L.V. Besteiro, T. Liedl, M.A. Correa-Duarte, Z. Wang, A. Govorov, Chiral plasmonic nanocrystals for generation of hot electrons: Toward polarization-sensitive photochemistry, Nano Letters, 19 (2), pp 1395–1407 (2019).

Tailoring the Chiral Response of Achiral Nanostructures Using Structured Light

Peter Banzer

Max Planck Institute for the Science of Light, Erlangen, Germany
Institute of Optics, Information and Photonics, Friedrich-Alexander-University Erlangen-Nuremberg
*corresponding author, E-mail: peter.banzer@mpl.mpg.de

Abstract

By utilizing engineered highly confined light for excitation, we show that an achiral nanosphere can scatter like a chiral dipole. While the input beam carries neither spin nor orbital angular momentum, we take advantage of the complex polarizabilities of an achiral spherical silicon particle.

1. Introduction

The recent interest in exotic dipole moments such as transversely spinning [1], Huygens [2-6] and Janus dipoles [5,6] has been an important driving force in nanophotonics research, contributing to the understanding of light-matter interaction and opening up new routes towards photon traffic control at the nanoscale [3-5]. In our work, we now investigate an important member of this zoo of electromagnetic dipole moments, i.e. the chiral dipole conceptually known from the interaction of circularly polarized light with chiral molecules or artificial nanostructures. Usually, the chiral dipole is a direct consequence of the twisted path of electrons in helically shaped chiral nano-entities, fixing also their handedness and optical response.

2. Structured Light-Matter Interactions – Exciting Chiral Dipoles in Achiral Nanoscturctures

In our experiments, we now show that a chiral dipolar mode consisting of parallel electric and magnetic dipole moments phase shifted with respect to each other by pi/2 can also be excited, with full tunability of handedness and strength, in an individual achiral nano-antenna [7]. This dipole represents a fundamental mode in the helicity basis and it exhibits maximum chirality. Here, we excite the mode with a locally linearly polarized beam carrying neither spin nor orbital angular momentum, taking advantage of the complex polarizabilities of an achiral spherical silicon particle. The scattered light, however, carries both, spin and orbital angular momentum, which can be manipulated spectrally. In particular, we can even tune the sign of the helicity/chirality of the mode, by changing the excitation wavelength, a feature which cannot be observed for fundamental modes of chiral plasmonic structures. Our study shows that the excitation and appearance of chiral dipoles is not restricted to chiral nanostructures, but they can also be excited and very flexibly controlled in achiral systems using structured light.

3. Conclusions

In this presentation, we highlight the excitation of chiral dipoles in achiral nanostructures, and survey other interesting related aspects of the interaction of structured light with individual nanoparticles [8].

References

[1] A. Aiello, P.Banzer, M. Neugebauer, G. Leuchs, From transverse angular momentum to photonic wheels, *Nature Photonics* 9: 789-795, 2015.

[2] I. Staude, A. E. Miroshnichenko, M. Decker, N. T. Fofang, S. Liu, E. Gonzales, J. Dominguez, T. S. Luk, D. N. Neshev, I. Brener, and Y. Kivshar, , *ACS Nano* 7: 7824, 2013.

[3] M. Neugebauer, P. Wozniak, A. Bag, G. Leuchs, P.Banzer, Polarization Controlled Directional Scattering for Nanoscopic Position Sensing, *Nature Communications* 7: 11286, 2016.

[4] A. Bag, M. Neugebauer, P. Woźniak, G. Leuchs, P.Banzer, Transverse Kerker Scattering for Ångström Localization of Nanoparticles, *Physical Review Letters* 121: 193902, 2018.

[5] M. F. Picardi, A. V. Zayats, and F. J. Rodriguez-Fortuno, Janus and Huygens dipoles: Near-field directionality beyond spin-momentum locking, *Physical Review Letters* 120: 117402, 2018.

[6] M. F. Picardi, M. Neugebauer, J. S. Eismann, G. Leuchs, P. Banzer, F. J. Rodriguez-Fortuno, A. V. Zayats, Experimental demonstration of linear and spinning Janus dipoles for polarisation and wavelength selective near-field coupling, *arXiv*:1901.07236v1, 2019.

[7] J. S. Eismann, M. Neugebauer, P. Banzer, Exciting a chiral dipole moment in an achiral nanostructure, *Optica* 5: 954-959, 2018.

[8] S. Nechayev, J. Eismann, G. Leuchs, P. Banzer, Orbital-to-Spin Angular Momentum Conversion Employing Local Helicity, *Physical Review B* 99: 075155, 2019.

Theory of chiral transport in chiral crystals

Shuichi Murakami[1,2,3]

[1]*Department of Physics, Tokyo Institute of Technology*

[2]*TIES, Tokyo Institute of Technology* [3]*CREST, JST*

In crystals with helical structure such as tellurium (Te) [1], we propose that a current along the helical axis induces an orbital magnetization [2,3] as well as spin magnetization. In crystals without inversion symmetry, such as chiral crystals, each Bloch eigenstate has an orbital magnetization, but their sum vanishes in equilibrium. We show that in the presence of the current, the electron distribution becomes off-equilibrium, giving rise to nonzero orbital magnetization. We can call this effect an orbital Edelstein effect, because this effect is similar to the Edelstein effect, where the current induces spin polarization in crystals without inversion symmetry.

This effect is analogous to solenoids in classical electrodynamics (Fig. 1(a)). Within this analogy to solenoids, we quantify this effect by introducing a dimensionless parameter ξ, which represents a number of turns within the unit cell when regarded as a classical solenoid. Then we found that ξ is largely enhanced when the system is in the Weyl semimetal phase [2,3]. Here the Weyl semimetal phase [4] is allowed by broken inversion symmetry. Moreover, we propose a similar effect for phonons. In crystals, each phonon eigenmode has angular momentum due to rotational motions of the nuclei (Fig. 1(b)), but their sum is zero in equilibrium. Meanwhile a heat current in the Te crystal induces a nonzero total angular momentum [5]. We evaluate this effect for GaN and Te by ab initio calculation, and propose experiments to measure this effect (Fig. 1(c)).

[1] M. Hirayama, R. Okugawa, S. Ishibashi, S. Murakami, and T. Miyake, Phys. Rev. Lett. 114, 206401 (2015).

[2] T. Yoda, T. Yokoyama, and S. Murakami, Sci. Rep. 5, 12024 (2015).

[3] T. Yoda, T. Yokoyama, and S. Murakami, Nano Lett. 18, 916 (2018).

[4] S. Murakami, New J. Phys. 9, 356 (2007).

[5] M. Hamada, E. Minamitani, M. Hirayama, S. Murakami, Phys. Rev. Lett. 121, 175301 (2018).

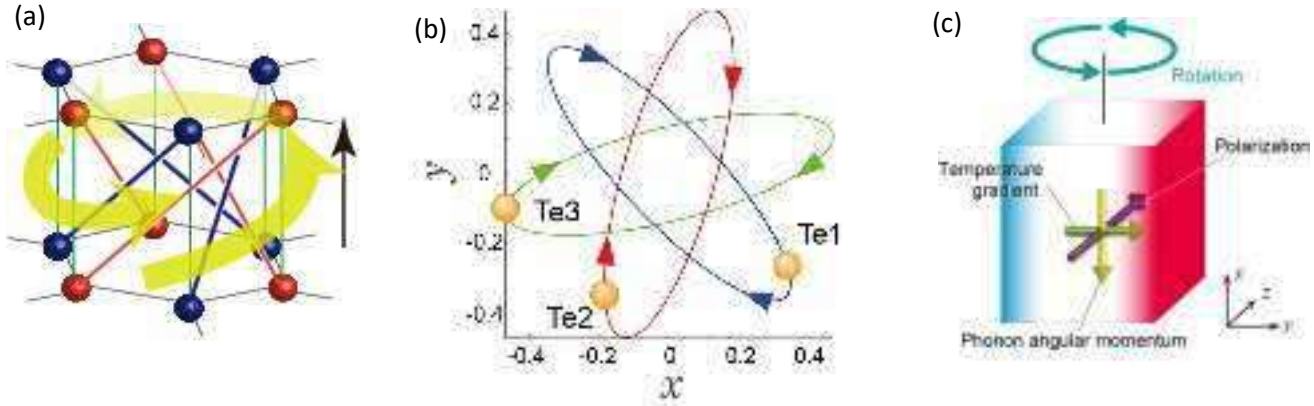


Fig. 1. (a) Schematic picture of the orbital Edelstein effect. (b) Rotational motion for a phonon mode in tellurium. (c) Proposed measurement for phonon Edelstein effect.

Stability and dynamics of skyrmions in multiferroic transition metal halides

Maxim Mostovoy and Alessio Pozzi

Zernike Institute for Advanced Materials, University of Groningen, Groningen, The Netherlands
*corresponding author, E-mail: m.mostovoy@rug.nl

Abstract

We study non-collinear magnetic orders in a transition metal dihalide with competing exchange interactions. We find an unusual defect with the skyrmion topology carrying both magnetic and electric dipole moments, which is stable in uniform and modulated magnetic phases of this material. We study dynamics of these skyrmions induced by spin-orbit torques and by the magnetoelectric coupling to an applied electric field.

1. Introduction

Mott insulators with competing Heisenberg exchange interactions form a new class of materials where topological magnetic defects, such as skyrmions, can exist in absence of inversion symmetry breaking [1-4]. Skyrmions in centrosymmetric materials have more degrees of freedom and show more complex dynamics than skyrmions in chiral magnets. In addition, the electric polarization induced by non-collinear spin textures couples the topological magnetic defects to an applied electric field [5]. This magnetoelectric coupling allows for the electric control of skyrmions in Mott insulators accompanied by low energy losses.

Transition metal halides form an interesting class of multiferroic frustrated magnets that can host skyrmions. These layered van der Waals materials allow for exfoliation down to monolayers and hold promise of new spintronic applications [6]. Competing exchange interactions between transition metal ions result in a variety of magnetic phases, including non-collinear spiral states that induce an electric polarization [7,8]. The interplay between the magnetic orders can be controlled by doping, gating, magnetic and electric fields [9]. We study theoretically stability of skyrmion crystals and isolated skyrmions in Fe-doped $NiBr_2$.

2. Phase diagram

First, we determine the intra- and interlayer exchange constants in $NiBr_2$ using the experimentally measured critical values of the magnetic field applied in the *ab* plane for the transitions between the spiral, canted antiferromagnetic, antiferro-fan and field-polarized states of this material [10]. We then obtain a magnetic phase diagram of $Fe_xNi_{1-x}Br_2$ in the out-of-plane magnetic field for various values of the uniaxial anisotropy, which can be tuned by Fe doping [11]. The phase diagram contains the vertical spiral, conical cycloidal spiral, canted antiferromagnetic and field-polarized states. Importantly, the skyrmion crystal phase is suppressed by the relatively strong antiferromagnetic interlayer exchange interactions. The relative displacement of the skyrmion triangular lattices in neighboring layers found for weak interlayer interactions [12] cannot stabilize the three-dimensional skyrmion crystal in $Fe_xNi_{1-x}Br_2$.

3. Topological defects

We found two types of stable topological defects with the skyrmion topology: (i) antiferromagnetic skyrmion tubes with the sign of the in-plane spin component alternating from layer to layer and (ii) skyrmions with topological charge ± 1 localized in a single layer. Although the antiferromagnetic skyrmion tubes are stable in a wider part of the phase diagram than the single-layer skyrmions, the latter topological defects are of more practical interest as they are much easier to create. We found the regions of stability of the single-layer skyrmions in the field-polarized, canted antiferromagnetic and periodically modulated conical spiral phase.

4. Skyrmion dynamics

Dynamics of the single-layer skyrmions is coupled to their helicity dynamics. In the uniform ferro- and antiferro-magnetic phases, the helicity angle increases linearly with time and the skyrmion center-of-mass undergoes a circular motion. In the cyloidal conical spiral phase, the skyrmion trajectory is straight: it moves in the direction normal to the spiral wave vector. The skyrmion motion can be excited by the spin-orbit torque in heterostructures of the magnetic insulator with a heavy metal conductor. Alternatively, the electric polarization induced by non-collinear spin textures can be used to move skyrmions in the conical spiral state.

5. Conclusions

Although the antiferromagnetic interlayer interactions in Fe-doped $NiBr_2$ are strong enough to suppress the skyrmion crystal phase, they allow for skyrmion defects with the topological charge localized in a single layer. These single-

layer skyrmions move under applied spin-orbit torques and oscillating electric fields, which makes them potentially useful for magnetic memory and data processing applications.

Acknowledgements

M.M. acknowledges Vrije FOM-programma "Skyrmionics".

References

[1] T. Okubo, S. Chung, H. Kawamura, Multiple-q states and the skyrmion lattice of the triangular-lattice Heisenberg antiferromagnet under magnetic fields, *Phys. Rev. Lett*. 108: 017206, 2012.

[2] A. O. Leonov, M. Mostovoy, Multiply periodic states and isolated skyrmions in an anisotropic frustrated magnet, *Nature Commun*. 6: 8275, 2015; 8: 14394, 2017.

[3] S. Hayami, S.-Z. Lin, C. D. Batista, Ginzburg-Landau theory for skyrmions in inversion-symmetric magnets with competing interactions, *Phys. Rev. B* 93: 184413, 2016.

[4] Y. A. Kharkov, O. P. Sushkov, M. Mostovoy, Bound states of skyrmions and merons near the Lifshitz point, *Phys. Rev. Lett.* 119: 207201, 2017.

[5] S-W. Cheong, M. Mostovoy, Multiferroics: a magnetic twist for ferroelectricity, *Nature Materials* 6: 13, 2007.

[6] M. A. McGuire, Crystal and Magnetic Structures in Layered, Transition Metal Dihalides and Trihalides *Crystals* 7: 121, 2017.

[7] Y. Tokunaga *et al*., Multiferroicity in $NiBr_2$ with long wavelength cycloidal spin structure on a triangular lattice, *Phys. Rev. B* 84: 060406, 2011.

[8] T. Kurumaji *et al*., Magnetoelectric responses induced by domain rearrangement and spin structural change in triangular-lattice helimagnets NiI_2 and CoI_2. *Phys. Rev. B* 87: 014429, 2013.

[9] S. Jiang, J. Shan, K. F. Mak, Electric-field switching of two-dimensional van der Waals magnets. *Nature Materials* 17: 406, 2018.

[10] K. Katsumata, K. Sugiyama, M. Date, Experimental observation of the antiferro–fan transition in $NiBr_2$. *J. Phys. Soc. Jpn.* 52: 3312, 1983.

[11] M. W. Moore, P. Day, Magnetic phase diagrams and helical magnetic phases in $M_xNi_{1-x}Br_2$ (M = Fe, Mn): a neutron diffraction and magneto-optical study, *J. Solid State Chem.* 59: 23, 1985.

[12] S. Z. Lin, C. D. Batista, Face centered cubic and hexagonal close packed skyrmion crystals in centrosymmetric magnets, *Phys. Rev. Lett.* 120: 077202, 2018.

Magnetic and chemical steering of chiral light at the nanoscale

Alexandre Dmitriev

Department of Physics, University of Gothenburg, Gothenburg 41258, Sweden

E-mail: alexd@physics.gu.se

A major challenge facing nanophotonics is the poor dynamic tunability. A functional adaptive nanophotonic element would feature the real-time large tunability of transmission and/or reflection of light's intensity and/or polarization, or the light's propagation direction over a broad range of wavelengths, and would be robust and easy to integrate. Several approaches have been explored so far including mechanical deformation [1-3], thermal [4] or refractive index [5, 6] effects, and all-optical switching [7, 8]. Building on our previous advances in nanofabrication [9, 10] and the combination of the plasmonic and ferromagnetic materials (magnetoplasmonics) [10-15], we devise an ultra-thin chiroptical surface, built on 2D nanoantennas, where the chiral light transmission is controlled by the externally applied magnetic field with tunability exceeding 100%. This is done by the magnetic steering of the chiral near-field of the nanoantennas. We explore this further by building the dynamic chiroptical surfaces with all-dielectric nanoantennas.

Combining plasmon and molecular resonances [16], we use a practical combination of the large array of magnetoplasmonic antennas and the thin layers of molecular photoswitches to get insight into the plasmon-molecular strong coupling and the associated polaritonic phototransformation chemistry. Further, we probe the opportunities, provided by the combination of chiral nanoantennas and the enantioselective phototransformations in chiral photoswitches.

References

[1] J. Y. Ou et al., An electromechanically reconfigurable plasmonic metamaterial operating in the near-infrared, *Nature Nanotechnol.* **8**, 252 (2013).
[2] J. Valente et al., Reconfiguring photonic metamaterials with currents and magnetic fields, *Appl. Phys. Lett.* **106**, 111905 (2015).
[3] N. I. Zheludev and E. Plum, Reconfigurable nanomechanical photonic metamaterials, *Nature Nanotechnol.* **11**, 16 (2016).
[4] J. Y. Ou et al., Reconfigurable photonic metamaterials, *Nano Lett.* **11**, 2142 (2011).
[5] A. K. Michel et al., Using low-loss phase-change materials for mid-infrared antenna resonance tuning, *Nano Lett.* **13**, 3470 (2013).
[6] Q. Wang et al., Optically reconfigurable metasurfaces and photonic devices based on phase change materials, *Nature Photon.* **10**, 60 (2015).
[7] R. F. Waters et al., Optically switchable photonic metasurfaces, *Appl. Phys. Lett.* **107**, 081102 (2015).
[8] M. Papaioannou et al., Two-dimensional control of light with light on metasurfaces, *Light: Science & Applications* **5**, e16070; doi:10.1038/lsa.2016.70 (2016).
[9] H. Fredriksson et al., Hole-mask colloidal lithography, *Adv. Mater.* **19**, 4296 (2007).
[10] K. Lodewijks et al., Multiscale conformal pattern transfer, *Sci. Rep.* **6**:28490, DOI: 10.1038/srep28490 (2016).
[11] I. Zubritskaya et al., Active magnetoplasmonic ruler, *Nano Lett.* **15**, 3204 (2015).
[12] N. Maccaferri et al., Ultrasensitive and label-free molecular-level detection enabled by light phase control in magnetoplasmonic nanoantennas, *Nat. Commun.* **6**: 6150 (2015).
[13] K. Lodewijks et al., Magnetoplasmonic design rules for active magneto-optics, *Nano Lett.* **14**, 7207 (2014).
[14] Z. Pirzadeh et al., Plasmon−interband coupling in nickel nanoantennas, *ACS Photonics* **1**, 158 (2014).
[15] V. Bonanni et al., Designer magnetoplasmonics with nickel nanoferromagnets, *Nano Lett.* **11**, 5333 (2011).
[16] R. Toftegaard et al., Metal-enhanced 1270 nm-singlet oxygen phosphorescence, *Angew. Chem. Int. Ed.* 47, 6025 (2008).

Circular Dichroism and Spontaneous Chiral Symmetry Breaking in Rotational Particles

Deng Pan[1]*, Hongxing Xu[2], F. Javier García de Abajo [1,3],

[1]ICFO-Institut de Ciencies Fotoniques, The Barcelona Institute of Science and Technology, 08860 Castelldefels (Barcelona), Spain
[2]School of Physics and Technology, Wuhan University, Wuhan 430072, China
[3] ICREA-Institució Catalana de Recerca i Estudis Avançats, Passeig Lluís Companys 23, 08010 Barcelona, Spain
*corresponding author, E-mail: Deng.Pan@icfo.eu

Abstract

We predict that rotating nano-rings and solid nanoparticles show different optical circular dichroisms, and when optically trapped by an unpolarized blue-detuned laser above a certain intensity the void particle starts rotating spontaneously.

1. Introduction

The interaction between light and the mechanical motion of nano-objects is fundamentally important, as recognized by the 2018 Nobel Prize awarded for the development of optical tweezer [1]. Light can exert forces and torques on such objects, and for example, a circularly polarized light beam can induce rotation on a nanoparticle due to conservation of angular momentum [2]. The optical response of the rotating particle is fully described by its polarizability $\alpha(\omega)$ when it is much smaller than the light wavelength. However, the polarizabilities of rotating nano-objects have not been rigorously studied in quantum theory, in part because of the complexity of the quantization of the mechanical rotation.

2. Results

We focus on the optical responses of rotating rings [Fig. 1(a) and (b)] and disks [Fig. 1(c) and (d)]. Applying quantum mechanics, we find the optical polarizabilities of the particles to depend on the thermal population of their internal electronic states. As shown in Fig. 1(a), the energy spectrum of electrons inside a ring in the rest frame is parabolic (solid curve), but for a rotating ring the thermal population is determined by the electronic energy in the frame rotating with the ring (dashed curve). The thermal population of the electrons in a rotating disk can also be determined similarly [Fig. 1(c)]. We use these considerations to calculate the polarizabilities of the ring and disk using the random-phase approximation. The results are shown in Fig. 1(b) and (d). The rotating ring exhibits a strong CD and the resonance splitting equals the rotation frequency Ω, while the disk almost does not possess CD at small Ω.

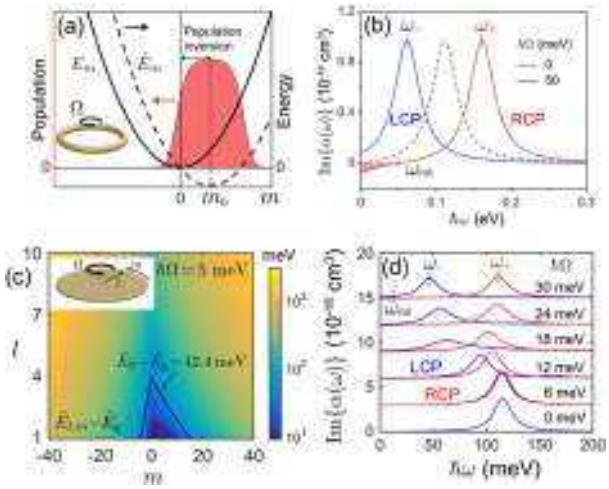


Figure 1: (a) Energy spectrum and thermal population of electrons in a rotating ring. (b) Polarizabilities of a ring (radius R=8 nm, with 80 electrons) rotating at different frequencies. (c) Energy spectrum in a rotating disk (radius R=12 nm, 80 electrons). The black curve shows the Fermi level. (d) Polarizabilities of the ring in (c) rotating at different frequencies.

When illuminating a rotating ring using an unpolarised light beam, the CD leads to an optical torque on the ring [Fig. 2(a)]. When the laser is red-detuned with respect to the resonance frequency ω_0, the optical torque accelerates the rotation of the ring, so the rotational degree of freedom is effectively "heated" [Fig. 2(b)]. Interestingly, the ring at rest is not mechanically stable, as shown by the temporal dynamical evolution in Fig. 1(c), where a small rotation velocity due to any fluctuation is amplified by the "heating" effect until the optical torque is cancelled by a thermal friction torque [3] (red dots). This spontaneous rotation can be regarded as spontaneous chiral symmetry breaking in a nonequilibrium system.

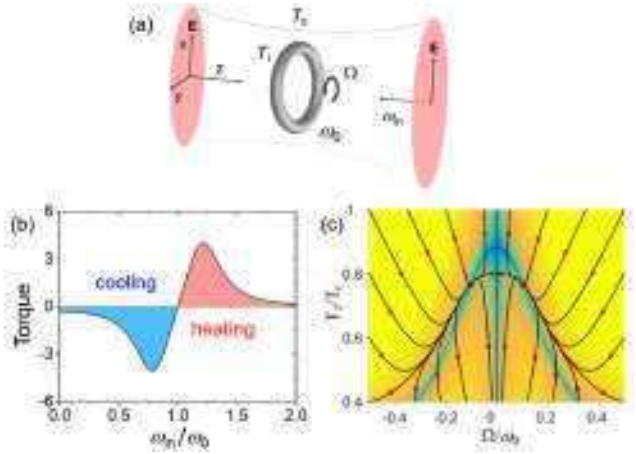


Figure 1: (a) Illustration of a rotating ring under linearly polarized or unpolarized illuminations. (b) Torque experienced by the ring for different light frequencies. (c) Temporal evolution for the ring at different initial rotating frequencies Ω and material temperatures T_1.

3. Conclusions

In this work, we rigorously derive the polarizabilities of rotating nanoparticles using quantum theory. Our results show that rotating nano-rings and solid nanoparticles (e.g., nanodisks) exhibit different optical circular dichroisms (CDs). From the knowledge of CDs of the particles, we predict that a motionless nano-ring exposed to a red-detuned illumination is not a stable configuration and must rotate spontaneously.

Acknowledgements

This work has been supported in part by the Spanish MINECO (MAT2017-88492-R and SEV2015-0522), ERC (Advanced Grant 789104-eNANO), the Catalan CERCA Program, and Fundació Privada Cellex.

References

[1] A. Ashkin, Acceleration and trapping of particles by radiation pressure, *Phys. Rev. Lett.* 24: 156 (1970).

[2] N. B. Simpson N B, *et al.* Mechanical equivalence of spin and orbital angular momentum of light: an optical spanner, *Opt. Lett.* 21: 52 (1997).

[3] A. Manjavacas, F. J. García de Abajo, Vacuum friction in rotating particles, *Phys. Rev. Lett.* 105: 113601 (2008).

Metamaterials and Photonic Crystals for THz Science and Technology

Gate-controlled Optical Properties in Graphene Based Metasurfaces

Teun-Teun Kim[1,2*], Hyeon-Don Kim[3], Hyunjun Kim[4], Sang Soon Oh[5], Bumki Min[4], Shuang Zhang[6]

[1]Center for Integrated Nanostructure Physics (CINAP), Institute for Basic Science (IBS), Suwon, Korea
[2]Sungkyunkwan University, Suwon, Korea
[3]Department of Applied Nano mechanics, KIMM, Daejeon, Korea
[4]Department of Mechanical Engineering, Korea Advanced Institute of Science and Technology (KAIST), Daejeon, Korea
[5]School of Physics and Astronomy, Cardiff University, Cardiff, United Kingdom
[6]School of Physics and Astronomy, University of Birmingham, Birmingham, United Kingdom
*corresponding author, E-mail: t.kim@skku.edu

Abstract

We experimentally demonstrate gate-controlled optical properties including an amplitude of anomalously refracted light and group delay of light with graphene integrated metamaterials with different design rules. The graphene based metasurfaces are expected to provide an important applications such as ultrathin lenses, slow light devices and ultrasensitive sensors and switched.

1. Introduction

Metamaterials, which consist of artificially structured building blocks allow us to manipulate optical properties in ways that would not be possible with materials in nature. Unfortunately, however, very feature that makes these devices so useful, structurally dependent optical properties, also limits their potential for dynamically manipulating electromagnetic waves as micro/nano objects are difficult to modify post fabrication. It has been shown that graphene-based optoelectronic devices can be realized and they have superior merit to compare with conventional semiconductor-based ones for application in the terahertz frequency range. For example, graphene-based metamaterial terahertz modulators provide better modulation not only transmission amplitude and phase but also polarization [1,2]. In this talk, I will review our recent work on electrically controllable optical properties by integrating atomically thin, 2D graphene layer onto 2D functional metallic metasurfaces, so called metasurfaces [3,4].

2. Results

2.1. Amplitude modulation of anomalously refracted light

The metasurfaces consisting of U-type aperture antennas is shown in Fig. 1 (a). For the unit-cell structure with optical axis rotated by angle θ, the transmission coefficients can be represented using the Jones matrix in the basis of right-handed and left-handed circular polarization:

$$T_{\mathrm{Cir.}} = \begin{bmatrix} T_{\mathrm{RR}} & T_{\mathrm{RL}} \\ T_{\mathrm{LR}} & T_{\mathrm{LL}} \end{bmatrix} = \frac{1}{2}\begin{bmatrix} (T_{xx}+T_{yy}) & (T_{xx}-T_{yy})e^{i2\theta} \\ (T_{xx}-T_{yy})e^{-i2\theta} & (T_{xx}+T_{yy}) \end{bmatrix} \quad (1)$$

Here T_{XY} represent the transmission coefficients, where the first subscript indicates the polarization (x or y for linearly polarized and R or L for circularly polarized wave) of transmitted wave and the second subscript indicates the polarization of the incident wave. It is shown that the cross-polarized component T_{RL} possesses a phase discontinuity $e^{i2\theta}$, which is a Pancharatnam-Berry (PB) phase. Therefore, the wave front of the cross-polarized light can be simply manipulated by rotating the U-types of antennas. When the terahertz waves incident normal direction, the refraction angle can be calculated as:

$$\alpha_t = \sin^{-1}((\lambda/2\pi)\, \mathrm{d}\Phi/\mathrm{dx}). \quad (3)$$

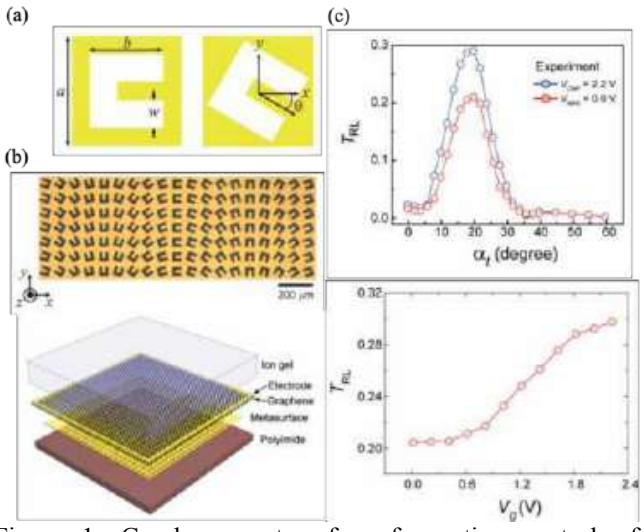


Figure 1: Graphene metasurface for active control of amplitude of anomalously refracted light.

Figure 1 (b) shows the fabricated graphene metasurface with a linear phase gradient. An ion-gel layer is used as a gate-dielectric material. At 1.15 THz, 30 % of right handed

circularly polarized wave is converted to left circularly polarized wave at refraction angle $\alpha_t = 20°$ and it is observed that this refracted cross-polarized wave is effectively controlled by the variation of an applied voltage (Fig. 1 (c)). The maximum modulation depth for refracted T_{RL} is measured to be 28%.

2.2. Active control of group delay

Electromagnetically induced transparency (EIT) is a well-known quantum phenomenon. A remarkable feature of EIT is the drastic slow-down of the group velocity of light. Recently, EIT-like effect can be observed in classical metasurface system without complex experimental setup including laser stability, strong coupling laser power, and low-temperature. Figure 2 (a) shows graphene EIT metasurface consists of bilayer metallic EIT metamaterial, a single-layer graphene, and an ion-gel gate-dielectric layer. Figure 2 (b) shows the measured and simulated transmission of the graphene EIT metasurface as a function of the gate voltages. More than 51 % of transmission of THz wave at 0.75 THz is measured and by increasing gate voltage to graphene layer the transparency peak can be gradually reduced. As a result, the group delay which is characterized as:

$$t_g = -\mathrm{d}\phi/\mathrm{d}\omega \qquad (4)$$

is delayed by 3.1 ps and effectively tuned by changing the gate voltage with tuning range of 3.3 ps. Where ϕ is the phase and ω is the angular frequency of the THz pulse.

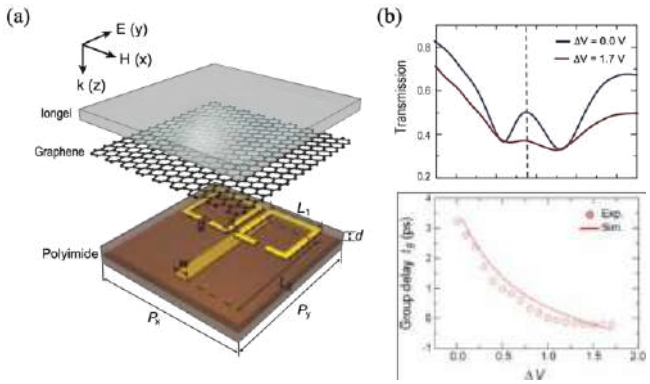


Figure 1: Graphene metasurface for active control of light speed.

3. Conclusions

In conclusion, we have experimentally demonstrated an electrically tunable optical properties with graphene EIT metamaterial at the THz regime. Benefiting from the electric control of optical properties, the proposed graphene metamaterials may provide opportunities in the design of various applications not only for THz regime but also extended to mid-infrared regime.

Acknowledgements

This work was supported by the Institute for Basic Science (IBS-R011-D1), the Marie-Curie International Incoming Fellowships (ref 626184). The work was also supported by the center for Advanced Meta-Materials (CAMM) funded by Korea Government (MSIP) as Global Frontier Project (NRF-2014M3A6B3063709), the European Research Council Consolidator Grant (TOPOLOGICAL), the Royal Society, the Wolfson Foundation, and Horizon 2020 Action Project No. 734578 (D-SPA).

References

[1] S. H. Lee, M. Choi, T.-T. Kim, et al. Switching terahertz waves with gate-controlled active graphene metamaterials. *Nature Materials*, *11*(11): 936–941, 2012.

[2] T.-T. Kim, S. S. Oh, H.-D. Kim, H.-S. Park, O. Hess, B. Min, and S. Zhang, Electrical access to critical coupling of circularly polarized waves in graphene chiral metamaterials. *Science Advances*, 3: 1701377, 2017

[3] T.-T. Kim, H. Kim, M. Kenney, H.-S. Park, H.-D. Kim, B. Min, and S. Zhang, Amplitude Modulation of Anomalously Refracted Terahertz Waves with Gated-Graphene Metasurfaces, *Advanced Optical Materials*, 6: 1700507, 2018.

[4] T.-T. Kim, H.-D. Kim, R. Zhao, S. S. Oh, T. Ha, D. S. Chung, Y. H. Lee, B. Min, and S. Zhang, Electrically Tunable Slow Light Using Graphene Metamaterials, *ACS Photonics*, 5 (5): 1800–1807. 2018.

High Performance Spintronic Terahertz Emitter Enabled by Metal–Dielectric Photonic Crystal and Metamaterials

Zheng Feng[1,2], Dacheng Wang[1,2], Haifeng Ding[3], Jianwang Cai[4], Wei Tan[1,2]

[1]Microsystem and Terahertz Research Center, China Academy of Engineering Physics, Chengdu, China
[2]Insititute of Electronic Engineering, China Academy of Engineering Physics, Mianyang,China
[3]National Laboratory of Solid State Microstructures and Department of Physics, Nanjing University, Nanjing, China
[4] Beijing National Laboratory for Condensed Matter Physics and Institute of Physics, Chinese Academy of Sciences, Beijing, China
*corresponding author, E-mail: fengzheng@mtrc.ac.cn

Abstract

Spintronic terahertz (THz) emitter has attracted great interest recently[1-4]. Here, we introduce two popular optical concepts, photonic crystal and metamaterials, to improve the performance of the emitter. By utilizing the metal–dielectric photonic crystal structure, the conversion efficiency of spintronic THz emitter is improved due to the enhanced absorption of pumped fs laser. By integrating spintronic THz emitter with metamaterials, the THz emission with tunable polarization is demonstrated in a single device.

1. Introduction

Spintronic THz emitter was firstly demonstrated in 2013, which is based on the spin related effects in ferromagnetic/nonmagnetic (FM/NM) heterostructures[1]: (i) a femtosecond laser pulse impinges on the FM/NM heterostructure, inducing ultrafast spin currents into the NM layer from the FM layer; (ii) transient charge currents are generated by the inverse spin Hall effect, leading to THz emission out of the structure. The new type emitter is broadband (up to 30 THz), compact, low cost, and magnetic field controllable, etc. Since then, efforts have been made in optimizing the material composition and structure geometry, the conversion efficiency has been improved close to that of ZnTe crystal[2-4].

One of the drawbacks of the current designs is the rather limited laser absorption - more than 50% energy is wasted and the conversion efficiency is thus limited. Here, we theoretically propose and experimentally demonstrate a novel device, metal-dielectric photonic crystal spintronic THz emitter ,that fully utilizes the laser intensity and significantly improves the conversion efficiency[5]. One of the unique advantages of the spintronic emitter is that the linear polarization orientation of emitted THz wave can be easily tuned via external magnetic field. We integrate spintronic THz emitter with metamaterials, where metamaterials are designed to act as broadband THz quarter-wave plate[6], and consequently the polarization state of the emitted THz wave can be switched between linear and circular by rotating the magnetic field in the individual device.

2. Results and Discussions

Figure 1a shows the schematic of metal–dielectric photonic crystal type spintronic THz emitter. It is composed of periodic metal–dielectric films, [dielectric interlayer/NM_1/FM/NM_2]n, on MgO substrate, where n denotes the number of repeats. Multiple scatterings and interference occurs when laser light propagates along the structure, which can be tailored by adjusting the thickness of the period (d) and the number of repeats (n). In principle, the reflection and transmission could be suppressed simultaneously, thus maximizing the laser absorption in the metal layers, which improves the conversion efficiency. Transfer-matrix method is employed for the theoretical calculations and the structure design. According to the theoretical design, we experimentally fabricate a series of samples with different periods and repeats. In this work, we choose W(1.8 nm)/Fe(1.8 nm)/Pt(1.8 nm) as the single repeat THz emitter, which exhibits the largest THz emission efficiency in our experiments, and SiO_2 for the dielectric interlayer. The measured laser absorbance and the THz amplitude show one-to-one correspondences with the theoretical calculations (Figure 1b). At the optimal conditions, the experimentally obtained conversion efficiency of the photonic crystal structures is about 1.7 times as high as that of the single-repeat spintronic THz emitter (Figure 1c), demonstrating the validity of the proposed method.

Figure 2a shows the schematic of the metamaterial integrated spintronic THz emitter. It is composed of a metal–dielectric photonic crystal spintronic THz emitter and a metamaterials, which are fabricated on the opposite sides of the MgO substrate, respectively. The metamaterials consist of a sandwiched structure, comprising of two layers of metallic wire gratings and three polyimide films, which act as a broadband THz quarter-wave plate. Accordingly, the polarization state of the THz wave generated from the

spintrnic emitter can be tailored depending on the initial orientation of linear polarization. As shown in Figure 2b and Figure 2c, the emitted THz wave varies from linearly polarized light to circularly polarized light as the magnetic field orientation varies from 45 º to 0 º.

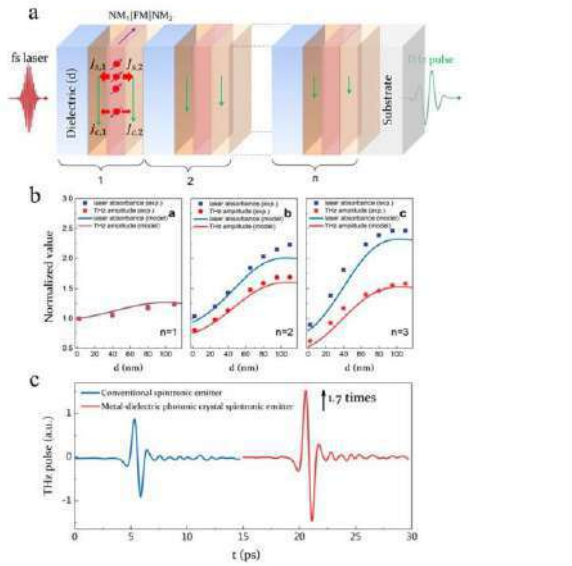


Figure 1: a. Schematic of the metal–dielectric photonic crystal spintronic THz emitter; b. Normalized THz pulse amplitude (red) and femtosecond laser absorbance (blue) as the functions of SiO_2 thickness d for different repeats; c. THz pulse amplitude comparison between conventional and metal-dielectric photonic crystal spintronic emitter.

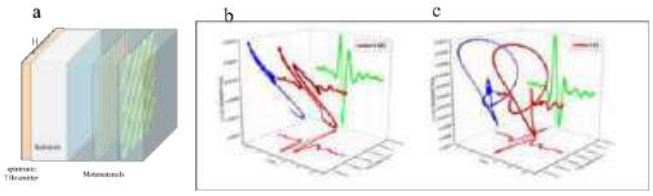


Figure 2: a. Schematic of the metamaterial integrated spintronic THz emitter; b.The emitted THz wave is linearly polarized when H=45 º ; c. The emitted THz wave is circularly polarized when H=0 º.

3. Conclusions

In conclusion, metal–dielectric photonic crystal structure has been investigated to enhance the laser absorption in the spintronic THz emitter, and thus improve the conversion efficiency. Meanwhile, a polarization-tunable terahertz emitter that integrates spintronic THz emitter and metamaterials has been demonstrated. This work opens a new pathway to improve the performance of spintronic THz emitter from the perspective of optics.

Acknowledgements

This work was supported by Science Challenge Project (Grant No. TZ2018003), the National Natural Science Foundation of China (Grants Nos. 11504345, 11504346, 51571109, 11734006, and 11674379), the National Key R&D Program of China (Grant Nos.2017YFA0303202 and 2018YFA0306004), and the National Basic Research Program of China (Grant No. 2015CB921403).

References

[1] Kampfrath T, Battiato M, Maldonado P, Eilers G, Nötzold J, Mährlein S, et al. Terahertz spin current pulses controlled by magnetic heterostructures. Nature nanotechnology. 2013;8(4):256.

[2] Seifert T, Jaiswal S, Martens U, Hannegan J, Braun L, Maldonado P, et al. Efficient metallic spintronic emitters of ultrabroadband terahertz radiation. Nature photonics. 2016;10(7):483-8.

[3] Yang D, Liang J, Zhou C, Sun L, Zheng R, Luo S, et al. Powerful and tunable THz emitters based on the Fe/Pt magnetic heterostructure. Advanced Optical Materials. 2016;4(12):1944-9.

[4] Wu Y, Elyasi M, Qiu X, Chen M, Liu Y, Ke L, et al. High - Performance THz Emitters Based on Ferromagnetic/Nonmagnetic Heterostructures. Advanced Materials. 2017;29(4).

[5] Feng Z, Yu R, Zhou Y, Lu H, Tan W, Deng H, et al. Highly Efficient Spintronic Terahertz Emitter Enabled by Metal–Dielectric Photonic Crystal. Advanced Optical Materials. 2018;6(23):1800965.

[6] Cong L, Xu N, Gu J, Singh R, Han J, Zhang W. Highly flexible broadband terahertz metamaterial quarter-wave plate. Laser & Photonics Reviews. 2014;8(4):626-32.

Photonic Crystal Waveguide Technologies for Terahertz Applications

Masayuki Fujita

Graduate School of Engineering Science, Osaka University, Toyonaka, Japan
E-mail: fujita@ee.es.osaka-u.ac.jp

Abstract

Terahertz waves, which are located in the region between radio and light waves, have attracted a great deal of interest in the interdisciplinary field of photonics and electronics. This study presents recent progress on photonic-crystal waveguide devices for advanced applications to the terahertz region.

1. Introduction

Photonic crystals are composed of dielectric materials with periodic refractive index distributions on scales comparable to the wavelengths [1, 2]. They are analogous to solid-state crystals with periodic potential distributions. Appropriate photonic-crystal designs exhibit a photonic bandgap in which no optical modes can exist. Introducing an artificial defect in a photonic crystal by disturbing the periodicity can produce compact and low-loss photonic components. These can be used not only to develop integrated devices [3] but also to manipulate radiation from matter [4]. In particular, two-dimensional photonic-crystal slabs with high refractive index contrasts (semiconductor/air) are promising for practical applications because of their strong optical confinement in simple, thin planar structures [5, 6].

This study presents recent progress on photonic-crystal waveguide devices for the terahertz (THz) region [7–18], which is located between the radio and light-wave frequencies (0.1–10 THz) and has attracted much attention in the interdisciplinary field of photonics and electronics for advanced applications on sensing and communications [19–21].

2. Low-loss THz-integrated platform

Currently, most existing THz application systems are composed of bulky and complex discrete components. Although metallic transmission lines based on conventional electronics are candidates for THz-integrated technology, the propagation loss is high (~10 dB/cm) in the THz region because of high absorption loss in metals. To overcome this critical loss issue, metal-free photonic waveguides can be used for routing THz waves. Photonic-crystal slab waveguides composed of only high-resistivity silicon is promising for this concept [7]. Ultralow-loss (< 0.1 dB/cm) waveguides using a photonic-crystal slab have been successfully demonstrated at the 0.3-THz band [8]. In addition to loss management, very broadband (approximately 10% relative to the center frequency) dispersion control is required for various applications because the absolute frequency of a THz wave is approximately three orders smaller than that of near-infrared light. The dispersion engineering of photonic crystal has yielded simultaneous low-loss and low-dispersion waveguides as well as high-speed communications at 36 Gbit/s [9].

For a practical integrated platform, development of a low-loss interface to connect the waveguide is critical. An adiabatic tapered silicon structure integrated with a photonic-crystal waveguide was applied to efficient couplers for a metallic hollow waveguide [8], which is standard for present THz equipment, and for a THz fiber link [10]. In addition, this type of tapered structure [11] along with a microresonator [12] and gradient index lens using an effective medium [13] integrated with a photonic-crystal waveguide were applied to a free space coupler (i.e., an antenna for wireless communications).

3. Development of THz functionalities

Active functions including THz-signal generation, detection, frequency conversion, and modulation can be integrated with a photonic-crystal platform. Resonant tunneling diodes (RTDs) based on compound semiconductors are promising THz-active devices because of their capabilities of fundamental THz oscillation [22, 23] and sensitive THz-wave detection [23] at room temperature. A major challenge lies in mode and impedance matching between the RTD and photonic-crystal waveguide for efficient coupling because of the large difference in their dimensions. A metallic tapered-slot coupling structure integrated with an RTD chip with an exponential characteristic profile provides an adiabatic impedance change from the RTD to the photonic-crystal waveguide to achieve high coupling efficiency (approximately 50%) with broadband operation (~40 GHz) [14].

Because of the low-loss nature of a photonic crystal, a high-Q THz microcavity (> 10,000) was developed [15]. These cavities were integrated with a waveguide and applied to high-sensitive sensing applications at 0.1-THz [16] and 0.3-THz bands [15]. Strong coupling between the high-Q cavity and RTD manipulates the THz oscillation beyond the performance of the RTD electric circuit [17].

Frequency routing functions can be implemented by a compact diplexer based on a photonic-crystal waveguide directional coupler and a photonic heterostructure [18]. Three-channel operation with a bandwidth greater than 5 GHz were realized in a 0.3-THz band [7]. The number of channels can be increased using a tandem structure of a diplexer.

4. Conclusion

This study reported on the recent progress of silicon photonic-crystal waveguides as a future integrated platform for sub-THz applications. The platform is scalable to higher THz frequencies to take advantage of the larger absolute bandwidth.

Acknowledgements

This work was supported in part by the Core Research for Evolutional Science & Technology (CREST) program of Japan Science and Technology Agency (JST) (#JPMJCR1534), and a Grant-in-Aid for scientific research from the Ministry of Education, Culture, Sports, Science, and Technology of Japan (#17H01764).

References

[1] E. Yablonovitch, Inhibited spontaneous emission in solid-state physics and electronics, *Phys. Rev. Lett.* 58: 2059–2062, 1987.

[2] S. John, Strong localization of photons in certain disordered dielectric superlattices, *Phys. Rev. Lett.* 58: 2486–2489, 1987.

[3] T. Baba, Photonic crystals remember the light, *Nat. Photon.* 1: 11–12, 2007.

[4] S. Noda, M. Fujita, T. Asano, Spontaneous-emission control by photonic crystals and nanocavities, *Nat. Photon.* 1: 449–458, 2007.

[5] M. Fujita, S. Takahashi, Y. Tanaka, T. Asano, S. Noda, Simultaneous inhibition and redistribution of spontaneous light emission in photonic crystals, *Science* 308: 1296–1298, 2005.

[6] R. Kakimi, M. Fujita, M. Nagai, M. Ashida, T. Nagatsuma, Capture of a terahertz wave in a photonic-crystal slab, *Nat. Photon.* 8: 657–663, 2014.

[7] W. Withayachumnankul, M Fujita, T. Nagatsuma, Integrated silicon photonic crystals towards terahertz communications, *Adv. Optical Mater.* 6: 1800401-1–1800401-7, 2018.

[8] K. Tsuruda, M. Fujita, T. Nagatsuma, Extremely low-loss terahertz waveguide based on silicon photonic-crystal slab, *Opt. Express* 23: 31977–31990, 2015.

[9] X. Yu, M. Sugeta, Y. Yamagami, M. Fujita and T. Nagatsuma, Simultaneous low-loss and low-dispersion in a photonic-crystal waveguide for terahertz communications, *Appl. Phys. Express* 12: 012005-1–012005-5, 2019.

[10] X. Yu, Y. Hosoda, T. Miyamoto, K. Obata, J.-Y. Kim, M. Fujita, T. Nagatsuma, Terahertz fibre transmission link using resonant tunnelling diodes integrated with photonic-crystal waveguides, *Electron. Lett.* 55: 2019. doi.org/10.1049/el.2018.7686.

[11] W. Withayachumnankul, R. Yamada, M. Fujita, T. Nagatsuma, All-dielectric rod antenna array for terahertz communications, *APL Photon.* 3: 051707-1–051707-1, 2018.

[12] W. Withayachumnankul, R. Yamada, C. Fumeaux, M. Fujita, T. Nagatsuma, All-dielectric integration of dielectric resonator antenna and photonic crystal waveguide, *Opt. Express* 25: 14706–14714, 2017.

[13] D. Headland, W. Withayachumnankul, R. Yamada, M. Fujita, T. Nagatsuma, Terahertz multi-beam antenna using photonic crystal waveguide and Luneburg lens, *APL Photon.* 6: 126105-1–126105-18, 2018.

[14] X. Yu, R. Yamada, J.-Y. Kim, M. Fujita and T. Nagatsuma, Integrated circuits using photonic-crystal slab waveguide and resonant tunneling diode for terahertz communication, *Proc. PIERS*, Toyama, Japan, pp. 599–605, 2018.

[15] K. Okamoto, K. Tsudura, S. Diebold, S. Hisatake, M. Fujita, T. Nagatsuma, Terahertz sensor using photonic crystal cavity and resonant tunneling diodes, *J. Infrared Millim. Terahertz Waves* 38: 1085–1097, 2017.

[16] S. M. Hanham, C. Watts, W. J. Otter, S. Lucyszyn, and N. Klein, Dielectric measurements of nanoliter liquids with a photonic crystal resonator at terahertz frequencies, *Appl. Phys. Lett.* 107: 032903-1–032903-5, 2015.

[17] X. Yu, J.-Y. Kim, M. Fujita, T, Nagatsuma, Highly stable terahertz resonant tunneling diode oscillator coupled to photonic-crystal cavity, *Proc. APMC2018*, Kyoto, Japan, pp. 114–116, 2018.

[18] M. Yata, M. Fujita, T. Nagatsuma, Photonic-crystal diplexers for terahertz-wave applications, *Opt. Express* 24: 7835–7849, 2016.

[19] T. Nagatsuma, S. Hisatake, M. Fujita, H. H. N. Pham, K. Tsuruda, S. Kuwano, J. Terada, Millimeter-wave and terahertz-wave applications enabled by photonics, *IEEE J. Quantum Electron.* 52: 0600912-1–0600912-12, 2016.

[20] T. Nagatsuma, G. Ducournau, C. C. Renaud, Advances in terahertz communications accelerated by photonics, *Nat. Photon.* 10: 371-379, 2016.

[21] D. M. Mittleman, Twenty years of Terahertz imaging, *Opt. Express* 26: 9417–9431, 2018.

[22] M. Asada, S. Suzuki, Room-temperature oscillation of resonant tunneling diodes close to 2 THz and their functions for various applications, *J. Infrared Millim. Terahertz Waves* 37: 1185–1198, 2016.

[23] S. Diebold, K. Nishio, Y. Nishida, J. Kim, K. Tsuruda, T. Mukai, M. Fujita, T. Nagatsuma, High-speed error-free wireless data transmission using a terahertz resonant tunnelling diode transmitter and receiver, *Electron. Lett.* 52: 1999–2001, 2016.

Photonic Crystal Resonators as Bio-liquid Sensing Platforms in the Terahertz Band

Stephen M. Hanham[1,2*], Clare Watts[2], M. M. Ahmad[3], William J. Otter[3], Stepan Lucyszyn[3], and Norbert Klein[2]

[1]Department of Electronic, Electrical and Systems Engineering, University of Birmingham, Birmingham, UK
[2]Department of Materials, Imperial College London, London, UK
[3]Department of Electrical and Electronic Engineering, Imperial College London, London, UK
*corresponding author, E-mail: stephen.hanham@ieee.org

Abstract

We describe the development of high quality (Q) factor photonic crystal resonators (PCRs) integrated with microfluidic systems to form the basis of highly sensitive liquid sensing platforms for the terahertz band. The strong confinement of the terahertz field in combination with the high Q-factor provided by the PCR allows the measurement of the dielectric properties of sub-nanoliter liquid volumes. We demonstrate the utility of this approach by measuring the complex permittivity of several bio-liquids at 100 GHz.

1. Introduction

PCRs have a well-established ability to achieve ultra-high quality (Q)-factors while simultaneously confining optical and infrared light to near- or sub-wavelength volumes. This feature makes them ideal sensors for samples with volumes less than λ^3. In the terahertz band, PCRs are less well developed despite the possibility of offering some of the highest Q-factors at room-temperature.

In this paper, we demonstrate the realization of several different types of PCRs operating at 100 and 200 GHz. We show that these resonators when combined with microfluidics allow the extremely sensitive detection of a liquid analyte's complex permittivity through enhancement of the strength of interaction between the liquid and the PCR's resonant mode.

2. High-Q terahertz PCRs

We can have experimentally demonstrated both microbeam and slab type PCRs for the low terahertz band and they will now be discussed individually.

2.1. THz Microbeam PCRs

A 1D or microbeam PCR can be fabricated from a rectangular dielectric slab waveguide by exploiting the transverse waveguide (TE) bandgap induced in the waveguide through the introduction of a linear array of cylindrical air holes. Through careful design of the hole radii and positions, a localized defect state can be created which supports a resonant mode with a ultra-high Q-factor [1].

We have experimentally demonstrated microbeam PCRs operating at 100 and 200 GHz [2], recently achieving Q-factors as high as 22,000. Fig. 1(a) shows one of the fabricated microbeam PCRs. The central microbeam is suspending using a series of supporting struts which electromagnetically isolates it from its environment, reducing dielectric losses and maximizing its Q-factor.

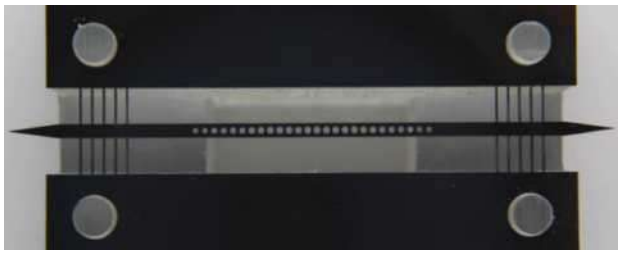


Figure 1: A one-dimensional microbeam PCR with a resonant frequency of 100 GHz.

2.2. THz Slab PCRs

A commonly implemented PCR is the slab PCR, which exploits the 2D TE bandgap created in a dielectric substrate when a periodic array of air holes is introduced. We realized a PCR resonating at W-band by creating a L3 cavity defect (three omitted holes) in a triangular lattice of holes etched in a high resistivity silicon substrate as shown in Fig. 2. The resonant defect was excited using a W1 defect waveguide, created by omitting a line of holes in the lattice. A Q-factor of approximately 11,900±500 was demonstrated, limited by the dielectric loss in the silicon [3].

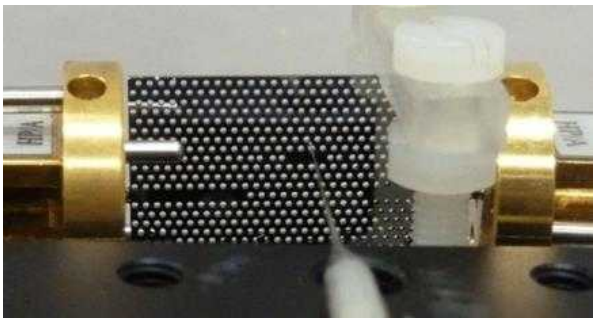


Figure 2: A two-dimensional photonic crystal slab resonator designed for W-band operation suspended between two waveguide flanges. A capillary tube is used to flow liquids through the field of the resonant mode.

2.3. PCR Fabrication

Both the microbeam and slab PCRs were fabricated using the Bosch process to perform deep reactive-ion etching (DRIE) of the 525 µm thick silicon wafer (resistivity >10 kΩ·cm) to realize the high aspect ratio holes with nearly vertical sidewalls.

3. Liquid Sensing

The PCRs were integrated with microfluidic systems to enable their use as liquid sensing platforms. A microfluidic syringe pump and quartz capillaries with 100-200 µm diameter were used to flow liquid analytes close to or through the high intensity region of the electric field of the PCR's resonant mode.

The introduction of the liquid analyte modifies the resonant modes properties. Perturbation theory can be used to relate a change in the PCR's resonant frequency Δf and reciprocal Q-factor $\Delta(1/Q)$ to the complex permittivity ϵ_s of a liquid analyte introduced into the field of the PCR. By assuming a quasi-static approximation for the electric field inside the liquid sample, the following analytical expression can be derived [4]

$$\frac{\Delta f}{f_0} + \frac{i}{2}\Delta\left(\frac{1}{Q}\right) \approx -A\frac{\epsilon_s - B}{\epsilon_s + \epsilon_q} \qquad (1)$$

where ϵ_s and ϵ_q are the liquid sample and quartz capillary permittivies, respectively, and A and B are the coefficients determined through fitting the measured response of binary solutions of water-ethanol solutions of known permittivity.

3.1. Bio-liquid and cell sensing

Once the system is calibrated and the fitting coefficients determined, the PCR can then be used to characterize the permittivity of unknown liquid analytes. As an initial demonstration, we characterize the constituents of human blood at 100 GHz using the slab PCR. We prepared cell suspensions of white (0.5% vol.) and red (50% vol.) blood cells and measured relative complex permittivities of 8.6±0.4+i(14.2±2) and 8.2±0.4+i(11.4±2), respectively. The blood plasma was measured to have a permittivity of 8.7±0.4+i(13.6±2).

3.2. Toward single biological cell sensing

The sensitivity provided by the use of a high-Q PCRs can be leveraged for the detection of sub-wavelength particles in a liquid. An important application of this is the dielectric measurement of single biological cells in a culture medium. To achieve this, we have designed improved PCRs which confine the field to smaller modal volumes and improved the microfluidics to allow smaller diameter capillary tubes to reduce the liquid interaction volume. Initial measurements have shown this approach to be capable of detecting individual cells. The potential advantage of this approach is that it allows non-invasive, label-free and contactless cell analysis to be made in real-time

4. Conclusions

We have demonstrated microbeam and slab type PCRs for the terahertz band, realizing Q-factors as high as 22,000 and limited by dielectric loss in the silicon. By combining these resonators with microfluidic systems, we have created sensing platforms for the measurement of the dielectric properties of nanoliter and sub-nanoliter quantities of liquids. This result represents a step towards a lab-on-a-chip device for the analysis of bio-liquids at terahertz frequencies

Acknowledgements

This work was financially supported by grant EP/M001121/1 from the UK's Engineering and Physical Sciences Research Council (EPSRC).

References

[1] Q. Quan and M. Loncar, "Deterministic design of wavelength scale, ultrahigh Q photonic crystal nanobeam cavities," *Opt. Exp.*, vol. 19, no. 19, pp. 18529–18542, Sep. 2011.

[2] S. M. Hanham, M. M. Ahmad, S. Lucyszyn, and N. Klein, "LED-Switchable High-Q Packaged THz Microbeam Resonators," *IEEE Trans. Terahertz Sci. Technol.*, vol. 7, no. 2, pp. 199–208, Mar. 2017.

[3] W. J. Otter, S. M. Hanham, N. M. Ridler, G. Marino, N. Klein, and S. Lucyszyn, "100 GHz ultra-high Q-factor photonic crystal resonators," *Sens. Actuators, A*, vol. 217, pp. 151–159, 2014.

[4] S. M. Hanham, C. Watts, W. J. Otter, S. Lucyszyn, and N. Klein, "Dielectric measurements of nanoliter liquids with a photonic crystal resonator at terahertz frequencies," *Appl. Phys. Lett.*, vol. 107, no. 3, p. 32903, Jul. 2015.

Singular graphene metasurfaces for broadband absorption

Paloma A. Huidobro*, E. Galiffi, J.B. Pendry

Imperial College London

*corresponding author, E-mail: p.arroyo-huidobro@imperial.ac.uk

Abstract

Metasurfaces can be formed by structuring a plasmonic surface at the subwavelength scale (see Fig. 1) and yield to richer interactions with external electromagnetic radiation than conventional gratings.

1. Introduction

In this talk conformal transformations will be discussed to design plasmonic metasurfaces, focusing in the case where these transformations have singular points. This gives rise to singular metasurfaces which have continuous spectra rather than the discrete set of peaks characteristic of conventional gratings [1].

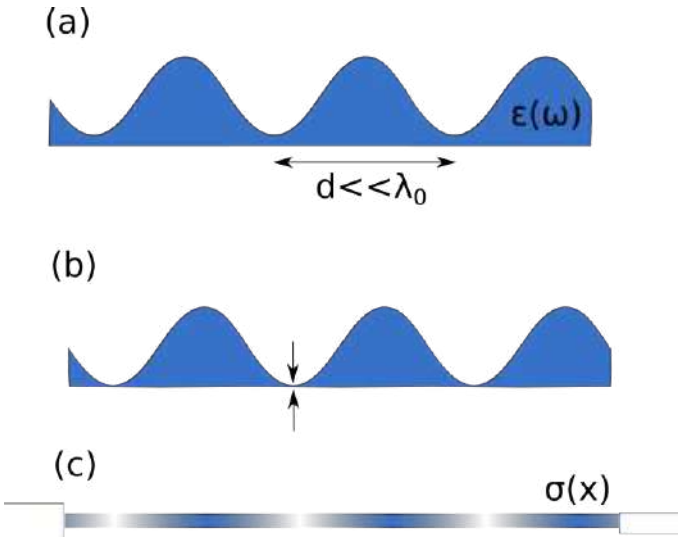


Figure 1: (a) A plasmonic surface structured at the subwavelength scale. (b) Surface with touching points which forms a singular metasurface. (c) In the limit of infinitesimal thickness, the singular plasmonic metasurface in (b) represents grapheme with modulated conductivity. The conductivity is suppressed in the singular points.

2. Singular graphene metasurfaces

2.1 Designing singular metasurfaces

Figure 1(a) shows a plasmonic grating designed from a translationally invariant slab through the conformal transformation given by,

$$z' = \frac{d'}{2\pi}\log\left(\frac{1}{e^{2\pi z/d} - iw_0} + iy_0\right)$$

This equation maps a length d of a translationally invariant slab placed at x_0 in frame z into a grating of period d' in frame z'. This is done by successively mapping the slab into an annulus, then to an off-centered annulus and finally to the grating [2]. A singular grating can be designed by taking the inversion center iw_0 very close to the inner annulus, and at the same time renormalizing the whole grating by $d' \to \infty$. This results in a grating schematically depicted in Fig. 1b.

Such plasmonic grating can represent graphene if the grating thickness is mapped to the conductivity, which varies periodically and is vanishingly small at the grating valleys, see Fig. 2.

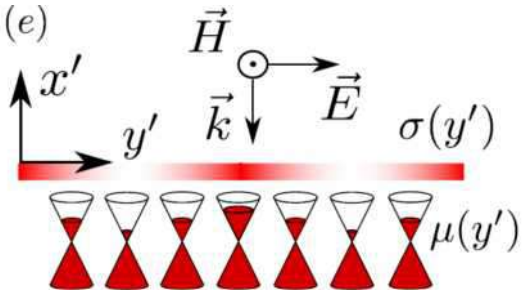


Figure 2: p-polarized light incident on a modulated graphene sheet with vanishing conductivity at the grating valleys.

2.2 Broadband absorption

Non-singular metasurfaces [2] support the excitation of a discrete set of surface plasmon modes, appearing as absorption peaks in their spectrum. As the valley-point conductivity is reduced, more and more peaks can be excited, and the resonances get closer together. Each of this excitations consists of surface plasmon modes featuring extreme confinements close to the singular point. When the metasurface approaches the singular limit, many resonances merge into a broad peak. In this limit, a wealth of surface plasmon resonances merge into a continuum of modes, which can strongly couple to external radiation over a broad range of frequencies, as shown in Fig. 3. These atom-thick metasurfaces then act as broadband absorbers, able to efficiently harvest THz radiation over fractional bandwidths approaching 200% [3,4].

3. Conclusions

This talk will discuss how singular metasurfaces can be designed using analytical tools provided by transformation optics. Broadband absorbers based on singular graphene metasurfaces will be presented.

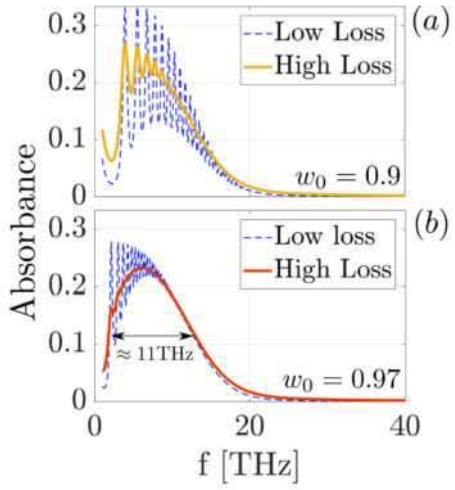


Figure 3: Absorption spectrum of singular graphene metasurfaces. The resonance peaks merge into a continuum once the resistive broadening reaches the spacing between the modes.

Acknowledgements

P.A.H. and J.B.P. acknowledge funding from the Gordon and Betty Moore Foundation. E.G. acknowledges a studentship in the Centre for Doctoral Training on Theory and Simulation of Materials at Imperial College London funded by the EPSRC (EP/L015579/1).

References

[1] J.B. Pendry, P.A. Huidobro, Y. Luo and E. Galiffi, "Compacted dimensions and singular plasmonic Metasurfaces", Science, 358(6365), 915-917 (2017).

[2] P.A. Huidobro, M. Kraft, R. Kun, S.A. Maier and J.B. Pendry, "Graphene, plasmons and transformation optics", Journal of Optics 18, 044024 (2016).

[3] E. Galiffi, J. B. Pendry and P.A. Huidobro, "Broadband THz absorption with singular graphene metasurfaces", ACS Nano, 12 (2), 1006-1013 (2018).

[4] E. Galiffi, J. B. Pendry and P.A. Huidobro, "Singular graphene metasurfaces", EPJ Appl. Metamat. 6, 10 (2019).

Terahertz Spoof Surface Plasmon Polaritons: Modelling, Design, and Experimental Characterization

Mehmet Unlu[1]

[1]Department of Electrical and Electronics Engineering, TOBB University of Economics and Technology, Ankara, Turkey
*corresponding author, E-mail: munlu@etu.edu.tr

Abstract

In this paper, we report the latest progress on the modelling, design, and characterization of the spoof surface plasmon polariton (sSPP) waveguides (WG) for the terahertz band. We will summarize our approach on the empirical modelling of the effective dielectric constant, extraction of the lumped-element circuit model, and realization of fixed-length delay lines using sSPP WGs. To the best of our knowledge, this is first extensive characterization that can be used for advanced sSPP circuit design for the terahertz band.

1. Introduction

Surface plasmon polaritons (SPP) are surface waves that propagate at the boundary of a dielectric and metal. Starting from the date that they have been discovered in 1950s [1], these extraordinary waves have attracted a lot of interest due to their ability to confine and guide the incoming light, which could make it possible to develop miniaturized photonic circuits [2, 3]. It is also possible to structure the metal surface so that the electric field is strongly enhanced around these structures, and a huge signal enhancement can be achieved, which is vital for sensing applications [4].

Surface plasmon polaritons do not exist at the microwave, millimeter-wave, and terahertz bands due to the perfect electric conductor (PEC)-like behavior of the metals at these bands. However, it was shown by Pendry *et al.* [5] that surface waves showing SPP-like behavior can exist at the dielectric-metal boundaries. Structuring the metal surface can allow the designer to control the propagation properties of these surface waves, which are mostly called as the "spoof" surface plasmon polaritons (sSPP). There have been a significant number of studies presented on sSPP engineering for the microwave band in the last few years including modelling [14], filters [6], metasurfaces [7], couplers [8], power dividers [9], antennas [10], switches, mode splitters, and sensors [11].

sSPP structures can also be used for promising applications in the terahertz band [12]. sSPP waveguides can be utilized for the miniaturized terahertz integrated circuits with improved signal integrity, thanks to their high confinement. In addition to that, sSPP waves can be employed for localized signal enhancement, which will significantly improve sensitivity for terahertz sensing applications. Despite these unprecedented possibilities, a limited number of studies have been reported so far that deeply investigate the properties of the sSPP waves for the terahertz band, few of which include experimental verification [13]. However, a detailed investigation and modelling of the sSPP waves is required for the development of the terahertz integrated systems.

In this talk, we will present our latest progress on the development of the sSPP waveguides for the terahertz band. We will first introduce our approach on modelling the most design critical parameter for the design of the sSPP waveguides, namely the effective dielectric constant. Then, we will present some sSPP delay lines examples for the terahertz sSPP phase shifters and reconfigurable circuits. We will also present a lumped-element circuit model for the terahertz sSPP waveguides. Finally, we will give some examples of the reconfigurable sSPP circuits for the terahertz band.

Acknowledgements

This work was supported by TUBITAK under grant 115E219 and TUBA under grant GEBIP 2015.

References

[1] R. H. Ritchie, Plasma losses by fast electrons in thin films, *Phys. Rev.* 106: 874–881, 1957.

[2] J. Pendry, Playing tricks with light, *Science* 285: 1687–1688, 1999.

[3] W. L. Barnes, A. Dereux, T. W. Ebbesen, Surface plasmon subwavelength optics. *Nature*, 424: 824, 2003.

[4] S. M. Nie and S. R. Emery, Probing single molecules and single nanoparticles by surface- enhanced Raman scattering, *Science* 275: 1102–1106, 1997.

[5] J. B. Pendry, L. Martin-Moreno, and F. J. Garcia-Vidal, Mimicking surface plasmons with structured surfaces, *Science* 305: 847-848, 2004.

[6] H. C. Zhang, T. J. Cui, Q. Zhang, Y. Fan, and X. Fu, Breaking the Challenge of Signal Integrity Using Time-Domain Spoof Surface Plasmon Polaritons, *ACS Photonics* 2: 1333–1340, 2015.

[7] G. Dong *et al.*, Wideband helicity dependent spoof surface plasmon polaritons coupling metasurface based on dispersion design, *Sci. Rep.* 6: 38460, 2016.

[8] J. Duan *et al.*, High-efficiency chirality-modulated spoof surface plasmon meta-coupler, *Sci. Rep.* 7: 1354, 2017.

[9] S. Zhou *et al.*, Spoof Surface Plasmon Polaritons Power Divider with Large Isolation, *Sci. Rep.* 8: 5947, 2018.

[10] A. Kianinejad, Z. N. Chen, C.-W. Qiu, A Single-Layered Spoof-Plasmon-Mode Leaky Wave Antenna with Consistent Gain, *IEEE Trans. Antennas Propag.* 65: 681–687, 2017.

[11] X. Chen and W. Fan, Ultrasensitive terahertz metamaterial sensor based on spoof surface plasmon. *Sci. Rep.* 7: 2092, 2017.

[12] C. R. Williams *et al.*, Highly confined guiding of terahertz surface plasmon polaritons on structured metal surfaces, *Nat. Photon.* 2: 175, 2008.

[13] Y. Liang *et al.*, On-chip sub-terahertz surface plasmon polariton transmission lines with mode converter in CMOS, *Sci. Rep.* 6: 30063, 2016.

[14] M. A. Unutmaz and M. Unlu, Modelling of the effective dielectric constant of planar spoof surface plasmon polariton waveguides, *Electron. Lett.* 53: 1418–1420 2017.

THz Metasurfaces for Spatial Beam Modulation and Chemical Identification

Polina Stefanova, Rhiannon Lees, Andreas K. Klein, Michael D. Cooke, Andrew J. Gallant, and Claudio Balocco*

Department of Engineering, Durham University, Durham, United Kingdom
*corresponding author, E-mail: claudio.balocco@durham.ac.uk

Abstract

The wavelength of THz radiation enables the use of metasurfaces which are both compact and easy to manufacture using conventional photolithography. This contribution addresses two specific applications: the optical control of an amplitude and phase THz modulator, and the fabrication of large-area disposable split-ring resonators on plastic and paper for chemical identification. All experiments were carried out using a vector network analyser with THz extenders operating in the frequency range 0.75-1.1 THz.

1. Introduction

Metamaterials operating in the THz region can take advantage of the relatively short wavelength to produce compact structures, and of the fabrication methods typical of the semiconductor and micro electro-mechanical system (MEMs) industry. The minimum features are of the order of a few microns, which can be easily achieved by the photolithographic processes often available in research institutions.

This contribution addresses two specific applications which have been explored at the THz laboratory in Durham in recent months: the optical control of the properties of metasurfaces for THz amplitude and phase modulation, and the manufacturing of disposable metasurfaces on flexible substrates, plastic and paper, for chemical analysis.

Optically controlled THz modulators are desirable for their fast switching speeds, which find application in real-time THz imaging and in future high data rate communication devices. Nevertheless, their use is limited by the poor modulation depth, which requires high optical powers in the order of several W/cm^2 [1]. Optically controlled THz modulators may exploit the photoconductive nature of a near-intrinsic semiconductor, which reduces the THz transmissivity when is illuminated by light with a photon energy above its bandgap [2]. The measured average change in transmission due to photo illumination for high-resistivity floating-zone (HR-FZ) silicon in the range between 0.75 and 1.1 THz was measured to be approximately 0.72 dB (equivalent to a modulation depth of 7.8%), with a normal illumination of 200 mW/cm^2 of unpolarised white light. This is too small for any realistic application; however an increase in optical power would require large sources and bulky heat sinks. Nevertheless, resonating metasurfaces can be incorporated on the semiconductor substrate to improve the modulation efficiency. The response of the material to electromagnetic excitation can be tuned by changing the geometry of the cells. The resonance in this type of metasurfaces can be designed to exhibit exotic properties, such as a negative refractive index, invisibility and zero-thickness [3]. As resonant metamaterials are highly susceptible to changes in the substrate, an increase in modulation depth at their resonance is expected.

The sensitivity of resonant metasurfaces to the substrate can also be exploited for chemical detection and analysis. In this case the aim is to use cost-effective materials, such as paper and plastic, and fabrication techniques which can be easily scaled up. As an example, tumor markers are necessary for a correct cancer diagnosis. The speed and accuracy of these tests can potentially be improved using metasurfaces which resonate at the specific frequencies of these markers. Due to the need to keep samples sterile, it is also highly desirable to make the substrates easy to be dispose of. While paper-based sensor technology has been driven forwards in recent years, the paper fibres result in an uneven surface, which causes the small resonant features to lay on the substrate in an unideal way. In addition to this, paper does not lend itself well to conventional fabrication techniques. Nevertheless, photolithography on paper has been demonstrated with micrometre feature sizes [4]. Other methods such as printing, screen printing [5] and stencil and spray [6] are also potentially viable.

2. Results and Discussion

The reported experimental results were taken using a Keysight vector network analyser (VNA) with Virginia Diodes extenders operating in the 0.75-1.1 THz frequency range. All the designs of the resonant metasurfaces were optimised by 3D finite-difference time-domain (FDTD)

simulations, using both a commercial package, Lumerical, and our own code, Lucifer [7].

2.1. Optically controlled THz modulators

Figure 1 shows two common types of resonant structures fabricated on HRFZ silicon: the first type (Fig. 1a) is the classic split-ring resonator (SRR); the second type (Fig. 1b) is a conductively coupled joint supercell (JSRR), consisting of two connected square split rings.

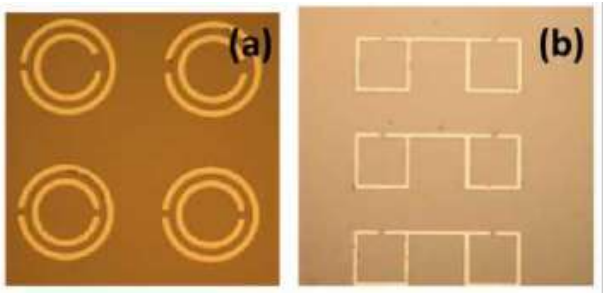


Figure 1: SSR (a) and JSRR (b) fabricated on HRFZ silicon.

Figure 2 shows the measured amplitude modulation as the metasurface in Fig. 1b was intermittently illuminated by white light, with a measured maximum modulation depth of over 400% at resonance.

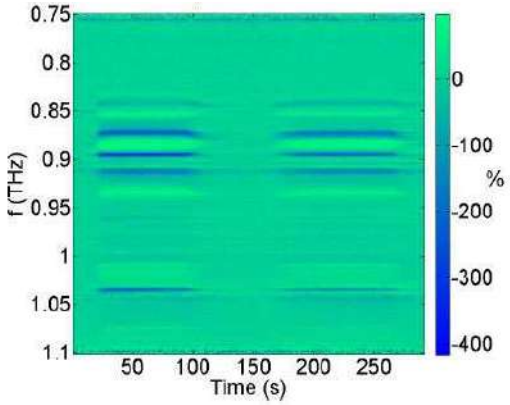


Figure 2: Measured amplitude modulation of JSRR.

A phase modulation of over 130º was also observed, which opens interesting applications if this modulator were used in the Fourier plane of a THz system.

2.2. Metasurfaces on plastic and paper

Figure 3 shows two different metasurfaces on plastic and paper. The structure in Fig. 3a, on paper, was optimised as a broadband stopband filter, with a centre frequency of approximately 0.9 THz. The structure in Fig. 3b is a more conventional single SRR on a plastic (PEN) substrate.

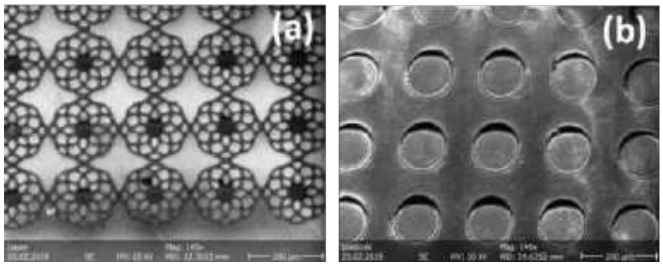


Figure 3: A broadband bandstop filter (a) and single SSR (b) on paper.

The advantage of using paper is that the chemical to be analysed can be absorbed in the paper fibres. Moreover functionalisation of paper can increase sensitivity to specific elements. We have also successfully coupled the resonant structures on a plastic substrate to a sheet of paper containing the analyte, combining the benefit of the flat plastic, resulting in sharper features, and the availability of an absorbing materials.

3. Conclusions

To summarise, we have reported on the use of THz metasurfaces for enhancing the modulation depth of THz modulators (above 400%) and for chemical detection using disposable paper and plastic substrates.

Acknowledgements

We wish to acknowledge financial support from the Durham Doctoral Studentship scheme and the Engineering and Physical Sciences Research Council under grant RP/N509462/1.

References

[1] Busch S., Scherger B., Scheller M., and Koch M. "Optically controlled terahertz beam steering and imaging"Opt. Lett. 37, 1391-1393 (2012).

[2] Rahm M , Li J-S., Padilla W. "THz Wave Modulators: A Brief Review on Different Modulation Techniques", J. Infrared Millim. Terahertz Waves 34,1-27 (2013).

[3] Kshetrimayum, R. S., "A Brief Introduction to Metamaterials", IEEE Potentials 23, 44-46, (2004).

[4] Cooke, M. D. and Wood, D. "Fabrication of micron scale metallic structures on photo paper substrates by low temperature photolithography for device applications" J. Micromechanics Microengineering 25, 115017 (2015).

[5]. Aydin Sadeqi, H. R. N. and Sonkusale, S. "Low-cost metamaterial-on-paper chemical sensor" Opt. Express 25, 16092–16100, (2017).

[6]. Hu Tao, Logan R. Chieffo and Omenetto, F. G. "Metamaterials on paper as a sensing platform" Adv. Mater. 23, 3197–3201, (2011).

[7] Lucifer, a 3D FDTD simulator. Code available under GPL license at: https://github.com/claudiobalocco/lucifer

High-Performance Metamaterial-Inspired Quasi-Optical Instrumentation for THz Range

Sergei A. Kuznetsov[1,2,3]*, Victor N. Fedorinin[1], Andrey V. Arzhannikov[2,3]
Alexander N. Gentselev[3], Pavel A. Lazorskiy[2], and Nazar A. Nikolaev[4]

[1]Rzhanov Institute of Semiconductor Physics SB RAS, Novosibirsk Branch "TDIAM", Novosibirsk, Russia
[2]Physics Department, Novosibirsk State University, Novosibirsk, Russia
[3]Budker Institute of Nuclear Physics SB RAS, Novosibirsk, Russia
[4]Institute of Automation and Electrometry SB RAS, Novosibirsk, Russia
*corresponding author, E-mail: SAKuznetsov@nsm.nsu.ru

Abstract

We review the results of extensive R&D activity focused on elaborating high-performance quasi-optical components of THz instrumentation using plasmonic metamaterials. Practical solutions for frequency filters of different types, non-profiled focusing devices, phase/polarization transformers, ultra-thin metasurface absorbers and metasurface-based radiation detectors, thin-film and SEIRA sensors are presented. The issues of design optimization, technological fabrication, and spectral characterization of the developed devices alongside with their practical applications are considered.

1. Introduction

Overlapping the frequencies from 0.1 to 10 THz, the terahertz band of the electromagnetic spectrum has been experiencing a rapid progress in the last decade stimulated by advancement in methods of THz generation and detection [1, 2]. Weakly developed in the past due to technological limitations, this spectral range attracts much interest both in fundamental and applied research owing to unique potentialities of THz waves unachievable for adjoining infrared (IR) and microwave (MW) domains. A relatively large penetration depth into various optically opaque materials, absence of ionizing effects, attainability of mm/submm spatial resolution acceptable for imagining of concealed targets, high sensitivity to metallic and water-containing media, existence of rotational and vibrational "fingerprints" in organic molecules, and high information capacity make THz radiation promising for security, non-destructive testing, environmental monitoring, communications, biomedical diagnostics, etc.

It is noteworthy that plasmonic metamaterials enables noticeably extending functional properties of THz devices breaking the limits of classical optics. In particular, subwavelength plasmonic structures allows implementing very thin and high-performance quasi-optical components, which fabrication can be easily realized using well-proven photolithographic or other micromachining techniques of micrometer accuracy. Elaborated for the THz band and highly demanded in the market of THz instrumentation, such cost-effective solutions facilitate the more rapid development of optical, IR, and MW technologies.

In this contribution we consider practical examples of various metamaterial-inspired quasi-optical devices and components operating at frequencies from 100 GHz to several THz and providing amplitude, phase, and polarization manipulation of radiation beams in different applications. We discuss frequency filters, quarter- and half-wave plates, planar focusing structures, absorbers and absorber-based detectors, sensors of thin-film analytes. Both novel instrumental solutions and the improved conventional ones are presented.

2. Developed THz components and devices

All the metamaterial-inspired THz components and devices discussed in this work are implemented as single- or multi-layer plasmonic structures based on frequency selective surfaces (FSSs) or metasurfaces (MSs). The complete development cycle includes: a) electromagnetic modeling using ANSYS EM Suite, methods of moments, and equivalent circuit methods; b) structure fabrication using UV-, X-ray, or E-beam lithography; c) spectral characterization with BWO-, TDS, or FT-spectrometers.

The detailed description of the employed methods and techniques is given in [3-5].

2.1. Frequency filters

Stimulated by experiments with quasi-optical frequency demultiplexing and spectral measurements of broadband THz radiation from electron-beam plasmas [6], we mastered technological routes to fabricate high-performance FSS/MS-filters of the following types:

2.1.1. Band-pass filters (BPFs)

Assembled from free-standing patterned copper foils produced by electroplating [5], these multilayer structures have a multiplex (non-interference) configuration. The entire device set includes 25 BPFs with shifted spectral

bands overlapping the range of 0.1–5 THz. Each BPF exhibits a high peak transmittance in the passband (~90%) at the fractional bandwidth (FWHM) of 12–20%. It is worth highlighting that due to a proper design of the FSS/MS pattern, the BPF out-of-band transmission is maintained at the level of –30–50 dB up to IR frequencies with no spurious transmission peaks.

2.1.2. Low-pass filters (LPFs)

The LPFs are represented by interference structures with 6-10 layers of capacitive patch-like FSSs/MSs patterned on polypropylene (PP) substrates and stacked together by means of a hot-pressing technique. The LPFs provide –30–40 dB of THz attenuation above their cut-on frequencies positioned between 0.25 and 2 THz. Originally, the LPFs were developed to suppress spurious absorption bands in MS absorbers integrated with our spectrometric pyro-detectors. We also successfully applied the LPFs to TDS measurements in the low-frequency regime to show a noticeable improvement of a S/N ratio and shortening the data acquisition time.

2.1.3. High-pass filters (HPFs)

The HPFs are implemented as thick single-layer structures of a wavelength-comparable thickness ranging from 0.3 to 1 mm. The HPFs strongly attenuate frequencies below the cut-off, which in our case can be selected within 0.2–1 THz. The topology of hexagon-shaped through holes separated by narrow crosspieces is utilized in the HPF design [7]. The HPFs are produced with one of 2 methods: a) via through-thickness lithographic patterning of a PMMA wafer with hard X-rays followed by its entire surface metallization (so-called "pseudometallic" structures [7, 8]); b) via reactive ion etching of low-resistivity silicon.

2.2. Planar focusing devices

The planar focusing devices are realized in 2 variants: a) as high-aspect-ratio "pseudometallic" structures with through holes of spatially-dependent dimensions operating in transmission [8]; b) as low-aspect-ratio grounded PP-backed MSs operating in reflection [9]. Due to electromagnetic optimization and holographic technique used in phase synthesis, we reach the diffraction efficiency of 75-90% when focusing 0.3–1 THz waves to focal areas of desired shapes.

2.3. Phase/polarization transformers

The phase and polarization transformers investigated in this work are implemented in single and bilayer configurations using anisotropic PP-based MSs operating in the range of 0.1–0.6 THz and exhibiting low absorption losses. Herein, we present a design of an efficient frequency filter with polarization discrimination using a MS of the half-wave plate type, and also consider a THz ellipsometer operating at 0.14 THz which exploits original quarter-wave plate elements based on self-complementary MSs.

2.4. Resonant absorbers and absorber-based detectors

We undertook extensive investigations of high-performance ultra-thin MS absorbers designed for narrow-band operation at frequencies from 0.1 to 1 THz and applicable to wavelength-selective (at 3-6% bandwidth) spectrometric detectors of a thermal type [5, 10]. In addition, we demonstrate a cost-effective industry-oriented technology of MS-absorber-based pyroelectric sensors and pyro-sensor arrays with tailored spectral and polarization responsivities.

Acknowledgements

This work was partially supported by the Russian Foundation for Basic Research (RFBR Grants No. 18-29-20066 and 18-02-00232). The authors also gratefully acknowledge the Shared Equipment Centers of the Novosibirsk State University and the Institute of Automation and Electrometry SB RAS for instrumental support of THz measurements.

References

[1] K.-E. Peiponen et al, *Terahertz spectroscopy and imaging*. *Springer series in optical sciences*, vol.171, Berlin Heidelberg: Springer-Verlag, 2013.

[2] H.-J. Song, T. Nagatsuma, *Handbook of terahertz technologies: devices and applications*, Singapore: Pan Stanford Publishing Pte Ltd, 2015.

[3] S.A. Kuznetsov et al., Development and characterization of quasi-optical mesh filters and metastructures for subterahertz and terahertz applications, *Key Eng*. *Mat*., 437: 276-280, 2010.

[4] M. Navarro-Cia et al., Route for bulk millimeter wave and terahertz metamaterial design, *IEEE J*. *Quantum Electr*. 47(3): 375−385, 2011.

[5] S.A. Kuznetsov et al., Microstructured frequency selective quasi-optical components for submillimeter-wave applications, *Proc*. *EuMC 2014*, Rome, Italy, pp. 881–884, 2014.

[6] M.K.A. Thumm et al., Generation of high-power sub-THz waves in magnetized turbulent electron beam plasmas, *J*. *Infrared, Millimeter, and Terahertz Waves* 35(1): 81−90, 2014.

[7] S.A. Kuznetsov et al., Implementation of high-pass subterahertz filters using high-aspect-ratio polimeric structures, *Optoelectron*. *Instrum*. *Data Process*. 53(1): 88−95, 2017.

[8] A. N. Gentselev et al., Fabrication of quasi-optical selective elements for the terahertz range in the form of pseudometallic structures via deep X-ray lithography, *J*. *Surf*. *Investigation* 11 (4): 710−720, 2017.

[9] S.A. Kuznetsov et al., Planar holographic metasurfaces for terahertz focusing, *Sci*. *Rep*. 5: 7738, 2015.

[10] S.A. Kuznetsov et al., Ultra-thin metasurface absorbers for subterahertz band: theoretical aspects and detector applications, *Proc*. *EuMC 2018*, Madrid, Spain, pp. 416– 419, 2018.

All-dielectric metasurfaces for terahertz science and technology

Willie J. Padilla[1], and Kebin Fan[1]

[1] Department of Electrical and Computer Engineering, Duke University, Durham, NC 27708, United States of America
*corresponding author, E-mail: willie.padilla@duke.edu

Abstract

All-dielectric metasurfaces are useful for investigation of new devices for terahertz science and technology. Scattering effects ranging from high absorption and Huygens' reflect arrays to bound-states-in-the-continuum (BIC) suggest their use for applications. We experimentally demonstrate several all-dielectric metasurfaces which realize: high transmission Huygens' structures, high absorptive devices for imaging, and dynamic surfaces with optical control. The all-dielectric metasurfaces we explore consists of arrays of high dielectric geometrical shapes, and may support a number of eigenmodes of either odd or even symmetry.

1. Introduction

Electromagnetic all-dielectric metasurfaces (DMSs) consist of one functional layer of dielectric resonator arrays, and are a versatile platform for exploration of a myriad of unconventional physical scattering responses ranging from high absorption and Huygens' arrays to bound-states-in-the-continuum (BIC) and zero rank absorbers (ZRAs). Dielectric metasurfaces realize several advantages over their metal-based counterparts, i.e. zero Ohmic loss, high temperature operation, and low thermal conductivity. Notably, like metal-based metasurfaces, DMSs support two dipole like modes – one a magnetic mode and the other electric – both of which are tunable with geometry. Therefore, dielectric metasurfaces possess much of the salient features generally attributable to metal-based metamaterials, without the disadvantages listed above.

We developed a few technology demonstration systems using DMS operating at THz frequencies. We also demonstrate dynamic control of a DMS through photodoping, suggesting applications ranging from high speed filtering to frequency diverse imaging.

2. Simulation and Experimentation

The metasurface is simulated using full-wave 3D electromagnetic software, with a frequency domain solver (finite element method). We also use two-port S-parameter simulations, where the two ports were set symmetrically with respect to the mid-plane of the unit cell, and periodic boundaries were used on all sides. Eigenvalue simulations are also performed permitting extraction of the modes complex frequency. Metasurfaces may be simulated with and without material loss, which permits us to determine the individual pieces of scattering and dissipative loss in the structures. We use silicon or zirconium dioxide (also called zirconia) as the base materials for all-dielectric metasurfaces, and – in some studies – use a slight silicon boron doping. The metasurfaces were fabricated by deep reactive ion etching and we use polydimethylsiloxane (pdms) or extruded polystyrene as support substrates, or use silicon interconnects between unit-cells to make the metasurface free-standing. The all-dielectric metasurfaces are characterized by various methods including a vector network analyzer, terahertz time-domain spectrometer, or a Fourier transform spectrometer.

Two examples of metasurfaces are shown in Fig. 1, a zirconia zero-rank absorber [1] and a silicon metasurface which supports high Q-factor bound-states-in-the-continuum modes [2].



Figure 1: Two examples of fabricated all-dielectric metasurfaces. The left is an optical photo of a zero-rank absorber fashioned from zirconia, and the right is a free-standing silicon metasurface which realized high Q-factor BIC modes.

We demonstrate dynamic control of the amplitude and phase of transmitted light. Two different optical sources are used – a 980nm LED [3] and an ultra-fast titanium sapphire laser producing radiation at a wavelength of 800nm. We obtain a transmitted phase of 120 degrees with transmission modulation of over 99.9%. Theoretical analysis and numerical simulations coupled with temporal coupled mode theory indicate that the tuning is due to a substantial increase in the material dissipation rate of the odd eigenmode of the structure. [4] This serve to lift the degeneracy of the odd and even eigenmodes, while simultaneously destroying the critical coupled state.

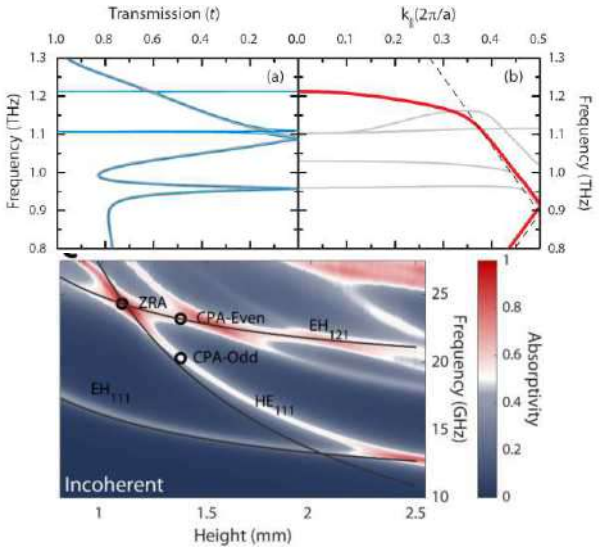


Figure 2: The top panel (a) shows a dispersion diagram calculated from S-parameter simulation showing the high Q BIC mode as the blue curve. Top panel (b) shows a corresponding eigenmode dispersion diagram identifying the mode giving rise to the BIC state. Bottom panel shows the frequency and height dependence of the zero rank absorber – denoted as ZRA – which coincides with the overlap of the even and odd modes of a coherent perfect absorber.

In Figure 2 we present simulations of the BIC metasurface (top) and the ZRA (bottom). The high-Q BIC mode can only be coupled to by breaking the symmetry of the system. We thus use off-normal THz light which allows us to realize a high-Q mode in transmission at 1.2 THz (blue curve top left of Fig. 2). However, normally incident light (grey curve) does not couple to the mode and there signature of the BIC in transmission. The top right panel in Fig. 2 shows a dispersion diagram which uncovers the origin of the BIC mode. We find that the metasurface supports a surface leaky mode, which gets band-folded at the Brillouin zone and returns to the zone center at 1.2 THz. The leaky mode cannot be driven at normal incidence, and thus oblique incident light is needed to drive the mode and thus the BIC.

The bottom panel of Fig. 2 shows a color map showing high absorption (red colors) as a color map vs height of the metasurface absorbers and frequency in THz. There are two main modes – an even hybrid mode termed CPA-Even and an odd hybrid mode termed CPA odd – here CPA stands for coherent perfect absorber. Each one of these modes may act as a coherent perfect absorber for even (CPA-even) and odd (CPA-odd) symmetric light incident on the absorber. However, when these two modes are degenerate, then the coherency of incident light is not relevant as an absorber fashioned at this height (1.1mm) and operating at this frequency can absorb both even and odd symmetric incident light – this is what we term a zero-rank absorber. Temporal coupled mode theory shows that the scattering matrix of the ZRA is nullity, whereas the scattering matrix of the coherent perfect absorbers (CPAs) is not zero. Thus the ZRA may absorb even, odd, or incoherent light, whereas the CPA may only absorb either odd or even symmetric light.

3. Discussion

Coupled mode theory and S-parameter simulations are used to elucidate the mechanism underlying physics and dynamics of the metasurfaces shown here. Similar to metal-based metamaterials, both systems may be scaled in size to operate in nearly any band of the electromagnetic spectrum. The dynamic terahertz photonic systems studied here show wide tunability and versatility which are not limited to the spectral range demonstrated, offering a new path for reconfigurable metasurface applications.

4. Conclusions

Our all-dielectric metasurface is an ideal platform to investigate unconventional physics in electromagnetic wave absorbing systems. The demonstration of a dynamic all-dielectric structure highlights a new strategy for controlling metasurfaces, and highlights a potential path to achieve reconfigurability for future applications.

Acknowledgements

This work was financially supported by the Department of Energy (DOE) (DE-SC0014372).

References

[1] Jonathan Y. Suen, Kebin Fan, and W.J. Padilla, A Zero-Rank, Maximum Nullity Perfect Electromagnetic Wave Absorber, *Advanced Optical Materials* 1801632 (2019).

[2] Kebin Fan, Ilya V. Shadrivov, and W.J. Padilla, Dynamic bound states in the continuum, *Optica* **6**, 169 (2019).

[3] Kebin Fan, Jingdi Zhang, Xinyu Liu, Gu-Feng Zhang, Richard D. Averitt and W.J. Padilla, Phototunable Dielectric Huygens' Metasurfaces, *Advanced Materials* **30**, 1800278 (2018).

[4] Xianshun Ming, Xinyu Liu, Liqun Sun, and Willie J. Padilla, *Degenerate critical coupling in all-dielectric metasurface absorbers*, Optics Express **25**, 24658 (2017).

Recent progress in the development of efficient semiconductor based THz sources

E.U. Rafailov[1], A. Gorodetsky[2], T. Gric[3], N. Bazieva[1]

[1]School of Engineering and Applied Science, Aston University, UK
[2]Department of Chemistry, Imperial College London, London SW7 2AZ, UK
[3]Department of Electronic Systems, Vilnius Gediminas Technical University, Vilnius, Lithuania
*corresponding author, E-mail: e.rafailov@aston.ac.uk

Abstract

Quantum-dot semiconductor structures have been used mostly in laser development. However, the unique properties of QD have allowed us to exploit it in the development of THz light source. Here we review our recent progress in generation of CW and pulsed THz radiation from QD based photoconductive antennae. The development of an ultra-compact, efficient, room temperature THz source based on QD structures is possible.

1. Introduction

Novel materials, notably quantum-dot (QD) semiconductor structures, offer the unique possibility of combining exploitable spectral broadening of both gain and absorption with ultrafast carrier dynamic properties [1]. Thanks to these characteristics, QD-based devices have enhanced the properties of CW devices as well as the development of compact ultrashort pulse lasers and provided a fertile ground for ultrafast science and technology.

2. Discussions

In this paper we review recent progress in generation of CW and pulsed THz radiation from QD based photoconductive antennae (PCA) pumped by ultrafast and dual wavelength semiconductor lasers. QD-PCA substrate incorporates InAs QDs in a GaAs matrix, thus keeping semiconductor carrier mobility at higher levels than is typical for SI GaAs, while QDs themselves serve as lifetime shortening centres, allowing to achieve sub-picosecond operation similar to LT-GaAs. Thus, such substrates combine the advantages and lack the disadvantages of GaAs and LT-GaAs, which are the most popular materials so far, and thus can be used for both CW and pulsed THz generation. Moreover, by engineering the design of the QD structure, effective pump wavelengths can be tuned in the range between 0.9-1.3 μm, which is well beyond the GaAs energies, hence compact and relatively cheap ultrafast and narrow line double-wavelength semiconductor and fibre pump lasers can be used for pumping such antennae for both pulsed and CW THz generation [2], [3].

However, antennae possess a low coefficient of optical-to-terahertz conversion due to the carrier screening effect and low quantum efficiency. To overcome these limitations, an optical nano-antennae technique can be employed. Optical nano-antennae are resonant nanostructures capable of transforming incident optical waves in a strong near-field. Such nano-antennae can be used to enhance the electric field and increase the absorption cross section in the active layers of the photoconductive antenna. We present our recent results on enhancement of THz generation in QD based log-periodic PCA with silver nano-antennae embedded in the antenna gap. Our first results demonstrated that using silver spheroid nano-antennae fabricated by a relatively simple method, can increase the coefficient of optical-to-terahertz conversion up to 4 times [4].

We also performed numerically investigation of THz photoconductive antennas based on optimized plasmonic nanostructures and studied the absorption enhancement of silver and transparent-conducting oxides (TCO) nanocylinders with different diameters by means of effective medium approximation. This study reports on the stronger enhancement in case of TCO nanocylinders. The results show that resonant absorption amplitude and wavelength are dramatically affected by the thickness of the nanostructure as well as by the distances between nanocylinders [5]. In case of TCO nanocylinders, absorption enhancement for NIR wavelengths, being relevant for present THz generation setup, reaches up to 5-fold leading to 25-fold increase in THz radiation.

3. Conclusions

In conclusion the development of an ultra-compact, efficient, room temperature THz source is possible. The inclusion of multiple bandgap-engineered semiconductor materials and quantum-confined structures enables additional pump absorption energy ranges and ultrafast charge carrier dynamics, crucial in the efficient generation of THz radiation.

Acknowledgements

E.U.R. acknowledges support from EPSRC (Grant EP/R024898/1) and Russian Science Foundation (Grant No. 18-15-00172). A.G. acknowledges support from Russian Foundation for Basic Research (research project No 18-07-01492a).

References

[1] E.U.Rafailov, M.A.Cataluna, W.Sibbett, Nature Photonics, 1, 395 (2007)

[2] R. Leyman, A.Gorodetsky, N.Bazieva, G.Molis, A.Krotkus, E.Clarke, E.U. Rafailov, Laser and Phot Review, 8, 1–8, 2016

[3] K.A. Fedorova, A. Gorodetsky, E.U. Rafailov, IEEE Journal of Selected Topics in Quantum Electronics, 23(4), 1900305, 2017

[4] S.Lepeshov, A.Gorodetsky, A.Krasnok, N.Toropov, T.A. Vartanyan, P.Belov, A.Alu, E.U. Rafailov, Scientific Report, SciRep, v.8, 6624, 2018

[5] T. Gric, A. Gorodetsky, A. Trofimov, E. Rafailov, "Tunable Plasmonic Properties and Absorption Enhancement in Terahertz Photoconductive Antenna Based on Optimized Plasmonic Nanostructures", J. of Infrared Millimeter and Therahertz waves, v.39(10) p. 1028-1038, 2018

Exploiting the Vacuum State in Materials with Plasmonic-to-Dielectric State Transition in Terahertz Gratings and Metasurfaces

Andriy E Serebryannikov[1,2,*], Akhlesh Lakhtakia[3,4], and Guy A E Vandenbosch[1]

[1]ESAT-TELEMIC, Katholieke Universiteit Leuven, 3000 Leuven, Belgium
[2]Faculty of Physics, Adam Mickiewicz University, 61-614 Poznań, Poland
[3]NanoMM–Nanoengineered Metamaterials Group, Department of Engineering Science and Mechanics, Pennsylvania State University, University Park, Pennsylvania 16802, USA
[4]Material Architecture Centre and Department of Electronics Engineering, Indian Institute of Technology (BHU), Varanasi, Uttar Pradesh 221005, India
*corresponding author, E-mail: aserebry@esat.kuleuven.be

Abstract

Certain materials exhibit dynamically controllable transitions from the plasmonic state to the dielectric state, traversing through intermediate states. Components made of such materials disappear electromagnetically in the vacuum state, except for ohmic loss. We have demonstrated the use of two materials, InSb and graphene-dielectric metamaterial in reflection gratings, transmission gratings, and metasurfaces for on-off switching operations that rely on the vacuum state or somehow deviate from it.

1. Introduction

Electric, magnetic, and thermal control of electromagnetic constitutive parameters of materials such as InSb, VO_2, graphene, and ITO are often investigated for the realization of tunable and switchable devices operating in diverse spectral regimes. Materials with the capability of transition from the plasmonic state [$\mathrm{Re}(\varepsilon_r) < 0$] to the dielectric state [$\mathrm{Re}(\varepsilon_r) > 0$] have attracted particular attention, with focus on achieving the maximum contrast between $\min\{\mathrm{Re}(\varepsilon_r)\} = \varepsilon_a < 0$ and $\max\{\mathrm{Re}(\varepsilon_r)\} = \varepsilon_b > 0$. Such a wide range encompasses the zero-permittivity state [$\mathrm{Re}(\varepsilon_r) = 0$] and the vacuum state [$\mathrm{Re}(\varepsilon_r) = 1$]. Whereas the zero-permittivity state has been extensively investigated this century, the vacuum state was only recently identified [1] despite it being the more distinguishable of the two intermediate states.

Ideally, the device components made of a material in the vacuum state disappear for electromagnetic purposes, so that an efficient on-off switching scenario can be achieved [1]. In this talk, our main objective is to demonstrate the capability of two selected materials for on-off switching of deflection in reflection and transmission modes in the THz spectral regime. The two materials are InSb [1,2] and a graphene-dielectric multilayer metamaterial [3], with thermal control applicable to the first one and electric control to the second.

2. Results and Discussion

We first revisited the effect of ohmic loss in the chosen materials by comparing the realistic case and the hypothetical cases of larger and smaller (including zero) losses. The goal was to assess the possibility of using these materials in (i) reflection gratings, (ii) transmission gratings, and (iii) as resonators in uniform and gradual metasurfaces. Ohmic loss is a critical issue for both transmission gratings and resonators. Based on computed data, we determined which ranges of values of $\mathrm{Im}(\varepsilon_r)$ are still acceptable for reflection gratings, transmission gratings and metasurfaces, and thus assessed the usefulness of both chosen materials.

The potentially realizable on-off switching scenarios may include but are not restricted to those based on vacuum-to-plasmonic-state transition, vacuum-to-high-ε_b-dielectric transition, and vacuum-to-zero-permittivity state transition.

2.1. Indium Antimonide (InSb)

The reflection grating shown in the inset of Fig. 1 enables nearly perfect deflection. The device comprises InSb microrods of square cross-section on a SiO_2 buffer layer ($\varepsilon_{SiO2} = 2.25$) backed by a metallic reflector. The relative permittivity ε_{InSb} of InSb can be varied at THz frequencies in a wide range, due to strong sensitivity to the temperature T. The grating period is $L = 80.22$ μm. At 3.135 THz frequency and $T = 315$ K, the grating disappears in an electromagnetic sense because $\varepsilon_{InSb} = 1.015+i0.234$ then, and only specular reflection occurs. When the temperature is lowered to 275 K, $\varepsilon_{InSb} = 9.72+i0.095$ and the –1th-order nonspecular reflection is very strong. Temperature-controlled on-off switching of deflection is thus possible in the reflection mode.

Next, the SiO_2 substrate was replaced by InSb, the metallic reflector was removed, the period was changed to 62.66 μm, and the remaining geometrical parameters were also adjusted. At 4.58 THz frequency, $\varepsilon_{InSb} = 12.88+i0.0305$ at $T = 275$ K but $\varepsilon_{InSb} = 1.577+i0.154$ at $T = 355$ K. The –1th-order nonspecular transmission is very strong at 275 K but very weak at 355 K. Temperature-controlled on-off switching of deflection is thus possible in the transmission mode. Ohmic loss in InSb may not permit the –1th-order transmittance to be higher when $\mathrm{Re}(\varepsilon_{InSb}) = 1$.

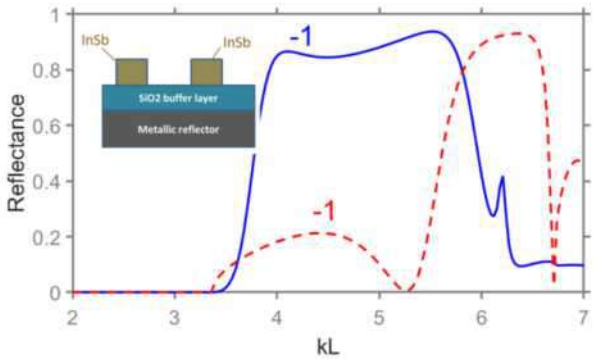


Figure 1: Reflectance of order $m = -1$ of a grating comprising InSb microrods of square cross-section on a SiO_2 buffer layer backed by a metallic reflector at $T = 275$ K (solid blue line) and $T = 315$ K (dashed red line), when the angle of incidence is 60 deg. The grating period $L = 80.22$ μm and k is the free-space wavenumber.

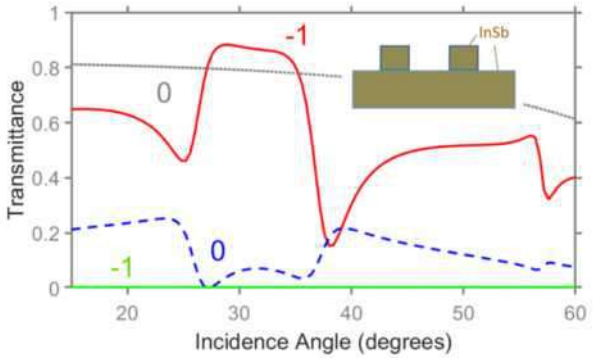


Figure 2: Transmittances of orders $m = 0$ and $m = -1$ of a grating comprising InSb rods of square cross-section on an InSb substrate at $T = 275$ K (solid red and dashed blue lines) and $T = 355$ K (dotted black and dash-dotted green lines), when the frequency is 4.58 THz. The grating period $L = 62.55$ μm.

Changes in temperature on the order of 10 K or 20 K can be sufficient to achieve a dramatic change of the diffraction characteristics, provided that the geometric parameters are properly chosen [1]. The role of the vacuum state in the tunability of a gradual meta-array composed of microrods similar to the ones in Figs. 1 and 2 has also been investigated.

2.2. Graphene-Dielectric Multilayer Metamaterial

Next, we consider two different devices comprising a graphene-dielectric multilayer metamaterial, with constitutive and geometric parameters given by Khromova *et al*. [3]. In the first device, the metamaterial is used as a substrate for a uniform two-dimensional array of dielectric resonators (microrods), as shown in the left panel of Fig. 3. By varying the Fermi energy level from 80 meV to 20 meV, the metamaterial's relative permittivity can be changed from $\varepsilon_a \approx -2.5$ to $\varepsilon_b \approx 2.2$, according to the model given in Ref. 3. The resonances of the individual microrods and, thus, the transmission and reflection characteristics of the whole device are affected. Using the results obtained for the uniform (non-gradual) arrays, we estimated the potential of the graphene-dielectric multilayer substrates in tunable deflection of THz waves by nonuniform (gradual) metasurfaces composed of such resonators. Finally, the case when the resonators are embedded in a tunable metamaterial substrate was considered; see the right panel of Fig. 3. A comparison of these two devices is being carried out.



Figure 3: Schematic views of (left) a nonperiodic array of Si microrods with a graphene-dielectric metamaterial as the substrate and (right) a periodic array of Si microrods embedded in a slab of the graphene-dielectric metamaterial.

3. Conclusion

To summarize, materials with plasmonic-to-dielectric state transition and vacuum state as one of the intermediate states allow us to make some components of a whole device on-off switchable. The presented examples show how the intermediate vacuum state is connected with the switch-off regime, when gratings and metasurfaces may disappear electromagnetically. In reflection mode, the tunable components of the studied structures may be weakly sensitive to the ohmic loss which acquires greater importance for transmission-mode devices. Both InSb and the graphene-dielectric multilayer metamaterial are suitable materials in the THz regime.

Acknowledgements

This work has been supported by EU Horizon-2020 via Marie Skłodowska-Curie IF program (grant no. 708200 – ADVANTA), NCN, Poland (DEC-2015/17/B/ST3/ 00118 – Metasel), and the Charles Godfrey Binder Endowment at Penn State.

References

[1] A. E. Serebryannikov, A. Lakhtakia, M. Aalizadeh, E. Ozbay, and G. A. E. Vandenbosch, Temperature-mediated invocation of the vacuum state for switchable ultrawide-angle and broadband deflection, *Sci Rep* 8:15044, 2018.

[2] J. Han and A. Lakhtakia, Semiconductor split-ring resonators for thermally tunable terahertz metamaterials. *J Modern Opt* 56:554–557, 2009.

[3] I. Khromova, A. Andryieuski, and A. Lavrinenko, Ultrasensitive terahertz/infrared waveguide modulators based on multilayer graphene metamaterials. *Laser Photon Rev* 8:916–923, 2014.

Graphene based terahertz optoelectronics

Coskun Kocabas

University of Manchester, School of Materials and National Graphene Institute
E-mail: coskun.kocabas@manchester.ac.uk

Abstract

Advances in terahertz (THz) research and technology, has bridged the gap between radio-frequency electronics and optics. More efficient control of THz waves would highly benefit noninvasive, high-resolution imaging and ultra-fast wireless communications. However, lack of active materials in THz spectrum, hinders the realization of these technologies. Graphene, 2d-crystal of carbon atoms, is a promising candidate for reconfigurable THz optoelectronics due to its unique electronic band structure which yields gate-tunable broad-band optical response. In this talk I will present our experimental work on graphene based devices for controlling intensity, phase and polarization of terahertz waves. These new modulation mechanisms could pave the way for developing active THz optoelectronic systems.

sm, and magnetoelectricity: Separate phenomena and joint effects in me

Chiral (excitation of) spin waves in ferromagnetic films and spheres

T. Yu[1], S. Sharma[1], Y.M. Blanter[1], and G. E. W. Bauer[1,2]

[1]Kavli Institute of NanoScience, Delft University of Technology, The Netherlands
[2]Institute for Materials Research, Tohoku University, Sendai, Japan

Surface waves of ferromagnetic films and spheres propagate only in one direction, with a handedness governed by the vector product of magnetization and surface normal [1,2]. This chirality gives rise to for example the spin conveyor belt effect [3].
I report our theoretical efforts to understand, control, and find applications for chiral spin waves [4,5] and chirally excited conventional spin waves [4-6] in yttrium iron garnet, an insulating ferrimagnet with exceptionally high magnetic quality. We compare our results with available experiments [6,7].

[1] L. R. Walker, Phys. Rev. **105**, 390 (1957).
[2] R. W. Damon and J. R. Eshbach, J. Phys. Chem. Solids **19**, 308 (1961).
[3] T. An et al., Nat. Mat. **12**, 549 (2013).
[4] S. Sharma, Y. M. Blanter, and G. E. W. Bauer, Phys. Rev. B **96**, 094412 (2017); Phys. Rev. Lett. **121**, 087205 (2018); and unpublished
[5] T. Yu, C. Liu, H. Yu, Y. M. Blanter, G. E. W. Bauer, arXiv:1901.09182 and unpublished.
[6] J. A. Haigh et al., Phys. Rev. B **97**, 214423 (2018).
[7] J.L. Chen et al., Phys. Rev. Lett. **120**, 217202 (2018) and unpublished.

Spin waves and electromagnetic waves in photonic-magnonic crystals

Jarosław W. Kłos[1], Igor L. Lyubchanskii[2], Yuliya S. Dadoenkova[3], Maciej Krawczyk[1], Nataliya N. Dadoenkova[3]

[1]Faculty of Physics, Adam Mickiewicz University in Poznań, 61-614 Poznań, Poland
[2]Donetsk Physical and Technical Institute of the National Academy of Sciences of Ukraine, Ukraine
[3]Ulyanovsk State University, 432017 Ulyanovsk, Russian Federation
*corresponding author, E-mail: klos@amu.edu.pl

Abstract

In the periodic structures combining the ferromagnetic and dielectric elements, both the spin waves and electromagnetic waves can propagate characterized by the dispersion relations with magnonic and photonic band gaps (MBGs and PBGs), respectively. These hybrid structures called photonic-magnonic crystals (PMCs) can be used to enhance the magneto-optical interactions. We calculated the MBG and PBG structures in 1D PMC and discussed the enhancement of Faraday rotation and cross-polarized contribution to Goos-Hänchen shift resulting from the periodicity in the structure under consideration.

1. Introduction

In this paper, we are considering a new type of 1D structure of similar type in which the periodically arranged magnetic layers (constituting a magnonic crystal (MC)) are spaced by dielectric multilayers (finite-size dielectric photonic crystal (PC)). Thus, the whole system has a double periodicity, which generates complex PBGs and MBGs. Its multifunctional properties manifest themselves by the possibility of simultaneous propagation of both electromagnetic waves (EMWs) and spin waves (SWs) [1-3].

In the considered structures the EMWs can be highly localized in magnetic layers when their frequencies correspond to the frequencies from the stop band of the finite-size PC. For such modes we can observe enhancement of magneto-optical (MO) interaction (resulting e.g. in the increase of Faraday rotation) and we expect to find the noticeable interaction between the SWs and the EMWs.

2. Photonic-magnonic crystal

The exemplary structure of 1D PMC is presented in Fig.1. We considered the structure where the dielectric ferrimagnetic layers (made of yttrium iron garnet (YIG)) are separated by nonmagnetic SiO_2/TiO_2 multilayers. The dielectric multilayers SiO_2/TiO_2 are thin enough to couple dipolar SWs in YIG layers. We investigated the case when the magnetization is saturated and oriented in the plane of the YIG layers which are, on the other hand, transparent for EMWs.

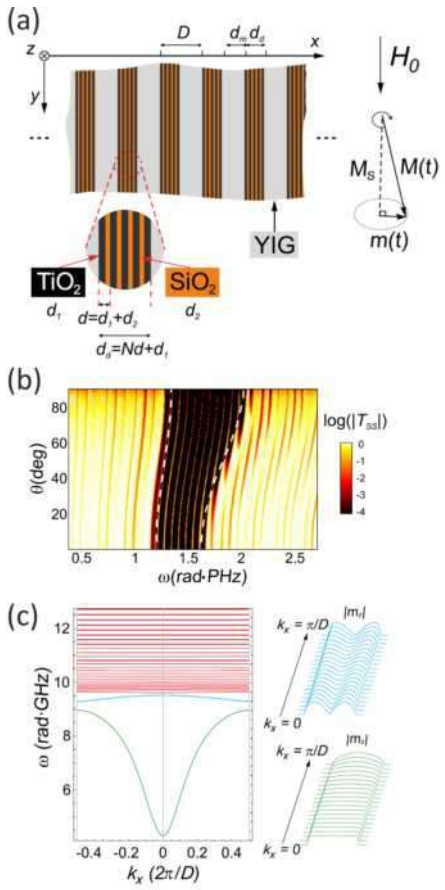


Figure 1: (a) The considered 1D PMC acting as magnonic and photonic crystal. The parameters d_m, d_d, and $D=d_m+d_d$ denote the thicknesses of the magnetic, or complex non-magnetic layers, and the period of the whole structure, respectively. (b) The transmittivity spectra log|T_{SS}| of a PMC with dielectric composite layers of structure $(TiO_2/SiO_2)^N$ with N=5 subperiods as a function of the incidence angle and frequency of the EMW. The dotted lines denote the PBG edges for the infinite dielectric PC with the unit cell (TiO_2/SiO_2) (for the details see [1, 2]). (c) The SW dispersion and profiles in YIG layer.

For the structure presented in Fig.1 we found the dispersion relations of dipolar SWs in simple 1D layered MC and the dispersion relations of the EMWs for complex PMC where the double periodicity is manifested in the splitting of the bands of SiO_2/TiO_2 PC into minibands and in the presence of weakly dispersive bands of the modes in the PBG of SiO_2/TiO_2 PC [1]. We call these modes as inside-PBG modes. The similar problem was investigated for a PMC with complex unit cell which contains two magnetic layers with different thicknesses [4].

3. Faraday rotation and Goose-Hänchen effects in photonic-magnonic crystal

We analyzed theoretically the Faraday rotation (FR) and the Goose-Hänchen (GH) effect (lateral shift of the transmitted Gaussian wave packet) for the near-infrared electromagnetic beams in PMC. These effects can be enhanced for inside-PBG modes which are confined in the magnetic layers. The presence of the linear magnetoelectric coupling in the magnetic layers can result in a significant increase of the FR (see Fig.2c) and in a vanishing of the positive maxima of the cross-polarized contribution to the GH shift (see Fig.3b).

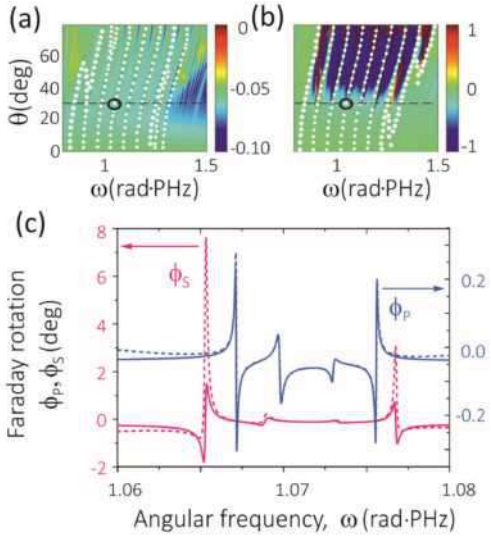


Figure 2: The evolution of the FR angles of (a) *p*-polarized and (b) *s*-polarized incident light, respectively, with frequency ω and incidence angle θ for the photonic structure $[M(AB)^4A]^5M$ (where M is YIG layer and A,B are SiO_2, TiO_2 layers.) The white dots depict the positions of the PBG edges and the inside-PBG modes. (c) Fine structure of the FR angles in dependence on frequency for selected inside-PBG modes at the incidence light angle θ=30 deg. Blue lines (pink lines) correspond to *p*- (*s*-) polarized light. We considered the magneto-electric constant $\alpha = 0$ (solid lines) and $\alpha = 30$ ps·m^{-1} (dotted lines) [4].

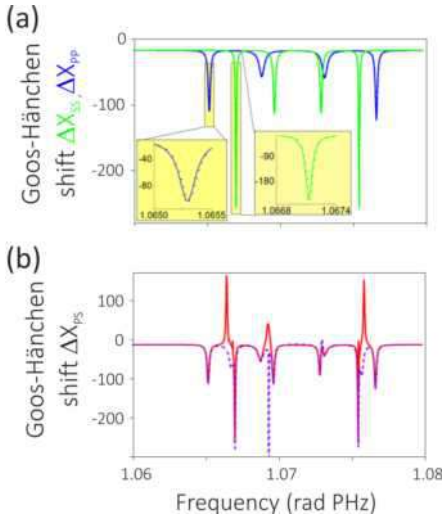


Figure 3: The GH shift vs frequency for (a) *s-s*, *p-p* transmission and for (b) *p-s* (*s-p*) transmission for selected inside-PBG modes at the incidence light angle θ=30 deg. We considered the same structure as in Fig.1 and Fig.2 for the cases when the magneto-electric constant $\alpha = 0$ (solid lines) and $\alpha = 30$ ps·m^{-1} (dotted lines) [5].

Acknowledgements

The study has received financial support from: the National Science Centre of Poland – grant No. UMO-2016/21/B/ST3/00452, and the Ministry of Science and Higher Education of the Russian Federation – grant No. 3.7614.2017/9.10.

References

[1] J. W. Kłos, M. Krawczyk, Y. S. Dadoenkova, N. N. Dadoenkova, I. L. Lyubchanskii, Photonic-magnonic crystals: Multifunctional periodic structures for magnonic and photonic applications, *J. Appl. Phys*. 115: 174311 (2014).

[2] J. W. Klos, M. Krawczyk, Y.S. Dadoenkova, N. N. Dadoenkova, and I. L. Lyubchanskii, Spin waves and electromagnetic waves in photonic-magnonic crystals, *IEEE Trans. Mag.* 50: 2504404 (2014).

[3] Y. S. Dadoenkova, N. N. Dadoenkova, I. L. Lyubchanskii, J. W. Klos, and M. Krawczyk, Confined states in photonic-magnonic crystal, *J. Appl. Phys*. 115, 073903 (2016).

[4] Y. S. Dadoenkova, N. N. Dadoenkova, I. L. Lyubchanskii, J. W. Klos, and M. Krawczyk, Faraday Effect in Bi-Periodic Photonic-Magnonic Crystals, *IEEE Trans. Mag*. 53: 2501005 (2017).

[5] Y. S. Dadoenkova, N. N. Dadoenkova, J. W. Kłos, M. Krawczyk and I. L. Lyubchanskii, Goos-Hänchen effect in light transmission through biperiodic photonic-magnonic crystals, *Phys. Rev. A* 96: 043804 (2017).

Toroidal Resonances and Reconfigurable Chiral Responses in Kirigami Metamaterials

Liqiao Jing[1], Zuojia Wang[2*], Bin Zheng[1,3] and Hongsheng Chen[1,3]

[1]Key Laboratory of Advanced Micro/Nano Electronic Devices & Smart Systems of Zhejiang, Zhejiang University, Hangzhou 310027, China
[2]School of Information Science and Engineering, Shandong University, Jinan 250100, China
[3]State Key Laboratory of Modern Optical Instrumentations, The Electromagnetics Academy at Zhejiang University, Zhejiang University, Hangzhou 310027, China
*corresponding author, E-mail: z.wang@sdu.edu.cn

Abstract

We demonstrate the excitation of multipolar resonances in kirigami metamaterial and the switching of electromagnetic properties among various chiral states. Single-band, dual-band, and broadband circular polarizers with reconfigurable performance are realized by steering the electric, magnetic and toroidal dipolar response. The underlying mechanism is explained and calculated via detailed analysis of the excited multipoles. With the ongoing development of micromanufacturing techniques, our findings may offer an alternate approach to lightweight, reconfigurable, and deployable metadevices.

1. Introduction

Metamaterials and metasurfaces are artificial materials engineered at the subwavelength scale to achieve electromagnetic functionalities[1, 2]. To date, one of the remaining difficulty is the large shape modification of the artificial structures, rendering them nonreconfigurable in various electromagnetic functionalities. Several methods have been utilized to dynamically control the optical properties of metamaterials, such as capacitors[3], semiconductors[4], phase change materials[5] and ferromagnetic/ferroelectric materials[6]. However, compared with the surrounding media and metamaterial constituents, most of these methods suffer from a limited tuning range because the variation is usually very small. Recently, origami provides an alternative approach to construct strong, lightweight, and tunable three-dimensional (3D) blocks from flat sheets[7, 8]. By applying prescribed sequences of folds to flat surfaces, researchers demonstrated flexible and efficient control over mechanical[7], electronic[9], acoustic[10], and electromagnetic functionalities[11]. Although the design capacity of origami is remarkable, achieving complex target shapes with only folds is mathematically challenging. Therefore, combining cut and fold together, namely, the technique of *kirigami*, would be a promising platform to design multifunctional metamaterials with less structural complexity.

In this talk, we will review our recent results on kirigami metamaterials[12], whose chiral responses can be flexibly controlled by the arrangement of meta-atoms and properly design kirigami. Three types of kirigami-based chiral metamaterial will be presented and the underlying multipolar responses with be discussed. We will also envision the future applications of the kirigami technique, as well as the origami one, in reconfigurable electromagnetic devices.

2. Results

The schematic illustration of the kirigami metamaterials is presented in Fig. 1. We start with an achiral two-dimensional (2D) metasurface consisting of periodically arranged meta-atoms. Only electric dipolar responses exist in the transverse plane, indicating no macroscopic chiral effect. Subsequently, the 2D metasurface is transformed into 3D geometries by introducing cuts at the boundary between neighboring meta-atoms. Through kirigami, parallel and anti-parallel electric and magnetic dipoles can be constructed, as well as the excitation of toroidal dipoles. As a result, various chiral polarizers can be realized (Fig. 2). Type-I kirigami metamaterial reaches high circular dichroism (CD) in a single band. Type-II kirigami metamaterial has two resonant frequencies where the handedness of the chirality is opposite. More intriguingly, the bandwidth of the chiroptical response can be improved by exciting a toroidal dipolar resonance, so as the Type-III kirigami metamaterial shows. Furthermore, the chirality of all three devices can be flexibly reversed by changing the folding direction of the kirigami process. The reconfigurable circular dichroism generated by toroidal dipoles offers an alternative approach to broadband chiroptical responses beyond the widely adopted methods based on parallel electric and magnetic dipoles. Circular dichroisms of 0.88, 0.94 and 0.92 have been experimentally observed for single-band, dual-band and broadband configurations, respectively. Due to the scaling properties of Maxwell's equations, the proposed strategy for reconfigurable electromagnetic performance can be extended to other frequencies, from

millimeter-scale architectures in microwave regimes to tunable metasurfaces in terahertz regimes. If it is combined with advanced micro technologies, such as electro-mechanical-systems (MEMS), we expect the kirigami metamaterials could find promising applications in terahertz sensors and detectors.

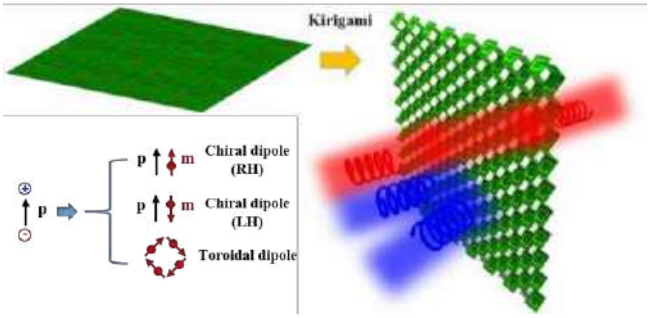


Figure 1. Kirigami metamaterials as a platform to steer the multipolar manipulation and reconfigurable chiroptical responses.

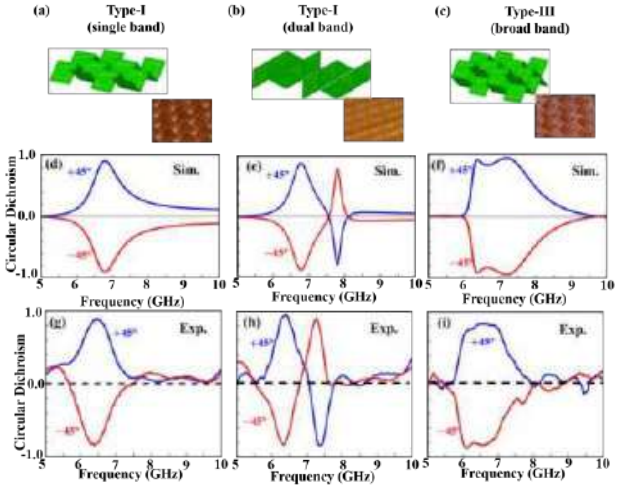


Figure 2. Electromagnetic performance of three types of kirigami-based chiral metamaterials. (a, d, g) Type-I device for single-band chiral resonances. (b, e, h) Type-II device for dual-band behaviors. (c, f, i) Type-II device for broadband behaviors.

3. Conclusions

We have proposed and demonstrated a general class of kirigami-based chiral metamaterials whose electromagnetic functionalities can be switched between nonchiral and chiral states. By introducing cuts and selecting the connection points between neighboring meta-atoms, 2D achiral metasurfaces can be deformed to 3D shapes with enhanced chiroptical responses. Highly efficient single-band, dual-band and broadband circular polarizers have been experimentlly demonstrated. The underlying mechanism has been confirmed by detailed analyses of the excited electrical, magnetic and toroidal dipoles. Compared with the technique of origami, kirigami allows for the practitioner to exploit cuts in addition to folds to achieve large deformations and create complex 3D objects.

Acknowledgements

This work was sponsored by the National Natural Science Foundation of China under Grant No. 61625502, No. 61574127, No. 61601408, No. 61775193 and No. 11704332, the ZJNSF under Grant No. LY17F010008, the Top-Notch Young Talents Program of China, the Fundamental Research Funds for the Central Universities, and the Innovation Joint Research Center for Cyber-Physical-Society System.

References

[1] Y. Liu and X. Zhang, Metamaterials: a new frontier of science and technology, Chem. Soc. Rev. **40**, 2494, 2011.
[2] N. Yu and F. Capasso, Flat optics with designer metasurfaces, Nat. Mater. **13**, 139, 2014.
[3] K. Aydin and E. Ozbay, Capacitor-loaded split ring resonators as tunable metamaterial components, J. Appl. Phys. **101**, 024911, 2007.
[4] K. Boulais, D. Rule, S. Simmons, F. Santiago, V. Gehman, K. Long, and A. Rayms-Keller, Tunable split-ring resonator for metamaterials using photocapacitance of semi-insulating GaAs, Appl. Phys. Lett. **93**, 043518, 2008.
[5] M. J. Dicken, K. Aydin, I. M. Pryce, L. A. Sweatlock, E. M. Boyd, S. Walavalkar, J. Ma, and H. A. Atwater, Frequency tunable near-infrared metamaterials based on VO 2 phase transition, Opt. Express **17**, 18330, 2009.
[6] L. Kang, Q. Zhao, H. Zhao, and J. Zhou, Magnetically tunable negative permeability metamaterial composed by split ring resonators and ferrite, Opt. Express **16**, 8825, 2008.
[7] Z. You, Folding structures out of flat materials, Science **345**, 623, 2014.
[8] Y. Chen, R. Peng, and Z. You, Origami of thick panels, Science **349**, 396, 2015.
[9] Z. Song *et al*., Origami lithium-ion batteries, Nat. Commun **5**, 3140, 2014.
[10] S. Babaee, J. T. Overvelde, E. R. Chen, V. Tournat, and K. Bertoldi, Reconfigurable origami-inspired acoustic waveguides, Sci. Adv **2**, e1601019, 2016.
[11] Z. Wang, L. Jing, K. Yao, Y. Yang, B. Zheng, C. M. Soukoulis, H. Chen, and Y. Liu, Origami-Based Reconfigurable Metamaterials for Tunable Chirality, Adv. Mater. **29**, 1700412, 2017.
[12] L. Jing, Z. Wang, B. Zheng, H. Wang, Y. Yang, L. Shen, W. Yin, E. Li, and H. Chen, Kirigami metamaterials for reconfigurable toroidal circular dichroism, NPG Asia Materials **10**, 888, 2018.

Cavity optomagnonics with magnetic quasi-vortices

Alto Osada[1*]

[1]Komaba Institute for Science, The University of Tokyo, Tokyo, Japan

Abstract

We investigate Brillouin scattering of whispering gallery modes, or optical vortices, by various magnetostatic modes, or magnetic quasi-vortices, both being supported inside a ferromagnetic sphere. As a consequence of conservation of angular momenta, Brillouin scattering becomes reciprocal or nonreciprocal, depending on the orbital angular momentum of the magnetic quasi-vortex. Observed experimental results are reasonably explained by the conservation of angular momenta, and the possible enhancement of Brillouin scattering by the use of optical cavity is inferred.

1. Introduction

Cavity optomagnonics has emerged recently as an activity to pursue the possibility of enhancing spin-light coupling [1, 2, 3, 4, 5, 6, 7, 8, 9], which is inherently weak due to unavoidable mediation of spin-orbit coupling of an electron, by the use of an optical cavity. A ferromagnetic sphere, in this perspective, is an excellent venue for the investigation since it supports optical whispering gallery modes (WGMs) and magnetostatic Walker modes inside the sphere itself [see Fig. 1(a)], equipping them with high quality factors [1, 2, 3, 4, 8].

Moreover, these optical and magnetostatic modes can be regarded respectively as optical vortex and magnetic quasi-vortex, which are typical topological excitations characterized by topological charges or orbital angular momenta. Thus, the system of cavity optomagnonics using a ferromagnetic sphere also provides a suitable platform for exploring the novel physics emerged from the interaction between topological excitations. It is expected that in the interaction between optical vortex and magnetic quasi-vortices, spin and orbital angular momenta are passed from one to the other. This, combined with the broken time-reversal symmetry of the material, can result in the nonreciprocal phenomena [7, 9]. Hence, the cavity optomagnonics may serve as a new approach to opto-spintronics, chiral quantum optics and topological photonics.

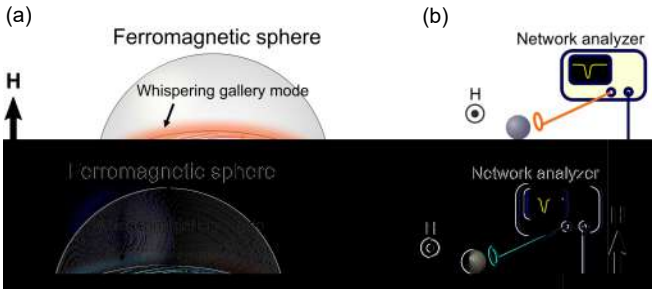


Figure 1: (a) Schematic illustration of the cavity optomagnonics involving whispering gallery modes and Walker modes. (b) Schematics of the experimental setup for the observation of Brillouin scattering. HWP: half-wave plate, PBS: polarization beam splitter, Amp.: microwave amplifier.

2. Nonreciprocal and reciprocal Brillouin scatterings

Experiments are conducted with the setup schematically shown in Fig. 1(b). Laser light with the wavelength of 1550 nm is evanescently coupled to WGMs via a prism, and then Brillouin-scattered by Walker modes. Walker modes possess their frequencies around 7 GHz and are excited by microwaves from a loop coil, in the presence of magnetic field ~ 0.25 T applied perpendicular to the sheet. The incident and scattered light, which are coupled out of the WGM in the same path, possess different polarization state, so that a half-wave plate and a polarization beam splitter make them interfere to generate beat signal. This beat signal manifests itself as the signal of the Brillouin scattering under investigation. The signal is detected by a high-speed photodetec-

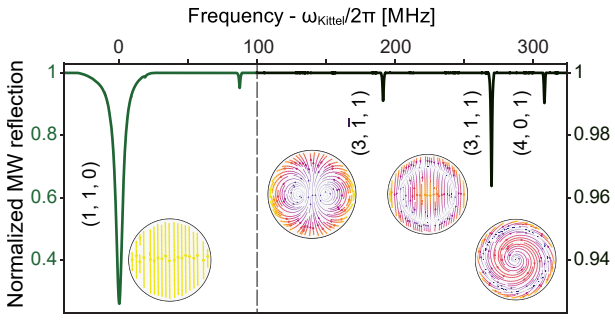


Figure 2: Normalized microwave reflection spectrum with the mode indices assigned to the Walker modes of our interest. Along the horizontal axis, the relative frequency to the Kittel-mode frequency $\omega_{\mathrm{Kittel}}/2\pi$ is used. The transverse-magnetization distributions of the assigned modes are also shown. Note that the spectra below (green, left axis) and above (black, right axis) 100 MHz are separately scaled.

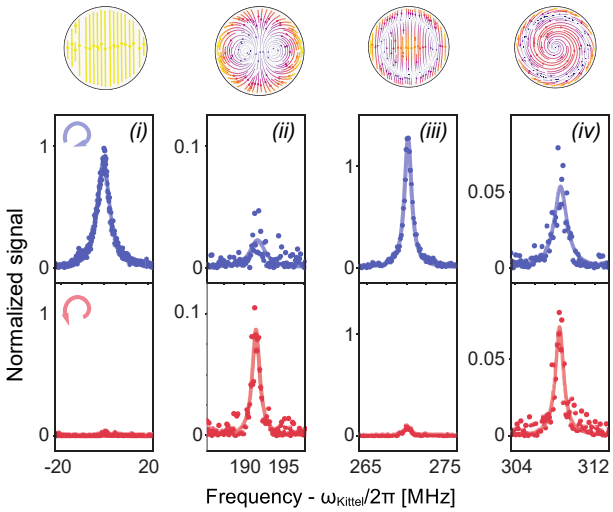


Figure 3: The signals of the Brillouin scattering of the CCW (red) and the CW (blue) WGMs by (i) $(1,1,0)$, (ii) $(3,\bar{1},1)$, (iii) $(3,1,1)$ and (iv) $(4,0,1)$ Walker modes. Solid lines are Lorentzian fittings to the data as a guide to the eye.

tor, which gives us information about the strengths of the Brillouin scatterings by various Walker modes.

The microwave reflection spectrum is displayed in Fig. 2. Along the horizontal axis, the relative frequency to the Kittel-mode frequency $\omega_{\mathrm{Kittel}}/2\pi$ is used. The transverse-magnetization distributions of the assigned $(1,1,0)$, $(3,\bar{1},1)$, $(3,1,1)$ and $(4,0,1)$ modes are also shown. Note that the spectra below (green, left axis) and above (black, right axis) 100 MHz are separately scaled.

Corresponding to the observed Walker modes, signals of Brillouin scattering by the them are observed, as presented in Fig. 3. Red (bottom) and Blue (top) plots are the signals obtained when counterclockwise (CCW) and clockwise (CW) WGMs are used in the experiment. It can be seen that the signal of the Brillouin scattering is larger for CW WGM with $(1,1,0)$ and $(3,1,1)$ modes with vanishing OAM, whereas it is larger for CCW WGM when $(3,\bar{1},1)$ mode is involved, where the OAM reads 2. Furthermore, $(4,0,1)$ mode, whose OAM is 1, results in the absence of the noticeable difference whichever WGM is used. These peculiar behavior can be clearly explained by taking conservation of spin and orbital angular momenta into account, by which together with the experimental results deepens the understandings of the system of cavity optomagnonics.

3. Cavity-enhanced Brillouin scattering

According to the theoretical consideration, the Brillouin scattering of the CW WGM by $(1,1,0)$ (Kittel) mode is resonantly enhanced by WGM, This cavity enhancement can be achieved when a suitable pair of WGMs of the same orbital angular momentum possess the frequency difference equal to the Kittel-mode frequency. Figure 4 shows the plot of Brillouin-scattering signal versus the Kittel-mode frequency tuned by magnetic field. The data and fitting endorse the presence of resonant peak when above condition is satisfied, in agreement with the theory.

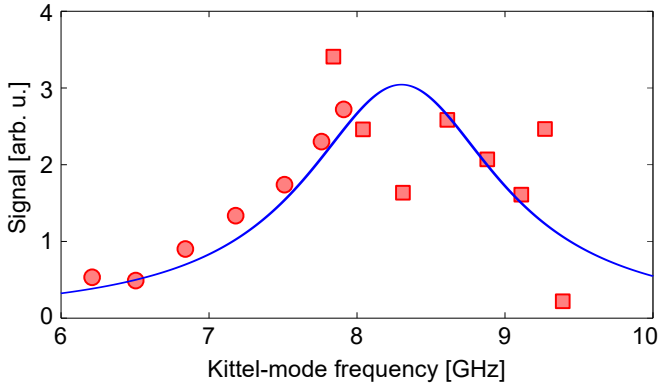


Figure 4: The signals of the Brillouin scattering of the CW WGM by $(1,1,0)$ (Kittel) mode whose frequency is tuned by applied magnetic field. Solid line is a Lorentzian fitting to the data where only the peak height is used as a free parameter.

4. Conclusions

Cavity optomagnonics using a ferromangetic sphere has been proven to be an interesting platform to investigate Brillouin scattering of optical vortices by magnetic quasi-vortices, which could be enhanced by the presence of optical cavity. In accordance with the theory, conservation of angular momenta resulted in the pronounced or absence of nonreciprocity depending on the orbital angular momentum of magnetic quasi-vortex. This work may provide novel approaches to fields such as opto-spintronics and chiral photonics.

References

[1] J. A. Haigh et al., Phys. Rev. A, **92**, 063845 (2015).

[2] A. Osada et al., Phys. Rev. Lett. **116**, 223601 (2016).

[3] X. Zhang et al., Phys. Rev. Lett. **117**, 123605 (2016).

[4] J. A. Haigh et al., Phys. Rev. Lett. **117**, 133602 (2016).

[5] S. V. Kusminskiy, H. X. Tang, and F. Marquardt, Phys. Rev. A, **94**, 033821 (2016).

[6] T. Liu et al., Phys. Rev. B, **94**, 060405(R) (2016).

[7] S. Sharma, Y. M. Blanter, and G. E. W. Bauer, Phys. Rev. B, **96**, 094412 (2017).

[8] A. Osada et al., Phys. Rev. Lett. **120**, 133602 (2018).

[9] A. Osada et al., New J. of Phys. **20**, 103018 (2018).

3D near-field circular dichroism measured by optical force

Masayuki Hoshina[1], Nobuhiko Yokoshi[1], Hajime Ishihara[1,2*]

[1]Department of Physics and Electronics, Osaka Prefecture University, Sakai, Japan
[2]Division of Frontier Materials Science, Osaka University, Toyonaka, Japan
*corresponding author, E-mail: ishi@mp.es.osaka-u.ac.jp

Abstract

We theoretically demonstrate an unnoticed role of the three-dimensional (3D) superchiral structure in the near-field circular dichroism (NF-CD), and propose a scheme of 3D NF-CD measurement near plasmonic chiral field by using the optical force exerted on a tip of the atomic force microscope (AFM), which cannot be performed by aperture-type scanning near-field optical microscope (SNOM) because of its 2D character of the field measurement.

1. Introduction

The interplay between the optical chirality and matter systems is essential for the analysis of matter chiral properties. Circular dichroism (CD), which is the difference in absorption of left- and right-circularly polarized light for substances, is a standard measure of matter chirality. In order to overcome the weakness of the intrinsic absorption cross section of molecules, recently, the superchiral fields near metallic structures is paid great attention[1, 2]. Near the metallic structure, a chiral asymmetry is greatly enhanced, and clear CD of a few molecules can be obtained[3, 4]. Actually, the various nanostructures have been reported to generate superchiral fields and huge optical activity[5, 6, 7, 8]. However, these studies measure the extinction of the propagating light through the target, i.e., measure the far-field component of the CD (FF-CD) signal. In order to extract the full potential of nanoscale superchiral fields and elucidate microscopic chiral properties of single molecules, direct measuring of NF-CD is crucial. To this end, we propose an approach utilizing optical force exerted on a metallic scanning probe. Importantly, the proposed method is sensitive to the longitudinal component (z-component) of polarization in the chiral near-fields through the optical force on the nano-probe tip.

2. Model and method

We assume that the probe tip is fixed to open end of the cantilever, and the optical force is evaluated. Indeed, the similar methods have succeeded in obtaining the super-resolution imaging of the sample surface[9]. We calculate the map of the optical force exerted on the scanning probe with left- or right-handed circularly polarized incident light. The time-averaged optical force acting on the metallic probe is calculated[10]. We scan the probe on the gap area of the four gammadions (see Fig. 1(a)). Under top of the tip is set at z = 5 nm. We set the incident light intensity to be $1\mathrm{kW/cm^2}$.

3. Results

We should note that the optical force is approximately proportional to the gradient of the field intensity. (In the present case, the scattering and absorbing forces are much smaller than the gradient force.) In the present analyses, we compare the maps of field gradient and optical forces. Figure 1(b) shows the map of the optical-force difference between illuminated by the LCP and RCP light. In Fig. 1 (c) and (d), we show the field gradients along z-direction for the field with xy-polarization and z-polarization, respectively. Here, we can see that the map in Fig.4 (b) well reproduces Fig. 4 (c) inside the gap area because the longitudinal component is weak in this region. However, on the edges of the metallic structures, the gradient of the longitudinal component becomes remarkably large as seen in Fig.4 (d). This situation is well reflected in the corner regions in Fig.4 (b). (Note that the color in the corner regions in Fig. 4(b) is strikingly different from that in Fig. 4 (c) with adjusted color bar scale.) Thus, we see that force map well provides information of the contribution from the longitudinal component.

4. Discussion

Here, we should note that the position dependence of the electric fields and the field intensity in itself are affected by the probe tip and generally different from those in the absence of the tip. However, the obtained information provides significant insight into the spatial structures of NF-CD indicated in Fig. 1. This result encourages the study for more detailed analyses of the force map to obtain the 3D NF-CD information including the case in the presence of the targeted molecules on the metallic structures in the next step.

5. Conclusions

We have proposed a scheme for 3D NF-CD measurement by utilizing the optical force exerted on the probe tip. Our demonstration shows that the superchiral fields near the

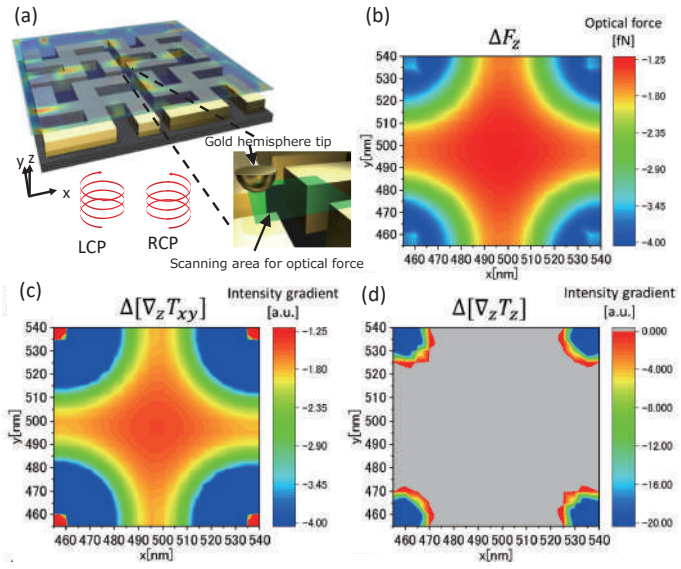


Figure 1: (a) Calculation model. Incident light is left- or right-handed circularly polarized plane wave and propagates along z axis and has left- or right-handed circular polarization. We allocate calculation space of $1000 \times 1000 \times 250\mathrm{nm}^3$ and discretize the space with cubes whose sizes are $5 \times 5 \times 5\mathrm{nm}^3$. The CD signal is the summation of field intensity of the sample surface. Thickness of gammadion is 100 nm. Enlarged view of optical-force scanning area near center gap of metallic structure is shown. (b) Difference between scanning force map of z component with LCP and RCP light. (c, d) Difference between z differential of xy- (c) and z-component (d) transmitted light intensity.

metallic nanostructures include rich longitudinal component that makes a great difference between NF-CD and FF-CD spectra, and the obtained force map well reproduces the 3D NF-CD map including z-component polarization. The understanding of NF-CD stereoscopically will advance the plasmonic chiral sensing and optical chiral manipulation to the next stage.

Acknowledgement

The authors thank Y. Togawa, S. Hashiyada and H. Okamoto for their fruitful discussions. This work was supported in part by JSPS KAKENHI Grant Number JP16H06504 for Scientific Research on Innovative Areas "Nano-Material Optical-Manipulation".

References

[1] Y. Tang and A. E. Cohen, "Optical chirality and its interaction with matter," *Physical review letters*, vol. 104, no. 16, p. 163901, 2010.

[2] E. Hendry, T. Carpy, J. Johnston, M. Popland, R. Mikhaylovskiy, A. Lapthorn, S. Kelly, L. Barron, N. Gadegaard, and M. Kadodwala, "Ultrasensitive detection and characterization of biomolecules using superchiral fields," *Nature nanotechnology*, vol. 5, no. 11, p. 783, 2010.

[3] A. Kuzyk, R. Schreiber, Z. Fan, G. Pardatscher, E.-M. Roller, A. Högele, F. C. Simmel, A. O. Govorov, and T. Liedl, "DNA-based self-assembly of chiral plasmonic nanostructures with tailored optical response," *Nature*, vol. 483, no. 7389, p. 311, 2012.

[4] J. Kumar, H. Eraña, E. López-Martínez, N. Claes, V. F. Martín, D. M. Solís, S. Bals, A. L. Cortajarena, J. Castilla, and L. M. Liz-Marzán, "Detection of amyloid fibrils in parkinson's disease using plasmonic chirality," *Proceedings of the National Academy of Sciences*, vol. 115, no. 13, p. 3225, 2018.

[5] A. Papakostas, A. Potts, D. Bagnall, S. Prosvirnin, H. Coles, and N. Zheludev, "Optical manifestations of planar chirality," *Physical review letters*, vol. 90, no. 10, p. 107404, 2003.

[6] M. Kuwata-Gonokami, N. Saito, Y. Ino, M. Kauranen, K. Jefimovs, T. Vallius, J. Turunen, and Y. Svirko, "Giant optical activity in quasi-two-dimensional planar nanostructures," *Physical review letters*, vol. 95, no. 22, p. 227401, 2005.

[7] B. Bai, Y. Svirko, J. Turunen, and T. Vallius, "Optical activity in planar chiral metamaterials: Theoretical study," *Physical Review A*, vol. 76, no. 2, p. 023811, 2007.

[8] X. Yin, M. Schäferling, B. Metzger, and H. Giessen, "Interpreting chiral nanophotonic spectra: the plasmonic born–kuhn model," *Nano letters*, vol. 13, no. 12, p. 6238, 2013.

[9] J. Yamanishi, Y. Naitoh, Y. Li, and Y. Sugawara, "Heterodyne frequency modulation in photoinduced force microscopy," *Physical Review Applied*, vol. 9, no. 2, p. 024031, 2018.

[10] T. Iida and H. Ishihara, "Force control between quantum dots by light in polaritonic molecule states," *Physical review letters*, vol. 97, no. 11, p. 117402, 2006.

Chirality Generation in Discrete Silicon Nanostructures

Xin Zhao[1] and Björn M. Reinhard[1,*]

[1]Department of Chemistry and The Photonics Center, Boston University, Boston, United States
*corresponding author, E-mail: bmr@bu.edu

Abstract

Silicon nanostructures provide morphology-dependent resonances that can be tuned across a wide wavelength range, which makes them versatile building blocks for higher order photonic molecules. Electromagnetic interactions between individual building blocks in silicon-based photonic molecules provide additional degrees of freedom for enhancing and controlling light-matter interactions. In this presentation we will review recent studies from our laboratory aimed at generating enhanced optical chirality densities in achiral structures.

1. Introduction

Depending on their precise morphology silicon nanostructures sustain a wide range of optical modes in the visible range of the electromagnetic spectrum. For instance, high refractive index silicon nanoparticles provide both magnetic and electric Mie resonances, and silicon nanorods can sustain additional guided modes.[1,2] If the diameter of the silicon nanowires is small, these modes can have a significant mode volume outside of the nanowire. Due to this field penetration of the ambient medium, higher functionality can be achieved by incorporating the individual silicon building blocks into higher order structures with sufficiently short spacing between the building blocks to allow for strong electromagnetic interactions. We will describe in this presentation recent progress from our laboratory to utilize silicon nanostructures (see for example Figure 1) to generate same sign near-field chirality enhancement and to boost chiral light-matter interactions.

2. Generating Near-Field Chirality in Silicon Nanowire Dimers

The spectra of silicon nanowires are dominated by weakly confined hybrid HE modes, described the nomenclature $HE_{l,m}$ with 2l intensity maxima around the circumference of the nanowire and m maxima along the radial direction.[1] The fundamental $HE_{1,1}$ mode is two-fold degenerate with *E*-field components pointing either into x- or y- direction: $HE_{1,1x}$ and $HE_{1,1y}$. Importantly, this degeneracy is removed if the two nanowires are localized in close vicinity to each other, and the leaky *E*-fields of the wires show different interactions along different directions.[3] If we assume the two nanorods to be arranged along the x-axis then the x-component of the *E*-field associated with a mode show a much richer interaction than along the y-axis. As the *E*-field along the x-axis penetrates the neighboring silicon nanowire, the refractive index of the *E*x component is effectively higher than that of the *E*y component due the the presence of the second high refractive index silicon nanorod. One important consequence of this birefringence that leads to differences in the refractive index between *E*x and *E*y components of the propagating modes is that the associated modes build up a phase difference as they travel along the nanowire. Importantly this phase difference will increase with increasing propagation length of the nanowire. In other words, the length of the fabricated nanowires provides opportunities to control the accumulated phase difference.

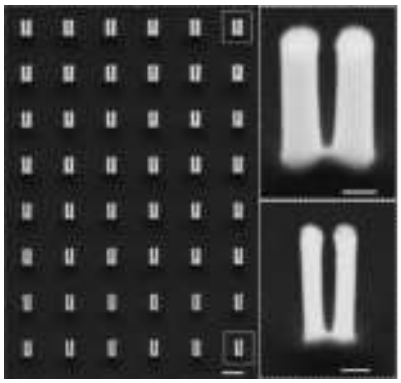


Figure 1. SEM images of silicon nanowire dimers generated by reactive ion etching. The images show an array with increasing wire radius from 55 nm (bottom) to 90 nm (top) in steps of 5 nm. Insets show magnified views of marked dimers. Scale bar = 1 micron in the array image and 200 nm in the insets. Reproduced with permission from X. Zhao and B.M. Reinhard, *ACS Photonics* **4**, 2265 (2017). Copyright American Chemical Society.

The ability of an electromagnetic field to enhance chiral light-matter interactions depends on the chirality density, *C*:[4,5]

$$C = -\tfrac{1}{2}\,\omega\varepsilon_0\,\mathrm{Im}(\boldsymbol{E}^{*}\cdot\boldsymbol{B}) \qquad (1)$$

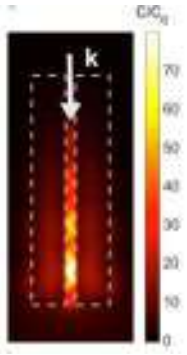


Figure 2: Simulated near-field optical chirality for silicon nanowire dimers (length: 2 microns, radius: 70 nm, separation: 40 nm) with an incident polarization $\theta=\pi/4$ relative to nanowire-nanowire axis. Reproduced with permission from X. Zhao and B.M. Reinhard, *ACS Photonics* **4**, 2265 (2017). Copyright American Chemical Society.

where *E* and *B* are electric and magnetic field, respectively. According to this relationship, it is clear that the near-field chirality depends on the alignment of electric and magnetic fields and the phase shift between electric and magnetic field. In dimers of silicon nanowires the presence of orthogonal $HE_{1,1x}$ and $HE_{1,1y}$ modes from two adjacent nanowires whose electric and magnetic compounds accumulate a relative phase shift, γ, as they propagate along the nanowire provides opportunities for achieving the correct alignment of *E* and *B* fields of the propagating modes to enhance the near-field chirality. We will demonstrate in this presentation that silicon nanowires and other silicon nanostructures can generate robust same sign chirality near-fields under illumination with linearly polarized light.

Figure 2 shows a finite difference time domain (FDTD) simulation of *C* in the plane between two 2 micron long silicon nanowires (140 nm diameter) with a spacing of 40 nm. The incident light polarization is $\pi/4$ (relative to the nanowire-nanowire axis). The simulations clearly confirm a strong near-field chirality in the gap between the two silicon nanowires.

We will discuss and characterize the fundamental working principles underlying optical chirality generation in dimers of silicon nanowires and other silicon-based photonic molecules.

3. Discussion

Silicon nanostructures provide tunable resonances over a broad spectral range as well as a high degree of mechanical and thermal stability. Their physical properties together with the availability of accurate top-down fabrication strategies for integrating them into higher order structures makes silicon nanostructures ideal building blocks for nanoscale optical antennas in the visible range of the electromagnetic spectrum. In this presentation we will discuss recent examples from our laboratory of how discrete silicon nanoantennas can be generated that provide exquisite control over the optical near-field chirality. Our fabrication strategies will be discussed and the underlying electromagnetic working principles will be characterized through combination of optical spectroscopy and electromagnetic simulations.

4. Conclusions

Silicon nanostructures that can provide both electric and magnetic field enhancements are versatile building blocks for generating chiral field enhancements in achiral antennas. The ability to enhance optical chirality in achiral structures with linear light polarization provides unique opportunities for enhancing chiral light-matter interactions and, thus, paves the way to detecting molecular chirality with higher sensitivity than is currently possible.

Acknowledgements

This project was partially supported by the National Science Foundation under CHE-1609778.

References

(1) Seo, K.; Wober, M.; Steinvurzel, P.; Schonbrun, E.; Dan, Y.; Ellenbogen, T.; Crozier, K. B. Multicoloroed Verical Silicon Nanowires. *Nano Lett.* **2011**, *11*, 1851.

(2) Abujetas, D. R.; Paniagua-Dominguez, R.; Sanchez-Gil, J. A. Unraveling the Janus Rule of Mie Resonances and Leaky/Guided Modes in Semiconductor Nanowire Absorption for Enhanced Light Harvesting. *ACS Photonics* **2015**, *2*, 921.

(3) Zhao, X.; Alizadeh, M. H.; Reinhard, B. M. Generating Optical Birefringence and Chirality in Silicon Nanowires. *ACS Photonics* **2017**, *4*, 2265.

(4) Tang, Y.; Cohen, A. E. Optical chirality and its interaction with matter. *Phys. Rev. Lett.* **2010**, *104*.

(5) Tang, Y.; Cohen, A. E. Enhanced enantioselectivity in excitation of chiral molecules by superchiral light. *Science* **2011**, *332*.

Generalization of the Optical Chirality to Arbitrary Media

J. Enrique Vázquez-Lozano* **and Alejandro Martínez**

Nanophotonics Technology Center, Universitat Politècnica de València, Camino de Vera s/n, 46022 Valencia, Spain
*corresponding author, E-mail: juavazlo@ntc.upv.es

Abstract

Motivated by recent theoretical results concerning energy, momentum, angular momentum, and optical helicity of electromagnetic waves in dispersive and lossless media, here we address a parallel derivation for the optical chirality, extending it so as to include dissipative effects as well. Looking into the mathematical structure of the continuity equation, we find a new general expression for the optical chirality density in lossless and lossy dispersive media, which may be applied to any medium, including dielectrics, plasmonic nanostructures, and metamaterials.

1. Introduction

Chirality is a geometrical property that allows us to describe objects that cannot be superimposed with their mirror image. This property is ubiquitous in nature at many different scales, with a special role at the molecular level, since enantiomers may behave very differently. Besides physical objects, chirality can also be exhibited by electromagnetic (EM) waves. In this context, as originally introduced by Tang and Cohen [1], optical chirality is a fundamental property of light that determines the degree of the handedness of optical fields in free space:

$$\mathcal{C}_{\text{vacuum}} \equiv \left[\varepsilon_0 \boldsymbol{\mathcal{E}} \cdot (\nabla \times \boldsymbol{\mathcal{E}}) + \mu_0 \boldsymbol{\mathcal{H}} \cdot (\nabla \times \boldsymbol{\mathcal{H}})\right]/2, \quad (1)$$

where ε_0 and μ_0 are the permittivity and permeability of vacuum, respectively, and $\boldsymbol{\mathcal{E}}(\mathbf{r},t)$ and $\boldsymbol{\mathcal{H}}(\mathbf{r},t)$ are the local, time-dependent electric and magnetic fields. This formula has been successfully used in circular-dichroism measurements for the experimental detection and characterization of chiral biomolecules by superchiral fields (i.e., fields with optical chirality larger than that due to circularly polarized light) [2, 3], thus confirming its physical significance and the feasibility for practical applications. Nonetheless, mainly due to the mismatch between the scales of the illuminating wavelength and the typical size of chiral molecules, the chiroptical responses are generally very weak [1].

Recent advances in nanofabrication have led to nanostructured metamaterials and plasmonic systems that tremendously boost chiral light-matter interactions. Indeed, the occurrence of strong optical chirality relies on the complexity of the EM-field distribution, and thus metallic nanostructures have been considered as the best-suited platforms for investigating chiroptical effects [4]. Still, it is certainly surprising that contributions of material dispersion as well as dissipation have mostly been ignored.

2. Continuity equation for optical chirality

Aiming to get the optical chirality density in dispersive media, we will first address the most complete form of its conservation law. In the presence of charges and/or currents, conservation laws are to be expressed through the continuity equations. Therefore, just as for the energy conservation (derived from the Poynting vector), for the optical chirality one must start by defining its flux density:

$$\boldsymbol{\mathcal{F}} \equiv \left[\boldsymbol{\mathcal{E}} \times (\nabla \times \boldsymbol{\mathcal{H}}) - \boldsymbol{\mathcal{H}} \times (\nabla \times \boldsymbol{\mathcal{E}})\right]/2. \quad (2)$$

Here it is worth remarking that, so far the literature concerning optical chirality has been mostly dealing with EM fields in free space [1, 5]. Then, we can often find several expressions for the chirality flux density where the fields $\boldsymbol{\mathcal{B}}$ and $\boldsymbol{\mathcal{H}}$ are used interchangeably yielding the same results. However, this does not occur in dispersive media, and special care should be taken in dealing with EM fields either in free-space ($\boldsymbol{\mathcal{E}}$ and $\boldsymbol{\mathcal{H}}$), or within a medium ($\boldsymbol{\mathcal{D}}$ and $\boldsymbol{\mathcal{B}}$). Be that as it may, the chirality flux density as defined in Eq. (2) is in fact used in Ref. [6], and coincides with that originally introduced by Tang and Cohen [1] for EM fields in free space. Then, taking the divergence it follows that

$$\nabla\cdot\boldsymbol{\mathcal{F}} = -[\boldsymbol{\mathcal{E}}\cdot\partial_t(\nabla\times\boldsymbol{\mathcal{D}}) + \boldsymbol{\mathcal{H}}\cdot\partial_t(\nabla\times\boldsymbol{\mathcal{B}}) + \mathcal{S}_{\mathcal{J}}]/2, \quad (3)$$

where $\mathcal{S}_{\mathcal{J}} = \boldsymbol{\mathcal{E}}\cdot(\nabla\times\boldsymbol{\mathcal{J}})$ is the current-related source-like contribution. Taking into account the mathematical structure of the continuity equation, Eq. (3) can be recast as

$$\nabla\cdot\boldsymbol{\mathcal{F}} + \partial_t\mathcal{C} = \mathcal{S}, \quad (4)$$

where the optical chirality density and the source-like terms have been defined as

$$\mathcal{C} \equiv \left[\boldsymbol{\mathcal{E}}\cdot(\nabla\times\boldsymbol{\mathcal{D}}) + \boldsymbol{\mathcal{H}}\cdot(\nabla\times\boldsymbol{\mathcal{B}})\right]/2, \quad (5)$$

$$\mathcal{S} \equiv \left[\partial_t\boldsymbol{\mathcal{E}}\cdot(\nabla\times\boldsymbol{\mathcal{D}}) + \partial_t\boldsymbol{\mathcal{H}}\cdot(\nabla\times\boldsymbol{\mathcal{B}}) - \mathcal{S}_{\mathcal{J}}\right]/2. \quad (6)$$

The above expressions represent the most general result for the conservation law of optical chirality without restrictions on the nature of the medium [7]. Still, on account of the dispersion-related terms, they differ considerably from those ones previously established [1, 5, 6].

3. Optical chirality density in dispersive media

For monochromatic EM fields, $\boldsymbol{\mathcal{E}} = \text{Re}\left[\mathbf{E}(\mathbf{r})e^{-i\omega t}\right]$ and $\boldsymbol{\mathcal{H}} = \text{Re}\left[\mathbf{H}(\mathbf{r})e^{-i\omega t}\right]$, the time-averaged optical chirality density is usually given by [1, 2, 3, 4, 5]:

$$C_{\text{vacuum}} = \frac{\omega}{2c^2}\text{Im}[\mathbf{E}\cdot\mathbf{H}^*], \quad (7)$$

where bold letters stand for complex field amplitudes and the asterisk denotes complex conjugation. However, this expression is only valid for optical fields in free space. Inspired by recent works examining dispersive features of several dynamical properties such as energy, momentum, angular momentum and helicity [8, 9], here we report on the optical chirality in lossless and lossy dispersive media [7]. Specifically, building on previous treatments addressing the electromagnetic energy density in a lossless dispersive medium (giving rise to the so-called Brillouin's formula), we are able to find a similar expression accounting for the optical chirality density in lossless dispersive media:

$$C_{\text{lossless}} = \text{Re}[n(\omega)\tilde{n}(\omega)]C_{\text{vacuum}} = \frac{\omega}{2}\frac{\text{Im}[\mathbf{E}\cdot\mathbf{H}^*]}{v_p(\omega)v_g(\omega)}, \quad (8)$$

where v_p and v_g, are the phase and group velocities, respectively, which can be given in terms of the refractive index $n(\omega)$ and the corresponding dispersion-modified group index $\tilde{n}(\omega) \equiv n(\omega) + \omega\,[\partial n(\omega)/\partial\omega]$.

According to the Kramers-Kronig relations, a more realistic description of dispersive media requires careful considerations of dissipative effects as well. However, in a lossy dispersive medium, there are certain frequency ranges where the physical meaning of the group velocity turns out to be somewhat unclear. Hence, in order to avoid misleading outcomes, the analysis of the optical chirality has to be carefully carried out from a material standpoint. Assuming a medium whose material parameters can be fitted by Lorentzian line shapes, and looking into the underlying mathematical structure of the continuity equation [Eq. (4)], it can be demonstrated that the optical chirality density in a lossy dispersive medium reads as [7]

$$C_{\text{lossy}} = \frac{\omega}{4c^2}\text{Im}[(\varepsilon(\omega)\mu_{\text{eff}}(\omega) + \varepsilon_{\text{eff}}(\omega)\mu^*(\omega))\mathbf{E}\cdot\mathbf{H}^*], \quad (9)$$

where ε_{eff} and μ_{eff} are the real-valued effective parameters:

$$\left\{\begin{matrix}\varepsilon_{\text{eff}}(\omega)\\ \mu_{\text{eff}}(\omega)\end{matrix}\right\} \equiv 1 + \sum_n (\chi_n' + 2\omega\chi_n''/\gamma_n), \quad (10)$$

with $\chi = \chi' + i\chi''$ being either the electric or magnetic susceptibilities. As shown in Fig. 1, both lossless and lossy approaches yield similar results, but they significantly differ in spectral regions with high absorption and anomalous dispersion. This fact should be accounted for and examined in experiments considering chiroptical interaction between light and metamaterials or plasmonic nanostructures.

4. Conclusions

We have provided insights into the theoretical derivation of the optical chirality in lossless and lossy dispersive media. Our results are perfectly consistent with that originally introduced for EM fields in free space, and should be enormously relevant for the development of advanced chiroptical applications, mainly in the context of lossy media such as plasmonic systems and metamaterials, whose chiral properties are currently receiving strong attention.

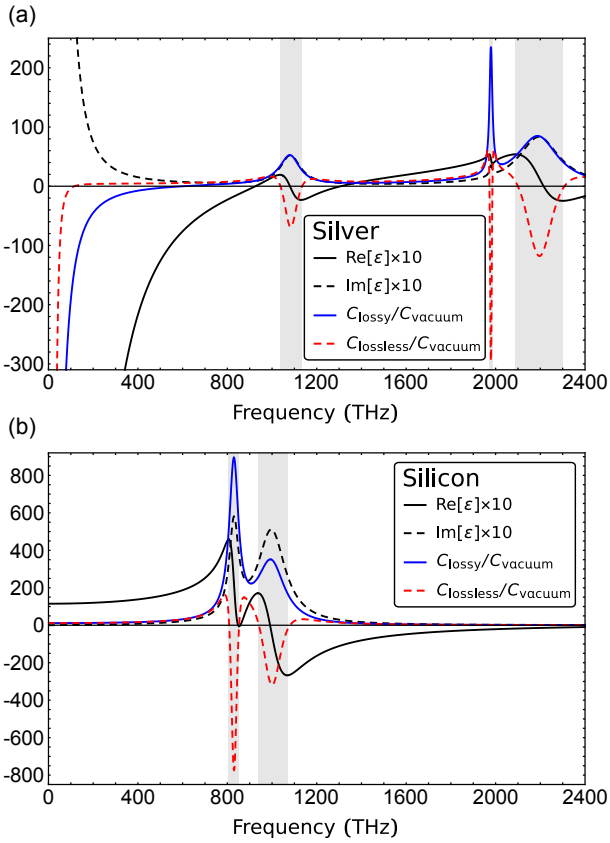


Figure 1: Optical chirality density for (a) silver, and (b) silicon. For comparison we represent the results for lossless (red dashed lines) [Eq. (8)] and lossy (blue solid lines) [Eq. (9)] dispersive media in terms of C_{vacuum} [Eq. (7)].

Acknowledgement

We acknowledge funding from contract No. TEC2014-51902-C2-1-R (MINECO/FEDER, UE).

References

[1] Y. Tang, A.E. Cohen, *Phys. Rev. Lett.* 104: 163901, 2010.

[2] E. Hendry *et al.*, *Nat. Nanotechnol.* 5: 783–787, 2010.

[3] Y. Tang, A.E. Cohen, *Science* 332: 333–336, 2011.

[4] M. Schäferling, *Chiral Nanophotonics*, Springer, Berlin, 2017.

[5] K.Y. Bliokh, F. Nori, *Phys. Rev. A* 83: 021803, 2011.

[6] L.V. Poulikakos *et al.*, *ACS Photonics* 3: 1619–1625, 2016.

[7] J.E. Vázquez-Lozano, A. Martínez, *Phys. Rev. Lett.* 121: 043901, 2018.

[8] K.Y. Bliokh, A.Y. Bekshaev, F. Nori, *Phys. Rev. Lett.* 120: 243605, 2018.

[9] F. Alpeggiani *et al.*, *Phys. Rev. Lett.* 120: 243605, 2018.

Chiral terahertz wave emission from the Weyl semimetal TaAs

Y. Gao[1], Y. Qin[1], Y. P. Liu[1], Y. L. Su[1], S. Kaushik[2], E. J. Philip[2], X.Chen[2], Z. Li[3, 4], H. Weng[4, 5], D. E. Kharzeev[2, 6, 7], M. K. Liu[2], and J. Qi[1*],

[1]State Key Laboratory of Electronic Thin Films and Integrated Devices, University of Electronic Science and Technology of China, Chengdu 610054, China
[2]Department of Physics and Astronomy, Stony Brook University, Stony Brook, New York 11794, USA
[3]State Key Laboratory for Artificial Microstructure and Mesoscopic Physics, Beijing Key Laboratory of Quantum Devices, Peking University, Beijing 100871, China
[4]Beijing National Laboratory for Condensed Matter Physics, Institute of Physics, Chinese Academy of Sciences, Beijing 100190, China
[5]Songshan Lake Materials Laboratory, Guangdong 523808, China
[6]Department of Physics, Brookhaven National Laboratory, Upton, New York 11973-5000, USA
[7]RIKEN-BNL Research Center, Brookhaven National Laboratory, Upton, New York 11973-5000, USA
[*]Author e-mail address: jbqi@uestc.edu.cn

Abstract

We discover strong coherent terahertz emission from the Weyl semimetal TaAs and demonstrate unprecedented manipulation over its polarization and chirality on femtosecond (fs) timescale. Such controllability is achieved via polarization-dependent, colossal ultrafast photocurrents in TaAs generated using the circular and/or linear photogalvanic effect.

1. Introduction

Ultrafast currents can cause terahertz emission in the terahertz (THz) frequency regime, where it is difficult to control the ellipticity and chirality over a broad spectral range [1-4]. A promising way to achieve these tasks is to generate the chiral photocurrents using the novel topology of band structures where electrons demonstrate unique spin-momentum locking [5-7]. It has been shown experimentally that both the circular photogalvanic effect (CPGE) [8] and linear photogalvanic effect (LPGE) [9] can lead to the colossal DC photocurrents exist in the Weyl semimetal (WSM) TaAs. Here, we investigate THz emission process due to the ultrafast photocurrents in TaAs, and reveal a new route to realize the generation and control of the broadband elliptically polarized THz waves.

2. Results and discussions

We mainly focus on the results obtained from the TaAs (112) single crystal. Figure 1(a) illustrates the THz emission spectroscopy. $\hat{x}$ is along the [-110] direction. The sample was excited by the laser pulses (duration ~80 fs, center wavelength 800 nm) from a Ti:sapphire amplifier (repetition rate 1 KHz) under ~ 3° angle of incidence with a beam diameter of 1.5 mm (full-width at half intensity maximum). A typical pump power of 25 mW was used. The THz electric field was detected by electro-optic sampling, with probe pulses from the same laser co-propagating with the terahertz field through an electro-optic crystal, which is the ZnTe(110) with a thickness of 0.4 mm. All measurements were performed at room temperature in a dry-air environment with relative humidity < 5%. Within our pump power range, the THz peak field strength can reach up to ~1 kV/cm.

The excitation given by pump pulse on the surface of TaAs initiates a transient photocurrent. According to the Maxwell equations, an ultrafast change in the current density $\vec{j}(z,t)$ on the picosecond (ps) timescale will result in electromagnetic radiation in the THz spectral range (1 THz = 1 ps^{-1}) [10]. The transient THz electric field $\vec{E}(t)$ is generated with a polarization parallel to the direction of the current. Therefore, one can directly detect the time-domain spectra $\vec{E}(t)$ of the THz radiation as a probe for the ultrafast sheet current density given by $\vec{J}(t) = \int dz\vec{j}(z,t)$. The THz electric field $\vec{E}(t)[= E_x(t)\hat{s} + E_{yz}(t)\hat{p}]$ consists of two components along two perpendicular directions. Measurement of $E_x(t)$ and $E_{yz}(t)$ by the EO sampling provides access to the sheet current density $\vec{J}(t)$ owing inside the sample.

Figure 1(b) and (c) show time-domain THz far-field EO signal component $S_x(t)$ along the $\hat{s}$ direction, detected for various settings of pump polarization via rotating the =λ/4 or λ/2 waveplate, characterized by the angle θ or ϕ. Here, ↔ (θ = 0°), ↻ (θ =45°), and ↺ (θ = 135°) represent the *p*, right-handed, and left-handed circularly polarized light, respectively. Clearly, both the magnitude and temporal shape of the THz waveform $S_x(t)$ depend strongly on the

light polarization. The key observation is that signals $S_x(t)$ taken with right- (↻) and left-handed (↺) circularly polarized light are completely out of phase. A similar observation was found for the 45° and 135° linearly polarized light in Figure 1(c). The helicity-dependent signals arise from the CPGE, while the signals depending on the linear polarization originates from the LPGE.

Figure 1(d) shows EO signal component $S_{yz}(t)$ along the $\hat{p}$ direction. Both the magnitude and temporal shape of the THz waveform $S_{yz}(t)$ remain the same nearly as the pump polarization changes. $S_{yz}(t)$ is almost polarization-independent and differs substantially from $S_x(t)$. S_{yz} has a thermal origin. Such distinct S_x and S_{yz} components lead to a elliptically polarized transient THz field $\boldsymbol{S}(t)$. Clearly, the chirality of $\boldsymbol{S}(t)$ can be manipulated by changing the polarization state of the pump light.

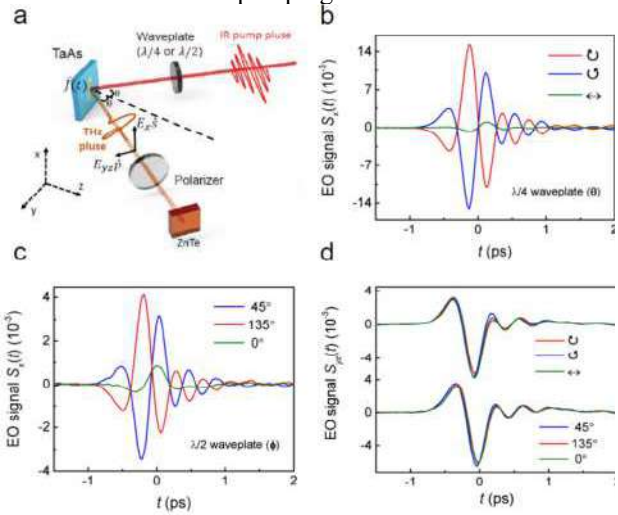


Figure 1: (a). Schematic of the THz emission spectroscopy. Excitation of a fs laser pulse with an incident angle Θ≈3° onto a TaAs single crystal initiates a photocurrent burst and, consequently, emission of a THz pulse. (b). Typical THz EO signal component $S_x(t)$ along the $\hat{s}$ direction was measured at various settings for pump polarization via rotating the λ/4 waveplate. (c). Typical THz EO signal component $S_x(t)$ along the $\hat{s}$ direction was measured at various settings for pump polarization via rotating the λ/2 waveplate. (d). Typical THz EO signal component $S_{yz}(t)$ along the $\hat{p}$ direction was measured at various settings for pump polarization via rotating the =λ/4 or λ/2 waveplate.

3. Conclusions

Strong THz emission due to the colossal ultrafast photocurrent response generated following excitation by near-infrared light was observed in WSM TaAs. Changing the circular or linear polarization of pump light can switch the polarization state of the broadband THz waves including the chirality.

Acknowledgements

This research is supported by the National Natural Science Foundation of China (Grants No. 11734006 and No. 11674369), the National Key Research and Development Program of China (No. 2016YFA0300600 and 2018YFA0305700), the Science Challenge Project of China (TZ2016004), and the National Postdoctoral Program for Innovative Talents (Projects No. BX201700012, funded by China Postdoctoral Science Foundation). This work is also supported in part by the U.S. Department of Energy under Awards DE-SC-0017662 (E.J.P. and D.E.K.), DE-FG-88ER40388 (S.K. and D.E.K.), and DE-AC02-98CH10886 (D.E.K.).

References

[1] N. Amer, W. C. Hurlbut, B. J. Norton, Y. S. Lee, and T. B. Norris, Generation of terahertz pulses with arbitrary elliptical polarization. *Appl. Phys. Lett.* 87, 221111 (2005).

[2] X. Lu, and X. C. Zhang, Generation of elliptically polarized terahertz waves from laser-induced plasma with double helix electrodes. *Phys. Rev. Lett.* 108, 123903 (2012).

[3] W. M. Wang, P. Gibbon, Z. M. Sheng, and Y. T. Li, Tunable circularly polarized terahertz radiation from magnetized gas plasma. *Phys. Rev. Lett.* 114, 253901 (2015).

[4] Z. Zhang *et al*. Manipulation of polarizations for broadband terahertz waves emitted from laser plasma laments. *Nat. Photonics* 12, 554 (2018).

[5] M. Z. Hasan, and C. L. Kane, Topological insulators. *Rev. Mod. Phys.* 82, 3045 (2010).

[6] X. -L. Qi, and S. -C. Zhang, Topological insulators and superconductors. *Rev. Mod. Phys.* 83,1057 (2011).

[7] H. Weng, R. Yu, X. Hu, X. Dai, and Z. Fang, Quantum anomalous Hall effect and related topological electronic states. *Adv. Phys.* 64, 227 (2015).

[8] Q. Ma *et al*. Direct optical detection of Weyl fermion chirality in a topological semimental. *Nat. Phys.* 13, 842-847 (2017).

[9] G. B. Osterhoudt *et al.* Colossal Bulk Photovoltaic Effect in a Weyl Semimetal. arXiv:1712.04951 (2018).

[10] T. Kampfrath *et al.* Terahertz spin current pulses controlled by magnetic heterostructures. *Nat. Nanotechnol.* 8, 256-260 (2013).

Photonic Orbital Angular Momentum Transfer and Magnetic Skyrmion Rotation

Wenrui Yang[1], Huanhuan Yang[1], Yunshan Cao[1], and Peng Yan[1,*]

[1]School of Electronic Science and Engineering and State Key Laboratory of Electronic Thin Films and Integrated Devices, University of Electronic Science and Technology of China, Chengdu 610054, China
*corresponding author, E-mail: yan@uestc.edu.cn

Abstract

We predict a photonic orbital angular momentum transfer effect, by studying the dynamics of magnetic skyrmions subject to Laguerre-Gaussian optical vortices, which manifests a rotational motion of the skyrmionic quasiparticle around the beam axis. The topological charge of the optical vortex determines both the magnitude and the handedness of the rotation velocity of skyrmions. The twisted light beam acts as an optical tweezer to displace skyrmion motions.

1. Introduction

A skyrmion is a swirling noncoplanar texture originally introduced by Skyrme a half century ago, as a hypothetical particle in the baryon theory [1], and later was observed in many condensed matter systems, such as liquid crystals, superfluids, and chiral magnets. The magnetic skyrmion, a topologically protected spin texture with a quantized topological charge, has been a prominent topic of spintronics since the first experimental observations of skyrmion lattices in bulk noncentrosymmetric magnets [2, 3] and thin films [4]. Depending on the magnetization rotation, three distinct types of skyrmions have been observed experimentally, referred to as Néel skyrmion, Bloch skyrmion and antiskyrmion. The manipulation of skyrmions is of great importance and interest: skyrmions can be driven by spin-polarized current, magnetic field or electric-field gradients, temperature gradients, and spin waves. However, the genuine skyrmion Hall effects tend to result in skyrmion accumulations at the edge of devices, although strongly coupled bilayer-skyrmions were proposed hopefully to overcome the problem. Crystal imperfections on the other hand may capture or stop skyrmions. These difficulties hinder the precise manipulation of the skyrmion motion by the mentioned control methods. Thus, it should be very interesting and important if one can find other effective control methods and principles to manipulate skyrmions in magnetic thin films.

Since the theoretical work of Poynting and the experiments by Beth, it has been known that light can carry angular momentum that is associated with circular polarization and arises from the spin of individual photons and is termed spin angular momentum. Following the pioneering work by Allen et al., it was realized that light can also carry orbital angular momentum (OAM) with helical phase fronts characterized by an $\exp(il\varphi)$ azimuthal phase dependence. Such twisted lights have a phase dislocation on the axis that is sometimes referred to as an optical vortex. A number of demonstrations and applications of twisted lights have been brought forward. They range from optical data storages to quantum communications, and black holes, among others. Optical vortices with high OAM have been achieved using spiral phase plates, computer-generated holograms, mode conversions, spatial light modulators, etc.

In this work, we let skyrmions enter the field of OAM. We theoretically propose to use Laguerre-Gaussian (LG) optical vortices to manipulate the skyrmion dynamics via the OAM transfer [5]. A rotational motion of an isolated skyrmion is found. We show that the topological charge l of the optical vortex plays a key role in driving the skyrmion motion: a positive l brings about an anticlockwise rotation of skyrmions around the beam axis, while a negative l results in a clockwise one. Finally, we demonstrate that optical vortices like tweezers can grip a skyrmion to overfly large-scale defects in magnetic films to avoid being captured.

2. Model and results

We consider an isolated Néel skyrmion whose magnetization dynamics generally is modeled by the Landau-Lifshitz-Gilbert (LLG) equation. The total effective field consists of isotropic exchange coupling, uniaxial anisotropy, the interfacial Dzyaloshinskii-Moriya interaction favoring Néel skyrmions, and the optical vortex field. Finite temperature effects can be taken into account by including a Gaussian stochastic magnetic field satisfying fluctuation-dissipation theorem. We focus on skyrmion dynamics at zero temperature, if not stated otherwise.
To demonstrate the time evolution of the skyrmion motion, we solved numerically the full LLG equation using the micromagnetic simulation codes MuMax3. We used magnetic parameters for Pt/Co/AlOx system. In Figs. 1(a1)-(a9), we observe an anticlockwise rotation of the skyrmion about the beam center due to an application of an optical

vortex with OAM quantum number l = +5. To prove that the rotational motion is indeed due to the OAM transfer from optical vortices to the skyrmion, we provide two more numerical evidences: (i) we reverse the helicity of the optical vortex from l = +5 to l = -5 without changing the rest parameters. Figures 1(b1)-(b9) demonstrate a striking reversal of the rotation direction of skyrmions, as expected.

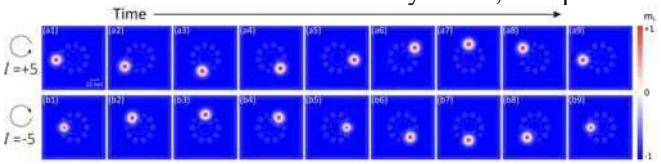


Fig. 1: Time evolution of an isolated Néel skyrmion under optical vortices with OAM quantum number l = +5 (a1)-(a9) and l = -5 (b1)-(b9). The time intervals between successive snapshots in two cases are 0.8 ns and 0.5 ns, respectively. A positive (negative) topological charge induces an anticlockwise (clockwise) rotation of a skyrmion around the beam axis.

The rotation velocity of skyrmions as a function of the driving frequency is shown in Fig. 2(a). The velocity linearly increases with the frequency below 1.5 GHz and sharply decreases then. The peak is due to the resonance between the skyrmion circular frequency and the vortex frequency. Higher frequency indicates more diluted photon number density, thus reducing the OAM transfer and lowering the skyrmion velocity drastically. Figure 2(b) shows the OAM dependence of the skyrmion velocity which is shown to be sensitive to l.

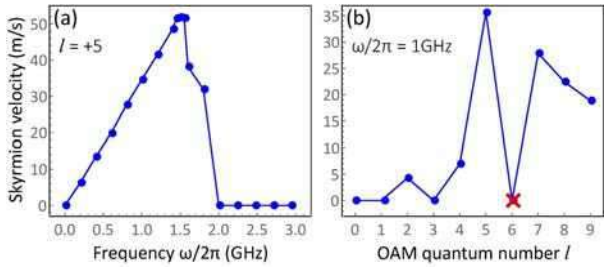


Fig. 2: Skyrmion velocity as a function of the driving frequency (a) and the topological charge (b) of optical vortices. The red cross stamps a skyrmion annihilation. The minus sign of the velocity is dropped.

3. Conclusions

In summary, we proposed an all-photonic orbital angular momentum transfer mechanism to manipulate magnetic skyrmions. This OAM transfer can effectively drive the skyrmion rotation around the beam axis. The mechanism applies not only to ferromagnetic skyrmions but also to antiferromagnetic ones. Our proposal opens the door for all-optical manipulations of magnetic skyrmions by harvesting the OAM of twisted lights and raises the challenge to generate micron-/submicron-focused optical vortices. Other types of vortex beams such as electron vortices and their acoustic counterparts without breaking the diffraction limit are also promising candidates to drive skyrmion rotations via magnetoelectric and magnetoelastic couplings, respectively. These should be interesting subjects for future research.

Acknowledgements

We thank H.Y. Yuan and Z.Y. Wang for useful discussions. This work was supported by the National Natural Science Foundation of China (Grants No. 11604041 and 11704060), the National Key Research Development Program under Contract No. 2016YFA0300801, and the National Thousand-Young-Talent Program of China.

References

[1] T.H.R. Skyrme, A unified field theory of mesons and baryons, Nucl. Phys. 31, 556 (1962).

[2] S. Mulbauer, B. Binz, F. Jonietz, C. Pfleiderer, A. Rosch, A. Neubauer, R. Georgii, and P. Boni, Skyrmion lattice in chiral magnet, Science 323, 915 (2009).

[3] X.Z. Yu, Y. Onose, N. Kanazawa, J.H. Park, J.H. Han, Y. Matsui, N. Nagaosa, and Y. Tokura, Real-space observation of a two-dimensional skyrmion crystal, Nature 465, 901 (2010).

[4] S. Heinze, K. von Bergmann, M. Menzel, J. Brede, A. Kubetzka, R. Wiesendanger, G. Bihlmayer, and S. Blugel, Spontaneous atomic-scale magnetic skyrmion lattice in two dimensions, Nat. Phys. 7, 713 (2011).

[5] W. Yang, H. Yang, Y. Cao, and P. Yan, Photonic Orbital angular momentum transfer and magnetic skyrmion rotation, Opt. Express 26, 8778 (2018).

Chiral quantum photonics

Rotenberg, Nir[1,*]

[1]Center for Hybrid Quantum Networks (Hy-Q), Niels Bohr Institute, University of Copenhagen, Denmark
*corresponding author, E-mail: nir.rotenberg@nbi.ku.dk

Abstract

We report on recent advances in the field of chiral quantum optics, focusing on experimental implementations using solid-state quantum emitters such as quantum dots. In particular, we discuss how chiral quantum light-matter interactions can form the basis for deterministic spin-photon interfaces and enable non-reciprocal photonic devices.

1. Introduction

One of the recent consequences of our ability to finely structure the photonic landscape using advanced nanofabrication techniques is the emergence of the field of chiral quantum optics [1]. At the heart of chiral light-matter interactions lies our ability to structure the local electric field polarization of waveguides such that, at certain points, it is circular, but with opposite handedness for the counter-propagating modes. A circular dipole – that is, one that can be thought of as being composed of two orthogonal linear dipoles oscillating 90 degrees out of phase – placed at such a location, will therefore couple well to light propagating in one of these modes, leading to directional radiation [2]. Amazingly, this chiral interaction is a purely electronic phenomenon that occurs in symmetric structures. This stands in stark contrast to light-matter interactions with chiral structure and metamaterials, where the directionality derives from the combined electric and magnetic response of the system.

2. Chiral quantum photonics

The transition dipoles of solid-state quantum emitters such as quantum dots can be circularly oriented, for example in the case of the neutral exciton in an external magnetic field or the spin-states of a charged exciton. The ensuing chiral-light matter interactions with these emitters, when embedded at the correct positions within waveguides, can therefore be used to control and initialize their spins [3] and for the basis for non-reciprocal photonic circuits [4] such as optical circulators, isolators or even quantum networks that operate at the single photon- and single emitter-level [1].

Acknowledgements

We gratefully acknowledge financial support from the European Research Council (ERC Advanced Grant 'SCALE'), Innovation Fund Denmark (Quantum Innovation Center 'Qubiz'), the Danish Research Infrastructure Grant (QUANTECH) and the Danish Council for Independent Research (grant number 4184-00203).

References

[1] P. Lodahl, *et al.*, Chiral quantum optics, *Nature* 541: 473−480, 2017.

[2] B. le Feber, N. Rotenberg and L. Kuipers, Nanophotonic control of circular dipole emission, *Nature Commun.* 6: 6695, 2015.

[3] R.J. Coles, *et al.*, Path-dependent initialization of a single quantum dot exciton spin in a nanophotonic waveguide, *Phys. Rev. B* 95: 121401(R), 2017.

[4] I. Söllner, *et al.*, Deterministic photon-emitter coupling in chiral photonic circuits, *Nature Nanotech.* 10: 775−778, 2018.

Chiral electric transport effects in topological solitons

Fabian Lux[1], Jonathan Kipp[1], Matthias Redies[1], Jan-Philipp Hanke[1], Frank Freimuth[1], Stefan Blügel[1], and Yuriy Mokrousov[1,2*]

[1]Peter Grünberg Institut and Institute for Advanced Simulation, Forschungszentrum Jülich and JARA, 52425 Jülich, Germany
[2]Institute of Physics, Johannes Gutenberg University Mainz, 55099 Mainz, Germany
*corresponding author, E-mail: y.mokrousov@fz-juelich.de

Abstract

Chiral magnetic systems gain more and more relevance for future information technology. Aside from the now famous proposal of skyrmionic information bits, recent publications suggest possible applications in the field of neuromorphic computing in the form of skyrmionic reservoirs, which rely on the non-linear magnetoresistance. Despite its practical importance, a general physical understanding of the electrical transport through chiral magnets is yet to be reached. Experimental studies of the Hall conductivity in chiral magnets commonly face the challenge of how to decompose the measured signal into several parts with a clear physical interpretation. Theoretical investigations on the other hand struggle with the complex electronic structure, especially in the case of isolated topological solitons. Inspired by our recent work on the orbital magnetism of chiral magnets [1, 2, 3], we demonstrate how semiclassical gradient expansion in combination with tight-binding modelling of the electronic structure can shed some light on the classification of Hall effects in chiral magnets. These results may open up new perspectives for the all-electrical detection of non-collinear magnetic structures such as skyrmions, hopfions and chiral bobbers [4].

Acknowledgement

We gratefully acknowledge computing time on the supercomputers JUQUEEN and JURECA at Jülich Supercomputing Center, and at the JARA-HPC cluster of RWTH Aachen. We acknowledge funding under SPP 2137 “Skyrmionics” of Deutsche Forschungsgemeinschaft (DFG). This work has been also supported by the DFG through the Collaborative Research Center SFB 1238, as well as by the DARPA TEE program through grant MIPR# HR0011831554 from DOI.

References

[1] F. Lux, F. Freimuth, S. Blügel and Y. Mokrousov, Engineering chiral and topological orbital magnetism of domain walls and skyrmions, *Communications Physics* 1:60, 2018.

[2] J.-P. Hanke, F. Freimuth, A. K. Nandy, H. Zhang, S. Blügel and Y. Mokrousov, Role of Berry phase theory for describing orbital magnetism: From magnetic heterostructures to topological orbital ferromagnets, *Physical Review B* 94:121114, 2016.

[3] J.-P. Hanke, F. Freimuth, S. Blügel and Y. Mokrousov, Prototypical topological orbital ferromagnet γ-FeMn, *Scientific Reports* 7:41078, 2017.

[4] M. Redies, F. R. Lux, J.-P. Hanke, P. M. Buhl, G. P. Müller, N. S. Kiselev, S. Blügel, and Y. Mokrousov, Distinct magnetotransport and orbital fingerprints of chiral bobbers, *arXiv:1811.01584v3*, 2018.

Switchable topological spin textures at a coherent oxide interface

Kathrin Dörr[1*], Martin Koch[1], Lukas Bergmann[1], Sujit Das[1], Stefano Agrestini[2], Igor Maznichenko[1], Nicolas Gauquelin[3] and Diana Rata[1]

[1]Institute of Physics, Martin Luther University Halle-Wittenberg, Halle, Germany
[2]ALBA Synchrotron Light Source, Barcelona, Spain
[3]EMAT, University of Antwerp, Antwerp, Belgium
*corresponding author, E-mail: kathrin.doerr@physik.uni-halle.de

Abstract

Complex conducting oxide ferromagnets, $La_{0.7}Sr_{0.3}MnO_3$ and $SrRuO_3$, are shown to form a Ru exchange spring at their coherent interface when grown on $SrTiO_3$(001) substrates. In low magnetic fields, non-coplanar, topologically non-trivial spin textures arise and can be switched, as is demonstrated based on magnetization and x-ray magnetic circular dichroism data.

1. Introduction

Engineering interfacial magnetism opens pathways to topologically non-trivial spin textures, an approach often utilized in metallic heterostructures. Interfaces of magnetic oxides, due to their complexity, are much less understood regarding the characteristics and physical origins of spin textures. They offer strong potential for novel types of spin structures as well as alternative tools for tuning them. For example, intimate links between lattice and electronic degrees of freedom can enable efficient control of interfacial magnetic anisotropy [1], exchange coupling [2] and Dzyaloshinskii-Moriya (DM) interaction [3] which are together responsible for the formation of spin textures.

In this work, the spin textures are formed at interfaces between two well-studied conducting oxide ferromagnets, $La_{0.7}Sr_{0.3}MnO_3$ and $SrRuO_3$. Such interfaces are chemically abrupt and show immense strength of antiferromagnetic Ru-O-Mn exchange coupling [4]. Magnetization depth profiling using polarized neutron reflectivity suggested a non-collinear spin configuration [5]. Different growth sequences of the ferromagnets have been shown to lead to crucially different interfacial spin orders [2]. Here, we introduce an interface with topologically non-trivial spin textures switchable in small magnetic fields.

2. Results and Discussion

$La_{0.7}Sr_{0.3}MnO_3$ (LSMO) and $SrRuO_3$ (SRO) layers of thicknesses between 4 und 20 unit cells (uc) have been grown on TiO_2-terminated $SrTiO_3$(001) (STO) substrates by pulsed laser deposition. Structural characterization by x-ray diffraction and scanning transmission electron microscopy revealed coherently strained films with sharp LSMO-SRO interfaces chemically terminated by MnO_2 for the growth sequence of SRO/LSMO/STO(001). Magnetization vs temperature and magnetic field has been measured in a superconducting quantum interference device magnetometer. X-ray magnetic circular dichroism (XMCD) was measured at the BL29 BOREAS beamline at the ALBA synchrotron, providing element-specific magnetization loops. The impact of chemical interface termination on interfacial Mn-O-Ru exchange coupling was calculated using density functional theory (DFT) [2].

Fig.1 summarizes field-dependent low-temperature magnetization M(H) data of a sample series with varied SRO thickness. Note the magnetic transition near $\mu_0 H_T$ = 2 T for thicker SRO layers ($d_{SRO} \geq 14$ uc) which vanishes for $d_{SRO} \leq 10$ uc. In contrast to earlier interpretations, our thickness-dependent data reveal rigid antiferromagnetic exchange coupling of Mn and Ru across the interface. A reversible rotation of interfacial Ru spins occurs driven by the in-plane magnetic field (Fig.2). Hence, a so-called exchange spring of ~10 uc thickness is formed in the SRO layer. The transition at H_T originates from field-induced reversal of the interface-far top part of the SRO layer.

Further support for the spin texture sketched in Fig.2 is derived from element-specific XMCD magnetization loops (Fig.3, recorded at 60 K). Complete XMCD data of Ru and Mn for bilayers, including both growth sequences, were published in [2]. While (interface-far) SRO coherently strained to STO(001) has large magnetic anisotropy with an easy axis canted out-of-plane [6], the interfacial Ru spins lie mostly in the film plane. This is derived from the fact that Mn spins coupled at 180° to Ru spins have very weak out-of-plane remanence (Fig.3). (Domains have been excluded as cause of that since Ru keeps a large remanence caused by the top part of the layer.) The reversed Mn loop sense with negative remanence is a consequence of the antiferromagnetic coupling to SRO. The very low switching field notable in Fig.3a results from relaxing the Ru exchange spring which twists or relaxes depending on the balance between SRO magnetic anisotropy plus exchange energies and field-dependent Zeeman energies dominated by LSMO.

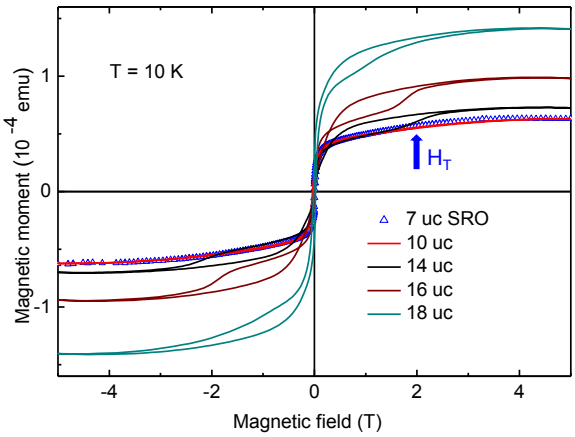


Figure 1: Magnetization of SRO/LSMO/STO(001) bilayers with thicknesses of 7 – 18 uc SRO and 9 uc LSMO .

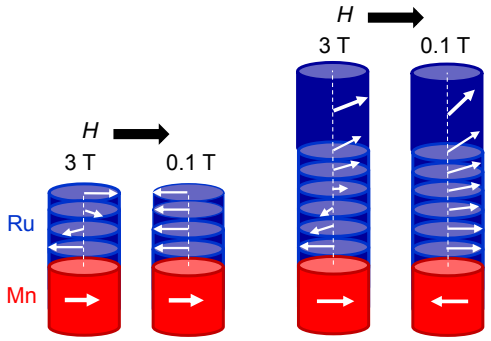


Figure 2: Spin configuration of the exchange spring in an in-plane magnetic field of 3 T and 0.1 T, respectively. Left side: SRO film of less than 10 uc thickness. Right side: SRO thickness of ≥ 14 uc. The vertical canting increases with SRO thickness.

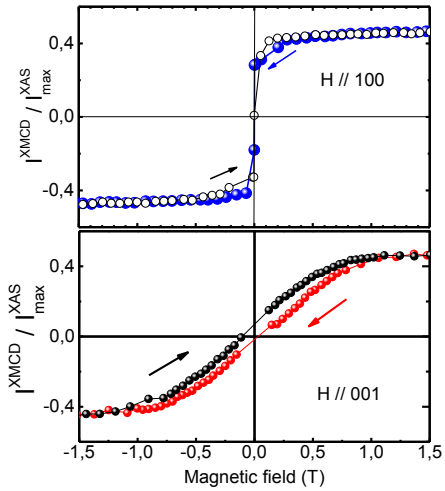


Figure 3: Mn magnetization loops derived from Mn L_3 edge XMCD at 60 K. Field along pseudocubic 100 in-plane direction (grazing incidence at 20°) and 001 out-of-plane direction.

Spin textures like that in Fig.2 resemble a Bloch wall parallel to the film plane with a gradual out-of-plane spin canting. They are non-coplanar in magnetic fields which twist the exchange spring and, thus, fulfill the criterion of Nagaosa [7] for being topologically non-trivial. If there is a sufficiently strong DM interaction in SRO, one expects a dominating chirality of the exchange spring. Additionally, the interfacial exchange spring is associated with (local) electric polarization like that of type II multiferroics [8] which is, however, screened in the conducting SRO. Thus, coherent interfaces between magnetic oxides bare potential for engineering topologically non-trivial and multiferroic spin textures. I will also discuss our current insights into the preconditions for forming such spin textures.

3. Conclusions

A coherent interface between complex oxide ferromagnets, $La_{0.7}Sr_{0.3}MnO_3$ and $SrRuO_3$, is shown to form an exchange spring which enables low-magnetic-field switching of topologically non-trivial and electrically polar spin textures. Thus, interface engineering of magnetic oxides with strong electron correlation offers unexplored terrain for topology-based or magnetoelectric functionalities of electronic devices.

Acknowledgements

The research was supported by Deutsche Forschungsgemeinschaft (DFG), SFB 762 *Functional Oxide Interfaces*, project A9.

References

[1] Z. Liao et al., Controlled lateral anisotropy in correlated manganite heterostructures by interface-engineered oxygen octahedral coupling, *Nat. Mater.* 15:425, 2016.

[2] S. Das et al., Low-field switching of non-collinear spin textures at $La_{0.7}Sr_{0.3}MnO_3$-$SrRuO_3$ interfaces, *Phys. Rev. B* 99: 024416, 2019.

[3] L. Wang et al., Ferroelectrically tunable magnetic skyrmions in ultrathin oxide heterostructures, *Nat. Mater.* 17:1087-1094, 2018.

[4] M. Ziese et al., Tailoring magnetic interlayer coupling in $La_{0.7}Sr_{0.3}MnO_3$-$SrRuO_3$ superlattices, *Phys. Rev. Lett.* 104: 167203 (2010).

[5] J. H. Kim et al., Competing interactions at the interface between ferromagnetic oxides revealed by spin-polarized neutron reflectivity, *Phys. Rev. B* 86: 180402(R), 2012.

[6] G. Koster et al., Structure, physical properties and applications of $SrRuO_3$ thin films, *Rev. Mod. Phys.* 84:253, 2012.

[7] N. Nagaosa, X. Z. Yu, Y. Tokura, Monopoles and skyrmions, *Philos. Trans. R. Soc. A* 370:5806, 2012.

[8] H. Katsura, N. Nagaosa, A. V. Balatsky, Spin current and magnetoelectric effect in noncollinear magnets, *Phys. Rev. Lett.* 95: 057205, 2005.

Magnetoelectricity of Micromagnetic Structures and Chirality

Alexander Pyatakov[1], Daria Kulikova[1], Elena Nikolaeva[1], Tatiana Kosykh[1], Alexey Kaminskiy[1], Wei Ren[2], Athinarayanan Sundaresan[3], Anatoly Zvezdin[4]

[1] M.V. Lomonosov Moscow State University, Leninskie gori, Moscow, Russia
[2] Materials Genome Institute, Physics Department, Shanghai University, Shanghai 200444, China
[3]Jawaharlal Nehru Centre for Advanced Scientific Research, Bangalore, India
[4] A.M. Prokhorov General Physics Institute, Moscow, Russia

*corresponding author, E-mail: pyatakov@physics.msu.ru

Abstract

The electric-field-induced nucleation of magnetic inhomogeneities is discussed. This magnetoelectric effect can develop in accordance to both chirality-dependent and chirality-insensitive scenarios related to two different mechanisms of magnetoelectricity.

1. Introduction

Chiral magnetic structures such as a spin cycloids [1], [2], homochiral domain walls [3],[4] skyrmions [5]–[8] and magnetic bubble domains [9], [10] are the subject of extensive research during the last decade. They demonstrate chirality-dependent behavior like spin-current-driven motion due to the spin-transfer torque effect [4], [7]. In this report we will focus on another property of these magnetic structures: the magnetoelectricity.

The magnetoelectric behavior was observed as the electric-field-driven motion of domain walls [11], and Bloch lines [12], as a nucleation of the bubble domains by electrically charged tip electrode [13], [14], and as the voltage control of skyrmion bubbles nucleation and annihilation [9], [10]. The mechanisms of these effects are disputable [15], [16] and they can be divided in two groups: chirality-sensitive electric tuning of Dzyaloshinskii-Moriya interaction [10], [17] and chirality-independent magnetic anisotropy modulation by electric field [9], [15]. Based on the experimental data obtained in iron garnet films we will illustrate the characteristic features of both type of the mechanisms.

2. Experimental methods

The 11-micron-thick iron garnet film with chemical composition $(BiLu)_3(FeGa)_5O_{12}$ grown on (210) $Gd_3Ga_5O_{12}$ substrate was used. The saturation magnetization was $4\pi MS$=44G. Uniaxial, orthorhombic and cubic anisotropy constants were respectively: Ku=1054 erg/cm^3, Ko-rh= erg/cm^3, Kc=1016 erg/cm^3.

The atomic force microscope cantilever tip was used as a source of the high gradient electric field: applying 100V to it results in electric field of 1MV/cm in micron-sized region near the tip.



Figure 1: The electric field control of magnetic domain structure with atomic force microscope cantilever tip [18]: a) the initial domain structure b) bubble domain nucleation from the single domain state [14].

3. Experimental results and discussion

In analogy to the electric–field induced bubble domain nucleation (fig.1) observed in [13,14] the tip electrode also nucleates magnetic inhomogeneities in this sample (Fig.2). They have specific gray color different from yellow/green contrast of domains. However there are striking differences compared to the magnetoelectric effects observed in [13,14]:

- The nucleation of the magnetic inhomogeneity is observed in spontaneous magnetic state, in contrast to the bubble domain nucleation (fig.1 b) no special magnetic bias is needed (fig.2a);
- In contrast to the electric-field-nucleated bubble domains observed in [13,14] this magnetic inhomogeneity always attracts to the tip: no chirality dependent motion is observed;
- The application of the voltage to the tip electrode leads also to the domain wall image widening and coalescence of the “island” with the wall (fig.2 b).

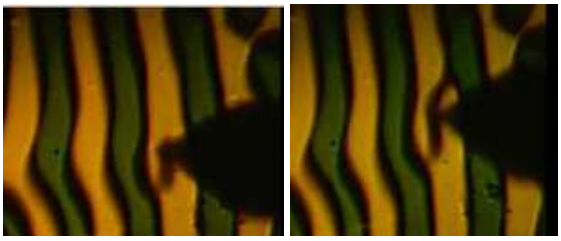


Figure 2: a) the nucleation of easy-plane phase by electric field b) the coalescence of the inhomogeneity with the domain wall

4. Conclusions

The electric-field induced domain structure transformation described above manifests itself as a nucleation of the island of new phase with the easy-axis anisotropy. In contrast to the effect of bubble nucleation [13,14] it is not chirality dependent and corresponds to the mechanisms described in [15]. The chirality dependent domain wall attraction or repulsion is observed only upon applying in-plane magnetic field that imposes the certain direction of magnetization direction: opposite for the opposite sides of the domain.

Acknowledgements

The support from Russian Foundation for Basic Research #18-52-80028 Brics_t and # 19-52-53020 is acknowledged.

References

[1] S.-W. Cheong and M. Mostovoy, *Nat. Mater.*, 6: 13–20, 2007.

[2] M. Bode *et al.*, *Nature*, 447: 190–3, 2007.

[3] M. Heide, G. Bihlmayer, and S. Blügel, *Phys. Rev. B*, 78: 140403, 2008.

[4] S. Emori, U. Bauer, S. Ahn, E. Martinez, and G. S. D. Beach, *Nat. Mater.*, 12: 611–616, 2013.

[5] U. K. Rössler, a N. Bogdanov, and C. Pfleiderer, *Nature*, 442: 797–801, 2006.

[6] S. Heinze *et al.*, *Nat. Phys.*, 7: 713–718, 2011.

[7] A. Fert, V. Cros, and J. Sampaio, *Nat. Nanotechnol.*, vol. 8, no. 3, pp. 152–156, 2013.

[8] P. Hsu, A. Kubetzka, A. Finco, N. Romming, K. von Bergmann, and R. Wiesendanger, "Electric-field-driven switching of individual magnetic skyrmions," *Nat. Nanotechnol.*, vol. 12, pp. 123–126, 2016.

[9] M. Schott *et al.*, "The Skyrmion Switch: Turning Magnetic Skyrmion Bubbles on and off with an Electric Field," *Nano Lett.*, vol. 17, no. 5, pp. 3006–3012, 2017.

[10] T. Srivastava *et al.*, "Large-Voltage Tuning of Dzyaloshinskii-Moriya Interactions: A Route toward Dynamic Control of Skyrmion Chirality," *Nano Lett.*, vol. 18, no. 8, pp. 4871–4877, 2018.

[11] A. P. Pyatakov *et al.*, "Micromagnetism and topological defects in magnetoelectric media," *Physics-Uspekhi*, vol. 58, no. 10, pp. 981–982, 2015.

[12] A. P. Pyatakov, V. I. Belotelov, D. P. Kulikova, N. E. Khokhlov, Z. A. Pyatakova, and A. V. Nikolaev, "Magnetoelectricity in topological magnetic textures," *J. Magn. Magn. Mater.*, vol. 440, no. December 2016, pp. 60–62, 2017.

[13] D. P. Kulikova, A. P. Pyatakov, E. P. Nikolaeva, A. S. Sergeev, T. B. Kosykh, and Z. A. Pyatakova, "Nucleation of Magnetic Bubble Domains in Iron Garnet Films by Means of an Electric Probe," *JETP Lett.*, vol. 104, no. 3, pp. 197–200, 2016.

[14] D. P. Kulikova *et al.*, "The Mechanisms of Electric Field-Induced Magnetic Bubble Domain Blowing," *Phys. Status Solidi - Rapid Res. Lett.*, vol. 12, p. 1800066, 2018.

[15] G. V Arzamastseva, A. M. Balbashov, F. V Lisovskii, E. G. Mansvetova, A. G. Temiryazev, and M. P. Temiryazeva, "Properties of epitaxial (210) iron garnet films exhibiting the magnetoelectric effect," *J. Exp. Theor. Phys.*, vol. 120, no. 4, pp. 687–701, 2015.

[16] I. S. Veshchunov *et al.*, "Direct Evidence of Flexomagnetoelectric Effect Revealed by Single-Molecule Spectroscopy," *Phys. Rev. Lett.*, vol. 115, no. 2, p. 27601, Jul. 2015.

[17] A. P. Pyatakov, A. S. Sergeev, F. A. Mikailzade, and A. K. Zvezdin, "Spin flexoelectricity and chiral spin structures in magnetic films," *J. Magn. Magn. Mater.*, vol. 383, pp. 255–258, Jun. 2015.

[18] A. P. Pyatakov, "Magnetoelectricity goes local: From bulk multiferroic crystals to ferroelectricity localized on magnetic topological textures," *Phys. B Condens. Matter*, vol. 542, 2018.

Title

Theory for Ultrafast Control of Spin Current and Spin Textures with AC Fields

Author

Masahiro Sato

Department of Physics, Ibaraki University, Mito, Ibaraki, Japan

Abstract

Laser science and technology have been rapidly developed in the last decades. The application of laser to solids is being one of the hottest topics in condensed-matter physics. Particularly, the significant development of intense terahertz (THz) laser science has accelerated the study of controlling magnetism with THz laser because the photon energy in THz regime is comparable to the energy of magnetic excitations. The control of magnetism with laser [1] has also attracted much attention as a large branch of spintronics [2].

Interestingly, theoretical methods for nonequilibrium systems have also been developed in recent years, and they have a high potential to capture laser-driven nonequilibrium dynamics. Applying such methods, we have theoretically explored/proposed several ways of controlling magnetism with electromagnetic waves. For instance, based on the concept of Floquet engineering [3], we have proposed some methods of controlling spin currents, spin spiral orders, and magnetizations with circularly polarized THz lasers [4]. We have also showed the ultrafast ways of generating a class of topological spin textures (such as skyrmions) in (chiral) magnets with topological light waves (such as vortex beams) [5]. Furthermore, we show that a DC spin current can be generated if we apply AC electromagnetic fields to noncentro-symmetric magnetic insulators (This phenomenon may be viewed as a spin-current version of solar cell) [6]. In the conference, I would like to report some of the above results, especially, focusing on the generation of spin current and spin textures.

[1] A. Kirilyuk, A. V. Kimel, and T. Rasing, Rev. Mod. Phys. **82**, 2731 (2010).

[2] *Spin Current*, edited by S. Maekawa, *et al* (Oxford Univ. Press, 2012).

[3] See, for example, T. Mikami, S. Kitamura, K. Yasuda, N. Tsuji, T. Oka, and H. Aoki, Phys. Rev. B **93**, 144307 (2016); A. Eckardt, Rev. Mod. Phys. **89**, 011004 (2017).

[4] S. Takayoshi, M. Sato, and T. Oka, Phys. Rev. B **90**, 214413 (2014); M. Sato, S. Takayoshi, and T. Oka, Phys. Rev. Lett. **117**, 147202 (2016).

[5] H. Fujita, and M. Sato, Phys. Rev. B **95**, 054421 (2017); Phys. Rev. B **96**, 060407(R) (2017).

[6] H. Ishizuka and M. Sato, arXiv:1811.10617.

Chiral Optomagnonics with Polarized Light in Magnetic Insulators

Igor Proskurin[1,2], Alexander S. Ovchinnikov[2], Jun-ichiro Kishine[3], Robert L. Stamps[1]

[1]Department of Physics and Astronomy, University of Manitoba, Winnipeg, Canada
[2]Institute of Natural Sciences and Mathematics, Ural Federal University, Ekaterinburg, Russia
[3]Division of Natural and Environmental Sciences, The Open University of Japan, Chiba, Japan
*corresponding author, E-mail: Igor.Proskurin@umanitoba.ca

Abstract

Several questions related to the interaction of magnetic excitations with polarized electromagnetic fields will be considered. We are going to discuss how chirality of spin waves can be introduced in analogy to the optical zilch, how chiral electromagnetic fields can be used to generate magnon spin currents, and couple to the collective degrees of freedom via the magneto-optical interactions.

1. Spin wave chirality in antiferromagnetic insulators

After Lipkin's original discovery of a new conservation law for the electromagnetic field in vacuum [1], it was realized that similar to geometric objects, dynamical fields can be characterized by chirality. In particular, free electromagnetic field can be described by locally conserving pseudoscalar that is even under the time reversal and odd under the spatial inversion transformations. Recently, this quantity, which is known in the literature as optical chirality or Lipkin's "zilch", attracted attention in chiral optics and plasmonics after Tang and Cohen demonstrated its relation to the asymmetry in light-matter interactions [2].

Based on the formal analogy between the electrodynamics and the low-energy magnetization dynamics in antiferromagnets, we demonstrate that the concept of optical chirality can be generalized on antiferromagnetic spin waves, which, similar to light, are doubly degenerated with respect to two polarization directions. This fact allows us to use the method of nongeometric symmetries originally developed for the Maxwell's equations and to find the conservation law for spin-wave chirality [3].

Similar to the case of light interacting with chiral medium [2], we show the relation between spin-wave chirality and asymmetry in the magnetic excitation energy absorption rate in an antiferromagnet, which host a pure spin current. The latter plays a role of the symmetry breaking mechanism and lifts the degeneracy between left- and right- polarized spin waves [3]. We find that injection of the spin current inside an antiferromagnetic insulator, creates the difference in population numbers of thermally excited left- and right-polarized magnons thus generating nonzero chirality inside the material.

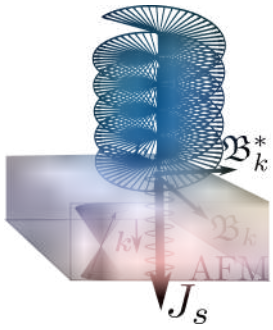


Figure 1: Circularly polarized light creates a direct magnon spin photocurrent $\boldsymbol{J}_s$ in the antiferromagnetic insulator along the direction of light propagation, which direction is controlled by the helicity of light $\sim \mathfrak{B} \times \mathfrak{B}^*$, where $\mathfrak{B}$ is the magnetic vector of the incident wave.

2. Optical excitation of spin photocurrents

Antiferromagnetic insulators are promising candidates with which to address the problem of creating and transmitting spin currents. Spin currents in these materials, carried by magnons, can be generated in several different ways, e. g. thermally excited using spin Seebeck/Nernst effects or pumped from the neighboring ferromagnetic insulator. Ultrafast optical excitation of coherent magnon dynamics is another prominent area, which lies in the basis of optospintronics – a direction targeting optical control of spin states in magnetic materials [4].

We propose a new mechanism for generating spin currents in antiferromagnetic insulators by optical excitation of spin dynamics [5]. The mechanism involves polarized light and is motivated by the photogalvanic effect in metals, where circularly polarized light can produce a direct electron photocurrent, which direction depends on the polarization. We suggest that an analogous nonlinear effect exists for antiferromagnetic insulators wherein the total spin of light and spin waves is conserved. In consequence, a spin angular momentum is expected to be transferred from photons to magnons so that a circularly polarized electromagnetic field will generate a direct magnon spin current, as shown in Fig. 1. We also discuss geometric contributions to the magnon photocurrents, which appear for materials with complex lattice structures and Dzyaloshinskii-Moriya interactions, where it is possible to use linearly polarized

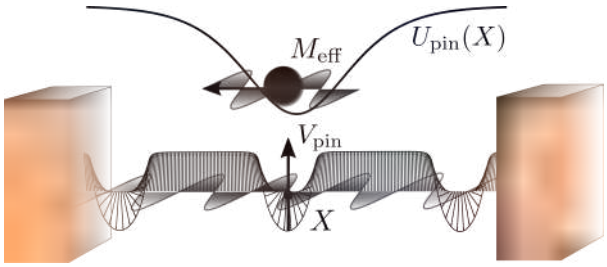


Figure 2: Chiral soliton lattice with the pinning potential at the center inside the cavity resonator and the corresponding effective mechanical model of a particle in the potential energy profile of magnetic pinning.

light to produce magnon spin currents.

3. Optomechanics of collective excitations in topological spin textures

Cavity optomechanics is an established field that studies mutual effects between the electromagnetic radiation pressure and mechanical degrees of freedom. It covers an impressive variety of phenomena such as optical damping/antidamping, laser cooling, parametric instability and chaotic dynamics, optomechanical entanglements, and quantum information protocols for numerous mechanical systems ranging from moving mirrors to cold atoms [6]. Finding new potential areas for application of cavity optomechanics is a relevant problem from both technological and fundamental viewpoints.

Here, we would like to discuss how topological spin textures in magnetic insulators may serve as an effective mechanical subsystems for optomechanical experiments. It is known that low-energy collective dynamics of such magnetic structures as domain walls in ferromagnets or soliton lattices in chiral helimagnets can be described in terms of several effective mechanical degrees of freedom known as collective variables thus making them behave analogously to massive mechanical particles. By adding a pinning potential to defects and magnetic impurities, we obtain a magnetic analogue of a mechanical oscillator, which frequency is determined by the pinning strength. We demonstrate [7] that such oscillator can feel the electromagnetic radiation pressure via magneto-optical interactions (such as inverse Faraday and Cotton-Mutton effects) effectively leading to the same effective Hamiltonian that is used in cavity optomechanics[8]. Moreover, using the inverse Faraday effect, it is possible to make the effective optomechanical coupling sensitive to the helicity of light, which makes the magnetic texture analogous to the chiral oscillator interacting with polarized cavity electromagnetic field (see Fig. 2).

Low damping of some magnetic insulators together with GHz range of oscillator frequencies make it possible to address quantum regime of oscillator dynamics, challenging in pure mechanical systems, which maybe useful for application quantum information processing.

Acknowledgement

I.P. is supported by the Ministry of Education and Science of the Russian Federation, Grant No. MK-1731.2018.2, and by the Russian Foundation for Basic Research (RFBR), Grant No. 18-32-00769. R.L.S. acknowledges the support of the Natural Sciences and Engineering Research Council of Canada (NSERC).

References

[1] D. M. Lipkin, Existence of a new conservation law in electromagnetic theory, *J. Math. Phys.* 5: 696, 1964.

[2] Y. Tang and A. E. Cohen, Optical Chirality and Its Interaction with Matter, *Phys. Rev. Lett.* 104: 163901, 2010.

[3] I. Proskurin, R. L. Stamps, A. S. Ovchinnikov, and J. Kishine, Spin-Wave Chirality and Its Manifestations in Antiferromagnets, *Phys. Rev. Lett.* 119: 177202, 2017.

[4] T. Jungwirth, X. Marti, P. Wadley, and J. Wunderlich, Antiferromagnetic spintronics, *Nat. Nanotechnol.* 11: 231 2016.

[5] I. Proskurin, A. S. Ovchinnikov, and J. Kishine, R. L. Stamps, Excitation of magnon spin photocurrents in antiferromagnetic insulators, *Phys. Rev. B* 98: 134422, 2018.

[6] M. Aspelmeyer, T. J. Kippenberg, and F. Marquardt, Cavity optomechanics, *Rev. Mod. Phys.* 86: 1391, 2014.

[7] I. Proskurin, A. S. Ovchinnikov, and J. Kishine, R. L. Stamps, Excitation of magnon spin photocurrents in antiferromagnetic insulators, *Phys. Rev. B* 98: 220411, 2018.

[8] S. Viola Kusminskiy, H. X. Tang, and F. Marquardt, Coupled spin-light dynamics in cavity optomagnonics, *Phys. Rev. A* 94: 033821, 2016.

Manifestation of the spatial Kramers-Kroning relations in plasmonic chiral metasurface

Leeju Singh[1,*], Shmuel sternklar[1], Yuri Gorodetski[1,2],

[1]Electrical engineering and electronics department, Ariel University, Ariel 40700, Israel

[2]Mechanical engineering and Mechatronics department, Ariel University, Ariel 40700, Israel

*corresponding author, E-mail: Leezu.me@gmail.com

Abstract

Light-matter interactions can exhibit a strong dissymmetry in chiral structure specifically, the phase and amplitude can be strongly affected by altering the chirality strength. The Kramers-Kronig relation between the imaginary and the real part of the index prescribes the connection between the two measurable effects of the optical activity, namely the optical rotation dispersion (ORD) and the circular dichroism (CD). Our results establish a basis for the development of the meta-surface that incorporates structural local chirality for phase modulation.

1. Introduction

Structures with subwavelength dimensions exhibit unusual behavior when they interact with electromagnetic (EM) waves and can be utilized for a variety of novel applications. In particular such behavior arises when the interaction between the metal surface irregularities and the incident light results in the excitation of a surface confined evanescent waves called surface plasmon polaritons (SPPs) [1]. Chiral nanostructures that support SPPs play a crucial role in improving the sensitivity of spectroscopic properties [2],[3]. Thus, the understanding of the underlying physical concepts is important to realize the desired tuning. Recently, it has been shown that chiral metamaterials exhibit extraordinary capabilities in controlling and manipulating the polarization states of light. For example, 2D arrays of planar chiral structures of gammadion-shaped metal nanoparticles produced by broken front-back symmetry exhibit a large CD and a giant optical activity [2] exceeding significantly those of conventional three dimensional materials. Particularly, gold nanostructures are widely used in the photonics and plasmonic integrated circuits aiming to manipulate the light at the nanoscale. Leakage radiation microscopy (LRM) is a surface sensitive optical technique that is especially useful for imaging of the SPP propagation with small changes of light polarization. The interaction of metallic nanostructures may depend on the design parameters of the structure such as length, width, periodicity and film thickness. In addition, one can tune the transmitted light polarization by changing the period of the structure and design.

In this study we use the LRM technique to collect and analyze the transmission through the structure of the right and left circularly polarized light as a function of the structure chirality and periodicity. This shall be the basis for the future analysis of the SPP excitation and propagation dependence on the chiral structure parameters. We have fabricated gold chiral rectangular planar structure by using FIB method and have demonstrated optical rotation [3] and circular dichroism [4] in direct transmission that strongly depends on the structure period. We also verified the existence of the Krammers-Kronig's connection between the measured spatial ORD and the CD in our structure.

2. Experimental part

The samples were fabricated by using focused ion beam (FIB) on a 100 nm thick Au film deposited on glass cover slips. Eeach array consisted of two rectangular apertures (250 nm length by 100 nm) that were shifted with respect to each other exactly by one length. The sample was illuminated by a 780 nm laser beam pre-focused by a 10X objective (NA =

0.4 and the leakage radiation was then collected through objective with NA = 1.25 (50X). The incident light's polarization was set to 45 degrees with respect to the array main axes and the emerging beam was then analyzed by a similar polarizer. We rotated the second polarizer to find the

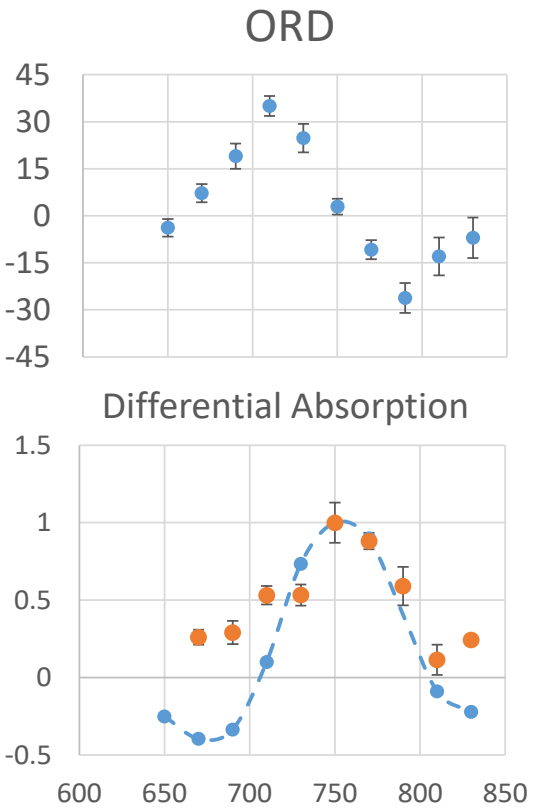


Fig. 1 Optical activity measurements. (a) – Linear polarization rotation versus the structure period. (b) – Differential absorption of the chiral metasurface versus the structure period. The dashed line represents the theoretically predicted absorption line evaluated using KK relations.

angle at which the maximum intensity at the exit was obtained. This polarization rotation angle was plotted as a function of the structure period to form the ORD of the structure. We note a characteristic bi-resonance behavior expected from optically active materials.

In the additional experiment we illuminated the structure with a circularly polarized light. For each handedness of the illumination we measured the transmitted intensity, I_R and I_L for right and left handed light respectively, and plotted the normalized value of the differential absorption, $\Delta = I_R - I_L$. This provided us the spatial CD spectrum of the structure. In Fig.1 we demonstrate the two measurements together as a function of the spatial period of the grating, Λ. Despite some noise, due to the depolarizing effects and fabrication imperfections, one can clearly recognize the resonance peak at 750 nm period. This period corresponds to the plasmonic wavelength and apparently leads to a resonant coupling of the chiral unit cells producing the enhancement of the optical activity.

Finally we use the spatial ORD data obtained in the first experiment to calculate the expected CD values by Krammer's-Kronig relations and obtain a perfect matching between observed and the measured results. We then conclude that our chiral metasurface behaves as an artificial chiral medium with the resonant chiral response obtained due to a collective plasmonic effect. Moreover, the rotation and the CD achieved in these experiments are unusually strong which leads to an additional conclusion, that our structures can be utilized to alter the light's polarization. This leads us to future research in the improvement of the chiral symmetry structure.

Acknowledgements

We acknowledge the Ministry of Science Technology and Space of Israel for the financial support in this project and Ariel University for the travel grant.

References

[1] B. L. D. Barron, "Symmetry and Molecular Chirality," pp. 189–223, 1986.

[2] M. Kuwata-Gonokami *et al.*, "Giant optical activity in quasi-two-dimensional planar nanostructures," *Phys. Rev. Lett.*, vol. 95, no. 22, pp. 1–4, 2005.

[3] S. Takahashi *et al.*, "Giant optical rotation in a three-dimensional semiconductor chiral photonic crystal," vol. 21, no. 24, pp. 421–425, 2013.

[4] S. Takahashi, T. Tajiri, Y. Ota, J. Tatebayashi, S. Iwamoto, and Y. Arakawa, "Circular dichroism in a three-dimensional semiconductor chiral photonic crystal," *Appl. Phys. Lett.*, vol. 105, no. 5, pp. 1–5, 2014.

Electromagnetic responses, dynamics, and superconductivity emerging from multipole order

Hikaru Watanabe[1], Atsuo Shitade[2], Akito Daido[1], Jun Ishizuka[1], and *Youichi Yanase[1]

[1]Department of Physics, Kyoto University, Kyoto, Japan
[2]RIKEN, Center for Emergent Matter Science, Wako, Japan
*corresponding author, E-mail: yanase@scphys.kyoto-u.ac.jp

Abstract

We will discuss electromagnetic responses, dynamics, and superconductivity arising from odd-parity multipole order. Combining group theoretical analysis, numerical calculation of microscopic models, local thermodynamics, we reveal intriguing properties of electromagnetic multipole states with spontaneous inversion symmetry breaking. Candidate materials are proposed by analyzing the existing experimental data.

1. Introduction

A concept of multipole moment has been established in the classical electrodynamics. In solid state electron systems, entanglement of spin, orbital, and sublattice degrees of freedom is described by the multipole moment, and spontaneous multipole order is a ubiquitous phenomenon in strongly correlated electron systems.

First, we present a group theoretical classification of multipole order in solids. Intriguing duality between the real space and momentum space multipole order parameters is revealed for odd-parity multipole order which spontaneously breaks space inversion symmetry. More than 110 odd-parity magnetic multipole materials are identified by the magnetic representation theory.

Second, emergent cross-correlated responses of elasticity, electricity, and magnetism are clarified by using real-space and k-space representations of multipole moment. In addition to the group theoretical classification, we provide a fully quantum mechanical formula for the odd-parity magnetic monopole, quadrupole and toroidal dipole moment, from which magnetoelectric (ME) effect can be quantitatively estimated.

Third, application to the antiferromagnetic spintronics is studied. Using the magnetic representation theory and magnetic space group analysis, antiferromagnetic domain switching by electric current is proposed.

Finally, exotic superconducting phases induced by the odd-parity multipole fluctuation are explored. Near the quantum critical point, spin-triplet superconductivity is stabilized by the effective interaction mediated by the magnetic multipole fluctuations. Then, a Z_2 topological superconducting state is identified. Multipole quantum criticality may be a route to the topological superconductivity.

2. Classification theory of multipole order

We carried out group-theoretical classification of the even-parity/odd-parity multipole order [1,2]. Multipole order parameter in cubic, tetragonal, and hexagonal systems has been classified by point-group symmetry. Classification in other crystal groups is straightforwardly obtained by compatibility relations. Even though real compounds are sometimes too complicated to see the relevant multipole moment characterizing the ordered state, we can identify the multipole order parameter by group-theoretical analysis.

3. Cross-correlated responses

Compounds with ferroic odd-parity magnetic multipole order are also called magnetoelectric materials since the electromagnetic crossed correlation appears. The magnetoelectricity has been extensively studied in the research field of multiferroic materials, and then the candidates should be insulating to hold well-defined electric polarization reversible by external electric fields. On the other hand, the odd-parity multipole order also leads to nontrivial electronic structures such as spontaneous emergence of spin-momentum locking and asymmetric band distortions in itinerant systems. Accordingly, characteristic electromagnetic responses may occur in metallic states. To explore intriguing phenomena in both metallic and insulating odd-parity multipole states we show the group theoretical classification of various electromagnetic response tensors and reveal their close relationship with multipole moment [2].

4. Quantum mechanical formula

We derive a quantum-mechanical formula of the spin and orbital magnetic monopole, toroidal, and quadrupole moments in periodic crystals by using the gauge-covariant gradient expansion [3,4]. We also prove a direct relation between the multipole moment and ME susceptibility for insulators at zero temperature. It indicates that the multipole moment is a microscopic origin of the ME effect. Using the formula, we quantitatively estimate these quantities for room-temperature antiferromagnetic semiconductors $BaMn_2As_2$ and $CeMn_2Ge_{2-x}Si_x$. We find that the orbital contribution to the ME susceptibility is comparable with or

even dominant over the spin contribution. We also formulate what we call gravitomagnetoelectric (gravito-ME) effect, in which the magnetization is induced by a temperature gradient. Although the Kubo formula for the gravito-ME effect provides an unphysical divergence at zero temperature, we prove that the correct susceptibility is obtained by subtracting the spin magnetic multipole moment from the Kubo formula. It vanishes at zero temperature and is related to the ME susceptibility by the Mott relation. We explicitly calculate the gravito-ME susceptibility in a Rashba ferromagnet and show its experimental feasibility.

5. Antiferromagnetic spintronics

Antiferromagnets are robust to external electric and magnetic fields, and hence are seemingly uncontrollable. Recent studies, however, realized the electrical manipulations of antiferromagnets by virtue of the antiferromagnetic Edelstein effect. We present a general symmetry analysis of electrically switchable antiferromagnets based on group-theoretical approaches [5]. Furthermore, we identify a direct relation between switchable antiferromagnets and the ferrotoroidic order. The concept of ferrotoroidic order clarifies the unidirectional nature of switchable antiferromagnets and provides a criterion for the controllability of antiferromagnets. The scheme may pave a way for perfect writing and reading of switchable antiferromagnets.

6. Superconductivity

Using a microscopic calculation and symmetry argument we reveal superconductivity in the vicinity of parity-violating magnetic order [6]. We show unconventional superconductivity induced by an odd-parity magnetic multipole fluctuation in a two-dimensional two-sublattice Hubbard model motivated by Sr_2IrO_4. We find that even-parity superconductivity is more significantly suppressed by spin-orbit coupling than that in a globally noncentrosymmetric system. Consequently, two odd-parity superconducting states are stabilized by magnetic multipole fluctuations in a large spin-orbit coupling region. Both of them are identified as Z_2 topological superconducting states. Our finding implies a new family of odd-parity topological superconductors. Candidate materials are proposed.

Acknowledgements

This work is supported by a Grant-in-Aid for Scientific Research on Innovative Areas “J-Physics” (Grant No. JP15H05884) and “Topological Materials Science” (Grants No. JP16H00991 and No. JP18H04225) from the Japan Society for the Promotion of Science (JSPS), and by JSPS KAKENHI (Grants No. JP15K05164, No. JP15H05745, and No. JP18H01178). H. W. and A. D. are supported by a JSPS research fellowship.

.

References

[1] Hikaru Watanabe and Youichi Yanase, "Magnetic hexadecapole order and magnetopiezoelectric metal in $Ba_{1-x}K_xMn_2As_2$" Phys. Rev. B. 96, 064432 (2017).

[2] Hikaru Watanabe and Youichi Yanase, "Group-theoretical classification of multipole order: emergent responses and candidate materials" Phys. Rev. B 98, 245129 (2018).

[3] Atsuo Shitade, Hikaru Watanabe, and Youichi Yanase, "Theory of Orbital Magnetic Quadrupole Moment and Magnetoelectric Susceptibility", Phys. Rev. B 98, 020407(R) (2018).

[4] Atsuo Shitade, Akito Daido, amd Youichi Yanase, "Theory of spin magnetic quadrupole moment and temperature-gradient-induced magnetization", Phys. Rev. B 99, 024404 (2019).

[5] Hikaru Watanabe and Youichi Yanase, "Symmetry analysis of current-induced switching of antiferromagnets", Phys. Rev. B 98, 220412(R) (2018).

[6] Jun Ishizuka and Youichi Yanase, "Odd-parity multipole fluctuation and unconventional superconductivity in locally noncentrosymmetric crystal", Phys. Rev. B 98, 224510 (2018).

Biomacromolecular Charge Chirality Detected Using Chiral Plasmonic Nanostructurese

Marion Rodier, Maryam Hajji and Malcolm Kadowala*

[1]School of Cheimstry, University of Glasgow, Joseph Black Building, Glasgow, G12 8QQ, UK,
*corresponding author, E-mail: malcolm.kadodwala@glasgow.ac.uk

Abstract

The spatial distribution of charge at the solvent exposed surfaces of complex biomacromolecules such has proteins, define electrostatic properties that control intermolecular interactions, which govern function. To date there is no known phenomenon that allows the surface charge distributions to be directly characterised. Information is restricted to that provided by modelling of proteins with both known structures and sequences. We show this essential but currently "*invisible*" property, can be detected by monitoring the chiroptical response of protein-plasmonic nanostructure complexes. To illustrate the unique capabilities of the phenomenon it has been used to discriminate between two forms of the same enzyme, type II dehydroquinase (DHA), which have the identical structures, but differing primary sequences. The different sequences results in the two forms having dramatically different surface charge distributiosns. The two form are indistinguishable with conventional chiroptical spectroscopy (*i.e.* circular dichroism) which are sensitive to secondary structure. However the DHQ-chiral plasmonic complexes of the two forms display different chiroptical properties. The phenomenon is rationalised with a simple model, validated by numerical simulations, whereby the surface charge of a protein induces an asymmetric mirror charge distribution within the surface region of a gold chiral plasmonic nanostructure. This causes a differentially change in the chiroptical response of left and right handed structures, which is dependent on the properties of distribution. The reported phenomenon affords a route by which changes in surface charge can be detected without prior knowledge of protein structure and sequence. Thus providing a new tool for understanding interactions between biomolecular materials.

Skyrmions, Antiskyrmions and Bobbers: Novel particles in chiral magnets

Markus Hoffmann[1], Bernd Zimmermann[1], Gideon P. Müller[1,2], Christof Melcher[3]
Nikolai S. Kiselev[1], Filipp Rybakov[4,5], Aleksandr Borisov[5],
Fengshan Zheng[6], András Kovács[6], Rafal E. Dunin-Borkowski[6] and Stefan Blügel[1*]

[1]Peter Grünberg Institut and Institute for Advanced Simulation, Forschungszentrum Jülich and JARA, 52425 Jülich, Germany
[2]Science Institute of the University of Iceland, VR-III, 107 Reykjavík, Iceland
[3]Department of Mathematics I & JARA FIT, RWTH Aachen University, 52056 Aachen, Germany
[4]Department of Physics, KTH-Royal Institute of Technology, Stockholm, Sweden
[5]M.N. Miheev Institute of Metal Physics of Ural Branch of Russian Academy of Sciences, Ekaterinburg, Russia
[6]Ernst Ruska-Centre for Microscopy and Spectroscopy with Electrons and
Peter Grünberg Institute, Forschungszentrum Jülich, 52425 Jülich, Germany
*corresponding author, E-mail: s.bluegel@fz-juelich.de

Abstract

Chiral magnets are an emerging class of topological matter harbouring localized and topologically protected vortex-like magnetic textures called skyrmions, which are currently under intense scrutiny as a new entity for information storage and processing. Chirality in magnetism is introduced through the chiral symmetry breaking Dzyaloshinskii-Moriya interaction, which arizes through the spin-orbit interaction in magnets with structural bulk and interface inversion asymmetry. We have shown that chiral magnets cannot only host skyrmions but also antiskyrmions and chiral bobbers as localized magnetization particles. We present a multiscale approach relating the electronic structure to an atomistic spin-lattice model and further to micromagnetic models by means of density-functional calculations, derive practical criteria for their occurrence and coexistence with skyrmions and minimizing the energy on a mesoscopic scale applying varying spin-relaxation methods. We conjecture on possible materials for antiskyrmions and give experimental evidence for bobbers. The technology potential of having two distinctly different stable particles will be discussed.

1. Introduction

After the discovery of skyrmions – nanoscale localized and topologically protected vortex-like magnetic textures – in bulk magnets [1] and at surfaces [2] – the research field of chiral magnetism developed to one of the most active fields of magnetism and spintronics as skyrmions promise to be the new information-carrying particle in future low-power information and communication technology. Skyrmions in chiral magnets may appear as isolated solitons or condensed in regular lattices. Their stability results from the Dzyaloshinskii-Moriya interaction (DMI), which breaks the chiral symmetry of the magnetic structure. The energy and size is determined by the competition between the Heisenberg, Dzyaloshinskii-Moriya (DMI), and Zeeman interaction together with the magnetic anisotropy energy (MAE) here expressed in terms of the spin-lattice model applied to an interface geometry:

$$\begin{aligned} H &= -\sum_{ij} J_{ij}\,(\mathbf{S}_i \cdot \mathbf{S}_j) - \sum_{ij} \mathbf{D}_{ij} \cdot (\mathbf{S}_i \times \mathbf{S}_j) \\ &\quad - \sum_{i} \mathbf{B} \cdot \mathbf{S}_i + \sum_{i} K_{\perp} (\mathbf{S}_i \cdot \hat{\mathbf{e}}_z)^2 \end{aligned} \tag{1}$$

with classical spin $\mathbf{S}$ of length one at atomic sites i, j and the corresponding microscopic pair J_{ij}, $\mathbf{D}_{ij}$ and on-site $K_{\perp}$ interactions. The DMI results from the spin-orbit interaction and is only non-zero for solids lacking bulk ($\mathbf{r} \nrightarrow -\mathbf{r}$) or structure inversion symmetry ($z \nrightarrow -z$). With respect to future applications, interfaces offer a great variety of options for optimizing and controlling magnetic the parameters J, $\mathbf{D}$, K: Variation of the interface composition [3, 4], of the interface crystal symmetry [5], as well as the fabrication of interlayers [6] and multilayers [7, 8] such as to obtain skyrmions with sizes and temperature stability suitable for technology, e.g. in the context of the race track memory.

2. Methodology

To understand the stabilization mechanism of skyrmions, to predict and design their properties in setups for technological use by theoretical models, *ab initio* spin-lattice models (1) proved to be a very powerful approach to realistically describe non-collinear magnets, single skyrmions and skyrmions lattices in experimentally realized systems. In such a model the parameters for an *ab initio* spin-lattice model are obtained directly from the total energy of the electronic structure by density functional theory, e.g. applying the `FLEUR` code [9], and the magnetic ground state as well as metastable states are found for example by spin-dynamics or Monte-Carlo methods using the recently developed `SPIRIT` code [10]. The long-wave length limit leads to micormagnetic energy functional whose mathematical analysis allows a rigerous examination the micromagnetic energy landscape.

3. Results

We employed this approach and developed the Skyrmion à la carte concept [7], prediciting the properties (size, stability, Curie temperatures) of skyrmions in thin films at surfaces [2, 3, 7], interfaces [4], multilayer [7, 8], exchange bias-systems [6] to optimize the properties of skrymions.

In chiral magnets the presence of the DMI commonly prevents the stability and coexistence of topological excitations of different types. In a recent work [5] we extended the scope of skyrmions to antiskyrmions and introduced a classification scheme partitioning chiral magnets into isotropic rank-three DM bulk and rank-two DM film magnets, described by an isotropic DM interaction expressed by a single DMI constant in the micromagnetic theory, for which antiskyrmions are stable only for bulk crystals with certain point group symmetries. Newly introduced are the anisotropic rank-two DMI film magnets, where skyrmions and antiskyrmions can coexist, while the sign of the determinant of the micromagnetic DM matrix determines which of the two has the lower energy. Finally, zero determinant indicates a rank-one DMI material, for which skyrmions and antiskyrmions have the same energy. Employing the methodology introduced above we conjecture that a Fe double on W(110) provides a possible system that hosts antiskyrmions.

Recently, we were able to extend the scope of skyrmions to a second class of particles, the chiral magnetic bobber (CB), first through theoretical analysis [11, 12] and then veryfied experimentally by the direct observation in thin films of B20-type FeGe by means of quantitative off-axis electron holography [13]. The CB is a localized three-dimensional hybrid particle on the nanoscale composed of both the smooth magnetization texture of skyrmions an a Bloch point, singularity in the micromagnetic theory of smooth magnetizations textures playing the role of a monopole. The interaction of electrons with such hybrid-objects. e.g. to understand how to move CB by spin currents is subject to ongoing investigations.

Acknowledgement

Deutsche Forschungsgemeinschaft (DFG) provides funding to N.K. and S.B. through SPP 2137 “Skyrmionics”, to S.B. through the Collaborative Research Centers SFB 1238, to Ch.M. through grant no. ME 2273/3-1. B.Z. and S.B. acknowledge funding from the European Union’s Horizon 2020 research and innovation programme under grant agreement number 665095 (FET-Open project MAGicSky). G.P.M. acknowledges funding from the Icelandic Research Fund (grant no. 152483-052). Ch.M. and S.B. acknowledge seed-fund support from JARA-FIT. M.H. and S.B. acknowledge the DARPA TEE program (#HR0011831554) from DOI for funding. We acknowledge computing time at the HLRN supercomputer as well as JURECA supercomputer (projects jias1a and jias1f) of Jülich Supercomputing Centre and JARA-HPC of RWTH Aachen University.

References

[1] S. Mühlbauer, B. Binz, F. Jonietz, C. Pfleiderer, A. Rosch, A. Neubauer, R. Georgii, & P. Böni, Skyrmion Lattice in a Chiral Magnet, *Science* **323**, 915 (2009)

[2] S. Heinze, K. von Bergmann, M. Menzel, J. Brede, A. Kubetzka, R. Wiesendanger, G. Bihlmayer, & S. Blügel, Spontaneous atomic-scale magnetic skyrmion lattice in two dimensions. *Nature Phys.* **7**, 713 (2011).

[3] A. Belabbes, G. Bihlmayer, F. Bechstedt, S. Blügel, & A. Manchon, Hund’s Rule-Driven Dzyaloshinskii-Moriya Interaction at $3d$-$5d$ Interfaces, *Phys. Rev. Lett.* **117**, 247202 (2016).

[4] B. Zimmermann, W. Legrand, D. Maccariello, N. Reyren, V. Cros, S. Blügel, & A. Fert, Dzyaloshinskii-Moriya interaction at disordered interfaces from ab initio theory: robustness against intermixing and tunability through dusting, *Appl. Phys. Lett.* **113**, 232403 (2018).

[5] M. Hoffmann, B. Zimmermann, G. P. Müller, D. Schürhoff, N. S. Kiselev, C. Melcher, & S. Blügel, Antiskyrmions stabilized at interfaces by anisotropic Dzyaloshinskii-Moriya interactions, *Nat. Commun.* **8**, 308 (2017).

[6] A. Nandy, N. S. Kiselev, & S. Blügel, Interlayer Exchange Coupling: A General Scheme Turning Chiral Magnets into Magnetic Multilayers Carrying Atomic-Scale Skyrmions, *Phys. Rev. Lett.* **116**, 177202 (2016).

[7] B. Dupé, G. Bihlmayer, M. Böttcher, S. Blügel, & S. Heinze, Engineering skyrmions in transition-metal multilayers for spintronics, *Nature Commun.* **7**, 11779 (2016).

[8] H. Jia, B. Zimmermann, & S. Blügel, First-principles investigations of chiral magnetic properties in multilayers: {Rh/Co/Pt} and {Pd/Co/Pt}, *Phys. Rev. B* **98**, 144427 (2018).

[9] http://www.flapw.de

[10] https://github.com/spirit-code/spirit

[11] F. N. Rybakov, A. B. Borisov, S. Blügel, & N. S. Kiselev, New Type of Stable Particlelike States in Chiral Magnets, *Phys. Rev. Lett.* **115**, 117201 (2015).

[12] F. N. Rybakov, A. B. Borisov, S. Blügel, & N. S. Kiselev, New spiral state and skyrmion lattice in3 D model of chiral magnets, *New J. Phys.* **18**, 045002 (2016).

[13] F. Zheng, F. N. Rybakov, A. B. Borisov, D. Song, S. Wang, Z.-A. Li, H. Du, N. S. Kiselev, J. Caron,A. Kovács, M. Tian, Y. Zhang, S. Blügel, & R. E. Dunin-Borkowski, Experimental observation ofchiral magnetic bobbers in B20-type FeGe, *Nature Nanotech.* **13**, 451 (2018).

Ultrafast Magnetic Recording with Terahertz Light

I. Radu[1, *], M. Shalaby[2], M. Hennecke[1], D. Engel[1], C. von Korff Schmising[1], A. Tsukamoto[3], C.P. Hauri[4] and S. Eisebitt[1]

[1]Max Born Institute Berlin, Max-Born-Str. 2A, 12489 Berlin, Germany
[2]Key Laboratory of Terahertz Optoelectronics, Advanced Innovation Center for Imaging Technology CNU, Beijing 100048, China
[3]College of Science and Technology, Nihon University, 7-24-1 Funabashi, Chiba, Japan
[4]Paul Scherrer Institute, 5232 Villigen, Switzerland
*corresponding author: radu@mbi-berlin.de

Abstract

We report on the first demonstration of THz-driven ultrafast magnetization switching of a magnetically ordered material using intense, single-cycle THz pulses. The magnetization switching process evolves on a few picoseconds timescale as probed by time-resolved magneto-optics in visible spectral range. Our findings reveal a fully deterministic switching event occurring upon each single-shot THz excitation of the ferrimagnetic GdFe alloy.

Using light to control the magnetic order parameter on ultimate time and length scales is a core research activity of modern magnetism [1,2]. Of particular interest for both fundamental and applied science is the use of femtosecond (fs) laser pulses to fully switch the magnetization orientation of a spin ensemble on ultrashort time scales [3,4].

A novel yet less explored approach towards controlling the magnetization and spin dynamics is the use of intense THz pulses (photon energies in the meV range) as an ultrafast external stimulus.

Here, we report on *the first demonstration of ultrafast magnetization switching of a spin-ordered material using single-cycle, intense THz pulses* at a central frequency of 2 THz. In particular, by employing intense THz radiation from a table-top THz source [5] to photo-excite a ferrimagnetic GdFe alloy and magneto-optics in visible spectral range to probe the subsequent magnetization changes, we reveal:

(i) a single-shot magnetization switching process driven by linearly polarized THz pulses *i.e.* the so-called toggle magnetization reversal, as shown in Figure 1
(ii) an ultrafast magnetization switching event investigated in time domain using a THz pump-MOKE probe approach.

Our findings indicate a highly efficient non-equilibrium energy transfer from the driving THz pulse to the spin system that leads to a magnetization switching event occurring on a few picoseconds timescale. Our results demonstrate a fully deterministic control of magnetization using single THz pulses, paving the way for an entire class of new experiments employing light-spin interactions at THz frequencies.

Acknowledgements

Funding from German Ministry for Education and Research (BMBF) through project 05K16BCA (Femto-THz-X) is gratefully acknowledged. C.P. Hauri acknowledges funding from SNSF through project IZKSZ2_162129.

References

[1] A. Kirilyuk, A.V. Kimel, and Th. Rasing, Ultrafast optical manipulation of magnetic order, *Review Modern Physics* 82: 2731, 2010

[2] K. Carva, P. Balaz and I. Radu, Laser-induced ultrafast magnetic phenomena, in *Handbook of Magnetic Materials*, vol. 26, 291-463, Elsevier, 2017.

[3] I. Radu et al., Transient Ferromagnetic-like state mediating ultrafast reversal of antiferromagnetically coupled spins, *Nature* 472: 205–208, 2011.

[4] T. Ostler et al., Ultrafast heating as a sufficient stimulus for magnetization reversal in a ferrimagnet, *Nature Communications* 3: 666, 2012.

[5] M. Shalaby and C.P. Hauri et al., Demonstration of a low-frequency three-dimensional terahertz bullet with extreme brightness, *Nature Communications* 6: 5976, 2015.

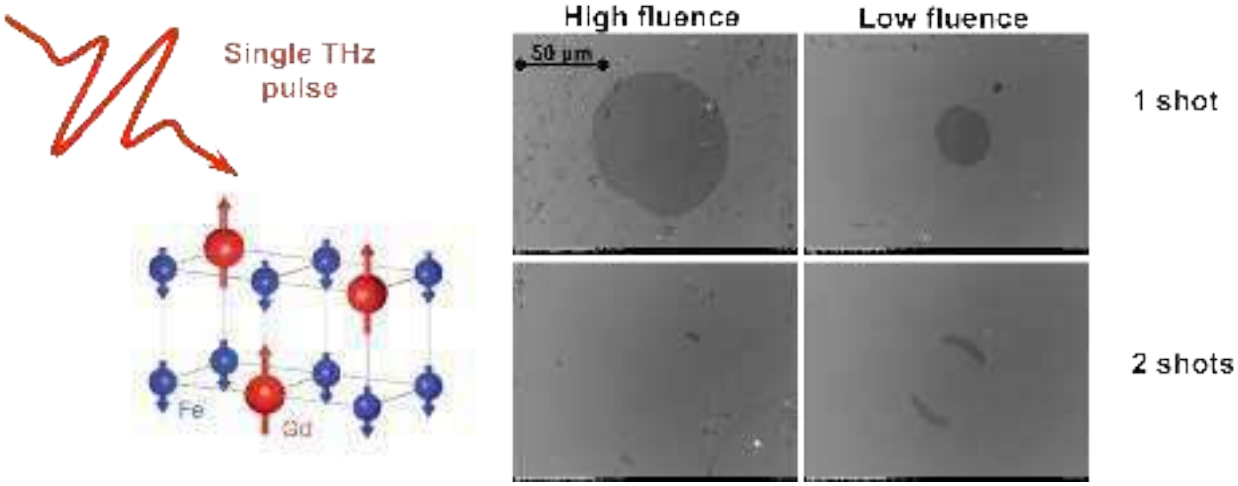


Figure 1: (Left) Pictorial view of the single-shot THz excitation of ferrimagnetic GdFe alloy **(Right)** MOKE microscopy images of GdFe obtained upon photo-excitation with one (upper panels) and two subsequent (lower panels) THz pulses (2 THz central frequency) at two different fluences. We observe magnetization switching for every single-shot THz pulse exposure *i.e.* toggle magnetization switching.

Spatio-Temporal Conductivity Modulation: A Pathway Towards CMOS Compatible, Low Loss, Magnetic-Free Non-Reciprocity

Aravind Nagulu, Negar Reiskarimian, Tolga Dinc, and Harish Krishnaswamy*

Dept. of Electrical Engineering, Columbia University, New York, NY 10027, USA
* To whom correspondence should be addressed (email: harish@ee.columbia.edu)

Abstract

Magnetic-free non-reciprocity using spatio-temporal modulation has gained a lot of attention in the recent years. Some approaches use permittivity modulation, but feature a large form-factor or high loss due to small modulation contrasts of permittivity. More recent approaches leverage much larger conductivity modulation contrasts available in CMOS to achieve drastically smaller form-factors and low-loss non-reciprocity across wide range of operating frequencies. Here we review recent progress on spatio-temporal conductivity-modulation, which enabled non-reciprocal components operating from radio frequencies to millimeter-waves in a CMOS platform.

1. Introduction

A medium with symmetric transmission of electromagnetic waves between two spatially separated points is referred as a reciprocal medium. Various theorems of reciprocity has been formulated over the years, including the work of Green (electrostatics), Rayleigh (dynamic systems), Helmholtz (optics, acoustics) and Lorentz (electromagnetics). Non-reciprocal components, such as circulators, isolators, gyrators and non-reciprocal phase-shifters, are critical for various applications ranging from radio frequencies (RF) to optical frequencies, including communications, radar, imaging and sensing. Traditionally, non-reciprocity has been achieved by using magnetic materials such as ferrites, which lose their reciprocity under the application of an external biasing magnetic field. Unfortunately, such materials are not compatible with existing semiconductor manufacturing processes and, therefore, lead to large form-factors and high implementation costs. In recent years, there has been progress on breaking reciprocity through time-variance. At RF, initial approaches have focused on permittivity modulation using modulated varactors (variable capacitors)[1, 2]. However, varactors have a weak modulation ratio ranging between 2-4, a weak modulation index directly translates to a large device size over which modulation must be performed or narrow transmission bandwidths if resonances are employed for miniaturization. Consequently, these approaches resulted in designs that exhibit a trade-off between loss, size and bandwidth.

Recently, we found that high conductivity modulation ratios ($10^3 - 10^5$) of transistors acting as electronic switches can be levaraged to realize a rich set of unique non-reciprocal properties, including wide-band gyration, isolation and circulation [3, 4, 5, 6]. In this abstract, we will cover our recent research on using commutated circuits to break reciprocity and build high-performance passive circulators operating from RF to mm-wave frequencies in CMOS. We will describe the fundamental physical principles, as well as the designs of our four generations CMOS circulators [3, 4, 5, 6].

2. Spatio-Temporal Conductivity Modulation

2.1. Non-Reciprocity Using Commutated Multipath Networks

Fig. 1(a) consists a 2-port commutated multipath network realized using N identical branches containing a shunt capacitance in each branch. The set of switches left and on the right are modulated using non-overlapping pulses each having the period T_s and the width of T_s/N. When the time constant $\tau = Z_0C >> T_s/N$ (Z_0 is the input/output port impedance), the structure behaves as a high-Q filter (commonly known as N-path filter) and is commonly used to realize a compact on-chip bandpass filter. In Ref. [3], we have shown that applying a relative phase shift to the non-overlapping clocks driving the left and right switch sets imparts a non-reciprocal phase-shift to the signals traveling in the forward and reverse directions since they see a different ordering of the phase-shifted switches. *Essentially, the two-port N-path filter with a clock phase shift of $\pi/2$ realizes an electrically-infinitesimal gyrator with transmission response $\pm\pi/2$.* Later a 3-port circulator is realized by embedding the gyrator transmission line loop within a length of 3λ/4 and by placing 3 ports with a relative circumferential distance of $\lambda/4$ (see Fig. 1(a)). The combination of the non-reciprocal phase shift of the N-path filter with the reciprocal phase shift of the transmission line results in constructive interference in clockwise direction and destructive interference in counter-clockwise direction.

2.2. 25 GHz Swithced-Transmission-Line Based Non-Reciprocal Circulator

Inspired by the N-path-filter-based RF circulator, we proposed a generalized conductivity modulation concept using switched transmission lines [4]. The concept, shown in Fig. 1(b), consists of two sets of differential mixer-quad switches on either end of a differential transmission-line delay. The switches are modulated using square wave clocks with a frequency ω_m, and the relative phase shift between the clocks is $T_m/4$, which is also equal to the delay pro-

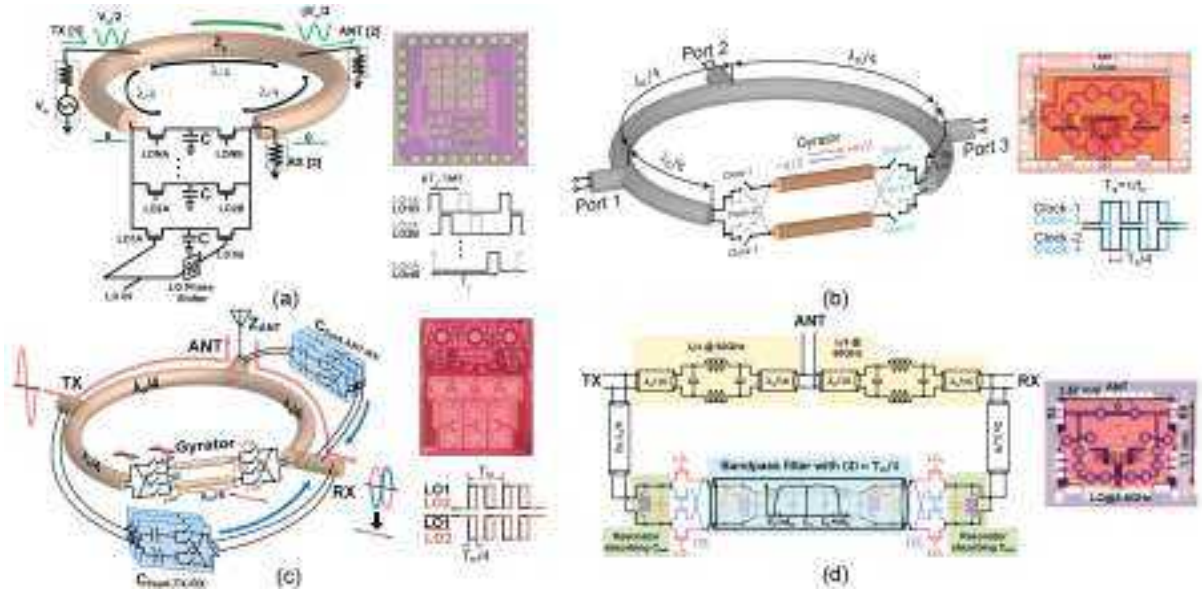


Figure 1: Conceptual diagrams and chip micro-photographs of our conductivity-modulation-based circulators: (a) RF circulator employing staggered commutation in multipath networks [3]. (b) 25 GHz switched-transmission-line circulator [4]. (c) RF switched-transmission-line circulator with >1W power-handling and inductor-free isolation tuning capability [5]. (d) 60 GHz switched-band-pass-filter circulator [6].

vided by the transmission line. For this structure, waves traveling from left to right experience the transmission-line delay with no sign flips in both halves of the clock period. On the other hand, waves traveling from right to left experience the transmission-line delay along with one sign flip. This additional sign flip produces an infinitely broadband 180° non-reciprocal phase difference, i.e., an infinitely broadband gyrator.

The infinite bandwidth of the gyrator implies that the signal frequency and the modulation frequency are completely decoupled. This feature was exploited to realize a mm-wave (25GHz) fully-integrated passive circulator in 45nm SOI CMOS, shown in Fig. 1(b) [4], by modulating the switches at 1/3rd of the operating frequency (8.33GHz). The lowering of the modulation frequency, as well as the need for 50% duty-cycle clocks made this high frequency implementation feasible.

2.3. Highly Linear 1 GHz Non-Reciprocal Circulator with Loss-Free, Inductor-Free Isolation Tuning

Fig. 1(c) shows the architecture of a highly-linear RF circulator, which uses the feature of lowering the modulation frequency to enhance the power handling and linearity of the circulator at 1GHz operating frequency. The switches were modulated at 333MHz for 1GHz operation, and such a low modulation frequency enables the usage of the thick-oxide devices in 180nm SOI CMOS technology to boost power handling. This implementation notably improves linearity and power handling of the CMOS citculator by 10-100$\times$ when compared with our prior implementations [5]. The TX-RX isolation of all shared-antenna interfaces, even circulators, is limited by the matching of the antenna port, which necessitates an antenna tuning mechanism. Traditionally, magnetic circulators are followed by antenna tuners. In this work, inbuilt isolation tuning is achieved by implementing digitally programmable differential feed capacitor banks between TX-RX and ANT-RX ports. The ability to compensate a VSWR of up to 1.85 (and beyond) was demonstrated in this work.

2.4. 60 GHz Circulator Based On Switched-Bandpass-Filter

Theoretically, the switched-transmision-line structure has no loss and infinite bandwidth. In practice, however, they are limited by the switch ON resistance R_{ON} and parasitic capcitance C_{OFF} and the product $R_{ON}C_{OFF}$ is constant for a given semiconductor technology. Hence during the deign process, there exists an trade-off between the losses from R_{ON} and C_{OFF}. In this work, we break this unfavorable trade-off between R_{ON} and C_{OFF} by recognizing that the mixing products are centered around the input frequency f_{in}, and therefore, a bandpass filter (BPF) with quarter-wave group delay is sufficient to preserve them. The bandpass filter exploited here includes shunt-LC resonators at the input and output of an 8-section LC ladder (Fig. 1(d)). The shunt LC resonators allow for the absorption of larger switch capacitance, allowing for a lower R_{ON}, while still allowing enough bandwidth in the BPF to sustain the dominant mixing products, thus allowing low R_{ON} loss as well as low filtering losses due to parasitic capacitance (Bragg loss). In our 60GHz circulator, the loss and power handling are improved by 1.3 dB and 9 dB respectively by using the switched-bandpass-filter approach.

Acknowledgement

This work was supported by DAPRA ACT and SPAR programs.

References

[1] N. Estep *et al.*, *Nature Physics*, vol. 10, no. 12, pp. 923–927, 2014.

[2] S. Qin *et al.*, *IEEE Trans. Microw. Theory Techn.*, vol. 62, no. 10, pp. 2260–2272, Oct 2014.

[3] N. Reiskarimian *et al.*, in *Nature Commun.*, vol. 7, no. 4, Apr 2016.

[4] T. Dinc *et al.*, in *Nature Commun.*, vol. 8, no. 10, Oct 2017.

[5] A. Nagulu *et al.*, in *2018 IEEE RFIC*, Jun 2018.

[6] A. Nagulu and H. Krishnaswamy, in *2019 IEEE International Solid-State Circuits Conference - (ISSCC)*, Feb 2019, pp. 446–448.

ogy in photonic crystals, metamaterials, and metasurfaces: physics and

Topological valley transport on the surface of biaxial hyperbolic metamaterials

Ruo-Yang Zhang, C. T. Chan*

Department of Physics, Hong Kong University of Science and Technology, Hong Kong, China
*corresponding author, E-mail: phchan@ust.hk

Abstract

On the iso-frequency surfaces of a homogeneous biaxial hyperbolic metamaterial, there exist four doubly degenerate diabolic points, which are protected by *PT* and mirror symmetries and can be utilized as valley degrees of freedom. By introducing chiral or gyroelectric material perturbations, we can lift the degeneracy at the diabolic points, and control the existence and chirality of the gapless Fermi arc at each valley. In particular, we can achieve topological valley-dependent helical transport for surface-arc waves.

1. Introduction

The concept of "valley", originating from semiconductor physics, refers to the local extrema in the band structures, and has been used as a new degree of freedom to manipulate the transport of electromagnetic waves [1,2]. It is also known that in Weyl and other nodal semimetal systems, the nonzero charges of the topological nodes ensures the existence of Fermi-arc surface states. It has been shown that fascinating surface wave transport effects can be achieved by manipulating the Fermi-arc dispersion, such as surface wave negative refraction [3], and helical transport using spin-polarized Fermi arcs [4]. In this work, we introduce valley degrees of freedom (VDF) to control the chirality of Fermi arcs, and achieve novel transport effects.

2. Results

An ideal platform for valley topological effect is biaxial hyperbolic metamaterials (BHMs)[5,6]. Similar to ordinary biaxial dielectric crystals, a BHM with the permittivity $\ddot{\varepsilon}_h = \mathrm{diag}(\varepsilon_x, \varepsilon_y, \varepsilon_z)$ ($\varepsilon_z < 0 < \varepsilon_x < \varepsilon_y$) possesses four doubly degenerate diabolic points on the iso-frequency surface, which are stabilized by the quantized Berry phase $\gamma = i\oint \langle \psi | \nabla_{\mathbf{k}} | \psi \rangle \cdot d\mathbf{k} = \pi$ encircling the degenerate point (see Fig. 1) and are protected by both the combined parity time-reversal (*PT*) symmetry and the mirror symmetry (M_y) about the plane of $y = \mathrm{const}$. By breaking both *PT* and M_y symmetries, the diabolic points will be gapped, and the hyperbolicity of the media ensures the appearance of complete momentum-gaps. The spatial dispersion near a diabolic point, $\mathbf{k}^{\mathrm{d}} = (k_x^{\mathrm{d}}, 0, k_z^{\mathrm{d}})$, can be described by the eigen-equation $\mathcal{H}\psi = \delta k\, \psi$ with a 2D Dirac Hamiltonian:

$$\mathcal{H} = s_x s_z v_f \left(\delta k_1 \hat{\sigma}_0 - \delta k_1 \hat{\sigma}_1 - \delta k_2 \hat{\sigma}_2 \right) + m(s_h, s_v)\hat{\sigma}_3 , \qquad (1)$$

where $\delta\mathbf{k} = \delta k_1 \mathbf{e}_1 + \delta k_2 \mathbf{e}_2 + \delta k \mathbf{e}_3$ denotes the displacement from the diabolic point ($\mathbf{e}_3$ is along the direction of $\mathbf{k}^{\mathrm{d}}$); $s_x = \mathrm{sgn}(k_x^{\mathrm{d}})$, $s_z = \mathrm{sgn}(k_z^{\mathrm{d}})$ label the quadrants of the four valleys; $v_f = \frac{1}{2}[(1-\varepsilon_y/\varepsilon_x)(\varepsilon_y/\varepsilon_z - 1)]^{1/2}$ is the Fermi velocity; and $m(s_x, s_z)$ is the valley-dependent mass. The integration of Berry curvature over a semi-infinite Dirac cone

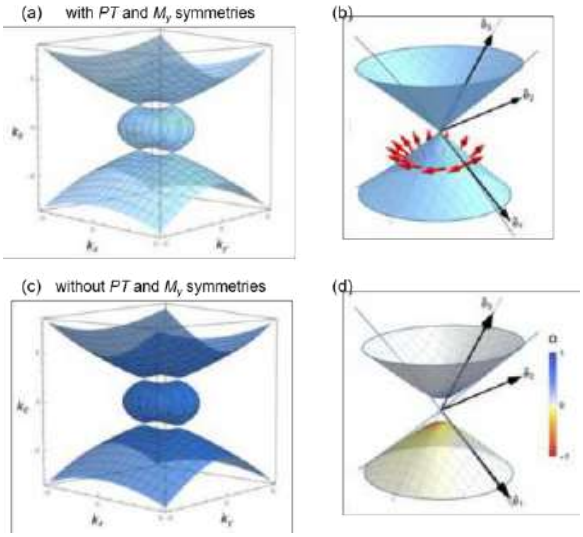


Figure 1: Iso-frequency surface of a BHM (a) with and (c) without *PT* and M_y symmetries. (b,d) Enlarged view around a diabolic point and a gapped valley respectively. The red arrows in (b) denote the eigen-polarization of electric field around the diabolic point. The polarization changes a π phase after winding around the diabolic point, which corresponds precisely to the Berry phase of the circle. The color on the surface in (d) represents the Berry curvature distribution.

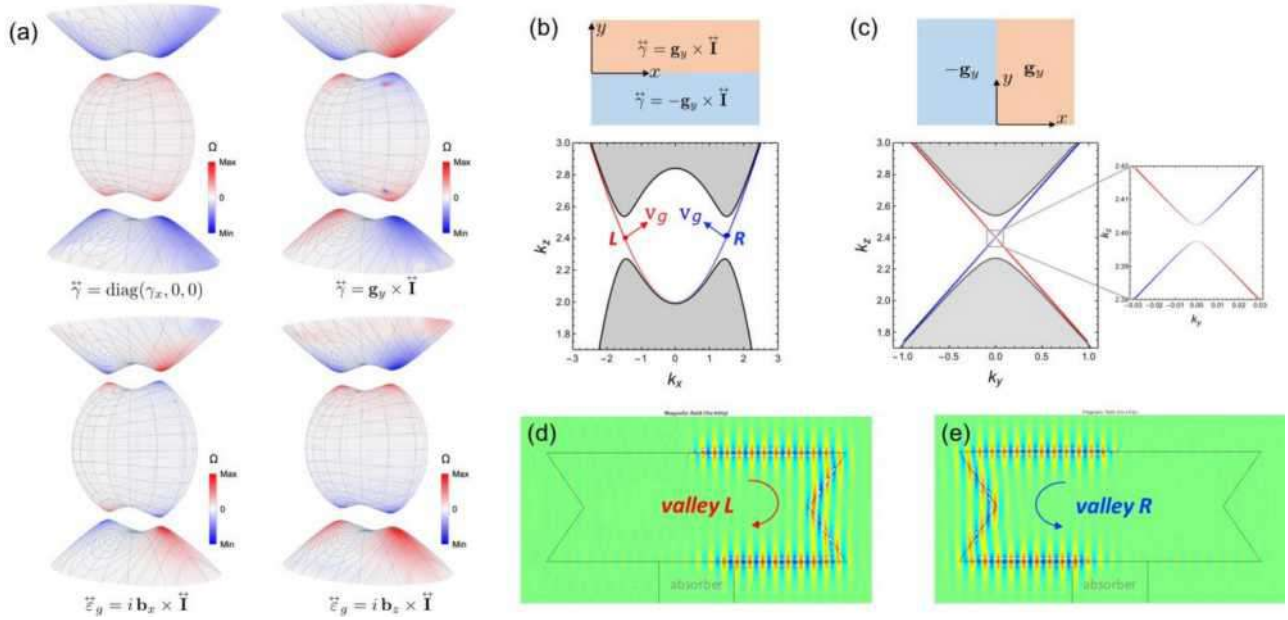


Figure 2: (a) Four kinds of material perturbations that can break both PT and My symmetries, where the colors on the iso-frequency surface show the distributions of the Berry curvature. (b,c) Valley-polarized Fermi arcs at $xz-$ and $yz-$ interfaces of two BHMs with opposite antisymmetric chiral coupling, where red and blue colors correpond to left and right valleys respectively. (d,e) Valley dependent helical transport of Fermi-arc surface waves.

tends to a half-integer topological invariant, the valley Chern number, determined by the sign of the effective mass: $C_V = \text{sign}(m)/2$. For two hyperbolic media facing at the interface of $y=0$, the difference between valley Chern numbers of two sides, $\nu = s_x s_z [C_V(y>0) - C_V(y>0)]$, predicts the existence and chirality of a gapless Fermi arc in the k_z-gap at each valley.

The effective mass $m(s_h, s_v)$ depends on the mechanism of symmetry breaking. We have investigated different mechanisms: (1) bianisotropic chiral coupling with either a diagonal chiral term $\ddot{\gamma} = \text{diag}(\gamma_x, \gamma_y, \gamma_z)$ or an anti-symmetric chiral term $\ddot{\gamma} = \mathbf{g}_y \times \ddot{I}$; (2) gyroelectric effect induced by magnetic field either along x-or z-direction $\ddot{\varepsilon} = \ddot{\varepsilon}_h + i\mathbf{b}_i \times \ddot{I}$ ($i = x, z$), which shows different valley Chern number distributions in Fig.2(a). Letting two hyperbolic media with different perturbations join at an interface, a full control of topological multi-valley transport, namely manipulating the existence and chirality of Fermi arcs at any specific valleys, can be achieved. In particular, for the interface of two BHMs with opposite antisymmetric chiral coupling, the Fermi arcs associated with left and right valleys in the same k_z bulk gap have opposite chirality as shown in Fig.2(b). Even if the interface is parallel to y axis, the crossover of the two Fermi arcs only induces an extremely tiny gap (see Fig.2(c)). This enables us to realize valley Hall effect using the Fermi-arc states. The full-wave simulations in Fig.2(d,e) manifest that the Fermi-arc surface waves possess valley-dependent helical transport feature and are immune from sharp-corner scattering.

3. Conclusions

We demonstrated that valley-dependent gapless Fermi arcs can emerge at the interface of two BHMs without *PT* and M_y symmetries, and valley Hall effect are realized using the Fermi-arc surface waves. Furthermore, the chirality of the Fermi arc at each valley can be individually controlled via introducing different kinds of material perturbations, hence this platform can be utilized to achieve multiple-valley topological transport.

Acknowledgements

This work was supported by the Research Grants Council of Hong Kong (AoE/P-02/12).

References

[1] T. Ma and G. Shvets, All-Si valley-Hall photonic topological insulator, *New J. Phys.* 18 025012, 2016.

[2] J.-W. Dong et al. *Nat. Mater.* 16:298-302, 2016.

[3] Hailong He et al. *Nature*, 560:61, 2018.

[4] Guo, Qinghua, et al. *Phys. Rev. Lett.* 119:213901, 2017.

[5] W. Gao et al. *Phys. Rev. Lett.* 114:037402, 2015.

[6] W. Gao, F. Fang, Y. Liu, S. Zhang, *Light Sci. Appl.* 4: e328, 2015.

Observations of Polarization Vortices in Momentum Space

Yiwen Zhang[1], Ang Chen[1], Wenzhe Liu[1], Chia Wei Hsu[3], Bo Wang[1], Fang Guan[1], Xiaohan Liu[1] Lei Shi[1*], Ling Lu[2], Jian Zi[1]

[1] Department of Physics, Fudan University, 200433, Shanghai, China
[2] Institute of Physics, Chinese Academy of Sciences, Beijing 100190, China
[3] Department of Applied Physics, Yale University, New Haven, Connecticut 06520, USA
*corresponding author, E-mail: lshi@fudan.edu.cn

As one of the most fundamental topological excitations in nature, vortices are widely known in hair whorls as the winding of hair strings, in fluid dynamics as the winding of velocities, in superconductors and superfluid as the winding of order parameters. However, vortices have hardly been observed other than those in the real space. Using a home-made polarization-resolved momentum-space imaging spectroscopy, we experimentally observed vortices in momentum space, as the winding of far-field polarization vectors in the first Brillouin zone of periodic plasmonic structures. We completely mapped out the band structure, lifetime and polarization states of all radiative states. The momentum space vortices were experimentally identified by their winding patterns in the polarization-resolved iso-frequency contours and their diverging radiative quality factors. Such polarization vortices, leading to high Q factor modes so called bound states in the continuum (BIC), can exist robustly on any periodic systems of vector fields, while they are not captured by the existing topological band theory developed for scaler fields. Our results also inspire that the non-trivial topological effects could be also found in photonic crystals assumed to be topologically trivial in the past.

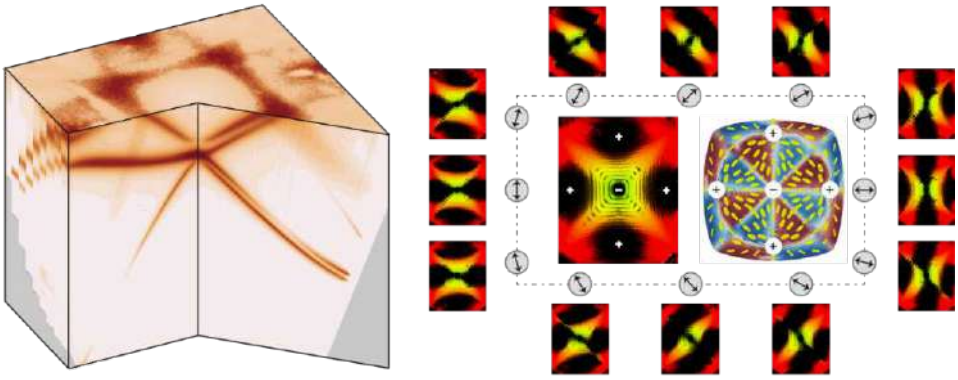


Figure Left: Bandstructure of a plasmonic crystal with simple square lattice. Right: Extinction map of the band of interest in the FBZ, obtained by summing 20 isofrequency contours. Different colors correspond to different wavelengths, with the color map shown in inset. Center plot: The polarization-averaged data and Measured polarization state distribution. Outer plots: The polarization-resolved data; the arrows aside, the direction of the polarizer.

References

[1] "Observation of optical vortices in momentum space," *Phys. Rev. Lett.* 120, 186103 (2018)

Optimal distance above ENZ-materials for fluorescence inhibition: Insight from a perturbative analysis of the surface Green function.

C. Silvestre[1], E.R. Méndez[2], A. Vial[1],G. Lerondel[1], A. Bruyant[1], and Rémi Vincent[1*]

[1]Light, nanomaterials and nanotechnology, ICD CNRS,
University of technology of Troyes, 12 Rue Marie Curie, 10004 Troyes, France
[2]Centro de investigación científica y de educación superior de Ensenada,
Carretera Ensenada-Tijuana No. 3918, Ensenada B.C, 22860, México
*corresponding author, E-mail: remi.vincent@utt.fr

Abstract

We study theoretically and numerically the electromagnetic response of a dipole near an Epsilon-near-zero (ENZ) surface. Explicit analytical expressions are given for the LDOS near a plane surface. A criterion for evaluating the threshold height above (below) which radiative (non-radiative) processes dominate is established. We found results elucidating the origin of LDOS cancellation. By the determination of an optimal spacer thickness between the ENZ substrate and a dipole emitter, the obtained results can be used to strongly augment the lifetime of the emitter.

1. Introduction

The development of near-field optics has led to an important number of applications involving the control of light emission. In this context, considering the electromagnetic environment is crucial for an accurate description of the physical mechanisms involved. In particular, when light sources are in the vicinity of a complex electromagnetic background, the emission properties of the source are modified. Therefore, considering the advances in nanofabrication of the last decades and microscopy techniques with sub-wavelength resolution, it is possible to of study near-field interactions in the visible and infra-red region of the spectrum. The case of a half-space system is of particular importance, as it can be considered the simplest structured electromagnetic background.

The electromagnetic Green function plays an important role in absorption and emission processes. Indeed, the Green function gives the local density of optical states (LDOS). The LDOS provides spectroscopic information and is independent of the illumination modes. In the case of the 'half-space' system, a rigorous solution for the Green function exists in reciprocal space [1]. As the rigorous solution requires some care in its evaluation, approximate solutions based on the method of images [2] are frequently used, the so-called *Image-Dipole* model (IDM).

We study the contribution of the substrate to the modification of the local density of optical states (LDOS) using a short-distance expansion (SDE) of the Green function. General trends for radiative and non-radiative contributions to the LDOS are discussed and examples of application of the formalism are given for ϵ-near-zero (ENZ) materials.

2. Green function formalism for a particle in a half-space background

In a half-space geometry, a plane interface separates a medium with refractive index n_1 ($z > 0$) from another with refractive index n_2 ($z < 0$). For the sake of simplicity, we will consider the case in which the emitter is located in the upper medium with refractive index n_1.

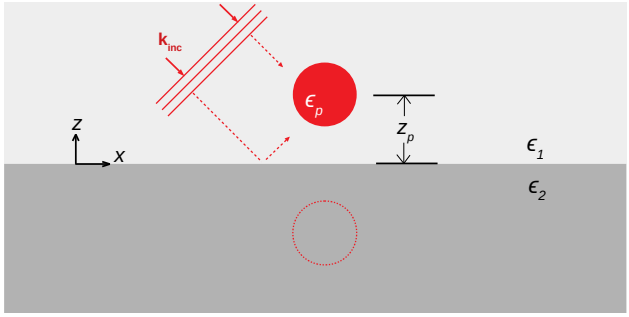


Figure 1: Schematic representation of a small particle above a plane interface. The particle interacts directly with an incident plane wave and with the field reflected at the interface. The dashed circle in the substrate represents the main idea of the image dipole moment (IDM), in which the surface is replaced by an 'image' charge on the substrate side.

The Green function associated to the half-space geometry, in the region $z > 0$, has two contributions: the dipole fields of a homogeneous medium (direct contribution) and those coming from the reflection at the interface (reflected contribution). A rigorous solution for the field scattered by a point dipole in the presence of the plane interface was obtained by Sommerfeld [1] in the context of radiowave propagation. The general procedure for obtaining such a solution relies on transforming the Green function from direct to reciprocal space. For our purposes, we write the half-space Green function as

$$\mathbf{G}^{HS}(\mathbf{r},\mathbf{r}') = \mathbf{G}^{0}(\mathbf{r},\mathbf{r}') + \mathbf{G}^{R}(\mathbf{r},\mathbf{r}'), \qquad (1)$$

with

$$\mathbf{G}^R(\mathbf{r},\mathbf{r}') = \int_0^\infty \int_0^{2\pi} \frac{q\,\mathrm{d}q\,\mathrm{d}\phi(q)}{2\pi\kappa(q)} \mathbf{D}(q) e^{i\Phi(q)} \quad (2)$$

and

$$\Phi(q) = q\mathcal{R}\cos\phi(q) + i\kappa(q)\mathcal{Z}. \quad (3)$$

Here $\mathbf{G}^0$ is the Green function of a homogeneous medium with refractive index n_1 and λ the free-space wavelength. The tensor $\mathbf{D}(q)$ is related to the dielectric properties of each medium. An analytic solution for the so-called Sommerfeld integral in equation (2) is not known and it is necessary to evaluate it numerically. The integral, however can be approximated as [4]

$$\mathbf{G}^R(\mathbf{r},\mathbf{r}) \approx \frac{1}{32\pi k_1^2 z^3} \sum_{l=1}^{N} (2k_1 z)^l \boldsymbol{\mathcal{K}}^{(l)}. \quad (4)$$

for small $k_1 z$. We have used the fact that $\mathcal{R} = 0$ and $\mathcal{Z} = 2z$. The dyadic $\boldsymbol{\mathcal{K}}^{(l)}$ contains the coefficients of the lth-order term.

2.1. Local density of optical states near a plane interface

The local electromagnetic density of states (LDOS) $\rho(\mathbf{r})$ is proportional to the imaginary part of the Green tensor, they are related through the expression [3]

$$\rho^{HS}(\mathbf{r}) = \frac{6\omega}{\pi c^2} \mathrm{Tr}\Im\{\mathbf{G}^{HS}(\mathbf{r},\mathbf{r})\} \quad (5)$$

and represents the density of electromagnetic modes at frequencies $\omega \pm \delta\omega$ and position $\mathbf{r}$. If the dipole has a preferential orientiation, one may define a *projected* LDOS $\rho_{\mathbf{u}}^{HS}(\mathbf{r})$ as

$$\rho_{\mathbf{u}}^{HS}(\mathbf{r}) = \frac{6\omega}{\pi c^2} \Im\{\mathbf{u}\cdot\mathbf{G}^{HS}(\mathbf{r},\mathbf{r})\cdot\mathbf{u}\}, \quad (6)$$

where $\mathbf{u}$ is a vector containing the dipole's orientation. Using equation (1), the LDOS modification can be expressed as

$$\tilde{\rho}(\mathbf{r}) = 1 + \frac{6\pi}{k_1} \Im\{\mathbf{G}^R(\mathbf{r},\mathbf{r})\}. \quad (7)$$

In this expression we defined $k_1 = n_1(\omega/c)$ and the corresponding LDOS as $\rho_1 = 6n_1\omega^3/(\pi c^2)$. A similar normalization is used for $\rho_{\mathbf{u}}$.

3. Discussion

Using the formalism described above, the zz component of $\mathbf{G}^R$ and the normalized projected LDOS $\tilde{\rho}_z$. are studied for ϵ-near-zero substrates. In particular, the SDE is used to identify radiative and non-radiative contributions to the LDOS. These contributions are separated by their dependence, in each case, with the distance z of the dipole to the substrate. In this context, the SDE provides extremely useful information regarding the dependence of the LDOS with the macroscopic dielectric properties of the substrate and upper medium, on the wavelength of emission and on the position of the emitter above the substrate.

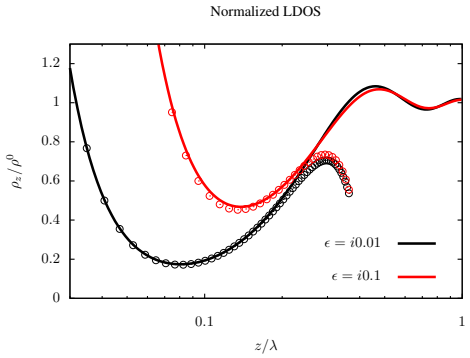


Figure 2: Exact (solid lines) and approximate (symbols) reflected Green function. The valley represents the suppresion of the LDOS for two distinct susbtrates.

4. Conclusions

Considering a dipole above an ENZ substrate, we found that if non-radiative effects are weak compared to the radiative ones, significant suppression of the LDOS can occur for the projected LDOS, i.e. $\tilde{\rho}_z < 1$ (see fig. 2). We analysed these suppression effects using the SDE of the *reflected* Green function. We find the necessary conditions to considerably suppress the LDOS and identify the particular term in the SDE that is responsible for the cancellation. Exacts calculations have been performed in order to validate the SDE. We also found that a third-order approximation accounts for the LDOS cancellation, with the order $\mathcal{O}(x^3)$ being responsible for the suppression. For sufficiently weak absorbing substrates, we find that the seventh-order approximation can describe accurately the cancellation process up to $z \approx \lambda/7$. Minimum values for the normalized LDOS $\tilde{\rho}$ on the order of a few percent were found for realistic materials.

Acknowledgement

C. S. C. is grateful for the financial support from the Grand Est region.

References

[1] A. Sommerfeld, ber die Ausbreitung der Wellen in der drahtlosen Telegraphie. *Annalen der Physik*, 333(4), 665-736, 1909.

[2] J.D. Jackson, Classical electrodynamics. John Wiley & Sons, 2007.

[3] L. Novotny & B. Hecht, (2012). Principles of nano-optics. Cambridge university press, 2012.

[4] G.Y. Panasyuk, J. C. Schotland, and V. A. Markel, Short-distance expansion for the electromagnetic half-space Green's tensor: general results and an application to radiative lifetime computations. *Journal of Physics A: Mathematical and Theoretical*, 2009.

Inverse design and demonstration of on-chip ultracompact multimode silicon photonic devices

Weijie Chang[1], Xinshu Ren[1], Longhui Lu[1], and Minming Zhang[1,2]

[1] School of Optical and Electronic Information, Huazhong University of Science and Technology, Wuhan 430074, China
[2] Wuhan National Laboratory for Optoelectronics, Huazhong University of Science and Technology, Wuhan 430074, China
*corresponding author, E-mail: mmz@hust.edu.cn

Abstract

We demonstrate several inverse-designed ultracompact and highly functional silicon devices based on digital subwavelength structures for on-chip optical interconnects, including mode multiplexer, dual mode power splitter, multimode waveguide crossing and multimode bent waveguide. An improved direct-binary-search-based inverse design method is utilized to optimize digital nanophotonic devices. Besides, an efficient inverse design approach based on digitized adjoint method is also discussed. The footprint of the devices we demonstrate is about two order of magnitude smaller than that of conventional ones, which has great potential for application in high-density integrated on-chip optical interconnects.

1. Introduction

Mode-division multiplexing (MDM) has provided an effective approach to further increase the transmission capacity of on-chip optical interconnect [1]. A variety of key building blocks based on conventional waveguides have been extensively reported typically including mode multiplexer, multimode waveguide crossing and multimode bent waveguide. The conventional waveguide based devices exhibited high performance and large fabrication tolerance. However, due to the limit of adiabatic evolution or weak-coupling strength, the conventional schemes suffer from relatively large scale, which may not be suitable for high-density integrated MDM systems. Recently, inverse design method potentially offers a new route to optimize refractive index distributions at the nanoscale and provide a promising platform for designing ultracompact and highly functional nanophotonic devices simultaneously [2,3]. However, the present inverse-designed silicon structures usually have random and complex etching patterns and may suffer from fabrication errors significantly.

In this work, we propose lag effect-insensitive digital subwavelength (SW) structure and utilize an improved direct-binary-search-based inverse design method to realize several ultracompact digital nanophotonic devices. The footprint of these devices is about two order of magnitude smaller than that of conventional ones.

2. ultracompact multimode silicon devices

As a proof of concept, ultracompact multiplexer and multimode waveguide crossing are demonstrated by improved inverse design method [4,5]. In addition, a digitized adjoint method is also discussed.

2.1. Multimode multiplexer

On-chip mode (de)multiplexer ((DE) MUX) is one of the most essential elements in MDM systems. Various mode multiplexer schemes based on conventional silicon waveguides have been proposed typically including asymmetric directional couplers (ADCs), multimode interferometers (MMI), or asymmetric Y-junction. Although these schemes have proved to be promising, they usually suffer from a relatively large footprint of tens or hundreds of μm^2 for two mode MUX due to adiabatic evolution or weak-coupling strength. As shown in Figs. 1(a) and (b), small branching angle (<9°) is required for satisfying adiabatic evolution in conventional asymmetric Y-junction scheme, which leads to a large scale. As a result, we theoretically discuss the feasibility of realizing a SW asymmetric Y-junction with a large divergence angle for mode conversion. A mode conversion factor (MCF) is used to evaluate the effect of mode conversion, and mode conversion occurs when the MCF is greater than approximately 0.43. By engineering material index and manipulating phase profiles of light at the nanoscale using the digital SW structures, we realize SW asymmetric Y-junctions with large divergence angles to reduce the device footprint greatly.

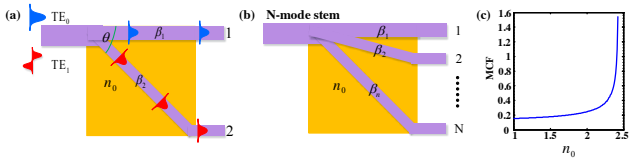


Fig. 1. (a) and (b)Working principles for two-mode (De) MUX and N-mode (De) MUX based on conventional waveguides asymmetric Y-junctions, respectively. (c) Mode conversion factor (MCF) as a function of the refractive index of the material.

An improved direct-binary-search-based (DBS) inverse design method is utilized to optimize digital SW structure MUX. Our simulation results indicate that a better device performance can be achieved by manually presetting an initial pattern like a conventional waveguide Y-junction rather than a random initial pattern in the DBS optimization algorithm. And we also find that the optimum pattern will automatically converge to a pattern equivalent to a SW asymmetric Y-junction with high performance. In this way, we demonstrate a three-mode SW MUX occupied 3.6 × 4.8 μm^2 as preset in Fig. 2.

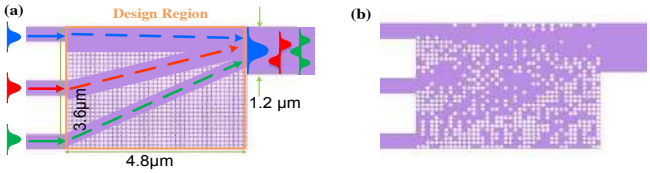


Fig. 2. (a) Schematic of the three-mode MUX based on SW structure asymmetric Y-junction. (b) The optimized device pattern for the manually-set initial pattern.

2.2. Multimode waveguide crossing

Multimode waveguide crossing is an essential component for realizing a densely integrated MDM optical network. Recently, the self-image effect of conventional multimode-interference (MMI) couplers has been utilized to realize the dual mode waveguide crossing. Unfortunately, the severe self-image position offset between the fundamental modes and first-order modes in conventional waveguide leads to a relatively large coupling length. However, digital SW structure could provide an additional design degree of freedom to optimize the mode effective index to realize same self-image lengths for individual modes. By engineering the refractive indices of the lateral claddings and changing the widths of MMI couplers, the same self-image beat lengths of both modes for SW-assisted MMI couplers could be expected to be achieved theoretically, as is shown in Fig. 3(c).

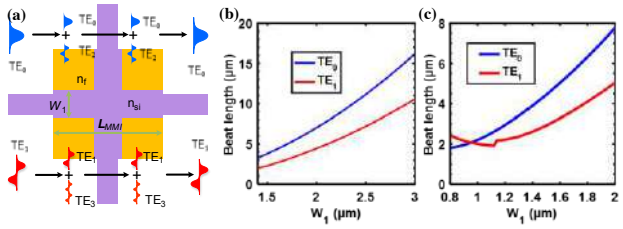


Fig. 3. (a) Schematic illustration of for the dual-mode waveguide crossing. (b) and (c) Self-image beat lengths of both modes for conventional waveguide-based MMI coupler and SW structure-assisted one as a function of W_1, respectively.

Similarly, the improved DBS-based inverse design method is also utilized to optimize the device. The manually set initial and optimized patterns are shown in Figs. 4(a) and 4(b), relatively. In this way, an ultra-compact and highly functional dual-mode waveguide crossings was demonstrated using inverse design method.

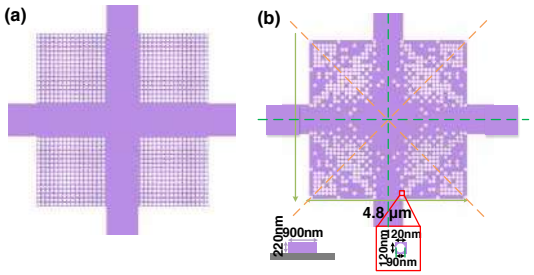


Fig. 4. (a) and (b) manually set initial and optimized patterns for the digital SW-based dual mode waveguide crossing, relatively.

2.3. Digitized Adjoint Method

To improve the efficiency of inverse design for large scale and high-performance "digital" subwavelength nanophotonic devices, We also present a digitized adjoint method. We design a single-mode 3-dB power divider and a dual-mode demultiplexer to demonstrate the digitized adjoint method for single-object and dual-object optimizations, respectively. The optimization comprises three stages, a first stage of continuous variation for an "analog" pattern, a second stage of forced permittivity biasing for a "quasi-digital" pattern, and a third stage for a multi-level digital pattern. Compared with conventional DBS method, the proposed digitized adjoint method can improve the design efficiency by about 5 times, and the performance optimization can reach approximately the same level using the ternary pattern. The digitized adjoint method takes the advantages of adjoint sensitivity analysis and digital subwavelength structure and provides a new route for efficient and high-performance design of compact digital subwavelength nanophotonic devices, which may be attractive for inverse design of large-scale digital nanophotonic devices.

3. Conclusions

In summary, we exploit an improved DBS-based inverse design method to realize several ultracompact digital nanophotonic devices. The digitized adjoint method is also discussed to improve the efficiency of inverse design. By flexibly engineering index at the nanoscale and exhibiting robustness, digital SW structures offers a route to design ultracompact and highly functional nanophotonic devices, which has great potential for application in high-density integrated on-chip optical interconnects.

Funding

National Natural Science Foundation of China (61775069) and the Technology Innovation Program of Hubei Province of China (2018AAA037).

References

[1] C. Li, D. Liu, and D. Dai, "Multimode silicon photonics," Nanophotonics-Berlin (2018)

[2] B. Shen, P. Wang, R. Polson, and R. Menon, "An integrated-nanophotonics polarization beamsplitter with 2.4 × 2.4 μm2 footprint," Nat. Photonics 9(6), 378–382 (2015).

[3] A. Y. Piggott, et al, "Inverse design and demonstration of a compact and broadband on-chip wavelength demultiplexer," Nat. Photonics 9(6), 374–377 (2015)

[4] W. Chang, et al., "Ultra-compact mode (de) multiplexer based on subwavelength asymmetric Y-junction," Optics Express 26, 8162 (2018).

[5] W. Chang, et al., "Ultracompact dual-mode waveguide crossing based on subwavelength multimode-interference couplers," Photonics Research 6, 660-665 (2018).

Design of Photonic Topological Insulators Using Density Based Topology Optimization

Rasmus E. Christiansen[1], **Fengwen Wang**[1], **Ole Sigmund**[1], **Søren Stobbe**[2]

[1] Department of Mechanical Engineering, Technical University of Denmark,
Nils Koppels Allé 404, DK-2800 Kgs. Lyngby, Denmark
[2] Department of Photonics Engineering, DTU Fotonik, Technical University of Denmark,
Building 343, DK-2800 Kgs. Lyngby, Denmark
*corresponding author, E-mail: raelch@mek.dtu.dk

Abstract

We provide a novel photonic topological insulator design (PTI) exhibiting the quantum-spin-Hall effect, which, as opposed to previous designs, is conceived using numerical optimization of the transmission through PTI edge states. Specifically, we use topology optimization to maximize the transmission of light through a carefully configured model domain composed of two photonic crystal phases. This leads to a numerically generated PTI, which features larger bandgaps than previously predicted for planar PTIs and excellent suppression of backscattering from sharp bends.

1. Introduction

Time-reversal-invariant photonic topological insulators (PTIs) support pseudo-spin-dependent edge states with bi-directional propagation and robustness against certain classes of disorder [1, 2]. Such properties are obviously desirable in many applications in chip-scale photonics where controlled propagation and low losses are essential. However, designing a PTI is highly non-trivial as it requires inversion of band symmetries around a band gap and thus the designs for dielectric planar PTIs available in the literature have so far been obtained using cleaver ideas and painstaking trial and error [3, 4, 5] . We present a completely different approach to the design of PTIs where the problem is formulated as an inverse problem which we solve using density-based topology optimization [6, 7, 8]. Our approach allows tailoring PTIs for different figures of merit, such as operational wavelength, bandwidth, transmission, etc. Further, our approach allows for imposing any symmetry in the constituent unit cells among other possibilities.

This talk provides a brief description of the topology-optimization method, an in-depth description of the proposed design procedure, and analyses of selected PTIs, designed using the proposed approach.

2. The Method

A classical electromagnetic model is assumed for the light,

$$\nabla \times (\nabla \times \mathbf{E}(\mathbf{r})) - k_0^2 \epsilon_r(\mathbf{r}) \mathbf{E}(\mathbf{r}) = \mathbf{S}(\mathbf{r}), \quad \mathbf{r} \in \mathbf{\Omega} \in \mathbb{R}^2.$$

with $\mathbf{E}$ denoting the electric field, $k_0 = \frac{2\pi\nu}{c}$ the free-space wave number with ν being the frequency and c the speed of light in vacuum, ϵ_r the relative permittivity and $\mathbf{S}_e$ a source. The two-dimensional model domain $\mathbf{\Omega} \in \mathbb{R}^2$ is truncated using a perfectly matched layer [9].



Figure 1: Conceptual sketch of the design-model domain, $\mathbf{\Omega}$. The edge (bulk) of the PC phases constituting the PTI are colored orange (yellow) and black (grey). The input/output ports are denoted P1-P4 and the arrows indicate power flow.

The PTI structure consists of two periodic hexagonal photonic crystals (PCs) with a zig-zag interface. In the design problem, the two PCs are placed in $\mathbf{\Omega}$ as sketched conceptually in figure 1. The problem of designing the PTI is formulated as an inverse problem and solved for a set of frequencies using density-based topology optimization [6]. In the design process, the material configuration constituting the PCs is changed iteratively in order to simultaneously maximize the transmission of energy from P1 to P2 and P4 and minimize the transmission to P3 while ensuring that both PC phases exhibit bandgaps at the targeted frequencies by enforcing a set of inequality constraints. By achieving negligible transmission from P1 to P3 and high transmission from P1 to P2 and P4, a behaviour identical to that of a PTI, configured as shown in figure 1, is obtained.

After the design procedure is completed, the band-structure for a supercell containing both PCs and their interface is computed. This is done to validate that a pair of counter-rotating pseudo-spin edge states exists inside the bulk-bandgap region at the targeted frequencies, confirming the successful design of a time-reversal invariant PTI.

3. Discussion

A PTI consisting of a silicon membrane ($\epsilon_{\mathrm{r,Si,reduced}} = 9.61$) with air holes ($\epsilon_{\mathrm{r,air}} = 1$) is designed using the proposed

approach. Both PC phases are initiated from the structure shown in figure 2**A**, C_{6v}-symmetry is imposed on the PC unit cells, and the frequencies $\nu \in \{184\text{ THz}, 187\text{ Thz}\}$ are targeted in the design process. The two PC phases constituting the final PTI design are shown in figure 2**B**-2**C**.

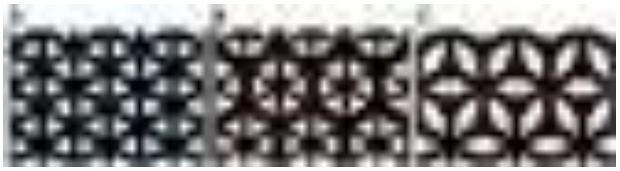


Figure 2: **(A)** Initial and **(B-C)** final distribution of Si (Black) and air (white) for the PCs constituting the PTI. The hexagonal unit cell is outlined in red.

In order to demonstrate the directional pseudo-spin dependent energy transport supported by the PTI, a chiral TE-polarized dipole source is placed at the interface between the two PC phases while varying the chirality from clockwise to counter-clockwise. The $\mathbf{H}_z$-component of the resulting field (shown for $|\mathbf{H}_z| > 0.05$) is plotted in figure 3**(A)** and 3**(B)**, respectively. It is clearly seen that the right-handed (left-handed) chirality excites the edge state with positive (negative) pseudo-spin travelling to the left (right).



Figure 3: **(A-B)** Chiral emission for **(A)** clockwise and **(B)** counter-clockwise excitation. Field propagation along the PTI interface **(C)** past four 120^{o} bends and **(D)** along a straight channel. The H_z-field component is shown for $\nu = 184$ Thz, overlaid on the PTI-structure.

A numerical demonstration of the back-scattering robustness offered by the PTI is shown in figures 3**C** and 3**D**. The former showing a field propagating along the PTI interface from left to right past four 120^{o} bends and the latter showing a field of equal amplitude propagating along a straight edge. From the figures it is seen that negligible back-scattering occur at the bends, in fact an energy loss of less than 0.07 dB per bend is computed. In a further set of calculations (not shown) we find that the relative bandgaps of the two crystal phases are 19% and 6% and we obtain a directional beta-factor $> 99\%$. [10]

4. Conclusion

A novel PTI is proposed and analysed along with the topology-optimization-based approach used in its design. The resulting structure features large bulk bandgaps, very low bending losses, and a very high degree of direction emission. The proposed design approach may be used to devise novel PTIs and/or to tailor them to maximize different figures of merit, such as operational bandwidth and/or energy transmission.

Acknowledgement

The authors acknowledge support from NATEC (NAnophotonics for Terabit Communications) Centre (Grant No. 8692) and the Villum Foundation Young Investigator Programme.

References

[1] L. Lu and J. D. Joannopoulos and M. Soljačić, Topological photonics *Nature photonics* 8:821-829, 2014

[2] A. B. Khanikaev and G. Shvets Two-dimensional topological photonics *Nature photonics* 11:763-773, 2017

[3] L.-H. Wu, and X. Hu, Scheme for Achieving a Topological Photonic Crystal by Using Dielectric Material, *Physical Review Letters* 114:223901, 2015

[4] S. Barik and H. Miyake and W. DeGottardi and E. Waks and M. Hafezi Two-dimensionally confined edge states in photonic crystals *New Journal of Physics* 18:113013, 2016

[5] T. Ma and G. Shvets, All-Si valley-Hall photonic topological insulator *New Journal of Physics* 18:025012, 2016

[6] M. P. Bendsøe and O. Sigmund, Topology Optimization, *Springer*, 2003

[7] R. E. Christiansen and F. Wang and O. Sigmund Topological Insulators by Topology Optimization *Submitted*, 2018

[8] J. S. Jensen and O. Sigmund, Topology optimization for nano-photonics, *Laser & Photonics Reviews* 5:308-321, 2011

[9] J.-P. Berenger, A Perfectly Matched Layer for the Absorption of Electromagnetic Waves, *Journal of Computational Physics* 114: 185–200, 1994.

[10] P. Lodahl and S. Mahmoodian and S. Stobbe and A. Rauschenbeutel and P. Schneeweiss and J. Volz and H. Pichler and P. Zoller, Chiral Quantum Optics, *Nature* 541:473, 2017

Optically Tunable Epsilon-Near-Zero Metamaterials

Surya Ayyagari, Alireza R. Rashed, Humeyra Caglayan *

Photonics Laboratory, Tampere University, 33720, Tampere, Finland
*Humeyra Caglayan, E-mail: humeyra.caglayan@tuni.fi

Abstract

In this study, we obtained epsilon-near-zero metamaterial at visible range by designing and fabricating a metal–dielectric multilayer anisotropic hyperbolic metamaterial. To do this, we experimentally characterize and extract the permittivity from the TMM (transfer matrix method). Later, we show by optically pumping with fs pulses at a proper wavelength the ENZ point of the structure alters, in comparison to the linear case. The change in the effective permittivity happens in the order of unity, leading to ultrafast light induced refractive index change.

1. Introduction

Optical metamaterials such as hyperbolic metamaterials (HMMs) have a unique property that exhibits high-k modes due to hyperbolic dispersion and the existence of epsilon-near-zero (ENZ) point in their electromagnetic spectral range. Beside the existence of ENZ point, HMMs can enhance the radiative recombination rate (spontaneous emission) of quantum emitters. Recently, people have investigated deeply the linear properties of ENZ metamaterials. Such investigations lead to achieve a broad range of applications such as novel waveguiding regimes and controlling the radiation pattern of electromagnetic sources [1-2]. In addition, the experimental evidences are presented for the role of ENZ metamaterials to affect the optical nonlinearity. Such affect demonstrates the efficient third harmonic generation and nonlinear Kerr index n_2 for TCO (transparent conductive oxides) materials and HMMs [3-5]. Our approach relies on modification of complex effective refractive index of the designed HMM in the visible spectral range which leads to the generation of the higher order nonlinear refractive index (Δn). Consequently, such modification in the effective refractive index changes the reflectance and transmittance properties.

2. Results

The HMM structure was fabricated on 0.5 mm (500 µm) thick substrate of fused silica (FS). The metal-dielectric stack (4 pairs of 16 nm thick Au and 32 nm thick TiO2) was deposited by using electron-beam deposition technique (see Figure 1). Deposition rate was kept below 0.2nm/sec for Au and below 0.16 nm/sec for TiO2 in order to achieve a homogenous surface of the layers.

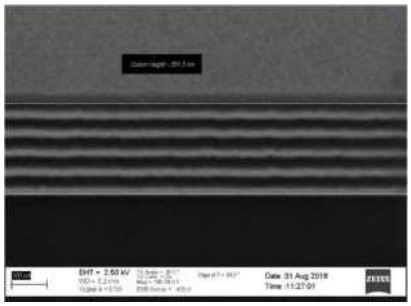


Figure 1: The SEM image of the fabricated sample showing the alternative layers of Au (16 nm) and TiO2 (32 nm).

Linear characterization

We have extracted the reflection and transmission properties of the designed HMM by using Transfer matrix method (TMM) as well as Lumerical FDTD software. Later, the linear optical properties of the fabricated HMM experimentally are investigated. The reflection and transmission measurements are done under a white lamp illumination and by using CCD spectrometer (Figure 2).

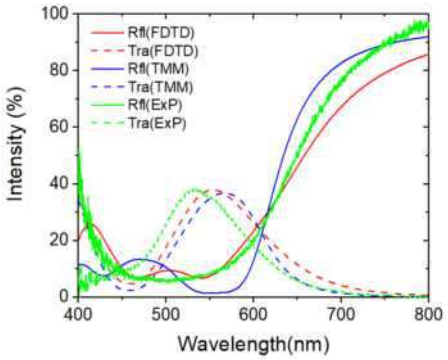


Figure 2: Comparison of reflectance and transmittance of HMM experiment (green), TMM (blue) and FDTD simulation (red).

Nonlinear characterization

In order to see the nonlinear response of the HMM, we have measured the change in reflectivity $\Delta R/R_{lin}$ (Figure 3) and transmissivity $\Delta T/T_{lin}$ (data not shown here) of the structure by optically inducing a pump signal. This characterization is done in a pump-probe spectroscopy system, in such a way that pump signal is fixed at a single wavelength with varied powers, while the broad band probe beam is varied temporally with respect to the pump beam.

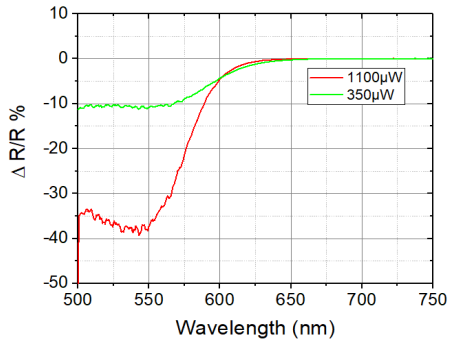


Figure 3: Nonlinear reflectivity (after pumping) as function of probe wavelength at 350μw and 1100μw with a fixed pump wavelength.

The pump-induced nonlinear refractive index change is given by $\Delta n = (n_{pump} - n_{lin}) \approx n_2 I$ [6], where I is the intensity of the optical pump and n_2 is the Kerr nonlinear refractive index. n_{pump} and n_{lin} stand for refractive index values after and before pumping, respectively. which are retrieved from the experimental data.

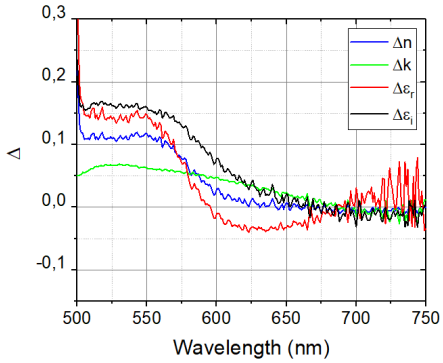


Figure 4: Change in the real part of nonlinear refractive index (red), imaginary part of nonlinear refractive index (green), real part of change in permittivity (red) and imaginary part of change in permittivity with respect to the linear case (non pumped).

3. Discussion

Figure 3 and 4 show evidently the modification of the reflectance and transmittance properties of the pumped structure, as a result of the effective refractive index change. Such change of the index refraction in turn is responsible for the modification of ENZ wavelength of the excited structure.

4. Conclusions

In this work, we have shown the ability to exploit the ENZ regime, for effectively tuning the optical properties of a metamaterial with simple design, operating in the visible range. The applied nonlinear change in the index of refraction leads to an ultrafast light induced metal to dielectric phase change at the ENZ region. The ability to access ultrafast light induced refractive index changes represents a new paradigm for the nonlinear optics.

Acknowledgements

This work is supported by "COMPETITIVE FUNDING TO STRENGTHEN UNIVERSITY RESEARCH PROFILES funded by Academy of Finland, decision number 301820".

References

[1] H Hajian, E Ozbay, H Caglayan "Beaming and enhanced transmission through a subwavelength aperture via epsilon-near-zero media" *Scientific reports,* 7.1 (2017):4741.

[2] Minn, Khant, et al. "Excitation of epsilon-near-zero resonance in ultra-thin indium tin oxide shell embedded nanostructured optical fiber." *Scientific reports* 8.1 (2018): 2342.

[3] Alam, M. Zahirul, Israel De Leon, and Robert W. Boyd. "Large optical nonlinearity of indium tin oxide in its epsilon-near-zero region." *Science* 352.6287 (2016): 795-797.

[4] Kaipurath, R. M., et al. "Optically induced metal-to-dielectric transition in Epsilon-Near-Zero metamaterials." *Scientific reports* 6 (2016): 27700.

[5] Caspani, Lucia, et al. "Enhanced nonlinear refractive index in ε-near-zero materials." *Physical review letters* 116.23 (2016): 233901.

[6] Boyd, Robert W. *Nonlinear optics*. Elsevier, 2003.

Experimental demonstration of topological photonic states based on composite left/right-handed coupled ring resonators

Zhiwei Guo, Yong Sun*, Haitao Jiang, and Hong Chen

MOE Key Laboratory of Advanced Micro-Structured Materials, School of Physics Science and Engineering, Tongji University, Shanghai, 200092, China
*corresponding author, E-mail: yongsun@tongji.edu.cn

Abstract

The array of two-dimensional coupled ring resonators is a typical system to realize the photonic and acoustic topological insulators with robust one-way transportation against defects and impurities. In this work, we theoretically propose and experimentally demonstrate the photonic analogue of quantum spin Hall effect in an improved broadband anomalous Floquet topological insulator in microwave regime, taking advantage of efficient and backward coupling between composite left/right-handed metamaterial rings resonators.

1. Introduction

Diversified coupled ring resonators (CRRs) arrays as suitable platforms for the study of topological photonic have been paid much attention. In these platforms, the roles of pseudo-spins with opposite directions are played by the clockwise and anti-clockwise propagations of the light [1]. Based on CRR arrays, the optimized topological optical devices with high-performance, such as delay lines, optical isolators, lase, have been proposed as the key components in optical communication systems. In particular, in 2013, Liang and Chong theoretically revealed that a lattice of optical ring resonators can exhibit a topological insulator phase even if all bands have zero Chern number [2]. Instead of delicately tuning the aperiodic couplings of the inter-resonators, this simplified structure is periodic because of the identical coupled ring resonators [2]. Inspired by this anomalous Floquet topological insulator, the topological edge states with T-symmetry have been experimentally measured by using a surface plasmon structure [3]. Furthermore, this novel topological edge mode also has been theoretically proposed [4] and experimentally demonstrated [5] in acoustic system. Nevertheless, it should be pointed out that the coupling between site rings in CRR array need be strong for the anomalous Floquet topological insulator. The widely used solution is to insert a coupler ring between two site rings. However, the strong coupling achieved in this way will rely on the resonance of the coupler ring, which severely limits the band width of the strong-coupling regime.

In this work, we propose a broadband anomalous Floquet topological insulator in microwave regime using a square array of metamaterial rings, and experimentally demonstrate the photonic analogue of QSHE. Different from the narrowband strong coupling relying on the resonance of the additional coupler ring, the broadband high efficient coupling is realized by utilizing a directional coupler made of the composite right/left-handed (CRLH) transmission line (TL) metamaterials. We construct a square array of CRRs with CRLH TL metamaterials, and measure the photonic topological edge states. In each individual ring resonator, the roles of opposite pseudo-spins are played by the clockwise and anti-clockwise propagations of the electromagnetic waves. It should be noted that the directional coupler inserted into the site rings supports the backward wave coupling. Therefore, the direction of energy flow in each ring is same for a given pseudo-spin state. We also investigate the robustness of edge states against a variety of perturbations. Our finding not only pave a new way to realize the broadband topological photonic device.

2. Band structure and the gapless edge modes in the topological structure

The scheme of our designed array of CRLH ring resonators is shown in Fig. 1. The size of our fabricated sample is 4×5 unit cells. Different from the previous schemes, every ring resonator in Fig. 1 belongs to the site ring except that two U-

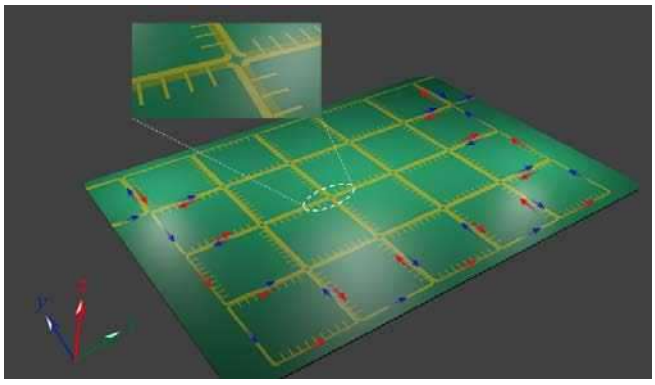


Figure 1: The schematic of CRLH ring resonators. The size of our fabricated sample is 4×5 unit cells. The right-handed material (simple line strips) and left-handed material (complex branched strips) connect successively in a ring structure.

shape waveguides play the roles of input and output ports, respectively. As an improved platform with backward coupling between the unit cells, the mediated coupler ring is not needed in the structure, as is shown in Fig. 1. In our proposed periodic rings array, there are two-fold degenerate modes in each resonator ring that correspond to a twofold pseudo-spin degree of freedom. By setting the position of input port, clockwise and anti-clockwise circulating photonic modes (e.g., two kinds of pseudo-spins) can be selectively excited along the opposite directions. In this work, we construct CRLH ring resonators based on TLs. TLs, as a good experimental platform, have been used to realize the effective medium with arbitrary parameters, quantum-optics-like systems and even the topological photonic structures. At first we use distributed composite CRLH TLs to design left-hand metamaterial with the negative refraction and backward wave-vector coupling. Next, the strong coupled ring resonators can be constructed by connecting left- and right-hand TLs in sequence. At last, the square array of CRLH coupled ring resonators can be established, as is schematically shown in Fig. 1.

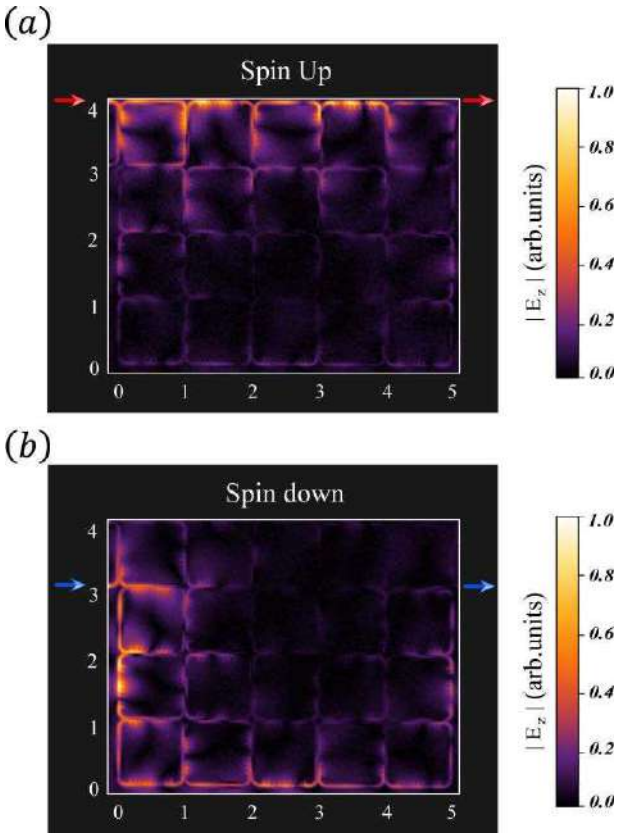


Figure 2: Measured 2D vertical electric field distributions of the one-way edge states at 2.56 GHz. The exciting position of the pseudo-spin-up (pseudo-spin-down) edge state is marked by the red (blue) arrow.

In the next we experimentally demonstrate the selectively excited pseudo-spin one-way edge states. We can find that the pseudo-spin-up edge state will propagate along the upper edge while the pseudo-spin-down edge state will propagate along the lower edge, as are shown in Fig. 2(a) and Fig. 2(b), respectively. The decay phenomenon of the topological edge states mainly comes from the absorption of the CRLH TLs.

3. Discussion

Our results pave a new way to realize the broadband topological photonic device with topological protection. Moreover, by using the mechanisms of multiple scattering in single negative metamaterials and effective negative coupling coefficient, our design also can be extended to higher frequencies and acoustics systems.

4. Conclusions

In conclusion, based on TLs, we propose an improved platform of photonic analogue of QSHE by using a square array of CRLH ring resonators, in which the mediated coupler ring is not needed and the topological edge state has a broadband property. Our experimental demonstration of the selectively excited one-way edge states will further enrich the design of anomalous Floquet topological insulator and may pave the way to design novel photonic topological devices.

Acknowledgements

This work is supported by the National Key Research Program of China (2016YFA0301101), National Natural Science Foundation of China (NSFC) (11674247, 61621001, 11504236, 11474220, 91850206 and 11774261); Shanghai Science and Technology Committee (17ZR1443800, 18ZR1442900, and 18JC1410900); and the Fundamental Research Funds for the Central Universities.

References

[1] M. Hafezi, E. A. Demler, M.D. Lukin, and J. M. Taylor, Robust optical delay lines with topological Protection, *Nat. Phys.* 7: 907, 2011.

[2] G. Q. Liang and Y. D. Chong, Optical resonator analog of a two-dimensional topological insulator, *Phys. Rev. Lett.* 110: 203904, 2013.

[3] F. Gao, Z. Gao, X. Shi, Z. Yang, X. Lin, J. D. Joannopoulos, M. Soljačić, H. Chen, L. Lu, Y. Chong, and B. Zhang, Probing the limits of topological protection in a designer surface plasmon structure, *Nat. Commun.* **7**: 11619, 2016.

[4] C. He, Z. Li, X. Ni, X. C. Sun, S. Y. Yu, M. H. Lu, X. P. Liu, and Y. F. Chen, Topological phononic states of underwater sound based on coupled ring resonators, *Appl. Phys. Lett.* 108: 031904, 2016.

[5] Y. G. Peng, C. Z. Qin, D. G. Zhao, Y. X. Shen, X. Y. Xu, M. Bao, H. Jia, and X. F. Zhu, Experimental demonstration of anomalous Floquet topological insulator for sound, *Nat. Commun.* 7: 13368, 2016.

Topological edge modes in all-dielectric kagome photonic crystals

Stephan Wong[1], Matthias Saba[2,3], Ortwin Hess[2], Sang Soon Oh[1*]

[1]School of Physics and Astronomy, Cardiff University, Cardiff CF24 3AA, United Kingdom
[2]The Blackett Laboratory, Department of Physics, Imperial College London, London SW7 2AZ, United Kingdom
[3]Adolphe Merkle Institute, University of Fribourg, Chemin des Verdiers 4, 1700 Fribourg, CH
*corresponding author, E-mail: OhS2@cardiff.ac.uk

Abstract

Photonic topological insulators are promising as a new photonic platform due to the unidirectional edge states insensitive to bendings and fabrication imperfections. A recently prososed all-dielectric perturbed honeycomb photonic crystal, however, intrinsically suffers from back-reflection due to the symmetry breaking at the interface. Here, we propose an all-dielectric photonic topogical insulator based on the kagome lattice geometry in which the topological edge modes do not undergo back reflection for termination along the Γ-K direction.

1. Introduction

Topological insulators (TI) enables a variety of exotic properties due to their correspondence between global, bulk properties of a material and their local properties at the egdes. This is known as the bulk-edge correspondance and it guarantees topologically protected edge modes at the interface between two topologically distinct materials with interesting features such as unidirectional propagation and robustness against bendings and fabrication imperfections. The photonic counterpart, known as photonic topological insulator (PTI) [1], is even more promising for real-life applications because it is easier to study and design.

Many different topologically non-trivial photonic designs have been proposed using non-reciprocal systems [2], complex metamaterials [3], etc. However, most of the PTIs are either complicated to fabricate or require strong magnetic fields. Recently, a deformed honeycomb-based topological photonic crystal (PhC) [4] that emulates the quantum spin Hall effect (QSHE) has gained interest due to its simplicity of fabrication compared to other PTIs. However the time-reversal anti-unitary operator $\mathcal{T}^2 = -\mathbb{1}$, which is required for well-defined orthogonal spin up/down channels, is constructed on the basis of the six-fold rotation (C_6) operator of the crystal. Therefore the edge modes intrisically suffer from back reflection due to the crystallographic symmetry breaking at the interface which leads to the coupling of the two spin channels showing an anti-crossing behaviour in their dispersion.

In this paper, we propose an all-dielectric PTI which is a deformed kagome-based [5] photonic crystal composed of dielectric rods. The proposed design emulates the so-called quantum valley Hall effect (QVHE) [6] and exhibits edge modes which do not intrisically suffer from backscattering at the interface but instead are sensitive to its termination.

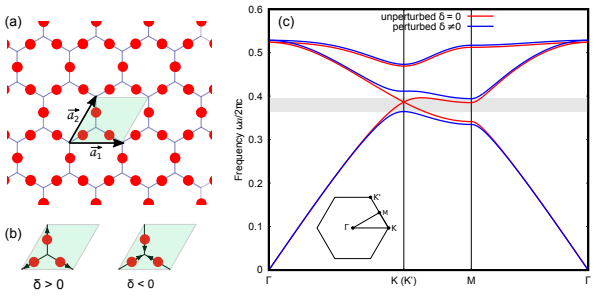


Figure 1: (a) Schematic of a kagome lattice. (b) The arrows denote the perturbation generated by shifting the rods away (left) or closer (right) to each other. (c) Band structure of the kagome lattice for the unperturbed (solid red line) and perturbed (solid blue line) cases with the lattice constant $a = 1\mu m$, rod diameter $d = 0.1a$ and permittivity $\varepsilon = 12$.

2. Results

Figure 1(a) shows the proposed kagome-like photonic crystal with the rod on the middle of the edges of the hexagons. Due to the hexagonal symmetry, its corresponding photonic band structure has a linear degeneracy at the K an K′ points (Fig. 1(c)). We consider transverse magnetic (TM) poarlization which has the magnetic field components in the 2D plane. The unit cell is composed of three rods and the geometric perturbation to lift the degeneracy is such that the rods get closer (negative perturbation $\delta < 0$) or away (positive perturbation $\delta > 0$) starting from their shared corner of the hexagons (see Fig. 1(b)): $\mathbf{r}' = (1 \pm \delta)\mathbf{r}$ where $\mathbf{r}$ is a vector taken from the corner of hexagon to the adjacent rod. Applying the methodology detailed in [7] to the hexagonal space group, i.e. the plane group $p6mm$ (17), one gets the corresponding effective Hamiltonian:

$$\mathcal{H}_{\text{kagome}} = \begin{pmatrix} \mathcal{W}_K & 0 \\ 0 & \mathcal{W}_{K'} \end{pmatrix} \tag{1}$$

where $\mathcal{W}_{K/K'} = \pm \boldsymbol{h} \cdot \boldsymbol{\sigma}$ are the Weyl Hamiltonians close to the K/K′ point $(\delta k_x, \delta k_y)$ with $\boldsymbol{h} = (-\delta k_y, \delta, \delta k_x)$ and $\boldsymbol{\sigma} = (\sigma_1, \sigma_2, \sigma_3)$ the Pauli matrix vector. The conservation of translation symmetry with the geometric perturbation,

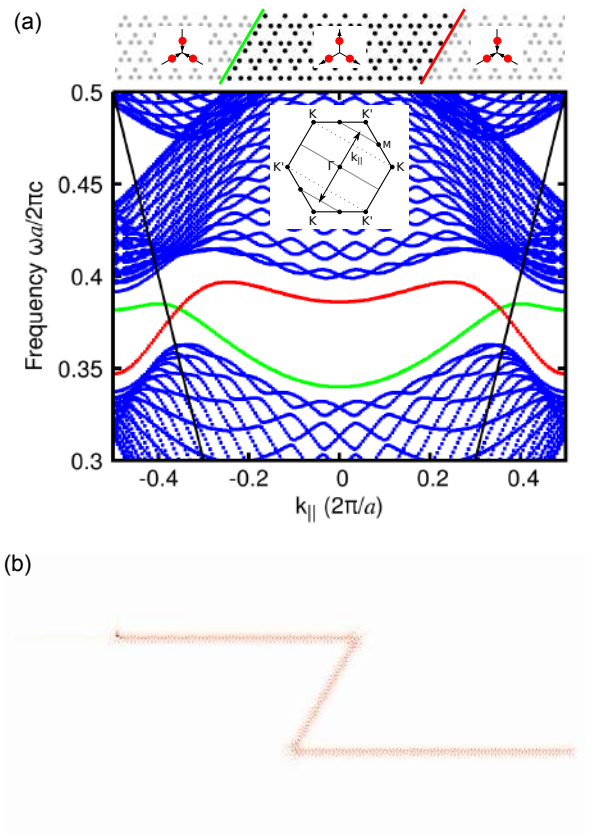


Figure 2: (a) Projected band structure for the interface between two topologically distinct kagome photonic crystals ($\delta = \pm 0.15$) along Γ-K termination. Inset shows the $k_{\|}$ sweep direction. (b) Power profile for the edge modes excited in the Z-shaped bending structure.

i.e. the lattice constant remains the same, leads to distinct and well-defined K and K′ point which was not the case for the perturbed honeycomb case [4]. More importantly, it gives an effective Hamiltonian which is necessarily block-diagonalizeed in two Weyl Hamiltonians (see Eq. (1)) in the same way as in the Kane-Mele Hamiltonian. One can therefore infer that the K (K′) point plays the role of some pseudo-spin up (down) channels, known as the valley degree of freedom.

As a consequence, at the interface, where the C_{6v} is broken, as long as the K and K′ points remain distinct, there is no coupling between the two pseudo-spin channels. From the expression of the kagome Hamiltonian $\mathcal{H}_{\text{kagome}}$, it becomes evident that a non-trivial Weyl charge is located at the K and K′ points and will be opposite because $\mathcal{W}_K = -\mathcal{W}_{K'}$. Additionally the Weyl charge at the K (or K′) will be opposite for opposite perturbations. This gives opposite valley Chern number for opposite perturbation. As a consequence of the bulk-boundary correspondence, edge modes are guaranteed at the interface between two joined kagome photonic crystals with opposite perturbations. Figure 2(a) shows the supercell band strucutre for a termination along the Γ-K direction. Because K and K′ are not projected on the same point along the $k_{\|}$ line, there is no intervalley coupling, leading to a crossing for the edge mode dispersion. Furthermore, for the case of a Γ-K termination, edge modes lie close to or below the light line, thus improving mode confinement to the fabricated surface substantially without the need of sub- and superstrate mirrors.

Figure 2(b) shows the power profile propagation along the interface of the type denoted by red lines in Fig. 2(a) with two bendings. Since the termination keeps Γ-K direction, the light propapagtes without back reflection for a finite wavelength range where the edge modes exist.

3. Conclusions

In summary, we have introduced a new kagome-like photonic topogical insulator which does not suffer from backscattering at the interface but instead depends on its termination. We showed the crossing behaviour of the edge modes using the band calculations for Γ-K termination directions, and have demonstrated the possibility of achieving vertical confinment due to edge modes below the light line.

Acknowledgement

This work is part-funded by the European Regional Development Fund through the Welsh Government.

References

[1] L. Lu, J. D. Joannopoulos, and M. Soljačić, "Topological photonics," *Nature Photonics*, vol. 8, no. 11, pp. 821–829, oct 2014.

[2] F. D. M. Haldane and S. Raghu, "Possible realization of directional optical waveguides in photonic crystals with broken time-reversal symmetry," *Physical Review Letters*, vol. 100, no. 1, pp. 1–4, 2008.

[3] A. B. Khanikaev, S. H. Mousavi, W.-K. Tse, M. Kargarian, A. H. MacDonald, and G. Shvets, "Photonic topological insulators." *Nature materials*, vol. 12, no. 3, pp. 233–9, mar 2013.

[4] L.-H. Wu and X. Hu, "Scheme for Achieving a Topological Photonic Crystal by Using Dielectric Material," *Physical Review Letters*, vol. 114, no. 22, p. 223901, 2015.

[5] M. Mekata, "Kagome: The story of the basketweave lattice [1]," *Physics Today*, vol. 56, no. 2, pp. 12–13, 2003.

[6] K. Qian, D. J. Apigo, C. Prodan, Y. Barlas, and E. Prodan, "Topology of the valley-Chern effect," *Physical Review B*, vol. 98, no. 15, p. 155138, 2018.

[7] M. Saba, J. M. Hamm, J. J. Baumberg, and O. Hess, "Group Theoretical Route to Deterministic Weyl Points in Chiral Photonic Lattices," *Physical Review Letters*, vol. 119, no. 22, p. 227401, nov 2017.

Approaching the fundamental limits of heat transfer at the nanoscale: the surprisingly limited role of inverse design

Prashanth Venkataram, Sean Molesky, Weiliang Jin, and Alejandro W. Rodriguez
Department of Electrical Engineering, Princeton University

Radiative heat exchanged between bodies at the nanoscale can surpass blackbody limits on thermal radiation by orders of magnitude due to contributions from evanescent electromagnetic fields, which carry no energy to the far-field. Such super-Planckian emission is known to depend strongly on both material and geometric properties. However, the relative importance and interplay of these two facets and their fundamental limitations remain open questions. While guiding principles have thus far assumed utility in the possibility of improvements (beyond planar media) through nanoscale texturing, thus far trial-and-error explorations and large-scale optimization procedures have failed to surpass the performance of ideal (unstructured) metals [1–3]. In this talk, I will present fundamental limits to near-field radiative heat transfer in resonant media [4]. We will show that at any given wavelength, multiple scattering between proximate bodies severely limits the marginal utility of nanoscale texturing for the purpose of enhancing near-field heat transfer, beyond shifting the resonant response of bulk materials to selective wavelengths. While compact bodies can benefit from stronger material response (larger indices of refraction and smaller losses) up to a size-dependent threshold, leaving room for applications of inverse design to discover optimal geometries, the near-field heat transfer between extended structures is shown to scale very weakly (logarithmically) with increased material response, and to be practically reached by planar materials at the surface polariton condition. The existence of tight bounds for heat transfer has ramifications for the performance of thermophotovoltaics, nanoscale cooling, and other thermal devices operating in the near field [5].

[1] W. Jin, R. Messina, and A. Rodriguez. “Overcoming limits to near-field radiative heat transfer in uniform planar media through multilayer optimization”. Optics Express, 25(13):293277, 2017.
[2] Weiliang Jin, S. Molesky, Z. Lin, and A. W. Rodriguez. “Material scaling and frequency-selective enhancement of near-field radiative heat transfer for lossy metals in two dimensions via inverse design”. Physical Review B (Rapid Comm.), 99:041403, 2019.
[3] Sean Molesky, Zin Lin, Weiliang Jin, Alexander Piggott, Jelena Vuckovic, and Alejandro W. Rodriguez. “Inverse Design in Nanophotonics”. Nature Photonics, 12 659-670, 2018
[4] Prashanth S. Venkataram and Alejandro W. Rodriguez. “Fundamental limits to near-field radiative heat transfer and the limited role of nanostructuring”. arXiv:1903.07968, 2019.
[5] Bai Song, Anthony Fiorino, Edgar Meyhofer, and Pramod Reddy. “Near-field radiative thermal transport: From theory to experiment”. AIP Advances 5, 053503, 2015.

Topology Optimization of Photonic Crystals and Large-area Metasurfaces

Zin Lin[1] and Steven G. Johnson[1]

[1] Department of Mathematics, Massachusetts Institute of Technology, 77 Massachusetts Avenue, Cambridge MA 02138, USA
*corresponding author, E-mail: zinlin@mit.edu

Summary

Recent developments in computational freeform inverse design [1] have provided a fertile landscape of structures and topologies for nanophotonics. However, simply dumping millions of parameters into a simulation can easily lead to intractable computational problems. Fortunately, a given engineering problem often admits many different mathematical formulations, and by carefully matching the formulation to the available electromagnetic solvers and optimization algorithms one can set the stage for extraordinarily flexible automated design. In this talk, we will show that, with careful consideration and reformulation of the design problem, powerful inverse design techniques can be successfully applied to a multitude of interesting problems ranging from designing exotic spectral features in photonic crystals [2,3] to beam-forming and manipulation through multi-layered metasurfaces [4,5].

Acknowledgements

U. S. Army Research Office through the Institute for Soldier Nanotechnologies (W911NF-13-D-0001)

References

[1] Molesky, S., Lin, Z., Piggott, A. Y., Jin, W., Vucković, J., & Rodriguez, A. W. (2018). Inverse design in nanophotonics. *Nature Photonics*, *12*(11), 659.

[2] Lin, Z., Pick, A., Lončar, M., & Rodriguez, A. W. (2016). Enhanced spontaneous emission at third-order Dirac exceptional points in inverse-designed photonic crystals. *Physical review letters*, *117*(10), 107402.

[3] Lin, Z., Christakis, L., Li, Y., Mazur, E., Rodriguez, A. W., & Lončar, M. (2018). Topology-optimized dual-polarization Dirac cones. *Physical Review B*, *97*(8), 081408.

[4] Lin, Z., Groever, B., Capasso, F., Rodriguez, A. W., & Lončar, M. (2018). Topology-optimized multilayered metaoptics. *Physical Review Applied*, *9*(4), 044030.

[5] Lin, Z., Liu, V., Pestourie, R., & Johnson, S. G. (2019). Topology optimization of freeform large-area metasurfaces. *arXiv preprint arXiv:1902.03179*.

Optimal metasurfaces: Theory and inverse design

Owen D. Miller[a]

[a]Department of Applied Physics and Energy Sciences Institute, Yale University, New Haven, Connecticut 06511, USA

ABSTRACT

We use two approaches to design best-in-class metasurfaces: large-scale computational optimization, i.e. "inverse design," to find optimal configurations of thousands of geometrical degrees of freedom, and analytical bounds, to discover fundamental limits that cannot be exceeded. The two ideas work in tandem: analytical bounds suggest areas ripe for orders-of-magnitude improvement, while computational design can identify structures exhibiting such improvements. In the area of optical superresolution, where one wants to created sub-diffraction-limited optical beams with maximal intensity, we develop a quadratic-programming framework and analytical expressions for the maximum intensity of any sub-diffraction-limited optical beam, and we use inverse design to discover metasurface structures operating close to these limits. Conversely, in the realm of broadband metasurface lenses, where no such bounds are known, we use inverse design to discover high-numerical-aperture, high-efficiency, broad-bandwidth metalenses.

1. SUPERRESOLUTION

Free-space optical beams with large focal-point intensities and arbitrarily small spot sizes are a long-sought goal[1–3] for applications from imaging[4–8] to 3D printing,[9,10] for which nanostructured lenses have enabled recent experimental breakthroughs.[11,12] Here, we derive fundamental limits to free-space optical-beam concentration, revealing the maximum possible focal-point intensity (related to the well-known "Strehl ratio"[13,14]) for any desired spot size. For waves incident from any region of space—generated by scattering structures, spatial light modulators, or light sources of arbitrary complexity—we show that the non-convex beam-concentration problem can be transformed to a quadratic program[15] with easily computable global optima. By honing in on the two essential degrees of freedom—the field intensity at the focal point, and its average over a ring at the desired spot size—optimal beam concentration can be further simplified to a rank-two optimization, resulting in *analytical* upper bounds in the far zone. For very small spot sizes G, which are most desirable for transformative applications, we show that the focal-point intensity must decrease proportional to G^4, a scaling within the exact bounds that cannot be overcome through any form of wavefront engineering. The bounds have an intuitive interpretation: the ideal field profile at the exit surface of an optical beam-shaping device must have maximum overlap with the fields radiating from a dipole at the origin yet be orthogonal to the fields emanating from a current loop at the spot size radius. We compare theoretical proposals and experimental demonstrations to our bounds, and we find that there is significant opportunity for order-of-magnitude intensity enhancements at those small spot sizes. We use "inverse design",[16–19] a large-scale computational-optimization technique, to design metasurfaces that generate nearly optimal wavefronts and closely approach our general bounds.

Consider a beam generated by almost any means. The physics underlying the extent to which such a beam is concentrated spatially in free space is distilled to its essence by the electromagnetic equivalence principle:[20] the (arbitrarily complex) interactions in the beam-generation process can be replaced by appropriate effective currents on a closed surface in free space. By this principle, the beam-generation problem is equivalent to asking: what is the maximum spatial concentration of a beam generated by electric and magnetic surface currents radiating in free space? We consider fields and currents at a single temporal frequency ω ($e^{-i\omega t}$ time evolution), and simplify

Further author information: (Send correspondence to O.D.M.)
O.D.M.: E-mail: owen.miller@yale.edu

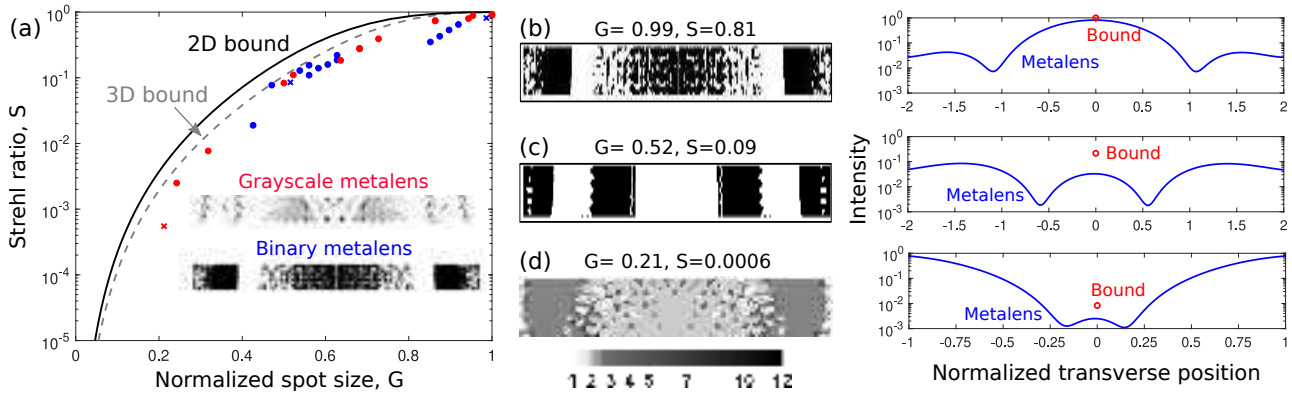


Figure 1. Inverse design of metasurfaces operating near the fundamental limits to sub-diffraction-limited optical beams.

the expressions to follow by encapsulating the electric and magnetic fields ($\mathbf{E}$, $\mathbf{H}$) and currents ($\mathbf{K}_{\text{eff}}$, $\mathbf{N}_{\text{eff}}$) in 6-vectors ψ and ξ, respectively:

$$\psi = \begin{pmatrix} \mathbf{E} \\ \mathbf{H} \end{pmatrix}, \quad \xi = \begin{pmatrix} \mathbf{K}_{\text{eff}} \\ \mathbf{N}_{\text{eff}} \end{pmatrix}. \tag{1}$$

The fields ψ emanating from the effective currents ξ distributed across the "exit" surface A are given by the convolution of the currents with $\mathbf{\Gamma}$, the 6×6 free-space dyadic Green's function: $\psi(\mathbf{x}) = \int_A \mathbf{\Gamma}(\mathbf{x}, \mathbf{x}')\xi(\mathbf{x}')$. Thus, the currents comprise the degrees of freedom determining the beam shape, and finding the maximum focal intensity at a single point for any desired focal spot size now reduces to determining the optimal effective currents. We will assume the underlying equations can be solved by any standard electromagnetic discretization scheme,[21] and we will write the matrix versions with the same symbols but without position arguments. For example, $\psi = \mathbf{\Gamma}\xi$ is the matrix equivalent of the Green's-function convolution, with ψ and ξ vectors and $\mathbf{\Gamma}$ a matrix. The total intensity at any point in free space, summing electric and magnetic contributions, is given by the squared norm of ψ:

$$\begin{aligned} I(\mathbf{x}) = |\psi(\mathbf{x})|^2 &= \int_A \int_A \xi^\dagger(\mathbf{x}'')\mathbf{\Gamma}^\dagger(\mathbf{x}, \mathbf{x}'')\mathbf{\Gamma}(\mathbf{x}, \mathbf{x}')\xi(\mathbf{x}') \\ &= \xi^\dagger \mathbf{\Gamma}^\dagger \mathbf{\Gamma} \xi. \end{aligned} \tag{2}$$

We now formulate the maximal-concentration question as a constrained optimization problem. The ideal optical beam has maximum focal intensity at a point (set at $\mathbf{x} = 0$), zero field along some spot-size contour $\mathcal{C}$, and a total propagating power P not exceeding an input value of P_0. Thus, the maximum focal intensity, and the ideal effective currents generating it, solve the optimization problem:

$$\begin{aligned} \underset{\xi}{\text{maximize}} \quad & I(\mathbf{x} = 0) = \xi^\dagger \mathbf{\Gamma}_0^\dagger \mathbf{\Gamma}_0 \xi \\ \text{subject to} \quad & \psi(\mathbf{x})\big|_{\mathcal{C}} = \mathbf{\Gamma}_{\mathcal{C}} \xi = 0 \quad \text{and} \quad P \le P_0, \end{aligned} \tag{3}$$

where the "0" and $\mathcal{C}$ subscripts indicate whether $\mathbf{\Gamma}$ and ψ are evaluated (in the appropriate basis) at the origin or at the spot-size contour, respectively. Attempting to directly solve Eq. (3) is infeasible: the $\mathbf{\Gamma}_0^\dagger \mathbf{\Gamma}_0$ matrix is positive semidefinite (which is nonconvex under maximization[22]), the equality constraint prevents the use of Rayleigh-quotient-based approaches,[23] and the power constraint is difficult to write in a simple linear or quadratic form.

We will not work through the detailed derivation of the following results, but we will note that the nonconvexity of the problem can be bypassed through multiple transformations. The results of those transformations are the following bounds. The general bound, which actual applies in any medium, in the near-field/near-zone/far-zone/etc., is:

$$I \le \mu^\dagger \left[\mathbf{\Gamma}_0 \mathbf{\Gamma}_0^\dagger - \mathbf{\Gamma}_0 \mathbf{\Gamma}_{\mathcal{C}}^\dagger \left(\mathbf{\Gamma}_{\mathcal{C}} \mathbf{\Gamma}_{\mathcal{C}}^\dagger \right)^{-1} \mathbf{\Gamma}_{\mathcal{C}} \mathbf{\Gamma}_0^\dagger \right] \mu, \tag{4}$$

where $\mathbf{\Gamma}_0$ is the Green's function from the exit surface to the focal point, $\mathbf{\Gamma}_\mathcal{C}$ is the Green's function evaluated over the contour in space where the field should be zero, and μ is the polarization vector of the optimal field at the focal point. Equation (4) represents a key theoretical result of our work. Although it may have an abstract appearance, it is a decisive global bound to the optimization problem, requiring only evaluation of the known free-space dyadic Green's function at the maximum-intensity point, the zero-field contour, and the effective-current exit surface. The matrix in the square brackets is a 6×6 matrix, whose largest eigenvector represents the optimal polarization. And the structure of Eq. (4) has simple physical intuition: the maximum intensity of an unconstrained beam would simply focus as much of the effective-current radiation to the origin, as dictated by $\mathbf{\Gamma}_0\mathbf{\Gamma}_0^\dagger$, but the constraint required zero field on $\mathcal{C}$ necessarily reduces the intensity by an amount proportional to the projection of the spot-size field ($\mathbf{\Gamma}_\mathcal{C}$) on the field at the origin ($\mathbf{\Gamma}_0$).

Figure 1 depicts the results of many design optimizations. Figure 1(a) compares unique optimal designs at spot sizes ranging from 1 down to 0.21 to the bounds described above; strikingly, the designed metalenses closely approach the bound for all spot sizes, with the best designs achieving 90% of the maximum possible intensity. In Fig. 1(b) three specific designs are shown alongside the resulting field profiles in their focal planes. The intensity does not perfectly reach zero but is forced to be significantly smaller than the peak intensity through a penalty constant. It is difficult to explain exactly how the computationally designed metasurface patterns achieve nearly optimal focusing; for spot sizes close to 1, the variations in material density suggest an effective gradient-index-like profile that offers lens-like phase variations across the device width, though the scattering effects of the front and rear surfaces renders such explanations necessarily incomplete. The depicted design with $G = 0.21$ exhibits to our knowledge the smallest spot size of any theoretical proposal to date.

REFERENCES

[1] McCutchen, C. W., "Superresolution in Microscopy and the Abbe Resolution Limit," *Journal of the Optical Society of America* **57**(10), 1190–1192 (1967).

[2] Stelzer, E. H. K., "Beyond the diffraction limit?," *Nature* **417**, 806–807 (jun 2002).

[3] Zheludev, N. I., "What diffraction limit?," *Nature Materials* **7**(6), 420–422 (2008).

[4] Gustafsson, M. G. L., "Nonlinear structured-illumination microscopy: Wide-field fluorescence imaging with theoretically unlimited resolution," *Proceedings of the National Academy of Sciences* **102**(37), 13081–13086 (2005).

[5] Betzig, E., Patterson, G. H., Sougrat, R., Lindwasser, O. W., Olenych, S., Bonifacino, J. S., Davidson, M. W., Lippincott-Schwartz, J., and Hess, H. F., "Imaging Intracellular Fluorescent Proteins at Nanometer Resolution," *Science* **313**, 1642–1645 (sep 2006).

[6] Rust, M. J., Bates, M., and Zhuang, X., "Sub-diffraction-limit imaging by stochastic optical reconstruction microscopy (STORM)," *Nature Methods* **3**(10), 793–795 (2006).

[7] Hell, S. W., "Far-field optical nanoscopy," *Science* **316**(5828), 1153–1158 (2007).

[8] Huang, B., Wang, W., Bates, M., and Zhuang, X., "Three-Dimensional Super-Resolution Imaging by Stochastic Optical Reconstruction Microscopy," *Science* **319**(5864), 810–813 (2008).

[9] Lipson, H. and Kurman, M., [*Fabricated: The new world of 3D printing*], John Wiley & Sons (2013).

[10] Chia, H. N. and Wu, B. M., "Recent advances in 3D printing of biomaterials," *Journal of Biological Engineering* **9**(1), 4 (2015).

[11] Huang, F. M. and Zheludev, N. I., "Super-resolution without evanescent waves," *Nano Letters* **9**(3), 1249–1254 (2009).

[12] Rogers, E. T., Lindberg, J., Roy, T., Savo, S., Chad, J. E., Dennis, M. R., and Zheludev, N. I., "A super-oscillatory lens optical microscope for subwavelength imaging," *Nature Materials* **11**(5), 432–435 (2012).

[13] Strehl, K., "Über luftschlieren und zonenfehler," *Zeitschrift für Instrumentenkunde* **22**, 213–217 (1902).

[14] Born, M. and Wolf, E., [*Principles of optics: electromagnetic theory of propagation, interference and diffraction of light*], Elsevier (2013).

[15] Bertsekas, D. P., [*Nonlinear programming*], Athena Scientific, Belmont, MA, 3rd ed. (2016).

[16] Jensen, J. S. and Sigmund, O., "Topology optimization for nano-photonics," *Laser and Photonics Reviews* **5**(2), 308–321 (2011).

[17] Miller, O. D., *Photonic Design: From Fundamental Solar Cell Physics to Computational Inverse Design*, PhD thesis, University of California, Berkeley (2012).

[18] Bendsoe, M. P. and Sigmund, O., [*Topology optimization: theory, methods, and applications*], Springer Science & Business Media (2013).

[19] Molesky, S., Lin, Z., Piggott, A. Y., Jin, W., Vucković, J., and Rodriguez, A. W., "Inverse design in nanophotonics," *Nature Photonics* **12**, 659–670 (nov 2018).

[20] Kong, J. A., [*Theory of electromagnetic waves*], Wiley-Interscience, New York (1975).

[21] Jin, J.-M., [*Theory and computation of electromagnetic fields*], John Wiley & Sons (2011).

[22] Boyd, S. and Vandenberghe, L., [*Convex optimization*], Cambridge university press (2004).

[23] Horn, R. A. and Johnson, C. R., [*Matrix analysis*], Cambridge university press, 2nd ed. (2013).

Modelling, simulation and optimization of metasurfaces

Designing nanophotonic structures using conditional-deep convolutional generative adversarial network

Sunae So[1], and Junsuk Rho[1,2,*]

[1]Department of Mechanical Engineering, Pohang University of Science and Technology (POSTECH), Pohang 37673, Republic of Korea
[2]2Department of Chemical Engineering, Pohang University of Science and Technology (POSTECH),Pohang 37673, Republic of Korea
*corresponding author, E-mail: jsrho@postech.ac.kr

Abstract

A data-driven design approach based on deep-learning is introduced in nanophotonics to reduce time-consuming iterative simulations. We report the first use of conditional deep convolutional generative adversarial network to design nanophotonic antennae that are not constrained to a predefined shape. For given input reflection spectra, the network provides desirable designs in the form of images. Numerical simulation results obtained from the generated designs agree well with the input reflection spectrum. The results provide a noteworthy contribution in nanophotonics.

1. Introduction

Recently, data-driven design approaches have been proposed to replace a time-consuming iterative optimization method on designing nanophotonic structures [1, 2]. These approaches use artificial neural networks(NNs) to design nanophotonic structures. Previous studies first set the shape, such as multilayers [1] or H-antenna [2] of structures to be predicted, then trained NNs to provide output structural parameters that achieve desired optical properties. Once the NNs are trained, they provide the corresponding design parameters without additional iterative simulations. Such attempts have greatly reduced the effort and computational costs of designing nanophotonic structures. So far, these approaches have only been applied to conditions in which basic structures are predefined where only structural parameters are predictable[3].

Here, we provide the first use of conditional deep convolutional generative adversarial network (cDCGAN) [4] to design nanophotonic structures [5]. cDCGAN is recently developed algorithm to solve the instability problem of GAN, which provides much stable Nash equilibrium solution. The generated designs are presented as images, so they provide essentially arbitrary possible design for desired optical properties which are not limited to specific structures. Our research provides designs of a $64 \times 64 -$ pixels probability distribution function (PDF) in a domain size of 500 nm $\times$ 500 nm, which allows $2^{64\times64}$ degrees of freedom of design.

2. Results and Discussion

2.1. Deep-learning procedure

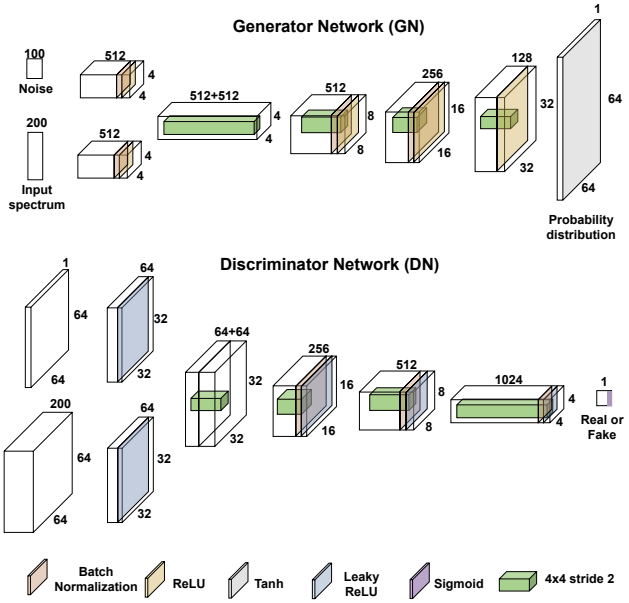


Figure 1: Schematic of the cDCGAN architecture to suggest designs of structures. GN is composed of a transposed CNN to generate structural images, and DN consists of conventional CNN to distinguish real designs from generated designs. Each layer introduces nonlinear activation functions (ReLU, Tanh, Leaky ReLU and Sigmoid) according to the guideline of Radford et al [4].

We implement cDCGAN algorithm using Pytorch framework. The cDCGAN architecture to design nanophotonic structures is presented in Figure 1. A generator network (GN) is composed of four transposed convolutional neural networks (CNNs) layers that consist of 1024, 512, 256, 128, and 1 channel, respectively; a discriminator network (DN) is a convolutional neural network with four hidden layers. GN takes inputs both the 100×1 size random noise (z) which generates appropriate design images, and the 200×1 size input spectrum which directs to generate a design that satisfies the condition. GN generates a design on a $64 \times 64 -$ pixels probability distribution function (PDF) in a 500 nm $\times$ 500 nm physical domain. The gener-

ated design is again fed into DN to be discriminated from ground-truth designs. GN is trained to generate a superficial authentic design to deceive DN, and DN is trained to distinguish ground-truth designs from the design generated by GN.

2.2. Network Evaluation

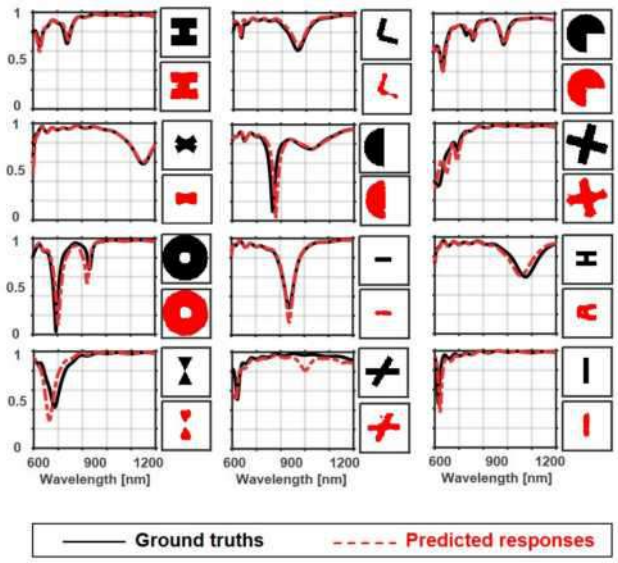


Figure 2: 12 examples of cDCGAN suggested images and their simulation results. Each panel is composed of reflection spectra and their corresponding structural cross-sectional images. The upper-right structural images are ground-truth designs (black) and the lower-right images are suggested images by cDCGAN (red). The left spectra show desired input spectra (black solid lines) that we fed into the network and predicted responses obtained from the suggested designs (red dotted lines).

The trained cDCGAN is evaluated on test data that were not used in previous training or validation steps. The randomly chosen test results are shown in Figure 2. Ground-truth designs of various nanophotonic antennae (upper-right panel in Figure 2 and corresponding suggested PDFs (lower-right panel in Figure 2) show good qualitative agreement. For the quantitative evaluation of the suggested PDFs, FDTD simulation based on those suggested designs are conducted. The PDFs were converted to binary designs to be imported into the simulations. Reflection spectra of the suggested images agree well with given input spectra. We introduce a mean absolute error (MAE) criterion,

$$l_{\text{error}} = \frac{1}{n}\sum_{i=1}^{n}|Y_i - \hat{Y}_i| \quad (1)$$

to quantitatively measure the accuracy of the model by comparing the predicted response with ground truth of input spectrum. The average MAE error of 12 test samples is 0.0322, which supports that the trained network can essentially provide appropriate structural design that has desired reflection spectrum.

3. Conclusion

This study demonstrates the first use of a cDCGAN to design nanophotonic structures. The two networks of GN and DN in cDCGAN competitively learn to suggest appropriate designs of nanophotonic structures that have desired optical properties of reflection. Our cDCGAN is not limited to suggesting predefined structures, but can also generate new designs. It has numerous design possibility with $2^{64\times64} = 2^{4096}$ degrees of freedom. Although our examples set the thickness of each layers and the material type of antenna, they can also be added as output parameters to be suggested. This modification would allow artificial intelligence to be used to design nanophotonic devices completely independently, and would thereby greatly reduce the time and computational cost of designing them manually. We believe that our research findings will lead to rapid development of nanophotonics by solving the main problem of designing structures.

Acknowledgement

S.S acknowledges global Ph.D fellowship (NRF-2017H1A2A1043322) from the NRF-MSIT, Korea.

References

[1] D. Liu, Y. Tan, E. Khoram, Z. Yu, Training deep neural networks for the inverse design of nanophotonic structures, *ACS Photonics* 5: 1365–1369, 2018.

[2] I. Malkiel, A. Nagler, M. Mrejen, U. Arieli, L. Wolf, H. Suchowski, Plasmonic nanostructure design and characterization via Deep Learning, *Light: Sci. Appl.* 7: 60, 2018.

[3] Z. Liu, D. Zhu, S. Rodrigues, K.T. Lee, W. Cai, A generative model for the inverse design of metasurfaces, *Nano Lett.* 18: 6570-6576, 2018.

[4] A. Radford, L. Metz, S. Chintala, Unsupervised representation learning with deep convolutional generative adversarial networks, *arXiv preprint* arXiv:1511.06434, 2015.

[5] S. So, J. Rho, Designing nanophotonic structures using conditional-deep convolutional generative adversarial network, *in review*.

Generalized Brewster conditions and bound states in the continuum in metal and all-dielectric metasurfaces through a coupled electric/magnetic dipole model

D. R. Abujetas[1], J. J. Senz[2], J. A. Sánchez-Gil[1,*]

[1]Instituto de Estructura de la Materia (IEM-CSIC), Consejo Superior de Investigaciones Científicas, Madrid, Spain
[2]Donostia International Physics Center, Donostia, Spain
*corresponding author, E-mail: j.sanchez@csic.es

Abstract

We derive a coupled electric and magnetic dipole (iCEMD) theoretical formulation to describe the optical properties of a periodic array consisting of one/several electric/magnetic dipoles per unit cell. In the case of high refractive index cylinders described by their lowest-order Mie resonances, this formulation yields analytical expressions for the reflectance and transmittance. In this regard, we show that although a zero back-scattering condition can never be achieved for individual cylinders, when they are arranged in a periodic array their mutual interaction leads to a generalized Brewster effect in such a nanorod-based metasurface. We also exploit this formulation to investigate symmetry-protected bound states in the continuum in arrays of dimers consisting of detuned resonant dipoles. Indeed, we demonstrate analytically that robust BICs emerge from Fano resonances when dipole detuning vanishes, as a universal behavior occurring regardless of dipole position within the unit cell. We also propose a scheme to engineer angularly-selective BICs with single magnetic-dipole resonance meta-atoms, called Brewster-like quasi BICs.

1. Introduction

In recent years, high-refractive index (HRI) nanophotonic structures are attracting a widespread interest [1], mostly due to the strong magnetic dipole resonances found in the visible and telecomm spectral ranges for HRI nanoparticles, which make them especially appealing to tailor light at the nanoscale, as an alternative to plasmonic nanostructures. HRI nanostructures are being used as building blocks of metasurfaces [2] which can be seen as ultrathin gratings whose thickness and periodicity are small compared to a wavelength in the surrounding media. Metasurfaces have been shown to be relevant in a variety of applications. As an example of particular interest, properly designed all-dielectric metasurfaces, based on HRI spheres or disks, exhibit zero reflectivity, a generalized Brewster effect, potentially for any angle, wavelength and polarization of choice [3, 4]. At normal incidence, the effect is related to the absence of backscattering from small dielectric spheres or disks at the, so-called, first Kerker condition. In contrast, homogeneous HRI cylinders do not fulfill the first Kerker condition due to the mismatch between the local electric and magnetic density of states.

In addition, bound states in the continuum (BICs) have attracted much interest lately in photonics for their (theoretically) infinite Q factor. These states are leaky modes that in a certain limit of some parameter space cannot couple to any radiation channel [5]. In order to trap light in such nearly-zero-linewidth electromagnetic modes, a common approach is to exploit metasurfaces [6, 7]: outgoing specular channels can be suppressed by tuning the parameters of the system in various manners, leading to symmetry-protected BICs.

2. Coupled electric/magnetic dipole theory for metasurfaces

In order to explore all this fascinating phenomenology in metasurfaces, we have theoretically investigated the reflection from and transmission through a periodic array of electric and magnetic dipoles. To this aim, a coupled electric (ED) and magnetic dipole (MD) formulation for infinite planar arrays (iCEMD) has been developed where the electric and magnetic polarizabilities are given by the meta-atom response. In particular, if the meta-atoms consist of HRI cylinders (see Fig. 1) described by the two lowest-order Mie resonances in both polarizations, general analytical expressions are explicitly derived for reflection and transmission, the optical theorem, and the Kerker conditions of the cylinder array [8]. The formulation can be applied to any array of HRI subwavelength wires across the electromagnetic spectrum, as long as the wire response can be reasonably described by the lowest order longitudinal/transverse electric/magnetic polarizibilities. Moreover, we have also extended the iCEMD formulation to account for actual 3D metasurfaces with arbitrary ED/MD meta-atoms upon numerically solving the required lattice sums.

3. Generalized Brewster effect in HRI cylinder metasurfaces

First, we will show that, although a zero back-scattering condition can never be achieved for individual cylinders (as mentioned above), when they are arranged in a periodic array their mutual interaction leads to a generalized Brewster effect in a nanorod-based metasurface. This is done through our iCEMD analytical approach, which describes the reflection/transmission of a periodic array of HRI nanorods in full

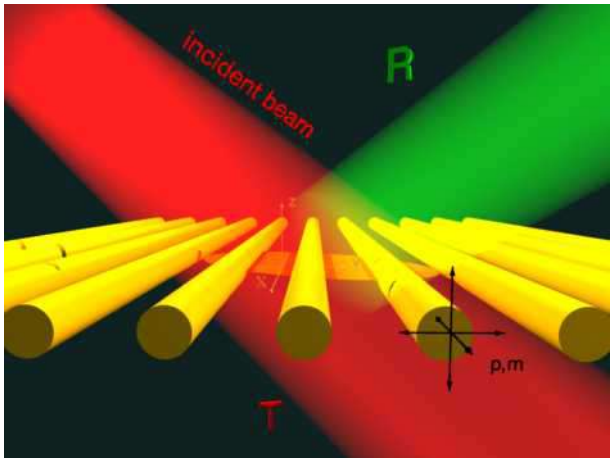


Figure 1: Schematic of the HRI cylinder metasurface wherein generalized Brewster effects are investigated.

agreement with exact numerical calculations [8].

4. BICs in coupled dipole metasurfaces

We will also show that simple metasurface configurations support robust, symmetry-protected BICs. On the basis of the iCEMD mentioned above [8], a variety of scenarios is investigated where single/double meta-atoms can be simply described by a combination of various EDs and/or MDs. First, an ED-dimer array is shown to yield a BIC at normal incidence as the dipole detuning parameter vanishes; this has been experimentally verified through Au-rod dimer metasurface in the THz domain [9].

Second, an array of single perpendicular MDs exhibits a so-called Brewster BIC at normal incidence, which evolves into a quasi-BIC at oblique incidence with a rich phenomenology as the (non-degenerate) MD is tilted. We will show that a high-refractive-index disk metasurface in the GHz domain in turn provides clear experimental evidence of such Brewster quasi-BICs [10].

Acknowledgement

The authors acknowledge the Spanish Ministerio de Ciencia, Investigación y Universidades through LENSBEAM (FIS2015-69295-C3-2-P, FIS2015-69295-C3-3-P), NANOTOPO (FIS2017-91413-EXP), and FPU PhD Fellowship FPU15/03566).

References

[1] A. García-Etxarri, R. Gómez-Medina, L. S. Froufe-Pérez, C. López, L. Chantada, F. Scheffold, J. Aizpurua, M. Nieto-Vesperinas, and J. J. Sáenz, Strong magnetic response of submicron Silicon particles in the infrared, *Opt. Express* 19: 4815, 2011.

[2] P. Genevet, F. Capasso, F. Aieta, M. Khorasaninejad, and R. Devlin, Recent advances in planar optics: from plasmonic to dielectric metasurfaces, *Optica* 4: 139, 2017.

[3] R. Paniagua-Domínguez, Y.F. Yu, A.E. Miroshnichenko, L.A. Krivitsky, Y.H. Fu, V. Valuckas, L. Gonzaga, Y.T. Toh, A.Y.S. Kay, B. Luk'yanchuk, and A.I. Kuznetsov, Generalized Brewster effect in dielectric metasurfaces, *Nat. Commun.*7: 10362, 2016.

[4] W. Liu, and A.E. Miroshnichenko, Beam steering with dielectric metalattices, *ACS Photonics* 5: 1733, 2018.

[5] C.W. Hsu, B. Zhen, J. Lee, S.-L. Chua, S.G. Johnson, J.D. Joannopoulos, and M. Soljačić, Observation of trapped light within the radiation continuum, *Nature* 499: 188–191, 2013.

[6] K. Koshelev, S. Lepeshov, M. Liu, A. Bogdanov, and Y. Kivshar, Asymmetric Metasurfaces with High-Q Resonances Governed by Bound States in the Continuum, *Phys. Rev. Lett.* 121: 193903, 2018.

[7] S.T. Ha, Y.H. Fu, N.K. Emani, Z.Pan, R.M. Bakker, R. Paniagua-Domínguez, and A.I. Kuznetsov, Directional lasing in resonant semiconductor nanoantenna arrays, *Nat. Nanotechnol.* 13: 1042–1047, 2018.

[8] D.R. Abujetas, J.A. Sánchez-Gil, and J.J. Sáenz, Generalized Brewster effect in high-refractive-index nanorod-based metasurfaces, *Opt. Express* 26: 31523, 2018.

[9] D.R. Abujetas, N. van Hoof, S. ter Huurne, J.G. Rivas, and J.A. Sánchez-Gil, From Fano resonances to bound states in the continuum in dipole arrays at THz frequencies, http://arxiv.org/abs/1901.03122

[10] D.R. Abujetas, A. Barreda, F. Moreno, J.J. Sáenz, A. Litman, J.-M. Geffrin, and J.A. Sánchez-Gil, Brewster quasi bound states in the continuum in all-dielectric metasurfaces from single magnetic-dipole resonance meta-atoms, http://arxiv.org/abs/arxiv:1902.07148

Optimized 3D metasurface for maximum light deflection at visible range

Mahmoud M. R. Elsawy[1*], Stéphane Lanteri[1], Régis Duvigneau[1], Peinan Ni[2], Gauthier Brière[2], and Patrice Genevet[2]

[1]INRIA, 06902 Sophia Antipolis Cedex, France
[2]CNRS, CRHEA, Université Côte d'Azur, rue Bernard Gregory, Sophia Antipolis, Valbonne, France
*corresponding author, E-mail: mahmoud.elsawy@inria.fr

Abstract

In this contribution, we use two different efficient global optimization techniques in order to optimize 3D real life gradient metasurface based on GaN semiconductor. Our results show that we can achieve more than 87% of diffraction efficiency at the visible regime using only 150 solver calls for optimizing 12 parameters. Our methods seem to be more efficient than other optimization techniques that require costly simulations, especially for 3D structures. The optimized structure will be fabricated and characterized experimentally.

1. Introduction

The field of metasurface has drawn a lot of attention in the last few years, because of the offered degrees of freedom that provide nearly a full control of the light properties in a very short propagation distance with high resolution [1, 2, 3]. The complexity of the problem, the wide parameter space, and the new fabrication capabilities, make the direct modelling problem insufficient and the use of inverse design is mandatory to achieve the maximum desired performance [4]. Several optimization methodologies have been used in the field of metasurfaces, including local and global search methods. The former, require fewer iterations, however, they can be stuck in local maxima/minima, the later is more general and is suitable for optimizing large parameter space. Nevertheless, most of the global techniques used in the metasurface designs require large number of solver calls, which make them inapplicable for modelling 3D real-life designs that require 3D solvers. The main target of this contribution is to find an optimal geometry for 3D gradient metasurface made of GaN nano-ridges (see the inset in Fig. 1) in order to achieve a maximum light deflection (in the same plane of incidence) with a specific angle at $\lambda = 600\ nm$. We choose GaN semiconductor due to its negligible losses and due to its high refractive index in the visible regime, which make it ideal nanoresonator (phase-shifters) for metasurface designs [1, 3].

Here, we use two different efficient global optimization techniques based respectively on advanced evolution strategies and statistical learning. The first one is the covariance matrix adaptation evolution strategy (CMA-ES) [5]. The CMA-ES has been gaining a lot of attention since it requires fewer cost function evaluations compared to the other evolutionary algorithms like genetic algorithms (GA) [4, 6] especially for 3D designs that require expensive simulations. The second method is the Efficient Global Optimization (EGO) algorithm [7]. The EGO algorithm is based on the surrogate modelling, that is to say, replacing the complex or costly evaluation process by a simpler and cheaper model [7] to reduce dramatically the computational cost (number of calls for the electromagnetic solver). We use our rigorous Discontinuous Galerkin Time Domain (DGTD) solver from the DIOGENES software suite dedicated to computational nanophotonics [8] together with the optimization algorithms, in order to achieve a maximum diffraction efficiency ($\eta(n, m)$, where n, m are the mode indices) at $\lambda = 600\ nm$. We consider a normal incident

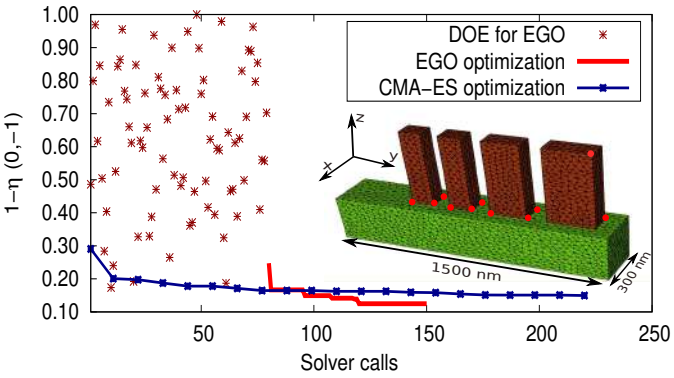


Figure 1: Optimization process using the EGO (red curve) and the CMA-ES (dark blue curve) methods as a function of the solver calls. The dark red points represent the DOE for the EGO. The inset shows the geometry under consideration, green region for the substrate (Al_2O_3), GaN ridges are shown in red. The 12 red circles represent the optimization parameters.

plane-wave with electric field polarized in the y-direction, and we aim to maximize the diffraction efficiency of the first order mode $\eta(0, -1)$ (deflect light in the same plane of incidence y-z plane). Thus, we consider a sub-wavelength period in the x-direction ($300\ nm$), and we consider a period of $1500\ nm$ in the y-direction, as it can be seen in the inset shown in Fig. 1. We restrict ourselves to rectangular shapes made of GaN semiconductor, in which the position and x and y thicknesses together with the height of the ridges need to be optimized. The 12 optimized parameters

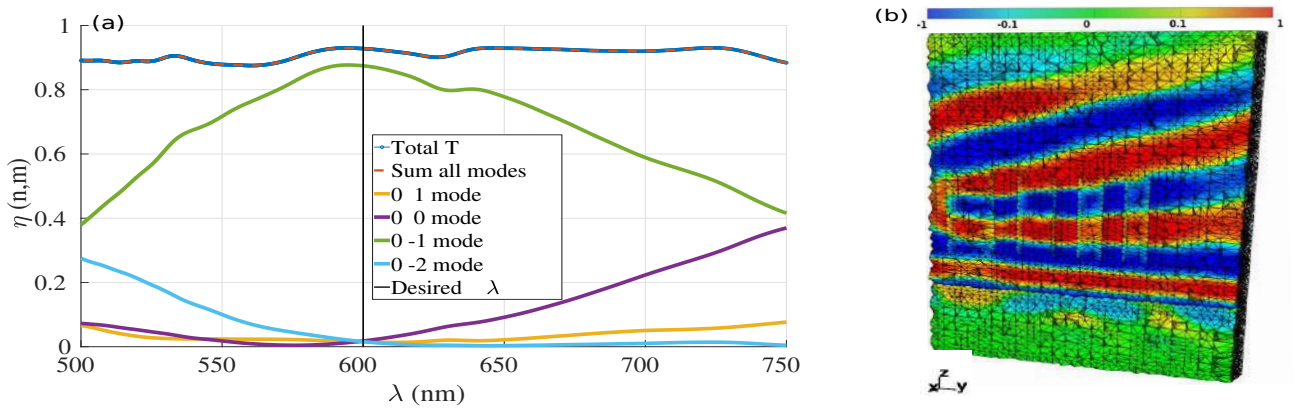


Figure 2: (a): Diffraction efficiency $\eta(n,m)$ for the main modes as a function of the wavelength, the total transmission is shown in blue. (b); $\Re e(E_y)$ obtained from our DGTD solver [8] at $\lambda = 600nm$.

are represented by the red circles in the inset of Fig. 1.

In Fig. 1, we show the results obtained using our optimization techniques. First, for the EGO model, the dark red points represent the design of experiment (DOE) obtained before the optimization process in the EGO model. Based on these points, a surrogate model is constructed and will be used during the optimization process to find a global minimum below the best point found in the DOE process. More precisely, after only 150 iterations (solver calls), we optimized 12 parameters and obtained a diffraction efficiency around 87% at $\lambda = 600\ nm$, which is sufficient for us at least at this moment, since we need to make a compromise between the number of iterations and the maximum diffraction efficiency obtained. The diffraction efficiency of the main modes, and total transmission as a function of the wavelength can be obtained in Fig. 2(a). As it can be seen, at $\lambda = 600\ nm$, nearly all the light is concentrated at the first order mode which is inferred in Fig. 2(b). Second, in Fig. 1, we show the results obtained from CMA-ES (dark blue curve). We have found that after 200 iterations, we obtain a point in which the diffraction efficiency is above 85%, but still the EGO provides a better point than the CMA-ES, at least below 200 iterations.

In conclusion, we used our global optimization techniques to optimize 3D gradient metasurface. Our results reveal that we can get up to 87% of diffraction efficiency by optimizing 12 different parameters using only 150 iterations. Our techniques seem to be more efficient than the usual global optimization methods [6] available in the literature in which numerous simulations are required for achieving optimized geometries. Based on the above results, the optimized geometry will be fabricated and characterized experimentally using our modern and efficient fabrication techniques.

References

[1] P. Genevet, F. Capasso, F. Aieta, M. Khorasaninejad, and R. Devlin, "Recent advances in planar optics: from plasmonic to dielectric metasurfaces," *Optica*, vol. 4, no. 1, pp. 139–152, 2017.

[2] S. Sun, K.-Y. Yang, C.-M. Wang, T.-K. Juan, W. T. Chen, C. Y. Liao, Q. He, S. Xiao, W.-T. Kung, G.-Y. Guo, *et al.*, "High-efficiency broadband anomalous reflection by gradient meta-surfaces," *Nano letters*, vol. 12, no. 12, pp. 6223–6229, 2012.

[3] N. Schmitt, N. Georg, G. Brière, D. Loukrezis, S. Héron, S. Lanteri, C. Klitis, M. Sorel, U. Römer, and P. Genevet, "Optimization and uncertainty quantification of gradient index metasurfaces," *Optical material express* vol. 9, pp. 892–910 (2019)

[4] S. Molesky, Z. Lin, A. Y. Piggott, W. Jin, J. Vuckovic, and A. W. Rodriguez, "Outlook for inverse design in nanophotonics," *arXiv preprint arXiv:1801.06715*, 2018.

[5] N. Hansen, S. Muller, and P. Koumoutsakos, "Reducing the time complexity of the derandomized evolution strategy with covariance matrix adaptation (CMA-ES)," *Evolutionary Computation*, vol. 11, no. 1, pp. 1–18, 2003.

[6] V. Egorov, M. Eitan, and J. Scheuer, "Genetically optimized all-dielectric metasurfaces," *Optics express*, vol. 25, no. 3, pp. 2583–2593, 2017.

[7] D. Jones, "A taxonomy of global optimization methods based on response surfaces," *Journal of Global Optimization*, vol. 21, pp. 345–383, 2001.

[8] *DIOGENES: A Discontinuous-Galerkin based software suite for nano-optics*. https://diogenes.inria.fr/.

[9] Zhenpeng Zhou, Juntao Li, Rongbin Su, Beimeng Yao, Hanlin Fang, Kezheng Li, Lidan Zhou, Jin Liu, Daan Stellinga, Christopher P Reardon, et al. Efficient silicon metasurfaces for visible light. *ACS Photonics*, 4(3):544–551, 2017.

[10] David Sell, Jianji Yang, Evan W Wang, Thaibao Phan, Sage Doshay, and Jonathan A Fan. Ultra-high-efficiency anomalous refraction with dielectric metasurfaces. *ACS Photonics*, 5(6):2402–2407, 2018.

Numerical dipoles method for light scattering by disordered metasurfaces

Maxime Bertrand[1], Alexis Devilez[1], Jean-Paul Hugonin[2], Philippe Lalanne[1], and Kevin Vynck[1*]

[1]LP2N, CNRS, IOGS, Univ. Bordeaux, 33400 Talence, France
[2]LCF, CNRS, IOGS, Univ. Paris-Saclay, 91127 Palaiseau, France
*corresponding author, E-mail: kevin.vynck@institutoptique.fr

Abstract

We propose a novel numerical method to efficiently and accurately model the optical response of disordered metasurfaces, consisting of large ensembles of non-spherical nanoparticles in a stratified medium, including in cases where the nanoparticles are in the near field of a surface or of each other.

1. Introduction

Disordered metasurfaces, consisting of resonant colloidal nanoparticles – or meta-atoms – deposited onto or incorporated into layered media (Fig. 1a), provide a very rich panel of optical features, such as frequency-selective wide-angle light absorption [1], controlled light coupling between free-space modes and guided modes in an optical stack [2] and strong light localization [3], which may be exploited for a wide range of photonic applications, from thin-film photovoltaics to lighting, to environmental sensing. This richness of optical properties comes from the nanoparticles themselves, their interaction with one or several interfaces and their mutual interaction with neighboring nanoparticles.

Theoretically or numerically predicting the optical properties of disordered metasurfaces has however remained a challenge so far due to the difficulty to simulate coherent phenomena occurring both at the scale of an individual nanoparticle and at the scale of the nanoparticle ensemble. Nanoscale phenomena are typically investigated using brute-force Maxwell's equations solvers (FDTD, finite-elements, ...), however these approaches can hardly deal with large ensembles of nanoparticles distributed in a large volume. This problem may instead be solved efficiently with a T-matrix formalism, where the incident and scattered fields are decomposed on a basis of vector spherical harmonics, however this method becomes very limited as soon as strong near-field interactions (between nanoparticles or between a nanoparticle and an interface) take place. Efforts are currently undergoing to overcome this limitation [4].

2. Results

The numerical method that we propose relies on finding a small set of fictitious electric and magnetic dipoles, described by a complex polarizability tensor, that can reproduce the near field scattered by an arbitrary nanoparticle for any excitation (planewave, point dipole source) at a given wavelength [5]. The polarizability tensor is obtained by solving a numerical inverse problem. Contrary to generalized multipole methods and alike [6], in which the inverse problem is solved by imposing specific boundary conditions on the surface of the scattering element, our method relies on a series of electromagnetic simulations, which can be performed with an arbitrary Maxwell equations solver, to find the polarizability tensor that reproduces the scattered field on *any* surface around the nanoparticle. It is therefore very general and versatile. Once this is done, the multiple scattering problem where nanoparticles are in the near-field of each other or of a surface can be solved via a classical Green tensor formalism [7].

The validity of our method is illustrated here with the example of a long silicon cylinder. The polarizability tensor of a set of 10 numerical dipoles regularly arranged along the cylinder principal axis was obtained from a data set of finite-element simulations (COMSOL Multiphysics) performed for an individual cylinder embedded in a *uniform* medium with refractive index 1.5 (glass). Figure 1b shows a comparison of the field scattered by the cylinder when placed in the near field of a gold substrate, as predicted by our method (left) and by the finite-element method (right), for an incident planewave. An excellent agreement is observed. In Ref. [5], we also demonstrate our capability to simulate large disordered ensembles of such cylinders incorporated into a metal-dielectric optical stack.

Acknowledgement

This work has been carried out with financial support from the IdEx Bordeaux LAPHIA (ANR-10-IDEX-03-02) under the project X-STACKS, and from the French National Agency for Research (ANR) under the project NanoMiX (ANR-16-CE30-0008).

References

[1] A. Moreau, et al., Controlled-reflectance surfaces with film-coupled colloidal nanoantennas, *Nature* Vol. 492, No. 7427, pp. 86–89, 2012.

[2] A. Jouanin, J.-P. Hugonin, P. Lalanne, Designer colloidal layers of disordered plasmonic nanoparticles

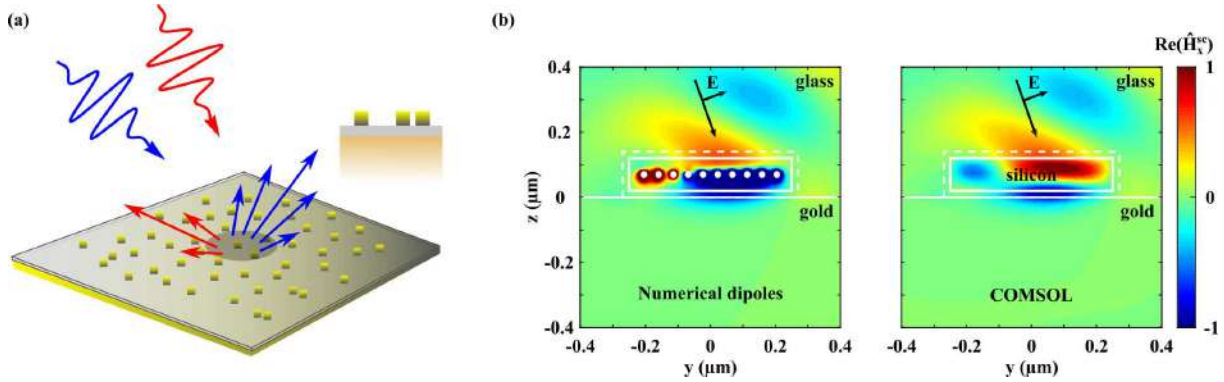


Figure 1: **(a)** Example of a disordered metasurface, consisting of metallic nanocubes deposited on a metallo-dielectric stack, that may be modelled with our numerical method. **(b)** Validity of the method (adapted from Ref. **??**). A long silicon cylinder (L = 500 nm, d = 100 nm) embedded in glass is placed 20 nm above a gold layer and illuminated by a TM planewave at λ = 580 nm and 20 degree incidence. 10 numerical dipoles are equally distributed along the cylinder principal axis. The scattered field predicted by our numerical method (left) outside the cylinder is in excellent agreement with the one obtained with the COMSOL Multiphysics (right).

for light extraction, *Advanced Functional Materials* Vol. 26, No. 34, pp. 6215–6223, 2016.

[3] V. Krachmalnicoff, et al., Fluctuations of the local density of states probe localized surface plasmons on disordered metal films, *Phys. Rev. Lett.* Vol. 105, No. 18, 183901, 2010.

[4] A. Egel, Y. Eremin, T. Wriedt, D. Theobald, U. Lemmer, G. Gomard, Extending the applicability of the T-matrix method to light scattering by flat particles on a substrate via truncation of Sommerfeld integrals, *J. Quant. Spect. Rad. Trans.* Vol. 202, pp. 279–285, 2017.

[5] M. Bertrand, A. Devilez, J.-P. Hugonin, P. Lalanne, K. Vynck, submitted, 2019.

[6] T. Wriedt, Generalized multipole techniques for electromagnetic and light scattering, *Elsevier* 1999.

[7] M. Paulus, O. J. F. Martin, Green's tensor technique for scattering in two-dimensional stratified media, *Phy. Rev. E* Vol. 63, No. 6, 066615, 2001.

Designer hyperbolic nanostructures for thermo-plasmonic bio-medical applications using finite element and finite difference time domain methods

Nicolò Maccaferri[1,2*]

[1]Istituto Italiano di Tecnologia, Via Morego 30, 16163, Genova, Italy
[2]Physics and Materials Science Research Unit, Université du Luxembourg, 165, avenue de la Faïencerie, L-1511, Luxembourg
*corresponding author, E-mail: nicolo.maccaferri@uni.lu

Abstract

Novel optical designs and architectures that modify the optical power flow through plasmonic nanostructures represent a crucial step towards a nanoscale manipulation of light-matter interactions. One of the main drawbacks of plasmonic nanostructures is the superposition of scattering and absorption processes and, more in general, the difficulties of controlling scattering and absorption separately. For guiding light, for instance, it is essential that the photonic or plasmonic circuit does not have a high absorption, while for other kind of applications, such as photo-acoustic imaging, it is essential that the light is absorbed rather than scattered. To this aim sophisticated approaches have been developed often based on antenna's design enabled by modern commercial CADs. The ideal solution would be an architecture and/or material which allows to control individually the absorption and scattering band through a clear physical concept, and possibly to tune the relative spectral position and modes strength. Here, we show how hyperbolic meta-antennas overcome these limitations [2]. We present a detailed numerical study where, by means of finite element and finite difference time domain methodologies, we design nanostructured meta-antennas which enable a full control of absorption and scattering of light. Furthermore, the proposed hyperbolic meta-antennas are directional and show both polarization and angular independence, which is an important property if the meta-antennas are dispersed in solvents or grown on different kind of surfaces. The powerful numerical approaches used in this work allow the design of novel nanostructured metamaterials suitable for practical applications spanning, for instance, from thermal emission manipulation, theragnostic nano-devices, optical trapping and nano-manipulation, non-linear optical properties, plasmon-enhanced molecular spectroscopy, photovoltaics and solar-water treatments.

References

[1] A. Poddubny, I. Iorsh, P. Belov, Y. Kivshar, Hyperbolic metamaterials, *Nat. Photon.* 7: 958-967, 2013.
[2] N. Maccaferri, Y. Zhao, T. Isoniemi, M. Iarossi, A. Parracino, G. Strangi, F. De Angelis, Hyperbolic Meta-Antennas Enable Full Control of Scattering and Absorption of Light, *Nano Lett.* 10.1021/acs.nanolett.8b04841, 2019.

Perfect Penetrable Cloaking Using Arbitrary-Shape Bianisotropic Metasurfaces

Mojtaba Dehmollaian[1*] and Christophe Caloz[2]

[1]School of Electrical and Computer Engineering, University of Tehran, Iran
[2]Poly-Grames Research Center, Polytechnique Montréal, Montreal, Quebec, Canada
*corresponding author, E-mail: m.dehmollaian@ut.ac.ir

Abstract

This paper combines Integral Equations (IEs) and Generalized Sheet Transition Conditions (GSTCs) with bianisotropic susceptibility tensors, to compute the wave scattering by cylindrical metasurfaces of arbitrary cross sections. It applies this technique to a newly introduced form of cloaking, *penetrable cloaking*, which is more realistic than transformation-electromagnetics cloaking. It shows that for a given object, properly synthesized gain-less and loss-less susceptibilities can perfectly cloak the object.

1. Introduction

Metasurface technology has been increasingly developed in recent years. A recent overview of the concept, design and applications of metasurfaces may be found for instance in [1].

Practical applications involve a variety of *curved* objects (e.g., [2]), requiring proper analysis tools. For example, [3] presents wave scattering by multilayered spherical shells using the method of moments (MoM) combined with tensor boundary conditions (TBCs). Generalized Sheet Transition Conditions (GSTCs) have been recently applied to the numerical study of circular-cylindrical [4], spherical [5], and arbitrarily-curved metasurfaces [6] using different analysis techniques [7].

This paper presents a generalization of the GSTC-IE/MoM technique for cylindrical metasurfaces of arbitrary cross section, and illustrates it with the example of the perfect bianisotropic penetrable cloaking of an elliptical object.

2. Computational Formulation

Fig. 1 shows the two-dimensional problem of interest, the analysis of wave scattering by a metasurface cavity of arbitrary cross section illuminated by an arbitrary source. The exterior and interior media, respectively labeled 1 and 2, have permittivities and permeabilities (ε_1, μ_1) and (ε_2, μ_2).

2.1. Generalized Sheet Transition Conditions (GSTCs)

Let us assume that the metasurface has only *transverse* electric and magnetic surface polarization densities, $\vec{P}_\parallel$ and $\vec{M}_\parallel$. In this case, the harmonic $(e^{-i\omega t})$ GSTCs reduce to [1]

$$\hat{n}\times\Delta\vec{E} = i\omega\mu_0\vec{M}_\parallel, \quad \hat{n}\times\Delta\vec{H} = -i\omega\vec{P}_\parallel, \qquad (1)$$

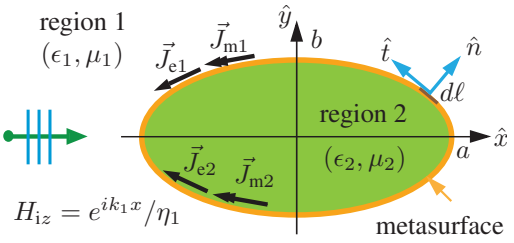


Figure 1: Scattering by a metasurface cavity using equivalent electric and magnetic currents.

where Δ denotes the difference of the fields at both sides of the metasurface, and

$$\vec{M}_\parallel = [M_t, M_z]' = \overline{\overline{\chi}}_{\mathrm{me}\,\parallel}\cdot\vec{E}_{\parallel,\,\mathrm{av}}/\eta_0 + \overline{\overline{\chi}}_{\mathrm{mm}\,\parallel}\cdot\vec{H}_{\parallel,\,\mathrm{av}}, \quad (2a)$$

$$\vec{P}_\parallel = [P_t, P_z]' = \varepsilon_0\overline{\overline{\chi}}_{\mathrm{ee}\,\parallel}\cdot\vec{E}_{\parallel,\,\mathrm{av}} + \overline{\overline{\chi}}_{\mathrm{em}\,\parallel}\cdot\vec{H}_{\parallel,\,\mathrm{av}}/c, \quad (2b)$$

where $\overline{\overline{\chi}}_{\mathrm{mm}\,\parallel}$, $\overline{\overline{\chi}}_{\mathrm{me}\,\parallel}$, $\overline{\overline{\chi}}_{\mathrm{em}\,\parallel}$ and $\overline{\overline{\chi}}_{\mathrm{ee}\,\parallel}$ are the surface susceptibilitiy tensors, and "av" denotes the average of the fields at both sides of the metasurface [1]. Eqs. (1) with (2) form two vector equations in terms of the four unknown vectors $\vec{E}_{\parallel 1}$, $\vec{H}_{\parallel 1}$, $\vec{E}_{\parallel 2}$ and $\vec{H}_{\parallel 2}$ in the local coordinate system (n, t, z).

2.2. Integral Equations (IEs)

According to the Huygens principle, the fields scattered by the metasurface outside/inside the metasurface enclosure are the convolution of the equivalent electric and magnetic polarization currents $\vec{\mathcal{J}}_{\mathrm{e,m}}(\vec{\rho})$ with the dyadic Green function of the corresponding medium $\overline{\overline{\mathcal{G}}}_{1,2}(\vec{\rho},\vec{\rho}')$ as [8]

$$\overline{\mathcal{E}}^{\mathrm{s}}_l(\vec{\rho}) = \oint\left(ik_l\eta_l\,\overline{\overline{\mathcal{G}}}_l\cdot\overline{\mathcal{J}}_{\mathrm{e}l}(\vec{\rho}') - \overline{\overline{\mathcal{F}}}_l\cdot\overline{\mathcal{J}}_{\mathrm{m}l}(\vec{\rho}')\right)d\ell', \quad (3)$$

where $l = 1, 2$ is the medium number and $\overline{\overline{\mathcal{F}}}_l(\vec{\rho},\vec{\rho}') = \nabla\times\overline{\overline{\mathcal{G}}}_l$. If the source is in region 1, then $\overline{\mathcal{E}}^{\mathrm{s}}_1 = \overline{\mathcal{E}}_1 - \overline{\mathcal{E}}_{\mathrm{i}}$ and $\overline{\mathcal{E}}^{\mathrm{s}}_2 = \overline{\mathcal{E}}_2$, where $\overline{\mathcal{E}}_1$ and $\overline{\mathcal{E}}_2$ are the total electric fields in regions 1 and 2, respectively, and $\overline{\mathcal{E}}_{\mathrm{i}}$ is the incident field, all in the global coordinate system (x, y, z). Using duality, similar IEs exist for the total magnetic fields, $\overline{\mathcal{H}}_1$ and $\overline{\mathcal{H}}_2$.

We want to express global coordinate system electric and magnetic polarization currents $\vec{\mathcal{J}}_{\mathrm{e,m}}(\vec{\rho})$ in terms of the four unknown vectors $\vec{E}_{\parallel 1}$, $\vec{H}_{\parallel 1}$, $\vec{E}_{\parallel 2}$ and $\vec{H}_{\parallel 2}$, expressed

in the local coordinate system. First, we express the global-system electric current densities $\vec{\mathcal{J}}_{\rm e1}(\vec{\rho})$ in terms of local-system electric currents $\vec{J}_{\rm e1}$ as $\vec{\mathcal{J}}_{\rm e1}(\vec{\rho}) = \overline{\overline{T}}(\vec{\rho}) \cdot \vec{J}_{\rm e1}$ with

$$\overline{\overline{T}}'(\vec{\rho}) = \begin{pmatrix} \hat{x}\cdot\hat{t} & \hat{y}\cdot\hat{t} & 0 \\ 0 & 0 & 1 \end{pmatrix}. \tag{4}$$

Second, we express the local-system current densities in terms of local-system magnetic tangential fields as $\vec{J}_{\rm e1} = \hat{n} \times \vec{H}_{\parallel 1} = H_{1t}\hat{z} - H_{1z}\hat{t} = \overline{\overline{\rm N}} \cdot \vec{H}_{\parallel 1}$, where $\overline{\overline{\rm N}}$ is the 2 by 2 matrix $[0, -1; 1, 0]$. As a result, we have $\vec{\mathcal{J}}_{\rm e1,2}(\vec{\rho}) = \pm\overline{\overline{T}}(\vec{\rho}) \cdot \overline{\overline{\rm N}} \cdot \vec{H}_{\parallel 1,2}$. Similarly, $\vec{\mathcal{J}}_{\rm m1,2}(\vec{\rho}) = \mp\overline{\overline{T}}(\vec{\rho}) \cdot \overline{\overline{\rm N}} \cdot \vec{E}_{\parallel 1,2}$.

Now, upon multiplying both sides of (3) by $\overline{\overline{T}}'$, we obtain the electric fields in the local coordinate systems [e.g., $\vec{E}_{\parallel 1} = \overline{\overline{T}}'(\vec{\rho}) \cdot \vec{\mathcal{E}}_1(\vec{\rho})$]. This way, Eqs. (3) and their counterparts for the magnetic fields are all given in terms of the tangential fields $\vec{H}_{\parallel 1}$, $\vec{E}_{\parallel 1}$, $\vec{H}_{\parallel 2}$, and $\vec{E}_{\parallel 2}$. We find $E_{1z} - E_{\rm iz}$ and E_{2z} and $H_{1z} - H_{\rm iz}$ and H_{2z} from Eqs. (3) and their counterparts for the magnetic fields, as the four solutions of the four scalar (or two vector) integral equations.

2.3. Combined GSTCs-IEs/MoM

Combining the two pairs of vector equations given by the GSTCs (1) and IEs (3) forms a system of four equations in four unknowns, the tangential fields [8]. Once they are determined, the IEs provide the fields everywhere in space.

3. Application : Penetrable Cloaking

3.1. Bianisotropic Loss/Gain-less Metasurface

Let us assume that a TE$_z$ plane wave (i.e., $\vec{H}_{\rm iz} = e^{+ik_1 x}/\eta_1$) is illuminating the object. The reciprocal, passive, and lossless metasurface [9] has nonzero purely real $\chi_{\rm ee}^{tt}$ and $\chi_{\rm mm}^{zz}$, and purely imaginary $\chi_{\rm em}^{tz} = -\chi_{\rm me}^{zt}$, given by

$$\chi_{\rm mm}^{zz} = A\, t_y^2 \sin\alpha, \quad \chi_{\rm ee}^{tt} = B \sin\alpha, \tag{5a}$$

$$\chi_{\rm em}^{tz} = -\chi_{\rm me}^{zt} = iB\, t_y\, (\eta_1 - \eta_2) \cos\alpha/2\eta_0, \tag{5b}$$

where $\alpha = (k_1 - k_2)x$, $A = 2T/\left(k_0 D \eta_0\right)$, $B = A\eta_0^2/\eta_1\eta_2$, $T = \sqrt{\eta_2/\eta_1}$, $D = t_y/\eta_1(1 + (\eta_1 + \eta_2)/(2\sqrt{\eta_1\eta_2})\cos\alpha)$, and t_y is the y-component of the tangential unit vector $\hat{t}$.

3.2. Numerical Results

We illustrate a metasurface-coated elliptic cylinder with major and minor axes $2a/\lambda_2 = 4$ and $2b/\lambda_2 = 2$, and non-magnetic media with $\epsilon_{\rm r1} = 1$ and $\epsilon_{\rm r2} = 4$. Figs. 2(a)-(c) show the synthesized susceptibilities $\chi_{\rm ee}^{tt}$, $\chi_{\rm mm}^{zz}$, and $\chi_{\rm em}^{tz}$. Inserting these susceptibilities into the IEs provides the magnetic fields shown in Fig. 2(d), exhibiting the expected perfectly unperturbed phase fronts.

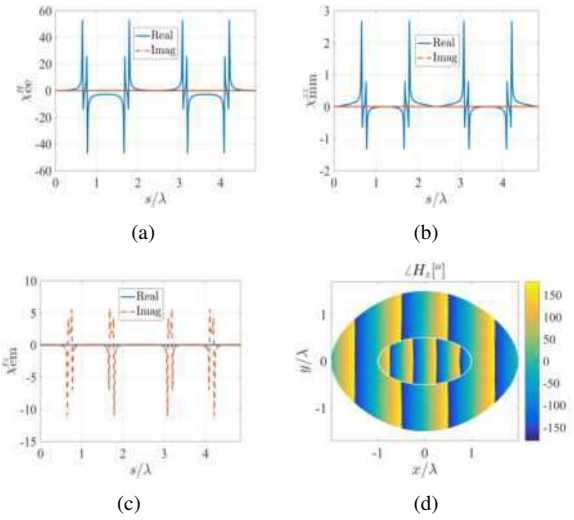


Figure 2: Bianisotropic susceptibilities (a) $\chi_{\rm ee}^{tt}$, (b) $\chi_{\rm mm}^{zz}$, and (c) $\chi_{\rm em}^{tz} = -\chi_{\rm me}^{zt}$ along the boundary of the metasurface s/λ. (d) Phase of the total magnetic field inside and outside of the cloaked elliptical cylinder, coated by the metasurface.

References

[1] K. Achouri and C. Caloz, Design, concepts, and applications of electromagnetic metasurfaces, *Nanophotonics*, vol. 7, no. 6, pp. 1095-1116, 2018.

[2] G. Moreno , A. B. Yakovlev , H. Mehrpour Bernety, D. H. Werner, H. Xin, A. Monti, F. Bilotti, and A. Alù, Wideband elliptical metasurface cloaks in printed antenna technology, *IEEE Trans. Antennas Propag.*, vol. 66, no. 7, pp. 3512-3525, 2018.

[3] E. Topsakal, J. L. Volakis, and D. C. Ross, Surface integral equations for material layers modeled with TBCs, *Radio Sci.*, vol. 37, no. 4, 2002.

[4] S. Sandeep and S. Y. Huang, Simulation of circular cylindrical metasurfaces using GSTC-MoM, *arXiv:1804.03472v1*, 2018.

[5] X. Jia, Y. Vahabzadeh, C. Caloz, and F. Yang Synthesis of spherical metasurfaces based on susceptibility tensor GSTC, *IEEE Trans. Antennas Propag.*, 2019.

[6] J. Yi Han Teo, L. Jie Wong, C. Molardi, and P. Genevet, Controlling EM fields at boundaries of arbitrary geometries, *Phys. Rev. A* 94, 023820, 2016.

[7] Y. Vahabzadeh, N. Chamanara, K. Achouri, and C. Caloz, Computational analysis of metasurfaces, *IEEE J. Multiscale and Multiphys. Comput. Techn.*, vol. 3, 2018.

[8] M. Dehmollaian, N. Chamanara, and C. Caloz, Wave scattering by a cylindrical metasurface cavity of arbitrary cross-section: Theory and applications, *arXiv preprint arXiv:1808.09530*, 2018.

[9] G. Lavigne, K. Achouri, V. S. Asadchy, S. A. Tretyakov, and C. Caloz, Susceptibility derivation and experimental demonstration of refracting metasurfaces without spurious diffraction, *IEEE Trans. Antennas Propag.*, vol. 66, no. 3, pp. 1321-1330, 2018.

Effective transmission conditions for an array of locally resonant inclusions

Kim Pham[1], **Agnès Maurel** [2] **and Jean-Jacques Marigo**[3]

[1] IMSIA, CNRS, ENSTA ParisTech, 828 Bd des Maréchaux, 91732 Palaiseau, France
[2] Institut Langevin, CNRS, ESPCI ParisTech, 1 rue Jussieu, 75005 Paris, France,
[3] LMS, Ecole Polytechnique, Route de Saclay, 91120 Palaiseau, France
*corresponding author, E-mail: kim.pham@ensta-paristech.fr

Abstract

We study the scattering of waves by a single row of resonant inclusions, of the Mie type. An effective model based on matched asymptotic analyzed is used to account for the small thickness of the array. Hence, instead of the effective bulk parameters (permittivity and permeabilty), we end up with interface parameters entering in jump conditions for the electromagnetic fields; among these parameters, one is frequency dependent and encapsulates the resonant behavior of the inclusions. Our effective model is validated by comparison with results of full wave calculations.

1. Introduction

Starting in the 1990's with the pioneering work of [1] in the context of elasticity, resonant structures with subwavelength unit cells have been proposed in the context of electromagnetism [2], and in a unified mathematical context [3]. In this case, the resonances are attributable to an inclusion placed in the unit cell and presenting a high contrast in its material properties with respect to the surrounding matrix. These resonances often referred to as Mie resonances occur at frequencies producing a wavelength in the inclusion comparable to the inclusion size (and this size is much smaller than the incident wavelength). The ability of these so-called locally resonant structures to forbid the wave propagation has been exhibited and the forbidden band gaps have been interpreted in terms of an effective negative parameter being the mass density in elasticity and the permeability in electromagnetism. Since then, locally resonant materials have been intensively studied for applications including the design of efficient wave shields, see *e.g.* [3] or absorbers of small thicknesses, see *e.g.* [4].

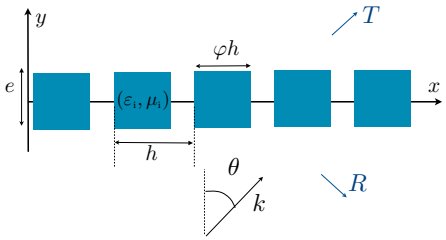


Figure 1: Scattering by an array of locally resonant inclusions with permittivity $\varepsilon_{\rm i}$ and permeability $\mu_{\rm i}$ (in the air).

Motivated by the design of compact metamaterial devices and following the intuitive argument that each local resonator vibrates almost like an independent unit, structures involving a single row of resonators or few rows have been thought, see *e.g.* [5]. In this case, interrogating the bulk response of the device becomes questionable. Indeed, when the number of cells is too small, the metamaterial device is dominated by boundary layer effects and the response of its bulk, in terms of effective parameters, is not pertinent anymore; the failure of the effective medium theories for thick structures has been illustrated in [6]. Here, we extend these works to the case of an array composed of a single row of locally resonant inclusions (Fig. 1).

2. The actual and the effective problems

We consider transverse electric polarized waves propagating in the air and interacting with a row of inclusions with relative permittivity $\varepsilon_{\rm i}$ and permeability $\mu_{\rm i}$ (and we set for the air $\varepsilon = \mu = 1$). In the case where $\varepsilon_{\rm i}\mu_{\rm i} \gg 1$, the wavelength inside the inclusions is much smaller than in the air, and resonances of the Mie type are possible. In this case, asymptotic analysis can be conducted which result in an effective interface model, see [7], where the array of resonant inclusions are replaced by jump conditions of the form

$$\left\{ \begin{array}{l} [\![E]\!]_e = h\mathcal{B}\,\overline{\partial_y E}, \\ [\![\partial_y E]\!]_e = h\mathcal{S}\,\overline{\partial_{yy} E} + h\mathcal{C}\,\partial_{xx}\overline{E} - h\mathcal{D}(k)\,k^2\,\overline{E}, \end{array} \right. \tag{1}$$

where we defined, for any field f, $[\![f]\!]_e \equiv f^+ - f^-$ and $\overline{f} \equiv (f^+ + f^-)/2$, with $f^\pm \equiv f(x, \pm e/2)$. The effective parameters $(\mathcal{B}, \mathcal{C}, \mathcal{S})$ depend only on the geometry of the inclusions while $\mathcal{D}(k)$ has an additional dependence on the frequency and it is the parameter which encapsulates the possible resonances of the Mie type. For instance, for rectangular shape of inclusion, as we shall consider in the numerical example, we have $\mathcal{S} = \frac{e}{h}(1-\varphi)$, $\mathcal{B} = \frac{e/h}{1-\varphi} - \frac{2}{\pi}\log\left(\cos\frac{\pi\varphi}{2}\right)$, $\mathcal{C} \simeq \frac{\pi}{8}(1-\varphi)^2\left(1 - e^{-\frac{8e}{(1-\varphi)\pi h}}\right)$ and

$$\mathcal{D}(k) = \varepsilon_{\rm i}\frac{e\varphi}{h}\left[1 - \sum_n \alpha_n^2 \frac{k_{\rm i}^2}{k_{\rm i}^2 - k_{{\rm i},n}^2}\right], \tag{2}$$

with for $n = (n_1, n_2)$, $k_{{\rm i},n}^2 = \left(\frac{n_1\pi}{e}\right)^2 + \left(\frac{n_2\pi}{h\varphi}\right)^2$ the wavenumbers at the resonances and $\alpha_n = \frac{8}{\pi^2 n_1 n_2}$.

3. Fano resonances

In our homogenized problem, the region $|y| < e/2$ is disregarded and the wavefield satisfies (1) for $|y| > e/2$; a solution of this problem for an incident plane wave at oblique incidence θ reads

$$E = \begin{cases} \left[e^{\mathrm{i}k(y+e/2)\cos\theta} + Re^{-\mathrm{i}k(y+e/2)\cos\theta}\right] e^{\mathrm{i}kx\sin\theta}, \\ Te^{\mathrm{i}k(y-e/2)\cos\theta}\, e^{\mathrm{i}kx\sin\theta}, \end{cases} \tag{3}$$

for $y < -1/2$ and $y > e/2$ respectively. Next, applying the jump conditions (1) yields the scattering coefficient

$$\begin{cases} R = -\dfrac{1}{2}\left(\dfrac{z_1}{z_1^*} - \dfrac{z_2}{z_2^*}\right), \quad T = \dfrac{1}{2}\left(\dfrac{z_1}{z_1^*} + \dfrac{z_2}{z_2^*}\right), \\ z_1 \equiv 1 + \dfrac{ikh}{2}\,\mathcal{B}\cos\theta, \\ z_2 \equiv \cos\theta + \dfrac{ikh}{2}\left(\mathcal{S}\cos^2\theta + \mathcal{C}\sin^2\theta + \mathcal{D}(k)\right), \end{cases} \tag{4}$$

where z^* denotes the complex conjugate of z.

We report in Fig. 2 the variations of the reflection coefficients against the dimensionless frequency kh, R^{num} being computed numerically and R from (4) (the incidence is $\theta = 40°$). In the range $kh \in [0, 1]$, the first monopolar resonance for $n = (1, 1)$ in (2) is visible (it occurs for $k_{\text{i}}h = 8.9$ whence $kh \simeq 0.9$, resulting in a wavelength within the inclusions being about half the inclusion length). The agreement between R^{num} and its homogenized counterpart R is good, about 2% and this accuracy is the same for any incidence θ up the grazing incidence (results not reported). The resonance of the inclusions produces sharp variations of the reflection with a typical Fano resonance curve characterized by a perfect transmission followed by a perfect reflection. Results including the attenuation due to losses in the dielectric will be presented, with the same accuracy of the effective model to reproduce the scattering properties in the actual problem.

4. Concluding remarks

There are at least two natural extensions of the present study that we shall discuss. We have considered waves in a binary structures but the present work can be extended to ternary structure, as proposed in [8]. This extension may be of particular interest when locally resonant materials are considered in the acoustic case; as previously said, this is obtained in practice considering binary or ternary structures mixing fluids and elastic materials, thus for which the conversions between shear and longitudinal waves have to be accounted for. We believe that this is the key point to properly describe the negative index material reported in this context [9].

The second extension is technically much demanding. Our result has a serious limitation, already mentioned in [2]. The analysis holds for resonances with non zero mean value (namely, n_1 and n_2 odd in (2)). Although these resonances have a higher quality factor and thus are much more sensitive to losses, the accuracy of the homogenized solution would be enhanced if one is able to account for them. This requires to develop the model up to higher order and this is not incremental.

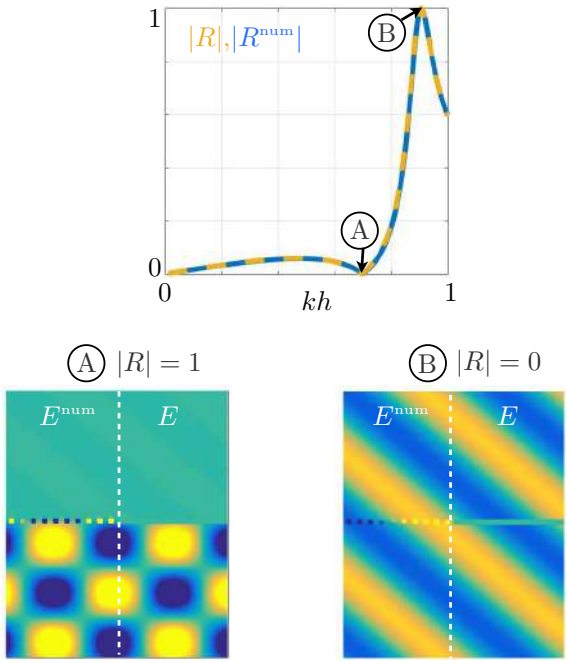


Figure 2: Fano resonance of a row of resonant Mie scatterers in the air ($\varepsilon = 100$, $\varphi = 0.5$, $e/h = 0.5$). Reflection coefficient $|R|$ against kh computed numerically (plain line) and from (4) (dotted line). The wavefields A at $kh = 0.7$ realizing perfect reflection and B at $kh = 0.9$ realizing perfect transmission (numerics and from (3) in both cases).

References

[1] J.-L. Auriault, Curr. Topics Ac. Res. I, 63-90, 1994.

[2] D. Felbacq and G. Bouchitté, PRL **94**(18),183902, 2005.

[3] V.V. Zhikov, Sbornik: Math., **191**(7), 973, 2000.

[3] C. Goffaux *et al.*, PRL, **88**(22), 225502, 2002.

[4] T. Brunet, J. Leng, and O. Mondain-Monval, **342**(6156), 323–324, 2013.

[5] H. Zhao, J. Wen, D. Yu and X. Wen, J. Appl. Phys., **107**(2), 023519, 2010.

[6] M. Lapine, R.C. McPhedran and C.G. Poulton, Phys. Rev. B, **93**(23), 235156, 2016.

[7] K. Pham, A. Maurel and J.-J. Marigo, JMPS, **106**, 80-94, 2017.

[8] Z. Liu, X. Zhang, Y. Mao, Y.Y. Zhu, Z. Yang, C.T. Chan, and P. Sheng, Science, **289**(5485, 1734-1736, 2000.

[9] Y. Ding, Z. Liu, C. Qiu, and J. Shi, Jing, Phys. Rev. Lett., **99**(9) 093904, 2007.

Biosensor chip based on VCSELs and gold grating

Yiyang Xie[1], Chen Xu[2], Qiang Kan[2], Beijv Huang[2], and Hongda Chen[2]

[1]Key Laboratory of Optoelectronics Technology (Beijing University of Technology) Ministry of Education, Beijing 100124, China
[2]Institute of Semiconductor, Chinese Academy of Sciences, Beijing 100083, China

*corresponding author, E-mail: xieyiyang@bjut.edu.cn,xuchen58@bjut.edu.cn

Abstract

We combine gold grating with vertical cavity surface emitting lasers to realize a prototype of miniaturized chemical/biosensor. The advantage of such chips include compact size, low cost and low power consumption, long life time, stable performance, easy to make array and multi-flux test, and label-free sensing. The finite difference time domain method is employed to model the transmission signal from the chips. It is believed that the biosensor chip has potential applications in health care, clinical diagnostics, and environmental monitoring.

1. Introduction

Vertical cavity surface emitting lasers (VCSELs) are key devices in optical fiber communication systems and 3D sensing in iPhone due to their important characteristics such as high modulation bandwidth, circular beam shape, small divergence angles, low power consumption, easy to integrate and make arrays, as well as high reproducibility in fabrication. To obtain a new type high sensitivity and high stability biochemical sensors, the gold grating have been integrated on the top surface of the VCSEL to realize the integration of the sensing material and the light source and then the sensors have both the advantages of the VCSEL and gold grating. Three-dimensional finite difference time domain (FDTD) algorithm simulations are utilized to explore their transmission spectra and steady-state field intensity distributions of the sensors to calculate the sensitivity. The design sensitivity of the sensors has been reached 10^6 nW/ RIU and the VCSELs have been produce by using normal semiconductor processes. After that, the gold grating was fabricated on the top surface of the VCSELs by using the focus ion beam (FIB). The sensing performances of the sensor were characterized via transmission light output power with different refractive index samples. The exosome interaction experiment was also adopted to verify the sensitivity of the surface binding reaction. Through four steps modification, the exosome specificity detection has been achieved and the exosome has been found very well combined on the gold nanoslit array. It is believed that the biosensor chip has potential applications in health care, clinical diagnostics, environmental monitoring, especially, cancer biomarker testing.

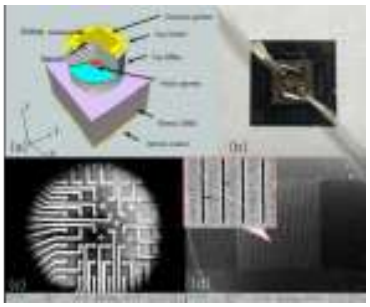


Figure 1.The structure of the biosensor chips (a) the schematic of the VCSEL with integration grating, (b) the micrograph of the chips with Microfluidic, (c) the VCSEL array of the chips, (d) the gold grating on the top surface of the VCSEL.

2. Design and fabrication

We first describe the fabrication of biosensor chips shows in Figure 1. A VCSEL epitaxial structure with 850 nm emission wavelength has been grown on an n-GaAs substrate. It contains 22.5-pairs of p-type top DBRs and 34.5-pairs of n-type bottom DBRs. Both DBRs consist of $Al_{0.9}Ga_{0.1}As/Al_{0.12}$ $Ga_{0.88}As$ except for a 30-nm $Al_{0.98}Ga_{0.02}As$ oxidation layer inserted in the bottom of top DBRs. The mesas were formed by $SiCl_4/Ar/Cl_2$ inductively coupled plasma reaction ion etching (ICP-RIE) down to the active region, using SiO_2 as the etching mask. Then the $Al_{0.98}Ga_{0.02}As$ layer was selectively oxidized to form the needed shape oxide aperture. After that, top ohmic (Ti/Au) ring contacts were patterned and bottom ohmic (Au/Ge/Ni/Au) contacts were formed. The devices were then annealed using rapid thermal annealing at 430 °C for 35 sec. After that, a chip with 8×8 VCSEL array has been successful produced and the size of the chip is 1cm×1cm. And then a 50 nm-thick gold film was deposited on the output window of the VCSEL. To isolate the chip and the metal film, a 500nm thick SiO_2 was inserted between the chip and the metal film. We employed focused ion-beam milling to fabricate gold grating structures on the metal film and the period and width of the gratings are shown in the table1, respectively. To test the property of the sensing chip and inject the medium, a microchannel was fabricated by using micro-replication technology. After that the PDMS

layers with microchannel and VCSEL with Au nanoslit array are bonded together and the SPR biosensor chip has been successful fabricated.

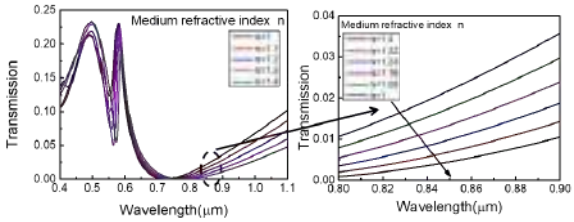


Figure 2. Gold grating transmission spectra for different medium refractive index. The Grating period is 350 nm, both the thickness and the slit width of the grating are 50nm.

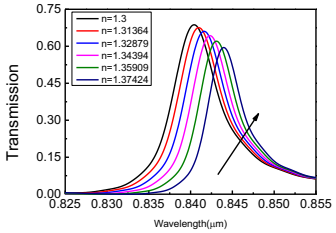


Figure 3. Gold grating transmission spectra for different medium refractive index. The Grating period is 570 nm, both the thickness and the slit width of the grating are 50nm.

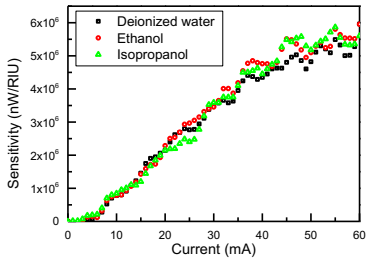


Figure 4. The sensitivity curve with different refractive index samples reference as air.

3. Results and discussion

In current biosensor architecture, the wavelength of the incident beam is fixed at 850 nm, and the beam is incident on the plasmonic aperture approximately normal to the surface. Consequently, we employ the intensity modulation principle to measure the strength of the coupling between the incident light wave and an SP mode at a single wavelength and a fixed narrow range of incident angles [19]. The intensity of transmitted light wave serves as the sensor output. Here we employ liquids with different refractive indices to demonstrate the sensitivity of the plasmonic VCSEL structure. The refractive index was varied from 1 to 1.5, as shown in Figure 2 and 3. There one signal channel to observe the surface property changes is transmission signal channel. When the output window is covered by a metal grating, the transmission properties can be tuned through the change of the refractive index on top of the nanostructures. the output beam will be monitored by the photodiode. When the signal changes because of the refractive index change at the window surface, we observe a change in signal from the photodiode. In this case, a chemical/biosensor function could be achieved by observing the transmission light signal.

The sensing performances of the sensor were characterized via transmission light output power in four kinds of refractive index samples shows in Figure 4. The highest sensitivity reaches 4×10^6 nW/RIU.

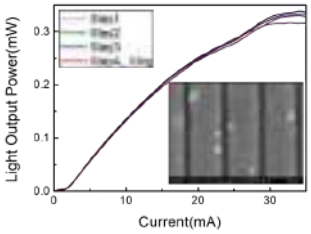


Figure 5. The four steps Biomolecule binding light output power of the biosensor chip, and the insert image is the SEM of the exosome.

4. Conclusions

A intensity detection sensor chip based on VCSEL was proposed. In the sensing chip VCSELs and gold grating are integrated together. Three-dimensional finite difference time domain algorithm simulations are utilized to explore their transmission spectra to calculate the sensitivity of Au grating. The simulation results are in agreement with the experiment. The highest sensitivity of the VCSEL based SPR sensor reaches 4×10^6 nW/. The exosome specificity detection has been achieved and the exosome has been found very well combined on the gold grating. The biosensor chip has the merits of VCSELs and may have potential applications in health care, clinical diagnostics, environmental monitoring, and cancer biomarker testing.

Acknowledgements

This work was supported by National Key R&D Program of China (2018YFA0209000); National Natural Science Foundation of China (61604007,61874145, 61774175); Beijing Natural Science Foundation (4182012,4172009); Beijing Municipal Commission of Education (KM201810005029).

References

[1] Q.Q. Gan, and F.D. Bartoli, Surface-plasmon-coupled semiconductor diode laser package for refractive index sensing, Optics Letters 34: 2180-2182, 2009.

[2] D. Kang, B.Gai, B. Thompson, S.M. Lee, N. Malmstadt,and J. Yoon, Flexible Opto-Fluidic Fluorescence Sensors Based on Heterogeneously Integrated Micro-VCSELs and Silicon Photodiodes, ACS Photonics,pp.912-916,2016

[3] J.Yuan, Y. Xie, Z.Geng, C. Wang, H. Chen, Q. Kan, H.Chen, Enhanced sensitivity of gold ellipticnanohole array biosensor with the surface plasmon polaritons coupling, Optical Materials Express, 5(4):818-826, 2015.

Beam Steering Chip based on VCSEL

Guanzhong Pan[1], Chen Xu[1], Yiyang Xie[1], Weiling Guo[1], Baolu Guan[1], Beijv Huang[2], and Hongda Chen[2]

1Key Laboratory of Optoelectronics Technology (Beijing University of Technology) Ministry of Education, Beijing 100124, China
2Institute of Semiconductor, Chinese Academy of Sciences, Beijing 100083, China
*corresponding author, E-mail: xuchen58@bjut.edu.cn; xieyiyang@bjut.edu.cn

Abstract

Beam steering devices have wide applications in both military and civil fields. The ultimate goal for such devices is to reduce their size, weight, and power consumption. A novel electrically controlled micro beam-steering chip based on coherently coupled VCSEL array integrated with liquid crystal optical phased array was achieved. One-dimensional beam steering was successfully realized. Such a highly integrated beam steering system has high compactness, small size, simple packaging, which could be transformative for various sensing and imaging applications.

1. Introduction

Beam steering devices are essential for a variety of applications in both military and civil fields such as LiDAR, communication, sensing and imaging. The ultimate goal for such devices is to reduce their size, weight, and power consumption, so that they can be mounted on, e.g. drones and autonomous cars [1]. However, most of the reported beam steering devices have the problem that the laser source in the device is spatially separate from the phase shifter [2-5], e. g. optical phased array (OPA), with optics, waveguide, or optical fiber in between, resulting in difficult miniaturization, large size, complex packaging, and low coupling efficiency.

In this paper, we propose a novel electrically controlled integrated beam steering chip based on in-phase coherently coupled VCSEL array (CCVA) and liquid crystal OPA. First, we use the simple and low-cost proton implantation technology to fabricate large-area in-phase CCVAs with uniform near-field to act as the coherent laser source for the chip. Then, taking advantage of the planar structure of the CCVA, the liquid crystal OPA is directly integrated on the CCVA by conventional process. The coherent light generated by the in-phase CCVA is uniformly and normally incident into the OPA without going through any optical elements, fibers, or waveguides, leading to high compactness, small size, simple packaging, and high coupling efficiency. One dimensional beam steering with a field of view of 2.19° has been realized. Larger deflection angle and two dimensional beam steering can be achieved by proper design and optimization of the chip's structure. Such a highly integrated beam steering chip has high compactness, small size, simple packaging, and high coupling efficiency, which could be transformative for various LiDAR, communication, sensing and imaging, and many other applications.

2. Device design and fabrication

A schematic structure of the beam steering chip based on a 4×4 square CCVA is shown in Fig. 1. Fig. 1 (a) is the three-dimensional schematic sketch of the chip, and Fig. 1 (b) is the cross-section view of the chip along the A-A' direction in Fig. 1 (a).

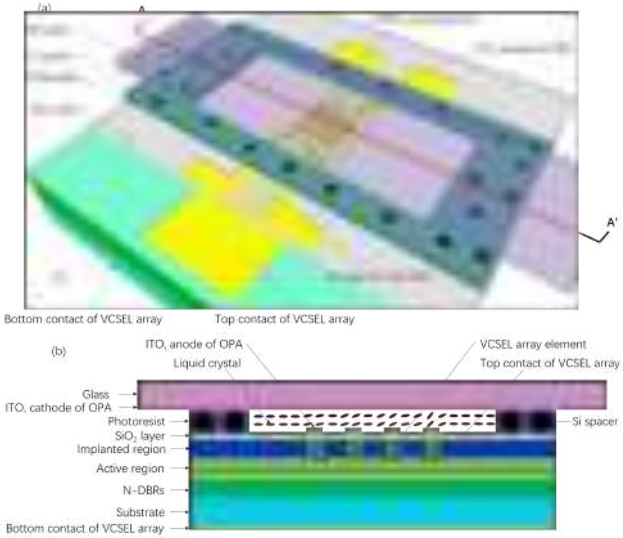


Figure 1: (a) Schematic structure of the beam steering chip based on a 4×4 square CCVA. (b) The cross-section view of the chip along the A-A' direction.

The chip consist of a 4×4 VCSEL array and a 1×4 LCOPA. The element dimension of the VCSEL array is 6 μm×6 μm and the inter-element spacing is chosen as 8 μm to achieve phase-locking among elements [6]. Proton implantation was performed to define the VCSEL array elements. An 800 nm-thick SiO_2 layer was deposited on the surface of the VCSEL array to realize electrical isolation between the VCSEL array and the LCOPA. Then, four ITO

strips with a width of 6 μm and a spacing of 8 μm formed by sputtering and wet etching were situated well atop the VCSEL array elements correspondingly, and act as the four anodes of the LCOPA. An ITO glass were used as the common cathode of the LCOPA. Between the ITO anode and the cathode is a LC layer ($\varepsilon_{//}$ = 11.9 and $\varepsilon_{\perp}$=3.2) with 10 μm thickness. Therefore, by applying voltage to the ITO positive and negative electrodes of each unit of the LCOPA, the LC molecules in between are rotated and the effective refractive index of the LC is changed, so that the phase of the light that going through the LCOPA unit is modulated. By controlling the voltages applied to each unit, the phase difference between units can be adjusted, so that electrically controlled beam steering can be realized. The area of the region where beam steering takes place is only about 95 μm×95 μm.

3. Discussion

The measured threshold current of the 4×4 VCSEL array is about 30 mA. The far-field pattern of the array measured at 34 mA is shown on the left top in Fig. 2, from which the coherence characteristics that the optical energy is mainly concentrated in the on-axis central lobe surrounded by several weaker secondary lobes can be seen clearly, indicating that the array is operating in the in-phase mode [6]. The applied voltages to the four ITO positive electrodes of the LCOPA are denoted by (V_1, V_2, V_3, V_4). Fig. 2 shows the measured beam steering results under different voltage conditions. As can be seen, when (V_1, V_2, V_3, V_4)=(0V, 0V, 0V, 0V), the far-field of the chip has no deflection. When (V_1, V_2, V_3, V_4)=(0.4V, 0.8V, 1.2V, 1.6V), the far-field of the chip is steered upward with a deflection angle of 0.13°. By increasing the applied voltages to (0.5V, 1.0V, 1.5V, 2.0V), the far-field of the chip is further steered upward with a larger deflection angle of 0.56°. When (V_1, V_2, V_3, V_4)=(0.6V, 1.2V, 1.8V, 2.4V), the deflection angle reaches to 1.34°. On the contrary, when (V_1, V_2, V_3, V_4)=(2.4V, 1.8V, 1.2V, 0.6V), the beam is steered downward with a deflection angle of 0.85°, giving a 2.19°. Larger deflection angle and two dimensional beam steering can be achieved by proper design and optimization of the chip's structure.

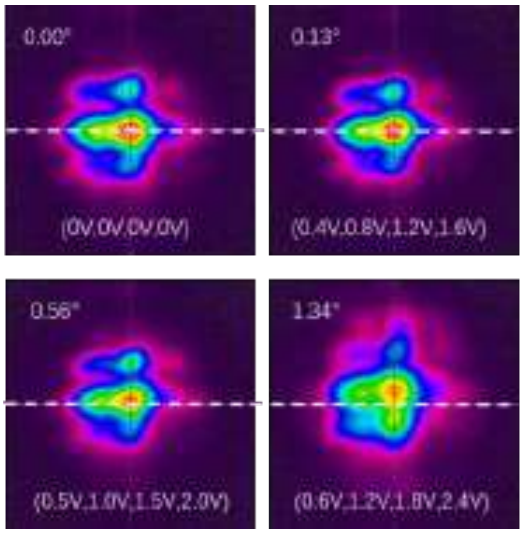


Figure 2: Measured beam steering results under different voltage conditions.

4. Conclusions

A novel integrated electrically controlled beam steering chip based on coherently coupled VCSEL array and liquid crystal optical phased array is proposed, which has successfully realized one-dimensional beam steering. The laser source is directly integrated with the LCOPA in the chip, leading to high coupling efficiency, high compactness, and simple packaging. Thus, the chip can meet the trend of integration and miniaturization of photoelectric systems.

Acknowledgements

This work was supported by National Key R&D Program of China (2018YFA0209000); National Natural Science Foundation of China (61874145, 61604007, 61774175,); Beijing Natural Science Foundation (4172009, 4182012); Beijing Municipal Commission of Education (KM201810005029).

References

[1] M. J. R. Heck, Highly integrated optical phased arrays: photonic integrated circuits for optical beam shaping and beam steering, *Nanophotonics* 6: 93–107, 2016.

[2] P. F. McManamon, T. A. Dorschner, D. L. Corkum, L. J. Friedman, D. S. Hobbs, M. Holz, S. Liberman, H. Q. Nguyen, D. P. Resler, R. C. Sharp, and E. A. Watson, Optical phased array technology, *Proc. IEEE* 84: 268–298, 1996.

[3] D. Engström, M. J. O'Callaghan, C. Walker, and M. A. Handschy, Fast beam steering with a ferroelectric-liquid-crystal optical phased array, *Appl. Opt.* 48: 1721, 2009.

[4] K. Van Acoleyen, K. Komorowska, W. Bogaerts, and R. Baets, One-dimensional off-chip beam steering and shaping using optical phased arrays on silicon-on-insulator, *J. Lightwave Technol.* 29: 3500-3505, 2011.

[5] J. Sun, E. Timurdogan, A. Yaacobi, E. S. Hosseini, and M. R. Watts, Large-scale nanophotonic phased array," *Nature* 493: 195–199, 2013.

[6] G. Pan, Y. Xie, C. Xu, M. Xun, Y. Dong, J. Deng, and J. Sun, Large-Scale Proton-Implant-Defined VCSEL Arrays With Narrow Beamwidth, *IEEE Electron Device Lett.* 39: 390–393, 2018.

Modelling of Nonlinear Metasurfaces: Second-Harmonic Generation and Kerr Effect

Karim Achouri[1], **and Olivier J. F. Martin**[1]

[1]Nanophotonics and Metrology Laboratory, Department of Microengineering,
École Polytechnique Fédérale de Lausanne, Route Cantonale, 1015 Lausanne, Switzerland
*corresponding author, E-mail: karim.achouri@a3.epfl.ch

Abstract

We present a nonlinear metasurface modelling framework based on the generalized sheet transition conditions (GSTC). It may be used to synthesize or analyse the scattering behavior of second- and third-order metasurfaces. We specifically study second-harmonic generation (SHG) and the Kerr effect. This framework is formulated in the frequency-domain and provides the relationships between the metasurface linear and nonlinear susceptibilities and the fields interacting with it.

1. Introduction

The emergence of (linear) metasurfaces along with the progress of nanofabrication technologies have paved the way for ever more elaborate wave-manipulation operations and hence complex metamaterial structures. Following these advances, nonlinear metasurfaces have naturally appeared as a logical outgrowth of conventional linear metasurfaces. However, the tremendous increase of degrees of freedom provided by nonlinear responses compared to linear ones, requires an adequate set of theoretical tools to efficiently model these structures. The purpose of this work is hence to develop a general modelling framework for second- and third-order nonlinear metasurfaces, which takes into account all possible fields interactions.

2. Modelling of Nonlinear Metasurfaces

A metasurface, whether it is linear of nonlinear, may generally be modelled as a zero-thickness homogeneous sheet consisting of electric and magnetic polarizations. Such a sheet may produce discontinuities in the electromagnetic field, which are effectively modelled by the generalized sheet transition conditions (GSTC) [1–5] For a metasurface lying in the xy-plane at $z = 0$, the GSTC are given by

$$\mathbf{z} \times \Delta\mathbf{H} = \frac{\partial}{\partial t}\mathbf{P} - \mathbf{z} \times \nabla M_z, \tag{1a}$$

$$\mathbf{z} \times \Delta\mathbf{E} = -\mu_0 \frac{\partial}{\partial t}\mathbf{M} - \frac{1}{\epsilon_0}\mathbf{z} \times \nabla P_z, \tag{1b}$$

where $\mathbf{P}$ and $\mathbf{M}$ are electric and magnetic polarization densities, respectively, and the operator Δ refers to the difference of the fields on both sides of the metasurface.

For the past few years, the GSTC have been extensively used to model linear bianisotropic metasurfaces [3–5] but they are also perfectly suited for nonlinear operations, as demonstrated in [6–9]. In this work, we present how the frequency-domain GSTC may be applied to model second-harmonic generation (SHG) and the third-order nonlinear Kerr effect.

2.1. Second-Harmonic Generation

Second-harmonic generation is a second-order nonlinear process, where the nonlinear medium scatters light with a frequency that is twice that of the exciting pump [10]. In the case of nonlinear metasurfaces, this effect is typically modelled by assuming that the pump is not depleted [6–9]. Accordingly, we may treat the pump as a constant source of power, which excites nonlinear responses on the metasurface. The frequency-domain GSTC, which thus apply to SHG read

$$\mathbf{z} \times \Delta\mathbf{H}^{2\omega} = j2\omega\mathbf{P}^{2\omega} - \mathbf{z} \times \nabla M_z^{2\omega}, \tag{2a}$$

$$\mathbf{z} \times \Delta\mathbf{E}^{2\omega} = -j2\omega\mu_0\mathbf{M}^{2\omega} - \frac{1}{\epsilon_0}\mathbf{z} \times \nabla P_z^{2\omega}, \tag{2b}$$

where the superscripts 2ω refers to second-harmonic light with ω being the frequency of the pump. The polarization densities may be expressed as

$$\mathbf{P}^{2\omega} = \mathbf{P}_{\text{lin}}^{2\omega} + \mathbf{P}_{\text{nl}}^{2\omega}, \tag{3a}$$

$$\mathbf{M}^{2\omega} = \mathbf{M}_{\text{lin}}^{2\omega} + \mathbf{M}_{\text{nl}}^{2\omega}, \tag{3b}$$

where the linear components ("lin"), which read

$$\mathbf{P}_{\text{lin}}^{2\omega} = \epsilon_0\overline{\overline{\chi}}_{\text{ee}} \cdot \mathbf{E}_{\text{av}}^{2\omega} + \epsilon_0\eta_0\overline{\overline{\chi}}_{\text{em}} \cdot \mathbf{H}_{\text{av}}^{2\omega}, \tag{4a}$$

$$\mathbf{M}_{\text{lin}}^{2\omega} = \overline{\overline{\chi}}_{\text{mm}} \cdot \mathbf{H}_{\text{av}}^{2\omega} + \frac{1}{\eta_0}\overline{\overline{\chi}}_{\text{me}} \cdot \mathbf{E}_{\text{av}}^{2\omega}, \tag{4b}$$

correspond to the interactions of the light at 2ω with the metasurface, while the nonlinear components ("nl"), which are given by

$$\begin{aligned}\mathbf{P}_{\text{nl}}^{2\omega} =& \frac{1}{2}\epsilon_0\big(\overline{\overline{\chi}}_{\text{eee}} : \mathbf{E}_{\text{av}}^{\omega}\mathbf{E}_{\text{av}}^{\omega} + \eta_0\overline{\overline{\chi}}_{\text{eem}} : \mathbf{E}_{\text{av}}^{\omega}\mathbf{H}_{\text{av}}^{\omega} \\ &+ \eta_0^2\overline{\overline{\chi}}_{\text{emm}} : \mathbf{H}_{\text{av}}^{\omega}\mathbf{H}_{\text{av}}^{\omega}\big),\end{aligned} \tag{5a}$$

$$\begin{aligned}\mathbf{M}_{\text{nl}}^{2\omega} =& \frac{1}{2}\big(\eta_0\overline{\overline{\chi}}_{\text{mmm}} : \mathbf{H}_{\text{av}}^{\omega}\mathbf{H}_{\text{av}}^{\omega} + \overline{\overline{\chi}}_{\text{mem}} : \mathbf{E}_{\text{av}}^{\omega}\mathbf{H}_{\text{av}}^{\omega} \\ &+ \frac{1}{\eta_0}\overline{\overline{\chi}}_{\text{mee}} : \mathbf{E}_{\text{av}}^{\omega}\mathbf{E}_{\text{av}}^{\omega}\big),\end{aligned} \tag{5b}$$

represent the nonlinear sources excited by the pump. In these expressions, the subscript "av" refers to the average of the fields on both sides of the metasurface and η_0 is the vacuum impedance. In (4), the tensors $\overline{\overline{\chi}}$ represent linear susceptibilities evaluated at 2ω, while in (5) they represent nonlinear susceptibilities evaluated at ω. To be very general, these expressions take into account all possible combinations of electric/magnetic excitations and responses.

Combining (3) to (5) into (1), specifying the fields to be that of normally propagating plane waves, and solving for the forward ($+z$) and backward ($-z$) second-harmonic waves scattered by the metasurface yields

$$\mathbf{E}_{\text{bw}}^{2\omega} = \frac{1}{\epsilon_0}\overline{\overline{\text{C}}}_1 \cdot \mathbf{P}_{\text{nl}}^{2\omega} + \eta_0 \overline{\overline{\text{C}}}_2 \cdot \bar{\bar{\text{J}}} \cdot \mathbf{M}_{\text{nl}}^{2\omega}, \tag{6a}$$

$$\mathbf{E}_{\text{fw}}^{2\omega} = \frac{1}{\epsilon_0}\overline{\overline{\text{C}}}_3 \cdot \mathbf{P}_{\text{nl}}^{2\omega} - \eta_0 \overline{\overline{\text{C}}}_4 \cdot \bar{\bar{\text{J}}} \cdot \mathbf{M}_{\text{nl}}^{2\omega}, \tag{6b}$$

where the tensors $\overline{\overline{C}}$ contain the linear susceptibilities and are provided in [9]. Relations (6) may either be used to homogenize and thus retrieve the nonlinear susceptibilities of a metasurface, or to predict the second-harmonic light scatter by a nonlinear metasurface with known susceptibilities.

2.2. Kerr Effect

The Kerr effect is a third-order nonlinear process, which typically occurs in centrosymmetric structures and where the response of the medium is modulated proportionally to the field intensity [10]. Here, we restrict our attention to the case of the AC Kerr effect, where the modulation of the medium is due to the light beam itself and not an external DC field. We also ignore the generation of third-harmonic light and thus consider only the interactions between the metasurface and the light at frequency ω. This transforms (1) into

$$\mathbf{z} \times \Delta\mathbf{H} = j\omega\mathbf{P} - \mathbf{z} \times \nabla M_z, \tag{7a}$$

$$\mathbf{z} \times \Delta\mathbf{E} = -j\omega\mu_0\mathbf{M} - \frac{1}{\epsilon_0}\mathbf{z} \times \nabla P_z, \tag{7b}$$

where the polarizations may be expressed in a similar fashion as in (3) except that all terms are evaluated at the frequency ω. From a general perspective, the nonlinear polarizations are now given by

$$\begin{aligned}\mathbf{P}_{\text{nl}}^{\omega} = \frac{3}{4}\epsilon_0\big(&\overline{\overline{\chi}}_{\text{eeee}} \vdots \mathbf{E}_{\text{av}}^{-\omega}\mathbf{E}_{\text{av}}^{\omega}\mathbf{E}_{\text{av}}^{\omega} + \eta_0\overline{\overline{\chi}}_{\text{eeem}} \vdots \mathbf{E}_{\text{av}}^{-\omega}\mathbf{E}_{\text{av}}^{\omega}\mathbf{H}_{\text{av}}^{\omega} \\ &+ \eta_0^2\overline{\overline{\chi}}_{\text{eemm}} \vdots \mathbf{E}_{\text{av}}^{\omega}\mathbf{H}_{\text{av}}^{-\omega}\mathbf{H}_{\text{av}}^{\omega} + \eta_0^3\overline{\overline{\chi}}_{\text{emmm}} \vdots \mathbf{H}_{\text{av}}^{-\omega}\mathbf{H}_{\text{av}}^{\omega}\mathbf{H}_{\text{av}}^{\omega}\big),\end{aligned} \tag{8a}$$

$$\begin{aligned}\mathbf{M}_{\text{nl}}^{\omega} = \frac{3}{4}\big(&\eta_0^2\overline{\overline{\chi}}_{\text{mmmm}} \vdots \mathbf{H}_{\text{av}}^{-\omega}\mathbf{H}_{\text{av}}^{\omega}\mathbf{H}_{\text{av}}^{\omega} + \eta_0\overline{\overline{\chi}}_{\text{memm}} \vdots \mathbf{E}_{\text{av}}^{-\omega}\mathbf{H}_{\text{av}}^{\omega}\mathbf{H}_{\text{av}}^{\omega} \\ &+ \overline{\overline{\chi}}_{\text{meem}} \vdots \mathbf{E}_{\text{av}}^{-\omega}\mathbf{E}_{\text{av}}^{\omega}\mathbf{H}_{\text{av}}^{\omega} + \frac{1}{\eta_0}\overline{\overline{\chi}}_{\text{meee}} \vdots \mathbf{E}_{\text{av}}^{-\omega}\mathbf{E}_{\text{av}}^{\omega}\mathbf{E}_{\text{av}}^{\omega}\big),\end{aligned} \tag{8b}$$

where the superscripts $-\omega$ indicate that we consider a negative frequency to satisfy the condition that the nonlinear polarizations be at frequency ω. Since the fields must be real, we have that $\mathbf{E}(-\omega) = \mathbf{E}^*(\omega)$ [10]. This implies that the polarizations (8), of a metasurface exhibiting low loss and low reflection, may essentially be expressed in terms of the incident light intensity. For instance, an isotropic nonlinear metasurface illuminated with a normally incident x-polarized plane wave would exhibit the nonlinear polarizations

$$P_{x,\text{nl}}^{\omega} = \frac{3}{2}I\eta_0\epsilon_0\big(\chi_{\text{eeee}} + \chi_{\text{eeem}} + \chi_{\text{eemm}} + \chi_{\text{emmm}}\big)E_{x,\text{av}}^{\omega}, \tag{9a}$$

$$M_{y,\text{nl}}^{\omega} = \frac{3}{2}I\eta_0\big(\chi_{\text{mmmm}} + \chi_{\text{memm}} + \chi_{\text{meem}} + \chi_{\text{meee}}\big)H_{y,\text{av}}^{\omega}, \tag{9b}$$

where we have used $E_{x,\text{av}} = \eta_0 H_{y,\text{av}}$ and $E_{x,\text{av}}H_{y,\text{av}}^{*} = 2I$. From these expressions, one may easily obtain the transmitted field in terms of the susceptibilities following similar procedures as those described in [5, 9].

Acknowledgement

We gratefully acknowledge funding from the European Research Council (ERC-2015-AdG-695206 Nanofactory).

References

[1] M. M. Idemen, *Discontinuities in the Electromagnetic Field*. John Wiley & Sons, 2011.

[2] E. F. Kuester, M. Mohamed, M. Piket-May, and C. Holloway, "Averaged transition conditions for electromagnetic fields at a metafilm," *IEEE Trans. Antennas Propag.*, vol. 51, no. 10, pp. 2641–2651, Oct 2003.

[3] K. Achouri, M. A. Salem, and C. Caloz, "General metasurface synthesis based on susceptibility tensors," *IEEE Trans. Antennas Propag.*, vol. 63, no. 7, pp. 2977–2991, Jul. 2015.

[4] K. Achouri, B. A. Khan, S. Gupta, G. Lavigne, M. A. Salem, and C. Caloz, "Synthesis of electromagnetic metasurfaces: principles and illustrations," *EPJ Applied Metamaterials*, vol. 2, p. 12, 2015.

[5] K. Achouri and C. Caloz, "Design, concepts, and applications of electromagnetic metasurfaces," *Nanophotonics*, vol. 7, no. 6, pp. 1095–1116, 2018.

[6] A. Rose, S. Larouche, E. Poutrina, and D. R. Smith, "Nonlinear magnetoelectric metamaterials: Analysis and homogenization via a microscopic coupled-mode theory," *Phys. Rev. A*, vol. 86, p. 033816, Sep 2012.

[7] A. Rose, D. Huang, and D. R. Smith, "Nonlinear interference and unidirectional wave mixing in metamaterials," *Phys. Rev. Lett.*, vol. 110, p. 063901, Feb 2013.

[8] X. Liu, S. Larouche, and D. R. Smith, "Homogenized description and retrieval method of nonlinear metasurfaces," *Optics Communications*, vol. 410, pp. 53 – 69, 2018.

[9] K. Achouri, G. D. Bernasconi, J. Butet, and O. J. F. Martin, "Homogenization and scattering analysis of second-harmonic generation in nonlinear metasurfaces," *IEEE Trans. Antennas Propag.*, vol. 66, no. 11, pp. 6061–6075, Nov 2018.

[10] R. W. Boyd, "Nonlinear optics," in *Handbook of Laser Technology and Applications (Three-Volume Set)*. Taylor & Francis, 2003, pp. 161–183.

Different Photonic Structures via Inverse-Design Algorithm

Döne Yılmaz, Mediha Tutgun, Ahmet M. Alpkılıç, Yusuf A. Yılmaz and Hamza Kurt

Department of Electrical and Electronics Engineering,
TOBB University of Economics and Technology, Ankara, Turkey

Abstract

In this work, we present various photonic structures generated by the inverse design algorithm. The computational method is used to obtain various photonic phenomena such as negative refraction, optical filtering and wavelength selectivity. The high performances of the designed structures reveal that the objective-first inverse-design algorithm is an effective and successful computational design approach for the realization of the photonic devices.

Keywords: Objective-first, inverse-design algorithm, optical notch filters, negative refraction, wavelength demultiplexer.

1. Introduction

In the design of photonic medium, the algorithms have recently attracted a lot of interest [1,2]. Inverse design algorithms enable the formation of the spatially varied structure in an easily way without much depending on intuition. Considering many parameters such as efficiency and functionality in device performances, a more comprehensive and controlled design method rather than intuitive method has been needed. Therefore, the inverse design method, also known as objective-first method, has emerged in the literature [3]. The objective-first inverse design algorithm is an effective optimization method that has been successfully applied to many linear and nonlinear photonic devices. In this design methodology, performance metrics of desired electromagnetic fields that can be revealed by targeted nanophotonic devices are first defined as the objective parameters in the cost function, then the dielectric distribution of the structure is iteratively obtained.

2. The Applications of Algorithm

The negative index medium, optical notch filter and wavelength demultiplexer (WDM) are achieved by the nonconventional design manner. The design details and results are presented in the following sections.

2.1. Negative Refraction

Anomalous light behaviors in photonic mediums such as bending, confining, and backward propagation provide different novel applications. The negative refraction as one of the peculiar properties of light propagation is practical to design effective super lens, prism and high-pass filters [4]. In contrast to conventional mediums, the incident and refracted electromagnetic wave are on the same side of the interface normal in the negative index mediums which means the reversion of the Snell's law. In literature, the negative refraction has been achieved by using metamaterials and photonic crystals [4-5]. In this part of the study, this extraordinary refraction effect is revealed by designing disarranged medium with the computational method.

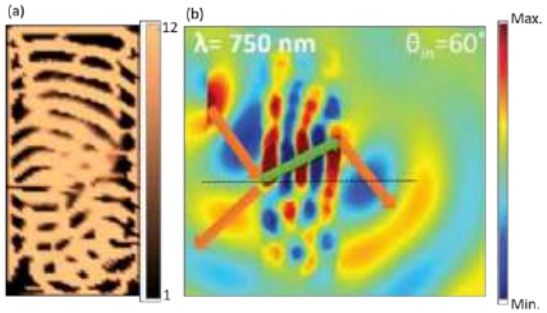


Figure 1: (a) The dielectric constant distribution of the design. (b) The electromagnetic response of the structure at the wavelength of λ=750 nm and incident angle of θ_{in}=60°.

The photonic medium with dimensions of 1.33 μm × 3.55 μm given in Fig. 1(a) has been designed at the wavelength of λ=750 nm for the transverse-electric (TE) polarization owing to additional constraints in the inverse-design algorithm. The performance of the structure has been evaluated through the finite-difference time-domain (FDTD) method. When the properly adjusted oblique Gaussian beam is incident to the interface, the negative refraction phenomenon has arisen in the dielectric structure. Figure 1(b) shows the magnetic field distribution of the propagating wave in the inhomogeneous photonic medium. While the structure routes the wave in the oblique direction, the light conserves its wavefronts. In addition, the output light direction at the structure termination is the same as the route of the incidence in accordance with the Snell's law. As a result, the negative refraction phenomenon is realized at the visible range by using the objective-first algorithm.

2.2. Notch Filter Design

The photonic notch filters are used in many applications like broadband wireless communications and satellite systems [6]. For the first time in the literature, on-chip photonic notch filter design is performed by effective manipulation of the objective-first algorithm. The Notch filter is designed in the visible range to drop frequencies around 545.077 THz. The dielectric constant distribution of the Notch filter is shown as Fig. 2(a) with dimensions of 2.32 µm x 1.40 µm. As shown in the figure, the frequency range that is intended

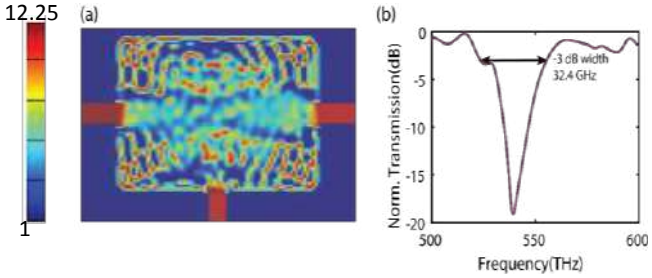


Figure 2: (a) The notch filter design dielectric distribution with dimensions of 4.44 µm x 2.96 µm. (b) Transmission spectrum at the range of 500-600THz.

to be blocked is transferred to the defined discharge port below the design area. The normalized transmission graph of the design is presented in Fig. 2(b). As can be seen in the figure, at the targeted point the attenuation of almost -20 dB is provided. The frequency at which the 50% attenuation is achieved (-3 dB) is measured as 32.4 GHz. The proposed optical Notch filter with great performance is a good candidate to be utilized in integrated photonic circuits.

2.3. Wavelength Demultiplexer (WDM)

WDM designs with a channel configuration of 1×4 are presented in Fig. 3. The designs are elongated along the propagation direction of the added channels, resulting in a footprint of 2.80 µm × 4.60 µm. A continuous distribution of 1×4 T-junction WDM is shown in Fig. 3(a). Figure 3(b)

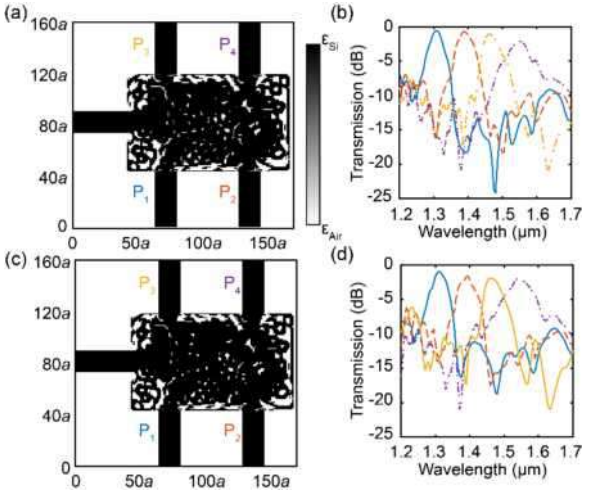


Figure 3: (a) All-dielectric 1×4 T-junction WDM with continuous distribution, (b) normalized transmission efficiency of (a), (c) WDM with binary distribution obtained through the level-set method, (d) normalized transmission efficiency of (c).

shows transmissions in the range [1.20—1.70] µm, where the design possess ultimately yields high transmission efficiencies at the specified wavelengths: -0.57 dB at 1.31 µm, -0.71 dB at 1.39 µm (E-band), -1.25 dB at 1.47 µm (S-band), and -2.11 dB at 1.55 µm. The dielectric distribution of the binary structure resulting from the level-set method for the structure in Fig. 3(a) is shown in Fig. 3(c), and the normalized transmission efficiencies are given in Fig. 3(d). The transmission efficiencies of the level-set binary structure presented in Fig. 3(d) are -0.92 dB at 1.31 µm, -1.65 dB at 1.39 µm, -2.07 dB at 1.47 µm, and -2.23 dB at 1.55 µm. The resulting devices exhibited ultra-high transmission, small footprint, low crosstalk, and relatively narrow channel spacing, all of which are very important for a variety of applications in integrated photonics.

3. Conclusions

We have demonstrated that it is possible to obtain the photonic device applications in the complex media via the objective-first inverse algorithm. Besides being compact, the proposed devices work with high performance at the design spectrum. Since the algorithm provides unconventional design capability with an acceptable simulation time, it has great potential to be used in new generation designs in the future.

Acknowledgments

The authors acknowledge the financial support of the Scientific and Technological Research Council of Turkey (TUBITAK) (116F200). H.K. also acknowledges the partial support of the Turkish Academy of Sciences.

References

[1] Seliger, P., Mahvash, M., Wang, C., and Levi, A., "Optimization of aperiodic dielectric structures", *J. Appl. Phys.* 100: 34310- 34316, 2006.

[2] Elesin, Y., Lazarov, B. S., Jensen, J. S., and Sigmund, O. "Design of robust and efficient photonic switches using topology optimization," *Photonics and Nanostructures - Fundamentals and Applications* 10: 153165, 2012.

[3] Lu, J., and Vuckovic, J., "Objective-first design of high-efficiency, small footprint couplers between arbitrary nanophotonic waveguide modes", *Opt. Express*, 20, 7221, 2012.

[4] T. Baba, H. Abe, T. Asatsuma and T. Matsumoto, "Photonic Crystal Negative Refractive Optics," *J. Nanosci. Nanotechnol.* 10: 1533-1542, 2010.

[5] V. Veselago, L. Braginsky, V. Shklover, and C. Hafner, "Negative Refractive Index Materials," *J. Comput. Theor. Nanosci* 3: 1-30, 2006.

[6] J. Ge, H. Feng, G. Scott, and M. P. Fok, "High-speed tunable microwave photonic notch filter based on phase modulator incorporated Lyot filter," *Opt. Lett.* 40: 48, 2015.

[7] M. Tutgun, A. M. Alpkilic, Y.A. Yilmaz, A. Yeltik, D. Yilmaz, and H. Kurt, "On-chip photonic filter design via objective-first algorithm", Proc. SPIE 10743, Optical Modeling and Performance Predictions X, 107430M (2018).

Y. A. Yılmaz, A. M. Alpkilic, A. Yeltik, D. Yilmaz, M. Tutgun, and H. Kurt, "Parametric study of wavelength demultiplexers designed via objective-first algorithm", Proc. SPIE 10720, Nanophotonic Materials XV, 1072004 (2018).

Inverse Design and Optimization along Machine Learning for Metasurfaces

Samad Jafar-Zanjani[1], and Hossein Mosallaei[1*],

[1] Metamaterials Lab, Department of ECE, Northeastern University, Boston, Massachusetts 02115, USA
*corresponding author, E-mail: hosseinm@ece.neu.edu

Abstract

Despite many advantages, performance of the conventional optical metasurfaces is not yet satisfactory, in terms of their functionality, frequency and angular response, and efficiency, due to the limitations imposed by their constituent units of canonical shape. In this summary we propose more sophisticated geometries, such as binary-pattern unit-cells, along with adaptive genetic algorithm multi-objective optimization, to overcome the limitations of the conventional metasurfaces and pave the way for efficient inverse design by machine leaning algorithms.

1. Introduction

As optical metasurfaces become increasingly pervasive the expectations from them are becoming progressively complex[1, 2]. Metasurface building blocks (BBs) have been mostly limited thus far to nano-scatterers with canonical shapes. The limited number of structural parameters in conventional BBs do not support the growth rate of metasurfaces and limits them to mostly a single functionality with narrow frequency and angular response.

To overcome the mentioned limitations, one needs to choose more sophisticated BBs with increased structural degrees of freedom, such as binary pattern BBs. Here, we propose a powerful evolutionary optimization method, adaptive genetic algorithm (AGA)[4], to handle the inherent difficulties that arise in designing the binary-pattern metasurfaces. We also demonstrate that surplus data generated by the AGA technique can be employed by machine learning algorithms to facilitate efficient inverse design of metasurfaces.

2. Adaptive Genetic Algorithm

In the most general case, a multi-objective optimization problem can be expressed as an attempt to maximize a fitness function

$$\max_{\mathbf{p}\in\mathbb{R}} \mathcal{F}(\mathbf{p}) \tag{1}$$

where $\mathbf{p} = (p_1, p_2, ..., p_n)$ is a vector representing the parameter space and the fitness function, $\mathcal{F}(\mathbf{p})$, can be represented as a weighted sum of the sub-objective functions:

$$\mathcal{F}(\mathbf{p}) = W_1 \times f_1(\mathbf{p}) + W_2 \times f_2(\mathbf{p}) + ... + W_n \times f_n(\mathbf{p}). \tag{2}$$

In the AGA method we start with an initial set of weights (W_i's) in eq. 2, and employ the conventional genetic algorithm (GA)[3] to maximize the corresponding $\mathcal{F}(\mathbf{p})$. During the course of the optimization, if an objective update criterion is met, the fitness function is updated and the optimization proceeds until the stop criteria is satisfied.

3. Binary-Pattern Plasmonic Metasurface

As an example of the application of the AGA method, in this section we present the results of the optimization of a binary-pattern plasmonic metasurface, working at 120 THz. We have taken advantage of an in-house developed GPU-enabled FDTD solver for electromagnetic characterization of the metasurface. Unit-cell of the inverse-designed metasurface is illustrated in Fig. 1. Here, we optimize one quarter of the binary pattern with 10×10 pixels. The fitness function is considered as

$$\begin{aligned}\mathcal{F}(\mathbf{p}) = W_\varphi \times \exp[-6.0\,(\varphi(\mathbf{p}) - \varphi_{\text{target}})^2] \\ + W_a \times \exp[-4.0\,(1.0 - A(\mathbf{p}))^2]\end{aligned} \tag{3}$$

In this application, the reflection phase is of extreme importance for achieving different functionalities, such as beam-steering and lensing. Therefore, in the AGA optimization, we first optimize the unit-cells to achieve sample phase levels from 0 to 2π. In other words, initial weighting coefficients in eq. 3 are considered as $W_\varphi = 1.0$ and $W_a = 0.0$. Once an acceptable value for the initial fitness function has been achieve by GA optimization, we update the fitness function to include a small weight for the amplitude of the reflection, which is of lower priority compared to the reflec-

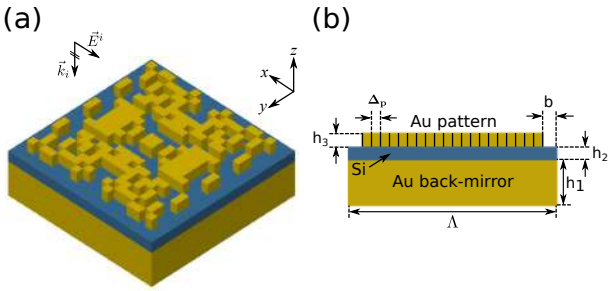


Figure 1: Unit-cell of the optimized plasmonic metasurface. (a) Perspective, and (b) side views of the unit-cell. Parameters: h_1=100 nm, h_2=30 nm, h_3=30 nm, Δ_p = 25 nm, b=25 nm, Λ = 550 nm [4].

tion phase, but, is crucial for improving the efficiency of the metasurface. More specifically, the weighting coefficients have been updated to $W_\varphi = 0.7$ and $W_a = 0.3$.

We further design a reflect-array consisting of the optimized BBs to bend a normally incident beam to an arbitrary direction at 120 THz. Figure 2 (a) depicts the 8×8 super-cell of the reflect-array. Reflection pattern of the reflect-array is also presented in Fig. 2, showing a beam very close to the targeted direction.

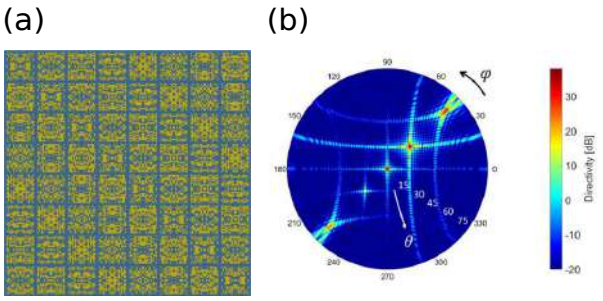


Figure 2: (a) Designed super-cell of the metasurface to reflect a normally incident beam to $(\theta_0, \varphi_0) = (30°, 45°)$. Reflection pattern of the designed metasurface, showing a main-lobe very close to the targeted direction at $(\theta, \varphi) = (28.6°, 45°)$ [4].

In addition to presented application, AGA method has been successfully employed to tackle other complicated applications including: A dual-beam aperiodic leaky-wave antenna, which diffract TE and TM excitation waveguide modes to arbitrary directions, and A dual-band visible-transparent IR-emitting metasurface. These applications will be elaborated during the presentation.

4. GA Surplus Data and Neural Network Based Inverse Design

Evolutionary optimization methods provide a valuable dataset that can be employed to conceive an image of the solution domain. As an example, surplus GA data corresponding to the binary-pattern plasmonic metasurface in the previous section is illustrated in Fig. 3. A uniform amplitude of around 0.4 is achievable with reflection phase samples from 0 to 2π. Alternatively, one can choose to work with highest amplitude at each sample phase, for achieving highest possible reflection efficiency, at the price of some spurious side-lobes.

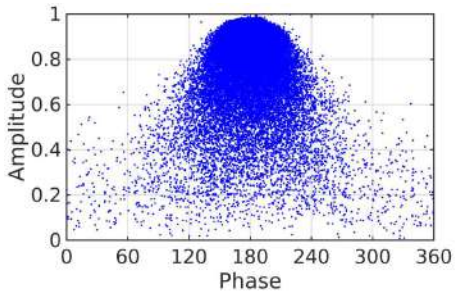


Figure 3: GA data corresponding to the binary plasmonic metasurface [4].

GA data can also be used to facilitate neural network based inverse design of metasurfaces. To demonstrate this concept, authors have recently proposed machine learning for efficient inverse design of an all-dielectric diffractive metagrating with parameterized units of arbitrary shape, defined by 16 radii values. A high-performance in-house developed RCWA solver is used to map the radii to the diffraction efficiencies (DEs) of the metagrating. 90,000 sample units in 8 categories have been solved to generate a diverse training dataset. A 3-layer artificial neural network (ANN) has been trained to yield a network function, which can mimic the response of the metagrating in much faster fashion than direct solution of the Maxwell's equations. Taking advantage of the obtained network function, we have been able to inverse design the metagrating orders of magnitude faster than brute-force optimization.

5. Conclusions

We have demonstrated the AGA technique as a powerful multi-objective evolutionary optimization method for designing binary-pattern metasurfaces. Inverse design of a binary-pattern plasmonic reflect-array with high tolerance to fabrication imperfections have been presented as an application of the AGA technique. We have explored more applications that will be presented in the conference. Finally, we have shown that the surplus GA data, can give an intuitive image of the solutions domain, and be used in new-age algorithms, such as, machine learning.

Acknowledgement

This work is supported in part by U.S. Air Force Office of Scientific Research (AFOSR)(FA9550-18-1-0354).

References

[1] W. T. Chen, et al, Broadband achromatic metalens for focusing and imaging in the visible, *Nature nanotechnology* 13(3): 220, 2018.

[2] M. Khorasaninejad, F. Capasso, Versatile multifunctional photonic components, *Science* 358(6367): eaam8100, 2017.

[3] J. M. Johnson, Y. Rahmat-Samii, Genetic algorithms in engineering electromagnetics, *IEEE Antennas and propagation Magazine*: 39(4):7-21, 1997.

[4] S. Jafar-Zanjani, H. Mosallaei, Adaptive genetic algorithm for optical metasurfaces design, *Scientific reports* 8(1): 11040, 2018.

[5] S. Inampudi, H. Mosallaei, Neural network based design of metagratings, *Applied Physics Letters* 112(24): 241102, 2018.

Multiple scattering by complex objects: revisiting the methods of fictitious sources

Anthony Gourdin[1,2], Patrice Genevet[3], Didier Felbacq[1]

[1]Univ Montpellier, L2C CNRS, Montpellier, France
[2]SAFRAN Electronics & Defense, Paris, France
[3]Université Côte d'Azur, CRHEA CNRS, Valbonne, France
*corresponding author, E-mail: didier.felbacq@umontpellier.fr

Abstract

We present a numerical method allowing to solve efficiently the Maxwell system in the presence of many obstacles. Each obstacle is characterized by a scattering matrix written in an adapted basis. The scattered field is then represented by fictitious sources. This approach is mixed with a fast multiple algorithm in order to deal with several different obstacles.

1. Introduction

The recent advances in the field of metasurfaces [1], have led to an increasing interest in the numerical methods that can deal with a large number of different resonators arranged along periodic or aperiodic patterns. Several methods can be used to obtain the scattered field. Two main categories can be singled out: on one hand, those who use a modal expansion, such as multiple scattering methods or the Fourier Modal Method or on another hand, those who use a discretization in direct space (such as the FDTD or the FEM).

We propose here a mixed approach where the field scattered by one obstacle is obtained through any available method (boundary integral equation, finite volume, DDA...). Then, a modal basis adapted to the scatterer is obtained by solving for the eigenfunctions of the Laplace-Beltrami operator on the boundary of the scatterer. This allows to express the exterior Calderòn operator and to represent the scattering matrix. The scattered field outside the obstacle has then an integral expression in terms of fictitious sources and can be used in a multiple scattering scheme.

2. Description of the method

The method used here to compute the field scattered by one obstacle is the DDA

2.1. Numerical computation of the scattering matrix

Let us consider an obstacle Ω that is connected and has a smooth boundary. It is characterized by its relative permittivity ε (it needs not be constant inside Ω).

Given an incident harmonic field (E^i, H^i) with pulsation ω, the field (E^s, H^s) scattered by the obstacle can be computed by using the Discrete Dipole Approximation.

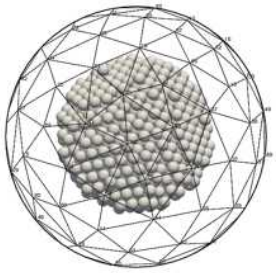


Figure 1: Delaunay triangulation enclosing the DDA. See image source.

The point is to be able to characterize the obstacle by pre-computing its scattering matrix [2], that is, the linear operator relating the scattered field to the incident one

$$(E^s, H^s) = \mathcal{S}(\omega)(E^i, H^i)$$

In order to do so, a basis of incident fields is needed. That is, we are going to compute the scattered field for a finite number of incident fields and then, the field scattered for an arbitrary incident field will be obtained as a linear combination of previously computed fields. The accuracy of the methods is linked to the number of elements of the incident field basis. in order to choose an efficient basis, we first note that in order to know the field everywhere, it suffices to know it on the surface of the obstacle, see Figure 1. Indeed, the scattered electric field can be written

$$E^s(r) = \frac{iZ_0}{k}\nabla\times\nabla\times\int_S g_0(k|r-r'|)m^s dS + \quad (1)$$

$$\nabla\times\int_S g_0(k|r-r'|)j^s dS \quad (2)$$

where $m^s = n\wedge E^s|_{\partial\Omega}$, $j^s = n\wedge H^s|_{\partial\Omega}$ are the tangential traces of the fields on the boundary of Ω, and the Green function g_0 is $g_0(x) = \frac{e^{ikx}}{4\pi x}$. This allows to compute the fields everywhere in space once they are known on the boundary of the obstacle.

It is to be noted that the information given by m^s and j^s is redundant since these functions are related by the so-called exterior Calderòn operator [3] $C^e(\omega) : m^s \longrightarrow j^s$. Using this operator, the integral formulation can be written by using m^s only. In the same way, the incident field

admits an integral representation involving m^i only by use of the exterior Calderòn operator. In order to obtain an efficient representation of the scattering matrix, we need to be able to decompose the functions defined on the boundary of the obstacle as well as the Calderón operators. In the case of a sphere, a natural basis is that of the spherical harmonics $Y_l^m(\theta, \phi)$. These functions are eigenfunctions of the angular part of the Laplacien in spherical coordinates, which is nothing else than the Laplace-Beltrami operator on the sphere [5]. These functions can be generalized to any sufficiently obstacle with regular boundary precisely as eigenfunctions of the Laplace-Beltrami operator $-\Delta_{\partial\Omega} Y_n = \lambda_n Y_n$. There are efficient numerical methods to compute these functions [6]. Given this basis, it is possible to obtain a basis for tangent fields to Ω. This is a generalization of the so-called vector harmonics

$$\mathbf{Y}_{1n} = (\lambda_n)^{-1/2} \mathrm{curl}_{\partial\Omega} Y_n,\ \mathbf{Y}_{2n} = (\lambda_n)^{-1/2} \nabla_{\partial\Omega} Y_n. \tag{3}$$

The set $\{\mathbf{Y}_{ln}, l = 1, 2,\ n = 1, \ldots\}$ form a (hilbertian) basis. This can be used to represent the tangential trace of the field in the form

$$m^s = \sum_{ln} m^s_{ln} \mathbf{Y}_{ln},\ m^i = \sum_{ln} m^i_{ln} \mathbf{Y}_{ln} \tag{4}$$

and the scattering matrix relates (m^i_{ln}) to (m^s_{ln}).

2.2. Several obstacles from a point of view of the multiple scattering

Now that we know how to characterize each object n by a scattering matrix S, we put our interest in how we can solve a problem with several objects.

Dealing with the interaction between all the N objects directly represents an algorithm scaling as N^2. An algorithm [7] called Multi- Level Fast Multipole Method (MLFMM) was developed to reduce the computational complexity.

This algorithm divides the entire domain that contains all of the scatterers into nested subdomains of cubic shape, until there is only one scatterer by subdomain. The interactions are then represented via a tree. In the lower branch of the tree, the scatterers interact directly with the other scatterers in the immediate neighborhood, whereas in the higher branches, the interactions are treated by means of multipoles.

Our approach is particularly suited to this algorithm since the field are represented by means of fictitious sources. The field scattered by a cluster of obstacles can be easily represented by fictitious sources situated on the boundary Γ of a domain comprising the cluster, once the field radiated by each obstacle is known. More precisely, given the tangential traces m^s_k for a collection of obstacle $k = 1 \ldots N$, there is a transfer operator $\mathcal{T}$ relating this traces to that on Γ. The numerical representation of $\mathcal{T}$ involves the evaluation of the free space Green function on predetermined points, a calculation that can be easily precomputed.

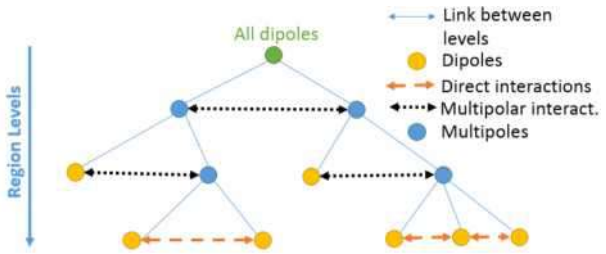


Figure 2: FFM interactions.

3. Conclusion

The proposed method allows to compute the field scattered by many, possibly different, scatterers in an efficient way since the electromagnetic behavior of each different scatterer can be pre-computed before solving the multiple scattering problem. This leads to efficient optimisation codes that usually require many iterations. It is to be noted that the present method does not assume any specific position for the scatterers. For instance, scatterers deposited on a surface or a plane can be considered.

Acknowledgement

This research was conducted under the financial support of SAFRAN Electronics & Defense and the French Procurement Defense Agency (grant CIFRE-DEFENSE n° 005/2017/DGA).

References

[1] P. Genevet, F. Capasso, F. Aieta, M. Khorasaninejad, and R. Devlin, Recent advances in planar optics: from plasmonic to dielectric metasurfaces,*Optica*, 4: 139-152, 2017.

[2] D. Felbacq and G. Bouchitté, Homogenization of a set of parallel fibers, *Waves Ramdom Media*, 7: 245-256, 1997.

[3] M. Cessenat, *Mathematical methods in electromagnetism*, World Scientific, Singapore, 1996.

[4] J. C. Nedelec, *Acoustic and electromagnetic equations*, Springer-Verlag, New York, 2001.

[5] S. Rosenberg, *The Laplacian on a Riemaniann Manifold*, Cambridge University Press, Cambridge, 1997.

[6] Martin Reuter, Silvia Biasotti, Daniela Giorgi, Giuseppe Patane, Michela Spagnuolo, Discrete Laplace-Beltrami Operators for Shape Analysis and Segmentation, *Computers & Graphics* 33: 381-390, 2009.

[7] T. Hrycak and V. Rokhlin, An improved fast multipole algorithm for potential fields, *SIAM J. Sci. Comp.*,19: 1804-1826, 1998.

Global Topology Optimization Networks (GLOnets) for Metasurface Design

Jonathan A Fan[1]

[1] Department of Electrical Engineering, Stanford University, Stanford, CA USA
E-mail: jonfan@stanford.edu

Abstract

I will introduce a new method for designing ultra-high efficiency metamaterials using global topology optimization networks (GLOnets). These networks combine deep generative neural networks with adjoint-based topology optimization to perform a global search and topology optimization within the design space. Importantly, these concepts utilize a population-based approach to optimize a distribution of device instances, which ensures that the full design space is properly sampled and vetted during network training. These hybrid algorithms that combine machine learning with physical calculations will set the stage for big data approaches to assist in defining the next generation of nano-based optical devices.

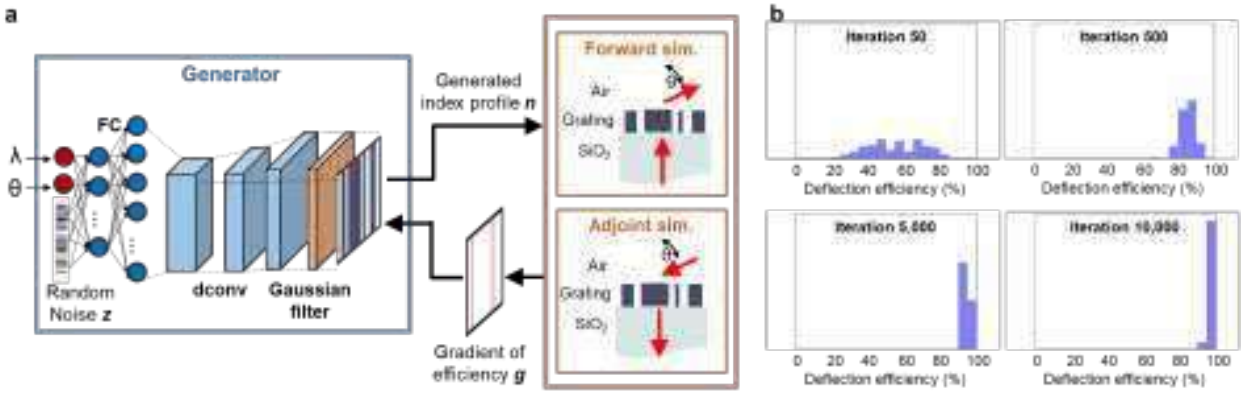


Fig. 1 GLOnets for metasurface design. (a) Architecture of GLOnets. A conditional generative neural network combines with adjoint-based optimization algorithms to perform device design. (b) Histogram plot of the efficiencies of a distribution of devices over the course of optimization. As the optimization iteration number increases, the device efficiency distribution narrows and converges towards high efficiency values.

Metasurface-based Light Sources, Modulators, and Detectors

Dielectric metasurfaces for holography, color printing and crypto-display

Junsuk Rho[1,2*]

[1]*Department of Mechanical Engineering, Pohang University of Science and Technology, Pohang, 37673, Republic of Korea*

[2]*Department of Chemical Engineering, Pohang University of Science and Technology, Pohang, 37673, Republic of Korea*

**jsrho@postech.ac.kr*

Miniaturization is a main stream in modern technology, but reduction of conventional optical components accompanies performance degradation that limits the minimum feature size of optical devices. Metasurfaces that consist of ultrathin subwavelength antenna arrays can be a promising solution because metasurfaces provide an effective way to control phase and amplitude without constraints on the device size. Metahologram is one of the most promising applications of phase-control metasurfaces because fundamental limitations of conventional holograms such as twin images can be removed by metaholograms due to their sub-wavelength pixel size. Early metahologram research has achieved high efficiency by tailoring electric and magnetic dipole resonances through adjusting unit structure shapes [1] or materials [2]. As a result, silicon becomes main material for metaholograms due to high refractive index in the visible as well as CMOS compatibility. Metaholograms have enabled further applications such as a polarization independent broadband beam splitter [3] and random point-cloud generator for 3D detection [4]. On the other hand, amplitude-control metasurfaces realize sub-wavelength color printing. These are based on absorptive resonance determined by structure shapes, thus, it is possible to make a metasurface have different colors by incident polarization enabling cryptographic applications [5]. In this case, silicon still shows higher efficiency than typical plasmonic metasurfaces [6]. Comprehensive metasurfaces that enable to control both phase and amplitude have also been realized by adjusting unit structure configurations. The hologram resolution can be drastically improved by controlling complex amplitude using X-shaped nanostructures [7]. It is also possible to achieve both functions of holography and color printing in a single metasurface [8]. In the future, metasurface research will be expanded to a practical region by large-scale fabrication and tunability incorporating with active materials such as 2D and organic materials [9].

References

1. Z. Li*, I. Kim* *et al*., *ACS Nano* **11**, 9382-9389 (2017).
2. G. Yoon *et al*., *ACS Photonics* **5**, 1643-1647 (2018).
3. G. Yoon *et al*., *Sci. Rep.* **8**, 9468 (2018).
4. Z. Li *et al*., *Light: Sci. & Appl.* **7**, 63 (2018).
5. J. Jang *et al*., *Adv. Opt. Mater.* **7**, 1801070 (2019).
6. M. Kim*, I. Kim*, J. Jang* *et al.*, *Appl. Sci.* **8**, 982 (2018).
7. G. Lee *et al*., *Nanoscale* **10**, 4237-4245 (2018).
8. G. Yoon *et al*., *ACS Nano* **12**, 6421-6428 (2018).
9. I. Kim*, G. Yoon*, J. Jang* *et al*., *ACS Photonics* **5**, 3876-3895 (2018).

Dynamic Formation of Ultra-Small Images via Metasurfaces

Khosro Zangeneh Kamali[1], Lei Xu[2], Jonathan Ward[1], Kai Wang[1], Guixin Li[3], Andrey E. Miroshnichenko[2], Dragomir Neshev[1], and Mohsen Rahmani[1,*]

[1]Nonlinear Physics Centre, The Australian National University, Canberra, ACT 2601 Australia
[2]School of Engineering and Information Technology, University of New South Wales, Canberra, ACT 2600, Australia
[3]Department of Materials Science and Engineering, Shenzhen Institute for Quantum Science and Engineering, Southern University of Science and Technology, Shenzhen 518055, China.
*corresponding author, E-mail: mohsen.rahmani@anu.edu.au

Abstract

A new technique to achieve image tuning in a reversible fashion by dielectric metasurfaces, composed of subwavelength silicon resonators, is demonstrated. We show that by controlling the temperature of a metasurface we can tune the encoded transmission pattern. To this end, we have designed and fabricated two sets of nanoresonators composed of non-concentric silicon disks with a hole that exhibit spectrally close sharp Fano resonances and forming a Yin-Yang pattern, with a full control on the contrast.

1. Introduction

Today, increasing the resolution of miniaturized displays is an important technological challenge for small gadgets. The further need for improving the resolution in images and displays, together with higher compactness, has motivated scientists to exploit novel alternatives, such as metasurfaces, allowing substantial improvements to the current technologies. Recently, many techniques have been proposed for tuning metasurfaces. Changing phase state of structured materials by laser illumination [1] offers reversible tuning in metasurface functions, but suffers from the challenges to achieve intermediate states in the output. Hydrogenation/dehydrogenation of metasurfaces is another novel tuning technique [2], however this process is relatively slow. Doping materials [3] can be used for changing the behavior of the metasurface, however it is not reversible. Utilizing free carrier plasma effect [4-6] can be achieved in plasmonic and semiconductor nanostructures in designs, however, it introduces high optical loss which limits the tunability. Tuning the metasurface response can also be achieved by covering the metasurface with liquid crystal [7] however this method revokes the access to the surface of nanostructures that forbids some applications, such as sensing.

Nevertheless, none of the aforementioned approaches have been used for image tuning. Recently, some research works have presented manipulating and decoding the output waveforms of the metasurface to construct an image [8, 9]. However, with the proposed imaging techniques, the dynamic tuning on the spatial of distribution of light in images has remained a challenge. Here, we propose a novel tuning technique that is compatible for image tuning. It is known that the thermo-optical effect of dielectrics can be used to alter the refractive index and subsequently optical responses of bulk materials [10, 11]. Such a rarely used degree of freedom provides a great platform for tuning the optical properties of nanostructures. Moreover, temperature control has never been used, as a versatile tool, to tune the contrast of the constructed image.

Here, we exploit heating and cooling for controlling the contrast of an image constructed by metasurfaces. For obtaining a tunable image with high switching contrast image, we employ Fano Resonance (FR) concept [12, 13] to exhibit a narrow-band resonance that is ideal for achieving very high transmission contrast [14]. This contrast is formed by transmission through the metasurface that is designed to filter the light at certain wavelengths. Our technique does not require external stimulator such as altering the polarization or angle of the illumination, or refractive index of environment. Silicon is chosen because of its high refractive index and pronounced thermo-optical properties. [10, 11]. For demonstration of the concept, we have chosen an Yin-Yang image that contains a binary region: bright and dark [14].

2. Results and Discussions

For building blocks of the Yin-Yang pattern, non-concentric disk and hole nanostructures are proposed (Fig. 1a). These building blocks exhibit sharp Fano resonances, therefore being opaque at a certain wavelength. Thus, the image construction is determined by type and arrangement of building blocks and the image contrast is determined by the resonance features of them. The experimentally measured transmission spectra of building blocks type A and B at temperatures 22°C, 75°C and 125°C are plotted in the Fig. 1b. As can be seen, the increment of the temperature, can lead to the optical transparency of one building block and opaqueness in the other at λ = 784 nm. When the metasurface is at room temperature, Types A and B transmit 25% and 75% of the light, respectively. But when the metasurfaces temperature reaches 125˚C, Types A and B transmit 75% and 40% of the light, respectively. This reversible transmission behavior effectively leads to a reversible contrast of the image.

The images of the Yin-Yang pattern at target illumination λ = 784 nm, in different temperatures, can be seen in Fig.4c. As expected, by changing the temperature from 22˚C to 125˚C, a dynamic reversible image can be observed, sweeping itself from one state to another, with exhibiting no contrast in the intermediate state. Point (i) is recorded image at 22˚C, where building block type A is opaque, while building block type B transmits the light, therefore the contrast is very clear. Point (ii) represents the temperature, at which the contrast is negligible. Experimentally this point is at 75˚C. And finally, Point (iii), shows the case, where one can see an opposite contrast, when building block type A is transparent and building block type B is opaque. In the proposed image tuning method, more shades and image states can be achieved by simply including different resonator building blocks in the image. Alongside this, it is worth noting that by employing the localized heating technology such as the one developed for anti-fog windows, this technique can find various applications in functional transparent displays, tunable tinting windows, tunable optical filters and optical switches.

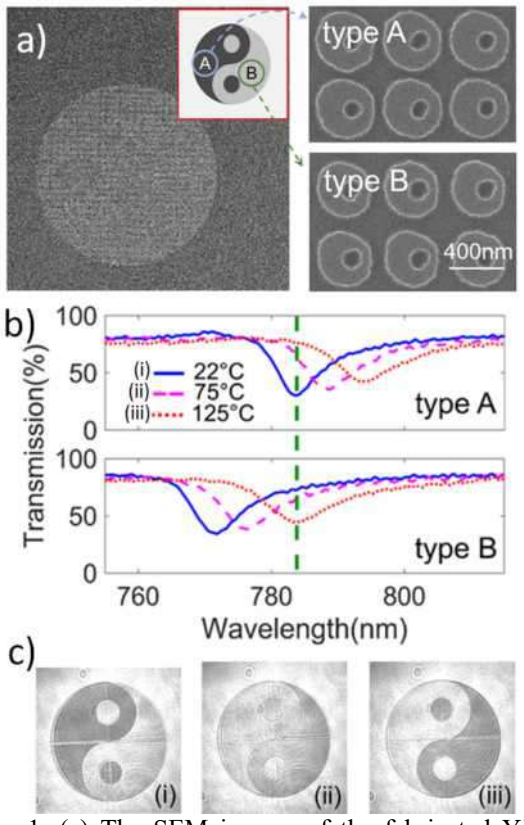


Figure 1: (a) The SEM images of the fabricated Yin-Yang pattern. The location of building blocks types A (r_{small} = 60 nm, r_{large} = 190 nm), and B (r_{small} = 56 nm, r_{large} = 183 nm) are identified in the inset, accompanied by magnified SEM images. (b) Experimentally measured transmission of the building blocks type A and B at wavelength 784 nm in different temperatures. (c) The images obtained at 784 nm in temperatures of (i) 22°C, (ii) 75°C and (iii) 125°C, respectively.

3. Conclusions

In summary, a Yin-Yang pattern, consisting of two building blocks possessing different resonant wavelengths, has been used to demonstrate the contrast control. Due to high quality factor of the FR, a slight modification in the metasurfaces temperature, results in a large transmission contrast. Sweeping temperature from 22˚C to 125˚C, was used as a versatile tool to completely control the contrast of the image, where binary building blocks of the image become transparent or opaque, separately and reversibly. This type of thermally tunable metasurfaces can be fabricated in larger dimensions and encompasses more integrated building blocks with different resonances, which leads to the formation of an image with more shades (dynamic range) and details. The proposed mechanism for designing tunable metasurfaces paves the road for applications such as real time displays, optical switches, passive temperature sensors and selective illumination systems.

Acknowledgements

The authors acknowledge the funding support provided by the Australian Research Council (ARC). The authors also appreciate the use of Australian National Fabrication Facility (ANFF)—the ACT Node.

References

[1] C. C. Hung, T. M. Lun, C. Jie, W. P. Chieh, C. Yi Hao, W. Hsiang Chu, C. Ting Yu, H. W. Ting, W. H. Jun, S. Greg, T. D. Ping, Laser Photon. Rev. 10: 1063, 2016.

[2] J. Li, S. Kamin, G. Zheng, F. Neubrech, S. Zhang, N. Liu, Sci. Adv. 4: 1704338, 2018.

[3] T. Lewi, P. P. Iyer, N. A. Butakov, A. A. Mikhailovsky, J. A. Schuller, Nano Lett. 15: 8188, 2105.

[4] Y. Yao, R. Shankar, M. A. Kats, Y. Song, J. Kong, M. Loncar, F. Capasso, Nano Lett. 14: 6526, 2014.

[5] Y.-W. Huang, H. W. H. Lee, R. Sokhoyan, R. A. Pala, K. Thyagarajan, S. Han, D. P. Tsai, H. A. Atwater, Nano Lett: 16: 5319, 2016.

[6] A. Howes, W. Wang, I. Kravchenko, J. Valentine, Optica 5: 787, 2018.

[7] A. Komar A, R. Paniagua-Domínguez, A. Miroshnichenko, Y. Yu, Y. Kivshar, A. Kuznetsov, D. Neshev, ACS Photonics 5:1742, 2018.

[8] X. Zang, F. Dong, F. Yue, C. Zhang, L. Xu, Z. Song, M. Chen, P.-Y. Chen, S. Buller Gerald, Y. Zhu, S. Zhuang, W. Chu, S. Zhang, X. Chen, Adv. Mater 30: 1707499, 2018.

[9] J. Bar-David, L. Stern, U. Levy, Nano Lett. 17: 1127, 2017.

[10] R. Mohsen, X. Lei, M. A. E., K. Andrei, C. Rocio, C. Haitao, Z. Yair, K. Sergey, Z. Guoquan, N. D. N., K. Y. S., Adv. Funct. Mater. 27: 1700580, 2017.

[11] J. Ward, K. Z. Kamali, L. Xu, G. Zhang, A. E. Miroshnichenko, M. Rahmani, Beilstein J. Nanotechnol. 9: DOI 10.3762/bjnano.9.44, 2018.

[12] A. E. Miroshnichenko, S. Flach, Y. S. Kivshar, Rev. Mod. Phys. 82: 2257, 2010.

[13] B. Luk'yanchuk, N. I. Zheludev, S. A. Maier, N. J. Halas, P. Nordlander, H. Giessen, C. T. Chong, Nat. Mater. 9: 707, 2010.

[14] K. Kamali, L. Xu, J. Ward, K. Wang, G. Li, A. E. Miroshnichenko, D. N. Neshev, M. Rahmani, Accepted to be published in Small

Metasurface Based Arbitrary Polarization Control and Its Applications

Xianzhong Chen*, Chunmei Zhang, Yuttana Intaravanne

School of Engineering and Physical Sciences, Heriot-Watt University, Edinburgh, UK
*corresponding author, E-mail: x.chen@hw.ac.uk

Abstract

Like amplitude and phase, polarization is a fundamental property of light, whose spatial distribution can be used to record, process and store information. Optical metasurfaces have shown unprecedented capabilities in the manipulation of the light's polarization profile, providing an unusual approach for image encryption. A novel metasurface platform has been demonstrated to hide an image into the polarization profile of a light beam.

1. Introduction

A laser beam usually has a homogeneous polarization after passing through a polarizer, while a vector beam has an inhomogeneous distribution of polarization in the transverse plane perpendicular to propagation. Vector beams have been recognized as a promising future technology in quantum memories, particle trapping, and high-resolution lithography. However, despite tremendous advances in the fundamental principles of vector beams (e.g., Mobius strip, Poincare sphere beams), the real-life applications remain limited, mainly because of complexity of the experimental system and the inability to arbitrarily manipulate polarization state of light at subwavelength scale. Thus far, metasufaces have been demonstrated to generate vector beams, such as radially or azimuthally polarized cylindrical beams, and arbitrary spatial polarization profiles. However, none of the metasurfaces demonstrated previously can be used to encode images in the polarization profiles. In order to overcome the present technical limitation of resolution and fundamental challenge of arbitrary polarization manipulation, we propose and experimentally demonstrate that, by precisely manipulating the spatially variant polarization states of a laser beam with an ultrathin metasurface, we can hide a high-resolution image within a laser beam. In this talk, we are going to introduce a metasurface platform for the arbitrary polarization manipulation for encoding various types of images, including a high-resolution grayscale image [1], a quick response (QR) code [2] and a color image [3].

2. Results

The structured beam that used to hide an image is created by a metasurface illuminated by the laser light at normal incidence. A linear polarizer is used to seek the hidden image in the generated structured beam. According to Malus' Law, when completely plane polarized light is incident on the analyzer, the intensity of the light transmitted by the analyzer is directly proportional to the square of the cosine of angle between the transmission axes of the analyzer and the polarizer.

To hide the portrait of James Clark Maxwell, a single reflective metasurface is used to continuously manipulate the superposition of two beams with opposite circular polarization states. The reflective metasurface consists of a gold ground layer, a silicon dioxide (SiO_2) spacer layer, and a top layer of gold nanorods. The generated structured light has a very specific polarization in the light beam, thus the electromagnetic field oscillates differently for different parts of the beam. In order to visualize the hidden image in the polarization topology of the laser beam, we reveal the grayscale of the image by using an analyzer (linear polarizer). In doing so, we do not directly observe the spatially-variant polarization profile of the laser beam but rather indirectly confirm its existence through the intensity profile (grayscale image) behind the analyzer. Figure 1 shows the simulation and experiment results. Because the theoretical amplitude of the two beams are exactly the same, no image is observed in the beam without the aid of the analyzer. The experimental result indicates that the image-hidden functionality is unambiguously realized. Similarly, a QR code can also be hidden in the polarization profile of a light beam.

We also demonstrate a metasurface platform for simultaneously encoding color and intensity information into the wavelength-dependent polarization profile of a light beam. Unlike typical metasurface devices in which images are encoded by phase or amplitude modulation, the color image here is multiplexed into several sets of polarization profiles, each corresponding to a distinct color, which further allow polarization-modulation induced additive color mixing. This unique approach features the combination of wavelength selectivity and arbitrary polarization control down to a single subwavelength pixel level. Upon the illumination of a linearly polarized light beam with multiple wavelengths, a color image is revealed after the light beam passes through a dielectric metasurface and a linear optical polarizer. The dielectric metasurface consists of silicon nanoblocks "meta-atoms" with different in-plane orientations and sizes on a fused silica substrate, which can be used to generate the desired polarization profile for two

different colors, with locally controlled intensity profile. We design two wavelength-selective polarization profiles for producing the polarization-encoded color images based on additive color mixing. Each supercell responds to a specific wavelength upon the illumination of a light beam containing red and green colors. The supercell represents a pixel of a mixed-color image with brightness of each color being individually controlled. Figure 2 shows the simulation and experimental results upon the illumination of linearly polarized red and green light.

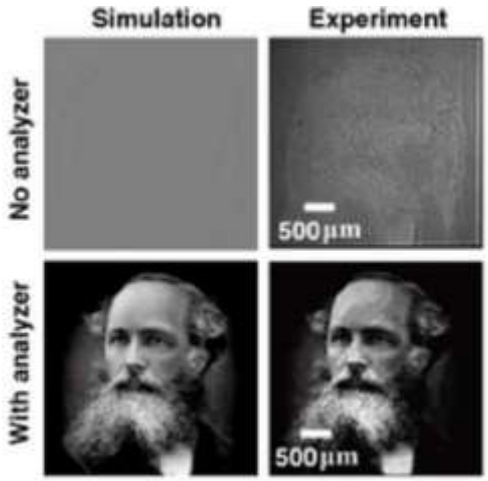


Figure 1: The simulated and experiment results with and without the analyzer.

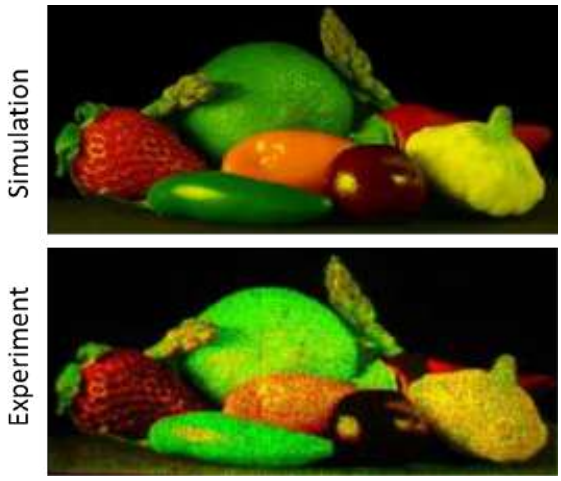


Figure 2: Simulated and experimental results of the full-color-like image.

3. Discussion

The obtained image shows how the electric field is oriented in the beam profile of the laser beam. These hidden images demonstrate the rich polarization structure that a light beam can possess at subwavelength scales. The precise control over the polarization state of light is faithfully mapped onto the intensity profile for each color, according to the famous Malus Law. The encoding approach for polarization and color may open a new avenue for novel, effective color display elements with fine control over both brightness and contrast, and may have significant impact for high-density data storage, information security, and anti-counterfeiting.

4. Conclusions

Our approach provides a novel route to hide a high-resolution grayscale image in the polarization topology of a laser beam. The dielectric metasurface having the ability to encode a spatially-varying and wavelength-selective polarization profile may provide a viable route for generating structured beams that unveil high-resolution color images with well-defined brightness and contrast.

Acknowledgements

This work is supported by Engineering and Physical Sciences Research Council of the United Kingdom (Grant Ref: EP/P029892/1).

References

[1] F. Yue, C. Zhang, X.-F. Zang, D. Wen, B. D. Gerardot, S. Zhang, X. Chen, High-resolution grayscale image hidden in a laser beam, *Light Sci. Appl.* 7: 17129, 2018.

[2] C. Zhang, D. Wen, F. Yue, Y. Intaravanne, W. Wang, X. Chen, Optical metasurface generated vector beam for anticounterfeiting, *Phys. Rev. Applied* 10: 034028, 2018

[3] X. Zang, F. Dong, F. Yue, C. Zhang, L. Xu, Z. Song, M. Chen, P. Chen, G. S. Buller, Y. Zhu, S. Zhuang, W. Chu, S. Zhang, X. Chen, Polarization encoded color image embedded in a dielectric metasurface, *Adv. Mater.* 30: 1707499, 2018.

Dielectric Metasurfaces for Ultrathin Half Waveplates

Yuttana Intaravanne, Xianzhong Chen*

School of Engineering and Physical Sciences, Heriot-Watt University, Edinburgh, UK
*corresponding author, E-mail: x.chen@hw.ac.uk

Abstract

Traditional half waveplates are not suitable for device miniaturization and system integration due to their large volume. The unprecedented capability of metasurfaces in the manipulation of light's polarization at subwavelength scale has provided an approach to develop ultrathin half waveplates. We developed an ultrathin half waveplate and evaluated its performance in term of conversion efficiency, phase retardation, and polarization rotation. Although our samples cannot be a perfect half waveplate, they can function as a quarter waveplate at some wavelengths.

1. Introduction

A half waveplate (HWP) is commonly used to control or rotate the polarization state of the linearly polarized light into two times of the angle of incident with respect to the fast axis (2α), where the refractive index along this direction is lower than that along the other. Traditional HWPs are made of birefringent materials (e.g., quartz, calcite, mica, magnesium fluoride, or sapphire), which can cover the optical range from ultraviolet to mid-infrared regions. However, these types of waveplate are very bulky so that there are not good for device miniaturization and system integration. Optical metasurfaces have provided an unusual approach to develop ultrathin HWPs in the optical range. Recently, Zang et al. have experimentally demonstrated a dielectric metasurface approach to hide an image into the polarization profile of a light beam [1]. Each nanopillar in the ultrathin device acts as a HWP. The performance of the HWPs influence the desired performance of the designed devices, so how to design, evaluate and improve their performance is a key step.

2. Results

The key idea for design and optimizing the dimension of nanopillars is shown in Figure 1(a). Each nanopillar was designed to generate a phase retardation (Δφ) of 180° as a function of HWP with a high efficiency at wavelength (λ) of 550 nm. Each nanopillar was designed to have a pixel size (p) of 360 nm along two orthogonal directions. The nanopillars are 310 nm high (h), 100 nm long (l), and 75 nm wide (w) oriented in a horizontal axis. To develop the sample as shown in Figure 1(b), amorphous silicon nanopillars sitting on a quartz substrate were fabricated. The fabricated sample was characterized by using the experimental setup diagram shown in Figure 1(c) in order to evaluate the performance in terms of conversion efficiency, phase retardation, and polarization rotation.

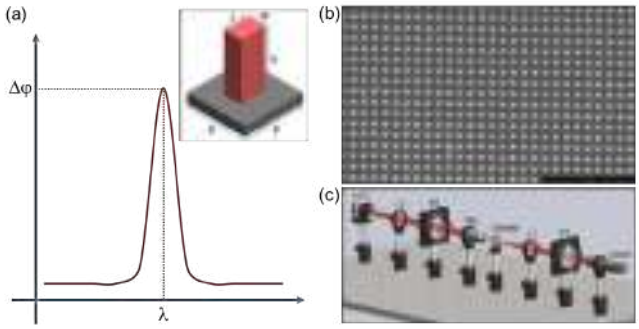


Figure 1: (a) The dependence of phase retardation on the wavelengths; (b) SEM image of the sample used in this work; (c) The experimental setup diagram for characterization of the sample.

Conversion efficiency is a very important parameter, which is defined as the ratio between the optical power with desired polarization rotation and the transmitted power [1]. The obtained conversion efficiency of the sample is shown in Figure 2(a). The experimental result shows that the operating wavelength is at 580 nm, which is shifted by 30 nm when compared to the designed wavelength. At this wavelength, the conversion efficiency is 89.60%. As shown in Figure 2(b), the sample was designed to generate the phase retardation of 180° whereas the real sample provides the phase retardation of 142.40° at wavelength of 580 nm. Similar to a perfect HWP (phase retardation 180°) that can generate a polarization rotation of 2α, but there is a slight difference in the polarization rotation for the fabricated samples due to the difference of the phase retardation (142.40°), Figure 2(c). All collected data from optical measurement was also plotted and compared with the simulation results as shown in Figure 2(d).

Although our samples cannot be a perfect HWP, it can function as a quarter waveplate at some wavelengths. Therefore, the Figure 2(b) was recalled and considered at the wavelengths that can generate the phase retardation of 90°. The corresponding wavelengths are around 562 nm and 602 nm for this sample.

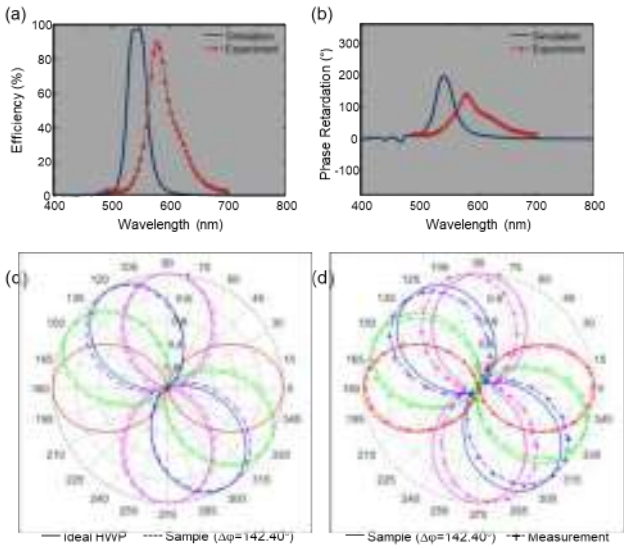


Figure 2: The comparison between simulation and experiment. (a) Phase retardation; (b) conversion efficiency; Polarization rotation, (c) ideal HWP versus our sample, and (c) our sample (simulation) versus measurement for the angle of fast axis 90° (red), 75° (green), 60° (blue), and 45° (magenta).

3. Discussion

The slight difference in the phase retardation between the simulation and experiment is due to the imperfection of the fabricated sample. The phase retardation can be increased by increasing the height of the amorphous silicon layer with the current geometry of the nanopillars unchanged or optimizing the feature size of the nanopillars with the current height unchanged. Furthermore, the shifting of the operating wavelength can be tuned by controlling the length and width of the nanopillars as reported by Zang et al. [1]. Ultrathin HWPs with spatially variant fast axes (orientation of nanopillars) at subwavelength scale are very attractive for the generation of arbitrary polarization profile for image encryption, including high resolution grayscale image [1], color image [2], and a quick response (QR) code [3].

4. Conclusions

In summary, we designed and developed an ultrathin HWP based on a dielectric metasurface. The performance of the ultrathin HWPs was evaluated in the terms of conversion efficiency, phase retardation and polarization rotation. Good agreement between measurement and simulation was found. Solutions on how to improve the device quality were given and future applications of nanopillars in polarization manipulation were also discussed.

Acknowledgements

This work is supported by Engineering and Physical Sciences Research Council of the United Kingdom (Grant Ref: EP/P029892/1).

References

[1] X. Zang, F. Dong, F. Yue, C. Zhang, L. Xu, Z. Song, M. Chen, P. Chen, G. S. Buller, Y. Zhu, S. Zhuang, W. Chu, S. Zhang, X. Chen, Polarization encoded color image embedded in a dielectric metasurface, *Adv. Mater.* 30: 1707499, 2018.

[2] F. Yue, C. Zhang, X.-F. Zang, D. Wen, B. D. Gerardot, S. Zhang, X. Chen, High-resolution grayscale image hidden in a laser beam, *Light Sci. Appl.* 7: 17129, 2018.

[3] C. Zhang, D. Wen, F. Yue, Y. Intaravanne, W. Wang, X. Chen, Optical metasurface generated vector beam for anticounterfeiting, *Phys. Rev. Applied* 10: 034028, 2018

Tunable and Reconfigurable Mid-Infrared Metasurfaces

Clayton Fowler[1], Sensong An[1], Mikhail Y. Shalaginov[2], Yifei Zhang[2], Bowen Zheng[1], Hong Tang[1], Hang Li[1], Tian Gu[2], Juejun Hu[2], and Hualiang Zhang[1*]

[1]ECE Dept., University of Massachusetts Lowell, Lowell, Massachusetts, USA
[2]MSE Dept., Massachusetts Institute of Technology, Cambridge, Massachusetts, USA
*corresponding author, E-mail: hualiang_zhang@uml.edu

Abstract

High-index dielectric Huygens' metasurfaces offer a means to create compact, high-performance infrared optical devices such as lenses, filters, beam-deflectors, waveplates and so on for applications where quality components are difficult to come by. The functionality of such devices could be vastly expanded by creating reconfigurable designs that enable switching and dynamic behavior. We detail how to design reconfigurable Huygens' surfaces, demonstrate some devices operating in the mid-IR, and discuss technical challenges and possible future developments.

1. Introduction

In the infrared range, there are numerous applications (astronomy, biomedical imaging, security, night-vision, missile-detection, etc.), which suffer from expensive, unwieldly, or low-quality bulk optical devices. Phase-gradient metasurfaces, or Huygens' surfaces [1], have strong potential to overcome these limitations, and can be used to create ultra-thin optical components with a high degree of precision for manipulation of electromagnetic (EM) wavefronts [2]. Huygens' surfaces can be constructed as a 2D array of subwavelength dielectric structures, which have been manufactured from a high refractive index material. The high index of refraction allows the structures (i.e. meta-atoms) to support magnetic and electric multipoles [3], that when excited, cause a temporal delay for incoming EM waves. The responses of these multipoles change with the geometry of a meta-atom, which provides a means of tuning the phase of an EM wave. A set of meta-atoms that adequately covers the full 2π phase range can be arranged along a surface in an appropriate pattern to produce meta-optical devices, such as lenses, filters, waveplates, polarizers, beam deflectors, and so on.

Although the control of EM waves enabled by metasurfaces is considerable, applications often call for multiple device functionality or dynamic behavior (such as zooming) that would ordinarily be unattainable by a single metasurface (or often any other type of optical component). Reconfigurable optical components are capable of such performance, but current devices depend on mechanical adjustment, which is slow, or make use of liquid crystals, which can be unstable when the device is in motion. As a solution to this challenge, we introduce building meta-atoms from a material, such as $Ge_2Sb_2Se_4Te$ (GSST), whose index of refraction can be controlled via a reversable thermally induced phase change between amorphous and crystalline states [4]. The heat necessary to induce the phase change can be supplied electrically to individual meta-structures, allowing the creation of the first electrically tunable solid-state infrared devices.

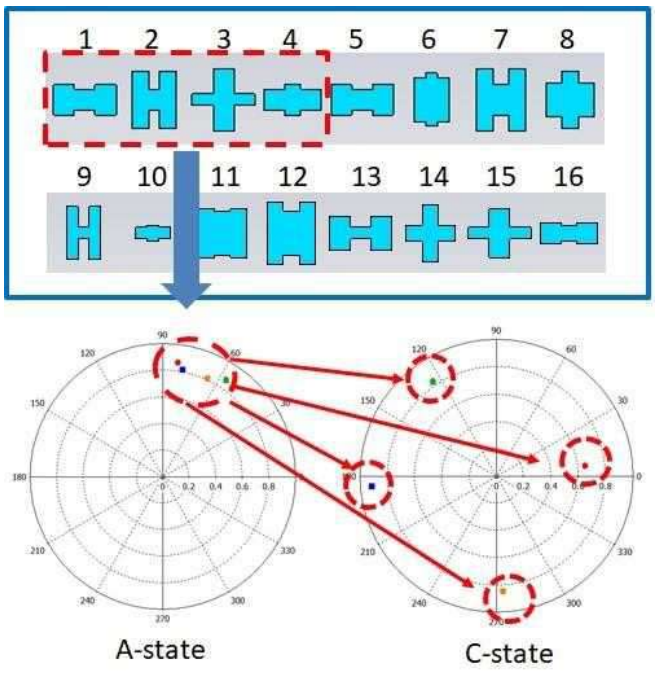


Figure 1: Example of reconfigurable meta-atoms for a 2-bit design. Atoms 1-4 have approximately the same phase in the amorphous (A) state but exhibit a roughly 90 degree phase progression in the crystalline (C) state. Atoms 5-8 behave similarly but are offset by 90 degrees from atoms 1-4 in the amorphous state. The remaining atoms continue in this manner so that full 2π coverage is available in both A and C states.

2. Reconfigurable Huygens' Surface Design

Complete control of the phase of an incoming EM wave requires many more meta-atoms for a reconfigurable Huygens' surface than for an ordinary one. The case of a phase increment of 90 degrees between meta-atoms would allow only modest wave manipulation. 16 meta-atoms are needed for this so-called 2-bit design (Fig. 1), as compared to only 4 that would be needed for an ordinary non-tunable Huygens's surface. A 3-bit design, which is more efficient and allows for better wavefront control by reducing the phase increment to 45 degrees, would require 64 structures (as compared to 8), and so on.

With a suitable set of reconfigurable meta-atoms, many devices can be constructed from appropriate arrangements such as determined by the Generalized Snell's Law of Refraction [5] (Equation (1)) or applying Fermat's Principle. Equation (2) is the metasurface phase distribution, φ(r), required for lenses [6], which we have used to construct a meta-lens with a focal spot that changes from 0.5 mm in the amorphous phase to 1.0 mm in the crystalline phase (Fig. 2 and Fig. 3).

$$n_t \sin\theta_t - n_i \sin\theta_i = \frac{1}{k}\frac{d\varphi}{dx} \quad (1)$$

$$\varphi(r) = k\left(\sqrt{r^2+f^2} - f\right) \quad (2)$$

3. Discussion

While there is great potential to create a wide variety of reconfigurable optical devices that would be superior to the current state of the art, there are some technical challenges to be overcome. For example, 3-bit and higher designs require a large number of suitable structures to be found, for which it can be increasingly challenging to obtain the proper performance for both states of matter. This challenge can be even more formidable for designs requiring broadband response. Additionally, fully electrical control over each structure becomes more difficult as the size of the surface is increased. We will demonstrate our approaches to overcome these challenges.

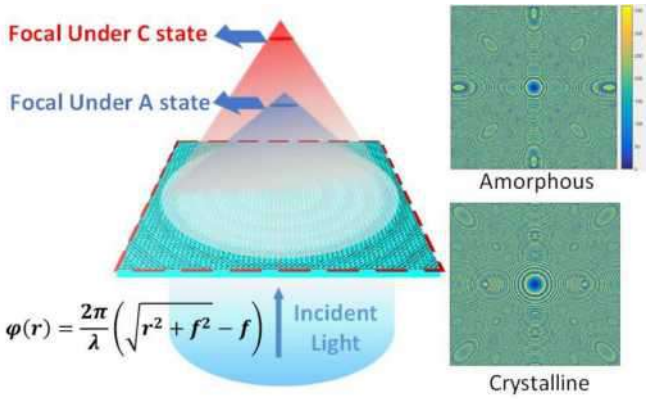


Figure 2: A reconfigurable meta-lens for which the focal point is different for amorphous and crystalline states. The meta-atoms must be properly selected so that the phase-equation for the lens is satisfied to give the desired focal point for each state.

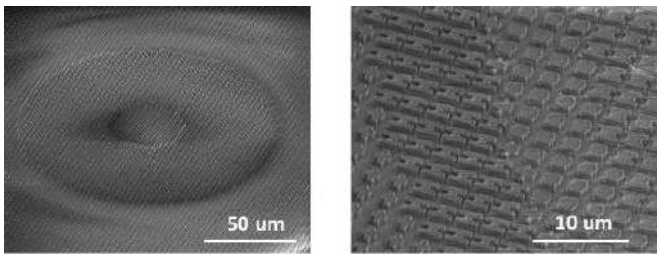


Figure 3: SEM images of a GSST-based reconfigurable meta-lens.

4. Conclusions

Huygens' surfaces have the potential to be used for high-quality, thin, and reconfigurable infrared flat optical devices. We will demonstrate how a reconfigurable Huygens' surface can be obtained and present some devices we have developed, such as lenses, polarizers, waveplates, and beam deflectors with tunable/reconfigurable responses. We also discuss more complex devices under development such as reconfigurable filters and dynamic zoom lenses.

Acknowledgements

This work is supported by the Defense Advanced Research Projects Agency EXTREME program under Agreement No. HR00111720029.

References

[1] M. Decker *et al*., "High-Efficiency Dielectric Huygens' Surfaces," vol. 3, no. 6, pp. 813-820, 2015.

[2] L. Zhang *et al*., "Ultra-thin high-efficiency mid-infrared transmissive Huygens meta-optics," *Nature Communications*, vol. 9, no. 1, p. 1481, 2018/04/16 2018.

[3] A. I. Kuznetsov, A. E. Miroshnichenko, Y. H. Fu, J. Zhang, and B. Luk'yanchuk, "Magnetic light," *Scientific Reports*, Article vol. 2, p. 492, 07/04/online 2012.

[4] Y. Zhang *et al*., "Extreme Broadband Transparent Optical Phase Change Materials for High-Performance Nonvolatile Photonics," *arXiv e-prints*, Available: https://arxiv.org/abs/1811.00526v2

[5] N. Yu *et al*., "Light Propagation with Phase Discontinuities: Generalized Laws of Reflection and Refraction," vol. 334, no. 6054, pp. 333-337, 2011.

[6] F. Aieta *et al*., "Aberration-Free Ultrathin Flat Lenses and Axicons at Telecom Wavelengths Based on Plasmonic Metasurfaces," *Nano Letters*, vol. 12, no. 9, pp. 4932-4936, 2012/09/12 2012.

High-dimensional vectorial metasurface holography

Lingling Huang[1], Ruizhe Zhao[1], Basudeb Sain[2], Qunshuo Wei[1], Chengchun Tang[3,4], Xiaowei Li[5], Thomas Weiss[6], Yongtian Wang[1], Thomas Zentgraf[2]

[1] School of Optics and Photonics, Beijing Institute of Technology, Beijing, 100081, China
[2]Department of Physics, University of Paderborn, Warburger Straße 100, 33098 Paderborn, Germany
[3]Institute for Quantum Science and Engineering, Shenzhen, 518055, China
[4]Department of Physics, Southern University of Science and Technology, Shenzhen, 518055, China
[5]Laser Micro/Nano-Fabrication Laboratory, School of Mechanical Engineering, Beijing Institute of Technology, Beijing 100081, China
[6]4th Physics Institute and Research Center SCoPE, University of Stuttgart, Pfaffenwaldring 57, 70569 Stuttgart, Germany
*corresponding author, E-mail: huanglingling@bit.edu.cn

Abstract

Information and image multiplexing based on the polarization states of the light is a powerful tool that can be easily realized with optical metasurfaces. Here, we have demonstrated a novel method for achieving high-dimensional vectorial holography based on birefringent all-dielectric metasurfaces to explore the full capacity of polarization. By considering the anisotropy property and extra design freedom of rotation matrix, together with smart multiplexing algorithms for establishing quantified related phase profiles, high-dimensional multichannel polarization multiplexed holograms have been successfully achieved using the simplest nanofin as the building block. Compared to previously demonstrated metasurface multiplexed holograms that can only be switched between two states by two orthogonal polarization for the light, here all combinations within twelve polarization channels in total can be obtained.

1. Introduction

The practical realization of metasurface holograms relies on the encoding of holographic profiles on ultrathin meta-atoms which can possess strong light-matter interaction within ultrashort distance. Many efforts by incorporating novel holographic related functionalities such as beam shaping and ghost imaging into metasurfaces have been done. Meanwhile, for the purpose of optimizing the tremendous information capability of metasurface holograms, multiplexing techniques are highly desired including color holograms, polarization multiplexing and hybrid multiplexing. Among the mentioned multiplexing techniques, polarization multiplexing is an attractive method due to the polarization sensitive ability of such artificially tailored meta-atoms. However, the full capacity of all polarization channels (input/output polarizations) has not been explored yet. This limits the improvement of the information capacity stored in metasurface holograms and restricts the versatile functionality of holographic-based optical devices.

Here, we demonstrate a novel method for achieving multichannel vectorial holography and show its potential for obtaining dynamic displays and high-security applications. We explore birefringent metasurfaces for the complete control of polarization channels with the freedom of designing both the polarization dependent phase shift and polarization rotation matrix. We show that although the target holographic phase profiles have quantified phase relations they can process very different information within different polarization manipulation channels. The reconstructed vectorial images can be switched with negligible cross-talk by selecting the desired combination of input/output polarization states. The set of the reconstructed images can conceive absolutely different meanings and therefore hosts unique merits for encryption. Our demonstrated multiplexing method may lead to a new frontier for applications related to dynamic holographic displays, switchable optical devices, data storage and optical encryption/anti-counterfeiting, to be compatible with most optical systems that operate in transmission. Furthermore, our proposed method can also be adapted to arbitrary spin to orbital angular momentum conversion or other types of polarization/phase modulation and enhance the information capacity.

2. Result

We comparatively study two schemes of multiple polarization channels (from orthogonal two channels to twelve channels) by using birefringent dielectric metasurfaces, as shown in Figure 1. We show that polarization and angle multiplexed holograms can be achieved by utilizing nanofins of different cross-sections but without rotation (Fig. 1a). Two sets of off-axis holographic images can be generated with two orthogonal states. However, by considering the flexibility of designing the entire Jones matrix, we can achieve more multiplexed functionalities with complete control of polarization and

phase (Fig. 1b). Three independent images (we choose the words “holography”, “meta”, and “surface” as the reconstructed images) can be reconstructed successfully with high resolution and high fidelity for different combinations of the input and output polarization channels. All combinations of these three images in a total of twelve different polarization channels can be observed (“meta” + “holography”, “meta” + “surface”, “ surface” + “holography” and “meta” + “surface” + “holography”) with satisfactory efficiencies. In addition, the reconstructed images exhibit vectorial feature for the polarization state of the different words in analogy to optical vector beams.

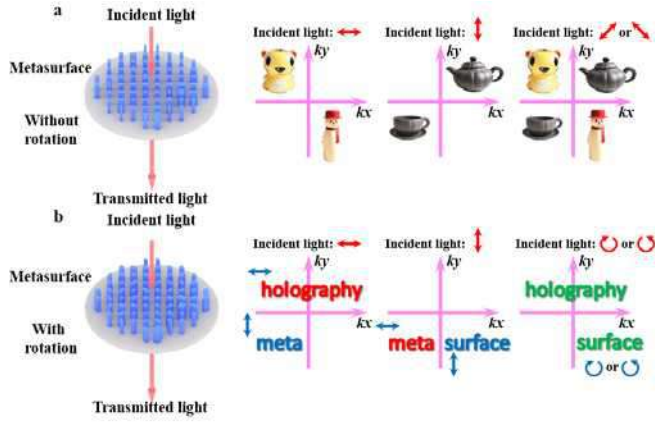


Figure 1: Schematic illustrations of polarization multiplexed holograms based on dielectric metasurfaces. The red and blue arrows indicate the polarization of incident light and the transmission axis of polarizer placed behind the metasurfaces sample.

We demonstrate such method also allows encrypting different original images that can be superimposed at the same spatial location. Such superposition has the ability to convey an absolutely different meaning in the reconstructed image and can be used to provide an alterable information content of the image, that is, encryption, as shown in Figure 2. We choose a dice as our original image. The dice has six faces that are represented by the number of pips on the surface. Interestingly, by using a suitable selection of different combinations of the input/output polarization states, a different number of pips (from one to six) can be observed. This kind of illusion of viewing different sides of the dice results from the increased multiplexing capability of our method that can encode of up to six different images for the various combinations of polarization states.

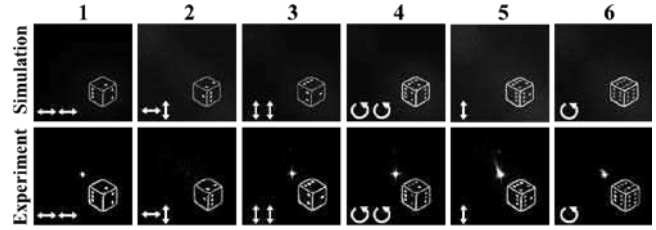


Figure 2: Simulated and experimental results for the reconstruction of a dice with different faces up.

3. Conclusion

In summary, such high-dimensional vectorial metasurface hologram can be applied in holographic display and encryption. Only by using the correct polarization keys the receiver will get the exact information delivered (as for the dice case). An even higher flexibility can be obtained by further increasing the complexity of the images together with a detailed analysis of the reconstructed vectorial image properties. Further application of arbitrary spin to angular momentum conversion and various phase modulation/beam shaping can be achieved accordingly.

4. Reference

1. Zhao, R., Sain, B., Wei, Q., Tang, C., Li, X., Weiss, T., Huang, L., Wang, Y., Zentgraf, T. Multichannel Vectorial Holographic Display and Encryption. Light: Science & Applications 7:95 (2018).

Terahertz Photonic Devices Employing Graphene-based Hybrid Metasurfaces

Peter Q. Liu

Department of Electrical Engineering, University at Buffalo, the State University of New York, Buffalo, USA
E-mail: pqliu@buffalo.edu

Abstract

Graphene has emerged in recent years as a versatile material for photonic devices operating in the infrared to terahertz (THz) spectral region. In particular, the large tunability of carrier density and the high carrier mobility of graphene allow this two-dimensional material to support tunable THz surface plasmon polaritons with exceedingly high field localization and enhancement as well as relatively long lifetime. The compatibility of graphene with a wide range of materials and various micro- and nano-fabrication processes also makes integrating graphene-based structures with other structures/devices relatively straightforward. In this invited talk, we will present several types of THz photonic devices we developed in recent years, including modulators and detectors, which employ graphene-based hybrid structures (e.g. metasurfaces) to achieve enhanced light-matter interactions and hence improved device performances.

Nanophotonic Enhancement of Light Out-Coupling for Deep-UV LEDs

Phillip Manley[1,2*], Martin Hammerschmidt[3], Sven Burger[2,3] and Christiane Becker[1]

[1]Helmholtz-Zentrum Berlin für Materialien und Energie GmbH, Kekuléstraße 5, 12489 Berlin, Germany
[2]Zuse Institute Berlin, Takustraße 7, 14195 Berlin, Germany
[3]JCMwave GmbH, Bolivarallee 22, 14050 Berlin, Germany
*corresponding author, E-mail: phillip.manley@helmholtz-berlin.de

Abstract

We present a concept for rapidly evaluating different nanostructures for enhanced out-coupling of light from light emitting diodes in the deep ultra violet wavelength region. The scattering matrix for a given nanostructured interface is calculated by means of rigorous simulations combined with a Brillouin zone sampling technique to minimize the number of required simulations. We then use the scattering matrix to evaluate the out-coupling for a source with an arbitrary angular distribution.

1. Introduction

Light emitting diodes (LEDs) based on AlN and operating in the deep ultra violet (DUV) wavelength regime (200-360 nm) represent a promising technology for a multitude of applications. These include air and water purification, optical data storage, sterilization, sensing and spectroscopy [1, 2]. Compared to established mercury lamps, LEDs have the advantages of miniaturization, they can be produced with different operating wavelengths and they can provide a lower energy consumption [3].

In order to make this a reality, the optical extraction of light emitted inside the LED must be as high as possible. For a simple planar AlN on sapphire substrate system, the expected light extraction to air is around 7%. We will present concepts for increasing this extraction efficiency. In order to increase this efficiency, the Al/sapphire interface may be nanostructured as shown in fig. 1(a).

Nanostructuring can increase the transmission from the AlN semiconductor into the sapphire substrate via wave optical effects such as diffraction. In order to optimize efficiently, a method of quickly evaluating the effectiveness of a given structure is needed. To this end,we present a method by which the total transmission at the AlN/sapphire interface can be obtained with a minimum number of simulations. This allows for an optimization of the transmission with minimal computational cost.

2. Method

In order to obtain the transmission through the AlN/sapphire interface for a source with an arbitrary angular distribution inside the AlN semiconductor, the transmission for each incident angle and polarization is required. For nanostructures with 2D periodicity in plane of the interface, the transmission taking into account all wave optical effects can be determined using the finite element method (FEM). In this case we use the commercial software package JCMsuite [4].

However, solving for each incident angle is a costly process. In order to accelerate the speed of simulations we exploit two factors based on the k space considerations. Simulating for all incident angles is equivalent to simulating for sources with k vectors with transverse components lying withing the Fermi circle $k_\perp < nk_0$. Where k_0 is the vacuum wave-number and n is the refractive index of the incident material. Figure 1 shows points sampled within the first Brillouin zone (BZ) for a geometry with hexagonal periodicity in the transversal plane. If the structure presents a symmetry in the transverse plane, then the BZ can be further reduced to the irreducible Brillouin zone (IBZ). This means that all points lying within the first BZ but outside of the IBZ can be reached by applying the symmetry operators of the respective point group to points within the IBZ.

The second property used in order to reduce the number of simulations is the Bloch periodicity of the k space inside the Fermi circle. Figure 2(a) shows a sampling of points inside the Fermi circle (note the symmetry operations previously considered have already been applied, restricting the points to the wedge shown). Also shown are the 1st and higher order BZs which are represented by the lattice pattern of hexagons. In fig. 2(c) the points are colored by subset. For each subset, the position of each point in k space is related by translation of a reciprocal lattice vector. This means that the points share a common Bloch periodicity. When performing calculations using the FEM, multiple sources with the same Bloch periodicity may be evaluated using the same system matrix. In the case presented here, only four families are present. This means only four matrix inversions need to be performed to sample all the k points shown. Since the matrix inversion is the most costly part of a given FEM simulation, this reduces the computational cost significantly.

3. Discussion

Circular structures in a hexagonal arrangement, such as for a photonic crystal, are commonly used for nanostructuring in LEDs. This geometry presents a C6 symmetry, mean-

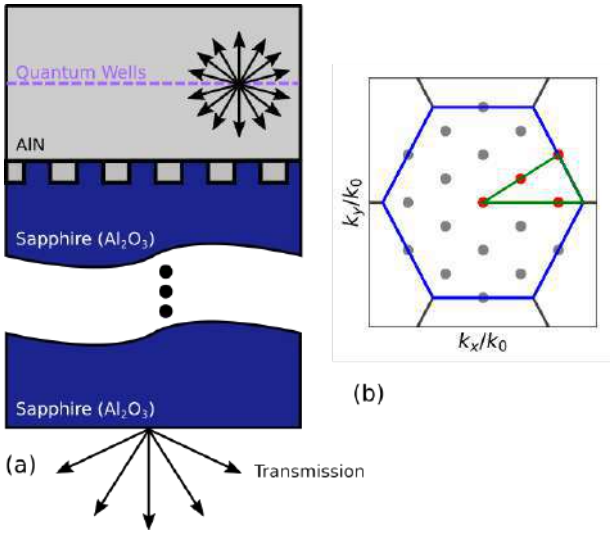


Figure 1: (a) The basic structure of a DUV LED. Light is emitted in the AlN layer and travels through the sapphire substrate to be transmitted at the lower interface to air. A schematic of a nanostructure at the AlN/sapphire interface is shown. (b) An arbitrary sampling (points) of the first Brillouin zone (blue hexagon) for a geometry with in-plane hexagonal symmetry. The irreducible Brillouin zone (green triangle) allows the number of sampling points to be reduced to those highlighted in red.

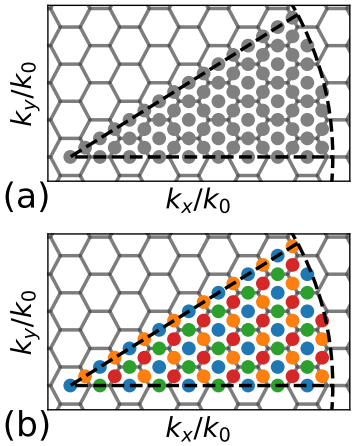


Figure 2: (a) A sampling (points) of the symmetry cone within the Fermi circle for a geometry with in-plane hexagonal symmetry. (b) the sampling from (a) recolored by Bloch family. There are four families present (blue,green,red,orange).

ing that the number of required simulations is reduced by a factor of 12 (fig. 1(b)).

Exploitation of the Bloch families depends heavily on the relationship between the pitch of the periodic structure and the wavelength of light. For DUV LEDs, the pitch is generally much larger than the wavelength of light due to experimental constraints on the nanostructuring processes. For the case of a 265 nm free space wavelength and 1000 nm pitch, the speedup of simulation time is $\sim$ 20. This is especially useful since FEM simulations become more costly when the pitch of the simulated device is larger than the wavelength.

Using these two factors, obtaining a scattering matrix to use for evaluating the performance of a nanostructured AlN/sapphire interface can be sped up by a factor of ~ 240. Thereby considerably accelerating the speed at which different structures can be evaluated. We will further discuss how an estimate for the light extraction can be obtained via a simple matrix scheme and the physical mechanisms which contribute to the enhanced light extraction.

4. Conclusions

We have presented a method of evaluating different nanostructures for enhanced out-coupling of light from light emitting diodes in the deep ultra violet wavelength region. This entails calculating the scattering matrix via finite element simulations. Due to the large size of the structures compared to the wavelength of light, these simulations are costly. We were able to reduce the amount of simulations required by a factor of ~ 240 by sampling k space at regular intervals defined by the reciprocal lattice vectors.

Using the scattering matrix allows the for a rapid optimization of the light extraction from an DUV LED for a source with an arbitrary angular distribution.

Acknowledgement

P. Manley acknowledges funding from the Helmholtz Innovation Lab HySPRINT, which is financially supported by the Helmholtz Association. We acknowledge the German Federal Ministry of Education and Research for funding within the project SnAPSHOTs (grant no. 01IO1806 and 01IO1807). Part of the work was done at the Berlin Joint Lab for Optical Simulations for Energy Research (BerOSE).

References

[1] Z. Arturas, M. Shur, and R. Gaska, *Introduction to Solid-State Light*. Wiley, 2002.

[2] S. F. Chichibu and S. Nakamura, *Introduction to nitride semiconductor blue lasers and light emitting diodes*. CRC Press, 2014.

[3] C. Pernot, M. Kim, S. Fukahori, T. Inazu, T. Fujita, Y. Nagasawa, A. Hirano, M. Ippommatsu, M. Iwaya, S. Kamiyama, I. Akasaki, and H. Amano, "Improved efficiency of 255–280 nm AlGaN-based light-emitting diodes," *Applied Physics Express*, vol. 3, no. 6, p. 061004, 2010.

[4] J. Pomplun, S. Burger, L. Zschiedrich, and F. Schmidt, "Adaptive finite element method for simulation of optical nano structures," *physica status solidi (b)*, vol. 244, no. 10, pp. 3419–3434, 2007.

Electric-Field-Induced Second Harmonic Generation from Organic Polymer

Shumei Chen[1], King Fai Li[2], Guixin Li[2*], Kok Wai Cheah[3], and Shuang Zhang[1*]

[1]School of Physics & Astronomy, University of Birmingham, Birmingham, B15 2TT, UK
[2]Department of Materials Science and Engineering, Shenzhen Institute for Quantum Science and Engineering, Southern University of Science and Technology, Shenzhen, 518055, China
[3]Department of Physics, Hong Kong Baptist University, Kowloon Tong, Hong Kong

* Corresponding author, Email: ligx@sustc.edu.cn; s.zhang@bham.ac.uk

Abstract

Here, we report giant tuneability of EFISH signal from a subwavelength thick polymer film sandwiched by a transparent electrode and a metallic mirror. By exploiting band-edge enhanced third-order nonlinear susceptibility from the organic conjugated polymer, we successfully demonstrate a gigantic EFISH effect with modulation ratio up to 422%/Volt at pumping wavelength of 840 nm. The band-edge enhanced EFISH opens new avenues for modulating the intensity of SHG signals, and for controlling nonlinear electro-optic interaction in nanophotonic devices.

1. Introduction

Dynamic control of nonlinear optical signal may have important applications in optical modulation and switching. Various switching technologies based on Kerr or free carrier nonlinearities in semiconductor materials have been developed using the all-optical control scheme. Alternatively, the control of nonlinear optical signal can be realized by using electro-optic interactions. For example, the electric-field-induced SHG (EFISH), which was proposed in early 1960s, provides an alternative route for designing nonlinear optical modulators.[1] In EFISH process, an external static electric field can be mixed with the fundamental wave (FW) to produce SHG in nonlinear optical materials with large third-order susceptibilities. Because the symmetry of the nonlinear optical materials has less restrictions on third-order processes as compared to second-order processes, EFISH process has been extensively exploited in various media such as optical crystals,[1],[2] electrolytic solutions,[3] metal-oxide-semiconductors,[4] organic devices,[5] silicon waveguides,[6] and photonic metamaterials.[7]-[9] It was demonstrated that the efficiency of EFISH signal could be greatly improved by utilizing the backward phase matching technique in plasmonic metamaterials[9] and quasi-phase matching in silicon waveguides[6]. EFISH was recently realized by electrostatic doping in two-dimensional (2D) materials. Specifically, electrically tuneable SHG was theoretically studied using plasmonic resonances in doped graphene nanoislands[10] and experimentally realized based on strong exciton charging effects in monolayers of WSe_2.[11] The electric field controlled SHG in 2D materials also have many limitations. For example, SHG predicted from graphene nano islands strongly relies on the heavy doping of charge carriers, and thus imposes critical requirements on the fabrication of graphene monolayers. In addition, the electric field enabled modulation depth of SHG from the WSe_2 transistor is less than 3%/Volt, which limits its potential applications as nonlinear optical modulators.

2. Results and Discussions

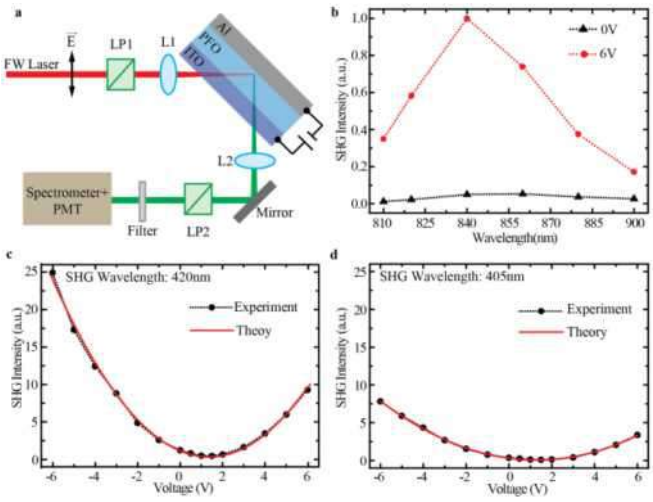


Figure 1. Nonlinear optical properties of ITO/PFO/Aluminium with applied voltages. (a) Configuration of SHG measurement, The TM-polarized FW (the) is obliquely incident onto the ITO/PFO/Aluminium device at angle of 45°. L1 and L2 are lenses; LP1 and LP2 are polarizers. (b) Characterization of the spectral response of H-polarized SHG from ITO/PFO/Aluminium with and without applied voltages. (c) The SHG intensity as a function of the applied voltages is plotted for SHG wavelength at 420 nm. (d) The SHG intensity as a function of the applied voltages is plotted for SHG wavelength at 405 nm. In the case of positive and negative voltages, ITO layer serves as anode and cathode, respectively.

We study the electric field induced SHG from the ITO/PFO/Aluminium device by applying a DC voltage (U) to the ITO and aluminium electrodes. As shown in Fig. 1a, ITO layer can be used as either an anode ($U > 0$) or a cathode ($U < 0$). To avoid the damage of the EFISH device, the spectral measurement of EFISH signal for DC voltage only up to $U = 6$ volt is carried out (red dot line with circles in Fig. 1b) for TM-polarized FW at incident angle of 45°.

Compared to the case of U = 0 (black dot line with triangles in Fig. 1b), one can see that the applied electric field can greatly boost the efficiency of SHG. To better understand the mechanism and the efficiency of the EFISH process, we plot the electric field induced SHG intensity versus the applied voltage *U* at the fundamental wavelength of 840 nm and 810 nm in Figs. 1c and 1d, respectively. At the resonant wavelength of 840 nm, the SHG always has the highest efficiency for EFISH device regardless of the applied DC electric field. When *U* is swept from zero to 6 Volts, the intensity of SHG initially drops to a minimum value of $I_{2\omega}$ = 0.489 (a.u.) at *U* = 1.5 Volt and then grows quickly to $I_{2\omega}$ = 9.29 (a.u.) at *U* = 6 Volts. This corresponds to a SHG modulation depth $I_{2\omega}(U=6)/[\Delta U \cdot I_{2\omega}(U=1.5)]$ ~ 422%/Volt, with $\Delta U = 4.5$ Volt in this case. This modulation depth is much higher than that in the conventional EFISH devices or the electric controlled SHG from WSe_2.[10] Also, the modulation depth of electric field controlled SHG from plasmonic metamaterials[7],[8] and WSe_2[11] is less than 0.9%/Volt and 3%/Volt, respectively. If a reversed voltage is applied to the device, the trend of EFISH shows a very different behavior; the intensity SHG keeps increasing when *U* is swept from zero to -6 Volt, and the measured modulation depth of SHG has a negative value of ~ -335%/Volt. In comparison, the electric field controlled modulation depth of SHG in WSe_2 devices is negative for both positive and negative biases. A very similar optical response was observed from the EFISH measurement at a non-resonant wavelength of 810 nm Fig. 1d. The measured EFISHG dependence over the applied electric field can be perfectly explained by the theory, and the relative values of effective $\chi^{(2)}$ and $\chi^{(3)}$ of the EFISH device can be retrieved by fitting the measured EFISH curves using Eq. 1, as shown in Figs. 1c and 1d. The ratio between the effective $\chi^{(2)}$ and $\chi^{(3)}$ is found to be 1.6271 V/m and 1.4451 V/m for fundamental wave at 840 nm and 810 nm, respectively.

3. Conclusions

This work opens new avenues for designing organic conjugated polymer based electric field controlled SHG with giant modulation depth. It is expected that through the integration of plasmonic metamaterials, metasurfaces into the current EFISH device, the performance such as modulation depth and efficiency of SHG will be further enhanced, indicating the great potentials in applications such as electro-optic modulators.

Acknowledgements

This work was financially supported by National Natural Science Foundation of China (11774145), Marie Curie Individual Fellowship (H2020-MSCA-IF-703803-NonlinearMeta) and the European Research Council Consolidator Grant (TOPOLOGICAL).

References

[1] Terhune, R. W., Maker, P. D. & Savage, C. M. Optical harmonic generation in calcite. *Phys*. *Rev*. *Lett*. **8,** 404–406 (1962).

[2] Maker, P. D. & Terhune, R. W. Study of optical effects due to an induced polarization third order in the electric field strength. *Phys*. *Rev*. **137**, A801–A818 (1965).

[3] Lee, C., Chang, R. & Bloembergen, N. Nonlinear electroreflectance in silicon and silver. *Phys*. *Rev*. *Lett*. **18,** 167–170 (1967).

[4] Lüpke, G. Characterization of semiconductor interfaces by second-harmonic generation. *Surf*. *Sci*. *Rep*. **35**, 75–161 (1999).

[5] Manaka, T. & Iwamoto, M. Optical second-harmonic generation measurement for probing organic device operation. *Light: Sci*. *& Appl*. ***5***, e16040 (2016).

[6] Timurdogan, E., Poulton, C. V., Byrd, M. J. & Watts, M. R. Electric field-induced second-order nonlinear optical effects in silicon waveguides. *Nat*. *Photon*. **11**, 200-206 (2017).

[7] Cai, W., Vasudev, A. P. & Brongersma, M. L. Electrically controlled nonlinear generation flight with plasmonics. *Science* **333**, 1720–1723 (2011).

[8] Kang, L. *et al*. Electrifying photonic metamaterials for tunable nonlinear optics. *Nat*. *Commun*. **5,** 4680 (2014).

[9] Lan, S. *et al*. Backward phase-matching for nonlinear optical generation in negative-index materials. *Nat*. *Mater*. **14,** 807–811 (2015).

[10] Cox, J. D. & Garcia de Abajo, F. J. Electrically tunable nonlinear plasmonics in graphene nanoislands. *Nat*. *Commun*. **5,** 5725 (2014).

[11] Seyler, K. L. et al. Electrical control of second harmonic generation in a WSe_2 monolayer transistor. *Nat*. *Nanotech*. ***10, 407–411*** (2015).

[12] Yap, B. K., Xia, R. D., Campoy-Quiles, M., Stavrinou, P. N. & Bradley, D. D. C. Simultaneous optimization of charge-carrier mobility and optical gain in semiconducting polymer films. *Nat*. *Mater*. **7**, 376-380 (2008).

Transmissive metasurface lens for a mid-wavelength infrared detectors and focal plane arrays

Alexander Soibel,[1*] Shuyan Zhang,[2,3] Sam A. Keo,[1] Dan Wilson,[1] Sir Rafol, Alan She,[2] David Z. Ting,[1] Federico Capasso[2] and Sarath D. Gunapala[1]

[1] Jet Propulsion Laboratory, California Institute of Technology, 4800 Oak Grove Dr., Pasadena, CA
[2] School of Engineering and Applied Sciences, Harvard University, Cambridge, MA
*[3] Singapore Bioimaging Consortium, A*STAR, 11 Biopolis Way, Singapore 138667.*
**corresponding author, E-mail: asoibel@jpl.nasa.gov*

Abstract

In this work, we successfully demonstrated flat optical concentrators operating in mid-wavelength infrared (MWIR) spectral range.[1] The optical concentrators are solid immersion polarization-independent transmissive metasurface lens designed to operate in the 3-5μm band. These 30μm diameter lenses were tested using a JPL-developed MWIR camera showing very good optical characteristics with a small focal spot size and focal length of about 150μm. This demonstration is the first step in the realization of infrared detectors monolithically integrated with flat lenses.

1. Introduction

High operating temperature of mid- and long-wavelength infrared imagers can be achieved by integrating detectors with optical concentrators that increase optical collection area while keeping detectors volume constant. The most common way to realize optical concentrators is by integrating spherical microlens with detectors but this technology is not well developed in mid- and long-infrared. Recently, a new class of optical components dubbed metasurfaces has been invented.[2,3] These components are based on inhomogeneous arrays of optical resonators with subwavelength separation. These metasurfaces offer novel approach for realization of optical concentrators that can be monolithically integrated with infrared detectors as well as small pixels of infrared focal plane arrays (FPAs).

These metalenses need to feature specific characteristics to enable their integration with FPAs. The lens needs to be transmissive and of the immersion type to focus light in the detector materials. The lens also needs to be fabricated on the backside of the detector so it is made of the same material as the detector wafer substrate (GaSb, InSb or CdTe). Hence, the fabrication process needs to be compatible with the detector manufacturing. Furthermore, it has to be scalable to the size of microlens arrays and robust to avoid issues with FPA uniformity and operability. Finally, similar to many other applications, the lens should have a high focusing efficiency, work for all incident polarizations and be broadband (e. g. 3 – 5 μm or 8 – 12 μm).

2. Design and fabrication

Here we developed a transmissive metalens focusing light from air into the substrate material. The metalens consists of circularly shaped posts etched directly into a GaSb substrate (Fig. 1). The circular shape of the posts ensures that the designs work for all incident light polarizations. The phase change in the dielectric resonators relies on the control of the scattering properties of ultrathin subwavelength scale optical resonators. By varying the diameter of the posts, a phase coverage of 2π and a relatively high and uniform transmission amplitude response can be achieved. The phase profiles of the metalenses were realized by placing these subwavelength posts with varying post diameter at fixed edge-to-edge separation.

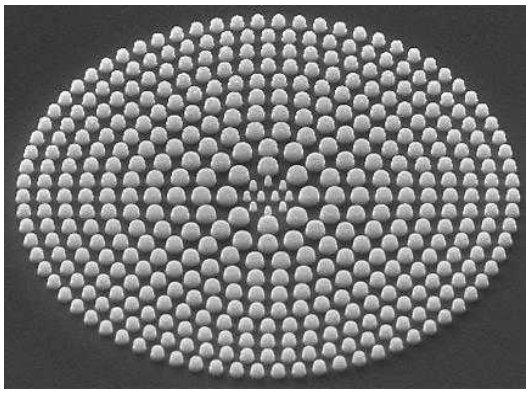


Figure 1: SEM image of a single metalens. Individual posts are clearly visible.

We fabricated a 10 × 10 metalens arrays with each metalens having a 30 μm in diameter and a focal spot size of 10 μm. For fabrication of the metalenses, the substrates were first prepared by solvent clean (IPA and acetone), oxygen plasma ash, and buffered oxide etch. Then a hard mask made of SiNx was deposited on the wafer. The metalenses were patterned by electron-beam lithography using a ZEP520A resist with a film thickness of around 500 nm. After the resist development, the hard mask was etched with CF_4 and O_2 using an inductively-coupled plasma (ICP) system (Plasma-Therm ICP etching system). Prior to the metalens

© 2019 California Institute of Technology. Government sponsorship acknowledged

etching, samples were mounted on substrate carriers with a thermal conductive-cooled adhesive medium. The GaSb was etched with a mixture of Cl_2, BCl_3, and Ar in an ICP etching system. The hard mask was then removed.

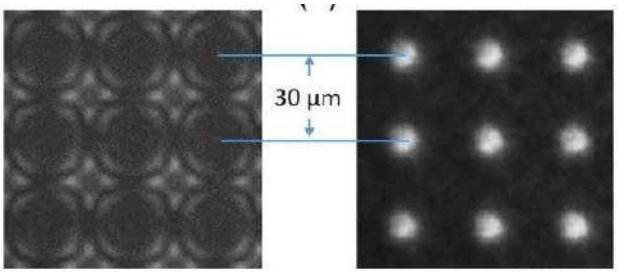


Figure 2: IR camera images of a 3x3 subsection of metalens array. (Left) Camera was focused on the metalenses. The center-to-center distance of the neighboring metalenses is 30 µm. (Right) Camera image at the focal plane showing the intensity enhancement

3. Measurement results

The blackbody at 1273K was used as the infrared source and metalenses were placed after the bandpass filter with the posts facing the bandpass filter. Imaging was performed with a 36x reflective microscope objective and an MWIR infrared camera. The infrared camera with the attached microscope objective was mounted on a translational stage and moved along the optical axis (z).

Figure 2 shows acquired IR images of the metalens array taken at different z values after subtracting the background intensity taken when the objective was blocked. z =0 µm was set when the camera was focused on the metalens [Fig. 2 left]. The metalens shapes are clearly visible. The camera assembly was then moved away from the metalens in 1 µm steps. Figure 2 (right) is the camera image taken at the focal plane of the metalens array.

We analyzed the measured normalized intensity and found the measured full beam waist is 16.4 µm for spectral range of 3-5 µm. This value is greater than the diffraction-limited spot size which is possibly caused by the incident light not being single wavelength and normal incidence and also fabrication imperfections. The measured focal length of the metalens, f = 153 µm, was constant for in the spectral band of 2.95–4 µm. The designed value is f = 153 µm. As the wavelength increases further, the focal length decreases to f = 130 µm. However, the percentage change is relatively small $\Delta f/f<14.6\%$ for $\lambda>4\mu m$.

Metalenses act as optical concentrators to collect incident light and focus it onto the active area (pixel size) of the FPA pixel unit cell (pixel pitch size) after propagating through the substrate material; hence, the device responsivity is increased. To quantify the focusing power of the metalenses, we measured the focusing efficiency and the intensity enhancement of the metalens as an optical concentrator. The focusing efficiency was defined as the optical power over the pixel size of 10 µm at the focus divided by the incident power over the pixel pitch size of 30 µm. The maximum focusing efficiency measured is 52% with the bandpass filter BP-3390-345 nm. In the simulation, the average focusing efficiency is 70% over a wavelength range of 3–5 µm and the maximum focusing efficiency is 80%. The loss in the simulation mainly comes from the reflection at the GaSb/air interface. The focusing efficiency can be improved by matching the optical impedance of the planar device with that of free space and/or depositing a layer of anti-reflection coating.

4. Conclusions

In summary, we demonstrated a type of metalens that operates as a solid-immersion lens, i.e., incident light is focused into the substrate material. The metalenses comprising GaSb posts were fabricated directly on the backside of GaSb substrates, making it compatible with backside illuminated IR FPAs. To keep the detector volume small, our metalenses are 30 µm in diameter corresponding to the FPA pixel pitch size and only 2 lm thick which are much smaller than the typical size of microlenses and microspheres for FPAs. The metalens has a constant focal length in 3–4 µm spectral range and has a small focal length variation over the incident wavelength range (3–5 µm). Metalens shows intensity enhancement of around three times at the focus indicating a potential to improve responsivity of the FPAs. In particular, the demonstrated 10 ×10 metalens array proves the scalability of this approach for FPAs. Our demonstration opens a path to the realization of high operating temperature IR detectors and FPAs monolithically integrated with flat and lightweight

5. Acknowledgements

The authors thank Xinghui Yin for helpful discussions and A. Shapiro-Scharlotta, F. Y. Hadaegh and R. Howard for encouragement and support. This work was supported by the Center Innovation Fund, Space Technology Mission Directorate, National Aeronautics and Space Administration. Shuyan Zhang thanks A*STAR Singapore for support through the National Science Scholarship. Part of this research was carried out at the Jet Propulsion Laboratory, California Institute of Technology, under a contract with the National Aeronautics and Space Administration.

References

[1] S. Zhang, Alexander Soibel, Sam A. Keo, Daniel Wilson, Sir. B. Rafol, David Z. Ting, Alan She, Sarath D. Gunapala, and Federico Capasso, Solid-immersion metalenses for infrared focal plane arrays, Appl. Phys. Lett. 113, 111104 (2018)

[2] N. Yu, P. Genevet, M. A. Kats, F. Aieta, J.-P. Tetienne, F. Capasso, and Z. Gaburro, "Light propagation with phase discontinuities: Generalized laws of reflection and refraction," Science 334, 333 (2011).

[3] N. Yu and F. Capasso, "Flat optics with designer metasurfaces," Nat. Mater. 13, 139 (2014).

High-performance, All-dielectric Metasurfaces in the Ultraviolet Regime

Cheng Zhang[1,2,*], Shawn Divitt[1,2], Qingbin Fan[3], Wenqi Zhu[1,2], Amit Agrawal[1,2], Ting Xu[3], and Henri J. Lezec[1]

[1]Physical Measurement Laboratory, National Institute of Standards and Technology, Gaithersburg, MD, 20899, USA
[2]Maryland Nanocenter, University of Maryland, College Park, MD, 20742, USA
[3]College of Engineering and Applied Sciences, Nanjing University, Nanjing, 210093, China
*corresponding author, E-mail: cheng.zhang@nist.gov

Abstract

I will present our recent efforts of achieving an assortment of low-loss all-dielectric metasurfaces operating down to a record-short deep-UV wavelength of 266 nm, with efficiencies up to 72%.

In this talk, I will show how low-loss, all-dielectric metasurfaces operating at UV wavelengths down to the deep-ultraviolet range can be implemented using Hafnium Oxide (HfO_2), an amorphous dielectric material most commonly exploited as a high static dielectric constant (high-k) material in integrated circuit fabrication, that is characterized by a wide-bandgap. We develop a unique Damascene fabrication process, involving both low-temperature atomic layer deposition (ALD) of HfO_2 onto patterned resist and back etching with Argon ion milling, to achieve high-aspect-ratio HfO_2 nanostructures with straight and smooth sidewall profiles. We first demonstrate a variety of polarization-independent UV metasurface devices having distinct functionalities, namely diffraction-limited focusing lenses (metalenses), hologram projectors (metaholograms) and self-accelerating beam generators, operating at two near-UV wavelengths (364 and 325 nm) with efficiencies as high as 72%. Scaling down metasurface critical dimensions, we achieve metaholograms operating with high efficiencies at a record-short, deep-UV wavelength of 266 nm. Finally, we demonstrate 266-nm, spin-multiplexed metasholograms of greater degree of geometric complexities, with efficiencies up to 61%. Our work paves the way towards low form factor and multifunctional UV flat optical systems.

Gate-tunable Conducting Oxide Epsilon-near-zero Metasurfaces with Active Nonlinear and Quantum Responses

Aleksei Anopchenko[1], Subhajit Bej[1], Sudip Gurung[1], Khant Minn[1], Jingyi Yang[1], and Ho Wai Howard Lee[1,2,*]

[1]Department of Physics and Baylor Research and Innovation Collaborative (BRIC), Baylor University, Waco, TX 76798, United States
[2]The Institute for Quantum Science and Engineering, Texas A&M University, College Station, TX 77843, United States
*corresponding author, E-mail: Howard_Lee@Baylor.edu

Abstract

The optical response of epsilon-near-zero (ENZ) materials has been a topic of significant interest in the last few years as the electromagnetic field inside media with near-zero permittivity has been shown to exhibit unique optical properties, including strong electromagnetic wave confinement, non-reciprocal magneto-optical effects, and abnormal nonlinearity. These ultrathin ENZ materials are promising for the enhancement of quantum emission for optical sensing and enhanced absorption/emittivity for energy harvesting.

This talk will review our recent development on a gate-tunable conducting oxide epsilon-near-zero metasurfaces [1-5]. I will present our recent development on the use of gate-tunable materials, transparent conducting oxides, to demonstrate an electrically tunable ultrathin ENZ perfect absorber enabled by the excitation of ENZ modes. In addition, I will present the active control of emissive properties of quantum emitters and enhanced optical nonlinearity in hybrid ENZ-plasmonic heterostructures.

Acknowledgements

This work was supported in part by the Young Faculty Award Program from Defense Advanced Research Projects Agency (grant number N66001-17-1-4047), AFOSR-AOARD (Award number: FA2386-18-1-4099), and the Robert A. Welch Foundation (Award number: AA-1956-20180324).

References

[1] Y. W. Huang, H. W. Lee, R. Sokhoyan, R. Pala, K. Thyagarajan, S. Han, D. P. Tsai, and H. A. Atwater, "Gate-tunable conducting oxide metasurfaces," *Nano Lett.* **16**, 5319-5325 (2016).

[2] A. Anopchenko, L. Tao, C. Arndt, H. W. Lee, "Field-effect tunable and broadband Epsilon-near-zero perfect absorbers with deep subwavelength thickness," *ACS Photonics* **5**, 2631 (2018).

[3] A. Anopchenko, S. Gurung, L. Tao, C. Arndt, H. W. Lee, "Atomic Layer Deposition of Ultra-thin and smooth Al-doped ZnO for Zero-Index Photonics", *Materials Research Express,* **5**, 014012 (2018).

[4] K. Minn, A. Anopchenko, J. Yang, H. W. Lee, "Excitation of epsilon-near-zero resonance in ultra-thin indium tin oxide shell embedded nanostructured optical fiber," *Nature Scientific Reports* **8**, 2342 (2018).

[5] J. Yang, I Ghirmire, P. C. Wu, S. Gurung, C. Arndt, D. P. Tsai, H. W. Lee, "Photonic crystal fiber metalens", Nanophotonics 8, 443-449 (2019).

Metasurface Light Sources and Modulators Based on Kerker Effects

Austin Howes[1], Zhihua Zhu[2], Wenyi Wang[2], Joshua R. Nolen[3], Ivan I. Kravchenko[4], Richard Haglund[1], Joshua Caldell[5], Jason Valentine[5*]

[1]Department of Physics and Astronomy, Vanderbilt University, Nashville, Tennessee, USA
[2] Department of Electrical Engineering and Computer Science, Vanderbilt University, Nashville, Tennessee, USA
[3]Interdisciplinary Materials Science Program, Vanderbilt University, Nashville, Tennessee, USA
[4]Center for Nanophase Materials Science, Oak Ridge National Laboratory, Oak Ridge, Tennessee, USA
[5]Department of Mechanical Engineering, Vanderbilt University, Nashville, Tennessee, USA
*corresponding author, E-mail: jason.g.valentine@vanderbilt.edu

Abstract

The first Kerker condition states that spectrally overlapped, and equal strength, electric and magnetic dipole modes will result in cancellation of the backscattered field. In this talk, I will outline how this effect, and related Kerker effects, can be harnessed in all-dielectric modulators and light sources. In the case of modulators this allows for high on-state transmission and large modulation depth. In absorbing metasurfaces this effect can be used to realize near-unity absorption leading to efficient thermal emitters.

1. Introduction

In 1983 Kerker *et. al.* published a paper in which scattering of a sphere with $\mu \neq 1$ was studied [1]. One of the observations of this study was that spectrally overlapped and in-phase electric and magnetic dipole modes result in cancelation of the backscattered field. This is known as the first Kerker condition. In the absence of absorption, this results in unity transmission with each scatterer corresponding to a "Huygens' source" allowing for tailoring of the wavefront [2].

In this talk, I will outline how this effect can be used to realize optical modulators with high on-state transmission [3]. Modulation of such surfaces can come in the form of carrier injection or through the use of phase change media such as vanadium dioxide (VO_2). In both cases, large modulation depth can be achieved by working close to the epsilon near-zero (ENZ) point of the medium. I will also discuss Kerkers' first condition when employing highly absorbing media, such as silicon carbide (SiC). In this case, the presence of two resonances allows for critical coupling and unity absorption without the use of a reflecting backplane, as is commonly employed in metamaterial perfect absorbers.

2. Metasurface Modulators

In Fig. 1a we provide a schematic of a metasurface unit cell comprising a cylindrical resonator made from silicon with a thin bus bar connecting the resonators. These resonators

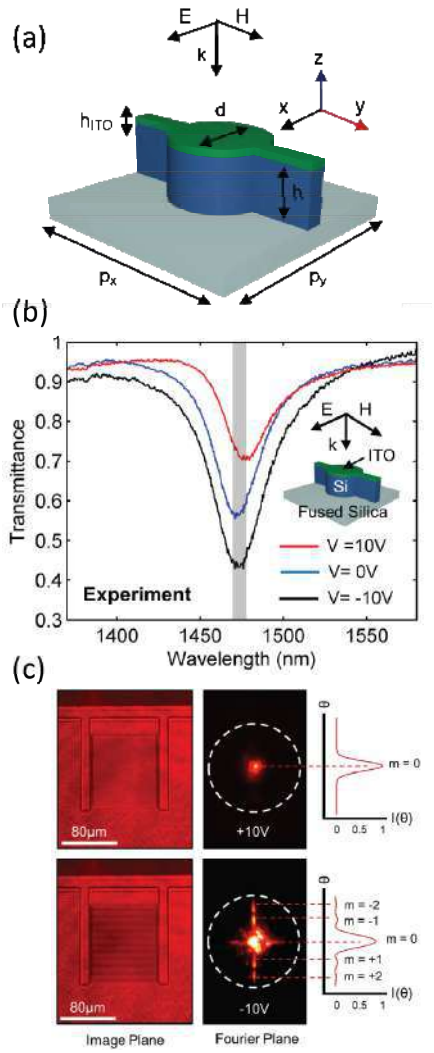


Figure 1: (a) Schematic of Huygens metasurface modulator. (b) Experimental transmission spectra as a function of bias. (c) Metasurface patterned into reconfigurable diffraction grating.

are designed to operate near the first Kerker condition such that backscattered light is cancelled. Active modulation of the metasurface is achieved by placing a thin film of indium tin oxide (ITO) on top of the resonator. By tuning the coupling between the resonators and the ENZ point of the ITO thin film, active control over the transmission amplitude is achieved. This results in near-unity transmission in the on-state. Upon moving the ITO film through its ENZ point, absorption is increased reducing transmission, as shown in Fig. 1b. Spatially patterning the modulated area allows one to create beam steering devices such as diffraction gratings as shown in Fig. 1c. While we will focus on transmission modulation, use of lower loss ENZ films may allow this approach to be translated into phase modulators in the future.

I will also discuss implementing these surfaces with VO_2 to achieve dynamic modulation. In this case, the larger absorption of the VO_2 results in larger modulation depth. One interesting application of such metasurfaces are optical limiters as such films have high, and spectrally flat, transmission in the on-state. When the metasurfaces are heated, for instance by an incident laser, a narrow stop band emerges with a modulation depth greater than 30dB. While working at the ENZ point of VO_2 results in the largest modulation depth the film can be designed at other frequencies with only a slight decrease in modulation depth.

3. Metasurface Absorbers and Thermal Emitters

While most Mie resonance-based metasurfaces employ low-loss constituents there are certain applications that could take advantage of absorption loss, such as thermal emitters and photodetectors. In the second half of the talk I will discuss spectrally overlapped electric and magnetic resonances in the presence of strong dispersion and absorption. While the first Kerker condition results in unity forward scattering in the absence of loss, we show that in a material of high dispersion, permittivity, and loss this condition can result in a uniquely strong and narrow absorption peak.

We accomplish such metasurfaces experimentally by employing 3C-SiC nanopillar arrays. The electric and magnetic dipole resonances are overlapped in the high index, and high absorption, region around the transverse optic (TO) phonon. We demonstrate an absorptance of 78% with a quality factor of 170. This design has one of the highest quality factors of any thermal emitter at this wavelength range while also still possessing near-unity absorptivity. In addition, the resonators have a deep sub-wavelength size due to the high refractive index near the TO phonon which results in a relatively angle insensitive response, unlike past work on SiC gratings.

References

[1] M. Kerker, D. S. Wang, and C. L. Giles, "Electromagnetic scattering by magnetic spheres," J. Opt. Soc. Am. 73, 765–767 (1983).

[2] M. Decker, I. Staude, M. Falkner, J. Dominguez, D. Neshev, I. Brener, T. Pertsch, Y. Kivshar, "High-Efficiency Dielectric Huygens Surfaces," Adv. Opt. Mater., 3, No. 6, pp.813-820 (2015).

[3] A. Howes, W. Wang, I. Kravchenko, J. Valentine, "Dynamic Transmission Control Based on All‐Dielectric Huygens Metasurfaces," Optica 5, No. 7, pp. 787-792 (2018).

High-efficiency coupling and reshaping of surface plasmon with metasurfaces

Xiaoer Li[1#], Zhuo Wang[2#], Shaohua Dong[1], Sixiong Yi[1], Yizhen Chen[1], Huijie Guo[2], Fuxin Guan[2], Qiong He[2], Lei Zhou[2], and Shulin Sun[1]*

[1]Department of Optical Science and Engineering, Fudan University, Shanghai 200433, China
[2] Department of Physics, Fudan University, Shanghai 200433, China
[#]X. Li and Z. Wang contributed equally to this work
*corresponding author, E-mail: sls@fudan.edu.cn

Freely controlling the surface plasmon polaritons (SPPs) is always an issue of photonic researches. While traditional approaches to excite and reshaping SPPs are widely utilized for a long time, they still suffer from some inherent challenges, e.g., low-efficiency, limited functionalities and huge size. While gradient metasurfaces exhibit strong abilities to control electromagnetic waves, most of previous works are devoted to modulate far-field EM waves [1-3]. Meanwhile, some metasurfaces are proposed to either couple the SPPs [4-6] or control the wavefronts of SPPs [7, 8] with very high efficiency. However, the metadevice with these two distinct functionalities merged together are rarely reported. Here, we propose a new scheme to simultaneously excite and reshape the SPPs with a single meta-device. Moreover, the chirality of input propagating waves can be utilized as a flexible freedom to modulate the wavefronts of the excited SPPs [9, 10]. Moreover, the wavefronts of the excited SPPs can be flexibly modulated to the totally independent forms, e.g., surface plasmon focusing and deflection, by simply changing the polarizations of impinging light. Our idea is successfully demonstrated by full wave simulations and near-field experiments. Our work may stimulate many near-field related applications, e.g., SPP holograms, complex SPP beam generations, super resolution imaging, enhanced non-linear effect, and so on.

References

[1] N. Yu, P. Genevet, M. a. Kats, F. Aieta, J.-P. Tetienne, F. Capasso, and Z. Gaburro, Science 334, 333 (2011).

[2] Weijie Luo, Shiyi Xiao, Qiong He, Shulin Sun, and Lei Zhou, Advanced Optical Materials 3, 1102 (2015).

[3] Hongchen Chu, Qi Li, Bingbing Liu, Jie Luo, Shulin Sun, Zhi Hong Hang, Lei Zhou and Yun Lai, Light: Science & Applications 7, 50 (2018).

[4] S. Sun, Q. He, S. Xiao, Q. Xu, X. Li, and L. Zhou, Nature Materials 11, 426 (2012).

[5] Wujiong Sun, Qiong He, Shulin Sun, and Lei Zhou, Light: Science & Applications 5, e16003 (2016).

[6] J. Duan, H. Guo, S. Dong, T. Cai, W. Luo, Z. Liang, Q. He, L. Zhou & S. Sun, Scientific Reports 7, 1352 (2017).

[7] S. Dong, Y. Zhang, H. Guo, J. Duan, F. Guan, Q. He, H. Zhao, L. Zhou, and S. Sun, Physical Review Applied 9, 014032 (2018).

[8] S. Dong, Z. Wang, H. Guo, F. Guan, X. Li, Q. He, H. Zhao, L. Zhou, and S. Sun, EPL 122, 67002 (2018).

[9] X. Li, Z. Wang, S. Dong, et al., submitted.

[10] Z. Wang, X. Li, et al, submitted.

Structural Color for Displays and Imaging

Electrically tunable multicolored filter based on plasmonic nanoscale phase retarder and liquid crystals

Luc Driencourt[1], Dimitrios Kazazis[2], Yasin Ekinci[2], François Federspiel[3], Richard Frantz[3], Rolando Ferrini[1], and Benjamin Gallinet[1,*]

[1]Centre Suisse d'Electronique et de Microtechnique (CSEM SA), Muttenz, Switzerland
[2]Paul Scherrer Institut (PSI), Villigen, Switzerland
[3]Rolic Technologies Ltd., Allschwil, Switzerland
*corresponding author, E-mail: Benjamin.gallinet@csem.ch

Abstract

An electrically tunable filter based on a nanoimprinted plasmonic phase retarder and liquid crystal cell is reported. A plasmon resonance and its abrupt phase jump yield structural colors between crossed polarizers. A range of 8V is enough to access to more than half of the area covered by standard RGB filters in CIE color coordinates with a single filter. Such approach is foreseen in particular to increase the spatial resolution of display devices.

1. Introduction

Surface plasmon resonances in metallic nano-structures enable the confinement and manipulation of the electromagnetic field well below the diffraction limit, thus opening new paradigms for phase and polarization control of light. An electrically tunable filter covering a large area in CIE coordinates is reported here. This effect is achieved by design and fabrication of plasmonic nanostructures showing a strong and spectrally narrow birefringence effect. The color transmitted through the device can be actively controlled by liquid crystals.

2. Discussion

The basic working principle of the device is shown in Fig. 1. A plasmonic phase retarder can generate different colors in transmission when placed between crossed polarizers and the output polarization is rotated [1]. The plasmonic phase retarder consists of a periodic array of deep-subwavelength metallic nanowires (50nm width), in order to have a stable optical response as a function of the incidence angle. The light polarized across the nanowires (TM) excites a plasmon resonance, while the other polarization (TE) does not induce a resonance. Here, a first entrance polarizer prepares the incident light in a polarization state oriented at 45° from the nanowires orientation. A phase retardation between TM and TE polarization yields an elliptically polarized light in transmission. A polarization analyzer based on liquid crystal cells allows to project the transmitted light onto a polarization state whose orientation depends on the applied voltage. Interferences between the different birefringent contributions lead to a color effect. As a result, the transmitted light has different colors depending on the applied voltage.

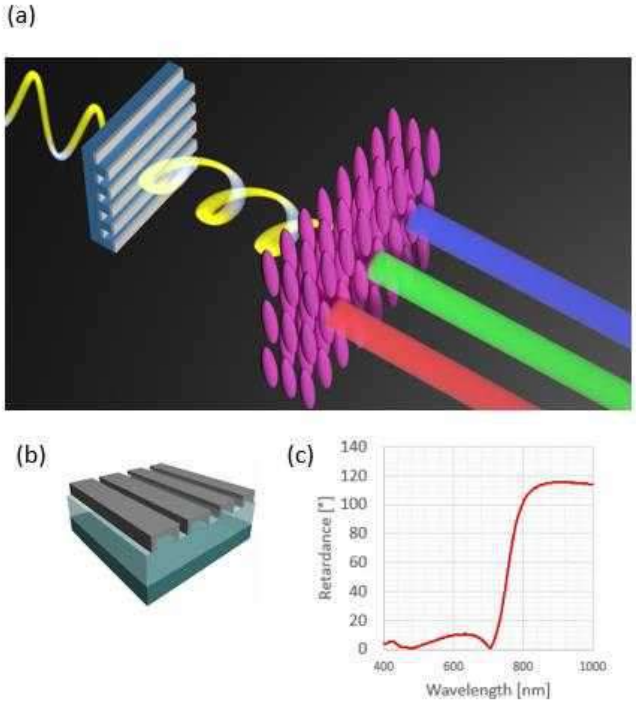


Figure 1: (a) Plasmonic retarder between in a polarizer and a liquid crystal based polarization analyzer, allowing to generate a variety of colors as a function of the voltage applied to the liquid crystal cell. (b) Plasmonic phase retarder made of a deep subwavelength array of silver nanowires. (c) Measured phase retardance between polarization along and across the wires.

In order to ensure the applicability to large area production, UV nanoimprint lithography (UV-NIL) and thin film coatings have been used to fabricate the plasmonic phase retarder, which are both wafer-scale and roll-to-roll compatible methods. The nanoimprint master consists in a periodic grating over an area of 30x30 mm^2 fabricated with electron beam lithography (EBL). A 100 mm Si wafer was initially covered with 20 nm of Cr in a blanket deposition by electron beam evaporation. A thin ~100 nm PMMA layer was subsequently spin-coated onto the Cr layer and exposed by EBL. The wafer was developed and the pattern

transferred from the PMMA layer onto the Cr layer by plasma etching. The PMMA layer was subsequently stripped and the grating pattern transferred into the Si wafer by inductively coupled plasma reactive ion etching (ICP-RIE), resulting in a well-controlled and anisotropic etch [2]. Finally the Cr mask was removed by Cl-based plasma etching, generating the UV-NIL master. A plasmonic phase retarder has been fabricated by UV-NIL of the grating master and evaporation of a silver thin film, followed by an encapsulation. The evaporation is performed with an angle, so that a self-shadowing effects prevents full coverage of the surface. The resulting structure is sketched in Fig. 1b and consists in a periodic array of silver nanowires with a cross section forming an inverted U-shape. This particular shape shows a high degree of tunability of the plasmon resonance position given the constraints of a sub-wavelength periodicity, and also enables a higher degree of transmission. Multiple interfering resonances are observed so that the peak transmission can reach >70%. Measurements of the phase retardation between the transmitted TM and TE fields (Fig. 1c) show a strong phase variation at the plasmon resonance at 750nm.

Placed between a polarizer oriented at 45° from the nanowires orientation and a liquid crystal cell, the transmission spectrum of the plasmonic phase retarder can be tuned with the voltage applied to the liquid crystal cells. For a low voltage, the polarization transmitted through the liquid crystal cell is oriented along the gratings lines. For higher voltage, the light transmitted through the liquid crystal cell is oriented across the grating lines and the resulting spectrum has a dip in transmission, which is the signature of a plasmon resonance at 725nm. At a voltage of 8V, a full rotation of the polarization by 180° has been spanned. The corresponding colors are shown in the CIE plot of Fig. 2a. A large range of colors can be spanned using this approach. Compared to a system where the analyzing polarization is rotated mechanically, the colors are similar for a low voltage up to 5.5V and diverge for higher voltages. The different originates from the appearing of Michel-Lévy colors in the birefringent liquid crystal cells. Therefore, only a voltage of 8V is enough to obtain a large number of different colors. In Fig. 2b, different colors have been selected at particular voltages, showing in particular that orange, magenta, purple, blue, turquoise, green and yellow can be obtained. Further colors ranging from orange to more saturated purple and blue can be obtained for higher voltages (from 9V to 20V), corresponding to a larger contribution of the Michel-Lévy interference colors. However, these colors require more time to be generated which reduces their applicability to a display device with high frequency.

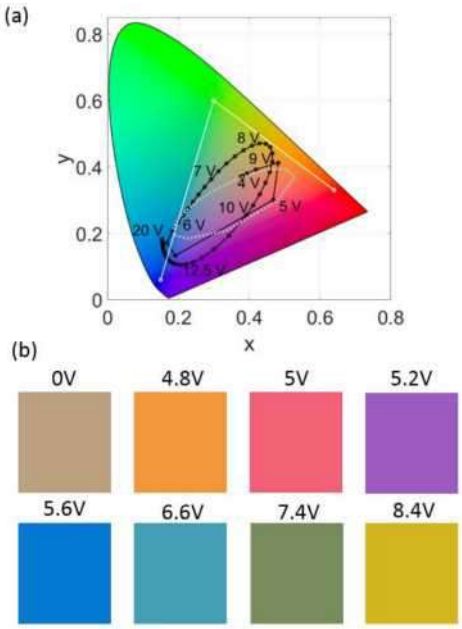


Figure 2: (a) CIE plot of color range spanned by the system. White: colors obtained by mechanical rotation of an analyzing polarizer. Black: colors obtained by increasing the voltage applied to the liquid crystal cell from 0V to 20V. (b) Colors at particular voltages.

3. Conclusions

We performed the design, fabrication and characterization of plasmonic phase retarders with spectrally narrow phase variations. Starting with the fabrication of a high resolution master using electron beam lithography, an upscalable nanoimprint and thin film coating process flow has been used to fabricate the plasmonic retarders. We have shown the tunability of their transmitted colors using liquid crystal cells, which paves the way towards their implementation in displays [3]. In particular, a range of 8V is enough to access to more than 50% of the area covered by standard RGB filters in CIE color coordinates with a single filter. Such approach is foreseen in particular to increase the spatial resolution of display devices.

Acknowledgements

Funding from Nano Argovia and Swiss Nanoscience Institute Basel (SNI) under A12.13 is gratefully acknowledged.

References

[1] L. Dümpelmann, A. Luu-Dinh, B. Gallinet, L. Novotny, Four-fold color filter based on plasmonic phase retarder, *ACS Photonics* 3: 190−196, 2016.

[2] L.-T. Tseng, D. Kazazis, X. Wang, C. M. Popescu, A. P. G. Robinson, Y. Ekinci, *under review*.

[3] L. Shao, X.L. Zhuo, J. Wang, Advanced Plasmonic Materials for Dynamic Color Display, *Adv. Mat.* 30: 1704338, 2018.

Hybrid Plasmonic and Electrochromic Displays

Magnus P Jonsson

Organic Photonics and Nanooptics group, Laboratory of Organic Electronics, Department of Science and Technology, Linköping University, Sweden

E-mail: magnus.jonsson@liu.se

I will here present our recent results on reflective displays, with focus on developing and understanding hybrid plasmonic and electrochromic systems for electronic paper in color.

Electrochromic systems have potential to enable highly important applications for society, such as smart windows and various types of energy-efficient displays and labels for use in, for example, internet-of-things devices, electronic readers, and advertisement boards.

In part of our research, we study organic electrochromic conducting polymers. These materials are popular for electrochromics due to advantages such as low-cost and compatibility with high throughput and low-temperature processing. Furthermore, they can provide superior switching speeds and optical memory compared with common inorganic alternatives. Our recent studies demonstrate that they can be used in various types of devices, including free-standing electrochromic paper, infrared electrochromic systems, and greyscale picture-to-picture displays.[1,2,3]

Conducting polymers, however, cannot provide good control of the reflected color, but are typically limited to black and white functionality (or blue and white). By contrast, plasmonic metasurfaces are capable of providing highly reflective surfaces with vibrant colors, which is ideal for reflective displays in color. We studied such plasmonic metasurfaces based on the abundant metals aluminum and copper, instead of the more commonly used gold and silver.[4] The metasurfaces were capable of providing high-quality colors in reflection, covering all the primary RGB colors and enabling accurate reproduction of color photographs. Combining these metasurfaces with electrochromic polymers then enabled the development of switchable plasmonic devices.[4] In brief, we utilized the variable transparency of electrochromic polymers to control the reflection from underlying colorful plasmonic metasurfaces. Besides these works, I would also like to present our yet unpublished research addressing the need for solution-processable fabrication methods not only of the conducting polymer layers, but also of the plasmonic metasurfaces.

Acknowledgements

The research on plasmonic displays is performed in collaboration with Dr. Dahlin at Chalmers University of Technology and RISE Acreo, and supported by the Swedish Foundation for Strategic Research. We also acknowledge financial support from the Wenner-Gren Foundations, the Swedish research council, the ÅForsk Foundation and the Swedish Government Strategic Research Area in Materials Science on Functional Materials at Linköping University (Faculty Grant SFO-Mat-LiU No 2009 00971).

References

[1] R. Brooke, J. Edberg, X. Crispin, M. Berggren, I. Engquist and M.P. Jonsson, Greyscale and paper electrochromic polymer displays by UV patterning, *Polymers* 2019, 11, 267

[2] A. Malti, R. Brooke, X. Liu, D. Zhao, P. Andersson Ersman, M. Fahlman, M.P. Jonsson, M. Berggren and X. Crispin, Free-standing electrochromic paper, *Journal of Materials Chemistry C* 2016, 4, 9680-9686

[3] R. Brooke, E. Mitraka, S. Sardar, M. Sandberg, A Sawatdee, X. Crispin and M.P. Jonsson, Infrared Electrochromic Conducting Polymer Devices, *Journal of Materials Chemistry C* 2017, 5, 5824-5830

[4] K. Xiong, D. Tordera, G. Emilsson, O. Olsson, U. Linderhed, M.P. Jonsson, and A.B. Dahlin, Switchable Plasmonic Metasurfaces with High Chromaticity Containing Only Abundant Metals, *Nano Letters* 2017, 17 (11), 7033–7039

Optimizing electrochromism for plasmonic electronic paper: Inorganic vs organic

Marika Gugole[1], Oliver Olsson[1], José Montero Amenedo[2], Kunli Xiong[1], Gunnar A. Niklasson[2], and Andreas Dahlin[1]

[1] Department of Chemistry and Chemical Engineering, Chalmers University of Technology, 41296 Göteborg, Sweden
[2] Department of Engineering Sciences, Solid State Physics, The Ångström Laboratory, 751 21 Uppsala, Sweden

Abstract

The combination of plasmonic nanostructures and electrochromic materials for dynamic color generation has been of interest in recent years due to the possibility to make reflective displays in full color with extremely low power consumption compared to emissive displays. We show a comparison between two electrochromic materials, tungsten trioxide (inorganic) and PProDOT-Me_2 (organic), for electrical modulation of the resonantly reflected light from plasmonic nanostructures. The comparison focuses on achievable contrast, switching speed, coloration memory and power consumption.

1. Introduction

Plasmonic metasurfaces with conjugated polymers have been used to generate dynamic color control in reflection mode [1][2]. The metasurfaces consist of three solid films made by evaporation: 150 nm silver film, for high reflection, an alumina spacer layer which tunes the reflective color (via Fabry-Pérot interference) and a 20 nm gold film where short-range ordered 150 nm nanoholes are prepared by colloidal lithography. These structures can generate vibrant red, green and blue colors which may be used as pixels in a reflective display. To switch the colors on and off, conjugated polymers with tunable optical absorption have been used [1]. However, there is room for improvements regarding the contrast, the switching speed, the coloration stability and power consumption.

Among materials which have electrochromic properties, we chose to compare the best inorganic and organic ones for full transparent/black switching across the visible. The first is tungsten trioxide (WO_3), an inorganic electrochromic material that has been used in smart windows applications for many years [3]. It shows high contrast over the whole visible spectrum up to >50% [4] and long lifetime [5]. The second is PProDOT-Me_2, reported to show highest contrast among all polymers (close to 78%) [6] and fast switching speed [7].

2. Results and discussion

Fig.1 shows a schematic of the structure used for the comparison. Bleached and colored state correspond to a voltage of 1 V and -1 V respectively vs Ag/AgCl. A Pt wire is used as counter electrode. WO_3 is switched using 1 M $LiClO_4$ /Propylene Carbonate as electrolyte while PProDOT-Me_2 using 0.1 M Tetrabutylammonium perchlorate/ Acetonitrile.

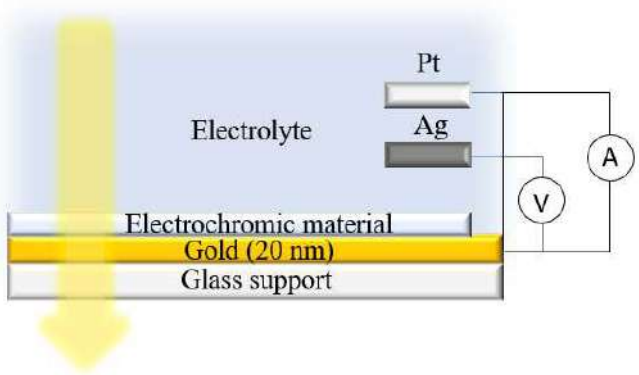


Figure 1: Schematic of the 3 electrodes setup.

In Fig.2, transmission spectra of 285 nm WO_3, approximately 200 nm PProDOT-Me_2 and the bare gold substrate before deposition (sputtering of WO_3 and electropolymerization of PProDOT-Me_2) are reported. WO_3 shows a contrast of 22% in the red region (660 nm), 32% in the green region (520 nm) and 25% in the blue region (490 nm). PProDOT-Me_2 shows a contrast of 7% in the red region, 15% in the green region and 11% in the blue region. Although the contrast does not seem to reach values comparable with, for example, black and white paper (around 50%) [8], both are reported to have potential to reach higher contrast [3][6] and data is here presented for transmission mode. Results will improve after optimization of the electrochemical polymerization of PProDOT-Me_2 and thickness of the films. The ideal thickness is around 200 nm for PProDOT-Me_2 and 300 nm for WO_3 in transmission, which are a good compromise between high contrast and transparent bleached state. In

reflection, they will differ by approximately a factor of 2 as the light passes through the film twice.
The switching speed of PProDOT-Me_2 is on the order of hundreds of ms, while for WO_3 in the order of a few seconds which is acceptable for devices displaying stationary images.
Coloration memory of WO_3 and PProDOT-Me_2 is on the order of a few minutes. It is defined as the time required for the contrast to drop by 10% while no voltage is applied. The maximum contrast can then be restored with a short voltage pulse.
The power consumption per switch is, on average, 4 mJ/cm^2 per full switch for PProDOT-Me_2 and 30 mJ/ cm^2 per full switch for WO_3.

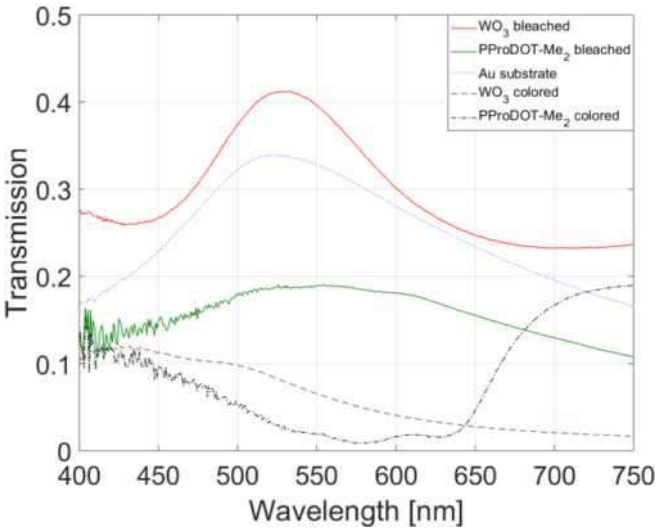


Figure 2: Transmission in colored and bleached state of 285 nm WO_3 and PProDOT-Me_2. The dotted line is the transmission of the gold substrate before deposition of the films.

3. Conclusion

Both WO_3 and PProDOT-Me_2 show promising results. The contrast of 285 nm thick WO_3 reaches a maximum value of 32%, and of 18% for 200 nm thick PProDOT-Me_2. For the optimal thicknesses of WO_3 (300 nm) and PProDOT-Me_2 (200 nm) the contrast should reach values >50%.
The switching speed of WO_3 is on the order of a few seconds, while the switching speed of PProDOT-Me_2 is on the order of a few hundreds of ms. Both switching speed are suitable for displaying stationary images.
The coloration memory of both WO_3 and PProDOT-Me_2 is on the order of a few minutes and the full contrast can be restored with a short voltage pulse.
The power consumption for full switch is 30 mJ/ cm^2 for WO_3 and 4 mJ/cm^2 for PProDOT-Me_2. More accurate evaluation of the power consumption will consider the short voltage pulse needed to restore the full contrast.

Acknowledgements

We acknowledge the Department of Microtechnology and Nanoscience – MC2 Laboratory.

References

[1] XIONG, Kunli, et al. Plasmonic metasurfaces with conjugated polymers for flexible electronic paper in color. Advanced Materials, 2016, 28.45: 9956-9960.

[2] XIONG, Kunli, et al. Switchable plasmonic metasurfaces with high chromaticity containing only abundant metals. Nano letters, 2017, 17.11: 7033-7039.

[3] NIKLASSON, Gunnar A.; GRANQVIST, Claes G. Electrochromics for smart windows: thin films of tungsten oxide and nickel oxide, and devices based on these. Journal of Materials Chemistry, 2007, 17.2: 127-156.

[4] GREEN, Sara, et al. Electrochromism in nickel oxide and tungsten oxide thin films: Ion intercalation from different electrolytes. Solar Energy Materials and Solar Cells, 2009, 93.12: 2050-2055.

[5] WEN, Rui-Tao; GRANQVIST, Claes G.; NIKLASSON, Gunnar A. Eliminating degradation and uncovering ion-trapping dynamics in electrochromic WO 3 thin films. Nature materials, 2015, 14.10: 996.

[6] WELSH, Dean M., et al. Enhanced contrast ratios and rapid switching in electrochromics based on poly (3, 4-propylenedioxythiophene) derivatives. Advanced Materials, 1999, 11.16: 1379-1382.

[7] OTLEY, Michael T., et al. Color-Tuning Neutrality for Flexible Electrochromics Via a Single-Layer Dual Conjugated Polymer Approach. Advanced Materials, 2014, 26.47: 8004-8009.

[8] XIONG, Kunli, et al. Active control of plasmonic colors: emerging display technologies. Reports on Progress in Physics, 2019, 82.2: 024501.

Nano-structured optical surfaces based on ultrathin materials for displays and sensing

Bruno Paulillo[1], Rinu Maniyara[1], Juan Rombaut[1], Kavitha Kalavoor Gopalan[1], Nestor Bareza[1], Valerio Pruneri[1,2]

[1]ICFO—Institut de Ciències Fotòniques, The Barcelona Institute of Science and Technology, Castelldefels (Barcelona), Spain.
[2]ICREA—Institució Catalana de Recerca i Estudis Avançats, Barcelona, Spain
*corresponding author, E-mail: bruno.paulillo@icfo.eu

Abstract

Optical structures based on nano-structured ultrathin materials offer unprecedented flexibility in molding light propagation for a variety of applications from the visible to the infrared range. In this talk we will discuss our recent work on optical surfaces that combine large-area graphene and/or ultra-thin (<10 nm) metal films with scalable nano-patterning techniques (dewetting, nano-imprint). Their applications include transparent electrodes, glass functional nano-structures for displays, and plasmonic metasurfaces for surface-enhanced sensing.

Tunable All-dielectric Metasurface for Color Printing

Xin Liu[1,2], Zhao Huang[1,2], Jianfeng Zang[1,2,*]

[1]School of Optical and Electronic Information, Huazhong University of Science and Technology, Wuhan, China
[2]Innovation Institute, Huazhong University of Science and Technology, Wuhan, China
*corresponding author, E-mail: jfzang@hust.edu.cn

Abstract

Color printing has drawn tremendous attention as a promising candidate in display and security technology. Plasmonics nanostructures has been intensively investigated and opened up a way to achieve color printing at deep-subwavelength scales. However, plasmonics suffers from intrinsic loss and heating effect. Dielectric materials with low loss and strong mie resonance become a promising candidate to fabricate metasurface for color printing. Here, we demonstrate all-dielectric Si nanoring metasurfaces (SRMs) for generating high saturation colors by tuning structure parameters.

Introduction

Colors are everywhere in our daily lives and play important roles in art works, signal indicators and decoration industry due to their abilities for information transfer and aesthetic expression. Among various mechanisms to generate colors, structure color, which directly generates colors by manipulation of light absorption and scattering utilizing nanostructures, has shown great promise in next generation imaging, display and security technology. Metallic nanostructures that possess the property of surface plasmon resonance open up a way to generate structural colors at deep-subwavelength scales. Recent studies show that array of small isolated metal nanoparticles can produce different colors. Such plasmonic colors have extremely high spatial resolution and are robust under ambient effect [1]. Plasmonic colors can therefore be used in security engineering and high-density data storage. However, plasmonics has intrinsic drawbacks such as high optical losses, heating effect, and incompatibility with semiconductor nano-fabrication processes, which reduces color quality and impedes its spread and applications. Dielectric and semiconductor materials with high refractive indices can be promising alternatives for structure color generation due to low loss and strong mie resonance [2]. Qinghai Song et al. demonstrate TiO2 metasurfaces for full color printing utilizing the electric and magnetic resonances [3].

Here, we demonstrate all-dielectric Si nanoring metasurfaces (SRMs) for full-color printing. Because of the strong local field enhancement due to Mie resonance, high reflection peaks have been obtained within the entire visible region. By carefully tuning the outer diameter, inner idameter of nanoring, and the distance between nanorings, the recorded colors were widely distributed in the a standard CIE 1931 chromaticity diagram map and match the R, G, B colors very well. Our approches will be important in applications of imaging and data storage.

Discussion

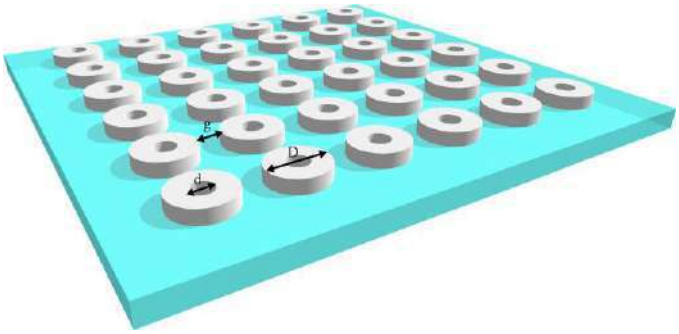


Figure 1: Illustration of the metasurface for color printing. The parameters D、d and g denote the outer diameter、inner diameter and the spacing between the adjacent ring.

As depicted in Fig 1, the metasurface is composed of Si nanoring on PDMS substrate in square lattice. We invetigate the individual influence of the outer diameter, inner diameter and the spacing between the adjacent ring on the reflection spectra, which determine the reflected color. As depicted in Fig 2, with the increasing of the outer diameter, the spectra show red shift. With the increasing of the inner diameter, the spectra show blue shift. With the increasing of the spacing, the spectra split to two evident peaks. These are related to the interaction between the Si resonators.

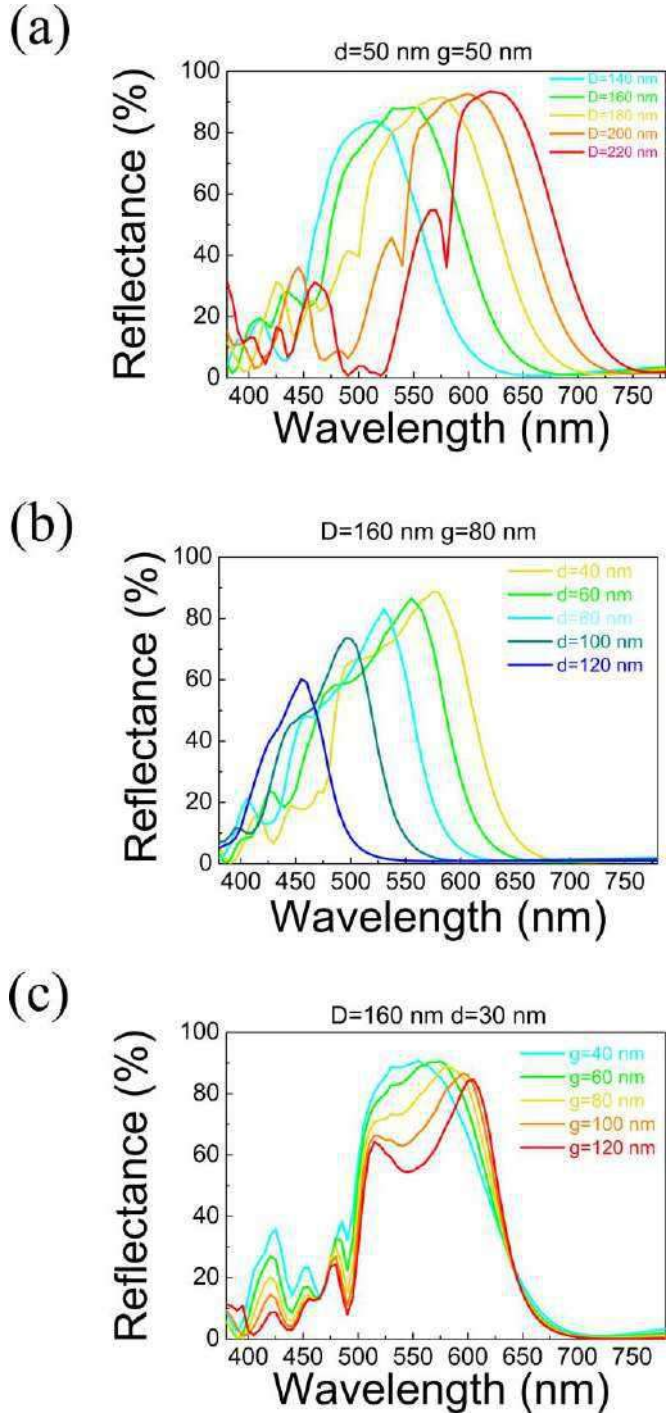


Figure 2: (a) The effect of the outer diameter on the reflection. (b) The effect of the inner diameter on the reflection. (c) The effect of the spacing on the reflection.

Conclusions

In summary, we demonstrate all-dielectric Si nanoring metasurfaces (SRMs) for color printing. By varying the parameters, the reflection spectra can be tuned, which is suitable for color printing.

Acknowledgements

This work is supported by the National Natural Science Foundation of China (51572096).

References

[1] K. Kumar, H. Duan, R. S. Hegde, S. C. W. Koh, J. N. Wei,J. K. W. Yang, Printing Colour at the Optical Diffraction Limit, Nat. Nanotechnol.,7,557-561,2012.

[2] Z. Dong, J. Ho, Y. F. Yu, Y. H. Fu, R. Paniagua-Dominguez, S. Wang, A. I. Kuznetsov,J. K. W. Yang, Printing Beyond sRGB Color Gamut by Mimicking Silicon Nanostructures in Free-Space, Nano Lett.,17,7620-7628,2017.

[3] S. Sun, Z. Zhou, C. Zhang, Y. Gao, Z. Duan, S. Xiao,Q. Song, All-Dielectric Full-Color Printing with TiO2 Metasurfaces, ACS Nano,11,4445-4452,2017.

High-Density Data Storage with Plasmonic Color Metapixels

Alexander V. Kildishev[1*], Maowen Song[1,2], Di Wang[1], Zhaxylyk A. Kudyshev[1], Honglin Yu[2], Alexandra Boltasseva[1], and Vladimir M. Shalaev[1]

[1]Birck Nanotechnology Center, School of Electrical and Computer Engineering,Purdue University, United States
[2]Key Lab of Optoelectronic Technology and Systems of Education Ministry of China, Chongqing University, China
*corresponding author, E-mail: kildishev@purdue.edu

Abstract

The plasmonic color metapixels have attracted increasing interest in the area of sensing and information technologies, including high-density data storage. We experimentally demonstrate plasmonic nanostructructures that significantly expand the number of degrees of freedom for tuning the output colors and encoding more information states in a single metapixel. Departing from the Morse-style sequential reading, a set of the plasmonic antennas orientation angles inside each metapixel is simultaneously mapped onto a unique color code and then translated into a corresponding state. Such information-multiplexing holds a great promise for high-density data storage, already exceeding the capacity of conventional optical disks.

1. Overview and Discussion

Accounting for the Global Datasphere that is predicted to exponentially explode from its 33 ZB (1 ZB = 10^{21}Byte) level in 2018 to 175 ZB by 2025 puts forward challenging technological tasks [1]. These challenges concern all branches of the modern information technologies. In the optical data storage, the storage density is fast approaching its theoretical limit, and the cost-per-bit is struggling to improve with increasing storage capacity [2]. In this talk, we offer designs and experimental demonstrations of optical metapixels that enable advanced optical data storage, based on structured color generation. Excitation of resonant modes encodes discrete topological states of metapixel designs into highly diverse colors, broadly increasing the information capacity that can be stored in an individual pixel. The combination of high color diversity with high spatial resolution enables robust, highly discernible color codes generated with metapixels. We also discuss an advanced parallel read-out system for rapid data acquisition unattainable with conventional optical data storage techniques. This is a important advancement beyond the approaches inherited from the Morse times (in 1837, Samuel Morse developed an early version of the Morse code) in the modern data storage – DVD and Blue-Ray disks – where dots and dashes are still translated from a reflected binary dash-dot sequence into meaningful content. So instead of using either dots or dashes, topologically-different nanostructures are employed in individual pixels. In the talk, we also review the structured colors that have attracted increasing interest to applications pertinent to optical displays, sensors, and cryptography due to their high spatial resolution and mechanical/chemical stability. Recently, such structured colors and especially plasmonic colors applications have generated much attention due to the increasing demand in optical steganography and cryptography techniques [4].

2. Conclusions

Thus, advancing from the Morse-style sequential reading, we associate the prime objective of the plasmonic color metapixels with the paradigm of storing and reproducing meaningful information with colors, where a set of the topological states inside each pixel area is mapped onto a unique set of colors and then decoded. Application of Artificial Intelligence techniques for optimizing the metapixels discernible with minimalistic hyperspectral filtering are also discussed. We conclude that the information-multiplexing metapixels hold a great promise for high-density data storage, advanced imaging steganography, and optical cryptography.

Acknowledgement

The authors acknowledge support by the AFOSR MURI Grant (FA9550-14-1-0389). Support for the advanced numerical modeling and optimization (A.V.K. and Z.A.K.) was provided by the DARPA/DSO Extreme Optics and Imaging (EXTREME) program (HR00111720032).

References

[1] D. Reinsel, J. Gantz, J. Rydning, *The Digitization of the World. From Edge to Core*, IDC White Paper, US44413318, 2018.

[2] *White Paper: Archival Disc Technology*, Sony, Panasonic, 2nd Edition, July 2018.

[3] M. Gu, X. Li, and Y. Cao, Optical storage arrays: a perspective for future big data storage, *Light. Sci. Appl.*, 3: e177 EP, 2014.

[4] M. Song, Z. A. Kudyshev, H. Yu, A. Boltasseva, V. M. Shalaev, and A. V. Kildishev, Achieving full-color generation with polarization-tunable perfect light absorption, *Opt. Mater. Express* 9: 779–787, 2019.

Light manipulation by natural photonic structures in diatom microalgae

Johannes Goessling[1] and Martin Lopez-Garcia[1*],

[1] Natural and Artificial Photonic Structures Group, Nanophotonics Department
INL- International Iberian Nanotechnology Laboratory, Braga, Portugal
*corresponding author, E-mail: martin.lopez@inl.int

Abstract

In this work we communicate an experimental investigation of the photonic properties of nano-porous silicate exoskeletons of diatom microalgae. We demonstrate that such natural structures can function as a wavelength selective light coupler and waveguide. The brilliant colors produced under certain illumination conditions could be the visual side-effects of an important underlying biological principle, *i.e.* manipulation of the photonic environment inside the cell to optimize light capture and photosynthesis.

1. Introduction

Recent research demonstrated that some plants evolved photonic structures that can modulate their photosynthetic efficiency [1]. However, this phenomena has not been yet described in algae. Interestingly, structural coloration is widespread in algae, but has been scarcely studied from a photonics perspective [2][3]. On this study we unveil the effect of photonic structures in diatom microalgae light harvesting.

Diatoms are a class of unicellular microalgae encompassing more than 10,000 species. They are responsible for a quarter of carbon fixation by photosynthesis, and thereby of global importance as basal species in aquatic food webs. One outstanding feature of diatoms is a silicate exoskeleton named the frustule, perforated by periodic nanostructures like pores, honeycomb chambers or grids. The frustule has photonic properties and might facilitate photosynthesis in aquatic environments [4].

We studied the optical properties of a large centric diatom species (*Coscinodiscus granii*, Fig. 1a/b) by Fourier image spectroscopy in of reflected/transmitted configuration, which facilitate wavelength and angular dependent characterization at microscale. The frustule of this species has a well-defined hexagonal photonic crystal 2D lattice on a cylindrical symmetry (Fig. 1c/d).

2. Discussion

The highly ordered nano-porous structure of the silicate diatom frustule has been suggested to have a photonic behaviour. However, it is still debated how and why such structures are formed by diatoms. Possible biological functions of the periodic frustule lattice are discussed in the literature, *e.g.* mechanical strengths as a defence against predation, filtering of harmful agents such as virus and bacteria, or light manipulation for optimized photosynthesis.

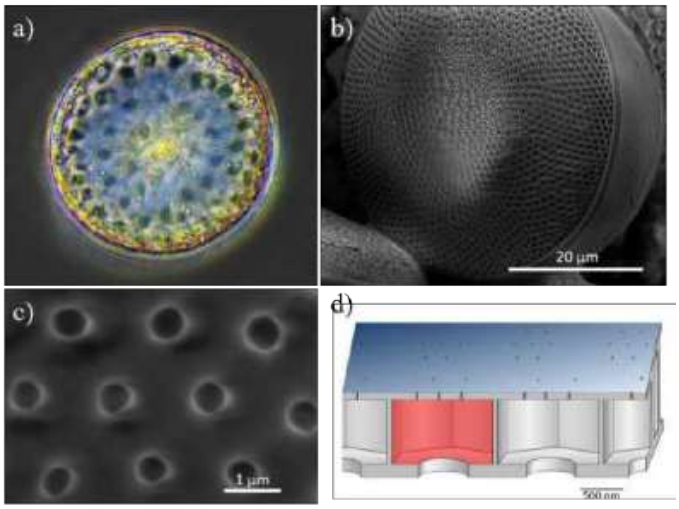


Figure 1. a) Single cell specimen of the diatom *Coscinodiscus granii* under epi-illumination white light microscopy. b) SEM image of the frustule (silica extra-cellular structure). c) Detail of the hexagonal lattice showing cylinder shaped holes on the silica exoskeleton. d) Internal 3D structure of the frustule in conceptual illustration.

We present an advanced morphological characterization of live diatoms and oxidized frustules using Environmental-SEM and Focus Ion Beam (FIB), respectively. We observed two hexagonal lattices at the external (cribrum) and internal (foramen) side of the frustule. These two lattices seem to cause various photonic effects related to their different lattice structure. The detailed morphological 3D characterization of the frustule also revealed a honeycomb chamber inside the frustule wall. On the base of this advanced 3D morphological reconstruction, we developed a numerical model that can explain the experimental data on frustule photonic properties. In fact, our optical model suggests that light confinement could take place at the frustule providing a wave guiding channel for a more

efficient light distribution to other parts of the cell. Moreover, our microscatterometry measurements suggest a blue-shift in the photonic response of the frustule (Fig. 2), which could be related to wave-guiding that could facilitate redistribution of more energetic light within the cell. However, the coupling effects to single modes described by the optical model have not yet been observed in experimental measurements (Fig. 2). This might in future be solved by increased spectral and/or angular resolution of the setup in this natural photonic crystal slab.

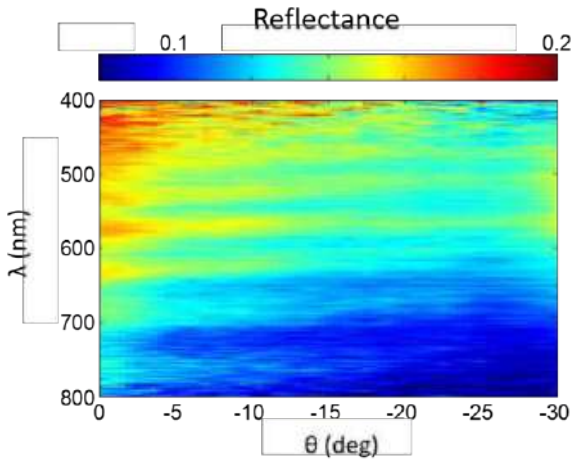


Figure 2. Reflectance of a frustule in air as shown in Fig 1b. The measurement was performed by Fourier image spectroscopy with white light and a circular spot of ≈40 μm diameter.

3. Conclusions

Our work explain the major features in the photonic response of a diatom frustule. Moreover, our data are supported by theoretical models which allows us to infer non-trivial photonic and biological properties of the microalgae such as wave guiding of the incoming light. In conclusion, our results suggest that the frustule may be understood as a photonic environment in which a highly efficient natural photocatalytic process, *i.e.* photosynthesis, takes place. Also, the photonic properties of the frustules could be a source of inspiration in light harvesting technologies suchas new designs for more effective photocatalytic reactors.

References

[1] M. Jacobs, M. Lopez-Garcia, O.-P. Phrathep, T. Lawson, R. Oulton, and H. M. Whitney, *"Photonic multilayer structure of Begonia chloroplasts enhances photosynthetic efficiency"* Nat. Plants **2**, 16162 (2016).

[2] M. Lopez-Garcia, N. Masters, H. E. O'Brien, J. Lennon, G. Atkinson, M. J. Cryan, R. Oulton, and H. M. Whitney, "Light induced dynamic structural color by intracellular 3D photonic crystals in brown algae" *Science Advances. 4(April),* eaan8917 (2018).

[3] C. J. Chandler, B. D. Wilts, J. Brodie, and S. Vignolini, "Structural Color in Marine Algae" *Adv. Opt. Mater*. **5**(5), 1600646 (2017)..

[4] J. W. Goessling, Y. Su, P. Cartaxana, C. Maibohm, L. F. Rickelt, E. C. L. Trampe, S. L. Walby, D. Wangpraseurt, X. Wu, M. Ellegaard, and K. Michael, "Structure-based optics of centric diatom frustules : modulation of the in vivo light field for efficient diatom photosynthesis," *New Phytol.* (219), 122–134 (2018).

Acknowledgements

JG acknowledges the support of the H2020-MSCA-COFUND-2015 program and MLG would like to acknowledge the support of the project (POCI-01-0145-FEDER-031739) co-funded by FCT and COMPETE2020.

Dual-color plasmonic filters

E. Heydari, [1] **J. Sperling,** [1] **S. Neale**[1] **and A.W. Clark**[1*]
[1]School of Engineering, University of Glasgow, UK
[*]corresponding author: Alasdair.clark@glasgow.ac.uk

Abstract- We demonstrate a plasmonic approach to high-density optical data storage. We employ dual-color plasmonic nano-pixels to encode two information sets into a single arrays of metal nano-apertures.

The ability to effectively separate discrete colors from white-light lies at the heart of how we record and view optical information; whether that be the arrangement of colored inks in painting and printing applications, or the spectral filters that enable many modern image display and recording technologies. Structural color systems based on engineered nanophotonic materials have emerged as an appealing alternative to absorptive dyes [1]. Among these examples are color filters based on plasmonic resonances. Filters such as these are promising candidates for applications in sub-wavelength color printing [1], image recording [2], anti-counterfeiting [3], and data storage [4].

Using asymmetric cross-shaped nano-apertures in a thin film of aluminum, we demonstrate a method for patterning full-color images and codes, at subwavelength resolutions, that exhibit dual, polarization-dependent information states. Each aperture is engineered to exhibit 2 plasmonic colors that can be individually tuned across the sRGB spectrum. This enables us to encode 2 arbitrary information sets using a single nano-aperture array. We show that using a standard optical microscope, color separation can be controlled down to 2x2 nano-pixels while retaining polarization selectivity. The maximum data density we can achieve using this technique is approximately 1.46 Gb/cm^2, with the added ability to further encode each of those pixels using the full visible-color spectrum.

Acknowledgements. The work was supported by the Royal Academy of Engineering (grant 10216/103) and the EPSRC (grants EP/P51133X/1 and EP/N016874/1).

References

[1] K. Kumar, H. Duan, R. S. Hegde, S. C. W. Koh, J. 6N. Wei, and J. K. W.Yang, "Printing Colour at the Optical Diffraction Limit", *Nature Nanotechnology*, 7, 557-561 (2012).
[2] S. P. Burgos, S. Yokogawa, H. A. Atwater, "Color Imaging Via Nearest Neighbor Hole Coupling in Plasmonic Color Filters Integrated onto a Complementary Metal-Oxide Semiconductor Image Sensor", *ACS Nano*, 7, 10038-10047 (2013).
[3] Y. H. Zheng, C. Jiang, S.H. Ng, Y. Lu, F. Han, U. Bach, J. J. Gooding, "Unclonable Plasmonic Security Labels Achieved by Shadow-Mask-Lithography-Assisted Self-Assembly", *Advanced Materials*, 28, 2330-2336 (2016).
[4] M. Gu, X.P. Li, Y. Y. Cao, "Optical Storage Arrays: A Perspective for Future Big Data Storage", *Light-Science & Applications,* 3 (2014).

Tunable spherical colloidal photonic pigments with non-iridescent structural color

Laurinda Areias[1], José Paulo S. Farinha[1]

[1]CQE & CQFM-IN, Instituto Superior Técnico, Universidade de Lisboa, Lisboa, Portugal
*presenting author: laurinda.areias@tecnico.ulisboa.pt

Abstract

Colloidal photonic crystals exhibit shining structural coloration that arises from the modulation of electromagnetic waves by means of Bragg reflection from photonic stop bands, originated from the periodical arrangement of nanoparticles.
We develop uniformly sized spherical colloidal photonic pigments that exhibit structural coloration throughout the visible spectrum light range, from differently sized colloidal building blocks synthesized by emulsion polymerization.
Spherical photonic pigments were obtained upon self-assembly of colloidal nanoparticles inside monodispersed emulsion droplets generated by soft-lithography microfluidics.

1. Introduction

Structural colors[1] are based on diffraction, scattering, and dispersion of light as a result of its interaction with structured materials[2]. Materials with structural color shows no photobleaching and can generate a wide range of colors in non-toxic and environmentally friendly ways. Depending on their behavior with respect to the angle of observation, structural color can be iridescent and non-iridescent. The former offers color generated from structures that contain periodically arranged nano- or microparticles and depend on the observation angle. These are called photonic crystals[3]. By contrast, the latter possess a quasi-ordered arrangement of colloids (photonic glass) and offers the opposite: angle-independent color, where the arrangement of the colloidal particles show a glassy structure with a short-range order[4]. these find a wide range of potential applications including reflective displays, colorimetric sensors, textiles, etc. In this study, non-iridescent spherical colloidal photonic crystals were fabricated by means of microfluidic droplet technology from soft-lithographic techniques. Differently sized highly monodispersed polymeric nanoparticles were synthesized by emulsion polymerization. Self-assembly of polymeric nanoparticles in the spherical confinement of emulsion droplets is induced by controlled temperature and stirring conditions. In order to break long range order, we added small amounts of black polydopamine nanoparticles to the emulsion droplets, that also act as incoherent light scattering absorbers, originating highly bright and non-iridescent photonic pigments.

2. Methodology and Results

Spherical photonic pigments were obtained from W/O emulsion droplets, generated in PDMS microfluidic devices. Dispersed aqueous phase is composed of a suspension of polymeric nanoparticles at 16% wt; continuous oil phase is composed of hexadecane with 3% SPAN 80 surfactant. Upon water evaporation, droplets shrunk, and polymeric nanoparticles self-assemble into ordered structures.
Highly monodispersed spherical photonic pigments with sizes between 40-60 μm in diameter were obtained (figure 1A), from nanoparticles that self-assemble in face centered cubic structures (figure1 B, shows the hexagonal arrangement of nanoparticles on the surface of the microsphere). Polymeric nanoparticles with sizes from 173 to 333 nm in diameter, originated photonic pigments that spans the entire visible spectrum light range (figure 1C).

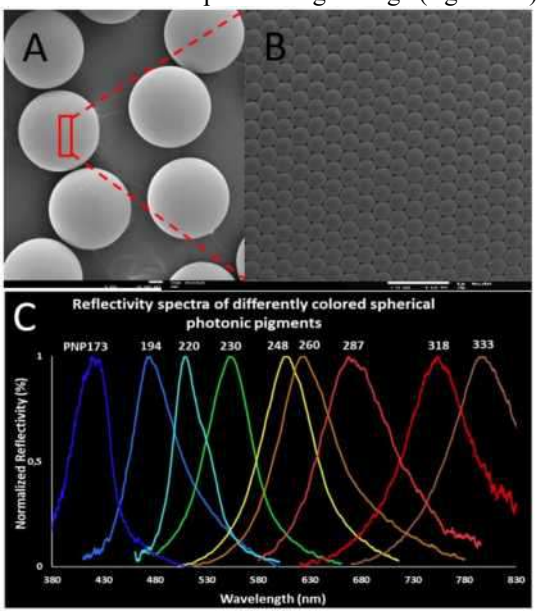


Figure 1: A) Spherical photonic pigments of 55 μm in diameter; B) Hexagonal close packed arrangement of polymeric nanoparticles (290 nm diameter) in photonic pigment surface; C) Reflectance spectra obtained for the 111 plane of structurally colored spherical photonic pigments, composed of differently sized polymeric nanoparticles.

2.1. Prediction of photonic stop band

The theoretical maximum reflectance wavelength of the photonic pigments can be calculated based on Bragg´s law of diffraction modified with Snell's law:

$$\lambda_{max} = 2d_{hkl}\, n_{eff} \sqrt{1 - \frac{sin^2\theta}{n_{eff}^2}}, \quad (1)$$

$$n_{eff}^2 = f_1 n_1^2 + f_2 n_2^2, \quad (2)$$

$$d_{111} = \sqrt{\frac{2}{3}} \times D, \quad (3)$$

where n^2_{eff} is the average refractive index of the photonic structures. For polymeric nanoparticles in air we calculate the average refractive index from the volume fractions occupied by nanoparticles and air (f_1 and f_2, generally 74% and 26%, respectively, for close-packed fcc structures) and their respective refractive index (n_1 and n_2). The lattice spacing for the 111 plane is given by equation 3, where D corresponds to polymeric nanoparticles diameter.

The calculated maximum reflectance wavelength λ_{max} (eq. 1), are comparable to those obtained experimentally (table 1).

Table 1: Calculated *vs* Experimental maximum Wavelength reflected by photonic pigments

PNP Diameter (nm)	**173**	**194**	**220**	**230**	**248**	**260**	**287**	**318**	**333**
Calculated λ_{max} (nm)	436	489	555	580	625	655	723	801	839
Experimental λ_{max} (nm)	400	480	527	551	602	622	670	763	800

2.2. Non-iridescent colored photonic pigments

Upon addition of small amounts of polydopamine nanoparticles (93 nm diameter), a quasi-ordered structure is developed in contrast with the long-range order of photonic crystals. By applying Fast Fourier Transform (*FFT*) to the SEM images, a frequency domain is obtained, where the appearance of sharp spots at certain frequencies indicate the existence of structural periodicity. Comparing the pattern before and after addition of polydopamine nanoparticles, we confirm that the as-prepared structures have only short-range order. Figure 2 compare the *FFT* pattern of a photonic crystal pigment (A) and the corresponding photonic glass (B), upon addition of PD nanoparticles (highlighted in yellow circles).

The absence of long-range order is also noticed in angle resolved reflectance measurements, were light hits the sample at 45º and reflected signal is collected from 0 to 75º. From 0º to 75º viewing angles, only a slightly shift towards the blue, around 45 nm, is observed for the maximum reflected wavelength, as expected for non-iridescent structurally colored photonic pigments.

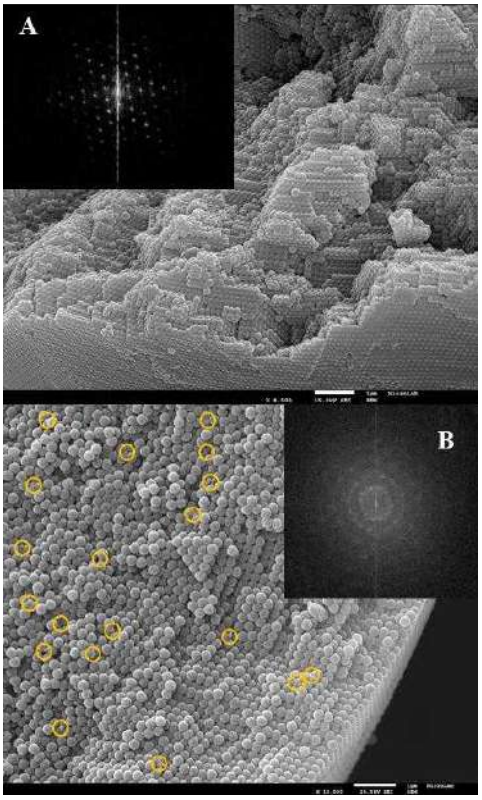


Figure 2: Periodic (A) *vs* random arrangement (B) of colloidal polymeric nanoparticles in photonic pigments.

3. Conclusions

Spherical non-iridescent photonic pigments were successfully obtained by combining microfluidics soft-lithography and temperature induced colloidal self-assembly of highly monodispersed polymeric nanoparticles. The obtained pigments provide a platform for future color and displays applications.

Acknowledgements

This work was partially supported by FCT-Portugal and COMPETE (FEDER) within project PTDC/CTM-POL/3698/2014 and UID/NAN/50024/2013. L. A. also thanks FCT for a ChemMat Doctoral Program PhD grant, PD/BD/113533/2015.

References

[1] Kinoshita, S., Yoshioka, S. & Miyazaki, J. Physics of structural colors. *Rep. Prog. Phys*. **71**, 076401 (2008).

[2] Marcelo, G., Areias, L. R. P., Maçoas, E., Mendicuti, F., Valiente, M., Martinho, J. M. G. & Farinha, J. P. S. Structural color and rheology of self-assembled poly (N-isopropylacrylamide-methacrylic acid) microgels in water. *Eur. Polym. Jour.* 113, 349-356 (2019).

[3] Cong, H. et al. Preparation of iridescent colloidal crystal coatings with variable structural colors. *Opt. Express*. **21**, 17831–17838 (2013).

[4] Shi, L. et al. Amorphous Photonic Crystals with Only Short-Range Order. *Adv. Mater.* **25**, 5314–5320 (2013).

Enhancing the purity of reflective structural colors with bilayer hybrid absorbers and investigation of solution process via electrodeposition of thin-films

L. Jay Guo, Saurabh Acharya, Zhengmei Yang, Chengang Ji

Department of Electrical Engineering and Computer Science
The University of Michigan, Ann Arbor, MI, 48109, USA

Abstract:
In recent years, structural colors based on optical interference effects of layered structures and resonance of nanostructures have received increasing interest due to their various advantages over traditional colorant-based pigmentations [1]. However, these structures typically involve sub-wavelength patterns that require complicated and time-intensive fabrication techniques such as e-beam lithography and focused ion beam milling, which significantly limit their large-scale feasibility. In comparison, planar thin-film structures based on Fabry-Pérot (F-P) cavity resonances can create wide-range colors by simply varying the spacer layer thickness. Their fabrication procedures only require physical vapor deposition tools (e.g., evaporation or sputtering systems), which have advantages of low cost and high scalability.

In many applications, structural colors of high purity and brightness are desired. Here we present a general strategy of selecting the appropriate material and thickness of each layer to create high-purity reflective colors in a classic asymmetric Fabry-Pérot cavity structure based on a dielectric-absorber-dielectric-metal multilayered configuration. Guided by the derived complex refractive index of the ideal absorber layer, an effective absorbing bilayer medium consisting of two ultrathin lossy films is used to improve the color purity of reflective colors by suppressing the reflection in the undesired color range with the enhanced optical absorption. Highly-purity red, green, and blue reflective colors are designed and experimentally demonstrated employing different effective bilayer absorbers. Due to the high refractive index of the dielectric material, the colored structures exhibit great angle-robust appearance up to ±60°. The generalized design principles and the proposed method of using effective bilayer absorbers open up new avenues for realizing high-purity thin-film structural colors with more materials selections.

Such multilayered structural colors could be fabricated using roll-to-roll deposition techniques [2]. Although they have been successfully adapted into pigment flakes for decorative paints, these special paints exhibiting a metallic appearance with high color purity are still too costly for wide-scale applications [3]. To address this issue, we developed a simple, inexpensive, and non-toxic bench-top electrodeposition process for the fabrication of structural color based on multilayer films at ambient conditions. This process avoids the need for expensive vacuum-based equipment and is compatible with highly non-planar substrates of arbitrary shape, size and roughness. Asymmetric metal-dielectric-metal structures were achieved by sequential electrodeposition of smooth gold, thin cuprous oxide, and finally thin Au on conductive substrates, forming an effective asymmetric Fabry-Pérot cavity. Different colors of high brightness were achieved by simply tuning the thickness of the electrodeposited middle cavity layer. Due to the high refractive index of the cuprous oxide dielectric layer, the vividness of the generated colors was invariant to viewing angle. This work is the first demonstration of solution-processed, electrodeposited metal-dielectric-metal

film stacks and highlights the clear advantages of this approach over traditional deposition or assembly methods for preparing colored films, and can be applied directly to curved surfaces.

References

[1] R. W. Sabnis, "Color filter technology for liquid crystal displays," *Displays*, *20*, 119-129 (1999).

[2] K. -T. Lee, C. Ji, D. Banerjee, L. J. Guo, "Angular- and polarization-independent structural colors based on 1D photonic crystals," *Laser Photon. Rev.*, *9*, 354-362 (2015).

[3] T. Masuda, Y. Kudo, D. Banerjee, "Visually Attractive and High-Power-Retention Solar Modules by Coloring with Automotive Paints," *Coatings, 8*, 282 (2018).

Skin-like Full-Color Angle Independent Plasmonic Reflective

Pablo Manuel Cencillo Abad, Debashis Chanda

NanoScience Technology Center, Dept. of Physics, CREOL, College of Optics and Photonics,
University of Central Florida, Florida, USA

Abstract

Tuning plasmonic light absorption with liquid crystal (LC), the color reflected from a nanostructured surface can be changed as a function of voltage. The engineered plasmonic surface allows complete LC reorientation and maximum overlap between plasmonic fields and LC, enabling large tunability across the entire visible spectrum.

Acoustic Metamaterials in the audible frequency range

Using mean flow to make a broadband acoustic diode

Vassos Achilleos, Yves Aurégan* and Vincent Pagneux

Laboratoire d'Acoustique de l'Université du Mans, CNRS, Le Mans Université,
Avenue Olivier Messiaen, 72085 Le Mans Cedex 9, France
*corresponding author, E-mail: yves.auregan@univ-lemans.fr

Abstract

A mean flow in a waveguide can cause significant changes in wave propagation. Among the effects of flow (possibility of creating an acoustic gain [1], changes in the characteristics of the metamaterials located in the waveguide [2], etc.), the flow can be used as a vectorial field that break reciprocity in order to make a broadband acoustic diode. In this context, we demonstrate theoretically and experimentally that an acoustic diode can be manufactured in a flow duct by slowing down the acoustic wave. In the slow sound region, the effective sound velocity can be so low that no waves can propagate against the flow while propagation is still possible in the direction of flow. Sound is slowed down by putting locally reacting tubes in the duct wall. This phenomenon can occur over a wide range of frequencies that can be extended to very low frequencies.

1. Introduction

An acoustic diode is a device that allows acoustic waves to travel in one direction but not in the opposite direction. This type of device is quite difficult to achieve because the reciprocity is difficult to break in a conventional acoustic system. To obtain this reciprocity break, non-linearity, temporal invariance break or polarization of the system with a vector field can be used. The use of a mean flow in an acoustic system adds a vector field that breaks reciprocity. In this article we show that the use of a compliant wall material emphasizes this effect over a wide frequency range.

2. Model

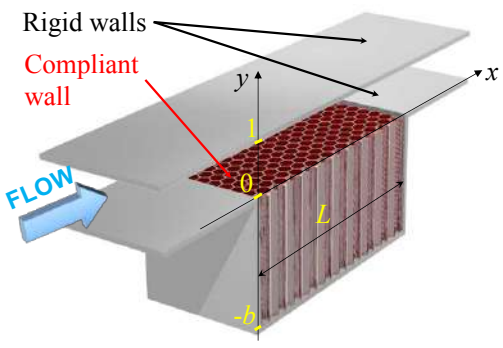


Figure 1: Sketch of a waveguide with a liner of height b.

When considering the propagation of sound in a 2D waveguide with a uniform flow, the 2D convected wave equation and boundary conditions are written [3]:

$$\begin{cases} D_t^2\phi - \nabla^2\phi & \text{for} \quad 0 < y < 1 \\ \partial_y\phi = 0 & \text{for} \quad y = 1 \\ \partial_y\phi = D_t(CD_t\phi) & \text{for} \quad y = 0 \end{cases} . \qquad (1)$$

where $\phi(x, y, t)$ is the normalized acoustic velocity potential in the duct, $D_t = \partial_t + M\partial_t$ is convective derivative, M is the Mach number and $C = \tan(b\omega)/\omega$ is the normalized compliance of a wall composed of reactive tubes (see Fig. 1). The parameter b is the ratio between the height of the tubes and the height of the duct.

Looking for solutions propagating in the x direction in the form $\exp(i(-\omega t + kx))$, leads to the dispersion equation expressed as a function of the frequency in the moving frame $\Omega = \omega - Mk$:

$$\mathcal{D}(\omega, k) = \alpha \tanh(\alpha) - \frac{\tan(b\omega)}{\omega}\Omega^2 = 0, \qquad (2)$$

where $\alpha = k^2 - \Omega^2$.

3. Dispersion relation

The real solutions of of the dispersion equation (2) are given in Fig. 2. Without flow, there are two solutions for each frequency and the liner introduces a dispersion relation with a quarter-wavelength resonance ($\omega_R = \pi/2b$). For low frequencies, the dispersion relation can be approximated by $\omega = k/\sqrt{1+b}$, leading to a phase velocity $c_b = 1\sqrt{1+b}$ which is always smaller than the free space normalized velocity $c_0 = 1$. Thus the presence of the liner on the wall of a wave guide produces slow sound.

When a mean flow flow is present (blue curves in Fig. 2) the solutions of the dispersion relation (2) have a richer structure (see also [3]). Starting from the low frequency regime (for instance ω_1 in Fig. 2), the Eq. (2) has four real solutions corresponding to four propagating modes. Two of them, which we call acoustic, approach $k = 0$ as $\omega \to 0$, and they propagate in both directions with the slow sound velocity c_b corrected by the convective effects. The other two modes do not exist without flow and we further on refer to them as dispersive modes. In this low frequency regime both the dispersive modes travel in the direction of the mean flow (positive slope). Beyond a critical frequency ω_c, two of the solutions collide and disappear and for higher frequencies ($\omega > \omega_c$) for instance ω_2 in Fig. 2, the system

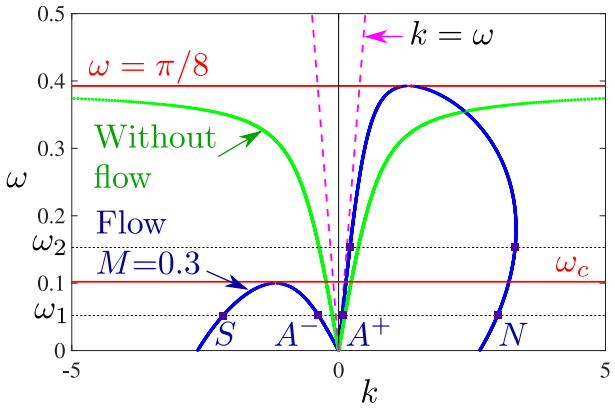


Figure 2: Real solutions of the dispersion equation (2) when $b = 4$ with and without flow ($M = 0.3$).

supports only two modes that are traveling in the flow direction.

In summary, in the presence of flow above a liner, for frequencies below ω_c, acoustic propagation is possible in both directions while for frequencies above ω_c acoustic propagation is only possible in the direction of flow. This principle can be used to build a broadband diode because ω_c can be set to zero when $M > 1/\sqrt{1+b}$.

4. Experimental results

To experimentally perform a diode, a compliant wall composed of thin tubes with a honeycomb structure is used (see Fig. 3 -a). The thickness of the honeycomb structure is such that the ratio between the height of the tubes and the height of the duct is $b = 10/3$. The diode is flush mounted in a rigid rectangular channel between two measuring sections (upstream and downstream) which allows the determination of the incoming and outgoing waves on both sides of the diode. Two acoustic sources, on both sides of the system, provide two different acoustic states of the system to evaluate the four elements of the scattering matrix for plane waves (transmission and reflection coefficient in both directions). The measured transmission coefficients are shown in Fig. 3-b in the case without flow and in the case of grazing flow with a mean Mach number equal to $M = 0.3$.

Without flow, the transmission coefficient displays some oscillations at low frequencies that are due to standing waves along the length L of the material. Due to the decreasing of the effective sound velocity when the frequency approaches the quarter-wavelength resonance ($f_r = c_0/4H = 1715$ Hz), the transmission coefficient is supposed to oscillate increasingly rapidly until it reaches the bandgap. This effect is partially masked in this experiment by the dissipative effect in the material. With flow, the diode effect can be clearly see by considering the difference in the transmission coefficients according to the direction of the wave propagation. In the flow direction, the transmission is slightly larger than without flow but against the flow the transmission is substantially reduced. For frequencies

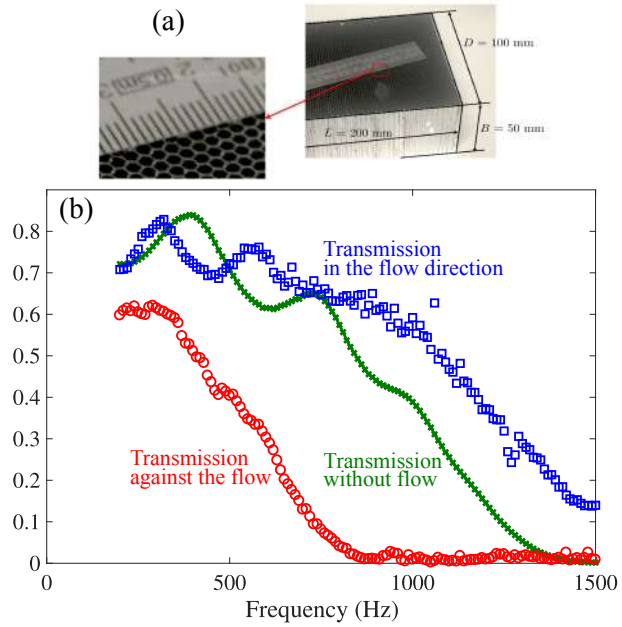


Figure 3: (a) Picture of the compliant material. (b) Experimental transmission coefficient of the diode with and without flow.

higher than 850 Hz, no significant transmission against the flow can be measured showing a blockage of the transmission against the flow as predicted by the model for supercritical conditions.

5. Conclusions

The diode effect in audible acoustics has been theoretically demonstrated and experimentally confirmed. The next steps will be to take better account of the dissipative effect and the boundary layer effect in order to extend this unilateral propagation to very low frequencies.

References

[1] Y. Aurégan, V. Pagneux, P T -Symmetric Scattering in Flow Duct Acoustics *Physical Review Letters* 118 (17) 174301, 2017.

[2] Y. Aurégan, M. Farooqui, J.-P. Groby, Low frequency sound attenuation in a flow duct using a thin slow sound material *Journal of the Acoustical Society of America* 139 (5) EL 149–153, 2016.

[3] Y. Aurégan, V. Pagneux, Slow sound in lined flow ducts *Journal of the Acoustical Society of America* 138 (2) 605–613, 2015.

Perfect absorption using sparse arrays of Helmholtz resonators

Jean-François Mercier[1], **Agnès Maurel** [2] **and Kim Pham**[3]

[1] Poems, CNRS, ENSTA ParisTech, INRIA, 828 Bd des Maréchaux, 91762 Palaiseau, France,
[2] Institut Langevin, CNRS, ESPCI ParisTech, 1 rue Jussieu, 75005 Paris, France,
[3] IMSIA, CNRS, ENSTA ParisTech, 828 Bd des Maréchaux, 91732 Palaiseau, France
*corresponding author, E-mail: jean-francois.mercier@ensta.fr

Abstract

We inspect the influence of the spacing on the resonance of a periodic arrangement of Helmholtz resonators for which an effective model is derived. It is shown that the strength of the resonance is enhanced when the array becomes sparser, which provides a degree of freedom to control the radiative damping of the array. This is of particular interest since it does not affect the resonance frequency nor the damping due to losses within each resonator; besides, it does not affect the total thickness of the array. We show that it can be used for the design of a perfect absorbing walls.

1. Introduction

Originally studied for their musical properties [1], the Helmholtz resonators are the most classical resonators for the acoustic waves. When organized in two or three dimensional arrays, they are known to have a collective behavior which has been used for several applications, including the improvement of edifice sonority [2]. With the development of metamaterials, it has been promoted to a key piece in devices as perfect absorbers efficient in the low frequency regime [3]. Here, we use an effective model derived in [4] to study the influence of the array spacing, from compact to sparse arrays. This model provides the reflection coefficient of the array in a close form, and a comprehensive picture of the wave pattern inside the resonators (in particular the pressure amplitude is correctly predicted). We shall use that the strength of the resonance can be tuned by the spacing h. The idea is intuitive: for a sparse array the resonance is close to that of a single resonator and it turns out that the collective effect of closer resonators weakens their resonance. This provides a degree of freedom to tune the radiative damping without affecting the damping due to the losses, this latter being related to the geometry of a single resonator, not to the array spacing. Thus, when the losses are accounted for, the two dampings can be tuned independently to reach the so-called critical coupling condition realizing perfect absorption.

2. The effective model

The two-scale homogenization of the array of Helmholtz (see Fig. 1) resonators has been presented in [4]. It provides an equivalent anisotropic medium replacing the region of the cavity where the wave equation reads as

$$\frac{\partial^2 p}{\partial y^2} + k_{\rm c}^2 p = 0, \tag{1}$$

where $k_{\rm c}$ is the wavenumber in the cavities, being possibly complex when the losses are accounted for (and $k_{\rm c} = k$ in the lossless case). The acoustic velocity $\mathbf{u} = (u, v)$ reads as $u = 0$, $v = \varphi_{\rm c}\partial_y p$. Eventually, the effect of the necks is encapsulated in non intuitive jump conditions, namely

$$[\![p]\!] = h\mathcal{B}\,\overline{v}, \quad [\![v]\!] = -\,h\mathcal{C}\,\frac{\partial^2 \overline{p}}{\partial x^2} \;-\; e\varphi_{\rm n} k_{\rm n}^2\,\overline{p}. \tag{2}$$

In the above expressions, we have defined the jump of f

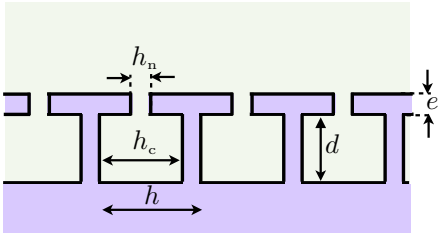


Figure 1: Array of Helmholtz resonators, with the aspect ratios $\varphi_{\rm c} = h_{\rm c}/h$ and $\varphi_{\rm n} = h_{\rm n}/h$. A compact array corresponds to $h_{\rm c} \sim h$, a sparse array to $h_{\rm c} \ll h$.

being $[\![f]\!] \equiv f_{|y=0} - f_{|y=-e}$, and its mean value $\overline{f} \equiv \frac{1}{2}\left(f_{|y=0} + f_{|y=-e}\right)$. Then, $k_{\rm n}$ refers to the wavenumber in the neck, being possibly complex valued in the lossy case (and $k_{\rm n} = k$ otherwise). In principle, the interface parameters $(\mathcal{B}, \mathcal{C})$ are deduced from elementary problems that have to be solved numerically, but good estimates of $(\mathcal{B}, \mathcal{C})$ are given by

$$\begin{cases} \mathcal{B} \simeq \dfrac{e}{h\varphi_{\rm n}} - \dfrac{1}{\pi}\log\left(\sin\left(\pi\dfrac{\varphi_{\rm n}}{2}\right)\sin\left(\pi\dfrac{\varphi_{\rm n}}{2\varphi_{\rm c}}\right)\right), \\ \mathcal{C} \simeq \dfrac{\pi}{16}\,\varphi_{\rm n}^2. \end{cases} \tag{3}$$

Eventually, the boundary condition to be applied at the bottom of the cavities at $y = -D$ with $D = e + d$ remains the condition of rigid wall (zero normal velocity) which holds all along the anisotropic equivalent medium, namely

$$\frac{\partial p}{\partial y}(x, -D) = 0. \tag{4}$$

3. Realization of a perfect absorbing wall

For an incident wave $p^{\text{inc}}(x,y) = e^{-\mathrm{i}\alpha y + \mathrm{i}\beta x}$ ($\alpha = k\cos\theta$, $\beta = k\sin\theta$), the solution $p(x,y)$ of the effective problem (1)-(4) reads $p(x,y) = A\cos k_{\text{c}}(y+D)e^{\mathrm{i}\beta x}$ for $-D < y < -e$, and $p(x,y) = \left(e^{-\mathrm{i}\alpha y} + Re^{\mathrm{i}\alpha y}\right)e^{\mathrm{i}\beta x}$, for $y > 0$. The amplitude A in the cavity and the reflection coefficient R are given in [4], and the approximate expressions

$$R \simeq \frac{k_r t_r - \frac{1}{h_{\text{c}}\mathcal{B}} - (i-\delta_{\text{V}})\alpha_{\text{RD}} + i\alpha_{\text{VD}}}{k_r t_r - \frac{1}{h_{\text{c}}\mathcal{B}} + (i-\delta_{\text{V}})\alpha_{\text{RD}} + i\alpha_{\text{VD}}},$$
$$A_{\text{c}} \simeq \frac{\frac{2}{h_{\text{c}}\mathcal{B}\cos k_{\text{c}}d}}{k_r t_r - \frac{1}{h_{\text{c}}\mathcal{B}} + (i-\delta_{\text{V}})\alpha_{\text{RD}} + i\alpha_{\text{VD}}}, \tag{5}$$

allow to exhibit the balance between the radiative damping $\alpha_{\text{RD}} = \frac{k_r}{k}\frac{t_r}{\cos\theta h\mathcal{B}}$ and the viscous losses $\alpha_{\text{VD}} = \delta_{\text{V}} k_r t_r$, where we have defined $k_{\text{c}} = k_r + ik_i$, $\tan(k_{\text{c}}d) = t_r + it_i$ and $\delta_{\text{V}} = (k_i/k_r + t_i/t_r)$. The losses are due to viscothermal effects and following *e.g.* [5], they are written $k_{\text{c,n}} = k\left(1 + \frac{1+\mathrm{i}}{\sqrt{k}}\alpha_{\text{c,n}}\right)$, with $\alpha_{\text{c}}, \alpha_{\text{n}}$ defined by $\alpha_{\text{c,n}} = \sqrt{\frac{\nu}{c}}\left(1 + \frac{\gamma-1}{\sqrt{P_r}}\right)\frac{1}{h_{\text{c,n}}}$, with in the air $P_r = 0.7$ the Prandtl number, $\nu = 1.5\ 10^{-5}$ m^2.s^{-1} the kinematic viscosity, $c = 340$ m.s^{-1} the sound speed and $\gamma = 1.4$ the heat capacity of air, hence $\alpha_{\text{c,n}} = 3.10^{-4}/h_{\text{c,n}}$ m$^{-1/2}$. Perfect absorption is obtained at the critical coupling, when the losses balance the leakage $\alpha_{\text{VD}} = \alpha_{\text{RD}}$ and when this condition is compatible with that of the slightly shifted resonance $k_r t_r = \frac{1}{h_{\text{c}}\mathcal{B}} - \delta_{\text{V}}\alpha_{\text{RD}}$. In order to fulfill these two conditions, we need two degrees of freedom which are provided by (k,h), although it is not guarantied that a solution can be found for any geometry of the resonators. We report the absorption $(1-|R|)$ computed numerically against (k,h) in Fig. 2 for $e = 0.6$ cm and for $e = 2.4$ cm. In both cases, the perfect absorption is obtained for relatively low kh value: $k = 0.191$ cm^{-1}, $h = 9.165$ cm for $e = 0.6$ cm and $k = 0.126$ cm^{-1}, $h = 5.65$ cm for $e = 2.4$ cm, well predicted by the effective model (white plain circles).

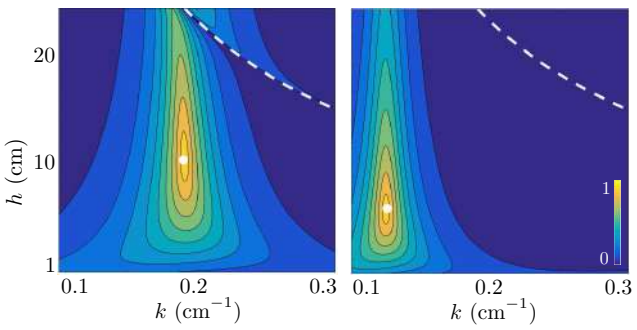


Figure 2: Absorption $(1-|R|)$ for an array of resonators ($h_{\text{c}} = 1$ cm, $d = 5$ cm, $h_{\text{n}} = 1/3$cm) (a) $e = 0.6$ cm revealing a perfect absorption $|R| = 0$ for $h = 9.165$ cm and $k = 0.191$ cm^{-1}. (b) $e = 2.4$ cm; $|R| = 0$ for $h = 5.65$ cm, $k = 0.126$ cm^{-1}.

Finally, the sensitivity of the perfect absorption on h is illustrated in Fig. 3 where we report the wavefields for the same Helmholtz resonators arranged on an array with spacing $h = 9.2$ cm (realizing perfect absorption) and with a spacing h= 3 cm. To get a perfect absorption for a spacing $h = 3$ cm, we should use $e = 7$ cm (and for a spacing $h = 1$ cm, e about 15 cm).

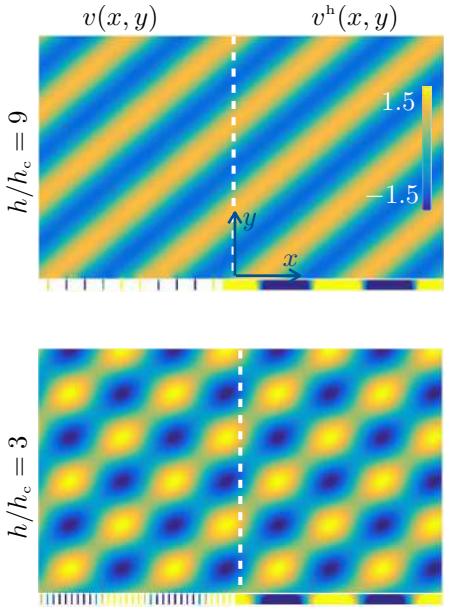


Figure 3: Acoustic pressure fields for an incident wave ($kh_{\text{c}} = 0.19$, $\theta = 40°$) on an array of Helmholtz resonators ($d/h_{\text{c}} = 5$, $e/h_{\text{c}} = 0.6$, $h_{\text{n}}/h_{\text{c}} = 0.3$); each panel contains the homogenized solution (right half panel) and the solution given by direct numerics (left half panel). (a) $h/h_{\text{c}} = 9.2$ realizing perfect absorption, (b) $h/h_{\text{c}} = 3$ for comparison.

References

[1] H. Helmholtz, On the sensations of tone, Courier Corporation, 2013.

[2] J.C. Valière, B. Palazzo-Bertholon, J.D. Polack, and P. Carvalho, Acoustic pots in ancient and medieval buildings, Acta Acustica united with Acustica, **99**(1), 70-81, 2013.

[3] N. Jiménez, W. Huang, V. Romero-García, V. Pagneux, and J.-P. Groby, Ultra-thin metamaterial for perfect and quasi-omnidirectional sound absorption, Appl. Phys. Lett. **109**(12), 121902, 2016.

[4] A. Maurel, J.-J. Marigo, J.-F. Mercier and K. Pham, Modelling resonant arrays of the Helmholtz type in the time domain, Proc. R. Soc. A, **474**(2210), 20170894, 2018.

[5] O. Richoux, A. Maurel and V. Pagneux, Disorder persistent transparency within the bandgap of a periodic array of acoustic Helmholtz resonators, J. App. Phys. **117**(10), 104902, 2015.

Effective transmission conditions across a resonant bubbly metascreen

Kim Pham[1], Jean-François Mercier[2], Daniel Fuster[3], Agnès Maurel[4] and Jean-Jacques Marigo[5]

[2] IMSIA, CNRS, ENSTA ParisTech, 828 Bd des Maréchaux, 91732 Palaiseau, France
[2] Poems, CNRS, ENSTA ParisTech, INRIA, 828 Bd des Maréchaux, 91762 Palaiseau, France,
[3] Institut d'Alembert, CNRS, Univ. Paris 6, 4 place Jussieu, 75005 Paris, France,
[4] Institut Langevin, CNRS, ESPCI ParisTech, 1 rue Jussieu, 75005 Paris, France,
[5] Laboratoire de Mécanique des Solides, CNRS, Ecole Polytechnique, 91120 Palaiseau, France,
*corresponding author, E-mail: kim.pham@ensta-paristech.fr

Abstract

We study the propagation of acoustic waves through a thin bubbly screen. The analysis is conducted in the time domain and preserves the non linear response of the bubbles; it provides an effective model involving a jump of the normal velocity coupled to an equation of the Rayleigh-Plesset's type for the bubble radius. Numerical implementation of the effective model allows us to discuss the influence of the distance between bubbles within the screen and that of the non linearities.

1. Introduction

In 1985, Caflisch and co-workers analyzed the wave propagation in bubbly liquids [1] offering a rigorous mathematical framework to the former analysis developed by [2]. Using asymptotic analysis, they derived an effective wave equation involving a continuous version of the bubble radius satisfying an equation of the Rayleigh-Plesset's type.

In some practical situations, the region of bubbles is reduced to one or a few layers (Fig. 1). The most famous example are the anechoic tiles, codenamed Alberich, developed during the Second World War by the german marine; these tiles are the building blocks of a rubber net containing bubbles used to block the signals of sonars. It is also the case of bubble nets used to protect underwater structures from damage by underwater explosions or those created by some of the marine mammals to catch fish. Recently, these metascreens with subwavelength thickness have been revisited in the context of metamaterials. Resonant bubbles are the equivalent of split rings in electromagnetism and by designing judiciously their structuration, it is possible to obtain exotic properties as those obtained for their electromagnetic counterparts, see *e.g.* [3].

To describe such a thin screen, we conduct an asymptotic analysis which results in effective transmission conditions (instead of an effective wave equation); while the pressure is continuous across the screen, the normal velocity satisfies a non intuitive transmission condition involving a continuous version of the bubble radius satisfying an equation of the Rayleigh-Plesset's type. The calculations are performed in the time domain and preserving the non linear behavior of the bubble oscillations. We present numerical results which exemplify the influence of the spacing between bubbles and of the non-linearities on the propagation of an acoustic wave train.

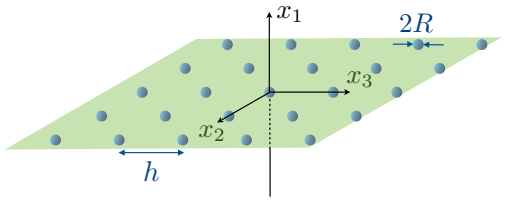


Figure 1: The actual problem of a bubbly screen in the $x_1 = 0$-plane with spacing h.

2. The actual and the effective problems

We start with the Euler equations which apply both in the air bubbles and in the surrounding fluid, namely

$$\begin{cases} \dfrac{\partial \rho}{\partial t} + \text{div}\,(\rho \mathbf{u}) = 0, \quad \rho\left(\dfrac{\partial \mathbf{u}}{\partial t} + (\mathbf{u}\cdot\nabla)\mathbf{u}\right) = -\boldsymbol{\nabla} p, \\ \quad \nabla \wedge \mathbf{u} = 0. \end{cases} \tag{1}$$

For a nearly incompressible liquid and a perfect gas under adiabatic transformations, the equations of state are written in the form $p_{\text{tot}} = P_{\text{eq}} + p = P_{\text{eq}} + c_\ell^2(\rho - \rho_\ell)$, in the liquid and $p_{\text{tot}}/P_{\text{eq}} = (\rho/\rho_{\text{g}})^\gamma$ in the gas, with $c_{\text{g}}^2 = \gamma P_{\text{eq}}/\rho_{\text{g}}$, where $\rho_{\ell,\text{g}}$ and $c_{\ell,\text{g}}$ are the mass density and the sound speed in the fluid and in the gas at the equilibrium with pressure P_{eq}, and with γ the adiabatic index. Eventually, the waves hitting the bubble i produce its oscillation, hence a time variation of its radius $R_i(t)$ around R_{eq}, its value at equilibrium. At the interface with the liquid, the radius of the bubble i is dictated by the condition $\mathbf{u}(\mathbf{x},t)\cdot\mathbf{n} = \dot{R}_i(t)$, where the dot denotes the time derivative. The homogenization procedure relies on a multiple scale analysis which leaves us with an effective problem in which the bubbly screen has disappeared, the derivation is detailed in [4]. In the liquid, for a low Mach number, $(p, \mathbf{u})$ satisfy

$$\frac{\partial p}{\partial t} + \rho_\ell c_\ell^2 \text{div}\mathbf{u} = 0, \quad \rho_\ell \frac{\partial \mathbf{u}}{\partial t} = -\boldsymbol{\nabla} p, \quad \nabla \wedge \mathbf{u} = 0, \tag{2}$$

with the initial and radiation conditions being the same as in the actual problem. The effect of the bubbly screen is reduced to effective transmission conditions which read as

$$\begin{cases} [\![p]\!] = 0, \quad [\![u_1]\!] = \dfrac{4\pi R^2}{h^2}\,\dot{R}, \\ \rho_\ell \left(R\ddot{R} + \dfrac{3}{2}\dot{R}^2 \right) + \dfrac{\rho_{\rm g} c_{\rm g}^2}{\gamma} \left(1 - \left(\dfrac{R_{\rm eq}}{R} \right)^{3\gamma} \right) = -p_{|x_1=0}, \end{cases} \tag{3}$$

where $[\![p]\!] = p(0^+, \mathbf{x}', t) - p(0^-, \mathbf{x}', t)$ (with $\mathbf{x}' = (x_2, x_3)$), the same for $[\![u_1]\!]$. The discontinuity of the normal velocity is thus related to the bubble oscillation whose effective radius is dictated by an equation of the Rayleigh-Plesset's type.

3. Numerical results

To inspect the characteristics of the effective model, we set the physical constants to: $\rho_l = 10^3$ Kg.m^{-3}, $c_\ell = 1\,500$ m.s^{-1}, $\gamma = 1.4$, $R_{\rm eq} = 10^{-5}$ m and $P_{\rm eq} = 0.225$ atm., and we consider an initial Gaussian pulse of the form

$$P_{\rm in}(x_1, t_{\rm ini}) = \Delta P \; e^{-(x_1 - x_{\rm ini})^2/\sigma^2}. \tag{4}$$

With a wavelength at the resonance $\lambda_{\rm M} = 10^{-2}$ m (and $T = \lambda_{\rm M}/c_\ell \sim 6.10^{-6}$ s), we use $\sigma = \lambda_{\rm M}/10 = 10^{-3}$ m (and $T_\sigma = T/10$ s). Making use of the above numerical values, the parameter κ measuring the strength of the interaction is given by $\kappa \simeq 10^4 \; \frac{(R_{\rm eq}/h)^2}{\Delta P/P_{\rm eq}}$, and we illustrate below the effects of the array spacing h and of the non-linearities on the propagation.

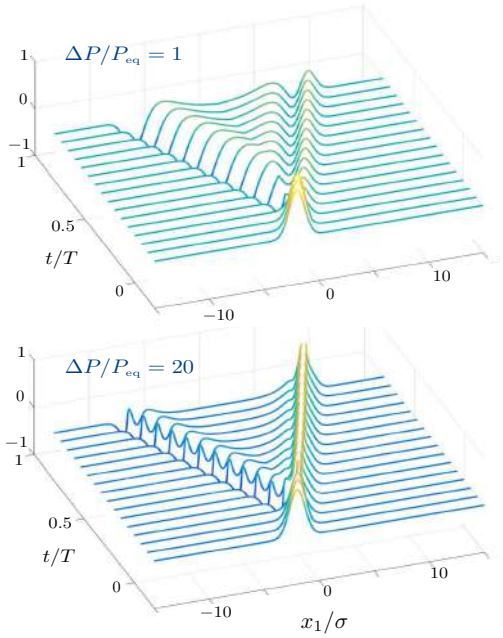


Figure 2: Propagation of an initial Gaussian pulse for $\Delta P/P_{\rm eq} = 1$ and 20. The pulse reaches the bubbly screen at $x_1 = 0$, $t = 0$.

To begin with, we report in Fig. 2 time series of the acoustic wave trains during propagation for $h/R_{\rm eq} = 20$ and increasing $\Delta P/P_{\rm eq} = 1$ (in the linear regime) and 20 (in the non linear regime). For larger ΔP, we observe that the reflected signal is smaller in amplitude, while the transmitted signal ressembles more and more to the initial pulse. This is attributable to the fact that pressure pulses with increasing amplitude produce more important bubble compression hence an apparent smaller scattering cross section. As a result the screen becomes invisible for large pressure amplitudes, as illustrated in Fig. 3(a). Varying now the distance h between the bubble, we observe that the screen becomes transparent for increasing h, see Fig. 3(b). In both cases, the weakening of the scattering strength of the bubbly screen occurs while the bubble oscillations are (i) of higher amplitude and (ii) less and less damped, see [4].

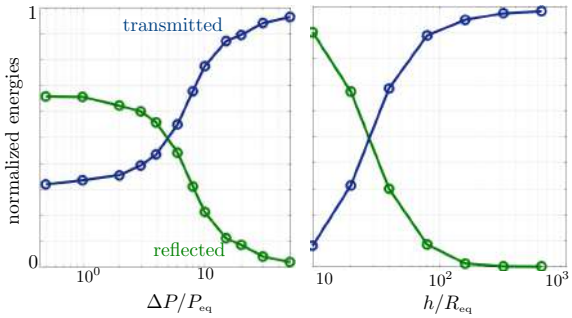


Figure 3: Normalized reflected and transmitted energies (a) against $\Delta P/P_{\rm eq}$ for $h/R_{\rm eq} = 20$, and (b) against $h/R_{\rm eq}$ for $\Delta P/P_{\rm eq} = 10^{-3}$.

4. Conclusions

The interaction of acoustic waves with a screen made of a thin layer of bubbles can be described by an effective model which reduces the effect of the bubbly screen to transmission conditions on the acoustic pressure and normal velocity. The numerical implementation of this effective model shows that the effect of the screen is weakened when the bubbles oscillate in a non linear regime or when their relative distance is large. Straightforward extensions of the present study would account for the surface tension and for the viscosity. A more demanding extension is to conduct the analysis to higher orders to account for the arrangement of the bubbles within the screen.

References

[1] R.E. Caflisch, M.J. Miksis, G. Papanicolaou and L. Ting, J. Fluid Mech. **160**, 1-14, 1985.

[2] L. Van Wijngaarden, J. Fluid Mech. **33**(3), 465-474, 1968.

[3] V. Leroy, A. Strybulevych, M. Lanoy, F. Lemoult, A. Tourin and J.H. Page, Phys. Rev. B **91**(2), 020301, 2015.

[4] K. Pham, J.-F. Mercier, D. Fuster, A. Maurel and J.-J. Marigo, submitted.

Sound absorbing metafluid inspired by cereal straws

W. Huang[1], L. Schwan[1], V. Romero-García[1], J.-M. Génevaux[1], and J.-P. Groby[1*]

[1]Laboratoire d'Acoustique de l'Université du Mans, LAUM - UMR CNRS 6613, Le Mans Université, Avenue Olivier Messiaen, 72085 LE MANS CEDEX 9, France.
*corresponding author, E-mail: Jean-Philippe.Groby@univ-lemans.fr

Abstract

Used as building biomaterials for centuries, cereal straws are known for their remarkable acoustic performances in sound absorption. Yet, their use as fibrous media disregards their internal structure made of nodes partitioning stems. Here, we show that such nodes can impart negative acoustic bulk modulus to straw balls when straws are cut on either side of a node. Large spectral bandgaps and slow sound regimes are theoretically predicted and experimental results from impedance tube measurements on an idealised 3D-printed sample layer perfectly capture these physical behaviours. Perfect absorption is achieved at wavelengths 13 times larger than the thickness of the metafluid layer, and slow sound entails an increased density of states causing a cascade of high absorption peaks.

1. Introduction

Particularly interesting in acoustic and thermal insulation are cereal straws such as wheat, reed or rattan. Attention was mainly paid to the effects of the length, concentration, and relative orientations of the straws on sound absorption. While arrays of straws were usually idealised as classical visco-thermal fluids made of either solid or completely hollow straws, closer examination of cereal straws reveals that nodes within the stem partition the straw into tubular segments. Therefore, when cutting straws on either side of a node, the resulting pieces are neither solid obstacles in the path of the acoustic wave, nor open hollow straws channelling the flow, but rather double quarter-wavelength resonators (QWR) separated by the node. Based on this observation, we designed a metafluid inspired by the cereal straws (MCS) made of the periodic repetition of double QWR, see Fig. 1.

2. Critical coupling and perfect absorption

The slow sound effect induced by the fundamental resonance of the double QWR and the inherent losses of the MCS can be used to design finite size perfect absorber samples. For the sake of comparison, the absorption of the equivalent anisotropic fluid inspired by cereal straws (FCS) in the absence of the QWR [1], that is when $r_i = 0$ and hence $\phi_j = 0$ for $j \in \{1, 2\}$, is also plotted. On the one hand, the frequencies of the Fabry-Perot resonances drastically decrease due to the slow sound regime of the MCS.

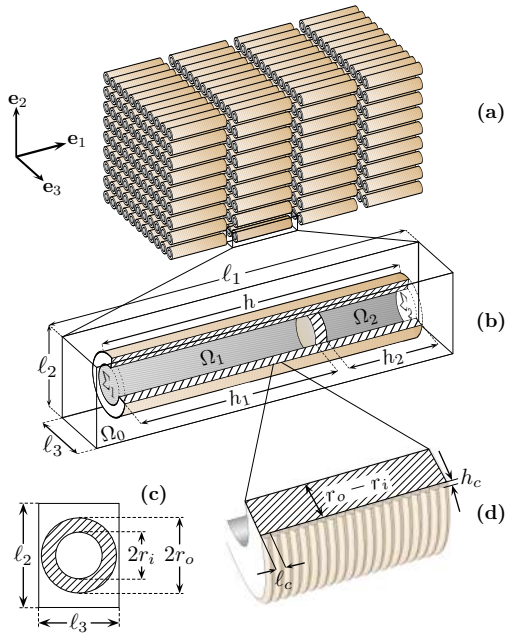


Figure 1: **Schematic of the idealised Metafluid inspired by cereal straws.** (a) Representation of the Ω-periodic arrangement of the double Quarter-Wavelength Resonators (QWRs) elements. (b) Details of the unit cell. (c) Details of the QWR opening. (d) Zoom at the corrugation of the walls.

As a consequence, these resonances occur for wavelengths much larger than the structure thickness, i.e., the MCS becomes deeply sub-wavelength. On the other hand, the MCS layer behaves as an open lossy and resonant system, characterised at the resonant frequencies, by both the leakage rate of energy (i.e., the coupling of the resonant elements with the propagating medium) and the inherent losses. In the reflection problem, the balance between the leakage and the losses activates the condition of critical coupling, enabling a perfect impedance matching to the background medium, and therefore generating a perfect energy absorption [2]. The layer sample analysed here has been designed so that the layer of thickness $L = 13\ell_3 = 109.2$ mm is critically coupled to air under plane wave excitation at normal incidence with $\lambda_e = 13L$ in the principal direction $\mathbf{e}_3$. Figure 2(a) shows the complex frequency plane for the FCS sample. The pairs of pole/zero represent the different Fabry-

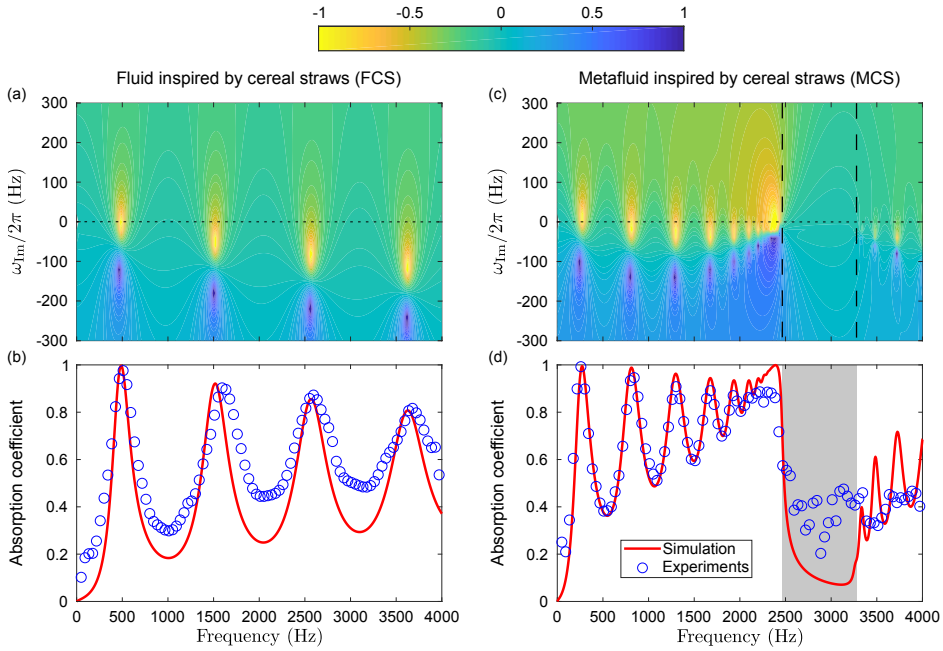


Figure 2: **Complex frequency planes representing** $\log(|R|^2)$ **for the FCS (a) and for the MCS (c).** Absorption coefficients (theoretical prediction in continuous red line, experiments in open circles) for the FCS (b) and for the MCS (d).

Perot resonances of the system. Complementary, Fig. 2(b) depicts the theoretical predictions and the experimental results of the absorption coefficient for the FCS sample. Both the pairs of pole/zero and the absorption peaks appear almost equally spaced in frequency, approximatively following the typical harmonic series $\{1, 3, 5, 7, \ldots\}$ of the quarter-wavelength resonances of a rigidly backed layer, because the system is weakly dispersive. Figure 2(c) and 2(d) respectively show the complex frequency plane and the absorption coefficient for the MCS sample. The absorption peaks and the pairs pole/zero are not anymore equally spaced in frequency due to the strong dispersion introduced by the resonances of the double QWR. Here, we pay attention to the frequencies below the band gap. The first absorption peak appears at 272 Hz. More importantly, we observe perfect absorption for the first absorption peak (experimentally 99.6 % at 258 Hz), where the corresponding wavelength equals to 13 times the slab thickness. Thus, this system represents a sub-wavelength perfect absorber. A cascade of nearly perfect absorption peaks, due to the higher order Fabry-Perot resonances, is produced and perfectly graspers by the theory. Each of these nearly perfect absorption peak is associated with a low quality factor resonance arising from the coupling with viscous and thermal diffusion tailored by the concentration of double QWR and the corrugation. These low quality factors strongly contribute to enhance the absorption between two consecutive peaks.

3. Conclusions

The metafluid inspired by cereal straws has been theoretically and experimentally reported for sub-wavelength perfect sound absorption. A straw bale constitued of straws cutted on either side of a node is idealised by a three-dimensional periodic reptition of tightly packed double QWR. This idealised straw bale is homogenised, exhibiting slow sound regime enabling to increase of the density of state in the subwavelength regime together with viscous and thermal diffusion through the arrangement of stems. The designed MCS possess a 99.6% absorption peak at 258 Hz, which corresponds to a wavelength 13 times larger than that of the slab thickness. The design of the present MSC offers both a comprehensive explanation of the acoustic properties of bio-sourced materials, such as wheat, reed, or rattan and large perspectives for the design of bio-inspired metafluid, notably through its anisotropy.

Acknowledgement

This work was funded by the PAVNat project, RFI *Le Mans Acoustique*, Région Pays de la Loire. This article is based upon work from COST Action DENORMS CA15125, supported by COST (European Cooperation in Science and Technology).

References

[1] D. Torrent, J. Sánchez-Dehesa, Sound scattering by anisotropic metafluids based on two-dimensional sonic crystals, *Phys. Rev. B* 17: 174104, 2009.

[2] N. Jiménez, W. Huang, V. Romero-García, V. Pagneux, J.-P. Groby, Ultra-thin metamaterial for perfect and quasi-omnidirectional sound absorption, *Appl. Phys. Lett.* 109: 121902, 2016.

Scattering by arrays of open ended resonators

Agnès Maurel [1], Jean-François Mercier[2] and Kim Pham[3]

[1] Institut Langevin, CNRS, ESPCI ParisTech, 1 rue Jussieu, 75005 Paris, France,
[2] Poems, CNRS, ENSTA ParisTech, INRIA, 828 Bd des Maréchaux, 91762 Palaiseau, France,
[3] IMSIA, CNRS, ENSTA ParisTech, 828 Bd des Maréchaux, 91732 Palaiseau, France
*corresponding author, E-mail: agnes.maurel@espci.fr

Abstract

We study the interaction of acoustic waves with arrays of cavities open at both ends. This is done owing to an effective model which provides explicit expressions of the reflection and transmission coefficients. Here, this is used to provide the relations required to produce zero reflection situation which are known to be surrounded by rapid variations of the scattering coefficients. The influence of the symmetry or asymmetry of the array is discussed.

1. Introduction

In electromagnetism, mushroom structures on a ground plane have attracted a lot of attention due to their capacity to produce high impedance boundaries [1]; in acoustic, similar structures are arrays of Helmholtz resonators. More recently, mushroom metamaterials open at both ends (with no ground plane) have been shown to enable interesting properties [2]. Here, we consider similar structures in acoustics consisting in arrays of cavities open at both ends (Fig. 1). For small openings, the backscattering is in general large but large variations of scattering can be observed in the vicinity of zero reflection configurations of practical interest, including Fano resonances. Such arrays have many free geometrical parameters, in particular for asymmetric configuration; thus it is meaningful to use approximate models to help in their designs. In [3], we have derived an effective model which accurately reproduces the scattering properties of such arrays. In the effective model, the wave in the region of the cavities satisfies $\frac{\partial^2 p}{\partial y^2}+k^2 p=0$ with p the acoustic pressure, while across the regions of the necks, jump conditions apply. At the entrance of the array, we have

$$[\![p]\!]=h\mathcal{B}_1\overline{u},\quad [\![u]\!]=-h\mathcal{C}_1\frac{\partial^2 p}{\partial x^2}-e_1\varphi_1 k^2\overline{p},\qquad (1)$$

where $[\![f]\!]=f^+-f^-$, $\overline{f}=\frac{1}{2}(f^+-f^-)$ with $f^-=f(x,0)$ and $f^+=f(x,e_1)$ and where $(\mathcal{B}_1,\mathcal{C}_1)$ are parameters well approximated by

$$\mathcal{B}_1=\frac{e_1}{h\varphi_1}-\frac{1}{\pi}\log\left(\sin\frac{\pi\varphi_1}{2}\sin\frac{\pi\varphi_1}{2\varphi}\right),\quad \mathcal{C}_1=\frac{\pi\varphi_1^2}{16}.\qquad (2)$$

The same condition holds at the exit of the array $1\to 2$ and $f^-=f(x,e_1+d)$ and $f^+=f(x,\ell)$, with $\ell=e_1+e_2+d$.

2. Scattering properties

For an incident plane wave, the solution of the effective model reads as

$$p(x,y)=e^{ik_x x}\times\begin{cases} e^{ik_y y}+Re^{-ik_y y}, & y<0,\\ Ae^{iky}+Be^{-iky}, & e_1<y<\ell-e_2,\\ Te^{ik_y(y-\ell)}, & y>\ell,\end{cases}\qquad (3)$$

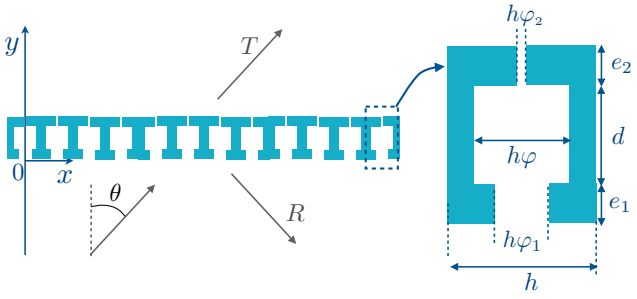


Figure 1: Scattering of an array of open ended resonators.

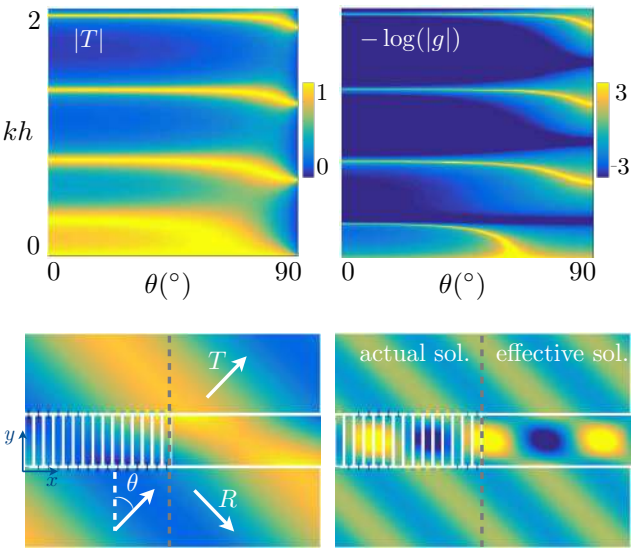


Figure 2: Perfect transmission for a symmetric array of resonators. Top panels: transmission spectrum and homogenized prediction (7). Bottom panels: velocity fields at the two first perfect transmissions for $\theta=45°$.

with $k_y = k\cos\theta$, $k_x = k\sin\theta$. Applying the 4 jump conditions (1) gives (R, A, B, T) as solution of the system

$$\begin{pmatrix} -\alpha_1^* & \gamma_1^* & \gamma_1 & 0 \\ \beta_1 & \delta_1 & -\overline{\delta_1} & 0 \\ 0 & \gamma_2 e^{ikd} & \gamma_2^* e^{-ikd} & -\alpha_2^* \\ 0 & \overline{\delta_2} e^{ikd} & -\delta_2 e^{-ikd} & -\beta_2 \end{pmatrix} \begin{pmatrix} R \\ A \\ B \\ T \end{pmatrix} = \begin{pmatrix} \alpha_1 \\ \beta_1^* \\ 0 \\ 0 \end{pmatrix}. \tag{4}$$

where * means complex conjugate and where

$$\begin{cases} \alpha_1 = 1 + \dfrac{i}{2} h\mathcal{B}_1 k_y, \quad \beta_1 = k_y + \dfrac{i}{2}\left(h\mathcal{C}_1 k_x^2 - e_1\varphi_1 k^2\right), \\ \gamma_1 = 1 + \dfrac{i}{2} h\varphi\,\mathcal{B}_1 k, \quad \delta_1 = \varphi k + \dfrac{i}{2}\left(h\mathcal{C}_1 k_x^2 - e_1\varphi_1 k^2\right), \end{cases} \tag{5}$$

(the same for index 2). It is easy to see that the condition $R = 0$ is possible if the following condition is satisfied

$$Z_1 = Z_2^*, \quad \text{with } Z_1 = e^{ikd}\,\frac{\alpha_1\delta_1^* + \beta_1^*\gamma_1}{\alpha_1\delta_1 - \beta_1^*\gamma_1^*}, \tag{6}$$

the same for Z_2. This condition is not easy to satisfy since Z is complex. To begin with, we consider symmetric arrays, for which it is sufficient that $Z_1 = Z_2$ is real. In this case, we find the condition that $g(k,\theta) = 0$ with

$$g(k,\theta) = \mathcal{D}(\theta)\; k - \tan kd\left(1 - \cos^2\theta\left(\frac{1}{\varphi^2} - \mathcal{B}_1^2 (kh)^2\right)\right), \tag{7}$$

with $\mathcal{D}(\theta) = 2\varphi\left(\mathcal{B}_1\cos^2\theta + \mathcal{C}_1\sin^2\theta - e\varphi_1\right)$. Hence, for any θ, a set of k-values produce zero reflection. This is illustrated in Fig. 2 where we reported $|T|$ against θ and kh for a symmetric array ($\varphi = 0.7$, $d/h = 5$ and $\varphi = 0.1$, $e/h = 0.3$); the accuracy of the condition (7) is better than 5% in the reported range.

We now move to asymmetric arrays; by simple inspection of (6), zero reflections appears to be possible if $\mathcal{B}_1 \simeq \mathcal{B}_2$. Hence, for a given geometry of the first necks (φ_1, e_1), a relation between e_2 and φ_2 is obtained, with

$$e_2 \simeq e_2^{\mathrm{G}} = h\varphi_2\left(\mathcal{B}_1 + \log\left(\sin\frac{\pi\varphi_2}{2}\sin\frac{\pi\varphi_2}{2\varphi}\right)\right). \tag{8}$$

The accuracy of the above expression is exemplified in Fig. 3 where we report $|R|$ computed numerically against kh and e_2/e_2^{G} for $\varphi_2 = 0.05$ (otherwise $\varphi = 0.7$, $d/h = 5$ and $\varphi_1 = 0.2$, $e_1/h = 0.6$).

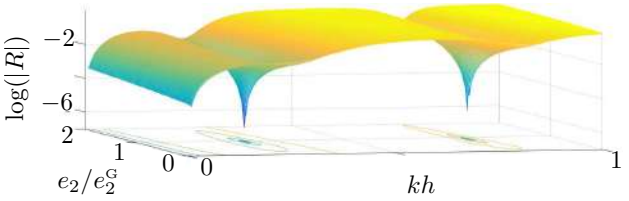


Figure 3: Perfect transmission for asymmetric arrays. With e_2 as free parameter, $|R| = 0$ is obtained for $e_2 \sim e_2^{\mathrm{G}}$ according to (8).

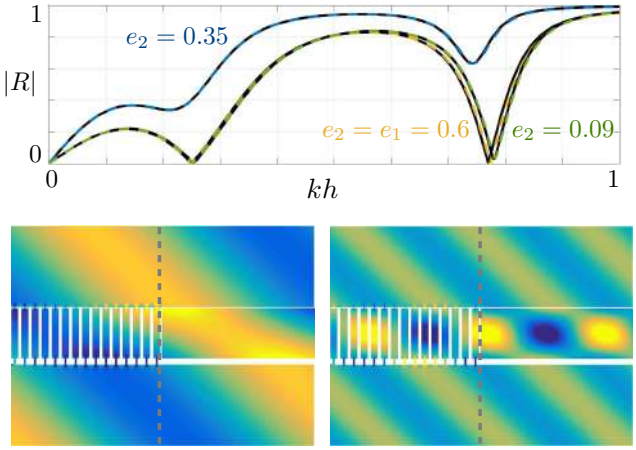


Figure 4: Perfect transmission for a asymmetric array. Top panels : $|R|$ against k for a symmetric array and for 2 asymmetric ones ($e_2 = 0.09$ close to e_2^{G} in (7), and $e_2 = 0.35$); numerics (plain black lines) and from the effective model (dotted lines). Bottom panels: same representation as in Fig. 2 for $e_2/h = 0.09$.

Eventually, we report in Fig. 4 the reflection curves for asymmetric arrays (i) realizing zero reflection in green ($e_2 = 0.09$ from Fig. 3, and $e_2^{\mathrm{G}} = 0.1$), (ii) in blue unable to produce zero reflection for $e_2 = 0.35$ and (iii) for a symmetric array by setting $e_2 = e_1$ and $\varphi_2 = \varphi_1$.

3. Conclusion

We have exemplified the interest of effective models to predict the acoustic properties of arrays with specific symmetries. When a symmetry is lost, a new degree of freedom is available. This may be of interest to design an array with specific properties; however, this make the actual problem more cumberstone to analyze. We shall discuss (i) the acoustic properties of a mushroom type array, with disconnected cavities in three dimensions and (ii) other properties of such arrays, notably the possible appearance of Fano resonances already observed in [2].

References

[1] D. Sievenpiper, L. Zhang, R. Broas, N. Alexopolous, and E. Yablonovitch, High-impedance electromagnetic surfaces with a forbidden frequency band, IEEE Trans. Microw. Theory Techn., **47**(11) 2059-2074, 1999.

[3] A. Maurel, J.-J. Marigo, J.-F. Mercier and K. Pham, Modelling resonant arrays of the Helmholtz type in the time domain. Proc. R. Soc. A, **474**(2210), 20170894, 2018.

[2] D. E. Fernandes, S. I. Maslovski,G. W. Hanson,2 and M.G. Silveirinha Fano resonances in nested wire media, Phys. Rev. B. **88**, 045130, 2013.

Deep Sub-wavelength Materials for Controlling Sound Diffusion: Experimental Validation of Metadiffusers

E. Ballestero[1], N. Jiménez[2], J.-P. Groby[2], S. Dance[1] and V. Romero-García[2*],

[1]London South Bank University, Department of The Built Environment,
90 London Road, London, SE16LN, United Kingdom.
[2]Consejo Superior de Investigaciones Científicas (CSIC), Universitat Politècnica de València,
Camino de Vera S/N, 46085, València, Spain.
[3]Laboratoire d'Acoustique de l'Université du Mans, LAUM - UMR 6613 CNRS, Le Mans Université,
Avenue Olivier Messiaen, 72085 LE MANS CEDEX 9, France.
*corresponding author, E-mail: vicente.romero@univ-lemans.fr

Abstract

This work reports the experimental validation of a deep-subwavelength material for sound diffusion named metadiffuser. Metadiffusers are rigidly backed slotted panels, each slit being loaded by an array of Helmholtz resonators (HRs) introducing strong dispersion in the slits and slow sound conditions. Therefore, the effective thickness of the panel is dramatically reduced down-shifting its quarter wavelength resonance in the deep-subwavelength regime. By tuning the geometry of the metamaterial, the reflection coefficient profile can be tailored to obtain a custom reflection phase. In this work we validate a metadiffuser based on a quadratic residue sequence, producing a uniform scattering function, so that the reflecting waves are dispersed in many different directions by the subwavelength metadiffuser of thickness $\lambda_0/34$ (where λ_0 is the wavelength of the design frequency).

1. Introduction

Sound diffusers are locally-reacting reflecting surfaces with spatially dependent reflection coefficient designed to produce uniform scattering, i.e., the reflected waves by these surfaces are scattered in many different directions [1]. Therefore, diffusers present a uniform far field magnitude, i.e. a uniform magnitude Fourier transform of its spatially dependent reflection coefficient distribution. The generation of spatially dependent reflecting surfaces is commonly achieved by using phase grating diffusers, also known as Schröeder's diffusers [2], that are rigidly-backed slotted panels where each slit acts as a quarter wavelength resonator. However, Schröeder diffusers are limited by their depths, which becomes large at low design frequencies. This results in thick and heavy panels, limiting the use of phase grating diffusers at low-frequencies where the wavelength of sound in air is of the order of several meters.

In this work, we present the experimental validation of the concept of metadiffusers which are deep-subwavelength thickness diffusers based on slow sound acoustic metamaterials [3, 4, 5] to dramatically reduce the thickness of Schröeder diffusers. By tuning the geometry of the HRs and the thickness of the slits, the phase of the reflection coefficients can be tailored to those of usual diffusers but with extremely deep subwavelength structures. We present the validation of a metadiffuser based on the one presented in a previous work of some of the authors of the current abstract [1].

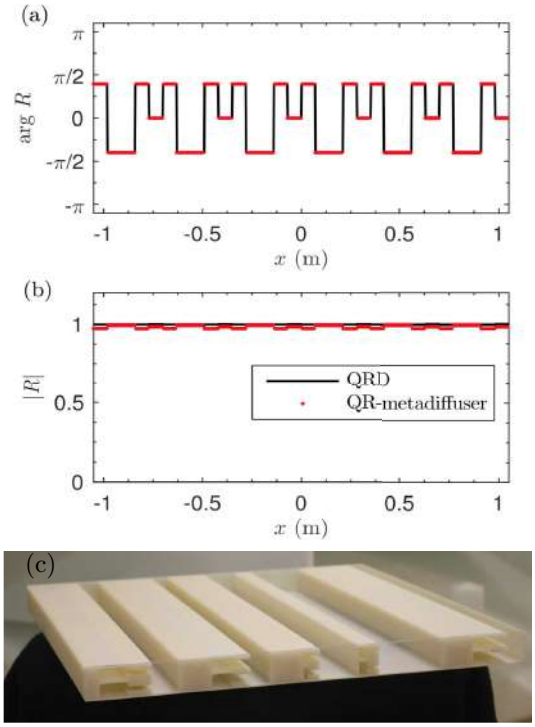


Figure 1: (a) Phase and (b) magnitude of the spatially-dependent reflection coefficient of a QRD (black line) and the QR-metadiffuser (red doted). Picture the analyzed metadiffuser (b).

2. Design of metadiffusers

A quadratic residue diffuser (QRD) is made from a numerical sequence given by $s_n = n^2 \mathrm{mod} N$, where mod is the

least non-negative remainder of the prime number N. If the phase grating diffuser is based on quarter wavelength resonators (wells), the depths of the wells are given by $L_n = s_n\lambda_0/2N$, where λ_0 is the design wavelength. A classical QRD with $N = 5$ and total thickness of $L = 27.4$ cm with side $Nd = 35$ cm could be designed for a frequency of 500 Hz. The resulting reflection coefficient could be mimicked by a metadiffuser structure as shown in Figs. 1(a,b). Perfect agreement is found between the reflection coefficients of the meta-QRD and the target phase. The picture of the designed metadifuser is shown in Fig. 1(c), with a deep sub-wavelength thickness of $L = 2$ cm.

3. Experimental set-up

The metadiffuser is experimentally tested in the anechoic chamber of the Laboratoire d'Acoustique de l'Université du Mans (LAUM). The metadiffuser is excited by a maximum length sequence (MLS) radiated by a source placed at 2 m from it at 90° of incidence. The metadiffuser is placed on a turning table covering all the azimutal angles. The scattering pressure field, p_s, is evaluated in the polar angles, along a semi-circumference of 1 m radius centered in the center of the metadiffuser. Therefore all the scattering directions can be captured by the experimental set-up. The scattering field is obtained by Fourier transforming the impulse response of the system after windowing it in the corresponding time period in order to remove the direct sound from the source.

4. Results

We evaluated a single repetition of the meta-QRD and an equivalent rigid panel of the same dimensions. Figure 2 shows the experimental results for the evaluated meta-QRD (in red lines) and for the rigid panel (in blue lines). In both cases the experimental scattered field, $p_s(\theta)$ is plotted. Two different frequencies are evaluated. The first one at 700 Hz, where the meta-QRD behaves as a rigid panel. The second frequency, at 1500 Hz, shows the spreading of the acoustic energy in all the directions produced by the meta-QRD.

5. Conclusion

The concept of metadiffuser as a design of deep subwavelength locally reacting surfaces with tailored acoustic scattering was experimentally validated, demonstrating the potential of the metadiffusers to be used in critical listening environments. Due to their deep-subwavelength nature, the thickness of the panels can be strongly reduced. In the context of smart building design and sustainability, metadiffusers can be used to save space and to produce lightweight materials, improving the performance of the acoustic solutions using less resources. Moreover, the proposed designs have the potential to meet the aesthetic requirements that are mandatory for modern auditoria design.

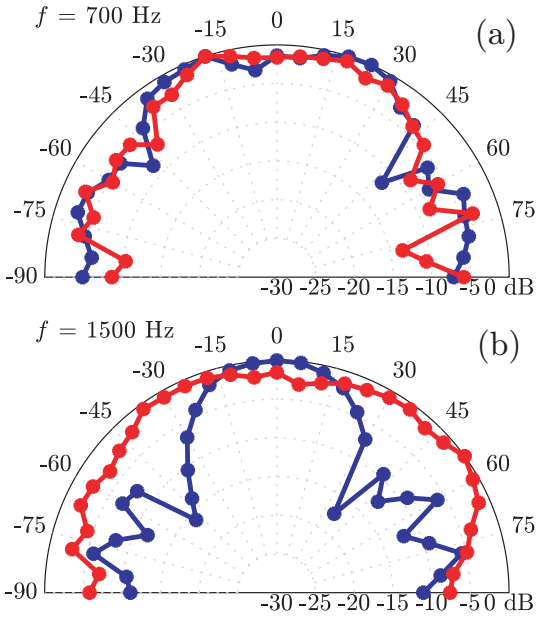


Figure 2: Experimental polar plots of the scattered acoustic field, $p_s(\theta)$, for (a) 700 Hz and (b) 1500 Hz. Blue line (Red line) represents the experimental evaluation of the far field of a flat square rigid panel (meta-QRD) of dimensions 35×35 cm^2.

6. Acknowledgement

The authors gratefully acknowledge the ANR-RGC META-Room (ANR-18-CE08-0021) project and the project HYPERMETA funded under the program Étoiles Montantes of the Région Pays de la Loire. This article is based upon work from COST (European Cooperation in Science and Technology) Action DENORMS CA15125, supported by COST (European Cooperation in Science and Technology).

References

[1] N. Jiménez, T. J. Cox, V. Romero-García and J.-P. Groby, Metadi users: Deep-subwavelength sound diffusers, *Sci. Rep.*, 7, 5389, 2017.

[2] Schröder, M. R. Diffuse sound reflection by maximum length sequences. *Jour. Acous. Soc. Am.*, 57, 149-150 (1975).

[3] Groby, J.-P., Huang, W., Lardeau, A. and Aurégan, Y. The use of slow waves to design simple sound absorbing materials, *J. Appl. Phys.*, 117, 124903 (2015).

[4] V. Romero-Garcá, G. Theocharis, O. Richoux, and V. Pagneux, Use of complex frequency plane to design broadband and sub-wavelength absorbers. *Jour. Acous. Soc. Am.*, 139, 3395-3403 (2016).

[5] N. Jiménez, W. Huang, V. Romero-García, V. Pagneux, and J.-P. Groby, Ultra-thin metamaterial for perfect and quasi-omnidirectional sound absorption. *Appl. Phys. Lett.*, 109, 121902 (2016).

Stealth Acoustic Materials for Scattering Cancellation

V. Romero-García[1*] , N. Lamothe[1], G. Theocharis[1], O. Richoux[1] and L.M. Garcia-Raffi[2],

[1]Laboratoire d'Acoustique de l'Université du Mans, LAUM - UMR CNRS 6613, Le Mans Université, Avenue Olivier Messiaen, 72085 LE MANS CEDEX 9, France.
[2] Universitat Politècnica de València, Camí de vera s/n, 46022, València, Spain.
*corresponding author, E-mail: vicente.romero@univ-lemans.fr

Abstract

We report a material that suppresses the acoustic scattering for a given set of incident wave vectors. This stealth acoustic material consists of multiple scatterers, rigid diaphragms, located in an air-filled acoustic waveguide. The experimental results are in good agreement with the theory. The robustness and the generality of the results motivate potential applications in wave physics.

1. Introduction

The control of the scattering of waves represents a major topic of interest in acoustics, photonics, and electromagnetism, due to the vast possibilities in fundamental physics with potential applications. In particular complex media [1, 2] and recently metamaterials [3], have been shown as potential candidates to control the scattering of different types of waves.

Recently, stealth distributions of scatterers [4] that are -counterintuitively- disordered, hyperuniform, and highly degenerate have been exploited to show novel thermodynamic and physical properties as for example broadband and omnidirectional band gaps for electromagnetic [5] or elastic waves [6]. These materials are designed by using the structure factor, which is a physical parameter proportional to the scattered energy. This structure factor can be controlled by the position of the scatterers in the stealth distribution.

In this work we construct disordered stealth configurations by engineering the material properties in a controlled manner in such a way that the system prevents scattering only at prescribed wavelengths with no restrictions on any other wavelengths. In particular we focus on the suppression of the Bragg scattering of the corresponding periodic case and make the structured system transparent for a broad-band range of frequencies. The inverse problem to generate the configuration of multiple scatterers with a specific scattering properties is non-trivial, as multiple solutions are conceivable. The approach is based on the optimization of the structure factor which, in the Born approximation, can be used as the outcome of a scattering experiment. The configuration of multiple scatterers is used to construct an one dimensional (1D) stealth structure made of rigid diaphragms embedded in an air-filled wave-guide (as shown in Fig. 1). The system is analytically analyzed by using the Transfer Matrix Method (TMM). Full wave numerical simulations have been done by using Finite Element Method (FEM). The system is analyzed considering the intrinsic viscothermal losses of the system. Experiments are performed to validate the theoretical results

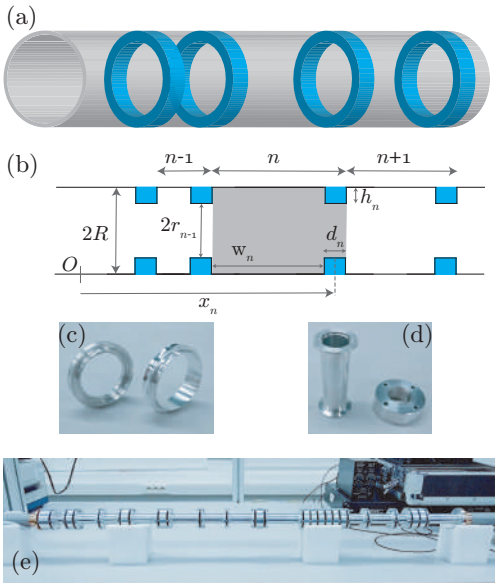


Figure 1: Schematics of both a three dimensional view (a) and the cross section (b) of the cylindrical waveguide along the n-th diaphragm. (c-e) Experimental set-up. (c) Connections: left diaphragme and flat connection for empty tube. (d) Separators. (e) Picture of the stealth material.

2. Main results

In Fig. 2(a) we represent the scattering coefficients of the periodic distribution of scatterers. The Bragg scattering of the finite structure is shown. Figure 2(b) shows the scattering coefficients of the designed stealth material (Fig. 1(e)) in the lossless case. The reflection coefficient is dramatically reduced and the transmission is almost one for the target range of frequencies (yellow area). We notice that in this lossless case, the reflection coefficients from both sides of the sample must be equal, $R^+ = R^-$. We analyze now the lossy case. Numerical, theoretical and experimental results are compared in Figs. 2(c) and 2(d). In this case, as

the stealth material is not symmetric, $R^+ \neq R^-$, but being reciprocal $T^+ = T^- = T$. We start by analyzing the results for the system excited from the right side (forward direction, Fig. 2(c)). In the optimized frequency band, the values of the reflection coefficient are nearly zero while the transmission coefficient has been reduced with respect to the lossless case. However the coefficients keep the flat behavior also shown in the lossless case. In order to check the transparency of the stealth material, we compare its transmission coefficients with the corresponding empty waveguide. In the optimized range of frequencies the transmission of the stealth material matches the transmission of the empty tube in very good agreement between numerics, analytics and experiments. As in the lossless case, out of the optimization range, the system is not transparent. One of the properties of the structure factor is that the scattered intensity should be the same in opposite directions even if the configuration of multiple scatterers conforming the stealth material is not symmetric, i.e., the reflection coefficient from both sides of the structure should be equal. Figure 2(d) analyzes the same coefficients as Fig. 2(c) but evaluated for the backward incidence direction, having a similar behavior as the opposite direction. Figure 2(e) shows that the difference between the amplitudes of the reflection coefficients evaluated from each side of the stealth material is less than 3% in the whole frequency range.

3. Conclusions

These preliminary results provide new insights into the nature of wave control by amorphous structures being the basis for future applications in acoustics and more generally in wave physics. It is worth noting here that the methodology is general and can be applied for any type of wave.

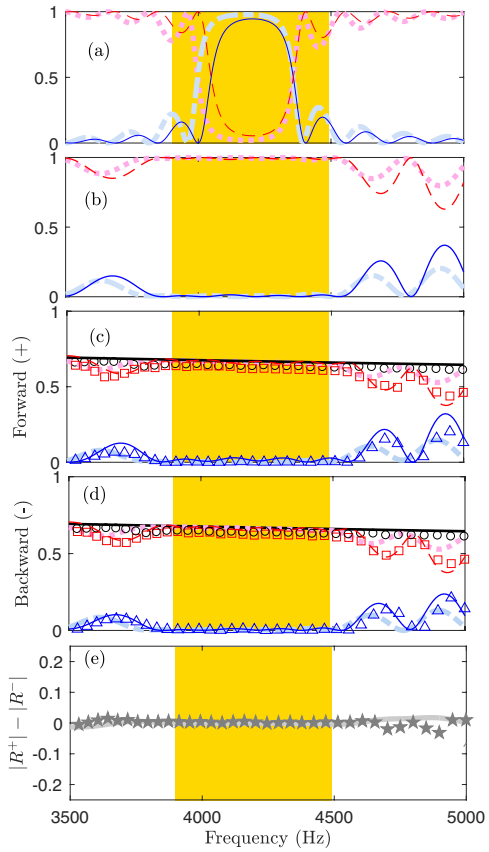


Figure 2: Analysis of the scattering produced by the stealth material. In the Figure the transmission, T^2, [reflection, R^2,] analytically and numerically calculated are represented by the shaded pink (▪ ▪ ▪) and red dashed (− −) lines respectively [shaded blue (▪ ▪ ▪) and blue continuous (−) lines respectively] and the experimental values are represented by red squares (□) [blue triangles (△)]. (a) Scattering coefficients of (a) the periodic distribution in the lossless case, (b) the stealth material in the lossless case, (c) and (d) the stealth material in the lossy case excited from the forward and backward incidence directions respectively. Black (−) continuous line and black circles (◯) represent the transmission coefficient of the empty waveguide, theoretical and experimental values respectively. (e) $|R^+| - |R^-|$ from the TMM (▬) and experimental results (★).

Acknowledgement

This work has been funded by RFI Le Mans Acoustique in the framework of the APAMAS project, by the project HYPERMETA funded by the Région Pays de la Loire as well as by the Ministerio de Economía y Competitividad (Spain) and European Union FEDER through project FIS2015-65998-C2-2-P. This article is based upon work from COST Action DENORMS CA15125, supported by COST.

References

[1] A. Ishimaru, *Wave Propagation and Scattering in Random Media*, Oxford University Press, New York, (1997).

[2] Diederik S. Wiersma, *Nat. Photonics*, 7 (2013).

[3] N. Engheta and R.W. Ziolkowski, eds., *Metamaterials: Physics and Engineering Explorations*, Wiley-IEEE Press, (2006).

[4] Salvatore Torquato, *Random Heterogeneous Materials: Microstructure and macroscopic properties*, Springer, (2002).

[5] W. Man, M. Florescu, E. P. Williamson, Y. He, S. Rez, B. Hashemizad, Y. C. Leung, D. R. Liner, S. Torquato, P. M. Chaikin, and P. J. Steinhardt, Isotropic band gaps and freeform waveguides observed in hyperuniform disordered photonic solids, *PNAS*, 110, 15886 (2013).

[6] G. Gkantzounis, T. Amoah, and M. Florescu, Hyperuniform disordered phononic structures, *Phys. Rev. B*, 95, 094120 (2017).

Sound Transmission Loss through a Phononic Crystal Panel: Prediction and Validation

Bart Van Damme*[1], Armin Zemp[1], Sepide Ahsani[2,3], Lucas Van Belle[2,3], Claus Claeys[2,3], and Elke Deckers[2,3]

[1]Laboratory for Acoustics/Noise Control, Empa, Materials Science and Technology, Duebendorf, Switzerland
[2]KU Leuven, Department of Mechanical Engineering, Leuven, Belgium
[3]DMMS Lab, Flanders Make
*corresponding author, E-mail: bart.vandamme@empa.ch

Abstract

Acoustic metamaterials and phononic crystals are often presented as improved materials for vibration and acoustic isolation. Calculating the dispersion relation, typically done using the assumption of periodic boundary conditions on a single unit cell, leads to accurate knowledge of frequency bands with high wave attenuation inside the structure. However, structural band gaps in a metamaterial plate do not necessarily lead to high sound transmission losses, since acoustic transmission is not only governed by wave processes. In the low frequency range, isolation is governed by the wall's mass, above the coincidence frequency out-of-plane wave attenuation is responsible for the sound transmission loss. In this paper, the case of a sandwich panel with a core consisting of periodic stiffeners is considered. A suitable geometry is defined based on structural band gap analysis. Consequently, the sound transmission loss under diffuse excitation is predicted, and compared to values measured on a realistic sample in an accredited testing facility.

1. Introduction

Metastructures are an established way to achieve elastic wave attenuation in plates. Two common approaches are: adding an array of resonators onto the plate, or altering the material in a regular pattern. The first path leads to narrow band gaps around the eigenfrequency of the resonators, which are to be placed less than a wavelength away from each other [1]. The latter method results in Bragg scattering of elastic waves, leading to destructive interference under certain propagation directions in broad frequency bands [2]. However, the band gaps only occur at wavelengths comparable to or larger than the structural period, hence it is hard to achieve low frequency attenuation. Moreover, since the forbidden frequencies are direction dependent, the existence of omnidirectional band gaps is not ensured.

In this paper, we present a phononic crystal plate with increased acoustic isolation properties compared to a plate with equal mass but without periodicity. The isolation is quantified by the sound transmission loss (STL), which is the sound power reduction as a function of frequency when the panel is excited by a diffuse sound field. Bending waves in the considered sandwich plate are scattered by a periodic arrangement of stiffeners in the core. The band gap frequencies are calculated using unit cell analysis. Subsequently, the STL is predicted by a hybrid Wave Based - Finite Element Unit Cell method. The results are validated by a standardized measurement on a representatively large sample.

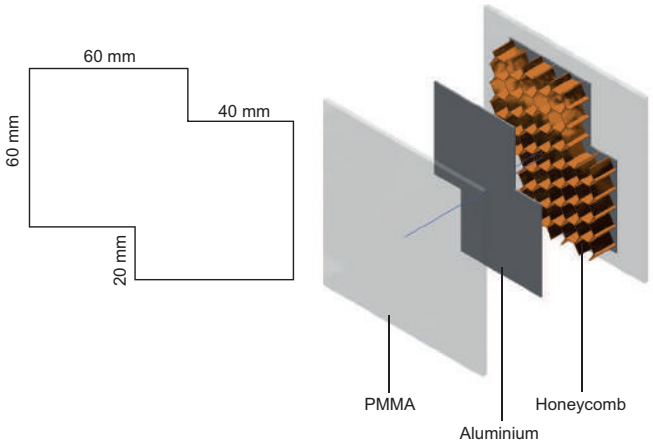


Figure 1: Geometry of the stiffener blocks (left) and assembly of a unit cell, consisting of PMMA shells and an aluminium honeycomb core (right)

2. Sandwich panel geometry and materials

Beams with periodically varying bending stiffness exhibit a series of band gaps with high flexural wave attenuation coefficients [3, 4]. Similarly, a plate with a rectangular pattern of stiffeners is expected to attenuate out-of-plane waves in certain frequency bands.

In order to achieve efficient wave scattering, the bending stiffness contrast between soft and hard parts should be as large as possible. We therefore propose a sandwich structure with outer shells made out of 3 mm PMMA plates ($E = 1.8$ GPa, $\rho = 1280$ kg/m^3). The shells are spaced by octagonal blocks made out of an aluminium sandwich material (face thickness 1 mm, $E = 40$ GPa) with an aluminium honeycomb core (15 mm). The difference in Young's moduli between PMMA and aluminium ensures a

large enough bending stiffness contrast. The core blocks are arranged in a square pattern with a unit cell size of 120 mm. Their dimensions are given in Fig. 1.

3. Modelling

3.1. Dispersion relation calculation

The wave dispersion is calculated according to the method proposed by Mace and Manconi [5]. A finite element model of a single unit cell is set up in ANSYS 18.2. The degrees of freedom of the right (top) edge are related to those of the left (bottom) edge according to the Bloch theorem:

$$q_R = \exp(ik_{Bx}d_x)q_L, q_T = \exp(ik_{By}d_y)q_B.$$

Using these relations, the degrees of freedom in the slave nodes at the right and top edges can be eliminated from the equations, resulting in reduced mass and stiffness matrices M_r and K_r. The reduced matrices are a function of the Bloch wave vector $\vec{k_B} = (k_{Bx}, k_{By})$. The corresponding eigenfrequencies ω can be found as the eigenvalues of the homogeneous system

$$K_r - \omega^2 M_r = 0.$$

3.2. Sound transmission loss

The STL of the infinite periodic structure is predicted using the hybrid Wave Based - Finite Element (WB-FE) UC method [6] coupling the structural FE UC model to two semi-unbounded periodic acoustic WB domains, above and below the structure. The upper acoustic domain is excited by an impinging acoustic plane wave. The pressure field in the acoustic domains is described using an expansion of wave functions that fulfil the governing Helmholtz equation, the Sommerfeld radiation condition and the Bloch-Floquet boundary condtions. Using a direct hybrid WB-FE coupling strategy, a system of equations is obtained, which is solved for the nodal degrees of freedom in the FE domain and the wave function contributions in the WB domain. The latter are used to calculate transmission coefficients τ and thus the STL = $-10log10(\tau)$ of the infinite periodic structure.

4. STL measurement

The sound transmission loss was measured according to European Standard EN-ISO-10140-1 [7]. The separation wall is placed between two reverberant rooms, thereby ensuring a diffuse field excitation. The STL value can be measured as the difference in sound pressure levels between both rooms L_1 and L_2, corrected by a term involving the size of the window (S) and the absorption surface of the rooms (A) as STL$= L_1 - L_2 + 10\log(S/A)$.

5. Conclusions

The use of phononic crystal plates to achieve a higher STL is not trivial for several reasons. Firstly, wave attenuation in the plate is not the only mechanism for the total acoustic isolation. Moreover, the elastic wave band gaps are not omnidirectional, and their contribution to the acoustic radiation has to be investigated more closely. In this work, calculations of the dispersion relations and sound transmission loss in a diffuse field are compared to STL measurements. This approach gives insight in the interaction between structural and acoustic properties.

Acknowledgement

The research of E. Deckers is funded by a postdoctoral grant form the Research Foundation - Flanders (FWO). This research was partially supported by Flanders Make, the strategic research centre for the manufacturing industry. The research of S. Ahsani is funded by an Early Stage Researcher grant within the European Project VIPER Marie Curie Initial Training Network (GA675441).
This article is based on work from COST Action DENORMS CA15125, supported by COST (European Cooperation in Science and Technology).

References

[1] C. C. Claeys, K. Vergote, P. Sas, and W. Desmet, On the potential of tuned resonators to obtain low-frequency vibrational stop bands in periodic panels, *Journal of Sound and Vibration*, vol. 332, no. 6, pp. 1418–1436, 2013.

[2] P. A. Deymier, *Acoustic metamaterials and phononic crystals*, Berlin, Heidelberg: Springer, 2013.

[3] L. Liu and M. I. Hussein, Wave Motion in Periodic Flexural Beams and Characterization of the Transition Between Bragg Scattering and Local Resonance, *Journal of Applied Mechanics*, vol. 79, no. 1, p. 011003, 2012.

[4] B. Van Damme and A. Zemp, Measuring dispersion curves for bending waves in beams: a comparison of spatial fourier transform and inhomogeneous wave correlation, *Acta Acustica united with Acustica*, vol. 104, no. 2, p.228-234, 2018.

[5] B. R. Mace and E. Manconi, Modelling wave propagation in two-dimensional structures using finite element analysis, *Journal of Sound and Vibration*, vol. 318, no. 4-5, pp. 884–902, 2008.

[6] E. Deckers, S. Jonckheere, L. Van Belle, C. Claeys, and W. Desmet, Prediction of transmission, reflection and absorption coefficients of periodic structures using a hybrid wave based - finite element unit cell method, *Journal of Computational Physics*, vol. 356, pp. 282–302, 2018.

[7] En ISO 10140-2 Messung der Schalldämmung von Bauteilen im Prüfstand - Teil 2: Messung der Luftschalldämmung, 2010.

On the use of plate-type metamaterial to experimentally highlight a hiding zone in Density Near Zero acoustic metamaterial

Matthieu Malléjac[1*], Aurélien Merkel[2], José Sánchez Dehesa[3], Johan Christensen[2], Vincent Tournat[1], Vicent Romero-García[1], and Jean-Philippe Groby[1]

[1]Laboratoire d'Acoustique de l'Université du Mans, LAUM - UMR 6613 CNRS, Le Mans Université, Avenue Olivier Messiaen, 72085 Le Mans Cedex 9, France
[2]Department of Physics, Universidad Carlos III de Madrid - Avenida de la Universidad, 28911 Leganés (Madrid), Spain
[3]Universitat Politècnica de València, Camino de Vera s/n, ES-46022 València, Spain
*corresponding author, E-mail: matthieu.mallejac@univ-lemans.fr

Abstract

Acoustic metamaterials composed of a periodic arrangement of plates or membranes in the air are of growing practical interest because of their peculiar properties such as the possibility to obtain zero dynamic mass density. The aim of this work is to experimentally, numerically and theoretically report and characterize the anomalous propagation of sound waves in a one-dimensional periodic system of thin elastic clamped plates emphasizing a hiding zone due to the near zero density regime.

1. Introduction

Density Near Zero (DNZ) acoustic metamaterials have drawn lots of attention in the last decades. One way to achieve the DNZ condition is to arrange periodically thin clamped elastic plates in the air [1]. Due to the strong dispersion around the band gap produced in such a system, zero mass density occurs. The phase velocity tends to infinity in the lossless case, leading to an effective quasistatic field distribution in the metamaterial. Interesting applications are then exhibited such as energy super-squeezing and tunneling in narrow duct [2] or non delayed propagation. Independently of the channel length or the twisting of the guide, a wave impinging the structure can propagate along the metamaterial without being delayed and with a high transmission. DNZ metamaterials can also lead to efficient cloaking effect as it has been studied numerically in a 2 dimensionnal lossless case in [3]. At the zero phase delay frequency, in the DNZ region, a propagating wave is not impacted by the presence of the scatterer. However, losses, not avoidable in reality, can be dramatically important in such systems and therefore drastically modify the metamaterial behavior. We thus propose an experimental evidence of this hiding zone in a one dimensional Density-Near-Zero material and an investigation on the inherent limits to these losses.

2. Experimental evidence of anomalous propagation

2.1. Set-up

The proposed system is composed of a periodic arrangement of 6 thin plastic plates clamped in a circular waveguide of inner radius $R_a = 1.5$ cm. The unit cell is built of a clamped plate of thickness $h = 102$ μm surrounded by two air cavities of length $L_{gap}/2 = 0.5$ cm. The transmission and reflection coefficients measured in a 4 microphones impedance tube allow to retrieve the metamaterial effective properties [4, 5]. Two different extraordinary features are explored here: the non-delayed propagation and the scatterer hiding efficiency.

2.2. Non-delayed propagation

Transfer matrix, Full-wave simulations (FEM), and measurements show that the 6 plates metamaterial exhibits a zero effective dynamic mass density. Furthermore, in this vanishing frequency region, the structure presents a zero phase of the transmission coefficient resulting from propagation without phase change. The non-delayed propagation is thus robust to losses (mostly from the plates), which are solely responsible for a decrease of the transmission (one in the lossless case), an increase of the reflection (zero in the lossless case), and a shift of both the zero density and the zero phase frequencies.

A circular diaphragm, playing the role of scatterer is then embedded into the plate metamaterial. The diaphragm alone induces a phase delay to the incident wave. The phase of the diaphragm transmission coefficient varies from -0.05π to -0.4π rad in [10 500] Hz. Adding the 6 plates metamaterial allows the phase to vanish in the DNZ region. The zero phase (non-delayed propagation) frequency depends on the aperture radius R_d of the diaphragm as shown by Fig. 1.

2.3. Hiding zone

Moreover, the DNZ metamaterial allows to hide the scatterer. At the zero phase frequency, the transmission and

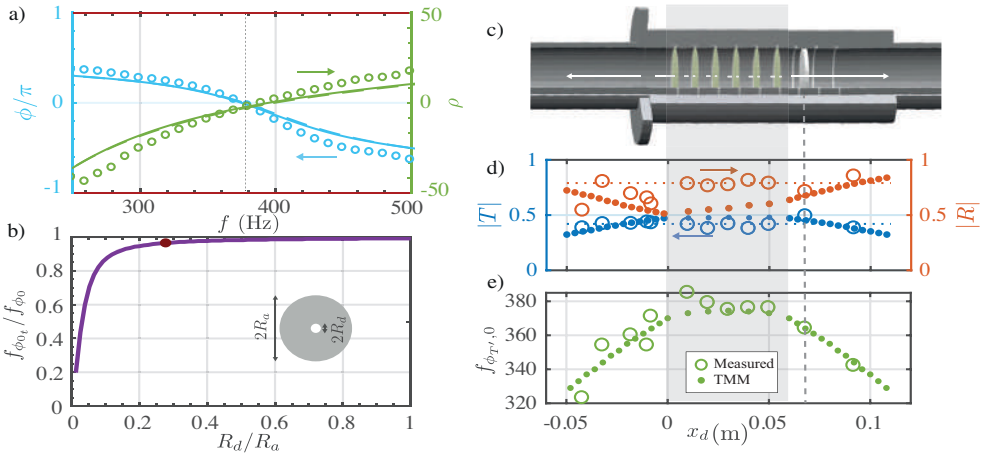


Figure 1: 6 plates metamaterial behavior with an embedded $L_d = 2$ mm thick annular diaphragm ; a) phase of the transmission coefficient (light blue) and real part of the effective dynamic mass density (green color) of the total system (metamaterial alone with an embedded diaphragm of aperture $R_d = 4$ mm). Circle markers, dashed line and solid line correspond respectively to the measurements, the Full-wave simulations and the TMM. b) relative frequency shift (ratio of the zero phase frequency of the total system to the one of the metamaterial alone) versus the diaphragm towaveguide radii ratio, from TMM. d) Transmission (blue color), reflection (red color) coefficients modulus at the zero phase frequency, and e) zero phase frequency values (green) of the total system for several diaphragm positions x_d inside and outside the metamaterial. The dots correspond to the TMM results and the circles to measurements. Dotted red and blue horizontal lines show respectively the measured reflection and transmission values of the 6 plates metamaterial alone at $f_{\phi_{t,0}}$

reflection values of the total system remain equal to the ones of the plate arrangement alone. In the lossless case, wherever the diaphragm along the material is placed, it remains hidden and does not impact neither the transmission nor the reflection. The plate arrangement with an embedded scatterer behaves as an homogeneous and symmetric material in the lossless case. Losses inherent to such a system modify this anomalous hiding behavior. Reflection slightly increases when the diaphragm position is moved away from the metamaterial entrance as illustrated by Fig. 1d-e). The metamaterial also becomes asymmetric in reflection ($R^+ \neq R^-$ whereas $T^+ = T^- = T$)).

The DNZ metamaterial has also an effect outside the metamaterial. The diaphragm can be placed in a unit cell distance from the metamaterial appendicular zones, in the transition layer, without impacting the transmission.

3. Conclusions

This work investigates experimentally, numerically, and theoretically the impact of losses, not avoidable in reality, on the DNZ behavior of a plate-type metamaterials. Even if losses results in a decrease of the transmission through the metamaterial, the non-delayed propagation is robust and has been measured. An hiding zone has also been experimentally shown in the DNZ region.

Acknowledgement

This abstract is based upon work from COST Action DENORMS CA15125, supported by COST (European Cooperation in Science and Technology)

References

[1] F. Bongard, H. Lissek, J.R. Mosig, Acoustic transmission line metamaterial with negative/zero/positive refractive index, *Physical Review B - Condensed Matter and Materials Physics* 82:24–26, 2010.

[2] R. Fleury, A. Alù, Extraordinary sound transmission through density-near-zero ultra-narrow channels, *Physical Review Letters* 111:1–5, 2013.

[3] Y. Gu, Y. Cheng, J. Wang, X. Liu, Controlling sound transmission with density-near-zero acoustic membrane network, *Journal of Applied Physics* 118,2015

[4] B.H. Song, J.S. Bolton, A transfer-matrix approach for estimating the characteristic impedance and wave numbers of limp and rigid porous materials, *The Journal of the Acoustical Society of America* 107: 1131–1152, 2000.

[5] M. Niskanen, J.-P. Grobyn A. Duclos, O. Dazel, J.-C. Le Roux, N. Poulain, T. Huttunen, T. Lähivaara, Deterministic and statistical characterization of rigid frame porous materials from impedance tube measurements, *The Journal of the Acoustical Society of America* 2407, 2017

Unidirectional zero sonic reflection in passive Partity-Time symmetric Willis media

Aurélien Merkel[1*], Vicent Romero-García[2], Jean-Philippe Groby[2], Jensen Li[3], and Johan Christensen[1*]

[1]Department of Physics, Universidad Carlos III de Madrid, Avenidad de la Universidad 30, 28911 Legans (Madrid), Spain.
[2]LAUM UMR-6613 CNRS, Le Mans Université, Avenue Olivier Messiaen, 72085 Le Mans Cedex 9, France.
[3]Department of Physics, The Hong Kong University of Science and Technology, Clear Water Bay, Hong Kong, China.
*corresponding authors, E-mail: amerkel@inst.uc3m.es, johan.christensen@uc3m.es

Abstract

In an effective medium description of acoustic metamaterials, the Willis coupling plays the same role as the bianisotropy in electromagnetism. Willis coupling have not only emerged to obtain physically meaningful effective parameters, but also to describe media presenting asymmetry in reflection. Asymmetries in reflection have also been made possible by considering the Parity-Time symmetry. In this work, we theoretically, in accordance with experimental results, show that a passive Willis media can be mapped onto Parity-Time symmetric systems [1].

1. Introduction

Waves irradiating onto a passive reciprocal medium usually display symmetric transparency in that the transmittance does not depend on the side at which the waves are launched. In contrast, if the elementary building units of the medium involved lack intrinsic inversion symmetry, then the reflectance depends on the side of the slab from which the waves are irradiated. Commonly, for electromagnetic waves, such asymmetric responses are known to occur in bianisotropic media, which are important in applications comprising unidirectional radiation, single-sided light detection, and emission. An analog picture for the case of sound is provided through the cross coupling between strain and velocity in so-called Willis media.

2. Acoustic effective Willis medium

In an one-dimensional, along the z-axis, cylidrincal acoustic waveguide, the effective constitutive matrix $\mathbf{M}_{\mathbf{eff}}$ of a reciprocal Willis media with the time convention $e^{-i\omega t}$ has the following form [2]

$$\frac{\partial}{\partial z}\Pi\begin{pmatrix} P \\ U \end{pmatrix} = i\omega\begin{bmatrix} S\rho_0 c_0/K_{\text{eff}} & \chi \\ -\chi & \rho_{\text{eff}}/(S\rho_0 c_0) \end{bmatrix}\begin{pmatrix} P \\ U \end{pmatrix}, \quad (1)$$

where the Poynting operator is defined by

$$\Pi = \begin{pmatrix} 0 & 1 \\ 1 & 0 \end{pmatrix}. \quad (2)$$

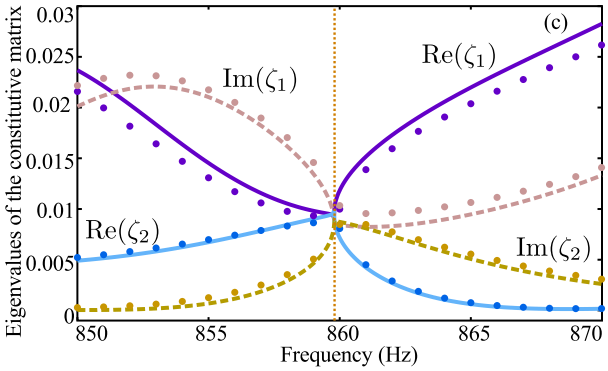


Figure 1: Theoretical (continuous curves) and experimental (dots) eigenvalues $\zeta_{1,2}$ of the constitutive matrix $\mathbf{M}_{\mathbf{eff}}$. The EP where the eigenvalues coalesce is marked with an orange vertical line.

and where $P \equiv P^{'}/(\rho_0 c_0)$ with $P^{'}$ being the acoustic pressure, ρ_0 is the mass density and c_0 is the speed of sound in the background medium, $U \equiv SU^{'}$ with $U^{'}$ being the acoustic velocity and S being the cross-section of the cylindrical waveguide, χ is the Willis coupling parameter, and ρ_{eff}, K_{eff} represent the effective mass density and bulk modulus, respectively.

3. Exceptional point in passive Willis media

Taking the case of acoustic waveguide side-loaded by two quarter-wavelength resonators with two distinct resonance frequencies, the eigenvalues $\zeta_{1,2}$ of the constitutive matrix $\mathbf{M}_{\mathbf{eff}}$ coalesce at approximately 860 Hz, as can be seen in Fig. 1, demonstrating the formation of an exceptional point.

At this exceptional point, the constitutive matrix $\mathbf{M}_{\mathbf{eff}}$ can be mapped onto a conventional 2×2 $\mathcal{PT}$-symmetric system matrix of the form

$$\Upsilon_{PT} = \begin{pmatrix} a + i\Delta\gamma & i\kappa \\ -i\kappa & a - i\Delta\gamma \end{pmatrix}, \quad (3)$$

where a, $\Delta\gamma$ and κ are real numbers. The mapping is performed through a gauge transformation comprising a shift

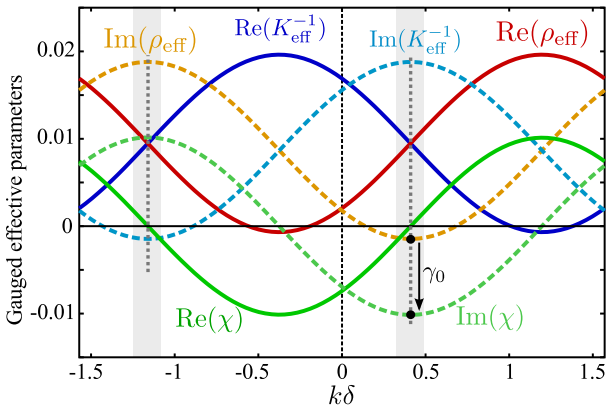


Figure 2: Gauge transformation of Eq. (4) comprising the elements of the constitutive matrix $\mathbf{M}_{\text{eff}}$ at the EP. The gauge transformation maps the constitutive matrix onto a $\mathcal{PT}$-symmetric matrix $\Upsilon_{PT} + i\gamma_0\mathbf{I}$, where $\text{Re}(\chi) = 0$, marked with vertical gray dotted lines in the gray areas

in the $\mathcal{P}$ operation associated an average loss bias, and has the form [3]

$$\begin{aligned}\mathbf{M}_{\text{eff}} &= U_u \begin{pmatrix} a + i\Delta\gamma + i\gamma_0 & i\kappa \\ -i\kappa & a - i\Delta\gamma + i\gamma_0 \end{pmatrix} U_u^{-1}, \\ &= U_u(\Upsilon_{PT} + i\gamma_0\mathbf{I})]U_u^{-1}, \end{aligned} \tag{4}$$

where γ_0 is a gauge biasing the system with an average level of losses, $\mathbf{I}$ is the identity matrix, and U_u is the propagator matrix

$$U_u = \begin{pmatrix} \cos(k\delta) & i\sin(k\delta) \\ i\sin(k\delta) & \cos(k\delta) \end{pmatrix}. \tag{5}$$

The propagator matrix is an unitary gauge transformation, which maps ideal $\mathcal{PT}$-symmetric systems such as γ_{PT} of symmetric $\mathcal{P}$ operation, that is, $z \to -z$, which is a mirror operation at the center of the cell onto shifted $\mathcal{PT}$-symmetric systems accommodating the generalized $\mathcal{P}$ operation $z \to 2\delta - z$, where δ is the distance to center of the cell. This gauge transformation is exposed in Fig. 2.

4. Discussion

This exceptional point translates into an unidirectional reflectionless propagation, which is of primary importance for sound absorption because, if combined with coherent perfect absorption, it results in an unidirectional perfect absorber. Further, our present findings can lead to a deeper insight into the unidirectional invisibility phenomena, altogether showing how the Willis coupling broadens the possibilities of embracing both worlds of acoustic metamaterials and $\mathcal{PT}$ symmetry physics at once to achieve unprecedented control of sound and vibrations.

Acknowledgement

J.C. acknowledges the support from the European Research Council (ERC) through the Starting Grant No. 714577 PHONOMETA and from the MINECO through a Ramón y Cajal grant (Grant No. RYC-2015-17156). J.-P. Groby and V. Romero García gratefully acknowledge the support from the ANR Project METAUDIBLE No. ANR-13-BS09-0003 co-founded by ANR and FRAE and the support from the RFI Le Mans Acoustique (Région Pays de la Loire) PavNat project. This article is based upon work from COST Action DENORMS CA15125, supported by COST (European Cooperation in Science and Technology). JL would like to acknowledge support from Research Grants Council of Hong Kong (Project number 16302218).

References

[1] Aurélien Merkel, Vicent Romero-García, Jean-Philippe Groby, Jensen Li and Johan Christensen Unidirectional zero sonic reflection in passive $\mathcal{PT}$-symmetric Willis media, *Phys. Rev. B* 98: 201102(R), 2018.

[2] Caleb F. Sieck, Andrea Alù, and Michael R. Haberman Origins of Willis coupling and acoustic bianisotropy in acoustic metamaterials through source-driven homogenization, *Phys. Rev. B* 96: 104303, 2017.

[3] James Gear, Yong Sun, Shiyi Xiao, Liwen Zhang, Richard Fitzgerald, Stefan Rotter, Hong Chen, and Jensen Li, Unidirectional zero reflection as gauged parity-time symmetry, *New J. Phys.* 19: 123041, 2017.

Acoustic cloaking and self-cloaking inside ducts using liners

Maaz Farooqui*, Yves Aurégan, Vincent Pagneux

Laboratoire d'Acoustique de l'Université du Mans,
Centre National de la Recherche Scientifique (CNRS), Le Mans Université,
Avenue Olivier Messiaen, 72085 Le Mans Cedex 9, France
*corresponding author, E-mail: maaz.farooqui@univ-lemans.fr

Abstract

Acoustic cloaking for backscattering reduction is proposed inside ducts in the audible range where plane waves are bended around the object using liner surface modes. It is shown that a slowly varying resonant liner forms a dumb zone in which an object of any shape can be rendered acoustically invisible for a wide range of frequencies. The cloaking band is a function of the impedance and height of the obstacle relative to the duct. For smooth shaped obstacles, there is an ability of the object to help hide itself, which increases the cloaking frequency band (self-cloaking).

1. Introduction

Rendering an obstacle hidden from the scattering of electromagnetic, acoustic or elastic waves has recently been a subject of particular interest because of its promising applications [1]. However, its manufacturing and broadband performance is still a challenging task. Recently, cloaking an obstacle located inside a waveguide was shown in the case of microwaves [2] and it has also be widely applied in spoof plasmon waveguide [3]. In this work, we first show that, by using a smooth axial variation of the wall impedance, it is possible to create a zone of silence in a duct. The purely reactive impedance gradually transforms a plane acoustic wave in the duct into an acoustic surface wave. This results in a bending of the acoustic wave towards the liner with a slower effective propagation velocity. In addition, we show that an obstacle with a smooth cross section variation can be cloaked even if it is outside the silence zone. This effect is called self-cloaking [4].

2. Cloaking in ducts

We consider the sound propagation in a two dimensional channel, see Fig. 1. The lower wall is rigid while the upper wall is described by a varying admittance $Y(x)$. When the distances are non-dimensioned by the height of the channel H, the Helmholtz equation, governing the propagation of the acoustic pressure p, is:

$$\Delta p + k^2 p = 0 \tag{1}$$

where ω is the frequency and c_0 is the sound velocity and $k = \omega H/c_0$ is the Helmholtz number. The boundary conditions are $\partial_y p = 0$ for $y = 0$ and $\partial_y p = Yp$ for $y = 1$. For a uniform admittance Y, the solution is searched under the form $p = A\cosh(\alpha y)\exp(\mathrm{i}(-\omega t+\beta x))$ where $\alpha^2 = \beta^2 - k^2$ which leads to the dispersion relation $Y = \alpha\tanh(\alpha)$. For a rigid wall, $Y = 0$, at low frequencies, only the plane wave can propagate thus $\alpha = 0$ when $k < \pi$ (Fig. 2(a)). If the admittance is positive and, is slowly varying compared to the sound wavelength, the local value of α increases as Y increases. It means that the wave is more and more concentrated against the wall, see Fig. 2(b). A silence zone is then created near the wall opposite to the admittance. In order to verify the cloaking efficiency with a smooth scatterer, Fig. 2(d) depicts the reflection coefficient $|R|$ for a smooth elliptical obstacle. The cloaking band in this case is from $\pi/4 \leqslant k \leqslant \pi/2$. The admittance only (green) curve corresponds to a lined duct and the cloaked (red) corresponds to lined duct with an obstacle.

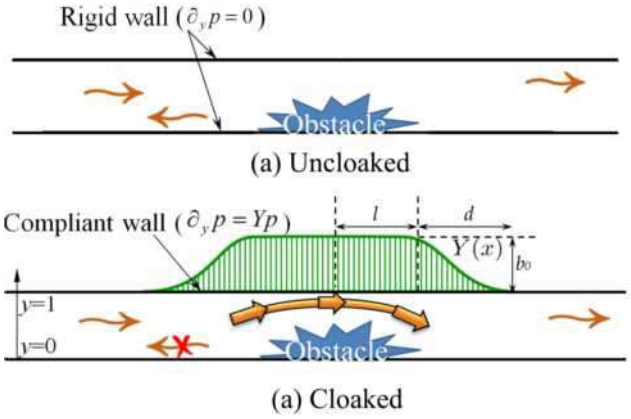


Figure 1: Schematic description of an obstacle in a duct with admittance (a) Uncloaked (hard duct), (b) Cloaked (duct with liner)

One way to realize a liner is by using small closed tubes whose lossless admittance can be written as $Y(x,k) = k\tan[kb(x)]$. When $kb \ll 1$, the admittance can be approximated by $Y = k^2 b$ and the phase velocity of the wave is given by $c_\phi = (1+b)^{-1/2}$ implying that the wave velocity is reduced compared to sound velocity. When the frequency k approaches the first resonant frequency of the tubes given by $k_r b = \pi/2$, the admittance and α goes to ∞. Thus, for frequencies slightly less than k_r, the wave decreases exponentially from the wall being transformed into a surface

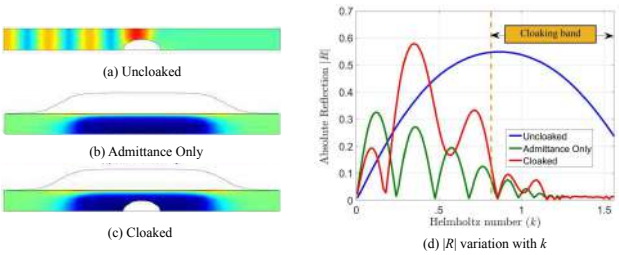


Figure 2: Response of a smooth elliptical obstacle (height=0.5, width=1) with admittance parameters ($l = 6$ and $d = 2$), Absolute pressure field at k=1.38 for (a) Uncloaked, (b) Admittance only and (c) Cloaked case, (d) Reflection coefficient $|R|$ for uncloaked (blue), Admittance only (green) and cloaked (red) cases

wave. Near k_r, the phase velocity and the effective wavelength of the wave goes linearly to zero. The propagation is then highly dispersive. The admittance profile is taken under the form $b(x) = \frac{b_0}{2}\left[\tanh\left(\frac{x+l}{d}\right) - \tanh\left(\frac{x-l}{d}\right)\right]$, where the maximum tube height has been arbitrarily fixed to $b_0 = 1$ and the two parameters l and d allow to tune separately the length of the admittance zone and maximal slope of the axial change in admittance.

3. Self-Cloaking in ducts

The parameter α gives the exponential decay of the pressure from the wall. The bending of the wave towards the liner is controlled by this parameter. The height of the channel H_0 between the obstacle and the liner, decreases with increasing height of the obstacle. This region follows a local dispersion relation of the form $k\tan(kb) = \alpha\tanh(\alpha H_0)$. The decrease in H_0, increases the α and therefore the presence of the obstacle helps to concentrate (push) the wave towards the compliant wall. This effect is called self-cloaking and it improves the efficiency of the cloaking for smoothly varying obstacle. The shape of the obstacle in this case is chosen to be: $h(x) = \frac{h_0}{2}(1 + \cos(\frac{\pi x}{L}))$. The results are shown in Fig. 3. An almost complete reflection is obtained in the uncloaked case at low frequencies ($k \simeq 0.25$) as seen in Fig. 3(a). For such a low frequency, the admittance variation alone is unable to generate a significant dumb/shadow zone. But when a smooth obstacle is added to the admittance (Fig. 3(b)), the reflected energy $|R|^2$ decreases drastically for the entire frequency band $0.25 < k < \pi/2$ demonstrating the self-cloaking effect. The cloaking band is then considerably increased compared to sharp obstacles where this self-cloaking effect cannot be seen due to the reflection induced by any sudden change in the geometry.

4. Conclusion

In this work, we report a broadband acoustic cloak to suppress backscattering inside ducts using liner surface modes. By using a smooth variation in wall admittance of a duct which does not produce reflection, it is possible to create a silent zone in which acoustic waves can not penetrate. For

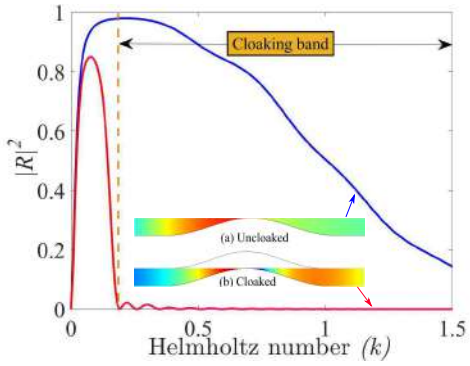


Figure 3: Visualization of self-cloaking phenomenon for a smooth cosine obstacle ($h_0 = 0.98$, $b_0 = 1$, $L = 8.25$), Real part of pressure fields at k=0.25 for, (a) Uncloaked case, (b) Self-cloaked duct. (d)$|R^2|$ for uncloaked (blue) and self-cloaked (red) cases.

an object which is half the height of the duct and with a liner made of tubes of the same height as the duct, this effect occurs at frequencies between the resonance frequency f_r of the liner and $2f_r/3$, which is a wide frequency band compared to other conventional cloaking techniques. When the object is smooth enough, the presence of the object broadens the cloaking bandwidth which is termed self-cloaking. The novelty of this cloaking, made simply from a resonant wall, contrasts with other cloaking techniques that are more complex to perform and lack broadband performance.

Acknowledgement

This work was supported by the "Agence Nationale de la Recherche" international project FlowMatAc No. ANR-15-CE22-0016-01.

References

[1] D. Schurig, J. Mock, B. Justice, S. A. Cummer, J. B. Pendry, A. Starr, and D. Smith, "Metamaterial electromagnetic cloak at microwave frequencies," *Science*, vol. 314, no. 5801, pp. 977–980, 2006.

[2] C. Gu, Y. Xu, S. Li, W. Lu, J. Li, H. Chen, and B. Hou, "A broadband polarization-insensitive cloak based on mode conversion," *Scientific reports*, vol. 5, p. 12106, 2015.

[3] A. Pors, E. Moreno, L. Martin-Moreno, J. B. Pendry, and F. J. Garcia-Vidal, "Localized spoof plasmons arise while texturing closed surfaces," *Physical review letters*, vol. 108, no. 22, p. 223905, 2012.

[4] M. Farooqui, Y. Aurégan, and V. Pagneux, "Using liner surface modes in acoustic ducts to make obstacles reflectionless," *Manuscript submitted to Scientific Reports*, 2019.

Experimental observation of topological edge waves in a two-dimensional Su-Schrieffer-Heeger acoustic network

Li-Yang Zheng[1], Vassos Achilleos[1], Olivier Richoux[1], Georgios Theocharis[1], and Vincent Pagneux[1]

[1]LAUM, UMR-CNRS 6613, Le Mans Université, Av. O. Messiaen, 72085 Le Mans, France
*corresponding author, E-mail: liyang.zheng.etu@univ-lemans.fr

Abstract

In this work, we propose an acoustic realization of two-dimensional Su-Schrieffer-Heeger model by constructing a network structure for sound wave, and we observe experimentally the existence of topological edge waves. A tight-binding model is used to describe the acoustic wave dynamics in the network, and topological edge waves are predicted on the boundary of the network. Moreover, we experimentally confirm the existence of topological edge wave.And a good agreement is found between the experiment and simulation results. The observation of topological edge waves in the acoustic network provides a flexible platform for the study of topological properties of sound waves.

1. Introduction

Recently, the study of novel topological phase with a zero Berry curvature has been attracted a lot of attention in different two-dementional (2D) systems [1, 2, 3]. In such systems, a 2D Su-Schrieffer-Heeger (SSH) model is proposed by extending the one-dementional SSH chain of identical atoms with alternating strengths of bonds in both $x-$ and $y-$directions. Different from most topologically nontrivial systems, which require a non-vanishing Berry curvature, the existence of topological phase of a 2D SSH model exhibits a fractional wave polarization characterized by the 2D Zak phase [1]. In this work, we propose an acoustic realization of the 2D SSH model, and experimental investigate the topological edge waves.

2. Results

The tight-binding model of a two-dimensional (2D) Su$-$Schrieffer$-$Heeger (SSH) model is depicted in Fig. 1(a), where identical mass points are arranged in a square lattice (lattice constant $2L$) with alternating coupling terms s and t in both $x-$ and $y-$directions. The unit cell of the 2D SSH model containing four mass points (marked as α, β, γ and δ) is labelled by the black-dashed box in Fig. 1(a).

2.1. Model

To realize the 2D SSH model in experiment, two kinds of rigid square blocks of width $L_1 = 0.01$ m, $L_2 = 0.013$ m, and height $\mathrm{H}_2 = 0.03$ m are fabricated as shown in Fig. 1(b). A plate of thickness $\mathrm{H}_1 = 0.02$ m is applied as the substrate to hold the blocks in a square lattice. By placing a same size of glass plate (thickness $\mathrm{H}_1 = 0.02$ m) on the top of the blocks, i. e., Fig. 1(c), a 2D experimental sample for sound wave is constructed. A close view of the unit cell of the experimental structure (lattice constant $2L = 0.025$ m) is illustrated in Fig. 1(d) by the white-dashed box. It can be seen that the block of size L_2 placed in the center of the unit cell is surrounded by 8 blocks of size L_1. This leads to two kinds of air channels of the width S_1 (orange bonds) and S_2 (blue bonds) between blocks, and four junctions connecting the channels as marked by α, β, γ and δ in Fig. 1(d). By extending the unit cell into a xy plan, e. g., 4 m $\times$ 2 m in experiment, a 2D acoustic network structure for sound wave is completed. This network is an acoustic realization of the 2D SSH model due to the fact that the acoustic pressure on the junctions interact with those on its neighboring junctions by alternating widths of channels in the $x-$ and $y-$directions. Therefore, the couplings of pressures between neighboring junctions can be tuned by the widths of air channels S_1 and S_2, which also determine the existence of nontrivial topological phase of the network.

2.2. Dispersion curves

For the experimental network, the values of S_1 and S_2 are fixed to be $S_1 = 0.025$ m, and $S_2 = 0.01$ m. Figure 2(a) shows the dispersion relation of the same parameters. Four propagating branches (blue curves) and two full gaps around 550 Hz and 900 Hz can be found. For comparison, we implement the COMSOL calculation by considering the same unit cell of the network, and the corresponding band structure (red curves) is shown in Fig. 2(b). A good agreement can be achieved between the two cases.

As had been reported in previous 2D SSH model, in the acoustic network, when $S_1 > S_2$, the network exhibits nontrivial topological phase and support topological edge states on the boundaries. To see the existence of edge waves, we investigate a super cell containing 8 unit cells along the y axis,and the edges of the super cell are set to be open, namely the pressure at the opened channels is zero. The dispersion curves from theory for the super cell is shown in Figs. 2(c). Two edge branches marked as black curves

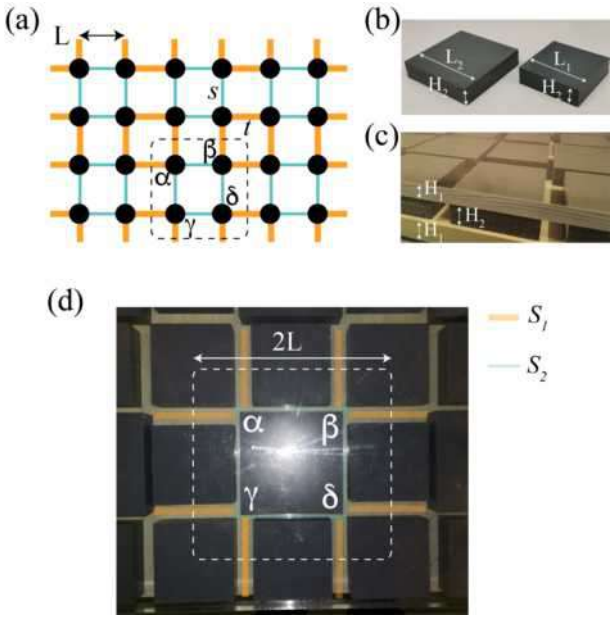


Figure 1: (a) Schematic presentationsof the two-dimensional (2D) Su-Schrieffer-Heeger (SSH) model. (b) Two building blocks for the 2D acoustic SSH network. (c) Side view of the experimental sample. (d) A close view of the unit cell of the acoustic SSH network.

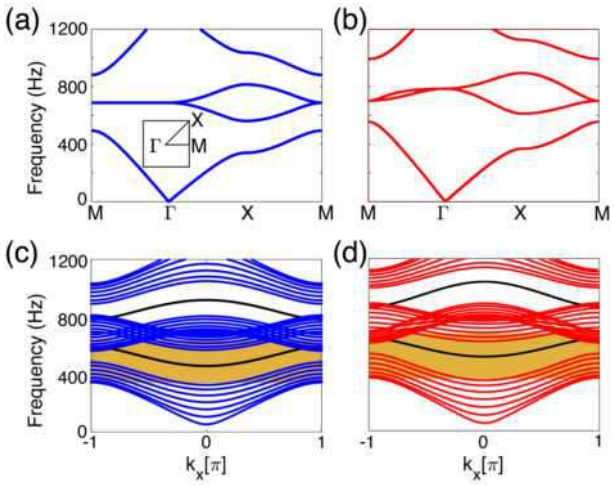


Figure 2: Dispersion curves of the unit cell from (a) tight-binding model, (b) COMSOL calculation. Dispersion curves of edge waves from (c) tight-binding model, (d) COMSOL calculation.

can be observed. For the sake of comparison, the dispersion curves obtained by COMSOL is shown in (e), where two edge wave branches also present in the bulk gaps.

2.3. Experiment

The schematic illustration of the experimental sample and set-up are shown in Fig. 3(a). First of all, we experimentally observe the band gap by putting the source at position $\mathcal{A}$ as marked in Fig. 3(a), and a sweep signal from 300 Hz to 800 Hz is generated from the source. We focus on the line $x = 24$ (red line), and measure the pressures of all the junctions on the line. The measured amplitude of the signal (in dB) is plotted in Fig. 3(c). The results of COMSOL by simulating the same experimental process is shown in Fig. 3(d). It can be see that in both cases that there is a bulk gap around the frequency range $\sim 540 - 620$ Hz. However, sound waves are observed to be localized near the edge $y < 2$, suggesting the the existence of bulk gap and the localization of sound pressure on the edges.

To further confirm the existence of edge waves, we put the source at position $\mathcal{B}$ as marked in Fig. 3(a), and a harmonic signal of 570 Hz is sent from the source. We focus on three lines $x = 8$, $x = 18$, and $x = 24$, noted by green, blue and red lines, respectively. And he pressures of all the junctions on those lines are measured. Figure 3(b) shows the pressure field distributions (absolute value) of each line. It can be seen sound energy is localized on the edges but vanished fast in the bulk, exhibiting the edge wave property. Figure 3(e) shows the edge wave profile a into the bulk obtained by measurement. It has a excellent agreement with Fig. 3(f) which is obtained by COMSOL calculation.

3. Conclusions

In this work, a 2D SSH model is realized by an acoustic network structure, and the existence of topological edge waves is experimentally observed. The study of this work can pave the way for the study of the experimental observation of higher-order topological modes [4] in acoustic systems.

Acknowledgement

This work has been funded by the APAMAS, Sice CIty LMac, and the Acoustic Hub projects.

References

[1] F. Liu, K. Wakabayashi, Novel topological phase with a zero Berry curvature, *Phys. Rev. Lett.* 118, 076803, 2017.

[2] F. Liu, H.-Y. Deng, K. Wakabayashi, *Phys. Rev. B*, 97, 035442, 2018.

[3] S. Liu, W. Gao, Q. Zhang, S. Ma, L. Zhang, C. Liu, Y. J. Xiang, T. J. Cui, and S. Zhang, *Research*, vol. 2019, Article ID 8609875, 8 pages, 2019.

[4] H. Xue, Y. Yang, F.Gao, Y. Chong, B. Zhang, Acoustic higher-order topological insulator on a kagome lattice, *Nature Materials*, volume 18, pages:108112, 2019.

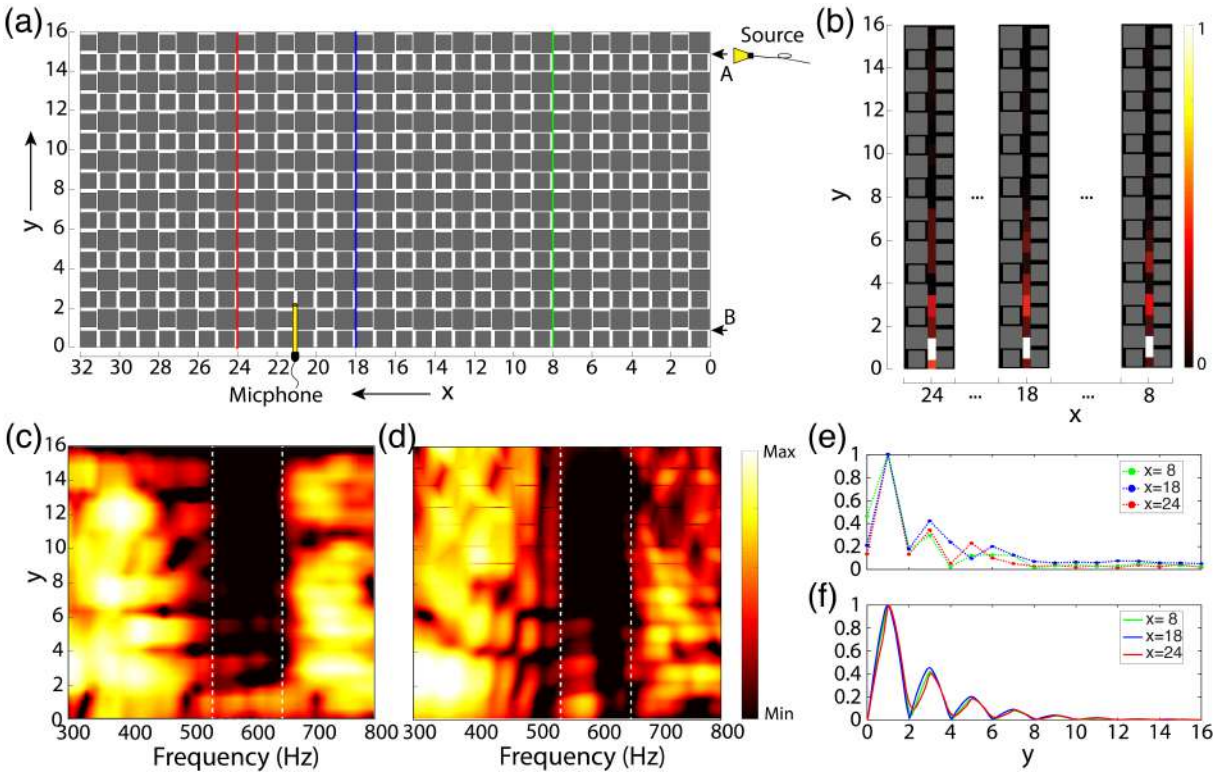


Figure 3: (a) Schematic presentations of sample and set-up. (b) Pressure field distributions of sound wave at 570 Hz for the three lines marked by colors in (a). Measurement of band gap in (c) from measurement, in (d) from COMSOL simulation. The edge wave profiles of 570 Hz from (e) measurement and (f) COMSOL.

Acoustic antennas based on the topological insulators

Zhiwang Zhang[1,2], Ye Tian[1], Ying Cheng[1,*], Xiaojun Liu[1,*] and Johan Christensen[2,*]

[1] Department of Physics, Collaborative Innovation Center of Advanced Microstructures, Nanjing University, Nanjing 210093, China
[2] Universidad Carlos III de Madrid, ES-28916 Leganés, Madrid, Spain
*corresponding author, E-mail: chengying@nju.edu.cn; liuxiaojun@nju.edu.cn;johan.christensen@uc3m.es

Abstract

Realizing directional acoustic signal transmittance and reception robust against surrounding noise and competing signals is crucial in many areas such as communication and detection for medical and industrial purposes. Here we show how topological acoustic valley transport can be designed to enable a unique beamforming mechanism that renders a super-directive needle-like sound radiation and reception pattern, which offers new ways to control sound with improved performance and functionalities that are highly desirable for versatile applications.

1. Introduction

For many animals, like dolphins, can produce directional acoustic wave beams of about 16° in width for detecting and tracking prey with high resolution in a blind and noisy environment [1-3]. Unlike dolphins, the function of human's acoustic communication system is given by the conventional outer ear and mouth structures, which are based on the acoustic horn concept rather than an acoustic lens, thus bringing forth sound emission/reception of poor directivity to/from almost every direction. In addition, duplex-devices both with the ability of emitting and receiving signals remain a great challenge in both physics and engineering. Therefore, there is a great need to develop a novel scheme and functional devices for super-directional duplex acoustic communication that can overcome the limitations of current acoustic technologies.

On the other hand, "topological acoustics" has attracted considerable attention over the past two years due to the fascinating quantum-like effects in acoustic systems [4-13], which originates from studies of condensed-matter states [14, 15]. Here we extend the concept of topological order to acoustic communication, and report a super-directional topological acoustic antenna (TAA) for audible sound based on VHTIs.

2. Results

The valley-polarized edge states observed above originate inherently from valley-projection, which guarantees reflection-free out-coupling from the topological interface into the free-space [16]. We begin by demonstrating the directional emission into free-space of out-coupled edge states along both positive- and negative-type interfaces in TAAs. As shown in Fig. 4, the direction of the outgoing beam into air depends on the type of valley (K or K′) from which the edge state is projected. Hence, sound waves that are launched from left to right along the negative-type interface are projected from the K valley (Fig. 4A), and conversely along the positive-type interface are projected from the K′ valley (Fig. 4D). To illustrate the refraction of the radiated beam, we draw the equifrequency curves in free-space (black dashed circle in Fig. 4A/4D) and the BZ (black solid regular hexagon in Fig. 4A/4D) on a scale that represents the relative magnitudes of the wavevectors of the incident and refracted waves. By matching the parallel component of the incident wavevector $\boldsymbol{K}$ on to the equifrequency curve of free-space, one is able to find the propagation direction of the radiated beam. The theoretical refraction angle $\theta^{-}_{\text{theory}}$ (for the negative-type interface) can be quantitatively determined by the phase-matching condition $\boldsymbol{k}\cdot\boldsymbol{e}_{\text{term}}=\boldsymbol{K}\cdot\boldsymbol{e}_{\text{term}}$,ultimately giving rise to a refraction angle. Likewise, at the same frequency, analytically we calculate the refraction angle for the positive-type interface TAA shown in Fig. 4D to be $\theta^{+}_{\text{theory}}=7.47°$. In order to verify this analysis, we scanned the far-field radiation pattern within an angular range as shown in Fig. 4, both by means of numerical simulations and measurements. We obtain, for the TAA having the negative-type interface, refraction angles as predicted $\theta^{-}_{\text{sim}}=-67.86°$ and measured $\theta^{-}_{\text{exp}}=-69°$shown as seen in Fig. 4B. With the positive-type interface we obtain: $\theta^{+}_{\text{sim}}=7.74°$ and $\theta^{+}_{\text{exp}}=6°$, shown in Fig. 4E. Additionally, as shown in the insets of these figures, we measure the pressure signals in the time-domain, in each case, both refraction angles $\theta^{+/-}_{\text{exp}}$ are considered, -69° and 6°. These results show that the super-directional out-coupled edge states indeed obey the valley-projected selection rule with time, such that the TAA with the negative (positive)-type interface suppresses sound refraction with positive (negative) angles. Lastly, as illustrated in Fig. 4C and Fig. 4F through the experimentally observed far-field energy spectra, we emphasize that the proposed acoustic antenna functions in the entire topological band gap spanning between 8.30 – 9.31 kHz.

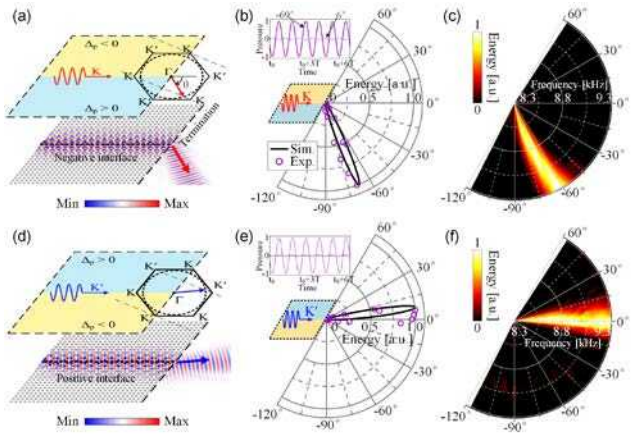


Figure 2: Super-directional sound radiation by out-coupling of valley-polarized edge states from the TAA. (A) *k*-space analysis on the out-coupling of K projected edge states along the negative-type (zigzag) interface. Black solid hexagon represents the 1st BZ and the black dashed circle shows the dispersion in air. Bottom panel: the simulated distribution of pressure fields at the frequency f = 8.66 kHz. (B) Simulated and measured far-field pattern with normalized energy emerging the negative-type interface at f = 8.66 kHz. Inset: pressure signals in the time-domain measured at -69° and 6°. T=1/f is the time period of sound wave. (C) Experimentally detected spectral relation between the acoustical energy and the directional angle within the entire topological band gap. (D to F) Corresponding analysis on the out-coupling of K′ projected edge state along the positive-type (zigzag) interface.

3. Conclusions

To sum up, theoretically and experimentally we proposed valley-Hall topological insulators acting efficiently as sound transmitting and receiving antennas, of which the structure is based on a Kagome lattice made of epoxy resin rods. Based on such platform, we have experimentally put forward a prototype topological acoustic antenna that is capable of out-coupling and sustaining valley-polarized edge states permitting energy efficient communication. The proposed duplex antenna not only supports super-directive needle-like sound radiation with less than a 10° beamwidth, but also achieves anti-interference sound reception in various acoustic environments while being immune to white noise. This topological acoustic antenna provides the unique possibility to advance communication technologies such and hands-free smartphones and noise-immune hearing aids, but also to improve sonar applications with highly directional collimated beams and underwater communications at efficient energy levels.

Acknowledgements

This work was supported by National Key R&D Program of China (2017YFA0303702), NSFC (11674172, 11574148, and 11474162), Jiangsu Provincial NSF (BK20160018), the Fundamental Research Funds for the Central Universities (020414380001) and Nanjing University Innovation and Creative Program for PhD candidate (CXCY17-11). J.C. acknowledges the support from the European Research Council (ERC) through the Starting Grant 714577 PHONOMETA and from the MINECO through a Ramón y Cajal grant (Grant No. RYC-2015-17156).

References

[1] W. A. Yost and G. Gourevitch, *Directional Hearing* (Springer-Verlag New York Inc., New York, 1987).
[2] W. W. L. Au, *The Sonar of Dolphins* (Springer-Verlag New York, Inc., New York, 1993).
[3] Y. Zhang, Z. Song, X. Wang, W. Cao, and W. W. L. Au, Phys. Rev. Appl. **8**, 064002 (2017).
[4] Z. Yang, F. Gao, X. Shi, X. Lin, Z. Gao, Y. Chong, and B. Zhang, Phys. Rev. Lett. **114**, 114301 (2015).
[5] A. B. Khanikaev, R. Fleury, S. H. Mousavi, and A. Alù, Nat. Commun. **6**, 8260 (2015).
[6] R. Fleury, A. B. Khanikaev, and A. Alu, Nat. Commun. **7**, 11744 (2016).
[7] C. He, Z. Li, X. Ni, X.-C. Sun, S.-Y. Yu, M.-H. Lu, X.-P. Liu, and Y.-F. Chen, Appl. Phys. Lett. **108**, 031904 (2016).
[8] Z. Yang and B. Zhang, Phys. Rev. Lett. **117**, 224301 (2016).
[9] Z. Zhang, Q. Wei, Y. Cheng, T. Zhang, D. Wu, and X. Liu, Phys. Rev. Lett. **118**, 084303 (2017).
[10] Q. Wei, Y. Tian, S. Y. Zuo, Y. Cheng, and X. J. Liu, Phys. Rev. B **95**, 9, 094305 (2017).
[11] J. Lu, C. Qiu, L. Ye, X. Fan, M. Ke, F. Zhang, and Z. Liu, Nat. Phys. **13**, 369 (2017).
[12] Z. Zhang, Y. Tian, Y. Cheng, X. Liu, and J. Christensen, Phy. Rev. B **96**, 241306 (2017).
[13] Z. Zhang, Y. Tian, Y. Cheng, Q. Wei, X. Liu, and J. Christensen, Phys. Rev. Appl. **9**, 034032 (2018).
[14] D. Hsieh, D. Qian, L. Wray, Y. Xia, Y. S. Hor, R. J. Cava, and M. Z. Hasan, Nature **452**, 970 (2008).
[15] Z. Qiao, J. Jung, Q. Niu, and A. H. MacDonald, Nano Lett. **11**, 3453 (2011).
[16] M. Tzuhsuan and S. Gennady, New J. Phys. **18**, 025012 (2016).

Effective Decay Coefficient of Low Frequency Sound in Phononic Crystals with Viscous Background

Martin Ibarias[1], Jesús Arriaga[1*], and Arkadii Krokhin[2]

[1]Instituto de Física, Benemérita Universidad Autónoma de Puebla, Puebla, Mexico
[2] Department of Physics, University of North Texas, Denton, Texas, USA
*corresponding author, E-mail: arriaga@ifuap.buap.mx

Abstract

The decay coefficient of sound propagating through a phononic crystal of solid rods in a viscous fluid is calculated in the low-frequency limit for arbitrary Bravais lattice and arbitrary cross-section of the rods. The decay coefficient exhibits anisotropy and anomalous frequency dependence. Strong enhancement of losses in a phononic crystal is due to viscous boundary layers formed near each solid scatterer.

1. Introduction

Exponential dissipative decay of sound amplitude ($\sim e^{-\gamma x}$) in pure water is weak. For a plane wave the decay coefficient $\gamma_0 = \frac{\omega^2(4\eta/3+\xi)}{2\rho_0 c_0^3}$ grows with frequency as ω^2 and it is linear over the viscosity coefficients η and ξ. Even for frequencies, in the region around 100 kHz, the propagation length $1/\gamma_0$ is about several kilometers. Such low dissipative losses can be safely neglected. However, near a solid boundary a viscous layer of thickness $\delta = \sqrt{2\eta/(\omega\rho_0)}$ is formed. Within this layer the acoustic energy dissipates much faster than in a free fluid. Each reflection from solid-fluid interface is accompanied by energy losses that scale as $\sqrt{\eta\omega}$ [1]. Multiple reflections strongly increase the energy losses. Thus, a phononic crystal is a dissipative metamaterial. Since the viscous losses in many cases is the main factor that limits the efficiency of acoustic device, it is of principal interest to develop a feasible method for calculation of the decay coefficient γ or the effective viscosity of phononic crystals.

In solid-solid phononic crystal dissipation can be described phenomenologically by introducing imaginary part of elastic moduli of the constituents. This approach was developed in Ref. 2. A microscopic approach based on Navier-Stokes equation was proposed in Ref. 3. Scattering of sound by a homogenized cluster of solid circular cylinders arranged in a square lattice was calculated and the effect of viscosity on scattering cross-section was analyzed [3].

Here we propose a method of calculation of the decay coefficient $\gamma = \dot{Q}/2(c_{eff}E)$ in solid-fluid phononic crystal assuming that the dissipation occurs only in the viscous fluid. Here c_{eff} is the effective speed of sound in homogenized phononic crystal. In the low-frequency limit the dispersion of sound is linear, $\omega = c_{eff}k$, with $c_{eff} = c_{eff}(\mathbf{n})$ being independent of ω but in lattices with low rotational symmetry it depends on the direction of propagation $\mathbf{n}$[4]. Acoustic energy E is obtained by integration of $\rho V^2/2$ over the area of the unit cell $A_c = A_0 + A_a$, containing viscous fluid ($\rho = \rho_0$) and solid rod ($\rho = \rho_a$)

$$E = \frac{\rho_0}{2}\int_{A_0} V^2(\mathbf{r})d\mathbf{r} + \frac{\rho_a}{2}\int_{A_a} V^2(\mathbf{r})d\mathbf{r}\,. \quad (1)$$

The power dissipated at a given point in fluid is defined by the gradients of velocity. If the viscous layer is well localized near the solid rod, i.e. $\delta \ll d$, where d is the lattice period, the following approximation is valid for the energy $\dot{Q}$ dissipated per unit length within the unit cell [5]

$$\dot{Q} = \frac{1}{2\sqrt{2}}\sqrt{\rho_0\eta\omega}\oint_L V^2(\mathbf{r})dl \quad (2)$$

Here the integration runs over the contour L which is the circumference of the solid rod. The dissipated energy in Eq. (1) is calculated in the lowest approximation over low viscosity η, therefore the velocity $\mathbf{V}(\mathbf{r})$ in Eqs. (1) and (2) is obtained from the dynamical equation for *inviscid* fluid. The latter is the Euler equation for pressure $p(\mathbf{r})$. The velocity is expressed through the scalar quantity $p(\mathbf{r})$ as $\mathbf{V}(\mathbf{r}) = \frac{\nabla p}{i\omega\rho(\mathbf{r})}$. The pressure is expanded over the plane waves and in the low-frequency limit the coefficients of this expansion can be calculated [4]. Calculating the integrals in Eq. (1) and (2) in the limit $\omega \ll c_{eff}/d$ (i.e. below the band gap) the following result was obtained for the decay coefficient:

$$\gamma(\mathbf{n}) = \frac{L_0\sqrt{\rho_0\eta\omega}}{2A_c\bar{\rho}c_{eff}(\mathbf{n})}\frac{M(\mathbf{n})}{N(\mathbf{n})}. \quad (3)$$

Here L_0 is the length of the contour L, $\bar{\rho} = f\rho_a + (1-f)\rho_0$, and f is the filling fraction of the rods. The quantities $M(\mathbf{n})$ and $N(\mathbf{n})$ are represented by series over the reciprocal lattice vectors $\mathbf{G}$

$$M(\mathbf{n}) = \rho_{ij}^{-1}\rho_{il}^{-1}n_j n_l + 2\rho_{ij}^{-1}n_j n_l\sum_{\mathbf{G}\neq 0}L^*(\mathbf{G})[\nu(\mathbf{G})\delta_{il} - a_{il}(\mathbf{G})] + n_j n_l\sum_{\mathbf{G},\mathbf{G}'\neq 0}L^*(\mathbf{G}+\mathbf{G}')\big[\nu(\mathbf{G})\delta_{ij} - a_{ij}(\mathbf{G})\big][\nu(\mathbf{G}')\delta_{il} - a_{il}(\mathbf{G}')], \quad (4)$$

$$N(\mathbf{n}) = \rho_{ij}^{-1}\rho_{il}^{-1}n_j n_l + 2\rho_{ij}^{-1}n_j n_l \frac{\rho_a-\rho_0}{\bar{\rho}}\sum_{\mathbf{G}\neq 0} F^*(\mathbf{G})[\nu(\mathbf{G})\delta_{il} - a_{il}(\mathbf{G})] + n_j n_l \frac{\rho_a-\rho_0}{\bar{\rho}}\sum_{\mathbf{G},\mathbf{G}'\neq 0} F^*(\mathbf{G}+\mathbf{G}')\big[\nu(\mathbf{G})\delta_{ij} - a_{ij}(\mathbf{G})\big][\nu(\mathbf{G}')\delta_{il} - a_{il}(\mathbf{G}')]. \quad (5)$$

Here $\rho_{ij}^{-1}$is the tensor of the inverse effective mass

$$\rho_{ij}^{-1} = \bar{\nu}\,\delta_{ij} - \sum_{\mathbf{G},\mathbf{G}'\neq 0} G_i G'_j \nu(\mathbf{G})\nu(-\mathbf{G}')[\mathbf{G}\cdot\mathbf{G}'\nu(\mathbf{G}-\mathbf{G}')]^{-1}, \quad (6)$$

$\nu(\mathbf{G})$ are the Fourier coefficients in the expansion of the periodic function $\rho^{-1}(\mathbf{r})$, $\bar{\nu} = \frac{f}{\rho_a} + \frac{1-f}{\rho_0}$, and the matrix

$$a_{ij}(\mathbf{G}) = \sum_{\mathbf{G}',\mathbf{G}''\neq 0} G'_i G''_j \nu(\mathbf{G}-\mathbf{G}')\nu(\mathbf{G}'')[\mathbf{G}'\cdot\mathbf{G}''\nu(\mathbf{G}'-\mathbf{G}'')]^{-1}. \quad (7)$$

The lattice form factors, $L(\boldsymbol{G})$ and $F(\mathbf{G})$ are related to integration over the contour L, $L(\mathbf{G}) = \frac{\mathbf{1}}{\boldsymbol{L_0}}\oint_L e^{-i\mathbf{G}\cdot\mathbf{r}}dl$ and the area of the cross-section of the rod A_a, $F(\mathbf{G}) = \frac{1}{A_c}\int_{A_a} \boldsymbol{e}^{-i\mathbf{G}\cdot\mathbf{r}}d\mathbf{r}$.

2. Discussion and Results

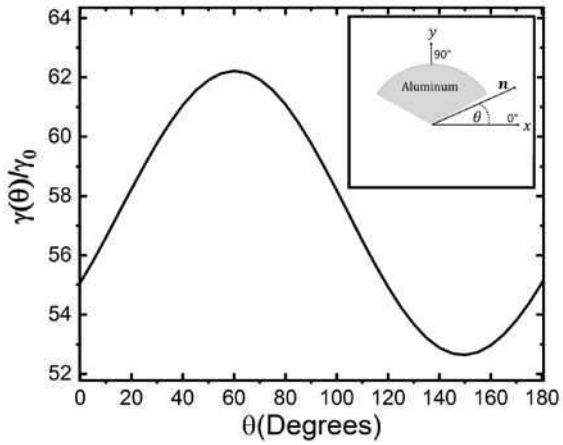


Figure 1: Angular dependence of the normalized decay coefficient for a phononic crystal of asymmetric Al rods embedded in water. The inset shows the unit cell with period of 5.5 mm, and the radius of the 120° circle sector is 2.2 mm. The angle θ shows the direction of propagation of sound wave of frequency 200 kHz.

Equations (3)-(7) were used for calculation of the decay coefficient for phononic crystal of asymmetric rods in water. The result is shown in Fig. 1. In this phononic crystal sound decays ~60 times faster than in free water due to formation of viscous boundary layer near each Al rod. The rate of decay depends on the direction of propagation, i.e. a phononic crystal with asymmetric unit cell behaves like an anisotropic viscous metamaterial. Note that the effective mass is also anisotropic. The frequency dependence of the effective decay coefficient is different from that in pure viscous fluid. The $\sqrt{\omega}$-scaling of $\gamma(\omega)$ is a clear evidence that the viscous layer give the principal contribution to dissipation of sound. The ω^2-dependence of the decay coefficient observed in a viscous fluid[5] is suppressed due to much stronger dissipation in the viscous layers, while they occupy much less volume.

Phononic crystal shown in the inset was used in Ref. [6] for demonstration of nonreciprocity in a system with broken *PT*-symmetry. The decay coefficient calculated in the lowest approximation is reciprocal, $\gamma(\mathbf{n}) = \gamma(-\mathbf{n})$ since the distribution of velocities $\mathbf{V}(\mathbf{r})$ is calculated neglecting viscosity, i.e. the *T*-symmetry is not broken.

Acknowledgements

This work was supported by an EFRI grant No. 1741677 from the National Science Foundation, and by Conacyt México under grant A1-S-23120.

References

[1] L. M. Brekhovskikh and O. A. Godin, *Acoustics of Layered Media I*, 2nd Ed., Springer, 1998.

[2] M. I. Hussein, Theory of damped Bloch waves in elastic media, *Phys. Rev. B* 80, 212301, 2009.

[3] E. Reyes-Ayona, D. Torrent, and J. Sánchez-Dehesa, Homogenization theory for periodic distributions of elastic cylinders embedded in a viscous fluid, *J. Acoust. Soc. Am*. 132, 2896, 2012.

[4] A. A. Krokhin, J. Arriaga, and L. N. Gumen, Speed of Sound in Periodic Elastic Composites, *Phys. Rev. Lett*. 91, 264302, 2003.

[5] L.D. Landau, and E.M. Lifshitz, *Fluid Mechanics*, 2nd Ed., Elsevier, Oxford, 1984.

[6] E. Walker, *et al*., Nonreciprocal Linear Transmission of Sound in a Viscous Environment with Broken P Symmetry, *Phys. Rev. Lett.* 120, 204501, 2018.

Acoustic demultiplexer based on Fano and induced transparency resonances in slender tubes

Abdelkader Mouadili[1], El Houssaine El Boudouti[2], Bahram Djafari-Rouhani[3]

[1]LPMCER, Département de Physique, Faculté des Sciences et Techniques de Mohammedia, Université Hassan II, Casablanca, Morocco
[2]LPMR, Département de Physique, Faculté des Sciences, Université Mohammed I, Oujda, Morocco
[3]IEMN, UMR CNRS 8520, Département de Physique, Université de Lille, 59655 Villeneuve d'Ascq, France
*corresponding author, E-mail: elboudouti@yahoo.fr

Abstract

We give an analytical demonstration of the possibility to realize a simple phononic demultiplexer based on Fano and acoustic induced transparency resonances. The demultiplexer consists of a Y-shaped waveguide with an input line and two output lines. Each output line contains two stubs grafted either at a given position or at two positions far from the input line. We derive in closed form the expressions for a selective transfer of a single propagating mode through one line keeping the other line unaffected.

1. Introduction

Fano and EIT (Electromagnetically Induced Transparency) resonances [1, 2, 3] have an atomic origin, but they have been the subject of several studies in classical systems such as coupled micro-resonators [4, 5, 6], photonic waveguides [7, 8, 9, 10, 11], acoustic slender tube waveguides and solid-liquid multilayers[12, 13, 14, 15, 16, 17, 18, 19, 20, 21] as well as plasmonic nonostructures [22, 23, 24, 25, 26]. Fano resonance can be explained as the product of two processes of constructive and destructive wave interferences that give rise to a resonance followed by an antiresonance over a narrow frequency range and can be manifested by an asymmetrical profile shape. In the transmission spectra, the Fano profile appears as a maximum near to a transmission zero [27, 28]. When the Fano resonance falls between two antiresonances (two transmission zeros) it becomes EIT. In optics this phenomenon has shown potential applications to realize slow light and data storage of optical information [29, 30, 31, 32]. Fano and EIT resonances are originally the product of a coupling between one or more discrete states and a continuum [3].

In general, to create this type of resonances in classical systems, one directly or indirectly connects two or more resonators with a waveguide. Among the simple structures giving a clear theoretical and experimental demonstration of such resonances, one can cite a guide connected with two lateral resonators at the same point (called a cross structure) or two different positions (called U-shaped structure). In acoustics the U-shaped structure was first studied by El Boudouti et al. [12] to show Fano and AIT (the acoustic analogue of EIT) resonances. A few years later, the same structure was studied by Santillan et al. [13] to demonstrate AIT resonances and delayed sound. More recently, cross and U-shaped structures have been the subject of interest by Merkel et al. [14] to experimentally show AIT and Fano resonances as well as the possibility to realize perfect absorption with such structures. Similar structures but with multiple stubs have been proposed by Long et al.[33] to realize multiband and broadband absorbers for low-frequency sound. It is worth mentioning that cross and U-shaped photonic structures based on coaxial cables have been studied both theoretically and experimentally[10, 11] in the radio-frequency domain. In addition, the cross structure has been proposed to study a Y-shaped demultiplexer based on EIT resonances[34]. This demultiplexer consists on one input line and two output lines, each one containing a cross-shaped resonator.

Acoustic demultiplexers based on phononic crystals with different defects has been realized either through what is called add-drop filters[35, 36] or multi-port channels[37, 38]. Recently, three-port acoustic network has been used to study subwavelength control of absorption [39] using resonators on each channel. Also, Three- and four-port configurations in presence of a resonator at the common junction have been designed such that the incoming waves are first coherent perfectly channeled to other channel before manipulating it to absorption [40]. In this paper we propose two Y-shaped acoustic demultiplexers with two different configurations: the first structure is based on the cross-shape structure (Fig. 1) and the second one is based on the U-shape structure (Fig. 7). The demultiplexers in these two devices are based on AIT and Fano resonances. The aim consists of demonstrating the possibility of finding analytically the appropriate lengths of the different waveguide resonotars in order to reach total transmission in one output line keeping the other lines unaffected. The demultiplexers proposed in this study have several advantages over those based on phononic crystals[37, 38], such as: i) the simplicity of the device manufacturing where only two resonators are needed on each output line instead of a periodic structure with a given defect, ii) the simplicity of the structure enables a full analytical calculation which allows to deduce

the exact expressions of the different lengths of the waveguides to achieve a perfect demultiplexing. iii) The possibility of increasing the quality factor of the filtered resonances to infinite values by detuning the lengths of the two stubs. This property is a feature of Fano and induced transparency resonances that does not exist in standard phononic crystals with defects in which filtering is performed using finite width Breit-Wigner resonances[37, 38, 41]. It should be pointed out that the validity of our results is subject to the requirement that the cross section of the slender tubes being negligible compared to their length and to the propagation wavelength. The assumption of monomode propagation is then satisfied.

The rest of the paper is organized as follows: in section 2 we shall give the analytical expressions of the lengths of the tubes that enables to realize a perfect demultiplexing for the cross structure. These analytical results are obtained from an analysis of the transmission and reflection coefficients and will be illustrated by numerical applications in standard acoustic slender tubes[13]. Section 3 gives the same results as in section 2 but for U-structure. The last section contains the concluding remarks.

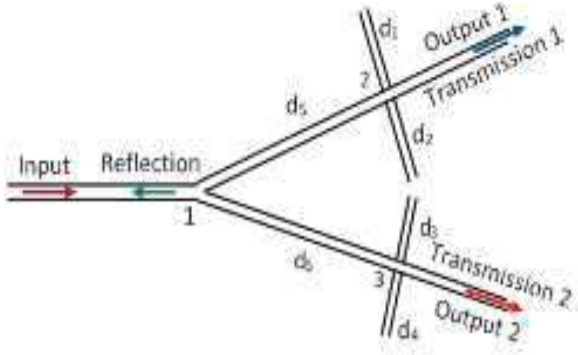


Figure 1: Schematic representation of a Y-shaped demultiplexer with one input line and two output lines. Two stubs are grafted at the same position along each output line. The geometrical parameters are defined in the text.

2. Demultiplexer based on cross structure

2.1. Transmission and reflection coefficients

Consider the structure shown in Fig. 1, this structure is composed of an input line and two output lines, all fixed at point 1. The first output line contains two stubs of lengths d_1 and d_2 inserted on the same site 2 at a distance d_5 from the input 1. Likewise, the second output line contains two stubs of lengths d_3 and d_4 inserted on the same site 3 at the distance d_6 from the input 1. The possibility of realizing an AIT type resonance in a simple cross structure composed of two resonators of lengths d_1 and d_2 connected at one point along an infinite waveguide, has been the subject of several previous works [12, 13, 14]. In a cross structure, the AIT resonance is obtained by the entire stub of lengths $d_0 = d_1 + d_2$. This resonance is trapped between two transmission zeros induced by the two elementary stubs of length d_1 and d_2.

The calculation of the transmission and reflection coefficients is carried out using the Green's function method[42]. For simplicity, all waveguides are assumed being characterized by the same characteristic impedance $Z = \frac{\rho v}{S}$ where $\rho = 1.2Kg/m^3$ and $v = 342m/s$ are respectively the density and velocity of the fluid inside the slender tubes (namely, air) and $S = 3.14cm^2$ is the section of the guide. We have chosen the same parameters as those used in the experimental work by Santillan and Bozhevolnyi[13]. However, the resonators are supposed to be simple stubs instead of Helmholtz resonators with narrow neck in order to get analytical expressions for a perfect demultiplexing (see below), otherwise the calculation becomes cumbersome and only numerical simulation can be performed.

The analytical expressions of the transmission coefficients t_1 and t_2 along fisrt and second output lines and the reflection coefficient r in the input line are obtained using the same procedure of calculation as for photonic waveguides[34]. We shall avoid the details of these calculations and give below the expressions of t_1, t_2 and r in closed form, namely

$$t_1 = \frac{2C_1C_2(-C_6C_3C_4 + S^{'}S_6 + jC_3C_4S_6)}{\chi_1 + j\chi_2}, \quad (1)$$

$$t_2 = \frac{2C_3C_4(-C_5C_1C_2 + SS_5 + jC_1C_2S_5)}{\chi_1 + j\chi_2}. \quad (2)$$

and

$$r = -\frac{\xi_1 + j\xi_2}{\chi_1 + j\chi_2} \quad (3)$$

where

$$\xi_1 = C_1C_2C_3C_4(S_5S_6 - C_5C_6) + C_1C_2S^{'}C_6S_5 + C_3C_4SC_5S_6 + SS'S_5S_6 \quad (4)$$

$$\xi_2 = C_1C_2C_3C_4S_0 + C_1C_2S^{'}C_5C_6 + C_3C_4SC_5C_6 - S_0SS^{'} \quad (5)$$

$$\chi_1 = 3C_1C_2C_3C_4(S_5S_6 - C_5C_6) + C_1C_2S'(S_0 + C_5S_6) + C_3C_4S(S_0 + C_6S_5) - SS'S_5S_6 \quad (6)$$

$$\chi_2 = C_1C_2C_3C_4(3C_6S_5 + 3C_5S_6) + (C_5C_6 - 2S_5S_6)(C_1C_2S' + C_3C_4S) - S_0SS^{'} \quad (7)$$

and $C_i = \cos(kd_i)$, $S_i = \sin(kd_i)$ (i = 1-6), $S = \sin(k(d_1 + d_2))$, $S^{'} = \sin(k(d_3 + d_4))$, $S_0 = \sin(k(d_5 + d_6))$. $k = \omega/v$ is the wave-vector of the sound wave in the slender tubes and ω is the angular frequency.

In the absence of loss, the transmission coefficients in the two output lines are given respectively by $T_1 = |t_1|^2$

and $T_2 = |t_2|^2$ while the expression of the reflection R in the input line is given by $R = |r|^2$. The transmission and reflection coefficients satisfy the energy conservation: $T_1 + T_2 + R = 1$.

2.2. Numerical results and discussions

Now, we are able to choose the precise parameters of the system to obtain a complete transmission in the two output lines with neighboring frequencies. Indeed, from Eqs. (1), (2) and (3), one can show easily that in order to realize $|T_1| = 1$, $T_2 = 0$ and $R = 0$, one should have $C_3C_4 = 0$ (i.e., $C_3 = 0$ or $C_4 = 0$), $S = 0$ and $C_6 = 0$. Similarly, in order to realize $|T_2| = 1$, $T_1 = 0$ and $R = 0$, one should have $C_1C_2 = 0$ (i.e., $C_1 = 0$ or $C_2 = 0$), $S' = 0$ and $C_5 = 0$. Now, in order to realize both $T_1 = 1$ and $T_2 = 1$ at two different and neighboring frequencies, we can show after some algebraic calculations that the six lengths d_1, d_2, d_3, d_4, d_5 and d_6, should satisfy the following conditions:

$$d_1 = \frac{d_0}{2} - \frac{\delta}{2} \tag{8}$$

$$d_2 = d_5 = \frac{d_0}{2} + \frac{\delta}{2} \tag{9}$$

$$d_3 = d_6 = \frac{d_0}{2} \tag{10}$$

$$d_4 = \frac{d_0}{2} + \delta, \tag{11}$$

where we have introduced a detuning parameter $\delta = d_2 - d_1 \neq 0$ between the two stubs along the output 1 (Fig. 1). This is a necessary and sufficient condition to realize an AIT resonance along the output 1. In addition, along this study we shall fix the length of the two stubs (i.e., $d_0 = d_2 + d_1$) which fixes the position of the AIT resonance along the output 1.

In order to illustrate the results above, we present in Fig. 2 the variation of the transmission coefficients T_1 and T_2 and the reflection coefficient R as a function of the frequency f for different values of $\delta = d_2 - d_1$ around $\delta = 0$ and for $d_0 = 8.57cm$. The choice of the length of $d_0 = d_1 + d_2$ enables to fix the frequency of the first AIT resonance induced by the two stubs along the first output at $\omega d_0/v = \pi$ (i.e., around $f_0 = 2000Hz$ as in Ref.[13]). Similarly, the length of the two stubs along the second line $d'_0 = d_3 + d_4$ is chosen such that the second resonance induced by the later stubs falls at the vicinity of the one induced by the former stubs. In particular, we have chosen the same parameter δ representing the detuning between the AIT resonances and at the same time the separation between the transmission zeros of each AIT resonance (i.e., $d'_0 - d_0 = d_2 - d_1 = d_4 - d_3 = \delta$). Figure 2 clearly shows that when the transmission along the first output (continuous curve) reaches unity ($T_1 = 1$), the transmission along the second output T_2 (discontinuous curve) and the reflection R (dotted curve) vanish (i.e., $T_2 = R = 0$). Similarly, when the transmission along the second output line (discontinuous curve) reaches unity ($T_2 = 1$), the transmission

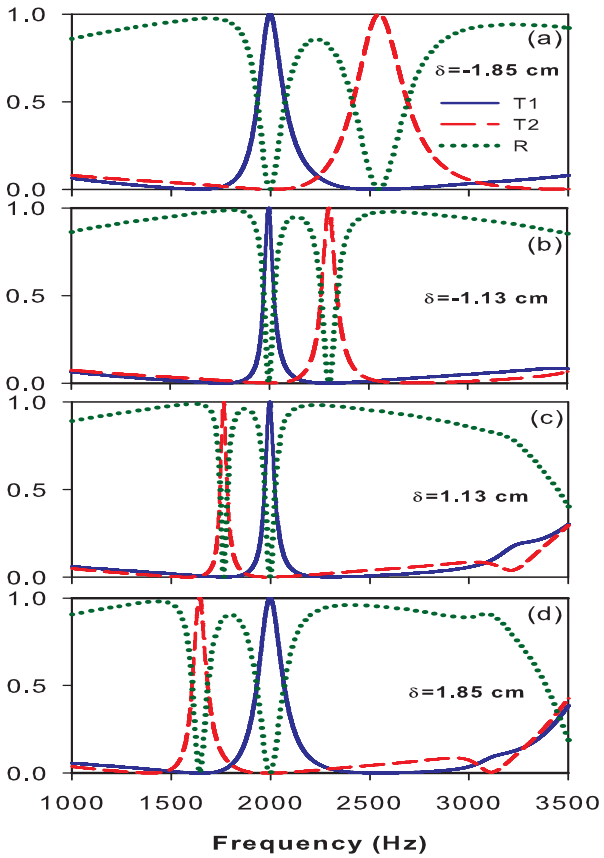


Figure 2: Variation of the transmission along the output 1 (continuous curve), the output 2 (discontinuous curve) and the reflection in the input (dotted curve) of the demultiplexer as a function of frequency f for different values of $\delta = d_2 - d_1$ and for $d_0 = d_1 + d_2 = 8.57cm$.

along the first output line T_1 (continuous curve) and the reflection R (dotted curve) vanish (i.e., $T_1 = R = 0$). As mentioned above, the AIT resonance in the first output falls at the same frequency $f_0 \simeq 2000Hz$ for all δ values, its width decreases when δ decreases and disappears for $\delta = 0$ (Fig. 2). In addition, the shape and width of the AIT resonance changes slightly when δ becomes negative (i.e., for a permutation of both stubs 1 and 2). The position and width of the resonance along the second line strongly depend on δ.

Indeed, since the first resonance AIT has two transmission zeros around $f_0 = 2000Hz$, the position of the second AIT resonance falls above $f_0 = 2000Hz$ for $\delta < 0$ (Figs. 2(a),(b)), crosses the first resonance at $\delta = 0$ and reappears below $f_0 = 2000Hz$ for $\delta > 0$ (Figs. 2(c), (d)). This is illustrated in Fig. 3 where we have given the variation of the frequencies f_1 and f_2 of both resonances for different values of δ. It can be noted that the frequency f_1 of the resonance along the first line remains constant at f_0 regardless the value of δ, whereas the frequency f_2 of the second resonance falls above f_0 for δ negative ($\delta < 0$) then it reappears below f_0 when δ becomes positive ($\delta > 0$). The crossing

between the two resonances takes place for $\delta = 0$.

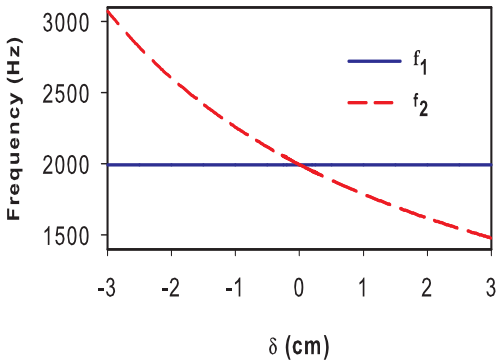


Figure 3: Variation of the frequency of the two AIT resonances along the two output guides as a function of δ.

Figure 4 gives the quality factor Q of the two resonances as a function of δ. We remark that the quality factor is almost the same for both resonances; it decreases very rapidly as a function of δ and tends to infinity when δ tends to zero. This kind of resonance (with infinite lifetime) is called *bound in continuum state*[43], it represents a stationary mode in the cross stubs and do not interact with the incident waves in the main waveguides.

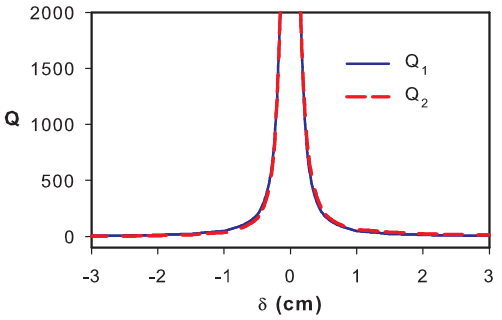


Figure 4: Variation of the quality factors Q_1 and Q_2 of the AIT resonances as a function of δ.

In the previous results we have neglected the effect of loss on the AIT resonances. In Fig. 5 we have given the same transmission spectra as in Fig. 2(b) but in presence of damping. We have considered the same damping due to viscosity and thermal conduction in the resonators as in the experimental work by Santillan and Bozhevolnyi[13]. One can see that the transmission does not reach unity because of the attenuation of sound in the guides, the energy transmitted remains less than 80% in both branches. Also, the effect of absorption on the amplitude of the AIT resonances becomes very important for resonances with narrow width.

In order to analyze the spatial localization of the different modes that can be filtered or stopped by the demultiplexer, we have calculated the displacement field along the two output lines of the system[42]. Figure 6 gives the square modulus of the displacement field $|U|^2$ for the resonance $f_1 = 2000Hz$ with $\delta = -1.85cm$, i.e., $d_1 = 5.21cm$, $d_2 = d_5 = 3.36cm$, $d_3 = d_6 = 4.285cm$, $d_4 = 2.435cm$ (Fig. 2(a)). This mode corresponds to a filtered mode (full curve) in one line and a stopped mode (dashed curve) in the other line (Fig. 2(a)). Figure 6 shows that the mode $f_1 = 2000Hz$ is transferred along the output 1 (Fig. 6(a)), whereas it is stopped along the output 2 (Fig. 6(b)). The transfer of this mode along the output 1 is due to the excitation of both stubs of lengths d_1 and d_2 along this line as it illustrated in Fig. 6(c), whereas its stopping along the second line is due to the excitation of the stationary mode of only the stub of length $d_4 = 2.435cm$ as shown in Fig. 6(d). Similar results are obtained for the the resonance mode $f_2 = 2544Hz$, but this time the transfer occurs along the second line through the excitation of its double stubs of lengths d_3 and d_4, whereas the wave is stopped along the first line as a consequence of the excitation of the mode of one of its stubs of length $d_2 = 3.36cm$. These results clearly show how the lengths of the finite guides constituting the demultiplexer should be chosen appropriately in order to transfer a wave in one line keeping the other line unaffected.

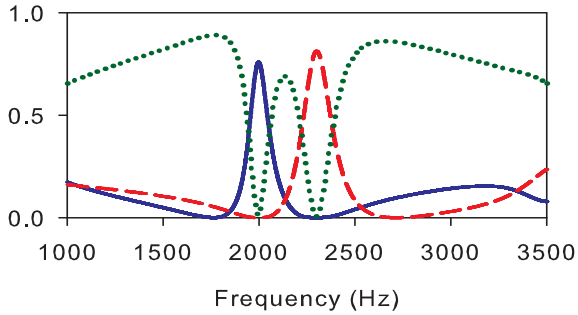


Figure 5: Same as in Fig. 2(b) but in presence of loss in the slender tubes.

3. Demultiplexer based on U-structure

As mentioned above, the U-shaped resonator along a waveguide was the subject of several studies in acoustics by different authors[12, 14]. In particular, it was shown that such structures can present two types of resonances: AIT-type resonances when the two resonators have different lengths and Fano resonances when the two resonators have the same lengths. In this section we consider the U-shaped demultiplexer composed of an input line and two output lines, all connected at the same point 1 (Fig. 7). On the first output line we connect two lateral stubs of lengths d_1 and d_2 separated by a distance d_0. The stub of length d_1 is inserted in the site 2 at a distance d_5 from the input 1 and the stub of length d_2 is inserted in the site 3 at a distance

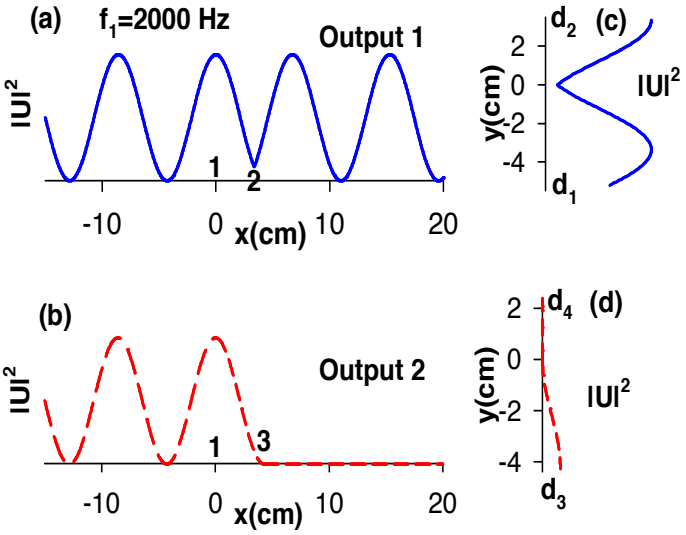


Figure 6: Square modulus of the displacement field $|U|^2$ (in arbitrary units) versus the space position along the output 1 (a) and the output 2 (b) for $f_1 = 2000Hz$. (c) and (d) show the behavior of $|U|^2$ along the vertical stubs in each line. 1, 2 and 3 indicate the entrance and the exit along each line (Fig. 1)

$d_5 + d_0$ from input 1. Similarly, the second output line contains two lateral stubs of lengths d_3 and d_4 separated by a distance d_0'. The stub of length d_3 is inserted in the site 4 at the distance d_6 from the input 1 and the stub of length d_4 is inserted in the site 5 at a distance $d_6 + d_0'$ from the input 1 (Fig. 7).

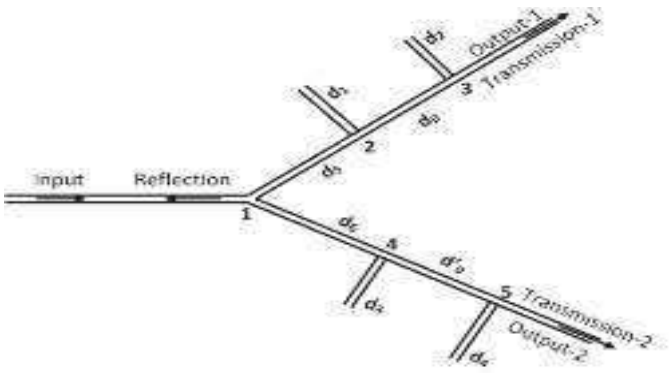


Figure 7: Schematic representation of a Y-shaped demultiplexer with one input line and two output lines. Two stubs are grafted at two different positions along each output line. The geometrical parameters are defined in the text.

The calculation of the transmission and reflection coefficients for the demultiplexer based on U-shaped structure can be performed in the same way as in section 2 using the Green's function method[42], however the corresponding expressions are more cumbersome. Therefore, we shall give only the conditions that should be satisfied by all the guides in order to realize perfect demultiplexing. Also, we shall distinguish two different cases depending on whether the stubs along each output line are slightly different which gives rise to AIT resonances or identical which gives rise to Fano resonnaces.

3.1. Demultiplexer based on AIT resonances

As already demonstrated in previous works [12, 14], in order to get AIT resonance with such structures, we should take the lengths of the two stubs along one guide slightly different (i.e., $\delta = d_2 - d_1 \neq 0$). In addition, along this study we will fix the total length of the two stubs along the first output line such that $d_0 = d_2 + d_1$ which fixes the position of the AIT resonance along this line. Now, in order to achieve total transmission for two neighboring frequencies along the two output lines, the lengths of the different guides should be taken as follows:

$$d_1 = \frac{d_0}{2} + \frac{\delta}{2}, \tag{12}$$

$$d_2 = d_5 = \frac{d_0}{2} - \frac{\delta}{2}, \tag{13}$$

$$d_3 = d_6 = \frac{d_0}{2}, \tag{14}$$

$$d_4 = \frac{d_0}{2} - \delta, \tag{15}$$

$$d_0' = d_3 + d_4 = d_0 - \delta. \tag{16}$$

Figure 8 presents the variation of the transmission coefficients T_1 and T_2 and the reflection coefficient R as a function of the frequency f for different values of δ around $\delta = 0$. We can see clearly that for each δ, when the transmission along the first output line (continuous curve) reaches unity ($T_1 = 1$), the transmission along the second output line T_2 (discontinuous curve) and the reflection R (dotted curve) cancel out each other (i.e., $T_2 = R = 0$). Similarly, when the transmission along the second line (discontinuous curve) reaches unity ($T_2 = 1$), the transmission along the first line T_1 (continuous curve) and the reflection R (dashed curve) vanish (i.e., $T_1 = R = 0$). As mentioned above, the AIT resonance in the first output line falls at the same frequency for all δ values, its width decreases as δ decreases and disappears for $\delta = 0$ (Fig. 8), giving rise to bound in continuum states[43]. In addition, the shape and width of the AIT resonance change slightly when δ becomes negative (i.e., for a permutation of both stubs 1 and 2). The position and width of the resonance along the second line strongly depend on δ.

Indeed, as the first AIT resonance has two transmission zeros around $f_0 = 2000Hz$, the position of the second AIT resonance falls above $f_0 = 2000Hz$ for $\delta < 0$, cross the first resonance at $\delta = 0$ and reappears below $f_0 = 2000Hz$ for $\delta > 0$. This behavior is similar to the one obtained in Fig. 3 for the cross-structure where the crossing between the two resonances takes place for $\delta = 0$. Also, the variation of the quality factor Q of the two AIT resonances in the two outputs lines as a function of δ, follows the same behavior as in Fig. 4. In particular, Q increases rapidly when the absolute value of δ decreases and tends towards infinity when δ tends to zero.

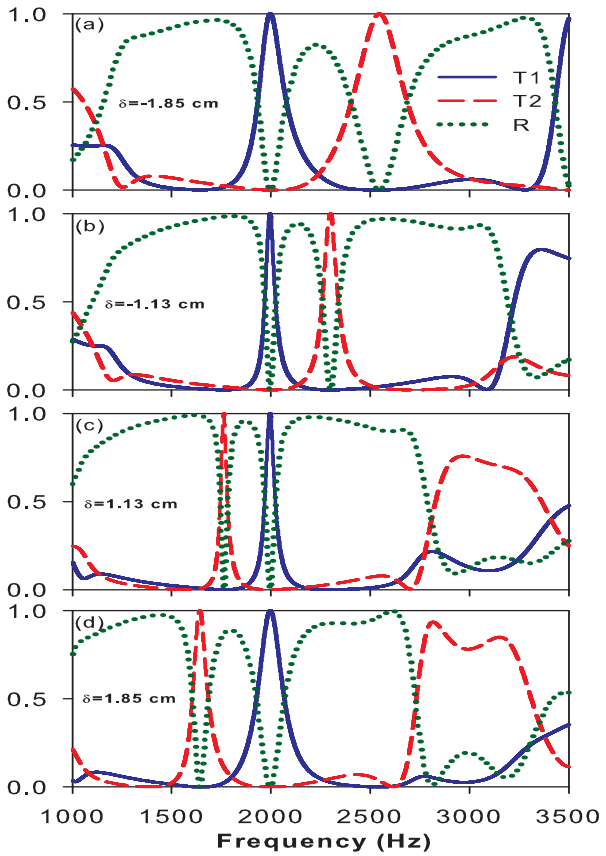


Figure 8: Variation of the transmission along the output 1 (continuous curve), the output 2 (discontinuous curve) and the reflection in the input (dotted curve) of the demultiplexer as a function of the frequency f for different values of δ and for $d_0 = d_1 + d_2 = 8.57cm$.

3.2. Demultiplexer based on Fano resonances

As mentioned in Ref.[12], in order to achieve a Fano resonance, one should take both stubs with identical lengths, but slightly different from $\frac{d_0}{2}$ (i.e., $d_1 = d_2 \neq d_0/2$) along the first output line. Similarly, we should take $d_3 = d_4 \neq d_0'/2$ along the second output line. The explicit expressions of the eight different lengths d_1, d_2, d_3, d_4, d_5, d_6 and d_0' should satisfy the following equations in order to obtain a total transmission along one output line keeping the other line unaffected

$$d_1 = d_2 = \frac{d_0}{2} + \varepsilon, \tag{17}$$

$$d_5 = d_2, \tag{18}$$

$$d_3 = d_4 = \frac{d_0}{2} + \frac{\varepsilon}{2}, \tag{19}$$

$$d_0' = d_0 + 3\varepsilon, \tag{20}$$

$$d_6 = d_3 \tag{21}$$

where ε represents the detuning between the lengths of the different guides constituting the demultiplexer. Figure 9 gives the variation of transmission coefficients T_1 and T_2 and reflection coefficient R as a function of frequency the f for different values of ε around $\varepsilon = 0$. From Fig. 9 one can see that both resonances are of Fano type, that is a resonance near a transmission zero. In addition, both resonances present different asymmetric line shapes (i.e., opposite Fano parameters[1]) in order to achieve a full transmission in one line and no signal in the other line. We can notice that for $\varepsilon = -0.925cm$ for example (Fig. 9(a)), the transmission along the first output (continuous curve) is unity ($T_1 = 1$) at $f = 1803Hz$, the transmission along the second output T_2 (discontinuous curve) and the reflection R (dotted curve) vanish (i.e. $T_2 = R = 0$). Similarly, when the transmission along the second line (discontinuous curve) reaches unity ($T_2 = 1$) at $f = 1640Hz$, the transmission along the first line T_1 (continuous curve) and the reflection R (dashed curve) vanish (i.e., $T_1 = R = 0$). Also, there exists a frequency between the two resonances for which the reflection along the input line reaches almost unity ($R \simeq 1$), while the transmission along the first line T_1 (continuous curve) and the transmission along the second line T_2 (discontinuous curve) vanish (i.e., $T_1 \simeq T_2 \simeq 0$). This behavior does not exist in the case of AIT resonances (Fig. 8). In addition, we can see that for $\varepsilon < 0$, the resonance in the second line falls below the one in the first line (Fig. 9(a)) and when ε increases both resonances fall close to each other and their widths decrease (Fig. 9(b)). For $\varepsilon = 0$, both resonances fall at the same frequency (around 2000 Hz), their widths vanish giving rise to bound in continuum states[43]. For $\varepsilon > 0$, the resonance in the second line falls above the one in the first line (Fig. 9(c)); its width increases when ε increases (Fig. 9(d)). These results are summarized in Fig. 10 where we have plotted the frequencies of both resonances as function of ε. We can see that contrary to Fig. 3, the frequencies of both Fano resonances depend on ε. Also, the quality factors of the two resonances (not shown here) are almost identical and tend to infinity when ε tends to zero. Finally, the amplitude of the filtered resonances in Figs. 8 and 9 can be affected considerably when loss is taken into consideration in particular for narrow resonances as in Fig. 5.

4. Conclusion

In this work we have studied a Y-shaped acoustic demultiplexer based on two different configurations. The first demultiplexer is based on a cross structure, in this case we used the AIT-type resonances presented by such structures to realize a perfect demultiplexing. We have given the analytical expressions of the lengths of the different guides to achieve a total transmittance in one output line canceling at the same time the reflection and transmission in the other lines. By taking into account the loss in the guides, we have shown that the property of demultiplexing still remains valid, however the amplitude of the output signal does not reach unity. In the second configuration we have studied the U-shaped structure for the design of the demultiplexer. In this case, we have shown two possibilities of demultiplexing by using either AIT symmetrical resonances or

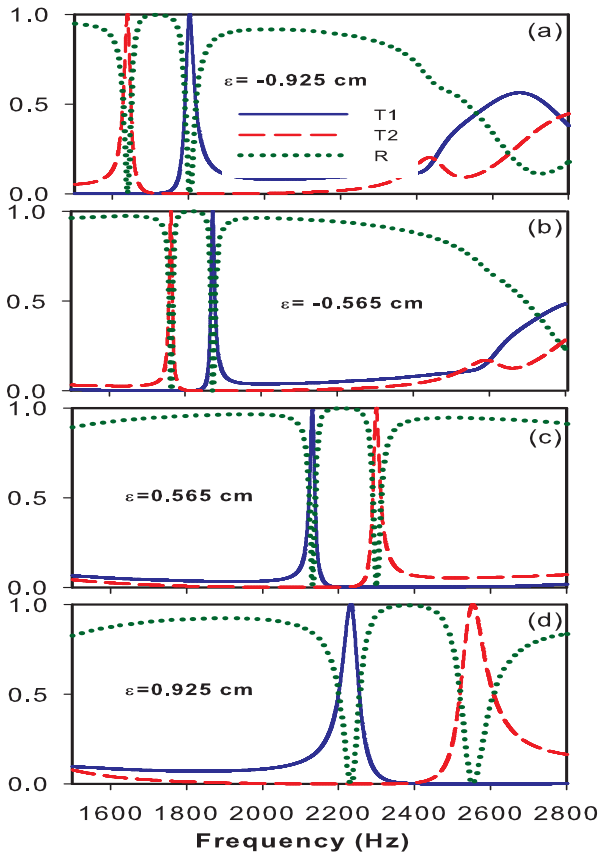


Figure 9: Variation of the transmission spectra along the output 1 (continuous curve), the output 2 (discontinuous curve) and the reflection in the input (dotted curve) of the demultiplexer as a function of the frequency f for different values of ε and for $d_0 = d_1 + d_2 = 8.57cm$.

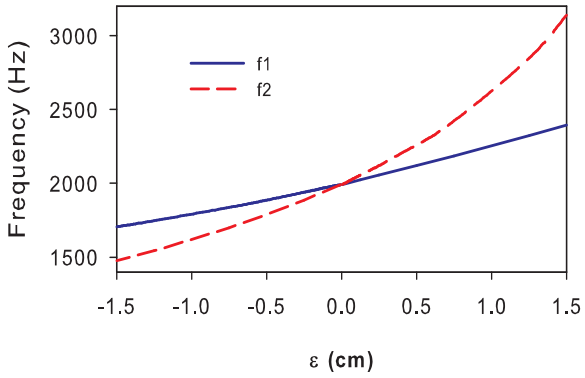


Figure 10: Variation of the frequencies of the two Fano resonances as a function of ε.

Fano asymmetrical resonances. In both cases we have determined analytically the expressions of the lengths of the different guides to get the total transmission in one output line keeping the other lines unaffected. For both demultiplexers, we have shown that the frequencies of the filtered resonances as well as their widths (i.e., the quality factors) can be tuned by appropriately choosing the lengths of the different waveguides constituting these systems. The confinement of the filtered and stopped resonances along each line are shown through an analysis of the displacement field. The experimental results predicted in this work can be easily validated by simple experiments in the audible frequency range[13, 14, 33].

References

[1] U. Fano, Phys. Rev. **124**, 1866 (1961)

[2] For a review, see M. Fleischhauer1, A. Imamoglu, and J. P. Marangos, Rev. Mod. Phys. **77**, 633 (2005)

[3] S. E. Harris, Phys. Today **50**, 36 (1997)

[4] M. Tomita, K. Totsuka, R. Hanamura, and T. Matsumoto, J. Opt. Soc. Am. B **26**, 813 (2009)

[5] Y-F Xiao, M. Li, Y-C Liu, Y. Li, X. Sun, and Q. Gong, Phys. Rev. A **82**, 065804 (2010)

[6] B-B Li, Y-F Xiao, C-L Zou, X-F Jiang, Y-C Liu, F-W Sun, Y Li, and Q Gong, Appl. Phys. Lett. **100**, 021108 (2012)

[7] X. Yang, M. Yu, D.-L. Kwong, and C. W. Wong, Phys. Rev. Lett. **102**, 173902 (2009).

[8] Y. Sato, Y. Tanaka, J. Upham, Y. Takahashi, T. Asano and S. Noda, Nature Photonics **6**, 56 (2012)

[9] N. Caselli, F. Intonti, F. La China, F. Biccari, F. Riboli, A. Gerardino, L. Li, E. H. Linfield, F. Pagliano, A. Fiore, and M. Gurioli, Nature Comm. **9**, 396 (2018).

[10] A. Mouadili, E.H. El Boudouti, A. Soltani, A. Talbi, A. Akjouj and B. Djafari-Rouhani, J. Appl. Phys. **113**, 164101 (2013).

[11] A. Mouadili, E.H. El Boudouti, A. Soltani, A. Talbi, B. Djafari-Rouhani, A. Akjouj and K. Haddadi, J. Phys.: Condens. Matter **26**, 505901 (2014).

[12] E. H. El Boudouti, T. Mrabti, H. Al-Wahsh, B. Djafari-Rouhani, A. Akjouj, and L. Dobrzynski, J. Phys.: Condens.Matter **20**, 255212 (2008).

[13] A. Santillán and S. I. Bozhevolnyi, Phys. Rev. B **84**, 064304 (2011)

[14] A. Merkel, G. Theocharis, O. Richoux, V. Romero-Garcia and V. Pagneux, Appl. Phys. Lett. **107**, 244102 (2015).

[15] M. Amin, A. Elayouch, M. Farhat, M. Addouche, A. Khelif, and H. Bağci, J. Appl. Phys. **118**, 164901 (2015).

[16] Y. Jin, E. H. El Boudouti, Y. Pennec, B. Djafari-Rouhani, J. Phys. D Appl. Phys. **50**, 425304 (2017).

[17] F. Zangeneh-Nejad and R. Fleury, Phys. Rev. Lett. **122**, 014301 (2019).

[18] I. Quotane, E. H. El Boudouti, and B. Djafari-Rouhani, Phys. Rev. B **97**, 024304 (2018).

[19] M. Vinod, G. Raghavan, V. Sivasubramanian, Sci. Rep. 8, 17706 (2018).

[20] M. Oudich, B. Djafari-Rouhani, B. Bonello, Y. Pennec, S. Hemaidia, F. Sarry, and D. Beyssen, Phys. Rev. Appl. **9**, 034013 (2018).

[21] Y. Jin, Y. Pennec and B. Djafari-Rouhani, J. Phys. D: Appl. Phys. **51**, 494004 (2018).

[22] B. Luḱyanchuk, N. I. Zheludev, S. A. Maier, N. J. Halas, P. Nordlander, H. Giessen and C. T. Chong, Nature Mater. **9**, 707 (2010).

[23] J. Wu, B. Jin, J. Wan, L. Liang, Y. Zhang, T. Jia, C. Cao, L. Kang, W. Xu, J. Chen, and P. Wu, Appl. Phys. Lett. **99**, 161113 (2011).

[24] L. Yang, J. Wang, L. Z. Yang, Z. D. Hu, X. Wu, and G. Zheng, Sci. Rep. **8**, 2560 (2018).

[25] S. Simoncelli, Y. Li, E. Cortes, and S. A. Maier, Nano Lett. **18**, 3400 (2018).

[26] T. Huang, S. Zeng, X. Zhao, Z. Cheng, and P. P. Shum, Photonics **5**, 23 (2018).

[27] R. Ghaffarivardavagh, J. Nikolajczyk, S. Anderson, and X. Zhang, Phys. Rev. B **99**, 024302 (2019).

[28] Fano Resonances in Optics and Microwaves: Physics and Applications, E. Kamenetskii, A. Sadreev, A. Miroshnichenko, Springer (2018).

[29] For a review, see I. Novikova, R. L. Walsworth, and Y. Xiao, Laser Photonics Rev. **6**, 333 (2012) and references therein.

[30] C. Liu, Z. Dutton, C. H. Behroozi, and L.V. Hau, Nature **409**, 490 (2001).

[31] L. V. Hau, S. E. Harris, Z. Dutton, and C. H. Behroozi, Nature **397**, 594 (1999).

[32] O. Katz, and O. Firstenberg, Nature Commun. **9**, 2074 (2018).

[33] H. Long, Y. Cheng, and X. Liu, Appl. Phys. Lett. **111**, 143502 (2017)

[34] A. Mouadili, E. H. El Boudouti, A. Soltani, A. Talbi, K. Haddadi, A. Akjouj and B. Djafari-Rouhani, J. Phys. D: Appl. Phys. **52**, 075101 (2019).

[35] Y. Pennec, B. Djafari-Rouhani, J. O. Vasseur, H. Larabi, A. Khelif, A. Choujaa, S. Benchabane, and V. Laude, Appl. Phys. Lett. **87**, 261912 (2005).

[36] B. Rostami-Dogolsara, M. K. Moravvej-Farshi, and F. Nazari, Phys. Rev. B **93**, 014304 (2016).

[37] Y. Pennec, B. Djafari-Rouhani, J. O. Vasseur, A. Khelif, and P. A. Deymier, Phys. Rev. E **69**, 046608 (2004)

[38] B. Rostami-Dogolsara, M. Kazem Moravvej-Farshi, F. Nazari, J. Mol. Liq. **281**, 100 (2019)

[39] O. Richoux, V. Achilleos, G. Theocharis and I. Brouzos, Sci. Rep. **8**, 12328 (2018).

[40] X. Zhang, C. Meng and Z. Yang, Sci. Rep. **7**, 13907 (2017).

[41] W. M. Robertson, I. Shirk and E. Campbell, AIP Advances **9**, 035013 (2019)

[42] V. Vasseur, A. Akjouj, L. Dobrzynski, B. Djafari-Rouhani and E.H. El Boudouti, Surf. Sci. Rep. **54**, 1 (2004).

[43] C.W. Hsu, B. Zhen, A.D. Stone, J.D. Joannopoulos and M. Soljačić, Nat. Rev. Mater. **1**, 16048 (2016).

A bottom-up approach towards metamaterials and plasmonics

Spherically Confined Self-Assembly of Molecular Bottlebrushes – A Facile Route to Hierarchical Photonic Pigments

Richard M. Parker, Dong-Po Song, Tianheng H. Zhao, Giulia Guidetti and Silvia Vignolini*

[1] Department of Chemistry, University of Cambridge, Cambridge, UK.
[2] Tianjin Key Laboratory of Composite and Functional Materials, Tianjin University, Tianjin, China.
*corresponding author, E-mail: sv319@cam.ac.uk

Abstract

Hierarchical, structurally-coloured materials offer a wide variety of visual effects that cannot be achieved with standard pigments or dyes. However, their fabrication requires simultaneous control over multiple length-scales. Here we present a robust strategy for the fabrication of hierarchical photonic pigments *via* the confined self-assembly of bottlebrush block copolymers within emulsified microdroplets. The resultant highly-ordered concentric lamellar structure gives rise to a near perfect photonic multi-layer in the solid-state, with reflectivity up to 100%. Our system is particularly suited for the scalable production of photonic pigments, arising from their rapid assembly mechanism and size-independent, tuneable colour.

1. Introduction

Structurally-coloured materials are ideal candidates for photonic pigments, as they offer the possibility to manipulate the visual appearance in terms of both the colour and scattering response. Such effects are also found in nature, where vivid and metallic colours are often the result of intricate nano- and micro-scale structural motifs.[1] Recently, the fabrication of photonic pigments from hierarchically-assembled photonic materials has been demonstrated by restricting the self-assembly of either colloidal particles[2,3] or liquid crystals[4,5] within the confined geometry of a micron-sized droplet. However, despite being extensively studied, such systems usually have strong intrinsic limitations in terms of formulation and scalability, which limits real-world application. Block copolymers provide a promising alternative for bottom-up fabrication of photonic structures.[6] In particular, bottlebrush block copolymers (BBCPs), where a highly extended backbone is densely grafted with polymer branches, are well-suited for photonic materials as they can form lamellae with domain spacings large enough to produce a strong reflection in the visible spectrum.[7,8] Here we present our recent work into the confinement of BBCPs within spherical microdroplets to yield intensely-coloured, hierarchical photonic pigments.[9]

2. Results and Discussion

A series of (poly(norbornene)-*graft*-poly(styrene))-*block*-(poly(norbornene)-*graft*-poly(dimethylsiloxane)) bottlebrush block copolymers were prepared with number average MW of 3.3, 4.1 and 7.1 MDa. To produce hierarchical photonic pigments, the BBCPs were geometrically-confined within monodisperse microdroplets, generated in a single step within a flow-focusing microfluidic device as a chloroform-in-water emulsion. Upon drying, vivid, monochromatic microspheres were produced (**Figure 1**). The trend in reflected colour correlates with the MW of the constituent BBCP,[8] with blue, green and red microspheres produced. Optical microscopy on an individual microsphere revealed a brightly-coloured reflection spot, with a corresponding sharp peak in the reflectance spectrum. This intense reflection, up to 100% reflectivity relative to a silver mirror, is due to a highly-ordered concentric multi-layer lamellar structure within the microsphere, as confirmed by electron microscopy.

The evolution of structural colour within the droplet was

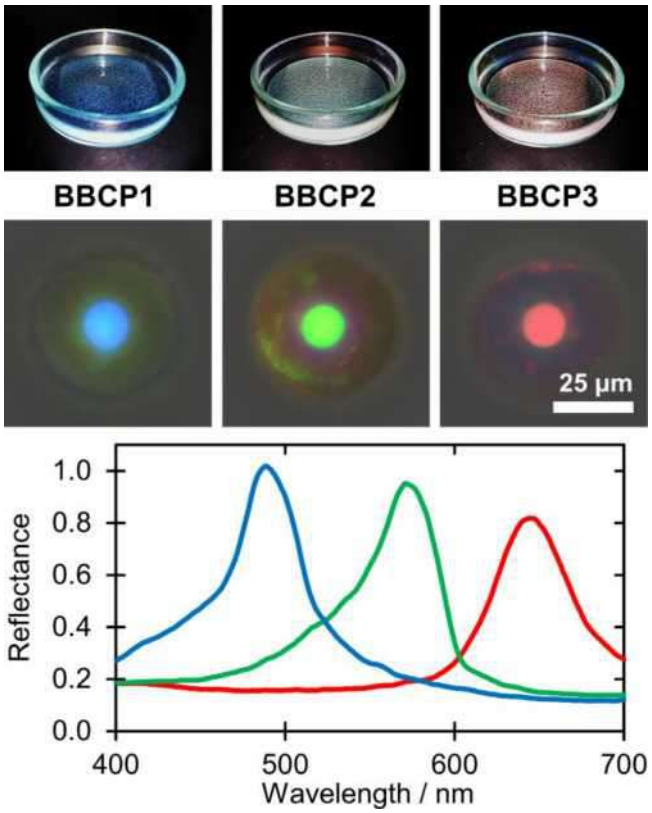


Figure 1: Blue, green and red hierarchical photonic pigments prepared from BBCP1-3 respectively (*top*) and the corresponding reflectance spectra for individual BBCP microspheres (*bottom*).

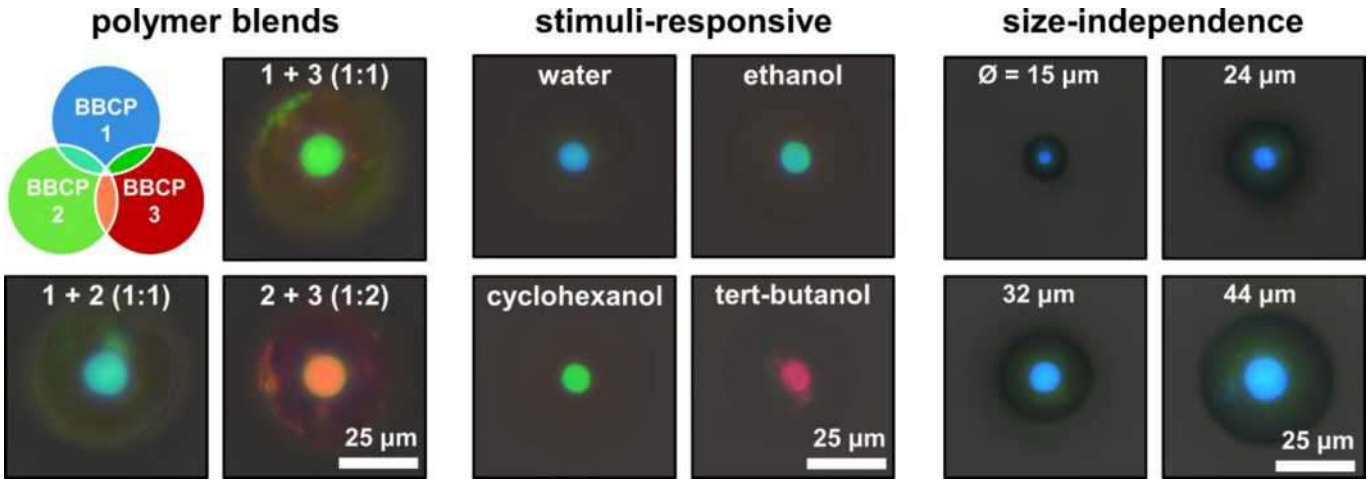


Figure 2: Polymer blends of BBCP1-3 result in intermediate coloured microspheres (*left*); responsive colour shifts arise from solvent-selective swelling of BBCP1 microspheres (*centre*); and polydisperse microspheres of BBCP1 are monochromatic (*right*).

monitored in real-time and correlated to the self-assembly process, where it was observed that the liquid-liquid droplet interface directs the assembly of the lamellar structure, promoting long-range concentric ordering and ensuring high reflectance from the microsphere by restricting any defects or disorder to the core. Furthermore, the choice of surfactant was found to be critical on this interfacially-templated process.

The colour can also be controlled by formulating microdroplets containing binary polymer blends,[7] with the colour of the blended microspheres lying between that of the two constituent BBCPs (**Figure 2**). This allows for a broad spectrum of photonic pigments to be readily prepared. Given that the colour reflected from a microsphere depends on the periodicity of the lamellae, the colour is also responsive to swelling in specific solvents. For example, BBCP1 microspheres were observed to reversibly shift from blue to red upon immersion in alcohols with decreasing – due to selective swelling of the poly(dimethylsiloxane) domains. The BBCP microspheres are also highly tolerant to the inclusion of contrast-enhancing additives, e.g. carbon black.

To understand the scalability of the fabrication process, the role of the drying rate was explored: microspheres formed in <30 min, were brightly coloured with longer drying times (e.g. 2 days) only leading to slightly higher reflectance and less observable defects. To explore the role of size on the optical properties, highly polydisperse microspheres were prepared by vortex-assisted emulsification. It was found that the reflected colour and as such the underlying microsphere nanostructure was not affected by the size of the templating microdroplet. Finally, the microspheres were embedded within a transparent matrix to evaluate the consequences of its hierarchical structure – only 2 wt.% of polydisperse BBCP2 microspheres were required to give a visibly green and non-iridescent colour under diffuse illumination.

3. Conclusions

We report a scalable approach for the fabrication of photonic pigments *via* the confined self-assembly of BBCPs. The obtained microspheres show strong, sharp reflectance peaks, with tuneable and responsive colours, arising from a well-ordered concentric multi-layer photonic structure. The self-assembly process is robust, with high tolerance to the initial droplet geometry and drying rate. The strong templating effect of the droplet interface, combined with the high surface-to-volume ratio leads to unprecedented long-range ordering of the lamellae, resulting in up to 100% reflectivity. As such, BBCP microspheres have great potential as photonic pigments to be used as a replacement for colorants in e.g. automotive paints or in photonic displays.

Acknowledgements

ERC [ERC-2014-STG H2020 639088], BBSRC [David Phillips Fellowship BB/K014617/1], EPSRC [1525292; EP/N016920/1; EP/R511675/1], National Natural Science Foundation of China [51873098] and the Winton Programme for the Physics of Sustainability.

References

[1] V. E. Johansen, O. D. Onelli, L. M. Steiner, S. Vignolini, *Functional Surfaces in Biology III: Diversity of the Physical Phenomena*; Springer International Publishing, 2017; 53–89.
[2] N. Vogel et al., *Proc. Natl. Acad. Sci.* **2015**, *112*, 10845.
[3] J. G. Park, S. H. Kim, S. Magkiriadou, T. M. Choi, Y. S. Kim, V. N. Manoharan, *Angew. Chemie Int. Ed.* **2014**, *53*, 2899.
[4] S. S. Lee, S. K. Kim, J. C. Won, Y. H. Kim, S. H. Kim, *Angew. Chemie Int. Ed.* **2015**, *54*, 15266.
[5] J. Noh, H.-L. Liang, I. Drevensek-Olenik, J. P. F. Lagerwall, *J. Mater. Chem. C* **2014**, *2*, 806.
[6] M. Stefik, S. Guldin, S. Vignolini, U. Wiesner, U. Steiner, *Chem. Soc. Rev.* **2015**, *44*, 5076.
[7] G. M. Miyake, V. A. Piunova, R. A. Weitekamp, R. H. Grubbs, *Angew. Chemie Int. Ed.* **2012**, *51*, 11246.
[8] B. R. Sveinbjörnsson, R. A. Weitekamp, G. M. Miyake, Y. Xia, H. A. Atwater, R. H. Grubbs, *Proc. Natl. Acad. Sci.* **2012**, *109*, 14332.
[9] D.-P. Song, T. H. Zhao, G. Guidetti, S. Vignolini, R. M. Parker, *ACS Nano* **2019**, DOI: 10.1021/acsnano.8b07845.

Nanoparticle clusters as building blocks for bottom-up metasurfaces

A. Baron, R. Dezert, R. Elancheliyan, O. Mondain-Monval, P. Barois and P. Richetti

[1]University of Bordeaux, CNRS, CRPP, UMR 5031, 115 avenue Schweitzer, F-33600 Pessac, France
*corresponding author, E-mail: alexander.baron@u-bordeaux.fr

Abstract

We present spherical clusters, composed of dielectric or metallic inclusions, as a new kind of efficient and isotropic Huygens sources. We demonstrate that this design overlapping electric and magnetic resonances excited at visible frequencies. They may serve as building blocks for metasurface applications. We investigate their possible uses in high transmittance devices requiring a local phase control, and in thin absorber metalattices. They are particularly suited to bottom-up fabrication and self-assembly, offering an alternative to the classical lithographically fabricated metasurfaces.

1. Introduction

Recent progress in electromagnetic metasurfaces has shown that by arranging tailored Huygens sources on a plane, high-transmittance surfaces could be produced to spatially control the wavefront of light and thereby construct flat optical components[1,2]. Huygens sources are characterized by highly asymmetric forward-scattering that results from the constructive interferences between the radiation of several modes. A Huygens dipole for instance is obtained by overlapping the radiation patterns of orthogonally oriented electric and magnetic dipoles of same amplitude and phase.

It has been shown recently that isotropic Huygens dipoles and multipoles could be obtained with colloidal particles [1]. The proposed systems are composed of clusters of nanoparticles and typically operate at optical frequencies.

The aim of our work is to propose design recipes of three-dimensional Huygens sources that may subsequently be used as individual building blocks for metasurfaces. We shall overview several Huygens particles and metasurface designs as well as review potential fabrication routes.

2. Clusters of nanoparticles as Huygens sources

Huygens dipoles and multipoles can be achieved artificially by creating spherical clusters of plasmonic or dielectric nano-inclusions. Such systems actually enable the independent tailoring of the electric and magnetic dipole/multipole moments both in frequency and in amplitude. This tuning is determined by the volume fraction and total amount of inclusions in the cluster. Furthermore, our numerical calculations – based on the T-matrix method [4] - show that they may be used to produce phase gradient metasurfaces, flat lenses or perfect absorbers and that the cluster concept is scalable to any wavelength. Our most important result is that the denser cluster geometries present giant scattering cross-section efficiencies that surpass the maximum achievable value by a theoretical spherical dielectric particles, as predicted by Mie theory.

Two typical designs are shown in Fig. 1. They consist in one case of a plasmonic cluster in one case and a dielectric cluster in the other. The scattering cross-sections of the particles when illuminated by an incident plane wave are plotted. In both cases broadband and resonant Huygens dipoles are obtained by overlapping the electric and magnetic dipole resonances. This shows that the cluster system is very versatile versatile. We provide several examples of structures to illustrate that both dipolar or extremely broadband sources can be achieved with either metallic or dielectric inclusions. Our approach to obtain such sources relies on the engineering of the refractive index of the structure, by varying the nature, amount, size, and volume fraction of inclusions.

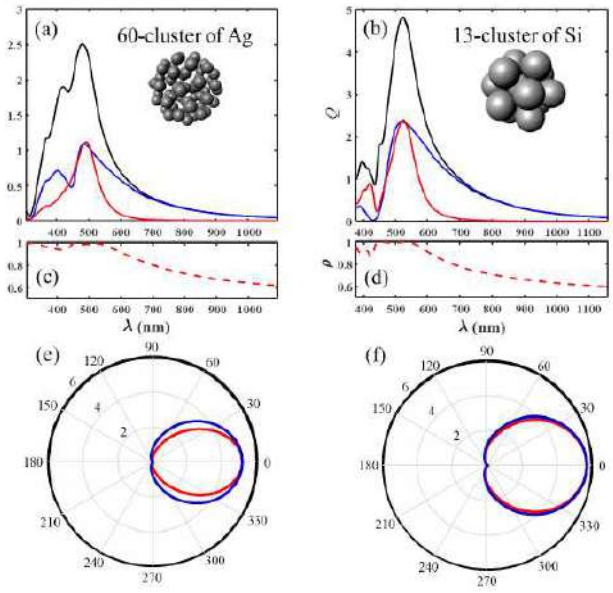


Figure 1: Two designs of Huygens sources made of spherical clusters. (a) (and (b)) Scattering cross-section efficiency (black: total, blue: electric, red: magnetic)

spectrum of a cluster made of 60 silver inclusions (13 silicon inclusions) of 15 nm (40 nm) in radius. (c) and (d) are the corresponding fraction of total energy scattered in the forward direction for the Ag and Si clusters respectively, when illuminated by a plane wave. (e) and (f) are the respective scattering diagrams in the E-plane (in blue) and H-plane (in red). Figure adapted from Dezert et al[Dezert].

3. From Colloidal Clusters to metasurfaces

When organized into 2D metalattices, Huygens sources allow to arbitrarily control transmitted waves [2]. Functionalities such as focusing, beam detection, vortex beam generation, holography, are widely explored in the literature. Our full wave numerical simulations show that silicon clusters periodically organized can induce a phase modulation of the transmitted wave in the full range between 0 and 2π, therefore unlocking beam shaping applications. On the other hand, lossy Huygens sources can be exploited to optimize light absorption [3]. Our work reveals the possibility to perfectly absorb an incident wave with an incident plane wave with an array of clusters. Systems based on dielectric as well as plasmonic structures will be presented.

4. Bottum-up fabrication routes

From an experimental point of view, clusters are particularly well-suited to bottom-up fabrication and self-assembly. They can be synthetized by making emulsions of two immiscible phases, one of which contains the nanoparticle inclusions. Therefore, they offer an alternative to the classical lithographically fabricated Huygens meta-atoms and can be made in large volumes. Examples of such synthesized particles will be shown. Figure 2 is an SEM image of preliminary attempts at fabrication of such clusters. Experimental characterizations of these systems will also be presented.

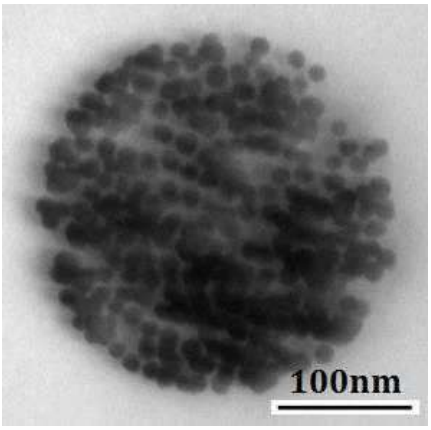


Figure 2: Scanning Electron Microscope image of preliminary clusters of gold inclusions assembled by following the emulsification route.

5. Conclusion

The cluster structure is a rich system as it is scalable and has tunable optical properties. Clusters are particularly suited to bottom-up fabrication and self-assembly, and can be synthetized in large amounts using a simple emulsification process. Furthermore, the ability to make Huygens systems from colloidal engineering separates the synthesis of the nanoresonator from the metasurface fabrication. Therefore, they offer an alternative to classical lithographically made Huygens meta-atoms and can be produced in very large quantities.

Acknowledgements

This work is supported by the LabEx AMADEus (ANR-10-LABX-42) in the framework of IdEx Bordeaux (ANR-10-IDEX-03-02), France.

References

[1] M. Decker, I. Staude, M. Falkner, J. Dominguez, D. Neshev, I. Brener, T. Pertsch, and Y. Kivshar, High-efficiency dielectric Huygens' surfaces, *Adv. Opt. Mater*. 3: 813-820, 2015.

[2] F. Aieta, M. A. Kats, P. Genevet, and F. Capasso, Multiwavelength achromatic metasurfaces by dispersive phase compensation, *Science* 347:1342-1345 (2015).

[3] R. Dezert, P. Richetti, and A. Baron, Isotropic Huygens dipoles and multipoles with colloidal particles, *Phys. Rev. B*, 96:180201 (2017).

[4] Mackowski D W, & Mishchenko M I 1996. Calculation of the T matrix and the scattering matrix for ensembles of spheres. *JOSA A*, 13: 2266-2278 (1996)

DNA-Based Self-Assembly of Plasmonic Nanoantennas

Sébastien Bidault

Institut Langevin, ESPCI Paris, CNRS, PSL University, Paris, France
E-mail: sebastien.bidault@espci.fr

Abstract

DNA nanotechnology provides numerous degrees of freedom to create hybrid plasmonic nanostructures for surface enhanced fluorescence and optical biosensing. We review some of our recent results.

Results and Discussion

Short DNA strands can be used as robust and versatile templates to produce plasmonic nanostructures with a fully controlled chemical environment. They allow the parallel production of millions of copies of gold particle dimers linked by a single DNA strand with gaps that can be controlled at the nanometer scale (Figure 1-a) [1]. In particular, a known number of fluorescent dye molecules can be easily introduced in such plasmonic antennas at the position where optical fields are strongly enhanced and confined. For instance, we demonstrated the deterministic introduction of individual fluorescent molecules in the gap between 40 nm gold particles and achieved single photon emission with decay rates enhanced by more than two orders of magnitude (Figure 1-b) [2].

The coupling between single dye molecules and plasmonic gap antennas can be further optimized by selecting nanostructures where the transition dipole of the emitter is aligned with the gold particle dimer axis [3]. Importantly, the efficiency of DNA-templated optical antennas can be optimized by increasing the size of the gold particles (60 nm – 80 nm) to enhance the excitation and emission rates of single fluorescent molecules by two orders of magnitude while reaching quantum yields as high as 70 % [4]. Furthermore, by introducing two dye molecules that act as a FRET (Förster resonant energy transfer) pair, we show how field confinement in plasmonic antennas allows the modulation of non-radiative energy transfer processes [5].

The flexibility of DNA-based self-assembly also means that the morphology of the produced nanostructures can be modulated in-situ. For instance, the DNA template can feature a secondary structure, such as a hairpin loop, in order to actively modulate the distance between gold particles when introducing a specific DNA strand [6]. Importantly, single nanostructure scattering spectroscopy provides a direct estimation of interparticle distances in gold nanoparticle dimers linked by a short DNA double-strand [1]. This spectroscopic information can be inferred from simple widefield measurements on a calibrated color camera (figure 1-c) [7]. This allows us to monitor optically how the interparticle distance between 40 nm gold particles can be tuned, between 20 nm and ~1 nm, when modifying the local ionic strength. In particular, we use this spectroscopic technique to analyze the morphological stability of hybrid gold-DNA nanostructures when tuning the surface chemistry of gold particles or the local temperature [8, 9]. These results also open numerous perspectives for the active tuning of DNA-templated plasmonic nanoantennas under controlled physicochemical stimuli.

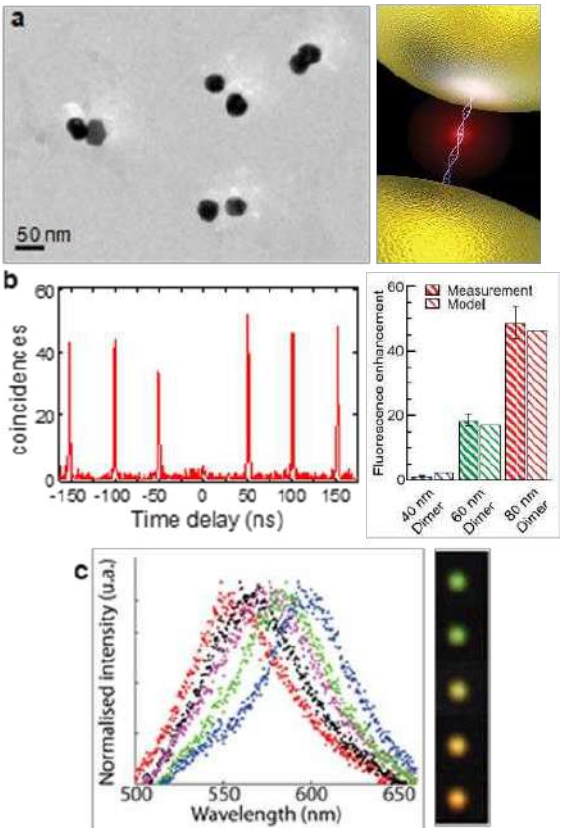


Figure 1: (a) Cryo-EM image of 40 nm AuNP dimers linked by a 30 base-pair DNA strand. (b) Photon antibunching from a single molecule in the center of a 40 nm AuNP dimer and average fluorescence enhancement values obtained with dimers of 40 nm / 60 nm and 80 nm gold particles. (c) Evolution of the scattering signal from a single 40 nm AuNP dimer, when increasing the salt concentration, measured with a confocal spectrometer (left) or a color camera (right).

References

[1] M. P. Busson, B. Rolly, B. Stout, N. Bonod, E. Larquet, A. Polman and S. Bidault, *Nano Lett.* 11, 5060, 2011

[2] M. P. Busson, B. Rolly, B. Stout, N. Bonod and S. Bidault, *Nat. Commun.* 3, 962, 2012

[3] M. P. Busson and S. Bidault, *Nano Lett.* 14, 284, 2014

[4] S. Bidault, A. Devilez, V. Maillard, L. Lermusiaux, J.-M. Guigner, N. Bonod, and J. Wenger, *ACS Nano* 10, 4806, 2016

[5] S. Bidault, A. Devilez, P. Ghenuche, B. Stout, N. Bonod, and J. Wenger, *ACS Photonics* 3, 895, 2016

[6] L. Lermusiaux, A. Sereda, B. Portier, E. Larquet, and S. Bidault, *ACS Nano* 6, 10992, 2012

[7] L. Lermusiaux, V. Maillard, and S. Bidault, *ACS Nano* 9, 978, 2015

[8] L. Lermusiaux, and S. Bidault. *Small* 11, 5696, 2015

[9] L. Lermusiaux, and S. Bidault. *Langmuir* 34, 14946. 2018

Self-Assembled Plasmon-Upconversion Nanoclusters for Cancer Theranostics

Wounjhang Park*

Department of Electrical, Computer & Energy Engineering, University of Colorado, Boulder, CO, USA
University of Colorado Cancer Center, Aurora, CO, USA
*corresponding author, E-mail: won.park@colorado.edu

Abstract

Nanoclusters of upconversion nanoparticle and gold nanorod are synthesized by a modified PEGylation process and further conjugated with antibody to epidermal growth factor receptor to target bladder cancer. They are then used to simultaneous imaging and optoporation aided chemotherapy of bladder cancer with high selectivity.

1. Introduction

Upconversion nanoparticles (UCNPs) have recently gained research interest due to several favorable characteristics. Because UCNPs upconvert lower energy photons in the near-infrared (NIR) region into higher energy photons in the visible, they provide distinct advantages of no autofluorescence, deeper tissue penetration, and minimal tissue damage. Furthermore, in contrast to conventional fluorescent probes such as organic dyes and quantum dots, UCNPs do not exhibit photobleaching or blinking. Compared to two-photon fluorescence or second harmonic generation, upconversion efficiency of UCNP is many orders of magnitude higher.

Plasmonic nanostructures are well known for their ability to enhance local field and have been studied to enhance upconversion. Negotiating the tradeoff between the plasmonic enhancement and the unavoidable quenching, however, is an on-going challenge [1]. A promising alternative direction is to use plasmonic-upconversion nanoclusters for multifunctionality, rather than upconversion enhancement. In this approach, one must still deal with metal losses but enjoys greater freedom of engineering.

2. Results and Discussion

2.1. Synthesis of nanoclusters

We use a modified PEGylation process to synthesize nanoclusters of UCNPs and gold nanorods (AuNRs). First, UCNPs are made water soluble by using polymer, poly(maleic anhydride-alt-1-octadecene) (PMAO). When reacted with NH_2-PEG-SH and NH_2-EtOMe, PMAO turns amphiphilic and binds with UCNPs. NH_2-PEG-SH provides thiols for further reaction with gold while the NH_2-EtOMe acts as a stabilizer to minimize aggregation of UCNPs. Then, the coated UCNPs bind with AuNRs through the gold-thiol bonding process. The AuNRs used in this work have an average width of 11 nm and length of 43 nm and has a localized surface plasmon near 800 nm [2]. It is noted that the plasmon resonance is not matched with either absorption or emission of UCNP, as the primary goal of this work is not to enhance upconversion but to achieve multifunctionality – upconversion luminescence for imaging/detection and plasmon-induced optoporation for therapeutics. Thus, we use small-size, detuned AuNRs for minimal luminescence quenching. As shown in Fig. 1, we achieved well-controlled synthesis of UCNP-AuNR nanoclusters and importantly UCNPs did not show any quenching.

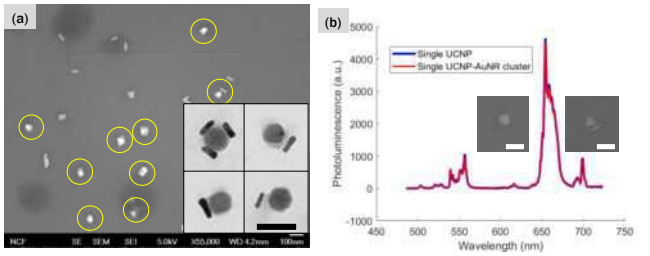


Figure 1. (a) Electron microscopy images of UCNP-AuNR nanoclusters. A low magnification SEM image reveals successful UCNP-AuNR conjugation yield of 34%. The inset shows higher magnification TEM images of the UCNP-AuNR clusters. Scale bars indicate 100 nm. (b) Upconversion PL spectra of single UCNP and UCNP-AuNR nanocluster consisting of one UCNP and one AuNR. There is no significant PL quenching due to the addition of a single AuNR. Scale bar indicates 100 nm.

2.2. Cancer targeting and imaging

The UCNP-AuNR nanoclusters were then functionalized with C-225, an antibody to epidermal growth factor receptor (EGFR) via the standard EDAC reaction. Human bladder cancer cells are known to over-express EGFRs while normal urothelial cells don't. Thus, when C-225 antibodies are present on UCNP surface, the nanoparticle will specifically bind to bladder cancer cell. The selective binding of C-225 conjugated UCNP-AuNR nanoclusters was tested by treating a mixture of EGFR-positive (A549) and EGFR-negative (H520) cells, a well-established model of EGFR expression, with the UCNP-AuNR nanoclusters. Figure 2(a) shows non-overlapping

green (EGFR-positive) and red (EGFR-negative) fluorescence, clearly demonstrating selective binding of our nanoclusters to the EGFR-positive cells only. This mixture of EGFR-positive and EGFR-negative cells is a good representative of the *in vivo* situations where EGFR-positive cancer cells are scattered in the midst of EGFR-negative normal cells. Figure 2(a) therefore serves as a powerful evidence that the UCNP-AuNR nanoclusters will selectively bind only to the EGFR-expressing cancer cells in the eventual human application.

Next, we demonstrate the high-contrast upconversion luminescence imaging capability of the UCNP-AuNR nanoclusters. Figure 2(b) shows an upconversion fluorescence image of T24T bladder cancer cells, an EGFR-positive cell line, treated with our nanoclusters. Unlike the conventional fluorescence imaging, there is no background autofluorescence, providing high contrast.

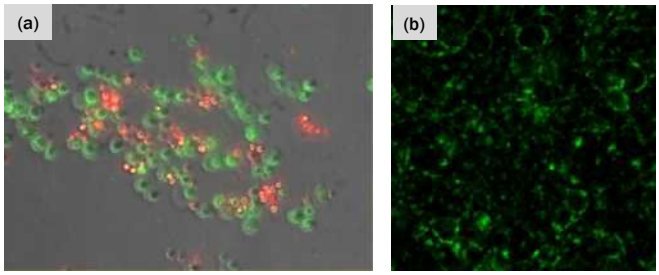


Figure 2. (a) Fluorescence micrograph of a mixture of A549 (EGFR-positive) and H520 (EGFR-negative) cells. (b) Upconversion fluorescence micrograph of T24T cells conjugated with UCNP-AuNR nanoclusters.

2.3. Targeted chemotherapy

We now demonstrate simultaneous upconversion imaging and optoporation capability. As shown in Figure 3(a), bladder cancer cells are identified clearly by the green upconversion fluorescence signal. We then irradiate only the region within the yellow circle with a femtosecond laser (energy of 8 pJ). The high peak power of the laser coupled with strong plasmon resonance of AuNR induces nano-cavitation which in turn results in membrane disruption. This process, often called optoporation, is first demonstrated with red dyes. As depicted by Figure 3(a), we observe a bright red fluorescence, resulting from dyes entering the cells and becoming fluorescent. It should be noted that the UCNP-AuNR mediated optoporation is highly localized and does not affect the neighboring cells. This is in contrast to photothermal ablation which could affect the neighboring cells due to heat dissipation.

Next we demonstrate the efficacy of the optoporation-based selective chemotherapy. For this, we design an experiment where we use sub-clinical dosages of cisplatin and monitor the cell viability for 24 hours after femtosecond laser irradiation. The cell viability is measured by fluorescence microscopy in which we use a dye that stains only the dead cells. As shown in Figure 3(b), we achieve cell viability below 20% with only 30 min of exposure of 1.5 μM of cisplatin when we utilize optoporation to enhance the chemotherapy drug intake, while the control samples (nanoclusters+laser but no cisplatin and cisplatin+laser but no UCNP-AuNRs) maintain viability of over 60%. The effectiveness of our nanocluster is evident from the fact that effective cell killing is achieved with a much shorter incubation time and a substantially lower chemotherapy drug concentration than previous reports. Both the shorter incubation time and lower dosage of chemotherapy drug are critical requirements for clinical applications because a lower dosage will reduce adverse side effects and 2 hours is known to be the longest intravescical treatment time tolerated in humans.

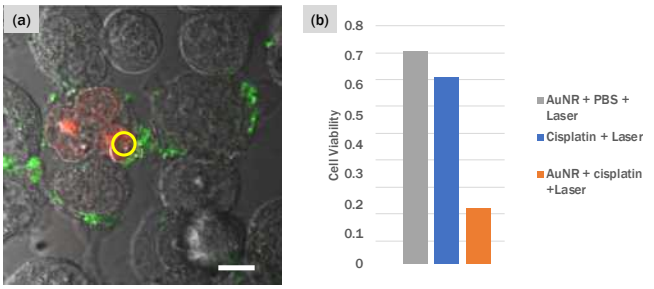


Figure 3. (a) Fluorescence micrograph of a bladder cancer cell treated with both UCNP-AuNR and femtosecond laser. (b) Cell viability for three groups of cells: nanocluster+laser, cisplatin+laser and nanocluster+ cisplatin+laser.

3. Conclusions

We demonstrate efficient coupling of UCNPs with AuNRs through a PEGylation process. The new PEGylation process allows the formation of highly stable UCNP-AuNR nanoclusters and further functionalization with antibodies for active targeting of bladder cancer. We demonstrated the capability of simultaneous upconversion imaging and targeted chemotherapy enabled by selective optoporation. Upconversion imaging provides high-contrast images leading to high sensitivity detection of cancer. Upon detection, a subsequent irradiation by femtosecond laser results in a highly selective optoporation. This then enables highly targeted chemotherapy, which results in cell death with sub-clinical dosages of chemotherapy drug.

It should be noted that we have demonstrate the cell targeting in a mixture of EGFR-positive and EGFR-negative cells, which is a good representation of in vivo situation. Also, we have used active targeting with EGFR antibody and accomplished cell targeting within 2 hours. This is important because 2 hours is generally considered the longest intravesical treatment time tolerated in human. Our approach thus shows a promising pathway to highly targeted bladder cancer treatment compatible with the current clinical practice.

References

[1] W. Park, D. Lu, and S. Ahn, Chem. Soc. Rev. **44**, 2940 (2015).

[2] S. K. Cho, K. Emoto, L. J. Su, X. Yang, T. W. flaig, and W. Park, Journal of Biomedical Nanotechnology **10**, 1267 (2014).

Correlated disordered nanostructures embedded in flexible film

Frédéric Hamouda, Gil Cardoso, Saber Hammami, and Béatrice Dagens

Centre de Nanosciences et de Nanotechnologies, CNRS, Univ. Paris-Sud, Université Paris-Saclay, C2N – 10 Boulevard Thomas Gobert, 91120 Palaiseau - France

*corresponding author, E-mail: beatrice.dagens@c2n.upsaclay.fr

Abstract

Metallic or dielectric nanostructures (NSs) modify the reflectance spectrum of functionalized glass surfaces and allow multiple or localized staining without using complex surface treatments. Here, we present the fabrication of metallic and dielectric NSs embedded in a flexible poly(dimethylsiloxane) (PDMS) film to modify its reflectance spectrum. The NSs are positioned with correlated disordered arrangements to avoid light diffraction and diffusion. PDMS enables fabrication of functionalized flexible and repositionable film which conforms to the shape of rigid transparent supports.

1. Introduction

Due to the increased interest for controlling the reflectance property of material surfaces for several optical applications during these last year, the research has been intensified to develop novel methods to nanostructure surfaces with nanowires, nanorods, nanodisks, or nanopillars with conical or pyramidal shapes[1-4]. The choice of materials, metals or dielectrics, as well as the dimensions of nanostructures depend on the required optical properties. In the field of solar cells silicon nanowires are commonly used to reduce reflection through destructive interference [5-7]. At the opposite, the reflectance of transparent display must be increased head-up display and augmented reality systems [8] in that respect thanks to the metal nanostructuration the reflectance spectrum and the apparent color can be controlled with a high spatial resolution down to subwavelengh dimension. In order to avoid any diffraction and diffusion effects, the NSs are arranged following a correlated disorder. Besides, for a different objective, a substrate with fully random metallic nanoparticles has been proposed as a transparent display revealing a blue image by scattering effect in the plane of the substrate [9]. Patterned flexible films with micro and nanostructures allow other functions compared to rigid substrates. Authors report the interest of poly(dimethylsiloxane) PDMS for its mechanical, optical and physical properties and to obtain flexible functionalized film for different optical applications [10,11]. It is elastic, flexible and transparent. Its flexibility permits a good conformity on non-planar surface. For these points we propose to present a new manufacturing method to embed metallic and dielectric NSs with a correlated disordered arrangement in a flexible PDMS film.

2. Fabrication

The objective is to embed NSs in a flexible 2 mm thick PDMS film. Metallic and dielectric NSs are firstly fabricated by electron beam lithography. For metallic nanostructures, manufacturing process is schematized in Figure 1. E-beam lithography is made on molybdenum sacrificial layer (Fig. 1a) by a Nanobeam (NB4) system with an accelerating voltage of 80 Kv and a current of 2 nA. Preliminary step is a spin-coated PMMA A2 resist on molybdenum sacrificial layer deposited on a silicon substrate by sputtering. An Ag layer is deposited on lithographied resist and followed by a lift-off process (Fig. 1b). PDMS is then coated to embed metallic nanoparticles (NPs) in flexible substrate before a bake (Fig 1c).

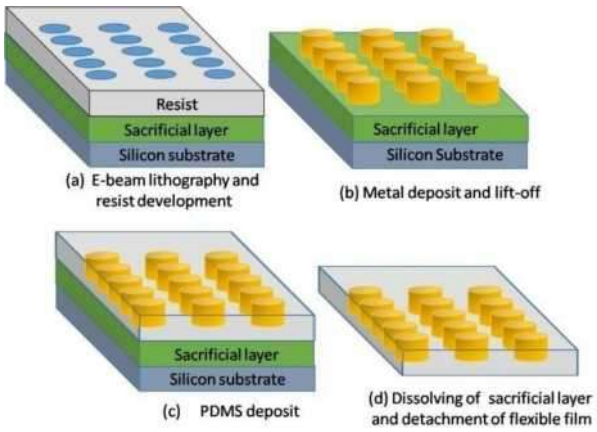


Figure 1: Scheme of the developed process.

The usage of soluble sacrificial layer is necessary to successfully transfer the NPs to the PDMS film with no mechanical peeling. Flexible film with metallic nanostructure grating is separated from silicon substrate after dissolution of molybdenum in H_2O_2 (Fig. 1d).

In the case of dielectric NSs, amorphous silicon (aSi) is deposited on molybdenum sacrificial layer before e-beam lithography, and a metallic mask is fabricated by lift-off

before reactive ionic etching of the aSi layer. Transfer of the Si NSs follows then the same process as in the case of metallic NSs.

3. Correlated disorder

Following our previous work [8], the NSs have been arranged according to a correlated disorder. The design of correlated disorder has been determined by using centroidal Voronoi tessalation algorithm applied on an initially random arrangement [12]. It is characterized by the structure factor (Fig. 2, right) determined by calculating the Fourier transform of the NS assembly pair correlation function. The structure factor is equal to zero for kD values lower than ~2π: considering that k is the projection of wavevector 2π/λ and D the average distance between NSs, diffusion effect will be reduced for wavelength higher than ~D.

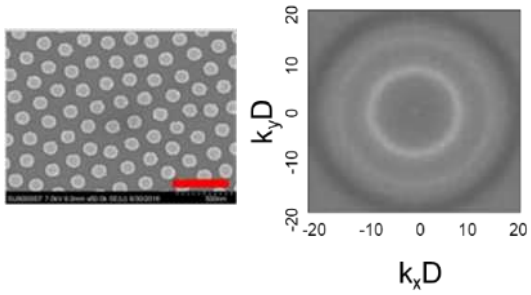


Figure 2: SEM image of correlated disorder arrangement of silver NPs, and calculation of the structure factor (Fast Fourier Transform of the pair correlation function).

We have fabricated such assembly in the case of D~250nm for metallic NSs [8], and we have checked improvement of reflectance at λ =590nm with no parasitic diffusion neither diffractive effects. We will show preliminary results obtained in the case of similar NSs embedded in PDMS.

4. Conclusions

We have developed a new technological process in order to embed metallic or dielectric nanostructures in PDMS: the process is based on sacrificial layer, without requirement of mechanical peeling. In order to obtain transparent functionalized substrates without diffusion and diffraction effects, the nanostructures are arranged following a correlated disorder arrangement. Such flexible and repositionable substrates can be used in many applications like augmented reality or glazing functionalization.

Acknowledgements

This work was done with the CTU IEF-MINERVE facility and partly supported by the RENATECH network and the General Concil of Essonne. It has been also supported by the ANR funded project PLANISSIMO (ANR-12-NANO-0003).

References

[1] Y-Ch. Lee, C-C. Chang, Y-Y.Chou,*Fabrication of broadband anti-reflective sub-micron structures using polystyrene sphere lithography on a Si substrate*,Photonics and Nanostructures-Fondamentals and applications 12: 16-22, 2014.

[2] F. Saffih, C. Con, A. Alshammari, M. Yavuz, B. Cui, *Fabrication of silicon nanostructures with large taper angle by reactive ion etching*, Wiley, J. Vac. Sci. Technol. B 32(6), Nov/Dec 2014.

[3] H. Yi, Y. Wensheng, T. Xinyu, H.Lijun, *Study on silicon nanopillars with ultralow broadband reflectivity via maskless reactive ion etching at room temperature*,Materials Science & Engineering B 223:153-158, 2017.

[4] M. Khorasaninejad, J Walia, S. S. Saini, *Enhanced first-order Raman scattering from arrays of vertical silicon nanowires*,Nanotechnology 23: 275706 (7pp), 2012.

[5] Hui Fang, Xudong Li, Shuang Song, Ying Xu, Jing Zhu, *Fabrication of slantingly-aligned silicon nanowire arrays for solar cell applications*, Nanotechnology 19: 255703 (6pp), 2019.

[6]L. Tsakalakos, J. Balch, J. Fronheiser, B. A. Korevaar, O. Sulima, J. Rand, *Silicon nanowire solars cells*,Appl. Phys. Lett 91: 233117, 2017.

[7]AvraKundu, Sonali Das, S. M. Hossain, Swapan K. Datta, HiranmaySaha,*Tapered silicon nanopillars for enhanced performance thin film solar cells*,Energie Procedia 54: 389-399, 2014.

[8] H. Bertin, Y. Brûlé, G. Magno, T. Lopez, P. Gogol, L. Pradere, B. Gralak, D. Barat, G. Demesy, B.Dagen,*Correlated Disordered Plasmonic Nanostructures Arrays for Augmented Reality*, ACS Photonics: 5, 7, 2661-2668 , 2018.

[9] C. W. Hsu, B. Zhen, W. Qiu, O. Shapira, B. G. Delacy, J. D. Joannopoulos, M. Slojacic, *Transparent display enabled by resonant nanoparticle scattering*, Nat. Commun., 5: 4152, 2014

[10] X. Dai, A. Messanvi, H. Zhang, C. Durand, J. Eymery, C. Bougerol, F. H. Julien, M. Techernycheva, *Flexible Light-Emitting Diodes Based on Vertical Nitride Nanowires*,Nano Lett. 15: 6958-6994, 2015.

[11]D. Visser, S. B. Basuvalingam, Y. Desieres, S. Anand, *Optical properties and fabrication of dielectric metasurfaces based on amorphous silicon nanodisk arrays*, Optical Express Vol. 27, No.4, 2019.

[12] Du, Q.; Faber, V.; Gunzburger, M. CentroidalVoronoiTessellations: Applications and Algorithms. *SIAM review***1999**, *41(4)*, 637–676.

Ligand-free synthesis of gold nanoparticles incorporated within oriented cylindrical block copolymer films : towards optical metamaterials

Florian Aubrit,[1,2] Fabienne Testard, [1] Aurélie Paquirissamy, [1] Frédéric Gobeaux, [1] Xuan Wang,[2] Frédéric Nallet, [2] Philippe Fontaine, [3] Virginie Ponsinet, [2] Patrick Guenoun,[1,*]

[1]*LIONS, NIMBE, CEA, CNRS, Université Paris-Saclay, CEA-Saclay F-91191 Gif-sur-Yvette Cedex*
[2]*Centre de Recherche Paul Pascal, Université de Bordeaux, UPR CNRS 8641, Pessac*
[3] *Synchrotron SOLEIL, L'Orme des Merisiers, Saint-Aubin-BP 48, F-91192 Gif-sur Yvette Cedex*
*corresponding author, E-mail: : patrick.guenoun@cea.fr

Abstract

We report a method to incorporate non-functionalized gold nanoparticles (AuNPs) in oriented cylindrical phases of poly(styrene)-b-poly(vinylpyridine) (PS-b-PVP) block copolymers, perpendicular to a substrate. The combination of AFM, TEM, GISAXS and spectroscopy allows complete characterization of the nanocomposites. AuNPs are produced by the ultra-sound reduction of a gold salt in the copolymer solution, prior to the deposition of the films by spin-coating. The AuNPs are found to be located within the PVP cylinders exclusively. The seeded-growth of these pre-formed AuNPs by a further ultra-sound treatment produced plasmonic AuNPs (up to d =10 nm). For perpendicular cylinders, the PVP domains are swollen without any change in their orientation. Ellipsometric optical properties of these plasmonic AuNPs embeded into oriented cylinders show a definite extinction in reflectivity at a precise energy and incidence angle.

1. Introduction

Hybrid nanocomposites including noble metal nanostructures have gained great interest due to their unique optical, properties.[1] They are essential elements of nanophotonics which explore the possibility of modulating light propagation with a very small amount of matter using nanoscale phenomena. The occurrence of plasmons at metal/dielectric interfaces is indeed one of the key phenomena used in nanophotonics towards the fabrication of nanostructured noble metal–dielectric materials and surfaces. In this context, increasing interest focuses on the incorporation of gold nanoparticles (AuNPs) into block copolymer (BCP) matrices, which allows the combination of the localized surface plasmon resonance[2] of the AuNPs with the ability of the BCP to self-assemble into well-organized 3D nanostructures,[3] such as lamellae, cylinders or spheres. Here, we report on the formation of PS-b-PVP films organized in cylindrical mesophases and containing AuNPs, a geometry akin to hyperbolic ones which are very promising for providing unusual wave propagation.[4] The incorporation of AuNPs in polymer was performed by a two step procedure: (1) the AuNPs were produced by sonication of the solution prior to (2) casting of films. This synthesis method avoids adding extra-species such as a ligand or a reducing agent in the solution. We also proved the efficiency of the seeded-growth method to obtain larger AuNPs exhibiting plasmon resonance. The processes of sonication and spin-coating of a gold-containing copolymer solution allow for an easy and controllable formation of self-organized plasmonic hybrid films. The full characterization of the perpendicular of PS-b-P4VP and PS-b-P2VP was achieved by Atomic Force Microscopy(AFM), Transmission Electron Microscopy (TEM) and Grazing-Incidence Small-Angle X-ray Scattering (GISAXS) experiments. First optical characterization of these films was achieved by variable angle spectroscopic ellipsometry. In particular, p-polarized visible radiation incident on the films containing the plasmonic nanoparticles presents an extinction accompanied by a phase jump at a specific wavelength and incidence angle. Furthermore, these wavelengths and angles were found to depend on the nanoparticle size.

2. Experimental

2.1. Materials

Two different diblock copolymers of poly(styrene)-block-poly-(4-vinylpyridine) (PS-b-P4VP) and one diblock copolymer of poly(styrene)-block-poly(2-vinylpyridine) (PS-b-P2VP) were purchased from Polymer Source, Inc., and used as received. Gold(III) chloride ($AuCl_3$, 99.99%) and sodium bromide (NaBr) were purchased from Sigma Aldrich and used as received.

2.2. Film preparation

The PS_{48}-b-$P4VP_{25}$ and PS_{27}-b-$P4VP_7$ copolymers were dissolved in a mixture of toluene/tetrahydrofurane (THF) in order to yield 1 wt% solutions. These solutions were spin-cast at 2000 rpm for 1 minute to yield ~100 nm-thick films. The residual solvent in the spin-cast films was removed by placing the films in vacuum for 2 h. For some samples, solvent annealing in vapors of a mixture chloroform/ethanol (10 : 1) was performed for 1 min at 60°C. The films were then quickly removed from the vapor chamber and dried with nitrogen and finally placed in vacuum for 2 h.

2.3. In situ formation of gold nanoparticles (AuNPs) by sonication

Copolymer solutions were prepared as described above and then mixed with a 0.1 M $AuCl_3$ solution in toluene in order to obtain various gold/pyridine molar ratios (from Au/Pyr = 0.1 to Au/Pyr = 5.5). The solution was protected from light and stirred overnight. AuNPs were synthetized by sonication in a bath (Elmasonic P30H, 37 kHz, 120W) for a given time (from 1 to 10 min) at room temperature. The films were then spin-cast as described above. Seeded growth kinetics were studied by adding more gold salt (Au/Pyr = 0.2, each addition) in the copolymer solution containing the previously formed AuNPs (initially with a ratio of Au/Pyr = 0.5). The mixture was sonicated again to grow metallic gold on the surface of the AuNPs. This process of gold addition/sonication was repeated four times, in order to get AuNPs bigger in size.

2.4. Characterization

Atomic Force Microscopy, Transmission Electron Microscopy and GISAXS were used as described in Ref. 5.

3. Results and Discussion

Addition of a gold salt ($AuCl_3$) in the PS_{27}-b-$P4VP_7$ copolymer solution and further sonication leads to the formation of AuNPs as demonstrated by UV/visible spectroscopy, evidencing the decrease of the Au(III) peak at 325 nm. TEM image (Fig. 1) of a dropcast film from the solution shows that the AuNPs formed by sonication were confined inside the P4VP domains, due to the affinity between gold and the pyridine group of P4VP. The average NP diameter determined by image analysis on the TEM micrographs was found to be 2–3 nm and could reach up to 10 nm after the seeded growth process was used. The conservation of the perpendicular orientation of cylinders when AuNPs are incorporated in the PS27-b-P4VP7 films was evidenced by AFM, TEM and GISAXS experiments, leading to an anisotropic structure with plasmonic features localized in perpendicular cylinders. Only a moderate increase of the cylinders diameter due to AuNPs incorporation was measured. At different growth steps of the gold nanoparticles by sonication, the films were studied using variable angle spectroscopic ellipsometry. The information contained in the ellipsometry data can be represented as the (Ψ, Δ) angle pair of the complex ratio of p and s polarized reflectivities $r = r_p/r_s = \tan(\Psi)_\exp(i\Delta)$. The ellipsometric data of the films, show the existence of a cancellation of the ellipsometric intensity angle Ψ, while the ellipsometric phase angle Δ jumps abruptly of more than 180° at a given incidence angle and photon energy. In the example shown in Fig. 2, for the film with the AuNPS obtained by two growth cycles (AuNP diameter of 7 nm), this specific behavior occurs at an incident light energy of 2.55 eV and an incidence angle of Θ = 65°.

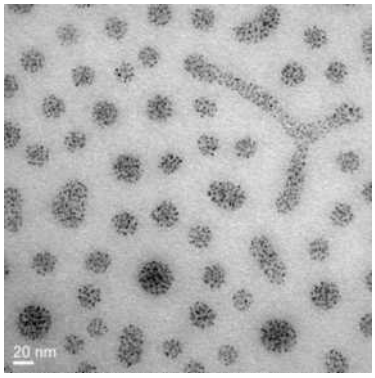


Fig. 1 : TEM picture proving AuNPs insertion in oriented polymer cylinders

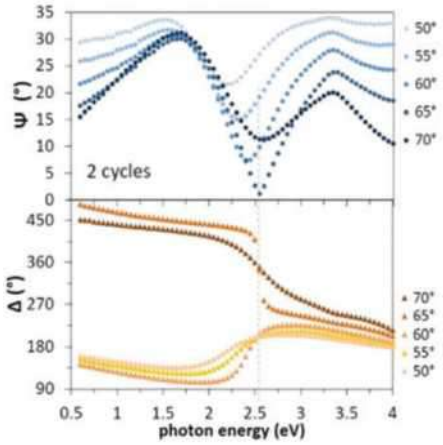


Fig. 2 : Annulation of Ψ and a jump in Δ are visible for an energy of 2.55 eV (λ = 486 nm) and an angle of incidence of Θ = 65°.

4. Conclusions

We produced anisotropic films of the block copolymer PS-b-PVP containing in situ synthetized plasmonic AuNPs of controlled sizes between 2 nm and 4 nm aligned along oriented cylinders. This method offer a very controlled way for easily inserting dense population of small sized AuNPs (2 nm) in an organic nanostructured film. Finally, we demonstrate promising optical properties of these hybrid films since they exhibit a sharp extinction accompanied by a phase jump at a specific wavelength and incidence angle.

References

[1] M.-C. Daniel and D. Astruc, *Chem. Rev*., 104 : 293, 2004

[2] W. L. Barnes, A. Dereux and T. W. Ebbesen, *Nature*, 424 : 824. 2003

[3] F. S. Bates and G. H. Fredrickson, *Phys. Today*, 52 : 32, 1999

[4] C.L. Cortes, W. Newman, S. Molesky & Z. Jacob, *J. Opt.,* 14 :063001, 2012

[5] F. Aubrit, F. Testard, A. Paquirissamy, F. Gobeaux, X. Wang, F. Nallet, P. Fontaine, V. Ponsinet, P. Guenoun, *Journal of Materials Chemistry C,* 6 : 8194-8204, 2018

Second-harmonic generation from metal oxide metasurfaces and photonic crystals

Flavia Timpu[1], Viola Valentina Vogler-Neuling[1], Rachel Grange[1]

[1]Optical Nanomaterial Group, Institute for Quantum Electronics, ETH Zurich, Switzerland
*corresponding author, E-mail: ftimpu@phys.ethz.ch

Abstract

We fabricate barium titanate metasurfaces from thin films and woodpile photonic crystals from nanoparticles to exploit the bulk optical nonlinearities of this non-centrosymmetric metal oxide. We demonstrate efficient second-harmonic generation in both devices, which shows the potential of top-up and bottom-up fabrication for nonlinear versatile flat photonics.

1. Introduction

Metasurfaces and photonic crystals have the ability to reshape the wavefront over the scale of few wavelengths [1]. Thus, it is possible to modify the phase, amplitude and polarization of a wave using quasi-two-dimensional devices. Currently, metasurfaces with nonlinearities are mostly made of metals [2] or semiconductors [3]. These materials can suffer from high ohmic losses or absorption from the visible to the near ultraviolet (NUV) range. Additionally, in the case of metal metasurfaces, their second order nonlinearities such as second harmonic generation (SHG) originate mostly from their surfaces and asymmetric shapes, which limits their nonlinear conversion efficiency.
Here, we use the dielectric metal oxide barium titanate ($BaTiO_3$, BTO), which is transparent from the NUV to the infrared range and has high second order susceptibilities. Due to the high refractive index of BTO, single BTO nanostructures have both magnetic and electric resonances [4], which can be combined to obtain novel properties such as tailored emission directivity. Based on the properties of single BTO nanoparticles, we design and fabricate BTO metasurfaces and photonic crystals by top-up and bottom-up approaches.

2. Results and discussion

2.1. Top-up fabrication

We deposit layers of BTO (Fig. 1a) by pulsed laser deposition. The crystal structure of the layer is determined by XRD measurements (Fig. 1b), while the thickness and its refractive index are measured by ellipsometry (Fig. 1c). We etch the BTO layer by a top-down fabrication method using inductively coupled plasma (ICP). The obtained metasurfaces (Fig. 1d) consist of a square lattice of nanodisks with variable heights, radii and periods. The measurement of the reflectance and transmittance are in good agreement with the simulations, which indicates that the refractive index is not altered by the fabrication process.

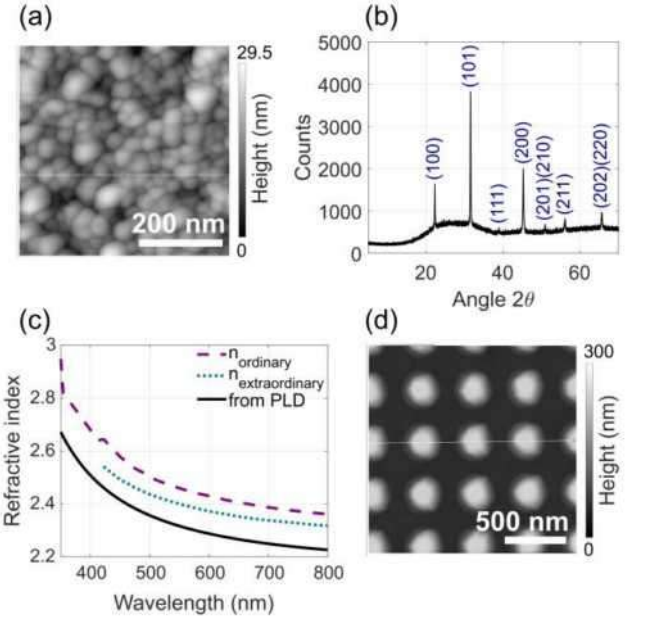


Figure 1: (a) AFM of a PLD grown BTO layer. (b) XRD measurement of the PLD grown BTO layer. The reflection peaks are labeled with the corresponding crystallographic planes of BTO. The continuum is caused by the amorphous glass substrate below the layer. (c) Measured refractive index of the BTO layer (solid black line). The ordinary (dashed purple line) and extraordinary (dotted blue line) refractive indices for bulk BTO are shown for comparison. (d) AFM of a BTO metasurface.

2.2. Bottom-up fabrication

We demonstrate a bottom-up soft nanoimprint lithography [5] fabrication technique to obtain nonlinear photonic crystals starting from dispersions of BTO nanoparticles (NPs) (Fig. 2a) and a sol-gel precursor. We use a silicon master mold to produce PDMS daughter molds. The PDMS molds are placed on dispersion layers spin coated on a glass substrate. This is followed by exposure to a UV lamp to cure the particle-sol-gel precursor solution in the mold in the form of woodpiles and removal of the PDMS mold. We stack several BTO NP woodpiles

using planarization layers (Fig. 2b), which are finally removed by calcination. We measure a photonic band gap at 560 nm by detecting the transmittance of the BTO woodpile photonic crystal.

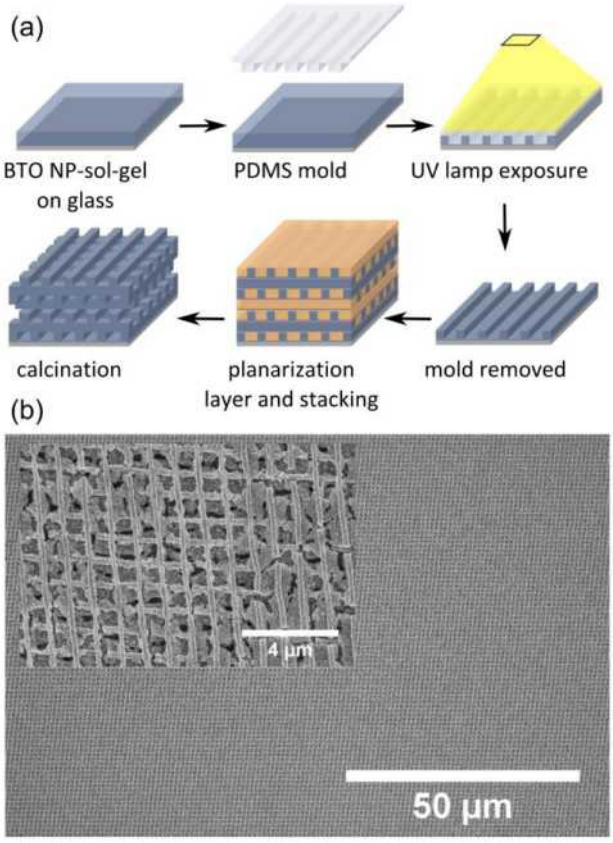


Figure 2: (a) Schematic of the soft nanoimprinting lithography process used to fabricate BTO woodpiles starting from a BTO NP-sol-gel precursor solution. (b) SEM micrograph showing two stacked layers of BTO woodpiles.

2.3. Second harmonic generation

We measure the SHG efficiency from the BTO metasurfaces and BTO woodpile photonic crystals in a home-built SHG transmission microscope. In the case of the BTO metasurface, we observe an enhanced SHG signal compared to the original unpatterned layer of BTO (Fig. 3 a-b). This enhancement appears because the incident electric field is confined in the volume of the BTO nanostructure and also due to the formation of SHG diffraction orders. In case of the BTO woodpile photonic crystals, we observe that the SHG efficiency is reduced at the photonic band gap at 560 nm, as the light is trapped in the photonic crystal (Fig. 3c).

3. Conclusions

We showed that nonlinear BTO periodic nanostructures such as metasurfaces or photonic crystals can be fabricated from BTO grains or nanoparticles. Following the demonstration of SHG emission shown in this work, we will investigate if further properties of bulk BTO are present in BTO nanostructures.

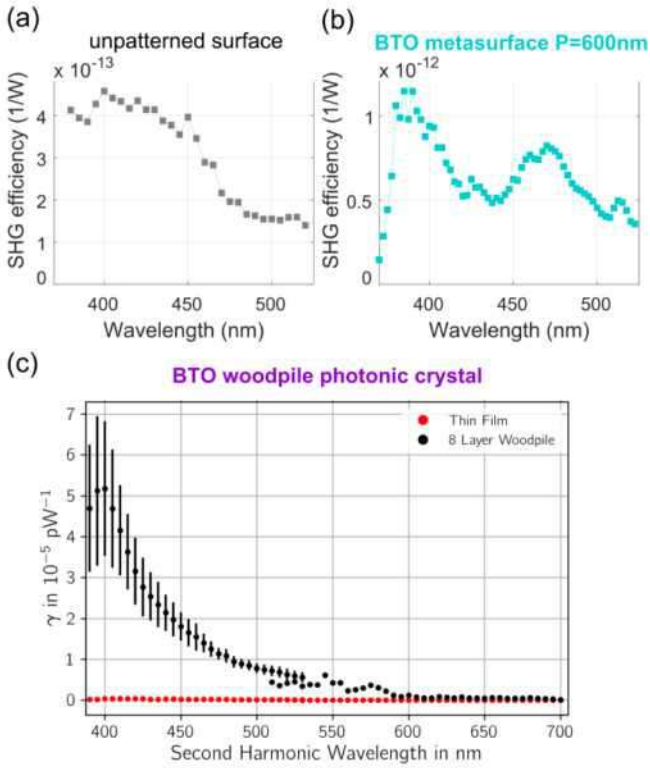


Figure 3: (a) SHG efficiency of the unpatterned BTO layer. (b) SHG efficiency of the a BTO metasurface consisting of disks with a radius of 160 nm and a period of 600 nm. (c) SHG emission efficiency of a 8-layer BTO woodpile photonic crystal compared to an unpatterned layer of BTO NP-crosslinked sol-gel layer.

Acknowledgements

We thank M. Trassin and M. Fiebig for the fabrication of the BTO layers by PLD.

References

[1] S. Jahani, Z. Jacob, All-dielectric metamaterials, *Nat. Nanotechnol*. 11: 23–36 (2016).

[2] K. O'Brien, H. Suchowski, J. Rho, et al., Predicting nonlinear properties of metamaterials from the linear response, *Nat. Mater*. 14: 379–383 (2015).

[3] S. Liu, S. Saravi, G. A. Keeler, et al., Resonantly enhanced second-harmonic generation using III-V semiconductor all-dielectric metasurfaces, *Nano Lett*. 16: 5426 – 5432 (2016).

[4] F. Timpu, A. Sergeyev, N. R. Hendricks, R. Grange, Second-Harmonic Enhancement with Mie Resonances in Perovskite Nanoparticles, *ACS Photonics* 4: 76–84 (2017).

[5] M. R. Beaulieu, N. R. Hendricks, J. J. Watkins, Large-Area Printing of Optical Gratings and 3D Photonic Crystals Using Solution-Processable Nanoparticle /Polymer Composites, *ACS Photonics* 1(9): 799–805 (2014).

Leaky Mode Engineering for Spectral Light Conversion Enhancement on Silicon Photonic Crystal Slabs

Doguscan Ahiboz[1], Phillip Manley[1,2], Christiane Becker[1],
[1]Helmholtz Zentrum Berlin für Materialien und Energie, Berlin, Germany
[2]Zuse Institute Berlin, Berlin, Germany
*corresponding author, E-mail: doguscan.ahiboz@helmholtz-berlin.de

Abstract

We designed and produced two-dimensional Silicon photonic crystal slabs on glass operating at near-infrared wavelengths. By tuning the slab thickness, we were able to systematically adjust the spectral position of leaky modes associated with strong near field enhancement effects, over several hundreds of nanometers. Near and far field characteristics of the photonic crystal slabs were examined numerically and experimentally. Proper design yields 100-fold enhanced near fields at 1550 nm enabling efficient photon up-conversion in future solar energy and telecommunication devices.

1. Introduction

Photon up-conversion, a non-linear spectral light converting process, consist of (i) the absorption of multiple low frequency photons, and (ii) emission of a single high frequency photon by fluorescent materials, such as nano-particles. Up-conversion materials are of interest in bio photonics for background-free sensing [1], photovoltaics enabling the utilization of near infrared sub-bandgap photons of the absorbing material [2] as well as in telecommunication [3]. However, an efficient spectral light conversion process often requires high excitation intensities limiting its applicability in case of one-sun illumination and/or the detection of highly diluted substances. Advanced optical light management methods, such as engineering the leaky modes of photonic crystals (PhC) can open up practical applications by significantly enhancing excitation and emission of the electromagnetic radiation. By interaction of photon up-conversion materials placed on the surface of the PhCs with leaky modes the spectral conversion efficiency can be significantly increased. However, feasibility of large area application, reproducibility and being coast efficient is crucial for a PhC slab to be as a simple technological platform facilitating aforementioned applications. In this study, we have designed and realized Si PhC slabs, which exhibit leaky modes resonant with specific NIR wavelengths, by taking advantage of (i) non-toxicity, (ii) well developed technology, (iii) large area applicability, and (iv) high dielectric constant contrast with air of Si. Spectral and angular dependence of the near field enhancement factor and far-field behavior of leaky modes of the Si PhC slab were examined theoretically by optical simulations based on the Finite Element Method (FEM). Moreover, the far-field behavior of the leaky modes of the produced PhCs was experimentally measured by angle-resolved directional transmission (ARDT) measurements. The simulations and experimental angle resolved transmission and reflection results agree very well. The produced PhCs are hence a promising platform for enhanced photon up-conversion in bio photonics and photovoltaics

2. Methods

2.1. Development of silicon photonic crystal slabs

Photonic crystal slabs were developed by a soft nano–imprinting lithography (NIL) based method. Hexagonal nano-pillar lattice were transferred to sol-gel spin coated 5 cm x 5 cm glass substrates from a master structure by a PDMS mold. The transferred pattern was UV cured prior to thermal curing at 600°C in order to form hexagonal silicon oxide (SiO_x) nano-pillar array. Amorphous Si (a-Si) with various thickness (84 nm to 125 nm) were deposited on the imprinted substrate by electron beam (e-beam) deposition method. After the deposited Si layer crystallized at 600°C under N_2 flow, the nano-pillars were etched successively by chemically and mechanically. Consequently, smooth and uniform Photonic crystal hole slabs were formed whose surface is imaged by scanning electron microscopy (SEM) and demonstrated in figure 1.

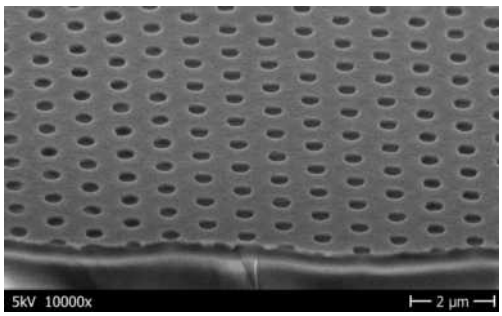


Figure 1: SEM image of the 84 nm silicon photonic crystal slab with lattice constant of 1000 nm.

2.2. Optical Simulation

The simulated electric field enhancement was obtained via finite element simulations using the commercial software JSMsuite. Periodic boundary conditions were applied in the

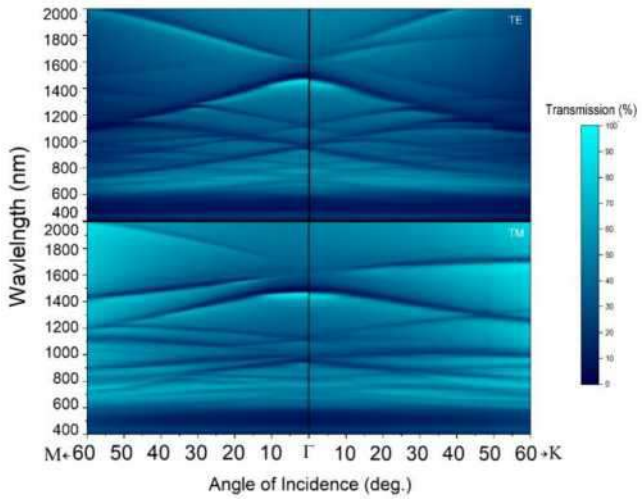


Figure 2: Angle-resolved transmission measurement results of a 125 nm Si PhC slabs with lattice constant of 1000 nm.

x-y plane, while transparent (perfectly matched layer) boundary conditions were used.

3. Results and Discussion

ARDT measurement is an effective technique which is capable of detection of resonant features originated from radiative resonance between leaky modes of a photonic crystal and incident radiation [4]. We experimentally detect spectral position of the leaky modes of the PhC slabs by ARDT measurements between 400 nm and 2000 nm. The measurements were performed by sweeping the angle of incidence from 0° to 60° by 2° steps through the high symmetry directions Γ → K and Γ →M with TE and TM polarized light in order to reveal spectral features of the leaky modes. The strong resonance features spanning NIR spectrum of the measured transmission spectra in figure 2 reveal the spectral distribution of the leaky modes. Furthermore, the simulated field enhancement with respect to the Si Slab thickness is shown in figure 3 for the 1550nm TE polarized radiation incident with varying angle of incidence between 0° to 60° on Si PhC slabs. The simulation results show that it is possible to enhance the field significantly, up to 100 times, inside the volume over the surface of the Si PhC slab either by changing the angle

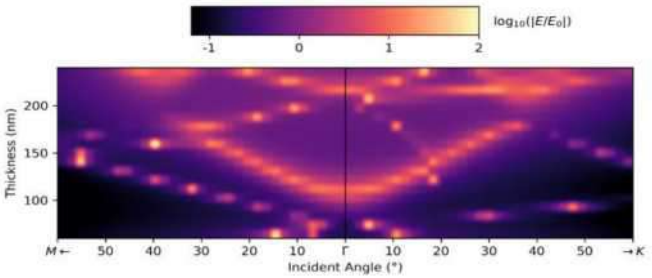


Figure 3: Simulated field enhancement of the Si PhC slabs with varying thickness (from 50 nm to 250 nm). E_o and E are amplitude of the 1550 nm TE polarized incident radiation and field over the Si PhC slab, respectively.

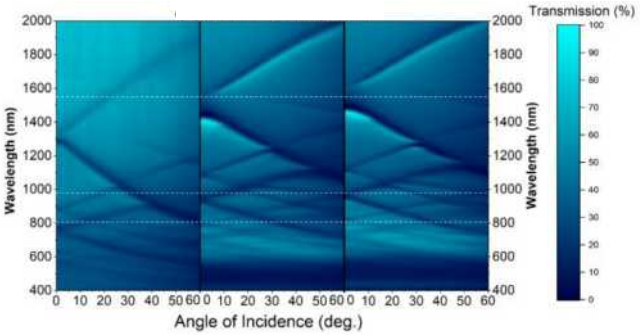


Figure 4: Angle-resolved directional transmission of the PhC slabs with various slab thickness (84 nm-106 nm-125 nm, left to right) in the M direction under TE polarization. (The dashed white lines guide the three important wavelengths, 808 nm-980nm-1550nm for the applications).

of incidence or thickness of the slab. However, most of the practical applications require light incident close to the normal incidence. Therefore, the leaky modes of the PhC slabs with various slab thicknesses were also experimentally studied by considering the resonant features around normal incidence. The measured resonance patterns of the Si PhC slabs in the figure 4, which shift towards to longer wavelength with the increasing Si slab thickness, demonstrate that how effectively spectral position of the leaky modes can be tuned and engineered by adjusting the slab thickness.

4. Conclusion

In summary, a feasible and large area applicable production procedure of Si PhC slab, whose leaky modes are resonant with external electromagnetic radiation, were demonstrated. Furthermore, the demonstrated production method makes us enable to tune resonant wavelengths of the leaky modes of Si PhC by changing an easily accessible experimental parameter (Si slab thickness). Thus, the produced Si PhC slabs can serve as a platform to enhance UC process at 1550 nm for telecommunication and photovoltaic applications.

References

[1] S. Wen, J. Zhou, K. Zheng, A. Bednarkiewicz, X. Liu, D. Jin, Advances in highly doped upconversion nanoparticles, *Nat. Commun.* 9: 2415 – 2426, 2018.

[2] T. Trupke, M. A. Green, P. Würfel, Improving solar cell efficiencies by up-conversion of sub-band-gap light, *J. Appl. Phys.* 92: 4117 – 4122, 2002.

[3] R. Hostein, R. Braive, M. Larqué, K.-H. Lee, A. Talneau, L. Le Gratiet, I. Robert-Philip,I. Sagnes, A. Beveratos, Room temperature spontaneous emission enhancement from quantum dot in photonic crystal slab cavities in the telecommunications C band, *J. Appl. Phys.* 94: 123101, 2008.

[4] S. Fan, J. D. Joannopoulas Analysis of guided resonances in photonic crystal slabs, *Phys. Rev. B* 65: 235112 1 – 8, 2002.

Silicon Particles with Optical Magnetic and Electric Mie Scattering: from the Synthesis to the Assembly of a Metamaterial

Maria Letizia De Marco[1*], Taizhi Jiang [2], Jie Fang[3], Benoît Miller[1],Brian Korgel[2], Yuebing Zheng[3], Philippe Barois[4], Glenna L. Drisko[1] and Cyril Aymonier[1]

[1] Institut de Chimie de la Matière Condensée de Bordeaux-CNRS, 87 Avenue du Dr Albert Schweitzer, 33608, Pessac, France
[2] Department of Chemical Engineering, 1 University Station C0400, University of Texas at Austin, Austin TX, 78712
[3]Department of Mechanical Engineering, Materials Science and Engineering Program, 204 E. Dean Keeton Street, C2200, University of Texas at Austin Austin, TX, 78712
[4] Centre de Recherche Paul Pascal-CNRS, 115 Avenue du Dr Albert Schweitzer, 33600 Pessac, France
*corresponding author, E-mail: marialetizia.demarco@icmcb.cnrs.fr

Abstract

Silicon particles with sub-wavelength dimensions support intense electric and magnetic dipole scattering in the visible spectrum. They are one of the best candidates for the assembly of optical metamaterials. We propose a high through-put synthesis for the production silicon particles with Mie scattering in the visible spectrum. The produced particles have been assembled into a thin film by dip-coating. The optical properties of the individual particles and of the films have been characterized by single particle scattering, static light scattering and ellipsometry.

1. Introduction

Silicon particles have gained increasing interest in the community of metamaterials, as ideal building blocks for all-dielectric optical metamaterials. Dielectric metamaterials, based on Mie scattering, are a good alternative to plasmonic metamaterials, whose scattering efficiency is hindered by absorption losses in the visible spectrum [1], [2]. Mie theory describes the field scattered from a dielectric particle as a summation of magnetic and electric multipole resonances, called optical modes. The lowest frequency mode is the magnetic dipole scattering. The following higher frequency mode is the electric dipole scattering. The magnetic and electric dipole modes are very intense for silicon particles scattering visible light, thanks to the low imaginary part of silicon's refractive index at optical frequencies [2]. To exhibit visible magnetic and electric dipole scattering, Si particles should range between approximately 75 and 250 nm [3]. Today, the main obstacle to all-dielectric optical metamaterials is the manufacturing of Si particles of appropriate size and morphology.

Zywietz *et al.* synthetized silicon particles, with controlled size and crystallinity, by laser printing of a Si wafer [4]. These particles exhibit magnetic and electric dipole scattering of visible light. Although this method succeeded in producing particles with the right size and crystallinity for optical scattering, it is not an efficient strategy.

In fact, to produce enough particles to assemble a material, a high throughput synthesis is required. Typically, bottom-up techniques respond to this requirement. To date, it is possible to produce small Si particles (1-15 nm) or large micrometer and sub-micrometer particles (300 – 2 μm) by bottom-up techniques [3], while the fabrication of Si particles in the right size range for optical dipole scattering remains an unaccomplished challenge.

The high throughput is not the only requirement to be met. Since the scattering wavelength depends on particles' size [3], a batch of Si particles should be monodispersed in order to be apt for the assembly of a metamaterial. Moreover, monodisperse spheres auto-assemble very easily, forming ordered structures. P. Moitra and co-workers already proved that the auto-assembly of sub-micrometer spherical particles is an efficient method for the realization of a large scale dielectric meta-surface [1].

In this paper, we propose a modification of the synthesis published for the first time by L. E. Pell *et al.*, [5] in order to produce monodispersed Si particles with visible magnetic and electric dipole scattering. The scattering properties of individual particles have been characterized by single particle scattering. Complementary static light scattering measurements have been performed on the colloidal suspensions of Si particles, to assess the quality of each batch in terms of size dispersion. In fact, if the size dispersion is too broad, no sharp peaks can be detected, and therefore the sample is not ideal for the assembly of a metamaterial.

Finally, thin films have been deposited by dip-coating, starting from a colloidal suspension of Si particles. The optical properties of the films have been characterized by ellipsometry.

2. Experimental

2.1 Material synthesis

Amorphous silicon particles were synthetized by thermal pyrolysis of trisilane in supercritical hexane, using a Ti grade 2 batch reactor, according to a procedure published by L.E. Pell et al. [5]. All the reactions were carried out at 460°C, for 10 minutes. Once the reactor is cooled to room temperature, the particles are collected and washed three times with chloroform.

2.2 Material characterization

The size and size distribution of Si particles was characterized by scanning electron microscopy, using a Zeiss Supra 40 VP, operated at 5 kV. Single particle's scattering spectra have been collected using a set-up consisting of an inverted microscope equipped with a halogen white light source, a spectrophotometer and a ccd detector. Scattering spectra were collected between 400 and 1000 nm.

3. Results and discussion

The decomposition of trisilane in supercritical hexane has proven an ideal method for the production of Si spherical particles with Mie resonances in the near infrared region [6]. In this work, we attempt to reduce the size of Si particles, in order shift the electric and magnetic dipole scattering in the visible region.
The particle's size can be tuned by adjusting the initial concentration of trisilane, as shown in the graph below (in figure 1).

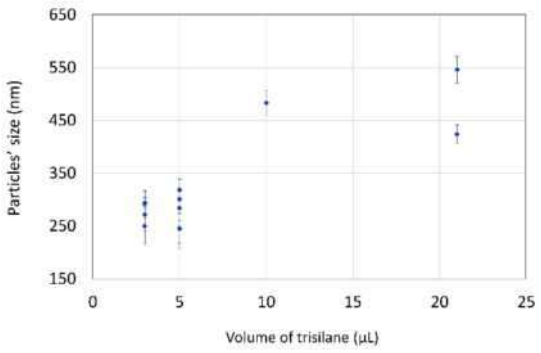


Figure 1: Effect of the quantity of trisilane on particles' size

When a concentration of trisilane of 4 mM (corresponding to a volume of trisilane of 5 µL) is used, particles with size smaller than 400 nm can be obtained. When the concentration is further decreased to 2,4 mM (corresponding to a volume of trisilane of 3 µL), the particles' size does not decrease sensibly. Therefore, for this study, we focused on a trisilane concentration of 4 mM. The produced particles, with size between 300 and 350 nm, exhibit magnetic and electric scattering in the visible spectrum (figure 2).

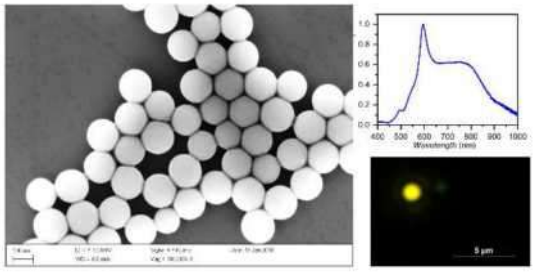


Figure 2: SEM image of particles realized by thermal decomposition of trisilane in supercritical hexane. The average size is 320 ± 28 nm (left). Scattering spectrum (top right) and dark field microscopy (bottom right) of a Si particle with diameter of approximately 300 nm.

1. Conclusions

Silicon particles with optical electric and magnetic dipole scattering have been synthetized according to an efficient bottom-up approach. This method is ideal for the assembly of optical metamaterials or metasurfaces, as it produces particles with a narrow size dispersion with a relatively high throughput.

References

[1] P. Moitra, B. A. Slovick, W. Li, I. I. Kravchencko, D. P. Briggs, S. Krishnamurthy, Large Scale All-Dielectric Metamaterial Perfect Reflector, *ACS Photonics* 2: 692−698, 2015.

[2] I. Staude, J. Schilling, Metamaterials Inspired Silicon Nanophotonics, *Nat. Photon.* 11: 274-284, 2017

[3] M. L. De Marco, S. Semlali, B. A. Korgel, P. Barois, G. L. Drisko, C. Aymonier, Silicon Based Optical Metamaterials: Focus on the Current Synthesis Challenges, *Angew. Chem. Int. Ed.,* 57: 4478-4498, 2018.

[4] U. Zywietz, A. B. Evlyukhin, C. Reinhardt, B. N. Chichkov, Laser printing of silicon nanoparticles with resonant optical electric and magnetic responses, Nat. Commun., 5: 3402-3409, 2014

[5] L.E. Pell, A. D. Schriker, F. V Mikulec, B. A. Korgel, Synthesis of Amorphous Si Colloids by Trisilane Thermolysis in High Temperature Supercritical Solvents, *Langmuir*, 20: 6546–6548, 2004

[6] L. Shi, J. T. Harris, R. Fenollosa, I. Rodriguez, X. Lu, B. A. Korgel, F. Meseguer, Monodisperse Silicon Nanocavities and Photonic Crystals with Magnetic Response in the Optical Region Nat. Commun., 4 : 1904-1911, 2013

Photonic crystal phosphors: materials meet structures for efficient color conversion

Tae-Yun Lee[1,2], Jongho Lee[1,2], Yeonsang Park[3], Kyung-Sang Cho[3], Kyungtaek Min[4], and Heonsu Jeon[1,2,5,*]

[1]Department of Physics and Astronomy, Seoul National University, Seoul 08826, Republic of Korea
[2]Inter-university Semiconductor Research Center, Seoul National University, Seoul 08826, Republic of Korea
[3]Samsung Advanced Institute of Technology, Suwon 16678, Republic of Korea
[4]Department of Nano-Optical Engineering, Korea Polytechnic University, Siheung 15073, Republic of Korea
[5]Institute of Applied Physics, Seoul National University, Seoul 08826, Republic of Korea
*corresponding author, E-mail: hsjeon@snu.ac.kr

Abstract

Phosphor material is reconfigured into a lateral photonic crystal structure such that the light-matter interaction can be enhanced, resulting in an improved color conversion efficiency. Following conceptual demonstrations, red and green photonic crystal phosphor plates are stacked in multiplicity on top of a blue light-emitting diode to generate white light of high quality and efficiency.

1. Introduction

The importance of phosphors has been revived with the emergence of phosphor-capped white light-emitting diodes (LEDs), where a GaN-based blue LED chip is combined with phosphor materials so that light with a wide emission bandwidth is generated cost-effectively. Phosphor development, however, has been predominantly materials-oriented and is quickly approaching its limitation. For a paradigm-shift in phosphor research, the authors' group proposed and demonstrated, called photonic crystal (PhC) phosphors [1]. The basic idea behind PhC phosphors is to structurally engineer phosphor materials into periodic PhCs. A key point in the PhC phosphor design is to tune the associated photonic band-edge (PBE) modes to the phosphor excitation wavelength and thus to induce an enhancement in phosphor excitation efficiency.

2. Device fabrication

Our PhC phosphor consisted of a lateral one-dimensional (1D) PhC backbone as an array of Si_3N_4 strip lines on a fused quartz substrate, with densely packed CdSe–CdS–ZnS core–shell–shell colloidal quantum dots (CQDs) coated atop (Fig. 1). After the substrate was diced into 1 cm × 1 cm square pieces, a 1D PhC grating pattern with the period of $\Lambda \approx 300$ nm and a duty-cycle of ~50% was obtained by laser interference lithography, followed by the pattern transfer down to the Si_3N_4 layer using $CF_4/O_2/N_2$ reactive-ion etching. CdSe– CdS–ZnS core–shell–shell CQDs, which were synthesized chemically, were dispersed in cyclohexane solution at 1.0 wt% and spin-coated at 2000 rpm to form a dense CQD film with no apparent void. A reference phosphor was prepared by spin-coating CQDs directly on a flat substrate, which resulted in a planar CQD film with a CQD amount equal to that of the PhC phosphor.

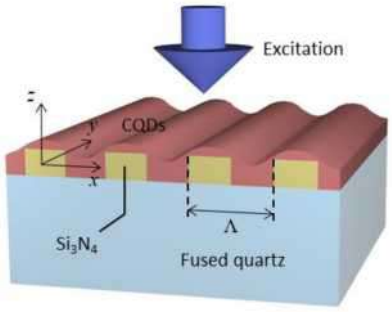


Figure 1: Schematic of the CQD 1D PhC phosphor structure in perspective, where cross-sectional structure and the groovy surface morphology are illustrated.

3. Fluorescence enhancement

Fluorescence spectra were measured for both the PhC and reference phosphors as functions of excitation wavelengths in the 410–510 nm range, which are summarized in Fig. 2. As can be seen from the figure, the fluorescence intensity for the PhC phosphor varies significantly with a strong enhancement for the excitation wavelength range of 430–480 nm, whereas the reference phosphor exhibits almost no variation. The fluorescence enhancement factor reaches its maxima 4.1 at 454 nm and 3.6 at 462 nm, which we attribute to two PBEs at the Brillouin zone center. These observation results are highly consistent with computer simulations based on the finite difference time-domain method.

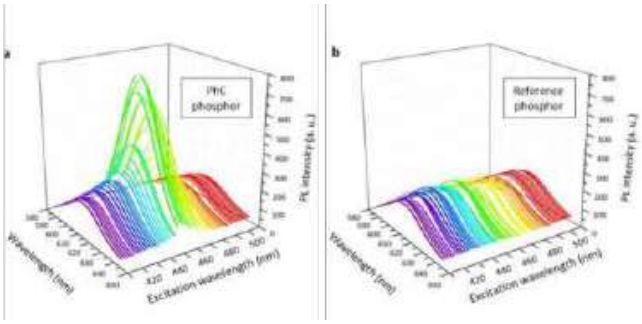


Figure 2: CQD fluorescence spectra for the PhC phosphor (a) and the reference phosphor (b), measured at various excitation wavelengths. All spectra were taken for TE-polarized excitation.

4. White light generation

To demonstrate the viability and applicability of the technology, we prepared two batches of PhC phosphors using red (620 nm) and green (530 nm) CQDs and stacked them on top of a blue LED chip (450 nm) to produce high-quality white light efficiently—thus economically [2]. The two kinds of PhC phosphors are almost identical in terms of structure (except for the CQDs used) as they are excited at the same wavelengths by the same blue LED chip. We were able to generate a quality white light with the chromaticity coordinates (0.332, 0.341) using a stack sequence of PhC-R3G11, which stands for 3 red PhC phosphor plates and 11 green PhC phosphor plates on the blue LED chip. The same stack sequence of the reference phosphor plates, Ref-R3G11, exhibits the chromaticity coordinates (0.216, 0.206), which is strongly bluish white. It required significantly more phosphor plates to produce the ideal chromaticity coordinates (0.333, 0.333) only using the reference phosphor plates: Ref-R5G16. Figure 3 shows the photographs taken from the three kinds of stack sequences.

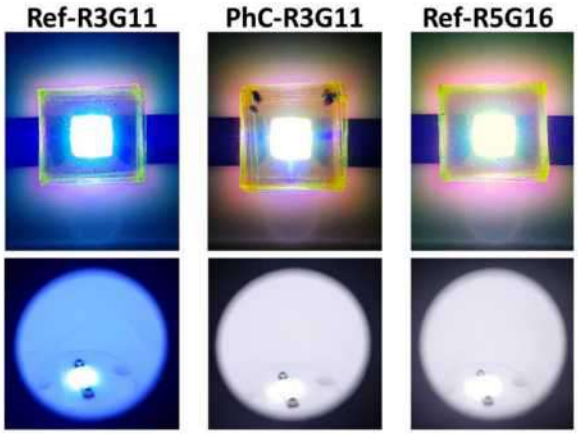


Figure 3: Photographs of LED+phosphor assemblies Ref-R3G11, PhC-R3G11, and Ref-R5G16 taken from directly above the sample assemblies (upper) and through the output port of the integrating sphere (lower).

5. Discussion

We have successfully demonstrated the concept and viability of the PhC phosphors, a totally new and paradigm-shifting approach for next-generation phosphors. Yet there still remain issues to be further refined and improved before the PhC phosphors can be accepted as an industrial standard, which include the elimination of excitation polarization dependence.

References

[1] K. Min, H. Jung, Y. Park, K.-S. Cho, Y.-G. Roh, S. W. Hwang, H. Jeon, Colloidal quantum dot photonic crystal phosphor: nanostructural engineering of phosphor for enhanced color conversion, *Nanoscale 9*: 8703, 2017.

[2] J. Lee, K. Min, Y. Park, K.-S. Cho, H. Jeon, Photonic crystal phosphors integrated on blue LED chip for efficient white light generation, *Adv*. *Mater*. *30*: 1703506, 2018.

Cooperative Energy Transfer Controls the Spontaneous Emission Rate Beyond Field Enhancement Limits

Mohamed ElKabbash[1], Tigran V. Shahbazyan[3], Jesse Berezovsky[1], Francesco De Angelis[2] and Giuseppe Strangi[1,2,4,*]

[1.] *Department of Physics, Case Western Reserve University, 10600 Euclid Avenue, Cleveland, Ohio, USA.*

[2.] *IIT - Istituto Italiano di Tecnologia, via Morego 30, 16163 Genova, Italy.*

[3.] *Department of Physics, Jackson State University, Jackson, Mississippi 39217, USA.*

[4.] *CNR-NANOTEC, Istituto di Nanotecnologia and Department of Physics, University of Calabria, Italy.*

giuseppe.strangi@case.edu.

Quantum emitters located in proximity to a metal nanostructure individually transfer their energy via near-field excitation of surface plasmons. The energy transfer process increases the spontaneous emission (SE) rate due to plasmon-enhanced local field. Here, we demonstrate significant acceleration of quantum emitter SE rate in a plasmonic nano-cavity due to cooperative energy transfer (CET) from plasmon-correlated emitters. The accelerated SE rate exceeds the rate acceleration experienced by individual emitters due to local field enhancement[1-2]. Using an integrated plasmonic nano-cavity, we realize up to six-fold enhancement in the emission rate of emitters coupled to the same nano-cavity on top of the plasmonic enhancement of the local density of states. The radiated power spectrum retains the plasmon resonance lineshape and frequency, with the peak amplitude proportional to the number of excited emitters indicating that the observed cooperative SE is distinct from superradiance[3]. Plasmon-assisted CET offers unprecedented control over the SE rate and allows to dynamically modulate the spontaneous emission rate at room temperature enabling an SE rate based optical modulator.

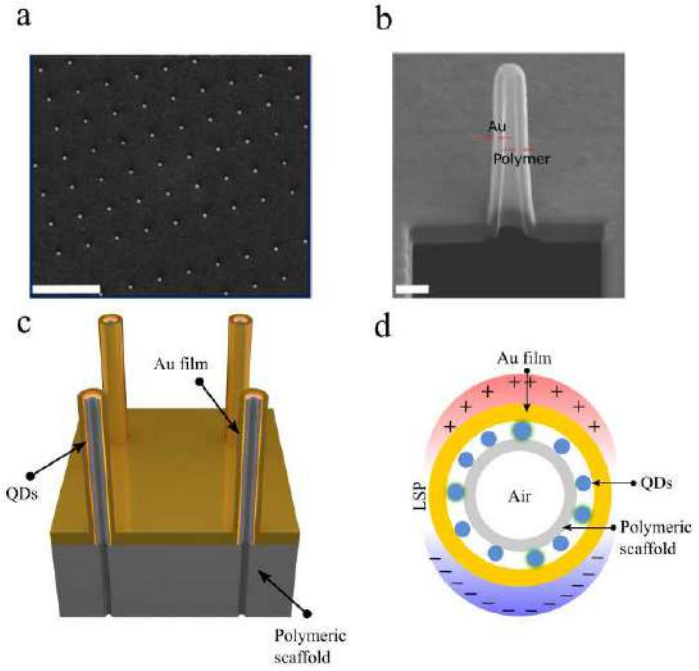


Figure 1: (a) SEM image of plasmonic nanocavity (PNC) array (scale bar= 5 mm). (b) SEM image of a cross-section of a single PNC that was cut using focused ion beam FIB (scale bar = 100 nm). (c) Schematic of the nano-pillar PNC. The quantum dots (QDs) are spin-coated on a polymeric scaffold, then an Au layer is deposited. (d) Schematic of a cross-section of a single nanopillar.

Here, we report the experimental observation of a cooperative SE from an ensemble of *N* excited quantum emitters (QEs) resonantly coupled to a plasmon nanocavity (PNC) acting as a plasmonic antenna[4]. We observe up to six-fold increase of the ensemble SE rate relative to the plasmonic LDOS enhancement which is linear in the excitation power. Simultaneously, the measured photoluminescence spectrum retains the plasmon resonance lineshape while the overall emission intensity increases linearly with the excitation power. These observations imply that the radiation is emitted by the plasmonic antenna following cooperative energy transfer (CET) from excited QEs. The linear dependence of the ensemble SE rate on the number of excited QEs (as opposed to total number of emitter) has not been observed previously. Such dependence as well as the incoherent nature of CET mechanism that does not require coherence buildup, in contrast to super-radiance[2], provides a unique possibility for dynamically controlling the SE rate in the *same* electromagnetic environment by varying excitation power[4]. We experimentally exploit CET to dynamically control SE rate by modulating the excitation power, resulting in *reversible* increase and decrease of the SE rate at room temperature, which was only possible in previous works using complex photonic devices at cryogenic temperatures. The cooperative enhancement of the ensemble SE rate takes place on top of the plasmon LDOS enhancement for individual emitter's SE rate paving the way towards SE rate control beyond field enhancement limits. This is particularly important for short-distance optical communication, to increase the modulation rate, and for optical data storage where faster SE rate increases data reading speed.

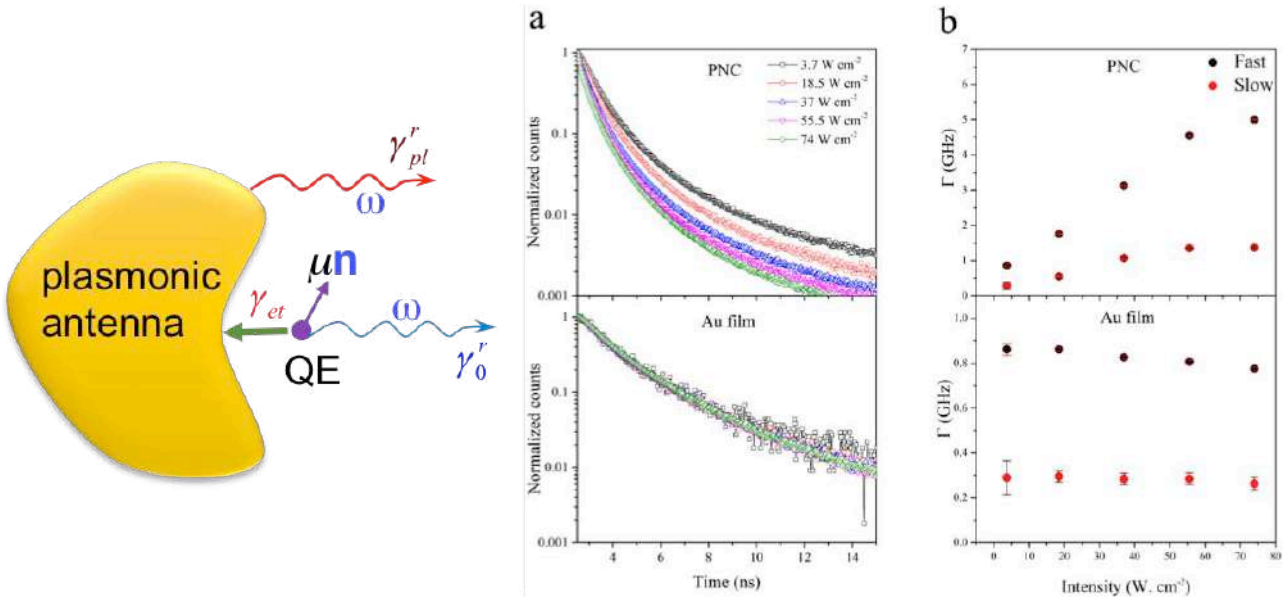


Figure 2: ***Left*** - Illustration of the energy transfer process at the basis of the CET. Incident light excites QDs that, subsequently, transfer their energy to excite localized surface plasmons (LSPs) which decay into a photon. ***Right*** - (a) Measured time-resolved photoluminescence for five different excitation intensities for the PNC (Top) and the reference Au film (Bottom). The SE lifetime is intensity dependent only for the PNC. (b) The fitted SE rate fast component (black spheres) and slow component (red spheres) for the PNC (Top) and for the reference Au film (Bottom). The fast and slow SE rate components vary by modifying *N*. The SE rate is linearly proportional to the excitation intensity.

REFERENCES

[1] E. M. Purcell, H. C. Torrey, and R. V. Pound, Physical Review **69**, 37 (1946).

[2] R. H. Dicke, Physical Review **93**, 99 (1954).

[3] T. V. Shahbazyan, Phys Rev Lett **117**, 207401 (2016).

[4] M.K. Elkabbash, T.V. Shahbazyan, J. Berezovsky, F. De Angelis, G. Strangi, Phys Rev Lett Under revision **(2019)**.

Metasurfaces atop Self-Assembled Metamaterials

Ullrich Steiner

March 18, 2019

The replication of the triply periodic morphology of suitable self-assembled triblock-terpolymers into plasmonic metals has been used for the manufacture of optical metamaterials. While the chiral morphology of the single gyroid holds promise for negative refraction, several aspects of this metamaterial are yet not well understood. One issue poses the termination of the tri-continuous bulk morphologies at the two surfaces. Using a combination of simulations and experiments we show that the termination of the gyroid surface breaks the cubic symmetry of the bulk morphology, inducing a strong linear dichroism. Furthermore, certain terminations lead to the creation of surface cavities that support localise plasmon modes [1].

This presentation discusses the various aspects of the interplay of surface and bulk modes in polymer self-assembled metamaterials and gives an outlook to the further development of these materials.

[1] James A. Dolan, Raphael Dehmel, Angela Demetriadou, Yibei Gu, Ulrich Wiesner, Timothy D. Wilkinson, Ilja Gunkel, Ortwin Hess, Jeremy J. Baumberg, Ullrich Steiner, Matthias Saba, and Bodo D. Wilts. Metasurfaces atop metamaterials: Surface morphology induces linear dichroism in gyroid optical metamaterials. *Advanced Materials*, 31(2):1803478, 2019.

Synthesis and characterization of plasmonic nanostructures

Plasmonic Horizon in Noble Metal Nanosponges

Thomas A. Klar[1]

[1] Institute of Applied Physics, Johannes Kepler University Linz, 4040 Linz, Austria

Abstract

Local electron-hole recombination in gold nanosponges can coherently excite plasmonic hot-spots only within a horizon given by the lifetime of localized plasmons and the finite speed carrying the information that a plasmon has been created.

1. Introduction

Gold nanosponges are three dimensionally (3D) fully percolated nanoparticles that consist of gold and air filaments of about 20 nm diameter and a diameter of the envelope in the range of 100 to 250 nm [1]. Such gold nanosponges are found to support broadband plasmonic resonances in the visible and the NIR. However, a simple assignment of an effective-medium permittivity to the nanosponges turns out to be impossible, despite the deep subwavelength size of their percolations. Scattering from individual Au nanosponges exhibits significant polarization dependence, even if the sponges show a circular circumference. This suggests that the internal pattern of each individual sponge needs to be respected to describe their optical properties correctly [2].

2. Gold intrinsic photoluminescence

Bulk gold shows photoluminescence (PL) with a negligible quantum yield of $\sim 10^{-10}$ [3], which can, nevertheless, be increased by several orders of magnitude in case of gold nanoparticles [4]. This bears, for instance, huge potential to use noble metal nanoparticles as fluorescent and unbleachable dyes in bio-imaging. The enhancement of the PL yield is commonly attributed to nanoparticle plasmons. Tuning the shape or geometry of gold nanostructures (e.g. via reducing the distance between two nanoparticles) allows for redshifting both the scattering and the PL spectra. However, while the scattering cross section increases with a plasmonic redshift, the PL yield decreases, indicating that the common simple picture of a plasmonically boosted gold luminescence turns out to be more subtle. Hence, we systematically varied the distance between the tips of two gold bipyramids on the nanometer scale using AFM manipulation and recorded the PL and the scattering spectra for each separation. We found that the PL intensity decreases as the interparticle coupling increases. This anticorrelation is explained by a theoretical model where both the gold-intrinsic d-band hole recombination probabilities as well as the field strength inside the nanostructure are considered. Besides, we not only observe PL supported by dipolar plasmon resonances, but also measure PL supported by higher order plasmonic modes, in accordance with simulations [5].

3. Plasmonic Horizon

Combining both preliminary works, that on sponges and that on PL, together, we can now investigate what we call the plasmonic horizon. The gold intrinsic photoluminescence events are the most nanoscopic light bulbs to excite localized plasmons, basically localized on one unit cell. We argue that such nanoscopic light bulbs are a useful tool to investigate the plasmonic horizon [6]. This is formed by the short lifetime of a plasmon (on the order of 6 fs) and the finite speed with which the information that a plasmon has been created can be transported. This actually leads to the fact that a localized creation of a plasmon cannot reach throughout a plasmonic nanosponge larger than 120 nm in diameter within the lifetime of the plasmon. Based on this hypothesis, we can explain the fact that intermediately sized nanosponges of about 150 nm in diameter show a polarization dependent scattering, but far less polarization dependence in the PL spectra [6].

References

[1] Wang, D.; Schaaf, P., Nanoporous Gold Nanoparticles. *J. Mater. Chem. 22*:5344-5348, 2012.

[2] Vidal, C.; Wang, D.; Schaaf, P.; Hrelescu, C.; Klar, T. A., Optical Plasmons of Individual Gold Nanosponges. *ACS Photonics 2*:1436-1442, 2015.

[3] Mooradian, A., Photoluminescence of Metals. *Phys. Rev. Lett. 22*:185-187, 1969.

[4] Boyd, G. T.; Yu, Z.; Shen, Y. R., Photoinduced Luminescence from the Noble Metals and Its Enhancement on Roughened Surfaces. *Phys. Rev. B 33*:7923-7936, 1986.

[5] Sivun, D.; Vidal, C.; Munkhbat, B.; Arnold, N.; Klar, T. A.; Hrelescu, C., Anticorrelation of Photoluminescence from Gold Nanoparticle Dimers with Hot-Spot Intensity. *Nano Lett. 16*:7203, 2016.

[6] Vidal, C.; Sivun, D.; Ziegler, J.; Wang, D.; Schaaf, P.; Hrelescu, C.; Klar, T. A., Plasmonic Horizon in Gold Nanosponges. *Nano Lett. 18*:1269-1273, 2018.

Liquid Crystalline Metasurfaces for Spin Control of Light

Yan Jun Liu[1,*], Zhen Yin[1], Yue Shi[1], Ruiheng Peng[1], Guixin Li[2], and Dan Luo[1],

[1]Department of Electrical and Electronic Engineering, Southern University of Science and Technology, Shenzhen 518055, China.
[2]Department of Materials Science and Engieering, Southern University of Science and Technology, Shenzhen 518055, China.
*corresponding author, E-mail: yjliu@sustc.edu.cn

Abstract

Patterning nano-objects is an exciting interdisciplinary research area in current materials science, arising from new optical and optoelectronic properties and the need to device miniaturization. Nowadays, the optical, electromagnetic and mechanical properties of a material can be well-tuned via artificial design over its composition and shape in principle. However, this is still kept challenging and costly for complex engineering at the nanoscale. Here we demonstrate a facile and low-cost fabrication of silver nanoparticle metasurface with a holographic technique. Mimicking the liquid crystal molecules, the silver nanoparticles show a well-observed polarization-directed shape-dependent nanoparticle growth and large-area interference-patterned nanoparticle assembly. The silver nanoparticle metasurface possesses excellent chiroptical properties that can be further used for spin control of light. This facile, large-area, cost-effective metasurface creation technique could open pathways for the new synthesis of chiral metamaterials with a large degree of freedom control of the nanounit (i.e., nanoparticles) and the resulting chiroptical properties.

Au nanorods based core@shell SERS tags with incorporated Raman reporters

Vitaly Khanadeev[1,*], Boris Khlebtsov[1,2], Snezhana Kushneruk[2], Nikolai Khlebtsov[1,2]

[1]Institute of Biochemistry and Physiology of Plants and Microorganisms Russian Academy of Sciences, Saratov, Russia
[2]Saratov National Research State University, Saratov, Russia
*corresponding author, E-mail: khanadeev@gmail.com

Abstract

In this work, we investigated the effect of synthetic parameters on the formation of a detectable gap inside SERS tags consisting of gold nanorods coated by 4-nitrobenzenethiol (NBT) and gold or silver shell. We found that the presence of a detectable intermetallic gap inside AuNR@NBT@Au nanoparticles can be tuned by synthetic parameters. For AuNR@NBT@Ag nanoparticles the intermetallic gap is indistinguishable. However, indirect experiments confirm that NBT molecules are inside the particles.

1. Introduction

SERS tags were developed as new type of probes for bioimaging [1]. SERS tags contain plasmon-resonant nanoparticles and Raman reporter molecules located in areas of high local electromagnetic field (so-called "hot spots"). With the optimal choice of nanoparticles, reporter molecules and the wavelength of the laser irradiation, such tags demonstrate a significant increase in the SERS signal from reporter molecules and have a stronger optical response compared to quantum dots and fluorescent molecules [2]. The localization of reporter molecules in a thin intermetallic gap inside the SERS tags led to the formation of so-called gap-enhanced Raman tags (GERTs) [3]. These tags have several important advantages. First, the incorporated molecules are protected from desorption and from external environment. Secondly, such tags demonstrate a more intensive SERS signal in comparison with SERS tags with surface adsorption of molecules. The SERS signal from reporter molecules inside GERTs is enhanced due to intense electromagnetic field inside the gap between metal surfaces. Indeed, for GERTs with a gold shell, it is possible to detect the gap using transmission electron microscopy [4]. However, for SERS tags with a gold core and complete silver shell, according to literary data, it is still impossible to detect a gap inside.

The aim of this work was to investigate the effect of synthetic parameters on the formation of a detectable gap inside the SERS tags with gold and silver shell. We also investigated the dependence of SERS signal on the presence of the gap inside SERS tags.

2. Materials and methods

2.1. Nanoparticle synthesis

Gold nanorods with a plasmon resonance at about 800 nm were synthesized as described previously [5]. After removing excess of reagents by double centrifugation, 4-nitrobenzenethiol (NBT) Raman reporter molecules were adsorbed on the surface of gold nanorods by the method from [4] followed by removing excess of unreacted NBT by triple centrifugation.

2.2. Silver and gold shell formation

Slow synthesis of silver shell on NBT-coated gold nanorods was performed by reduction of silver nitrate by ascorbic acid at 70C during three hours. For fast growth, sodium hydroxide was added to this mixture and the reaction lasted for 10 minutes at room temperature.

Gold shell on AuNRs@NBT was slowly synthesized by regrowth protocol for gold nanorods [6] during twelve hours. Fast growth of gold shell was performed by reduction of hydrogen tetrachloroaurate by ascorbic acid in cetyltrimethylammonium bromide solution under vigorous sonication during twenty minutes.

After shell formation all SERS tags were washed by double centrifugation and resuspension in water.

3. Discussion

3.1. Nanoparticle characterization

According to TEM data initial gold nanorods have average L=42.1±7.1 nm, d=11.2±2.3 nm. TEM images of SERS tags with incorporated NBT molecules are presented at the Fig.1. On the TEM images SERS tags with a silver shell, the gold nanorod inside is clearly seen (Fig.1 (a, b)). For fast synthesized gold shell, the gold rod inside is also visible due to the presence of a thin gap (Fig.1 (c)). For slowly synthesized gold shell, the gap and the initial rod are not observed (Fig.1 (d)). It should be mentioned, that a distinct gap inside SERT tags is observed only in the case of fast synthesized gold shell (Fig.1 (c)). Thus, for SERS tags with gold shell it is possible to tune the presence of the intermetallic gap inside particles whereas for tags with

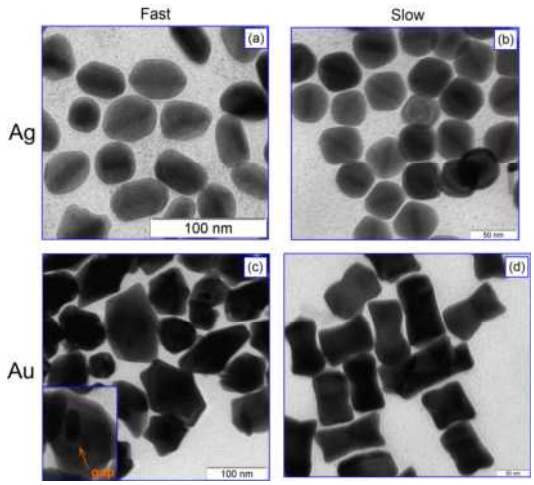


Figure 1: TEM images of AuNRs@NBT, coated by silver shell by fast (a) and slow (b) growth and coated by gold shell by fast (c) and slow (d) growth.

silver shell it remains impossible and these SERS tags, in good agreement with the literature data, always have no detectable gap.

3.2. SERS measurements

The measured SERS spectra for synthesized SERS tags are presented in Figure 2. To estimate the SERS properties of tags we calculated the SERS enhancement factor (EF) which is equal to the ratio of SERS intensity to Raman intensity normalized to the number of excited reporter molecules [7]:

$$EF = \frac{I_{SERS} / N_{SERS}}{I_{Raman} / N_{Raman}}. \qquad (1)$$

For calculations we used the peak intensity at 1345 cm^{-1}. As a result, slow and fast formation of silver shell led to EF increase to 5.6×10^4 and 9.5×10^4, respectively. Fast and slow

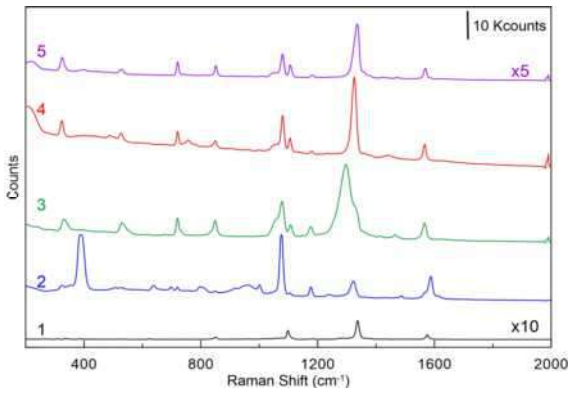


Figure 2: The Raman spectrum of 100 mM NBT solution (1) and SERS spectra of AuNRs@NBT coated by fast (2) and slowly (5) formed silver shell and by fast (3) and slowly (4) synthesized gold shell.

formation of the gold shell resulted in the EF values of 3.9×10^5 and 4.4×10^5, respectively.

It is worth noting that for SERS tags with a gold shell, the presence of a detectable gap does not affect the SERS EF. For SERS tags with silver shell the gap is not observed. However, with the addition of sodium borohydride, the SERS spectrum does not change (data not presented). This means that NBT molecules are protected and located inside the SERS tags.

4. Conclusions

In this work we report on synthesis of gold nanorod-based SERS tags with incorporated NBT molecules. By varying the synthetic protocol for gold shell, we received SERS tags with inner gap or without it. For SERS tags with silver shells, the gap is always indistinguishable, although our indirect experiments confirm that the NBT molecules are inside the particles and are protected from the environment. For gold shell in both cases (with or without a gap), the SERS enhancement factor is about 4×10^5. SERS enhancement factor decreases in the row: AuNRs@NBT@AuSlow - AuNRs@NBT@AuFast – AuNRs@NBT@AgFast - AuNRs@NBT@AgSlow. To understand the SERS mechanism in the absence of a gap inside the nanoparticles, further research is required.

Acknowledgements

This work was supported by the Russian Scientific Foundation (project no. 18-14-00016) and by RFBR grants nos. 18-52-7803 and 17-02-00075. The work of VK was supported by the grant from the President of the Russian Federation.

References

[1] Y. Wang, B. Yan, L. Chen, SERS tags: novel optical nanoprobes for bioanalysis, *Chem. Rev.* 113: 1391−1428, 2013.

[2] E.S. Allgeyer; A. Pongan, M. Browne, M.D. Mason, Optical signal comparison of single fluorescent molecules and Raman active gold nanostars, *Nano Lett.* 9: 3816–3819, 2009.

[3] J.W. Kang, P.T.C. So, R.R. Dasari, D.-K. Lim, High resolution live cell Raman imaging using subcellular organelle-targeting SERS-sensitive gold nanoparticles with highly narrow intra-nanogap, *Nano Lett.* 15: 1766–1772, 2015.

[4] S. Wang, Z. Liu, C. Bartic, H. Xu, J. Ye, Improving SERS uniformity by isolating hot spots in gold rod-in-shell nanoparticles, *J. Nanopart. Res.* 18: 246, 2016.

[5] B. Khlebtsov, V. Khanadeev, T. Pylaev, N. Khlebtsov, A new T-matrix solvable model for nanorods: TEM-based ensemble simulations supported by experiments, *J. Phys. Chem. C* 115: 6317-6323, 2011.

[6] B.N. Khlebtsov, V.A. Khanadeev, J. Ye, G.B. Sukhorukov, N.G. Khlebtsov, Overgrowth of gold nanorods by using a binary surfactant mixture, *Langmuir* 30: 1696-1703, 2014.

[7] E.C. Le Ru, E. Blackie, M. Meyer, P.G. Etchegoin, Surface enhanced Raman scattering enhancement factors: a comprehensive study, *J. Phys. Chem. C* 111: 13794-13803, 2007.

Recent advances in the bottom-up approach to artificial optical magnetism

Philippe Barois[1*], Alexandre Baron[1], Romain Dezert[1], Etienne Duguet[2], Rajam Elancheliyan[1], Véronique Many[2], Olivier Mondain-Monval[1], Virginie Ponsinet[1], Serge Ravaine[1], Philippe Richetti[1] and Mona Treguer-Delapierre[2]

[1] Centre de Recherche Paul Pascal, CNRS-Université de Bordeaux, UMR5031, 33600 Pessac, France
[2] Institut de Chimie de la Matière Condensée de Bordeaux, CNRS-Université de Bordeaux, UMR5026, 33600 Pessac, France
*corresponding author, E-mail: barois@crpp-bordeaux.cnrs.fr

Abstract

We present several routes towards the generation of artificial optical magnetism in visible light. Our bottom-up strategies combine nano-chemistry for the fabrication of optically resonant building blocks and colloidal self-assembly for the fabrication of macroscopic 2D or 3D materials. Basically, two types of optical resonators are investigated, namely plasmonic and Mie resonators. In the first type, we show that the magnetic response can be optimized by a proper design of plasmonic nano-clusters. In the second type, the challenge is to produce nanoparticles of high refractive index. We show that the bottom-up approach enables the large-scale production of metallic nanoclusters exhibiting strong magnetic Mie resonances in visible light.

1. Introduction

The generation of artificial optical magnetism at high frequencies ranging from microwaves to visible wavelengths is one of the major breakthrough in the field of metamaterials. Major successes have been obtained in the top-down approach whereby sub-wavelength elements are imprinted or carved on a substrate. In visible light, the bottom-up approach based on the large-scale synthesis of nano-sized optical resonators has proved its ability to produce a bulk magnetic material exhibiting non-natural values of the magnetic permeability. In this material, the resonators called "plasmonic rasberries" consist of a set of plasmonic nanoparticles evenly, but randomly distributed around a dielectric core nanoparticle. The ratio of the magnetic to electric dipole scattering cross-section of a single raspberry is about 1/3 and the magnetic permeability of the assembled bulk metamaterial ranges from 0.8 to 1.45 μ_0 units[1].

In order to increase the magnetic response of the metamaterial, we investigate in this work novel morphologies guided by numerical simulations of various plasmonic nano-clusters. We show experimentally that a significant increase of the magnetic dipole can be obtained by a well-controlled geometrical organization of twelve plasmonic satellites onto the dielectric core[2]. Moreover, we show that a simple emulsification process can be used to synthesize large amounts of plasmonic clusters exhibiting a large and tunable magnetic response.

These new results open the way to the fabrication of bulk magnetic metamaterials of large or zero permeability, and of Huyghens metasurfaces based on optical resonators of equal electric and magnetic response over a broad frequency range.

2. Plasmonic dodecapods

In the plasmonic raspberry model of Simovski and Tretyakov, a dense corona of metallic nanoparticles are randomly distributed at the surface of a dielectric core[3]. Guided by numerical simulations, chemical routes have been developed to place 12 metallic satellites onto the faces of a dodecahedron (Fig. 1).

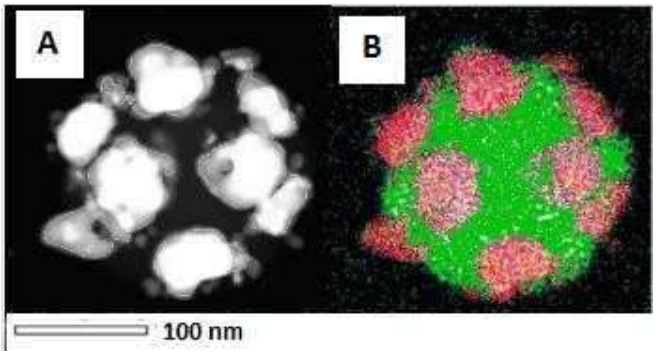


Figure 1: A - Scanning electron micrographs of the plasmonic dodecapods. B – Elemental analysis showing silica (green) and gold (red).

The optical response of the dodecapods (DDPs) has been measured by a polarization-resolved static light scattering. The ratio of the magnetic to electric scattering is shown in Fig. 2. It is increased by a factor >3 when compared to plasmonic raspberries of the same size with the same amount of gold.

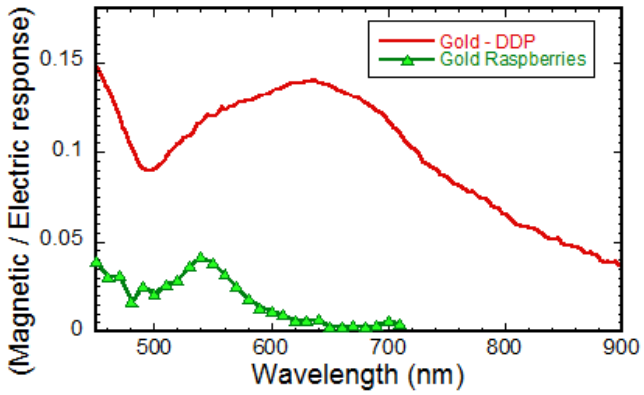


Figure 2. Magnetic to electric scattering response of gold dodecapods (red line) and gold raspberries of the same size (green line with triangles).

3. Metallic clusters

The magnetic Mie resonance of a spherical particle constitutes another source of strong magnetic scattering. It is obtained when the wavelength inside the particle matches its diameter. A high value of the refractive index of the particle is then required to keep its size well below the wavelength in vacuum.

Crystalline silicon is a good candidate and strong chemical efforts are currently developed to synthesize silicon nanoparticles of controlled size[4,5]. Another option was proposed in which the high refractive index results from the plasmonic resonance of a metallic nano-cluster[6].

A controlled emulsification process, sketched in Fig. 3, can be used to synthesize dense clusters of gold nanoparticles which exhibit the targeted magnetic Mie-resonances. A suspension of gold nanoparticles is first emulsified in a continuous phase. In a second step, the solvent of the emulsion droplets is evaporated. The ratio of the magnetic to electric response, measured by static light scattering on the final clusters, reaches 30 to 60%, well above the highest values obtained for gold raspberries and gold dodecapods (see Fig. 2).

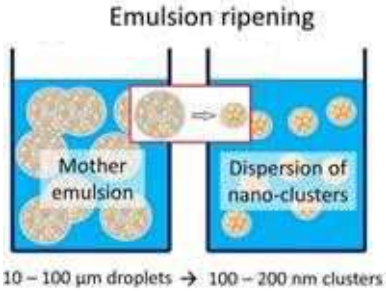


Figure 3: Sketch of the emulsion ripening process used for the formulation of NP-clusters..

These new clusters are good candidates for the fabrication of Huyghens' sources in which the electric and magnetic scattering display equal strength[7].

4. Conclusions

Nanochemistry and colloidal physics can be used to synthesize different types of nanoclusters exhibiting high levels of optical magnetism in visible light. The bottom-up approach enables cost-effective, large-scale production of such magnetic resonators, hence opening the way to the fabrication of 2D and 3D magnetic metamaterials.

Acknowledgements

This work was supported by the LabEx AMADEus (ANR-10-LABX-42) and IdEx Bordeaux (ANR-10-IDEX-03-02), i.e. the Investissements d'Avenir programme of the French government managed by the Agence Nationale de la Recherche.

References

[1] S. Gomez-Graña *et al*., "Hierarchical self-assembly of a bulk metamaterial enables isotropic magnetic permeability at optical frequencies", *Mater. Horiz.* **3**, 596 (2016).

[2] V. Many *et al*., "High optical magnetism of dodecahedral plasmonic meta-atoms". *Nanophotonics*, 2018. DOI: 10.1515/nanoph-2018-0175.

[3] C.R. Simovski and S.A. Tretyakov. "Model of isotropic resonant magnetism in the visible range based on core-shell clusters". Phys. Rev B **79**, 045111 (2009).

[4] S. Jahani and Z. Jacob, "All-dielectric metamaterials". *Nat Nanotech*. 11, 23–36 (2016).

[5] M.-L. De Marco *et al*., "C. Silicon-based dielectric metamaterials: focus on the current synthetic challenges". *Angew Chem Int Ed*. **57**, 2–23 (2018).

[6] C. Rockstuhl *et al*., "Design of an Artificial Three-Dimensional Composite Metamaterial with Magnetic Resonances in the Visible Range of the Electromagnetic Spectrum". Phys. Rev. Lett. **99**, 017401 (2007).

[7] R. Dezert *et al*. "Isotropic Huygens dipoles and multipoles with colloidal particles". Phys Rev B **96**, 180201(R) (2017).

Laser implantation of plasmonic nanoparticles into glass

Jürgen Ihlemann[1], Jörg Meinertz[1], Maximilian Heinz[2], Manfred Dubiel[2]

[1]Laser-Laboratorium Göttingen e.V., Göttingen, Germany
[2]Martin-Luther-Universität Halle-Wittenberg, Halle, Germany
*corresponding author, E-mail: juergen.ihlemann@llg-ev.de

Abstract

UV-laser irradiation of gold-coated glass leads to gold nanoparticle formation and, at sufficiently high laser fluence, to incorporation or implantation of these particles into the glass. A characteristic plasmon absorption peak around 550 nm is observed. Gold particles in SiO_2-glass are obtained by implanting gold into SiO_x that is subsequently oxidized to SiO_2 Spatially defined particle implantation is achieved by structured irradiation.

1. Introduction

The generation and controlled arrangement of metallic nanoparticles is very important for the fabrication of plasmonic devices. Silver and gold nanoparticles in glasses are attracting particular attention since the wavelength of their surface plasmon resonance (SPR) is in the visible spectral range, making such materials promising candidates for applications in optoelectronics and nanoplasmonics. Typically, silver nanoparticles in sodium silicate glasses are prepared by $Ag^+ \leftrightarrow Na^+$ ion exchange process and subsequent thermal or laser treatment. However, this method does not allow creating nanoscaled arrays of particles localized in a certain way. Furthermore, this method is not suitable for gold.

2. Laser implantation of gold into soda lime glass

As glass cannot be doped with a sufficient concentration of gold, for the near-surface formation of gold particles in glass the following method is applied: The glass surface is coated with a thin gold film and subsequently irradiated with a pulsed excimer laser [1]. Moderate laser fluences lead to dewetting of the gold film and particle formation. At sufficiently high fluence, the particles are in part or completely embedded or implanted into the glass (Fig. 1). Using an ArF excimer laser (wavelength 193 nm) at a fluence below the threshold of ablation, gold nanoparticles are formed and partially implanted into the glass as can be seen from the colored appearance of the irradiated areas (Fig. 2) and the plasmon resonance peak in the absorption spectra (Fig. 3). After wiping off the loosely sticking particles, the remaining effect is only due to the implanted particles.

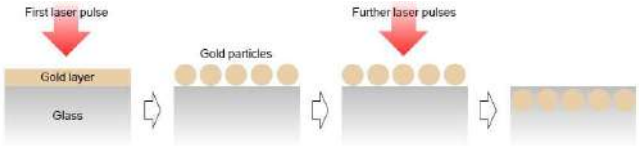


Figure 1: Scheme of laser induced particle formation and implantation.

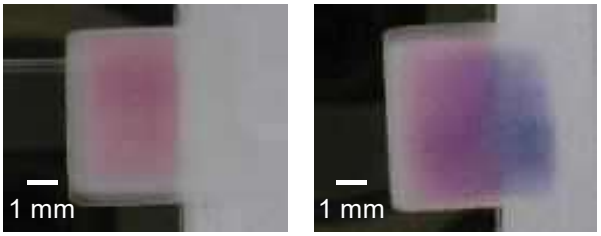


Figure 2: Laser irradiated areas (193 nm, 140 mJ/cm², 10 pulses) on the air side (left) and the bath side (right) of soda lime float glass coated with 70 nm Au [1]. On the right side of each image, the non-implanted gold has been removed by wiping with a dry cloth.

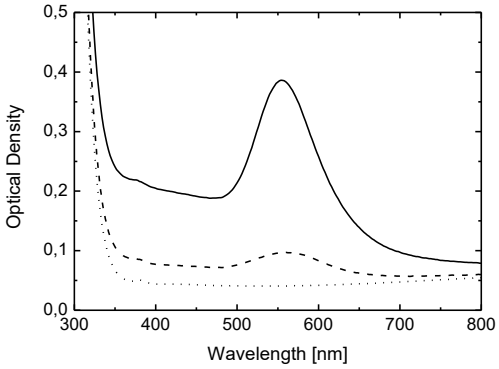


Figure 3: Optical extinction spectra as a result of irradiating the gold coated tin bath side by 10 laser pulses at 140 mJ/cm^2. Spectra recorded before cleaning (solid line) and after cleaning (dashed line) of the laser spots with acetone; dotted line: basic glass.

3. Laser implantation of gold into fused silica

For the implantation of gold into pure fused silica, fluences of about 1 J/cm² at 193 nm laser wavelength are required. Using a SiO_x ($x \approx 1$) coated SiO_2-substrate, the implantation of gold into this coating can be accomplished at significantly lower fluences starting from 0.2 J/cm² (Fig. 4) [2]. Particles with diameters in the range of 10 to 60 nm are implanted to a depth of about 40 nm as identified by transmission electron microscopy (Fig. 5). An additional high temperature annealing step in air [3] leads to the oxidation of SiO_x to SiO_2, without influencing the depth distribution of the particles significantly. Absorption spectra show a characteristic plasmon resonance peak at 540 nm. Thus, pure silica glass (SiO_2) with near surface incorporated plasmonic particles can be fabricated with this method. Such material systems may be useful for example as robust substrates for plasmonic applications.

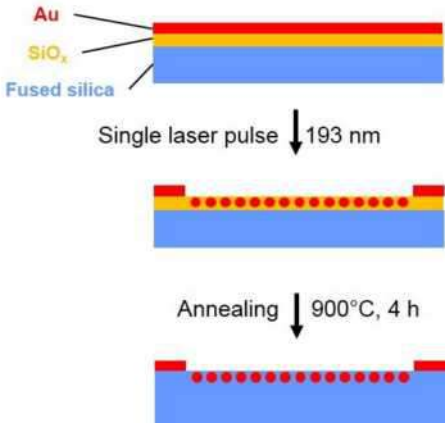


Figure 4: Scheme of the laser induced implantation of gold nanoparticles into SiO_x with subsequent oxidation of the matrix to SiO_2.

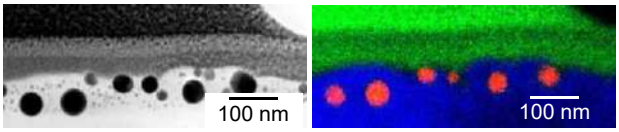


Figure 5: Transmission electron micrograph of laser implanted gold nano particles (left), EDX-analysis: Red = Au, Blue = Si/O, Green = Pt as cover layer (right) [2] (M. Seibt, Univ. Göttingen).

4. Spatial arrangement of nanoparticles

To achieve the implantation of nanoparticles in specifically defined areas, the laser irradiation is performed in a mask projection setup (Fig. 6). To obtain a linear grating consisting of implanted and non-implanted lines, a linear phase mask is applied, which is imaged onto the sample utilizing only the +/- first diffraction orders leading to a linear interference pattern. A resolution down to 1 µm wide lines and spaces is obtained this way (Fig. 7) [4].

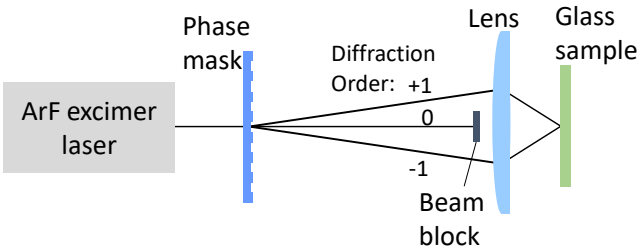


Figure 6: Laser irradiation set-up for structured (line pattern) illumination.

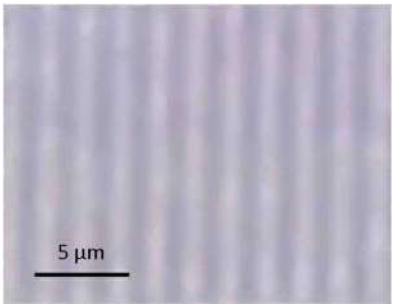


Figure 7: Microscope image (transmitted light) of a line pattern obtained by structured irradiation of Au-coated glass (bath side) using a 40µm-phase mask and a fluence of 400 mJ/cm², 50 pulses [4]. Dark and bright lines represent the implanted and non-implanted regions. (Recorded after cleaning the surface with acetone.)

Acknowledgements

Financial support by Deutsche Forschungsgemeinschaft, grant number Du 214/14-1, and Bundesministerium für Wirtschaft und Energie, grant number 16KN047223 is gratefully acknowledged.

References

[1] M. Heinz, V.V. Srabionyan, L.A. Avakyan, A.L. Bugaev, A.V. Skidanenko, V.V. Pryadchenko, J. Ihlemann, J. Meinertz, C. Patzig, M. Dubiel, L.A. Bugaev, Formation and implantation of gold nanoparticles by ArF-excimer laser irradiation of gold-coated float glass, *Journal of Alloys and Compounds* 736: 152-162, 2018.

[2] H. Stolzenburg, P. Peretzki, N. Wang, M. Seibt, J. Ihlemann, Implantation of plasmonic nanoparticles in SiO_2 by pulsed laser irradiation of gold films on SiO_x-coated fused silica and subsequent thermal annealing, *Applied Surface Science* 374: 138-142, 2016.

[3] T. Fricke-Begemann, J. Meinertz, R. Weichenhain-Schriever, J. Ihlemann, Silicon suboxide (SiO_x): laser processing and applications, *Applied Physics A* 117: 13-18, 2014.

[4] M. Heinz, J. Meinertz, M. Dubiel, J. Ihlemann, Excimer laser induced spatially resolved formation and implantation of plasmonic particles in glass, *Nanomaterials* 8: 1035-1-10, 2018.

Plasmonic nanoparticles synthesized by laser ablation and their antibacterial activity

M. Fernández-Arias[1], M. Boutinguiza[1], J. del Val[1], A. Riveiro[1], R. Comesaña[2], F. Lusquiños[1], J. Pou[1*]

[1] Applied Physics Dpt., University of Vigo, EEI, Lagoas-Marcosende, Vigo, E-36310, Spain

[2] Materials Eng., Applied Mech., and Construction Dpt., University of Vigo, Lagoas-Marcosende, E-36310, Vigo, Spain

*corresponding author, E-mail: jpou@uvigo.es

Abstract

Plasmonic nanoparticles have been of great interest as a subject of investigation due to their unique property of absorbing and scattering strongly certain frequency of light. This capacity of interacting with light makes plasmonic nanoparticles profusely used in many applications and produced following different methods and strategies. In this work we present the results of producing silver and copper nanoparticles by laser ablation in liquid and their capacity as antimicrobial agents.

1. Introduction

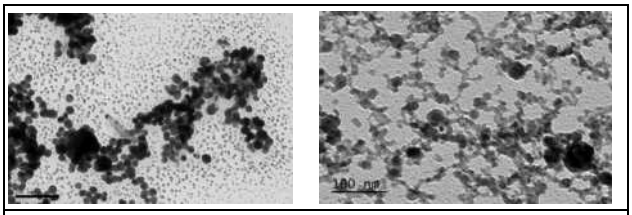
Nanoparticles and nanostructures of noble metals have received great attention in recent years due their unusual optical, electronic, and thermal properties. Their high specific surface area together with the corresponding quantum effects provide them new properties compared to those of material bulk. The new exceptional physical and chemical properties of noble metal nanoparticles make them very used and investigated in a wide variety of areas, such as nanomedicine [1], sensing and biosensing [2], photothermal therapy [3], drug delivery [4, 5], etc.

The physicochemical properties of noble metal nanoparticles are determined by different aspects like size, shape, composition crystallinity, presence of impurities, degree of aggregation, etc., which are highly affected by the nanoparticle processing method.

There is a wide range of methods and techniques for producing nanoparticles, which can be mainly classified into chemical, physical and biological processes [6-8]. Most of these methods use stabilizing molecules or other chemicals, which can result in the contamination of the synthesized particles. Laser ablation in liquids or in gas atmosphere enables obtaining nanoparticles with controlled size and without contaminants. On the other hand, regarding toxicity and antibiotic resistance it is well known that noble metal nanoparticles present some advantages over the organic compounds used for disinfection [9]. In this work we report the results of synthesising copper and silver nanoparticles by laser ablation in water and their antibacterial capacity against the growth of *Staphylococcus aureus* and *Lactobacillus Salivarius*, which play an important role in biofilm formation [10].

2. Experimental

Foils of Ag and Cu with 99.99% of purity were used as targets to be ablated. The laser beam was focused on the target to give a spot size about 0.15 mm diameter. The laser source consisted in a diode-pumped Nd:YVO_4, providing 15 ns pulses at 532 nm, 20 kHz, and 0.30 mJ of pulse energy. The morphology and microstructure of the synthetized nanoparticles were investigated by FESEM (JEOL-JSM-6700F) and HRTEM (JEOL-JEM 2010 FEG). The UV-Vis absorption was measured with a Hewlett Packard HP 8452 spectrophotometer. Antibacterial activity against *Staphylococcus aureus* and *Lactobacillus Salivarius* was assessed by minimal inhibitory concentration assays.



a) b)

Figure 1: Silver (a) and Copper (b) nanoparticles obtained by laser ablation in water.

3. Results and discussions

In both cases the formation mechanism of the obtained nanoparticles in water is basically the same. The laser beam is focused on the upper surface of the submerged foil (Ag-Cu) heating up the target above its melting point, while the surrounding liquid is evaporated, which can react with the ejected species from the target, giving the final nanoparticles. Given the parameters of the used laser and its

intensity on the target (10^8 W/cm^2), plasma plume can be formed and consequently different species such as ions, atoms and droplets confined by the liquid, nucleate and grow by coalescence to form the final nanoparticles. Figure 1 (a and b) shows the appearance of Ag and Cu nanoparticles obtained under the same conditions in water. The obtained nanoparticles show rounded shape and a tendency to agglomeration. This effect can be explained by the overlapping of the ablated material and the following pulse. All the obtained particles are crystalline. Regarding Ag nanoparticles, crystalline phases of metallic Ag and AgO_2 have been detected, while in the case of Cu the colloid is predominantly dominated by the presence of CuO, since Cu is much more reactive than Ag. This result is in agreement with the UV-Vis absorption spectra of the obtained colloidal solutions as can be observed from figure 3. The peak about 400 nm is characteristic of surface plasmon resonance of spherical Ag nanoparticles, while the peak about 220 nm is due to the inter-band transitions indicating the formation of CuO.

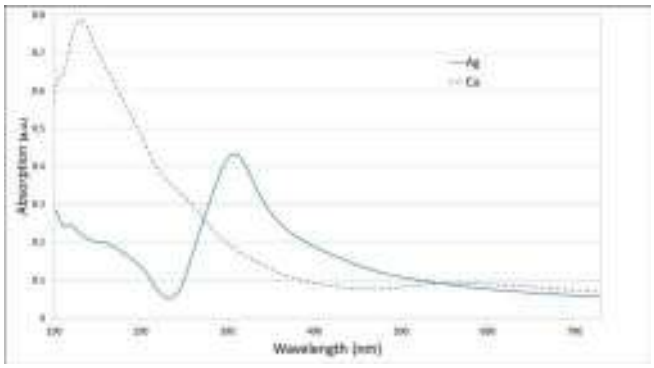


Figure 3: UV-vis spectra of Ag and CuO colloidal solutions obtained by laser ablation in water.

Antimicrobial activity of the obtained solutions was evaluated through standard Optical Density measurements at wavelength of 600 nm (OD600). *Staphylococcus aureus* and *Lactobacillus Salivarius*, were cultured in in MRS broth (Scharlab SL, Spain). Cultures were incubated for 12 h at 37 °C before each assay. Bacterial suspensions were seeded onto agar plates. The agar plates were then incubated at 37 º C for 12-18 h and the colony forming units (CFU) were counted. As result both kind of particles exhibited high bactericidal capacity with reduction of CFU with regard to the control plates.

4. Conclusions

Colloidal solutions of Ag and Cu nanoparticles have been synthesized by laser ablation in water. All obtained nanoparticle are crystalline and present oxidation, especially the case Cu ones. All the obtained nanoparticles showed good bacterial activity against *Staphylococcus aureus* and *Lactobacillus Salivarius*.

Acknowledgements

Authors would like to thank Prof. J. Gil and his team at UIC and UPC for performing the bactericidal tests.
This work was partially supported by the EU research project Bluehuman (EAPA_151/2016 Interreg Atlantic Area), Government of Spain (MAT2015-71459-C2-P (MINECO/FEDER), and Xunta deGalicia (ED431B 2016/042, ED481D 2017/010, ED481B 2016/047-0).

References

[1] I. Fratoddi et al. Electronic Properties of a Functionalized Noble Metal Nanoparticles Covalent Network. J. Phys. Chem. C 121 (2017), 18110–18119.

[2] J.N. Anker et al. Biosensing with plasmonic nanosensors. Nat. Mater., 7 (2008), pp. 442-45.

[3] M. Perez-Hernandez et al. Dissecting the molecular mechanism of apoptosis during photothermal therapy using gold nanoprisms. ACS Nano, 9 (2015), pp. 52-6.

[4] P. Prosposito et al. Hydrophilic silver nanoparticles with tunable optical properties: application for the detection of heavy metals in water. Beilstein J. Nanotechnol. 7 (2016), 1654–1661.

[5] A. Bearzotti et al. Hydrophobic Noble Metal Nanoparticles: Synthesis, Characterization and Perspectives as Gas Sensing Materials. Procedia Eng. 120 (2015), 781–786.

[6] K.H. Tseng et al. Continuous synthesis of colloidal silver nanoparticles by electrochemical discharge in aqueous solutions, J. Nanopart. Res. 13 (2011) 1865–1872.

[7] A. Panacek et al. Silver colloid nanoparticles: synthesis, characterization, and their antibacterial activity, J. Phys. Chem. B (2006) 16248–16253.

[8] M.N. Nadagouda et al. Microwave-assisted green synthesis of silver nanostructures, Acc. Chem. Res. 44 (2011) 469–478.

[9] MJ Hajipour et al. Antibacterial properties of nanoparticles. Trends Biotechnol., 30 (2012), 499–511.

[10] M.S. Kang et al. Antimicrobial activity of Lactobacillus salivarius and Lactobacillus fermentum against Staphylococcus aureus. Pathogens and Disease, 75 (2017), ftx009

Bottom-up fabrication for ultradense, ultraclean plasmonic ensembles

Francesco Bisio[1,*], Michele Magnozzi[2,3], Marzia Ferrera[2], Remo Proietti Zaccaria[4,5], Alessandro Alabastri[6], and Maurizio Canepa[2]

[1]CNR-SPIN, Corso Perrone 24, Genova Italy
[2]OptMatLab, Dipartimento di Fisica, Università di Genova, Via Dodecaneso 33, Genova, Italy
[3]INFN, Sezione di Genova, Via Dodecaneso 33, Genova, Italy
[4] Cixi Institute of Biomedical Engineering, Ningbo Institute of Materials Technology and Engineering, Chinese Academy of Sciences, Ningbo, China
[5]Istituto Italiano di Tecnologia, Via Morego 30, 16163 Genova, Italy
[6] Department of Electrical and Computer Engineering, Rice University, Houston, TX, USA
*corresponding author, E-mail: Francesco.bisio@spin.cnr.it

Abstract

Bottom-up fabrication methods surely represent a niche within the broad field of nanofabrication of plasmonic structures, yet what they lack in terms of structure complexity is more than compensated by the ability to affordably produce ultradense, highly-packed and ultraclean structures over large areas. In this contribution we will review some of the most intriguing physics of spontaneously-arranged plasmonic nanostructures.

1. Introduction

More often than not, the success in a plasmonic experiment depends on the ability to finely control the morphology of the nanostructures involved. In this sense, there has been a clear evolution from pioneering experiments, that necessarily had to rely on bottom-up system fabrication towards more and more sophisticated top-down approaches, that allow to fabricate virtually any conceivable structure. Stating that lithography has made other fabrication methods obsolete would however grossly misjudge the impact of bottom-up techniques in present-day plasmonics. Experimental methods like chemical synthesis or self-organization are indeed able to achieve an atomic-level control of the system morphology that is so far unparalleled. Such a fine control can be fruitfully exploited in dedicated experiments with fundamental but also technological appeal.

In this contribution, we will provide an overview of recent experiments performed on 2-dimensional (2D) ultradense arrays of metallic nanoparticles (NPs) realized by self-organized template-assisted deposition. The generality of the method in terms of the target metal, and the possibility to obtain ultrafine and closely-spaced NPs was exploited to push the high-energy limit of plasmonics with ultraclean Al NPs [1,2], fabricate highly sensitive detectors with plentiful electromagnetic hot-spots [3], and exploit ultraclean environments for sample characterization [4].

2. Experimental

2.1. Fabrication

The systems under scrutiny are 2D arrays of metal NPs obtained by template-assisted physical deposition followed by thermal dewetting.

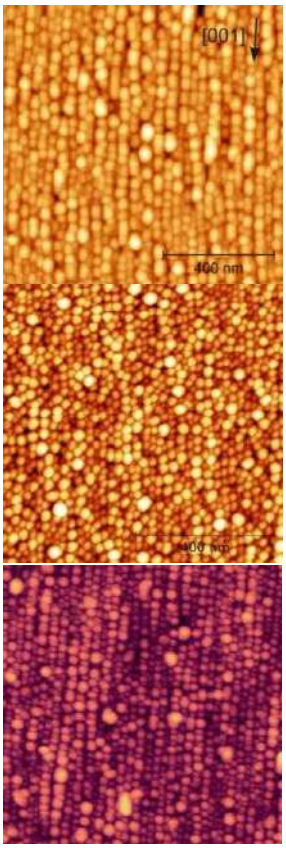


Figure 1: 2D arrays of metallic nanoparticles supported on nanopatterned insulating substrates. Top to bottom the images (1×1 μm^2) refer to Au, Ag and Al, respectively.

The arrays were fabricated depositing the target material onto the self-organized nanometric uniaxial sawtooth pattern

that develops upon high-temperature homoepitaxial growth onto LiF(110) substrates [5].

Few nm of metal (typ.<5nm) were deposited at room temperature in high vacuum by molecular beam epitaxy at 60° of incidence with respect to the surface normal, and the samples were subsequently annealed at T=670 K in order to induce the thermal dewetting. Selected examples of array morphology are reported in Fig.1.

Top to bottom, the arrays consist of Au, Ag and Al NPs. As apparent, the NPs are densely packed on the substrate, with small interparticle spacing and plentiful electromagnetic hot-spots. The typical NP size achievable is of the order of 10-30 nm, whereas the areal density typically exceeds 10^{11} NP/μm^2. The arrays are homogeneous over the whole sample area (typ. 1 cm^2), making it straightforward to measure their properties without resorting to microscopy. This makes it incidentally easier to investigate these systems in technically-challenging environments such as vacuum, liquids etc.

2.2. Plasmonic Response

In Figure *2* we report transmission spectra of 2D arrays of Au, Ag and Al NPs (yellow, blue, red symbols, respectively).

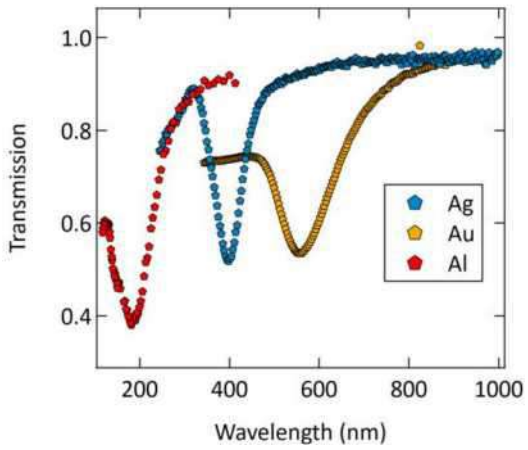


Figure 2: transmittance spectra of 2D arrays of Al (red), Ag (blue) and Au NPs (yellow).

The marked transmission dip in the spectra is the fingerprint of the Localized Surface Plasmon Resonance (LSPR) excitation in the arrays. The LSPR falls within the visible range for Au, across the UV-VIS for Ag and in the deep UV for Al. Here the ability to produce ultraclean and fine particles has been instrumental to push the LSPR energy of Al NPs to an unprecedented, and unsurpassed, value of 6.9 eV [1]. Also, the high density of NPs allows the realization of electromagnetically-coupled plasmonic resonators, whose collective LSPR is spectrally narrower than the incoherent superposition of individual resonances. The method easily lends itself to fabricate more complex materials in NP form, such as composition-graded nanoalloys. There, the LSPR response smoothly varies across the spectrum while maintaining an invariant morphology (Figure 3*: transmission spectra of arrays of NPs of Au_xAg_{1-x} with a spatially-graded composition*.). Such systems can be fruitfully exploited as hyper-SERS platforms for ultrasensitive detection [3].

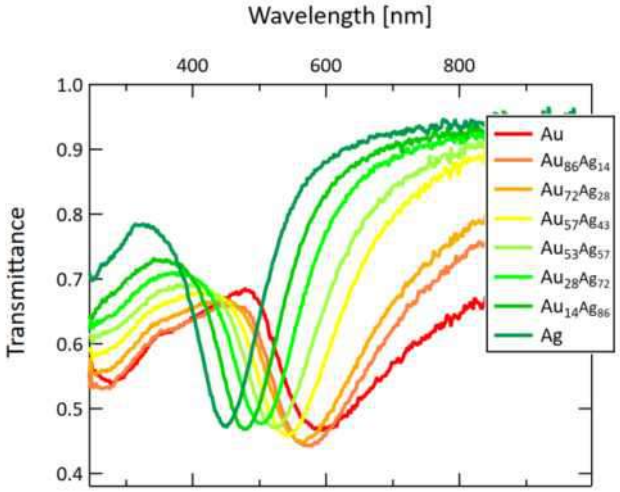


Figure 3: transmission spectra of arrays of NPs of Au_xAg_{1-x} with a spatially-graded composition.

Acknowledgements

We acknowledge support from the Ministero dell'Istruzione, dell'Università e della Ricerca (PRIN NEWLI, n.2015CL3APH) and from the Compagnia di San Paolo (proj. PanLab).

References

[1] F. Bisio, R. Proietti Zaccaria, R. Moroni, G. Maidecchi, A. Alabastri, G. Gonella, A.Giglia, L. Andolfi, S. Nannarone, L. Mattera, M. Canepa "Pushing the High-Energy Limit of Plasmonics" ACS Nano 8 (2014) 9239.

[2] G. Maidecchi, G. Gonella, R. Proietti Zaccaria, R. Moroni, L. Anghinolfi, A.Giglia, S. Nannarone, L. Mattera, Hai-Lung Dai, M. Canepa, F.Bisio "Deep Ultraviolet Plasmon Resonance in Aluminum Nanoparticle arrays" ACS Nano 7 (2013) 5834.

[3] Proietti Zaccaria, R., Bisio, F., Das, G., Maidecchi, G., Caminale, M., Vu, C.D., De Angelis, F., Di Fabrizio, E., Toma, A., Canepa, M., Plasmonic Color-Graded Nanosystems with Achromatic Subwavelength Architectures for Light Filtering and Advanced SERS Detection, ACS Applied Materials and Interfaces, 8 (2016) 8024-8031.

[4] Michele Magnozzi, Marzia Ferrera, Lorenzo Mattera, Maurizio Canepa and Francesco Bisio, Plasmonics of Au nanoparticles in a hot thermodynamic bath, Nanoscale, 11 (2019) 1140-1146.

[5] A. Sugawara and K. Mae, Surface morphology of epitaxial LiF(110) and CaF2(110) layers, Journal of Vacuum Science & Technology B 23, 443 (2005).

Plasmonic nanoparticles for molecular detection

David Zopf, Angelina Pittner, Cornelia Arnold, Stephan Kastner, Andre Dathe, Matthias Thiele, Jacqueline Jatschka, Thomas Schneider, Ondrej Stranik, Andrea Csaki, and Wolfgang Fritzsche*

Leibniz Institute of Photonic Technology (IPHT) Jena, Germany
*corresponding author, E-mail: wolfgang.fritzsche@ipht-jena.de

Abstract

A reliable, sensitive and cost-efficient molecular detection could have a broad field of bioanalytical applications in fields ranging from clinical diagnostics over food safety to environmental applications. We describe here the use of localized surface plasmon resonance (LSPR), an effect based on collective oscillations of conduction electrons in gold nanoparticles under visible light irradiation, in order to realize a label free and multiplexed molecular detection.

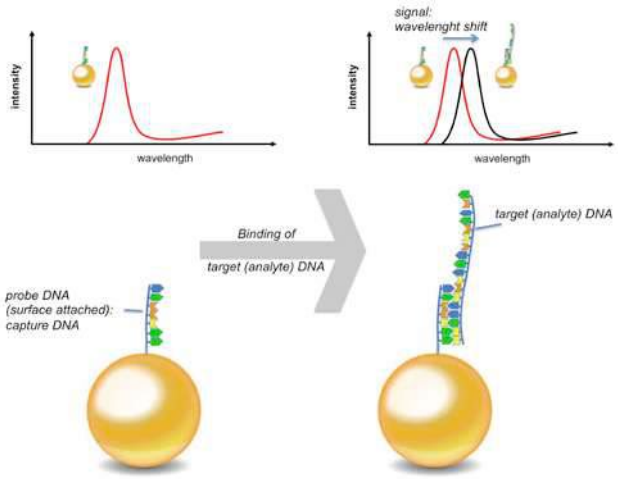


Fig. 1: Scheme of LSPR detection. Left: A gold nanoparticle is acting as sensor, when modified with single-stranded capture DNA. Right: When complementary target (analyte) DNA is present, it will bind, and thereby change the refractive index (and so the LSPR resonance), which is read out in the spectrum (top).

1. Introduction

The detection of target molecules of interest is an important prerequisite for our modern life in order to keep and enhance the standard of living. It includes a vast range of applications, e.g. in the fabrication of goods and food, in medicine, but also in environmental protection and a variety of other applications. Although there is a long tradition in various technical approaches, there is still room for improvement regarding key parameters such as sensitivity, specificity, but also throughput and cost-efficiency. Any significant improvement in one of these factors enables a widening of the application field (or even opening a new one), so there is a constant quest for novel and superior approaches.

Over time, methods that do not rely on the use of labels or markers were preferred due to cost, time and robustness isses connected with such additional elements. Especially the often lower sensitivity for label-free methods could be a limiting factor. Beside mechanical (quartz crystal microbalance and relating resonator methods), also electrochemical (electrical as well as optical methods have been studied for this purpose.

2. LSPR in bioanalytics

In bioanalytics, methods based on the interaction of visible light with the conduction electrons in thin metal (often gold) layers, which are called surface plasmon resonance (SPR), are often used. However, this approach requires rather complex realization of the incoupling of light into the metal-dielectric interface like prisms or gratings. Moreover, in its basic type, it is limited to one channel, making multiplexing complicate. A further development lead to a similar effect in metal nanostructures, resulting in localized surface plasmon resonance (LSPR). Here, a resonance can be observed spectroscopically, the wavelength position depends on factors related to particle properties (material, size, shape) and the environment [1]. The latter parameter is based on the refractive index of the space surrounding the particle. If the particle is utilized as biosensor, it is functionalized by receptor molecules, such as single stranded DNA (complementary to a desired target DNA). If one monitors now the LSPR of this structures during incubation with sample solutions, the binding of present target DNA would change the refractive index on the particles surface, and induce a measurable signal (wavelength shift), which is used as sensoric signal, and can be correlated to the presence of target molecules. A proof-of-principle of this approach for DNA detection was conducted on individual, single gold nanoparticle sensors [2]. In comparison with SPR, LSPR is sensing in a much more limited distance around the particles, which can be approximated by the particle diameter, in contrast to the hundreds of nm and more in the case of SPR [3]. This limited distance leads to a significantly decreased background signal in the case of typical biomolecular binding reactions which happen in the range of 5-10 nm distances.

3. Multiplexed LSPR

In the field of biomolecular detection, often a series of similar assays is oft interest, like in the identification of the kind of antibody present, or the pathogenic species out of a whole family of organisms like E. coli. In such cases, single assays are not sufficient, and have to be paralleled. One possible approach to address this problem is the microarray (or chip) format, where an array of receptors is located on the substrate surface, and incubated with a solution containing (a mixture of) target molecules. Here, usually labeled molecules are used, such as by fluorescence (during previous PCR steps) in the case of DNA/RNA. Using LSPR, a similar miniaturized concept could be realized, with the advantage of avoiding the labels. Therefore, nanoparticles were chemically synthesized using conventional as well as microfluidic approaches [4], and arrayed on a glass substrate using a dispensing spotter [5].

In order to read-out the whole array in one step, a Fourier transform imaging spectrometer based on a Michelson interferometer was set up and demonstrated to be able to detect changes in the refractive index on the nanoparticles surfaces [6]. Finally, it could be shown that the instrument is able to detect and identify various DNA sequences from pathogenic funghi with this approach [7], demonstrating the proof-of-principle of this promising innovative method for multiplexed molecular detection.

Acknowledgements

Funding of the research projects WaterChip (01DQ16009A) and DesPAC (01DH17058) and InfectoGnostics (13GW0096F) by the Federal Ministry of Education and Research Germany as well as DFG (FR 1348/31-1) and DAAD (PPP 57397547), is gratefully acknowledged.

References

[1] A. Csaki, O. Stranik, W. Fritzsche: Localized surface plasmon resonance based biosensing. Expert Review Of Molecular Diagnostics 18, 279-296 (2018)

[2] T. Schneider, N. Jahr, J. Jatschka, A. Csaki, O. Stranik, W. Fritzsche: Localized surface plasmon resonance (LSPR) study of DNA hybridization at single nanoparticle transducers, J Nanopart Res 15, 1531 (2013)

[3] J. Jatschka, A. Dathe, A. Csaki, W. Fritzsche, O. Stranik: Propagating and localized surface plasmon resonance sensing - a critical comparison based on measurements and theory. Sensing and BioSensing Research 7, 62-70 (2016)

[4] M. Thiele, A. Knauer, D. Malsch, A. Csaki, T. Henkel, J.M. Köhler, W. Fritzsche: Combination of microfluidic high-throughput production and parameter screening for efficient shaping of gold nanocubes using Dean-flow mixing. Lab on a Chip 17, 1487-1495 (2017)

[5] A. Pittner, S. Wendt, D. Zopf, A. Dathe, N. Grosse, A. Csáki, W. Fritzsche and O. Stranik: Fabrication of micro-patterned substrates for plasmonic sensing by piezo-dispensing of colloidal nanoparticles. Analytical and Bioanalytical Chemistry, in press (2019)

[6] D. Zopf, J. Jatschka, A. Dathe, N. Jahr, W. Fritzsche, O. Stranik: Hyperspectral imaging of plasmon resonances in metallic nanoparticles. Biosensors and Bioelectronics 81, 287-293 (2016)

[7] D. Zopf, A. Pittner, A. Dathe, N. Grosse, A. Csáki, K. Arstila, J. Toppari, W. Schott, D. Dontsov, G. Uhlrich, W. Fritzsche and O. Stranik: Plasmonic nanosensor array for multiplexed DNA-based pathogen detection. ACS Sensors, 4, (2), 335-343 (2019)

Anisotropic noble metal nanoparticles coated by SiO_2 and ZrO_2 nanolayer for SHINERS environmental analysis

Jan Krajczewski[1*], Andrzej Kudelski[1]

[1]Faculty of Chemistry, University of Warsaw, 02-093 Warsaw
*corresponding author, E-mail: jkrajczewski@chem.uw.edu.pl

Abstract

In this contribution we report synthesis of some silver and gold nanoparticles having spherical, decahedral and bipyramidal shape which have been covered with various protecting layers. Optical and structural properties of obtained nanomaterials was examined. It was found that the zirconia protecting layer exhibits significantly better durability in corrosive environmental conditions than standard silica nanolayer. Obtained nanoparticles were applied as optical nanoresonators for shell-isolated nanoparticle-enhanced Raman scattering (SHINERS) measurements of various pesticidies.

1. Introduction

Nanoparticles from metals from the 11 group in specific manner interact with light. Incident light with appropriate frequency excites collective oscillation of electron plasma, so called surface plasmon resonance (SPR). This leads to high local enhancement of the electromagnetic field. Therefore, such nanoparticles could be applied to enhance efficiency of some weak optical effects (like Raman scattering) which intensity depends on the intensity of the electromagnetic field. Theoretical calculations showed that the highest enhancement occurs on sharp tops and edges in case of anisotropic nanoparticles or in the gap between nanoparticles. Therefore, application of anisotropic plasmonic metal nanoparticles allows to rich significantly higher enhancement factor what allow to detect analytes in lower concentration range. However, direct interaction between metallic surfaces and some analytes could lead to their denaturation. Therefore, in some cases, nanometric layers of protecting oxide are deposited on nanoparticles surface. A protective layer keeps nanoparticles from agglomeration and prevents direct interaction between metallic surfaces and analyte molecule.

2. Experimental

Gold bipyramids were obtained due to seed mediated growth method described by Weizmann et al. [1]. In the first step gold nanoseeds were formed by the reduction of $AuCl_4^-$ ions by sodium borohydride. In the second step spherical nanoseeds growth in solution containing cetyltrimethylammonium bromide (CTAB) as stabilizing agent by reducing $AuCl_4^-$ ions by weak redactor - ascorbic acid.

The decahedral silver nanoparticles were synthesized by photochemical transformation [2]. In the first step small semi spherical nanoseeds were formed by the reduction of silver ions by sodium borohydride in the presence of sodium citrate and L-arginine. After 10 minutes, the obtained sol of silver nanoseeds was transferred into a cylindrical glass reactor and illuminated by 470 nm light under constant stirring for 5 h at 35 °C.

Spherical gold and silver nanoparticles were obtained due to standard citrate method.

In most cases silica layer was deposited on plasmonic cores due to decomposition of tetraethoxysilane (TEOS) catalyzed by ammonia. Alternatively, nanometric silica layer was obtained by the decomposition of Na_2SiO_3 in the acidified solution.

Zirconia layer were deposited according to the method reported by Krajczewski et al. [3]. In the first step the surface of nanoparticles was modified by L-arginine. Then, some portion of cyclohexene was added what leads to formation of two phase solution. To upper, organic phase, some amount of (3-mercaptopropyl)trimethoxysilane was added under stirring. After 30 minutes organic layer was carefully separated. Nanoparticles were stirred and redispersed in absolute ethanol .Then, appropriate amount of zirconia(IV) isopropoxide was added. Solution was vigorously stirred for 15 minutes, then nanoparticles were centrifuged and suspended in distilled water.

3. Discussion

Optical and structural properties of synthesized nanomaterials were carefully examined. Fig. 1. presents TEM micrographs of decahedral silver nanoparticles before and after deposition of silica layer.

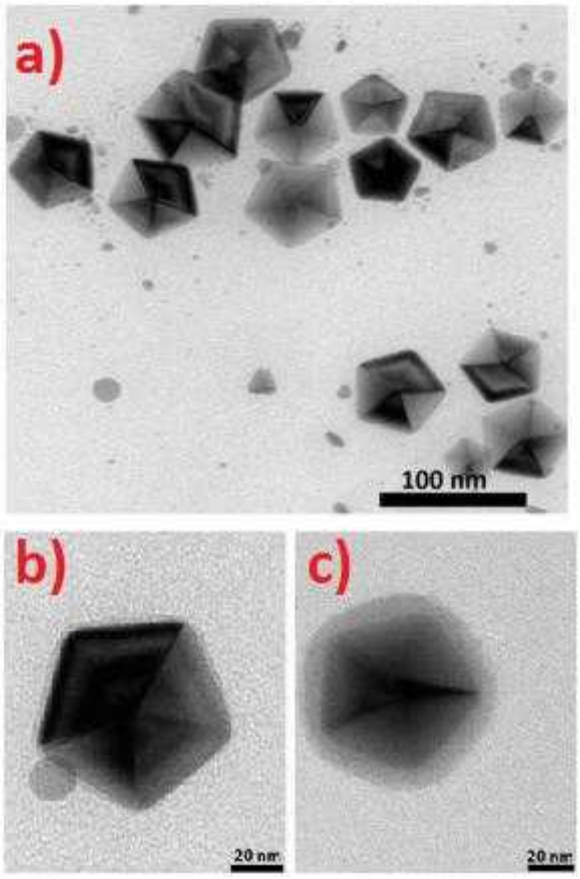


Figure 1: TEM micrographs of decahedral silver nanoparicles: a) before deposition of silica layer, b) after deposition of 3 nm thick silica layer, c) after deposition of 10 nm thick silica layer.

Obtained nanostructures were tested as SHINERS nanoresonators. To do this, the same amount of various nanoparticles were dropped on chemisorbed monolayer of p-mercaptobenzoic acid on platinum plate. Then, SHINERS spectra was recorded. It was found that suitably thin protective layer do not dump electromagnetic field so much and nanoparticles still could be applied as nanoresonators. We found using dipyramidal gold nanostructures coated by silica layer, that we are able to detect thiram pesticide in trace amounts on tomato skin (12 ng/cm^2).

4. Conclusions

In this work we presented various methods of synthesis of anisotropic silver and gold nanoparticles. Optical and structural properties were studied. Plasmonic cores were coated by nanometric protective layer of various oxides like silica, zirconia. Stability in various environmental conditions was tested. Finally, obtained nanoparticles were applied as SHINERS nanoresonators. It was found that the anisotropic noble metal nanoparticles coated by nanometric silica layer could be used to detect trace amount of pesticide like thiram or methyl parathion.

Acknowledgements

This work was financed from the funds of the National Science Centre (Poland) allocated on the basis of decision number DEC-2013/11/B/ST5/02224. J.K. thanks the Faculty of Chemistry, University of Warsaw for its financial support.

References

[1] J. H. Lee, K. J. Gibson, G. Chen, Y. Weizmann, Bipyramid-templated synthesis of monodisperse anisotropic gold nanocrystals, Nat. Commun. 6:1-9, 2015

[2] B. Pietrobon, M. McEachran, V. Kitaev, Synthesis of size-controlled faceted penta-gonal silver nanorods with tunable plasmonic properties and self-assembly of thesenanorods, ACS Nano 3:21–26, 2009

[3] J. Krajczewski, H. Abdulrahman, K. Kołątaj, A. Kudelski, Zirconium(IV) oxide: New coating material for nanoresonators for shell-isolated nanoparticle-enhanced Raman spectroscopy, Spectrochim. Acta A, 193:480-485, 2018

Synthesis, characterization and application of novel bifunctional magneto - plasmonic nanocomposites

Jan Krajczewski[1*], Karol Kołątaj[1], Andrzej Kudelski[1]

[1]Faculty of Chemistry, University of Warsaw, 02-093 Warsaw
*corresponding author, E-mail: jkrajczewski@chem.uw.edu.pl

Abstract

Herein we describe synthesis of some magneto - plasmonic nanocomposites consisting of Fe_2O_3 and various plasmonic nanoparticles. Optical and structural properties of obtained materials are carefully examined. TEM micrographs and XRD measurements confirmed formation of magneto - plasmonic nanocomposites. Application of external magnetic field allows to obtained highly organized substrate for repetitive SERS measurements, which allows to eliminate the so - called ,,coffee - ring effect", involving peripheral accumulation of nanoparticles.

1. Introduction

Gold and silver metal nanoparticles in a specific manner interact with light. Irradiation wit incident light with appropriate frequency leads to excitation of collective oscillations of electron plasma, so called surface plasmon resonance (SPR). This leads to local high enhancement of electromagnetic field. Therefore, such nanoparticles could be applied to enhance efficiency of weak optical effects (like Raman scattering) which efficiency depends on intensity of the electromagnetic field. Theoretical calculation showed that the highest enhancement occurs on sharp tops and edges in case of anisotropic nanoparticles or in the gap between two nanoparticles. Therefore, application of anisotropic plasmonic metal nanoparticles allows to rich significantly higher enhancement factor what allows to detect analytes in lower concentration range. Moreover, coupling of anisotropic plasmonic metal nanoparticles with magnetic Fe_2O_3 nanoparticles leads to formation of bifunctional nanomaterials. In our study we report that application of magneto - plasmonic nanocomposite allows to prepare of highly organized substrate for SERS measurements.

2. Experimental

Magnetic Fe_2O_3 nanoparticles were prepared according to co-precipiate method proposed by Makovec et al. [1]. Solution of $FeSO_4$ and $FeCl_3$ was stirred, then appropriate amount of concentrated ammonia was added, during vigorously stirring. After 30 minutes next portion of ammonia was added, and pH of solution reached 11.6. Obtained nanoparticles were washed by distilled water twice.

Fe_2O_3 nanoparticles were functionalized with (3-aminopropyl)triethoxysilane (APTMS). Briefly, APTMS was added to the as-prepared sol of Fe_2O_3 to obtain a final concentration of APTMS equal to 0.1 M, and the obtained mixture was stirred for 24 hours. This led to a reaction between the Fe_2O_3 and APTMS – the methoxy groups of APTMS react with the hydroxyl groups at the surface of Fe_2O_3 forming strong Fe-O-Si bonds.

The decahedral silver nanoparticles were synthesized by photochemical transformation [2]. In the first step small semi spherical silver nanoseeds were formed by the reduction of silver ions by sodium borohydride in a presence of sodium citrate and L-arginine. After 10 minutes, the obtained sol of silver nanoseeds was transferred into a cylindrical glass reactor and illuminated by 470 nm light under constant stirring for 5 h at 35 °C.

The silver nanocubes were prepared using a method developed by Xia et al. [3]. 60 ml of anhydrous ethylene glycol was heated at 160 °C for 1.5 h. Next, sodium sulfide and polyvinylpyrrolidone was added to solution. In the last step 5 ml of a 0.3 mM $AgNO_3$ solution in ethylene glycol were added to the boiling ethylene glycol, and the reaction mixture was boiled for another 20 min. Then, the reaction was quickly suspended by immersing the reaction flask in a mixture of ice and water. The resulting nanoparticles were then centrifuged with acetone three times and re-dispersed in water.

The hollow gold nanoparticles were synthesized using cobalt nanoparticles as sacrificial templates [4]. In first step cobalt nanoparticles were prepared due to reduction of cobalt salt by sodium borohydride. Subsequently, to formed cobalt nanoparticles, some amount of $HAuCl_4$ solution was added. Gold hollow nanoparticles was formed due to galvanic replacement mechanism.

In order to prepare magneto - organic nanocomposite plasmonic nanoparticles were added to a solution of APTMS-functionalized Fe_2O_3 nanoparticles, shaken gently, and left for 30 minutes. After this time, the agglomerates formed were concentrated by a magnetic field and then concentrated agglomerates were re-dispersed in water.

3. Discussion

Optical and structural properties of synthesized nanomaterials were carefully examined. Fe_2O_3 colloid is brown; however, after attachment to the γ-Fe_2O_3 nanostructures of various plasmonic nanoparticles the magneto - plasmonic conglomerate obtained took another distinctive color, depending on the plasmonic nanoparticles used. In a strong magnetic field, the color of the nanocomposite associated with the plasmonic nanoparticles is "transferred" to the sediment formed, leaving the solution colorless. Re-dispersing the sediment of the nanocomposites leads to sols that display a color typical for the attached plasmonic nanostructures. This indicates that the plasmonic nanoparticles are strongly connected to their magnetic counterpart. Fig. 2. present TEM micrographs of magneto - plasmonic nanocomposite with cubic and decahedral silver nanoparticles.

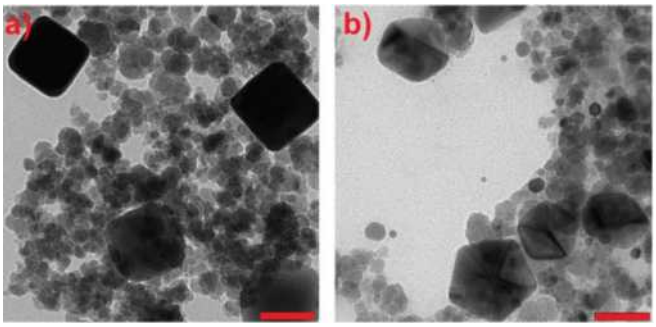


Figure 1: TEM micrographs of nanocomposites with: (a) cubic–Ag, (b) decahedral–Ag nanoparticles.

Obtained nanostructures were applied as highly organized substrate for repetitive SERS measurements. SERS measurements were carried out for few chosen analytes. Application of magneto - plasmonic nanocomposite provide low detection limit (for example of 18 ng/cm^2 for malachite green).

4. Conclusions

In this work we propose an easy and very efficient method for preparing conglomerates of magnetic Fe_2O_3 nanoparticles with various noble metal nanoparticles. Noble metal nanoparticles was attached to the Fe_2O_3 nanoparticles via organic linker (APTMS). As far as we know synthesized composites are the first examples of magnetic composites containing well defined anisotropic metallic nanostructures. The magnetic-plasmonic conglomerates have been used as highly organized substrate for SERS measurements.

Acknowledgements

Dr. Marcin Pisarek (Institute of Physical Chemistry, Polish Academy of Sciences) is acknowledged for her assistance in the XPS measurements. This work was financed out of funds of the National Science Centre, Poland, No. 2017/25/B/ST5/01997. J.K. thanks the Faculty of Chemistry, University of Warsaw for its financial support.

References

[1] M. Tadic, S. Kralj, M. Jagodic, D. Hanzel, D. Makovec, Magnetic properties of novel superparamagnetic iron oxide nanoclusters and their peculiarity under annealing treatment, *Appl. Surf. Sci.* 322:255–264, 2014

[2] B. Pietrobon, M. McEachran, V. Kitaev, Synthesis of size-controlled faceted penta-gonal silver nanorods with tunable plasmonic properties and self-assembly of thesenanorods, *ACS Nano* 3:21–26, 2009

[3] A. R. Siekkinen, J. M. McLellan, J. Chen, Y. Xia, Rapid synthesis of small silver nanocubes by mediating polyol reduction with a trace amount of sodium sulfide orsodium hydrosulfide, Chem. Phys. Lett. 432:491-496, 2006

[4] A. M. Schwartzberg, T. Y. Olson, Ch. E. Talley, J. Z. Zhang, Synthesis, Characterization, and Tunable Optical Properties of Hollow Gold Nanospheres, J. Phys. Chem. B, 110:19935–19944, 2006

Light management in solar cells

Subwavelength High Refractive Index Dielectric structures for photovoltaic applications

Ángela I. Barreda[1], Amélie Litman[2], Francisco González[1], Pablo Albella, Jean-Michel Geffrin[2] and Fernando Moreno[1]

[1]Group of Optics, Department of Applied Physics, University of Cantabria, Cantabria 39005, Spain
[2]Aix-Marseille Univ, CNRS, Centrale Marseille, Institute Fresnel, Marseille, France
*corresponding author, E-mail: morenof@unican.es

Abstract

High Refractive Index Dielectric (HRID) nanostructures have become an alternative to metallic ones in the VIS-NIR due to their low-losses and magnetic response. In addition, they can be basic units in applications where directionality control of the scattered radiation is required. Here, we show that aggregates of subwavelength HRID particles, under strong electromagnetic interaction, can be efficient scattering units for redirecting the incident radiation towards a photosensitive substrate. Applications for optimizing the efficiency of photovoltaic devices (solar cells) are envisaged.

1. Introduction

High Refractive Index Dielectric (HRID) nanoparticles (NPs) have been vastly investigated in the last years due to their low-losses in the VIS-NIR ranges and also because of their unusual magnetic response in spite of being non-magnetic materials [1]. Scattering directionality exhibited by these structures manifest due to the coherent effects between their electric and magnetic resonances. Kerker *et al* established that under certain conditions of the electric permittivity and magnetic permeability, scattered radiation can be concentrated either in the forward or backward region, being null or almost null in the backward or forward direction. This corresponds to the *First Kerker* (*Zero-Backward*) condition or *Second Kerker* (*near Zero-Forward*) condition [2], respectively. The first experimental evidence of these directionality effects was carried out in the microwave region [3] and its conclusions can be extrapolated to the nanometric scale because of the scalability of Maxwell equations (in this work we will keep the millimetric range for analogy to previous research). A lot of effort has been done to control the directionality properties of HRID subwavelength (SW) structures. More complex geometries (dimers, trimers or even oligomers) have been explored. In particular, it was shown that dimers of SW HRID spherical particles, with strong electromagnetic interaction, can redirect the incident radiation in the forward direction more efficiently than an isolated particle. A new Scattering Directionality Condition (SDC), denoted as *near Zero-Backward* (a 180º rotation of the traditional *near Zero-Forward* condition) shows up [4] due to the coupling effects between the components of the dimer. With respect to the *Zero-Backward* condition, it can be observed independently of the interaction effects between the particles. This suggests that by means of this dimer scattering unit, it is possible to achieve two spectral regions where the incident radiation is forward scattered, being null or almost null in the backward direction. They are observed at the frequencies corresponding to the *Zero-Backward* and *near Zero-Backward* conditions, respectively. Here, we analyze the electromagnetic behavior of isolated and aggregates (two (dimer), four and five particles) of HRID SW particles, placed on a dielectric monolayer/multilayer substrate of known optical properties with the objective of analyzing their performance for energy harvesting applications with photovoltaic devices.

2. Results

In general, SDCs are affected by the presence of the substrate. When its refractive index is moderately low (for instance, glass with $n_s \sim 1.5$), the SDCs can still be observed. However, as the substrate refractive index increases, SDCs are hardly fulfilled [5].

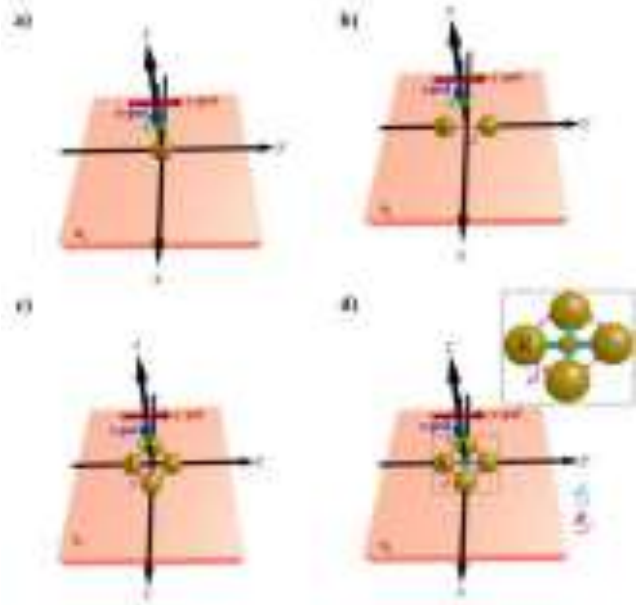


Figure 1. The different analyzed geometries of SW HRID structures on a monolayer substrate. a) One particle, b) dimer, c) four particles and d) five particles. The particle gap distance is d = 3 mm. For the five-particle configuration, the distance between the side particles and the central one is d_2 = 0.85 mm. The particles radii correspond to R = 9 mm, except for the central particle in d), which is R_2 = 5 mm. Their electric permittivity is $\varepsilon = 15.7 + 0.3i$.

All the analyzed geometries are illuminated by a plane wave propagating along the −*z*-axis and linearly polarized along the *x*- or *y*-axis.

To analyze how the presence of a substrate, with known optical properties, affects the electromagnetic radiation reaching the substrate when one of the previous nanostructures is located on it, we evaluate the parameter, defined as $f_{subs} = Q_{sca\ subs}/Q_{sca}$ [6]. $Q_{sca\ subs}$ and Q_{sca} are the normalized scattering cross-section for radiation scattered into the substrate by the structure and its total normalized scattering cross-section, respectively. Physically, f_{subs} represents the fraction of radiation that is scattered into the substrate. In Table 1 we show f_{subs} integrated over the range q = [0.6, 1.2] (q is the size parameter) for the different configurations (see Fig. 1) when located on a monolayer dielectric substrate of refractive index n_s = [1.5, 3.5]. Also, different polarizations of the incident radiation are considered (all the structures are illuminated by a plane wave propagating along the -*z*-axis and linearly polarized along the *x*- or *y*-axis).

Table 1. f_{subs} (%), integrated over all q values (q = [0.6, 1.2]) for different substrate refractive indices n_s. Different particles configurations and polarizations of the incident radiation are considered.

Geometry	n_s = 1.5	2.0	2.5	3.0	3.5
Isolated	38.65	36.25	33.35	30.93	28.88
Dimer pol y	40.48	36.37	32.53	29.61	27.25
Dimer pol x	37.47	35.07	32.12	29.60	27.44
4 particles	39.17	35.80	32.42	29.61	27.27
5 particles	41.17	38.02	34.59	31.69	29.25

As n_s increases, f_{subs} decreases for all the studied geometries and polarizations of the incident radiation. This decrease is more notorious when the electromagnetic interaction between the particles is strong (i.e. for an exciting plane wave linearly polarized along the *y*-axis and the configurations corresponding to four and five particles). For moderately low values of n_s (i.e. 1.5), the largest values of f_{subs} are obtained for the cases where the interaction effects are strong. This is because of the *near Zero-Backward* condition. However, with the exception of the five-particle geometry, for substrates made of silicon (n_s = 3.5, typical photovoltaic silicon layer in solar cells), the behavior is the opposite: f_{subs} is higher for the isolated particle and the dimer illuminated by a plane wave linearly polarized along the *x*-axis (weak interaction effects). The fact that the five-particle geometry provides the highest f_{subs} values, regardless of the value of n_s, is due to the large enhancements of the electric field in the particle gaps, which increase the absorption of radiation in the substrate. For the isolated particle and the four- and five-particle geometries, f_{subs} is the same independently of the polarization of the impinging wave, due to symmetry. For n_s = 1.5, it is possible to redirect the incident radiation towards the substrate more efficiently by using aggregates. However, for n_s = 3.5, the isolated particle works better than aggregates. This is because of two different factors. On the one hand, for moderately low n_s, SDCs can be achieved. Due to the *near Zero-Backward* condition, f_{subs} is larger for aggregate configurations than for the isolated one. Nevertheless, for high values of n_s, SDCs are not fulfilled. On the other hand, as n_s increases, the reflection at the air-substrate interface increases too. To take advantage of this new SDC (*near Zero-Backward* condition) to optimize the performance of solar cells, we analyzed the electromagnetic behavior of the different configurations of HRID particles on a multilayer substrate. In particular, we place two antireflection dielectric layers on the photosensitive silicon substrate. The purpose of this multilayer structure is two-fold. First, by means of this graded-index coating, the reflection of the incident radiation is minimized. Second, the SDCs can be recovered as the difference in refractive index between air and the first antireflection layer is lower than between air and silicon. We have shown that for two antireflective layers, it is possible to recover the SDCs and obtain values of f_{subs} for silicon substrates similar to those corresponding to a glass monolayer substrate.

3. Conclusions

In this work, we have evidenced that by using aggregates of subwavelength HRID particles with strong electromagnetic interaction, it is possible to redirect the incident radiation towards the photovoltaic silicon layer more efficiently than with isolated HRID particles. This is because of a new SDC, the *near Zero-Backward*. In order to take advantage of the SDCs for increasing the fraction of radiation scattered towards a silicon substrate, an antireflection multilayer coating should be used. In addition, thanks to this graded-index multilayer, the reflection at the air-substrate decreases. This research supports optimization of solar cells performance.

Acknowledgements

AIB thanks the U. Cantabria for her PhD grant. Authors thank support of SODERCAN through the Research Vicerrectorate of the U. Cantabria.

References

[1] A. García-Etxarri, *et al.*, Strong magnetic response of submicron silicon particles in the infrared, *Opt. Express* 19: 4815–4826, 2011.

[2] M. Kerker, D. S. Wang, C. L. Giles, Electromagnetic scattering by magnetic spheres, *J. Opt. Soc. Am.* 73: 765–767, 1983.

[3] J. M. Geffrin, *et al*., Magnetic and electric coherence in forward-and back-scattered electromagnetic waves by a single dielectric subwavelength sphere, *Nat. Commun.* 3: 1–8, 2012.

[4] A. I. Barreda, *et al*., On the scattering directionality of a dielectric particle dimer of high refractive index, *Sci. Rep.* 8: 7976, 2018.

[5] J. Van de Groep, A. Polman, Designing dielectric resonator on substrates: Combining magnetic and electric resonances, *Opt. Express* 21: 26285–26302, 2013.

[6] K. R. Catchpole, A. Polman, Design principles for particle plasmon enhanced solar cells, *Appl. Phys. Lett.* 93: 191113, 2008.

Nanophotonic enhanced perovskite-silicon solar cell devices

Christiane Becker[1], Phillip Manley[1,2], Klaus Jäger[1,2], David Eisenhauer[1], Johannes Sutter[1], Steve Albrecht[1], Kaibo Zheng[3], Tõnu Pullerits[3], and Sven Burger[2]

[1]Division Renewable Energies, Helmholtz-Zentrum Berlin für Materialien und Energie GmbH, Berlin, Germany
[2]Computational Nanooptics Group, Zuse Institute Berlin, Berlin, Germany
[3]Division Chemical Physics, Lund University and NanoLund, Lund, Sweden
*corresponding author, E-mail: christiane.becker@helmholtz-berlin.de

Abstract

Perovskite-silicon tandem solar cells are a promising concept for overcoming the limits of conventional silicon single-junction technology. Light management is doubtless a key issue for further boosting efficiency. We discuss the impact of photonic nanostructures on the optical performance of perovskite-silicon devices. We experimentally and numerically demonstrate shallow antireflective nanotextures, which are compatible with perovskite solution processing. We further showcase enhanced photon up-conversion using perovskite nanoparticles interacting with photonic nanostructures and discuss the applicability for spectral conversion of sunlight.

1. Introduction

Single-junction silicon solar cells are currently dominating the photovoltaic market, but they more and more approach the theoretical power conversion efficiency limit of 29.4%. Perovskite-silicon tandem solar cells are at present the most investigated concept to overcome this limit and to further boost efficiency [1]. Optimized light management is a key issue to tap the full potential of such tandem solar cells as often planar interfaces lead to undesired reflective losses and still large parts of the solar irradiance remain unused. Nanostructures with dimensions comparable to the wavelength of light enable systematic control of the light-matter interaction and are hence a promising measure for improving the optical performance of solar energy devices.
Here, we experimentally and numerically investigate two different optical characteristics of photonic nanostructures in order to improve the performance of perovskite-silicon tandem solar cells. First, we develop shallow sinusoidal nanotextures at the interface between perovskite top and silicon bottom cell. We show that these structures not only reveal excellent broadband anti-reflective properties but also demonstrate the compatibility with perovskite solution processing, so far yielding highest single-junction efficiencies. We further consider a second characteristic of such nanophotonic structures: enormous near-field enhancement effects can occur when momentum and energy of the incident light and of a leaky mode of the photonic nanostructure match. We harvest these enhanced near-fields in order to increase the two-photon pumped photoluminescence of perovskite nanoparticles placed on a silicon photonic crystal structure. We sketch the way to efficient photon up-conversion in order to harvest so far unused near infrared parts of the solar spectrum.

2. Experimental and numerical methods

In order to meet the constraints for solar cell processing, we exclusively apply nanopatterning techniques allowing for large-area fabrication and high throughput, namely, nanoimprint-lithography in combination with dry- and/or wet-chemical etching. We implement shallow sinusoidal nanotextures with 500 to 750 nm period into the surface of silicon wafers. Perovskite thin films can be spin-coated onto this textured surface (see Fig. 1a). We further fabricate large-area silicon photonic crystal slabs for photon up-conversion experiments with perovskite nanoparticles (Fig. 1b). Optical simulations are performed using a commercial software (JCMsuite) based on the finite element method (FEM) and the rigorous solution of Maxwell's equations.

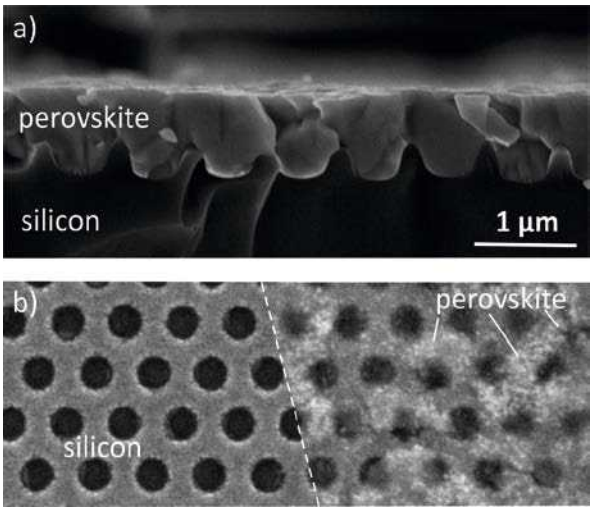


Figure 1: a) Spin-coated perovskite film on a silicon wafer with shallow nanotextured surface. b) Silicon photonic crystal slab without (left) and with (right) $CsPbBr_3$ perovskite nanoparticle coating.

3. Results and discussion

3.1 Perovskite-silicon tandem solar cells

Planar interfaces in perovskite-silicon tandem solar cells often cause large reflective losses. We investigate by optical FEM simulations how well shallow sinusoidal nanotextures, which are compatible with perovskite solution processing (see Fig. 1a), can reduce reflection. Figure 2 shows the simulation domain as well as the absorption in different layers of the tandem device. With 500 nm texture period and height, optical reflection and parasitic absorption losses amount to 3.8 mA/cm^2 current density only.

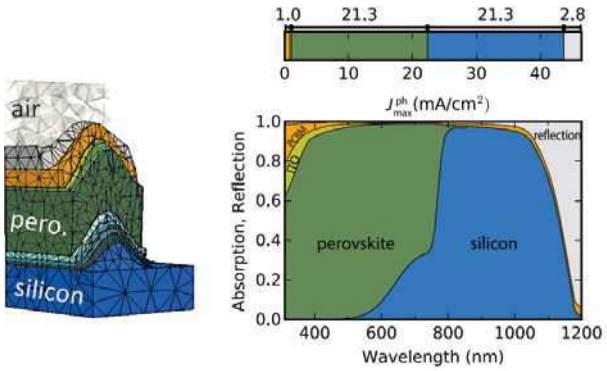


Figure 2: (Left) Simulation domain for optical FEM simulations of a 500 nm - periodic sinusoidal textured 2-terminal perovskite-silicon tandem solar cell. (Right) Absorption profile and associated theoretical current density. A maximum achievable matched current density of 21.3 mA/cm^2 and power conversion efficiency of 31.8% can be reached (from [2]).

3.2 Spectral up-conversion

Spectral conversion in low light intensity conditions can significantly increase the thermodynamic limiting efficiency of solar cells by harnessing near infrared parts of the solar spectrum. Light confinement on photonic nanostructures permits decreasing the required irradiance level for photon up-conversion processes.

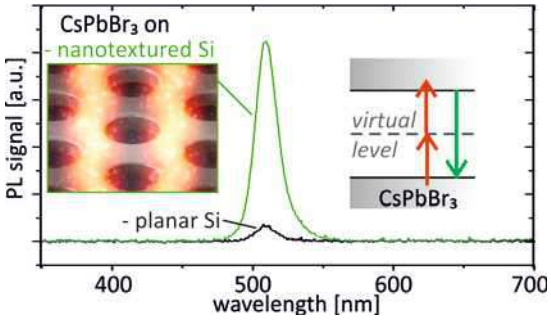


Figure 3: Photoluminescence signal of $CsPbBr_3$ nanoparticles on a nanostructured (green) and on a bulk (black) silicon film excited at λ = 925 nm. The left inset exemplifies a simulated 3D electric field energy distribution (from [3]). The right inset illustrates the underlying two-photon absorption process (from [4]).

Figure 2 shows the two-photon excited photoluminescence of $CsPbBr_3$ perovskite nanoparticles. By interaction with a leaky mode of a silicon photonic crystal slab as shown in Fig. 1b, a 15-fold enhanced photoluminescence is observed for an excitation at center wavelength 925 nm despite rather broadband excitation conditions (FWHM = 40 nm). Future design of photonic nanostructures aims at light confinement at λ > 1200 nm for up-conversion of to date unused parts of the solar spectrum.

4 Conclusions

We investigated the impact of photonic nanostructures on the optical performance of perovskite-silicon tandem devices experimentally and numerically. Shallow nanotextures promise both, a strong anti-reflective effect as well as compatibility with perovskite spin-coating. Strong near-fields on silicon nanostructures are found to boost photon up-conversion in perovskite nanoparticles.

Acknowledgements

We thank Carola Klimm from Helmholtz-Zentrum Berlin for SEM imaging. We thank the German Federal Ministry of Education and Research (grant no. 01IO1806), the Helmholtz Association (Helmholtz Innovation Lab HySPRINT) and the Swedish Research Council for funding. The simulation results were obtained within the Berlin Joint Lab on Optical Simulations for Energy Research (BerOSE) of Helmholtz-Zentrum Berlin für Materialien und Energie GmbH, Zuse Institute Berlin and Freie Universität Berlin..

References

[1] M. Jošt, E. Köhnen, A. Belen Morales-Vilches, B. Lipovšek, K. Jäger, B. Macco, A. Al-Ashouri, J. Krč, L. Korte, B. Rech, R. Schlatmann, M. Topič, B. Stannowski, Steve Albrecht, Textured interfaces in monolithic perovskite/silicon tandem solar cells: advanced light management for improved efficiency and energy yield, *Energy & Environmental Science* 11:3511-3523, 2018

[2] D. Chen, P. Manley, P. Tockhorn, D. Eisenhauer, G. Köppel, M. Hammerschmidt, S. Burger, S. Albrecht, C. Becker, K. Jäger, Nanotextured perovskite-silicon tandem solar cells, *Journal of Photonics for Energy* 8: 022601, 2018

[3] C. Barth, C. Becker, Machine learning classification for field distributions of photonic modes, *Communications Physics* 1: 58, 2018

[4] C. Becker, S. Burger, C. Barth, P. Manley, K. Jäger, D. Eisenhauer, G. Köppel, P. Chabera, J. Chen, K. Zheng, T. Pullerits, Nanophotonic enhanced two-photon absorption of perovskite quantum dots, *ACS Photonics* 5: 4668−4676, 2018

Nanostructuring photovoltaic cells: How to push some limits.

Mahmoud H. Elshorbagy[1,2], Alexander Cuadrado[1], and Javier Alda[1]

[1] Applied Optics Complutense Group. University Complutense of Madrid.
Faculty of Optics and Optometry. Ave. Arcos de Jalón, 118. 280367 Madrid. Spain.
[2] Minia University. Physics Department. Faculty of Science. El-Minya. Egypt.
* corresponding author, E-mail: javier.alda@ucm.es

Abstract

Advances in photovoltaics are mostly a quest for higher efficiency in the energy conversion for low-cost solar panels. This can be attainable by different strategies dealing with complex arrangements of materials to cover the whole spectrum. We have followed a different way by tailoring the geometry and subwavelength structures of auxiliary layer terminating the photovoltaic cell. This approach needs the full understanding of the interaction of light with nanostructures on ultra-thin films. The physical mechanisms involved in the proposed arrangement are funneling and guiding effects. The cell type platform able to support this nanostructures is selected as the one with larger margin of improvement, i.e., amorphous Si hydrogenated cells. This contribution shows how a proper dimensional and material set-up can increases the short circuit current more than 50%.

1. Introduction

When talking about effciiency in a solar cell, the short circuit current, J_{SC}, is the variable to watch once the material selection has been done [1]. This parameter can be increased by customizing the geometry and selecting carefully the material of the front and back auxiliary layer of the cell. The goal is to have as much possible amount of light interacting with the active layer of the structure. Then, charge carriers are routed towards electrodes to establish a current deliverable to an outer circuit. This simple scenario is limited by the constrains imposed by charge mobility, free mean path, and usable spectral windows of the materials of the active layer. Besides, the fabrication constrains may jeopardize some good performance parameters of the involved materials. Then, geometry is playing a decisive role in the pursue of a higher efficiency.

Even though, multi-junction solar cells have established world record figures in efficiency, we have preferred to move towards the lower end of the pack, and see how a cheap technology can benefit from a dedicated and optimized design of the layers around the active region. Amorphous silicon hydrogenated cells (a-Si:H) in their classical and ultra-thin version are well capable of improvement. Their modest efficiency of around 10% is balanced with its low cost and easiness of fabrication. They are affected by a main issue related with the degradation due to the Staebler-Wronski effect (SWE) that strongly affect the charge carrier availability [2].

Nanostructures and metasurfaces have been proposed to induce plasmonic effect that increases the absorption of the cell [4, 3]. Part of the effort is pointed towards the reduction of the light lost at the front interface. This requires the addition of antireflection coating that makes an impedance matching of the involved wave propagation and directs radiation to the inner layers of the cell. Also, we can fold the active layer of ultra-thin cell to trigger guiding and funneling mechanisms that expand the light interaction longer within the active layers [5, 6]. Another option to improve the performance of the cell is to channel light through nanostructured slots towards the active layer. In this contribution we will make a description of these geometries to show how metasurfaces can help solar cell technology to jump over the limits of previous technologies.

2. Geometric and material arrangement for a-Si:H cells

The starting point of the design is the commercial a-Si:H cell (see left layout in figure 1). This is composed of several layers stacking with plane-parallel interfaces. Each one of these layers contribute to the total short circuit current in different ways. In the right plot of Fig. 1 we show these contributions to the total absorption of the cell. However, the only radiation generating current is the one that is absorbed at the active layer. Actually, the relation between the calculated absorption and the short-circuit current is given as

$$J_{\rm SC} \int \frac{q}{hc} A(\lambda) \Phi_{\rm AM1.5}(\lambda) d\lambda,$$

where q is the electron charge, c is the speed of light in vacuum, h is the Planck's constant, $\Phi_{\rm AM1.5}(\lambda)$ is the solar spectral irradiance in terms of the wavelength, λ, and $A(\lambda)$ is the spectral absorption rate that is directly related with the electric field distribution at the active layer as

$$A(\omega) = \frac{1}{2} \omega \epsilon'' |E(\omega)|^2$$

that is written in terms of the frequency, ω and depends on the electric field distribution, $E(\omega)$ and the imaginary part of the dielectric constant of the active layer material ϵ''. All these variables can be computed and accounted for using computational electromagnetism tools. Our analysis

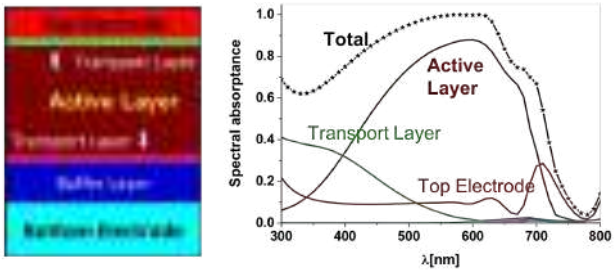


Figure 1: Left: Geometric and material arrangement of an amorphous-Si:H solar cells. Right Individual contribution of the layers composing the cell. The black star-line represents the total absorption. The portion that contributes to the short-circuit current is the absorption happening at the active layer (brown line).

has been made through a Finite Element Method package (COMSOL Multiphysics).

A first approach to improve the absorption at the active layer is to decrease light reflected back from the top electrode. This is possible by an antireflection coating that takes the form of a one dimensional subwavelength dielectric grating. The geometry of the grating makes possible to generate highly directional nanobeams that route radiation towards the active layer. An additional design that involves a two dimensional arrangement is presented here as a collection of nanoholes. They work as injectors that funnel light again towards the active layer, increasing absorption and improving the short-circuit current.

The same material arrangement presented in figure 1 is applicable to an ultra-thin a-Si:H solar cell. The main difference is the thickness of the active layer that is reduced from 350 nm to 150 nm. This thinning of the active layer benefits the charge carrier separation, mitigates SWE, but it also decreases the absorption of the active layer for wavelengths above 450 nm. To compensate this loss, we design a periodic corrugated template where the ultra-thin structure is deposited on conformally

Each one of the previously presented alternatives have their own advantages and a comparison among them. Their performance, in terms of the short-circuit current, is reported in Table 1 for comparison. We may see that the improvement in J_{SC} is larger than 30% for regular 350 nm thick cells, and more than 50% for ultra-thin cells. This better performance is obtained by taking into account light propagation within nanostructures. The main physical mechanism explaining this increase are: the generation of nanojets, and the guiding and funneling effects due to the existence of whole and the structural corrugation of the cell.

3. Conclusions

The performance of amorphous Silicon cells can be greatly improved by nanostructuring their geometrical arrangement. The front contact can be textured to avoid reflections and direct light towards the active layer. When even the active layer is shaped with slots, the funneling of the radiation towards these inner layers increases absorption, and the short-circuit current also increases. For ultra-thin a-Si:H cells, it is still possible to take advantage of the radiation behavior in the subwavelength domain if the whole cell structure is corrugated. The improvement of the short-circuit current is high enough to encourage researcher towards this approach.

Table 1: Short circuit current, J_{SC}, for the analyzed design.

Cell type (a-Si:H)	J_{SC} mA/cm^2
Reference	11.70
Nano-triangle ARC	15.68
Funneling holes	15.60
Reference ultra-thin	8.98
Textured ultrathin	13.64

Acknowledgements

This contribution has been possible thanks to the support of the Ministry of Higher Education of Egypt and the Ministerio de Economiía y Competitividad of Spain through the project TEC2013-40442.

References

[1] M. A. Green, K. Emery, Y. Hishikawa, W. Warta, and E. W. Dunlop, "Solar cell efficiency tables (version 45), Prog. Photovoltaics Res. Appl. **23**(1), 19 (2015).

[2] D. Staebler, and C. Wronski, "Reversible conductivity changes in discharge-produced amorphous Si, Appl. Phys. Lett. **31**(4), 292294 (1977).

[3] K. Huang, Q. Wang, X. Yan, K. Hu, M. Yu, and X. Shen, "Demonstration of enhanced absorption in thin film si solar cells with periodic microhemisphere hole arrays", Opt. Commun. **315**, 7982 (2014).

[4] J.N. Munday, H.A. Atwater, "Large integrated absorption enhancement in plasmonic solar cells by combining metallic gratings and antireflection coatings", Nano Lett. **11**(6), 21952201 (2010).

[5] M. H. Elshorbagy, K. Abdel-Hady, H. Kamal, and J. Alda, "Broadband anti-reflection coating using dielectric Si_3N_4 nanostructures. Application to amorphous-Si-H solar cells", Opt. Comm. **390**, 130-136 (2017).

[6] M. H. Elshorbagy, and J. Alda, "Funneling and guiding effects in ultrathin aSi-H solar cells using one-dimensional dielectric subwavelength gratings", J. Photon. Energy **7**(1), 017002 (2017).

[7] A. Vora, J. Gwamuri, J. M. Pearce, P. L. Bergstrom, D. Ö. Güney, "Multi-resonant silver nano-disk patterned thin film hydrogenated amorphous silicon solar cells for staebler-wronski effect compensation", J. App. Phys. **116** (9) 093103 (2014).

Complex epsilon-near-zero materials enhances light absorption in ultra-thin solar cells

Marcella Bonifazi, Valerio Mazzone, Andrea Fratalocchi,

PRIMALIGHT, Faculty of Electrical Engineering; Applied Mathematics and Computational Science,
King Abdullah University of Science and Technology (KAUST), Thuwal, Saudi Arabia
*corresponding author, E-mail: andrea.fratalocchi@kaust.edu.sa

Special session SP19: Light management in solar cells.

Abstract

We engineered an epsilon-near-zero (ENZ) material from suitably disordered metallic nanostructures. We experimentally demonstrate that this nanomaterial increases up to a record value the absorption of ultra-thin light harvesting films at visible and infrared wavelengths with a broadband enhancement of 170% in the external quantum efficiency (EQE). In addition, we developed a cost-effective fabrication process that make these materials suitable to large scale production.

1. Introduction

Recently, many efforts have been devoted to enhance the performances of light harvesting systems and colloidal quantum dots (CQD) revealed itself to be most valuable approach in enhancing the performances of light harvesting systems. In fact, CQDs are used in a wide range of devices, from photodetectors [1] to photovoltaic and photo-JFET devices [2] because they are cost-effective and have size-tunable emission. On the other hand, one of the biggest restraint with these materials is the compromise between the charge carrier extraction and the light absorption [3].
Different approaches have been proposed to overcome this limitation [4], but coupling light directly into the active layer by micro-structuring the substrate and introducing plasmonic nanostructures in CQD layer, seems to be the most effective [5]. The main drawback of this technology is that often most of the energy is localized inside the metal.

Here we present a new class of broadband epsilon-near zero (ENZ) materials based on disordered plasmonic nanostructures. These structures are able to localize broadband radiation within ultra-thin light harvesting films, greatly enhancing their absorption [6]. A theoretical investigation based on transformation optics allows us to obtain a material design effective for harvesting purposes Figure 1(a-b). In fact, these ENZ materials slow down light on scale smaller than the charge diffusion length and dramatically enhance the absorption. in addition to that, an innovative fabrication process make it suitable for large scale production.

2. Discussion

We developed a large scale process to fabricate suitable complex disordered ENZ metallic structures with completely controllable features. Figure **??**a shows SEM cross sections of a fabricated sample, assembled by an electroplating process that grows a random networks of gold (Au) nanowires from a flat metallic Au substrates. By using an exact analysis based on transformation optics, we demonstrate that the complex metallic network of Figure 1a is exactly equivalent to a flat metallic panel with a series of ENZ nano-regions on top (Figure 1c), connected by areas of high dielectric constant. When a thin layer of absorptive material is deposited on top of the ENZ nanostructures, incoming radiation gets trapped inside the ENZ material, originating a quasi-static field localized in areas of $10 - 100$ nm in proximity of the metal. In a series of AFM, Photoconductive AFM (PC-AFM) and Photoluminescence excitation (PLE) measurements, which are illustrated in Fig. 1d-e, we investigate the impact of ENZ nanostructures on the broadband absorption of an ultra-thin CQD film of $50 - 300$ nm thickness. Figure 1d reports the PC-AFM map of one region of a sample, he spatial current distribution is illustrated as a pseudocolor in the plot and is superimposed on the surface topography of the sample, which is obtained by AFM. We observe a great current enhancement on the peak of the structures, where the ENZ regions are formed. To further prove that the electromagnetic localization happen proximity of the peaks of our nanostructures, figure 1e show a TEM image of our metasurface. It is clear that the light is concentrated in the bright areas near the tips and, in particular, it is shown that most of the radiation is collected in the active material side. Figure 1f, shows the results of PLE experiments, which measure the absorption increase in the CQD region for different electroplating times.
For CQD thicknesses between $50 - 300$ nm, we experimentally observed a dramatic absorption enhancement ($\approx 400\%$) when compared to the PLE signal from an equivalent planar configuration, which becomes completely flat in the visible and infrared regions.
Thanks to its peculiar characteristics this innovative light harvesting device based on ultra-broadband ENZ material can be easily combined with ultra-thin absorptive film,

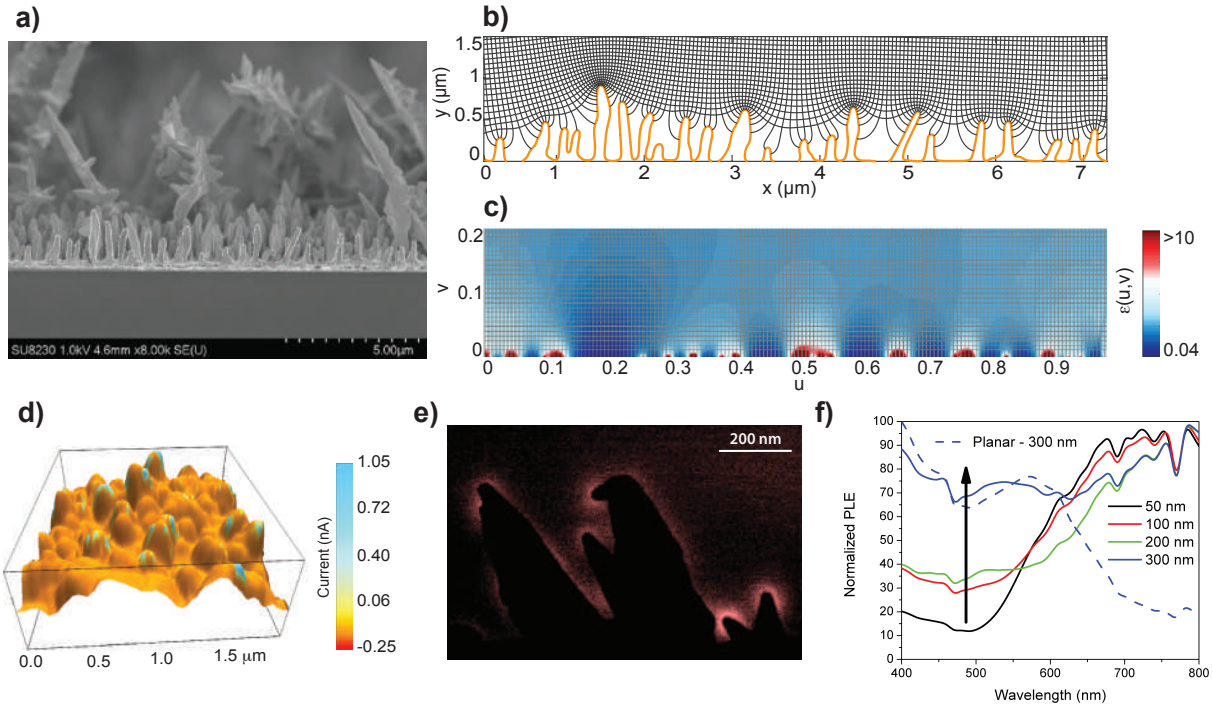


Figure 1: **ENZ materials design**: a) SEM cross section of a nanostructured sample, b) 2D reconstructed cross section of the profile, c) equivalent ENZ representation of the random disordered structures illustrated in panel b. **Photoconductive AFM, TEM and PLE measurements.** d) Photocurrent distribution plotted over surface profile, e) TEM measurements show a concentration of electromagnetic radiation near the tips of the nanostructures, f) PLE signals of 50-300 nm CQD film deposited on ENZ nanostructures

achieving very high efficiency in light absorption.

References

[1] Konstantatos, G., et al, Ultrasensitive solution-cast quantum dot photodetectors, *Nature*, Vol. 442, 180-183, 2006.

[2] Chuang, C.-H. M., et al, Improved performance and stability in quantum dot solar cells through band alignment engineering, *Nat. Materials*, Vol. 13, 796-801, 2014.

[3] Labelle, A. J., et al, Conformal fabrication of colloidal quantum dot solids for optically enhanced photovoltaics, *ACS Nano*, Vol. 9, 5447-5453, 2015.

[4] Barkhouse, D. A. R., et al, Depleted bulk heterojunction colloidal quantum dot photovoltaics, *Adv. Materials*, Vol. 23, 3134-3138, 2011.

[5] Labelle, A. J., et al., Colloidal quantum dot solar cells exploiting hierarchical structuring, *Nano Letters*, Vol. 15, 1101-1108, 2015.

[6] Labelle, A. J, et al., Broadband epsilon-near-zero reflectors enhance the quantum efficiency of thin solar cells at visible and infrared wavelengths, *ACS Applied Materials and Interfaces*, Vol. 9, 5556-5565, 2017.

Correlation between Light Absorption and External Quantum Efficiency of Metamaterial Perfect Absorber Solar Cell

Wakana KUBO[1*]

[1]Tokyo University of Agriculture and Technology (TUAT),
Department of Electrical and Electronic Engineering, 5-208, 2-24-16, Naka-cho, Koganei-shi, Tokyo 184-8588, Japan
*corresponding author, E-mail: w-kubo@cc.tuat.ac.jp

Abstract

We examined the light absorption properties and device performance of the metamaterial perfect absorber (MPA) solar cell in order to clarify the contribution of plasmonic light confinement effect on the solar cell device performance. The metamaterial perfect absorber solar cell exhibited the enhanced external quantum efficiency (EQE) at the wavelength where the MPA can confine light into the active layer. This result is an evidence that the enhancement in EQE is strongly correlated to the light confinement acquired by MPA.

1. Introduction

Plasmonic solar cells have been intensively investigated since they have been proposed. [1] The researchers expect an enhancement in the device performance owning to the light absorption enhancement of the active materials acquired by plasmonic electromagnetic fields created at the vicinity of the metal nanostructures, followed by an improvement in the device performance.

In fact, there are some papers reporting enhancements in the device performance of plasmonic solar cells. Some of them showed the increase of device performances; however, the enhancements of EQE were observed at all of the absorption wavelength range of the active materials regardless of the plasmonic resonance wavelength. [2, 3] These results raise questions concerning the contribution of plasmons on the enhanced device performance of plasmonic solar cells.

Here, we propose to introduce metamaterial perfect absorber (MPA) into organic thin-film solar cell to clarify the contribution of plasmons on the device performance. Metamaterial perfect absorber consists of two distinct metallic structures sandwiching a thin dielectric film as a spacer, and it can confine the magnetic fields into the dielectric layer as a result of the coupling between the metallic nanostructure and the metallic film. The advantage of the MPA structure is that its position adjustability of the strong light confinement into active materials of solar cells. Proper designing and accurate fabrication of MPA configuration will enable us to adjust the light confinement mode of the configuration to the absorption wavelength of the active materials. And it cannot be realized by dispersed plasmonic nanostructures.

We fabricated a MPA solar cell by using top-down technique, and examined its light absorption properties and device performance. In previous investigations, we have found the MPA configuration can enhance the light absorption of the thin-film organic solar cells. [4-6] In this report, we compared the light absorption enhancement of the MPA solar cell with its device performance, and discussed the effect of plasmons on the device performance of the MPA solar cell.

2. Experimental section

A schematic of the MPA solar cell is shown in Fig. 1 (a). The solar cell consists of indium tin oxide (ITO), zinc oxide (ZnO), photoelectric conversion layer Poly[2,6-(4,4-bis-(2-ethylhexyl)-4H-cyclopenta [2,1-b;3,4b']dithiophene alt 4,7 (2,1,3 benzothiadiazole)):[6,6]-phenyl-C71-butyric acid methyl ester (PCPDTBT:$PC_{71}BM$), molybdenum oxide

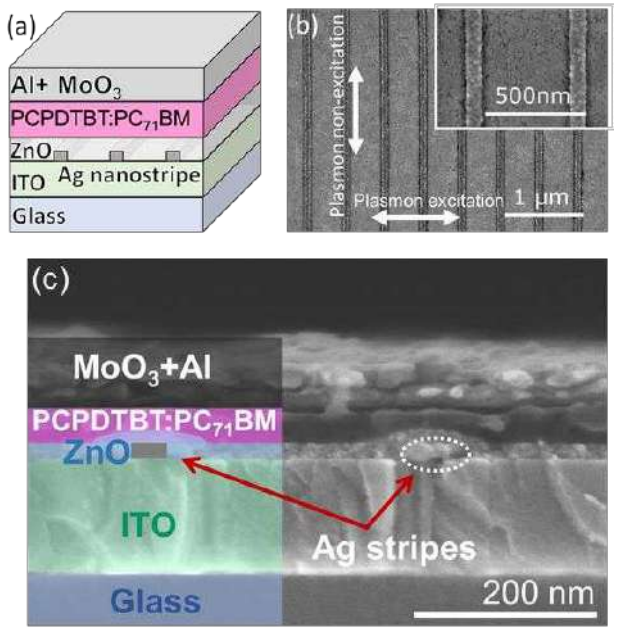


Figure 1: (a) Schematic of metamaterial perfect absorber solar cell, (b) SEM images of silver nanostripes, and (c) cross-sectional SEM image of the metamaterial perfect absorber solar cell.

(MoO_3), and aluminum (Al). In this research, a periodic silver nanostripe (Ag NS array) was used as a metal nanostructure (Fig. 1 (b)). The Ag NS has a width, pitch, and height of 82, 500, and 20 nm, respectively. Ag NS shows polarization dependence. Therefore, the extinction ratio of the plasmon excitation polarization to the plasmon non-excitation polarization was defined as the absorption enhancement (AE) factor. To examine the device performance, the external quantum efficiency (EQE) was measured. The EQE ratio was calculated by dividing the EQE measured under plasmon excitation polarization by the EQE measured under plasmon non-excitation polarization. The EQE ratio was compared with the AE factor.

3. Results and Discussion

Figure 2 (a) shows the absorption spectrum of PCPDTBT:PC_{71}BM, the active materials has an absorption edge around 1000 nm. The red line in Fig. 2 (b) represents the AE factor of the MPA solar cell. Absorption enhancement factor larger than the unity means that the absorption of the MPS solar cell is enhanced. Figure 2 (b) shows that the absorption enhancements were mainly observed at 650 and 880 nm. The blue line in Fig. 2 (b) represents the IPCE ratio of the MPA solar cell, and showed a deterioration of the device performance at 690 nm and an enhancement at 880 nm. In order to clarify the correlation between the light absorption enhancement and device performance of the cell, we calculated the magnetic field distributions by COMSOL Multiphysics finite-element solver. Figure 2 (c) shows the magnetic field distribution calculated at 650 nm where the absorption enhancement and the remarkable device deterioration were observed. Figure 2 (c) represents the light was confined at ITO side, resulting in a deterioration of the device performance due to a decrease of light absorption of the PCPDTBT:PC_{71}BM layer. On the other hand, Fig. 2 (d), a magnetic field distribution at 880 nm, where the enhancements in the light absorption and EQE ratio were observed, shows the light confinement into the PCPDTBT:PC_{71}BM layer. This light confinement in the active layer resulted in an enhancement of the EQE enhancement of the MPA solar cell via the light absorption increase of the active layer.

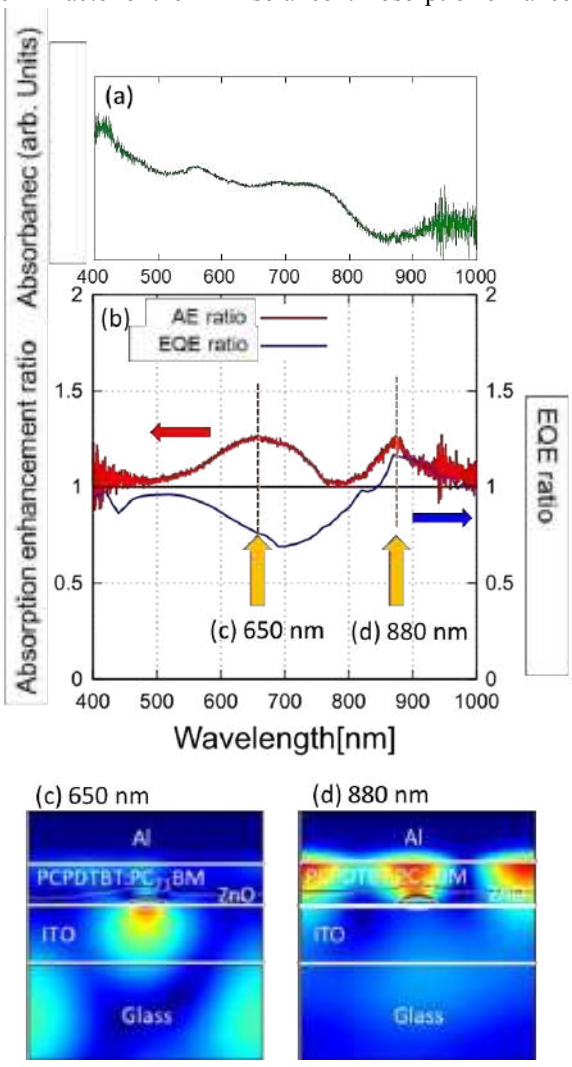


Figure 2. (a) Absorption spectrum of PCPDTBT:PC_{71}BM layer, (b) a comparison of the absorption enhancement with an IPCE ratio of the metamaterials perfect absorber solar cell, and magnetic field distributions calculated at (c) 650 nm and (d) 880 nm.

4. Conclusions

We clarified the contribution of the plasmonic light confinement properties on the device performance of a thin-film organic solar cell for the first time. These results will pave the way to propose highly efficient plasmonic solar cells.

Acknowledgements

The author is grateful to Prof. Takayuki Okamoto, RIKEN in Japan, for fruitful discussions.

References

[1] H.A. Atwater, A. Polman, Plasmonics for improved photovoltaic devices, *Nat. Mater.*, 9 (2010) 205-213.

[2] Y.S. Hsiao, S. Charan, F.Y. Wu, F.C. Chien, C.W. Chu, P.L. Chen, F.C. Chen, Improving the Light Trapping Efficiency of Plasmonic Polymer Solar Cells through Photon Management, *J. Phys. Chem. C*, 116 (2012) 20731-20737.

[3] D.D.S. Fung, L. Qiao, W.C.H. Choy, C. Wang, W.E.I. Sha, F. Xie, S. He, Optical and electrical properties of efficiency enhanced polymer solar cells with Au nanoparticles in a PEDOT-PSS layer, *J. Mater. Chem.*, 21 (2011) 16349-16356.

[4] T. Isegawa, T. Okamoto, M. Kondo, S. Katsumata, W. Kubo, P3HT:PC_{61}BM solar cell embedding silver nanostripes for light absorption enhancement, *Opt. Commun.*, 441 (2019) 21-25.

[5] W. Kubo, Y. Yokota, T. Tanaka, Au nanodot lattices with well-controlled size and density for thin organic solar cells, *phys. status solidi RRL*, 9 (2015) 348-352.

[6]W. Kubo, Effect of Au nanoparticles on PCPDTBT:PC_{71}BM device performance with fair comparisons, *Phys. Status Solidi a-Applications and Materials Science*, 214 (2017).

Ultrathin Semiconductor Superabsorbers from the Visible to the Near Infrared

Pau Molet Bachs, Juan Luis Garcia-Pomar, Cristiano Matricardi, Miquel Garriga, Maria Isabel Alonso and Agustín Mihi

Institut de Ciència de Materials de Barcelona (ICMAB-CSIC), Campus de la UAB, 08193 Bellaterra, Catalonia, Spain

*amihi@icmab.es

Abstract

In this work[1], we present a strategy that achieves broadband optimal absorption in arbitrarily thin semiconductor materials for all energies above their bandgap. Our strategy follows an easy and scalable fabrication route enabled by soft nanoimprinting lithography with seamless integration in many optoelectronic fabrication procedures.

1. Introduction

The achievement of ultrathin films that strongly interact with light, absorbing photons over a wide spectral range is of central importance for applications such as sensing, energy harvesting, or biology among others. Strong broadband absorption is challenging in view of the intrinsic limitation in the absorption coefficient of every material, which is especially deleterious for infrared wavelengths. Many wave optics based designs are being currently investigated to surpass this limitation, from photonic crystals[2,3] to plasmonics and microresonators. All these architectures[4–6] provide new and exciting means of confining light in sub-wavelength thin films. Nevertheless**,** the absorption enhancements exhibited are typically restricted to a specific frequency range or mostly take place in the metal part. In sum, a photonic architecture capable of increasing the absorption of a semiconductor throughout its entire absorption coefficient has hitherto, remained elusive.

In our work, we demonstrate a germanium photonic architecture deposited on a metal film acting as a metasurface. Our metasurface sustains the simultaneous excitation of Fabry-Perot resonances, Brewster modes and plasmonic-photonic modes that result in an omnidirectional enhanced absorption in a Ge ultra-thin film of 70 nm from 400 nm until 1500 nm. This represents an unprecedented advance in broadband light harvesting, well beyond previous reports (see Figure 1).

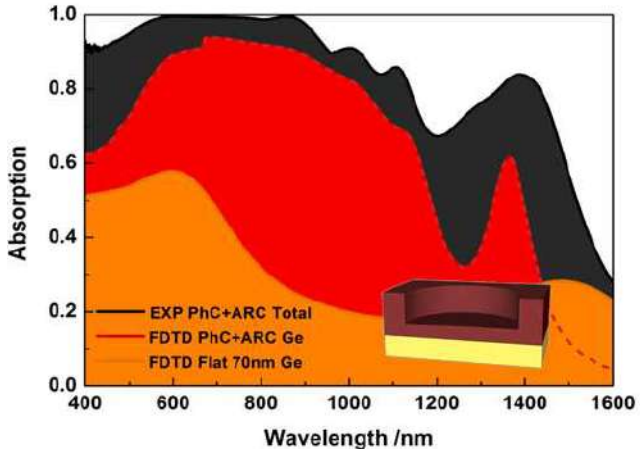


Figure 1: Total absorption of the Nanostructured 70 nm dielectric superabsorber (Black) and absorption in the Germanium (Red) vs the absorption of a flat film of germanium over gold with the same thickness (70 nm) (Orange). Inset: Cross section scheme of the photonic structure.

The key aspects of our findings are:

1. The **absorption in the metasurface exceeds over 100%** that of a flat a-Ge film on gold over an impressive **bandwidth of 1100 nm**. Moreover, the high refractive index of the Ge renders the absorption profile of the metasurface **independent to the angle of incidence** of the incident light.
2. We provide the **key design guidelines to tune the absorption profile** of the metasurfaces and the physical origin beneath each resonant mode sustained by the architecture. With these findings, we show metasurfaces exhibiting strong broadband absorption (appealing to PV community) or NIR absorption peaks reaching 100% at the telecommunication windows (interesting to the photodetection field).
3. Remarkably, we fabricated the **16-mm^2 Ge metasurfaces via nanoimprinting lithography**[7], the most promising method for mass-produced nanostructures. This inexpensive and large area technique adds feasibility to the exciting photonic properties described in the manuscript (Figure 2).

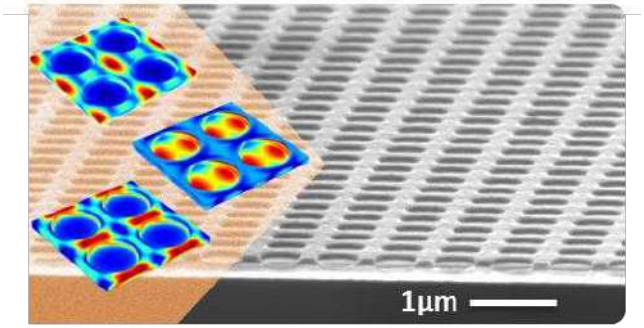


Figure 2: SEM Tilted cross-section image of the photonic architecture and the electric field concentration for its maximum absorption peaks.

Conclusions

In summary, we demonstrate an 81% of total integrated absorption over a broad spectral range in an 80 nm germanium photonic crystal built on a gold layer. Through a rational design of the architecture, the absorption in the active layer exceeds over 100% that of a flat 80 nm a-Ge film on gold. Furthermore, the high refractive index of the semiconductor renders the absorption profile of the metasurface independent to the angle of incidence. The fabrication of these photonic structures follows a highly scalable nanoimprinting technique, which adds to the appeal of the enhanced optical properties described herein. We believe this metasurface has a tremendous potential for light harvesting applications such as photodetection, photocatalysis and photovoltaics.

Acknowledgements

We thank the Spanish Ministry of Economy and Competitiveness (MINECO) for its support through Grant MAT2016-79053-P. AM was funded by a Ramón y Cajal fellowship (RYC-2014-16444). The work at ICMAB was carried out under the auspices of the Spanish Severo Ochoa Centre of Excellence programme (grant SEV-2015-0496). This project has received funding from the European Research Council (ERC) under the European Union's Horizon 2020 research and innovation programme (grant agreement No 637116).

References

[1] P. Molet, J. L. Garcia-Pomar, C. Matricardi, M. Garriga, M. I. Alonso, A. Mihi, *Advanced Materials* **2018**, *30*, 1705876.

[2] T. Ochiai, K. Sakoda, *Physical Review B* **2001**, *63*, 125107.

[3] S. Fan, J. D. Joannopoulos, *Physical Review B* **2002**, *65*, 235112.

[4] Q. Zhao, J. Zhou, F. Zhang, D. Lippens, *Materials Today* **2009**, *12*, 60.

[5] P. Spinelli, M. A. Verschuuren, A. Polman, A. Polman, K. J. Vahala, *Nature Communications* **2012**, *3*, 692.

[6] A. Mihi, F. J. Beck, T. Lasanta, A. K. Rath, G. Konstantatos, *Advanced Materials* **2014**, *26*, 443.

[7] Y. Xia, G. M. Whitesides, *Angewandte Chemie International Edition* **1998**, *37*, 550.

Next generation solar cells and photodetectors with III-V nanowires

Anna Fontcuberta i Morral[1,2]

[1]Laboratory of Semiconductor Materials, Institute of Materials, School of Engineering, Ecole Polytechnique Fédérale de Lausanne, Lausanne, Switzerland
[2]Institute of Phhysics, School of Basic Sciences, Ecole Polytechnique Fédérale de Lausanne, Lausanne, Switzerland
*corresponding author, E-mail: anna.fontcuberta-morral@epfl.ch

Abstract

Nanowires are filamentary crystals with a tailored diameter ranging from few to ~100 nm. The special geometry and tailored dimensions result in photonic properties providing great potential in applications requiring enhanced light absorption. We will review how these properties can be used in different configurations for both photo-detection and energy harvesting applications.

1. Introduction

Semiconductor nanowires have attracted an increasing amount of attention thanks to their special properties. Especially interesting is the growth of III-V nanowires on silicon as they naturally allow the integration of the functionalities of the III-V and Si platforms. The dimensions and shape of the nanowires render them ideal for a variety of applications in photonics. The needle-like shape results also in a high degree of polarization response: light absorption is very low for incoming light polarized across the nanowire axis, while it is very high for light polarized along the nanowire axis. In this talk we will show it is possible to vary the intrinsic absorption and emission properties by engineering their size and/or by coupling the nanowires to plasmonic nanostructures.

2. Results

Nanowires are filamentary structures with a tailored diameter between the few and ~100 nm. They can be obtained in a freestanding manner or aligned on a substrate. Figure 1 shows scanning electron micrographs of compound semiconductor nanostructures considered here. Fig. 1a-e elucidates freestanding GaAs nanowire arrays on a silicon substrate with a tailored diameter down to 10 nm [1-3]. They can be used as absorber for a single or dual solar cell. We will explain how the absorption properties depend on the nanowire diameter and interwire distances [4,5] and how an array of nanowires of different compositions can act as a multiple-junction solar cell with conversion efficiencies up to 47% [6].

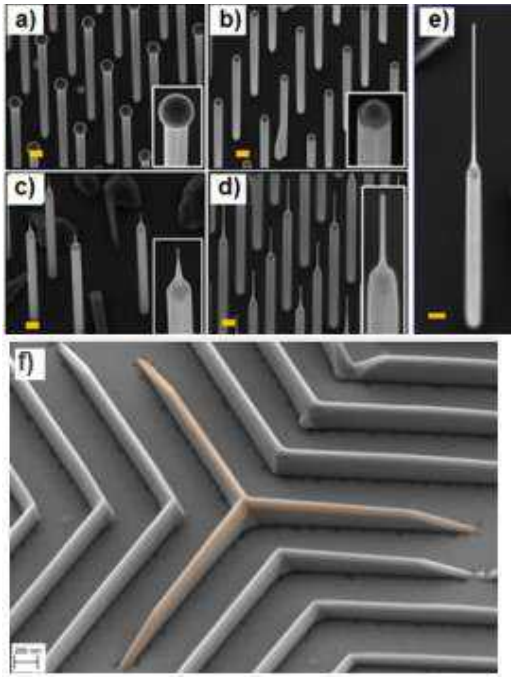


Figure 1: Scanning electron micrographs of types of nanostructures investigated here. a) GaAs nanowire array on silicon [1,2] b) droplet shrinkage; c) Further evolution of the tip resulting in conically tapered GaAs nanoneedles; d-e) Straight, ~10 nm radius nanowires on top of thicker nanowire stems The scale bar corresponds to 200 nm [3]. f) GaAs nanoscale membrane networks with an InAs nanowire ontop [9].

We will then move to the use of freestanding structures for photodetection. Here, we will elucidate how the contacting scheme can provide a base for ultra-fast detection in the GHz regime [7].

Finally, we will explain how nanowires can also be used in their horizontal configuration for highly efficient photodetectors. Here, due to the reduced absorption cross-section in horizontal nanowires, coupling of the semiconductors with plasmonic structures is the key to guarantee high absorption [8,9].

3. Conclusions

In conclusion, we report how one-dimensional structures can be used for efficient and fast light absorption both for applications in photovoltaics and photodetection. The photonic principles can be applied from the UV down to the MIR range of the electromagnetic spectrum.

Acknowledgements

AFiM thanks funding by the ERC Starting grant UpCon and SNF Consolidator Grant (BSCGI0-157705).

References

[1] J. Vukajlovic-Plestina et al, Nano Lett. 'Engineering the Size Distributions of Ordered GaAs Nanowires on Silicon' Nano Lett. 17, pp. 4101 (2017).

[2] W. Kim et al, 'Bistability of contact angle and its role in achieving quantum-thin self-assisted GaAs nanowires' Nano Lett. 18, pp. 49 (2018).

[3] J. Vukajlovic-Plestina et al, 'Fundamental aspects to localize self-catalyzed III-V nanowires on silicon' Nature Comm. 10, pp. 869 (2019).

[4] P. Krogstrup, H.I. Jørgensen, M. Heiss, O. Demichel, J.V. Holm, M. Aagesen, J. Nygard, Anna Fontcuberta i Morral, 'Single nanowire solar cells beyond the Shockley-Queisser limit' Nature Photonics 7, pp.306-310 (2013).

[5] M. Heiss et al, 'III–V nanowire arrays: growth and light interaction', Nanotech. 25, pp. 014015 (2014).

[6] A. Dorodnyy, E. Alarcon-Llado, V. Shklover, C. Hafner, A. Fontcuberta i Morral, J. Leuthold, 'Efficient multi-terminal spectrum splitting via a nanowire array solar cell' ACS Photonics 2, pp. 1284, 2015.

[7] A. Dorodnyy et al 'Plasmonic photodetectors' IEEE J. Sel. Top. Quant. Elec. 24, pp. 1-13 (2018).

[8] M. Ramezani, A. Casadei, G. Grzela, F. Matteini, D. Rüffer, A. Fontcuberta i Morral, J. Gomez-Rivas 'Hybrid semiconductor nanowire-mettallic Yagi-Uda antennas' Nano Lett 15, pp.4889, 2015.

[9] A. Casadei, E. Alarcon-Llado, F. Amaduzzi, E. Russo-Averchi, D. Rüffer, M. Heiss, L. Dal Negro, A. Fontcuberta i Morral, 'Polarization response of nanowires à la carte' Scientific Reports 5, pp.7651, 2015.

[10] M. Friedl et al 'Template-assisted scalable nanowire networks' Nano Lett. 18, pp. 2666 (2018).

Total internal reflection using nano-gratings for enhancing the optical response of perovskite solar cells.

Eduardo López-Fraguas*[1], Braulio García-Cámara[1], and Ricardo Vergaz[1]

[1]GDAF-UC3M, Displays and Photonic Applications Group, Universidad Carlos III de Madrid, Madrid, Spain.
*corresponding author, E-mail: edlopezf@ing.uc3m.es

Abstract

In this work, we propose the use of a simple transmission diffraction nano-grating to improve the optical absorption of a perovskite solar cell through the Total Internal Reflection (TIR) phenomenon in the active layer, enlarging the optical path and the photon absorption rate. We design the structure close to the active layer to avoid further optical losses. Although we considered perovskite solar cells, this can be also extended to other types like silicon or organic solar cells.

1. Introduction

The perovskite solar cells are one of the most promising recent technologies in the field of solar cells, due to the remarkable efficiency increment that they have shown in the last years, as well as their easy fabrication [1]. The use of roughness and nanostructured layers in perovskite solar cells are a typical way to increase their efficiency [2]. The searching of optical effects to enhance the light injection in the active layer usually takes into account nanostructured contact layers.

The larger the distance between the nanostructure and the active layer, the lower the intensity of the desired effect. Thus, our motivation in this work is to produce a diffractive effect by nanostructuring a layer as close as possible to the active perovskite layer, but still allowing the appearance of other interesting effects, such as directional scattering or dielectric resonances, which can improve further the light confinement and thus, the effective absorption.

We base our proposal in nanostructuring the TiO_2 electron transport layer of a perovskite thin-film solar cell, a technique that can be performed just by applying photolithography to the FTO contact layer prior to TiO_2 deposition. With this structure, we induce diffraction effects to achieve a Total Internal Reflection (TIR) in the opposed interface of the perovskite active layer. Thus, the increment of the optical path will lead to the enhancement of the absorption and by this effect, the increment of the short-circuit current. Further effects that increase light confinement are possible due to the dielectric nature of the nanostructure.

2. Simulation setup

In this study, we have modelled the optical behavior of a thin-film perovskite solar cell. The starting point is taken from [3], where they performed an analysis of a Methylammonium Lead Iodide ($CH_3NH_3PbI_3$) solar cell, using TiO_2 as an electron transport layer and without a hole transport layer. They finished the cell with two electrodes, one of gold (rear electrode) and other of Fluorine doped Tin Oxide (FTO, transparent front electrode). This simple thin-film planar structure shows a maximum short-circuit current J_{SC} of 16.43 mA/cm^2 at a certain thickness.

We propose a modification of this structure including a nano-grating in the interlayer between the FTO and TiO_2 layer, in order to obtain a diffraction effect without changing any parameter of the remaining cell. We show a schematic slice of the proposed cell at Fig.1.

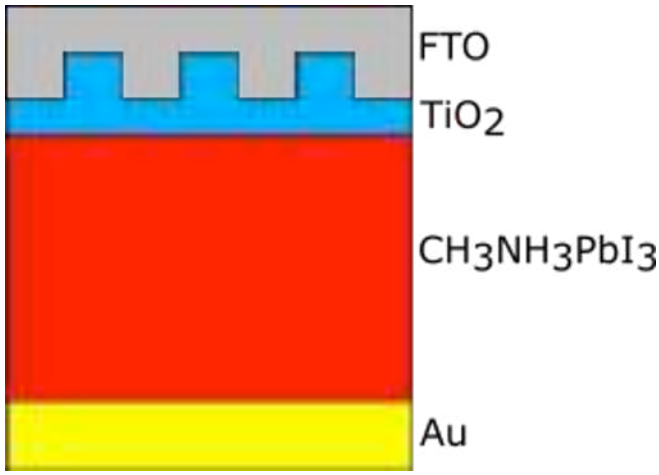


Figure 1: Solar cell structure with the embedded nano-grating.

When light impinges in this structure from top to bottom, it produces a diffraction effect that we are going to study, in order to achieve TIR inside the active layer, and thus increasing the optical path and absorption into it.

We have used the software COMSOL Multiphysics © to take into account both diffraction effects and all the possible absorption and losses that can appear in the interfaces and layers.

3. Theoretical calculations

The problem of the optical path in solar cells has important concerns due to the interface effects. From a classical point of view, and using the Snell's law, (Eq.1), we can determine the refracted angle of an incident ray of light impinging in an interface between two different materials, with different refraction indices (n_i and n_o) as follows:

$$n_i \cdot sin\theta_i = n_o \cdot sin\theta_o \quad (1)$$

If the output angle (refracted beam) is 90º, we will have the TIR phenomenon. Taking this into account, we can determine the minimum input angle (θ_i) to produce TIR (Brewster's angle) using Eq. (2):

$$\theta_i = sin^{-1}\left(\frac{n_o}{n_i}\right) \quad (2)$$

On the other side, we can calculate the output angle of the *m* mode (θ_m) from a diffraction grating by using Eq. (3):

$$a \cdot sin\theta_m = m \cdot \lambda \quad (3)$$

Where *a* is the pitch of the grating, *m* is the diffraction order and λ is the wavelength of the light.

By combining these two effects, we can adjust the diffraction grating dimensions in order to tune its output angle, choosing the range in which it produces an incident angle in the next interface over the TIR angle, previously calculated.

4. Results

As both angles, Θ_i and Θ_m are wavelength dependent (Eq. 2 and 3), we can plot their dependence with wavelength using different grating dimensions. As an example, Fig. 2 shows the result of a diffraction pitch of a = 1 μm, with certain arbitrary dimensions in the rest of the layers. We can see that there are certain conditions (wavelength over 480 nm) in which we can achieve a TIR condition, i.e., the Θ_m is bigger than the obtained Θ_i.

This result demonstrates that we can tune the dimensions of the proposed nanostructured TiO_2 in order to achieve an improvement of the optical path. Our preliminary results show that an enhancement higher than a 10% in J_{SC} respect to the planar structure is achieved, taking advantage of both the increment in the optical path and a light confinement effect in the perovskite layer.

We will show the optimization of this structure with dimensions easily achievable through simple fabrication techniques, as well as some alternatives based on the dielectric resonances that allow directionality control.

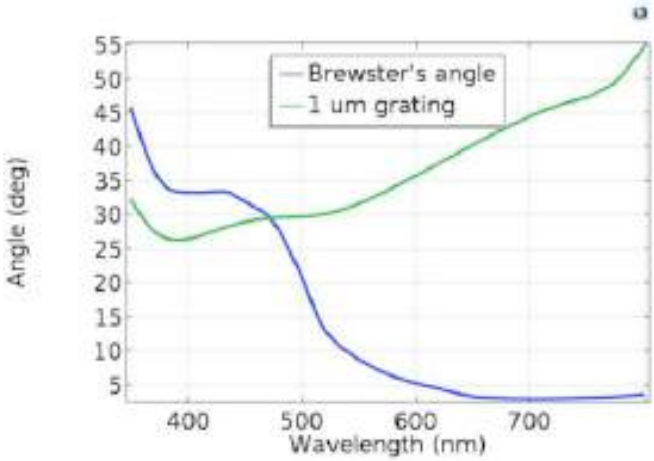


Figure 2: Output grating angle versus Brewster's angle. TIR condition appears for wavelengths higher than 480 nm.

5. Conclusions

We propose the introduction of a nanostructure in TiO_2 layer of a perovskite planar thin-film solar cell. The fabrication of this structure is a relatively easy task, if a photolithography technique is applied to the FTO previously to TiO_2 deposition, or alternatively a nanoimprint technique is applied over the TiO_2 layer. A dimension tuning of this simple grating can produce a performance of it in which the Brewster angle is achieved in the other active layer interface, thus increasing the optical path, and besides producing a light confinement in the active layer. We will show the improvements in short-circuit current that it produces for several configurations.

Acknowledgements

This work was supported by the Spanish Ministerio de Economía y Competitividad TEC2016-77242-C3-1-R Grant (AEI/FEDER, UE funds) and Comunidad de Madrid SINFOTON-CM Research Program (S2013/MIT-2790). ELF wants to express his gratitude to the Ministerio de Educación y Formación Profesional for his doctoral grant (FPU research fellowship Ref. FPU17/00612).

References

[1] M. I. H. Ansari, A. Qurashi, M. K. Nazeeruddin, Frontiers, opportunities, and challenges in perovskite solar cells: A critical review, *Journal of Photochemistry and Photobiology C: Photochemistry Reviews* 35 1–24, 2018.

[2] W. Qarony, M. I. Hossain, A. Salleo, D. Knipp, and Y. H. Tsang, Rough versus planar interfaces: How to maximize the short circuit current of perovskite single and tandem solar cells, *Materials Today Energy* 11 106-113, 2019.

[3] K. Fu, Q. Zhou, Y. Chen, J. Lu, and S.-E. Yang, The simulation of physical mechanism for HTM-free perovskite organic lead iodide planar heterojunction solar cells, *J. Opt.* 17 105904, 2015.

Novel perforated all-dielectric metamaterials

Alexey A. Basharin[1,2]

1 National University of Science and Technology (MISiS), The Laboratory of Superconducting metamaterials, 119049 Moscow, Russia
2 National University of Science and Technology (MISiS), Department of Theoretical Physics and Quantum Technologies, 119049 Moscow, Russia
*corresponding author: Alexey.basharin@misis.ru

Abstract-In this report we discuss a novel type of perforated silicon metamaterials, possessing toroidal and anapole mode in visible spectral range due to destructive interference between electric and toroidal dipole moments. This type of metamaterial is simple fabrication process without complicated 3D toroidal geometry and exhibits a desirable physical effects like multipolar interactions. We shown how does it possible to split toroidal and electric dipoles excitation by changing geometry of metamolecules.

Some insights on the light management in halide perovskite solar cells and optoelectronic devices

Iván Mora-Seró[1,*]

[1] Institute of Advanced Materials (INAM), Universitat Jaume I, Castelló 12006, Spain

*corresponding author, E-mail: sero@uji.es

Abstract

In this presentation some insights about light management in halide perovskite optoelectronic devices is provided. The introduction of light scattering nanoparticles can enhance the perovskite solar cell photocurrent by the improvement of performance by the incorporation of Au nanoparticles cannot be always assigned to plasmonic effects but to interface modification. The outstanding properties of halide perovskites can also be used to develop other optoelectronic devices as light amplifiers and photodetectors.

1. Introduction

Halide perovskite are receiving a huge attention in the recent few years. Undoubtedly this attention is mainly due to the outstanding power conversion efficiencies, surpassing 24%,[1] reported for photovoltaic devices, fabricated with polycrystalline films from low cost techniques. This outstanding performance is based in the excellent properties of halide perovskite materials presenting direct bandgap with high light absorption coefficient, and a benign defect physics, allowing low recombination rates even in polycrystalline films.

As an optoelectronic device the light management plays a very important role, and the light conversion performance can be increased for example incorporating light scattering nanoparticles. Another way that has been explored in order to increase the performance is to use metallic nanoparticles to take advantage of the plasmonic properties. Here, we highlight the necessity of a systematic characterization in order to rule out another effects rather than the light management to justify the performance increase.

Finally, the outstanding optical properties can be use to develop alternative optoelectronic devices as light amplifiers and photodetectors.

2. Results and Discussion

In this presentations we provide some insights about the light management in perovskite solar cells and optoelectronic devices. First we will discuss about light scattering as an efficient way of light management in perovskite solar cells. One of the classical configurations of perovskite solar cells is the n-i-p configuration using as electron transporting material (ETM) a compact TiO_2 with a mesoporous TiO_2 scaffold deposited on top. For a long time this configuration produced the record perovskite solar cell performance as the mesoporous scaffold helps in the perovskite crystallization and also decreases the recombination rate.[2] We have observed that the incorporation of SiO_2 nanoparticles into the TiO_2 mesoporous scaffold, see Figure 1, enhances the light scattering improving the photocurrent of perovskite solar cells and consequently the final photoconversion efficiency.[3] Large SiO_2 produce higher scattering but this effect has to be properly balanced with layer morphology, the loss in transparency, and the reduction of the effective refractive index by the introduction of the SiO_2 nanoparticles. The addition of SiO_2 also affects the slow processes in the perovskite solar cell.

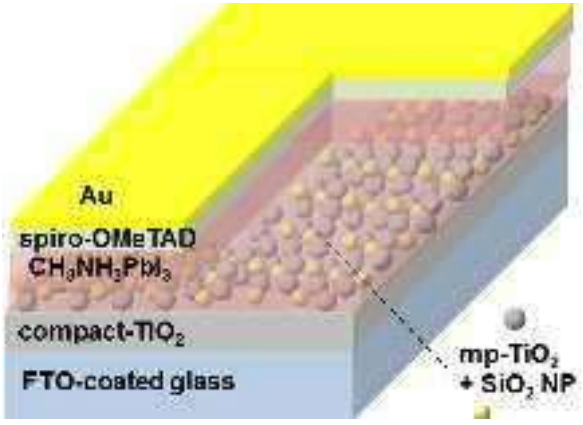


Figure 1: Perovskite solar cell adding SiO_2 nanoparticles into the TiO_2 mesoporous scaffold, using TiO_2 and spiro-OMeTAD as electron and hole selective contacts respectively.[3]

This study indicates a way in which light management can be used to improve perovskite performance. There are other ways in which light management can help in the increase of perovskite solar cell performance, but it is necessary to clearly stablish a causality effect with light management and exclude other possible effects as the modification of

morphology or affecting the interfacial properties. There are different examples in the literature where the use plasmonic effects of metallic nanoparticles are claimed to be the origin of performance enhancement observed after the addition of these nanoparticles. Here, we show that it is needed to be cautious to associate the effects observed by the addition of metallic nanoparticles with a plasmonic effect without further analysis as there are other ways in which this particles can affect the perovskite solar cell performance. Here we show that the efficiency enhancement observed by the addition of core/shell Au/SiO_2 nanoparticles added at the interface between TiO_2 ETM and the perovskite layer are not due to plasmonic effect but to a modification of the interfacial properties.[4]

Finally, the outstanding optical properties of halide perovskite will be used to develop other optoelectronic devices as light amplifiers[5] and light amplifiers couple with photodetectors,[6] in both rigid and flexible substrates.

Acknowledgements

The work was supported by European Research Council (ERC) via Consolidator Grant (724424 - No-LIMIT).

References

[1] https://www.nrel.gov/pv/assets/pdfs/best-research-cell-efficiencies-190416.pdf

[2] M. Anaya, W. Zhang, B. C. Hames, Y. Li, F. Fabregat-Santiago, M. E. Calvo, H. J. Snaith, H. Miguez, I. Mora-Sero, *Journal of Materials Chemistry C* **2017**, 5, 634.

[3] N. Aeineh, A.-F. Castro-Méndez, P. J. Rodriguez-Cantó, R. Abargues, E. Hassanabadi, I. Suarez, A. Behjat, P. Ortiz, J. P. Martínez-Pastor, I. Mora-Seró, *ACS Omega* **2018**, 3, 9798.

[4] N. Aeineh, E. M. Barea, A. Behjat, N. Sharifi, I. Mora-Seró, *ACS Applied Materials & Interfaces* **2017**, 9, 13181.

[5] I. Suárez, E. J. Juárez-Pérez, J. Bisquert, I. Mora-Seró, J. P. Martínez-Pastor, *Adv. Mater.* **2015**, 27, 6157.

[6] I. Suárez, E. Hassanabadi, A. Maulu, N. Carlino, C. A. Maestri, M. Latifi, P. Bettotti, I. Mora-Seró, J. P. Martínez-Pastor, *Advanced Optical Materials* **2018**, 6, 1800201.

Nanophotonic tools for exploring low-energy excitations in nanomateria

Probing Plasmons, Phonons, and Phase-Change Materials with Synchrotron Infrared Nanospectroscopy

Hans A. Bechtel[1*], Omar Khatib[1,2], Stephanie N. Gilbert Corder[1,3], Mengkun Liu[3], Markus B. Raschke[2], Michael C. Martin[1], and G. Lawrence Carr[4]

[1]Advanced Light Source, Lawrence Berkeley National Laboratory, Berkeley, CA USA
[2]Departments of Chemistry, Physics and JILA, University of Colorado, Boulder, CO USA
[3]Department of Physics and Astronomy, Stony Brook University, Stony Brook, NY USA
[4]National Synchrotron Light Source II, Brookhaven National Laboratory, Upton, NY USA
*corresponding author, E-mail: habechtel@lbl.gov

Abstract

Synchrotron infrared nanospectroscopy (SINS) combines the broad bandwidth and brightness of synchrotron infrared radiation with scanning near-field optical microscopy (s-SNOM) to enable vibrational spectroscopy spanning the entire mid-infrared region with < 20 nm spatial resolution. By using fast, sensitive custom-modified detectors, we have extended the wavelength range into the far-infrared, enabling direct probing of the tunable plasmon response in a gated graphene device and phonon modes in phase-change materials, such as VO_2 and SmS.

1. Introduction

Infrared (IR) spectroscopy continues to be a powerful analytical method to probe molecular vibrations, low-energy electronic excitations, and related collective surface plasmon, phonon, or other polaritonic resonances in a variety of natural and engineered systems. Diffraction and the long wavelengths of infrared light have traditionally limited the spatial resolution of infrared techniques to the micron scale, thereby preventing measurements of nanoscale heterogeneity. The development of near-field IR techniques has changed this paradigm, opening the nanoscale to infrared analysis. Here, we highlight synchrotron infrared nanospectroscopy (SINS), which is a variant of scattering type, scanning near-field optical microscopy (s-SNOM) with synchrotron IR radiation as the light source [1]. The high spectral irradiance and large bandwidth of synchrotron radiation combined with s-SNOM enables broadband infrared spectroscopy with a wavelength independent spatial resolution of < 25 nm, a dramatic improvement over diffraction limited techniques by several orders of magnitude. The Advanced Light Source (ALS) at Lawrence Berkeley National Laboratory operates two infrared beamlines (Beamlines 2.4 and 5.4) with SINS instruments that are freely available to users with an approved scientific proposal. The technique has been widely applied to a growing range of applications in physics, chemistry, biology, materials, geology, atmospheric, and space sciences. We discuss the technical aspects of the technique and highlight several SINS measurements of plasmons, phonons, and phase-change materials.

2. SINS Experiment

2.1. Experimental Layout

A typical SINS experiment (Fig. 1) is based on an asymmetric Michelson interferometer, in which half of the incident synchrotron light is focused onto a metallic tip of an atomic force microscope (AFM), scanning in nanometer proximity to the sample, and the elastically scattered light is collected and directed onto an IR detector. The conductive tip effectively acts as an optical antenna by localizing and scattering the optical field in the near-field region of its nanoscopic apex, yielding a spatial resolution limited by the tip radius. The other half of the incident synchrotron radiation is directed to a moving reference mirror. The reflected light interferes with the tip-scattered light on the detector, creating a distance-dependent interference pattern that is Fourier-transformed to yield the near-field amplitude and phase spectra. Far-field background scattered light is reduced by demodulating the detected signal at higher harmonics of the tip-tapping frequency.

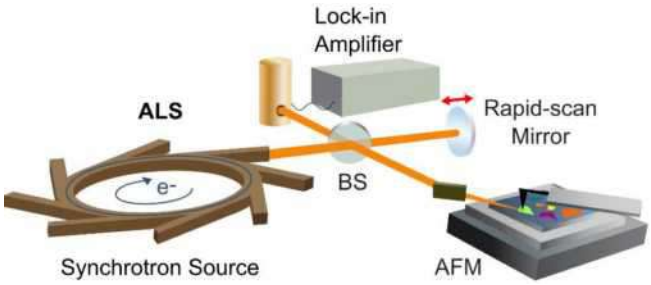


Figure 1: SINS experimental diagram

2.2. Spectral range

Synchrotron radiation from a bend magnet is spectrally broad, spanning the far-IR to x-ray regime. Thus, the primary bandwidth limitations for SINS measurements are

the beamsplitter and detector, not the source. For mid-IR applications, KBr/Ge or ZnSe beamsplitters are used in combination with mercury cadmium telluride (MCT) detectors. The highest sensitivity MCT detectors have frequency cutoffs around 700 cm^{-1}, but the spectral range can be extended to frequencies near 500 cm^{-1} through different doping, albeit at the expense of detector sensitivity. We have recently expanded the spectral range into the far-IR by customizing a Ge:Cu detector with high bandwidth electronics [2]. When used in combination with a silicon or KRS-5 beamsplitter, this liquid helium-cooled detector has a low-frequency cutoff at 320 cm^{-1} (Fig. 2).

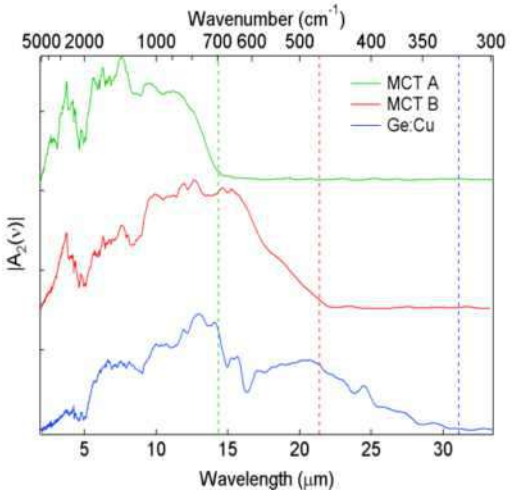


Figure 2: SINS 2nd harmonic amplitude spectra on a gold reference mirror with different detectors.

3. Examples

The extension of SINS measurements to the far-IR opens up a new nanospectroscopic window to directly probe far-IR electronic and lattice excitations, including the low energy free carrier response, surface phonon polariton waves and optical phonons in oxides and ultrathin van der Waals materials, skeletal deformations and conformational vibrations in molecular systems, and the highly tunable plasmonic regime of graphene plasmons.

3.1 Phase-Change Materials

Gilbert Corder *et al*. [3] used SINS to characterize different phases of SmS, a strongly correlated heavy fermion system that undergoes a semi-conductor-to-semimetal phase transition at modest pressures (6.5 kbar). The authors used contact-mode AFM to apply pressure to induce and control the local phase transition, and used a combination of SINS and laser-based s-SNOM to probe the nanoscale phase separation and locally probe the plasmonic resonances in the IR and visible regions. SINS spectra show an exciton peak at 468 cm^{-1} that blueshifts in the strained regions, caused by lowering of the 5d t_{2g} band, and subsequent transfer of 4f electrons into the hybridized state, increasing the baseline reflectivity. Access to the indirect gap and exciton resonances of the pristine and lithographically strained phases allowed the authors to distinguish the transitioned phases, which is not immediately clear at visible frequencies due to the golden color being present in both IV and fully metallic SmS.

3.2 Graphene Plasmons

Graphene has paved the way for a new generation of 2D optoelectronic materials by virtue of its inherently tunable IR and THz plasmonic response. Khatib *et al*. [2] used SINS to probe the full voltage-dependent nanospectroscopic IR plasmonic response in a pristine monolayer graphene flake (Fig. 3). At negative voltages, they observed a significant enhancement of the SINS amplitude and phase response and a nearly full suppression for high positive voltages above +50 V, approaching the intrinsic response of the underlying SiO_2 (black curve). This behavior is consistent with gate tuning of the Drude free carrier response superimposed with the plasmon absorption in graphene. The spectral behavior and enhancement near the SiO_2 resonances indicate a hybridization and strong coupling between graphene plasmons and the substrate surface phonons.

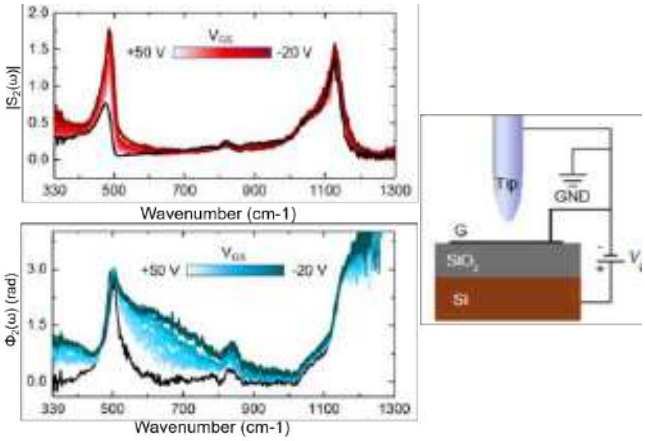


Figure 3: SINS amplitude (upper panel) and phase spectra (lower panel) at different gate voltages of a graphene device on SiO_2, showing tuning of the plasmon response.

Acknowledgements

This research used resources of the Advanced Light Source, which is a DOE Office of Science User Facility under contract no. DE-AC02-05CH11231.

References

[1] H. A. Bechtel, E. A. Muller, R. L. Olmon, M. C. Martin, M. B. Raschke, Ultrabroadband infrared nanospectroscopic imaging, *PNAS* **111**, 7191 (2014).

[2] O. Khatib, H.A. Bechtel, M.C. Martin, M.B. Raschke, G.L. Carr, Far infrared synchrotron near-field nanoimaging and nanospectroscopy, *ACS Photonics*, **5**, 2773 (2018).

[3] S.N. Gilbert Corder *et al*. Near-field spectroscopic investigation of dual-band heavy fermion metamaterials, *Nature Communications*, **8**, 2262 (2017).

Between photonics and electronics: is THz the promised land of graphene technologies?

Alessandro Tredicucci[1,2,*]

[1]Dipartimento di Fisica "E. Fermi", Università di Pisa, largo Pontecorvo 3, Pisa, Italy
[2]NEST Scuola Normale Superiore and Istituto Nanoscienze-CNR, Piazza San Silvestro 12, Pisa, Italy
*corresponding author, E-mail: alessandro.tredicucci@unipi.it

Abstract

Its peculiar band structure and electron transport characteristics naturally suggest graphene could offer a perfect platform for a new generation of high-performance devices operating in the THz range of the electromagnetic spectrum. This talk will review recent results in the development of high-speed modulators and plasmonic detectors; it will also discuss perspectives towards the implementation of graphene-based deeply sub-wavelength THz emitters and lasers.

1. Graphene-based THz devices

Graphene is attracting considerable attention for a variety of photonic applications, including fast photodetectors, transparent electrodes in displays and photovoltaic modules, and saturable absorbers. Owing to its high carrier mobility, gapless spectrum, tunable chemical potential, and frequency-independent absorption coefficient, it has been recognized as a very promising element for the development of detectors and modulators operating in the Terahertz (THz) region of the electromagnetic spectrum, which is still severely lacking in terms of solid-state devices [1].

In the last few years, progress in the realization of graphene-based THz photonic devices has advanced very rapidly. In this talk I will focus in particular on the realization of THz detectors based on antenna-coupled graphene field-effect transistors (FETs) [2,3], discuss the various mechanisms involved in their operation, and examine extension to other 2D materials and integration into future THz cameras. I will also address the development and applications of electrically switchable metamaterial devices [4] as well as the prospects for the use of graphene in a new generation of THz sources, either directly as active element, or as waveguide optical component (for instance acting as saturable absorber in laser mode-locking) [5]. Finally, schemes to implement coherent control of absorption in graphene and the possible entailing device / diagnostic applications will be analyzed [6].

References

[1] A. Tredicucci, M.S. Vitiello, Device concepts for graphene-based terahertz photonics, *IEEE J. Sel. Top. Quantum Electron.* 20: 130-138, 2014.

[2] L. Vicarelli, M.S. Vitiello, D. Coquillat, A. Lombardo, A.C. Ferrari, W. Knap, M. Polini, V. Pellegrini, A. Tredicucci, Graphene field-effect transistors as room-temperature terahertz detectors, *Nature Mat.* 11: 856-871, 2012.

[3] A.A. Generalov, M.A. Andersson, X. Yang, A. Vorobiev, J. Stake, A 400-GHz Graphene FET Detector, *IEEE Trans. Terahertz Sci. Technol.* 7: 614-616, 2017.

[4] R. Degl'Innocenti, S.J. Kindness, H.E. Beere, D.A. Ritchie, All-integrated terahertz modulators, *Nanophotonics* 7: 127-144, 2018.

[5] V. Bianchi, T. Carey, L. Viti, L. Li, E.H. Linfield, A.G. Davies, A. Tredicucci, D. Yoon, P.G. Karagiannidis, L. Lombardi, F. Tomarchio, A.C. Ferrari, F. Torrisi, M.S. Vitiello, Terahertz saturable absorbers from liquid phase exfoliation of graphite, *Nature Comm.* 8: 15763, 2017.

[6] S. Zanotto, F. Bianco, V. Miseikis, D. Convertino, C. Coletti, A. Tredicucci, Coherent absorption of light by graphene and other optically conducting surfaces in realistic on-substrate configurations, *APL Photonics* 2: 016101, 2017.

Extraordinarily transparent compact metallic metamaterials

Vincenzo Giannini[1,2*]

[1] Instituto de Estructura de la Materia (IEM-CSIC), Consejo Superior de Investigaciones Científicas, Madrid, Spain
[2]Department of Physics, Imperial College London, London, UK
*corresponding author, E-mail: v.giannini@csic.es

Abstract

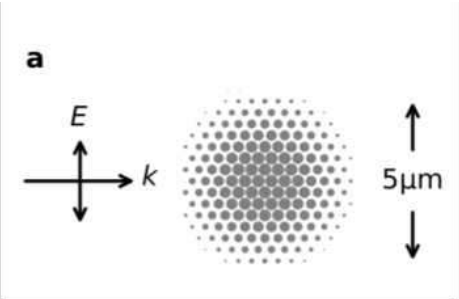
Nanostructured bulk metals can be more transparent than glass and for a bigger range of frequencies. We show that the transparency can go from the near infrared to any smaller photon energy. Also, we can easily tune and design the refractive index.

1. Introduction

Metals are highly opaque, yet we show theoretically and experimentally that densely packed arrays of metallic nanoparticles can be more transparent to infrared radiation than dielectrics such as germanium, even for arrays that are over 75% metal by volume.

Despite strong interactions between the metallic particles, these arrays form effective dielectrics that are virtually dispersion-free, making possible the design of optical components that are achromatic over ultra-broadband ranges of wavelengths from a few microns up to millimetres or more. Furthermore, the local refractive indices may be tuned by altering the size, shape, and spacing of the nanoparticles, allowing the design of gradient-index lenses that guide and focus light on the microscale (see figure a).

The electric field is also strongly concentrated in the gaps between the metallic nanoparticles, and the simultaneous focusing and squeezing of the electric field produces strong 'doubly-enhanced' hotspots (see figure b) which could boost measurements made using infrared spectroscopy and other non-linear processes over a broad range of frequencies, with minimal heat production.



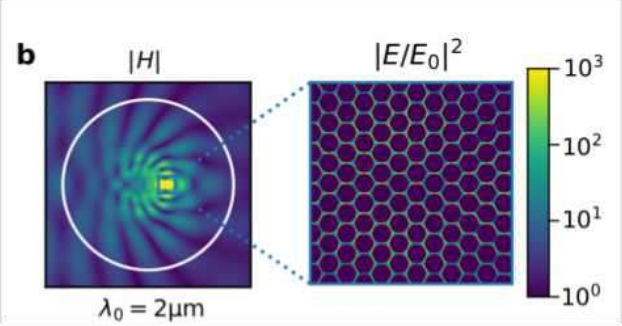


Figure 1: (a) Schematic of a 'concentrator' gradient-index lens composed of gold nanocylinders on a triangular lattice with 50nm site-to-site separation (b) Magnetic near-fields and broadband 'doubly-enhanced' electric field hotspots

1.1. Transparency

The underlying physics of the transparency of densely packed metal metamaterials can be understood by considering how the electrons in metals and dielectrics respond to an electric field. In metals, free electrons are driven to the surfaces until the field generated by the build up of surface charges cancels the applied field within the metal.

On the other hand, the electrons within dielectrics are bound to their parent molecules or atoms, which polarise in the presence of an electric field.

Although the metallic particles comprising the artificial dielectrics possess free electrons, these particles can be regarded as the 'meta-molecules' or '-atoms' as the electrons are only free to move within the confines of the metallic particles, effectively mimicking a dielectric. It is worth noting that this effect is not connected with the creation of plasmonics bands due to the array periodicity.

2. Conclusions

In conclusion, low-loss effective dielectrics can be constructed from arrays of metallic nanoparticles. These arrays are highly transparent, at times even exceeding the transparency of real dielectrics renowned for their transparency to low energy radiation, such as germanium, and can be tuned locally by controlling the size, shape, and spacing of the particles.

Furthermore, and in contrast to metamaterials designed upon resonant effects, the effective index is essentially constant for all wavelengths greater than about 2 um. This al-

lows the design of optical devices to guide or enhance light over an extremely broad range of frequencies, essentially without an upper bound on wavelength.

Acknowledgement

V.G. acknowledges the Consejo Superior de Investigaciones Cientfícas (INTRAMURALES 201750I039).

References

[1] Samuel J. Palmer, Xiaofei Xiao, Nicolas Pazos-Perez, Miguel A Correa-Duarte, Stefan A Maier, Richard V. Craster, Ramon A. Alvarez-Puebla, Vincenzo Giannini

arXiv preprint arXiv:1811.08796

Nonlinear THz response of graphene plasmonic structures

Stephan Winnerl[1]*, M. Mehdi Jadidi[2,3], Matt Chin[2], Angelika Seidl[1], Harald Schneider[1], Manfred Helm[1], H. Dennis Drew[2], Thomas E. Murphey[2], and Martin Mittendorff[4]

[1]Helmholtz-Zentrum Dresden-Rossendorf, 01328 Dresden, Germany
[2]University of Maryland, College Park, 20742 MD, USA
[3]Columbia University, New York, 10027 NY, USA
[4]Universität Duisburg-Essen, Fakultät für Physik, 47051 Duisburg, Germany
*corresponding author, s.winnerl@hzdr.de

Abstract

Ribbons and discs based on doped graphene feature strong tunable plasmonic resonances. We show that excitation with THz radiation results in strong changes of transmission, even at moderate pump fluences. The response is due to a broadening and redshift for the plasmonic absorption line as charge carriers are heated. The response time is determined by the cooling of carriers, which is of the order of 10 ps.

1. Introduction

Optoelectronic effects in graphene have been studied extensively in a wide spectral range, in particular also in the THz frequency region. Making use of plasmonic effects in tailored micro- and nanostructures allows one to enhance the absorption at particular frequencies and to tune the resonance frequency by the structure size and the doping level, respectively [1]. This, together with spatial localization of the excitation, makes plasmonic effects attractive for optoelectronic device applications such as detectors, modulators, saturable absorbers or frequency multipliers [2].
Here we focus on time resolved studies of nonlinear effects in graphene based ribbons and discs.

2. Experimental

Various arrays of graphene ribbons and discs (typical size ~1 µm in arrays covering 1.5 × 1.5 mm^2) have been fabricated by electron beam lithography and subsequent oxygen-plasma etching. For one set of samples graphene grown by chemical-vapor deposition (CVD) was transferred to SiO_2/Si substrates. In these samples the plasmon resonance can be tuned by controlling the carrier concentration via a back-gate voltage [3]. Quasi-freestanding bilayer graphene of high structural quality grown epitaxially by thermal decomposition of SiC on the (0001) side and subsequent hydrogen intercalation is the base of another set of ribbons [4,5] and also discs. The linear absorption of the samples was characterized by Fourier transform infrared spectroscopy. The epitaxial samples exhibit stronger resonant absorption (35 %) compared to the CVD grown sample (18 %) and a four-times narrower Lorentzian linewidth. Comparing the results with calculations based on the Drude model yields a mobility of 3600 cm^2(Vs)$^{-1}$ and a carrier concentration of 9×10^{12} cm^{-2} for the quasi-freestanding epitaxial layers.
Single-color pump probe experiments were performed using a free-electron laser as a source of intense narrowband tunable THz pulses. The samples were kept at 15 K in a He flow cryostat.

3. Results and Discussion

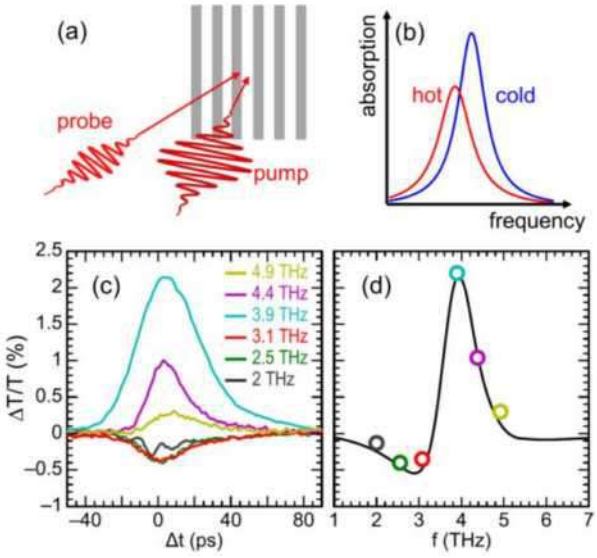


Figure 1: Principle of the pump-probe experiment on ribbon samples (a). Sketch of the redshift and broadening of the plasmonic absorption (b). Pump-induced transmission as a function of time delay for various frequencies (c). Maximal pump-induced transmission change (d). The circles are experimental data (see part (c)), the line is calculated based on the hot-carrier model. Part (c) and (d) are adapted from Ref. [4].

The pump-induced change in transmission was measured in the experiments at different spectral positions within the plasmonic resonance.

In one set of experiments the polarization of both the pump and the probe beam were orientated perpendicular to the ribbons in order to make use of the plasmonic resonance. The pump-induced change in transmission changed proportionally the square-root of the pump fluence, thus providing relatively strong signals at low fluence. For example, a transmission change of 5 % was achieved by excitation with 0.5 $\mu J/cm^2$ for the epitaxial sample.

To investigate the spectral response in a reliable quantitative manner, the pump polarization was oriented along the direction of the ribbons, while the probe polarization was kept perpendicular. Consequently, the excitation occurs via free-carrier heating, which is spectrally almost flat in the range of plasmonic absorption line. The probe pulse, however, still measures the plasmonic response of the heated electron system. The results are depicted in Fig. 1c-b for epitaxial ribbons with a resonance frequency of 3.9 THz. Induced absorption occurs below resonance, while induced transmission is observed at resonance and above resonance.

The results can be explained by a nonlinear hot-carrier response of the thermalized electronic system. Heating of the electron gas by THz radiation requires the chemical potential to drop, in order to conserve the number of free carriers. Furthermore a broadening is induced by the increasing electron scattering rate for supercollision cooling [6]. A thermodynamic model that takes these effects into account provides excellent agreement with the experimental findings [4], cf. Fig. 1d.

Finally, first experiments were carried out on discs of quasi-freestanding bilayer graphene. Here, a plasmonic response is induced for all orientations of linearly polarized radiation. Particularly strong induced transmission is observed for circularly polarized radiation. For the case of circularly copolarized radiation a change in transmission of 2 % is reached for pumping with just 20 nJ/cm^2. Furthermore we show that discs are an ideal system to study nonlinear effects that go beyond the hot carrier response and stem directly from the non-equilibrium excitation.

4. Conclusions

We demonstrate strong nonlinear THz plasmonic response in graphene ribbons and discs. High quality samples provide particularly strong pump-induced transmission. The results from the ribbons are well explained by a hot carrier model, which predicts a red-shift and broadening of the plasmonic absorption by an increase of the electron temperature.

References

[1] A. N. Grigorenko, M. Polini, K. S. Novoselov, *Graphene plasmonics*, Nature Photon. **6**, pp. 749-758, 2012.

[2] L. Ju, B. S. Geng, J. Horng, C. Girit, M. Martin, Z. Hao, H. A. Bechtel, X. G. Liang, A. Zettl, Y. R. Shen, F. Wang, *Graphene plasmonics for tunable terahertz metamaterials*, Nature Nanotechnol. **6**, pp.630-634 2011.

[3] M. M. Jadidi, J. C. König-Otto, S. Winnerl, A. B. Sushkov, H. D. Drew, T. E. Murphy, and M. Mittendorff, *Nonlinear terahertz absorption of graphene plasmons*, Nano Lett. 16, pp.2734-2738, 2016.

[4] M. M. Jadidi, K. M. Daniels, R. L. Myers-Ward, D. K. Gaskill, J. C. König-Otto, S. Winnerl, A. B. Sushkov, H. D. Drew, T. E. Murphy, and M. Mittendorff, *Optical control of plasmonic hot carriers in graphene*," ACS Photonics **6**, pp.302–307, 2019.

[5] K. M. Daniels, M. M. Jadidi, A. B. Sushkov, A. Nath, A. K. Boyd, K. Sridhara, H. D. Drew, T. E. Murphy, R. L. Myers-Ward, and D. K. Gaskill, *Narrow plasmon resonances enabled by quasi-freestanding bilayer epitaxial graphene*, 2D Mater. **4**, 025034 , 2017.

[6] J. C. Song, M. Y. Reizer, and L. S. Levitov, *Disorder-assisted electron-phonon scattering and cooling pathways in graphene*, Phys. Rev. Lett. **109**, 106602, 2012.

In-Plane Anisotropic and Ultra-Low Loss Polaritons in a Natural van der Waals Crystal

Javier Taboada-Gutiérrez[1], Weiliang Ma[2], Pablo Alonso-González[1], Shaojuan Li[2], Alexey Y. Nikitin[3,8], Jian Yuan[2], Javier Martín-Sánchez[1], Iban Amenabar[4], Peining Li[4], Saül Vélez[4,5], Christopher Tollan[4], Zhigao Dai[6], Yupeng Zhang[6], Sharath Sriram[7], Kourosh Kalantar-zadeh[7], Shuit-Tong Lee[2], Rainer Hillenbrand[4,8], Qiaoliang Bao[2,6]

1. Departamento de Física, Universidad de Oviedo, 33007 Oviedo, Spain
2. Institute of Functional Nano and Soft Material (FUNSOM), Jiangsu Key Laboratory for Carbon-Cased Functional Materials and Devices, and Collaborative Innovation Center of Suzhou Nano Science and Technology, Soochow University, Suzhou 215123, China
3. Donostia International Physics Center (DIPC), 20018 San Sebastián, Spain
4. CIC nanoGUNE, 20018 San Sebastian, Spain
5. Department of Materials, ETH Zürich, 8093 Zürich, Switzerland
6. Department of Materials Science and Engineering, and ARC Centre of Excellence in Future Low-Energy Electronics Technologies (FLEET), Monash University, Clayton, Victoria 3800, Australia
7. School of Engineering and the Micro Nano Research Facility, RMIT University, Melbourne, Australia
8. IKERBASQUE, Basque Foundation for Science, 48011 Bilbao, Spain

Abstract

Polaritons – hybrid light-matter excitations – play a crucial role in fundamental and applied sciences, as they enable nanoscale control of light. Polaritons with anisotropic propagation along the surface of vdW materials have been predicted, caused by in-plane anisotropic structural and electronic properties. Here we report anisotropic polariton propagation along the surface of α-MoO_3, a natural vdW material using infrared nano-imaging and nano-spectroscopy techniques. In-plane anisotropic polaritons could enable directional and strong light–matter interactions, in applications such as bio-sensing, among others.

1. Introduction

Anisotropic optical materials exhibit numerous distinctive and non-intuitive optical phenomena such as negative refraction, hyper-lensing, wave-guiding and enhanced quantum radiation, which have been demonstrated typically with artificial hyperbolic metamaterials. However, further progress is limited by optical losses and the complexity of metamaterial fabrication.

The recent emergence of low-loss vdW materials opens the door to achieving anisotropic optical phenomena naturally, because their layered crystal structure leads to an intrinsic and strong out-of-plane (perpendicular to the layers) optical anisotropy. Prominent examples are hyperbolic phonon polaritons (PhPs)—infrared light coupled to lattice vibrations in layered polar materials—in hexagonal boron nitride (h-BN), which exhibit long lifetimes, ultra-slow propagation and hyper-lensing effects. Interestingly, when the layers of a vdW material are anisotropic (that is, when the permittivities along orthogonal in-plane directions are different), the polaritons are expected to propagate along the layers with an in-plane anisotropic dispersion. When the permittivities are different but of the same sign, the polaritons possess an elliptic in-plane dispersion, in which the iso-frequency contours (slices in two-dimensional (2D) wavevector space (kx, ky) of constant frequency ω) describe ellipsoids. When the signs are different, the polaritons possess an in-plane hyperbolic dispersion, in which the iso-frequency contours are open hyberboloids. Only recently, PhPs with in-plane hyperbolic dispersion have been demonstrated by fabricating an artificial metamaterial out of h-BN flakes [1].

Theory predicts polaritons with both in-plane anisotropies even for natural materials that exhibit an in-plane anisotropy of their electronic or structural properties. However, their experimental observation and verification has so far been elusive. Here we present the first images of in-plane elliptic and hyperbolic polaritons. We found them in thin slabs of α-phase molybdenum trioxide (α-MoO_3), a natural vdW polar semiconductor [2].

2. Discussion

To explore the polaritonic response of α-MoO_3, we performed polariton interferometry using scattering-type scanning near-field optical microscopy (s-SNOM, Fig. 1a). A vertically oscillating metallized atomic force microscopy (AFM) tip is illuminated with p-polarized infrared light of frequency ω and field E_{inc} while scanning an α-MoO_3 flake. The tip acts as a polariton launcher and scatterer, since it concentrates the incident field at its apex allowing polariton excitation but also scatters the polaritons reflected to the far field. The polaritons excited by the tip propagate away and are back-reflected at the flake edges, giving rise to interference fringes with a λ/2 spacing. Figure 1b shows s-

SNOM near-field amplitude images of an α-MoO_3 flake with thickness d = 250 nm taken at ω = 990 cm^{-1} and ω = 900 cm^{-1}. At 990 cm^{-1} (upper image in Fig. 1b), we observe that the fringe periodicity largely depends on the propagation direction, being λ_x = 950 nm and λ_y = 1200 nm for the [100] and [001] crystal directions. Apart from the deep subwavelength-scale polariton confinement $\lambda_{x,y} << \lambda_0$=11.1 μm. This anisotropy becomes even more marked at ω = 900 cm^{-1} (lower image in Fig. 1b), where the fringes are seen only parallel to the [001] direction. Accordingly, we assign each of these measurements to each of the two Reststrahlen Bands: an upper one (Fig. 1b upper panel), the so-called elliptical regime and a lower one (Fig. 1b lower panel), the so-called hyperbolic regime.

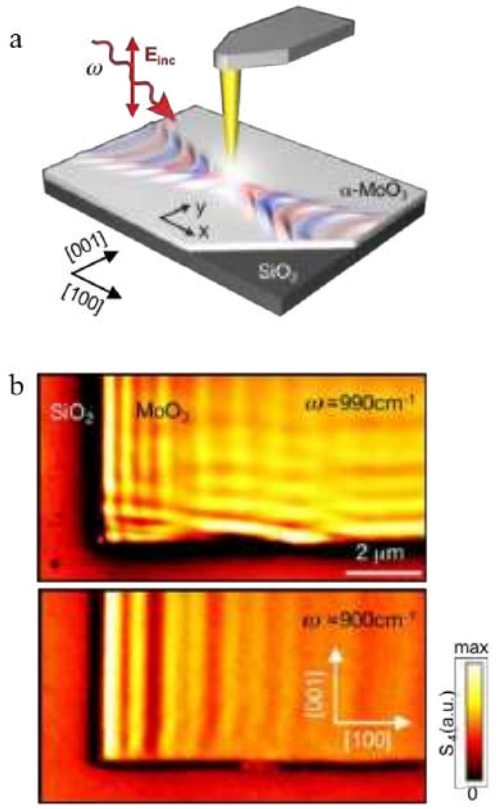


Figure 1: a, Schematic of the s-SNOM experimental configuration used to image an α-MoO_3 flake. A metallized AFM tip (yellow) is illuminated by p-polarized infrared light of frequency ω and electric field E_{inc}. It launches polaritons, which are back-reflected at the flake edges and subsequently scattered by the tip. The tip-scattered field is detected by a distant detector. **b**, Near-field amplitude images s4 of an α-MoO_3 flake with thickness d = 250 nm at illuminating frequencies ω = 990 cm^{-1} (top panel) and ω = 900 cm^{-1} (bottom panel).

For a better understanding of these phenomena, we model the α-MoO_3 as a 2D conductivity layer of negligible thickness compared to the incident wavelength surrounded with two dielectric half-spaces. This model also allows us to extract the unknown α-MoO_3 permittivity at infrared frequencies. We corroborate the model and the permittivity values extracted by performing numerical simulations of near-field images of an α-MoO_3 flake on SiO_2. From our analysis, we find $\varepsilon_{xx,yy}>0$ and $\varepsilon_{zz}<0$ for the elliptic regime and $\varepsilon_{xx}<0$ and $\varepsilon_{yy,zz}>0$ for the hyperbolic regime. Furthermore, we find negative phase velocity for phonon polaritons in the elliptical regime and positive phase velocity for phonon polaritons in the hyperbolic regime.

Regarding phonon polariton lifetimes, τ, we measured record-high polariton lifetimes of 8 ps. Which are more than one order of magnitude larger than that of graphene plasmons and four times larger than that of isotopically enriched h-BN. We obtain the lifetime according to $\tau=L/v_g$, where L is the decay length and v_g the group velocity. Decay lengths are calculated fitting s-SNOM profiles to a exponentially decaying sine-wave function and group velocities are worked out by applying a numerical derivative to the ω-k phonon polariton dispersion (being ω the incident wavelength and k the phonon polariton wavenumber)

3. Conclusions

In short, we have shown for the very first time in-plane anisotropic phonon polariton propagation in α-MoO_3 (both elliptical and hyperbolic), with record-high phonon polariton lifetimes. Moreover, we have extracted the sign of the phonon polaritons phase velocity and the values of the α-MoO_3 permittivity at IR wavelengths. This finding may establish a route to directional control of light and light-matter interactions at the nanoscale.

Acknowledgements

We acknowledge support from the European Research Council under Starting Grant 715496, 2DNANOPTICA, and we also acknowledge support through the Clarín Programme from the Government of the Principality of Asturias and a Marie Curie-COFUND grant (PA-18-ACB17-29)

References

[1] P. Li et al. Infrared hyperbolic metasurface based on nanostructured van der Waals materials. *Science* 23 Feb 2018 Vol. 359, Issue 6378, pp. 892-896.

[2] W. Ma et al. In-plane anisotropic and ultra-low-loss polaritons in a natural van der Waals crystal, *Nature*, 562, pages 557–562 (2018).

Highly anisotropic phonon polaritons in natural biaxial hyperbolic van der Waals alpha-MoO_3

Zebo Zheng, Huanjun Chen*

State Key Laboratory of Optoelectronic Materials and Technologies, Guangdong Province Key Laboratory of Display Material and Technology, School of Electronics and Information Technology, Sun Yat-sen University, Guangzhou, China.

*corresponding author, E-mail: zhengzb5@mail.sysu.edu.cn

Abstract- We show that the van der Waals α-MoO_3 can support naturally in-plane hyperbolic phonon polariton at mid-infrared frequencies. Because α-MoO_3 is a biaxial crystal with three different Reststrahlen bands, where the permittivity is negative due to its lattice vibrations. Interestingly, due to the minimal spectral overlap between these bands, the material is hyperbolic in its natural state. However, unlike previously investigated uniaxial hyperbolic materials, the permittivities along all three axes are different, so in-plane hyperbolic dispersion is also observed.

Hyperbolic materials refer to those media exhibit permittivity tensor having one principal component with opposite sign with respect to the other two axes. They have been extensively studied for their exotic optical properties, particularly the highly confined electromagnetic fields with arbitrarily high momenta *(1)*. This concept can be directly generalized to 2D media, where surface waves or guided waves are considered, and implemented using hyperbolic metasurfaces (HMSs) *(2)*. These are flat photonic nanopatterned structures that support guided waves with in-plane hyperbolicity and can control the two-dimensional light propagation in unconventional way, giving rise to a variety of intriguing optical phenomena such as all-angle negative refraction, greatly enhanced photonic density of states, and wavefronts with concave curvatures *(3)*. The necessity of patterning, however, typically leads to strong optical losses, and limits the actual confinement that can be reached. Furthermore, the electromagnetic responses of the HMSs are governed by the permittivity tensors that are derived from the effective medium theory, which is only valid in the long-wavelength limit where the structural periodicity is much smaller than the incidence wavelength. Consequently, the hyperbolic dispersion is constrained to a very small region in the reciprocal space, leading to rather limited electromagnetic wavevectors. Such an issue can in principle be alleviated by reducing the structural periodicities of the metasurfaces down to sub-10 nm scale. However, this should happen without bringing in additional surface roughness or defects, which is a great challenge for nano-fabrication techniques. Thus, the quest for a natural medium that can be used to achieve in-plane hyperbolicity without nanopatterning is a very important open problem in nanophotonics.

In a recent study, we demonstrated highly confined hyperbolic phonon polaritons (PhPs) in a new type of vdW semiconducting crystal, alpha-phase molybdenum trioxide (α-MoO_3), grown by the thermal–physical-deposition method *(4)*. Herein, we show that vdW α-MoO_3 is actually a type of natural biaxial hyperbolic crystal and that it exhibits pristine in-plane hyperbolic dispersion in the mid-infrared range. First, we proposed a universal three-dimensional analytical dielectric and dispersion model for describing the hyperbolic PhPs in α-MoO_3. Secondly, by utilizing the high-resolution optical scanning near-field nano-imaging techniques, the phonon polariton modes are launched, guided, and manipulated within the different hyperbolicity bands in thin α-MoO_3 crystal flakes. In particular, the concave wavefront of a polaritonic mode originating from the in-plane hyperbolicity of the flake is directly imaged, which is an unmistakable signature of the preserved three-dimensional hyperbolicity of this 2D material. In addition, we measured for the first time the whole dispersion relations of the hyperbolic PhPs corresponding to the three Reststrahlen bands of α-MoO_3 by combining scattering-type near-field scanning optical microscopy (s-SNOM) and photo-induced force microscopy (PiFM) techniques. Furthermore, potential applications of vdW α-MoO_3 in focusing and manipulating mid-infrared electromagnetic fields at the nanoscale are demonstrated *(5)*.

The homogenous biaxial hyperbolic vdW α-MoO_3 crystal investigated here offers the prospect of planar nanophotonics without the need for complex nanopatterning, which is unavoidable in 2D artificial counterparts. The unique biaxial hyperbolicity can provide opportunity for controlling the nanoscale interactions in a direction-dependent manner. For example, Controlling and manipulation of dipole–dipole interactions with more freedom and the broadband super-Planckian thermal emission due to its high photonic density of states in mid-infrared region. This effect can pave the way for engineering the thermal emission at nanoscale. On the other hand, in principle, the wavevectors of the guided electromagnetic waves attained within α-MoO_3 are only limited by the atomic crystalline periodicity; thus, very strong electromagnetic confinement can be reached. The confinement and manipulation of electromagnetic fields at the

nanoscale can be further enriched by introducing sophisticated nanostructures. Moreover, α-MoO_3 is also a semiconductor, which demonstrates the potential for applications of hyperbolic media in active optoelectronic devices because of their excellent electrical transportation characteristics, the tunability of their physical characteristics by external doping, and their high optical-to-electrical conversion efficacy.

References

[1] A. Poddubny, I. Iorsh., P. Belov, Y. Kivshar, "Hyperbolic metamaterials". *Nat. Photonics* 7, 958–967 (2013).

[2] N. Yu, F. Capasso, "Flat optics with designer metasurfaces". *Nat. Mater.* 13, 139–150 (2014).

[3] A. V. Kildishev, A. Boltasseva, V. M. Shalaev, "Planar photonics with metasurfaces". *Science* 339, 1232009 (2013).

[4] Z. Zheng, W. Xie, H. Chen, S. Deng, N. Xu, "Highly confined and tunable hyperbolic phonon polaritons in van der Waals semiconducting transition metal oxides". *Adv. Mater.* 30, 1705318 (2018).

[5] Z. Zheng, A. Ambrosio, S. Deng, H. Chen, "A mid-infrared biaxial hyperbolic van der Waals crystal". *arXiv*:1809.03432 (2018).

Non Linear Single-Particle and Plasmonic Terahertz Properties of 3D Topological Insulators

Paola Di Pietro[1], Federica Piccirilli[2], N. Adhlakha[1], Andrea Perucchi[1], and Stefano Lupi[3,*]

[1]Elettra Sincrotrone Trieste, S.S.14 Km 163,5 in AREA Science Park
IT-34149 Basovizza, Trieste (IT)
[2]CNR-IOM, S.S.14 Km 163,5 in AREA Science Park
IT-34149 Basovizza, Trieste (IT)
[3]INFN and Department of Physics, Sapienza University of Rome, P.le A. Moro 2, 00185 Rome, Italy
*stefano.lupi@roma1.infn.it

Abstract

The terahertz properties of Bi_2Se_3 3D Topological Insulator have been studied in the 0.2-5 THz spectral range. The linear response is described in terms of a Drude term and plasmon modes mainly related to the surface Dirac conducting states characterizing the low-energy electrodynamics of Bi_2Se_3. The intrinsic non linearity of Dirac states, when excited by strong THz fields, provide either harmonic generation and strong plasmon softening, opening the use of TIs for photonic devices.

Introduction

3D Topological Insulators (TIs) are quantum electronic materials characterized by an insulating electronic gap in the bulk, whose opening is due to strong spin-orbit interaction, and gapless surface states at their interfaces. Surface states in TIs are metallic, characterized by a Dirac dispersion, showing a chiral spin texture, and protected from back-scattering by the time-reversal symmetry. Dirac carriers in TIs are characterized by a Fermi energy of about 300 meV substaining single particle and plasmon excitations in the terahertz region of the electromagnetic spectrum [1]. In this paper we have studied the linear and non-linear electromagnetic properties of Bi_2Se_3 thin films. These films with a thickness from 10 to 100 nm, have been grown by Molecular Beam Epitaxy technique and show a high purity with a very low number of defects and Se out of stoichiometry [2]. This provided the possibility to observe by Angular Resolved Photoemission (ARPES) well defined Dirac cones at the Bi_2Se_3 surface with a reduced contribution from bulk bands to their low-energy electrodynamics [2].

1. Experiments

Single particles and plasmon modes have been observed in transmission by using THz radiation from 200 GHz to 5 THz. Linear spectroscopy has been performed through the radiation emitted by the SISSI THz/Infrared beamline at the Elettra Synchrotron facility in Trieste, Italy [3]. Non linear spectroscopy has been instead performed at the THz high-intensity facility TeraFermi@Elettra, producing sub-ps THz pulses with an associated electric field up to 2 MV/cm [4]. Non linear optical properties has been measured vs. the THz electric field through a home-made Michelson interferometer [4]. In Fig.1 we show the experimental apparatus for non linear spectroscopy.

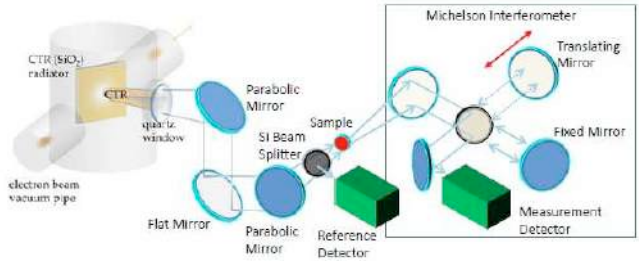


Figure 1: The non linear spectroscopy apparatous. The high-intensity THz radiation produced through a Transition Radiation mechanism (CTR) is focalized on Bi_2Se_3 thin films by parabolic mirrors and then the transmitted spectra vs. THz intensity is measured through a Michelson interferometer.

2. Discussion

We observe a strong THz electric field dependence of both the single particle (Drude) and collective (plasmon) modes of low-energy electrodynamics of Bi_2Se_3 films. In particular,

the single-particle term when excited by a strong THz pulse is renormalized transfering spectral weight at high frequency thus realizing an effective mechanism for harmonic generation in the THz region. Plasmon modes are also modified generating a strong softening of their central frequencies. Both effects are associated to Dirac carriers generated by the non trivial topology of Bi_2Se_3.

3. Conclusions

THz measurements on Bi_2Se_3 topological insulator show a strong non linear response associated to Dirac carriers. This opens the possibility to use Bi_2Se_3 thin films for photonic devices like harmonic generators and frequency converters.

References

[1] P. Di Pietro, M. Ortolani, O. Limaj, A. Di Gaspare, V. Giliberti, F. Giorgianni, M. Brahlek, N. Bansal, N. Koirala, S. Oh, P. Calvani and S. Lupi, Nat. Nanotechnology 8, 556 (2013).

[2] N. Bansal, Y. S. Kim, Brahlek, E. Edrey, S. Oh, Phys. Rev. Lett. 109, 116804 (2012).

[3] S Lupi, A Nucara, A Perucchi, P Calvani, M Ortolani, L Quaroni, JOSA B 24 (4), 959-964 (2007).

[4] P. Di Pietro, N. Adhlakha, F.Piccirilli, L. Capasso, C. Svetina, S. Di Mitri, M. Veronese, F. Giorgianni, S. Lupi, A. Perucchi Synchrotron Radiation News 30, 36 (2017).

Photonic Crystals for Nano-Light in Twisted Bilayer Graphene

D.N. Basov
Columbia University

500 W 120 Street New York, NY USA

Abstract: Atomically relaxed twisted bilayer graphene hosts periodic arrays of topological conducting channels that act as a photonic crystal for surface plasmons.

Graphene is an atomically thin plasmonic medium that supports highly confined plasmon polaritons, or nano-light, with very low loss. Electronic properties of graphene can be drastically altered when it is laid upon another graphene layer, resulting in a moiré superlattice. The relative twist angle between the two layers is a key tuning parameter of the interlayer coupling in thus obtained twisted bilayer graphene (TBG). We studied propagation of plasmon polaritons in TBG by infrared nano-imaging. We discovered that the atomic reconstruction occurring at small twist angles turns the TBG into a natural plasmon photonic crystal for propagating nano-light. This discovery points to a pathway towards controlling nano-light by exploiting quantum properties of graphene and other atomically layered van der Waals materials instead of arduous top-down nanofabrication. (Science 362, 1153–1156 (2018)).

Imaging ultrafast dynamics on the nanoscale with terahertz scanning tunneling microscopy

Frank Hegmann

Department of Physics
4-183 CCIS
University of Alberta
Edmonton AB T6G 2E1
Canada

E-mail: hegmann@ualberta.ca

The ability to directly probe ultrafast phenomena on the nanoscale is essential to our understanding of excitation dynamics on surfaces and in nanomaterials. Recently, a new ultrafast scanning tunneling microscope technique that couples terahertz pulses to the scanning probe tip of an STM was demonstrated (THz-STM), showing photoexcitation dynamics of a single InAs nanodot with simultaneous 0.5 ps time resolution and 2 nm spatial resolution under ambient conditions. Operation of THz-STM in ultrahigh vacuum now makes it possible to spatially-resolve sub-picosecond dynamics of single molecules and silicon surfaces with atomic precision. THz-STM also makes it possible to coherently control currents at the tunnel junction, as well as drive tunnel currents exceeding 100 GA/cm2 through a single atom over sub-picosecond time scales. However, more work is needed to better understand the nature of terahertz-pulse-induced tunnel currents and nanoscale photoexcitation dynamics in various material systems using THz-STM. This talk will discuss how ultrafast THz-STM works, recent progress, operation in ambient versus UHV, and how THz-STM can provide new insight into ultrafast dynamics on the atomic scale, which is essential for the development of novel silicon nanoelectronics, nanophotonics, and molecular-scale devices operating at terahertz frequencies.

asmonics and Nanophotonics Based on 2D Materials: Graphene and Bey

Surface plasmon-polaritons in deformed graphene layer

Maksim Usik[1], Igor Bychkov[1,2], Olga Kharitonova[1], Vladimir Shavrov[3], Dmitry Kuzmin[1,2]

[1]Chelyabinsk State University, Department of Radio-Physics and Electronics, Chelyabinsk, Russian Federation
[2]South Ural State University (National Research University), Chelyabinsk, Russian Federation
[3] Kotelnikov Institute of Radio-engeneering and Electronics of RAS, Moscow, Russian Federation
*corresponding author, E-mail: usikmo95@gmail.com

Abstract

In this work, we theoretically investigated the excitation of surface plasmon-polaritons (SPPs) in deformed graphene by attenuated total reflection method. We considered the Otto geometry for SPPs excitation in graphene. Efficiency of SPPs excitation strongly depends on the SPPs propagation direction. The frequency and the incident angle of the most effective excitation of SPPs strongly depend on the polarization of the incident light. Our results may open up new possibilities for strain-induced molding flow of light at nanoscales.

1. Introduction

Graphene is one of the materials which allow reaching the most possible miniaturization of nowadays devices just a one atomic layer of thickness. Moreover, it has a lot of non-trivial physical properties ranging from mechanical to optical. For plasmonic applications it is important that graphene carrier concentration can be tuned by chemical doping or applying an electric field, which allow varying its electrodynamic properties from highly conductive to dielectric. This feature makes graphene a very promising material for flatland photonics and plasmonics [1, 2].

For practical applications, it is highly desirable to have the effective tools for control of SPPs characteristics. Usually, this goal may be achieved by introducing into plasmonic structure some optically active materials [3, 4]. In contrast to such approach graphene may show an optical activity itself: its optical properties may be effectively manipulated by electric [5] and magnetic [6] field, by topological manipulations [7] or by deformations [8].

Despite a large number of works devoted to electric and magnetic field manipulation by SPPs in graphene, the impact of deformations on the plasmonic properties is not investigated enough. In this paper we investigated the excitation of SPPs on non-elastically deformed graphene (see Fig. 1). We found that such a structure shows high anisotropy of reflectance from graphene layer orientation (or orientation of deformations). Our results may pave the way for new straintronic methods of nanoscale light control.

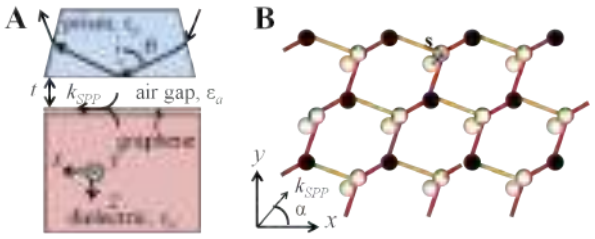


Figure 1: Surface plasmon-polaritons in deformed graphene may be excited in Otto configuration (**A**). Non-elastic deformation of graphene layer leads to anisotropy of propagating SPPs with respect to propagation direction (**B**).

2. Discussion

In this work, we theoretically investigated the excitation of surface plasmon-polaritons (SPPs) in deformed graphene by attenuated total reflection method. We considered the Otto geometry for SPPs excitation in graphene layer under external strain. We calculated the light reflectance from the structure, which allows concluding what part of the energy of the incident wave has passed into the excitation of SPPs.During the work, we investigated plasmonics of deformed graphene lattice, as illustrated in Fig. 1 (**B**). The optical conductivity tensor for this modified graphene lattice has non-zero off-diagonal components [8] $\sigma_{xy} = \sigma_{yx} = 2\sigma_0(\omega)\beta s_x/a$ and modified diagonal components $\sigma_{xx,yy} = \sigma_0(\omega)[1 \pm 2\beta s_y/a]$, where $\sigma_0(\omega)$ is graphene conductivity, β the electron Gruneisen parameter, s_x and s_y are the components of relative displacement of graphene sub-lattice $\vec{s}$. A possible scenario for such deformation could occur in graphene grown on a substrate with an appropriate combination of lattice mismatch between the two crystals [9].

Color maps of the reflectance are shown on Fig. 2. One can see that in the deformed graphene the excitation pattern of surface plasmons differs from that of undeformed graphene. Excitation of SPPs by TM-incident wave is more efficient at lower frequencies. For TE-polarized incident wave excitation of SPPs occurs more significantly and at higher angles of incidence θ.



Figure 2: Color maps of the reflectance: a) unstrained graphene, TM-polarized incident wave; b) unstrained graphene, TE-polarized incident wave; c) deformed graphene ($\vec{s}/a = (0.04, 0.03)$), TM-polarized incident wave; d) deformed graphene ($\vec{s}/a = (0.04, 0.03)$), TE-polarized incident wave.

Figure 3: Reflectance spectrum of the system for several values of propagation angles in the x-y plane.

Fig. 3 shows that by changing the angle of propagation α with respect to deformation vector $\vec{s}$, one can control the intensity of excitation of surface plasmons. There is also a coincidence of the system behavior at $\alpha = 0$ and $\alpha = \pi/2 - arctan(s_y/s_x)$.

As usually for graphene-based plasmonics, the frequency range for SPPs excitation varies from THz to mid-infrared depending on graphene chemical potential [1, 2]. At the frequencies corresponding to the condition of intraband electron transitions in graphene (i.e. when $\hbar\omega \approx 2\mu_{ch}$), imaginary part of its conductivity becomes negative (or, equivalently, its dielectric permittivity becomes positive) which means that graphene can not support any SPPs. We should note also that attenuated total reflection method is based on resonant phase matching between incident light and propagating SPPs. This means that change of graphene chemical potential (by external gate voltage, for example) will lead to breaking of phase matching condition and to significant change (increasing) in the reflectance.

3. Conclusions

The calculations have shown that the deformed graphene is a good basis for the excitation of plasmons not only by TM-polarized waves, but also by TE-polarized incident waves, which is impossible to observe in an undeformed layer of graphene for THz frequency range. The frequency and angle of the most effective excitation of plasmons strongly depend on the polarization of the incident electromagnetic wave. This opens up new possibilities for controlling electromagnetic radiation on nanoscale.

Acknowledgement

The work was financially supported in part by RFBR (16-37-00023, 16-07-00751, 16-29-14045, 17-57-150001, 19-07-00246), Act 211 Government of the Russian Federation (contract 02.A03.21.0011).

References

[1] Kuzmin D.A., Bychkov I.V., Shavrov V.G., Temnov V.V., *Plasmonics of magnetic and topological graphene-based nanostructures*, Nanophotonics. 2018;7(3):597.

[2] Chen P.-Y., Argyropoulos Ch., Farhat M., Gomez-Diaz J.S., *Flatland plasmonics and nanophotonics based on graphene and beyond*, Nanophotonics 2017;6(6):1239.

[3] Temnov V.V., Armelles G., Woggon U. et al., *Active magneto-plasmonics in hybrid metalferromagnet structures*, Nat. Photonics. 2010;4:107.

[4] Kuzmin D.A., Bychkov I.V., Shavrov V.G., *Magnetic field control of plasmon polaritons in graphene-covered gyrotropic planar waveguide*, Opt Lett. 2015;40:2557.

[5] Gusynin V.P., Sharapov S.G., *Transport of Dirac quasiparticles in graphene: Hall and optical conductivities*, Physical Review B 2006;73:245411.

[6] Crassee I., Levallois J., Walter A.L., et al., *Giant Faraday rotation in single- and multilayer graphene.*, Nat Phys. 2010;7:48.

[7] Gomez-Diaz J.S., Tymchenko M., Al A., *Hyperbolic metasurfaces: surface plasmons, light-matter interactions, and physical implementation using graphene strips*, Opt Mater Expr. 2015;5:246047.

[8] Oliva-Leyva M., Naumis G.G., *Effective Dirac Hamiltonian for anisotropic honeycomb lattices: Optical properties*, Phys. Rev. B 2016;93:035439.

[9] Lee S.-M., Kim S.-M., Na M., et al., *Materialization of strained CVD-graphene using thermal mismatch*, Nano Research. 2015;8:2082.

Second harmonic generation in graphene-based hyperbolic metasurface

Olga Kharitonova[1], Igor Bychkov[1,2], Maksim Usik[1], Vladimir Shavrov[3], Dmitry Kuzmin[1,2,*]

[1]Chelyabinsk State University, Department of Radio-Physics and Electronics, Chelyabinsk, Russian Federation
[2]South Ural State University (National Research University), Chelyabinsk, Russian Federation
[3] Kotelnikov Institute of Radio-engeneering and Electronics of RAS, Moscow, Russian Federation
*corresponding author, E-mail: kuzminda@csu.ru

Abstract

In this work, the phenomenon of second-harmonic generation in a hyperbolic metasurface based on graphene strips was investigated. Existence of phase matching between surface plasmon-polaritons (SPPs) at fundamental and second harmonic frequencies was shown. The phase matching condition may be satisfied just for certain angles of SPPs propagation. The dependencies of this angle on frequency and filling factor are investigated.

1. Introduction

Graphene (2D honeycomb-like lattice of carbon atoms) allows reaching the most possible miniaturization of just one atomic layer for nowadays devices. Its electromagnetic properties may be easily tuned from highly conductive to almost dielectric by tuning the carrier concentration. This feature makes graphene a very promising material for flatland photonics and plasmonics [1, 2].

Densely packed array of graphene stripes may support a hypebolic surface plasmon-polaritons (SPPs), which attracts researchers attention by exciting optical properties [3, 4, 5]. Such an array forms a hyperbolic metasurface (HMSs). It supports highly localized low-loss SPPs, providing drastic increase of the light-matter interactions near the surface. Moreover, HMSs allow the very effective manipulation by SPPs varying from routing them towards specific directions within the sheet, dispersion-free propagation (canalization), and to the negative refraction.

Here, we consider the pecularities of second harmonic generation (SHG) in graphene-based metasurfaces (see Figure 1), when the metasurface works in hyperbolic regime for both fundamental and second harmonic frequencies.

2. Results and Discussion

Electrodynamic properties of the above-mentioned metasurface may be described by diagonal conductivity tensor with the following components: $\sigma_{xx}^{eff} = (L\sigma\sigma_c)/(W\sigma_c + G\sigma)$, $\sigma_{yy}^{eff} = \sigma W/L$.

With this conductivity tensor, solving Maxwell's equations with the boundary conditions of electric field strength continuity for tangentional components and jump of tangentional magnetic field strength due to currents in metasurface, one may calculate the dispersion relation of propagating SPPs:

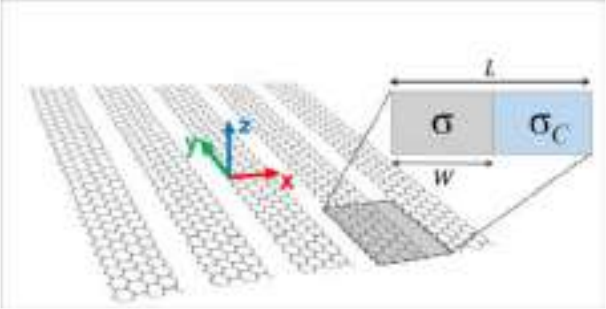


Figure 1: Scheme of graphene-based metasurface formed by graphene stripes with the conductivity σ and air gaps characterized by capacity-like conductivity σ_C. Graphene stripes have a width W, the gap width is G, the periodicity of the structure is L.

$$\left(q_x^2 - k_0^2\right)\sigma_{xx} + (q_y^2 - k_0^2)\sigma_{yy} = 2i\gamma\omega\left(\varepsilon_0 + \frac{\mu_0\sigma_{xx}\sigma_{yy}}{4}\right) \quad (1)$$

where $\gamma^2 = q_x^2 + q_y^2 - k_0^2$, $k_0 = \omega/c$, ω is an angular frequency (time-dependence $\propto exp(-i\omega t)$ is assumed), SPPs propagates with the wavevector lying in $xy-$plane $q = (q_x, q_y)$.

Solving this dispersion relation for both fundamental and second harmonic frequencies, it is possible to calculate an isofrequency contours and define the phase matching condition $2q_\omega = q_{2\omega}$.

Let us consider the structure with $L = 50nm, W = 15nm$. Figure 2 shows an isofrequency contours calculated for such a structure at frequency 10 THz. One can see, that the phase matching condition is satisfied for certain angles of SPPs propagation.

This phase matching angle depends on frequency and geometrical parameters of the structure. Figure 3 shows the behaviour of phase matching angle under variation of frequency and for fixed geometrical parameters. One can see that the phase matching angle changes with the frequency in wide angular range.

As usually for graphene-based plasmonics, the frequency range for SPPs excitation varies from THz to mid-infrared depending on graphene chemical potential μ_{ch} [1, 2]. At the frequencies corresponding to the condition of intra-band electron transitions in graphene (i.e. when $\hbar\omega \approx$

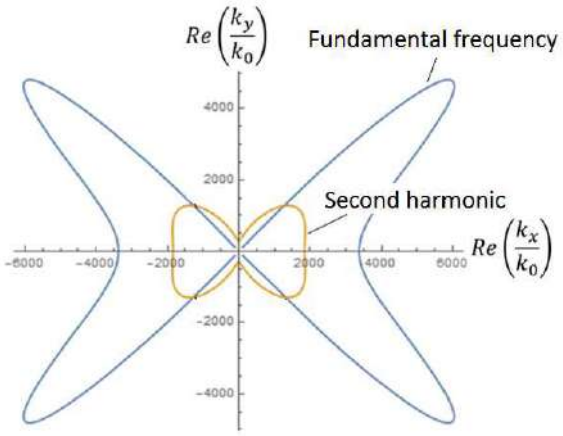


Figure 2: Isofrequency contours of SPPs propagating along the metasurface at fundamental and second harmonic frequency. Phase matching condition corresponds to the intersection points.

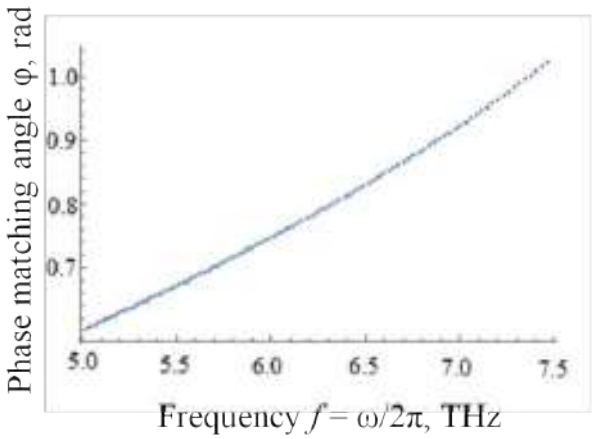


Figure 3: Frequency dependence of phase matching angle.

$2\mu_{ch}$), imaginary part of its conductivity becomes negative (or, equivalently, its dielectric permittivity becomes positive) which means that graphene can not support any SPPs. This means that change of graphene chemical potential (by external gate voltage, for example) will lead to breaking of phase matching condition.

3. Conclusions

We have theoretically investigated a phase matching condition for SHG in graphene-based hyperbolic metasurfaces. We have found that it is possible to observe a SHG from SPPs at fundamental frequency to SPPs at doubled frequency, when the metasurface works in hyperbolic regime at both frequencies. Phase matching condition may be observed just for certain angles of propagation for SPPs. Phase matching angle depends significantly from frequency, geometrical parameters of the structure and properties of graphene.

Acknowledgement

The work was financially supported in part by RFBR grants (16-37-00023, 16-07-00751, 16-29-14045, 17-57-150001, 19-07-00246).

References

[1] Kuzmin D.A., Bychkov I.V., Shavrov V.G., Temnov V.V., *Plasmonics of magnetic and topological graphene-based nanostructures*, Nanophotonics. 2018;7(3):597.

[2] Chen P.-Y., Argyropoulos Ch., Farhat M., Gomez-Diaz J.S., *Flatland plasmonics and nanophotonics based on graphene and beyond*, Nanophotonics 2017;6(6):1239.

[3] Gomez-Diaz J.S., Tymchenko M., Alu A., *Hyperbolic plasmons and topological transitions over uniaxial metasurfaces*, Phys. Rev. Lett. 2015;114:233901.

[4] Gomez-Diaz J.S., Tymchenko M., Alu A., *Hyperbolic metasurfaces: surface plasmons, light-matter interactions, and physical implementation using graphene strips*, Optical Materials Express. 2015;5:2313.

[5] Gomez-Diaz J.S., Alu A., *Flatland Optics with Hyperbolic Metasurfaces*, ACS Photonics. 2016;3:2211.

[6] Crassee I., Levallois J., Walter A.L., et al., *Giant Faraday rotation in single- and multilayer graphene.*, Nat Phys. 2010;7:48.

[7] Gomez-Diaz J.S., Tymchenko M., Al A., *Hyperbolic metasurfaces: surface plasmons, light-matter interactions, and physical implementation using graphene strips*, Opt Mater Expr. 2015;5:246047.

Graphene Plasmonic Slot Photodetector on Silicon-on-insulator with High Responsivity

Zhizhen Ma[1], Mario Miscuglio[1], and Volker J. Sorger[1,*]

[1] Department of Electrical and Computer Engineering, The George Washington University, 800 22nd St NW, Washington, DC 20052, USA
*corresponding author, E-mail: sorger@gwu.edu

Abstract

Graphene has extraordinary electro-optic properties and is therefore a promising candidate for monolithic photonic devices such as photodetectors. However, the integration of this atom-thin layer material with bulky photonic components usually results in a weak light-graphene interaction leading to large device lengths limiting electro-optic performance. In contrast, here we demonstrate a plasmonic slot graphene photodetector on silicon-on-insulator platform with high-responsivity given the 5 μm-short device length. We observe that the maximum photocurrent, and hence the highest responsivity, scales inversely with the slot width. Using a dual-lithography step, we realize 15 nm narrow slots that show a 15-times higher responsivity per unit device-length compared to photonic graphene photodetectors. Furthermore, we reveal that the back-gated electrostatics is overshadowed by channel-doping contributions induced by the contacts of this ultra-short channel graphene photodetector. This leads to quasi charge neutrality, which explains both the previously-unseen offset between the maximum photovoltaic-based photocurrent relative to graphene's Dirac point and the observed non-ambipolar transport. Such micrometer compact and absorption-efficient photodetectors allow for short-carrier pathways in next-generation photonic components, while being an ideal testbed to study short-channel carrier physics in graphene optoelectronics.

Here, we report the design and characterization of a plasmonic slot graphene photodetector monolithically integrated on silicon-on-insulator. While our plasmonic slot design results in a comparable (absolute) responsivity compared to that of plasmonic graphene detectors recently reported by Ding et al., the underlying physics and relative performances are substantially different as discussed below; in brief our design utilizes hybrid slot plasmonic mode with a smallest slot width (15 nm) to date. Interestingly, the maximum photo-absorption is achieved for smallest plasmonic gap. To understand the short-channel effect of this novel design, we investigate a symmetric metal-contact work-function concept, which therefore requires a bias voltage to extract the photo-carriers. However, the generality of our observed results and short-channel explanation hold true for both the symmetric and the asymmetric metal work-function case. Our structure sits on top of the silicon-on-insulator (SOI) epitaxy layer. Besides providing a different integration method to the plasmonic graphene PD with conventional photonic integrated circuit, the silicon layer can be used as a back gate to achieve two device operation regimes (i.e. bolometric effect or photovoltaic effect) thus this PD design allows for dual operation (positive or negative photocurrent) depending on the gate voltage. Multiple devices with a variety of geometric dimension have been fabricated and studied, and the device featuring the smallest plasmonic slot gap size (15 nm) showed the highest responsivity of 0.35 A/W while being only 5 μm short and a bias of 0.2 V. This is about 15-times more efficient per device length than integrating graphene onto an SOI waveguide, enabled by the strong light-graphene interaction enhancement from the narrow plasmonic slot structure. As expected this device also shows broadband (here 100 nm tested) operation. We believe this compact yet high-responsivity photo-detector enables next-generation optoelectronics specifically for both dense integration and short temporal delays.

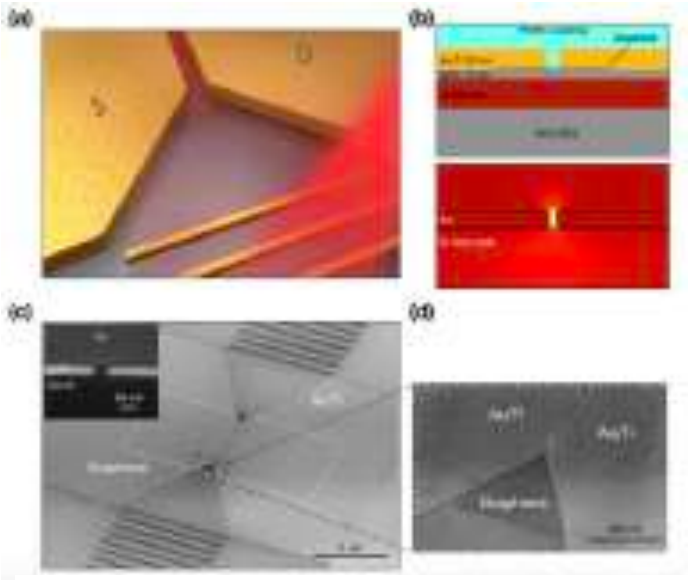


Figure 1. *(a) 3-dimensional representation of the photodetector. (b) Cross sectional schematic of the device, where the Ti/Au metallic structures are in close proximity to each other for forming the plasmonic slot waveguide, as well as serving as the source-drain contact, while the p-doped SOI device layer silicon is used for back gate with a thin silica layer in between. (c) SEM image of fabricated photodetector, graphene is underneath the metal structure and the cross-sectional image as inset, here is a slot with slot gap width W = 30 nm and length L = 5 μm. (d) Zoom in view of the tapered region and slot, note that the graphene layer is slightly extended out from the slot region for a few hundreds of nanometers to ensure lithography alignment.*

For graphene-based photodetectors, three different compelling mechanisms contribute to the photo-response, namely photo-thermoelectric (PTE) effect, photo-bolometric (PB) effect and photovoltaic (PV) effect. The PTE effect relies on the photon induced electron temperature difference between two different graphene doping regions, which is usually achieved by designing an asymmetric energy band profile from different material doping or spatially placing the photosensitive region away from the symmetric part (36). However, in our design, the same metal combination (Ti/Au) is used for the plasmonic slot which is simultaneously used to contact graphene. This results in a symmetric band diagram across

the active region, and therefore minimizes the contributions from PTE effect. Instead, a competing PB and PV effect is observed due to their inverse photocurrent polarity; that is, the PB contributes to a negative photocurrent due to the increased channel resistance from smaller mean free path for heated carriers, whereas photo-generated carriers from PV reduce the channel resistance. By varying the gate voltage to change the channel doping level, two distinct PB dominant vs. PV dominant regions were found for our devices (Fig. 2). Furthermore, this short-channel detector shows that the PV generated photocurrent peak (minimized PB) does not coincide with the same gate bias where the Dirac point. This is due to the metal-induced short-channel doping of the graphene sheet, which is no longer a negligible effect for devices with such short channel length, i.e. the physical channel length (slot width W) is shorter than the charge transfer region L_{ct}.

In view of our results, here we compare the device performance in term of device compactness (1/device length) and responsivity per bias to the state of art integrated graphene photodetectors. In general, the photonic graphene integrated PD requires a larger device footprint to achieve significant absorption in graphene, due to the dimension mismatch between graphene and dielectric waveguide, hence a small mode overlap. For plasmonic PDs, for both PB and PV effect driven device, our short-channel device shows a higher responsivity-per-bias compared to recently

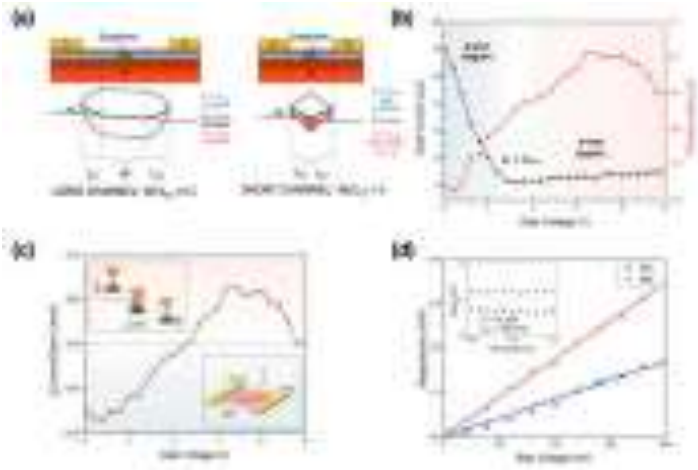


Figure 2. *Ultra-narrow plasmon slot graphene photodetector physics and measurement. (a) Band diagram for long and short channel device. For the short-channel detector, because of the small W/L_{ct}, the charge transfer region has a significant influence on the channel. (b) Measurement of photocurrent and dark current (I_{sd}) from the photodetector (V_{sd} = 0.1V), the photocurrent changes sign when the photovoltaic effect is stronger than bolometric effect. 8 μW optical signal at 1310 nm wavelength was coupled into the plasmonic slot structure, and the source-drain current and photocurrent under different gating voltage was measured with a static bias voltage of 0.1 V (c) Change of current, two peaks are observed in different polarity for either bolometric effect and PV effect dominant*

reported graphene plasmonic detectors, despite the fact that the absolute absorption area is smallest in our device. We believe this superior responsivity per bias, along with the compact device footprint is a direct result of the ultra-short slot width W amongst these plasmonically enhanced PDs enabling higher absorption per unit device length and a shorter carrier drift path. To summarize, in addition to the device demonstration, our photocurrent measurements provides considerable insightful details on the transport in short channel devices, highlighting the role of the metal-graphene junctions and the governing mechanism in the charge transport region. We measure that under different back-gate voltage, the ultra-short graphene channel, in fact, displays a large mismatch between the channel net charge neutrality point and the Dirac point for graphene due to a significant influence of the metal contact doping into the ultra-short channel detector. This translates to a pronounced shift between the peak in PC and the Dirac Point, here reported for the first time. Also, the peculiarity of the short channel transport mechanism combined with the electrostatic doping, allows two distinct non-competing operation regimes having response in inversed polarities, which enables more system level functionality when integrated with PICs. Moreover, we provide the device performance, as function of the width of the slot. Smaller slot width yields a stronger field confinement, which ultimately leads to a larger photoresponse.

In conclusion, hereby, we demonstrated an ultra-compact graphene based plasmonic slot detector with a responsivity of 0.35 A/W and 0.17 A/W for bolometric and photovoltaic effect, respectively. This high responsivity was due to enhanced absorption in graphene enabled by the strong mode confinement in the ultra-short slot width, which is significantly smaller than the charge transfer region. We show that the voltage-bias normalized responsivity is not only the highest measured-to-date in integrated graphene photodetectors, but this ultra-narrow slot design also enables the most compact device to-date. Moreover, our work provides an alternative approach for integrated graphene plasmonic detectors, which could lead to engineering an entire class of short-channel optoelectronic devices for dense integrated photonic circuits.

References

1. Z. Ma, K. Kikunage, H. Wang, S. Sun, R. Amin, M. Tahersima, M. Miscuglio, H. Dalir, V. J. Sorger, “Compact Graphene Plasmonic Slot Photodetector on Silicon-on-insulator with High Responsivity”, ***arXiv***, 1812:00894 (2018).

5. V.S. is supported by AFOSR (FA9550-17-1-0377) and ARO (W911NF-16-2-0194).

vel guided wave configurations with nanostructures for emerging applica

Photonic nanojet generated by dielectric multi-material microstructures.

Oksana Shramkova*, Laurent Blondé, Valter Drazic, Bobin Varghese, Valérie Allié

Technicolor Research & Innovation, Cesson Sévigné, France
*corresponding author, E-mail: Oksana.shramkova@technicolor.com

Abstract

In this paper we study high-intensity nanojet (NJ) beams generated at the output of dielectric multi-material elements. The proposed method for generating condensed optical NJ beams relies on the complex electromagnetic phenomenon associated with the light diffraction on the edges of constitutive parts of the studied system embedded in a host medium with lower refractive index. The possibility of NJ shift and deviation in the near zone of such a microstructure illuminated by a plane wave is demonstrated via a double-material microstructure. We examine the dependence of NJ beam behavior and orientation on the materials and dimensions of the constitutive parts.

1. Introduction

The photonic NJ is a highly focused beam of light formed in proximity to the shadow surface of illuminated transparent dielectric particles with a size/diameter comparable or somewhat larger than the wavelength of the incident optical radiation [1]. The interest ~~to~~ of the NJ effect is mostly related to the promises of its practical applications in multiple emerging application domains, including optical sensors, light communication systems, spectroscopy, optical trapping and manipulation. In this connection, the question of controlled NJ characteristics' manipulation attracts a growing interest.

The physics of photonic NJs generated by spherical or cylindrical particles was studied using the Mie theory [2]. The analytical method of investigation of the near field focusing phenomenon for arbitrary-shaped microstructures was proposed in [3]. The latest studies have shown that both the NJ shape and intensity depend significantly on the shape, size and optical properties of the generating microparticles [1,4,5]. In a recent paper [6], we reported that the beam geometry and field intensity enhancement can be tuned by varying the curvature of the edge line of dielectric microstructures. The photonic NJ is created due to the constructive interference of edge diffracted waves from different segments of the edge line. The formation of a curved ~~a~~ photonic jet, named "photonic hook", by a single-material structure was discussed in [7]. The authors present a dielectric cuboid with the addition of a wedge-shaped prism made of the same material. It was also demonstrated that if the NJ is produced by a multi-material composite (for example a radially inhomogeneous particle consisting of several concentric shells with different refractive indices or graded refractive index material) the NJ characteristics can be changed significantly [8,9].

In this work we demonstrate a solution for the design of a NJ focusing component capable of deviating the focused beam in the near zone. The proposed solution is based on a combination of different dielectric materials. The possibility to control the deviation direction and the intensity of the generated NJ beam by changing the parameters of such system was considered.

2. Problem statement

Let us consider the cuboid geometry. A cross-sectional view of the double-material NJ element is schematically illustrated in Fig. 1. The proposed microstructure combines two dielectric materials, having different refractive indexes, in such a way that all the NJ beams, originating from different edges (associated with different blocks/layers) of the system, recombine and contribute to the formation of a total NJ beam. The structure parts are made of lossless isotropic dielectric materials. It is assumed that the double-material dielectric system with refractive indexes n_2 and n_3 ($n_2 > n_3$) is embedded in a homogeneous dielectric host media with a refractive index $n_1 < n_3$. The structure is illuminated by a TM-polarized plane wave propagating in the positive z-axis direction from below.

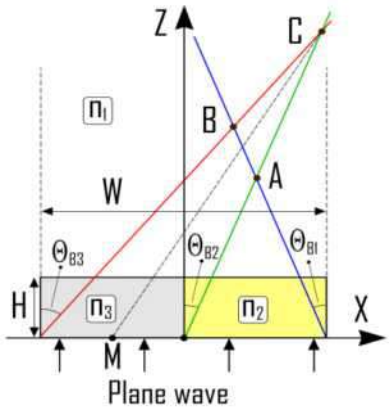


Figure 1: Geometry of the system.

Our analysis shows that the angles of deviation of the NJ beams caused by diffraction of a plane wave on the edges with a base angle of 90° (vertical edge in the example) are determined mainly by the ratio of indexes of the two media in contact:

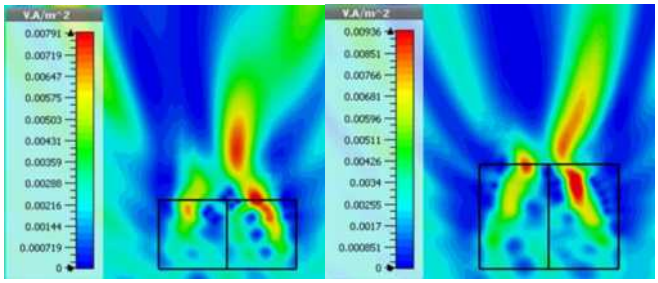
$$\Theta_{Bj} \approx \frac{90^\circ - \Theta_{TIRj}}{2}, \qquad (1)$$

where $\Theta_{TIR1} = \sin^{-1}\left(\frac{n_1}{n_2}\right)$, $\Theta_{TIR2} = \sin^{-1}\left(\frac{n_3}{n_2}\right)$, $\Theta_{TIR3} = \sin^{-1}\left(\frac{n_1}{n_3}\right)$ are the critical angles of refraction, j=1,2,3. Let us note that the length and intensity of these three NJ beams are different. The maximal intensity and minimal length correspond to the beam with highest ratio between the refractive indexes in the expression for Θ_{TIRj}.

To explain the behavior of total NJ radiated by the double-material microstructure we should determine the points of intersection of these initial NJs associated with the edges of the system and radiated at the angles Θ_{B1}, Θ_{B2} and Θ_{B3}.

3. Parametric study

To analyze the features of the generated NJ beam we consider data for a 2D double-material microlens computed using software package CST MICROWAVE STUDIO. It was obtained that the position of the NJ hot spot is determined by the sizes and refractive indexes of the constitutive parts.



(a) (b)

Figure 2. Power density distribution in xz-plane at λ=550*nm* for the systems with parameters: n_1=1, n_2=1.8, n_3= 1.6, W= 1200*nm,* (a) H=600*nm;* (b) H=900*nm*.

For the microstructure with total width $W \le \lambda$ we observe a NJ beam shift towards the part with lower refractive index n_3. Changing the refractive index n_3 we can tune the position of the NJ hot spot. The NJ hot spot position in x does not depend on the height H of the system. Increasing the total width of the microelements ($W > \lambda$) we can distinguish two cases corresponding to different ratios between the refractive indexes of constitutive materials. For $n_3 < \sqrt{n_1 n_2}$, the behavior of NJ beam will be similar to the $W \le \lambda$ case and changing n_3 we just observe the NJ hot spot shift. This similar behavior is observed in Fig. 2a for a double-material microlens with $n_3 > \sqrt{n_1 n_2}$ and $H<H_A$ with H_A defined as the z-coordinate of point A (see Fig. 1) corresponding to the intersection between the NJs generated by the edges of the part with refractive index n_2. For $n_3 > \sqrt{n_1 n_2}$ and $H \ge H_A$ we get the deviation of the total NJ beam towards the part with higher refractive index n_2 (Fig. 2b). It was demonstrated that in this case the generated NJ will be parallel to the line MC, where point M corresponds to the middle of the second part with lower refractive index n_3 and point C is the crossing point of the NJs generated by the external edges of the microstructure.

4. Conclusions

Our analysis has revealed that diffraction of a plane wave on a microlens based on the combination of different dielectric materials, can result in a deviation of the NJ away from the normal direction. The position of the NJ hot spot, angle of deviation, intensity and shape of NJ beam can be controlled by the refractive indexes and sizes of the constitutive parts. We also demonstrate that in a case of small particles having a total width less than the wavelength the NJ beam can be shifted from the axis of symmetry of the system by tuning the parameters of the blocks.

References

[1] B. S. Luk'yanchuk, R. Paniagua-Dominguez, I.Minin, O.Minin, Z. Wang, Refractive index less than two: photonic nanojets yesterday, today and tomorrow, *Opt. Mat. Expr.* 7: 1820-1847, 2017.

[2] A. Heifetz, S.-C. Kong, A.V. Sahakian, A. Taflove, and V. Backman, Photonic nanojets, *J. Comp. Theor. Nanosc.* 6: 1979-1992, 2009.

[3] P. D. Terekhov, K. V. Baryshnikova, Yu. A. Artemyev, A. Karabchevsky, A. S. Shalin, and A. B. Evlyukhin, Multipolar response of nonspherical silicon nanoparticles in the visible and near-infrared spectral ranges, *Phys. Rev. B* 96: 035443, 2017.

[4] V. Pacheco-Pena, M. Beruete, I. V. Minin, O. V. Minin, Terajets produced by dielectric cuboids, *Appl. Phys. Lett.* 105: 084102, 2014.

[5] A. Darafsheh, D. Bollinger, Systematic study of the characteristics of the photonic nanojets formed by dielectric microcylinders, *Opt.Commun.* 402: 270-275, 2017.

[6] A. Boriskin, V. Drazic, R. Keating, M. Damghanian, O. Shramkova, L. Blondé, Near field focusing by edge diffraction, Opt. Lett. 43: 4053, 2018.

[7] S. Angeleene, A. Karabchevsky, I. V. Minin, O. V. Minin, S. V. Sukhov, A. S. Shalin, 'Photonic Hook' based optomechanical nanoparticle manipulator, *Sci. Rep.* 8:2029, 2018

[8] Yu. Shen, L. V. Wang, J.-T. Shen, Ultralong photonic nanojet formed by a two-layer dielectric microsphere, *Opt.Lett.* 39: 4120, 2014.

[9] X. Mao, Ya. Yang, H. Dai, D. Luo, B. Yao, S. Yan, Tunable photonic nanojet formed by generalized Luneburg lens, *Opt. Expr.* 23: 026426, 2015.

Topological Phase Transitions in Guiding Photonic Systems

Zhaxylyk A. Kudyshev[1], Vladimir M. Shalaev[1], Alexandra Boltasseva[1], and Alexander V. Kildishev[1]

[1]*School of Electrical and Computer Engineering and Birck Nanotechnology Center, Purdue University, USA*
E-mail: shalaev@purdue.edu, aeb@purdue.edu, kildishev@purdue.edu

Abstract

Precise control over the topology of guiding systems is critical for photonic applications, such as topologically protected memory/logic and quantum communication devices. Within this work, we show that by integrating modulators with a photonic waveguide system, it is possible to realize ultrafast control over topologically nontrivial photonic states. We can achieve this task by combining a system of modulators with a silicon resonator array, enabling unparalleled optical/electrical control over the topology of the system with a synthetic magnetic field.

1. Introduction

Light control in photonic systems and improved robustness to imperfections or disorder are in high demand. Recently it has been shown that by breaking time-reversal symmetry in photonic systems, it is possible to realize topologically protected states which are resistant to perturbations and back-scattering. This effort has resulted in an increased interest in a new class of topologically ordered optical systems - photonic topological insulators [1,2,3]. Some of the approaches to realize topologically protected photonic states include using metamaterials exhibiting a magneto-optical/nonlinear responses, engineering photonic crystal dispersion, as well as introducing synthetic magnetic field for photons. Precise control of topologically protected states can potentially open new frontiers of light-matter interaction and lead to many applications, such as topologically protected memory/logic devices, compact optical isolators, unidirectional waveguide systems, and numerous quantum communication applications.

2. Discussion

There are numerous ways of synthesizing gauge magnetic field in a photonic system. Here, we utilize the approach proposed in [4] and use a 2D array of coupled ring resonators (Fig. 1d). These "site" resonators are coupled by evanescent fields to the ring waveguides, which provide transfer to their nearest neighbors, while "link" waveguides are detuned from resonance wavelength, thus making all the energy confined in the site rings. External gauge magnetic field is synthesized by shifting one of the link waveguides located horizontally between the site rings, in the vertical direction by offset ξ. With this shift, photons going anticlockwise (clockwise) around the plaquette acquire a phase shift of $\alpha\left(-\alpha\right)$, $\alpha = 2\pi\phi = 4\pi n_{\mathrm{mod}}\xi / \lambda$. The Hamiltonian of such system can be written as,

$$H_0 = \sum_{x,y} \hat{a}^{\dagger}_{x,y}\hat{a}_{x,y} - J\sum_{x,y}\begin{pmatrix} \hat{a}^{\dagger}_{x+1,y}\hat{a}_{x,y}\mathrm{e}^{-iy\alpha} + \hat{a}^{\dagger}_{x,y}\hat{a}_{x+1,y}\mathrm{e}^{iy\alpha} + \\ \hat{a}^{\dagger}_{x,y+1}\hat{a}_{x,y} + \hat{a}^{\dagger}_{x,y}\hat{a}_{x,y+1} \end{pmatrix}.$$

Here $\hat{a}^{\dagger}_{x,y}$ ($\hat{a}_{x,y}$) is a creation (annihilation) operator at a (x, y) site, and J is the effective tunneling rate between resonators. Figure 1 shows that a finite size system of coupled resonators with the gauge field supports topologically protected edge state as well as bulk states.

Within this work, we propose employing a system of modulators to achieve tunability of the gauge magnetic field

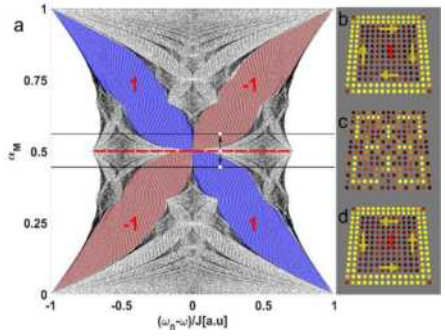


Fig.1 (a) Hofstadter butterfly spectrum for a 15×15 resonator system. Eigenfunctions of the three different states: (b) $\alpha_M^{(1)} = 0.45$ - topologically protected state with unity Chern number C_{+1}, (c) $\alpha_M^{(2)} = 0.5$ (trivial state), (d) $\alpha_M^{(3)} = 0.55$ - topologically protected state with negative Chern number C_{-1}. Arrows show direction of propagation of probability currents in corresponding edge states.

by modulating the effective refractive index of the link waveguides, i.e., to tune the Aharonov-Bohm phase α, and hence, to control the topology. There are different ways of introducing phase modulation into a silicon-on-insulator waveguide. We consider the use of either thermal modulation of titanium nitride or optical/electrical nonlinear modulation

of transparent conducting oxides (TCOs) for ultrafast control of topology of the system.

Using the transfer matrix method, we analyze a dynamically tunable platform that integrates a thermal heater with a photonic system and comprises an array of 15×15 site microring resonators. To enable the gauge magnetic field $\alpha_M^{(1)} = 0.45$ the geometric offset of the link waveguides should be $\xi = 215\,\mathrm{nm}$. *Thermal heaters are off:* this regime corresponds to topological protection state $\alpha_M^{(1)}$ with C_{+1} Chern number. Figure 2a shows field distribution of 15×15 resonator array at a working wavelength of $\lambda = 1.305\,\mu m$. Following the prediction of the tight-binding model, this state enables backscattering-free clockwise propagation of the topologically protected edge mode. *An input power of 25 mW is applied to each thermal heater* to realize topological phase transition which brings the system into the trivial state with $\alpha_M^{(2)} = 0.5$. All of the supported modes at this state are topologically trivial and correspond to bulk modes. Figure 2b depicts the field distribution corresponding to $\alpha_M^{(2)}$ -state. *By applying an input power of 50 mW,* we realize topological phase transition that places the system into the topologically protected ($\alpha_M^{(3)} = 0.55$) state with C_{-1}. Figure 3c shows the topologically protected edge mode at this state; it corresponds to counter-clockwise propagating, backscattering-free edge mode.

3. Conclusions

In this work, we demonstrate the concept of the tunable topological phase transition realized in a photonic system arranged of a coupled ring resonator array. We show that by integrating an array of modulators in the system, it is possible to introduce an additional propagation phase, superimposed on top of the phase shift created by a geometrical offset of the link couplers. This approach opens up a new way to precise control over gauge magnetic field, which in turn leads to flexible, on-demand control over the topology of the photonic guiding systems.

Acknowledgments

This work was supported in part by U.S. Department of Energy (DE-SC0017717), AFOSR (FA9550-18-1-0002) and DARPA/DSO Extreme Optics and Imaging (EXTREME) program (HR00111720032).

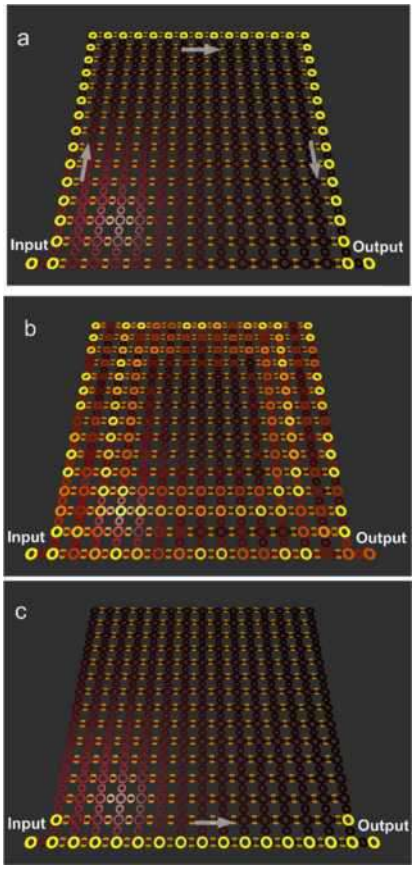


Fig.3 (a)-(c) Field distributions of a 15×15 resonator array for three different cases at a working wavelength of 1.305 μm: (a) topological protection state is achieved when all the thermal heaters are off; (b) topologically trivial state corresponds to an input power of 25 mW applied to each heater; and (c) topologically protected state that corresponds to an input power of 50 mW applied to each heater.

References

[1] M. C. Rechtsman, et al., Photonic Floquet topological insulators, *Nature* 496: 196, 2013.

[2] Z. Wang, et al., Observation of unidirectional backscattering-immune topological electromagnetic states. *Nature* 461: 772–775, 2009.

[3] A. B. Khanikaev, et al., Photonic topological insulators, *Nature Mat.* 12: 233-239, 2013

[4] M. Hafezi, et al., Robust optical delay lines with topological protection. *Nature Phys.* 7: 907–912, 2011

Light Propagation in Synthetic Photonic Lattices in the Presence of Disorder

Stanislav A. Derevyanko

Department of Electrical and Computer Engineering,
Ben Gurion University of the Negev, Beer Sheva 84105, Israel
*corresponding author, E-mail: stasd@bgu.ac.il

Abstract

We discuss recent results for Anderson localization in synthetic photonic lattices. We present the results for the spectra and both dynamic and modal participation number for systems with both phase and coupling static disorder.

1. Introduction

Recently the topic of synthetic dimension attracted much attention in the field of photonics [1]. The concept of synthetic photonic dimension allows one to use extra degrees of freedom either via the frequency space of coupled resonators or pulse time-multiplexing in coupled fibre loops in addition or even instead of traditional geometric dimensions. In particular time multiplexing can realize different multicomponent synthetic photonic lattices (SPL) that can model a variety of physical systems: from geometric mesh lattices to discrete time random walks [2, 3]. The dynamics of light in coherent SPLs is now quantified extremely well both theoretically and experimentally. On the other hand the effects of disorder on pulse evolution in such systems is a much less studied area. Here we present some recent theoretical results on Anderson localization in SPLs for both random phase and coupling modulation [4, 5, 6].

2. Theoretical model

Synthetic photonic lattices can be realized either by considering two linearly coupled fibre loops of unequal length [3] or an array of waveguides which are periodically coupled together in discrete interval [2]. The discrete "time" variable has either the meaning of the round trip number in a loop or the number of a physical layer in a mesh. For each round trip or layer number m the system is completely described by a two-component vector $\mathbf{X}^m = (U_n^m, V_n^m)$ where discrete index $n = 1, ..., N$ counts the time lag position in the two loops or array cites in the effective mesh. The dynamical evolution of the state of the system amounts to iterating a unitary map $\mathbf{X}^{m+1} = \mathcal{U}\mathbf{X}^m$ between the round trips. General localization properties in such systems can be studied by looking at the eigenstates of this step operator defined as solutions of $\mathcal{U}\mathbf{X} = z\mathbf{X}$, $(|z| = 1)$.

There are several ways in which disorder can be introduced into the system: either by inserting phase modulator(s) into one or both fibre loops thus realizing phase disorder [4] or/and modulating the coupling coefficient between the loops (e.g. via integrated Mach-Zehnder interferometers with switching time of 100 ns or less). Motivated by this we consider a generic static eigenproblem [3, 4, 5, 6]:

$$\begin{aligned} zU_n &= e^{i\phi_\uparrow(n)}\left(\cos\theta_{n+1}\, U_{n+1} + i\,\sin\theta_{n+1}\, V_{n+1}\right) \\ zV_n &= e^{i\phi_\downarrow(n)}\left(\cos\theta_{n-1}\, V_{n-1} + i\,\sin\theta_{n-1}\, U_{n-1}\right) \end{aligned} \tag{1}$$

where it is assumed that random phases due to phase modulators $\phi_{\uparrow\downarrow}(n)$ are i.i.d. uniformly distributed in the interval $[-\Phi_*, \Phi_*]$ with the parameter Φ_* serving as the effective strength of disorder. The effective angles θ_n are responsible for the coupling and are also assumed i.i.d. uniform in the interval $[\pi/4 - \theta_*, \pi/4 + \theta_*]$. The pulse in the longer loop (U_n) "overshoots" the location over one round trip by one time position similarly as the pulse in the longer loop V_n undershoots by the same amount. The dynamical evolution of the field distribution in both loops is obtained by iterating the map in the r.h.s. of Eq.(1).

3. Results and discussion

Theoretical results on Anderson localization for pure phase ($\theta_* = 0$) or coupling ($\Phi_* = 0$) disorder were obtained previously in Refs. [4, 5, 6]. It is known that in the presence of phase disorder all eigenstates are localized while in the case of pure coupling disorder there exist delocalized states near the band centre which however have minimal effect on pulse spreading due to their small overlap with the localized initial pulse [6]. Here we concentrate on the most general case of mixed disorder. In order to quantify localization phenomenon we study the so-called participation number (PN) defined for the shorter loop as $P_U = (\sum_n |U_n|^2)^2 / \sum_n |U_n|^4$ and similarly for V. The PN serves as a measure of localization length in both loops and can be defined for each mode (modal PN) or in the dynamical settings where a single pulse introduced in an upper/lower loop evolves between round trips thus leading to dynamical PN $P_{U/V}$. The results of both types of simulations runs are given in Fig.1. The numerical simulation of the pulse evolution was performed by iterating the map with $N = 500$ time positions (synthetic mesh points) subject to periodic boundary conditions. The results were averaged over an ensemble of 50 realizations of combined phase and coupling disorder. The left panel was obtained by numerical diagonalization of system (1) calculating the PN for each mode/loop and selecting the maximum value corresponding to the least localized mode. In the second pane we consider a pulse inserted in the shorter

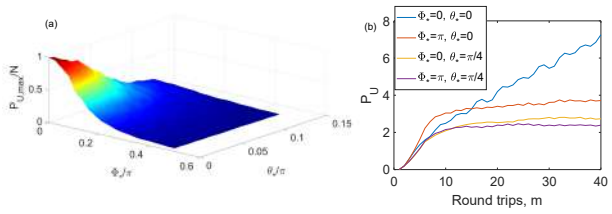


Figure 1: (a) The maximum normalized modal participation number P_U/N as a function of phase and coupling disorder levels. (b) The dynamical arrest of pulse spreading for different types of disorder signifying the onset of Anderson localization

loop at position $n_0 = N/2 = 250$ and follow the evolution of the dynamical PN for different types of disorder. For brevity only the results for the shorter loop (U_n) are shown. It is seen that the minimal participation ratio (minimum spread) is achieved largely by the coupling disorder alone and adding phase disorder contributes less than 10% to further delocalization. The ratio of the asymptotic levels of PN for two separate types of disorder is found to be: $P_{as}(\text{phase})/P_{as}(\text{coupling}) \approx 1.35$.

The typical SPL spectra are given in Fig. 2 (a). We plot quasi-energies β (the effective propagation constants) given by the relation $\exp(i\beta_j) = z_j$ for j-th eigenmode. Without disorder there is a bandgap of the size $\Delta = \pi/2$ corresponding to the well known spectrum given by $\cos\beta = (1/\sqrt{2})\cos(k)$ where k is a properly normalized wavevector spanning a well-defined Brillouin zone $[-\pi, \pi]$. As the disorder is switched on the band-gap starts to close. Note however that the the coupling disorder alone does not appear to be able to close the gap completely as opposed to the phase disorder which manifests itself more strongly. The dependence of the bandgap on disorder levels is given on the second panel of Fig.(2).

4. Conclusions

To conclude, we have quantified the phenomenon of Anderson localization in synthetic photonic lattices subject to most general type of disorder combining both random phase and coupling modulation. It is shown that phase localization effects are generally much stronger than those of the fluctuating coupling coefficient. In the case of pure coupling disorder the bandgap between the Floquet-Bloch modes is still open although diminished almost by a factor of 2. In both cases the disorder arrests the pulse propagation although the asymptotic participation number for the coupling disorder is found to be smaller signifying stronger localization.

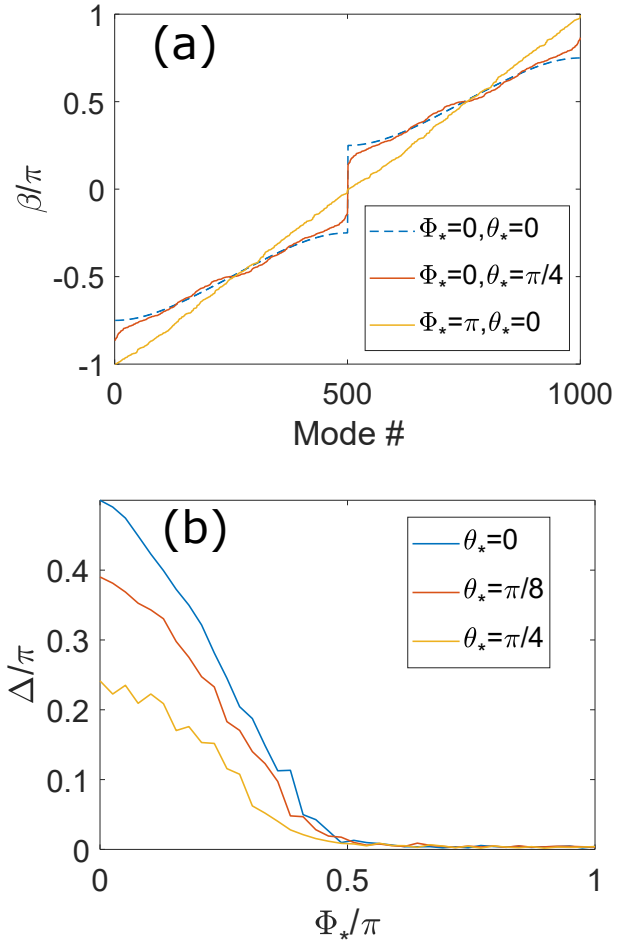


Figure 2: (a) The spectra of system (1) for different levels and types of disorder. (b) The dependence of the bandgap on the disorder levels.

References

[1] L. Yuan, Q. Lin, M. Xiao, and S. Fan, Synthetic dimension in photonics, *Optica* 5: 1396–1405, 2018.

[2] M.A. Miri, A. Regensburger, U. Peschel, and D.N. Christodoulides, Optical mesh lattices with $\mathcal{PT}$ symmetry, *Phys. Rev. A* 86: 023807, 2012.

[3] A. Regensburger, C. Bersch, B. Hinrichs, G. Onishchukov, A. Schreiber, C. Silberhorn, and U. Peschel, Photon propagation in a discrete fiber network: an interplay of coherence and losses, *Phys. Rev. Lett.* 108: 233902, 2011.

[4] I.D. Vatnik, A. Tikan, G. Onishchukov, D.V. Churkin, and A.A. Sukhorukov, Anderson localization in synthetic photonic lattices, *Sci. Rep.* 7: 4301, 2017.

[5] S. Derevyanko, Anderson localization of a onedimensional quantum walker, *Sci. Rep.* 8: 1795, 2018.

[6] A.V. Pankov, I.D. Vatnik, D.V. Churkin, and S.A. Derevyanko, Anderson localization in synthetic photonic lattice with random coupling, *Opt. Express* 27:4424–4434, 2019.

Towards an integrated quantum photonics platform on GaAs

L. Dusanowksi[1], Christof. P. Dietrich[1], Andrea Fiore[3], Mark Thompson[4], Martin Kamp[1], Sven Höfling[1,2]

[1] Technische Physik, Physikalisches Institut and Wilhelm Conrad Röntgen-Center for Complex Material Systems, Universität Würzburg, Am Hubland, 97074 Würzburg, Germany

[2] SUPA, School of Physics and Astronomy, University of St Andrews, North Haugh, St Andrews KY16 9SS, United Kingdom

[3]Eindhoven University of Technology, 5600 MB Eindhoven, The Netherlands

[4] Centre for Quantum Photonics, H. H. Wills Physics Laboratory and Department of Electrical and Electronic Engineering, University of Bristol, Woodland Road, Bristol BS8 1UB, United Kingdom

*Corresponding author: *sven.hoefling@physik.uni-wuerzburg.de*

Quantum information processing is a rapidly developing research field. The exploitation of quantum bits instead of classical bits offers key advantages for future technologies including secure communication and ultra-fast computation. Lab-size experiments on quantum information processes have already proven the validity of its concepts. However, any wide spread utilization will require dense integration of functionalities. This requires the realization of semiconductor integrated quantum photonic circuits on a single semiconductor chip with embedded sources, photon processing units and detectors on the single photon level. Among the different material platforms currently being investigated, direct-bandgap semiconductors and particularly gallium arsenide (GaAs) offer the widest range of functionalities, including single and entangled-photon generation by radiative recombination, low-loss routing, electro-optic modulation and single-photon detection. We review recent achievements in quantum integrated photonic components and circuits based on the GaAs technology platform [1]. All key functionalities, including single-photon sources and single-photon detectors, integrated auto-correlators and tuneable Mach-Zehnder interferometers have been realized and tested. These results lay the foundation for a fully-functional and densely integrated quantum photonic technology based on GaAs components.

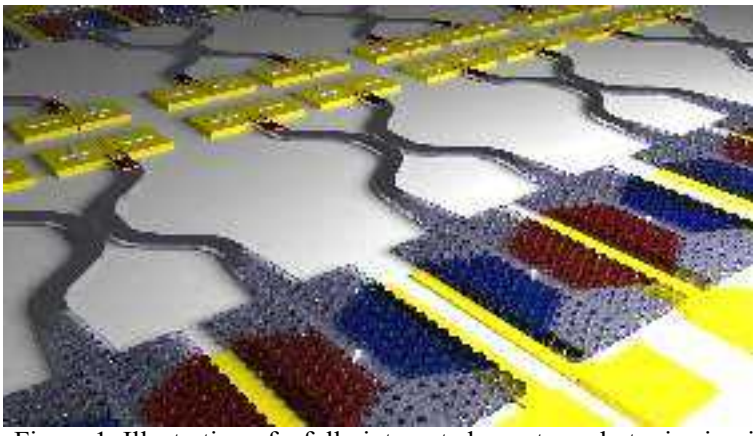


Figure 1: Illustration of a fully integrated quantum photonic circuits.

References

[1] C. P. Dietrich, A. Fiore, M. G. Thompson, M. Kamp, S. Höfling, "GaAs integrated quantum photonics: Towards compact and multi-functional quantum photonic integrated circuits", Laser & Photonics Reviews 10, 870 (2016) (2016).

Biosensing using Metamaterials and Plasmonics

Holey metal films for sensing applications - Impact of nonlocality on extraordinary optical transmission

Christin David[1*], **Johan Christensen**[2]

[1]Madrid Institute for Advanced Studies in Nanoscience (IMDEA Nanoscience), Madrid, Spain
[2]Instituto Gregorio Millán Barbany, Universidad Carlos III de Madrid, Leganés (Madrid), Spain
*corresponding author, E-mail: christin.david@imdea.org

Abstract

Electron-electron interactions in metals are neglected in classical electrodynamics. Though short-ranged, they can have a remarkable impact on the optical response of metals. The excitation of additional pressure waves and anomalous diffraction lead to a substantial change in the bandstructure and electromagnetic fields supported by a nonlocal holey metal film with respect to the classical local response approximation even at large geometrical parameters. In contrast to homogeneous nonlocal metal films, spatial dispersion is found to emerge also at normal incidence.

1. Introduction

First principle methods can accurately describe atomistic matter, but they are strongly restricted in the maximum system size that can be described with available computational ressources [1, 2, 3]. Theoretical efforts continue to pursue the extension of classical electrodynamics to scalable, semi-classical descriptions, which allow describing much larger systems. In recent years, experiments to verify effects stemming from the quantum nature of free electrons in metal nanoparticles were made [4, 5, 6]. For instance, the Generalized Nonlocal Optical Response (GNOR) [7, 8] is based on coupling the hydrodynamic equation for the interacting, free electron gas to the electromagnetic wave equation [9, 10]. Hereby, the dynamics of the free electron gas at the nanoscale is corrected to include Coulomb interaction and diffusion effects via $\vec{D}(\vec{k},\omega) = \epsilon(\vec{k},\omega)\vec{E}(\vec{k},\omega)$ instead of using the common local response approximation $\vec{D}(\omega) = \epsilon(\omega)\vec{E}(\omega)$ of classical electrodynamics, excluding the aforementioned short-ranged electron-electron interactions. This has recently been extended towards two-fluid models for semiconductors (separating electron and hole dynamics) [11, 12], as well as electrolytes (separating the dynamics of positive and negative ions) [13]. Such nonlocal effects are inherently nonlinear.

Here, we consider two-dimensional, subwavelength hole arrays in metal films, which are equally a source of nonlocal electron dynamics. We discuss the impact of spatial dispersion in plasmonic crystal films using GNOR extending established periodic crystal concepts such as the Rigorous Coupled Wave Analysis (RCWA) [9, 14, 15].

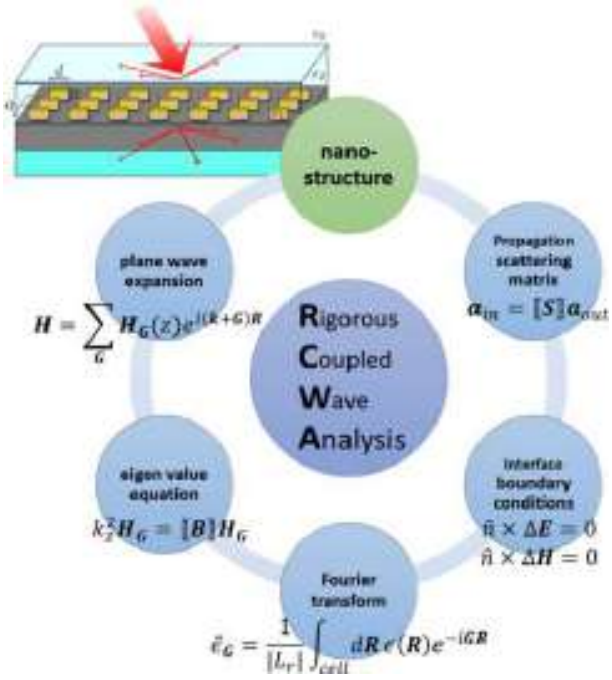


Figure 1: Illustration of the modules in the (two-dimensional) RCWA to perform electromagnetic simulations on complex, nanostructured devices such as holey metal films.

2. Discussion

Figure 1 depicts the different modules within RCWA. Different geometries are addressed via the Fourier transform of the permittivity describing a unit cell of the structure. Multilayers, homogeneous or structured, are combined with propagation steps using an iterative scattering matrix scheme. Introducing electron interaction effects alters parts of the standard modules. However, by evaluating the additional boundary condition given by the hydrodynamic equation in a first step, we can find a formulation that does not alter the iterative scheme of the propagation steps of the scattering matrices [9]. However, they add an additional, scalar eigenvalue equation which increases the computational effort moderately.

The excitation of additional pressure waves and anomalous diffraction leads to a substantial change in the band-

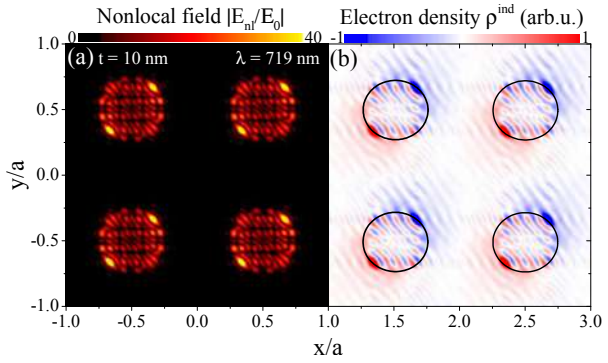


Figure 2: (a) Contribution of the nonlocal mode ($D = 0$) to the electric field $E_n l$ at the front surface for holey gold films with a lattice constant of $a = 200$ nm, a radius of $r = 0 : 25a$, and a thickness of $t = 10$ nm at a resonance frequency of $\lambda = 719$ nm. (b) Induced charge density for this case. Note that $k_x = k_y = 10^{-4} 2\pi/a$.

structure and electromagnetic fields supported by a nonlocal holey metal film with respect to the classical local response approximation, see Fig.2, even at surprisingly large geometrical parameters. In contrast to homogeneous nonlocal metal films [16], spatial dispersion emerges also at normal incidence. We discuss in detail the dependence on different illumination parameters and geometrical configurations of holey metal films. Assuming the presence filling of the holes with a dielectric of larger refractive index, we also discuss the shift of nonlocal features with the dielectric constant.

3. Conclusions

This impacts many concepts and applications in photonics such as imaging and extraordinary optical transmission (EOT). This contributes to the understanding of spatial dispersion in promising building blocks for photonic circuits, bio-chemical sensing and spectroscopy.

References

[1] J. Zuloaga, E. Prodan, and P. Nordlander, "Quantum description of the plasmon resonances of a nanoparticle dimer," *Nano Lett.*, vol. 9, pp. 887–891, 2009.

[2] J. Lermé, B. Palpant, B. Prével, E. Cottancin, M. Pellarin, M. Treilleux, J. L. Vialle, A. Perez, and M. Broyer, "Optical properties of gold metal clusters: A time-dependent local-density-approximation investigation," *Eur. Phys. J. D*, vol. 4, pp. 95–108, 1998.

[3] K. J. Savage, M. M. Hawkeye, R. Esteban, A. G. Borisov, J. Aizpurua, and J. J. Baumberg, "Revealing the quantum regime in tunnelling plasmonics," *Nature*, vol. 491, no. 7425, pp. 574–577, 2012.

[4] J. A. Scholl, A. L. Koh, and J. A. Dionne, "Quantum plasmon resonances of individual metallic nanoparticles," *Nature*, vol. 483, no. 7390, pp. 421–427, 2012.

[5] C. Ciracì, R. T. Hill, J. J. Mock, Y. Urzhumov, A. I. Fernández-Domínguez, S. A. Maier, J. B. Pendry, A. Chilkoti, and D. R. Smith, "Probing the ultimate limits of plasmonic enhancement," *Science*, vol. 337, pp. 1072–1074, 2012.

[6] S. Raza, T. Christensen, M. Wubs, S. I. Bozhevolnyi, and N. A. Mortensen, "Nonlocal response in thin-film waveguides: Loss versus nonlocality and breaking of complementarity," *Phys. Rev. B*, vol. 88, no. 11, p. 115401, 2013.

[7] N. A. Mortensen, S. Raza, M. Wubs, T. Søndergaard, and S. I. Bozhevolnyi, "A generalized non-local optical response theory for plasmonic nanostructures," *Nat. Commun.*, vol. 5, p. 3809, 2014.

[8] S. Raza, S. I. Bozhevolnyi, M. Wubs, and N. A. Mortensen, "Nonlocal optical response in metallic nanostructures," *J. Phys. Cond. Matter.*, vol. 27, no. 18, p. 183204, 2015.

[9] C. David, J. Christensen, and N. A. Mortensen, "Spatial dispersion in two-dimensional plasmonic crystals: Large blueshifts promoted by diffraction anomalies," *Phys. Rev. B*, vol. 94, no. 16, p. 165410, 2016.

[10] C. David and J. Christensen, "Extraordinary optical transmission through nonlocal holey metal films," *Applied Physics Letters*, vol. 110, no. 26, p. 261110, 2017.

[11] J. R. Maack, N. A. Mortensen, and M. Wubs, "Size-dependent nonlocal effects in plasmonic semiconductor particles," *EPL (Europhysics Letters)*, vol. 119, no. 1, p. 17003, 2017.

[12] J. R. Maack, N. A. Mortensen, and M. Wubs, "Two-fluid hydrodynamic model for semiconductors," *Phys. Rev. B*, vol. 97, no. 11, p. 115415,2018.

[13] C. David, "Two-fluid, hydrodynamic model for spherical electrolyte systems," *Scientific Reports*, vol. 8, no. 1, p. 7544, 2018.

[14] D. M. Whittaker and I. S. Culshaw, "Scattering-matrix treatment of patterned multilayer photonic structures," *Phys. Rev. B*, vol. 60, pp. 2610–2618, 1999.

[15] V. Liu and S. Fan, "S4 : A free electromagnetic solver for layered periodic structures," *Computer Physics Communications*, vol. 183, pp. 2233–2244, 2012.

[16] C. David, N. A. Mortensen, and J. Christensen, "Perfect imaging, epsilon-near zero phenomena and waveguiding in the scope of nonlocal effects," *Sci. Rep.*, vol. 3, p. 2526, 2013.

Tunable SiC Metasurface for Mid-infrared Biochemical Detection

Zhao Huang[1,2], Xin Liu[1,2], Jianfeng Zang[1,2,*]

[1]School of Optical and Electronic Information, Huazhong University of Science and Technology, Wuhan, China
[2]Innovation Institute, Huazhong University of Science and Technology, Wuhan, China
*corresponding author, E-mail: jfzang@hust.edu.cn

Abstract

The mid-infrared (MIR) spectral range offers various applications in chemical detection, food safety and biosensing. However, trace detection still remains challenge due to weak light–matter interaction between infrared light and nanoscale molecules. Fortunately, polar dielectrics have ability to achieve optical sub-diffraction confinement and in the MIR spectral range through surface phonon polariton (SPhP) modes. Here, we demonstrate SiC nanoring metasurfaces to achieve high local field enhancement and control the detection frequency by varying structure parameters.

Introduction

The mid-IR to THz spectral ranges offers a wealth of potential applications in astronomy, thermal radiation and imaging [1]. Among various applications, biological detection is particularly important because it closely related to human safety and health. However, the weak light–matter interaction between infrared light and nanoscale molecules reduces the detection efficiency. Fortunately, polar dielectrics possess ability to achieve sub-wavelengh confinement in the mid-IR band through the stimulation of surface phonon polariton (SPhP) modes, which can be used to fabricate nanophotonics devices in MIR applications [2, 3]. Here we demonstrate 4H-SiC nanoring metasurfaces for MIR detection and sensing. Because of the strong local field confinement, the interaction between light and moleculars are significantly enhanced. By tuning the outer radius, inner radius, and the period of metasurfaces, the nearly full Reststrahlen band can be effectivily utilized.

Discussion

The SPhP modes excited in 4H-SiC are stimulated between the transverse optical phonon (TO) frequencies at 797 cm−1 (12.5 μm) and the longitudinal optical phonon (LO) frequencies at 973 cm−1 (10.3 μm), referred as Reststrahlen band. 4H-SiC nanoring metasurfaces can provide localized SPhP modes with low optical losses, high field confinement and broad band spectral tunability. Finite element theory (FET) simulations were performed with optical constants of 4H-SiC from Handbook of Optics. The metasurfaces are illumanited by p-polarized plane wave within the xz-plane at an incident angle of 25°. A typical reflection spectra from FEM calculation are shown in Fig. 1a with outer radius r_o=0.5 um, inner radius r_i=0.25 um, and period p=3 um. Four reflection valleys are attributed to the excitation of SPhP modes. Fig. 1b and 1c demonstrate the normalized electric field intensity at first and second valleys. Strong field enhancement is obtained around SiC nanoresonators, which can be applied to improve detection sensitivity.

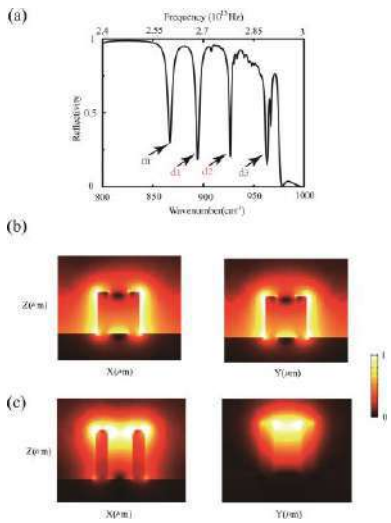


Figure 1: (a) simulation reflection spectra of 0.5 μm outer radius, 0.2 μm inner radius and 1 μm high 4H-SiC nanorings on a square lattice with 3μm period. (b) Normalized electric field intensity in the x = 0 plane and y = 0 plane for the m mode and d1 mode, respectively.

As discussed previously, the occurrence of monopole (m) stimulated by the vertical component of electric field is attributed to the negative permittivity of both the nanoring resonators and the underlying SiC substrate. Apart from the monopolar mode, three transverse dipolar modes (d1, d2 and d3) are excited by the inplane electric field. According to interaction between nanoring resonantors and substrate, the first two dipolar modes are identified as bonding mode and last dipolar mode is identified as antibonding mode. As depicted in Fig 2a and Fig 2b, bonding mode corresponds to the condition that like charges distributed in both nanoring

resonantors and substrate, while antiboding mode corresponds to the condition that dissimilar charges distributed in nanoring resonantors and substrate respectively.

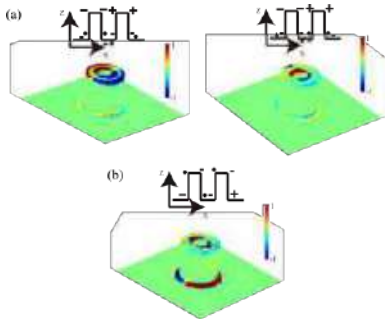


Figure 2: 3D views of the charge density of three transverse dipolar modes. The insets show schematic charge configurations of one nanoring for the corresponding modes, with "+" and "–" denoting the charges. (a) d1 and d2 modes. (b) d3 mode.

By varing outer radius, inner radius, period of SiC nanoring metasurfaces, four resonance modes can be effectively tuned throughout the Reststrahlen band. Fig 3 demonstrates the tunability of SiC nanoring metasurface.

Conclusions

In summary, we demonstrate that SiC nanoring metasurfaces exhibit excitations of monoloar resonances and dipoloar resonances. This intriguing resonances offer strong field confinement around the nanoring resonators. Furthermore, we detailly study all the modes supported in these metasurfaces and state their spectral dependence on the structure parameters through simulations. This work shows that SiC nanoring metasurface provide promising candidates in mid-IR nanophotonics.

Acknowledgements

This work is supported by the National Natural Science Foundation of China (51572096).

References

[1] J. D. Caldwell, L. Lindsay, V. Giannini, I. Vurgaftman, T. L. Reinecke, S. A. Maier, and O. J. Glembocki, Low-loss, infrared and terahertz nanophotonics using surface phonon polaritons，*Nanophotonics*，4，44-68，2015.

[2] Y. Chen, Y. Francescato, J. D. Caldwell, V. Giannini, T. W. W. Maß, O. J. Glembocki, F. J. Bezares, T. Taubner, R. Kasica, M. Hong, and S. A. Maier, Spectral Tuning of Localized Surface Phonon Polariton Resonators for Low-Loss Mid-IR Applications，*ACS Photonics*，1，718-724，2014.

[3] O. J. G. Y. Joshua D. Caldwell, J. P. L. J. Francisco J. Bezares, and N. D. B. L. Virginia D. Wheeler, Low-Loss, Extreme Sub-Diffraction Photon Confinement via Silicon Carbide Localized Surface Phonon Polariton，*Nano Letters*，13，3690-3697，2013.

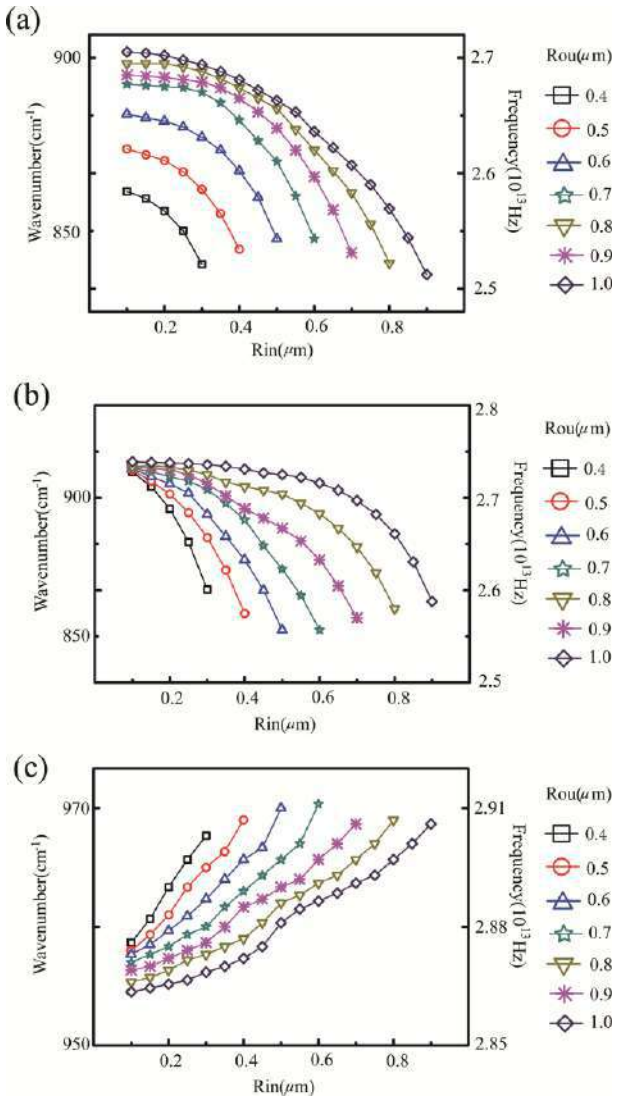


Figure 3 : Spectral positions for (a) monopolar mode, (b) dipolar mode 1 and (c) dipolar mode 3 of SiC nanoring metasurfaces as the function of the inner radius and outer radius.

Engineered Lab-On-Fiber SERS Optrodes based on Nanosphere Lithography

Giuseppe Quero[1], Gianluigi Zito[2], Stefano Managò[2], Francesco Galeotti[3], Marco Pisco[1], * Anna Chiara De Luca[2, *] Andrea Cusano[1]

[1]*Optoelectronic Division – Eng. Dept., University of Sannio, 82100 Benevento, Italy*
[2]*Institute of Protein Biochemistry, National Research Council, 80131, Napoli, Italy*
[3]*Institute for Macromolecular Studies, National Research Council, 20133, Milan, Italy*
*corresponding author, E-mail: marco.pisco@unisannio.it, a.deluca@ibp.cnr.it

Abstract

We report on the development of repeatable surface enhanced Raman scattering (SERS) probes realized onto optical fiber tips (OFTs) through nanosphere lithography. We first evaluated the SERS performances pertaining to different patterns with different nanosphere diameters and gold thicknesses, then the SERS-OFT performance. The analysis allowed us to identify the most promising SERS platform, exhibiting an Enhancement Factor of 4×10^5 and a SERS measurements variability lower than 10%. Current activities are devoted to realize Lab-on-fiber SERS probes for human Thyroglobulin, a protein marker of differentiated thyroid cancer.

1. Introduction

SERS is an analytical technique that allows the detection of molecules at extremely low concentrations and with high specificity. The unique advantages offered by optical fibres represent a valuable platform for SERS sensors in biological and biomedical applications. Additionally, the use of self-assembly fabrication approaches to realize reproducible SERS active surfaces on the optical fiber tips can provide a significant technological advancement by granting low fabrication costs and high throughput.

Recently, the use of self-assembly in combination with optical fiber technology has been strongly revisited and revitalized. Indeed, alongside the "Lab on Fiber" technological advancements in the use of conventional lithographic approaches on the optical fiber tip, self-assembly techniques have progressed and have been demonstrated as a reliable tool for the fabrication of regular nanostructures on the optical fiber tip [1-2]. Lithographic processes based on breath figures formation or nanosphere self-assembly [3-5] have been successfully used to create well ordered and regular metallo dielectric patterns on the fiber tip. In particular, in a recent work, after assessing the process repeatability, proof of principle of the SERS ability of close-packed arrays (CPA) of polystyrene (PS) nanospheres, covered by thin films of gold, has been provided [5]. With regards to the selection of the optical fiber, an ideal fiber probe should have low dopant concentration in the fiber core, high numerical aperture (NA), and small core size, in order to reduce the background and to maximize both the collection efficiency and the coupling between the fiber and the Raman spectrometer. Nonetheless, these parameters are not independent and the "a priori" identification of the optimum configuration among different commercial fiber probes is not trivial.

Starting from the promising results achieved in terms of reproducible metallo-dielectric patterns on the optical fiber tip, we first investigated the SERS performances through the evaluation of the Enhancement Factor (EF). Then, we selected several commercially available optical fibers and tested them to identify the best fiber platform providing the best performances in terms of Raman excitation/collection efficiency and related background. Current work is devoted to the functionalization of the identified fiber probes for the ex-vivo detection of human Thyroglobulin.

2. Experimental results

In order to measure the performances of the SERS surfaces, independently from the selected fiber probe,

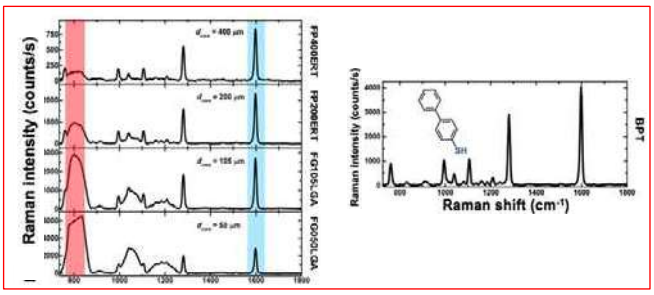


Figure 1. Raman spectrum from 100 mM BPT solution through different optical fibers and, at the bottom, Raman spectrum from the BPT solution with the Raman microscope without the fibers.

we fabricated the SERS samples in planar configuration (on the coverslip slides, quartz CFQ-2557, UQG Optics, 150 μm thickness). The fabrication process follows the procedure described in ref [5]. In order to estimate the EF of the fabricated SERS active surfaces, we used the biphenylthiol (BPT) monolayer as benchmark analyte. The resulting EF as function of the CPA diameter and gold thickness, revealed that the highest measured EF of 4.0×10^5 can be achieved with the CPA geometry characterized by a PS diameter of 500 nm and nominal gold thickness of 30 nm. The different SERS substrates were investigated also in terms of repeatability by mapping the intensity of the BPT band at 1590 cm^{-1} within the same sample (intra-sample) and among different samples (inter-sample). Also in this case, the best repeatability has registered for the CPA samples with PS diameter of 500 nm and nominal gold thickness of 30 nm.

With regard to the selection of the most suitable fiber probe, we collected commercially available fibers with a core of pure silica and operating in the visible spectral range with different core diameter (ranging from 50 up to 400 μm), different cladding materials (fluorine-doped silica or hard polymer) and different NAs (from 0.22 up to 0.5). We show the Raman spectra (Figure 1), in the range between 750-1800 cm^{-1}, obtained by illuminating the BPT solution, and collecting the scattered light through different optical fiber probes. When we use the fiber FG050LGA and FG105LGA, the silica band at 800 cm^{-1} is particularly intense obscuring the BPT peak due to ν(S-C) around 757 cm^{-1}. Similarly, also the three BPT peaks in the wavenumber region 950-1100 cm^{-1} have an unfavorable signal-to-background ratio. Interestingly, when we use the fibers with larger core diameter (FP200ERT and FP400ERT) and larger NA the interference with the silica Raman bands decreases and even the small BPT band at 757 cm^{-1} becomes visible. As a result, a good compromise to have a high intensity for the BPT fingerprint (which requires a small fiber core diameter) and a low silica background (which requires a fiber with large diameter) can be reached with the optical fiber FP200ERT, which maximizes the difference between the signal and the background.

3. Conclusions

In conclusion, we investigated the possibility to engineer Lab-on-Fiber SERS optrodes in order to provide advanced and repeatable SERS substrates integrated on the optical fiber tip. To this aim, we assessed the performances in terms of true EF pertaining to SERS substrates composed of hexagonally CPAs of PS nanospheres with different diameter (d = 500, 750, 1000 nm) and different gold film thickness (h = 20, 30, 40 nm). Additionally, the different SERS substrates were investigated in terms of SERS intensity repeatability (intra- and inter-samples). As a second important step towards engineering of the SERS optrode, Raman excitation/collection efficiency and related background pertaining to different commercially available optical fibers were investigated using a reference BPT solution as benchmark. As a result, we found that CPA geometry with PS diameter of 500 nm and nominal gold thickness of 30 nm exhibited the best performance and we selected the fiber probe with core in pure silica, 200 μm diameter and high numerical aperture (i.e. 0.5) because it offered a favorable trade-off between collection efficiency and background. Following these developments, current activities are devoted to the assessment and exploitation of the investigated sensing platform for human Thyroglobulin detection.

References

[1] F. Galeotti, et al Nanoscale, 2018, 10, 22673
[2] Vaiano, P. et al Laser Photonics Rev. 2016, 10, 922.
[3] Pisco, M.; Galeotti, F.; Quero, G.; Iadicicco, A.; Giordano, M.; Cusano, A. Miniaturized sensing probes based on metallic dielectric crystals self-assembled on optical fiber tips. ACS Photonics 2014, 1, 917–927.
[4] Pisco M. et al Light: Science & Applications 6, e16229 (2017).
[5] Quero, G. et al Sensors 2018, 18, 680.

Photonics for space systems and propulsion

Metal Oxide Meta-optical Solar Reflector for Space Applications

Kai Sun[1,2], Wei Xiao[1,2], Yudong Wang[1,2], Mirko Simeoni[3], Alessandro Urbani[3], Sandro Mengali[3], Fausto Lucantonio[4], Marco Ivagnes[4], Maksim Zalkovskij[5], Brian Bilenberg[5], C.H. (Kees) de Groot[2], Otto L. Muskens[1,*] ,

[1]School of Physics and Astronomy, University of Southampton, Southampton, UK
[2]School of Electronics and Computer Science, University of Southampton, Southampton, UK
[3]Consorzio C.R.E.O., L'Aquila, Italy
[4]Thales Alenia Space, L'Aquila, Italy
[5]NIL Technology, Kongens Lyngby, Denmark
*corresponding author, E-mail: O.Muskens@soton.ac.uk

Abstract

Optical solar reflectors (OSRs) play a crucial role in the thermal control of a spacecraft. We present novel meta-surface-based OSRs using metal oxides, e.g. Al-doped zinc oxide (AZO) and vanadium dioxide (VO_2). Our AZO-based meta-OSRs have been optimized for a high infrared emittance and low solar wavelength absorption. VO_2-based meta-OSRs have demonstrated a superior emittance tunability and lower solar absorption than the planar film. Both meta-OSRs have been comprehensively tested for their robustness required by space applications.

Keywords: meta-surface, radiative cooling, perfect absorption, plasmonics, optical solar reflectors, transparent conductive oxide.

1. Introduction

Optical solar reflectors (OSRs) play a crucial role in the thermal control of a spacecraft since they are the physical interface between the thermal management system and the space environment. To avoid solar heating and achieve radiative cooling, an ideal OSR is required to reflective all energies in the UV/Vis/NIR spectrum and emit those at the thermal infrared spectrum (blackbody radiation spectrum). OSRs are conventionally formed through quartz tiles or silver-coated fluorinated ethylene propylene (FEP) foils. The former suffers for its poor mechanical robustness and launch cost and the latter is constraint for its low lifetime at harsh space environment. Therefore, there is a need for a thin-film technology using durable, radiation resistance hard coatings.

Recently, metal oxides have been investigated for their suitability in infrared plasmonics [1]. In this work, we report the results of H2020 Meta-reflector and Smart-Flex projects on a meta-optical solar reflector (Meta-OSR) based on Al-doped Zinc Oxide (AZO) and a smart Meta-OSR based on VO_2. Here, VO_2 is used for its thermochromic characteristics as dielectric below transition temperature and metallic above transition temperature and therefore forms a smart meta-OSR with a tunability against temperature change.

2. Results and Discussions

The proposed structure is a traditional Salisbury screen consisting of a stack of three layers: the metal back reflector, the dielectric spacer layer and the TCO meta-surface [2] [3]. The performance of an OSR is defined by its solar spectrum absorption (α) and infrared spectrum emittance at 300 K (ε). The emittance, ε, is defined as the averaging emissivity weighted by the theoretical blackbody spectrum at the operating temperature (T) in Kelvin:

$$\epsilon = \frac{\int_{\lambda_\varrho}^{\lambda_1} \varepsilon_\lambda(T) P(\lambda, T) d\lambda}{\int_{\lambda_\varrho}^{\lambda_1} P(\lambda, T) d\lambda} \quad (1)$$

where λ is the thermal conductivity, B(λ, T) is the blackbody spectral distribution at temperature T, given by Plank's equation.

2.1. AZO-based Meta-OSRs

Figure 1a shows the proposed AZO-based meta-OSRs on flexible foil fabricated through nanoimprint patterning technique. The foil in the figure is 80 mm × 80 mm and the AZO array is designed as 1350 nm square with a gap of 250 nm. Figure 1b shows the UV/VIS and FTIR absorption spectra of a meta-OSR with an array of square varying from 750 to 1350 nm and a gap of 150 nm. The solar and 200 K black body spectrum are also presented as references. Infrared absorption are seen broader for square array than the planar film owning to the plasmonic resonance whilst the UV/Vis absorption are consistent in Fabry-Perot fringes. The optimized OSR gives an alpha of 0.16 and epsilon of 0.79. With a further UV reflective cladding, the performance can be further improved to alpha of 0.12 and epsilon of 0.80 and these performance well meet the requirement of space applications.

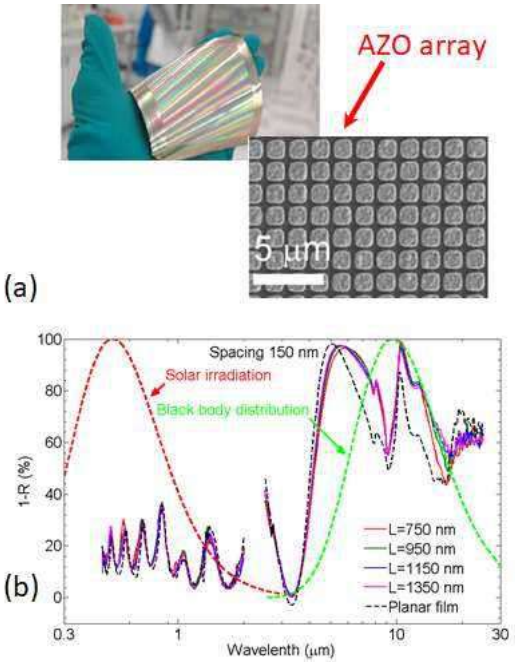


Figure 1: (a) AZO meta-OSRs fabricated on an 80×80 mm^2 flexible substrate and plan SEM micrograph of the AZO array, (b) UV/Vis/Infrared absorption spectra of an AZO meta-OSR with varying feature size and a gap of 150 nm.

2.2. VO_2-based smart OSRs

Figure 2a shows the UV/VIS and FTIR absorption spectra of a VO_2-based smart meta-OSR with an array of VO_2 squares of 2.8 µm and a gap of 0.5 µm measured at 25°C and 80°C. The infrared absorption is significantly increased when temperature is increased to 80°C. For smart OSRs, the emittance tunability ($\Delta\varepsilon$) is the figure-of-merit. Figure 2b shows extracted $\Delta\varepsilon$ as a function of square size at different gaps. Meta-OSRs for all feature size with a gap of 0.5 µm achieve higher $\Delta\varepsilon$ than planar film, whilst the $\Delta\varepsilon$ improvement decreases with the increase of gap size and even below the planar film. This is attributed to the reduction of VO_2 filling ratio of the whole surface. The best smart-OSR gives an emittance tunability of 0.49. In addition, the reduction of VO_2 coverage would positively contribute to a lower solar absorption.

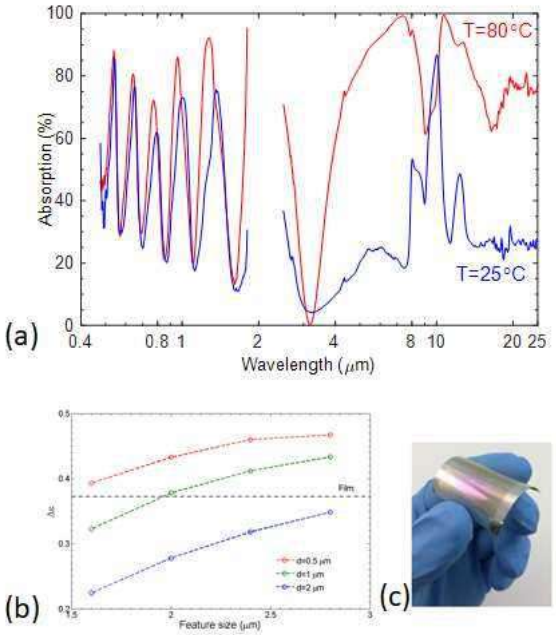


Figure 2: (a) UV/Vis/Infrared absorption spectra of a VO_2 smart meta-OSR with a feature size of 2.8 um and gap of 0.5 um measured at 25 and 80°C, (b) emittance tunability as a function of feature size at different gaps and (c) smart OSRs fabricated on flexible Ti foil.

3. Conclusions

We report metal oxide based meta-OSRs for space applications. The fabricated AZO meta-OSR shows an improved performance than the planar structure and the best structure shows an infrared emittance ε of 0.79 and solar absorption α of 0.16. The fabricated VO_2 smart meta-OSR show a superior emittance tunability Δε of 0.49. Both meta-OSRs have been demonstrated to be able for scaling up to large area flexible substrate through nanoimprint. Comprehensive robust tests have been performed to test their durability at harsh space environment.

Acknowledgements

This work was financially supported by through Horizon 2020 projects META-REFLECTOR and SMART-FLEX.

References

[1] M. Abb, Y. Wang, N. Papasimakis, C. H. de Groot, O. L. Muskens, Surface-Enhanced Infrared Spectroscopy Using Metal Oxide Plasmonic Antenna Arrays, *Nano Lett*. 14 (1), 346 - 352 (2014)

[2] K. Sun, C. A. Riedel, Y. Wang, A. Urbani, M. Simeoni, S. Mengali, M. Zalkovskij, B. Bilenberg, C.H. de Groot, O. L. Muskens, Metasurface optical solar reflectors using AZO transparent conducting oxides for radiative cooling of spacecraft, ACS Photon. 5, 495-501 (2017)

[3] K. Sun, C. A. Riedel, A. Urbani, M. Simeoni, S. Mengali, M. Zalkovskij, B. Bilenberg, C.H. de Groot, O. L. Muskens, VO_2 thermochromic metamaterial-based smart optical solar reflector. ACS Photon. 5, 2280-2286 (2018)

Reflectivity control devices for solar sail actuation

Jeremy N. Munday[1,2]

[1]Department of Electrical and Computer Engineering, University of Maryland, College Park, MD, 20742, USA
[2] Institute for Research in Electronics and Applied Physics, University of Maryland, College Park, MD, 20742, USA
*corresponding author, E-mail: jnmunday@umd.edu

Abstract

Radiation pressure from the sun can exert a force on spacecrafts that can either be beneficial, in the case of solar sail propulsion, or harmful, in the case of satellites in predefined orbits. Thus, there is a need for a way to control this radiation pressure. Here we present our latest work on switchable reflectivity materials to actively control the radiation pressure exerted on a spacecraft to enable real-time attitude control and maneuvering. We will discuss our first generation proof-of-concept devices, preliminary space environment testing, and provide a future outlook for this technology.

1. Introduction

Solar sails offer an opportunity for a cubesat-scale, propellant-free spacecraft technology to enable long-term and long-distance missions not capable with traditional methods. In principle, to propel such a craft, no mechanically moving parts, thrusters, or propellant are needed. However, in practice, attitude control is still performed using traditional methods involving reaction wheels and propellant ejection, which severally limits mission lifetime and increases costs. For example, the current state of the art solutions implored by the recent Near- Earth Asteroid Scout mission couple the solar sail subsystem with a state of the art propellant ejection gas system. However, gas thrusters have a limited supply of propellant, which reduces the lifetime of the mission to less than three years.

To replace the traditional gas thruster system for attitude control, we are using propellantless attitude control through an electrically switchable optical film [1]. The technology is based on a polymer-dispersed liquid crystal (PDLC), similar to IKAROS; however, my switching between transparent and diffusely reflective (rather than switching between specular and diffuse reflection) upon application of a voltage, a factor of >4 improvement is achieved. This technology removes the need for propellant, which will reduce weight and cost while improving performance and lifetime.

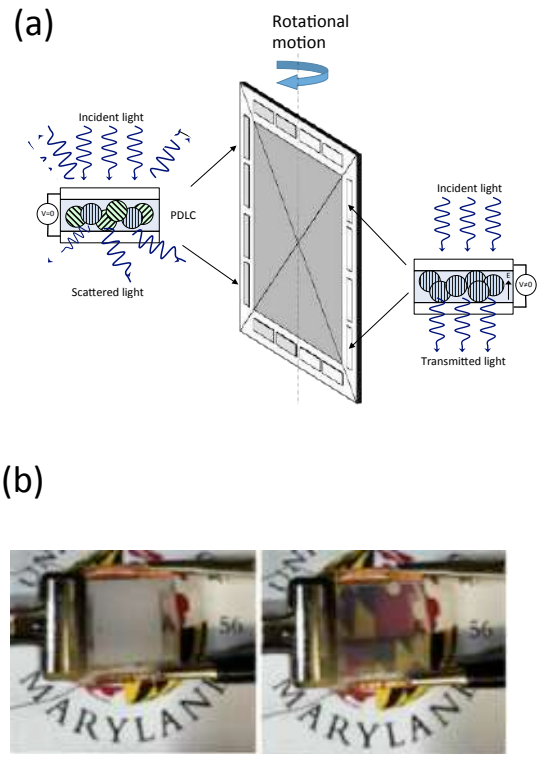


Figure 1: Reflective control device. (a) Schematic of a solar sail incorporating polymer dispersed liquid crystal (PDLC) devices along the edge to actively modify the radiation pressure. (b) PDLC device in operation changing between diffusely reflective (left) and transparent (right) states.

2. Discussion

The ability to control radiation pressure could enable a wide-variety of functionalities for solar sail missions. We have previously performed experiments to measure the radiation pressure on microcantilevers [2] and have recently exploited the wave nature of light to create optical forces that take advantage of interference effects in thin films [3]. Further, we have shown that PDLCs can be combined with photovoltaic materials to allow for self-powering of dynamically switchable reflectivity [4], which may have additional advantages in space missions.

3. Conclusions

In summary, the ability to actively control the reflectivity of materials may provide significant advantages over traditional actuation methods for advanced solar sail technologies.

Acknowledgements

The authors acknowledge financial support for this project from a NASA Early Career Faculty Award (No. NNX12AQ50G) and a NASA Smallsat Partnership Award (No. NNX15AW53A). The authors also thank Tiffany Russell Lockett, Andrew Heaton, Keats Wilkie, and Les Johnson for many helpful suggestions, comments, and discussions about solar sails.

References

[1] Dakang Ma, Joseph Murray and Jeremy N. Munday, Controllable Propulsion by Light: Steering a Solar Sail via Tunable Radiation Pressure, *Adv. Opt. Mat.*, **5**, 1600668, 2017.

[2] Dakang Ma, Joseph L. Garrett and Jeremy N. Munday, Quantitative measurement of radiation pressure on a microcantilever in ambient environment, *Appl. Phys. Lett.* **106**, 091107, 2015.

[3] Dakang Ma and Jeremy N. Munday, Measurement of wavelength-dependent radiation pressure from photon reflection and absorption due to thin film interference, *Scientific Reports*, **8**, 15930, 2018.

[4] Joseph Murray, Dakang Ma, and Jeremy N. Munday, Electrically Controllable Light Trapping for Self-Powered Switchable Solar Windows, *ACS Photonics*, **4**, pp. 1–7, 2017.

Relative and Absolute Phase Control of Lasers

Firooz Aflatouni[1,*]

[1]Department of Electrical and Systems Engineering, University of Pennsylvania
*corresponding author, E-mail: firooz@seas.upenn.edu

Abstract

In this paper a review of our work on optical phased arrays and laser stabilization systems is presented. The relative phase between semiconductor lasers are controlled through heterodyne phase locked loops forming a laser phased array. An integrated Pound-Drever-Hall stabilization system is presented that reduced the frequency noise of a commercially available laser by more than 25dB. In another PDH chip, the linewidth of a distributed feedback laser is reduced from 246 kHz to 7 kHz using an off-chip resonator.

1. Introduction

Relative phase control of lasers has many applications such as realization of high power efficient light sources though coherent power combining of multiple semiconductor lasers, phase modulation and demodulation, and laser phased arrays. To control the relative phase between semiconductor lasers, an array of lasers can be phase locked to a reference laser using an array of electro-optical phase locked loops (EOPLL), where the relative phases between the semiconductor lasers can be adjusted electronically [1][2]. Using this method, we have implemented a laser phased array and demonstrated beam-steering [3].

Absolute phase control of a semiconductor laser, where the laser phase noise is reduced, has many applications from coherent communication to spectroscopy and sensing. One method often used for laser phase noise reduction (and stabilization) is the Pound-Drever-Hall (PDH) method, where the frequency of a laser is measured using an optical frequency reference and the error signal in the electrical domain is fed back to the laser suppressing the frequency fluctuations of the laser. We have demonstrated an integrated PDH system, where an on-chip Mach−Zehnder interferometer is used as the frequency reference to reduce the frequency noise of semiconductor lasers by more than 25 dB [4]. In another work, we have implemented a PDH chip that reduced the linewidth of a distributed feedback laser from 246 kHz to 7 kHz using an off-chip resonator [5].

2. Relative optical phase control

Figure 1(a) shows the block diagram of a 2-element laser array where each laser is phase locked to a reference laser using a heterodyne EOPLL. In each EOPLL, the beat-note between the reference laser and the semiconductor laser (SCL) is amplified and down-converted using a heterodyning RF reference. Under the lock condition, the phase difference between the two lasers can be set by the phase of the RF reference [2]. The instantaneous relative phase between the two SCLs is detected by photo-detecting their beat-note after the beam-splitter. The photo-current is injected to the control voltage of a voltage controlled oscillator (VCO) shifting the heterodyning frequency of EOPLL 2 correcting for this relative instantaneous phase error. Figure 1(b) shows the beam-steering performed using the two-element laser phased array.

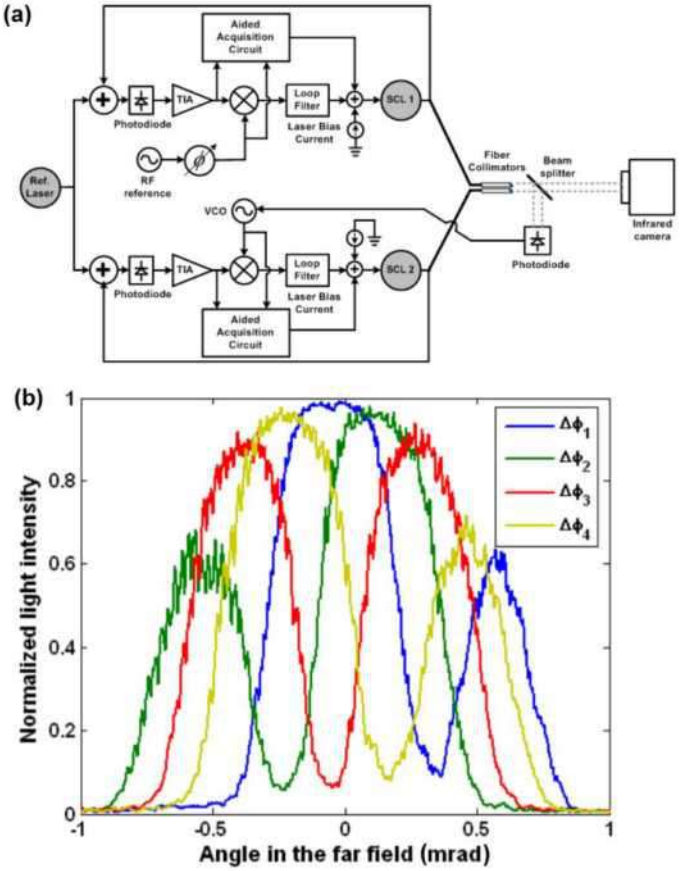


Figure 1.(a)Block diagram of the 2-element laser phased array. (b) The horizontal far-field intensity distributions demonstrating beam-steering by electronic phase shifts of $\Delta\varphi_1 = 0$, $\Delta\varphi_2 = 90^o$, $\Delta\varphi_3 = 180^o$, and $\Delta\varphi_4 = 270^o$.

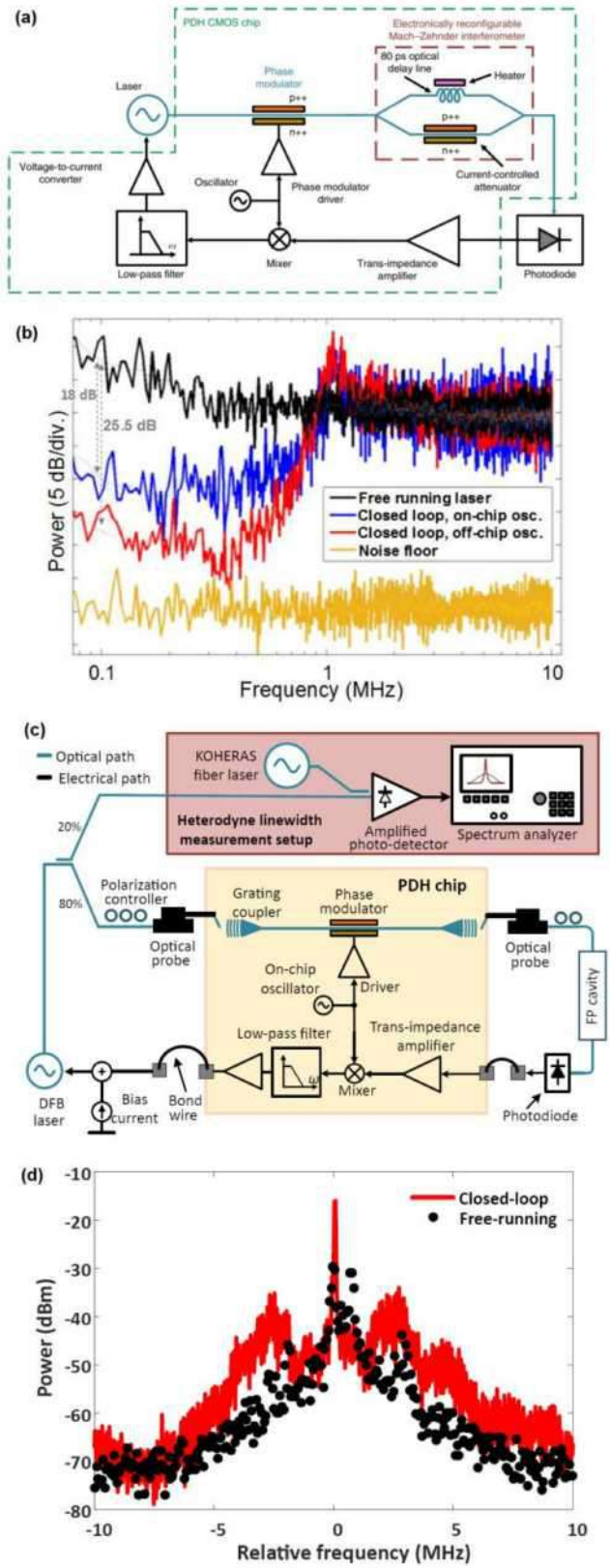


Figure 2.(a)Block diagram of the integrated PDH system with on-chip MZI reference. (b) The laser frequency noise before and after PDH stabilization. (c)Heterodyne linewidth measurement setup, and (d) The FWHM laser spectral linewidth measurement.

3. Absolute phase control of lasers

Figure 2(a) shows the block diagram of the implemented on-chip PDH system. An electrical local oscillator (LO) is used to modulate the output of the laser using a modulator generating sidebands around the carrier frequency. The phase modulated signal passes through the reference MZI. The MZI output is photo-detected and converted to a voltage and mixed with the output of the LO. The mixer output is low-pass filtered, and injected to the gain section of the laser to close the PDH feedback loop. Figure 2(b) shows the frequency noise of the laser before and after PDH stabilization where a 25.5dB frequency noise reduction is observed. Figure 2(c) shows the block diagram of the integrated PDH system with an off-chip Fabry-Perot cavity as the frequency reference.

Fig 2(d) shows the beat-note spectrum for free-running and PDH stabilized cases, where the FWHM linewidth of the free-running DFB laser (emitting 12 dBm) is reduced by a factor of 35 (from 246 kHz to 7 kHz). The resolution bandwidth for these measurements was set to 10 kHz.

Acknowledgements

The chip fabrications were supported by MOSIS Services.

References

[1] F. Aflatouni, O. Momeni, and H. Hashemi, A heterodyne phase locked loop with GHz acquisition range for coherent locking of semiconductor lasers," *IEEE Custom Integrated Circuit Conference*, 463-466, 2007.

[2] F. Ashtiani and F. Aflatouni, An integrated electro-optical phase locked loop for highly tunable high resolution optical synthesis, *Optics Express*, vol. 24, no. 14, pp. 16171-16181, 2017.

[3] F. Aflatouni and H. Hashemi, An electronically controlled optical phased array, in *IEEE International Microwave Symposium,* WEPN-6, 2012.

[4] M. Idjadi and F. Aflatouni, Integrated Pound-Drever Hall laser stabilization system in silicon, *Nature Communications* 8, 1209, 2017.

[5] M. Idjadi and F. Aflatouni, Laser Spectral Linewidth Reduction Using an Integrated Pound-Drever-Hall Stabilization System in 180 nm CMOS SOI," *IEEE Radio Frequency Integrated Circuits,* 2019.

Passively Actuated Thermal Coating for Radiative Controlled Homeostasis

Philip W.C. Hon[1], Ahmed Morsy[2], Virginia D. Wheeler[3], Michael Barako[1], Vladan Jankovic[1], Michelle Povinelli[2], Luke A. Sweatlock[1]

[1]NG Next Northrop Grumman Corporation, 1 Space Park Drive, Redondo Beach, CA. 90278, USA
[2]Ming Hsieh Department of Electrical Engineering and Center for Energy Nanoscience, University of Southern California, Los Angeles, CA. 90089-0106, USA
[3]U.S. Naval Research Laboratory, Washington, D.C. 20375, United States

*corresponding author, E-mail: Philip.Hon@northropgrummannext.net

Abstract

Spacecraft temperature stability and control is achieved using bulky solutions, like thermal heat pipes or technologies that use moving parts like mechanical louvres. Thermal control surfaces are an attractive alternative since they are mechanically compliant and solid-state solutions. We present micro-patterned silicon coated with a phase change material as a passive thermal control surface.

1. Introduction

Given the large external temperature variations in space ranging from 150K to 400K [1], spacecraft thermal control coatings play a critical role in spacecraft thermal management. Design, fabrication and optimization of these devices requires an in-depth understanding of the thermal coating's solar absorptance and hemispherical emittance. Conventional solutions include thermal heat pipes [2,3] and mechanical louvers [4], while current state of the art coatings include electrically actuated electrochromic devices [5]. For select applications with zero solar irradiance incident on a spacecraft's particular facet, i.e. solar absorptance is not a concern, we present an alternative passive thermal control coating that can maintain a target temperature coinciding with the transition temperature of the incorporated phase change material. In this design we use micro-patterned features coated with a phase change material to achieve thermal stability via passive, thermally actuated emissivity changes and show a 10x difference between high and low temperature states.

2. Achieving Dynamic Emissivity

To achieve passive thermal regulation, appreciable emissivity differences in the thermal coating above and below a target temperature must be achieved. To demonstrate the concept, we use vanadium dioxide (VO_2), a phase change material, that exhibits appreciable electrical and optical refractive index swings between its dielectric and metallic states, delineated by a phase transition temperature of 68 ºC [6].

2.1. Material and Optical Design

Our design consists of an array of electromagnetic impedance tapering silicon (Si) micro-cones coated with a thin layer of VO_2. Transfer matrix method simulations were used to sweep through the parameter space (VO_2 thickness, micro-cone height and pitch) to capture the broadband (2.5 µm to 30 µm) emissivity response. Shown in Fig. 1 is the emissivity response of an optimal design with micro-cone height, h = 10 µm, lattice constant, a = 1 µm, VO_2 thickness, t = 40 nm and Si substrate thickness, t_{sub} = 300 µm.

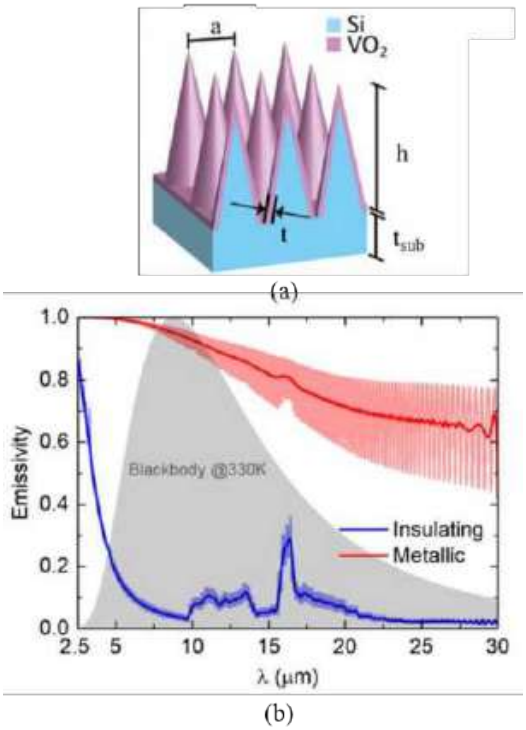


Figure 1: Physical design parameters for the (a) VO_2 coated silicon micro-cones and (b) its emissivity below and above the phase transition temperature.

.

3. Thermal Balance

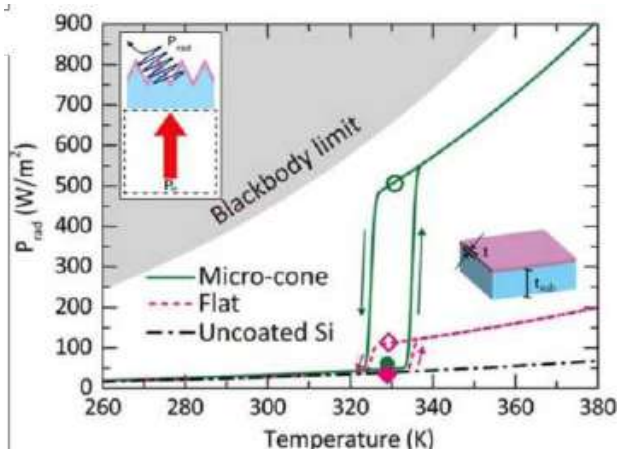


Figure 2: The temperature dependent model in [7] with the assumption of a 10 K wide phase transition is used to calculate the radiated power for the micro-cone coated, thin-film and uncoated, flat silicon substrate

Taking the angle-averaged emissivity from the TMM simulations, we then calculate the radiated thermal power across the 2.5 µm to 30 µm spectral range as detailed in [7]. Fig 2 shows the total radiated power calculated for the micro-cone coated device exhibiting a P_{rad} of 517 W/m^2 for the metallic (unfilled green circle) and 56 W/m^2 for the insulating (filled green circle) states at 330 K. For comparison, an uncoated silicon substrate and coated thin-film substrate are considered, as well. The uncoated Si exhibits zero thermal regulation while the VO_2 coated micro-cones, exhibit thermal regulation, but with a much smaller dynamic range between its metallic (unfilled pink diamond) and insulating (filled pink diamond) states, respectively.

4. Conclusions

We have investigated and shown a viable realization for thermal control using passive thermal coatings. Although, we have chosen a specific phase change material and micro-feature in this investigation, the design concept can be applied more broadly for other applications with specific target temperatures. Our device exhibits 20x improvement in temperature stability relative to an uncoated silicon substrate. This passive, solid-state solution could augment or replace current thermal radiatively cooled mechanical solutions.

References

[1] V. L. Pisacane, Fundamentals of Space Systems, JHU/APL Series in Science and Engineering, 1994.

[2] Lashley, C., Krein, S., and Barcomb, P., Deployable Radiators - A Multi-Discipline Approach, SAE Technical Paper 981691, 1998.

[3] Perotto, V., Tavera, S., Goncharov, K., Orlov, A. et al., Development of Improved 1500 W Deployable Radiator with Loop Heat Pipe, SAE Technical Paper 2000-01-2458, 2000.

[4] T. D. Swanson and G. C. Birur, NASA thermal control technologies for robotic spacecraft, Appl. Therm. Eng. 23, 1055–1065 (2003).

[5] P. Chandrasekhar, et. al., Variable-Emittance Infrared Electrochromic Skins Combining Unique Conducting Polymers, Ionic Liquid Electrolytes, Microporous Polymer Membranes, and semiconductor polymer coatings for spacecraft thermal control, NASA Publications 2014

[6] Marc Currie, Michael A. Mastro, and Virginia D. Wheeler, Characterizing the tunable refractive index of vanadium dioxide, Opt. Mater. Express **7**, 1697-1707 (2017)

[7] Shao-Hua Wu, Mingkun Chen, Michael T. Barako, Vladan Jankovic, Philip W.C. Hon, Luke A. Sweatlock, and Michelle L. Povinelli, Thermal homeostasis using microstructured phase-change materials, Optica 4, 1390-1396 (2017)

Approved for Public Release: NG19-0306

Optical rectification and resonant absorption in active nonlinear metasurfaces

(Invited talk in SP23: "Photonics for space systems and propulsion")

R. M. Osgood[1*], M. Kang[2], K-B. Kim[2], Y. Ait-El-Aoud[1], S. Dinneen[1], S. Kooi[3], G. Fernandes[4], J. M. Xu[4]

[1]US Army CCDC-Soldier Center, USA

[3]Seoul National University, Republic of Korea

[4]Insitute for Soldier Nanotechnologies, MIT, USA

[4]Brown University, USA

[*]corresponding author: richard.m.osgood.civ@mail.mil

Abstract- Rectifying stripe-teeth metasurfaces, consisting of nanorectenna arrays with plasmonic near-infrared resonances, coupled to vertical Metal-Insulator-Metal (MIM) diodes having an insulating barrier layer, were designed and their current-voltage (I-V) measurements analyzed. Effects of barrier heights, thickness, dielectric constant, and effective mass on the I-V curves were examined. The nanorectenna arrays were illuminated by visible and near-infrared laser beams, which shifted their I-V curve, indicating rectifying power production. An interesting large increase in the forward bias current is much greater than what is attributable to structural effects and plasmonic field-enhancement. We attribute it to a novel optical rectification mechanism: out-of-equilibrium "hot-electron" energy distribution due to plasmonic resonant absorption by the optical Au nanowire antennas.

In a semiconductor, absorption is limited by the band gap. An array of nonlinear receivers or "microrectennas" could rectify any desired portion of the infrared frequency spectrum, very efficiently converting the incident THz field to direct current. Vertical metal-insulator-metal (MIM) diodes have produced power from optical-frequency fields, when coupled to an asymmetric metamaterial planar stripe-teeth Al or Ag array lying above the vertical diode. We recently published a model of MIM diodes and their predicted current-voltage (I-V) characteristics and rectification[1].

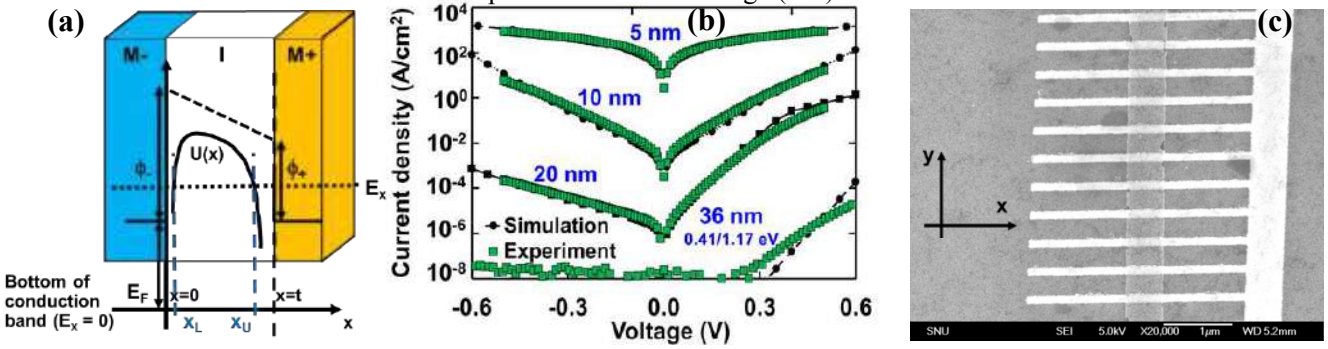


Figure 1: (a) CCDC-Soldier Center model of a rectifying MIM diode; metal (-) electrode has the larger barrier height, and the "I" region is the barrier layer (thickness t) with a potential function U(x). (b) Model agrees with experiment over eleven orders of magnitude, for four different barrier (oxide) thicknesses for both forward bias (V < 0) and reverse bias (V > 0)[1]. (c) Plan view electron microscopy image of Au nanowire antenna-coupled-Al/Al_2O_3/Au diodes, showing Au stripe-teeth array (brightly-colored; teeth are along the x-axis) and overlapping Al counter-electrode (transparent stripe along y). Vertical MIM diodes form at the intersection of the Al stripe and Au teeth.

These stripe-teeth arrays are similar to stripe arrays that have demonstrated near-perfect absorption in the infrared,[2] except that "teeth" along the x-axis are designed to resonate in the visible and produce an enhanced resonant a.c. z-field, determined by the length of the tooth, into the substrate. This optical rectification produced a d.c. voltage

and direct current, which is extracted by the stripes. The z- field was rectified by the vertical diode, composed of $Al/Al_2O_3/Au$, with Al_2O_3 fabricated by atomic layer deposition (ALD). Barrier heights (substantially lower than the ideal Al_2O_3-Au and -Al barrier heights), thickness, dielectric constant, and effective mass were all fitted to match the I-V curves. Barrier heights and thickness lower than expected values could be caused by roughness of the ALD-deposited Al_2O_3. The barrier asymmetry rising from the work function differences at the interfaces, $\Delta\phi$, was estimated to be ~ 0.25 eV.

The unilluminated I-V curve (black curve in Fig. 2a) is nonlinear, asymmetric due to $\Delta\phi$, and centered at V=0. When laser-illuminated, the curve shifts away from V=0, indicating that power is produced (there is a short circuit current and an open circuit voltage), and also the forward bias current changes not only amplitude but also shape in response to the laser illumination. The unusual forward bias current change near resonance (in the red) suggests that this is related to the antenna resonant absorption. Considering photon energy alone, photon-assisted tunneling would be stronger in the blue. The increase in the forward bias current is unusual, and different from what straightforward MIM modeling would anticipate (simple voltage shift ΔV).

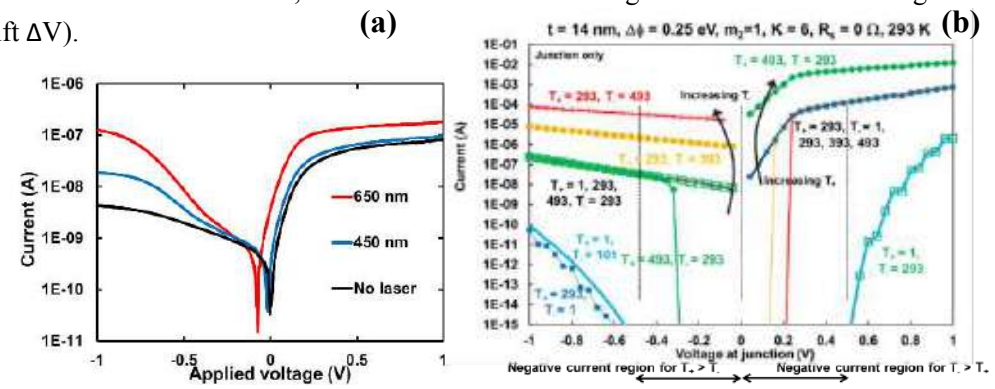


Figure 2: (a) Dependence of I-V curves on visible wavelength excitation of Au nanowire antenna-coupled-$Al/Al_2O_3/Au$ MIM diodes. (b) CCDC-Soldier Center modeling explaining large increase in forward bias current with out-of-equilibrium electron energy distribution (effective temperatures shown with corresponding forward bias current) due to plasmonic excitation in the (-) electrode. The effect of out-of-equilibrium electron energy distribution in the (+) electrode, basically just on the reverse bias current, is also shown.

The shift of ΔV can be explained using the quantum rectification formulism of Tucker *et. al.*[3] The large increase in the forward bias current can be explained by the excitation of electrons in the (-) (Au) nanoantennas out of equilibrium at plasmonic resonance to dominate the current, while there is little absorption in the large-area Al. A subtle but crucial difference exists between the single-electron treatment of photon-assisted tunneling in the literature and the out-of-equilibrium electron reservoir here, characterized by effective temperatures given in Fig. 2b, although both might be referred to as "hot electron plasmonics".[4] For the reverse bias current that flows from (+) to (-) in Fig. 1a, an electron distribution characterized by a high effective temperature in the (–) layer won't strongly affect the current, since the thermally excited electrons aren't primarily responsible for the current. This will be discussed with the aid of a full analysis and model of the I-V curves of nano-/micro-rectenna arrays, their responsivities to illumination, along with power and data beaming to these and related nano-enhanced metasurface receivers, for space and terrestrial applications.

REFERENCES

1. R. M. Osgood, *et. al.*, "Conduction and rectification in NbOx- and NiO-based metal-insulator-metal diodes," *J. Vac. Sci. Tech. A*, 34: 051514 – 051527, 2016.
2. C. Wu, *et.al.* "Large-area wide-angle spectrally selective plasmonic absorber," *Phys. Rev. B*, 84: 075102-7, 2011.
3. J. R. Tucker and M. J. Feldman,"Quantum detection at millimeter wavelengths," *Rev. Mod. Phys.*, 57: 1055-1114, 1985.

4. H. Chalabi *et. al*. “Hot-Electron Photodetection with a plasmonic nanostripe antenna,” *Nano Letts.,* 4: 1374-1380, 2014.

Simulating the Dynamic Structural Stability of Ultrathin Lightsails

Michael D. Kelzenberg* and Harry A. Atwater

California Institute of Technology, Pasadena, CA
*corresponding author, E-mail: mdk@caltech.edu

Abstract

Laser-propelled lightsails have been proposed as a technologically viable means of deploying interstellar space probes. Here, we investigate the dynamic structural stability of such light sails, treating the sail as a free membrane rather than a rigid body. Using realistic values for strength and modulus, we show that spin-stabilized paraboloid lightsails can in principle exhibit mechanical stability and beam-riding behavior.

1. Introduction

The Breakthrough Starshot Initiative was announced in 2016 as a $100M philanthropic effort to develop technologies and lay the foundations for launching humankind's first interstellar probe. [1] Scientists and engineers around the world are being challenged to build a 1-gram interstellar probe ("nanocraft") that will travel 4.2 light years to reach Proxima Centauri B, the nearest known habitable-zone exoplanet, within ~20 years of launch. To accelerate the nanocraft to the required speed of $0.2c$, a ~10 m^2 lightsail will be propelled by radiation pressure from an earth-based or earth-orbiting laser ("light beamer") at incident power densities approaching 10 GW/m^2, over the course of ~10 minutes (i.e., ~10,000 Gs of acceleration). This concept for interstellar exploration has been studied in great detail by Lubin et al. [2]

A lightsail suitable for acceleration to relativistic speeds must satisfy several challenging requirements, including: (1) the materials themselves must be capable of reflecting high intensity light (potentially over a wide range of angles) without overheating; (2) the sail must be stable under acceleration and not deviate from the beam path; and (3) the sail must be strong enough to retain its shape and avoid crumpling or tearing under rapid acceleration. A study investigating the first requirement has resulted in a short list of candidate materials combining low absorption with high reflectivity, including crystals such as Si and diamond, 2-dimeinsional transition metal dichalcogenides of W and Sn, and amorphous materials including a-Si and SiO_2. [3] Certain reflector shapes, including cones [4, 5], hyperboloids [6], and paraboloids [7] have been predicted to offer stable beam-riding behavior. Nanophotonic designs for lightsails have also been proposed, which allow lightsail surfaces to achieve beam-riding stability. [8] However, these prior studies treated the lightsail as a rigid body, which is likely a poor assumption for meter-scale membranes made from <100nm thick materials and thus will offer negligible out-of-plane stiffness.

Here, we turn our attention to the dynamic mechanical performance of unconstrained lightsail membranes to investigate whether design approaches such as those referenced above can be realized with real materials, which have finite stiffness and strength. We develop a computational numerical approach to simulate sheets of thin materials, considering their linear elastic behavior in the time domain. In this initial report, we present simulations of non-rigid paraboloid lightsails.

2. Approach

We construct a triangular surface mesh to model the lightsail membrane. Vertices of the mesh are assigned positions along the desired (e.g., paraboloid) surface, with their spacing chosen to yield reasonably uniform edge length and aspect ratio among the triangles. The mesh is formed by Delaunay triangulation, then an array of unique edges is constructed to model the elastic behavior of the membrane. An example simulation mesh is plotted in Figure 1.

Each vertex is assigned a mass based on the membrane thickness, the area of the adjoining triangles, and the material density. Each edge is assigned a linear elastic coefficient (i.e., spring constant) based on the edge length, the membrane thickness, the area of the adjoining triangles, and the material's Young's modulus. This simplistic approach neglects the bending stiffness and the shear modulus of the material, but provides a reasonable first-order glimpse into the behavior of ultrathin membranes under tensile loading, which is the predominant type of loading for most lightsail applications of interest. Future efforts can improve upon this approach by considering the full linear elastic behavior of the lightsail material(s), and by considering non-isotropic material properties.

To simulate the acceleration and deformation of the lightsail, and the stability of its trajectory, we implement a finite-difference time-domain approach wherein we calculate the forces acting upon each mesh vertex, then calculate the resulting change in position and velocity over a finite time step $\Delta\tau$. By choosing sufficiently small $\Delta\tau$, such that the propagation of the membrane's vibrational modes can be simulated with high precision on our computational platform, we can obtain reasonable predictions of the lightsail's dynamic behavior.

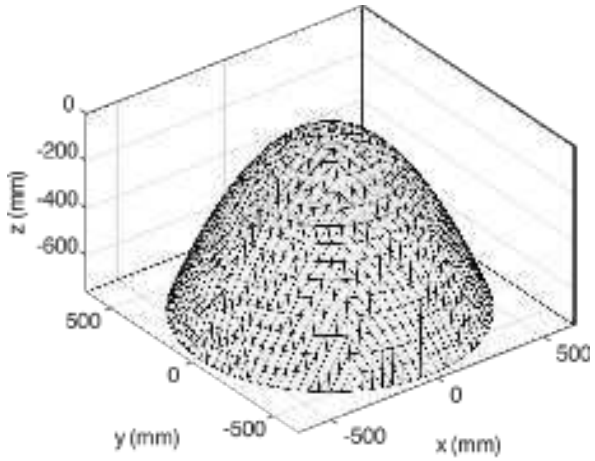


Figure 1. Example simulation mesh for a paraboloid lightsail comprising 1536 triangular elements.

In addition to simulating the mechanical response of the lightsail, we also calculate the temperature of the sail by assuming a fixed value of absorption (10^{-5}), emissivity (0.8), thermal conductance, and heat capacity. We use values for crystalline Si for the latter properties, neglecting its anisotropy. We consider first-order thermal expansion by using a linearized coefficient of thermal expansion (CTE), again using a value of 2.3 corresponding to Si at room temperature. Future work can improve this approach by more accurately calculating the optical properties based on the sail's composition and design, and taking into account the local angle of incidence. Furthermore, it should be noted that these and other properties can vary greatly with temperature, and that a linearized model may be inadequate to accurately describe these variations.

Finally, we consider the tensile strength of the material by comparing the instantaneous strain of each mesh edge to the materials fracture strain given by the ratio of its ultimate tensile strength to its Young's modulus. If this strain is exceeded, we conclude that the membrane has failed and thus would be inadequate for interstellar propulsion. For illustrative purposes, we allow the simulation to continue for some time, deleting all edges that have failed (and their adjacent triangles) from the calculation of optical and mechanical forces in the membrane. Note that this is not intended to accurately model the propagation of structural failure within the membrane.

3. Results

Results of a simulation of a paraboloid lightsail are shown in Figure 2. We have used material properties roughly corresponding to those of crystalline Si, neglecting its anisotropy, and assume a sail thickness of 43 nm (corresponding to ~ 1 g/m^2 areal mass density). We found that spin-stabilization is required to prevent the paraboloids from collapsing immediately upon the application of the accelerating forces. The figure depicts the acceleration of a lightsail having ~1 m^2 effective initial aperture area. The paraboloids are initially offset from the beam centerline to illustrate their beam-riding stability.

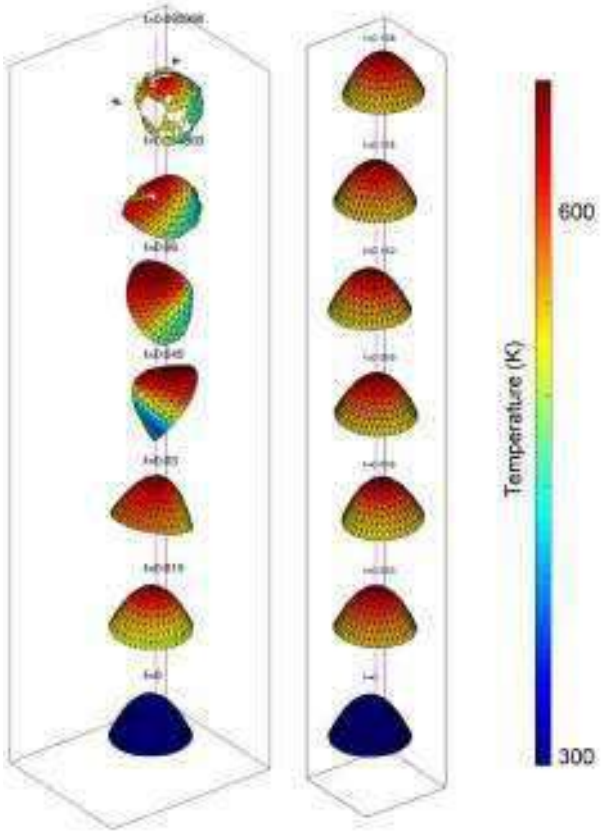


Figure 2. Results of simulations showing the shape and temperature of the lightsail mesh at various times during acceleration. The lightsail on the left was spin-stabilized at 30 Hz, which was inadequate to prevent it from toppling in the beam. The structure on the right is identical but spin-stabilized at 100 Hz, enabling it to the beam path through the simulation duration of 1.0 seconds. Each depiction of the mesh is plotted at the same relative scale; however, the z-position has been arbitrarily shifted to stack the images for presentation. The magenta line depicts the centerline of the accelerating beam, which is Gaussian with width equal to the initial paraboloid radius, intensity of 1 GW/m^2, and is offset from the paraboloid's initial centroid by 20% of the paraboloid radius to illustrate beam-riding stability.

References

[1] *Breakthrough Starshot Initiative*. Available: https://breakthroughinitiatives.org/initiative/3

[2] P. Lubin, "A roadmap to interstellar flight," *JBIS,* vol. 69, pp. 40-72, 2016.

[3] H. A. Atwater *et al.*, "Materials challenges for the Starshot lightsail," *Nat Mater,* vol. 17, no. 10, pp. 861-867, Oct 2018.

[4] Z. Manchester and A. Loeb, "Stability of a Light Sail Riding on a Laser Beam," *The Astrophysical Journal Letters,* vol. 837, no. 2, p. L20, 2017.

[5] E. Popova, M. Efendiev, and I. Gabitov, "On the stability of a space vehicle riding on an intense laser beam," *Mathematical Methods in the Applied Sciences,* vol. 40, no. 4, pp. 1346-1354, 2017.

[6] P. Srinivasan *et al.*, "Stability of laser-propelled wafer satellites," in *SPIE Optical Engineering + Applications*, 2016, vol. 9981, p. 11: SPIE.

[7] A. Davoyan, *In preparation,* 2019.

[8] O. Ilic and H. A. Atwater, "Self-stabilizing photonic levitation and propulsion of nanostructured macroscopic objects," *Nature Photonics,* vol. 13, no. 4, pp. 289-295, 2019/04/01 2019.

Exotic Meta-media - Spatial, Non-local and Other Novel Responses

Sensitivity of layered structures in critical conditions

Agnès Maurel [1], Kim Pham[2] and Jean-François Mercier[2]

[1] Institut Langevin, CNRS, ESPCI ParisTech, 1 rue Jussieu, 75005 Paris, France,
[2] IMSIA, CNRS, ENSTA ParisTech, 828 Bd des Maréchaux, 91732 Palaiseau, France
[3] Poems, CNRS, ENSTA ParisTech, INRIA, 828 Bd des Maréchaux, 91762 Palaiseau, France,
*corresponding author, E-mail: agnes.maurel@espci.fr

Abstract

We conduct two-scale homogenization of multilayered structures composed of nonmagnetic isotropic materials. The resulting effective model involves a relation between the electric field and electric displacement and non intuitive transmission conditions at the interfaces with the surrounding media. In transverse electric polarization, the model reduces to a fully local model and in transverse magnetic polarization, classical non local terms appear. Comparaison with direct numerics show that the model is accurate up to the critical conditions near total reflection.

1. Introduction

We present a generalization of the homogenization procedure presented in [1] for transverse electric polarized waves in a dielectric layered structure. It was shown that conducting this approach at the third order results in a fully local effective model, with an effective wave equation involving a permittivity frequency dependent and effective transmission conditions involving a parameter which depends only on the layer terminating the structure. Near the critical conditions of total internal reflection reported in [2], this model has been shown to capture the scattering properties of the actual structure with an accuracy less than 1% up to $kd \sim 1$ (Fig. 1). Here, the procedure is performed on the Maxwell equations in three dimensions. The resulting model involved a generalized relation between the electric field $\boldsymbol{E}$ and the electric displacement field $\boldsymbol{D}$, revealing local and spatial dispersion of the effective medium. The transmission conditions between the effective medium and the surrounding media are in general non local well, in the sense where they involve tangential derivative of the fields. Expectedly, we recover the model of [1] in transverse electric polarization. For transverse magnetic polarization, the effective model reveals anisotropy and spatial dispersion by means of a fourth order spatial derivative of the magnetic field; it is also non local in the transmission condition.

2. The effective model

We start with the Maxwell equations in the dielectric (non magnetic) structure

$$\left\{ \begin{array}{l} \mathrm{rot}\boldsymbol{H} = \partial_t \boldsymbol{D}, \quad \mathrm{rot}\boldsymbol{E} = -\partial_t \boldsymbol{H}, \\ \mathrm{div}\boldsymbol{D} = \mathrm{div}\boldsymbol{H} = 0, \quad \text{with } \boldsymbol{D} = \varepsilon \boldsymbol{E}, \end{array} \right. \tag{1}$$

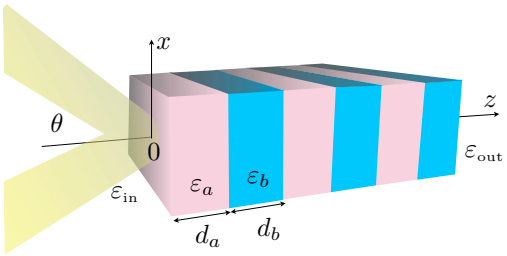


Figure 1: Multilayer structure illuminated by a plane wave near the critical angle of total reflection (wavenumber k and incidence θ).

and $\varepsilon = 1, \varepsilon_a, \varepsilon_b$ is a function of z. The effective model aims to describe the fields $(\boldsymbol{E}, \boldsymbol{D}, \boldsymbol{H})$ in an average sense which results in (a) an effective medium for $z > 0$ being homogeneous, anisotropic and possibly non local and (b) effective transmission conditions which in general differ from the usual continuities of $\boldsymbol{H}$, of the normal component of $\boldsymbol{D}$ and of the tangential component of $\boldsymbol{E}$. The model is a generalization of that in [1] which hold for transverse electric polarized waves (with $\boldsymbol{E}(x,z)$ polarized along $\boldsymbol{e}_y$). Below we report the resulting model in the harmonic regime (with time dependence $e^{-i\omega t}$ in the air where we set the velocity to unity, and $k = \omega$ is the wavenumber).

$$\left\{ \begin{array}{l} \mathrm{rot}\boldsymbol{H} = -ik\boldsymbol{D}, \quad \mathrm{rot}\boldsymbol{E} = ik\boldsymbol{H}, \\ \mathrm{div}\boldsymbol{D} = \mathrm{div}\boldsymbol{H} = 0 \end{array} \right. \tag{2}$$

with, for $z < 0$ $\boldsymbol{E} = \boldsymbol{D}$ and for $z > 0$

$$\boldsymbol{E} = \begin{pmatrix} \varepsilon_{\parallel}^{-1}(k) - \alpha\partial_{xx} & -\alpha\partial_{xy} & 0 \\ -\alpha\partial_{xy} & \varepsilon_{\parallel}^{-1}(k) - \alpha\partial_{yy} & 0 \\ \beta\partial_{xz} & \beta\partial_{yz} & \varepsilon_{\perp}^{-1}(k) \end{pmatrix} \boldsymbol{D} \tag{3}$$

where (α, β) are non dimensional constant parameters which depend on the structure of the multilayer. Next, the usual transmission conditions read as $[\![\boldsymbol{H}]\!] = [\![E_x]\!] = [\![E_y]\!] = [\![D_z]\!] = 0$ are replaced by effective transmission conditions of the form

$$\left\{ \begin{array}{l} [\![\boldsymbol{H}]\!] = -ia\,k\,\boldsymbol{e}_z \times \overline{\boldsymbol{E}}, \\ [\![E_x]\!] = b\partial_x \overline{D_z}, \; [\![E_y]\!] = b\partial_y \overline{D_z}, \\ [\![D_z]\!] = a\left(\partial_x \overline{E_x} + \partial_y \overline{E_y}\right), \end{array} \right. \tag{4}$$

where (a, b) are constant parameters which depend only on the arrangement of the layer terminating the structure (at $z = 0$ and at $z = \ell$). In the above relation, for a field $F(x, y, z)$ being discontinuous, say at $z = 0$, we defined $\overline{F} = \frac{1}{2}(F(x, y, 0^+) + F(x, y, 0^-))$.

• The case of TE polarized waves– If we consider $\boldsymbol{D}$ and $\boldsymbol{E} = E(x, z)\boldsymbol{e}_y$ along $\boldsymbol{e}_y$ (hence $H_y = 0$), then (2) reduces to a 2D problem in (x, z); accounting for (3) and for the transmission conditions (4),the problem reads as

$$\begin{cases} (\partial_{xx} + \partial_{zz})E + \varepsilon_{\parallel}(k)k^2 E = 0, \\ [\![E]\!] = 0, \quad [\![\partial_z E]\!] = a\, k^2 E. \end{cases} \tag{5}$$

• For TM polarized waves, $\boldsymbol{H} = H(x, z)\boldsymbol{e}_y$ and where $E_y = 0$, (2), (3) and (4) simplify to

$$\begin{cases} \varepsilon_{\perp}^{-1}(k)\partial_{xx}H + \varepsilon_{\parallel}^{-1}(k)\partial_{zz}H - \gamma\, \partial_{xxzz}H + k^2 H = 0, \\ [\![H]\!] = -a\, (\overline{ikE_x}), \quad [\![ikE_x]\!] = -b\, \partial_{xx}\overline{H}, \end{cases} \tag{6}$$

with $\gamma = (\alpha + \beta)$ and $ikE_x = \partial_z H$ for $z < 0$ and $ikE_x = (\varepsilon_{\parallel}^{-1}(k) - \alpha\, \partial_{xx})\partial_z H$ for $z > 0$.

3. Numerical validation of the effective model

We inspect the scattering properties of the actual structures in the case of all dielectric layers ($\varepsilon_{\rm a} > 0$, $\varepsilon_{\rm b} > 0$) and in that of metal-dielectric succession ($\varepsilon_{\rm a} < 0$, $\varepsilon_{\rm b} > 0$). The solution of the actual problem is calculated numerically and it is compared to that given by the effective model which is given in a close form. We report in Fig. 2 the transmission at moderate $kd = 0.5$ value for the succession of layers considered in [1, 2]. The anomalie is visible with different scattering for the direct order (a structure starting with a layer a) and the inverse order (starting with a layer b); as a result, the classical EMA fails in capturing this sensitivity to the layer arrangement (dotted grey lines). In comparison, our effective model is 0.1% accurate in both cases (additional results can be found in [1]).

We report in Fig. 3 an additional and interesting result coming from [3]; in this reference, a model based on the transmission through a metal-dielectric structure is analyzed through an operator effective medium theory involving electric dipoles, chirality and magnetic and electric quadrupoles. In the case $kd = 2$, that is when thickness d is not much less than the incident wavelength. The authors remark that their model is not very accurate but ir catches the resonances of the exact solution. They conclude that other homogenization models considered cannot be used at all outside their applicability ranges. What we show in Fig. 3 is that our model has exactly the same accuracy as the operator effective model of [3] which suggests an equivalence between both models, which is not immediate to establish.

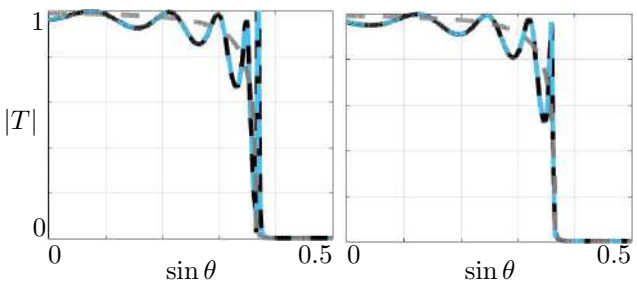


Figure 2: Transmission against $\sin\theta$ for all dielectric structures the case reported in [2], $\varepsilon_{\rm in} = 4$, $\varepsilon_{\rm out} = 3$, $\varepsilon_{\rm a} = 5$, $\varepsilon_{\rm b} = 1$, $d_{\rm a} = d_{\rm b}$ and $kd = 0.5$, $N = 20$, direct (left) and inverse (right) order. Direct numerics (plain black lines) and effective model (dotted blue lines).

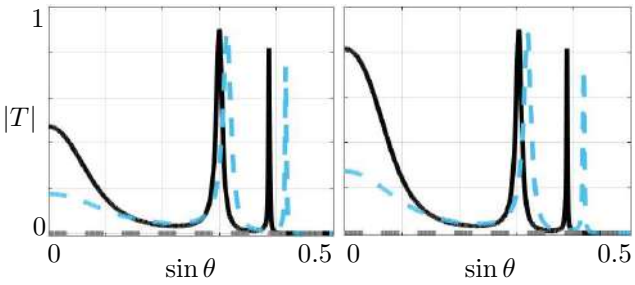


Figure 3: Transmission against $\sin\theta$ for metal-dielectric structure, as reported in [3], $\varepsilon_{\rm in} = 1$, $\varepsilon_{\rm out} = 0.215$, $\varepsilon_{\rm a} = -3$, $\varepsilon_{\rm b} = 2.25$, $d_{\rm a} = d_{\rm b}$ and $kd = 2$, $N = 10$; same representation as in Fig. 2.

References

[1] A. Maurel and J.-J. Marigo, Sensitivity of a dielectric layered structure on a scale below the periodicity: A fully local homogenized model, Phys. Rev. B, **98**(2), 024306, 2018.

[2] H.H. Sheinfux, I. Kaminer, Y. Plotnik, G. Bartal and M. Segev, Subwavelength multilayer dielectrics: ultrasensitive transmission and breakdown of effective-medium theory, Phys. Rev. Lett. **113**(24), 243901, 2014.

[3] V. Popov, A.V. Lavrinenko and A. Novitsky, Operator approach to effective medium theory to overcome a breakdown of Maxwell Garnett approximation, Phys. Rev. B, **94**(8), 085428, 2016.

Simultaneous amplification and attenuation of plane waves and surface waves possible using nanoengineered materials

Tom G. Mackay[1,2,*], **Akhlesh Lakhtakia**[2,3,4]

[1] School of Mathematics and Maxwell Institute for Mathematical Sciences, University of Edinburgh, Edinburgh EH9 3FD, UK
[2] *NanoMM — Nanoengineered Metamaterials Group*, Department of Engineering Science and Mechanics, The Pennsylvania State University, University Park, PA 16802–6812, USA
[3] Material Architecture Center, Indian Institute of Technology (BHU), Varanasi 221005, India
[4] Department of Electronics Engineering, Indian Institute of Technology (BHU), Varanasi 221005, India
*corresponding author, E-mail: T.Mackay@ed.ac.uk

Abstract

Electromagnetic plane waves are attenuated by dissipative materials and amplified by active materials. However, by virtue of judicious design, certain nanoengineered materials may be neither wholly dissipative nor wholly active. In such materials, whether plane waves are amplified or attenuated can depend upon the direction of propagation or on the polarization state. The prospects of achieving simultaneous amplification and attenuation of plane waves and surface waves have been established theoretically and numerically using a variety of nanoengineered materials, including homogenized composite materials and nanostructured thin films.

1. Introduction

Tantalizing technological opportunities, and illuminating fundamental insights, can be offered by nanoengineered materials with exotic optical properties [1], as exemplified by metamaterials [2] and certain homogenized composite materials (HCMs) [3]. Our focus here is on amplification and attenuation in such materials. It is well known that active materials may be used to overcome the debilitating effects of dissipation in metamaterials [4, 5, 6, 7]. However, it is less well known that by judiciously combining active and dissipative component materials, the resulting composite material can simultaneously support both amplification and attenuation. A survey is presented here of recent results concerning nanoengineered materials, including HCMs, which exhibit simultaneous amplification and attenuation.

2. Homogenized composite materials

The electromagnetic attributes of an assembly of electrically small spheroidal particles, randomly distributed but identically aligned, made from isotropic dielectric materials, are indistinguishable from those of a homogeneous uniaxial dielectric material [3]. Furthermore, if one of the component materials is active but the other component material is dissipative, then plane waves propagating in the resulting HCM in certain propagation directions may be amplified but plane waves propagating in other propagation directions may be attenuated [8]. Similarly, a multilayer of alternate active and dissipative thin sheets may be electromagnetically indistinguishable from a homogeneous birefringent continuum which can control plane-wave polarization states [9]. Also, HCMs arising from certain active and dissipative component materials can simultaneously amplify incident light of one linear polarization state whilst attenuating incident light of the orthogonal polarization state [10]. This effect can be extended to circular polarization states in the case of chiral HCMs: that is, a chiral HCM may be conceptualized that can simultaneously amplify circularly polarized light of one handedness whilst attenuating circularly polarized light of the other handedness [11].

3. Electromagnetic surface waves

Combinations of active and dissipative materials also give rise interesting results when electromagnetic surface waves [12] are considered. For example, suppose one considers the propagation of surface-plasmon-polariton (SPP) waves [13] guided by the planar interface of an isotropic metal and an active uniaxial dielectric material, for the case in which the optic axis of the uniaxial partnering material lies wholly in the interface plane. By judicious choice of the constitutive parameters of the partnering materials, one can find that SPP waves propagating in certain directions in the interface plane are amplified but the SPP waves propagating in other directions are attenuated [14]. Furthermore, a critical propagation direction exists for which the SPP wave is neither amplified nor attenuated. Analogous results arise for (i) Dyakonov waves [15, 16] supported by the planar interface of two dielectric materials, one of which is anisotropic and the other is isotropic [17]; and (ii) electromagnetic surface waves somewhat akin to SPP waves and somewhat akin Dyakonov waves supported by the planar interfaces of certain isotropic chiral materials [18, 19].

4. Closing remarks

The adjectives 'active' and 'dissipative' must be applied with caution when one considers certain nanoengineered materials, because under some circumstances amplification and attenuation may be supported simultaneously. Materials that simultaneously support amplification and dissipation are promising for applications in optical communications and noise reduction, for examples.

References

[1] R. Vajtai, ed., *Springer Handbook of Nanomaterials* (Springer, 2013). https://doi.org/10.1007/978-3-642-20595-8

[2] R.M. Walser, Electromagnetic metamaterials, Proc. SPIE **4467**, 1 (2001). https://doi.org/10.1117/12.432921

[3] T.G. Mackay and A. Lakhtakia, *Modern Analytical Electromagnetic Homogenization* (Morgan & Claypool, 2015).

[4] S. Wuestner, A. Pusch, K.L. Tsakmakidis, J.M. Hamm, and O. Hess, Overcoming losses with gain in a negative refractive index metamaterial, Phys. Rev. Lett. **105**, 127401 (2010). https://doi.org/10.1103/PhysRevLett.105.127401

[5] Z.-G. Dong, H. Liu, T. Li, Z.-H. Zhu, S.-M. Wang, J.-X. Cao, S.-N. Zhu, and X. Zhang, Optical loss compensation in a bulk left-handed metamaterial by the gain in quantum dots, Appl. Phys. Lett. **96**, 044104 (2010). https://doi.org/10.1063/1.3302409

[6] G. Strangi, A. De Luca, S. Ravaine, M. Ferrie, and R. Bartolino, Gain induced optical transparency in metamaterials, Appl. Phys. Lett. **98**, 251912 (2011). https://doi.org/10.1063/1.3599566

[7] L. Sun, X. Yang, and J. Gao, Loss-compensated broadband epsilon-near-zero metamaterials with gain media, Appl. Phys. Lett. **103**, 201109 (2013). https://doi.org/10.1063/1.4831768

[8] T.G. Mackay and A. Lakhtakia, Dynamically controllable anisotropic metamaterials with simultaneous attenuation and amplification, Phys. Rev. A **92**, 053847 (2015). https://doi.org/10.1103/PhysRevA.92.053847

[9] A. Cerjan and S. Fan, Achieving arbitrary control over pairs of polarization states using complex birefringent metamaterials, Phys. Rev. Lett. **118**, 253902 (2017). https://doi.org/10.1103/PhysRevLett.118.253902

[10] T.G. Mackay and A. Lakhtakia, Polarization-state-dependent attenuation and amplification in a columnar thin film, J. Opt. (UK) **19**, 12LT01 (2017). https://doi.org/10.1088/2040-8986/aa9127 Erratum **20**, 019501 (2018). https://doi.org/10.1088/2040-8986/aa9ec3

[11] T.G. Mackay and A. Lakhtakia, Simultaneous amplification and attenuation in isotropic chiral materials, J. Opt. (UK) **18**, 055104 (2016). https://doi.org/10.1088/2040-8978/18/5/055104

[12] J.A. Polo Jr., T.G. Mackay, and A. Lakhtakia, *Electromagnetic Surface Waves: A Modern Perspective* (Elsevier, 2013).

[13] J.M. Pitarke, V.M. Silkin, E.V. Chulkov, and P.M. Echenique, Theory of surface plasmon and surface-plasmon polaritons, Rep. Prog. Phys. **70**, 1–87 (2007).

[14] T.G. Mackay and A. Lakhtakia, Simultaneous existence of amplified and attenuated surface-plasmon-polariton waves, J. Opt. (India) **47**, 527–533 (2018). https://doi.org/10.1007/s12596-018-0481-y

[15] F.N. Marchevskiĭ, V.L. Strizhevskiĭ, S.V. Strizhevskiĭ, Singular electromagnetic waves in bounded anisotropic media, Sov. Phys. Solid State **26**, 911–912 (1984).

[16] M.I. D'yakonov, New type of electromagnetic wave propagating at an interface, Sov. Phys. JETP **67**, 714–716 (1988).

[17] T.G. Mackay and A. Lakhtakia, Simultaneous existence of amplified and attenuated Dyakonov surface waves, Opt. Commun. **427**, 175–179 (2018). https://doi.org/10.1016/j.optcom.2018.06.050

[18] J. Noonan and T.G. Mackay, On electromagnetic surface waves supported by an isotropic chiral material, Opt. Commun. **434**, 224–229 (2019). https://doi.org/10.1016/j.optcom.2018.11.001

[19] M. Naheed, M. Faryad and T.G. Mackay, Electromagnetic surface waves guided by the planar interface of isotropic chiral materials, J. Opt. Soc. Am. B (at press).

Nonlocal homogenisation of centro-symmetric optical metamaterials

Karim Mnasri[1], Fatima Z. Goffi[2], Michael Plum[2], Carsten Rockstuhl[1,3]

[1]Institute of Theoretical Solid State Physics, Karlsruhe Institute of Technology, Wolfgang-Gaede-Str. 1 76131 Karlsruhe Germany
[2]Institute for Analysis, Karlsruhe Institute of Technology, Englerstr. 2 76131 Karlsruhe Germany
[3]Institute of Nanotechnology, Karlsruhe Institute of Technology, P.O. Box 3640 76021 Karlsruhe Germany
*corresponding author, E-mail: karim.mnasri@kit.edu

Abstract

Homogenising metamaterials with local constitutive relations frequently fails when the characteristic length scale of the metamaterial is no longer much smaller than the wavelength. To improve the situation, we consider nonlocal constitutive relations and demonstrate an improvement in the effective description of metamaterials. We discuss the dispersion relations, the additional interface conditions, and study the emerging reflection and transmission coefficients. We validate our model by testing it on selected metamaterials of interest by comparing the electromagnetic response from a slab.

1. Introduction

The characterisation of optical metamaterials (MMs) is an important task in the field of electromagnetism. It provides us not only a fundamental, physical understanding of the wave propagation inside complex media, but also offers a guideline for tuning and for a targeted engineering of the electromagnetic response from the MM. Particularly interesting in the last years are materials with a negative index of refraction. This phenomena usually appears when the material has metallic inclusions and sustains a magnetic resonance that translates to a resonant magnetic susceptibility at the effective level. To homogenise the MM, the lateral period of the structure has to be much smaller than the wavelength of light. However, frequently it is only smaller than the wavelength. In such sitze regime the introduction of effective material parameters requires to track the information of the spatial derivatives of the mean fields as well [1]. Simply because the field variation across the unit cell cannot be neglected anymore as the structures are too large for that. Therefore, an effective medium approach that retains spatial dispersion is required. In other terms, spatial dispersion means that the auxiliary fields, $\mathbf{D}$ and $\mathbf{H}$, linearly depend on the macroscopic fields $\mathbf{E}$ and $\mathbf{B}$ and on their spatial derivatives, with spatially independent coefficients - the effective material parameters. This goes beyond the usually considered local responses, or local constitutive relations, which have been extensively studied in the past [2]. However, local approaches show severe limitations when the wavelength is only slightly longer than the lattice size, because the field of light at one position polarizes the material at a distant position, which is only captured by considering nonlocal constitutive relations. It is the purpose of our work, that we review, to establish a framework for the homogenization of MMs that considers such strong spatial dispersion (SSD).



Figure 1: Fishnet MM. We consider a biperiodic structure with periods $\Lambda_x = \Lambda_y = 600\,\text{nm}$ and consider an extension of the thin film in z direction of $200\,\text{nm}$. The fishnet consists of rectangular holes with the width $w_x = 100\,\text{nm}$ and $w_y = 316\,\text{nm}$. They consist in a stack of layers made of two $45\,\text{nm}$ Ag layers separated by a thin dielectric spacer, $30\,\text{nm}$ of MgF_2, with $n_{\text{MgF}_2} = 1.38$.

2. Material Model and Results

To homogenise optical MMs with nonlocal constitutive relations, we proposed a macroscopic model for materials in Ref. [3]. For the sake of simplicity, we do not consider MMs that mix TE and TM polarisations. The MMs we consider are intrinsically achiral and are invariant under spatial inversion. As a consequence, the effective response function, that shall respect the same symmetry as the original structure, will only contain even derivatives of the electric field. An example of a structure that undergoes a negative index behaviour is the Fishnet MM. It is a bi-periodic structure consisting of a stack of two perforated metallic layers separated by a dielectric spacer and embedded in a nondispersive host medium (See Fig. 1). Our model for nonlocality is

$$\begin{aligned}\mathbf{D}(\mathbf{r},\omega) =& \boldsymbol{\epsilon}(\omega)\mathbf{E}(\mathbf{r},\omega) + \nabla\times\boldsymbol{\alpha}(\omega)\nabla\times\mathbf{E}(\mathbf{r},\omega) \\ &+ \nabla\times\nabla\times\boldsymbol{\gamma}(\omega)\nabla\times\nabla\times\mathbf{E}(\mathbf{r},\omega)\,, \quad (1)\end{aligned}$$

where $\boldsymbol{\epsilon}(\omega), \boldsymbol{\alpha}(\omega)$, and $\boldsymbol{\gamma}(\omega)$ are spatially independent effective material parameters. Bear in mind that the material is intrinsically non-magnetic, i.e., $\mathbf{H}(\mathbf{r},\omega) = \mathbf{B}(\mathbf{r},\omega)$.

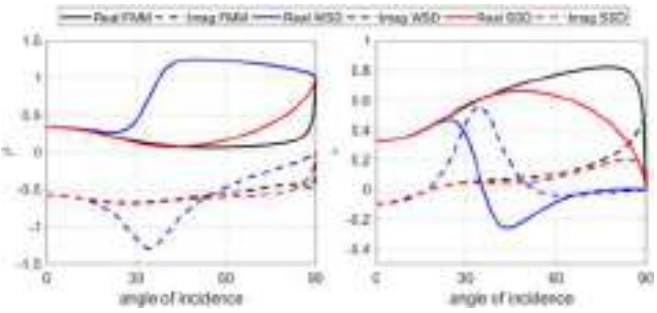


Figure 2: Reflection (left) and transmission (right) coefficients from one fishnet layer at a selected frequency of $k_0 = 4.2414\ \mu\text{m}^{-1}$. The solid (dashed) curves represent the real (imaginary) part. The reference curves obtained from the FMM are in black while the blue curves are obtained from considering the local and the red ones for the case of nonlocal approach. The red curves show a good agreement with the the reference curves up to $50°$. Meanwhile, the blue curves, which are obtained from WSD, are showing only an agreement within the paraxial regime.

However, $\boldsymbol{\alpha}(\omega)$ can be transformed, by means of a gauge transformation, to a local magnetic permeability that leads to artificial magnetization in such MMs. This is a consequence of finite-size structures where currents in a closed loops can be formed. The tranformation reads $\alpha_i(\omega) = \frac{1-\mu_i(\omega)}{k_0^2\mu_i(\omega)}$, where $\mu_i(\omega)$ is the i-th component of the local, effective magnetic permeability. The parameter $\boldsymbol{\gamma}(\omega)$, however, is the actual nonlocal parameter associated to SSD.

We have solved the wave equation and discussed it's multiple solutions in Ref. [3]. In particular, in contrast to local constitutive relation where only a single forward propagating mode is sustained for a given pair of transverse wave vector component and frequency, two plane wave solutions emerge in nonlocal materials. To unambiguously fix their amplitudes at an interface, additional interface conditions have to be introduced. We derived these additional interface conditions by means of weak formulations in Ref. [3]. For practical reasons, we have calculated the necessary Fresnel matrix to analytically express the reflection and transmission from a slab. In order to validate our model as well as our derived additional interface conditions, we compare the results produced by our homogenization approach against full wave numerical simulations. We consider topical subjects such as the Fishnet as well as basic structures, e.g., spheres on a cubic lattice and wire media. Recent results can be found in Ref. [4]. In the conference, we will show the actual improvements in capturing the reflection and transmission coefficients from slabs with different thicknesses in the propagation direction and show that the nonlocal approach leads to more robust results compared to the local one. We will discuss the retrieved material parameters $\boldsymbol{\epsilon}(\omega)$, $\boldsymbol{\alpha}(\omega)$, and $\boldsymbol{\gamma}(\omega)$ in depth as well.

The numerical data for the complex reflection and transmission coefficients of the fishnet MM have been calculated with the Fourier Modal Method (FMM) and are depicted in Fig. 2 (black curves), exemplary at the resonance frequency where the Fishnet has a negative index but depending on the angle of incidence. The comparison of this reference data to the reflection and transmission coefficients calculated using both local and nonlocal material laws is based on a least absolute deviations fit by optimizing the effective material parameters present in the respective model. We notice in Fig. 2 that the nonlocal model covers a larger parameter space of validity. The reflection and transmission coefficients evaluated with the retrieved effective material parameter are shown in blue for the local (WSD) and in red for the nonlocal (SSD) approach. Significant improvement can be seen when considering nonlocality. The local approach is only in agreement with the reference in the paraxial regime, while the nonlocal approach goes up to $50°$. This implies that retaining nonlocal constitutive relations is required for a realistic homogenization.

3. Conclusion

To conclude, we have seen that local constitutive relations turn out to become insufficient beyond the paraxial regime for selected MMs. This insufficiency could be lifted by introducing nonlocal material parameters. We discussed the additional interface conditions and the reflection and transmission coefficients from a slab and compared those to the response of an actual structure. We have also shown the importance of the introduction of advanced material properties in order to guarantee a more realistic homogenization. Exemplary, we demonstrated the improvement on the fishnet material, but improvements in other structure, e.g., spheres on a cubic lattice or wire media structures are visible too.

Acknowledgement

We gratefully acknowledge financial support by the Deutsche Forschungsgemeinschaft (DFG) through CRC 1173. K. Mnasri also acknowledges support from the Karlsruhe School of Optics and Photonics (KSOP).

References

[1] L.D. Landau and E.M. Lifshits, *Electrodynamics of Continuous Media,* 2nd edition, Oxford, England: Pergamon Press, 1984.

[2] I. Semchenko, A. Serdyukov, A. Sivola and S. Tretyakov, *Electromagnetics of Bi-Anisotropic Materials: Theory and Applications*, Routledge, 2001.

[3] K. Mnasri, A. Khrabustovskyi, C. Stohrer, M. Plum, and C. Rockstuhl, Phys. Rev. B **97**, 075439 (2018).

[4] K. Mnasri, A. Khrabustovskyi, M. Plum, and C. Rockstuhl, Phys. Rev. B **99**, 035442 (2019).

Challenging the foundations of electromagnetism: the excitation fields D and H

Jonathan Gratus[1,2,*], **Paul Kinsler**[1,2], **Martin W. McCall**[3]

[1]Lancaster University, Physics department, Lancaster LA1 4YB, UK
[2]The Cockcroft Institute, Sci-Tech Daresbury, Daresbury WA4 4AD, UK
[3]Department of Physics, Imperial College London, Prince Consort Road, London SW7 2AZ, UK
*corresponding author, E-mail: j.gratus@lancaster.ac.uk

Abstract

Maxwell's equations contain two auxiliary "excitation" fields, namely (D,H). These not only contain a gauge freedom, but have no way of being directly measured; as can be demonstrated by considering H inside a permanent magnet. This (D,H) freedom even allows us to defy global charge conservation in topologically non-trivial spacetimes (e.g. if a black hole forms and evaporates). We can also better understand the constitutive axion terms, and explore the possibility of a new treatment of electromagnetic current.

1. Introduction

Maxwell's equations do not feature the actual values of the excitation fields, but only their derivatives. As a result there is debate in the literature [1, 2] as to whether excitations $\boldsymbol{D}$ and $\boldsymbol{H}$ really are physical fields which can be directly measured, or simply a potential for the charge and current. As shown in fig. 1 (see also [3]) the $\boldsymbol{H}$-field in a permanent magnet can either be parallel or anti-parallel to the $\boldsymbol{B}$-field, depending on which constitutive model used you might choose. This is in stark contrast with the unambiguously physics electromagnetic fields $\boldsymbol{E}$ and $\boldsymbol{B}$, where the integrated fields can be measured inside a material using the Aharonov-Bohm effect.

It is easy to see that Maxwell's equations are invariant if we add a gauge $(\phi_{\mathrm{g}}, \boldsymbol{A}_{\mathrm{g}})$ to the excitation fields

$$\boldsymbol{D} \to \boldsymbol{D} + \nabla \times \boldsymbol{A}_{\mathrm{g}} \quad \text{and} \quad \boldsymbol{H} \to \dot{\boldsymbol{A}}_{\mathrm{g}} + \nabla \cdot \phi_{\mathrm{g}} \qquad (1)$$

This new gauge freedom, is distinct from the gauge freedom associated with the potential for $(\boldsymbol{E}, \boldsymbol{B})$.

2. A New Hope

There are two questions which arise naturally when we drop the existence of $\boldsymbol{D}$ and $\boldsymbol{H}$. How do we prescribe the constitutive relations, and what consequence arise as a result?

Our new approach re-evaluates the fundamental basis of the macroscopic Maxwell's equations, bypassing the excitation fields completely, and instead directly connecting the electromagnetic field to the current. The constitutive relation for this new type of media combines Gauss's Law, Maxwell-Ampère, and the constitutive tensor; all being

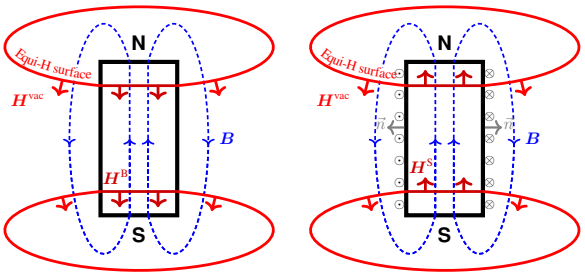


Figure 1: A comparison between the distinct models for the $\boldsymbol{H}$ fields in two standard pictures of magnetism: the bulk response model $\boldsymbol{H}^{\mathrm{B}} = \mu^{-1}\boldsymbol{B} - \boldsymbol{H}_{\mathbf{c}}$ (left), and the surface current model $\boldsymbol{H}^{\mathrm{S}} = \mu^{-1}\boldsymbol{B}$ and $\boldsymbol{\sigma}^{\mathrm{S}}_{\mathrm{b}} = \boldsymbol{n} \times \boldsymbol{H}_{\mathbf{c}}$ (right). Observe the direction of the $\boldsymbol{H}$ field inside the magnet. Figure used from [3] under the CCBY license.

represented instead by new functions $(\Psi^E_\rho, \Psi^B_\rho, \Psi^E_J, \Psi^B_J)$. Maxwell's equations now become

$$\nabla \cdot \boldsymbol{B} = 0\,, \qquad \nabla \times \boldsymbol{E} + \dot{\boldsymbol{B}} = 0\,,$$
$$\Psi^E_\rho(\boldsymbol{E}) + \Psi^B_\rho(\boldsymbol{B}) = \rho \quad \text{and} \quad \Psi^E_J(\boldsymbol{E}) + \Psi^B_J(\boldsymbol{B}) = \boldsymbol{J} \qquad (2)$$

The functions $(\Psi^E_\rho, \Psi^B_\rho, \Psi^E_J, \Psi^B_J)$ cannot be modelled as tensors as they involve derivatives. Instead, we will present the alternative rules they must obey, notably the requirements of conservation of charge. A careful analysis of the symmetries of $(\Psi^E_\rho, \Psi^B_\rho, \Psi^E_J, \Psi^B_J)$ shows that, in the homogeneous non-dispersive case, they possess 55 free parameters: 20 more that the standard constitutive tensor. These fall into two classes.

Four of the new parameters describe the axion response of the material. If one were to express these in terms of the excitation fields, they would be of the form

$$\begin{aligned} \boldsymbol{D}_{\mathrm{ax}} &= (t\zeta_t + x\zeta_x + y\zeta_y + z\zeta_z)\,\boldsymbol{B} \\ \text{and} \qquad \boldsymbol{H}_{\mathrm{ax}} &= -(t\zeta_t + x\zeta_x + y\zeta_y + z\zeta_z)\,\boldsymbol{E} \end{aligned} \qquad (3)$$

where t is time, (x, y, z) are the usual Cartesian coordinates and $(\zeta_t, \zeta_x, \zeta_y, \zeta_z)$ are the four axionic material constants. In the traditional approach, these would not be considered as valid terms in the homogeneous constitutive tensor, but, in contrast, when substituted into Maxwell's equations they

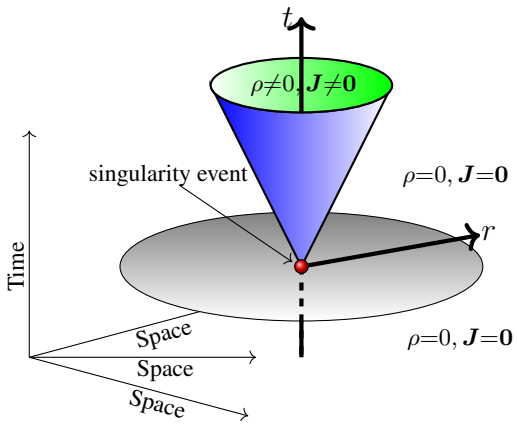


Figure 2: An event is excised from spacetime. The resulting non-trivial topology, together with the non existence of $(\boldsymbol{D}, \boldsymbol{H})$ breaks charge conservation.

give a perfectly valid homogeneous axionic response, i.e.

$$\begin{aligned} \nabla \cdot \boldsymbol{D}_{\text{ax}} &= \boldsymbol{\zeta} \cdot \boldsymbol{B} \\ \text{and} \qquad \nabla \times \boldsymbol{H}_{\text{ax}} - \dot{\boldsymbol{D}}_{\text{ax}} &= -\boldsymbol{\zeta} \times \boldsymbol{E} - \zeta_t \, \boldsymbol{B} \end{aligned} \tag{4}$$

Thus we can model a medium with an axionic response together with a simple constant permittivity ε and permeability μ. Maxwell's equations (2) become

$$\begin{gathered} \nabla \cdot \boldsymbol{B} = 0\,, \quad \nabla \times \boldsymbol{E} + \dot{\boldsymbol{B}} = 0\,, \quad \varepsilon \nabla \cdot \boldsymbol{E} - \boldsymbol{\zeta} \cdot \boldsymbol{B} = \rho \\ \text{and} \quad \mu^{-1} \nabla \times \boldsymbol{B} - \varepsilon \dot{\boldsymbol{E}} + \boldsymbol{\zeta} \times \boldsymbol{E} + \zeta_t \, \boldsymbol{B} = \boldsymbol{J} \end{gathered} \tag{5}$$

An interesting feature of such a medium is that electromagnetic wave with longitudinal components can propagate.

The remaining 51 parameters include the usual 35 given in the standard constitutive tensor. However they also give 16 *new* types of electromagnetic response. A traditional analysis could quite reasonably set these to zero, as they do not couple to electric charge or current. However, there is no reason why they *cannot* couple to something, and if that something did exist it would be interpretable as a new type of current and charge. We will briefly examine this exotic possibility, noting that in traditional notation it can been seen as arising from a (new) distinction that can be made between different instances of the same field components.

3. What are the consequences?

Although the arguments above are theoretic, it is possible to propose thought experiments where they have incontrovertible physical consequences. We will describe how (cf. [4]), given that a forming and evaporating black hole can create a topologically non-trivial spacetime, local charge conservation is no longer sufficient to also guarantee global charge conservation. As an example, in figure 2 we replace the evaporated black hole lifecycle with a simplified analogue, i.e. a spacetime with a single event removed. Before this event there is no charge or current, but, a nonzero charge nevertheless emanate from it. Another consquence is that if a charge passes through a wormhole, it need not leave that wormhole charged, as is traditionally believed.

4. Conclusion

We have challenged the notion that the excitation fields $(\boldsymbol{D}, \boldsymbol{H})$ are measurable fields, interpreting them instead as gauge fields for the current. We have given a new model of the constitutive relations, which bypasses the need to define $(\boldsymbol{D}, \boldsymbol{H})$. Analysing these relations we see there are an additional 20 parameters. Four of these are axions, while the remaining 16 require a new charge and current field.

We have shown that the consequence of these new relations mean that electromagnetic wave can have a longitudinal component and that we can break global charge conservation.

Acknowledgement

JG and PK are grateful for the support provided by STFC (the Cockcroft Institute ST/G008248/1 and ST/P002056/1) and EPSRC (the Alpha-X project EP/N028694/1). PK would like to acknowledge the hospitality of Imperial College London.

References

[1] J. J. Roche B and H, the intensity vectors of magnetism: A new approach to resolving a century-old controversy *American Journal of Physics* 68:5, 438-449 2000.

[2] F. W. Hehl, Y. N. Obukhov A gentle introduction to the foundations of classical electrodynamics: The meaning of the excitations (D,H) and the field strengths (E, B) *arXiv:physics/0005084*

[3] J. Gratus, P. Kinsler, M. W. McCall, Maxwell's (D, H) excitation fields: lessons from permanent magnets *European Journal of Physics.* 40, 025203 (2019).

[4] J. Gratus, P. Kinsler, M. W. McCall, Evaporating black-holes, wormholes, and vacuum polarisation: must they always conserve charge? Foundations of Physics (Under review) 2018

Electron Spill-Out Effects on Strong Light-Matter Coupling in Plasmonic Systems

Radoslaw Jurga[1,2], **Khalid Muhammad**[1], **Fabio Della Sala**[1,3], **Cristian Ciracì**[1*]

[1]Center for Biomolecular Nanotechnologies, Istituto Italiano di Tecnologia, via Barsanti 14, 73010, Arnesano, Italy
[2]Dipartimento di Matematica e Fisica, Universitá del Salento, via Monteroni, 73100, Lecce, Italy
[3]Institute for Microelectronics and Microsystems (IMM-CNR), Campus Ecotekne, 73100, Lecce, Italy
*corresponding author, E-mail: cristian.ciraci@iit.it

Abstract

At sub-nanometer length-scale, nonlocal and quantum effects are expected to influence the interaction between emitters and plasmonic systems, which unavoidably requires to go beyond classical models. Here, we apply state-of-the-art quantum hydrodynamic theory to investigate the quantum effects on strong coupling of a point-dipole emitter placed nearby metallic particles. In order to understand the effects of the quantum hydrodynamic model on the plasmon-emitter coupling, we compare our results with the conventional local response approximation and Thomas-Fermi hydrodynamic theory.

1. Introduction

Strong coupling in light-matter interactions requires enhanced optical field and small cavity volumes. Latest developments in the nanotechnology and nanofabrication techniques allow to engineer metallic structures supporting localized surface plasmons able to squeeze light in ever smaller nanovolumes, thus, offering an excellent platform to explore strong electromagnetic coupling in a plasmonic cavity. A quantum emitter placed inside a few-nanometer plasmonic gap shows a drastic change [1] in its radiation dynamics compared to bare metal films. Such light-atom interactions are of particular interest in quantum computation, biosensing, nanolasing and active plasmoinc applications. When coupling of a photon emitter with the surrounding plasmonic cavity is large enough so that the energy exchange happens before it is lost (or decayed) in the system, it is possible to enter the strong coupling regime where the emitter can reversibly exchange photons with the environment, hence leaving a signature in the optical emission spectra widely known as Rabi splitting [2, 3, 4].

Significantly large optical field confinement can be achieved in metallic structures with a few-nanometer or even subnanometer interparticle distances. At such small length scales, nonlocal and quantum effects come into play, which may have a non-negligible impact on the optical behavior the system [5, 6, 7]. When a quantum emitter is brought to close proximity of such nanostrucuters, more dramatic changes can be expected in its emission spectra due to nonlocal and quantum effects. Many studies have highlighted the impact of nonlocality on light-matter interactions in the strong coupling regime [4, 8, 9]. These nonlocal effects cannot be predicted in the framework of classical electrodynamics as revealed in several experiments [10, 11] and, thus, necessitating the development of efficient analytical and numerical models for correct description of electron dynamics.

2. Discussion

We investigate nonlocal and quantum effects on the optical properties of a photon emitter placed in a close proximity of plasmonic particles in tunneling regime by employing state-of-the-art quantum hydrodynamic theory (QHT). That is, the plasmonic system is considered in its complex dynamic including nonlocal effects, electron spill-out and tunneling, while the emitter is approximated as a point dipole.

The QHT can be summarized by the equation of motion of the electron gas written as a relation between the electric polarization $\mathbf{P}$ and the electric field $\mathbf{E}$ [5, 6, 7]

$$\frac{en_0}{m}\boldsymbol{\nabla}\left(\frac{\delta G[n]}{\delta n}\right)_1 - \frac{e}{m}\boldsymbol{\nabla}\cdot\sigma^{(\mathrm{kxc})} + \left(\omega^2 + i\gamma\omega\right)\mathbf{P} = -\varepsilon_0\omega_\mathrm{p}^2\mathbf{E}, \tag{1}$$

where e and m are respectively the magnitude of the charge and the mass of the electron, n the spatially dependent electron density, n_0 the equilibrium density, γ the phenomenological damping rate and ω_p the plasma frequency. The energy functional $G[n]$ contains the Thomas-Fermi and the von Weizsäcker kinetic energy functionals and a local-density approximated exchange-correlation energy term[6]. Eq. (1) includes an additional term $\sigma^{(\mathrm{kxc})}$, the viscoelastic kinetic-exchange-correlation tensor whose full expression is given in Ref. [7]. Its main effect is to take into account the nonlocal broadening of the spectra, especially relevant for geometries with small features[7].

Coupled to the continuity equation and Maxwell's equations, Eq. (1) describes the nonlocal optical response of metals, takes into account the charge spill-out and the size-dependent spectra broadening. The equilibrium density n_0 is computed self-consistently and fed as input into the QHT linear response equation.

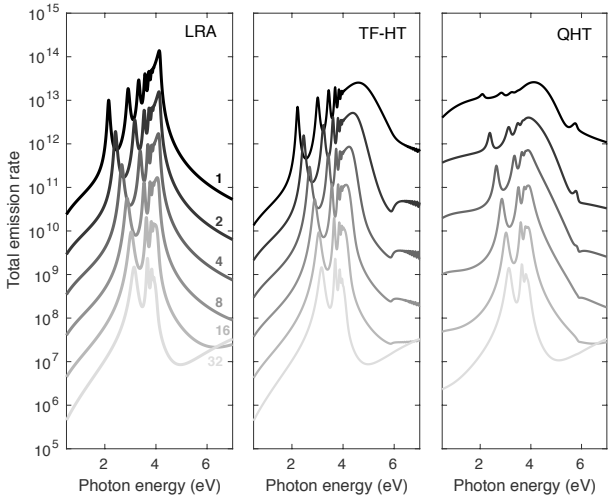


Figure 1: Decay rates of a dipole between a 40 nm Na sphere dimer for different gap sizes (from 1 to 32 nm).

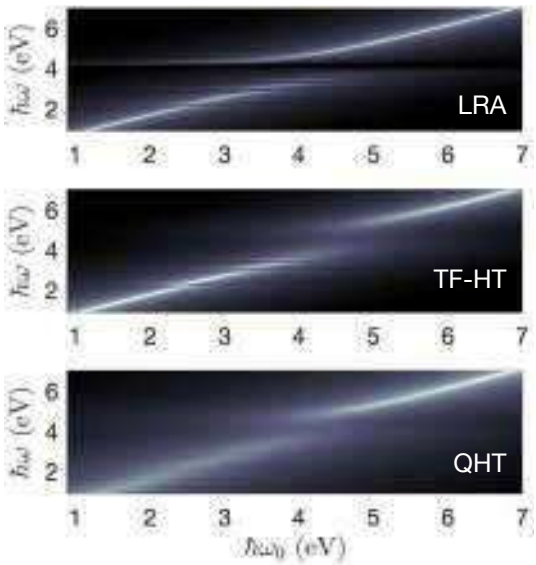


Figure 2: Dipole spectra for the same structure as a function of the emitter frequency ω_0. The results are computed within the local response approximation (LRA), Thomas-Fermi hydrodynamic theory (TF-HT) and quantum hydrodynamic theory (QHT).

Our results show that the impact of nonlocal and quantum effects on the fluorescence properties in configurations where metals are separated by gaps of a few nanometers might be drastic (Figure 1). Systems that are characterized by very small mode volumes, are the ones that are likely to display strong coupling at room temperature. The investigation of their impact in the strong coupling regime shows that depending on the specific material properties QHT may show a decrease in the threshold oscillator strength required to observe Rabi splitting (Figure 2) with respect to models in which the spill-out is neglected [9].

3. Conclusions

In the limit of the point-dipole approximation for the emitter considered here, nonlocality and quantum effects increase the oscillator strength threshold at which Rabi splitting can occur. This increase is caused by a decrease of the total decay rate, which is lower and broader when the QHT is used to describe the plasmonic environment.

References

[1] N. Kongsuwan *et al.*, "Suppressed Quenching and Strong-Coupling of Purcell-Enhanced Single-Molecule Emission in Plasmonic Nanocavities," *ACS Photonics*, 5: 186–191, 2017.

[2] S. Savasta, R. Saija, A. Ridolfo, O. Di Stefano, P. Denti, and F. Borghese, "Nanopolaritons: Vacuum Rabi Splitting with a Single Quantum Dot in the Center of a Dimer Nanoantenna," *ACS Nano*, 4: 6369–6376, 2010.

[3] L. Novotny, "Strong coupling, energy splitting, and level crossings: A classical perspective," *American Journal of Physics*, 78: 1199–4, 2010.

[4] M. M. Dvoynenko and J.-K. Wang, "Revisiting strong coupling between a single molecule and surface plasmons," *Opt. Lett.*, 38: 760–762, 2013.

[5] G. Toscano, *et al.*, "Resonance shifts and spill-out effects in self-consistent hydrodynamic nanoplasmonics," *Nat. Comm.*, 6: 7132, 2015.

[6] C. Ciracì and F. Della Sala, "Quantum hydrodynamic theory for plasmonics: Impact of the electron density tail," *Phys. Rev. B*, 93: 205405, 2016.

[7] C. Ciracì, "Current-dependent potential for nonlocal absorption in quantum hydrodynamic theory," *Phys. Rev. B*, 95: 245434, 2017.

[8] R. Filter, C. Bösel, G. Toscano, F. Lederer, and C. Rockstuhl, "Nonlocal effects: relevance for the spontaneous emission rates of quantum emitters coupled to plasmonic structures ," *Opt. Lett.*, 39: 6118–6121, 2014.

[9] R. Jurga, S. D'Agostino, F. Della Sala, and C. Ciracì, "Plasmonic Nonlocal Response Effects on Dipole Decay Dynamics in the Weak- and Strong-Coupling Regimes," *J. Phys. Chem. C*, 121: 22 361–22 368, 2017.

[10] K. J. Savage, M. M. Hawkeye, R. Esteban, A. G. Borisov, J. Aizpurua, and J. J. Baumberg, "Revealing the quantum regime in tunnelling plasmonics," *Nature*, 491: 574–577, 2012.

[11] C. Ciracì *et al.*, "Probing the ultimate limits of plasmonic enhancement," *Science*, 337: 1972–1074, 2012.

Spatial dispersion and local field effects in metamaterials

A.A. Tishchenko[1,2]

[1]National Research Nuclear University "MEPhI", Russia
[2]National Research Center "Kurchatov Institute", Russia
*corresponding author, E-mail: tishchenko@mephi.ru

Abstract

In this report I discuss correlation between two key phenomena in metamaterials: spatial dispersion – non-local response of material – and local field effects. I consider 1D, 2D and 3D systems of interacting objects (meta-atoms), and two types of response functions: response to the macroscopic field existing in the system, which leads directly to the dielectric function, like the Clausius-Mossotti one; and the response to the field of external sources. The analysis is given for two competing approaches: i) the widely used description via two independent dielectric and magnetic functions, and ii) more general but less popular description through the tensor of dielectric function embracing both dielectric and magnetic properties.

1. Introduction

The phenomenon of spatial dispersion of dielectric function – the dependence of dielectric properties of a material from the wave vector, which is explained by the non-localness of the response of the material - was first mentioned, probably, by Gerzenshtein as early as in 1952 [1]. Since then this phenomenon has been widely investigated. It is usually assumed to be most pronounced in plasma [2], because of high electron mobility, but in fact plays key role near zeros of dielectric function, when spatial dispersion provides us with new types of electromagnetic waves in condensed matter [3]. It is also well-known to be responsible for the natural optical activity of some crystals (or gyrotropy). It proves, however, that the spatial dispersion is absolutely fundamental phenomenon, which is necessary, for instance, for the high temperature superconductivity to exist (the condition $\varepsilon(\mathbf{q},0)<0$ must be satisfied) [4]. The spatial dispersion plays a vital part in violation of the Kramers-Kronig relations [4], which are, in a sense, even more fundamental then basic Maxwell's equations, because they are caused directly by the causality principle.

Though the role of spatial dispersion in metamaterials is very well known [5, 6], its potentialities has not been exhausted. Interestingly, recently Im with coauthors have reinterpreted a dielectric bi-layer as a monolayer with non-local properties that change as the angle of the incident wave varies [7]; this effect makes this effective matching layer a promising 'quarter-wave' layer, i.e. very good candidate for ideal active anti-reflection coating.

On the other hand, for the microscopic properties of metamaterial to be calculated, one needs to calculate first the local fields, acting at the points in which the meta-atoms are. This problem can be solved within the so-called local field approach that operates with double-particle distribution functions, taking into account the effects of interaction in system of many particles. This method is then naturally suitable for taking into account the mutual disposition of the single meta-atoms, i.e., the structure of the material.

In this report I show how the local field effects lead to the non-locality of dielectric response of materials, and show it by the examples of 1D, 2D and 3D systems. Below are represented the generalized expressions linking dielectric function of metamaterial with microscopic properties of constituent meta-atoms and the double-particle distribution function defining the inner structure of the material.

2. Some analytics

Let us consider dielectric properties of the material consisting of meta-atoms – small objects that are characterized by the polarizability $\alpha_{ij}(\omega)$. This value can have non-zero imaginary part, and can be tensor, which would suit for anisotropic meta-atoms. Based on the Maxwell's equations, it is not hard to obtain the expressions linking the exact microscopic field $E_i^{mic}(\mathbf{r},\omega)$, the field external of sources $E_i^0(\mathbf{r},\omega)$, and the local field $E_j^{loc}(\mathbf{R}_a,\omega)$, i.e. the field acting at the points in which the meta-atoms are disposed

$$E_i^{mic}(\mathbf{r},\omega)=E_i^0(\mathbf{r},\omega)+\hat{A}_{ij}\,E_j^{loc}(\mathbf{R}_a,\omega). \qquad (1)$$

Here tensor operator $\hat{A}_{ij}$ describes the contribution of the matter. Further, two types of averaging are used: the conventional one giving the average macroscopic field $\mathbf{E}$

$$E_i=E_i^0+\hat{B}_{ij}E_j^{loc}, \qquad (2)$$

and the second one, being obtained with the help of averaging with double-particle distribution function, which reads

$$E_i^{loc}=E_i^0+\hat{C}_{ij}E_j^{loc}. \qquad (3)$$

Combined solving of two these let one to find the different answers, depending on the dimensionality of the structure considered. For example, in case of 3D structure (infinite volume filled up with meta-atoms) it reads

$$\varepsilon_{ij}(\mathbf{q},\omega)=\delta_{ij}+4\pi n\alpha_{ik}(\omega)t^{-1}_{kj}(\mathbf{q},\omega), \quad (4)$$

where

$$t_{ij}(\mathbf{q},\omega)=\delta_{ij}- \\ -4\pi n\left\{\alpha_{ij}(\omega)+\int d^3l\frac{l_i l_s-l^2\delta_{is}}{l^2-k^2}\alpha_{sj}(\omega)f(\mathbf{l}-\mathbf{q})\right\} \quad (5)$$

and $f(\mathbf{l}-\mathbf{q})$ is a Fourier-image of the radial distribution function.

In case of 2D structure (infinite surface filled up with meta-atoms) is reads

$$\varepsilon_{ij}(\mathbf{q},\mathrm{z},\omega)=\delta_{ij}+4\pi n\alpha_{ik}(\omega)t^{-1}_{kj}(\mathbf{q},\mathrm{z},\omega), \quad (6)$$

where

$$t_{ij}(\mathbf{q},z,\omega)=\delta_{ij}+ \\ +4\pi n\int d^3lS_{ik}(\mathbf{l},\omega)\alpha_{kj}(\omega)\eta(l_z)f(\mathbf{l}_{\|}-\mathbf{q})\exp\{il_z z\} \quad (7)$$

and the functions $\eta(l_z)$ and $f(\mathbf{l}_{\|}-\mathbf{q})$ are parts of the Fourier-image of the radial distribution function as well. Note, that in Eqs. (6) and (7) vector $\mathbf{q}$ is two-dimensional in contrast to Eqs. (4) and (5) in which it is 3D.

For example, in the long-wave limit, when the wavelength exceeds considerably the size of single meta-atoms (which is totally natural case for metamaterials), Eq. (6) becomes much simpler, with main values of tensor ε_{ij}:

$$\varepsilon_{\|}(z,\omega)=1+\frac{4\pi n\alpha_{\|}(\omega)\eta(z)}{1-\pi n\alpha_{\|}(\omega)\xi(z)}, \\ \varepsilon_{\perp}(z,\omega)=\frac{1+2\pi n\alpha_{\perp}(\omega)\xi(z)}{1+2\pi n\alpha_{\perp}(\omega)\left(\xi(z)-2\eta(z)\right)}, \quad (8)$$

and the value

$$\xi(z)=\int d^2l_{\|}f(\mathbf{l}_{\|})l_{\|}\exp\{-|z|l_{\|}\} \quad (9)$$

contains the information about the structure, while

$$\eta(z)=\left(4\pi b^2\right)^{-1/2}\exp\left\{-\frac{z^2}{4b^2}\right\} \quad (10)$$

is the function, describing distribution of meta-atoms near the surface given by $z=0$, b is the effective width of this quasi-monolayer.

Along with that, the system of Eqs. (2) and (3) let us find the expression linking the local field with the external one:

$$E^{loc}_i(\mathbf{r},\omega)=\left(\frac{\delta_{ij}-e_i e_j}{1-\pi n\alpha_{\|}(\omega)\xi(z)}+ \right. \\ \left. +\frac{e_i e_j}{1+2\pi n\alpha_{\perp}(\omega)\xi(z)}\right)E^0_j(\mathbf{r},\omega), \quad (11)$$

where e_i is the i-th component of the vector normal to the surface. The expressions like Eq. (11) are very useful for the wide range of practical problems to be solved. For example, the problems of generation radiation by the charged particles beams from metasurfaces are solved more or less easily, see, e.g. [8, 9]. Moreover, it is very promising for the High-Resolution Cathodoluminescence Spectroscopy and Electron Energy Loss Spectroscopy – instruments that are being developed very actively nowadays [10].

3. Conclusions

The real report will contain not only the detailed discussion of what has been said above, but also the issues mentioned in the abstract: the comparison between two close in nature, but differing from point of view of analytics approaches, dealing with i) two independent dielectric and magnetic functions, and ii) the tensor of dielectric function embracing both dielectric and magnetic properties; the description for 1D systems (chains of meta-atoms – meta-wires); discussion of the difficulties concerning the existence of the boundaries in 3D case: here the theory allows obtaining dielectric function, including the so-called natural change of surface properties, caused by the change in the symmetry in formation of local fields near the surface (see, e.g., [11]) – but the expression linking the local field through the external one has been an unsolvable problem, being a stumbling block on the way of many practically interesting applications.

Acknowledgements

This research was supported by the Competitiveness Programme of National Research Nuclear University "MEPhI" and partially by the Ministry of Science and Education of the Russian Federation, grant №3.2621.2017/4.6.

References

[1] M.E. Gerzenshtein, *ZhETF* **22**, 303 (1952).

[2] A.A. Rukhadze, V.P. Silin, Linear electromagnetic phenomena in a plasma, *Sov. Phys. Usp.* **5**, 37 (1962).

[3] M.V. Gorkunov, M.I. Ryazanov, Unknown additional electromagnetic waves in crystal near absorption lines, *Laser Physics* **8**, 502 (1998).

[4] D.A. Kirzhnits, Are the Kramers-Kronig relations for dielectric permittivity of a material always valid? Sov. Phys. Usp. **19**, 530 (1976).

[5] V.M. Agranovich, Yu.N. Gartstein, Spatial dispersion and negative refraction of light, *Phys.Usp.* **49**, 1029 (2006).

[6] A.K. Sarychev, V.M. Shalaev, *Electrodynamics of Metamaterials*, World Scientific, 2007.

[7] K. Im, J.-H. Kang, Q-H. Park, Universal impedance matching and the perfect transmission of white light, Nature Photonics **12**, 143 (2018).

[8] M.I. Ryazanov, M.N. Strikhanov, A.A. Tishchenko, Local field effect in diffraction radiation from a periodical system of dielectric spheres, Nucl. Instr. and Meth. B **266**, 3811 (2008).

[9] D.Yu. Sergeeva, A.A. Tishchenko, M.N. Strikhanov, Microscopic theory of Smith-Purcell radiation from 2D photonic crystal, Nucl. Instr. Meth. B **402**, 206 (2017).

[10] F.J. García de Abajo, Optical Excitations in Electron Microscopy, Rev. Mod. Phys. **82**, 209−275 (2010).

[11] O.V. Porvatkina, A.A. Tishchenko, M.N. Strikhanov, Permeability tensor for a metamaterial adjacent to a metal, Applied Physics A **123**, 2 (2017).

Electromagnetic clocks at the rim of metamaterial black holes

Sophie Viaene[1*], Vincent Ginis[2], Jan Danckaert[2], Ortwin Hess[1], and Philippe Tassin[3]

[1] The Blackett Laboratory, Department of Physics, Imperial College London, South Kensington Campus, Prince Consort Road, London SW7 2AZ, UK
[2] Applied Physics Research Group, Vrije Universiteit Brussel, Pleinlaan 2, B-1050 Brussels, Belgium
[3] Department of Physics, Chalmers University of Technology, SE-412 96 Gteborg, Sweden
*corresponding author, E-mail: sophie.viaene@imperial.ac.uk

Abstract

It is notoriously difficult to emulate black hole physics with experiments on earth. This is especially true when emulating the event horizon, which requires controlling materials or experimental settings in time. In contrast, here, we show that hallmark phenomena such as a gravitational red shift can be imposed by a static metamaterial black hole. To this end, we solve for the spontaneous emission rate of a two-level emitter inside a metamaterial black hole, which serves as an electromagnetic clock.

1. Emulating black holes

The Schwarzschild geometry is the oldest and simplest solution of the Einstein field equations in general relativity. It describes how particles are affected by the gravitational pull of heavy spherical objects such as the earth, stars, black holes, and centres of galaxies [1, 2]. Black holes are particularly interesting deformations of space and time because of their nonreciprocal behaviour, i.e., their gravitational pull is so strong that within a Schwarzschild radius nothing can escape from it. The appearance of such an event horizon strongly depends on the observer. Co-moving observers who cross the event horizon of the black hole would not experience anything out of the ordinary, except that they would be unable to return. However, static observers at a large distance from the black hole would see quite a few extraordinary things, such as a gravitational red shift [7], an apparent slowing down of light [2], and Hawking radiation from the black hole [3].

Research on analogue systems of black holes has an impressive reach, encompassing a variety physics theories such as the physics of moving condensates [8], spatio-temporally modulated metamaterials [10], filaments in optically pumped nonlinear media [11], and atomic ensembles imposing slow light [12]. All of these proposals are based on the implementation of an artificial event horizon with time-dependent material properties, thus hoping to observe Unruh-Hawking radiation [9]. Besides these advanced proposals, which have given rise to much debate, there are several proposals of simplified electromagnetic emulations [5, 6, 13], such as refractive index distributions and waveguide-based proposals with singularities, that mimic the ray dynamics near a black hole. In particular, the singularities result in a rapidly varying phase, i.e., a phase catastrophe, and a low group velocity that prevents light from crossing them [12, 16, 17]. Hence, these singular systems emulate the viewpoint of an external observer at infinity, who is never able to see inside the event horizon.

2. Electromagnetic clocks

In this contribution, we show how transformation-optical metamaterials based on the Schwarzschild geometry [4, 5, 6] can emulate Schwarzschild black holes in a way that goes beyond ray dynamics. The idea is to capture the dynamic properties of the metamaterial black holes, such as the gravitational red shift and the slowing down of electromagnetic phenomena, by making use of an electromagnetic clock that consists of a two-level emitter, as visualized in Fig. 1. The two-level emitter with dipole moment $\mathbf{d}$ is put at different radial distances r from the metamaterial black hole, with the usual permittivity and permeability distributions outside an event horizon with Schwarzschild radius R_s

$$\bar{\bar{\varepsilon}} = \mathrm{diag}\left(1, (1-\mathrm{R_s/r})^{-1}, (1-\mathrm{R_s/r})^{-1}\right) = \bar{\bar{\mu}}. \quad (1)$$

Note that the dipole moment can be either parallel ($||$) or perpendicular ($\perp$) to the radial unit vector. For each distance, the spontaneous emission rate of the electromagnetic clock is determined by two contributions to Fermi's golden rule at a transition frequency ω_{eg}:

$$\gamma = \frac{\pi\omega_{eg}}{3\hbar\epsilon_0} \underbrace{\left|-e\langle\psi_e\left|\mathbf{r}\cdot\mathbf{n_d}\right|\psi_g\rangle\right|^2}_{|\mathbf{d}_{eg}|^2} \underbrace{3\sum_{\mathbf{k}\lambda}\left|\mathbf{n_d}\cdot\mathbf{u}_{\mathbf{k}}^{(\lambda)}\right|^2\delta\left(\omega_{\mathbf{k}}-\omega_{eg}\right)}_{\rho(\omega_{eg})}. \quad (2)$$

The first contribution by the transition dipole moment with orientation $\mathbf{n_d}$ is determined by the overlap integral between the excited state $|\psi_e\rangle$ and the ground state $|\psi_g\rangle$ orbitals. Our analytical calculations and finite-element simulations of the Schrödinger equation for the emitter inside the metamaterial show that its effective permittivity distribution deforms the orbitals in an exact, non-perturbative, and geometrical way, but only when the effective mass of the emitter $\bar{\bar{m}}$ is engineered to be anisotropic, i.e., $(1-R_s/r)m_{||} =$

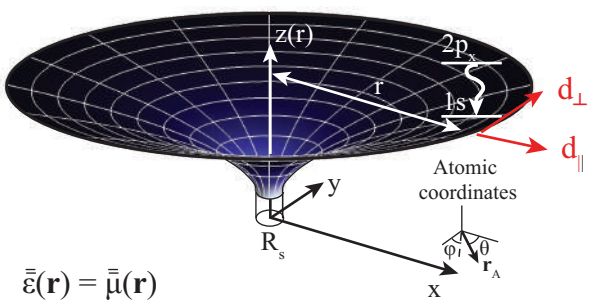


Figure 1: Visualization of a Schwarzschild black hole, with an effective measure of length along the surface. A two-level emitter with a dipole moment $\mathbf{d}$ parallel ($||$) or perpendicular ($\perp$) to the radial direction is put at various distances from the event horizon ($r = R_s$) to probe the spontaneous emission rate.

$m_\perp$. This provides an additional equivalence relation, complementing those of transformation optics.

The second contribution is due to the partial density of states (PDOS), i.e., the distribution of photons $\mathbf{u}_\mathbf{k}^\lambda$ with quantum numbers $\mathbf{k}$ and polarization λ. Usually, it is assumed that the photons are coordinate-transformed plane waves [20]. Here, however, the plane wave expansion of the PDOS is incompatible with the spherically symmetric event horizon. We have developed an expansion based on vector spherical harmonics that does impose appropriate boundary conditions.

Overall, we show that a time-independent metamaterial black hole can modify emission rates and emission frequencies through a joint engineering of electronic (effective mass) and optical properties (transformation-optical metamaterials) in space.

Acknowledgement

S. V. and V. G. acknowledge fellowships from the Research Foundation Flanders (FWO-Vlaanderen). Work at Chalmers was partially supported by Vetenskapsrådet under grant No. 201603603. Work at Imperial College London was partially supported by the COST action MP1403 on Nanoscale Quantum Optics.

References

[1] K. Schwarzschild, On the gravitational field of a point mass according to Einstein's theory, *Sitzungsber. Preuss. Akad. Wiss., Phys. Math*, 2016.

[2] S. M. Caroll, *Spacetime and geometry. An introduction to general relativity*, Addison Wesley, New York, 2004.

[3] L. Susskind, The paradox of quantum black holes, *Nat. Phys.* 2: 665, 2006.

[4] J. B. Pendry, D. Schurig, D. R. Smith, Controlling electromagnetic fields, *Science* 312: 1780–1782, 2006.

[5] U. Leonhardt, Optical conformal mapping, *Science* 312: 1777–1780, 2006.

[6] D. A. Genov, S. Zhang, X. Zhang, Mimicking celestial mechanics in metamaterials, *Nat. Phys.* 5: 687, 2009.

[7] C. Chin-Wen, D. B. Hume, T. Rosenband, D. J. Wineland, Optical clocks and relativity, *Science* 329: 1630–1633, 2010.

[8] J. Steinhauer, Observation of self-amplifying Hawking radiation in an analogue black-hole laser, *Nat. Phys.* 10: 864, 2014.

[9] W. G. Unruh, Experimental black-hole evaporation?, *Phys. Rev. Lett.* 46: 1351, 1981.

[10] R. Schützhold, W. Unruh, Hawking radiation in an electromagnetic waveguide?, *Phys. Rev. Lett.* 95: 031301, 2005.

[11] J. Drori, Y. Rosenberg, D. Bermudez, Y. Silberberg, U. Leonhardt, Observation of stimulated Hawking radiation in an optical analogue, *Phys. Rev. Lett.* 122: 010404, 2019.

[12] U. Leonhardt, A laboratory analogue of the event horizon using slow light in an atomic medium, *Nature* 415: 406, 2002.

[13] C. Sheng, H. Liu, Y. Wang, S. N. Zhu, D. A. Genov, Trapping light by mimicking gravitational lensing, *Nat. Photon.* 7: 902, 2013.

[14] H. Chen, R. Miao, M. Li, Transformation optics that mimics the system outside a Schwarzschild black hole, *Opt. Expr.* 18: 15183–15188, 2010.

[15] A. Aubry, D. Y. Lei, A. I. Fernández-Domínguez, Y. Sonnefraud, S. A. Maier, J. B. Pendry, Plasmonic light-harvesting devices over the whole visible spectrum, *Nano Lett.* 10: 2574–2579, 2010.

[16] J. B. Pendry, P. A. Huidobro, Y. Luo, E. Galiffi, Compacted dimensions and singular plasmonic surfaces, *Science* 358: 915–917, 2017.

[17] K. L. Tsakmakidis, O. Hess, R. W. Boyd, X. Zhang, Ultraslow waves on the nanoscale, *Science* 358: eaan5196, 2017.

[18] L. Novotny, B. Hecht, *Principles of nano-optics*, Cambridge university press, Cambridge, 2012.

[19] S. Viaene, *Exploring metamaterial horizons: New concepts and geometrical tools for the description of advanced electromagnetic phenomena*, VUB press, Brussels, 2018.

[20] J. Zhang, M. Wubs, P. Ginzburg, G. Wurtz, A. V. Zayats, Transformation quantum optics: designing spontaneous emission using coordinate transformations, *J. Opt.* 18: 044029, 2016.

Electromagnetic Wave generation and Amplification mediated via Artificial Materials.

Rebecca Seviour[1] and Simon Foulkes[1]

[1] Accelerator Research Group, University of Huddersfield, West Yorkshire, UK
*corresponding author, E-mail: r.seviour2@hud.ac.uk

Abstract

In this paper we examine the use of artificial electromagnetic media to mediate interactions between electromagnetic waves and charged particle beams. Where we consider the physics and application of interaction between artificial media and electron beams, and how this interaction can be used to create novel sources and amplifiers of EM waves.

1. Introduction

The realisation of artificial electromagnetic materials began a hundred years before the term "metamaterial" was introduced, with the work of Rayleigh and Bose in the 1890s. Although the first practical applications did not appear until the 1940s with the pioneering work of Kock[3], who considered these constructs as artificial dielectric materials. Renewed interest in these materials arose with the work of Pendry[4] on metamaterials. The term metamaterial was coined by Rodger Walser defined a metamaterial as; "*...macroscopic composites having man-made, three-dimensional, periodic cellular architecture designed to produce an optimised combination, not available in nature, of two or more responses to specific excitation*". Where the subwavelength scale of the cells in the metamaterial make the whole composite macroscopically uniform and treatable as an artificial material. Artificial electromagnetic materials, such as metamaterials, essential create an arbitrary, engineered, phase shift of an incident wave across the unit cell, which enables the dispersion relation of the media to be engineered in a controlled way.

To date numerous papers have been published on the electromagnetic properties of metamaterials at low power levels. In this paper we examine advances that have been made in studying metamaterials as slow wave structures for active electron beam-driven microwave devices. We discuss structures that do satisfy the Waslers definition of a metamaterial and those that do not, that offer novel engineered dispersion relations to discover novel beam/wave interactions that can be exploited for new technologies.

In this paper we bring together advances that have been made in studying metamaterials as slow wave structures for active electron beam-driven devices. We consider the ability of the sub wave length geometries to with stand high power, and we consider two scenarios where metamaterials are for EM amplification and for EM generation. In both configurations for effective energy transfer between beam and EM wave the phase velocity of the wave must approximately match the velocity of the electron beam. Where this is achieved by engineering the dispersion of the wave through the material to tailor the interaction between electron beam and wave.

2. Traveling Wave Amplification

In this section of the paper we consider the application of metamaterials to Traveling Wave Tubes (TWT). In a conventional TWT amplification of an EM wave is achieved by passing the EM wave to be amplified through a Slow Wave Structure (SWS) simultaneously with an electron beam, where wave and beam pass through the structure with similar velocities. Resulting in an interaction between beam transferring energy from beam to wave. In a conventional Waveguide TWT this is achieved by folded the waveguide (see figure 1)[5] to slow down the wave, generating Spatial Harmonics Wave Components parallel to the beam. The SHWC interact with the beam resulting in energy transfer.

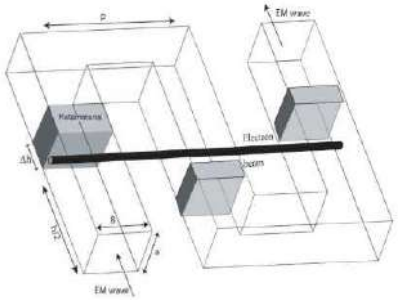


Figure 1: The traveling wave structure considered here, consisting of a folded waveguide with a metamaterial insert, the electron beam passes through the middle of the structure. Figure taken from [6].

To ensure that the phase of the EM field is the same at each point wave and beam interact, the wave takes the long path around the folded wave guide, hence the period in the beam frame of reference is half the geometrical period of the structure shown in figure 1. In a conventional TWT the dispersion relation, frequency of operation and size of device are all determined by the physical dimensions of the

device. By inserting a metamaterial at the interaction points between wave and beam the metamaterial enables both the tailoring of the dispersion relation and an arbitrary phase shift of the wave [6].

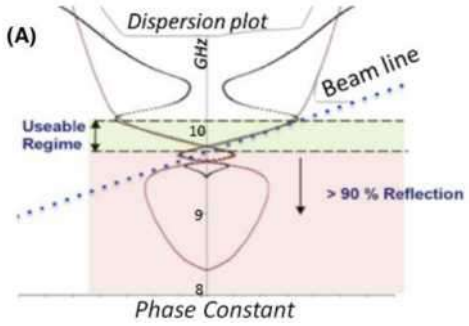


Figure 2: Dispersion curve for a waveguide loaded with metamaterial, the dotted line represents the electron beam line.

Figure 2 show the dispersion relation for a waveguide loaded with metamaterial, in the case presented the material has both negative permittivity and permeability at around 10GHz, as can be seen by the anomalous dispersion shown in fig2. The interaction of the loaded waveguide with perpendicular beam is shown by the dotted line. The power exchanged between wave and beam can be calculated via the perturbation approach of Madeys theory[6]. Figure 3 presents the results of the power exchange between wave and beam vs frequency for several beam energies, calculated via Madeys theory. As can be seen for different frequencies/voltages the configuration can act either as an amplifier taking energy from the beam into the wave, or as an accelerator taking energy from the wave into the beam.

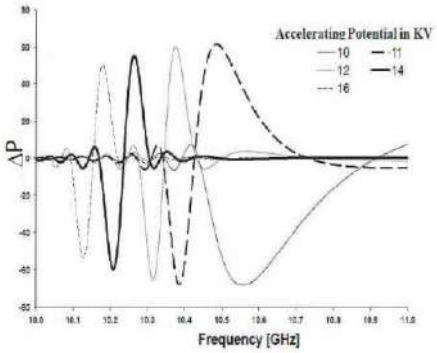


Figure 3: Increase in EM power due to interaction with an electron beam, for different electron beam energies. Figure taken from [6].

3. Traveling Wave Amplification

In this section of the paper we consider the application of metamaterials as an RF source. Where in the configuration we present a circular waveguide loaded with metamaterial shown in fig4. The metamaterial used in this configuration is a complementary split ring resonator, an all metal metamaterial. The media is "wrapped" into a cylinder around the electron beam. In this particular configuration we consider a thin gyro electron beam as a 20keV 500μA.

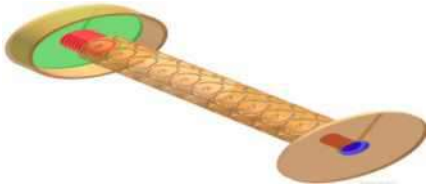


Figure 4 Circular waveguide loaded with metamaterial, where the beam passes on axis shown in red.

To examine the interaction between beam wave and metamaterials model the system of fig 4 was modelled using the particle-in-cell finite difference time domain simulation software MAGIC. The result of the interaction between wave and beam are shown in figure 5. Figure 5 shows that the system loaded with metamaterial triggers a strong EM wave production, where as the empty system produces negligible EM wave production.

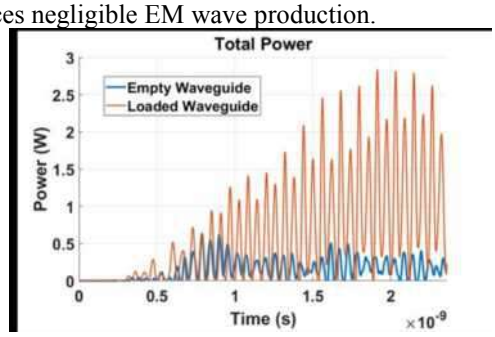


Figure 5: Power as a function of time for both a metamaterial loaded waveguide and an empty waveguide of fig 4.

4. Conclusions

We see that a metamaterial TWT can offer an additional factor to controlling the gain-frequency characteristics, compared to the conventional TWT. The ability to arbitrarily control the phase shift of the wave with the metamaterial enables us to consider oversized or undersized Although this approach does have the disadvantages that the bandwidth is Limited.

Acknowledgements

The authors would like to thank the AFOSR and the EPSRC for their support in undertaking the work presented.

References

[1] Rayleigh. Phil. Mag., 5, 34, pp 481, 1892

[2] J. C. Bose, Proc R. Soc. Lon., 63, 146, 1898.

[3] W. E. Kock, Bell System Technical J, 27, pp58, 1948.

[4] J.B. Pendry, A.J. Holden, D.J. Robbins and W.J. Stewart, Magnetism from conductors and enhanced nonlinear phenomena, IEEE Trans Microw Theory Tech, 47, 2075-2084, 1999.

[5] A.F. Harvey, Periodic and guiding structures at microwave frequencies, IRE Trans Microwave Theory Tech 8 (1960), p. 30-61.

[6] Y. Tan and R. Seviour, Europhys.Lett.87:34005,2009

Omnidirectional impedance match and its applications based on effective nonlocal media

Jie Luo[1], Yun Lai[2]
[1]College of Physics, Optoelectronics and Energy & Collaborative Innovation Center of Suzhou Nano Science and Technology, Soochow University, Suzhou 215006, China
[2]National Laboratory of Solid State Microstructures, School of Physics, and Collaborative Innovation Center of Advanced Microstructures, Nanjing University, Nanjing 210093, China
*corresponding author, E-mail: laiyun@nju.edu.cn

Abstract

In this work, we first demonstrate that pure dielectric photonic crystals can be used to realize effective nonlocal media with omnidirectional impedance matching effect, which allow near 100% transmission of light for all incident angles. Then, we show that by adding some loss into such effective nonlocal media, omnidirectional and broadband absorption can be realized with near 100% efficiency. We believe that the nonlocality enables new freedoms for light manipulation beyond the local medium framework.

1. Introduction

Transparent media are the foundation of almost all optical instruments, such as optical lens, etc. However, perfect transparency has never been realized in natural transparent solid materials such as glass because of the impedance mismatch with free space or air. As a consequence, there generally exist unwanted reflected waves at the surface of a glass slab, as illustrated in Fig. 1(a). It is well known that non-reflection only occurs at a particular incident angle for a specific polarization, which is known as the Brewster angle effect [1]. Our question is: is it possible to extend the Brewster angle from a particular angle to a wide range of or all angles, so that there is no reflection for any incident angle.

In addition, the virtual image formed by a glass slab placed in air is usually blurred to a certain extent [Fig. 1(a)]. Such a blur indicates the aberration of virtual images, and is caused by the mismatch of equal frequency contours (EFCs) between air (grey lines) and the glass (blue lines).

In this work, we propose to utilize the spatial dispersive effective parameters of pure dielectric PhCs to realize perfectly transparent media with omnidirectional impedance matching, which allows near 100% transmission of light at all incident angles. The equal frequency contours (EFCs) of such PhCs are designed to be elliptical and "shifted" in the k-space, and thus contain strong spatial dispersions. We demonstrate that at certain frequency regimes, such PhCs can allow maximal amount of light to pass through and create aberration-free virtual images. Moreover, we show that by adding some loss into such effective nonlocal media, omnidirectional and broadband absorption can be realized with near 100% efficiency. Based on this principle, photonic crystals composed of a large variety of dielectric materials can become perfect absorbers at a broad spectrum range.

2. Ultratransparent media with omnidirectional impedance matching effect

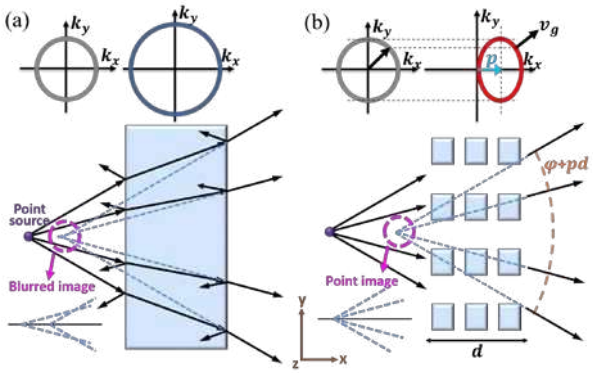


Figure 1: (a) Virtual image formation through a glass slab, with general reflection and aberration. (b) Aberration-free virtual image formation through an ultratransparent PhC without any reflection due to omnidirectional impedance matching. The black arrows and blue dashed lines in represent the light rays from a point source, and the back tracing lines, respectively. The yellow dashed curves in (b) indicate equal phase surfaces of transmitted rays. The inset graphs show the corresponding EFCs.

First, we find that omnidirectional impedance matching can be realized by utilizing effective medium with nonlocal parameters, i.e. permittivity and permeability that are dependent on the incident angle [2-4]. Interestingly, such an effective medium can be realized by using pure dielectric PhCs [5]. Moreover, the EFC of the ultratransparent PhC can be tuned to be a shifted ellipse (red lines) with the same height of the EFC of air (grey lines). By using ray optics, we prove that such an EFC endows the valuable ability of forming aberration-free virtual images, as presented in Fig.

1(b).

Because of the shift of EFC, the PhC is beyond the local medium framework, and effective parameters are nonlocal (i.e. spatially dispersive). Interestingly, such nonlocality leads to additional phase modulation pd, where p is the shift magnitude and d is the slab thickness [Fig. 1(b)].

In addition, numerical calculations confirm that such a PhC exhibits almost complete transparency (T>99%) for nearly all incident angles ($-89^{o}, 89^{o}$).

3. Omnidirectional perfect absorbers

Next, we show that when there is loss in the ultratransparent media with omnidirectional impedance matching effect, light energy will be gradually absorbed, as illustrated in Fig. 2. Therefore, this concept provides a straightforward way to realize omnidirectional near-perfect absorption by bulk materials without surface decoration [6].

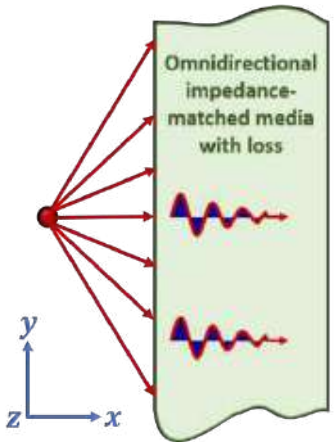


Figure 2: Illustration of an omnidirectional near-perfect absorber consisting of omnidirectional impedance-matched media with a small amount of material loss.

For demonstrations, we simulated the distribution of electric fields when a point source is placed in front of the multilayer absorber, as presented in Fig. 3. It is seen that the radiated wave in the left side (air) is a well-defined cylindrical wave with no interference pattern induced by any reflection. This again confirms the omnidirectional characteristic of the mutilayer absober.

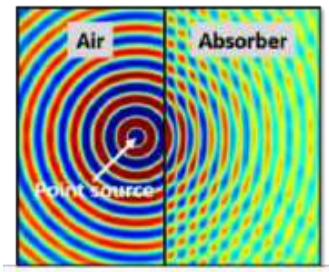


Figure 3: The simulated distribution of electric fields when a point source is placed in front of the multilayer absorber.

4. Conclusions

In summary, we show that ultratransparent media with omnidirectional impedance matching effect can be realized by using pure dielectric PhCs with spatial dispersions. Moreover, by introduction appropriate material losses into such impedance-matched media, broadband and omnidirectional perfect absorbers can be realized.

Acknowledgements

National Key R&D Program of China (2017YFA0303702), National Natural Science Foundation of China (61671314, 11574226, 11634005 and 11704271), Natural Science Foundation of Jiangsu Province (BK20170326), Natural Science Foundation for Colleges and Universities in Jiangsu Province of China (17KJB140019), the Priority Academic Program Development (PAPD) of Jiangsu Higher Education Institutions.

References

[1] J. D. Jackson, *Classical Electrodynamics*, Wiley, New York, 1975.

[2] J. Luo, Y. Yang, Z. Yao, W. Lu, B. Hou, Z. H. Hang, C. T. Chan, and Y. Lai, Ultratransparent media and transformation optics with shifted spatial dispersions, *Phys. Rev. Lett.* 117: 223901, 2016.

[3] Z. Yao, J. Luo, and Y. Lai, Photonic crystals with broadband, wide-angle, and polarization-insensitive transparency, *Opt. Lett.* 41: 5106, 2016.

[4] Z. Yao, J. Luo, and Y. Lai, Illusion optics via one-dimensional ultratransparent photonic crystals with shifted spatial dispersions, *Opt. Express* 25: 30931, 2017.

[5] J. D. Joannopoulos, S. G. Johnson, J. N. Winn, and R. D. Meade, *Photonic Crystals: Molding the Flow of Light*, Princeton University Press, Princeton, 2008.

[6] J. Luo, and Y. Lai, Near-perfect absorption by photonic crystals with a broadband and omnidirectional impedance-matching property, *Submitted*.

Modeling large scale metamaterials for elastic waves control

Bogdan Ungureanu[1], Stéphane Brûlé[2], Younes Achaoui[2], Stefan Enoch[2], Richard Craster[1], and Sébastien Guenneau[2]

[1]Department of Mathematics, Imperial College London, London, UK
[2]Aix Marseille Univ, CNRS, Centrale Marseille, Institut Fresnel, Marseille, France
*corresponding author, E-mail: b.ungureanu@imperial.ac.uk

Abstract

We've studied and proposed to apply the large scale metamaterials properties, which are based on the negative values of the Bulk modules K and G; the Young modulus, of longitudinal elasticity, as well as on the negative mass density, in order to obtain elastic waves control. These negative values are obtained with the help of the local resonance of the elementary cells that lead to very dispersive properties of the metamaterials.

1. Introduction

We use scaled-up configurations of metamaterials for the control of very low frequency elastic waves, with application in seismic wave protection by designing meter-scale locally resonant elementary cells that lead to very dispersive metamaterials properties and low frequency stop bands, associated with negative values of Bulk moduli K and G, Young modulus E and mass density in the frequency range of interest for earthquake engineers (0,1 – 10 Hz).

2. Methods and contribution

In order to optimize the location of low frequency resonances associated with the stop band of interest for civil engineering, see Figure 1, we propose asymptotic estimates of eigenfrequencies. Equation (1) is an asymptotic estimate of eigenfrequency of a resonator and it encapsulates the density, shear modulus and bulk modulus of the material constituting a resonator, to optimize the location of low frequency resonances associated with the stop bands [1].

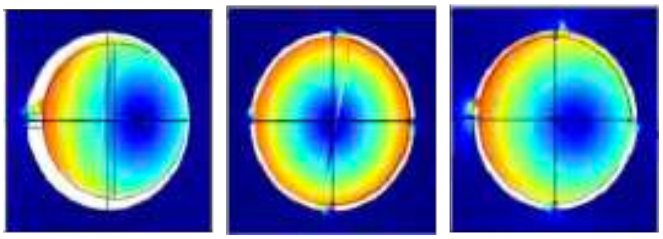


Figure 1: First mode of iron spheres connected to concrete via 1 (left), 6 identical (middle), 6 asymmetric (right) iron ligaments [1].

$$f = \frac{1}{4\pi}\sqrt{\frac{\mu}{4\rho}\frac{\lambda+\mu}{\lambda+2\mu}\sum_{i=1}^{N}\frac{h_i^2}{R^3 l_i}}, \qquad (1)$$

We also introduced in [2] the concept of auxetic seismic metamaterials where our goal was to tune low frequency stop bands as we please, thanks to a negative Poisson's coefficient, which makes unit cells contract when an axial force is applied, contrary to common, isotropic, elastic, natural materials, which have values of the Poisson coefficient constrained between 0 and 0.5, meaning that they laterally expand when an axial load is applied. In [2], we discovered that auxetic features of our specially designed seismic metamaterials permit to open very large band gaps at frequencies compatible with seismic waves.

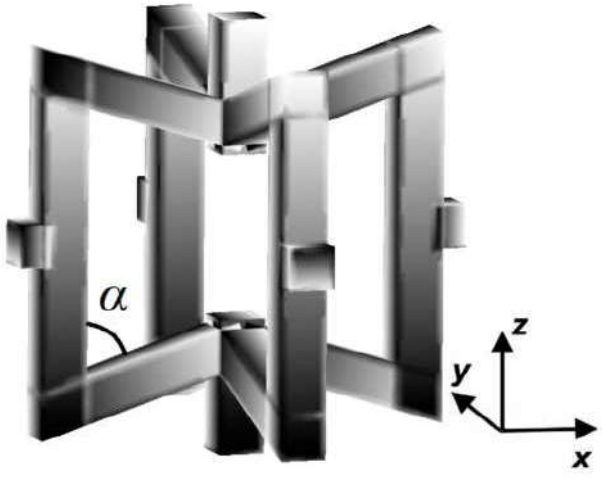


Figure 2: Auxetic bow-tie element consisting of a concrete frame in air [2].

Such mechanical metamaterials are already known [3], and become increasingly topical, but were never used for seismic wave protection. In [2], we further proved that the sign and the value of the resulting Poisson's coefficient, and

even the frequency of the band gaps, can be controlled by the angle made between elements of the frame within an elementary cell.

Another promising avenue to produce a radical change of the seismic reverberations is the creation of an artificial anisotropy by including, into a city map, some elements of different geometries, which are either full or empty. On a small scale, one could envision a design of a seismic cloak by controlling the soil artificial anisotropy with inertial resonators, buried in soil like in Figure 1, or simply placed above the soil like in Figure 3. This method inspired from earlier work on invisibility cloaks, requires some creative thinking at the interface between computer vision and artificial intelligence in mathematics and civil engineering and geophysics. As a result of a collaborative work within a multidisciplinary international team [4], we proposed an even more futurist urban design of metacities that could protect themselves from deleterious seismic waves [5]. Our proposal of transformed urbanism is born from the observation in urban seismology that some city layouts already exploit building resonances and site-city interaction to mitigate the propagating seismic field. We propose that this can be simply achieved via a spatially varying index (characterizing a quasi-conformal city map), which accounts for interaction between earthquake ground motion and multiple buildings in urban regions.



Figure 3: Creating an artificial anisotropy with inertial resonators judiciously placed within or above soil (Photo taken in Singapore).

3. Conclusions

In conclusion, we have seen that inertial resonators, which were introduced 20 years ago to achieve some acoustic neutrality [6] (this somewhat predates the field of cloaking), can be used to design seismic metamaterials that shield [1], or even detour [4,5], deleterious elastodynamic waves. Some large scale version of auxetic media that display a dynamically negative Poisson ratio, could prove useful to engineer new types of buildings' foundations. The future of seismic metamaterials is bright.

Acknowledgements

Bogdan Ungureanu acknowledge funding of European Union (MARIE SKŁODOWSKA-CURIE ACTIONS project Acronym/Full Title: METAQUAKENG - Metamaterials in Earthquake Engineering - MSCA IF - H2020) (Award No: MATH_P74520).

References

[1] Y. Achaoui, B. Ungureanu, S. Enoch, S. Brûlé, and S. Guenneau, *Extreme Mechanics Letters* **8**, 30, 2016.

[2] B. Ungureanu, Y. Achaoui, S. Enoch, S. Brûlé, and S. Guenneau, *EPJ Applied Metamaterials* **2**, 17, 2016.

[3] G. Milton and A. Cherkaev, *Journal of Engineering Materials and Technology*, **117**, 483-493, (1995).

[4] S. Brûlé, B. Ungureanu, Y. Achaoui, A. Diatta, R. Aznavourian, T. Antonakakis, R. Craster, S. Enoch, and S. Guenneau, *Innov. Infrastruct. Solut.* **2**, 20, 2017.

[5] B. Ungureanu, S. Guenneau, Y. Achaoui, A. Diatta, M. Farhat, H. Hutridurga, R.V. Craster, S. Enoch and S. Brûlé, *Special Issue of EPJAM -Metamaterials 2018* (in press).

[6] D. Bigoni, S. K. Serkov, M. Valentini, and A. B. Movchan, *Int. J. Solids Struct.* **35**, 3239, 1998.

Exotic symmetry-induced effects in photonic and phononic systems

Mehul Makwana[1,2], Richard Craster[1], Sebastien Guenneau[3], Kun Tang[4], Patrick Sebbah[4,5], Gregory Chaplain[1] and Kin Ian Lo[1]

[1]Department of Mathematics, Imperial College London, London SW7 2AZ, UK
[2]Multiwave Technologies AG, 3 Chemin du Prê Fleuri, 1228, Geneva, Switzerland
[3]Aix−Marseille Univ, CNRS, Centrale Marseille, Institut Fresnel, Marseille, France
[4]Department of Physics, The Jack and Pearl Resnick Institute for Advanced Technology, Bar-Ilan University, Ramat-Gan 5290002, Israel
[5]Institut Langevin, ESPCI ParisTech CNRS UMR7587, 1 rue Jussieu, 75238 Paris cedex 05, France
*corresponding author, E-mail: mehul.makwana07@imperial.ac.uk

Abstract

Predictive theory to geometrically engineer materials in continuum systems to have desired symmetry-induced effects is developed here by bridging the gap between quantum and continuum descriptions. We emphasise a predictive approach, the strength of which is demonstrated by the ability to design well-defined broadband edge states, valley-Hall networks and anisotropic quasicrystalline effects. We solely use semi-analytical models; this means we can concentrate cleanly upon issues such as group theory, and its influence upon the effects we see, without numerical distractions.

1. Introduction

Guiding waves, splitting, and redirecting them between channels, and steering waves around sharp bends in a robust and lossless manner is of interest across many areas of engineering and physics. Recent advances based upon ideas originating from topological insulators, translated to Newtonian wave systems, have inspired great interest. In particular, geometrically engineering valley-Hall photonic and phononic crystals to direct waves along interfaces in a robust tuneable manner has shown much potential. Herein, we elucidate the core concepts of these effects as well as a myriad of other exotic symmetry-induced phenomena. The group theoretic concepts used throughout transcend specific physical systems, hence, we opt to use easily solvable semi-analytical models.

2. Models

We choose to illustrate our theory within the context of flexural waves upon thin structured elastic plates, by doing so we emphasise the continuum nature of the model and show the generality of the basic ideas. These displacement eigenmodes are governed by the (non-dimensionalised) Kirchhoff-Love (K-L) equation

$$\left(\nabla_{\mathbf{x}}^2\left[\beta\left(\mathbf{x}\right)\nabla_{\mathbf{x}}^2\right]-\mu(\mathbf{x})\omega_{\boldsymbol{\kappa}}^2\right)\psi_{n\boldsymbol{\kappa}}=F(\mathbf{x}),\qquad(1)$$

and the reaction forces at the point constraints $F(\mathbf{x})$ introduce the dependence upon the direct lattice. This model has considerable advantages in terms of being almost completely explicit, and additionally the Green's function is nonsingular; this leads to highly resolved solutions that enable us to interpret the results accurately. We shall also make use of a model that consists of the Helmholtz equation and periodic arrangements of small inclusions upon which the field is taken to be zero. The scatterers are then thin perfectly condicting wires or soft scatterers within acoustics.

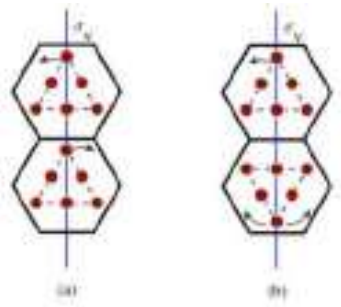


Figure 1: The geometric creation of the three distinct interfacial edge states relies upon broken threefold symmetry.

3. Periodic structures

3.1. Hexagonal

3.1.1. Theory

Geometrical valley-Hall interfacial modes are contingent upon gapping Dirac cones [1]. In two-dimensional systems, there are only three symmetry sets that are guaranteed to yield Dirac cones, all of which occur on hexagonal lattices. These three cases are distinguised by their point groups at $\Gamma=(0,0)$ in Fourier space; these are C_{6v}, C_6, C_{3v}. We demonstrate that from these, three distinct edge states can be intelligently constructed (Fig. 1); two of these are imbued with a chiral flux that results in enhanced robustness against defects [2]. These interfacial states alongside the design paradigm espoused in [2] enables us to construct highly-efficient energy networks for classical systems(Fig. 2). The interfacial modes, within these networks, travel between geometrically distinct regions.

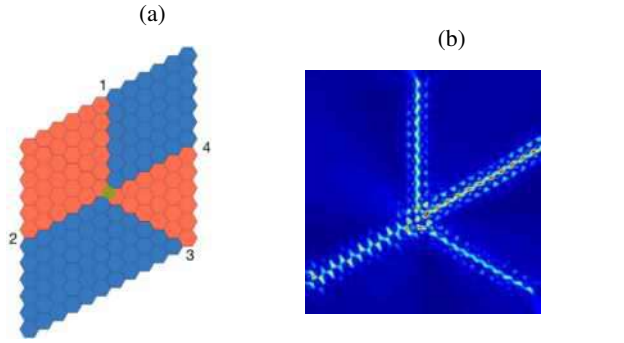


Figure 2: Different coloured regions in panel (a) represent geometrically distinct regions; source location indicated by green circle. Resulting scattered field shown in panel (b). Geometrically distinct interfaces result in edge states with different modal shapes.

3.1.2. Experiments

Experimental results based upon the earlier geometrical theory will also be shown for a metallic plate tesselated with magnets (Fig. 3). This experiment utilises the C_{3v} case within a pinned plate model [2].

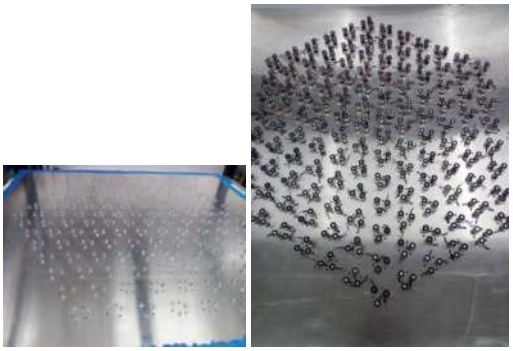


Figure 3: Structured elastic plate tesselated with magnets.

3.2. Square structures

The most commonly used models within the valleytronics community are based upon the hexagonal lattice. These are the only $2D$ structures that yield symmetry-induced Dirac cones. However, due to symmetry constraints, these hexagonal structures only produce valley-Hall energy-splitters that partition energy two-ways; we rectify this with an intelligently engineered three-way robust energy-splitter, the geometrical design of which is based upon the square lattice (Fig. 4). The resulting three-way broadband energy-splitter is shown within the contexts, of both, optics and elasticity [3, 4].

4. Aperiodic structures

The efficiency of the models used allow us to explore more exotic symmetry-induced phenomena; specifically, anisotropy within quasicrystals. We consider a structure pe-

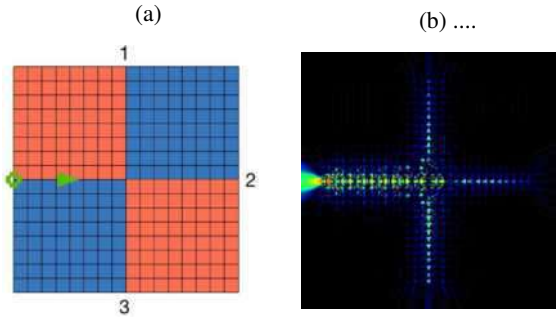


Figure 4: Demonstration of an optical valley-Hall three-way energy-splitter.

riodic in some higher- dimensional space and then project it down to lower dimensional space where it becomes quasi-periodic. Quasicrystals possess broad band-gaps and demonstrate anisotropy with rotational symmetries that are unobtainable within periodic structures. Combining our semi-analytical models with a fully-fledged quasicrystalline generator allows for the efficient generation of exotic quasicrystalline patterns (Fig. 5).

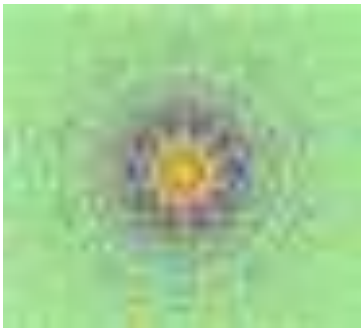


Figure 5: Scattered 10-fold rotationally symmetric pattern. 10-dimensional periodic structure projected down onto a 2-dimensional plane.

References

[1] M. Makwana and R. V. Craster,
Geometrically navigating topological plate modes around gentle and sharp bends, *Phys Rev. B* 98: 184105, 2018.

[2] M. Makwana and R. V. Craster,
Designing multidirectional energy splitters and topological valley supernetworks, *Phys Rev. B* 98: 235125, 2018.,

[3] M.. Makwana and G. J. Chaplain,
Tunable three-way topological energy-splitter, *arXiv:1901.01937v2*,

[4] M. Makwana, R. V. Craster and S. Guenneau,
Novel topological beam-splitting in photonic crystals, *arXiv:1902.00072v2*,

Structured and topological photonic fields

Visible vector beams using dielectric metasurfaces

Antonio Ambrosio[1], Yao-Wei Huang[2], Noah A. Rubin[2], Federico Capasso[2]

[1]Center for Nanoscale Systems, Harvard University, Cambridge, Massachusetts
[2]Harvard John A. Paulson School of Engineering and Applied Sciences, Harvard University, Cambridge, Massachusetts

*corresponding author, E-mail: ambrosio@seas.harvard.edu

Abstract

Recently, dielectric metasurfaces J-plate [1] allowed the most general conversion from any pair of orthogonal polarization states to the conjugate states with any value of orbital angular momentum. This is possible by controlling simultaneously the propagation phase, the Pancharatman-Berry (PB) phase and the form birefringence of each single element of the metasurface.
J-plates can be used to generate structured light with both complex intensity as well as optical field distributions.

1. Introduction

Propagation phase and PB-phase can be independently controlled in a metasurface made of different size and differently oriented nano-elements that have all the same form birefringence value. In this way, propagation phase and PB-phase can be used independently. Arbitrary phase profiles can be then designed for illuminating circularly polarized light of opposite handedness. In the case of conversion of spin angular momentum to orbital angular momentum, this approach allows to impart arbitrary and different values of orbital angular momentum to opposite handedness circularly polarized light. Simple analytical solutions can be found for the propagation phase and the PB phase as a function of the azimuthal angle at the device plane.
However, the conversion scheme can be made more general [2] since any two orthogonal polarization states can be converted to the conjugate states with arbitrary value of angular momentum. There are in general no simple analytical solutions in this case. It is instead necessary to: (1) find the Jones matrix that represents the transformation; (2) solve for the linear eigenpolarizations on which to impart the characteristic phase shifts along x and y; (3) find the right element (from a library of simulated nano-elements) that in a specific position of the metasurface plane does the right transformation (polarization and phase).

2. Discussion

Figure 1 shows an example of a J-plate realization for circularly polarized beams that are converted into two helical modes with topological charge +3 and +4. Figure 1(a) shows the emerging beam representation on a high-order poincare sphere (HOPS) [3].

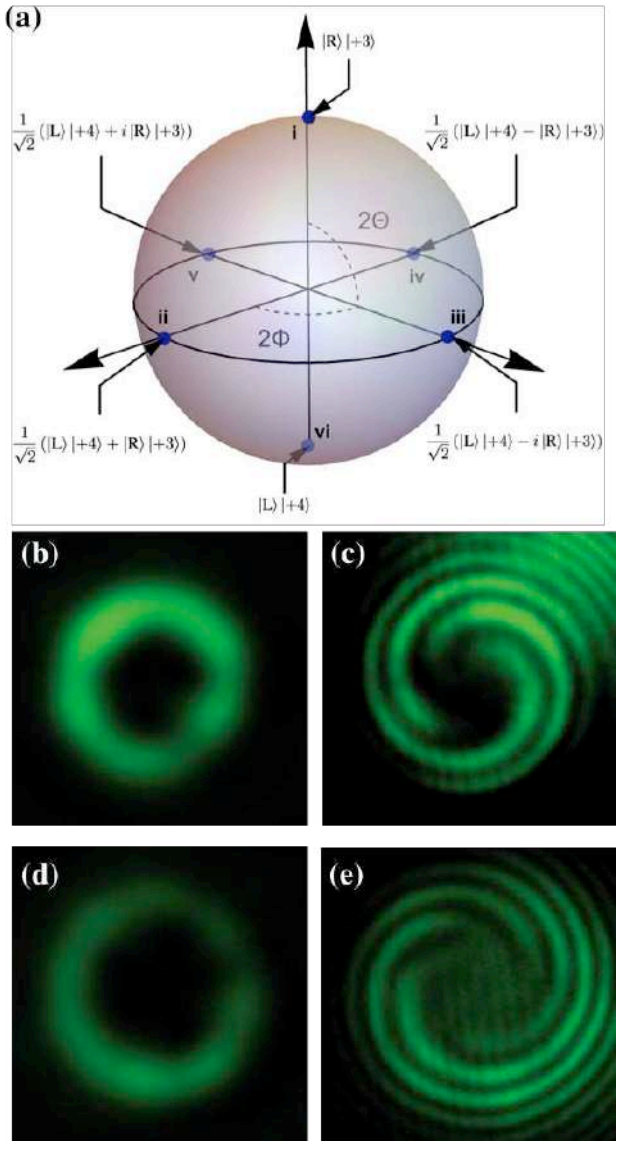


Figure 1: (a) Representation of the polarization base and orbital angular momentum modes on the high-order

Poincare sphere. (b) Intensity profile of a topological charge +3 beam imparted by a J-plate on a left-circularly polarized beam. (c) Interference with a spherical reference wave. (d) The same J-plate converts a right-circularly polarized beam into a beam with orbital angular momentum +4. (e) interference of the beam in (d) with a reference spherical wave.

The north and the south poles of the sphere are the right-circularly polarized beam with topological charge +3 and the left-circularly polarized beam with topological charge +4, respectively. For these vortex beams, the intensity profile and the spiral interference with a reference plane wave are showed in figures 1(b-e). When linearly polarized light illuminates the device, both vortex beams are generated producing characteristic structured intensities along the beam propagation.

3. Conclusions

In a dielectric J-plate, at each position (x, y) occupied by a nano-element, the birefringence, the overall phase delay and the orientation of the optical axes are controlled independently and simultaneously. This in fact results into a inhomogeneous distribution of phase delays, birefringence and axes orientation that cannot be obtained with any other single device.

Acknowledgements

This work was performed in part at the Center for Nanoscale Systems (CNS), a member of the National Nanotechnology Coordinated Infrastructure (NNCI), which is supported by the National Science Foundation under NSF award 1541959. CNS is part of Harvard University.

References

[1] R. Devlin, A. Ambrosio, N. Rubin, J.P.B. Mueller, F. Capasso, Arbitrary spin-to–orbital angular momentum conversion of light, *Science* 358, 896, 2017.

[2] J.P.B. Mueller, N. Rubin, R. Devlin, B. Groever, F. Capasso, Metasurface Polarization Optics: Independent Phase Control of Arbitrary Orthogonal States of Polarizaion, *Phys. Rev. Lett.* 118, 113901, 2017.

[3] G. Milione, H. I. Sztul, D. A. Nolan and R. Alfano, Higher-Order Poincaré Sphere, Stokes Parameters, and the Angular Momentum of Light, *Phys. Rev. Lett.* 107, 053601, 2011.

Optical spin and orbital angular momentum effects in multiple Laguerre-Gaussian beams

M. Babiker[1*], K. Koksal[1,2] , V. E. Lembessis[3] , J. Yuan[1]

[1]Department of Physics, University of York, Heslington, York YO10 5DD, England
[2]Physics Department, Bitlis Eren University, Bitlis 13000, Turkey
[3]Quantum Technology Group, Department of Physics and Astronomy, College of Science, King Saud University, Riyadh 11451, Saudi Arabia
**Corresponding author Email: m.babiker@york.ac.uk*

Abstract

The physics arising from the orbital angular momentum (OAM) as a significant property of twisted light is enhanced considerably when combined with optical spin. The superposition of multiple beams involving twisted light in any desired geometry can in principle be generated in the laboratory, giving rise to optical fields that are rich in both total amplitude and total phase. Their effects on the dynamics of atoms immersed in them as well as the exchange of angular momentum in their interactions with matter are highlighted.

Introduction

The role of the optical spin (wave polarisation) of multiple `untwisted' light in laser atom cooling and trapping is well known and has been shown to give rise to axial polarisation gradients [1]. It is also the basis for efficient laser cooling of atoms down to ultra-low temperatures. Light field distributions arising from the superposition of multiple twisted beams in one, two, and three space dimensions can, in principle, be created in the laboratory using computer-generated holograms. Inevitably the wave polarisations of the individual participating twisted beams collectively determine the overall vector field distributions.

This talk aims to highlight the effects for a variety of beam scenarios, including co- and counter-propagating beams of various combinations of wave polarizations and in various focusing arrangements, including shifted focused beams[2]. In practice the field intensity which controls the trapping presents regions of trapping sites. However, for the one- and two-dimensional cases, even multiple beams with the same linear polarizations show an interesting dependence of the overall phase function on the individual amplitude distributions, as well as the individual phase functions. The influence of the Gouy and curvature effects on the interference is highlighted for the case of multiple highly twisted, but axially shifted, Laguerre-Gaussian beams, in which case the interference leads to regions where there is a finite number of atom trapping sites.

References

[1] M. Babiker, D. L. Andrews and V. E. Lembessis "Atoms in complex twisted light", *Journal of Optics* **21**, 013001-013068 (2019).

[2] K. Koksal et al, "Axially shifted moderately focused Laguerre-Gaussian beams" *(under preparation* 2019).

Microwave magnetoelectric photonics based on magnetic-dipolar-mode resonators

E. O. Kamenetskii and A. Davidov

Microwave Magnetic Laboratory, Department of Electrical and Computer Engineering,
Ben Gurion University of the Negev, Beer Sheva, Israel.
*corresponding author, E-mail: kmntsk@bgu.ac.il

Abstract

Microwave magnetoelectric photonics bridges microwave engineering, optoelectronics and magnetoelectric-coupling effects. Recently, it was shown that with use of quasi-2D ferrite disks with magnetic-dipolar-mode (MDM) oscillations one can observe near-field chirality in microwaves. The fields originated from a MDM ferrite disk, called magnetoelectric (ME) fields, carry both spin and orbital angular momentums. They are characterized by power-flow vortices and non-zero helicity. With use of MDM ferrite resonators we have unique microwave photonics devices.

1. Introduction

In increasing the capabilities of the optical and microwave techniques further into the subwavelength regime, quasistatic resonant structures has attracted considerable interest. Electromagnetic responses of electrostatic plasmon resonances in optics and magnetostatic magnon resonances in microwaves give rise to a strong enhancement of local fields near the surfaces of subwavelength particles [1]. We propose to realize subwavelength confinement in microwaves by using dipolar-mode (magnetostatic) magnon oscillations in ferrite-disk particles. Our studies of interactions between microwave electromagnetic fields and small ferrite particles with magnetic-dipolar-mode (MDM) oscillations show strong localization of electromagnetic energy. MDM oscillations in a ferrite disk are at the origin of topological singularities resulting in Poynting vector vortices and symmetry breakings of the microwave near fields. The energy, spin and orbital angular momenta of MDM oscillations constitute the key physical quantities that characterize the *magnetoelectric-field* (ME-field) configurations. In small ferromagnetic-resonance samples, macroscopic quantum coherence can be observed. Long range magnetic dipole–dipole correlation can be treated in terms of collective excitations of the system. In a case of a quasi-2D ferrite disk, the quantized forms of these collective matter oscillations – the MDM magnons – were found to be quasiparticles with both wave-like and particle-like behaviors, as expected for quantum excitations [2].

2. MDM-ME microwave photonics devices

We show that new subwavelength microwave structures can be realized based on a system of interacting MDM ferrite disks. Wave propagation of electromagnetic signals in such structures is characterized by topological phase variations. Unidirectional ME field resonant tunneling is observed due to the distinguishable topology of the ‘forward’ and ‘backward’ ME field excitations.

2.1.1. MDM-disk arrays

Interactions of microwave fields with an MDM ferrite disk and MDM-disk arrays open a perspective for creating engineered electromagnetic fields with unique symmetry properties [3].

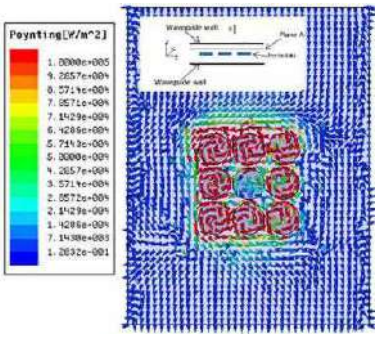


Figure 1: The power-flow-density distribution on a vacuum plane (plane A) for a structure of the in-plane nine-particle array with a center of symmetry. An insert shows a TE10-mode rectangular waveguide with a ferrite-disk array.

2.1.2. MDM-ME ferrite sensors and microwave microscops

Strong energy concentration and unique topological structures of the near fields originated from the MDM resonators allow effective measuring material parameters in microwaves, both for ordinary structures and objects with chiral properties. Development of such subwavelength sensors for direct microwave characterization of microscopic material structure with application to biology and nanotechnology is a subject of high importance. The shown ME-field sensing is addressed to microwave biomedical diagnostics and pathogen detection and to

deepen our understanding of microwave biosystem interactions. It can be also important for an analysis and design of microwave chiral metamaterials [2 – 7].

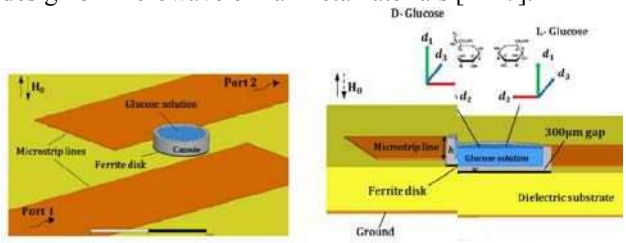


Figure 2: Experimental setup for near-field characterization of chiral parameters based on MDM-ME ferrite sensors.

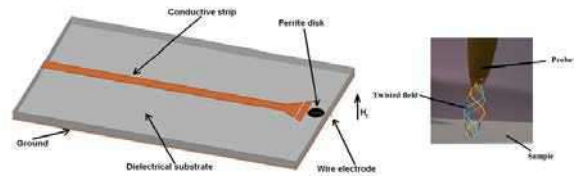


Figure 3: MDM-ME microwave microscope and the twisted structure of the probe near field.

2.1.3. MDM-ME microwave antennas

Based on a small microwave antenna with a MDM ferrite resonator, we observe the topological ME effects in far-field microwave radiation. We show that the microwave far-field radiation can be manifested with a torsion structure where an angle between the electric and magnetic field vectors varies. We discuss the question on observation of the regions of localized ME energy in far-field microwave radiation [8, 9].

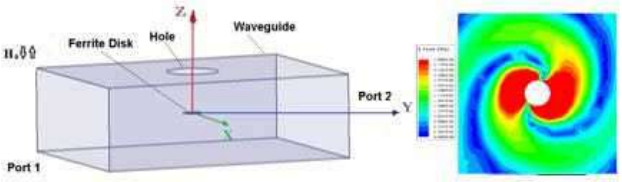


Figure 4: MDM-ME microwave antenna and the near-field topology

3. Conclusion

Microwave ferrite structures with a reduced dimensionality brings into play new effects, which should be described based on the quantized picture and demonstrate the properties of artificial atomic structures. The subwavelength confinement of the fields due to ferrite particles with MDM oscillations is related to the field quantization and symmetry breakings. A distinctive feature of the near fields originated from MDM ferrite particles – the ME fields – is the presence of the helicity structure. Use of subwavelength MDM fields with energy localization and symmetry breakings opens a perspective for novel near- and far-field microwave applications. Unique topological properties of these fields can be used to study specific structural effects in natural and artificial materials. Presently, direct detection of biological structures in microwave frequencies and understanding of the molecular mechanisms of nonthermal microwave effects is a problem of a great importance. The question of effective characterization of chemical and biological objects in microwaves can be solved when one develops special sensing devices with microwave chiral probing fields. We showed that small ferrite-disk resonators with MDM oscillations may create microwave superchiral fields with strong subwavelength localization of electromagnetic energy. Based on such properties of the fields, we propose a novel near-field microwave sensor with application to material characterization, biology, and nanotechnology. Generation of far-field orbital angular momenta from near-field chirality of MDM structures is another subject of a great interest in microwaves. This will allow creation of localized microwave radiation with spin and orbital angular momentums. Such propagating twisted microwave fields can be used for material studies and communication systems with topological-phase modulation.

References

[1] E. O. Kamenetskii, Quasistatic oscillations in subwavelength particles: Can one observe energy eigenstates?, *arXiv:1811.03314*.

[2] E. O. Kamenetskii, Quantization of magnetoelectric fields, *J. Mod. Opt.*, DOI: 10.1080/09500340.2019.1589005 (2019).

[3] E. O. Kamenetskii, M. Sigalov, and R. Shavit, Manipulating microwaves with magnetic-dipolar-mode vortices, *Phys. Rev. A* 81: 053823, 2010.

[4] E. O. Kamenetskii, R. Joffe, and R. Shavit, Microwave magnetoelectric fields and their role in the matter-field interaction, *Phys. Rev. E* 87: 023201, 2013.

[5] R. Joffe, E. Kamenetskii, and R. Shavit, Novel microwave near-field sensors for material characterization, biology, and nanotechnology, *J. Appl. Phys*. 113: 063912, 2013.

[6] E. Kamenetskii, E. Hollander, R. Joffe, and R. Shavit, "Unidirectional magnetoelectric-field multiresonant tunneling," *J. Opt.* 17: 025601, 2015.

[7] E. Hollander, E. O. Kamenetskii, and R. Shavit, Microwave chirality discrimination in enantiomeric liquids, *J. Appl. Phys*. 122: 034901, 2017.

[8] M. Berezin, E. O. Kamenetskii, and R. Shavit, Magnetoelectric-field microwave antennas: Far-field orbital angular momenta from chiral-topology near fields, *Prog. Electromag. Res. B* 68: 141–157, 2016.

[9] Topological magnetoelectric effects in microwave far-field radiation, *J. Appl. Phys*. 120: 033104, 2016.

Optical helicity gratings

Koen van Kruining[1], Robert P. Cameron[2], and Jörg B. Götte[3,4*]

[1]Max Planck Institute for the Physics of Complex Systems, Dresden, Germany
[2]Department of Physics, University of Strathclyde, Glasgow, Scotland, UK
[3]College of Engineering and Applied Sciences, Nanjing University, Nanjing, China
[4]School of Physics and Astronomy, University of Glasgow, Glasgow, Scotland, UK
*corresponding author, E-mail: Joerg.Goette@glasgow.ac.uk

Abstract

We introduce the concept of two- and three-dimensional optical helicity lattices wherein the helicity of light alternates amidst a homogenous electric part of the optical field energy density. Many of our lattices show regions of bright superchirality, where locally the helicity is larger than the modulus square of the electric field. Our helicity gratings create the possibility of trapping ultracold chiral molecules specific to their enantiomer in adjacent lattice sites.

1. Introduction

In optics helicity is a pseudoscalar which characterises locally the handedness of light [1, 2]. Similar to the varying intensity structure of conventional optical lattices it is possible to create helicity lattices by superimposing plane waves. To study the interaction of molecules with a varying helicity density landscape in isolation we construct helicity lattices with a homogenous energy density of the electromagnetic field by using orthogonal polarisations for the constituent plane waves [2].

In this way it is possible to construct one- and two- dimensional helicity lattices with two and three plane waves respectively. This suggests in turn that it is impossible to construct three-dimensional helicity lattices with a homogeneous energy density as there are at most three mutually orthogonal polarisations in space. However, if we relax the condition of a homogenous energy density to apply only to the electric part and not the magnetic one, it is possible to construct larger superpositions for which the interference terms in the electric field cancel. In this manner a three-dimensional helicity lattice with a homogeneous electric part of energy density can be constructed [3].

2. Construction of superpositions

We work in the classical electrodynamics in free space and consider superpositions of N plane waves, each of which has the same angular frequency $\omega = ck$. For a superposition of N waves the resulting electric and magnetic fields are

$$\mathbf{E} = \mathrm{Re}\ \tilde{\mathbf{E}} = \mathrm{Re}\left(\sum_{j=1}^{N} \tilde{\mathbf{E}}_j e^{i(\mathbf{k}_j\cdot\mathbf{x}-\omega t)}\right), \quad (1)$$

$$\mathbf{H} = \mathrm{Re}\ \tilde{\mathbf{H}} = \mathrm{Re}\left(\tfrac{1}{\mu_0\omega}\sum_{j=1}^{N} \mathbf{k}_j \times \tilde{\mathbf{E}}_j e^{i(\mathbf{k}_j\cdot\mathbf{x}-\omega t)}\right).$$

The complex amplitudes $\tilde{\mathbf{E}}_j$ define the polarisations, amplitudes and phases of the waves. Because light's polarisation is transverse $\tilde{\mathbf{E}}_j \cdot \mathbf{k}_j = 0$ has to hold for all plane waves.

2.1. Interference cancellation

The mean square of the electric field is given by

$$\frac{\omega}{2\pi}\int_0^{\frac{2\pi}{\omega}} \mathbf{E}\cdot\mathbf{E}dt = \frac{1}{2}\tilde{\mathbf{E}}\cdot\tilde{\mathbf{E}}^* = \frac{1}{2}\left(\sum_{j=1}^{N}\tilde{\mathbf{E}}_j\cdot\tilde{\mathbf{E}}_j^* + \sum_{i=1}^{N}\sum_{j\neq i}\tilde{\mathbf{E}}_i\cdot\tilde{\mathbf{E}}_j^* e^{i(\mathbf{k}_i-\mathbf{k}_j)\cdot\mathbf{x}}\right). \quad (2)$$

If this is to be homogeneous, the second sum must vanish. The most obvious way to achieve this is to choose the constituent plane waves such that no two interfere, in which case $\tilde{\mathbf{E}}_i\cdot\tilde{\mathbf{E}}_j^* = 0\ \forall\ i \neq j$. This can be done for at most three plane waves because there are three orthogonal polarisation directions possible. In this paper we recognise that it is also possible, however, to allow multiple pairs of waves to interfere, provided the associated interference patterns cancel. To appreciate this, suppose that there exists within the superposition a pair $(i \neq j)$ of interfering waves, with the spatial periodicity of the associated interference pattern being dictated by the wavevector difference $\mathbf{k}_i - \mathbf{k}_j$. If another pair $(i' \neq j')$ of interfering waves with the same wavector difference $\mathbf{k}_i - \mathbf{k}_j = \mathbf{k}_{i'} - \mathbf{k}_{j'}$ can be identified, giving an associated interference pattern with the same spatial periodicity, then the two interference patterns will cancel provided that $\tilde{\mathbf{E}}_i\cdot\tilde{\mathbf{E}}_j^* + \tilde{\mathbf{E}}_{i'}\cdot\tilde{\mathbf{E}}_{j'}^* = 0$. The same reasoning applies for more than two pairs of interfering waves with the same wavevector difference. It is this trick that allows us to superpose more than three plane waves whilst keping the mean square of the electric field homogeneous.

3. Superchirality

The definition of helicity density stems from plasma physics and is known for arbitrary light fields in vacuum and for an arbitrary medium with linear response. As we are considering only monochromatic light fields we can use the simpler expression $\mathcal{H} = \frac{1}{2}\mathrm{Im}(\tilde{\mathbf{E}}\cdot\tilde{\mathbf{H}}^*)/c\omega$. The helicity density is bounded between $\pm\frac{1}{4\omega}(\epsilon_0\tilde{\mathbf{E}}\cdot\tilde{\mathbf{E}}^* + \mu_0\tilde{\mathbf{H}}\cdot\tilde{\mathbf{H}}^*)$.

For a superposition of N plane waves one has

$$\mathcal{H} = \frac{-i}{4c\omega} \sum_{i,j=1}^{N} (\tilde{\mathbf{E}}_i \cdot \tilde{\mathbf{H}}_j^* - \tilde{\mathbf{E}}_j^* \cdot \tilde{\mathbf{H}}_i) e^{i(\mathbf{k}_i - \mathbf{k}_j)\cdot \mathbf{x}}. \quad (3)$$

When all waves are linearly polarised, the terms with $i = j$ are zero and only the 'interference terms' remain.

Typically, our helicity lattices show regions of superchirality, that is regions where the local helicity density exceeds the mean square of the electric field $\sqrt{\epsilon_0\mu_0}|\mathrm{Im}(\tilde{\mathbf{E}} \cdot \tilde{\mathbf{H}}^*)| > \epsilon_0 \tilde{\mathbf{E}}^* \cdot \tilde{\mathbf{E}}$ [4]. Previous realizations of superchiral light relied on interference to create dark regions where the mean square of the electric field is smaller than the helicity density, but our lattices exhibit bright regions of superchirality, where locally the helicity density exceeds the homogenous modulus square of the electric field $\sup\left(\sqrt{\epsilon_0\mu_0}|\mathrm{Im}(\tilde{\mathbf{E}} \cdot \tilde{\mathbf{H}}^*)|\right) > \sup\left(\epsilon_0 \tilde{\mathbf{E}}^* \cdot \tilde{\mathbf{E}}\right)$. That is, the local helicity is large compared to the squared electric field anywhere.

4. Explicit examples

In this section our graphics of the helicity structure will be $4 \times 4 \times 4$ wavelengths large and we use blue for negative helicity and red for positive helicity. We will show diagrams to illustrate the superpositions for which we plot the helicity density. In these diagrams, gray arrows indicate wavevectors and electric field polarizations are indicated with yellow arrows. Green arrows to indicate the magnetic polarizations are included for reference, as well. Mutually cancelling pairs of interference terms are indicated by red lines, and interference terms contributing to the inhomogeneous helicity density are shown as black dashed lines.

5. Conclusion

Apart from being an optics curiosity, noninterfering superpositions of more than three waves raise new mathematical challenges and provide new ways to probe and manipulate chiral matter, such as the ability to trap ultracold atoms specific to their enantiomer in neighbouring sites of a helicity lattice.

Acknowledgement

RPC's contribution was supported by the EPSRC and the Leverhulme Trust. JBG's contribution was supported by the National Key Research and Development Program of China.

References

[1] R.P. Cameron, J.B. Götte, S.M. Barnett, A.M. Yao. Chirality and the angular momentum of light, *Phil. Trans. R. Soc. A* **375**, 20150433, 2017.

[2] R.P. Cameron, A.M. Yao, S.M. Barnett, Discriminatory optical force for chiral molecules, *New J. Phys.* **16**, 013020, 2014.

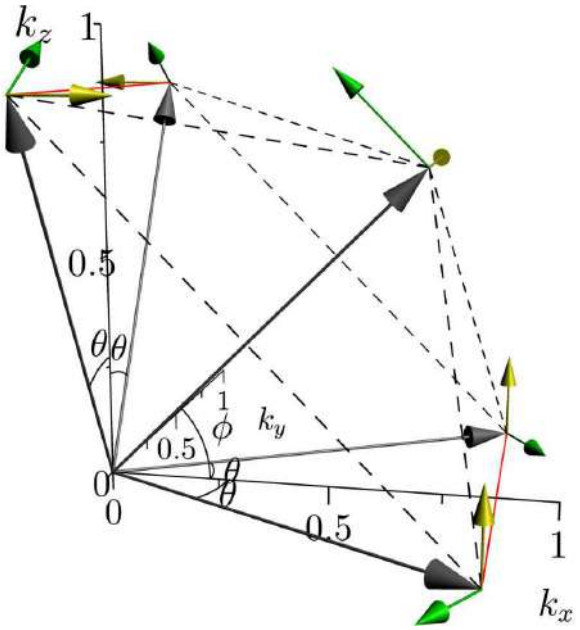


Figure 1: Example of a five-wave noninterfering superposition. Figure adopted from [3].

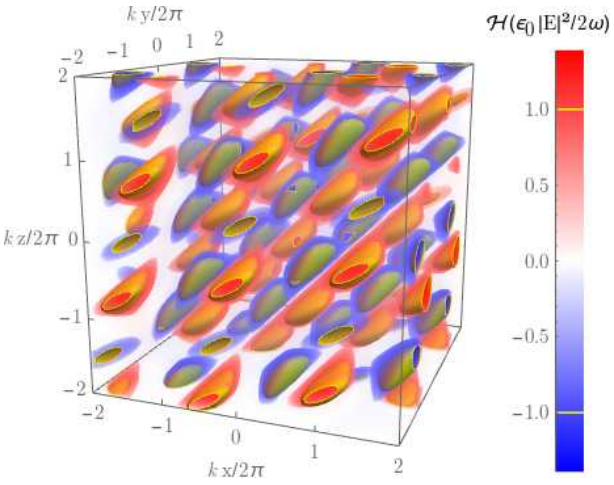


Figure 2: The three-dimensional helicity lattice resulting from the superposition in Fig. 1. The superchiral regions are enclosed by the yellow surfaces. At about half a wavelength in length they are surprisingly large. Figure taken from [3].

[3] K. van Kruining, R.P. Cameron, J.B. Götte, Superposition of up to six plane waves without electric field interference, *Optica* **5**, 1091, 2018.

[4] Y. Tang, A.E. Cohen, Optical chirality and Its Interaction with Matter, *Phys. Rev. Lett.* **104**, 163901, 2010.

Skyrmion structure in vector beams

**Sijia Gao*, Jörg B Götte, Fiona Speirits,
Neal Radwell, Sonja Franke-Arnold, and Stephen M Barnett**

School of Physics and Astronomy, University of Glasgow, Scotland, U.K.
*corresponding author, E-mail: s.gao.2@research.gla.ac.uk

Abstract

Vector beams have both a spatially varying amplitude and polarization, for light, or spin direction for electrons. Associated with these we find a topological feature, the skyrmion number, that is robust against any deformation during propagation. The simplest way to map out this feature is to use the associated skyrmion field. This is a transverse or divergence-less field and so has neither sources nor sinks. Mapping out the skyrmion field for these beams reveals constraints on the manner in which vector beams can be manipulated.

1. Skyrmion number

Skyrmions were introduced by Skyrme in 1962 [1] as a topological soliton for the pion field, aimed at explaining the stability of hadrons. Although this idea is not part of the mainstream particle theory, it has been adopted widely in many areas of physics including quantum liquids [2], magnetic materials [3, 4], and in the study of fractional statistics [5]. Recently they have been found in optics by the controlled interference of plasmon polaritons [6]. We show here that freely propagating paraxial beams in the form:

$$|\Psi(\mathbf{r})\rangle = \frac{u_0(\mathbf{r})\,|P\rangle + u_1(\mathbf{r})\,|V\rangle}{\sqrt{|u_0(\mathbf{r})|^2 + |u_1(\mathbf{r})|^2}}, \qquad (1)$$

also possess a non-trivial skyrmion field and with it an integer skyrmion number. Here $u_0(\mathbf{r})$ and $u_1(\mathbf{r})$ are two orthogonal spatial modes. The states $|P\rangle$ and $|V\rangle$ represent either any two orthogonal spin directions for the electron or any two orthogonal directions on the Poincaré sphere for a light beam.

Skyrmions are characterized by the topological integer n, the skyrmion number, which can be evaluated as a surface integral of the form

$$n = \frac{1}{4\pi}\oint_S \mathbf{M}\cdot\left(\frac{\partial \mathbf{M}}{\partial x}\times\frac{\partial \mathbf{M}}{\partial y}\right)dxdy, \qquad (2)$$

where $\mathbf{M}$ is the unit vector in the local effective magnetization field. For structured beams, this is the Bloch vector for electron beams or Poincaré vector for optical beams.

When the spatial modes $u_0(\mathbf{r})$ and $u_1(\mathbf{r})$ are two Laguerre-Guassian beams with the same focus but different winding number ℓ_+ and ℓ_- respectively, as depicted in Fig. 1, we find the simple value:

$$n = \ell_+ - \ell_-. \qquad (3)$$

In a more complicated case where although $u_0(\mathbf{r})$ and $u_1(\mathbf{r})$ are still both Laguerre-Guassian beams, their ratio $v(\mathbf{r})$ is more complicated and has the general form

$$v(\mathbf{r}) = f(\rho, z)e^{i\theta(\rho,z)}e^{i\ell_\Delta\phi}, \qquad (4)$$

where ℓ_Δ is the difference between the winding numbers of $u_0(\mathbf{r})$ and $u_1(\mathbf{r})$ while f and θ are real functions of coordinates ρ and z. We find the skyrmion number is

$$n = \ell_\Delta\left(\frac{1}{1+f^2(0,z)} - \frac{1}{1-f^2(\infty,z)}\right). \qquad (5)$$

We note that this does not depend on the specific orientation of the spin or polarization, indeed performing a global spin or polarization rotation does not change this result.

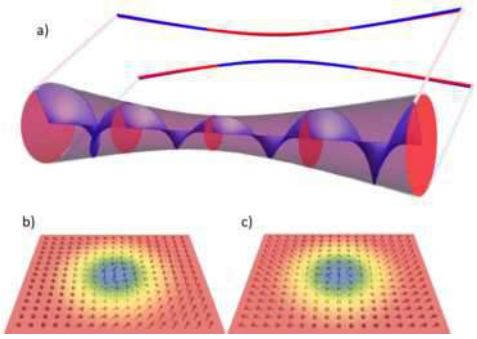


Figure 1: This is a illustration of the paraxial beam given in Equation (1), when the two spatial modes are Laguerre-Guassian modes with $\ell_+ = 1$ and $\ell_- = 0$ focusing at the same point: a) A schematic diagram of the beam; b) The $\mathbf{M}$ vector field when the phase difference is $\frac{\pi}{2}$; c) The $\mathbf{M}$ vector field when there is no phase difference between u_0 and u_1.

2. Skyrmion field

We can also understand the skyrmion number as the flux of a vector field, the skyrmion field, in the z direction. The general form of this skyrmion field is

$$\Sigma_i = \frac{1}{2}\varepsilon_{ijk}\varepsilon_{pqr}M_p\frac{\partial M_q}{\partial x_j}\frac{\partial M_r}{\partial x_k}. \qquad (6)$$

It is not difficult to verify that this field is divergence-less, which means that the associated field lines can form loops but have no sources nor sinks. This means that the field can neither be created or destroyed and that, for example, the creation of a beam with a total flux of the skyrmion field 1 is accompanied by the creation of a further beam with a total flux of skyrmion field -1. We note that the skyrmion field, being divergence-less, can be written as a curl of another vector field. We evaluate this quantity and note its similarity to the velocity field in the theory of superfluids [2].

Acknowledgement

This work was supported by a Royal Society Research Professorship, grant number RP150122, and by the UK Engineering and Physical Science Research Council, grant number EP/R00826/1.

References

[1] T. H. R. Skyrme, "A unified field theory of mesons and baryons," *Nuclear Physics*, vol. 31, pp. 556–569, 1962.

[2] D. Vollhardt and P. Wölfle, *The superfluid phases of helium 3*. Courier Corporation, 2013.

[3] A. Bogdanov and U. Rößler, "Chiral symmetry breaking in magnetic thin films and multilayers," *Physical review letters*, vol. 87, no. 3, p. 037203, 2001.

[4] N. Romming, C. Hanneken, M. Menzel, J. E. Bickel, B. Wolter, K. von Bergmann, A. Kubetzka, and R. Wiesendanger, "Writing and deleting single magnetic skyrmions," *Science*, vol. 341, no. 6146, pp. 636–639, 2013.

[5] F. Wilczek, *Fractional statistics and anyon superconductivity*. World scientific, 1990, vol. 5.

[6] S. Tsesses, E. Ostrovsky, K. Cohen, B. Gjonaj, N. Lindner, and G. Bartal, "Optical skyrmion lattice in evanescent electromagnetic fields," *Science*, vol. 361, no. 6406, pp. 993–996, 2018.

Charge and spin dynamics driven by topological photonic fields.

Jonas Wätzel[1]*, and Jamal Berakdar[1]

[1] Institute for Physics, Martin-Luther-University Halle-Wittenberg, 06099 Halle, Germany
*corresponding author, E-mail: jonas.waetzel@physik.uni-halle.de

Abstract

We consider the spin-dependent charge dynamics in quantum nanostructures in response to radiation fields with a topologically non-trivial wave fronts. We find that optical vortices, i.e. fields with spatially varying phase of the wave front, are well suited as a versatile tool for the ultrafast generation and control of spin accumulations. Vector beams with spatially varying polarization state induce rather different types of charge and spin dynamics. For instance, radially polarized vector beams drive radially breathing charge-density oscillations via electric-type quantum transitions while azimuthally polarized beams trigger a dynamic Aharonov-Bohm effect leading to an oscillating magnetic moment without affecting the charge dipolar transitions at all.

1. Introduction

The experimental availability of structured light fields for a large set of parameters fueled the intense recent research in this area. Structured fields with topologically non-trivial wave fronts have be employed for applications ranging from optical tweezers for microscale objects to electronics and life sciences, quantum information or optical telecommunications. Especially light pulses carrying orbital angular momentum (OAM) enable the photo-mechanics of moving, trapping and rotating nanostructured objects as wells as atoms or molecules. Further, such beams were used to study otherwise inaccessible angular momentum states of atoms and solids. In addition, spin-orbit interaction allows a coupling to the spin of the angular momentum that has been transferred from the photons to the charge, which opens the way for using structured light for optospintronic applications, as will be discussed in this contribution in more detail.

On the other hand, vector beams exhibit a fundamentally different behavior in driving quantum matter. While their intensity profile is similar to optical vortices and OAM carrying beam, a radially and azimuthally polarized vector beams for instance do not trigger a unidirectional charge current in a quantum system but mainly radially-breathing charge response or a transient magnetic response.

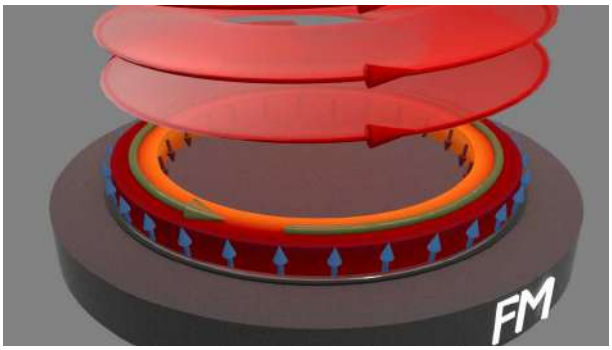


Figure 1: Schematics of the light-driven spin Hall effect. A focused THz optical vortex beam (red circles) excites a circulating current $\boldsymbol{j}$ (green arrow) upon the transfer of optical OAM to charge carriers confined in the quantum ring. Due to the spin-orbit interaction the circular orbital motion is accompanied by a drift spin-polarized current to ring edges. This leads to an accumulation of spin polarized charge density (indicated by arrows) at the ring boundaries which can act for example with a torque on an interfaced magnet.

2. All-Optical Generation of the Spin-Hall current by optical vortices

For the emergence of photo-induced spin Hall current (SHE) the spin-orbit coupling is crucial. Working within the Lorentz-gauge for vector potential of the incident light beam and accounting for the surrounding phonon bath, we evaluate the time evolution of the light-induced spin-dependent charge dynamics. To this end, we use within the single-particle picture the Hamiltonian

$$\hat{H}(t) = \hat{H}_0 + \hat{H}_{\rm int}(t) + \hat{H}_{\rm ph} + \hat{H}_{\rm B} \qquad (1)$$

where the unperturbed carriers in a quantum ring with confinement potential $V(r)$ are described by $\hat{H}_0$. The coupling to the laser fields is given in terms of $\hat{H}_{\rm int}(t)$ while the phononic environment is characterized by the electron-phonon coupling $\hat{H}_{\rm ph}$, and the bath $\hat{H}_{\rm B}$. More details on the Hamiltonians can be found in the full paper [2].

Generally, the irradiation by a THz optical vortex leads to a directed circulating photocurrent that emerges due to the resonant excitation of the charge carriers and the simultaneous transfer of the OAM to them [1]. Moreover, a full-numerical solution of the three-dimensional Schrödinger equation extended to the spin degree of freedom reveals an accumulation of the spin-polarized circulating currents at

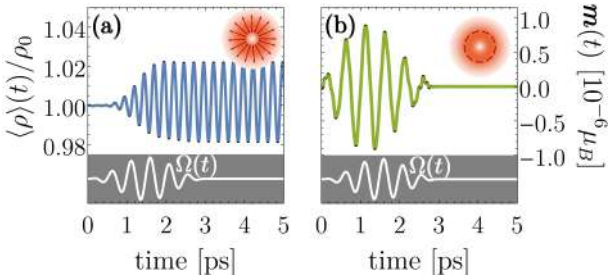


Figure 2: Numerical simulation of a few-electron quantum ring irradiated by a vector beam. (a) the case of the radial polarization reveals a radial charge oscillations. (b) Azimuthally polarized vector beams trigger a dynamical Aharonov-Bohm effect characterized by the emergence of an oscillating magnetic moment.

the opposite ring boundaries, as indicated in the schematics in Fig. 1. This laser-driven charge and spin accumulation at the edges is a type of a spin-Hall effect that in our case, depends on the transferred OAM [2], which can be characterized by the spin Hall angle [2].

3. Ring-confined charge dynamics driven by vector beams

As already noted in the introduction, although vector beams share some common features with vortex beams carrying orbital angular momentum, like the intensity profile, their effect on charge carriers is fundamentally different. As evidenced by our numerical simulations of a quantum ring irradiated by a vector beam with radial and azimuthal polarization, the internal angular momentum state can not be changed. However, the radially polarized vector beam (RVB) triggers via electric transitions radial charge oscillations which one can interpret as a symmetric breathing charge-density cloud. We note that such a collective charge excitation is non-dipolar in contrast to the usage of spatially homogeneous laser fields. The evaluated local dipole moment is the same in all radial directions and oscillates with a frequency characterized by the energy difference between the radial sublevels of the quantum structure (cf. Fig. 2). As a result, the averaged total dipole moment is zero:

$$\boldsymbol{d}(t) = \int \mathrm{d}\boldsymbol{r}\, \rho_e(\boldsymbol{r},t)\boldsymbol{r} = 0 \qquad (2)$$

where $\rho_e(\boldsymbol{r},t)$ is the driven charge density. Furthermore, this charge response to the incident light field is of an electric-type [3].

In contrast, for the azimuthally polarized vector (AVB) beam we demonstrated that the associated electric contribution to the light-matter Hamiltonian $\hat{H}_{\mathrm{int}}(t)$ vanishes in the cylindrically symmetric geometry since $\boldsymbol{r}\cdot\boldsymbol{E}(\boldsymbol{r},t)=0$. Thus, the AVB induces no electric (dipole) moment. In Fig. 2 we present the results of a full-numerical simulations which can be interpreted by first-order perturbation theory. It can be shown that the main contribution to the light-induced current is given by circulating currents:

$$j_\varphi(\boldsymbol{r},t) = \frac{e^2}{m_0}\rho_e(\boldsymbol{r},t) f_{\mathrm{AVB}}(r)\Omega(t)\sin(\omega t) \qquad (3)$$

where $f_{\mathrm{AVB}}(r)$ describes the radial profile of the AVB, $\Omega(t)$ is the temporal envelope of the pulse and ω the central frequency. As a consequence, the charge density oscillates with the frequency of the driving vector beam field which means that, beyond transient effects, no directional time-averaged current is induced in φ-direction. The oscillating circularly currents give rise to an oscillating magnetic moment $\boldsymbol{m}(t) = 1/2\int \mathrm{d}\boldsymbol{r}\,\boldsymbol{r}\times\boldsymbol{j}(\boldsymbol{r},t)$ which is shown in Fig. 2. In line with the analytical predictions, the build-up and decay times are locked to the applied external field. Furthermore, the interaction is of a magnetic-type and represents a dynamical Aharonov-Bohm effect.

4. Conclusion

The present contribution represents an overview of new effects akin to the interaction of topologically non-trivial photonic fields with quantum matter. Both, charge and spin degrees of freedom of the confined carriers are affected in a unique way. It is well-known that optical vortices transfer OAM to charge carriers if the requirements on symmetry and energy landscape are fulfilled. In combination with the spin-orbit coupling an all-optical spin Hall effect can be generated.

Vector beams share some features with optical vortices but the corresponding fundamental light-matter interaction reveals marked differences. No angular momentum transfer is possible and no electric dipole moment can be induced for the systems that we studied. Nevertheless, we find interesting and remarkable effects on the charge carriers: radially polarized vector beams trigger via non-dipolar electric transitions radial charge oscillations while azimuthally polarized vector beams generate via a magnetic interaction oscillating magnetic moments.

References

[1] J Wätzel, J Berakdar, Centrifugal photovoltaic and photogalvanic effects driven by structured light, *Sci. Rep.* **6**: 21475, 2016.

[2] J Wätzel, J Berakdar, All-optical generation and ultrafast tuning of non-linear spin Hall current, *Sci. Rep.* **8**: 17102, 2018.

[3] J Wätzel, J Berakdar, Magnetoelectric response of quantum structures driven by optical vector beams, *Phys. Rev. B* **99**: 085425, 2019.

Interaction of an Archimedean spiral structure with twisted light

Richard M. Kerber[1], Jamie M. Fitzgerald[2], Xiaofei Xiao[2], Stefan A. Maier[2,4], Vincenzo Giannini[2,5], Doris E. Reiter[1] and Sang Soon Oh[3*]

[1]Institut für Festkörpertheorie and Center for Multiscale Theory and Computation (CMTC), Universität Münster, D-48149 Münster, Germany
[2]Department of Physics, Imperial College London, London SW7 2AZ, United Kingdom
[3]School of Physics and Astronomy, Cardiff University, Cardiff CF24 3AA, United Kingdom
[4]Nanoinstitute Munich, Ludwig-Maximilians-Universität München, D-80539 München, Germany
[5]Instituto de Estructura de la Materia (IEM-CSIC), Consejo Superior de Investigaciones Científicas,E-28006 Madrid, Spain
*corresponding author, E-mail: OhS2@cardiff.ac.uk

Abstract

Light-matter interaction between a structured light and metallic structures allows for interesting plasmonic mode excitation with its unique selections rules. Importantly, the selection rule depends on the size of the structures and the shape of the structured light. Here, we compare two Archimedean spirals consisting of bent gold nanorods with different sizes when illuminated by an orbital angular momentum light. We show the vortex generation and conrol for a micrometer-sized spirals.

1. Introduction

In a gold nanoplate with Archimedean spiral shape grooves, a vortex of the surface plasmon polariton (SPP) field can be formed at the centre of the Archimedean spiral [1, 2, 3]. There is an optical analogue of the SPP vortex field, known as orbital angular momentum (OAM) light which has a vortex at the beam axis with non-zero OAM. A difference between SPP vortex and OAM light is that while for the SPP the field is confined at the two-dimensional surface and the evanescent SPP have an imaginary wavevector perpendicular to the interface and thus the confinement is associated with a transverse spin, OAM light has a real wavevector also with a component pointing along the propagation direction.

Due to the ability of encoding information in its optical phase, the OAM light has become attractive for quantum information and communication technologies. For these applications, it is essential to implement an efficient generation and detection of the OAM. Therfore, various plasmonic structures have been proposed and the light-matter interaction in these structures has been studied intensively [4, 5]. In this work, we explore the interaction of OAM light with Archimedean spiral metalic structures. We show that the Archimedean spiral structure offers the possibility to generate a vortex in the free optical field by considering a micrometer-sized structure made of bent gold nanorods. Moreover, we further analyse the resonance behaviour for a nanometer-sized structure illuminated by OAM light.

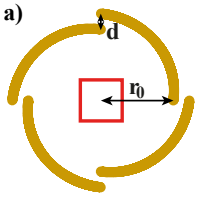


Figure 1: Geometry of the Archimedean spiral structure with $m = 4$ elements in the xy-plane.

2. Theory

2.1. Archimedean spirals

An Archimedean spiral is a spiral whose radius increases when making a rotation following the polar equation

$$r(\phi) = r_0 + \tilde{d}\frac{\phi}{2\pi} \tag{1}$$

where r_0 is the starting radius and after one rotation the radius has increased by the distance $\tilde{d}$. This definition of an Archimedean spiral can be generalized by dividing a single rotation into m elements. Then the radius r_m for each element is given by

$$r_m(\phi) = r_0 + d\frac{mod(m\phi, 2\pi)}{2\pi} \tag{2}$$

where d is the distance between the starting point of the one element and the end point of the other element and mod is the modulus function that gives the remainder of the division of $m\phi$ by 2π. An example of a segmented Archimedean spiral ($m = 4$) is shown in Fig. 1.

2.2. Orbital angular momentum light

In general, a light carries both SAM and OAM. SAM of light is associated with polarization s that is the difference in phase between the two electric filed components on a plane perpendicular to the light propagation direction. While a plane wave light has zero OAM, a structured light can have non-zero OAM if it has a phase change along

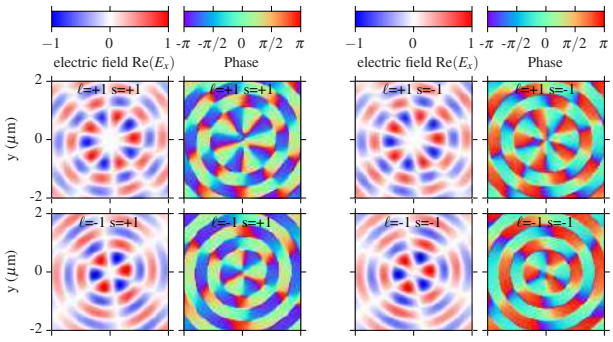


Figure 2: Electric field component $Re(E_x)$ and phase of the scattered electric field of an Archimedean spiral with $m = 4$ elements for plane wave excitation with varying polarization $s = \pm 1$.

the azimuthal direction around the beam axis. The OAM is quantified by the integer number ℓ and the OAM light is also called 'twisted light' because it has a helical wavefront. Although several different mathematical descriptions are employed for a radial dependence, we here consider Bessel beams because they are exact solutions of Maxwell equations.

3. Results

3.1. Micrometer-sized spiral

First, we consider an excitation with an OAM light beam with $\ell = \pm 1$ as well as different polarizations $s = \pm 1$. The different rows in Fig. 2 display the fields for excitation with varying OAM $\ell = \pm 1$ and the two columns correspond to the different signs of polarization $s = \pm 1$. Let us look at an excitation with positive polarization $s = \pm 1$ (left) and an OAM light beam with $\ell = +1$ in the first row and $\ell = -1$ in the second row. We find a vortex in the centre of the spiral, but the number of maxima is 5 for $\ell = +1$ and 3 for $\ell = -1$. In agreement with the number of maxima, the phase shows 5 and 3 jumps, respectively meaning that the topological charge of the vortex is $v = 5$ and $v = 3$. This indicates that the topological charge of the vortex v in a m-segmented Archimedean spiral can be calculated by

$$v = |m + \ell|. \tag{3}$$

Interestingly, the topological charge v does not depend on s with $s = -1$ leading to the same behaviour as $s = +1$.

3.2. Nanometer-sized spiral

Next, we look into whether an Archimedean spiral structure also can have a strong optical response at nanometer scales. In this nanometer-sized spiral case, localized surface plasmon resonances are expected to dominate the optical response [6]. For rotationally arranged nanoantennas, the resonances induced by OAM light can be very different to an excitation with plane waves and the resonance behaviour strongly depends on both the OAM and polarization of the light beams [4]. We found that the resonances are of different type compared to the excitation of plane wave and are thus classified as dark modes, which have a quadrupolar and an azimuthal character excited by OAM light of the parallel and anti-parallel class, respectively.

4. Conclusions

In conclusion, we have considered the interaction of OAM light with a metallic Archimedean spiral structure. Depending on the scale of radius in comparison to the excitation wavelength the Archimedean spiral behaves differently. For a micrometer-sized spiral, an optical vortex can be generated in the centre of the spiral and the topological charge can be controlled by the OAM value of the exciting field, while it is independent from the handedness of polarization. For a nanometer-sized Archimedean spiral, the optical response is dominated by the near-field and we found pronounced resonances originating from localized SSPs.

Acknowledgement

This work is part-funded by the European Regional Development Fund through the Welsh Government.

References

[1] Y. Gorodetski, a. Niv, V. Kleiner, and E. Hasman, "Observation of the Spin-Based Plasmonic Effect in Nanoscale Structures," *Physical Review Letters*, vol. 101, no. 4, pp. 1–4, jul 2008.

[2] H. Kim, J. Park, S. W. Cho, S. Y. Lee, M. Kang, and B. Lee, "Synthesis and dynamic switching of surface plasmon vortices with plasmonic vortex lens," *Nano Letters*, vol. 10, no. 2, pp. 529–536, 2010.

[3] J. Park, S.-W. Cho, B. Lee, S.-Y. Lee, and H. Kim, "Coupling of spin and angular momentum of light in plasmonic vortex," *Optics Express*, vol. 20, no. 9, p. 10083, 2012.

[4] R. M. Kerber, J. M. Fitzgerald, X. Xiao, S. S. Oh, S. A. Maier, V. Giannini, and D. E. Reiter, "Interaction of an Archimedean spiral structure with orbital angular momentum light," *New Journal of Physics*, vol. 20, no. 9, p. 095005, sep 2018.

[5] R. M. Kerber, J. M. Fitzgerald, S. S. Oh, D. E. Reiter, and O. Hess, "Orbital angular momentum dichroism in nanoantennas," *Communications Physics*, vol. 1, no. 1, p. 87, dec 2018.

[6] V. Giannini, A. I. Fernández-Domínguez, S. C. Heck, and S. A. Maier, "Plasmonic Nanoantennas: Fundamentals and Their Use in Controlling the Radiative Properties of Nanoemitters," *Chemical Reviews*, vol. 111, no. 6, pp. 3888–3912, jun 2011.

Controlling Internal Quantum States of Subwavelength Systems with Optical Vortices

Andrei Afanasev[1*], Maria Solyanik-Gorgone[1]

[1]Department of Physics, The George Washington University, Washington, DC, USA
*corresponding author, E-mail: afanas@gwu.edu

Abstract

Quantized optical vortices, or the twisted photons, may carry pre-set amounts of angular momentum along their direction of propagation, thus allowing for quantum transitions otherwise forbidden for conventional plane-wave light. We address the question of the angular momentum transfer to internal degrees of freedom of quantum systems excited by the twisted photons, and discuss appropriate polarization observables. We will show that interactions of such beams generate parity-conserving single spin asymmetries due to presence of an orbital angular momentum, showing in circular dichroism even in the isotropic atomic matter. We extend our theory approach to the case of semi-conductor quantum dots and demonstrate associated spin-orbit effects for spin injection of photoelectrons in bulk GaAs.

1. Introduction

Conservation of angular momentum in the interaction of the photons with quantum systems leads to well-known selection rules that control allowed quantum states of the excited physical system. Quantized optical vortices, or the twisted photons, defy some of the known quantum selection rules. As was shown theoretically [1,2] and demonstrated experimentally with single trapped ^{40}Ca ions [3,4], Zeeman sublevels of the excited atomic states are populated differently under twisted light, with the quantum transition probability strongly depending on the radial distance to the optical vortex axes at sub-wavelength scales. Moreover, in the field of the optical vortex, the conventional multipole transitions (e.g., E2-, M1) can be separated by mapping the dependence on the atom's radial position within a vortex [5], thus providing a novel tool for multipole analysis.

2. Results and Discussion

In this work, we consider quantum states in III-V semiconductor (GaAs) excited by a twisted photon carrying total angular momentum along the direction of propagation equal to m_γ. First considered were a semiconductor quantum dot (QD), for which we employed an atom-like approach outlined in Refs.[1,2]. The results of calculations are shown in Figure 1.

Next, we developed a theory approach to spin transfer by twisted photons to photoelectrons in bulk GaAs. We show

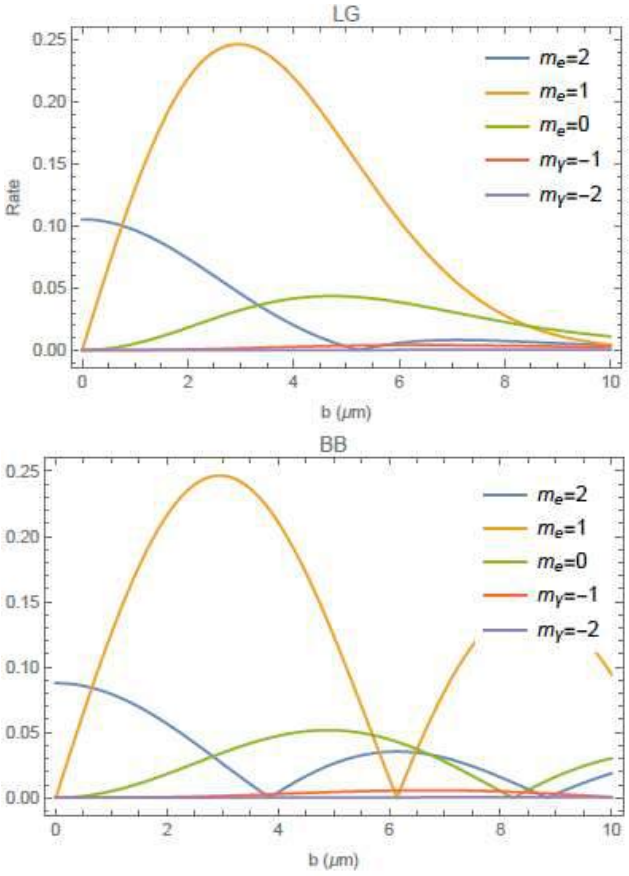


Figure 1: Quadrupole transition rates for photo-excitation of a QD by Laguerre-Gauss (top plot) and BB (bottom plot) the twisted photons of wavelength λ= 550nm, which corresponds to the spatial dimensions of QD of the order $R_0 \approx 10$nm

that spin polarization of the photoelectrons, that find wide applications in spintronics and polarized electron sources for particle accelerators, is in fact altered by the combined effect of orbital angular momentum and spin of the incident photons. The results, as shown in Figure 2, demonstrate that the polarization is different from plane-wave photon case (that is equal to ±50% for unstrained GaAs for given circular polarization), while the difference strongly depends on the location of the photoelectron with respect to the vortex center, similarly to atom or QD cases.

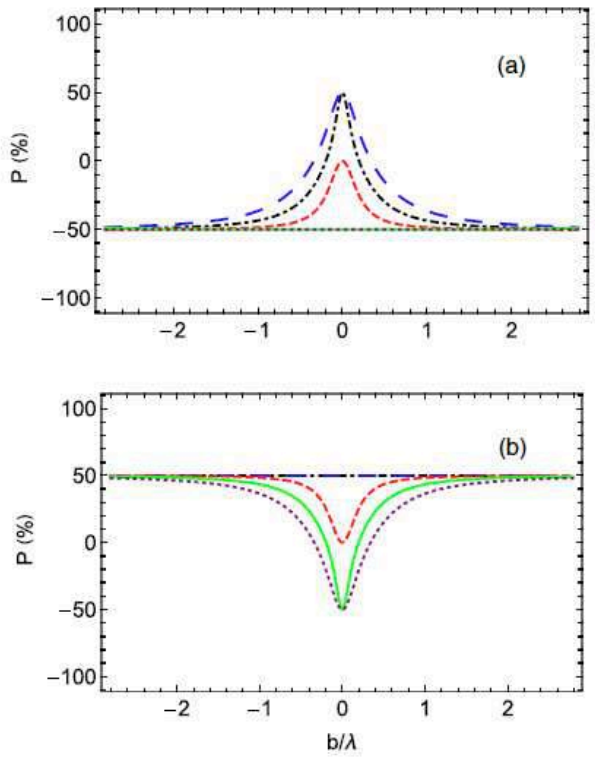


Figure 2: Photoelectron polarization in bulk GaAs sample as a function of the electron's distance to the optical vortex center b measuren in units of photon's wavelength; (a) right circular polarization (b) left circular polarization. Long-dashed blue line is photons total angular momentum projection $m_\gamma = -2$, dot-dashed black is $m_\gamma = -1$, dashed red is $m_\gamma = 0$, solid green is $m_\gamma = 1$, dotted purple is $m_\gamma = 2$. See Ref. [5] for details of calculation.

3. Conclusions

We show theoretically that twisted photon beams have the capability of transferring the angular momentum degrees of freedom to electrons in semiconductors. The transfer signature may be observable in the form of altered angular momentum selection rules for the artificial atoms (i.e., quantum dots) or photoelectron polarization.

Acknowledgements

This work was partially supported by ARO Grant Award No. W911NF-19-1-0022.

References

[1] A. Afanasev, C. E. Carlson, and A. Mukherjee, Off-axis excitation of hydrogenlike atoms by twisted photons, *Phys. Rev. A*: 88, 033841, 2013.

[2] A. Afanasev, C. E. Carlson, and A. Mukherjee, High-multipole excitations of hydrogen-like atoms by twisted photons near a phase singularity, *J. Opt.:* 18, 074013, 2016.

[3] C. T. Schmiegelow, J. Schulz, H. Kaufmann, T. Ruster, U. G. Poschinger, and F. Schmidt-Kaler, Transfer of optical orbital angular momentum to a bound electron, *Nature Comm.:* 7, 12998, 2016.

[4] A. Afanasev, C. E. Carlson, C. Schmiegelow, J. Schulz, F. Schmidt-Kaler, and M. Solyanik, Experimental verification of positiondependent angular-momentum selection rules for absorption of twisted light by a bound electron, *New J. Phys.:* 20, 023032, 2018.

[5] M. Solyanik-Gorgone, A. Afanasev, Spin polarization of photoelectrons in GaAs excited by twisted photons, *Phys. Rev. B*: 99, 035204, 2019.

Nonreciprocal and Topological Photonics

Experimental realization of valley-Hall photonic topological insulators with dual-band kink states

Q. Chen[1], L. Zhang[1], M. He[1], Y. Yang[2], H. Wang[3], and H. Chen[1]

[1]State Key Laboratory of Modern Optical Instrumentation, College of Information Science and Electronic Engineering, Zhejiang University, Hangzhou 310027, China.
[2]Division of Physics and Applied Physics, School of Physical and Mathematical Sciences, Nanyang Technological University, 21 Nanyang Link, Singapore 637371, Singapore.
[3]Marine electronics Institute, Zhejiang University, Hangzhou 310027, China

Email: Q. Chen: qiaolu_chen@163.com, H. Chen: hansomchen@zju.edu.cn.

Abstract

Valley, as a binary degree of freedom in valleytronics, has been attracting great interests because of its distinctive topological behaviors and potential applications in information processing. Recently, the concept of valley has been introduced into photonic systems, and has motivated the study of valley-Hall photonic topological insulators (PTIs), which could support topological kink states at non-trivial domain walls. However, in the previous valley-Hall PTIs, the kink states only work at a single frequency band, limiting potential applications in multiband waveguides, filters, communications, and so forth. To overcome this challenge, we experimentally realize a valley-Hall PTI based on an inversion-breaking graphene-like structure in a substrate-integrated microwave circuitry, where the topological kink states exist at two separated frequency bands. Both the simulated and experimental results verify the existence of topological dual-band kink states. Moreover, the kink states are robust against the sharp bends of the internal domain wall with negligible inter-valley scattering. Our work may pave the way for multi-channel substrate-integrated photonic devices with high efficiency and high capacity for information communications and processing.

Experimental Discovery of Photonic Nodal Chains

Rongjuan Liu[1*], Qinghui Yan[1,2], Zhongbo Yan[3], Boyuan Liu[1], Hongsheng Chen[2], Zhong Wang[3,4], Ling Lu[1]

[1]Institute of Physics, Chinese Academy of Sciences/Beijing National Laboratory for Condensed Matter Physics, Beijing, China
[2]College of Information Science and Electronic Engineering, State Key Laboratory of Modern Optical Instrumentation, Zhejiang University, Hangzhou, China
[3]Institute for Advanced Study, Tsinghua University, Beijing, China
[4]Collaborative Innovation Center of Quantum Matter, Beijing, China
*corresponding author, E-mail: liurj@iphy.ac.cn

Abstract

We theoretically predict and experimentally observe nodal chains in a metallic-mesh photonic crystal across the entire Brillouin zone. These nodal chains are protected by mirror symmetry and have a frequency variation of less than 1%. We use angle-resovled transmission measurements to probe the projected bulk dispersion and perform Fourier-transformed field scans to map out the dispersion of the drumhead surface state. Our results establish an ideal nodal-line material for further study of topological line degeneracies with non-trivial connectivity. **Keywords: Nodal Chains, Photonic crystal, Angle-resolved transmission measurements**.

1. Introduction

Three-dimensional Weyl and Dirac nodal points have attracted widespread interest across multiple disciplines and in many platforms but allow for few structural variations. In contrast, nodal lines can have numerous topological configurations in momentum space, forming nodal rings, nodal chains, nodal links and nodal knots. However, nodal lines are much less explored because of the lack of an ideal experimental realization. In order to prompt the progress of the researches on nodal lines, we theoretically predict and experimentally observe nodal chains in a metallic-mesh photonic crystal.

2. Theoretical design

A nodal line is the extrusion of Dirac cone, arguably the most intriguing two-dimensional band structure, into three-dimensional momentum space. They share the same local Hamiltonian $H(\mathbf{k}) = k_x\sigma_x + k_y\sigma_z$, that can be protected by the PT symmetry forbidding the mass term of σ_y in the whole Brillouin zone. A single nodal line forms a closed ring, due to the periodicity of the Brillouin zone. And a nodal chain can be formed by two nodal rings touching at one point. The local chain Hamiltonian can be written as $H(\mathbf{k}) = k_x\sigma_x + (k_xk_z + m_z)\sigma_z$, when $m_z = 0$ which can be guaranteed by the mirror symmetry $\mathrm{M}_z = \sigma_x$. According to the symmetry, we designed a metallic-mesh three-dimensional photonic crystal in fig. 1a. The fig. 2b shows the structure of chains in the Brillouin zone.

3. Experimental observation

3.1. Experimental sample

In experiment, we adopted aluminium as the material of choice for its high conductivity, low weight and low cost. The lattice constant is 11.6mm, and the rod width is 2mm. the sample is stacked with nine identical layers and each layer has 30×30 unit cells. The final size for one layer is 37cm×37cm×10.44cm.

3.2. Observation of bulk states by angle-resolved transmission measurement

We carried out angle-resolved transmission to measure the nodal-chain bulk states. A similar set-up as in ref. [1] is used. Figure 1 c-f show two measured and the corresponding theoretical results when the measured angle is 0°, 15°, 30°, and 45°. The experimental results are in good agreement with theory, which prove the realization of photonic nodal chains in experiment through the observation of bulk states.

3.3. Observation of surface states by field-scanning measurement

A nodal-line material is known to support a drumhead surface state, which is a sheet of surface dispersion enclosed by the projected nodal-line bulk state in the surface Brillouin zone. We performed Fourier-transformed field scans to measure the surface states of our nodal-chain sample. Figure 1 g and h show the theoretical surface dispersion and the experimentally observed surface dispersion, which agree with each other very well. It further proves the topological property of nodal chains.

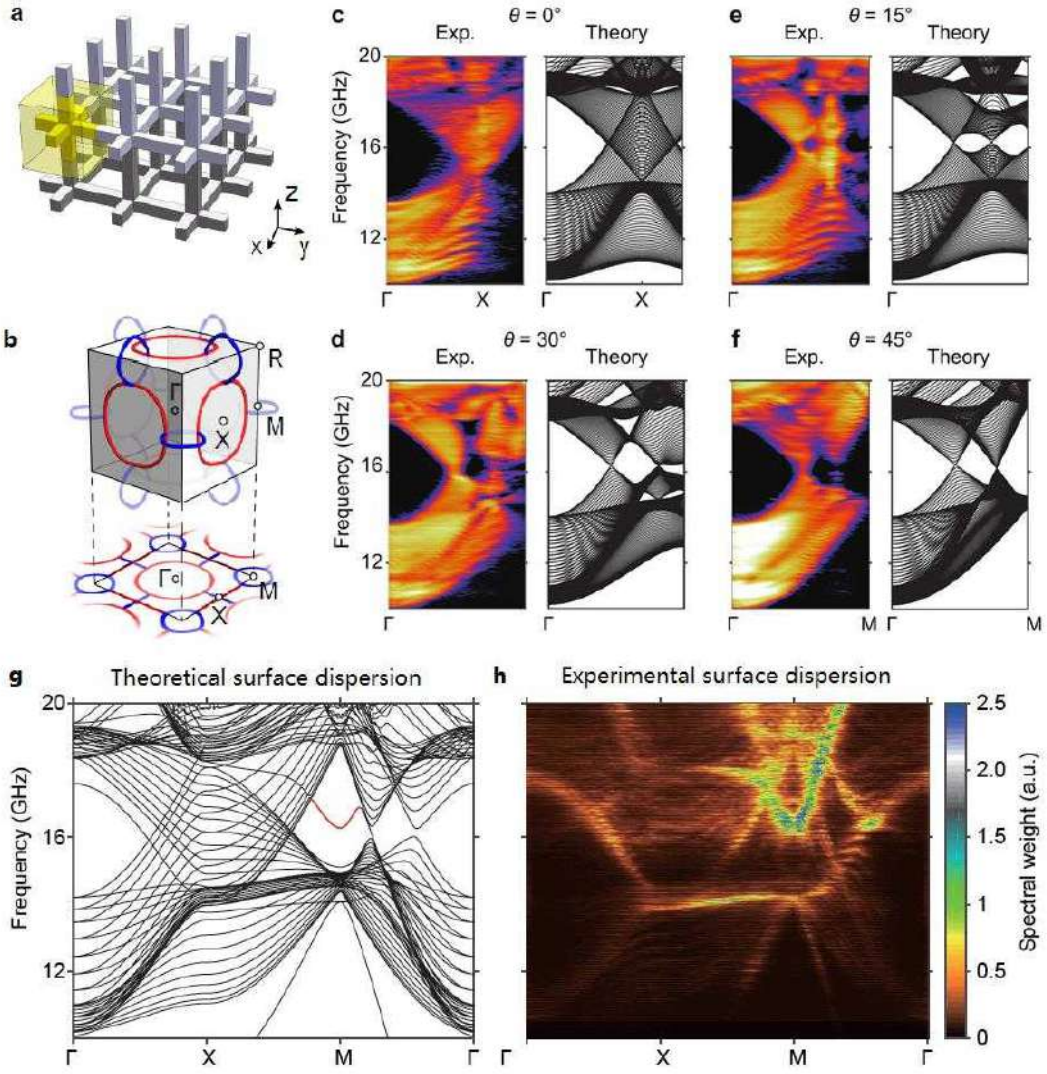


Figure. 1 a: the metallic-mesh three-dimensional photonic crystal; b: the structure of nodal chains in the Brillouin zone; c-f: the measured projected band structures at different angles by angular-resolved transmission and the corresponding theorectical results. g and h: the theorectial and experimental surface dispersions.

4. Conclusions

We proved the discovery of photonic nodal chains through the measurements of bulk states and surface states in experiment. Our finding may inspire searches for ideal nodal lines in other material platforms, and stimulate experimental realization of non-trivial nodal-line structures, such as nodal links and nodal knots.

Acknowledgements

We thank Yang He, Chen Fang and Hongming Weng for discussions. The authors were supported by the National Key R&D Program of China under Grant Nos 2017YFA0303800 and 2016YFA0302400 and by NSFC under Project Nos 11721404.

References

[1] L. Lu, et al, Experimental observation of Weyl points, *Science* 349: 622−624, 2015.

Theory of Chiral Edge State Lasing in a 2D Topological System

Matteo Seclì[1*], Massimo Capone[1,2], and Iacopo Carusotto[3]

[1]International School for Advanced Studies (SISSA), Via Bonomea 265, I-34136 Trieste, Italy
[2]CNR-IOM Democritos, Via Bonomea 265, I-34136 Trieste, Italy
[3]INO-CNR BEC Center and Dipartimento di Fisica, Università di Trento, I-38123 Povo, Italy
*corresponding author, E-mail: matteo.secli@sissa.it

Abstract

We numerically simulate a Harper-Hofstadter model equipped with broadband optical gain, with the goal of extracting those general features of the lasing regime resulting from the chirality of the edge modes. We find ultraslow relaxation times well above threshold and, depending on the shape of the amplifying region, the opening of a convective instability region in which the competition between the two chiral edge modes emerges more clearly.

1. Introduction

Topological insulators are materials that behave as insulators in the bulk but have conducting edges; these edges have to ability to host a topologically protected conductance which is immune to disorder and backscattering impurities. A recent idea is to provide a topological insulator with some gain and then exploit the topological protection of its edge modes in order to possibly improve the emission of laser devices; experiments on top of 1D and 2D topological insulators have appeared in the last couple of years [1–5].

The goal of our study is to identify those features that stem directly from the chirality of the lasing edge modes, and therefore are peculiar to topological lasers only. This is done in a general way by not choosing a model tied to a specific platform and by focusing only on the basic effects.

2. Model

As we want to focus only on the topological nature of the lasing modes, we consider here the bosonic Harper-Hofstadter (HH) model [6, 7] without any loss of generality:

$$H = \sum_{m,n} \Big\{ \omega_0 a^\dagger_{m,n} a_{m,n} - J\big(a^\dagger_{m,n} a_{m+1,n} + e^{-i2\pi\vartheta m} a^\dagger_{m,n} a_{m,n+1} + \text{h.c.}\big)\Big\}, \quad (1)$$

where ω_0 is the on-site energy, J is the hopping amplitude and $a_{m,n}$ is the photon field at the lattice site (m, n). The hopping along y has an x-dependent phase, proportional to the flux $\vartheta = p/q$ of the synthetic magnetic field. For $\vartheta = 1/4$ (as in the present discussion) the system has two bandgaps, each of them equipped with a topological edge mode; these two modes have opposite chiralities.

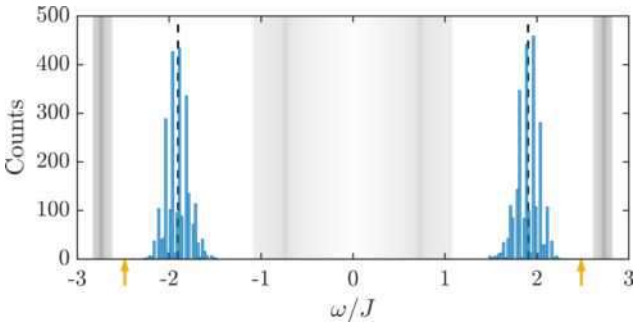


Figure 1: Histogram of the lasing frequency for WEG. The dashed lines indicate the average values, while the orange arrows indicate the lasing frequency for a 1×15 PEG. The gray shading indicates the density of bulk states.

We then simulate the time-evolution of the classical field amplitudes, with the addition of on-site losses $\gamma_{m,n} \equiv \gamma$ and a broadband, saturable gain with spatial profile determined by $P_{m,n}$ [8]:

$$\dot{a}_{m,n} = -i\,[a_{m,n}, H] + \left(\frac{P_{m,n}}{1+\beta|a_{m,n}|^2} - \gamma\right) a_{m,n}. \quad (2)$$

3. Results

We've simulated the system in two different configurations: a *whole edge gain* (WEG) configuration, in which we amplify the whole 1-site-thick edge of the lattice, and a *partial edge gain* (PEG) configuration, in which we amplify only a 1-site-thick strip of sites on one of the edges [8].

In the WEG configuration, we've witnessed the presence of a slowly-fading intensity "bump" that travels along the edge with group velocity v_g; this bump is generated by the initial noisy state of the system but cannot be expelled from the edge due to the topological protection of the mode, resulting in long-time intensity oscillations of the laser emission.

Furthermore we observe that the lasing frequency, albeit unique for each realization, is randomly chosen from relatively broad distributions (Figure 1); this is actually common in ring lasers, where the modes are quantized with periodic boundary conditions. These modes are again selected depending on the initial noisy state, while the k-dependent spatial overlap between the edge modes and the amplify-

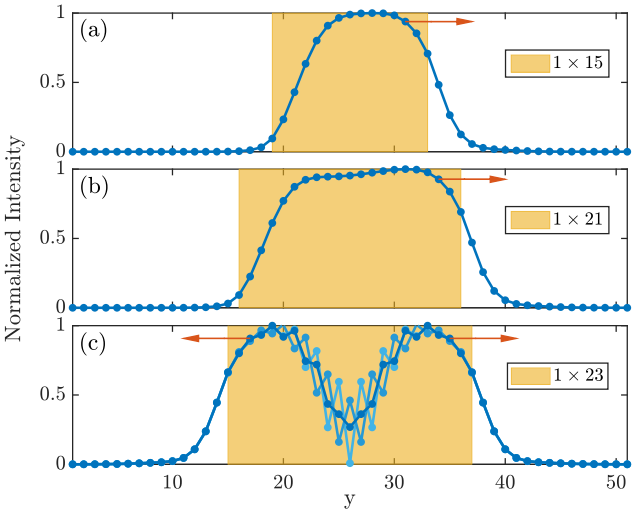


Figure 2: Intensity profiles along the $x = 1$ edge for different strip lengths (legends). The shaded area indicates the amplifying region, while the red arrows indicate the chirality of the mode.

ing region produces a frequency-dependent effective gain, which is (roughly) maximized at the center of the bandgap.

In order to avoid these two effects, we can then try to amplify only part of the edge. In this PEG configuration, for a strip of moderate length, one indeed quickly finds a steady-state intensity profile with a single chirality (arrows in Figure 2(a-b)) and with a frequency which does not vary for different realizations (arrows in Figure 1).

In this case, however, the lasing threshold is much higher than in the WEG case because of the opening of a convective instability region. The threshold can be reduced by increasing the length of the amplifying strip, and the emission stays single-mode up to a certain critical length; after this point, the lasing profile splits into two sub-regions having opposite chiralities (Figure 2(c)) due to the competition between the two modes. The latter can be seen as wild temporal oscillations in the central overlap region, and can be suppressed by using a medium with a ω-dependent gain.

Future works will analytically explain the ultra-slow relaxation rate of the intensity bump observed in the WEG configuration within the general theory of collective modes of a laser [9] in terms of the k-dependent effective gain, and will explore the consequences of having an amplifying medium with a frequency-dependent gain.

Acknowledgements

We warmly acknowledge continuous exchanges with M. Wouters on the subject of convective and absolute instabilities. We are grateful to T. Ozawa and H. M. Price for stimulating discussions. I.C. acknowledges funding from Provincia Autonoma di Trento. M.C. acknowledges support from MIUR PRIN 2015 (Prot. 2015C5SEJJ001) and SISSA/CNR project "Superconductivity, Ferroelectricity and Magnetism in bad metals" (Prot. 232/2015).

References

[1] P. St-Jean, V. Goblot, E. Galopin, A. Lemaître, T. Ozawa, L. Le Gratiet, I. Sagnes, J. Bloch, and A. Amo, "Lasing in topological edge states of a one-dimensional lattice," *Nature Photonics*, vol. 11, no. 10, pp. 651–656, oct 2017.

[2] M. Parto, S. Wittek, H. Hodaei, G. Harari, M. A. Bandres, J. Ren, M. C. Rechtsman, M. Segev, D. N. Christodoulides, and M. Khajavikhan, "Edge-Mode Lasing in 1D Topological Active Arrays," *Physical Review Letters*, vol. 120, no. 11, p. 113901, mar 2018.

[3] H. Zhao, P. Miao, M. H. Teimourpour, S. Malzard, R. El-Ganainy, H. Schomerus, and L. Feng, "Topological hybrid silicon microlasers," *Nature Communications*, vol. 9, no. 1, p. 981, dec 2018.

[4] B. Bahari, A. Ndao, F. Vallini, A. El Amili, Y. Fainman, and B. Kanté, "Nonreciprocal lasing in topological cavities of arbitrary geometries," *Science*, vol. 358, no. 6363, pp. 636–640, nov 2017.

[5] M. A. Bandres, S. Wittek, G. Harari, M. Parto, J. Ren, M. Segev, D. N. Christodoulides, and M. Khajavikhan, "Topological insulator laser: Experiments," *Science*, vol. 4005, no. February, pp. 1–8, 2018.

[6] D. R. Hofstadter, "Energy levels and wave functions of Bloch electrons in rational and irrational magnetic fields," *Physical Review B*, vol. 14, no. 6, pp. 2239–2249, sep 1976.

[7] M. Hafezi, E. A. Demler, M. D. Lukin, and J. M. Taylor, "Robust optical delay lines with topological protection," *Nature Physics*, vol. 7, no. 11, pp. 907–912, nov 2011.

[8] M. Seclì, M. Capone, and I. Carusotto, "Theory of chiral edge state lasing in a two-dimensional topological system," *arXiv preprint*, jan 2019.

[9] M. Wouters and I. Carusotto, "Excitations in a Nonequilibrium Bose-Einstein Condensate of Exciton Polaritons," *Physical Review Letters*, vol. 99, no. 14, p. 140402, oct 2007.

Nonreciprocity, Isolation and Time-reversal Symmetry in Nonlinear Devices

David E. Fernandes[1] and Mário G. Silveirinha[2]

[1] Instituto de Telecomunicações, Departamento de Engenharia Electrotécnica, Universidade de Coimbra - Pólo II, 3030-290 Coimbra, Portugal
[2] University of Lisbon and Instituto de Telecomunicações, Avenida Rovisco Pais, 1, 1049-001 Lisboa, Portugal
*corresponding author, E-mail: dfernandes@co.it.pt

Abstract

Here we highlight that nonlinear devices that operate as "electromagnetic diodes" for individual port excitations, cannot possibly provide a robust optical isolation under a simultaneous port excitation. Moreover, in the lossless case, typical nonlinear structures, despite being nonreciprocal, are time-reversal invariant, and thereby are inherently bi-directional.

1. Introduction

In electromagnetism, reciprocity is a consequence of linearity and time-reversal symmetry [1]. Reciprocal systems are inherently bi-directional and thus some microwave devices that are used in telecommunications networks, such as isolators and circulators, must rely on nonreciprocal elements. Typically, a nonreciprocal response is obtained with a magnetic bias [2]. However, this solution may be impractical in highly-integrated photonic platforms, and other alternatives to obtain a nonreciprocal response have emerged, such as using nonlinear effects [3] and others [4]-[7].

The mushroom metamaterial may be regarded as a wire medium [8] loaded with square metallic patches [9]. It possesses unusual electromagnetic properties that may enable the negative refraction of light and near-field imaging [10], amongst many other applications. In the nonlinear regime, these structures can allow for the realization of absorbers of high-power signals [11] and can exhibit a strong bi-stable response, which can be used to realize electromagnetic switches [12]. Here, we explore the possibility of using a mushroom metamaterial loaded with nonlinear elements to realize an "electromagnetic diode", where the metamaterial is either nearly fully reflecting or almost transparent, depending on the excitation port [13]. We show that the nonlinear device does not provide port isolation in the scenario of a simultaneous excitation. Furthermore, in the lossless case the nonlinear metamaterial is time-reversal invariant, and thus is intrinsically bi-directional.

2. Diode Functionality vs. Port Isolation

Here we study the scattering of incoming plane waves by a nonlinear lossless asymmetric mushroom metamaterial slab. The plane waves illuminate the slab at both interfaces, as shown in Fig. 1a. We use the effective medium theory described in [12]-[13] to determine the nonlinear response of the lossless metamaterial to variations of the incident field amplitude at a fixed frequency The chosen frequency is close to the strongest resonance of the metamaterial, so that the current delivered to the nonlinear lumped element becomes highly sensitive to small variations of the excitation field [12]. In Fig. 1b we show the transmission coefficient of the mushroom metamaterial as a function of the amplitude of the incident field for the *individual* excitations of ports 1 and 2. As seen, the relation between the incident field and the transmission coefficients is not univocal, leading to a bi-stable hysteresis response. Remarkably, the two ports can have a strong asymmetric response. Particularly, when the metamaterial is operated in the hysteresis branch where the excitation field decreases from very large values to around $\left|E^{\text{inc}}\right| = 465\ \text{V/m}$, we have $|T_1|/|T_2| >> 1$ with $|T_1| \approx 1$. Thus, in this regime the mushroom metamaterial behaves as a "diode" for electromagnetic waves so that it is almost transparent for a top excitation and nearly completely opaque for a bottom excitation.

Importantly, for a simultaneous excitation of the two ports the structure no longer behaves as an electromagnetic diode. This is shown in panel c) of Fig. 1 for incident fields that guarantee that the wave scattered to port 1 has negligible amplitude in the 2nd time plateau, when any of the ports is individually excited (the relevant operating points are determined by the vertical dashed line of panel Fig. 1**b**). In contrast, Fig. 1c reveals that under a simultaneous excitation the scattered field is almost evenly distributed at both interfaces. Thereby, the port 1 is not isolated from port 2. Indeed, it is impossible to realize an isolator without material loss [13].

Furthermore, as theoretically shown in [13], in the lossless scenario the nonlinear device is time-reversal invariant and, thus, is inherently bi-directional, which is incompatible with the isolator functionality. This property

extends and generalizes the concept of "dynamic" reciprocity introduced in [14] to arbitrary variations in time of the incoming waves. At the conference, we will present a full time-domain analysis illustrating the invariance of the nonlinear lossless mushroom metamaterial slab under the time-reversal operation and its consequences.

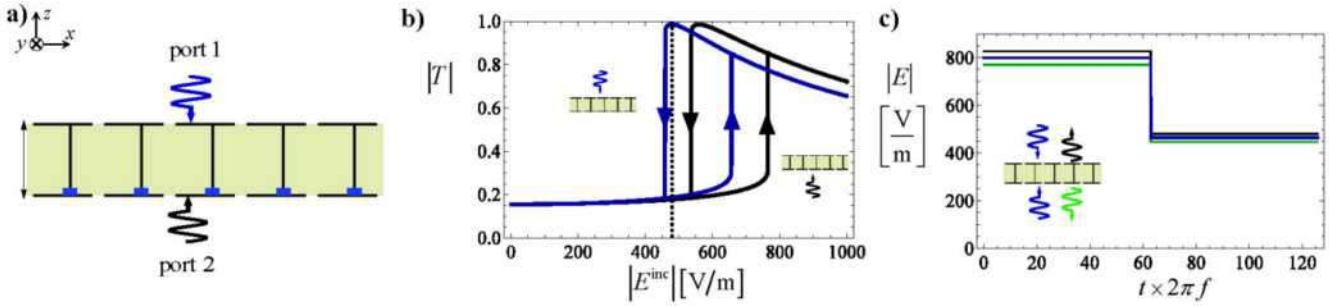


Figure 1: **a)** Geometry of the two-sided mushroom slab: the wires are embedded in air and connected to metallic patches through a nonlinear capacitors at the bottom interface, represented in the figure as blue rectangles, and through ideal short-circuits at the top interface. The lumped element is a parallel plate-type capacitor filled with a nonlinear Kerr-type dielectric. The details about all structural parameters are described in [12]-[13]. **b)** Transmission coefficient as function of the amplitude of the incident field. The arrows in the hysteresis loops indicate whether the excitation field amplitude is increasing or decreasing. The blue curves are for an excitation of port 1 and the black curves for an excitation of port 2. **c)** Envelope of the scattered field calculated at the top (black line) and bottom (green line) interfaces as a function of time. The time scale is normalized to the oscillation frequency *f*. The incident field (blue line) envelope has two plateaus: in the first plateau $\left|E^{\text{inc},1}\right| = \left|E^{\text{inc},2}\right| = 800\,\text{V/m}$, whereas in the second plateau $\left|E^{\text{inc},1}\right| = \left|E^{\text{inc},2}\right| = 465\,\text{V/m}$. For an individual excitation of the ports, the wave scattered to port 1 has negligible amplitude in the second plateau but for a simultaneous excitation it has amplitude comparable to that of the wave scattered to port 2.

3. Conclusions

We showed that the nonlinear mushroom-metamaterial may behave as an almost ideal electromagnetic-diode for individual port excitations. However, due to the inapplicability of the superposition principle the structure does not provide "isolation" between the two ports. In addition, typical lossless nonlinear devices are invariant under the time-reversal operation, and hence are intrinsically bi-directional [13].

Acknowledgements

This work is supported in part by the IET under the Harvey Engineering Research Prize and by Fundação para Ciência e a Tecnologia (FCT) under project PTDC/EEITEL/4543/2014 and UID/EEA/50008/2017, and by the European Regional Development Fund (FEDER), through the Competitiveness and Internationalization Operational Programme (COMPETE 2020) of the Portugal 2020 framework, Project, RETIOT, POCI-01-0145-FEDER-016432. D. E. Fernandes acknowledges support by FCT, POCH, and the cofinancing of Fundo Social Europeu under the fellowship SFRH/BPD/116525/2016.

References

[1] C. Caloz, A. Alù, S. Tretyakov, D. Sounas, K. Achouri, and Z.-L. Deck-Léger, Electromagnetic Nonreciprocity, *Phys. Rev. Applied* 10: 047001, 2018.

[2] Z. Wang, and S. Fan, Optical circulators in two-dimensional magneto-optical photonic crystals, *Opt. Lett.* 30: 1989–1991, 2005.

[3] M. Soljačić, C. Luo, J. D. Joannopoulos, and S. Fan, Nonlinear photonic crystal microdevices for optical integration, *Opt. Lett.* 28: 637-639, 2003.

[4] S. Lannebère, M. G. Silveirinha, Wave Instabilities and Unidirectional Light Flow in a Cavity with Rotating Walls, *Phys. Rev. A* 94: 033810, 2016.

[5] Z. Yu, and S. Fan, Complete optical isolation created by indirect interband photonic transitions, *Nat. Photon.* 3: 91-95, 2009.

[6] S. Tanaka, N. Shimomura, and K. Ohtake, Active circulators — the realization of circulators using transistors, *Proc. IEEE* 53: 260–267, 1965.

[7] T. A. Morgado, M. G. Silveirinha, Drift-induced Unidirectional Graphene Plasmons, *ACS Photonics* 5: 4253, 2018.

[8] P. A. Belov, R. Marques, S. I. Maslovski, I. S. Nefedov, M. G. Silveirinha, C. R. Simovski, and S. A. Tretyakov, Strong spatial dispersion in wire media in the very large wavelength limit, *Phys. Rev. B* 67: 113103, 2003.

[9] M. G. Silveirinha, Nonlocal homogenization model for a periodic array of ϵ-negative rods, *Phys. Rev. E* 73: 046612, 2006.

[10] M. G. Silveirinha, and A. B. Yakovlev Negative Refraction by a Uniaxial Wire Medium with Suppressed Spatial Dispersion, *Phys. Rev. B* 81: 233105, 2010.

[11] H. Wakatsuchi, S. Kim, J. J. Rushton, and D. Sievenpiper, Circuit-based nonlinear metasurface absorbers for high power surface currents, *Appl. Phys. Lett.* 102: 214103, 2013.

[12] D. E. Fernandes, and M. G. Silveirinha, Bistability in mushroom-type metamaterials, *J. of Appl. Phys.* 122: 014303, 2017.

[13] D. E. Fernandes, and M. G. Silveirinha, D. E. Fernandes, M. G. Silveirinha, Asymmetric Transmission and Isolation in Nonlinear Devices: Why They Are Different, *IEEE Antennas and Wireless Propag. Lett.* 17:1953-1957, 2018.

[14] Y. Shi, Z. Yu, and S. Fan, Limitations of nonlinear optical isolators due to dynamic reciprocity, *Nature Photon*. 9: 388, 2015.

Photonic analogues of the Haldane and Kane-Mele Models

Sylvain Lannebère[1*], **Mário G. Silveirinha**[1,2]

[1]Department of Electrical Engineering, University of Coimbra and Instituto de Telecomunicações, 3030-290 Coimbra, Portugal
[2]University of Lisbon – Instituto Superior Técnico, Department of Electrical Engineering, 1049-001 Lisboa, Portugal
*corresponding author, E-mail: sylvain.lannebere@co.it.pt

Abstract

We propose strict electromagnetic analogues of the Haldane and Kane-Mele models in photonic crystals made of dielectric cylinders with honeycomb symmetry embedded in a metallic background with a nonreciprocal spatially variable pseudo-Tellegen response. In addition, it is shown using a duality transformation that the Kane-Mele model can be implemented in a reciprocal system made of matched anisotropic dielectrics with identical permittivity and permeability.

1. Introduction

The Haldane model [1] played a fundamental role in the development of topological concepts in electronics. This model describes the electronic properties of a graphene-type material under the influence of a periodic magnetic field with zero-spatial average. Furthermore, the Haldane model is effectively at the origin of the theory of topological insulators: the Kane-Mele model [2, 3] consists of two copies of the Haldane model with opposite magnetic field. However, despite the numerous connections between topological electronics and photonics developed in recent years [4, 5], so far there is no precise electromagnetic counterpart of these models, mainly due to the difficulties to mimic an effective magnetic field for photons. Here we propose a strategy to implement both models in photonic crystals.

2. Photonic Haldane model

It was recently shown [6] that the electronic Haldane model can be implemented in a 2DEG under the influence of a periodic electrostatic potential $V(\mathbf{r})$ with the honeycomb symmetry and of a magnetic vector potential $\mathbf{A}(\mathbf{r})$ that breaks the time reversal symmetry (see Fig. 1a). It can be demonstrated, by using an analogy between the time-independent Schrödinger's equation describing this system and the 2D Maxwell equations, that a photonic analogue of the Haldane model can be implemented for TE-waves ($\mathbf{E} = E_z\hat{\mathbf{z}}$) in a photonic crystal with honeycomb symmetry made of air cylinders embedded in a metallic background and with a *spatially variable* magnetoelectric coupling tensor of the form $\overline{\overline{\xi}} = \overline{\overline{\zeta}} = \boldsymbol{\xi}(\mathbf{r}) \otimes \hat{\mathbf{z}} + \hat{\mathbf{z}} \otimes \boldsymbol{\xi}(\mathbf{r})$ [7] (see Fig. 1b). This type of nonreciprocal magnetoelectric coupling, known as a pseudo-Tellegen coupling [8], turns out to be the photonic equivalent of the effect of a magnetic field on electrons [9]. The obtained structure is a precise photonic analogue of the Haldane model, i.e. only the phase with dominant broken time reversal symmetry leads to a non-trivial topology and supports, in the whole band gap, unidirectional edge mode propagation protected against back-scatterings. To confirm this statement, the field in the 2D closed cavity depicted in Fig. 2a was computed with the finite-difference method (FDFD see [10]) under a dipole excitation and for frequencies in the band gap. As seen in Fig. 2b–c, the phase with a dominant broken time reversal symmetry is, as expected, topologically non trivial and supports unidirectional edge state whose direction of propagation is locked to the sign of the magnetoelectric coupling. Crucially, these topologically protected modes do not experience any backscattering at the corners of the cavity.

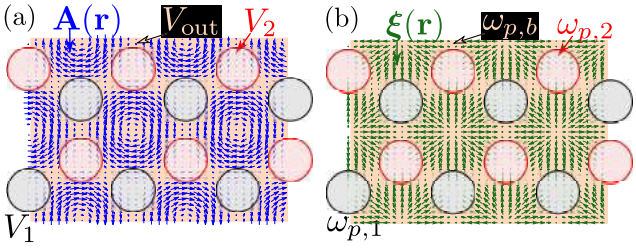


Figure 1: Schematic of (a) the electronic and (b) the equivalent photonic structure used to implement the Haldane model. The V_is and $\omega_{p,i}$s with $i = 1, 2$ are respectively the electrostatic potentials and plasma frequencies of the materials associated with the two different sublattices, V_{out} and $\omega_{p,b}$ are the electrostatic potential and the plasma frequency of the background material, and $\mathbf{A}$ and $\boldsymbol{\xi}$ are the spatially dependent magnetic vector potential and pseudo-Tellegen vector, respectively.

3. Photonic Kane-Mele model

By further imposing a matched permittivity and permeability in the same nonreciprocal system, it can be shown that TE and TM polarized waves become described by two copies of the previous model with opposite magnetoelectric coupling [7]. This paradigm constitutes an exact photonic analogue of the Kane-Mele model. Interestingly, it can be demonstrated [7, 11] that this nonreciprocal system is linked, through a duality transformation, to a much simpler

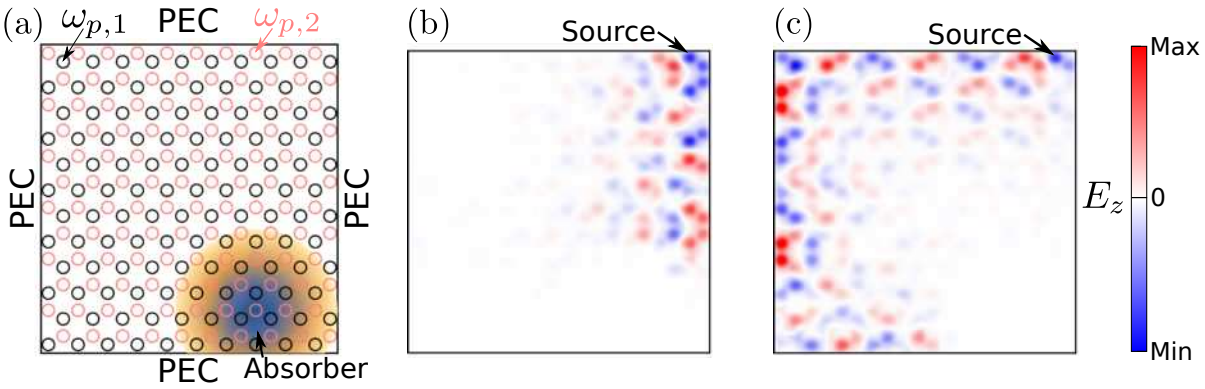


Figure 2: (a) Schematic of the simulated cavity: the photonic crystal of Fig. 1b with an absorber located at the right-bottom region and surrounded by PEC walls. For the sake of clarity the pseudo-Tellegen response $\boldsymbol{\xi}(\mathbf{r}) = \xi_0\hat{\boldsymbol{\xi}}(\mathbf{r})$ is not represented in the figure. The z-component of the electric field in a structure with $\omega_{p,1} = \omega_{p,2}$ and, $\xi_0 > 0$ in (b) and $\xi_0 < 0$ in (c).

reciprocal platform with the same edge-states. These findings evidenced the possibility of implementing the photonic Kane-Mele model with fully reciprocal materials made of matched non-bianisotropic dielectrics.

4. Conclusions

We used an analogy between the 2D Schrödinger and Maxwell equations to obtain an electromagnetic equivalent of the electronic Haldane and Kane-Mele models based on photonic artificial graphene with a spatially variable pseudo-Tellegen coupling. Interestingly, the Kane-Mele nonreciprocal platform is related through a duality transformation with a much simpler reciprocal system with the same edge states. Our analysis proves that the Kane-Mele model can be rigorously implemented using matched non-bianisotropic dielectrics and that such structures can support bi-directional edge states immune to back-scattering. Our findings make a connection between the fields of time-reversal invariant topological photonics, pseudomagnetic fields [12] and symmetry protected systems [11].

Acknowledgement

This work was partially funded by the IET under the A F

Harvey Engineering Prize, by Fundação para a Ciência e a Tecnologia under projects PTDC/EEI-TEL/4543/2014 and DL 57/2016/CP1353/CT0001.

References

[1] Haldane, F. D. M. Model for a Quantum Hall Effect without Landau Levels: Condensed-Matter Realization of the "Parity Anomaly". *Phys. Rev. Lett.* **61**, 2015–2018 (1988).

[2] Kane, C. L. & Mele, E. J. Quantum Spin Hall Effect in Graphene. *Phys. Rev. Lett.* **95**, 226801 (2005).

[3] Kane, C. L. & Mele, E. J. Z_2 Topological Order and the Quantum Spin Hall Effect. *Phys. Rev. Lett.* **95**, 146802 (2005).

[4] Khanikaev, A. B. *et al.* Photonic topological insulators. *Nat. Mat.* **12**, 233–239 (2013).

[5] Slobozhanyuk, A. *et al.* Three-dimensional all-dielectric photonic topological insulator. *Nat. Photonics* **11**, 130–136 (2017).

[6] Lannebère, S. & Silveirinha, M. G. Link between the photonic and electronic topological phases in artificial graphene. *Phys. Rev. B* **97**, 165128 (2018).

[7] Lannebère, S. & Silveirinha, M. G. Photonic analogues of the Haldane and Kane-Mele models. *arXiv:1902.04001* (2019).

[8] Serdyukov, A., Semchenko, I., Tretyakov, S. & Sihvola, A. Electromagnetics of bi-anisotropic materials: Theory and applications (2001).

[9] Jacobs, D. A., Miroshnichenko, A. E., Kivshar, Y. S. & Khanikaev, A. B. Photonic topological Chern insulators based on Tellegen metacrystals. *New J. Phys.* **17**, 125015 (2015).

[10] Lannebère, S. & Silveirinha, M. G. Effective Hamiltonian for electron waves in artificial graphene: A first-principles derivation. *Phys. Rev. B* **91**, 045416 (2015).

[11] Silveirinha, M. G. $\mathcal{P}\cdot\mathcal{T}\cdot\mathcal{D}$ symmetry-protected scattering anomaly in optics. *Phys. Rev. B* **95**, 035153 (2017).

[12] Liu, F. & Li, J. Gauge Field Optics with Anisotropic Media. *Phys. Rev. Lett.* **114**, 103902 (2015).

One-way surface plasmons in drift-current biased graphene

Tiago A. Morgado[1], Mário G. Silveirinha[1,2]

[1]Instituto de Telecomunicações and Department of Electrical Engineering, University of Coimbra, 3030-290 Coimbra, Portugal
[2]University of Lisbon, Instituto Superior Técnico, Avenida Rovisco Pais, 1, 1049-001 Lisboa, Portugal
*corresponding author, E-mail: tiago.morgado@co.it.pt

Abstract

We propose an innovative solution to break reciprocity and obtain one-way subwavelength light propagation. We theoretically demonstrate that the biasing of a graphene sheet by an electric drift current leads to the emergence of one-way surface plasmons. Our findings open interesting perspectives in nonreciprocal photonics and offer new opportunities to control the flow of light at the nanoscale.

1. Introduction

Lorentz reciprocity – a fundamental principle rooted in the linearity and invariance of Maxwell's equations under time-reversal symmetry [1-2] – is an intrinsic feature of the vast majority of photonic systems. This fundamental law imposes that the level of wave transmission in linear photonic systems is invariant under the swap of the source and receiver positions [2]. Yet, nonreciprocal devices with strong asymmetric wave transmissions (e.g., isolators and circulators) are of critical importance in optical systems.

Nonreciprocal responses are typically accomplished with magneto-optical materials (such as ferrites or other iron garnets) biased with a static magnetic field [3]. Remarkably, some of these nonreciprocal gyrotropic platforms are inherently topological and support unidirectional backscattering-immune chiral edge modes [4-5]. Nevertheless, the need of employing an external biasing circuit, as well as the relatively weak magneto-optical responses and their associated high losses in the terahertz and optical regimes, hamper the integration of such nonreciprocal components in highly-integrated photonic systems. For this reason, great efforts have been devoted to develop magnetic-free nonreciprocal photonic solutions fully compatible with modern nanophotonic systems [6-11]. Recently [12], we have proposed a novel and promising platform to break the Lorentz reciprocity and achieve magnetic-free nonreciprocal subwavelength light propagation. In particular, we have theoretically demonstrated in [12] that by biasing a graphene sheet with a drift electric current it is possible to achieve broadband regimes of unidirectional propagation of surface plasmons.

2. Results and Discussion

The system under study is illustrated in Fig. 1(a). It consists of a graphene sheet surrounded by a dielectric with relative permittivity $\varepsilon_{r,s}=4$ (e.g., SiO_2 or h-BN). The graphene sheet is traversed by a direct electric current created by a static voltage drop applied across the sheet.

As demonstrated by us in [13], in the presence of a drift current, the graphene conductivity associated with a longitudinal excitation (with in-plane electric field directed along x) is given by $\sigma_g^{\text{drift}}(\omega,k_x)\approx(\omega/\tilde{\omega})\sigma_g(\tilde{\omega},k_x)$, where $\tilde{\omega}=\omega-k_x v_0$ is the Doppler-shifted frequency, k_x is the wave number along x-direction (we only consider plasmons with $k_y=0$), v_0 is the drift velocity, and $\sigma_g(\omega,k_x)$ is the nonlocal zero-temperature graphene conductivity reported in [14-15]. Interestingly, in the presence of an electron drift (i.e., for $v_0\neq 0$) $\sigma_g^{\text{drift}}(\omega,k_x)\neq\sigma_g^{\text{drift}}(\omega,-k_x)$, and therefore, the electromagnetic response of the graphene sheet is nonreciprocal.

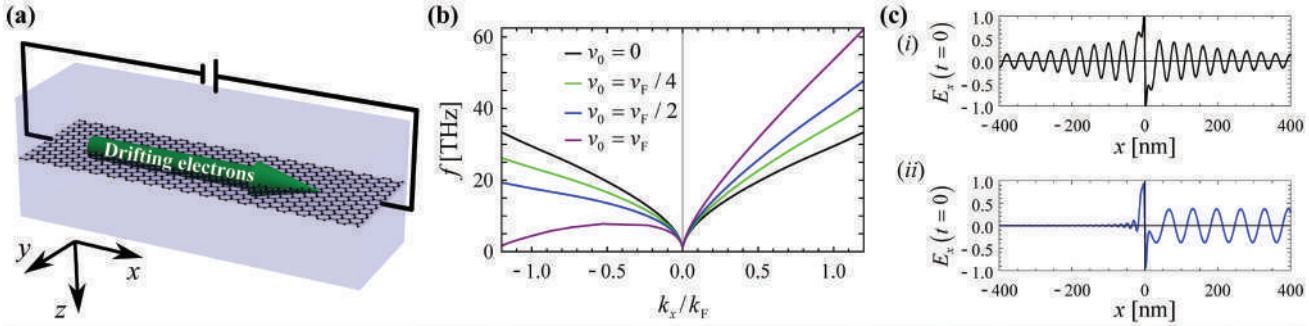


Figure 1: (a) A graphene sheet surrounded by a dielectric. A static voltage generator induces an electron drift in the graphene sheet. (b) Dispersion of the SPPs supported by the graphene sheet for several drift velocities v_0. (c) Snapshots in time of E_x (in arbitrary unities) as a function of x and for $z=0$ and frequency $f=30$ THz. (*i*) Without drift ($v_0=0$); (*ii*) With drift ($v_0=v_F/2$). The chemical potential of the graphene sheet is $\mu_c=0.1$ eV and the collision time is $\tau=170$ fs.

The dispersion characteristic of the SPPs supported by the drift-current biased graphene sheet can be obtained from $2i\omega\varepsilon_0\varepsilon_{\mathrm{r,s}}/\gamma_s - \sigma_{\mathrm{g}}^{\mathrm{drift}}(\omega, k_x) = 0$, where c is the speed of light in vacuum, and $\gamma_{\mathrm{s}} = \sqrt{k_x^2 - \varepsilon_{\mathrm{r,s}}(\omega/c)^2}$ is the transverse (along z) attenuation constant. Figure 1(b) depicts the dispersion characteristic of the SPPs for different drift velocities v_0. As expected, in the absence of the drift-current biasing ($v_0 = 0$), the graphene response is reciprocal, and thereby, the dispersion diagram is formed by two symmetric branches. In contrast, in the presence of a drift-current biasing, a clear symmetry breaking of the SPPs dispersion occurs. The degree of asymmetry of the dispersion diagram is more pronounced for higher drift velocities. Remarkably, the symmetry breaking caused by the drift-current biasing gives rise to broadband regimes of unidirectional propagation wherein the SPPs are allowed to propagate only along the $+x$ direction (the direction of the drift current).

To further demonstrate the emergence of a unidirectional propagation regime in the drift-current biased graphene, next we consider a scenario wherein the SPPs are excited by a near-field emitter. The SPP fields excited by the near-field emitter are calculated using the formalism of Ref. [12]. Figure 1(c) depicts the E_x-field as a function of x and for $z = 0$ for a near-field emitter located at $(x, z) = (0, 5\ \mathrm{nm})$. In the absence of a drift-current bias, two identical counter-propagating SPPs are clearly excited by the emitter (Fig. 1(c)(*i*)). Quite differently, when the graphene sheet is biased by a drift-current, the response of the system becomes strongly nonreciprocal and the SPPs propagate only along the direction of the drifting electrons ($+x$ direction) (Fig. 1(c)(*ii*)).

3. Conclusions

We have theoretically demonstrated that the electromagnetic response of a graphene sheet biased by a drift electric current is strongly nonreciprocal and enables the emergence of broadband regimes of one-way SPP propagation. In the talk, we will present these exciting results, as well as our most recent findings on this one-atom thick nonreciprocal plasmonic platform. In particular, we will also show that the drift-induced unidirectional graphene plasmons are protected against backscattering from obstacles and imperfections, similar to the "one-way" topologically protected chiral edge modes supported by topological photonic systems [4-5]. Furthermore, we will show that the drift-current biasing may provide optical gain, and thereby, may enable enhancing the propagation length of the graphene plasmons.

Acknowledgements

This work was partially funded by Fundação para a Ciência e a Tecnologia PTDC/EEI-TEL/4543/2014, by the IET under the A F Harvey Research Engineering Prize, and by Instituto de Telecomunicações under project UID/EEA/50008/2017. T. A. Morgado acknowledges financial support by Fundação para a Ciência e a Tecnologia (FCT) under the research contract with reference DL 57/2016/CP1353/CT0002 established with Instituto de Telecomunicações (IT) – Coimbra.

References

[1] H. B. Casimir, "On Onsager's principle of microscopic reversibility," *Rev. Mod. Phys* 17, 343-350, 1945.

[2] R. J. Potton, "Reciprocity in optics," *Rep. Prog. Phys.* 67, 717-754, 2004.

[3] M. Freiser, "A Survey of Magnetooptic Effects," *IEEE Trans. Magn.* 4, 152, 1968.

[4] L. Lu, J. D. Joannopoulos, M. Soljačić, "Topological photonics", *Nat. Photon.* 8, 821, 2014.

[5] Z. Wang *et al.*, "Observation of unidirectional backscattering-immune topological electromagnetic states," *Nature* 461, pp. 772-775, 2009.

[6] L. Fan *et al.*, "An all-silicon passive optical diode," *Science* 335, pp. 447–450, 2012.

[7] Z. Shen *et al.* "Experimental realization of optomechanically induced non-reciprocity," *Nat. Photon.* 10, pp. 657‑661, 2016.

[8] S. Lannebère, M. G. Silveirinha, "Wave instabilities and unidirectional light flow in a cavity with rotating walls," *Phys. Rev. A* 94, 033810, 2016.

[9] T. Kodera, D. L. Sounas, C. Caloz, "Artificial Faraday rotation using a ring metamaterial structure without static magnetic field," *Appl. Phys. Lett.* 99, 03114, 2011.

[10] Z. Yu and S. Fan, "Complete optical isolation created by indirect interband photonic transitions," *Nat. Photon.* 3, pp. 91-94, 2009.

[11] D. L. Sounas and A. Alù, "Non-reciprocal photonics based on time modulation," *Nat. Photon.* 11, pp. 774-783, 2017.

[12] T. A. Morgado, M. G. Silveirinha, "Drift-induced Unidirectional Graphene Plasmons," *ACS Photonics* 5(11), pp. 4253-4258, 2018.

[13] T. A. Morgado, M. G. Silveirinha, "Negative Landau damping in bilayer graphene," *Phys. Rev. Lett.* 119, 133901, 2017.

[14] F. H. L. Koppens, D. E. Chang, and F. J. García de Abajo, "Graphene Plasmonics: A Platform for Strong Light-Matter Interactions," *Nano Lett.* 11(8), 3370, 2011.

[15] X. Lin *et al.*, "All-angle negative refraction of highly squeezed plasmon and phonon polaritons in graphene-boron nitride heterostructures," *Proc. Natl. Acad. Sci. USA* 114, pp. 6717–6721, 2017.

Synthetic gauge fields and tilted Dirac cones in photonic honeycomb lattices

Omar Jamadi[1], Marijana Milicevic[2], Elena Rozas[3], Grazia Salerno[4], Tomoki Ozawa[5], Iacopo Carusotto[6], Gilles Montambaux[7], Luc Le Gratiet[2], Abdelmounaim Harouri[2], Isabelle Sagnes[2], Aristide Lemaître[2], Jacqueline Bloch[2], Alberto Amo[1*]

[1]Laboratoire de Physique des Lasers, Atomes et Molécules, CNRS-Université de Lille, F-59000 Lille, France
[32]Centre de Nanosciences et de Nanotechnologies (C2N), CNRS - Université Paris-Sud/Paris-Saclay, Palaiseau, France
[3]Dept. Física de Materiales & Inst. Nicolás Cabrera, Universidad Autónoma de Madrid, 28049 Madrid, Spain
[4]Center for Nonlinear Phenomena and Complex Systems, Univ. Libre de Bruxelles, B-1050 Brussels, Belgium
[5]Interdisciplinary Theoretical and Mathematical Sciences Program (iTHEMS), RIKEN, Wako, Saitama 351-0198, Japan
[6]INO-CNR BEC Center and Dipartimento di Fisica, Università di Trento, 38123 Povo, Italy
[7]Laboratoire de Physique des Solides, CNRS, Univ. Paris-Sud, Université Paris-Saclay, 91405 Orsay Cedex, France
*corresponding author, E-mail: alberto.amo-garcia@univ-lille.fr

Abstract

Strain engineering is a powerful tool to shape the dispersion of Dirac materials. Here we use a honeycomb lattice of coupled polariton micropillars to implement tilted photonic Dirac cones, including type-III cones. To do so, we introduce a spatial asymmetry in the hopping of photons in the x and y directions of the lattice. When the hopping presents a spatial gradient, an artificial gauge field for photons is engineered, and photonic Landau levels are observed.

1. Introduction

Two-dimensional Dirac materials, i.e. materials whose electronic energy bands present a Dirac cone, are revolutionizing electronics. The linear dispersion characteristic of the Dirac cones results in striking phenomena like Klein tunnelling, ballistic transport and weak anti-localisation. When adding strain in a material with Dirac cones, or when considering high orbital bands, it has been recently shown that tilted Dirac cones and artificial gauge fields can be implemented [1,2]. Bringing these properties to the photonics realm would enable the manipulation of photons in metamaterials and photonic lattices with novel properties. Moreover, the easy manipulation of the photonic dispersions in these systems brings the possibility of exploring new strategies to implement tilted Dirac dispersions.

A very suitable platform to study Dirac dispersions in photonics is lattices of polariton micropillars [3]. In a semiconductor micropillar, photons are confined in the three directions of space: in the vertical direction they are confined via upper and lower Bragg mirrors that surround a semiconductor spacer acting as an optical cavity (see Fig. 1). In the horizontal direction, photons are confined thanks to the index of refraction contrast between the semiconductor spacer and air. Photons in the micropillar present a gapped spectrum with quantized energy levels with s-, p-, d-, … symmetry. Photonic tunnelling between adjacent micropillars can be induced by making them overlap during the fabrication process. This feature has been used to explore bosonic Josephson physics [4]. When extending the coupling to one- and two-dimensional lattices, energy bands for photons can be engineered [5]. A remarkable case is that of a honeycomb lattice [3]. The bands emerging from the coupling of the s-modes of each micropillar are analogous to the electronic bands emerging from the p_z orbitals of graphene, and present Dirac cones for photons. The photonic p-bands have a richer spectrum with four bands, two of which are flat and the other two show Dirac crossings.

The micropillar lattices allow the control of the onsite energies via the size of each micropillar, the nearest-neighbours coupling t via the physical overlap of adjacent micropillars, and direct access to the dispersion and wave functions in simple photoluminescence experiments. They are thus ideal to explore Dirac Hamiltonians. Here we report the observation of tilted Dirac cones and the implementation

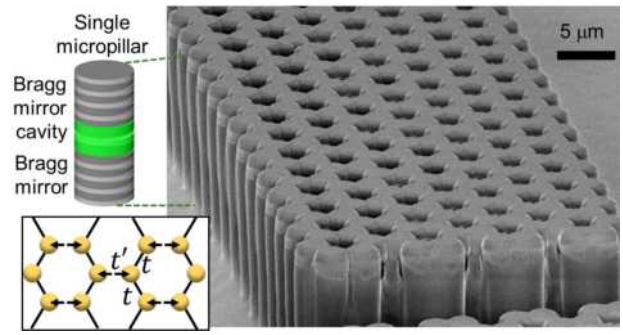


Figure 1. Scanning electron microscope image of a honeycomb lattice of micropillars with a gradient of hopping in the horizontal direction ($t'=t'(x)$).

of gauge fields in a honeycomb lattice of polariton micropillars via artificial strain engineering.

2. Discussion

Artificial strain can be engineered in honeycomb lattices of micropillars by engineering the hopping of photons between adjacent sites. Homogeneous uniaxial strain can be implemented by modifying one of the three couplings *t'*, with respect to the other two *t* (see Fig. 1), and keeping the same values all over the lattice. For the s-bands, increasing *t'* induces the displacement of the Dirac cones in the Brillouin zone until their merging at *t'*=2*t* [6]. In the p-bands, increasing *t'* with respect to *t* gives rise to the emergence of a new type of Dirac cones, so-called type-III. This kind of Dirac cone is characterised by the crossing of two linear dispersions, one of which is horizontal (a flat band). We provide direct experimental evidence of the engineering of such Dirac cone [7]. Materials with this kind of Dirac cone have been recently proposed as promising for the study of artificial black hole horizons [8].

Strain engineering is also an excellent technique to implement artificial gauge fields in Dirac materials. In 2010, F. Guinea and co-workers proposed that a trigonal strain gradient in a graphene layer would create a gauge field and give rise to the emergence of Landau levels in the absence of an external magnetic field [9]. Experimental evidence of this idea has been reported by measuring the local density of states in strained graphene lattices [10]. However, access to the eigenfunctions remains elusive in electronic experiments. This would provide key information on the artificial-gauge-field origin of the Landau levels. Indeed, the eigenfunctions of the Landau levels in electronic graphene subject to an external magnetic field present a sublattice-valley symmetry: in the K valley, the wavefunctions corresponding to the n=0 Landau level are localised in the A sublattice, while in the K' valley, they are localised in the B sublattice. In the case of an artificial gauge field induced by strain, the wavefunction of the n=0 Landau level is localised in the A sublattice, both for K and K' points. This is a consequence of the preservation of time-reversal symmetry in this case: the induced gauge field has opposite signs in both valleys.

We have followed the proposal of G. Salerno and co-workers [11] and implemented an artificial gauge field in a honeycomb lattice of micropillars by introducing a spatial gradient in the hopping *t'*. We observe the emergence of Landau levels and provide evidence of the sublattice asymmetry in the n=0 wavefunctions associated to the presence of the gauge field.

Our work goes well beyond previous reports of artificial gauge fields in lattices of coupled waveguides, in which the presence of Landau levels was evidenced via their localisation properties [12]. We report direct observation of the gapped flat bands associated to the Landau levels. This is a very promising framework to study flat band physics in two dimensions in the presence of nonlinearities. The semiconductor micropillars we use are actually in the strong coupling regime, in which photons are mixed with excitonic excitations in a quantum well embedded in the micropillar. The presence of the excitonic resonance provides significant photon nonlinearities which could be used to explore interaction effects in Landau levels.

References

[1] M. O. Goerbig, J.-N. Fuchs, G. Montambaux, and F. Piéchon, Tilted anisotropic Dirac cones in quinoid-type graphene and α-(BEDT-TTF)$_2$I$_3$, *Phys. Rev. B* 78:45415, 2008.

[2] A. A. Soluyanov, D. Gresch, Z. Wang, Q. Wu, M. Troyer, X. Dai, and B. A. Bernevig, Type-II Weyl semimetals, *Nature* 527:495, 2015.

[3] T. Jacqmin, I. Carusotto, I. Sagnes, M. Abbarchi, D. Solnyshkov, G. Malpuech, E. Galopin, A. Lemaître, J. Bloch, and A. Amo, Direct Observation of Dirac Cones and a Flatband in a Honeycomb Lattice for Polaritons, *Phys. Rev. Lett.* 112:116402, 2014.

[4] M. Abbarchi, A. Amo, V. G. Sala, D. D. Solnyshkov, H. Flayac, L. Ferrier, I. Sagnes, E. Galopin, A. Lemaitre, G. Malpuech, and J. Bloch, Macroscopic quantum self-trapping and Josephson oscillations of exciton polaritons, *Nat. Phys.* 9:275, 2013.

[5] C. Schneider, K. Winkler, M. D. Fraser, M. Kamp, Y. Yamamoto, E. A. Ostrovskaya, and S. Höfling, Exciton-polariton trapping and potential landscape engineering, *Rep. Prog. Phys.* 80:016503, 2017.

[6] G. Montambaux, F. Piéchon, J.-N. Fuchs, and M. Goerbig, Merging of Dirac points in a two-dimensional crystal, *Phys. Rev. B* 80:153412, 2009.

[7] M. Milićević, G. Montambaux, T. Ozawa, I. Sagnes, A. Lemaître, L. Le Gratiet, A. Harouri, J. Bloch, and A. Amo, Tilted and type-III Dirac cones emerging from flat bands in photonic orbital graphene, ArXiv:1807.08650, 2018.

[8] G. E. Volovik and K. Zhang, Black hole and hawking radiation by type-II Weyl fermions, *JETP Lett.* 104:645, 2016.

[9] F. Guinea, M. I. Katsnelson, and A. K. Geim, Energy gaps and a zero-field quantum Hall effect in graphene by strain engineering, *Nat. Phys.* 6:30, 2010.

[10] N. Levy, S. A. Burke, K. L. Meaker, M. Panlasigui, A. Zettl, F. Guinea, A. H. C. Neto, and M. F. Crommie, Strain-Induced Pseudo–Magnetic Fields Greater Than 300 Tesla in Graphene Nanobubbles, *Science* 329:544, 2010.

[11] G. Salerno, T. Ozawa, H. M. Price, and I. Carusotto, How to directly observe Landau levels in driven-dissipative strained honeycomb lattices, *2D Mater.* 2:034015, 2015.

[12] M. C. Rechtsman, J. M. Zeuner, A. Tunnermann, S. Nolte, M. Segev, and A. Szameit, Strain-induced pseudomagnetic field and photonic Landau levels in dielectric structures, *Nat. Phot.* 7:153, 2013.

Protected Edge Modes in Metasurface Junctions

Enrica Martini[1*], Mário G. Silveirinha[2], Stefano Maci[1]

[1]Department of Information Engineering and Mathematical Science, University of Siena, Siena, Italy
[2]Departamento de Engenharia Electrotécnica e de Computadores, University of Lisbon, Portugal
*corresponding author, E-mail: martini@dii.unisi.it

Abstract

This paper presents a new type of waveguide supporting robust propagation of an edge mode thanks to the property of parity, time-reversal and duality (PTD) symmetry. It consists of the combination of two dual parallel-plate waveguides with artificial impedance surfaces as sidewalls. In the particular case of PEC/PMC boundaries, a closed form solution is found for the supported mode through a mode matching procedure. Artificial impedance implementation through mushroom type metasurface is also discussed.

1. Introduction

Topological edge modes are immune to backscattering, and therefore exhibit robust scatter-free propagation along arbitrarily shaped pathways [1]. Topological protection normally requires nonreciprocal elements [2]. Recently, however, it has been shown that backscattering protection is also exhibited by unimodal structures which exhibit PTD-symmetry [3], *i.e.*, which are invariant under the composition of the parity, time-reversal and duality transformations. A PTD-symmetric guiding structure supporting an edge mode was recently proposed in [4]. It consists in the combination of two semi-infinite planar surfaces laid side by side and exhibiting complementary surface impedances. This structure supports a surface wave mode confined to the interface line between the two planes, with a wavenumber dependent on the surface impedance value. Although this surface wave mode is protected from backscattering thanks to the PTD symmetry property, the guiding structure may present radiation leakage, since it is not closed, and therefore a continuous spectrum of modes exists.

A unimodal PTD-symmetric edge waveguide can be obtained by coupling the structure in [4] with an identical one located at a certain distance, with opposite positions of the impedance surfaces, so as to preserve the PTD-symmetry. The resulting structure can be seen as the pairing of two parallel plate waveguides (PPWs) with dual impedance walls In the particular case in which the two surface impedances go to zero and infinity, respectively, the boundary conditions become of perfect electric conductor (PEC) and perfect magnetic conductor (PMC) type. For this structure, the expression of the supported mode can be derived in closed form, as shown in [5]. In particular, it is found that the edge mode is TEM, and it is the only supported mode from zero frequency to the frequency at which the height of the PPW is equal to λ/4, where λ is the wavelength of the dielectric contained in the PPW. This edge mode is protected against backscattering from any discontinuity that respects the PTD-symmetry, including transition to free space, if the PPW is empty.

2. PEC/PMC parallel plate waveguide junction

The geometry for the PEC/PMC edge waveguide structure is shown in Fig. 1. A difference of potential $2V$ is applied between the top and bottom PEC plates.

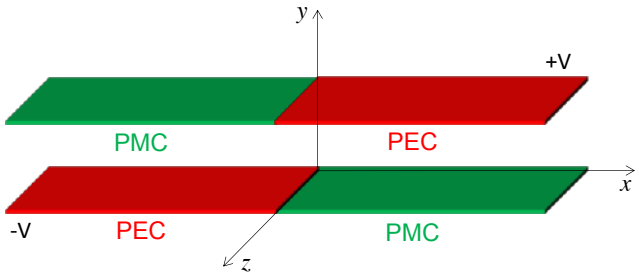


Figure 1: Geometry for the PEC/PMC edge waveguide structure.

Thanks to the TEM nature of the supported mode, the problem can be solved in the electrostatic regime. To this end, the electrostatic potential on either side of the interface x=0 is expanded into an infinite series of proper eigenfunctions. Then, continuity conditions are imposed at the interface, to obtain an infinite set of linear equations for the unknown expansion coefficients. For this particular structure, the linear system can be solved in closed form, leading to the following expression for the electrostatic potential:

$$\psi(x,y) = 2V\sum_{n=0}^{\infty} c_n e^{-\xi_n|x|}\left[\sin(\xi_n y)\ u(-x) - \cos(\xi_n y)u(x)\right] + \\ +2\,\mathrm{sgn}(x)V \qquad (1)$$

with

$$\xi_n d \equiv 2\pi n + \frac{\pi}{2}$$

$$c_n \equiv 0.7965 \frac{(2n)!}{(4n+1)(n!)^2 4^n} \qquad n = 0,1,2,... \tag{2}$$

The potential distribution and the corresponding electric field distribution across the waveguide cross section are shown in Fig. 2 and Fig. 3, respectively.

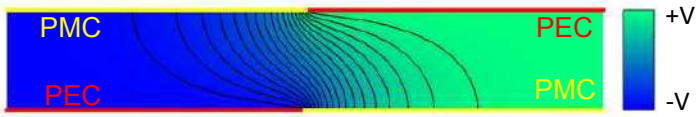


Figure 2: Potential distribution for the PEC/PMC edge waveguide.

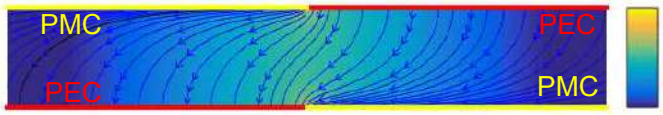


Figure 3: Electric field distribution for the PEC/PMC edge waveguide.

3. Implementation

In practice, impedance surfaces can be realized through metasurfaces. An example of metasurface which can mimic PMC behavior in a given frequency range is provided by mushroom type structures [6]. This kind of structure has been employed to design an edge waveguide based on the formulation provided in the previous section. The geometry for a single period of the edge waveguide is reported in Fig. 4. The unit cell of the mushroom structure has a size of 2.5mmx2.5mm, and the dielectric is Rogers RO3003 (ε_r=3). The PPW height is 3mm. This structure has been analyzed with the eigenmode solver of CST; it was found that it exhibits a unimodal band between 9.33GHz and 14.84GHz.

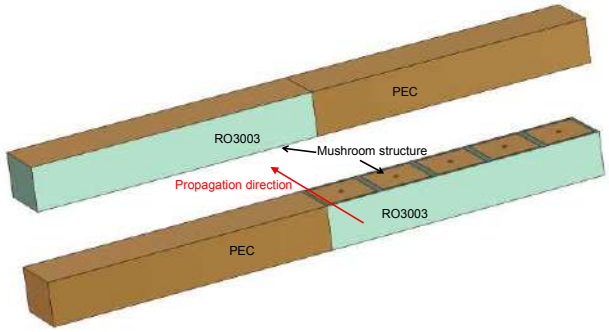


Figure 4: Geometry for the edge-waveguide structure based on mushroom MTS.

The electric field distribution at 13.66GHz is shown in Fig. 5. As it can be seen, in the region above the mushroom MTS the field behavior is close to the one found for the ideal PEC/PMC edge waveguide.

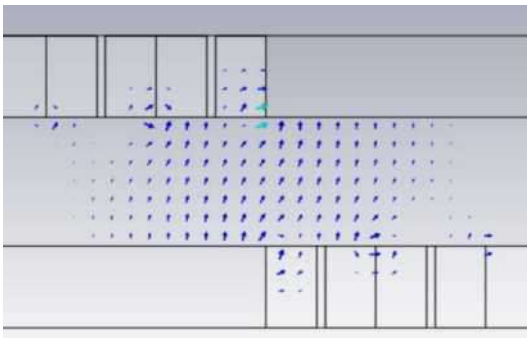


Figure 5: Electric field distribution in the cross-section of the edge-waveguide structure .

4. Conclusions

A PTD-symmetric edge waveguide structure consisting of a couple of PEC-PMC PPW has been analysed, and a closed-form solution has been found for the fundamental supported mode through a mode matching procedure. This mode is immune from backscattering from PTD-symmetric discontinuities, including the transition to free-space. Numerical results relevant to a practical implementation of the structure have also been presented.

References

[1] Z. Wang, Y. Chong, J. D. Joannopoulos, and M. Soljacic, "Observation of unidirectional backscattering-immune topological electromagnetic states," *Nature*, vol. 461, pp. 772–775, 2009.

[2] F. D. M. Haldane and S. Raghu, "Possible realization of directional optical waveguides in photonic crystals with broken time-reversal symmetry," *Phys. Rev. Lett.*, vol. 100, no. 1, p. 013904, 2008.

[3] M. G. Silveirinha, "PTD Symmetry protected scattering anomaly in optics," *Phys. Rev. B*, vol. 95, 035153, 2017.

[4] D. J. Bisharat, and D. F. Sievenpiper, "Guiding Waves Along an Infinitesimal Line between Impedance Surfaces, " *Phys. Rev. Lett.*, vol. 119, no. 10, 106802, Sept. 2017.

[5] E. Martini, M. G. Silveirinha and S. Maci, "Exact Solution for the Protected TEM edge mode in a PTD-Symmetric Parallel-Plate Waveguide," *IEEE Transactions on Antennas and Propagation*, vol. 67, no. 2, pp. 1035-1044, Feb. 2019.

[6] D. Sievenpiper, L. Zhang, R. F. J. Broas, N. G. Alexopolous, E. Yablonovitch, "High-impedance electromagnetic surfaces with a forbidden frequency band", *IEEE Trans. Microwave Theory Tech.* vol. 47, p. 2059, 1999.

First Principles Calculation of Topological Invariants by Means of the Photonic Green's Function

Filipa R. Prudêncio[1,2], and Mário G. Silveirinha[1]

[1]University of Lisbon – Instituto Superior Técnico and Instituto de Telecomunicações, Avenida Rovisco Pais 1, 1049-001 Lisbon, Portugal
[2]Instituto Universitário de Lisboa (ISCTE-IUL), Avenida das Forças Armadas 376, 1600-077 Lisbon, Portugal
*corresponding author, E-mail: filipa.prudencio@lx.it.pt

Abstract

The Chern topological numbers of a material platform are usually written in terms of the Berry curvature which depends on the normal modes of the system. Here, we use a gauge invariant Green's function method to determine from "first principles" the topological invariants of photonic crystals. The proposed formalism does not require the calculation of the photonic band-structure, and can be easily implemented using the operators obtained with a standard plane-wave expansion.

1. Introduction

Topological systems have fascinating and intriguing properties, which can lead to novel physical effects and phenomena [1-8]. The Chern topological numbers of a material system are usually written in terms of the Bloch eigenmodes. Thus, from a computational point of view, the numerical calculation of the Chern invariants is a rather complex problem: it generally requires finding the photonic band structure and all the Bloch states in the Brillouin zone. The problem is specially challenging in the case of periodic systems, e.g., nonreciprocal photonic crystals. In a few recent articles [6, 7] it was shown that the gap Chern numbers can alternatively be written in terms of the system Green's function. The theory is gauge invariant and does not require any detailed knowledge of the band structure or of the Bloch eigenstates. The method applies to both fermionic and bosonic platforms (even in case of material dispersion) and to non-Hermitian systems [6, 7]. Here, we illustrate the application of the formalism to ferrite photonic crystals. Specifically, we determine from first principles (i.e., without a tight-binding approximation) the gap Chern numbers of the photonic crystal relying on a plane wave expansion.

2. General formalism

Next, we briefly review the general Green's function formalism reported in [6, 7] to characterize the Chern invariants of photonic platforms. Consider a generalized eigenvalue problem of the form $\hat{L}_{\mathbf{k}} \cdot \mathbf{Q}_{n\mathbf{k}} = \mathcal{E}_{n\mathbf{k}} \mathbf{M}_g \cdot \mathbf{Q}_{n\mathbf{k}}$ (n=1,2,…), where $\hat{L}_{\mathbf{k}}$ and $\mathbf{M}_g$ are operators (possibly non-Hermitian). The operator $\hat{L}_{\mathbf{k}}$ is parameterized by the real wave vector $\mathbf{k} = k_x \hat{\mathbf{x}} + k_y \hat{\mathbf{y}}$ and the operator $\mathbf{M}_g$ is independent of $\mathbf{k}$. Here, $\mathbf{Q}_{n\mathbf{k}}$ are the generalized eigenstates of $\hat{L}_{\mathbf{k}}$ and $\mathcal{E}_{n\mathbf{k}}$ are the generalized eigenvalues. The system Green's function is defined by $\mathcal{G}_{\mathbf{k}}(\mathcal{E}) = i\left(\hat{L}_{\mathbf{k}} - \mathbf{M}_g \mathcal{E}\right)^{-1}$ [7]. The Green's function has poles at the eigenfrequencies $\mathcal{E} = \mathcal{E}_{n\mathbf{k}}$, but otherwise is an analytic function of frequency. The band gaps are vertical strips of the complex plane ($\mathcal{E}_L < \mathrm{Re}\{\mathcal{E}\} < \mathcal{E}_U$) where the Green's function is analytic. The gap Chern number is determined by [6, 7]:

$$\mathcal{C} = \frac{1}{(2\pi)^2} \iint_{B.Z.} d^2\mathbf{k} \int_{\mathcal{E}_{\mathrm{gap}}-i\infty}^{\mathcal{E}_{\mathrm{gap}}+i\infty} d\mathcal{E}\, \mathrm{Tr}\left\{\partial_1 \mathcal{G}_{\mathbf{k}}^{-1} \cdot \mathcal{G}_{\mathbf{k}} \cdot \partial_2 \mathcal{G}_{\mathbf{k}}^{-1} \cdot \partial_{\mathcal{E}} \mathcal{G}_{\mathbf{k}}\right\} \quad (1)$$

where $\partial_{\mathcal{E}} = \partial / \partial \mathcal{E}$ and $\mathcal{E}_{\mathrm{gap}}$ is some "frequency" in the gap. We denote $\partial_j \mathcal{G}_{\mathbf{k}}^{-1} = \partial \mathcal{G}_{\mathbf{k}}^{-1} / \partial k_j = -i\partial \hat{\mathbf{L}}_{\mathbf{k}} / \partial k_j$ (j=1,2) with $k_1 = k_x$ and $k_2 = k_y$. The integral in $\mathcal{E}$ is over the line $\mathrm{Re}\{\mathcal{E}\} = \mathcal{E}_{\mathrm{gap}}$ and $\mathrm{Tr}\{...\}$ stands for the trace operator.

3. Ferrite photonic crystal

Consider a ferrite photonic crystal formed by a hexagonal array of ferrites embedded in air [9], as illustrated in Fig.1. Assuming transverse electric (TE) polarization ($\mathbf{E} = E_z \hat{\mathbf{z}}$) and propagation in the *xoy* plane it can be shown that the secular wave equation is of the form $\hat{L}(-i\nabla) \cdot E_z = \mathcal{E} \mathbf{M}_g \cdot E_z$ with $\mathcal{E} = (\omega/c)^2$, $\mathbf{M}_g \cdot E_z \equiv \varepsilon E_z$ and

$$\hat{L} \cdot E_z \equiv -\partial_x \left[\frac{1}{\mu_{ef}} \partial_x E_z + \frac{-i\kappa}{\mu_{ef}\mu} \partial_y E_z\right] - \partial_y \left[\frac{1}{\mu_{ef}} \partial_y E_z + \frac{i\kappa}{\mu_{ef}\mu} \partial_x E_z\right]. \quad (2)$$

Thus, $\mathbf{M}_g$ is a multiplication operator and $\hat{L}(-i\nabla)$ is a differential operator. In the above, $\varepsilon = \varepsilon(x,y)$ is the permittivity, $\mu = \mu_{11}(x,y)$ and $\kappa = -i\mu_{12}(x,y)$ are the diagonal and anti-diagonal elements of the permeability tensor, respectively, and $\mu_{ef} = (\mu^2 - \kappa^2)/\mu$. For simplicity,

in this work we ignore material dispersion and take $\varepsilon = 12$, $\mu = 1$ and $\kappa = 0.9$. The Bloch modes associated with the wave vector $\mathbf{k}$ are of the form $E_z = e_z(x,y)e^{i\mathbf{k}\cdot\mathbf{r}}$ with $e_z(x,y)$ a periodic function that satisfies $\hat{L}_\mathbf{k}\cdot e_z = \mathcal{E}\mathbf{M}_g \cdot e_z$, with $\hat{L}_\mathbf{k} \equiv \hat{L}(-i\nabla + \mathbf{k})$. The band structure can be found using the plane wave method by expanding e_z into plane waves, $e_z = \sum_\mathbf{J} c_\mathbf{J}^E e^{i\mathbf{G}_\mathbf{J}\cdot\mathbf{r}}$ ($\mathbf{G}_\mathbf{J} \equiv j_1\mathbf{b}_1 + j_2\mathbf{b}_2$ is a generic reciprocal lattice primitive vector) [10]. Thus, the operators $\mathbf{M}_g$ and $\hat{L}_\mathbf{k}$ can be represented by matrices (in the simulations the plane wave expansion was truncated with $|j_i| \le N_{\max} = 3$). The Chern topological number can be calculated by feeding the matrices that are used in the plane wave method into the integral (1). The band structure of a photonic crystal formed by ferrite cylinders with radius $r = 0.2\sqrt{3}a$ is shown in Fig.2. As seen, there is a complete band-gap delimited by $1.13/a^2 < \mathcal{E} < 1.53/a^2$. The Chern number $\mathcal{C}$ is found through the numerical integration of Eq. (1) taking $\mathcal{E}_{\text{gap}} = 1.3257/a^2$ the mid-point in the gap. A generic wave vector in the Brillouin zone is of the form $\mathbf{k} \equiv \beta_1\mathbf{b}_1 + \beta_2\mathbf{b}_2$ with $|\beta_i| \le 1/2$ and generic $\mathcal{E}$ is of the form $\mathcal{E} = \mathcal{E}_{\text{gap}} + i\xi$. Figure 3a depicts the integrand of Eq. (1) as a function of β_1 for $\xi = 0$ and $\beta_2 = 1/3$ (solid line) and $\beta_2 = -1/3$ (dashed line). As seen, the integrand is peaked near $\beta_1 = \mp 2/3$, which corresponds to the coordinates of the K and K' points, respectively. This reveals that the topological charge is concentrated near the two Dirac points. The integral is numerically evaluated using the trapezoidal rule. The Brillouin zone is sampled with $N_1 = N_2 = N$ points. The integral along the imaginary axis is truncated at $|\xi| \le \xi_{\max} = 5/a^2$ and is sampled with $N_w = 2\times 50$ points. Figure 3b shows that for sufficiently large N the numerical result approaches $\mathcal{C} \approx 1$, consistent with the topological nature of the Chern number.

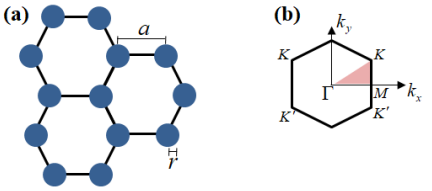


Figure 1: **(a)** Hexagonal array of ferrite cylinders. The distance between nearest neighbors is *a*. **(b)** First Brillouin zone of the 2D lattice.

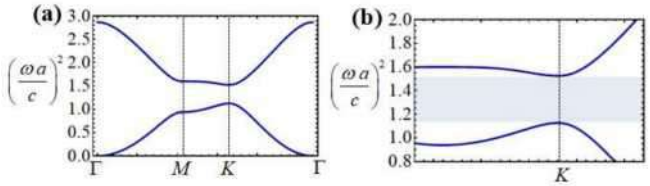


Figure 2: **(a)** Photonic band structure of the ferrite photonic crystal. **(b)** Zoom in of panel (a) around the K point.

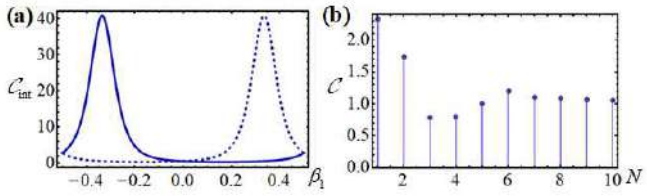


Figure 3: **(a)** Integrand of Eq. (1) [in arbitrary units] as a function of β_1. **(b)** The numerically calculated Chern number $\mathcal{C}$ as a function of N.

The computation time is on the order of a few minutes in a standard personal computer. At the conference, we will present additional examples and in particular we will discuss how the effect of loss impacts the topological properties of the material.

Acknowledgements

This work was supported by the IET under the A F Harvey Engineering Research Prize and by Fundação para Ciência e a Tecnologia (FCT) under project PTDC/EEITEL/4543/2014 and UID/EEA/50008/2017. F. R. Prudêncio acknowledges financial support by FCT under the Post-Doctoral fellowship SFRH/BPD/108823/2015.

References

[1] F. D. M. Haldane, S. Raghu, Possible realization of directional optical waveguides in photonic crystals with broken time-reversal symmetry, *Phys. Rev. Lett.*, 100: 013904, 2008.

[2] S. Raghu, F. D. M. Haldane, Analogs of quantum-Hall-effect edge states in photonic crystals, *Phys. Rev. A* 78: 033834, 2008.

[3] Z. Wang, Y. Chong, J. D. Joannopoulos, M. Soljačić, Observation of unidirectional backscattering immune topological electromagnetic states, *Nature* 461: 772, 2009.

[4] S. A. H. Gangaraj, M. G. Silveirinha, George W. Hanson, Berry phase, berry connection, and chern number for a continuum bianisotropic material from a classical electromagnetics perspective, *IEEE J. Multiscale and Multiphys. Comput. Techn.* 2: 3, 2017.

[5] M. Silveirinha, Bulk edge correspondence for topological photonic continua, *Phys. Rev. B* 94: 205105, 2016.

[6] M. G. Silveirinha, Topological classification of Chern-type insulators of the photonic Green function, *Phys. Rev. B* 97: 115146, 2018.

[7] M. G. Silveirinha, Topological theory of non-Hermitian photonic systems, *Phys. Rev. B*, 2019, (in press) available at arXiv:1901.01408.

[8] M. G. Silveirinha, Quantized angular momentum in topological optical systems, *Nature Communications* 10: 349, 2019.

[9] T. Ochiai, M. Onoda, Photonic analog of graphene model and its extension: Dirac cone, symmetry, and edge states, *Phy. Rev.* 80: 155103, 2019.

[10] K. Sakoda, *Optical Properties of Photonic Crystals*, Springer, Berlin, 2001.

Nanophononics and nanomechanics

Synthetic magnetic fields for on-chip phonons through nano-optomechanical interactions

John P. Mathew[1], Javier del Pino[2], and Ewold Verhagen[1,*]

[1]Center for Nanophotonics, AMOLF, Amsterdam, The Netherlands
*corresponding author, E-mail: verhagen@amolf.nl

Abstract

We demonstrate synthetic gauge fields for phonon transport in a nano-optomechanical platform. Employing time-modulated radiation pressure forces, we evidence nonreciprocal nanomechanical phase transfer. We show how this enables a new class of on-chip phononic topological insulators.

1. Introduction

Gauge fields are a subject of major interest in modern condensed matter physics, with fundamental implications ranging from the quantum Aharonov-Bohm effect to emergent topological phases of matter, to cite a few. The last few years have witnessed both experimental and theoretical effort in extrapolating these ideas to charge-less excitations such as photonic [1] and even macroscopic mechanical oscillator ensembles [2]. In contrast with electronics, where gauge-related phenomena can arise naturally as a result of real magnetic fields [3] gauge fields need to be artificially devised for charge-less excitations via structural-symmetry- or time-reversal-symmetry breaking [4]. The field of cavity optomechanics exploits the interaction, via radiation pressure force, of localized electromagnetic fields with micro- or nano-mechanical phononic modes. Remarkably, the high degree of controllability of these coupling could pave the way towards a suitable platform to extend non-trivial topological phenomena to mesoscopic on-chip applications via optomechanical circuits and arrays [5].

2. Results

Here we present a scalable, nanoscale optomechanical platform that enables the creation of a gauge field for phonons via optically-mediated dynamical modulation of the nanomechanical coupling. Our specific implementation consists of a sliced silicon photonics crystal nanobeam (cf. Fig 1a), supporting a defect-induced optical mode and two mechanical modes. The system is driven by an intensity-modulated field that tailors the radiation pressure force exerted on on the mechanical modes and enables readout by a probe field (see Fig 1b). Due to the large optical losses, the system is operated in the bad-cavity limit and phonons are therefore addressed instantaneously by optical forces.

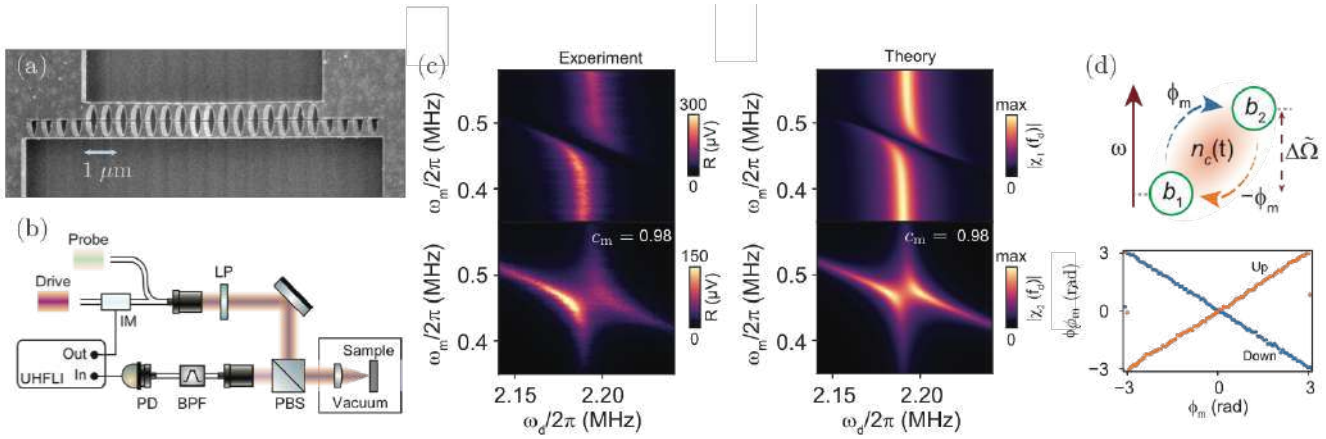


Fig. 1. (a) SEM image of a single optomechanical nanobeam device. The cavity mode, confined in the air gap between the two unequal halves of the nanobeam couples with its two fundamental mechanical eigenmodes. (b) Sketch of the experimental setup used. IM: intensity modulator, LP: linear polarizer, PBS: polarizing beam, splitter, BPF: optical bandpass filter, PD: photodiode, UHFLI: Ultra High Frequency Lock-In amplifier. The UHFLI enables modulation of the intensity of the driving laser and demodulation of the probe laser intensity. (c) The optomechanical interaction gives rise to an effective phonon transfer between the intra-nanobeam mechanical modes and induces a large Rabi splitting in agreement with the theoretical model. (d) Furthermore, hopping of excitations between the two modes (b1,b2) is accompanied by a non-reciprocal phase imprint (represented at the top), as observed by phase measurements at frequency of the transferred mode for up and down transfer processes under varying modulation phase φm (bottom).

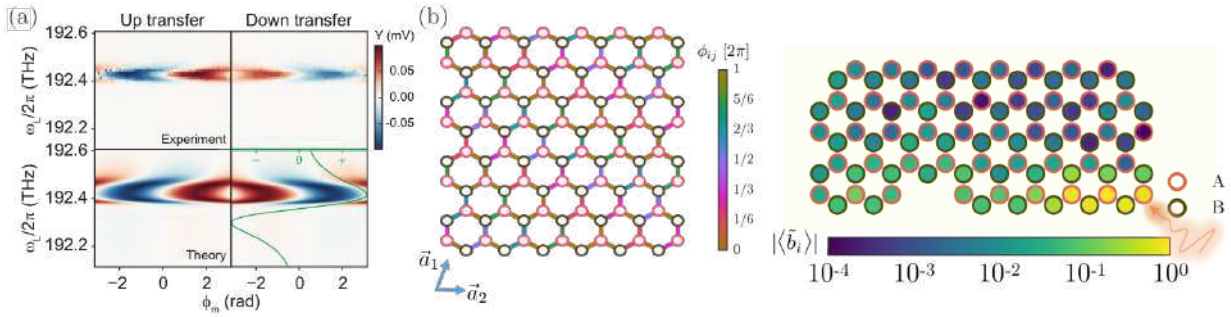


Fig. 2. (a) Quadrature response for up- and down-transfer pathways as a function of modulation phase and laser detuning. The theoretical response shows the imaginary part of the susceptibility of the transferred mode. The green curve and corresponding axis displays the calculated optical spring shift. (b) (left) Phase pattern (gauge choice) that could be imprinted on an honeycomb lattice encompassing many nanobeam unit cells containing each the two mechanical modes of interest, denoted as A and B. The phase is evolved between plaqueetes an amount of π/3, along lattice unit cell directions a1. (right) Phonon transmission probability displaying the edge state propagation under continuous excitation at the pointed position. A finite slab lattice including a defect, energetic disorder of ~0.5 %, and a ratio between direct coupling (next nearest neighbors) and modulated (nearest neighbors) of 5 % is considered.

By tuning the modulation frequency in resonance with the frequency splitting of the mechanical modes, we demonstrate theoretically and observe experimentally (see Fig 1c) the emergence of a population transfer pathway between mechanical modes characterized by a coupling tunable by optical driving parameters and a non-reciprocal phase imprint. The existence of a non-reciprocal gauge associated with this transfer is corroborated via measurements of the demodulated phase of the transfer signal at a fixed frequency, shown in Fig 1d. Further exploration as function of the laser detuning elucidates the paramount role of the optical spring effect in the transfer process. Fig 2a shows the measured phase evolution for the transferred mode and suggests an optimal condition for the gauge transfer process.

Finally, we demonstrate theoretically how a possible extension of our nanobeam device to an array encompassing many periodically arranged nanobeams, with spatially resolved input phases, could be exploited to synthetically engineer topological phases in an optomechanical network. In particular, by forming a honeycomb lattice of nanobeams as seen in Fig2b, we show a phononic analogue of an integer Quantum Hall topological insulator, signaled by chiral propagation of the edge modes. Numerical estimates indicate the robustness of edge state propagation over large lattice distances in such an array, even in the presence of disorder and direct mechanical couplings between the nanobeams, and suggest this device could be implemented within state-of-the art technology.

3. Conclusions

The aforementioned results therefore show how optomechanical arrays built upon nanobeam devices represents a promising avenue for topologically protected transport of phononic excitations. Similar ideas could be exported to chiral acoustic waveguides suitable for quantum applications [6], and topological heat currents [7].

Acknowledgements

This work is part of the research programme of the Netherlands Organisation for Scientific Research (NWO). The authors acknowledge support from the Office of Naval Research (grant no. N00014-16-1-2466), the European Research Council (ERC Starting Grant no. 759644-TOPP), and the European Union's Horizon 2020 research and innovation programme under grant agreement no. 732894 (FET Proactive HOT).

References

[1] T. Ozawa et al. "Topological Photonics", *arXiv*:1802.04173 (2018).
[2] R. Süsstrunk & S. D. Huber, "Observation of phononic helical edge states in a mechanical topological insulator", *Science* 349, 47 (2015). - S.D. Huber. "Topological mechanics", *Nature Physics* 12, 621 (2016).
[3] M. Z. Hasan and C. L. Kane, "Colloquium: Topological insulators", *Rev. Mod. Phys.* 82, 3045 (2010).
[4] K.Fang, Z.Yu and S. Fan, "Realizing effective magnetic field for photons by controlling the phase of dynamic modulation", *Nature Photonics* 6, 782 (2012).
[5] V. Peano, C. Brendel, M. Shmidt, and F. Marquardt. "Topological phases of sound and light". *Phys. Rev. X* 5, 031011 (2015)
[6] Q. Wei, Y. Tian, S. Zuo, Y. Cheng, and X. Liu, "Experimental demonstration of topologically protected efficient sound propagation in an acoustic waveguide network", *Phys. Rev. B* 95, 094305 (2017).
[7] Á. Rivas, M. Martín-Delgado, "Topological Heat Transport and Symmetry-Protected Boson Currents", *Sci. Rep.* 7, 6350 (2017).

Dispersive Measurements of Flux-Qubit States: Energy-Level Splitting and Beyond

Jeong Ryeol Choi*

Department of Physics, Kyonggi University, Yeongtong-gu, Suwon, Gyeonggi-do 16227, Republic of Korea
*corresponding author, E-mail: choiardor@hanmail.net

Abstract

The complete quantum solutions of the flux qubit-oscillator in the Fock state have been derived under the condition that the coupling strength is weak. The influence of parameters, such as the tunnel splitting, the coupling strength, the Josephson inductance, and the shunt capacitance, on the system was examined. In particular, upper and lower energy levels and the difference between them were analyzed in detail.

1. Introduction

Superconducting nanocircuits [1, 2] are simple quantum systems that can be potentially used for controlling universal quantum gates in quantum computers. According to the recent advance for realizing quantum-based technologies, these circuits became one of the main research subjects in quantum information science. As is well known, a basic unit for storing quantum information in quantum computers is qubit which is a two-level system. Several kind of qubits materialized on the basis of superconducting circuits are flux qubits, charge qubits, and phase qubits [1, 2]. We will focus on flux qubits in this work, which exhibit usual quantum properties such as discrete energy levels, entanglements, quantum interferences, and superposed quantum states.

The interaction of a two-level system with a harmonic oscillator became a highly emerging research topic over the years, while the operation of such an interacting system is actually the same as a single atom that has a large electric dipole moment coupled to the cavity mode of the microwave photons. Experimental realizations of not only flux qubits [3, 4] but also coherent tunable couplings between flux qubits [5] have been achieved. Moreover, the possibility of many other experimental manipulations with the flux qubit-oscillator upon rigorous theoretical backgrounds was also demonstrated.

Quantum dynamics of superconducting flux qubit-oscillators will be investigated in this work. Because the Hamiltonian for a superconducting flux qubit coupled to a harmonic oscillator is a somewhat complicated form, the direct evaluation of quantum solutions of the system is very difficult. For this reason, we do not know how to derive exact quantum solutions for this system yet. Only approximation and perturbation methods are available for treating the mechanics of qubit oscillators. In a conventional theory, rotating wave approximation (RWA) [6, 7] which neglects rapidly oscillating terms in the Hamiltonian is typically applied for this purpose. Although serious defects of this method in its application on quantum optics was well known from several decades ago [7, 8], this method is still potentially used because it provides solutions in a simple manner regardless of treating the field as classically or quantum mechanically.

In this work, we will use a different method which is the unitary transformation technique in order to increase the accuracy of the results. Unitary transformation with the matrix Hamiltonian will be performed without loss of the Hermitian nature of the matrix. The Hamiltonian can be simplified via such a transformation, leading to providing an easy way to identify the corresponding wave functions in the transformed system. This is our main strategy for deriving quantum solutions of the system in order to investigate the energy levels of the system.

2. Results

We consider a flux qubit coupled to a SQUID oscillator, which is illustrated in Ref. [3]. This coupling exhibits many interesting effects concerning the experiments of cavity quantum electrodynamics and ion/atom-traps, which facilitate the generation and detection of nonclassical states that are important in quantum devices. Further, such a coupling enables to produce a state entangled between multiple qubits, which are crucial in quantum-state engineering for quantum information processing [9]. This kind of entanglement is necessary in quantum computing, while the degree of the entanglement can be enhanced by increasing the relaxation time of the oscillator and/or the coupling strength [3]. The Hamiltonian of the system is composed of a qubit term, a harmonic oscillator term, and the term coupling between them.

The unitary transformation has been performed by two steps. From the first transformation, the Hamiltonian matrix was diagonalized. However, the evaluation of the Schrödinger equation in this transformed system in a straightforward way is still difficult because the transformed Hamiltonian is not so simple. For this reason, the second unitary transformation for further simplification has been carried out by introducing another unitary operator. The final Hamiltonian obtained through the two transformations is the coupling of two simple harmonic oscillators

of which we can easily identify the Schrödinger solutions.

We have analyzed the upper ($E_{n,+}$) and lower ($E_{n,-}$) energy levels of the qubit and the differences between them, $E_{n,\mathrm{d}}(= E_{n,+} - E_{n,-})$. We have confirmed that $E_{n,\pm}$ are represented in terms of modified angular frequencies $\omega_{\mathrm{p},\pm}$, respectively. $E_{n,\mathrm{d}}$ are smallest when $\varepsilon = 0$ where $\hbar\varepsilon$ is the qubit maximum persistent current, whereas they grow as the value ε increases. On the other hand, $E_{n,\mathrm{d}}$ do not vanish even when $\Delta = 0$, where $h\Delta$ is the minimum energy splitting. We have confirmed that $E_{n,\mathrm{d}}$ increase as Δ grows. By the way, $E_{n,\pm}$ decrease when the overall inductance L_{t} of the SQUID circuit increases. The informations developed here are useful for designing a flux qubit and a readout system of qubit signals.

We have also investigated the wave functions of the system. The wave functions $\psi_n(q,t)$ that are indispensable as a basic means for studying quantum features of the system were obtained. The overall wave function can be written as $\psi(q,t) = \sum_n c_n\psi_n(q,t)$ where c_n are nth coefficients with the condition $\sum_n |c_n|^2 = 1$. This wave function is necessary for investigating various quantum informational properties of the flux qubit system coupled to the oscillator and can be directly extended to more generalized states such as coherent, squeezed, and thermal states.

3. Conclusions

Quantum features of a flux qubit coupled to a harmonic oscillator have been investigated in this work. Energy-level splitting in the dispersive measurements of flux-qubit states has been analyzed. Because the Hamiltonian of the system is a somewhat complicated form, the mathematical treatment of the system is not an easy task. Hence, special mathematical tools for treating the Hamiltonian are necessary. We have used the unitary transformation method for this purpose.

We have easily identified quantum solutions (wave functions) in the transformed system because the transformed system is a simplified one. Eventually, by transforming the wave functions in the transformed system inversely, the wave functions in the original system were obtained. The full wave function is crucial as the basic tool for investigating quantum properties of the system. Various quantum characteristics of the qubit system can be analyzed by making use of the wave functions. For instance, one can evaluate not only fluctuations of the canonical variables, but also the expectation values of the Hamiltonian and other physical observables. The time behavior of the system can also be analyzed on the basis of the wave functions.

Acknowledgement

This research was supported by the Basic Science Research Program of the year 2018 through the National Research Foundation of Korea (NRF) funded by the Ministry of Education (Grant No.: NRF-2016R1D1A1A09919503).

References

[1] J. Clarke, F.K. Wilhelm, Superconducting quantum bits, *Nature* 453: 1031-1042, 2008.

[2] J.Q. You, F. Nori, Atomic physics and quantum optics using superconducting circuits, *Nature* 474: 589-597, 2011.

[3] I. Chiorescu, P. Bertet, K. Semba, Y. Nakamura, C.J.P.M. Harmans, J.E. Mooij, Coherent dynamics of a flux qubit coupled to a harmonic oscillator, *Nature* 431: 159-162, 2004.

[4] A. Wallraff, D.I. Schuster, A. Blais, L. Frunzio, R.S. Huang, J. Majer, S. Kumar, S.M. Girvin, R.J. Schoelkopf, Strong coupling of a single photon to a superconducting qubit using circuit quantum electrodynamics, *Nature* 431: 162-167, 2004.

[5] S.H.W. van der Ploeg *et al.*, Controllable coupling of superconducting flux qubits, *Phys. Rev. Lett.* 98: 057004, 2007.

[6] Y.-M. Wang, G. Du, J.-Q. Liang, Geometric phases in qubit-oscillator system beyond conventional rotating-wave approximation, *Chin. Phys. B* 21: 044207, 2012.

[7] B.J. West, K. Lindenberg, On the rotating wave approximation, *Phys. Lett. A* 102: 189-193, 1984.

[8] G.W. Ford, R.F. O'Connell, The rotating wave approximation (RWA) of quantum optics: serious defect, *Physica A* 243: 377-381, 1997.

[9] P. Bertet, I. Chiorescu, K. Semba, C.J.P.M. Harmans, J.E. Mooij, Dynamics of a qubit coupled to a harmonic oscillator, In: B. Ruggiero, P. Delsing, C. Granata, Y. Pashkin, P. Silvestrini (eds.), *Quantum Computing in Solid State Systems*, Springer, NY, 2006.

Picosecond acoustics of vanadium dioxide

Iaroslav Mogunov[1*], Anatolii Fedianin[1,2], Félix Fernández[3], Sergiy Lysenko[3], Anthony Kent[4], Alexey Scherbakov[1,5], Alexandra Kalashnikova[1] and Andrey Akimov[4]

[1]Ioffe Institute, 194021 St. Petersburg, Russia
[2]ITMO University, 197101 St. Petersburg, Russia
[3]Department of Physics, University of Puerto Rico, Mayaguez, Puerto Rico 00681, USA
[4]School of Physics and Astronomy, University of Nottingham, Nottingham NG7 2RD, UK
[5]Experimentelle Physik 2, Technische Universität Dortmund, D-44227 Dortmund, Germany
*corresponding author, E-mail: mogunov@mail.ioffe.ru

Abstract

Picosecond acoustics utilizes short strain pulses generated by pulsed lasers to determine and affect properties of solid media. This represents two challenges in the field - to achieve stronger strain-induced effects and to generate stronger yet shorter strain pulses. Here we examine if a medium with insulator-metal transition, such as vanadium dioxide VO_2, may facilitate addressing both challenges.

1. Introduction

Strain pulses with sub-nanosecond duration constitute the new non-thermal avenue for controlling properties of solids on nanometer and picosecond scales. Therefore there is a demand for new ways to generate such pulses with higher amplitudes and with control over pulse parameters, as well as new mechanisms and materials to make the impact of these pulses more prominent.

Generation of picosecond strain pulses is conventionally realized via rapid thermal expansion of thin metallic film following femtosecond laser excitation [1, 2]. Resulting pulses are as short as a few picoseconds with amplitudes up to 10^{-2} [2]. In semiconductors the strain pulse generation is commonly attributed to deformation potential rather than thermal expansion [3] leading to other durations and amplitudes of generated pulses. A material with insulator-metal transition would therefore allow an on-a-fly control of generated pulses. Among such materials the most potent is VO_2 which exhibits a *photo-induced ultrafast first-order* insulator-metal and structural phase transition (PIPT) [4, 9, 10].

Application of picosecond strain pulses has been shown to alter and control various properties of media on picosecond timescale. These include launching magnetization dynamics [5], generation of THz radiation [6] and electrical currents [7], etc. Still, picosecond strain pulses were not applied to study or control ultrafast phase transitions despite known role stationary strain has on their onset [8]. We start to fill this gap by showing the effect of picosecond strain on PIPT in VO_2 [9].

2. Experimental

2.1. Samples

For the strain pulse generation we used a 50 nm and 100 nm VO_2 films grown epitaxially by PLD on a r-cut Al_2O_3 substrate in $[100]_{M1}$ orientation (for details see [10]). On the other side of the substrate, a 50 nm Cr layer was deposited allowing photoelastic detection of generated pulses.

For evaluating the effect picosecond strain has on PIPT we used a layer of epitaxial VO_2 nanohillocks with $[020]_{M1}$ orientation grown by pulsed laser deposition (PLD) on a c-cut sapphire Al_2O_3 substrate (for details see [10]). The nanohillocks have height of 70 ± 20 nm and lateral size of 200 ± 60 nm. Here picosecond strain pulses were generated by 140 nm Al trancducer film deposited on the back side of the substrate.

2.2. Experiment layout

The laser source is a 170-fs Yb:$KGd(WO_4)_2$ regenerative amplifier with 5 kHz repetition rate and a central photon energy of 1.2 eV. For generation of picosecond pulses in VO_2, a conventional picoacoustics setup was used with two beams taken from the same laser source. One beam was incident on the VO_2 film acting as a pump to generate a strain pulse, the other passing via a motorized delay line was directed on the Cr film and served as a probe. We monitored the intencity of a reflected probe pulse as a function of the time delay at 295 K and 400 K.

To study the effect of strain pulses on PIPT the probe beam was incident on VO_2 nanohillocks and the pump beam was excitng the Al film. In order to induce PIPT in VO_2 we applied one more beam from the same source to directly excite the nanohillocks. Certain time delay was set between the moment of PIPT excitation and the moment of the strain pulse reaching VO_2.

3. Results and discussion

3.1. Generation of picosecond strain pulses in VO_2 film

First experiments on generation of strain pulses in 100 nm VO_2 film showed that these pulses after propagation through a 300 μm sapphire substrate have longer dura-

tion - up to 200 ps - for moderate pump beam fluence of J_{VO_2}=14 mJ/cm^2. Due to non-linear nature of strain pulse propagation in sapphire, longer pulse duration is one of the main markers for strong initial amplitude of the generated pulse [2].

Plotting the pulse duration and signal amplitude versus the fluence J of the laser pulse generating strain pulse in VO_2, we obtained a distinct deviation of the monotonous increase between the PIPT threshold J=J_T=2.3 mJ/cm^2 and saturation J=J_S=6.4 mJ/cm^2 fluencies obtained for this sample. This result is an indication of the alteration in pulse generation process due to PIPT.

Notably, the amplitude of the measured signals show a slight decrease with increasing fluence above J_T before starting to rise again. Our calculations show that such behavior could not be described solely by the change of parameters of heat-driven strain generation during the transition and the generated pulses are likely to be affected by lattice contraction in the growth direction $[100]_{M1}$ occuring during the PIPT. This provides a new tool to study PIPT in VO_2. For details and further analysis see [11].

3.2. Effect of picosecond strain pulses on PIPT

In these experiments we applied strain pulses with the largest amplitude we could get with Al transducer film, using pump beam fluence of 60 mJ/cm^2. After nonlinear propagation through sapphire [2] they had amplitude $\sim$0.1 % and duration $\sim$100 ps. The measured reflectivity change of VO_2 nanohillocks was attributed to photoelastic effect. Then we applied the laser beam to the VO_2 nanohillocks to excite the PIPT before arrival of the strain pulse in VO_2 and set it fluence larger than saturation value measured for this sample $J > J_S$=20 mJ/cm^2. Such fluence corresponds to a complete PIPT. The observed signal was the same as photoelastic response measured at T=360 K in temperature-induced metallic phase.

The main results were obtained for fluence of the beam exciting PIPT being lower than the saturation value but still higher than threshold $J > J_T = 6$ mJ/cm^2, which corresponds to incomplete PIPT with some nanohillocks remaining in insulator phase. The front of the strain pulse was the first to arrive in nanohillocks, and then - while the pulse had not yet left VO_2 - the PIPT was excited. We found that for such fluencies *the PIPT is sensitive to strain amplitude and sign presented at the moment of laser excitation*. Kinetics of the PIPT at longer times is found to be insensetive to the dynamical strain still present in the nanohillocks [9]. This result opens a prospective to control the PIPT in VO_2 by varying the moment of excitation with respect to the strain pulse profile. Timing excitation with the maximal compression/tension in the strain pulse we achieved $\sim$1 % suppression/enhancement of the PIPT, respectively.

Finally, we revealed that the strain affects the PIPT by changing the amount of VO_2 nanohillocks undergoing ultrafast phase transformation. The detailed analysis based on Landau phenomenological theory is presented elsewhere [9].

4. Conclusions

To conclude, we show that VO_2 possessing an ultrafast photo-induced insulator-metal and structural phase transition is a novel promising choice of a material for tunable generation of picosecond strain pulses. Moreover, the ultrafast phase transition in VO_2 can be successfully controlled by picosecond strain pulses on nanometer and picosecond scales.

Acknowledgement

Collaboration between Ioffe Institute and The University of Nottingham is supported by the RFBR Grant No. 17-52-10015 and the Royal Society Grant No. IEC\R2\170217. Work on strain pulse generation is partly supported by GosZadanie (Physical Sciences, direction 8, theme 8.5).

References

[1] C. Thomsen et al., Surface generation and detection of phonons by picosecond light pulses, *Phys. Rev. B* 34: 4129–4138, 1986.

[2] P.J.S. van Capel et al., Nonlinear ultrafast acoustics at the nano scale, *Ultrasonics* 56: 36–51, 2015.

[3] E.S.K. Young et al., Picosecond strain pulses generated by a supersonically expanding electron-hole plasma in GaAs, *Phys. Rev. B* 86, 155207, 2012.

[4] A. Cavalleri et al., Evidence for a structurally-driven insulator-metal transition in VO_2: A view from the ultrafast timescale, *Phys. Rev. B* 70, 161102(R), 2004.

[5] A.V. Scherbakov et al., Coherent Magnetization Precession in Ferromagnetic (Ga,Mn)As Induced by Picosecond Acoustic Pulses, *Phys. Rev. Lett.* 105, 117204, 2010.

[6] M.R. Armstrong et al., Observation of terahertz radiation coherentlygenerated by acoustic waves, *Nature Phys.* 5, 285–288, 2009.

[7] D.M. Moss et al., Ultrafast Strain-Induced Current in a GaAs Schottky Diode, *Phys. Rev. Lett.* 106, 066602, 2011.

[8] J.H. Park et al., Measurement of a solid-state triple point at the metal–insulator transition in VO_2, *Nature Lett.* 500, 431–434, 2013.

[9] Ia.A. Mogunov et al., Ultrafast Insulator-Metal Transition in VO_2 Nanostructures Assisted by Picosecond Strain Pulses, *Phys. Rev. Applied* 11, 014054, 2019.

[10] S. Lysenko et al., Photoinduced insulator-to-metal phase transition in VO_2 crystalline films and model of dielectric susceptibility, *Phys. Rev. B* 75, 075109, 2007.

[11] Ia.A. Mogunov et al., in preparation.

Controlling the vibrational quality factors of an individual supported nano-object by tuning its morphology

Aurélien Crut[1*], Fabio Medeghini[1], Romain Rouxel[1], Marco Gandolfi[2,3], Francesco Rossella[4], Paolo Maioli[1], Fabrice Vallée[1], Francesco Banfi[1], and Natalia Del Fatti[1]

[1] FemtoNanoOptics group, Univ Lyon, UCBL-CNRS, Institut Lumière Matière, Villeurbanne, France
[2] Dipartimento di Matematica e Fisica and I-LAMP, Università Cattolica del Sacro Cuore, Brescia, Italy
[3] Laboratory of Soft Matter and Biophysics, Department of Physics and Astronomy, KU Leuven, Leuven, Belgium
[4] NEST, Scuola Normale Superiore and Istituto Nanoscienze-CNR, Pisa, Italy
*corresponding author, E-mail: aurelien.crut@univ-lyon1.fr

Abstract

Acoustic damping of lithographed gold nanodisk vibrations was investigated using single-particle time-resolved spectroscopy. A strong influence of morphology (diameter/height ratio) on their vibrational quality factors was experimentally demonstrated and confirmed by numerical modeling. These findings thus open new possibilities for engineering the vibrational modes of nano-objects.

1. Introduction

The vibrational properties of nano-objects can be experimentally addressed using optics-based methods such as Raman and time-resolved spectroscopies, which enable the detection of a few vibrational modes and the measurement of their frequencies and, in certain conditions, of their damping rates. Experiments performed in the last 20 years in this field have clarified the dependence of vibrational frequencies on nano-object size, shape, crystallinity and environment [1]. In particular, their surprisingly accurate reproduction by continuum mechanics models, even in the case of ultrasmall (~1 nm) nanoparticles [2], has been demonstrated. However, many questions still remain open regarding the nature and efficiency of the mechanisms ruling vibrational damping. In contrast with vibrational frequencies, which are predominantly determined by intrinsic nano-object properties (e.g., composition, morphology and crystallinity) [1], damping rates are very sensitive to the properties of the nano-object/environment interface, which determine the efficiency with which acoustic waves are emitted from the nano-object. Additionally, a quantitative investigation of damping requires experiments on individual nano-objects to avoid the spurious inhomogeneous effects affecting measurements on nanoparticle assemblies. In this context, recent single-particle experiments performed on supported nano-objects have shown large interparticle fluctuations of vibrational damping rates, which were ascribed to variations of nanoparticle-substrate coupling [1], while those on suspended nanowires have evidenced the effect of intrinsic damping mechanisms, which become dominant when acoustic radiation by a nano-object is made inefficient [3]. In order to better understand vibrational quality factors, and in particular to investigate a possible dependence of damping rate on nano-object morphology, systematic time-resolved studies were performed on individual gold nanodisks (NDs) deposited on a sapphire substrate. NDs were chosen as their shape is characterized by only two dimensions, i.e., diameter D and height h (with their aspect ratio defined as η=D/h). Their production by electron lithography enables the easy variation of ND diameter and avoids the presence of surfactant molecules in their surroundings, which occurs for chemically synthesized nano-objects.

2. Linear and time-resolved optical experiments

Detection and optical characterization of NDs were performed using spatial modulation spectroscopy (SMS) [4], a quantitative single-particle technique based on the periodic displacement of a nano-object in the focal spot of a strongly focused light beam, which induces a modulation of the transmitted light power proportional to the extinction cross-section. The measured extinction spectra of individual NDs are dominated by their localized surface plasmon resonance (SPR), whose spectral position evolution with ND diameter was well reproduced by numerical simulations. NDs with a non-circular section could be identified from the significant polarization dependence of their extinction. They were found to present a more complex acoustic response (as compared to circular NDs) and were not considered for the vibrational damping investigations presented below.

Time-resolved experiments on individual NDs were performed by combining the SMS microscope with a two-color pump-probe setup based on a tunable Ti:Sa laser source delivering ~ 100 fs pulses. The output pulse train was split in two parts to generate the pump and the probe beams, a different wavelength being generated for one of them using second harmonic generation or an optical parameter oscillator. The measured time-resolved signals

contain contributions from the different relaxation mechanisms following sudden ND excitation by pump pulse absorption: ND internal thermalization (by electron-electron and electron-phonon scattering mechanisms), acoustic vibrations and cooling (by dissipation of the thermal energy injected by the pump pulse). The oscillating part of the signals, associated to ND vibrations, was selected and analyzed.

Depending on ND aspect ratio, this oscillating component contains contributions from one or two acoustic mode(s), whose frequencies f, damping times τ and quality factors $Q=\pi\tau f$ were estimated. Measurements evidenced the existence of two particular morphologies (at specific values of aspect ratio) presenting a pronounced enhancement of acoustic quality factors, namely close to $\eta\approx2.5$ (with $Q \approx 70$) and close to $\eta\approx6$ (with $Q \approx 30$) (Figure 1a). This complex dependence of vibrational quality factors on morphology was found to contrast with the simpler one of ND cooling dynamics, which was shown to be mostly controlled by ND thickness.

3. Analysis

To obtain a physical insight for these enhancements, the acoustic properties of gold NDs were explored by finite-element simulations in the frequency domain accounting for the inhomogeneous ND environment resulting from their deposition on a substrate. Perfectly matched layers were used at the border of the simulation domain to avoid spurious acoustic reflections, and vibrational spectra were obtained by computing the average elastic energy stored in a ND as a function of the frequency of a periodical excitation (a uniform stress being chosen, as it corresponds to the experimental case). Excited vibrational modes appear as Lorentzian resonances in the computed spectra, enabling the determination of their associated frequencies and quality factors.

This finite-element analysis sheds considerable light on the experimental observations listed above, yielding frequencies similar to those of the experimentally detected modes and thus providing access to their associated displacement fields. The low-frequency oscillation detected for $\eta<2.5$ was ascribed to a mode with a mostly vertical displacement (mainly affecting ND height), whose excitation amplitude quickly decreases at small η, in agreement with experiments. Conversely, the only oscillation detected for $\eta>3$ corresponds to a mode with a mostly radial displacement profile. A strong decrease of the elastic energy transfer at the ND/substrate interface occurs for this mode at $\eta\approx2.7$, leading to very high (>2000) computed Q value (Figure 1a). This is at the origin of measured Q values for $\eta\approx2.5$, unusually high for supported nano-objects. The experimental maximal Q value (70) remains however much smaller than the computed one, most probably because of intrinsic vibrational damping within the NDs [3].

Finite-element simulations were also performed for supported NDs with elliptical sections. These computations explained the richer acoustic response experimentally observed for NDs with a non-circular section. Indeed, they show that some vibrational modes not excited in the circular ND case become observable when the ND circular symmetry is broken. Moreover, the nature and associated displacement field of the additional detected modes could be understood by detailed comparison between experimental and simulated results.

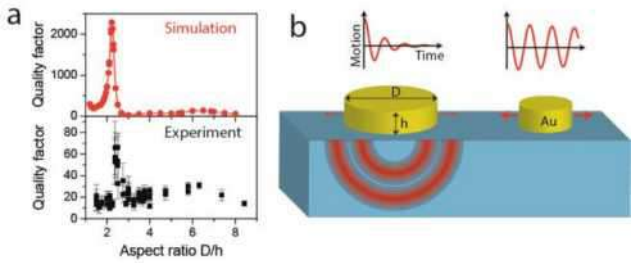


Figure 1. a) Maximal quality factors among the de vibrational modes detected in time-resolved experiments (bottom) and predicted in finite-element simulations (top). b) Schematic illustration of the morphology-dependent damping of ND vibrational modes.

4. Conclusions

In conclusion, this study demonstrates that the quality factors associated to the vibrational modes of a supported nano-object strongly depend on its morphology [5]. In particular, much longer vibrations occur for some specific geometries, as if the nano-object was "isolated" from the substrate (Figure 1b), a situation interesting for developing nanobalance applications and for quantifying the internal sources of vibrational damping.

References

[1] A. Crut, P. Maioli, N. Del Fatti, F. Vallée, Acoustic Vibrations of Nano-Objects: Time-Domain Investigation", Phys. *Rep.* **549**, 1, 2015.

[2] V. Juvé, A. Crut, P. Maioli, M. Pellarin, M. Broyer, N. Del Fatti, F. Vallée, Probing Elasticity at the Nanoscale: Terahertz Acoustic Vibration of Small Metal Nanoparticles", *Nano Lett*. **10**, 1853, 2010.

[3] T. A. Major, A. Crut, B. Gao, S. S. Lo, N. Del Fatti, F. Vallée, G. V. Hartland, Damping of the Acoustic Vibrations of a Suspended Gold Nanowire in Air and Water Environments, *Phys. Chem. Chem. Phys.* **15**, 4169, 2013.

[4] A. Crut, P. Maioli, F. Vallée, and N. Del Fatti, Linear and Ultrafast Nonlinear Plasmonics of Single Nano-Objects, *J. Phys. Condens. Matter* **29**, 123002, 2017.

[5] F. Medeghini, A. Crut, M. Gandolfi, F. Rossella, P. Maioli, F. Vallée, F. Banfi, N. Del Fatti, Controlling the Quality Factor of a Single Acoustic Nanoresonator by Tuning its Morphology, *Nano Lett.* **18**, 5159, 2018.

Following heat transport in 2D materials using ultrafast techniques

Klaas-Jan Tielrooij[1], Niels Hesp[2], Alexander Block[2], Matz Liebel[2], Aloïs Arrighi[1], Marianna Sledzinska[1], Sergio O. Valenzuela[1], Clivia Sotomayor Torres[1], Frank Koppens[2], Niek van Hulst[2]

[1]Catalan Institute of Nanoscience and Nanotechnology (ICN2), Barcelona Institute of Science and Technology, Bellaterra (Barcelona), Spain
[2]ICFO – The Institute of Photonic Sciences, Barcelona Institute of Science and Technology, Castelldefels (Barcelona), Spain
*corresponding author, E-mail: klaas.tielrooij@icn2.cat

Abstract

We have used various ultrafast optical and optoelectronic techniques to study thermal transport phenomena in 2D materials, in particular processes that take place on the femtosecond, picosecond and nanosecond timescale. These processes include the phonon-mediated cooling dynamics of hot electrons in graphene, as well as the thermal diffusion of different heat and charge carriers in graphene and semiconducting layered materials. We will discuss some previous and some ongoing results related to these topics.

1. Introduction

Two-dimensional materials have given rise to many interesting phenomena in the area of thermal transport, such as the large thermal conductivity of graphene [1], and strongly anisotropic heat transport in WSe_2 [2]. We will discuss a number of observations in this field, which were made possible using ultrafast optical and optoelectronic techniques. First, we will discuss time-resolved photocurrent measurements showing that near-field coupling between hot electrons in graphene and hyperbolic phonons in the surrounding hexagonal BN (hBN) layers dominates the hot-electron cooling dynamics [3, 4]. Second, we will discuss results obtained using spatiotemporal scanning on suspended flakes of semiconducting layered materials, where we follow heat and charge diffusion in time and space with femtosecond temporal and nanosecond spatial resolution.

2. Near-field electron-hyperbolic-phonon coupling in hBN-graphene-hBN stacks: super-planckian cooling

Absorbed light in graphene leads to heating of the electronic system on a timescale of tens of femtoseconds and to ultrafast generation of a photoresponse when the light is incident on a *pn*-junction. Using two femtosecond light pulses with a variable time delay incident on such a junction, one can study the heating-cooling dynamics of the electron system. In hBN-graphene-hBN stacks – currently the most promising architecture for electronic and optoelectronic graphene devices – we found that these cooling dynamic occur through a surprisingly efficient out-of-plane cooling mechanism [3, 4]. In this mechanism, the energy from hot graphene electrons is transferred through near-field radiation to hyperbolic phonon modes in the hBN layers above and below the graphene. This process is many orders of magnitude more efficient than Planckian radiation, owing to the large mode density of the hyperbolic phonons. The experimental observations are in agreement with the results of microscopic calculations based on this mechanism. Interestingly, when using thinner hBN encapsulation, the cooling time increases. Thus by changing the hBN hyperbolic phonon modes, the properties of nearby hot electrons in graphene are modified.

3. Heat diffusion through ultrafast spatiotemporal scanning

In ultrafast spatiotemporal scanning measurements, two femtosecond light pulses are incident on a material, while both the time delay as well as the spatial displacement between the two pulses is varied. Such measurements allow for extracting the diffusivity of different charge and/or heat carriers. We have applied this technique to suspended flakes of semiconductor layered materials. It is crucial to suspend the flakes, in order to avoid out-of-plane transport into a supporting substrate. Rather, we are exclusively sensitive to the in-plane diffusion of charge and/or heat. We will discuss our ongoing efforts into understanding the material parameters that influence the diffusivity of, in particular, excitons and phonons in these systems.

References

[1] A.A. Balandin et al., Superior thermal conductivity of single-layer graphene, *Nano Lett.* 8: 902−907, 2008.

[2] C. Chiritescu et al., Ultralow thermal conductivity in disordered layered WSe2 crystals, *Science* 315: 351−353, 2017.

[3] K.J. Tielrooij et al., Out-of-plane heat transfer in van der Waals stacks through electron-hyperbolic phonon cooling, *Nat. Nanotechnol.* 13: 41−46 , 2018.

[4] A. Principi et al., Super-Planckian electron cooling in a van der Waals stack, *Phys. Rev. Lett.* 118: 126804, 2017.

Anisotropic Thermal Magnetoresistance in Radiative Heat Transfer

A. Garcia-Martin*

[1]IMN-Instituto de Micro y Nanotecnología (CNM-CSIC), Isaac Newton 8, E-28760 Tres Cantos, Madrid, Spain
*corresponding author, E-mail: a.garcia.martin@csic.es

Abstract

Here, we predict a huge anisotropic thermal magnetoresistance (ATMR) in the near-field radiative heat transfer between magneto-optical particles when the direction of an external magnetic field is changed with respect to the heat current direction. We illustrate this effect with the case of two InSb particles where we find that the ATMR amplitude can reach values of up to 800% for a magnetic field of 5 T, which is many orders of magnitude larger than its spintronic analogue. This thermomagnetic effect could find broad applications in the field of ultrafast thermal management as well as magnetic and thermal remote sensing.

1. Discussion

The possibility to create and manipulate nanostructured materials encouraged the exploration of new strategies to control the electromagnetic properties without the need to modify its physical structure, i.e. by means of an external agent. An approach is the combination of magneto-optically active and resonant materials (e.g. plasmonic modes), where it is feasible to control the optical properties with magnetic fields in connection to the excitation of resonances [1] (magnetoplasmonics). It has been shown that these nanostructures can be employed to modulate the propagation wavevector of SPPs [2], which allows the development of label free sensors with enhanced capabilities [3-5] or to enhance the magneto-optical response in isolated entities as well as films, in connection with a strong localization of the electromagnetic field [6-8].
Here we will show that they also play a crucial role in the active control thermal emission and the radiative heat transfer (RHT) between objects in the near and far field regime [9-11].
In particular we will show that the Near Field RHT between two MO particles can be efficiently controlled by changing the direction of the magnetic field, in the spirit of the Anisotropic Magneto Resistance in spintronics. This phenomenon, which we term anisotropic thermal magnetoresistance (ATMR), stems from the anisotropy of the photon tunneling induced by the magnetic field. We discuss this effect through the analysis of the radiative heat exchange between two InSb particles, and show that the ATMR can reach amplitudes of 100% for fields on the order of 1 T and up to 1000% for a magnetic field of 6 T. These values are several orders of magnitude larger than in standard spintronic devices. More importantly, this thermomagnetic effect paves the way for exploring heat transfer physics at pico- and even subpicosecond time scales, which are even shorter than the relaxation time of heat carriers. Moreover, we show that the heat flux is very sensitive to the magnetic field direction, which makes this effect very promising for the development of a new generation of thermal and magnetic sensors.

References

[1] G. Armelles, et al., Adv. Opt. Mat. 1, 10 (2013)
[2] V.V. Temnov et al., Nat. Photon. 4, 107 (2010)
[3] B. Sepúlveda, et al., Opt. Lett. 31, 1085 (2006)
[4] M.G. Manera, et al., Biosens. Bioelectron. 58, 114 (2014)
[5] B. Caballero, et al., ACS Photonics 3, 203 (2016),
[6] N. de Sousa et al., Phys. Rev. B 89, 205419 (2014)
[7] N. de Sousa et al., Sci. Rep. 6, 30803 (2016)
[8] M. Rollinger et al., Nano Lett. 16, 2432-2438 (2016)
[9] E. Moncada-Villa, et al., Phys. Rev. B 92, 125418 (2015).
[10] R. M. Abraham Ekeroth, et al., Phys. Rev. B 95, 235428 (2017)
[11] R. M. Abraham Ekeroth, et al., ACS Photonics 5, 705 (2018).

Optomechanical coupling in the Anderson-localization regime

G. Arregui,[1,2,*] N. D. Lanzillotti-Kimura,[3] C. M. Sotomayor-Torres,[1,4] and P. D. García[1]

[1] *Catalan Institute of Nanoscience and Nanotechnology (ICN2), CSIC and BIST, Campus UAB, Bellaterra, 08193 Barcelona, Spain*
[2] *Dept. de Física, Universitat Autonoma de Barcelona, 08193 Bellaterra, Spain*
[3] *Centre de Nanosciences et de Nanotechnologies, CNRS, Univ. Paris-Sud, Université Paris-Saclay, C2N - Marcoussis, 91460 Marcoussis, France*
[4] *ICREA - Institució Catalana de Recerca i Estudis Avançats, 08010 Barcelona, Spain*

Many fundamental observations in physics ranging from gravitational wave detection to laser cooling of a nanomechanical oscillator into its quantum ground state rely on the interaction between the optical and the mechanical degrees of freedom. Due to the scaling dependance of the coupling strength with size, lithography-grown optomechanical crystals, purposely designed semiconductor nanostructures, are used to enhance the coupling between the electromagnetic field and the mechanical vibrations of matter at the nanoscale. The confinement strategy and spatial overlap between the two fields is typically engineered through controlled point or line defects in otherwise regular dielectric and acoustic lattices. A bottleneck of this strategy relies on the sensitivity of particularly high Q-factor cavities to uncontrolled imperfections appearing during the fabrication process [1, 2]. A less typical strategy to confine light and sound consists of exploiting such spatial fluctuations [3]; they give rise to strong multiple scattering which results in confinement by recurrent interference. Quality factors reaching $Q \sim 10^6$ have been observed in photonic crystal waveguides (PCW) [4, 5], thus competing in performance with engineered defects in the same platform while being inherently robust against disorder.

We have studied the localization properties of electromagnetic radiation and mechanical motion in disordered periodic-on-average silicon nanobeams [6]. In these systems, disorder localizes both fields which can interact with each other as in standard engineered cavity optomechanical systems [7]. Due to the inherently complext nature of the interference process, disorder lacks an a priori mechanism to co-localize both fields, limiting the maximum achievable coupling rate g_o in the Anderson-localization regime. To address this challenge, we propose using GaAs/AlAs vertical distributed Bragg reflectors with embedded geometrical disorder [8]. Due to a remarkable coincidence in the physical parameters governing light and motion propagation in these two materials, the equations for both longitudinal acoustic waves and normal-incidence light become practically equivalent for excitations of the same wavelength. This guarantees spatial overlap between the electromagnetic and displacement fields of specific photon-phonon pairs, leading to strong light-matter interaction. In particular, a statistical enhancement in the vacuum optomechanical coupling rate, g_o, is found.

The enhanced light-matter interaction induced by the co-localization of particular photon-phonon pairs allows exploring Anderson localization of high frequency ($\sim$ 20 GHz) phonons with cavity optomechanics techniques, using Anderson-localized optical modes as a probe for read-out. As opposed to optics, where excellent point sources exist granting direct access to the localized field [3], the direct spatial and spectral resolution of Anderson-localized elastic waves remains elusive. The lack of practical phonon transitions in the solid state and their limited far field radiation complicate the read out of confined states. The strong co-localization effect in GaAs/AlAs multilayered structures is therefore a promising resource to overcome this limitations and explore Anderson localization of phonons at frequencies so far unexplored, as well as a testbed to explore field-localization phenomena with coupled excitations.

* Electronic address: guillermo.arregui@icn2.cat

[1] D. Gerace and L. C. Andreani, Opt. Lett. **29**, 1897 (2004).
[2] M. Minkov and V. Savona. Scientific Reports **4**, 5124 (2014).
[3] P. D. García and P. Lodahl. Annalen Der Physik **529**, 1600351 (2017).
[4] J. Topolancik, B. Ilic, and F. Vollmer. Phys. Rev. Lett. **99**, 253901 (2007).
[5] G. Arregui, D. Navarro-Urrios, N. Kehagias, C. M. Sotomayor-Torres, and P. D. García. Phys. Rev. B **98**, 180202(R) (2018).
[6] P. D. García, R. Bericat-Vadell, G. Arregui, D. Navarro-Urrios, M. Colombano, F. Alzina, and C. M. Sotomayor-Torres. Phys. Rev. B **95**, 115129 (2017).
[7] M. Aspelmeyer, T. J. Kippenberg, and F. Marquardt. Rev. Mod. Phys. **86**, 1391 (2014).
[8] G. Arregui, N. D. Lanzillotti-Kimura, C. M. Sotomayor-Torres, and P. D. García. Phys. Rev. Lett. **122**, 043903 (2019).

Modulation of the THz Emission by a Quantum Cascade Laser using Coherent Acoustic Phonon Pulses

Anthony Kent*[1], Aniela Dunn[2], Caroline Poyser[1], Andrey Akimov[1], Paul Dean[2], A Giles Davies[2], Aleksandar Demic[2], Dragan Indjin[2], Lianhe Li[2], Edmund Linfield[2], Alexander Valavanis[2] and John Cunningham[2]

[1]School of Physics and Astronomy, University of Nottingham, Nottingham, UK
[2]School of Electrical and Electronic Engineering, University of Leeds, Leeds, UK
*corresponding author, E-mail: Anthony.Kent@Nottingham.ac.uk

Abstract

We use laser-generated coherent acoustic phonon (strain) pulses to modulate the electronic transport and THz emission of a 2.6 THz Ga(Al)As quantum cascade laser. The modulation amplitude is of the order of a few % and the rise time, limited by the measurement system response, is less than 1 nanosecond.

1. Introduction

As compact sources of intense THz radiation, quantum cascade lasers (QCLs) have applications in spectroscopy, imaging and communications. For a number of applications, it is essential to be able to modulate the THz emission, e.g.: for superimposing information, or to generate pulsed emission or tunable sidebands.

One way of modulating the QCL emission is to change the electrical pumping current [1]. A large modulation depth is possible and it is theoretically fast due to the ps electron dynamics of the QCL. However, the practical speed is limited by the ability to drive fast current changes in a highly reactive load. Another method is to use an electrically gated graphene-based modulator layer at the output of the QCL [2]. Depths of modulation up to 100% are possible with this method, but maximum modulation speeds have been limited to ~ 100 MHz, again due to the difficulty of driving reactive loads at high speed.

Here we describe an alternative method of QCL emission modulation using bulk acoustic (strain) waves consisting of coherent acoustic phonons with frequency ~ 100 GHz. Previously it was shown that short strain pulses could be used to modulate the electron transport in resonant tunneling devices at high speed [3]. This was due to transient changes to the device bandstructure, via the deformation potential electron–phonon interaction, as the strain pulse propagated through the device. Similar effects could be exploited to modulate a QCL, e.g. by changing the injection of electrons into the active region. The theoretical limit to the speed is the time it takes for the acoustic wave, travelling at the speed of sound, to travel through the resonant tunneling region, which is ~10 ps.

2. The experiment

The Ga(Al)As QCL structure designed to emit at about 2.6 THz was grown by molecular beam epitaxy on a semi-insulating GaAs substrate, and consisted of 88 repeat periods of the injector and active regions. The total thickness of the structure was about 14 microns. A QCL ridge, 2 mm long by 150 μm wide, was formed by etching and electrical contacts made to the top and back. The substrate was thinned to 150 μm and then polished, and a 100 nm aluminium thin film acoustic transducer deposited opposite the QCL ridge. The device was mounted in an optical cryostat, cooled to a temperature in the range 10 – 20 K and was pumped by 50-μs-duration current pulses of amplitude of up to I = 1.8 A and with a duty cycle 5%. The QCL emission was detected using a THz Schottky diode.

Single-cycle, bipolar, acoustic strain pulses, with an amplitude $\eta \leq 10^{-3}$ and duration ≈15 ps, were generated by exciting the transducer with ~100-fs-duration pulses from an amplified Ti:Sapphire laser, of 800 nm wavelength, with a repetition rate of 1 kHz (synchronized to the QCL pump current pulses), and average power in the range 1 – 10 mW. The generated acoustic pulses propagated across the substrate and entered the QCL stack, travelling vertically up through the structure to the top contact, whereupon they were reflected and travelled back down through the QCL stack. The acoustic-pulse-induced transient changes in the voltage across the QCL, $V(t)$, were extracted by using a bias tee in the DC pumping line and measured on a 12.5 GHz sampling oscilloscope. Changes in the intensity of the QCL THz light emission, $L(t)$, detected using the Schottky diode, were also displayed on the oscilloscope.

3. Results

Fig. 1 shows $V(t)$ and $L(t)$ measured for a QCL pumping current of 1.64 A. Time t = 0 is the moment of impact of the laser pulse on the acoustic transducer, the first acoustic responses occur at t = 32 ns, which is the time taken for the strain pulse to reach the QCL ridge. Further acoustic responses, decaying in amplitude, are seen to repeat with a period of 64 ns. These are due to multiple reflections of the

acoustic wave back and forth across the substrate. A closer look at the $V(t)$ response (inset to Fig. 1) shows that the duration of the signal is about 6 ns. This is the time it takes for the strain pulse to travel through the QCL ridge in each direction, before and after reflection at the gold top contact. The polarity of the QCL contact voltage response implies an increase in the resistance of the device as the strain pulse propagates through the device. The rise time of the $V(t)$ response is 0.8 ns, but this is apparently limited by the temporal response of the measurement system.

The corresponding $L(t)$ shows a fast negative spike (reduction of THz emission) during the propagation of the strain pulse through the device. This is followed by a recovery and electrical ringing due to the parasitic reactances of the setup. Comparing the amplitude of the initial negative spike with the quasi-DC response of the Schottky detector, we find the modulation depth is 6%.

4. Discussion

We observed that the acoustic pulse increases the electrical resistance and reduces the THz output of the QCL as it propagates through the device. We have developed a theoretical model of the interaction of the acoustic pulse with the QCL: in essence, the acoustic strain pulse can be considered as a propagating potential distortion of the band structure with amplitude $\eta\Xi_D$, where Ξ_D is the deformation potential constant (~ 10 eV in GaAs). As this passes through each period of the QCL structure, it detunes the resonant injection of electrons into the upper lasing level, thus affecting the transport and the THz emission. More detailed calculations show that the THz emission from the QCL may increase or decrease, depending on whether the QCL is biased at a current below or above the peak in the steady-state *L-I* curve as we have observed experimentally.

5. Conclusions

We have used laser generated picosecond acoustic (strain) pulses to modulate the THz emission from a QCL. The modulation depth obtained in our device was 6%, and the measured rise time of the QCL voltage response was 0.8 ns. However, the theoretical modulation speed is expected to be much higher: ~ 10 ps.

Acknowledgements

The authors acknowledge the support of this work by the UK Engineering and Physical Sciences Research Council, grant references: EP/M016161/1, EP/M01598X/1, and EP/P021859/1. We also acknowledge support of the Royal Society and the Wolfson Foundation.

References

[1] S. Barbieri, W. Maineult, S.S. Dhillon and C. Sirtori, *Appl. Phys. Lett.* **91**, 143510 (2007).

[2] G. Liang et al., *ACS photonics* **2**, 1559 (2015).

[3] E.S.K. Young, A.V. Akimov. M. Henini, L. Eaves and A.J. Kent, *Phys. Rev. Lett.* **108**, 226601 (2012).

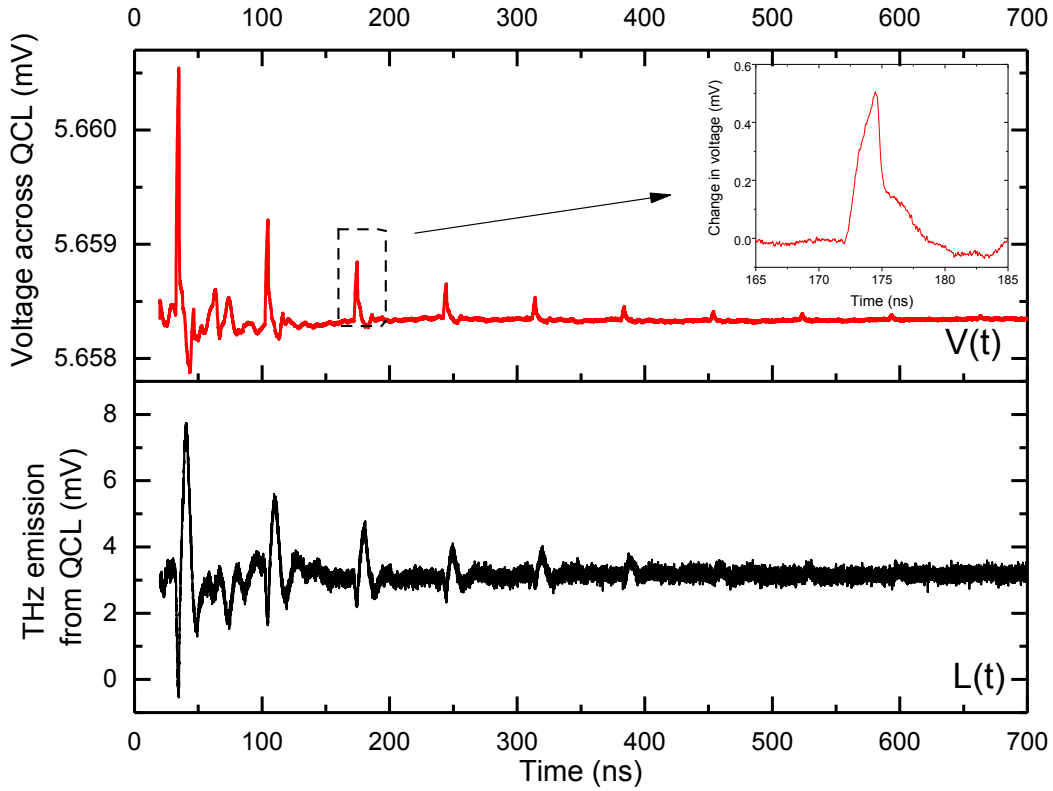


Figure 1: Temporal response of QCL voltage, $V(t)$, (red trace) and Schottky detector signal, ~ $L(t)$, (black trace) to incident strain pulses. The initial strain pulse, arriving at 32 ns, is generated by laser impact on the Al transducer at $t = 0$ and the following pulses are due to multiple reflections in the sample. The inset shows the detail of the $V(t)$ response to an incident acoustic pulse.

First principles calculation of the real-time dynamics of inter-valley electron-phonon coupling after photoexcitation

Felipe Murphy Armando[1], Éamonn Murray[2], Ivana Savic[1,3], Mariano Trigo[3], David Reis[3*], and Stephen Fahy[1,2]

[1]Tyndall National Institute, University College Cork, Ireland
[2]Department of Physics, University College Cork, Ireland
[3]Department of Physics and Department of Materials, Imperial College London, United Kingdom
[4]Department of Photon Science and Applied Physics, Stanford University, Stanford, California 94305, USA
*corresponding author, E-mail: philip.murphy@tyndall.ie

Abstract

We investigate the generation of phonons via inter-valley scattering by calculating the time-dependent relaxation of electrons and phonons on picosecond timescales in photo-excited GaAs, Ge and Bi. We simulate the time evolution of carriers and phonons based on first-principles band structure calculations, including electron-phonon and 3-phonon processes. We compare the simulations with data from time-resolved diffuse x-ray scattering experiments performed at the LCLS free-electron laser facility. We also compare our results in Bi to existing reflectivity experiments[1].

1. Introduction

Direct observation of out-of-equilibrium phenomena has only become possible recently, with the development of large scale free electron laser facilities, such as the LCLS in the US, SACLA in Japan, and FLASH in Germany, as well as ultra-fast probing techniques.[2, 3, 4] One such phenomena is the observation of the transfer of energy from optical sources, via electrons to atomic movement. These techniques provide an unprecedented way to benchmark the phenomena governing energy relaxation processes. To reach this advanced stage has required the development of both the ultra-fast X-ray scattering techniques[3, 5] and sophisticated first-principles electron and phonon scattering algorithms.[6, 7, 8, 9]

In this work, we calculate the phonon generation via electron-phonon scattering in Ge, GaAs and Bi. We compare our results in Ge to measurements of the diffuse X-ray scattering intensity near the Brillouin zone boundary, observed in a scattering geometry similar to that in Ref. [5], but with substantially higher resolution. In Bi, we compare our results of the carrier dynamics to reflectivity experiments in Bi nanomembranes.[1]

2. Summary of results

In Ge and GaAs we observe an increase in the intensity of the x-ray signal near the L-point in the Brillouin zone, over 3-5 ps, that lasts over 10ps. This is due to the non-thermal phonons generated by inter-valley scattering of hot carriers in the L and Δ valleys. We also observe other non-thermal features in the x-ray scattering intensity due to anharmonic phonon scattering. The observation of these phonons strongly depends on the material electronic band structure and is affected by the pump wavelength. In Bi our model accounts for the experimental observation of the relaxation of the reflectivity signal in 12-26 ps[1] after photo-excitation. We attribute this to electron-hole recombination via inter-valley electron-phonon scattering between the conduction bands at the L points and the valence band at the T point. The magnitude of this relaxation time suggests that the carriers are not relaxed within the period of the optical phonons, and thus do not adiabatically follow the phonon dynamics.

References

[1] Y. M. Sheu, Y. J. Chien, C. Uher, S. Fahy, and D. A. Reis, *Phys. Rev. B* 87, 075429, 2013.

[2] R. Corts, L. Rettig, Y. Yoshida, H. Eisaki, M. Wolf, and U. Bovensiepen, Phys. Rev. Lett. 107, 097002 (2011).

[3] M. Trigo, J. Chen, V. H. Vishwanath, Y. M. Sheu, T. Graber, R. Henning, and D. A. Reis, Phys. Rev. B 82, 235205 (2010).

[4] T. Popmintchev, *et al*, *Science* 336, 1287 (2012),

[5] M. Trigo, *et al*, *Nature Physics* 9, 790 (2013),

[6] A. Marini, S. Ponc, and X. Gonze, Phys. Rev. B 91, 224310 (2015).

[7] D. M. Fritz, *et al*, *Science* 315, 633 (2007).

[8] É. Murray and S. Fahy, Phys. Rev. Lett. 114, 055502 (2015).

[9] P. Maldonado, K. Carva, M. Flammer, and P. Oppeneer, Phys. Rev. B 96, 174439 (2017).

Study of the resonant modes of hypersonic acoustic cavities by an ultrafast pump-probe technique

Camille Lagoin, Daniel Garcia-Sanchez, Paola Atkinson, and Bernard Perrin*

Sorbonne Université, CNRS-UMR 7588, Institut des NanoSciences de Paris, F-75005 Paris, France
*corresponding author, E-mail: bernard.perrin@insp.jussieu.fr

Abstract

We used an ultrafast pump-probe technique to characterize the acoustic properties of semiconductor micropillars designed for optomechanics experiments. We described the way to measure quality factors as high as 35000 of a 20 GHz cavity mode with subharmonic resonant excitation by a femtosecond laser oscillator which has a repetition rate of 80 MHz. The spatial profile of the modes has also been investigated and discussed.

1. Introduction

Optomechanical devices working in the range of a few tens of GHz would be very useful since they can be used at much higher temperatures than MHz resonators and contribute to ultrafast information processing. Micropillar semiconductor GaAs/AlAs superlattice cavities which confine simultaneously optical and sound waves appeared as a promising tool a few years ago [1]. Frequency and spatial profiles of micropillar optical cavity modes have been studied many times [2] and large quality factors have already been evidenced. In contrast there are only a few numerical and experimental studies of their acoustical resonant modes [3,7]. Such measurements at 20 GHz are quite challenging: this frequency seems too large for conventional piezoelectric excitation and too low for ultrafast pump-probe technique. Indeed, the lifetime of the acoustic mode is expected to be of the order of hundreds of ns or more which is much larger than what can be studied with a mechanical optical delay line and much larger than the interval between two laser pulses of a femtosecond laser oscillator. In this work we used a subharmonic resonant excitation technique to overcome this difficulty.

2. Experiments

The planar acoustic cavities are obtained with two Bragg mirrors made of $\lambda/4$ GaAs/AlAs superlattices surrounding a $\lambda/2$ GaAs cavity; the whole device has been grown on GaAs wafers with thickness around 370 µm. Depending on the samples, the number of periods in the Bragg mirrors is 15, 20 or 25 and the fundamental resonant mode frequency is 16 or 20 GHz. The micropillars are obtained by etching the planar cavities; both circular and square section have been studied with typical diameter (or side length) going from 8 to 64 µm.

We studied the resonant modes of the acoustic cavities with an ultrafast pump-probe technique. Since the device works simultaneously as an optical and acoustical cavity we could have a complex interaction between the pump and the probe in a configuration where pump and probe are incident on the same side of the device. Thus we chose a configuration already used to study acoustic nanocavities [8] where pump and probe are incident on the opposite sides of the device. Opaque 60-nm Al films were deposited on the backside of the wafer and on the top of the cavities: the pump pulse excites a broad acoustic pulse which propagates through the wafer and through the cavity. To get rid of phonon-phonon interactions both in the substrate and the cavity we worked at 20K. The surface displacement of the cavity surface is probed with a Sagnac interferometer [9]: the top aluminum film prevents any photoelastic contribution to the detection process within the cavity.

The delay line of our setup works up to 12ns and we used the subharmonic resonant excitation of the acoustic cavity mode by tuning the repetition rate of the laser [9] to be able to measure decay times of the resonant oscillation of the order of hundreds of ns. The pump beam is modulated at a frequency f_{mod} = 1 or 2 MHz and a lock-in amplifier is used for the detection. Combining the in-phase X and out-of-phase components Y of the lock-in and taking account for the cumulative effects of the successive pump pulses, it is straightforward to show that, close to a resonant frequency mode, we obtain two signals

$$S^{\pm}(\tau) = X \pm iY \propto \frac{e^{-\tau/\tau_m} e^{2i\pi f^{\pm}\tau}}{1 - e^{-(\tau_m f_{rep})^{-1}} e^{2i\pi f^{\pm} f_{rep}^{-1}}}, \qquad (1)$$

where τ is the pump-probe delay, $f^{\pm} = f_m \pm f_{\mathrm{mod}}$, f_m and τ_m are the frequency and lifetime of the mode. Usually no resonant peak at f_m appears on the Fourier transform of $S^{\pm}(\tau)$ except when the ratio $f^{\pm} / f_{\mathrm{mod}}$ is very close to an integer n. Then, plotting the peak amplitude in terms of the repetition rate f_{rep} we obtain a lorentzian shape from which we can extract the resonance frequency $f_m = n \times f_{rep} \mp f_{\mathrm{mod}}$, the lifetime τ_m and the quality factor $Q = \pi f_m \tau_m$. Results for a planar cavity with 25 periods Bragg mirrors is reported on Fig. 1. The Lorentzian fit gives a lifetime of 550ns

corresponding to a quality factor of 35000, 3 times smaller than the theoretical expectation; the small bump on the right side is due to successive acoustic echoes in the substrate With this technique, it has been possible to study the seventh harmonic (112 GHz) of a fundamental mode at 16 GHz which corresponds to an integer n= 1400.

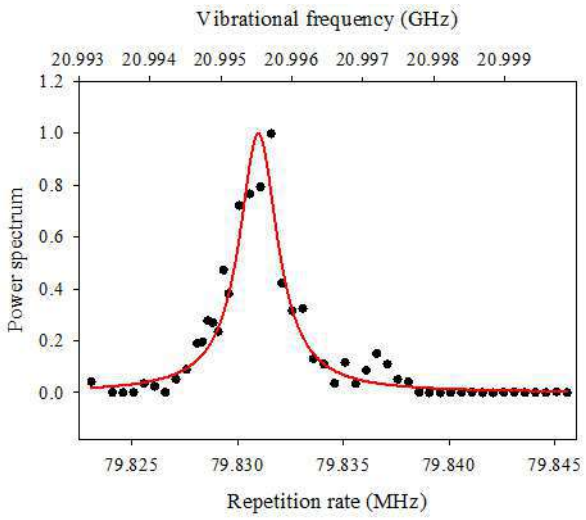


Figure 1: Peak amplitude of the power spectrum of the surface displacement of a planar cavity with 25 periods Bragg mirrors (black dots). The Q factor estimated from the fit(red line) is 35000 ($\tau_m = 550$ ns).

The same kind of results have been obtained in circular or square section micropillars with typical size ranging from 8 to 64 µm. For the largest (64 µm) and smallest (8 µm) micropillars we still obtain a Lorentzian shape scanning the repetition rate of the laser but in between it departs clearly from this behavior and we can highly suspect that we are also exciting other close resonant modes [6]. To check this possibility, we performed the following experiment:

In a first step, the acoustic pulse is incident on the middle of a 32 µm square micropillar. Scanning the repetition rate, we observed two peaks separated by $15.8KHz = 2f_{\mathrm{mod}/n}$ which corresponds to the two side bands of the pump $f^{\pm}$ in the excitation process (the pump is modulated at 2MHz and the integer $n=253$).

In a second step, we chose a repetition $f_{rep} = f^{-}/n$ and perform a probe scan through the top of the pillar to obtain the modes profile. The acoustic pulse is incident on the left side of the micropillar The black dots gives the resonance amplitude for the signal S^{-} ;the shape of the signal is clearly asymmetric with respect to the middle of the scan although the fundamental resonant mode should be symmetric. The red dots correspond to S^{+} ; the shape of the signal is more complex and evidences the fact that at least two side modes with higher frequencies are also excited.

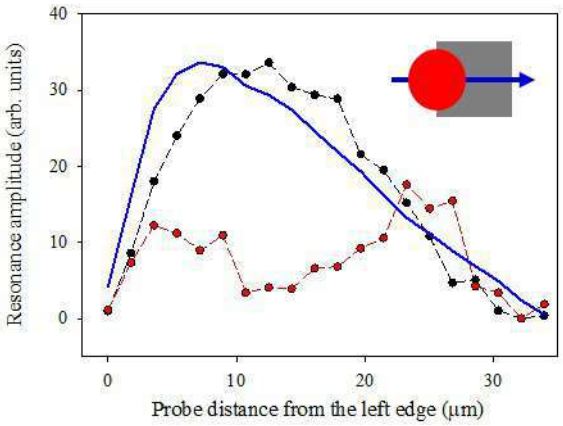


Figure 2: Asymmetric excitation of the resonant modes of a square section micropillar (32µm). The red circle in the inset corresponds to the pump position; black and red dots gives S^{-} and S^{+} in terms of the probe position along the blue arrow for a repetition rate of 79.9035MHz. The blue line is the maximum amplitude of the first acoustic echo.

3. Conclusions

It has been shown that very high acoustic quality factors can be measured with an ultrafast pump-probe technique and that a detailed investigation of the mode profile can be performed.

References

[1] A. Fainstein, N. D. Lanzillotti-Kimura, B. Jusserand, and B. Perrin, *Phys. Rev. Lett.* 110: 037403, 2013.

[2] G. Ctistis, A. Alex Hartsuiker, E. van der Pol, J. Claudon, et al., *Phys. Rev. B* 82: 195330, 2010.

[3] D. Garcia-Sanchez, S. Déleglise, J.-L. Thomas, P. Atkinson, C. Lagoin, B. Perrin, *Phys. Rev. A* 94 : 033813, 2016.

[4] F. R. Lamberti, Q. Yao, L. Lanco, et al., *Optics Express* 25 : 24437, 2017.

[5] S. Anguiano, A. E. Bruchhausen, B. Jusserand, et al., Phys. Rev. Lett. 118: 263901, 2017.

[6] S. Anguiano,1 P. Sesin,1 A. E. Bruchhausen,1 F. R. Lamberti, et al., *Phys. Rev. A* 98 : 063810, 2018.

[7] C. Lagoin, B. Perrin, P. Atkinson, D. Garcia-Sanchez, *Phys. Rev. B. Rapid Com. B* **99:** 060101, 2019.

[8] A. Huynh, N. D. Lanzillotti-Kimura, B. Jusserand, B. Perrin, et al., *Phys. Rev. Lett.* 97 : 115502, 2006.

[9] E. Péronne, N. Chuecos, L. Thevenard, and B. Perrin, *Phys. Rev. B* 95: 064306, 2017.

Bruchhausen, R. Gebs, F. Hudert, D. Issenmann, G. Klatt, et al., *Phys. Rev. Lett.* 106: 077401, 2011.

Dynamics of nanomechanical pillar resonators

Juliane Doster[1], Simon Hönl[1+], Heribert Lorenz[2], Philipp Paulitschke[2], and Eva M. Weig[1*]

[1]Department of Physics, University of Konstanz, Universitätsstraße 10, 78457 Konstanz, Germany
[2]Fakultät für Physik and Center for NanoScience (CeNS), Ludwig-Maximilians-Universität, Geschwister-Scholl-Platz 1, 80539 München, Germany
*corresponding author, E-mail: eva.weig@uni-konstanz.de
[+]present address: IBM Research – Zurich, Säumerstrasse 4, CH-8803 Rüschlikon, Switzerland

Abstract

We investigate inverted conical nanopillars as a mechanical resonators, considering their flexural modes. Nanopillars are well suited for dense integration into resonator arrays. Establishing coupling between neighboring nanopillars enables then the investigation of coupled resonator networks.

1. Introduction

Nanopillars are ideally suited as mechanical resonators in the scope of applications in sensing [1] as well as the investigation of phenomena such as collective dynamics. Inverted conical nanopillars, fabricated in a top-down process, allow access to a large frequency range. The inverted

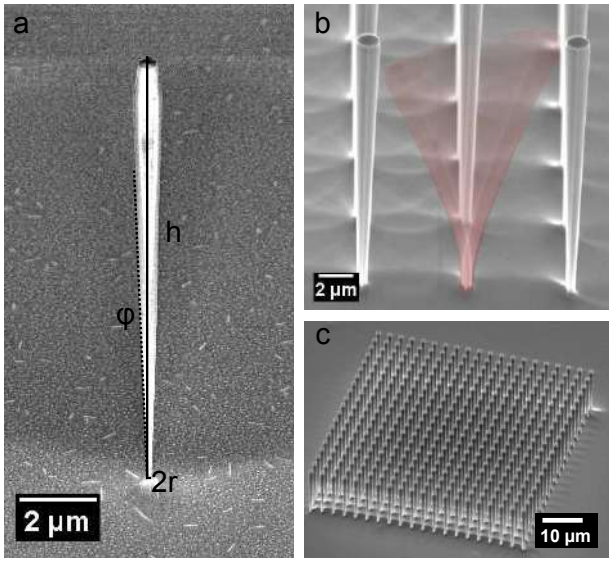


Figure 1: Scanning electron micrograph of **a**, resting nanopillar, **b**, moving nanopillar, and **c**, nanopillar array.

conical shape (cf. Fig. 1a) allows for extremely high flexibility at the clamping point of the resonators, as well as straightforward optical detection, owing to their relatively large heads.
Top-down fabrication of these nanopillars also allows for dense and well-controlled fabrication of nanopillar arrays. We investigate the dynamics of individual as well as the coupling between nanomechanical pillar resonators.

2. Experimental and results

Inverted conical GaAs nanopillars are fabricated in an electron beam patterning step combined with an anisotropic chlorine reactive ion etch. We investigate flexural modes as depicted in Fig. 1b exhibiting large amplitudes, which can be detected via SEM imaging as well as optical laser based detection. Top-down fabrication further allows frequency control through the geometry parameters (cf. Fig. 1a) of the nanopillar

$$\omega = \sqrt{\frac{E}{\rho}} G(r, b, h) \tag{1}$$

with geometry factor $G(r, b, h)$ [2]. We further examine intrinsic coupling between two neighboring nanopillars. Based on studies of mode hybridization as well avoided level crossings, we can control the coupling strength solely through the geometry of the nanopillars. [3]

3. Conclusion

Nanomechanical pillar resonators are well suited for the investigation of collective dynamics owing to their well controlled frequencies and the straight-forward integration into large arrays (cf. Fig.1c).

References

[1] P. Paulitschke, F. Keber, A. Lebedev, J. Stephan, H. Lorenz, S. Hasselmann, D. Heinrich, and E. M. Weig, *Ultraflexible Nanowire Array for Label- and Distortion-Free Cellular Force Tracking*, Nano Letters Article ASAP

[2] P. Paulitschke, N. Seltner, A. Lebedev, H. Lorenz, and E. M. Weig
Size-independent Young's modulus of inverted conical GaAs nanowire resonators Appl. Phys. Lett. 103, 261901 (2013)

[3] J. Doster, S. Hoenl, H. Lorenz, P. Paulitschke, and E. M. Weig, *Strong Strain-Induced Coupling between Nanomechanical Pillar Resonators*, arxiv:1812.08614 (2018)

Mechanical Synchronization of Optomechanical Oscillators

D. Navarro-Urrios[1]*, M. F. Colombano[2,3], G. Arregui[2,3], N. E. Capuj[4,5], A. Pitanti[6], J. Maire[2], S. Zanotto[6], A. Griol[7], A. Martinez[7], C. M. Sotomayor-Torres[2,8]

[1]MIND-IN2UB, Departament d'Enginyeria Electrònica i Biomèdica, Facultat de Física, Universitat de Barcelona, Martí i Franquès 1, 08028 Barcelona, Spain
[2]Catalan Institute of Nanoscience and Nanotechnology (ICN2), CSIC and BIST, Campus UAB, Bellaterra, 08193 Barcelona, Spain.
[3]Depto. Física, Universidad Autónoma de Barcelona, Bellaterra, 08193 Barcelona, Spain.
[4]Depto. Física, Universidad de La Laguna, 38200 San Cristóbal de La Laguna, Spain.
[5]Instituto Universitario de Materiales y Nanotecnología, Universidad de La Laguna, 38071 Santa Cruz de Tenerife, Spain.
[6]NEST, CNR - Istituto Nanoscienze and Scuola Normale Superiore, Piazza San Silvestro 12, 56127 Pisa, Italy
[7]Nanophotonics Technology Center, Universitat Politècnica de València, 46022 València, Spain.
[8]Catalan Institute for Research and Advances Studies ICREA, 08010 Barcelona, Spain.
*corresponding author, E-mail: dnavarro@ub.edu

Abstract

Our work thoroughly addresses the topic of synchronization of nanoscaled optomechanical (OM) oscillators.
We demonstrate for the first time synchronization of a pair of mechanically-coupled OM cavities by means of a set of unequivocal experiments. We also show that the collective dynamics can be controlled by externally actuating over a single oscillator. Therefore, these results set a solid basis for realizing reconfigurable networks of OM oscillators displaying collective dynamics dominated by weak mechanical coupling.

1. Introduction

In 1665 Lord Christiaan Huygens discovered that two pendulum clocks, hung from the same wooden structure, were oscillating in perfect consonance but in opposite directions, i.e. the clocks were synchronized in anti-phase.

Essential conditions for spontaneous synchronization between two dynamical systems are [1]: i) both of them are self-sustained oscillators, i.e., capable of generating their own rhythms; ii) the systems adjust their rhythm due to a weak interaction; and iii) the adjustment of rhythms occurs in a certain range of mismatch of the individual systems. To date, there has been only a handful of reports claiming synchronization in coupled OM cavities [2]-[4]. Most of these works are rather controversial [5], since the systems operate in a rather strong-optical-coupling regime that makes them indecomposable. Indeed, the coupled OM cavities share a common optical mode, which in addition prevents extracting the dynamics of each cavity cannot in an independent way. On the other hand, a couple of reports have reported long-range synchronization between OM cavities placed in different chips [6],[7]. The coupling mechanism in these cases relies on modulating the optical excitation of one of the cavities with an electro-optical-modulator that reproduces the dynamics of the other cavity.

2. Results and discussion

In this work, we report synchronization of the mechanical dynamics of a pair of OM oscillators weakly coupled mechanically and completely isolated optically. The OM oscillators are independently driven to a state of high amplitude, coherent and self-sustained mechanical motion (mechanical lasing from now on) using a self-pulsing dynamics [8],[9]. Although the coupling is bidirectional, the synchronization dynamics is nearly of a Master-Slave type, given that the amplitude of the coherent oscillations is considerably larger in one of the cavities. Simultaneous recording of the optical transmission temporal traces of each of the two cavities allows concluding that, in the synchronized state, they mechanically oscillate in anti-phase, which is in agreement with the predictions of our numerical model with reactive coupling. Finally, we demonstrate that, when the coupled system is in a synchronized state, it is possible to disable it while actuating over one of the cavities with a heating laser, so that both cavities oscillate independently.

The geometrical configuration of two OM oscillators can be upscaled to realize complex networks comprising many more nodes without substantially increasing the technological requirements. Our structures can be optically excited by a common laser source by exploiting thermo-optic effects while still maintaining the weak interaction requirement for synchronization. These results are the first step towards building networks of weakly coupled OM oscillators able to display collective dynamics susceptible to

be modified by addressing single structures with external perturbations, thus enhancing the performances of single nano-mechanical oscillator systems and constituting a novel architecture for neuromorphic computing applications.

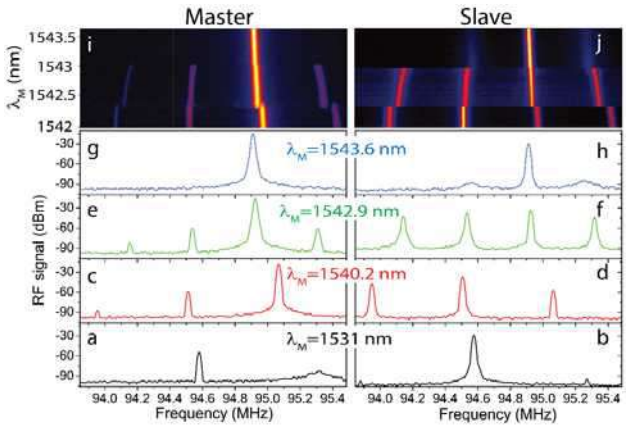


Figure 1: Synchronization of Optomechanical crystal oscillators in the frequency domain. a-h, Radio-frequency spectra of the optical transmission associated to the Master cavity (left panels) and the Slave cavity (right panels) for different values of the wavelength of the laser driving the Master cavity (λ_M). The wavelength of the laser driving the Slave cavity is fixed at λ_S=1529nm. i-j, Colour contour plots of the radio-frequency spectra as a function of λ_M of the Master and Slave cavities (i and j panels respectively).

Acknowledgements

This work was supported by the European Commission project PHENOMEN (H2020-EU-713450), the Spanish Severo Ochoa Excellence program and the MINECO project PHENTOM (FIS2015-70862-P). DNU, GA and MFC gratefully acknowledge the support of a Ramón y Cajal postdoctoral fellowship (RYC-2014-15392), a BIST studentship and a Severo Ochoa studentship, respectively.

References

[1] A. Pikovsky, M. Rosenblum, J. Kurths, Synchronization: A universal concept in nonlinear sciences (Cambridge Univ. Press, Cambridge, 2003).

[2] M. Zhang, G.S. Wiederhecker, S. Manipatruni, A. Barnard, P. McEuen, M. Lipson, Synchronization of micromechanical oscillators using light. Phys. Rev. Lett. 109, 233906 (2012).

[3] M. Zhang, S. Shah, J. Cardenas, M. Lipson, Synchronization and phase noise reduction in micromechanical oscillator arrays coupled through light. Phys. Rev. Lett. 115, 163902 (2015).

[4] M. Bagheri, M. Poot, L. Fan, F. Marquardt, H.X. Tang, Photonic cavity synchronization of nanomechanical oscillators. Phys. Rev. Lett. 111, 213902 (2013).

[5] M. H. Matheny, M. Grau, L.G. Villanueva, R.B. Karabalin, M.C Cross, M.L. Roukes, Phase synchronization of two anharmonic nanomechanical oscillators. Phys. Rev. Lett. 112, 014101 (2014). Supplementary Information file.

[6] S. Shah, M. Zhang, R. Rand, M. Lipson, Master-slave locking of optomechanical oscillators over a long distance. Phys. Rev. Lett. 114, 113602 (2015).

[7] S. Shah, M. Zhang, R. Rand, M. Lipson, Long-range synchronization of nanomechanical oscillators with light. Preprint at https://arxiv.org/abs/1511.08536 (2017).

[8] D. Navarro-Urrios, N. E. Capuj, J. Gomis-Bresco, F. Alzina, A. Pitanti, A. Griol, A. Martínez, and C. M. Sotomayor Torres, Sci. Rep. 5(1), 15733 (2015).

[9] D. Navarro-Urrios, N. E. Capuj, M. F. Colombano, P. D. García, M. Sledzinska, F. Alzina, A. Griol, A. Martínez, and C. M. Sotomayor-Torres, Nat. Commun. 8, 14965 (2017).

Stochastic and vibrational resonance with a driven electro-mechanical resonator

Guilhem Madiot[1], Franck Correia[1], Avishek Chowdhury[1], Sylvain Barbay[1], M. G. Clerc[2] and Braive Rémy[1,3*]

[1] Centre de Nanosciences et Nanotechnologies, CNRS, Palaiseau, France
[2] Departamento de Física, Facultad de Ciencias Físicas y Matemáticas, Universidad de Chile, Casilla 487-3, Santiago, Chile
[2] Université Paris Diderot – Paris 7, Paris, France

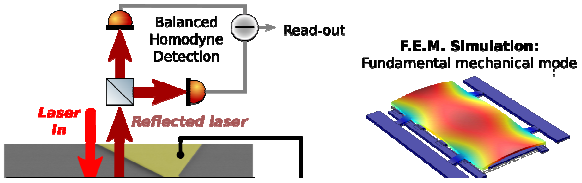
*corresponding author, E-mail: remy.braive@c2n.upsaclay.fr

Abstract

Stochastic resonance is a general phenomenon usually observed in one-dimensional, amplitude modulated, bistable systems. We show experimentally the emergence of phase stochastic resonance in the bidimensional response of a forced nano-electromechanical membrane by evidencing the enhancement of a weak phase modulated signal thanks to the addition of phase noise. Based on a general forced Duffing oscillator model, we demonstrate experimentally and theoretically that phase noise acts multiplicatively inducing important physical consequences. These results may open interesting prospects for phase noise metrology or coherent signal transmission applications in nanomechanical oscillators.

1. Stochastic with electromechanical resonator

Stochastic resonance whereby a small signal gets amplified resonantly by application of external noise has been introduced originally in paleoclimatology [1] to explain the recurrence of ice ages and has then been observed in many other areas including neurobiology [2, 3], electronics [4], mesoscopic physics [5], photonics [6, 7], atomic physics [8] and more recently mechanics [9, 10, 11]. Implementation of stochastic resonances involves generally three ingredients: (i) the existence of metastable states separated by an activation energy, as in excitable or bistable nonlinear systems, (ii) a coherent excitation, whose amplitude is however too weak to induce deterministic hopping between the states, and (iii) stochastic processes inducing random jumps over the potential barrier. In the classical picture of a bistable system, this corresponds to the motion of a fictive particle in a double-well potential periodically modulated in amplitude by the signal and subjected to noise [12]. When an optimal level of noise is reached, the system's response power spectrum displays a peak in the signal to noise ratio, unveiling the stochastic resonance phenomenon. The resonance occurs as a 'bona-fide' resonance in a frequency band around a signal frequency approximately given by the time-matching condition [13], i.e. when the potential modulation period is twice the mean residence time of the noise-driven particle. Experimental works on stochastic resonance are almost exclusively using amplitude modulation going along with additive amplitude noise or multiplicative amplitude noise [14, 15]. In this case, it corresponds to a pure one-dimensional effect.



phase noise observed on the bidimensional response of the oscillator (Fig. 2). This opens new avenues for stochastic resonance in bidimensional systems by allowing for instance stochastic amplification of mixed phase-amplitude modulated signals by complex value noise. We highlight that the system's response can be projected on any variable in phase space and that the amplification depends on the chosen basis. Finally, we derive a stochastic nonlinear amplitude equation for the forced stochastic Duffing oscillator, which describes qualitatively well our system (Fig. 2), and show that phase noise acts multiplicatively inducing important physical consequences.

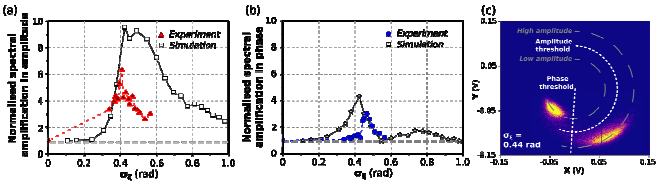


Figure 2 : Experimental (red triangles) and theoretical (open black squares) spectral amplification in amplitude R as a function of phase noise strength. (b) Experimental (blue circles) and theoretical (open black stars) spectral amplification in phase Φ as a function of phase noise strength. (c) Experimental polar plot for phase noise (0.44rad) with maximum amplification, highlighting the shape of the two stable points as well as the directions imprinted by the modulation on the input phase or amplitude. The two dashed grey lines are guide for the eyes indicating the two distinct amplitude states and the dotted white line highlights the threshold.

2. Vibrational resonance with electromechanical resonator

Similarly to stochastic resonance, vibrational resonance show up in non-linear resonators sustaining metastable states. Instead of using broad band noise, vibrational resonance is implemented with a high frequency modulation (between the low frequency modulation of the weak signal and the mechanical frequency of the resonator). Here, the gain factor also features a resonant-like behaviour, with a well pronounced maximum for optimal external driving amplitudes. The maximum achieved gain factor is 20 much higher than for stochastic resonance.

Vibrational resonance is governed by an amplitude condition. It occurs close to the transition from bistability to monostability, during which the effective potential of the slow variable evolves from a rapidly oscillating double well to a single well with a parametric dependence on the high-frequency signal amplitude and frequency. As such, this phenomenon has some features in common with parametric amplification near the critical point. The shape of gain achieved in vibrational resonance consequently reflects the (here symmetrical) shape of the parametric gain in the system. By numerically investigating the amplitude equation, we show that the strength of the high-frequency driving can tune the system such that the low amplitude signal drive makes the system jump between the two branches. It is the basic physical phenomenon at the origin of vibrational resonance. In the absence of high frequency amplitude modulation, the system stays in the lower branch and the response is quasi linear. When the driving is increased, the system is tuned into resonance and this corresponds to a large signal amplification, provided the modulation amplitude is large enough. The amplification displays a sharp transition corresponding to the tuning of the system into the bistable region. For still higher driving the system stays in the upper branch where the response is sublinear, thus leading to de-amplification.

3. Conclusions

We have demonstrated stochastic and vibrational resonance with a unique and driven electromechanical photonic crystal membrane. This versatile platform allows coupling several of them either optically or mechanically.

Multimode optomechanics has started to be explored in the last years for its promising applications in nonlinear signal processing. The use of coupled optical or mechanical modes can lead to interesting properties such as nonreciprocal states [16], spontaneous symmetry breaking [17] or noise-aided process which might have a strong impact in noise-assisted applications including signal processing or sensing.

Acknowledgements

This work is supported by the European Union's Horizon 2020 research and innovation programme under grant agreement No 732894 (FET-Proactive HOT).

References

[1] Gammaitoni et al, Rev. Mod. Phys. 70, 223 (1998)..

[2] Douglass et al, Nature 365, 337 (1993)

[3] Bezrukov et al, Nature 378, 362-364 (1995).

[4] Fauve et al, Physics Letters A 97, 5

[5] Hibbs et al,J. Appl. Phys. 77, 2582 (1995)

[6] McNamara et al, Phys. Rev. Lett. 60, 2626 (1988)

[7] Barbay et al, Phys. Rev. E 61, 157 (2000)

[8] Wilkowski et al, Phys. Rev. Lett. 85, 1839 (2000)

[9] Badzey et al, Nature 437, 995 (2005)

[10] Venstra et al Nat Commun 13 (2013)

[11] Monifi et al, Nat Photon 10, 399 (2016)

[12] Gammaitoni et al, Phys. Rev. Lett. 62, 349 (1989)

[13] Gammaitoni et al, Phys. Rev. Lett. 74, 1052 (1995)

[14] Gammaitoni et al, Phys. Rev. E 49, 4878 (1994)

[15] Qiao et al Phys. Rev. E 94, 052214 (2016)

[16] Miri et al, Phys. Rev. Applied **7**,064014 (2017)

[17] Miri et al, Phys. Rev. A **95**,053822 (2017)

Electromagnetically-optomechanically induced transparency in atom-photon-phonon system

He Hao[1], Juanjuan Ren[1], Fan Zhang[1], Qihuang Gong[1,2] and Ying Gu[1,2]

[1]State Key Laboratory for Mesoscopic Physics, Collaborative Innovation Center of Quantum Matter, School of Physics, Peking University, Beijing, 100871, China
[2]Collaborative Innovation Center of Extreme Optics, Shanxi University, Taiyuan, Shanxi, 020006, China
*Ying Gu, E-mail: ygu@pku.edu.cn

Abstract

We propose a scheme of atom-assisted cavity optomechanical system and demonstrate the electromagnetically-optomechanically induced transparency, where a transparent point appears as long as the satisfaction of two sets of two-photon resonance. Our work offers new insight for the tripartite coherent interaction among photon, phonon and atom, giving great exibility for manipulation of light and motivating the development of quantum information process.

1. Introduction

Cavity quantum electrodynamics (CQED) has provided a ubiquitous platform for the interaction between atoms and cavity fields at single quantum level. And the realization of cavity optomechanics has coupled cavity fields to mechanical resonators. Currently, motivated by the rapid development of quantum information network, the bridge of the CQED and optomechanics has been demonstrated[1]. A wide range of physics appears, and one of the most interesting phenomena is the analogous electromagnetically induced transparency (EIT) in hybrid systems.Since the first observation of EIT in atom gas[2], the analogous EIT phenomenon has been realized in various systems, ranging from the CQED, multi-microcavities systems to cavity optomechanics[3]. However, the analogous EIT phenomenon in the hybrid atom-photon-phonon system has been absent.

Here, we theoretically study an atom-photon-phonon system, consisting of a single Λ-type three-level atom and an optomechanical cavity, which is driven by strong lasers at the red sidebands (see Fig.1). The innovation of our model lies in the combination of two kinds of interactions in the atom-photon-phonon system, one is the interaction between the atom and the cavity mode, the other is the interaction between the sideband driven cavity mode and the mechanical mode. Based on the above considerations, we demonstrate electromagnetically-optomechanically induced transparency (EOMIT), where the transparent point appears in the condition of satisfaction of two sets of two-photon resonance. We explain the mechanism of EOMIT from the perspective of dressed state theory and find the property of EOMIT (e.g. transparent point, width of transparent window) can be effectively tuned by several system parameters including the coupling strength between cavity field and atom, Rabi frequency of atom, optomechanical cooperativity as well as relevant detunings.

2. Atom-photon-phonon model setup

As schematically shown in Fig. 1(a), we study a hybrid atom-photon-phonon system consisting of an optomechanical cavity and a Λ-type three-level atom. The atom is confined inside the cavity and its excited and grounds states are labeled as $|1\rangle$ and $|2\rangle$, $|3\rangle$, respectively. The atomic transition $|1\rangle \leftrightarrow |2\rangle$ with energy level difference $w_{12} = w_1 - w_2$ is coupled to the cavity field of frequency w_{cav} with coupling coefficient g and the detuning $\Delta_{cav} = w_{12} - w_{cav}$. While the transition $|1\rangle \leftrightarrow |3\rangle$ is driven by a classical, controllable field of frequency w_0 with Rabi frequency Ω and detuning $\Delta_0 = w_{13} - w_0$. Fig. 1(b) shows the driven lasers associated with the system, the lasers of frequence w_0 and w_d drive the atom and cavity respectively, while a weak laser with frequence w_p probes the resonance of the cavity. The whole couplings existed in the system is shown in Fig. 1(c).

Based on the above considerations, in a rotating frame, the Hamiltonian of the hybrid system reads:

$$\begin{aligned} H_I &= \hbar\Delta_{cav}\sigma_{11} + \hbar(\Delta_{cav} - \Delta_d)\sigma_{22} + \hbar(\Delta_{cav} - \Delta_0)\sigma_{33} \\ &\quad +\hbar(\Delta_d - \Delta_{cav})a^+a + \hbar w_m b^+b - \hbar G a^+a(b + b^+) \\ &\quad +\hbar(\Omega\sigma_{13} + ga\sigma_{12} + H.c.) + i\hbar\sqrt{2\eta r_a}[(\varepsilon_d a^+ - \varepsilon_d^* a) \\ &\quad +(\varepsilon_p a^+ e^{i(\Delta_p - \Delta_d)t} - \varepsilon_p^* a e^{-i(\Delta_p - \Delta_d)t})], \end{aligned}$$

where the detunings are defined as $\Delta_p = w_{12} - w_p$, $\Delta_d = w_{12} - w_d$, $\Delta_{cav} = w_{12} - w_{cav}$, $\Delta_0 = w_{13} - w_0$

3. Electromagnetically-optomechanically induced transparency

In the red resolved sideband, we get the intracavity field induced by the probe light as Eq. (1). For numerical work, we use parameters from recent experiments: $g = 1MHz, \Omega = 2MHz, r_a = 1MHz, r_{21} = 0.5MHz, r_{23} = r_m = 0.01MHz, \eta = 0.6$.

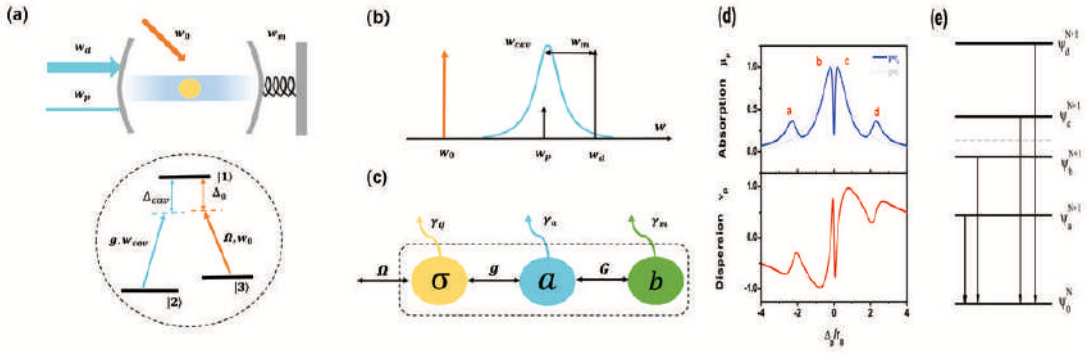


Figure 1: (a) Scheme of the considered hybrid system. Three-level atom in configuration showing the cavity (w_{cav}) and control (w_0) fields coupling the transitions $|2\rangle \longleftrightarrow |1\rangle$ and $|3\rangle \longleftrightarrow |1\rangle$, respectively, and relevant detunings. (b). Three optical fields, a driven laser (w_d) drives the cavity at red or blue sidebands with a mechanical frequency w_m offset from the cavity field, a second laser (w_p) probes the cavity resonance while a third laser (w_0) controls the transition $|3\rangle \longleftrightarrow |1\rangle$ in atom. (c) Schematic illustration of decay channels and couplings among photons(a), phonons(b) and atom(σ).(d) Absorption and dispersion spectra of propagating quantum light as a function of detuning $\Delta_p = w_p - w_{12}$. There are four peaks and a transparent window under the condition $\Delta_d = w_m$ and $\Delta_0 = \Delta_{cav} = 0$ (e) The atom-photon-phonon eigenstates structure for the hybrid quantum system.

$$\delta a = \frac{\sqrt{2\eta r_a}\varepsilon_p}{r_a + i(\Delta' + \Delta_p - \Delta_d) + \dfrac{G^2\overline{a}^2}{r_m + i(w_m + \Delta_p - \Delta_d)} + \dfrac{g^2}{r_{21} + i\Delta_p + \dfrac{\Omega^2}{r_{23} + i(\Delta_p - \Delta_0)}}}, \tag{1}$$

The effective cooperativity for optomechanical system $C = \dfrac{(G\overline{a})^2}{r_a r_m} = 4$. Figure 1(d) plots the absorption and dispersion spectrum of probe light as a function of detuning $\Delta_p = w_p - w_{12}$ with $\Delta_d = w_m$ and $\Delta_0 = \Delta_{cav} = 0$. It is shown that there are four peaks in the absorption spectrum and each peak corresponding to a steep slope in the dispersion spectrum. The position of each peak (a-d) locates at -2.29r_0, -0.18r_0, 0.18r_0 and 2.29r_0 respectively. Meanwhile, a transparent point appears under the condition $\Delta_d = w_m$ and $\Delta_0 = \Delta_{cav} = \Delta_p = 0$. We also give an explicit physical reason for the peaks and transparent point using the dressed state language, whose eigenstates are shown in Fig. 2(e).

4. Discussion

we also demonstrate that the transparent point can be tuned by the relevant detunings and the width of transparent window can be increased by the decreasing the coupling strength between cavity field and atom or increasing the Rabi frequency of atom and optomechanical cooperativity. The EOMIT can find its role in quantum state transduction and quantum memory. For example, the information carried by atom can be transfered to phonon with the help of photon, which has long coherence time and can be an ideal carrier for quantum memory. Also, the EOMIT has a positive effect to generating slow light as the width of transparent window can be controlled by atom, which is easy to implement in experiments.

5. Conclusions

We report the EOMIT in atom-assisted system and reveal the mechanism in terms of dressed state theory. Our work would bring great flexibility for manipulating light, which can be used for generating slow light and amplifying signal light.

References

[1] M. Cotrufo and A. Fiore, "Coherent Atom-Phonon Interaction through Mode Field Coupling in Hybrid Optomechanical Systems," Phy.Rev.Lett. **118**, 133603 (2018).

[2] K.-J. Boller, A. Imamoglu, and S. E. Harris, "Observation of electromagnetically induced transparency ," Phy.Rev.Lett. **66**, 2593 (1991).

[3] S. Weis, R. Rivire, S. Delglise, E. Gavartin, O. Arcizet, A. Schliesser, T. J. Kippenberg, "Optomechanically Induced Transparency ," Science **330**, 1520 (2010).

Ultrafast microscopy of the acoustic eigenmodes of a single nanoparticle

Yannick Guillet[1,2,*], Allaoua Abbas[1,2,3], Serge Ravaine[4] and Bertrand Audoin[1,2],

[1]Univ. Bordeaux, I2M, UMR 5295, F-33400 Talence, France
[2]CNRS, I2M, UMR 5295, F-33400 Talence, France
[3]Present address: Neta, Rue Franc¸ois Mitterand, F-33400 Talence, France
[4]CNRS, Univ. Bordeaux, CRPP, UMR 5031, F-33600 Pessac, France
*corresponding author, E-mail: yannick.guillet@u-bordeaux.fr

Abstract

Ultrafast acoustic spectroscopy of single nanoparticles appears as a promising way to probe the elastic properties of matter at GHz to THz frequencies[1] or to perform local in-depth elastic nanoscopy[2-3]. To date, ultrafast spectroscopy of the acoustic eigenmodes of nanoparticles are usually performed with single point measurements. For a nanosphere, the acoustic spectrum is then dominated by the purely radial breathing mode. However, the detection of acoustic eigenmodes involving a shear component of the particle surface displacement is highly desired to investigate the elastic properties of liquids[4], biological media[5] or nano-contacts[6-8] in the GHz to THz range. We demonstrate here that ultrafast microscopy of the acoustic eigenmodes of a single nanoparticle allows us to unveil such eigenmodes.

A movie of the picosecond dynamics of a single gold nanoparticle dropped on a silica substrate is recorded over 20 ns with an ultrafast pump-probe experiment. We demonstrate that spectro-imaging, i.e. the investigation of the spatially resolved acoustic spectrum, is ideally suited to push further the analysis of the vibrational landscape of the nanoparticle. This spectral analysis reveals a more complex acoustic spectrum of the nanoparticle and high order acoustic eigenmodes undetectable in single point measurements are detected. The frequency of these modes is shown to be influenced by the shear contact stiffness[9].

References

[1] A. Crut, P. Maioli, N. Del Fatti and F. Vallée, Phys. Rep. **549**, 1 (2015).

[2] C. Jean, L. Belliard, T. W. Cornelius, O. Thomas, Y. Pennec, M. Cassinelli, M. E. Toimil-Molares and B. Perrin, Nano Lett. **16**, 6592 (2016).

[3] F. Xu, Y. Guillet, S. Ravaine and B. Audoin, Phys. Rev. B **97**, 165412 (2018).

[4] D. Chakraborty, G. V. Hartland, M. Pelton and J. E. Sader, J. Phys. Chem. C **122**, 13347 (2018).

[5] T. Dehoux, M. Abi Ghanem, O. F. Zouani, M. Ducousso, N. Chigarev, C. Rossignol, N. Tsapis, M.-C. Durrieu and B. Audoin, Ultrasonics **56**, 160 (2015).

[6] J. Léopoldès and X. Jia, Phys. Rev. Lett. **105**, 266101 (2010).

[7] Y. Guillet, B. Audoin, M. Ferrié and S. Ravaine, Phys. Rev. B **86**, 035456 (2012).

[8] A. Vega-Flick, R. Duncan, S. Wallen, N. Boechler, C. Stelling, M. Retsch, J. Alvarado-Gil, K. Nelson and A. Maznev, Wave Motion **76**, 122 (2018).

[9] Y. Guillet, A. Abbas, S. Ravaine and B. Audoin, Appl. Phys. Lett. **114**, 091904 (2019).

Optomechanics with hybrid carbon nanotube resonators

Alexandros Tavernarakis[1], Alexandros Stavrinadis[1], Alex Nowak[1], Ioannis Tsioutsios[1], Adrian Bachtold[1], and Pierre Verlot[1,2]

[1]ICFO-Institut de Ciencies Fotoniques, The Barcelona Institute of Science and Technology, 08860, Barcelona, Spain
[2]School of Physics and Astronomy, University of Nottingham, Nottingham, NG7 2RD, United Kingdom
*corresponding author, E-mail: pierre.verlot@nottingham.ac.uk

Abstract

Nanomechanical systems are raising increasing attention. This is prominently due to their very low mass, yielding to much reduced sensitivity towards thermally induced decoherence. Here we report what appears the most extreme kind of nanomechanical resonator, consisting of a single-clamped carbon nanotube at the tip of which an efficient nano-optical scatterer has been added. Our system is reported the most sensitive ever demonstrated at room temperature. We also analyze the noise dynamics of our devices and reveal fundamental limitations of nanomechanical sensing.

1. Introduction

In twenty years, cavity optomechanics has established as a rapidly advancing research field aiming at developing macroscopic systems operating in the quantum regime (1). Important progress has been achieved in this direction, such as laser cooling of a macroscopic mechanical resonator in its groundstate(2), the demonstration of the quantum backaction in an interferometric measurement(3) and more recently the first evidence of quantum optomechanical entanglement(4).
Further exploring the quantum regime and extending the application range of optomechanical systems requires drastic suppression of decoherence, which remains the main source of limitation. Several approaches are being developed, aiming at reducing the thermal noise, including electromagnetic trapping(5), tethered resonators(6), and dissipation dilution(7).
Here we present a novel approach based on hybrid carbon nanotube resonators, consisting of single-clamp suspended carbon nanotube at the tip of which a nano-optical scatterer is grown(8). Sensitive optomechanical detection is demonstrated and dynamical backaction analysed. The force sensitivity is calibrated at the sub-attonewton level at room temperature for the first time, representing a two orders of magnitude improvement compared to previous report(6). The frequency noise dynamics is also analyzed, showing the fundamental impact of nonlinearities on nanomechanical sensing. Our work opens the path towards implementing quantum optomechanical technology at room temperature.

2. Results

2.1. Hybrid carbon nanotube resonator

Our hybrid carbon nanotube resonators (CNT) consists of singly clamped suspended carbon nanotube resonators at the tip of which a nanoparticle is subsequently grown. Details on the fabrication of our devices can be found elsewhere(8).

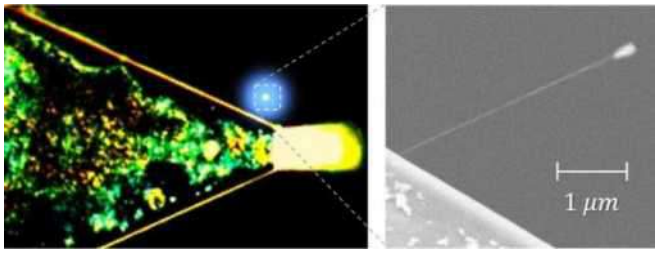


Figure 1 Hybrid Carbon Nanotube Resonator. Left: Optical micrograph showing the silicon microcantilever chip hosting a single-clamp hybrid carbon nanotube resonator (framed region). Right: Scanning Electron Micrograph showing the same device, featuring the platinum ball at the tip (bright region).

Our devices have typical masses, resonance frequencies and quality factors ranging from 10^{-21} kg to 10^{-18} kg, 10 kHz to 10 MHz and 10^2 to 10^4 range, respectively.

2.2. Optomechanical coupling

Our devices are mounted on a 3D nanopositioning stage placed in a vacuum chamber. A single-mode Helium-Neon laser is focused on the sample by means of an aspherical lens with numerical aperture NA=0.55. The light scattered by the tip of the device is collected in reflection by means of an optical circulator and further sent to a fast avalanche photodetector. When the device is off-centered from the laser beam waist, the backscattered becomes sensitive to its mechanical motion, therefore enabling nanomechanical detection (see Fig. 2(a)). Sweeping the frequency of a piezo-driven excitation around the mechanical resonance frequency of the device, one retrieves a harmonic behavior enabling to determine both mechanical resonance frequency and mechanical quality factor (upper curve, Fig. 2(b)). Turning the excitation off, a noise peak is revealed, driven by the ambient thermal fluctuations (lower curve on Fig. 2(b)).
Increasing the optical power up yields to the unexpected lowering of the nanomechanical fluctuations, as

demonstrated by the net decrease of the optomechanical spectrum area (see Fig. 2(c)). This is explained because of the presence of photothermal backaction, yielding to a cold damping force with negligible extra fluctuations being added. These results enable us to provide a direct calibration of the thermal force noise $S_{FF}=(0.7\ aN/Hz^{-1/2})^2$, that is the lowes ever reported thermal noise level for a solid state nanomechanical device operating at room temperature, 2 orders of magnitude lower compared to previous report(6)

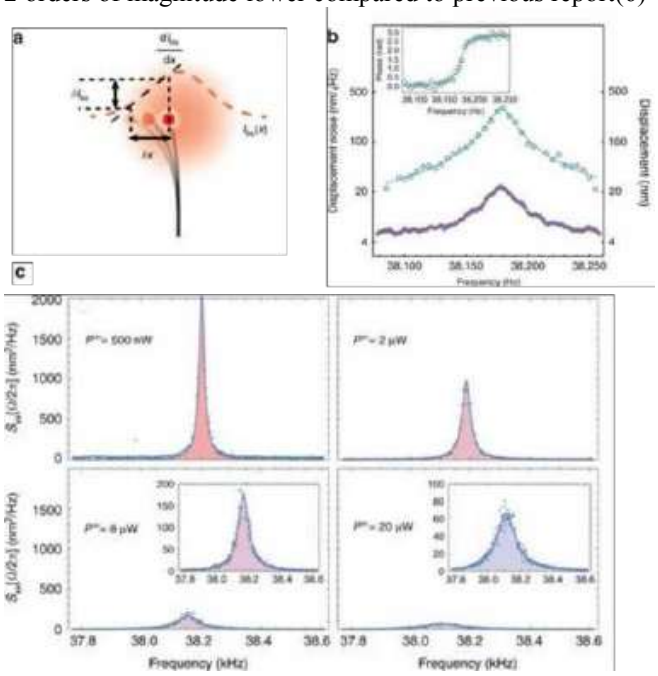


Figure 2 Optomechanical coupling with Hybrid CNT resonators. (a) Principle of the optomechanical detection. When being off-centered from the laser beam waist, the backscattered intensity fluctuations becomes sensitive to mechanical motion, enabling nanomechanical detection. (b) Piezo driven amplitude and phase response (upper curve and inset, respectively), and thermal noise (lower curve). (c) Photothermal backaction cooling for increasing incident optical powers.

2.3. Frequency noise dynamics

A regime of particular importance is that where the nanomechanical motion is coherently driven, which is at the basis of all phase-sensitive detection schemes (including e.g. scanning probe microscopy). The frequency noise of the nanomechanical device then becomes a prominent source of limitation, which has recently attracted intense attention. Here we report how the combined effect of intrinsically high thermally driven motion, nonlinear response and multimode nature of our devices generate frequency noise, acting as fundamental limits of nanomechanical sensing. We notably report the first demonstration of resonant squeezing, and the spectral broadening it induces on its paired, orthogonal vibration mode (see Fig. 3).

3. Conclusions

We have reported the first ultra-sensitive detection and control of a single-clamp carbon nanotube resonator. Our system is so far the most sensitive ever demonstrated at room temperature, opening novel perspective both in Science and Technology. We also demonstrat, intrinsic noise mechanisms, establishing fundamental limits of nanomechanical sensing.

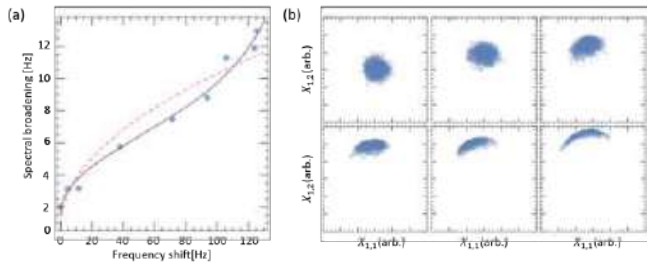


Figure 3 (a) Spectral broadening of the out-of-plane fundamental mode as a function of the frequency shift induced in presence of an increasing driving force applied to the in-plane mode. (b) Phase-space representation of the motion fluctuations of the in-plane mode in presence of an increasing piezo-drive, showing a strong squeezing of the noise distribution. The straight line on Fig. 3(a) corresponds to the full non-linear model, including squeezing of the in-plane fluctuations, whereas the dashed red line assumes unchanged fluctuations, to the lowest order.

Acknowledgements

The work at ICFO is supported by the ERC advanced grant 692876, the Foundation Cellex, the CERCA Programme, Severo Ochoa (SEV-2015-0522), the grant FIS2015-69831-P of MINECO, and the Fondo Europeo de Desarrollo Regional (FEDER). PV acknowledges support from the French National Research Agency (projects NOFX2015 ANR-15-CE09-0016 and QDOT ANR-16-CE09-0010) and from the ERC starting grant 758794 'Q-ROOT'.

References

1. Aspelmeyer M, Kippenberg TJ, Marquardt F. Cavity optomechanics. Reviews of Modern Physics. 2014;86(4):1391.
2. Chan J, Alegre TM, Safavi-Naeini AH, Hill JT, Krause A, Gröblacher S, et al. Laser cooling of a nanomechanical oscillator into its quantum ground state. Nature. 2011;478(7367):89–92.
3. Purdy TP, Peterson RW, Regal CA. Observation of radiation pressure shot noise on a macroscopic object. Science. 2013;339(6121):801–804.
4. Ockeloen-Korppi CF, Damskägg E, Pirkkalainen J-M, Asjad M, Clerk AA, Massel F, et al. Stabilized entanglement of massive mechanical oscillators. Nature. 2018;556(7702):478.
5. Gieseler J, Deutsch B, Quidant R, Novotny L. Subkelvin parametric feedback cooling of a laser-trapped nanoparticle. Physical review letters. 2012;109(10):103603.
6. Reinhardt C, Müller T, Bourassa A, Sankey JC. Ultralow-Noise SiN Trampoline Resonators for Sensing and Optomechanics. Physical Review X. 2016;6(2):021001.
7. Ghadimi AH, Fedorov SA, Engelsen NJ, Bereyhi MJ, Schilling R, Wilson DJ, et al. Elastic strain engineering for ultralow mechanical dissipation. Science. 2018;360(6390):764–768.
8. Tavernarakis A, Stavrinadis A, Nowak A, Tsioutsios I, Bachtold A, Verlot P. Optomechanics with a hybrid carbon nanotube resonator. Nature communications. 2018;9(1):662.

A self-assembled array of microspheres for radiative cooling

J. Jaramillo-Fernández[1,4], G. L. Whitworth [1] J. A. Pariente[2], P. D. García[1], C. López[2], and C. M. Sotomayor-Torres[1, 3]

[1]Catalan Institute of Nanoscience and Nanotechnology (ICN2),
CSIC and BIST, Campus UAB, Bellaterra, 08193 Barcelona, Spain
[2]Materials Science Factory, Instituto de Ciencia de Materiales de Madrid (ICMM),
c/Sor Juana Ins de la Cruz 3, 28049 Madrid, Spain
[3]ICREA - Institució Catalana de Recerca i Estudis Avancats, 08010 Barcelona, Spain
[4]Universitat Autonoma de Barcelona, 08193 Bellaterra, Spain.

*corresponding author, E-mail: Juliana.jaramillo@icn2.cat

Abstract

Implementing sustainable methods for cooling is urgent, due to global warming and the high energy consumption associated to modern cooling technologies. In this work, we propose self-assembled colloidal arrays as an energy-efficient solution for above-ambient radiative cooling. We show that the temperature of a crystalline silicon wafer is lower during daytime when the thermal emitter is placed on its surface. This structure can be used to remove heat passively from devices that currently undergo critical heating during operation.

1. Introduction

Today, temperature regulation at the macro and microscale is one of the major contributors to the energy demand of society [1]. Cooling is particularly energy-consuming, accounting for 15% of the global energy use and 10% of green-house gas emissions. Furthermore, a tenfold growth in the demand of cooling technologies is expected in the next 30 years, mainly due to global warming [2]. Here, we propose an array of SiO_2 microspheres on a Soda-lime slab as an above-ambient radiative cooler. This structure can improve the thermal performance of devices that undergo critical heating during operation without the need of additional energy or electricity for removing heat from a surface.

2. Methods and results

The working principle of the proposed cooling device is based on the interaction of the transverse optical phonons and equally polarized electromagnetic waves, which results in an intense evanescent field confined at the surface of a polar-dielectric interface. Such surface excitations, so called surface phonon polaritons (SPhP), have the ability to enhance thermal energy conduction [3], and, in the presence of a grating, they can be diffracted to the far-field as infrared thermal energy [4]. We also use the differential polar-dielectric boundaries from the spherical shape of the microspheres, that result in an effective impedance matching between the polar and the dielectric media (silica/air) over a large spectral range [5], for enhancing the emissivity of the material in the IR transparent window of the atmosphere. This passive thermodynamic mechanism evacuates heat from a hot surface and deposits it into outer space at 3K, which acts as a heat sink.

In this work, we will present a theoretical study using an in-house developed rigorous-coupled-wave analysis (RCWA) code was performed to predict the optimal colloidal structure which maximizes the emissivity in the atmospheric infrared transparency window for the greatest range of emission angles. Based on the theoretical results, we will show how an optimal thermal emitter can be used to passively radiate heat from a surface into the out space, cooling it down passibly, i.e. without external energy or electricity input.

3. Conclusions

In summary, we will present here a novel thermo-functional material for above-ambient passive radiative cooling. It consists of an array of SiO2. Our structure behaves as a nearly perfect thermal blackbody. We analyze its radiative cooling performance by measuring the temperature cycle of the proposed structure and we prove its performance as an above-ambient daytime cooler. So far a temperature difference of 12 K has been achieved for a thermal emitter on a bare silicon substrate using the proposed radiative cooler, which compares well with the 8 K temperature difference of a water tank reported for an 80 μm thick film of randomized glass-polymer hybrid metamaterial [6]..

‘Acknowledgements

The European Union’s Horizon 2020 research and innovation programme under the Marie Sklodoswa-Curie grant agreement Nº 665919 supported JJF and funded this project. Moreover, the research received funds from the

Spanish Minister of Science, Innovation and Universities via the Severo Ochoa Program (Grant No. SEV-2017-0706) as well as by the CERCA Programme / Generalitat de Catalunya. PDG is supported by a Ramon y Cajal fellowship nr. RyC-2015-18124.

References

[1] Y. Joshi and P. Kumar, Energy efficient thermal management of data centers, New York: *Springer Science & Business Media*, 2012.

[2] E. A. Goldstein, A. P. Raman, and S. Fan, Sub-ambient non-evaporative fluid cooling with the sky, *Nat. Energy*, **2,** 17143, 2017.

[3] Tervo, E. J., Adewuyi, O. S., Hammonds, J. S. & Cola, B. A. High thermal conductivity in polaritonic SiO 2 nanoparticle beds. *Mater. Horiz.* **3,** 434–441 ,2016.

[4] Joulain, K., Mulet, J.-P., Marquier, F., Carminati, R. and Greffet, J.-J. Surface electromagnetic waves thermally excited: Radiative heat transfer, coherence properties and Casimir forces revisited in the near field. *Surf. Sci. Rep.* 57, 59112 ,2005

[5] Zhu, L., Raman, A., Wang, K. X., Anoma, M. A. and Fan, S. Radiative cooling of solar cells. *Optica* 1, 3238, 2014.

[6] Y. Zhai et al., Scalable-manufactured randomized glass-polymer hybrid metamaterial for daytime radiative cooling, *Science*, 2017.

Topological states of acoustic phonons in semiconductor nanocavities

Martin Esmann[1*], F.R. Lamberti[1], G. Arregui[2], O. Ortíz[1], C. M. Sotomayor-Torres[2], I. Favero[3], O. Mauguin[1], B. Perrin[4], O. Krebs[1], L. Lanco[1], P. Senellart[1], C. Gomez-Carbonell[1], P. D. García[2], A. Lemaître[1],N. D. Lanzillotti-Kimura[1]

[1]Centre de Nanosciences et de Nanotechnologies (C2N), CNRS, Univ. Paris-Sud, Univ. Paris-Saclay, 91120 Palaiseau, France
[2]Catalan Institute of Nanoscience and Nanotechnology (ICN2),CSIC and BIST, Campus UAB, Bellaterra, 08193 Barcelona, Spain
[3]Matériaux et Phénomènes Quantiques, Université Paris-Diderot, CNRS UMR 7162,Sorbonne Paris Cité, 10 Rue Alice Domon et Léonie Duquet, 75013 Paris, France
[4] Institut de Nanosciences de Paris, Sorbonne Univ., CNRS UMR 7588, 75005 Paris, France
*corresponding author, E-mail: martin.esmann@c2n.upsaclay.fr

Abstract

We introduce the concept of topological invariants to nanophononics and implement a nanophononic semiconductor system supporting a robust topological interface state at 300GHz. We optically probe this mode through Brillouin spectroscopy and coherent phonon generation experiments. This type of topological interface states could become part of novel devices requiring resonant nanoacoustic structures such as compact integrated Brillouin light sources operating at ultrahigh frequencies.

Acoustic phonons constitute a versatile platform for the study of fundamental wave dynamics, including Bloch oscillations and other localization phenomena. Many of these studies were inspired by their counterparts in optics and electronics. In these fields, the consideration of topological invariants to control wave dynamics has already had a great impact for the generation of robust confined states. Interestingly, the use of topological phases to engineer nanophononic devices remains an unexplored and promising field.

Here, we introduce the concept of topological invariants to nanophononics and experimentally implement a nanophononic system supporting a robust topological interface state at 300 GHz [1]. The state is constructed through band inversion, i.e., by concatenating two semiconductor superlattices with inverted spatial mode symmetries [2]. The existence of this state is purely determined by the Zak phases of the constituent superlattices, i.e., the one-dimensional Berry phase.

We experimentally evidence these novel modes through Brillouin spectroscopy [1] and coherent phonon generation and detection using pulsed laser schemes [3]. The reported topological interface states could become part of novel devices requiring resonant nanoacoustic structures such as compact integrated Brillouin light sources operating at ultrahigh frequencies [4].

References

[1] M. Esmann, F. R. Lamberti, P. Senellart, I. Favero, O. Krebs, L. Lanco, C. Gomez Carbonell, A. Lemaître, N. D. Lanzillotti-Kimura, "Topological nanophononic states by band inversion," *Phys. Rev. B* **97,** 155422 (2018).

[2] M. Xiao, G. Ma, Z. Yang, P. Sheng, Z. Q. Zhang, C. T. Chan, "Geometric phase and band inversion in periodic acoustic systems," *Nat. Phys.* **11,** 240–244 (2015).

[3] G. Arregui, O. Ortíz, M. Esmann, C. M. Sotomayor-Torres, C. Gomez-Carbonell, O. Mauguin, B. Perrin, A. Lemaître, P. D. García, N. D. Lanzillotti-Kimura, "Coherent generation and detection of acoustic phonons in topological nanocavities," ***ArXiv181109781*** (2018). (APL Photonics accepted 2019)

[4] M. Esmann, F. R. Lamberti, A. Harouri, L. Lanco, I. Sagnes, I. Favero, G. Aubin, C. Gomez-Carbonell, A. Lemaitre, O. Krebs, *et al.*, "Brillouin Scattering in Hybrid Optophononic Bragg Micropillar Resonators at 300 GHz," ***ArXiv181205190*** (2018).

Ultrafast THz coherent excitation of optical and acoustic phonon modes in topological insulators

Vincent Juvé[1,*], Artem Levchuk[1], Matteusz Weis[1,2], Brice Arnaud[1], Gwenaelle Vaudel[1], Bartosz Wilk[2], Jacek Szade[2] and Pascal Ruello[1]

[1] Institut des Molécules et Matériaux du Mans, UMR CNRS 6283, Le Mans Université, 72085 Le Mans, France
[2] A. Chelkowski Institute of Physics, University of Silesia, Chorzów, Poland
*corresponding author, E-mail: vincent.juve@univ-lemans.fr

Abstract

Intense picosecond TeraHertz pulses are used to drive coherent phonons dynamics in nanometric films of topological insulators Bi_2Te_3 measured in time-resolved experiments. The possible coherent phonons excitation mechanisms are discussed.

1. Introduction

Over the last decade, the development of high-power ultrafast laser systems led to the emergence of ultrafast picoseconds Terahertz pulses, which provide a new tool for studying fundamental aspects of light-matter interactions [1]. For instance, THz-driven ballistic charge currents in semiconductors [2, 3], THz-induced dynamics in metallic ferromagnets [4] or High Harmonic Generation in solids [3] have been investigated. Topological insulators exhibit peculiar physical properties and are stated to be the next generation of electronics and spintronics devices [5]. Using low photon energy excitation with THz pulse opens new possibilities to study their electronic and lattice properties. Here, we demonstrate the possibility to generate both coherent optical and acoustic phonon modes with a picosecond THz pulse in the topological insulator Bi_2Te_3 with a photon energy ($\sim$2 meV) way below the material band gap ($\sim$200 meV). The latter was never observed in the literature at our knowledge.

2. Discussion

In our experiments, we study prototypical topological insulators Bi_2Te_3 in a THz pump/visible probe setup by measuring $\Delta T/T(\tau)$, the relative change of transmission of the visible probe as a function of the pump/probe delay τ. Both pump and probe pulses are generated by an amplified Ti:sapphire laser system (pulse energy 3 mJ and duration 120 fs, central wavelength 805 nm, repetition rate 1 kHz). The main fraction of the laser is used to induce optical rectification in a stoichiometric MgO-doped $LiNbO_3$ crystal by the tilted pulse front method [6, 7], which generates ultrashort single cycle THz pulses with a duration of around 1.6 ps (full width half maximum), a pulse energy of roughly 1μJ and a spectrum centered at 0.5 THz (photon energy of $\sim$2 meV) spanning frequencies from 0.2 to more than 1 THz. The remaining fraction is used as probe pulses at 402 nm wavelength obtained by frequency doubling in a BBO-crystal. The THz pulse impinges the sample at normal incidence while the probe's incident angle is roughly equal to 20°. The experiments were performed in air at room temperature. The growth of ultrathin Bi_2Te_3 nanofilms was performed by the Molecular Beam Epitaxy technique in the co-deposition mode on a freshly cleaved Mica subtract [8].

Typical transient is shown in the Fig. 1a) for a nanofilm of thickness 6 nm. The measured $\Delta T/T(\tau)$ exhibits a fast rise and a slower decay, reflecting the excitation and then the relaxation of hot carriers generated by the THz pulse. The initial electronic excitation process is not in the scope of the paper, but due to the sample growth method we expect to have carriers in the conduction band (n-doped), which can lead to electronic response in the transients due to THz excitation. We will focus here on the oscillating part of the signal exhibiting two different periods, which can be easily identified in the probe transmission change $\Delta T/T(\tau)$ and is related to coherent excitation of an optical phonon mode and of an acoustic phonon mode. Fig. 1b) displays the oscillatory signal and allows to extract the two different frequencies of 1.85 THz, which corresponds to the optical A1g phonon mode, and 0.18 THz, which corresponds to the fundamental breathing mode of the thin film. The latter reflects the elastic properties of the sample at the nanoscale. Similar measurements were performed in nanofilms with different thicknesses. The observed acoustic oscillation period increases with the film thickness as shown by Fig. 1c). In contrary, we did not measure any change in the optical phonon frequency.

The generation mechanisms of the optical and acoustic phonons modes are different. Concerning the optical raman-active A1g phonon mode, it has been recently shown that terahertz sum-frequency excitation can be an efficient way to excite raman-active mode with a terahertz pulse [10]. Concerning the fundamental breathing mode generation, it has been shown that thermoelasticity effect is negligible compare to electron-phonon deformation potential in a recent all optical pump/probe experiment [9]. However, the excitation process by a THz pulse is not established yet. In this communication, we will discuss the

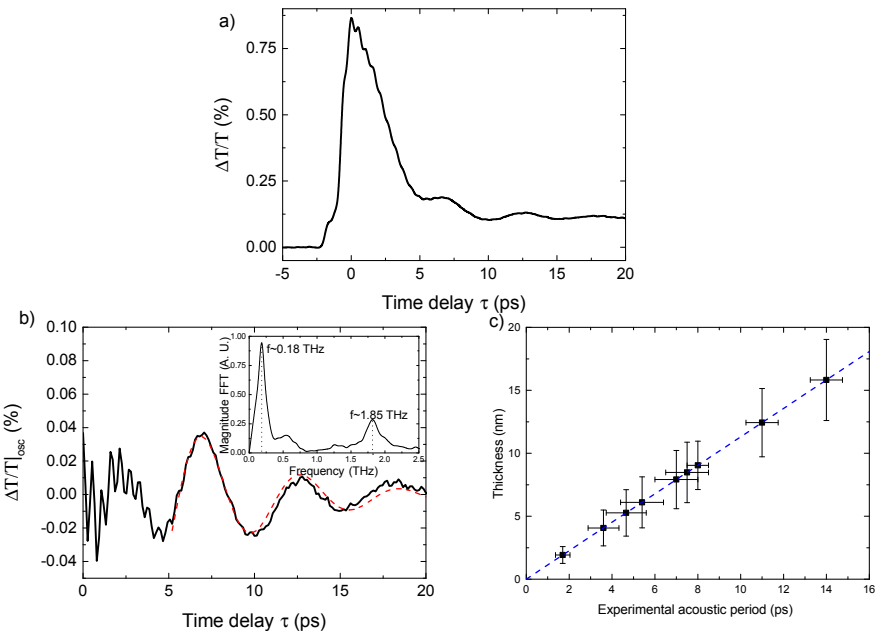


Figure 1: a) Typical experimental transient obtained for a nanometric Bi_2Te_3 film showing electronic and phonons ultrafast dynamics. b) Extracted oscillatory signal $\Delta T/T|_{osc}(\tau)$, which is composed of an optical phonon mode at a period of roughly 0.6 ps and an acoustic phonon mode at a period of 5.6 ps. The Red dashed line corresponds to a fit using a damped sine function. Inset: Fast Fourier Transform of $\Delta T/T|_{osc}(\tau)$ showing the frequencies of the optical (1.85 THz) and acoustic (0.18 THz) phonons modes. c) Periods of the acoustic vibrations measured in Bi_2Te_3 films as a function of their thicknesses. The thicknesses were deduced by using a sound velocity of 2260 m/s [9], which is depicted by the blue dashed line.

different possible excitation mechanisms for the coherent acoustic phonons generation.

Acknowledgement

Région Pays de la Loire and project NanoPlasMag.

References

[1] T. Kampfrath, K. Tanaka and K.A. Nelson, "Resonant and nonresonant control over matter and light by intense terahertz transients", Nature Photonics **7**, 680 (2013).

[2] W. Kuehn, P. Gaal, K. Reimann, M. Woerner, T. Elsaesser, and R. Hey, "Coherent Ballistic Motion of Electrons in a Periodic Potential", Phys. Rev. Lett. **104** 146602 (2010).

[3] O. Schubert, M. Hohenleutnee, F. Langer, B. Urbanek, C. Lange, U. Huttner, D. Golde, T. Meier, M. Kira, S.W. Koch and R. Huber, "Sub-cycle control of terahertz high-harmonic generation by dynamical Bloch oscillations", Nature Photonics **8**, 119 (2014).

[4] C. Vicario, C. Ruchert, F. Ardana-Lamas, P. M. Derlet, B. Tudu, J. Luning, and C. P. Hauri, "Off-resonant magnetization dynamics phase-locked to an intense phase-stable terahertz transient", Nature Photonics **7**, 720 (2013).

[5] J.E. Moore, "The birth of topological insulators", Nature, **464**, 194-198, (2010).

[6] H. Hirori, A. Doi, F. Blanchard, and K. Tanaka, "Single-cycle terahertz pulses with amplitudes exceeding 1 MV/cm generated by optical rectification in $LiNbO_3$", Applied Physics Letters **98**, 091106 (2011).

[7] J. Hebling, A. Stepanov, G. Almási, B. Bartal, and J. Kuhl, "Generation of 10μJ ultrashort terahertz pulses by optical rectification", Applied Physics B **78**, 593 (2004).

[8] M. Weis, K. Balin, J. Szade and P. Ruello, "Ultrafast light-induced Coherent Optical and Acoustic Phonons in few Quintuple Layers of Topological Insulators Bi_2Te_3", Physical Review B, **92**, 014301 (2015).

[9] M. Weis, B. Wilk, G. Vaudel, K. Balin, R. Rapacz, A. Bulou, B. Arnaud, J. Szade and P. Ruello, "Quantum size effect on charges and phonons ultrafast dynamics in atomically controlled nanolayers of topological insulators Bi_2Te_3", Scientific Reports **7**, 13782 (2017).

[10] S. Maehrlein, A. Paarmann, M. Wolf, T. Kampfrath, "Terahertz sum-frequency excitation of a Raman-active phonon". Physical review letters, **119**, 127402 (2017).

Pulsed Two-Dimensional Atomic Crystal Cavity Optomechanics

Yuhao Xu[1], Wen Chen[1], Shunping Zhang*[1], Hongxing Xu*[1,2]

[1]School of Physics and Technology, Center for Nanoscience and Nanotechnology, and Key Laboratory of Artificial Micro- and Nano-structures of Ministry of Education, Wuhan University, Wuhan 430072, China
[2]The Institute for Advanced Studies, Wuhan University, Wuhan 430072, China
*corresponding author, E-mail: spzhang@whu.edu.cn
*corresponding author, E-mail: hxxu@whu.edu.cn

Abstract

Molecular cavity optomechanics is a new description of surface enhanced Raman scattering, and in return, surface enhanced Raman spectroscopy provides a new method for constructing and studying high coupling strength cavity optomechanics system. Moreover, pulsed excitation with duration time shorter than the phonon decay time, along with two-dimensional atomic crystals with well-defined arrangement and lattice orientation, facilitates the quantitation and simultaneously resolution of the time scale and the space scale. Here we show some results based on such a platform.

1. Introduction

The vibrational properties of molecules can be used as feature for analysis detection. Owing to 'hot spot' effect, surface enhanced Raman spectroscopy (SERS) enable a sensitive way to realize single molecular detection [1,2]. The vibrational pumping regime in surface enhanced Raman scattering [3,4] links Raman active nanomaterials to cavity optomechanics [5]. In this paradigm, plasmonic nanocavities with blue (or red) detuned light excitation with respect to the cavity resonance wavelength would lead to the amplification (or cooling) of the vibration of molecules, showing as the nonlinear emission of the Stokes and Anti-Stokes Raman scattering. Raman process induced by such dynamic back action can be distinguished from normal Raman scattering by power- and wavelength- excitation dependence of anti-Stokes/Stokes intensity and its anomalous ratios. Nonlinear power dependence of SERS intensity based on a pulsed molecular optomechanics configuration has been demonstrated [6]. However, for the quantity and the orientation of molecules are hard to be manipulated, it is not precise enough to get the quantitative feature of such a molecules cavity optomechanics. In our previous work [7], we show the advantage of two-dimensional atomic crystals probe where the orientation of molecules is well defined naturally and the quantity of molecules can be estimated with smaller deviation.

2. Experiment and Result

Here, we adopt a molybdenum disulfide (MoS_2) spaced nanoparticle-on-mirror (MoS_2-NPOM) system with wavelength- and power-dependent SERS measurements (Fig. 1). In this configuration, two-dimensional monolayer MoS_2 is placed between an ultrasmooth gold film and a nanoparticle with an additional Al_2O_3 fabricated within the gap using atomic layer deposition. Atoms or molecules filled in the gap have a well-defined lattice orientation such that the lattice vibrations are precisely aligned with the plasmonic field components (Fig. 1). By means of grating and tunable filter sets, 50-fs pulses with full width at half maximum about 40 nm (80 MHz repetition rate) are spectrally filtered as pulses with full width at half maximum about 1.5 nm (Fig. 2b). By rotating the grating and tunable filter sets, we can get wavelength spanning the spectra of the pulses. In this way, we can achieve wavelength tunable excitation in narrow band. Furthermore, we can manipulate the resonance of cavity by changing the thickness of Al_2O_3 in surface coating and in gap. Finally, we get excitation of wide-range detuning condition. Our result show that the dark-field scattering spectrum remains nearly unmodified after the whole experiment. The Stokes/anti-Stokes (not simultaneously) spectra and the power dependence excited by wavelength of 800 nm (slightly blue detuned) are shown in Fig. 2.

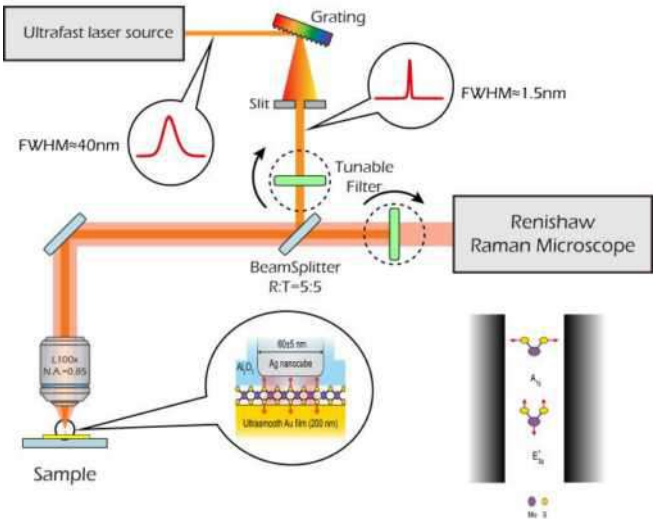


Figure 1: Schematic of surface-enhanced Raman excitation spectroscopy system as well as monolayer molybdenum disulfide (MoS_2) spaced nanoparticle-on-mirror.

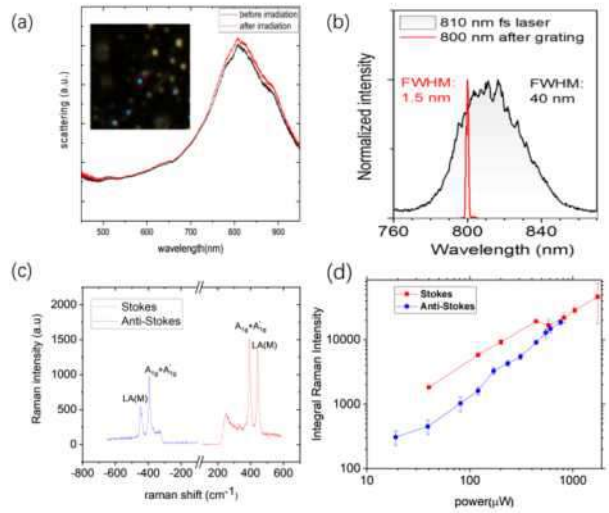


Figure 2: (a) Dark-field scattering from MoS_2 spaced single silver NPoM before (black) and after (red) pulse irradiation. The inset in shows the dark-field optical image. (b) Spectra of excitation source before (black) and after (red) filtered. (c) Stokes (red) anti-Stokes (blue) spectra. (d) Power dependence of Stokes/anti-Stokes.

3. Discussion

From present results, nonlinear anti-Stokes and linear Stokes emission are observed. Because anti-Stokes emission is likely disturbed by environment and nonlinear Stokes emission has its power threshold, here needs for deeper study before coming to a demonstrably conclusion. It is possible that the power we use now is not strong enough for MoS_2 crystal or the coupling of different atoms interfere and cancel. As expected, all the results have good repeatability. In summary, this two-dimensional atomic crystal spaced NPOM system combined with tunable pulsed excitation is a robust platform for quantitative instead of a qualitative research on molecular cavity optomechanics.

References

[1] Xu H, et al. Spectroscopy of Single Hemoglobin Molecules by Surface Enhanced Raman Scattering. Phys Rev Lett 83, 4357-4360 (1999).

[2] Xu H, et al. Electromagnetic contributions to single-molecule sensitivity in surface-enhanced Raman scattering. Phys Rev E 62, 4318-4324 (2000).

[3] K. Kneipp, Y. Wang, H. Kneipp, I. Itzkan, R. R. Dasari and M. S.Feld, Phys. Rev. Lett., 1996, 76, 2444–2447

[4] Maher R C, Galloway C M, Le Ru E C, et al. Vibrational pumping in surface enhanced Raman scattering (SERS) [J]. Chemical Society Reviews, 2008, 37(5): 965-979.

[5] Roelli P, Galland C, Piro N, et al. Molecular cavity optomechanics as a theory of plasmon-enhanced Raman scattering[J]. Nature nanotechnology, 2016, 11(2): 164.

[6] Lombardi A, Schmidt M K, Weller L, et al. Pulsed molecular optomechanics in plasmonic nanocavities: from nonlinear vibrational instabilities to bond-breaking[J]. Physical Review X, 2018, 8(1): 011016.

[7] Chen W, Zhang S, Kang M, et al. Probing the limits of plasmonic enhancement using a two-dimensional atomic crystal probe[J]. Light: Science & Applications, 2018, 7(1): 56.

Brillouin scattering in nanofibers

Jean-Charles Beugnot

Université Bourgogne Franche-Comté, Institut FEMTO-ST, CNRS UMR 6174, 25030 Besançon, France
*corresponding author, E-mail: jc.beugnot@femto-st.fr

Abstract

Brillouin light scattering is a fundamental interaction between light waves and small acoustic vibrations which gives rise to inelastic light diffusion with a frequency shift by an amount that corresponds to the acoustic phonon frequency [1]. Due to their strong light confinement capabilities, optical fibers have been early recognized as an ideal medium to exploit the Brillouin scattering for applications in e.g., lasers, telecommunications, microwave photonics and optical sensing [2,3].

Introduction

The rich and complex dynamics of light and sound interactions in tiny optical waveguides has recently gained much interest because of their experimental realization in emerging key areas of photonics.

For instance, we demonstrate recently for the first time the generation of a new class of surface acoustic waves in a subwavelength-diameter silica nanofibers and term this new effect as surface acoustic wave Brillouin scattering (SAWBS) [4]. In such thin silica wires, boundary conditions induce a strong coupling of shear and longitudinal displacements, resulting in a much richer dynamics of light interaction with hybrid acoustic phonons.

Using numerical simulations based on electrostriction and experimental results, we show that SAWBS results from the stimulated optical excitation of Rayleigh-type surface-ripple waves propagating at a velocity of 3400 m/s along the optical nanofibers surface and giving rise to new useful RF sidebands around 6 GHz in the scattering spectrum. As these new acoustic resonances are strongly sensitive to microwire surface, SAWBS opens new interesting opportunities for various sensor applications.

We proposed an original technique based on Brillouin backscattering that allows for the accurate diameter measurement of nanofibers [7].

Acknowledgements

This work was supported by the French “Investissements d’Avenir” program, project ISITE-BFC (contractANR-15-IDEX-0003) and Agence Nationale de la Recherche (FUNFILM-ANR-16-CE240010-03.

References

[1] R. W. Boyd, Nonlinear Optics, (Academic Press, Boston, 4th ed, 2009).

[2] G. Agrawal, Nonlinear fiber Optics (Academic Press, Boston, 5th ed., 2012).

[3] A. H. Hartog, An Introduction to Distributed Optical Fibre Sensors (CRC, 2018).

[4] J-C. Beugnot, S. Lebrun, G. Pauliat, H. Maillotte, V. Laude, T. Sylvestre “Brillouin light scattering from surface acoustic waves in a subwavelength-diameter optical fibre,” Nature communications, 5, (2014).

[5] A. Godet, A. Ndao, T. Sylvestre, V. Pecheur, S. Lebrun, G. Pauliat, J-C. Beugnot, and K. Phan Huy, "Brillouin spectroscopy of optical microfibers and nanofibers," Optica 4, 1232-1238 (2017).

Engineering and measuring thermal transport in nanowires

Marta De Luca[1], Milo Y. Swinkels[1], Claudia Fasolato [1], Daniel Vakulov[2], Erik P. A. M. Bakkers[2], Xavier Cartoixà[3], Riccardo Rurali[4], and Ilaria Zardo[1]

[1] Department of Physics, University of Basel, Klingelbergstrasse 82 CH-4056 Basel, Switzerland
[2] Department of Applied Physics, Eindhoven University of Technology, 5600 MB Eindhoven, The Netherlands
[3] Departament d'Enginyeria Electrònica, Universitat Autònoma de Barcelona, 08193 Bellaterra, Barcelona, Spain
[4] Institut de Ciència de Materials de Barcelona (ICMAB–CSIC), Campus de Bellaterra, 08193 Bellaterra, Barcelona, Spain
*corresponding author, E-mail: ilaria.zardo@unibas.ch

Abstract

The recently growing research field called "Nanophononics" deals with the investigation and control of vibrations in solids at the nanoscale. Phonon engineering leads to a controlled modification of phonon dispersion, phonon interactions, and transport [1]. Nonetheless, it requires new theoretical and experimental methods, especially when combined with low dimensional physics, which is one of the most promising routes for thermal management.

Nanowires (NWs) form an ideal template to study thermal transport behavior at the nanoscale thanks to the intrinsic 1D nature of transport in these materials, as well as the possibility to obtain different types of heterostructures, under different geometries, combining different materials and/or crystal structures that would not be possible in bulk materials [2]. However, measuring the thermal conductivity of single NWs is a non-trivial problem, for which a wide range of measurement schemes are currently being used, all with their respective advantages and disadvantages [2].
In this talk, we discuss how phononic properties can be engineered in nanowires and the challenges and progresses in the measurement of the thermal conductivity of nanostrcutures.
The concept of phonon engineering in NWs is exploited in superlattice (SL) NWs. We experimentally show that a controlled design of the NW phononic properties can be decided à la carte by tuning the SL period.
Furthermore, Raman thermometry is used to probe the temperature profile along the NWs upon application of a thermal grandient, enabling the differentiation between ballistic and diffusive flow regimes (Figure 1).

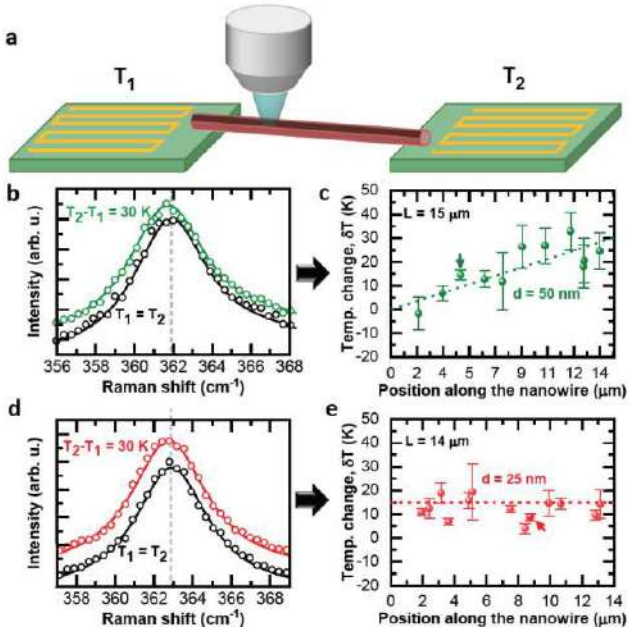


Figure 1: a) Illustration of the microdevice with NW used for the measurements of the thermal profile. A laser spot is moved along the wire and Raman spectra are acquired for T_1=T_2=300 K and T_1= 300 K, T_2= 300 K +ΔT . b) Spectra measured at the position indicated by the arrow in c for a NW with d = 50 nm and L = 15 μm. Solid lines are Lorentzian fits to the spectra. c) Resulting temperature profile along the NW while applying ΔT = 30 K using the Pt meander heaters. The dashed line is the expected profile for purely diffusive heat flow. d) and e) The same as b) and c) but for a NW with d = 25 nm and L = 14 μm. The dashed line in e is the expected profile for purely ballistic transport.

Acknowledgements

This project has received funding from the European Research Council (ERC) under the European Union's Horizon 2020 research and innovation programme (grant agreement No 756365) and from the Swiss National Science Foundation research grant (Project Grant No. 200021_165784)

References

[1] S. Voltz et al. Nanophononics: state of the art and perspectives, *Eur. Phys. J. B* 89: 15, 2016.

[2] M.Y. Swinkels and I. Zardo, Nanowires for heat conversion, *J. Phys. D: Appl. Phys.* 51: 353001, 2018.

Magnon-Phonon Coupling in Lateral Ferromagnetic Nanogratings

Alexey V. Scherbakov[1,2*], Felix Godejohann[1], Serhii M. Kukhtaruk[1,3], Dmytro D. Yaremkevych[1], Achim Nadzeyka[4], Andrew W. Rushforth[5], Dmitri R. Yakovlev[1,2], Andrey V. Akimov[5], and Manfred Bayer[1,2]

[1] Experimentelle Physik 2, Technische Universität Dortmund, 44227 Germany
[2] Ioffe Institute, Russian Academy of Sciences, 194021 St. Petersburg, Russia
[3] Department of Theoretical Physics, V.E. Lashkaryov Institute, 03028 Kyiv, Ukraine
[4] Raith GmbH, 44263 Dortmund, Germany
[5] School of Physics and Astronomy, University of Nottingham, NG7 2RD Nottingham UK
*corresponding author E-mail: Alexey.shcherbakov@tu-dortmund.de

Abstract

The talk gives an overview of the recent experiments with metallic ferromagnetic films, in which a nanoscale periodic pattern results in formation of the localized phonon modes of sub-THz frequencies. In the time-domain experiments, we investigate the effects related to the resonant interaction of the phonon and magnon modes excited by femtosecond laser pulses. A variety of experimental observations includes the phonon driving of the magnetization precession, the magnon driving of coherent phonons and the magnon-phonon strong coupling.

1. Introduction

Active search of the effective methods to manipulate spin and elastic excitations at the nanoscale has gained the interest to the magnon-phonon interaction in magnetically ordered materials. The most interesting phenomena are observed at conditions of the magnon-phonon resonance, when magnons and phonons with, both the same frequencies and wave vectors can form a hybridized state. Various effects related to the magnon-phonon interaction [1-4] have been recently observed in ferromagnetic dielectrics, which possess extremely weak damping for both phonons and magnons. In contrast, in ferromagnetic metals, where the damping is much stronger, the magnon-phonon interaction remains almost unexplored. In the present research, we overcome this limitation and show that a ferromagnetic metal can be a perfect platform for manipulating of magnons and phonons at the nanoscale. We use periodic nanoscale patterning of thin (Fe,Ga) layers to form the desirable phonon spectrum. The resonant interaction between the localized phonon modes and the modes of the discreet magnon spectrum yields bright experimental manifestations, which are observed directly in the time-resolved magneto-optical experiments.

2. Studied structures and experimental technique

The studied structures are based on an alloy of Iron and Gallium, i.e. Galfenol. The combination of the high Curie temperature (>900 K), the large saturation magnetization and the enhanced magnetostriction in this metallic ferromagnet allows studying the magnon-phonon interaction and related effects at ambient conditions [5-8]. The main studied structures are one-dimensional nanogratings formed by parallel grooves milled by focused ion beam (Raith Velion FIB-SEM) in $Fe_{0.81}Ga_{0.19}$ films of 60 and 120 nm thicknesses. The nanogratings have lateral size of 10×10 μm^2 and the following structural parameters: groove width a=100 nm, groove depth h=5÷25 nm, lateral period d=200 nm. The lateral pattern results in formation of the localized surface phonon modes in 10-20 GHz frequency range and adds the spatial harmonics with the in-plane wave vector $k=2\pi/d$ to the discreet magnon spectrum of a plain film.

In the experiment, the studied structures are excited by the 150-fs pump laser pulses (1050 nm, 80 MHz) focused to the spot of 10 μm diameter at the front side of a nanograting, or at its back side (through the GaAs substrate, which is transparent at this wavelength). The used excitation density is of ~1 mJ/cm^2. The response of a nanograting is measured by means of the probe laser pulses (780 nm, 150 fs, 80 MHz) focused at the nanograting front side to the spot of 1 μm diameter. The probe and pump lasers are synchronized with controlled detuning of their repetition rates (800 Hz in the performed experiments). This allows detecting the transient signals in the scheme of asynchronous optical sampling (ASOPS) [10] in the time window of 12.5 ns with the resolution limited by the probe pulse duration. We measure the transient reflectivity, $\Delta R(t)$, to monitor the coherent lattice vibrations and the transient polar Kerr rotation, $\Delta\Psi(t)$, which reflects the time evolution of the magnetization. By applying external magnetic field, **B**, we tune the magnon spectrum (its spectral content and position)

to achieve the resonant conditions for certain magnon and phonon modes.

3. Experimental results

As an example, Figure 1 shows the fast Fourier transforms (main panels) of the Kerr rotation signals $\Delta\Psi(t)$ (insets) measured in the plain film of 120-nm thickness [panel(a)] and in the nanograting with h=20 nm and d=200 nm milled in this film [panel (b)]. The transient signals reflect the precessional response of the magnetization on the femtosecond optical excitation. The signals and their FFTs are significantly different in the plain film and in the nanograting. The rapid (within ~100 ps) decay of $\Delta\Psi(t)$ in the plain film is determined by fast dephasing due to the contribution of the exchange magnon modes, which are clearly visible in the FFT spectrum (indicated by the arrows). In contrast to this, in the nanogratingthe magnetic response is determined by the localized phonon modes, which drive the magnetization precession within their lifetimes. In the presented experimental conditions, the phonon modes with frequencies f_{ph1} and f_{ph2} are in resonance with the two lowest magnon modes, which dominate in the precessional signal, while the other magnon modes are suppressed. The localized phonon modes have alternative (quasi-longitudinal and quasi-transverse) polarizations and significantly different spatial distributions. This allows controlling the phonon driving efficiency by spatial overlap of certain phonon and magnon modes at resonance. We show that at certain magnetic fields, only one of two phonon mode gives dominating contribution to the magnetization precession.

4. Conclusions

The experimental result presented above demonstrates the simplest effect, i.e. the resonant phonon driving of the magnetization precession, among other bright manifestations of the magnon-phonon interaction observed in our experiments. In the shallow nanograting we demonstrate the strong magnon-phonon coupling, which is manifested by anti-crossing of the magnon and phonon modes at the resonant conditions. We have also detected the 10-times amplification of the localized phonon mode driven by magnons at the magnon-phonon resonance. We demonstrate the interplay of these effects, which are controlled by the grating parameters and by direction and strength of the external magnetic field. We are convinced that our observations pave the way to effective manipulation of coherent spin and lattice excitations at the nanoscale.

Acknowledgements

The work was supported by the Bundesministerium für Bildung und Forschung through the project VIP+ ”Nanomagnetron” and in the frame of the International Collaborative Research Center TRR160 by the Russian Foundation for Basic Research (project 19-52-12065) and the Deutsche Forschungsgemeinschaft.

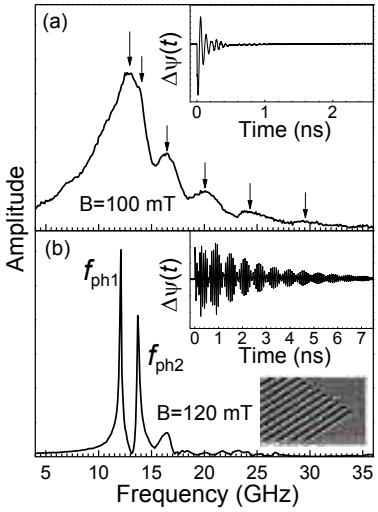


Figure 1: FFTs (main panels) of the transient Kerr rotation signals $\Delta\psi(t)$ (insets) measured in the plain $Fe_{0.81}Ga_{0.19}$ film of 120-nm thickness (a) and the nanograting with h=20 nm (b). The lower inset in (b) shows a scanning electron microscope image in the lower inset in (b).

References

[1] X. Zhang, C.-L. Zou, L. Jiang, and H. X. Tang, Cavity magnomechanics, *Sci. Advances* 2: e1501286, 2016.

[2] D. A. Bozhko et al., Bottleneck accumulation of hybrid magnetoelastic bosons, *Phys. Rev. Lett*. 118: 237201, 2017.

[3] J. Holanda, D. S. Maior, A. Azevedo, and S. M. Rezende, Detecting the phonon spin in magnon–phonon conversion experiments, *Nat. Phys.* 14: 500-506, 2018.

[4] H. Hayashi and K. Ando, Spin Pumping Driven by Magnon Polarons, *Phys. Rev. Lett.* 121: 237202, 2018.

[5] J. V. Jäger et al., Picosecond inverse magnetostriction in galfenol thin films, *Appl. Phys. Lett.* 103: 032409, 2013.

[6] J. V. Jäger et al., Resonant driving of magnetization precession in a ferromagnetic layer by coherent monochromatic phonons, *Phys. Rev. B* 92: 020404(R), 2015.

[7] V. N Kats et al., Ultrafast changes of magnetic anisotropy driven by laser-generated coherent and noncoherent phonons in metallic films, *Phys. Rev. B* 93: 214422, 2016.

[8] A. S. Salasyuk et al., Generation of a localized microwave magnetic field by coherent phonons in a ferromagnetic nanograting, *Phys. Rev. B* 97: 060404(R), 2018.

[9] A. Bartels et al., Ultrafast time-domain spectroscopy based on high-speed asynchronous optical sampling. *Rev. Sci. Instrum.* 78: 035107, 2007.

Two Level Systems at the surface of crystalline Nano-OptoMechanics

Mehdi Hamoumi[1], Chérif Belacel[1], Pierre Allain[1], William Hease[1], Aristide Lemaître[2], Giuseppe Leo[1] and Ivan Favero[1]

[1]Matériaux et Phénomènes Quantiques, CNRS, Université Paris-Diderot, Paris, France
[2] Centre de Nanosciences et Nanotechnologies, CNRS, Université Paris-Saclay, Palaiseau, France
* E-mail: ivan.favero@univ-paris-diderot.fr

Abstract

What ultimately limits mechanical dissipation of quantum nanomechanical resonators? The authors report on an experimental and theoretical investigation that consistently answers this question. The work is carried on crystalline semiconductor nano-devices, operated from cryogenic to room temperature, whose coherence properties are shown to be ruled by surface Two Level Systems. These fluctuating entities set the ultimate limit to the frequency-Q product of resonators, a widely used figure of merit for quantum operations.

Detailed summary

The physical origin of nanomechanical dissipation is a topic of curiosity and debate, motivated by a vast number of applications. Ultralow-dissipation nanomechanical resonators represent a key ingredient for optomechanics, which investigates the interaction of light and mechanical motion [1,2]. They are becoming crucial in weak-force resolution, mass sensing, and mesoscopic quantum operations, like mechanical state preparation or entanglement between mechanical systems.

Here we report on a systematic study of nanomechanical dissipation in high-frequency (≈300 MHz) semiconductor optomechanical disk resonators [3], in conditions where clamping and fluidic losses are negligible. Phonon-phonon interactions are shown to contribute with a loss background fading away at cryogenic temperatures (3 K). Atomic layer deposition of alumina at the surface modifies the quality factor of resonators, pointing towards the importance of surface dissipation. The temperature evolution is accurately fitted by two-level systems models, showing that the nanomechanical dissipation of resonators directly connects to microscopic material properties. Two-level systems, notably at surfaces, appear to rule the damping and fluctuations of high-quality crystalline nanomechanical devices, at all temperatures from 3 to 300K. The models lead to Q expectations beyond 10^9 at milliKelvin temperatures [3].

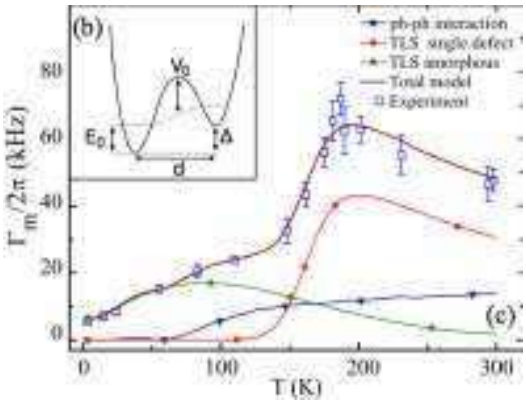


Figure 1: Mechanical energy dissipation rate of a nanomechanical resonator, measured (open symbols) and modeled using phonon-phonon interactions and TLS models.

References

[1] I. Favero and K. Karrai, Nat. Photonics 3, 201 (2009).
[2] M. Aspelmeyer, T. J. Kippenberg, and F. Marquardt, Rev. Mod. Phys. 86, 1391 (2014).
[3] M. Hamoumi, P. E. Allain, W. Hease, L. Morgenroth, B. Gérard, A. Lemaître, G. Leo and I. Favero. PRL **120**, 223601 (2018).

Surface waves beat phonons in polar ultra-thin films

Sebastian Volz[1]

[1] Laboratory for Integrated Micro-Mecatronic Systems, CNRS,
Institute of Industrial Science, The University of Tokyo, Tokyo, Japan
*corresponding author, E-mail: volz@iis.u-tokyo.ac.jp

Abstract

Thermal transport becomes less efficient as structures scale down since phonon-boundary scattering becomes predominant, therefore thermal management becomes more challenging in micro-electronic or optical devices. Here we aim at revealing the predominance of Surface Phonon-Polaritons (SPhPs) in thin film heat conduction. SPhPs are evanescent electromagnetic waves coupled to optical phonons and propagating along the interfaces of polar dielectrics. Through theoretical demonstration, SPhP propagation length reaches ten micrometers and SPhP spectral range reduces to the one of Surface Phonon-Polariton resonance in semi-infinite systems [1]. Consequently, SPhPs contribution to heat flux along a surface is usually found negligible

We have shown that thin film geometries allow for drastic changes in the surface evanescent electromagnetic field in terms of spectrum broadening and of propagation length. In thin silica films with thicknesses smaller than 1 micron, propagation length can reach centimeters and more, and evanescent waves exist in the full spectral range [2]. Our calculations predict that those two modifications yield guided radiative heat fluxes higher than the one carried by phonons.

Moreover, thermal conductivity contributed by SPhPs can be further enhanced by increasing temperature. Nevertheless no experimental result directly proves neither the existence of a SPhP heat channel nor the enhancement of thermal conductivity in thin film due to those carriers. We experimentally measure effective in-plane thermal conductivity of amorphous SiN thin films and show that it can indeed be significantly increased by surface SPhPs when the film thickness scales down.

References

[1] J. Ordonez-Miranda, L. Tranchant, T. Tokunaga, B. Kim, B. Palpant, Y. Chalopin, T. Antoni, and S. Volz, J. *Appl. Phys.*, 113(8):084311, 2013.

[2] S. Gluchko, B. Palpant, S. Volz, R. Braive, and T. Antoni, Thermal Excitation of Broadband and Long-range Surface Waves on SiO2 Submicron Film, *App. Phys. Lett.* 110:263108, 2017.

Phonon Engineered Detectors and Refrigerators

Mika Prunnila[1]

[1]VTT Technical Research Centre of Finland Ltd, P.O.Box 1000, FI-02044 VTT, Espoo, Finland
*corresponding author, E-mail: mika.prunnila@vtt.fi

Engineering of electron, photon and phonon thermal fluxes on small length scales is important for different ICT devices ranging from sensors to CMOS circuits. Mastering the different energy/particle channels at the nanoscale enable, especially, high sensitivity detectors and compact refrigerators. In this communication, we discuss on phonon engineering methodologies and physics for thermal radiation detectors and micro-coolers targeting to enhance their performance. Experimental realizations and results will be shown to back up our phonon engineering postulates and theoretical estimates.

Thermal radiation detectors (bolometers) are utilized in different application fields from chemical sensing to thermal imaging. Our main focus here will be on nano-thermoelectric detectors [1,2], where photon absorption can be boosted by nano-structured low heat capacity absorbers and thermal transduction can be enhanced by the methodologies of nano-scale thermoelectrics. Low heat capacity enables small thermal time constant and we will demonstrate fast and efficient thermal detector IR pixels operating at room temperature.

On the electro-thermal microcooler side we will show how phonon engineering can be adapted to significantly enhance refrigeration performance. We will show experimental results and also discuss the ultimate performance limits. Our working horse here is semiconductor-superconductor (Sm-S) junction. In the experimental proof-of-concept the refrigerated mass is suspended directly from these junctions. Thus the detrimental heat from due to phonons is defined by the Kapitza resistance at the junctions. We demonstrate significant thermal isolation and show electro-thermal cooling of 40 % [3]. This operation principle is in strong contrast to the conventional superconductive electro-thermal devices that operate against the volumetric electron-phonon coupling.

Acknowledgements

Collaborators listed as the co-authors of References 1-3 are gratefully acknowledged. This work has been financially supported by H2020 programme projects EFINED http://www.efined-h2020.eu/ (project number 766853) and MOS-QUITO (project number 688539) and Academy of Finland project QuMOS. This work was performed as part of the Academy of Finland Centre of Excellence program (project 312294).

References

[1] A. Varpula, A. Timofeev, A. Shchepetov, K. Grigoras, J. Hassel, J. Ahopelto, M. Ylilammi, M. Prunnila, *Thermoelectric detectors based on ultra-thin heavily doped single-crystal silicon membranes*, Appl. Phys. Lett. 110: 262101 (2017).

[2] A. Varpula, K. Grigoras, K. Tappura, A. Timofeev, A. Shchepetov, J. Hassel, J. Ahopelto and M. Prunnila, *Silicon Based Nano-Thermoelectric Bolometers for Infrared Detection*, Proceedings *2*: 894 (2018).

[3] E. Mykkänen, J. Lehtinen, L. Grönberg, A. Shchepetov, A. Timofeev, D. Gunnarsson, A. Kemppinen, A. Manninen, M. Prunnila, *Efficient thermionic operation and phonon isolation by a semiconductor-superconductor junction*. arXiv:1809.02994v1.

on-Hermitian Complex Systems: Photonics, Plasmonics and Metamater

Non-Hermiticity in optical microcavities

Jan Wiersig* **and Julius Kullig**

Institut für Physik,
Otto-von-Guericke-Universität Magdeburg
Postfach 4120, D-39016 Magdeburg, Germany
*corresponding author, E-mail: jan.wiersig@ovgu.de

Abstract

We discuss two aspects of non-Hermiticity in optical microcavities. First, we theoretically demonstrate third-order exceptional points in whispering-gallery cavities. Second, we reveal the role of mode nonorthogonality in the dynamics of waves propagating in open systems with localized losses.

1. Introduction

Optical microcavities are the key elements for modern light-emitting devices such as single-photon emitters, ultralow-threshold lasers, and sources of entangled photon pairs. An important subclass are whispering-gallery cavities, e.g. microdisks and microtoroids, where the light is trapped for a long time by total internal reflection at the boundary of the cavity. An optical mode in such a cavity therefore has a high quality factor $Q = \mathrm{Re}\,\omega/(-2\mathrm{Im}\,\omega)$, where ω is the complex-valued resonant frequency of the mode. Deforming or perturbing the boundary of whispering-gallery cavities can be beneficial for several applications, e.g. directional free-space light emission and mode discrimination, see [1] for a review.

Optical microcavities, and in fact all real physical systems, are open systems. The emerging field of "non-Hermitian physics" deals with the resulting phenomena such as mode nonorthogonality and spectral degeneracies, so-called exceptional points (EPs). In contrast to conventional degeneracies, at an EP not only eigenvalues but also the corresponding eigenstates of the non-Hermitian Hamiltonian coalesce [2]. A number of experiments have proven the existence of EPs in various physical systems including optical microcavities [3]. Applications of EPs are, for instance, ultrasensitive sensors for single-particle detection [4, 5] and orbital angular momentum microlasers [6]. Third-order EPs, involving three eigenstates, have been experimentally realized only recently using coupled acoustic cavities with asymmetric dissipation [7] and in parity-time-symmetric photonic molecules [8]. Of particular interest is the higher sensitivity to perturbations if compared to second-order EPs [8].

In this contribution, we discuss two aspects of non-Hermiticity in optical microcavities, namely third-order EPs and the role of mode nonorthogonality in the dynamics of propagating waves.

2. Third-order EPs in optical microcavities

One well-known mechanism to create second-order EPs in whispering-gallery cavities is asymmetric backscattering of light as reviewed in [9]. Here, we introduce two further mechanisms which allow to create third-order EPs in such systems.

The first example is an optical microdisk of radius R with a class of extremely weak boundary deformations, which weakly couple the given modes with azimuthal mode numbers $m > p > q$. Using a perturbative approach the specific deformation can be determined as [10]

$$\frac{r(\phi)}{R} = 1 + 2\epsilon_1 \cos\left[(m-p)\phi\right] + 2\epsilon_2 \cos\left[(p-q)\phi\right] + 2\epsilon_3 \cos\left[(m-q)\phi\right] + 2\sigma_p \cos\left(2p\phi\right) + 2\sigma_q \cos\left(2q\phi\right) \quad (1)$$

with polar coordinates (r, ϕ) and five independent deformation parameters ϵ_1, ϵ_2, ϵ_3, σ_p, σ_q which have to be adjusted to result in a third-order EP. Figure 1 shows the corresponding characteristic cubic root topology of the frequencies in the vicinity of the EP when two parameters are varied.

The second example is a microdisk with a concentrically layered refractive index profile. For a triple-layered cavity we verify and discuss the emergence of a third-order EP and its higher sensitivity to perturbations [11].

3. Role of nonorthogonality in systems with localized losses

Away from an EP, the dynamics of a wave packet in a microcavity (or in an open quantum system) can be described by a superposition of the modes (energy eigenstates). Naively, one would expect that the decay of the modes directly determine the decay of the total wave intensity. However, this is not the case for systems with localized losses, such as at the boundary of a microcavity without absorption in the bulk. Here, we demonstrate that the nonorthogonality of the modes plays the decisive role [12]. It can, to a large extent, compensate the initial decay of the modes leading to a transient power-law decay of the wave intensity with a potentially large exponent.

Acknowledgement

This work was financially supported by the German Research Foundation (DFG) through project No. WI1986/7-1.

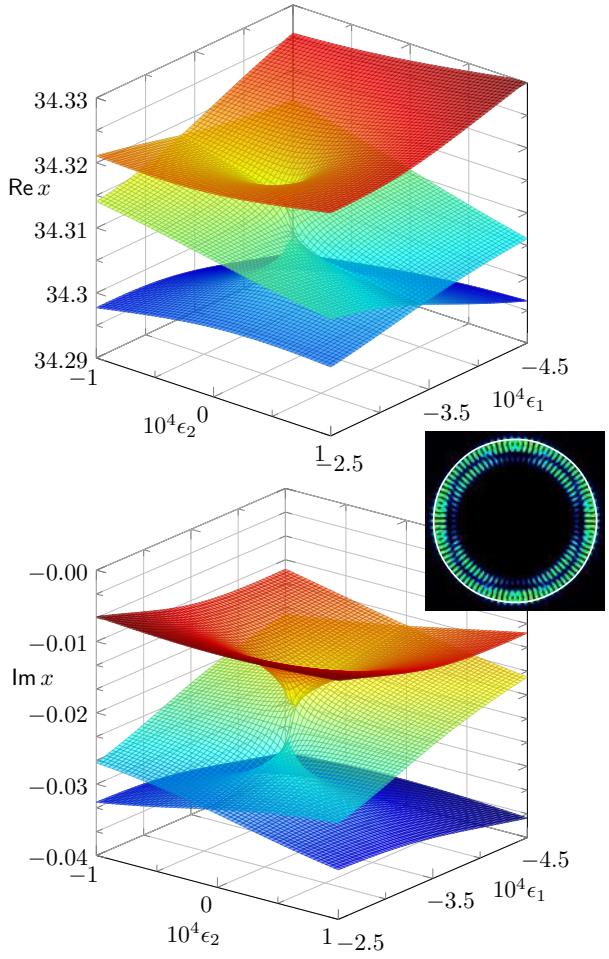


Figure 1: Real and imaginary part of the dimensionless frequency $x = \omega R/c$ of modes in the microdisk with boundary deformation (1). The parameters varied around the third-order exceptional point are ϵ_1 and ϵ_2. The other parameters are $\epsilon_3 \approx 0.001009$, $\sigma_p \approx 0.000157$, $\sigma_q \approx 0.000016$, $m = 46$, $p = 41$, and $q = 37$. The refractive index is $n = 1.5$. The inset shows the mode at the exceptional point. Note that the deformation is so weak that it cannot be seen with the naked eye.

References

[1] H. Cao and J. Wiersig, "Dielectric microcavities: Model systems for wave chaos and non-Hermitian physics," *Rev. Mod. Phys.*, vol. 87, pp. 61–111, 2015.

[2] T. Kato, *Perturbation Theory for Linear Operators*. New York: Springer, 1966.

[3] S.-B. Lee, J. Yang, S. Moon, S.-Y. Lee, J.-B. Shim, S. W. Kim, J.-H. Lee, and K. An, "Observation of an exceptional point in a chaotic optical microcavity," *Phys. Rev. Lett.*, vol. 103, p. 134101, 2009.

[4] J. Wiersig, "Enhancing the sensitivity of frequency and energy splitting detection by using exceptional points: application to microcavity sensors for single-particle detection," *Phys. Rev. Lett.*, vol. 112, p. 203901, 2014.

[5] W. Chen, Ş. K. Özdemir, G. Zhao, J. Wiersig, and L. Yang, "Exceptional points enhance sensing in an optical microcavity," *Nature*, vol. 548, pp. 192–196, 2017.

[6] P. Miao, Z. Zhang, J. Sun, W. Walasik, S. Longhi, N. M. Litchinitser, and L. Feng, "Orbital angular momentum microlaser," *Science*, vol. 353, pp. 464–467, 2016.

[7] K. Ding, G. Ma, M. Xiao, Z. Q. Zhang, and C. T. Chan, "Emergence, coalescence, and topological properties of multiple exceptional points and their experimental realization," *Phys. Rev. X*, vol. 6, p. 021007, 2016.

[8] H. Hodaei, A. Hassan, S. Wittek, H. Carcia-Cracia, R. El-Ganainy, D. Christodoulides, and M. Khajavikhan, "Enhanced sensitivity at higher-order exceptional points," *Nature*, vol. 548, pp. 187–191, 2017.

[9] J. Wiersig, "Non-Hermitian effects due to asymmetric backscattering of light in whispering-gallery microcavities," in *Parity-time Symmetry and Its Applications*, D. Christodoulides and J. Yang, Eds. Singapore: Springer, 2018, pp. 155–184.

[10] J. Kullig, C.-H. Yi, and J. Wiersig, "Exceptional points by coupling of modes with different angular momenta in deformed microdisks: A perturbative analysis," *Phys. Rev. A*, vol. 98, p. 023851, 2018.

[11] J. Kullig, M. Yi, C.-H. Hentschel, and J. Wiersig, "Exceptional points of third-order in a layered optical microdisk cavity," *New J. Phys.*, vol. 20, p. 083016, 2018.

[12] J. Wiersig, "Role of nonorthogonality of energy eigenstates in quantum systems with localized losses," *Phys. Rev. A*, vol. 98, p. 052105, 2018.

Coherent perfect absorber and laser for nonlinear waves

Vladimir V. Konotop[1*], Herwig Ott[2], and Dmitry A. Zezyulin[3]

[1]Departamento de Física and Centro de Física Teórica e Computacional,
Faculdade de Ciências, Universidade de Lisboa, Campo Grande 2, Edifício C8, Lisboa 1749-016, Portugal
[2]Department of physics and OPTIMAS research center, Technische Universität Kaiserslautern,
Erwin Schrödinger Straße, 67663 Kaiserslautern, Germany
[3]ITMO University, St. Petersburg 197101, Russia
*corresponding author, E-mail: vvkonotop@fc.ul.pt

Abstract

Coherent perfect absorber and laser for nonlinear waves are introduced. As an example, we consider an array of optical waveguides, in which waveguides with gain and absorption are incorporated. The results are generalized to setups with nonlinear active and absorbing waveguides, in particular, characterized by additional nonlinear dissipation or gain. Two-dimensional arrays are also considered.

1. Introduction

An optical optical media with localized dissipation or gain can coherently absorb incident radiation or emit waves. These phenomena are known in optics already for long time [1, 2]. Rapidly growing interest in such systems and their applications was triggered by more recent works (see e.g. [3, 4]), where, in particular, the physical properties of coherent lasing and absorption were related to the existence spectral singularities (SS) of the respective non-Hermitian potentials. In a notion of a coherent perfect absorber (CPA) and its interpretation as a time reversed laser was introduced. A Ss as a mathematical is known in literature since the original work [5] (the term SS was introduced in [6]).

By its definition a SS is a linear object: it characterizes interaction of linear waves with linear non-Hermitian potentials. Recently, in [7] there has been introduced a concept of a CPA for a nonlinear waves, as a *linear* localized potential totally absorbing *nonlinear* waves. In [7] this phenomenon was observed experimentally on matter waves loaded in an optical lattice where a dissipative potential was induced by a narrow electronic beam. Here we present theoretical consideration of optical systems implementing CPA and lasers for nonlinear waves.

2. Spectral singularities for nonlinear waves

Why SSs for nonlinear waves are challenging? (i) The "linear" arguments do not work: there is no well defined transfer matrix connecting left- and right- incident waves because the problems where either the incident or transmitted radiation is given, have different solutions. (ii) Interactions among the modes does not support interference in the linear sense. Thus results on scattering of monochromatic waves do not give any more an answer on the scattering of wave packets used in experiments, and no coherence arguments perfectly working in the linear case can be applied. (iii) Even if a CPA can exist in a nonlinear medium, its realization remains an open question because there are no general methods of determining parameters necessary for the observation of the phenomenon. (iv) Realization of plane waves may be practically impossible due to instabilities.

We argue that all above challenges can be overcome, and observation of a CPA or a laser in the nonlinear case, in a definite sense, can be even simpler that in the linear system. To this end, however we have to clarify these concepts.

The requirements for a nonlinear solution to be CPA or laser are reduced to the following properties: (i) it be stationary processes; (ii) it must be observed for monochromatic waves; (iii) it must consist of waves propagating respectively inwards and outwards of the non-hermitian potential, and (iv) it must have a linear limit, which is the CPA or laser in the conventional sense.

3. One-dimensional arrays

We consider two waveguide arrays placed in two (generally speaking different) left ("L") and right ("R") media and separated by an active or absorbing waveguide at the site $n = 0$ [Fig. 1]. The waveguides have Kerr nonlinearity χ (either positive or negative). The media determine the coupling coefficients (we consider them positive, $\kappa_{L,R} > 0$). Light propagation in such an array is described by the discrete nonlinear Schrödinger equations

$$\begin{aligned} &i\dot{q}_n + \kappa_L\left(q_{n-1} + q_{n+1}\right) + \chi|q_n|^2 q_n = 0, \quad \text{for } n \le -1,\\ &i\dot{q}_0 + \kappa_L q_{-1} + \kappa_R q_1 - i\frac{\gamma}{2}q_0 + \left(\chi - i\frac{\Gamma}{2}\right)|q_0|^2 q_0 = 0,\\ &i\dot{q}_n + \kappa_R\left(q_{n-1} + q_{n+1}\right) + \chi|q_n|^2 q_n = 0, \quad \text{for } n \ge 1. \end{aligned} \tag{1}$$

Here $\dot{q} = dq/dz$, z is the propagation distance, γ and Γ are linear and nonlinear gain ($\gamma > 0, \Gamma > 0$) or dissipation ($\gamma < 0, \Gamma < 0$).

Nonlinear solutions satisfying the requirements, formulated above reads

$$q_n = e^{i\beta z}\begin{cases} \rho e^{\pm ik_1 n} & \text{for } n \le 0,\\ \rho e^{\mp ik_2 n} & \text{for } n \ge 0. \end{cases} \tag{2}$$

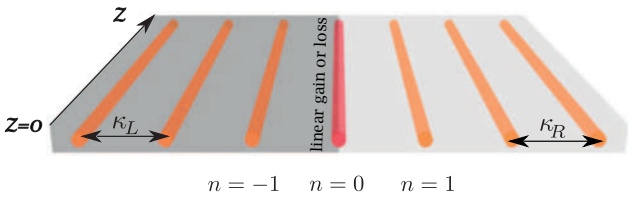


Figure 1: Schematic representation of an array of waveguides for observation of either a CPA (when the central waveguide is absorbing) or a coherent laser (when central waveguide is active). In a general situation the properties of the left and right media can be different; they are characterized by coupling constants κ_L (the left medium) and κ_R (the right medium)

The propagation constant of nonlinear solution reads

$$\beta = 2\kappa_L \cos k_1 + \chi\rho^2 = 2\kappa_R \cos k_2 + \chi\rho^2, \qquad (3)$$

and upper (lower) signs stand for CPA (lasing) solutions.

One finds that there exist the lower and the largest values of the loss and gain for which respectively CPA and lasing are possible:

$$\sqrt{2|\kappa_L^2 - \kappa_R^2|} < |\gamma + \Gamma\rho^2| \leq 2(\kappa_L + \kappa_R). \qquad (4)$$

Due to instabilities in the case of $\chi > 0$ ($\chi < 0$) only fast (slow) CPA or lasing of nonlinear waves can be observed.

4. Two-dimensional arrays

The above results are generalized to the two-dimensional (2D) waveguide arrays. Now a CPA or laser represents a discrete absorbing or lasing "layer" (a 1D array of waveguides). The field in each waveguide $q_{n,m}$ is specified by two indexes n and m. For fixed m and running n, one recovers the aD case considered above, while changing m establishes the second dimension. The absorbing or lasing layer is situated at $n = 0$ with m running through all integers. The media at both sides of the absorbing or lasing layer are considered equal. Such 2D array is modeled by

$$i\dot{q}_{n,m} + \kappa\Delta_2 q_{n,m} + \chi|q_{n,m}|^2 q_{n,m} = 0, \quad \text{for } n \neq 0,$$
$$i\dot{q}_{0,m} + \kappa\Delta_2 q_{0,m} - i\frac{\gamma}{2}q_{0,m} + \left(\chi - i\frac{\Gamma}{2}\right)|q_{0,m}|^2 q_{0,m} = 0$$

where $\Delta_2 q_{n,m} = q_{n-1,m} + q_{n+1,m} + q_{n,m-1} + q_{n,m+1}$.

The nonlinear CPA or lasing solution can be found as

$$q_{n,m}(z) = \rho e^{i\beta z + i\nu m \mp ik|n|} \qquad (5)$$

where $\nu \in (-\pi, \pi)$ is a free parameter tuning the angle of incidence (angle of emission) of the nonlinear wave with respect to the absorbing or lasing layer; $\beta = 2\kappa(\cos k + \cos\nu) + \chi\rho^2$ is the nonlinear propagation constant provided the condition $4\kappa \sin k = \mp(\gamma + \Gamma\rho^2)$ is satisfied. The upper and lower signs in (5) correspond to CPA and laser. We study the stability of the solution (5) and its evolution in the unstable case numerically.

5. Conclusion

We presented the generalization of the concept of spectral singularities on the case when a linear non-Hermitian potential is placed in a nonlinear medium, which without potential supports propagation stable monochromatic carrier waves of constant amplitude. Since both nonlinear CPA and and nonlinear laser solutions represent attractors, they are achieved along the evolution and thus do not require too demanding constraints on the initial conditions. Small initial deviations from the exact nonlinear solution are damped along the propagation. By reducing the intensity of the input beam it is possible to achieve the regime of linear CPA and laser, where the conditions of the destructive interference are satisfied automatically. The reported solutions can be used for rectification of the phase gradient and for the equalization of the amplitudes of input beams.

References

[1] [1] A. P. Khapalyuk, *Dokl. Akad. Nauk BelSSR* 6:301, 1962 (In Russian).

[2] [2] L. Poladian, Resonance mode expansions and exact solutions for nonuniform gratings, *Phys. Rev. E* 54: 2963, 1996.

[3] [3] A. Mostafazadeh, Spectral Singularities of Complex Scattering Potentials and Infinite Reflection and Transmission Coefficients at Real Energies *Phys. Rev. Lett.* 102:220402, 2009.

[4] [4] Y. D. Chong, L. Ge, H. Cao, and A. D. Stone, Coherent Perfect Absorbers: Time-Reversed Lasers, *Phys. Rev. Lett.* 105:053901, 2010.

[5] [5] M. A. Naimark, Investigation of the spectrum and the expansion in eigenfunctions of a nonselfadjoint operator of the second order on a semi-axis, *Tr. Mosk. Mat. Obs.* 3:181, 1954.

[6] [6] J. Schwartz, Some non–selfadjoint operators, *Comm. Pure Appl. Math.*, 13:609, 1960.

[7] [7] A. Müllers, B. Santra, C. Baals, J. Jiang, J. Benary, R. Labouvie, D. A. Zezyulin, V. V. Konotop, and H. Ott, Coherent perfect absorption of nonlinear matter waves, *Sci. Adv.* 4:eaat6539, 2018.

[8] [8] D. A. Zezyulin, H. Ott, and V. V. Konotop, Coherent perfect absorber and laser for nonlinear waves in optical waveguide arrays, *Opt. Lett.* 43:5901, 2018.

Proposal for a New Topological Laser

Xiao-Chen Sun and Xiao Hu

International Center for Materials Nanoarchitectonics (WPI-MANA)
National Institute for Materials Science (NIMS), Tsukuba 305-0044, Japan
*corresponding authors, E-mail: SUN.Xiao-Chen@nims.go.jp, HU.Xiao@nims.go.jp

Abstract

We propose theoretically to realize a ring laser based on honeycomb-type topological photonic crystals. Using the topological interface states as the cavity modes, we demonstrate a single-mode lasing over a large range of gain value. This lasing phenomenon is available up to frequencies of visible lights and is robust against disorders.

1. Introduction

Topological insulators have attracted much attention because of their quantized edge states [1], which also inspired the study of topological physics in bosonic systems [2-12]. Especially, the edge states of photonic topological insulators (PTIs) robust to disorders and immune to backscattering offer a huge potential in the design of optical devices. Very recently, several PTI lasers have been reported [13-15]. In this work, we construct topological interface states in the all-dielectric honeycomb-type photonic crystals [8-10] and use them for lasing in a ring cavity. As compared with previous works, our design can be realized with the matured processing technologies on photonic crystals.

2. Model

The topological ring cavity based on honeycomb-type photonic crystals is shown schematically in Fig. 1 [8-10]. We investigate the system by a tight-binding equation of motion, where the nontrivial topology of the photonic crystal in the inner part and the topological interface modes are derived by tuning the real-number hopping integrals.

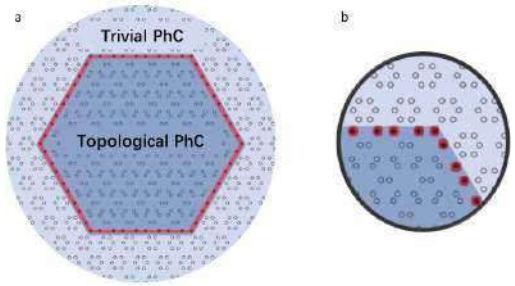


Figure 1: Schematics of the topological ring cavity used for lasing. The part inside the red hexagon is topological photonic crystal, and the outside part is the trivial photonic crystal, which is based on cylinders of a dielectric material with different deformations of honeycomb structures. Gains are introduced on the red sites along the interface.

3. Results

3.1. Single-mode lasing

In the ring cavity, the eigenmodes are given by the linear combinations of the $|p_{\pm}\rangle$ and $|d_{\pm}\rangle$ modes defined in the unit cell of honeycomb lattice [8], where the coefficients depend on the azimuthal angle [16]. Upon introducing gains, we find that the mode mostly uniform along the interface becomes lasing beyond a threshold gain and its intensity increases linearly with the gain value. Importantly, the single-mode lasing is achieved up to a gain as large as 25 times of the threshold value.

3.2. Robustness

We also find that our single-mode lasing is much more robust against disorders as compared with a laser formed by whispering-gallery ring cavity, while the intensities of these two cases are comparable in absence of disorders.

4. Conclusions

With the photonic topology generated by photonic crystals made of dielectric materials, the present design for robust ring laser can be fabricated by the matured semiconductor technologies. Our system is also expected to provide a good platform for the study on topology physics in non-Hermitian and nonlinear systems.

Acknowledgements

This work is supported by JSPS KAKENHI (No. 17H02913) and JST CREST (No. JPMJCR18T4).

References

[1] H. Weng, R. Yu, X. Hu, X. Dai, Z. Fang, Quantum anomalous Hall effect and related topological electronic states, *Adv. Phys.* 64: 227-282, 2015.

[2] F. D. M. Haldane, S. Raghu, Possible realization of directional optical waveguides in photonic crystals with broken time-reversal symmetry, *Phys. Rev. Lett.* 100: 013904, 2008.

[3] Z. Wang, Y. D. Chong, J. D. Joannopoulos, M. Soljacic, Reflection-free one-way edge modes in a gyromagnetic photonic crystal, *Phys. Rev. Lett.* 100: 013905, 2008.

[4] Z. Wang, Y. Chong, J. D. Joannopoulos, M. Soljacic, Observation of unidirectional backscattering-immune topological electromagnetic states, *Nature* 461: 772-775, 2009.

[5] M. Hafezi, E. A. Demler, M. D. Lukin, J. M. Taylor, Robust optical delay lines with topological protection, *Nat. Phys.* 7: 907-912, 2011.

[6] M. Hafezi, S. Mittal, J. Fan, A. Migdall, J. M. Taylor, Imaging topological edge states in silicon photonics, *Nat. Photon.* 7: 1001-1005, 2013.

[7] A. B. Khanikaev, S. H. Mousavi, W.-K. Tse, M. Kargarian, A. H. MacDonald, G. Shvets, Photonic topological insulators, *Nat. Mater.* 12: 233-239, 2013.

[8] L.-H. Wu, X. Hu, Scheme for Achieving a Topological Photonic Crystal by Using Dielectric Material, *Phys. Rev. Lett.* 114: 223901, 2015.

[9] Y. Li, Y. Sun, W. Zhu, Z. Guo, J. Jiang, T. Kariyado, H. Chen, X. Hu, Topological LC-circuits based on microstrips and observation of electromagnetic modes with orbital angular momentum, *Nat.Commun.* 9: 4598, 2018.

[10] Y. Yang, Y. F. Xu, T. Xu, H.-X. Wang, J.-H. Jiang, X. Hu, Z. H. Hang, Visualization of a Unidirectional Electromagnetic Waveguide Using Topological Photonic Crystals Made of Dielectric Materials, *Phys. Rev. Lett.* 120: 217401, 2018.

[11] C. He, X.-C. Sun, X.-P. Liu, M.-H. Lu, Y. Chen, L. Feng, Y.-F. Chen, Photonic topological insulator with broken time-reversal symmetry, *Proc. Natl. Acad. Sci. U.S.A.* 113: 4924-4928, 2016.

[12] C. He, X. Ni, H. Ge, X.-C. Sun, Y.-B. Chen, M.-H. Lu, X.-P. Liu, Y.-F. Chen, Acoustic topological insulator and robust one-way sound transport, *Nat. Phys.* 12: 1124-1129, 2016.

[13] B. Bahari, A. Ndao, F. Vallini, A. El Amili, Y. Fainman, B. Kanté, Nonreciprocal lasing in topological cavities of arbitrary geometries, *Science* 358: 636, 2017.

[14] G. Harari, M. A. Bandres, Y. Lumer, M. C. Rechtsman, Y. D. Chong, M. Khajavikhan, D. N. Christodoulides, M. Segev, Topological insulator laser: Theory, *Science* 359: eaar4003, 2018.

[15] M. A. Bandres, S. Wittek, G. Harari, M. Parto, J. Ren, M. Segev, D. N. Christodoulides, M. Khajavikhan, Topological insulator laser: Experiments, *Science* 359: eaar4005, 2018.

[16] G. Siroki, P. A. Huidobro, V. Giannini, Topological photonics: from crystals to particles, *Phys. Rev. B* 96: 041408, 2017.

Coherent perfect absorption in disordered media: experimental realization of the random anti-laser

Kevin Pichler[1,*], Matthias Kühmayer[1], Julian Böhm[2], Andre Brandstötter[1], Philipp Ambichl[1], Ulrich Kuhl[2], and Stefan Rotter[1]

[1]Institute for Theoretical Physics, Vienna University of Technology (TU Wien), Vienna, Austria
[2]Institut de Physique de Nice, Université Côte d'Azur, CNRS, Nice, France
*corresponding author, E-mail: kevin.pichler@tuwien.ac.at

Abstract

We report on the first experimental implementation of coherent perfect absorption in a disordered medium. With this process corresponding to the time-reverse of random lasing at threshold, our microwave experiment constitutes the first "random anti-laser". Our approach relies only on the multi-modal scattering matrix of the system based on which we achieve more than 99.78% absorption of the injected intensity. We expect our approach to be suitable for numerous applications in which waves need to be perfectly focused, routed or absorbed.

1. Introduction

One of the most successful concepts that has emerged from the field of non-Hermitian wave engineering so far is that of coherent perfect absorption [1-4] – an effect analogous to the time-reversal of coherent emission of radiation at the lasing threshold. Such coherent perfect absorbers (CPAs) have already been realized in a number of experiments [3,4], but have remained limited to setups involving simple slab geometries. Here we combine the concept of a coherent perfect absorber with the concept of random lasing [5]. A random laser is a disordered gain medium that is pumped sufficiently strongly to emit coherent laser light. Time-reversing such a single-mode random laser mode results in a highly complex wave state that impinges on the disordered structure and gets perfectly absorbed there (without any back-reflection to the asymptotic region). We build such a random anti-laser using a microwave setup and demonstrate its ability to absorb a suitably shaped incoming wavefront with close to perfect efficiency.

2. Theory

The crucial quantity behind the CPA concept is the scattering matrix that relates the injected fields to the outgoing ones, $\psi_{\text{out}} = \mathrm{S}\,\psi_{\text{in}}$. In Hermitian systems, zeros of the scattering matrix S are generally located in the upper half ($\mathrm{Im}(\upsilon) > 0$) of the complex plane of frequency υ, whereas poles are located in the lower half ($\mathrm{Im}(\upsilon) < 0$). Adding gain to the system moves the poles up towards the real υ-axis where the system turns into a random laser as soon as the first pole hits the real υ-axis. Also the opposite is possible: adding loss to the medium will turn it into a random anti-laser (disordered CPA) at those frequencies and loss values where one of the S-matrix zeros crosses the real υ-axis. At these parameter configurations, a random anti-laser mode ψ_{CPA} is an eigenstate of the scattering matrix S with eigenvalue $\lambda_{\text{CPA}} = 0$, i.e. $\mathrm{S}\,\psi_{\text{CPA}} = 0$, where ψ_{CPA} is the incoming radiation field and the empty 0-field is the outgoing one.

3. Experimental realization

Fig. 1a shows our experimental setup consisting of an aluminum waveguide where the disordered medium is implemented by 60 randomly placed cylindrical Teflon scatterers. Four transverse modes are open at the operation frequency, requiring four antennas on each side (left and right) to control all degrees of freedom of the injected microwave field. In the center of the scattering region we place a monopole antenna where the absorption strength can be tuned simply by varying the length of this central absorbing antenna inside the waveguide. This microwave setup allows us to measure the full scattering matrix of the disordered medium (including transmissions and reflections from both sides) as well as to inject arbitrarily shaped wavefronts into the disorder in a broad frequency interval.
Our experimental procedure to realize a random anti-laser is now the following: we first measure the S-matrix of the system as a function of frequency (in a broad interval to ensure that many S-matrix zeros are contained in it) and of the absorption strength of the central absorbing antenna (as determined by the penetration depth into the waveguide). In a next step, we evaluate the eigenvalues of these S-matrices and identify those parameter configurations for which the absolute value of the smallest S-matrix eigenvalue dips almost to zero. In the last step, we inject the S-matrix eigenstate with the smallest eigenvalue (the CPA state) into the system and evaluate its properties, in particular its degree of absorption.

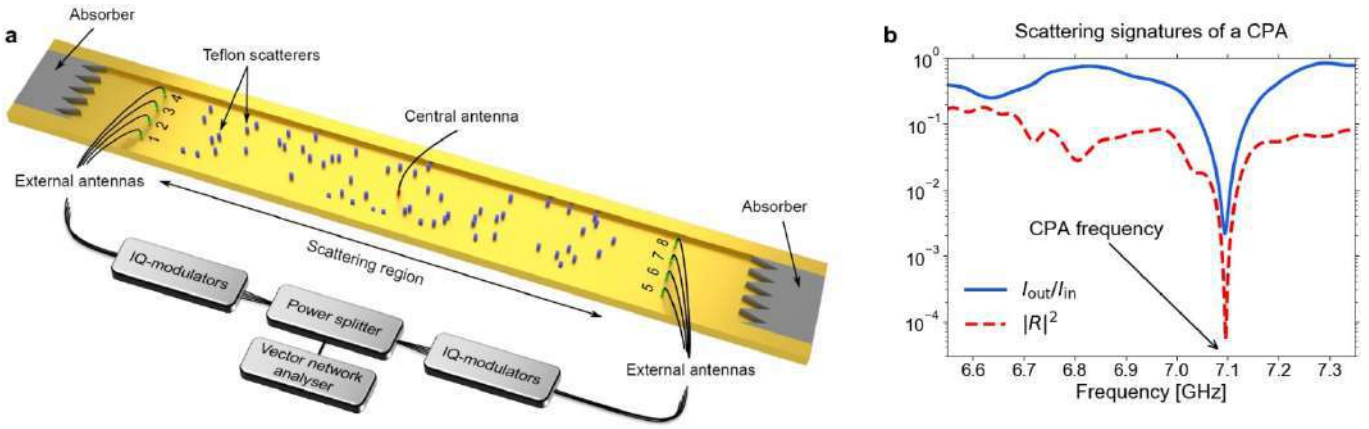


Figure 1: **(a) Experimental setup of the random anti-laser:** Microwaves are injected into an aluminum waveguide through eight external antennas (four on each side). The central scattering region of the waveguide contains a set of randomly placed Teflon scatterers simulating a disordered medium. A monopole antenna in the center of the disordered region (central antenna) provides a tunable absorption strength through which the CPA state is completely absorbed. **(b) Scattering signatures of a CPA state:** Incoming and outgoing intensities (I_{in} and I_{out}) of a CPA state injected by the external antennas compared to the reflection signal R measured at the central antenna when injecting microwaves there. Both the ratio I_{out}/I_{in} and the reflection coefficient $|R|^2$ show a pronounced minimum close to the CPA-frequency around 7.1 GHz.

4. Results and Discussion

Following the protocol outlined in section 3, we find CPA states where more than 99.78% of the injected intensity gets absorbed, as illustrated by the blue curve in Fig. 1b, where we show the ratio between the outgoing and the incoming microwave intensity (I_{out}/I_{in}) of a CPA state as a function of the signal frequency. We have also devised a number of independent tests that confirm unambiguously that we have indeed realized a disordered CPA rather than a coherent enhancement of absorption (CEA) [6]. For example, we expect that a CPA state is primarily absorbed by the central antenna (and less by global absorption in the metallic waveguide). Therefore, the time-reverse of this state should be a harmonic signal that enters through the central antenna without any back-reflection. Indeed, we find by injecting microwaves through the central antenna that its frequency-dependent reflection coefficient $|R|^2$ shows a pronounced minimum close to the frequency where we found the CPA state independently, see red dashed curve in Fig. 1b.

5. Conclusions

In summary, we present the first experimental realization of a random anti-laser, which provides proof of principle that coherent perfect absorption can also be realized in arbitrarily composed systems such as disordered media. We expect our findings [7] to be relevant for practical applications such as perfect focusing of electromagnetic signals and sound fields in complex environments such as in an office space or in biological tissue. Our results also serve as a bridge between the two highly active communities of wavefront shaping [8] and non-Hermitian physics [9].

Acknowledgements

K.P., M.K., A.B., P.A. and S.R. were supported by the Austrian Science Fund (FWF) through project I 1142- N27 (GePartWave). J.B. and U.K. were supported by the French Science Fund (ANR) through project GePartWave and by the European Union via the H2020 project OpenFet NEMF21.

References

[1] Y.D. Chong, L. Ge, H. Cao and A.D. Stone, *Coherent Perfect Absorbers: Time-Reversed Lasers*, Phys. Rev. Lett. **105**, 053901 (2010).

[2] S. Longhi, *PT-symmetric laser absorber*, Phys. Rev. A **82**, 031801 (2010).

[3] W. Wan, Y. Chong, L. Ge, H. Noh, A.D. Stone and Hui Cao, *Time-Reversed Lasing and Interferometric Control of Absorption*, Science **331**, 889–892 (2011).

[4] D.G., Baranov, A. Krasnok, T. Shegai, A. Alù and Y.D. Chong, *Coherent perfect absorbers: linear control of light with light*, Nat. Rev. Mater. **2**, 17064 (2017).

[5] D.S. Wiersma, *The physics and applications of random lasers*, Nat. Phys. **4**, 359–367 (2008).

[6] Y.D. Chong and A.D. Stone, *Hidden Black: Coherent Enhancement of Absorption in Strongly Scattering Media*, Phys. Rev. Lett. **107**, 163901 (2011).

[7] K. Pichler, M. Kühmayer, J. Böhm, A. Brandstötter, P. Ambichl, U. Kuhl and S. Rotter, *Random anti-lasing through coherent perfect absorption in a disordered medium*, Nature (accepted for publication).

[8] S. Rotter and S. Gigan, *Light fields in complex media: Mesoscopic scattering meets wave control*, Rev. Mod. Phys. **89**, 015005 (2017).

[9] R. El-Ganainy, K.G. Makris, M. Khajavikhan, Z.H. Musslimani, S. Rotter and D.N. Christodoulides, *Non-Hermitian physics and PT symmetry*, Nature Physics **14**, 11–19 (2018).

Encircling an exceptional point in waveguide structures and electrical circuits

Youngsun Choi,[1] Jae Woong Yoon,[2] Choloong Hahn,[3,4] Pierre Berini,[3,4,5] Jong Kyun Hong,[1] Yeonghwa Ryu,[1] and Seok Ho Song[1*]

[1] Department of Physics, Hanyang University, Seoul, Korea
[2]Electronics and Telecommunications Research Institute (ETRI), Daejeon, Korea
[3]School of Electrical Engineering and Computer Science, University of Ottawa, Canada
[4]Centre for Research in Photonics, University of Ottawa, Canada
[5]Department of Physics, University of Ottawa, Canada

Abstract- We discuss experimental results on dynamically encircling an exceptional point in coupled waveguides and electrical resonator circuit systems.

Recently, encircling an exceptional point (EP) and consequent time-asymmetric dynamics have attracted significant attention because it produces robust chirality. When a non-Hermitian system slowly changes to encircles an EP in a system's parameter space, time-dependent states undergo time-asymmetric evolution where final states differ depending on encircling direction. This chirality is robust to the parametric-path change as long as it encircles an EP. The time-asymmetric mode conversion has been experimentally demonstrated in the metallic waveguides and opto-mechanical systems [1, 2].

Here, we introduce two experimental demonstrations of dynamically encircling an EP. One is a Si-base waveguides coupler that produces broadband unidirectional mode conversion, and the other is an electrically tunable circuit system that enables observation of full dynamics in the time-domain.

In the waveguide experiment, two coupled waveguides are precisely designed to encircle an EP in the parameter space {ΔnR, ΔnI} by changing the width of waveguide and position of the side-patched slab waveguide that generates radiative loss. Symmetrically coupled mode is launched, output waveguide mode measured by the interferometric method for the forward and backward propagation direction. We observed unidirectional mode conversion over the full-telecommunication band.

In the circuit experiment, two RLC resonators having different dissipation rate coupled through a varactor diode which provides electrically tunable capacitance. One of the resonators also has a varactor diode to control its resonance frequency. Changing coupling strength and frequency detuning in time-domain, the proposed circuit is manipulated to encircles an EP. With the circuit system, we measured entire time-dependent state information during the system encircles an EP including non-adiabatic state jump which is not observed in the previous experiments.

Acknowledgements, This research was supported in part by the Global Frontier Program through the National Research Foundation of Korea funded by the Ministry of Science, ICT & Future Planning (NRF-2014M3A6B3063708), the Basic Science Research Program (NRF-2015R1A2A2A01007553), and the Presidential Post-Doc Fellowship Program (NRF-2017R1A6A3A04011896).

REFERENCES

[1] J. Doppler *et al.*, "Dynamically encircling exceptional points in a waveguide: asymmetric mode switching from the breakdown of adiabaticity," *Nature*, vol. 537, pp. 76–79, 2016.
[2] H. Xu, D. Mason, L. Jiang, and J. G. E. Harris, "Topological energy transfer in an optomechanical system with exceptional points," *Nature*, vol. 537, pp. 1–28, 2016.

Photonic topological insulator in synthetic dimensions

Eran Lustig[†1], Steffen Weimann[†2], Yonatan Plotnik[1], Yaakov Lumer[1], Miguel A. Bandres[3], Alexander Szameit[2] and Mordechai Segev[1]

[1]Physics Department and Solid State Institute, Technion–Israel Institute of Technology, Haifa, Israel
[2]Institut für Physik, Universität Rostock, Rostock, Germany
[3]CREOL, College of Optics and Photonics, University of Central Florida, Orlando, F, USA
*corresponding author, E-mail: msegev@technion.ac.il
[†]These authors contributed equally

Abstract

Topological physics enables protected transport along edges of materials. Interestingly, such edge transport can flow not only on edges in real-space, but also on the interface of a synthetic space, such as modal space or spin space. Here, we report the first experimental realization of photonic topological insulators in synthetic dimensions. Our work on these synthetic space concepts leads to combining high-dimensional physics and long-range connectivity with a plethora of optical phenomena such as PT-symmetry, Topological lasers and more.

1. Introduction

Topological insulators enable protected transport along edges of materials, offering immunity against scattering from disorder and imperfections. Traditionally, the underlying model for topological insulators is a spatial lattice in two or three dimensions. However, in recent experiments topological edge-states were observed in a lattice with one spatial dimension and one synthetic dimension - the intrinsic energy modes of cold atoms [1–3]. This striking phenomenon is related to high dimensional topological physics and long-range connectivity, due to the nature of the modal degree of freedom[4]. Soon thereafter, in photonics, topological transport in synthetic dimensions – photonic modes which are not intrinsic, were theoretically proposed[5,6]. These systems can exhibit high-dimensional phenomena such as four-dimensional quantum Hall effect and Weyl points along with applications such as topologically protected mode converters and more[7].

Here, we present the first experimental realization of photonic topological insulators in synthetic dimensions[8]. We demonstrate topologically protected transport of an optical wavepacket through a two-dimensional (2D) waveguide array, engineered such that it has one synthetic dimension in modal space, while its other dimension is in real space. This opens the door for experiments combining high dimensional physics and long-range connectivity with a plethora of physical phenomena ranging from PT-symmetry to Anderson localization and topological photonics. Our experimental realization can also lead to observing new phenomena in cold atoms[9].

2. Photonic topological insulator in synthetic dimensions

We describe our system as follows: consider a one-dimensional array of N evanescently-coupled waveguides arranged along the *y* axis (columns) and propagating in the *z* direction. This array has N propagating eigenmodes with different propagation constants, which form an equally-spaced ladder of modes in a synthetic space. To create a 1D lattice of coupled modes, we spatially oscillate the array along its longitudinal dimension (Fig.1a). Next, we can

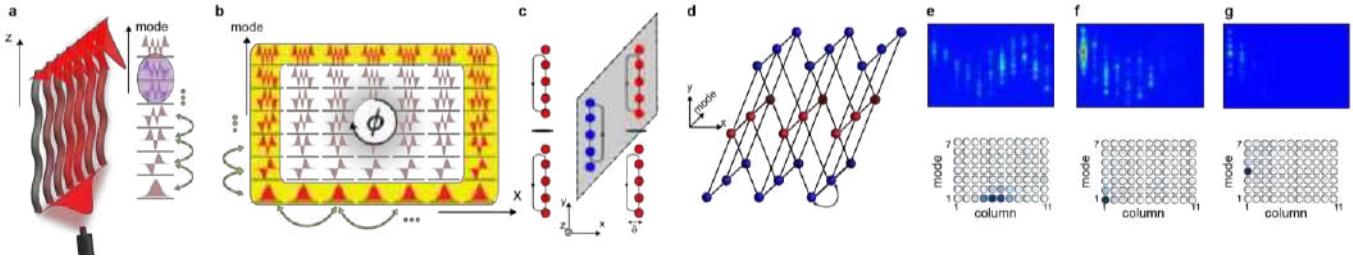


Figure 1: **(a)** A column of evanescently coupled waveguides oscillating spatially. The supermodes of the columns are coupled due to the oscillations of the waveguides. **(b)** *M* columns as in (a) placed next to each form a lattice in synthetic dimensions with one spatial and one modal degree of freedom (edge-state in yellow). **(c)** Columns arranged in a 2D lattice (unit cell in grey), the column oscillate along the black line lines, each column couples to four other columns during a period **(d)** The 3D geometry of the lattice of (c) in synthetic dimensions. **(e-g)** Experimental measurements of a propagating edge-state in synthetic dimensions as it is seen in real space (top), and the matching description of the propagation in synthetic space (bottom).

arrange M of these oscillating columns one next to the other. This adds a spatial dimension to the system (along the x axis). The first dimension is the supermode spectrum of each column, and the second dimension is the spatial location of the column in x. When the oscillations of the columns have a relative phase ϕ between one another, the light acquires a total phase of ϕ upon encircling a plaquette in synthetic space resulting in topological edgestates (Fig.1b). This approach allows increasing the dimensionality further by arranging 1D oscillating columns as the unit-cell of a 2D lattice (Fig.1c-d). Furthermore, long-range connectivity (which can lead to further dimensionality increase) can be achieved by adding more frequencies of oscillations.

We study experimentally the evolution of the edge states in our synthetic topological system, we propagate a paraxial beam at λ=633[nm] through the 2D lattice fabricated in fused silica. Our experimental results (Fig.1e-g(top)) show a wavepacket propagating on the edge of synthetic space. We show that it is robust to disorder and bypasses the corner of synthetic space (Fig.1e-g(bottom)). We hope our study will open the door for observing new high dimensional and long-range physics both in photonics and in cold atoms.

References

[1] O. Boada, A. Celi, J. I. Latorre & M. Lewenstein. Quantum simulation of an extra dimension. *Phys. Rev. Lett.* 108, 133001 (2012).

[2] M. Mancini. et al. Observation of chiral edge states with neutral fermions in synthetic Hall ribbons. *Science* 349, 1510 LP-1513 (2015).

[3] B. K. Stuhl, H.-I.-I. Lu,, L. M. Aycock, D. Genkina & I. B. Spielman. Visualizing edge states with an atomic Bose gas in the quantum Hall regime. *Science* 349, 1514 LP-1518 (2015).

[4] A. Celi. et al. Synthetic gauge fields in synthetic dimensions. *Phys. Rev. Lett*. 112, 43001 (2014)

[5] T. Ozawa, H. M. Price, N. Goldman, O. Zilberberg & I. Carusotto. Synthetic dimensions in integrated photonics: from optical isolation to four-dimensional quantum Hall physics. *Phys. Rev. A* 93, 43827 (2016).

[6] L. Yuan, Y. Shi & S. Fan. Synthetic dimension in photonics. *Opt. Lett.* 41, 741–4 (2016).

[7] L. Yuan, Q. Lin, M. Xiao, & S. Fan. Synthetic dimension in photonics. *Optica* 5, 1396–1405 (2018).

[8] E. Lustig, et al. Photonic Topological Insulator in Synthetic Dimensions. *Nature* (2019) Advanced online publication. https://doi.org/10.1038/s41586-019-0943-7.

[9] H. M. Price, T. Ozawa & N. Goldman, Synthetic dimensions for cold atoms from shaking a harmonic trap. *Phys. Rev. A* 95, 23607 (2017).

Exceptional-point parity-time symmetry based sensors: limitations due to fluctuations and noise

Christos Tserkezis[1], Christian Wolff[1], and N. Asger Mortensen[1,2,3*]

[1]Center for Nano Optics, University of Southern Denmark, Odense, Denmark
[2]Danish Institute for Advanced Study, University of Southern Denmark, Odense, Denmark
[3]Center for Nanostructured Graphene, Technical University of Denmark, Kongens Lyngby, Denmark
*corresponding author, E-mail: asger@mailaps.org

Abstract

We theoretically discuss limitations in the operation of sensors based on parity-time symmetric gain-loss resonator pairs initially operating near the exceptional point. In particular, we show how mesoscopic fluctuations in resonator pair ensembles produce a detuning in the frequencies of the constituent resonators, while thermal noise leads to an exponential divergence of the initial states. We therefore show that considerable effort is required in order to exploit the sensitivity of such sensors in its full potential.

1. Introduction

Parity-time symmetric systems of coupled gain-loss resonators operating near the exceptional point have been attracting considerable interest in recent years, as it has been proposed that extremely sensitive sensors can be designed, exploiting the energy splitting of the two coalescing eigenfrequencies, which scales with the square root of any perturbation [1]. However, this sensitivity can be as much of a curse for practical applications as it is a blessing, because even minor deviations of the operating point can lead the system away from the exceptional point, thus diminishing its sensitivity [2, 3], even if this, somehow ambigious, sensitivity is defined in the most favourable way [4]. Here we discuss how operation at the exceptional point and the applications that depend on it are affected by two fundamental issues that cannot be avoided in practice: sample-to-sample fluctuations in ensembles of resonator pairs, and (thermal) noise.

In what follows we consider a pair of resonators, one characterised by a damping rate $g/2$ and the other by an equal amount of gain. The two resonators are coupled through a coupling parameter κ and, within coupled-mode theory [5] their dynamics is described by a Schrödinger-like equation

$$\mathrm{i}\partial_t \begin{pmatrix} a_1(t) \\ a_2(t) \end{pmatrix} = \begin{pmatrix} \omega_1 - \mathrm{i}g/2 & \kappa \\ \kappa & \omega_2 + \mathrm{i}g/2 \end{pmatrix} \begin{pmatrix} a_1(t) \\ a_2(t) \end{pmatrix}, \quad (1)$$

where $a_i(t)$ $(i = 1, 2)$ are the complex amplitudes of the two resonator modes, and ω_i their corresponding eigenfrequencies. The eigenvalues of the above effective Hamiltonian can be obtained straightforwardly as

$$\Omega_\pm = \bar{\Omega} \pm \sqrt{1 - (G + \mathrm{i}\Delta)^2}, \quad (2)$$

where $\Omega = \omega/\kappa$, $G = g/2\kappa$, the central frequency $\bar{\Omega} = (\omega_1 + \omega_2)/2\kappa$, while the normalised detuning of the two resonances is denoted by $\Delta = (\omega_1 - \omega_2)/2\kappa$.

2. Fluctuations near the exceptional point

From Eq. (2) one immediately sees that, in the limit of low gain ($G \ll 1$), the imaginary part of the eigenvalues behaves as $\Omega''_\pm \simeq \mp G\Delta$. This means that the finite detuning breaks the parity-time symmetry associated with perfectly aligned resonators, for which the eigenvalues are purely real [6].

To further evaluate the role of fluctuations, we assume an ensemble of resonator pairs with a Gaussian distribution of the detuning parameter

$$P_0(\Delta) = \frac{1}{\sqrt{2\pi}\sigma} \exp(-\Delta^2/2\sigma^2), \quad (3)$$

where σ it the distribution variance. Such a distribution can be interpreted either as the result of fabrication tolerance or as originating from temporal fluctuations, assuming that an ergodic approximation to the system dynamics is valid. Then one can show [2] that the eigenfrequencies also acquire a relatively broad distribution around the exact solution of Eq. (2), as we schematically show in Fig. 1, described by

$$P(\Omega') \simeq \frac{1}{\sqrt{\sigma}} F\left(\frac{\Omega' - \bar{\Omega}}{\sqrt{\sigma}}\right), \quad (4)$$

where $F(x) = \left(\frac{8}{\pi}\right)^{1/2} |x| \exp\left(-\frac{1}{2}x^4\right)$, and Ω' is the real part of Ω.

3. Time evolution in the presence of noise

To explore the time evolution of the exceptional point in the presence of noise, we assume that the operating point of the system is perturbed by some time dependent real-valued fluctuation $\Lambda(\tau)$ ($\tau = \kappa t$ being a rescaled time) which can be represented as a Fourier integral

$$\Lambda(\tau) = \int_{-\infty}^{\infty} \mathrm{d}\omega b(\omega) \exp(-\mathrm{i}\omega\tau). \quad (5)$$

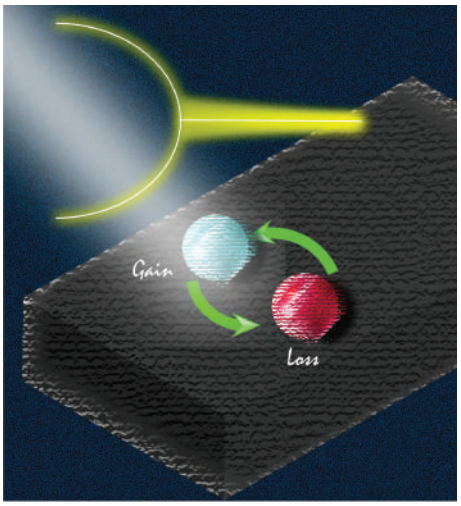


Figure 1: Artistic view of the blurring of the eigenfrequencies of the coupled gain-loss pair of resonators due to fluctuations.

The phase of the function $b(\omega)$ is assumed to fluctuate randomly and arbitrarily quickly in ω, while its modulus is a smooth function of ω [7]; it is connected to the fluctuation power spectrum $P_0(\omega)$ through $P_0(\omega) = |b(\omega)|^2$. We assume the overall fluctuation power to be finite, so $P_0(\omega)$ must cut off at high frequencies, and we distinguish between low-frequency and quasistatic fluctuations (drift), which are eliminated by a stabilisation circuit, and high-frequency fluctuations (noise). In other words, we assume that $\Lambda(\tau)$ vanishes in a neighbourhood of $\omega = 0$, if only to prevent the system from permanently drifting away from the exceptional point. Then $P_0 = 0$ for $|\omega| < \omega_{\text{min}}$. The characteristic auto-correlation function of the noise, $\Gamma(\tau)$, is approximated as a Dirac distribution

$$\Gamma(\tau) = \int_{-\infty}^{\infty} \mathrm{d}\tau' \Lambda(\tau')\Lambda(\tau'+\tau) \approx \zeta\delta(\tau), \qquad (6)$$

with the constant ζ formally given by $\zeta = \iint_{-\infty}^{\infty} \mathrm{d}\tau' \mathrm{d}\tau \Lambda(\tau')\Lambda(\tau'+\tau)$. Then one can show [3] that, after some characteristic time, the system enters a regime where the norm of any initial state grows exponentially, following to a very good accuracy the equation

$$|\Lambda\, a_i(\tau)| \approx \exp\left(\sqrt{2\zeta}\tau - 1\right). \qquad (7)$$

This means that a system with noisy system parameters can be operated at the exceptional point for a time no longer than $\tau_{\text{max}} = 1/\sqrt{2\zeta}$. A stabilization circuit could then try to stabilise the norm of the state, moving one system parameter away from the exceptional point, and the system will either settle at this new equilibrium point or the feedback circuit will become unstable and enter oscillations. Reduction in noise comes therefore at the price of increased tendency for oscillation of the system parameters (detuning, gain or loss).

4. Conclusions

In summary, we have theoretically explored how realistic experimental conditions affect the operation of sensors based on the exceptional point of parity-time symmetric gain-loss resonator pairs. We have shown that fluctuations, noise, and statistical averaging all rapidly lead the system away from the exceptional point. Maintaining operation at the exceptional point for long, experimentally relevant times, requires therefore careful design of an appropriate feedback system.

Acknowledgements

N. A. M. is a VILLUM Investigator supported by VILLUM Fonden (grant No. 16498). C. W. acknowledges funding from a MULTIPLY fellowship under the Marie Skłodowska-Curie COFUND Action (grant agreement No. 713694). The Center for Nano Optics is financially supported by the University of Southern Denmark (SDU 2020 funding).

References

[1] J. Wiersig, Enhancing the sensitivity of frequency and energy splitting detection by using exceptional points: application to microcavity sensors for single-particle detection, *Phys. Rev. Lett.* 112: 203901, 2014.

[2] N.A. Mortensen, P.A.D. Gonçalves, M. Khajavikhan, D.N. Christodoulides, C. Tserkezis, C. Wolff, Fluctuations and noise-limited sensing near the exceptional point of parity-time-symmetric resonator systems, *Optica* 5: 1342-1346, 2018.

[3] C. Wolff, C. Tserkezis, N.A. Mortensen, On the time evolution at a fluctuating exceptional point, *arXiv* 1810.08390v1, 2018.

[4] W. Langbein, No exceptional precision of exceptional-point sensors, *Phys. Rev. A* 98: 023805, 2018.

[5] S.H. Fan, W. Suh, J.D. Joannopoulos, Temporal coupled-mode theory for the fano resonance in optical resonators, *J. Opt. Soc. Am. A* 20: 569–572, 2003.

[6] R. El-Ganainy, K.G. Makris, M. Khajavikhan, Z.H. Musslimani, S. Rotter, D.N. Christodoulides, Non-Hermitian physics and PT symmetry, *Nature Phys.* 14: 11–19, 2018.

[7] M. Born, E. Wolf, *Principles of Optics*, Cambridge University Press, Cambridge, 1999).

Optical Amplifications at Non-Hermitian singularities

Q. Zhong[1], S. K. Ozdemir[2], A. Eisfeld[3], A. Metelmann[4] and R. El-Ganainy[1,5],

[1]Department of Physics and Henes Center for Quantum Phenomena, Michigan Technological University, Houghton, MI, 49931, USA
[2]Department of Engineering Science and Mechanics, Penn State University, University Park, PA, 16802, USA
[3]Max Planck Institute for the Physics of Complex Systems, Nöthnitzer Strasse 38, 01187 Dresden, Germany
[4]Department of Physics, Freie Universität, Arnimallee 14, 14195, Berlin, Germany
[5]Department of Electrical and Computer Engineering, Michigan Tech, Houghton, MI, 49931, USA

Abstract

We propose a new optical amplifier geometry based on exceptional points. Compared to its standard counterpart device, the proposed structure relaxes the limitation imposed by the gain-bandwidth product.

1. Introduction

Signal amplification is one of the most fundamental processes in optical science and engineering. Optical amplifiers (OAs) can be classified into traveling [1] or standing [2] waves devices . The former offers a larger bandwidth at the expense of the attainable gain values. On the other hand, the latter can have larger gain due to the power recycling in the resonator, allowing for a smaller device size. However, the resonant condition leads to a very narrow bandwidth. This fundamental limitations pertinent to cavity-based optical amplifiers is known as the gain-bandwidth product.

Here we introduce a new OA scheme based on optical resonators operating at exceptional points (EPs) – a special type of singularities at which two or more eigenstates coalesce [3, 4]. We show that the gain-bandwidth product of the proposed device scales differently from that of standard resonators, which leads to superior performance.

2. Setup and theoretical description

The proposed structure consists of a microring resonator coupled to two identical waveguides, one of which is terminated by a mirror, as shown in Fig. 1(a). Optical gain g is applied to the ring where the amplification process takes place. In the absence of any excitation, the above system is described by the following effective Hamiltonian [5]:

$$i\frac{d}{dt}\begin{bmatrix} a_{\rm cw} \\ a_{\rm ccw} \end{bmatrix} = H \begin{bmatrix} a_{\rm cw} \\ a_{\rm ccw} \end{bmatrix}, \quad H = \begin{bmatrix} \Omega & 0 \\ -2i\gamma r e^{i\phi} & \Omega \end{bmatrix} \tag{1}$$

Here r is the magnitude of the field reflection coefficient of the mirror, $\Omega = \omega - \omega_0 - i(2\gamma + \alpha - g)$ where ω and ω_0 are the input signal angular frequency and resonant frequency, respectively. Additionally, α and γ are the decay rates due to radiation/material loss, and coupling to waveguides, correspondingly. The Hamiltonian H is a non-diagonalizable

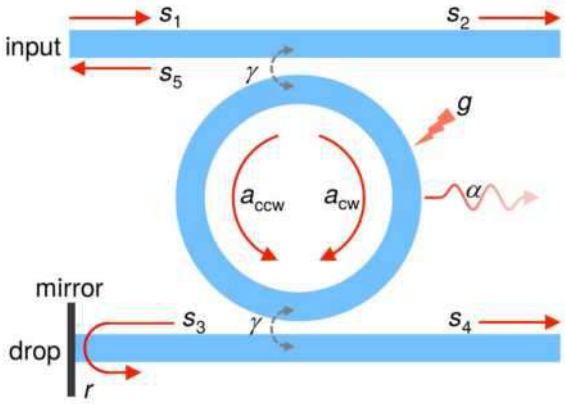


Figure 1: (Schematic of the proposed structure for an optical amplifier working at an EP that arises from the unidirectional coupling from the clockwise (CW) mode $a_{\rm cw}$ to the counterclockwise (CCW) mode $a_{\rm ccw}$.

Jordan matrix that features an EP [6]. By using the coupled mode theory, we obtain the scattering coefficient between the input and output ports:

$$s_{51} \equiv \frac{s_5}{s_1} = \frac{4re^{i\phi}\gamma^2}{[i(\omega-\omega_0)+2\gamma+\alpha-g]^2} \tag{2}$$

Note that this expression is valid only below the lasing threshold $g = 2\gamma + \alpha$. The maximum value of the amplification (at resonance) is $G_{\rm EP} \equiv \max[|s_{51}(\omega_0)|^2] = 16r^2\gamma^4/(2\gamma+\alpha-g)^4$. On the other hand, the bandwidth is given by $B_{\rm EP} = 2F(2\gamma+\alpha-g)$ with $F = \sqrt{\sqrt{2}-1}$. Compared to amplifiers based on diabolic points (DPs) that arise from Hermitian degeneracies, the bandwidth is reduced by a factor of F, while the gain is enhanced according to the quadratic relation $G_{\rm EP} = r^2 G_{\rm DP}^2$. This leads to the following expression for the gain-bandwidth product for the OA operating at an EP:

$$\chi_{\rm EP} \equiv \sqrt[4]{G_{\rm EP}} \cdot B_{\rm EP} = 4F\sqrt{r}\gamma \tag{3}$$

Equation (3) shows that the gain-bandwidth product for the EP regime scales differently than the case of DP, in which $\chi_{\rm DP} = \sqrt{G_{\rm DP}} \cdot B_{\rm DP} = 4\gamma$.

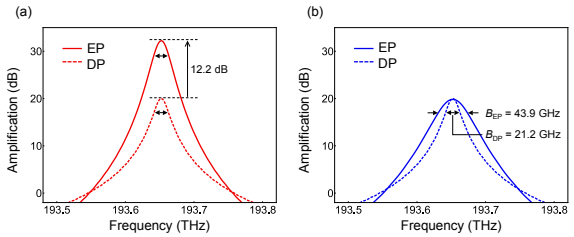


Figure 2: (a) and (b) present a comparison between the proposed EP-based amplifier and a standard device (without the mirror) for fixed bandwidth or gain), respectively. Evidently, the EP-based OA demonstrates better performance.

3. Results

To demonstrate the advantage of the proposed amplifier operating at an EP, we compare its performance with DP-based amplifier in two different situations: (1) When they both share the same bandwidth but have different maximum amplification; and (2) When they both exhibit the same maximum amplification but have different bandwidth. In both cases, we take $r \approx 1$. In the first scenario, we fix the bandwidth by choosing the pump values to be $\tilde{g}_{\rm EP} = F^{-1}\tilde{g}_{\rm DP} + 2(1 - F^{-1})$, where $\tilde{g} = (g - \alpha)/\gamma$. In our simulations, we used the same values for α but different gains γ. Under these conditions, the amplification enhancement is $G_{\rm EP}/G_{\rm DP} = 4F^4/(2 - \tilde{g}_{\rm DP})^2$. Similarly, in the latter case, the bandwidth enhancement factor (for fixed maximum amplification) is $B_{\rm EP}/B_{\rm DP} = \sqrt{2}F/\sqrt{2 - \tilde{g}_{\rm DP}}$ and the required pumping is $\tilde{g}_{\rm EP} = 2 - \sqrt{2(2 - \tilde{g}_{\rm DP})}$. Note that the EP-based OAs delivers a better performance only when $\tilde{g}_{\rm DP} > 2\sqrt{2}F^2 \approx 1.17$.

In order to confirm these predictions and explore realistic implementations, we consider a semiconductor-based optical structure having the following physical parameters: waveguide width w = 0.25 μm (for both the straight and the ring waveguides), ring radius R = 5 μm, edge-to-edge distance between the ring and either waveguides d = 0.15 μm. To implement the mirror, we assume a thin layer of silver with thickness of 100 nm. The material refractive index is $n_1 = 3.47$ (relevant to Si and AlGaAs implementations) and the background index is taken to be $n_2 = 1.44$ (silica for example). Figure 2 (a) and (b) present the comparison between the proposed EP-based amplifier and the standard device when DP $= 1.8$, where the clear advantage of the former is evident.

4. Conclusions

In conclusion, we have introduced a new design paradigm for optical amplifiers based on Jordan exceptional points. An important feature of the proposed structure is the unique scaling of its gain-bandwidth product which is different from standard amplifiers, and allows for achieving more gain or larger bandwidth of operation.

References

[1] K. Hattori, et al., "Erbium-doped silica-based waveguide amplifier integrated with a 980/1530 nm WDM coupler," Electr. Lett. **30**, 856-857 (1994).

[2] K. Amarnath, et al., "Electrically pumped InGaAsP-InP microring optical amplifiers and lasers with surface passivation," IEE Photon. Technol. Lett. **17**, 2280-2282 (2005).

[3] R. El-Ganainy, et al., "Non-Hermitian physics and PT symmetry," Nat. Phys. **14**, 11 (2018).

[4] L. Feng, R. El-Ganainy, L. Ge, "Non-Hermitian photonics based on paritytime symmetry," Nat. Photon. **11**, 053817 (2017).

[5] K. Vahala, *Optical Microcavities* (World Scientific, 2017).

[6] Q. Zhong, et al., "Sensing with exceptional surfaces: combining sensitivity with robustness," arXiv:1810.09417 (2018).

Controlling photonic systems via topological anomalies

Henning Schomerus[1*]

[1]Department of Physics, Lancaster University, Lancaster, UK
*corresponding author, E-mail: h.schomerus@lancaster.ac.uk

Abstract

Anomalies are the term by which we denote that topological states respond in characteristic ways to external probes. Here I show that such anomalies extend naturally to photonic systems, where they take on extra significance in the presence of gain and loss.

1. Introduction

The anomalous response of topological states to probes that break the underlying symmetries underpin the utility of these states in many prosepctive applications. Examples are unidirectional currents in response to external magnetic fields in the quantum Hall effect and analogous surface currents in Weyl and Dirac materials. In the original electronic setting, these topological states are protected by symmetries that are intimately related to the fermionic character, where charge is conserved and stable quasiparticle excitations emerge above the Fermi sea. None of these constraints are natural in photonic systems where loss, gain, nonlinearities and bosonic coherence are normal occurrences. In particular, the properties of photonic systems and operation modes of corresponding devices are often determined by a competition between modes of different life time, as dictated by the gain and loss. As I here set out, topological symmetry protection has a direct bearing on these effects, and offers practically useful tools to design and manipulate photonic components.

2. Making anomalies visible

To set the scene I consider a direct translation of a fermionic anomaly to the photonic setting. This is the chiral anomaly, which when realized in momentum space yields directed currents while when realized in real space yields characteristic intensity patterns. I discuss the realization of a real-space chiral anomaly in a fiber-optical photonic quantum walk [1] (see Fig 1). There, an interface between coin operations (determining the settings of polarizing beam splitters) gives rise to spatially confined states with alternating circular polarization patterns that switch around from round-trip to round-trip of the photonic signal through the circuit.

To understand the origin of these alternating patterns I point out that photonic quantum walks display an unexplored additional symmetry, akin to a supersymmetry (SUSY) but related to the unitary time evolution operator (hence a *unitary SUSY*). This extra symmetry gives rise to a third winding number, which complements the winding numbers known from chiral systems and determines the polarization patterns in the round trips.

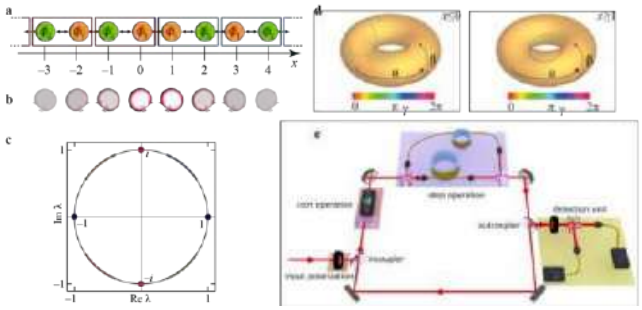


Figure 1: Supersymmetric polarization anomaly in a quantum walk. a) Coin operations. b) Polarization pattern pf the topological state. c) Quasienergy band structure of a topological phase. d) Color representation of winding around a 3-dimensional torus. e) Fibre-optical realization.

3. Gain and loss

Given the translation of fermionic anomalies to photonic structures, these states can now be manipulated in real space by gain and loss. I first discuss how the chiral symmetry extends to this case, and formally takes on the form of a charge-conjugation symmetry known from fermionic superconductors, but applied to an effectively nonhermitian Hamiltonian [2,3,4]. Gain and loss then directly influence the lifetime of the topological state, giving a precise meaning to the notion of a life-time anomaly. First proposed theoretically in [2] and [3], these life-time anomalies have now been realized in a wide range of active and passive photonic structures [5-11].

4. Classification and two-dimensional systems

Conventional classifications of fermionic topological systems invoke the spatial dimensionality of the system. Interestingly, by utilizing the effects of gain and loss described above the boundaries between these symmetry classes become less clear. I describe these complications for two-dimensional resonator arrays yielding the formation of nonhermitian bulk and surface Fermi arcs [12], Lieb lattices supporting gain/loss selected corner states [6] and compactons [13], and anomalous Landau levels [2,14]. Reassuringly, all these states still display anomalous features, which therefore serve as a unifying principle in the categorization of these systems.

5. Conclusions

Photonic topological systems offer many features that go beyond the original setting, with gain and loss being particularly prevalent and important. Under these circumstances one needs to revisit the notion of topological protection and robustness; for instances, in many cases the definition of topological quantum numbers becomes unclear. Against this backdrop it appears that anomalies offer a unifying principle that survives the transition to systems with gain and loss, and at the same time identifies the practically most useful features of the corresponding devices.

Acknowledgements

The theoretical work has been carried out in collaboration with N Yunger-Halpern, C Poli, S Malzard, E Cancellieri, and the groups of R El-Ganainy as well as V Vitelli. Experimental realizations of the theoretical concepts described here have been carried out in collaboration with the groups of S Barkhofen and C Silberhorn; F Mortessagne and U Kuhl; L Feng; and M Skolnick. Funding was received from ESPRC via Grant No. EP/N031776/1.

References

[1] S. Barkhofen, L. Lorz, T. Nitsche, C. Silberhorn, and H. Schomerus, Supersymmetric Polarization Anomaly in Photonic Discrete-Time Quantum Walks, Phys. Rev. Lett. 121, 260501 (2018).

[2] H. Schomerus and N. Yunger-Halpern, Parity Anomaly and Landau-Level Lasing in Strained Photonic Honeycomb Lattices, Phys. Rev. Lett. 110, 013903 (2013).

[3] H. Schomerus, Topologically protected midgap states in complex photonic lattices, Opt. Lett. 38, 1912-1914 (2013).

[4] S. Malzard, C. Poli, and H. Schomerus, Topologically Protected Defect States in Open Photonic Systems with Non-Hermitian Charge-Conjugation and Parity-Time Symmetry, Phys. Rev. Lett. 115, 200402 (2015).

[5] C. Poli, M. Bellec, U. Kuhl, F. Mortessagne, and H. Schomerus, Selective enhancement of topologically induced interface states in a dielectric resonator chain, Nat. Commun. 6, 6710 (2015).

[6] C. Poli, H. Schomerus, M. Bellec, U. Kuhl, and F. Mortessagne, Partial chiral symmetry-breaking as a route to spectrally isolated topological defect states in two-dimensional artificial materials, 2D Mater. 4, 025008 (2017).

[7] P. St-Jean, V. Goblot, E. Galopin, A. Lemaître, T. Ozawa, L. Le Gratiet, I. Sagnes, J. Bloch and A. Amo. Lasing in topological edge states of a one-dimensional lattice. Nat. Photonics 11, 651–656 (2017).

[8] H. Zhao, P. Miao, M. H. Teimourpour, S. Malzard, R. El-Ganainy, H. Schomerus, and L. Feng, Topological hybrid silicon microlasers, Nat. Commun. 9, 981 (2018).

[9] M. Parto, S. Wittek, H. Hodaei, G. Harari, M. A. Bandres, J. Ren, M. C. Rechtsman, M. Segev, D. N. Christodoulides, and M. Khajavikhan, Edge-Mode Lasing in 1D Topological Active Arrays, Phys. Rev. Lett. 120, 113901 (2018).

[10] Y. Ota, R. Katsumi, K. Watanabe, S. Iwamoto, and Y. Arakawa, Topological photonic crystal nanocavity laser, Communications Physics 1, 86 (2018).

[11] R. Yao, H. Li, B. Zheng, S. An, J. Ding, C.-S. Lee, H. Zhang, W. Guo, Electrically Tunable and Reconfigurable Topological Edge State Lasers, arXiv:1804.01587.

[12] S. Malzard and H. Schomerus, Bulk and edge-state arcs in non-Hermitian coupled-resonator arrays, Phys. Rev. A 98, 033807 (2018).

[13] C. E. Whittaker, E. Cancellieri, P. M. Walker, D. R. Gulevich, H. Schomerus, D. Vaitiekus, B. Royall, D. M. Whittaker, E. Clarke, I. V. Iorsh, I. A. Shelykh, M. S. Skolnick, and D. N. Krizhanovskii, Exciton Polaritons in a Two-Dimensional Lieb Lattice with Spin-Orbit Coupling, Phys. Rev. Lett. 120, 097401 (2018).

[14] H. Abbaszadeh, A. Souslov, J. Paulose, H. Schomerus, and V. Vitelli, Sonic Landau Levels and Synthetic Gauge Fields in Mechanical Metamaterials, Phys. Rev. Lett. 119, 195502 (2017).

PT symmetry in a Double Quantum Dot circuit-QED set-up

Manas Kulkarni[1], **Archak Purkayastha**[2], **Yogesh Joglekar**[3],

[1]International Center for theoretical Sciences, Tata Institute of Fundamental Research, Bangalore, India
[2]Trinity College Dublin, The University of Dublin, College Green, Dublin, Ireland
[3]Department of Physics, Indiana University Purdue University Indianapolis (IUPUI), Indianapolis, Indiana, USA

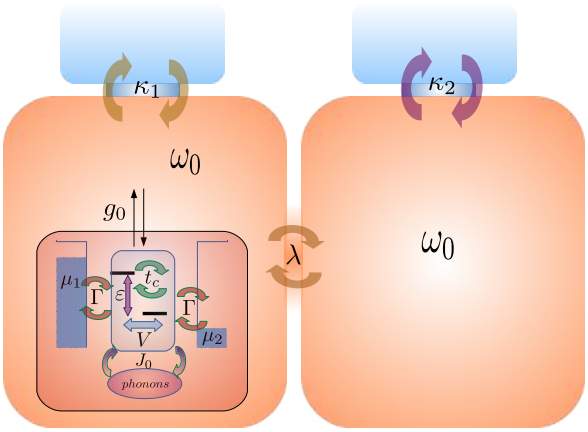


Figure 1: The set-up consists of two cavities connected to each other, with the left cavity having a double-quantum-dot out-of-equilibrium. The double-quantum-dot is configured to give a gain to the left cavity. If the gain is same as the loss of the right cavity, the bosonic system of the cavities have an effective $\mathcal{PT}$ symmetric dynamics.

Abstract

We show here that state-of-the-art double-quantum-dot circuit-QED (DQD-cQED) system can be controllably tuned to show non-Hermitian quantum dynamics governed by an effective PT -symmetric Hamiltonian. We show this by rigorously deriving the effective dynamics from a microscopic model of the set-up. This also reveals the effect of thermal and quantum fluctuations on the PT symmetric system.

1. The set-up

The schematic diagram of the set-up is given in Fig. 1. The DQD Hamiltonian is,

$$\hat{\mathcal{H}}_{DQD} = \frac{\varepsilon}{2}\left(\hat{n}_1 - \hat{n}_2\right) + V\hat{n}_1\hat{n}_2 + t_c\left(\hat{c}_1^\dagger\hat{c}_2 + \hat{c}_2^\dagger\hat{c}_1\right), \tag{1}$$

where $\hat{n}_\ell = \hat{c}_\ell^\dagger\hat{c}_\ell$, and $\hat{c}_\ell$ is the fermionic annihilation operator of the ℓth site. The DQD Hamiltonian can be diagonalized by the transforming to the fermionic operators $\hat{A}_\alpha$, which are related to $\hat{c}_\ell$ via the following transformaiton,

$$\begin{pmatrix}\hat{A}_1\\ \hat{A}_2\end{pmatrix} = \Phi\begin{pmatrix}\hat{c}_1\\ \hat{c}_1\end{pmatrix},\quad \Phi = \begin{pmatrix}\cos(\theta) & \sin(\theta)\\ -\sin(\theta) & \cos(\theta)\end{pmatrix},$$
$$\tan(\theta) = \frac{2t_c}{\varepsilon + \sqrt{\varepsilon^2 + 4t_c^2}}. \tag{2}$$

In the transformed basis, the system Hamiltonian is given by,

$$\hat{\mathcal{H}}_{DQD} = \frac{\omega_q}{2}(\hat{N}_1 - \hat{N}_2) + V\hat{N}_1\hat{N}_2,$$
$$\omega_q = \sqrt{\varepsilon^2 + 4t_c^2}, \tag{3}$$

where $\hat{N}_\alpha = \hat{A}_\alpha^\dagger\hat{A}_\alpha$.

The bosonic system Hamiltonian is

$$\hat{\mathcal{H}}_S^b = \omega_0(\hat{b}_1^\dagger\hat{b}_1 + \hat{b}_2^\dagger\hat{b}_2) + \lambda(\hat{b}_1^\dagger\hat{b}_2 + \hat{b}_2^\dagger\hat{b}_1) \tag{4}$$

The cavity-DQD coupling Hamiltonian is,

$$\hat{\mathcal{H}}^{fb} = g_0(\hat{c}_1^\dagger\hat{c}_1 - \hat{c}_2^\dagger\hat{c}_2)(\hat{b}_1^\dagger + \hat{b}_1). \tag{5}$$

All baths are modelled by non-interacting systems with infinite degrees of freedom. For the phononic bath and the baths attached to the bosonic cavities, the degrees of freedom are bosonic. For source and drain baths attached to the DQD, the degrees of freedom are fermionic. All system-bath couplings are bilinear except for the coupling to the phononic bath, which is given by

$$\hat{\mathcal{H}}_{DQD-ph} = \epsilon\left(\hat{n}_1 - \hat{n}_2\right)\sum_{s=1}^{\infty}\lambda_s\left(\hat{B}_s^\dagger + \hat{B}_s\right). \tag{6}$$

Here, $\hat{\mathcal{H}}_{ph} = \sum_{s=1}^{\infty}\Omega_s\hat{B}_s^\dagger\hat{B}_s$, is the phononic bath.

2. The effective $\mathcal{PT}$ symmetry

We consider the regime where,

$$V \gg \mu_1 \gg \frac{\omega_q}{2},\ \ \mu_2 \ll -\frac{\omega_q}{2},\ \ \kappa_1,\kappa_2,g_0,\Gamma,\lambda \ll \omega_0$$
$$\omega_0 \simeq \omega_q,\ \ \beta \gg 1/\omega_0,\ \ \Gamma \gg \kappa_1,\kappa_2. \tag{7}$$

After integrating out the fermionic part and the bosonic baths, we have the effective equations of motion for the

ω_0	8 GHz
g_0	60 MHz
Γ	90 MHz
μ_1	30 GHz
μ_2	-30 GHz
κ_1, κ_2	2 MHz
λ	20 MHz

Table 1: Set of parameters chosen for numerical plots. These parameters are very much within reach of the state-of-the-art experiments.

bosonic system,

$$\frac{d}{dt}\begin{pmatrix}\hat{b}_1\\ \hat{b}_2\end{pmatrix} = -i\hat{\mathbf{H}}_{eff}\begin{pmatrix}\hat{b}_1\\ \hat{b}_2\end{pmatrix} - i\begin{pmatrix}\hat{\xi}_1^b(t)+\hat{\xi}_A(t)\\ \hat{\xi}_2^b(t)\end{pmatrix}, \tag{8}$$

$$\mathbf{H}_{eff} = \begin{pmatrix}\omega_0 + i(\Delta N_{ss}\frac{g^2\Gamma}{\lambda^2+\Gamma^2} - \frac{\kappa_1}{2}) & \lambda\left(1+\frac{\Delta N_{ss}g^2}{\lambda^2+\Gamma^2}\right)\\ \lambda & \omega_0 - i\frac{\kappa_2}{2}\end{pmatrix},$$

where

$$g = g_0\sin(2\theta),\ \ \Delta N_{ss} = \langle\hat{N}_1\rangle_{ss} - \langle\hat{N}_2\rangle_{ss}. \tag{9}$$

where the $\langle ...\rangle_{ss}$ refers to the steady state expectation value of the corresponding fermion correlations when $g_0 = 0$. Associated with the gain is a fluctuation term, $\hat{\xi}_A(t)$ coming from the DQD, thereby satisfying the fluctuation dissipation relation.

The effective non-Hermitian Hamiltonian is $\mathcal{PT}$-symmetric if

$$\Delta N_{ss}\sin^2(2\theta) = \left(\frac{\lambda^2+\Gamma^2}{g_0^2\Gamma}\right)\left(\frac{\kappa_1+\kappa_2}{2}\right). \tag{10}$$

3. Conclusions and further (on-going) work

In this on-going work, we have been able to show that an extension of an already state-of-the-art quantum experimental set-up [1,2] can be tuned to show $\mathcal{PT}$-symmetric dynamics. The fundamental question of quantum fluctuations in such set-ups remain to be thoroughly explored. This is possible within the formalism we have developed.

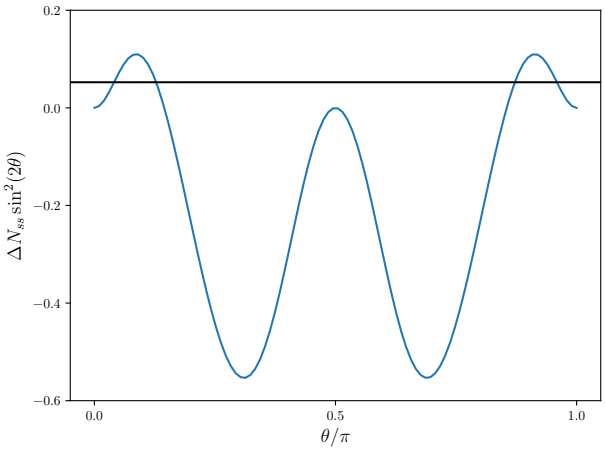
4. Acknowledgements

M. K. gratefully acknowledges the Ramanujan Fellowship SB/S2/RJN-114/2016 from the Science and Engineering Research Board (SERB), Department of Science and Technology, Government of India.

References

[1] Y.-Y. Liu, J. Stehlik, C. Eichler, M. J. Gullans, J. M. Taylor, and J. R. Petta, Science **347**, 285 (2015).

[2] Y.-Y. Liu, J. Stehlik, C. Eichler, X. Mi, T.R. Hartke, M.J. Gullans, J.M. Taylor, and J.R. Petta Phys. Rev. Lett. **119**, 097702 (2017).



$\mathcal{PT}$-symmetric points:

ε (GHz)	t_c (GHz)
7.7382	$\pm$1.0150
5.5467	$\pm$2.8825

Figure 2: $\Delta N_{ss}\sin^2(2\theta)$ vs θ as ε and t_c are varied under the constraint $\omega_q = \omega_0$, for parameters given in Table 1. The horizontal line shows the RHS of Eq. 10. The points at which the curve and the horizontal line meet, the effect dynamics of the cavity is $\mathcal{PT}$-symmetric. The value of ε and t_c at those points are given in the table. Other parameters: $\beta = 10$ (GHz)$^{-1}$.

Demonstration of a two-dimensional PT-symmetric crystal: Bulk dynamics, topology and edge states

Lukas J. Maczewsky[1,*], Mark Kremer[1], Tobias Biesenthal[1], Matthias Heinrich[1], Ronny Thomale[2], and Alexander Szameit[1]

[1]Institut für Physik,Universität Rostock, Germany
[2]Department of Physics and Astronomy, Julius-Maximilians-Universität Würzburg, Germany
*corresponding author, E-mail: lukas.maczewsky@uni-rostock.de

Abstract

We report the first implementation of a two-dimensional PT-symmetric crystalline structure. Using a novel isotropic loss mechanism in a photonic setting, we probe both bulk and edge properties, and study the interplay between PT-symmetry and topology in this system.

1. Introduction

One of the fundamental percepts of quantum mechanics is that in order to properly describe a physical system, its associated Hamiltonian has to be real-valued. The well-trodden path to fullfill this condition is to demand the Hamiltonian to be Hermitian. In their seminal work of 1988, Carl M. Bender and Stefan Boettcher showed that parity-time (PT) symmetric Hamiltonians may likewise exhibit real spectra [1]. As it turned out, these notions can be readily implemented in the field of photonics, where the associated complex-valued potentials translate to arrangements of refractive index, gain and loss for electromagnetic waves. Experiments along these lines allowed the verification of numerous hallmark features of PT symmetric systems [2]. However, to date, various technological challenges prevented researchers from going beyond arrangements with single spatial dimension. In this work, we present the first experimental realization and characterization of a two-dimensional PT-symmetric system utilizing photonic waveguide structures with judiciously tailored discrete refractive index landscape and tailored loss structure. In this vein, we explore a non-Hermitian 2D topological phase transition and its connection to the emergence of mid-gap sates.

2. PT-symmetric waveguide lattices

A system is PT-symmetric of its Hamiltonian H fulfills

$$[H, PT] \stackrel{!}{=} 0\,, \tag{1}$$

where P is the parity operator and T the time-reversal operator, respectively. Due to this relation, H and PT share the same set of eigenstates. A necessary condition arising from these demands is that $V(-\mathbf{r}) = V^*(\mathbf{r})$ holds for the complex potential V [1]. In the paraxial Helmhotz regime, the refractive index landscape plays the role of the quantum mechanical potential, hence [3]

$$n(x, -y) = n^*(x, y)\,. \tag{2}$$

Our system is based on photonic graphene, i.e. a honeycomb lattice of straight waveguides [4] as sketched in Fig.1 (a). In order to implement the above relation, we introduce differential loss to the two elements of the unit cell, as indicated by the blue and yellow shading in Fig.1 (a). Since this configuration is known to exhibit complex eigenvalues, i.e. reside in the phase of broken PT symmetry, we moreover apply a strain (τ) along the horizontal bonds (shown in Fig. 1(a)) to enforce unbroken PT symmetry. We realized these ideas by using the femtosecond laser writing technique [6]. In particular, repeated dwelling of the focal spot along the waveguide trajectory was used to create microscopic scatter centers that, at properly chosen concentrations, yield the desired additional isotropic loss (displayed in Fig. 1(b)). By adjusting the fill factor and the dwelling time, the propagation losses are continuously tunable in a wide range. In turn, the lattice strain is implemented by changing the ratio of the lattice site separations along the horizontal and diagonal bonds in Fig. 1(a), respectively.

In this vein, we were able to observe the transition from broken to unbroken PT-symmetry in a two dimensional system. As indicator, we made use of the fact that in the broken-PT phase, some eigenmodes experience loss, while others remain lossless. This results in a characteristic dependence of the overall output intensity on the specific site that was excited. In contrast, in the presence of the appropriate strain, all eigenvalues become real and no mode is experiencing loss. As a result, the output intensity no longer depends on the injection site. We experimentally verify this behaviour by extracting the standard deviation of the output intensities [7] when launching in 6 different lattice sites. The results are shown in Fig. 1(c), together with a theoretical graph calculated within the tight-binding approximations, clearly confirming the transition from 'broken' to 'unbroken' PT-symmetry.

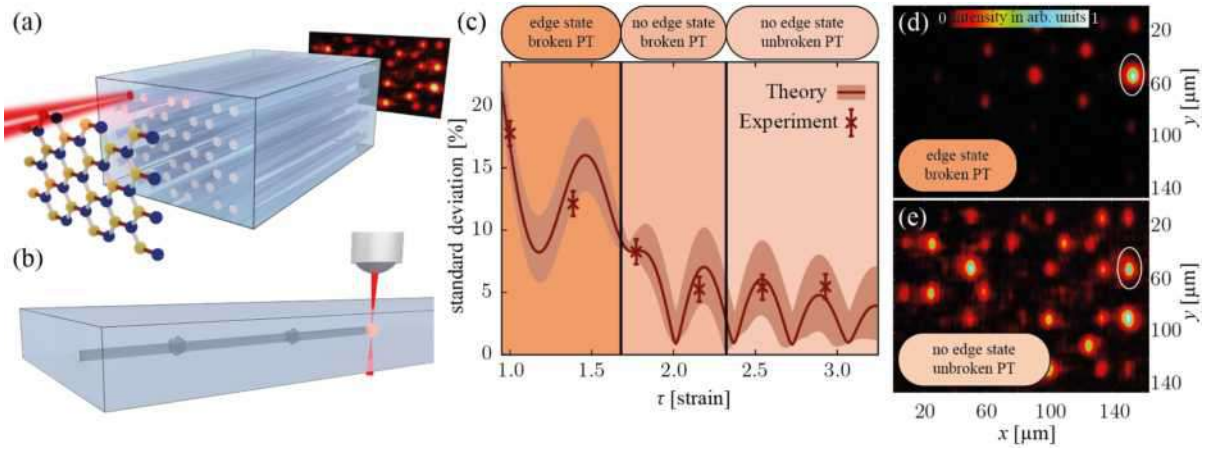


Figure 1: (a) Schematic of the investigated photonic graphene based structure. The yellow and blue colors of the lattice sites indicate different losses, while the red and gray connections indicate strained and unstrained bonds, respectively. (b) Illustration of the dwelling mechanism to induce precise amounts of artificial propagation losses. (c) Calculated and measured strain dependence of the standard deviation of the output power over 6 different single site excitations. (d) & (e) Exemplary intensity patterns of the end facet, illustrating the presence and absence of an edge state.

3. Discussion

As it turns out, this transition is closely linked to a topological phase transition, as indicated by the shading in Fig. 1(c). The topological characterization is retrieved from the winding number of a Su-Shrieffer-Heeger (SSH) model perpendicular to the edges [8], resulting in the presence (or absence) of a topological mid-gap state (i.e. an edge mode). In the Hermitian case, the topological invariant changes at a threshold strain of $\tau = 2$. However, as soon as gain/loss is introduced, this behavior changes, as displayed in Fig. 1(c). Furthermore, 'unbroken' PT-symmetry and the presence of an edge mode are mutually exclusive. This is the result of the second condition for PT-symmetry, mentioned above. Since the edge modes are not eigenstates of the PT operator, they inevitably break PT-symmetry. As the topological phase transition is linked to the presence or absence of these edge states, they can readily serve as its indicator. By quantifying the localization in terms of the fraction of a wave packet remaining within the marked edge waveguide (Fig. 1(d,e)), we find that this value drops from $(43.5 \pm 1)\%$ to $(6.3 \pm 1)\%$ as our system changes its phase.

4. Conclusions

In summary we have designed and experimentally realized a two-dimensional PT-symmetric crystalline structure based on photonic graphene. For this purpose we developed a new technology to introduce tunable artificial losses. In addition to observing the phase transition associated with the breaking of PT symmetry, we also shed light on its close connection to a second, topological phase transition. Our results pave the way towards a wide range of future investigations in high-dimensional non-Hermitian settings. Now, their combinations with nonlinearity or single-photon interference are in the reach of experiments.

References

[1] C.M. Bender and S. Boettcher, "Real spectra in non-Hermitian Hamiltonians having PT symmetry", Phys. Rev. Lett. **80**, 5243 (1998).

[2] R. El-Ganainy, K. Makris, M. Khajavikhan, Z. Musslimani, S. Rotter and D. Christodoulides, "Non-Hermitian physics and PT symmetry", Nature Physics, **14**, 11, (2018)

[3] S. Longhi, "Quantum-optical analogies using photonic structures", Laser Phot. Rev. **3**, 243 (2009).

[4] O. Peleg, G. Bartal, B. Freedman, O. Manela, M. Segev, and D. N. Christodoulides, "Conical Diffraction and Gap Solitons in Honeycomb Photonic Lattices", Phys. Rev. Lett. **98**, 103901 (2007).

[5] B. Zhen, C.W. Hsu, Y. Igarashi, L. Lu, I. Kaminer, A. Pick, S.-L. Chua, J.D. Joannopoulos, and M. Soljačić, "Spawning rings of exceptional points out of Dirac cones", Nature **525**, 354 (2015).

[6] A. Szameit, M. C. Rechtsman, O. Bahat-Treidel, and M. Segev, "PT-Symmetry in honeycomb photonic lattices", Phys. Rev. A **84**, 021806(R) (2011).

[7] S. Weimann, M. Kremer, Y. Plotnik, Y. Lumer, S. Nolte, K. G. Makris, M. Segev, M. C. Rechtsman, and A. Szameit, "Topologically protected bound states in photonic PT -symmetric crystals", Nature Mater. **16**, 433 (2017).

[8] K. Esaki, M. Sato, K. Hasebe, and M. Kohmoto, "Edge states and topological phases in non-Hermitian systems", Phys. Rev. B **84**, 205128 (2011)

Coherent absorption in non-Hermitian multilayers: when the weak controls the strong

Simone Zanotto[1], Giuseppe C. La Rocca[2], and Alessandro Tredicucci[1,3]

[1]Istituto Nanoscienze - CNR, and Laboratorio NEST, Piazza San Silvestro 12, 56127 Pisa, Italy
[2]Scuola Normale Superiore and CNISM, Piazza dei Cavalieri 7, 56126 Pisa, Italy
[3]Dipartimento di Fisica "E. Fermi", Università di Pisa, Largo Pontecorvo 3, 56127 Pisa, Italy
*corresponding author, E-mail: simone.zanotto@nano.cnr.it

Abstract

Controlling the flow of an intense light beam by means of a much weaker one is a dream whose realization may open the way to potentially disruptive data elaboration techniques. However, since light interacts with itself very weakly and only under precise circumstances, this task has proven elusive for long times. In this abstract we show that a loss-gain multilayer – either thin-film based or metasurface-based – may implement perfect, asymmetric, full-optical control if non-Hermitian photonics concepts are appropriately exploited.

The last decade welcomed the concept of *coherent perfect absorption* (CPA), where an appropriately tailored optical field is completely absorbed by an object which, under ordinary circumstances, would appear only partially opaque [1]. In the simplest, two-port CPA object, the relative phase and intensity of two input beams dictate the amount of light absorbed, which can switch from zero to unity (relative to input energy) thus implementing a perfect light-light switch [2]. However, when attempting to extend this concept to the situation where the phase of a weak beam is used to control the intensity of an intense beam, it turns out that unavoidable losses are present due to a fundamental limitation in the structure of the scattering matrix.

The key idea to overcome this kind of limitation stems from recent observations about photonic elements that contain both gain and loss. Actually, the co-presence of gain and loss, which mathematically results in non-Hermitian Hamiltonians, was first studied in the framework of theoretical quantum mechanics, particularly in the case of parity-time (PT) symmetric systems, since it leads to alternative theories about the mathematical nature of observables. These studies triggered a flourishing literature in the photonics community, since non-Hermitian and PT-symmetric permittivity landscapes imply extremely unusual solutions of the Maxwell equations and, consequently, novel photonic functionalities [3-5]. One of such phenomena is coherent absorption in loss/gain structures. In its simplest version it occurs when a two-port photonic device, like a multilayer that contains materials with both loss and gain, is illuminated with two coherent beams. The multilayer can either work in the ordinary, wavelength-scale regime (e.g., Fabry-Pérot resonator), or in the subwavelength regime, where conducting layers (e.g., natural ones like graphene or artificial ones like metasurfaces) are appropriately arranged (Fig. 1a). The overall output intensity from this object ($I_{out} = |s_1^-|^2 + |s_2^-|^2$) depends sinusoidally on the relative phase of the input beams ($\Delta\phi = \arg(s_1^+/ s_2^+)$), as illustrated in Fig. 1b. Notably, the minimum/maximum values of I_{out} depend on the relative intensity between the input beams, that in the figure is indicated with the parameter $x = (|s_1^+|^2 - |s_2^+|^2)/(|s_1^+|^2 + |s_2^+|^2)$. It can be shown that the curve that describes the phenomenon is an ellipse. As it can be noticed in the region $x > 0$, the object can act *either* as a lossy *or* a gainy component, depending only upon the externally imposed relative phase $\Delta\phi$. This observation has far-reaching consequences. Suppose indeed that one's interest is to switch an intense light beam with a much weaker one; this means that the system must operate at a point where $|x| \approx 1$.

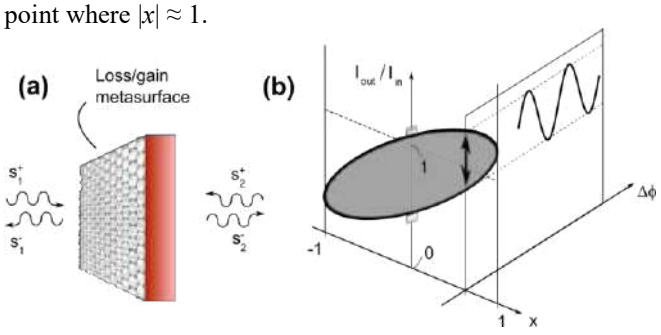


Figure 1. Panel (a), schematic of a loss-gain two-port coherent intensity control system. The loss and gain elements may be implemented, as illustrated here, by means of conducting sheets (graphene or metasurface), or by means of dielectric layers. Panel (b), normalized output intensity as a function of the relative phase $\Delta\phi$ between input beams and of the relative amplitude x .

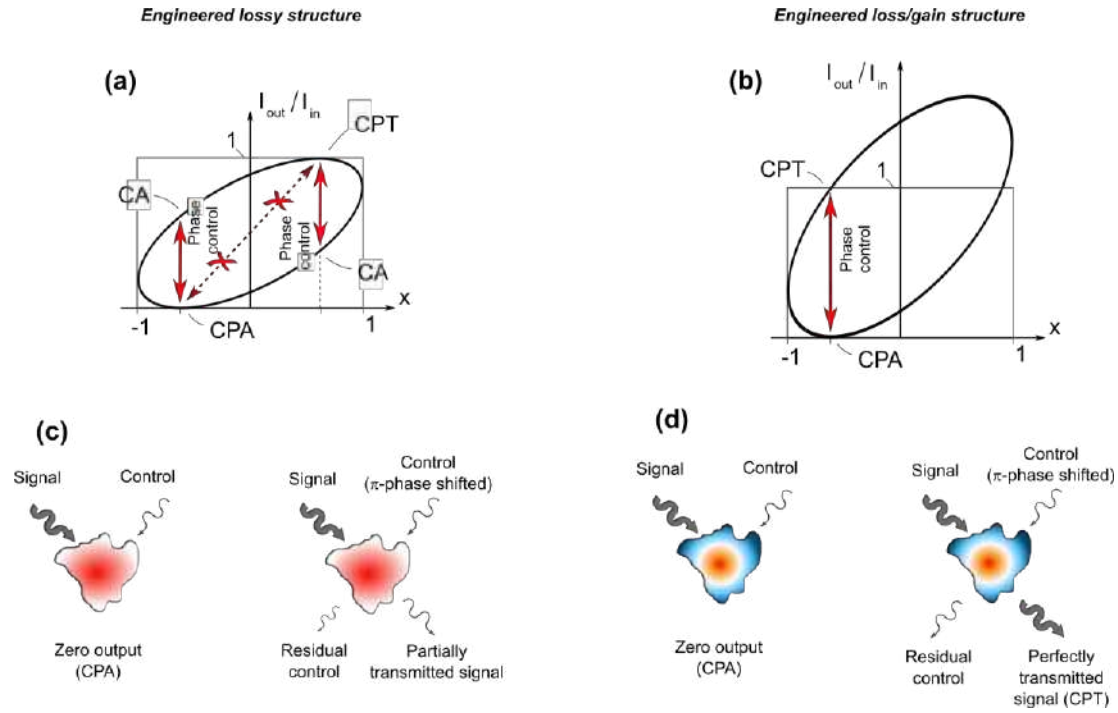


Figure 2. Optimal control of a strong signal by a weak beam in a structure with engineered loss (a, c) and with engineered loss and gain (b,d). In the structure with losses, the weak control beam can trigger a modulation from coherent perfect absorption (CPA) to coherent absorption (CA) or from coherent absorption (CA) to coherent perfect transparency (CPT). In no way it is possible to span from CPA to CPT, i.e., it is not possible that a weak beam can perfectly stop a strong beam without introducing some spurious losses in the system. Instead, if a structure with an engineered combination of loss and gain is employed, it is possible that a weak control beam perfectly switches on and off a strong signal beam having an arbitrarily large intensity (b,d).

Suppose also that the device only contains lossy elements. In order to have the largest possible modulation depth, one may think of appropriately engineering the ellipse shape, however, an ideal situation will never be reached due to a fundamental limitation. This is illustrated in Fig. 2a: because of energy conservation, the ellipse is constrained in the region $0 < I_{out}/I_{in} < 1$, and the phase control will only allow for a limited span of the output intensity. In other words, even if the ellipse is fully optimized, i.e., if the system is capable of both coherent perfect absorption *and* coherent perfect transparency (CPA and CPT), a sole relative phase control is not sufficient for an efficient switching of a strong beam by means of a weak beam.

This limitation can be overcome by relying on an appropriate loss/gain structure. Indeed, by these means the limitation dictated by energy conservation is lifted, and the ellipse shape can be engineered as illustrated in Fig. 2b. Now, simply sweeping by π the relative phase between the input beams will switch the strong signal off and on in a perfect way (Fig. 2d).

Numerical analysis on a prototypical structure, i.e., on a two-layer gain-loss slab, revealed that there exists a family of solutions to the problem, hence proving the feasibility of the CPA/CPT concept in a practical framework. We believe that this concept may prove useful in fully-optically controlled signal elaboration systems.

References

[1] Y. D. Chong, L. Ge, H. Cao, and A. D. Stone, *Coherent Perfect Absorbers: Time-Reversed Lasers,* Phys. Rev. Lett. **105**, 053901 (2010).

[2] H. Zhao, W. S. Fegadolli, J. Yu, Z. Zhang, L. Ge, A. Scherer, and L. Feng, *Metawaveguide for Asymmetric Interferometric Light-Light Switching,* Phys. Rev. Lett. **117**, 193901 (2016).

[3] S. Longhi, *Parity-time symmetry meets photonics: A new twist in non-Hermitian optics,* Euro Physics Lett. **120**, (2017).

[4] R. El-Ganainy, K. G. Makris, M. Khajavikhan, Z. H. Musslimani, S. Rotter, and D. N. Christodoulides, *Non-Hermitian physics and PT symmetry*, Nat. Phys. **14**, 11 (2018).

[5] B. Peng, Ş. K. Özdemir, F. Lei, F. Monifi, M. Gianfreda, G. L. Long, S. Fan, F. Nori, C. M. Bender, and L. Yang, *Parity–time-symmetric whispering-gallery microcavities,* Nat. Phys. **10**, 394 (2014).

PT-symmetric quantum optics

Friederike Klauck[1,*], Lucas Teuber[1], Marco Ornigotti[1], Matthias Heinrich[1], Stefan Scheel[1], and Alexander Szameit[1]

[1]Institute of Physics, University of Rostock, Rostock, Germany
*corresponding author, E-mail: Friederike.klauck@uni-rostock.de

Abstract

Photonics has become the primary testbed for Parity-Time-symmetric systems and a wide range of its implications in classical systems. However, the intersection between quantum optics and PT-symmetry remains largely uncharted. Here, we report on the first observation of quantum interference achieved by entangled biphotons in lossy directional couplers. We observe the generalized version of the well-known Hong-Ou-Mandel, and find that the underlying non-trivial loss distribution systematically displaces photon bunching with respect to the Hermitian case, as predicted by our theory.

1. Introduction

Parity-Time(PT)-symmetric physics have been intensely studied since their first description by Bender & Boettcher in 1998 [1]. Especially in photonics, numerous PT-symmetric effects and systems were investigated [2]. However, since all of those experiments were performed with classical light or single photons- the observation of a multi-particle quantum interference in PT symmetric arrangements remains elusive to this date. We close this gap by exploring two-photon interference in a lossy directional coupler and characterize the underlying generalized Hong-Ou-Mandel (HOM) interference [3].

In optics, complex potential landscapes such as required by PT symmetry can be implemented by establishing a symmetric real part of the refractive index in conjunction with an antisymmetric imaginary part (i.e. gain/loss) [4]. Optical waveguides are a particularly versatile tool to construct such distributions in a discrete framework. However, in the quantum regime, the introduction of gain would fundamentally change the character of a propagating quantum state by inevitably introducing thermal noise [5]. Instead, we make use of entirely passive systems: By choosing an appropriate loss distribution, the behavior of the system can be separated into a global loss factor and the desired dynamics of the PT-symmetric system [6]. The object of our following considerations is a passive PT-symmetric coupler, in which two waveguides interact over a distance z, see Fig. 1 A. Rapid undulations introduce Markovian effective losses, resulting in the desired complex refractive index distribution (B).

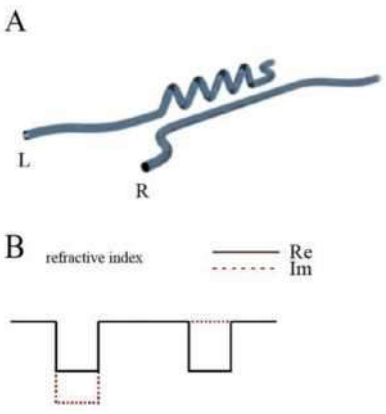


Figure 1: The lossy directional coupler. (A) In a pair of coupled waveguides, undulations selectively introduce losses to facilitate the desired effective complex index distribution illustrated in (B).

2. Theory of the PT-symmetric coupler

We theoretically describe light propagation in the lossy directional coupler by a quantum master equation in Lindblad form, i.e.

$$\partial_z \rho(z) = -\frac{i}{\hbar}[H,\rho] + \gamma\left(2\, a_L\, \rho\, a_L^\dagger + \{a_L^\dagger a_L, \rho\}_+\right) = \mathcal{L}\,\rho,$$

where γ is the loss rate in waveguide L. We chose a rigorous approach providing information on the full quantum state of the system based on a Lie algebra treatment. This yields an igen-deco mposition of the density matrix, and the resulting analytical solution for the intensities is plotted in Fig. 2.

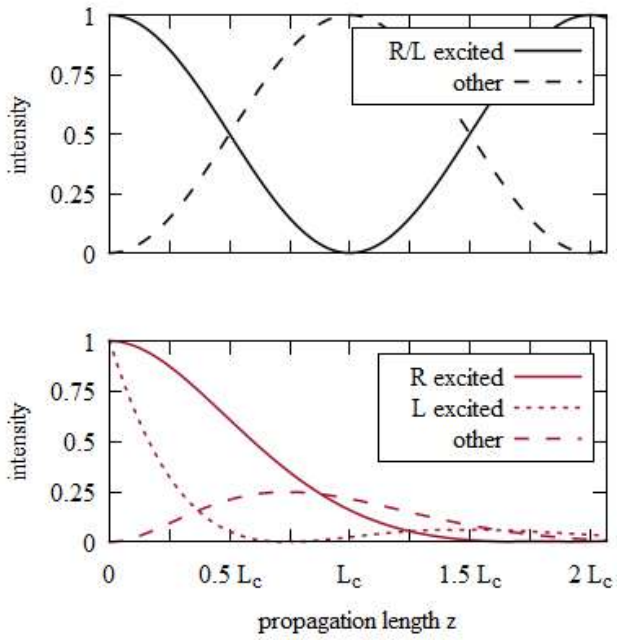


Figure 2: Analytical solution of the intensity in the directional coupler in the Hermitian case (red) and the PT-symmetric case (black).

In the conventional Hermitian case (black), the intensities evolve as sine- and cosine squared, and after half the coupling length L_c, the intensities in both waveguides are identical. In the PT-symmetric case, the evolution of light launched into the L or R waveguide differs strongly: For a |1,1> input state, the coincidence rate of finding the photons in different outputs is described by the density matrix:

$$\Gamma(z) = e^{-2\gamma z}\left(\frac{\gamma^2 - 4\,\kappa^2\,cos(\omega z)}{\omega^2}\right)^2.$$

Here, $\omega = \sqrt{4\,\kappa^2 - \gamma^2}$ is the damped oscillation frequency of the system. Our analytical solution holds for the unbroken PT-symmetry case, i.e. for losses that do not exceed twice the coupling. The resulting coincidence function is plotted in Fig. 3, in the Hermitian case the HOM dip occurs at half the coupling length. In the PT-symmetric case, the asymmetric loss alters the interference such that the minimum occurs after a shorter propagation length, as indicated by the dashed vertical lines. The region, which admits for photon bunching, is limited by the PT-symmetry breaking threshold and outlined in gray.

3. Measurement of the HOM-Dip in PT-symmetry

For the experiment, a set of lossy directional couplers of identical couplings with different propagation lengths was implemented to sample light at different z positions. A corresponding set of conventional Hermitian couplers served as baseline reference. The couplers were fabricated with a coupling constant of $\kappa = 0.25\ cm^{-1}$ and loss coefficient $\gamma = 0.2\ cm^{-1}$ for the probe wavelength of 815 nm light. As predicted by theory, the antisymmetric loss distribution leaves a distinct signature in the passive PT-symmetric couplers. For the correlation measurement, our experiments were conducted with photon pairs synthesized by type-I spontaneous parametric down conversion, the coincidences were recorded by avalanche photo detectors. The results are shown in Fig. 3.

4. Conclusions

In conclusion, we present the first observation of multi-particle quantum interference in a PT symmetric system. From our experiments, we find that coincidence minimum in the PT-symmetric case is systematically shifted and occurs earlier than in the Hermitian case, in close agreement with the theoretical predictions.

References

[1] C. M. Bender and S. Boettcher, Real Spectra in Non-Hermitian Hamiltonians Having PT Symmetry, *Phys. Rev. Lett.*, vol. 80, no. 24, pp. 5243–5246, Jun. 1998.

[2] R. El-Ganainy, K. G. Makris, M. Khajavikhan, Z. H. Musslimani, S. Rotter, and D. N. Christodoulides, Non-Hermitian physics and PT symmetry, *Nat. Phys.*, vol. 14, no. 1, pp. 11–19, Jan. 2018.

[3] C. K. Hong, Z. Y. Ou, and L. Mandel, Measurement of subpicosecond time intervals between two photons by interference, *Phys. Rev. Lett.*, vol. 59, no. 18, pp. 2044–2046, Nov. 1987.

[4] R. El-Ganainy, K. G. Makris, D. N. Christodoulides, and Z. H. Musslimani, Theory of coupled optical PT-symmetric structures, *Opt. Lett.*, vol. 32, no. 17, pp. 2632–2634, Sep. 2007.

[5] S. Scheel and A. Szameit, PT -symmetric photonic quantum systems with gain and loss do not exist, *EPL*, vol. 122, no. 3, p. 34001, Jun. 2018.

[6] M. Ornigotti and A. Szameit, Quasi PT -symmetry in passive photonic lattices, *J. Opt.*, vol. 16, no. 6, p. 065501, Jun. 2014.

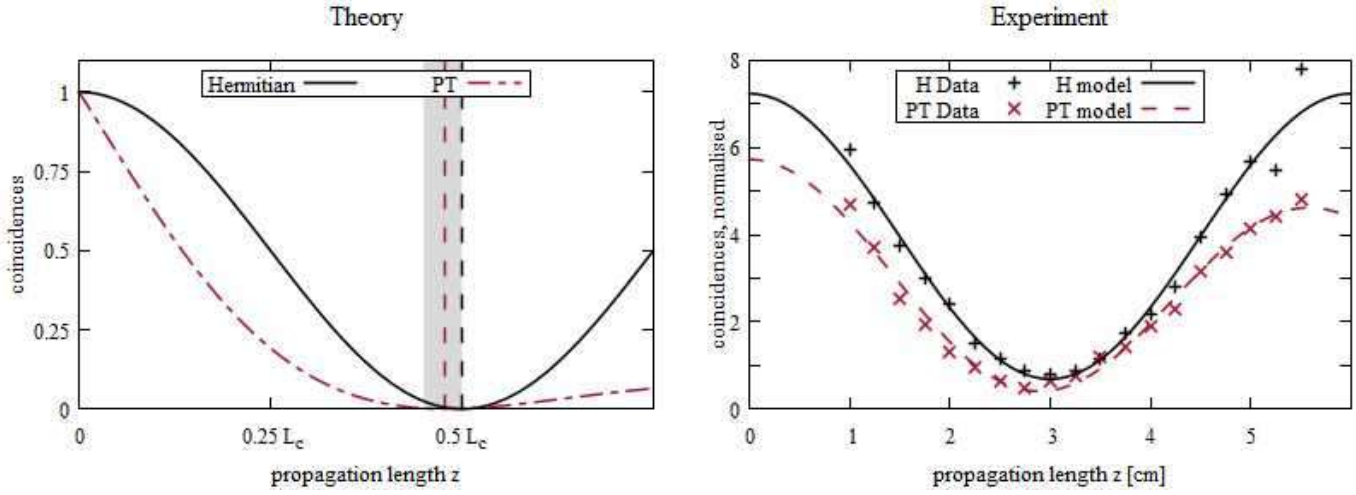


Figure 3: HOM Dip in PT symmetric systems. Dependence of the two-photon coincidence on the propagation length in the coupler. In the Hermitian case, the HOM dip has its minimum at half the coupling length. In contrast, PT-symmetry systematically displaces the dip minimum towards shorter propagation lengths, as indicated by the vertical dashed red line. In general, the minimum can occur anywhere in the grey region, which is bounded by the PT-symmetry breaking threshold. In the experiment, corresponding coincidence data were obtained for Hermitian and PT-symmetric couplers. We achieved a dip with a visibility of 87±2 % and the minimum at 3cm in the Hermitian case, and in the PT case 90±4 % at a position of 2.75cm.

Synthetic Dimensions, $\mathcal{PT}$-Symmetry and Nonlinearity in Photonic Mesh Lattices

A. L. M. Muniz[1], M. Wimmer[1], A. Bisianov[1], R. Morandotti[2] and U. Peschel[1*]

[1]Institute of Solid-State Physics and Optics, Friedrich Schiller University Jena, Max-Wien-Platz 1, 07743 Jena, Germany
[2]Institut National de la Recherche Scientifique–EMT, 1650 Boulevard Lionel-Boulet, Varennes, Québec J3X 1S2, Canada
*corresponding author, E-mail: ulf.peschel@uni-jena.de

Abstract

Using standard telecommunication equipment, we implement parity-time ($\mathcal{PT}$) symmetry in one- and two-dimensional synthetic lattices with tunable gain, loss and phase modulation. By exploiting its non-Hermitian dynamics, we realize different parity time symmetric configurations, observe unidirectional invisibility, $\mathcal{PT}$-Bloch oscillations and solitons in one- and two-dimensional lattices.

1. $\mathcal{PT}$-symmetry in 1D synthetic lattice

The $\mathcal{PT}$-symmetry in 1D synthetic lattice consists of two coupled fiber loops having slightly different lengths (ΔL=600 m) and periodically switching between gain and loss (see Fig 1a). Following the concept of time-multiplexing (1), subsequent pulses passing through the short and long loop cause a pulse to spread on a time mesh lattice with discrete arrival times being equivalent to positions in the spatial domain (see Fig. 1b,c). When a pulse travels through the long or short loop, it will not only step in time from m to m+1, but will also be slightly delayed thus hopping from position n to n+1 or n-1, respectively. The 1D $\mathcal{PT}$ lattice presents real-valued eigenvalues if a suitable phase modulation scheme (φ) is applied. By exploiting the fiber nonlinearity, a train of 20ns long retangular optical pulses having a Gaussian envelope inserted into the system forms a discrete $\mathcal{PT}$ soliton for higher input power. Its profile and behaviour follows the conservative self-trapped waves by the nonlinear Schroedinger equation (see Fig. 2a).

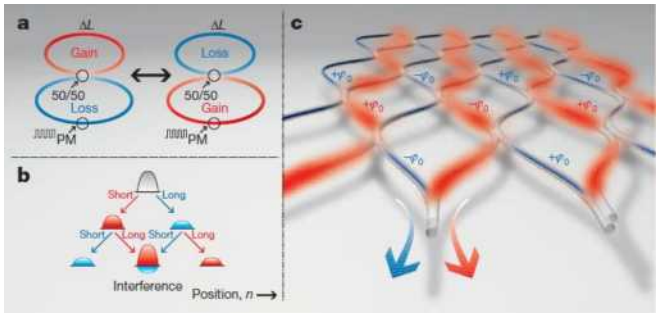


Fig.1: $\mathcal{PT}$-symmetry in 1D lattice. a) Two coupled fiber loops periodically switching between gain and loss. b) Pulse evolution in the network. c) Equivalent 1D $\mathcal{PT}$-symmetric lattice [1].

In general, its dynamics exhibits prominently features, such as unidimensional invisibility and $\mathcal{PT}$-symmetric saturable absorbers [2]. Also, $\mathcal{PT}$-Bloch oscillations in 1D lattice can be implemented by a time-dependent phase gradient $\varphi(m) = m\varphi_0$ (see Fig. 2b). Inserting a Gaussian wave packet in the broken $\mathcal{PT}$-symmetric configuration (without phase modulation), it is periodically amplified during Bloch oscillations due to the partially complex band structure. Interestingly, a new branch of Bloch oscillations appears (secondary emissions) each time the wave packet passes through an exceptional point (see left picture in fig. 2b). In contrast, for resonant Bloch gradient (π/31.0), a pseudo-Hermitian propagation is restored, where the total energy stays constant over many time steps [3] (see right picture in fig. 2b).

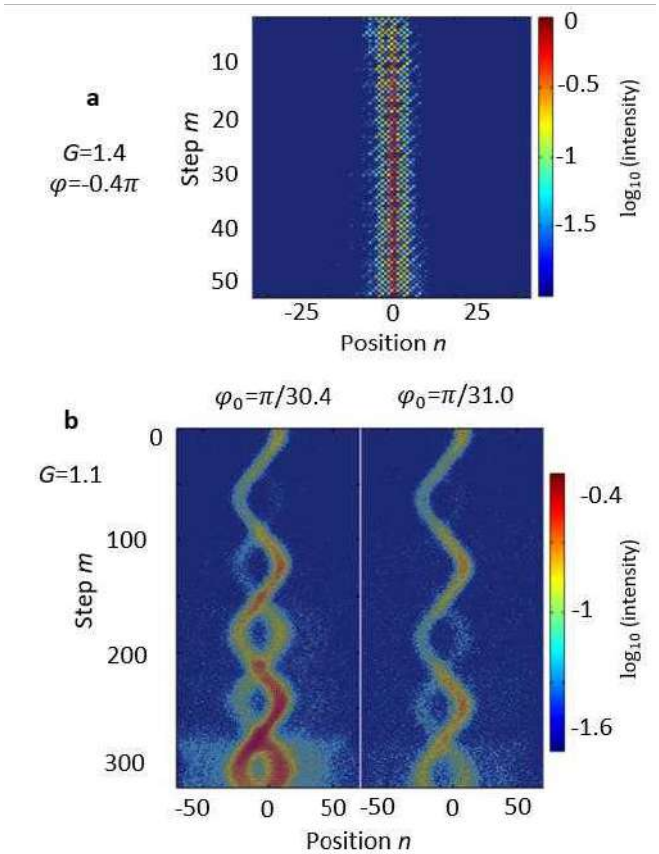


Fig. 2: a) 1D discrete $\mathcal{PT}$ soliton [2]. b) $\mathcal{PT}$-Bloch oscillations in 1D lattice [3].

2. $\mathcal{PT}$-symmetry in 2D synthetic lattices

Following a concept developed in [4], we present a novel protocol for realizing $\mathcal{PT}$-symmetry in two-dimensional synthetic lattices based on short and long-range coupling. Our experimental platform (see Fig. 3a) is based on two pairs of slightly dissimilar coupled fiber loops, where each fiber patch is approximately 30 km long. A synthetic 2D mesh lattice is implemented by exploiting a time multiplexing technique. As shown in Fig. 3a, an initial seed pulse is injected via a fiber optical coupler into the outer left loop and splits into two pulses at the first 50/50 coupler at the entrance of the two inner loops. The lengths of the inner two loops differ by $\Delta L_{\text{inner}} \approx 600$ m ($\Delta T_{\text{inner}}=3$ µs), while that of the outer loops by $\Delta L_{\text{outer}} \approx 6$ m ($\Delta T_{\text{outer}}=30$ ns). After passing through the second 50/50 coupler, the pulses are split into four that in turn propagate through the outer loops back to the first 50/50 coupler. In this stage, the ordered sequence of pulses arrives at the first coupler with a mean round trip time $T \approx 300$ µs and starts its journey again. Crucially, the pulse arrival time allows for a straightforward mapping from the temporal evolution through the fibers onto an equivalent 2D spatial mesh lattice (see Fig. 3b). By propagating through the inner long / short loop x increases / decreases by one, which is equivalent to a step to the right / left on the 2D synthetic lattice. Afterwards, by propagating through the outer long / short loop, y increases / decreases by one, respectively, and thus the pulse makes a step up / down on the lattice. In this way, any path through the 2D lattice can be interpreted as a combination of roundtrips through the four different loops. The arrival times of the pulses at the photodetector are measured, sampled electronically and mapped onto a 2D discrete lattice spanned by the x and y coordinates. A 2D $\mathcal{PT}$-symmetry can be realized by applying a balanced gain/loss space-dependent protocol on the lattice (red and blue circles in Fig. 3b). Additional, unbroken $\mathcal{PT}$-symmetry is only fulfilled when a phase modulation scheme is applied (light blue diagonal lines in Fig. 3b).

A specific-like region of the Brillouin zone can be excited by launching a train of rectangular pulses containing a Gaussian envelope $G(x,y)=A\exp[-(x^2+y^2)/w^2]$ along x- and y-axis (see Fig. 3c) with a variable amplitude (A) and a fixed width (w) of 6 positions (1/e drop of intensity). We realized a stable linear propagation in the 2D $\mathcal{PT}$-symmetric lattice (see Fig. 3d,e), which changed dramatically for higher power levels. Stable 2D solitons formed for input powers of about 1mW (see Fig. 3f,g), while higher power levels (above 4mW) caused a collapse of the field distribution (see Fig. 3h,i). The latter one causes a locally spontaneous $\mathcal{PT}$-symmetry breaking, leading to power increase and a nonlinearly self-accelerating localized spike, which is rather unusual for a discrete system.

Acknowledgements

The authors thanks support from German Research Foundation (DFG) through the International Research Training Group (IRTG) 2101, as well as an NSERC CREATE grant.

References

[1] Regensburger, A. *et al*. Parity–time synthetic photonic lattices. Nat. 488, p. 167–171 (2012).

[2] Wimmer, M. *et al*. Observation of optical solitons in PT-symmetric lattices. Nat. Comm. 6, 7782 (2015).

[3] Wimmer, M. *et al*. Observation of Bloch oscillations in complex PT-symmetric photonic lattices. Scient. Rep. 5, 17760 (2015).

[4] Schreiber, A. *et al*. A 2D quantum walk simulation of two-particle dynamics. Science 80. 336, 55–58 (2012).

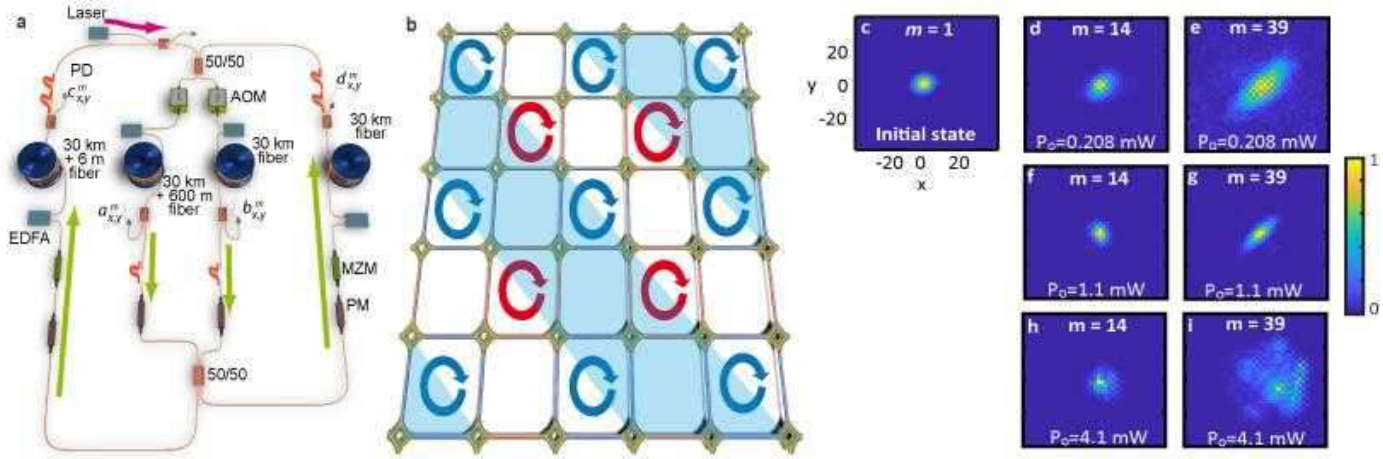


Fig. 2: Light propagation on a 2D mesh lattice. a) experimental set-up, b) equivalent 2D lattice (red and blue lattice arms display gain and loss; light blue regions denote a phase modulation). (c-i) Evolution of a broad excitation in the presence of a $\mathcal{PT}$-symmetry.

Chiral metamaterials with PT symmetry and beyond

Sotiris Droulias[1,2*], Ioannis Katsantonis[1,2], Maria Kafesaki[1,2], Costas M. Soukoulis[1,3], and Eleftherios N. Economou[1,4]

[1] Institute of Electronic Structure and Laser, Foundation for Research and Technology Hellas, 71110 Heraklion, Crete, Greece
[2] Department of Materials Science and Technology, University of Crete, 71003 Heraklion, Crete, Greece
[3]Ames Laboratory and Department of Physics and Astronomy, Iowa State University, Ames, Iowa 50011, USA
[4]Department of Physics, University of Crete, 71003 Heraklion, Crete, Greece
*corresponding author, E-mail: sdroulias@iesl.forth.gr

Abstract

Chiral systems impose circularly polarized waves which do not preserve their handedness under the combined space- and time- reversal operations and, as a result, seem to be incompatible with systems possessing PT symmetry. Here we show that in certain metamaterials, PT symmetric permittivity, permeability and chirality is possible; in addition, real eigenvalues are maintained even if the chirality goes well beyond PT symmetry, thus enabling advanced polarization control of PT symmetric systems.

1. Introduction

The concept of Parity-Time (PT) symmetry, which was originally introduced in the context of quantum mechanics [1] (referring to systems with a non-Hermitian Hamiltonian which commutes with the combined action of Parity and Time operators) was very quickly transferred in optics, where PT-symmetric systems can be more easily realized, by properly combining loss and gain media. This extension of PT-symmetry to optical systems led to novel phenomena, such as coherent perfect absorption, the PT-laser absorber, and anisotropic transmission resonances [2,3].

However, the combination of PT-symmetry and chiral metamaterials (i.e. metamaterials lacking any mirror symmetry plane [4]) remains highly unexplored. In this work we derive the necessary conditions for a chiral system to be PT-symmetric and we examine how the obtained general results are modified if PT invariance is imposed. To our surprise, we find that both the eigenvalues of the scattering matrix and the PT-related functionalities are still preserved, independently of whether the PT requirement is violated in chirality. This unexpected result turns out to be of utmost importance for chiral systems, because it allows retaining an unbroken PT phase with all its benefits and controlling the chirality simultaneously and independently from the PT-related functionalities. This finding enables new optical capabilities, such as anisotropic transmission resonances with polarization conversion and unidirectional polarization conversion with no reflection, as we demonstrate explicitly with simulations in realistic chiral metamaterials.

2. Conditions for PT-symmetric chiral systems

To find the conditions for PT-symmetry in chiral systems we cast Maxwell's equations into an eigenproblem with a Schrödinger-like Hamiltonian and we require that the Hamiltonian commutes with the PT operator [5]. The eigensolutions are circularly polarized waves, which change their handedness upon space reversal (x⟶-x, y⟶-y, z⟶-z), thus implying an apparent incompatibility of chiral systems with PT-symmetry. This limitation can be overcome if systems that respect a reduced spatial parity, such as space reflection by a plane (instead of a point), are considered. Such systems possess material parameters that change for example only along the z-direction (x⟶x, y⟶y, z⟶-z), as shown in Fig. 1; for waves propagating along the z-direction, we find that the conditions for the material parameters, so as to have a PT-symmetric chiral system are:

$$\begin{aligned} \varepsilon(z) &= \varepsilon^*(-z) \\ \mu(z) &= \mu^*(-z) \\ \kappa(z) &= -\kappa^*(-z) \end{aligned} \qquad (1)$$

In Eqs. (1) ε is the electric permittivity, μ the magnetic permeability and κ the chirality parameter, which connects the electric and magnetic fields in the chiral constitutive equations [6].

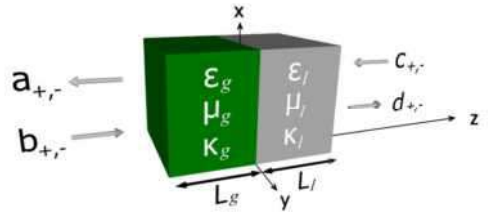


Figure 1: A system for the realization of PT-symmetric chiral structure. The necessary conditions are: $\varepsilon_g = \varepsilon_l^*$, $\mu_g = \mu_l^*$, $\kappa_g = -\kappa_l^*$ and L_g=L_l. The subscripts + and – in the amplitudes of the incoming (b,c) and outgoing (a,d) waves denote right-handed and left-handed circularly polarized waves (RCP/LCP), respectively.

3. Chiral systems with PT-symmetry and beyond

Below a critical value, the so-called Exceptional Point (EP), the eigenstates of non-chiral PT-systems are known to be unimodular, despite the presence of gain and loss (above the EP the system is not unitary anymore) [1-3]. Here, we find that in the presence of chirality the eigenvalues of the scattering matrix do not change, i.e. the EP is preserved, unaffected by chirality. Hence, characteristic phenomena related to PT-symmetry, such as unidirectional invisibility, can be tailored independently of chirality and can be expanded to account for circularly polarized waves.

In Fig. 2, we demonstrate the response of a non-magnetic ($\mu_g = \mu_l = 1$) system with $n_g = 2.2+0.15i$, $n_l = 2.2–0.15i$ ($n = \sqrt{\varepsilon\mu}$ and positive/negative imaginary part accounts for gain/loss) and $\kappa_g = –0.1–0.1i$, $\kappa_l = 0.1–0.1i$ (sign of imaginary part accounts for preferential absorption among Right/Left Circularly Polarized (RCP/LCP) waves). The two slabs have equal length $L_g = L_l \equiv L/2$ and the eigenvalues of the scattering matrix, as well as the transmitted and reflected power are shown as a function of the normalized frequency $\omega L/c$ (c is the vacuum speed of light). In T_{ij} (transmittance) and R_{ij} (reflectance) the subscript i (j) indicates the outgoing (incident) polarization (i, j: +/– accounts for RCP/LCP waves). For our system we find that $T_{+–} = T_{–+} = R_{++} = R_{––} = 0$ and that T_{++}, $T_{––}$ are the same regardless of the illuminated side. However, depending on the side from which the system is illuminated, different reflected powers can be achieved. In particular we find that $R_{L++} = R_{L––} \equiv R_L$ and $R_{R++} = R_{R––} \equiv R_R$, where the subscript L or R denotes incidence from 'Left' or 'Right', respectively.

In Fig. 2a $\kappa_g = -\kappa_l^*$, i.e. κ satisfies condition (1) and hence $\mathrm{Re}(\kappa)$ changes sign across the system, resulting overall in zero optical activity, $\theta = 0$. On the other hand $\mathrm{Im}(\kappa)$ preserves its sign across the entire system, resulting in nonzero ellipticity, $\eta \neq 0$, and hence $T_{++} \neq T_{––}$. Practically, after the operation point of zero reflection at $\omega L/c = 15.68$, there exist multiple reflectionless points with $\theta = 0$ and $\eta = 45$ deg. At those points full conversion of linearly polarized waves into circularly polarized waves occurs, the handedness of which is controlled by the sign of $\mathrm{Im}(\kappa)$.

In Fig. 2b $\kappa_g = \kappa_l^*$, i.e. κ does not satisfy condition (1). In this case only $\mathrm{Im}(\kappa)$ is spatially odd, leading to $\eta = 0$ (and $\theta \neq 0$) and $T_{++} = T_{––}$. This relaxed condition does not affect the eigenvalues λ of the scattering matrix, as predicted [6]. In this case the reflectionless operation points correspond to *unidirectional pure optical rotation of a linearly polarized wave*. At $\omega L/c = 15.68$, in particular, $\theta = 90$ deg., i.e. x-polarized waves are fully converted to y-polarized waves and are transmitted entirely without reflection.

4. Conclusions

We have shown that the combination of chirality with PT symmetry in ε and μ is possible in certain systems. The unexpected κ-independence of the PT-phase turns out to be of utmost importance, as it enables advanced polarization control of PT symmetric systems.

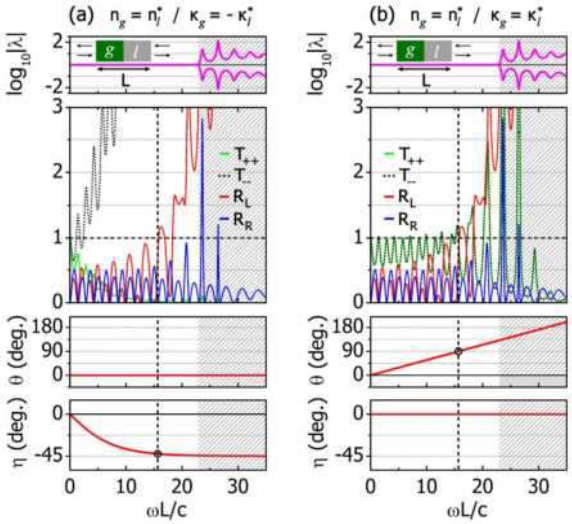


Figure 2: *PT*-chiral system of length L with $n = 2.2±0.15i$ ($n = \sqrt{\varepsilon\mu}$ and $\mu = 1$). The chirality is (a) $\kappa = ±0.1+0.1i$ and (b) $\kappa = 0.1±0.1i$. Top row: Eigenvalues λ of scattering matrix. Middle row: transmittance T_{++}, $T_{––}$ and reflectance R_L, R_R. Bottom rows: optical activity θ and ellipticity η. The shaded area denotes the broken *PT*-phase.

Acknowledgements

This work was supported by the Hellenic Foundation for Research and Innovation (HFRI) and the General Secretariat for Research and Technology (GSRT), under the HFRI PhD Fellowship grant (GA. no. 4820). It was also supported by the EU-Horizon2020 FET project Ultrachiral.

References

[1] M. Bender and Boettcher, Real spectra in non-Hermitian Hamiltonians having PT Symmetry, *Phys. Rev. Lett.* 80:5243, 1998.

[2] R. El-Ganainy, K. G. Makris, M. Khajavikhan, Z. H. Musslimani, S. Rotter and D. N. Christodoulides, Non-Hermitian physics and PT symmetry, *Nat. Phys.* 14:11, 2018.

[3] Li Ge, Y. D. Chong and A. D. Stone, Conservation relations and anisotropic transmission resonances in one-dimensional PT-symmetric photonic heterostructures, *Phys. Rev. A* 85:023802 2012.

[4] B. N. Wang, J. F. Zhou, Th. Koschny, M. Kafesaki, and C. M. Soukoulis, Chiral metamaterials: simulations and experiments, *J. Opt. A: Pure and Appl. Opt.* 11:14003, 2009.

[5] G. Castaldi, S. Savoia, V. Galdi, A. Alù, and N. Engheta, PT metamaterials via complex-coordinate transformation optics, *Phys. Rev. Lett.* 110:173901, 2013.

[6] S. Droulias, I. Katsantonis, M. Kafesaki, C. M. Soukoulis, and E. N. Economou, Chiral metamaterials with PT symmetry and beyond, *arXiv*:1811.05344, 2018.

Port swithing and replication in cyclic non-Hermitian arrays

B. M. Rodríguez-Lara[1,2,*], **Benjamín Jaramillo Ávila**[3]

[1]Tecnologico de Monterrey, Escuela de Ingeniería y Ciencias, Ave. Eugenio Garza Sada 2501, Monterrey, N.L., Mexico, 64849
[2]Instituto Nacional de Astrofísica, Óptica y Electrónica, Calle Luis Enrique Erro No. 1. Sta. Ma. Tonantzintla, Pue. C.P. 72840, Mexico
[3]CONACYT-Instituto Nacional de Astrofísica, Óptica y Electrónica, Calle Luis Enrique Erro No. 1. Sta. Ma. Tonantzintla, Pue. C.P. 72840, Mexico
*corresponding author, E-mail: bmlara@tec.mx, bmlara@inaoep.mx

Abstract

Abstract symmetries are a powerful framework to study propagation dynamics in photonic devices described by mode-coupling theory. We will show that the cyclic group can help us go beyond the nearest neighbor approximation in periodic multicore photonic devices. In addition, we will show that it is possible to design devices with cyclic composite symmetries that provide us with port replication. We will discuss how the cyclic repetition of a non-Hermitian dimer allows for port switching and replication.

1. Introduction

Symmetries play a fundamental role in physics, as they are connected to conservation laws. The mathematical framework to study continuous differentiable symmetries is Group Theory and it provides us with valuable tools to find analytic solutions to differential equations. Of course, the design of differential equations with a prescribed symmetry, where the solution is known, is also possible. Our program pushes for the latter in optics where quantum inspired symmetries have been used to engineer novel devices [1]. Photonic devices described by mode-coupling theory provide a perfect platform for design based on symmetry; e.g. multicore fibers, waveguide arrays, micro-ring arrays, etc.

Here, we will focus on a photonic device with cyclic symmetry, that is the, device remains invariant to discrite rotations, Fig. 1. We call the repetition photonic device a *black-box*. We assume that the internal dynamics of this *black-box* can be described by mode-coupling theory as well as the interactions between each of these *black-boxes*. Thus, the whole device can be described in terms of the block couple-mode matrix,

$$M = \begin{pmatrix} \boxed{B} & \boxed{G} & \cdots & \\ \boxed{G} & \boxed{B} & \cdots & \\ \vdots & \vdots & \ddots & \\ & & & \boxed{B} \end{pmatrix} \tag{1}$$

where the B blocks determine the dynamics of the *black-box* and the G blocks define the coupling between copies of the unit cell.

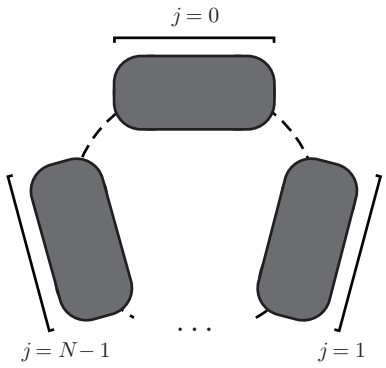


Figure 1: A cyclic array of N *black-box* photonic devices.

In the following, we will discuss the cyclic group, the symmetry related to discrete rotations, and show that it can help us go beyond nearest neighbor modelling in coupled mode theory. Then, we will show that we can use it as the foundation of composite symmetries that will allow for the replication of dynamics. In particular, we will focus on the cyclic repetition of a loss-based non-Hermitian dimer to show that there exists a reference frame where it is evident that the device possesses an underlying PT-symmetry, that we can use to control the dynamics in the photonic device. This allows us to design a device with different dynamics that can be controlled by the input state and will be replicated at the output of the device.

2. The model

Let us study first the underlying cyclic symmetry of the device. We have discusse in the past that it is possible to use the Fourier matrix [2],

$$[F]_{p,q} = \frac{1}{\sqrt{n}} e^{i\frac{2\pi}{n}(p-1)(q-1)}. \tag{2}$$

to diagonalize the coupled-mode matrix of a cyclic repetition of an identical unit cell. For an array of N identical guiding cores, it is possible to find the normal modes,

$$\vec{u}_j = F^\dagger \cdot \hat{e}_j, \tag{3}$$

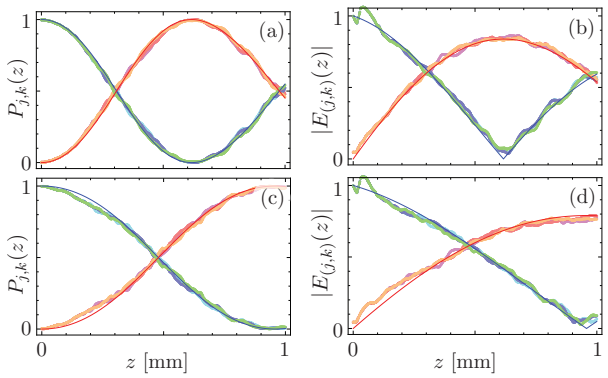


Figure 2: Propagation of the power and absolute value of the field amplitude in the effective and laboratory frames.

and their corresponding propagation constants,

$$\lambda_j = \begin{cases} 2\sum_{k=1}^{m-1}\left\{g_k\,\cos\left[\frac{\pi}{m}(j-1)k\right]\right\} + g_m(-1)^{j-1}, \\ 2\sum_{k=1}^{m}\left\{g_k\,\cos\left[\frac{2\pi}{2m+1}(j-1)k\right]\right\}, \end{cases} \quad (4)$$

where $m = N/2$ when N is even and $m = (N-1)/2$, considering all neighbor couplings g_k and the standard orthonomal basis $\hat{e}_j$. The duplicity of propagation constants is not an issued due to the fact that all the normal modes are mutually orthonormal.

As a unit cell, we will consider the non-Hermitian dimer,

$$M_d = \begin{pmatrix} n+2i\,\gamma & g_d \\ g_d & n \end{pmatrix}, \quad (5)$$

composed by two guiding cores with identical real part of the refractive index but one of them lossy, with a loss rate 2γ, and the other lossless. It is possible to show that an effective imaginary propagation constant $n_{bias} = n + i\gamma$ can be factored from the dynamics to provide an effective PT-dimer with gain/loss rate γ and the standard regimes PT-symmetric dimer [3, 4, 5].

The cyclic symmetry allows us to calculate an effective coupling matrix that is isolated block diagonal, the off-diagonal blocks become zero and the diagonal blocks become the matrix,

$$M_j = \begin{pmatrix} i\,\gamma & \Gamma_j \\ \Gamma_j^* & -i\,\gamma \end{pmatrix}, \quad (6)$$

where the effective couplign constants are given by $\Gamma_j = g_d + g_N e^{-i\frac{2\pi}{N}j}$. Choosing an adequately initial amplitude vector,

$$\mathcal{E}(0) \;=\; \frac{1}{\sqrt{N}}\sum_{j=0}^{N-1} e^{i\frac{2\pi}{N}aj}\hat{e}_j \otimes \mathcal{E}_D(0), \quad (7)$$

where the normalized vector field amplitude $\mathcal{E}_D(0)$ refers to the initial state that will impinge on each copy of the dimer, provides replication, up to a phase, of the dynamics provided by each of these isolated effective PT-symmetric dimers,

$$\mathcal{E}(z) \;=\; \frac{1}{\sqrt{N}}\sum_{p=0}^{N-1} e^{i\frac{2\pi}{N}jp}\hat{e}_p \otimes e^{iM_j z}\mathcal{E}_D(0), \quad (8)$$

in the composite system. In other words, a permutation of the phases in the initial field amplitudes controls the dynamics in the output.

3. Discussion

Figure 2 shows a comparison of analytic theoretical with finite element simulation results for a photonic device composed by three lossy-lossless dimers. We show port switching in the effective frame, Figure 2(a) where we normalize to the total instantaneous power, and the laboratory frame, 2(b) where we don't renormalize and the effect of losses is seen. Addionally, we can select a regime that provides port mixing in the effective, Figure 2(c), and laboratory, 2(d), frames.

4. Conclusions

The cyclic group as foundation for the design of composite photonic devices allows for port replication and dynamics switching if used in addition to unit cells showing different operation regimes. Control of the dynamics is provided by the relative phases in the input signal. We provided a simple example where the repetition of a lossy-lossless dimer provides switching and mixing of the input signals.

References

[1] B. M. Rodríguez-Lara, R. El-Ganainy, and J. Guerrero, Symmetry in optics and photonics: a group theory approach, *Sci. Bull.* 63: 244, 2018.

[2] B. Jaramillo Ávila, J. Naya Hernández, S. M. Toxqui Rodríguez, and B. M. Rodríguez-Lara Symmetric supermodes in cyclic multicore fibers Accepted in OSA Continuum (2019).

[3] C. E. Rüter, K. G. Makris, R. El-Ganainy, D. N. Christodoulides, M. Segev and D. Kip, Observation of paritytime symmetry in optics, Nature Physics 6: 192, 2010.

[4] B. M. Rodríguez-Lara and J. Guerrero, Optical finite representation of the Lorentz group, *Opt. Lett.* 40: 5682, 2015.

[5] J. D. Huerta Morales, J. Guerrero, S. López-Aguayo, and B. M. Rodríguez-Lara, Revisiting the optical PT-symmetric dimer, *Symmetry* 8: 83, 2016.

[6] D. J. Nodal Stevens, B. Jaramillo Ávila, and B. M. Rodríguez-Lara, Necklaces of PT-symmetric dimers, Photonics Research 6: A31, 2018.

Quantum criticality and nonequilibrium phases: topology in non-Hermitian physics

Yuto Ashida[1,2*], Shunsuke Furukawa[1], Masahito Ueda[1,3],

[1]Department of Physics, The University of Tokyo, Japan
[2] Department of Applied Physics, The University of Tokyo, Japan
[3] RIKEN CEMS, Japan
*corresponding author, E-mail: ashida@cat.phys.s.u-tokyo.ac.jp

Abstract

I will present our recent results on two distinct topological aspects of non-Hermitian physics. First, I discuss the unconventional quantum phase transition and critical phenomena in the parity-time-symmetric sine-Gordon model, which can be realized in ultracold atoms. Second, I talk about the role of topology in nonequilibrium phases of non-Hermitian systems and present a possible topological classification and its relevance to the Hatano-Nelson model.

1. Introduction

Studies of phase transitions and critical behavior in non-Hermitian systems date back to the discovery of the Lee-Yang edge singularity. On another front, the real-to-complex spectral phase transition has been found in a broad class of non-Hermitian Hamiltonians that satisfy parity-time (PT) symmetry. Recent experimental and theoretical studies on non-Hermitian systems in optics, metamaterials, and weakly interacting open quantum systems have already revealed their intriguing physical properties. However, the previous works mainly concern the classical (one-body) aspects and the role of strong correlations has yet to be clarified. Moreover, a generic aspect of topology in non-Hermitian systems has been largely unexplored. We aim to fill this gap and create a bridge between the fields of non-Hermitian physics and condensed-matter physics.

2. Results

2.1. Quantum criticality

Quantum critical phenomena originate from collective behavior of strongly correlated particles and lie at the heart of universal low-energy properties in many-body systems. The strong correlation between quantum particles is particularly prominent in a low-dimensional system. We identify what types of non-Hermitian perturbations are relevant to one-dimensional low-energy properties and address how they qualitatively alter the underlying quantum critical behavior [1]. Specifically, we show that, in the presence of the PT-symmetric non-Hermitian perturbation, a combination of spectral singularity and quantum critical point results in a nontrivial renormalization group fixed point

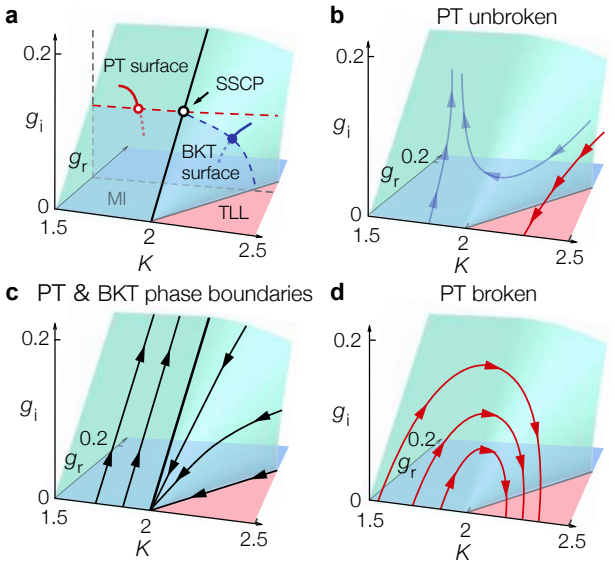


Figure 1: Quantum critical phenomena in PT-symmetric many-body systems. (a) 3D phase diagram in the parameter space (K, g_r, g_i), where K and g_r (g_i) characterize the strength of the inter-particle interaction and the depth of the real (imaginary) part of a complex potential, respectively. The Mott-insulator (MI) and Tomonaga-Luttinger Liquid (TLL) phases are separated by the surface of the topological Berezinskii-Kosterlitz-Thouless (BKT) transition for $K > 2$ and that of the PT transition for $K < 2$. (b) Hyperbolic RG flows in a PT-unbroken region ($g_i < g_r$), which reproduce the conventional flow diagram in the sine-Gordon model. (c) RG flows on the two phase boundaries separated by an unconventional fixed line (thick black line). (d) Anomalous RG flows in a PT-broken region ($g_i > g_r$), which violate the c-theorem. Along each flow, the TLL parameter K monotonically increases, indicating the anomalous enhancement of the superfluid correlation.

that has no counterpart in Hermitian systems. Moreover, we found anomalous renormalization group flows violating the c-theorem, which lead to enhancements of superfluid correlations in stark contrast to a topological transition in the Berezinskii-Kosterlitz-Thouless paradigm (see Fig. 1). Our field-theoretic arguments provide a universal

model-independent perspective to one-dimensional quantum critical phenomena subject to non-Hermiticity. The non-Hermiticity can naturally arise in the context of dissipation and continuous monitoring of ultracold atoms, and a concrete experimental setup to test our theoretical predictions has been proposed.

2.2. Nonequilibrium phases

We establish a systematic theoretical framework to characterize and classify non-Hermitian systems in terms of their topological aspects [2]. The two guiding principles are dynamical viewpoint as nonequilibrium phases and the constraint such that the energy spectrum neither touches nor crosses the base point (see Fig. 2). In particular, we study one-dimensional non-Hermitian lattices belonging to class A in detail, and identify the topological winding number and reveal an exotic bulk-edge correspondence. Historically, this model has been known as the Hatano-Nelson model. We also give a systematic classification based on K theory and obtain the periodic table. Time permitting, I will also discuss unconventional nonequilibrium quench dynamics and the subsequent thermalization in a PT-symmetric dissipative many-body lattice model [3, 4].

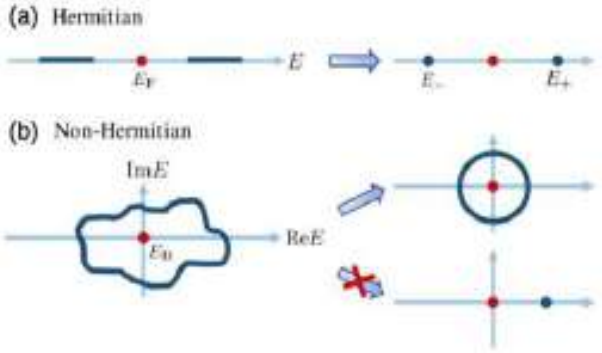


Figure 2: (a) Energy spectrum (thick lines and dots) of a Hermitian insulator. We can always perform band flattening, i.e., continuously deform the spectrum into $\{E_-, E_+\}$ with $E_- < E_F < E_+$, where E_F (red dot) is the Fermi energy. In particular, we can choose $E_\pm = \pm 1$ for $E_F = 0$. (b) Energy spectrum of a non-Hermitian system forming a loop that encircles a base point $E_B \in \mathbb{C}$. (In the figure, we set $E_B = 0$ for simplicity.) While the shape can be deformed continuously, the loop can never shrink to a single point without crossing the base point.

Acknowledgement

This work was supported by KAKENHI Grant No. JP18H01145 and a Grant-in-Aid for Scientific Research on Innovative Areas "Topological Materials Science" (KAKENHI Grant No. JP15H05855) from the Japan Society for the Promotion of Science. Y. A. was supported by the JSPS through Program for Leading Graduate Schools (ALPS) and acknowledges support from JSPS Grants No. JP16J03613.

References

[1] Y. Ashida, S. Furukawa, M. Ueda, Parity-time-symmetric quantum critical phenomena, *Nat. Commun.* 8, 15791, 2017.

[2] Z. Gong*, Y. Ashida*, K. Kawabata, K. Takasan, S. Higashikawa, M. Ueda, Topological phases of non-Hermitian systems, *Phys. Rev. X* 8, 031079, 2018.

[3] Y. Ashida, M. Ueda, Full-counting many-particle dynamics: nonlocal and chiral propagation of correlations, *Phys. Rev. Lett.* 120, 185301, 2018.

[4] Y. Ashida, K. Saito, M. Ueda, Thermalization and Heating Dynamics in Open Generic Many-Body Systems, *Phys. Rev. Lett.* 121, 170402, 2018.

Quasi-Normal-Mode Approach for Dissipative Systems - Classical and Quantum Regime

Kurt Busch [1,2,*]

[1] Humboldt Universität zu Berlin, AG Theoretische Optik & Photonik, 12489 Berlin, Germany
[2] Max-Born-Institut, 12489 Berlin, Germany
*corresponding author, E-mail: kurt.busch@physik.hu-berlin.de

Abstract

An approach is presented for modeling the response of localized electromagnetic resonators using quasi-normal modes, which represent the natural, dissipative modes of the resonators with complex frequencies. For many problems of interest in optics and nanophotonics, the quasi-normal modes constitute a powerful modeling tool, both in the classical and the quantum regime.

1. Introduction

On the classical level, and combined with a bi-orthogonal approach this approach provides a coherent, precise, and accessible derivation of the associated theory and leads to an efficient coupled-mode theory [1]. In turn, this enables an illustrative connection between different modeling approaches in the literature and allows for a multitude of applications.

On the quantum level, this approach leads to a novel quantization scheme for the electromagnetic field in dissipative and open systems [2]. Contrary to many "modes-of-the-universe" approaches that utilize the microscopic Maxwell equations together with a set of uncontrolled approximations, this scheme is based on the macroscopic Maxwell equations and thus leads to the correct classical limit. Applications for certain leaky and hybrid cavity-QED systems/effects including cavity enhanced spontaneous emission rates are developed and shown to agree well with corresponding semi-classical results.

Acknowledgements

KB acknowledges funding by the Deutsche Forschungs-gemeinschaft (DFG, German Research Foundation) – Projektnummer 182087777 - SFB 951.

References

[1] P.T. Kristensen, K. Herrmann, F. Intravaia, K. Busch, Modeling electromagnetic resonators using quasi-normal modes, *in preparation*, 2010.

[2] S. Franke, S. Hughes, M. K. Dezfouli, P. T. Kristensen, K. Busch, A. Knorr, M. Richter, Quantization of quasi-normal modes for open cavities and plasmonic cavity-QED, *arXiv:1808.06392*.

Bloch-oscillations in a lattice with passive PT-symmetry

Eva-Maria Graefe and Bradley Longstaff

Department of Mathematics, Imperial College London

Abstract

A tight-binding lattice with losses from every other lattice site is considered. In the absence of losses, if a static tilt is applied to the lattice the continuous dispersion relation is replaced by a discrete spectrum with equidistant spacings that lead to periodic dynamics. In particular, an initially broad wave packet will perform the famous Bloch oscillations, effectively mapping out the band structure of the untilted system. The presence of losses leads to a number of intriguing changes explored here.

1. The model

We consider a tight-binding lattice with losses from every other lattice site, that could be realised in a number of experimental setups, including cold atoms in optical lattices with particle losses or arrays of optical wave guides. This leads to a Schrödinger dynamics with an effective non-Hermitian Hamiltonian of the form

$$\hat{H} = -\sum_{j=-L}^{L-1} \left(|j+1\rangle\langle j| + |j\rangle\langle j+1|\right) + \frac{i\gamma}{4}\sum_{j=-L}^{L}\left((-1)^j - 1\right)|j\rangle\langle j|, \tag{1}$$

where the hopping element has been set to unity and where $\gamma \in \mathbb{R}$ denotes the loss rate. While the system has a passive PT-symmetry, this is broken for arbitrarily small loss rates, leading to two complex mini-bands, which below a critical loss strength are connected at exceptional points. We investigate the dynamics arising when applying an additional static tilt $\Delta \sum_{j=-L}^{L} j|j\rangle\langle j|$. A similar system has briefly been investigated before in [2] and [3].

2. Results

Here we show how the exceptional points in the band structure leave characteristic fingerprints in the dynamics of a broad beam, while remarkably there are no exceptional points in the spectrum of the full system including the tilt. We use semiclassical arguments developed in [1] to show how the dynamics maps out the real part of the dispersion relation, while inter-band transitions occur around the exceptional points in the dispersion relation. We provide an estimate for the percentage of population transfer by deriving an analytic solution to a non-Hermitian Landau-Zener problem approximating the bands around the exceptional point.

Acknowledgements

This research has been generously supported by the Royal Society via URF Grant. No. UF130339 and the European Research Council (ERC) under the European Union's Horizon 2020 research and innovation programme (grant agreement No 758453) as well as the Engineering and Physical Sciences Research Council via the Doctoral Training Partnership (Grant No. EP/M507878/1).

References

[1] T. Hartmann, F. Keck, H. J. Korsch, and S. Mossmann, Dynamics of Bloch oscillations, *New J. Phys.* 6: 2, 2004.

[2] S. Longhi, Bloch oscillations in complex crystals with PT symmetry, *Phys. Rev. Lett.* 103: 123601, 2009.

[3] Z. Turker and C. Yuce, Super Bloch oscillation in a PT symmetric system, *Phys. Lett. A* 360: 2260, 2016.

[1] E. M. Graefe, H. J. Korsch, and A. Rush, Quasiclassical analysis of Bloch oscillations in non-Hermitian tight-binding lattices, *New J. Phys.* 18: 075009, 20016.

Intensity fluctuations and mode correlations in strongly coupled nanolasers

A. M. Yacomotti[1], M. Marconi[1], A. Pan[2], F. Raineri[1], A. El Amili[2], J. A. Levenson[1] and Y. Fainman[2]

[1]Centre for Nanoscience and Nanotechnologies (CNRS/CN2 UMR 9001), 10 Boulevard Thomas Gobert, 91120 Palaiseau, France

[2]Department of Electrical and Computer Engineering

9500 Gilman Drive, University of California, La Jolla, CA 92093-0407

*corresponding author: alejandro.giacomotti@c2n.upsaclay.fr

Abstract-We investigate second order correlations in a bimodal nanolaser and relate them with mode-intensity fluctuations. We first discuss the predictions as a function of the system "size", determined by the inverse of the spontaneous emission (β) factor. The modal cross correlation decreases from $g_{i,j}^{(2)}=1$ in the "thermodynamic" limit ($\beta^{-1}>10^4$) to $g_{i,j}^{(2)}=2/3$ in the "mesoscopic" limit (β^{-1}~10-100). This is the consequence of flat potential transitions at the origin of large intermode energy fluctuations. We experimentally verify such a limit and confirm the flat potential scenario by means of probability distribution measurements of the mode population imbalance.

It is well established that the intensity correlations of a classical light beam cannot reach values below $g_{i,i}^{(2)}(\tau=0)=1$, where $g_{i,i}^{(2)}(\tau=0)$ is the second order coherence of a mode i at zero time delay (τ=0). As long as a multiple beam source is considered, such as the output of a coupled cavity array, the nature of the fluctuations is not only contained in the auto correlation properties of the beams (alternatively, modes), but also in the cross correlation features between them. For instance, independent single photon sources with indistinguishable photons are expected to verify $g_{i,j}^{(2)}(0)=0$ (i,j stand for the two sources), which is the manifestation of quantum interferences of the optical paths, usually known as photon coalescence in a Hong Ou Mandel experiment.

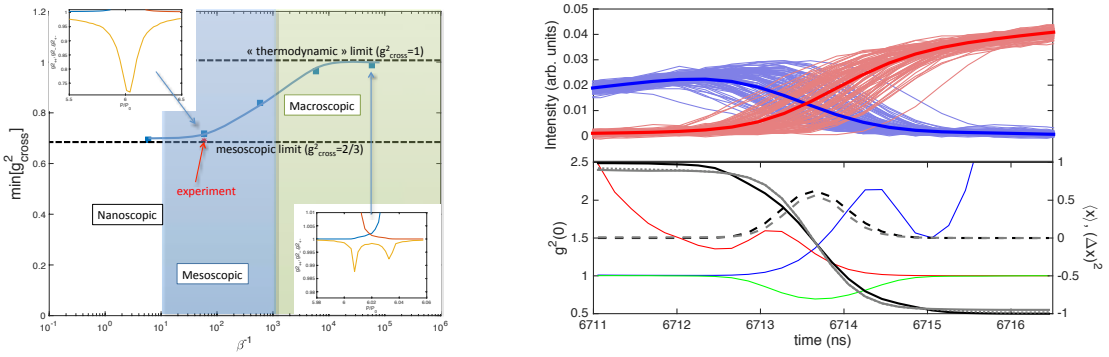


Figure 1: Left: Minima of second order cross correlation as a function of the β factor in coupled lasers. Blue squares: numerical simulations of a semiclassical model with Langevin noise. Right: Experimental second order mode correlations as the pump power is ramped up in time. Top: Intensity traces for bonding (B, blue) and antibonding (A, red) modes. Pump ramp duration=6 ns. Thick lines: average. Bottom: left axis, $g_{BB}^{(2)}$ (blue), $g_{AA}^{(2)}$ (red), and $g_{AB}^{(2)}$ (green) corresponding to 10^4 time traces; right axis,

mean values (solid) and variance (dashed lines) of the mode population imbalance.

As long as two independent classical fields are considered, the mutually incoherent phases lead to a limit of $g_{i,j}^{(2)}=0.5$ for independent sources. However, mode-to-mode interactions in coupled cavities can produce strong intermode intensity fluctuations, which can decrease the second order cross correlation functions to values significantly below 0.5, down to $g_{i,j}^{(2)}(0)=0$ in the general case. Here we show that two coupled nanolasers operating in the mesoscopic regime, $\beta\sim0.01$, exhibit a second order cross correlation of $g_{i,j}^{(2)} \approx 0.69$, compatible with the predicted 2/3 limit originated by flat potentials at the mode switch transition.

Figure 1 (left) shows the prediction of $g_{AB}^{(2)}$ in a two evanescently coupled cavity laser system ("B" and "A" refer to "bonding" and "antibonding" modes of the photonic dimer) as a function of the system "size", which can be defined as the inverse of the spontaneous emission (β) factor of the laser cavities. Clearly, $g_{i,j}^{(2)}$ tends to 1 in the thermodynamic limit ($\beta^{-1}>>1$), whereas a limit $g_{i,j}^{(2)}=2/3$ is observed for β^{-1}-values as small as ~10.

Figure 1 (right) shows experimental results of two lasing modes in a strongly coupled photonic crystal cavity nanolaser system [1,2] as the pump power is ramped up. A minimum of $g_{AB}^{(2)}\approx0.69$ can be observed at the mode switching point. Such a minimum coincides with a zero-crossing of $\langle x\rangle$, and a maximum of Δx, where x is the mode population imbalance $x=(I_B-I_A)/(I_B+I_A)$, in good agreement with the theoretical predictions of a mean field semiclassical model. Such a model predicts flat probability distributions of x at the switching point, which directly implies $g_{AB}^{(2)}=2/3$. In order to experimentally test such scenario, we have measured the probability distributions $P(x,I_{tot})$, Fig. 2. These get dramatically stretched at the switching point. As a result, $P(x,I_{tot})$ becomes flat at the switching point, which confirms the predictions. Note that other dynamical mechanisms of mode interactions such as mode bistability would result in bi-modal distributions rather than flat ones.

In conclusion we have shown, both theoretically and experimentally, a "mesoscopic" limit of the modal cross correlation functions of strongly evanescently coupled laser cavities, $g_{i,j}^{(2)}=2/3$. An avenue is now open to study correlations at the few photon level, which might exhibit quantum features such as photon entanglement.

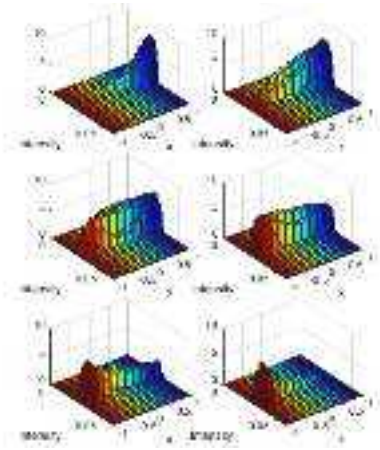


Figure 2: Joint histograms $P(x,I_{tot})$ for the results in Fig. 1 (log scale). Frames correspond to increasing pump powers at different times: from right-bottom to left-top corners t=6712.7, 6713.1, 6713.5, 6713.9, 6714.3, 6714.7.

Acknowledgements This work is supported by a public grant overseen by the French National Research Agency (ANR) as part of the "Investissements d'Avenir" program (Labex NanoSaclay, reference: ANR-10-LABX-0035) and (ANR-12-BS04-0011), as well as ANR UNIQ DS078 and RENATECH network.

REFERENCES

1. P. Hamel, et al., Nature Photonics **9**, 311–315 (2015)
2. M. Marconi, et al., Phys. Rev. X **8**, 011013 (2018)

Nonreciprocity, Chirality and PT-Symmetry in Photonics and Functional Materials

Avadh Saxena[1]

[1]*Theoretical Division, Los Alamos National Lab, Los Alamos, NM 87545, USA*

avadh@lanl.gov

The concepts of nonreciprocal properties in photonics as well as materials have recently become quite significant due to their technological implications [1]. In general, nonreciprocity arises due to mainly three reasons: nonlinearity, asymmetric property tensors and spatio-temporal modulation. However, it can be further enhanced in non-Hermitian (e.g. parity-time or PT-symmetric) and topological settings. For example, many useful properties of materials such as optical diode effect crucially depend on the interplay between chirality, reciprocity as well as broken spatial and temporal symmetries. One notable example is that of nonreciprocal directional dichroism. I will discuss the conditions for non-reciprocity of ferro-rotational order in a variety of materials and suggest the use of linear optical gyration and vortex beams as possible ways to detect ferro-rotational domains [2]. Next, I will discuss how to generalize the notion of vector order parameters to second- and higher-rank tensor order parameter. I will also elucidate how to achieve high-temperature optical diode effect. Finally, as a different example, I will consider a PT-symmetric photonic Kagome lattice [3], which is a two-dimensional network of corner-sharing triangles. At each lattice point a PT-symmetric dimer is placed, where a dimer represents a pair of strongly coupled waveguides. The frustrated coupling between waveguide modes leads to a dispersionless flat band consisting of spatially localized modes. The beam evolution in the waveguide array results in an oscillatory rotation of the optical power along the propagation direction. We also observe long-lived chiral structures that originate from the nearly flat bands of the Kagome structure when the lattice is subject to a narrow beam excitation.

References:

1. L. Bi, *MRS Bulletin,* **2018**, *43*, 407-412.
2. S.-W. Cheong, D. Talbayev, V. Kiryukhin and A. Saxena, *NPJ Quant. Mater.,* **2018**, *19*, 1-7.
3. G.-W. Chern and A. Saxena, *Opt. Lett.,* **2015**, *40*, 5806-5809.

Thermal-photonics for information and energy applications

Hybrid Plasmonics for Solar Energy Harvesting Through Radiative Heating

Mina Shiran Chaharsoughi, Dan Zhao, Daniel Tordera, Simone Fabiano, Xavier Crispin and Magnus P. Jonsson

Laboratory of Organic Electronics, Department of Science and Technology, Linköping University, Sweden
E-mail: mina.shiran@liu.se

Abstract

In this presentation, I will present our recent research on thermoplasmonics, with focus on hybrid plasmonic systems enabling radiation sensing and harvesting of energy from random light fluctuations.

Noble metal nanostructures have attracted much attention due to their unique optical properties. Enhanced light absorption in these nanostructures makes them ideal nano-sources of heat. While discrete nanostructures such as nanodisks have received much interests for thermoplasmonics, we showed that metal nanohole arrays can be as efficient light-driven heat sources, as used to create heat gradients and induce thermoelectric potentials over an ionic thermoelectric material.[1] Moreover, we demonstrate that the fast heating process in plasmonic nanostructures allows energy harvesting even from solar-light fluctuations, based on a hybrid device combining plasmonic nanodisks arrays with a pyroelectric material.[2] At the end, I will discuss our most recent study showing that merging these two aforementioned systems can provide interesting enhancement effects with regards to the rate of the thermoelectric response and the voltage derived from the device.[3]

Acknowledgements

We acknowledge financial support from the Wenner-Gren Foundations, the Swedish Research Council, the Swedish Foundation for Strategic Research, the Royal Swedish Academy of Sciences, the ÅForsk Foundation, and the Swedish Government Strategic Research Area in Materials Science on Functional Materials at Linköping University (Faculty Grant SFO-Mat-LiU no. 2009 00971).

References

[1] D. Tordera, D. Zhao, A. V. Volkov, X. Crispin, M. P. Jonsson, *Nano Lett.* **2017**, *17*, 3145.
[2] M. Shiran Chaharsoughi, D. Tordera, A. Grimoldi, I. Engquist, M. Berggren, S. Fabiano, M. P. Jonsson, *Advanced Optical Materials*. **2018**, *6*, 1701051.
[3] M. Shiran Chaharsoughi, D. Zhao, X. Crispin, S. Fabiano, M. P. Jonsson, *submitted*.

Near-infrared selective thermal emitter for thermo-photovoltaic energy conversion system

Takashi Asano*[1], Masahiro Suemitsu[1,2], and Susumu Noda[1]

[1]Department of Electronic Science and Engineering, Kyoto University, Kyoto, Japan
[2]Energy Technology Laboratories, Osaka Gas Co., Osaka, Japan
*corresponding author, E-mail: tasano@kuee.kyoto-u.ac.jp

Abstract

We report a near-infrared selective thermal emitter based on rod-type Si photonic crystals, which can be operated at temperatures above 1300 K. A thermo-photovoltaic energy conversion system using this selective thermal emitter is also discussed.

1. Introduction

Thermal emitters generally exhibit a broad spectrum and are widely used for various light sources from the far-infrared to the visible range. However, in many applications involving non-dispersive infrared sensing and thermo-photovoltaics (TPV), only a specific spectral component that is much narrower than the blackbody spectrum is utilized. Therefore, it is important to develop a narrow-bandwidth thermal emitter that achieves high emissivity at a target wavelength while suppressing emission at other wavelengths as much as possible to increase the energy utilization efficiency.

So far, we have developed selective thermal emitters based on simultaneous control of bare material absorption and photonic states [1-6]. Specifically, for spectroscopic applications in the mid- to long- wavelength infrared range, we utilized intersubband transitions in n-doped semiconductor quantum wells to control the bare absorption spectrum of a material, and fabricated a photonic crystal (PC) structure using such material to achieve a narrow thermal emission spectrum [1-2]. Ultrafast modulation (~MHz) of thermal emission has been also realized by changing the emissivity using an applied electric field [3]. For TPV applications, near-infrared selective emitters that can operate at high temperatures are important for the improvement of energy conversion efficiency. In this abstract, we discuss selective thermal emitters based on Si rod photonic crystals [5] and also discuss TPV systems that utilize them.

2. Emitter design

Thermal emission spectrum from an emitter can be controlled by varying the temperature and the emissivity spectrum. Emissivity spectrum can be controlled by selecting the bare absorption spectrum of the material consisting of the emitter, and by designing photonic states of the emitter. For TPV applications, it is important to suppress emissivity at wavelengths longer than the bandgap wavelength of the target photovoltaic (PV) cell to improve the system efficiency. In contrast, emissivity at wavelengths much shorter than the bandgap wavelength of the PV cells does not need to be suppressed because intensity of the blackbody radiation rapidly decreases at the shorter wavelength side of its peak. Figure 1 shows our strategy, where (A) an interband absorption of a semiconductor and (B) resonances of a photonic structure are combined to produce high emissivity at the near-infrared range and very low emissivity at longer wavelengths. Finally, the emissivity spectrum is shaped into a narrowband intensity spectrum by the falling tail of the blackbody spectrum, as shown in (C).

We utilized an interband transition of Si for (A) because Si has a high melting point of 1687 K and the bandgap is appropriate for near-infrared thermal emission. Fig. 2 (A) shows the theoretical absorption coefficient spectra of intrinsic Si at various temperatures calculated by taking into account both the interband transition and the free-carrier absorption owing to the intrinsic carriers generated at elevated

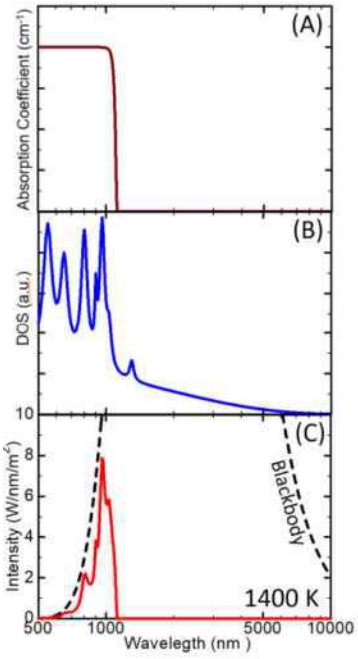


Figure 1: Strategy to obtain a narrowband selective thermal emission spectrum at the near-infrared wavelength. (A) Interband absorption spectrum of a semiconductor. (B) Photonic resonance of a micro structured emitter. (C) Emission intensity spectrum.

temperatures. It can be seen in the figure that the spectra exhibit step-like increases at wavelengths shorter than 1.2–1.5 μm, even at temperatures above 1000 K. For the control of the photonic resonance (B), we utilized rod-type PCs (Fig. 2 (B)). This structure exhibits resonance effects with a minimal Si filling factor, which is important for the suppression of non-resonant longer-wavelength emissions from the intrinsic free carriers generated at elevated temperatures.

Figure 3 shows examples of theoretical thermal emission spectra from the Si rod-type PC emitters at 1400 K. We designed two types of emitters: one was for Si PV cells (black solid line) and the other was for InGaAs or GaSb PC cells (gray solid line). It can be seen in the figure that near-infrared narrowband thermal emitters with suppressed longer wavelength components can be obtained.

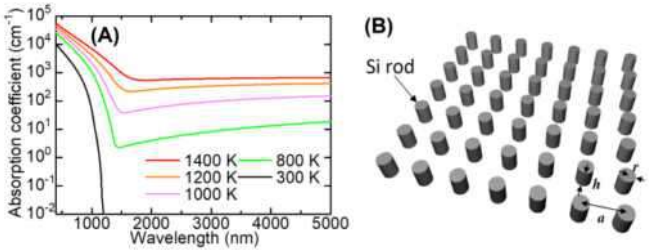


Figure 2: (A) Theoretical absorption coefficient spectra of intrinsic Si. (B) Photonic crystal consisting of a square array of Si rods.

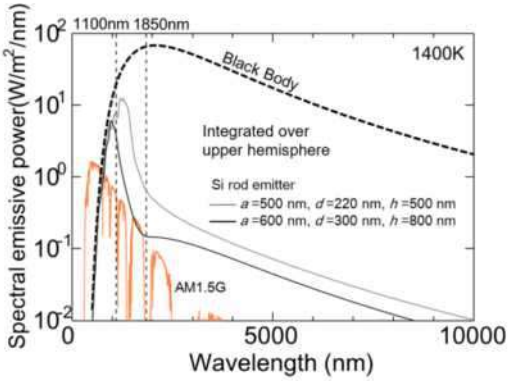


Figure 3: Theoretical thermal emission spectra of Si rod-type photonic crystal emitters for Si PV cells (black solid line) and InGaAs or GaSb PV cells (gray solid line).

3. Experiment

Figure 4 shows the experimental thermal emission spectrum of a Si rod-type PC emitter at 1400 K observed from the vertical direction [6]. The emitter was designed for InGaAs PV cells and fabricated on a MgO substrate. The MgO substrate is transparent at mid infrared region and resistant to high temperatures. It can be seen in the figure that thermal emission concentrated below ~1800 nm was experimentally obtained at the very high operating temperature of 1373 K. (We have previously realized Si-rod PC emitters for Si PV cells [5]).

In addition, we fabricated a TPV system by using the Si-rod PC emitters and PV cells, as schematically shown in Fig. 5. In this system, we placed InGaAs PV cells on both sides of the emitter, and formed reflectors at the backsides of the PV cells for the recycling of the spectral components not absorbed by the PV cells. The details, including energy conversion efficiency, will be discussed in the conference.

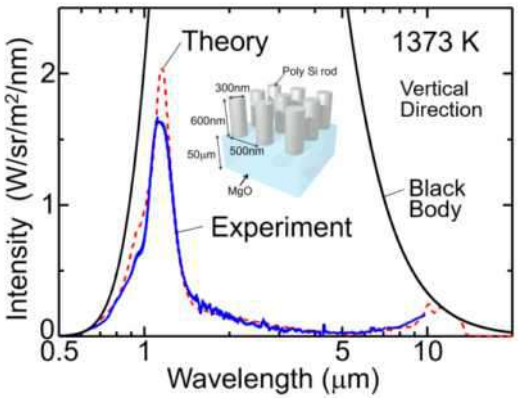


Figure 4: Experimental thermal emission spectrum of a Si rod-type photonic crystal emitter at 1373 K.

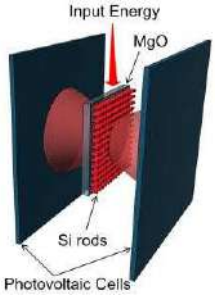


Figure 5: Schematic of TPV system utilizing a Si-rod photonic crystal emitter.

4. Conclusion

We have realized a near-infrared selective thermal emitter based on Si rod-type PCs on a MgO substrate, which can be operated at temperatures above 1300 K. A thermo-photovoltaic energy conversion system based on this emitter is also discussed.

Acknowledgements

This work was supported in part by Japan Society for the Promotion of Science (JSPS) Grant-in-Aid for Scientific Research (KAKENHI) grant no. 25220607 and 17H06125.

References

[1] T. Asano, K. Mochizuki, M. Yamaguchi, M. Chaminda, and S. Noda, *Opt. Exp.* **17**, 19190–203 (2009).

[2] M. De Zoysa, T. Asano, K. Mochizuki, A. Oskooi, T. Inoue, and S. Noda, *Nat. Photon.* **6**, 535-539 (2012).

[3] D. D. Kang, T. Inoue, T. Asano, S. Noda, *Appl. Phys. Lett.* **110**, 181109-1-4 (2017).

[4] T. Inoue, M. D. Zoysa, T. Asano, and S. Noda, *Nature Mat.* **13**, 928-931, (2014).

[5] T. Asano, M. Suemitsu, K. Hashimoto, M. De Zoysa, T. Shibahara, T. Tsutsumi, and S. Noda, *Sci. Adv.* **2**, e1600499-1-5 (2016).

[6] M. Suemitsu, T. Asano, M. De Zoysa, S. Noda, *Appl. Phys. Lett.* **112** (2018).

Near field based energy applications – thermophotovoltaics and photonic refrigeration by controlling the chemical potential of photons

Linxiao Zhu, Anthony Fiorino, Dakotah Thompson, Rohith Mittapally, Edgar Meyhofer, and Pramod Reddy

Abstract:
We will talk about our recent experiments of near-field based energy applications. First, we will show a 40-fold enhancement of thermophotovoltaic electricity generation rates by maintaining a nanoscale gap between a thermal emitter and a photovoltaic cell. Secondly, we will show the realization of photonic refrigeration by controlling the chemical potential of photons. We achieved net cooling on a planar device by suppression of radiation from a reverse-biased photodiode, and enhancement of photon transfer from the planar device.

Resonant laser processing for fabrication of nanobiophotonic devices

Xiaolong Zhu, Airidas Žukauskas, Andreas Raimund Stilling-Andersen, Anders Kristensen

DTU Healthtech, Technical University of Denmark, DK-2800 Kongens Lyngby
Presenting author: xizhu@dtu.dk

Abstract

Functional nanophotonic devices realized by the state-of-the-art nanofabrication technologies have offered the control of light with nanoscale precision, which are boomingly used in advanced bio-sensors and bio-imaging systems. Most of the functional nanophotonic devices rely on the ability to precisely control its individual meta-elements within the subwavelength scale. The absorption in metallic or dielectric elements provides a new route for photo-to-thermal conversions and processing. Here, we introduce a resonant laser processing (RLP) technique as a flexible photo-thermal post-writing technology for mass-customization of optical devices.

1. Introduction

Optical functional devices with photonic crystals, plasmonics or metasurfaces are designed photonic textures which have the capability of manipulating the amplitude, phase, polarization, activity, spin and quantum-entanglement of light. They can be made on metallic as well as dielectric or hybrid materials with the state-of-the-art nanofabrication facilities. Their optical properties are defined by the material composition, geometry, arrangement, orientation, topology and environment of each meta-element. The absorption in metallic or dielectric meta-elements provides an avenue for photo-to-thermal conversions. We developed a resonant laser processing (RLP) technique as a flexible post-writing technology for mass-customization of optical devices.[1-4] Strong on-resonance energy absorption under pulsed laser irradiation locally elevates the lattice temperature of individual optical meta-elements in an ultra-short time scale. In the RLP process, rapid melting allows for surface-energy-driven morphology changes and sintering or annealing of individual meta-elements with associated modification of the optical properties of the reflected and transmitted light from the devices. By controlling of the RLP process, we can manipulate the material and structural properties of the optical devices with a very high precision. Combined with the use of prefabricated large-area templates, RLP is a promising approach for the fabrication of next-generation low-cost optical devices for bio-sensors and bio-imaging systems.

2. Result and discussion

A light trap was born after the invention of the laser, it came to be known as optical tweezers for its direct applications in capturing things by light induced pressure and force. Nano-scaled optical metalens with dielectric and metallic structures are popular light tapping structures.[5,6]

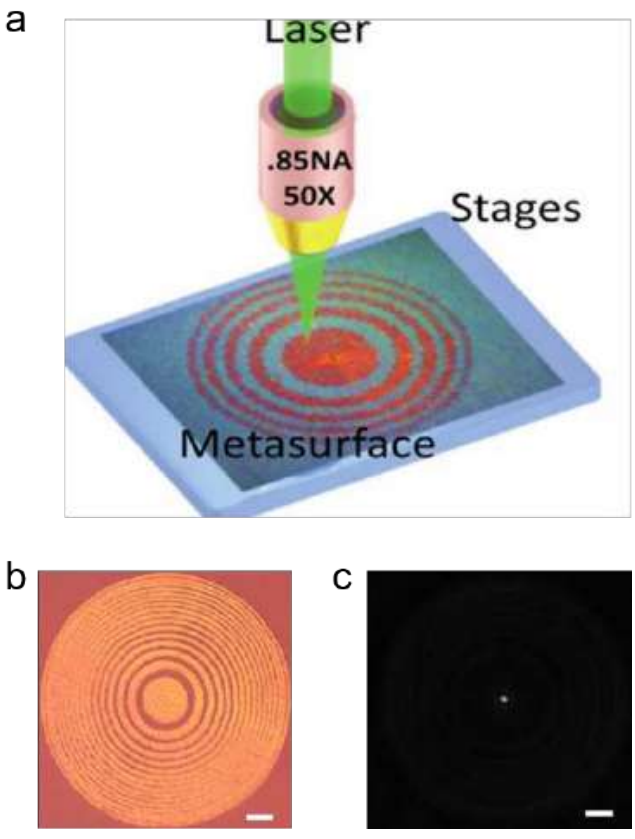


Figure 1: a. The concept of RLP, which is based on photo-to-thermal conversions and processing. b. Microscope image of ultrathin metalens printed onto silicon based metasurface templates. c. The characterized focus spot at the focus plane. Scale bars in b and c: 20 µm.

In this work, we report an in-line optofluidic light trapping device by introducing a metalens fabricated by nanosecond pulsed laser processing at the surface of a silicon metasurface.[7] We post-processed silicon based metasurfaces with morphology-dependent double resonances in the visible and in the near infrared. With the excitation of fundamental order resonance in the visible, the loss-assisted on-resonance photo-thermal melting of silicon ensures that the writing process only takes place at certain threshold, causing a resonance configured adaptive processing for resulting the desired metalens. Under coordinating the double-resonance phase matching condition dynamically, RLP in the visible allows for the morphology changes of the silicon metasurface with associated spatially modification of the optical phase and the transmittance in the near infrared by shifting the double-resonance coordinately.

Figure 1a shows the concept of laser printed flat optics by using a Nd:YAG laser (wavelength 532 nm, pulse length 2 ns)[4], illustrated by the writing of a Fresnel metalens on a silicon metasurface template comprising hybridized nanodisk and nanohole arrays[2]. Figure 1b presents an optical micrograph of the laser printed Fresnel metalens working at near infrared. We achieved a metalen with a full-wave-half-maximum of 2.29 um in the focus (Figure 1c), a focal length of 113 um and an efficiency of 16.98 %. The metalens is further integrated into an optofluidic devices for optical trapping experiments using a lasing wavelength of 1064 nm.[7]

3. Conclusions

In conclusion, as an alternative process to using state-of-the-art and expensive fabrication methods, we demonstrate that RLP is a powerful tool for the fabrication of ultrathin multi-functional optical devices. The concept of RLP makes the meta-optics closer to reality by providing a path for mass-production and ready-for-applications processes. This may pave the way of ultrathin flat optics into consumer nanobiophotonic products in the near future.

Acknowledgements

This work was supported by the European Commission project CHROMAVISION (Grant Agreement No. 665233) and X.Z. is funded by VILLUM Experiment (grant No. 17400) both supported by VILLUM FONDEN.

References

[1] Zhu, X.; Vannahme, C.; Højlund-Nielsen, E.; Mortensen, N. A.; Kristensen, A. Plasmonic colour laser printing. Nat. Nanotechnol. 2015, 11, 325−329.

[2] Zhu, X.; Yan, W.; Levy, U.; Mortensen, N. A.; Kristensen, A. Resonant-laser-printing of structural colors on high-index dielectric metasurfaces. Sci. Adv. 2017, 3, e1602487.

[3] Zhu, X.; Hedayati, M. K.; Raza, S.; Levy, U.; Mortensen, N. A.; Kristensen, A. Digital resonant laser printing: Bridging nanophotonic science and consumer products. Nano Today 2018, 18.

[4] Carstensen, M. S.; Zhu, X.; E. I., Oseze; Levy, U.; Mortensen, N. A.; Kristensen, A. Holographic resonant laser printing of flat optics using template plasmonic metasurfaces. ACS Photonics 2018, 5, 1665-1670.

[5] Tkachenko, G. et.al, Optical trapping with planar silicon metalenses Opt. Lett. 2018, 43, 3224-3227.

[6] Markovich, H.; Shishkin, I. I.; Hendler, N.; Ginzburg, P. Optical Manipulation along an Optical Axis with a Polarization Sensitive Meta-Lens. Nano Lett. 2018, 18, 5024−5029.

[7] Žukauskas, A.; Zhu, X.; Kristensen, A. Double-resonance-induced resonant laser printing of optical metalens for light trapping. 2019, In preparing.

Nanoscale Surface Thermal Hotspots of Vertical Antenna Arrays Activated by Mid-infrared Quantum Cascade Lasers

Andrea Mancini[1,2], Valeria Gliberti[3], Alessandro Alabastri[4], Eugenio Calandrini[5,6], Francesco De Angelis[6], Denis Garoli[6], and Michele Ortolani[1,3,*]

[1]Department of Physics, Sapienza University of Rome, Rome, Italy
[2] Nanoinstitute Munich, Ludwig Maximilian University, Munich, Germany
[3]Center for Life NanoScience (CLNS), Istituto Italiano di Tecnologia (IIT), Rome, Italy
[4]Department of Electrical and Computer Engineering, Rice University, Houston, United States
[5]Synchrotron SOLEIL, Saclay, France
[6]Plasmon Nanotechnology Department, Istituto Italiano di Tecnologia (IIT), Genoa, Italy
*corresponding author, E-mail: Michele.ortolani@roma1.infn.it

Abstract

Vertical antenna arrays of few-micron height and pitch, illuminated with a tunable mid-infrared laser, provide intense electric field hotspots far from the solid substrate. These hotspots do not suffer from the high thermal conductivity of the substrate and therefore, if a material with resonant vibrational fingerprint is present, thermal hotspots are generated, with local temperature increase of up to 100 K. Applications in nanoscale thermophoresis, photocatalysis and remote energy transfer are envisaged.

1. Introduction

Local photothermal effects produced by focused laser beams allow for fast and contact-less energy transfer to specific locations. In this context, plasmonic nanoantennas allow one to both circumvent the diffraction limit and obtain nanoscale thermal hotspots with very strong temperature gradients [1]. In the mid-infrared (IR) range, antenna arrays fabricated by lithography on solid substrates allow for the exploration of new designs for local heat generation, in which coherent enhancement of the e.m. field plays a key role [2].

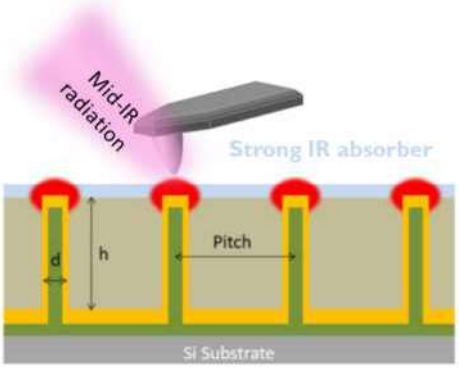


Figure 1. Sketch of the experimental setup. An AFM probe illuminated by a focused mid-IR tunable laser beam, senses the thermal expansion of a thin molecular layer on top of the vertical antenna array.

We have previously developed vertical antenna arrays for use as sensors based on the Surface Enhanced Infrared Absorption (SEIRA). Indeed, due to SEIRA, the strong apical electric field hotspots can become a thermal hotspot generator if an IR-absorbing material is placed at the antenna apex (see sketch in Figure 1) [3].

2. Experiment

Nanoscale surface thermal hotspots with local temperature up to 400 K (with a base temperature of 295 K) are obtained by focusing a mid-IR laser beam on the antenna array. The laser is an external-cavity tunable quantum cascade laser (MIRcat-xB by Daylight Solutions) continuously tuned around the vibrational absorption line of target molecules (wavenumber resolution is 1 cm^{-1}). Typical power in pulsed mode is up to 300 mW. The temperature increase is indirectly visualized by recording the photothermal expansion signal with a silicon cantilever probe for atomic force microscopy (AFM-IR, NanoIR2 by Anasys Instruments). The actual value of the temperature increase in a sphere of diameter 300 nm (red circles in Figure 1) is determined by comparison with thermal simulations.

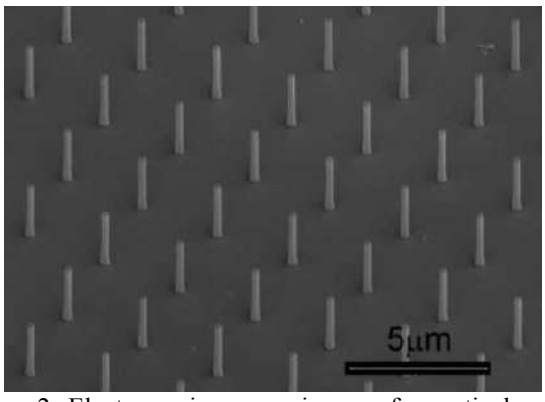


Figure 2: Electron microscope image of a vertical antenna array. Height is 2.7 μm. Antennas are fabricated by local amorphization of a polymer film by a focused ion beam, removal of the unexposed polymer, and gold evaporation.

The plasmonic structure consists in a square array of vertical gold-coated rods of height h = 2.7 μm, 250 nm in diameter, with an array pitch p = 4.0 μm (Figure 2). When illuminated with a monochromatic mid-infrared radiation beam at specific resonant frequencies, set by coherent enhancement designed by carefully selecting both p and h, the structure generates field-enhancement hotspots at the rod apexes. Embedding the antenna array in a polymer layer with low thermal conductivity, of thickness identical to the antenna height, results in a quasi-planar surface thermally isolated from the solid substrate. A strong IR-absorbing molecular layer (in this case, 120 nm thick film of hydrogen silsesquioxane, HSQ) is then located on top of the surface.

HSQ has a vibrational fingerprint at 1070 cm^{-1} (λ = 9.3 μm) whose intensity depends on the maximum temperature seen by the material [4], therefore the array was designed to resonate precisely at that IR wavelength. The absorption at 1070 cm^{-1} of the material portion located on top of each antenna, measured by AFM-IR, was found to depend on laser power (Figure 3): the HSQ material undergoes a smooth transition from amorphous to reticule when the temperature increases, and the peak intensity at 1070 cm^{-1} is a measure of the density of reticule bonds created by the temperature increase [4].

Finite-element simulations (COMSOL multiphysics, Figure 4) confirm that the T increase if of the order of 1 K/mW in the hotspot region of approximately 300 nm diameter.

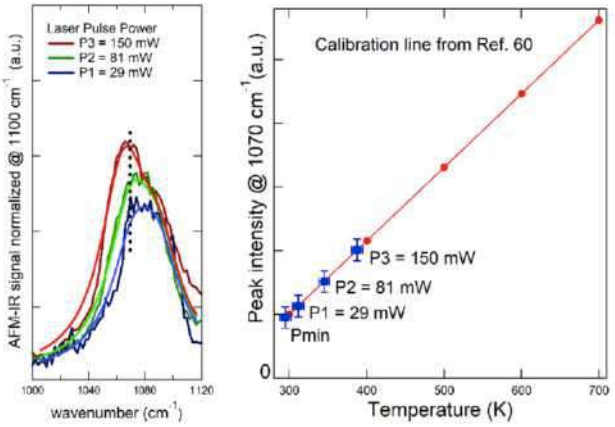


Figure 3. Photothermal expansion spectra of the HSQ film portion located on top of one of the antennas recorded as a function of quantum cascade laser power from 29 to 150 mW. The calibrated temperature dependence of the 1070 cm^{-1} peak indicates that temperatures around 400 K are reached in the nanoscale hotspot for 150 mW peak power.

3. Discussion

The use of SEIRA effect as photothermal transducer instead of electromagnetic field dissipation in the metal also solves a long-standing contradiction of the generation of nanoscale thermal hotspots using metal antennas anchored on a solid substrate: to maintain the absorbed thermal energy in a nanoscale region of space, the photothermal transducer should feature low thermal conductivity, but metal films and solid substrates generally feature high thermal conductivity. The fundamental mechanism of SEIRA heating is the non-radiative decay of highly excited vibrational states, which is physically different from plasmon dissipation. SEIRA heating does not take place in the metal, but in the molecules forming the dielectric layer on the of the antenna surface, which generally features low thermal conductivity. Therefore, with appropriate electromagnetic and thermal engineering, the contradiction can be solved and strong thermal hotspots can be obtained.

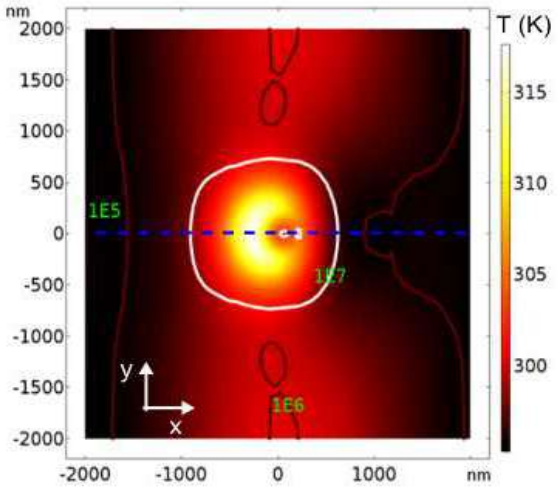


Figure 4. Simulated temperature increase at the surface of an embedded vertical antenna for input power of 19 mW and absorption coefficient of 1000 cm^{-1}. The numbers in green are isocurves of thermal gradient in K/m.

4. Conclusions

Local temperature increase of up to 100 K is obtained in hotspots with diameter around 300 nm at the apex of vertical antenna arrays with coherent plasmonic field enhancement in the mid infrared (λ = 9.3 μm). Applications in nanoscale thermophoresis, photocatalysis and remote energy transfer are envisaged.

References

[1] A. Mancini, V. Giliberti, A. Alabastri, E. Calandrini, F. De Angelis, D. Garoli and M Ortolani, Nanoscale thermal gradients activated by antenna-enhanced molecular absorption in the mid-infrared, *Appl. Phys. Lett.* 114: 023105, 2019.

[2] G. Baffou and R. Quidant, Thermo-plasmonics: using metallic nanostructures as nano-sources of heat, *Laser Photonics Rev.* 7: 171 2013.

[3] A. Mancini, V. Giliberti, A. Alabastri, E. Calandrini, F. De Angelis, D. Garoli and M Ortolani, Thermoplasmonic Effect of Surface-Enhanced Infrared Absorption in Vertical Nanoantenna Arrays, *J Phys. Chem. C.* 122: 13072–13081 (2018).

[4] D. L. Olynick et al., Electron-beam exposure mechanisms in hydrogen silsesquioxane investigated by vibrational spectroscopy and in-situ electron-beam-induced desorption, *J. Vac. Sci.Technol.B* 28:581, 2010.

Tunable Infrared Perfect Absorption in Bismuth-based Nanostructures for Thermal Photonics

Rosalía Serna[1], and Johann Toudert[1]

[1]Laser Processing Group, Instituto de Óptica, IO-CSIC, Madrid, Spain
*corresponding authors, E-mail: rosalia.serna@csic.es; johann.toudert@gmail.com

Abstract

Bismuth-based nanostructures present unique optical properties related with their giant near-infrared interband transitions. At longer wavelengths in the infrared, their giant refractive index and small extinction coefficient make them efficient light harvesters. In this presentation, we explore the potential of different kinds of bismuth-based nanostructures (nanospheres, nanocylinders and nanolayers) for achieving a spectrally tunable perfect absorption of light in the mid-to-far infrared and discuss the suitability of such nanostructures for thermal photonics.

1. Introduction

Bismuth (Bi) and its chalcogenides ($Bi_{1-x}Sb_xTe$, $Bi_{1-x}Sb_xSe$, $Bi_{1-x}Sb_xTe_{1-y}Se_y$) are becoming increasingly appealing to the photonics community owing to their unique optical properties.[1-3] Such properties arise from their peculiar electronic structure, which enables giant near-infrared interband transitions implying a negative dielectric permittivity in the ultraviolet-visible and a giant refractive index in the mid-to-far infrared.[1] Such features are especially relevant to efficiently harvest light in nanostructures, because of plasmonic effects and strong dielectric confinement, respectively. Up to now, many works have aimed at harnessing the ultraviolet-visible plasmonic properties of Bi-based nanostructures, especially for applications in photocatalysis[4,5] and for the development of thermally-switchable optical filters.[6] In contrast, very few works have aimed at exploring the optical properties of Bi-based nanostructures in the mid-to-far infrared and their potential for thermal photonics. In this presentation, we report the mid-to-far infrared optical properties of bulk Bi and its chalcogenides. We show that nanostructures of such materials are excellent candidates to achieve a perfect absorption of light tunable over the mid-to-far infrared. Finally, we discuss the implication of these findings for thermal photonics. In particular, we consider the applicability of such nanostructures for thermal camouflage and the spectral shaping of thermal radiation.

2. Results

2.1. Optical properties of Bi and its chalcogenides

It is only a few years ago that the bulk optical properties of Bi and its compounds have been characterized accurately. Especially, we reported for the first time the broadband characterization of the refractive index and extinction coefficient of Bi from the far infrared to the ultraviolet.[7] In a broad wavelength region from the mid infrared to the far infrared, it presents a giant refractive index ($n \sim 10$) and a small extinction coefficient ($k \sim 1$). Bi chalcogenides show comparable trends, yet with a slightly smaller n.[2]

2.2. Spectrally tunable perfect absorption in Bi-based nanostructures

Because of their giant refractive index and small extinction coefficient, such materials are outstanding candidates for achieving a strong absorption of infrared light in nanostructures around selected wavelengths. The absorption mechanism depends on the type of nanostructure involved. For 3d-confined nanostructures such as nanospheres or nanocylinders, absorption is achieved by lossy dielectric Mie resonances.[1] In 1d-confined nanostructures - or nanolayers - absorption can be achieved by designing resonant vertical cavities. In this presentation, we make an emphasis on the design of simple 1d- and 3d- confined Bi nanostructures enabling perfect absorption at selected wavelengths in the infrared. Especially, we demonstrate that very simple Bi/dielectric/metal resonant vertical cavities enable angle-independent perfect absorption in a Bi nanolayer more than 100 times thinner than the perfect absorption wavelength, and that such wavelength can be efficiently tuned from 3 to 20 μm by controlling the layer thicknesses. Such outstanding compactness and tunability stand on the surprising fractal interference mechanism of the cavity, which is enabled by the giant n and small k of Bi.[8]

3. Discussion

Achieving perfect absorption of light in nanostructures at selected wavelengths in the mid-to-far infrared is of utmost importance for thermal photonics. Combining nanostructures absorbing at different wavelengths enables the design of very thin coatings with tailored reflectance matching the spectral regions considered for thermal camouflage applications. Furthermore, according to Kirchhoff's law, such reflectance tailoring is also interesting for achieving very thin coatings with tailored infrared emissivity, and thus the spectral shaping of thermal radiation.[9]

4. Conclusions

The unique optical properties of Bi and its chalcogenides make Bi-based nanostructures excellent candidates for achieving the perfect absorption of light at selected wavelengths in the infrared. They can be therefore be used as the building blocks of very thin coatings presenting a tailored infrared reflectance and emissivity, as required for thermal camouflage and the spectral shaping of thermal radiation. Interestingly, such very thin coatings do not require complex patterning and can even be fabricated with lithography-free processes, in contrast with usual thermal photonics solutions such as metal-based metasurfaces.

Acknowledgements

This work was partially funded by the Spanish Ministry for Economy and Competitiveness through the project MINECO/FEDER TEC2015-69916-C2-1-R.

References

[1] J. Toudert, R. Serna, Interband transitions in semi-metals, semiconductors and topological insulators: a new driving force for plasmonics and nanophotonics [Invited], *Opt. Mater. Express* 7, 2299, 2017.

[2] D. Piccinotti, B. Gholipour, J. Yao, K.F. MacDonald, B.E. Hayden, N.I. Zheludev, Stoichiometric engineering of chalcogenide semiconductor alloys for nanophotonic applications, *Adv. Mater.* 1807083, 2019.

[3] J. Yin, H.N.S. Krishnamoorthy, G. Adamo, A.M. Dubrovkin, Y. Chong, N. Zheludev, C. Soci, Plasmonics of topological insulators at optical frequencies, *NPG Asia Materials* 9, e245, 2017.

[4] J. Toudert, R. Serna, M. Jiménez de Castro, Exploring the optical potential of nano-bismuth: tunable surface plasmon resonances in the near ultraviolet-to-near infrared range, *J. Phys. Chem. C* 116, 20530-20539, 2012.

[5] Y. Tian, J. Toudert, Nanobismuth: fabrication, optical, and plasmonic properties – emerging applications, *Journal of Nanotechnology* 3250932, 2018.

[6] M. Jiménez de Castro, F. Cabello, J. Toudert, R. Serna, E. Haro-Poniatowski, *Appl. Phys. Lett.* 105, 113102, 2015.

[7] J. Toudert, R. Serna, I. Camps, J. Wojcik, P. Mascher, E. Rebollar, and T.A. Ezquerra, Unveiling the far infrared-to-ultraviolet optical properties of bismuth for applications in plasmonics and nanophotonics, *J. Phys. Chem. C* 121, 3511-3521, 2017.

[8] J. Toudert, R. Serna, M. García Pardo, N. Ramos, R.J. Peláez, B. Maté, Mid-to-far infrared tunable perfect absorption by a sub-λ/100 nanofilm in a fractal phasor resonant cavity, *Opt. Express* 26, 34043 (2018)

[9] W. Streyer, S. Law, G. Rooney, T. Jacobs, D. Wasserman, Strong absorption and selective emission from engineered metals with dielectric coatings, *Opt. Expr*ess 21, 9113-9122, 2013.

Temperature dependent Mie resonances and spectral characteristics of semiconductor nanoparticles and their composites

Vaibhav Thakore[1,2*], Janika Tang[3], Kevin Conley[3], Tapio Ala-Nissila[3,4,5], and Mikko Karttunen[1,2,6]

[1]Department of Applied Mathematics, Western University, 1151 Richmond Street, London, Ontario N6A 5B7, Canada
[2]Center for Advanced Materials and Biomaterials Research, Western University, 1151 Richmond Street, London, Ontario N6A 5B7, Canada
[3]QTF Center of Excellence, Department of Applied Physics, Aalto University School of Science, FIN-00076, Aalto, Espoo, Finland
[4]Department of Physics, Brown University, Providence, Rhode Island 02912-1843, USA
[5]Interdisciplinary Centre for Mathematical Modelling, Department of Mathematical Sciences, Loughborough University, Loughborough LE11 3TU, UK
[6]Department of Chemistry, Western University, 1151 Richmond Street, London, Ontario N6A 5B7, Canada
*corresponding author, E-mail: vthakore@knights.ucf.edu

Abstract

Thermoplasmonic response of indirect (silicon, Si) and direct (gallium-arsenide, GaAs) bandgap semiconductor nanoparticles is studied and compared with the results from metallic (gold, Au) nanoparticles. Si nanoparticles present high values of quality factors for the resonances while the spectral selectivity of the absorption efficiency in GaAs nanoparticles is maintained at elevated temperatures in contrast to the Au nanoparticles. Furthermore, results from the multiscale modeling of plasmonically enhanced control of radiation using spherical semiconductor inclusions in a composite will also be presented.

1. Introduction

Plasmonically enhanced absorption or scattering of radiation on the mesoscale forms the basis of promising applications in a wide variety of fields such as: biosensing, photothermal therapy, photocatalysis, solvothermal chemistry, energy harvesting, magnetic recording for data storage, control of radiative heat transfer and so on [1, 2, 3]. In a majority of the applications based on plasmonics, the noble metals - Au and silver (Ag) - have been the materials of choice. However, it is also now widely acknowledged that these materials suffer from problems of poor thermal and chemical stability accompanied by significant dissipative losses under high-temperature conditions. These issues have thus prompted a quest for materials with better thermoplasmonic properties. In this regard, semiconductor micro- and nanoparticles have lately attracted a lot of attention because they exhibit low ohmic losses, are thermochemically more stable, and exhibit highly tunable plasmonic resonances through bandgap engineering, control over dopant concentration and dielectric environment. Here, we present results from our recent work on the multiscale modeling of plasmonically enhanced control of radiation in composites with semiconductor inclusions [1, 2]. Furthermore, a comparison of the size-dependent thermoplasmonic behavior of undoped indirect (Si) and direct (GaAs) bandgap semiconductor nanoparticles with the metallic (Au) particles that are characterized by a complete absence of the bandgap is also presented [1].

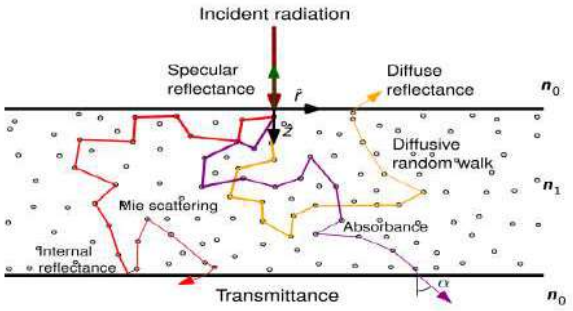


Figure 1: A schematic illustrating the Monte Carlo model of propagating photons inside composites with scattering inclusions for modeling the transport of the incident radiation. An infinitesimally thin beam of incident photons is scattered within the composite layer until the photons are absorbed or exit the system. The random distribution of small open circles represents the inclusions that serve as scattering and absorption centers for the photons. The photon weight is progressively decremented as it executes a random motion in the composite. The direction of photon exit from the composite is characterized by the angle α in the Monte Carlo model. This angle α varies with each random trajectory and for a large number of photons cumulatively gives rise to diffuse reflectance or transmittance. n_o and n_1 represent the refractive indices of the surrounding medium and the composite layer, respectively [2, 3].

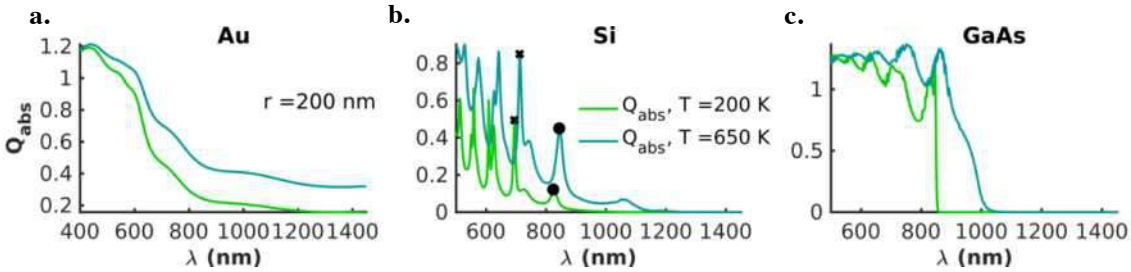


Figure 2: Mie absorption efficiency (Q_{abs}) as a function of the wavelength λ for (a) Au (Drude-Lorentz model), (b) Si and (c) GaAs nanoparticles of radii r = 200 nm at temperatures T = 200 and 650 K.

2. Theory and Methods

Multiscale modeling of radiation transport in micro/nanocomposites is carried out using a three-step process [2]. The first step involves the computation of the temperature dependent dielectric permittivities for Au, Si and GaAs. Next, these temperature dependent dielectric permittivities are employed to numerically compute the Mie scattering and absorption coefficients along with the asymmetry factor that determines the proportion of forward- to back-scattered radiation. These characteristic Mie parameters for a spherical nanoparticle of given size are then utilized in a Monte Carlo algorithm to determine the reflectance, absorbance and transmittance spectra for a micro- or nanocomposite with particle inclusions at a low volume fraction of 1-5% (Figure 1) [2]. For the Monte Carlo simulations, the real part of the refractive index of the composite layer is computed using the Effective Medium Theory.

3. Results and Discussion

A broadening and redshifting of the scattering and absorption resonances with an increase in the temperature and the particle radii is observed in nanoparticles of all three materials including Au, Si, and GaAs [1]. Our results indicate that semiconductor nanoparticles maintain the strength of their scattering and absorption resonances at high temperatures compared to the metallic Au nanoparticles (Figure 2). Enhanced absorption resonances at elevated temperatures are observed due to the phonon-mediated interband electronic transitions in the indirect bandgap Si nanoparticles at shorter wavelengths. On the other hand, the magnitude of the absorption resonances for the direct bandgap GaAs nanoparticles stays close to constant for similar wavelengths at higher temperatures. Si and GaAs nanoparticles exhibit Fano resonances, in both the scattering and absorption spectra, due to the presence of sharp higher order electric and magnetic Mie resonances against a background of broad quadrupole or dipole modes. The ratio of the radiative to dissipative damping decreases with an increase in temperature for all the nanoparticles. However, this ratio is observed to be about 1-2 orders of magnitude greater for the Si and GaAs nanoparticles. This points to the excessive heating of Au nanoparticles at elevated temperatures due to increased Drude damping of plasmonic resonances and enhanced absorption at longer wavelengths.

4. Conclusions

We have investigated the thermoplasmonic response of indirect (Si) and direct (GaAs) bandgap semiconductor nanoparticles and compared it to that of metallic (Au) nanoparticles [1]. Furthermore, we have studied the temperature dependent multiscale radiative transport in composites of these materials [2, 3]. Our results indicate that, unlike metallic nanoparticles, semiconductor nanoparticles allow for a much better control of radiation on the nanoscale because of the stability of their scattering and absorption resonances at elevated temperatures. This renders them particularly promising for thermoplasmonic applications such as solar thermophotovoltaics, photocatalysis, and solvothermal chemistry that require operating at high temperatures for desired optimal performance.

Acknowledgements

The authors gratefully acknowledge funding and support from the COMP CoE Program, Grant # 284621; QTF CoE Program, Grant # 312298; RADDESS Consortium Grant; the Aalto Energy Efficiency Research Program EXPECTS; the Aalto Science-IT project; the Discovery Grants and Canada Research Chairs Program of the Natural Sciences and Engineering Research Council of Canada; and Compute Canada (www.computecanada.ca).

References

[1] Vaibhav Thakore, Janika Tang, Kevin Conley, Tapio Ala-Nissila, Mikko Karttunen, Thermoplasmonic response of semiconductor nanoparticles – A comparison with metals, Adv. Theory Sim. 1800100, 2018.

[2] Janika Tang, Vaibhav Thakore, Tapio Ala-Nissila, Plasmonically enhanced reflectance of heat radiation from low-bandgap semiconductor microinclusions, *Sci. Rep.* 7, 5696, 2017.

[3] Kevin Conley, Vaibhav Thakore, Tapio Ala-Nissila, Plasmonically Enhanced Spectrally-sensitive Coatings for Gradient Heat Flux Sensors, *PIERS 2018*, Toyama, Japan, August 1-4, 2018.

Narrowband Photothermal Converters for Infrared Sensors

T. Nagao[1,2*], A. T. Doan[1,2], T. D. Dao[1] , S. Ishii[1], H. D. Ngo[1,2]

[1]National Institute for Materials Science, 1-1 Namiki, Tsukuba, Ibaraki 305-0044, Japan
[2]Hokkaido University, Kita-ku, Sapporo 060-0808, Japan
*corresponding author, E-mail: NAGAO.Tadaaki@nims.go.jp

Abstract

Wavelength-selective light absorbers and emitters, or spectroscopic energy transducers for light, are expected to provide wide variety of applications in energy harvesting, remote and perceptive sensors for IoT devices. Especially, narrowband perfect absorption and emission in the infrared (IR) region are critical prerequisites for modern spectroscopy and energy applications such as non-dispersive infrared (NDIR) gas sensors, multi-wavelength pyrometers, IR radiative heaters, and thermophotovoltaics. The technology to control thermal emission and absorption is rapidly progressing recently with the development in the field of plasmonics and metamaterials. In this talk, we demonstrate our methodology to achieve narrowband perfect absorption and thermal emission based on 2D and 3D nano architectures combined with IR plasmonic materials [1-6]. We introduce some of our recently developed uncooled infrared detectors combined with spectroscopic perfect absorbers for wavelength-selective infrared ray detection. The MIM metamaterial IR sensors with pyroelectric/thermoelectric detection exhibit resolutions better than 1um with wide acceptance angles. By adopting Gires-Turnois structures (asymmetric Fabry-Perot resonators), Tamm plasmon polariton, and aperiodic structures composed of low-loss dielectrics and metal reflectors, wavelength resolution better than 50 nm was achieved at operation wavelengths in the mid infrared region. The same design can be adopted also to narrowband thermal emitters when it is fabricated with refractive dielectrics and conductive ceramics.

1. Introduction

Perfect narrowband absorption and emission in the infrared (IR) region are critical prerequisites for modern spectroscopic applications such as multi-wavelength pyrometers, nondispersive infrared (NDIR) gas sensors, IR radiative heaters, and thermophotovoltaics. Within the past decade, artificial photonic structures, such as plasmonic metamaterials and photonic crystals, have been used to realize spectrally selective absorbers and emitters. We present our recent study on the development of perfect absorbers based on the metal-insulator-metal structures. We also discuss the design and the fabrication of narrowband perfect absorption based on several different layered structures, such as Gires–Tournois (GT) etalon (Assymetric Fabry-Perot resonator), Tamm-plasmon polariton, and aperiodic layered structures. The MIM metamaterial IR sensors with pyroelectric or thermoelectric detection exhibited resolutions better than 1um with wide acceptance angles. By adopting GT structure with, the wavelength resolution goes lower than 50 nm at resonance wavelength of 3-4 um. Such structures also shows sharp thermal emission when they are fabricated with refractory materials and heated at high temperatures. These devices will open a new avenue for potential applications in multiband temperature sensing, infrared-color imaging, and NDIR gas sensors for security gas sensors and combustion analysis.

2. Discussion

Figure 1a shows the photo of a fabricated four-wavelength detector, which has a width of 0.5 cm and length of 1 cm. This design demonstrates the hybrid plasmonic-pyroelectric device can be easily integrated on a standard CMOS platform and achieve multispectral selectivity without any additional bulky optical filters. **Figure 1b** shows the optical microscopy images of the top view and back view of a single sensing element with an active area of 200×200 μm. The sensing area is thermally well-isolated from the body of the device.

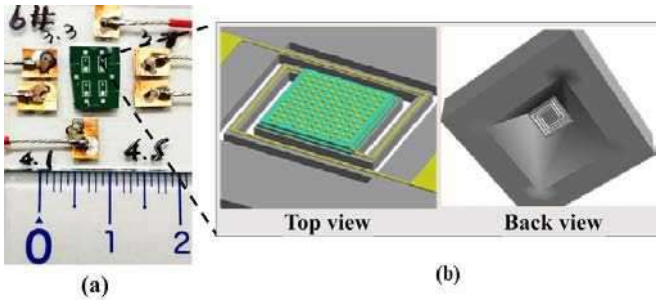


Figure 1. (a) photo of a fabricated four-wavelength detector. (b) Microscope images of top view and back view of a fabricated sensing patch for one wavelength.

The scanning electron microscope (SEM) images of the hexagonal arrays of Al disk resonators (**Figure 2 a-d**) shows that the Al disk array fabricated on top of the membrane structures is well-defined and homogeneously distributed. The simulated absorption spectra are shown in **Figure 2e**. The reflectivity spectra of the fabricated devices were measured using a Fourier transform infrared spectrometer with a microscope. The reflectance spectra were normalized with respect to the reflectance from a gold film. The absorptivity values were 0.92, 0.93, 0.85, 0.87 at 3.3, 3.7, 4.1 and 4.5 μm, and the wavelength resolution were 0.94, 1.02, 1.1, 1.2 μm FWHM, respectively. The fabricated device demonstrated the spectrally selective detection of IR radiation in the range of 3.3 to 4.5 μm, that locates in the atmospheric window, and exhibited the FWHMs in the

range of 0.9 to1.1 μm, and the spectral responsivities of 125-128 mV/W, respectively. These results demonstrate the feasibility and great potential for MEMS-based multispectral hybrid plasmonic-pyroelectric infrared detector with remarkable wavelength tunability, compactness, and high spectral resolution.

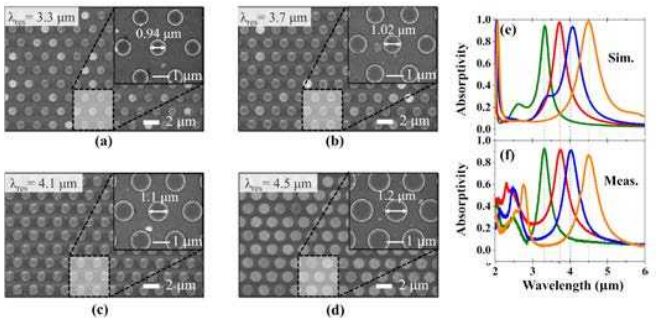


Figure 2. (a-d) Scanning electron microscope (SEM) images of the fabricated disk array patterns at four resonance wavelengths. (e), (f) Simulated and measured absorptivities of the perfect absorbers at four wavelengths.

Next we directly integrated a distributed Bragg reflector 3(SiO_2–Si)–SiO_2–based GT resonator onto a pyroelectric $LiTaO_3$ single-crystal slab [6]. We intentionally chose Al as the material for the back reflector for three reasons: first, it exhibits low-loss and high-optical response plasmonic properties similar to Au and Ag in the near-to-mid IR region; second, no adhesion layer is required to fix the oxide layer on Al; and third, Al is widely used as one of the industry-compatible base metals.

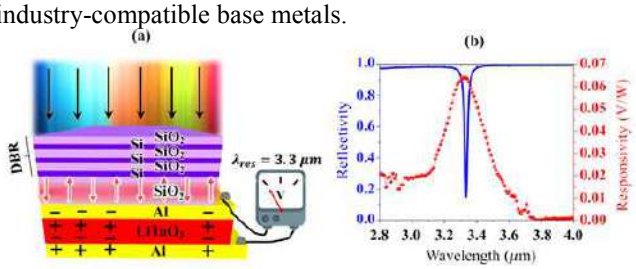


Figure 3. Gires-Tournois resonator-based narrowband pyroelectric IR detector fabricated by adopting DBR-cavity-metal design and loaded on LTO single crystal slab: (a) schematic illustration, (b) measured reflectivity and spectral responsivity[6].

The spectral responsivity curve exhibited an absorption peak at 3.3 μm, which matches to the absorption band of water and methane. The FWHM of the reflectivity spectra is as narrow as 22 nm, corresponding to a Q-factor of 151, which is two to four times higher than that of recently reported multilayered absorbers and detectors base on photothermal transduction. To the best of our knowledge, this is the first time that an on-chip GT resonator-based perfect absorber achieves such a high spectral resolution.

3. Conclusions

We have demonstrated that metal(disk)-insulator-metal(plate) structures and 1D layer structures, such as Gires-Tournois (GT) Asymmetric cavity structures, can be utilized as high-efficiency narrowband photothermal transducers working in the infrared region. The quad-wavelength pyroelectric microsensors were fabricated for multicolor IR sensing application and exhibited excellent wavelength selectivity. The GT layered structure exhibited very high wavelength selectivity with sharp resonant absorption at the vibrational peak of methane (3.3 μm) with an excellent quality factor of 151, which is higher than that of any layered-type un-cooled infrared detectors studied so far.

Acknowledgements

This work is partially supported by the JSPS KAKENHI (16H06364, 17K19045, 16F16315) and JST CREST (JPMJCR13C3) "Phase Interface Science for Highly Efficient Energy Utilization".

References

[1] T.D. Dao, S. Ishii, T. Yokoyama, T. Sawada, S. Ramu Pasupathi, K. Chen, Y. Wada, T. Nabatame, T. Nagao, ACS Photonics 3, 1271-1278 (2016).

[2] T. Yokoyama, T. D. Dao, K. Chen, S. Ishii, R. P. Sugavaneshwar, M. Kitajima, T. Nagao, Adv. Opt. Mater. 4 (12), 1987-1992 (2016).

[3] K. Chen, T. Dao, and T. Nagao, Sci. Rep. 7, 44069, (2017).

[4] K. Chen, T. Dao, S. Ishii, M. Aono, and T. Nagao, Advanced Functional Materials **42**, 6637-6643 (2015).

[5] T.D.Dao, K. Chen, S. Ishii, A. Ohi, T. Nabatame, M. Kitajima, and T. Nagao, ACS Photonics **2**, 964-970, (2015).

[6] T. A. Doan, T.D. Dao, S. Ishii, T. Nagao, Submitted to Opt. Exp.

Photothermal epoxy curing with plasmonic nanoparticles: From modeling to experiments

Alessandro Alabastri[1], Adam T. Roberts[2], Jian Yang[3], Matthew E. Reish[4], Naomi J. Halas[1,3,4], Peter Nordlander[1,3] and Henry O. Everitt[1,2]

[1] Dept. of Electrical and Computer Engineering, Rice University, Houston, TX 77005, USA
[2] U.S. Army CCDC Aviation & Missile Center, Redstone Arsenal, AL 35898, USA
[3] Dept. of Physics and Astronomy, Rice University, Houston, TX 77005, USA
[4] Oak Ridge Institute of Science and Education, Redstone Arsenal, AL 35898, USA
[4] Dept. of Chemistry, Rice University, Houston, TX 77005, USA

*corresponding author, E-mail: Henry.Everitt@rice.edu

Abstract

Epoxy materials are widely used for efficient bonding and repair of composite materials. Plasmonic nanoparticles can be employed as heat source to improve curing of epoxy films. We theoretically show how the nanoparticle-assisted photothermal curing is a four-stage process: a rapid plasmonic temperature increase, a slow curing initialization, a temperature increase due to cured epoxy direct light absorption and a final stage that completes the chemical transformation. Experiments confirm theoretical predictions and further demonstrate how the plasmon-assisted curing forms stronger bonds than conventional thermal curing.

1. Introduction

Composite materials have been replacing metals in several sectors (*e.g.* aviation, automotive, robotics) to improve performance. Unlike metals, composite materials often require heat during their assembly and lifecycle. For example, during repairing, high-temperature epoxy resins are regularly employed to bind composite materials. Usually this process requires oven heating, thus posing significant challenges when large parts need to be treated or when components include temperature sensitive materials. The possibility to selectively dissipate heat in localized regions to trigger the epoxy curing only where it is needed would be crucial in this field. When two composites need to be joined, the epoxy is deposited at their interface, and this is the only region which actually requires heat. Laser heating represents a possibility for the curing of buried junctions in the wavelength range where the composite is partially transparent to the radiation. However, the approach can be inefficient if the epoxy is a weak absorber in its uncured state. Recently, it has been shown that nanoparticles close to their plasmon resonance act as efficient heaters and enable *in situ* epoxy curing [1,2]. In our study we examine a different regime where plasmonic nanoparticles are combined with an epoxy resin transparent to laser radiation in its uncured state and absorptive upon curing [3]. This combination allows for an initial localized temperature increase through plasmonic nanoparticles followed by a self-reinforcing process given by the epoxy absorption. The synergetic effect allows the curing of buried junction at lower laser powers, thus preventing potential damages to components in proximity to the interface.

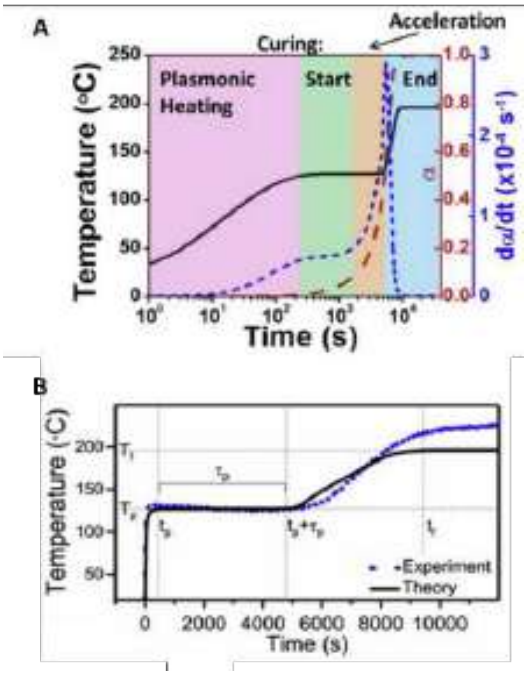


Figure 1: A - Temperature (solid black), curing state (dashed red) and curing rate (dotted blue) dependence on time (log scale) of a 40 nm Au nanoparticles covered FM 300 epoxy film. B - Comparison between experimental results (dotted blue) and theoretical calculations (solid black) for the temperature increase of a FM 300 epoxy film sample over time. An input power of P_{in} = 5 W/cm^2 and a nanoparticle density $\rho_{NP} = 2.2 \cdot 10^{10}$ NP/cm^2 are considered. [3]

The concept is of general interest since interrelated opto-thermal properties need to be analyzed whenever nanoparticles are placed in a temperature sensitive matrix, such as biological tissues, polymers or phase-changing media. Here we give a detailed theoretical time-dependent description of the steps involved in the nanoparticle-assisted photo-thermal curing process, identifying four major thermal

regimes. Experiments confirm theoretical predictions and, additionally, demonstrate how the resulting bonds are stronger than conventional thermal curing.

2. Results and discussion

The investigated system consists of a 2-dimensional random array of 40 nm Au nanoparticles (NPs) sandwiched between a supporting glass and a 0.2 mm epoxy film. The sample is laser irradiated at a wavelength of 532 nm while the temperature is measured through an infrared (IR) camera. A Finite Element Method (COMSOL) model has been developed to describe the electromagnetic and thermal processes accurately [3]. Fig. 1A shows the calculated temperature (black, solid), cure progress (red, dashed) and cure rate (blue, dotted) at the center of the epoxy film from the time the laser is switched ON until the resin is fully cured. Four distinct opto-thermal phases can be identified. (i) *Plasmonic heating (pink region)* – Temperature quickly increases due to the efficient heat dissipation in the nanoparticles: during this phase the cure progress is close to zero while the cure rate starts increasing. (ii) *Initial curing phase (green region)* – A first temperature plateau is reached at ~130°C where the cure begins while the curing rate remains approximately constant. (iii) *Acceleration phase (tan region)* – The curing rate reaches its peak due to the increasing optical absorption in the epoxy glue. As consequence, the cure state rapidly increases. (iv) *Final curing phase (light blue region)* – Both the heat generated in the NPs and within the epoxy are balanced by the heat exchanged with the background. The final temperature plateau (~200°C) is reached when the curing rate stops as the chemical transformation is complete. Fig. 1B shows the comparison between theoretically predicted and measured temperature in the case of a FM300 epoxy covered by a Au NPs array (2.2 NPs/cm^2) heated by a scanning laser at 532nm, with incident intensity 5W/cm^2. All four curing stages described above can be recognized in the temperature measurements.

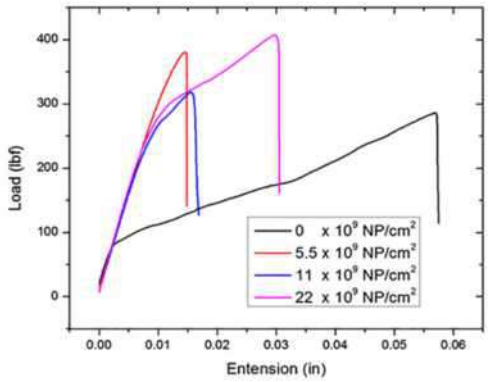


Figure 2: Lap shear measurements for four samples of increasing nanoparticle concentration: 0, 5.5·10^9 NP/cm^2, 1.1·10^{10} NP/cm^2, and 2.2·10^{10} NP/cm^2, following identical photocuring conditions of laser intensity (1.55 W/cm^2), illumination area (1 in x 1 in), and duration (30 min). [3]

To test the efficacy of the plasmonic NPs assisted bonding, four samples, partially cured using different NP concentrations, have been mechanically tested. The parameter of interest is the maximum load that a bonded junction can sustain. Fig. 2 shows lap shear measurements in which the samples were pulled along the bond axis until the bond broke. The sample cured employing the largest density of NPs (~22·10^9 /cm^2, pink line) failed at 1800 N (407 lbs). The sample cured without NPs failed at 1300 N instead. Further numerical analyses and experiments [3] confirm the important interrelations among the parameters employed for the process. The four curing stages can be tailored in terms of duration and temperature levels not only by modifying the laser power but also by changing the nanoparticle density, shape, and material. Different nanostructures can be considered to interact with radiation at different wavelengths, thus widening the range of applications of this approach.

3. Conclusions

We have theoretically and experimentally investigated how laser bonding of composite materials can take advantage of plasmonic nanoparticles for a better performing photo-curing process. The concentrated heat dissipated in the nanoparticles provide a localized thermal source which promotes a faster curing and leads to stronger bonds. Upon curing, the epoxy itself starts absorbing laser radiation in a self-sustaining heating process. The local nature of the efficient plasmon heat generation avoids the exposure of thermally sensitive parts to high temperatures and represents a major improvement for practical bonding of composite materials. Earth abundant materials (*e.g.* aluminum) and other epoxies may be utilized to ease the commercialization of this approach.

Acknowledgements

This work was partially supported by the Army's former Aviation and Missile Research, Development, and Engineering Center. MER is supported through the Oak Ridge Institute for Science and Education. The authors thank Sean Thompson, David Busby, and Lance Hall for the lap shear measurements. PN and JY acknowledge support from the Robert A. Welch Foundation under Grant C-1222, and NJH acknowledges support from the Robert A.Welch Foundation under Grant C-1220. PN, NJH, and HOE all acknowledge the Air Force Office of Scientific Research Multidisciplinary Research Program of the University Research Initiative (MURI FA9550-15-1-0022).

References

[1] A. T. Roberts, H. O. Everitt, Nanoparticle Assisted Laser Bonding in Composites, U.S. Army AMRDEC Tech. Reports RDMR-WD-15-17,1-30, 2015

[2] J. Dong, G.E. Firestone, J. R. Bochinski, L. I. Clarke, R. E. Gorga, *In situ* curing of liquid epoxy via gold-nanoparticle mediated photothermal heating, *Nanotechnology* 28, 065601, 2017.

[3] A. T. Roberts, J. Yang, M. E. Reish, A. Alabastri, N. J. Halas, P. Nordlander, H. O. Everitt, Plasmonic nanoparticle-based epoxy photocuring: A deeper look, *Materials Today*, https://doi.org/10.1016/j.mattod.2018.09.005 , 2018.

Thermo-plasmonics on vanadium oxide and silicon-based infrared sensor platforms

Xu Fang

[1]School of Electronics and Computer Science, University of Southampton, UK
E-mail: x.fang@soton.ac.uk

We present recent experimental and numerically simulated results in integrating plasmonic nanostructures with vanadium oxide and silicon thin films for developing infrared sensors with various functionalities. We also present a theoretical model, the modified Maxwell Garnett model, for interpreting hysteresis in vanadium dioxide.

A microbolometer is a type of photodetector that utilises the dependence of material resistivity on temperature in the light detection. Its unique properties such as extremely broadband response and room-temperature operation have led to its widespread use in various application. Its relatively simple sensor structure, at the same time, provides an ideal platform for nanoengineering.

We demonstrate both numerically and experimentally that plasmonic nanostructures fabricated on top of thin films of vanadium oxide and silicon, the two most commonly used sensing materials in microbolometers, regulate the distribution of light and heat at the nanoscale. This phenomenon is used to develop functionalities such as wavelength and polarisation sensitivity in the photodetection [1]. This result may be used to improve the performances of a variety of vision systems in the infrared.

We further present a theoretical model for interpreting optical hysteresis, where the optical properties of a material depends on not only the current temperature but also those in the history [2]. Hysteresis is a phenomenon that crucially affects the performances of vanadium oxide-based infrared sensors. The standard Maxwell Garnett model, a theoretical model widely used in effective medium analysis, is modified here to allow it to be used in hysteresis analysis. The model requires very few input parameters, providing a phenomenological approach to describing electromagnetic hysteresis in not only vanadium dioxide but also may other phase change materials.

[1] H. Takeya, J. Frame, T. Tanaka, Y. Urade, X. Fang & W. Kubo. Bolometric photodetection using plasmon-assisted resistivity change in vanadium dioxide. *Scientific Reports* 8, 12764 (2018).

[2] J. Frame, N. Green & X. Fang. Modified Maxwell Garnett model for hysteresis in phase change materials. *Optical Materials Express* 8, 1988 (2018).

Thermal emission engineering with confined plasmons in semiconductors

Angela Vasanelli, Simon Huppert, Yanko Todorov, Djamal Gacemi, Carlo Sirtori

Laboratoire de Physique de l'Ecole normale supérieure, ENS, Université PSL, CNRS, Sorbonne Université, Université Paris-Diderot, Sorbonne Paris Cité, Paris, France

Email: angela.vasanelli@ens.fr

Bulk plasmons are collective excitations of a three dimensional electron gas. As any quantum entity, also plasma waves undergo size confinement when they lay in a thin film with thickness smaller than their wavelength. The resulting confined plasmon modes are called Berreman or Ferrell – Berreman modes and they are coupled to free space radiation. Consequently, in the earliest works on plasmons, the confinement has been exploited to probe their existence through the measurement of transmittance, reflectance and absorbance of thin metallic films [1–4].

Bulk plasmons can also be confined in highly doped semiconductor layers. In this case Berreman modes are in the mid-infrared range, at wavelengths set by the doping, and are characterized by a sharp resonance with quality factor in order of 20 [5].

In the last years, we have established that Berreman modes are strongly coupled with mid-infrared radiation. We have demonstrated that, when a Berreman mode is coupled to a resonant microcavity mode, the ultra-strong light-matter coupling regime can be achieved up to room temperature, with a record value of 92% of the relative Rabi energy [6]. Furthermore, such a phenomenal interaction with the electromagnetic field appears also in the absence of a microcavity and it gives rise to superradiance [7].

In this talk we will present how the strong interaction of confined plasmons with the electromagnetic field has been exploited to engineer active and functional mid-infrared thermal emitters [8,9]. In our devices, based on highly doped GaInAs layers, the electron gas is excited by a current flowing in the layer plane, allowing frequency modulation of thermal emission up to 50 MHz. Optical emission is engineered by exploiting the strong interaction of the plasmons with the electromagnetic field. In the superradiant regime a critical coupling sets the plasmon radiative decay equal to the excitation rate (~ps^{-1}) [8]. This allows realizing directional and quasi-monochromatic incandescent sources without using any photonic structure, but only exploiting the superradiant nature of plasmons. On the other hand mid-infrared plasmons ultra-strongly coupled with the fundamental mode of a suitably designed metallic microcavity generate THz emission [6].

References

[1] R. A. Ferrell, Phys. Rev. **111**, 1214 (1958).
[2] A. J. McAlister and E. A. Stern, Phys. Rev. **132**, 1599 (1963).
[3] A. R. Melnyk and M. J. Harrison, Phys. Rev. Lett. **21**, 85 (1968).
[4] I. Lindau and P. Nilsson, Physica Scripta **3**, 87 (1971).
[5] B. Askenazi, A. Vasanelli, A. Delteil, Y. Todorov, L. C. Andreani, G. Beaudoin, I. Sagnes, C. Sirtori, New Journal of Physics **16**, 043029 (2014)
[6] B. Askenazi, A. Vasanelli, Y. Todorov, E. Sakat, J. J. Greffet, G. Beaudoin, I. Sagnes, C. Sirtori, ACS Photonics **4**, 2550 (2017)
[7] T. Laurent, Y. Todorov, A. Vasanelli, A. Delteil, I. Sagnes, G. Beaudoin, and C. Sirtori, , Phys. Rev Lett. **115,** 187402 (2015).
[8] S. Huppert, A. Vasanelli, T. Laurent, Y. Todorov, G. Pegolotti, G. Beaudoin, I. Sagnes, and C. Sirtori, ACS Photonics **2**, 1663 (2015)
[9] G. Frucci, S. Huppert, A. Vasanelli, B. Dailly, Y. Todorov, G. Beaudoin, I. Sagnes and C. Sirtori, New Journal of Physics **19**, 043006 (2017)

Dynamic and spatial multilevel control over emissivity with phase transition material

Qiang Li[1,*]

1State Key Laboratory of Modern Optical Instrumentation, College of Optical Science and Engineering, Zhejiang University, Hangzhou 310027, China

*corresponding author, E-mail: qiangli@zju.edu.cn

Abstract

Dynamic and successive control of thermal emissivity are critical problems for related applications such as radiative heat management and thermal camouflage. Previous experimental works have not explored the ability of spatial resolved emissivity control with large dynamic range and reconfigurability. In this work, phase transition material (vanadium dioxide, VO_2) as a dynamic element is deployed to enable dynamic emissivity modulation. Large dynamic range of emissivity during phase transition (0.2@insulator phase VO_2 and 0.9@metallic phase VO_2) is achieved with designed planar structured cavity. By exploiting the hysteresis of VO_2 partial phase transition, successive control of emissivity is partially achieved in this device which has shown spatial resolved multilevel emissivity modulation at ~69 ℃ in experiment. The results of this work show potential applications of phase transition material based devices in the field of thermal information management in a feasible way.

Porous Thermochromic Nano-composite for Smart Window Systems

Man Xu[1,2*], Charlotte Jansen[1,3], and Pascal Buskens[1,4,5]

[1]The Netherlands Organisation for Applied Scientific Research (TNO), Delft, The Netherlands
[2] ImPhys, Delft University of Technology, Delft, The Netherlands
[3]Leiden Institute of Chemistry, Leiden University, Leiden, The Netherlands
[4]Institute for Materials Research, Inorganic and Physical Chemistry, Hasselt University, Hasselt, Belgium
[5]Zuyd University of Applied Sciences, Heerlen, The Netherlands
*corresponding author, E-mail: man.xu@tno.nl

Abstract

Nano-porous thermochromic VO_2 thin film has been studied as a smart coating in a fenestration system to gain thermal modulation ability depending on the ambient temperature. Both analytical calculation and numerical simulations have been carried out to study the optical performance of the porous thin film. Additionally the functionality of the designed coating on glass has been characterized for the special needs of a smart window.

1. Introduction

About 40% of the primary energy used in the European Union is connected with the buildings sector. Up to 60% of the total energy loss of a building is coming from its windows. For achieving sustainable buildings, many fenestration systems have been proposed [1]. In our research, thermochromic material vanadium dioxide (VO_2) is explored for a smart window design.

VO_2 is a thermochromic material [2], that undergoes a reversible metal-semiconductor transition at a critical temperature (T_c) of 68˚C. Above T_c, VO_2 film is highly reflective for near-IR and functions as a heat barrier to reduce energy consumption due to cooling and air-conditioning. Thermochromic materials switch passively and therefore do not need an external switching system, leading to a simple and low cost smart window design. Even though decades of research on VO_2, the main challenges to further bring it to the market remain till this day: the high switching temperature T_c, low luminous transmittance T_{lum} and the solar modulation ability ΔT_{sol}. In this paper we propose a porous thin film construction of VO_2 thin film aiming to solve some of the above issues.

2. Porous VO_2 thin film and smart windows

T_c can be reduced by metal ion doping to the room temperature (20-30˚C). However, the doping often leads to low T_{lum} and undesirable ΔT_{sol}. To obtain higher T_{lum} and ΔT_{sol} various approaches have been developed, such as nanothermochromic [3], porous films [4, 5], biomimetic surface structures [6], multi-layered coating [7], etc. Nano-porous VO_2 structures can be relatively easily realized through coating process. The nano-porous thin film is a promising construction to increase the T_{lum} and to improve on the color appearance of the coating.

2.1. Design of functional nano-porous VO_2 thin films

The functionality of the coating for fenestration system can be quantified using luminous transmission T_{lum} and solar modulation ΔT_{sol}. Luminous transmission is defined as the transmission of the sunlight through a coating or a system in the visible light range:

$$T_{lum} = \frac{\int_\lambda \phi_{lum}(\lambda) \cdot T(\lambda) d\lambda}{\int_\lambda \phi_{lum}(\lambda) d\lambda} \quad (1)$$

where ϕ_{lum} is the sensitivity of human eye, T is the transmission spectrum and λ is the wavelength. The solar transmission can be defined as:

$$T_{sol} = \frac{\int_\lambda \phi_{sol}(\lambda) \cdot T(\lambda) d\lambda}{\int_\lambda \phi_{sol}(\lambda) d\lambda} \quad (2)$$

Where ϕ_{sol} is the solar spectrum. Then the solar modulation is the difference of the solar transmission of the thermochromic coating at high (above T_c) and low (below T_c) temperatures:

$$\Delta T_{sol} = T_{sol,low} - T_{sol,high} \quad (3)$$

2.2. Optical modelling of the nano-porous structure

When nano-pores are present in a thin film, the effective refractive index of the mixture medium can be calculated using effective medium approximations (EMAs) [8], those include Maxwell-Garnett (MG) theory, Lorentz-Lorenz (LL) model and Bruggeman (Br) theory. Then the porous thin film can be treated as a homogeneous thin layer in a multilayer system to calculate the transmission, reflection and absorption of the stack using any multilayer solver. To test the accuracy of the EMAs and to choose the most suitable model, the Finite Element Method based rigorous

full wave simulations are performed to compare the calculation results.

2.3. Results

The optical performance of the glass coated with nano-porous VO_2 thin film is calculated with both EMA plus transfer matrix method (TMM) and FEM solver COMSOL [9]. The comparison of the calculation results are shown in Figure 1.

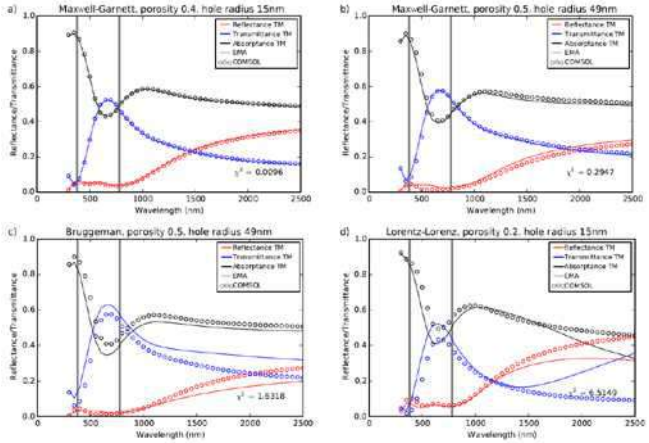


Figure 1: Comparison of the multilayer calculation results of using EMA+TMM and FEM.

We have found that the MG theory gives the best matching with FEM simulation result. Therefore it is chosen as the EMA for the rest of the calculation done in this paper.

2.4. Design for smart windows

For a smart thermal modulating coating on windows, the thin film or the coating should have $T_{lum,low} > 0.6$ and $\Delta T_{sol} > 0.1$. To achieve those goals, the porous VO_2 thin film has been studied for varying porosity and layer thickness and the results are shown in Figure 2.

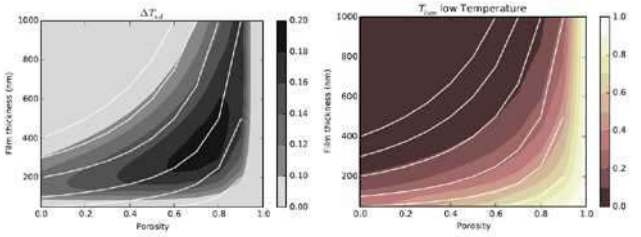
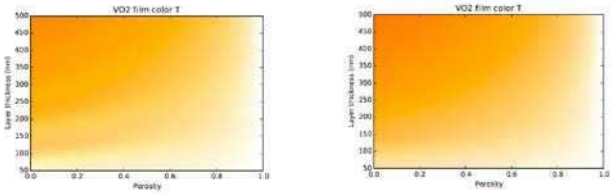


Figure 2: Left: ΔT_{sol} and right: $T_{lum,low}$ of the porous VO_2 thin film for varying porosity and layer thickness.

Furthermore, we have analyzed the color appearance of the coated glass using colorimetry [10]. The result is shown in Figure 3. The transmission color of the porous VO_2 thin film becomes more neutral when the porosity increases and layer thickness reduces as expected. The color neutrality is a very important aesthetic criteria for a fenestration system. However to make the system smart with thermal modulation ability, the coating should contain sufficient thickness and restricted porosity. A trade-off between those factors yields a design of a desired product.



(a) (b)

Figure 3: The color of a single layer coated glass in transmission at (a) low temperature and at (b) high temperature.

References

[1] M. Kamalisarvestani, R. Saidur, S. Mekhilef, and F.S. Javadi, Performance, materials and coating technologies of thermochromic thin film on smart windows, *Renewable and Sustainable Energy Reviews* 26, 353, 2013.

[2] F. Morin, Oxides which show a metal-to-insulator transition at the Neel temperature, *Physics Review Letters* 3, 34, 1959.

[3] S.-Y. Lia, G. A. Niklasson and C. G. Granqvist, "Nanothermochromics: Calculations for VO_2 nanoparticles in dielectric hosts show much improved luminous transmittance and solar energy transmittance modulation," *Journal of Applied Physics,* 108, 063525, 2010.

[4] M. Zhou, J. Bao, M. Tao, R. Zhu, Y. Lin, X. Zhang and Y. Xie, "Periodic porous thermochromic VO_2 (M) films with enhanced visible transmittance," *Chemical Communications,* 49, 6021, 2013.

[5] L. Hu, H. Tao, G. Chen, R. Pan, M. Wan, D. Xiong and X. Zhao, "Porous W-doped VO_2 films with simultaneously enhanced visible transparency and thermochromic properties," *Journal of Sol-Gel Science and Technology,* 77, 85–93, 2016.

[6] X. Qian, N. Wang, Y. Li, J. Zhang, Z. Xu and Y. Long, "Bioinspired Multifunctional Vanadium Dioxide: Improved Thermochromism and Hydrophobicity," *Langmuir,* 30, 10766–10771, 2014.

[7] L. M and J. Cho, "Better thermochromic glazing of windows with anti-reflection coating," *Thin Solid Films,* 365, 5, 2000.

[8] (2008) A. Navid and L. Pilon, Effect of polarization and morphology on the optical properties of absorbing nanoporous thin films, *Thin Solid Films* 516, 4159.

[9] https://www.comsol.com/comsol-multiphysics

[10] I. E. Commission et al., IEC 61966-2-1: Multimedia systems and equipment-Colour measurement and management-Part 2-1: Colour management-Default RGB colour space-sRGB, Geneva, Switzerland: International Electrotechnical Commission (1999).

Mid-IR emission at high modulation rates with incandescent metasurfaces

Leo Wojszvzyk[1], Anne-Lise Coutrot[1], Mondher Besbes[1], Jean-Paul Hugonin[1], Benjamin Vest[1] and Jean-Jacques Greffet[1]

[1]Laboratoire Charles Fabry, Institut d'Optique Graduate School, CNRS, Université Paris-Saclay, 91127 Palaiseau, France
*corresponding author, E-mail: jean-jacques.greffet@institutoptique.fr

Abstract

We report a numerical and experimental study of a metasurface patterned with arrays of nanowires, that reaches an emissivity close to 1 at 4 microns and can be operated at modulation rates up to 50 MHz.

1. Introduction

Light sources such as LEDs suffer from a significant decrease of their performances, in particular of their efficiency, when operated in the mid-infrared. In contrast, whereas it is easy to use thermal emission to generate blackbody radiation in the mid-infrared, the intrinsic slowness of the cooling of a thermal emitter generally prevents thermal sources from being modulated faster than a few hundreds of Hz. Here, we aim at developing incandescent sources operating a

2. Discussion

In this work, we use a different approach and circumvent the issue of cooling time by using tiny sub-wavelength thermal emitters [1] deposited on a cold substrate. The design is based on a local form of Kirchhoff law recently introduced [2]. We use 20 nm thick platinum wires that can cool down by thermal diffusion on a few nanosecond time scale so that they can be switched on and off up to a few tens of MHz. The dimensions of the wires and the spacer are designed to achieve total absorption at a given wavelength in the platinum. Using a local version of the Kirchhoff's law, we show that such a structure with good absorptivity also has a good emissivity in the IR.

Our design consists of a grating of thin platinum wires that act both as thermal emitters and as nanoantennas. Its dimensions are optimized to maximize the absorption cross-section of the wires in the infrared. Thus, we tailor the surface of a substrate to create a metasurface. Finally, we apply an electrical current to heat the wires by Joule effect. We report experimental data showing thermal emission in the mid-infrared using this process. By modulating the heating current at high frequencies, we observe a modulation of the thermal emission at rates up to 30 MHz.

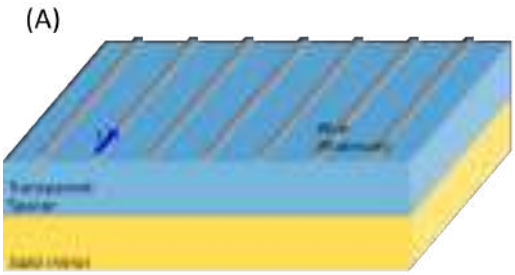


Figure 1: Design of the metasurface, with thin platinum wires forming a grating on a substrate surface. Electrical current can flow through the wires to heat them.

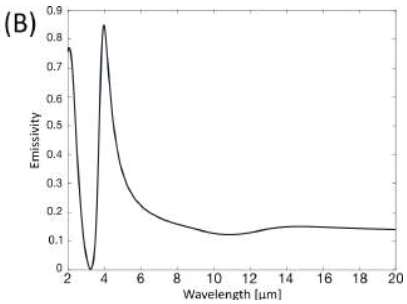


Figure 2: Numerical simulation of the emissivity of such a metasurface, with near-unity emissivity around 4 microns for appropriate dimensions

References

[1] Emilie Sakat, Leo Wojszvzyk, Jean-Paul Hugonin, Mondher Besbes, Christophe Sauvan, and Jean-Jacques Greffet, *Optica* **5**, 175 (2018).

[2] Jean-Jacques Greffet, Patrick Bouchon, Giovanni Brucoli, and François Marquier, *Phys. Rev. X* **8**, 21008 (2018).

Parity-Time and related symmetries in Photonics, Plasmonics, Acoustic

Chiral symmetry in non-Hermitian systems: product rule and Clifford algebra

Li Ge

Department of Physics and Astronomy, College of Staten Island, CUNY, Staten Island, NY 10314, USA
The Graduate Center, CUNY, New York, NY 10016, USA
corresponding author, E-mail: li.ge@csi.cuny.edu

Abstract

Chiral symmetry provides the symmetry protection for a large class of topological edge states. It exists in non-Hermitian systems as well, and the same anti-commutation relation between the Hamiltonian and the chiral operator, i.e., $\{H, \Pi\} = 0$, still warrants an energy spectrum that is now symmetric about the origin of the complex energy plane. Here we show two general approaches to construct chiral symmetry in non-Hermitian systems, with an emphasis on lattices with detuned on-site potentials that can vary in both their real and imaginary parts. One approach relies on the simultaneous satisfaction of both non-Hermitian particle-hole symmetry and a non-Hermitian bosonic anti-linear symmetry, while the other utilizes Clifford algebra satisfied by the Dirac matrices.

Chiral symmetry plays an important role in the study of topological phases of matter [1, 2]. It warrants that the energy spectrum of the system is symmetric about a well-defined energy level, such as the Fermi level or the energy of an uncoupled orbital, which is chosen as the zero energy. Recently [4, 3], the exploration of chiral symmetry in non-Hermitian systems [5] has also attracted fast growing interests, especially with the advent of topological photonics and lasers [6]. In non-Hermitian systems, the energy spectrum is complex in general, and chiral symmetry, defined by the anti-commutation relation of the Hamiltonian and a linear operator, warrants that the complex spectrum is symmetric about the origin of the complex energy plane. As a consequence, a non-Hermitian zero mode, with its energy right at the origin of the complex plane [3], can still exist similar to its Hermitian counterpart.

The easiest way to construct a non-Hermitian system with chiral symmetry is to start with a Hermitian system with two sublattices (such as in a tight-binding square or honeycomb lattice) and no detuning between onsite potentials. One then introduces asymmetric couplings that lift the Hermiticity of the system [3], which can be applied to both periodic [4] and non-periodic systems. This approach, however, does not utilize one important benefit provided by the non-Hermitian platforms in optics and photonics [5], namely, the availability and tunability of gain and loss, which is represented by an imaginary detuning between different lattice sites.

To eliminate such restrictions, we propose in this work two general approaches to construct non-Hermitian chiral symmetry. In the first approach we introduce a product rule where chiral symmetry, denoted by Π below, results from the simultaneous satisfaction of non-Hermitian particle-hole (NHPH) symmetry [3, 4, 7, 8, 9] and a non-Hermitian bosonic anti-linear symmetry. The former is defined similarly to its Hermitian counterpart, i.e., with the Hamiltonian H *anticommuting* with an *antilinear* operator Ξ; the latter is defined as a *commutation* relation between the Hamiltonian and an *antilinear* operator Λ, with parity-time symmetry [10] being a specific example. As we will exemplify below, the advantage of this approach lies in the fact that both NHPH symmetry and bosonic anti-linear symmetry are straightforward to implement in optics and related fields. One example is shown in Fig. 1.

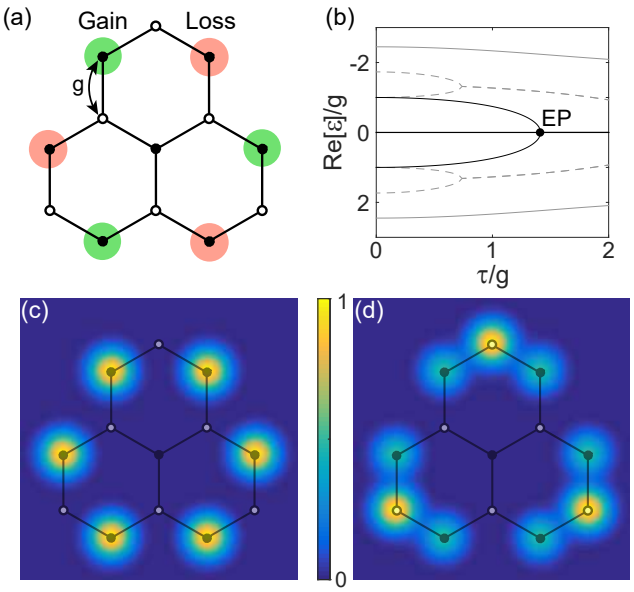


Figure 1: **Construction of non-Hermitian chiral symmetry by the product rule**. (a) Schematics of a finite honeycomb lattice with only nearest neighbor couplings. (b) Real part of the complex spectrum as a function of the gain and loss strength. Thick black line shows the existence of a zero mode with $\varepsilon = 0$. Black dot marks its exceptional point. (c) and (d) Spatial profile of this zero mode at $\tau = 0$ and the exceptional point in (b), respectively.

In the second approach, we discuss how Clifford algebra can be used to generate non-Hermitian chiral symmetry for 4×4 Hamiltonians, independent of NHPH and bosonic anti-linear symmetries. Through the discussion of several

examples, we show that the Dirac matrices can be arranged to maintain chiral symmetry in the presence of complex detunings between on-site potentials. Given by

$$\gamma^0 = \begin{pmatrix} \mathbf{1}_2 & 0 \\ 0 & -\mathbf{1}_2 \end{pmatrix},\ \gamma^j = \begin{pmatrix} 0 & \sigma_j \\ -\sigma_j & 0 \end{pmatrix}\ (j = 1, 2, 3) \tag{1}$$

in terms of the identity matrix and Pauli matrices, the Dirac matrices are used in the Dirac equation to describe relativistic quantum mechanics. Together with

$$\gamma^5 = \begin{pmatrix} 0 & \mathbf{1}_2 \\ \mathbf{1}_2 & 0 \end{pmatrix}, \tag{2}$$

they satisfy the Clifford algebra

$$\{\gamma^\mu, \gamma^\nu\} = 2\eta^{\mu\nu}\mathbf{1}_4 \quad (\mu, \nu = 0, 1, 2, 3, 5), \tag{3}$$

where $\eta^{\mu\nu}$ is a (diagonal) metric with signature $(+, -, -, -, +)$.

This defining property of Clifford algebra is particularly appealing in the construction of chiral symmetry: by designing the Hamiltonian as a superposition of the Dirac matrices, we have a straightforward way to determine its chiral operators. As a simple example, let us first consider

$$H = g_1\gamma^5 - g_2\gamma^1 \tag{4}$$

depicted schematically in Fig. 2(a), featuring one symmetric coupling and one asymmetric coupling. Using Eq. (3), we know immediately that its chiral operators can be $\gamma^0, \gamma^2, \gamma^3$ as well as $g_2\gamma^5 - g_1\gamma^1$ upon proper normalization. In addition, we also note that

$$\{\gamma^j\gamma^k, \gamma^l\} = 0 \tag{5}$$

holds when $j \neq k$ and $l = j$ or k (otherwise $\{\gamma^j\gamma^k, \gamma^l\} = 2\gamma^j\gamma^k\gamma^l$). Therefore, $\gamma^1\gamma^5$ is also a non-Hermitian chiral symmetry in this case.

If the Hamiltonian contains the product of two Dirac matrices, for example,

$$H = g_1\gamma^5 + g_2\gamma^0\gamma^1 \tag{6}$$

as shown in Fig. 2(b), it remains a simple task to verify that the chiral operators can be γ^0, γ^1 using Eq. (5). In addition, by noticing the relation

$$\{\gamma^j\gamma^k, \gamma^k\gamma^l\} = 0\ \ (j \neq l \neq k,\ k = 1, 2, 3), \tag{7}$$

we also identify $\gamma^1\gamma^5$ as another non-Hermitian chiral symmetry.

We will discuss more complicated constructions using Clifford algebra. Here we just note that the two examples given in Fig. 2 still have two sublattices without detuning. Therefore, we naturally expect them to have chiral symmetry with respect to the operator $P_A - P_B$, where $P_{A,B}$ are the sublattice projection operators. The difference of these two sublattice projection operators is exactly γ_0 in this case, but the more general analysis based on Clifford algebra has revealed that these systems have many more chiral operators of different forms.

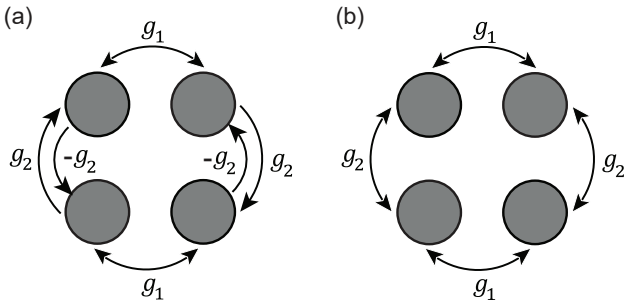


Figure 2: **Systems with non-Hermitian chiral symmetry constructed by simple combinations of the Dirac matrices**. The couplings g_1, g_2 are not restricted to be real.

References

[1] M. Z. Hasan and C. L. Kane, *Topological insulators*, Rev. Mod. Phys. **82**, 3045 (2010).

[2] X.-L. Qi and S.-C. Zhang, *Topological insulators and superconductors*, Rev. Mod. Phys. **83**, 1057 (2011).

[3] L. Ge, *Symmetry-protected zero-mode laser with a tunable spatial profile*, Phys. Rev. A **95**, 023812 (2017).

[4] S. Malzard, C. Poli, and H. Schomerus, *Topologically protected defect states in open photonic systems with non-Hermitian charge-conjugation and parity-time symmetry*, Phys. Rev. Lett. **115**, 200402 (2015).

[5] L. Feng, R. El-Ganainy, and L. Ge, Nat. Photon. **11**, 752–762 (2017).

[6] L. Lu, J. D. Joannopoulos, and M. Soljacic, *Topological photonics*, Nat. Photon. **8**, 821 (2014).

[7] K. Esaki, M. Sato, K. Hasebe, and M. Kohmoto, *Edge states and topological phases in non-Hermitian systems*, Phys. Rev. B **84**, 205128 (2011).

[8] B. Qi, L. Zhang, and L. Ge, *Defect States Emerging from a Non-Hermitian Flatband of Photonic Zero Modes*, Physical Review Letters. **120**, 093901 (2018).

[9] L. Ge, *Non-Hermitian lattices with a flat band and polynomial power increase [Invited]*, Photon. Res. **6**, A10–A17 (2018).

[10] C. M. Bender and S. Boettcher, *Real spectra in non-Hermitian hamiltonians having $\mathcal{PT}$ symmetry*, Phys. Rev. Lett. **80**, 5243 (1998).

Short Pulse Propagation in Quasi-PT-Symmetric Structure

Dmitri Tsvetkov[1], Vladimir Bushuev[1], Vladimir Konotop[2], and Boris Mantsyzov[1]*

[1] Department of Physics, M. V. Lomonosov Moscow State University, Moscow 119991, Russia
[2] Centro de Física Teórica e Computacional and Departamento de Física, Faculdade de Ciências, Universidade de Lisboa, Campo Grande, Ed. C8, Lisboa 1749-016, Portugal
*corresponding author, E-mail: bmantsyzov@gmail.com

Abstract

It is shown that inhomogeneous broadening of the spectral line of active impurities may sustain simultaneously parity (P) and time (T) symmetries of a medium, in a finite range of field frequencies, what is forbidden by the causality principle in media without broadening. If a spectral width of a propagating pulse is less than the inhomogeneous broadening, the medium for such a pulse becomes quasi-PT-symmetric. The effect of the broadband quasi-PT symmetry in a finite frequency domain, is illustrated by examples of unidirectional diffraction of pulses in Bragg and Laue geometries, propagating in photonic crystals.

1. Introduction

The concept of parity-time (PT) symmetry in the non-Hermitian optics requires delicate balance between real and imaginary parts of the dielectric permittivity [1,2]. The last requirement for the distribution of absorption and gain, described by the imaginary part of the dielectric permittivity, strictly speaking, is applicable for a given frequency of light. This point has fundamental importance in optical applications, in view of the causality principle. Mathematically, this is expressed through the Kramers-Kronnig relations, which can be satisfied only for isolated frequencies [3]. Therefore, the major development of the PT-symmetric optics is achieved, so far, within the paraxial approximation proposed in [2], rather than with optical pulses, as initially suggested in Ref. [1].

In the present work we show that imperfectness of atomic resonances may allow for sustaining PT symmetry in strongly dispersive media. The PT-symmetric optical properties are significantly restored for broadband radiation if the width of the pulse spectrum $\delta\omega$ is substantially less than the width of the inhomogeneously broadened spectral line γ_2^* of a resonant dispersive medium. We call it *quasi*-PT symmetry for broadband radiation [4]. Media with inhomogeneously broadened spectrum line are suitable for exploring short pulse dynamics in quasi-PT-symmetric environment.

2. Unidirectional zero diffraction and a spatially localized pulse dynamics in a quasi-PT-symmetric structure

Using spectral method [4] we solve the boundary diffraction problem of picoseconds pulse propagation in quasi-PT-symmetric photonic crystals (PhC) with strong material dispersion under condition of dynamical Bragg diffraction in Laue and Bragg schemes (Fig. 1) beyond the paraxial approximation.

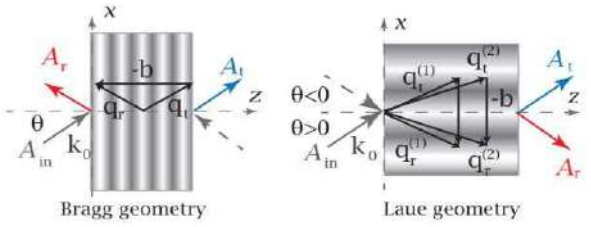


Figure 1: Schematic illustration of the Bragg (left panel) and Laue (right panel) diffractions [4]. Solid and dashed arrows show the central wave-vectors of the pulses incident from the left and right (Bragg diffraction) and with positive and negative incidence angles (Laue diffraction). Red and blue arrows correspond to the pulses reflected and transmitted by the PhC. The central wave-vectors of resonantly interacting waves in the PhC, $\mathbf{q}_t$ and $\mathbf{q}_r$, are also shown.

Figure 2 shows the amplitudes $|A_{t,r}(t)|$ illustrating the phenomenon of unidirectional diffraction reflection of an incident Gaussian pulse by a layered medium in the Bragg geometry for the left (upper row) and right (lower row) incidence at exact exceptional point (EP) and Bragg condition. The phenomenon consists in propagation of the pulse incident from the left hand side of the layered medium [Figs. 2(a) and 2(e)] with negligible reflection and strongly enhanced diffractionally reflected signal in the case of right incidence [Figs. 2(b) and 2(f)].

In presence of weak inhomogeneous broadening, a wide quasi-monochromatic nano-second pulse is totally transmitted [reflected] at the left, Fig. 2(a) [right Fig. 2(b)] incidence. However for the same medium but for a short

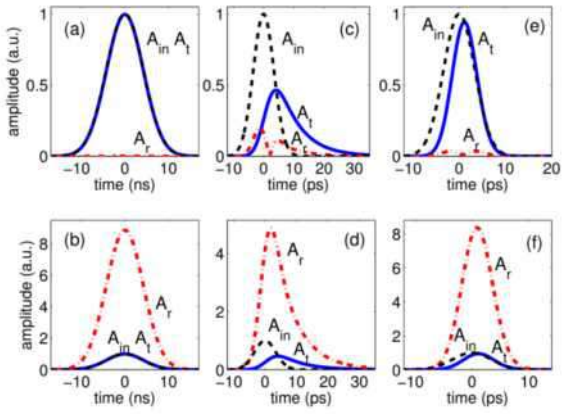


Figure 2: Temporal profiles of the transmitted (blue lines) and reflected (red lines) pulses generated by the incident Gaussian pulse (dashed line) upon left (upper row) and right (lower row) incidence [4]. In (a), (b) the duration of the incident quasi-monochromatic pulse $\tau = 6$ ns. In (c)-(f) the incident short pulse duration $\tau = 6$ ps; (c), (d) $\gamma_2^* \sim \delta\omega$ and (e), (f) $\gamma_2^* >> \delta\omega$.

pico-second pulse having spectral width $\delta\omega \sim \gamma_2^*$, the PT-symmetric effects are strongly suppressed. Now one observes partial transmission and reflection of the pulse for both left [Fig. 2(c), c.f. panel (a)] and right [Fig. 2(d), c.f. panel (b)] incidence. Transmitted and reflected pulses emerge strongly deformed. Significant increase of the inhomogeneous broadening, ensuring $\gamma_2^* >> \delta\omega$, results in enhancement of the unidirectional reflection: there is almost total transmission of the pulse for the left [Fig. 2(e)] and enhanced reflection for the right [Fig. 2(f)] incidence. In this last case, the Gaussian shape of the incident pulse is almost restored. So, we have demonstrated the restoration of effect of unidirectional diffraction for a short pulse in quasi-PT-symmetric PhC.

Under the quasi-PT-symmetric light-matter interaction, we describe the dynamics of a short spatially localized pulse propagating in the extended medium, when the length of propagation significantly exceeds the pulse size. The boundary problem of dynamical Bragg diffraction in the Laue geometry [Fig. 1 (right panel)] for a short laser pulse in a PhC with strong material dispersion is solved.

In Fig. 3(a) and Fig. 3(b), the intensity of the field of an extended quasi-monochromatic pulse with long duration $\tau = 100$ ps and the size $\tau c >> L$, where L is the PhC's thickness, is represented. If the angle of incidence is positive, the pulse propagates in a periodic Bragg structure with gain and loss as in a continuous conservative medium, i.e. without diffraction, absorption and amplification. The medium is transparent. With the sign of angle changing $\theta < 0$, Fig. 3(b), the pulse Bragg diffraction occurs, as well as its significant amplification and spatial expansion take place. This effect of unidirectional diffraction Bragg reflection disappears in dispersive media with the decreasing of pulse duration [$\tau = 1$ ps and $\gamma_2^* \sim \delta\omega$ in Fig. 3(c), (d)].

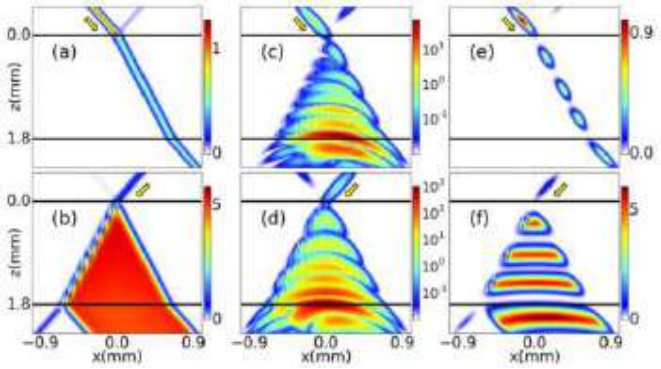


Figure 3: Snapshots of the intensity of the pulse field at EP for the positive (upper panels) and negative (lower panels) angles of incidence [4]. (a), (b) the Gaussian pulse with $\tau = 100$ ps; (c) – (f) $\tau = 1$ ps; $\gamma_2^* \sim \delta\omega$ in (c), (d) and $\gamma_2^* >> \delta\omega$ in (e), (f). The PhC's thickness $L = 1.8$ mm.

Under the quasi-PT-symmetric condition, $\gamma_2^* >> \delta\omega$, one can observe again the unidirectional Bragg reflection for spatially localized short pulse [Fig. 3(e), (f)].

3. Conclusions

We have demonstrated the dynamics of short spatially localized optical pulse propagation in quasi-PT-symmetric medium with strong material dispersion and beyond the paraxial approximation. In such a medium, the propagation of pulses with a finite frequency spectrum becomes possible due to a significant restoration of the PT-symmetric properties of the structure under the broadening of the spectral line of the resonant medium. This opens up great opportunities for controlling the pulse dynamics by means of small variations of the radiation frequency.

Acknowledgements

The work was supported by the RFBR (No 18-02-00556-a) (D.T., V.B., B.M.) and by the BASIS Foundation (D.T.).

References

[1] A. Ruschhaupt, F. Delgado, J.G. Muga, Physical realization of PT-symmetric potential scattering in a planar slab waveguide, J. Phys. A 38: L171, 2005.

[2] R. El-Ganainy, K.G. Makris, D.N. Christodoulides, Z. H. Musslimani, Theory of coupled optical PT-symmetric structures, Opt. Lett. 32: 2632-2634, 2007.

[3] A.A. Zyablovsky, A.P. Vinogradov, A.V. Dorofeenko, A. A. Pukhov, A. A. Lisyansky, Causality and phase transitions in PT -symmetric optical systems, Phys. Rev. A 89: 033808, 2014.

[4] D.M. Tsvetkov, V.A. Bushuev, V.V. Konotop, B.I. Mantsyzov, Broadband quasi-PT-symmetry sustained by inhomogeneous broadening of the spectral line, Phys. Rev. A 98: 053844, 2018; D.M. Tsvetkov, V.A. Bushuev, B.I. Mantsyzov, Optical pulse dynamics under quasi-PT-symmetry, Phys. Rev. A 99: 2019 (accepted).

Odd-PT-symmetric couplers

Vladimir V. Konotop[1*] and Dmitry A. Zezyulin[2]

[1]Departamento de Física and Centro de Física Teórica e Computacional,
Faculdade de Ciências, Universidade de Lisboa, Campo Grande 2, Edifício C8, Lisboa 1749-016, Portugal
[2]ITMO University, St. Petersburg 197101, Russia
*corresponding author, E-mail: vvkonotop@fc.ul.pt

Abstract

Parity-time-symmetric couplers with odd time reversal are introduced. In such systems the waveguides with gain and losses are coupled by anti-PT-symmetric media. We describe constraints imposed by the symmetry on spectral characteristics of the guided modes. As an application, we propose a coherent switch operating with a superposition of binary states. We also discuss coherent perfect absorption and lasing by non-Hermitian optical potentials embedded in such waveguides.

1. Introduction

During the last decade, parity-time ($\mathcal{PT}$) symmetric systems were in the focus of intensive studies in different branches of physics [1], and especially in optics [2, 3]. Until recently, the most of applications were concerned with the time reversal symmetry characterized by $\mathcal{T}^2 = 1$ (respectively $(\mathcal{PT})^2 = 1$), which in quantum mechanics corresponds to the physics of bosons (below it is referred to as even $\mathcal{PT}$ symmetry). Fermions, however are described by *odd* $\mathcal{PT}$ symmetry, where the time reversal operator obeys $\mathcal{T}^2 = -1$. In particular, this is the case of $\mathcal{T} = i\sigma_2\mathcal{K}$, with σ_2 being the Pauli matrix, and $\mathcal{K}$ being the element-wise complex conjugation [4]. It turns out that in optical (and more general, physical) systems such symmetry can be also realized [5, 6]. Such symmetry can be achieved in couplers that have balanced gain and loss, and the arms of which are connected by means of an anti-$\mathcal{PT}$-symmetric medium, i.e., medium characterized by the dielectric permittivity satisfying the relation [7]: $\varepsilon(x) = -\varepsilon^*(-x)$. Here we report on two examples of implementation and use of the odd $\mathcal{PT}$ symmetry.

2. Coherent switch.

Consider propagation of two birefringent waveguides coupled to each other by an anti-$\mathcal{PT}-$symmetric medium [5]. The electric fields are written as $\boldsymbol{E}_1 = [\boldsymbol{e}_1 A_1(z)\psi_1(\boldsymbol{r}) + \boldsymbol{e}_2 A_2(z)\psi_2(\boldsymbol{r})]e^{i(q-\delta)z}$, $\boldsymbol{E}_2 = [\boldsymbol{e}_3 A_3(z)\psi_3(\boldsymbol{r}) + \boldsymbol{e}_4 A_4(z)\psi_4(\boldsymbol{r})]e^{i(q+\delta)z}$. Here $\boldsymbol{r} = (x, y)$, $\psi_j(\boldsymbol{r})$ are transverse distributions of the modes, $A_j(z)$ are slowly varying field amplitudes, and 2δ is the mismatch between propagation constants in the waveguides. It is assumed that polarizations in each waveguide are mutually orthogonal: $\boldsymbol{e}_1 \cdot \boldsymbol{e}_2 = \boldsymbol{e}_3 \cdot \boldsymbol{e}_4 = 0$, and in different waveguides are mutually rotated by angle α, ensuring the relations $\boldsymbol{e}_1 \cdot \boldsymbol{e}_3 = \boldsymbol{e}_2 \cdot \boldsymbol{e}_4 = \cos\alpha$ and $\boldsymbol{e}_1 \cdot \boldsymbol{e}_4 = -\boldsymbol{e}_2 \cdot \boldsymbol{e}_3 = -\sin\alpha$ where α is the angle of mutual rotations of the polarizations in different waveguides.

The evolution equation for the slowly varying amplitudes $\boldsymbol{A} = (A_1, A_2, A_3, A_4)^\top$ ($\top$ stands for transpose) reads $i\dot{\boldsymbol{A}} = H_\delta \boldsymbol{A}$ where

$$H_\delta = \begin{pmatrix} \delta\sigma_0 & i\kappa C \\ i\kappa C^\dagger & -\delta\sigma_0 \end{pmatrix}, \; C = \begin{pmatrix} e^{-i\vartheta}\cos\alpha & -e^{i\varphi}\sin\alpha \\ e^{-i\varphi}\sin\alpha & e^{i\vartheta}\cos\alpha \end{pmatrix}$$

σ_0 is the 2×2 identity matrix, κ is the coupling between the waveguides, and φ and ϑ are the phase mismatches of the transverse distributions: $\psi_2 = \psi_1 e^{i\varphi}$, $\psi_4 = \psi_3 e^{i\vartheta}$. The guided eigenmodes modes are double-degenerated with the propagation constants, $b_\pm = \pm\sqrt{\delta^2 - \kappa^2}$, each having an invariant subspace spanned by two $\mathcal{PT}$-conjugate eigenvectors, $\boldsymbol{A}_\pm^{(1)}$ and $\boldsymbol{A}_\pm^{(2)} = \mathcal{PT}\boldsymbol{A}_\pm^{(1)}$.

The double-degeneracy of eigenstates is protected by the odd $\mathcal{PT}$ symmetry, i.e., in such a coupler, one simultaneously affects both modes with the same propagation constant. This allows one to perform switching between a superposition of binary states. We consider the coupler illustrated in Fig. 1. Two couplers, with $\delta \leftrightarrow -\delta$, are connected by two decoupled waveguides having balanced loss $-\Gamma$ and gain Γ, and a mismatch between the propagation constants $\pm\delta$. The lengths of the couplers are equal and chosen as $L = \pi/(2\sqrt{\delta^2 - \kappa^2})$. The decoupled segment which disrupts the odd $\mathcal{TP}$ symmetry has the length $\ell = \pi/(2\delta_0)$.

The field in the coupler is expressed through the evolution operators $U_{\pm\delta}(z, z + L) = -iH_{\pm\delta}/\sqrt{\delta^2 - \kappa^2}$. The evolution operator of the decoupled segment is: $U_0(z, z + \ell)$ =diag$(ie^{-\Gamma\ell}, ie^{-\Gamma\ell}, -ie^{\Gamma\ell}, -ie^{\Gamma\ell})$. The output (at $z = 2L + \ell$) and input (at $z = 0$) fields are related by:

$$\tilde{\boldsymbol{A}}_{\rm out} = U_{-\delta}(L + \ell, 2L + \ell)U_0(L, L + \ell)U_\delta(0, L)\tilde{\boldsymbol{A}}_{\rm in}.$$

The switch is controlled by Γ. Let the input signal with polarization $\tilde{\boldsymbol{A}}_{\rm in} = (\cos\chi, \sin\chi, 0, 0)^\top$ be applied to the waveguide 1. Then $\tilde{\boldsymbol{A}}_{\rm in}$ is characterized by a free parameter χ (the red vector at the input in Fig. 1). If the central waveguides are conservative, $\Gamma = 0$, the output signal is $\pi/2$-phase-shifted and is detected only at output of the first waveguide $\tilde{\boldsymbol{A}}_{\rm out}^{(0)} = i\tilde{\boldsymbol{A}}_{\rm in}$. If $\Gamma = \Gamma_{\rm sw} = \ell^{-1}\ln(\delta/\kappa)$,

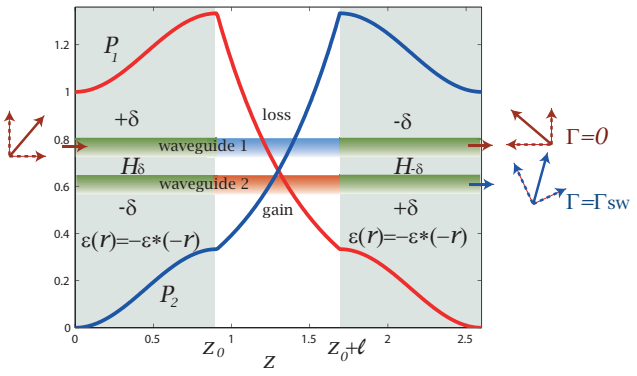


Figure 1: Schematic representation of the coherent switch. Shadowed domains correspond to anti-$\mathcal{PT}$-symmetric media. The central empty part illustrates the uncoupled waveguides with gain (red) and loss (blue). The polarization vectors at the output indicate (schematically) $\pi/2$-phase rotation of the non-switched signal (at $\Gamma = 0$, red), and switching of the superposition rotated by angle $-\alpha$ (at $\Gamma = \Gamma_{\rm sw}$, blue). Red and blue curves show power distributions in the first P_1 and second P_2 arms at $\Gamma_{\rm sw}$, obtained for $\delta = \delta_0 = 2$ and $\kappa = 1$.

the output-signal polarization is rotated by $-\alpha$ and is detected only in the second waveguide: $\tilde{\boldsymbol{A}}_{\rm out} = (0, 0, \cos(\chi - \alpha), \sin(\chi - \alpha))^\top$ (blue polarization vectors in Fig. 1). The ratio, i.e., χ, between the polarization components remains a free parameter. The power distributions, $P_{1,2}$ in the waveguides in regime of switching are shown by red and blue lines in Fig. 1.

3. Spectral singularities of an odd$-\mathcal{PT}-$symmetric coupler.

Now we consider stationary scattering problem for a two component field $\boldsymbol{\psi} = (\psi_1, \psi_2)^\top$: $H\boldsymbol{\psi} = k^2\boldsymbol{\psi}$ where k is the spectral parameter and the non-Hermitian Hamiltonian is given by

$$H = -\frac{d^2}{dx^2}\sigma_0 + \hat{U}, \quad \hat{U} = \begin{pmatrix} U_0(x) & V_2(x) \\ V_2(x) & U_1(x) \end{pmatrix}$$

with $U_{0,1}, V_2 \to 0$ at $x \to \pm\infty$ [6]. The Hamiltonian H is odd-$\mathcal{PT}$ symmetric if the conditions $U_0(x) = U_1^*(-x)$, and $V_2(x) = -V_2^*(-x)$ are satisfied.

Since the system is two-component the field asymptotics are gievn by

$$\boldsymbol{\psi}(x) \to a_1 e^{ikx}|\uparrow\rangle + a_2 e^{ikx}|\downarrow\rangle + a_3 e^{-ikx}|\uparrow\rangle + a_4 e^{-ikx}|\downarrow\rangle,$$
$$\boldsymbol{\psi}(x) \to b_1 e^{ikx}|\uparrow\rangle + b_2 e^{ikx}|\downarrow\rangle + b_3 e^{-ikx}|\uparrow\rangle + b_4 e^{-ikx}|\downarrow\rangle,$$

where $|\uparrow\rangle = (1,0)^\top$ and $|\downarrow\rangle = (0,1)^\top$ In terms of the column vectors $\boldsymbol{a} = (a_1, a_2, a_3, a_4)^\top$ and $\boldsymbol{b} = (b_1, b_2, b_3, b_4)^\top$ the transfer matrix M is defined as

$$\boldsymbol{b} = M\boldsymbol{a}, \quad M(k) = \begin{pmatrix} \mathcal{M}_{11}(k) & \mathcal{M}_{12}(k) \\ \mathcal{M}_{21}(k) & \mathcal{M}_{22}(k) \end{pmatrix},$$

where $\mathcal{M}_{ij}$ are 2×2 matrices.

Define $\Delta(k) = \det \mathcal{M}_{22}(k)$. There exist two types of the spectral singularities (SS). *Weak* SS is the (real) wavevector $k_\star$ at which $\Delta(k_\star) = 0$ while $\mathcal{M}_{22}(k)$ remains nonzero matrix. *Strong* SS $k_\star$ corresponds to the zero matrix $\mathcal{M}_{22}(k_\star) = (0)$. We show that that the SSs are self-dual, i.e. if $k_\star$ is a SS (for $k_\star > 0$ it corresponds to laser), then $-k_\star$ is a SS too (it corresponds to coherent perfect absorber (CPA)).

We illustrate laser and CPA based on odd$-\mathcal{PT}-$symmetry using a specific example of the non-Hermitian matrix potential $\hat{U}$ consisting of one waveguide with localized in the transverse direction gain and another waveguide with localized absorption, which are coupled by a antisymmetric medium which is also localized in transverse direction. We detect and consider weak self-dual SS and their splitting into complex-conjugate eigenvalues, the latter being the bound states characterized by propagation constants with real parts lying in the continuum. We also report a counter-intuitive restoration of the unbroken odd-$\mathcal{PT}$-symmetric phase subject to the increase of the gain-and-loss strength.

References

[1] [1] V. V. Konotop, J. Yang, and D. A. Zezyulin, Nonlinear waves in $\mathcal{PT}$-symmetric systems, *Rev. Mod. Phys.* 88:035002, 2016.

[2] [2] S. V. Suchkov A. A. Sukhorukov J. Huang, S. V. Dmitriev C. Lee, and Y. S. Kivshar, Nonlinear switching and solitons in PT-symmetric photonic systems, *Las. Photon. Rev.* 10:177, 2016.

[3] [3] R. El-Ganainy, K. G. Makris, M. Khajavikhan, Z. H. Musslimani, S. Rotter, and D. N. Christodoulides, Non-Hermitian physics and PT symmetry, *Nat. Phys.* 14:11, 2018.

[4] A. Messiah, *Quantum Mechanics* (Wiley, New York, 1966), Vol. II.

[5] V. V. Konotop, D. A. Zezyulin, Odd-Time Reversal PT Symmetry Induced by Anti-PT-Symmetric Medium, *Phys. Rev. Lett.* 120:123902, 2018.

[6] V. V. Konotop, D. A. Zezyulin, Spectral singularities of odd-PT-symmetric potentials. *Phys. Rev. A* 99: 013823, 2019.

[7] L. Ge and H. E. Türeci, Antisymmetric PT-photonic structures with balanced positive-negative-index materials, *Phys. Rev. A* 88:053810, 2013.

Coupled resonances with dynamic modulation for selective wavelength conversion

Galaad Altares Menendez, Bjorn Maes*

Micro- and Nanophotonic Materials Group, Faculty of Science,
University of Mons, Mons, Belgium
*corresponding author, E-mail: bjorn.maes@umons.ac.be

Abstract

We present a method to obtain efficient and selective frequency conversion using a system of two time-modulated cavities. This setup allows to tailor the conversion process by controlling important parameters such as the inter-cavity coupling and the external excitation frequency. We describe the process extensively, with for example an important role for the dynamic modes of the coupled system, the Floquet modes.

1. Introduction

In previous work, Ginis et al. [1] proposed a frequency comb generation principle based on time modulation, where the comb was generated from an incident plane wave via a time modulated graphene sheet. This mechanism is useful to create a wide range of frequencies. In our previous work [2] we expanded upon that idea using plasmonic resonances [3] in graphene ribbons to improve the efficiency and the tunability of the process. However, that setup was limited in the sense that it is difficult to target the generation of a specific frequency. In this work we use a system of two coupled cavities, allowing their interference to achieve selective frequency conversion. We study this system with temporal coupled mode equations [4], and show that the Floquet modes of the dynamic system play a crucial role for the conversion efficiency.

2. Setup and coupled mode theory

The system under investigation is sketched in Fig. 1(a). It consists of two cavities, each supporting one mode with amplitudes $a(t)$ and $b(t)$. These modes are coupled to each other via the coupling constant κ. In our case, the mode a is dark, while the mode b can radiate to the outside (and thus has a decay rate γ). A possible implementation using graphene plasmonic resonances in ribbon arrays with different widths is represented in Fig. 1(b). The coupled equations for this system are [5]:

$$\frac{da(t)}{dt} = i\omega_1 a(t) + i\kappa b(t) + s(t) \tag{1}$$

$$\frac{db(t)}{dt} = i\omega_2(t) b(t) + i\kappa a(t) - \gamma b(t) \tag{2}$$

where ω_1 and ω_2 are the resonance frequencies of the two cavities and $s(t)$ is the source. Note that the dark mode a is

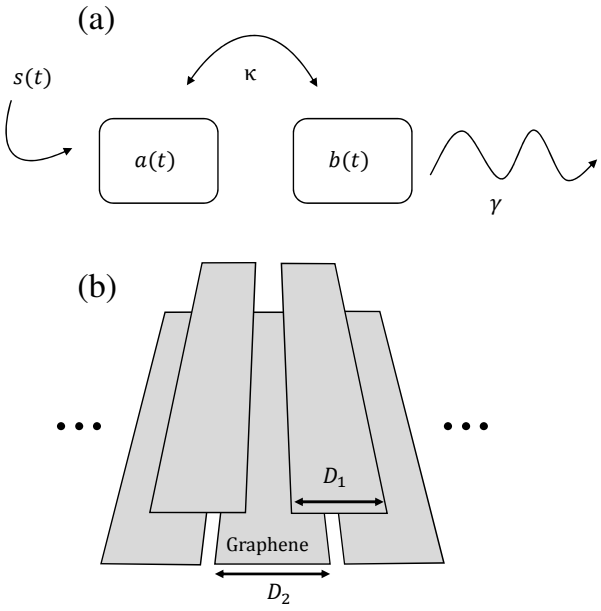


Figure 1: (a) Representation of the system of coupled resonances. (b) Potential implementation using two coupled arrays of graphene ribbons. Each cavity corresponds to a plasmonic resonance in the graphene array, where different ribbon widths (D_1 and D_2) provide different resonance frequencies. The ribbons are repeated in the horizontal direction creating two vertically offset gratings.

directly excited by the source, and that only the resonance frequency ω_2 is time-dependent, in particular:

$$\omega_2(t) = \omega_2 + \delta \sin(\Omega t) \tag{3}$$

where δ is the modulation amplitude and Ω is the modulation frequency.

3. Floquet modes

In the absence of time-modulation, the system eigenvalues are $\omega_\pm = \frac{\omega_1+\omega_2}{2} \pm \frac{1}{2}\sqrt{(\omega_1-\omega_2)^2+4\kappa^2}$. These two frequencies are represented as a function of κ in Figure 2 by the red dashed lines. However with the introduction of a time modulation, the system supports so-called Floquet modes [6] (blue lines in Fig. 2), analogous to the Bloch-modes in spatially periodic systems.

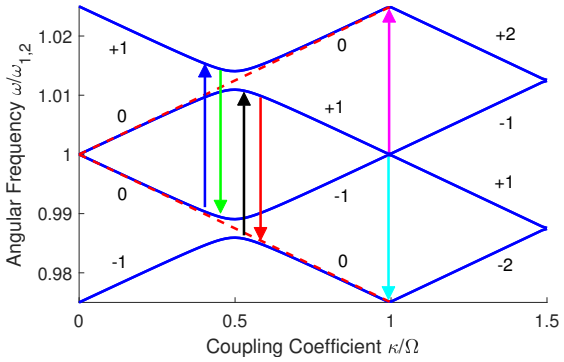


Figure 2: Dashed red lines: static resonance frequencies for the degenerate case ($\omega_{\pm} = \omega_{1,2} \pm \kappa$). Blue lines: Floquet modes of the system for the degenerate case, where $\omega_{1,2} = 2\pi \times 10^{13}$ rad/s, $\Omega = 2\pi \times 2.5 \times 10^{11}$ rad/s and $\delta = \Omega/2$.

The Floquet frequencies form a band structure and can exhibit anti-crossings, leading to bandgap-like features. The modulation amplitude δ is the parameter responsible for the bandgap size: a larger δ yields a wider anti-crossing. These modes play a crucial role in the frequency conversion efficiency.

4. Selective frequency conversion

The temporal modulation leads to the excitation of new frequencies in the system, organized as a comb. The frequency components inside the comb are always separated by the modulation frequency Ω, as seen in Fig. 3. We mainly focus on the first two generated sidebands ($\omega_0 \pm \Omega$ where ω_0 is the incident frequency). In general, we note that the frequency conversion process is much more efficient when the incident frequency is equal to a Floquet frequency.

Furthermore, the system parameters permit in some cases to achieve selective frequency conversion. In Fig. 3 for example, the frequency conversion to the upper sideband is clearly more efficient than the conversion to the lower sideband. Interestingly, this asymmetric conversion mainly happens when the source frequency is equal to a Floquet frequency at the edge of the anti-crossing ($\kappa = \Omega/2$). And this process is particularly efficient there, which is reminiscent of bandgap effects in Bragg structures.

In addition, it is also possible to efficiently convert with the same efficiency to both sidebands, leading to symmetric combs. This type of conversion mainly occurs around the first band crossing, when $\kappa = \Omega$ (see Fig. 2).

5. Conclusions

We describe how to achieve selective frequency conversion using a system of two time dependent coupled cavities. This process is particularly efficient at an anti-crossing, and different types of conversion can be achieved. This phenomenon is rather general and can be applied to any physical system of coupled resonances.

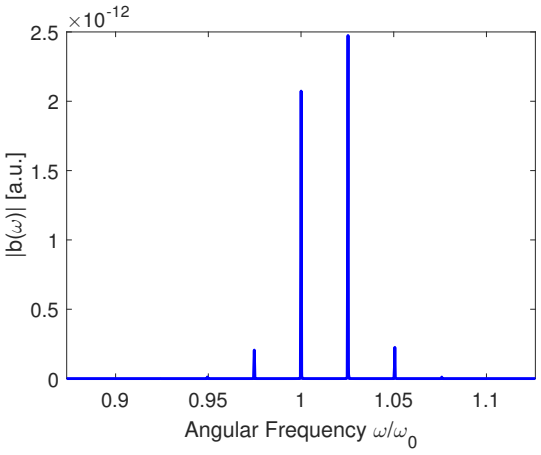


Figure 3: Comb produced by a set of parameters that maximizes upper frequency conversion ($\omega_0 = 0.9890\,\omega_{1,2}$). The conversion to the upper sideband ($\omega_0 + \Omega$) is more efficient than the conversion to the lower sideband ($\omega_0 - \Omega$) and as a result the comb is asymmetric.

Acknowledgement

Support by the Fonds pour la Formation à la Recherche dans l'Industrie et dans l'Agriculture (FRIA) and by the Fonds National de Recherche Scientifique (FNRS).

References

[1] V. Ginis, P. Tassin, T. Koschny, and C. M. Soukoulis, "Tunable terahertz frequency comb generation using time-dependent graphene sheets," *Phys. Rev. B*, vol. 91, p. 161403, 2015.

[2] G. Altares Menendez and B. Maes, "Frequency comb generation using plasmonic resonances in a time-dependent graphene ribbon array," *Phys. Rev. B*, vol. 95, p. 144307, 2017.

[3] M. Jablan, H. Buljan, and M. Soljačić, "Plasmonics in graphene at infrared frequencies," *Phys. Rev. B*, vol. 80, p. 245435, 2009.

[4] S. Fan, W. Suh, and J. D. Joannopoulos, "Temporal coupled-mode theory for the fano resonance in optical resonators," *J. Opt. Soc. Am. A*, vol. 20, no. 3, p. 569, 2003.

[5] A. Pick, Z. Lin, W. Jin, and A. W. Rodriguez, "Enhanced nonlinear frequency conversion and purcell enhancement at exceptional points," *Phys. Rev. B*, vol. 96, p. 224303, 2017.

[6] J. H. Shirley, "Solution of the schrödinger equation with a hamiltonian periodic in time," *Phys. Rev.*, vol. 138, pp. B979–B987, 1965.

Non-Hermitian transformations with optical metasurfaces

Andrey A. Sukhorukov[1*]
[1] Nonlinear Physics Centre, Research School of Physics and Engineering,
The Australian National University, Canberra, ACT 2601, Australia
[*]corresponding author: Andrey.Sukhorukov@anu.edu.au

Abstract. We present theoretical and experimental results demonstrating non-Hermitian transformation of classical and quantum states of light with ultra-thin dielectric metasurfaces. We introduce a new conceptual approach for implementing arbitrary complex birefringence with polarization-dependent transmission, based on tailored interference from specially engineered nano-resonators in the metasurface. The fabricated metasurfaces demonstrate new regimes of polarisation control for enhanced measurements and unconventional interference with classical and quantum light, and discuss analogies with Parity-Time symmetric transformations.

A new regime of non-Hermitian complex-valued birefringence has been recently suggested [1], extending the notion of real-valued birefringence through the specially introduced polarization-sensitive loss or gain. This can enable fundamentally new possibilities for polarization control, such as amplifying the angle between polarization vectors to improve detection sensitivity. However, a practical realization of complex-valued birefringence concept was missing. In particular, the theoretical approach in Ref. [1] was based on a complicated metamaterial with loss and gain, which is challenging to fabricate and not suitable for quantum applications.

Here, we report on a new conceptual approach for implementing arbitrary complex-valued birefringence with pairwise birefringent elements using high-index dielectric nanostructured metasurfaces. We formulate a practical design principle, which is optimal for achieving any desirable polarization transformation. While loss is inherently necessary for implementing non-Hermitian birefringent transformations, our all-dielectric metasurface design achieves the mathematically minimum required amount of loss through tailored diffraction without any material absorption.

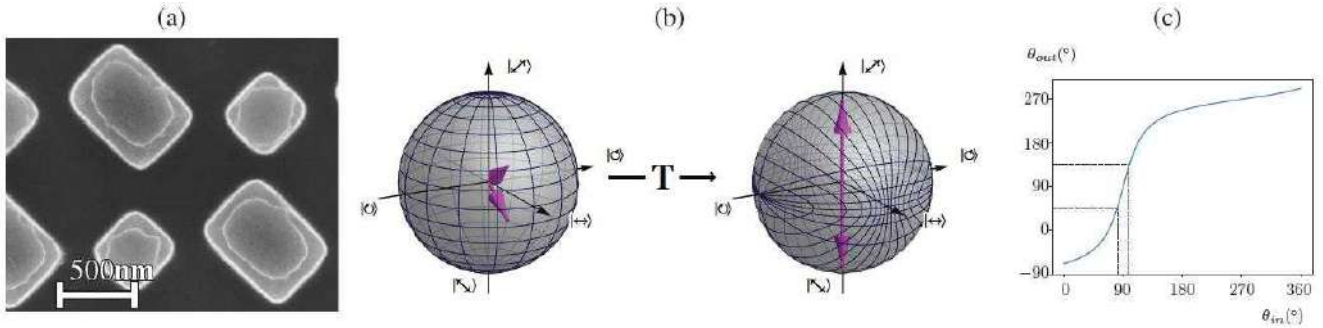


Fig. 1: (a) Scanning Electron Microscope (SEM) image of a representative unit cell composed of two different nanoresonators. (b) Transformation of polarization states with the complex-birefringent metasurface, visualized on a Poincare sphere. Two close input state vectors (purple arrows, left) are brought to orthogonal (right) after passing through the metasurface. (c) Output angular separation θ_{out} for a pair of input states with angle difference θ_{in} computed from experimental transfer matrix; dashed lines correspond to the states illustrated in (b).

We designed, fabricated and characterized amorphous silicon metasurfaces realizing complex birefringence, where diffraction is used as a loss channel. A scanning electron microscope (SEM) image is shown in Fig. 1(a). This design transforms a pair of very close input polarization states [Fig. 1(b, left)] into output orthogonally polarized states [Fig. 1(b, right)]. This polarisation mapping is enabled by the non-conservative transformation provided by the complex birefringence. Under the Stokes formalism of polarization states, this transformation is equivalent to the distortion of states on the surface of the Poincare sphere in a nonuniform manner [see grids in Fig. 1(b)]. Based on experimental measurements, we determine the dependence of the output angle (θ_{out}) between the polarization states on the relative input angle (θ_{in}), see Fig. 1(c). Depending on the angle between the input linear polarization states, the output angle of polarization difference can be either amplified (as marked by dashed lines, corresponding to Fig. 1(b)) or scaled down.

The metasurfaces realizing non-Hermitian complex-birefringent transformations can find applications for precise polarization measurements and state discrimination in classical and quantum optical platforms.

Acknowledgements. This presentation is based on results of collaborations driven by researchers who co-authored Refs. [2-4]

REFERENCES

1. A. Cerjan and S. H. Fan, "Achieving Arbitrary Control over Pairs of Polarization States Using Complex Birefringent Metamaterials," Phys. Rev. Lett. **118**, 253902 (2017).
2. K. Wang, S. S. Kruk, L. Xu, M. Parry, H. P. Chung, A. S. Solntsev, J. Titchener, I. Kravchenko, Y. H. Chen, Y. S. Kivshar, D. N. Neshev, and A. A. Sukhorukov, "Quantum metasurface for multi-photon interference and state reconstruction," Science **361**, 1104 (2018).
3. S. Lung, K. Wang, K. Z. Kamali, M. Rahmani, D. N. Neshev, and A. A. Sukhorukov, "Complex-Birefringent and Chiral Waveplates with Metasurfaces," submitted (2019).
4. N. Pedersen, K. Wang, S. Lung, and A. A. Sukhorukov, "Optimal Single Metagrating for Robust Polarization Measurements", submitted (2019).

Anisotropic exceptional points of arbitrary order

Yi-Xin Xiao[1,2], Zhao-Qing Zhang[2], Zhi Hong Hang[1,3], and C. T. Chan[2*]

[1]School of Physical Science and Technology, Soochow University, Suzhou 215006, China

[2]Department of Physics, Hong Kong University of Science and Technology, Hong Kong

[3]Institute for Advanced Study, Soochow University, Suzhou 215006, China

*corresponding author, E-mail: phchan@ust.hk

Abstract

A pair of anisotropic exceptional points (EPs) of arbitrarily high order are found in a class of random non-Hermitian systems carrying non-reciprocal hoppings. Both Eigenvalues and phase rigidity show different asymptotic forms near the anisotropic EPs in two orthogonal directions in the parameter space, making them anisotropic EPs. Some universal features are observed to govern the critical exponents of the phase rigidity near an anisotropic EP, which depend on the dimensions of the Hamiltonian. Such system has order-2 EPs forming multiple ellipses that converge to the two high-order EPs in the parameter space and these ellipses coalesce to form a ring of high-order EPs for some particular configurations.

1. Introduction

Non-Hermiticity can bring interesting new phenonmena [1]. Extensive research effort has been devoted to classical-wave systems involving material carrying gain/loss or having radiation leaking into open space. Exceptional points, at which both eigenvalues and eigenstates coalesce, often occur as square-root singularities and they account for many fascinating properties of non-Hermitian systems, including unusual reflection and transmission. In this work, we consider systems in which the non-Hermiticity comes from asymmetric hoppings between sites instead of the gain/loss usually considered in PT-symmetric non-Hermitian systems. We found that a pair of arbitrarily high order EPs exists in such systems even in the presence of randomness. Near the EPs, eigenvalues and phase rigidity exhibit anisotropic behaviors. The critical exponents of phase rigidity are found to certain universal rules. The two high-order EPs are the common vertices of multiple ellipses comprising order-2 EPs. For some configurations, a ring of high-order EPs occurs due to the coalescence of the ellipses.

Results

To illustrate the idea, let us consider a non-Hermitian system represented by a $N\times N$ Hamiltonian $H'=H+\lambda s_z^j$, where

$$H=\begin{pmatrix} 0 & \tau_1 & 0 & 0 & 0 \\ \tau_2 & 0 & \tau_1 & 0 & 0 \\ 0 & \tau_2 & 0 & \ddots & 0 \\ 0 & 0 & \ddots & \ddots & \tau_1 \\ 0 & 0 & 0 & \tau_2 & 0 \end{pmatrix}, \tag{1}$$

with $\tau_1=\tau-1,\tau_2=\tau+1$, and $s_z^j=S_z^j/j\hbar$ with S_z^j being the z component of the spin-j operator and $j=(N-1)/2$. The non-Hermiticity comes from asymmetric hoppings, $\tau_1\neq\tau_2$. Such systems can be realized by coupled ring resonators [2], electronic circuits [3] or cold atoms in optical lattices [4]. The eigenvalues are

$$E_m=2\sqrt{\tau^2-1}\cos\left(\frac{m\pi}{N+1}\right), m=1,2,\cdots,N. \tag{2}$$

All N eigenstates coalesce to a single one at $\tau=\pm1$ with eigenvalue $E=0$, leading to an EP of order N. In the (τ,λ) plane, $(\pm1,0)$ are two EPs of order N. These two EPs exhibit anisotropic behaviors in both eigenvalues and phase rigidity, which is defined by $R=\left\langle\psi^L\,|\,\psi^R\right\rangle$ with ψ^L (ψ^R) denoting left (right) eigenvectors. When $\lambda=0$, the eigenvalues of H' reduce to square-root forms given by Eq. (2). In contrast, eigenvalues take linear forms, i.e., $E_m=\lambda(j+1-m)/j$ when $\tau=\pm1$, where $m=1,2,\cdots,N$. Thus, eigenvalues exhibit different behaviors in different directions in the parameter space near an EP. Thus $(\tau,\lambda)=(\pm1,0)$ are two anisotropic EPs of order N for H'. To characterize eigenstates near an anisotropic EP,

we calculate the phase rigidity near the anisotropic EP at $(\tau,\lambda)=(1,0)$ in the (τ,λ) plane and find $R_i \propto |\delta|^{(N-1)/2}$ with $\Delta=\tau-1$ when $\lambda=0$, and $R_i \propto |\lambda|^{N-1}$ when $\tau=1$. The exponents of phase rigidity are respectively $(N-1)/2$ and $N-1$ in the two orthogonal directions, exhibiting anisotropic behaviors.

These EPs and their anisotropic behaviors persist even in the presence of certain types of disorder. We consider the following Hamiltonian with disorder,

$$H_{dis}=\begin{pmatrix} c_1\lambda & a_1\tau_1 & 0 & 0 & 0 \\ b_1\tau_2 & c_2\lambda & a_2\tau_1 & 0 & 0 \\ 0 & b_2\tau_2 & c_3\lambda & \ddots & 0 \\ 0 & 0 & \ddots & \ddots & a_{N-1}\tau_1 \\ 0 & 0 & 0 & b_{N-1}\tau_2 & c_N\lambda \end{pmatrix}, \quad (3)$$

where a_i, b_i, c_i are arbitrary real numbers with $a_i, b_i > 0$. When $a_i=b_i=1$ and $c_i=(j+1-i)/j$, H_{dis} reduces to $H'=H+\lambda s_z^j$. We find that $(\tau,\lambda)=(\pm1,0)$ remain anisotropic EPs even in the presence of randomness. All eigenvalues take the square-root form, which can be expressed as $E_i=\pm d_i\sqrt{\tau_1\tau_2}$ when $\lambda=0$, where d_i are constants. Near each anisotropic EP, say $(1,0)$, the eigenvalues of H_{dis} show anisotropic behaviors: $E_i \approx \pm d_i\sqrt{2\Delta}$ with $\Delta=\tau-1$ along $\lambda=0$, and $E_i=c_i\lambda$ along $\tau=1$. The critical exponents of phase rigidity are $(N-1)/2$ and $N-1$ for all eigenstates, independent of a_i, b_i, c_i.

2. Conclusions

For a class of random non-Hermitian systems carrying non-reciprocal hoppings, two high-order anisotropic EPs are found to be the converging point of multiple order-2 EP ellipses in the parameter space. For some particular configurations, the ellipses coalesce to form a ring of high-order anisotropic EPs.

Acknowledgements

This work was supported by the Research Grants Council of Hong Kong (AoE/P-02/12).

References

[1] R. El-Ganainy et al., *Nat. Phys.* 14, 11 (2017).

[2] S. Longhi et al., *Phys. Rev. B* 92, 094204 (2015).

[3] H. Jiang et al., *Arxiv*:1901.09399.

We observed multiple elliptical trajectories formed by order-2 EPs in the form of $\tau^2+A_i\lambda^2=1$ with A_i being some positive number, which share the two order-*N* EPs as their common vertices. The coalesced eigenvalues on each ellipse are proportional to λ, that is $E=B_i\lambda$. The values of A_i and B_i depend on the specific values of a_i, b_i, c_i.

If the values of a_i, b_i, c_i are taken so that the Hamiltonian have the following form

$$H^j=\tau s_x^j - i s_y^j + \lambda s_z^j, \quad (4)$$

where $s_\mu^j, \mu=x,y,z$ are spin matrices, all ellipses of order-2 EPs coincide and form a ring of order-*N* EPs: $\tau^2+\lambda^2=1$. Every point on the ring is an anisotropic EP.

We want to compare the order-N anisotropic EPs found in this work with conventional order-N EPs. The phase rigidity near the EP in the Hamiltonian H' behaves as $R_i \propto |\Delta|^{(N-1)/2}$ with $\Delta=\tau-1$ when $\lambda=0$. The exponent $\sigma=(N-1)/2$ is very different from $\sigma=(N-1)/N$ for the conventional order-*N* EPs. The difference results from distinct singular behaviors in the eigenvalues near an EP. For H', multiple pairs of square-root singularities, i.e., $\sqrt{\Delta}$, share the same EP, whereas for a conventional order-*N* EP, all eigenvalues are from a single *N*-th root singularity, i.e., $\sqrt[N]{\Delta}$.

[4] Z. Gong et al., *Phys. Rev. X* 8, 031079 (2018).

Topological protection and quantum noise in nonlinear photonic systems

Henning Schomerus[1*]

[1]Department of Physics, Lancaster University, Lancaster, UK
*corresponding author, E-mail: h.schomerus@lancaster.ac.uk

Abstract

Many prospective applications of topological photonics involve intrinsically nonlinear media, such as in lasers, plasmonic structures, or excitonic condensates. As I show here, one of the main underlying symmetries know from the linear context extends seamlessly to these situations. This allows us to precisely define topologically protected dynamically stable states, which either may be stationary states replicating zero modes, or power-oscillating states.

1. Introduction

Topological lasers and condensates [1-6] offer means to confine and manipulate coherent and collective states of light and matter in versatile ways. In particular, the confinement and coherent feedback can be obtained without mirrors based on suitable photonic lattice structures with small geometric adjustments. The original design of these systems relied on the hop that the topological protection of the cold-cavity modes has bearing for the above-threshold operation modes, which however strongly depend on the nonlinear response in the system. This poses the question whether topological protection persists under nonlinear conditions. In this work I provide a framework that answers this question both from a practical as well as from a fundamental perspective. The main ingredient is a dynamical extension of the topological symmetries known from the linear case. As it turns out, these considerations also have implications for the effects of quantum noise in these systems.

2. Origins and implications of nonlinearities

In topological lasers and condensates there are two main types of nonlinearities – those that change the lifetime of states, such as observed in gain saturation, and those that nonlinearly shift the resonance frequency, as e.g. captured by the line-width enhancement factor in lasers, or induced by excitonic interactions in exciton-polariton condensates. Bothe effects are not accounted for in the linear cold-cavity description of these systems. Consider e.g. a coupled-mode theory of a system with discretely coupled modes, as e.g. supported by microresonators, pillars, or waveguides in a structured system. Such systems display a chiral symmetry if the discrete components populate two mutually coupled sublattices A and B, such that

$$\omega A = T_{AB} B, \qquad \omega B = T_{BA} A,$$

with suitable coupling matrices T_{AB} and T_{BA} that we take to be real. The system then displays a chiral symmetry realized by the invariance $(A, B, \omega) \to (A, -B, -\omega)$. Hence the spectrum of such as system is symmetric in ω, and the corresponding topologically protected states are zero-modes with $\omega = 0$. In the presence of linear gain and loss, where

$$\omega A = i\Gamma_A A + T_{AB} B, \qquad \omega B = i\Gamma_B B + T_{BA} A,$$

we encounter an analogous invariance $(A, B, \omega) \to (A^*, -B^*, -\omega^*)$, which formally agrees with the charge-conjugation symmetry encounter in a superconductor [1,7,8] Zero modes now have a fixed frequency Re $\omega = 0$ but can have a variable life time from Im ω.

Spectral characterizations such as this are adapted to linear systems, but do not have a precise meaning in nonlinear systems. In that case, I propose to **directly study the dynamical problem** [9-11].

For illustration consider a system with real-space gain saturation, whose dynamical evolution is given by [9,10]

$$i\frac{dA}{dt} = i\Gamma_A(|A|^2)A + T_{AB} B, \qquad i\frac{dB}{dt} = i\Gamma_B(|B|^2)B + T_{BA} A,$$

with real nonlinear functions Γ describing the gain and loss. As we now can check directly, this system remains invariant under the substitution $(A(t), B(t)) \to (A^*(t), -B^*(t))$. This constitutes a dynamical symmetry between different solutions that persists in the nonlinear case. For stationary states with harmonic time dependence $\sim\exp(-i\omega t)$ it reduces to the nonhermitian charge conjugation symmetry above. The corresponding zero modes can be written with real amplitudes A and imaginary amplitudes B, thus display a characteristic spatial phase pattern. Furthermore, this dynamical formulation of symmetries allows for symmetry-protected cycles, where $(A(T/2), B(T/2)) = (A^*(0), -B^*(0))$. This gives rise to power-oscillating

solutions that are again protected by symmetry. These modes have been termed *twisted modes*, and do not have a counterpart in the linear system.

3. Extensions using geometric symmetries

It is also possible to identify situations in which similar considerations hold for the additional presence of nonlinear interactions that shift the resonance frequencies. Our main proposal employs the parity symmetry, and hence realizes a situation analogous to PT symmetric systems, but with the charge-conjugation symmetry C replacing T. This leads to systems of the form [11]

$$i\frac{dA}{dt} = i\Gamma(|A|^2)A + TB, \qquad i\frac{dB}{dt} = i\Gamma^*(|B|^2)B + TA,$$

where Γ is now complex but the same functions Γ and couplings T now appear in both equations. One now confirms that these equations remain invariant under the substitution $(A(t), B(t)) \rightarrow (B^*(t), -A^*(t))$. Based on these relations we can again define zero modes and we can now defined nonlinear zero modes and twisted modes.

4. Stability and noise

To assert whether such topologically protected dynamical states can be realized and observed in physical systems we need to consider their stability against perturbations. At the same time, such an analysis gives a characterization of these states in terms of their intrinsic levels and sensitivity to quantum noise. I present a detailed analysis in terms of Bogoliubov excitations, and show that the topological modes indeed display characteristic excitations and therefore provide a characteristic response to external probes. We find that these systems offer particularly favourable switching mechanism between the topological solutions, which can take the form of Hopf bifurcations [9,10] or infinite-period bifurcations [11].

5. Conclusions

The characterization of nonhermitian topology poses many challenges, which become even more pressing when nonlinearities are involved. As described in this work, a promising way forward is to ask whether symmetries exist between the stable dynamical solutions of the system [9-11]. Self-symmetric solutions provide a natural extension of the zero modes known from linear systems, while twisted modes displaying power oscillations define a new class of symmetry-protected solutions that do not have a linear counterpart. The proposed systems offer new switching mechanisms that make them attractive for device applications.

Acknowledgements

This work has been carried out in collaboration with S Malzard and E Cancellieri. Funding was received from ESPRC via Grant No. EP/N031776/1.

References

[1] Henning Schomerus, Topologically protected midgap states in complex photonic lattices, Opt. Lett. 38, 1912-1914 (2013).

[2] P. St-Jean, V. Goblot, E. Galopin, A. Lemaître, T. Ozawa, L. Le Gratiet, I. Sagnes, J. Bloch and A. Amo. Lasing in topological edge states of a one-dimensional lattice. Nat. Photonics 11, 651–656 (2017).

[3] H. Zhao, P. Miao, M. H. Teimourpour, S. Malzard, R. El-Ganainy, H. Schomerus, and L. Feng, Topological hybrid silicon microlasers, Nat. Commun. 9, 981 (2018).

[4] M. Parto, S. Wittek, H. Hodaei, G. Harari, M. A. Bandres, J. Ren, M. C. Rechtsman, M. Segev, D. N. Christodoulides, and M. Khajavikhan, Edge-Mode Lasing in 1D Topological Active Arrays, Phys. Rev. Lett. 120, 113901 (2018).

[5] Exciton Polaritons in a Two-Dimensional Lieb Lattice with Spin-Orbit Coupling, C. E. Whittaker, E. Cancellieri, P. M. Walker, D. R. Gulevich, H. Schomerus, D. Vaitiekus, B. Royall, D. M. Whittaker, E. Clarke, I. V. Iorsh, I. A. Shelykh, M. S. Skolnick, and D. N. Krizhanovskii, Phys. Rev. Lett. 120, 097401 (2018).

[6] C. E. Whittaker, E. Cancellieri, P. M. Walker, B. Royall, L. E. Tapia Rodriguez, E. Clarke, D. M. Whittaker, H. Schomerus, M. S. Skolnick, and D. N. Krizhanovskii, Effect of photonic spin-orbit coupling on the topological edge modes of a Su-Schrieffer-Heeger chain, Phys. Rev. B 99, 081402 (2019).

[7] C. Poli, H. Schomerus, M. Bellec, U. Kuhl, and F. Mortessagne, Partial chiral symmetry-breaking as a route to spectrally isolated topological defect states in two-dimensional artificial materials, 2D Mater. 4, 025008 (2017).

[8] S. Malzard, C. Poli, and H. Schomerus, Topologically Protected Defect States in Open Photonic Systems with Non-Hermitian Charge-Conjugation and Parity-Time Symmetry, Phys. Rev. Lett. 115, 200402 (2015).

[9] Simon Malzard and Henning Schomerus, Nonlinear mode competition and symmetry-protected power oscillations in topological lasers, New J. Phys. 20, 063044 (2018).

[10] Simon Malzard, Emiliano Cancellieri, and Henning Schomerus, Topological dynamics and excitations in lasers and condensates with saturable gain or loss, Opt. Express 26, 22506-22518 (2018).

[11] E. Cancellieri and H. Schomerus, PC-symmetry-protected edge states in interacting driven-dissipative bosonic systems arXiv:1811.09542 [physics.optics], accepted for publication in Phys. Rev. A (2019).

Nonlinear scattering by PT-symmetric layered periodic structures with gain and loss saturation effects

O. Shramkova[1*], G. Tsironis[2]

[1]Technicolor Research & Innovation, Cesson Sévigné, France
[2]University of Crete, Heraklion, Greece
*corresponding author, E-mail: Oksana.shramkova@technicolor.com

Abstract

We investigate the effect of gain saturation on scattering characteristics of PT-symmetric periodic stacks of the layers with balanced loss and gain. Closed form solutions for calculating the transmission and reflection of nonlinear system have been obtained. It is shown that the non-reciprocal response of the nonlinear medium depends on parameters of the stack, angles of wave incidence and saturation intensity. The effects of nonlinearity on the exceptional points and symmetry breaking are systematically examined.

1. Introduction

The discovery of parity-time (PT)-symmetric media, motivated by fundamental studies of PT -symmetric quantum Hamiltonians [1], has shown significant potential for advancing toward the goal of new metamaterial design. PT-symmetry can lead to many exotic features of optical systems, including double refraction, unidirectional invisibility, nonreciprocal propagation, coherent perfect absorption, selective lasing and other intriguing nonlinear effects [2-4]. A necessary condition for an optical structure to be PT- symmetric is that its complex refractive index distribution satisfies the condition $n(\vec{r}) = n^*(-\vec{r})$. However, the transition to a complex spectrum, which is called PT-symmetry breaking, appears upon the increase of the strength of imaginary part of $n(\vec{r})$.

To date, most of the studies in optical realizations of PT-symmetric media have connected stacked layers and films [5-8]. The research in this topic was primarily focused on the linear phenomena, whereas the nonlinear effects have attracted the growing interest only lately. The problem of plane wave scattering by the layered PT-symmetric grating with longitudinal distribution of loss and gain saturation inside the unit cell was explored in [9]. It was shown that the strong nonreciprocal response of the structure and the bistability effect depend on the gain and loss saturation value, on the value of input intensity and on the side of electromagnetic wave incidence. Moreover, gain and loss saturations can force the transition from broken symmetry phase to a PT-symmetric. To analyze the layered structure authors used the transfer matrix method dividing each layer of primitive cells into narrow stripes. As the result, the approximate expression of the output intensity, the reflection and transmission coefficients, as a function of the incident wave intensity, was obtained.

The aim of this paper is to explore the scattering characteristics of periodic layered structure with balanced distribution of loss and gain, when dispersion and saturation nonlinear effects are taken into account. We provide a nonlinear model describing the field evolution in the periodic semiconductor layered system in the presence of saturable gain. The obtained solution enable fast quantitative analysis of the incidence angle effect on the scattered field intensities.

2. Problem statement and main equations

Let us consider a finite PT-symmetric periodic stack composed of dielectric layers of identical thickness d and complex-conjugate dielectric permittivities $\varepsilon = \varepsilon' - i\varepsilon''$ and $\varepsilon^* = \varepsilon' + i\varepsilon''$ (ε' and ε'' are positive) corresponding to balanced gain (G) and loss (L) regions. The layers are of infinite extent in the x0y-plane. The system is PT-symmetric about z=0. Let plane wave be incident at angle Θ_i on a structure of thickness $L=2N$, where N is the number of structure periods. It is surrounded by linear homogeneous medium with dielectric permittivity ε_a as shown in Fig. 1.

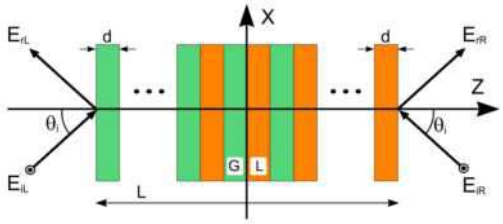


Figure 1: Geometry of the problem.

The complex nonlinearity we use were derived using the two-level model. By assuming that the intensity of propagating waves is much less than the saturation intensity, the nonlinear susceptibility can be expressed as [10]:

$$\chi_j \approx \varphi_j \frac{\delta_j - i}{1+\delta_j^2} + \varphi_j \frac{i-\delta_j}{\left(1+\delta_j^2\right)^2} \left| \frac{\vec{E}_j}{E_{sj}} \right|^2, \qquad (1)$$

where $\delta_j = \left(\omega^2 - \omega_{0j}^2\right) / \left(\omega\gamma_j\right)$ and ω_{0j} is the emission frequency, γ_j is the gain/absorption linewidth;

$\varphi_j = \alpha_j \frac{\omega_{0j}}{\omega}$, α_j is the dimensionless gain/absorption coefficient, $k_0 = \omega/c$. We use positive parameters α_1 and γ_1 when referring to the amplifying medium with $\mathrm{Im}\,\varepsilon_1(\omega) < 0$. To satisfy Kramers-Kronig relations, in the case of absorbing media with $\mathrm{Im}\,\varepsilon_2(\omega) > 0$ we take $\alpha_2 < 0$ and $\gamma_2 > 0$, which ensures the causality of dielectric permittivity.

Solving the non-homogeneous Helmholtz equation perturbatively under the assumption that the nonlinear terms are small, enforcing the boundary conditions of field continuity at the interfaces of the stacked layers and using the modified transfer matrix method we obtain the closed-form expressions for the reflection/transmission coefficient of the TM waves outgoing from the nonlinear PT-symmetric periodic stack. The nonreciprocity of the scattering process can be directly inferred from the analysis of the obtained expressions.

3. PT-symmetry breaking

To elucidate the features of nonreciprocal scattering by nonlinear non-Hermitian system with gain saturation, the scattering characteristics of the TM waves have been examined numerically. It was observed that the influence of nonlinearity leads to considerable differences between the scattering characteristics of the corresponding linear and nonlinear systems and are pronounced in the frequency range close to the emission frequency.

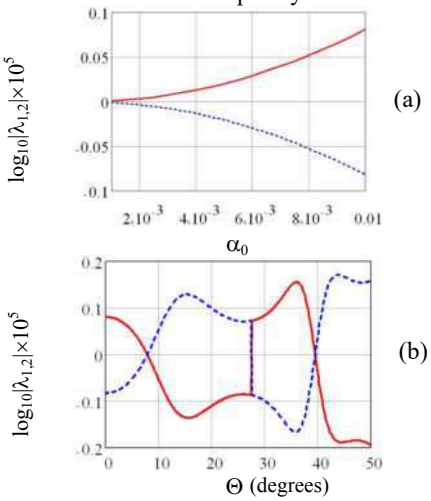


Figure 2: Eigenvalues of the S-matrix for the nonlinear system at $\varepsilon_{01} = \varepsilon_{02} = 10.9$, $\omega_{01} = \omega_{02} = \omega_0 = 1$ THz, $\gamma_1 = \gamma_2 = 0.066$ THz, , d = 0.2 mm, $\alpha_1 = |\alpha_2| = \alpha_0$, N=40, (a) - Θ= 0°; (b) – $\alpha_0 = 0.01$. Solid red lines correspond to the eigenvalues $\lambda_{1,}$ blue dashed lines are for λ_2.

To measure the breaking of *PT* symmetry, we use a scattering *S*-matrix [3]. To gain insight in the effect of the nonlinearity on the symmetry-breaking transition the eigenvalues $\lambda_{1,2}$ have been simulated at variable parameters of the system (Fig.2). The analysis of the eigenvalue spectrum dependence demonstrates that the *PT*-symmetry of nonlinear stack is broken, but we can get a set of points corresponding to the PT-symmetric phase of *S*-matrix changing the angle of electromagnetic wave incidence.

4. Conclusions

We have investigated the asymmetric and non-reciprocal features of the reflectance and transmittance of a multilayered structure with balanced distribution of loss and gain, when dispersion and saturation nonlinear effects are taken into account. The transition between symmetric and broken phases in the non-Hermitian system with gain and loss saturation effects has been considered.

References

[1] C. M. Bender and S. Boettcher, Real Spectra in Non-Hermitian Hamiltonians having PT symmetry, *Phys. Rev.Lett*. 80: 5243, 1998.

[2] K. G. Makris, R. El-Ganainy, D. N. Christodoulides, and Z. H. Musslimani, Beam dynamics in PT - symmetric optical lattices, *Phys. Rev. Lett.* 100: 103904, 2008.

[3] Y. D. Chong, L. Ge, and A. D. Stone, PT-symmetry breaking and laser-absorber modes in optical scattering systems, *Phys. Rev. Lett*. 106: 093902, 2011.

[4] M.-A. Miri, P. LiKamWa, and D. N. Christodoulides, Large area single-mode parity–time-symmetric laser amplifiers, *Opt. Lett.* 37: 764-766, 2012.

[5] S. Savoia, G. Castaldi, V. Galdi, A. Alu and N. Engheta, Tunneling of obliquely incident waves through PT-symmetric epsilon-near-zero bilayers, *Phys. Rev. B* 89: 085105, 2014

[6] H. Alaeian, J. A. Dionne, Non-Hermitian nanophotonic and plasmonic waveguides, *Phys. Rev. B* 89: 075136, 2014.

[7] O.V. Shramkova, G.P. Tsironis, Scattering properties of PT- symmetric layered periodic structures, *J. Opt.* 18: 105101, 2016.

[8] J. Gear, F. Liu, S. T. Chu, S, Rotter, J. Li, Parity-time symmetry from stacking purely dielectric and magnetic slabs, *Phys. Rev. A* 91: 033825, 2015.

[9] P. Witoński , A. Mossakowska-Wyszyńska, P. Szczepański, Effect of Nonlinear Loss and Gain in Multilayer PT-Symmetric Bragg Grating, *IEEE Journal of Quantum Electronics* 53: 2100111, 2017.

[10] A. Marini, A.V. Gorbach, D.V. Skryabin, A.V. Zayats, Amplification of surface plasmon polaritons in nonlinear medium with full saturation susceptibility model, Opt. Lett. 34: 2864-2866, 2009.

[11] O.V. Shramkova, A. G. Schuchinsky, Nonlinear scattering by anisotropic dielectric periodic structures, *Adv. in OptoEl.* 2012: Article ID 154847, 2012.

Regularization of broad-area lasers by non-Hermitian potentials

M. Botey[1], W. W. Ahmed[2], Judith Medina[1], R. Herrero[1], Ying Wu[2], and K. Staliunas[1,3]

[1]Departament de Física, Universitat Politècnica de Catalunya (UPC), Barcelona, Catalonia
[2]King Abdullah University of Science and Technology (KAUST), Saudi Arabia
[3]Institució Catalana de Recerca i Estudis Avançats (ICREA), Barcelona, Catalonia
[*]corresponding author: muriel.botey@upc.edu

Abstract- It was recently shown that arbitrary non-Hermitian optical potentials based on local Parity-Time (PT-) symmetry may control the flow of light, due to the asymmetric mode coupling. We propose periodic non-Hermitian potentials to efficiently regularize the complex spatial dynamics of broad-area semiconductor (BAS) lasers and Vertical-Cavity Surface-Emitting Lasers (VCSELs). Light generated from the entire active layer is concentrated on the structure axis, confined in an intense central narrow beam opening the path to design compact, bright broad-area lasers.

Semiconductor lasers are compact and efficient coherent light sources yet being generally unstable due to their large aspect ratio and to the lack of a transverse mode control mechanism. Spatial random fluctuations and spatiotemporal instabilities degrade the spatial beam quality and laser coherence [1]. This intrinsic instability gives rise to different nonlinear modal interactions such as filamentation and hole burning, limiting possible applications. Common techniques to control the complex dynamics of BAS and VCSELs semiconductor lasers generally compromise their compactness while reducing the power conversion efficiency.

The present paper proposes a novel solution to the need for a general physical mechanism to stabilize the complex dynamics of semiconductor lasers, while improving the beam quality emission. In recent years, non-Hermitian spatially modulated materials have provided a flexible platform to manipulate light wave dynamics. Simultaneous refractive index and pump modulations have already shown the capability to suppress spatial instabilities in nonlinear optical systems, particularly in BAS and VECSEL devices [2]. A remarkable class of such materials is the one globally holding PT- symmetry [3], which may be regarded as particular class of non-Hermitian systems fulfilling spatial Kramers-Kronig relations [4]. Such materials allow unidirectional light transport arising from the unidirectional mode coupling. In turn, it was shown that local PT-symmetry may lead to light localization and enhancement at a selected point [5] or complex potential may be specially designed using a local Hilbert transform, to control flow of light favoring arbitrary vector fields directionality using periodic, quasiperiodic or random background potentials [6].

We now show how axisymmetric non-Hermitian potentials efficiently regularize VCSELs radiation achieving a stable bright emission, see Figs 1.a-e. Dephased periodic (radial) refractive index and gain-loss modulations accumulate the generated light from the entire active layer and concentrate it around the structure axis to emit narrow beams. We perform a comprehensive analysis to explore the maximum central intensity enhancement and concentration regimes. We observe such lasers can be operated in stationary or pulsating oscillatory regime depending on the relative amplitude and phase of the index and gain-loss modulations. The results indicate stabilization occurs coinciding when the coupling between transverse modes is inwards, while

not fulfilling perfect PT-symmetry. We also apply an analogous scheme to control and improve the spatiotemporal dynamics in BAS lasers, see Figs.1e-f. In the proposed modulated BAS devices, the structure in divided into two half-spaces with two symmetric PT-symmetric potentials, by introducing a modulation both in the pump and refractive index. The generated light is directed towards the symmetry axis, see Fig.1g, forming a narrow and bright and temporally stable emitted beam, see Fig.1h.

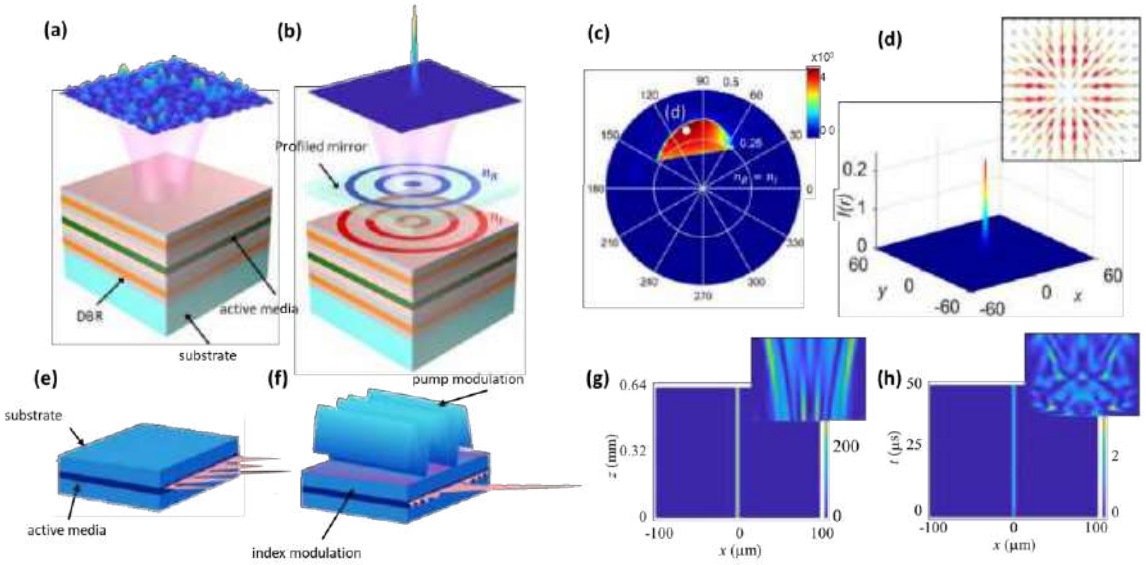


Fig. 1 (a)/b) Complex irregular/bight and narrow beam emission form conventional/structured broad-area VCSELs; (blue, n_R: index, red, n_I: gain-loss); (c) concentration factor C=[$I(r=0)$.Area]/ $\int I(r)dr$ in parameter space (n_I, ϕ); (d) intensity profile in stationary state., and transverse field flow around the center, showing the unidirectional inward radial coupling. (inset) (e)/(f) Complex irregular/bright and narrow emission from conventional/structured BAS lasers; (g) spatial intensity distribution within the BAS laser; (h) temporal evolution of the output intensity profile of the modulated BAS laser and the same intensity profiles for an unstable BAS laser (insets).

The study uncovers rich possibilities for various configurations which could be extended beyond periodic non-Hermitian potentials assuming different random, quasiperiodic complex profiles of the background potential. The reported field regularization effect is universal, and we expect the proposed mechanism to be applicable to regularize the radiation from actual broad aperture lasers and microlasers.

We acknowledge the European Union Horizon 2020 Framework Programme (H2020) EUROSTARS (E10524 HIP-Laser).

REFERENCES

1. J. Othsubo, Semiconductor Lasers: Stability, Instability and Chaos (Springer, Heidelberg, 2013).
2. R. Herrero, M. Botey, M. Radziunas, and K. Staliunas, Opt. Lett. 37, 5253 (2012), S. Kumar, R. Herrero, M. Botey, and K. Staliunas, Opt. Lett. 39, 5598 (2014)
3. C. M. Bender and S. Boettcher, Phys. Rev. Lett. 80, 5243 (1998),
4. S. A. R Horsley, M. Artoni, and G. C. La Rocca. Nat. Phot. 9.7, 436 (2015)
5. W. W. Ahmed, R. Herrero, M. Botey, and K. Staliunas, Phys. Rev. A 94, 053819 (2016).
6. W. W. Ahmed, R. Herrero, M. Botey, Z. Hayran, H. Kurt, and K. Staliunas, Phys. Rev. A 97, 033824 (2018).
7. W. W. Ahmed, R. Herrero, M. Botey, Y. Wu and K. Staliunas, arXiv:1902.04915 [physics.optics]

Active parity-time symmetric and exceptional point structures

Choloong Hahn,[1,2] Youngsun Choi,[3] Jae Woong Yoon,[4] Seok Ho Song,[3] and Pierre Berini[1,2,5,*]

[1]School of Electrical Engineering and Computer Science, University of Ottawa, Canada
[2]Centre for Research in Photonics, University of Ottawa, Canada
[3]Department of Physics, Hanyang University, Seoul, Korea
[4]Electronics and Telecommunications Research Institute (ETRI), Daejeon, Korea
[5]Department of Physics, University of Ottawa, Canada
[*]corresponding author: berini@eecs.uottawa.ca

Abstract

We discuss recent progress on active parity-time symmetric plasmonic systems. We discuss interactions based on encircling-an-exceptional-point, which are reciprocal in the linear regime, but become nonreciprocal in the nonlinear regime over a very broad optical bandwidth. We present an implementation based on plasmonic waveguides incorporating an IR140-doped PMMA gain medium.

Synthetic optical materials having a carefully-structured complex refractive index distribution, following non-Hermitian Hamiltonian analogs, have attracted significant attention because of their interesting optical behaviour [1]. Such materials enable functions such as uni-directionality, non-reciprocity, and unconventional beam dynamics.

The interplay between gain and loss, especially in low-loss (long-range) plasmonic systems is interesting because parity-time (PT) symmetric and exceptional point systems become readily accessible, leading to practical experimental demonstrations. Example systems include plasmonic waveguide Bragg gratings incorporating structured and unstructured gain media enabling distributed feedback lasing [2], and single-sided reflection [3]. Single-sided diffraction as a holographic lattice transitions through the exceptional point is also an interesting phenomenon [4].

We show that interactions based on encircling-an-exceptional-point, which are reciprocal in the linear regime, may become nonreciprocal in the nonlinear regime over a very broad optical bandwidth (limited mainly by the bandwidth of the nonlinearity) [5]. Recent experiments in passive Si-based optical waveguides confirm modal evolution that trace out adiabatic and anti-adiabatic parametric paths around an exceptional point [6].

We describe a plasmonic coupled-waveguide structure that combines an encircling-an-exceptional-point parametric evolution with a gain saturation nonlinearity (following the theory of [5]), and discuss progress on the experimental realization of the concept, aiming towards an integrated on-chip asymmetric amplifier.

References

[1] R. El-Ganainy, K. G Makris, M. Khajavikhan, Z. H. Musslimani, S. Rotter, D. N. Christodoulides, "Non-Hermitian physics and PT symmetry," *Nature Photonics* 14, 11 (2017)

[2] E. Karami Keshmarzi, R. N. Tait, and P. Berini, "Single-mode surface plasmon distributed feedback lasers," *Nanoscale* 10, 5914 (2018).

[3] C. Hahn, E. Karami Keshmarzi, S. H. Song, C. H. Oh, N. Tait, P. Berini, "Unidirectional Bragg Gratings Using Parity-Time Symmetry Breaking in Plasmonic Systems," *IEEE J. Sel. Top. Quant. Electr*. 22, 4600712 (2016)

[4] C. Hahn, Y. Choi, J. W. Yoon, S. H. Song, C. H. Oh, P. Berini, "Observation of exceptional points in reconfigurable non-Hermitian vector-field holographic lattices," *Nature Communications* 7, 12201 (2016)

[5] Y. Choi, C. Hahn, J. W. Yoon, S. H. Song and P. Berini, "Extremely broadband, on-chip optical nonreciprocity enabled by mimicking nonlinear anti-adiabatic quantum jumps near exceptional points," *Nature Communications* 8, 14154 (2017).

[6] J. W. Yoon, Y. Choi, C. Hahn, G. Kim, S. H. Song, K.-Y. Yang, J. Y. Lee, Y. Kim, C. S. Lee, J. K. Shin, H.-S. Lee, P. Berini, "Time-asymmetric loop around an exceptional point over the full optical communications band," *Nature* 562, 7725 (2018)

Nonreciprocal Passive Acoustic Structures with Broken PT-Symmetry

Arkadii Krokhin[1*], Yurii Zubov[1], Jyotsna Dhillon[1], Andrey Bozhko, Ezekiel Walker[2], Arup Neogi[1]

[1]Department of Physics, University of North Texas, 1155 Union Circle #311277, Denton, TX 76203
[2]Echonovus Inc., 1800 S Loop 288, Denton, TX 76205
*corresponding author, E-mail: arkady@unt.edu

Abstract

Nonreciprocal transmission of sound through a phononic crystal with asymmetric metal rods in viscous background (water) is studied within a wide range of frequencies. Nonreciprocity in transmission is observed if sound wave propagates along the directions with broken P-symmetry. The transmission remains reciprocal along the P-symmetric direction. Experiments are performed for periodic and disordered samples. In the latter case the nonreciprocity is observed for localized states in the regime of exponentially weak transmission.

1. Introduction

Two common concepts of nonreciprocity in sound propagation are based on nonlinear effects and on local circulation of fluid. Both types of acoustic systems have been successfully fabricated in the recent years. Nonlinearity is introduced through specially designed electronic circuits which connect linear scatterers [1, 2]. In active acoustic devices, the *T*-symmetry is usually broken due to rotation of the background fluid that in the case of local vortices becomes topologically equivalent to presence of external magnetic field [3], and in the case of global rotation leads to Doppler shift [4]. Practical realization of both concepts requires additional devices to be installed with their own power sources. Here, we explore viscosity of fluid as a natural factor of T-symmetry breaking and propose a passive nonreciprocal acoustic device.

2. Periodic structure

Reciprocity theorem is hold for wave equation due to time-reversal symmetry. In viscous fluid acoustic oscillations of local velocity $\mathbf{v}(\mathbf{r})$ follow the Navier-Stokes equation, which is not time-reversible,

$$\rho\ddot{v}_i - \frac{\partial}{\partial x_i}(\lambda\nabla\cdot\mathbf{v}) = \frac{\partial}{\partial x_k}\left[\eta\left(\frac{\partial\dot{v}_i}{\partial x_k} + \frac{\partial\dot{v}_k}{\partial x_i} - \frac{2}{3}\delta_{ik}\nabla\cdot\dot{\mathbf{v}}\right)\right] + \frac{\partial}{\partial x_i}(\xi\nabla\cdot\dot{\mathbf{v}}), \quad i = x, y, z. \tag{1}$$

Here $\rho = \rho(\mathbf{r})$ is the mass density, $\lambda(\mathbf{r})$ is the bulk elastic modulus, and $\eta(\mathbf{r})$ and $\xi(\mathbf{r})$) are the viscousity coefficients.

However, broken T-symmetry does not necessarily lead to nonreciprocity. Here we demonstrate that the necessary condition for nonreciprocal propagation in a viscous fluid is broken P-symmetry, which can be achieved by introducing asymmetric scatterers in a viscous environment. The experiment was done with a phononic crystal of Al rods in water [5]. The rods have asymmetric cross-section as shown in Fig. 1. The measured transmission spectrum shown in Fig. 2 exhibits signatures of strong nonreciprocity if sound wave propagates along axis of broken P-symmetry (axis y).

Unlike this, the spectra of transmission along axis x are practically reciprocal, while T-symmetry remains bro-

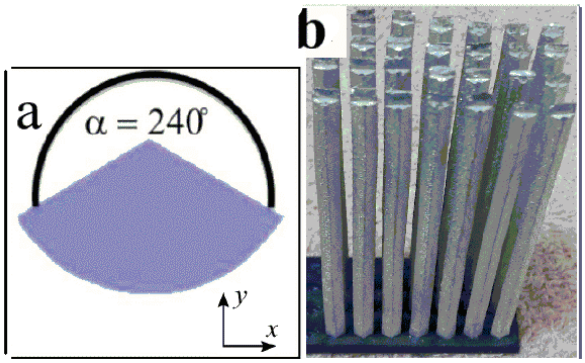


Figure 1: Phononic crystals used for the measurements of acoustic transmission. (a) Square unit cell with period 5.5 mm. The angle α is a measure of broken P-symmetry. The radius of the arc is 2.2 mm. The P-symmetry is broken along the vertical axis and it holds along the horizontal axis. (b) Sample with 4×7 rows of unanodized aluminum rods.

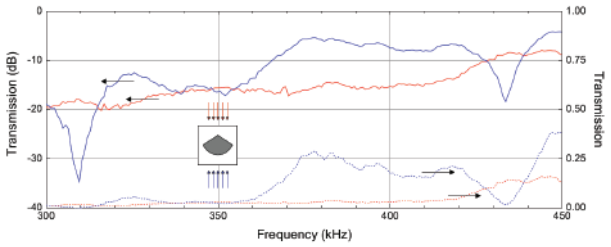


Figure 2: The transmission spectra of the phononic crystal of unanodized rods shown in Fig 1 Solid lines show the transmission plot in logarithmic scale with left vertical axis. Dotted lines show the linear transmission with right vertical axis. The nonreciprocity level is about 10-15 dB within the transmission bands. Insert shows orientation of the unit cell with respect to the direction of the incoming wave.

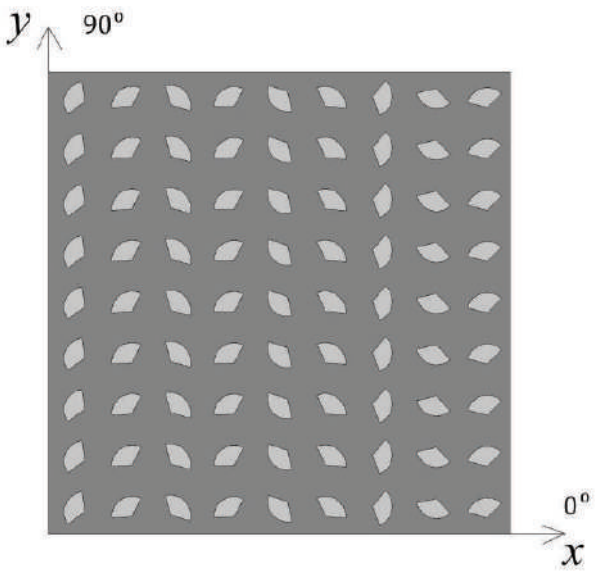


Figure 3: Disordered phononic crystal of 9×9 aluminum rods used in the experiments on sound transmission. Along the x-axis the rods are completely disoriented producing strong disorder. Direction along the positive axis x (y) corresponds to $0°$ ($90°$).

ken by viscous losses. But due to P-symmetry these losses are the same for two opposite directions. Thus, the nonreciprocity is not manifested.

3. Disordered structure

The asymmetric scatterers may be arranged in a structure which is periodic along one direction and disordered along another, see Fig. 3. Since P-symmetry is broken along both directions the corresponding transmission spectra are nonreciprocal. Due to specific arrangement of the scatterers the transport properties along axis x of this 2D system are the same as for truly one-dimensional disordered system. Then all the eigenstates are exponentially localized and the logarithm of transmission decays linearly with sample length. The latter property was measured experimentally and simulated numerically. The results presented in Fig. 4a. In the experiment it is impossible to separate decay due to viscous losses from that due to disorder. Numerical results obtained for viscous and inviscid water clearly show that the viscous decay gives small contribution. Thus, the linear decay presented by red symbols in Fig. 4a is a signature of Anderson localization of sound. Nonreciprocity in the regime of localization is manifested in slightly different slopes of the lines in Fig. 4b, i.e. in different localization lengths observed for the opposite directions of incoming sound wave.

Acknowledgement

This work is supported by EFRI grant No. 1741677 from the National Science Foundation.

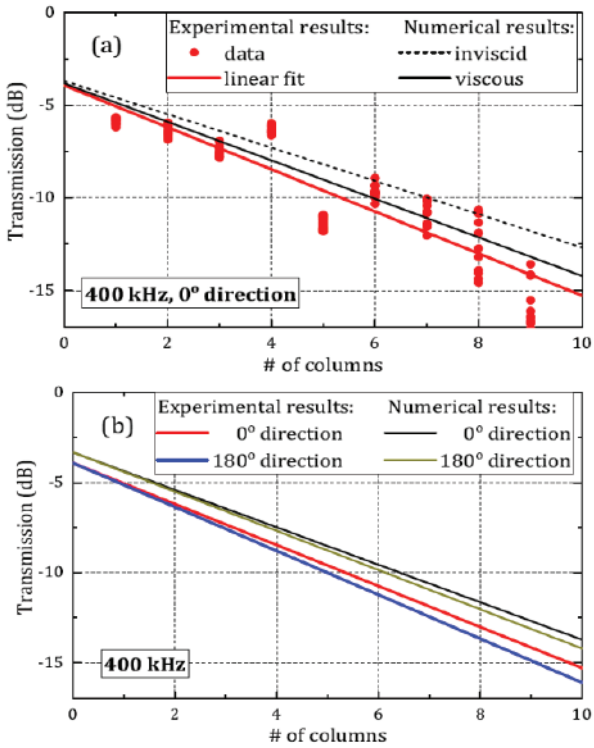


Figure 4: Transmission coefficient (in dB) along the direction of broken P-symmetry (axis y) vs sample length. Slope of the linear fit is proportional to the inverse localization length l^{-1}. (a) Comparison of experimental and numerical results obtained for $0°$ direction. (b) Linear fit of the transmission coefficient obtained for two opposite direction of propagation ($0°$ and $180°$) along axis x (along disorder). Lines in (b) are offset vertically for clarity.

References

[1] B.-I. Popa, S.A. Cummer, Non-reciprocal and highly nonlinear active acoustic metamaterials, *Nat. Commun.* 5: 3398, 2014.

[2] Y. Hadad, Jason C. Soric, A. Khanikaev, and A. Alù, Self-induced topological protection in nonlinear circuit arrays, *Nat. Electronics*, 1: 178, 2018.

[3] Zh. Yang, F. Gao, X. Shi, X. Lin, Zh. Gao, Y. Chong, and B. Zhang, Topological acoustics, *Phys. Rev. Lett.*, 114: 114301, 2015.

[4] R. Fleury, D.L. Sounas, C.F. Sieck, M.R. Haberman, and A. Alù, Sound isolation and giant linear nonreciprocity in a compact acoustic circulator, *Science* 343: 516, 2014.

[5] E. Walker, A. Neogi, A. Bozhko, Yu. Zubov, J. Arriaga, H. Heo, J. Ju, and A.A. Krokhin, Nonreciprocal linear transmission of sound in a viscous environment with broken P symmetry, *Phys. Rev. Lett.* 120: 204501, 2018.

Active Electroacoustic Resonators and their Application to Non-Hermitian Acoustics

Romain Fleury

Laboratory of Wave Engineering, School of Electrical Engineering, EPFL, Station 11, 1015 Lausanne, Switzerland

Email: romain.fleury@epfl.ch

We will discuss our recent experimental progress on developing active acoustic resonators that provide independently tunable acoustic properties, namely the possibility to control at will their resonance frequency, absorption losses, and radiative losses. We will describe how this can be achieved using electroacoustic systems such as loudspeakers, by employing a real-time single sensor feedback control strategy similar to what is used for broadband acoustic impedance control [1], but adapted using a demodulation/modulation scheme to provide a more flexible control of the complex impedance. We will present measurements on a single controlled meta-atom for which the resonance frequency, as well as radiative and non-radiative quality factors, can be tuned independently. We will also demonstrate the possibility to target a given value of the input impedance of the resonator, which allows us to design acoustic metamaterials with any scattering potentials, including non-Hermitian. We will discuss an application example for such active acoustic meta-atoms to the observation of constant-amplitude waves through a disordered non-Hermitian metamaterial, a concept developed by collaborators at TU Wien [2,3] and validated in our laboratory [4].

References

1. E. Rivet, S. Karkar and H. Lissek, "Broadband Low-Frequency Electroacoustic Absorbers Through Hybrid Sensor-/Shunt-Based Impedance Control," in IEEE Transactions on Control Systems Technology **25**, 63-72 (2017).
2. K. G. Makris, A. Brandstötter, P. Ambichl, Z. H. Musslimani, and S. Rotter, "Wave propagation through disordered media without backscattering and intensity variations," Light: Science & Applications **6**, e17035 (2017).
3. P. Sebbah, "Scattering media: A channel of perfect transmission," Nature Photonics News & Views **11**, 337 (2017).
4. E. Rivet et al, "Constant-pressure sound waves in non-Hermitian disordered media", Nature Physics **14**, 942 (2018).

Chiral-reversing vortex radiation at the exceptional point of a plasmonic nanocavity

Ren-Min Ma[1], Xing-Yuan Wang[1], Hua-Zhou Chen[1], Suo Wang[1], Li Ge[2], Shuang Zhang[3],

[1] *School of Physics, Peking University, Beijing 100871, China*

[2] *Department of Engineering Science and Physics, College of Staten Island, CUNY, NY 10314, USA*

[3] *School of Physics and Astronomy, University of Birmingham, Birmingham, B15 2TT, UK*

The radiation of an emitter does not depend only on its intrinsic properties but also on the surrounding photonic environment, the notion of which is essential in the developments of lasers, quantum optics and other light-matter interaction related fields. However, in conventional wisdom, an emitter radiates into photonic eigenstates in the weak coupling regime and does not alter the property of the latter. Here, we report a counterintuitive phenomenon where the radiation field of a dipole in a parity-time symmetric ring resonator displays the opposite handedness to the coalesced eigenstate of the system (Fig. 1) [1]. This finding, to the best of our knowledge, is the first time the wave function of a Jordan vector is revealed in a physical system. We employ this phenomenon to construct vortex radiation with controllable topological charge from a single quantum dot embedded plasmonic nanocavity, demonstrating an enhancement of the Purcell factor by three orders of magnitude. Our scheme enriches the intriguing physics of an exception point in the quantum region and may open a new paradigm for chiral quantum optics and vortex lasers at nanoscale.

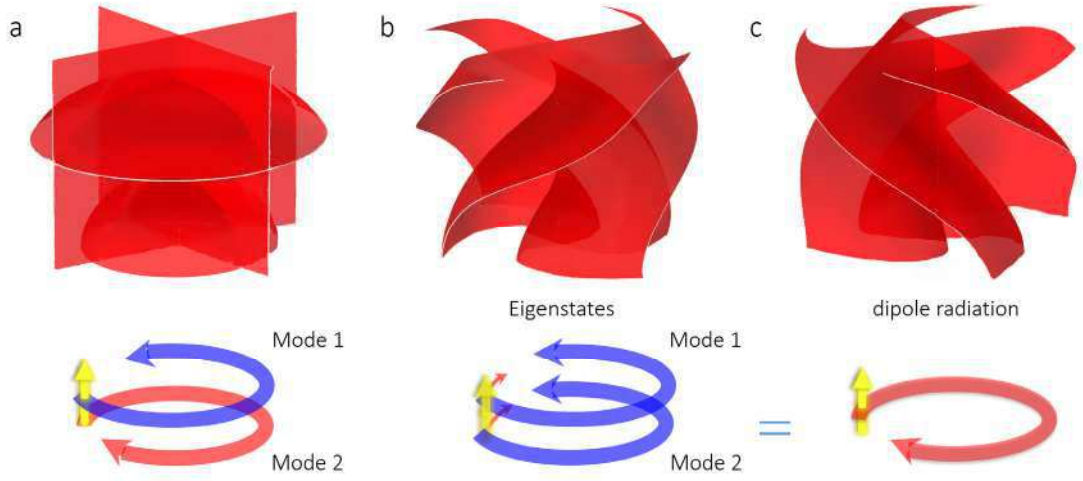


Fig. 1. Chiral-reversing dipole radiation by eigenstates phase locking. The radiation field pattern (isosurface of $E_\rho = 0$) of a **(a)** dipole emitter inside a normal ring cavity, of **(b)** the coalesced eigenstate of a ring cavity operating close to an exceptional point, and of **(c)** a dipole emitter inside a ring cavity operating close to an exceptional point.

[1] X. Y. Wang *et al.,* arXiv: [1707.01055] (2017).

Electrically injected DFB laser based on the Parity-Time symmetry concept

V. Brac de la Perrière[1], Q. Gaimard[1], H. Benisty[2], A. Ramdane[1], A.Lupu[1,*]

[1]Centre de Nanosciences et de Nanotechnologies, CNRS, Univ. Paris-Sud, Université Paris-Saclay, C2N – 10 Boulevard Thomas Gobert – 91120 Palaiseau cedex, France

[2] Laboratoire Charles Fabry de l'Institut d'Optique, CNRS, Univ. Paris Saclay, 2 Ave Augustin Fresnel, 91127 Palaiseau Cedex, France

*corresponding author, E-mail: anatole.lupu@c2n.upsaclay.fr

Abstract

The principle of Parity-Time symmetric optics is exploited for realization of electrically injected single frequency DFB lasers based on industry-adopted design and fabrication approaches. Experimental evidence is provided for "unidirectional" gain discrimination mechanism induced by the complex refractive index Bragg grating. This is expected to enhance lasers' resistance to parasitic optical feedback. The experimental results showing an apparent correlation between the gratings real-to-imaginary phase shift and the laser feedback resistance are corroborating theoretical prediction.

1. Introduction

The advent of the concept of Parity-Time (PT) symmetry and the progress in nanofabrication technologies, ~~witnessed~~ triggered the appearance during the past decade of new type of artificial optical materials where the refractive index (real and imaginary) ñ(r) behaves akin the complex potential of the original idea [1]. Since then, academic teams have achieved demonstrations that make use of integrated optics as a laboratory vehicle but without genuine industrial perspective [2-6].

The aim of the present work is to exploit asymmetric reflection properties of Parity-Time symmetric Bragg gratings (PTSBG) to enhance the resistance of distributed feedback (DFB) lasers to the optical feedback, in the spirit of the IEEE 802.3 standard for isolator-free sources in optical networks. Due to the narrow-band "unidirectional" reflection of PTSBG introducing an additional gain discrimination mechanism, it is expected that the coherence of such a laser would be highly tolerant with respect to the parasitic reflections along the optical path [7,8]. This is one of the worst network impairment issues, currently addressed by the costly means of garnet-based optical isolators.

2. Results and discussion

Based on the same gain medium, index-coupled (IC), loss-coupled and complex-coupled (CC) DFB lasers with different phase shifts between loss and index grating profiles were fabricated, using industry-adopted design and fabrication approaches. The complex-coupled Bragg grating is achieved through the technological realization combining a metallic Bragg grating ensuring modulation of the imaginary part of the complex effective index profile with a shifted dielectric Bragg grating modulating the real part of the effective index profile (Fig. 1a).

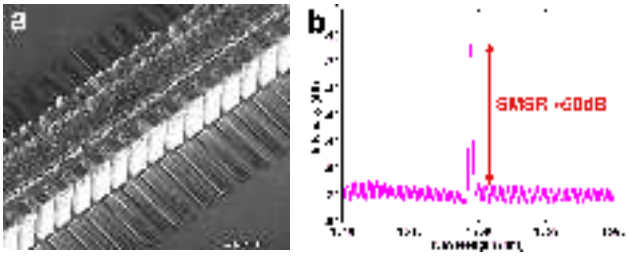


Fig. 2. a) SEM view of PTSBG with $\pi/2$ phase shifted dielectric and metallic Bragg gratings; b) Emission spectrum of PTSBG DFB laser at 1549.5 nm.

The characterization of the fabricated CC DFB lasers showed a reduction in threshold compared to equivalent third-order loss-coupled DFB lasers, and improved single frequency operation and yield compared to third-order index-coupled DFB lasers. High spectral purity laser emission with typical side mode suppression ratio (SMSR) ~50dB, as shown in Fig. 1b, was demonstrated.

Real and imaginary parts of the effective index modulation as well as reflection spectral response were investigated by external optical probing of the laser cavities, the former in order to refine the guidance modelling of this particular geometry, and the latter to assess the impact of the phase shift. The specific phase shift of a quarter period, matching the PT-symmetric configuration, is found to show highly asymmetric mode selection, with unidirectional amplification in reflection.

The resistance of the CC DFB lasers to external optical feedback was further investigated. The obtained results show an apparent correlation between the gratings phase shift and the feedback resistance. In contrast, no significant improvement was found with respect to IC DFB lasers.

Strategies for the optimization of the Bragg grating complex index profile aiming to achieve performances beyond the current state of the art for DFB lasers will be discussed.

3. Conclusions

This first milestone on the application of PT-symmetry to the design and fabrication of DFB lasers compatible with industrial fabrication provide interesting prospects on the improvement of existing technologies. This work reinforces the interest of this concept for the design of feedback tolerant DFB lasers, and their integration in an all PT-symmetric laser-modulator system.

Acknowledgements

Funding by the French Agence Nationale pour la Recherche (project "PARTISYMO", contract number N° ANR-18-CE24-0024) is acknowledged by A.L., A.R. and H.B.

References

[1] C. M. Bender and S. Boettcher, "Real spectra in non-Hermitian Hamiltonians having PT-symmetry," Phys. Rev. Lett. 80, 5243 (1998).

[2] C. E. Rüter, K. G. Makris, R. El-Ganainy, D. N. Christodoulides, M. Segev, and D. Kip, "Observation of parity–time symmetry in optics," Nature Phys. 6, 192–195 (2010).

[3] L. Feng, Y.-L. Xu, W. S. Fegadolli, M.-H. Lu, J. E. Oliveira, V. R. Almeida, Y.-F. Chen, and A. Scherer, "Experimental demonstration of a unidirectional reflectionless parity-time metamaterial at optical frequencies," Nat. Mater. 12, 108–113 (2012).

[4] B. Peng, Ş. K. Özdemir, S. Rotter, H. Yilmaz, M. Liertzer, F. Monifi, C. M. Bender, F. Nori, L. Yang, "Loss-induced suppression and revival of lasing," Science 346, 328-332 (2014).

[5] H. Hodaei, M.-A. Miri, M. Heinrich, D. N. Christodoulides, and M. Khajavikhan, "Parity-time-symmetric microring lasers," Science 346, 975–978 (2014).

[6] P. Miao, Z. Zhang, J. Sun, W. Walasik, S. Longhi, N. M. Litchinitser, and L. Feng, "Orbital angular momentum microlaser," Science, 353, 464-467 (2016).

[7] Y. Zhu, Y. Zhao, J. Fan, and L. Zhu, "Modal Gain Analysis of Parity-Time-Symmetric Distributed Feedback Lasers," IEEE Journal of Selected Topics in Quantum Electronics 22, 1-7 (2016).

[8] C. Ke, X. Li, Y. Xi, "Parity-time symmetric complex-coupled distributed feedback laser with excellent immunity to external optical feedback," AIP Advances 7, 035010 (2017).

Metamaterials/Metasurfaces in Dirac/Kane Plasmons

Controlling the THz Dirac plasmon in Bi_2Se_3 Topological Insulator at the TeraFERMI beamline

Paola Di Pietro[1*], Andrea Perucchi[1], Nidhi Adhlakha[1], Federica Piccirilli[2], Seangshik Oh[3], Alessandra Di Gaspare[4] and Stefano Lupi[5]

[1]Elettra-Sincrotrone Trieste S.C.p.A. Area Science Park, SS 14km 163.5 Trieste, Italy
[2]CNR-IOM Trieste c/o Area Science Park – Basovizza SS 14km 163.5 Trieste, Italy
[3]Department of Physics and Astronomy Rutgers, State University of New Jersey, 136 Frelinghuysen Road, Piscataway, NJ 08854-8019, United States
[4]NEST, Istituto Nanoscienze, CNR, Scuola Normale Superiore, Piazza S. Silvestro 12, Pisa, Italy
[5]CNR-IOM Dip. di Fisica, Univeristà di Roma Sapienza, P.le Aldo Moro 5, Roma, Italy
*corresponding author, E-mail: paola.dipietro@elettra.eu

Abstract

Bi_2Se_3 is one of the most studied Topological Insulator. Thanks to its pretty large band gap and unique Dirac cone in the energy-momentum dispersion, Bi_2Se_3 mirrors indeed a representative candidate for investigating the electrodynamics of Dirac fermions in a graphene-like material.

Collective oscillations of Dirac electrons, i. e. Dirac surface plasmons, in a topological insulator have been demonstrated to exist for the first time in Bi_2Se_3 in 2013 [1]. The Dirac plasmonic dispersion has been measured in five samples of Bi_2Se_3 thin films on sapphire substrate patterned with micro-ribbons of width from 2 to 20 μm. The actual plasmonic resonance has been extracted from FTIR measurements and compared to the theoretical Dirac dispersion, finding a very good agreement.

Recently, we addressed the intrinsic nonlinearity of Bi_2Se_3 Topological Insulator, due to its linear Dirac energy-momentum dispersion. As in graphene, nonlinear properties like saturable absorption and harmonic generation have been shown in a topological insulator in [2]. Moreover, theoretical papers proved the nonlinear effects even on a patterned topological insulator, predicting a softening of the surface plasmon in presence of tens kV/cm of electric field.

The THz beam provided by our beamline TeraFERMI at the Free Electron Laser (FEL) Fermi at Elettra in Trieste (Italy) [3] provides very intense THz electric field in the MV/cm range. TeraFERMI was built up in 2015 at the seeded FEL Fermi, which works in a single pass-single bunch mode at 10 or 50 Hz, covering the spectral range from 100 to 4 nm. TeraFERMI is based on a Coherent Transition Radiation source that provides high intense, broadband and short (about 1 ps) pulses. Such a THz beam can push nonlinear materials well into their nonlinear regime. The beamline experimental setup fulfills the capability to address nonlinear regime by measuring both fluence-dependent transmission/reflection spectra and pump-probe response.

Particularly, the case of Dirac plasmon in Bi_2Se_3 perfectly fits with the potentiality of TeraFERMI. Here we show the THz control of the Dirac plasmon by TeraFERMI electric field. Our data of two samples of Bi_2Se_3 thin films on sapphire substrate with micro-ribbons of 4 and 20 μm exhibit a redshift of the plasmonic resonance with respect to the incoming electric field. This is the first demonstration of Dirac plasmon tunability with THz light in a topological insulator.

References

[1] P. Di Pietro *et al*., Nature Nanotechnology 8, 556 (2013).

[2] F. Giorgianni *et al*., Nature Communications 7, 11421 (2016).

[3] P. Di Pietro *et al*., Synchrotron Radiation News 30, 4 (2017).

Ratchet and magneto-ratchet phenomena excited by THz radiation in semiconductor nanostructures and graphene with lateral superlattices

Sergey Ganichev[1]

[1]Terahertz Center, University of Regensburg, 93040 Regensburg, Germany
*corresponding author, E-mail: sergey.ganichev@ur.de

Abstract

The paper overviews experimental and theoretical studies of terahertz radiation induced ratchet and magnetic ratchet effects in graphene and semiconductor nanostructures with a lateral superlattice (SL). We show that the ratchet photocurrent induced in such samples is caused by the combined action of a spatially periodic in-plane potential and the spatially modulated radiation due to the near field effect of light diffraction. The magnetic quantum ratchet effect is observed in diluted magnetic heterostructures and additionally requires an external magnetic field applied normal to the sample surface. We present symmetry arguments allowing a phenomenological analysis of the respective phenomena, then outline the microscopic theory and finally discuss the main experimental findings.

1. Introduction

Generally, nonequilibrium spatially-periodic noncentrosymmetric systems are able to transport particles in the absence of an average macroscopic force. The directed transport in such systems, known as ratchet effect, has a long history and is relevant for different fields of physics, for review see e.g. [1, 2, 3, 4, 5]. If this effect is induced by electromagnetic radiation it is usually referred to as photogalvanic effect [6]. A novel situation emerges if a lateral superlattice is superimposed upon a two dimensional electron system (2DES): THz radiation shined through a periodic grating, drives the ratchet current through the modulated 2DES, for reviews see e.g. [3, 5].

We begin the review with a short overview on the structures and methods used for the study of THz radiation induced ratchet effects in semiconductor nanostructures and graphene with a lateral one-dimensional potential. Then we give an introduction to the basic concepts and present experimental findings.

2. Terahertz radiation induced ratchet effects

Modulated potentials have been obtained fabricating either a sequence of metal stripes or inter-digitated comb-like dual-grating-gate (DGG) structures, both on top of a 2DES. Examples of such structures deposited on graphene are shown in Fig. 1. By applying different voltages to the two gratings, we can control the photocurrent behaviour for different structure asymmetry, carrier type and density.

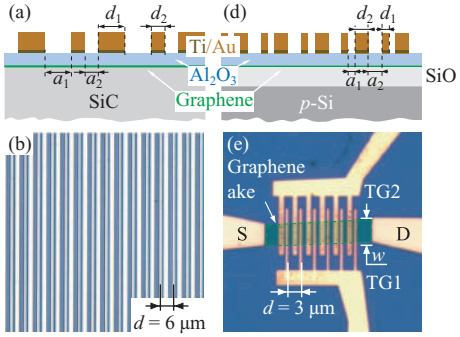


Figure 1: Cross section, photograph and sample geometry sketch of metal finger structure deposited on large area epitaxial graphene, see panel (a) and (b), and interdigitated grating gates deposited on the exfoliated monolayer graphene flake, see panel (c) and (d). Here, $d_{1,2}$ and $a_{1,2}$ are the width of metal stripes and the spacing in-between, respectively.

We present experimental results obtained on such systems demonstrating that the radiation induced total current steams from the superposition of the polarization independent Seebeck ratchet effect and ratchet effects being sensitive to the plane of polarization of linearly polarized light and, in the case of circularly polarized light, to the photon helicity [3, 5, 7].

A typical behaviour of the ratchet photocurrents upon variation of back gate potential is shown in Fig. 2 for graphene structures for several combinations of top gate voltages. These data reveal that the ratchet photocurrent reflects the degree of asymmetry induced by different top gate potentials and vanishes for a symmetric profile. The latter is obtained for $U_{TG1} = -2$ V compensating the build-in potential caused by the metal stripes deposited on top of graphene.

The experimental data are analyzed for the electronic and plasmonic ratchets taking into account the calculated potential profile and the near field acting on carriers in 2DES. We present the theory of ratchet effects stemming from the combined action of the lateral periodic potential and the in-plane pumping by the THz field modulated by the near-field diffraction. We formulate the model in terms of the classical Boltzmann equation for the electron distribution function, show the position of this model with re-

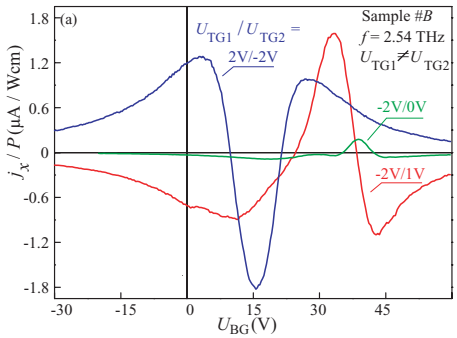


Figure 2: Back gate voltage dependence of the photocurrent in graphene normalized on the radiation intensity measured for three sets of unequal top gate potentials.

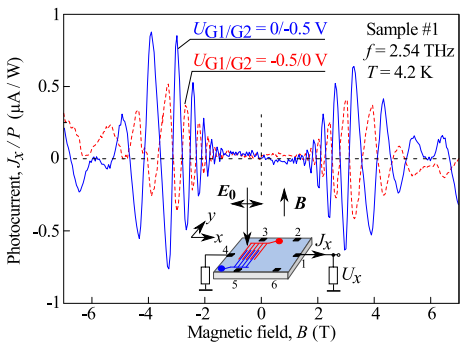


Figure 3: Normalized photocurrent J_x/P as a function of the magnetic field B measured in (Cd,Mn)Te QW sample #1 for two combinations of the gate voltages. Solid blue line show the data for the gate voltages $U_{\rm G1} = 0$ and $U_{\rm G2} = -0.5$ V and the dashed red line for $U_{\rm G1} = -0.5$ V and $U_{\rm G2} = 0$, the setups denoted as $U_{\rm G1/G2} = 0/-0.5$ V and $U_{\rm G1/G2} = -0.5/0$ V. The vertical dashed line indicates zero magnetic field. The inset illustrates the experimental setup.

spect to other electronic ratchets, and propose a model picture to interpret the observed photocurrents.

3. Magnetic quantum ratchet effects

Magnetic quantum ratchet effects, for review see [8], have been recently observed in (Cd,Mn)Te/(Cd,Mg)Te diluted magnetic heterostructures and CdTe/CdMgTe QWs superimposed with lateral asymmetric superlattices [9]. We show that application of an external magnetic field B along the growth direction results in the ratchet current exhibiting sign-alternating $1/B$-periodic oscillations with amplitudes immensely larger than the ratchet signal at zero magnetic field, Fig. 3. The photocurrent consists of the polarization insensitive Seebeck ratchet, as wellas of the polarization sensitive magnetic quantum ratchet current, whose direction and magnitude are determined by the orientation of the THz electric field (linear magnetic ratchet effect) and/or by the direction of the field rotation (circular magnetic ratchet effect). We show that the observed magneto-oscillations with enhanced photocurrent amplitude result from Landau quantization and, for (Cd,Mn)Te at low temperatures, from the exchange enhanced Zeeman splitting in diluted magnetic heterostructures.

Acknowledgement

The support from the DFG priority program SFB 1277 (project A04) and the Volkswagen Stiftung Program is gratefully acknowledged.

References

[1] P. Reimann, Brownian motors: Noisy transport far from equilibrium, *Phys. Rep.*: 361, 57–265, 2002.

[2] P. Hänggi and F. Marchesoni, Artificial Brownian motors: Controlling transport on the nanoscale *Rev. Mod. Phys.*: 81, 387–442, 2009.

[3] E. L. Ivchenko and S. D. Ganichev, Ratchet effects in quantum wells with a lateral superlattice, *JETP Lett.*: 93, 673–682, 2011.

[4] S. Denisov, S. Flach, and P. Hänggi, Phys. Rep. **538**, 77 (2014). Tunable transport with broken space-time symmetries, *Phys. Rep.*: 538, 77-120, 2014.

[5] S.D. Ganichev, D. Weiss, and J. Eroms, THz electric field driven electric currents and ratchet effects in graphene (review), *Annalen der Physik* 529: 1600406(1)–1600406(13), 2017.

[6] E.L. Ivchenko and S.D. Ganichev, *Spin Photogalvanics* in *Spin Physics in Semiconductors*, ed. M.I. Dyakonov, Springer, 2016.

[7] P. Olbrich, J. Kamann, M. König, J. Munzert, L. Tutsch, J. Eroms, D. Weiss, M.-H. Liu, L. E. Golub, E. L. Ivchenko, V. V. Popov, D. V. Fateev, K. V. Mashinsky, F. Fromm, Th. Seyller, and S. D. Ganichev, Terahertz ratchet effects in graphene with a lateral superlattice, *Phys. Rev. B*: 93, 075422(1)–075422(15), 2016.

[8] G. V. Budkin, L. E. Golub, E. L. Ivchenko, and S. D. Ganichev, Magnetic ratchet effects in a two-Dimensional electron gas (review), *JETP Lett.*: 104, 649–656, 2016.

[9] P. Faltermeier, G.V. Budkin, J. Unverzagt, S. Hubmann, A. Pfaller, V.V. Bel'kov, L.E. Golub, E.L. Ivchenko, Z. Adamus, G. Karczewski, T. Wojtowicz, V.V. Popov, D.V. Fateev, D.A. Kozlov, D. Weiss, and S.D. Ganichev, Magnetic quantum ratchet effect in (Cd,Mn)Te- and CdTe-based quantum well structures with a lateral asymmetric superlattice, *Phys. Rev. B*: 95, 155442(1)–155442(12), 2017. See also *Physica E*: 101, 178–187, 2018.

Massless Dirac fermions in III-V semiconductor quantum wells

Sergey S. Krishtopenko[1*], Wilfried Desrat[1], Christophe Consejo[1], Sandra Ruffenach[1], Benoit Jouault[1], Wojciech Knap[1], Fernando Gonzalez-Posada[2], Guilhem Boissier[2], Eric Tournié[2] and Frédéric Teppe[1]

[1]Laboratoire Charles Coulomb, Université de Montpellier, CNRS, 34095 Montpellier, France.
[2]Institut d'Electronique et des Systèmes, Université de Montpellier, CNRS, 34000 Montpellier, France.
*corresponding author, E-mail: sergey.krishtopenko@umontpellier.fr

Abstract

We report on massless Dirac fermions in two-dimensional system based on III-V semiconductors. Using a gated Hall bar made on a three-layer InAs/GaSb/InAs quantum well, we restore the Landau levels fan chart by magnetotransport and unequivocally demonstrate a gapless state in our sample. Measurements of cyclotron resonance at different electron concentrations directly indicate a linear band crossing. Analysis of experimental data allows us not only determing velocity of the massless fermions but also demonstrating significant non-linear dispersion at high energies.

1. Introduction

Since relativistic Dirac-like character of charge carriers was demonstrated in monolayer graphene [1], two-dimensional (2D) massless Dirac fermions (DFs) are intensively studied in condensed matter physics. There are several systems [2] from graphene-like 2D materials (silicene, germanene, etc.) or high-temperature d-wave superconductors to the surfaces of three-dimensional (3D) topological insulators, in which the presence of 2D massless DFs was revealed. Their universal features, such as suppressed backscattering [3], Klein tunneling [4], or their specific response to impurities and magnetic field [5] hold great promises for new nano-scale electronic devices.

Among quantum well (QW) systems, a single-valley spin-degenerate Dirac cone at the Γ point of Brillouin zone was theoretically predicted [6,7] and experimentally observed [8] in HgTe/CdTe QWs. At a critical width, the band gap in these QWs vanishes and the band structure changes from trivial into inverted. The key advantage of QWs over other systems is based on the ability to adjust DFs velocity by adjusting the strain and thickness of the layers. It allows varying the ratio between kinetic energy and Coulomb interaction, which results in a rich variety of phenomena involving massless DFs [9]. However, the massless DFs in HgTe QWs appear only at a fixed temperature, since the temperature changes open a band gap resulting in a non-zero rest-mass of the particles [10-14].

Alternative III-V semiconductor QWs, in which massless DFs have been theoretically predicted, are symmetric three-layer InAs/$Ga_xIn_{1-x}Sb$/InAs QWs confined between wide-gap AlSb barriers [15]. Depending on their layer thicknesses, these QWs host trivial, quantum spin Hall insulator and gapless state. However, in contrast to the HgTe QWs, the three-layer QWs have a temperature-insensitive band-gap, as it has been recently shown by terahertz spectroscopy [16]. Another expected difference of massless DFs in InAs/$Ga_xIn_{1-x}Sb$/InAs QWs is the large tunability of quasiparticle's velocity, which can be varied from $1\cdot10^5$ m/s to $7\cdot10^5$ m/s depending on x and the layer thicknesses [15]. The latter offers the possibility not only to tune the electronic properties [3,4,6] of the DFs but also to achieve specific non-trivial states induced by electron-electron interaction [17-19].

2. Outline of the talk

In this work, we report striking evidence of the presence of massless Dirac fermions in InAs/GaSb/InAs QWs embedded between AlSb barriers. Measuring magnetoresistance of a gated Hall bar, we restore the Landau level (LL) fan chart in our sample, as firstly performed by Büttner et al. [8] in HgTe QWs. Our experimental data clearly evidence a gapless state. We also measure cyclotron resonance (CR) at different electron concentrations varied by bipolar persistent photoconductivity (PPC) inherent for InAs-based QWs [20-22]. The latter is also known as an optical gating and allows one changing an electron concentration in the QW by several times. By analyzing the dependence of the cyclotron mass as a function of the concentration, the massless DF velocity is deduced. To analyze these data, we use both realistic band structure calculations based on an eight-band Kane model [15] and analytical approach involving a simplified Dirac-like Hamiltonian [7]. Experimental dispersion of the massless DFs is in good agreement with realistic band structure calculations.

Acknowledgements

This work was supported by MIPS department of Montpellier University through the "Occitanie Terahertz Platform", by the Languedoc-Roussillon region via the "Gepeto Terahertz platform" and the ARPE project "Terasens" and by the CNRS through "Emergence project

2016" and LIA "TeraMIR'. MBE growth of the samples was performed within the French program "Investments for the Future" (ANR-11-EQPX-0016).

References

[1] K.S. Novoselov, A.K. Geim, S.V. Morozov et al. Two-dimensional gas of massless Dirac fermions in graphene. *Nature* 438: 197, 2005.

[2] T.O. Wehling, A.M. Black-Schaffer, A.V. Balatsky. Dirac materials. *Adv. Phys*. 63: 1, 2014.

[3] A.H. Castro Neto, F. Guinea, N.M.R. Peres et al. The electronic properties of graphene. *Rev. Mod. Phys*. 81: 109, 2009.

[4] C.W.J. Beenakker. Colloquium: Andreev reflection and Klein tunneling in graphene. *Rev. Mod. Phys*. 80: 1337, 2008.

[5] K.S. Novoselov, A.K. Geim, S.V. Morozov et al. Electric field effect in atomically thin carbon films. *Science* 306: 666, 2004.

[6] L.G. Gerchikov, A.V. Subashiev. Interface states in subband structure of semiconductor quantum wells. *Phys. Status Solidi B* 160: 443, 1990.

[7] B.A. Bernevig, T.L. Hughes, S.-C. Zhang. Quantum spin Hall effect and topological phase transition in HgTe quantum wells. *Science* 314: 1757, 2006.

[8] B. Büttner, C.X. Liu, G. Tkachov et al. Single valley Dirac fermions in zero-gap HgTe quantum wells. *Nat. Phys*. 7: 418, 2011.

[9] V.N. Kotov, B. Uchoa, V.M. Pereira et al. Electron-electron interactions in graphene: Current status and perspectives. *Rev. Mod. Phys*. 84: 1067, 2012.

[10] S. Wiedmann, A. Jost, C. Thienel et al. Temperature-driven transition from a semiconductor to a topological insulator. *Phys. Rev. B* 91: 205311, 2015.

[11] S.S. Krishtopenko, I. Yahniuk, D. B. But et al. Pressure- and temperature-driven phase transitions in HgTe quantum wells. *Phys. Rev. B* 94: 245402, 2016.

[12] F. Teppe, M. Marcinkiewicz, S.S. Krishtopenko et al. Temperature-driven massless Kane fermions in HgCdTe crystals. *Nat. Commun*. 7: 12576, 2016.

[13] M. Marcinkiewicz, S. Ruffenach, S.S. Krishtopenko et al. Temperature-driven single-valley Dirac fermions in HgTe quantum wells. *Phys. Rev. B* 96: 035405, 2017.

[14] A.M. Kadykov, S. S. Krishtopenko, B. Jouault et al. Temperature-induced topological phase transition in HgTe quantum wells. *Phys. Rev. Lett*. 120: 086401, 2018.

[15] S.S. Krishtopenko, F. Teppe, Quantum spin Hall insulator with a large bandgap, Dirac fermions, and bilayer graphene analog. *Science. Adv*. 4: eaap7529, 2018.

[16] S.S. Krishtopenko, S. Ruffenach, F. Gonzalez-Posada et al. Temperature-dependent terahertz spectroscopy of inverted-band three-layer InAs/GaSb/InAs quantum well. *Phys. Rev. B* 97: 245419, 2018.

[17] D.I. Pikulin, T. Hyart. Interplay of exciton condensation and the quantum spin Hall effect in InAs/GaSb bilayers. *Phys. Rev. Lett*. 112: 176403, 2014.

[18] J.C. Budich, B. Trauzettel, P. Michetti. Time reversal symmetric topological exciton condensate in bilayer HgTe quantum wells. *Phys. Rev. Lett*. 112: 146405 2014.

[19] L. Du, X. Li, W. Lou, G. Sullivan et al. Evidence for a topological excitonic insulator in InAs/GaSb bilayers. *Nat. Commun*. 8: 1971, 2017.

[20] C. Gauer, J Scriba, A Wixforth et al. Photoconductivity in AlSb/InAs quantum wells. *Semicond. Sci. Technol*. 8: S137, 1993.

[21] V.I. Gavrilenko, A.V. Ikonnikov, S.S. Krishtopenko et al. Persistent photoconductivity in InAs/AlSb heterostructures with double quantum wells. *Semiconductors* 44: 616, 2010.

[22] K.E. Spirin, K.P. Kalinin, S.S. Krishtopenko et al. Features of the persistent photoconductivity in InAs/AlSb heterostructures with double quantum wells and a tunneling-transparent barrier. *Semiconductors* 46: 1396, 2012.

Far and Mid IR lasers based on Dirac heterostructures HgTe/CdHgTe

Sergey Morozov*

[1]Institute for Physics of Microstructures RAS, Nizhny Novgorod, Russian Federation
*, E-mail: more@ipmras.ru

Abstract

We report on stimulated emission at wavelengths up to 20μm from HgTe/HgCdTe quantum well heterostructures with wide-gap HgCdTe dielectric waveguide, grown by molecular beam epitaxy on GaAs(013) substrates. The mitigation of Auger processes in structures under study is exemplified, and the promising routes towards the 20–50 μm wavelength range, where HgCdTe lasers may be competitive to the prominent emitters, are discussed.

1. Introduction

The problem of developing compact terahertz (THz)/long-wavelength emitters is one of the hottest topics in the applied physics. There is a spectral «gap» λ = 20 – 60 μm in which no quantum cascade lasers (QCLs) are available (except for several specific wavelengths near 20 μm), since the majority of QCLs are based on A3B5 materials with strong lattice absorption in this spectral region. Among compact semiconductor lasers, only lead salt lasers cover a part of this gap (up to 46 μm), but their figures of merit are rather low due to formidable problems in growth technology. On the other hand, modern MBE delivers high quality HgTe/CdHgTe quantum well (QW) structures that allow tailoring the bandgap for interband transitions at λ = 20 – 60 μm and have TO phonon frequencies low enough to enter this wavelength range. In addition, HgTe/CdHgTe structures offer strongly non-parabolic dispersion law resembling that of graphene but with finite gap and finite carrier masses that set a considerable energetic threshold for Auger processes.

2. Results and discussion

We report on stimulated emission at wavelengths up to 20μm at 20K and 2.8 – 3.5 μm at 210K from HgTe/HgCdTe quantum well heterostructures with wide-gap HgCdTe dielectric waveguide, grown by MBE on GaAs(013) substrates. The mitigation of Auger recombination (AR) in structures under study is exemplified, and the promising routes towards the 20–50μm wavelength range, where HgCdTe lasers may be competitive to the prominent emitters, are discussed. The next one we conclude that Peltier cooled operation is feasible in lasers based on such structures, making them of interest for spectroscopy applications in the atmospheric transparency window from 3 to 5 μm. We demonstrate stimulated emission (SE) under pulsed and cw optical pumping from HgTe/CdHgTe QWs at wavelengths as long as 11 – 20 μm [1-3], which is almost fourfold increase over previous works. We show that a significant increase in operating temperature (by ~80 K) and wavelength is possible by introducing the additional strain in QW structure to modify the carrier spectrum in the valence band due to suppression AR. We show that the side maxima, arising in the valence band when the QW width is increased, is a critical issue for radiative properties of the material

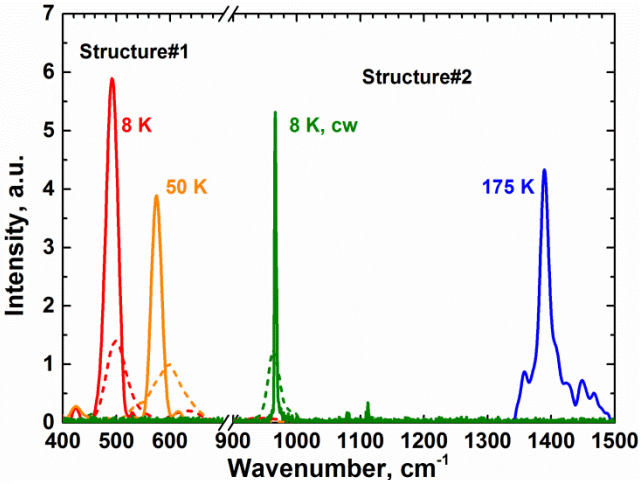


Fig.1. Stimulated emission spectra for structures under study at different temperatures (solid curves). SE was obtained under pulsed pumping with 2300 nm wavelength and 10 kW/cm2 intensity for Structure#1 (T = 8K, T = 50K) and 65 kW/cm^2 for Structure#2 at 175K. SE at cw excitation with 7W/cm2 intensity at 900 nm wavelength is presented for Structure#2 at 8K. Dash curves show PL spectra obtained with the same cw pumping source at 5 W/cm^2 intensity for Structure#1 (T = 8K, T = 50K) and 1 W/cm^2 for

since they enhance AR. On the other hand, implementing narrow HgTe/CdHgTe is performed to suppress the AR and increase the operating wavelength and operating temperature

of HgCdTe based lasers far-infrared from 10 to 20 μm. Experimental results agree well with theoretical calculations of energetic threshold for AR performed in the framework of Kane 8x8 Hamiltonian model as were performed in [4, 5].

Implementing such structures, we demonstrate stimulated emission (SE) under pulsed [1-3] and continuous wave (cw) (Fig. 1) optical pumping at wavelengths as long as 9.5 – 19.5 μm, which is almost fourfold increase over previous works. Being recalculated to the equivalent threshold current, the threshold is only 500 A/cm2 for $\lambda = 20$ μm at 8K – 45K. In principle, such low threshold current density allows development of continuous wave diode lasers. We show that the side maxima, arising in the valence band when the QW width is increased, is a critical issue for radiative properties of the material since they enhance Auger processes. We show that a significant increase in operating temperature (by ~80 K) and wavelength is possible by introducing the additional strain in QW structure to modify the carrier spectrum in the valence band. Using Kane 8x8 Hamiltonian and Bernevig-Hugh- Zhang four-band model to calculate radiative and Auger recombination times, respectively. Carrier lifetime measurements agree well with the calculated data. The subnanosecond carrier lifetimes have been explored via the pumpprobe measurements of a sample's transmission [3]. For HgCdTe QW with 20 meV, corresponding to 4.8 THz frequency, the carrier lifetime is no less than 100 ps for carrier density of 10^{11} cm^{-2} that is sufficient to achieve population inversion. One can estimate a threshold pumping intensity of 10 kW/cm^2 for an optically pumped laser exploiting such QWs as an active media. Thus, implementing narrow HgTe/CdHgTe is the promising route to suppress the Auger recombination and increase the operating wavelength of HgCdTe based lasers in far-infrared/THz (20 – 60 μm) range.

Acknowledgements

This work was supported by the Russian Science Foundation under Grant # 17-12-01360.

References

[1]. S.V. Morozov, V.V. Rumyantsev, M.A. Fadeev, M.S. Zholudev, K.E. Kudryavtsev, A.V. Antonov, A.M. Kadykov, A.A. Dubinov, N.N. Mikhailov, S.A. Dvoretsky, and V.I. Gavrilenko, Stimulated emission from HgCdTe quantum well heterostructures at wavelengths up to 19.5 μm. Appl. Phys. Lett., 2017. 111(19): p. 192101.

[2]. S.V. Morozov, V.V.Rumyantsev, A.M. Kadykov , A.A. Dubinov, K.E. Kudryavtsev, A.V. Antonov, N.N. Mikhailov, S.A. Dvoretskii, V.I. Gavrilenko. Long wavelength stimulated emission up to 9.5 μm from HgCdTe quantum well heterostructures. Appl. Phys. Lett., 2016, Vol. 108, P. 092104.

[3]. S. Ruffenach, A. Kadykov, V. V. Rumyantsev, J. Torres, D. Coquillat, D. But, S. S. Krishtopenko, C. Consejo, W. Knap, S. Winnerl, M. Helm, M. A. Fadeev, N. N. Mikhailov, S. A. Dvoretskii, V. I. Gavrilenko, S. V. Morozov, and F. Teppe. HgCdTe-based heterostructures for terahertz photonics. APL MATERIALS 5, 035503 (2017).

[4]. F. Teppe, M. Marcinkiewicz, S. S. Krishtopenko, S. Ruffenach, C. Consejo, A. M. Kadykov, W. Desrat, D. But, W. Knap, J. Ludwig, S. Moon, D. Smirnov, M. Orlita, Z. Jiang, S. V. Morozov, V.I. Gavrilenko, N. N. Mikhailov, S. A. Dvoretskii. Temperature-driven massless Kane fermions in HgCdTe crystals. Nature Communications, 2016, Vol. 7, P. 12576.

[5]. A. M. Kadykov, S. S. Krishtopenko, B. Jouault, W. Desrat, W. Knap, S. Ruffenach, C. Consejo, J. Torres, S. V. Morozov, N. N. Mikhailov, S. A. Dvoretskii, and F. Teppe. Temperature-Induced Topological Phase Transition in HgTe Quantum Wells. Physical Review Letters 120, 086401 (2018).

Graphene based field-effect transistors as tunable plasmonic interferometers for terahertz radiation detection

G. E. Fedorov[1*], D. Svintsov[1], D. Bandurin[1,2], I. Gayduchenko[3], G. Goltsman[3]

[1]Moscow Institute of Physics and Technology (State University), Russia
[2]School of Physics, University of Manchester, United Kingdom
[3]Department, Moscow State University of Education (MSPU), Russian Federation
*corresponding author, E-mail: gefedorov@mail.ru

Abstract

1. Plasmons, collective oscillations of electron systems, can efficiently couple light and electric current, and thus facilitate developing many optoelectronic devices. Despite considerable effort, it has proven challenging to implement plasmonic devices operating at terahertz frequencies. With lowering the operation frequency down to the THz domain, momentum relaxation rate has to be below the plasmon frequency, which, in turn, requires ultra-high electron mobility. The material capable to meet this challenge is graphene that has been proved to support long-lived electrically tunable plasmons.

2. Introduction

Here we report on plasmon-assisted resonant detection of terahertz radiation by antenna-coupled graphene transistors that act as both plasmonic Fabry-Perot cavities and rectifying elements. We demonstrate this long-sought resonant regime [1] using field effect transistors (FETs) based on high-quality van der Waals heterostructures. In particular, we employ graphene encapsulated between hexagonal boron nitride (hBN) crystals which have been shown to provide the cleanest environment for long-lived graphene plasmons [2-4]. Exploiting the gate-tunability of plasmon velocity, we switch our detectors between more than 10 resonant modes, and use this functionality to measure plasmon wavelength and lifetime [5].

In addition to their potential applications in high-responsivity detection and on-chip spectroscopy of the THz radiation, our devices also represent a convenient tool to study plasmons under conditions where other approaches may be technically challenging. Due to their compact size and far-field coupling, our photodetectors can easily be employed to carry out plasmonic experiments in extreme cryogenic environments and in strong magnetic fields, as well in studies of more complex van der Waals heterostructures. As an example, we apply our approach to probe plasmons in graphene/hBN superlattices and unveil collective modes of charge carriers in moiré minibands.

References

[1] 1. Dyakonov, M. & Shur, M. Detection, mixing, and frequency multiplication of terahertz radiation by two-dimensional electronic fluid. IEEE Trans. Electron Devices 43, 380–387 (1996).

[2] 2. Woessner, A. et al. Highly confined low-loss plasmons in graphene-boron nitride heterostructures. Nat. Mater. 14, 421–425 (2015).

[3] 3. Alonso-González, P. et al. Acoustic terahertz graphene plasmons revealed by photocurrent nanoscopy. Nat. Nanotechnol. 12, 31–36 (2016).

[4] 4. Ni, G. et al. Fundamental limits to graphene plasmonics. Nature 557, 530–533 (2018).

5. D. Bandurin, et al., Resonant Terahertz Detection Using Graphene Plasmons, Nature Communications, 9, 5392 (2018).

Quantum phenomena with collective excitations in confined systems

A. Vasanelli[1], S. Huppert[1], Y. Todorov[1], D. Gacemi[1], and C. Sirtori[1]

[1]Laboratoire de physique de l'École Normale Supérieure & CNRS, 75005 Paris, France 7162, 75013 Paris, France
*corresponding author, E-mail: carlo.sirtori@ens.fr

Elementary excitations in dense media are renormalized by their mutual interaction, giving rise to quasiparticles with new collective properties. Such renormalization occurs for instance in highly doped semiconductor layers where Coulomb interaction ties together all single electronic excitations and gives rise to a bright collective mode [1] with a huge optical dipole. These excitations correspond to confined plasmons.

In the past few years we have investigated electronic many-body states in quantum wells as a valuable platform to probe some of the most fundamental phenomena of quantum electrodynamics, which are usually the realm of atomic physics. Indeed, each many-body electronic state is a bosonic quasi-particle confined perpendicularly to the plane of the quantum well. While considering the first two energy levels of the harmonic ladder, the quasi particle can be regarded as a macro-atom carrying all the interaction with the electromagnetic field [2]. When such an excitation is coupled to a microcavity mode, it reaches straightforwardly the ultra-strong light- matter coupling regime [5] at room temperature. Furthermore, identical macro-atoms located in spatially separated quantum wells, within a sub-wavelength distance, have a huge interaction with the vacuum field by exchanging real and virtual photons [3]. This results into a superradiant mode displaying a large cooperative Lamb shift [4]. Finally, we have observed experimental signatures on the energy spectrum of these many-body states that arise from its size confinement. This effect produces a set of energy resonances given by the folding of the excitation dispersion.

All these fundamental quantum effects have been investigated in optoelectronic devices [7], paving the way towards a new generation of devices in which light-matter interaction is tailored by collective phenomena.

References

[1] A. Delteil et al., Phys. Rev. Lett. 109, 246808 (2012).
[2] S. Huppert et al., Phys. Rev. B 94, 155418 (2016)
[3] M. O. Scully, Phys. Rev. Lett. 102, 143601 (2009)
[4] G. Frucci, et al. New Journal of Physics 19, 043006 (2017)
[5] C. Ciuti et al., Phys. Rev. B 72, 115303 (2005).
[6] B. Askenazi et al., New Journal of Phys. 16, 043029 (2014); B. Askenazi et al., ACS Photonics 4, 2550 (2017)
[7] T. Laurent et al., Phys. Rev. Lett. 115, 187402 (2015).

Emergent optoelectronic functionality in low dimensional non-centrosymmetric semiconductors

Yijin Zhang[1*], Toshiya Ideue[2], Masaru Onga[2], Feng Qin[2], Ryuji Suzuki[2], Alla Zak[3], Reshef Tenne[4], Jurgen H. Smet[1], and Yoshihiro Iwasa[2,5]

[1]Max Planck Institute for Solid State Research, Stuttgart, Germany
[2]Department of Applied Physics, University of Tokyo, Tokyo, Japan
[3]Faculty of Science, Holon Institute of Technology, Holon, Israel
[4]Department of Materials and Interfaces, Weizmann Institute of Science, Rehovot, Israel
[5]CEMR, RIKEN, Wako, Japan
*corresponding author, E-mail: y.zhang@fkf.mpg.de

Abstract

Transition-metal dichalcogenides (TMDs) are exemplary low-dimensional semiconductors. By breaking the inversion symmetry inherent in their bulk crystals, various exotic physical phenomena have been realized. We studied electrical responses under light illumination in such non-centrosymmetric TMDs belonging to a few different point groups, and observed a large photovoltaic effect induced by the reduction of the crystal symmetry.

1. Introduction

The unit cell of bulk TMDs is composed of two layers. The inversion centre in the unit cell is located at the van der Waals gap. The inversion symmetry can be broken simply by isolation of monolayers, and/or application of external electric field. Many peculiar phenomena and functionalities have been realized in such non-centrosymmetric TMDs [1-3]. The bulk photovoltaic effect (BPVE) is one of the fundamental physical phenomena that requires inversion symmetry breaking which is not studied in TMDs so far [4]. This effect can be distinguished from the ordinal photovoltaic effect that is observed at the interface of two different species, for instance, *p-n* junctions and metal-semiconductor Schottky junctions, because the BPVE does not require any interface.

Monolayer TMDs have a non-centrosymmetric D_{3h} crystal symmetry. Materials in this point group should exhibit BPVE upon irradiation of linearly polarized light [4]. Circularly polarized light will not induce BPVE due to the mirror and rotational symmetries. These remnant symmetries are broken when 2D sheets are rolled up to form quasi-one dimensional tubular structure (Fig. 1). BPVE is expected regardless of the optical polarization of the incident light when mirror and rotational symmetries are broken [4]. Here, we studied the BPVE in WS_2, a representative member of TMDs, in three different forms, namely, centrosymmetric bilayer and non-centrosymmetric monolayer as well as nanotube (NT).

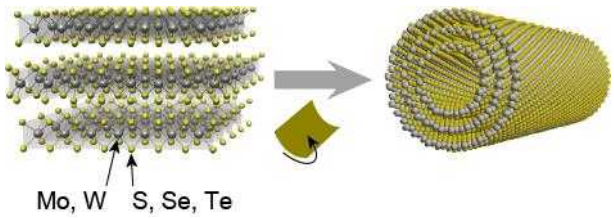


Figure 1: Schematics of 2D and quasi-1D TMDs.

2. Experiment

WS_2-NTs were chemically synthesized [5] and then dispersed on a SiO_2/Si++ substrate. Isolated nanotubes were selected under an optical microscope. WS_2 flakes were mechanically exfoliated by an adhesive tape from single crystals grown via chemical vapour transport (CVT) [6]. The electrodes were patterned using electron-beam lithography. After its development, Cr (5 nm) and Au (200 nm) were evaporated.

The WS_2-NTs used in this study have multiwall and hollow core as shown in the representative transmission electron microscopy (TEM) image in Fig. 2a. Their outer diameter is in average 100 nm. The electron diffraction (Fig. 2b) indicates that the chirality of each layer of the wall is different. A detailed characterization of the WS_2-NTs can be found in literatures [5,7].

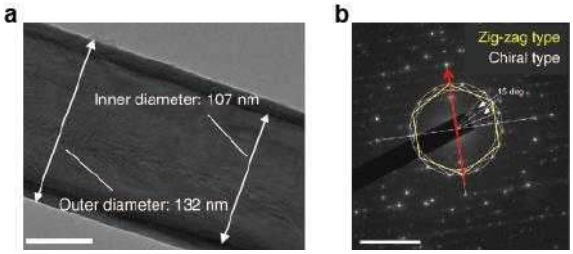


Figure 2: Characterization of WS_2-NT. (a) TEM image. The scale bar equals 50 nm. (b) EDX pattern. The scale bar equals 5 cm^{-1}.

All measurements were performed under high vacuum conditions at room temperature. Samples were placed under a home-built optical microscope and are illuminated by laser with one of following three wavelengths: 532nm, 632.8 nm, or 730 nm, through an x50 objective. The wavelength of 632.8 nm is almost resonant to the direct gap energy of WS_2 [7,8]. The laser spot size is approximately 1-2 μm as determined from a fit of the laser profile to Gaussian. The electrical signal were acquired using a source-measure unit under continuous illumination.

3. Results and discussion

I-V characteristics at dark and under light illumination were mainly studied. The *I-V* curve at dark passes through the origin, while under illumination finite short-circuit current (I_{sc}) and open-circuit voltage (V_{oc}) are recognized. This fact indicates the existence of the photovoltaic effect in WS_2-NTs.

Although the laser spot size is about half of the separation between two electrode, the photovoltaic effect due to charge separation at the Schottky barrier contacts may occur if the diffusion length is in the micro-meter scale. In order to assess this possibility, I_{sc} was recorded while the laser spot was scanned from one of two electrodes toward the other. If the observed photovoltaic effect is induced by the charge separation at the Schottky barrier, $|I_{sc}|$ increases with the laser spot approaching electrodes. In addition, the sign of I_{sc} should reverse between two electrodes. We found that the spatial dependence of I_{sc} in WS_2-NT does not match the feature of Schottky barrier photovoltaic effect discussed above, suggesting the existence of the BPVE. As a comparison, a WS_2 monolayer device with similar lateral dimension is fabricated as well. The spatial dependence of I_{sc} in this monolayer device is consistent with the Schottky barrier photovoltaic effect.

The BPVE in TMD monolayers are likely quite small and buried in the features of the Schottky photovoltaic effect, since the group theory does predicts BPVE in TMD monolayers [4]. In contrast, BPVE in WS_2-NT is largely enhanced and overwhelms features from Schottky photovoltaic effect. Considering the small absorbance of the WS_2 monolayer as well as the small diameter of WS_2-NT, the total photon absorption in WS_2 monolayer is about half of that in WS_2-NT assuming 100 % absorption in WS_2-NT. Nevertheless, the BPVE, evidenced from the I_{sc} when the laser spot is away from contacts, in WS_2-NT is more than orders in magnitude larger than that in WS_2 monolayer. Both WS_2 monolayer and NT have non-centrosymmetric structure. However, the former is non-polar while the latter is polar. Therefore, the large enhancement of the BPVE in WS_2-NT is likely owing to the polar structure.

4. Conclusions

We discovered a bulk photovoltaic effect in WS_2-NT. The large suppression of the similar effect in WS_2 monolayer implies the importance of the polar crystal structure beyond the mere inversion symmetry breaking.

Acknowledgements

Authors acknowledge M. Kühne, H. Isobe, M. Nakamura, N. Ogawa, and D. Zhao for fruitful discussions, and S. Göres, Y. Stuhlhofer, J. Geurs, and Y. Kim for technical assistance.

References

[1] Y. J. Zhang, T. Oka, R. Suzuki, J. T. Ye, and Y. Iwasa, Electrically Switchable Chiral Light-Emitting Transistor, *Science* 344: 725-728, 2014.

[2] K. F. Mak, K. L. McGill, J. Park, and P. L. McEuen, The valley Hall effect in MoS_2 transistors, *Science* 344: 1489-1492, 2014.

[3] W. Z. Wu, L. Wang, Y. L. Li, F. Zhang, L. Lin, S. M. Niu, D. Chenet, X. Zhang, Y. F. Hao, T. F. Heinz, J. Hone, and Z. L. Wang, Piezoelectricity of single-atomic-layer MoS_2 for energy conversion and piezotronics, *Nature* 514: 470-474, 2014.

[4] B. I. Sturman, Fridkin, V. M., *The Photovoltaic and Photorefractive Effects in Noncentrosymmetric Materials*, Gordon and Breach Science Publishers, 1992.

[5] F. Qin, W. Shi, T. Ideue, M. Yoshida, A. Zak, R. Tenne, T. Kikitsu, D. Inoue, D. Hashizume, and Y. Iwasa, Superconductivity in a chiral nanotube, *Nature Commun.* 8: 14465, 2017.

[6] W. Shi, J. T. Ye, Y. J. Zhang, R. Suzuki, M. Yoshida, J. Miyazaki, N. Inoue, Y. Saito, and Y. Iwasa, Superconductivity Series in Transition Metal Dichalcogenides by Ionic Gating, *Sci. Rep.* 5: 11534, 2015.

[7] L. Yadgarov, B. Visic, T. Abir, R. Tenne, A. Y. Polyakov, R. Levi, T. V. Dolgova, V. V. Zubyuk, A. A. Fedyanin, E. A. Goodilin, T. Ellenbogen, R. Tenne, and D. Oron, Strong light-matter interaction in tungsten disulfide nanotubes, *Phys. Chem. Chem. Phys.* 20: 20812-20820, 2018.

[8] J. A. Wilson and A. D. Yoffe, Transition Metal Dichalcogenides Discussion and Interpretation of Observed Optical, Electrical and Structural Properties, *Adv. Phys.* 18: 193-335, 1969.

s High Efficiency Detectors and Sources for Field-Ready Quantum Nano

Limits to the fidelity of on-demand single photon sources using quantum dot-cavity systems

S. Hughes[1]

Department of Physics, Queen's University, Kingston, Ontario, Canada K7L 3N6

Abstract—

A quantum dot coupled to an optical cavity has recently proven to be an excellent source of on-demand single photons. We investigate the factors associated with pulsed excitation that can limit simultaneous efficiency and indistinguishability, including excitation of multiple excitons, multi-photons, and pump-induced dephasing, and find for realistic single photon sources that these effects cause degradation of the source figures-of-merit comparable to that of phonon scattering. We also compare and contrast semiconductor cavity systems with metallic resonator systems.

The use of photons as easily manipulated quanta for quantum information processing applications, as well as fundamental studies, has led to the desire to create high-fidelity sources which can produce single photons "on demand" [1–3]. The single photon source (SPS) should produce photons efficiently (ideally, where each trigger pulse produces one and only one photon) which are of an indistinguishable quantum character (i.e., a pure quantum state), in addition to other desirable parameters including scalability and source stability over time. Semiconductor quantum dots coupled to an optical cavity have recently proven to be an excellent source of on-demand single photons [4–8]. Typically, applications require simultaneous high efficiency of the source and quantum indistinguishability of the extracted photons. While much progress has been made, both in suppressing background sources of decoherence and utilizing cavity-quantum electrodynamics to overcome fundamental limitations set by the intrinsic exciton-phonon scattering inherent in the solid-state platform [9, 10], the role of the excitation pulse has been often neglected.

This talk will discuss the key factors associated with pulsed excitation that can limit simultaneous efficiency and indistinguishability, including excitation of multiple excitons, multi-photons, and pump-induced dephasing. We will show that, for realistic SPSs, the role of pulse excitation causes degradation of the source figures-of-merit comparable to that of intrinsic phonon scattering. We present rigorous open quantum system polaron master equation models of quantum dot dynamics under a time-dependent drive which incorporate non-Markovian effects of both photon and phonon reservoirs, and explicitly show how coupling to a high Q-factor cavity suppresses multi-photon emission in a way not predicted by commonly employed models. We then use our findings to summarize the criteria that can be used for single photon source optimization [11]. We also show how short pulses manifest in a time-dependent Purcell factor that is suppressed during the pulsed excitation process, causing a departure from the usual Fermi's golden rule.

Nanoplasmonic resonators offers another class of "cavity system" that can enhance the light-matter interactions for SPS applications, and there have been various works published on how to increase the Purcell factor as well as on how to increase the output (radiative) beta factor [12, 13]. Huang *et al.* [14] demonstrated room-temperature SPS emission from QDs coupled to plasmonic nanocavities, using silver nanocubes, and measured impressive Purcell factors in excess of 500; and Lyamkina *et al.* [15] showed how one can deterministically integrate semiconductor quantum emitters with plasmonic nano-devices, demonstrating enhanced spontaneous emission of single near-surface (<10 nm) InAs quantum dots. Most of these metal resonator works agree that two of the most important metric for efficient SPSs are the Purcell factor and output beta factor or quantum efficiency; unfortunately, these two properties are not mutually exclusive, even at the level of a single mode. In terms of the single photon purity [8, 16], fast SPS emission and suppression of multi-photon emission with $g^{(2)}(0) < 0.1$ has been achieved by quasi-resonant excitation at low excitation power. However, to the best of our knowledge there has not yet been any reported measurements of the two-photon interference for metal based SPSs, which is required to quantify the indistinguishability of the emitted photons. Using a recent quantization scheme for quasinormal modes [17] (the dissipative modes for any open-cavity structure [18]), we will highlight the main challenges for metal based SPSs and compare these with semiconductor cavity systems.

[1]Work carried out in collaboration with Chris Gustin, Mohsen Kamandar Dezfouli, Sebastian Franke, Martin Richter, and Andreas Knorr.

References

[1] P. Senellart, G. Solomon, and A. White, "High-performance semiconductor quantum-dot single-photon sources," *Nat. Nanotech.*, vol. 12, pp. 1026–1039, 2017.

[2] M. Müller, et al., "Quantum-dot single-photon sources for entanglement enhanced interferometry," *Phys. Rev. Lett.*, vol. 118, p. 257402, 2017.

[3] A. J. Shields, "Semiconductor quantum light sources," *Nat. Photon.*, vol. 1, pp. 215–223, 2007.

[4] S. Buckley, K. Rivoire, and J. Vučković, "Engineered quantum dot single-photon sources," *Rep. Prog. Phys.*, vol. 75, p. 126503, 2012.

[5] X. Ding, et al., "On-demand single photons with high extraction efficiency and near-unity indistinguishability from a resonantly driven quantum dot in a micropillar," *Phys. Rev. Lett.*, vol. 116, p. 020401, 2016.

[6] N. Somaschi et al., "Near-optimal single-photon sources in the solid state," *Nat. Photon.*, vol. 10, pp. 340–345, 2016.

[7] Y.-M. He, et al., "Deterministic implementation of a bright, on-demand single-photon source with near-unity indistinguishability via quantum dot imaging," *Optica*, vol. 4, p. 802, 2017.

[8] X. Liu, T. Asano, S. Odashima, H. Nakajima, H. Kumano, and I. Suemune, "Bright single-photon source based on an InAs quantum dot in a silver-embedded nanocone structure," *Applied Physics Letters*, vol. 102, p. 131114, Apr. 2013.

[9] J. Iles-Smith, D. P. S. McCutcheon A. Nazir, and J. Mørk, "Phonon scattering inhibits simultaneous near-unity efficiency and indistinguishability in semiconductor single-photon sources," *Nat. Phot.*, vol. 11, pp. 521–526, 2017.

[10] C. Roy and S. Hughes, "Phonon-dressed mollow triplet in the regime of cavity quantum electrodynamics: Excitation-induced dephasing and nonperturbative cavity feeding effects," *Phys. Rev. Lett.*, vol. 106, p. 247403, 2011.

[11] C. Gustin and S. Hughes, "Pulsed excitation dynamics in quantum-dot–cavity systems: Limits to optimizing the fidelity of on-demand single-photon sources," *Phys. Rev. B*, vol. 98, jul 2018.

[12] C. Belacel, B. Habert, F. Bigourdan, F. Marquier, J.-P. Hugonin, S. Michaelis de Vasconcellos, X. Lafosse, L. Coolen, C. Schwob, C. Javaux, B. Dubertret, J.-J. Greffet, P. Senellart, and A. Maitre, "Controlling Spontaneous Emission with Plasmonic Optical Patch Antennas," *Nano Letters*, vol. 13, pp. 1516–1521, Apr. 2013.

[13] H. Siampour, S. Kumar, and S. I. Bozhevolnyi, "Nanofabrication of Plasmonic Circuits Containing Single Photon Sources," *ACS Photonics*, vol. 4, pp. 1879–1884, Aug. 2017.

[14] T. B. Hoang, G. M. Akselrod, and M. H. Mikkelsen, "Ultrafast Room-Temperature Single Photon Emission from Quantum Dots Coupled to Plasmonic Nanocavities," *Nano Letters*, vol. 16, pp. 270–275, Jan. 2016.

[15] A. A. Lyamkina, K. Schraml, A. Regler, M. Schalk, A. K. Bakarov, A. I. Toropov, S. P. Moshchenko, and M. Kaniber, "Monolithically integrated single quantum dots coupled to bowtie nanoantennas," *Optics Express*, vol. 24, pp. 28936–28944, Dec. 2016.

[16] N. Livneh, M. G. Harats, D. Istrati, H. S. Eisenberg, and R. Rapaport, "Highly Directional Room-Temperature Single Photon Device," *Nano Letters*, vol. 16, pp. 2527–2532, Apr. 2016.

[17] S. Franke, S. Hughes, M. K. Dezfouli, P. T. Kristensen, K. Busch, A. Knorr, and M. Richter, "Quantization of quasinormal modes for open cavities and plasmonic cavity-QED," *arXiv:1808.06392 [cond-mat, physics:physics, physics:quant-ph]*, Aug. 2018.

[18] P. T. Kristensen and S. Hughes, "Modes and Mode Volumes of Leaky Optical Cavities and Plasmonic Nanoresonators," *ACS Photonics*, vol. 1, no. 1, pp. 2–10, 2014.

Generating and routing single photons in GaAs nanophotonic circuits

Leonardo Midolo

Center for Hybrid Quantum Networks (Hy-Q), Niels Bohr Institute, University of Copenhagen, Blegdamsvej 17, 2100-DK Copenhagen Denmark
corresponding author, E-mail: midolo@nbi.ku.dk

Abstract

We report the latest advances in controlling single-photon emission and routing using photonic integrated circuits with embedded quantum dots. These include methods for performing on-chip resonance fluorescence, actively routing photons within a chip, and efficiently couple them into optical fibers. These results constitute key steps to develop scalable emitter-photon interfaces with high efficiency and coherence.

1. Introduction

In recent years, semiconductor quantum dots (QDs) in GaAs have been suggested as a promising alternative to, e.g., spontaneous parametric down-conversion, for single-photon generation and quantum information processing, mainly due to their ability to provide on-demand photon emission and near-unity coupling to optical waveguides [1]. Nevertheless, the integration in GaAs circuits, and the solid-state nature of the emitters, make it highly challenging to simultaneously fulfill all the requirements for coherent emission, routing, and processing of single photons. The most prominent technological challenge is to boost the total efficiency of photonic qubits, which demands a fully-integrated approach with nearly lossless devices. Here, we report some of the recent efforts that we have taken towards improving the excitation schemes for QDs and to implement active routing of single photons within a GaAs optical circuit.

2. Waveguide-based resonance fluorescence

Generating highly indistinguishable photons requires pumping the QDs with resonance fluorescence excitation schemes. This is commonly achieved by focusing a laser on the QD, tune it to an individual excitonic transition, and extinguish its signal using cross-polarized detection. Here, we present a novel method to excite the emitter without a free-space objective, i.e., with an entirely waveguide-based approach relying on multi-mode waveguides where the laser and the emitter couple to two distinct optical modes in a controllable way. We achieve an extinction ratio between resonance fluorescence and pump photons higher than >100 using a simple on-chip mode filtering technique. The indistinguishability is measured via a Hong-Ou-Mandel experiment, which results in >90% visibility of interference between two consecutively emitted photons. Such approach enables realistic pathways for removing free-space optical setups for exciting the emitters, since both the laser pump and the emitted photons can be coupled to a chip with, e.g., high-efficiency gratings [2].

3. Nanomechanical routing of single photons

Another important functionality is to scale up the number of photons that can be emitted by a single QD. To achieve this goal, a key requirement is to develop reconfigurable circuitry that does not introduce excessive loss or emitter decoherence. Such circuitry would enable routing and switching photons into different optical channels, enabling spatial de-multiplexing of photons. The existing routing mechanisms, based on thermo-optic and electro-optic effects are too slow or require very large footprints, limiting both scalability and efficiency. We report a nanomechanical single-photon router based on gap-variable directional couplers, with electro-mechanically controllable splitting ratio. Such device enables us to route single photons emitted by embedded QDs with extinction ratios >20 dB and nW-level power consumption. The reduced device footprint (<30 μm^2) and the small dimension involved, allow us to achieve sub-microsecond switching time (~370 ns) and a total insertion loss of 0.67 dB/switch [3]. These results are key to implementing networks of re-configurable quantum gates and schemes for on-chip de-multiplexing with more than 10 photons.

Acknowledgements

We gratefully acknowledge financial support from the European Research Council (ERC Advanced Grant 'SCALE') and the Danish Council for Independent Research (grant number 4184-00203).

References

[1] P. Lodahl, S. Mahmoodian, and S. Stobbe, Interfacing single photons and single quantum dots with photonic nanostructures, *Rev. Mod. Phys.* 87: 347, 2015.

[2] X. Zhou *et al.* High-efficiency shallow-etched grating on GaAs membranes for quantum photonic application, *Appl. Phys. Lett.* 113: 251103, 2018.

[3] C. Papon *et al.* Nanomechanical single-photon routing, *arXiv preprint* arXiv:1811.10962, 2018.

Engineering Photon-pair Sources for Integrated Quantum Technologies

Gary F. Sinclair, Will McCutcheon, Imad I. Faruque, John G. Rarity

School of Physics, HH Will Physics Laboratory, University of Bristol, Bristol, BS8 1TL, United Kingdom
*corresponding author, E-mail: gary.f.sinclair@bristol.ac.uk

Abstract

The on-chip generation of quantum states of light is a fundamental requirement for integrated photonic quantum technologies. Many photonic integrated chip platforms exhibit an intrinsic material nonlinearity which can be used for quantum state generation. We focus on engineering photon-pair sources in silicon photonics. This platform offers the ability to construct photonic circuits of unparalleled size and complexity. Nonetheless, careful engineering of the classical and quantum source physics is needed to construct high-performance sources for next-generation quantum technology applications.

1. Introduction

Engineering the quantum state of light on-chip is a key enabling technology for quantum photonic applications. Two complementary routes to generating photons on-chip have been pursued: single-photon emitters (quantum dots, colour centres, etc) and parametric photon-pair sources. We choose to develop parametric sources that make use of the intrinsic material nonlinearity of silicon to generate photon-pairs through the process of spontaneous four-wave mixing (SFWM). These sources can be integrated with complex photonic and electronic circuits, with zero-change required to the fabrication process [1]. Motivated by the goal of large-scale linear optics quantum computing and quantum simulation, ever-larger demonstrations of on-chip quantum information processing (QIP) have been performed [2]. Nonetheless, current large-scale demonstrations employ basic source designs that fall short of the stringent performance requirements necessary for a scalable monolithically integrated QIP platform. In particular, current designs achive only limited purity and heralding efficiency, and require both off-chip spectral filtering and single photon detection. Although there has been a wealth of theoretical research into advanced source designs, this has largely focussed on improvements in the purity only and has yet to be experimentally demonstrated. Currently, the most advanced demonstration of on-chip photon-pair generation has demonstrated an interference visibility of $72\,\%$ between two independent ring resonator sources [3]. We examine the system-level requirements for photon-pair sources for QIP applications and report developments that we believe will overcome the limitations of current source designs.

2. Source Engineering

2.1. System-level requirements

Any QIP platform will have to be robust to errors. Although the exact error thresholds are dependent on the encoding scheme used we can identify system-level source metrics that will have to be targeted for linear optical QIP:

- single photons: parametric sources produces photon-pairs probabilistically. Nonetheless, heralding with number-resolving detectors and active multiplexing should allow the creation of a near deterministic single-photon source [4].
- heralding efficiency: the efficiency with which a photon can be heralded is limited by the detection efficiency, source design (photon extraction efficiency) and material and waveguide scattering losses.
- heralded photon purity: the purity of the heralded photon sets an upper limit on the nonclassical interference visibility, which is a fundamental requirement for the high-fidelity operation of quantum gates.
- low noise: the low conversion efficiency between pump photons and generated photon-pairs typically demands $> 100\,\mathrm{dB}$ pump rejection filtering. The monolithic integration of single-photon detectors and sources on-chip, will require high-extinction on-chip filtering and engineering of the optical environment around sources to contain scattered light and avoid blinding of on-chip detectors.

2.2. Technical requirements

The system-level requirements for a QIP photonic source can be translated into technical requirements for our parametric photon-pair source designs, some of which we discuss below.

2.2.1. Schmidt mode engineering

Parametric sources produce photons in pairs. Due to energy and momentum conservation constraints, these photon-pairs will in general exhibit spectral correlations that can be described by the bi-photon state [5]:

$$|\psi\rangle = \int \psi(\omega_1, \omega_2)\hat{a}_1^\dagger(\omega_1)\hat{a}_2^\dagger(\omega_2)d\omega_1 d\omega_2|\mathrm{vac}\rangle. \qquad (1)$$

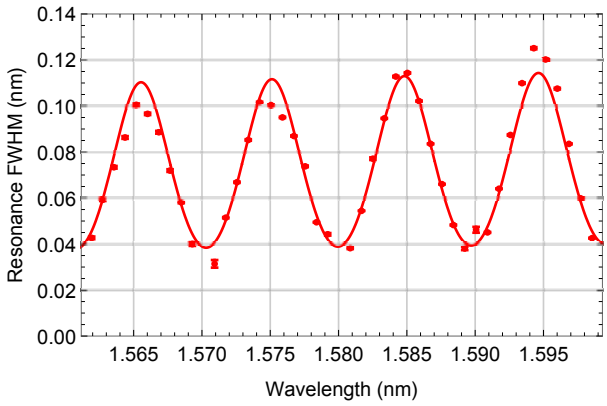


Figure 1: Modification of the resonance linewidths of a ring resonator source to improve heralded photon purity (dots - experimental data, solid line - model fit).

By the *Schmidt decomposition* it is always possible to write this as the sum of factorisable photon-pair states:

$$|\psi\rangle = \sum_i \lambda_i \hat{A}_1^\dagger(\omega_1)\hat{A}_2^\dagger(\omega_2)|\text{vac}\rangle, \qquad (2)$$

where λ_i are the *Schmidt values* and $\hat{A}_i^\dagger$ are creation operators on the broadband single-photon modes. This expansion provides a convenient basis from which to calculate the purity of the heralded single-photon state : $\mathcal{P} = \sum_i |\lambda_i|^4$. The engineering of spectral correlations to improve source purity has been the focus of significant research. Standard ring-resonator designs exhibit a upper-limit to the purity of 93 % and designs have been proposed that overcome this limit [6]. We demonstrate chromatically coupled ring-resonators that show strong modulation of the resonance linewdith, allowing modification of the Schmidt modes for enhanced heralded photon purity (see Fig 1).

2.2.2. *parasitic nonlinearities*

Photon-pair generation occurs via the process of SFWM due to the third-order optical nonlinearity of silicon. However, this material nonlinearity will also give rise to a variety of parasitic nonlinearities, such as self- and cross-phase modulation (SPM, XPM) and two-photon absorption (2PA). We have explored the effects of parasitic nonlinearities on the photon-pair generation rate and purity [7]. We have also investigated the effect of parasitic loss due to 2PA on the heradling efficiency of a source and its variation with temperature [8].

3. Conclusions

Engineering parametric photon-pair sources for QIP applications will require a system-level approach to the requirements of a monolithically integrated platform. We are engineerig photon-pair sources that satisfy the full range of classical and quantum engineering challenges necssary for scalable on-chip QIP in a silicon photon platform.

Acknowledgement

This work was supported by the Engineering and Physical Sciences Research Council (EPSRC EP/L024020/1).

References

[1] C.M. Gentry, J.M. Shainline, M.T. Wade, M.J. Stevens, S.D. Dyer, X.-G. Zeng, F. Pavanello, T. Gerrits, S.W. Nam, R.P. Mirin, M.A. Popović, Quantum-correlated photon pairs generated in a commercial 45 nm complementary metal-oxide semiconductor microelectronic chip *Optica*, 2, 1065, 2015.

[2] J.-W. Wang, S. Paesani, Y. Ding, R. Santagati, P. Skrzypczyk, A. Salavrakos, J. Tura, R. Augusiak, L. Mančinska, D. Bacco, D. Bonneau, J.W. Silverstone, Q. Gong, A. Acín, K. Rottwitt, L.K. Oxenløwe, J.L. O'Brien, A. Laing, M.G. Thompson, Multidimensional quantum entanglement with large-scale integrated optics, *Science* 360: 285–291, 2018.

[3] I.I. Faruque, G.F. Sinclair, D. Bonneau, J.G. Rarity, M.G. Thompson, On-chip quantum interference with heralded photons from two independent micro-ring resonator sources in silicon photonics *Opt. Express*, 26, 20379, 2018.

[4] A.L. Migdall, D. Branning, S. Castelletto, Tailoring single-photon and multiphoton probabilities of a single-photon on-demand source *Phys. Rev. A*, 66, 053805, 2002.

[5] C.K. Law, I.A. Walmsley, J.H. Eberly, Continuous Frequency Entanglement: Effective Finite Hilbert Space and Entropy Control, *Phys. Rev. Lett.*, 84: 5304, 2000.

[6] Z. Vernon, M. Menotti, C.C. Tison, J.A. Steidle, M.L. Fanto, P.M. Thomas, S.F. Preble, A.M. Smith, P.M. Alsing, M. Liscidini, and J.E. Sipe, Truly unentangled photon pairs without spectral filtering, *Opt. Lett.*, 42: 3638–3641, 2017.

[7] G.F. Sinclair, M.G. Thompson, Effect of self- and cross-phase modulation on photon pairs generated by spontaneous four-wave mixing in integrated optical waveguides, *Phys. Rev. A*, 94, 063855, 2016.

[8] G.F. Sinclair, N.A. Tyler, D. Sahin, J. Barreto, M.G. Thompson, Temperature dependence of the Kerr nonlinearity and two-photon absorption in a silicon waveguide at 1.55m, *arXiv:1809.00237*, 2018.

Metrology for single-photon detectors and sources

Angela Gamouras

National Research Council Canada,
Ottawa, Canada
*corresponding author, E-mail: angela.gamouras@nrc-cnrc.gc.ca

Abstract

National metrology institutes around the world have been working to provide characterization techniques and reference standards for few-photon technologies including single-photon detectors and sources. As advances are made towards on-chip integration of single-photon sources, detectors, and other optical components, methodologies for effectively characterizing these quantum integrated circuits will need to be developed. This presentation will discuss ongoing efforts in this area, including the need for consistency in the measurement of performance metrics for deterministic and probabilistic single-photon sources.

1. Introduction

Few-photon technologies have extended from applications in quantum information science (e.g. quantum computing, quantum cryptography, etc.) to numerous areas including spectroscopy, single molecule detection, remote sensing, and monitoring the environment [1]. These quantum technologies depend on the accurate detection of single photons, and in some cases rely on specific parameters for the individual photons themselves. Current and future implementations of quantum information and communication technologies will only be as effective as our measurement capabilities. National metrology institutes have developed several characterization techniques for single-photon detectors [2, 3], and now with commercially available devices for quantum key distribution [4], these methodologies have been extended to these systems [5]. As the quality of single photons from solid-state quantum emitters improves [6, 7] and as photonic integrated circuits begin to incorporate sources and detectors on a single chip [8, 9], additional efforts are being made to address the need for robust metrics when characterizing these devices.

References

[1] C. J. Chunnilall, I. P. Degiovanni, S. Kück, I. Müller, A. G. Sinclair, Metrology of single-photon sources and detectors: a review, *Optical Engineering* 53 (8), 081910, 2014.

[2] S. V. Polyakov and A. Migdall, High accuracy calibration of photon-counting detectors 'on demand', *Proc. of SPIE* 6583, 65830A, 2007.

[3] G. Porrovecchio, M. Šmid, M. López, H. Hofer, B. Rodiek, S. Kück, Comparison at the sub-100 fW optical power level of calibrating a single-photon detector using a high-sensitive, low-noise silicon photodiode and the double attenuator technique, *Metrologia*, 53, 1115, 2016.

[4] https://www.idquantique.com/quantum-safe-security/products/

[5] ETSI GS QKD 004 V1.1.1 Quantum Key Distribution (QKD) Component characterization: characterizing optical components for QKD systems, ETSI, Group Specification, May 2010.

[6] P. Senellart, G. Solomon, A. White, High-performance semiconductor quantum-dot single-photon sources, *Nature Nanotechnology*, 12, 1026, 2017.

[7] D. Dalacu, P. Poole, R. Williams, Nanowire-based Sources of Non-classical Light, *Nanotechnology*, Accepted Manuscript, 2019.

[8] J. M. Shainline, S. M. Buckley, N. Nader, C. M. Gentry, K. C. Cossel, J. W. Cleary, M. Popović, N. R. Newbury, S. W. Nam, and R. P. Mirin, Room-temperature-deposited dielectrics and superconductors for integrated photonics, *Optics Express* 25, 10322, 2017.

[9] R. Gourgues, I. E. Zadeh, A. W. Elshaari, G. Bulgarini, J. W. N. Los, J. Zichi, D. Dalacu, P. J. Poole, S. N. Dorenbos, and V. Zwiller, Controlled integration of selected detectors and emitters in photonic integrated circuits, *Optics Express* 27, 3710, 2019.

High efficiency entangled photon sources and single photon detectors based-on semiconductor nanowires

Michael E. Reimer[1,*], Arash Ahmadi[2], Mohd Zeeshan[1], Simon Daley[1], Nachiket Sherlekar[2], Bradley van Kasteren[1], Burak Tekcan[1], Sandra J. Gibson[1], Andreas Fognini[3], Klaus Jons[4], Val Zwiller[4], Dan Dalacu[5] and Philip J. Poole[5]

[1]Institute for Quantum Computing and Department of Electrical & Computer Engineering, University of Waterloo, ON N2L 3G1, Waterloo, Canada
[2]Institute for Quantum Computing and Department of Physics & Astronomy, University of Waterloo, Waterloo, ON N2L 3G1, Canada
[3]Kavli Institute of Nanoscience Delft, Delft University of Technology, Delft 2628 CJ, The Netherlands
[4]Department of Applied Physics, Royal Institute of Technology (KTH), AlbaNova University Center, SE - 106 91 Stockholm, Sweden
[5]National Research Council of Canada, Ottawa, ON K1A 0R6, Canada
*corresponding author, E-mail: mreimer@uwaterloo.ca

Abstract

Semiconductor nanowires offer a powerful platform for engineering light at the nanoscale by controlling their size and shape in order to guide light efficiently and minimize undesired reflections. In this work we have shaped the nanowires with a unique tapering to realize bright quantum dot based entangled photon sources and high efficiency single photon detectors with high speed and timing resolution over an unprecedented bandwidth.

1. Introduction

In the first part of the talk I will discuss the on-demand generation of entangled photon pairs with a quantum dot in a tapered nanowire waveguide [1-3]. These results will be put in perspective with respect to state-of-the-art entangled photon sources with the viewpoint of going beyond in the future towards near-unity fidelity and efficiency. Reaching near-unity fidelity and efficiency has proven elusive with leading photon technologies due to the probabilistic nature of the generation process.

In the second part of the talk I will present our recent results towards efficient single-photon detectors based-on semiconductor nanowire p-n junction arrays operating at room temperature [4]. Due to the unique nanowire shape and device design we achieve broadband high-efficiency photodetection from the UV to the near infrared with peak efficiencies exceeding 80%. Such capability is beneficial for numerous applications including remote sensing of low power signals, acquiring high resolution images at long range and quantum communication, and advantageous for sensing applications requiring portability.

Acknowledgements

We acknowledge funding from the Canada First Research Excellence Fund and Industry Canada to support this work.

References

[1] M.A.M. Versteegh *et al.*, Observation of strongly entangled photon pairs from a nanowire quantum dot, *Nature Commun.* **5**, 5298 (2014).

[2] K.D. Jöns *et al.*, Bright nanoscale source of deterministic entangled photon pairs violating Bell's inequality, *Scientific Reports* **7**, 1700 (2017).

[3] A. Fognini *et al.*, Path to perfect photon entanglement with a quantum dot, arXiv:1710.10815 (2017).

[4] S.J. Gibson *et al.*, *Nature Nanotechnol.* **14**, 473–479 (2019).

Impact of ultrasmall capacitance for OE/EO conversions using photonic crystals

Masaya Notomi[1, 2, 3], Kengo Nozaki[1,2], Shinji Matsuo[2,4], Akihiko Shinya[1,2]

[1]Nanophotonics Center, Nippon Telegraph and Telephone Corporation, Atsugi, Japan
[2]NTT Basic Research Laboratories, Nippon Telegraph and Telephone Corporation, Atsugi, Japan
[3]Department of Physics, Tokyo Institute of Technology, Tokyo, Japan
[4] NTT Device Technology Laboratories, Nippon Telegraph and Telephone Corporation, Atsugi, Japan
*corresponding author, E-mail: notomi@phys.titech.ac.jp

Abstract

We have realized a photodetector whose capacitance is less than 1 fF by using InP-based buried-heterostructure photonic crystal platform. We show that this ultrasmall-capacitance photodetector enables an amplifier-free and bias-free photoreceiver, which generates sufficiently-large on-chip output voltage without use of any electric power. In addition, we have also realized a electro-optic modulator whose capacitance is also less than 1 fF, which shows record-low consumption energy (42aJ/bit). Recently, we have integrated a fF photodetector with a fF electro-optic modulator via load resistor, which presents three-terminal optical nonlinear (transistor-like) functionalities, such as switching with signal gain. We believe these achievements pave the way to a novel form of optoelectronic information processing which has OE/EO conversions with very fine granularity.

1. Introduction

Traditionally, optical-to-electrical (OE) and electrical-to-optical (EO) conversions are considered as energy-consuming parts in optoelectronic signal processing systems. Generally, we should decrease the number of OE/EO conversions to make efficient optoelectronic systems. In this presentation, we are going to demonstrate that it is indeed possible to greatly improve the efficiency and latency of OE/EO conversions by making the capacitance of OE/EO converters small. Our recent achievement shows that the energy cost of OE/EO conversions can be reduced down to fJ/bit level, which is comparable or even smaller than the energy cost of cutting-edge photonic devices [1].

Although the gate capacitance of CMOS transistors have been decreased year by year, down to less than fF levels. The capacitance of conventional photonic devices such as photodetectors (PDs) and electro-optic modulators (EOMs) are still rather large (100 fF to pF range). Recently, however, we have succeeded in reducing the capacitance of PDs and EOMs down to less than 1 fF by use of buried-heterostructure photonic crystal technologies.

2. fF photodetector

Figure 1 shows our fF-PD based on a buried heterostructure photonic crystal waveguide with a laterl p-i-n junction [2]. As a result of the strong light confinement achieved by photonic crystals, its electrostatic size is extremely small, and the estimated device capacitance is as small as 0.6fF. More importantly, the fF-PD exhibits excellent performance as regards the bandwidth (f_{3dB} = 29 GHz, 40Gbps NRZ operation), the responsivity (1A/W), and the dark current (< 100 pA), despite of its small size. We have monolithically integrated this fF-PD with a load register, and experimentally demonstrated surprisingly large light-to-voltage conversion efficiency (4 kV/W) without any electric amplifier [2].

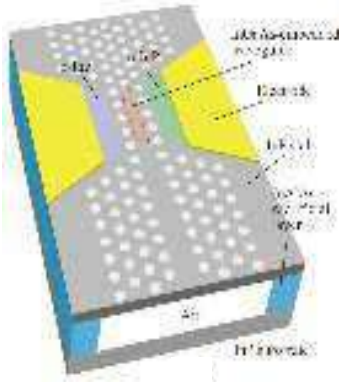


Fig. 1. Schematic of fF-PD based on a photonic crystal.

In addition, we have demonstrated that a photonic crystal PD can be operated at high frequency (20 Gbps) even under a forward bias condition. This should enable zero-bias operation with a large load resistor (such as 7 kΩ). This suggests that this tiny PDs can be operated at high frequency without any electric power [3, 4].

The fF PD has also another advantage in terms of its noise characteristics because it is free from thermal noise from electric amplifiers [4].

3. fF electro-optic modulator

With the same scenario as the previous section, it is possible to reduce the device capacitance of EOMs. Figure 2 shows our fF-EOMs based on a buried heterostructure photonic crystal waveguide (a) and nanocavity (b). Owing to the strong light confinement of photonic crystals, we have achieved the energy cost of 1.8 fJ/bit for (a), which is the smallest value for waveguide-based EOMs [5]. Furthermore, the nanocavity-based EOMs (b) present extreme small capacitance (0.6 fF) and can be operated at 40 Gbps with the record-low energy cost (42 aJ/bit), which is the smallest value for any types of optical modulators [6].

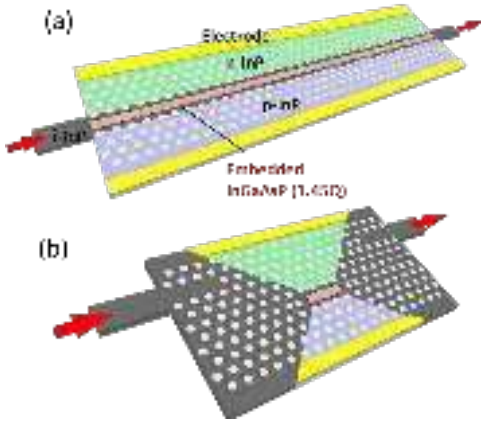


Fig. 2. Schematic of waveguide-based (a) and nanocavity-based EOMs within a photonic crystal.

4. fF optoelectronic integration

Recently, we have integrated a fF PD and a fF EOM via a load resistor as shown in Fig. 3 [6]. Such optoelectronic integration (O-E-O device) has been known to realize an optical three-terminal transistor-like device which essentially functions as an all-optical nonlinear processing device, but the previous O-E-O devices suffered from the large capacitance, thereby leading to substantially large energy cost or slow operation speed. In the present study, we have solved these problems by directly integrating fF OE and EO devices n the photonic crystal platform and achieved excellent various coordinated nonlinear operation at 10 Gbps. We have experimentally verified that the total device capacitance of this O-E-O device is about 2 fF, which is the first experimental demonstration of optoelectronic integration at fF level as far as we know. Furthermore, the required optical pulse energy for this nonlinear device is 1.6 fJ/bit. More importantly, this O-E-O device exhibits a signal gain of 3.6 dB, which has been difficult to achieve in conventional all-optical devices.

5. Summary

We believe that fF OE/EO conversion technologies may have an impact on various optical information processing systems. Since we have tended to think that we have to reduce the number of OE/EO conversions to realize efficient processing systems, the present result may lead to a certain paradigm change because we may be able to incorporate OE/EO conversion in a very fine granularity scale. For example, it may become meaningful to consider OE/EO conversion even within a computation circuit, leading to novel optoelectronic computation scheme.

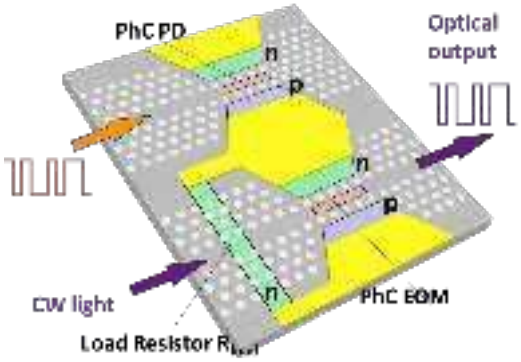


Fig. 3. Schematic of fF O-E-O three-terminal device.

Acknowledgements

We acknowledge financial support from the Japan Science and Technology Agency(JST) through the CREST program under Grant No. JPMJCR15N4.

References

[1] M. Notomi, K. Nozaki, A. Shinya, S. Matsuo, E. Kuramochi, “Toward fJ/bit optical communication in a chip”, Opt. Commun. Vol. 314 , pp. 3-17 (2014).

[2] K. Nozaki, S. Matsuo, T. Fujii, K. Takeda, M. Ono, A. Shakoor, E. Kuramochi, and M. Notomi , "Photonic-crystal nano-photodetector with ultrasmall capacitance for on-chip light-to-voltage conversion without an amplifier", *Optica*, vol. 3, pp. 483-492 (2016).

[3] K. Nozaki, A. Shakoor, S. Matsuo, T. Fujii, K. Takeda, A. Shinya, E. Kuramochi, and M. Notomi "Ultralow-energy electro-absorption modulator consisting of InGaAsP-embedded photonic-crystal waveguide," *APL Photonics* 2, 056105 (2017).

[4] K. Nozaki, S. Matsuo, A. Shinya, and M. Notomi, "Amplifier-Free Bias-Free Receiver Based on Low-Capacitance Nanophotodetector", *IEEE J. Sel. Topics Quantum Electron*., vol. 22, p. 4900111, 2018

[5] Kengo Nozaki, S. Matsuo, T. Fujii, K. Takeda, A. Shinya, E. Kuramochi, and M. Notomi, "Forward-biased nanophotonic detector for ultralow-energy dissipation receiver", *APL Photonics* 3, 046101 (2018)

[6] K. Nozaki, S. Matsuo, T. Fujii, K. Takeda, A. Shinya, E. Kuramochi, and M. Notomi, "Femtofarad optoelectronic integration demonstrating energy-saving signal conversion and nonlinear functions", *Nature Photonics* (2019). DOI: 10.1038/s41566-019-0397-3.

Plasmonics: Fundamentals and Application

Tailoring Induced Plasmonic Circular Dichroism in Hybrid Nanostructures with Different Geometric Configurations

Wei Zhang[1]

[1]Institute of Applied Physics and Computational Mathematics, P. O. Box 8009 (28), Beijing 100088, P. R. China
*corresponding author, E-mail: zhang_wei@iapcm.ac.cn

Abstract

We investigate various ways of tailoring the induced circular dichroism in nanostructures with different geometric configurations (end-to-end, side-by-side assembly nanorod configurations or nanorod with core-shell structure) and explore the key factors affecting the chiroptical responses. It is revealed that the interplay between the local field enhancement and backaction, and the morphology of the nanorod with core-shell structure play important roles in the chiral properties of the hybrid nanostructures.

1. Introduction

The chiral optical properties of various systems are of great importance in understanding biological processes and have many applications. Hybrid nanostructures of different geometric configurations, such as end-to-end, side-by-side assembly nanorod configurations, core-shell structured nanorod with different morphology/aspect ratio, show different chiroptical properties. They provide us much opportunities of exploring the keys factors affecting the chiral responses. Our theoretical and experimental studies indicate that the interaction between the molecules and metallic nanorod can be modulated by geometric configurations and leads to tunable chiral optical properties[1,2]. Our work not only sheds light on understanding the relationship between the configuration of plasmonic nanostructure assemblies and geometry-manipulated circular dichroism (CD), but also paves the way for predictive design of plasmonic biosensors or other nanodevices with controllable optical activities from the UV to the NIR light range.

2. The induced plasmonic circular dichroism in different assembly configurations

We systematically study the optical properties of the chiral cysteine-directed assemblies of Au@Ag core–shell nanocrystals (CSNCs) and Au/Ag nanorods with end-to-end (ETE) and side-by-side (SBS) configurations. We consider core-shell nanocrystal assemblies (with ETE or SBS configuration) incorporating the dipole of cysteine (CYS) at the center of the gaps. The dominant contribution of CD comes from CYS-induced plasmonic circular dichroism (PCD). The CD signal of the nanocrystals is given by the difference of optical absorption (Q_{CSNC}) between the left/right circularly polarized fields, that is, $CD_{CSNC} = Q^{L}_{CSNC} - Q^{R}_{CSNC}$ with $Q_{CSNC}^{L/R} \propto \int dV(E_0 + E_D^{L/R}) * \cdot (E_0 + E_D^{L/R})$, $E_D^{L/R}(r, r_D) = G(r, r_D) p_D^{L/R}(r_D)$, where E_0 is the incident field and $E_D^{L/R}$ is the induced field due to CYS, $E_0 + E_D^{L/R}$ is the local field on the nanocrystal, $G(r,r_D)$ (r, r_D are the coordinate centers of the CSNC and cysteine) reflects the distance dependence of the backaction of cysteine on the CSNC. The anisotropic factor can be obtained as $g=CD_{CSNC}/Abs_{CSNC}$. The theoretical and experimental results are shown in table 1.

Table 1: The comparison between theoretical and experimental results of anisotropic factor g for different geometric configurations (end-to-end versus side-by-side assembly configurations, and different aspect ratios).

	AR	Size(a*b*c) [nm]	g_{EE}/g_{SS} (TH)	g_{EE}/g_{SS} (EXP)
Au@Ag d=2.0nm	3.8	28.5*7.5*7.5	1.37	1.70
	3.5	29.5*8.5*8.5	3.39	3.14
	3.2	30.5*9.5*9.5	3.80	3.25
Ag d=2.0nm	1.58	15.0*9.5*9.5	3.31	3.47
Au d=3.5nm	3.71	26.0*7.0*7.0	0.69	0.64

Our studies show that the PCD response of Au, Ag, and Au@Ag CSNC assemblies is the combined contribution from both the electromagnetic field effect at the hotspots and the geometry-dependent electromagnetic backaction. Thus, different geometric configurations (ETE & SBS) lead to different electromagnetic fields at hotspots and backaction amplitudes, which brings about interesting geometry-dependent chiral characteristics for Au@Ag CSNC, Ag and Au NR assemblies.

3. Tuning the chiroptical properties by the morphology of nanorod with Au-CYS-Au core-shell structures

We perform studies of the chiral properties of the nanorod with Au- cysteine (CYS)-Au core-shell structures. The core-shell structured nanorod has different morphology depending on the concentration of CYS. We propose an effective medium approach consisting of a Au NR core, a chiral molecular shell and outer shell of Au or mixture of Au and solution. The effective dielectric permittivity $\varepsilon_{B@A}$, for core material A with inner geometric factor $L^{(1)}$ and shell material B with outer geometric factor $L^{(2)}$ is

$$\varepsilon_{A@B} = \varepsilon_B \frac{1-(1-L^{(2)})fG}{1+L^{(2)}fG}, \quad G = \frac{\varepsilon_B - \varepsilon_A}{L^{(1)}\varepsilon_A + (1-L^{(1)})\varepsilon_B}.$$

The absorption of nanoparticle can be calculated based on the formula

$$C_{abs} = k \cdot \mathrm{Im}\left[V_{A@B} \frac{\varepsilon_{A@B} - \varepsilon_B}{L^{(2)}\varepsilon_{A@B} + (1-L^{(2)})\varepsilon_B} \right].$$

The CD signal is the difference between the absorption of left and right circularly polarized light. In the calculation based on above formula, we first obtain $\varepsilon_{Au@CYS}$by using the values of ε_{Au} and ε_{CYS}. Then we use the formula again to calculate $\varepsilon_{(Au@CYS)@Au/sol}$. $\varepsilon_{Au/sol}$ is calculated based on the Bruggeman effective media theory.

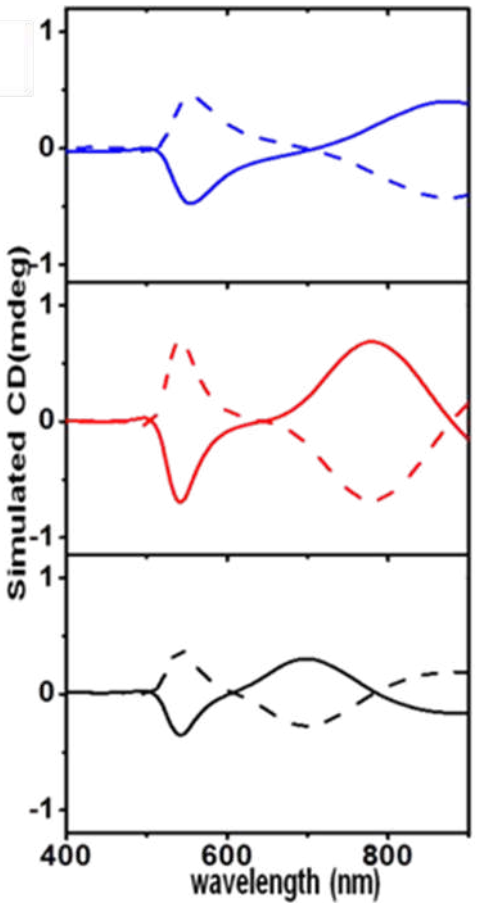


Figure 1: The circular dichroism for nanorod with Au-CYS-Au core-shell structures in the presence of different concentration of CYS: 0.4μM; 0.04μM; 4nM.

Our studies show that the induced circular dichroism from CYS and the related morphology lead to nonmonotonic dependence of circular dichroism on the concentration of CYS as shown in figure 1.

4. Conclusions

We have performed systematic studies of induced circular dichroism of nanostructure with different assembly configurations and/or core-shell structures. We have found that the interplay between the local field enhancement and backaction, and the morphology of the nanorod determine the chiral responses of the hybrid nanostructures.

Acknowledgements

I acknowledge the collaboration of Dang Yuan Lei, Kwok-Yin Wong, Zhi Yong Bao, Jiyan Dai, Qiang Zhang, Kwun Hei Ho, Siqi Li, Cheuk Ho Chan, Guangchao Zheng, Jorge Perez-Juste, Ruolan Du, Wei Liu, Lawrence Yoon Suk Lee, and the support from National Key Research and Development Program of China (2017YFA0303400), National Natural Science Foundation of China (11774036), NSFC-RGC (Grant No.11861161002).

References

[1] Z. Y. Bao, J. Dai, Q. Zhang, K. H. Ho, S. Li, C. H. Chan, W. Zhang* and D. Y. Lei*, Geometric modulation of induced plasmonic circular dichroism in nanoparticle assemblies based on backaction and field enhancement, *Nanoscale* 10: 19684−19691, 2018.

[2] G. Zheng, Z. Bao, J. Pérez‐Juste, R. Du, W. Liu, J. Dai, W. Zhang*, L. Y. Suk Lee*, K.-Y. Wong*, Tuning the morphology and chiroptical properties of discrete gold nanorods with amino acids, *Angew. Chem. Int. Ed.*, 57: 16452 –16457, 2018.

Strong coupling between plasmonic meta-atoms and plasmonic surface bloch waves

Chun-Yuan Wang[1,2] , Yungang Sang[3], Xinyue Yang[3], Soniya S. Raja[1], Haozhi Li[3],Yufeng Ding[3], Shuoyan Sun[3],Chang-Wei Cheng[1], Hyeyoung Ahn[4], Chih-Kang Shih[2,†], Shangjr Gwo[1,5†], Jinwei Shi[3,†]

[1]Department of Physics, National Tsing-Hua University, Hsinchu 30013, Taiwan
[2]Department of Physics, The University of Texas at Austin, Austin, Texas 78712, USA
[3]Department of Physics and Applied Optics Beijing Area Major Laboratory, Beijing Normal University, Beijing 100875, P.R.C.
[4] Department of Photonics, National Chiao-Tung University, Hsinchu 30010, Taiwan
[5] Research Center for Applied Sciences, Academia Sinica, Nankang, Taipei 11529, Taiwan
[†]corresponding author, E-mail: shijinwei@bnu.edu.cn

Abstract

A strong coupling system is realized by using silver nanogrooves as meta-atoms and surface Bloch waves launched by periodic nanogroove arrays. This system is found to be analogous to electronic band structure in solids but with more flexibility. Due to directly sharing the free electrons in the metallic medium, the plasmonic gap modes coherently couple with surface Bloch waves when they overlap with each other in real- and momentum-space. A giant Rabi splitting on the order of 400-500 meV can be experimentally achieved.

1. Introduction

Plasmonic metamaterials have unique properties to manipulate and amplify optical process at subwavelength scales. Metasurface is a class of metamaterials with one layer of artificially engineered structure. The building block, the meta-atom, is typically made of metallic nanostructure. By designing their spatial arrangement one can obtain the desired collective modes, in a manner analogous to how atomic levels are coupled in the solid to form the electronic band structure. In real solids, valence states and core levels are separated in energy space, leading to little coupling between them. In periodic plasmonic metasurfaces, we show that the energy levels of the localized (plasmonic meta-atoms) and delocalized (plasmonic surface Bloch wave) surface plasmon polaritons (SPPs) based on nanogroove array on silver single crystal can be tuned independently. This tunability then lead to spectacularly strong coupling between them with a Rabi splitting as high as 420 meV. Localized plasmonic resonance (LSPR) coupled with surface lattice resonance (SLR) based on discreet nano structures, such as nanodisks or nanowires, had been reported before, but only moderate Rabi Splitting was observed. The coupling between them is through electric field and photon, and the corresponding free electrons are still localized in nanodisk or nanowires. Hence, in this work, we present a coupling system of nanogroove array on silver substrate (free electrons can be shared each other and propagate without scattering field as coupling media) to be analogous to electronic band structure in solid state physics, as well as obtain giant Rabi Splitting via strong coupling.

2. Results

Figure 1a shows the schematic diagram between groove-LSPR and lattice-SPP. From a microscopic perspective, if the LSPR and lattice-SPP are separated in energy-momentum space, or the LSPR is broadband (low plasmon density), this groove array can be seen as well-known SPP grating coupler, and we can get general SLR on the grating and SPPs away from the grating. However, if the LSPR is narrowband (high plasmon density), and overlapped with lattice-SPP in energy and momentum space, it could achieve strong coupling and plasmon energy state can be separated with a gap (Rabi splitting).

To systematically study the strong coupling in such groove array, we fabricated 17 gratings on single crystalline Ag plate using FIB milling, as shown in Fig. 1b. The groove depth is fixed at 140 nm, and the pitch varies from 154 nm to 730 nm. Figure 2 shows some typical angle-resolved reflectance spectra and corresponding fitting results. From the fitting results we can see clear strong coupling between groove-LSPR (linewidth ~160 meV) and the lattice-SPP (linewidth ~150 meV) , and the maximum Rabi splitting is as big as 420 meV, which to our knowledge, is the biggest value in pure plasmonic system.

3. Discussion

Due to the strong coupling, plasmons are hybridized to the upper and lower branch modes. The electric field within the gap is completely parallel to the surface, and there is

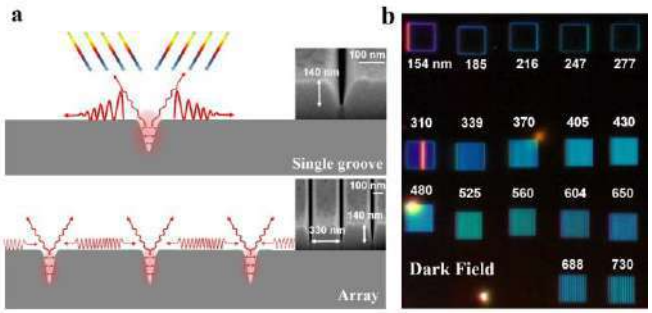


Fig. 1. Scheme of the strong coupling in metallic groove array and sample fabrication. (a) Top: a single groove generates relatively narrow band localized surface plasmon resonance (LSPR) when the incident light is in resonance with the groove mode. The LSPR then acts as an efficient source to launch SPPs along both sides. Bottom: a groove array (grating) generates lattice-SPPs collectively. When the lattice-SPP is in resonance with LSPR, strong coupling between these modes will happen. Insets: SEM images of single groove and an array. (b) Dark field images of 17 gratings fabricated on single crystalline silver plate, with fixed groove depth and increasing pitches. The centers of the images change from dark to a certain color. The size of each grating is about 7 μm.

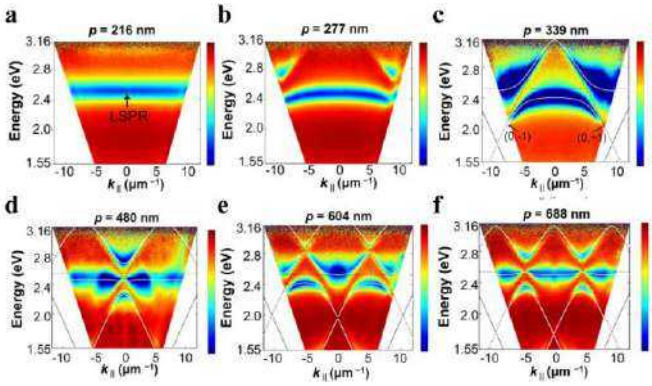


Fig. 2. Typical angle-resolved reflectance spectra obtained in the experiment. (a-f) The pitch increases from 216 nm to 688 nm, showing the evolution of the strong coupling. The black dashed curves denote the original groove-LSPR and two lattice-SPPs. The white curves are the fitting results (eigen modes) using coupled mode theory.

basically no electric field within the groove at zero detuning, resulting a nearly unit reflection. In the strong coupling region, the on-resonance dipole moment replaces the ordinary off-resonance dipole moment to generate the lattice-SPP. In hybridized states, the SPPs generated by all the groove FP modes form the lattice-SPPs and propagating along the surface, and interact back to the groove-LSPRs. The whole process is done through the high confinement of parallel parallel electric field in nanogroove and sharinge the same free electrons in continue metal. In comparison, for the case of discrete nanoparticle array, the coherent oscillation in lattice is done by scattering light from local oscillator with point spread function coupled to neighbor nanoparticle in phase with incident light.

The lattice bandgap is enlarged to quasi bandgap by strong coupling with LSPR within a small range of wave vector. The experiment shows that the lattice bandgap leads to weakening the intensity of middle branch (Fig. 2), and the corresponding weighting fractions from the fitting results show the localized plasmon energy transfer to upper and lower branches resulting to quasi bandgap. Furthermore, the maximum Rabi splitting happens while the upper and lower branches having the same weighting fraction of compositions from any of the coupling modes (LSPR, lattice-SPP (0, +1) and lattice-SPP (0, –1)). Again, it is also located at point of three modes crossing each other in energy-momentum space. By engineering the pitch size, the lattice bandgap can be tuned and matched to the LSPR mode forming the giant Rabi splitting and quasi bandgap, which always occurs at Γ point (p = 480 nm) and Brillion zone boundary (p = 688 nm). It is hard to realize engineering the band structure in nature material but can be done in metasurface.

4. Conclusions

To sum up, we have fabricated 17 GSLR samples of plasmonic meta-atom system and studied the strong coupling of the metallic groove arrays to be analogized forming the electron band structure in solid. Giant Rabi splitting over 420 meV was observed using both angle tuning and pitch tuning. The mechanism of such giant Rabi splitting was based on strong parallel electric field within the grooves and especially sharing the same free electrons between lattice-SPP and groove-LSPR. Furthermore, three modes crossing and coupling each other in energy-momentum space by tuning the pitch further enhance the Rabi splitting and forming quasi-bandgap. It realizes obtaining and engineering the artificial band-structure through meta-atom system and plasmonic Bloch wave. This meta-atom system has potential to be a device with adding electric gate to modulate the artificial band-structure and apply in many fields, such as solar energy device, nano laser, all optical switch and modulator, sensor, nonlinear optics devices and enhanced chemical reaction.

Acknowledgements

This work is supported by the NSFC (11774035, and 11674032) and is partially sponsored by Beijing Cooperative Construction Project. The authors acknowledge financial support from the Ministry of Science and Technology (MOST) in Taiwan (MOST 105-2112-M-007-011-MY3, MOST 104-2112-M-009-007-MY3, MOST-105-2112-M-007-032-MY3, MOST-105-2119-M-007-027, and MOST-105-2633-M-007-003).

Chiral Weak and Strong Photon-Emitter Coupling in Coupled Photonic Structures

Fan Zhang[1], Juanjuan Ren[2], Lingxiao Shan[1,3], Xueke Duan[1]
Yan Li[1,4], Tiancai Zhang[3,4], Qihuang Gong[1,2,4], and Ying Gu[1,2,4]

[1]State Key Laboratory for Mesoscopic Physics, Collaborative Innovation Center of Quantum Matter, Department of Physics, Peking University, Beijing 100871, China
[2]Beijing Academy of Quantum Information Sciences, Beijing 100193, China
[3]State Key Laboratory of Quantum Optics and Quantum Optics Devices, Institute of Opto-Electronics, Shanxi University, Taiyuan 030006, China
[4]Collaborative Innovation Center of Extreme Optics, Shanxi University, Taiyuan, Shanxi 030006, China
*corresponding author, E-mail: ygu@pku.edu.cn

Abstract

To bridge the gap between the cavity quantum electrodynamics and chiral photon-emitter coupling, we propose the coupled photonic crystal and metallic nanoparticle structure, where through strong local field with high helicity, both weak and strong couplings between the circularly polarized emitter and photons are obtained with almost the unidirectional photons propagating, which can be utilized in directional quantum light sources.

1. Introduction

Cavity quantum electrodynamics (CQED) studies the light-matter interaction at a single quanta level [1, 2]. In traditional CQED, by compressing the optical mode volume into the region of several hundreds of micrometers, weak and strong couplings have been achieved. Recently, through reducing the optical mode volume into micro/nano scale, the CQED has achieved great success in photonic crystals, plasmonic nanocavities, whispering guided resonantors, and various hybrid photonic systems, which paves a way to nanolaser, on-chip quantum devices, and scalable quantum networks.

Besides the ultrasmall mode volume, transversely confined light in the photonic structures induces the local spin of light, whose handedness has a one-to-one relation with respect to the propagation direction of the optical field enforced by time-reversal symmetry. If one puts a circularly polarized emitter in these structures, the propagation direction of the emitted photons will be locked by the handedness of local spin, so-called the chiral photon-emitter coupling [3]. Hence, the propagation isolation of photons is able to avoid the signal disturbance and improve transmission efficiency, which can be utilized in some nonreciprocal quantum information components, e.g., chiral entanglement, quantum gates, switchings, isolators, and circulators.

However, in the coupling between the circularly polarized emitter and photons, to simultaneously realize the strong interaction of photon-emitter and propagation direction lock of photons at the nanoscale, which will bring novel applications in nonreciprocal quantum devices, has not been reported yet.

2. results

Here, by combining the advantages of the CQED and chiral coupling, we propose the coupled structure consisting of W1 PC and Ag nanoparticle (AgNP), where high quality nanocavities are formed to guarantee an achievement of both weak and strong couplings [4]. Through strong local field with high helicity in nanocavities, coupling strength of photon-emitter can be greatly enhanced, accompanied by almost unidirectional propagation of emitted photons. In weak coupling regime, total decay rate reaches over $4000\gamma_0$ (γ_0 is the spontaneous emission rate in vacuum), among which the rate of photon emission into the PC waveguide is $124\gamma_0$, which is one order larger than that with only W1 PC. While for the strong coupling, by using a low loss band-edge mode, the linewidth of fluorescence spectra of Rabi splitting is about one-tenth of that with only the AgNP. For both cases, $\sim 95\%$ photons propagate unidirectionally. Moreover, though the mode design, the coupled structure is capable of routing different wavelength photons into opposite propagation directions.

3. Conclusions

In summary, we have established a photonic interface of chiral CQED by proposing the coupled photonic crystal and plasmon nanoparticle structure. We state that the key element of chiral CQED is the joint action of strong local field and its high helicity, which provides a strengthened light-emitter coupling with good directionality of emitted photons. The results bridge the fields of the CQED and the chiral coupling, which greatly enriches the contents of light-emitter interaction at the nanoscale. By combining the advantages of these two fields, we provide a possible platform in coupled photonic structures for nonreciprocal quantum light sources, quantum circuits, and scalable quantum network.

Acknowledgement

This work is supported by the National Key R&D Program of China under Grant No. 2018YFB1107200, and by the National Natural Science Foundation of China under Grants No. 11525414 and No. 11734001.

References

[1] S. Haroche, D. Kleppner, Cavity quantum electrodynamics. Phys. Today 42, 24-30 (1989).

[2] R. Miller, T. E. Northup, K. M. Birnbaum, A. Boca, A. D. Boozer, H. J. Kimble, Trapped atoms in cavity QED: coupling quantized light and matter. J. Phys. B 38, S551-S565 (2005).

[3] P. Lodahl, S. Mahmoodian, S. Stobbe, A. Rauschenbeutel, P. Schneeweiss, J. Volz, H. Pichler, P. Zoller, Chiral quantum optics. Nature 541, 473480 (2017).

[4] F. Zhang and Y. Gu et al. ArXiv:1808.07210v1.

Optical and spectroscopic properties of large scale and flexible plasmonic metasurfaces by colloidal self-asssembly

Tobias A.F. König[1,2,*]

[1]Leibniz-Institut für Polymerforschung Dresden e.V., Institute of Physical Chemistry,
Hohe Str. 6, 01069 Dresden, Germany.
[2]Technische Universität Dresden, Physical Chemistry,
Technische Universität Dresden, Bergstr. 66b, 01062 Dresden, Germany
*corresponding author, E-mail: koenig@ipfdd.de

Abstract

For the next generation of optical computing, a novel and cost efficient approach is needed. This future development requires both tailored control over nanometer-sized building blocks on large area and a fundamental understanding of the strong as well as coherent coupling mechanisms [1, 2]. Currently, practical demonstrations are scarce, and are limited in terms of how many devices may be fabricated in parallel. To realize fabrication on a larger scale, a synergy between optical metasurfaces and colloidal self-assembly will be leveraged. This requires, on the one hand, applying concepts from metamaterials and, on the other hand, using pre-existing quantum emitter and plasmonic nanoparticle building blocks, which form an organized structure on large area by reducing their free energy [2-4]. We discuss our recent achievements in finite-difference time-domain modelling, large area self-assembly of tailored building blocks as well as time and space resolved optical characterization to fabricate cost-efficient, programmable and up-scalable photonic devices.

1. Plasmonic metasurfaces by colloidal self-assembly

Self-assembly methods show a clear advantage in comparison to size-, time-limited and cost-intensive electron (ion) beam or pick-and-place methods, such as optical tweezers and scanning probe microscopy. On the other hand, self-assembly mechanisms are programmable, scalable and robust; this makes this method very important for applications in electronics, sensing and optics.

Metsurfaces are artificial structures, which obtains its properties from a two dimensional periodic structure and not properties of the individual components [4]. We define such individual component as plasmonic atom (Figure 1a). Thus isolated plasmonic atom of various size can be fabricated using a surface-supported overgrow process. At this technique the microscope glass slide with gold nanoparticle was carefully withdrawn from the growing solution [5]. Thus plasmonic atom can be a metallic nanoparticle of various diameter, shape and material [6-8]. Mie-theory calculations of a gold nanoparticle in water show an increase as well as red-shift in the effective absorption cross section.

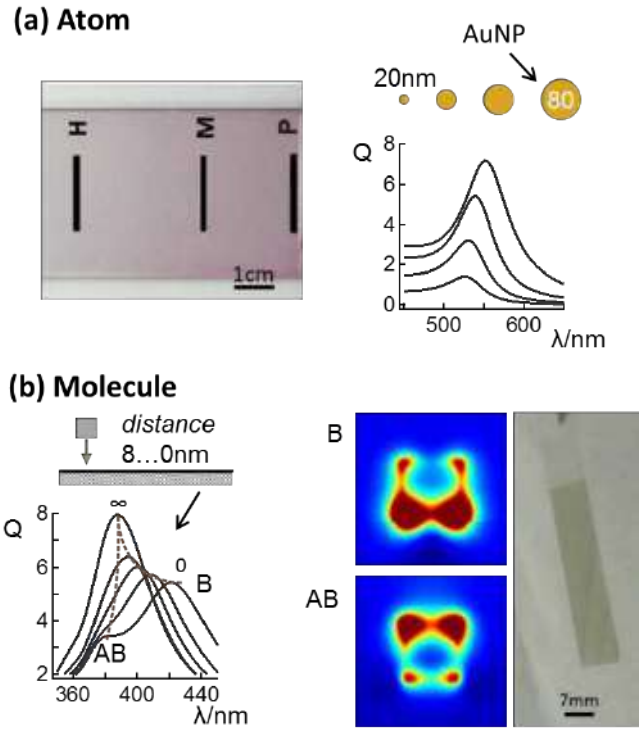


Figure 1 Colloidal atoms and polymers by directed self-assembly: *Well-defined plasmonic colloids or (a) atoms can be rationally assembled into (b) molecules. (a) A substrate-supported grows of gold nanoparticle[5] and simulated extinction cross-section (Q) of various diameters. (b) Substrate induced hybridization into bounding and anti-bounding plasmon modes, which can be fabricated by Langmuir Blodgett technique. Copyright 2014, American Chemical Society.*

Figure 1b shows a plasmonic molecule, which can be excited by a simple break of symmetry using a dielectric substrate. Such plasmonic hybridization into bonding and anti-bonding mode is a result of the coherent coupling between the dipolar and quadrupolar resonance [9]. Especially the anti-bonding mode shows superiors sensing properties [10]. Add one particle step wise to another particle results in red-shift of the plasmonic resonance until

the radiative damping gets dominant [2]. Such plasmonic oligomers (particle number greater than one and less than 10) and plasmonic polymers (particle number greater than 10) can be fabricated using template-assisted self-assembly [3] (Figure 2a). Among other applications such particle chain assemblies can be used to propagate light below the diffraction limit [11, 12]. Moreover, such colloids can be assembled into a periodic structure where the plasmon resonance can coherently couple to the diffraction mode of the grating. Such interaction results in a high quality surface lattice mode (see Figure 2b). This plasmonic crystals (hexagonal packed) can be fabricated using a floating method at a water air interface to achieve centimeter squared coverage [13].

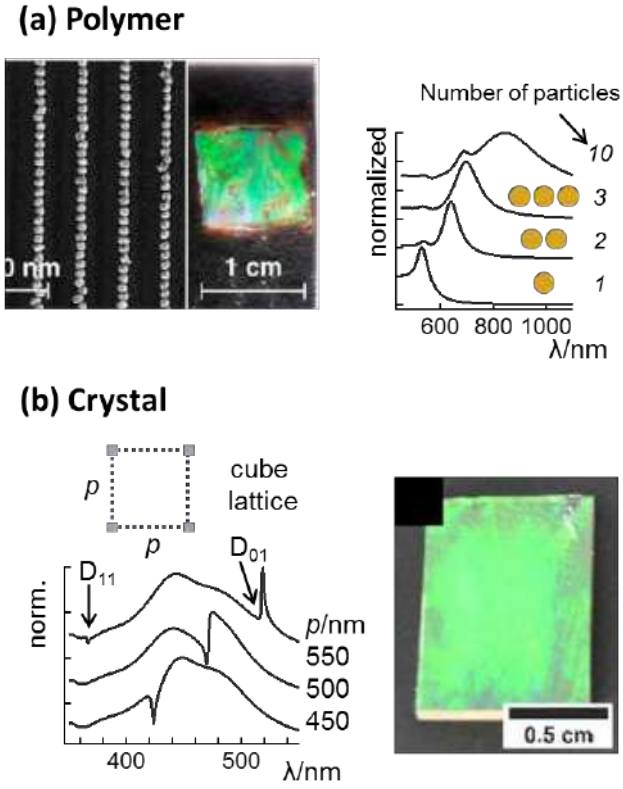


Figure 2 ***Colloidal metasurfaces by directed self-assembly:*** *Well-defined plasmonic colloids or atoms can be rationally assembled into molecules, (a) polymers and (b) crystals. (a) Template-assisted self-assembly of gold nanoparticle chains [3] and optical properties of various particle length. (b) Lattice induced hybridization by first and second diffraction mode (surface lattice resonance) and self-assembly by floating method. (a,b) Adapted with permission.*

2. Spectroscopic properties of plasmonic metasurfaces

Similar how a chemist designs its molecules, polymers and crystals, we design our colloidal metasurfaces for photonic applications. The key is that each atom can be replaced by single particle source such as fluorescent particle or quantum dot. This approach opens up a large horizon in coherent coupling of the singe photon sources with the plasmonic system to achieve unique optical properties. Recently, we infiltrated fluorescent emitters (rhodamine B) into the silica shelled gold nanoparticle. In close contact to metallic substrate the colloidal particle results in a colloid-to-film coupled nanoantenna (nanocavity) with enhanced radiative properties [6]. Thus nanometer sized, high-quality and up-scalable gain nanoantenna at a reasonable price is the first step into colloidal nanophotonic devices.

Acknowledgements

This project was financially supported by the Volkswagen Foundation through a Freigeist Fellowship to TAFK. The author acknowledge the Deutsche Forschungsgemeinschaft (DFG) within the Cluster of Excellence Center for Advancing Electronics Dresden' (cfaed) and DFG Sachbeihilfe (Projektnummer 404818834) for financial support.

References

1. F. G. Goßler, A. M. Steiner, O. Stroyuk, A. Raevskaya, and T. A. F. König, "Active Plasmonic Colloid-to-Film Coupled Cavities for Tailored Light-Matter Interactions," J. Phys. Chem. C **accepted** (2019).
2. M. Mayer, M. J. Schnepf, T. A. F. König, and A. Fery, "Colloidal Self-Assembly Concepts for Plasmonic Metasurfaces," Advanced Optical Materials **0**, 1800564 (2018).
3. C. Hanske, M. Tebbe, C. Kuttner, V. Bieber, V. V. Tsukruk, M. Chanana, T. A. F. König, and A. Fery, "Strongly coupled plasmonic modes on macroscopic areas via template-assisted colloidal self-assembly," Nano Lett. **14**, 6863-6871 (2014).
4. M. Mayer, M. Tebbe, C. Kuttner, M. J. Schnepf, T. A. F. König, and A. Fery, "Template-assisted colloidal self-assembly of macroscopic magnetic metasurfaces," Faraday discussions (2016).
5. M. B. Müller, C. Kuttner, T. A. F. König, V. V. Tsukruk, S. Förster, M. Karg, and A. Fery, "Plasmonic Library Based on Substrate-Supported Gradiential Plasmonic Arrays," ACS Nano **8**, 9410-9421 (2014).
6. M. Schnepf, J., Y. Brasse, F. R. Goßler, A. M. Steiner, J. Obermeier, M. Lippitz, A. Fery, and T. A. F. König, "Single Particle Spectroscopy of Radiative Processes in Colloid-to-Film-Coupled Nanoantennas," in *Z. Phys. Chem.*(2018), p. 1593.
7. M. Tebbe, C. Kuttner, M. Mayer, M. Maennel, N. Pazos-Perez, T. A. F. König, and A. Fery, "Silver-Overgrowth-Induced Changes in Intrinsic Optical Properties of Gold Nanorods: From Noninvasive Monitoring of Growth Kinetics to Tailoring Internal Mirror Charges," J. Phys. Chem. C **119**, 9513-9523 (2015).
8. M. Mayer, A. M. Steiner, F. Röder, P. Formanek, T. A. F. König, and A. Fery, "Aqueous Gold Overgrowth of Silver Nanoparticles: Merging the Plasmonic Properties of Silver with the Functionality of Gold," Angewandte Chemie International Edition **56**, 15866-15870 (2017).
9. T. A. F. König, R. Kodiyath, Z. A. Combs, M. A. Mahmoud, M. A. El-Sayed, and V. V. Tsukruk, "Silver Nanocube Aggregates in Cylindrical Pores for Higher Refractive Index Plasmonic Sensing," Part. Part. Syst. Charact. **31**, 274-283 (2014).
10. T. A. F. König, P. A. Ledin, J. Kerszulis, M. A. Mahmoud, M. A. El-Sayed, J. R. Reynolds, and V. V. Tsukruk, "Electrically Tunable Plasmonic Behavior of Nanocube–Polymer

Nanomaterials Induced by a Redox-Active Electrochromic Polymer," ACS Nano **8**, 6182-6192 (2014).
11. F. N. Gür, C. P. T. McPolin, S. Raza, M. Mayer, D. J. Roth, A. M. Steiner, L. Löffler, A. Fery, M. L. Brongersma, A. V. Zayats, T. A. F. König, and T. L. Schmidt, "Efficient energy propagation through self-assembled gold nanoparticle chain waveguides," arXiv **1712.09141** (2017).
12. F. N. Gür, C. P. T. McPolin, S. Raza, M. Mayer, D. J. Roth, A. M. Steiner, M. Löffler, A. Fery, M. L. Brongersma, A. V. Zayats, T. A. F. König, and T. L. Schmidt, "DNA-Assembled Plasmonic Waveguides for Nanoscale Light Propagation to a Fluorescent Nanodiamond," Nano Lett. **18**, 7323-7329 (2018).
13. K. Volk, J. P. S. Fitzgerald, P. Ruckdeschel, M. Retsch, T. A. F. König, and M. Karg, "Reversible Tuning of Visible Wavelength Surface Lattice Resonances in Self-Assembled Hybrid Monolayers," Advanced Optical Materials **5**, 1600971 (2017).

Extraordinary Transmission and Polarization Control of Cavity Modes in Thue-Morse Gold Nanocavities

Antonio De Luca[1,6], Rakesh Dhama[2],Vincenzo Caligiuri[3], Lucia Petti[4], Alireza R. Rashed[5], Massimo Rippa[4], Raffaella Lento[6], Roberto Termine[6], Humeyra Caglayan[5]

[1]Department of Physics, University of Calabria, 87036 Rende, Italy
[2]School of Electronic Engineering, Bangor University, Bangor, LL57 1UT, UK
[3]Istituto Italiano di Tecnologia
[4]CNR, Institute of Applied Sciences and Intelligent Systems, 80072 Pozzuoli, Italy
[5]Laboratory of Photonics, Tampere University of Technology, 33720 Tampere, Finland
[6]CNR Nanotec, 87036 Rende, Italy
*corresponding author, E-mail: antonio.deluca@unical.it

Abstract

Plasmonic quasi-periodic structures are well-known to exhibit several surprising phenomena with respect to their periodic counterparts, due to their long-range order and higher rotational symmetry [1]. Thanks to their specific geometrical arrangement, plasmonic quasi-crystals offer unique possibilities in tailoring the coupling and propagation of surface plasmons through their lattice, unabling a plethora of fascinating phenomena. In this work we investigate the extraordinary transmission phenomenon occurring in specifically patterned Thue-Morse gold nanocavities and the polarization dependence of their cavity modes.

1. Introduction

The control and manipulation of light-matter interaction through metallic nanoapertures enables several applications in plasmonic biosensing, tunable and selective wavelength filters, increased signal in surface enhanced Raman spectroscopy for single molecule detection, and near-field optics. Furthermore, tailoring plasmonic resonances in particularly designed nanoplasmonic devices, surface plasmons (SPs) have also been exploited as information carriers, thanks to their ability to confine, concentrate, and channel light through subwavelength structures. However, it is well-known that far-field measurements can not clearly distinguish the role of SPs, due to the bound nature of their electromagnetic field, whose salient features arise in the near-field propagating regime. Scanning near-field optical microscopy (SNOM) enables the opportunity to visualize the surface plasmon-mediated mechanisms as well as the enhanced transmission phenomenon through particular patterned structures, beyond the diffraction limit. In this framework, quasi-crystals (QCs) exhibit long-range order and higher rotational symmetry, but no translational one, demonstrating to special features with respect to their periodic counterparts. Here we report on near and far-field spectral properties of quasi-periodic plasmonic gold nanocavities (NCs), obtained by patterning a Thue-Morse (T-M) array of nanoholes in a polymeric film and evaporating a thin gold layer on the fabricated QC. This type of configuration allows unique coupling possibilities between propagating and localized surface plasmons. We demonstrate Extraordinary Transmission (EOT) through subwavelength T-M patterned nanocavities, as a consequence of the strong coupling between surface plasmon polaritons (SPPs) and cavity plasmon resonances (CPRs). SNOM investigations confirm that NCs are the only source of transmitted light via SPPs strong coupling with CPRs in such subwavelength quasi-structures. Furthermore, this plasmonic coupling enables polarization and size-dependent cavity modes in T-M structures with increased nanocavities diameter, causing the appearance of surface plasmon pattern waves which reduces the overall EOT effect.

2. Results and Discussion

T-M patterned structures with different diameters (Ø), as well as a dodecagonal structure, have been fabricated by means of a nanolithography procedure reported in [2] (Fig. 1a). Scanning electron microscopy (SEM) images confirm the fabrication of T-M and dodecagonal quasi-periodic patterns (see Figure 1b,c). Figure 1d reports the schematic and beam path of the SNOM system used to perform near- and far-field optical experiments in transmission mode. The optical investigation of the quasi-periodic nanocavities has been performed by means of a SNOM (Alpha 300S by WITec) used in confocal transmission mode. The acquired transmitted signal has been compared and normalized to that of an unpatterned gold film of the same thickness ($\lambda_{exc} = 532nm$). We observe a 3.15-fold and a 2.9-fold enhancement in PMT counts in the case of samples with diamters of 250 and 400nm (Sample-A and -B). On the contrary, transmitted signals through samples with larger diameters (500 and 750nm, sample-C and -D) are comparable

with the reference. Same behavior has been obtained in far-field with an un-coherent white light. To better understand

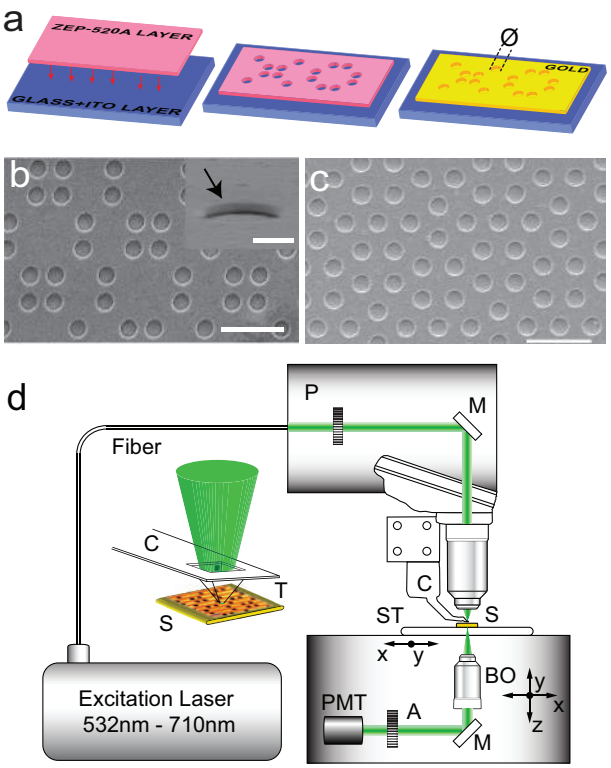


Figure 1: (a) T-M patterned plasmonic nanocavities. (b)-(c) SEM images of the T-M nanocavities. (d) Schematic of SNOM instrument for near- and far-field optical experiments. Inset: Cantiliver and SNOM tip.

the physics behind this enhanced transmission mechanism and to investigate localization of electromagnetic fields inside the obtained NCs, SNOM technique has been used in order to obtain super-resolution imaging, beating the optical diffraction limit. A linearly polarized laser beam (532 nm) has been tunnelled through an Al-coated aperture SNOM tip, with a diameter of about 60 nm, in order to collect near-field information. Figure 2 reports the topographic (a, b) and transmitted optical near-field images (c, d) of sample-B and -C (diameters 400 and 500nm), respectively, showing the formation of different cavity modes. The incident polarization induces the appearance of donut-type modes in sample-B, whereas three intense spots are present in sample-C. We performed numerical simulations, based on the finite difference time domain (FDTD) method, on all the different T-M structures, obtaining very good results.[3] Some ellipsometric measurements have been performed in order to highlight the presence of particular modes related to the quasi-crystal structure.

3. Conclusions

In conclusion, this work explores the fascinating and unexpected near- and far-field optical phenomena observed in quasi-periodic structures. Patterned plasmonic nanocavities make such quasi-periodic structures very particular and enable the strong coupling between surface plasmon polaritons propagating on the gold surface with the cavity resonances of each nanocavity. We demonstrated enhanced transmission mechanism via polarization-independent near-field responses in the subwavelength Thue-Morse arrays of plasmonic nanocavities and report the ellipsometric response of these structures.

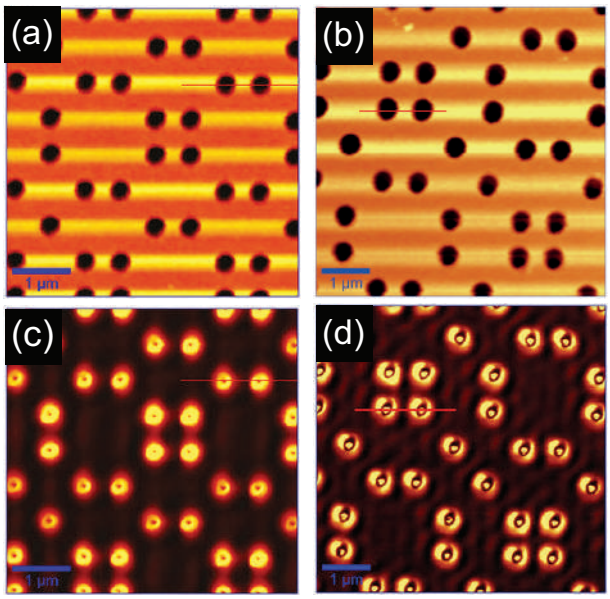


Figure 2: (a) T-M patterned plasmonic nanocavities. (b)-(c) SEM images of the T-M nanocavities. (d) Schematic of SNOM instrument for near- and far-field optical experiments. Inset: Cantiliver and SNOM tip.

References

[1] H. Gao, J. Henzie, and T. W. Odom, "Direct evidence for surface plasmon-mediated enhanced light transmission through metallic nanohole arrays," *Nano Letters*, vol. 6, no. 9, pp. 2104–2108, 2006.

[2] M. Rippa, R. Castagna, M. Pannico, P. Musto, E. Bobeico, J. Zhou, and L. Petti, "Plasmonic nanocavities-based aperiodic crystal for protein-protein recognition sers sensors," *Optical Data Processing and Storage*, vol. 3, p. 54, 2017.

[3] R. Dhama, V. Caligiuri, L. Petti, A. R. Rashed, M. Rippa, R. Lento, R. Termine, H. Caglayan, and A. De Luca, "Extraordinary effects in quasi-periodic gold nanocavities: Enhanced transmission and polarization control of cavity modes," *ACS Nano*, vol. 12, no. 1, pp. 504–512, 2018, pMID: 29178780. [Online]. Available: https://doi.org/10.1021/acsnano.7b07076

Optically Thin Plasmonic Nanohole Metasurfaces: Fano Interferences and Strong Coupling

Evan S H Kang and Magnus P Jonsson

Laboratory of Organic Electronics, Department of Science and Technology, Linköping University, Sweden
E-mail: evan.kang@liu.se

Abstract

In this presentation, I will present our recent research on optically thin plasmonic nanohole metasurfaces.

Plasmonic nanohole metasurfaces have been intensely investigated due to their usefulness in multitude of applications, including biosensors, optical trapping, light-to-heat conversion, and strongly coupled systems. Introducing nanohole arrays in metal films has been regarded as responsible for both extraordinary optical transmission (EOT) for opaque films (≈200 nm) and suppressed transmission for ultrathin films (≈10 nm). Accordingly, plasmon resonances were assigned to transmission peaks for thick films and to transmission dips for ultrathin films. For the intermediate film thicknesses, however, the lack of consensus on the resonance assignment often results in misinterpretation of results and impedes our understanding of underlying physics.

I will first demonstrate the evolution from suppressed to enhanced optical transmission through nanohole arrays with increasing metal film thickness using Fano description. Here, I will also discuss how to define the true plasmon resonances, which can be far from both peaks and dips observed in transmission spectra [1]. Based on our results, I then explore strong plasmon-exciton coupling phenomena in optically thin hybrid nanohole metasurfaces [2]. Distinct features of optically thin hybrid systems including directional absorption will be discussed.

Acknowledgements

We acknowledge financial support from the Wenner-Gren Foundations, the Swedish Research Council, the Swedish Foundation for Strategic Research, the Royal Swedish Academy of Sciences, the ÅForsk Foundation, and the Swedish Government Strategic Research Area in Materials Science on Functional Materials at Linköping University (Faculty Grant SFO-Mat-LiU no. 2009 00971).

References

[1] E. S. H. Kang, H. Ekinge, and M. P. Jonsson, Plasmonic Fanoholes: on the gradual transition from suppressed to enhanced optical transmission through nanohole arrays in metal films of increasing film thickness. *Opt. Mater. Express* 9**:**1404–1415, 2019.

[2] E. S. H. Kang, S. Chen, S. Sardar, D. Tordera, N. Armakavicius, V. Darakchieva, T. Shegai, and M. P. Jonsson, Strong Plasmon-Exciton Coupling with Directional Absorption Features in Optically Thin Hybrid Nanohole Metasurfaces. *ACS Photonics* 5**:**4046–4055, 2018.

Plasmon Enhancement of Luminescence Upconversion

Wounjhang Park*

Department of Electrical, Computer & Energy Engineering, University of Colorado, Boulder, CO, USA
University of Colorado Cancer Center, Aurora, CO, USA
*corresponding author, E-mail: won.park@colorado.edu

Abstract

This paper presents a comprehensive theoretical framework for plasmon enhancement of luminescence upconversion and also a systematic experimental study demonstrating the enhancement mechanisms. Finally, metal-insulator-metal design was used to achieve a record high 1200x enhancement in upconversion.

1. Introduction

Upconversion luminescence materials combine two or more low energy photons to generate single high energy photons. This nonlinear upconversion is most efficiently achieved by energy transfer upconversion or excited state absorption via long-lived intermediate energy levels of the upconversion luminescence material. Unlike the nonlinear susceptibility based upconversion mechanisms, such as high harmonic generation or optical parametric oscillation, upconversion luminescence can occur with low power excitation and with an incoherent excitation source, and thus has applications in photovoltaics, displays, bioimaging and therapeutics.

Upconversion nanoparticles (UCNPs) are particularly useful for biomedical applications as they have excellent photostability, narrow emissions bands with high color purity, and low cytotoxicity. Additionally, the near-infrared excitation falls within the biological transparency window allowing for deep penetration into biological tissue. However, a wide spread use requires a much improved upconversion efficiency, for which plasmonic nanostructures are ideally suited. This paper presents the theoretical foundation of plasmon enhancement of upconversion, experimental results demonstrating the enhancement mechanism and a metal-insulator-metal structure exhibiting over 1000x enhancement.

2. Results and Discussion

2.1. Theory of plasmon enhanced upconversion

Luminescence upconversion involves three distinct physical processes: absorption, energy transfer and emission. For absorption, the absorption cross section is given by[1]

$$\sigma = c\mu_o \omega \,\mathrm{Im}\{\alpha\}\frac{|\mathbf{E}|^2}{|\mathbf{E}_0|^2}$$

where c is speed of light, μ_o is vacuum permeability, ω is angular frequency, α is atomic polarizability and $\mathbf{E}$ and $\mathbf{E}_0$ are local and incident field, respectively. Emission rate depends on the photon density of states, which can be estimated by the Green dyadic,[1]

$$\rho = \frac{6\omega}{\pi c^2}\left[\hat{\mathbf{n}}_d \cdot \mathrm{Im}\{\overleftrightarrow{\mathbf{G}}(\mathbf{r_0}, \mathbf{r_0}; \omega)\} \cdot \hat{\mathbf{n}}_d\right]$$

where $\overleftrightarrow{\mathbf{G}}$ is the Green dyadic and $\hat{\mathbf{n}}_d$ is the unit vector along the dipole orientation. Alternatively, radiation rate can also be calculated by evaluating the total radiated power from a classical dipole, which is known to accurately predict quantum mechanical radiation rate with a difference of a constant factor. Finally, energy transfer rate is also determined by the Green dyadic,[1]

$$w_{ET} = \frac{2\pi}{\hbar^2}\frac{\omega^2}{\epsilon_o c^2}\left|\mathbf{d}_A^* \cdot \overleftrightarrow{\mathbf{G}}(\mathbf{r_A}, \mathbf{r_D}; \omega) \cdot \mathbf{d}_D\right|^2$$

These transition rates can then be linked together in a set of rate equations containing all states involved in upconversion.[2] Solutions of the rate equations provide the full description of the upconversion processes and how they are affected by plasmonic nanostructures.

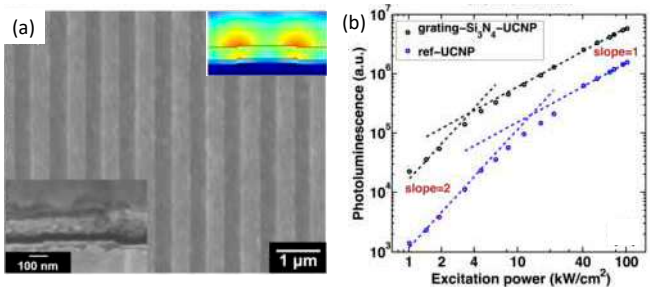


Figure 1. (a) Scanning electron microscope (SEM) images of silver nanograting structure. Inset: (bottom-left) cross-sectional SEM imaging of silver nanograting, Si_3N_4 spacer layer and UNCP layer. (top-right) Simulated field profile at the plasmon resonance wavelength of 980 nm. (b) Upconversion photoluminescence intensity as a function of excitation power density for the reference and nanograting samples.

2.2. Experimental study

For systematic experimental study of plasmon enhanced upconversion, we use a simple silver nanograting structure (Figure 1a). Nanograting is fabricated by the laser interference lithography (LIL) and 100 nm thick UCNP layer is deposited by a layer-by-layer technique. A 30 nm thick Si_3N_4 layer is deposited between silver and UCNPs to alleviate quenching. The upconversion luminescence intensity exhibits the classical quadratic power dependence in the weak excitation regime and linear in the strong

excitation regime. The quadratic power dependence is a signature for two-photon upconversion process and when the intermediate energy level saturates, the power dependence becomes linear. This system exhibits an overall enhancement of 16x and 3x of the green luminescence in the weak and strong excitation regimes, respectively. The rate equation analysis indicates that we have an absorption enhancement of 3x and energy transfer enhancement of 1.7x in this system. To further investigate the energy transfer process, we conducted a more detailed time-resolved study probing the decay and rise of upconversion luminescence. The results are summarized in Figure 2, which show that the energy transfer rate can be enhanced by a factor of 1.7 while the energy transfer efficiency is enhanced by 50%.[3] This study confirms the rate equation analysis conducted on the luminescence intensity results.

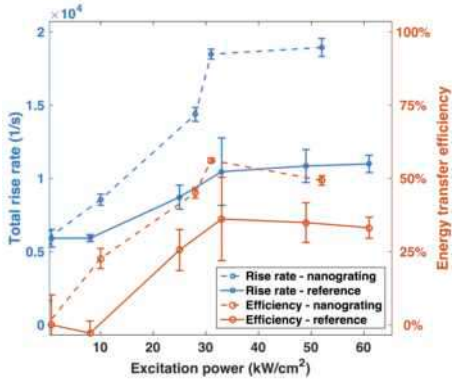


Figure 2. The blue curves referring to the left y-axis correspond to the rise rate of UCNPs on silver nanograting (dash line) and on silver film (solid line) respectively for different excitation power densities. The red curves refereeing to the right y-axis correspond to the internal upconversion efficiency of UCNPs on silver nanograting (dash line) and on silver film (solid line) respectively for different excitation power densities.

2.3. Metal-insulator-metal structure

Our previous study clearly suggests that the absorption enhancement provides the greatest overall upconversion enhancement thanks to the quadratic scaling. Metal-insulator-metal (MIM) design is one of the most effective structure for strong light confinement and thus absorption enhancement. We therefore conduct numerical simulations to optimize the MIM geometry to achieve resonance at 980 nm and thus maximize enhancement in absorption. MIM structures are fabricated using LIL. Briefly, LIL is used to create a nanohole array on a photoresist film on silicon substrate. We then sequentially deposit gold, UCNPs and gold layers on top, followed by lift-off to produce MIM arrays on silicon (Figure 3a). Optionally, we can detach the MIMs from the silicon substrate and disperse them in water to create MIM colloidal solutions for biological applications using a simple lift-off process we recently demonstrated.[4]

We then conduct steady state and transient photoluminescence (PL) spectroscopy over a wide range of excitation power densities. The PL intensity show quadratic power dependence in the weak excitation regime while becoming linear in the strong excitation regime as the intermediate level begins to saturate. Comprehensive electrodynamic simulations and a thorough analysis of the rate equations are performed to quantify the effects of plasmon enhancement and quenching and we obtained excellent agreement between the theoretical predictions and the experimental results. The maximum enhancement factor is around 1200, which is the highest value ever reported for upconversion enhancement. Finally, we use poly-vinyl alcohol to lift off all MIMs from the silicon substrate and disperse them in water. We then use the colloidal MIM for cancer cell imaging. Figure 3(b) shows the composite image obtained by overlaying a brightfield micrograph of bladder cancer cells and the upconversion fluorescence micrographs under 980 nm excitation. Compared to free UNCPs, we observe comparable fluorescence intensity using approximately 1000 times smaller concentration of MIMs. This result is consistent with the over 1000-fold enhancement observed in the PL measurements for MIMs on the silicon substrate.

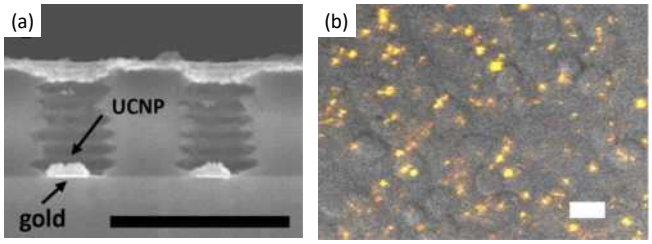


Figure 3. (a) Cross-sectional scanning electron micrograph (SEM) of nanoholes filled with gold and UCNPs. (scale bar: 1 μm). (b) Fluorescence micrograph of bladder cancer cells treated with gold-UCNP-gold MIM particles.

3. Conclusions

We present a comprehensive theoretical framework describing the plasmon enhancement of luminescence upconversion. Quantum electrodynamic theory describes light-matter interaction at each ion while rate equation provides a description for the interplay among various processes involved in upconversion. By a series of photoluminescence and time-resolved photoluminescence spectroscopy, we demonstrate the mechanism responsible for the overall enhancement of upconversion in a plasmonic nanostructure. Based on the fundamental understanding, we designed an MIM structure exhibiting strong local field enhancement and consequently absorption enhancement. A record high 1200x enhancement was achieved and the MIMs have been used to demonstrate fluorescence imaging of cancer cells.

References

1 Park, W., Lu, D. & Ahn, S. Plasmon enhancement of luminescence upconversion. *Chem. Soc. Rev.* **44**, 2940-2962.
2 Lu, D. *et al.* Plasmon Enhancement Mechanism for the Upconversion Processes in $NaYF_4$:Yb^{3+},Er^{3+} Nanoparticles: Maxwell versus Förster. *ACS Nano* **8**, 7780-7792.
3 Lu, D., *et al.* Experimental demonstration of plasmon enhanced energy transfer rate in $NaYF_4$:Yb^{3+},Er^{3+} upconversion nanoparticles. *Sci. Rep.* **6**, 18894.
4 Das, A., *et al.* Over 1000-fold enhancement of upconversion luminescence using water-dispersible metal-insulator-metal nanostructures. *Nat. Comm.* **9**, 4828.

Emission spectra of plasmon-exciton hybrid systems: A simple model

Xiaoguang Li

Institute for Advanced Study,
Shenzhen University, Shenzhen, 518060, China
*corresponding author, E-mail: xgli@szu.edu.cn

Abstract

Absorption spectra of a plasmon-exciton hybrid system can be qualitatively or even quantitatively studied by using the classical or quantum model with coupled oscillators. However, the emission spectra of plasmon-exciton hybrid systems are still largely unexplored, which presumably is due to the relatively slow emission process frequently interfered by other faster transition channels. Here, we describe a simple phenomenological model, which can evaluate both the absorption and emission spectra by selectively excluding some transitions during the emission process.

1. Introduction

The couplings between the metal plasmon and molecular exciton in metal-molecule hybrid systems have been extensively studied in the past two decades. The absorption spectra of the hybrid systems have been well explored in different systems from weak to strong coupling regimes [1], and can be well described by using the classical or quantum model with coupled oscillators [2, 3, 4]. For the emission process, we may expect that it has the same spectral line-shape as the absorption because it is basically the time reversal process of the absorption. Clearly, we know that it is not true for the individual molecule system because the fast vibrational relaxation usually occurs before the emission. Some intriguing features for the emission of hybrid systems, including the peak shifting and splitting, have been observed in the earlier studies [5, 6], and the discrepancy between the absorption and emission can be clearly seen [6]. Here, we present a simple phenomenological model to simultaneously capture the characteristics of both the absorption and emission spectra.

2. Model description

To evaluate both the absorption and emission, we start from the model introduced in our previous study for the absorption of the hybrid system [4]. Based on the linear response theory, the non-interacting response function of the hybrid system can be written as

$$\chi^0 = \begin{pmatrix} \frac{n_p}{\omega-\omega_p^-} & 0 \\ 0 & \frac{n_e}{\omega-\omega_c^-} \end{pmatrix} \tag{1}$$

where the subscripts p and c stands for the plasmon and exciton, respectively, n_i indicates the density, and $\omega_i^- = \omega_i - \Gamma_i/2$ with ω_i and Γ_i standing for frequency and linewidth of the corresponding state, respectively. Then, the interaction between the plasmon and excitons is introduced as

$$K = \begin{pmatrix} 0 & V_{pc}^* \\ V_{pe} & 0 \end{pmatrix} \tag{2}$$

and the plasmon-exciton interacting response function χ of the hybrid system is obtained from the Dyson equation as

$$\chi = \frac{\chi^0}{1-\chi^0 K} = \begin{pmatrix} \chi_{pp} & \chi_{pc} \\ \chi_{cp} & \chi_{cc} \end{pmatrix}. \tag{3}$$

The function χ_{ij} indicates the response of state i to the excitation on the state j. For example, χ_{pc} indicates the response of the dipole exciton to the field added on the plasmon. The induced charge density is linearly depended on the external field as

$$\rho_{ind} = \begin{pmatrix} \rho_p \\ \rho_e \end{pmatrix} = \chi V_{ext} = \begin{pmatrix} \chi_{pp} & \chi_{pc} \\ \chi_{cp} & \chi_{cc} \end{pmatrix} \begin{pmatrix} V_p \\ V_c \end{pmatrix}, \tag{4}$$

where V_i indicates the coupling between the state i and external field, and ρ_p and ρ_c are the induced charge oscillation on the metal and molecule. The absorption of the system depending on the charge oscillation out of phase with the external field is obtained as

$$\sigma = Im\left[\begin{pmatrix} V_p^* & V_c^* \end{pmatrix} \begin{pmatrix} \rho_p \\ \rho_c \end{pmatrix}\right] = Im(V_p^*\rho_p + V_c^*\rho_c). \tag{5}$$

As the time reversal process of the absorption, the emission is expected to give the same spectral line-shape as the absorption. However, the emission process will be largely disturbed by some fast nonradiative processes, including the Landau damping of the plasmon and the vibrational relaxation of the molecule. Due to the vibrational relaxation, the emission peak of the molecule will red-shift to lower energy. By incorporating this effect, we could use an exciton with lower energy ω_c coupled with the plasmon, which would give a spectrum with different peak shifting as in the absorption. For the Landau damping, we expect that it will quickly change the induced charge density ρ_p in the metal, and thus largely modify the emission spectrum.

3. Discussion

We consider the whole emission process involving three consecutive steps: the absorption, decoherence, and emission with new coherent hybrid state. First, the absorption spectrum of the hybrid system is evaluated as shown

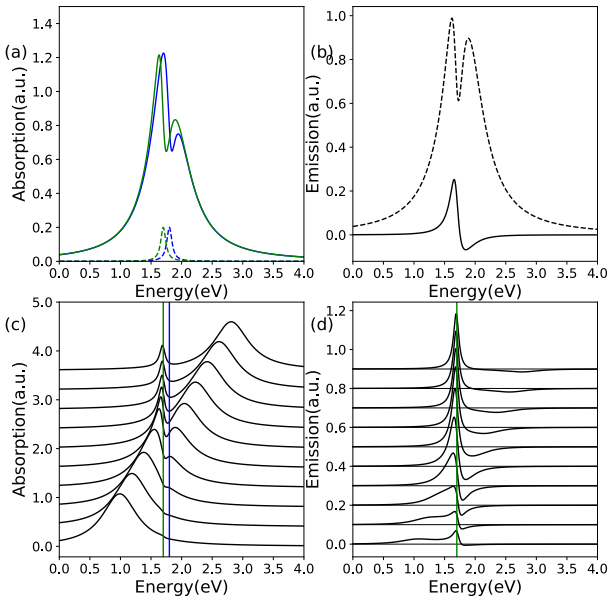


Figure 1: (a) The absorption spectra for hybrid system with the plasmon energy at $\omega_p = 1.8$ eV, and exciton energy at 1.8 eV (blue) and 1.7 eV (green). (b) The emission spectra for ρ_p and ρ_c. The absorption (c) and emission (d) spectra (vertically shifted) for the plasmon energy from 1.0 to 2.8 eV. The coupling strength are chosen as $V_p = 0.6$ and $V_c = V_{pc} = 0.1$ for both excitons. The linewidth for plasmon and exciton are 0.7 and 0.1 eV, respectively.

in Fig.1(a), where the spectra of the plasmon coupled with two different excitons have been shown. The blue solid line indicates the absorption due to the plasmon coupled with the exciton at 1.8 eV. We assume that the exciton will exhibit Stokes shift by losing 0.1 eV energy due to the vibrational relaxation, and thus gives the intrinsic emission peak at 1.7 eV. The absorption induces charge oscillation on the metal and molecules, forming the coherent wave packet oscillating between plasmon and exciton states. In the next step, the coherence will be lost very quickly due to the plasmon damping [7], as well as the vibrational relaxation of the exciton. After this decoherence, we believe the radiative process is then dominated by the charge oscillation on the molecule only, and thus the emission spectrum is evaluated similar as absorption spectrum except that we consider only the term involving ρ_c in Eq. (5). In Fig.1(b), we separate the absorption spectrum of the plasmon coupled with the exciton at 1.7 eV into the ρ_c (solid line) and ρ_p (dashed line) parts. As the energy of the plasmon changes from 1.0 eV to 2.8 eV, we show the full absorption results [Fig. 1(c)] and the ρ_c part only spectra [Fig. 1(d)], which are considered as the emission spectra.

The emission spectra show negative region due to the interference contribution mentioned in our earlier studies [4]. This issue can be fixed by introducing finite contribution from the ρ_p part, which should be more carefully discussed in the future studies. Figure 1(d) shows that as the plasmon energy red-shifts across the intrinsic energy of the emitted exciton, the emission peak will slightly red-shift and then exhibit a large linewidth broadening at the large detuning energy. Essentially, the emission is launched by the charge oscillation on the molecule, and the spectrum includes the direct emission of the molecule and the emission by first transfer energy to plasmon. The later one induce the peak shifting and broadening. It is intriguing to notice that both the features of the emission peak shifting and spitting as the plasmon energy change have been observed in the earlier study [5].

4. Conclusions

In summary, we develop a simple phenomenological model to deal with the absorption as well as emission of the strongly coupled plasmon-exciton systems. We hope the present result could stimulate more efforts along this direction.

Acknowledgement

This work was supported by National Natural Science Foundation of China (Grant No. 11874268).

References

[1] X. Li, L. Zhou, Z. Hao, and Q.-Q. Wang, *Plasmon-Exciton Coupling in Complex Systems*, *Advance Optical Materials*, 6: 1800275, 2018.

[2] A. Manjavacas, F. J. García de Abajo, and P. Nordlander, *Quantum Plexcitonics: Strongly Interacting Plasmons and Excitons*, *Nano Letters* 11: 2318, 2011.

[3] P. Törmä and W. L. Barnes, *Strong coupling between surface plasmon polaritons and emitters: a review*, *Reports Prog. Phys.* 78: 013901, 2015.

[4] S. J. Ding, X. Li, F. Nan, Y. T. Zhong, L. Zhou, X. Xiao, Q. Q. Wang, and Z. Zhang, *Strongly Asymmetric Spectroscopy in Plasmon-Exciton Hybrid Systems due to Interference-Induced Energy Repartitioning*, *Physical Review Letters* 119: 177401, 2017.

[5] K. Tanaka, E. Plum, J. Y. Ou, T. Uchino, and N. I. Zheludev, *Multifold enhancement of quantum dot luminescence in plasmonic metamaterials*, *Physical Review Letters* 105: 227403, 2010.

[6] M. Wersall, J. Cuadra, T. J. Antosiewicz, S. Balci, and T. Shegai, *Observation of mode splitting in photoluminescence of individual plasmonic nanoparticles strongly coupled to molecular excitons*, *Nano Letters* 17: 551, 2017.

[7] P. Vasa, W. Wang, R. Pomraenke, M. Lammers, M. Maiuri, C. Manzoni, G. Cerullo, and C. Lienau, *Real-time observation of ultrafast Rabi oscillations between excitons and plasmons in metal nanostructures with J-aggregates*, *Nature Photonics* 7: 128, 2013.

Optical Diversity of Metal Nanoparticles Modified by Stilbene Compounds: Plasmon Coupling, Raman Resonance Enhancement and Fluorescence Quenching

Elena Solovyeva*, Alexey Smirnov, Olga Odintsova, Vlad Deev

Chemistry Institute, Saint-Petersburg State University, Saint-Petersburg, Russia
*corresponding author, E-mail: solovyeva.elena.v@gmail.com, e.solovieva@spbu.ru

Abstract

In this work, we investigated the optical properties and surface chemistry of gold and silver nanoparticles modified by mono- and 4,4'-bifunctional stilbene compounds. Based on SERS spectra, UV-vis and TEM data, the linking of nanoparticles accompanied by plasmon coupling was revealed for 4,4'-diaminostilbene but remains under question for 4,4'-dimercaptostilbene. Ligand to metal charge transfer, occurring exclusively in the regions of plasmon coupling, was established. Analytical enhancement factors were calculated. Optical activity of modified nanoparticles was also investigated by fluorescent spectroscopy.

1. Introduction

The noble metals nanoparticles (NPs) have unique property known as localized surface plasmon resonance arising in result of interaction of light with the conduction electrons. The individual plasmonic nanoparticles can be assembled in various patterns for creation of promising metamaterials. The surface structures with short interparticle gap are the most preferable due to plasmon coupling providing a higher optical activity. The linking of metal NPs by organic modifiers is one of the powerful chemical approaches for fabrication of substrates with closely spaced NPs. The molecules having two functional groups on the opposite ends usually serve as the organic linkers. The excellence of bifunctional linkers is that they allow not only controlling the interparticle distance [1] but also creating the highly ordered spatial networks of NPs or nanocrystals [2-3].

This work represents the continuation of previous study of linking the metal NPs by stilbene derivatives [4]. Here, we consider extended list of mono- and 4,4'-bifunctional stilbene compounds and an influence of molecular structure on the optical properties of modified NPs. The investigation of organic modifiers with various degrees of substitution but close in a chemical nature allowed to distinguish the contributions from the effect of plasmon coupling and resonance charge transfer into enhancement of Raman scattering. This achievement is significant as for fundamental describing of plasmon coupling effect as for the correct assessment of capabilities for analytical detection.

2. Experimental

The initial Ag and Au NPs were prepared in the colloidal state by a reduction from the salts in accordance with the standard procedures. Their further modification was carried out by a quantitative addition of methanol solution of stilbene compound under vigorous stirring. To obtain the NPs with different surface coverage, the solutions with various modifier concentrations were used. 4,4'-diaminostilbene (DAS), 4,4'-dimercaptostilbene (DMS), 4,4'-dibromostilbene (DBS), and 4-aminostilbene (AS) were used for the modification of Ag and Au NPs.

The surface enhanced Raman scattering (SERS) spectra were acquired on a LabRam HR800 (Horiba Jobin Yvon) spectrometer using 488 and 633 nm excitation lines. The ultraviolet-visible (UV-vis) absorption spectra were recorded on a UV-1800 (Shimadzu) spectrophotometer with quartz cell of 1.0 cm path length. The emission spectra were registered on a Fluorog (Horiba Jobin-Yvon) spectrometer. The images of silver nanoparticles were obtained with a Zeiss Libra 200FE transmission electron microscope (TEM) at an accelerating voltage of 200 kV.

3. Discussion

A surface coverage by organic modifiers can strongly influence on the properties of metal NPs. Therefore, the NPs with different numbers of molecular adlayers have to be considered for firstly applied modifiers. SERS response registered from NPs modified by stilbene derivatives showed two types of dependence on surface coverage. As can be seen from Fig. 1, the non-monotonous curve is characteristic for bifunctional 4,4'-stilbene derivatives, namely DAS and DMS, which are able to chemisorb on a surface. For DBS, which functional groups have a weaker affinity to the metal surface, the type of dependence turned out to be the same as for stilbene derivative with a single substitution. Regular growth of SERS intensity with increasing concentration corresponds to conventional Langmuir's adsorption without significant transformations in the molecular adlayers while the non-monotonous change testifiers the more complex processes occurring on the interface.

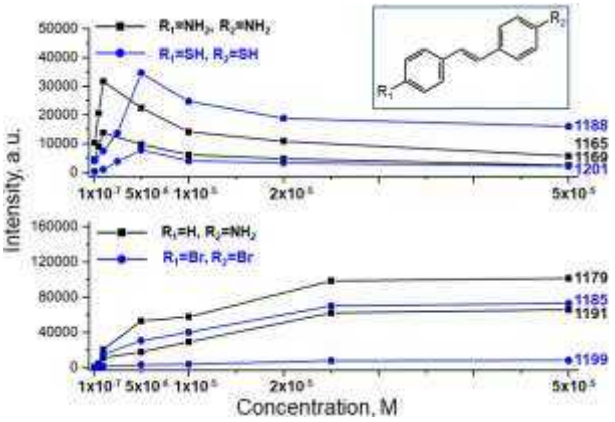


Figure 1: Dependence of SERS intensity of ν_{16} and ν_{15} vibrational bands on concentration for stilbene compounds under investigation.

The nanoparticle agglomerates observed on TEM images and appearance of long-wavelength band in the absorption spectra of Ag NPs modified by DAS clearly showed the formation of linked NPs at submonolayer coverage [3]. But it is not so obvious in case of DMS. The type of SERS spectra dependence on surface coverage evidences about possible linking, but TEM and UV-vis data did not give the reliable proofs. Despite the literature data talking about linking Ag NPs via DMS bridges [5], another possible reason of observed spectral changes can conclude in the reorientation of DMS molecules from convex to unbent state. A resonance character of Raman enhancement was established in the case of DAS adsorbed in the regions of plasmon coupling. Ligand to metal charge transfer was revealed based on the UV-vis data and overtones appeared at the higher wavenumbers in the SERS spectra. To differentiate the contributions to SERS signal from plasmon coupling, charge transfer and ordinary electromagnetic mechanism, the analytical enhancement factors (AEF) were calculated (Table 1). The advantage in Raman enhancement in case of linked NPs is four orders of magnitude due to plasmon coupling.

Table 1: Analytical enhancement factors for selected Raman bands of stilbene dyes adsorbed on Ag NPs.

Stilbene dye	Raman band, cm^{-1}	SERS band, cm^{-1}	AEF
DAS@2AgNPs	1178	1165	8.2×10^4
	1193	1169	4.2×10^5
DAS@AgNP	1178	1180	1.4×10^1
	1193	1194	0.6×10^1
DMS@AgNP	1181	1183	1.6×10^5
	1195	1201	7.5×10^4
AS@AgNP	1181	1180	2.9×10^2
	1195	1192	1.8×10^2
DBS@AgNP	1183	1186	3.3×10^2
	1191	1198	2.1×10^2

An optical activity of modified NPs was also investigated by fluorescent spectroscopy. Different responses were revealed for NPs linked by DAS and single NPs covered by AS. Fluorescent quenching corresponding to linear dependence on NPs concentration correlated with the Stern-Volmer equation was obtained only for AS.

4. Conclusions

In accordance with the obtained data, the following important findings were made: i) at sub-monolayer surface coverage, bifunctional aminostilbenes coordinate with two Ag nanoparticles simultaneously that leads to the plasmon coupling in the obtained agglomerates. The stilbene derivatives with single substitution adsorb on metal nanoparticles by ordinary layer-by-layer way; ii) plasmon coupling gives the additional contribution in the Raman enhancement of four orders of magnitude; iii) the ligand to metal charge transfer may arise exclusively in the regions of plasmon coupling even if it is absent on the uniformly amplifying surface. Generally, this work represents the simple method to controllable effect on the structural, plasmonic and optical properties of noble metal nanoparticles by the new class of modifiers based on stilbene compounds.

Acknowledgements

This work was supported by the Russian Science Foundation (grant № 17-73-10209). The authors acknowledge the Resources Centers of Saint-Petersburg State University: the Center for Optical and Laser Materials Research and Center for Chemical Analysis and Materials Research, the Interdisciplinary Center for Nanotechnology.

References

[1] L. Guerrini, I. Izquierdo-Lorenzo, R. Rodriguez-Oliveros et. al, α,ω-Aliphatic Diamines as Molecular Linkers for Engineering Ag Nanoparticle Clusters: Tuning of the Interparticle Distance and Sensing Application, *Plasmonics* 5: 273−286, 2010.

[2] R. Matassa, G. Familiari, E. Battaglione, C. Sibilia, G. Leahu, A. Belardini, I. Venditti, L. Fontana, I. Fratoddi, Electron Microscopy Reveals Soluble Hybrid Network of Individual Nanocrystal Self-Anchored by Bifunctional Thiol Fluorescent Bridges, *Nanoscale* 8: 18161−18169, 2016.

[3] Y. Bu, S. J. Park, S.-W. Lee, Diamine-linked array of metal (Au, Ag) nanoparticles on glass substrates for reliable surface-enhanced Raman scattering (SERS) measurements, *Curr. Appl. Phys.* 14: 784–789, 2014.

[4] E.V. Solovyeva, E.V. Ubyivovk, A.S. Denisova, Effect of diaminostilbene as a molecular linker on Ag nanoparticles: SERS study of aggregation and interparticle hot spots in various environments, *Coll. Surf. A.* 528: 542−548, 2018.

[5] N. Guarrotxena, Y. Ren, A. Mikhailovsky, Raman Response of Dithiolated Nanoparticles Linkers, *Langmuir* 27(1): 347−351, 2011.

Tuning phase matching conditions in second harmonic generation via the excitation of higher order plasmonic mode in waveguides

Ning Liu[1*] and Brian Corbett[2]

[1] Department of Physics and Bernal Institute, University of Limerick, Co. Limerick, Ireland
[2] Tyndall National Institute, University College Cork, Cork, Ireland
*corresponding author, E-mail: ning.liu@ul.ie

Abstract

Plasmonic waveguides, with characteristic strong electric field confinement at the dielectric-metal interface, have found many applications in nonlinear optics. However, the dispersion relationship of fundamental plasmonic mode works against the phase matching condition required for strong second harmonic generation. Here we show that by exciting higher order plasmonic modes, phase matching condition can be satisfied in plasmonic waveguides.

1. Introduction

Because of the strong electric field confinement present in plasmonic waveguides, researchers have been trying to take advantages of the field enhancement for various nonlinear processes. Among them, second harmonic generation (SHG) has been explored on metallic structures along and on the combination of nonlinear materials and metallic structures. Non-centrosymmetric compound III-V semiconductors such as GaInP are known to have strong nonlinear coefficients. For nonlinear semiconductor waveguides in close vicinity to metal, strong SHG is expected. However, realistic semiconductor material possesses nonlinear dispersion relationship ($k_{2\omega} \neq 2k_{\omega}$) [1]. For surface plasmon propagation at semiconductor-metal interface, the difference between $k_{2\omega}$ and $2k_{\omega}$ is further widened [2]. In other words, the coherent length of SHG is extremely short, usually within few microns. It is therefore necessary to find a proper phase matching mechanism to fully exploit the strong field enhancement and high nonlinear coefficients of the semiconductor-metal waveguides.

2. Results and Discussion

In order to reduce the propagation loss inherent to the metal substrate, an air-semiconductor waveguide-insulator-metal hybrid plasmonic waveguide geometry is applied. A quaternary AlGaInP multi-layer structure is used for the nonlinear waveguides [3]. A laser beam is edge coupled into the waveguide. When a proper polarization angle of the laser beam is chosen, higher order plasmonic mode are excited [4], where phase matching condition can be achieved for SHG, as shown in Fig. 1.

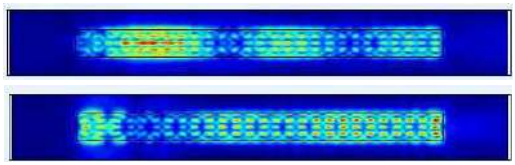


Figure 1: (a) SHG from plasmonic mode without proper phase matching condition, (b) SHG from plasmonic mode with proper phase matching condition.

This phase matching mechanism also depends on the dimension of the waveguides and the crystal orientation of the material.

3. Conclusion

In summary, we have explored the possibility of using higher order plasmonic waveguided modes to achieve phase matching in SHG of nonlinear hybrid plasmonic waveguides. This study further widens the applications of plasmonic waveguides in integrated plasmonic circuits.

Acknowledgements

N. L. acknowledge the support by Science Foundation Ireland Career Development Award 17/CDA/4733 and National Access Programme #444.

References

[1] S. Buckley, M. Radulaski, J. Petykiewicz, K. G. Lagoudakis, J. -H. Kang, M. Brongersma, K. Biermann, J. Vučković, Second-Harmonic Generation in GaAs

Photonic Crystal Cavities in (111)B and (001) Crystal Orientations, *ACS Photonics* 1: 516-523, 2014.

[2] H. Wei, D. Pan, S. P. Zhang, Z. P. Li, Q. Li, N. Liu, W. H. Wang, H. X. Xu, Plasmon Waveguiding in Nanowires, *Chem. Rev.*, 118: 2882–2926, 2018.

[3] N. Liu, A. Gocalinska, J. Justice, F. Gity, I. Povey, B. McCarthy, M. Pemble, E. Pelucchi, H. Wei, C. Silien, H. X. Xu, and B. Corbett, Lithographically defined, room temperature low threshold red-emitting subwavelength hybrid plasmonic lasers, *Nano Lett.* 16: 7822–7828, 2016.

[4] N. Liu, H. Wei, J. Li, Z. X. Wang, X. R. Tian, A. L. Pan, H. X. Xu, Plasmonic Amplification with Ultra-High Optical Gain at Room Temperature, *Sci. Rep*. 3: 1967, 2013.

Quasicrystal Photonic Metasurfaces for Radiation Control of Second Harmonic Generation

Yutao Tang[1,2,3], Junhong Deng[1,2], King Fai Li[1,2], Mingke Jin[1], Jack Ng[3], and Guixin Li[1,2]*

[1]Department of Materials Science and Engineering, Southern University of Science and Technology, Shenzhen 518055, China
[2]Shenzhen Institute for Quantum Science and Engineering, Southern University of Science and Technology, Shenzhen, China
[3]Department of Physics and Institute of Computational and Theoretical Studies, Hong Kong Baptist University, Hong Kong
*corresponding author, E-mail: ligx@sustc.edu.cn

Abstract

Nonlinear optical quasicrystal metasurfaces to control the radiation of the second harmonic generation (SHG) will be presented. The metasurfaces are based on the geometric phase controlled plasmonic meta-atoms with local rotational symmetry, which are ordered quasiperiodically according to two quasicrystalline tilings. We found that the far field radiation of SHG waves are determined by both the tiling schemes and the local symmetry of meta-atoms. The proposed concept may open new avenues for designing nonlinear optical sources with metasurface crystals.

1. Introduction

Metasurfaces, as the two-dimensional artificially engineered surfaces, have enabled abundant optical functionalities and hold great potentials for applications in integrated optics thanks to their compactness and flexibilities of design. In the context of linear optics, how to elaborately order the meta-atoms in metasurfaces is vital for realizing specific optical functionalities such as focusing, beam-splitting, generation of optical vortex, etc. In addition to the periodic lattices, the adoption of quasicrystalline structure may also bring new degrees of freedom to the optical functions of metasurfaces, e.g. the Penrose-type plasmonic metasurfaces have been used for symmetry-induced optical isotropy [1] or linear optical phase control [2].

Recently, the research of optical metasurface goes into nonlinear optical regime. The key issues in this field mainly involve how to control the amplitude, phase and polarization of light in nonlinear optical processes. Strong localization of electromagnetic waves in vicinity of the metasurface can be used to boost the efficiency of SHG, third harmonic generation and four-wave mixing, etc. There has also been strong interests to locally control the phase of nonlinear waves by using electric poling method, but only until recently, they can be continuously manipulated with the help of nonlinear geometric P-B phase of meta-atoms [3,4]. Apart from this, the nonlinear polarizations can also be well controlled by the local symmetry of meta-atom and the polarization of fundamental wave (FW).

Now it is timely to pay more attentions to the relationship between local and global symmetries of metasurfaces, which may introduce new degrees of freedom to control the nonlinear optical radiation in the far field. As shown in Fig. 1, we take the advantages of both the nonlinear P-B phase controlled meta-atoms and various quasicrystal tiling schemes to construct the nonlinear optical quasicrystal metasurface (NOQCM).

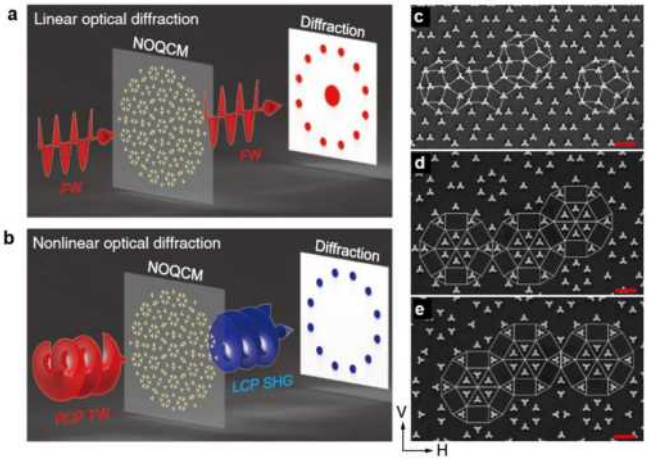


Figure 1 : Illustration of the linear and nonlinear optical diffractions of the nonlinear metasurface (a-b). The SEM images show (c) the Penrose-type metasurface, (d) the asymmetric HQC metasurface and (e) the symmetric HQC metasurface. Scale bars, 1 μm.

2. Design and Fabrication of NOQCMs

The nonlinear meta-atoms used to construct the NOQCM is a gold nanostructure with three-fold (C3) rotational symmetry. As the inversion symmetry is broken in the C3 meta-atom, SHG is allowed and could be greatly enhanced when the localized plasmon resonance of the fundamental wave (FW) is excited. The gold meta-atoms are then ordered according to two quasiperiodic tilings, namely the famous Penrose tiling, and the newly proposed hexagonal quasicrystalline (HQC) tiling [5]. Compared to the extensively investigated Penrose structures, the HQC metasurface we designed is the first experimental

demonstration of its kind. To make use of the P-B phase, two distinct orientation distribution of the meta-atoms are deployed to form different HQC metasurfaces, one is asymmetric (Fig. 1d) and the other symmetric (Fig.1e). The NOQCMs are fabricated by using standard electron beam lithography followed by the metal lift-off process.

3. Far Field Radiation of the NOQCM

The far field radiation the nonlinear optical quasicrystal metasurfaces is investigated in both linear and nonlinear optical regimes (Fig. 2). For the linear optical experiment, the unpolarized laser beam of wavelength 635nm is normally incident onto the metasurfaces. In the transmission direction, diffraction patterns with ten-fold and six-fold rotational symmetries are observed for the Penrose and HQC metasurfaces, respectively. The diffraction patterns from the symmetric and asymmetric design of HQC samples in Fig. 2b and 2c are almost identical. This is mainly because that the incident light is propagating along the optical axis of the C3 meta-atom and its polarization state is insensitive to the orientation directions of the meta-atoms. As is expected, the global symmetry regarding how to order the meta-atoms plays vital roles in determining the linear optical diffraction of the quasicrystal metasurfaces.

Based on the measured spin dependent SHG responses (not presented), the nonlinear far field radiation of the Penrose and HQC metasurfaces are measured at the resonant fundamental wavelengths of 1275 nm and 1250 nm, respectively. The FW is left circular polarized, while the SHG of right circular polarization is recorded. It is found that the ten-fold and six-fold rotational symmetries of optical diffraction pattern also exist in the nonlinear optical regime. However, a phenomenon worth to be mentioned is that the SHG diffraction pattern of the symmetric HQC metasurface (Fig. 2f) exhibits significant peripheral spots, but its central spot disappears. A theoretical dipole radiation model, enhanced with the nonlinear P-B phase theory, is then developed for interpreting the far field nonlinear optical radiations. The calculated far field radiation patterns (not shown) of the NOQCMs are well consistent with the experimental results. An easy way to understand the missing central spot in Fig. 2f is the destructive interference of the SHG waves produced by adjacent C3 meta-atoms in Fig. 1e, such interference is utilized in ref. [6] to encode an image.

4. Conclusions

In summary, we have designed and fabricated nonlinear optical quasicrystal metasurfaces by assembling the geometric P-B phase controlled plasmonic meta-atoms into the macroscopic quasicrystal lattices. We successfully demonstrate that the nonlinear SHG radiation in the far field can be manipulated by both the local and global symmetries of the metasurface crystals. It is anticipated that the concept of quasicrystal metasurfaces not only represent novel strategy for controlling far field nonlinear optical radiations, but also offers an integrated platform for quantum information processing, optical modulation, all-optical optical switching and so on.

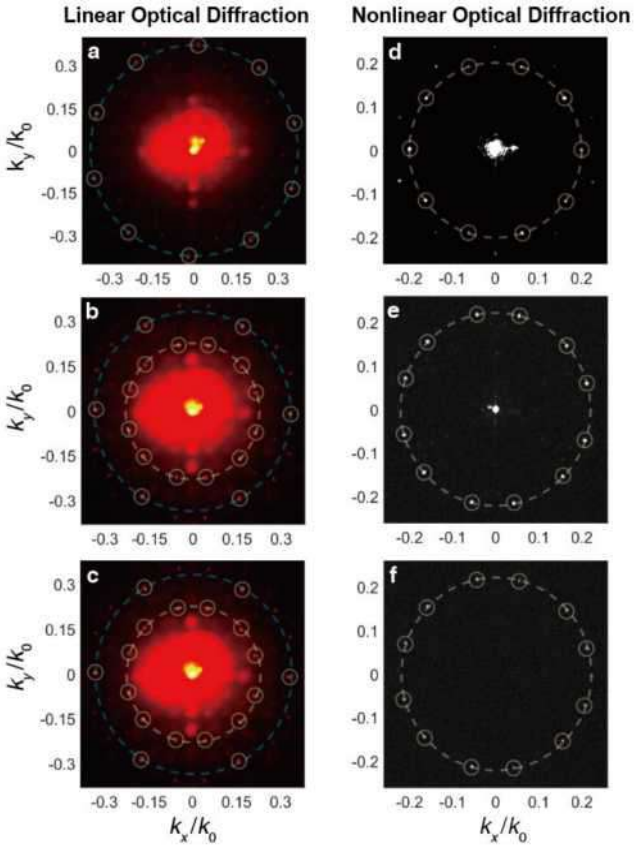


Figure 2: Experimental results of the linear and nonlinear far field radiation of the NOQCMs as shown in Fig. 1c-d.

Acknowledgements

This research was supported by the Guangdong Provincial Innovation and Entrepreneurship Project (2017ZT07C071), Applied Science and Technology Project of Guangdong Science and Technology Department (2017B090918001), National Natural Science Foundation of China (11774145) and Natural Science Foundation of Shenzhen Innovation Committee (JCYJ20170412153113701).

References

[1] S. S. Kruk *et al.*, Optical metamaterials with quasicrystalline symmetry: Symmetry-induced optical isotropy. *Phys. Rev. B* **88**, 201404 (2013).

[2] I. Yulevich *et al.*, Optical Mode Control by Geometric Phase in Quasicrystal Metasurface. *Phys. Rev. Lett.* **115**, 205501 (2015).

[3] G. Li *et al.*, Continuous control of the nonlinearity phase for harmonic generations. *Nat. Mater.* **14**, 607-612 (2015).

[4] G. Li, S. Zhang, T. Zentgraf, Nonlinear photonic metasurfaces. *Nat. Rev. Mater.* **2**, 17010 (2017).

[5] Dotera, S. Bekku, P. Ziherl, Bronze-mean hexagonal quasicrystal. *Nat. Mater.* **16**, 987-992 (2017).

[6] F. Walter, G. Li, C. Meier, S. Zhang, T. Zentgraf, Ultrathin Nonlinear Metasurface for Optical Image Encoding. *Nano Lett.* **17**, 3171-3175 (2017).

Energy of plasmonic photocatalytic sites

Emiliano Cortés[1]

[1]Chair in Hybrid Nanosystems, Nanoinstitut München, Fakultät für Physik,
Ludwig-Maximilians-Universität München, 80799 München, Germany
*corresponding author, E-mail: Emiliano.Cortes@lmu.de

Abstract

Plasmonic photocatalysts hold the potential of transforming visible light into chemical energy [1]. Here we performed a spectral screening study on the energy of the extracted hot-holes in a 80 nm Au nanoparticle that photocatalyze an electro-polimerization reaction. We demonstrate that Landau damping is the absorption channel that leads to the most energetic carriers for plasmonic photocatalysis [2].

1. Introduction

Single-particle techniques are key to unearth the underlying mechanisms of hot-carrier generation, transport and injection as well as to disentangle the role of the temperature increase and the enhanced near field at the nanoparticle-molecule interface [2, 3]. Gaining a nanoscopic insight of these processes and their interplay could aid in the rational design of plasmonic photocatalysts.

Here, electrochemistry and single-particle dark-field microscopy and spectroscopy are combined to study the role of a photoexcited Au nanoparticle (AuNP) in the electro-oxidation of aniline to polyaniline. Electrochemistry provides a way to control the energy of the electrons in the metal nanoparticle and at the same time allows to compute the overpotential needed for the electrochemical reaction to proceed. This also serves as a method to quantify the photocatalytic effect of the illuminated AuNP.

2. Discussion

Wavelength-dependence studies show that the overall energy requirements of the electrochemical reaction can be reduced up to ~35% when exciting the NP at it plasmon resonance. In order to understand the mechanism behind this photocatalytic effect, a single particle nanothermometry technique based on anti-stokes photoluminescence emission is implemented. It is shown that even if the total absorbed energy at each excitation wavelength is the same, the reactivity of the hot-holes follow the plasmon resonance profile. The effective energy of the reactive hot holes is in the range of 0.028eV to 0.24eV. These results shed light on the role of the absorption processes in plasmonic photocatalysts and the maximum energy of the reactive hot holes at the surface of a 80 nm AuNP.

Our spectral screening study allowed us to explore the influence of the different absorption channels in the final energy of the extracted hot-holes. Four different mechanisms of carrier generation through plasmon decay have been identified – interband absorption, phonon (or defect) assisted absorption, electron-electron scattering assisted absorption, and Landau damping (or surface collision assisted absorption). The excitation wavelength determines the relative contribution of each mechanism and therefore the energy distribution of the generated carriers. We found that the maximum energy of the carriers is reached when Landau damping is the favored excited channel.

3. Conclusions

Here we shed light on an important aspect of plasmonic photocatalysis by measuring the energy of the generated hot-holes in a single 80 nm gold nanoparticle. We found that the extracted energy of the hot-holes is about 0.24 eV. Among the different absorption pathways that can lead to hot-carrier generation in plasmonic nanoparticles, we found that Landau damping – a surface collision process – is responsible for producing the most energetic carriers. Single-particle measurements allowed to disentangle the role of temperature increase, intense electromagnetic near fields and hot carriers for an electro-polymerization reaction. These results could aid in the rational design of plasmonic photocatalysts with highly energetic reactive-sties.

Acknowledgements

E.C. acknowledge financial support from the European Commission through the ERC-STG 802989.

References

[1] E. Cortés. Activating Plasmonic Chemistry, *Science* 362, 28, 2018.

[2] E. L. Pensa, J. Gargiulo, A. Lauri, S. Schlücker, E. Cortés, S.A. Maier. Spectral screening of the energy of hot holes over a particle plasmon resonance, *Nano Letters*, just accepted, 2019.

[3] S. Simoncelli, E. L. Pensa, T. Brick, J. Gargiulo, A. Lauri, J. Cambiasso, Y. Li, S. A. Maier, E. Cortés. Monitoring plasmonic hot-carrier chemical reactions at the single particle level, Faraday Discuss., DOI: 10.1039/ c8fd00138c, 2019

Continuously tuning the coupling strength of bow-tie nanoantennas by strain variation

Florian Labile[1,2], Dominik A. Gollmer[1,2], Simon Dickreuter[1,2], Dieter P. Kern[1,2], and Monika Fleischer[1,2]

[1]Institute for Applied Physics, Eberhard Karls University of Tübingen, Germany
[2]Center for Light-Matter Interaction, Sensors and Analytics LISA+, Eberhard Karls University of Tübingen, Germany
*corresponding author, E-mail: monika.fleischer@uni-tuebingen.de

Abstract

Plasmonic coupling effects show a strong distance dependence for few nanometer gaps. The coupling of individual nano-bowties is reversibly tuned by fabricating antennas on flexible polymers, enabling their use as plasmon rulers or strain sensors.

1. Introduction

The coupling strength and spectral positions of the plasmon resonances of gap antennas strongly depend on the respective gap distance [1]. Creating antenna dimers such as bowties with gaps down to less than 10 nm allows for high electric near-fields in the gap region that can be used as highly confined sensing volumes. When attempting to evaluate the spectral characteristics of different antennas with similar gaps however, the comparison is strongly hampered by the unavoidable nanoscale fluctuations between nominally identical antennas due to the limits of the nanofabrication processes [2]. Therefore the strategy to prepare bowtie nanoantennas on flexible substrates is pursued, such that studies of the gap dependence can be performed at the individual nanostructure level.

2. Discussion

In this presentation the fabrication of sparse arrays of gold nano-bowtie antennas on flexible PDMS (polydimethyl-siloxane) substrates is illustrated. The samples are prepared by electron beam lithography and a lift-off process on a silicon sample with a thin sacrificial chromium layer. In the subsequent transfer process, a sheet of PDMS is placed on top of the nanostructures, and the chromium is dissolved, leaving the bowties on the surface of the PDMS. Individual nano-bowties are then investigated by dark-field spectros-copy using a pinhole to select only the signal from single structures. This way the reversible spectral properties of bowties under different amounts of strain are demonstrated, and the spectral features are assigned via comparison to numerical simulations [3]. In Figure 1, an example of the spectra of a bowtie antenna with a 12 nm gap under 0%, 25% and 50% strain are shown, increasing the gap width to 18 nm. The spectra can be modeled by Lorentzian fits, showing the presence of three plasmonic modes at different wavelengths. The mode at the shortest wavelengths close to 700 nm corresponds to an excitation of the base of the bowtie and is only little affected. The central mode is hardly visible. The longest wavelength mode results from an excitation of the bowtie along its long axis and is strongly influenced by the coupling conditions between the two bowtie triangles.

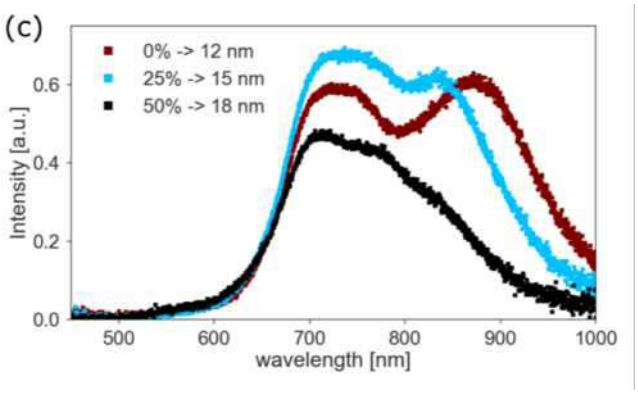


Figure 1: Change in the spectral properties corresponding to the scheme in Fig. 2 (a) due to hybridization and coupling. Image adapted from [3].

By suitable orientation of the nanostructures either parallel or perpendicular to the direction of strain, an increasing strain level can lead to either increasing or decreasing gap widths, see Figure 2. When strain is applied perpendicular to the bowtie axis, the original lithographically defined gap size can be further decreased due to the necking of the flexible substrate.
This way, gaps in the single digit nanometer regime can be reached and further investigated. The resonance wavelength of the coupling mode is shifted according to an exponential power law. Evaluating the spectral shift of the coupling mode in terms of this plasmonic ruler equation [4], the structures have the potential to act as strain sensors. Starting with few nanometer gaps, the regime of quantum plasmonics comes within reach.

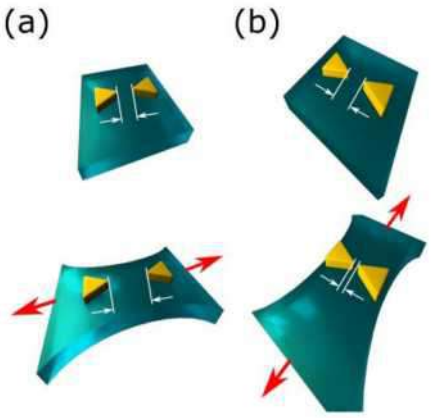


Figure 2: Schematic of (a) longitudinal stretching vs. (b) lateral necking of individual bow-tie antennas, changing their gap widths under applied strain. Images adapted from [3].

3. Conclusions

By preparing bowtie antennas on flexible substrates, the coupling strength within one and the same individual nano-antenna can be continuously and reversibly tuned. An increasing blue- or redshift is observed when the strain in the direction of the bowtie's long axis is increased or decreased, respectively. The opposite behavior can be induced by rotating the bowtie by 90° relative to the strain. In this configuration the pre-defined gaps can be further minimized.

Acknowledgements

Financial support by the German Research Foundation (DFG) under Grant number FL670/7-1 is gratefully acknowledged.

References

[1] T. Maurer, J. Marae-Djouda, U. Cataldi, A. Gontier, G. Montay, Y. Madi, B. Panicaud, D. Macias, P.-M. Adam, G. Lévêque, T. Bürgi, R. Caputo, The beginnings of plasmomechanics: towards plasmonic strain sensors, *Front. Mater. Sci.* 9(2): 170, 2015.

[2] S. Dickreuter, D. P. Kern, M. Fleischer, Single particle dark-field spectroscopy of spherical dimers with down to sub-10 nm gaps fabricated by the annealing of nano-pillars, *Nanophotonics* 7: 1317, 2018.

[3] F. Laible, D. A. Gollmer, S. Dickreuter, D. P. Kern, M. Fleischer, Continuous reversible tuning of the gap size and plasmonic coupling of bow tie nanoantennas on flexible substrates, *Nanoscale* 10: 14915, 2018.

[4] P. K. Jain, W. Huang, M. A. El-Sayed, On the universal scaling behaviour of the distance decay of plasmon coupling in metal nanoparticle pairs: a plasmon ruler equation, *Nano Lett.* 7: 2080, 2007.

Out-of-equilibrium dynamics of silver: saturated nonlinear response

Andrea Marini[1,*], Alessandro Ciattoni[2], and Claudio Conti[3,4]

[1]Department of Physical and Chemical Sciences, University of L'Aquila, Via Vetoio, 67100 L'Aquila, Italy
[2]Consiglio Nazionale delle Ricerche, CNR-SPIN, Via Vetoio 10, 67100 L'Aquila, Italy
[3]Department of Physics, University Sapienza, Piazzale Aldo Moro 5, 00185, Rome, Italy
[4]Institute for Complex Systems (ISC-CNR), Via dei Taurini 19, 00185, Rome, Italy
*corresponding author, E-mail: andrea.marini@aquila.infn.it

Abstract

Starting from the Fokker-Planck-Landau theory of electron collisions, we derive a novel set of hydrodynamical equations accounting for the ultrafast dynamics of silver, demonstrating that absorption saturates owing to the quenching of electron collisions. Our results hold great potential for mitigating absorption of plasmonic materials, thus opening novel avenues for the development of low-loss plasmonic circuits and solid-state attosecond pulse sources along with ultra-efficient nonlinear control at the nanoscale by near-zero index media.

1. Introduction

Plasmonic materials and metamaterials (MMs) have attracted over the last decade a great deal of interest owing to their capacity to confine light down to the nanoscale. Such a peculiar property ensues from the coupling between photons and plasma waves excited within plasmonic media such as metals, transparent conductors, or graphene enabling the excitation of surface plasmon (SP) modes. The tight confinement provided by SP modes in plasmonic media and MMs has opened several possibilities to enhance light-matter interaction and nonlinear optical processes, enabling the control and manipulation of light at the nanoscale along with the development of nano-sized optical interconnects, super-resolution techniques, surface-enhanced spectroscopy, and optical cloaking.

Most of the above mentioned innovative applications have been developed thanks to the continuous advances in nanofabrication techniques, which have exploited mainly noble metals as plasmonic materials, particularly gold and silver owing to the lower scattering rate of free electrons as compared to other metals. However, except for sensing and surface-enhanced spectroscopy where metal absorption only limits the resonance quality factor, the amount of loss in current plasmonic devices such as interconnects, switches, modulators, and detectors is far too high for practical applications. More recently, graphene, oxides and nitrides, and polar dielectrics have risen as promising materials for infrared plasmonics with smaller absorption owing to the lower electron density. Further strategies for loss mitigation involve quenching of interband absorption via self-induced-transparency plasmon solitons [1], reduction of surface roughness, and embedding gaining media in plasmonic setups. The ultrafast response of plasmonic media to sub-picosecond temporal pulses of electromagnetic (EM) radiation generally involves heating of electrons and the lattice with a complex dynamics involving exchange of energy from hot electrons to the lattice via electron-phonon scattering. Heating is a primary consequence of absorption and is generally undesirable since it leads to material damage. Reducing the time-duration of EM pulses to the femtosecond regime is a promising strategy to quench absorption and heating since it enables the achievement of high peak intensity with reduced transfer of energy to hot electrons. Here, we investigate the ultrafast nonlinear dynamics of plasmonic media under excitation by temporal pulses of EM radiation with duration of few femtoseconds. Start-

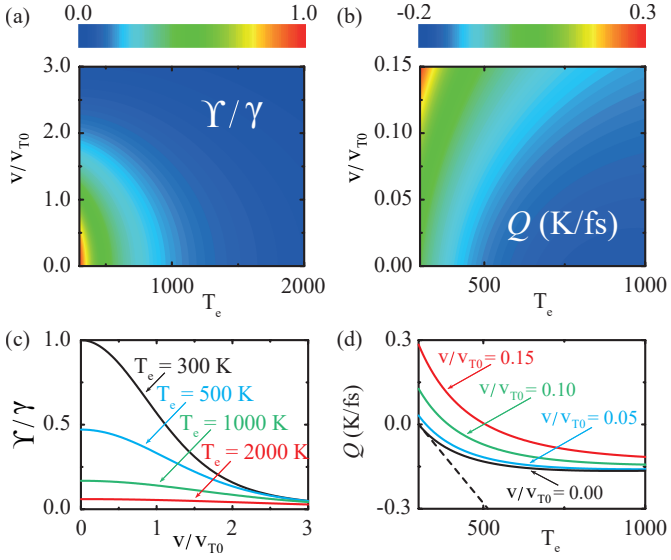


Figure 1: Parametric nonlinear dependency of (a,c) rescaled nonlinear damping Υ/γ and (b,d) heating rate Q over the rescaled average velocity $\mathrm{v}/\mathrm{v}_{\mathrm{T0}}$ and OOE plasma temperature T_{e}. The plots are made at ambient lattice temperature $T_0 = 300$ K and refer to silver, so that $\omega_{\mathrm{P}} = 14$ fs^{-1}, $\gamma = 32$ ps^{-1}, and $\gamma_{\mathrm{th}} = 1.4$ ps^{-1}. The dashed black line in (d) indicates the linear limit of plasma temperature relaxation $Q \simeq -\gamma_{\mathrm{th}}(T_{\mathrm{e}} - T_0)$ for vanishing velocity $\mathrm{v} \to 0$.

ing from the Boltzmann equation for the electron plasma, and accounting for electron-electron and electron-phonon collisions through the full collisional integral, we derive a novel set of hydrodynamical equations (HDEs) describing electron collisions beyond the standard damping approximation [2]. We find a complex analytical expression for the effective electron damping that depends nonlinearly on the electron current and reduces to the Drude-like damping in the limit of small driving intensity, while it quenches for high driving peak intensity owing to the reduced Coulomb interaction of electrons with ions.

2. Discussion

Borrowing the Fokker-Planck-Landau theory of collisions we model electron dynamics in plasmonic materials beyond the RTA. We solve the Boltzmann equation following the method of moments, which enables us to obtain a hierarchy of hydrodynamical equations that are fully equivalent to the FPLE. Since we are interested only on the zero [electron density $\int \mathrm{d}\mathbf{w} f(\mathbf{r},\mathbf{w},t) = n(\mathbf{r},t)$, such that $\int \mathrm{d}\mathbf{r} n(\mathbf{r},t) = N$], first [current density $\int \mathrm{d}\mathbf{w}\mathbf{w} f(\mathbf{r},\mathbf{w},t) = n(\mathbf{r},t)\mathbf{v}(\mathbf{r},t)$], and second [energy density $(m/2)\int \mathrm{d}\mathbf{w}|\mathbf{w}-\mathbf{v}|^2 f(\mathbf{r},\mathbf{w},t) = (3/2)n(\mathbf{r},t)k_\mathrm{B}T_\mathrm{e}(\mathbf{r},t)$] moments, we truncate the hierarchy by neglecting higher-order moments obtaining the solution

$$f(\mathbf{r},\mathbf{w},t) \simeq \frac{n(\mathbf{r},t)m^{3/2}}{[2\pi k_\mathrm{B}T_\mathrm{e}(\mathbf{r},t)]^{3/2}} \mathrm{e}^{-\frac{m|\mathbf{w}-\mathbf{v}(\mathbf{r},t)|^2}{2k_\mathrm{B}T_\mathrm{e}(\mathbf{r},t)}}. \quad (1)$$

The moments $n(\mathbf{r},t)$, $\mathbf{v}(\mathbf{r},t)$, and $T_\mathrm{e}(\mathbf{r},t)$ satisfy the hydrodynamical equations (HDEs)

$$\partial_t n + \nabla\cdot(n\mathbf{v}) = 0, \quad (2a)$$

$$\partial_t \mathbf{v} + (\mathbf{v}\cdot\nabla)\mathbf{v} + \frac{3k_\mathrm{B}}{mn}\nabla(nT_\mathrm{e}) = \frac{1}{m}\mathbf{F}_\mathrm{eff} - \Upsilon\mathbf{v}, \quad (2b)$$

$$\partial_t T_\mathrm{e} + \frac{2}{3}T_\mathrm{e}\nabla\cdot\mathbf{v} + \mathbf{v}\cdot\nabla T_\mathrm{e} = Q, \quad (2c)$$

where

$$\Upsilon(\mathbf{r},t) = \gamma\frac{3\mathrm{v}_{\mathrm{T}0}^3}{2\mathrm{v}^2\mathrm{v}_\mathrm{T}}\left[\mathcal{F}(\mathrm{v}/\mathrm{v}_\mathrm{T}) - \mathrm{e}^{-\frac{\mathrm{v}^2}{\mathrm{v}_\mathrm{T}^2}}\right], \quad (3a)$$

$$Q(\mathbf{r},t) = \gamma_\mathrm{th}\frac{M\mathrm{v}_{\mathrm{T}0}^3}{2k_\mathrm{B}\mathrm{v}_\mathrm{T}}\left[\mathcal{F}(\mathrm{v}/\mathrm{v}_\mathrm{T}) - \frac{T_\mathrm{e}\mathrm{v}_{\mathrm{T}0}^2}{T_0\mathrm{v}_\mathrm{T}^2}\mathrm{e}^{-\frac{\mathrm{v}^2}{\mathrm{v}_\mathrm{T}^2}}\right], \quad (3b)$$

$\mathbf{F}_\mathrm{eff} = -e\mathbf{E} - e\mathbf{v}\times\mathbf{B}$ is the external effective force, $\mathrm{v}_\mathrm{T}(T_\mathrm{e}) = \sqrt{2k_\mathrm{B}(T_0/M + T_\mathrm{e}/m)}$ and $\mathrm{v}_{\mathrm{T}0} = \mathrm{v}_\mathrm{T}(T_0)$ are the OOE and equilibrium thermal velocities, respectively, $\gamma_\mathrm{th} = 2m\gamma/(m+M)$, $\gamma = 8\pi C_\mathrm{ei} n_0\sqrt{M/m(m+M)}/3(2\pi k_\mathrm{B}T_0)^{3/2}$, and $\mathcal{F}(\mathrm{v}/\mathrm{v}_\mathrm{T}) = (\sqrt{\pi}\mathrm{v}_\mathrm{T}/2\mathrm{v})\mathrm{erf}(\mathrm{v}/\mathrm{v}_\mathrm{T})$. The parametric functions $\Upsilon(\mathrm{v},T_\mathrm{e})$ and $Q(\mathrm{v},T_\mathrm{e})$ are depicted in Fig. 1 for silver. The novel HDEs reported above in Eqs. (2) constitute a substantial extension of traditional HDEs used to model the EM response of plasmonic materials, where $\Upsilon \simeq \gamma$. Note that, in the limit of small electron current $\mathrm{v}/\mathrm{v}_\mathrm{T} << 1$ and electron heating $T_\mathrm{e} - T_0 << T_0$, Eq. (3a) reduces to $\Upsilon \simeq \gamma$ (see Fig. 1), thus recovering the RTA, while Eq. (3b) reduces to $Q \simeq -\gamma_\mathrm{th}(T_\mathrm{e} - T_0)$, which describes relaxation towards equilibrium via electron-phonon scattering. Conversely, our results indicate that damping Υ quenches for $\mathrm{v}/\mathrm{v}_{\mathrm{T}0} >> 1$ (see Figs. 1a,c).

3. Conclusions

In conclusion, starting from the Boltzmann equation in the weak coupling assumption, we have developed a novel set of hydrodynamical equations able to describe the ultrafast nonlinear dynamics of electrons in silver. We find that the collision-induced damping quenches for ultrashort pulses with infrared carrier wavelength and peak intensities of the order of GW/cm^2, leading to absorption saturation. Although ultrafast nonlinear dynamics in metals has been experimentally investigated by several groups, typically these studies have focused on EM pulses with time duration > 100 fs. Furthermore the inherently high dispersion of silver leads to efficient temporal broadening of the EM pulse over propagation and intraband absorption saturation has not been observed yet. We conclude that dispersion management techniques and temporal plasmon solitons can constitute promising strategies for counterbalancing temporal dispersion and enabling absorption mitigation in silver-based plasmonic devices, thus opening novel avenues for the development of low-loss plasmonic circuits.

Acknowledgement

A.M. acknowledges support from the Rita Levi Montalcini Fellowship (grant number PGR15PCCQ5) funded by the Italian Ministry of Education, Universities and Research (MIUR), and from the Marie Curie Individual Fellowship OUTNANO (grant number 746774). A.C. acknowledges the U.S. Army International Technology Center Atlantic for financial support (grant number W911NF-14-1-0315). C.C. acknowledges the H2020 QuantERA Quomplex project (grant number 731743).

References

[1] A. Marini and F. Biancalana, Ultrashort self-induced transparency plasmon solitons, *Phys. Rev. Lett.* 110, 243901 (2013).

[2] A. Marini, A. Ciattoni and C. Conti, Out-of-equilibrium electron dynamics of silver driven by ultrafast electromagnetic fields - a novel hydrodynamical approach, *Faraday Discuss.*, 2018, DOI: 10.1039/C8FD00153G

Single-molecule sensing mediated by localized plasmon resonances

Peter Zijlstra, Rachel Armstrong, Michael Beuwer, Matej Horacek, Yuyang Wang
Eindhoven University of Technology, Department of Applied Physics and Institute for Complex Molecular Systems, De Rondom 70, 5612 AP, Eindhoven, The Netherlands
Author e-mail address: p.zijlstra@tue.nl

Abstract: I will outline recent advances in the plasmon-enhanced detection of single molecules and their application toward single-molecule biosensing and single-molecule biophysical studies.

Future optical sensors should report quantitative and reliable data with high signal-to-noise ratio on short timescales. Single-molecule sensing holds great promise to achieve this because the digital signals allow for the detection of very low concentrations, whereas single-molecule sensitivity gives access to different populations in a seemingly homogeneous distribution. Optical detection of single molecules mostly relies on their fluorescence because of the high contrast of this technique against the background. However, the majority of native biomolecules such as proteins hardly fluoresce at all, requiring a different approach for their detection. Plasmon-enhanced detection circumvents the need for labelling by allowing direct optical detection of weakly emitting and completely non-fluorescent species.

In the past decade several mechanisms for plasmon-enhanced single-molecule detection have been demonstrated, including (1) by plasmonically enhancing the emission of weakly fluorescent biomolecules, or (2) by monitoring shifts of the plasmon resonance induced by single-molecule interactions. I will outline recent advances in both approaches at the single-particle and single-molecule level, and will describe their application toward biosensing and single-molecule biophysics.

Collective effects on periodic arrays of plasmonic nanostructures

Alejandro Manjavacas[1,*]

[1]Department of Physics and Astronomy, University of New Mexico, Albuquerque, USA
*corresponding author, E-mail: manjavacas@unm.edu

Abstract

We will discuss some interesting effects arising from the collective interaction in periodic arrays nanostructures.

1. Discussion

Periodic arrays are an exceptionally interesting arrangement for plasmonic nanostructures due to their ability to support strong collective lattice resonances, which arise from the coherent multiple scattering enabled by the array periodicity. Thanks to these exceptional properties, periodic arrays are being exploited in a wide variety of applications, including ultrasensitive biosensing, nanoscale light emission, and color printing, to cite a few [1]. In this talk, we will discuss the response of arrays with multi-particle unit cells using an analytical approach based on plasmon hybridization, which provides a simple an efficient way to design periodic arrays with engineered properties [2], as the ones depicted in Figure 1. We will also discuss how the interplay between the response of the individual constituents and the collective interaction determines the ultimate limits of the field enhancement provided by these systems. We will finish by addressing the effect that the presence of edges, as well as disorder, have on the response of these systems [3].

Acknowledgement

We acknowledge the UNM Center for Advanced Research Computing for computational resources used in this work. This work has been sponsored by the U.S. National Science Foundation (Grant ECCS-1710697).

References

[1] V. G. Kravets, A. V. Kabashin, W. L. Barnes, and A. N. Grigorenko, "Plasmonic surface lattice resonances: A review of properties and applications," *Chem. Rev.*, vol. 118, no. 12, pp. 5912–5951, 2018.

[2] S. Baur, S. Sanders, and A. Manjavacas, "Hybridization of lattice resonances," *ACS Nano*, vol. 12, pp. 1618–1629, 2018.

[3] L. Zundel and A. Manjavacas, "Finite-size effects on periodic arrays of nanostructures," *J. Phys.: Photonics*, vol. 1, no. 1, p. 015004, 2019.

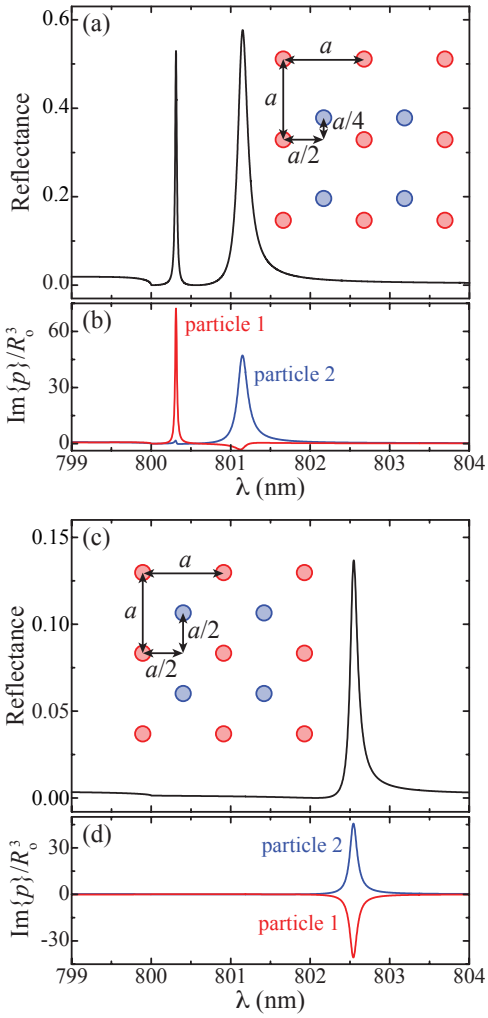


Figure 1: Plasmonic arrays with multi-particle unit cells. (a) Reflectance of a square array with period $a = 800\,\text{nm}$ and two particles per unit cell, arranged as shown in the inset. Both particles are silver nanoshells with silica cores. The inner and outer radii are $R_i = 40\,\text{nm}$, $R_o = 50\,nm$ for particle 1 and $R_i = 50\,\text{nm}$, $R_o = 60\,\text{nm}$ for particle 2. (b) Imaginarypartofthe dipole induced in particle 1 (red curve) and particle 2 (blue curve). (c),(d) Same as (a),(b) but for the array shown in the inset of (c). These results show how, by controlling the relative positions of particle 1 and 2 within the unit cell, it is possible to engineer the response of the array. (Figure adapted from [2]).

The role of the thermo-optic nonlinearity of metals in plasmonic-assisted photocatalysis

Ieng Wai Un[1], Yonatan Dubi[2], Yonatan Sivan[1]

[1]Unit of Electro-optic Engineering, Ben-Gurion University, Israel, [2] Department of Chemistry, Ben-Gurion University, Israel,

*corresponding author, E-mail: sivanyon@bgu.ac.il

Abstract

We show that a failure to account for the thermo-optic nonlinear response of the metals leads to significant overestimates of the temperature developing in illuminated metal-dielectric composites used for photocatalysis. This error is then frequently interpreted incorrectly as non-thermal (i.e., "hot") electrons action. As an alternative, we provide a purely thermal self-consistent model that explains the observed experimental data.

The possibility to use high energy (aka "hot") electrons in illuminated plasmonic nanostructures for applications such as photo-catalysis, sensing, up-conversion attracts a lot of interest recently. A complete theoretical model of this problem should account for the non-equilibrium nature of the electron distribution in the metal, but also for the possibility of both the electrons and the underlying lattice to heat up under continuous wave (CW) illumination. As shown in a series of recent works [1,2], the latter thermal effects dominate completely the photo-catalysis, whereas the non-thermal effects (associated with the so-called "hot" electrons) are more than a billion times weaker. A critical review of some of the most famous experimental papers on the topic has shown that the thermal effects in those papers were grossly underestimated, leading to an incorrect interpretation of the results as due to "hot"-electron action [2,3,4]. A re-interpretation of the experimental data in those papers with a purely thermal model provided an essentially perfect fit to all experimental data (with the bare minimum of fitting parameters) [2,3,4].

The model used so far in [3,4] assumed that the temperature of the plasmonic nanostructure grows linearly with the incoming intensity. However, for sufficiently high intensities, the temperature of the metal and environment rises significantly so that their permittivities are modified significantly with respect to their room temperature values. This, in turn, causes the scattering to be modified with respect to the linear prediction. This thermo-optic nonlinear response was studied in detail for a single spherical particle in [5,6], but so far, not for metal particle composites.

Here, we perform detailed numerical calculations of the temperature of such particle composites at high temperatures, which include the temperature dependence of the metal and host permittivities, as well as the thermal conductivity of the host both for monochromatic and pulsed illumination schemes. We show that the temperature developing in the composites can be even 50% lower than the linear prediction employed so far in [3,4]. As a confirmation, we show that the predictions of the simulations are in good agreement with the temperatures extracted from several papers reporting experimental measurements of temperatures and reaction rates. This further strengthens the interpretation of plasmonic effects in photocatalysis as purely thermal effects (rather than as the result of non-thermal ("hot") electron action) and emphasizes the difficulty in an experimental isolation of these "hot" electron effects from stronger, far more conventional and well-established effects.

References

[1] Y. Dubi, Y. Sivan, ""Hot" electrons in metal nanostructures – non-thermal carrier or heating?", ArXiv https://arxiv.org/abs/1810.00565.

[2] Y. Sivan, I.W. Un, Y. Dubi, "Assistance of metal nanoparticles in photocatalysis – nothing more than a classical heat source", Faraday Discussions, in Press (2019).

[3] J. Baraban, I.W. Un, Y. Dubi, Y. Sivan, "Comment on "Quantifying hot carrier and thermal contributions in plasmonic photocatalysis", Science, under review.

[4] Y. Dubi, I.W. Un, Y. Sivan, "Thermal effects - an alternative mechanism for plasmonic-assisted photo-catalysis", submitted.

[5] Y. Sivan, S.-W. Chu, "Nonlinear plasmonics at high temperatures", Nanophotonics 6, 317-328 (2017).

[6] I. Gurwich, Y. Sivan, "A metal nanosphere under intense continuous wave illumination – a unique case of non-perturbative nonlinear nanophotonics", Phys. Rev. E 96, 012212 (2017).

Backward groove-regulated light wave resonance inside a subwavelength metallic slit

Jian-Shiung Hong and Kuan-Ren Chen*

Department of Physics, National Cheng Kung University, Tainan 70101, Taiwan
*corresponding author, E-mail: chenkr@phys.ncku.edu.tw

Abstract

Grooves patterned at the exit side of a subwavelength metallic slit are known to manipulate the transmitted light profile. We study the groove effect and find a backward coupling mechanism. The transmitted light is scattered by the grooves and then re-enters into the slit. This causes a phase delay of the reflected wave and is considered a reduction in the resonant film thickness. The traveling wave in the slit can be more in phase to significantly enhance the transmission.

1. Introduction

The optical response of subwavelength structures in metal films [1] is extensively studied to understand the enhanced transmission mechanism. For a single subwavelength slit pierced in a metal film, the forward coupling of the incident light causes the funneling of the incident energy to enhance the light transmission [2]. Grooves patterned at the entrance side of the film can further increase the channeling of the incident light into the slit [3]. The transmitted light through the slit can be forward coupled with the grooves patterned at the exit side of the film to affect the light spatial distribution in the exit space, such as controlled beaming [4] and beyond-limit focusing [5]. The mechanism for a subwavelength slit and coupling grooves at the exit side is well studied [6].

We analytically study the effect of the exit-side grooves and discover a novel backward coupling mechanism that causes a part of the scattered light to flow back into the slit to change the resonance condition. This backward coupling mechanism can increase the phase of the wave reflected at the exit boundary in the case studied. As a result, the film thickness at resonance is effectively reduced. The roundtrip wave can be made more in resonance so as to significantly enhance the transmission.

2. Reflection at the slit exit

Figure 1(a) shows a subwavelength slit in a metal film patterned with multiple grooves. Without loss of generality, the film is made of a perfect electric conductor (PEC). A p-polarized wave of wavelength λ_0 is incident inside the slit. After the transmission, it is both radiated into free space and scattered by the grooves [6].

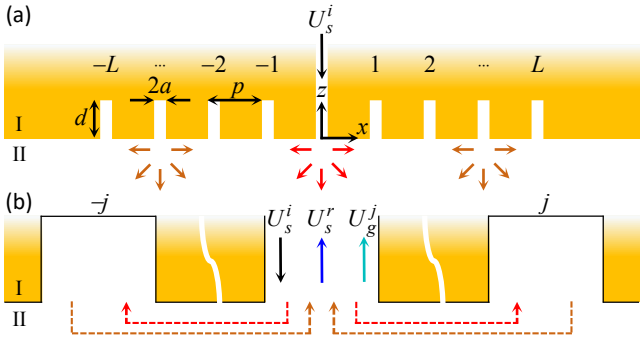


Figure 1: (a) Schematic of a slit and a number of grooves in a PEC film. (b) Reflected wave at the exit interface of the slit and scattered wave by the $\pm j$th grooves coupled into the slit.

Suppose that the system is divided into two regions: region I for $z > 0$ and region II for $z < 0$. By defining the boundary magnetic field U_0^l and its normal derivative DU_0^l at each opening for l from $-L$ to L, we obtain a set of equations based on Green's theorem:

$$\sum_{k=-L}^{L} I_{0,k} DU_0^k = 2 - \frac{i}{k_0} DU_0^0, \tag{1a}$$

$$\sum_{k=-L}^{L} I_{l,k} DU_0^k = \frac{1}{k_0} \cot(k_0 d) DU_0^l, \tag{1b}$$

where

$$I_{l,k} = \frac{i}{2} \int_{kp-a}^{kp+a} H_0^{(1)}(k_0|x - lp|)dx. \tag{2}$$

Now, we analyze the field in the slit. Given $U_0^0 = 2 - (i/k_0)DU_0^0$ for $|x| < a$, Eq. (1a) indicates

$$U_0^0 = 1 + \frac{k_0 I_{0,0} - i}{k_0 I_{0,0} + i} + \frac{2i}{k_0 I_{0,0} + i} \sum_{j=1}^{L} I_{0,j} DU_0^j. \tag{3}$$

We obtain that the first term is the incident field, the second term represents the field reflected at the interface of the slit exit, and the third term indicates the sum of the fields scattered by the $\pm j$th grooves as the radiated cylindrical wave from the grooves to the slit

opening for j from one to L and coupled backward into the slit. We illustrate the reflection inside the slit and this backward coupling from the $\pm j$th grooves in Fig. 1(b). The slit-reflected field and the groove-scattered fields will propagate away from the interface.

The sum of the fields are considered as the effectively reflected field by the interface. We assume that the effective reflection coefficient is r_L. The field inside the slit can be expressed as $U_1(x,z) = U_s^i(x,z) - r_L U_s^i(x,0)\exp(ik_0 z)$. By comparing this expression at $z = 0$ with Eq. (3), we obtain $r_L = r_0 + r_g^L$, where

$$r_0 = -\frac{k_0 I_{0,0} - i}{k_0 I_{0,0} + i}, r_g^L = \frac{-2i}{k_0 I_{0,0} + i}\sum_{j=1}^{L} I_{0,j} D U_0^j \quad (4)$$

are the intrinsic slit reflection coefficient and the contribution coefficient from the grooves, respectively. In our case, we obtain $\arg(r_L)$ is increased with L.

3. Resonance inside the slit

In the slit of thickness b, the effectively reflected wave at the exit interface is again reflected at the entrance interface and the reflection coefficient at the interface is r_0 without the patterned grooves. Due to the reflection at both interfaces, an incident plane wave on the slit will travel in roundtrips after the transmission through the entrance interface. Suppose that the magnetic field of the incident plane wave at $z = b$ is $U_b^i = \exp(-ik_0 b)$. For $0 \le z \le b$, the magnetic field in the slit is

$$U_s(z) = U_b^i t_0 e^{ik_0 b}\frac{e^{-ik_0 z} - r_L e^{ik_0 z}}{1 - r_L r_0 e^{i2k_0 b}}, \quad (5)$$

where $t_0 = 2i/(k_0 I_{0,0} + i)$ is the transmission coefficient of the entrance interface. The electric field is obtained from $E_{xs}(z) = (-i/k_0)\partial_z U_s(z)$. The transmittance from the roundtrip-wave model is $T_s = \mathrm{Re}\{-E_{xs}(z)U_s^*(z)\}$.

The resonance condition is satisfied when

$$2k_0 b_{\mathrm{res},q} + \arg(r_L) + \arg(r_0) = 2q\pi, \quad (6)$$

where q is a positive integer and $b_{\mathrm{res},q}$ is the film thickness at resonance. As L increases, $b_{\mathrm{res},q}$ will be slightly reduced due to the increased phase of r_L in our case. For a film thickness b slightly smaller than $b_{\mathrm{res},q}$, the roundtrip wave inside the slit will be closer to the resonance condition so that more incident energy can be transmitted. Figure 2 shows the resultant transmittance T_s yielded for each L when b is 6% of λ_0 smaller than $b_{\mathrm{res},1}$. We obtain that, in addition to the enhanced transmission when $L = 0$ [2], significant 70% more incident energy is transmitted.

4. Conclusions

We discovered a backward coupling mechanism for the grooves patterned at the exit side of the metal film

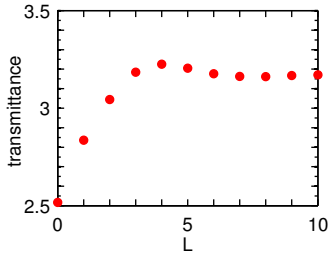


Figure 2: Transmittance T_s at the slit exit.

to regulate the resonance. The phase of the effective reflection coefficient is increased for the case studied. Our analysis based on the roundtrip-wave model shows that the increased phase causes an effective reduction of the film thickness required to satisfy the resonance condition. As a result, the roundtrip wave in a slit of the film thickness being slightly smaller than that of resonance can be more in phase so as to transmit significantly more light energy.

Acknowledgement

Ministry of Science and Technology, Taiwan, and National Center for High-performance Computing.

References

[1] T. W. Ebbesen, H. J. Lezec, H. F. Ghaemi, T. Thio, and P. A. Wolff, "Extraordinary optical transmission through sub-wavelength hole arrays," *Nature*, vol. 391, no. 6668, pp. 667–669, 1998.

[2] J.-W. Li, J.-S. Hong, W.-T. Chou, D.-J. Huang, and K.-R. Chen, "Light funneling profile during enhanced transmission through a subwavelength metallic slit," *Plasmonics*, vol. 13, no. 6, pp. 2249–2254, 2018.

[3] F. J. García-Vidal, H. J. Lezec, T. W. Ebbesen, and L. Martín-Moreno, "Multiple paths to enhance optical transmission through a single subwavelength slit," *Phys. Rev. Lett.*, vol. 90, no. 21, p. 213901, 2003.

[4] H. J. Lezec, A. Degiron, E. Devaux, R. A. Linke, L. Martin-Moreno, F. J. Garcia-Vidal, and T. W. Ebbesen, "Beaming light from a subwavelength aperture," *Science*, vol. 297, no. 5582, pp. 820–822, 2002.

[5] K. R. Chen, "Focusing of light beyond the diffraction limit of half the wavelength," *Opt. Lett.*, vol. 35, no. 22, pp. 3763–3765, 2010.

[6] L. Martín-Moreno, F. J. García-Vidal, H. J. Lezec, A. Degiron, and T. W. Ebbesen, "Theory of highly directional emission from a single subwavelength aperture surrounded by surface corrugations," *Phys. Rev. Lett.*, vol. 90, no. 16, p. 167401, 2003.

Confining plasmon-exciton interaction in individual nanocavity

Jiawei Sun[1], Huatian Hu[1], Di Zheng[2], Daxiao Zhang[2], Shunping Zhang,*[,2] and Hongxing Xu,*[, 1,2]

[1]The Institute for Advanced Studies, Wuhan University, Wuhan 430072, China.

[2]School of Physics and Technology, Center for Nanoscience and Nanotechnology, and Key Laboratory of Artificial Micro- and Nano-structures of Ministry of Education, Wuhan University, Wuhan 430072, China.

*corresponding author, E-mail: spzhang@whu.edu.cn
*corresponding author, E-mail: hxxu@whu.edu.cn

Abstract

The highly-confined nanogap plasmons in nanocube-over-mirror (NCOM) system possess huge enhancement of electric field and local density of states (LDOS)[1, 2], and these fascinating properties make NCOM to be an idea platform to study the light-matter interaction. Here, we demonstrate the coupling between the neutral excitons in monolayer TMDs and the magnetic plasmons in NCOM. In this geometry, we found that huge PL enhancement and Rabi splitting are achieved simultaneously, whereas the circular emission of PL can be manipulated by shifting the plasmon resonance through depositing alumina layers.

1. Introduction

Transition metal dichalcogenides (TMDs) are widely atrracted due to its fascinating optical and electric properties. The transition dipole moment $\boldsymbol{\mu}$ of monolayer TMDs is huge, which facilitating the light-matter coupling[3, 4]. Here, we found that coupling between excitons in monlayer WSe_2 and magnetic plasmon mode in NCOM reached internediate regime. And huge PL enhancement (~1700 times) and Rabi splitting were achieved simultaneously. Such huge PL enhancement mainly comes from the enhancement of emission (~410 times) process. Another facinating property of monolayer TMDs is the valley selection rule[5], which make the PL emission preserve the same chirality as the circular polarized excitaiton light. Here we found that the circular emission of the MoS_2 can be manipulated by the magnetic plasmon in NCOM. The circular polarization of the PL was enhanced but negative due to the plasmon modulation.

2. Results and discussion

Figure 1a shows the sample geometry of the NCOM coupled with monolayer WSe_2. Normalized scattering spectra for different alumina deposition were shown in Figure 1b. The scattering spectra was taken by a s-polarized light, because the s-polarized light can excite a pure magnetic mode rather than the dipole-dipole mode according to our recent research[2]. An apparent splitting of the scattering spectra (highlighted by a grey dashed line) at the exciton peak position was found. After fitting the scattering spectra with the two coupled-oscillators model, we found a 35.0 meV Rabi splitting (shown in Figure 1c). The splitting is smaller than the plasmon linewidth (~120 meV) but comparable with the exciton linewidth (~40 meV), indicating that the coupling between the magnetic plasmon mode and excitons in WSe_2 is in the intermediate regime. Besides, the PL spectra (shown in 1d) demonstrate a huge enhancement of PL was achieved in this system. So in this system, the Rabi splitting and PL enhancement can be achieved simultaneously. The real enhancement of PL due to the interaction with magnetic plasmon mode reaches nearly 1700 times. 410 times of the PL enhancement comes from the emission if we take out the PL enhancement coming from the excitation process. Such high emission brightness of excitons is owing to that the coupling is just in the intermediate regime[6].

A monolayer MoS_2 was used to couple with the NCOM, the sample geometry is shown in Figure 2a. The plasmon resonance was shifted by coating alumina on top of the silver nanocube (shown in Figure 2b). We excited the sample with a 633 nm left circular (σ^-) light, and then we collected the left circular and right circular (σ^-) light respectively. The PL intensity against the plasmon resonance is shown in Figure 2c. We then calculate the circular polarization according to $\rho = \frac{I(\sigma^-) - I(\sigma^+)}{I(\sigma^-) + I(\sigma^+)}$. So we can see that the circular polarization can be tuned very well by coating the alumina. A circular polarization nearly -18% can be realized which is much higher than the background (~5%) MoS_2 without silver nanocubes on it, but this circular polarization changed its sign. This manipulation of the circular polarization is probably due to the tilt angle between the bottom side of the silver nanocube and horizontal plane.

3. Conclusions

In conclusions, we demonstrate that huge emission enhancement and Rabi splitting can be achieved simultaneously in the NCOM coupled with monolayer WSe_2 system. Besides, the circular emission from the monolayer

MoS_2 can be manipulated by the magnetic plasmon mode in NCOM. Meanwhile, the circular polarization changed with shifting the plasmon resonance by alumina depositing. We believe that NCOM coupled with TMDs system is an ideal platform for the study of light-matter interaction.

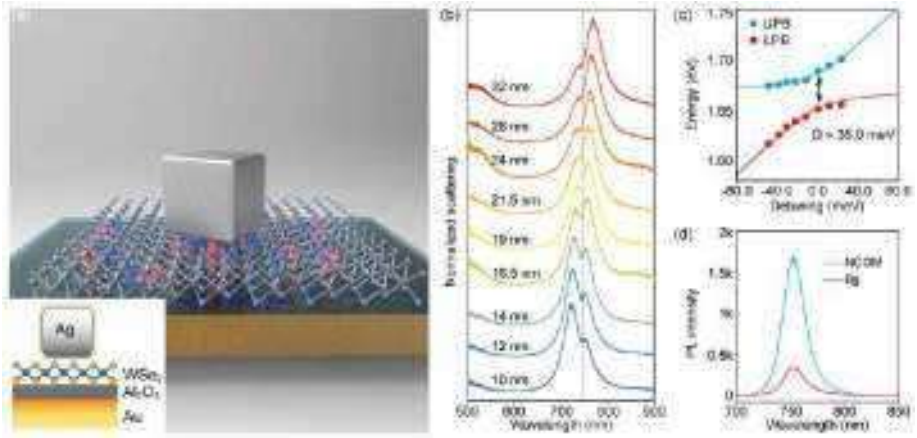


Figure1. (a) The sample geometry of the NCOM coupled with monolayer WSe_2. (b) Normalized scattering spectrum taken by s-polarized light for a NCOM coupled with a monolayer WSe_2. Alumina coating changing from 10 nm to 32 nm. (c) Plots of energy of upper plexciton branch (UPB) and lower plexciton branch (LPB) against detuning. (d) The PL spectra of the monolayer WSe_2 with (cyan) and without (red) the silver nanocube.

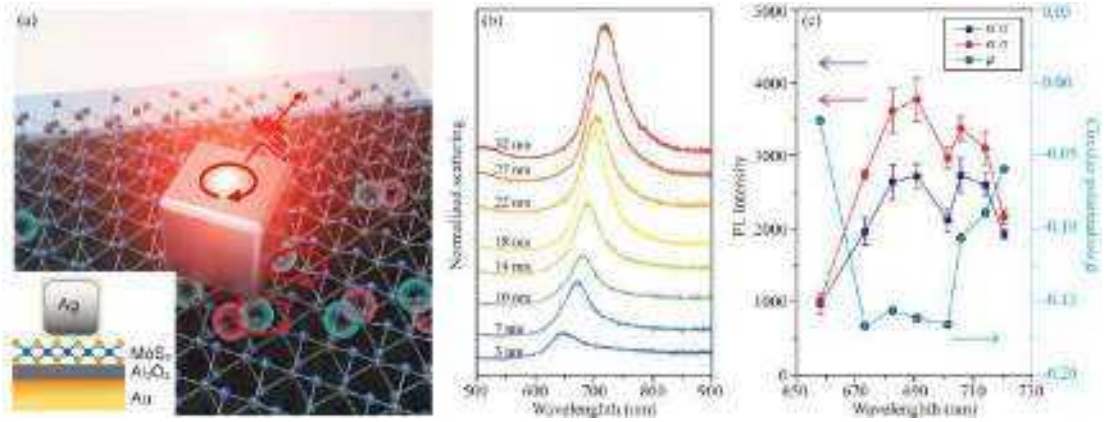


Figure 2. (a) The sample geometry of the NCOM coupled with monolayer MoS_2. (b) Normalized scattering spectra for a single silver nanocube over ultra-smooth gold film coupled with monolayer MoS_2. Alumina coating changing from 3 nm to 32 nm. (c) Helicity-resolved PL intensity and circular polarization of the NCOM coupled with monolayer MoS_2 against plasmon resonance. Excitation light is 633 nm σ^- circular polarized light.

References

1. Lassiter, J.B., et al., *Plasmonic waveguide modes of film-coupled metallic nanocubes.* Nano Letters, 2013. **13**(12): p. 5866-5872.
2. Sun, J., et al., *Light-Emitting Plexciton: Exploiting Plasmon-Exciton Interaction in the Intermediate Coupling Regime.* ACS Nano, 2018. **12**(10): p. 10393-10402.
3. Zheng, D., et al., *Manipulating coherent plasmon-exciton interaction in a single silver nanorod on monolayer WSe_2.* Nano Letters, 2017. **17**(6): p. 3809-3814.
4. Kleemann, M.E., et al., *Strong-coupling of WSe_2 in ultra-compact plasmonic nanocavities at room temperature.* Nature Communications, 2017. **8**(1): p. 1296.
5. Xiao, D., et al., *Coupled spin and valley physics in monolayers of MoS_2 and other group-VI dichalcogenides.* Physical Review Letters, 2012. **108**(19): p. 196802.
6. Hugall, J.T., A. Singh, and N.F. van Hulst, *Plasmonic cavity coupling.* Acs Photonics, 2018. **5**(1): p. 43-53.

Plasmoemission: Nonlinear Electron Emission from Surface Plasmon Polaritons

Frank-J. Meyer zu Heringdorf, Daniel Podbiel, Philip Kahl, Pascal Dreher, David Janoschka

Faculty of Physics and CENIDE, University of Duisburg Essen, Duisburg, Germany
*corresponding author, E-mail: meyerzh@uni-due.de

Abstract

The time-resolved investigation of surface plasmon polaritons by means of photoelectron imaging after femtosecond laser pulse excitation has developed into a mature technique over the last years. By using a normal-incidence geometry in a photoemission electron microscope it has become possible to record slow-motion movies of surface plasmon propagation and to spatio-temporally resolve standing plasmon waves. Analyzing the energy distribution of emitted electrons shows that above threshold ionization and strong-field emission from plasmonic foci is possible.

1. Introduction

Surface plasmon polaritons (SPPs) are longitudinal waves in the electron system of selected metal surfaces that are coupled to an oscillating electric field with unique properties. Imaging of SPPs in time and space can be accomplished by means of time-resolved nonlinear photoemission microscopy (PEEM). Figure 1 (a) shows a sketch of the experimental setup used at the University of Duisburg-Essen. A commercial low-energy electron microscope (ELMITEC GmbH) is operated in photoemission mode. Femtosecond laser pulses from a Ti:Sapphire oscillator (central wavelength $\lambda = 800\,\mathrm{nm}$, pulse duration $< 15\,\mathrm{fs}$) impinge on the sample along the surface normal and liberate electrons by means of a nonlinear emission process. The emitted electrons pass through an electron-optical magnification system where they can also be energy-filtered. Ultimately, the spatial distribution of the emitted electrons is imaged on a screen.

For the experiment discussed here, we start with a polycrystalline Ag film and use a focused Ga ion beam to mill grooves with the shape of concentric circles into the film. A cross-section through a resulting structure is sketched in Fig. 1 (b). At the grating couplers on the left and right of Fig. 1 (b) the femtosecond laser pulses are coupled into SPPs that propagate across the surface and that are imaged in our normal-incidence pump-probe PEEM experiment [1]. Since the laser pulse intensity is approximately equal across the milled structure, each laser pulse simultaneously excites SPPs on either side of the grating coupler. Here, we will only discuss the SPPs that are propagating towards each other, i.e., towards the center of the coupler. The circular shape of the grating coupler ensures focusing of the SPPs into the center of the circle. The innermost ring of the grating coupler has a diameter of $40\,\mu\mathrm{m}$ by design,

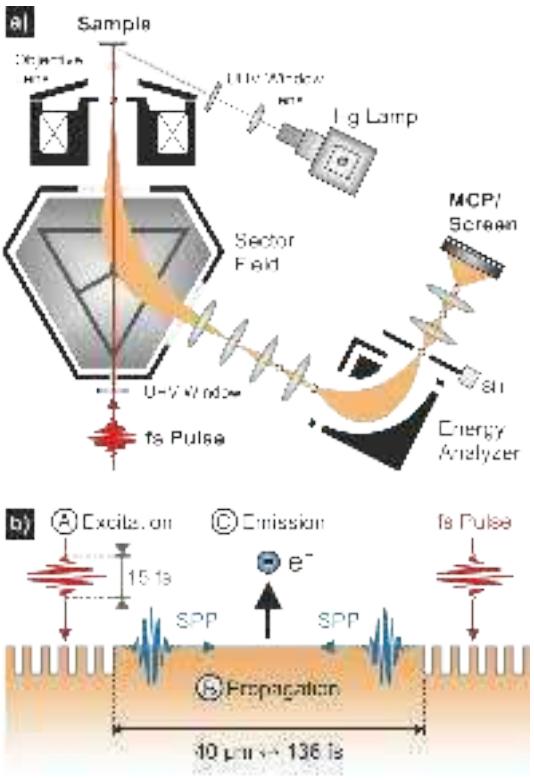


Figure 1: Experimental concept. (a) a commercial low energy electron microscope is operated in photoemission mode. The sample is illuminated by femtosecond laser pulses that liberate electrons from the surface by means of a nonlinear emission process. After optional energy filtering the spatial distribution of the electrons is imaged on a screen. (b) sketch of the experimental situation. A fs laser pulse excites two SPP pulses that propagate towards each other and meet in the center after the exciting fs laser pulse has decayed. Electron emission from the center of the structure is due to the transiently formed standing SPP wave.

which implies that the counter-propagating SPPs, advancing with a phase-velocity of 97.9% of the speed of light in vacuum [2] ($v_p \approx 293.5\,\mathrm{nm/fs}$) need approximately $68\,\mathrm{fs}$ to arrive in the center of the circle. At this time the exciting $< 15\,\mathrm{fs}$ laser pulse is already over. When the two counter-propagating SPPs transiently form a standing wave in the center of the ring, any electron emission (in addition to the photoemission background) must be explained by electron emission from the SPP. To semantically distin-

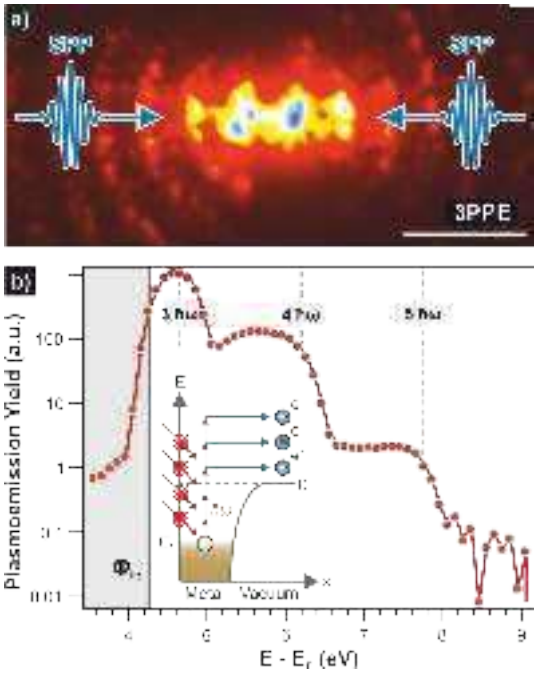


Figure 2: Plasmoemission from a SPP focus. (a) Energy-filtered PEEM image showing third order emission in the center of the circular grating coupler. The highest electron yield is observed near the focus spot. The concentric fringes surrounding the focus originate from a standing SPP wave and resemble a spacing of $\lambda_S/2$. The scalebar has a length of $1\,\mu$m. (b) Energy distribution of electrons emitted from the focus. To overcome the work function, at least a third order process is necessary. The spectrum also shows fourth and fifth order emission. The inset illustrates the mechanism of this above-threshold ionization, where more energy quanta are absorbed from the SPP field than would be required to just overcome the work function barrier.

guish the well-known two-photon photoemission from the described mechanism of emission from the SPP, the latter mechanism was coined *plasmoemission* [3].

In our experiment with the circular grating coupler, the combination of SPP focusing and spatio-temporal separation of light and SPP allows us to study electron emission from strong plasmonic fields in more detail. Figure 2 shows experimental results obtained near the focus of the SPP. Panel (a) shows an energy-filtered image with the focus in the center. The two counter-propagating SPPs coming from the left and from the right meet in the center of the circular grating coupler and form a standing wave with fixed positions of nodes and anti-nodes. As electrons are emitted from the anti-nodes of the transverse part of the SPPs standing wave electric field [**?**], concentric phase-fronts with a separation of half the SPP wavelength, $\lambda_S/2$ are visible. Due to the focusing, the SPP field strength and the emitted electron yield close to the focus are much stronger than at other areas on the surface.

Inserting an aperture into one of the conjugate image planes within the microscope's beam path, centering the aperture on the focus point, and analyzing the energy of the emitted electrons from the focus point provides further information about the emission mechanism. Figure 2 (b) shows an energy spectrum of the electrons emitted from the focus. The energy scale has been offset using the literature value of the work function of polycrystalline Ag of $\Phi_{lit} = 4.26\,\text{eV}$ [4]. As the energy of SPP quanta is only $E_S = \hbar\omega = 1.55\,\text{eV}$, any emission process below third order is suppressed because of the work function of the sample. The energy spectrum in Fig. 2 (b) shows unexpectedly high electron energies and exhibits several distinct steps that are separated by E_S in energy. Emitted electrons with such high energies can be explained by higher order nonlinear emission processes. The higher the order of the process, the lower the emission probability, and accordingly, the steps in the spectrum resemble replicas of the Fermi-edge for the different emission orders. Note that the quantitative determination of the electron temperature is not possible due to the limited energy resolution of the used energy filter.

In the spectrum of Fig. 2 (b), emission of up to the fifth order is observed. The inset in Fig. 2 illustrates this above threshold ionization in an energy-level picture. Not only can we unambiguously conclude from the data that the nonlinear electron emission is caused by plasmoemission, but we can also demonstrate that the SPP field in the focus is strong enough to enhance nonlinear emission pathways.

In conclusion, focusing of SPPs with appropriate excitation structures provides a promising pathway to study highly nonlinear electron emission. Improving the focus quality and enhancing the SPP excitation will push the system into the plasmonic strong-field regime, where field emission becomes the dominating emission channel. Such experiments are currently under way.

Acknowledgement

We gratefully acknowledge financial support from the Deutsche Forschungsgemeinschaft (DFG) through programs SFB 616, SPP 1391, and CRC 1242 (project number 278162697–SFB 1242).

References

[1] P. Kahl et al., Direct Observation of Surface Plasmon Polariton Propagation and Interference by Time-Resolved Imaging in Normal-Incidence Two Photon Photoemission Microscopy. *Plasmonics* 13: 239–246, 2018

[2] P. B. Johnson and R. W. Christy, Optical Constants of the Noble Metals, *Phys. Rev. B* 6: 4370–4379, 2010

[3] D. Podbiel et al., Imaging the Nonlinear Plasmoemission Dynamics of Electrons from Strong Plasmonic Fields, *Nano Lett.* 17: 6569–6574, 2017

[4] A.W. Dweydari and C.H.B. Mee, Work Function Measurements on (100) and (110) Surfaces of Silver. *Phys. Stat. Sol. (a)* 27: 223-230, 1975.

Emission Pathways for Electrons in Surface Plasmon Enhanced Photoemission

David Janoschka [1*], Pascal Dreher[1], Timothy J. Davis[1,2], Frank-J. Meyer zu Heringdorf[1]

[1] Faculty of Physics and CENIDE, University of Duisburg-Essen, Lotharstrasse. 1, 47057 Duisburg, Germany
[2] School of Physics, University of Melbourne, Parkville Victoria 3010, Australia
*corresponding author, E-mail: david.janoschka@uni-due.de

Abstract

In surface plasmon polariton-enhanced nonlinear photoemission from gold surfaces, several pathways can lead to the emission of electrons. In addition to the well-established two-photon absorption, emission purely from the plasmonic field can occur. More complex emission mechanisms come into play when there are interferences between the surface plasmon polariton and a probing femtosecond laser pulse. Here we use a pump-probe experiment to describe how the different contributions of plasmon and probing laser field can be disentangled.

1. Introduction

Electron emission from metal surfaces under illumination by light proceeds by simultaneous or subsequent absorption of one or more photons, depending on the intensity of the incident light and the work function of the metal. Likewise, in the presence of surface plasmon polaritons (SPPs), the electrons can absorb energy from the plasmon wave and also be ejected from the metal surface. Figure 1 (a) illustrates these two possible emission pathways in an energy diagram. Both have been isolated and identified in the past, and they were referred to as photoemission and plasmoemission, respectively [1]. When both SPP and light fields are simultaneously present, it is more difficult to separate photon-related from SPP-related contributions to the overall emission yield. Here, we demonstrate that such separation can be achieved by using photo-emission electron microscopy combined with optical pump-probe techniques. We show that in a pump-probe experiment with individual control over the pump- and probe-pulse intensities different emission mechanisms would be distinguishable by their characteristic nonlinearities.

2. Experiment

We use time-resolved nonlinear photoemission electron microscopy (PEEM) and combine it with a Ti:Sapphire laser to observe SPPs in a pump-probe experiment. In such an experiment, as sketched in Figure 1 (b), a first linearly polarized (pump) laser pulse incident on a grating coupler excites a SPP which then propagates across the surface. A time-delayed second linearly polarized (probe) laser pulse interferes constructively with the SPP pulse and locally increases the nonlinear photoemission yield. Given the velocity of the SPP (almost the speed of light in vacuum) it is clear that such an experiment requires femtosecond time scales. In our case, the used laser pulses are < 15 fs short, and the relative precision in the time delay (Δt) between pump- and probe pulse is of the order of 50 attoseconds. We use focused ion-beam milled grating couplers to effectively convert our $\lambda = 800$ nm laser pulses into SPPs. For the single-crystalline Au(111) platelets that we are using as plasmonic material, such excitation results in long-range SPPs of a wavelength of ≈ 780 nm. Since the work function of the Au platelets is of the order of 5.3 eV, we have to deposit a submonolayer of Cs prior to our experiments in order to enable a two photon (or two plasmon) emission process.

3. Results and Discussion

Figure 2 shows a result from a time-resolved experiment at a pump-probe delay time of $\Delta t \approx 70$ fs. The grating coupler used for excitation of the SPP is on the left, next to a static wave pattern that is due to the interference of the pump beam with the SPP it excites. Further away from the

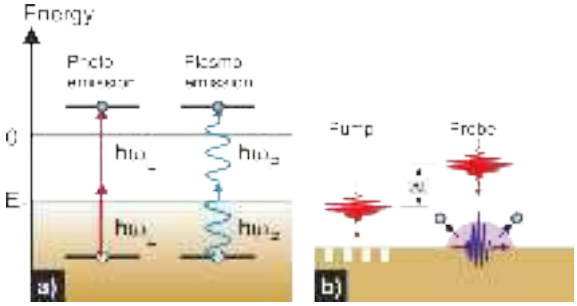


Figure 1: SPP based nonlinear photoemission. (a) Energy level diagram indicating how electrons can be liberated from a solid either by absorption of two photons (photoemission) or two plasmons (plasmoemission). (b) Illustration of the pump-probe experiment. A fs laser pump-pulse (red) excites a fs SPP pulse (blue), which propagates across the surface and becomes probed by a second (delayed) fs laser pulse. In the interaction region of the probe-pulse with the SPP (purple), the interference leads to a spatially modulated pattern of emitted electrons.

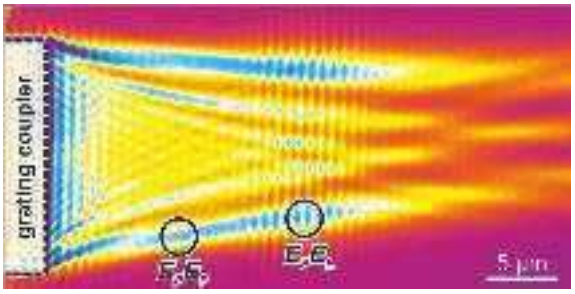


Figure 2: Example of a pump-probe PEEM image at a delay-time of $\Delta t \approx 70\,\text{fs}$. A SPP is launched from the grating coupler on the left by the pump-pulse. The SPP propagates to the right and emits electrons by plasmoemission ($E_P E_P$). When the probe-pulse arrives at the surface, the SPP has already propagated by $15 - 20\,\mu$m. The time-dependent interference between the propagating SPP and the oscillating laser field causes a spatial modulation of the emitted electron yield ($E_P E_L$).

coupler a modulation of the background intensity is visible (labeled by $E_P E_P$) that resembles the near-field diffraction pattern of a slit. At a distance $15 - 20\,\mu$m away from the grating coupler, a prominent wave intereference pattern is formed (labeled by $E_P E_L$). Unlike all other features in the experiment, the location of this interference pattern depends on delay time.

To better understand the different elements that contribute to the overall electron yield in Fig. 2, we describe the contrast as the temporal integral of the time-dependent coherent superposition of all electric fields at the surface [2]. Due to the normal-incidence geometry for our laser pulses relative to the surface plane, the light field has no spatial dependence. Furthermore, we only consider SPPs that were created by the pump pulse, and we neglect any SPPs that would be created by the probe laser pulse. In a one-dimensional description the expected yield is then given by

$$Y(r, \Delta t) \propto \int |E_P(r,t) + E_L(t + \Delta t)|^4 \, dt. \qquad (1)$$

This yield model can be independently applied for the transverse and the longitudinal part of the SPPs' electric field [1]. For the pump-probe experiment described here, a discussion of the longitudinal fields is sufficient [3]. Expanding Eq. (1) highlights several individual emission paths

$$Y \propto \int E_L^4 + 4E_L^3 E_P + 6E_L^2 E_P^2 + 4E_L E_P^3 + E_P^4 \, dt. \quad (2)$$

Note that in Eq. (2) the position and time-dependence were suppressed for clarity. The E_L^4 contribution simply accounts for a two photon photoemission background. In the same way, the E_P^4 term describes the time-integrated plasmoemission from the longitudinal field of the SPP. The remaining three terms are interferences between the longitudinal SPP field and the probe laser pulse. The $E_L^2 E_P^2$ term describes an emission process where both a photon and a plasmon are absorbed by the electron before it can be liberated from the Au. The $E_L^3 E_P$ and $E_L E_P^3$ are more complex emission pathways. All the interference terms have in common, however, that for an experiment they predict different scaling behaviour for both SPP strength and laser pulse strength.

To disentangle the contributions of the individual terms to the emission, we thus measured the electron yield at the point of overlap of the probe and SPP pulses as functions of both the probe and SPP pulse intensities. Key to achieving these measurements is the fact that the SPP intensity is determined by the strength of the pump pulse that can be adjusted independently of the probe pulse. In this manner we can experimentally verify the presence of all the individual electron emission pathways suggested by Eq. (2).

4. Conclusion

In our study we identified both experimentally and theoretically the emission pathways for electrons in SPP enhanced nonlinear photoemission. By adjusting the SPP and laser field strength independently, we were able to experimentally verify the existence of all theoretically predicted pathways. Several emission mechanisms exist, into which SPP and laser pulse enter with different exponents. While this can be easily understood in a semi-classical electrodynamic picture, our study paves the way for a deeper understanding of SPP-light interference at a more fundamental level.

Acknowledgement

We gratefully acknowledge financial support from the Deutsche Forschungsgemeinschaft (DFG) through programs SFB 616, SPP 1391, and CRC 1242 (project number 278162697–SFB 1242). Samples with Au platelets were provided by B. Frank & H. Giessen from the University of Stuttgart (Germany).

References

[1] D. Podbiel, Ph. Kahl, A. Makris, B. Frank, S. Sindermann, T. J. Davis, H. Giessen, M. Horn-von Hoegen and F. Meyer zu Heringdorf, Imaging the Nonlinear Plasmoemission Dynamics of Electrons from Strong Plasmonic Fields, *Nano Lett.* 17: 6569–6574, 2017.

[2] A. Kubo, N. Pontius, and H. Petek, Femtosecond Microscopy of Surface Plasmon Polariton Wave Packet Evolution at the Silver/Vacuum Interface, *Nano Lett.*, 7: 470–475, 2007.

[3] D. Podbiel, P. Kahl, and F.-J. Meyer zu Heringdorf, Analysis of the contrast in normal-incidence surface plasmon photoemission microscopy in a pump–probe experiment with adjustable polarization, *Appl. Phys. B* 122: 90, 2016.

Silicon Photonic Integrated Circuits

Hybrid on silicon photonics for light amplification and Fanoenhanced electro-optical modulation at telecom wavelengths

Jianhao Zhang[1,2], John Röhn[3], Xavier Le Roux[1], Carlos Alonso-Ramos[1], Mathias Berciano[1], Delphine Marris-Morini[1], Sailing He[2], Zhipei Sun[3], Laurent Vivien[1], and Eric Cassan[1]

[1] Centre for Nanoscience and Nanotechnology (C2N), CNRS, University Paris-Sud, University Paris-Saclay, 91405 Orsay cedex, France
[2] Centre for Optical and Electromagnetic Research, Zijingang Campus, Zhejiang University, Hangzhou 310058, China
[3] Department of Electronics and Nanoengineering, Aalto University, Tietotie 3, FI-00076 Espoo, Finland
*corresponding author, E-mail: eric.cassan@u-psud.fr

Summary

The challenges to be solved in silicon photonics at telecom wavelengths are still of several kinds. Among these, two important locks concern the realization of integrated optical amplifiers essential for re-amplifying attenuated signals, and the realization of fast electro-optical modulators (>>10GHz) with low power consumption (<1fJ/bit) [1]. The approaches used in the literature to address these two locks have led to a wealth of proposals and works, including the hybrid integration of III/V semiconductors on silicon by sticking vignettes or full plate, or more rarely by monolithic growth. This solution, based directly on pre-existing mature solutions, raises co-integration problems, both in terms of materials and photonic integration (coupling of Si guide light to III/V guides, etc.), but has already demonstrated several very solid proposals. However, it presents difficulties related to the complexity of processes and technologies, without integration into a complete CMOS process flow [1].

In this context, our presentation will summarize our recent contributions on the two key functions mentioned above. Our approach to light amplification is based on the integration of Erbium-doped materials and brings a strong innovation to the field through the integration of state-ofthe-art active materials combined with a proper choice of slot silicon nitride waveguides. We report ultra-high onchip optical gain in Erbium-based hybrid slot waveguides with a monolithic, CMOS-compatible and scalable atomiclayer deposition (ALD) process. The nature of ALD provides a versatile tool to atomic scale engineering of the gain layer properties and an efficient integration with SiN waveguides and other photonic structures. We demonstrate 20dB/cm of modal gain at λ=1.53μm, which opens up very interesting perspectives for the creation of light sources and their transcription into various integrated system-level functions [2].

In another complementary direction, the signals thus produced or amplified must be encoded by electro-optical modulation for the realization of optical links. We started from the observation that beyond the physical mechanisms leading to index modulation by refraction, a significant part of the contribution to the energy dissipation of the modulators was due to the type of resonators or interferometers used. An electro-optical modulator exploiting the plasma effect (refraction on free carriers) and integrating a phase modulator into a Mach-Zehnder interferometer geometry, for example, consumes several ps/bit. This is mainly due to the size of the interferometer (several mm), which brings back high structural capacities. The use of nanoresonators, such as nanobeam cavities, provides a very significant downscaling factor but is still insufficient to achieve the targeted consumption levels (about 1 fs/bit). The reason lies in the classical form of the optical resonances used (Lorentzians), which leads to a necessary strong modulation to detune the resonance from its maximum. We have recently shown that a complete paradigm shift could be achieved in the consumption of plasma electro-optical modulators when an asymmetric Fano resonance is considered. We have specially proposed and designed an original Fano cavity structure based on the electromagnetic coupling of two pre-existing resonances in a single silicon guide geometry [3]. This single guide geometry offers a generic platform of Fano cavities directly applicable to the production of electro-optical modulators characterized by a set of merit factors superior to those obtained previously due to the very abrupt transmission of the Fano resonance. All these results will be detailed and supplemented at the conference by the most recent experimental results obtained.

Acknowledgements

ANR SITQOM project, POPSTAR ERC

References

[1] D. Thomson, A. Zilkie, J. E Bowers, T. Komljenovic, G. T Reed, L. Vivien, D. Marris-Morini, E. Cassan, L. Virot, J.-M. Fédéli, “Roadmap on silicon photonics”, Journal of Optics 18(7), 073003 (2016).

[2] J. Rönn, W. Zhang, A. Autere, X. Le Roux, L. Pakarinen, C. Alonso-Ramos, A. Säynätjoki, H. Lipsanen, L. Vivien, E. Cassan, Z. Sun, “Ultra-high onchip optical

gain in erbium-based hybrid waveguides", Nature Communications, 10:432 (2019).
[3] J. Zhang, X. Leroux, E. Durán-Valdeiglesias, C. Alonso-Ramos, D. Marris-Morini, L. Vivien, S. He, E. Cassan, "Generating Fano Resonances in a Single-Waveguide Silicon Nanobeam Cavity for Efficient Electro-Optical Modulation", ACS Photonics 5 (11), 4229-4237 (2018).

Scaling of monolayer 2D photonic crystal surface emitting lasers for 3D integrated photonics (Invited)

Weidong Zhou and Xiaochen Ge

Department of Electrical Engineering

University of Texas at Arlington, Arlington, Texas, USA

(wzhou@uta.edu)

Abstract:

Free-space coupled membrane photonic devices are highly desirable for 3D optical interconnects, free space communications, imaging, sensing, and ranging applications. Based on transfer printing processes, heterogeneously integrated active photonic crystal devices can be built on the common silicon platform. In this talk, I will report recent progresses related to hybrid integrated photonic crystal surface-emitting membrane lasers on silicon substrate, based on QW gain material and transition metal dichalcogenide monolayers. Issues to be discussed related to thermal performance, charge injection, and scaling towards energy efficient optical interconnects.

Submitted to: **SP33. Silicon Photonic Integrated Circuits**

Power Efficient Thermal Optical Tunable Grating Coupler Based on Silicon Photonic Platform

Lifeng Chen[1*]

[1] State Key Laboratory of Optoelectronic Materials and Technologies, Sun Yat-sun University, Guangzhou 510275, China
*corresponding author, E-mail: chenlf37@mail.sysu.edu.cn

Abstract

We demonstrate a tunable grating coupler with low power consumption, fabricated via a standard complementary metal–oxide–semiconductor process. The grating coupler locates on a freestanding silicon-on-insulator strip waveguides. The air gap between the grating structure and the silicon substrate enhances the heating efficiency. We achieve a central wavelength thermal shift of 55 nm with 19.5 mW input power, a tuning efficiency of 2.82 nm/mW. The dynamic response with rise time and fall time are 0.16 ms and 0.74 ms, respectively.

1. Introduction

Silicon-on-insulator (SOI) is recognized as one of the most attractive platforms for photonic integrated circuits (PICs) due to the compatibility with CMOS foundries, as well as the potential of low-power, high-capacity interconnects for electronic-photonic integrated circuits (EPICs) [1]. To couple the guided mode from a SOI platform to a single mode fiber, one can use a grating couple that eliminate the index mismatch between two modes. However, in practice, the central wavelength of grating coupler could vary randomly due to many reasons [2-4]. For photonic integrated circuits, this variation introduces significant optical losses. A tunable grating coupler that can dynamically change central wavelength is ideal to compensate the wavelength drifts. Most common ways of making tunable grating couplers are changing the refractive index of the grating via thermal-optical effect [5] or using micro-electro-mechanical system (MEMS) actuation [6]. Nevertheless, they suffering from high power consumption (0.23 nm/mW) [5] or narrow tuning range [6]. Here, we introduce a new tunable grating coupler design based on an efficient thermal tuning principle, by employing micro-heaters and freestanding silicon-on-insulator strip waveguides. As a result, this design significantly enhanced the thermal tuning efficiency by one order of magnitude compare to previous demonstrations.

2. Results

The schematic diagram of the tunable grating device shown in Fig. 1. A TE-mode focused grating coupler is located on a 220 nm SOI platform, and suspended from the silicon substrate (Fig. 1(a)). We remove the whole Si substrate and part of silicon under the coupler to form a thermal insulation

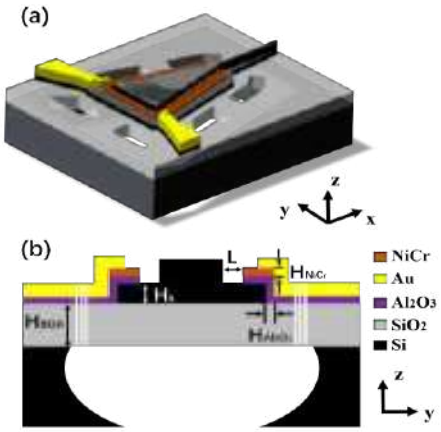


Fig. 1. (a) Three-dimensional schematic diagram of tunable grating coupler. (b) Cross section view of the device. The distance between the micro-heater and the grating, L, is 2μm to avoid the metal-induced absorption. The NiCr thickness H_{NiCr} and silicon layer thickness H_{BOX} is 150 nm and 2 μm, respectively.

buffer layer, shown as a cross-section diagram in Fig. 1(b). SiO_2 supporting arms are surrounding the suspended grating coupler. A zig-zag-shaped heater locates on the side of the grating region to heat up the device. We pattern and use a higher resistivity metal (NiCr) near the grating region where thermal tuning is required, and a lower resistivity metal (Ti-Au) making conductive arms on the sides. A thin electrical insulation layer (Al_2O_3) with 10-nm thickness is sandwiched between the heater and silicon, also provides efficient heat conduction from the heater to silicon substrate.

Fig. 2 investigates the theoretical power-thermal efficiency difference between air buffered and non-air buffered grating coupler, based on the Poisson's Equation. Fig. 2(a) and (b) shows the air buffered grating coupler has more than 300K higher temperature achieved at same heating power of 20mW. In Fig. 2(c) we confirmed this difference increases as heating power increase. And Fig. 2(d) shows the center wavelength shifts at different heating power, ranging from 1530nm to 1600nm in 20mW power increment.

Fig. 3 shows the fabricated devices in SEM (a) and optical (b) view, and characterization results via optical transmission measurements. The width of the etching windows and micro heater is 7 μm and 1.5 μm, total footprint of the device is about 81 μm by 100 μm including a 24 μm length taper serving as a mode field transformer from ridge waveguide to

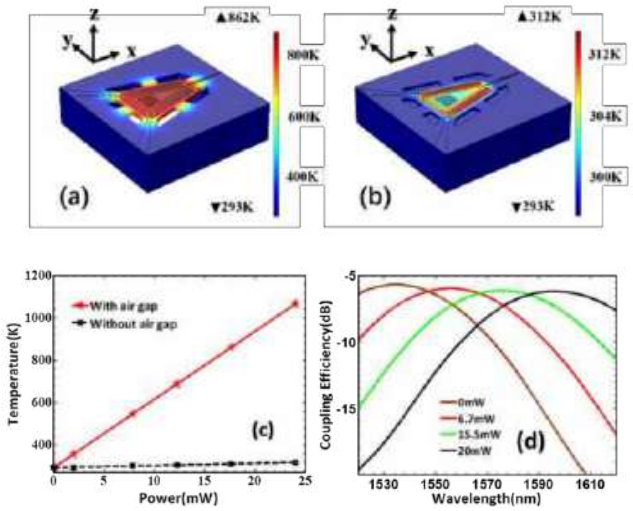


Fig. 2. The calculation of temperature field distribution at the same power for the device (a) with air gap and (b) without air gap thermal isolation; (c) the temperature change of grating coupler as a function of heating power change for two cases; (d) the coupling spectra of the air buffered grating coupler at different heating power.

strip waveguide. Fig. 3(c) shows the measured coupling spectra of the tunable grating coupler under different heating power. The maximum coupling efficiency at different heating power varies between -7 dB and -6.5 dB is due to the dispersion of silicon's thermo-optic effect [7]. The 1 dB bandwidth is around 30 nm within heating power range. Moreover, the central wavelength is shifting from 1535 nm the 1590 nm while heating power is increasing from 0 mW to 19.5 mW, well matched to the simulation results. Fig. 3 (d) shows a plot of the central wavelength versus the heating The dynamic response of the tunable grating coupler, shown in Fig.4, is investigated by applying a square-wave electrical power. The thermal tuning efficiency, extracted from the slope of the curve, is approximately 2.82 nm/mW.signal from a signal generator with a 100 Hz and 50% duty cycle, the high and low level is 2V and 0V. The heating (10%-90%) and

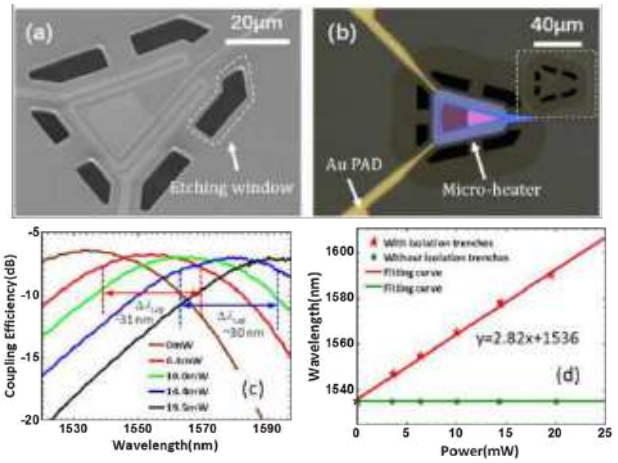


Fig. 3 (a) SEM image of the fabricated device. (b) Optical microscope image of tunable grating coupler. (c) Measured coupling spectra of the tunable grating coupler for different voltages. (d) Central wavelength shift for the applied heating power

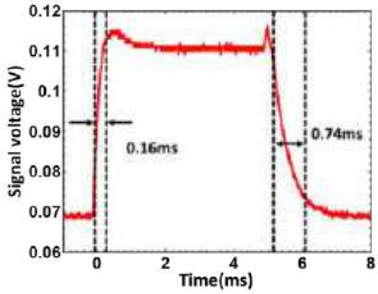


Fig. 4. Temporal response of the tunable grating coupler showing the heating and cooling response times

cooling (90%-10%) times were estimated to be 0.16 ms and 0.74 ms, respectively.

3. Conclusions

In summary, we have designed and demonstrated a tunable grating coupler capable of changing the central wavelength with low power consumption on the SOI platform using the direct heating method and thermal isolation designs. The tunable range of central wavelength is 55 nm (from1535 nm to 1590 nm) at a heating power from 0 to 19.5 mW, and a efficiency of 2.82 nm/mW has achieved. The response time of this device is 0.16 ms (the heating time) and 0.74 ms (the cooling time). This coupling efficiency can further be optimized by depositing and patterning overlay amorphous silicon. Moreover, the manufacturing procedure is highly scalable and fully CMOS-compatible.

Acknowledgements

We thank the engineers of State Key Laboratory of Optoelectronic Materials and Technologies at Sun Yat-sen University.

References

[1]B. Jalali and S. Fathpour, "Silicon photonics," J. Lightwave Technol., vol. 24, no. 12, pp. 4600-4615, 2006.

[2]D. Taillaert, et al, "An out-of-plane grating coupler for efficient butt-coupling between compact planar waveguides and single-mode fibers," IEEE Journal of Quantum Electronics., vol. 38, no. 7, pp. 949-955, 2002.

[3]Y.H. Ding, et al, "Fully etched apodized grating coupler on the SOI platform with −0.58 dB coupling efficiency," Opt. Lett., vol. 39, no. 18, pp. 5348-5350, 2014.

[4]J.H. Zou, et al, "Ultra efficient silicon nitride grating coupler with bottom grating reflector," Opt. Express., vol. 23, no. 20, pp. 26305-26312, 2015.

[5]J. H. Kim, et al, "Tunable Grating Couplers for Broadband Operation Using Thermo-Optic Effect in Silicon," IEEE Photon. Technol. Lett., vol. 27, no. 21, pp. 2304-2307, 2015.

[6] C. P. Ho, et al, "Tunable Grating Coupler by Thermal Actuation and Thermo-Optic Effect," IEEE Photon. Technol. Lett., vol. 30, no. 17, pp. 1503-1506, 2018.

[7] R. F. Aguinaldo, "Silicon Photonics with Applications to Data Center Networks," Ph.D. Dissertation, University of California, San Diego, (2014).

Lithium Niobate Michelson Interferometer Modulator on Silicon-On-Insulator Platform

Xinlun Cai[1*]

[1] State Key Laboratory of Optoelectronic Materials and Technologies, Sun Yat-sun University, Guangzhou 510275, China
*corresponding author, E-mail: caixlun5@mail.sysu.edu.cn

Abstract

We demonstrate a lithium niobate Michelson interferometer (MI) modulator on silicon-on-insulator platform with half the voltage-length product (Vπ·L) compare to silicon based Mach-Zehnder interferometer (MZI). A single MI modulator shows the electro-optic modulation efficiency of 1.2V·cm and insertion loss of 3dB. The -3dB electro-optic bandwidth is approximately 16 GHz, and the optical eye diagrams, operating at 30 Gbit/s and 40 Gbit/s, with dynamic extinction ratios are measured at 10 dB and 6.8 dB respectively.

1. Introduction

Silicon photonics on the silicon-on-insulator (SOI) platform is the most promising technology in CMOS foundries [1]. However, optical modulation in the silicon material mainly relies on free-carrier plasma dispersion effect, which leads to high absorption losses and nonlinear voltage response [2]. Lithium niobate (LiNbO3, LN) shows potential in electro-optic (EO) modulation due to its physical properties: large EO coefficient (30pm/V), strong Pockles effect, wide bandgap (wide transparency window), and good temperature stability [3]. Nevertheless, commercial bulk LN modulators are still based on indiffused or proton-exchange waveguide with low refractive index contrast and low EO modulation efficiency (typically Vπ·L>10 V·cm). Previous research work shows the thin film based Lithium niobate on insulator (LNOI) has emerged as a promising platform for micro-structuring devices [4-5]. The cross-section of LNOI photonic waveguide is less than 1μm^2, which lead to small mode size and tight mode confinement. More recently, integrated LN modulator with low loss, low drive voltage and high bandwidth have been demonstrated [6]. In this work, we take advantage of thin film LNOI platform and design a MI modulator, which using loop waveguides as mirror reflectors and half the Vπ·L than a MZI modulator.

2. Results

Fig.1 shows the design layout of a hybrid Si/LN MI modulator. The MI modulator consists of one 2×2 3dB Si MMI, two etched LN arm waveguides, and two 1×2 3dB MMI connecting two silicon waveguide loop mirrors. The hybrid Si/LN modulators consist of silicon waveguide layer, LN waveguide modulation layer, VACs and gold microwave electrode. The device is fabricated through wafer bonding technology by benzocyclobuten (BCB). The top LN waveguides is formed by dry-etching x-cut 600-nm thick LN membrane (NANOLN), and was connected with the bottom Si waveguide layer through VACs. Light can be coupled from Si inverse taper to LN ridge waveguide in high coupling efficiency.

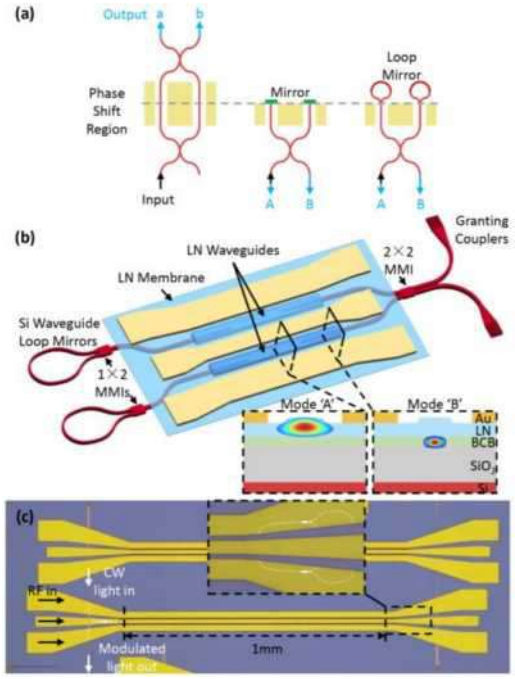


Fig. 1. (a) Schematics of a traditional MZI modulator (left), a traditional MI modulator (middle) and an integrated MI modulator with two loop waveguide mirrors (right). (b) The hybrid Si/LN MI modulator, and insets are cross-section views of calculated optical TE0 modes in (mode 'A') the modulation region and (mode 'B') the beginning of VAC. (c) Top view image from microscope of the fabricated 1-mm-long MI modulator. The white dash lines indicating the silicon waveguides. The devices are located under Au electrodes.

To evaluate the performance of a MI modulator, we performed half wave voltage (Vπ) measurements with a 100-kHz triangular voltage sweep for both MZI and MI. Fig. 2 shows the results for both case, we keep the same waveguide and electrodes design. In Fig. 3(a) the 3-mm-long MZI modulator has an 8.4V mod voltage difference for a pi phase shift in signal, corresponding to 2.5 V·cm of Vπ·L. While this value drop to half (1.2 V·cm) in the 1-mm-long MI modulator, and keeping a DC extinction ratio of >25 dB (see inset). This indicates the MI structure has doubled modulation efficiency compare to the MZI structure.

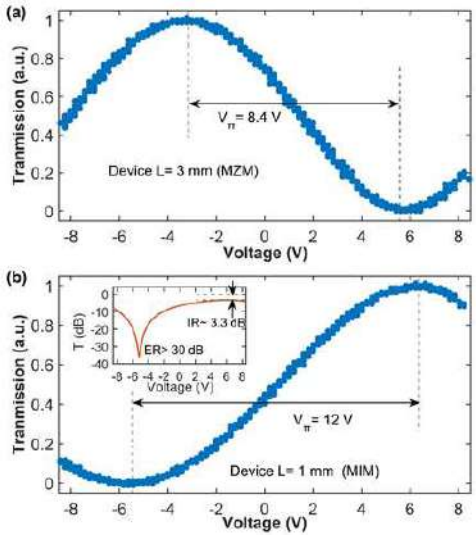


Fig. 2. 100 kHz triangular voltage scan of (a) a 3-mm-long MZI modulator and (b) a 1-mm-long MI modulator with the similar waveguides and electrodes design.

Fig. 3 shows the non-return-to-zero (NRZ) open eye diagrams at 30 Gbit/s and 40 Gbit/s to evaluate the high-speed digital data transmission performance of the device. The analog signals are generated by Agilent E8257D and amplified by SHF 807 to peak-to-peak voltage (Vpp) of 6.1V before sending to a modulator. Eye diagrams are obtained from wide-bandwidth oscilloscope (Agilent DCA-X 86100D) without additional compensations. When the modulator is biased at just below the quadrature point, we measured the dynamic extinction ratios are 10 dB at 30Gbit/s and 6.8 dB at 40Gbit/s, which are shown in Fig. 3 (a) and (b). Our devices operate at data rates higher than 3dB EO bandwidth because of the high-quality electrical signal system. The energy consumption of a MI modulator can be estimated by $Wbit = (Vpp/2)2/(BR)$, where B is the bit-rate and R is the 50Ω load. At bit-rate of 40 Gbit/s, the energy consumption of MI modulator is approximately 4.6 pJ/bit.

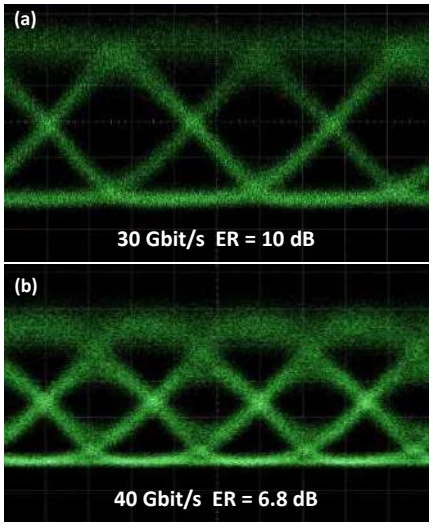


Fig. 3. The measured optical open eye diagrams at (a) 30 Gbit/s and (b) 40 Gbit/s under bias voltage at little lower than the quadrature point. The dynamic extinction ratios are 10 dB and 6.8 dB, respectively.

3. Conclusions

We demonstrate a hybrid silicon and lithium niobate MI modulator in a compact footprint (0.1 mm^2) with doubled modulation efficiency compare to a MZI modulator. The insertion loss of a 1-mm long MI modulator is less than 3dB, and the lowest figure of merit Vπ·L in monolithic LN platform of 1.2 V·cm is achieved. This allows a COMS-level voltage when the modulation length increase to 5mm while keeping the data transmission in Gbit/s range. In the high-speed data transmission experiment, we show an open optical eye diagram data rates up to 40 Gbit/s with 6.8dB extinction ratio. As the LN platform is proposed to be a good candidate for high-speed linear quantum key distribution (QKD)[24] applications, our design will satisfy the requirements of efficient and high-speed QKD system. Moreover, for the hybrid Si/LN platform, it is ideal for integrated microwave photonic (MWP) devices on SOI circuits.

Acknowledgements

Acknowledgements belong here.

References

[1] G. T. Reed and A. P. Knights, Silicon photonics: an introduction (John Wiley & Sons, 2004).
[2] Q. Xu, B. Schmidt, S. Pradhan, and M. Lipson, "Micrometre-scale silicon electro-optic modulator," Nature 435, 325 (2005).
[3] E. L. Wooten, K. M. Kissa, A. Yi-Yan, E. J. Murphy, D. A. Lafaw, P. F. Hallemeier, D. Maack, D. V. Attanasio, D. J. Fritz, G. J. McBrien, and D. E. Bossi, "A review of lithium niobate modulators for fiber-optic communications systems," IEEE J. Sel. Top. Quantum Electron. 6, 69-82 (2000).
[4] D. Janner, D. Tulli, M. Garcia-Granda, M. Belmonte, and V. Pruneri, "Micro-structured integrated electro-optic LiNbO3 modulators," Laser Photon. Rev. 3, 301-313 (2009)
[5] A. Boes, B. Corcoran, L. Chang, J. Bowers, and A. Mitchell, "Status and Potential of Lithium Niobate on Insulator (LNOI) for Photonic Integrated Circuits," Laser Photon. Rev. 12, 19 (2018).
[6] C. Wang, M. Zhang, X. Chen, M. Bertrand, A. Shams-Ansari, S. Chandrasekhar, P. Winzer, and M. Lončar, "Integrated lithium niobate electro-optic modulators operating at CMOS-compatible voltages," Nature 562, 101-104 (2018).
[7] C. Wang, M. Zhang, B. Stern, M. Lipson, and M. Loncar, "Nanophotonic lithium niobate electro-optic modulators," Opt. Express 26, 1547-1555 (2018).

Plasmonics in Silicon Photonics for Microwave Photonics

Y. Salamin[1,*], W. Heni[1], P. Ma[1], Y. Fedoryshyn[1], B. Baeuerle[1], A. Josten[1], C. Haffner[1], M. Baumann[1], B. Cheng[1], T. Watanabe[1], M. Burla[1], A. Emboras[1], D. L. Elder[2], L. R. Dalton[2], and J. Leuthold[1]

[1]Institute of Electromagnetic Fields (IEF), ETH Zurich, 8092 Zurich, Switzerland
[2]Department of Chemistry, University of Washington, Seattle, WA 98196-1700, USA
*corresponding author, E-mail: salaminy@ethz.ch

Abstract

We show how plasmonics can be integrated with the silicon photonics platform to enable new electro-optic devices. Different active materials are integrated with a plasmonic slot waveguide technology to achieve highest speed modulators and photodetectors on a lowest footprint. It is discussed how the unique properties offered by plasmonics enables new opportunities for the field of microwave photonics.

1. Introduction

Plasmonics has early on promised a revolution in the field of optics [1]. Plasmonics can offer smallest confinement with highest field intensities [2]. In combination with nonlinear materials, sub-wavelength confinement enables strongest light-matter interactions [3] allowing new optoelectronic devices with ultra-compact footprints [4]. The advantages offered by plasmonics have enabled a variety of new devices, finding applications in optical interconnects [5], microwave photonics [6], sensing [7] and atomic-scale devices [8, 9]. In particular, owing to its compact footprint, plasmonics can offer unprecedented bandwidths for optical modulators [10, 11] and photodetectors [12, 13]. The unique advantages offered by plasmonics in terms of high-speed and low footprint capabilities are essential for high-speed fiber-wireless applications [14].

Virtual fibers – high-capacity fiber-wireless links – become economically interesting for dense urban or residential areas, such as shown in Fig. 1. The last few meters of a fiber-to-the-home link is bridged by a high-capacity wireless link. Low-cost and compact devices consuming low energy are required to make such applications practical. Most fiber-to-wireless transmitters and receivers rely on high-speed electronics. With the wireless carrier frequency shifting towards the millimeter-wave and terahertz spectrum [14], the electronics becomes very costly and complex. It is therefore of great interest to have electro-optic devices capable of directly converting the optical signal to the wireless domain and vice-versa.

Here, we show how plasmonics can enable new devices for the fields of microwave photonics. In particular, we show how the plasmonic-organic platform [15], which combines plasmonic slot waveguides with organic nonlinear materials, can enable new wireless receivers for high-data-rate millimeter wave links without consuming any electrical



Figure 1: Application scenario for high-capacity fiber-wireless link. Inset showing the microwave plasmonic mixer (Ref. 6).

power. In addition, we show a new type of high-speed photodetector based on amorphous germanium taking advantage of plasmonics to achieve highest speed and efficiency.

2. Microwave Plasmonic Devices

To realize direct wireless-to-optical and optical-to-wireless converters for future high-capacity wireless links, electro-optic modulators and photodetectors with bandwidths going beyond 100 GHz are required. Integrated plasmonics is a promising platform for such electro-optic devices.

2.1. Microwave Plasmonic Mixer

Combining the strong modulation efficiency of recently demonstrated plasmonic modulators with a resonant antenna allows one to directly modulate the phase of an optical carrier by a wireless signal [6, 7]. The structure of the device is shown in the inset of Fig. 1. The plasmonic subwavelength waveguide enables confinement of the optical mode and the wireless signal to a sub-100 nm gap. This leads to an almost perfect overlap of both signals resulting in a very strong nonlinear interaction. Such a device was used in the demonstration of a transparent fiber-wireless link transmitting 10 and 20 Gbit/s over wireless distances of 1 and 5 m [6]. The demonstrated wireless receiver required no electrical power.

2.2. High-speed Plasmonic Photodetector

The speed limitation of photodetectors is defined by its RC time constant and transit time, i.e. time required for carriers to be extracted. Plasmonics enables to shrink the size of the active region to sub-100 nm. This way, very fast carrier dynamics can be achieved. In addition, the metal forming the plasmonic slot waveguide is simultaneously used as electrical contact. This reduces the resistance and capacitance of the device dramatically. A meta-semiconductor-metal plasmonic waveguide photodetector with amorphous germanium as the active material was proposed, see Fig. 2. An electro-optic bandwidth beyond 100 GHz was measured with an internal quantum efficiency of 36% [12]. The device was used in a data reception experiment, receiving up to 72 Gbit/s on-off keying (OOK) data which was only limited by the available equipment. New generation of detectors have already shown the possibility for 100 Gbit/s OOK reception [13].

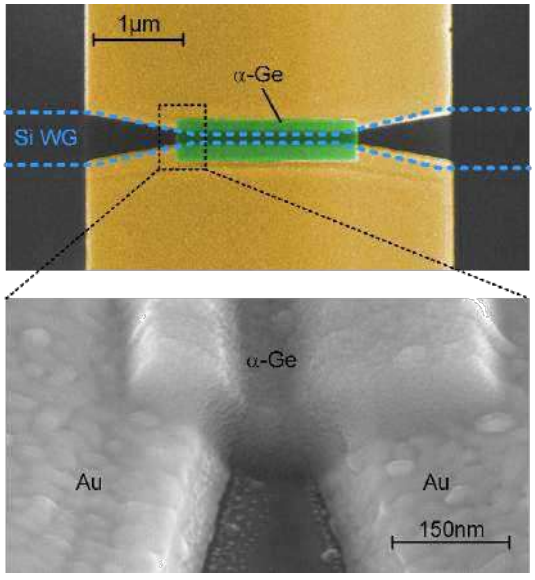


Figure 2: Plasmonic photodetector (Ref. 12).

Acknowledgements

This work was carried out partially at the Binnig and Rohrer nanotechnology Center (BRNC) and in the FIRST lab cleanroom facility at ETH Zurich. The European ERC PLASILOR (670478), NSF (DMR-1303080) and the AFOSR (FA9550-15- 1-0319) projects are acknowledged for partial funding of the work.

References

[1] M. L. Brongersma and V. M. Shalaev, "The Case for Plasmonics," *Science,* vol. 328, no. 5977, pp. 440-441, 2010.

[2] D. K. Gramotnev and S. I. Bozhevolnyi, "Plasmonics beyond the diffraction limit," *Nature Photon.,* Review Article vol. 4, p. 83, 2010.

[3] M. P. Nielsen, X. Shi, P. Dichtl, S. A. Maier, and R. F. Oulton, "Giant nonlinear response at a plasmonic nanofocus drives efficient four-wave mixing," *Science,* vol. 358, no. 6367, pp. 1179-1181, 2017.

[4] M. Ayata *et al.*, "High-speed plasmonic modulator in a single metal layer," *Science,* vol. 358, no. 6363, pp. 630-632, 2017.

[5] C. Hoessbacher *et al.*, "Optical Interconnect Solution With Plasmonic Modulator and Ge Photodetector Array," *IEEE Photon. Technol. Lett.,* vol. 29, no. 21, pp. 1760-1763, 2017.

[6] Y. Salamin *et al.*, "Microwave plasmonic mixer in a transparent fibre–wireless link," *Nature Photon.,* vol. 12, no. 12, pp. 749-753, 2018.

[7] Y. Salamin *et al.*, "Direct Conversion of Free Space Millimeter Waves to Optical Domain by Plasmonic Modulator Antenna," *Nano Lett.,* vol. 15, no. 12, pp. 8342-8346, 2015.

[8] A. Emboras *et al.*, "Atomic Scale Photodetection Enabled by a Memristive Junction," *ACS Nano,* vol. 12, no. 7, pp. 6706-6713, 2018.

[9] A. Emboras *et al.*, "Atomic Scale Plasmonic Switch," *Nano Lett.,* vol. 16, no. 1, pp. 709-714, 2016/01/13 2016.

[10] C. Hoessbacher *et al.*, "Plasmonic modulator with >170 GHz bandwidth demonstrated at 100 GBd NRZ," *Opt. Express,* vol. 25, no. 3, pp. 1762-1768, 2017.

[11] S. Ummethala *et al.*, "Terahertz-to-Optical Conversion Using a Plasmonic Modulator," in *CLEO*, San Jose, California, 2018, p. STu3D.4: Optical Society of America, 2018.

[12] Y. Salamin *et al.*, "100 GHz Plasmonic Photodetector," *ACS Photon.,* vol. 5, no. 8, pp. 3291-3297, 2018.

[13] P. Ma *et al.*, "Plasmonically Enhanced Graphene Photodetector Featuring 100 Gbit/s Data Reception, High Responsivity, and Compact Size," *ACS Photon.,* vol. 6, no. 1, pp. 154-161, 2019.

[14] H. Shams and A. Seeds, "Photonics, Fiber and THz Wireless Communication," *Opt. Photon. News,* vol. 28, no. 3, pp. 24-31, 2017/03/01 2017.

[15] C. Haffner *et al.*, "Plasmonic organic hybrid modulators—scaling highest speed photonics to the microscale," *Proc. IEEE,* vol. 104, no. 12, pp. 2362-2379, 2016.

Heterogeneously integrated membrane III-V/Si photonic devices

Tatsurou Hiraki[1,2], Takuma Aihara[1], Koji Takeda[1,2], Takuro Fujii[1,2], Hidetaka Nishi[1,2], Takaaki Kakitsuka[1,2], Tai Tsuchizawa[1,2], Hiroshi Fukuda[1,2], and Shinji Matsuo[1,2]

[1]NTT Device Technology Labs, NTT Corporation, Kanagawa, Japan
[2]NTT Nanophotonics Center, NTT Corporation, Kanagawa, Japan
*Corresponding author, e-mail: tatsurou.hiraki.gu@hco.ntt.co.jp

The Si photonics platform is attractive for fabricating compact and low-cost optical transceivers with low power consumption. On the platform, heterogeneous integration of III-V semiconductors is the key technology for integrating high-efficiency Mach-Zehnder modulators and laser diodes. Here, we review our recent work on heterogeneously integrated III-V/Si Mach-Zehnder modulators and lasers with a membrane III-V semiconductor structure, which provides a high optical confinement factor for low power consumption and easy integration with Si waveguide circuits.

Fig. 1(a) shows a schematic of the membrane InGaAsP/Si Mach-Zehnder modulator [1]. The Mach-Zehnder modulator has a metal-oxide-semiconductor (MOS) capacitor structure with 100-nm-thick n-type InGaAsP, 10-nm-thick SiO_2, and 110-nm-thick p-type Si layers. By accumulating the majority carriers at the semiconductor/SiO_2 interfaces, the phase of the lightwave is mainly modulated by the large carrier plasma effect and band filling effect of the n-type InGaAsP layer. Thanks to the large optical confinement factor with the membrane structure, a large overlap between the optical mode field and carrier distribution is obtained. In addition, the high electron mobility of the n-type InGaAsP layer is beneficial for small free-carrier absorption. The fabricated device showed $V_\pi L$ of 0.09 Vcm and the phase shifter loss of around 2.6 dB/mm. Both the $V_\pi L$ and phase shifter loss are much smaller than those of conventional Si MOS capacitor Mach-Zehnder modulators.

Fig. 1(b) shows a schematic of the lateral current injection membrane laser diode on the Si waveguide [2]. The thickness of the laser diode (0.23 μm) is much smaller than that of the conventional laser diode (~2 μm). Since the effective refractive index of the membrane InP-based layer is comparable to that of the typical ~200-nm-thick Si waveguide layer, the membrane laser diode efficiently couples to widely developed Si photonics circuits. The fabricated 500-μm-long distributed feedback laser diode showed a threshold current of ~6 mA and a fiber coupled output power of 4.6 mW in the C band. Thanks to the small active volume and low effective refractive index of the membrane layer, low threshold current and efficient optical coupling to the Si waveguide were obtained.

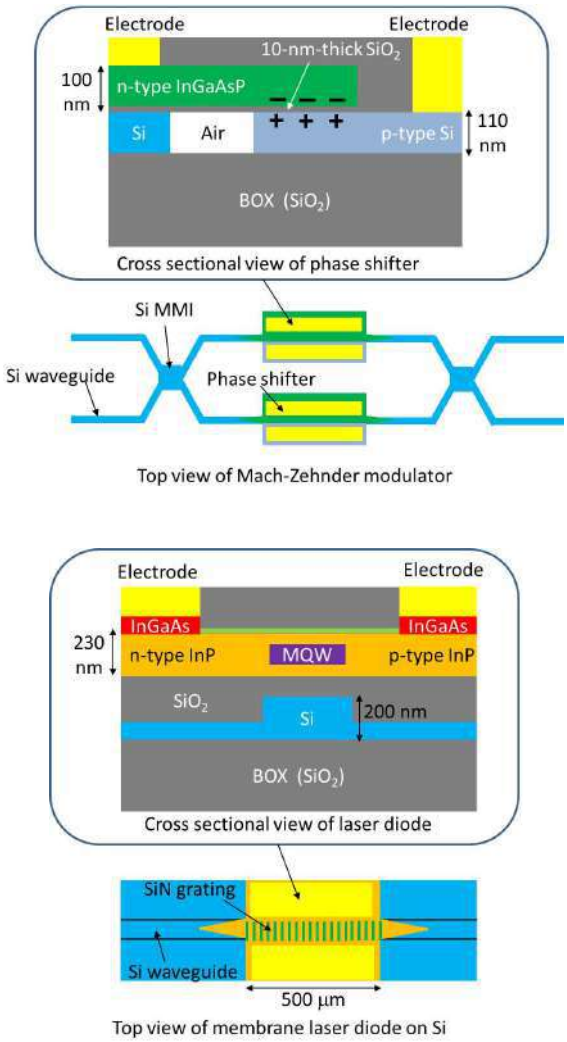


Fig. 1 Schematics of (a) membrane InGaAsP/Si Mach-Zehnder modulator and (b) membrane laser diode.

Acknowledgements

Part of these research results were achieved by “R&D on optical PLL device for receiving and monitoring optical signals”, Commissioned Research of the National Institute of Information and Communications Technology (NICT), JAPAN.

References

[1] T. Hiraki, T. Aihara, K. Hasebe, K. Takeda, T. Fujii, T. Kakitsuka, T. Tsuchizawa, H. Fukuda, and S. Matsuo, Heterogeneously integrated III-V/Si MOS capacitor Mach-Zehnder modulator, *Nature Photonics* 11: 482-485, 2017.

[2] T. Aihara, T. Hiraki, K. Takeda, K. Hasebe, T. Fujii, T. Tsuchizawa, T. Kakitsuka, and S. Matsuo, *OFC 2108*, W3F.4, 2018.

Silicon Integrated Quantum Photonics

Yunhong Ding[1,2]*, Davide Bacco3[1,2], Karsten Rottwitt5[1,2], Mark Thompson[4], Jian Wang[3], and Leif K. Oxenløwe6[1,2]

[1]Department of Photonics Engineering, Technical University of Denmark, 2800 Kgs. Lyngby, Denmark
[2]Center for Silicon Photonics for Optical Communication (SPOC), Technical University of Denmark, 2800 Kgs. Lyngby, Denmark
[3]State Key Laboratory for Mesoscopic Physics and Collaborative Innovation Center of Quantum Matter, School of Physics, Peking University, Beijing 100871, China
[4]Quantum Engineering Technology Labs, H. H. Wills Physics Laboratory and Department of Electrical and Electronic Engineering, University of Bristol, BS8 1FD, Bristol, United Kingdom
*corresponding author, E-mail: yudin@fotonik.dtu.dk

Abstract

Quantum photonics opens a new era of technology revolution deeply embedded in quantum mechanism. Silicon integrated quantum photonics is of particular interest able to integrate mass of quantum photonic components on a single silicon chip. Here we present our recent work on silicon photonics for advanced quantum applications, including high-dimensional quantum quantum key distribution, high-dimensional quantum entanglement, and Hong-Ou-Mandel interference of two independent lasers on silicon for quantum communication.

1. Introduction

Over the past decades, free space optics has greatly pushed the research of quantum photonics and its applications in quantum key distribution, quantum simulation, and quantum computation. Silicon photonics, able to integrate a large amount of photonic components in a single chip with complementary metal-oxide semiconductor (CMOS) compatible fabrication process, is a versatile platform for development of quantum technologies with intrinsic stability, high precision, and dense integration [1]. Here we present our recent work on silicon integrated quantum photonics, including high-dimensional (HiD) chip-to-chip quantum key distribution (QKD) with high photon information efficiency and enhanced noise-resilience, on-chip creation and manipulation of HiD-quantum entanglement states, and Hong-Ou-Mandel (HOM) interference of two independent semiconductor lasers on silicon necessary for measurement device independent (MDI) quantum communication.

2. Quantum key distribution

QKD is an attractive quantum technology that shares secret keys between two parties (Alice and Bob) with ultimate security. Traditional QKD is based on binary signal formats (qubits), such as the BB84 protocol, and information efficiency is limited to 1 bit/photon. HiD-QKD employing HiD quantum states (qudits) provides higher information efficiency (>1 bit/photon) and better noise resilience [2]. However, implementing HiD-QKD with traditional free-space optics is extremely challenging in terms scalability and stability, which can be effectively handled by silicon photonics. As shown in Fig. 1(a), Alice chip is able to create any four-dimension quantum state within three mutually unbiased basis (MUBs) M0, M1 and M2,

$$\mathrm{M0}=\begin{Bmatrix}|A\rangle+|B\rangle\\|A\rangle-|B\rangle\\|C\rangle+|D\rangle\\|C\rangle-|D\rangle\end{Bmatrix}\quad \mathrm{M1}=\begin{Bmatrix}|A\rangle+|C\rangle\\|A\rangle-|C\rangle\\|B\rangle+|D\rangle\\|B\rangle-|D\rangle\end{Bmatrix}\quad \mathrm{M2}=\begin{Bmatrix}|A\rangle+|D\rangle\\|A\rangle-|D\rangle\\|B\rangle+|C\rangle\\|B\rangle-|C\rangle\end{Bmatrix} \quad (1)$$

where $|A\rangle$, $|B\rangle$, $|C\rangle$, and $|D\rangle$ represent the quantum states related to the four individual cores of a multi-core fiber. The HiD quantum states are sent through a multicore fiber (MCF) and received by Bob chip, who is able to receive the quantum states in any of three MUBs. With standard QKD protocol,

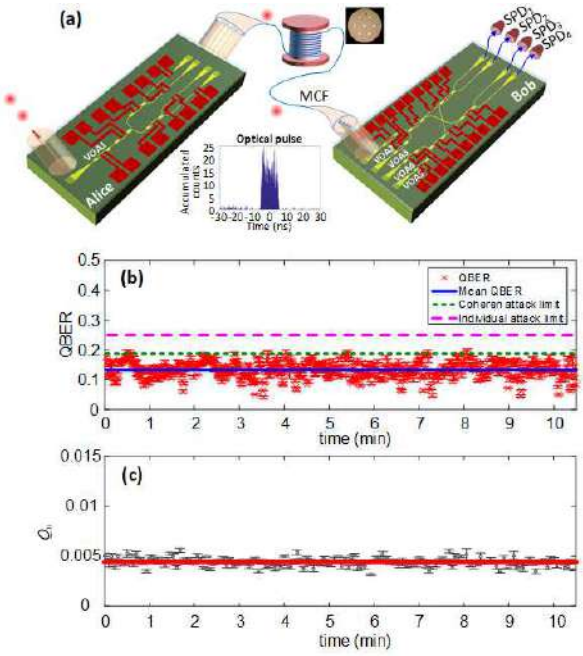


Fig. 1. (a) Schematic of HiD chip-to-chip QKD over MCF. (b) QBER and (c) stability of the QKD system.

we achieved low quantum bit error rate (QBER) below bothcoherent attack limit and indivisual attack limit, as presented in Fig. 1(b) and (c).

3. High dimensional quantum entanglement

Apart from the promising potential of qudits in quantum communication, as presented above, qudits can also be used to strengthen the violations of generalized Bell and Einstein-Podolsky-Rosen (EPR) steering inequalities [4], provide richer resources for quantum simulation, and offer higher efficiency and flexibility in quantum computing. Previous work on qudits entanglement systems incur limitations in terms of controllability, precision, and universality, which represent bottlenecks for further developments of HiD technologies. We demonstrate a large-scale silicon quantum photonic circuit to implement qudit entanglement [5], as shown in Fig.2(a) and 2(b), which can generate and manipulate HiD entanglement state with certified dimensionality up to 14, providing an experimental platform for the development of multidimensional quantum technologies.

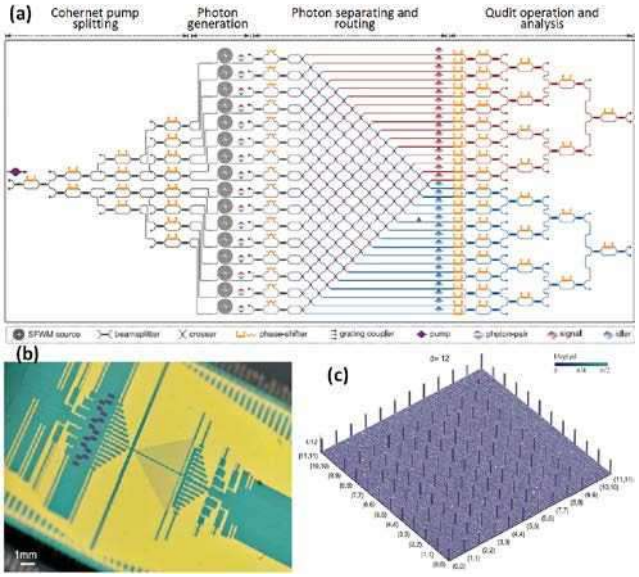


Fig. 1. (a) Schematic on-chip generation and manipulation of HiD quantum entanglement state. (b) fabricated silicon quantum chip, and (c) experimental quantum state tomography of generated 12-dimensional quantum state, indicating a fidelity of 81%.

4. High dimensional quantum entanglement

Despite the great potentials of QKD, practically implementations are always imperfect, which opens loopholes that undermine the security of the protocol. A well-known example is the detector side channel attack, which can be exploited to hack QKD systems [6]. To tackle this vulnerability, measurement device independent QKD (MDI-QKD) was introduced and demonstrated [7, 8], where a third untrusted party, i.e., Charlie, performs a Bell-state measurement on the quantum states sent by the two trusted parties, i.e., Alice and Bob, allowing them to establish a secret key based on time-reversed entanglement. A successful implementation of MDI-QKD requires high-visibility two-photon interference, i.e. HOM interference, between Alice's and Bob's quantum states. When the single photons are replaced with weak-coherent pulses (WCPs),

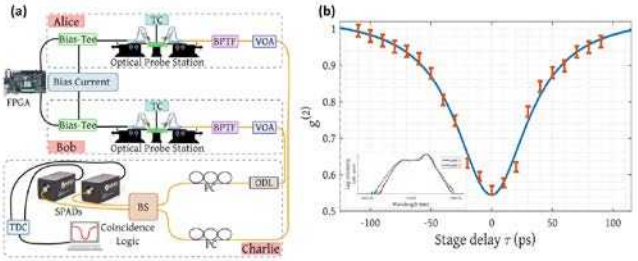


Fig. 1. (a) Experimental setup to study HOM interference between WCPs generated by gain-switched III–V on silicon waveguide integrated lasers. (b) HOM dip between WCPs generated by independent gainswitched III–V on silicon waveguide integrated lasers, showing a visibility $V = 46 \pm 2\%$. The inset shows the OSA trace of the laser pulses. Both lasers show similar spectral profiles centered at 1534.5 nm and ~400 pm in width.

HOM interference still occurs, but with a diminished visibility of 50%. We obtained, for the first time, to the best of our knowledge, high-visibility HOM interference between WCPs generated by independent gain-switched III–V on silicon waveguide integrated lasers (see Fig. 3(a)) [9]. Experimental visability of $V = 46 \pm 2\%$ is achieved, as shown in Fig. 3(b), paving the way towards implementation of metropolitan QKD networks based on silicon photonics with fully integrated WCP sources.

Acknowledgements

The work is supported by the Danmarks Grundforsknings-fond (DNRF) (123), FP7 People: Marie-Curie Actions (PEOPLE) (609405), and Horizon 2020 Framework Programme (H2020) (731473).

References

[1]. N. C. Harris, G. R. Steinbrecher, M. Prabhu, Y. Lahini, J. Mower, D. Bunandar, C. C. Chen, F. N. C. Wong, T. Baehr-Jones, M. Hochberg, S. Lloyd, and D. Englund, Nat. Photonics 11(7), 447–452 (2017).

[2]. Y. Ding, D. Bacco, K. Dalgaard, X. Cai, X. Zhou, K. Rottwitt, and L. K. Oxenløwe, npj Quantum Information, 3, 25 (2017).

[3]. V. Karimipour, A. Bahraminasab, and S. Bagherinezhad, "Quantum key distribution for d-level systems with generalized bell states," Phys. Rev. A 65, 042320 (2002).

[4]. A. Salavrakos, R. Augusiak, J. Tura, P. Wittek, A. Acín, and S. Pironio, Phys. Rev. Lett. 119, 040402 (2017).

[5]. J. Wang, S. Paesani, Y. Ding, R. Santagati, P. Skrzypczyk, A. Salavrakos, J. Tura, R. Augusiak, L. Mančinska, D. Bacco, D. Bonneau, J. W. Silverstone, Q. Gong, A. Acín, K. Rottwitt, L. K. Oxenløwe, J. L. O'Brien, A. Laing, and M. G. Thompson, Science 360, 285-291 (2018).

[6]. L. Lydersen, C. Wiechers, C. Wittmann, D. Elser, J. Skaar, and V. Makarov, Nat. Photonics 4, 686 (2010).

[7]. H.-K. Lo, M. Curty, and B. Qi, Phys. Rev. Lett. 108, 130503 (2012).

[8]. H.-L. Yin, T.-Y. Chen, Z.-W. Yu, H. Liu, L.-X. You, Y.-H. Zhou, S.-J. Chen, Y. Mao, M.-Q. Huang, W.-J. Zhang, H. Chen, M. J. Li, D. Nolan, F. Zhou, X. Jiang, Z. Wang, Q. Zhang, X.-B. Wang, and J.-W. Pan, Phys. Rev. Lett. 117, 190501 (2016).

[9]. C. Agnesi, B. Da Lio, D. Cozzolino, L. Cardi, B. Ben Bakir, K. Hassan, A. Della Frera, A. Ruggeri, A. Giudice, G. Vallone, P. Villoresi, A. Tosi, K. Rottwitt, Y. Ding, and D. Bacco, Opt. Lett. 44, 271-274 (2019).

Application opportunities for Field-Programmable Photonic Integrated Circuits

Daniel Pérez-López*, Prometheus DasMahapatra, José Capmany,
[1]Photonics Research Labs, Universitat Politècnica de València, Spain
*corresponding author, E-mail: dperez@iteam.upv.es

Abstract

The advent of a new generation of programmable photonic integrated circuits (PICs) has paved the path for cost-effective solutions for a wide variety of applications which employ at least one photonic-based subsystem. Here, we review the main characteristics of programmable PICs and analyze their trade-offs and performance in the different fields of application: telecommunications, datacentres, radio-over-fiber, microwave photonics processing, high-performance computing and sensing.

1. Introduction

Integrated photonics is the science and technology that enables the integration of a large number of waveguide elements and specific devices/performance blocks in order to perform optical processing on a chip. Traditionally, both, industry and academia have mainly focused on the design and optimization of Application Specific Photonic Integrated Circuits (ASPICs) whereby all the stages involved in the development of a PIC are tailored to optimize the chip performance, power budget, consumption, and footprint [1]. This strategy involves the optimization of photonic-based systems through multiple time-consuming cycles of custom design, fabrication, packaging and testing, leading to solutions that are far from being cost-effective for low and moderate volumes. Only very large volumes benefit from economies of scale, but such applications are not there yet, beyond datacenter interconnects and transceivers [2].
A paradigm shift in PIC design explores the development of multipurpose programmable circuits [3-5]. This aims at designing generic integrated optical hardware configurations which, by suitable programming, can implement a variety of functionalities that can be extended to basic or more complex operations in many application fields, enabling a new generation of field-programmable PICs that will potentially offer cost-effective and ready-to-use programmable solutions.

2. Field-Programmable Photonic Integrated Circuits

A field-programmable PIC integrates a large number of programmable components that can be configured via software. In such PICs, we can find two subcategories: The first one deals with fixed circuit topologies and targets very few applications. They allow a limited degree of reconfiguration by only affecting certain design parameters. The second category comprises of a more versatile approach, enabling both the modification of circuit topology and design settings. A recently proposed architecture is the Field-Programmable Photonic Arrays (FPPA) as illustrated in Figure 1. FPPAs include a subset of components or high-performance building blocks (HPBs) that are often present in different optical processing system architectures for undertaking specific tasks: delay lines, beam-splitters, optical filters, dispersive components, (de)-multiplexers, as well as optical sources, amplifiers and electro-optic modulators and photodetectors, to cite a few. All of them are interconnected to a reconfigurable optical core that enable the (1) smart and flexible routing between the desired components, allowing the user to define their custom circuit scheme and (2) the synthesis of conventional processing blocks constructed using Tunable Basic processing Units as primitive blocks [4].

This scheme enables the use of a generic hardware for multi-functional processing and applications.

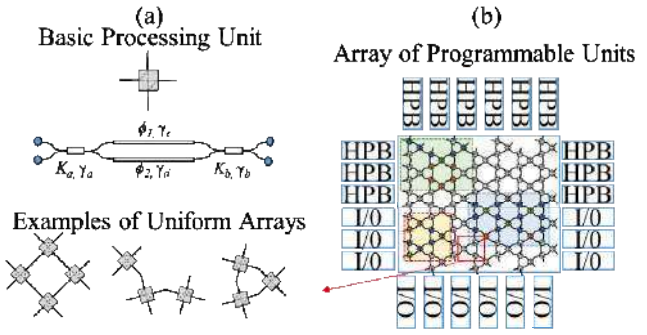


Figure 1: (a)Top-Level description of the basic processing units that build up the Field-Programmable Photonic array (b) Implementation and hardware embodiment of the photonic design,

Once designed, the FPPA workflow is detailed in a very recent article, [3]. It starts with the initial *application initialisation* or circuit configuration together with the main targeted specifications, followed by an area and performance optimization, the *technology mapping*, and *place and route* tasks and *final evaluation*. The steps contained in the generic design flow can be done automatically either by the software layer or, the user, or by a mixture of both, depending on the autonomation and the capabilities of the FPPA software tier.

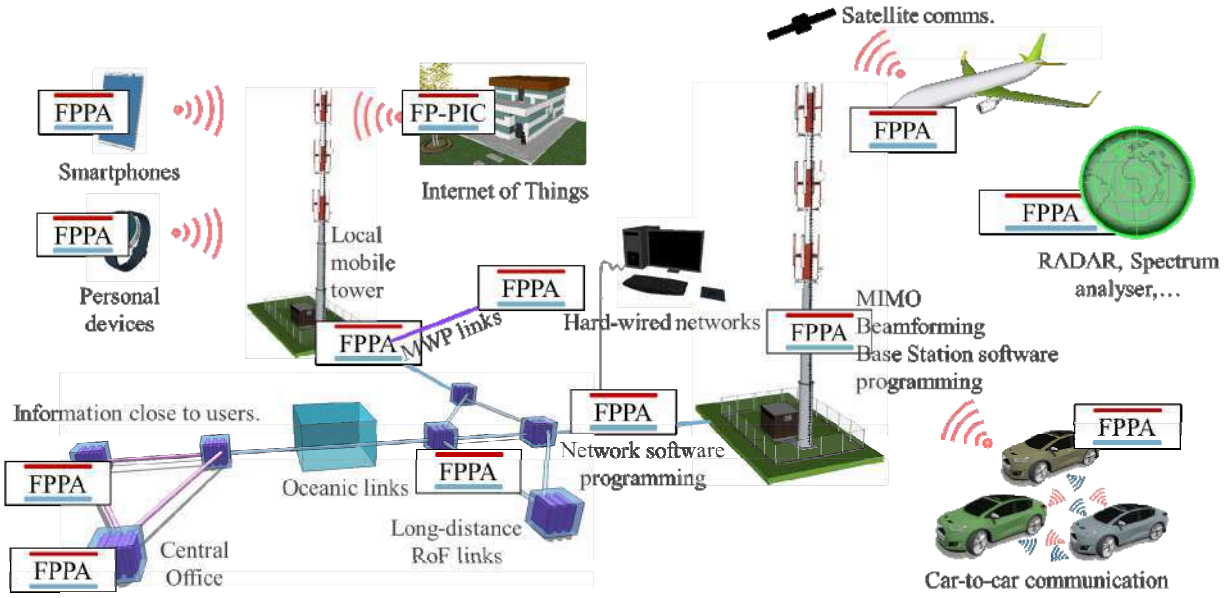


Figure 2: Application scenarios of Field-Programmable Photonic Arrays.

3. Applications

Programmable photonics and FPPAs in particular can find applications in any field requiring optical processing functionalities either in fixed or dynamic conditions, as shown in Figure 2. In this section we list and briefly analyse the potential implementation in different fields:

Telecommunications and datacentres: Future communication scenarios and protocols demands a higher degree of flexibility. The FPPAs can be programmed to perform optical interconnects between their optical ports, smart routing of the different channels and software-defined commutation for software-defined networks. In this sector, advanced FPPAs can be employed to a new generation of flexible transceivers and software-defined networks engines.

Radio-over-fiber and microwave photonics for wireless communications: FPPAs incorporating electro-optical components can be programmed to perform the interfacing between these two physical domains, provide flexibly in band and functionality [5]. In addition, FPPA architecture allows the potential implementation of multiband / multichannel capability.

High-performance computing: a set of integrated beam-splitters can be interconnected to define any linear optical operation [6]. This capability is being employed by state-of-the-art demonstrators. FPPAs can be programmed for these multiport interferometry tasks.

Sensing: In this field, several photonic integrated circuits have been proposed for both the direct implementation of sensing functions and as interrogator systems to feed and process the information in the optical domain. The FPPAs can potentially be employed in the last scenario.

4. Conclusions

Here, we have reviewed the main definitions associated with general-purpose, field-programmable photonic integrated circuits. They are proposed as a platform to realize a wide variety of applications that deal with or employ optical signal processing.

Acknowledgements

The authors acknowledge financial support by the ERC ADG-2016 UMWP-Chip, the Generalitat Valenciana PROMETEO 2017/017 research excellency award, and the COST Action CA16220 EUIMWP.

References

[1] Soref, R.A., "Silicon photonics technology: past, present, and future", Proc. SPIE 5730, Optoelectronic Integration on Silicon II, (7 March 2005); doi: 10.1117/12.585284;

[2] Inniss D., and Rubenstein, R., “Silicon Photonics: Fueling the next information revolution,” Morgan Kaufmann; 1 edition (2016).

[3] Pérez, D., Gasulla, I., & Capmany, J. “Field-programmable photonic arrays,” Optics express, 26(21), (2018). 27265-27278.

[4] Pérez, D., Gasulla, I., Crudgington, L., Thomson D. J., Khokhar, A. Z., Li K., Cao W., Mashanovich G. Z. and Capmany, J., “Multipurpose silicon photonics signal processor core,” Nature Comm., Vol. 8, no. 636, (2017).

[5] Pérez, D., Gasulla, I., & Capmany, J. (2018). Toward Programmable Microwave Photonics Processors. *Journal of Lightwave Technology*, *36*(2), 519-532.

[6] Clements, W. R., Humphreys, P. C., Metcalf, B. J., Kolthammer, W. S., and Walmsley. I. A., “Optimal design for universal multiport interferometers.” Optica 2016, 3, 1460-5.

Laser Processing of Amorphous Semiconductors on Planar Substrates for Photonic and Optoelectronic Applications

Ozan Aktas[1,*], Yohann Franz[1], Antoine F. J. Runge[2], Stuart J. MacFarquhar[1], Swe Z. Oo[3], Vinita Mittal[3], Antulio Tarazona[1], Harold M. H. Chong[3], Sakellaris Mailis[4], and Anna C. Peacock[1]

[1]Optoelectronics Research Centre, University of Southampton, Southampton, UK
[2]Institute of Photonics and Optical Science (IPOS), School of Physics, University of Sydney, Sydney, Australia
[3]School of Electronics and Computer Science, University of Southampton, Southampton, UK
[4]Department of Photonics and Quantum Materials, Skolkovo Institute of Science and Technology, Moskovskiy, Russia
*corresponding author, E-mail: O.Aktas@soton.ac.uk

Abstract

We report results of laser processing on amorphous silicon and silicon-germanium films deposited on planar substrates. Pre-patterned a-Si waveguides were recrystallized and reflowed to enhance their material and optical properties. Formation of millimeter long crystal grains and surface roughness of 0.52 nm enable optical losses to become as low as 5.3 dB/cm. Laser-driven phase separation in the binary alloy of a-SiGe allows fabrication of composition graded microstructures with Si-rich and Ge-rich regions. A composition tuning capability of 40% was demonstrated.

1. Introduction

Polycrystalline semiconductor materials have the potential to exhibit both optical and electronic functionalities that are comparable with single crystal platforms, but with much more flexibility in the fabrication process. However, to obtain good quality of polycrystalline materials, the process temperatures need to be higher than 900 ºC [1], rendering them incompatible with CMOS devices. We have developed a laser processing method for the fabrication of low loss p-Si waveguides with a low thermal budget [2].

Another set of material for laser processing is binary semiconductor alloys such as SiGe, which have attracted a growing interest of the photonics industry over the past few years, due to their tunable material, electrical and optical properties. Bandgap and optical properties of $Si_{1-x}Ge_x$ can be modified by changing the material composition through x [3]. Laser inscription of compositional microstructures in crystalline SiGe core silica clad fibres has been recently shown during the local heating of the core by a CO_2 laser [4]. However, spatial control of the phase separation in SiGe alloys for fabrication of photonic devices has yet to be demonstrated on planar substrates.

2. Fabrication

The fabrication process of a-Si films begins with the formation of a 4.6 µm thick thermally grown buried oxide layer on top of the c-Si substrate. A thin film of a-Si with a thickness of 480 nm is then grown using a hot-wire chemical vapor deposition (HWCVD) technique with silane (SiH_4) as the only precursor. HWCVD allows low temperature deposition at 320 ºC with low hydrogen concentration. Following the deposition, e-beam lithography and plasma etching were used to pattern a series of straight waveguides with widths of 0.5 µm, 1 µm, 1.5 µm and 2 µm in the a-Si film.

The a-SiGe films were directly fabricated on silicon wafers, which were dipped in buffered hydrofluoric acid (HF) for 3 minutes to remove the native oxide before deposition. Then, 400 nm thick SiGe films were deposited by plasmon enhanced chemical vapour deposition (PECVD) using SiH_4 (5 sccm) and GeH_4 (50 sccm) precursors with an RF power of 15 W at a pressure of 300 mTorr and a temperature of 200 ºC. Initial atomic content of Ge is 60%.

3. Laser processing

Laser processing of a-Si and a-SiGe films was carried out with the setup shown in Figure 1. The light source is an Argon ion laser emitting continuous wave (CW) radiation at 488 nm with a maximum power of 350 mW. The setup includes 3D motorized stages capable of programmed movements at speeds ranging from 0.01 mm/s up to 100 mm/s. The power was adjusted using a polarization cube and a half wave plate. The beam was focused on the top surface of the samples using 10x and 20x objective lens to produce a spot diameter of 4.7 µm and 2.5 µm, respectively. A pellicle beam splitter, a CCD camera and a white light source were used to image the surface of the samples.

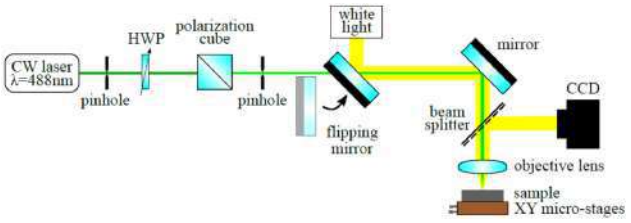


Figure 1: Schematic of experimental set-up for laser processing. HWP is half-wave plate.

4. Material and optical characterizations

Micro focus X-ray diffraction (XRD) with a highly collimated beam provided by a synchrotron source was used to assess the presence of crystals in the laser-processed regions and collect information about their length, orientation and lattice constant. The XRD setup was established in a grazing incidence configuration to avoid strong diffraction from the c-Si substrates. In addition, X-ray fluorescence spectroscopy was used to access spatial distribution of Ge in the p-SiGe tracks. We also performed a set of micro-Raman spectroscopy measurements before and after laser processing. The line width of the Raman peaks were used to optimize power levels and scan speeds. The optical quality of the p-Si waveguides was assessed by measuring the linear propagation losses using the standard cut-back technique.

5. Results and Discussion

5.1. Laser crystallization and reflowing of amorphous silicon waveguides

As a consequence of the complete melting during laser annealing, the a-Si waveguides were reshaped while in liquid state by surface tension that acts on the liquid-air interface. Therefore, the initially rectangular cross section of the a-Si waveguide forms a semi-circular shape, as shown in Figure 2. Here, the SEM micrograph in (a) is an un-processed 2 µm wide a-Si waveguide, whilst the SEM micrograph in (b) is a 2 µm wide p-Si waveguide, which has been laser processed with 200 mW at 0.1 mm/s.

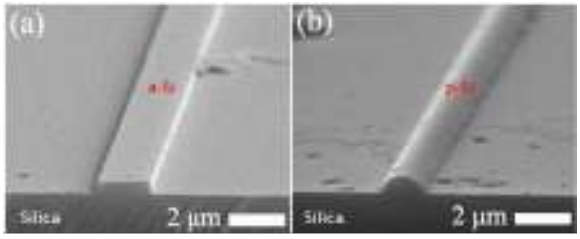


Figure 2: SEM micrographs shows cross-section of a 2µm wide waveguide before (a) and after (b) laser processing.

Micro-Raman spectroscopy, Secco etching and X-ray diffraction measurements reveal the high crystalline quality of the processed waveguides with the formation of millimeter long crystal grains. Optical losses as low as 5.3 dB/cm have been measured, indicating their suitability for the development of integrated circuits.

5.2. Laser inscription of composition graded polycrystalline silicon-germanium microstructures

Laser assisted melting of SiGe alloys induces phase segregation of Si and Ge atoms producing Si-rich and Ge-rich regions. Our results show that the spatial profile and amount of phase segregation in the Si-Ge thin films can be engineered by controlling the scan speed of the laser. Depending on the scan speed, two different types of spatial redistribution for Ge can be achieved as shown in Figure 3. Speeds below a threshold (5 mm/s) result in Si-rich regions at the centre of the track. However, above the threshold speed, a Ge-rich region is obtained at the centre between two lower index Si-rich lateral regions, which can help to promote optical waveguiding in the Ge-rich core. Moreover, higher Ge content can be obtained by using higher scan speeds. We have control over the size, composition gradient and direction of p-SiGe microstructures written by the laser.

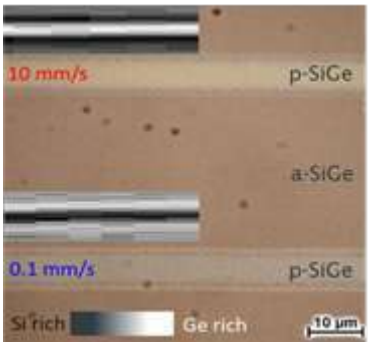


Figure 3: Optical microscope image shows two polycrystalline tracks inscribed in an amorphous SiGe film on c-Si wafer by a CW Ar+ ion laser at different scan speeds. Inset pictures show speed dependent spatial redistribution of Ge as given by the X-ray fluorescence intensity of Ge.

6. Conclusions

We have demonstrated laser processing of amorphous semiconductors on planar substrates to fabricate low loss p-Si waveguides and composition graded p-SiGe microstructures. A key feature of our technique is the low thermal budget, which makes it compatible with CMOS fabrication processes. Laser processing of semiconductors can pave the way for various photonic and optoelectronic devices to be used in novel integrated platforms.

Acknowledgements

The authors thank Diamond Light Source staff for their assistance on beamline I18, and the Engineering and Physical Sciences Research Council (EPSRC) for funding.

References

[1] J. S. Orcutt, S.D. Tang, S. Kramer, K. Mehta, H. Li, V. Stojanovic, Low-loss polysilicon waveguides fabricated in an emulated high-volume electronics process, *Opt. Express* 20: 7243−7254, 2012.

[2] Y. Franz, A. F. J. Runge, Swe Z. Oo, G. Jimenez-Martinez, N. Healy, A. Khokhar, A. Tarazona, H. M. H. Chong, S. Mailis, A. C. Peacock, Laser crystallized low-loss polycrystalline silicon waveguides, *Opt. Express* 27: 4462-4470, 2019.

[3] G. Pethuraja, R. Welser, A. Sood, C. Lee, N. Alexander, H. Efstathiadis, P. Haldar, J. Harvey, Effect of Ge Incorporation on Bandgap and Photosensitivity of Amorphous SiGe Thin Films, *Mater. Sci. and Appl.* 3: 67-71, 2012.

[4] D. A. Coucheron, M. Fokine, N. Patil, D. W. Breiby, O. T. Buset, N. Healy, A. C. Peacock, T. Hawkins, M. Jones, J. Ballato, U. J. Gibson, Laser recrystallization and inscription of compositional microstructures in crystalline SiGe-core fibres, *Nat. Commun.* 7: 13265, 2016.

Microresonator Soliton frequency combs

Tobias J. Kippenberg
EPFL, Switzerland

Optical frequency combs[1,2] provide equidistant markers in the IR, visible and UV and have become a pivotal tool for frequency metrology and are the underlying principle of optical atomic clocks, but are also finding use in other areas, such as broadband spectroscopy or low noise microwave generation. In 2007 a new method to generate optical combs was discovered based on high Q optical microresonators[3,4]. Such microresonator frequency combs have since then emerged as a new and widely investigated method with which combs can be generated via parametric frequency conversion of a continuous wave (CW) laser inside a high Q resonator via the Kerr nonlinearity. Over the past years the a detailed understanding of the comb formation process has been gained, and regimes identified in which dissipative temporal solitons (DKS) can be generated, that not only provide low noise optical frequency combs but moreover give access to femtosecond pulses. Such DKS have unlocked the full potential of soliton micro-combs by providing access to fully coherent and broadband combs and soliton broadening effects. Dissipative Kerr solitons have now been generated in a wide variety of resonators, including those compatible with photonic integration based on silicon nitride (Si_3N_4). We will discuss the DKS regime, first discovered in crystalline resonators, and our current understanding including the observation of the breather soliton regime, the influence of avoided mode crossings on breather and the repetition rate, as well as methods to deterministically access the single soliton regime. Taken together this has enabled to reliably access single soliton states in photonic chip based resonators, in particular those utilizing the photonic damascene process. Dissipative Kerr solitons enable to obtain combs that can span more than a full octave using soliton induced Cherenkov radiation, which extends the combs bandwidth and power in the spectral wings via dispersive waves. Such DKS have been enabled to count the cycles of light, allow 2f-3f self referencing. Using such soliton Kerr optical frequency combs in a SiN microresonator we have recently demonstrated with the group of C. Koos (KIT) massively parallel coherent communication, with dual combs for both the source and as massively parallel LO for the coherent receiver [1]. Moreover, we have demonstrated using a pair of photonic chip based frequency combs dual comb distance measurements, with record acquisition rates due to the combs large mode spacing (100 GHz). Recent work moreover has shown that DKS can be extended to the biological imaging window at 1 micron, relevant for e.g. Raman spectral imaging or OCT. Soliton microcombs have the potential to advance timekeeping, metrology or telecommunication by providing a technology amenable to full photonic integration, low power consumption and large comb bandwidth and repetition rate.

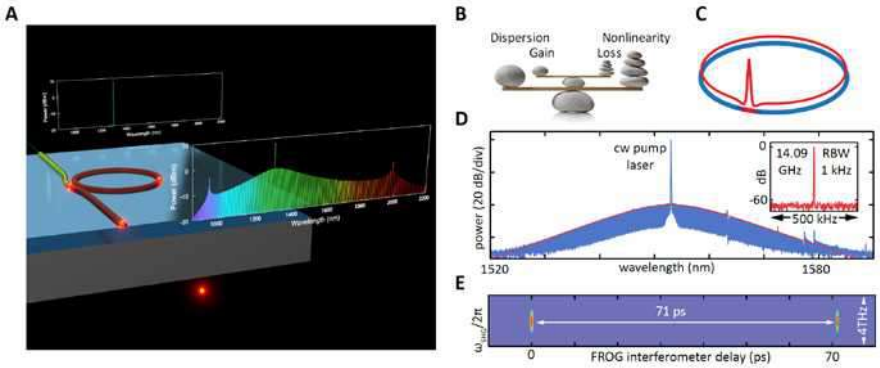


Figure 1 : Dissipative Kerr solitons in microresonators. (B) Principle of a DKS that balances dispersion and nonlinearity, as well as parametric gain and cavity loss. (C) temporal dissipative soliton waveform envelope in a microresonator (D) First demonstration of a DKS in a crystalline microresonator. (E) The FROG profile of a single DKS.

1 Cundiff, S. T. & Ye, J. Colloquium: Femtosecond optical frequency combs. *Rev. Mod. Phys.* **75**, 325-342 (2003).
2 Udem, T., Holzwarth, R. & Hansch, T. W. Optical frequency metrology. *Nature* **416**, 233-237 (2002).
3 Del Haye, P. *et al.* Optical frequency comb generation from a monolithic microresonator. *Nature* **450**, 1214 (2007).
4 Kippenberg, T. J., Holzwarth, R. & Diddams, S. A. Microresonator-based optical frequency combs. *Science* **332**, 555-559, doi:10.1126/science.1193968 (2011).
5 Del'Haye, P. *et al.* Octave Spanning Tunable Frequency Comb from a Microresonator. *Physical Review Letters* **107**, doi:10.1103/PhysRevLett.107.063901 (2011).
6 Herr, T. *et al.* Universal formation dynamics and noise of Kerr-frequency combs in microresonators. *Nature Photonics* **6**, 480-487, doi:10.1038/nphoton.2012.127 (2012).
7 Alnis, J. *et al.* Thermal-noise-limited crystalline whispering-gallery-mode resonator for laser stabilization. *Physical Review A* **84**, doi:10.1103/PhysRevA.84.011804 (2011).
8 Kudryashov, A. V. *et al.* Terabit/s data transmission using optical frequency combs. **8600**, 860009, doi:10.1117/12.2003701 (2013).
9 Wang, C. Y. *et al.* Mid-infrared optical frequency combs at 2.5 mum based on crystalline microresonators. *Nature communications* **4**, 1345, doi:10.1038/ncomms2335 (2013).10 Herr, T. *et al.* Temporal solitons in optical microresonators. *Nature Photonics* **8**, 145-152, doi:10.1038/nphoton.2013.343 (2013).

Fano resonances in optics and microwaves: Physics and application

Tunable Fano resonances in the radiative decay rate of a dipole emitter near a graphene-coated nanowire

Tiago J. Arruda[1], Romain Bachelard[2], John Weiner[1], and Philippe W. Courteille[1]

[1]São Carlos Institute of Physics (IFSC), University of São Paulo (USP), São Paulo, Brazil
[2]Department of Physics, Federal University of São Carlos (UFSCar), São Paulo, Brazil
*corresponding author, E-mail: tiagojarruda@gmail.com

Abstract

We study radiative transition rates for different orientations of a dipole emitter near a graphene-coated nanowire. We show that Fano resonances appear in the Purcell factor as a function of frequency. Furthermore, the Fano lineshape can be tailored and electrically tuned by varying the distance between emitter and cylinder and by modulating the graphene chemical potential. This gate-voltage-tunable Fano resonance leads to a resonant enhancement and suppression of light emission in the far-infrared range of frequencies.

1. Introduction

The modification of the spontaneous-emission rate of a quantum emitter induced by its interaction with environment is generally referred to as the Purcell effect [1]. First described in the context of cavity quantum electrodynamics [2], the Purcell effect finds applications where controlling and manipulating light emission and absorption in subwavelength structures is crucial [3], such as, e.g., high efficiency single-photon sources [4] and microcavity light-emitting devices [5]. Recently, graphene has become a promising alternative material to enhance the Purcell factor in subwavelength structures due to its unique optical properties, such as strong localized surface plasmon resonances with relatively lower losses than noble metals [6]. Furthermore, graphene exhibits strong light-matter interaction in two-dimensional atomically thin layers of carbon atoms [7], and it also offers magnetic, electrical, or chemical tunability of its conductivity from terahertz up to midinfrared frequencies [8].

Here, based on the full-wave Lorenz-Mie theory of circular cylinders, we study the spontaneous-emission rate of a point dipole emitter near a graphene-coated nanowire. By varying the distance between emitter and cylinder, the radiative decay rate associated with the dipole moment oriented orthogonal to the cylinder axis is shown to exhibit a Fano line shape as a function of the emission frequency; conversely, a dipole moment oriented parallel to the cylinder axis exhibits a Lorentzian line shape. The appearance of a Fano line shape is a signature of interference between a localized plasmon resonance at the graphene coating and a broad dipole resonance acting as a radiation background [9, 10]. More importantly, the Fano asymmetry parameter is proportional to the graphene chemical potential. This allows one to control enhancement and suppression of spontaneous emission by a gate voltage. For the interested reader, the explicit analytical connection between Fano resonances in the Lorenz-Mie theory of core-shell scatterers and radiative decay rates of a dipole emitter in the vicinity of a graphene-coated nanofiber can be found in Ref. [1].

2. Discussion and results

Let us consider a pointlike emitter located at position $\mathbf{r}'$ in the vicinity of a uniform graphene-coated nanowire in free space, with inner radius a and outer radius $b < r'$. We assume a dielectric core made of a lossless material with permittivity $\varepsilon_{\rm d} = 3.9\varepsilon_0$ and radius $a = 100$ nm. Since the graphene monolayer is a two-dimensional electromagnetic material and its thickness ($b - a \approx 0.5$ nm) is much smaller than the radius of the dielectric core, we can treat it as a conducting film [11].

To simplify our discussion, let us consider the limiting case $kr' \ll 1$, i.e., the system composed by cylinder and emitter together is diameter-subwavelength, and hence can be described as a dipole-type system. With this assumption, we can simplify the expressions of the radiative decay rates normalized to free space. For each dipole moment orientation in relation to the cylindrical coordinate system (r, φ, z), we have after some algebra

$$\frac{\Gamma_r^{\rm rad}(r',\omega)}{\Gamma_0} \propto \frac{\left[X(\omega) + F_+(r')\right]^2}{[X(\omega)]^2 + 1}, \tag{1a}$$

$$\frac{\Gamma_\varphi^{\rm rad}(r',\omega)}{\Gamma_0} \propto \frac{\left[X(\omega) + F_-(r')\right]^2}{[X(\omega)]^2 + 1}, \tag{1b}$$

where we have defined

$$X(\omega) \equiv \frac{\omega - \omega_+}{\gamma/2},\ F_\pm(r') \equiv \pm\frac{b^2}{r'^2}\frac{(\omega_+ - \omega_-)}{\gamma/2}, \tag{2}$$

$$\omega_\pm \equiv \sqrt{\frac{e^2\mu_{\rm c}}{\pi\hbar^2 b(\varepsilon_{\rm d} \pm \varepsilon_0)}}, \tag{3}$$

with $\omega_{\rm res} = \omega_+$ for the resonance and $\omega_{\rm inv} = \omega_-$ for the antiresonance. The quantities $\mu_{\rm c}$ and γ are the graphene chemical potential and the damping rate ($\gamma \ll \omega$), respectively. Since we are interested in the frequency range where the localized surface plasmon resonance occurs, we can

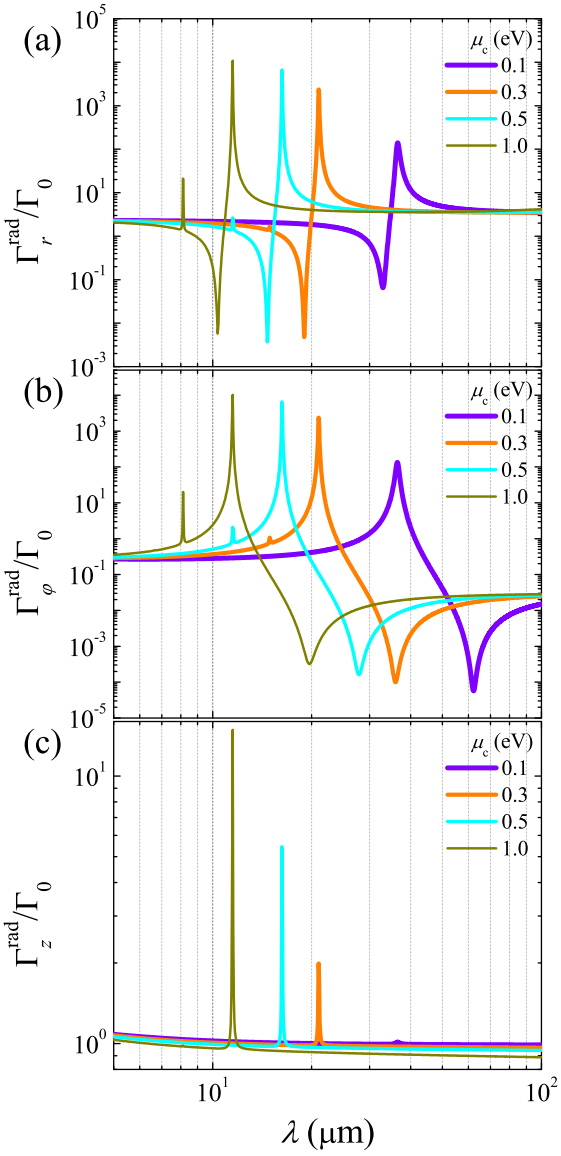


Figure 1: Radiative decay rates for a dipole emitter near a graphene-coated dielectric nanowire of radius $a = 100$ nm at $T = 300$ K. The distance between emitter and cylinder is $\Delta r = 10$ nm. The plots show the influence of the graphene chemical potential μ_c on the Fano line shapes in (a) Γ_r^{rad} and (b) Γ_φ^{rad}, and on the Lorentzian line shape in (c) Γ_z^{rad} at the vicinity of the localized surface plasmon resonance.

consider that Γ_z^{rad} has a Lorentzian line shape as a function of ω: $(\Gamma_z^{rad} - \Gamma_0) \propto \Gamma_0/(X^2+1)$. This Lorentzian line shape is related to the fact that Γ_z^{rad} depends only on the transverse-magnetic mode, see Ref. [1].

The Fano asymmetry parameter given in Eq. (2) depends explicitly on the distance $\Delta r = r' - b$ between emitter and cylinder. More importantly, we see that $F_\pm(r') \propto \sqrt{\mu_c}$, which implies that both enhancement and suppression of the Purcell factor can be tuned by the chemical potential. In practice the graphene chemical potential can be dynamically controlled by an applied static electric field (gate voltage) through the graphene/dielectric interface [8].

Using the analytical expressions derived in Ref. [1], we show in Fig. 1 the plots of radiative decay rates associated with a dipole emitter at $\Delta r = 10$ nm from the graphene-coated nanowire. By increasing the chemical potential from $\mu_c = 0.1$ eV to 1.0 eV, we show that the Fano line shape is blueshifted. At the same time, the maximum enhancement of decay rates increases two orders of magnitude for $\Gamma_r^{rad}(\lambda_{res})$ and $\Gamma_\varphi^{rad}(\lambda_{res})$ [Figs. 1(a) and 1(b), respectively] and one order of magnitude for $\Gamma_z^{rad}(\lambda_{res})$ [Fig. 1(c)].

3. Conclusion

We have shown that the enhancement and suppression of the radiative decay rate of a point dipole emitter near a graphene-coated nanowire can be tuned by the graphene chemical potential monitored by a gate voltage. The Fano asymmetry parameter of radiative decay rates, which determines the degree of asymmetry of the Fano line shape, is shown to be proportional to the square root of the chemical potential and depends strongly on the distance between dipole emitter and cylinder for a dipole moment oriented along φ direction. For a dipole moment oriented along z direction, the interaction between dipole emitter and graphene is weak, leading to a Lorentzian line shape in the radiative decay rate. The strong dependence of decay rates on the graphene chemical potential can be explored to enhance or suppress the radiative decay response of a plasmonic system by dynamically controlling the Fano resonance via a gate voltage.

Acknowledgement

T.J.A., R.B., and Ph.W.C. hold Grants from São Paulo Research Foundation (FAPESP) (Grants No. 2015/21194-3, No. 2014/01491-0, and No. 2013/04162-5, respectively).

References

[1] T.J. Arruda, R. Bachelard, J. Weiner, P.W. Courteille, Tunable Fano resonances in the decay rates of a point-like emitter near a graphene-coated nanowire, *Phys. Rev. B* 98: 245419, 2018.

[2] E.M. Purcell, Spontaneous emission probabilities at radio frequencies, *Phys. Rev.* 69: 681, 1946.

[3] R. Carminati, A. Cazé, D. Cao, F. Peragut, V. Krachmalnicoff, R. Pierrat, Y. De Wilde, Electromagnetic density of states in complex plasmonic systems, *Surf. Sci. Rep.* 70: 1, 2015.

[4] D.E. Chang, A.S. Sørensen, E.A. Demler, M.D. Lukin, A single-photon transistor using nanoscale surface plasmons, *Nat. Phys.* 3: 807, 2007.

[5] Q. Gu, B. Slutsky, F. Vallini, J.S.T. Smalley, M.P. Nezhad, N.C. Frateschi, Y. Fainman, Purcell effect in sub-wavelength semiconductor lasers, *Opt. Express* 21: 15603, 2013.

[6] G.W. Hanson, E. Forati, W. Linz, A.B. Yakovlev, Excitation of terahertz surface plasmons on graphene surfaces by an elementary dipole and quantum emitter: Strong electrodynamic effect of dielectric support, *Phys. Rev. B* 86: 235440, 2012.

[7] F.H.L. Koppens, D.E. Chang, F.J. García de Abajo, Graphene plasmonics: A platform for strong light-matter interactions, *Nano Lett.* 11: 3370, 2011.

[8] A. Vakil, N. Engheta, Transformation optics using graphene, *Science* 332: 1291, 2011.

[9] T.J. Arruda, A.S. Martinez, F.A. Pinheiro, Unconventional Fano effect and off-resonance field enhancement in plasmonic coated spheres, *Phys. Rev. A* 87: 043841, 2013.

[10] T.J. Arruda, R. Bachelard, J. Weiner, S. Slama, P.W. Courteille, Fano resonances and fluorescence enhancement of a dipole emitter near a plasmonic nanoshell, *Phys. Rev. A* 96: 043869, 2017.

[11] M. Naserpour, C. J. Zapata-Rodríguez, S. M. Vuković, H. Pashaeiad, and M. R. Belić, Tunable invisibility cloaking by using isolated graphene-coated nanowires and dimers, *Sci. Rep.* 7: 12186, 2017.

Fano Resonances in Dimer Nanoantennas: Switching and Directionality Effects

Ángela I. Barreda[1], Hassan Saleh[2], Amélie Litman[2], Francisco González[3], Jean-Michel Geffrin[2], and Fernando Moreno[3]

[1]Nanophotonics Technology Center, Universitat Politècnica de València, Valencia 46022, Spain
[2]Aix-Marseille Univ, CNRS, Centrale Marseille, Institute Fresnel, Marseille, France
[3]Group of Optics, Department of Applied Physics, University of Cantabria, Cantabria 39005, Spain
*corresponding author, E-mail: anbargo@ntc.upv.es

Abstract

Directionality properties of subwavelength High Refractive Index Dielectric particles make them good candidates for controlling the direction of the scattered radiation. Here, we show experimentally, in the microwave range, that a dimer unit made of such materials can optimize the performance of solar cells by redirecting the incident radiation to the photosensitive layer. In addition, we demonstrate its utility for building operational switching devices.

1. Introduction

Metallic particles smaller than the incident wavelength have been vastly analyzed for many different applications, like Surface Enhanced Spectroscopies (SERS or equivalent techniques), biosensing, solar energy harvesting, etc [1]. However, their inherent ohmic losses limit their performance. High Refractive Index Dielectric (HRID) particles, like silicon, germanium or other semiconductor compounds [2] in the NIR, have been proposed as an alternative to solve this issue. Their most important advantages come from their low-losses and their magnetic response in spite of being non-magnetic materials [3]. Also, the coherent effects between electric and magnetic spectral resonances give rise to directionality properties. Kerker *et al.* established that for a point-like particle and under certain conditions of its electric permittivity and magnetic permeability, incident radiation can be concentrated in the forward (backward) direction, being null (almost null) in the exact backward (forward) one [4,5]. This situation corresponds to the Zero-Backward (near Zero-Forward) or First Kerker condition (Second Kerker condition). In this work, we show that by means of a dimer of HRID particles and controlling the distance between them, it is possible to observe in the dipolar regime, two spectral regions where the incident radiation is mainly scattered in the forward direction. These ranges correspond to the Zero-Backward condition (also observed for either isolated particle or a particle cluster, when there is no electromagnetic interaction between its components) and to a new "near Zero-Backward" condition (originated by the interaction effects between the particles) [6]. This fact finds its major application for optimizing the performance of solar cells. For eccentric metallo-dielectric core-shell particles [7] and asymmetric dimers [8], the incident radiation can be redirected to certain directions respect to forward or backward. This effect can be used for building switching devices. Here, we analyze this by means of a symmetric homogeneous dimer of HRID spherical particles [9]. We demonstrate that the scattered intensity at 90º from the incident direction can be null or maximum by playing with the polarization of a single frequency excitation and with a dimer whose components are close enough to interact in a controlled way.

2. Results

2.1. Directionality properties

For a HRID dimer of spherical particles, it is possible to find, in the dipolar regime, two spectral regions where the incident radiation is scattered in forward. They correspond to the Zero-Backward condition and to a new "near Zero-Backward" condition. The interaction effects between the particles are responsible for the last one, which is a 180º "rotated" version of the near Zero-Forward condition. In particular, a Fano-like resonance (originated by the interference between both the sharp magnetic and the broad electric dipolar modes) gives rise to this new Scattering Directionality Condition (SDC).

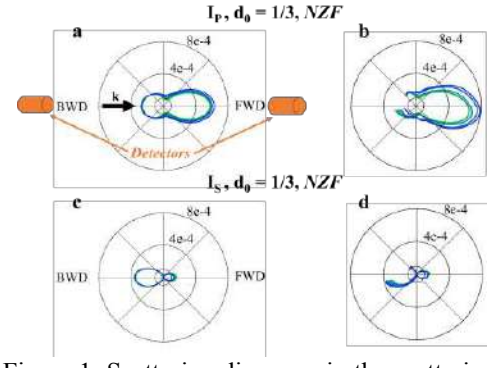


Figure 1: Scattering diagrams in the scattering plane at the near Zero-Forward (NZF) condition for a HRID dimer. The radii of the particles are $R_1 = R_2 = 9$ mm and their dielectric permittivity is $\varepsilon_1 = \varepsilon_2 = 15.7+0.3$. The distance between both components of the dimer is $d = 3$ mm ($d_0 = 1/3$). (a-b) Longitudinal configuration. (c-d) Transverse configuration. The theoretical and experimental results are shown in left and right columns, respectively. The black arrow represents the

direction of the impinging radiation (***k***). The orange cylinders indicate the detectors positions. BWD stands for Backward Direction and FWD stands for Forward Direction.

In Fig. 1, we show the scattering diagrams at the frequencies where the near Zero-Forward condition holds for d_0 = 1/3 and both polarizations of the incident radiation (longitudinal (I_P, polarization along the axis dimer) and transverse (I_S, polarization perpendicular to the axis dimer) configurations). d_0 is a parameter, which takes into account the interaction effects between the particles, defined as $d_0 = d/R$, being d the distance between both components of the dimer (gap) and R their radius.

2.2. Switching effect

The switching effect is produced by the spectral evolution of one of the natural resonances (the dipolar magnetic) of the isolated particle to an asymmetric shape resonance (Fano-like) as the particle interaction increases. This behavior can be observed in Fig. 2, where we show the spectral evolution of the scattered intensity at 90º for longitudinal and transverse polarizations of the incident radiation. We also plot the behavior of the linear polarization degree at 90º, P_L(90º) [5]. The analysis is carried out for two different distances between the particles d_0 = 2 (weak interaction effects between the particles) and d_0 = 1/3 (strong interaction effects).

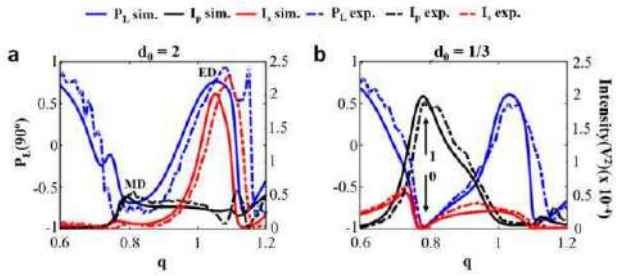


Figure 2: Scattered intensity in far-field at 90º and linear polarization degree at right angle scattering configuration (P_L(90º)) for a HRID dimer of spherical particles as a function of the size parameter q ($q = 2\pi R/\lambda$). Particles radii $R_1 = R_2$ = 9 mm and dielectric permittivity $\varepsilon_1 = \varepsilon_2$ = 15.7+0.3. The distance between both components of the dimer is d = 18 mm (d_0 = 2) and d = 3 mm (d_0 = 1/3). It is illuminated by a plane wave linearly polarized parallel (I_P) or perpendicular (I_S) to the scattering plane. (a) Simulation and measurement for d_0 = 2. (b) Simulation and measurements for d_0 = 1/3. (MD = Magnetic dipole resonance, ED = Electric dipole resonance). Simulations (solid line). Simulations (solid line). Measurements (dash line). P_L(90º) blue line. I_S (red line). I_P (black line). The low and high states are indicated with the 0 and 1 arrows respectively.

3. Conclusions

In this work, we have evidenced different applications of a dimer of HRID spherical particles. In particular, we have analyzed the utility of these structures for optimizing the performance of actual photovoltaic cells. With a HRID dimer unit, it is possible to find two spectral ranges in the dipolar region, where the incident radiation is forward scattered. They correspond to the Zero-Backward condition and to a new "near Zero-Backward" condition, which is a "rotated" version of the traditional near Zero-Forward condition. We have also shown the possibility of using this scattering unit as a new block for building operational switching devices whose on/off state only depends on the polarization of the incident radiation. Both applications are a consequence of the excitation of Fano-like resonances due to electromagnetic interaction between the particles.

Acknowledgements

AIB acknowledges financial Support by the European Commission under Project THOR H2020-EU-829067. Authors thank support of SODERCAN through the Research Vicerrectorate of the U. Cantabria.

References

[1] P. Prasad, *Nanophotonics*, John Wiley & Sons, Inc., Hoboken, New Jersey, 2004.

[2] D. G. Baranov, *et al*., All-dielectric nanophotonics: the quest for better materials and fabrication techniques, *Optica* 4: 814-825, 2017.

[3] A. García-Etxarri, *et al.*, Strong magnetic response of submicron silicon particles in the infrared, *Opt. Express* 19: 4815–4826, 2011.

[4] M. Kerker, D. S. Wang, C. L. Giles, Electromagnetic scattering by magnetic spheres, *J. Opt. Soc. Am.* 73: 765–767, 1983.

[5] J. M. Geffrin, *et al*., Magnetic and electric coherence in forward-and back-scattered electromagnetic waves by a single dielectric subwavelength sphere, *Nat. Commun.* 3: 1–8, 2012.

[6] A. I. Barreda, *et al*., On the scattering directionality of a dielectric particle dimer of high refractive index, *Sci. Rep.* 8: 7976, 2018.

[7] A. I. Barreda, *et al*., Light guiding and switching using eccentric core-shell geometries, *Sci. Rep.* 7: 1–10, 2017.

[8] P. Albella, T. Shibanuma, S. A. Maier, Switchable directional scattering of electromagnetic radiation with subwavelength asymmetric silicon dimers, *Sci. Rep*. 5: 1–8, 2015.

[9] A. I. Barreda, *et al*., Electromagnetic polarization controlled perfect switching effect with high refractive index dimers and the beam-splitter configuration, *Nat. Commun*. 8: 1–8, 2017.

Trapped light states in spatially dispersive plasmonic nanostructures

Solange V. da Silva[1], Tiago A. Morgado[1], Mário G. Silveirinha[1,2]*
[1]Instituto de Telecomunicações and Department of Electrical Engineering, University of Coimbra, 3030-290 Coimbra, Portugal
[2]University of Lisbon, Instituto Superior Técnico, Avenida Rovisco Pais, 1, 1049-001 Lisboa, Portugal
*corresponding author, E-mail: solange@co.it.pt

Abstract

It was shown some time ago that open bi-layered plasmonic nanostructures may support trapped light states with infinite lifetimes. Counterintuitively, here we prove that spatially dispersive effects may relax the material and geometrical conditions required for the formation of embedded eigenstates in plasmonic systems.

1. Introduction

In the last years, several research groups have shown that it may be possible to have optical bound states with infinite oscillation lifetimes within the radiation continuum (embedded eigenstates) in open unbounded structures (see review [1] and references therein). However, a complete suppression of the radiation loss is typically only possible when the material structures are infinitely extended in space. In contrast, in a recent work [2], we demonstrated that the embedded eigenstates can as well be formed in compact three-dimensional (3D) nanostructures, e.g., a core-shell nanoparticle made of a dielectric core and an epsilon-near-zero (ENZ) shell [2]. Our proposal was also explored by other groups [3-4].

In [2-6] the plasmonic ENZ shell was assumed to have a local electromagnetic response, i.e., the permittivity is only frequency-dispersive and has no wave-vector dependence. However, it is known that the nonlocal effects may affect considerably the response of nanosized plasmonic particles [7]. In particular, one may heuristically expect that charge diffusion may create additional difficulties to the formation of embedded eigenstates. Surprisingly, here we prove that it is precisely the opposite, and that the spatial dispersion effects in the plasmonic shell offer new opportunities to trap light in open resonators.

2. Spatially dispersive meta-atom

Figure 1(a) depicts the meta-atom geometry: a bi-layered sphere embedded in air. The internal layer (core region) and the outer layer (shell) have respectively radii R_1 and R_2. The core material (e.g. air) has a standard dielectric response characterized by the relative permittivity ε_1. The shell is made of a material with plasmonic response. To account for the nonlocal effects in the plasmonic shell, we use the hydrodynamic (drift-diffusion) model [7]. A spatially-dispersive plasma supports three plane-wave natural modes with a spatial dependence of the type $e^{i\mathbf{k}\cdot\mathbf{r}}$: two transverse modes and also a longitudinal mode [7]. The transverse modes see a relative permittivity described by a standard Drude-type model $\varepsilon_{2,\mathrm{T}}(\omega)=\varepsilon_\infty-\omega_\mathrm{p}^2/\left[\omega(\omega+i\omega_\mathrm{c})\right]$, where ω_p is the plasma frequency, ω_c is the collision frequency, and ε_∞ is the high-frequency relative permittivity (we take $\varepsilon_\infty=1$). On the other hand, the longitudinal mode sees a permittivity which is frequency and wave-vector dependent, described by $\varepsilon_{2,\mathrm{L}}(\mathbf{k},\omega)=\varepsilon_\infty-\omega_\mathrm{p}^2/\left[\omega(\omega+i\omega_\mathrm{c})-\beta^2k^2\right]$ [7], where $\beta^2=3/5\,v_\mathrm{F}^2$ and v_F is the Fermi velocity. Since the nanoparticle has spherical geometry (Fig. 1(a)), we can write the electromagnetic fields in all the regions of space in terms of spherical Bessel functions **Erro! A origem da referência não foi encontrada.**. To calculate the TM^r embedded eigenstates supported by the nanoparticle, we impose the

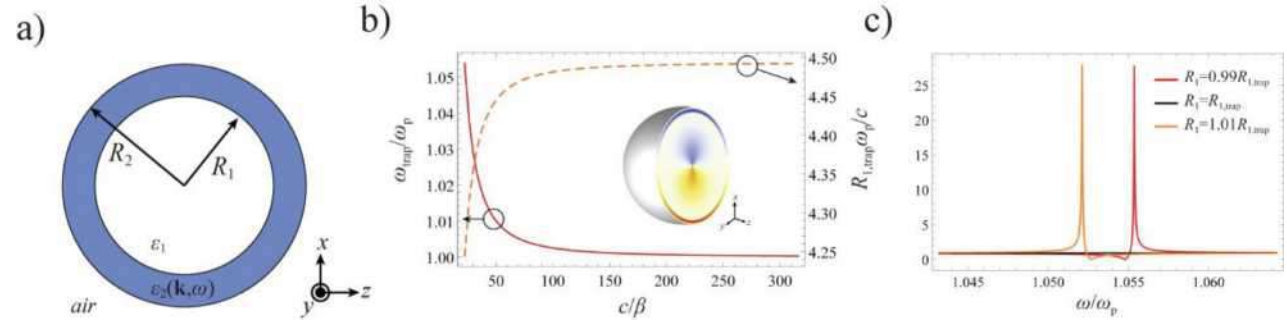


Figure 1: (a) Geometry of the open bi-layered spherical meta-atom. The shell is made of a plasmonic spatially dispersive material while the core material is a standard dielectric. (b) Embedded eigenstate frequency (solid red line) and optimal core radius (dashed orange line) as a function of the locality strength. The inset shows a time snapshot of the radial electric field $E_r(t=0)$ in the meta-atom. (c) Mie coefficient $\left|a_1^{\mathrm{TM}}\right|$ in the core region as a function of the normalized frequency ω/ω_p and for different values of the internal radius. The meta-atom parameters are $c/\beta=\sqrt{10^3}$, $R_2/R_{1,\mathrm{trap}}=1.1$, $\varepsilon_1=1$, and $\omega_\mathrm{c}=0$.

classical boundary conditions at the interfaces. Due to the additional longitudinal mode, it is also necessary to ensure that the normal component of the electric conduction current vanishes at the interfaces of the spatially dispersive plasma [2, 7]. This procedure yields a 6×6 homogeneous linear system of the form $\mathbf{M}\cdot\mathbf{x}=0$. The frequencies of oscillation $\omega=\omega'+i\omega''$ ($\omega''\le0$) of the natural modes of oscillation are calculated by solving a characteristic equation $D\left(\omega,R_1,\varepsilon_1,R_2,\omega_\mathrm{p},\beta\right)\equiv\det\left(\mathbf{M}\right)=0$, with $D=D'+iD''$ complex-valued.

3. Properties of the embedded eigenstates

In the local limit ($\beta=0$), the embedded eigenstates can be formed only when the shell has $\varepsilon_2=0$, i.e. when $\omega=\omega_\mathrm{p}$ [2]. In this case, the TM^r waves see the ENZ shell as a PMC wall. Thus, the embedded eigenstates can emerge if and only if $\omega=\omega_\mathrm{p}$ coincides with one of the eigenfrequencies of the equivalent PMC cavity. The geometrical condition for the formation of an embedded eigenstate with dipolar-type symmetry (see inset of Fig. 1(b)) is $R_1=R_{1,0}\equiv4.49c\Big/\left(\omega_\mathrm{p}\sqrt{\varepsilon_1}\right)$ [2].

In contrast, in the nonlocal case ($\beta\neq0$), the condition $\omega=\omega_\mathrm{p}$ does not lead to the formation of eigenstates. Remarkably, we find that the pair of equations $D'=0$ and $D''=0$ has always a real-valued solution in frequency. The solution ω_trap (oscillation frequency) and $R_{1,\mathrm{trap}}$ (optimal core radius) is associated with an embedded eigenstate characterized by the parameters $\left(\varepsilon_1,R_2,\omega_\mathrm{p},\beta\right)$. The obtained solutions are depicted in Fig. 1(b) as a function of c/β. The results show that for small values of c/β (i.e. for strong nonlocal effects), ω_trap can be significantly different from ω_p. This means that the eigenstates may be formed for frequencies $\omega\neq\omega_\mathrm{p}$, for which the the shell permittivity can significantly differ from zero ($\varepsilon_{2,\mathrm{T}}\neq0$). Thus, nonlocal effects clearly relax the formation of the eigenstates by avoiding the need of a singular material response. Furthermore, the optimal core radius $R_{1,\mathrm{trap}}$ may differ considerably from the local value $R_{1,0}$ for strongly nonlocal responses, relaxing thereby also the geometrical condition.

4. Meta-atom response under external excitation

Suppose now that the meta-atom is excited by a linearly polarized plane wave. The Mie coefficients that determine the fields scattered by the bi-layered nanoparticle can be calculated by solving the system of equations $\mathbf{M}\cdot\mathbf{x}=\mathbf{b}$, with $\mathbf{b}$ a vector determined by the incident wave. In Fig. 1(c) we depict the variation of the first (electric-dipole) Mie coefficient in the core region $\left|a_1^{\mathrm{TM}}\right|$ with frequency for three different values of the core radius R_1. The results show that for values of R_1 different from the optimal $R_{1,\mathrm{trap}}$, the Mie coefficient has a strong resonant behavior with a Fano-type line shape. On the other hand, when R_1 is exactly coincident with $R_{1,\mathrm{trap}}$, there is no resonance and $\left|a_1^{\mathrm{TM}}\right|=1$ due to a pole-zero cancellation [2]. This behavior is fully consistent with the emergence of an embedded eigenstate in the meta-atom.

5. Conclusions

We theoretically demonstrated that open core-shell meta-atoms may support embedded eigenstates even if diffusion effects in the plasmonic shell are fully considered. Surprisingly, the diffusion effects relax the conditions required to suppress the radiation loss, as it is no longer necessary that the permittivity of the shell vanishes as in the local case. At the conference, we will show that the same material shell can potentially trap light for multiple frequencies.

Acknowledgements

This work was partially funded by the IET under the A F Harvey Engineering Research Prize, by Fundação para Ciência e a Tecnologia (FCT) under Project PTDC/EEITEL/4543/2014 and by Instituto de Telecomunicações (IT) under Project No. UID/EEA/50008/2017. S. S. acknowledges financial support by FCT/POPH and the cofinancing of Fundo Social Europeu under the PhD fellowship SFRH/BD/105625/2015. T. M. acknowledges financial support by FCT under the research contract with reference DL 57/2016/CP1353/CT0002 established with IT – Coimbra.

References

[1] C. W. Hsu, B. Zhen, A. D. Stone, J. D. Joannopoulos, M. Soljacic, Bound States in the continuum, *Nat. Rev. Mater.* 1: 16048, 2016.

[2] M. G. Silveirinha, Trapping light in open plasmonic nanostructures, *Phys. Rev. A* 89: 023813, 2014.

[3] F. Monticone and A. Alù, "Embedded Photonic Eigenvalues in 3D Nanostructures," *Phys. Rev. Lett.* **112**, 213903 (2014).

[4] I. Liberal and N. Engheta, "Nonradiating and radiating modes excited by quantum emitters in open epsilon-near-zero cavities," *Sci. Adv.* **2**, e1600987, 10 (2016).

[5] S. Lannebère, M. G. Silveirinha, Optical meta-atom for localization of light with quantized energy, *Nat. Commun.* 6: 8766, 2015.

[6] S. Silva, T. A. Morgado, M. G. Silveirinha, Discrete light spectrum of complex-shaped meta-atoms, *Radio Sci.* 53: 144-153, 2018.

[7] C. David, F. J. G. de Abajo, Spatial Nonlocality in the Optical Response of Metal Nanoparticles, *J. Phys. Chem. C* 115: 19470-19475, 2011.

Silent enhancement of SERS signal without increasing the hot spot intensity

Mehmet Emre Tasgin[1]

[1]Institute of NuclearSciences, Hacettepe University, 06800 Ankara, Turkey

Abstract

Nanostructures enhance nonlinear response, such as surface enhanced Raman scattering (SERS), by localizing the incident field into hot spots. The localized hot spot field can be enhanced even further when linear Fano resonances (FR) take place in a double resonance scheme. On the other hand, hot spot enhancement is limited with the break-down of the molecule and the tunnelling regime. We present a method which can circumvent these limitations. Our analytical model and solutions of 3D Maxwell equations show that: enhancement due to the localization can be further multiplied by a factor of 3 orders of magnitude. Moreover, this can be performed without increasing the hot spot intensities which also avoids the modification of the Raman modes. Unlike linear Fano resonances, we create the path interference in the nonlinear response. We demonstrate on a single equation that enhancement takes place due to the cancellation in the denominator of the SERS response [1].

1. Introduction

Metal nanostructures (MNSs) can localize incident radiation in nm-size hot spots. The trapped field, as plasmon polarization, can be enhanced several orders of magnitude compared to the incident one. This yields an enhancement also in the nonlinear effects, such as surface enhanced Raman scattering (SERS) or second harmonic generation. SERS phenomenon has imaging applications in all fields of science, from chemistry to tumor targeting. This is because, SERS spectrum is material specific and can be used in identification.

There are quite recent, interesting, studies on the further enhancement of SERS. (i) A double resonance scheme, where exciting and the Raman-converted frequencies are aligned with two plasmon resonances, is shown to enhance [2] several orders of magnitude more. This is because, both the input and output hot spots localize the two fields resonantly. (ii) More recent studies cleverly combined this phenomenon with linear Fano resonances. It is well-known that Fano resonances enhance the localized field more, called as dark-hot resonances. Researchers showed that when the input and output frequencies are aligned with two linear Fano resonances in a double resonance scheme, i.e. double Fano resonance scheme, SERS signal can be enhanced even further on top of the double resonance scheme [3].

These two developments carried the SERS imaging at a new stage. Both methods, (i) and (ii), rely on the enhancement of the localized hot spot field more. On the other hand, it is experimented that strong hot spot fields can (a) modify the Raman modes of the samples, (b) burn the sample. Moreover, (c) tunneling regime in the nanogaps can avoid the further enhancement of the hot spot fields.

2. Summary

In this work [1], we present a method which can increase the SERS signal 3 order of magnitude, but can leave the hot spot intensities unchanged. That is, our method multiplies the SERS signal in a double resonance scheme by 3 orders, without heating the sample! In spite of the linear Fano resonances, we adopt the Fano resonances in the nonlinear response. Path interference takes place in the nonlinear response. On a single equation, Eq. (1), we show that this enhancement takes place due to the cancellation in the denominator of the SERS response, $\alpha_{\rm R}$, without affecting the linear response, α.

$$\tilde{\alpha}_{\rm R} = \frac{-i\chi\varepsilon_{\rm ph}^{*}}{\beta_{\rm ph}^{*}\Big([i(\Omega_{\rm R}-\omega_{\rm R})+\gamma_{\rm R}]-\frac{|f|^2 y}{[i(\omega_{eg}-\omega_{\rm R})+\gamma_{eg}]}\Big)-|\chi|^2|\tilde{\alpha}|^2}\tilde{\alpha} \quad (1)$$

$$\omega_{eg}^{*} = \omega_{\rm R} + \frac{|f|^2 y}{2(\Omega_{\rm R}-\omega_{\rm R})} - \sqrt{\frac{|f|^4|y|^2}{4(\Omega_{\rm R}-\omega_{\rm R})^2} - \gamma_{\rm eg}^2}. \quad (2)$$

An auxiliary quantum emitter (QE) or a MNS supporting a long-live dark plasmon mode is coupled to a metal nanoparticle (MNP)-dimer, see Fig. 1. Auxiliary QE couples only to the plasmon mode of the MNP-dimer. The choice of the level spacing for this auxiliary QE affects the SERS signal dramatically. when one chooses the level spacing ω_{eg} as in Eq. (2), the extra term cancels the nonresonant term in the denominator of Eq. (1). We also perform 3D simulations with the exact solutions of the Maxwell equations. We observe that the enhancement, predicted by the basic model, Eq. (1), is present in Fig. 2.

Acknowledgement

I acknowledge support from Hacettepe BAP grant no FBB-2017-13389 and TUBA GEBIP Award.

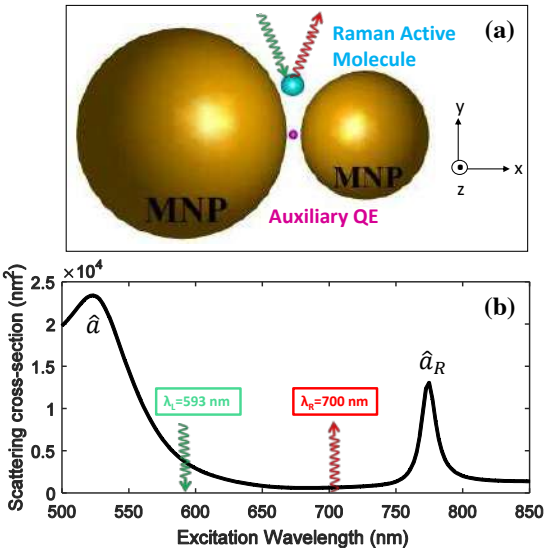


Figure 1: Figure is from Ref. [1]. (a) The setup we use in the 3D solutions of Maxwell equations. A gold MNP dimer, of radii 90 nm and 55 nm, creates a hot spot in the 4 nm gap. A Raman-active sphere of 4 nm radius (blue) is placed close to the dimer hot spot for producing the SERS signal. We place an auxiliary QE (purple) also in the vicinity of the dimer, for enhanced interaction with the $\hat{a}_{\rm R}$ plasmon mode. We move it along the z-direction when we desire to decrease the plasmon-auxiliary QE coupling, f. (b) Linear response of the dimer shows two plasmon peaks at Λ=530 nm and $\Lambda_{\rm R}$=780 nm. System is excited by a $\lambda_{\rm L}$=593 nm laser and a Stokes shifted signal emerges at $\lambda_{\rm R}$=700 nm. $\lambda_{\rm L}$ and $\lambda_{\rm R}$ overlap with Λ and $\Lambda_{\rm R}$, respectively. The λ_{eg} of the molecule is chosen to couple with the $\hat{a}_{\rm R}$-mode, see Fig. 2a. We use parameters similar to (b) in producing an accompanying simulation within our simple model. Experimental data of gold (dimer) and a Lorentzian dielectric function (auxiliary QE), in MNPBEM [4], are used for the 3D simulations.

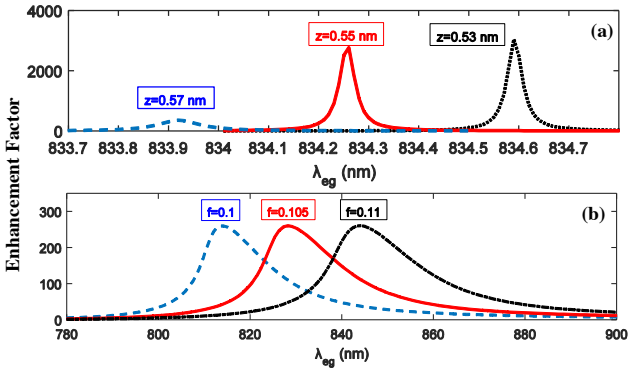


Figure 2: Figure is from Ref. [1]. Enhancement of the SERS signal with the presence of the auxiliary QE (purple) in Fig. 1. We plot the EFs with respect to the level spacing ($\lambda_{eg} = c/\omega_{eg}$) of the auxiliary QE interacting with the $\hat{a}_{\rm R}$ plasmon mode, (Fig. 1b). Interaction of the auxiliary QE decreases with larger separations (z) to the hot spot. (a) Solutions of the 3D Maxwell equations for the system depicted in Fig. 1. EFs for SERS are calculated for three different positions of the auxiliary QE, z=0.53, 0.55 and 0.57 nm. The position of optimum $\lambda^*_{eg} = c/\omega^*_{eg}$, where maximum EF appears, shifts to larger wavelengths. Optimum λ^*_{eg} ≈834 nm, is far away from the Stokes signal (700 nm). An enhancement due to a linear FR would yield maximum enhancement at $\lambda_{eg} \approx 700$ nm. Enhancement originates from the interference in the conversion paths as predicted by Eqs.(1)-(2). Intensities of both hot spots are unchanged. (b) Simulation of the EF using our simple model with the parameters similar to Fig. 1b. Simulations are for the presence of an auxiliary QE. We observe the similar behavior in the position of optimum λ^*_{eg}, even though several complications involve in 3D simulations (a).

References

[1] S. Postaci, B. C. Yildiz, Alpan Bek, M. E. Tasgin, Silent enhancement of SERS signal without increasing the hot spot intensity, Nanophotonics **7**, 16871695 (2018).

[2] Y. Chu, M. G. Banaee, and K. B. Crozier, Double-resonance plasmon substrates for surface-enhanced Raman scattering with enhancement at excitation and stokes frequencies, ACS Nano **4**, 2804 (2010).

[3] J. Ye, F. Wen, H. Sobhani, J. B. Lassiter, Pol Van Dorpe, P. Nordlander, and N. J. Halas, Plasmonic nanoclusters: near field properties of the Fano resonance interrogated with SERS," Nano Letters **12**, 1660 (2012).

[4] BEM simulations, http://physik.uni-graz.at/ uxh/mnpbem/html/mnpbem_ug_bemsimulations.html, accessed: 2017-09-22.

Coupled-Wave Model of Bound States in the Continuum in Diffraction Gratings and Integrated Diffractive Structures

Dmitry A. Bykov*, Evgeni A. Bezus, and Leonid L. Doskolovich

Image Processing Systems Institute — Branch of the Federal Scientific Research Centre "Crystallography and Photonics" of Russian Academy of Sciences, Samara, Russia
Samara National Research University, Samara, Russia
*corresponding author, E-mail: bykovd@gmail.com

Abstract

We study coupled-wave model describing optical properties of diffraction gratings and rectangular ridges located on a slab waveguide. The proposed model enables obtaining simple and accurate formulas for the complex transmission and reflection coefficients of the considered structures. By analyzing these expressions, we analytically show that these structures support bound states in the continuum (BICs). We obtain simple closed-form expressions describing the positions (frequencies and wave numbers) of the BICs emerging in the considered structures.

1. Introduction

In recent years, investigation of the bound states in the continuum (BICs) has attracted considerable attention in photonics (see the review paper [1] and references therein). The BICs are eigenmodes that have an infinite lifetime though the structure supporting them has open scattering channels. The leakage into these channels is canceled either due to symmetry reasons or by means of parameter tuning [1]. Small deviation from the BIC condition makes it possible to obtain resonators with arbitrarily high quality factors. This makes the BICs promising for practical applications in lasing, sensing, and filtering [1].

In the present work, we study theoretically and numerically the formation of BICs in very simple photonic structures consisting of either a single dielectric ridge or diffraction gratings located on a dielectric slab waveguide [2]. We show that such structures support high-Q resonances and bound states in the continuum. We present simple coupled-wave model that rigorously proves the existence of the BICs and predicts their spectral and angular locations. According to the derived models, the BIC formation is associated with the coupling between the different eigenmodes of the considered structures.

2. Ridge on a slab waveguide

Let us consider a rectangular ridge located on a slab waveguide [see Fig. 1(a)]. We will consider diffraction of the fundamental TE-polarized guided mode obliquely incident on the ridge. One can choose the angle of incidence in such a way that the out-of-plane scattering is completely suppressed [2]. In this case, the considered structure has only two scattering channels corresponding to the reflected and transmitted slab waveguide modes.

The ridge region [see Fig. 1(a)] can be considered as a segment of a slab waveguide having a greater thickness, thus supporting different guided modes. We will consider the case when the "thicker" waveguide supports only fundamental TE and TM modes with effective refractive indices n_{TE} and n_{TM}. In this case, the considered structure exhibits pronounced resonant properties.

Figure 1(c) shows the reflectance of a TE-polarized mode upon diffraction by a ridge vs. the angle of incidence θ and the ridge width w. The spectrum, which was calculated using the aperiodic Fourier modal method, exhibits several resonant lines with their width narrowing to zero at several points. This suggests the presence of the BICs in the considered structure. Figure 1(d) showing the quality factor of the resonance vs. the ridge width w proves the existence of the BICs [2, 3].

3. Coupled-wave model

To describe resonant optical properties of the considered structure, we developed the following coupled-wave model.

Let the incident wave have unit amplitude. We denote the unknown reflected mode amplitude by R. Inside the ridge, we consider a TE mode propagating to the right (amplitude U_1), a TE mode U_2 propagating to the left, and, similarly, two TM modes: V_1 and V_2.

The considered modes are coupled at the edges of the ridge. By equating the complex amplitudes of the modes at the edges of the ridge, we obtain the coupled-wave model of the considered structure:

$$\begin{cases} U_1 = \mathrm{e}^{\mathrm{i}\phi}\left(r_1 U_2 + r_c V_2 + t\right), \\ V_1 = \mathrm{e}^{\mathrm{i}\psi}\left(r_c U_2 + r_2 V_2 + t_c\right), \\ U_2 = \mathrm{e}^{\mathrm{i}\phi}\left(r_1 U_1 + r_c V_1\right), \\ V_2 = \mathrm{e}^{\mathrm{i}\psi}\left(r_c U_1 + r_2 V_1\right), \\ R = tU_2 + t_c V_2 + r. \end{cases} \tag{1}$$

Here, r and t are the reflection and transmission coefficients of the incident TE mode; r_1 and r_2 denote the reflection coefficients of the U and V modes; r_c and t_c are the cross-polarization reflection and transmission coefficients. The

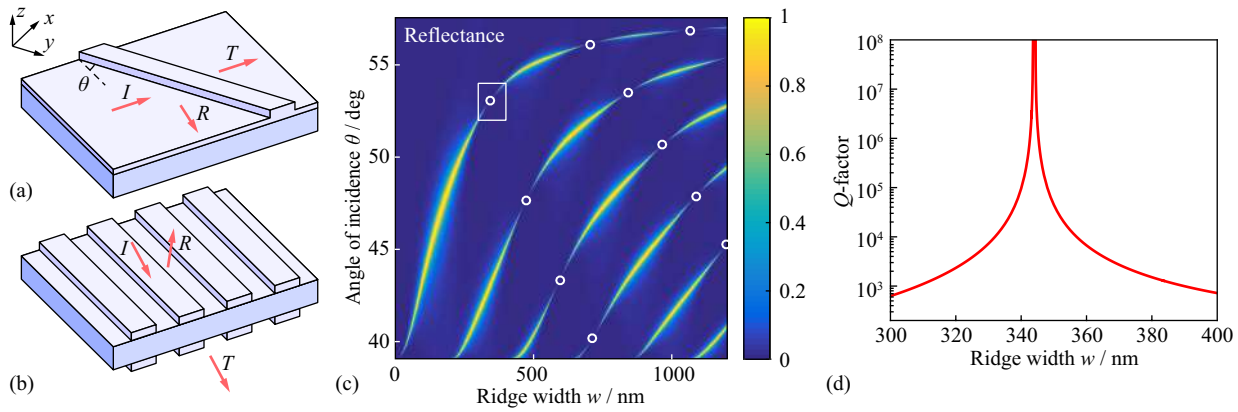


Figure 1: Considered structures: (a) a ridge on a slab waveguide and (b) a symmetric guided-mode resonant grating. (c) w–θ ridge reflection spectrum. (d) Quality factor of the mode vs. the ridge width w.

exponents describe the phase change of TE and TM modes acquired upon propagation between the edges of the ridge.

By eliminating U_1, U_2, V_1, and V_2 from the system (1), we can represent the reflection coefficient R in the form of a fraction. This fraction provides a good approximation of the reflection spectrum of the structure [Fig. 1(c)]. The BICs appear when both the numerator and denominator of this fraction vanish [2]. One can show that this happens when ϕ and ψ take the form

$$\phi = \pi m + \arg\frac{t_c}{r_c t - r_1 t_c}, \quad \psi = \pi l + \arg\frac{t}{r_c t_c - r_2 t}, \quad (2)$$

where m and l are positive integers.

Having calculated the phases, one can obtain closed-form expressions for the ridge width w and angle of incidence θ providing the BIC:

$$w = \frac{1}{k_0}\sqrt{\frac{\phi^2-\psi^2}{n_{\mathrm{TE}}^2-n_{\mathrm{TM}}^2}}, \quad \sin\theta = \sqrt{\frac{\phi^2 n_{\mathrm{TM}}^2 - \psi^2 n_{\mathrm{TE}}^2}{(\phi^2-\psi^2)n_1^2}}, \quad (3)$$

where n_1 is the effective refractive index of the incident mode, and $k_0 = \omega/\mathrm{c}$ is the free-space wave number. The BIC positions predicted using these equations are shown with white circles in Fig. 1(c). The predicted positions are in perfect agreement with the presented simulation results. Let us note that similar equations for ω and k_y providing the BIC positions for a fixed ridge width w can also be obtained.

4. Grating on a slab waveguide

Let us now consider a different structure: a pair of gratings separated by a slab waveguide [see Fig. 1(b)]. We consider the diffraction of a plane wave on this structure, being interested in the amplitudes of the 0-th reflected and transmitted diffraction orders. The grating is assumed subwavelength, so that all other diffraction orders are evanescent.

In the case of oblique incidence of light one can choose the wavelength and angle of incidence in such a way that *inside* the slab the -1-st diffraction order is evanescent, whereas the $+1$-st and the 0-th diffraction orders are propagating. In this case, the model presented in the previous section can be utilized with the difference that instead of the TE and TM modes, the Fabry-Perot and the quasi-guided mode of a the slab are considered. Therefore, equations similar to Eqs. (1)–(3) can be used to describe the reflection and transmission coefficients. The closed-form BIC conditions can also be derived.

5. Conclusions

We have shown that a simple couple wave model can be used to describe and predict the BICs in simple photonic structures, including a ridge on a slab waveguide and guided-mode resonant gratings. Similar models can be developed for diffraction gratings and integrated diffractive structures having different symmetries and geometries.

Acknowledgement

This work was funded by Russian Foundation for Basic Research (project nos. 18-37-20038 and 16-29-11683; numerical simulations) and by Ministry of Science and Higher Education of the Russian Federation (State assignment to the FSRC “Crystallography and Photonics” RAS; coupled-wave model).

References

[1] C. W. Hsu, B. Zhen, A. D. Stone, J. D. Joannopoulos, M. Soljačić, Bound states in the continuum, *Nat. Rev. Mat.* 1: 16048 (13 pp.), 2016.

[2] E. A. Bezus, D. A. Bykov, L. L. Doskolovich, Bound states in the continuum and high-Q resonances supported by a dielectric ridge on a slab waveguide, *Photon. Res.* 6: 1084–1093, 2018.

[3] C. L. Zou, J. M. Cui, F. W. Sun, X. Xiong, X. B. Zou, Z. F. Han, G. C. Guo, Guiding light through optical bound states in the continuum for ultrahigh-Q microresonators, *Laser Photon. Rev.* 9: 114–119, 2015.

The passive and active controls of Fano resonances in metasurfaces

Shuo Du[1,2], Zhe Liu[1,3], Junjie Li [1,2,4], Changzhi Gu [1,2]

[1] Beijing National Laboratory for Condensed Matter Physics, Institute of Physics, Chinese Academy of Sciences, Beijing, China
[2] School of Physical Sciences, CAS Key Laboratory of Vacuum Physics, University of Chinese Academy of Sciences, Beijing, China
[3] Niels Bohr Institute, University of Copenhagen, Blegdamsvej, Copenhagen, Denmark
[4] Songshan Lake Materials Laboratory, Dongguan, Guangdong, China
*corresponding author, E-mail: czgu@iphy.ac.cn

Abstract

We report the passive and active approaches to manipulate the properties of Fano resonances in metasurfaces. By passively tailoring the height of one arm during fabrication, double Rabi splitting caused by strong coupling of triple Fano resonances are observed in the unique 3D folded metallic resonators. Besides, by introducing the non-volatile chalcogenide phase-change material, the Fano resonances of can be actively controlled. These resonance properties are preservable, and have promising prospects in sensors, switches and modulators.

1. Introduction

Fano resonance is a common resonant scattering phenomenon of metasurfaces[1]. It can be generated in the interference between near fields of building blocks with different resonant modes. By manipulating the coupling of these modes, the properties of Fano resonances can be controlled consequently. In general, tailoring the geometrical parameters in the process of fabrication is the passive control of resonances[2], and the electromagnetic properties are fixed after fabrication. However, most of works in passive method are focus on the tuning the properties of individual resonance and neglecting the control of interaction in multiple resonances. Another method is active manipulation. By introducing the functional materials, such as semiconductor, graphene and liquid crystal, the dynamic control of resonances can be achieved. However, these materials are volatile, which means once the stimulus are removed the resonance properties will return to their initial state. Here we develop the methods of passive and non-volatile active controls of Fano resonances by varing the geometric parameters in the process of fabrication and introducing the phase-change material in nano-rsonators.

2. Passive control

First, we use the unique 3D folding process to tailor the geometric parameter of nano-resonators[3], achieving the passive control of the interaction in multiple Fano resonances[4]. By only varying the height of one arm of asymmetric spilt-ring resonators (SRRs), the resonance wavelength of one of three Fano resonances moves to and strongly interacts with the others. This interaction satisfies the strong coupling criterion, and two Rabi splittings are observed from it.

3. Non-volatile active control

Secondly, for the case of active control method, we introduce Ge2Sb2Te5 (GST) as the non-volatile functional material[5] in nano-resonators. The Fano resonances are designed at optical communication wavelength, and we modulate the properties of them simply by heating. The GST has distinct permittivity in different phase states, by which the resonance properties, such as resonance wavelength and amplitude, of resonators are controlled precisely. And the modulated properties are preservable even when the simulus are removed. Such repeatable dynamic metasurfaces are highly promising for the applications, such as active swiches and modulators.

4. Conclusion

The properties of Fano resonances in nano-resonators can be manipulated by tailoring their near field interaction passively or actively. By passive control, we demonstrate the strong coupling between multiple Fano resonances. And by introducing GST into the resonator units, the active and non-volatile active control on Fano resonances are implemented.

Acknowledgements

This work is supported by the National Key Research and Development Program of China under Grant Nos. 2016YFA0200400 and 2016YFA0200800; the National Natural Science Foundation of China under Grants Nos. 61888102, 91323304, 11674387, 11504414, 11574369, 11574385, 11574368 and 61390503; Strategic Priority

Research Program and Key Research Program of Frontier Sciences, CAS, Grant No.XDB07020200 and No.QYZDJ-SSW-SLH042.

References

[1] A.E. Miroshnichenko, S. Flach, Y.S. Kivshar, Fano resonances in nanoscale structures, *Reviews of Modern Physics* 82: 2257-2298, 2010.

[2] D.R. Chowdhury, A.K. Azad, W. Zhang, R. Singh, Near Field Coupling in Passive and Active Terahertz Metamaterial Devices, *IEEE Transactions on Terahertz Science and Technology* 3: 783-790, 2013.

[3] A. Cui, Z. Liu, J. Li, T.H. Shen, X. Xia, Z. Li, Z. Gong, H. Li, B. Wang, J. Li, H. Yang, W. Li, C. Gu, Directly patterned substrate-free plasmonic "nanograter" structures with unusual Fano resonances, *Light-Science & Applications* 4: e308, 2015.

[4] Z. Liu, J. Li, Z. Liu, W. Li, J. Li, C. Gu, Z.Y. Li, Fano resonance Rabi splitting of surface plasmons, *Sci Rep* 7: 8010, 2017.

[5] C. Li, W. Zhu, Z. Liu, S. Yan, R. Pan, S. Du, J. Li, C. Gu, Tunable near-infrared perfect absorber based on the hybridization of phase-change material and nanocross-shaped resonators, *Applied Physics Letters* 113: 231103, 2018.

Interference of Multipolar Lattice Resonances in Plasmonic Crystal Excited by Structured Light

Keiji Sasaki*, Hiroki Kitajima, and Kyosuke Sakai

Research Institute for Electronic Science, Hokkaido University, Sapporo, Japan
*corresponding author, E-mail: sasaki@es.hokudai.ac.jp

Abstract

We report interference of dipolar, quadrupolar, and higher-order multipole lattice resonances in plasmonic crystal structures. We theoretically demonstrate that such bright- and dark-mode lattice resonances in finite-sized, square-lattice arrays of metal nanodisks can be excited by both vertically-incident, linearly-polarized Gaussian beam and cylindrical vector beam having orbital angular momentum. The simulation result shows that spatial distributions of the lattice resonances in the plasmonic crystal exhibit characteristic patterns with the chirality that conserve the chirality of the incident light and the excited plasmonic fields of individual nanodisks.

1. Introduction

Plasmon damping and losses limit the enhancement of the localized plasmonic field and thus represent one of the main barriers to the evolution of plasmonics into a prominent technology. It should be possible to reduce damping by controlling the material properties, whereas radiative losses can be managed by the following two approaches. The first approach is to exploit the dark modes of the localized plasmon. We have recently reported a method of exciting dark-mode multipole plasmons by using vortex beams with specific angular momentum [1-3]. The second approach to managing radiative losses is to take advantage of the lattice resonances in periodic metal nanoparticles, i.e., plasmonic crystals, in which collective resonances are mediated by the diffractive coupling of localized plasmons. In this presentation, we report a combination of the two above approaches applied to the management of radiative losses, taking advantage of multipolar dark lattice resonances, which can be excited from free space. We theoretically demonstrate that the quadrupole lattice resonances in square lattice plasmonic crystals composed of nanodisks can be excited both by vertically incident cylindrical vector (CV) beam and by a linearly polarized Gaussian beam. The spatial distributions of the lattice resonances in the plasmonic crystal exhibit characteristic patterns where the chirality of the spatial patterns conserve the chirality of the incident structured light and the excited plasmonic fields in the individual nanodisks.

2. Results and discussion

Figure 1 shows the model used in our calculations. For simplicity, we consider a square lattice plasmonic crystal in a homogeneous background with a refractive index of n = 1.0. The structure consists of 9 x 9 array of gold nanodisks with diameter of 400 nm and thickness of 30 nm, which yields localized plasmon peaks at approximately 800 nm. The lattice period (L = 700 nm) is set such that normally incident light along the z direction is diffracted in the *x* or *y* directions (first-order grating) at wavelength of ~800 nm. A CV beam shown in the inset of Fig. 1 and a linearly polarized Gaussian beam were chosen to excite different lattice resonances. The polarization of the CV beam is linear at all points, although the direction of the electric field vector depends on the spatial position.

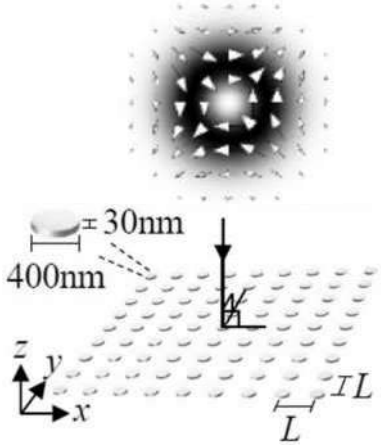


Figure 1. Square-lattice plasmonic crystal consisting of 9 x 9 gold nanodisks. The inset shows the cross-section of incident cylindrical vector beam. The arrows indicate the electric field vectors.

When the CV beam is used as the excitation beam (Fig. 2(a)), the near-field electric field intensity spectrum integrated over the *x*-*y* plane exhibits two clear peaks, as shown in Fig. 2(g): a narrow peak at 805 nm (quadrupole mode) and a broad peak at 1040 nm (dipole mode). The full width at half maximum (FWHM) of the quadrupole resonance is ~30 nm, which is much narrower than the FWHM of ~80 nm for a single isolated nanodisk. This result indicates that the lattice resonance decreases the radiative

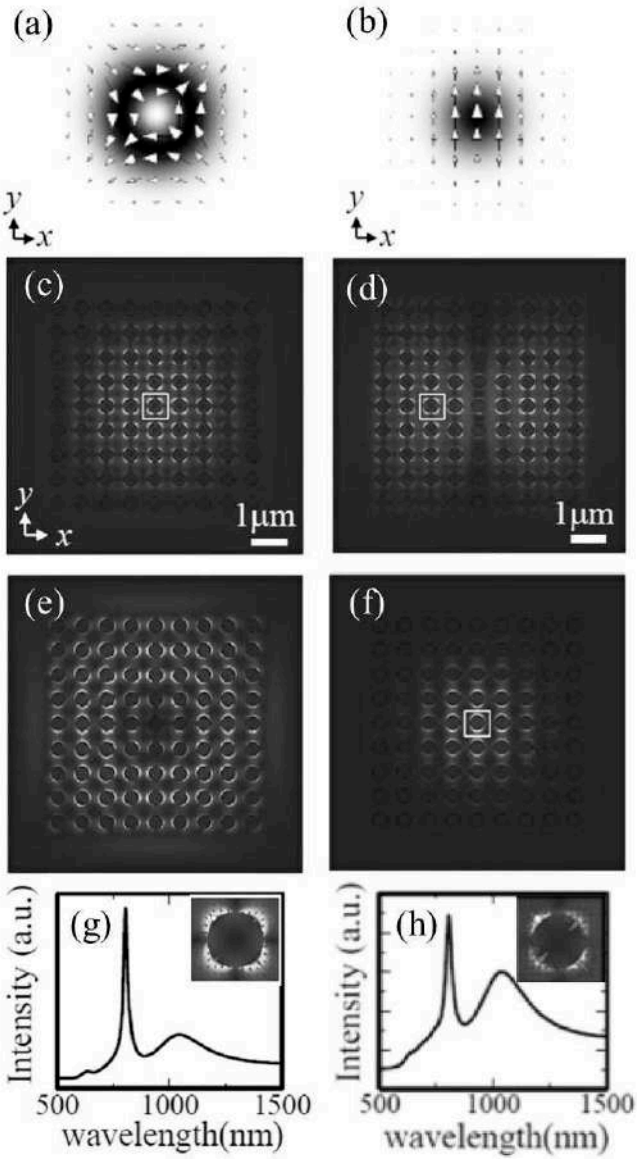


Figure 2. Cross-section profiles of (a) vertically-incident cylindrical vector (CV) beam and (b) linearly-polarized Gaussian (G) beam. Electric field norm distributions of plasmonic crystal excited by (c) CV- and (d) C-beams at 805 nm, (e) CV- and (f) C-beams at 1064 nm. Near-field intensity spectra at the hot spots under the excitation with (g) CV- and (h) G-beams. The insets in (g) and (h) show detailed views of the near-field profiles inside the white boxes in (c) and (d), respectively.

loss even in a finite crystal with a 9 x 9 nanodisk array. The peak intensity reaches a very large value of more than 5 x 10^4. Figure 2(c) shows the near-field distribution at 805 nm, in which the single-lobed envelope function peaks at the center, even though the incident beam has a ring-shaped intensity profile. In contrast, the near-field distribution at 1040 nm shown in Fig. 2(e) exhibits a ring-shaped envelope function corresponding to a higher-order mode, with a dipole-like intensity profile on each nanodisk. The axis of the dipole on each disk is parallel to the electric field vector of the incident beam, as shown in Fig. 2(a). An inset of Fig. 2(g) shows a detailed view of the electric field profile around the central nanodisk of Fig. 2(c), thus indicating that this 805 nm lattice resonance corresponds to quadrupole mode.

The quadrupole lattice resonance is excited even using a Gaussian incident beam (Fig. 2(b)). Figure 2(h) shows the corresponding integrated intensity spectrum, in which there are two clear peaks: a narrow quadrupole peak at 805 nm and a broad dipole peak at 1040 nm. The near-field distribution at 805 nm in Fig. 2(d) shows a double-lobed higher-order envelope function along the x axis with a quadrupole profile around the nanodisks. Although it is not apparent from the figure, the phases of the left and right-hand parts are π shifted with respect to each other. As a result, the quadrupole mode is cancelled out, and only a small dipole mode can be observed in the central column. The detailed field distribution around the nanodisk indicated by the white square corresponds to quadrupole mode, as shown in the inset of Fig. 2(h). At 1040 nm, the near-field distribution exhibits dipole lattice resonances with a single-lobed fundamental envelope function, as shown in Fig. 2(f).

3. Conclusions

We showed that the quadrupole lattice resonances in a square lattice, finite-sized plasmonic crystal can be excited by vertically incident light beams. Both cylindrical vector beams and a Gaussian beam can excite dipole and quadrupole lattice resonances with broad and sharp peaks, respectively. In addition, there are considerable differences in the envelope distribution functions of the dipole and quadrupole lattice resonance fields. These results indicate that the two modes overlap and interfere with each other in space and frequency. The combination of the dark mode and lattice resonance leads to lower radiative losses than dipole localized surface plasmon resonances. Our scheme allows for the exploitation of low radiative loss plasmon resonances with many hot spots by using an incident beam from free space. This finding may pave the way for novel light-matter interactions that require a narrow spectral line width or wide field distributions.

Acknowledgements

This work was supported by JSPS KAKENHI (Grant Numbers JP16H06506, JP18H05205, and JP18H03882) and the Nanotechnology Platform (Hokkaido University).

References

[1] K. Sakai, K. Nomura, T. Yamamoto, and K. Sasaki, Excitation of multipole plasmons by optical vortex beams, *Scientific Reports*, 5, 8431, 2015.

[2] K. Sakai, K. Nomura, T. Yamamoto, T. Omura, and K. Sasaki, Quadrupole lattice resonances in plasmonic crystals excited by cylindrical vector beams, *Scientific Reports* 6, 34967, 2016.

[3] K. Sakai, T. Yamamoto, and K. Sasaki, Nanofocusing of structured light for quadrupolar light-matter interactions, *Scientific Reports* 8, 7746, 2018.

Highly-efficient nonlinear image tuning through magnetic dipole quasi-BIC ultra-thin resonators

Lei Xu[1*], Khosro Zangeneh Kamali[2], Lujun Huang[1], Mohsen Rahmani[2], Alexander Smirnov[3], Rocio Camacho-Morales[2], Yixuan Ma[4], Guoquan Zhang[4], Matt Wolley[1], Dragomir Neshev[2], and Andrey E. Miroshnichenko[1]

[1]School of Engineering and Information Technology, University of New South Wales, Canberra ACT 2600, Australia
[2]Nonlinear Physics Centre, The Australian National University, Canberra ACT 2601, Australia
[3]Institute of Applied Physics, Russian Academy of Science, Nizhny Novgorod 603950, Russia
[4]The MOE Key Laboratory of Weak-Light Nonlinear Photonics, School of Physics and TEDA Applied Physics Insitute, Nankai University, Tianjin 300457, China
*corresponding author, E-mail: lei.xu@unsw.edu.au

Abstract

We propose an ultra-thin silicon metasurface supporting a high-quality quasi-bound-state-in-the-continuum (BIC) generated by the collective magnetic dipole (MD) resonance excited in the subdiffractive periodic systems. Such quasi-BIC MD state leads to a robust near-field enhancement and a significant boost of the nonlinear process, resulting in measured 500-fold enhancement of third-harmonic emission in comparison to the conventional silicon disk metasurface. We further demonstrate the highly-efficient dynamical switching experimentally over nonlinear images via polarisation and wavelength control, opening the way for various applications in highly-efficient nonlinear metadevices including tunable laser, tunable displays, nonlinear imaging.

1. Introduction

Nonlinear nanophotonics, aiming for the efficient generation and control of nonlinear properties of light in the nanoscale structures, is a rapidly developing research field benefiting applications such as chip-based light sources, nanolasers, optoelectronic devices, imaging, etc. High-index dielectric nanostructures have emerged as a promising tool to boost the nonlinear processes through efficient nanoscale light manipulation based on the control over both optically-induced electric and magnetic Mie-type resonances [1, 2], offering great potential for future on-chip applications in the nonlinear regime [3, 4]. MD resonance supported by dielectric nanostructures has been widely used to enhance the nonlinear frequency conversion due to the associated strong near-field enhancement and large mode volume. BICs, being originally predicted by von Neumann and Wigner in 1929 [5], have been extensively studied in different fields of wave physics including acoustics, microwaves and nanophotonics [6]. An ideal BIC manifests as itself via diverging Q-factor with complete suppression of the radiation of the state to the free space. By breaking the symmetry of the system which supports a symmetry-protected BIC, one can transform an ideal BIC to a quasi-BIC with finite Q-factor. It allows obtaining an energy exchange with the external modes and manifests itself as a sharp Fano resonance in the optical response spectrum [6]. Through the mechanism of BIC, one can merely control and tune the radiation damping rate and thus the width of the resonance. BIC-inspired mechanism provides a useful tool to engineer and tailor the line width and Q-factor flexibly and allows directly excite the quasi-BICs by free propagation plane waves, making it a novel platform for nanophotonics applications.

Here, by taking the advantages of both Mie resonators and BIC states, we design ultra-thin resonant silicon disk metasurface supporting high-quality quasi-BIC MD state leading to a strong near-field enhancement inside the nanoresonators. we further demonstrate highly-efficient dynamical nonlinear image tuning through designed quasi-BIC MD resonators.

2. Results and Discussions

Our designed metasurface is composed of silicon nanodisk supporting out-of-plane MD resonance which is a symmetry-protected BIC state. The thickness and period of our metasurface are 53 nm and 840 nm, respectively. We introduce an off-centred hole to open a radiation channel and transform the ideal-BIC MD state into quasi-BIC MD state which can be excited directly under normal pump irradiation. The silicon metasurface is optimised to support a quasi-BIC MD state at a near-infrared wavelength around 1345 nm with spectral full-width-at-half-maximum (FWHM) around 12 nm, which matches the spectral width of our used laser to expect maximum coupling and nonlinear signal generation. By measuring the linear transmission spectrum of the metasurface under plane wave normal incidence as shown in Figure 1a, we observed a pronounced asymmetric Fano line shape with a narrow dip around $\lambda = 1345$ nm, indicating the excitation of the quasi-BIC-MD state. We then perform the third-harmonic spec-

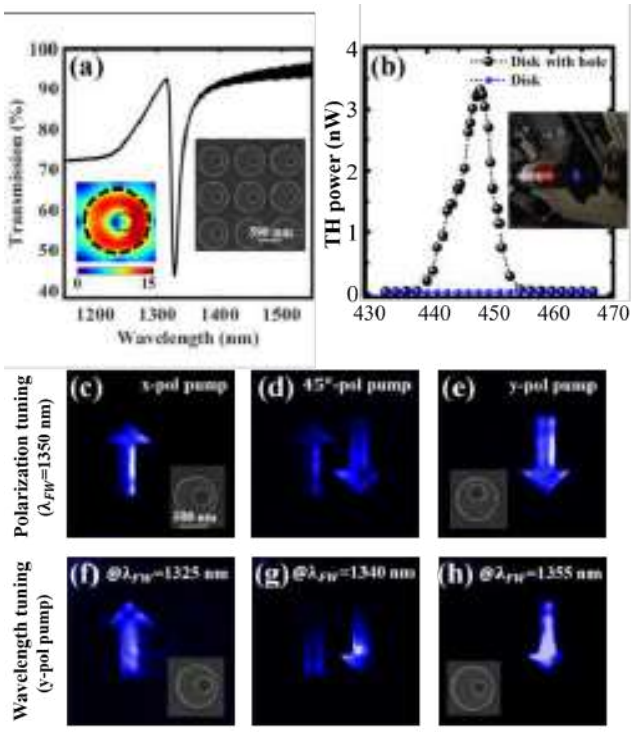


Figure 1: (a) Experimentally measured linear transmission spectrum. The inset shows the calculated electric near-field distribution in the x-y plane at the resonance (left) and the SEM image of the fabricated sample (right), respectively. (b) Experimentally measured THG spectra of the sample. The inset shows a photographic image of the TH emission from the sample. Nonlinear image tuning in the designed metasurfaces is demonstrated by polarisation (c-e) and wavelength tuning (f-h), respectively.

troscopy measurement as shown in Fig. 1(b). The TH signal can be dramatically enhanced in the optimised disk-hole metasurface at the quasi-BIC-MD state, resulting in more than 500-fold enhancement as compared with the silicon disk metasurface. This leads to an estimated total TH conversion efficiency in the order of 10^{-5} under peak pump intensity only $\mathrm{I}_0 = 1.0\ \mathrm{GW/cm^2}$.

Such high-quality quasi-BIC MD states provide a powerful platform to efficiently control the nonlinear emission spatially. We further encode two images into the metasurface, i.e., tuning the geometry of the nanodisks and holes to support resonances at different wavelength position or under different pump excitation polarisation conditions. Due to the spatial asymmetry of such quasi-BIC-MD states, we first encode two images of arrow $\uparrow$ and $\downarrow$ indicating the opposite directions through the metasurface for disks with x-off-centered hole and disks with y-off-centered hole, respectively. The width and length of the arrow is about 20nm and 90nm, respectively. By varying the pump from x-polarization to y-polarization, it is possible to separately excite the quasi-BIC MD states supported by the two images. Thus, one can read out the encoded image through the generated nonlinear signal (Fig. 1c-e). As the spectral position and width of such quasi-BIC MD state can be engineered effectively through geometric tuning of the nanoresonators, the nonlinear image tuning can also be achieved directly through wavelength tuning as shown in Fig. 1f-h, where the two images are encoded into the nanoresonators with quasi-BIC MD state at different spectral positions (at 1325 nm and 1355 nm).

3. Conclusions

In summary, we have demonstrated an ultra-thin resonant silicon metasurface supporting high-Q quasi-BIC MD state. Due to strong light confinement inside the nanoresonators originating from the BIC-MD nature, we have shown that such quasi-BIC MD state can significantly enhance the nonlinear process. We further demonstrated a nonlinear image switching through polarisation- and wavelength-tuning methods, respectively. Our results underpin nonlinear nanophotonics applications such as tuneable displays, tuneable nanolasing and on-chip integrated metadevices with multi-functionalities.

Acknowledgement

The authors acknowledge the funding support provided by the Australian Research Council (ARC) and UNSW Scientia Fellowship program. The authors also appreciate the use of Australian National Fabrication Facility (ANFF)the ACT Node.

References

[1] A. I. Kuznetsov, A. E. Miroshnichenko, M. L. Brongersma, et al, Optically resonant dielectric nanostructures, *Science* 354, aag2472, 2016.

[2] M. Rahmani, L. Xu, A. E. Miroshnichenko, et al, Reversible Thermal Tun-ing of All-Dielectric Metasurfaces, *Adv. Funct. Mater.* 1700580, 1700580 2017.

[3] Y. Yang, W. Wang, A. Boulesbaa et al, Nonlinear fano-resonant dielectric metasurfaces, *Nano Lett.* 15, 73887393, 2015.

[4] L. Xu, M. Rahmani, K. Zangeneh Kamali, et al, Boosting third-harmonic generation by a mirror-enhanced anapole resonator, *Light. Sci. & Appl.* 7, 44 2018.

[5] J. von Neuman and E. Wigner, Uber merkwrdige diskrete Eigenwerte. Uber das Verhalten von Eigenwerten bei adiabatischen Prozessen, *Physikalische Zeitschrift* 30, 467470 1929.

[6] C. W. Hsu, B. Zhen, A. D. Stone, J. D. Joannopoulos, and M. Soljačić, Bound states in the continuum, *Nat. Rev. Mater.* 1, 16048, 2016.

High-Q modes in a single dielectric nonspherical nanocavity

Lujun Huang[1*], Lei Xu[1], Mohsen Rahamani[2], Dragomir Neshev[2], and Andrey E Miroshnichenko[1],

[1]School of Engineering and Information Technology, University of New South Wales, Canberra, Australia
[2]Nonlinear Physics Centre, Australia National University, Canberra, Australia
*corresponding author, E-mail: lujun.huang@unsw.edu.au

Abstract

High index dielectric nanostructures support both electric and magnetic multipole resonances. In real applications, it is desirable to achieve high-quality optical resonances to have a high-Q factor within a small volume of a material. Here, we demonstrate the high-Q factor resonant modes in a single nonspherical dielectric nanocavity (i.e. rectangular nanowire, cuboid, and disk) by exploring quasi-bound states in the continuum. We find that the high-Q modes only occur at a specific size aspect ratio, around which avoided crossing (or crossing) feature appears for pair modes. The Q factor can be up to 2.31×10^4 for square nanowire (n=4) with $a/\lambda_0<1$. Multipole analysis on the high Q eigenmode indicates that radiation is significantly suppressed in the limited eigenchannels. High Q modes are verified experimentally via scattering spectrum.

1. Introduction

Dielectric metamaterial has been promised as an alternative candidate to realise the CMOS compatible with all dielectric nanophotonics [1]. Similar to the metallic structures supporting plasmonic resonance, dielectric structures can also provide both electric and magnetic resonances (known as Mie-type resonances). The dissipative loss for dielectric materials, however, is much lower than the counterpart of plasmonic materials. Due to these two unique properties, the performance of photonic and optoelectronic devices can be significantly improved by taking advantage of dielectric materials [2]. The tremendous research effort has been conducted to study the resonant properties of a single dielectric nanocavity beyond analytical Mie theory based on finite difference time domain (FDTD) approach [3]. In our previous work [4], we clarified the resonant mode properties of a single dielectric nonspherical nanocavity from the perspective of eigenmodes and demonstrated that its optical properties are governed by the eigenvalue of the leaky modes the structures support.

Moreover, the eigenvalue of leaky modes shows a linear dependence on the size ratio of structures (i.e. rectangular nanowire (NW) or cuboid). The intuitive understanding of leaky modes may open a new door in studying the optical resonance of dielectric resonator. For example, ultrahigh Q modes are always desired to enhance light-matter interaction, which was proposed for a single dielectric cylinder recently by exploring quasi-bound state in continuum (BIC) [5]. However, how to find a high-Q mode remains unanswered in single dielectric nonspherical nanocavity.

In this work, we report the general rule of thumb to find out the high Q mode in a single nonspherical nanocavity (i.e. rectangular NW, cuboid, and disk). For rectangular NW under the transverse electric (TE) polarization with electric field parallel to the axis of NW, the supercavity modes only appear for pair modes TE(m,l) and TE(m-2,l+2) or TE(m,l) and TE(m+2,l-2) accompanied by the avoided crossing features of real part of eigenvalue between these two modes at given size ratio R (named as critical ratio). Following these general rules, we can immediately find many high-Q modes. The Q factor can be high to 2.3×10^4 for square NW while the width of NW is smaller than the resonant wavelength. The extreme good confinement of the electric field can be ascribed to the suppression of radiation in limited leaky channels or radiation quenching to a minimum from the momentum space. This conclusion can also be generalised to rectangular NW with transverse magnetic (TM) polarisation, single cylinder with finite thickness and cuboid. Moreover, we also experimentally verify high Q mode of single Si NW from scattering spectrum. Our results may find the applications in boosting the light-matter interaction, such as nonlinear optics effect and laser.

2. Results and Discussions

We start with considering the eigenmode (named leaky mode) of rectangular NW with a refractive index n=4 under the TE polarization. Assuming the width and height of nanowire are a and b, respectively. The size ratio of NW is defined as $R=b/a$. The leaky mode is feature by complex eigenvalue $N=n\omega b/c=N_{real}-iN_{imag}$, in which ω is complex eigenfrency of eigenmode and c is the speed of light. The Q factor can be obtained from $Q= N_{real}/(2\times N_{imag})$. Previously, we have demonstrated that the eigenmode supported by the dielectric nanostructure plays the dominant role in governing its optical properties. Moreover, linear dependence between N_{real} and size ratio R has been shown for mode TE(m,l), in which m and l are the maximum number of electric field within the NW. In the following section, we will demonstrate that high Q and low Q modes only appear at the critical ratio of NW in the pair modes TE(m,l) and TE(m-2,l+2) or TE(m,l) and TE(m+2,l-2),

which suggests that the parity of two modes must be same? The pair modes here are divided into three categories: (1) Type I: m=l-2; (2) Type II: m>l-2; (3) Type III: m<l+2. Fig.1a-b shows N_{real} and quality (Q) factor as a function of size ratio R for mode TE(3,5) and TE(5,3) which belongs to Type I. Interestingly, Q factor reaches maximum value 3300 at R=1 for TE(3,5) while the avoided crossing occurs for real part of complex eigenvalue in these two modes. It is worth of noting that the mode TE(3,5) and TE(5,3) will interchange with each other while the size ratio larger than one based on the definition of eigemode. Other high Q modes fallen within the category of Type I, such as TE(1,3) and TE(2,4), can be found at same critical ratio R=1.

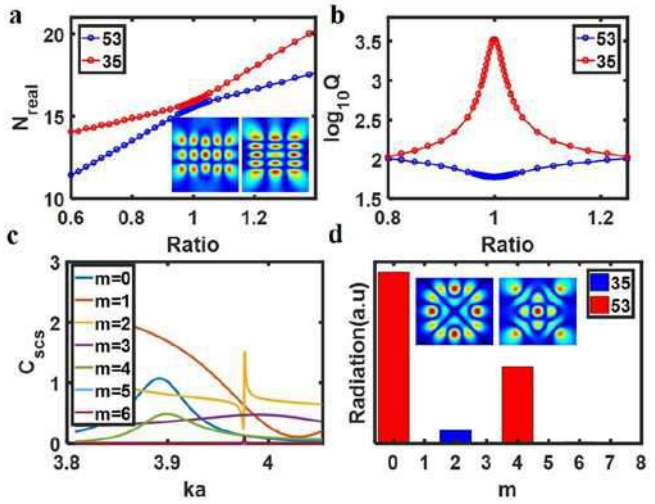


Figure 1: (a) Real part of eigenvalue for modes TE(3,5) and TE(5,3) as a function of size ratio. (b) Q factor of modes TE(3,5) and TE(5,3) as a function of size ratio. (c) Scattering cross section contributed by monopole, dipole, quadrupole, and other multipoles. (d) Multipole analysis on the eigenfield for two modes.

3. Discussion

In order to explore the physical origin of the high-Q mode, we perform multipole analysis to separate the scattering contribution of different eigenchanels [6]. Here, we consider the case of NW at oblique incidence (θ=15°) with TE polarization to excite all the eigenmodes of NW. Fig.1c shows scattering efficiency contributed by multipoles for square NW. Two resonant peaks can be observed at ka=3.89 and ka=3.97, which are related to the low Q mode TE(5,3) and high Q mode TE(3,5). The scattering efficiency around ka=3.97 is mainly contributed by the quadrupole (m=2), and weakly contributed by the multipoles (m=6). Due to the interference between them, scattering efficiency contributed by m=2 displays Fano line shape. In contrast, both monopole and octupole play the major role in the scattering efficiency around ka=3.89 for low Q mode. In addition, we also perform the multipole analysis on the eigenfield for these two modes, which is shown in Fig.1d. Interestingly, the main radiation channels are quadrupole (m=2) and multipole (m=6) for TE(3,5) while they are monopole(m=0) and octupole (m=4), which well matches the result in the scattering spectrum. Moreover, it is also worth of noting that the monopole has large leakage rate than that of quadrupole and multipole. This also explains why TE(5,3) has much larger radiation than that of TE(3,5). In fact, high Q mode can be found in a similar way for the NW with TM polarization, cylinder with finite thickness and cuboid.

4. Conclusions

In summary, we report the upper limit of the Q factor for single dielectric nonspherical nanocavity by exploring quasi BIC. The quality factor of resonant mode can reach maximum only when avoided crossing (or crossing) features are displayed between pair modes for TE (or TM) cases in single NW, and magnetic (or electric) modes in single cuboid (disk). Such a high Q factor can be attributed to the quenching of limited radiation channels. Also, the electric (magnetic) field in momentum space is reduced to a minimum at critical size aspect ratio, indicating the limited radiating capability of the modes. This unique high Q property is experimentally demonstrated from the scattering spectrum of single Si NW. Our findings provide a general guiding principle to design extreme high Q mode with relatively small material volume and may find the applications in lasing, biosensor and enhancing light-matter interactions.

Acknowledgements

The authors acknowledge the funding support provided by the Australian Research Council (ARC) and UNSW Scientia Fellowship program.

References

[1] A. Kuznetsov, A. E. Miroshnichenko, M. Brongersma, Y. Kivshar, and B. Luk'yanchuk, Optically resonant dielectric nanostructures, *Science* 354: aag2472, 2016.

[2] M. Khorasaninejad, W. T. Chen, R. C. Devlin, J. Oh, A. Y. Zhu, and F. Capasso, Metalenses at visible wavelengths: Diffraction-limited focusing and subwavelength resolution imaging, *Science* 352:1190-1194, 2016.

[3] Y. Kivshar, and A. E. Miroshnichenko, Meta-optics with Mie resonances, *Optical and Photonics News* 28, 24-31, 2017.

[4] L. Huang, Y. Yu, and L. Cao, General modal properties of optical resonances in subwavelength nonspherical dielectric structures, *Nano.Lett* 13,3559-3565, 2013

[5] M. Rybin, K. Koshelev, Z. Sadrieva, K. Samusev, A. Bogdanov, R. Nicole, M. Limonov and Y. Kivshar, High-Q supercavity modes in subwavelength dielectric resonator, *Phys. Rev. Lett* 119,243901, 2017.

[6] P. Grahn, A. Shevchenko, and M. Kaivola, Electromagnetic multipole theory for optical nanomaterials, *New. J. Phys* 14, 093033, 2012.

Spin-Polarized Directive Coupling of Light and Near-Field Amplification at the Bound States in the Continuum of a Transparent Photonic Crystal

Gianluigi Zito,[1*] Silvia Romano,[2] Stefano Managó,[1] Stefano Cabrini,[3] Giuseppe Calafiore,[3] Anna Chiara De Luca,[1] Erika Penzo,[3] Vito Mocella[2]

[1] National Research Council IBP, Via Pietro Castellino, Naples, 80131, Italy
[2] National Research Council IMM, Via Pietro Castellino, Naples, 80131, Italy
[3] Molecular Foundry, Lawrence National Laboratory of Berkeley, Berkeley, CA 94720, USA
*corresponding author, E-mail: g.zito@ibp.cnr.it

Abstract

Spin-polarized directive coupling of light is an intriguing property of topological photonic structures. Associated to the quantum spin Hall effect of light, it results from the transverse spin angular momentum density of inhomogeneous optical fields. We observed a resonantly-enhanced spin-directive coupling of light at bound states in the continuum (BICs) of nanoscale photonic crystal slabs. The application of BICs for achieving a non-plasmonic enhancement of the fluorescence emission and Raman scattering is also discussed.

1. Introduction

Spin-polarized directive coupling of light can be achieved with helical optical modes of photonic topological insulators and basically with inhomogeneous optical fields like surface waves manifesting spin-momentum locking [1, 2]. Herein, we discuss the experimental observation of spin-directive coupling in the Bloch's wave components of a symmetry-protected bound state in the continuum (BIC) [3]. The waves are amplified by the the resonance and easily detected and outcoupled form the system, which consists of a photonic crystal (PhC) thin slab made of transparent silicon nitride (Si_3N_4). We show that BICs are characterized by a transverse spin angular momentum (SAM) density not only in the trivial evanescent regions of the cladding but also inside the confining dielectric material. We observe emergent surface waves propagating along the symmetry axes of the PhC at the BIC, whose intensity depends on the input polarization. Specifically, the helicity of the input circular polarization determines the intensity of the wave along a specific direction of propagation, intensity revealing a mirror-symmetry breaking despite the *non* chiral nature of the geometry. We interpret the phenomenon by considering the spin-momentum locking associated to the transverse SAM.

Our experimental results point out the possibility of a BIC-enhanced spin-directive coupling of light. Potential multi-platform implementations are envisaged. Indeed, the near-field amplification of the BIC evanescent tail over the large PhC surface can be used in a synergistic fashion to amplify the spontaneous emission properties and Raman scattering of molecules. We discuss some results recently achieved in this direction by our group.

2. Results

2.1. Spin-directive coupling at the BIC

We studied a dielectric geometry consisting of a square lattice of cylindrical air holes etched in a thin film of Si_3N_4 between air and a supporting quartz (SiO_2) coverslip. Numerical modeling was carried out using a rigorous coupled wave approach (RCWA). Figure 1 shows the electromagnetic field at the BIC and input SAM dependence. Top and bottom panels refers to RCP and LCP incident radiation, respectively. The grey region reproduces the Si_3N_4 elementary volume. A BIC mode obtained for h = 144 nm is represented in the unit cell. The vector map of the field $\boldsymbol{E}$ shows its character of surface wave with longitudinal components also inside the confining dielectric material. The colormap is associated to magnetic field intensity $|H|^2$, whose z-cross section is that of evanescent waves (asymmetric in the cladding). Comparing top and bottom Poynting vector maps, we can see that the propagation direction of the wave along the x-axis (a similar behavior occurs also along the y-axis) depends on the helicity of the input. The colormap is associated to the energy density. The yellow arrows are a guide to the eye. The SAM density $\boldsymbol{S} = \mathrm{Im}\left[\epsilon_0 \boldsymbol{E}^\star \times \boldsymbol{E} + \mu_0 \boldsymbol{H}^\star \times \boldsymbol{H}\right]/4\omega$ associated to this BIC mode has transverse components with respect to $\boldsymbol{\Pi}$ [2]. This significant transverse SAM, not only at the interfaces but also inside the nanoscale slab, is associated to the orientation of the Poynting vector, which can be seen in detail in Fig. 1**e-f**. From the asymmetry of the mode profile along the $z-$axis in Fig. 1 it is clear that the surface waves have different amplitude at the interfaces. Along a given direction, say x-axis in Fig. 1, in one way there will be more light than the way back for a given input circular polarization, with a reversed behavior for the opposite input helicity. Therefore, we can expect that the main surface wave out-coupled again in the free space at fixed direction will be characterized by a different field intensity depending on the input spin causing a breaking of the planar mirror symmetry of the system even at

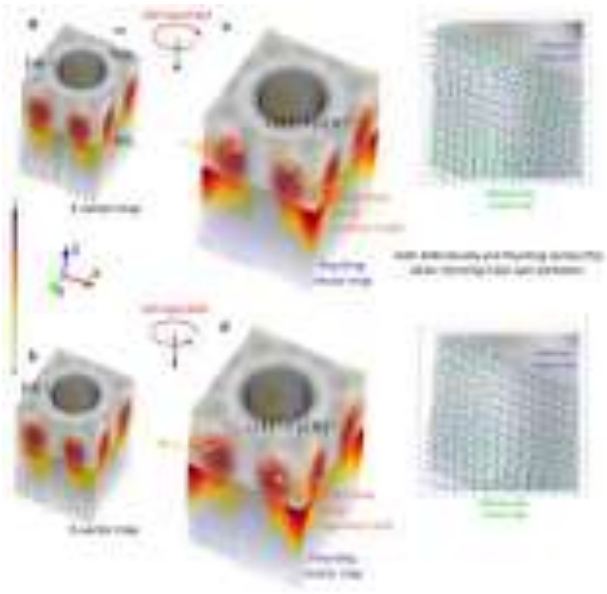


Figure 1: (a, b) BIC mode profiles and electric field vector maps, Poyinting vector maps (c, d) and corresponding SAM maps (e, f), respectively, for RCP and LCP input plane waves.

normal incidence, producing a macroscopic spin-polarized directive coupling. Experimental details will be given on site.

2.2. Near-field amplification at the BIC

The electromagnetic field confinement in BIC resonators occurs in the direction normal to the periodicity plane and no cavity is needed. For a transparent resonator, probe molecules or materials of interest on the PhC surface can experience a significantly amplified optical near field [4] useful in nonlinear processes and sensing applications [5, 6, 7]. However, the extremely precise alignment at normal incidence defines a stringent bottleneck limiting microscopic applications. On the other hand, for BICs based on resonance trapping mechanism the Q-factor dependence on the wavevector allows a significant amplification also with a microscopy interrogation, as our preliminary results point out. We found that BICs can be effectively used in standard microscopy for practical applications. We observed an enhancement of 10^3 fold of both fluorescence emission and Raman scattering processes within a range of 100 nm from the PhC surface [5]. Finally, we take advantage synergistically of the BIC pre-amplification of the surface plasmon gain provided by a model plasmonic system placed on the PhC. We observed an increase of the gain of surface-enhanced Raman scattering of more than one order of magnitude by resonant matching of the localized surface plasmon resonance (LSPR) with the BIC field. Our results may open the avenue to a BIC-enhanced microscopy thanks to a simple, loss-free nanostructured glass, useful in many kind of biological investigations.

3. Discussion

In this summary, we outlined several results obtained applying large-area PhC nanoscale slabs working at the BIC point. The BIC resonator is capable of mediating the coupling to emergent surface waves having a well-defined linear momentum and transverse SAM. The asymmetry observed in the intensity of the side waves - the first four fundamental Bloch's waves of the mode - is ascribed to transverse SAM. The advantage of the BIC mode is the resonant enhancement of the light scattered by the PhC and characterized by such a spin-polarized directive propagation.
A BIC resonator may also provide a strong near-field amplification. This may lead to metasurface multiplatform applications, also favored by the large scale collective character of the BIC, which makes it robust against defects. Indeed, we studied the possibility of standard optical microscopy interrogation of a BIC-based open cavity resonator for fluorescence and Raman scattering enhancement. In contrast to plasmonic nanostructures characterized by absorption losses, the photonic crystal is a loss-free, transparent and extended dielectric platform. We foresee the possibility of versatile biological investigations for several applications.

Acknowledgement

Funding: AIRC IG Grant 21420.

References

[1] A. B. Khanikaev, G. Shvets, Two-dimensional topological photonics, *Nat. Photonics* 11(12):763, 2017.

[2] K. Y. Bliokh, D. Smirnova, F. Nori, Quantum spin Hall effect of light, *Science* 348:1448–1451, 2015.

[3] A. Kodigala, T. Lepetit, Q. Gu, B. Bahari, Y. Fainman, B. Kanté, Lasing action from photonic bound states in continuum, *Nature*, 541:196–199, 2017.

[4] V. Mocella, S. Romano, Giant field enhancement in photonic resonant lattices, *Phys. Rev. B* 92:155117, 2015.

[5] Romano, S. *et al.* Surface-Enhanced Raman and Fluorescence Spectroscopy with an All-Dielectric Metasurface. *J. Phys. Chem. C* 122(34), 19738–19745, 2018.

[6] Romano, S. *et al.* Label-free sensing of ultralow-weight molecules with all-dielectric metasurfaces supporting bound states in the continuum. *Phot. Research* 6(7), 726–733, 2018.

[7] Romano, S. *et al.* Optical biosensors based on photonic crystals supporting bound states in the continuum.*Materials* 11(4), 526, 2018.

Superchirality, circular dichroism bands and singular value resonances of a minimal dielectric metasurface

Simone Zanotto[1]

[1]Istituto Nanoscienze - CNR, and Laboratorio NEST, Piazza San Silvestro 12, 56127 Pisa, Italy
*corresponding author, E-mail: simone.zanotto@nano.cnr.it

Abstract

We show that a metasurface having the simplest pattern that implements 2d-chirality shows circular dichroism band structure and superchiral near fields. These features occur in correspondence to the resonances of the singular value spectrum. In particular, Fano-like structures in the transmission spectrum are correlated with anomalies of the singular value and of the singular vector polarization states.

Electromagnetic fields which carry chirality – in their simplest form, left- and right-circularly polarized plane waves – deserve huge interest as they interact with matter chirality, enabling for instance to discriminate enantiomers in chemistry, which are ultimately connected with key features of living organisms. Indeed, many biomolecules have a specific sense of handedness, and it is not yet clear why nature has decided to go in that precise direction. From more applicative points of view, pharmaceutical industry constantly seeks for effective methods to discriminate stereoisomers, where chiral light-matter interaction could prove useful [1,2].

To date, the most common technique to prepare and analyze chiral light is to employ birefringent plates and linear polarizers that convert light to and from linear polarization, as almost no effective sources nor direct detectors of chiral light exist. Last advances in nanotechnology are however revolutionizing chiral optical devices [3,4]. Far- and near-field chiral electromagnetic responses have been indeed observed in a variety of artificially structured systems, where the shape of the machined elements must have a three-dimensional character if proper chirality has to be attained, because of the requirement of the absence of any mirror symmetry plane. While many proposed structures rely on volumetric fabrication techniques, which suffer from either scarce throughput or limited flexibility, less demanding fabrication technologies -- i.e., planar technologies -- may be also employed, as witnessed by some reports. For instance, a dielectric film with a non-centrosymmetric partially etched planar pattern was proposed as a simple gateway towards strong chiro-optical phenomena [5].

Indeed, there is a wide interest in developing subwavelength-patterned high-index dielectrics, both for applications and for fundamental research: from one side, they enable the synthesis of flat lenses, polarimeters, spectrometers, and computer-generated holograms; from another side, they exhibit a variety of intriguing phenomena such as Fano lineshapes, perfect forward scattering, geometric phase effects, and bound states in the continuum resonances.

In this work we report on the observation of photonic bands in a chiral metasurface, highlighting that the chiral response shows fingerprints of both guided wave and locally resonant phenomena. The object under investigation is an extremely simple 2d-chiral dielectric metasurface: a slab perforated with L-shaped holes. While not being 3d-chiral, it shows interesting features such as chiro-optical far-field response at normal incidence and the possibility to excite superchiral near-fields with unpolarized light.
The objects under investigation have the layout depicted in Fig. 1. They consist of a 220 nm thick gallium arsenide membrane, patterned with L-shaped holes arranged over a square lattice. We characterized the sample by performing polarization-resolved transmission over a broad band covering the near infrared wavelength between 1 and 2 um. Fig. 1b represents such spectra. The spectra consist of a series of quite narrow dips, some of them having different shapes and depths depending on the polarization state of the incident light. From the transmittances for left (right) circularly polarized light, the transmission circular dichroism can be defined. This quantity is plotted in Fig. 1c. Here, the traces labeled *front incidence* and *back incidence* have been collected from the same sample, but illuminated from either the top surface or the bottom surface.

As it can be noticed from Fig. 1b, the transmittance spectral features are Fano resonances, arranged in multiplets whose nature becomes clearer when an angularly-resolved analysis is performed. Such an analysis revealed the presence of a photonic band structure. Curiously, such band structure also manifested itself on the circular dichroism spectrum, where intrinsic chirality fingerprints stand out.

What is more, we performed a singular-value decomposition analysis of the transmission matrix: this analysis is more suited than an eigenvalue analysis since the T-matrix of this device is not unitary. Indeed, despite the membrane does not absorb any light (at the wavelengths of interest), some light is lost in reflection.

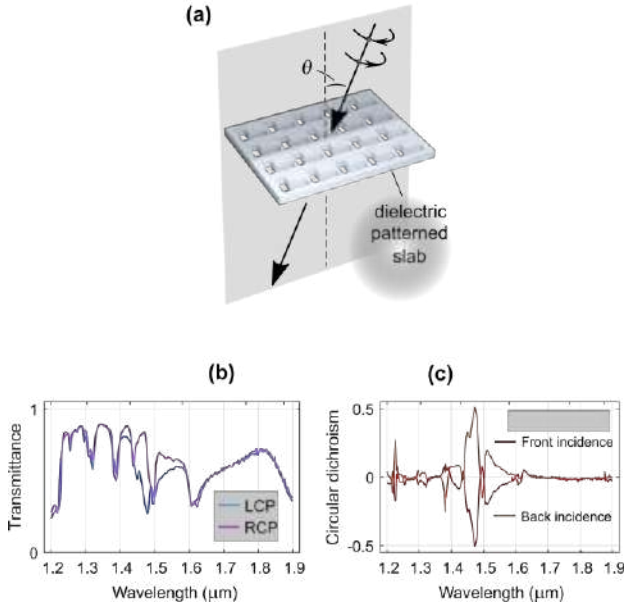


Figure 1: This is the figure caption. Color figures are acceptable.

This novel type of analysis revealed that resonant features in the singular value spectra, and in the spectra of the polarization states of the singular vectors, are strongly correlated with the features observes in the polarization-resolved transmission and in the circular dichroism. In addition, we noticed that appropriate algebraic manipulation of the SVD expressions allow to decouple the metasurface operation into a trivial one (i.e., a geometric rotation of the reference frame), and a non-trivial one, that constitutes the "core" of the metasurface operation.

Acknowledgements

The author kindly acknowledges the support of Alessandro Pitanti, prof. Alessandro Tredicucci, prof. Giuseppe C. La Rocca, Giacomo Mazzamuto, Sara Nocentini, and Francesco Riboli who supported the work at various stages. This work was in part supported by the European Commission through the project PHENOMEN (H2020-EU-713450).

References

[1] Y. Tang and A. E. Cohen, *Enhanced Enantioselectivity in Excitation of Chiral Molecules by Superchiral Light,* Science **332**, 333 (2011).

[2] A. Vázquez-Guardado and D. Chanda, *Superchiral Light Generation on Degenerate Achiral Surfaces,* Phys. Rev. Lett. **120**, 137601 (2018).

[3] M. Hentschel, M. Schäferling, X. Duan, H. Giessen, and N. Liu, *Chiral Plasmonics,* Sci. Adv. **3**, 1 (2017).

[4] J. T. Collins, C. Kuppe, D. C. Hooper, C. Sibilia, M. Centini, and V. K. Valev, *Chirality and Chiroptical Effects in Metal Nanostructures: Fundamentals and Current Trends,* Adv. Opt. Materials **1700182**, (2017).

[5] A. Y. Zhu, W. T. Chen, A. Zaidi, Y. Huang, M. Khorasaninejad, V. Sanjeev, C. Qiu, and F. Capasso, *Giant intrinsic chiro-optical activity in planar dielectric nanostructures*, Light Sci. Appl. **7**, 17158 (2018).

Hybrid plasmonic-dielectric resonant waveguide grating for diffraction with high color purity

Giorgio Quaranta[1], Olivier J. F. Martin[2], and Benjamin Gallinet[1,*]

[1]Centre Suisse d'Electronique et de Microtechnique (CSEM SA), Muttenz, Switzerland
[2]Nanophotonics and Metrology Laboratory (NAM), Swiss Federal Institute of Technology, Lausanne (EPFL), 1015 Lausanne, Switzerland
*corresponding author, E-mail: Benjamin.gallinet@csem.ch

Abstract

A hybrid dielectric-plasmonic waveguide grating enabling highly color-selective first order diffraction is reported. The effect is achieved by means of waveguide resonances and a Fano-like interference with the continuum formed by grating diffraction orders. This work shows the promising use of hybrid structures for taking the best features of both plasmonic and dielectric grating resonances for designing highly integrated optical devices such as spectrometers or optical security features.

1. Introduction

Plasmonic waveguides and resonant waveguide gratings have been a subject of extensive research for a few decades, showing promising optical properties relying on the Fano interference effect. In particular, filtering has been achieved thanks to the extraordinary optical transmission effect, implemented for imaging and spectral imaging devices [1]. In parallel, resonant waveguide gratings have been used for their filtering and coupling properties into thin film waveguides [2]. The search for full control of polarization, amplitude and phase of the electromagnetic field from planar surfaces remains of high interest, especially for the development of highly integrated photonic systems. Here, we report on a hybrid dielectric-plasmonic resonant waveguide grating which enables highly color-selective first order diffraction in a multimode light guide, which could be used for e.g. spectrometry or as an optical security feature.

2. Discussion

The system investigated in this work is sketched in Fig. 1a. A periodic sub-wavelength grating on glass susbtrate is coated with a thin silver film, followed by a coating of silica, with a thickness typically ranging up to 200nm. The silver layer alone supports a surface plasmon (SPP) mode, which is altered by the presence of the thin silica film into a hybrid dielectric waveguide-plasmon mode, named hybrid mode in the following. At a given wavelength, the incident light is diffracted by the grating and coupled into the hybrid mode with wavevector $\mathbf{k}_w$:

$$\mathbf{k}_W = \mathbf{k}_{in,t} + \frac{2\pi}{\Lambda}\hat{x}, \qquad (1)$$

where $\mathbf{k}_{in,t}$ is the tangential component of the incident wavevector in the grating plane. Several optical paths are available for the hybrid mode for outcoupling. It can be outcoupled by the same grating to the zeroth order of reflection or transmission such that:

$$\mathbf{k}_{out,t,0} = \mathbf{k}_W - \frac{2\pi}{\Lambda}\hat{x} = \mathbf{k}_{in,t}. \qquad (2)$$

Alternatively, it can be evanescently coupled into the substrate without action of the grating, with the resulting wavevector corresponds to the one of the first order of diffraction:

$$\mathbf{k}_{out,t,1} = \mathbf{k}_W = \mathbf{k}_{in,t} + \frac{2\pi}{\Lambda}\hat{x}. \qquad (3)$$

The hybrid mode is the resonant mode in this system.

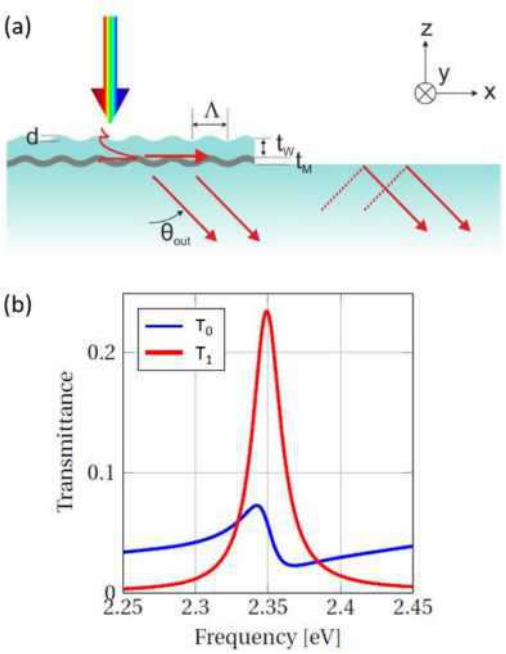


Figure 1: (a) Wavelength selective coupling in a highly multimode light guide using a hybrid plasmonic-dielectric resonant waveguide grating. The incident light is coupled by grating diffraction into a hybrid surface plasmon-dielectric waveguide mode and released into the substrate. (b) The interference between the direct diffracted light and the light coupled into a waveguide mode yields a Fano interference in the zeroth and first order of diffraction.

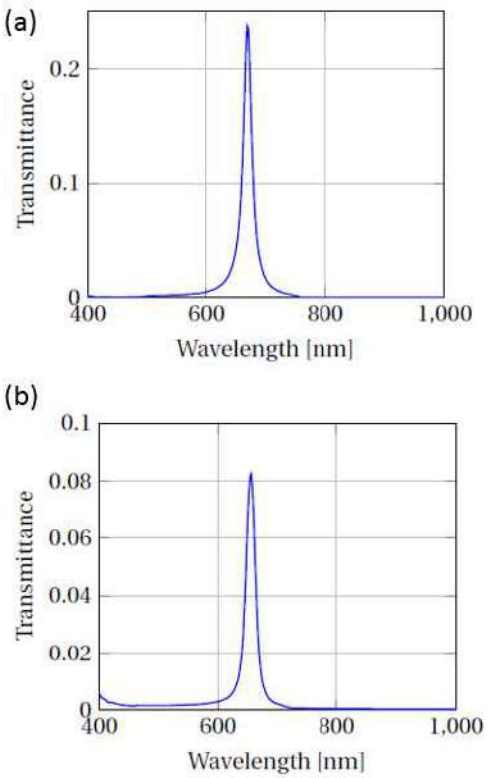


Figure 2: (a) Numerical calculation and (b) measurement of first order diffraction efficiency spectrum under TM polarization.

Other non-resonant optical paths include direct zeroth and first order of transmission, with tangential wavevectors equal to $\mathbf{k}_{in,t}$ and $\mathbf{k}_{in,t}+(2\pi/\Lambda)\,\hat{x}$, respectively. The interaction between the SPP mode and the continuum of zeroth and first order diffraction leads to a Fano-like interference with different asymmetry parameters, as shown in the rigorous coupled wave analysis (RCWA) calculations in Fig. 1(b).. The grating fabrication has been performed with electron beam lithography into a silicon wafer, which has been used as a replication template for UV-NIL on glass. After silver and silica coating, the first order diffraction efficiency in the substrate has been measured as a function of the wavelength (Fig. 2). It shows an isolated peak at the resonance wavelength with a very weak amplitude at other wavelengths, a signature of the resonance effect. In order to achieve high color purity, the coupling from free space to the waveguide should be small, which implies a low grating corrugation depth (typically in the order of 50nm and below). Overall, the grating depth and silver coating thickness are chosen to achieve the critical coupling condition, optimizing the diffraction amplitude in the first order of diffraction. Fig. 3a shows the peak wavelength and outcoupling angle obtained as a function of the silica coating thickness and period. In general a large range of design possibilities is available using this approach. Figures 3b and 3c show an example of application, in which a white light beam with large angle divergence is transformed into a set of angularly separated quasi-monochromatic light beams.

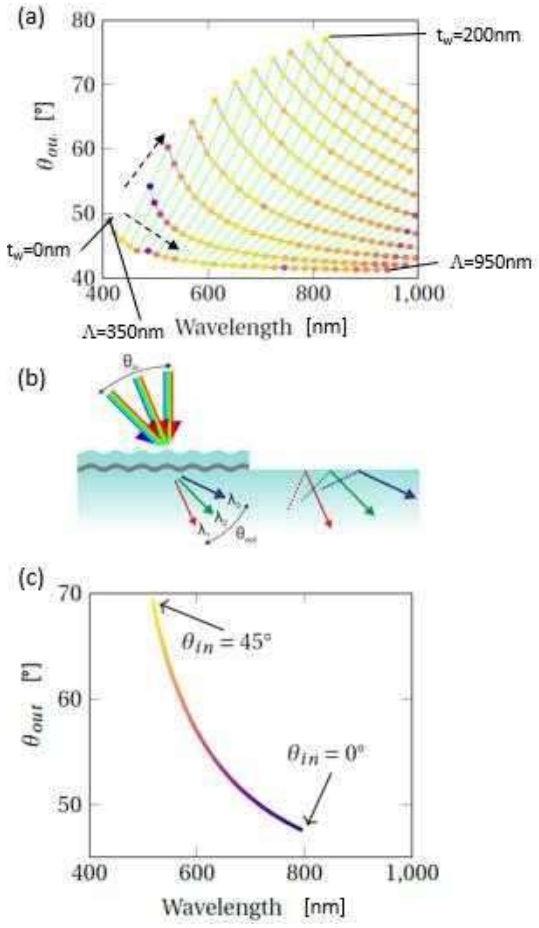


Figure 3: (a) Diffracted angle and wavelength related to the diffraction peak as a function of dielectric waveguide thickness t_w and the period. (b-c) Separation of incident white light with a large range of incidence angles into a set of quasi-monochromatic diffracted beams.

3. Conclusions

A highly color-selective diffraction and coupling into a multimode light guide has been achieved by means of waveguides resonances and a Fano-like interference with the continuum of grating diffraction orders. This work shows the promising use of hybrid structures for taking the best features of both plasmonic and dielectric grating resonances for designing highly integrated optical devices such as spectrometers or optical security features.

References

[1] S. Yokogawa, S.P. Burgos, H.A. Atwater, Plasmonic Color Filters for CMOS Image Sensor Applications, *Nano Letters* 12: 4349−4354, 2014.

[2] G. Quaranta, G. Basset, O.J.F. Martin, B. Gallinet, Recent advances in resonant waveguide gratings, *Laser and Photonics Reviews* 12: 1800017, 2018.

[3] B. Gallinet, T. Siegfried, H. Sigg, P. Nordlander, O.J.F. Martin, Plasmonic radiance: probing structure at the Angström scale with visible light, *Nano Letters* 13: 497-503, 2013.

Acoustic topological Fano resonances

Farzad Zangeneh-Nejad, and Romain Fleury

Laboratory of Wave Engineering, School of Electrical Engineering, EPFL, Station 11, 1015
*corresponding author, E-mail: romain.fleury@epfl.ch

Abstract

We report the observation of acoustic topological Fano resonance, and demonstrate their robustness to imperfections. By going beyond the performance degradations caused by inadvertent flaws occurring during fabrication process, such topologically protected Fano resonances pave the way for a new generation of reliable wave-based devices such as ultrafast switches or modulators , efficient lasers, perfect absorbers, and highly precise interferometers.

1. Introduction

Fano resonance is a ubiquitous classical wave phenomenon, commonly found in various branches of science and engineering like atomic and solid states physics [1], electromagnetism [2], circuits [3], photonics [4], and acoustics [5]. While originally developed to explain the inelastic scattering of electrons from helium, Fano resonances have recently attracted a great deal of interest by virtue of their myriad engineering applications. As a matter of fact, the ultra-sharp spectral feature of Fano resonances has established the basis for chains of prominent technology-oriented devices such as low threshold lasers [6], low energy switches, ultrafast modulators, high quality factor filters, compact electromagnetically induced transparency (EIT) devices, ultrathin perfect absorbers, and highly accurate interferometers.

Apart from its steepness, the peculiar asymmetric line shape of Fano-type resonances is known to be excessively sensitive to environmental changes, a characteristic which has enabled the realization of highly sensitive sensors [7,8]. Such sensitivity, however, is not always desirable, when such resonances are intended for the applications other than sensing. In such cases, even slight changes in structural features such as the disorder and imperfection caused inevitably during fabrication process are highly detrimental and degrade the performance of the device severely.

The recently proposed concept of topological insulators [9], however, offers an unprecedented solution to overcome the challenges associated with inadvertent, or even deliberate, structural impurities. Topological insulators are a class of materials exhibiting insulating behavior in their bulk, yet they allow conduction along their edges. The paramount feature of topological insulators, however, relies on the fact that these conduction edge states are invulnerable to broad imperfection as they are protected by the topology of the bulk material.

Here, we demonstrate how topological insulators can be leveraged to make Fano resonances robust against impurities. Towards this goal, we first investigate the unexplored physics of the topological bound states which may happen to coexist within the continuum spectrum of the edge states of a topological insulator. We then describe how such bound states can give rise to topological Fano-type resonances, protected against broad structural deformations. Such robust Fano resonances constitute a promising framework for a large variety of efficient and fabrication-insensitive Fano-type devices.

2. Results

We start with considering the topological edge states that form at the phase transition interface of the SSH array shown in Fig. 1a. The system consists of cylindrical rods embedded inside an acoustic parallel plate waveguide. Considering the symmetry of the system under study, one can categorize the corresponding edge states into two classes: the edge state stemming from the bound state in the continuum of waveguide (BIC) and those originating from the radiation modes. Fig. 3a (second and third panels) illustrate the profile of these two different types of edge states, respectively. For future references, we entitle the first and second types as dark and bright edge states, respectively. Such appellation is inspired by the fact that the dark edge state possesses much narrower resonance linewidth (or lower leakage) compared to the bright edge states [10]. We note that by scaling the lattice constant, one can readily adjust the frequency of the bright edge state [10]. Here, we have subtly chosen the lattice constant in a way that the bright edge mode occurs in the neighboring of the dark edge mode. Consequently, when performing the scattering experiment, the dark edge mode coexists in the resonance continuum of the bright edge mode, creating an ultra-sharp and asymmetric Fano resonance as observed in Fig. 3a (fourth panel). Note that if the mirror symmetry had been preserved, the dark edge mode would be hidden in the spectrum (the dashed red line), forming a topological bound state in the continuum of the bright edge mode.

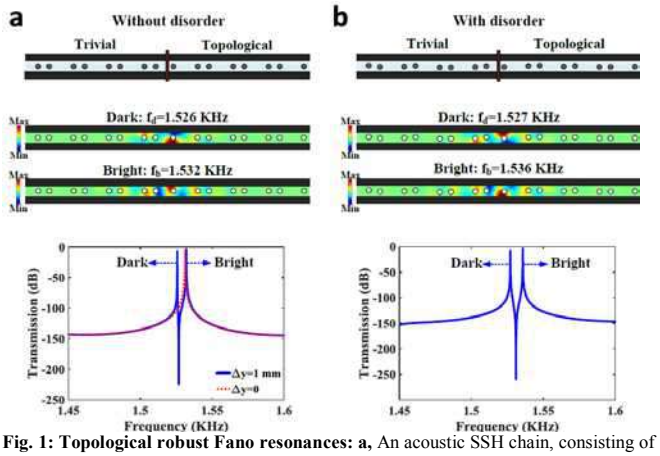


Fig. 1: Topological robust Fano resonances: a, An acoustic SSH chain, consisting of a series of cylindrical rods embedded inside an acoustic parallel plate waveguide. Two types of edge states will subsequently be formed at the interface: those originating from the radiation modes (the bright edge state) and the one stemming from the BIC mode. By scaling the lattice constant, one can conveniently enforce the bright edge state occurs in the neighboring of the dark one so as to achieve the Fano-type resonance (the solid blue line). **b,** Same as panel a but for a largely disordered configuration. Since both the bright and the dark resonances have topological nature, the resulting Fano resonance is protected against the disorder by the topology of the bulk insulators. The interested reader in referred to [10] for more information regarding the topological nature of the system and its robustness.

We now move onto to examine the robustness of the obtained Fano resonance against structural deformation. Intuitively, since both of the bright and dark resonances have topological nature, the resulting Fano resonance is expected to be protected against disorder by the topological order of the surrounding insulators. To examine such robustness, we randomly change the positions of the obstructing circles to achieve the largely disordered system of Fig. 3b (first panel). The mode profile of the resulting dark and bright edge states are shown in Fig. 3b, second and third panels, respectively. Notice that the resonance frequencies of both bright and dark resonances are not significantly affected by the disorder owing to their topological nature. The resulting Fano resonance is therefore expected to negligibly deviate from its ideal case. This is evident from the transmission spectrum of the waveguide in Fig. 3b (fourth panel), confirming the high robustness of such kinds of Fano resonances. Such reliability offers promising perspectives for the realization of various fabrication-insensitive Fano-resonance-based devices such as low-threshold lasers, ultrafast modulators and switches, and perfect absorbers.

3. Conclusions

We introduced and the concept of topological Fano resonance. Our findings demonstrate the superior robustness of topological Fano resonances over trivial Fano resonances. Topology guarantees the peculiar Fano line shape to occur in the desired frequency range, as long as the level of disorder is not strong enough to close the surrounding topological band gaps. Remarkably, such topological Fano resonances are still sensitive to environmental changes, a characteristic which may allow for a new generation of sturdy sensors. Our results shows that achieving a topological Fano resonance does not require tight geometrical tolerances, very different from trivial Fano resonances. We believe that the concept of topological Fano resonance can offer new perspectives in broad range of applicative fields, including, but not limited to, photonic, plasmonic, sensing, all-optical signal processing, or biomolecular detection.

Acknowledgements

This work was supported by the Swiss National Science Foundation (SNSF) under Grant No. 172487.

References

[1] O. Újsághy, J. Kroha, L. Szunyogh, and A. Zawadowski, Phys. Rev. Lett. **85**, 2557

[2] A. Bärnthaler, S. Rotter, F. Libisch, J. Burgdörfer, S. Gehler, U. Kuhl, and H. J. Stöckmann, Phys. Rev. Lett. **105**, (2010).

[3] B. Luk'Yanchuk, N. I. Zheludev, S. A. Maier, N. J. Halas, P. Nordlander, H. Giessen, and C. T. Chong, Nat. Mater. **9**, 707 (2010).

[4] A. E. Miroshnichenko, S. Flach, and Y. S. Kivshar, Rev. Mod. Phys. **82**, 2257 (2010).

[5] E. H. El Boudouti, T. Mrabti, H. Al-Wahsh, B. Djafari-Rouhani, A. Akjouj, and L. Dobrzynski, J. Phys. Condens. Matter **20**, (2008).

[6] S.L. Chua, Y. Chong, A. D. Stone, M. Soljacic, and J. Bravo-Abad, Opt. Express **19**, 1539 (2011).

[7] C. Wu, A. B. Khanikaev, R. Adato, N. Arju, A. A. Yanik, H. Altug, and G. Shvets, Nat. Mater. **11**, (2012).

[8] F. Zangeneh-Nejad and R. Safian, IEEE Sens. J. (2016).

[9] C. L. Kane and E. J. Mele, Phys. Rev. Lett. **95**, (2005)

[10] F. Zangeneh-Nejad and R. Fleury, Phys. Rev. Lett. (2019).

Coupling regimes in a complex of two rods: from core-shell particle to dimer

Alexey A. Dmitriev[1*] **and Mikhail V. Rybin**[1,2]

[1]Department of Physics and Engineering, ITMO University, St Petersburg 197101, Russia
[2]Ioffe Institute, St Petersburg 194021, Russia
*corresponding author, E-mail: alexey.dmitriev@metalab.ifmo.ru

Abstract

We study coupling regimes in a system made of two infinite dielectric rods with the same frequency of dipole Mie resonances. We present simulated scattering spectra in three configurations: a core-shell particle, an eccentrically coated rod and a dimer. We track the evolution of spectra as the distance between the rods is varied and discuss the coupling regimes.

1. Introduction

Photonic structures operate due to resonances in their constituent elements. The strength of coupling between the resonances determines whether the corresponding mode would be local or distributed among multiple particles [1]. A core-shell particle is an example of a photonic structure operating on local resonances. Their interaction is described as a Fano resonance leading to scattering cancellation [2]. Photonic oligomers, on the contrary, support hybridized modes [3]. Each type of coupling has its own advantages and disadvantages for specific applications. Thus, it is crucial to reveal conditions for the transition between the weak and strong coupling regimes in different photonic structures.

Here we study coupling regimes in a system consisting of two infinite dielectric rods. We start with a configuration when the rods are placed coaxially forming a core-shell particle. Then we "pull" the core out of the shell by increasing the distance between the centers of the rods. We identify two possible configurations here: (i) the smaller rod is eccentrically embedded inside the bigger one, and (ii) the rods are separated by an air gap, forming a dimer.

2. Simulation of the scattering spectra

To study the coupling regimes we consider the problem of the scattering of a plane wave on a system made of two infinite dielectric rods. The rods have the radii R and r, with R being greater than r, and the refractive indices n_1 and n_2 with n_1 being less than n_2. We choose the refractive indices so as to tailor the dipole Mie resonance to the same frequency for both rods. The distance d between the centers of the rods is varied to make one of the following configurations: (i) $d = 0$ for a core-shell particle, (ii) $0 < d \leq (R - r)$ for an eccentrically coated rod and (iii) $d \geq (R + r)$ for a dimer.

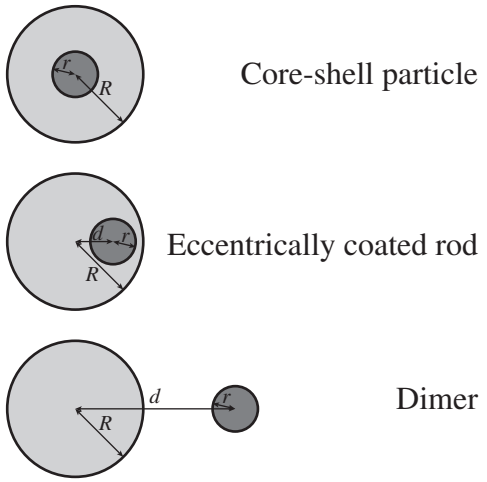


Figure 1: A sketch of the system under study. We consider two infinite dielectric rods matching one of the following configurations: a core-shell particle ($d = 0$), an eccentrically coated rod ($0 < d \leq R - r$) or a dimer ($d \geq R + r$).

To simulate the scattering we use a rigorous coupled-multipole method also known as multiple scattering theory (MST). The method is based on rewriting each multipole of scattered field as a multipole expansion in the vicinity of another scatterer, so as to account for all subsequent scattering events. This allows us to write down a system of equations on the scattered multipole amplitudes and to solve it. We use this approach to formulate a generalized Lorentz – Mie theory for an array of rods embedded into a bigger rod. To do this, we write down the multiple scattering equations and rewrite the scattering fields as a multipole expansion around the center of the enclosing rod. By imposing field continuity conditions on the boundary between the enclosing rod and air, we can work out the scattering matrix of this complex treated as a single scatterer. Then we use the 2D optical theorem [4] to calculate the scattering cross-section from the scattered multipole amplitudes. The theorem reads

$$C_{\text{ext}} = 2\sqrt{\frac{\pi}{k}}\left(\text{Im}\{f(0)\} - \text{Re}\{f(0)\}\right), \qquad (1)$$

where $f(0)$ is the forward scattering amplitude normalized to the amplitude of plane wave.

3. Results of simulation

We show the results of our simulations in Fig. 2. Solid lines correspond to the "longitudinal" configuration with the centers of rods put along the direction of incidence. We note that reversing the direction of incidence does not change the spectra. Dotted lines show the "transverse" configuration with the centers of rods put perpendicularly to the incidence direction.

At infinitely large distances (labeled $d \to \infty$ in the figure) the rods scatter light independently. Spectra in both configurations demonstrate a single peak at the size parameter of $kR = 0.25$ corresponding to two-fold degenerated dipole Mie resonances, which are tailored to the same frequency for both rods. When the distance between the rods is decreased, (see the curve labeled $d = 100r$ in the figure) the scattering spectra start to exhibit fringes (oscillations), which correspond to Fabry–Perot-like modes appearing between the rods [4, 6]. We note that the "frequency" of the oscillations in the longitudinal configuration is two times larger than in the transverse configuration, due to the symmetry forbidding the excitation of odd modes in the latter one.

At the distance $d = 25r$ (we show $d \leq 10r$ for better clarity) the rods enter the strong coupling regime, which is characterized by splitting of the Mie resonance [5, 6]. This splitting appears due to hybridization of the eigenmodes of the rods. The lower peak corresponds to the symmetric hybridized mode, while the higher one is the antisymmetric mode. The latter peak is not observed in the spectra for the transverse configuration due to the symmetry. The splitting increases as the distance between rods is decreased.

The distance $d = 4r$ corresponds to the case of touching rods. To study the coupling at even smaller distances, we consider the eccentrically coated rod configuration with $d \leq 2r$. Here the spectra for the longitudinal configuration show the same behavior: they exhibit the peaks corresponding to the symmetric and the antisymmetric modes with the splitting increasing as the distance decreases. At the core-shell particle regime ($d = 0$) the spectra for the longitudinal and the transverse configurations coincide.

4. Conclusion

We have performed simulations of scattering spectra of two infinite dielectric rods the same dipole Mie resonance frequency and different radii in three configurations: a dimer, an eccentrically coated rod and a core-shell particle. We have compared the spectra for two scattering geometries. As the distance between the rods is decreased, the weak-to-strong coupling regime transition occurs. The strong coupling regime is characterized by splitting of the dipole peak into a duplet of a symmetric and an antisymmetric modes. After the smaller rod is embedded into the larger one to form an eccentrically coated rod configuration, the longitudinal configuration shows the same behavior.

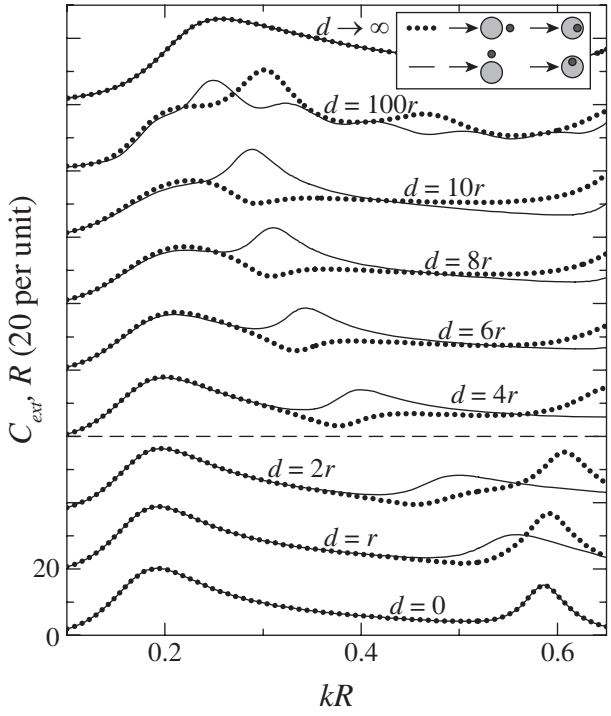


Figure 2: Scattering spectra of two rods in case of dimer ($d \geq 4r$), eccentrically coated rod ($0 < d \leq 2r$) and core-shell particle ($d = 0$). The spectra are shifted up along the y-axis.

Acknowledgement

We acknowledge a support of the Ministry of Education and Science of the Russian Federation (Project 3.1500.2017/4.6).

References

[1] Mikhail F. Limonov, Mikhail V. Rybin, Alexander N. Poddubny, and Yuri S. Kivshar. Fano resonances in photonics. *Nature Photonics*, 11(9):543–554, 2017.

[2] Pai-Yen Chen, Jason Soric, and Andrea Alù. Invisibility and cloaking based on scattering cancellation. *Advanced Materials*, 24(44):OP281–OP304, 2012.

[3] Arseniy I. Kuznetsov, Andrey E. Miroshnichenko, Mark L. Brongersma, Yuri S. Kivshar, and Boris Luk'yanchuk. Optically resonant dielectric nanostructures. *Science*, 354(6314):aag2472, 2016.

[4] Alexey A. Dmitriev and Mikhail V. Rybin. Coupling regimes of high-index dimer. In *Days on Diffraction (DD) 2018*, 71–75. IEEE, 2018.

[5] Linyou Cao, Pengyu Fan, and Mark L. Brongersma. Optical coupling of deep-subwavelength semiconductor nanowires. *Nano Letters*, 11(4):1463–1468, 2011.

[6] Alexey A. Dmitriev and Mikhail V. Rybin. Strong optical coupling combines isolated scatterers into dimer. *(to be published)*

Fano resonances and exceptional points in waveguides and quantum conductors

Alexander Gorbatsevich[1,2*], Nikolay Shubin[1,2], Vladimir Kapaev[1], and Alexander Friman[1]

[1]P.N.Lebedev Physical Institute, Solid State Physics Department, Moscow, Russia
[2]National Research University of Electronic Technology – MIET, Zelenograd, Moscow, Russia
*corresponding author, E-mail: aagor137@mail.ru

Abstract

We present a unified theory, which makes it possible to study on a unique theoretical platform diverse issues concerning resonances in complex classical as well as quantum systems including Fano resonances and exceptional points, collapse of Fano resonances and bound states in the continuum. We support the main results of our theory by numerical simulations of a real electromagnetic waveguides and discuss difference between classical and quantum description of Fano resonances.

1. Introduction

Scattered waves can exhibit either constructive or destructive interference resulting in transmission maximum (resonance) or minimum (antiresonance) correspondingly. Both types of interference phenomena take place in Fano resonances, which appear in scattering of continuum states by a (quasi) localized resonant state [1]. Fano resonances are ubiquitous in complex classical and quantum systems such as plasmonic and dielectric nanostructures, semiconductor heterostructures, photonic crystals, metamaterials and metasurfaces, optomechanical resonators, waveguide sensors, molecular conductors etc. [1,2]. Hence design and fabrication of such structures with desired resonance properties are of primary importance both for fundamental science and applications. In the present report we address this problem on the basis of a recently developed unified theory of resonances and bound states in the continuum [3]. General results of Ref. [3] are supported by means of modal plane wave expansion (PWE) and finite difference time domain (FDTD) numerical simulations.

2. Unified tight-binding theory of (anti)resonances

In Ref. [3] a scattering problem was studied for a quantum conductor or a waveguide in tight binding approximation and a universal formula for the transparency T was derived:

$$T(\omega)=\frac{P^2(\omega)}{P^2(\omega)+Q^2(\omega)}, \qquad (1)$$

where P and Q are some functions of photonic frequency (electron energy). It was shown that Q can be determined as the characteristic determinant of some auxiliarly non-Hermitian Hamiltonian, which can be straightforwardly deduced from Fano-Feshbach non-Hermitian Hamiltonian:

$$Q(\omega)=\det\left(\hat{I}\omega-\hat{H}_{aux}\right). \qquad (2)$$

Expression (1) is exact within the framework of tight-binding approximation irrespective to number of the neighbors taken into account. Real eigenvalues of $\hat{H}_{aux}$ and roots of Q (2) exactly determine perfect transmission resonances (1). Non-Hermitian operators can possess real eigenvalues under the condition of *PT*-symmetry (here P – space inversion and T – time reversal operators) [4]. *PT*-symmetry can be broken under variation of internal system parameter at the *exceptional point* (EP) of the system. At EP two real eigenvalues coalesce and turn into a pair of complex conjugate. From Eq. (1) it follows that at EP two perfect resonances coalesce and turns into a single resonance with transparency less then unity.

In simply connected (linear) system P does not depend on frequency and can be written as a product of intersite couplings. Transmission (1) in this case does not possess zeroes and turns into Breit-Wigner expression near single resonance. In multiply connected systems P becomes frequency (energy) dependent and its roots determine antiresonances. Closely spaced roots of P and Q describe a typical Fano resonance. Poles of the transparency coincide with poles of scattering matrix. Therefore the compact expression (1) makes it possible to perform consistent study of bound states in the continuum (BIC) [5], which are related to the poles of scattering matrix on real axis. From Equation (1) it follows that BIC occurs if and only if P and Q share the same real root. Hence BIC emerges as a result of collapse of Fano resonance accompanied by coalescence of resonance and antiresonance. Depending on multiplicity of the P and Q roots we can also consider BIC either as a Breit-Wigner resonance or as an antiresonance with zero width.

3. Fano supernodes near exceptional points

Near EP of an auxiliary Hamiltonian transparency (1) forms a broad resonance window. As it was shown in Ref. [3] function P under some conditions can be expressed as the characteristic determinant of another non-Hermitian Hamiltonian as well. This Hamiltonian can possess EP either, near which the transparency is characterized by a window of almost zero transparency – Fano supernode. It was shown that multiple transmission zeros (Fano supernodes) can provide a great enhancement in the ZT parameter of a thermoelectric transformer [6]. These supernodes can be predicted by the simplest tight-binding model with nearest neighbor approximation in transmission spectra of various molecular conductors with equal side groups placed along the conductor. Unfortunately, they are not robust against taking into account next nearest neighbors or Coulomb correlation effects [7]. Coalescence of antiresonances provides different nature of the Fano supernodes formation and they might be more robust against through-space couplings and many-body correlations. As an example consider a double-chain system with two sites in each chain (inset in Fig. 1). Taking into account next nearest neighbor couplings only shifts the supernode position rather than destructs it (Fig. 1).

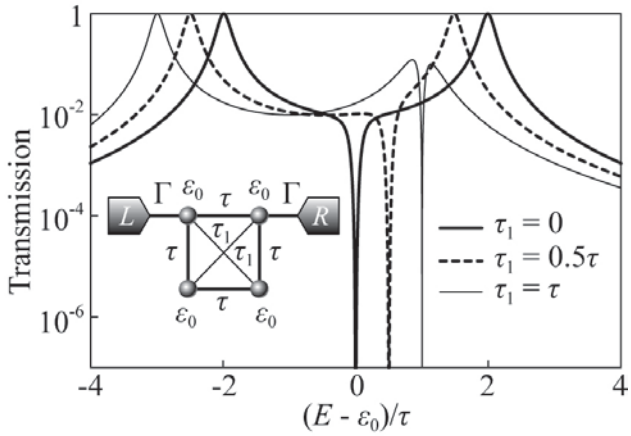


Figure 1: Fano supernodes. Transmission spectrum of the double chain system with two sites in each chain (inset) with next nearest neighbors couplings taken into account.

4. Coalescence of Fano resonances in numerical simulations of electromagnetic waveguides

We use two techniques of electromagnetic fields simulation: FDTD and modified PWE. FDTD calculations of EM waves in a structure with sharp Fano resonances raise some difficulties such as necessity of long emitting sources due to large resonance buildup times. To avoid time consuming FDTD simulations we use a modified PWE technique for coarse estimation of the resonances positions. The PWE approach uses radiation boundary conditions and gives us realistic data for infinite long waveguides with a finite resonator. The results of numerical simulation of the simplest waveguide structure are presented in Fig. 2. We also studied temporal evolution of electromagnetic fields during BIC formation by means of FDTD technique. It should be noted that due to the difference in the conditions for the bound state existence in quantum mechanics and electromagnetic cavity modes formation the simulation of Fano resonances in quantum and classical theory possesses the essential differences.

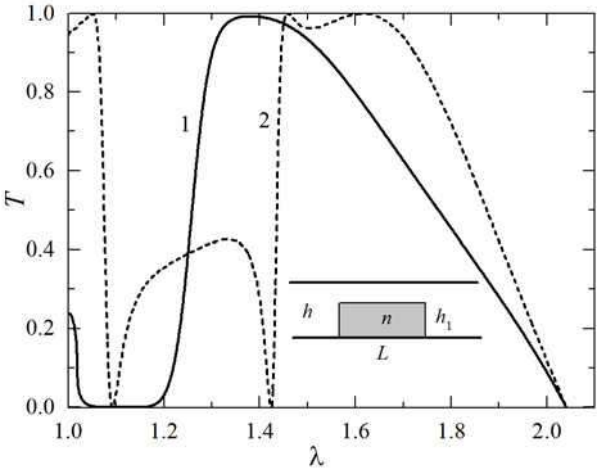


Figure 2: Transmission spectrum demonstrating coalescence of Fano resonances in metallic waveguide with dielectric insert n=2, h=1, L=0.5, 1 – h_1=0.46, 2 – 0.60.

5. Conclusions

In the present report we show that design rules can be formulated that makes it possible to construct electromagnetic waveguides with diverse and controllable properties of Fano resonances ranging from collapse of Fano resonances, resulting in BIC formation, to coalescence of Fano resonances accompanied by emergence of wide reflection windows.

Acknowledgements

The authors acknowledge the partial support from Russian Ministry of Science and Education and Presidium of RAS.

References

[1] E. Kamenetskii, A. Sadreev, A. Miroshnichenko *Fano resonances in optics and microwaves*, Springer International Publishing, 2018.

[2] M.F. Limonov, M.V. Rybin, A.N. Poddubny et al, Fano resonances in photonics, *Nature Photonics* 11: 543−554, 2017.

[3] A.A. Gorbatsevich and N.M. Shubin, Unified theory of resonances and bound states in the continuum in Hermitian tight-binding models, *Phys. Rev. B* 96: 205441, 2017.

[4] C.M. Bender, Making sense of non-Hermitian Hamiltonians, *Rep. Prog. Phys.* 70: 947, 2007.

[5] C.W. Hsu, B. Zhen, A.D. Stone et al, Bound states in the continuum, *Nat. Rev. Mat.* 1: 16048, 2016.

[6] J.P. Bergfield, M.A. Solis, and C.A. Stafford, Giant thermoelectric effect from transmission supernodes, *ACS Nano* 4 (9): 5314−5320, 2010.

[7] G.C. Solomon, J.P. Bergfield, C.A. Stafford et al, When "small" terms matter: Coupled interference features in the transport properties of cross-conjugated molecules, *Beilstein J. Nanotechnol.* 2: 862−871, 2011.

Bound States in the Continuum in Hybrid Photonic-Plasmonic-Structures

Shaimaa I. Azzam[1], Vladimir M. Shalaev[1], Alexandra Boltasseva[1], and Alexander V. Kildishev[1]

[1]School of Electrical and Computer Engineering and Birck Nanotechnology Center, Purdue University, West Lafayette, IN 47907, USA
E-mail: shalaev@purdue.edu, aeb@purdue.edu, kildishev@purdue.edu

Abstract

This work investigates the formation of bound states in the continuum (BICs) in a system of coupled plasmonic grating and a photonic waveguide. Aside from the conventional symmetry-protected BICs that appear at the band edge, the hybrid system also supports Friedrich-Wintgen BICs that are formed in the vicinity of the avoided crossing of strongly-coupled plasmonic and photonic modes. The radiative quality factors of the BIC states diverge to infinity which makes them perfect candidates for many applications.

1. Introduction

Since their first realization in optical systems [1], bound states in the continuum (BICs) have been achieved in a large number of loss-free optical platforms [2, 3]. However, their realization in systems with losses has been very limited [4].
In this work, we strongly-couple the plasmons modes of a silver grating and the photonic modes in a dielectric waveguide which results in an avoided crossing with Rabi frequency of 150 meV [5]. This system allows us to access different types of BICs such as symmetry-protected plasmonic BIC, and symmetry-protected photonic BIC which appear at normal incidence. Also, we can observe Friedrich-Wintgen BIC that are formed due to the destructive interference between different resonances. Besides BIC states which are dark states with theoretically infinite radiative quality factors, "near-BIC" regime is where very high quality-factors can still be attained in the vicinity of BICs is very important. Resonances in the near-BIC regime can be excited by free propagating plane waves and are generally more robust and practical to work with.

2. Discussion

In Fig. 1(a), we show the proposed hybrid system. The plasmonic grating is made of silver on top of a thick (100 nm) silver film. The periodic ridges of the grating are 30-nm high and 100-nm wide. The period of the grating is 400 nm, and the top silica layer has a refractive index of 1.45 and is 500-nm thick. The polarization of the incident light is directed along the grating wires (TM) to enable the excitation of the surface plasmon modes. Figure 2(b) shows the reflectance spectra with varying incident angles. At the normal incidence, we can notice the vanishing of the linewidth at two different wavelengths. The first is of the plasmonic resonance (upper branch ~ 700nm) which we call symmetry-protected plasmonic BIC. The second is the vanishing of the linewidth of the photonic resonance (~532 nm) which is called symmetry-protected photonic BIC. Both plasmonic and photonic symmetry-protected states disappear at the normal incidence due to the incompatibility of the symmetry of the state with the outgoing field. The second type of BICs formed in our hybrid system are the Friedrich-Wintgen BIC resulting from the strong coupling and the destructive interference of the photonic and the plasmonic modes. In Fig. 1(b), the BIC appears close to the avoided crossing at an angle of 11.4°. In all cases, photonic and plasmonic symmetry-protected BICs and the off- Friedrich-Wintgen BIC, the linewidths of the resonances disappear, and the radiative Q-factor diverges as a signature of the formation of a BIC.

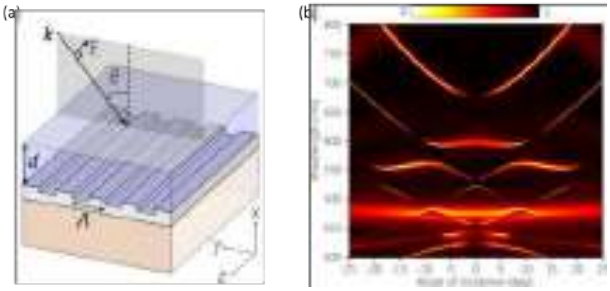


Figure 1: (a) Schematic of a plasmonic grating coupled to a silica waveguide. (b) Reflectance spectra as a function of the incident angle showing the different types of BICs. At an incident angle of 0°, multiple symmetry-protected BICs are observed. The Friedrich-Wintgen BIC appears near the strong coupling point at an angle of 11.4°.

To showcase the nature of the interacting modes in the hybrid structure, the electric field distributions at 1° angle of incidence and variable wavelengths are plotted in Fig. 2. Fig. 2(a, b) show the fields at 521.3 nm and 536.3 nm wavelength, respectively, which indicated mainly photonic

nature in the 500 nm-wide slab waveguide. On the contrary, the electric field at 599.5 nm, Fig. 2(c), is purely plasmonic. Also, varying the thickness of the photonic slab waveguide changes the number of supported modes and hence dramatically alter the band diagram of the hybrid structure. This opens a multitude of opportunities for application requiring band gap engineering by controlling the dispersion of the plasmonic component, or the photonic one, or both in the hybrid design.

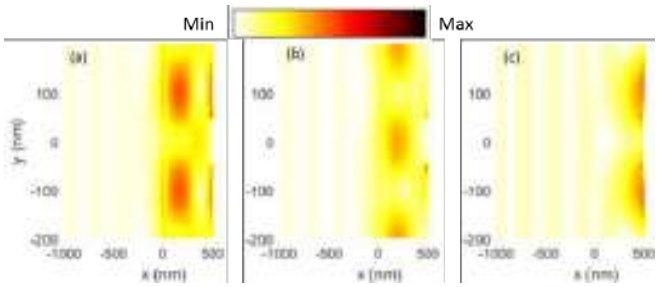


Figure 2: Electric field distribution at an angle of incidence of 1° and wavelength of (a) 521.3 nm, (b) 536.4 nm, and (c) 599.5 nm.

Moreover, we can notice from Fig. 1(b) that the system supports slow light, not only at the band edge (normal incidence), but also, at arbitrary values for the angle of incidence. More interestingly, the spectral bandwidth along which the slow light can be supported is substantially increased. As noted from Fig. 1(b), the slow light band at ~600 nm expands from -10° to 10° and that at ~560 nm from 7° to 20°. Therefore, the hybrid structure is capable of selecting the central angle at which the slow light exists, extending its angular span, and providing means to select where the slow light is supported spectrally.

3. Conclusions

In conclusion, we have explored the formation of BICs in hybrid systems with a realistic intrinsic loss. Due to the strong coupling of plasmonic and photonic modes and their destructive interference, the losses are significantly reduced due to the suppression of radiation. Two different types of BICs are accessible in the hybrid plasmonic-photonic system due to the symmetry incompatibility with the radiation as well as the destructive reactions of resonances. A distinct characteristic of the Friedrich-Wintgen BIC achieved in this study is that it originates from the interference of two resonances with different natures. Besides, we also demonstrated that the hybrid system studied exhibits strong coupling with large Rabi splitting, optical bandgap engineering and slow light with sizeable spectral robustness.

Acknowledgements

The authors acknowledge the support by the U.S. Department of Energy (DOE), Office of Basic Energy Sciences (BES), Division of Materials Sciences and Engineering under Award DE-SC0017717.

References

[1] D. C. Marinica and A. G. Borisov, and S. V. Shabanov. "Bound states in the continuum in photonics." *Phys. Rev. Lett.* 100: 183902, 2008.

[2] C.W. Hsu, B. Zhen, J. Lee, S.-L. Chua, S.G. Johnson, J.D. Joannopoulos, and, M. Soljacĭc, "Observation of trapped light within the radiation continuum," *Nature*, 499: 188−91, 2013.

[3] C.W. Hsu, B. Zhen, A.D. Stone, J.D. Joannopoulos, and M. Soljačić, "Bound states in the continuum," *Nat. Rev. Mater.*, 1: 16048, 2016.

[4] F. Monticone, and A. Alu. "Embedded photonic eigenvalues in 3D nanostructures." *Phys. Rev. Lett.* 112: 213903, 2014.

[5] S. I Azzam, V. M Shalaev, A. Boltasseva, A. V Kildishev, "Formation of Bound States in the Continuum in Hybrid Plasmonic-Photonic Systems," *Phys. Rev. Lett.* 121: 253901, 2018

Multiple Fano Feature due to Optical Bound States in the Continuum

Dmitrii N. Maksimov* and Evgeny N Bulgakov

Reshetnev Siberian State University of Science and Technology, Krasnoyarsk, Russia
*corresponding author, E-mail: mdn@tnp.krasn.ru

Abstract

We consider light scattering by 2D arrays of dielectric spheres arranged into the triangular lattice. It is demonstrated that the scattering spectra exhibit a complicated picture of Fano resonances. The Fano features are explained as a signature of bound states in the continuum (BICs). It is found that an in-Gamma BIC induces off-Gamma BICs due to different scaling laws for real and imaginary parts of the resonant eigenfrequency, the latter being parabolic while the former form a Dirac cone.

Multipolar properties of bound states in the continuum supported in all-dielectric metasurfaces

Yi Xu[1]

[1] Department of Electronic Engineering, College of Information Science and Technology, Jinan University, Guangzhou 510632, China
*corresponding author, E-mail: yi.xu@osamember.org

Abstract

We study the multipolar properties of bound states in the continuum of all-dielectric metasurfaces which are consisted of periodic silicon nanodisks. Such bound states in the continuum can be regarded as the discrete states (subradiant modes) which involves in forming high-Q Fano resonances. By reconstructed the Fano line shape utilizing the induced multipole moments in one unit cell, we reveal the important roles of multipolar bound states in the continuum play in forming such Fano resonances.

1. Introduction

Wavelength scale dielectric nanoparticles can support Mie type resonances manifested themselves as electromagnetic multipole resonances [1]. It might even support exotic phenomena in the scattering of electromagnetic waves, such as the nonradiative anapole mode [2] and ideal magnetic dipole scattering [3]. If these Mie type resonators are arranged in a periodic way, a metasurface is formed and guide resonances can be triggered under the suitable excitation condition [4]. Such high-Q Fano resonances are attractive as they can be used in many electromagnetic applications, such as optical modulator, optical filter and optical switch [4]. In general, all of these Fano resonances are featured with sharp asymmetry line shapes, which can be easily detected in the far-field. However, less attention is paid to the near-field electromagnetic distributions of various high-Q guided resonances while they do exhibit interesting and distinct multipole features [5].

Herein, we study the multipolar properties of eigenmodes with infinite Q factors supported in an all-dielectric metasurface which is consisted of periodic arranged silicon nanodisks shown in Fig. 1 (a). Such BIC can be tuned into leaky resonances with ultrahigh Q factors. By decomposing the induced multipole moments in one unit cell, we reveal the important roles of multipolar bound states in the continuum play in forming various kinds of leaky resonances. We further discuss potentials applications, such as lasing, sensing and enhancing optical nonlinearity, by utilizing different kinds of multipolar bound states in the continuum.

2. Results

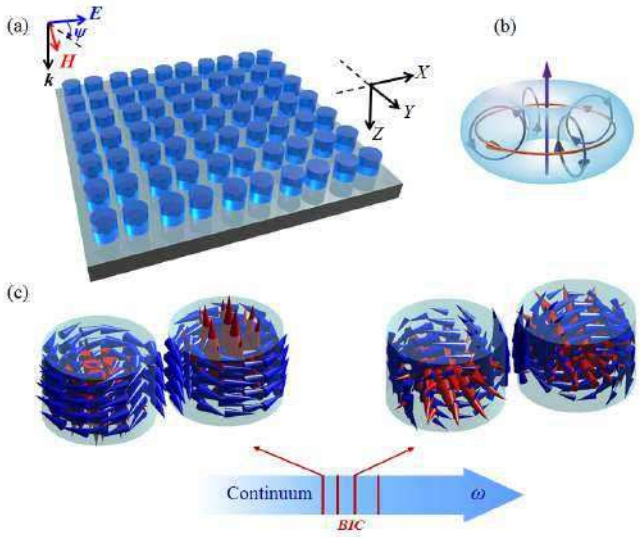


Figure 1: (a) Schematic of an all-dielectric metasurface supporting multipolar bound states in the continuum (BIC). Periodic silicon dimer nanodisks arranged in a square lattice are placed on a quartz substrate. (b) Schematic of a toroidal dipole (TD) moment. (c) Two TD BIC eigenmodes of the metasurface with their TD moments along the Y axis and Z axis, respectively. We only show the electromagnetic field inside the particles. The blue/red arrows stand for the electric/magnetic field vectors.

Without loss of generality, we show that an all-dielectric metasurface consisted of periodic silicon dimer nanodisks arranged in a square lattice supports various kinds of Bloch modes with infinite life time. Such BIC states manifest themselves as distinct electromagnetic multipolar modes in the near-field. In particular, two toroidal dipole (TD) BIC modes, which exhibit a particular localized current distribution as shown in Fig. 1 (b), can be found in this structure. Because of the special localized current distribution of the TD moment [6], these two TD BIC modes are quite unique and possess giant electric field enhancement in free space [5], i.e. on the surface and in the gap of the metasurface, as shown in Fig. 1 (c).

3. Conclusions

In summary, we demonstrate that all-dielectric metasurface supports BIC modes with distinct multipolar properties. By manipulating the symmetry properties of either the excitation field or the structure, we can transform these BIC modes into the leaky Fano resonances with ultrahigh-Q factors. We can further fine tune the Q factors of these BIC modes and their associated near-field enhancement. At the same time, the multipolar properties of BIC modes can find applications in many branches of physics, including, but not limited to, lasing and ultrasensitive biosensors. Our results and methods are quite general and they can be applied to a variety of areas in wave physics.

Acknowledgements

The authors also are thankful for the financial support from National Natural Science Foundation of China (Grants No. 11674130, No. 91750110, and No. 11704156) and Natural Science Foundation of Guangdong Province, China (Grants No. 2016A030306016 and No. 2016TQ03X981).

References

[1] A. I. Kuznetsov, A. E. Miroshnichenko, M. L. Brongersma, Y. S. Kivshar, B. Luk'yanchuk, Optically resonant dielectric nanostructures, *Science* 354: aag2472,2016.

[2] A. E. Miroshnichenko, A. B. Evlyukhin, Y. F. Yu, R. M. Bakker, A. Chipouline, A. I. Kuznetsov, B. Luk'yanchuk, B. N. Chichkov, and Y. S. Kivshar, Nonradiating anapole modes in dielectric nanoparticles, *Nat. Commun*. 6:8069,2015.

[3] T. Feng, Y. Xu, W. Zhang, and A. E. Miroshnichenko, Ideal magnetic dipole scattering, *Phys. Rev. Lett*. 118:173901,2017.

[4] S. Fan and J. D. Joannopoulos, *Phys. Rev. B* 65:235112,2002.

[5] Y. He, G. T. Guo, T. H. Feng, Y. Xu, and A. E. Miroshnichenko, Toroidal dipole bound states in the continuum, *Phys. Rev. B* 98, 161112(R),2018.

[6] N. Papasimakis, V. A. Fedotov, V. Savinov, T. A. Raybould, and N. I. Zheludev, Electromagnetic toroidal excitations in matter and free space, *Nat. Mater*. 15: 263–271,2016.

Asymmetric to symmetric line-shape transition of guided-mode resonance enabled by cross-polarization filtering

Jiaxin Lv, Jicheng Jin, Xuefan Yin, and Chao Peng*

State Key Laboratory of Advanced Optical Communication Systems and Networks, Peking University, Beijing, China
*Corresponding author, E-mail: pengchao@pku.edu.cn

Abstract

The guided-mode resonance in photonic crystal slab, also known as bound state in the continuum (BIC), usually exhibits as sharp asymmetric Fano profile owing to the interaction between the discrete localized state and the continuum state. The transition from asymmetric Fano lineshape to symmetric Lorentz lineshape could be achieved by suppressing this non-resonance continuum state. In this work, we demonstrate a measurement technique for this purpose. Nearly symmetric lineshape is observed and we utilize it as thermo-optic phase shifter.

1. Introduction

It is well-known that the guided-mode resonance (GMR) in photonic crystal (PhC) slab behaves as Fano resonance because of the inteference between the directly reflected light and the radiation of resonance [1][2]. From physics point of view, the GMR is essentially a photonic bound state in the continuum (BIC), an ubiquitous pheomenon that exists in many wave systems. The reflected light only carries trivial information, and hence, usually becomes an obstruction to characterize the resonance mode itself which should be in symmetric Lorentz lineshape. In this work, we demonstrate a measurement technique that suppresses the reflections beyond from optical resonance, by applying two orthogonal aligned polarziers. Almost symmetric lineshape has been observed, showing the transition from Fano resonance to Lorentz resonance.

Further, we demonstrate a novel phase manipulation functionality based on the GMR in PhC. Specifically we adopt a pair of micro-heaters to modify the refractive index of the PhC area, and hence, the resonance peak moves thermal-optically and the phase of returned light also varies. About ~1.2π phase shift is directly observed from the shifting of fringes in the interference patterns by using Michelson interferometer.

2. Principle

The principle of lineshape transition is described as following. A normalized Fano profile can be written as:

$$I = \frac{1}{1+q^2}\frac{(\varepsilon+q)^2}{\varepsilon^2+1} \qquad (1)$$

Where ε refers to the normalized frequency and q is a shape parameter. Fig.1 (a) shows the degree of symmetry profile changes as q varies, owing to the relative strength between the localized and the continuum state [3]. In such model, the complex amplitude is given as:

$$A = \frac{1}{\sqrt{1+q^2}}\frac{j(\varepsilon+q)}{j\varepsilon+1} \qquad (2)$$

Considering a realistic Fano resonance in the PhC slab, the quantities A and q depend on the transmission and reflection of the slab [1], as:

$$A = \frac{jr(\varepsilon+\frac{t}{r})}{j\varepsilon+1}, q = \frac{t}{r} \qquad (3)$$

It can be noticed that the phase changes 2π for asymmetric lineshape and π for symmetric lineshape, when ε changes from -∞ to +∞.

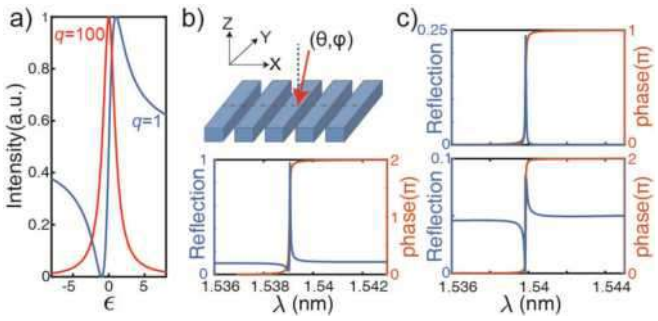


Figure 1. (a) Fano resonance with different q. The profile is sharply asymmetric when q=1 and becomes quite symmetric when q=100 since the localized state hardly couples with the continuum state; (b) Fano resonance in PhC. S-polarized incident light θ =1.14°; (c) Incident light θ =1.14°, φ =0.57°.

3. Measurement setup

The measurement system for high-Q resonance observation is schematically illustrated in Fig.2. A tunable laser working at 1550 nm wavelength generates an incident light which goes through the objective lens firstly and shines on the PhC sample. The reflected light is collected by the same objective lens, transformed by a group of 4F lens systems, and then imaged onto the CCD camera. The resonance

spectrum is measured by a high-sensitive photodiode (PD) while precisely sweeping the incident wavelength [4].

Since we are expecting to observe high-Q resonance, its radiation power is quite weak and easily immersed into background noise. The optical surfaces in the measurement system, such as the lens surfaces (objective lens surface in particular), bottom surface of the SOI slab, also contribute unwanted residual reflections that deteriorate the resonance signal. Such reflections can be effectively suppressed by using a "cross-polarization-filtering" technique. Specifically, since the reflections almost keep the same polarization as the incidence while the optical resonance itself doesn't. Two perpendicularly aligned polarizers stop most of the reflections but let part of resonance pass. An almost symmetric, Lorentz-shape-like resonance peak is observed, which represents the resonance property directly.

The phase response can also be measured by using such setup. As shown in Fig.2, the incidence is split by the beam splitter (BS1). One part is reflected by a gold mirror, regarded as "reference light", the other part returns from the sample, and denoted as "signal light". Obviously, those two beams form a Michelson interferometer. Interference fringes can be observed at the CCD to characterize of their phase difference.

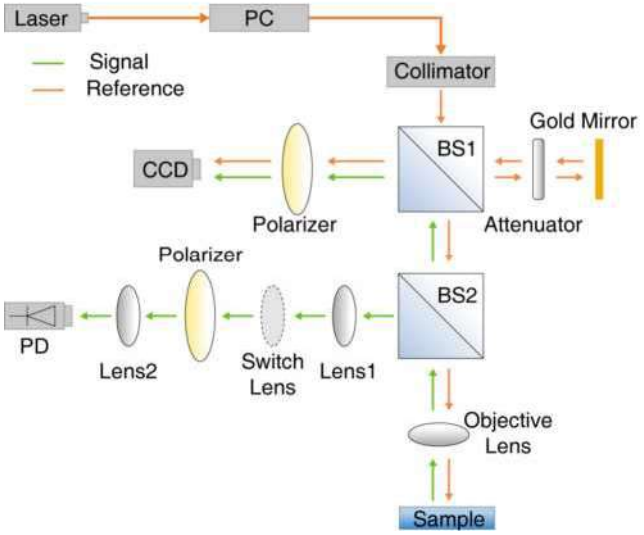


Figure 2. Schematic of the measurement setup.

4. Results

We fabricate the sample as shown in Fig.3 (a). It is an one-dimensional grating lying on silicon-on-insulator (SOI) wafer and a pair of S-shape metal strips working as micro-heaters [4]. The grating contains 200 bars and in footprint of 110 μm × 300 μm. Metal micro-heaters are deposited by 25 nm of titanium and 60 nm of gold. By turning the direction of polarizers, an almost symmetric Lorentz lineshape is obtained from measurement setup and Q-factor is estimated as ~12000 (Fig.3.b).

The refractive index of PhC is modified as heating. When the voltage turns from 0 V to 5.4 V, the resonance peak shifts from 1539.72 nm to 1540.66 nm, which corresponds to ~1.2π phase shift, extracted from the moving of interference fringes.

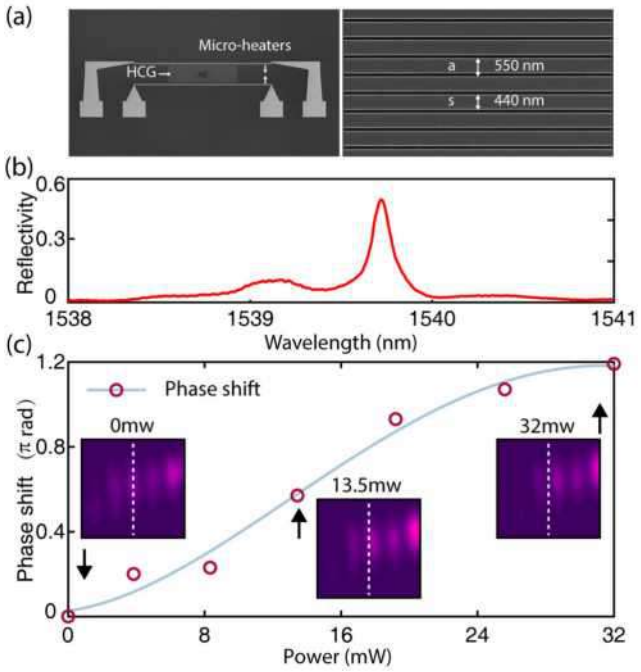


Figure 3. (a) SEM images of PhC device; (b) Reflectivity spectrum; (c) Phase response under heating.

5. Conclusions

We demonstrate a practically useful technique to suppress the residual reflections beyond from guided-mode resonance, and the lineshape transits from asymmetric Fano-like to symmetric Lorentz-like. A thermal-optic phase shifter based on PhC is realized. Such method characterizes the optical resonance itself, and could be useful in many related fields.

Acknowledgements

This work was supported by the National Natural Science Foundation of China (NSFC) under grant No. 61575002, and by the State Key Laboratory of Advanced Optical Communication Systems and Networks, China.

References

[1] Fan, S. et al. Temporal coupled-mode theory for the Fano resonance in optical resonators. J. Opt. Soc. Am. A 20, 569 (2003).

[2] Limonov, M. F. et al. Fano resonances in photonics. Nat. Photon. 11, 543 (2017).

[3] Galli, M. et al. Light scattering and Fano resonances in high-Q photonic crystal nanocavities. Appl. Phys. Lett. 94, 071101 (2009).

[4] Lv, J. et al. Demonstration of a thermo-optic phase shifter by utilizing high-Q resonance in high-index-contrast grating. Opt. Lett. 43, 827 (2018).

Light-Matter Interaction in Antenna-based Infrared Nanocavities

Andrea Toma*

Istituto Italiano di Tecnologia, Via Morego 30, 16163 Genova, Italy
*corresponding author, E-mail: andrea.toma@iit.it

Abstract

Antenna-based resonant nanocavities can efficiently couple to other excitations/quasi particles of similar energy, giving rise to strong signal enhancement in the infrared spectral domain. In this framework, Fano-like interferences can be successfully exploited for promoting mid-infrared and THz spectroscopic studies of molecules and/or nanomaterials at extremely low concentrations.

1. Introduction

Optical antennas are playing a fundamental role in many applications ranging from enhanced spectroscopies [1] to in vivo molecular imaging [2] and non-linear interactions. Their success relies on the strong field enhancement generated in the close proximity of the structure, when the excitation of plasmon resonances is promoted. A significant number of experimental investigations have been carried out in the last decades to completely describe the electromagnetic (EM) properties of metallic structures such as nanostars, bow-tie antennas, nanoshells etc., which are now efficiently employed to address practical questions in life sciences and nano-medicine.
Within this context, infrared resonant dipole antennas coupled through nanogaps [3-5] have emerged as promising architectures for improving infrared light-matter interaction, pushing the detection limit towards the single-few units.

2. Discussion

Here we would like to report our investigations on antenna enhanced infrared spectroscopy, spanning from mid-infrared detection of medically relevant molecular species to THz sensing of nano-localized quantum dots [3,5]. In both cases, when the vibrational excitation is efficiently coupled to the nanostructure resonance, the combined system shows a clear interference feature in the extinction spectra, which can be clearly ascribed to a Fano-like hybridization.

Specifically designed nanoantenna dimers with different interparticle distances (down to the 10 nm range) were prepared by electron beam lithography and optically characterized using a Fourier-transform IR microscope, coupled to a thermal glow-bar source -for the mid-IR spectral window- or to synchrotron light (ELETTRA Trieste) in the case of THz measurements.

The efficiency of antenna-based platform in enhancing infrared spectroscopy has been further improved by decoupling the antenna structures from the underlying substrate, thus allowing a more pronounced EM field concentration and spatial overlap with the analyte/ nanomaterial under investigation [6]. The advantages of a "free-standing" configuration for sensing applications have been demonstrated by monitoring the vibrational signal of test molecules, achieving a signal enhancement of an order of magnitude higher than the planar counterparts.

Finally, the conjugation between vibrational modes and confined optical resonances has been extended towards the strong coupling regime [5], where intensified light-matter interaction promotes the formation of new vibro-polariton bands, which no longer belong to light or matter in a separate way.

References

[1] C. D'Andrea, J. Bochterle, A. Toma, et al. Optical Nanoantennas for Multiband Surface-Enhanced Infrared and Raman Spectroscopy, *ACS Nano* 7: 3522, 2013.

[2] H. Xin, B. Namgung, L. P. Lee, Nanoplasmonic optical antennas for life sciences and medicine, *Nat. Rev. Mats.* 3: 228, 2018.

[3] A. Toma, S. Tuccio, M. Prato, et al. Squeezing Terahertz Light into Nanovolumes: Nanoantenna Enhanced Terahertz Spectroscopy (NETS) of Semiconductor Quantum Dots, *Nano Lett.* 15: 386, 2015.

[4] C. Huck, F. Neubrech, J. Vogt, A. Toma, et al. Surface-Enhanced Infrared Spectroscopy Using Nanometer-Sized Gaps, *ACS Nano* 8: 4908, 2014.

[5] X. Jin, A. Cerea, G. C. Messina, et al. Reshaping the phonon energy landscape of nanocrystals inside a terahertz plasmonic nanocavity, *Nat. Commun.* 9: 763, 2018.

[6] C. Huck, A. Toma, F. Neubrech, et al. Gold Nanoantennas on a Pedestal for Plasmonic Enhancement in the Infrared, *ACS Photonics* 2: 497 2015.

Theory of Fano Resonances in the electromagnetic scattering from two-dimensional bodies.

Carlo Forestiere[1], Giovanni Gravina[1,2],Giovanni Miano[1] Mariano Pascale [1,3], Roberto Tricarico[1,3]

[1] Università degli Studi di Napoli Federico II, via Claudio 21, Napoli, 80125, Italy
[2]Italian Air Force Academy, Via San Gennaro, Agnano 30, 80078 Pozzuoli Napoli
[3]ICFO Institut de Cincies Fotniques, 08860 Castelldefels, Barcelona, Spain
*corresponding author, E-mail: carlo.forestiere@unina.it

Abstract

The electromagnetic modes and the resonances of homogeneous, finite size, two-dimensional bodies are examined in the frequency domain by a rigorous full-wave approach. The presence of vortex current modes is demonstrated. The presence of Fano resonances in the scattering from a Si disk of size comparable to the incident wavelength is demonstrated and the interferencing mode behind them are shown.

1. Introduction

In the last ten years, the rise of two-dimensional materials has attracted a great amount of interest in the field of plasmonics and photonics. In terms of electrical properties, they range from the insulating hexagonal boron nitride and semiconducting transition metal dichalcogenides, to semi metallic graphene. In this work, the electromagnetic modes and the resonances of homogeneous, finite size, two-dimensional bodies are examined in the frequency domain by a rigorous full wave approach based on an integro-differential formulation of the electromagnetic scattering problem. Open and closed surfaces are considered.

2. Formulation of the problem

We use the concept of material independent modes [1, 2]. The current modes and the corresponding eigen-conductivities are solution of a linear eigenvalue problem. The eigen-conductivity σ_n corresponding to the current mode $\mathbf{J}_n$ is the value that the surface conductivity of the body, normalized to the vacuum admittance $1/\zeta_0$, should have so that the current mode $\mathbf{J}_n$ is a free source solution of the Maxwell equations. The current modes and the corresponding eigen-conductivities only depend on the geometry of the body and on the frequency, they are independent of the surface conductivity σ_n. We found that the real part of the eigen-conductivity is proportional to the radiation losses of the current mode; hence, it is always negative. The imaginary part is proportional to the difference between the time average of the magnetic energy and the time average of the electric energy of the mode hence it may be either negative or positive, depending on the shape of the 2D body and on the normalized body size kl_c, where l_c is the characteristic length of the body and $k = 2\pi/\lambda$. The existence of vortex current modes in addition to source-sink current modes (no whirling modes), which describe plasmonic oscillations, is demonstrated.

The source-sink current modes, which in the long wavelength limit ($kl_c \to 0$) are irrotational, are characterized by a number of sources and sinks of the field lines that is conserved as the ratio between the characteristic linear dimension of the body and the wavelength kl_c increases. Similarly, the vortex current modes, which in the long wavelength limit are solenoidal, are characterized by a number of vortexes of the field lines that is conserved. Important topological features of the current modes, such as the number of sources and sinks, the number of vortices, the direction of the vortices are preserved as the size of the body and the frequency vary. The surface current density induced on the body by an external excitation $\mathbf{E}_{inc}$ is represented in terms of the current modes

$$\mathbf{J} = \sum_{n=1}^{\infty} \frac{\sigma_n}{\sigma_n - \zeta_0 \sigma} \langle \mathbf{J}_n^* | \sigma \mathbf{E}_{inc} \rangle \mathbf{J}_n \qquad (1)$$

The expansion coefficient of each current mode is equal to $\sigma_n/(\sigma_n - \zeta_0\sigma) < \mathbf{J}_n^* | \mathbf{E}_{inc} >$. The resonant frequency of the mode is the frequency for which $\sigma_n/(\sigma_n - \zeta_0\sigma)$ is maximum. This expansion reveals the important physical mechanisms involved in the electromagnetic scattering and can greatly improve the way it is understood and optimized. For instance, unlike the source-sink current modes, in open surfaces the vortex current modes can be resonantly excited only in materials with positive imaginary part of the surface conductivity. Illustrative examples for open surfaces (disk, equilateral triangle, rectangle) and a closed surface (spherical surface) will be given. The scattering efficiency and the amplitude of the near electric field of a disk with either positive or negative imaginary part of the surface conductivity will be presented and analysed, the presence of Fano resonances will be highlighted.

3. Results and Discussion

Now an example of material with positive imaginary part of the surface conductivity is considered: a dielectric thin disk with relative permittivity $\varepsilon_r = 16$ (silicon), radius $l =$

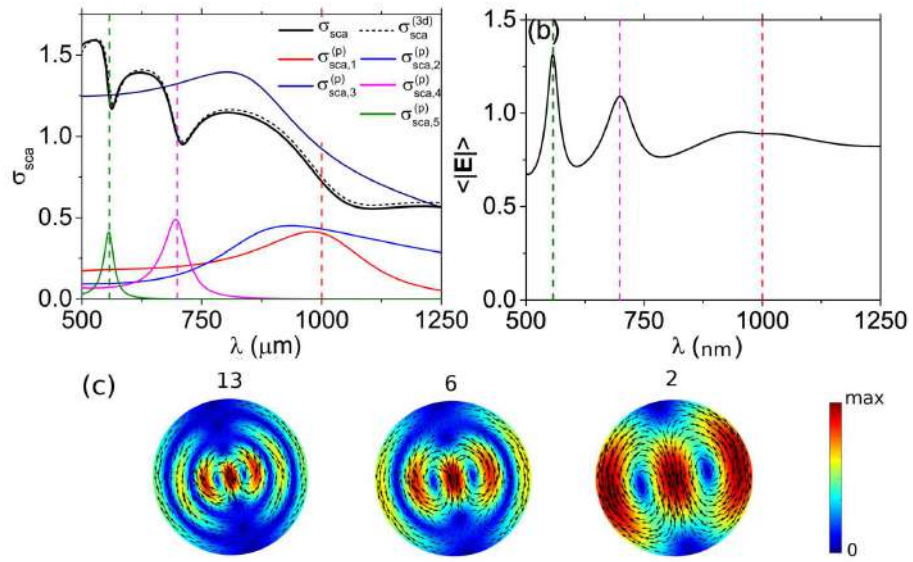


Figure 1: Scattering efficiency (a) and averaged near field enhancement (b) of a silicon thin disk with radius $l = 500nm$ and thickness $\Delta = 19.2nm$, illuminated by a linearly polarized plane wave propagating normally to the disk. The vertical dashed lines indicate the positions of the resonant wavelengths of the three vortex modes shown in panel (c). The partial scattering cross sections of the most important current modes that contribute to the scattered field are shown: $\sigma^{(p)}_{v,2}$, $\sigma^{(p)}_{v,2}$, $\sigma^{(p)}_{v,2}$ are the partial scattering efficiency of the three resonant vortex current modes shown in (c), while $\sigma^{(p)}_{ss,1}$,$\sigma^{(p)}_{ss,1'}$ are the partial scattering efficiencies of the off resonant first source-sink current mode, which is double degenerate. The dashed line in the panel (a) indicates $\sigma^{(3d)}_{sca}$ the values of the scattering efficiency obtained by using a three dimensional full wave numerical code.

500 nm and thickness $\Delta = 19.2$ nm . The electromagnetic field scattered by it in the wavelength range from $0.5\ \mu m$ to $1.25\ \mu m$ is analysed. The incident electromagnetic field is a plane wave linearly polarized, propagating normally to the disk. Since the disk thickness t is much smaller than its radius and the wavelength, the thin disk may be represented as a circle with equivalent surface conductivity given by

$$\zeta_0 \sigma = x \left(\frac{\Delta}{l} \right) (\varepsilon_r - 1)\, i \tag{2}$$

Fig. 1 (a) shows the scattering efficiency (black line). A very good agreement is found between the scattering cross sections obtained by using the expression 1 and the scattering cross section obtained by means of a full wave three-dimensional numerical code. This fact again validates the solution 1 and the computation of the current modes and the eigen-conductivities. Several current modes contribute to the scattered electromagnetic field. The vertical dashed lines in Fig. 1 (a) indicate the values of the resonant wavelengths of the vortex current modes shown in Figure 1 (c), $\lambda_2 = 980nm$, $\lambda_6 = 696nm$ and $\lambda_{13} = 556nm$. Besides these resonant modes, the first two source-sink current modes of the disk contribute to the scattered field. These two degenerate modes are off resonance because their eigen-conductivities are bounded in the region of complex plane with the imaginary part belonging to the interval $(-2.95, 0.238)$ regardless of l/λ , while the imaginary part of $\zeta_0\sigma$ varies between 1.45 and 3.61. Even if these modes are off resonance, their coupling amplitudes with the plane wave are very high because they have a strong electric dipole moment. To highlight the contribution of the most important current modes, Figure 1(a) also shows the partial scattering efficiencies defined as the scattering efficiency obtained by considering only one mode at a time. The partial scattering efficiencies $\sigma^{(p)}_{v,2}$, $\sigma^{(p)}_{v,6}$, $\sigma^{(p)}_{v,13}$ are relevant to the three vortex current modes shown in 1 (c); $\sigma^{((p)}_{ss,1}$ and $\sigma^{(p)}_{ss,1'}$ are, instead, the partial scattering efficiency of the first source-sink current modes. The destructive interferences between the broad source-sink modes and one of the narrow vortex current mode shown in 1 (c) give rise to the Fano resonances around $\lambda = 1106nm$, $\lambda = 711nm$ and $\lambda = 563nm$. Figure 1 (b) shows the averaged amplitude of the electric field on the disk surface. The vertical dashed lines always indicate the values of the resonant wavelengths of the vortex current modes shown in Figure 1 (c).

References

[1] C. Forestiere, G. Miano, Material-independent modes for electromagnetic scattering, *Physical Review B* 94 (20), 201406, 2016.

[2] C. Forestiere, G. Gravina, G. Miano, M. Pascale, R. Tricarico, Electromagnetic modes and resonances of two-dimensional bodies *arXiv preprint arXiv:1811.03857*, 2018

Bound States and Resonances in Lattice Models

Ya Yan Lu

Department of Mathematics,
City University of Hong Kong, Kowloon, Hong Kong
corresponding author, E-mail: mayylu@cityu.edu.hk

Abstract

In this paper, we develop a general theory for bound states and resonances in locally distorted infinite or semi-infinite tight-binding lattice models. These models can be realized as waveguide arrays. We propose a finite linear matrix eigenvalue problem for computing all bound states and resonant modes. For bound states in the continuum, we establish a necessary and sufficient condition for their existence, and study their robustness with respect to structural perturbations.

1. Introduction

There is currently a significant interest in studying optical bound states in the continuum (BICs). Strong resonances appear when system parameters are slightly perturbed from their perfect values for the existence of a BIC. Applications of the BICs are either based on enhanced local fields caused by the strong resonances or the far-field (collapsing Fano) resonance features in transmission, reflection or other spectra. Infinite or semi-infinite tight-binding lattice models with local distortions are useful discrete models for a number of physical applications. In particular, they can be realized as waveguide arrays and have been used in theoretical and experimental studies on BICs [1, 2, 3, 4]. These studies are concerned with a few specific and relatively simple configurations. To the best of our knowledge, there is no general theory about BICs on such lattice models. Although most current works on optical BICs are related to physical structures that can only be analyzed by solving Maxwell's equations rigorously, the study of lattice models helps to gain physical insight and provides useful guidelines for analyzing more complicated structures.

2. Theory

For a locally distorted semi-infinite tight-binding lattice, the governing equation can be written as

$$A\mathbf{x} = \lambda\mathbf{x}, \tag{1}$$

where $\mathbf{x} = [x_1, x_2, ...]^T$ is an infinite vector, $A = \begin{bmatrix} A_n & L \\ L^T & T \end{bmatrix}$, A_n is an $n \times n$ real symmetric matrix, L is an $n \times \infty$ matrix with only one nonzero entry $L_{n1} = 1$, and T is an infinite tridiagonal matrix with 1's immediately below and above the main diagonal. That is,

$$L = \begin{bmatrix} 0 & 0 & \dots & \dots \\ \vdots & \vdots & & \\ 0 & 0 & \dots & \dots \\ 1 & 0 & \dots & \dots \end{bmatrix}, \quad T = \begin{bmatrix} 0 & 1 & & \\ 1 & 0 & 1 & \\ & 1 & \ddots & \ddots \\ & & \ddots & \ddots \end{bmatrix}.$$

The matrix T corresponds to a semi-infinite tight-binding lattice with identical hopping rates (with are normalized as 1) and identical potentials (which become 0 after a shift to λ). From Eq. (1), one gets $x_{j+2} + x_j = \lambda x_{j+1}$ for $j \geq n$. For $\lambda \in (-2, 2)$, we have propagating solutions $x_j = C_1\mu^j + C_2\mu^{-j}$ for a complex μ on the unit circle. If μ is chosen such that μ^j represents an incoming wave, then a scattering problem can be defined by setting $C_1 = 1$. The coefficient C_2 is an unknown related to the reflection coefficient. The continuous spectrum is the interval $[-2, 2]$.

A general eigenmode of Eq. (1) is required to satisfy

$$x_j = C_2\mu^{-j} = x_n\mu^{n-j}, \quad j \geq n, \tag{2}$$

for any μ satisfying $\mu^2 + 1 = \lambda\mu$. A bound state is an eigenmode such that $\sum |x_j|^2 < \infty$. For the special case $x_n = 0$ (thus $x_j = 0$ for all $j \geq n$), the eigenmode is a compact bound state. If $x_n \neq 0$, a (non-compact) bound state must satisfy $|\mu| > 1$. A resonant mode is always non-compact ($x_n \neq 0$), and it corresponds to a complex μ such that μ^{-j} is an outgoing wave. It can be shown that the eigenmodes satisfy the following matrix eigenvalue problem:

$$\begin{bmatrix} A_n & -J^T \\ J & \mathbf{0} \end{bmatrix} \mathbf{u} = \mu\mathbf{u}, \tag{3}$$

where $J = [I_{n-1}, \mathbf{0}]$ is an $(n-1) \times n$ matrix and it can be obtained by adding a zero column to the $(n-1) \times (n-1)$ identity matrix. The eigenvalue problem (3) has $2n-1$ eigenvalues, since the size of the matrix in the left hand side is $(2n-1) \times (2n-1)$. A zero eigenvalue of Eq. (3) does not correspond to a "physical" eigenmode that must satisfy Eq. (2). Non-zero eigenvalues of Eq. (3) can be classified as: (1) BICs, (2) compact bound states outside the continuum (BOCs), (3) non-compact BOCs, (4) improper modes, (5) resonant modes, and (6) time-reversal of resonant modes.

Since the matrix in Eq. (3) is real, the eigenvalues μ are either real or complex conjugate pairs. A complex conjugate pair $\{\mu, \overline{\mu}\}$ on the unit circle (of the complex μ plane)

corresponds to one BIC. It has to be compact and the corresponding λ is in $(-2, 2)$. A complex conjugate pair inside the unit circle corresponds to a resonant mode and its time-reversal. The time-reversal of a resonant mode is an eigenmode with an incoming wave from infinity. These modes are always non-compact and the corresponding λ is complex. It can be proved that Eq. (3) cannot have a complex conjugate pair outside the unit circle. A real eigenvalue μ satisfying $|\mu| > 1$ always gives a bound state. In that case, $\lambda = \mu + 1/\mu$ is real and $|\lambda| > 2$. If the corresponding eigenvector gives $x_n \neq 0$, the eigenmode is a non-compact BOC. If $x_n = 0$, it is a compact BOC. A real eigenvalue μ in $(-1, 1)$ must be classified according to x_n. If $x_n \neq 0$, it corresponds to an improper mode that grows exponentially as $j \to \infty$. If $x_n = 0$, it is a compact BOC.

Compact eigenmodes must satisfy

$$A_n \mathbf{x}_n = \lambda \mathbf{x}_n, \quad x_n = 0, \tag{4}$$

where $\mathbf{x}_n = [x_1, x_2, ..., x_n]^T$. Both BICs (which are always compact) and compact BOCs satisfy Eq. (4). If we let

$$A_n = \begin{bmatrix} B & \mathbf{c} \\ \mathbf{c}^T & d \end{bmatrix}, \quad \mathbf{x}_n = \begin{bmatrix} \mathbf{y} \\ x_n \end{bmatrix}, \quad \mathbf{y} = \begin{bmatrix} x_1 \\ \vdots \\ x_{n-1} \end{bmatrix}.$$

then the compact modes satisfy

$$B\mathbf{y} = \lambda \mathbf{y}, \quad \mathbf{c}^T \mathbf{y} = 0. \tag{5}$$

Using Eq. (5), the compact modes can be easily solved. If $\lambda \in (-2, 2)$, the solution is a BIC, and if $|\lambda| > 2$, it is a compact BOC. It is interesting to note that if the matrix B (or A_n) has a multiple eigenvalue, then compact modes always exist. Since B is symmetric, the eigenspace corresponding to a multiple eigenvalue has dimension larger than 1, and it is always possible to choose a non-zero vector $\mathbf{y}$ in the eigenspace such that $\mathbf{c}^T \mathbf{y} = 0$. For a multiple eigenvalue of A_n, it is always possible to choose a vector in the eigenspace with zero entry at the bottom. The BICs of [2] and [4] are examples of multiple eigenvalues.

The BIC of [3] is symmetry-protected. We can use Eq. (5) to understand symmetry-protected BICs (and compact BOCs). Let P be a real $(n-1) \times (n-1)$ matrix such that $P^2 = I$, we say the structure is symmetric if

$$PB = BP, \quad P^T \mathbf{c} = \mathbf{c}. \tag{6}$$

In that case, the eigenvectors of matrix B must satisfy (or can be chosen to satisfy, for multiple eigenvalues) either $P\mathbf{y} = \mathbf{y}$ (symmetric) or $P\mathbf{y} = -\mathbf{y}$ (anti-symmetric). An anti-symmetric mode corresponds to a symmetry-protected bound state. Since $\mathbf{c}^T \mathbf{y} = \mathbf{c}^T P P \mathbf{y} = (P^T \mathbf{c})^T (P\mathbf{y}) = -\mathbf{c}^T \mathbf{y}$, we have $\mathbf{c}^T \mathbf{y} = 0$. As usual, the symmetry-protected compact bound states are robust to symmetry-preserving perturbations. That means, if we perturb B and $\mathbf{c}$ such that Eq. (6) remains valid, then we have an anti-symmetric compact bound state with a slightly different λ.

In general, a perturbation of the structure will turn a BIC to a resonant mode. Using Eq. (3), the complex μ of the resonant mode can be calculated. If the strength of the perturbation is δ, the Q-factor of the resonant mode is usually $O(1/\delta^2)$. However, if we add one parameter depending on δ, it is possible to preserve the BIC. More precisely, assuming the structure described by matrix B and vector $\mathbf{c}$ has a BIC with eigenvector $\mathbf{y}$ and eigenvalue $\lambda \in (-2, 2)$, and if B is perturbed to $B + \delta B_1$ where B_1 is a real symmetric matrix and $\mathbf{y}$ is not an eigenvetor of B_1, $\mathbf{c}_1$ is a given vector such that $\mathbf{c}_1^T \mathbf{y} \neq 0$, then for small but arbitrary δ, there is a β, depending on δ, such that the system corresponding to $B + \delta B_1$ and $\mathbf{c} + \beta \mathbf{c_1}$ also has a BIC. This is quite similar to propagating BICs on periodic structures [5]. In that case, when the structure is perturbed (preserving the required symmetries), a BIC continue to exist, but only for a slightly different Bloch wavenumber.

3. Conclusion

For locally distorted tight-binding lattice models, we developed a general theory for computing and analyzing bound states (in or outside the continuum) and resonant modes. Formulated as a finite matrix eigenvalue problem, all modes can be easily calculated and BICs can be easily obtained. Based on the new formulation, we developed perturbation theories for BICs. In particular, special perturbations that preserve the BICs are obtained.

Acknowledgement

The author is partially supported by the Research Grants Council of Hong Kong Special Administrative Region, China (CityU 11304117).

References

[1] K.-K. Voo and C. S. Chu, Localized states in continuum in low-dimensional systems, *Phys. Rev. B* 74: 155306, 2006.

[2] S. Longhi, Bound states in the continuum in a single-level Fano-Anderson model, *Eur. Phys. J. B* 57: 45–51, 2007.

[3] Y. Plotnik, O. Peleg, F. Dreisow, M. Heinrich, S. Nolte, A. Szameit, and M. Segev, Experimental observation of optical bound states in the continuum, *Phys. Rev. Lett.* 107: 183901, 2011.

[4] S. Weimann,Y. Xu, R. Keil,A. E. Miroshnichenko, A. Tünnermann, S. Nolte, A. A. Sukhorukov, A. Szameit, and Y. S. Kivshar, Compact surface Fano states embedded in the continuum of waveguide arrays, *Phys. Rev. Lett.* 111: 240403, 2013.

[5] L. Yuan and Y. Y. Lu, Bound states in the continuum on periodic structures: perturbation theory and robustness, *Opt. Lett.* 42: 4490–4493, 2017.

Reaching dark mode condition in a system of gain-loss assisted coupled resonators

A. Lupu[1*], V. Klimov[2], H. Benisty[3], A. Uskov[2], and A. Ramdane[1]

[1]Centre de Nanosciences et de Nanotechnologies, CNRS, Univ. Paris-Sud, Université Paris-Saclay, C2N – 10 Boulevard Thomas Gobert – 91120 Palaiseau cedex, France

[2] P.N. Lebedev Physical Institute, Russian Academy of Sciences, 119991 Moscow, Russia

[3] Laboratoire Charles Fabry de l'Institut d'Optique, CNRS, Univ. Paris Saclay, 2 Ave Augustin Fresnel, 91127 Palaiseau Cedex, France

*corresponding author, E-mail: anatole.lupu@c2n.upsaclay.fr

Abstract

A generic model of two antennas type dissimilar resonators coupled both via near-field and far-field coupling with active gain and/or loss media is considered. Conditions required for hitting the dark mode operation are established. It is shown that tuning the material gain level is effective in cancelling the detrimental effect of deviations from nominal values of resonant elements unavoidably caused by fabrication imperfections. The considered approach can be used for the implementation of high-contrast tunable metasurfaces.

1. Introduction

One of the most promising applications of metallic nano-resonators is their use as sensors for the detection of biological or chemical species adsorbed on their surface. The sensing detection limit and accuracy is expected to be greatly enhanced when operating at the exceptional point (EP) [1,2] or by using narrow width spectral features associated with Fano-type resonance occurring in the near vicinity of a dark mode (DM) [3]. Experimentally however, achieving operation right at the EP or DM is far from being trivial [4,5]. Unavoidable fabrication imperfections result in deviation of the geometrical size of nanoresonators and of their spatial positioning off nominal ones. Adjunction of a fine tuning mechanism in the system is then required. Conventional tuning mechanisms rely on the variation of the resonant elements refractive index, achieved either thanks to micro-mechanical actuators or through electrically addressable means such as electro-refractive effect, charge density variation and temperature change. The aim of the current contribution is to explore a different approach, where the tuning mechanism relies on the variation of the imaginary part of the refractive index that can be achieved through gain or absorption modulation in resonant nano-resonators.

2. Couple mode theory model

To this end we consider a system of two coupled antennas type resonators with resonant frequencies ω_1 and ω_2 and material gain or absorption rate g_1 and g_2, as well as radiation decay rates γ_1 and γ_2 [6]. The scattering matrix of such system is:

$$S = C + iV\left[\omega I - H_{eff}\right]^{-1} V^{\dagger} \qquad (1)$$

where C is the background scattering which does not interact with resonator, V is the radiation-resonator coupling. The effective Hamiltonian H_{eff} can be described as:

$$H_{eff} = \begin{bmatrix} \omega_1 & \kappa \\ \kappa^* & \omega_2 \end{bmatrix} + i\begin{bmatrix} \gamma_1 & \gamma_0 \\ \gamma_0^* & \gamma_2 \end{bmatrix} + i\begin{bmatrix} g_1 & 0 \\ 0 & g_2 \end{bmatrix} \qquad (2)$$

It is assumed that the coupling coefficient κ related to near-field evanescent tunneling is real, while the radiative (far-field) coupling to the environment provided by $i\gamma_0 = i\sqrt{\gamma_1\gamma_2}$ is imaginary. The eigenvalues $\omega_{\pm}$ of H_{eff} are poles of the S scattering matrix and correspond to sharp features in the spectral response. While most of the parameters (ω_i, γ_j, κ) entering in H_{eff} can be engineered by design, they can take only fixed values especially in metallic nano-resonators. Once fabricated it is not possible to adjust any more their frequency, their radiative decay rate or coupling strength between them. The only experimentally available degrees of freedom are the incident light frequency and also the material gain (loss) gain level g_j that can be varied either by means of electrical current injection or optical pumping.

3. Results and discussion

3.1. Operation at the exceptional point

The first point of our analysis concerns examination of the requirements for attaining an EP. The real and imaginary parts of ω_+ and ω_- eigenvalues coalesce at the EP when the following conditions are simultaneously fulfilled:

$$\delta = \omega_1 - \omega_2 = -2\gamma_0 \text{ and } \kappa = \left(\gamma_1 + g_1 - \gamma_2 - g_2\right)/2 \qquad (3)$$

As it can be seen, the target resonators detuning δ depends solely on the radiative coupling. Thus, δ cannot be adjusted through gain variation to attain exactly the EP. This is at variance with the use of gain to bring the κ-induced splitting to zero at an EP in the PT-symmetry context. In addition, operation at the EP is also a poor option in terms of the large gain it requires. A high quality factor resonance at the EP implies $\mathrm{Im}(\omega_{\pm}) \to 0$. This only occurs at the condition $\gamma_1 + g_1 = \gamma_2 + g_2 = 0$. In other words, the gain of each resonator should exactly compensate its radiative losses. As

will be shown below, DM operation is more favorable since it requires much less gain (temporal gain, in Haus' theory).

3.2. DM operation without threshold gain condition

The DM condition corresponds to the cancellation of the imaginary part of antisymmetric mode [3]. It requires to simultaneously satisfy the condition for resonators detuning:

$$\delta = \frac{\kappa\gamma_0\left(\gamma_1 + g_1 - \gamma_2 - g_2\right)}{\left(\gamma_1\gamma_2 + g_1g_2 + \gamma_1g_2 + \gamma_2g_1\right)} \qquad (4)$$

as well as either of the two conditions of Eq.(5) below:

$$\gamma_1 g_2 + \gamma_2 g_1 + g_1 g_2 = 0 \qquad (5a)$$

$$\kappa^2 + \gamma_1\gamma_2 + \gamma_1 g_2 + \gamma_2 g_1 + g_1 g_2 = 0 \qquad (5b)$$

Eq. (5a) corresponds to the "thresholdless" gain operation for reaching the DM. Indeed, considering that $g_1>0$ is the absorption loss level in the first resonator, it directly follows from Eq. (5a) that the second resonator gain must obey:

$$g_2 = -\frac{\gamma_2 g_1}{\gamma_1 + g_1} \qquad (6a)$$

In the limit of $g_1 << \gamma_1$, $g_2 \to -g_1(\gamma_2/\gamma_1)$. This means that in theory the required gain level g_2 can be arbitrary small, even much lower than the loss g_1, provided that $\gamma_2 << \gamma_1$. Another remarkable feature is that the gain condition given by Eq.(5a) is independent of the coupling strength κ. Though detuning δ between resonators expressed by Eq. (4) is sensitive to κ, its deviation from nominal value can be adjusted through either variation of the gain level g_2 or loss level g_1. This is illustrated by Fig. 1a representing evolution of the real and imaginary parts of eigenvalues $\omega_\pm$ as a function of ω_2 for a fixed ω_1 value and three different values of g_2 [lower, equal or higher than gain g_2 given by Eq. (6a)].

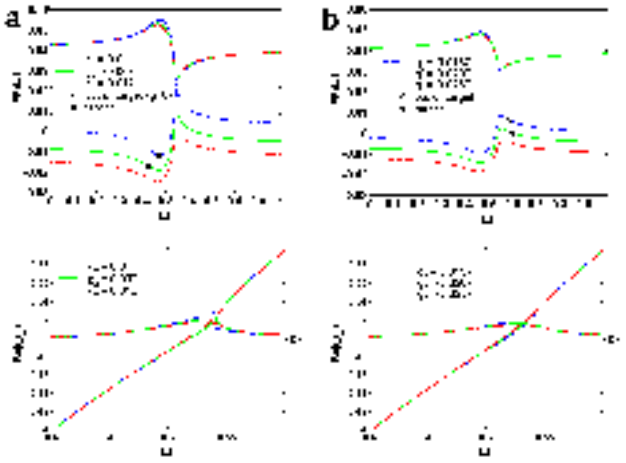


Figure 1: Evolution of $\mathrm{Im}(\omega_\pm)$ and $\mathrm{Re}(\omega_\pm)$ as a function of ω_2 with ω_1=0.5, γ_1=0.03, γ_2=0.015, κ=0.0175; g_1=0.01. Target DM indicated by bold black point. a) "thresholdless" DM regime; b) DM regime with threshold gain condition.

3.3. DM operation with threshold gain condition

The evolution of $\mathrm{Re}(\omega_\pm)$ and $\mathrm{Im}(\omega_\pm)$ as a function of ω_2 for a fixed value of ω_1 and corresponding to the DM regime defined by Eq. 5(b) is shown in Fig. 1(b). In contrast to the previously considered case, the DM condition is now attained at the upper point of the $\mathrm{Im}(\omega_-)$ branch. As follows from Eq. 5(b) this is achieved when:

$$g_2 = -\frac{\kappa^2 + \gamma_1\gamma_2 + \gamma_2 g_1}{\gamma_1 + g_1} \qquad (6b)$$

In the limit $\kappa \to 0$ and $g_1 \to 0$ the lowest "threshold" gain for reaching DM is $g_2 = -\gamma_2$. It corresponds to the compensation by gain of the radiative losses in the second resonator. Note also that same lowest gain $g_2 = -\gamma_2$ can be achieved when $g_1 >> \gamma_1$ while $\kappa \to 0$. Obviously this operation regime in terms of gain "cost", much less favorable than the "thresholdless DM" one, but still more advantageous compared to the operation at the EP.

4. Conclusions

Tunability mechanisms based on gain or loss variation in a system of two coupled antenna-type nano-resonators were considered. Conditions corresponding to the operation in the dark mode regime were identified. It was found that the optimal configuration in terms of lowest gain to be supplied corresponds to a system composed of gain and loss resonators with highly asymmetric radiative rates (γ_2/γ_1) and detuned resonance frequencies. The considered approach can be exploited for the implementation of tunable metasurfaces with high-contrast.

Acknowledgements

Funding by the French Agence Nationale pour la Recherche (project "PARTISYMO", contract number N° ANR-18-CE24-0024-01) is acknowledged by A.L., A.R. and H.B.

References

[1] A. Kodigala, T. Lepetit, and B. Kanté, "Exceptional points in three-dimensional plasmonic nanostructures," Phys. Rev. B 94(20), 201103 (2016).

[2] M. Sakhdari, M. Farhat, & P. Y. Chen, "PT-symmetric metasurfaces: wave manipulation and sensing using singular points," New Journal of Physics 19(6), 065002 (2017).

[3] 3. T. Lepetit, E. Akmansoy, J.-P. Ganne, & J.-M. Lourtioz, "Resonance continuum coupling in high-permittivity dielectric metamaterials," Phys. Rev. B 82, 195307 (2010).

[4] N. A. Mortensen, P. A. D Gonçalves, M. Khajavikhan, D. N. Christodoulides, C. Tserkezis, & C. Wolff, "Fluctuations and noise-limited sensing near the exceptional point of PT-symmetric resonator systems," Optica 10(5), 1342-1346 (2018).

[5] V. Brac de la Perrière, Q. Gaimard, H. Benisty, A. Ramdane, & A. Lupu, "Restoring robust binary switching operation and exceptional point using long-period grating-assisted Parity-Time symmetric couplers," accepted J. Phys. D: Appl. Phys. (doi.org/10.1088/1361-6463/ab11b4)

[6] A. Kodigala, T. Lepetit, and B. Kanté, "Engineering resonance dynamics of plasmon hybridized systems," J. Appl. Phys. 117, 023110 (2015).

Rigorous modal analysis of photonic micro and nanoresonators

Philippe Lalanne[1], Wei Yan[2]

[1]LP2N, Institut d'Optique Graduate School, CNRS, Univ. Bordeaux, 33400 Talence, France
[32]Institute of Power Engineering, Computational Science Research Center, Jeju, Korea
*corresponding author, E-mail: *Philippe.lalanne@institutoptique.fr*

Abstract

The most general motion of a system is a superposition of its normal modes, or eigenstates. For Hermitian system, classical normal mode theory applies. For non-Hermitian systems, presently a lot of progress is done to describe the response of optical micro and nanoresonators in their quasinormal mode basis. We have developed a rigorous modal analysis of electromagnetic resonators with unprecedented generality and report numerical results for the general case of 3D resonators, made of dispersive materials on substrate with guiding layers.

1. Introduction

Modes are central in physics, chemistry ... In optics, modes are self-consistent electromagnetic field distributions in waveguides, optical resonators or in free space (plane waves, Hermite–Gaussian modes …). In waveguide and free space, they are well documented in the literature, as shown by several textbooks on Fourier optics and optical waveguide theory (Vassalo, Snyder & Love, Marcuse, Collin).

We cannot find any textbook on the modal theory of resonators, although nanoresonances play an essential role in current developments in nanophotonics, e.g., optical metasurfaces, integrated optics, optical sensing, photovoltaic devices... The reason is due to mathematical difficulties, see details in the recent review article [1], and especially to the fact that optical resonators are non-Hermitian systems; their physics is not driven by classical normal modes that can be normalized by their energy, but by quasinormal modes (QNMs) with complex frequencies.

In 2013, a general method was proposed to normalize the quasinormal modes of any resonator [1], generalizing earlier works for simple 1D geometries or spheres [2-3]. From that time, the research on the modal theory of resonator has increased at a fast rate. The same year, a freeware was launched [4]. The freeware can be used by any Maxwell equation solver (surface integral methods, volume integral methods, finite element methods, other Fourier expansion, finite element methods with and without PMLs). The only exception seems to be the FDTD method. This year, the fist benchmark paper [5] on the computation and normalization of quasinormal modes has been published. The publication, coauthored by 20 researchers from 9 institutions, benchmarks several methods for three geometries of wide interest in modern optics: a two-dimensional plasmonic crystal, a two-dimensional metal grating, and a three-dimensional nanopatch antenna on a metal substrate. We are close to elaborate standards for the computation of resonance modes. Presently, about 10 theoretical groups in the world are developing a modal theory for analyzing light scattering by resonators, see the recent review article published on the subject that gathers the contribution of all in a comprehensive way [6]. Progress is impressive.

Hereafter, we report on our recent work that provides a significant improvement of the state of the art, with respect to several point, the most important being the versatility and the generality of the theory and the numerical results obtained for complicated structures.

2. Main result

The theory has been reported in a recent paper [7] that we summarize hereafter. Of particular importance in the present context is the successful generalization of the auxiliary-field method, originally proposed for simulating dispersive media with finite difference time-domain simulations [8] and computing the band diagram of dispersive crystals [9], to compute the quasinormal modes of open resonators with finite element methods.

- The quasinormal modes are defined in an extended basis that comprises the electric **E** and magnetic **H** fields, like before, but which additionally comprises the polarisation **P** and current **J** fields. For the first time it is thus the whole resonance eigenstates that are computed: the modes disentangle the resonance associated to the geometry (basically associated to the **E** and **H** fields) and the resonance associated to the material (basically associated to the **P** and **J** fields).
- This allows us to successfully implement a quasinormal mode solver that efficiently computes the eigenstates of photonic and plasmonic resonators. The associated freeware QNMEig that relies on a COMSOL Multiphysics computational platform can be downloaded on the website of the group.
- On the theoretical side, another important consequence of the auxiliary-field method is a net physical interpretation of temporal dispersion, which lead us to

derive orthogonality relations in the augmented formulation for resonances made of dispersive media. Such a derivation that was not possible in earlier works with unspecified dispersion relation [6] leads to the important proposition of closed-form expressions for the eigenstate excitation coefficients.

- The following figure shows the results obtained for a silver nanobullet deposited on a Si slab and illuminated from the far-field by a plane wave. It compares the prediction of the far-field and guided-mode radiation diagrams obtained with the freeware and with classical simulations performed with COMSOL. The complexity of the present geometry, unprecedented in modal analysis, is due to the fact that the quasinormal modes not only leak in free space but also in the guided modes of the Si slab.

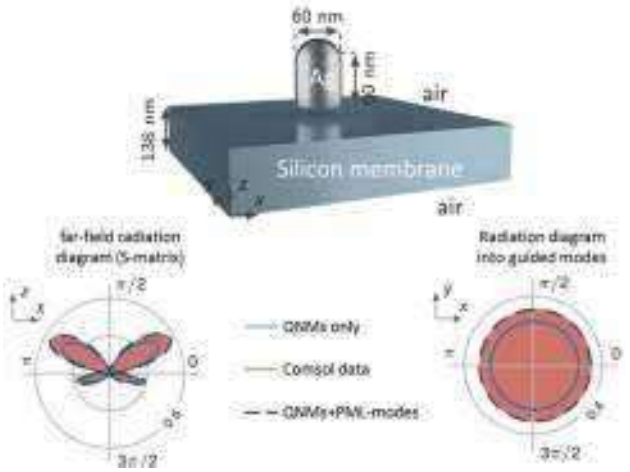


Figure 1. Ag nanobulet on a Si slab illuminated by a plane wave. More details are found in [7].

3. Conclusions

The modal theory of optical resonators has recently achieved very important improvements, to such an extend that it can be considered as mature nowadays. Refinements are on the road and they can be expected to lead to improved convergence and thus to very powerful numerical tools.

We believe that the joint effort in numerics and theory greatly expands the capabilities of analyzing electromagnetic resonance in nanophotonics, offering increased physical insight and improved computational speed.

With respect to the physics of light interaction with micro and nanoresonators, the new theory that rely on a mathematically-safe normalization of the quasinormal modes leads to a quantitative understanding of how light interact with non-hermitian systems. Many basics can be revisited, sometimes significantly, including the definition of cavity Q's (please take for a moment a critical view on how to define the energy stored inside a photonic crystal cavity or a nanoantenna) [6] and of the mode volume [1,8], an accurate formula for the Purcell effect [1], the strong coupling of a quantum emitter and a cavity mode [6], cavity perturbation theory [] cavity perturbation theory, Fano lineshapes.

Acknowledgements

PL would like to thank Wei Yan (Westlake University, China), Christophe Sauvan and Jean-Paul Hugonin (Institut d'Optique, France), Boris Gralak and André Nicolet (Institut Fresnel, France), Femius Koenderink (AMOLF), Massimo Gurioli (LENS), and Marin Soljačić (MIT). He thanks the ANR-16-CE24-0013 that gathers four French groups with the objective of developing the quasinormal mode theory of optical resonators. He also acknowledges the support from the LabEx LAPHIA, the Direction Générale de l'Armement (DGA) and of INRIA.

References

[1] C. Sauvan, J.P. Hugonin, I.S. Maksymov and P. Lalanne, *Theory of the spontaneous optical emission of nanosize photonic and plasmon resonators*, Phys. Rev. Lett 110, 237401 (2013).

[2] B. J. Hoenders, *On the completeness of the natural modes for quantum mechanical potential scattering*, J. Math. Phys. **20**, 329 (1979).

[3] P. T. Leung, S. Y. Liu, and K. Young, *Completeness and orthogonality of quasinormal modes in leaky optical cavities*, Phys. Rev. A **49**, 3057 (1994).

[4] Q. Bai, M. Perrin, C. Sauvan, J.P. Hugonin and P. Lalanne, *Efficient and intuitive method for the analysis of light scattering by a resonant nanostructure*, Opt. Express **21**, 27371 (2013).

[5] P. Lalanne, W. Yan, A. Gras, C. Sauvan, J.-P. Hugonin, M. Besbes, G. Demesy, M. D. Truong, B. Gralak, F. Zolla, A. Nicolet, F. Binkowski, L. Zschiedrich, S. Burger, J. Zimmerling, R. Remis, P. Urbach, H. T. Liu, T. Weiss, *Quasinormal mode solvers for resonators with dispersive materials*, J. Opt. Soc. Am. A **36**, 686-704 (2019).

[6] P. Lalanne, W. Yan, K. Vynck, C. Sauvan and J.-P. Hugonin, *Light interaction with photonic and plasmonic resonances*, Laser Photonics Rev. **12**, 1700113 (2018).

[7] W. Yan, R. Faggiani, P. Lalanne, *Rigorous modal analysis of plasmonic nanoresonators*, Phys. Rev. B **97**, 205422 (2018).

[8] R. M. Joseph, S. C. Hagness and A. Taflove, *Direct time integration of Maxwell's equations in linear dispersive media with absorption for scattering and propagation of femtosecond electromagnetic pulses*, Opt. Lett. **16**, 1412 (1991).

[9] A. Raman and S. Fan, *Photonic band structure of dispersive metamaterials formulated as a Hermitian eigenvalue problem*, Phys. Rev. Lett. 104, 087401 (2010).

[10] K. G. Cognée, W. Yan, F. La China, D. Balestri, F. Intonti, M. Gurioli, A. F. Koenderink, and P. Lalanne, *Mapping Complex Mode Volumes with Cavity Perturbation Theory*, Optica **6**, 269-273 (2019).

[11] J. Yang, H. Giessen, P. Lalanne, *Simple Analytical Expression for the Peak-Frequency Shifts of Plasmonic Resonances for Sensing*, Nano Lett. **15**, 3439 (2015)

Magnetic interactions and transport properties of parallel coupled magnetic molecules in presence of spin-orbit interactions.

S. Alwan and J. Fransson*

Department of Physics and Astronomy, Uppsala university, Uppsala, Sweden

*corresponding author: Jonas.Fransson@physics.uu.se

Abstract-Parallel coupled quantum dots embedded in a tunnel junction is a typical system that exhibits Fano resonances. Here, we consider magnetic molecules in a similar geometry and consider the electronically mediated magnetic interactions between the localized spins as function of the gate and bias voltages. In particular, we demonstrate that spin-orbit coupling enables an additional control parameter for the Fano resonances. Depending on the phase of the spin-orbit interaction, the asymmetry of the Fano resonance can be shifted from, e.g., dip-peak to peak-dip. This property leads to dramatic variations in the exchange parameters, and the anisotropic interactions are shown to be particularly sensitive to such variations.

Previous predictions of electrical and thermal control of magnetic exchange interactions between localized spin moments in, e.g., magnetic molecules have revealed the ability to fine tune gate and bias voltages in order to deliberately go between regimes of ferromagnetic and anti-ferromagnetic exchange [1–3]. These studies have been focused on serially coupled molecules in which it is well known that interference phenomena such as Fano resonances are normally not occurring. In quantum dots coupled in parallel, however, Fano resonances are known to exist and are well captured within the traditional two-path structure, see e.g., [4], which serve as a prerequisite for the effect. Here, we consider the electronically mediated magnetic interactions between the localizes spin in magnetic molecules. In particular, we address the dependence of the magnetic interactions on the gate and bias voltages between the leads. In a quite similar fashion as in the serially coupled system, we show that the exchange interaction can be controllably fine tuned between ferromagnetic and anti-ferromagnetic by means of the external control variables. In addition to this control, we also show that sudden absences of the exchange are correlated with Fano resonances and since the transport properties are deeply connected with the magnetic configuration of the spin dimer, this provides a unique way to study the Fano interference phenomena and its influence on magnetic systems.

REFERENCES

1. Fransson, J, Ren, J, and Zhu, J.-X. “Electrical and Thermal Control of Magnetic Exchange Interactions”, *Phys. Rev. Lett.*, Vol. 113, 257201, 2014.
2. Saygun, T, Bylin, J, Hammar, H, and Fransson, J, “Voltage-Induced Switching Dynamics of a Coupled Spin Pair in a Molecular Junction”, *Nano Lett.*, Vol. 16, 2824–2829, 2016.
3. Vasquez Jaramillo, J D, and Fransson, J, “Charge Transport and Entropy Production Rate in Magnetically Active Molecular Dimer”, *J. Phys. Chem. C*, Vol. 121, 27357–27368, 2018.
4. Fransson, J and Balatsky, A. V., “Exchange interaction and Fano resonances in diatomic molecular systems”, *Phys. Rev. B*, Vol. 75, 153309, 2007.

Disordered metamaterials: Strong interactions, subradiance and field localization

Stewart D. Jenkins[1], Nikitas Papasimakis[2], Salvatore Savo[2,3], Nikolay I. Zheludev[2,4], Janne Ruostekoski[1,5*]

[1]Mathematical Sciences and Centre for Photonic Metamaterials, University of Southampton, Southampton SO17 1BJ, United Kingdom
[2]Optoelectronics Research Centre and Centre for Photonic Metamaterials, University of Southampton Southampton SO17 1BJ, United Kingdom
[3]TetraScience Inc., 114 Western Ave, Boston, MA, 02134
[4]Centre for Disruptive Photonic Technologies School of Physical and Mathematical Sciences and The Photonics Institute, Nanyang Technological University, Singapore 637378, Singapore
[5]Department of Physics, Lancaster University, Lancaster, LA1 4YB, United Kingdom
*corresponding author, E-mail: j.ruostekoski@lancaster.ac.uk

Abstract

We provide detailed comparisons between experimental findings and numerical simulations of large cooperatively interacting, spatially disordered metamaterial arrays, consisting of asymmetrically split rings. Simulation methods fully incorporate strong field-mediated inter-meta-atom interactions between discrete resonators and statistical properties of disorder, while approximating the resonators' internal structure. Despite the large system size, we find a qualitative agreement between the simulations and experiments, and characterize the microscopic origins of the observed disorder response. Our microscopic description of macroscopic electrodynamics reveals how the response of disordered arrays with strong field-mediated interactions is inherently linked to their cooperative response to electromagnetic waves where the multiple scattering induces strong correlations between the excitations of individual resonators. We show how the effects of disorder and cooperative interactions are mapped onto the transmission resonance in the far field spectrum. In the near field response we find substantially increased standard deviation of the Purcell-enhancement with disorder, making it increasingly likely to find collective excitation eigenmodes with very high Purcell factors that are also stronger for magnetic than electric excitations. We show that disorder can dramatically modify the cooperative response of the metamaterial even in the presence of strong dissipation losses as is the case for plasmonic systems.

1. Introduction

Disordered media and propagation of waves through them is a ubiquitous theme across physics. While metamaterials have so far been almost solely based on regularly structured resonator arrays, there is an increasing interest in extending these also to the realm of disordered systems, where disorder is introduced either in the form of inhomogeneous broadening or as random perturbations in the resonator positions. Whereas the former can affect the strength of inter-

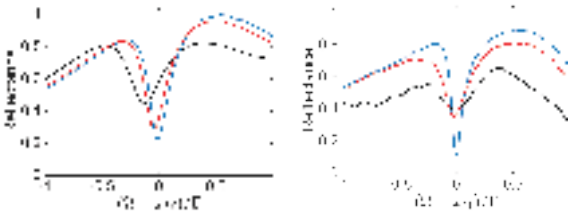


Figure 1: Far field spectrum of microwave and optical plasmonic arrays with varying degree of disorder. The backscattered intensity from the microwave array (a) as calculated by the theoretical model and (b) measured in the experiments. The blue lines represent scattering from ordered arrays, and the red and black lines represent scattering from arrays with an increasing disorder.

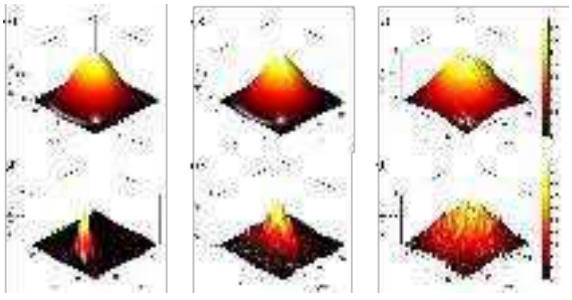


Figure 2: The effects of density on the collective uniform magnetic eigenmode. Excitations of a single eigenmode with vayring lattice spacing a for regular (a-c) and disordered (d-f) ASR arrays. The corresponding lattice spacings (in the units of a wavelength) are a = 0.28 (a,d), 0.83 (b,e), and 1.4 (c,f).

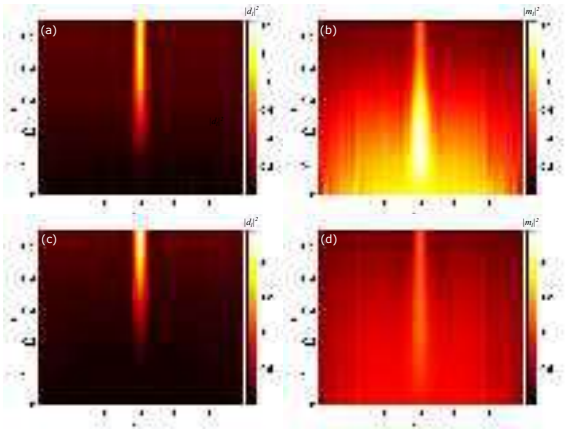


Figure 3: Localized meta-molecule excitations in numerical simulations. Electric (a,c) and magnetic (b,d) dipole excitations of the most strongly excited meta-molecule and its neighbouring meta- molecules for microwave (a-b) and plasmonic (c-d) arrays as a function of the disorder. The colormaps present averages over all realizations.

actions between the resonators, the latter can lead to qualitative changes in the response of the resonator array. We study the near- and far-field responses of positionally disordered metamaterial arrays consisting of asymmetrically split rings (ASRs). Our approach includes numerical simulations of the full metamaterial array, where each meta-atom is considered individually, and experimental near-and far-field measurements. We show how the response of disordered system is inherently linked to strong field-mediated interactions between the resonators that induce correlations between the excitations of different resonators and cannot be described by effective continuous medium theories of electrodynamics. We find that the dramatic difference between the responses of regular and disordered arrays manifests itself most clearly in the microscopic properties of collective radiative excitation eigenmodes. Our findings indicate that this sensitivity of the cooperative response on disorder strength depends heavily on dissipation losses. In the case of low-loss (microwave) ASR arrays, manifestations of disorder-induced collective phenomena are readily observed. On the other hand, careful engineering of the metamolecule properties allows the observation of such phenomena even in the case of plasmonic, lossy metamaterial systems operating in the optical part of the spectrum.

2. Disorder responses

In Fig. 1 we show the far field spectrum for different strengths of disorder. The reflection spectrum displays a Fano resonance that directly conveys information on the collective radiative excitation eigenmodes of the system. The cooperative response of the metamaterial array is sensitive to the density of the resonators as illustrated in Fig. 2

Numerically simulated near-field localization for different strengths of disorder is shown in Fig. 3. The effects of disorder on the Purcell factors in terms of the collective excitation eigenmodes is described in Fig. 4.

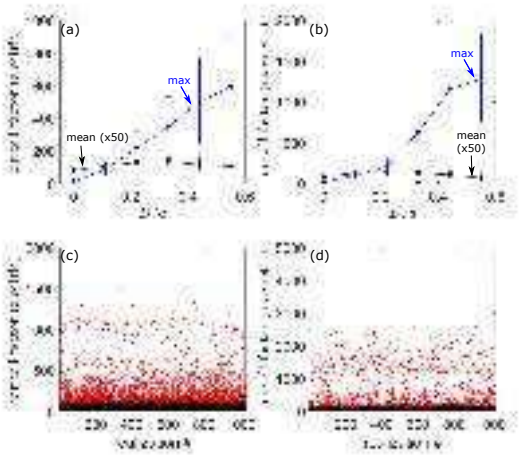


Figure 4: Purcell enhancement in plasmonic metamaterial arrays. (a-b) Average (black) and maximum (blue) Purcell factor for electric (a) and magnetic (b) dipole excitations as a function of disorder. The average is calculated over 1024 different realizations and over all modes of each realization, and it has been multiplied by a factor of 50. The maximum Purcell factors have been calculated by finding the maximum value for each realization and then averaging over all 1024 realizations. The errorbars correspond to the standard deviation of the average and maximum Purcell factor across different realizations. (c-d) Purcell factors for electric (c) and magnetic (d) dipole excitation for different realizations and for two different degrees of disorder. Each point in the graphs corresponds to the Purcell factor of a single mode of a single realization.

3. Conclusions

We have characterized the effects of spatial disorder in near- and far-field response in terms of collective excitation eigenmodes in strongly interacting, cooperatively radiating metamaterial arrays.

Acknowledgement

We acknowledge financial support from the EPSRC, the Leverhulme Trust, the Royal Society, and the MOE Singapore Grant No. MOE2011-T3-1-005.

References

[1] S. D. Jenkins *et al.*, Strong interactions and subradiance in disordered metamaterials, Phys. Rev. B **98**, 245136 (2018).

[2] N. Papasimakis *et al.*, Cooperative field localization and excitation eigenmodes in disordered metamaterials, Phys. Rev. B **99**, 014210 (2019).

Photonic crystal structures treated by the resonant state expansion

Sam Neale and Egor A. Muljarov

School of Physics and Astronomy, Cardiff University, Cardiff CF24 3AA, United Kingdom

The resonant state expansion (RSE) is a novel rigorous method for calculating resonant states (RSs) of a photonic system [1]. These are the eigensolutions of Maxwell's wave equation (MWE) with outgoing boundary conditions. Using a complete set of RSs of a simpler system as a basis, the RSE makes a mapping of MWE onto a linear eigenvalues problem, determining the full set of the RSs of a complex system.

In addition to higher numerical efficiency [2,3] compared to other computational methods, the RSE provides an intuitive physical picture of resonant phenomena, capable of explaining features observed in optical spectra. So far the RSE has been applied to finite open optical systems of different geometry and dimensionality, as well as to homogeneous and inhomogeneous planar waveguides [3]. Very recently, the RSE was generalized to magnetic, chiral and bi-anisotropic optical systems [4], enabling its further application to metamaterials. The RSE has been also used in first perturbation order for photonic crystal (PC) structures to describe the refractive index sensing [5], and a rigorous analytic normalization of the RSs in PC structures has been presented [5,6].

Here, we develop a PC-RSE, a new rigorous approach for accurate calculation of RSs in planar PC structures using a homogeneous slab as basis system. The periodicity of PC structures mixes all possible Bragg harmonics. Therefore, the basis RSs have to be taken with different in-plane wave numbers. As a result, the Green's function of MWE has branch cuts in the complex frequency plane, which have to be taken into account in the PC-RSE along with the RSs. This presents the major complication of the PC-RSE which we have dealt with by splitting the cuts into series of discrete, artificial cut states added for completeness to the basis of RSs [3]. Using for illustration a dielectric slab periodically modulated in one direction, we demonstrate the accuracy and efficiency of the PC-RSE for finding the RSs of photonic crystals.

We further study bound states in the continuum (BIC) of a dielectric photonic-crystal slab. We show in particular how different types of RSs of a homogeneous slab contribute to BIC and compare these contributions with other resonances of the photonic-crystal system, such as waveguide, quasi-guided [7] and Fabry-Perot modes.

[1] E. A. Muljarov, W. Langbein, and R. Zimmermann, Europhys. Lett. **92**, 50010 (2010).
[2] M. B. Doost, W. Langbein, and E. A. Muljarov, Phys. Rev. A **90**, 013834 (2014).
[3] S. V. Lobanov, G. Zoriniants, W. Langbein, and E. A. Muljarov, Phys. Rev. A **95**, 053848 (2017).
[4] E. A. Muljarov and T. Weiss, Opt. Lett. **43**, 1978 (2018).
[5] T. Weiss, M. Mesch, M. Schäferling, H. Giessen, W. Langbein, and E. A. Muljarov, Phys. Rev. Lett. **116**, 237401 (2016).
[6] T. Weiss, M. Schäferling, H. Giessen, N. A. Gippius, S. G. Tikhodeev, W. Langbein, and E. A. Muljarov, Phys. Rev. B **96**, 045129 (2017).
[7] S. G. Tikhodeev, A. L. Yablonskii, E. A. Muljarov, N. A. Gippius, and T. Ishihara, Phys. Rev. B **66**, 045102 (2002).

Interaction between dielectric particles enhances the Q-factor

Evgeny Bulgakov[1,2], Konstantin Pichugin[1], Almas Sadreev[1]

[1]Kirensky Institute of Physics, Federal Research Center KSC Siberian Branch, RAN, Krasnoyarsk 660036, Russia
[2] Reshetnev Siberian State University of Science and Technology, 660037, Krasnoyarsk, Russia
corresponding author, E-mail: almas@tnp.krasn.ru

Abstract

We study behavior of resonant modes with a distance between two identical dielectric cylinders and disks. We reveal two basic scenarios of evolution of resonances with the distance between the cylinders. For larger distances and respectively weaker interaction of particles the resonances are bound around the Mie resonances and evolve by spiral way. For shorter distances and respectively stronger interaction the resonances bypass the Mie resonances. Both scenarios demonstrate considerable enhancement of the Q factor compared to the case of isolated particle.

1. Introduction

It is rather challenging for optical resonators to support resonances of simultaneous subwavelength mode volumes and high Q factors. The traditional way for increasing the Q factor of optical cavities is a suppression of leakage of resonance mode into the radiation continua. That is achieved usually by decreasing the coupling of the resonant mode with the continua by the use of metals, photonic band gap structures, or whispering-gallery-mode resonators. All of these approaches lead to reduced device efficiencies because of complex designs, inevitable metallic losses, or large cavity sizes. On the contrary, all-dielectric subwavelength nanoparticles have recently been suggested as an important pathway to enhance capabilities of traditional nanoscale resonators by exploiting the multipolar Mie resonances being limited only by radiation losses [1, 2].

The decisive breakthrough came with the paper by Friedrich and Wintgen [3] which put forward the idea of destructive interference of two neighboring resonant modes leaking into the continuum. Based on a simple generic two-level model they formulated the condition for the bound state in the continuum (BIC) as the state with zero resonant width for crossing of eigenlevels of the cavity or avoided crossing of resonances. This principle was later explored in open plane wave resonator where the BIC occurs in the vicinity of degeneracy of the closed integrable resonator [4].

However, these BICs exist provided that they embedded into a single continuum of propagating modes of a directional waveguide. In photonics the optical BICs embedded into the radiation continuum can be realized by two ways. The first way is realized in an optical cavity coupled with the continuum of 2d photonic crystal (PhC) waveguide [5] that is an optical variant of microwave system [4]. Alternative way is the use periodic PhC systems (gratings) or arrays of dielectric particles in which resonant modes leak into a restricted number of diffraction continua [6, 7, 8, 9, 10]. Although the exact BICs can occur only in infinite periodical arrays, the finite arrays demonstrate resonant modes with the very high Q factor which grows quadratically [11] or even cubically [12] with the number of particles (quasi-BICs). Even arrays of five dielectric particles demonstrate the Q factor exceeding the Q factor of individual particle by six orders in magnitude [13].

Isolated subwavelength high-index dielectric resonators are more advantageous from an applied point of view to achieve high Q resonant modes (super cavity modes) [2, 14, 15]. Such super cavity modes originate from avoided crossing of the resonant modes, specifically the Mie-type resonant mode and the Fabry-Pérot resonant mode under variation of the aspect ratio of the dielectric disk which could result in a significant enhancement of the Q factor. It is worthy also to notice the idea of formation of long-lived, scar like modes near avoided resonance crossings in optical deformed microcavities [16]. The dramatic Q factor enhancement was predicted by Boriskina [17, 18] for avoided crossing of very highly excited whispering gallery modes in symmetrical photonic molecules of dielectric disks on a surface.

In the present paper we consider a similar way to enhance the Q factor by variation of the distance between two identical dielectric cylinders and coaxial disks as sketched in Fig. 1 As different from papers [16, 17, 18, 19, 20] we consider the avoided crossing of low excited resonant modes (monopole, dipole and quadruple) with variation of the distance between two cylinders. Because of lifting of the axial symmetry many Mie resonances contribute into the resonances of two cylinders which show two basic scenarios of evolution with the distance, bound to the Mie resonances and unbound. The same scenarios show the resonances of two coaxial dielectric disks however with those difference that for small distance between them there might be avoided crossing of different resonances of the isolated disk.



(b)

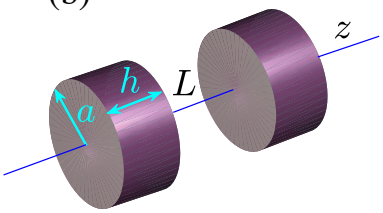


Figure 1: Two parallel dielectric cylinders (a) and coaxial disks (b).

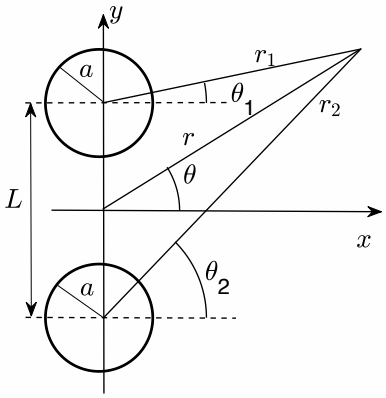


Figure 2:

2. Avoided crossings under variation of the distance between two cylinders

The problem of scattering of electromagnetic waves from two parallel infinitely long dielectric cylinders ketched in Figs. 2 was solved long time ago in papers [21, 22, 23]. The solutions for electromagnetic field, the component of electric field directed along the cylinders $\psi = E_z$ outside the cylinders are given by

$$\psi_1 = \sum_n A_{1n} H_n^{(1)}(kr_1) e^{in\theta_1}, \quad (1)$$
$$\psi_2 = \sum_n A_{2n} H_n^{(1)}(kr_2) e^{in\theta_2}. \quad (2)$$

Inside the cylinders we have

$$\psi_1 = \sum_n B_{1n} J_n(\sqrt{\epsilon} kr_1) e^{in\theta_1}, \quad (3)$$
$$\psi_2 = \sum_n \sum_n B_{2n} J_n(\sqrt{\epsilon} kr_2) e^{in\theta_2}. \quad (4)$$

By means of the Graf formula [24]

$$H_n^{(1)}(kr_1) e^{in\theta_1} = \sum_m i^{n-m} H_{m-n}^{(1)}(kL) J_m(kr_2) e^{im\theta_2}, \quad (5)$$
$$H_n^{(1)}(kr_2) e^{in\theta_2} = \sum_m i^{n-m} H_{m-n}^{(1)}(kL) J_m(kr_1) e^{im\theta_1}, \quad (6)$$

the total field $\psi = \psi_{inc} + \psi_1 + \psi_2$ can be written completely in the coordinate system of either cylinder.

Applying the boundary conditions at $r_j = a$ leads to [21, 23]

$$A_{1n} = i^n S_n(k) \sum_m i^{-m} H_{n+m}(kL) A_{2n},$$
$$A_{2n} = i^n S_n(k) \sum_m i^{-m} H_{n+m}(kL) A_{1n}, \quad (7)$$

where S_n are the scattering matrix amplitudes for the isolated cylinder

$$S_n(k) = \frac{\sqrt{\epsilon} J_m'(\sqrt{\epsilon} ka) J_m(k) - J_m'(k) J_m(\sqrt{\epsilon} k)}{H_m^{(1)'}(k) J_m(\sqrt{\epsilon} k) - \sqrt{\epsilon} J_m'(\sqrt{\epsilon} k) H_m^{(1)}(k)}. \quad (8)$$

The resonances are given by the complex roots of the following equation

$$Det[\hat{M}^2 - I] = 0 \quad (9)$$

where matrix elements $\hat{M}$ is given by Eq. (7) and equal

$$M_{mn} = S_m(k) i^{m-n} H_{m+n}(kL) \quad (10)$$

and I is the unit matrix. In what follows the dimensionless complex eigenvalues k are measured in terms of c/a where c is the light velocity and a is the radius of cylinders and L is measured in terms of a. .

In general Eq. (9) has an infinite number of complex resonant frequencies $k = k_r - i\gamma_r$. The total view of the dependence of resonant eigenvalues is shown in Fig. 3 which demonstrates complicated evolution of resonant poles against the distance between the cylinders. First of all one can see the major part of the resonances are unbound bypassing the Mie resonances of the isolated cylinder marked by crosses which are collected in Fig. 4. Second, there are a small part of resonances which are bound around the Mie resonances with smaller imaginary parts.

Let us consider the asymptotic behavior of resonances for $L \to \infty$. By use of asymptotical behavior of the Hankel functions [25] we have for matrix (10) the following

$$M_{mn} \sim \sqrt{\frac{2}{\pi kL}} e^{i(kL - \pi/4)} S_m(k) (-1)^n. \quad (11)$$

Let us take the eigenvector of matrix $\widehat{M}$ $\overrightarrow{\psi}^+ = (\psi_1, \psi_2, \psi_3, \ldots)$. Then Eq. (9) takes the following form

$$\sqrt{\frac{2}{\pi kL}} e^{ikL} S_m(k) \sum_n (-1)^n \psi_n = \pm \psi_m, \quad (12)$$

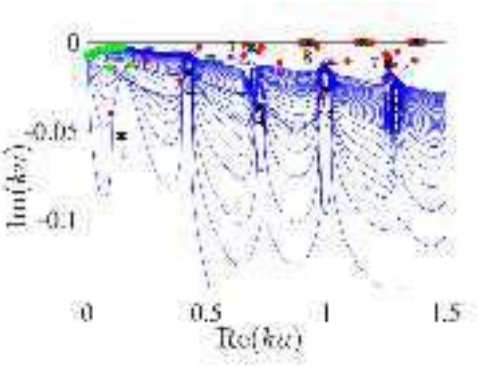


Figure 3: The behavior of resonant frequencies vs the distance between cylinders. Open green circles correspond $L = 1000a$, closed red circles correspond to minimal distance $L = 2a$, where a is the radius of cylinders and black crosses are the Mie resonances shown in the next Fig. 4.

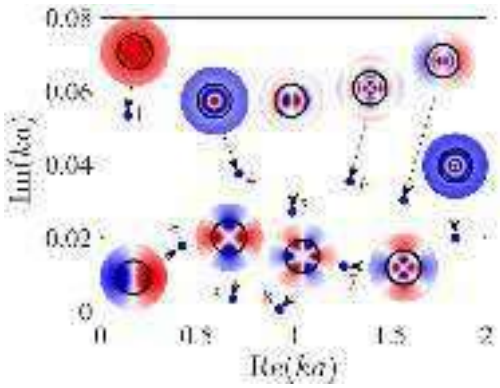


Figure 4: The Mie resonant complex eigenfrequencies (close circles) and corresponding resonant modes (the component E_z) of isolated cylinder.

which has the solution provided that

$$\sqrt{\frac{2}{\pi kL}}e^{ikL}\sum_n(-1)^n S_n(k) = \pm 1. \qquad (13)$$

For the absolute value we have

$$\frac{2e^{\gamma_n L}}{\pi|k_n|L} = \frac{1}{|\sum_n(-1)^n S_n(k)|^2} \qquad (14)$$

where $\gamma_n = -2\mathrm{Im}(k_n)$. The resonances of the isolated cylinder are given by poles of the S-matrix, i.e., by equation $\frac{1}{S_m(k)} = 0$. Therefore from (14) it follows that, first, the resonances of two cylinders do not converge to the resonances of the isolated cylinder. Second, because of finite value of right hand side of Eq. (14) the line widths and resonance positions limit to zero at $L \to \infty$. Therefore we can conclude that the resonances of two dielectric cylinders do NOT limit to the Mie resonances of the isolated cylinders at $L \to \infty$. The reason is related to to the exponential factor $\exp(\gamma_n L)$ of the resonant modes (the Gamov states) at large distances between the cylinder.

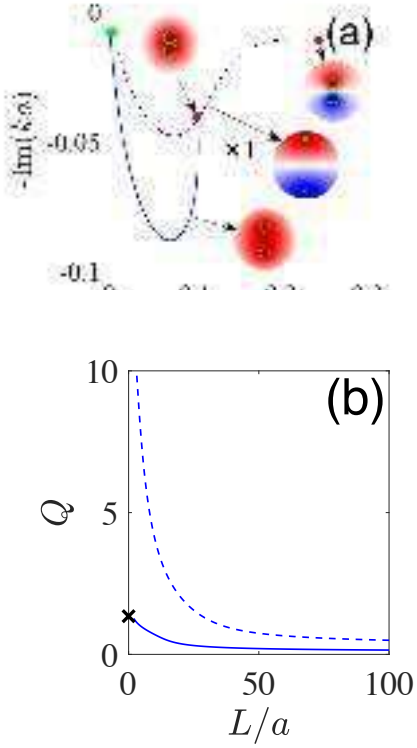


Figure 5: Evolution of resonant frequencies and monopole resonant modes $\psi_{s,s/a}$ (a) and the Q factors (b) with the distance between the cylinders. Solid/dash lines show symmetric/antisymmetric resonant frequencies. Closed circles correspond to $L = 2a$, open circles correspond to $L = 1000a$ and cross corresponds to the monopole Mie resonance 1.

Next, we consider the behavior of some typical resonances in Fig. 4 in detail from the limiting case $L = 2a$ to $L = 1000a$. Due to the symmetry of the system relative to $x \to -x$ and $y \to -y$ the resonant modes can be classified as $\psi_{\sigma;\sigma'}$ where the indices $\sigma = s, a$ correspond to the symmetric and antisymmetric modes respectively. We start with the first two lowest symmetric and antisymmetric monopole resonant modes $\psi_{s;s/a}$. Fig. 5 (b) shows that the Q factor of the antisymmetric monopole resonance exceeds the Q factor of the isolated cylinder by one order in magnitude. The reason for that follows from the Mie resonances shown in Fig. 4. As seen from Fig. 5 (a) at the closest distance between the cylinders $L = 2a$ the symmetric resonant mode becomes the monopole mode with corresponding Q factor close to the Q factor of isolated cylinder which is rather low as marked by cross in Fig. 5 (b). At the same time the antisymmetric mode of two cylinders at $L = 2a$ becomes the dipole resonance which as seen from Fig. 4 has the Q factor exceeding the Q factor of the monopole Mie resonance by one order in magnitude. The next resonances illustrate that the evolution of resonances strongly

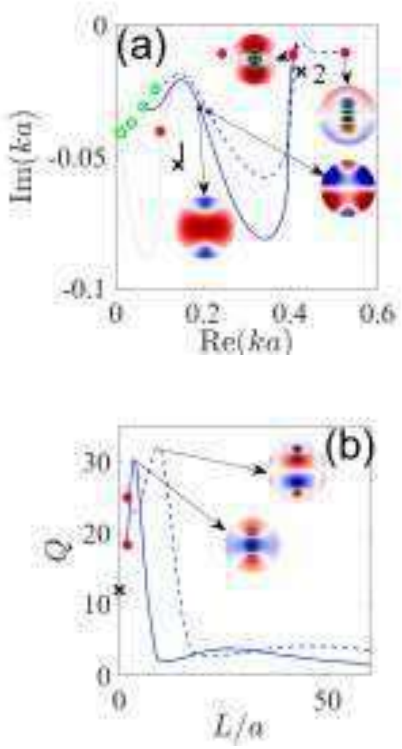


Figure 6: The same as in Fig. 5 for the dipole resonant modes $\psi_{s;s/a}$ symmetric relative to $x \to -x$. Cross marks the Mie resonance (a) and respectively Q factor of the isolated cylinder (b).

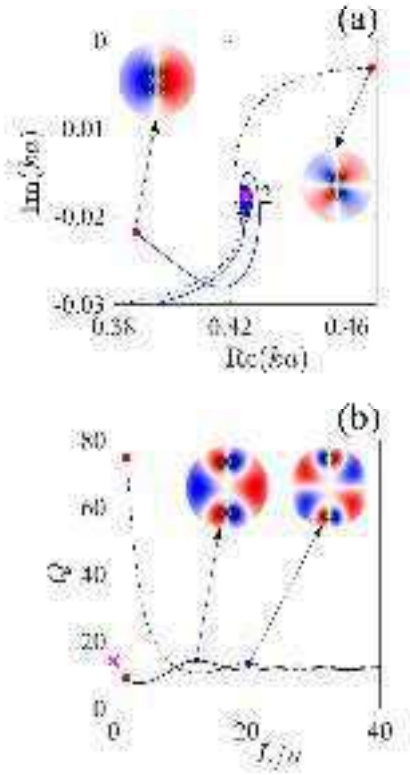


Figure 7: The same as in Fig. 6 for the dipole resonant modes $\psi_{a;s/a}$ antisymmetric relative to $x \to -x$.

depend on interaction between the cylinders via the radiating Mie resonances. The general expressions and physical origin of the coupling of dielectric resonators was considered in Refs. [26, 27, 28]. The coupling constant can be written as [27]

$$\kappa = \int dv[\epsilon(\overrightarrow{r}) - 1]\overrightarrow{E}_1^* \overrightarrow{E}_2 \qquad (15)$$

where $\overrightarrow{E}_{1,2}$ are normalized solutions by the factor $\sqrt{\int \epsilon(\overrightarrow{r})|\overrightarrow{E}_{1,2}|^2 dv}$. Here the indices 1 and 2 imply the resonant modes of the corresponding dielectric particles. The coupling constant is determined by overlapping of resonant modes which in turn depend on the distance between the particles and prevailing direction of radiation of the modes.

That conclusion is well illustrated by the Mie dipole resonant modes which are degenerate. The first dipole Mie resonant mode, symmetric relative to $x \to -x$, radiates prevalently towards the neighboring cylinder as shown in insets in Fig. 6 while the second antisymmetric dipole Mie resonant mode radiates away from the neighboring cylinder as shown in insets of Fig. 7. As a result the interaction in former case turns out stronger compared to the latter case as it follows from Eq. (15). That explains why the evolution of resonances shown in Fig. 6 (a) is similar to the case of interaction via the monopole resonant modes in Fig. 5 while the evolution of resonances in Fig. 6 is bound to the Mie dipole resonance 2 as seen from Fig. 6 (a). Respectively the gain in the Q factor in the former case is smaller than in the latter case as seen from Figs. 6 (b) and 7 (b).

With further increase of the distance L the resonance bypasses the monopole Mie resonance 1 of the isolated cylinder. As a result the solution of the Maxwell equations becomes close to the resonant mode $\psi_{s;s/a}$. That rule for the solutions when the resonances bypass the Mie resonances is fulfilled for all other resonances as one can see from Fig. 8. Similar evolution scenarios can be observed for the quadruple resonances shown in Fig. 9 (a). In this case the Mie resonant mode radiates from one cylinder to another that gives rise to interaction between cylinders stronger than the case of the modes $\psi_{a;s/a}$ shown in Fig. 8 (c). Both cases result in interaction weaker than the case of dipole Mie resonances. As a result in both cases one can observe that the resonances are bound around the Mie quadruple resonance 3 shown in Fig. 4 for distances from $L = 2a$ to $L = 350a$. However, in the first case of stronger interaction between the cylinders the resonances $\psi_{s;s/a}$ go away from the initial Mie resonance 3 and consequently go to zero bypassing the Mie resonance 2 as seen in Fig. 4. meanwhile in the second case of weaker interaction the resonances $\psi_{a;s/a}$ remain bound around the quadruple Mie resonance 3 as shown in Fig. 9 (c). The dependence of the Q factor on L is shown in Fig. 9 (b) and (d).

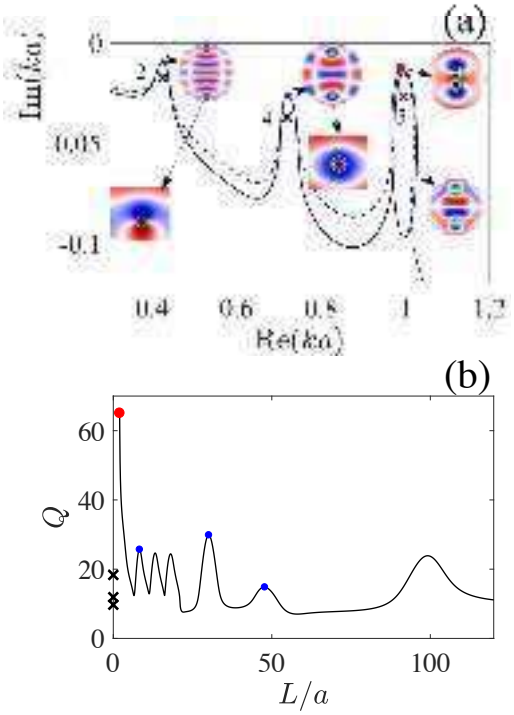


Figure 8: Evolution of symmetric and antisymmetric hybridizations of higher Mie dipole resonant modes (a) and respective Q factors (b) with the distance.

3. Avoided crossings in system of two coaxial disks

In the present section we consider two identical coaxial disks as sketched in Fig. 1 (b) each of them having the aspect ratio not obligatory tuned to the optimal Q-factor as in [14, 15]. The coaxial disks have the advantage that all resonant modes are classified by the azimuthal index $m = 0, 1, 2, \ldots$ because of the axial symmetry. Therefore one can consider subspaces with definite m separately. In the present paper we follow the case $m = 0$ for which the solutions are separated by polarization with $H_z = 0$ (E modes) and $E_z = 0$ (H modes). In what follows we consider the H-modes. In general the resonant modes and their eigenfrequencies are given by solving the time-harmonic source-free Maxwell's equations [29, 30]

$$\begin{pmatrix} 0 & \frac{i}{\epsilon}\nabla\times \\ -i\nabla\times & 0 \end{pmatrix} \begin{pmatrix} \mathbf{E}_n \\ \mathbf{H}_n \end{pmatrix} = k_n \begin{pmatrix} \mathbf{E}_n \\ \mathbf{H}_n \end{pmatrix} \qquad (16)$$

where $\mathbf{E}_n$ and $\mathbf{H}_n$ are the EM field components defined in Ref. [30] as quasinormal modes which are also known as resonant states [31, 32] or leaky modes [33]. It is important that they can be normalized and the orthogonality relation can be fulfilled by the use of perfectly matched layers (PMLs) [30]. With the exception of very restricted number of symmetrical particles Eq. (16) can be solved only numerically. The eigenfrequencies are complex $k_n a = \omega_n + i\gamma_n$ where a is the disk radius. In what follows the light velocity is taken unit. Fig. 10 shows resonant frequencies of the isolated disk complimented by insets with the resonant modes

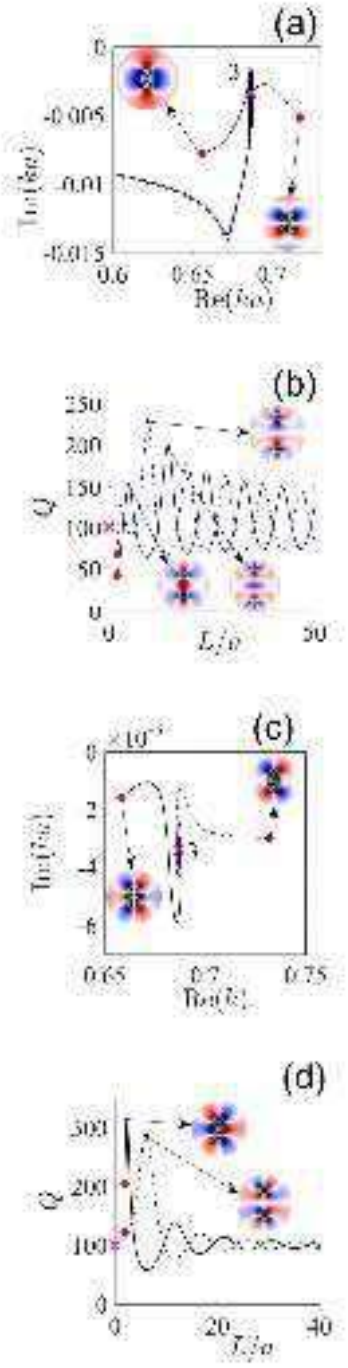


Figure 9: The evolution of quadruple resonant modes under vs the distance. Crosses mark the Mie resonances shown in Fig. 4. Red closed circle marks the case of the smallest distance and open green circle marks the distance $L = 1000a$.

(only the component E_ϕ is shown). There are modes with nodal surfaces crossing the z-axis and the modes with nodal surfaces crossing the plane $z = 0$. They correspond to the Fabry-Perot resonant modes and the radial Mie modes by the terminology introduced in paper [14].

Fig. 11 shows the solutions of Eq. (16) for the case of

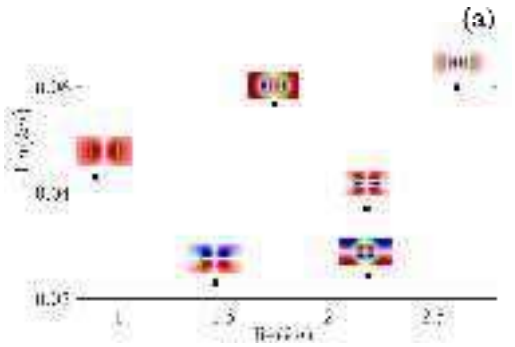


Figure 10: The resonant eigenfrequencies (close circles) and corresponding resonant modes (the component E_ϕ of isolated dielectric disk with the height $h = a$ and permittivity $\epsilon = 40$.

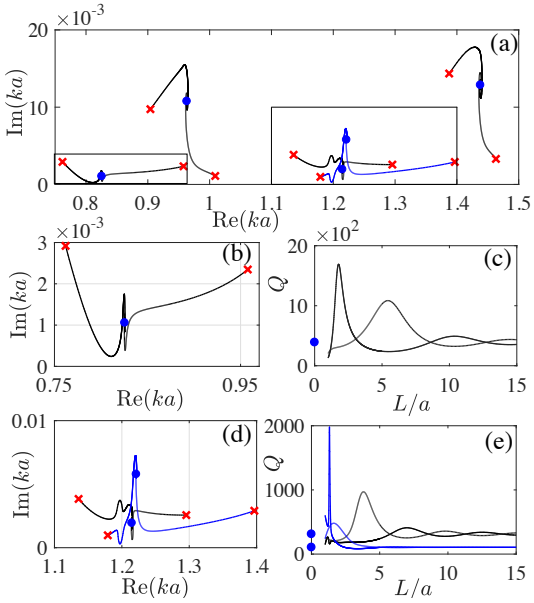


Figure 11: (a) The behavior of resonant eigenfrequencies under variation of the distance between the disks L with the $\epsilon = 40, a = h$. (b) and (d) zoomed areas highlighted in (a) with symmetric (solid lines) and antisymmetric (dash lines) resonant modes. (c) and (e) show the behavior of the Q factor vs the distance for corresponding insets at the left. Closed circles mark the eigenfrequencies of isolated disks and respectively the Q factors while crosses mark the limiting case $L = h$ when two disks stick together.

two coaxial dielectric disks as dependent on the distance L between the disks. The necessity to use PMLs restricts the distance between the disks which is to be considerably less than the distance between the PMLs in the z-direction.

In spite of an illusive complexity in Fig. 11 the zoomed pictures reveal remarkably simple behavior of resonant frequencies in the form of a spiral convergence of the eigenfrequencies to the resonant frequencies of the isolated disk marked by closed circles. However, when the disks approach close enough to each other the spiralling behavior is replaced by strong repulsion of resonant frequencies because of interaction enhancement.

In order to quantitatively evaluate this interaction we start consideration with an isolated disk for which the matrix of derivatives in Eq. (16) becomes diagonal with the complex eigenfrequencies k_n in the eigenbasis presented in Fig. 10. It is reasonable to assume that for enough separation between disks the matrix is still diagonal with pairs of degenerate k_n shown in Fig. 11 by blue closed circles. As the distance between the disks is reduced the interaction between the disks via the resonant modes splits the degenerate resonant modes k_n giving rise to an avoided crossing. We also assume also that the value of splitting much less than the distance between the different k_n. These assumptions are justified numerically as shown in insets of Fig. 11, however, for only in definite domains of the frequency k around the resonances of the isolated disk where spiral behavior of the resonant frequencies takes place. In the framework of these assumptions we can use two-level approximation for the Hamiltonian matrix in Eq. (16) for each resonance k_n [16, 30, 15]

$$H^{(n)}_{eff} = H^{(0)}_{eff} + V = \begin{pmatrix} k_n a & 0 \\ 0 & k_n a \end{pmatrix} + \begin{pmatrix} u_n & v_n \\ v_n & u_n \end{pmatrix}, \quad (17)$$

where v_n is responsible for interaction between the disks via the resonant modes while u_n is the result of the backscattering by the first disk. Therefore one can expect that $arg(v_n) = \omega_n L/a, \quad arg(u_n) = 2\omega_n L/a$. Fig. 12 shows the behavior of the absolute value and phase both of the matrix elements. The matrix elements v_n and u_n can be easily found from numerically calculated resonances shown in Fig. 11

$$k^{(n)}_{a,s} a = k_n a + u_n \pm v_n, \quad (18)$$

as $v_n = \frac{k^{(n)}_s - k^{(n)}_a}{2}, u_n = \frac{k^{(n)}_s + k^{(n)}_a}{2} - k_n$. From Fig. 12 one can evaluate that the interaction term in (17)

$$v_n \sim \frac{e^{ik_n L}}{L^2}, u_n \sim \frac{e^{2ik_n L}}{L^4}. \quad (19)$$

The distance behavior (19) is observed with a good accuracy for all resonances shown in Fig. 12, however, for only spiral convergence of the resonances. Numerically calculated behavior of the matrix elements v_n and u_n for $n = 2$ is shown in Fig. 12. In spiralling around the resonances of the isolated disk the hybridized resonant eigenmode is given by symmetric and antisymmetric combinations of the resonant modes of the isolated disk

$$\psi_{s,a}(\vec{r}) = \psi_n(\vec{r} - \frac{1}{2}L\vec{e}_z) \pm \psi_n(\vec{r} + \frac{1}{2}L\vec{e}_z) \quad (20)$$

where $\vec{e}_z$ is the unit vector along the z-axis and $\psi_n(\vec{r})$ are the corresponding resonant modes of the isolated disk shown in the insets in Fig. 10.

At first the resonant frequencies slowly spiral away from the limiting point given by k_n. Respectively the Q factor in Fig. 11 (c) demonstrates oscillating behavior exceeding the Q factor of the isolated disk a few times. As

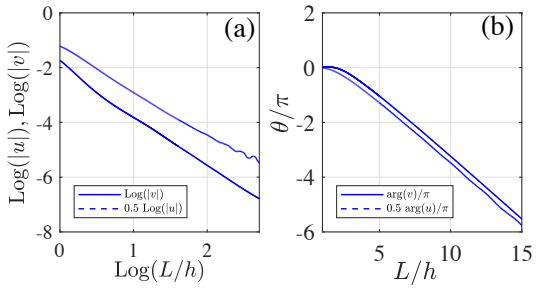


Figure 12: Dependence of the matrix elements v_n and u_n on the distance between disks L.

the disks approach each other the spiral behavior of the pair of resonances $k_{s,a}^{(n)}$ is replaced by strong repulsion as shown Fig. 11 (b). Fig. 11 (d) shows a remarkable feature caused by the avoided crossing of resonances with different n. To be specific there is an avoided crossing of symmetric resonances $k_s^{(2)}$ and $k_s^{(5)}$ according to enumeration in Fig. 10. Because of the same symmetry these resonances undergo typical avoided crossing with a considerable decrease of the imaginary part of the resonant frequency and correspondingly enhancement of the Q factor by one order in magnitude. Respectively the two-mode approximation (17) breaks down.

It is interesting to trace the behavior of resonances and the Q factors for the aspect ratio $h/a \approx 1.0395$ and $\epsilon = 12$ for which the isolated disk shows the maximal Q factor. The results are presented in Fig.13. One can see that with decrease of the distance between the disks we have the same spiralling behavior of the hybridized resonances around the resonances of the isolated disks which is terminated by strong repulsion of the symmetric and antisymmetric resonances for $L \to h$. However, we don't see a pronounced effect of the avoiding crossing of hybridized resonances with different n and respectively have no enhancement of the Q factor by one order in magnitude as it was achieved for the aspect ratio $a/h = 1$ (see Fig. 12 (e)).

Up to now we considered the permittivity $\epsilon = 40$ and $a = 1cm$ (ceramic disks) that enters the resonant frequencies into the THz range. Finally, we consider $\epsilon = 12$ (silica disks) and $a = h = 1\mu$ with the resonant frequencies in the optical range. Results of computations are presented in Fig. 14 which shows that there is no qualitative difference between the ceramic disks with $\epsilon = 40$ and silica disks with $\epsilon = 12$. Similar to Fig. 11 and Fig. 13 we observe spiral behavior of the resonant frequencies for the enough distance between the disks. But what is more remarkable we also observe an avoided crossing of the resonances with different indices as shown in Fig. 14 (d) with corresponding strong enhancement of the Q factor by one order in magnitude (Fig. 14 (e)).

4. Conclusions

For the isolated dielectric cylinder we have well known Mie resonances specified by azimuthal index $m = 0, \pm 1, \pm 2, \ldots$ (monopole, dipole, quadruple *etc* resonances) due to axial symmetry. Two parallel cylinders have no axial symmetry and therefore the solutions of the homogeneous Maxwell equations are given by series of the Bessel (inside) or Hankel (outside cylinders) functions in m. By the use of Graf formula the coefficients in series satisfy linear algebraic equations and can be easily found [21, 22, 23]. However, there were no studies on the behavior of resonances of two cylinders in dependence on the distance between them except the studies of the Q factor for extremely highly excited resonances, whispering gallery modes by Boriskina [17, 18]. The study presented in this paper reveals surprisingly rich evolution of the resonances with the distance that can be described by two scenarios. In the first scenario the resonances subsequently bypass the Mie resonances. Each time when the resonance is close to a Mie resonance the resonant mode inside the cylinders takes the field profile of the corresponding Mie resonant mode. At the same time the Q factor achieves maximal magnitudes. It is worthy to notify recent publication by Abdrabou

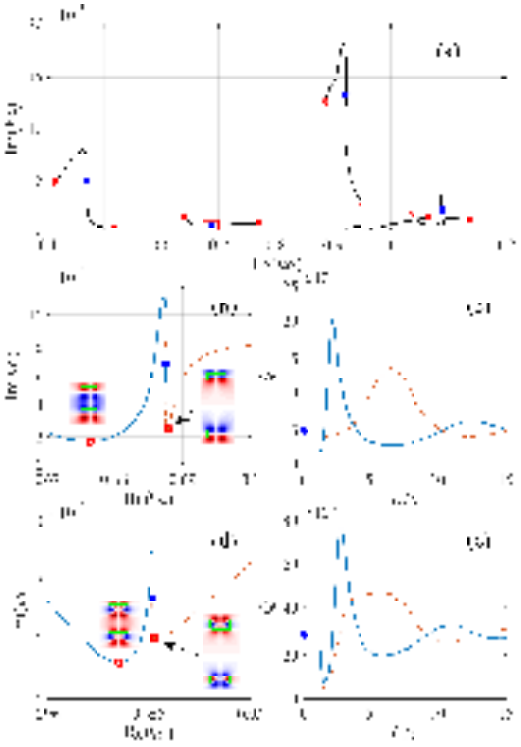


Figure 13: (a) Behavior of resonant eigenfrequencies under variation of the distance between the disks L with $\epsilon = 40$ (ceramics in THz range) and the aspect ratio $a/h = 0.7$. (b) and (d) zoomed areas highlighted in (a) with symmetric (solid lines) and antisymmetric (dash lines) hybridization (20) of resonant modes of the isolated disk. (c) and (e) show behavior of the Q factor vs the distance for corresponding insets at the left. Closed circles mark the eigenfrequencies of isolated disks and respectively the Q factors while crosses mark the limiting case $L = a$ when the two disks stick together.

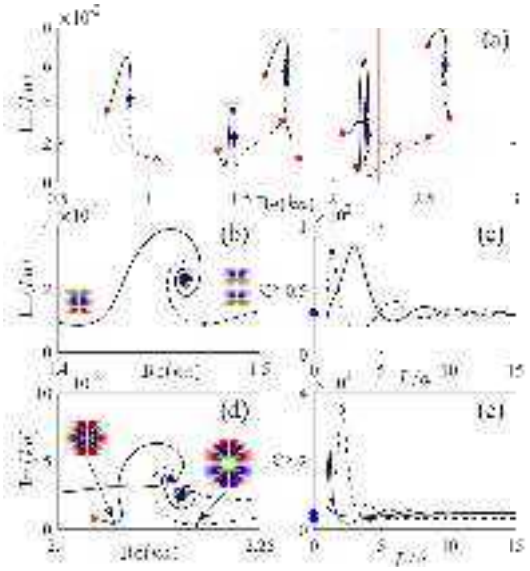


Figure 14: (a) Behavior of resonant eigenfrequencies under variation of the distance between the disks L with $\epsilon = 12$ (silica in optical range) and aspect ratio $a/h = 1$. (b) zoomed area highlighted in (a) with symmetric (solid lines) and antisymmetric (dash lines) hybridization (20) of resonant modes of the isolated disk. (c) shows behavior of the Q factor vs the distance for corresponding insets at the left. Closed circles mark the eigenfrequencies of isolated disks and respectively the Q factors while crosses mark the limiting case $L = a$ when two disks stick together.

and Ya Yan Lu [35] in which exceptional points for resonant states were achieved for variation of the distance between dielectric cylinders.

The evolution of resonances bound by the Mie resonances follows the second scenario and typical for the higher resonances with $m = 2, 3, \ldots$. It is interesting that the dipole resonance which leaks aside from the other cylinder bears features of the both families. When the leakage from the first cylinder is directed to the second cylinder, the overlapping (15) exceeds the coupling of the Mie dipole resonant modes which leakage aside the the cylinders. As a result in the first case the resonances consequently bypass the Mie resonances while in the second case the resonances are bound to the dipole Mie resonance of isolated cylinder. For variation of the distance the Q factor shows oscillating behavior with maxima which can exceed the Q factor of the isolated cylinder three times. That enhancement is typical for all types of resonances except the monopole resonance which demonstrates enhancement by one order in magnitude.

5. Discussions

The recept to enhance the Q factor by means of the avoided crossing of resonances is well known. Friedrich and Wintgen [3] were the first who investigated the quantitative influence of the interference of resonances on their positions and widths. Moreover, in the framework of two-level effective Hamiltonian they found out that one of the widths can turn to zero to identify the BIC. A single isolated dielectric particle of finite dimensions can not trap light because of the infinite number of radiation continua or diffraction channels [10]. However, for sufficiently large refractive index the particle shows distinctive resonances with the Q-factors which can be substantially enhanced owing to the avoided crossing of the resonances under variation of the aspect ratio of the disk [14, 15]. Technologically, it might be challengeable to vary the size of the disk in the optical range. In the present paper we propose to vary the distance between two coaxial disks that is preferable from the experimental viewpoint. Continuous variation of the distance gives rise to an avoided crossing of the resonances due to interaction between the disks through radiating resonant modes.

Although in the present paper we considered only dielectric cylinders and disks, it is clear that the phenomenon of the avoided crossing and respective enhancement of the Q factor would occur with particles of arbitrary shape when the distance between them is varied. The case of two coaxial disks simplifies computations because the solutions with different angular momentum m are independent. In the present paper we have presented only the case $m = 0$ because of a possibility to consider separately E and H polarizations.

Acknowledgement

We acknowledge discussions with A.A. Bogdanov and D.N. Maksimov.This work was partially supported by RFBR grant 19-02-00055 and Ministry of Education and Science of Russian Federation (state contract N 3.1845.2017/4.6).

References

[1] A.I. Kuznetsov, A.E. Miroshnichenko, M.L. Brongersma, Yu.S. Kivshar and B. Luk'yanchuk, Optically resonant dielectric nanostructures, *Science*, 354: 2472, 2016.

[2] K. Koshelev, A. Bogdanov, and Yu. Kivshar, Meta-optics and bound states in the continuum, *Science Bull.*, 17: 065601, 2018.

[3] H. Friedrich and D. Wintgen, Interfering resonances and bound states in the continuum, *Phys. Rev. A*, 32: 3231–3242 (1985).

[4] A.F. Sadreev, E.N. Bulgakov, and I. Rotter, Bound states in the continuum in open quantum billiards with a variable shape, *Phys. Rev. B*, 73: 235342 (2006).

[5] E.N. Bulgakov and A.F. Sadreev, Bound states in the continuum in photonic waveguides inspired by defects, *Phys. Rev. B*, 78: 075105 (2008).

[6] S.P. Shipman and S. Venakides, Resonant transmission near non robust periodic slab modes, *Phys. Rev. E*, 71: 026611 (2005).

[7] D. C. Marinica, A. G. Borisov, and S.V. Shabanov, Bound States in the Continuum in Photonics, *Phys. Rev. Lett.*, 100: 183902 (2008).

[8] Chia Wei Hsu, Bo Zhen, J. Lee, Song-Liang Chua, S.G. Johnson, J.D. Joannopoulos, and M. Soljačić, Observation of trapped light within the radiation continuum, *Nature*, 499: 188–191 (2013).

[9] E.N. Bulgakov and A.F. Sadreev, Bloch bound states in the radiation continuum in a periodic array of dielectric rods, *Phys.Rev. A*, 90: 053801 (2014).

[10] E.N. Bulgakov and A.F. Sadreev, Bound states in the continuum with high orbital angular momentum in a dielectric rod with periodically modulated permittivity , *Phys. Rev. A*, 96: 013841 (2017).

[11] Z.F. Sadrieva, M.A. Belyakov, M.A. Balezin, P.V. Kapitanova, E.A. Nenasheva, A. F. Sadreev, and A.A. Bogdanov, Experimental observation of a symmetry-protected bound state in the continuum in a chain of dielectric disks, *Phys. Rev. A*, 99: 053804 (2019).

[12] E.N. Bulgakov and A.F. Sadreev, High- Q resonant modes in a finite array of dielectric particles, *Phys. Rev. A*, 99: 033851 (2019).

[13] A. Taghizadeh and Il-Sug Chung, Quasi bound states in the continuum with few unit cells of photonic crystal slab, *Appl. Phys. Lett.*, 111: 031114 (2017).

[14] M.V. Rybin, K.L. Koshelev, Z.F. Sadrieva, K. B. Samusev, A. A. Bogdanov, M. F. Limonov and Yu. S. Kivshar, High-Q Supercavity Modes in Subwavelength Dielectric Resonators, *Phys. Rev. Lett.*, 119: 243901 (2017).

[15] A.A. Bogdanov, K.L. Koshelev, P.V. Kapitanova, M.V. Rybin, S.A. Gladyshev, Z.F. Sadrieva, K.B. Samusev, Yu.S. Kivshar, and M. F. Limonov, Bound states in the continuum and Fano resonances in the strong mode coupling regime, *Adv. Photonics*, 1: 016001 (2019).

[16] J. Wiersig, Formation of long-lived, scarlike modes near avoided resonance crossings in optical microcavities, *Phys. Rev. Lett.*, 97: 253901 (2006).

[17] S. V. Boriskina, Theoretical prediction of a dramatic Q-factor enhancement and degeneracy removal of whispering gallery modes in symmetrical photonic molecules, *Opt. Lett.*, 31: 338–340 (2006).

[18] S.V. Boriskina, Coupling of whispering-gallery modes in size-mismatched microdisk photonic molecules, *Opt. Lett.*, 32: 1557–1559 (2007).

[19] J. Unterhinninghofen, J. Wiersig, and M. Hentschel, Goos-Hanchen shift and localization of optical modes in deformed microcavities, *Phys. Rev. E*, 78: 016201 (2008).

[20] M. Benyoucef, J.-B. Shim, J. Wiersig, and O. G. Schmidt, Quality-factor enhancement of supermodes in coupled microdisks, *Opt. Lett.*, 36: 1317–1319 (2011).

[21] G.O. Olaofe, Scattering by Two Cylinders, *Radio Science*, 5: 1351–1360 (1970).

[22] J.W. Young and J.C. Bertrand, Multiple scattering by two cylinders, *J. Acoust. Soc. Am.*, 58: 1190–1195 (1975).

[23] Tak-Goa Tsuei and P.W. Barber, Multiple scattering by two parallel dielectric cylinders, *Appl. Opt.*, 27: 3375–3381 (1988).

[24] K. Yasumoto and H. Jia, Modeling of Photonic Crystals by Multilayered Periodic Arrays of Circular Cylinders, in book *Electromagnetic Theory and Applications for Photonic Crystals*, MIT Press, Cambridge, 2006.

[25] M. Abramowitz and I.A. Stegun, *Handbook of Mathematical Functions*, National Bureau of Standards, 1964.

[26] I. Awai and Y. Zhang, Coupling coefficient of resonators - An intuitive way of its understanding, *Electronics and Communications in Japan (Part II: Electronics)*, 90: 11–18 (2007).

[27] S.Y. Elnaggar, R.J. Tervo, and S.M. Mattar, General expressions and physical origin of the coupling coefficient of arbitrary tuned coupled electromagnetic resonators, *J. Appl. Phys.*, 118: 194901 (2015).

[28] A. Tayebi and S. Rice, Superradiant and Dark States in Non-Hermitian Plasmonic Antennas and Waveguides, arXiv: 1812.10057v1 (2018).

[29] J.D. Joannopoulos, R.D. Meade, and J.N. Winn, *Photonic Crystals: Molding the Flow of Light*, Princeton Univ.Press, 1995.

[30] P. Lalanne, Wei Yan, K. Vynck, C. Sauvan, and J.-P. Hugonin, Light Interaction with Photonic and Plasmonic Resonances, *Laser & Photonics Reviews*, 12: 1700113 (2018).

[31] R.M. More and E. Gerjuoy, Properties of Resonance Wave Functions, *Phys. Rev. A*, 7: 1288–1303 (1973).

[32] E.A. Muljarov, W. Langbein, and R. Zimmermann, Brillouin-Wigner perturbation theory in open electromagnetic systems, *Europhys. Lett.*, 92: 50010 (2010).

[33] A.W. Snyder and J.D. Love, *Optical Waveguide Theory*, Springer, 1984.

[34] E.N. Bulgakov and A.F. Sadreev, Bound states in the continuum with high orbital angular momentum in a dielectric rod with periodically modulated permittivity, *Phys. Rev. A*, 96: 013841 (2017).

[35] A. Abdrabou and Ya Yan Lu, Exceptional points for resonant states on parallel circular dielectric cylinders, J. Opt. Soc. Am. B, 36: 1659–1667 (2019).

Magneto-plasmonics

Ultra-wideband graphene circulators for THz region

Victor Dmitriev[1], Samara Leandro Matos da Silva[1,2], Wagner Castro[1,3],

[1]Department of Electrical Engineering, Federal University of Para, PO Box 8619, Agencia UFPA, 66075-900, Belem, Para, Brazil
[2]Federal University of Tocantins, 77842-838, Araguana, Tocantins, Brazil
[3]Cyberspace Institute, Federal Rural University of Amazonia, Belm 66077-830, Brazil
*corresponding author, E-mail: samaraleandro@uft.edu.br

Abstract

3-port and 4-port THz circulators are discussed. The circulators are based on graphene placed on a two-layer dielectric substrate. The circulation behaviour is defined by application of a DC magnetic field normal to the graphene plane. We discuss the choice of the physical and geometrical parameters which provide octave frequency band of these components.

1. Introduction

Nonreciprocal components are indispensable part of many microwave [1] and optical systems. The existing publications show that the bandwidth of the graphene-based circulators in THz region can be of $(10-20)\%$ [2]. Usually, they have rather complicated structure [3, 4]. The suggested in this work circulators have very simple design which presents the magnetized junction of three strip graphene waveguides. We discuss the principal parameters which define the bandwidth and their influence on the bandwidth. The calculations are fulfilled by a full-wave electrodynamic method. Our approach gives recipes to engineer the edge-guided circulators with octave frequency band.

2. Problem description

The geometries and coordinate system used for the analysis are shown in Fig. 1. In the 3-port circulator (Fig. 1 (a)) the device is formed by a central magnetized region and three waveguides symmetrically connected to it. Analogously, in the 4-port circulator, the four waveguides are symmetrically coupled to the central region (Fig. 1 (b)). The third device, also a 4-port circulator (Fig. 1 (c)), is equivalent to combination of two T-circulators. The width of the guides is indicated by w and R is the radius of the circumference that define the curvature of the central region of the devices. The thicknes of the graphene is d, of silica (SiO_2) is h_1, and of silicon (Si) is h_2. The permittivity of SiO_2 is 2.09 and Si is 11.9.

3. Numerical modeling of graphene

The electric conductivity tensor of graphene is modeled by using the semiclassical approach based on the Boltzmann transport equation. This model is described by simple equations and fits well in THz frequency region.

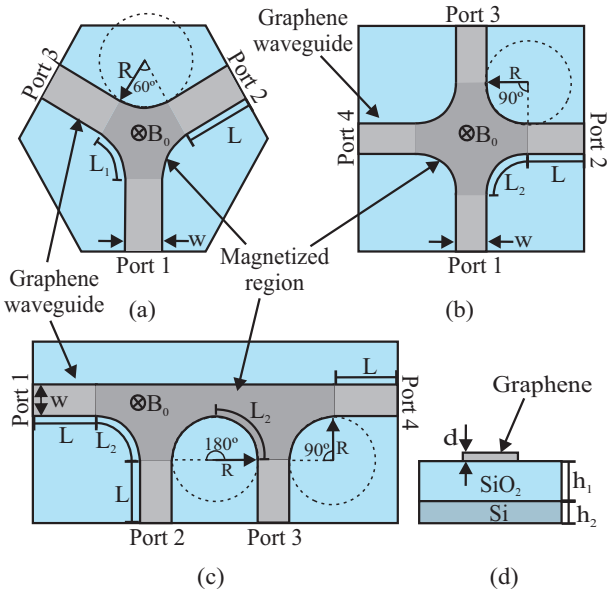


Figure 1: Sketch of graphene circulator, (a) top view, (b) side view, B_0 is DC magnetic field.

The graphene conductivity tensor can be written as follows:

$$[\sigma_s] = \begin{bmatrix} \sigma_{xx} & -\sigma_{xy} \\ \sigma_{xy} & \sigma_{xx} \end{bmatrix}. \quad (1)$$

The parameters of the conductivity tensor are given in [5]:

$$\sigma_{xx} = \frac{q_e^2 \mu_c}{\pi\hbar^2} \frac{1/\tau - i\omega}{\omega_c^2 - (\omega + i1/\tau)^2}, \quad (2)$$

and

$$\sigma_{xy} = -\frac{q_e^2 \mu_c}{\pi\hbar^2} \frac{\omega_c}{\omega_c^2 - (\omega + i1/\tau)^2}, \quad (3)$$

where q_e is the charge of the electron, $\hbar$ is reduced Planck constant, ω_c the angular cyclotron frequency, τ relaxation time, w the angular frequency incident and μ_c the chemical potential of graphene. The angular cyclotron frequency is defined by $\omega_c = q_e B_0 v_F^2/\mu_c$, where B_0 represents the DC magnetic field and v_F the Fermi velocity $v_F \approx 9.5 \times 10^5\ m/s$. In this work we will use the parameter $\tau = 0.9\ ps$ [6].

Analogously to that used in ferrite devices [1] we can define the graphene gyrotropy parameters, from the param-

eters $Re\{\sigma_{xy}\}$ and $Im\{\sigma_{xx}\}$ which define the losses in it.

$$g = \frac{Re\{\sigma_{xy}\}}{Im\{\sigma_{xx}\}} = \frac{\omega_c}{\omega}\frac{(\omega^2 - \omega_c^2 - (1/\tau)^2)}{(\omega^2 - \omega_c^2 + (1/\tau)^2)}. \quad (4)$$

4. Numerical Results

The numerical results were obtained by the commercial software Comsol Multiphysics [7]. Bandwidth was calculated as an intersection of frequency bands corresponding to the reflection which is less than $-10\ dB$, the transmission which is better than $-2\ dB$ and the isolation higher than $-15\ dB$. From Fig. 2 one can see that, in the band of $(2.5 \div 4.5)$ THz, the circulator has a good matching, S_{11} is better than $-10\ dB$, in the band of $(2.65 \div 4.2)$ the level of isolation is less than $-15\ dB$ and the insertion loss is better than $-2\ dB$ in the band of $(2.5 \div 4.05)$. Thus, the resultant bandwidth is 42%.

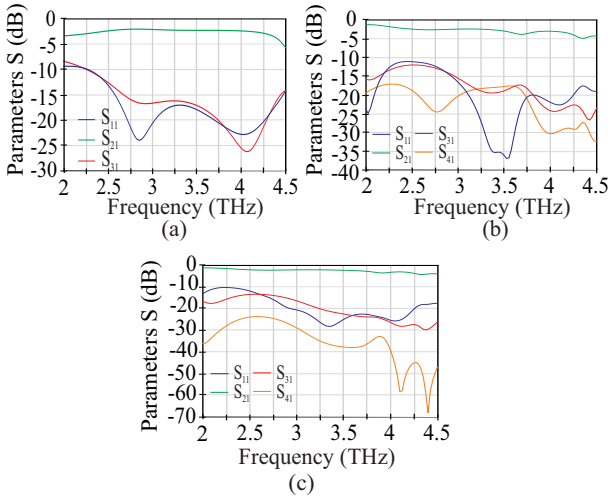


Figure 2: Transmission, reflection and isolation coefficients (a) for the 3-port circulator, (b) for the 4-port circulator (Fig. 1 (b)) and (c) for the 4-port circulator (Fig. 1 (c)), $w = 2\ \mu m$, $R = 2.75\ \mu m$, $B_0 = 1.5\ T$ and $\mu_c = 0.15\ eV$.

In Fig. 3 we present the distribution of the electric field component E_z for the discussed circulators for the frequency $2.85THz$.

5. Conclusions

The discussed circulators possess the record bandwidth which is twice as much as the published ones. For example, the 3-port circulator works in the 42% frequency band and even can achieve octave band. Thus, the presented components are characterized by a very high bandwidth and good characteristics of transmission and isolation. They can be used in integrated THz circuits. The presented methodology can be also used in the infrared frequency range.

Acknowledgement

This work was supported by Brazilian agency CNPq.

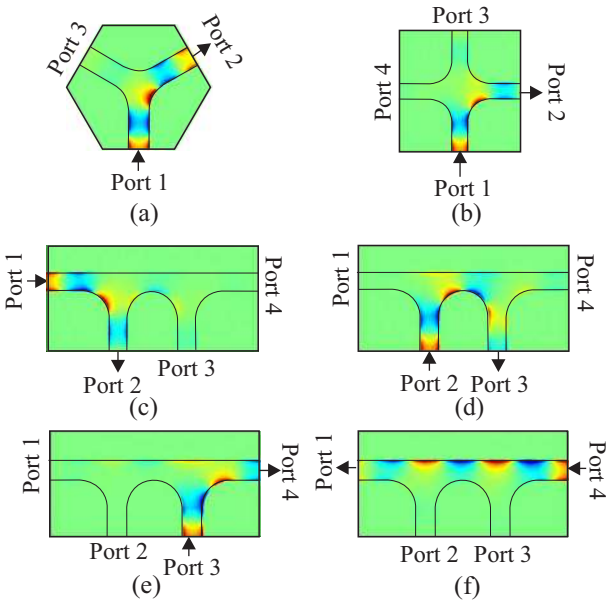


Figure 3: E_z distribution in circulators. Parameters used $w = 2\ \mu m$, $R = 2,75\ \mu m$, $B_0 = 1.5\ T$ and $\mu_c = 0.15\ eV$.

References

[1] J. Helszain, *The Stripline Circulators: Theory and Practice,* Wiley, Hoboken, 2008.

[2] V. Dmitriev, and W. Castro, *Dynamically Controllable Terahertz Graphene Y-Circulator,* IEEE Transactions on Magnetics, vol.55, no. 2, pp. 4001712-4001724, Fev. 2019.

[3] X. Lin, Y. Xu, B. Zhang, R. Hao, H. Chen and E. Li, *Unidirectional surface plasmons in nonreciprocal graphene,* New Journal of Physics, vol. 15, no. 11, pp. 113003-113018, Nov. 2013.

[4] V. Nikkhah, A. Bakhtafrouz, M. Maddahali and S. K. Dezaki, *Three-port graphene-based electromagnetic circulator in the terahertz and infrared frequency ranges with a very low loss and wideband response*, JOSA B, vol. 35, no. 8, pp. 1754-1763, Jul. 2018.

[5] G. P. A. Dias and N. M. M. R. Peres. *An Introduction To Graphene Plasmonics,* World Scientific, Hackensack, 2016.

[6] A. Principi, and G. Vignale, *Intrinsic lifetime of Dirac plasmons in graphene,* Phys. Review B, vol. 88, no. 19, pp. 195405-195420, 2013.

[7] www.comsol.com

Plasmon-induced inverse Faraday Effect and switchable routers and modulators in magneto-plasmonic structures

Joachim Herrmann[1], Song-Jin Im[2], Ji-Song Pae[2], Chol-Song Ri[2], Kum-Song Ho[2], Yong-Ha Han[2]

[1]Max-Born-Institute for Nonlinear Optics and Short Pulse Spectroscopy, Berlin, Germany

[2] Kim Il Sung University, Pyongyang, Democratic People's Republic of Korea

Recently, the inverse Faraday Effect (IFE) has attracted much attention because of its potential impact for ultrafast all-optical switching of magnetization in thin magnetic films induced by ultrafast pulses [1] which opens the possibility for magnetic data storage with unprecedented speed. In order to enable sub-wavelength spatial resolution for magnetic recording we study a modified version- the plasmon-induced IFE- in which instead of free space circular polarized optical pulses free running surface-plasmon-polaritions (SPP) generated by incident linearly polarized input pulses induce a quasi-static magnetic field. SPPs exhibit a longitudinal component of the electric field, therefore the vector product of E and its complex conjugate E* do not vanishes. This means that in an opto-magnetic material quasi-static magnetic fields can also be induced by running SPPs. We present analytical and numerical results for the computation of the induced magnetic field distributions by SPPs in a metal-insulator-metal

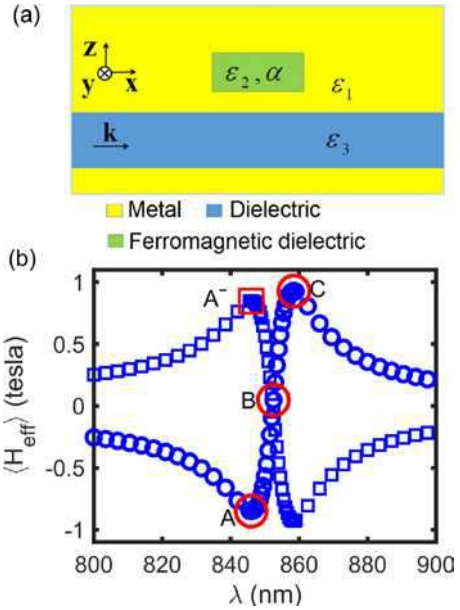


Fig. 1. Scheme (a) and averaged effective magnetic field vs the wavelength (b).

plasmonic waveguide with an isolator layer composed from a ferromagnetic dielectric and show that the magnetization of a magnetic area can be reversed within sub-ps time in such nano-confined waveguides. The magnetization can be switched back by SPPs propagating into the opposite direction. Besides we study a magneto-optical dielectric cavity side-coupled to a metal-insulator-metal (MIM) waveguide (Fig.1a). The average effective magnetic field *H*eff denotes the average value over the magneto-optical cavity [the green part of Fig.1a). *H*eff is sensitive to the wavelength near the resonance and perceives a sign change [the points A and C of Fig.1b). It becomes zero at the exact resonance [the point B of Fig. 1(b)]. The sign of *H*eff is also reversed for backward-propagating SPPs (point A^- in Fig.1b). The cavity resonance wavelength is determined by the length of the cavity. This could open up a mechanism for multilevel 3D magnetic recording by using several layers including opto-magnetic cavities with varying resonance wavelength in every layer addressed by using multi-wavelength optical pulses.

The back-reaction of the IFE on the plasmon propagation leads to a new type of ultrafast third-order nonlinearity with a nonlinear susceptibility exceeding the optical Kerr effect of typical dielectric materials by five orders of magnitude and that of gold by two orders of magnitude [3]. We derive analytical expressions for IFE-related nonlinear susceptibility for a ferromagnetic dielectric/metal interface and for a dielectric/hybrid metal-ferromagnetic interface.

In a second part of the talk we propose and study a magnetically controlled switchable plasmonic router with 99-%-high contrast [4]. In metal films surrounded by a ferromagnetic

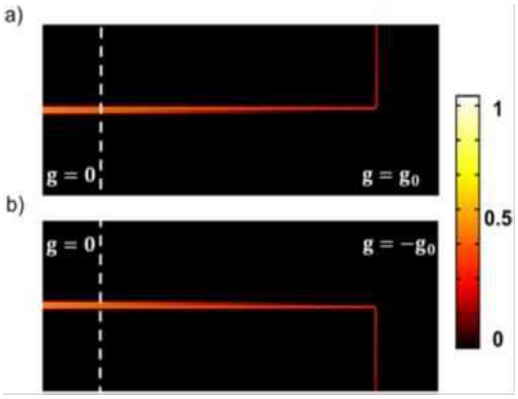


Fig 2. Numerical results for the magnetic field distribution for a gyration g=0.026 (a) and g=-0.026 (b), respectively.

dielectric an external magnetic field in the transverse direction can induce a significant spatial asymmetry of mode distribution. Superposition of the odd and the even asymmetric modes over a certain distance leads to a concentration of the energy on one interface which is switched to the other interface by magnetic field reversal. In Fig. 2 numerical results for the magneto-plasmonic waveguide show a high-contrast modulation and channel switching by the magnetic field reversal. We estimate the modulation contrast defined by the ratio of powers through the two channels in dependence on the gyration g and the wavelength λ. The numerical results well agree with the analytically predicted results. The power splitting ratio is tunable by controlling the external magnetic field and reaches a value larger than 20 dB, which corresponds a contrast 99% over a broad wavelength range from 770nm to 820nm.

Finally, we propose and study a novel type of plasmonic resonators based on a metal-insulator-metal waveguide and above the upper thin metallic layer a side-coupled magneto-optical disk controlled by an external magnetic field [5]. The wave-number change and the transmission can be tuned by altering the magnetic field and reversible on/off switching of the running SPP modes by a reversal of the direction of the external magnetic field is demonstrated. Fig, 3(a) and 3(b) show the distribution of the magnetic field component of the SPPs at a gyration g=-0.03 and g=0.03, respectively. As seen by changing the direction of the magnetic field, the SPP transmission is switched from an off to an on state via the changed interference pattern.

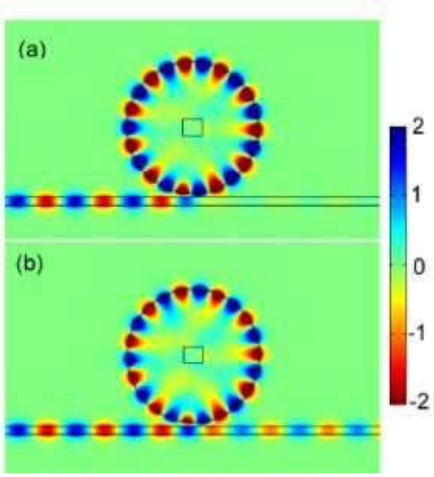


Fig. 3.Distribution of the SPP magnetic field component for g= -0.03 and g=0.03, respectively.

References:
[1] C.D. Stanciu et al., Phys. Rev. Lett. 99, 047601 (2007),
[2] Song-Jin Im et al. Phys. Rev. B 99, 041401 (R) (2019).
[3] Song-Jin Im et al. Phys. Rev. B96, 165437 (2017).
[4] Kum-Song Ho et al. Scientific Reports 8:10584 (2018),
[5] Ji-Song Pae et al .Phys. Rev. B 98, 041406 (R) (2018).

Second Harmonic Generation in Hyperbolic Magneto-Plasmonic Metasurfaces

Dmitry A. Kuzmin[1,2,*], Igor V. Bychkov[1,2], Vladimir G. Shavrov[3] and Vasily V. Temnov[4]

[1]South Ural State University (National Research University), 76 Lenin Prospekt, Chelyabinsk 454080, Russian Federation
[2]Chelyabinsk State University, Br. Kashirinykh Street 129, 454001 Chelyabinsk, Russian Federation
[3]Kotelnikov Institute of Radio-engeneering and Electronics of RAS, 11/7 Mokhovaya Str., Moscow 125009, Russian Federation
[4]Institut des Molécules et Matériaux du Mans, CNRS UMR 6283, Université du Maine, 72085 Le Mans cedex, France
*corresponding author, E-mail: kuzminda@csu.ru

Abstract

In this work we propose a new class of hyperbolic magneto-plasmonic metasurface for second harmonic generation (SHG). We discuss three possible realizations of such a metasurfaces, which based on non-linear magneto-plasmonic multilayers. Theoretical models for investigation of SHG in abovementioned realizations are performed.

1. Introduction

Nowadays, hyperbolic plasmonics attracts researchers' attention by its exciting optical properties [1-6]. Hyperbolic metasurfaces (HMSs) support highly localized low-loss surface plasmon-polaritons (SPPs), providing drastic increase of the light-matter interactions near the surface. Moreover, HMSs allow the very effective manipulation by SPPs varying from routing them towards specific directions within the sheet, dispersion-free propagation (canalization),

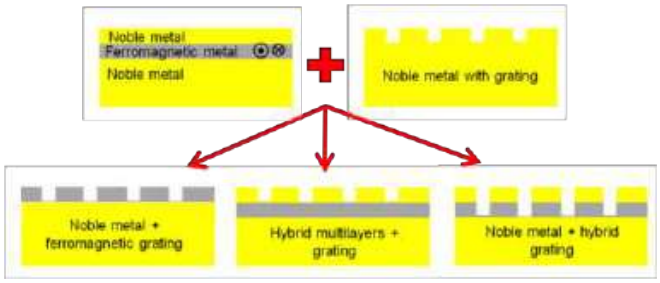


Figure 1: Hyperbolic magneto-plasmonic metasurfaces may be created by combination of principles of hybrid metal-ferromagnet magneto-plasmonic nanaostructures and hyperbolic metasurface realized by subwavelength grating. Depending on position of ferromagnet layer and grating depth it is possible to construct tree structures.

and to the negative refraction.

The usual realization of HMSs is constructing the surface which behaves as a dielectric (has a capacitive impedance) in one direction and as a metal (has an inductive impedance) in the orthogonal one. In the hyperbolic regime plasmons propagate as a very narrow beam along the specific direction and electromagnetic energy became localized near metasurface even stronger than for "usual" elliptic SPPs.

Recently, non-linear magnetooptical properties of rectangular array of nickel dimers featuring a nanoscale gap have been investigated [7]. Taking advantage of different periods of the investigated array in two orthogonal in-plane directions, a novel regime for the nonlinear Wood's anomaly, when the structure exhibits grating properties exclusively at the second harmonic wavelength $\lambda/2$ but not at the fundamental wavelength λ, has been identified. In this nonlinear regime the Wood's anomaly is characterized by an order-of-magnitude larger effect in intensity redistribution between the diffracted beams, as compared to the linear case.

The general trend of increasing light-matter interactions near the surface in hyperbolic regime allows us suppose that non-linear magneto-plasmonic effects in magneto-plasmonic HMSs should have some non-trivial features as well.

Here, we investigate a second harmonic generation (SHG) (including magneto-induced SHG) in magneto-plasmonic HMSs, when the periodicity of the metasurface is much smaller than both fundamental and second harmonic wavelengths.

2. Hyperbolic magneto-plasmonic metasurfaces

Usually HMSs are realized by deeply subwavelength grating of plasmonic (metallic) surface [1-6]. For non-linear magneto-plasmonics, metal-ferromagnet multilayer structures have a great potential [8]. Hyperbolic magneto-plasmonic metasurface may be constructed by combination of these two ideas, i.e. by subwavelength grating of magneto-plasmonic multilayers. Here, depending on the

position of ferromagnet and grating depth three variants are possible (see Figure 1 for details): noble metal covered by ferromagnetic metasurface (similar structure has been investigated recently [7], but for non-hyperbolic regime), hybrid metal-ferromagnet structure covered by noble metal based metasurface, and noble metal covered by hybrid metal-ferromagnet metasurface (similar structures have been investigated in [9], but not for hyperbolic regime as well).

Taking into account very interesting and promising properties of such kind of metasurfaces in non-hyperbolic regime, it is highly desirable to investigate the behavior of all the effects in hyperbolic regime of metasurface.

3. Discussion

In order to investigate SHG in hyperbolic magneto-plasmonic MSs, theoretical model based on effective medium approximation has been performed. In contrast to hybrid metal-ferromagnet plasmonic structure, hyperbolic magneto-plasmonic MSs will have a highly anisotropic dielectric permittivity tensor. This leads to significantly anisotropic SHG signal (with respect to SPPs propagation direction).

In directions where SPPs cannot propagate, SHG signal will have the similar behavior as for the system without the metasurface, while in directions where canalization of SPPs observed SHG signal significantly increase.

In contrast to usual hybrid metal-ferromagnet multilayers, proposed structure will have an additional surfaces for SHG signal caused by grating. For hybrid metal-ferromagnet multilayers non-magnetic SHG is caused by z-component of non-linear polarization P_z at all the interfaces (z-axis is perpendicular to the interfaces, x- and y- axis lies in-plane), while magnetic SHG is caused by P_x. For noble metal covered by ferromagnetic metasurface and for noble metal covered by hybrid metal-ferromagnet metasurface an additional z-component of non-linear polarization will be induced by interfaces between magnetic metal and air in grating. In turn, for hybrid metal-ferromagnet structure covered by noble metal based metasurface, and for noble metal covered by hybrid metal-ferromagnet metasurface an additional x-component of non-linear polarization will be induced by interfaces between non-magnetic metal and air in grating.

4. Conclusions

We have proposed and theoretically investigated new class of hyperbolic magneto-plasmonic metasurfaces for SHG. These structures may have an increased both magnetic and non-magnetic SHG signal. Highly anisotropic properties of such structures may open the door for directional SHG and magnetic control of SHG directivity. Existence of additional grating-caused interfaces may allow geometrical tuning of the interference between magnetic and non-magnetic impact in SHG.

Acknowledgements

The work was financially supported in part by RFBR (16-37-00023, 16-07-00751, 16-29-14045, 17-57-150001), Act 211 Government of the Russian Federation (contract № 02.A03.21.0011).

References

[1] J. S. Gomez-Diaz, M. Tymchenko, A. Alù, Hyperbolic plasmons and topological transitions over uniaxial metasurfaces, *Phys. Rev. Lett.* 114: 233901, 2015.

[2] J. S. Gomez-Diaz, M. Tymchenko, A. Alù, Hyperbolic metasurfaces: surface plasmons, light-matter interactions, and physical implementation using graphene strips, *Optical Materials Express* 5: 2313-2329, 2015.

[3] J. S. Gomez-Diaz, A. Alù, Flatland Optics with Hyperbolic Metasurfaces, *ACS Photonics* 3: 2211–2224, 2016.

[4] A. Nemilentsau, T. Low, G. Hanson, Anisotropic 2D materials for tunable hyperbolic plasmonics, *Phys. Rev. Lett.* 116: 066804, 2016.

[5] A. V. Kildishev, A. Boltasseva, V. M. Shalaev. Planar photonics with metasurfaces, *Science* 339: 1232009, 2013.

[6] A. A. High, R. C. Devlin, A. Dibos, et al., Visible-frequency hyperbolic metasurface, *Nature* 522: 192, 2015.

[7] N.-M. Tran, I.-O. Chioar, A. Stein, et al., Observation of the nonlinear Wood's anomaly on periodic arrays of nickel nanodimers, *Physical Reviews B* 98: 245425, 2018.

[8] I. Razdolski, D. Makarov, O. D. Schmidt, et al., Nonlinear surface magnetoplasmonics in Kretschmann multilayers, *ACS Photonics* 3: 179, 2016.

[9] G. Armelles, L. Bergamini, N. Zabala, et al., Metamaterial Platforms for Spintronic Modulation of Mid-Infrared Response under Very Weak Magnetic Field, *ACS Photonics* 5: 3956, 2018.

Enhancement of Faraday rotation of iron thin layers on periodic array of Al nanocylinders

Taisuke Atsumi[1], Shunsuke Murai[1*], Katsuhisa Tanaka[1*]

[1] Graduate School of Engineering, Kyoto University, Kyoto, Japan
*corresponding author, E-mail: tanaka@dipole7.kuic.kyoto-u.ac.jp(KT), murai@dipole7.kuic.kyoto-u.ac.jp(SM)

Abstract

Diffractive plasmonic nanostructures sustain both localized surface plasmon polaritons (LSPPs) and optical diffraction in the plane of the array, i.e., lattice plasmon. Although such structure combined with magnetic materials can largely enhance magnetooptical (MO) effects, the plasmonic material utilized for MO enhancement is limited to Au. In this study, we fabricated diffractive array composed of Al nanocylinders and succeeded in enhancement of Faraday rotation of Fe layer deposited on the array at spectrally shorter range (blue to green) of visible light.

1. Introduction

It has been demonstrated that diffractive plasmonic nanostructures can largely enhance MO effects[1-3]. Such systems include periodic one-dimensional gratings and two-dimensional nanoparticle/nanohole arrays of plasmonic metals combined with magnetic materials, which support lattice plasmons, i.e., the radiative coupling between LSPPs via light diffraction. These systems utilize two kinds of resonances for MO enhancement; not only the LSPPs that accumulate light in the vicinity of the metallic surface to enhance MO effect locally, but the light diffraction that traps light inside the MO-active region and enhances light-matter interaction. In this sense, diffractive plasmonic nanostructures possess advantages of both LSPP-based system and diffraction-based, i.e., magnetophotonic crystals [4, 5], systems. In addition, these systems enjoy advanced properties including wavelength-selective MO enhancement by the periodicity of the gratings and arrays [6, 7].

In spite of high degree of freedom in engineering the MO effect, the material used for diffractive plasmonic nanostructures has been limited to Au thus far. This restricts the tunability of enhancement to the spectral region where Au shows plasmonic behavior, typically optical wavelength $\lambda > 600$ nm. In this study, we fabricated Al nanocylinder array to obtain enhanced MO effect at shorter spectral regions. The array was designed to show lattice mode around $\lambda = 500$ nm, overlapping with LSPPs of Al nanocylinders. As a MO-active material, Fe was deposited on top of the array and Faraday effect was examined. We compared the MO enhancement to that of the Fe layer on the nanocylinder array of Si and SiO_2 with the design identical to the Al nanocylinder array.

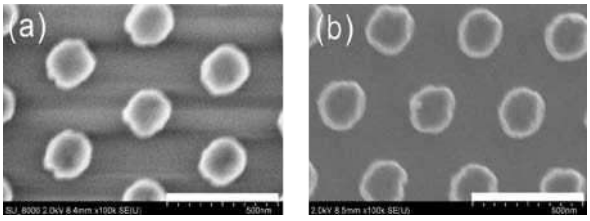


Figure 1: SEM images of the Al nanocylinder array; (a) before and (b) after deposition with 7.5 nm Fe. Scale bar = 500 nm.

2. Experiment

2.1. Sample fabrication

Al nanocylinders arranged in a triangle lattice with a period $p = 400$ nm was fabricated using nanoimprint lithography in combination with reactive ion etching (RIE), as described elsewhere [8]. The designed height (H) and diameter (D) of the nanocylinder were $H = 150$ nm and $D = 200$ nm, respectively. Si nanocylinder arrays were fabricated by the combination of nanoimprint lithography and Si deep etching, from the polycrystalline Si with a 200 nm thick on silica glass substrate. SiO_2 nanocylinder arrays were fabricated by the combination of nanoimprint lithography and RIE, by directly depositing resist on the silica substrate. The same mold was used in nanoimprint process for all the fabrications so that the design of the Al, Si and SiO_2 nanocylinder arrays were identical to each other. Fe thin layer (7.5 nm thickness) was deposited on the nanocylinder arrays by electron beam deposition under 4.0×10^{-4} Pa.

Zeroth-order optical transmittance was measured by UV-visible-near infrared spectrophotometer, (V770, JASCO). Wavelength-dependence of Faraday rotation angle (θ_F) was measured at room temperature by the polarization modulation technique using a commercial measurement system (K-250, JASCO).

3. Results and Discussion

Figure 1(a) shows scanning electron microscopic (SEM) image of Al nanocylinder array prepared on silica glass substrate. Al cylinders with D = 200 nm are arranged in triangle lattice with P = 400 nm. Figure 1(b) illustrates the SEM image of Al nanocylinder array on which 7.5 nm thick Fe layer was deposited. The diameter of each cylinder becomes larger by the Fe deposition.

Figure 2 compares θ_F and transmittance of the Fe layer on the Al nanocylinder array. The transmittance of Fe layer on the array is less than that on the flat substrate because of the additional extinction by the Al nanocylinders. The vertical dotted lines denote the condition of in-plane diffraction calculated by using a refractive index of glass (n = 1.46). A kink is found in the optical transmission indicating the occurrence of in plane diffraction. A modulation in θ_F is found at around the in-plane diffraction condition, and the magnitude in θ_F of the Fe layer on the Al nanocylinder array is larger than that on a flat silica glass in most of the spectral range measured. In Faraday rotation spectrum, θ_F of 7.5 nm thin Fe layer on the Al nanocylinder array has two local maxima at λ = 403 and 503 nm, which are associated with SPPs and the in-plane light diffraction, respectively.

For the Fe layer on the Si nanocylinder array (Fig. 3), the value of θ_F for the Fe layer deposited on the array is similar to that on the flat substrate, and a modulation is found around the spectral range of diffraction anomaly. A comparison between Figs. 2 and 3 clearly suggests that the Al nanocylinder array possesses a higher ability to enhance Faraday rotation compared to the Si nanocylinder array.

4. Conclusions

We designed the diffractive array of Al nanocylinders and enhanced MO effect of Fe layer deposited on the top of the nanocylinders. Two local maxima appear in Faraday rotation spectrum, one is due to LSPP (λ = 403 nm) and the other is lattice mode (λ = 503 nm). A comparison with Si nanocylinder array proves that LSPPs peculiar to Al show higher ability to enhance Faraday rotation, although Si could enhance the Faraday effect under optimal designs. This work clarified the advantages of Al nanocylinder array to tune the MO effect in blue to green region of the spectrum, which cannot be achieved by Au nanostructures reported thus far.

Acknowledgements

This work was partly supported by the Nanotechnology Hub, Kyoto University, the National Institute for Material Science and Nanotech CUPAL. The work was also financially supported by JSPS KAKENHI (Grant-in-Aid for Scientific Research(A)) Grant Number JP17H01320..

References

[1] J.Y. Chin *et al.*, Nonreciprocal plasmonics enables giant enhancement of thin-film Faraday rotation, *Nat Commun*, **4** (2013) 1599.

[2] A.V. Baryshev *et al.,* Tunable plasmonic thin magneto-optical wave plate, *Journal of the Optical Society of America B*, **33** (2016) 1399-1405.

[3] D. Floess *et al.*, Plasmonic Analog of Electromagnetically Induced Absorption Leads to Giant Thin Film Faraday Rotation of 14°, *Physical Review X*, **7** (2017) 021048.

[4] V.I. Belotelov *et al.*, Magnetophotonic intensity effects in hybrid metal-dielectric structures, *Phys Rev B*, **89** (2014) 045118.

[5] J.M. Caicedo *et al.*, Magnetophotonic Response of Three-Dimensional Opals, *ACS Nano*, **5** (2011) 2957-2963.

[6] S. Sadeghi *et al.*, Enhanced Faraday rotation in one dimensional magneto-plasmonic structure due to Fano resonance, *J Magn Magn Mater*, **451** (2018) 305-310.

[7] H. Uchida *et al.*, Large enhancement of Faraday rotation by localized surface plasmon resonance in Au nanoparticles embedded in Bi:YIG film, *J Magn Magn Mater*, **321** (2009) 843-845.

[8] Y. Kawachiya *et al.*, Collective plasmonic modes excited in Al nanocylinder arrays in the UV spectral region, *Opt Express*, **26** (2018) 5970-5982.

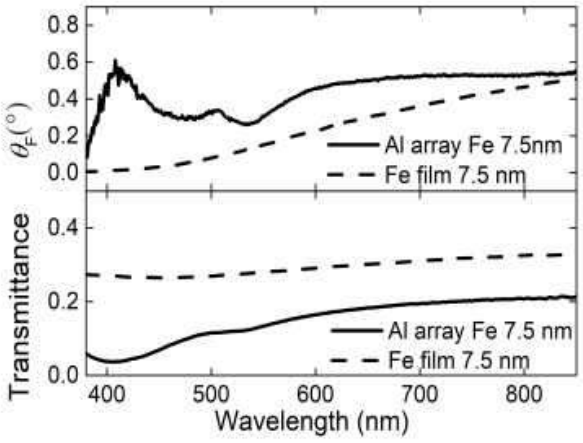


Figure 2: Faraday rotation angle, θ_F, (top panel) and transmittance (bottom) of Al nanocylinder array on which 7.5 nm Fe layer was deposited. Faraday rotation angle and transmittance of the Fe thin layer on a flat SiO_2 substrate are also shown.

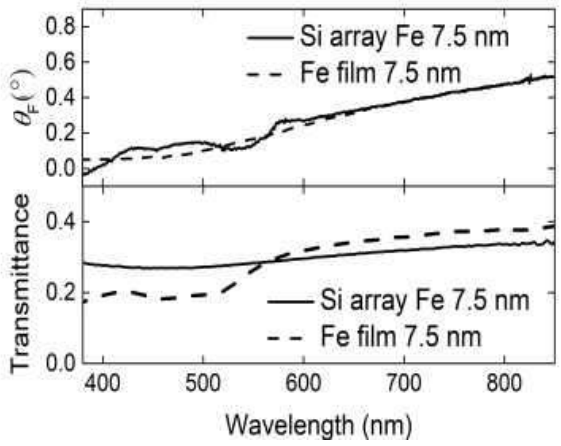


Figure 3: Faraday rotation angle, θ_F, (top panel) and transmittance (bottom) of Si nanocylinder array on which 7.5 nm Fe layer was deposited. Faraday rotation angle and transmittance of the thin Fe layer on a flat SiO_2 substrate are also shown.

Versatile $Tb_{18}Co_{72}$ magnetoplasmonic nanooptical antennas

Richard Rowan-Robinson[1], J. Hurst[1], A. Čiučiulkaitė[1], I-A. Chioar[1], M. Pancaldi[2*], P. Vavassori[2], P. M. Oppeneer[1], A. Dmitriev[3], V. Kapaklis[1]

[1]Department of Physics and Astronomy, Uppsala University, Uppsala, Sweden
[2]CIC nanoGUNE Consolider, San Sebastian, Spain
[3]Department of Physics, University of Gothenburg, Gothenburg, Sweden
*present address: Department of Physics, Stockholm University, Stockholm, Sweden

Abstract

We demonstrate the fabrication and measurement of hybrid magnetoplasmonic Au/$Tb_{18}Co_{72}$ nanoantennas. Tb_xCo_{1-x} alloys have been shown to exhibit all-optical switching and the merging with plasmonics could yield routes to optical switching of single nanomagnetic elements. The structures exhibit a dramatic enhancement of the Faraday effect when localized surface plasmons (LSPs) are excited. An angular dependence is observed, whereby the sign and magnitude of the Faraday effect can by tuned through the mutual combination of incidence wavelength and incidence angle.

1. Introduction

Nanoscale confinement of light with the aid of plasmonics has stimulated research towards a number of future technologies including on-chip micro- and nanosensor arrays [1], super-resolution imaging and designer flat-optics [2]. Within this field, active plasmonics, wherein the optical properties can be tuned in real time by an external stimulus are of great interest. Here, magnetoplasmonics provides a promising avenue to achieve real-time dynamic plasmonic devices with the use of an external magnetic field.

In this work, we demonstrate the incorporation of plasmonics with magnetic materials which exhibit all-optical switching [3]. Plasmonics can increase the efficiency of the all-optical switching effect whilst simultaneously allowing switching of individual nanoscopic elements. Furthermore, the use of Tb_xCo_{1-x} alloys which have perpendicular magnetic anisotropy, reduces the magnetic field required to orient the magnetization out of the plane of the film, as is required to measure the Faraday effect.

2. Discussion

Thin films of Au(80nm)/$Tb_{18}Co_{72}$(20nm)/Al_2O_3(3nm) were patterned into ordered arrays of nanoantennas. We use a top-down approach to fabricate large area ordered arrays of magnetoplasmonic nanocone antennas. Using electron beam lithography a nanodisk *hard*-mask is patterned on the Au/$Tb_{18}Co_{72}$ film. After the Ar^+ ion milling process it is shown that the nanoantennas exhibit a conical profile. A schematic of the antenna structure is shown in the inset of Fig.1, with the plasmonic body of Au (yellow) and $Tb_{18}Co_{72}$ (blue) forming the nanocone tip. The latter is ferri-magnetic at room temperature, exhibiting perpendicular magnetic anisotropy. By tuning the mask diameter, either complete or truncated nanocones are produced. The base-diameters range between 150 to 220nm.

The Faraday rotation and ellipticity was extracted as a function of wavelength, nanoantenna diameter and incidence angle. The spectral Faraday rotation measured at normal incidence is shown in Fig. 1. An enhancement of the Faraday rotation and ellipticity is observed at the LSP resonance. This LSP is very sensitive to the base-diameter of the nanostructure, shifting to longer wavelengths as the diameter increases. This behavior is confirmed by finite element simulations of both the optical and magneto-optical response using the software package COMSOL™.

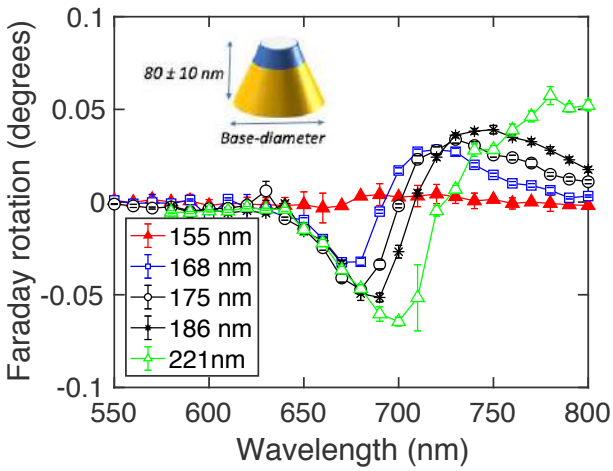


Figure 1: Spectral dependence of the Faraday rotation, demonstrating the magneto-optical plasmonic enhancement associated with the excitation of LSPs in the Au/$Tb_{18}Co_{72}$ nanoantennas.

In addition, these arrays of nanoantennas shows a strong angular dependence for the Faraday effect (not shown), whereby the Faraday effect can be suppressed, enhanced or even undergo a sign change by an angular rotation of the sample incidence plane of just 10 degrees. This effect is strongly dependent on the wavelength and differs between the various base-diameter nanoantennas.

3. Conclusions

We have demonstrated the integration of an amorphous transition ferri-magnetic-rare earth alloy with nanophotonics. The $Tb_{18}Co_{72}$ nanoantennas maintain the perpendicular magnetic anisotropy and remain magnetic at room temperature, thus confirming the potential for integrating plasmonics with all-optical switching materials. The magnetoplasmonic nanoantenna arrays are highly versatile, exhibiting a strong enhancement of the magneto-optical activity at the LSP resonance. In addition, a strong angular dependence of the Faraday effect is observed, indicating a potential dynamic tunability of such devices.

Acknowledgements

The author would like to acknowledge A. Friedel for their contributions to the measurements.

References

[1] Brolo, A. G. Plasmonics for future biosensors. *Nature Photonics* **6**, 709–713 (2012).

[2] Yu, N. & Capasso, F. Flat optics with designer metasurfaces. Nat Mater 13, 139–150 (2014).

[3] Mangin, S. et al. Engineered materials for all-optical helicity-dependent magnetic switching. Nature Materials 13, 286–292 (2014).

Transverse magnetic routing of light emission in hybrid plasmonic semiconductor structures

Lars Klompmaker[1*], Felix Spitzer[1], Alexander N. Poddubny[2], Ilya A. Akimov[1,2], Leonid V. Litvin[3], Ralf Jede[3], Grzegorz Karczewski[4], Maciej Wiater[4], Tomasz Wojtowicz[5], Dmitri R. Yakovlev[1,2], and Manfred Bayer[1,2]

[1]Experimentelle Physik 2, Technische Universität Dortmund, 44221 Dortmund, Germany
[2]Ioffe Institute, Russian Academy of Sciences, 194021 St. Petersburg, Russia
[3]Raith GmbH, 44263 Dortmund, Germany
[4]Institute of Physics, Polish Academy of Sciences, PL-02668 Warsaw, Poland
[5]International Research Centre MagTop, Institute of Physics, Polish Academy of Sciences, PL-02668 Warsaw, Poland
*corresponding author, E-mail: lars.klompmaker@tu-dortmund.de

Abstract

We report on transverse magnetic routing of light emission (TMRLE) from excitons in a diluted-magnetic-semiconductor quantum well. The strongest directionality is achieved for a quantum well located several tens of nm apart from a metal-semiconductor interface. At such distance the quantum well is coupled to surface plasmon polaritons that carry large transverse spin and are efficiently controlled by the magnetic field direction. We observe directionality of up to $60\,\%$ for the emission detected from the grating side. When the distance between emitter and surface is large, the transverse spin is caused by the far-field interference effect and the routing is weak. The effect is studied in different geometries regarding the orientation of the plasmonic grating towards excitation and detection.

1. Introduction

Different magneto-optical phenomena such as the Faraday and Kerr effect are widely used to control the polarization and intensity of transmitted or reflected light rays. Significant enhancements of these magneto-optical effects has been achieved recently by combining magnetic and plasmonic materials[1, 2]. Additionally, gaining control over the intensity and propagation direction of emitted light is important for many domains of modern optics. We report a new class of emission phenomena where directionality is established perpendicular to an external magnetic field and show a significantly enhanced directionality of up to $60\,\%$ in hybrid plasmonic semiconductor structures.

TMRLE requires two key features to be fulfilled: first, the optical selection rules of the light source need to be modified by the magnetic field, which is an intrinsic property of any emitter in magnetic materials. In this case we use circularly polarized excitons in a magnetic quantum well as light source. Second, the emitted light should have nonzero transverse spin (angular momentum) $\boldsymbol{S} \parallel x \perp \boldsymbol{k}$. This is true for a quantum well (QW) located in the vicinity of a surface because the mirror symmetry is broken, leading to spin-momentum locking. As a result a far-field effect for directionality emerges: Interference takes place between the directly emitted and reflected electromagnetic waves. The reflection occurs at the back side of the structure. The interfering beams originate from the same dipole and propagate along the same direction in free space outside the sample. The phase between interfering beams is determined by the helicity of the dipole in yz-plane, changing with the magnetic field. The result is directional emission.

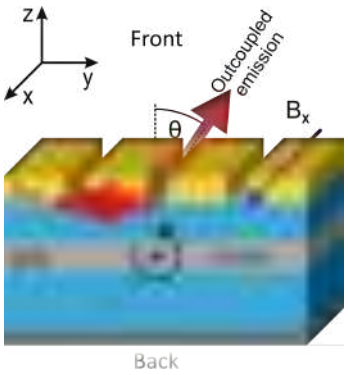


Figure 1: Schematic presentation of transverse magnetic routing of light emission in hybrid plasmonic semiconductor. The emitter is circularly polarized in the yz-plane and radiatively emit into SPP, which is out-coupled to the right.

The directionality can be enhanced in the near field with the QW layer being located in close proximity to a semiconductor/metal interface supporting surface plasmon polaritons (SPP). In this case the excitons emit into SPPs as shown in Fig. 1. SPPs carry transverse spin S_x with $S_x > 0$ for right-going and $S_x < 0$ for left-going waves. The spin of generated SPPs is pinned to the magnetic field $\boldsymbol{S} \parallel \boldsymbol{B}$ due to the modified selection rules for exciton emission, allowing magnetic control over the direction of SPP propagation and subsequent directional emission into free space by using a metalic grating. Furthermore, we show that far field effects due to superposition of electromagnetic waves diffracted at the metallic grating also contribute to the directionality of the emission.

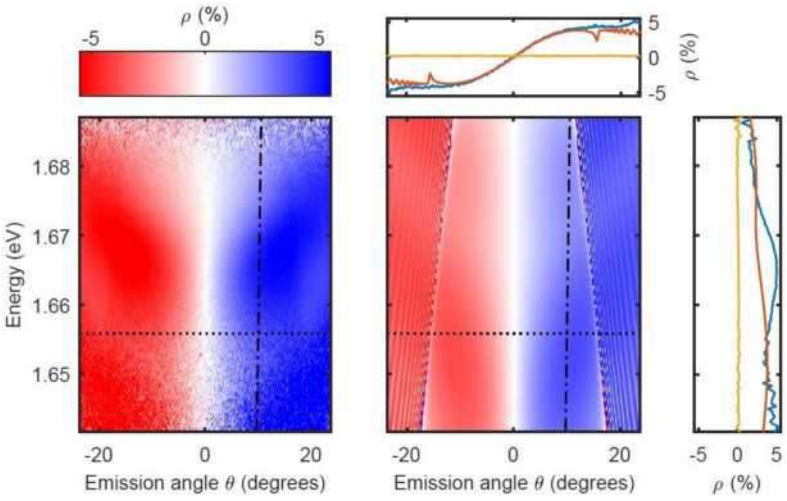


Figure 2: Angle- and spectrally-resolved directionality measurement of the near field effect depicted in Fig. 1. Left and right coloured panels correspond to the measured and calculated $\rho(\hbar\omega, \theta)$-patterns, respectively.

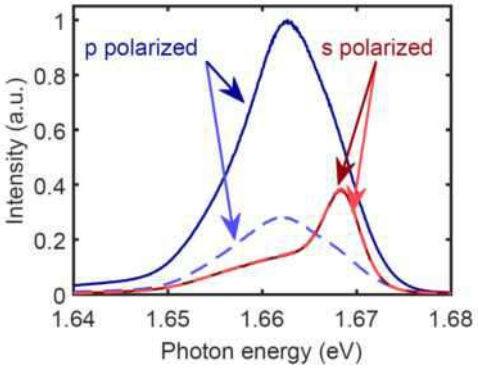


Figure 3: Measured intensities at $T = 2\,\mathrm{K}$, $B_x = \pm 1.5\,\mathrm{T}$, $\theta = 15°$ yielding $\rho = 60\,\%$ directionality in p-polarization, negligible effect in s-polarization.

2. Results

We measure the strength of the magnetic field induced changes in photoluminescence (PL) intensity by the quantity

$$\rho = \frac{I_+(\theta) - I_-(\theta)}{I_+(\theta) + I_-(\theta)}, \tag{1}$$

comparing the detected light intensities I_+ / I_- for magnetic fields in positive or negative x-direction respectively at different emission angles θ. As light source we use a CdMnTe / CdMgTe quantum well structure with large Zeeman splitting and thus strong circular polarization degree in a magnetic field. On top of this structure, rectangular gold gratings with $250\,\mathrm{nm}$ grating period are applied for supporting SPPs. The emitted light is detected in a Fourier imaging setup with the sample being placed inside a liquid helium flow cryostat at $B_x = 520\,\mathrm{mT}$, $T = 10\,\mathrm{K}$.

Figure 2 shows an exemplary measurement of SPP-supported directional emission in p-polarization of up to $\rho = 5\,\%$ for the structure with $32\,\mathrm{nm}$ spacer between QW and the metallic grating. Left and right colored panels correspond to measured and calculated $\rho(\hbar\omega, \theta)$-patterns, respectively. The side plots at the calculated pattern shows cross-sections along fixed photon energy $\hbar\omega = 1.656\,\mathrm{meV}$ (upper plot) as indicated by the dotted line or along fixed angle $\theta = 10°$ (right plot) as indicated by the dash-dotted line. In these plots blue curves correspond to cross-sections of experimental data and red curves to calculation results. Yellow curves in the side plots show the absence of $\rho(\theta)$ in s-polarization. The measurements show that ρ is an odd function with respect to emission angle ($\rho(\theta) = -\rho(-\theta)$). Thus, in our case the magneticfield-induced variation of the PL intensity is fully determined by the TMRLE with directionality $C(\hbar\omega, \theta) = \rho(\hbar\omega, \theta)$.

The effect is significantly enhanced by placing the sample in a bath cryostat, reaching $\rho = 60\,\%$ at $T = 2\,\mathrm{K}$, $B_x = \pm 1.5\,\mathrm{T}$ and $\theta = 15°$. This is shown in Fig. 3 where solid and dashed lines of the same colour correspond to intensity at opposite magnetic field directions. For larger spacer the effect due to SPP assisted emission disappears and far field effects with a magnitude of about 10 – 100 times smaller take place.

Directionality of emitted light is also present for backside detection. In this case the relative contribution of SPP assisted emission is getting smaller with respect to the overall exciton signal. This results in a decrease of the TMRLE magnitude by about 5 times compared to frontside detection. At the same time the far-field effect due to interference of direct and reflected emission is getting weaker in case of backside detection.

References

[1] V.V. Temnov et al., "Active magneto-plasmonics in hybrid metal-ferromagnet structures", *Nature Photonics* 4: 107–111, 2010.

[2] V.I. Belotelov et al., "Enhanced magneto-optical effects in magnetoplasmonic crystals", *Nature Nanotechnology* 6: 370–376, 2011.

[3] F. Spitzer et al., "Routing the emission of a near-surface light source by a magnetic field", *Nature Physics* 14: 1043–1048, 2018.

Nonlinear and parametric magneto-elastic dynamics in ferromagnetic nanostructures

Vladimir Vlasov[1*], Anton Golov[1], Alexandr Alekhin[2], Alexey Lomonosov[2], Leonid Kotov[1], Dmitry Kuzmin[3,4], Igor Bychkov[3,4], and Vasily Temnov[2]

[1]Syktyvkar State University named after Pitirim Sorokin, Syktyvkar, Russia
[2]Institut des Molecules et Materiaux du Mans, UMR CNRS 6283, Le Mans Universite, Le Mans, France
[3]Chelyabinsk State University, Chelyabinsk, Russia
[4] South Ural State University (National Research University), Chelyabinsk, Russia
*corresponding author, E-mail: vlasovvs@syktsu.ru

Abstract

This work investigates theoretically nonlinear and parametric magneto-elastic interactions between surface acoustic waves and magnetization in ferromagnetic thin films and nanoparticles. Excitation of magnetic oscillations by elastic waves is calculated within the framework of a theoretical model based on the Landau-Lifshitz-Gilbert (LLG) equations dynamically driven via magneto-elastic interactions. In particular, we report on a theoretical investigation of magnetization switching in polycrystalline Ni nanoparticles induced by ultrashort pulses of surface acoustic waves.

1. Introduction

Studying the interactions of surface acoustic waves (SAWs) with magnetization in thin ferromagnetic films is motivated by beautiful physics and new principles of magnetic recording [1,2]. Nonresonant magneto-elastic switching in micrometer-sized cobalt bars using MHz-frequency SAWs has been demonstrated by Davis at al. [3]. Here we explore an alternative route of magneto-elastic switching using single broadband acoustic SAW pulses of picosecond duration. In our previous work, we have predicted the phenomenon of the acoustically induced magnetization switching in Terfenol thin films using ultrafast acoustic strain pulses characterized by the relatively large strain amplitude of 1 % [4]. Although acoustic pulses with such huge amplitude can be generated under strong excitation conditions [5], the energy barrier between the meta-stable states in Terfenol (determined by the competition of magneto-elastic, magnetocrystalline and magnetic shape anisotropies) cannot be easily tuned.

2. Main effects and equations

Let us consider a thin ferromagnetic film deposited on a nonmagnetic dielectric substrate with a constant magnetic field applied in the sample plane. Short acoustic pulses propagating at the surface of a solid can be generated by absorption of short laser pulses in a thin subsurface layer. This results in a transient and spatially inhomogeneous heating profile and subsequent generation of thermoelastic stress. This excites various acoustic modes in substrate, two of them can propagate along the surface: surface skimming longitudinal (SSLW) and Rayleigh surface acoustic wave (SAW).

Excitation of FMR precession by elastic waves has been calculated within the framework of a theoretical model taking into account the Landau-Lifshits-Gilbert (LLG) dynamics and the equations for transient elastic deformations. The effective magnetic field consists of the external DC magnetic field (with an arbitrary in-plane orientation with respect to elastic wavevectors), demagnetizing field, and a time-dependent magnetoelastic field. The latter is determined by SAW and SSLW strain elements. The equations for the magnetic oscillations induced by elastic waves have been derived by perturbation theory. The parametric interaction of elastic waves with ferromagnetic resonance leads to SAW+SSLW and SSLW+SSLW harmonic generation. The magnetic precession amplitude dependences on the DC magnetic field at different angles between the DC magnetic field and the direction of acoustic k-vector were obtained.

We consider also a polycrystalline Ni nanoparticle in a shape of an ellipsoidal disc with a long axis a, short axis b and thickness c. Such structures can be routinely fabricated from thin nickel films by electron or ion beam lithography. It is important to notice that such nanoparticles, produced by lithography techniques, stick to the surface and their mechanical adhesion is the same as that of a continuous thin film. Introducing the Cartesian coordinates, we can set the y axis to be parallel to the long axis of the ellipse. The particle is placed in a permanent magnetic field H pointing along the x axis. Short acoustic transients with propagate along the x axis. The free energy density of an elliptical ferromagnetic nanoparticle consists of Zeeman, demagnetization and magneto-elastic terms. We can tune the free energy density by different means. For example, its demagnetization term depends on demagnetizing factors, therefore it can be modified by varying the aspect ratio a/b of the nanoparticle. In the presented analysis, we use the

following particle dimensions: a=150 nm, b=100 nm, c=20 nm. The choice of these dimensions is arbitrary, but it fulfills certain requirements. First, such dimensions ensure that the magnetization is in a single-domain state and provide the volume of the nanoparticle to obtain the energy barrier between the metastable states. Second, the small axis of the ellipse remains much smaller than the spatial extent of the acoustic SAW pulse and justifies the assumption of spatially homogeneous strain acting on the nanoparticle. Third, as long as the lateral dimensions of the nanoparticle are large compared to its thickness, i.e. $a,b>>c$, the simulations will still be valid for nanodiscs for cases with the same aspect ratio a/b=1.5.

Variation of the external magnetic field provides another flexible tool to change the structure of the free energy density. In the absence of the external magnetic field or for small H, the free energy F possesses two minima corresponding to two meta-stable states of defined magnetization direction. Upon an increase of H, these minima merge into a single minimum, corresponding to the alignment of the magnetization along the external magnetic field. Dynamic perturbations of the bi-stable nanomagnet described above may result in magnetization switching. In this study we are particularly interested in the influence of transient elastic deformations induced by picosecond SAW pulses. Energies required for magnetization switching are expected to approach the fundamental Landauer limit of kT ln 2=17 meV, i.e. the minimum energy required to record a single bit of information at T=300 K.

3. Conclusions

We investigated the phenomenon of magnetization excitation in films and reversal (switching) in elliptical nanomagnets induced by ultrashort pulses of surface acoustic waves. The areas of the parametric and direct excitations on the static magnetic field and amplitude of the strain were revealed. In the case of magnetization switching in nanoparticle the switching threshold between two metastable single-domain magnetization states depends on the amplitude and duration of SAW pulses, the magneto-elastic coupling efficiency and the height of the potential barrier between these states. The latter is determined by the magnetic shape anisotropy of an elliptical nanomagnet, which depends on its dimensions and the amplitude of the external magnetic field. The key point is tuning the height of the potential barrier between the metastable energy minima using weak magnetic fields easily accessible in the experiments. Our geometry, where the magnetic nanoparticle is driven by short SAW pulses, is complimentary to similar objects driven by quasi-monochromatic excitations and displaying bifurcations and chaos. Ultimate speed limits of magneto-acoustic switching can be investigated solving LLG equations driven by dynamic SAW strains. The 10^{-4} SAW-switching threshold for elliptical Ni nanomagnets appears to be significantly lower as compared to highly magnetostrictive thin films of Terfenol-D switchable by ultrashort longitudinal acoustic pulses with amplitudes 10^{-2} propagating in the direction perpendicular to the surface [4]. At first glance this observation may be surprising because of the 20 times larger magnetostriction coefficient in Terfenol-D. However, the much longer 300 ps duration of SAW pulses as compared to [4] and the magnetic tunability of the height of the potential barrier between the states overcompensate the lower efficiency of magneto-elastic coupling in nickel. It is quite straightforward that the SAW-induced switching threshold of Terfenol-D elliptical nanomagnets of similar dimensions should drop below 10^{-5} making the investigated configuration suitable for low-power acoustic transducers.

Acknowledgements

The work was financially supported by Strategie internationale "NNN-Telecom" and the Acoustic HUB de la Region Pays de La Loire, ANR-DFG "PPMI-NANO" (ANR-15-CE24-0032 and DFG SE2443/2), RFBR (17-57-150001, 17-02-01138, 19-02-00682), Act 211 Government of the Russian Federation (contract 02.A03.21.0011), PRC CNRS-RFBR "Acousto-magneto-plasmonics", Deutsche Forschungsgemeinschaft (AL2143/2-1).

References

[1] J. Janusonis, C.-L. Chang, T. Jansma, A. Gatilova, V. Vlasov, A. Lomonosov, V. Temnov, and R. Tobey, *Phys. Rev. B* 94, 024415 2016.

[2] C. Chang, A. Lomonosov, J. Janusonis, V. Vlasov, V. Temnov, and R. Tobey, *Phys. Rev. B* 95, 060409 2017.

[3] S. Davis, J. A. Borchers, B. B. Maranville, and Adenwalla, *J. Appl. Phys.* 117, 063904 2015.

[4] O. Kovalenko, T. Pezeril, and V. V. Temnov, *Phys. Rev. Lett.* 110, 266602 2013.

[5] V. V. Temnov, C. Klieber, K. A. Nelson, et al., *Nature Comm.* 4, 1468 2013.

[6] V. S. Vlasov et al., *Phys. Rev. B* (under review)

Optical isolators based on magnetoplasmonic subwavelength gratings

Sevag Abadian, Giovanni Magno, Vy Yam, Béatrice Dagens

Centre de Nanosciences et de Nanotechnologies, CNRS, Univ. Paris-Sud, Université Paris-Saclay, C2N – 91120 Palaiseau, France

Optical isolators are one-way devices allowing light to pass only in one direction. They are elementary components to protect laser diodes against spurious back reflections or to build functions like optical circulators. Here we propose a metal-dielectric non-reciprocal waveguide that may pave the way toward the conception of compact integrated isolators. The challenge is to design integrated optical isolator with low footprint, high isolation ratio and low insertion losses. Fig. 1(a) depicts a 3D sketch of the proposed structure which includes a one dimensional (1D) subwavelength periodic gold plasmonic grating. The latter is located on one side of a magneto-optical (MO) dielectric Bismuth Iron Garnet (BIG) waveguide. These elements are placed on top of a non-MO Gallium Gadolinium Garnet (GGG) substrate and buried in SiO_2 superstrate. In this configuration non-reciprocal transmission of the TE fundamental mode is obtained by applying a vertical static magnetic field (inducing vertical magnetization in BIG layer).

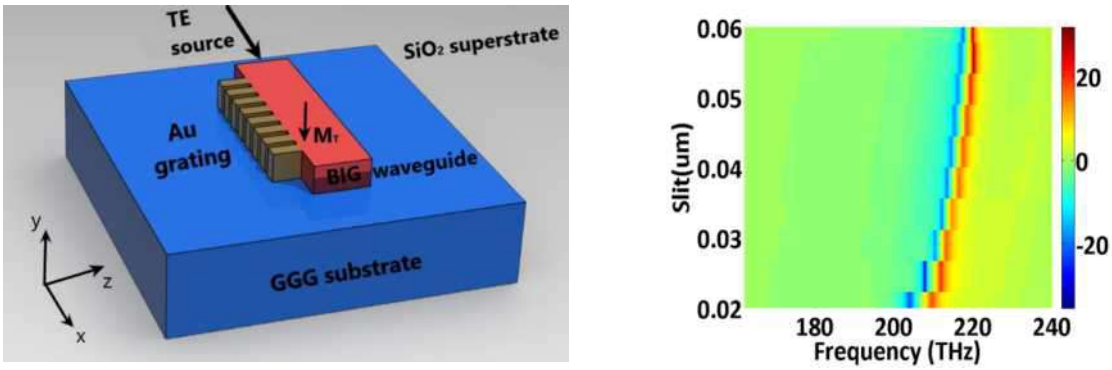


Fig. 1: (a) A gold grating on one side of a MO dielectric BIG waveguide placed on a non-magnetic substrate GGG and buried inSiO_2. Magnetization M_T is applied vertically in the BIG layer and a TE source is used. (b) represents the Isolation ratio in dB versus the grating slit width and the wavelength for a device length of 3µm for a grating width of 0.13µm. Red and blue areas underline the resonances.

In this work, the enhancement of the TMOKE (Transverse MO Kerr Effect), arising from the coupling of grating and plasmonic resonances with guided modes, is studied in order to achieve efficient isolation. The numerical investigation has been performed by means of FDTD simulations. In non-guided configuration it has been observed that, when extraordinary optical transmission (EOT) occurs in deep-subwavelength plasmonic gratings placed on top of a MO substrate, a giant enhancement of the MO effect is achieved [1,2]. Here, in the case of integrated guided device, Fig. 1(b) shows the blueshift of the isolation curve peaks (defined as the difference in transmission in the forward and backward directions) as the slit widths increases from 0.03µm to 0.07µm, when a structure with ten gold gratings having a thickness of 0.13 µm is considered. To account for the losses, crucial in isolators, we define a figure of merit (FoM) as the ratio of isolation to insertion losses. The figure of merit calculated for the same structure shows a maximum value of 1.9dB, at λ=1373 nm.

To further investigate the behavior of our structure, hereinafter we consider larger grating thicknesses in order to exploit the existence of both the horizontal and the vertical Fabry Perot modes within the grating slits. To unveil the different optical mechanisms occurring in this structure a set of bandstructure simulations were performed on a unitary cell (with periodic boundary condition) [3].

Fig. 2(a) represents the band diagram of the proposed structure when p=0.3µm, s=0.04µm and h=0.9µm. Dashed white lines correspond to SiO_2, GGG and BIG lightlines. We can distinguish a set of propagating modes, identified as the TE waveguide mode (see label '1'), and a SPP mode (see label '2'), as well as a third, second and first order horizontal Fabry Perot flat bands (labels '3', '4' and '5', respectively).

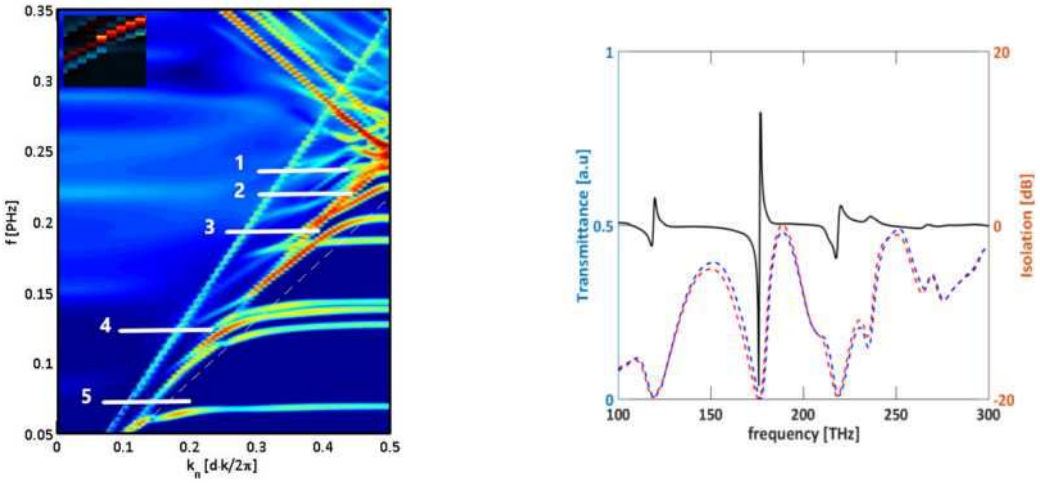


Fig. 2: (a) Bandstructure for $+M_T^{sat}$ for period 0.3µm, slit width of 0.04µm and gold width of 0.9µm. Inset: superimposed band structures for $+M_T^{sat}$ and $-M_T^{sat}$ at the vicinity of the interaction of the SPP with the third order FP mode. (b) Transmission (red, blue) and Isolation ratio (black) in dB versus wavelength for a device length of 3µm.

By inspecting the bandstructure in Fig. 2(a), we can see that the SPP mode interacts with the flat band near the third order horizontal Fabry Perot mode. This reflects on the amplitude of the isolation curve shown in Fig. 2(b) at f=180THz. Finally, the inset in Fig. 2(a) depicts the superimposed band structures for $+M_T^{sat}$ and $-M_T^{sat}$. We clearly observe the existence of a difference between the wave vectors for waves propagating in forward and backward directions, at the vicinity of the interaction between the guided TE mode, SPP mode and the Fabry Perot resonance housed inside the slit.

The spectral position of the slit resonances can be predicted by considering the response of an equivalent FP-like slab resonator: a layer with an index n_{eff}, the same thickness as the gold grating and sandwiched between SiO_2 and the BIG waveguide. The effective index n_{eff} is given by the fundamental TE mode of the whole transverse structure which is represented in Fig. 3(a).

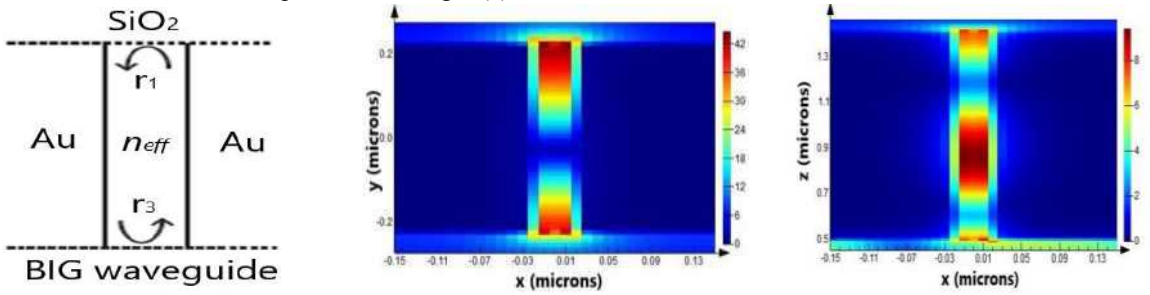


Fig. 3: (a) Transverse structure consisting of gold/SiO_2/gold waveguide and its extension into a resonant cavity by introduction of the garnet and SiO_2 media is shown schematically. (b) and (c) respectively represent the vertical and horizontal electric field profiles of the third Fabry Perot mode confined in the cavity with the SiO_2 gap set to 0.04µm, frequency 180 THz.

The location of the cavity resonances is then found by expressing round-trip resonance [4]:

$$2k_0 n_{eff} h_1 + \varphi_{r_1} + \varphi_{r_3} = 2n\pi, \quad n \in Z$$

Where h_1 is the length of the Fabry Perot cavity, in this case it is the width of the gold grating and φ_{r_i} is the reflection phase shift of the slit mode at both ends of the cavity.

As preliminary result we have identified that vertical Fabry Perot modes seem to have stronger impact than the horizontal ones on the device isolation ratio.

In this work, we have numerically shown that when a MO-BIG waveguide is coupled to a gold grating adjacent to it, surface plasmon polaritons may strongly enhance transverse magnetic-optical Kerr effect especially when guided TE modes interact with slit FP modes. The TMOKE effect can be tuned by optimization of grating geometry and opens the prospect of achieving an integrated isolator for TE mode.

References

[1] V. Belotelov, I. Akimov, M. Pohl, V. Kotov, S. Kasture, A. Vengurlekar, A. Gopal, D. Yakovlev, A. Zvezdin, and M. Bayer, "Enhanced magneto-optical effect in magnetoplasmonic crystal," Nature Nanotech. 6, 370–376 (2011).

[2] L. Halagacka, M. Vanwolleghem, F. Vaurette, J. Ben-Youssef, J. Pistora, K. Postava, and B. Dagens, "Magnetoplasmonic nanograting enables optical nonreciprocity sign reversal," Opt. Expr. 26(24), pp. 31554-31566 (2018).

[3] G. Magno, V. Yam, B. Dagens, "Integrated magneto-plasmonics for non-reciprocal optical devices," ECIO 2017, 3-5/04/17, Eindhoven.

[4] Y. Ding, J. Yoon, M. Javed, S. Song, and R. Magnusson, "Mapping surfaceplasmon polaritons and cavity modes in extraordinary optical transmission," Photonics Journal, IEEE 3, 365 –374 (2011).

THz graphene four-port circulators with elliptic resonators

Victor Dmitriev[1], Gabriel Barros[1], Thiago Oliveira[1], Wagner Castro[1,2]

[1]Department of Electrical Engineering, Federal University of Pará, PO Box 8619, 66075-900, Belém, Pará, Brazil
[2]Cyberspace Institute, Federal Rural University of Amazonia, 66077-830, Belém, Pará, Brazil
*corresponding author, e-mail: gabriel.barros@itec.ufpa.br

Abstract

We investigate four-port circulators for THz region which present two parallel graphene waveguides with SPP modes and a magnetized resonator of elliptic form. The waveguides and the resonator are placed on a two-layer dielectric substrate. The working principle of the device is based on the rotating dipole resonance of the magnetized graphene resonator. Numerical simulations demonstrate good parameters of the circulators.

1. Introduction

Circulators are nonreciprocal components frequently used in microwave and optical systems for different purposes [1]. One of their main applications is protection of vulnerable sources from parasitic reflections in other circuit elements. Usually, they are based on different physical effects in waveguides with magneto-optical materials (one of such circulators in the photonic crystal technology is described in [2]). In this work, we investigate four-port circulators for THz region which present two parallel graphene waveguides with SPP modes and a magnetized disk or ring graphene resonator of elliptic form.

2. Circulator Description

The geometries of the circulators are presented schematically in Fig. 1 for the graphene resonators in the form of elliptic disk and ring. A magnetized resonator is placed between two identical parallel graphene waveguides with surface plasmon-polariton (SPP) modes. In the resonator for a given external DC magnetic field, two rotating modes can exist. The wave with the central frequency in port 1 propagates in waveguide 2 and excites the anticlockwise rotation mode in the resonator. This rotating mode, in its turn, excites the waveguide 1. The SPP mode in this waveguide appears in port 2. The wave entering in port 2, passes directly to port 3 without excitation of the resonator. Due to two-fold rotational symmetry, the physical processes in port 3 and in port 4 run their course analogously. Thus, the device provides the circulation $1\to2\to3\to4\to1$. In our analysis, we start with a circular geometry and then make small changes to come to elliptic one.

3. Optical Conductivity Tensor

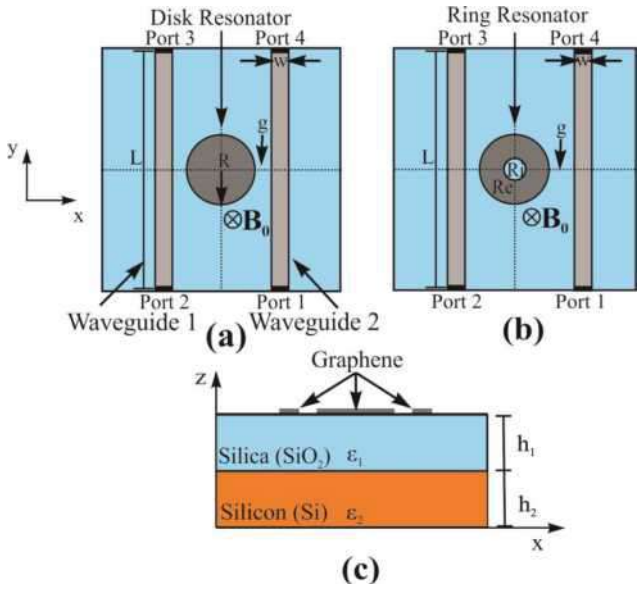


Figure 1: Front view of circulators with disk (a) and ring (b) resonators, side view (c).

With applied DC magnetic field B_0, the 2D tensor of conductivity is as follows:

$$[\sigma_s]=\begin{pmatrix}\sigma_{xx} & -\sigma_{xy}\\ \sigma_{xy} & \sigma_{xx}\end{pmatrix}, \tag{1}$$

where $\sigma_{yy}=\sigma_{xx}, \sigma_{yx}=-\sigma_{xy}$. The components of the tensor are:

$$\sigma_{xx}=\frac{2D}{\pi}\frac{1/\tau-\imath\omega}{\omega_c^{\,2}-(\omega+\imath/\tau)^2}, \tag{2}$$

$$\sigma_{xy}=\frac{2D}{\pi}\frac{\omega_c}{\omega_c^{\,2}-(\omega+\imath/\tau)^2}, \tag{3}$$

where σ_0 is the conductivity of graphene, $D=2\sigma_0\varepsilon_F/\hbar$ is the Drude weight, $\hbar$ is the reduced Planck's constant, $\omega_c=eB_0v_F^2/e_F$ is the cyclotron frequency, ε_F is related to chemical potencial of graphene, e is the electron charge, τ

is the relaxation time, ω is the frequency of incident wave, v_F is the Fermi velocity, B_0 is the magnetic field and $i = \sqrt{-1}$.

We consider the graphene monolayer with a finite thickness Δ and the conductivity tensor given by $[\sigma_v] = [\sigma_s]/\Delta$, where $[\sigma_s]$ are tensor components (2) and (3). In our simulations, we use $\Delta = 1$ nm. The artificial parameter Δ is used only for calculation purposes and the numerical calculations were made for the following data: $\mu_c = 0.15$ eV, $B = 0.8$ T and $\tau = 0.9$ ps [3].

4. Numerical Results

The device in Fig. 1 (a) consists of the disk graphene resonator with radius R=600 nm and two symmetrical parallel graphene waveguides with the width w=200 nm and the length L=4210 nm. The resonator is magnetized by a magnetic field of normal direction to the graphene resonator along the z-axis, the waveguides are coupled laterally to the resonator with the gap g=2.5nm. In Fig. 1(b) a similar device with ring resonator is shown. The relation of internal and external radius in the circular ring is s = R_i/R_e. In the example below, R_e = 600 nm and R_i = 150 nm, s=0.25. The graphene elements are placed on a dielectric substrate composed of SiO_2 and Si layers with $h_1 = h_2$ thicknesses equal to 5000nm and relative permittivity 2.09 and 11.9, respectively.

The numerical results were obtained by using the commercial software Comsol Multiphysics [4]. We consider the resonators with a small eccentricity. The frequency characteristics of the disk circulator are shown in Fig. 2. Fig. 3 demonstrates the frequency responses for the ring case. The field distributions of the electric field with the disk structure are shown in Fig. 4(a) and Fig. 4(b), and for the ring one in Fig. 4(c) and Fig. 4(d) for the cases with excitation of different ports. The central frequency of the disk circulator is 5.09 THz, and 4.61 THz for the ring one. In the disk structure, we used the ellipse with eccentricity of 3% of the value of R and for the ring one of 7% of the value of R.

The device based on disk resonator has the coefficient of transmission around -4.0 dB, isolation of port 4 is -10.2 dB, the isolation of port 3 is -45 dB and the reflection coefficient of -25.8 dB for excitation at port 1 and DC magnetic field is B = 0.8T.

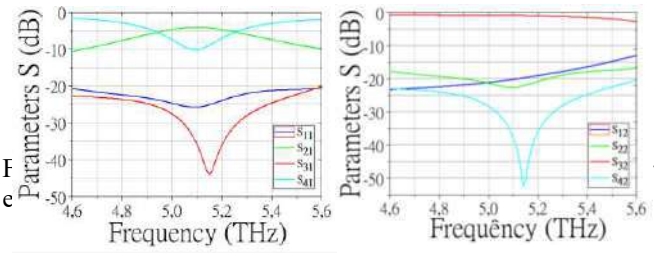


Figure 2: Frequency responses of ring circulator for excitation at port 1 and 2.

The device based on ring resonator has the transmission coefficient around -4.0 dB, the isolation of port 4 -8.7 dB, isolation of port 3 of -29.7 dB and reflection coefficient of -40.3 dB for excitation at port 1. DC magnetic field is B = 0.8T.

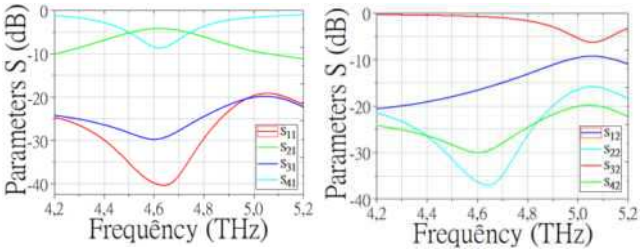


Figure 3: Frequency responses of ring circulator for excitation at port 1 and 2.

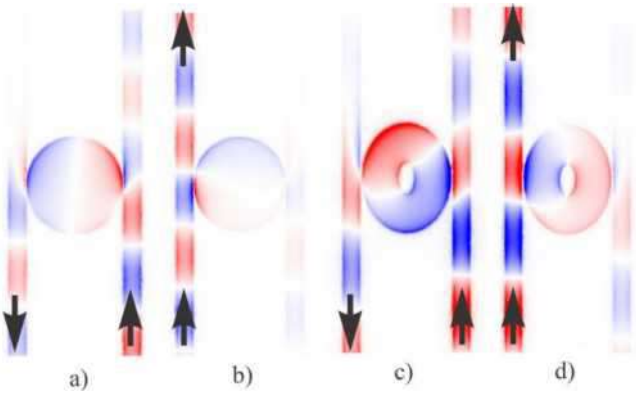


Figure 4: E_z field distribution for disk and ring circulators.

5. Conclusions

We analyzed two types of four-port graphene circulators operating in THz region. These devices have a very simple structure composed of graphene elements placed on a dielectric substrate, with resonators of different geometries. The simulations of the devices demonstrated that the circulators possess good isolation and matching. The insertion losses can be reduced by optimization of the physical and geometrical parameters.

Acknowledgements

This work was supported by Brazilian agency CNPq.

References

[1] J. Helszain, "Waveguide Junction Circulators: Theory and Practice", *John Wiley and & Sons, New York*, 1998.

[2] Wang, Z & Fan, S. "Suppressing the effect of disorders using time-reversal symmetry breaking in magneto-optical photonic crystals: an illustration with a four-port circulator" *Photonics and Nanostructures-Fundamentals and Applications*, *4*.3: 132-140. 2006

[3] A. Principi, and G. Vignale, "Intrinsic lifetime of Dirac plasmons in graphene", *Physics Review B, vol. 88, no. 19, pp. 195405-195420, Nov 2013.*

[4] www.comsol.com.

Magnetoplasmonic Modulators for Integrated Optics

C. J. Firby* and A. Y. Elezzabi

Ultrafast Optics and Nanophotonics Laboratory, Department of Electrical and Computer Engineering,
University of Alberta, Edmonton, Alberta T6G 1H9, Canada
*corresponding author, E-mail: firby@ualberta.ca

Abstract

Incorporating magnetic materials into plasmonic devices facilitates unique nonreciprocal phenomenon and highly nonlinear temporal dynamics in integrated nanoplasmonic circuitry. In this work, we review some of our recent advances in the development of magnetoplasmonic waveguide devices. Specifically, we demonstrate that integrating magnetic garnets as the core of plasmonic waveguide platforms allows for the development of unique optical phase and intensity modulators which are vital for integrated plasmonic networks.

1. Introduction

Nonreciprocal elements are crucial for integrated optical networks, as they be used to manipulate the flow of light in a circuit, provide unique mechanisms through which modal properties can be tailored, or facilitate unique modulator designs. As such, it is imperative to develop such components in the plasmonic regime. In optics, nonreciprocity is typically introduced by incorporating magnetic materials. Since plasmonic waveguide devices are inherently limited by the propagation losses of their metallic constituents, employing ferromagnetic metals, which are exceptionally lossy, only exacerbates these issues. Thus, a promising solution involves incorporating magneto-optical (MO) garnets, such as yttrium iron garnet or its derivatives (e.g., bismuth-substituted yttrium iron garnet or Bi:YIG, and cerium–substituted yttrium iron garnet, or Ce:YIG), into plasmonic structures. Such materials are dielectrics that are characterized by low absorption around the telecom wavelength of 1550nm, high magneto-optical parameters, and low saturation magnetizations, making them ideal candidates for plasmonic integration.

In this work, we review some of our recent designs for novel integrated magnetoplasmonic devices. By integrating magneto-optic garnets into plasmonic waveguide architectures, unique functionalities can be realized. Specifically, we design and numerically analyze devices such as a plasmonic phase shifters, isolators, and unique modulators such as a magnetoplasmonic analog to the electrical clock-multiplier, and an RF mixer.

2. Background

Incorporating magnetic garnets into waveguide architectures and subsequently magnetizing them via static external magnetic fields ($\mathbf{H}_{static}$) can generate a number of unique effects on a propagating optical mode. If the magnetic garnet is magnetized transverse to the direction of propagation, a nonreciprocal phase shift will be imparted onto the optical mode. This implies that the propagation constant will differ for both forward and backward propagating modes. These unique effects can be modeled by considering the fully asymmetric permittivity tensor of the magnetic garnet [1]:

$$\varepsilon_r = \begin{bmatrix} n_{YIG}^2 & -ig_z & ig_y \\ ig_z & n_{YIG}^2 & -ig_x \\ -ig_y & ig_x & n_{YIG}^2 \end{bmatrix} \tag{1}$$

where n_{YIG} is the refractive index of the garnet, and $\mathbf{g}(\mathbf{M}) = \langle g_x, g_y, g_z \rangle$ is the gyration vector of the material, and $\mathbf{M}$ is the magnetization vector.

Furthermore, the magnetization of a material, and thus the magneto-optic phenomena, can be actively modulated via the application of time varying magnetic fields, $\mathbf{h}(t)$. In such scenarios, the magnetization will evolve in accordance with the Landau-Lifshitz-Gilbert model of magnetization dynamics [2]:

$$\begin{aligned} \frac{d\mathbf{M}}{dt} = &- \frac{\mu_0\gamma_0}{1+\alpha^2}[\mathbf{M} \times (\mathbf{H}_{static} + \mathbf{h}(t))] \\ &- \frac{\mu_0\gamma_0\alpha}{M_S(1+\alpha^2)}\mathbf{M} \times [\mathbf{M} \times (\mathbf{H}_{static} + \mathbf{h}(t))] \end{aligned} \tag{2}$$

where μ_0 is the permeability of free space, γ_0 is the gyromagnetic ratio, M_S is the saturation magnetization, and α is the Gilbert damping constant. As such, a variety of novel structures are investigated via fully vectorial 3D finite-difference-time-domain (FDTD) simulations.

3. Results and discussion

3.1. Phase shifter

First, we examine the simplest structure to incorporate magneto-optical effects into a plasmonic platform: the dielectric-loaded plasmonic waveguide [3]. By incorporating a rectangular ridge of Bi:YIG onto an Ag transmission line, we show that the NRPS can be tailored to be as high as 6.99rad/mm. Furthermore, by passing transient current pulses through the underlying transmission line, the corresponding magnetic field pulses can modulate the magnetization, and hence the NRPS within the device. We show

that the device is capable of providing dynamic phase shifts up to 0.33rad within the propagation length of 49μm.

3.2. Isolator

The inherent limitation on the attainable phase shift in the previous dielectric loaded plasmonic waveguide device is the short propagation length of the magnetoplasmonic mode. As such, the waveguide architecture can be modified to produce a device that can provide a useful $\pi/2$ NRPS within its propagation length. Specifically, we consider the popular long-range dielectric-loaded plasmonic waveguide geometry, with a core of Ce:YIG, thin film of Ag, and buffer layers of Si_3N_4 and Al_2O_3 on a SiO_2 substrate. We demonstrate that this waveguide architecture can provide a NRPS of 3.11rad/mm, which can impart a useful $\pi/2$ phase shift within only 505.6μm, which is far less than the 3.14mm propagation length of the mode. This waveguide architecture can be used within a Mach-Zehnder interferometer (MZI) configuration, biased by buried SmCo permanent magnets, to develop a magnetoplasmonic optical isolator [4]. We show that this isolator design produces isolation ratios of 22.82dB with low insertion losses of only 2.51dB.

3.3. Clock multiplier

The aforementioned MZI configuration can lead to the development of unique modulator geometries as well. Specifically, we show that one can construct the plasmonic equivalent of an electrical clock multiplier by employing Bi:YIG in a long-range dielectric loaded plasmonic waveguide MZI, in conjunction with two adjacent Ag transmission lines to apply transient magnetic fields [5]. In such a device, the applied fields can be tailored to excite resonant precession of the magnetization within the MZI arms, and thus, correspondingly excites a continuous oscillation of both the NRPS, and the MZI output. Tuning the magnetic field parameters can yield continuous optical intensity oscillations between 279.9MHz and 5.6GHz with 16.26dB modulation depth, and can multiply the exciting electrical pulse frequency up to 2.1×10^3 times.

3.4. RF mixer

While previous applications considered transient electrical pulses driving the NRPS in magnetoplasmonic devices, driving the same MZI geometry with continuous RF signals can modulate the output intensity in a highly nonlinear manner. This is due to the nonlinear dynamics prescribed by Eqn. 2. By examining the frequency spectrum of the modulated transmission signal, we observe that RF mixing and nonlinear frequency generation occur [6]. Specifically, driving the Bi:YIG magnetization with a single sinusoudal signal can generate harmonics of the driving frequency, as well as frequency splitting into sidebands and down-conversion. Furthermore, by exciting the magnetoplasmonic MZI with two RF signals, the nonlinear behavior produces various mixed frequencies of the inputs.

4. Conclusions

In conclusion, we have reviewed a number of novel magnetoplasmonic devices. By incorporating Bi:YIG and Ce:YIG into magnetoplasmonic waveguides, we have shown that active phase shifters can be formed, and furthermore, these nonreciprocal phase shifters can be incorporated into MZI geometries to produce a plasmonic isolator, an analog to an electrical clock multiplier, or a nonlinear RF mixer. These devices are envisioned as critical building blocks in future nanoplasmonic networks.

Acknowledgement

This work was funded by the Natural Sciences and Engineering Research Council of Canada.

References

[1] A. K. Zvezdin and V. A. Kotov, *Modern Magnetooptics and Magnetooptical Materials* (IOP Publishing, 1997).

[2] R. F. Soohoo, *Microwave Magnetics* (Harper & Row, 1985).

[3] C. J. Firby and A. Y. Elezzabi, "High-speed nonreciprocal mangetoplasmonic waveguide phase shifter," *Optica* **2**(7), 598-606 (2015).

[4] C. J. Firby and A. Y. Elezzabi, "Magnetoplasmonic isolators utilizing the nonreciprocal phase shift," *Opt. Lett.* **41**(3) 563-566 (2016).

[5] C. J. Firby and A. Y. Elezzabi, "A magnetoplasmonic electrical-to-optical clock multiplier," *Appl. Phys. Lett.* **108**(5), 051111 (2016).

[6] C. J. Firby and A. Y. Elezzabi, "Magnetoplasmonic RF mixing and nonlinear frequency generation," *Appl. Phys. Lett.* **109**(1), 011101 (2016).

Layer-selective All-Optical Magnetization Switching in Plasmonic Magnetic Heterostructure

Daria Ignatyeva[1,2,*], Carl Davies[3,4], Daria Sylgacheva[1,2], Arata Tsukamoto[5], Hiroki Yoshikawa[5], Pavel Kapralov[2], Andrey Kirilyuk[4], Vladimir Belotelov[1,2], and Alexei Kimel[3,6]

[1]Faculty of Physics, Lomonosov Moscow State University, Moscow, Russia
[2]Russian Quantum Center, Moscow, Russia
[3]Radboud University, Institute for Molecules and Materials, Nijmegen, The Netherlands
[4]Radboud University, FELIX Laboratory, The Netherlands
[5]College of Science and Technology, Nihon University, Chiba, Japan
[6]Moscow Technological University (MIREA), Moscow, Russia
*corresponding author, E-mail: ignatyeva@physics.msu.ru

Abstract

We propose and experimentally demonstrate a novel approach for all-optical control and switching of magnetization states of individual layers in the multilayered GdFeCo structures utilizing the excitation of the surface plasmon polaritons. Surface plasmon polaritons provide us an efficient tool to tailor light energy distribution inside the multilayered structure with GdFeCo layers, and thus for addressed magnetization reversal in the particular layer of the whole structure without any impact on the other layers.

1. Introduction

GdFeCo is a ferrimagnetic material which magnetization state can be all-optically controlled by laser pulses [1]. Moreover, it is a unique material since its magnetization could be switched by means of femtosecond laser pulses in the absence of the external magnetic field [2]. The effect originates from the peculiar ultrafast dynamics of the exchange coupled Gd and Fe sub-lattices having different relaxation times [3]. The important thing found is that all-optical magnetization reversal depends on the laser pulse energy density absorbed by the layer and has a threshold below which the layer does not switch magnetization [4]. Among the most fascinating effects observed in GdFeCo is all-optical helicity-dependent switching which is a difference of the threshold fluence required for magnetization reversal for opposite circular polarization states of the pump. The phenomenon of circular magnetic dichroism explains the observed effect, thus confirming the principal role of the absorption in the all-optical magnetization reversal [4]. Due to this helicity-dependence, one can switch the domains of one magnetization direction without any impact on the domains with the opposite direction.

As the all-optical magnetization switching takes place at picosecond time scale, it is very promising for the data storage applications at ultrafast recording rates. GdFeCo film could be as thin as a few nanometers, the most serious limitations of record density are imposed by the size of the optical laser spot. Therefore, for practical applications it is crucial to find the methods of increase the record density for such films. Multilayered GdFeCo structure could open the door for the multifold record density increase. However, up to nowadays, there was no way how to perform magnetization reversal in only one particular layer without making impact to the other ones.

In this work we present the method of layer-selective all-optical switching in GdFeCo multilayered structure utilizing the excitation of the surface plasmon polaritons (SPPs). The energy of the SPPs is concentrated locally near the metal/dielectric interface where they are excited [5]. Therefore, SPPs present an efficient tool to tailor light energy distribution inside the multilayered structure, and thus for addressed magnetization reversal in the particular layer of the whole structure.

2. Layer-selective magnetization reversal in bilayer structure

We demonstrate the proposed approach in the following bilayer GdFeCo SPP-supporting structure: (glass substrate)- Si_3N_4(5nm)- $Gd_{26.0}Fe_{64.8}Co_{9.2}$(10 nm)- Si_3N_4(80 nm)- $Gd_{27.0}Fe_{63.9}Co_{9.1}$(10 nm)- Si_3N_4 (10 nm). For the SPP excitation, we use Kretschmann scheme with a 60-deg. SiO_2 prism attached to the glass substrate. The absence of exchange interaction between the two GdFeCo layers is achieved via the inclusion of the middle Si_3N_4(80 nm) layer, which width was tuned to achieve the significant difference in absorption of the top and bottom GdFeCo layers.

SPP excitation (at GdFeCo/air interface) and localization near the bottom GdFeCo layer is observed for p-polarized incident light, causing p-polarized femtosecond pulse being absorbed predominantly in this bottom layer. However, for the same angle of incidence of 60 deg. inside of the prism, and the same 800 nm wavelength of the pump, electromagnetic field distribution s- polarization is almost

the contrary. S-polarized incident pulse cannot excite SPP and is mostly absorbed in the top GdFeCo layer. Therefore, for the pump fluence exceeding the threshold value required for magnetization reversal, polarization is responsible for targeting of the certain layer where the magnetization would switch, without any impact on the other layer.

We have performed experimental investigation of the plasmonic-enabled layer-selective GdFeCo switching. Observation of magnetooptical state of each layer was possible due to the different contribution of each layer to polar magnetooptical Kerr effect (PMOKE) of the whole structure. The PMOKE hysteresis loop measured as the dependence on the external magnetic field showed four distinct PMOKE values corresponding to the four possible magnetization states of the bilayered GdFeCo structure. It made possible magnetooptical imaging of the pump impact on the magnetization state of each layer.

Obtained magnetooptical images (Fig.1) clearly show the difference in the targeting layer for p- and s- polarizations of light.

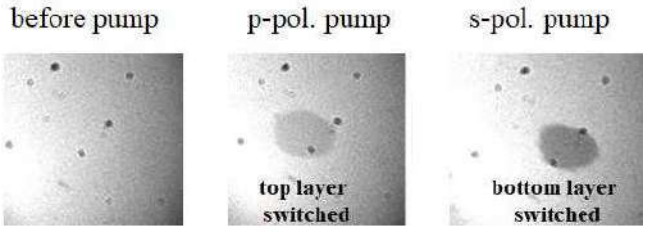


Figure 1: Magneto-optical image of GdFeCo structure after exposure to p- and s- polarized pump.

Explicit description of the experimental results on layer-selective switching in the bilayered structure could be found in Ref. [6]

3. Layer-selective magnetization reversal in multilayered GdFeCo structures

The demonstrated approach could be easily extended to the multilayered structures where the SPP resonances for different layers take place at different pump wavelengths or incidence angles. The most straightforward way to detune SPP resonances in the spectral range is to select the GdFeCo-surrounding dielectrics with different refractive indices for each GdFeCo layer of the multilayered structure. However, the broadness of the SPP resonances as well as high nonlinearity of the dielectrics with high refractive indices prevents from practical use this approach.

Way that is more efficient might be etching of GdFeCo layers to achieve gratings of different periods. Each grating period P in this case is responsible for the SPP resonance position determined as: $k_0 \sin\theta + 2\pi/P \cdot m = k_0 n_{spp}$, where k_0 is the wavenumber in free space, θ is the angle of incidence, m is the grating diffraction order (integer number), and n_{spp} is the effective SPP mode index. Therefore, variation of the GdFeCo grating period P makes the SPP resonances to be spectrally diverged, both in wavelength and angular spectra. This allows one to achieve all-optical layer-selective magnetization reversal using pump of different wavelengths (or angles) in multilayered GdFeCo structures.

4. Conclusions

We have proposed and demonstrated a novel concept of layer-selective all-optical magnetization reversal in bilayer GdFeCo structure based on the controllable accumulation of energy in a particular layer due to the SPP excitation. We have shown experimentally, that using a single shot of the femtosecond laser pulse one can all-optically reverse the magnetization state of only one layer determined by the polarization of the pump. This approach of all-optical layer targeting and magnetization reversal in GdFeCo could be easily extended to the layered structures with multiple GdFeCo layers where the SPP resonances are detuned from one another.

Acknowledgements

The work was supported by Russian Foundation for Basic Research 18-32-20225, from the European Union's Horizon 2020 research and innovation program under FET-Open Grant Agreement No. 713481 (SPICE), de Nederlandse Organisatie voor Wetenschappelijk Onderzoek (NWO), and from Grant-in-Aid for Scientific Research on Innovative Area, "Nano Spin Conversion Science", grant No. 26103004.

References

[1] R. Medapalli, I. Razdolski, M. Savoini, A.R. Khorsand, A. Kirilyuk, A. Kimel, A. Itoh, Efficiency of ultrafast laser-induced demagnetization in $Gd_xFe_{100-x-y}Co_y$ alloys, *Phys. Rev. B*, 86(5), 054442, 2012.

[2] C.D. Stanciu, F. Hansteen, A.V. Kimel, A. Kirilyuk, A. Tsukamoto, A. Itoh, T. Rasing, All-optical magnetic recording with circularly polarized light, *Phys. Rev. Lett.*, 99(4), 047601, 2007.

[3] I. Radu et al., Transient ferromagnetic-like state mediating ultrafast reversal of antiferromagnetically coupled spins, *Nature,* 472(7342), 205, 2011.

[4] A.R. Khorsand et al., Role of magnetic circular dichroism in all-optical magnetic recording, *Phys. Rev. Lett.*, 108(12), 127205, 2012.

[5] S.A. Maier, Plasmonics: fundamentals and applications. Springer Science & Business Media, 2007.

[6] D.O. Ignatyeva, C.S. Davies, D.A. Sylgacheva, A. Tsukamoto, H. Yoshikawa, P.O. Kapralov, A. Kirilyuk, V.I. Belotelov, and A.V. Kimel, Plasmonic all-optical layer-selective magnetic switching with a nanometer resolution (*submitted*, 2019)

Faraday Rotation Enhancement in Graphene Metasurfaces

J-M Poumirol[1], M. Tamagnone[2], T. M. Slipchenko[3], L. Martin-Moreno[4], J. R. Mosig[*], Alexey B. Kuzmenko[@].

[1] Department of Quantum Matter Physics, University of Geneva, Switzerland
[2] Harvard John A. Paulson School of Engineering and Applied Sciences, Cambridge, USA
[3]Instituto de Ciencia de Materiales de Aragon and Departamento de Fisica de la Materia Condensada, CSIC-Universidad de Zaragoza, Spain
[4]Laboratory of Electromagnetics and Antennas, EPFL de Lausanne, Switzerland
*corresponding author, E-mail: jean-marie.poumirol@unige.ch

Abstract

The magnetic circular dichroism and the Faraday rotation are the fundamental phenomena of great practical importance arising from the breaking of the time reversal symmetry by a magnetic field. In graphene those non-reciprocal phenomenons are linked to the cyclotron resonance, and as such appear at very low frequency [1], therefore limiting their potential for applications. In this work we studied both theoretically and experimentally the possibilities that graphene based metasurfaces offer for the control of the Faraday rotation and MCD. We studied various matasurfaces, both plasmonic [2] and photonic [3] and observed strong enhancement of the Faraday rotation at selected frequencies independently of the cyclotron resonance. We went further by showing that, depending on its design, each metasurface allows specific control over the frequency, amplitude and/or broadening of the non-reciprocal optical response of graphene [4], possibly forming the building blocks for future non-reciprocal optical elements from TeraHertz up to the mid infrared.

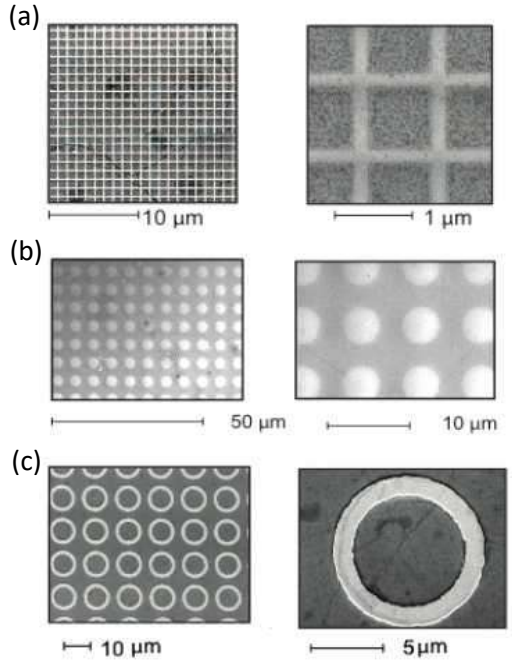


Figure 1: SEM pictures of different type of graphene metasurfaces

References

[1] L. I. Crassee, *et. al*., Nature Physics *7*, 48–51 (2011)

[2] J-M. Poumirol, Peter Q. Liu, T. M. Slipchenko, A. Y. Nikitin, L. Martin-Moreno, J. Faist & A. B. Kuzmenko, Nature Comm. 8, 14626 (2017)

[3] M. Tamagnone, C. Moldovan, J-M. Poumirol, A. B. Kuzmenko, A. M. Ionescu, J. R. Mosig, and J. Perruisseau-Carrier. Nature Comm.. 7, 11216 (2016)

[4] M. Tamagnone, T. M. Slipchenko, C. Moldovan, P. Q. Liu, A. Centeno, H. Hasani, A. Zurutuza, A. M. Ionescu, L. Martin-Moreno, J. Faist, J. R. Mosig, A. B. Kuzmenko, & J-M. Poumirol Physical Review B 97, 241410(R) (2018).

Ultrafast Magnetization Dynamics of CoFeB-based multilayer thin films with perpendicular anisotropy

Ana S. Silva[1], Simão P. Sá[1], Sergiy Bunyayev[1], Gleb Kakazei[1], Miguel Canhota[1], Miguel Miranda[1], Carlos Garcia[2], Iñigo J. Sola[3], Helder Crespo[1] and David Navas[1,*]

[1]Department of Physics and Astronomy, IFIMUP-IN, Faculdade de Ciências, Universidade do Porto, Porto, Portugal
[2]Department of Physics, Technical University Federico Santa María, 2390123 Valparaiso, Chile
[3]Laser Applications and Photonics group, Department of Applied Physics, University of Salamanca, E-37008 Salamanca, Spain

*corresponding author, E-mail: davidnavasotero@gmail.com

Abstract

Since the middle of the 1970s, thin films with perpendicular magnetic anisotropy (PMA) have been widely studied for recording media applications [1,2]. These systems can be designed with high thermal stability to avoid superparamagnetic behavior and with good writability [1], but this may raise the switching field above that which can be produced by currently available write heads. In order to overcome this limitation, other alternatives, such as perpendicular exchange coupled composite or exchange spring media, have been explored [3,4]. Perpendicular exchange spring systems consist of exchange-coupled hard and soft magnetic layers with respectively out-of-plane and in-plane easy magnetization axes. While the magnetically hard film provides thermal stability, the soft layer reduces the reversal field.

In this work, we studied [CoFeB/Pd] multilayer thin films as well as [CoFeB/Pd]/Co exchange spring structures by comparing time-resolved magneto-optical Kerr effect (TR-MOKE) measurements [5] with ferromagnetic resonance analysis (VNA-FMR). TR-MOKE measurements show a sudden drop within the first picosecond and a fast recovery (remagnetization) within a few picoseconds. This is followed by a clear oscillation or precession during a slower magnetization recovery (Figure 1 a). From the analysis of the precession behavior, we determined both the ferromagnetic resonance frequency ω_{FMR} and the effective Gilbert damping parameter α_{eff} (Figure 1 b). Both parameters have been compared with the results obtained from the VNA-FMR measurements.

Finally, the ultrafast demagnetization and the fast remagnetization processes within the initial 5 picoseconds have been analyzed. Measurements of the laser-induced demagnetization revealed a minimum at t ≈ 320 fs for the [CoFeB/Pd]5/Pd/Co(7Å) sample (Figure 1 c).

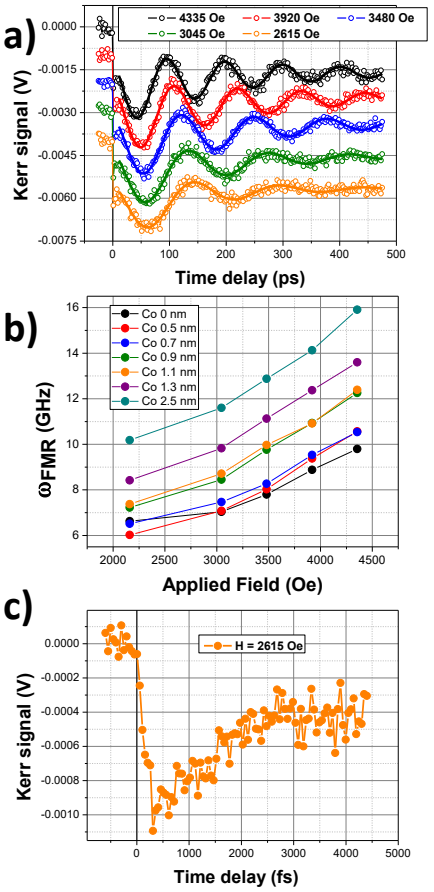


Figure 1: (a) TR-MOKE measurements at a pump laser fluence of 1.0 mJ/cm^2 on the [CoFeB/Pd]5 multilayer thin film and with different applied external magnetic fields (open symbols). The solid lines are the theoretical fittings. (b) Field dependence of the resonance frequency of the exchange spring systems. (c) Experimental demagnetization data of the [CoFeB/Pd]5/Pd/Co(7Å) exchange spring system.

Acknowledgements

The Portuguese team acknowledges the Network of Extreme Conditions Laboratories-NECL and Portuguese Foundation of Science and Technology (FCT) support through the projects NORTE-01-0145-FEDER-022096, MIT-EXPL/IRA/0012/2017, POCI-01-0145-FEDER-031302, EXPL/IF/01191/2013 (D.N.), EXPL/IF/00541/2015 (S.A.B.), EXPL/IF/00981/2013 (G.N.K). Authors acknowledge the support by the European Union Horizon 2020 Research and Innovation Programme under Marie Sklodowska-Curie Grant Agreement EU H2020-MSCA-RISE-2016 (No 734801).

References

[1] H. Richter, The transition from longitudinal to perpendicular recording, *J. Phys. D: Appl. Phys.* 40: R149-R177, 2007.

[2] R. Wood, Future hard disk drive systems, *J. Magn. Magn. Mater.* 321: 555-561, 2009.

[3] R. H. Victora and X. Shen, Composite media for perpendicular magnetic recording, *IEEE Trans. Magn.* 41: 537-542, 2005.

[4] H. J. Richter and A. Y. Dobin, Analysis of magnetization processes in composite media grains, *J. Appl. Phys.* 99, 08Q905, 2006.

[5] C.S. Gonçalves et al., A Dual-Colour Architecture for Pump-Probe Spectroscopy of Ultrafast Magnetization Dynamics in the Sub-10-femtosecond Range, *Sci. Rep.* 6: 22872, 2016.

Nonreciprocal magnetoplasmonic gratings

Rafael Cichelero, Mikko Kataja, Gervasi Herranz

[1] Institut de Ciència de Materials de Barcelona (ICMAB-CSIC), Campus de la UAB, Bellaterra, Catalonia, Spain
*corresponding author, E-mail: gherranz@icmab.cat

Abstract

Grating offer a solution towards integrated optical isolation by coupling optic fibers to on-chip waveguides. In this context, we study the interplay between diffraction and plasmons in magnetoplasmonic gratings, where broken time-reversal symmetry induces frequency shifts in energy and angular spectra of plasmon resonances. As a result, exceptionally large magneto-optic responses are seen in diffracted modes. Our results can be generalized to complex diffractive elements, such as metasurfaces, where they could find use in designing tunable nonreciprocal devices.

1. Introduction

Photonic or hybrid electronic/photonic circuits are considered to be a promising perspective for the next-generation of integrated devices [1]. This brings up the need for integrated nonreciprocal devices that could find use for optical isolation at small scales. Facing this need, there is an emergent activity that aims at achieving unidirectional light propagation along integrated optical waveguides. Additionally, optoelectronic devices are investigated, in which modulation and switching capabilities can be accomplished by electric control of the amplitude and phase of electromagnetic waves, using architectures based either on Mach-Zehnder interferometers or microring resonators. Therefore, the control of the properties of devices by electric fields is an active research field in nanophotonics.

Optical nonreciprocity is usually achieved by magneto-optic materials. However, as the relevant device length is reduced to very small scales in integrated devices, the magneto-optic activity –which is proportional to the amount of material–, is drastically reduced. It is therefore necessary to compensate the large reduction in size and magneto-optic activity with a large enhancement of the intrinsic response. Facing this challenge, a substantial research has been devoted to boost the intrinsic magneto-optical magnetoplasmonic devices [2]. Along these lines, metallic diffraction gratings have been studied in the context of magnetoplasmonic crystals where control on surface plasmon polaritons (SPPs) is exerted by external magnetic fields. Yet, the mutual interplay of plasmonics, magneto-optics and diffraction has not been addressed so far. Facing this challenge, we have been primarily concerned with the study of this interplay using the grating coupler structure as the basic device where to analyze the effect of diffraction and plasmonics on magneto-optic responses. Indeed, grating couplers are important devices in the perspective of integrated photonic applications, as they enable efficient coupling between light from optic fibers to on-chip waveguides offering easy integration on wafers and enabling communication with external units via optical links.

2. Angle-resolved reflectance Fourier spectroscopy

We studied the optical properties of magnetoplasmonic gratings using Fourier optics microscopy [3], which provides access to the band structure of photonic crystals. The working principles of the Fourier optics are based on the collimation of the light coming from a point source, so that a plane wave is projected into the detector, which is placed in the Fourier plane, in which the reflected light projects the reciprocal space response, providing the band structure of photonic structures. This way, the angular information can be recovered through a space-angular conversion, providing angle-resolved reflectance (ARR) maps. The Fourier spectroscopy approach can be adapted to the study of magnetoplasmonic gratings by reducing the beam spot size in the objective back aperture, so that diffracted modes can be analyzed independently, enabling the exploration of the interplay between plasmonic resonances and diffracted light. We used this approach to study selectively surface plasmon polaritons propagating along backward or forward directions, enabling us to easily assess their non-reciprocal magnetic modulation.

2.1.1. Magneto-optic response of individual SPP excitations

To assess the magneto-optic response, we measured the transverse magneto-optic Kerr effect (TMOKE) amplitude of Au/Co magnetoplasmonic gratings, measured from the ARR maps, obtained through the expression

$$\tau = \left[\frac{I(H_+) - I(H_-)}{I(H_{avg})}\right] \quad (1)$$

where $I(H_+)$, $I(H_-)$ are the reflected or diffracted intensity detected at opposite saturated magnetizations of Co (taken at $H_{+,-} \approx \pm 150$ Oe), and $I(H_{avg})$ is defined as the average of the absolute value of $I(H_+)$ and $I(H_-)$ over many hysteretic cycles. In our study we demonstrate that that large TMOKE signals are associated with individual forward- and backward- SPP propagating modes. Interestingly, we found remarkably large TMOKE responses (above 4%) enhanced by selectively excited propagating plasmons. This observation opens up interesting perspectives in nanophotonics, as it might be exploited in on-chip grating couplers to external optical links, eventually enabling one-way propagation in integrated photonic circuits.

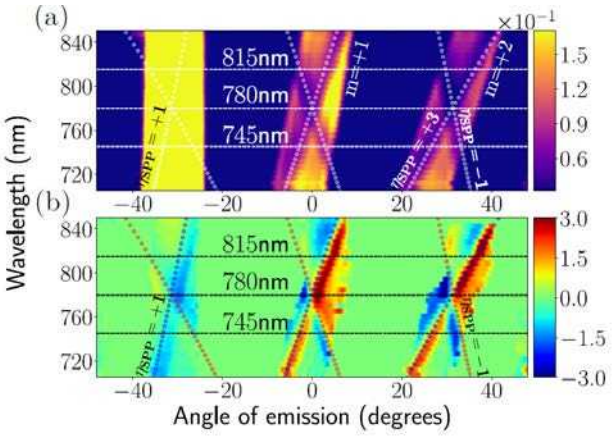


Figure 1: Panels (a) and (b) show, respectively, the reflectance and TMOKE angular resolved plots from off-angle excitations, in which the light beams arise from the specular reflection and diffraction modes, corresponding to a grating with periodicity of Δ = 1000 nm.

2.1.2. Magneto-optic response of SPP excitations under electric fields

In addition to magnetism, we also analyzed plasmon propagation and magneto-optic responses under the effects of electric fields after incorporation of ferroelectric materials into the magnetoplasmonic structures. For that purpose, we measured ARR maps under applied electric fields (Figure 2). We studied the particular case of Au/Co magnetoplasmonic gratings grown in combination with ferroelectric $BaTiO_3$ layers.

In line with our previous results, large magneto-optic signals – two orders of magnitude larger than intrinsic responses– arise from the SPP excitation. We show that, due to the presence of the ferroelectric layer, plasmon propagation can be modulated by electric fields enabling reversing the sign of magneto-optic signals. Thus, the combined integration of magneto-optical and ferroelectric materials enables control over non-reciprocal device properties by application of external electric fields, rather than magnetic fields, which could greatly simplify their integration into multifunctional nanophotonic devices.

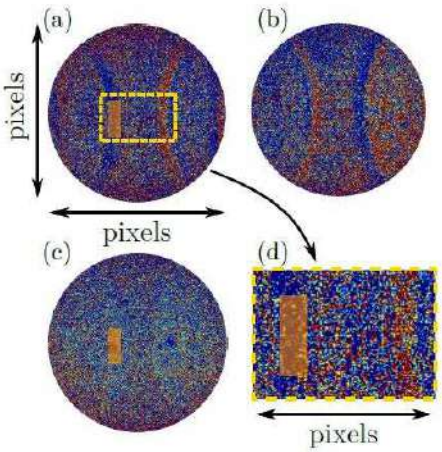


Figure 2: Panels (a)-(c) display the normalized average intensity in the Fourier plane for three polarization states. Plasmon resonances are visible in (a) and (b). Panel (a) shows an orange square, from which the normalized average intensity as a function of field is calculated. Panel (d) shows a zoom of the region where the plasmonic effects are extracted.

3. Conclusions

Large enhancements of the magneto-optic response are found in magnetoplasmonic grating couplers. This enhancement is due to magnetically-induced frequency shifts in the energy and angular spectra of plasmon resonances. Interestingly, these shifts can be modulated by electric fields via the control of the electric polarization of magnetoplasmonic gratings that incorporate ferroelectrics. The concepts presented here can be used to develop non-reciprocal devices that exploit diffraction in order to achieve tailored electromagnetic responses, opening up new avenues for active integrated nanophotonic devices.

Acknowledgements

We acknowledge financial support by the Spanish Ministerio de Economía y Competitividad through projects MAT2017-85232-R (AEI/FEDER,UE), Severo Ochoa (SEV-2015-0496), by the Generalitat de Catalunya (2017SGR 1377), by CNPq – Brazil, and by the European Comission (Marie Skłodowska-Curie IF EMPHASIS - DLV-748429).

References

[1] M. Hochberg, T. Baehr-Jones, Towards fabless silicon photonics, *Nat. Photonics* 4: 492 – 494, 2010.

[2] G. Armelles et al. Magnetoplasmonics: Combining Magnetic and Plasmonic Functionalities. *Adv. Opt. Mater.* 1: 10–35, 2013.

[3] R. Cichelero et al. Non-reciprocal diffraction in magnetoplasmonic gratings. Opt. Exp. 26: 34842-34852, 2018.

Naturally Hyperbolic and Chirality Too: The Optics of Antiferromagnets

Robert Stamps[1], Rair Macedo[2], Igor Proskurin[1],

[1]Department of Physics and Astronomy, University of Manitoba, Winnipeg, MB, Canada
[2]School of Physics and Astronomy, University of Glasgow, Glasgow, UK
*corresponding author, E-mail: robert.stamps@umanitoba.ca

Abstract

The optical properties of antiferromagnets and cavity magnonics of ferromagnets are discussed. The antiferromagentic system displays phenomena analogous to non-ferroic hyperbolic materials and meta-materials, with interesting possibilities for optical spintronics. The ferromagnet cavity system shows mode attraction and may also support an analogy to opto-mechanical cavity response.

Natural hyperbolic magnetic media exist in which optical effects such Goos-Hanchen shifts [1] and negative reflection [2] can be tuned by simply applying external magnetic fields. We discuss how this occurs in antiferromagnets and show that by rotating the easy axis of the crystal, the hyperbolic dispersion is rotated and the angle of refraction is modified and cannot be defined as simply negative and positive as is done in conventional hyperbolic media. The optical properties derived from the hyperbolic behaviour are also modified, and can result in slab focusing with a magnetic field dependence. An example is shown below in Figure 1, where negative refraction is predicted for light propagation through an antiferromagnet with frequency chosen such that there is competition between elements of the permeability tensor. [2]

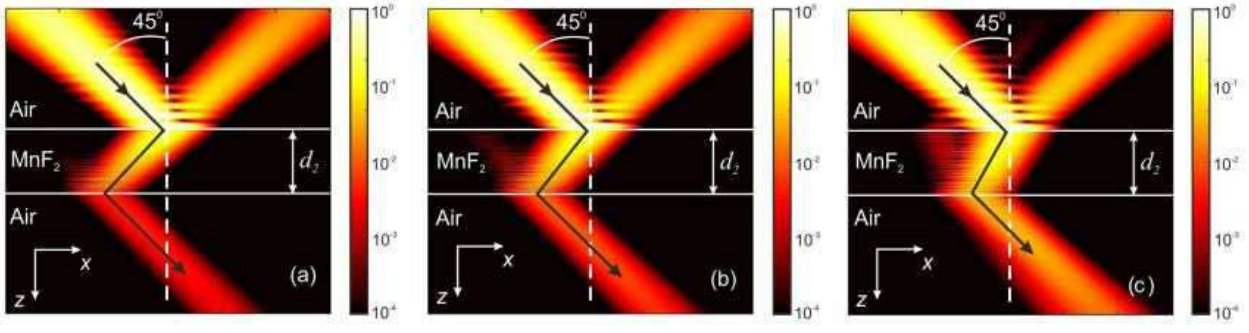


Figure 1. Illustration of negative refraction through an antiferromagnetic film for different applied magnetic field strnegths (after Ref. 2).

Magnetic polaritons in antiferromagnets are electromagnetic excitations coupled with spin degrees of freedom. Antiferromagnetic spin excitations can have properties that arise from a feature associated with their spin ordering that provides an analogy to right and left circular polarisation of optical radiation. This allows us to explore possibilities for unique coupling between optics and spintronics. [4,5] As first demonstrated by Tang and Cohen in chiral optics, the asymmetry in the rate of electromagnetic energy absorption between left and right enantiomers is determined by an optical chirality density. Here, we demonstrate that this effect can exist in magnetic spin systems. By constructing a formal analogy with electrodynamics, we show that in antiferromagnets with broken chiral symmetry, the asymmetry in local spin-wave energy absorption is proportional to a spin-wave chirality density, which is a direct counterpart of optical zilch.[4] We propose that injection of a pure spin current into an antiferromagnet may serve as a chiral symmetry breaking mechanism, since its effect in the spin-wave approximation can be expressed in terms of additional Lifshitz invariants. We use linear response theory to show that the spin current induces a nonequilibrium spin-wave chirality density.

Cavity electrodynamics can also be realised in the context of magnetic spin systems. [6-7] In contrast to the THz frequency excitations typical of antiferromagnets, we consider instead the microwave frequency properties of ferromagnets. In ferromagnetic resonance, the zero wavevector resonance mode can be driven by fields within a microwave cavity. The cavity modes can hybridize with the resonance modes and create level splitting that is tuned by an applied magnetic field. An example of an experimental geometry is shown below in Figure 2 along with example results for mode hybridisation. [7]

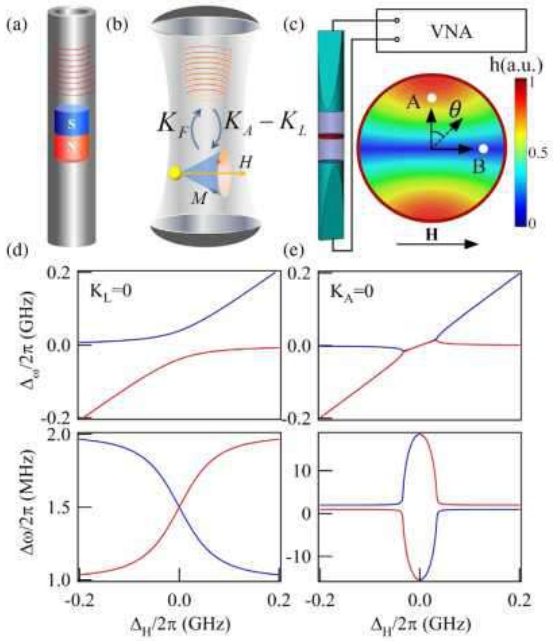


Figure 2. An example cavity geometry is shown in (a), (b) and (c), and examples of cavity and ferromagnetic resonance hybridization is shown in (d) and (e).

An interesting feature is the possibility of mode attraction, as observed in Ref. 7. We examine also possibilities for creating an analogy to optomechanical cavities using a topological excitation that can exist in magnetic spin systems. Topological soliton 'twists' can respond to optical pressure with natural frequencies determined by either structure or pinning. We predict mode repulsion and attraction processes, tunable with applied magnetic field, should exist for these systems also.

This work was supported in part through NSERC Natural Sciences and Engineering Research Council of Canada (NSERC). Cette recherche a été financée par le Conseil de recherches en sciences naturelles et en génie du Canada (CRSNG).

[1] R. Macêdo, T. Dumelow, and R. L. Stamps, Optics Express, 22, 28467 (2014)
[2] R. Macêdo, T. Dumelow, and R. L. Stamps,ACS Photonics 3, 9, 1670-1677, (2016)
[3] R. Macêdo, T. Dumelow, R. E. Camley and R. L. Stamps,ACS Photonics 5, 5086-5094, (2018)
[4] I. Proskurin, R.L. Stamps, A.S. Ovchinnikov, J. Kishine, Phys. Rev. Lett. 119, 177202 (2017)
[5] I. Proskurin, A.S. Ovchinnikov, J. Kishine, and R.L. Stamps, Phys. Rev. B 98, 134422 (2018)
[6] I. Proskurin, A.S. Ovchinnikov, J. Kishine, and R.L. Stamps, Phys. Rev. B 98, 220411(R) (2018)
[7] M. Harder, Y. Yang, B. M. Yao, C. H. Yu, J. W. Rao, Y. S. Gui, R. L. Stamps, and C.-M. Hu
Phys. Rev. Lett. 121, 137203 (2018

Nanoscale Localization of sub-Terahertz Spin Dynamics in Au/Garnet Magnetoplasmonic Crystals

Alexander L. Chekhov[1,§,*], Alexander I. Stognij[2], Takuya Satoh[3], Tatiana V. Murzina[1], Ilya Razdolski[4,†], and Andrzej Stupakiewicz[5]

[1]Department of Physics, Moscow State University, Moscow, Russia
[2]Scientific-Practical Materials Research Centre of the NASB, Minsk, Belarus
[3]Department of Physics, Kyushu University, Fukuoka, Japan
[4]Fritz Haber Institute of the Max Planck Society, Berlin, Germany
[5]Faculty of Physics, University of Bialystok, Bialystok, Poland
[§]Present address: Faculty of Physics, Free University Berlin, Berlin, Germany
[†]Present address: FELIX laboratory, Radboud University, Nijmegen, The Netherlands
*corresponding author, E-mail: chekhov@fhi-berlin.mpg.de

Abstract

We present results on ultrafast magnetization dynamics induced by the surface plasmon-polariton electric field in Au/iron-garnet magnetoplasmonic crystals [1]. The spin precession excited through the inverse Faraday effect demonstrates strong localization and efficiency enhancement by two orders of magnitude at the surface plasmon resonance. The mechanisms of the observed effect are discussed both analytically and numerically.

1. Introduction

Ultrafast spin dynamics is a research field of constantly growing interest. By coherently controlling the magnetic order of the solids, one can open possibilities for terahertz speed recording of information [2]. As new optical mechanisms for spin control are being developed [3], the problem of spatial localization still remains unsolved. At the same time, by using magnetoplasmonic structures one can excite surface plasmons in magnetic systems [4, 5, 6]. High spatial confinement and short lifetime of these excitations [7, 8] may help overcoming the localization problem [9].

One of the mechanisms for coherent spin control via optical fields is the inverse Faraday effect (IFE), when the light electric field induces a static magnetic field in a gyrotropic medium [10]:

$$H_k^{IFE} = \chi_{ijk}^m E_i E_j \sin\varphi, \qquad (1)$$

where χ_{ijk}^m is the magneto-optical susceptibility, E_i, E_j the electric field components and φ the phase delay between them. H_k^{IFE} is maximal for circularly polarized light and zero for linear polarization. Interestingly, the field structure of the surface plasmon polariton (SPP) is such, that it should produce strongly localized static IFE magnetic field on the timescale of the SPP lifetime. In this study we aim to utilize this unique combination of spatial and temporal localization of the magnetic field to control the spin dynamics in a transparent ferrimagnetic dielectric.

2. Experiment

For the experiment we fabricated an Au/garnet magnetoplasmonic crystal consisting of the 380 μm thick Gd-Yb-doped bismuth iron garnet single crystal ($Gd_{4/3}Yb_{2/3}BiFe_5O_{12}$, GdYbBIG)) covered with 50 nm Au grating with the period of 800 nm (Fig. 1). GdYbBIG is a ferrimagnetic dielectric, in which the exchange precession mode can be efficiently excited via the IFE (precession frequency is 0.41 THz) [11]. The sample was studied using a pump-probe setup with 800 nm probe and near-IR pump. The pump wavelength was tuned across the resonance for the SPP excitation at the Au/GdYbBIG interface. As schematically shown in Fig. 1, the SPP electric field rotates in the incidence plane as the SPP propagates along the Au/GdYbBIG interface and induces a static transversal IFE magnetic field localized on the scale of 100 nm.

By measuring the probe pulse Faraday rotation variation with respect to the time delay between the pump and probe, we were able to extract the amplitude and phase of the exchange precession mode for different pump pulse wavelengths. Spectrum of the exchange mode amplitude is shown in Fig. 2 for circular and linear pump polarizations.

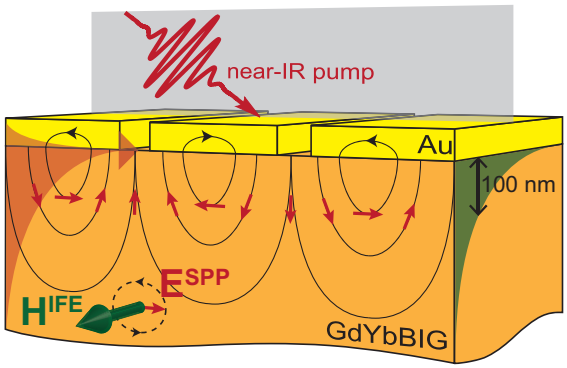


Figure 1: Illustration of the Au/GdYbBIG magnetoplasmonic crystal and the IFE mechanism for the SPP field.

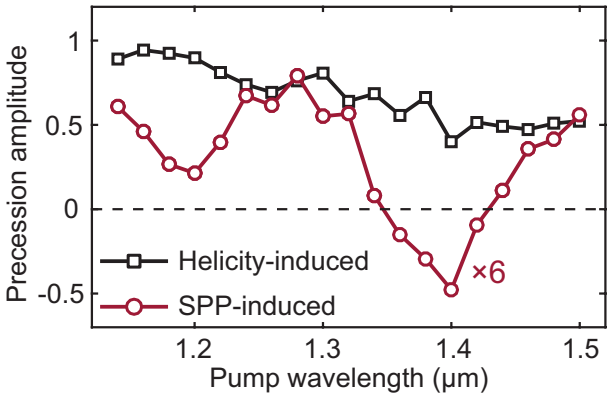


Figure 2: Exchange precession amplitude versus the pump wavelength for circular (black curve) and linear (red curve, multiplied by 6) pump polarizations. Adapted from [1].

3. Discussion

The precession amplitude spectrum for circularly polarized pump does not show any features, since no SPPs are excited and the precession is homogeneously induced in the bulk of the GdYbBIG crystal due to the helicity of the pump pulse. At the same time, for the linearly polarized pump the bulk IFE effect should be zero, while the SPP excitation should induce the static IFE magnetic field localized at the Au/GdYbBIG interface. Indeed, the precession amplitude spectrum in this case shows strong feature centered at 1400 nm (Au/GdYbBIG SPP excitation in the first diffraction order) and changes the sign (phase) of the precession.

We also confirm our findings with numerical simulations and demonstrate high localization of the SPP-induced IFE magnetic field on the scale of 100 nm. Using the precession amplitudes and the characteristic dimensions of the regions, where the probe pulse experiences rotation, we calculate the ratio between the precession excitation efficiencies for resonant (SPP excitation) and non-resonant (circularly polarized pump) cases. The SPP-induced IFE magnetic field turns out to be 10^2 times larger than that induced by the circularly polarized pulses in the bulk of the crystal.

4. Conclusions

Our findings demonstrate that the electric field of the SPP can induce a highly localized static magnetic field in gyrotropic medium that allows for efficient precession excitation in ferrimagnetic dielectrics.

References

[1] A.L. Chekhov, A.I. Stognij, T. Satoh, T.V. Murzina, I. Razdolski, and A. Stupakiewicz, Surface plasmon-mediated nanoscale localization of laser-driven subterahertz spin dynamics in magnetic dielectrics, *Nano Lett.* 18: 2970–2975, 2018.

[2] A. Kirilyuk, A.V. Kimel, and Th. Rasing, Ultrafast optical manipulation of magnetic order, *Rev. Mod. Phys.* 82: 2731–2784, 2010.

[3] A. Stupakiewicz, K. Szerenos, D. Afanasiev, A. Kirilyuk, and A.V. Kimel, Ultrafast nonthermal photomagnetic recording in a transparent medium *Nature* 542: 71–74, 2017.

[4] V.I. Belotelov et al. Enhanced magneto-optical effects in magnetoplasmonic crystals *Nat. Nanotechnol.* 6: 370–376, 2011.

[5] I. Razdolski et al. Nonlocal nonlinear magneto-optical response of a magnetoplasmonic crystal, *Phys. Rev. B* 88: 075436, 2013.

[6] A. L. Chekhov, V. L. Krutyanskiy, A. N. Shaimanov, A. I. Stognij, and T. V. Murzina, Wide tunability of magnetoplasmonic crystals due to excitation of multiple waveguide and plasmon modes, *Opt. Express* 22: 17762–17768, 2014.

[7] D. Bossini, V.I. Belotelov, A.K. Zvezdin, A.N. Kalish, and A.V. Kimel, Magnetoplasmonics and femtosecond optomagnetism at the nanoscale, *ACS Photonics*, 3: 1385–1400, 2016.

[8] I. Razdolski, A.L. Chekhov, A.I. Stognij, and A. Stupakiewicz, Ultrafast transport and relaxation of hot plasmonic electrons in metal-dielectric heterostructures, arXiv:1901.08887, 2019.

[9] T.-M. Liu et al. *Nano Lett.* 15: 6862–6868, 2015.

[10] L.P. Pitaevskii, Electric forces in a transparent dispersive medium, *Sov. Phys. JETP* 12: 1008–1013, 1961.

[11] S. Parchenko, A. Stupakiewicz, I. Yoshimine, T. Satoh, and A. Maziewski, Wide frequencies range of spin excitations in a rare-earth Bi-doped iron garnet with a giant Faraday rotation, *Appl. Phys. Lett.* 103: 172402, 2013.

Revealing the Coupling Mechanism of Plasmonic and Magneto-Optically Induced Near-Fields in Bi:YIG/Au nanostructures

Spiridon D. Pappas[1], Philipp Lang[1] and Evangelos Th. Papaioannou[1,*]

[1]Fachbereich Physik and Forschungszentrum OPTIMAS, Technische Universität Kaiserslautern, Erwin-Schrödinger-Strasse 56, 67663 Kaiserslautern, Germany.

*corresponding author, E-mail: papaio@rhrk.uni-kl.de

Abstract

We demonstrate the anomalous enhancement of the longitudinal magneto-optic Kerr effect of bismuth-substituted yttrium iron garnet films, induced by localized surface plasmons in embedded gold nanoparticles. We reveal the underlying mesoscopic near-field mechanism by quantifying the result of the mixing of the two localized plasmonic resonant modes on the magneto-optic response in the far-field. Our results pave the way to the design on demand of the magneto-optic response of similar hybrid structures.

1. Introduction

The field of magnetoplasmonics allows to explore the influence of the strong localization of light, enabled by resonant plasmonic structures, on the response of magneto-optically active adjacent materials [1,2,3]. Nowadays, it is generally accepted that the strong confinement of light in plasmonic structures results in large local field enhancements, which increase enormously the interaction of light with the magnetic material. However, no conclusive quantification of the effect has been discussed. Recently, first steps in this direction were taken by showing the correlation of near- and far-field effects to design the magneto-optic response of a magneto-plasmonic material [4]. Here, we focus on the origin of the magneto-optical/plasmonic interaction using nanoparticles that support localized surface plasmons (gold nanoparticles-AuNPs) embedded in ferri-magnetic dielectric layers composed of bismuth substituted yttrium iron garnet (Bi:YIG).

2. Results

For our study, the AuNPs are randomly distributed on the interface of the Bi:YIG and gadolinium gallium garnet (GGG) layers. The optical properties of this sort of system are mainly determined by Localized Surface Plasmon resonances (LSPs), rather than by geometrical-lattice resonances. The Au/Bi:YIG system has already attracted numerous theoretical and experimental [5, 6, 7] studies based on the Faraday and Polar Kerr Effect (P-MOKE) enhancement. However, the underlying near-field mechanism is not clarified while there is lack of studies on the anomalous longitudinal MOKE response (L-MOKE) induced by LSPs. The L-MOKE geometry, used in our study, is easy to be implemented and therefore quite attractive for technological applications.

The samples consist of AuNPs fabricated on top of a single crystalline GGG (111) substrate by post heating of a thin continuous Au film. On top of the AuNPs layer, the BiY2Fe5O12film is grown.

The Kerr rotation spectra measured with the aid of a spectroscopic Kerr effect setup operating in the longitudinal mode, by means of a Wollaston prism, combined with a balanced photodiode setup, mounted on a motorized rotational stage. The setup is fully automated and, with proper calibration, it can provide the Kerr rotation in absolute values.

Numerical calculations were based on the Finite Integration Technique (FIT) method, by using the CST Microwave Studio.

The Kerr rotation as a function of the light wavelength is shown in Fig. 1 for a reference Bi:YIG sample without AuNPs and for a Bi:YIG film containing AuNPs. The magneto-optical response of Bi:YIG in the optical and near-infrared region is attributed to the wings of the optical transitions occurring at photon energies of 2.8 and 3.3 eV (442 and 378 nm correspondingly). The main contribution is coming from the 3.3 eV transition band, which is largely affected by the Bi substitution, and less from the 2.8 eV band. Bi substitution increases both the oscillator strengths, as well as the splittings of the electronic transition bands. The Kerr rotation curves corresponding to both samples increases to high positive values for the low-wavelength spectral region, verifying the aforementioned points. For both samples exists a certain spectral region for which the Kerr rotation sign inverts. The spectral position of the zero-crossing is highly sensitive to the stoichiometry and the thickness of the film. For the sample containing AuNPs, the magneto-optical response of the Bi:YIG layer is strongly modified in the very broad optical region where the resonant localized surface plasmon phenomena take place. One sharp feature is located close to 625 nm, and a moderately broad one with an opposite sign at~700 nm.

As a generic conclusion, the experiment clearly shows a large anomalous modification of the magneto-optical response of Bi:YIG originating from LSPs.

2.1. Simulated Kerr rotation

In order to gain insight into the deeper mechanism of the observed anomalous magneto-optic activity, we need to answer the following question: Is the magneto-optic behavior of the hybrid Bi:YIG/AuNPs attributed to a possible modification of the off-diagonal elements of the dielectric tensor of Bi:YIG, caused by the intensified electric field of the LSPs, or is it simply attributed to the modification of the light scattering / absorption close to the resonant wavelength of the AuNPs?

For this, we calculated the reflectivity for s- and p-polarized light R_{ss} and R_{pp} respectively, as well as the polarization conversion efficiency R_{ps} and R_{sp} in the L-MOKE geometry. We furthermore studied the electric near-field components and attempt to correlate the magneto-optical far-filed spectral features with the magneto-optically induced near-fields. From the simulated data we can conclude that the sign of Kerr rotation in the far-field, as well as its absolute value in the LMOKE geometry, is an interplay between the main oscillating field resonances and the magneto-optically induced resonances. The Kerr rotation in the far-field is generated by the landscape of the near-field modifications of the magneto-optically induced fields.

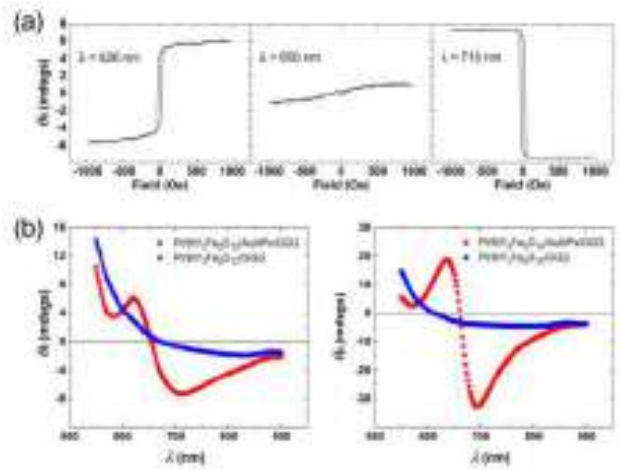


Figure 1: (a) Magnetic loops recorded in the longitudinal geometry for the BiY2Fe5O12/AuNPs/GGG sample at three different wavelengths. Scanning from low wavelength values, the amplitude of the magnetic loop is minimal at 650 nm and is subsequently inverted for higher wavelength values. (b) Dependence of the Kerr rotation as a function of wavelength, recorded for the samples with (red-solid circles) and without (blue-solid triangles) AuNPs for s- (left-side panel) and p- (right-side panel) polarized incident light. A large enhancement is observed when localized plasmons are present.

3. Conclusions

We make a step towards engineering the magneto-optical response of noble metal/magneto-optically active dielectric structures, by addressing the key question of how the localization of the electromagnetic field defines the magneto-optical enhancement in these structures. We achieve the latter by mapping the enhancement of the magneto-optically induced near-fields. Furthermore, we show how the magneto-optic behaviour of the hybrid Bi:YIG/AuNPs system can be reproduced computationally. Near-field simulations show that the far-field MOKE features are attributed to more than one LSP resonant mode. The different modes have different field orientations and signs, and this effectively alters the dielectric tensor elements of the magnetic material.

Acknowledgements

We gratefully acknowledge the Deutsche Forschungsgemeinschaft program SFB/TRR 173: SPIN+X Project B07.

References

[1] Armelles, G., Cebollada, A., García-Martín, A. and M. U. Gonzalez, Magnetoplasmonics: Combining Magnetic and Plasmonic Functionalities, *Adv. Opt. Mater.* Vol 1, 10−35, 2013.

[2] E. Melander, E. Östman, J. Keller, J. Schmidt, E. T. Papaioannou, V. Kapaklis, U. B. Arnalds, B. Caballero, A. Garcia-Martin, J. C. Cuevas, and B. Hjörvarsson, *Appl. Phys. Lett*. 101, 063107, 2012.

[3] I. Razdolski, D. G. Gheorghe, E. Melander, B. Hjörvarsson, P. Patoka, A. V. Kimel, A. Kirilyuk, E. Th. Papaioannou, and Th. Rasing, Nonlocal nonlinear magneto-optical response of a magnetoplasmonic crystal, *Phys. Rev. B* 88, 075436, 2013.

[4] M. Rollinger, P. Thielen, E. Melander, E. Östman, V. Kapaklis, B. Obry, M. Cinchetti, A. García Martín, M. Aeschlimann and E. Th. Papaioannou, Light Localization and Magneto-Optic Enhancement in Ni Antidot Arrays, *Nano Letters* Vol. 36, 2432–2438, 2016.

[5] S. Tomita, T. Kato, S. Tsunashima, S. Iwata, M. Fujii, and S. Hayashi, *Phys. Rev. Lett.* 96, 167402, 2006.

[6] G. Armelles, A. Cebollada, F. Garcia, A. Garcia-Martin, and N. de Sousa, *ACS Photonics* 3, 2427, 2016.

[7] B. Caballero, A. Garcia-Martin, and J. C. Cuevas, *Opt. Express* 23, 22238, 2015.

The Transverse Magneto-Optical Kerr Effect in Two-Dimensional Magnetoplasmonic Periodic and Quasicrystalline structures

Andrey Kalish[1,2*], Roman Komarov[1], Mikhail Kozhaev[2,3], Achanta Venu Gopal[4], Aman Agrawal[4], and Vladimir Belotelov[1,2]

[1]Faculty of Physics, Lomonosov Moscow State University, Moscow, Russia
[2]Russian Quantum Center, Moscow, Russia
[3]Prokhorov General Physics Institute of the Russian Academy of Sciences, Moscow, Russia
[4]Tata Institute of Fundamental Research, Mumbai, India
*corresponding author, E-mail: kalish@physics.msu.ru

Abstract

We report on the transverse magneto-optical Kerr effect in a two-dimensional magnetoplasmonic quasicrystal and compare it to the case of magnetoplasmonic crystals with different basic angles. The quasicrystalline structure provides resonant response with increased bandwidth.

1. Introduction

Quasicrystalline structures were experimentally discovered by Shechtman et al. [1], for which he was awarded the Nobel Prize in Chemistry in 2011. Quasicrystals are non-periodic but ordered structures [2]. Contrary to the periodic crystalline structures, they do not possess translational symmetry but have long-range ordering. For periodic structures the reciprocal lattice is given by an equidistant set of reciprocal vectors. Unlike periodic structures, the quasiperiodic ones are characterized by discrete but non-equidistant reciprocal lattices and corresponding unusual diffraction patterns.

Two-dimensional quasicrystalline structures can possess rotational symmetry C_n of orders, that are prohibited for periodic structures, such as n = 5, 7 and higher orders. An example of that is Penrose tiling that possesses C_5 rotational symmetry. Quasicrystalline substances are usually metallic alloys and they provide high hardness, low coefficient of friction, low thermal conductivity and wide optical absorption bands. Quasicrystals, like two-phase materials containing steel, have potential application as materials having high strength and plasticity at high temperatures and also as coatings, for example, for frying pans, solar energy absorbers and reflectors [2].

The concept of quasicrystals has been implemented in plasmonics as well. Plasmonic quasicrystals in the form of metal-dielectric nanostructures with quasicrystalline pattern that support excitation of surface plasmon-polaritons (SPP) were designed. Due to the discrete non-equidistant reciprocal space and the rotational symmetry of quasicrystals, a larger number of resonances associated with SPP modes appear and therefore such structures demonstrate a broadband optical response. Moreover, it is polarization-independent for the 2D structures [3]. The advantage of quasicrystalline structures over periodic and non-periodic ones is that they possess rich and designable reciprocal lattice that governs the optical diffraction and dispersion of the eigenmodes, and therefore offer designable broadband optical response. It comes from the fact that the reciprocal lattice is strongly dependent on the geometrical parameters of the structure, while for the periodic structures it is defined solely by the period.

The study of magnetoplasmonic quasicrystalline structures is also performed. In particular, the transverse magneto-optical Kerr effect (TMOKE) was shown to demonstrate multiband response in one-dimensional magneto-plasmonic crystals [4].

In the present work we present theoretical and experimental study of the TMOKE in a two-dimensional magnetoplasmonic quasicrystal as well as two-dimensional periodic structures.

2. Considered structures

The considered structures consist of metallic grating of these patterns and a smooth magnetic dielectric film. The periodic structures are formed by circle holes in metallic films with rombohedral lattice with different basic angles of 30, 36, 45, 60, 72 and 90 degrees. The quasi-crystalline structure is formed by superposition of five periodic lattices with basic angles 72 deg. rotated by 72 deg. with respect to each other. Such structure obviously possesses 10-fold rotational symmetry. The quasi-crystalline pattern is shown in Fig. 1.

The metal grating is made of gold with the thickness of 100 nm. The magnetic dielectric is a bismuth substituted iron-garnet film of composition $Bi_{1.5}Gd_{1.5}Fe_{4.5}Al_{0.5}O_{12}$ with the width of 80 nm, so that waveguide modes are not excited.

The light is TM-polarized and hits the sample from the metal side of the structure. The TMOKE in transmission is measured as $\delta = [T(M)–T(–M)]/T(0)$, where $T(M)$ is transmittance at magnetization equal to M.

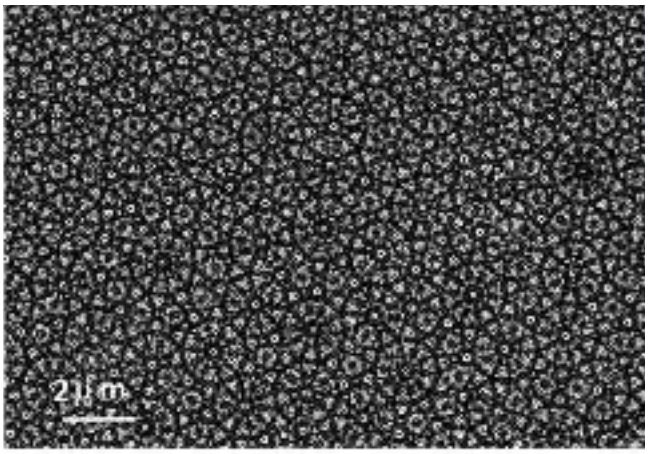
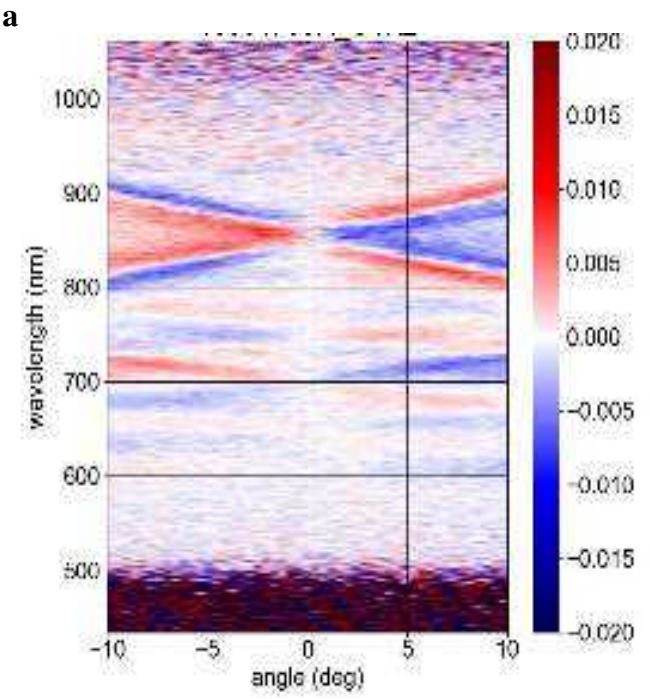


Figure 1: Quasi-crystalline pattern.

3. Results and discussion

Fig.2 shows the TMOKE for the quasicrystalline structure and for the plasmonic crystal with the basic angle of 72 degrees. The spectral position of the resonances are the same, which corresponds to theoretical consideration, as the quasicrystal is formed by superposition of similar crystalline structures. The width and the strength of the resonances are different because the quasicrystalline structure supports the greater number of plasmonic modes propagating in different directions.

Experiments also reveal that the resonance position changes when the basic angle changes.



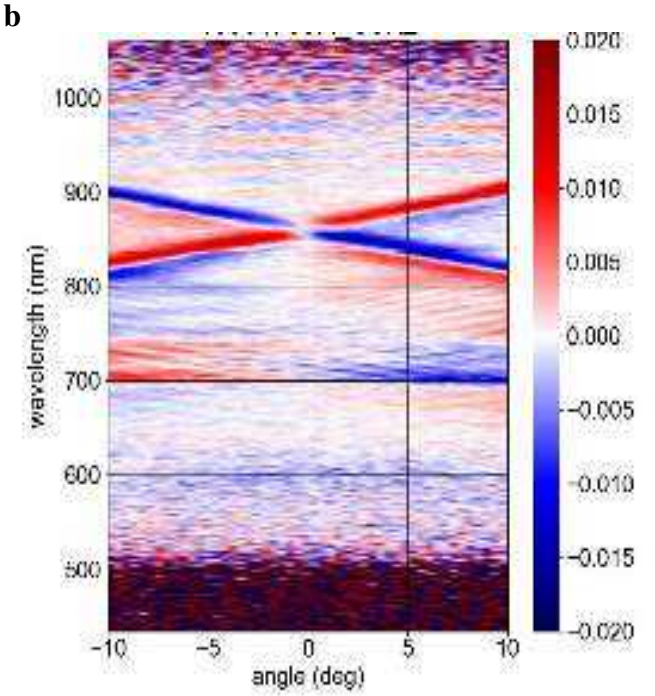


Figure 2: The TMOKE spectra for the quasicrystalline structure (a) and for the plasmonic crystal with the basic angle of 72 degrees (b).

Acknowledgements

This work was supported by the RFBR grant No. 19-02-00856.

References

[1] D. Shechtman, I. Blech, D. Gratias, J.W. Cahn, Metallic phase with long-range orientational order and no translational symmetry, *Phys. Rev. Lett.* 53, 1951, 1984.

[2] Yu.Kh. Vekilov, M.A. Chernikov, Quasicrystals, *Phys. Usp.* 53, 537, 2010.

[3] V.G. Achanta, Plasmonic Quasicrystals, *Prog. Quant. Electron.* 39, 1, 2015.

[4] A.N. Kalish, R.S. Komarov, M.A. Kozhaev, V.G. Achanta, S.A. Dagesyan, A.N. Shaposhnikov, A.R. Prokopov, V.N. Berzhansky, A.K. Zvezdin, V.I. Belotelov. Magnetoplasmonic quasicrystals: an approach for multiband magneto-optical response, *Optica* 5, 617, 2018.

Metasurfaces and 2D Metamaterials in microwave region

Experimental Realization of Tunable Microwave Coherent Perfect Absorber in Graphene-based Sandwich Structure

Jin Zhang and Weiren Zhu*

Department of Electronic Engineering, Shanghai Jiao Tong University, Shanghai, China
*corresponding author, E-mail: weiren.zhu@sjtu.edu.cn

Abstract

We exploit experimentally a graphene-based sandwich structure for the realization of tunable microwave coherent absorption. It is demonstrated that the coherent absorption can be tuned from 65% to 100% via changing the Fermi energy of graphene, in good accordance with numerical simulations and equivalent circuit model analysis.

1. Introduction

Coherent perfect absorption is a time-reversed process of lasing at threshold, where a pair of coherent waves could be totally absorbed in a medium/device, named as a coherent perfect absorber (CPA) [1]. The exclusive features of complete absorption of electromagnetic radiations in CPAs are of great interest for a wide range of applications, including radar cloaking, sensing, and molecular detection. Various types of CPAs have been realized in several platforms, including ultrathin metasurfaces, plasmonic surfaces and waveguides. Recently, another feasible method to realize CPAs is using graphene as the absorbing medium. The static CPA in graphene for microwave and visible spectra has been demonstrated experimentally [2-3]. Recent study also show that graphene would yield tunable absorption for terahertz radiation [4]. However, due to the limitation of conventional doping method, graphene-based tunable CPA has not been experimentally achieved in microwave yet.

In this paper, we realize the tunable perfect absorption of gigahertz radiations by exploiting the concept of coherent absorption within a graphene-based sandwich structure (GSS). Owing to the unique tunable characteristics of the GSS, experimental results show that the coherent absorption could be tuned from 65% to 100% by changing Fermi energy of the graphene film. This method provides additional degree of freedom in designing graphene based coherent absorber.

2. Structure and Analysis

Figure 1(a) gives a schematic representation of the GSS. Two graphene layers are separated by an electrolyte medium, where $h_e = 50$ μm is the distance between the two graphene layers. Applying a voltage bias between the top and bottom monolayer graphene polarizes the electrolyte and thus generates different polarities concentrating beside the graphene layers. In such a way, the graphene layers are electrostatically doped and the Fermi energy could be dynamically adjusted. In a coherent system as shown in Fig. 1(a), the complex output beams ($O_\pm$) from the GSS are related to the two input beams ($I_\pm$) through an S parameters matrix,

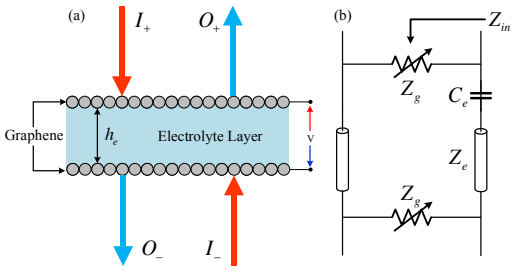


Figure 1: (a) Schematic of a GSS illustrated by two counter-propagating input beams($I_\pm$); $O_\pm$ are output beams. (b) Equivalent circuit model of the GSS with arrows indicating the voltage-variable elements.

$$\begin{bmatrix} O_+ \\ O_- \end{bmatrix} = \begin{bmatrix} S_{11} & S_{21} \\ S_{12} & S_{22} \end{bmatrix} \begin{bmatrix} I_+ \\ I_- \end{bmatrix}. \quad (1)$$

For simplicity, the scattering matrix can be simplified with $S_{11} = S_{22}$ and $S_{12} = S_{21}$, since the proposed CPA is a reciprocal structure with spatial symmetry. The equivalent circuit model of this graphene-based CPA is shown in Fig. 1(b). C_e represents the electrostatic capacitance of the electrolyte and Z_e represents the characteristic impedance of the electrolyte medium. The doping level of graphene layers defines graphene's surface resistance, Z_g, which could be expressed as

$$Z_{\mathrm{g}} = \frac{\pi\hbar^2\left(\omega - j\tau^{-1}\right)}{-j2e^2k_{\mathrm{B}}T}\log^{-1}\left[2\cosh\left(\frac{E_F}{2k_{\mathrm{B}}T}\right)\right], \quad (2)$$

where e is the electron charge, k_B is the Boltzmann constant, and $\hbar$ is the reduced Plank constant. τ and T represent the scattering rate and temperature. It is easy to know that the increase of the Femi level E_F in graphene will lead to the decrease of surface resistance Z_g. For example, the surface resistances of graphene are roughly 3000 Ω/sq and 80 Ω/sq for $E_F = 0$ eV and 1 eV, respectively. According to transmission line theory, the S parameters for this system can be calculated as:

$$S_{11} = \frac{Z_{\mathrm{in}} - \eta_0}{Z_{\mathrm{in}} + \eta_0}, \quad S_{12} = \frac{2Z_{\mathrm{in}}}{Z_{\mathrm{in}} + \eta_0}, \quad (3)$$

where Z_{in} and η_0 represent the input impedance and wave impedance of free space. Considering two coherent waves with identical amplitude normally incident on the two sides of GSS, the coherent absorption A_{co} can be written as [5]

$$\begin{aligned} A_{\text{co}} =& 1 - 2\left|S_{11}\right|\left|S_{12}\right|\left(1+\cos\Delta\phi\cos\Delta\varphi\right) \\ & -\left(\left|S_{12}\right|-\left|S_{11}\right|\right)^2 \end{aligned} \tag{4}$$

where $\Delta\phi$ is the phase difference between S_{11} and S_{12}, $\Delta\varphi$ is the phase difference of the beams I_+ and I_-.

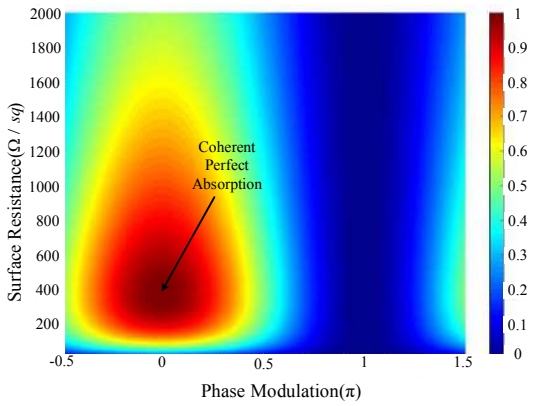


Figure 2: Coherent absorption as a function of phase modulation and surface resistance of graphene at 4 GHz.

In Fig. 2, we plot the false-color map of the coherent absorption spectra, showing the detailed dependence on the phase modulation $\Delta\varphi$ and graphene's surface resistance Z_g. It is seen that proper phase modulation ($\Delta\varphi = 0$) and surface resistance ($Z_g = 377\Omega/\text{sq}$) lead to a nearly perfect absorption at 4 GHz. This significant perfect absorption relies on the destructive interference that prevents the coherent beams from escaping the absorbing channel of the GSS, demonstrating complete suppression of the scattering outputs.

3. Experimental Results

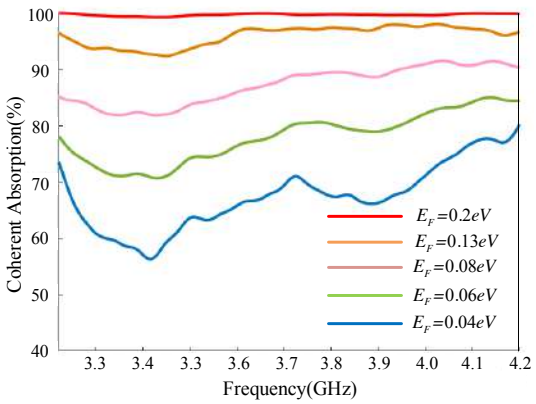


Figure 3: The measured tunable coherent absorption of double-layer GSS with variable Fermi energy.

The large-area monolayer graphene is synthesized by chemical vapor deposition on copper foil and then transferred onto a polyvinyl chloride substrate. The membrane soaked with ionic liquid is severed as electrolyte medium, which has a large electrochemical window that yields tunable Fermi energy on graphene. When a bias voltage is applied, the Fermi energy of graphene can be significantly changed. Two-layers GSS are used in our experiment that enables Z_{in} to match the wave impedance of free space. Then the reflection and transmission coefficients of the fabricated structure are measured in a two-port S-band waveguide system. Figure 3 shows the measured tunable coherent absorption spectra with variable Fermi energies. It is assumed that the phase modulation is fixed at $\Delta\varphi = 0$ for all the cases. It is seen that when the Fermi energy of graphene increasing from 0.04 to 0.2 eV, the coherent absorption increases correspondingly from about 65% to 100%. In particular, the coherent perfect absorption is realized when the Fermi energy is 0.2 eV.

4. Conclusion

In summary, we have shown that graphene sandwich structure can be employed for perfectly suppressing scattering of coherent microwave radiations. Furthermore, it is experimentally demonstrated that the coherent absorption of the GSS could be dynamically manipulated via changing the Fermi energy of graphene.

Acknowledgement

This work was supported by National Natural Science Foundation of China (61701303), Natural Science Foundation of Shanghai (17ZR1414300), and Shanghai Pujiang Program (17PJ1404100).

References

[1] Y. Chong, L. Ge, and A. D. Stone, Coherent perfect absorbers: time-reversed lasers, *Phys. Rev. Lett.* 105: 053901, 2010.

[2] S. Li, Q. Duan, and W. Wen, Perfect electromagnetic absorption atone-atom-thick scale, *Appl. Phys. Lett.*, 107: 181112, 2015.

[3] G. Pirruccio, L. Moreno, and G. Lozano, Coherent and broadband enhanced optical absorption in graphene, *ACS Nano*, 7: 4810–4817, 2013.

[4] N. Kakenov, O. Balci,and C. Kocabas, Observation of gate-tunable coherent perfect absorption of terahertz radiation in graphene, *ACS Photonics*, 3: 1531–1535, 2016.

[5] W. Zhu, F. Xiao, M. Kang, and M. Premaratne, Observation of gate-tunable Coherent perfect absorption in an all-dielectric metasurface, *Appl. Phys. Lett.*, 108: 121901, 2016.

Size influence of checkerboard-like wideband metamaterial absorbers

André Barka[1*], Xavier Begaud[2], Anne Claire Lepage[2], Stefan Varault[2]
Michel Soiron[3], Olivier Rance[2]

[1] *ONERA-DEMR, Université de Toulouse, 2 avenue Edouard Belin, 31055 Toulouse, France*
[2] *LTCI, Télécom ParisTech, Université Paris Saclay, 46 rue Barrault, 75013 Paris, France*
[3] *SART, 16, allée des Quatre Coins, 91190 Gif sur Yvette, France*
*corresponding author, E-mail: andre.barka@onera.fr

Abstract

Recently the performances of radar absorbing materials have been extended by designing new thin structures with wideband properties and large angles of incidence [1]. In this paper, the design and performances of such ultra-wideband microwave absorber of low thickness material developed within the framework of the SAFAS project (self-complementary surface with low signature) are confirmed with complementary quasi monostatic measurements and finite array simulations using Finite Element Tearing and Interconnecting domain decomposition methods (FETI).

1. Introduction

The innovative nature of the SAFAS project is based on the combined use of a self-complementary chessboard-like structure, a metasurface, and a WAIM layer, to make possible a dual polarized self-complementary connected array antenna [2] and, also, an ultra-wideband and wide-angle metamaterial absorber. The architecture of the absorber material that has been optimized in [3] is presented in Figure 1 and Figure 2. The lower part is the self-complementary structure (checkerboard) which inherently has a wideband behavior. The elementary cell of the absorber is given in Figure 2, where the metallic parts are drawn in grey. To achieve the absorption of the structure, resistive deposits were placed between each conducting patch of the checkerboard. This self-complementary structure is placed above a ground plane. To increase the bandwidth of the structure, a metasurface also using resistive deposit has been optimized and is located above the checkerboard. Finally, to minimize the impedance discontinuity between the absorber and free space and to provide wide angle and wideband frequency matching, a WAIM layer has been added at the top of the structure.

In this paper, additional simulations results of the absorber performances for several finite sizes of the array are presented. The simulations using the FACTOPO code developed at ONERA and equipped with a FETI-2LM solver ([4]) are carried out on High Performance Computer (HPC) provided by the GENCI consortium in France (Grand Equipement National en Calcul Intensif). New measurement results obtained with CAMERA@ONERA measurement facility are also presented to confirm the simulated predictions.

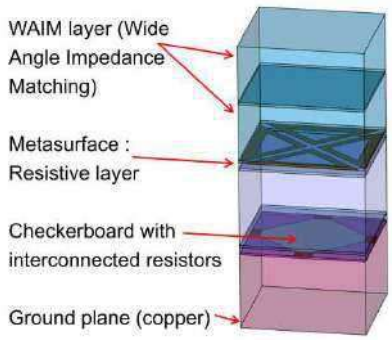


Figure 1: Multilayer absorber description (unit cell).

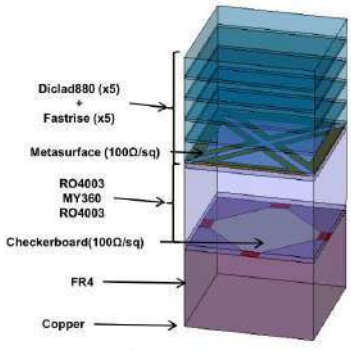


Figure 2: Nomenclature of each layer of the ultra-wideband absorber

2. Results and discussion

The absorber is composed with Copper as ground plane, Epoxy FR4 (glass-reinforced epoxy laminate, ε_r = 4.7, tan δ=0.02), RO4003 (woven glass reinforced hydrocarbon/ceramics, ε_r = 3.38 and tan δ = 0.0027) from Rogers, MY360 (woven glass PTFE, ε_r = 2.33 and tan δ = 0.0011) from Neltec and Diclad 880 (fiberglass reinforced

PTFE-based composites, ε_r = 2.2 and tan δ = 0.0009) from Rogers. The checkerboard is constituted by metallic patches etched on RO4003 material and connected at their corners with Resistor Foil NiCr (100 ohms per square) from Ticer Technologies. The metasurface is composed with the same Resistor Foil NiCr (100 ohms per square) etched on the second RO4003 material. The total thickness of the absorber is 11.5 mm.

Other material choices were possible but not reachable in the time line of the SAFAS project. It is therefore not an optimum but a compromise to validate a proof of concept.

The prototypes having the following dimensions (20 cm^2) and composed of 1600 cells were manufactured by CIRETEC (Figure 3). The simulations results presented in Figure 4 are obtained with ONERA's FACTOPO_fem-feti domain decomposition code [4]. The exact size of the array prototype 20 cm^2 fabricated with 1600 unit cells is simulated as well as virtual prototypes of 10 cm^2 (400 cells) and 30 cm^2 (3600 cells). These parametric studies on the size of the array show that the performances of the absorber are already obtained with a limited size of 10 cm^2. It is also observed a convergence of the RCS reduction in terms of bandwidth and magnitude starting from a prototype of size 20 cm^2.

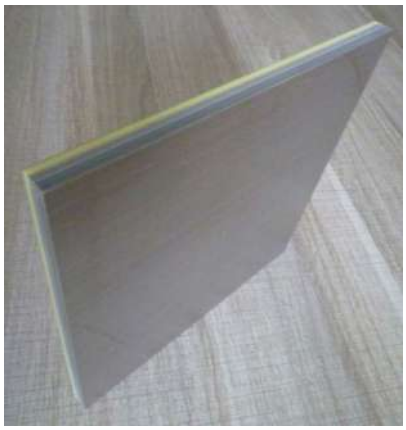


Figure 3: Prototype of the manufactured absorber.

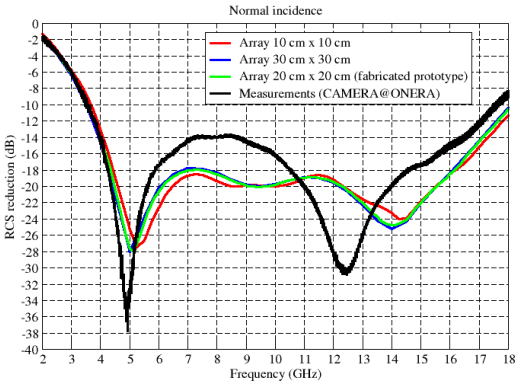


*Figure 4: F*inite array simulation results and measurements of the checkerboard-like absorber

Similar to what has been observed in previous works [1], at normal incidence (Figure 4) the FACTOPO@ONERA finite arrays simulation results give a bandwidth (-10dB) of 3.5-18 GHz while the CAMERA@ONERA measurement results give 3.7-17.5 GHz. These results seem different from each other but the behavior of the absorber is well observed on a very large bandwidth. The level of the two characteristic minima appearing at 5 GHz and 14 GHz in simulation is shifted around 4.9 GHz and 12.5 GHz in measurements. This frequency shift can be explained mainly by the cause of a poor estimation of the dielectric constants. The FR4 material is a low cost material and the dielectric constant is subject to significant fluctuations. This work seems to exclude the influence of the finite dimensions of the absorber in these frequency shifts. The level of the magnitude of the reflection coefficient between these two minima is higher in measurements than in simulations, and a poor estimation of the dielectric constant can also be the cause. Finally, it should be noted that these differences occur between -14 dB and -18 dB which are intrinsically low values.

3. Conclusions

New simulation results and complementary measurements of the SAFAS prototype presented in this paper confirm the overall performances of the absorber. These works are actually transposed to the domain of composite materials in the framework of the SAFASNAV project.

Acknowledgements

This research was funded by French Ministry of Defense (DGA), through the French National Research Agency (ANR) and Astrid Program in the framework of SAFAS project. Simulation results have been obtained using HPC resources from GENCI (Grant c2016107558).

References

[1] X. Begaud, A-C. Lepage, S. Varault, , M. Soiron, A. Barka, "Ultra-Wideband and Wide-Angle Microwave Metamaterial Absorber", Materials, Vol. 11, n° 10, 2045, 2018.

[2] S. Varault, M. Soiron, A. Barka, A-C. Lepage, X. Begaud, "RCS reduction with a Dual Polarized Self-Complementary Connected Array Antenna", IEEE Trans. Antennas Propag., vol. 65, n° 2, pp. 567-575, Dec. 2016.

[3] Begaud X., Varault S., Lepage A-C., Soiron M., Barka A., "Design of a thin ultra-wideband metamaterial absorber", Proceedings of the 2017 International Conference on Electromagnetics in Advanced Applications (ICEAA), Verona, Italy, 11-15 September 2017.

[4] F. X. Roux, A. Barka, "Block Krylov Recycling Algorithms for FETI-2LM Applied to Three-Dimensional Electromagnetic Wave Scattering and Radiation", IEEE Trans. Antennas and Propagation, Vol. 65 No. 04, April 2017.

Dynamically controlling focal point position with reconfigurable metasurface

Badreddine Ratni[1], Zhuochao Wang[2], Kuang Zhang[2], Xumin Ding[2], André de Lustrac[3,4], and Shah Nawaz Burokur[1]

[1]LEME, UPL, Univ Paris Nanterre, F92410 Ville d'Avray, France
[2]Department of Microwave Engineering, Harbin Institute of Technology, Harbin, 150001, China
[3]Centre de Nanosciences et de Nanotechnologies (C2N), CNRS, Univ. Paris-Sud, Université Paris-Saclay, 91120 Palaiseau, France
[4]UPL, Univ Paris Nanterre, 92410 Ville d'Avray, France
*corresponding author, E-mail: badreddine.ratni@parisnanterre.fr

Abstract

The phase distribution required along a metasurface in order to converge the energy to any desired spatial position is calculated. In order to dynamically control this convergence point, a planar reconfigurable metasurface has been developed. This structure is composed of meta-atoms that incorporate voltage-controlled varactor diodes. The dispersion responses of each unit cell are individually tailored for the reconfigurability mechanism. Experimental verifications performed on an active metasurface agree with theoretical calculations and validate the proposed concept.

1. Introduction

Electromagnetic (EM) wave control has become possible today thanks to metamaterials. In addition, in recent years a planar version of metamaterials called metasurfaces has been developed. These new structures present the main advantage of having reduced profile and therefore reduced losses [1]. By controlling the reflection and/or transmission characteristics of metasurfaces, they have been successfully implemented to generate anomalous reflection and refraction [2-3], to control the polarization [4], generation of vortex beams [5] and holograms [6].

2. Manipulating spatial energy distribution

In order to manipulate the spatial energy distribution of an EM wave, a general theoretical model has been developed recently [7]. This model allows calculating the phase distribution that should be applied along a metasurface in order to converge energy to any desired spatial position. This theoretical approach is based on a holography imaging technique. For that, we start by imposing a desired spatial distribution of the energy, and then we extract the phase profile that allows obtaining such desired configuration. In this work, we aim to design a reconfigurable converging mirror that allows controlling the focal point position. In this case, we define an elementary point source on the desired focal points (F = 50 and 120 mm in our case). Thereafter, Green function is used to calculate the electromagnetic fields that are generated by this elementary source. Then, we extract the phase distribution on the position of the metasurface, as illustrated in Fig. 1.

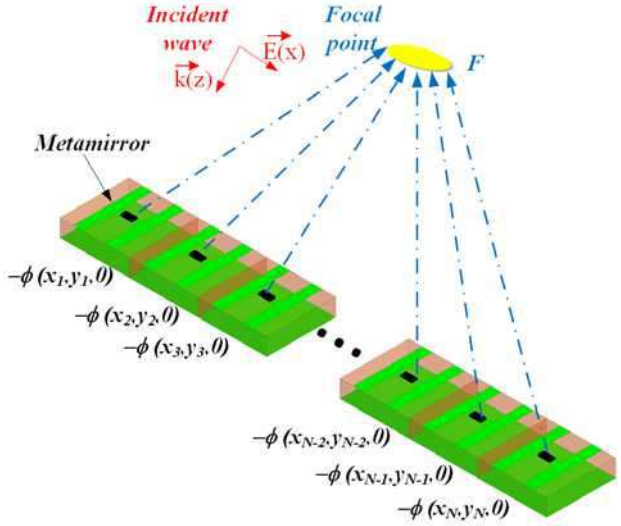


Figure 1: Schematic view of the design principle process for the manipulation of the spatial energy distribution.

3. Results

The calculated phase profiles, shown in Fig. 2, are applied to a reconfigurable metasurface that is composed of resonant meta-atoms. Each individual meta-atom incorporates a varactor diode that can be controlled by a DC voltage. By varying the applied bias voltage, the reflection phase response of each unit cell can be tuned and in this way, the calculated phase profiles can be applied to the whole structure. An electric field mapping distribution along *xoz* plane is then reconstructed and presented in Fig. 3(a). Energy spots are respectively obtained at the positions of 50 mm and 120 mm in calculations.

The phase profiles are implemented on the metasurface prototype by applying the corresponding bias voltage

profile. Measurements are performed and the experimental near-field distributions show the reconfigurability of the focal point, as presented in Fig. 3(b).

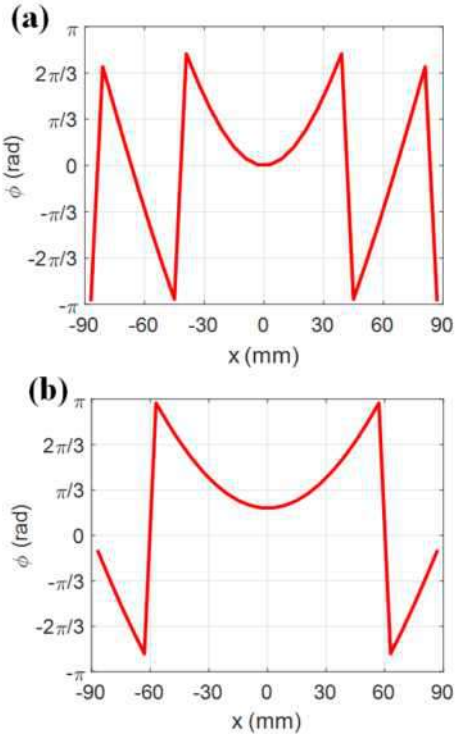


Figure 2: Calculated phase profiles for two different focal points F = 50 and 120 mm.

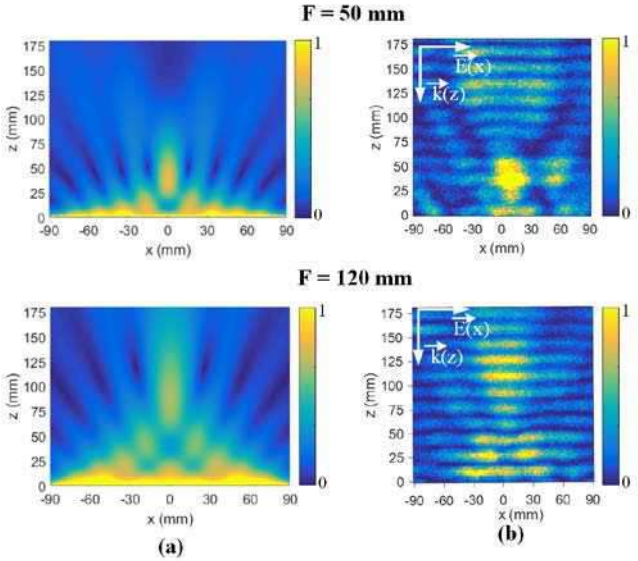


Figure 3: Mapping of intensity of the electric field for the two focal point along *xoz* plane. (a) Calculations. (b) Experimental.

4. Conclusions

To summarize, a phase distribution that allows to converge an EM wave to any desired spatial position has been calculated. In order to dynamically control this convergence point, a planar reconfigurable metasurface that incorporate voltage-controlled varactor diodes has been developed. Two focal points (F = 50 mm and 120 mm) have been tested and near-field measurements have been performed to validate the concept.

References

[1] C. L. Holloway, E. F. Kuester, J. A. Gordon, J. O'Hara, J. Booth, D. R. Smith, An overview of the theory and applications of metasurfaces: the two-dimensional equivalents of metamaterials, *IEEE Antennas Propag. Mag*. 54: 10-35, 2012.

[2] B. Ratni, A. de Lustrac, G.-P. Piau, S. N. Burokur, Active metasurface for reconfigurable reflectors, *Appl. Phys. A* 124: 104, 2018.

[3] B. Ratni, A. de Lustrac, G.-P. Piau, S. N. Burokur, Reconfigurable meta-mirror for wavefronts control: applications to microwave antenna, *Opt. Express* 26: 2613-2624, 2018.

[4] B. Ratni, A. de Lustrac, G.-P. Piau, S. N. Burokur, Electronic control of linear-to-circular polarization conversion using a reconfigurable metasurface, *Appl. Phys. Lett*. 111: 214101, 2017.

[5] K. Zhang, Y. Yuan, D. Zhang, X. Ding, B. Ratni, S. N. Burokur, M. Lu, K. Tang, Q. Wu, Phase-engineered metalenses to generate converging and non-diffractive vortex beam carrying orbital angular momentum in microwave region, *Opt. Express* 26: 1351-1360, 2018.

[6] Z. Wang, X. Ding, K. Zhang, B. Ratni, S. N. Burokur, X. Gu, Q. Wu, Huygens Metasurface holograms with the modulation of focal energy distribution, *Adv. Opt. Mater*. 8: 1800121, 2018.

[7] Z. Wang, X. Ding, K. Zhang, Q. Wu, Spacial energy distribution manipulation with multi-focus Huygens metamirror, *Sci. Rep*. 7: 9081, 2017.

Metasurface Surface-Wave Dispersion Analysis and Synthesis Technique

Karim Achouri[1], **and Olivier J. F. Martin**[1]

[1]Nanophotonics and Metrology Laboratory, Department of Microengineering,
École Polytechnique Fédérale de Lausanne, Route Cantonale, 1015 Lausanne, Switzerland
*corresponding author, E-mail: karim.achouri@a3.epfl.ch

Abstract

The proposed technique allows one to efficiently and quickly retrieve the dispersion diagram of a metasurface from its numerically simulated scattering parameters without resorting to a time-consuming numerical eigensolver. It may also be used to find the metasurface structure corresponding to desired surface-wave propagation characteristics.

1. Introduction

This work aims at relating the susceptibilities of a metasurface to its ability of supporting the propagation of surface-wave modes. To do so, an eigenvalue equation is formulated using the geometry depicted in Fig. 1, where the metasurface is modelled based on the generalized sheet transition conditions (GSTC) [1–4]. While several surface-wave

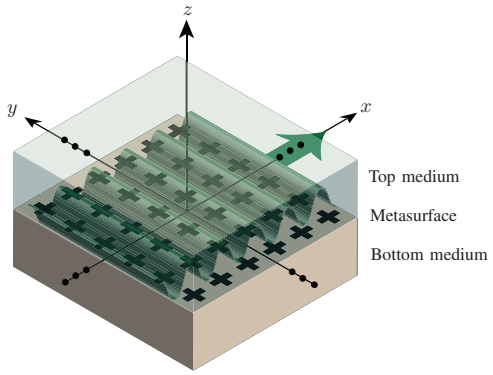


Figure 1: Surface wave propagating on a metasurface surrounded by two different media.

analysis techniques have already been developed, such as in [5–8], most of them are limited to impenetrable and anisotropic surfaces. The proposed technique alleviates these limitations as it may be applied to penetrable, impenetrable, anisotropic and bianisotropic structures.

2. Eigenvalue Problem

For a general bianisotropic metasurface lying in the xy-plane at $z = 0$, the GSTC read [1, 9]

$$\hat{\mathbf{z}} \times \Delta\mathbf{H} = j\omega\epsilon\overline{\overline{\chi}}_{\text{ee}} \cdot \mathbf{E}_{\text{av}} + jk\overline{\overline{\chi}}_{\text{em}} \cdot \mathbf{H}_{\text{av}}, \tag{1a}$$

$$\hat{\mathbf{z}} \times \Delta\mathbf{E} = -j\omega\mu\overline{\overline{\chi}}_{\text{mm}} \cdot \mathbf{H}_{\text{av}} - jk\overline{\overline{\chi}}_{\text{me}} \cdot \mathbf{E}_{\text{av}}, \tag{1b}$$

where $\overline{\overline{\chi}}_{\text{ee}}$, $\overline{\overline{\chi}}_{\text{mm}}$, $\overline{\overline{\chi}}_{\text{em}}$ and $\overline{\overline{\chi}}_{\text{me}}$ are respectively the electric, magnetic, magnetic-to-electric and electric-to-magnetic susceptibility tensors, the operator Δ refers to the difference of the fields between both sides of the metasurface while the subscript "av" refers to their arithmetic average.

A surface-wave eigenvalue problem may be formulated from (1) by defining the fields at $z = 0^+$ and $z = 0^-$ as that of TE and TM surface waves [4]. After substantial algebraic manipulations, we arrive at the eigenvalue problem defined by

$$\overline{\overline{M}} \cdot \mathbf{x} = k_z\mathbf{x}, \tag{2}$$

where $\overline{\overline{M}}$ is a matrix (provided in [4]) containing the metasurface susceptibilities and the media parameters, the eigenvalue k_z is the normal propagation constant of the surface wave and the eigenvector $\mathbf{x}^{\text{T}} = (A^{0^-}_{\text{TE}}, A^{0^-}_{\text{TM}}, A^{0^+}_{\text{TE}}, A^{0^+}_{\text{TM}})$ contains the amplitude of the TE and TM surface waves on the top and bottom sides of the metasurface.

Eigenvalues, k_z	Eigenvectors, $\mathbf{x}^{\text{T}}$	Propag. const., k_x
$\frac{2j}{\chi^{xx}_{\text{mm}}}$	$(-1,0,1,0)$ TE, symmetric, ω^-	$\pm\frac{\sqrt{4+k^2\chi^{2xx}_{\text{mm}}}}{\chi^{xx}_{\text{mm}}}$
$\frac{2j}{\chi^{xx}_{\text{ee}}}$	$(0,-1,0,1)$ TM, symmetric, ω^-	$\pm\frac{\sqrt{4+k^2\chi^{2xx}_{\text{ee}}}}{\chi^{xx}_{\text{ee}}}$
$-\frac{1}{2}jk^2\chi^{yy}_{\text{ee}}$	$(1,0,1,0)$ TE, asymmetric, ω^+	$\pm\frac{1}{2}k\sqrt{4+k^2\chi^{2yy}_{\text{ee}}}$
$-\frac{1}{2}jk^2\chi^{yy}_{\text{mm}}$	$(0,1,0,1)$ TM, asymmetric, ω^+	$\pm\frac{1}{2}k\sqrt{4+k^2\chi^{2yy}_{\text{mm}}}$

Table 1: Dispersion relations of anisotropic metasurfaces.

From (2), one may obtain the dispersion diagram of a metasurface using $k_x = \pm\sqrt{k^2 - k_z^2}$, where k_z is the eigenvalue of the problem and k is the propagation constant in the medium of interest. In this case, the susceptibilities in $\overline{\overline{M}}$ may be found from numerically simulated scattering parameters [3, 4]. Alternatively, the metasurface susceptibilities required to achieve a specified surface-wave propagation may be obtained by specifying k_z and $\mathbf{x}$, and solving (2) for the susceptibilities.

The case of anisotropic (birefringent) metasurfaces is of particular interest as it corresponds to most surface-wave guiding structures (it includes isotropic structures but excludes gyrotropic ones). Assuming that such an anisotropic

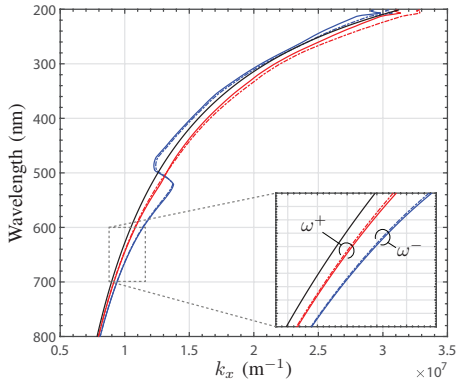


Figure 2: Dispersion diagram for a 60 nm thick gold slab. The black curve is the light line. The dashed curves correspond to the GSTC method and the solid curves correspond to the exact solutions.

metasurface is surrounded by the same medium on both sides, the system (2) may be easily solved and yields the 4 solutions provided in Table 1 corresponding to TE and TM, symmetric and asymmetric surface-wave modes.

Figure 2 compares the dispersion curves of a 60 nm thick gold slab obtained from the TM solutions in Table 1 and the exact solutions from Maxwell equations. Simi-

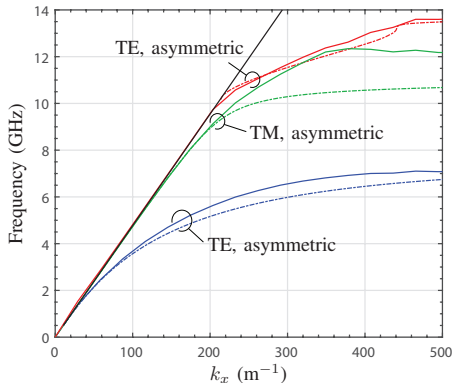


Figure 3: Dispersion diagram of a microwave metasurface. The black curve is the light line. The dashed curves correspond to the GSTC method and the solid curves correspond to the full-wave numerical solutions.

larly, Fig. 3 compares the dispersion curves of the three first surface-wave modes propagating on the microwave metasurface structure discussed in [4] obtained using Table 1 and the eigenmode solver of CST MWS. Both figures show good agreements.

We also have considered the case of bianisotropic (omega-type) metasurfaces. The solutions of (2) for this type of structures are given in Table 2. The main advantage of bianisotropic metasurfaces over anisotropic ones is their ability to independently control the amplitude of the surface waves on the top and bottom sides of the structure, as evidenced by the dependence of the eigenvectors on the susceptibilities.

Eigenvalues, k_z	Eigenvectors, $\mathbf{x}^{\mathrm{T}}$
$\frac{k^2\left(\chi_{\mathrm{em}}^{2yx}+\chi_{\mathrm{ee}}^{yy}\chi_{\mathrm{mm}}^{xx}\right)-4+C_{\mathrm{E}}}{4j\chi_{\mathrm{mm}}^{xx}}$	$\left(\frac{4jk\chi_{\mathrm{em}}^{yx}+C_{\mathrm{E}}}{k^2\left(\chi_{\mathrm{em}}^{2yx}+\chi_{\mathrm{ee}}^{yy}\chi_{\mathrm{mm}}^{xx}\right)+4},0,1,0\right)$
$\frac{k^2\left(\chi_{\mathrm{em}}^{2yx}+\chi_{\mathrm{ee}}^{yy}\chi_{\mathrm{mm}}^{xx}\right)-4-C_{\mathrm{E}}}{4j\chi_{\mathrm{mm}}^{xx}}$	$\left(\frac{4jk\chi_{\mathrm{em}}^{yx}-C_{\mathrm{E}}}{k^2\left(\chi_{\mathrm{em}}^{2yx}+\chi_{\mathrm{ee}}^{yy}\chi_{\mathrm{mm}}^{xx}\right)+4},0,1,0\right)$
$\frac{k^2\left(\chi_{\mathrm{em}}^{2xy}+\chi_{\mathrm{ee}}^{xx}\chi_{\mathrm{mm}}^{yy}\right)-4+C_{\mathrm{M}}}{4j\chi_{\mathrm{ee}}^{xx}}$	$\left(0,\frac{4jk\chi_{\mathrm{em}}^{xy}+C_{\mathrm{M}}}{k^2\left(\chi_{\mathrm{em}}^{2xy}+\chi_{\mathrm{ee}}^{xx}\chi_{\mathrm{mm}}^{yy}\right)+4},0,1\right)$
$\frac{k^2\left(\chi_{\mathrm{em}}^{2xy}+\chi_{\mathrm{ee}}^{xx}\chi_{\mathrm{mm}}^{yy}\right)-4-C_{\mathrm{M}}}{4j\chi_{\mathrm{ee}}^{xx}}$	$\left(0,\frac{4jk\chi_{\mathrm{em}}^{xy}-C_{\mathrm{M}}}{k^2\left(\chi_{\mathrm{em}}^{2xy}+\chi_{\mathrm{ee}}^{xx}\chi_{\mathrm{mm}}^{yy}\right)+4},0,1\right)$
$C_{\mathrm{E}}=\sqrt{k^4\chi_{\mathrm{em}}^{4yx}+2k^2\chi_{\mathrm{em}}^{2yx}(k^2\chi_{\mathrm{ee}}^{yy}\chi_{\mathrm{mm}}^{xx}-4)+(k^2\chi_{\mathrm{ee}}^{yy}\chi_{\mathrm{mm}}^{xx}+4)^2}$	
$C_{\mathrm{M}}=\sqrt{k^4\chi_{\mathrm{em}}^{4xy}+2k^2\chi_{\mathrm{em}}^{2xy}(k^2\chi_{\mathrm{ee}}^{xx}\chi_{\mathrm{mm}}^{yy}-4)+(k^2\chi_{\mathrm{ee}}^{xx}\chi_{\mathrm{mm}}^{yy}+4)^2}$	

Table 2: Dispersion relations for omega-type metasurfaces. The propagation constants, k_x, are easily calculated by solving $k^2=k_z^2+k_x^2$.

Acknowledgement

We gratefully acknowledge funding from the European Research Council (ERC-2015-AdG-695206 Nanofactory).

References

[1] K. Achouri, M. A. Salem, and C. Caloz, "General metasurface synthesis based on susceptibility tensors," *IEEE Trans. Antennas Propag.*, vol. 63, no. 7, pp. 2977–2991, Jul. 2015.

[2] K. Achouri, B. A. Khan, S. Gupta, G. Lavigne, M. A. Salem, and C. Caloz, "Synthesis of electromagnetic metasurfaces: principles and illustrations," *EPJ Applied Metamaterials*, vol. 2, p. 12, 2015.

[3] K. Achouri and C. Caloz, "Design, concepts, and applications of electromagnetic metasurfaces," *Nanophotonics*, vol. 7, no. 6, pp. 1095–1116, 2018.

[4] K. Achouri and O. J. Martin, "Surface-wave dispersion retrieval method and synthesis technique for bianisotropic metasurfaces," *arXiv preprint arXiv:1805.05116*, 2018.

[5] H. J. Bilow, "Guided waves on a planar tensor impedance surface," *IEEE Trans. Antennas Propag.*, vol. 51, no. 10, pp. 2788–2792, Oct 2003.

[6] R. Quarfoth and D. Sievenpiper, "Artificial tensor impedance surface waveguides," *IEEE Trans. Antennas Propag.*, vol. 61, no. 7, pp. 3597–3606, July 2013.

[7] A. M. Patel and A. Grbic, "Modeling and analysis of printed-circuit tensor impedance surfaces," *IEEE Trans. Antennas Propag.*, vol. 61, no. 1, pp. 211–220, Jan 2013.

[8] M. Li, S. Xiao, J. Long, and D. F. Sievenpiper, "Surface waveguides supporting both tm mode and te mode with the same phase velocity," *IEEE Trans. Antennas Propag.*, vol. 64, no. 9, pp. 3811–3819, Sept 2016.

[9] E. F. Kuester, M. Mohamed, M. Piket-May, and C. Holloway, "Averaged transition conditions for electromagnetic fields at a metafilm," *IEEE Trans. Antennas Propag.*, vol. 51, no. 10, pp. 2641–2651, Oct 2003.

Abnormal Refractions with Independent-Polarizations Enabled by Transmissive-Type Metasurface in Microwave Region

Kuang Zhang[1,2], Yueyi Yuan[1], Xumin Ding[1,2], Badreddine Ratni[2], Shah Nawaz Burokur[2], and Qun Wu[1]

[1] Department of Microwave Engineering, Harbin Institute of Technology, Harbin, 150001, China
[2] State Key Laboratory of Millimeter Waves, Nanjing, 210096, China
[3] LEME, UPL, Univ Paris Nanterre, F92410 Ville d'Avray, France
*corresponding author, E-mail: zhangkuang@hit.edu.cn

Abstract

In this paper, transmissive-type metasurfaces is proposed to independently refract the orthogonal circularly polarized wave in microwave region. Based on the combination of propagation phase and geometry phase principles, the opposite circularly polarized transmitted wave can be deflected into independent and arbitrary directions. Experimental measurement are conducted and effectively verified the feasibility of the proposed theory for artificial manipulation of circular polarization manipulation in microwave region.

1. Introduction

Polarization is one of the intrinsic attributes of planar electromagnetic (EM) wave [1]. Traditional methods of polarization manipulation are birefringence [2], photonic crystals [3], metasurfaces [4] and so on. The geometric phase also known as Pancharatnam-Berry phase can be employed to convert the left-/right-handed circular polarized (LHCP/RHCP) incident wave into its opposite circular handedness with totally symmetrical characteristics [5]. However, the inherent restrictions of this symmetry characteristic have limited the applications in wireless systems [6]. Various works have been proposed to figure out the symmetry limitation in orthogonal polarization manipulation of EM wave [7].

In this paper, transmissive meta-lens is proposed to realize polarization-independent refraction at microwave frequencies. Based on the library of unit cells for the full phase coverage, the meta-lens is composed of 8 unit cells with different constructions. The simulation and measurement results demonstrate that the desired polarization-independent refraction can be achieved in a wide frequency band, suggesting promising applications in wireless communication systems.

2. Principles and results

The schematic of polarization-independent refraction is shown in Fig. 1. Under the orthogonal circularly polarized incident waves, the transmitted wave can be refracted into different and independent directions by elaborately designed meta-lens.

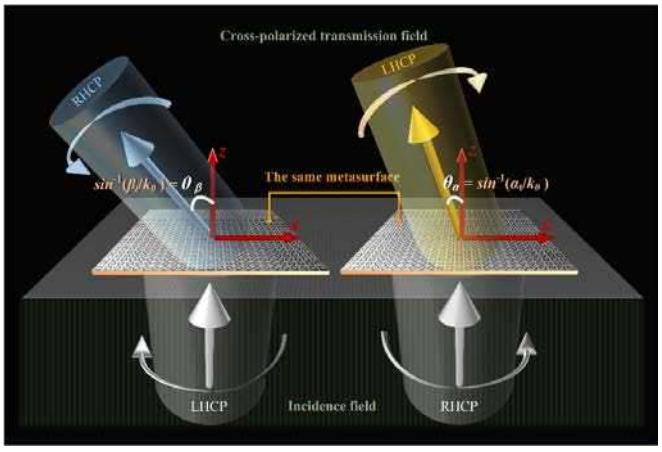


Figure 1: Schematic of proposed meta-lens for generating polarization-independent refracted wave with the illumination of orthogonal circularly polarized incident waves.

The asymmetry refraction between orthogonal circular polarizations is achieved by the combination of propagation phase and geometry phase, which can be described as:

$$\delta_x = \frac{1}{2}(\alpha_t + \beta_t)x \tag{1}$$

$$\delta_y = \frac{1}{2}(\alpha_t + \beta_t)x - \pi \tag{2}$$

$$\theta = \frac{1}{4}(\alpha_t - \beta_t)x \tag{3}$$

Where δ_x, δ_y represent the phase delays along x- and y-axis, θ shows the rotation angle of each unit cell, α_t and β_t are the phase gradient along x direction. Equation (1)-(3) illustrate the relationships between the coordination and required phase response of each unit cell, which provides the design scheme of proposed meta-lens.

In this paper, the phase gradients for circularly polarized incident waves are set as$\alpha_{t1} = 0.5k_0$ and $\beta_{t1} = 0.25k_0$, where k_0 is the wave number ($k_0 = 2\pi/\lambda_0$, $\lambda_0 = 30$ mm). According

to the generalized refraction laws, the transmitted refraction angle can be obtained as -30° and -14.5° with the illumination of LHCP and RHCP waves.

The constructed meta-lens is exhibited in Fig. 2(a) and the unit cell is composed of two metallic layers separated by a dielectric substrate. One of the utilized unit cells are simulated and analyzed shown in Fig. 2(b) and 2(c). It can be seen that the magnitude responses under orthogonal linearly polarized incidences are equal and higher than 0.9 at 10 GHz, while the difference of phase delays along x- and y-directions maintains π during the bandwidth, which guarantees the effective conversion of circular polarization at working frequency.

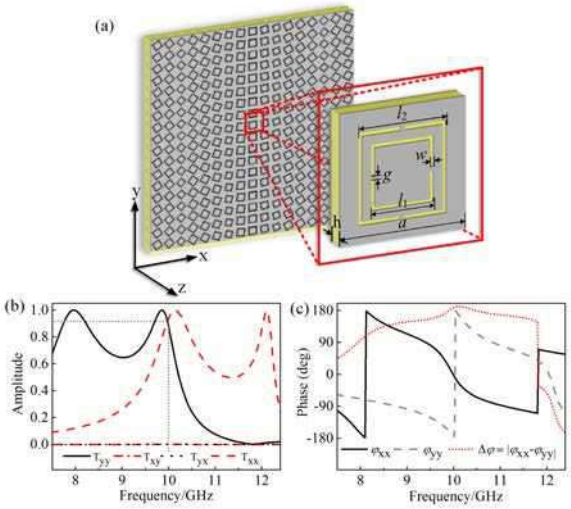


Figure 2: (a) The schematic of unit cell and proposed meta-lens. Simulated (a) magnitude responses and (b) phase responses under x- and y-linearly polarized incident waves.

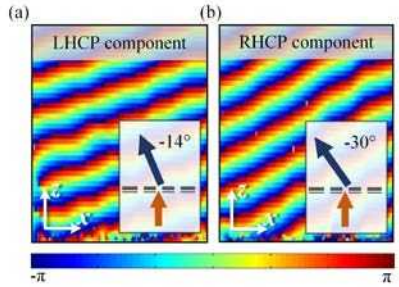


Figure 3: Simulated phase front distributions of cross-polarized transmit-ted wave under (a) RHCP and (b) LHCP incident waves, respectively.

In order to verify the performances of the designed meta-deflectors, full-wave simulations based on the finite difference time-domain technique (FDTD) are conducted at 10 GHz. The simulation results of asymmetrical refractions are shown in Fig. 3. It can be observed that under different circularly polar-ized incident wave, the transmitted wave are refracted into -30° and -14.5°, which are in accordance with the theoretical design.

The measured normalized far-field intensity distributions of the cross-polarized component under incidence with different polarizations are presented in Figs. 4(a) and 4(b), It can be observed that the operation bandwidth of proposed meta-lens is about 2.5 GHz with a relative band width of 25%, where the LHCP and RHCP components in transmitted field are deflected into required directions.

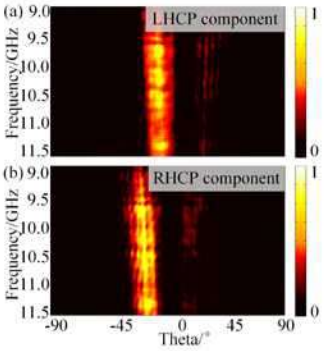


Figure 4: Measured normalized far-field distributions of cross-polarized transmitted wave under (a) RHCP and (b) LHCP incident waves, respectively.

3. Conclusions

To summarize, a general scheme to design broadband ultra-thin metasurface for polarization-independent manipulation of EM wave is presented in this paper. The simulated and measured results verify the designed meta-lens has ability to deflect transmitted waves into desired directions independently within a wide frequency range. The design method proposed in this paper shows great potential to meet various requirements of microwave wireless communication systems.

References

[1] M. Born and E. Wolf, “Principles of optics: electromagnetic theory of propagation, interference and diffraction of light,” Elsevier, 2013.

[2] T. Sato, K. Shiraishi, K. Tsuchida, and S. Kawakami, "Laminated polarization splitter with a large split angle," Appl. Phys. Lett. 61(22), 2633-2634 (1992).

[3] J. Sun and J. Li, "Terahertz wave polarization splitter using full band-gap photonic crystals," J. Infrared Millim. W. 36(3), 255-261 (2015).

[4] Y. Zhao, M. A. Belkin, and A. Alu, "Twisted optical metamaterials for planarized ultrathin broadband circular polarizers," Nat. Commun. 3, 870 (2012).

[5] C. C. Homes, G. L. Carr, R. P. S. M. Lobo, J. D. LaVeigne, and D. B. Tanner, "Silicon beam splitter for far-infrared and terahertz spectroscopy," Appl. Optics 46(32), 7884-7888 (2007).

[6] M. Khorasaninejad and K. B. Crozier, "Silicon nanofin grating as a miniature chirality-distinguishing beam-splitter," Nat. Commun. 5, 5386 (2014).

[7] 39. J. P. B. Mueller, N. A. Rubin, R. C. Devlin, B. Groever, and F. Capasso, "Metasurface Polarization Optics: Independent Phase Control of Arbitrary Orthogonal States of Polarization," Phys. Rev. Lett. 118(11), 113901 (2017).

Active Metasurfaces and Waveguiding with Photoexcited Graphene

Yuancheng Fan[1,2*], Fuli Zhang[1], and C. T. Chan[2]

[1]Key Laboratory of Space Applied Physics and Chemistry, Ministry of Education and
Department of Applied Physics, School of Science, Northwestern Polytechnical University, Xi'an, 710129 China
[2]Department of Physics and Center for Metamaterials Research,
The Hong Kong University of Science and Technology, Hong Kong, China
*corresponding author, E-mail: phyfan@nwpu.edu.cn

Abstract

The high intrinsic loss of graphene severely obstructs us from achieving high-quality resonance in various graphene metamaterials and metasurfaces. Here, we demonstrate that the photoexcited graphene, in which the quasi-Fermi energy of graphene changes corresponding to optical pumping, can boost the originally extremely weak plasmonic resonances in a graphene metasurface, showing remarkable modulations in the transmission. And it is also found the loss compensation in graphene is helpful in realizing long-range plasmonic waveguiding. Our work pioneers the possibilities of optically pumped graphene metasurfaces for significant enhancement of light-graphene interactions for various active meta-devices.

1. Introduction

Graphene is also promising for applications in photonics and optoelectronics. Much stronger confinement of surface plasmons at the atomic scale [1], implying that graphene is a novel platform for boosting light–matter interactions [2]. More importantly, the sensitivity of Fermi energy to the carrier density in the Dirac fermions results in ultrawide tunable space in responding external light fields, which makes it a feasible and outstanding platform for actively controllable plasmonics [3]. Graphene metasurfaces [4-7] were proposed to realize various tailorable functionalities. However, the optical loss of graphene hinders many practical applications of the 2D plasmonic excitations. The large real part of surface conductivity (i.e., the intrinsic loss) makes the propagating plasma decay fast and the local resonant plasmonic modes weakly excited, especially the magnetic dipolar mode in graphene-based plasmonic metasurfaces.

Fortunately, the unique band structure of graphene offers the possibility of a new mechanism for loss compensation. The gapless and linear dispersion of the 2D Dirac fermions could lead to negative dynamic conductivity in an ultrawide frequency range under optical pumping [8-10], which is significant for active photonics in 2D. The stimulated emission at the terahertz and near-infrared region has been experimentally demonstrated in graphene with inverted Dirac fermion population through time-resolved spectroscopy of fast nonequilibrium carrier relaxation dynamics. These findings support the significance of graphene in active photonics applications.

In this work, we theoretically study the loss compensation of resonant plasmonic excitations in photoexcited graphene metasurface and graphene plasmonic waveguide. It is well known that the coupling of magnetic dipoles of natural atoms to the external light field is much weaker compared to electric dipoles especially at optical frequencies. It is shown in the scattering spectra and local-field distributions that photoexcitaion is a promising route to compensate the resonantly enhanced energy dissipation in graphene metasurfaces. It is found that the difficultly excited magnetic resonance in passive graphene can be boosted in a photoexcited graphene metasurface with proper quasi-Fermi energy, and significant modulations in the transmission and absorption in the photoexcited graphene metasurfaces can be achieved. We also find the photoexcitation in graphene is helpful in realizing extended graphene plasmon propagation. Our work pioneers the way toward various practical applications based on the active and dynamic plasmonic excitations in graphene microstructures due to strong light–graphene interactions [11].

2. Results and Discussion

We first studied a magnetic metasurface in which the photoexcited monolayer graphene is patterned into a periodic array of split-ring resonators. We performed full-wave numerical simulations with a finite-element-method (FEM)-based electromagnetic package (COMSOL Multiphysics) to calculate the terahertz response of graphene metasurfaces. We first consider the resonant behavior of a photoexcited graphene metasurface at a temperature of 77 K. The transmission and absorption spectra of an unpumped graphene metasurface were studied in FEM simulations. It was found that the magnetic resonance of the photoexcited graphene metasurface is continuously strengthened as the pump beam is on, or the quasi-Fermi level increases from 0 meV to about 10 meV. Especially when the quasi-Fermi is 10.3 meV, a pronounced dip is observed from the transmission spectrum. The corresponding absorption and transmission are 39% and 8%, respectively, indicating that we can achieve a strong

modulation in the transmission through the photoexcited magnetic metasurface. The modulation depth is over 90% (the transmission changes from 99% to 8%).

The evolution of the loss compensation in different photoexcited graphene metasurfaces at 77 K is investigated by studying the on-resonance transmission and absorption (transmission and absorption at resonant frequencies). The on-resonance transmission and absorption are plotted as a function of the quasi-Fermi levels in Figure 1. As the excitation power of the pump beam is increased with the quasi-Fermi level changing from 0 to 10.3 meV, the on-resonance transmission undergoes a strong modulation from nearly unity to the minimum 8%, and the on-resonance absorption also undergoes a dramatic increment to the maximum 50% at the quasi-Fermi level of 10.2 meV. When the quasi-Fermi energy is further increased, the on-resonance transmission undergoes an increment reversely, and the photoexcited graphene metasurface becomes lasing with an amplified beam propagating through the SRRs. The on-resonance absorption becomes negative regarding the loss compensation in the magnetic resonant structure.

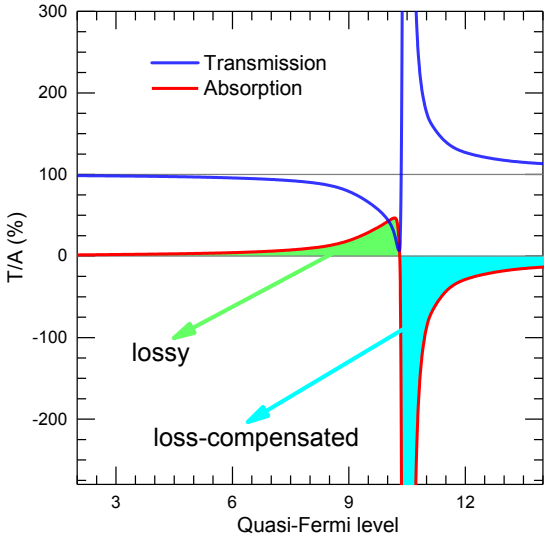


Figure 1: Magnetic resonances of photoexcited graphene metasurfaces with different quasi-Fermi levels. The on-resonance transmission (blue) and absorption (red, with lossy and loss-compensated regimes marked with green and cyan shadows) values are plotted as a function of the quasi-Fermi level.

Then we further studied the photoexcitation in a graphene plasmonic waveguide, we found that the loss-gain in graphene forms plasmonic cavities for enhancing the propagating length of graphene plasmons .

3. Conclusions

In summary, we studied the boosting the originally weak plasmonic resonances in graphene metasurfaces and plasmons in graphene waveguide via photoexcitation-induced inverted Dirac fermion population for intrinsic loss compensation. The proposed mechanism may also apply to all other 2D conductive materials in the format of various micro- and nanostructures. Our work therefore paves the way toward more efficient control of light with many potential applications.

Acknowledgements

This work was financially supported by the National Natural Science Foundation of China (NSFC) (Grants Nos. 11674266, 61505164, 61771402), the Science and Technology Plan of Shenzhen City (JCYJ20170817162221169), the Hong Kong Scholars Program (XJ2017006), and the Natural Science Basic Research Plan in Shaanxi Province of China (Program No. 2018JM6024).

References

[1] M. Jablan, H. Buljan, M. Soljačić, Plasmonics in graphene at infrared frequencies, *Phys. Rev. B* 80: 245435, 2009.

[2] F.H.L. Koppens, D.E. Chang, F.J. García de Abajo, Graphene Plasmonics: A Platform for Strong Light–Matter Interactions, *Nano Lett.* 11: 3370-3377, 2011.

[3] T. Low, P. Avouris, Graphene Plasmonics for Terahertz to Mid-Infrared Applications, *ACS Nano* 8: 1086-1101, 2014.

[4] P. Tassin, T. Koschny, C.M. Soukoulis, Graphene for Terahertz Applications, *Science* 341: 620-621, 2013.

[5] H. Cheng, S. Chen, P. Yu, W. Liu, Z. Li, J. Li, B. Xie, J. Tian, Dynamically Tunable Broadband Infrared Anomalous Refraction Based on Graphene Metasurfaces, *Adv. Opt. Mater.* 3: 1744-1749, 2015.

[6] P.A. Huidobro, M. Kraft, S.A. Maier, J.B. Pendry, Graphene as a Tunable Anisotropic or Isotropic Plasmonic Metasurface, *ACS Nano* 10: 5499-5506, 2016.

[7] Y. Fan, N.-H. Shen, F. Zhang, Q. Zhao, H. Wu, Q. Fu, Z. Wei, H. Li, C. M. Soukoulis, Graphene Plasmonics: A Platform for 2D Optics, *Adv. Opt. Mater.* 7: 1800537, 2019.

[8] V. Ryzhii, M. Ryzhii, T. Otsuji, Negative dynamic conductivity of graphene with optical pumping, *J. Appl. Phys.* 101: 083114, 2007.

[9] T. Li, L. Luo, M. Hupalo, J. Zhang, M.C. Tringides, J. Schmalian, J. Wang, Femtosecond Population Inversion and Stimulated Emission of Dense Dirac Fermions in Graphene, *Phys. Rev. Lett.* 108: 167401, 2012.

[10] P.-Y. Chen, J. Jung, ***PT*** Symmetry and Singularity-Enhanced Sensing Based on Photoexcited Graphene Metasurfaces, *Phys. Rev. Appl.* 5: 064018, 2016.

[11] Y. Fan, N.-H. Shen, F. Zhang, Q. Zhao, Z. Wei, P. Zhang, J. Dong, Q. Fu, H. Li, C.M. Soukoulis, Photoexcited Graphene Metasurfaces: Significantly Enhanced and Tunable Magnetic Resonances, *ACS Photonics* 5: 1612-1618, 2018.

Holographically-modulated metasurface leaky-wave antennas for multiple near-field focused spots manipulation

José Luis Gómez-Tornero*, and Miguel Poveda-García

Dep. Information and Communications Technologies, Technical University of Cartagena (UPCT), Spain
*corresponding author, E-mail: Josel.Gomez@upct.es

Abstract

This work describes a synthesis technique to generate multiple near-field focused beams in the microwave regime, using single-fed thin metasurface antennas. Using spatially-modulated leaky-wave theory and holographic principles, it is demonstrated how one can tailor the equivalent amplitude and phase aperture distributions of the waves emerging from the metasurface, so to precisely locate several independent near-field focused spots in the Fresnel region.

1. Introduction

Holographic surface antennas transform a reference surface wave which is bounded inside the thin patterned substrate, into a leaky wave which produces directive space radiation [1]. This relation between radio-frequency holography and modulated leaky-wave antennas (MLWAs), -also referred to as metasurfing-, has been applied for far-field focusing [1], and also for near-field (NF) focusing in the Fresnel zone. This type of MLWAs offering NF focusing, also known as leaky-wave lenses (LWL), were initially proposed for 1D [2]-[4] and later for 2D [5]-[8] metasurface antennas. As demonstrated, the engineered metasurface must be properly patterned by modulating the constitutive unit-cell dimensions along the antenna aperture, so to obtain the desired NF focused spot specifications: namely the focal point location and the half-power focal region size (depth of focus and focal width).

This design is even more challenging for the case of simultaneous multiple-focus synthesis, as recently pursued by some authors [9]-[13]. Phased-array antennas designs [9]-[12] need a beam-forming network to feed each individual radiators with optimum amplitude and phase for the multi-focusing synthesis. In [13], a reflective metasurface was proposed for multi-feed and multi-focus. Compared to these phased-arrays [9]-[12] and reflectarrays [13] designs, LWLs offer much simpler and integrated solutions which dispenses from beam forming networks and external feeders. As shown in Fig.1, a planar LWL uses a single integrated port to launch a travelling surface-wave, which is manipulated by the thin metasurface to create several independently controllable focal regions in the desired locations. Here we demonstrate for the first time the capability to synthesize several focused spots in the NF from a single-fed holographic LWL.

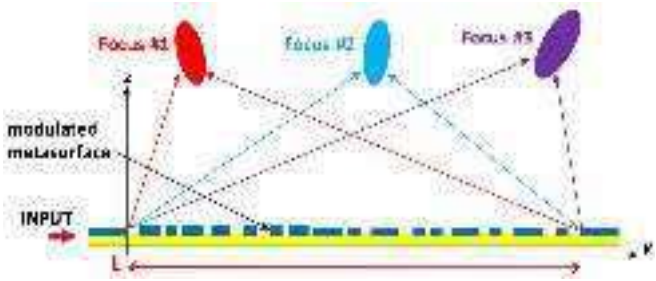


Figure 1: Scheme of a 1D LWL with a single feeding, creating three different focused spots in the Fresnel region.

2. Results

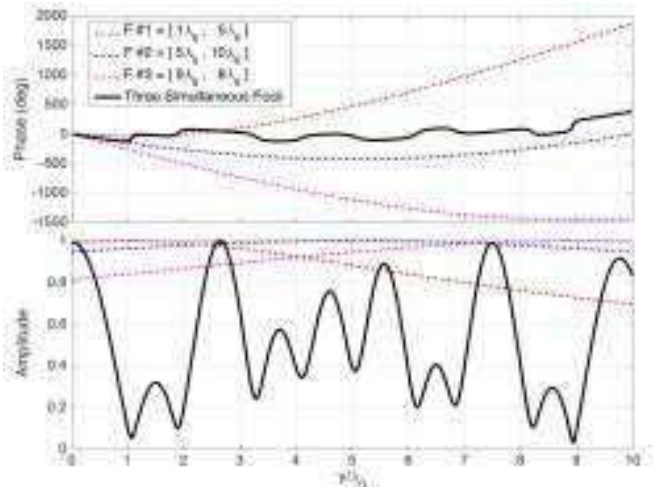


Figure 2: Individual and interference LWL aperture complex-field distribution (phase and amplitude).

The basic theory to synthesize *a single focused NF spot* located at the position $F_i=\{y_{Fi}, z_{Fi}\}$, using a LWL was described in [2]. The modulated LW must create a given phase and amplitude field distribution along the aperture length L. Fig.2 shows results for an aperture length $L=10\lambda_0$ (where λ_0 is the free-space wavelength), and for three different focal positions $F_1=\{1\lambda_0, 5\lambda_0\}$, $F_2=\{5\lambda_0, 10\lambda_0\}$, and $F_3=\{9\lambda_0, 8\lambda_0\}$. Using the holographic principle, we can superimpose the complex field distributions *for N focused spots* at the antenna aperture. The resulting holographic interference created by the complex addition of the three modulated LWs is plotted with thick black line in Fig.2.

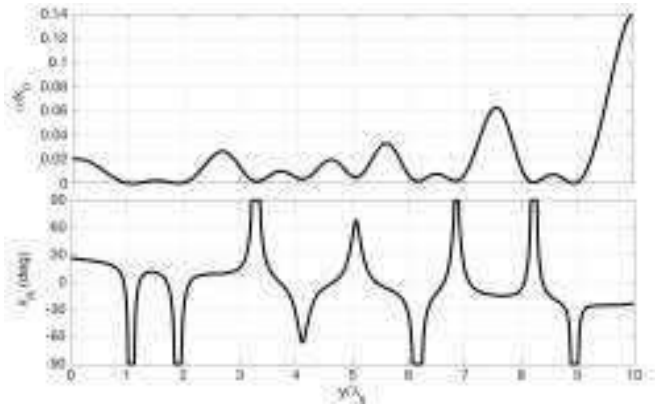


Figure 3: Modulation of the leaky-wave (LW) local leakage rate $\alpha(y)$ and scanning angle $\theta_R(y)$ to create the interference holographic complex field in Fig.2.

Then, this total holographic field at the LWL aperture can be generated by *a single modulated* LW, which local scanning angle and leakage rates, $\theta_R(y)$ and $\alpha(y)$, must be properly tapered along the LWL aperture as explained in [2] and shown in Fig.3. The last design step involves the translation of this LW electromagnetic modulation into geometrical modulation of a practical MLWA, as it was done in [3] for a holographic LWA in planar Substrate Integrated Waveguide (SIW) technology. The theoretical fields created by such MLWA are plotted in Fig.4, demonstrating the successful synthesis of three simultaneous focused spots at the prescribed focal points (indicated with red stars), located in the Fresnel region of the metasurface.

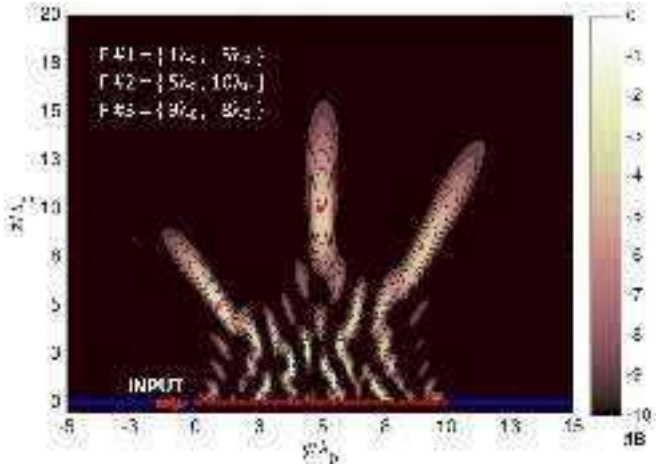


Figure 4: Simulated near-field intensity (in dB) created by the modulated leaky-wave in Fig.3.

3. Conclusions

It has been demonstrated for the first time that a single leaky wave modulated by a metasurface can radiate a holographic field which synthesizes several simultaneous focused spots in the Fresnel zone. Compared to more complex designs, the holographic leaky-wave lens (LWL) dispenses for more complex and bulky feeding network, since a single port can be used to launch the surface wave propagating through the hosting waveguide. More detailed results will be given in the full paper and the oral presentation.

References

[1] M. Nannetti, F. Caminita, and S. Maci, "Leaky-wave based interpretation of the radiation from holographic surfaces," in *Proc. Int. Symp. IEEE Antennas Propag. Society*, Jun. 2007, pp. 5813–5816.

[2] J. L. Gomez-Tornero, et al., "Frequency steerable two dimensional focusing using rectilinear leaky-wave lenses," *IEEE Trans. Antennas Propag*, vol. 59, no. 2, pp. 407-415, Feb. 2011.

[3] A. J. Martinez-Ros, J. L. Gómez-Tornero and G. Goussetis, "Holographic pattern synthesis with modulated substrate integrated waveguide line-source leaky-wave antennas," *IEEE Trans. Antennas Propag*., vol. 61, no. 7, pp. 3466-3474, July 2013.

[4] H. Yi, at al. "Flat terahertz reflective focusing metasurface with scanning ability," *Sci. Rep*., vol. 7, Jun. 2017, Art. no. 3478.

[5] J. L. Gomez-Tornero, D. Blanco, E. Rajo-Iglesias, N. Llombart, "Holographic surface leaky-wave lenses with circularly-polarized focused near-fields—Part I: Concept Design and Analysis Theory", *IEEE Trans. Antennas Propag*, vol. 61, no. 7, pp. 3475-3485, 2013.

[6] M. Ettorre. M. Casaletti, G. Valerio, R. Sauleau. L. L. Coq, S. C. Pavone, and M. Albani, "On the near-field shaping and focusing capability of a radial line slot array," *IEEE Trans. Antennas Propag*, vol. 62, no. 4, pp. 1991-1999. April 2014.

[7] I. Iliopoulos, M. Esquius-Morote, J. R. Mosig and M. García-Vigueras, "Near-field focusing employing sinusoidally modulated reactance surfaces," in EuCAP proceedings, pp.1-5, 2016.

[8] V. R. Gowda, M. F. Imani, T. Sleasman, O. Yurduseven and D. R. Smith, "Focusing microwaves in the Fresnel zone with a cavity-backed holographic metasurface," *IEEE Access*, vol. 6, pp. 12815-12824, 2018.

[9] J. Álvarez, et al., "Near field multifocusing on antenna arrays via non-convex optimization," *IET Microw. Antennas Propag*., vol. 8, no. 10, pp. 754–764, Jul. 2014.

[10] R. G.-Ayestaran, "Fast near-field multifocusing of antenna arrays including element coupling using neural networks," *IEEE Antennas and Wireless Propag. Lett*., vol. 17, no. 7, pp. 1233-1237, Jul. 2018.

[11] S. E. Bankov, "A bifocal focused two-dimensional frequency-scanned array," *Journal of Communications Technology and Electronics*, vol. 63, no. 9, pp. 968-979, 2018.

[12] R. G.-Ayestaran, J. Álvarez, and F. Las-Heras, "Design of non-uniform antenna arrays for improved near-field multifocusing," *Sensors*, vol. 19, no.3, pp. 645-664, 2019.

[13] S. Yu, H. Liu, and L. Li, "Design of near-field focused metasurface for high efficient wireless power transfer with multi-focus characteristics," *IEEE Trans. Industrial Electronics*, vol.66, no.5, pp.3993-4002, May 2019.

Advanced passive and active metasurfaces

Optical Metasurfaces for Designing Planar Cassegrain-Schwarzschild Objective

Xuan Liu[1,†], Junhong Deng[1,†], King Fai Li[1,†], Yutao Tang[1], Mingke Jin[1], Jing Zhou[2], Xing Cheng[1], Wei Liu[3,*] and Guixin Li[1,4,*]

[1]Southern University of Science and Technology, Department of Materials Science and Engineering, Shenzhen, China, 518055
[2]Beijing Normal University, Applied Optics Beijing Area Major Laboratory, Department of Physics, Beijing, China 100875
[3]National University of Defense Technology, College for Advanced Interdisciplinary Studies, Changsha, China, 410073
[4]Southern University of Science and Technology, Shenzhen Institute for Quantum Science and Engineering, Shenzhen, China, 518055
*Wei Liu, E-mail: wei.liu.pku@gmail.com, *Guixin Li, E-mail: ligx@sustc.edu.cn

Abstract

Curved reflective mirrors with inevitably bulky size play an indispensable role in widely-employed Cassegrain-type optical devices. Through substituting geometric phase based flat reflective metasurfaces for curved mirrors, here planar Cassegrain-type Schwarzschild objectives are obtained experimentally, with their achromatic focusing and imaging functionalities. The planar reflective objectives achieved are intrinsically free of residual light. Our designs can potentially reshape and simplify the core components of many microscope and telescope systems working over broadband spectral regimes.

1. Introduction

Optical mirrors are probably the most ubiquitous optical elements in both everyday infrastructures and scientific apparatus. The Cassegrain family of two-mirror configurations are employed in all conventional Cassegrain-type Schwarzschild objectives. The efficient phase tuning and beam redirections rely on the continuous geometric curvatures of the consisting elements, which inevitably result in cumbersome and costly optical devices.

The paradigm has been totally shifted with the explosively developing field of optical metasurfaces, which are composed of spatially variant meta-atoms on a planar interface and show unprecedented flexibility for optical wave manipulations. Among all the metasurface-based optical components, probably the most attractive and promising example is the planarized refractive objective lenses, which could consist of an individual metalens, metalens doublets, and other more sophisticated designs.

Here we investigate the simplest and most widely employed two-mirror reflective configuration and realize planar Cassegrain-type Schwarzschild objectives, of which both the functionalities of focusing and imaging with high efficiencies are experimentally demonstrated. The curved concave and convex primary and secondary mirrors in the conventional Schwarzschild objective are replaced by a pair of conjugated planar metasurfaces. The wavefront shaping and beam routing within the metasurface objective are achieved by the efficient tuning of the geometric Pancharatnam-Berry (PB) phase, which is inherent to a cascaded process of circular polarization transformations. Compared to the refractive metalenses based on geometric PB phase metasurfaces, our reflective design is intrinsically free of residual light. Moreover, the achromatic focusing property has been achieved by optimizing the phase profiles of the metasurface mirrors. It is expected that our work here can trigger an avalanche of investigations into reflective optical components, which can potentially set off the trend to reconstruct and refine many optical devices including microscopes, spectrometers, telescopes.

2. Designs of the Planar Schwarzschild Objective

The conventional Cassegrain-type Schwarzschild objective is shown schematically in Fig. 1a. The objective consists of one concave primary mirror and one convex secondary mirror. A judicious combination of designed geometry and spatial parameters for the two mirrors leads to a reflective Schwarzschild objective. A planar version of the Cassegrain-type Schwarzschild objective is shown in Fig. 1b, where the curved mirrors are replaced by two metamirrors made of flat metasurfaces with correspondingly converging and diverging optical functions. The required phase distributions upon reflections by the metamirrors are made possible by the geometric PB phase. To be more specific, upon each reflection, the originally left-/right-circularly polarized (LCP/RCP) light is converted to RCP/LCP light. As a result, upon the two successive rounds of reflections by the metamirrors, at the opposite sides of the metasurface objective the optical wave is of the same circular polarization [Fig. 1b]. In both the conventional and planar designs there is an aperture throughout the primary mirror. Figures 1c and 1d show the two-dimensional cross-section views of Figs. 1a and 1b for further clarity.

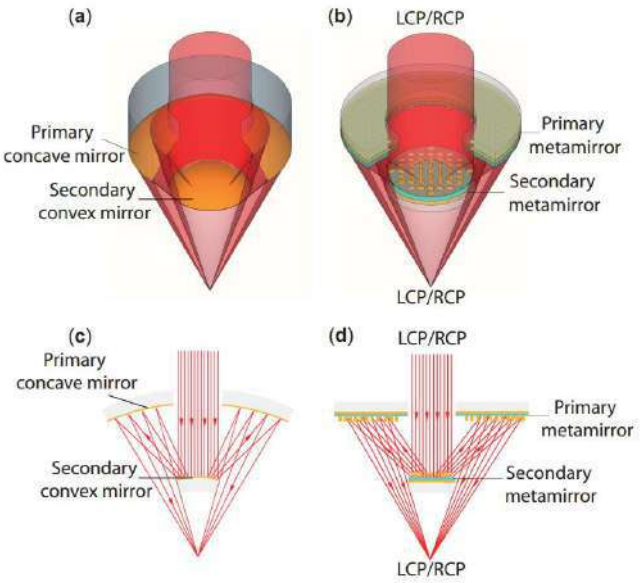


Figure. 1. Schematic illustration of curved and planar Cassegrain-type Schwarzschild Objectives. (a) The conventional objective, consisting of a concave primary mirror and a convex secondary mirror, focuses collimated incident light after being reflected twice. (b) The miniaturized planar counterpart of the conventional Schwarzschild objective, where the conventional curved mirrors are replaced by planar metamirrors with pre-designed gradient phase distributions. (c) and (d) are the two-dimensional cross-section views of objectives in (a) and (b), respectively. The red lines denote the trajectories of light rays.

3. Focusing Properties of the Planar Schwarzschild Objective

A planar Schwarzschild objective (N. A. = 0.1) with the two fabricated metamirrors can focus a LCP wave to a focal spot with the same polarization, as is schematically demonstrated in Fig. 1b. The focusing properties are experimentally characterized. Firstly, a collimated LCP incident light wave has been focused by the planar metasurface objective; then the focal spot is magnified through a 10× objective lens and a tube lens with f = 100 mm and finally is recorded with a CCD camera. The measured focal spots at λ = 780 nm and 633 nm are shown in Figs. 2a and 2d respectively, which are highly symmetric and can justify the excellent focusing property. The cross-sections of the focal spots are shown in Figs. 2b and 2e, with full-width at half-maximum (FWHM) of 3.15 μm and 2.83 μm at λ = 780 nm and 633 nm that exceeds the estimated Abbe limit (λ/(2×N. A.)). Figures 3c and 3f show the measured field profiles in the axis plane with the PM located at z = 0 at λ = 780 nm and 633 nm, respectively. The focal lengths are almost the same as each other at the two wavelengths, indicating the achievement of conventional dual-wavelength achromatic focusing capability. The measured focal lengths at both wavelengths are around z = 5.35 mm which is close to the designed value of $z = f$ = 4.98 mm, and the deviation is induced by the substrate effects that have not been considered in our theoretical analysis. The intensity distributions in Fig. 2 are shown in false-color, which are captured by a monochrome CCD camera.

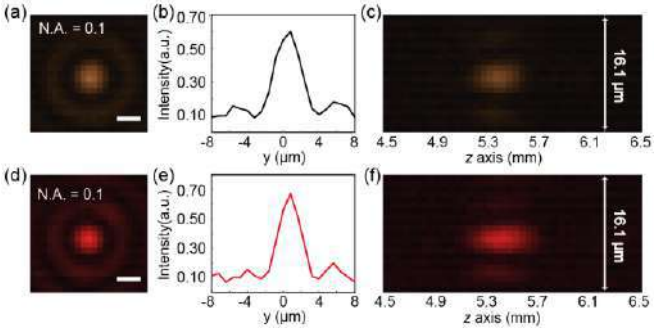


Figure. 2. Focusing properties of the planar Cassegrain-type Schwarzschild Objectives. N. A. = 0.1. (a, d) The measured intensity profiles at the focal plane (scale bar: 3μm). (b, e) The corresponding cross-sections of the focal spots along y direction, with FWHM of 3.15 μm, 2.83 μm, respectively. (c, f) The intensity profiles along the propagating axial plane. The wavelength of incident light is 780 nm in (a-c), and 633 nm in (d-f).

4. Conclusions

We have successfully incorporated flat optical elements made of plasmonic metasurfaces into classical Cassegrain-type reflective systems and demonstrate highly efficient planar Schwarzschild objectives that can be applied for achromatic focusing. We believe our work opens the door to metasurface-based revolutionary refinements and miniaturizations for not only refractive but also reflective optical systems. The fusion of refractive optical elements and planar meta-optics paves new avenues for manufacturing and reconstructing new types of microscopes, telescopes and other optical devices over much broader spectral regimes.

Acknowledgements

This research was supported by the National Natural Science Foundation of China (Grant No. 11774145 and 11404403), Guangdong Provincial Innovation and Entrepreneurship Project (Grant 2017ZT07C071), Applied Science and Technology Project of Guangdong Science and Technology Department (2017B090918001) and Natural Science Foundation of Shenzhen Innovation Committee (JCYJ20170412153113701).

References

[1] M. Born, E. Wolf, Principles of Optics: Electromagnetic Theory of Propagation, Interference and Diffraction of Light, 7th ed., (Cambridge University Press, Cambridge, New York, 1999).

[2] G. Zheng, H.Mühlenbernd, M. Kenney, G. Li, T. Zentgraf, and S. Zhang, Nat. Nanotechnol. 10, 308 (2015).

[3] M. Khorasaninejad, W. T. Chen, R. C. Devlin, J. Oh, A. Y. Zhu, and F. Capasso, Science 352, 1190–1194 (2016).

Ultra-low power thermo-optical switching in graphene metasurfaces

Joel D. Cox[1,2]

[1]Center for Nano Optics, University of Southern Denmark, Campusvej 55, DK-5230 Odense M, Denmark
[2]Danish Institute for Advanced Study, University of Southern Denmark, Campusvej 55, DK-5230 Odense M, Denmark
*corresponding author, E-mail: cox@mci.sdu.dk

Abstract

While plasmons in noble metal nanostructures facilitate strong nanoscale light-matter interactions, the overabundance of free electrons in these systems inhibits their tunability by weak external stimuli. Countering this limitation, the linear electronic dispersion in graphene endows the two-dimensional material with an enhanced sensitivity to doping electron density, enabling active tunability of its highly-confined plasmon resonances, and a low electronic heat capacity with a large thermo-optical response. Here we show that these properties combined enable significant optical modulation in isolated graphene nanostructures from the energy associated with just one of their supported plasmons. Our analysis is based on realistic, complimentary classical and quantum mechanical simulations, revealing that the energy associated with a single plasmon, absorbed in a small, lightly-doped graphene nanoisland, can sufficiently modify its electronic temperature and chemical potential to produce unity-order modulation of the optical response within sub-picosecond timescales, effectively shifting or damping the original plasmon absorption peak and thereby blockading subsequent excitation of a second plasmon. We further demonstrate that the proposed thermo-optical single-plasmon blockade consists in a viable ultra-low power all-optical switching mechanism for actively-tunable metasurfaces consisting of periodically-arranged doped graphene nanoislands, while their combination with quantum emitters could yield applications in biological sensing and quantum nano-optics.

1. Introduction

The ability of plasmons, the collective oscillations of conduction electrons, to intensify the electromagnetic fields upon which nonlinear optical phenomena superlinearly depend motivates fertile research efforts in nonlinear plasmonics to control light by light on the nanoscale [1]. In this context, engineered plasmonic near field enhancement from noble metal nanostructures has been enormously successful in bolstering the weak susceptibilities associated with coherent nonlinear processes while reducing the intensity threshold for optical switching [2], with engineered nonlinear plasmonic metasurfaces enabling a large nonlinear response from optically-thin structures [3]. However, despite impressive plasmonic enhancement, the realization of strong nonlinear optical interactions at ultra-low powers, ultimately down to the few- or single photon regime, remains elusive.

Here we propose that the combined large thermo-optical response and very low heat capacity originating from the unique conical dispersion of graphene can enable single plasmons strongly modulate the optical response. In particular, we explore scenarios where the energy of a single plasmon quanta ($\hbar\omega_{\rm p}$, where $\omega_{\rm p}$ is the plasmon resonance frequency), distributed among a finite number of electrons, can modify the local equilibrium temperature and chemical potential of a graphene nanoisland enough to produce observable changes in its supported plasmon resonances [4, 5]. Remarkably, in small graphene nanoislands doped with only a few electrons, we predict unity-order modulation of the optical response through single-plasmon absorption on ultrafast timescales, during the transfer of electronic energy to lattice vibrations. This phenomenon consists in an incoherent plasmon blockade, whereby the decay of a single excited plasmon suppresses the probability of exciting additional plasmons. We further demonstrate that this phenomenon enables ultra-low power optical modulation in nanopatterned graphene metasurfaces.

2. Results and Discussion

Optimal single-plasmon thermo-optical switching is achieved in small graphene nanoislands doped with a few electrons, necessitating a quantum-mechanical treatment of their electronic states and optical response [5]. Indeed, for nanohexagons containing $\sim$ 1000 or fewer carbon atoms, the Fermi energy does not well-describe the initial charging state in the presence of large energy gaps between discrete electronic states. We consider in Fig. 1 situations where an integral number of electrons $N_{\rm e}$ are added to a graphene nanohexagon, down to doping with only a few additional electrons. The absorption spectra shown in the upper row of Fig. 1 are dominated by quantum-finite size effects, where peaks associated with the HOMO-LUMO transition appear in the spectra even for undoped ($N_{\rm e} = 0$) structures. The excitation and decay of a single plasmon quantum at the frequency of this high-energy peak at various charging states results in even higher obtained electronic temperatures (see lower row of Fig. 1), which manifest prominently in the shift of the lower-energy plasmonic peak appearing for $N_{\rm e} > 0$ that dominates the response when $N_{\rm e} \gg 0$.

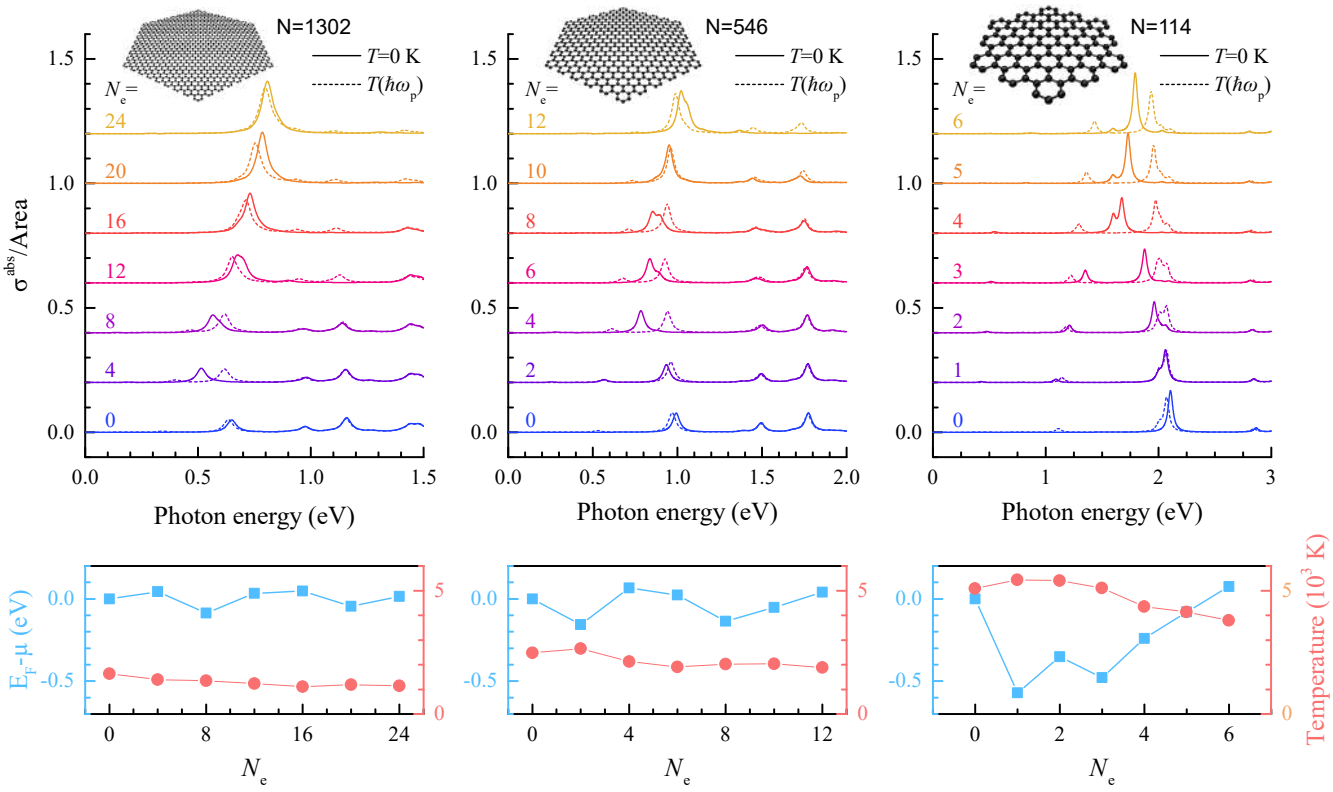


Figure 1: Thermo-optical switching by molecular plasmons. For graphene nanohexagons shown in the upper row containing N carbon atoms, with lateral sizes of 7.1 nm (left column), 4.5 nm (center column), and 2.0 nm (right column), we show in the center row the absorption spectra when the corresponding hexagon is doped with integral numbers of electrons $N_{\rm e}$, plotting in each case the spectrum before (solid curves) and after (dashed curves) the absorption of a single plasmon. For each hexagon we show in the lower row the chemical potential shift $E_{\rm F} - \mu$ (blue squares) and the electronic temperature (red circles) obtained upon absorption of energy $Q = \hbar\omega_{\rm p}$ associated with the dominant plasmon absorption peak in the $T = 0$ case for the considered doping charge.

A grand goal of nonlinear optics is the realization of an all-optical switch to produce light modulations in which the modulated light is phase-locked with the light *gate* signal. Our proposed switch does not preserve gate-signal phase coherence, but in exchange, it produces order-unity modulations with a single photon in a robust, integrable, solid-state platform (nanostructured graphene). The single-plasmon thermo-optical switching mechanism in nanostructured graphene is made possible by the intrinsically-low heat capacity of the 2D material and strong light-matter coupling of its electrically-tunable plasmon resonances, the latter enabling significant absorption even in very small structures containing only a few doping electrons. These properties are essential to achieve significant modifications in the optical response, which relies on the distribution of a finite plasmon energy among a small number of electrons to produce dramatic changes in the electronic temperature and the chemical potential. The change in optical response associated with single-plasmon absorption consists in ultra-low power all-optical switching for atomically-thin metasurfaces, which in combination with proixmal dipole emitters could open new avenues in optical sensing and quantum nano-optics.

Acknowledgement

The Center for Nano Optics is financially supported by the University of Southern Denmark (SDU 2020 funding). J.D.C was supported by VILLUM Fonden (grant No. 16498).

References

[1] J. A. Schuller, E. S. Barnard, W. Cai, Y. C. Jun, J. S. White, and Mark L. Brongersma, Plasmonics for extreme light concentration and manipulation, *Nat. Mater.* 9: 193–204, 2010.

[2] M. Kauranen and A. V. Zayats *Nat. Photon* 6: 737–748, 2012.

[3] Alexander Krasnok, Mykhailo Tymchenko, Andrea Alù, *Mater. Today* 21: 8–21, 2018.

[4] M. M. Jadidi et al., Nonlinear terahertz absorption of graphene plasmons, *Nano Lett.* 16: 2734–2738, 2016.

[5] J. D. Cox and F. J. García de Abajo, Transient nonlinear plasmonics in nanostructured graphene, *Optica* 5: 429–433, 2018.

Design of Meta-reflector by Deep Learning

Wei Xiao[1,2], Peter R. Wiecha[1], Kai Sun[1,2],C. H. de Groot[2], Otto L. Muskens[1]*,

[1.] Physics and Astronomy, University of Southampton, Southampton SO17 1BJ, United Kingdom
[2.] Electronics and Computer Science, University of Southampton, Southampton SO17 1BJ, United Kingdom
*corresponding author, E-mail: Wei.Xiao@soton.ac.uk; O.Muskens@soton.ac.uk

Abstract

Metamaterial absorbers have drawn lots of attentions due to their higher degree of freedom in geometry design for some specific applications compared with conventional multilayer absorbers. Recently, we have reported meta-surface optical solar reflectors (OSRs) based on metamaterial absorber, which can provide cost-effective high performance alternative to conventional OSRs in spaceship applications. However, the design and optimization of meta-reflectors unsurprisingly involve numerical simulations with wide range of multiple design variables and leads to a low computational efficiency. In this work, we adopted a deep learning technique to speed up the computational efficiency and demonstrated that the optical response of meta-reflectors can be directly predicted through machine deep learning for a given set of design parameter. In addition, an inverse design of meta-reflector can also be obtained for desired optical properties, which could provide a complete novel design strategy in the optical design. The proposed deep learning design technique is found to be promising for ultracompact nanophotonics device design.

1. Introduction

Meta-reflector is a flexible optical solar reflector with high reflection in visible range and broadband absorption (high emissivity) in the infrared based on meta-surface nanostructures, which can be used for the radiation cooling of spacecraft [1]. Compared with conventional multilayer optical solar reflectors, meta-reflectors could achieve an improved performance due to the excitation of plasmonic resonance [2-3]. The conventional way of designing meta-reflector is based on simulating a serial of different geometries [4], through solving the Maxwell's equation using commercial numerical software (COMSOL and FDTD). Recently, with the advance of computational techniques, Deep Learning (DL) becomes a powerful computational tool to solve problems and boost the developments, e.g. face recognition [5] and optical information storage [6]. Therefore, it is of interest to investigate deep learning capability on nanophotonic device design. Here, we present an innovative deep learning technique, which can predict the optical response of meta-reflectors with given design parameters and also predict design parameters for a given spectral response (inverse design).

2. Results and Discussion

2.1. Design of metareflector and training for neural networks

Figure 1 shows the schematic of a meta-reflector. The metareflector is designed using the Salisbury screen and consist of three layers, the bottom Al mirror layer as back-reflector, the middle dielectric layer of SiO_2 and the top patterned layer of Aluminum-doped Zinc Oxide (AZO), AZO is a Transparent Conductive Oxide (TCO) with a dielectric response in visible range and metallic response in infrared range. The device optimizations were done through varying three parameters, AZO feature gap (g), AZO feature width (w) and SiO_2 thickness (t). Using numerical simulations, 2000 datasets were generated with different gap (g), width (w) and thickness (t) to train the neural networks (deep learning).

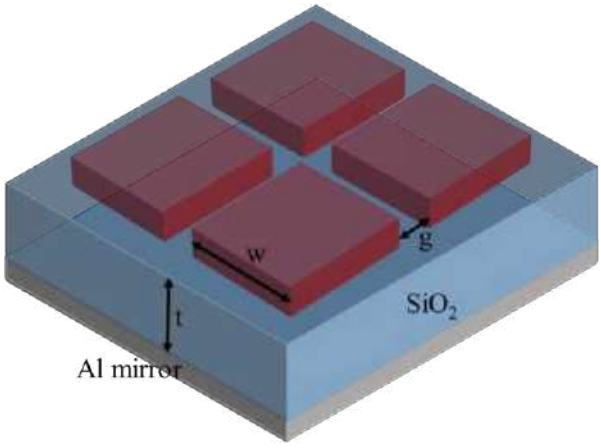


Figure 1: Schematic of a meta-reflector

2.2. Forward problem: Predict the reflectance spectrum

Initially, the neural network was trained to solve the forward problem, predicting the reflectance spectrum for a set of given parameters t, w, g, as shown in Figure 2. The reflectance generated by the trained neural network well agrees with that generated from FDTD numerical method over a wide range of wavelength for a given structure. Unlike numerical method through finite element method by solving Maxwell equation, deep learning method can obtain the response through a direct calculation using trained neural networks and this is highly advantageous in computational efficiency.

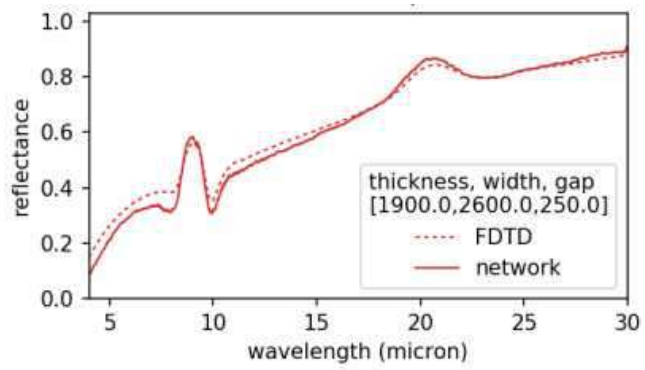


Figure 2: Meta-reflector reflection spectra of generated from the trained neural network and FDTD numerical method for a given design.

2.3 Inverse problem: Predict design parameters for a desired spectral response

In many cases, it would be more important to achieve a design with a desirable optical response and this makes an inverse design even more attractive than the forward design given by a numerical method. The trained neural network is therefore tested for it capability in finding the structure for a desirable response. Figure 3 shows reflectance comparison of the predicted structure through the trained neural network and the given arbitrary structure. Reflectance spectra of some random structures are also plotted for comparisons. The predicated parameter from the trained neural network shows the best fitting parameter with a thinner (800 nm) thickness than the preset one. This discrepancy provides an insight that similar performance can be achieved with a further compact design, which is essential to reduce fabrication costs and spaceship's launch costs.

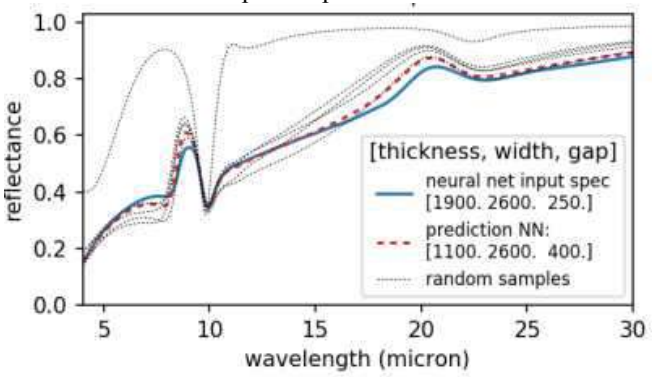


Figure 3: Meta-reflector reflection comparison between the trained neutral network predicted structure and the preset structure.

3. Conclusions

In conclusion, we have demonstrated that the deep learning can be used to predict the reflectance spectrum of a meta-reflector. The deep learning technique is highly advantageous over the conventional numerical method for its significantly improved computational efficiency and multi variable handling. Moreover, the deep learning neural network can also provide an inverse design capability to directly get the design structure for the desired optical response.

Acknowledgements

This work was financially supported by through Horizon 2020 project META-REFLECTOR, ID 687303, SMART-FLEX, DSTL MULTIMETA project.

References

[1].Sun, K., Riedel, C.A., Wang, Y., Urbani, A., Simeoni, M., Mengali, S., Zalkovskij, M., Bilenberg, B., De Groot, C.H. and Muskens, O.L., 2017. Metasurface optical solar reflectors using AZO transparent conducting oxides for radiative cooling of spacecraft. *ACS Photonics*, *5*(2), pp.495-501.

[2].Landy, N.I., Sajuyigbe, S., Mock, J.J., Smith, D.R. and Padilla, W.J., 2008. Perfect metamaterial absorber. *Physical Review Letters*, *100*(20), p.207402.

[3].Watts, C.M., Liu, X. and Padilla, W.J., 2012. Metamaterial electromagnetic wave absorbers. *Advanced Materials*, *24*(23), pp.OP98-OP120.

[4].Abb, M., Wang, Y., Papasimakis, N., De Groot, C.H. and Muskens, O.L., 2013. Surface-enhanced infrared spectroscopy using metal oxide plasmonic antenna arrays. *Nano letters*, *14*(1), pp.346-352.

[5].Parkhi, O.M., Vedaldi, A. and Zisserman, A., 2015, September. Deep face recognition. In *bmvc* (Vol. 1, No. 3, p. 6).

[6].Wiecha, P.R., Lecestre, A., Mallet, N. and Larrieu, G., 2019. Pushing the limits of optical information storage using deep learning. *Nature Nanotechnology*, p.1.

Vortex generation by graphene and near-zero index thin films

Alessandro Ciattoni[1] **and Andrea Marini**[2,*]

[1]Consiglio Nazionale delle Ricerche, CNR-SPIN, Via Vetoio 10, 67100 L'Aquila, Italy
[2]Department of Physical and Chemical Sciences, University of L'Aquila, Via Vetoio, 67100 L'Aquila, Italy
*corresponding author, E-mail: andrea.marini@aquila.infn.it

Abstract

We show that resonant subwavelength media illuminated by a circularly polarized beam produce optical vortices of order two in the opposite circularly polarized components of the reflected and transmitted fields as a consequence of enhanced spin-orbit interaction of light. Our theoretical predictions indicate that graphene and near-zero index media hold great potential as miniaturized active devices for the optical control of light orbital angular momentum.

1. Introduction

The exploitation and control of light orbital angular momentum (OAM) constitutes a novel and potentially disruptive technology for increasing the bandwidth of current telecommunication systems. Indeed, with respect to other mode division multiplexing schemes, OAM has the advantage of ease detection through phase-only optical elements along with a reported Tbit/s transmission capacity over both free space and optical fibers. In this context, spin-orbit interaction (SOI) of light is a very important research topic since it provides a tool for manipulating the spatial degrees of freedom of radiation by acting on its circular polarization state. As an example, reflected and refracted beams at a planar medium discontinuity experience a lateral shift which depends on the circular polarization state of the incident beam (spin-Hall effect). Another remarkable SOI effect is the generation of optical vortices from circularly polarized beams, a process accompanied by spin to orbital angular momentum conversion. Standard procedures to achieve vortex generation are focusing by high-numerical aperture lens, scattering by small particles, propagation along the optical axis of a uniaxial crystal, and propagation through semiconductor microcavities. Similar SOI effects involving Bessel beams have been considered in uniaxial crystals and at reflection and transmission by a planar interface between two homogeneous media. The advent of metamaterials has further increased the SOI research effort, mostly in the use of ultra-thin metasurfaces for manipulating the angular momentum of light and for vortex generation [1, 2, 3].

Near-zero index (NZI) media are nowadays attracting an increasing research interest owing to the very unconventional way they affect the electromagnetic radiation. The effective wavelength in NZI media is much larger than the vacuum wavelength and this entails a regime quite opposite to geometrical optics where the field is slowly-varying over relatively large portions of the bulk. Such feature has been exploited for squeezing electromagnetic waves at will, for tailoring the antenna radiation pattern and for enhancing nonlinear response of matter.

2. Discussion

Here we show that two-dimensional materials and near-zero index thin films can support vortex generation [4, 5]. We prove that such genuine SOI effect is physically due to the mutual difference between the dynamics of transverse magnetic and transverse electric fields upon reflection and transmission. As the majority of radiation SOI phenomena, the slab vortex generation is mainly a nonparaxial effect. On the other hand, we prove that vortex generation in the NZI regime is remarkably efficient even for incident paraxial beams in spite of the very small film thickness. Such phenomenology is unprecedent since paraxial vortex generation occurs only in uniaxial crystal and its efficiency requires very long samples whose thickness is comparable with the beam diffraction length (millimeters). Here, the crucial role is played by the physical ability of a NZI slab to turn a paraxial wave, incoming from vacuum, into a nonparaxial one within the bulk, its nonparaxiality triggering the predicted slab vortex generation. In addition we provide a first-principle theoretical approach able to describe the scattering of arbitrary tightly confined fields impinging on a generic two-dimensional medium. Our framework, which does not resort to any approximation on the vectorial electromagnetic field, is very similar in its kinematical traits to the description of a spin one quantum particle living in the atomically thin medium, whose orbital, spin and total angular momenta are the basic quantities allowing us to elucidate the physics of radiation matter interaction in the presence of two-dimensional materials. Rotational invariance is the key ingredient of our analysis and accordingly we find that the ensuing total angular momentum conservation rules radiation scattering. Indeed, the rotationally invariant electromagnetic coupling provided by the two-dimensional material, triggers photon transitions accompanied by an exchange between the orbital and spin angular momenta which is quantified by suitable selection rules. We further specialize our calculations to doped extended graphene, demonstrating that thanks to plasmon-enhanced SOI such an atomically-thin medium can generate efficiently optical vortices of order $m = \pm 2$ and actively

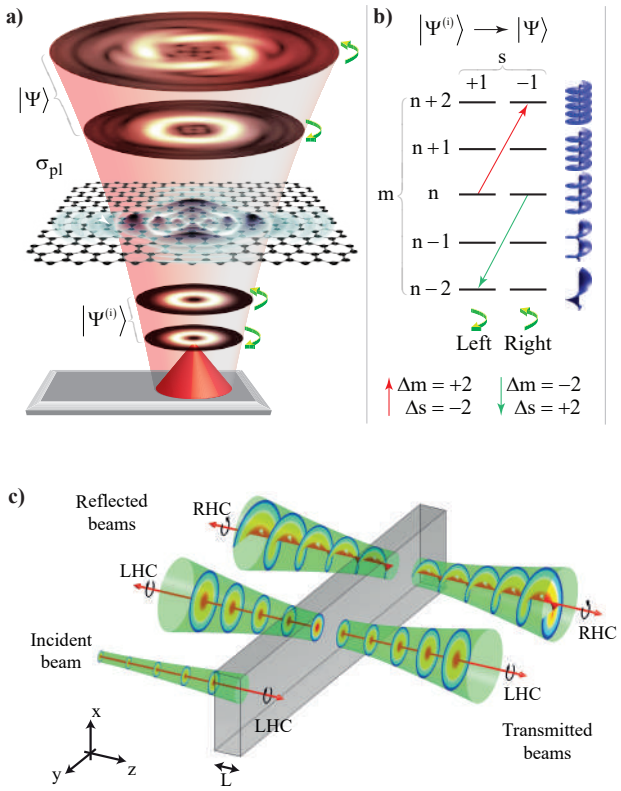


Figure 1: (a) Geometry of radiation scattering by graphene. The impinging field (represented by the abstract vector $|\Psi^{(i)}\rangle$) is radiated by a tip and it has both left and right handed polarized components. The circularly polarized components of the transmitted field (represented by the abstract vector $|\Psi\rangle$) display vortex photons not present in the incoming field. The high transverse confinement of the field emitted by the tip both enhances such vortex scattering process and enables the concurrent excitation of graphene plasmons whose charge oscillation is denoted with $\sigma_{\rm pl}$. (b) Vortex level scheme and fundamental scattering processes supported by graphene. A vortex (m, s) is characterized by the topological charge m (coinciding with its orbital angular momentum) and by the left/right circular polarization $s = \pm 1$ (coinciding with its spin). Graphene induces the transitions $(n, +1) \longrightarrow (n + 2, -1)$ (red arrow) and $(n, -1) \longrightarrow (n-2, +1)$ (green arrow). The selection rules $\Delta m = \pm 2$ and $\Delta s = \mp 2$ are a consequence of the conservation of the total angular momentum $j = m + s$ (i.e. the rotational invariance of the system). (c) Geometry of the vortex generation process by NZI subwavelength slabs. The incident beam is a LHC polarized beam with no topological charge. Both the reflected and the transmitted fields have LHC and RHC polarized components, the former being circularly symmetric and the latter containing a vortex of the second-order. The spatial separation in figure among such components is introduced for clarity purposes.

manipulate the mixing of different OAM states by means of the external gate voltage, thus enabling fast electrical processing of information stored in OAM states. In addition, we demonstrate that such a tunable mixing of OAM vortices of different order can be exploited to devise arbitrary subwavelength arrays of optical traps in the near field able to pin cold atoms into desired patterns, thus enabling the engineering of artificial materials at will.

3. Conclusions

In conclusion we show that resonant subwavelength materials like graphene and NZI media enable the generation of optical vortices at the nanoscale with unprecedentedly high efficiency and deep-subwavelength spatial features. We show that extended graphene is ideal since it hosts plasmons with long lifetime and high quality factor, increasing the vortex generation efficiency. Furthermore, thanks to the mixing and interference of distinct vortices, we demonstrate the ability of graphene to generate deep subwavelength optical lattices of arbitrary shape and pace of few nanometers, enabling to devise artificial media at will. Although future work is required to extend our results to the quantum regime, we envisage that they will constitute a solid theoretical ground for the development of nano-scaled active elements and logic gates for enhanced quantum computation based on hyper-entangled photon states.

Acknowledgement

A.M. acknowledges support from the Rita Levi Montalcini Fellowship (grant number PGR15PCCQ5) funded by the Italian Ministry of Education, Universities and Research (MIUR). A.C. acknowledges the U.S. Army International Technology Center Atlantic for financial support (grant number W911NF-14-1-0315).

References

[1] G. Li, M. Kang, S. Chen, S. Zhang, E. Y.-B. Pun, K. W. Cheah, and J. Li, *Nano Lett.* 13, 4148-4151 (2013).

[2] F. Bouchard, I. De Leon, S. A. Schulz, J. Upham, E. Karimi, and R. W. Boyd, *App. Phys. Lett.* 105, 101905 (2014).

[3] D. Hakobyan, H. Magallanes, G. Seniutinas, S. Juodkazis, and E. Brasselet, *Adv. Optical Mater.* 4, 306312 (2016).

[4] A. Ciattoni, A. Marini, and C. Rizza, *Phys. Rev. Lett.* 118, 104301 (2017).

[5] A. Ciattoni, C. Rizza, H.-W. H. Lee, C. Conti, and A. Marini, *Laser & Photon. Rev.* 12, 1800140 (2018).

Hiding a QR code in a Vector Light Beam

Chunmei Zhang, Yuttana Intaravanne, Wei Wang, Xianzhong Chen*,

School of Engineering and Physical Sciences, Heriot-Watt University, Edinburgh, UK
*corresponding author, E-mail: x.chen@hw.ac.uk

Abstract

As one of the important properties of light, polarization profile can be utilized to carry information. Metasurfaces have shown great potentials in manipulating the light propagation. In this paper we experimentally demonstrate a metasurface device which can encode a quick response (QR) code into the space-variant polarization profile of a laser beam. A linear polarizer is used to reveal the hidden QR code. This technology has potential application in anti-counterfeiting, security and so on.

1. Introduction

In the recent years, optical metasurfacs have been adopted to generate the vector beams with typical or even arbitrary polarization states [1-3]. Quick response (QR) code is two-dimensional barcode which has been widely used in the daily life. QR code usually consists black and white patterns with spatially varying intensity profile, which can be processed by a QR code reader. To further explore the capability and feasibility of the optical metasurfaces, we experimentally demonstrate a metasurface device upon which a QR code can be encoded into the spatially-variant polarization profile of the light beam.

2. Results

In our design, the vector beam that can be used to hide the QR code is generated by a reflective metasurface (Fig.1b), illuminated by a linearly polarized light beam at normal incidence. The polarization profile are space variant after the incident light is reflected by the metasurface. If adding an analyzer before the CCD camera, the hidden QR code can be revealed which is impossible without this analyzer. The standard electron-beam lithography is used to fabricate the designed metasurface, then followed by the lift-off process. The size of finished sample is 300 μm by 300 μm. The SEM image of part of the fabricated sample is shown in Fig.1a.
Since the sign of the geometric phase generated at the interface of metasurface depends on the helicity of the incident light, upon the illumination of the linearly polarized light which can be decomposed to two circularly polarized light beams with opposite helicity which will meet and interfere with each other, generating the desired polarization profile which is space variant. The simulation and experimental results with and without the analyzing polarizer are shown in Fig.1c and Fig.1d, for incidence wavelengths of 650nm and 540nm, respectively. The slight difference between experiment and simulation is due to the imperfection of the sample and measurement error. The QR code contains the information of our group website (http://nanophotonicslab.eps.hw.ac.uk/), which can be accessed by using a QR code reader such as a smart phone.

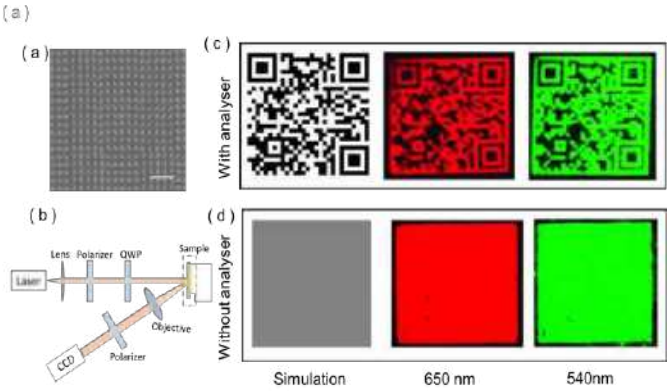


Figure 1. Simulation and experimental results. (a) SEM image of the fabricated sample. The scale bar is 1 μm. The size of fabricated sample is 300 μm by 300 μm. Each unit cell is 300 nm by 300 nm. (b) Schematic of experimental setup. QWP: quarter waveplate. Simulation and experimental results (c) with and (d) without the analyser.

We further characterize the device by studying the relationship between the obtained QR code images and the transmission axis of the analyzer. In the original design, the transmission axes of the polarizer (before the sample) and the analyser (after sample) are designed to be along the horizontal and vertical directions, respectively. Various QR codes are obtained by rotating the transmission axis of the analyser, while that of the polarizer is fixed along the horizontal direction. Fig.2 shows the simulation and experimental results when the rotation angles of the analyser (away from the designed direction) are 0, $\pi/4$, and $\pi/2$, respectively. It is interesting to find that those two QR codes for the analyser with orthogonal directions of transmission axis (0 and $\pi/2$) are complementary images, i.e., the brightest area becomes the darkest area and vice versa. This phenomenon can be explained from the point of Malus' law.

3. Discussion

The uniqueness of this multichannel metasurface device is that the black and white image the integration of totally

different functionalities onto a single device by the independent control of phase and polarization profile. In our demonstration the reconstructed holographic image is dependent on the polarization state of the incident light, while the hidden image is embedded in the inhomogeneous polarization distribution of the generated laser beam and can be revealed by using a linear polarizer.

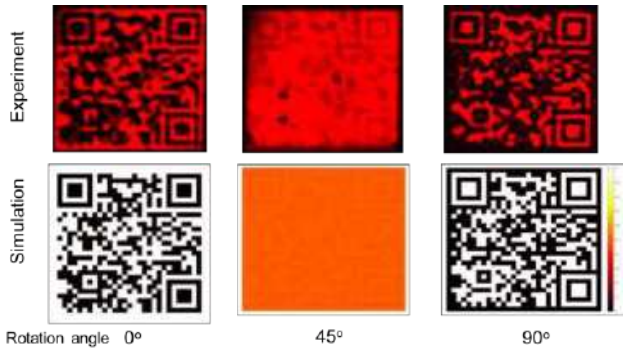


Figure 2. The dependence of experimental results on the rotation angles of the transmission axis of the analyser away from the vertical direction. The incident light is linearly polarized along the horizontal direction.

The demonstration of this new device will possess a unique advantage over traditional security holograms due to the combination of image-switchable functionality and the hidden image in the laser beam.

4. Conclusions

Optical metasurfaces provide the capability to generate inhomogeneous polarization states, providing a powerful tool to develop compact and novel device with unusual functionalities.We experimentally demonstrate a metasurface device which can generate space variant polarization distribution which is used here to hide a QR code into it. This study of the multichannel device based on the independent control of polarization makes this technique very attractive for compact optical devices with high density of functionalities.

Acknowledgements

This work is supported by Engineering and Physical Sciences Research Council of the United Kingdom (Grant Ref: EP/P029892/1).

References

[1].Yue, F., et al., Vector vortex beam generation with a single plasmonic metasurface. ACS photonics, 2016. 3(9): p. 1558-1563.

[2].Wang, L., et al., Active display and encoding by integrated plasmonic polarizer on light-emitting-diode. Scientific reports, 2013. 3: p. 2603.

[3].Yue, F., et al., High-resolution grayscale image hidden in a laser beam. Light: Science & Applications, 2018. 7(1): p. 17129.

Applying computer graphics techniques to optical metasurfaces: Broadband reflective metasurfaces for the visualisation of 3D effects

Diane J. Roth[1], Alexander E. Minovich[1], Guixin Li[2], Anatoly V. Zayats[1]

[1] Department of Physics and London Centre for Nanotechnology, King's College London, Strand, London WC2R 2LS, United Kingdom

[2] Department of Materials Science and Engineering and Shenzhen Institute for Quantum Science and Engineering, Southern University of Science and Technology, Shenzhen, 518055 China

*corresponding author, E-mail: diane.roth@kcl.ac.uk

Abstract

We report on the use of optical metasurfaces for the development of the concept of surface normal mapping to achieve the representation of 3D objects and shading effects. As a proof of principle, a flat diffuse metasurface imitating lighting and shading effects of a 3D cube was fabricated and characterised under incoherent illumination. The metasurface performs in a broad range of the visible spectrum, including the three main RGB wavelengths. Applications of these metasurfaces span from 3D security features and anti-counterfeiting to efficient optical diffusers.

1. Introduction

Dielectric and plasmonic metasurfaces provide excellent control over the shaping of optical wavefronts via the manipulation of polarisation, phase and amplitude of the light. Taking advantage of their subwavelength thicknesses, metasurfaces have shown to be a very promising technology in a variety of applications including beam steering and focusing, polarisation and angular momentum control, enhancement of nonlinear effects, as well as holographic information encoding for 3D displays [1-3]. Recently, the emergence of virtual reality and augmented reality technologies have led to the constant demand of effective techniques for the 2D visualisation of 3D objects. Normal mapping [4], for example, is widely used in computer graphics to create shading effects and recreate 3D-like features of surface textures, such as regular patterns, bumps or ripples. Normal maps are typically overlaid onto low resolution models to add fine geometric surface features, in order to increase the rendering speed of a 3D image. In this way, the brightness of different parts of the 3D object varies accordingly to the normal map, providing adequate shading to the object.

In this work, we designed an optical metasurface implementing diffuse reflection and using the concept of normal mapping to control its scattering properties. The metasurface, imitating the shading of a 3D cube, is designed so the "3D image" is displayed directly on the illuminated metasurface and its shading varies in response to the change in illumination angle.

2. Discussion

In order to transpose the computer graphics approach to the metasurface, the normal map of the 3D cube is created by controlling the phase distribution of the metasurface. To do so, a reflective metasurface design based on the Pancharatnam-Berry principle [5,6] was used. The phase controlling elements are aluminium nanorods placed above an aluminium film and separated from it by a MgF_2 dielectric spacer (Fig. 1). A superstrate of MgF_2 is used to prevent oxidation.

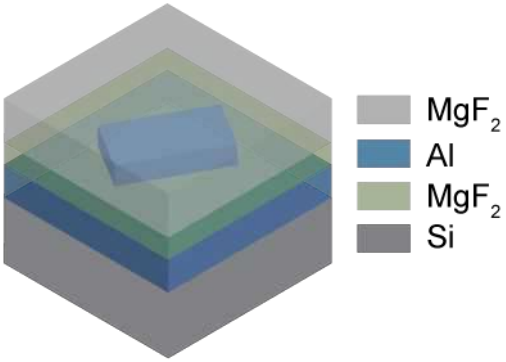


Figure 1: Schematic illustration of a metasurface unit cell.

In the experiments, the structure is illuminated by circularly polarised white light and the observation is performed in cross-polarised configuration. Images of the 3D object created are recorded for different illumination angles of the sample as well as different rotation angles. The metasurface is shown to exhibit a high scattering efficiency in a broad spectral range, including the main RGB wavelengths, and performs well for a wide range of illumination angles. Figure 2 shows images of different metasurface patterns for three different angles of rotation of the sample, observed at a normal to the metasurface pattern as the light source rotates

about the sample. The metasurface is illuminated at an angle of 30° with incoherent white light. It is shown that the metasurface behaves as a real 3D object when during rotation, the cube faces facing the light become brighter.

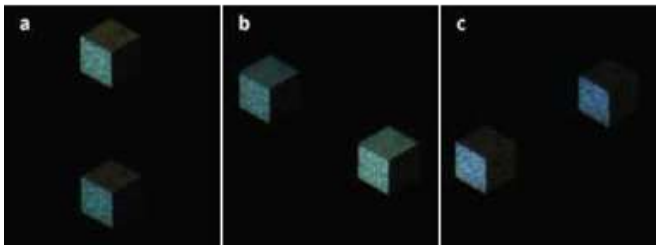


Figure 2: Images of different metasurface patterns under incoherent white light illumination. The rotation angles of the sample are 0° (a), 120° (b), and 240° (c). The structures are illuminated at the angle of incidence of 30°.

3. Conclusions

We have developed the concept of surface normal mapping for the visualisation of 3D objects and shading effects with optical metasurfaces. The designed metasurface, which provides an efficient control of diffuse scattering, performs under broadband incoherent illumination, including the main RGB wavelengths. The 3D images created via normal mapping based on optical metasurfaces provide an effective technology for 3D security features and anti-counterfeiting. This type of metasurfaces can also be useful in the design of efficient optical diffusers for display technology and etalons for metrology. Combination of metasurfaces with complex polarisation light states may provide additional degrees of freedom for multiplexing and active manipulation of images and optical information [7-9].

Acknowledgements

This work was supported in part by EPSRC (UK) and ERC iCOMM project (789340).

References

[1] A.V. Kildishev, A. Boltasseva, V.M. Shalaev, Planar photonics with metasurfaces, *Science*, 339, p.1232009, 2013.

[2] F. Capasso, N. Yu, Flat optics with designer metasurfaces, *Nature materials*, 13, p.139, 2014.

[3] A.E. Minovich, A.E. Miroshnichenko, A.Y. Bykov, T.V. Murzina, D.N. Neshev, Y.S. Kivshar, Functional and nonlinear optical metasurfaces, *Laser & Photonics Reviews*, 9, pp.195-213, 2015.

[4] F. Ganovelli, M. Corsini, S. Pattanaik, M. Di Benedetto, *Introduction to computer graphics: a practical learning approach*, CRC Press, 2015.

[5] G. Zheng, H. Mühlenbernd, M. Kenney, G. Li, T. Zentgraf, S. Zhang, Metasurface holograms reaching 80% efficiency. *Nature Nanotechnology*, 10, p.308, 2015.

[6] A.E. Minovich, M. Peter, F. Bleckmann, M. Becker, S. Linden, A.V. Zayats, Reflective metasurfaces for incoherent light to bring computer graphics tricks to optical systems, *Nano Letters*, 17, pp.4189-4193, 2017.

[7] A.V. Krasavin, P. Segovia, R. Dubrovka, N. Olivier, G. A. Wurtz, P. Ginzburg, A.V. Zayats, Generalization of the optical theorem: experimental proof for radially polarized beams, *Light: Science & Applications*, 7, p.36, 2018.

[8] G. Li, G. Sartorello, S. Chen, L.H. Nicholls, K.F. Li, T. Zentgraf, S. Zhang, A.V. Zayats, Spin and Geometric Phase Control Four-Wave Mixing from Metasurfaces, *Laser & Photonics Reviews*, 12, p.1800034, 2018.

[9] L. Du, A. Yang, A.V. Zayats, X. Yuan, Deep-subwavelength features of photonic skyrmions in a confined electromagnetic field with orbital angular momentum, *arXiv preprint arXiv:1806.04827,* 2018.

Plasmonic open systems: theory and applications

Shiyi Xiao[1], Jing Lin[2], Meng Qiu[2], Xiyue Zhang[2] , Huijie Guo[2], and Lei Zhou[2]*

[1]Key laboratory of Specialty Fiber Optics and Optical Access Networks, Shanghai University, Shanghai 200444, China
[2]Department of Physics, Fudan University, Shanghai 200438, China
*corresponding author, E-mail: phzhou@fudan.edu.cn
Presenting author, E-mail: shiyi_xiao@shu.edu.cn

Abstract

We present a bottom up coupled-mode-model from first principles (Maxwell's equations) to study the plasmonic open systems, where, all coupling parameters can be calculated by a directly integration of different optical modes. Based on this theory, we establish phase diagrams to systematically study the whole picture of optical response of interested systems. For example, designing meta-surface to realize wide-band optical transparent window (OTW) with diminished transmittance fluctuations.

1. Introduction

Over the past decades, many efforts were devoted to studying plasmonic open systems, particularly those consisting of multiple plasmonic resonators coupled in different ways. The latter can generate fascinating effects such as Fano resonance, Rabi oscillations, and plasmonic-induced transparency in different scenarios, which can have plenty of applications in practice. However, understanding the profound physics underlying these intriguing phenomena is far from satisfactory. While full wave simulations can numerically repeat experimental findings in most cases, they can offer very little physics, not mentioning the huge computing costs required. Meanwhile, many models (e.g., coupled-mode-theory (CMT)[1], Fano's formula[2], or effective circuit models[3], etc.) are intuitive enough to explain the underlying physics, they unfortunately require model parameters obtained from fitting with available experimental/simulation results, implying that they are empirical models which cannot predict unknown phenomena before performing simulations or experiments. The difficulties behind the slow theoretical development in such a field are ultimately due to the fact that the plasmonic coupled systems are complex open systems, in which not only different resonators are coupled with each other via near-field effect but also they can couple with external free space via far-field interactions.

Here, we present a bottom up coupled-mode-model from first principles (Maxwell's equations) to study the plasmonic open systems. Here, direct and indirect coupling parameters can be calculated by a directly integration of different optical modes. Our theory is fully justified by both full wave simulations and infrared experiments. Based on this theory, we establish phase diagrams to systematically study the whole picture of optical response of interested systems. For example, we can predict and design the complex meta-atoms with optimized local field enhancement or optimized quantum yield, which can be used in metasurface enabled fluorescence enhancement or other light mater interactions enhancement. Such a theoretical approach can be also used to design structures to realize wide-band optical transparent window (OTW) with diminished transmittance fluctuations. As an illustration, we design a 4-layer structure (with a total thickness 36 mm) through solving the proposed criterion, and experimentally demonstrate that it exhibits a flat OTW within 3.7 - 5 GHz with transmittance fluctuations smaller than 10% .

2. Theoretical framework of plasmonic open systems

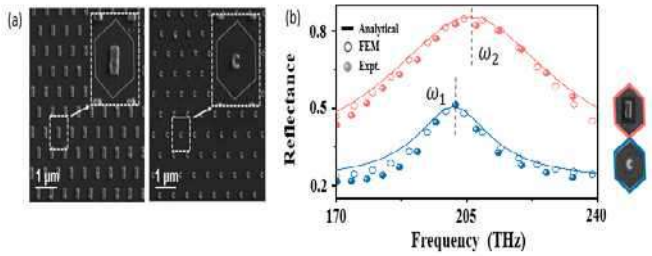


Figure 1 Comparison between experiment results (solid circle lines),FEM simulation results (open circle lines and theoretical prediction (red lines) on two different plasmonic open systems.

Before the presenting the analytical model, we briefly review the Hamiltonian form of Maxwell's equations for nanoparticles systems[4,5]. In analogy to the Schrödinger equation, the full-vector Maxwell's equations coupled with equation of motion for electron can be rewritten in a Hamiltonian form $\hat{\mathbf{H}}|\psi\rangle = \omega|\psi\rangle$, where the wave function is defined as $|\psi\rangle = [\boldsymbol{H}, \boldsymbol{E}, \boldsymbol{P}, \boldsymbol{V}]^T$ and the Hamiltonian operator is defined

$$\hat{\mathbf{H}} = \begin{pmatrix} 0 & -\frac{i}{\mu}\nabla\times & 0 & 0 \\ \frac{i}{\varepsilon_\infty}\nabla\times & 0 & 0 & -\frac{i}{\varepsilon_\infty} \\ 0 & 0 & 0 & i \\ 0 & i\omega_p^2\varepsilon_\infty & i\omega_0^2 & -i\Gamma_e \end{pmatrix} \quad (1)$$

Here $\boldsymbol{E}$ is the electric field, $\boldsymbol{H}$ is the magnetic field, $\boldsymbol{P} = [\varepsilon(\omega) - \varepsilon_0]\boldsymbol{E}$ is the polarization field, $\boldsymbol{V} = d\boldsymbol{P}/dt$ is the polarization field. We also note that the inner product is defined as $\langle\psi_1|\psi_2\rangle = \frac{1}{2}\int d\tau[\mu \boldsymbol{H_1^*}\cdot\boldsymbol{H_2} + \varepsilon_\infty \boldsymbol{E_1^*}\cdot\boldsymbol{E_2} + \omega_e^2(\omega_p^2\varepsilon_\infty)^{-1}\boldsymbol{P_1^*}\cdot\boldsymbol{P_2} + (\omega_p^2\varepsilon_\infty)^{-1}\boldsymbol{V_1^*}\cdot\boldsymbol{V_2}]$. Based on this Hamiltonian, the coupled mode model of plasmonic systems can be expressed by

$$-i\omega a_m = -i(\omega_m + t_m)a_m - \Gamma_m a_m + \sum_{n\neq m}(-it_{mn})a_n + \sum_{n\neq m} X_{mn}a_n + \sum_k \kappa_{mk}S_k \quad (2)$$

Where a_m, t_m and Γ_m is the amplitude, on-site correction, and radiation damping of the m-th plasmonic mode, X_{mn} and t_{mn} describes the far field and near field coupling, κ_{mn} denotes the coupling efficiency between m-th mode and k-th port. In order to verify our analytical model, we design and fabricated inferred nano-particles, we can see that the measured and theoretical calculation are in good agreement with each other, [see Fig. 1]. Such nice agreement unambiguously justified our validated our model analysis.

3. Application: mechanism and realization for flat optical transparent window

We now employ the CMT model to study the multilayer metasurfaces for the realization of flat optical transparent window. Solid lines in Fig. 1(d) depict the FDTD simulated transmittance/phase spectra of a slab formed by stacking N=4 such layers (N denotes the number of layers) with equal inter-layer distance, where the building block of metasurface the a metallic "H" shape inserted in subwavelength size metallic mesh. While the coupling between these layers indeed enlarges the total transmission band, strong fluctuations on both amplitude and phase exist inside the transmission band, especially at the high-frequency edge of the OTW [7].

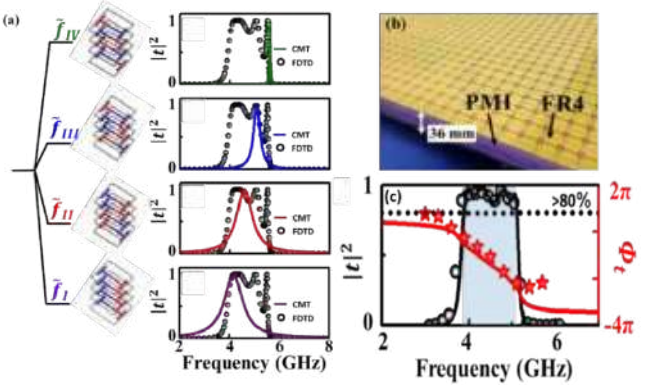


Figure 2. (a) Modes diagram depicting the collective modes for the N=4 stacked metasurface. (b) Photography of microwave samples. (c) Measured (symbols) and numerical-simulated (curves) transmittance and phase spectra of designed metasurface with flat transparent window.

We find that the peaks in the transmission spectrum of a coupled multilayer metasurfacce are closely related to the "collective" resonant modes supported by the system, which can be well controlled by the inter-layer couplings [Fig. 2(a)]. Such inherent link enables us to efficiently manipulate the shape of transmission spectrum via varying the inter-layer distances of the coupled multilayer system. As an illustration of our general theory, we applied it to design and fabricate a metasurface [Fig. 2(b)] exhibiting an optical transparency window with 3.7-5 GHz with diminished transmittance fluctuations, and demonstrated the idea by microwave experiments [Fig. 2(c)]. Our design approach is robust, intuitive, fast, and can have many applications in practice.

4. Conclusions

To summarize, we have established a highly efficient approach to study the plasmonic open systems. As an illustration of our general theory, we applied it to the design of a structure exhibiting an optical transparency window with a 3.7–5 GHz range with diminished transmittance fluctuations, and demonstrated the idea by microwave experiments. Our approach can have many applications in practice.

5. Acknowledgments

This work is supported by the National Natural Science Foundation of China (Grants Nos. 11704240, 11734007, 11474057, 11404063, and 11674068) and the Natural Science Foundation of Shanghai (Grants Nos. 17ZR1409500, 16ZR1445200, 16JC1403100).

References

[1] Joannopoulos, J. D., Johnson, S. G., Winn, J. N. & Meade, R. D. Photonic Crystals:Molding the Flow of Light 2nd edn (Princeton Univ. Press, 2008).

[2] Fano U. Effects of Configuration Interaction on Intensities and Phase Shifts. 1961 *Phys. Rev.* 124 1866.

[3] E. L. Norton, Constant Resistance Networks with Applications to Filter Groups, *Bell Syst. Tech. J.* 16, 178 (1937).

[4] Xi, B., H. Xu, Xiao. S., Zhou L. "Theory of coupling in dispersive photonic systems", *Phys. Rev. B*.83, 165115(2011).

[5] Aaswath Raman and Shanhui Fan, Photonic Band Structure of Dispersive Metamaterials Formulated as a Hermitian Eigenvalue Problem, *Phys. Rev. Lett.* 104, 087401 (2010).

[6] Lin, J., Meng, Q., Zhang, X., Guo, H., He, Q., Xiao S., & Zhou L. (unpublished).

[7] H. Guo, J. Lin, M. Qiu, J. Tian, Q. Wang, Y. Li, S. Sun, Q. He, S. Xiao and L. Zhou, "Flat optical transparent window: mechanism and realization based on metasurfaces", *J. Phys. D: Appl. Phy.* 51 074001 (2018).

Metasurface and Epsilon-near-zero Resonances on Optical Fiber

Jingyi Yang[1], Indra Ghimire[1], Khant Minn[1], Aleksei Anopchenko[1], Sudip Gurung[1], and Ho Wai Howard Lee[1, 2, *]

[1]Department of Physics, Baylor University, Waco, TX 76798, United States
[2]The Institute for Quantum Science and Engineering, Texas A&M University, College Station, TX 77843, United State
*Corresponding author, E-mail: Howard_Lee@baylor.edu

Abstract

Optical fiber is an excellent platform in guiding light, which has been widely employed for optical communication, imaging/sensing, and fiber lasers. Although a dielectric optical fiber is efficient for transmitting light, its functionality is limited by the geometry and dielectric material of fiber (Ge-doped silica for core and silica glasses for cladding). The mode size is limited by the diffraction limit of the dielectric core, and the numerical aperture is determined by the refractive index of the fiber materials. Meanwhile, the spot size right after the fiber is divergent and the intensity decreases dramatically with distance. However, the emergency of metasurfaces provides the opportunity of a variety of optical fiber innovations. In this presentation, we report an ultrathin optical metalens cascaded on the facet of a photonic crystal optical fiber that enables light focusing in the telecommunication regime (Fig. 1). In-fiber metalenses with designed focal lengths at the wavelength of 1550 nm are demonstrated [1]. The integration of an ultrathin metalens and optical fiber will pave the way of ultracompact in-fiber optical devices for optical imaging, sensing and fiber laser applications.

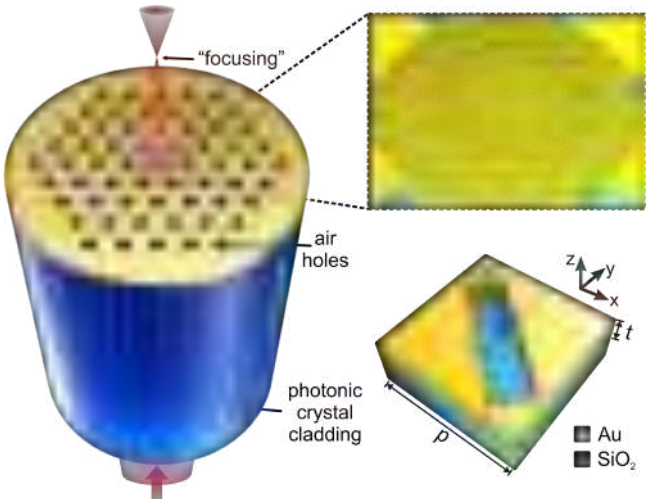


Fig. 1 Photonic crystal fiber metalens.

We also experimentally demonstrate a novel optical waveguide of side-polished optical fiber nano-coated with an ultrathin aluminum-doped zinc oxide (AZO) epsilon-near-zero film by atomic layer deposition technique. The AZO thin film with thickness of ~73 nm and ENZ wavelength of 1577 nm (real part of permittivity of the material crosses zero) is fabricated onto the D-shaped platform. Due to the evanescent field between the core mode and the mode supported by the AZO nano-layer, a highly confined ENZ mode in the AZO nano-film on the fiber could be excited (Fig. 2). We observed a resonant dip at the wavelength of ~ 1700 nm with strength of 8.2 dB in the measured transmission of 1.7cm long ENZ-fiber, showing a good agreement with the phase matching condition from the full-wave numerical simulation by considering the measured dispersion of the AZO thin film. Our results show the first experimental demonstration on the excitation of highly confined ENZ mode on optical fibers. These hybrid ENZ-optical fibers could be applied in zero-index photonic applications for studying enhanced ENZ nonlinear in fiber, quantum emission in ENZ media, and subwavelength mode enhanced in-fiber optical- and bio-sensing.

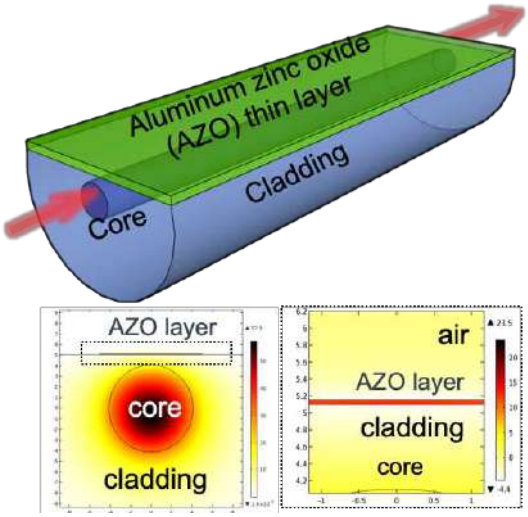


Fig. 2 Excitation of epsilon-near-zero mode on side-polished optical fiber.

Acknowledgements

The authors acknowledge the supports partially by the Robert A. Welch Foundation (Award number: AA-1956-20180324) and the Defense Advanced Research Projects Agency (grant number N66001-17-1-4047). The authors acknowledge the Center for Microscopy and Imaging (CMI) at Baylor University for technical support during the microscopy and image analysis.

References

[1] J. Yang, I. Ghimire, P.C. Wu, S. Gurung, C. Arndt, D.P. Tsai and H.W. Lee, Photonic crystal fiber metalens, *Nanophotonics* 8, 443-449 (2019).

[2] K. Minn et al. Excitation of epsilon-near-zero resonance in ultra-thin indium tin oxide shell embedded nanostructured optical fiber, *Nature Scientific Reports* 8, 2342 (2018).

[3] A. Anopchenko, et al. Atomic Layer Deposition of Ultra-thin and smooth Al-doped ZnO for Zero-Index Photonics, *Materials Research Express* 5, 014012 (2018).

Dynamic metamaterials

Bose-Einstein condensation and K-point lasing in a plasmonic lattice

Jani-Petri Martikainen, Antti Moilanen, Rui Guo, Aaro Väkeväinen, Marek Nečada, Konstantinos S. Daskalakis, Heikki T. Rekola, Aleksi Julku and Päivi Törmä[1]

[1]Department of Applied Physics, Aalto University, Finland
*corresponding author, E-mail: jani-petri.martikainen@aalto.fi

Abstract

We discuss our recent work on condensation phenomena on plasmonic lattices as well as K-point lasing in honeycomb lattices.

1. Experiment on Bose-Einstein condensation

A metal nanoparticle array gives rise to quasi-particles called surface plasmon polaritons (SSPs) which are a mixture of light and electron movement in metal. We demonstrate a Bose-Einstein condensate (BEC) of SPPs in a lattice of metallic nanoparticles [1] . Interaction of the SPPs with organic dye molecules induces thermalization by subsequent absorption and re-emission processes. With suitable lattice periodicity this interaction leads to condensation, which occurs at room temperature and in a picosecond timescale. The dynamics are studied in an experiment that utilizes the propagation of the modes and the open cavity character of the system, see Fig 1. Linewidth narrowing and increase of the spatial coherence of the mode is observed in response to onset of condensation. Transition from BEC to lasing is observed when the periodicity of the lattice is varied. We also discuss our more recent progress in this topic.

2. K-point lasing

We also study lasing at the high-symmetry points of the Brillouin zone in a honeycomb plasmonic lattice[2] with IR-792 dye as gain material. We demonstrate lasing,Fig.2, at the K points. By comparing polarization properties to

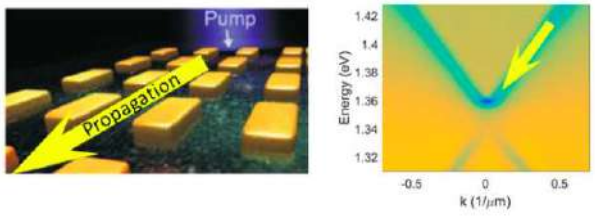


Figure 1: Propagating plasmonic modes undergo a redshift (decrease in energy) and eventually condense to the bottom of the energy band of the lattice. A typical nanorod sample and pump configuration is presented on the left. The dispersion relation of a nanoparticle array is presented on the right.

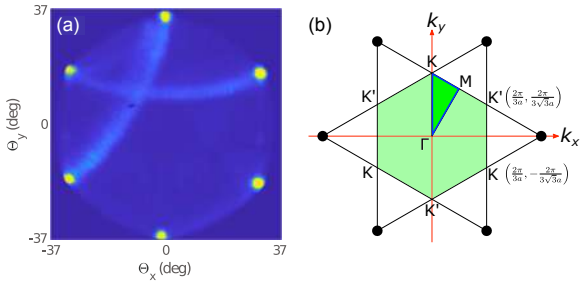


Figure 2: a) Angle resolved emission of the sample without any polarizer in detection. All six K-points are clearly visible. b) The first Brillouin zone (green area) of the honeycomb reciprocal lattice and its high symmetry points

T-matrix simulations, we identify the lasing mode as one of the singlets with an energy minimum at the K-point enabling feedback.

Acknowledgement

These works were supported by the Academy of Finland through its Centres of Excellence Programme (20122017) and under project numbers 284621, 303351 and 307419, and by the European Research Council (ERC-2013-AdG-340748-CODE). This is based on the work from COST Action MP1403 Nanoscale Quantum Optics, supported by COST (European Cooperation in Science and Technology). K.S.D. acknowledges financial support by a Marie Skłodowska-Curie Action (H2020-MSCA-IF-2016, project id 745115).

References

[1] T. Hakala *et al.*, Bose-Einstein condensation in a plasmonic lattice *Nature Physics* 14: 345365, 2018.

[2] R. Guo *et al.*, Lasing at K Points of a Honeycomb Plasmonic Lattice *Physical review Letters*, 122: 013901, 2019.

Functional all-dielectric nanophotonic: from colloidal syntesis to transition metal dichalcogenides nanoantennas

Ruggero Verre[1],* Nils Odebo-Länk[1], Denis Baranov[1], Timur Shegai[1] and Mikael Käll[1]

[1]Chalmers University of Technology, Physics Department, Göteborg, 41264, Sweden
corresponding author, E-mail: ruggero.verre@chalmers.se

Abstract

We present the first techniques able to fabricate solutions of all-dielectric nanoparticles with predefined shape and demonstrate that multilayer WS2 nanodisks support geometrical Mie resonances and new light-matter regimes not attainable by standard materials.

1. Introduction

Electromagnetic (EM) metasurfaces are structured material layers with subwavelength thickness that appears smooth to an impinging EM field because the feature spacing is small compared to the incident wavelength. In particular, the use of high-index dielectric (HID) nanoparticles as metasurface building blocks, or meta-atoms, allows for extremely flexible control of the optical properties by engineering their morphology. Similar to their metallic counterparts, HID nanoparticles support multiple resonances[1] and are able to efficiently convert propagating fields into sub-wavelength volumes. HID nanoparticles also have additional advantages, such as thermal stability, reduced Ohmic losses and CMOS fabrication compatibility. These features render HID metasurfaces highly interesting for applications like wavefront manipulation, light managment, directional antennas, light harvesting, ultra-fast optical switching and molecular sensing, to name a few.[2]

The diverse pool of potential applications highlights the need for flexible and cost-effective fabrication methods that would enable realization of large-scale nanostructured HID materials with well-defined physical and optical properties. Many of the available techniques have their limitation: lithographic methods cannot cover large areas and the features are generally planar. On the other hand, wet chemistry synthesis of HID nanoparticles is far from being as mature as for metal nanoparticles, several methods are capable of producing high quality spherical silicon particles with a range of sizes have been recently reported.

In this document, we first demonstrate a method for large-scale fabrication of different silicon nanostructures using a modified version of the hole-mask colloidal lithography (HCL) technique. Afterwards, we present a method for removing such Si particles from a supporting substrate and used it to realize colloidal HID solutions. We show that this methodology can be used to detach and dissolve nanoparticles of diverse shapes ranging from disks to chiral particles. In the final part of the document, we will discuss some applications of the different fabricated systems. It is important to note that this is the very first technique able to fabricate shaped high index dielectric nanoparticles in solutions and these can be used for optical trapping fundamental studies or to realize new type of systems.

Finally, it is demonstrated that patterned multilayer transition metal dichalcogenides are nanoparticles which support geometrical Mie resonance like standard high index materials. In addition, thanks to their excitonic response and optical anisotropy, this materials support novel light matter interactions not encountered with standard materials.

2. Metasurface fabrication

Figure 1a shows the basic principle for the fabrication of HID metasurfaces [1-2]. A sacrificial layer, for example a resist or a SiO2 film, is formed by spin coating or deposition, on top of a deposited Si film. Polystyrene beads are then dispersed on the substrate. After a thin metal film evaporation and tape stripping, a hole mask is formed. The sacrificial layer is then etched through the holes in the mask, followed by evaporation of hard mask (Ni or Cr) nanoparticles of a chosen shape. These hard mask particles can be transferred to the poly-Si film underneath by anisotropic etching.

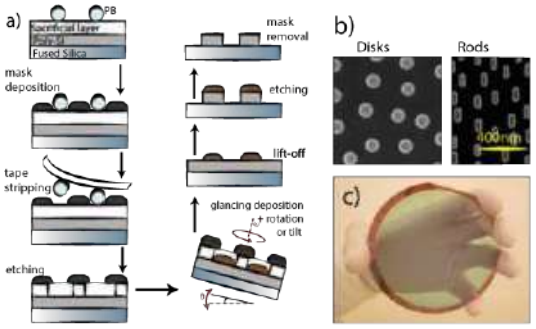


Figure 1:a) Schematic of HID metasurfaces fabrication. b) SEM images images of different HID metasurfaces and (c) picture of a 4-inch substrate covered with Si nanodisks.

The method described can be used to produce homogeneous metasurfaces over 4-inch wafers, as shown in Figure 1b. Most importantly, it is also highly versatile and capable of fabrication of nanoparticles of different shapes simply by changing the conditions for deposition of the Ni mask.

3. Colloidal solutions

The fabricated nanoparticles can be removed from the substrate to realize colloidal [2-3]. The as-fabricated metasurface is first dipped into a HF solution (5%) to selectively etch the substrate. Subsequently, diluted HF (0.1%) is drop-casted on the metasurface until the particles disperse into the solution. The HF solution is then left to evaporate. Finally, the particles are dispersed by sonication in an aqueous solution of cetrimonium bromide (CTAB, typically 1-5mM). The colloidal solution is stable for several months. Note that this method can in principle be adapted to substrates prepared by any large-scale fabrication method. The optical extinction measurements of the metasurface (b) and colloidal solution (d) composed of nanodisks, reveal the presence of tunable multiple resonances, typical of HID nanostructures.

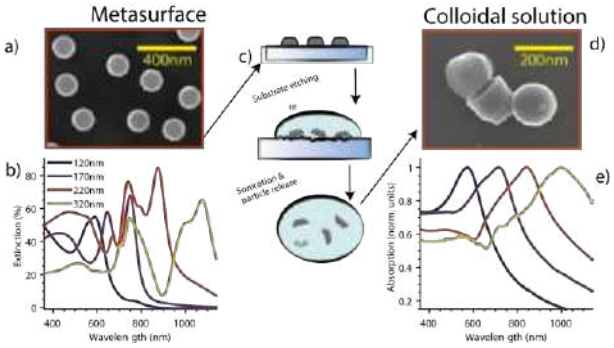


Figure2. From HID metasurface to colloidal solution. Using HF, the substrate supporting the Si nanoparticles can be etched. After HF dilution and evaporation, the particles can be released in solution by sonication, resulting in a colloidal suspension of HID nanoparticles. SEM image of a fabricated metasurface composed of Si nanodisks (a) and after redispersion onto a Si chip (d). The optical extinction spectra for nanodisks of different diameters on a substrate and in solution are shown in Figure b and e respectively.

4. TMDC nanoantennas

Finally, we have recently discovered and demonstrated that nanoparticles made of multilayers WS_2, a Van der Vaal's crystal typically used as a 2D material, also supports Mie resonances like standard high dielectric materials [4]. However, thanks to the rich exciton physics, the possibility of simple flake transfer on any host transfer and their anisotropic dielectric function, this material can be used as a platform capable of realizing new light-matter interaction regimes and whose potential still needs to be completely unveiled.

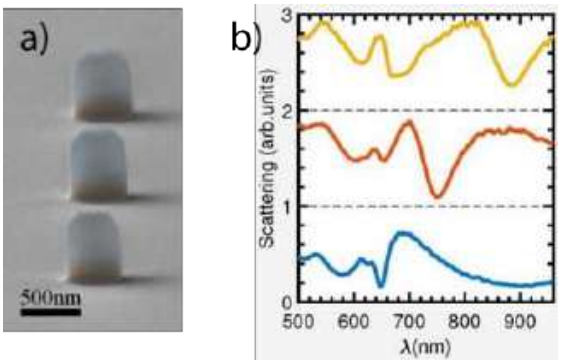


Figure 3. (a) Scanning electron microscope and single particle dark-field scattering made of nanodisks made of WS_2. We discovered that transition metal dichalcogenide nanodisks act as high-index dielectric Mie nanoresonators which a rich physics and multiple resonances.

References

[1] N. Odebo Länk, R. Verre, P.Johansson, M.Käll, Large-scale silicon nanophotonic metasurfaces with polarization independent near-perfect absorption, Nano Letter, 17 (2017)

[2] R. Verre, N. Odebo Länk, D. Andrén, H. Šípová, M. Käll, Large‐Scale Fabrication of Shaped High Index Dielectric Nanoparticles on a Substrate and in Solution, Advanced Optical Material, (2018)

[3] R. Verre, L. Shao, N. Odebo Länk, P. Karpinski, A.B Yankovich, T. J Antosiewicz, E. Olsson, M. Käll, Metasurfaces and colloidal suspensions composed of 3D chiral Si nanoresonators, Advanced materials, 29 (2017)

[4] Ruggero Verre, Denis G Baranov, Battulga Munkhbat, Jorge Cuadra, Mikael Käll, Timur Shegai, Transition metal dichalcogenide nanodisks as high-index dielectric Mie nanoresonator, arXiv: 1812.04076.

Magnetic field modulation of plasmon properties

Gaspar Armelles[1], Alfonso Cebollada[1], Fernando Garcia[1], Raquel Alvaro[1],

Maria Ujué Gonzalez [1], Luca Bergamini[2,3], Nerea Zabala[2] and Javier Aizpurua[2],

[1]Instituto de Micro y Nanotecnologia (IMN-CNM, CSIC), Madrid, Spain
[2]Materials Physics Center, CSIC-UPV/EHU and DIPC, San Sebastian, Spain
[3]Department of Electricity and Electronics, FCT-ZTF, UPV-EHU, Bilbao,Spain
*corresponding author, E-mail: gaspar@imm.cnm.csic.es

Abstract

Plasmonics has proven to be a powerful tool to improve the performance of optical devices. The possibility of modulating the emission, propagation and/or detection of radiation constitutes a promising aspect to expand the limits of the currently used technologies. In this sense, fast and contactless actuation on plasmon resonances via the Magneto-Optical (MO) effect has been put forward by the inclusion of ferromagnetic components into noble metal layers and nanostructures, yet up to now restricted to the visible and near-infrared ranges.

Recently it has been shown that this magnetic field modulation can be extended to the mid -IR and THz region by the use of the Magneto-Refractive (MR) effect, i., a change in the optical properties of the system by magnetic field controlled electrical resistivity1,2,3 . In this talk we will review the effect that a magnetic field has on the plasmon properties and in particular this new alternative for magnetic modulation in the mid and far IR range using different plasmonic metasurfaces.

References

1. G. Armelles et al. Optics Express 25,18784 (2017).
2. G. Armelles et al. ACS Photonics 5, 3956 (2018).
3. G. Armelles et al. Optical Materials Express 9, 923 (2019)..

Geometric Frustration in Arrays of Au Nanoelements

Ana Conde-Rubio[1,2], Arantxa Fraile Rodríguez[1,2], Francesc Pérez-Murano[3], André Espinha[4], Agustín Mihi[4], Xavier Batlle[1,2], Amílcar Labarta[1,2,*]

[1]Dpt. Física de la Matèria Condensada, Universitat de Barcelona, 08028 Barcelona, Spain
[2]Institut de Nanociència i Nanotecnologia, Universitat de Barcelona, 08028 Barcelona, Spain
[3]Institut de Microelectrònica de Barcelona (IMB-CNM, CSIC), Bellaterra, 08193, Spain
[4]Institut de Ciència de Materials de Barcelona (ICMAB, CSIC), Bellaterra, 08193, Spain
*corresponding author, E-mail: amilcar.labarta@ub.edu

Abstract

Inspired by frustrated magnetic systems, the effect of geometric frustration in the optical response of plasmonic arrays of Au nanoelements is studied. In particular, we show how the symmetry of the lattice can hamper the excitation of near-field dipolar modes among the nanoelements, favoring in turn the excitation of lattice collective modes. Both simulations and experimental results demonstrate that these systems behave as perfect absorbers in the visible and/or the near infrared and they exhibit a relatively extended time response.

1. Introduction

Geometric frustration has largely been studied in magnetism where the term refers to situations in which spins in one or more of the magnetic sub-lattices do not find a proper orientation to fully satisfy the interactions with the neighboring spins due to the actual geometry of the structure itself. This yields slow dynamics caused by an intricate energy landscape with lots of quasi-degenerate states. We introduced this concept in the field of plasmonics referring to situations in which the symmetry of the array does not favor a complete ferroelectric polarization of the gaps between neighboring elements [1]. Our goal is to favor the excitation of collective modes at the expense of the near-field interactions with prevailing dipolar character. We show that the key ingredients in settling the degree of geometric frustration of these lattices depend on the complexity of the system, that is, the number of sub-lattices of gaps with different spatial orientations (see Fig. 1(b)), together with the strength of the interactions among them. The former is related to the symmetry of both the lattice and the elements of the array. Furthermore, since the strength of the interactions among neighboring gaps depends on their areal density and inter-distances, the effect on the optical response of the array can also be modulated by changing both the size of the nanoelements and the pitch of the array.

Studies on the geometric dependence of the plasmonic response of arrays have already been reported [2,3], most of them exploiting the coupling through the gaps between close-lying structures. However, few works studied the dependence of the system's response on the lattice symmetry, and in particular, the interplay between low energy and high energy modes within those lattices [3]. Here, we go one step further and exploit multiple coupling in various hexagonal arrays of Au nanoelements to yield extended time response with echoed excitation of lattice modes at significantly longer times than in systems without frustration.

2. Results and discussion

We present experimental and numerical results for the optical response of three cases of hexagonal lattices of plasmonic nanoelements.

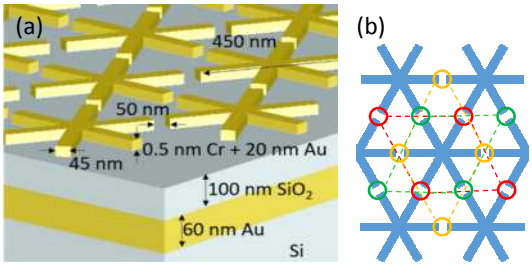


Figure 1: a) Scheme of the hexagonal array of Au asterisks. b) Unit cells for the three competing hexagonal sub-lattices of gaps among neighboring nanoelements.

2.1. Design

We studied a hexagonal array of Au disks, a honeycomb array of Au bars, and a hexagonal array of Au asterisks (see Fig. 1 for a scheme of the latter). Our structures are arranged in such a way that the elements strongly interact via near-field coupling thanks to the small gap between them. Also, we studied structures with metal-insulator-metal (MIM) configuration where the spacer was set to a quarter-wavelength thickness to achieve maximum absorption around the plasmon resonance for normal incidence (Fig. 1(a)).

2.2. FDTD simulations

Finite-Difference Time Domain (FDTD) simulations using the Lumerical FDTD Solutions package were carried out to calculate the absorption spectrum, the near-field intensity, the charge distribution, and the time evolution of the optical response.

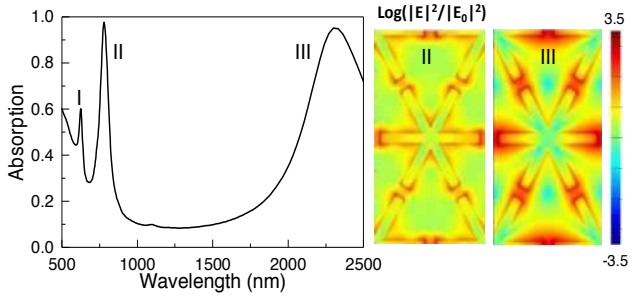


Figure 2: Absorption spectrum for a hexagonal array of asterisks. The two panels at the right-hand side show the electric field distribution corresponding to the peaks labeled as II and III in the figure.

The absorption spectra for the three lattices have common features [1,4]: All of them show a broadband in the near-infrared region (NIR) attributed to the dipolar excitation of the gaps, and higher order modes lying around the visible, which are associated with collective modes and correspond to sharp and high absorption peaks that in some cases can reach almost perfect absorbance. While the electric field associated with the NIR modes is mainly concentrated within the gaps, the high-energy modes exhibit electric field distributions around the whole nanoelements. These modes are also enhanced because of the cavity formed by the MIM stack. Figure 2 shows an example of this general behavior for a hexagonal array of asterisks.

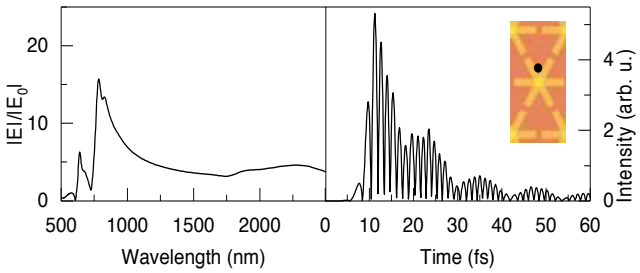


Figure 3: Spectral distribution and time evolution of the intensity of the electrical field at the point indicated in the inset for a hexagonal array of asterisks.

Figure 3 shows the time evolution of the magnitude of the electric field at a certain point of the lattice for the asterisk array [1]. Remarkably, the system remains active for over 70 fs after a pulse excitation of 8 fs and the main contributions to the spectral distribution are in the visible region corresponding to lattice excitations that are still shining after relatively long times.

We also evidence that this general behavior is shared too by other arrangements without triangular symmetry such as a square array of bars.

2.3. Experimental results

A set of samples with triangular symmetry were manufactured by electron beam lithography. Scanning Electron Microscopy (SEM) images are shown in Fig. 4(a-c) together with their corresponding extinction spectra (Fig. 4(d-f)) which are in qualitative agreement with the simulated ones.

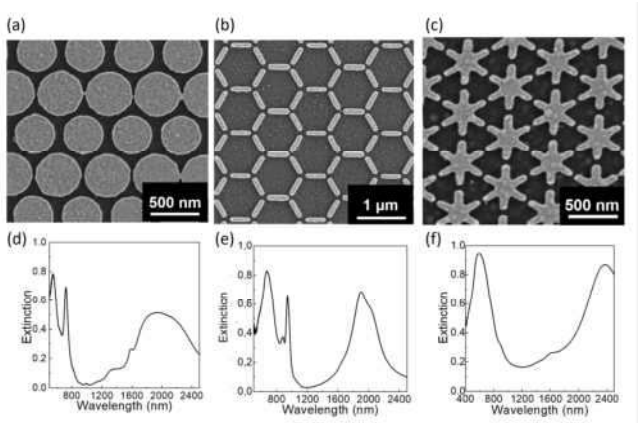


Figure 4: SEM images of three samples and the corresponding extinction spectra.

3. Conclusions

We show arrays of Au nanoelements with various lattice symmetries, all of them exhibiting high absorption sharp peaks in the visible and/or the NIR, as well as an extended time response of the collective modes due to the frustrated dipolar polarization of the gaps between the nanoelements [4]. This behavior, together with the fact that the electric field enhancement in these plasmonic arrays extends over very large areas, makes them suitable as enhancers for spectroscopies such as Raman and fluorescence that benefit from increased light absorption.

Acknowledgements

This work was supported by Spanish MINECO (MAT2015-68772- P project and A.C.R Ph.D. contract BES-2013-065377), the Spanish ICTS Network MICRONANOFABS, and EU FEDER funds.

References

[1] A. Conde-Rubio, A. Fraile Rodríguez, X. Borrisé, F. Perez-Murano, X. Batlle, A. Labarta, *Geometric frustration in a hexagonal lattice of plasmonic nanoelements*, Optics Express 26, 20211 (2018).

[2] A. D. Humphrey, W. L. Barnes, *Plasmonic surface lattice resonances on arrays of different lattice symmetry*, Phys. Rev. B 90, 075404 (2014).

[3] Y. Chen, J. Dai, M. Yan, M. Qiu, M. *Metal-insulator-metal plasmonic absorbers: influence of lattice*. Opt. Express 22, 30807–30814 (2014).

[4] A. Conde-Rubio, A. Fraile Rodríguez, A. Espinha, A. Mihi, F. Perez-Murano, X. Batlle, A. Labarta, *Geometric frustration in ordered lattices of plasmonic nanoelements*, Scientific Reports, accepted (2019).

Light modulating and detecting in on-chip plasmonic-graphene hybrid platforms

Sanshui Xiao[1,3,*], Hao Hu[1,2], Michael Galili[1,2], N. Asger Mortensen[3,4], Leif Katsuo Oxenløwe[1,2], and Yunhong Ding[1,2*]

[1]Department of Photonics Engineering, Technical University of Denmark, DK-2800, Kongens Lyngby, Denmark
[2]Center for Silicon Photonics for Optical Communications (SPOC), Technical University of Denmark, DK-2800, Kongens Lyngby, Denmark
[3]Center for Nanostructured Graphene (CNG), Technical University of Denmark, DK-2800, Kongens Lyngby, Denmark
[4] Center for Nano Optics and Danish Institute for Advanced Study, University of Southern Denmark, Campusvej 55, DK-5230, Odense M, Denmark.
*corresponding author, E-mail: saxi@fotonik.dtu.dk, yudin@fotonik.dtu.dk

Abstract

Graphene has offered a new paradigm for extremely fast and active optoelectronic devices. Here we present novel integrated graphene plasmonic devices for on-chip light modulating and detecting. The graphene plasmonic modulator shows high modulation depth and low insertion loss, and the graphene plasmonic waveguide photodetector has the bandwidth beyond 110 GHz and intrinsic responsivity of 360 mA/W.

1. Introduction

Graphene, a unique two-dimensional material, provides great potential in the realization of high-performance optoelectronic devices. In particular, significant efforts have been devoted to graphene modulators and photodetectors [1-6]. The distinct properties of graphene in terms of ultrahigh carrier mobility, zero bandgap property that enables wavelength-independent light absorption over a very wide spectral range, and tunable optoelectronic properties give rise to realize graphene devices with large spectral bandwidth and high speed. However, their performance is still limited by weak light-graphene interaction and large resistance-capacitance product. Here we present our recent results on graphene plasmonic hybrid platforms for on-chip light modulating and detecting, giving a promising way to realize on-chip interconnects with graphene plasmonic devices.

2. Results

Figure 1(a) shows the SEM image of our proposed graphene plasmonic waveguide modulator [7], where the plasmonic slot waveguide is coupled in/out by silicon waveguides with inverse tapering tips. The plasmonic waveguide can confine modes beyond diffraction limit, while at the same time suffering with large propagation loss. Here we propose plasmonic slot waveguides relying on the concept of leaky mode, giving us extremely low loss of 0.25dB/μm. The good alignment of the coupling part (between the silicon and plasmonic waveguide) leads to high in/out coupling efficiency of 1.45 dB.

Transmissions of the light at 1.55 μm through 20 μm-long leaky-mode graphene-plasmonic waveguides at different bias voltages are presented in Fig. 1(b) for two slot widths of 120 nm and 145 nm. One can find that the transmission through the graphene-plasmonic hybrid waveguides is

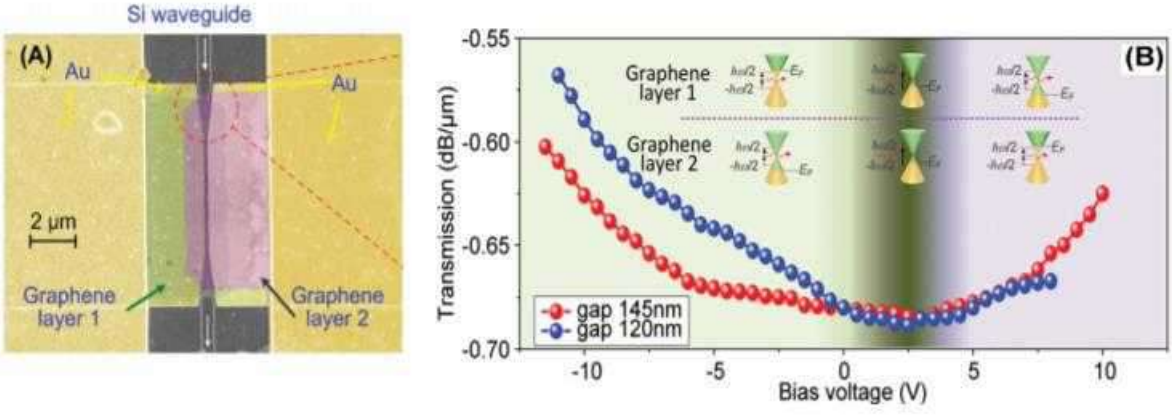


Figure 1: (A) False-color SEM image of the fabricated graphene-plasmonic slot hybrid waveguide. (B) Measured transmission as a function of bias voltage for 20 um-long plamonic slot waveguides with gaps of 145 nm and 120 nm.

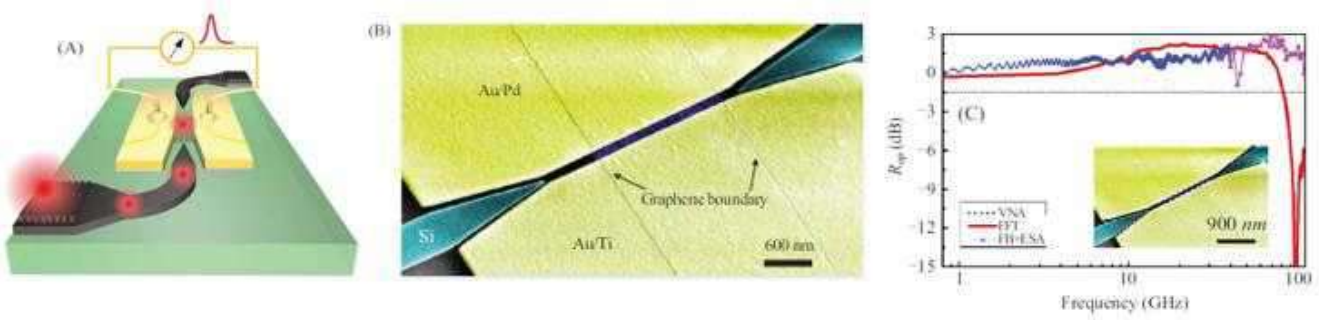


Figure 2. (a) Schematic of the proposed graphene-plasmonic hybrid photodetector (b) An example of fabricated graphene plasmonic photodetector with the graphene coverage length of 2.7 um (c) Its corresponding optical bandwidth measured by VNA, impulse response, and frequency beating with ESA at the bias voltage of 1.6V.

effectively tuned by applying bias voltages on the graphene. An efficient attenuation tunability of 0.13 dB/μm is achieved for the plasmonic slot width of 120 nm at low gating voltages. The modulation depth of 0.13 dB/μm achieved here exceeds that for reported graphene-plasmonic hybrid device [8].

Figure 2 shows our proposed ultra-compact, on-chip, and high-speed graphene photodetector based on a plasmonic slot waveguide [9]. The subwavelength confinement of the plasmonic mode gives rise to the enhanced light-graphene interactions, and the narrow plasmonic slot of 120 nm enables short drift paths for photogenerated carriers. The schematic of the proposed graphene plasmonic hybrid photodetector is shown in Fig. 2(A), where the light from a fiber is first coupled to a silicon waveguide through a grating coupler and further to the plasmonic slot waveguide by a short taper structure. Fig. 2(B) shows a fabricated graphene-plasmonic photodetector, where the dashed lines represent the graphene coverage boundary, and the corresponding optical bandwidth measured by VNA, impulse response, and frequency beating with ESA is presented at the bias voltage of 1.6 V, showing that the bandwidth is over 110GHz. Moreover, the use of chemical-vapour deposition (CVD)-growth graphene here allows for the scalable fabrication and we believe that our work greatly pushes the 2D material towards practical applications, e.g. in optical interconnects, high-speed optical communications, and so on.

3. Conclusions

We present novel integrated graphene plasmonic devices for on-chip light modulating and detecting, which shows a promising way to realize ultra-compact and high-speed optoelectronic devices for potential applications in on-chip interconnects.

4. Acknowledgements

The work is supported by the Center for Silicon Photonics for Optical Communication (SPOC, DNRF123), the Center for Nanostructured Graphene (CNG, DNRF103) both sponsored by the Danish National Research Foundation.

References

[1] F. Bonaccorso, Z. Sun, T. Hasan and A. C. Ferrari, “Graphene photonics and optoelectronics”, *Nature Photon.*, 4, 611 (2010).

[2] M. Liu, X.B. Yin, E. Ulin-Avila, B.S. Geng, T. Zentgraf, L. Ju, F. Wang, and X. Zhang, “A graphene-based broadband optical modulator”, *Nature* 474, 64 (2011).

[3] Y. Ding, X. Zhu, S. Xiao, H. Hu, L.H. Frandsen, N.A. Mortensen, and K. Yvind, “Effective electro-optical modulation with high extinction ratio by a grapheme-silicon microring resonator”, *Nano. Lett.,* 15, 4393 (2015).

[4] F. Xia, T. Mueller, Y. Lin, A. Valdes-Garcia, and P. Avouris."Ultrafast graphene photodetector," *Nature Nanotechnol* 4, 839–843 (2009).

[5] M. Ayata et al., "High-speed plasmonic modulator in a single metal layer," *Science* 358, 630–632 (2017).

[6] Y. Salamin et al. "100 GHz Plasmonic Photodetector," *ACS Photon*. 5, 3291-3297 (2018).

[7] Y. Ding, X. Guan, X. Zhu, H. Hu, S. I. Bozhevolnyi, L.K. Oxenloewe, N.A. Mortensen, S. Xiao, “Integrated graphene plasmonic electro-optical modulator based on leaky-mode slot waveguides”, *Nanoscale*, 9, 15576 (2017).

[8] D. Ansell, I. Radko, Z. Han, F. Rodriguez, S.I. Bozhevolnyi, and A.N. Grigorenko, “Hybrid graphene plasmonic waveguide modulators”. *Nature Commun*., 6, 8846 (2015).

[9] Y. Ding, Z. Chen, X. Zhu, K. Yvind, J. Dong, M. Galili, H. Hu, N. A. Mortensen, S. Xiao, and L. K. Oxenløwe, “Ultra-compact integrated graphene plasmonic photodetector with bandwidth over 110 GHz”, submitted (2018). arXiv:1808.04815

Nanoporous metamaterials as novel electrodes for enhanced in-vitro electrophysiology and toxicology

Michele Dipalo[1], Giovanni Melle[1,2], Laura Lovato[1], Andrea Jacassi[1], Francesca Santoro[4], Valeria Caprettini[1], Andrea Schirato[3], Alessandro Alabastri[3], Denis Garoli[1], Giulia Bruno[1,2], Francesco Tantussi[1] and Francesco De Angelis[1]*

[1]Istituto Italiano di Tecnologia, Genova, Italy
[2]Dipartimento di Informatica, Bioingegneria, Robotica e Ingegneria dei Sistemi. DIBRIS, Università degli Studi di Genova, 16145 Genova, Italy
[3]Department of Electrical and Computer Engineering, Rice University, Houston, TX, USA
[4]Center for Advanced Biomaterials for Healthcare, Istituto Italiano di Tecnologia, Naples 80125, Italy
*corresponding author, E-mail: francesco.deangelis@iit.it

Abstract

In the past decade, the scientific community could obtain the in-vitro recording of intracellular action potentials from large networks of electrogenic cells by exploiting 3D vertical nanostructures, such as nanopillars. Despite the high quality of the recordings, these techniques were not implemented in commercial products due to difficulties in the mass production of 3D nanostructures. Here, we show that intracellular action potentials can be acquired also with laser excitation of planar nanoporous metamaterials used as meta-electrodes of multi-electrode arrays. The fabrication of the meta-electrodes is extremely cost-effective and is compatible with large production, allowing for the fast and easy integration on commercial devices.

1. Introduction

The *in-vitro* characterization of electrogenic cells is a fundamental step to understand the functioning mechanisms of neuronal and cardiac cell cultures[1]. These data are acquired with multi-electrode arrays (MEA) that record extracellular action potentials from hundreds to thousands of cells simultaneously. However, the extracellular action potentials do not provide comprehensive details on the cell activity. In fact, to improve the quality of the obtainable information, the scientific community has developed new methodologies to achieve recordings of intracellular action potentials, which are significantly richer of information on the electrogenic activity of the cell and on its ion channels' status. For instance, the recording of intracellular action potentials allows for detecting changes in the functioning of ion channels due to the effects of drugs.

Almost all *in-vitro* intracellular recording techniques exploit 3D vertical nanopillars fabricated on the MEA electrodes to enhance the coupling with cells and to achieve intracellular access[2,3]. However, 3D nanostructures are not easily implemented on commercial devices because of difficulties in combining them with large and cost-effective production processes.

Here, we show that plasmonic nanoporous metamaterials can replace 3D nanopillars as efficient tools to porate the cellular membrane and to record intracellular action potentials, while preserving compatibility with large production processes. The membrane poration process exploits the fast-pulsed laser excitation of the metamaterial to produce plasmonic hot spots, which locally disrupts the cellular membrane and allows for accessing the intracellular compartment[4].

2. Discussion

Nanoporous metamaterials present several interesting properties for biological applications. On the one hand, they can efficiently absorb light radiation in the visible/near-infrared region and can concentrate it in plasmonic hot spots located in the nanogaps of the material. On the other hand, porous materials strongly promote cell adhesion due to the very high surface roughness. At the interface with such materials, the cellular membrane conforms to the rough surface and infiltrates the nanogaps in the nanoporous material. When exploited together, these features make it possible to porate the cellular membrane by exciting the porous metamaterial at the interface with cells. In fact, the cellular membrane is in tight adhesion in the nanogaps where the impinging radiation is concentrated and thus where the plasmonic enhancement is highest.

In figure 1a and 1b, we report SEM images of MEA electrodes coated with nanoporous platinum and nanoporous gold respectively. The electrodes do not present protruding vertical structures and show a planar configuration at the microscale. However, at the nanoscale, the materials present bumps and gaps with sizes down to 10-20 nm.

The use of a fast-pulsed laser in the near-infrared (NIR) region allows achieving cell poration without heating the biological sample[4]. In our experiments, we use a 1064 nm pulsed laser source with pulse duration of 8 picoseconds.

In figure 1c, we show superimposed intracellular action potentials of a HL-1 cardiac cell after the administration of 500 nM dofetilide, a known compound that slows down the repolarization phase and thus prolongs the action potential duration. The signals were recorded with a commercial MEA device and using plasmonic optoacoustic poration to enable intracellular recording. The traces show a high signal-to-noise ratio that allows for the precise characterization of the action potential shape.

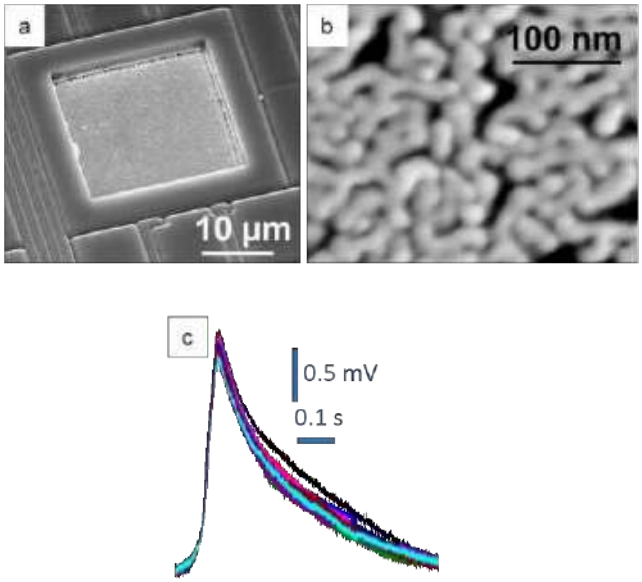


Figure 1: a) SEM image of a meta-electrode on a MEA commercial device based on CMOS technology. b) Close-up view of planar gold meta-electrodes with nanoporous surface. c) Superimposed intracellular action potentials of HL-1 cardiac cells after the administration of 500 nM dofetilide.

3. Conclusions

Here, we have shown that nanoporous metamaterials can be very effective tools in the field of *in vitro* electrophysiology. By means of fast-pulsed laser NIR radiation, the plasmonic properties of the metamaterials allow for disrupting the cellular membrane of cells cultured in tight adhesion on them. When the metamaterials are fabricated onto the electrodes of multi-electrode arrays, they provide a cost-effective and non-invasive tool for recording high-quality intracellular action potentials from large cultures of electrogenic cells.

Acknowledgements

The research that led to these results received funding from the European Research Council under the European Union's Seventh Framework Programme (FP/2007-2013)/ERC Grant Agreement no. [616213], CoG: Neuro-Plasmonics.

References

[1] Blinova K, Dang Q, Millard D, Smith G, Pierson J, Guo L, Brock M, Lu HR, Kraushaar U, Zeng H, Shi H, Zhang X, Sawada K, Osada T, Kanda Y, Sekino Y, Pang L, Feaster TK, Kettenhofen R, Stockbridge N, Strauss DG GG. *International Multisite Study of Human-Induced Pluripotent Stem Cell-Derived Cardiomyocytes for Drug Proarrhythmic Potential Assessment.* Cell Rep. 2018.

[2] Xie C, Lin Z, Hanson L, Cui Y, Cui B. *Intracellular recording of action potentials by nanopillar electroporation.* Nat Nanotechnol. Nature Publishing Group; 2012;7: 185–90.

[3] Robinson JT, Jorgolli M, Shalek AK, Yoon M-H, Gertner RS, Park H. *Vertical nanowire electrode arrays as a scalable platform for intracellular interfacing to neuronal circuits*. Nat Nanotechnol. 2012;7: 180–4.

[4] Dipalo M, Melle G, Lovato L, Jacassi A, Santoro F, Caprettini V, et al. *Plasmonic meta-electrodes allow intracellular recordings at network level on high-density CMOS-multi-electrode arrays*. Nat Nanotechnol. 2018, 13 (10), 965-971

Advances in Nanomechanical Metamaterials

Eric Plum[1,*], Dimitrios Papas[1], Jun-Yu Ou[1], Artemios Karvounis[1], Kevin F. MacDonald[1], and Nikolay I. Zheludev[1,2]

[1]Centre for Photonic Metamaterials & Optoelectronics Research Centre, University of Southampton, Southampton, SO17 1BJ, UK
[2]Centre for Disruptive Photonic Technologies, The Photonics Institute, Nanyang Technological University, Singapore 637371, Singapore
*corresponding author, E-mail: erp@orc.soton.ac.uk

Abstract

We report recent breakthroughs in nanomechanical metamaterials including (i) a giant acousto-optical effect, (ii) on/off switching of metasurfaces, (iii) selective electrical and optical actuation of metamaterials elements with sub-wavelength spatial resolution, (iv) phase-change metasurfaces with bistable optical and mechanical properties and (v) metamaterials tuned by electrostriction.

1. Introduction

The optical properties of metamaterials, and indeed any other material, depend strongly on the spatial arrangement of their components. This has enabled giant thermo-optical, electro-optical, magneto-electro-optical and nonlinear optical phenomena in photonic metamaterials fabricated on dielectric membranes of nanoscale thickness, where the nanostructure is rearranged by thermal, electrical, magnetic and optical forces [1]. Here we provide an overview focusing on recent advances.

2. Results

High-contrast modulation of light is of great practical importance. We observe giant acousto-optical modulation in a nanomechanical metamaterial that is actuated by ultrasound frequency vibrations. Such modulation exhibits strong nonlinearities and reaches relative reflectivity changes of up to 75% in a structure of only 100 nm thickness.

Exploiting electrostatic forces in nanomechanical metamaterial structures, we demonstrate novel approaches to electro-optical modulation based on (i) MEMS modulation of the interaction of light with a metasurface, essentially switching the metasurface on and off [2], and (ii) electrostriction in a nanomechanical metamaterial [3].

Dynamic control over optical properties at any point in space and time is arguably the ultimate metamaterials vision. We demonstrate both electrical and optical methods that enable selective actuation of nanomechanical metamaterial elements with sub-wavelength spatial resolution [4, 5].

Phase transitions enable bistable nanomechanical actuation associated with bistable optical properties. Exploiting phase change materials such as shape memory alloys [6] and chalcogenide glasses, we demonstrate nanomechanical metamaterials with optical memory functionalities.

3. Conclusions

In summary, we report recent advances in nanomechanical metamaterials, including light modulation based on acousto-optical, coherent electro-optical and electrostriction effects, optical and mechanical bistability based on phase transitions, and electric as well as optical nanomechanical actuation with sub-wavelength resolution.

Acknowledgements

This work is supported by the UK's Engineering and Physical Sciences Research Council (grant EP/M009122/1), the MOE Singapore (grant MOE2016-T3-1-006) and the U.S. Office of Naval Research (grant N62909-18-1-2026).

References

[1] N. I. Zheludev, E. Plum, Reconfigurable nanomechanical photonic metamaterials, *Nature Nanotech.* 11: 16, 2016.

[2] P. Cencillo-Abad, J. Y. Ou, E. Plum, N. I. Zheludev, Electro-mechanical light modulator based on controlling the interaction of light with a metasurface, *Sci. Rep.* 7: 5405, 2017.

[3] A. Karvounis, B. Gholipour, K. F. MacDonald, N. I. Zheludev, Giant electro-optical effect through electrostriction in a nano-mechanical metamaterial, *Adv. Mater.* 31: 1804801, 2019.

[4] P. Cencillo-Abad, J. Y. Ou, E. Plum, J. Valente, and N. I. Zheludev, Random access actuation of nanowire grid metamaterial, *Nanotechnology* 27: 485206, 2016.

[5] J. Y. Ou, E. Plum, N. I. Zheludev, Optical addressing of nanomechanical metamaterials with subwavelength resolution, *Appl. Phys. Lett.* 113 : 081104, 2018.

[6] Y. Nagasaki, B. Gholipour, J. Y. Ou, M. Tsuruta, E. Plum, K. F. MacDonald, J. Takahara, N. I. Zheludev, Optical bistability in shape-memory nanowire metamaterial array, *Appl. Phys. Lett.* 113 : 021105, 2018.

Epsilon-Near-Zero Resonant Tunneling Modes in Metal/Insulator/Metal nanocavities

Vincenzo Caligiuri[1], Milan Palei[1,2], Giulia Biffi[1,2], Sergey Artyukhin[1], Liberato Manna[1] and Roman Krahne[1]

[1]Istituto Italiano di Tecnologia, Via Morego 30, 16163 Genova, Italy
[2] Dipartimento di Chimica e Chimica Industriale, Università degli Studi di Genova, Via Dodecaneso, 31, 16146 Genova, Italy
*corresponding author, E-mail: Vincenzo.caligiuri@iit.it

Abstract

We demonstrate, theoretically and experimentally, the achievement of broadly customizable Epsilon-Near-Zero response in the whole visible range by using Metal/Insulator/Metal nano-cavities. The optical response of the proposed structures is modelled in both a classic and a quantum framework, elucidating the resonant tunneling nature of the Epsilon-Near-Zero (ENZ) response occurring at the cavity modes, clarifying the reason why they can be excited without any momentum matching. We also investigate the hybridization of the ENZ modes in multiple cavity systems, achieving broadly tailorable ENZ bands. As remarkable applications, we demonstrate how the proposed systems can be used as tunable superabsorbers, refractive index sensor and to enhance the photophysical performances of weakly coupled fluorophores.

1. Introduction

Metal/Insulator/Metal (MIM) waveguides constitute a versatile platform for light confinement at the nanoscale. Their optical response has been widely investigated in the past, since these structures revealed outstanding properties as plasmonic waveguides, color filter and superabsorbers. Recently, it has been demonstrated that these MIM nanocavities support ENZ response at their resonances. In this work we explore this scenario, investigating the occurrence of their ENZ response by means of a quantum approach. This new point of view provides great insight in the physics governing the optical response of MIM structures, elucidating that the MIM's resonances correspond to *resonant tunneling* modes occurring due to the zero wavevector given by the vanishing effective perrmittivity of the MIM. Remarkable implications of this conclusions are reflected in the possibility we demonstrate to use these structures as superabsorbers and refractive index sensors. We extend the treatment to the noticeable cases of MIMIM systems, demonstrating the possibility of coupling their ENZ response to $CsPbBr_3$ perovskites to enhance their photophysical response. In the end, we explore the possibility of engineering artificial metals with completely tailorable ENZ bands, via multiple MIM cavities systems.

2. Single MIM

The optical response of a Metal/Insulator/Metal (MIM) nanocavity is ellipsoemtrically detected, and its homogenized refractive index is calculated via a direct fitting of the ellipsometrical angles Ψ and Δ, demonstrating the occurrence of a vanishing effective dielectric permittivity in correspondence of the absorbance maxima (1-Transmission-Reflectance), corresponding to the modes of the cavity. The MIM system is modeled in a classic framework as a simple harmonic oscillator. Such an approach allows a quick and accurate calculation of the effective permittivity of the MIM, demonstrating the low-loss ENZ nature of the modes of the cavity. The optical response of the MIM nanocavity is then modeled in a quantum framework as a finite quantum well. This analogy provides deep physical insight in the behavior of the MIM system, demonstrating that the modes of the cavity correspond to *resonant tunneling* frequencies occurring thanks to the zero wavevector inside the MIM, due to its effective ENZ permittivity.

3. MIMIM and multicavity systems

A second MIM cavity is then fabricated on the top of the first one, to form a MIMIM system. Sharing the common central metal, the two cavities can exchange energy very efficiently, so that the hybridization and splitting of their resonance occurs, as shown in Figure 2.

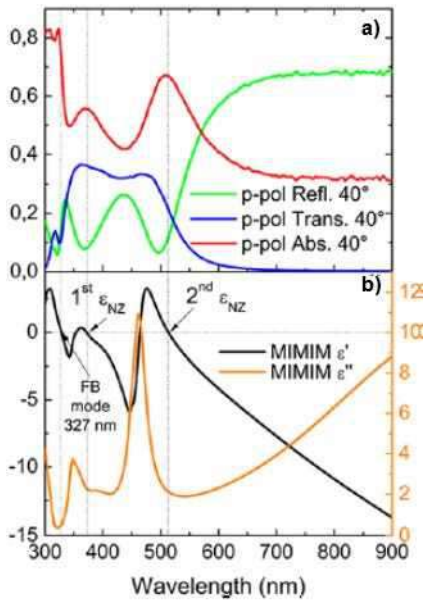


Figure 1: (a) Absorbamce, reflectance and transmittance of a MIMIM system, together with (b) its effective dielectric permittivity.

The MIMIM system is modeled as double quantum well, in analogy with many two level systems, so that an accurate analytical description of the dispersion of the MIMIM structure is provided. Ellipsometrical measures carried out over this system reveal the ENZ nature of the hybridized modes as well. The splitting of the two modes can be finely engineered by acting on the geometrical parameters of the resonators, in order to position the two resonances where desired within the complete visible range. The resonances of the MIMIM are tuned to match the absorbance and the emission of a $CsPbBr_3$ Perovskite placed in proximity of the MIMIM, demonstrating remarkable Purcell effect with consequent enhancement of its photophysical properties (photoluminescence, decay lifetime and quantum yield), as shown in Figure 3.

Multicavity systems made of several stacked MIMs are then analyzed to demonstrate how to engineer complete ENZ bands.

4. Conclusions

In conclusion, we investigated the optical response of metal/insulator multilayers in a quantum framework, revealing that the cavity modes correspond to resonant tunneling ENZ modes, occurring due to the vanishing wavevector inside the cavity. This approach allows to finely determine the dispersion of these structures, providing at the same time new insight on very well-studied systems. We demonstrate how such an approach can be extended towards the design of artificial metals with engineered ENZ bands. As remarkable applications, we demonstrate the possibility of using these structures as completely tailorable superabsorbers, refractive index sensors and as innovative platforms for the enhancement of the photophysical properties of fluorophores.

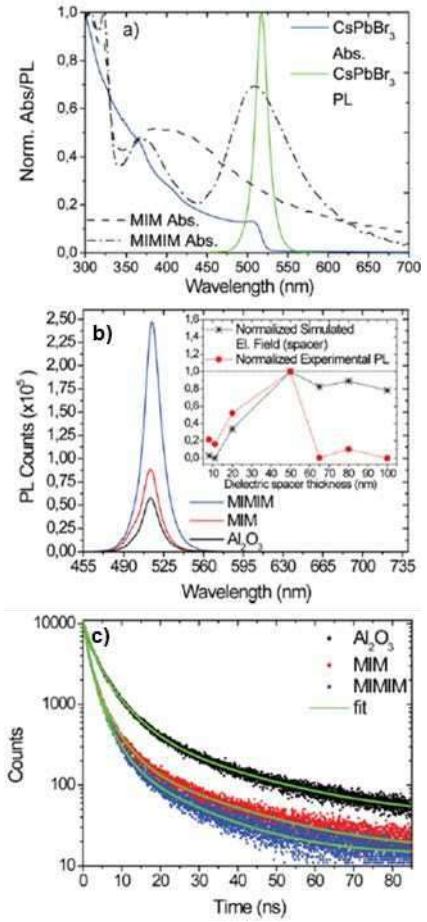


Figure 2: (a) Absorbance of the MIMIM system, tuned with the absorbance and emission of a $CsPbBr_3$ perovskite layer placed on the top of it. (b) Photoluminescence and (c) decay lifetime enhancement in the cases of pristine $CsPbBr_3$, MIM and MIMIM system.

Acknowledgements

The research leading to these results has received funding from the European Union under the Marie Skłodowska-Curie Grant Agreement COMPASS No. 691185.

References

[1] [1] J. A. Dionne, E. Verhagen, A. Polman, H. A. Atwater, Are negative index materials achievable with surface plasmon waveguides? A case study of three plasmonic geometries Opt. Express 2008, 16, 19001–19017.

[2] J. A. Dionne, L. A. Sweatlock, H. A. Atwater, A. Polman, Phys. Rev. B - Condens. Matter Mater. Phys. 2005, 72, 075405..

[3] Z. Li, S. Butun, K. Aydin, Large-Area, Lithography-Free Super Absorbers and Color Filters at Visible Frequencies Using Ultrathin Metallic Films ACS Photonics 2015, 2, 183–188.

[4] V. Caligiuri, M. Palei, M. Imran, L. Manna, R. Krahne, Planar Double-Epsilon-Near-Zero Cavities for Spontaneous Emission and Purcell Effect Enhancement ACS Photonics 2018,5, 2287–2294.

Ultrafast Laser-Induced Control of Interface-Induced Magnetic Anisotropy in Ferromagnetic Thin Films

Alexandra Kalashnikova[1]

[1]Ioffe Institute, 194021 St. Petersburg, Russia
E-mail: kalashnikova@mail.ioffe.ru

Abstract

Ultrafast laser-induced changes of magnetic anisotropy is the phenomenon allowing to excite and control dynamics of magnetization in a bulk, thin films, and nanostructures. We present our recent results on studies of ultrafast laser-induced thermal changes of magnetic anisotropy with emphasis put on contributions defining properties of thin and ultrathin films. We consider the laser-induced manipulation of perpendicular magnetic anisotropy in magnetic tunnel junctions, and of magneto-elastic domains in composite strain-mediated multiferroics.

1. Introduction

Excitation of magnetic media by femtosecond laser pulses yields a broad variety of ultrafast spin phenomena [1], from subpicosecond demagnetization [2] and full magnetization reversal [3] in metals to opto-magnetic effects in transparent dielectrics [4]. Recently, a particular interest arose to laser-induced *thermal* changes of magnetic anisotropy. Such mechanisms rely on a rapid laser-induced increase of temperatures of various subsystems of a medium and, therefore, can be realized in different materials, metallic [5, 6], semiconducting [7], and dielectric [8]. It has been shown, that such changes of magnetic anisotropy enable novel pathways for laser-induced switching of magnetization [9, 10, 11], launching spin pumping in spin-valve structure [12], driving multiple spin-wave modes in thin films [13], etc.

Here we present a review of our recent works on ultrafast laser-induced control of magnetic anisotropy in thin films of a ferromagnetic CoFeB alloy with emphasis put on contributions to the magnetic anisotropy related to the interfacial phenomena. In particular, we discuss how laser excitation can affect the strain-induced anisotropy and perpendicular anisotropy in thin and ultrathin CoFeB films.

2. Results and discussion

When a magnetic metallic film is excited by a femtosecond laser pulse, the energy is transferred to an electronic subsystem, and, upon electron-phonon relaxation, to a lattice. Increase of the temperatures of these two subsystems reach hundreds degrees, and a following cooling down can proceed on various timescales, from picoseconds for electrons to nanoseconds for a lattice. This, in particular, leads to an ultrafast demagnetization, i.e. decrease of the saturation magnetization M_s, and variations of magnetic anisotropy parameters $K_{1,u,...}$. When the external field is applied to a magnetic film, the total effective field setting the magnetization orientation is determined by the balance between the anisotropy $\sim K_{1,u...}$, and the Zeeman $\sim HM_s$ energies. Therefore, laser-induced changes of $K_{1,u,...}/M_s$ lead to abrupt reorientation of this field, thus triggering a magnetization precession. Angle by which the total effective field reorients determines the amplitude of the excited magnetization precession, while the strength of the changes and their relaxation times may affect the precession frequency. This simple macroscopic picture capturs the main features of the process of ultrafast changes of magnetic anisotropy and of the related excitation of magnetization precession. Therefore, in experiments, by studying the properties of the laser-driven precession, one can extract a valuable information about microscopic mechanisms underlying ultrafast laser-induced anisotropy changes.

2.1. Laser-induced changes of perpendicular magnetic anisotropy

In thin and ultrathin magnetic films, in particular in metallic films grown on oxide substrates, interfacial contribution to magnetic anisotropy may play a decisive role and, in particular, stabilize perpendicular magnetic anisotropy (PMA) [14]. In order to investigate a possible impact of ultrafast laser pulses on such structures, we studied the laser-induced excitation of magnetic tunnel junction structure formed by two layers of amorphous CoFeB separated by a 1.2-nm thick layer of MgO. The important feature of the studied structure is that one of the magnetic layers with a thickness of 1.2 nm is in a vicinity of the thickness-induced spin reorientation transition (SRT) due to the subtle balance between shape- and PMA-contributions to the magnetic anisotropy [15]. Upon excitation of such structure by a femtosecond laser pulses, the magnetization precession is observed. The precession excitation can be unambiguously ascribed to the laser-induced suppression of the PMA-contribution to the anisotropy. Owing to the proximity of SRT, the laser-induced changes of PMA are found to be very pronounced and affect not only the excitation of precession, but also the frequency of the latter. As a result, the laser-induced suppression of PMA enables tuning the precession frequency in a wide range, e.g. from 3 upto 6 GHz by changing the

pulse pulses fluence at a fixed applied field.

2.2. Laser-induced changes of magneto-elastic anisotropy

Amorphous CoFeB is a model material to investigate a laser-induced dynamics of another type of magnetic anisotropy – magnetoelastic one. We studied the structure consisting of a 50-nm thick layer of CoFeB deposited on a ferroelectric substrate $BaTiO_3$. Strain transfer from the ferroelectric domains in $BaTiO_3$ to the CoFeB layer imprints in the latter magnetic domains with anisotropy axes defined solely by magneto-elastic interactions [16]. Such system represents a composite multiferroic in which the magnetization can be controlled by applying electric voltage to a ferroelectric layer. We demonstrate excitation of the magnetization precession by femtosecond laser pulses in individual magnetic domains in the CoFeB layer of such the multiferroic structure. By analyzing the dependence of the excited precession on the orientation of external magnetic field relatively to the magneto-elastic anisotropy axis of a particular domain, we show that the precession is launched by the ultrafast laser-induced thermal changes of the magneto-elastic parameters. We suggest that such an approach paves a way for controlling magnetization in multiferroic micro- and nanostructures with high spatial and temporal resolutions provided by electric and optical stimuli, respectively.

3. Conclusions

We have demonstrated ultrafast laser-induced changes of magnetic anisotropy in thin-film structures based on CoFeB ferromagnetic alloys. We showed that in the ultrathin CoFeB/MgO layers with PMA, the latter can be efficiently suppressed due to laser-induced picosecond heating. Such an effect, in particular, allows realizing laser-driven tuning of the magnetization precession frequency. In teh mutiferroic structures CoFeB/$BaTiO_3$ we have realized laser-induced excitation of magnetization precession in individual micrometer-sized magnetic domains. We show that this is enabled by the ultrafast laser-induced thermal changes of magneto-elastic anisotropy.

Acknowledgement

The work has been partly supported by RSF grant No. 16-12-10485, and RFBR grants No. 18-02-00824 and 19-52-12065.

References

[1] A. Kirilyuk, A. V. Kimel, and Th. Rasing, Ultrafast optical manipulation of magnetic order *Rev. Mod. Phys.* 82: 2731, 2010.

[2] E. Beaurepaire, et al., Ultrafast Spin Dynamics in Ferromagnetic Nickel, *Phys. Rev. Lett.* 76: 4250–4253, 1996.

[3] T.A. Ostler, et al., Ultrafast heating as a sufficient stimulus for magnetization reversal in a ferrimagnet, *Nature Commun.* 3: 666, 2012.

[4] A. M. Kalashnikova, A. V. Kimel, R. V. Pisarev, Ultrafast optomagnetism, *Phys. Usp.* 58: 969–980, 2015.

[5] M. van Kampen, et al., All-Optical Probe of Coherent Spin Waves, *Phys. Rev. Lett.* 88: 227201, 2002.

[6] E. Carpene et al., Ultrafast three-dimensional magnetization precession and magnetic anisotropy of a photoexcited thin film of iron *Phys. Rev. B* 81: 060415(R), 2010.

[7] N. Tesařová et al., Direct measurement of the three-dimensional magnetization vector trajectory in GaMnAs by a magneto-optical pump-and-probe method, *Appl. Phys. Lett.* 100: 102403, 2012.

[8] L. A. Shelukhin, et al., Ultrafast laser-induced changes of the magnetic anisotropy in a low-symmetry iron garnet film, *Phys. Rev. B.* 97: 014422, 2018.

[9] J. A. de Jong et al., Coherent Control of the Route of an Ultrafast Magnetic Phase Transition via Low-Amplitude Spin Precession *Phys. Rev. Lett.* 108: 157601, 2012.

[10] D. Afanasiev et al., Laser Excitation of Lattice-Driven Anharmonic Magnetization Dynamics in Dielectric $FeBO_3$, *Phys. Rev. Lett.* 112: 147403, 2014

[11] C. S. Davies et al., Anomalously Damped Heat-Assisted Route for Precessional Magnetization Reversal in an Iron Garnet *Phys. Rev. Lett.* 122: 027202, 2019.

[12] A. P. Danilov, et al., Optically excited spin pumping mediating collective magnetization dynamics in a spin valve structure, *Phys. Rev. B.* 98: 060406(R), 2018.

[13] A. V. Scherbakov et al., Optical excitation of single- and multi-mode magnetization precession in Galfenol nanolayers, *arXiv:1812.01237*.

[14] B. Dieny and M. Chshiev, Perpendicular magnetic anisotropy at transition metal/oxide interfaces and applications *Rev. Mod. Phys.* 89: 025008, 2017.

[15] R. R. Gareev et al., The role of weak interlayer coupling in the spin-reorientation of perpendicular ultrathin Co-Fe-B/MgO-based heterostructures, *Appl. Phys. Lett.* 106: 132408, 2015.

[16] T. H. E. Lahtinen, et al., Pattern Transfer and Electric-Field-Induced Magnetic Domain Formation in Multiferroic Heterostructures, *Adv. Mater.* 23: 3187-3191, 2013.

Spiral metamaterials for terahertz magnetic field enhancement

Matteo Pancaldi[1], Debanjan Polley[1], Nanna Zhou Hagström[1], Matthias Hudl[1], Paolo Vavassori[2,3], Sergei Urazhdin[4], Clemens von Korff Schmising[5], Stefan Eisebitt[5,6], and Stefano Bonetti[1,7*]

[1]Department of Physics, Stockholm University, SE-106 91 Stockholm, Sweden
[2]CIC nanoGUNE, E-20018 Donostia-San Sebastian, Spain
[3]IKERBASQUE, Basque Foundation for Science, E-40013 Bilbao, Spain
[4]Emory University, Atlanta, GA 30322, United States of America
[5]MBI Max-Born Institute for Nonlinear Optics and Short Pulse Spectroscopy, D-12489 Berlin, Germany
[6]Institut für Optik und Atomare Physik, Technische Universität Berlin, D-10623 Berlin, Germany
[7]Università di Venezia "Ca Foscari", Italy
*corresponding author, E-mail: stefano.bonetti@fysik.su.se

Abstract

We designed a class of spiral thin-film antennas for enhancing, in the near field, the incident terahertz (THz) magnetic field. Indeed, using existing laser-based THz sources, our metamaterial geometry allows generating magnetic fields of the order of 2 T over a time scale of few picoseconds, enabling the investigation of nonlinear ultrafast spin dynamics in table-top experiments.

1. Introduction

In the last three decades, the development of high-power ultrafast table-top lasers represented a great experimental advance, as emphasized by the 2018 Nobel Prize in Physics. Indeed, these tools allow studying non-equilibrium dynamics in several systems on a sub-ps time scale, directly unveiling the foundations of the involved physical processes. In particular, ultrafast magnetism proved to be an exciting field of research after the groundbreaking experiments that showed the possibility of achieving sub-ps demagnetization of ferromagnetic materials by ultrafast optical excitation[1]. The use of visible radiation involves three main systems in the process: the electrons, the spins and the lattice[2]. Besides the clarity and the relevance of the experimental evidences, the interplay between these three systems makes the interpretation of the phenomenon quite complicate and highly debated[3].

Hence, to shed light on ultrafast demagnetization, a recent and successful approach consisted in the use of single-cycle THz radiation for triggering magnetization dynamics[4, 5]. Indeed, the magnetic field component of the THz radiation can couple directly to the spin degree of freedom, reducing the number of systems involved in the process. Through this capability, it is even possible to induce coherent precessional magnetization reversal ("ballistic switching") in metallic ferromagnets[6], which constitutes the fastest and most efficient switching method to be used, e.g., in magneto-recording media[7]. However, the peak THz magnetic field needed for ballistic switching is of the order of 1 T, whereas only about 0.33 T can be reached nowadays through optical rectification in table-top setups.

2. Discussion

For this purpose, we designed a class of thin-film metamaterials that can be patterned on top of the target sample for enhancing, in the near field, the incident THz magnetic field[8, 9]. Through finite element simulations, the asymmetric spiral geometry[9] resulted to be the best compromise between magnetic field uniformity and enhancement factor. Indeed, this metamaterial acts as a RLC circuit whose resonance frequency can be precisely defined by varying the characteristic geometrical parameters and the number of turns, so allowing the design to be adapted to the THz radiation to be used. Figs. 1(a)-(b) show the electric and magnetic field enhancements of an asymmetric spiral antenna tuned to have a resonance frequency of 1 THz, a typical value in THz pump-probe experiments[5]. The magnetic field enhancement, which is quite uniform in the central region of the spiral, can reach a factor of 40.

However, when performing time-resolved measurements with single-cycle pulses, the antenna bandwidth plays a major role, and the total enhancement results in a factor of 6, as shown in Fig. 1(c). This is not a drawback, since the balance between resonant enhancement and antenna bandwidth actually provides an effective design: the peak magnetic field of the amplified pulse is high enough for, e.g., testing ballistic switching in ferromagnetic materials, whereas the antenna bandwidth can be properly tuned to obtain a table-top near-field source of multicycle THz radiation driven by broadband THz pulses.

3. Conclusions

In conclusion, the asymmetric spiral antenna proved to be a flexible and effective design for obtaining THz magnetic field enhancement in table-top experiments. Not only our metamaterial can provide uniform enhancement of THz single-cycle pulses, but also constitutes a source of intense multicycle THz radiation.

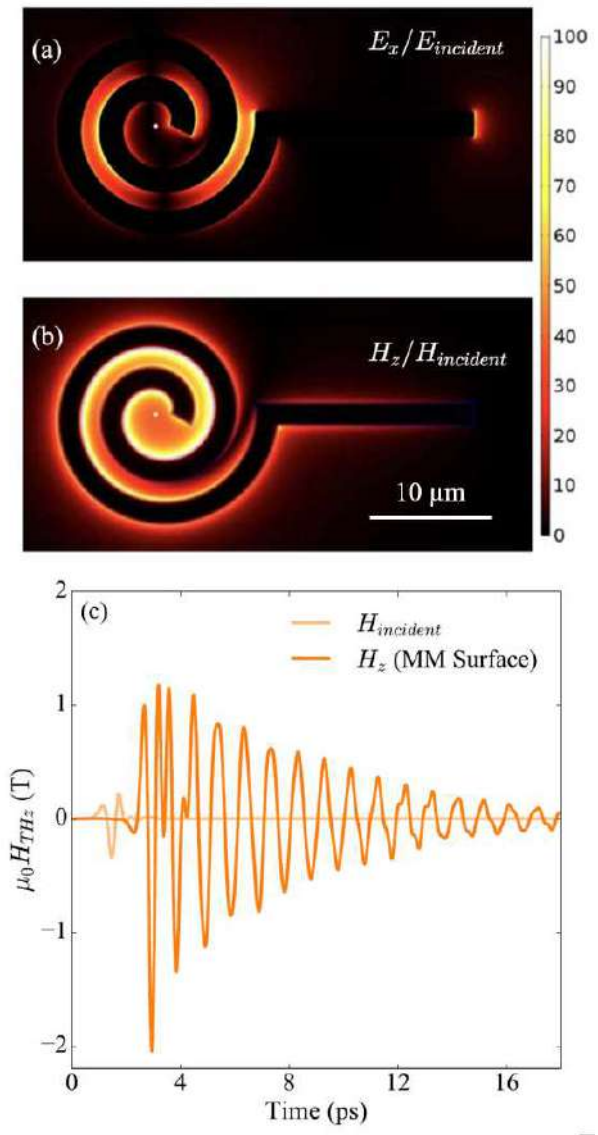


Figure 1: (a) Electric and (b) magnetic field enhancements for an asymmetric spiral antenna (100 thick Au) at the resonance frequency of 1 THz, as obtained from frequency-domain simulations. The incident radiation is linearly polarized along the direction of the spiral arm (horizontal in the figure). (c) Magnetic field profile (H_z) at the center of the spiral antenna, as obtained from time-domain simulations. The incident magnetic field $H_{incident}$ is visible in semi-transparent color between 0 and 3 ps. Adapted from Ref. [9].

References

[1] E. Beaurepaire et al., Ultrafast Spin Dynamics in Ferromagnetic Nickel, *Phys. Rev. Lett.* 76: 4250, 1996.

[2] [2] A. Kirilyuk et al., Ultrafast optical manipulation of magnetic order, *Rev. Mod. Phys.* 82: 2731, 2010.

[3] C. Dornes et al., The ultrafast Einstein-de Haas effect, *Nature* 565: 209, 2019.

[4] C. Vicario et al., Off-resonant magnetization dynamics phase-locked to an intense phase-stable terahertz transient, *Nat. Photon.* 7: 720, 2013.

[5] S. Bonetti et al., THz-Driven Ultrafast Spin-Lattice Scattering in Amorphous Metallic Ferromagnets, *Phys. Rev. Lett.* 117: 087205, 2016.

[6] S. J. Gamble et al., Electric Field Induced Magnetic Anisotropy in a Ferromagnet, *Phys. Rev. Lett.* 102: 217201, 2009.

[7] I. Tudosa et al., The ultimate speed of magnetic switching in granular recording media, *Nature* 428: 831, 2004.

[8] D. Polley et al., TH-driven demagnetization with perpendicular magnetic anisotropy: towards ultrafast ballistic switching, *J. Phys. D: Appl. Phys.* 51: 084001, 2018.

[9] D. Polley et al., Terahertz magnetic field enhancement in an asymmetric spiral metamaterial, *J. Phys. B: At. Mol. Opt. Phys.* 51: 224001, 2018.

Reprogrammable Nano-Optical Computing Using Metatronic Circuits

Mario Miscuglio[1,*], Joseph Crandall[1], Shuai Sun[1], Zhizhen Ma[1], Engin Kayraklioglu[1], Jeffery Anderson[1], Yousra Alkabani[1], Tarek A. El-Ghazawi[1], and Volker J. Sorger[1,*]

[1] Department of Electrical and Computer Engineering, The George Washington University, 800 22nd St NW, Washington, DC 20052, USA

*corresponding author, E-mail: sorger@gwu.edu

Abstract

The computing landscape has been dramatically perturbed due to the slowing to a halt of Moore's law, favoring the advancement of several non-VonNeauman architectures. Analog memory devices [1], neuromorphic photonics for deep learning applications [2–4], optical coprocessors for high speed convolutions [5,6] and quantum analog computers [7] are just some examples of currently used analog architectures which can tackle complex tasks more efficiently than a regular digital processor. The main advantage of analog computers is the ability to perform algebraic and integro-differential operations upon continuous signals, without a temporization, enabling efficient processing for specific operations. One of the mathematical tasks that can exploit these paradigms and could greatly benefit from using analog co-processor is solving Partial differential equation (PDE). In the past, analog processors, consisting of grids of resistive or reactive elements, were used to model the spatial distribution of physical quantities, in a speculative way to a finite difference approach. However, the complexities of an effective integration of a high speed programmable and concurrently energy efficient static-like analog mesh significantly reduced the advancement of this technology. Here, we demonstrate the realization of a nano-optic co-processor able to instantaneously solve partial differential equation. The proposed PDE processor is based on air grooves meshes, engraved in an Indium Tin oxide (ITO) substrate at epsilon-near-zero condition locally excited by the near field generated by a dipole. We show that this platform behaves as a lumped circuit [8–10], similarly to a resistive mesh, and can be configured to map a finite difference problem, thus providing a discretized solution of a PDE. Thanks to an unprecedented control of the ENZ position and material losses over ITO [11], we are able to provide a top-down approach for a monolithic integration of nano-optics circuits based only on opportunely processed ITO films. In details, we are able to obtain ITO films with tailored values of real and imaginary part of the dielectric constant, mimicking resistors and reactances in our nano-optic circuit, which operates in the IR telecommunication wavelength. Moreover, the elements of the circuit can be electrostatically tuned, by altering the carriers in a capacitor configuration [12–14] and therefore reprogrammed, aiming to solve a great variety of PDEs with different boundary conditions including Poisson Equation, Diffusion Equation and the Wave Equation. We further investigate the performance of our nano-optic processor by comparing the accuracy of the solution of PDE representing a heat transfer problem with the results obtained with finite difference approaches, demonstrating physical limit of the technology in terms of mesh density and size. We also prove that the circuit dimensions, contrary to a lumped circuit model, can be of the same size or exceed the dimension of the impinging radiation wavelength, while elements of the circuit being still locally coupled. We also show that, unlike resistive network, the operating bandwidth at which the circuit can be reprogrammed is decoupled from the physical dimensions of the circuit, thus obtaining high speed reconfiguration without trading off with solution accuracy. Ultimately, power consumption and footprint of the proposed metatronic circuit are evaluated and compared to those required by the state-of-the-art PDE analog co-processors, demonstrating orders of magnitude improvement with respect of speed, power, and size, while providing an accurate solution.

Our results open a significant pathway towards the realization of nano-optics reprogrammable co-processor able to efficiently solve complex problem, in particular for those systems where only small amounts of energy is available, while still demanding for high computation speed.

References

1. S. Ambrogio, P. Narayanan, H. Tsai, R. M. Shelby, I. Boybat, C. di Nolfo, S. Sidler, M. Giordano, M. Bodini, N. C. P. Farinha, B. Killeen, C. Cheng, Y. Jaoudi, and G. W. Burr, "Equivalent-accuracy accelerated neural-network training using analogue memory," Nature **558**, 60 (2018).
2. Y. Shen, N. C. Harris, S. Skirlo, M. Prabhu, T. Baehr-Jones, M. Hochberg, X. Sun, S. Zhao, H. Larochelle, D. Englund, and M. Soljačić, "Deep learning with coherent nanophotonic circuits," Nature Photonics **11**, 441–446 (2017).
3. A. N. Tait, T. F. de Lima, E. Zhou, A. X. Wu, M. A. Nahmias, B. J. Shastri, and P. R. Prucnal, "Neuromorphic photonic networks using silicon photonic weight banks," Scientific Reports **7**, 7430 (2017).
4. M. Miscuglio, A. Mehrabian, Z. Hu, S. I. Azzam, J. George, A. V. Kildishev, M. Pelton, and V. J. Sorger, "ALL-OPTICAL NONLINEAR ACTIVATION FUNCTION FOR," 13 (n.d.).
5. X. Lin, Y. Rivenson, N. T. Yardimci, M. Veli, Y. Luo, M. Jarrahi, and A. Ozcan, "All-optical machine learning using diffractive deep neural networks," Science **361**, 1004–1008 (2018).
6. J. Chang, V. Sitzmann, X. Dun, W. Heidrich, and G. Wetzstein, "Hybrid optical-electronic convolutional neural networks with optimized diffractive optics for image classification," Scientific Reports **8**, 12324 (2018).
7. S. Debnath, N. M. Linke, C. Figgatt, K. A. Landsman, K. Wright, and C. Monroe, "Demonstration of a small programmable quantum computer with atomic qubits," Nature **536**, (2016).
8. N. Engheta, A. Salandrino, and A. Alù, "Circuit Elements at Optical Frequencies: Nanoinductors, Nanocapacitors, and Nanoresistors," Physical Review Letters **95**, (2005).
9. Y. Li, I. Liberal, C. Della Giovampaola, and N. Engheta, "Waveguide metatronics: Lumped circuitry based on structural dispersion," Science Advances **2**, e1501790 (2016).
10. A. Alù and N. Engheta, "All Optical Metamaterial Circuit Board at the Nanoscale," Physical Review Letters **103**, (2009).
11. Y. Gui, M. Miscuglio, Z. Ma, M. T. Tahersima, S. Sun, R. Amin, H. Dalir, and V. J. Sorger, "Towards integrated metatronics: a holistic approach on precise optical and electrical properties of Indium Tin Oxide," arXiv:1811.08344 [physics] (2018).
12. R. Amin, R. Maiti, C. Carfano, Z. Ma, M. H. Tahersima, Y. Lilach, D. Ratnayake, H. Dalir, and V. J. Sorger, "0.52 V-mm ITO-based Mach-Zehnder Modulator in Silicon Photonics," arXiv:1809.03544 [physics] (2018).
13. H. W. Lee, G. Papadakis, S. P. Burgos, K. Chander, A. Kriesch, R. Pala, U. Peschel, and H. A. Atwater, "Nanoscale Conducting Oxide PlasMOStor," Nano Letters **14**, 6463–6468 (2014).
14. E. Feigenbaum, K. Diest, and H. A. Atwater, "Unity-Order Index Change in Transparent Conducting Oxides at Visible Frequencies," Nano Lett. **10**, 2111–2116 (2010).

Magnetic metamaterials

Vassilios Kapaklis

Department of Physics & Astronomy, Uppsala University, Sweden
E-mail address: vassilios.kapaklis@physics.uu.se

Metamaterials are artificial materials with an engineered periodic structure aiming in properties which cannot be found in nature. Lithographically nano-patterned magnetic materials can result in fascinating behaviour exploiting the magnetic dipolar interactions between individual elements. The emergent properties in such systems are distinctly different from those of their constituent components, driven by the collective dynamics of the interacting elements and respond to external stimuli such as magnetic fields or temperature. Further enhanced functionality can be realised exploiting the fact that the periodicity and element size in such nano-patterned magnetic arrays matches well the wavelengths of visible light, thus providing an ideal setting for the investigation of the interaction of light with magnetic metamaterials. I will present approaches for the fabrication of magnetic metamaterials using thin films. Recent works have demonstrated the creation of reconfigurable magnetic structures which undergo phase transitions and exhibit dynamics on adjustable length- and energy-scales [1-8]. The interaction of visible light with such structures also reveals the opportunity of "steering" light and altering optical properties using such magnetically reconfigurable metasurfaces [9-11].

References

1. V. Kapaklis et al., *New J. Phys.* **14**, 035009 (2012).
2. V. Kapaklis et al., *Nature Nanotechnology* **9**, 514 (2014).
3. S. Zhang et al., *Nature* **500**, 553 (2013).
4. L. Anghinolfi *et al*., Nature Communications **6**, 8278 (2015).
5. M. S. Andersson et al., *Scientific Reports* **6**, 37097 (2016).
6. C. Nisoli et al., *Nature Physics* **13**, 200 (2017).
7. E. Östman et al., *Nature Physics*, **14**, 375 (2018).
8. H. Stopfel *et al*., Phys. Rev. B **98**, 014435 (2018).
9. E. Melander et al., *Appl. Phys. Lett*. **101**, 063107 (2012).
10. M. Rollinger et al., *Nano Letters* **16**, 2432 (2016).
11. R. Rowan-Robinson *et al*., AIP Advances, *in press* (2019).

Localization of light in magnetophotonic structures for ultrafast magnetism

Vladimir I. Belotelov[1,2], Alexander I. Chernov[1], Mikhail A. Kozhaev[1,3], Daria O. Ignatyeva[1,2], Miguel Levy[4], Alexander N. Shaposhnikov[5], and Vladimir N. Berzhansky[5]

[1]Russian Quantum Center, 45, Skolkovskoye shosse, Moscow, Russia
[2]Faculty of Physics, Lomonosov Moscow State University, Leninskie Gory, Moscow, Russia
[3]Prokhorov General Physics Institute RAS, 38 Vavilov Street, Moscow, Russia
[4]Physics Department, Michigan Technological University, Houghton, Michigan, USA
[5]Vernadsky Crimean Federal University, 4 Vernadskogo Prospekt, Simferopol, Russia

*corresponding author, E-mail: belotelov@physics.msu.ru

Abstract

Optical control of the magnetization at ultrashort time scales attracts much attention in context of the data processing and spintronic applications. In this work we demonstrate the optical confinement in photonic microcavity that results in the significant increase of the inverse Faraday effect (IFE) within the magnetic layer. Along with that we show the light localization inside the dielectric sub-wavelength gratings in iron-garnet films that gives rise to the enhancement of the photo-magnetic effects.

1. Introduction

Optical manipulation of the magnetization at ultrashort time scales is of prime interest in context of the data processing and spintronic applications. Excitation with femtosecond laser pulses provides a new way for efficient control of spins at GHz and THz rates. Light localization is the additional way to enhance the light-matter interaction and also to manipulate the magnetic properties at sub-wavelength scales. All-dielectric structures in many aspects are more advantageous for the light localization since they provide optical resonances with high optical quality factors and allow excluding the thermal effects.

In this work, we investigate the influence of the optical confinement in two systems: magnetophotonic microstructures and dielectric sub-wavelength gratings, where in both the magnetic layer is iron-garnet film.

2. Experimental

The magnetophotonic microcavity consists of the magnetic film and two non-magnetic dielectric Bragg mirrors. The iron-garnet magnetic film includes two layers M1 and M2: the auxiliary 72-nm-thick $Bi_{1.0}Lu_{0.5}Gd_{1.5}Fe_{4.2}Al_{0.8}O_{12}$ layer and the main 210-nm-thick $Bi_{2.5}Gd_{0.5}Fe_{3.8}Al_{1.2}O_{12}$ layer. Each Bragg mirror consists of four pairs of alternating 76-nm-thick TiO_2 and 117-nm-thick SiO_2 layers grown on the fused quartz substrate.

The all-dielectric iron-garnet 1D gratings have been formed on the films by ion etching. The height and width of the pillars is around 200 nm, while the underneath film was left 75 nm thick, the period is around 450 nm. Magnetic film and the formed grating are located on the GGG substrate.

To investigate the magnetization precession we used the pump-probe experimental technique. The laser system (Newport Mai Tai HP Ti:Sapphire laser and Spectra-Physics Inspire Auto 100 optical parametric oscillator) emits at 80.54 MHz repetition rate pairs of 150-fs-pulses that are tunable in wavelength. The weaker probe pulse is used for observation of the magnetization dynamics through the direct Faraday effect, i.e. by measuring variation of the Faraday rotation angle, Ψ, caused by the magnetization precession. The average pump light energy fluence was set to 0.66 mJ/cm^2 An external magnetic field, **H**, was applied in-plane to saturate the magnetization.

3. Discussion

We first turn to the discussion of the magnetophotonic microcavity sample. The optical confinement of the cavity was used as a tool for enhancement of inverse magneto-optical effect. Basing on the approach of the optical excitation of magnetization precession by femtosecond laser pulses [1-4], we excite the magnetic layer inside the magnetophotonic microcavity and detect the significant increase of the IFE due to the concentration of the optical energy and angular momentum. The cavity mode is excited in the photonic band gap center at λ_0 = 642 nm (Fig. 1). Spectral dependence of the IFE on the laser pulse wavelength in the band gap of the magnetophotonic microcavity has a sharp peak that results in a significant enhancement of the IFE (Fig.1 bottom). Localization of light inside the microcavity leads to the 3D IFE enhancement in depth within the cylindrical regions with diameter of the laser spot and height as small as 30 nm inside of the magnetic layer. These excited volumes can be shifted along the sample depth via e.g. changing the frequency of the laser pulses.

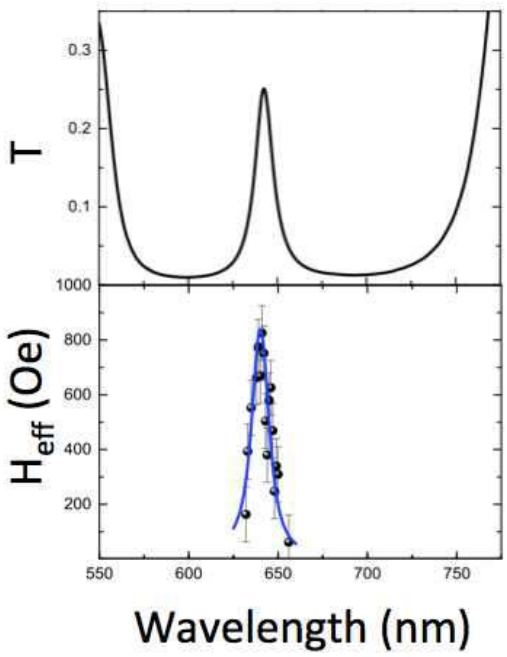


Figure 1: Top: optical transmittance spectrum of the magnetophotonic microcavity. The cavity mode is located in the photonic band gap. Bottom: Averaged over the thickness of the magnetic film the normal component of the IFE magnetic field versus the pump wavelength: found from the experimental data, $\langle H_{IFE} \rangle_{exp}$ (black spheres), and calculated from the electromagnetic field distribution, $\langle H_{IFE} \rangle_{calc}$ (blue curve).

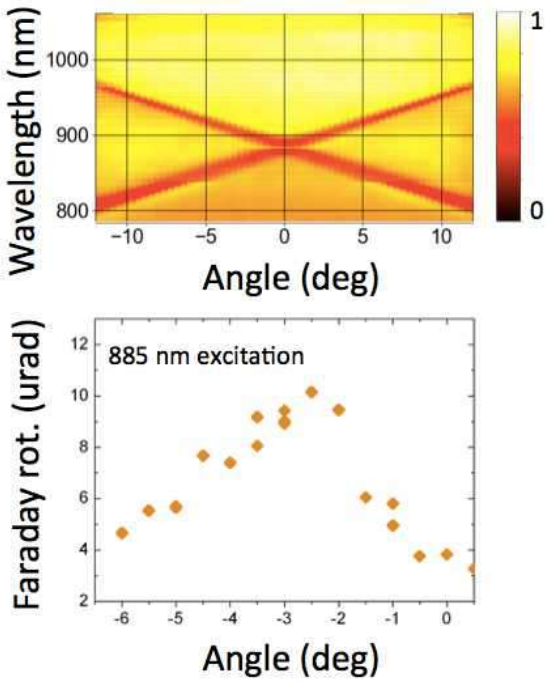


Figure 2: Top: optical transmittance spectrum of the 1D iron-garnet grating depending on the light incidence angle. Bottom: Faraday rotation intensity angle dependence.

Another type of structures that demonstrates the optical localization is the iron-garnet gratings that are formed by 1D grooves etched in the magnetic film. The formed all-dielectric structures allow us to demonstrate the sub-wavelength light localization. The transmission spectrum of the 1D grating depending on the light incidence angle is presented in Fig.2. Light localization results in the appearance of the waveguide modes that depend on the width and the period of the grooves. Taking in mind the waveguide mode distribution we excite the sample with linearly polarized femtosecond light pulses and trace the time-resolved change of the Faraday rotation indicating the magnetization precession at different light incidence angles with a fixed excitation wavelength. In the area close to the resonance we detect a more than 3 times enhancement of the Faraday rotation. Therefore, we demonstrate that the 1D iron-garnet grating is the platform for the study of the photo-magnetic effects enhancement.

4. Conclusions

Two systems, namely magnetophotonic microcavity and 1D gratings, both containing the iron-garnet as the magnetic material, have been used to demonstrate the enhancement of the inverse magneto-optical and photo-magnetic effects. In the case of the microcavity we show the 5-times IFE enhancement and the light localization of femtosecond laser pulses in 30 nm cylinder areas in depth of the magnetic layer. While in the all-dielectric sub-wavelength 1D gratings we detect the significant enhancement of the photo-magnetic effects with local light impact across the film thickness and in the transverse direction. For both systems excitation wavelength and polarization of the laser pulses determines the intensity of the effects and leads to the light localization that enhances the light-matter interaction. The obtained results can be a path for the new applications in magnonics.

Acknowledgements

The work was supported by Russian Science Foundation grant 17-72-20260.

References

[1] M A. Kozhaev, A. I. Chernov, D. A. Sylgacheva *et al.*, Sci. Rep. (2018) 8, 11435.

[2] A. I. Chernov, M. A. Kozhaev, I.V. Savochkin, *et al.*, Optics Letters (2017) 42, 279.

[3] A. I. Chernov, M. A. Kozhaev, A. K. Zvezdin, *et al.*, J. Phys. Conf. Ser. (2017) 869, 012020.

[4] M. Jackl, V. I. Belotelov, I. A. Akimov, *et al.*, Phys. Rev. X (2017) 7, 021009.

Control of Hot-Electron Dynamics: From Ballistic Collection to Ultrafast Hot-Hole Removal

Giulia Tagliabue[1,2,3,*], Joseph S. DuChene[1,2], Ravishankar Sundararaman[4], Harry A. Atwater[1,2,3]

[1]Thomas J. Watson Laboratory of Applied Physics, California Institute of Technology, Pasadena, CA 91125 United States.
[2]Joint Center for Artificial Photosynthesis, California Institute of Technology, Pasadena, CA 91125 United States.
[3]Laboratory of Nanoscience for Energy Technologies, EPFL, 1015 Lausanne, Switzerland.
[4]Department of Materials Science and Engineering, Rensselaer Polytechnic Institute, Troy, New York 12180, United States

*corresponding author, E-mail: giulia.tagliabue@epfl.ch

Abstract

Photo-doping of low dimensional materials with plasmonic hot carriers is a promising route for fast all-optical modulation of optoelectronic devices[1,2]. Hence understanding the fundamental processes involved in hot-electron generation, transport and thermalization is of crucial importance. Theoretical analysis of the quantum decay of surface plasmon polaritons, with and without phonons, showed that the prompt distribution of generated carriers is extremely sensitive to the band structure of the plasmonic material. In particular, the onset of interband transitions, occurring in the visible regime (around 2 eV) for most common plasmonic metals (Au, Cu, Ag), is expected to significantly modify the hot-carrier distributions[3]. Also, upon interband excitation of d-band metals such as Au and Cu, a high probability of very hot holes has been predicted[3]. In our work, we first focused on elucidating the role of plasmon excitation and metal band structure on the internal quantum efficiency of plasmonic photodetectors[4]. Next, we utilized ultrafast visible transient absorption spectroscopy to understand the effect of hot-hole removal on the thermalization process of hot electrons[5]. The choice of an appropriate experimental platform (Au/GaN heterostructures) combined with advanced theoretical methods enables unprecedented insight into the dynamics of plasmonic hot electrons.

References

[1] Kang, Y. , Najmaei, S. , Liu, Z. , Bao, Y. , Wang, Y. , Zhu, X. , Halas, N. J., Nordlander, P. , Ajayan, P. M., Lou, J. and Fang, Z. (2014), Plasmonic Hot Electron Induced Structural Phase Transition in a MoS_2 Monolayer. *Adv. Mater.*, 2014 26: 6467-6471.

[2] Zheyu Fang, Yumin Wang, Zheng Liu, Andrea Schlather, Pulickel M. Ajayan, Frank H. L. Koppens, Peter Nordlander, and Naomi J. Halas Plasmon-Induced Doping of Graphene, *ACS Nano* 2012 6 (11), 10222-10228.

[3] Brown, A. M.; Sundararaman, R.; Narang, P.; Goddard III, W. A.; Atwater, H. A. Nonradiative plasmon decay and hot carrier dynamics: effects of phonons, surfaces, and geometry. *ACS Nano* 10, 957-966 (2016).

[4] G Tagliabue, AS Jermyn, R Sundararaman, AJ Welch, JS DuChene, R Pala, AR Davoyan, P Narang, H A Atwater, Quantifying the role of surface plasmon excitation and hot carrier transport in plasmonic devices, Nature Communications 9 (1), 3394

[5] G. Tagliabue, JS. DuChene, M. Abdellah, A. Habib, Y.Hattori, K.Zheng, SE Canton, DJ Gosztola, W.H Cheng, R. Sundararaman, J Sá, HA Atwater, Ultrafast Studies of Hot-Hole Dynamics in Au/p-GaN Heterostructures, arXiv preprint arXiv:1810.04238

Self-assembled magnetic nanoparticles on plasmonic nanoantennas

G. Petrucci[1], O. Lysenko[2], E. Fantechi[1], C. Sangregorio[3,4], A. Dmitriev[2], F. Pineider[1]*
[1]INSTM and Dept. of Chemistry and Industrial Chemistry, University of Pisa, Italy
[2]Gothenburg University, Department of Physics, Gothenburg Sweden
[3]CNR-ICCOM, Sesto Fiorentino (FI), Italy
[4]INSTM and Dept. of Chemistry, University of Florence, Italy
*corresponding author, E-mail: francesco.pineider@unipi.it

Abstract

We show that chemically prepared cobalt ferrite nanoparticles can be selectively assembled on plasmonic gold nanodisks, thus forming a hybrid magnetic-plasmonic platform. Spectroscopic and field-dependent magneto-optical studies show an interesting behavior around the plasmon resonance frequency: the magneto-optical response of the gold disks is influenced quantitatively by the local magnetic field induced by the surrounding nanoparticles. We thus propose the idea of using plasmonic nanoantennas as optical local magnetic field sensors.

1. Introduction

Magnetoplasmonics is the research field dedicated to studying the effect of a static magnetic field on plasmon resonance [1]. In this paper we show how magnetoplasmonic effects can be used to gain information on the local magnetic fields generated by nanometric magnetic objects placed around plasmonic nanoantennas.
This has been achieved by selectively assembling chemically prepared colloidal nanoparticles on the gold surface of plasmonic nanodisks. Ligand-passivated cobalt ferrite nanoparticles (average diameter ~ 15 nm) were prepared by thermal decomposition of organometallic precursors [2]. This method affords highly crystalline, monodiperse spherical nanoparticles which can be efficiently dispersed in organic solvents. Gold nanodisks (diameter x height ~ 150x25 nm) were prepared by hole-mask colloidal lithography [3]. This highly parallel procedure yields gold nanostructures supported on glass over macroscopic areas. Hydrophobic interactions between the alkyl chains passivating the nanoparticle surface promote binding to the polarizable gold disks. On average, around 15-20 particles are attached to each nanodisk (Figure 1).

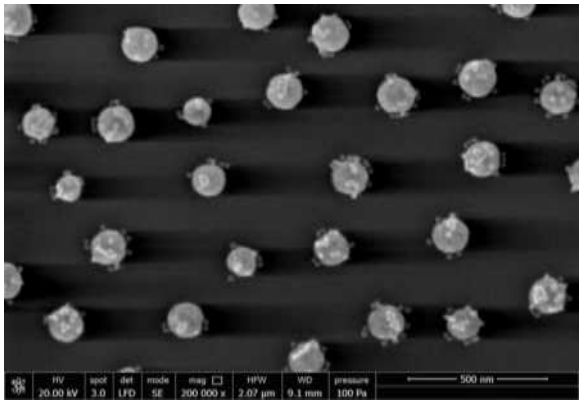


Figure 1: Scanning electron micrograph of magnetic nanoparticles assembled on plasmonic nanoantennas.

Magnetic circular dichroism (MCD) spectroscopy was used to characterize the hybrid system. Tuning both incoming light wavelength and applied field magnitude, a full map of this bidimensional parameter space can be investigated (Figure 2).

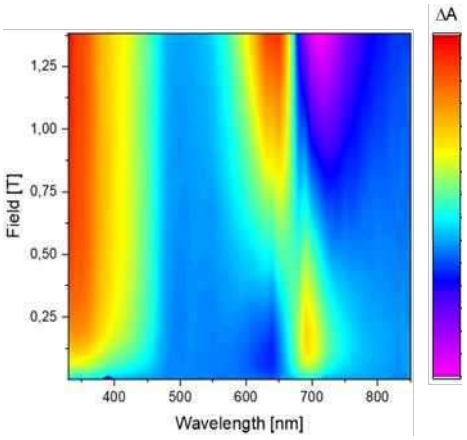


Figure 2: Magnetic circular dichroism (ΔA) intensity map of the magnetic nanoparticle-plasmonic nanoantenna hybrid system as a function of light wavelength and applied magnetic field.

2. Discussion

Two regimes in the low and high magnetic field can be seen in the plasmon resonance wavelength range, centered at 670 nm. This peculiar behavior arises from the different field dependence of the magnetic and plasmonic components of the hybrid: cobalt ferrite nanoparticles exhibit a saturating behaviour with respect to an external magnetic field. Gold nanoantennas, on the other hand, show a linear field dependence of their magneto-optical signal [4,5], which becomes dominant at high field values. Taking adventage of this different behavior of the two components, it is possible to separate the their respective spectroscopic footprints, as shown in Figure 3.

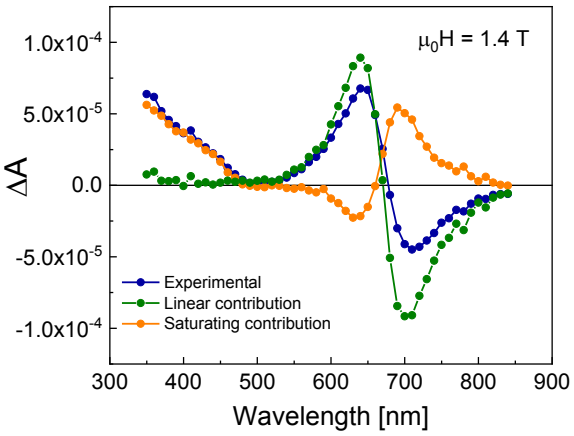


Figure 3: Separation of the experimental magnetic circular dichroism spectrum into linear and saturating contributions.

The linear contribution shows the derivative-like magnetoplasmonic signal arising from magnetic field modulation of plasmon resonance [4].
The saturating (*i.e.* magnetic) contribution shows a direct footprint of the magnetic nanoparticles in the 350-450 nm range, which is related to charge transfer processes of cobalt ferrite. A second, inverted derivative-like signal is found in the plasmon resonance range: this is not related to direct magneto-optical transitions of cobalt ferrite, but rather to an effect induced by them on plasmon resonance. Considering the assembly geometry of the nanoparticles around the disk, they can be divided into two populations: those standing around the disk and those lying on top of them. We assume that the latter population does not affect strongly plasmon resonance, since most of the near field localization of light is concentrated at the base of the disk (calculations not shown). Considering the nanoparticles adsorbed at the sides of the disks, we observe that their generated dipolar magnetic field is of opposite direction to that of the applied (magnetizing) field (Figure 4). We hypothesize that this opposite field component causes an inverted magnetoplasmonic response in the nanoantennas. Since the magnetoplasmonic signal scales linearly with the field, we can calculate the average magnetic field generated by the nanoparticles around each disk (~ 0.6 T).

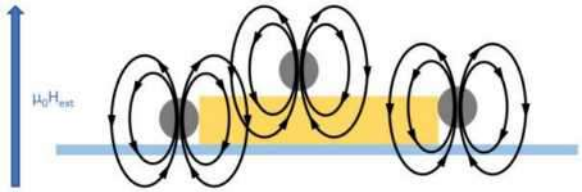


Figure 3: Sketch of the dipolar fields generated by magnetized particles around the nanoantenna.

3. Conclusions

We observed an anomalous behavior in the magneto-optical response of gold nanodisks when magnetic nanoparticles are adsorbed on their surface. We ascribe this behavior to dipolar fields generated by the particles, to which the plasmonic antenna responds locally.
We believe that, with proper optimization, this principle could be used to design (magneto-)optical readout systems for magnetic fields at the nanoscale.

Acknowledgements

This work has been supported by the European Union's Horizon2020 Research and Innovation program, Grant agreement No. 737709 (FEMTOTERABYTE) and by the University of Pisa, project PRA_2017_25.

References

[1] G. Armelles et al. Adv. Opt. Mater. 1 (2013) 10.
[2] S. Sun, H. Zheng, J. Am. Chem. Soc. 124 (2002) 8204.
[3] H. Fredriksson et al. Adv Mater. 19 (2007) 4297.
[4] F. Pineider et al. Nano Lett. 13 (2013) 4785.
[5] B. Sepulveda et al. Phys. Rev. Lett. 104 (2010) 147401.

Tunable and nonlinear metamaterials for circular polarization control

Kuniaki Konishi

Institute for Photon Science and Technology, The University of Tokyo, Tokyo, Japan
E-mail: kkonishi@ipst.s.u-tokyo.ac.jp

Abstract

Symmetry of material plays a crucial role in the polarization sensitive optical phenomena; thus it is important to design and control shapes of artificial nanostructures for developing devices for active polarization control. We have been developing methods of circularly polarized light control by using them. In this presentation, I introduce the recent progress of our study for controls of active THz polarization by active chiral metamaterials and second-harmonic generation with nonlinear metasurfaces with rotational symmetries.

1. Introduction

Circularly polarized light (CPL) sources are important for a variety of applications, such as circular dichroism spectroscopy, spin state control in materials, ultrafast magnetization control and so on. Metamaterials are promising candidates for ultra-small devices with a lot of flexibility in their design for CPL control. The symmetry of a material plays an especially crucial role in polarization sensitive optical phenomena; therefore it is necessary to employ metamaterials with appropriate symmetries to achieve circular polarization control. We have studied the effect of circular polarization in planar metamaterials. We demonstrated that chiral metamaterials which exhibit strong optical activity and found that active control of the structure can be used for THz polarization control with dynamic chirality switching. We also demonstrated that triangle-arrayed metamaterials, which have threefold rotational symmetries, exhibit a unique polarization effect in a second-order nonlinear process: a circularly polarized fundamental beam produces a counter-circularly polarized second-harmonic beam. In this presentation, the recent progress of our research related to these topics is shown.

2. Active Handedness-Switchable Metamaterial for THz Polarization Control

Active modulation of the polarized state of light is important for polarization-sensitive spectroscopy. In the THz frequency region, practical polarization-modulation devices for such purposes have been in demand. Active metamaterials are attracting attention [1], and especially, tunable chiral metamaterials are promising candidates. We present a new type of active chiral metamaterials whose optical activity is controlled by vertical deformation of a three-dimensional structure, engineered by micro electro mechanical system (MEMS) technology [2, 3].

The working schematic and a scanning electron microscope (SEM) image are shown in Figure 1(a). When a planar Archimedean spiral is actuated in the upward vertical direction, the spiral becomes left handed (LH) (Fig. 1a). A reversal of the direction provides a right-handed (RH) spiral, a mirror image of the LH spiral. This reversal achieves chirality switching while maintaining the enantiomeric symmetry. The spiral deformation modulates the polarization state of THz wave passing through it (Fig. 1b). To enhance the spatial dispersion, we employed a unique pneumatic force actuation, which provides a significantly larger deformation.

Planar Archimedean spirals are fabricated by gold thin film deposited on Si membrane, and direction of deformation is selected by the direction of N_2 pressure supply [3]. The microscopic images of the fabricated spiral metamaterial are shown in fig. 1(c)

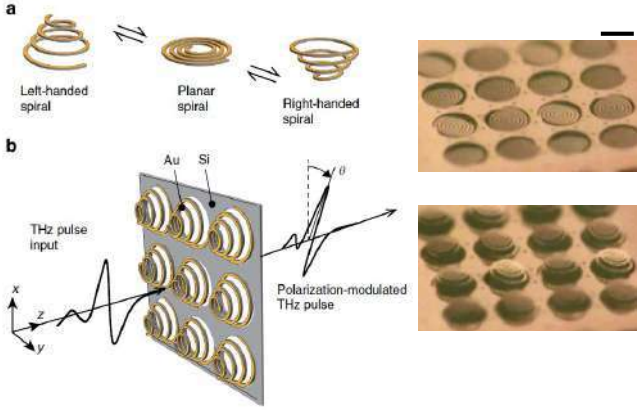


Figure 1: (a) Principle of enantiomeric chirality switching of the spiral structures (b) Configuration of spiral structures arrayed to form a chirality-switchable metamaterial. (c) Microscope images of the MEMS spirals in the pre-actuation and on-actuation states. The scale bar corresponds to 100μm. [3]

The optical activity of the device was investigated using THz time-domain spectroscopy. We observed that the amplitude of optical activity depends on the amplitude of

vertical defamation. Moreover, enantiomeric switching is realized by selecting the deformation direction, where the polarity of the optical activity is altered while maintaining the spectral shape. A polarization rotation as high as 28° is experimentally observed, thus providing a practical and compact polarization modulator for the terahertz range. In the THz regime where polarization devices are still lacking, the presented device can for example be used to create a simple and practical polarization-modulated THz imaging system when combined with other new types of THz devices, such as the THz camera [4].

3. Polarization-Controlled Circular Second-Harmonic Generation from Metamaterials with three-fold rotational symmetry

Nonlinear processes forbidden in homogeneous media can be allowed in metamaterials, thereby offering a unique opportunity to study the interplay between the shapes and mutual arrangements of individual nanostructures. This is especially important for second-order nonlinear optical phenomena and second-harmonic generation (SHG) in arrays of metal nanoparticles and has accordingly been investigated extensively [5].

It is attractive to handle the polarization state of the SH beam arbitrary by controlling that of the fundamental beam in properly designed metamaterials. It was known that circularly polarized SHG occurs from a counter-circularly polarized fundamental beam which propagates along a threefold rotational axis of a nonlinear optical crystal [6]. If the same relation holds between the polarization states of the fundamental and SH beams in nonlinear metamaterials, these materials will be an attractive solution for controlling SHG polarization. Therefore, we investigate SHG in a nonlinear metamaterial with threefold rotational symmetry [7].

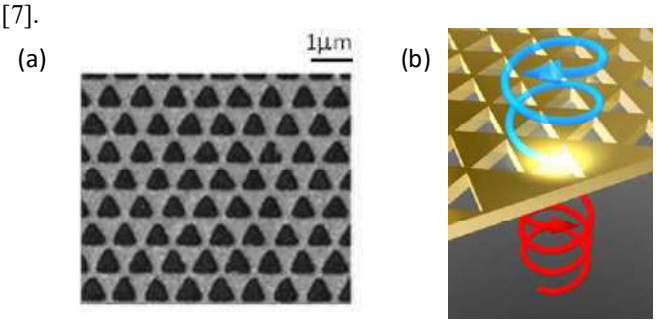


Figure 2: (a) SEM image of the sample with threefold rotational symmetry [7] (b) Schematics of circularly-polarized second-harmonic generation in metallic meta surface with threefold rotational symmetry.

Figure 2(a) shows a SEM image of a fabricated metal nanostructure with triangular-hole arrays, which possesses a threefold rotational symmetry axis. We measured the polarization properties of the SH beam generated by laser pulses with various polarization states and found that the SH beam was predominantly right circularly polarized when the fundamental was left circularly polarized, and vice versa, indicating that the helicity of the SH beam was opposite to that of the fundamental beam (schematics is shown in Fig. 2(b)). Such metallic nanostructures are recently attracting attention as a useful tool to control polarization in nonlinear processes referred as nonlinear photonics metasurface [8].

The presented relationships between polarization selection rules and rotational symmetries of nanostructures are of practical importance for developing wavelength-conversion devices that function in wavelength regions in which other methods of polarization control are unavailable. In the presentation, I would like to also introduce our recent progress on this point if possible.

Acknowledgements

These researches were performed in collaboration with Simoyama group at the University of Tokyo, and supported by the Photon Frontier Network Program, KAKENHI (25600109, 20104002, 18H01147), "Nanotechnology Platform" (project No. 12024046), and Project for Developing Innovation Systems of the Ministry of Education, Culture, Sports, Science and Technology (MEXT), Japan, by JSPS through its FIRST Program, and by JST, PRESTO Grant Number JPMJPR18G6, Japan. The EB photomask fabrication was performed using the EB lithography apparatus at the VLSI Design and Education Center (VDEC) of the University of Tokyo.

References

[1] N. I. Zheludev and Y. S. Kivshar, From metamaterials to metadevices, *Nat. mater.* 11: 917-924, 2010.

[2] T. Kan, A. Isozaki, N. Kanda, N. Nemoto, K. Konishi, M. Kuwata-Gonokami, K. Matsumoto, and I. Shimoyama, Spiral metamaterial for active tuning of optical activity, *Appl. Phys. Lett.* 102: 221906, 2013.

[3] T. Kan, A. Isozaki, N. Kanda, N. Nemoto, K. Konishi, H. Takahashi, M. Kuwata-Gonokami, K. Matsumoto, and I. Shimoyama, Enantiomeric switching of chiral metamaterial for terahertz polarization modulation employing vertically deformable MEMS spirals, *Nat. Commun.* 6: 8422, 2015.

[4] N. Nemoto, N. Kanda, R. Imai, K. Konishi, M. Miyoshi, S. Kurashina, T. Sasaki, N. Oda and M. Kuwata-Gonokami, High-Sensitivity and Broadband, Real-Time Terahertz Camera Incorporating a Micro-Bolometer Array With Resonant Cavity Structure, *IEEE Trans. THz Sci. Technol.* 6: 175, 2016.

[5] M. Kauranen and A. V. Zayats, Nonlinear plasmonics, *Nat. photon.* 6: 737-748, 2012.

[6] H. J. Simon and N. Bloembergen, Second-Harmonic Light Generation in Crystals with Natural Optical Activity, *Phys. Rev.* 171:1104-1114, 1968.

[7] K. Konishi, T. Higuchi, J. Li, J. Larsson, S. Ishii, and M. Kuwata-Gonokami, Polarization-controlled circular second-harmonic generation from metal hole arrays with threefold rotational symmetry, *Phys. Rev. Lett.* 112: 135502, 2014.

[8] G. Li, S. Zhang, and T. Zentgraf, Nonlinear photonic metasurfaces, *Nat. Rev. Mater.* 2: 17010, 2017.

Towards optically adjustable and rewriteable metasurfaces enabled by phase-change materials.

Andreas F. Hessler[1], Ann-Katrin U. Michel [1,2], Sebastian Meyer[1], Julian Pries[1] Yuan Yu[1], Thomas Kalix[1], Martin Lewin[1], Julian Hanss[1], Angela de Rose[1], Tobias W.W. Mass[1], Matthias Wuttig[1], Dmitry N. Chigrin[1,3] and Thomas Taubner[1]

[1]Institute of Physics (IA), RWTH Aachen University, Aachen, Germany
[2] *present address:* Optical Materials Engineering Laboratory, ETH Zurich, Zurich, Switzerland
[3]DWI – Leibniz Institute for interactive materials, Aachen, Germany
*corresponding author, E-mail: taubner@physik.rwth-aachen.de

Abstract

For arbitrarily programmable metasurfaces, a local change of the optical properties of each individual meta-atom is needed. We employ and compare different non-volatile phase-change materials (PCM) as switchable dielectric environment for meta-atoms. We show the fine-tuning of individual elements of a metasurface covered with a PCM by locally addressing them with laser pulses. Our materials and concepts can be applied to a multitude of already present metasurface designs.

1. Introduction

Despite their nanometer thickness, metasurfaces consisting of resonant metallic or dielectric nanostructures offer comprehensive control over light fields and allow for the creation, detection and transformation of light. Often, their optical functionality is only obtained at a fixed wavelength, determined by the geometric design and the material properties. For optimal functionality, they need to be freely programmable and have low optical losses.

Phase-change materials (PCMs) provide a switchable dielectric environment for resonant nanostructures, altering their resonance frequencies in a non-volatile, reversible way. PCMs have a high optical contrast between their amorphous and crystalline phases (Fig. 1a), while only exhibiting low optical losses in the infrared [1,2].

Active metasurfaces based on PCMs are thus promising building blocks for compact photonic components because they offer adjustable, designed functionality for the manipulation and control of light [2]. Among recent examples are polarization filters [3], beam steerers and lenses [4-6]. Conventionally, they feature multiple operation states by switching the whole phase-change material partially or fully between two states of drastically different optical properties via short electrical or optical pulses (Fig 1 b). Here, we take a different approach by using a visible light switching laser to crystallize sub-wavelength regions in an infrared (IR) metasurface (Fig. 1c). By varying the pulse parameters of the laser, we can control the size of the switched phase-change spot inside of each meta-atom. Thus, it will be possible to tune the amplitude and phase of the light everywhere on the metasurface and impart multiple complex functionalities onto the same metasurface.

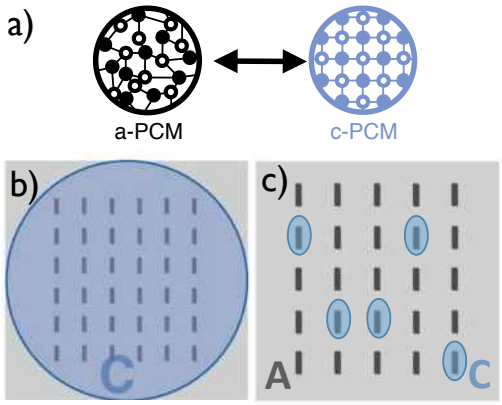


Figure 1: a) Reversible switching between amorphous (a-PCM) and crystalline (c-PCM) states of a phase-change material (PCM). b) Conventionally, all meta-atoms of a metasurface are altered in the same way by PCM switching. c) Our new approach allows for a direct optical addressing of individual meta-atoms within the metasurface.

2. Results

As proof of principle, we investigated an Al nanorod antenna array on a Si substrate covered by a thin film of the PCM $Ge_3Sb_2Te_6$ (GST-326) a protective capping layer of $(ZnS)_{80}$-$(SiO_2)_{20}$, similar to the sketches in Figure 1. These linear nanoantennas is used as a simple model system for

various kinds of meta-atoms. Upon phase change from the amorphous to the crystalline state, the real part of the GST-326 refractive index changes from $\underline{n}_A$ = 3.5 to $\underline{n}_C$ = 6.1 at 2000 cm^{-1}[1].

To demonstrate the effect of the position and size of crystalline volume inside of one meta-atom, we varied the size of elliptical crystalline spots centered on the antennas. Simulated relative reflection spectra of infinite periodic arrays with different C-spot sizes all show clear resonant behavior (Figure 2a**)**. Depending on the size of the C-spots (color coded for the long spot axis *l*), the resonance frequencies shift from ν_{res} = 2028 cm^{-1} in the amorphous case to 1692 cm^{-1} in the fully crystalline case. The larger the C-spot, the lower the resonance frequency ν_{res}. The measured relative reflectance spectra of differently switched 6x6 antenna arrays are shown in Figure 2b. The C-spot size has been controlled by adjusting the laser power employed to switch the material. The resonance frequency decreases with increasing spot size, from ν_{res} = 2006 cm^{-1} in the fully amorphous case down to ν_{res} = 1711 cm^{-1} for the largest spots.

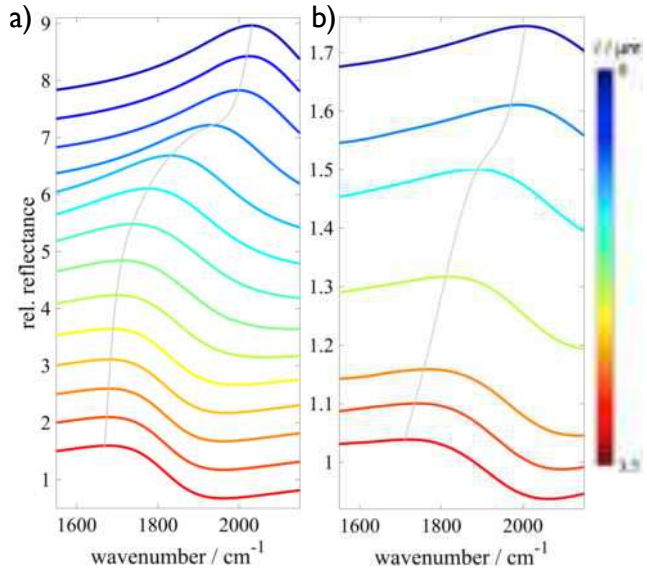


Figure 2: Simulated (a) and experimentally obtained reflectance spectra of identical linear nanoantennas which are differently addressed by switching a certain spot size (elliptical spot with long axis *l*) of the PCM.

3. Discussion

While the experimental spot-size dependent resonance shifting behavior qualitatively matches the predicted one, the total achieved shift at the maximum spot size is considerably smaller than simulated. Only after fully crystallizing the sample by annealing it in an oven at 180°C for 30 min, a comparable resonance shift was achieved. In order to understand this apparent difference, we have to investigate the three-dimensional nature of the optically induced crystallization and its consequences for the metasurface resonance tuning [7].

4. Conclusions

We show how we can fine-tune individual metallic infrared nanoantennas covered with the phase-change material $Ge_3Sb_2Te_6$ by locally addressing them with single visible laser pulses. Our work represents an advance towards actively programmable metasurfaces and the concept can be applied to a multitude of already present metasurface designs.

Acknowledgements

We acknowledge support by the German Federal Ministry of Education and Research (13N14151) and the DFG (German Science Foundation) SFB 917. A.-K.U.M. acknowledges funding from the RWTH scholarship for doctoral students, the ETH Zurich Postdoctoral Fellowship Program and the Marie Curie Actions for People COFUND Program. D.N.C. acknowledges a partial support by the DFG through the Heisenberg Fellowship (CH 407/7-2).

References

[1] A.-K.U. Michel, D.N. Chigrin, T.W.W. Maß, K. Schönauer, M. Salinga, M. Wuttig, and T. Taubner, Using Low-Loss Phase-Change Materials for Mid-Infrared Antenna Resonance Tuning. *Nano Letters* 13: 3470–3475, 2013.

[2] M. Wuttig, H. Bhaskaran and T. Taubner, Phase-change materials for non-volatile photonic applications, *Nat. Photon.* 11: 465–476, 2017.

[3] X. Yin, M. Schäferling, A.-K.U. Michel, A. Tittl, M. Wuttig, T. Taubner and H. Giessen, Active Chiral Plasmonics," *Nano Letters* 15: 4255–4260, 2015.

[4] X. Yin, T. Steinle, L. Huang, T. Taubner, M. Wuttig, T. Zentgraf and H. Giessen, Beam switching and bifocal zoom lensing using active plasmonic metasurfaces, *Light Sci Appl*. 6: e17016, 2017.

[5] Q. Wang, E.T.F. Rogers, B. Gholipour, C.-M. Wang, G. Yuan, J. Teng and N.I. Zheludev, Optically reconfigurable metasurfaces and photonic devices based on phase change materials, *Nat. Photon.* 10: 60–65, 2016.

[6] P. Li, X. Yang, T.W.W. Maß, J. Hanss, M. Lewin, A.-K.U. Michel, M. Wuttig and T. Taubner, Reversible optical switching of highly confined phonon-polaritons with an ultrathin phase-change material, *Nat. Mater*. 15: 870–875, 2016.

[7] A.-K.U. Michel, A. Hessler, S. Meyer, J. Pries, Y. Yu, T. Kalix, M. Lewin, J. Hanss, A. De Rose, T. W. W. Maß, M. Wuttig, D.N. Chigrin and T. Taubner, Advanced optical programming of individual meta-atoms beyond the effective medium approach, *submitted 2019*

Exploiting the polarization of nanoparticles near surfaces: position sensing, recoil optical forces, and full angular spectrum engineering

Lei Wei, Jack Kingsley-Smith, Michela F. Picardi, Anatoly V. Zayats, and Francisco J. Rodríguez-Fortuño

Department of Physics, King's College London and London Centre for Nanotechnology, London, United Kingdom
*corresponding author, E-mail: francisco.rodriguez_fortuno@kcl.ac.uk

Abstract

Small polarized nanoparticles exhibit remarkable electromagnetic properties even in the dipolar regime. The superposition of electric and magnetic dipoles on illuminated nanoparticles may result in far-field destructive interference and in near-field directionality, with applications on ultra-sensitive position sensing, optical forces due to recoil, and polarization control of the amplitude and phase of modal excitation in nearby waveguides. We describe our recent theoretical works on these applications.

1. Introduction

A small illuminated nanoparticle is polarized and scatters light. In general, this scattering can be studied via an expansion of electric and magnetic multipoles. If the particle is small compared to the wavelength, the lowest order electric and magnetic dipoles dominate the scattering fields. We conventionally describe dipolar modes as having the familiar toroidal radiation diagram; however, this description is naive as it assumes a single linear dipole component. In general, six different dipole components (p_x, p_y, p_z, m_x, m_y, m_z) may interfere coherently with each other, resulting in remarkable directionality properties of the nanoparticle. Much interest has surrounded the combination of electric and magnetic dipoles to create the so-called Huygens dipole, which exhibits far-field directionality with applications on metasurfaces. The use of circularly polarized dipoles as polarization-controlled directional sources of guided modes in nearby waveguides spurred huge interest with applications in light nanorouting, polarimetry and optical isolators. Recently, we showed that the combination of electric and magnetic dipoles can also be exploited for near-field directionalities [1], [2]. Practical ways of exciting all these dipoles may be: via engineering of the particle's polarizabilities, which enables controlling amplitude and phase of the different dipolar components, or by using structured illumination, which allows great control on the incident amplitude and phase of the electric and magnetic fields. In this work we summarize our recent research efforts in exploiting the properties of these particles for practical applications.

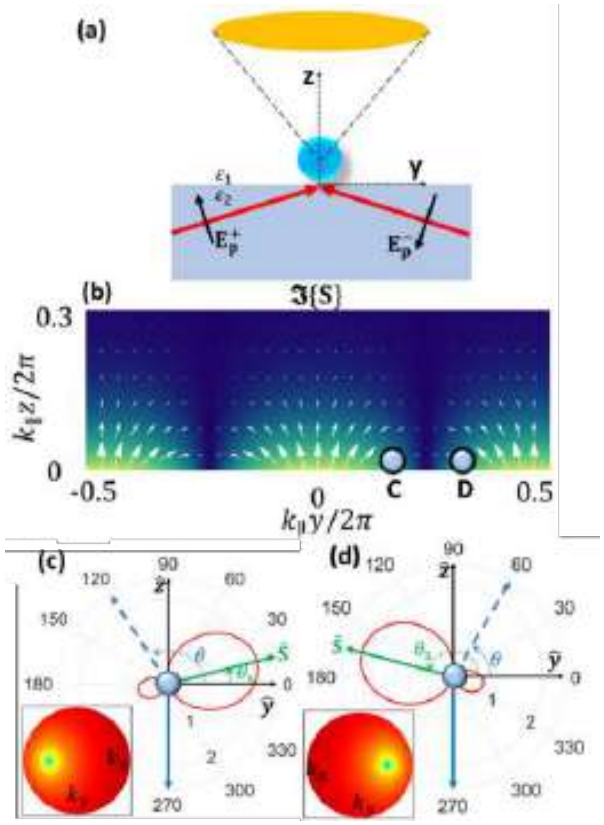


Figure 1: Illumination of a magnetoelectric particle with evanescent wave interference for position sensing. (a) Schematic of the proposed setup. (b) Map of interfering evanescent waves' Poynting vector (purely imaginary), with positions C and D separated by a distance λ/20. (c-d) Far-field radiation diagrams of the particle at locations C and D, respectively (showing YZ cut-plane and full half-space radiation diagram in the inset).

2. Far-field interference for position sensing

The interference of two evanescent waves, easily achieved by dual plane wave illumination in a total internal reflection setup (Fig 1a), gives rise to a remarkable interference pattern in which the Poynting vector may become purely imaginary [3] and changes rapidly its orientation with position along

the surface (Fig 1b). An engineered particle with electric and magnetic polarizabilities 90 degrees out of phase can be placed in this interference pattern to achieve perfect destructive interference in a specific far-field direction, whose angle is extremely sensitive to variations in the particle's position (Fig 1c), resulting in a practical method for position sensing [4].

3. Dipolar interference for optical forces

The far-field and near-field directional excitation enabled by dipole interference implies an imbalance in the net outgoing optical linear momentum, which necessarily requires the existence of recoil optical forces on the particles [5], such as that on a Huygens dipole near a surface (Fig 2).

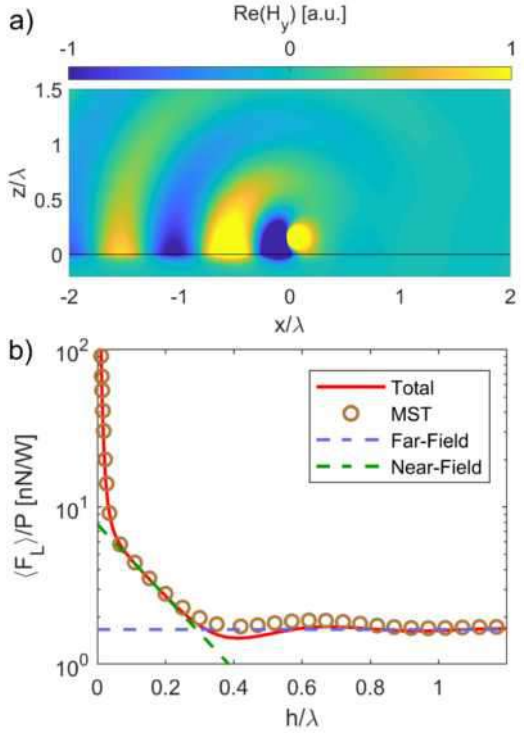


Figure 2: Optical forces of a Huygens dipole radiating near a plasmonic surface. (a) Electromagnetic fields of a Huygens dipole ($m_y = k_{SPP}\, c\, p_z$) at a distance 0.15λ over a surface of a metallic material (ε=−12+3i), exciting surface plasmons directionally due to near-field interference. (b) Resulting time-averaged lateral force F_L in the x-direction (normalized to the power radiated by the dipole) calculated analytically (line) and confirmed via Maxwell Stress Tensor integration (circles).

4. Engineering the full angular spectrum

Beyond simple dipoles such as circular, Huygens or Janus dipoles, we have endless possibilities. Fully exploiting the six degrees of freedom in dipolar sources enables a full control of their angular spectra, which can be applied for the directional excitation of modes with arbitrary amplitude, phases and even multimode control in nearby waveguides (Fig 3).

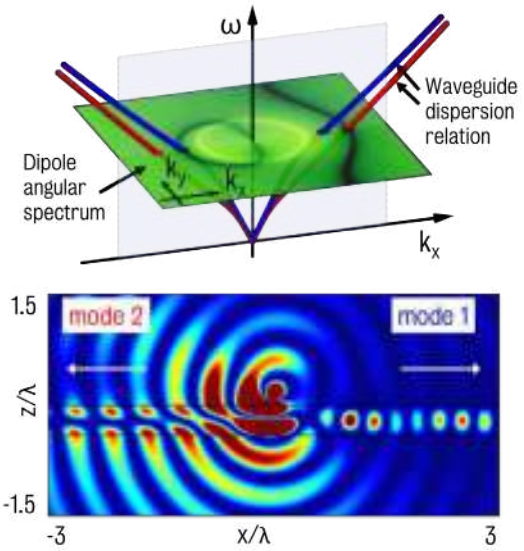


Figure 3: Dipolar angular spectrum engineering for full control of the excitation of nearby waveguided modes in terms of amplitude, phase and mode excited. (Top) Schematic of the idea, the angular spectrum can be designed in relation to the dispersion relation of the waveguide. (Bottom) Numerical simulation of designed dipole exciting different modes on different directions.

5. Conclusions

We have outlined several applications that arise from the deceptively simple system of a small particle near a surface or waveguide, from position sensing to optical forces. The advantage of using the dipole polarization is that these effects can be tuned via the illumination, potentially at ultrafast speeds.

Acknowledgements

European Research Council Starting Grant ERC-2016-STG-714151-PSINFONI, EPSRC (UK), Royal Society and the Wolfson Foundation.

References

[1] M. F. Picardi, A. V. Zayats, and F. J. Rodríguez-Fortuño, "Janus and Huygens Dipoles: Near-Field Directionality Beyond Spin-Momentum Locking," *Phys. Rev. Lett.*, vol. 120, no. 11, p. 117402, Mar. 2018.

[2] M. F. Picardi, M. Neugebauer, J. S. Eissman, P. Banzer, F. J. Rodríguez-Fortuño, and A. V. Zayats, "Experimental demonstration of linear and spinning Janus dipoles for polarisation and wavelength selective near-field coupling," *ArXiv*, p. 1901.07236, 2018.

[3] L. Wei, M. F. Picardi, J. J. Kingsley-Smith, A. V. Zayats, and F. J. Rodríguez-Fortuño, "Directional scattering from particles under evanescent wave illumination: the role of reactive power," *Opt. Lett.*, vol. 43, no. 14, p. 3393, Jul. 2018.

[4] L. Wei, A. V. Zayats, and F. J. Rodríguez-Fortuño, "Interferometric Evanescent Wave Excitation of a Nanoantenna for Ultrasensitive Displacement and Phase Metrology," *Phys. Rev. Lett.*, vol. 121, no. 19, p. 193901, Nov. 2018.

[5] J. J. Kingsley-Smith, M. F. Picardi, L. Wei, A. V. Zayats, and F. J. Rodríguez-Fortuño, "Optical forces from near-field directionalities in planar structures," *ArXiv*, Nov. 2018.

Lighting up magneto-optics to its limit with dark plasmons

Mario Zapata-Herrera[1,5*], Alberto López-Ortega[1], Nicolò Maccaferri[2], Matteo Pancaldi[3], Mikel Garcia1[2], and Paolo Vavassori1,[1,4]

1. CIC nanoGUNE, Donostia–San Sebastian 20018, Spain
2. Faculty of Science, Technology and Communication, Université du Luxembourg, Campus Limpertsberg L-1511, Luxembourg
3. Department of Physics, Stockholm University, SE-106 91 Stockholm, Sweden
4. IKERBASQUE, Basque Foundation for Science, Bilbao 48013, Spain
5. Facultad de Ciencias y Educación, Universidad Distrital Francisco José de Caldas, Cra 7 No. 40B-53, Bogotá, Colombia

*corresponding author, E-mail: m.zapata@nanogune.eu

Abstract

In this work we present a new strategy to actively enhance the magneto optical activity beyond its current limits by the excitation of a hybrid dark-bright modes in a magnetic-disk/metallic-ring plasmonic nanocavity.

1. Introduction

Magneto-plasmonic structures composed by arrangements of magnetic nanoantennas can be used for the active control of light polarization. Their unique optical properties arise from combining strong local enhancements of electromagnetic fields in surface plasmon excitations with the magneto-optical (MO) activity inherent to ferromagnetic materials that can be controlled by external magnetic fields.

Up to now, most studies exploiting metal magneto-plasmonic nanostructures focused on the effects of the scattered electromagnetic field due to the excitation of localized dipolar plasmonic resonances (LPRs). Indeed, dimeric and multilayered hybrid noble/ferromagnetic metals structures as well as purely ferromagnetic nanoantennas have demonstrated the possibility to control and amplify the MO properties via plasmonic excitations [1-3]. For a circular disk-like magneto-plasmonic nanoantenna, incident radiation of proper wavelength excites a LPR. When the nanoantenna is magnetic-field (H) activated, a second LPR is induced by the inherent MO activity. The MO-induced LPR (MOLPR) is driven by the LPR in a direction orthogonal to both H and the LPR. The ratio between the MOLPR and the LPR corresponds to the ratio between the response of orthogonal radiating electric dipoles that determine the magnetic-field induced polarization change of scattered light [4]. For typical metallic constituents, the electric dipole per unit volume associated to the MOLPR is about 2-orders of magnitude larger than that in a film or bulk magnetic material counterparts. This remarkable value represents the theoretical limit for the maximum achievable MO activity amplification. However, the MOLPR amplification results from a parallel enhancement of the electric dipole per unit volume associated to the LPR by typically 1-order of magnitude with respect to film or bulk counterparts. This simultaneous excitation of the LPR and MOLPR limits the maximum achievable enhancement of magnetic-field activated change in polarization to only 1-order of magnitude, as observed experimentally [1-3]. Thereby, using bright dipolar LPRs this 1-order of magnitude enhancement of MO activity represents a sort of fundamental upper limit that cannot be overcome, hindering the applications of magneto-plasmonics to active nanophotonics and flat-optics.

Here, we propose and demonstrate a strategy to overcome the aforementioned limitation based on a hybridization with high order multi-polar dark modes as a viable and powerful mean to amplify the magneto-optical activity of magneto-plasmonic nanoantennas and achieve an unprecedented active control of the light polarization under a magnetic field. Symmetry broken non-concentric magneto-plasmonic-disk/plasmonic-ring nanostructures are designed to enable the free-space light excitation of dark modes in the plasmonic-ring as well as their hybridization with the dipolar plasmonic resonance of the magneto-plasmonic disk.

2. Discussion

The magneto-optical response of a hybridized system composed by a non-concentering Nickel (permaloy) disk inside a gold (labeled as NCRD in Fig. 1) is drastically modified by the excitation of a hybrid dark-bright mode

resulting in an extraordinary amplification of the magneto-optical activity.

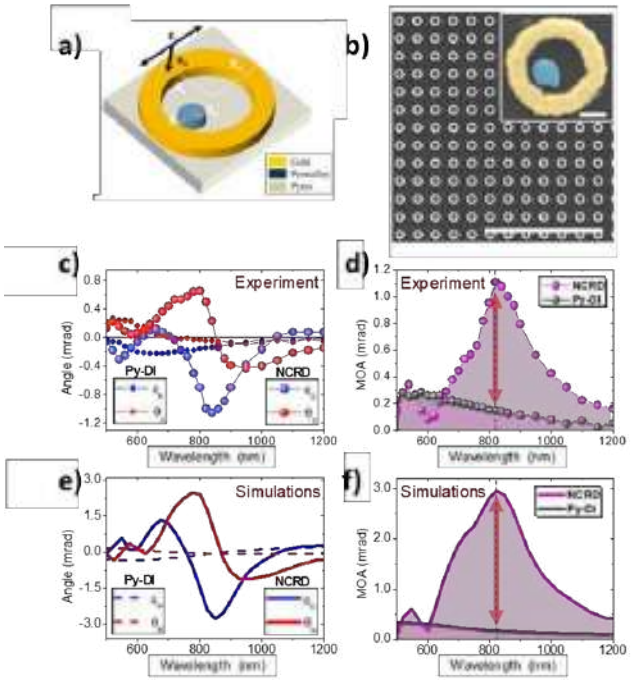


Figure 1: **a)** Schematic and **b)** realistic NCRD hybrid structure. **c)** and **e)** show the experimental results and simulation of the Kerr rotation and ellipticity, respectively. **d)** and **f)** show the magneto-optical (MOA) for the bare permaloy disk (Py) and the hybrid non-concentric ring-disk (NCRD)

This far more efficient magnetic field control of the polarization of light is explained by a large enhancement of the radiant magnetic-field activated magneto-optical bright dipole in the magneto-plasmonic nanoantenna driven by the low-radiant hybrid dark-bright mode. The subradiance of the hybrid mode arises from an overall reduction of the total dipole moment due to the antisymmetric coupling of the parent plasmons. While bare magneto-plasmonic nanoantennas enhance the magneto-optical response typically by 1 order of magnitude with respect to the corresponding film counterpart, in the present case the peculiar resonant mechanism leads to an observed enhancement approaching the theoretical limit of 2 orders of magnitude.

The experimental results showed in Fig 1. were complemented with a detailed study of the surface charge density maps and the strength of optical and magneto-optical electric dipoles using the Finite Element Method (FEM) implemented in the commercial COMSOL Multiphysics software in order to explain the mechanism behind. Simulations show that the MOA features are a consequence of the subradiant character of the hybrid mode that leads to an overall reduction of the total optical dipole moment.

3. Conclusions

High-order multi-polar dark plasmon resonances in magnetoplasmonic nanocavities can be used to achieve unprecedented enhancement of the magneto-activated optical response, beyond the present limitations of magnetoplasmonic nanoantennas, enabling a far more efficient active control of the light polarization under weak magnetic fields. The novel concept showed in this work opens a new path towards applications of magnetoplasmonics to a variety of fields ranging from active nanophotonics to sensing. This mechanism might have a huge impact on forthcoming photonic nanotechnologies based on plasmon-mediated local enhanced manipulation of electronic spin-currents opening excellent perspectives in disclosing novel opto-electronic phenomena.

Acknowledgements

This work was supported by the Spanish Ministry of Economy, Industry and Competitiveness under the Maria de Maeztu Units of Excellence Programme - MDM-2016-0618 and from the European Union under the Project H2020 FETOPEN-2016-2017 “FEMTOTERABYTE” (Project n. 737093).

References

[1] Chen, J. *et al.* Plasmonic Nickel Nanoantennas. *Small* **7**, 2341–2347 (2011).

[2] Maccaferri, N. *et al.* Anisotropic Nanoantenna-Based Magnetoplasmonic Crystals for Highly Enhanced and Tunable Magneto-Optical Activity. *Nano Lett.* **16**, 2533–2542 (2016).

[3] López-Ortega, A., Takahashi, M., Maenosono, S. & Vavassori, P. Plasmon induced magneto-optical enhancement in metallic Ag/FeCo core/shell nanoparticles synthesized by colloidal chemistry. *Nanoscale* **10**, 18672–18679 (2018).

[4] Maccaferri, N. *et al.* Tuning the Magneto-Optical Response of Nanosize Ferromagnetic Ni Disks Using the Phase of Localized Plasmons. *Phys. Rev. Lett.* **111**, 167401 (2013).

Ultrafast dynamics at fs-laser-excited magnetic meta-surfaces

Alexandr Alekhin and Vasily Temnov

Institut des Molecules et Materiaux du Mans, UMR CNRS 6283, Le Mans Universite, Le Mans, France
vasily.temnov@univ-lemans.fr

Interactions of femtosecond laser pulses with magnetic materials result in a large variety of physical phenomena from different fields of physics: nonlinear optics, magnetism, ultrafast spintronics, acoustics, shock waves and/or laser-induced phase transitions. From a metrological perspective different time scales associated with those transient phenomena can be measured with femtosecond temporal resolution in conventional all-optical pump-probe experiments utilizing linear and non-linear magneto-optical techniques. However, in a typical pump-probe experiment, absorption of ultrashort femtosecond laser pulse by an opaque magnetic material may trigger very complex dynamics including coherent and incoherent excitations of electronic, phononic and magnetic subsystems. Different underlying processes evolve on several time scales, and their characteristic time constants can be close to each other rendering the identification of the underlying mechanisms extremely challenging.

One of the ways to reduce the complexity of ultrafast optical measurements is to study the experimentally accessible monochromatic excitations and their interactions. To be more specific, here we are talking about the periodic oscillations of electromagnetic fields at the (fundamental, second harmonic, third harmonic etc.) optical frequencies, elastic deformations (surface acoustic waves) at MHz-THz frequencies and time-dependent perturbations of the magnetic order (ferromagnetic resonance, magneto-static or exchange-coupled magnon modes) oscillating at GHz-THz frequencies.

Apart from a trivial case of oscillating optical fields, the temporal periodicity of fs-laser-induced magnetic and acoustic dynamics is not granted. For example, the absorption of an ultrashort optical pulse in a magnetic material results in a famous phenomenon of ultrafast demagnetization [1]. However, under specific conditions dictated by the orientation of an external magnetic field, ultrafast demagnetization can trigger ferromagnetic resonance (FMR) precession and oscillating spin-wave resonances at elevated frequencies in ferromagnetic thin films [2,3].

At the same time, fs-laser excitation of opaque materials is signified by the thermo-elastic generation of single-cycle acoustic pulses with picosecond time duration [4], which may reach giant strain amplitudes up to 1%, strong enough to induce the nonlinear lattice dynamics at the nano-scale [5] or even switch magnetization in magnetostrictive thin films [6] and ferromagnetic nanostructures [7].

Monochromatic acoustic waves can be generated by fs-laser excitation of periodic gratings, either in the so-called transient grating geometry [8-9] or using permanent gratings [10]. The characteristic feature in these experiments is the possibility to excite monochromatic surface acoustic waves (SAWs) with frequencies determined by the grating periodicity and going up to a few tens of GHz when using deeply sub-wavelength periodic structures with periods of the order of 100 nm. This sub-wavelength spatial periodicity for magneto-acoustic studies represents the link between ultrafast magneto-acoustics and (magneto-)optics of meta-surfaces. The intrinsic possibility to bring the FMR-frequency in resonance with acoustic waves, for example using a proper combination of grating periodicity and the magnitude of an external magnetic field, can result in the resonant enhancement of the FMR precession [8-10], with the onset of parametric instabilities [9]. Whereas the experimental conditions to obtain large-amplitude FMR precession through the fs-laser mediated resonant magneto-elastic interactions have not yet been optimized, such technique would provide new possibility to modulate the optical properties of magnetic meta-surfaces. Given that the static nonlinear magneto-optical and/or magneto-plasmonic effects are more pronounced than the linear ones [11-14], it makes sense to go beyond the time-resolved measurements based on linear magneto-optical effects and probe dynamics of resonant magneto-acoustic interactions [8-10] with nonlinear magneto-optical detection schemes [11-14], hoping to develop real-life applications with magnetic meta-surfaces modulated on ultrafast time scales.

Acknowledgements

The work was financially supported by Strategie internationale "NNN-Telecom", ANR-DFG "PPMI-NANO" (ANR-15-CE24-0032 and DFG SE2443/2), PRC CNRS-RFBR "Acousto-magneto-plasmonics", Deutsche Forschungsgemeinschaft (AL2143/2-1).

References

[1] E. Beaurepaire at al., *Phys. Rev. Lett.*76: 4250, 1996.

[2] M. van Kampen et al., *Phys. Rev. Lett.* 88: 227201, 2002.

[3] R. Salikhov et al., *Phys. Rev. B*, 2019 (in print).

[4] C. Thomsen et al., *Phys. Rev. B* 34 : 4129, 1986.

[5] V. V. Temnov et al., *Nature Comm.* 4: 1468, 2013.

[6] O. Kovalenko et al., *Phys. Rev. Lett.* 110: 266602, 2013.

[7] V.S. Vlasov et al., *Phys. Rev. B, 2019 (under review)*

[8] J. Janusonis et al., *Phys. Rev. B* 94: 024415, 2016.

[9] C. Chang et al., *Phys. Rev. B* 95: 060409, 2017.

[10] C. Chang et al., *Phys. Rev. Applied* 10 : 034068, 2018.

[11] I. Razdolski et al., *ACS Photonics* 3: 179, 2016.

[12] V.V. Temnov et., *J. of Optics* 18, 0903002, 2016.

[13] L. Michaeli et al., *Phys. Rev. Lett.*118: 243904, 2017.

[14] M. Tran et al., *Phys. Rev. B* 98: 245425, 2018.

Single-shot all-optical switching in GdFeCo alloys using pulses of varying photon energies and durations

Carl S. Davies[1,*], Thom Janssen[1], Johan Mentink[2], Arata Tsukamoto[3], Alexey V. Kimel[2], Lex van der Meer[1], Andrzej Stupakiewicz[4], and Andrei Kirilyuk[1]

[1]FELIX Laboratory, Radboud University, Nijmegen, The Netherlands
[2]Institute of Molecules and Materials, Radboud University, Nijmegen, The Netherlands
[3]College of Science and Technology, Nihon University, Chiba, Japan
[4]University of Bialystok, Bialystok, Poland
*corresponding author, E-mail: c.davies@science.ru.nl

Abstract

We experimentally investigate how the process of deterministic all-optical switching in GdFeCo alloys depend on the properties of the optical pulse i.e. photon energy and pulse duration. We reveal that the switching of magnetization can be achieved using photons in the mid-infrared spectral range, and there exists a composition-dependent pulse-duration threshold above (below) which the switching fails (succeeds). To explain our findings, we develop a simple but elegant phenomenological theory of longitudinal magnetization dynamics.

1. Introduction

Ultrafast reversal of magnetization can generally be achieved through modifying either the magnetic properties (such as magnetic anisotropy[1]) or the magnetization length (i.e. demagnetization). Despite the fact that deterministic all-optical switching of GdFeCo was discovered more than half a decade ago[2], deep physical understanding of the process is still lacking. To date, GdFeCo is the only material known to exhibit ultrafast deterministic all-optical switching, whereby its net magnetization can be reversed upon exposure to a single femtosecond laser pulse in the absence of any bias magnetic field. Experimentally, it has been revealed[3] that the process evolves in the ferrimagnet GdFeCo via the simultaneous optically-induced demagnetization of both sublattices (gadolinium and iron-cobalt), giving rise to a transient ferromagnetic state on the picosecond timescale. Subsequently the magnetization of both sublattices reverse.

While this description has been supported by experimental measurements[2] and atomistic simulations[2], several recent findings have suggested that this description is incomplete. In particular, experiments shown in Ref. [4] have demonstrated that an ultrafast laser pulse is not a prerequisite for deterministic all-optical switching. Using a single pulse of duration 15 ps, for example, the authors in Ref. [4] were able to switch the magnetization of a particular alloy of GdFeCo. In addition, it is still an open question as to whether the photon energy represents an important constraint on the material process.

In this work, we experimentally investigate how the process of ultrafast helicity-independent all-optical switching evolves as a function of both the photon energy, the pulse duration and the chemical composition of GdFeCo. To explain our results, we expand on a simple but elegant mean-field theory. This model not only successfully reproduces our experimental findings, but provides a general formalism which should be able to predict and explain ultrafast all-optical switching in a wider array of materials.

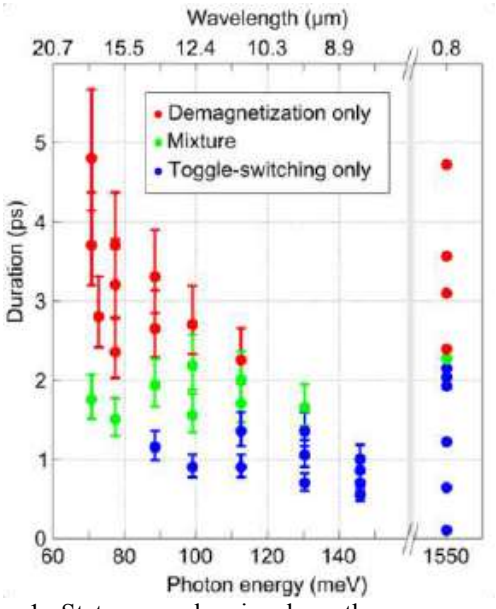


Figure 1: State map showing how the process of all-optical switching in $Gd_{24}(FeCo)_{76}$ evolves as function of both the photon energy and the pulse duration.

2. Experimental measurements

We perform experiments using optical pulses sourced from FELIX Laboratory in the mid-infrared spectral range.

Through magneto-optically imaging the effect of exposing different $Gd_x(FeCo)_{100-x}$ alloys to multiple pulses, we were able to identify that all-optical switching was largely unaffected by the photon energy (Figure 1). Moreover, we identified the existence of a composition-dependent pulse-duration threshold. For example, a pulse of duration 6 ps is capable of switching the magnetization in $Gd_{27}(FeCo)_{73}$, but incapable of doing the same in $Gd_{23}(FeCo)_{77}$. In the latter case, only demagnetization is observed.

3. Modelling deterministic all-optical switching

To explain our experimental results, we improve upon the phenomenological mean-field approach presented in Ref. [5]. Specifically, we solve the coupled equations of motion

$$\frac{dS_{Gd}}{dt} = \lambda_e\left(H_{Gd} - H_{Fe}\right) + \lambda_{Gd} H_{Gd}, \quad (1)$$

$$\frac{dS_{Fe}}{dt} = -\lambda_e\left(H_{Gd} - H_{Fe}\right) + \lambda_{Fe} H_{Fe}, \quad (2)$$

Where S_{Gd} and S_{Fe} are the temperature-dependent angular momenta of the gadolinium and iron sublattices respectively, and damping terms of different origin are represented by λ. The effective fields acting on the indicated gadolinium and iron site are given by a combination of the time-dependent heating and the composition-dependent inter- and intra-sublattice exchange interactions. The thermal load delivered by the optical pulse is essentially captured by a simple form of the two-temperature model, given by a rise time of τ and a subsequent exponential decay.

Using our mean-field approach, we successfully demonstrate that as one increases x, the pulse duration τ capable of achieving single-shot switching of magnetization increases monotonically. When using an ultrashort pulse, both sublattices demagnetize at substantially different rates, giving rise to switching via the formation of a transient ferromagnetic state. If the pulse instead has a duration on the order of picoseconds, the sublattices demagnetize at similar rates, predominantly exchanging angular momentum between each other. If the duration is too long however, we identify a peculiar evolutionary trajectory whereby the gadolinium sublattice actually becomes first to demagnetize fully[6]. This gives rise to a transient ferromagnetic state, with the magnetization Gd becoming parallel to the still-demagnetizing Fe sublattice. In this form, switching is forbidden. Using these trends, we are able to fully explain our experimental findings.

4. Conclusions

In summary, we have demonstrated that the photon energy plays no significant role in the process of deterministic all-optical switching of magnetization in GdFeCo. Rather, the key criterion lies in the pulse duration, whereby there exists an alloy-dependent threshold below/above which the ultrafast toggling succeeds/fails. We have expanded upon a phenomenological mean-field theory to successfully predict and explain this compositional dependence. Our results and explanatory model not only resolve fundamental questions concerning the origin and mechanism of all-optical toggle-switching, but could also potentially be used to predict and explain all-optical toggle-switching effects in a broader class of ferrimagnetic alloys.

Acknowledgements

The authors thank S. Semin, T. Toonen and all technical staff at FELIX for technical support. This research has received funding from de Nederlandse Organisatie voor Wetenschappelijk Onderzoek (NWO).

References

[1] C. S. Davies *et al*. Anomalously Damped Heat-Assisted Route for Precessional Magnetization Reversal in an Iron Garnet. *Phys*. *Rev*. *Lett*. 122, 027202 (2019).

[2] T. A. Ostler *et al*. Ultrafast heating as a sufficient stimulus for magnetization reversal in a ferrimagnet. *Nature Comms*. 3, 666 (2012).

[3] I. Radu *et al*. Transient ferromagnetic-like state mediating ultrafast reversal of antiferromagnetically coupled spins. *Nature* 472, 205 (2011).

[4] G. Gorchon *et al*. Role of electron and phonon temperatures in the helicity-independent all-optical switching of GdFeCo. *Phys*. *Rev*. *B* 94, 184406 (2016).

[5] J. H. Mentink *et al*. Ultrafast spin dynamics in multisublattice magnets. *Phys*. *Rev*. *Lett*. 108, 057202 (2012).

[6] U. Atxitia *et al*. Controlling the polarity of the transient ferromagneticlike state in ferrimagnets. *Phys*. *Rev*. *B* 89, 224421 (2014).

Electrochemical plasmonics
for dynamic control of optical properties of self-assembling metamaterials

J.B.Edel[1], A.A.Kornyshev[1*], A.R.Kucernak[1], Y.Ma[1], Y.Montelongo[1], D.Sikdar[1,2], M.Urbakh[3], L.Velleman[1], C.Zagar[1,4]

[1] Department of Chemistry, Imperial College London, Molecular Sciences Research Hub, White City, W12 0BZ London,UK
[2] Department of Electronics and Electrical Engineering, Indian Institute of Technology Guwahati, Guwahati-781039, India
[3] School of Chemistry, University of Tel Aviv, Tel Aviv 69978, Israel
[4] Department of Physics, Imperial College London, South Kensington, SW7 2AZ London, United Kingdom
*corresponding author, E-mail: a.kornyshev@imperial.ac.uk

Abstract

This talk will overview a new direction of research based on self-assembly of plasmonic nanoparticles at electrochemical liquid-liquid or solid-liquid interfaces. Optical properties of such systems can be varied in real time via voltage-control over the structure and density of the nanoparticle assemblies. Potential applications involve switchable mirror-windows, tunable color mirrors, optical cavities, and pixels.

1. Introduction

Progress in photonic metamaterials was made possible by advances in nanotechnology. Many of such materials, however, can only perform a single target function. Not surprisingly, already Meta-2014 was opened with a provocative statement: "The time of metamaterials is over… It is the time of tuneable metamaterials" (N. Zheludev). Realization of such platforms would allow properties of such functional metamaterials to be tuned in real-time, with major implications for absorbers in solar cells, antennae, super-lenses, cloaking, sensors –amongst others. Tunability can be reached by utilization of fine electrodynamic effects, controlling light by light, etc, but also via changing the structure of metamaterials in real time. To make the latter kind of tuning and switching fast, is a challenge, but not an unsolvable one. Our team pursued this direction of research, and its current status is summarised below.

2. Chemical tuning of nanoplasmonic meta-arrays

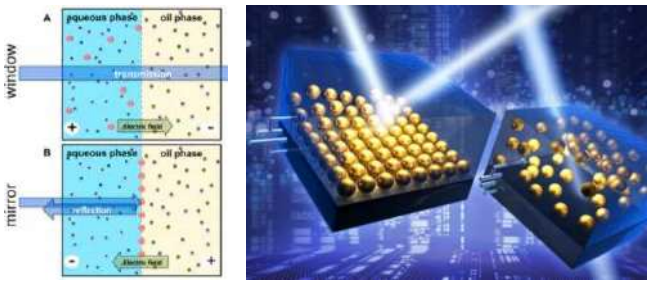
We responded to this challenge first with developing the 'nanotechnology-free' concept of chemically tunable self-assembly of plasmonic **n**ano**p**articles (NPs), such as quasi-2D arrays NPs at a liquid|liquid (LLI) and solid|liquid (SLI) interfaces [1,2]. We have demonstrated that such arrays could be used for ultrasensitive SERS detection of trace analytes –e.g. proxies for pollutants, illegal substances, terror agents – that get into 'hot spots' between NP's [3].

The array structure was controlled by tuning the composition of the solutions (electrolyte concentration or pH). Indeed, NPs are functionalized by ligands that dissociate, in the aqueous phase, leaving negative charges at their terminal groups. This is necessary to prevent NPs to agglomerate in the bulk of the solution, otherwise driven by Vand-der-Walls attraction. pH and electrolyte concentration control the repulsion between NPs. More basic pH will increase dissociation of ligands and thereby increase the charge. Increase of electrolyte concentration will decrease the Debye length and will weaken the repulsion.

Starting with arbitrary conditions that do not allow NPs' agglomeration in the bulk, we cannot expect them to come too close to each other at the surface. Still, they come much closer to each other there, than in the bulk: because of the strong driving force for them to be at the interface, they have to tolerate the proximity of each other. For instance, at an oil|water interface each individual NP strongly adsorbs, to block the energetically unfavorable contact between water and oil; the effect called 'capillary attraction'. One can obtain denser quai-2D monolayers of NPs by minimizing their charges down to and maximizing the electrolyte concentration up to the values that yet do not allow their agglomeration in the bulk. We have been able to establish the conditions of this fine balance.

We performed a complex study of the structure and optical properties of such NP arrays at DCE/water interface. Within the same setup, we performed a combination of grazing incidence, small angle X-ray scattering and in situ optical reflectivity. From the X-ray and optical data, we could determine (from a combination of experimental [4] and original theoretical [5] results) the average distance between NPs, the long-range order, and reflectivity –all as a function of concentration electrolytes, either of inorganic electrolyte in water, or organic electrolyte in oil. Incorporating the obtained values of array's 'lattice constants' into the theory of optical reflectance from such arrays [5], we could calculate the reflectance spectra for each electrolyte concentration and compare them with those measured in the same system [4]. The excellent match between the theory and experiments demonstrated that the *physics worked exactly as expected*! These studies gave us confidence that we could control these novel nanoplasmonic platforms by smart 'physical chemistry, i.e. generate tunable self-assembled metamaterials. But it was not a *real-time reversible control*.

3. Voltage-controlled tuning of meta-arrays and switching dynamics in electrochemical cells



A sketch of a self-assembled voltage-controlled of negatively charged Au NPs at electrified **i**nterface of **t**wo **i**mmiscible **e**lectrolytic **s**olutions (**ITIES**), in reflecting mode (left) and transmitting mode (right). Switching on- and off- reflection or modification of the reflection spectra can be achieved by controlling the density of charged nanoparticle arrays adsorbed at the interface through the variation of applied voltage.

It was clear to us, that *electrochemistry* will be the game changer here. At electrochemical interfaces, with tiny voltage variation, one can create localised electric fields that may dramatically change the structures of adsorbed NP arrays and their optical properties. We demonstrated this by creating the first electrically switcheable mirror based on voltage controlled self-assembly of functionalized gold NPs at the interface of two immiscible electrolytic solutions see video at https://youtu.be/68J0yLvrvJE) [6]. We have shown that it is possible to transition between a mirror and window and back again using a mere 0.5 V - voltage variation through its effect on the density of the NP arrays and their resulting optical response.

The reflectivity spectrum, the maximum of which is centered near the frequency of coupled localized plasmon resonances in NPs, gradually shifts to the blue and its intensivity gradually vanishes with reduction of the density of the NPs array, making the interface transparent. This process is controlled by the voltage drop across the interface: polarizing water positively, we invite negatively charged NPs to leave the potential wells at the interface and move to the aqueous bulk; polarizing water negatively we stimulate adsorption of NPs.

A switch of a different kind, based on voltage-controlled adsorption-desorption of NPs on a metal substrate, described earlier in detail theoretically [7], was reported in Ref. [8]. The difference of this system from the LLI case is as follows. Metallic electrode (in our study – silver, covered by thin protective film of titanium nitride) reflects light itself, but when covered by a dense array of plasmonic NPs (Au, in our case), an effect of resonance quenching of reflection by increased absorption of light in the NP-array|metallic substrate system turns on. These causes a dip in reflectivity spectrum, centered near the frequency of localized plasmons in NP. The latter shifts to the red, with denser population of the surface by NPs. All-in-all, some range of frequencies are get reflected less, and the mirror becomes colored. The density of NP arrays is again controlled by voltage: positively polarized electrode will cause stronger adsorption ('electrosorption') of negatively charged NPs, decreasing the average inter-NP distance. Through affecting this distance, voltage controls the color of the mirror.

Both for LLI and SLI, studying the evolution of the spectra with time, we learn about the kinetics of voltage-controlled adsorption/desorption of NP, by fitting the spectra to the theory that relates the latter with the density of NP arrays at the interface. Generally, reproduction by the theory [5,7] of the experimental data both for the LLI and SLI systems [6.8] is amazing; the theory itself, systematically tested againt COMSOL simulations, shows excellent correspondence with the latter.

A set of other interesting scenarios have been also considered (see e.g. [9,10]). Several other papers are submitted for publication, whereas the disclosure of some other results awaits patenting.

Acknowledgements

The project was supported by an Engineering and Physical Sciences Research Council Grant, "Electrotunable Molecular Alarm", EP/L02098X/1. J.B.E. also acknowledges receipt of European Research Council Consolidator Grant (NanoPD). Y.M. has been supported in part by a China Scholarship Council, Imperial Scholarship (201506320194).

References

[1] J.B.Edel, A.A.Kornyshev, M.Urbakh, "Self-Assembly of Nanoparticle Arrays for Use as Mirrors, Sensors, and Antennas," ACS Nano 7, 9526-9632 (2013).
[2] J.Edel, A.A.Kornyshev, A.Kucernak, M.Urbakh, "Fundamentals and applications of self-assembled plasmonic nanoparticles at interfaces", Chem. Soc. Rev. 45, 1581-1596 (2016).
[3] M.P. Cecchini, V.A. Turek, J. Paget, A.A. Kornyshev, J.B. Edel, "Self-assembled nanoparticle arrays for multi-phase trace analyte detection", Nature Materials 12, 165-171 (2013).
[4] L.Velleman, D.Sikdar, V.A.Turek, S.J.Roser, A.R.Kucernak, A.A.Kornyshev, J.B.Edel, "Tuneable 2D self-assembly of plasmonic nanoparticles at liquid|liquid interfaces", Nanoscale, 8, 19229 (2016).
[5] D.Sikdar, A.A.Kornyshev, "Theory of tailorable optical response of two dimensional arrays of plasmonic nanoparticles at dielectric interfaces", Sci. Rep. 6, #33712 (2016).
[6] Y.Montelongo, D.Sikdar, Y.Ma, A.J.S. McIntosh, L.Velleman, A.R.Kucernak, J.B.Edel, A.A.Kornyshev, "Electrotuneable nanoplasmonic liquid mirror", Nature Materials 16, 1127-1135 (2017).
[7] D.Sikdar, S.Bin Hasan, M.Urbakh, J.Edel, A.A.Kornyshev, "Unravelling the optical responses of nanoplasmonic mirror-on-mirror metamaterials", Phys.Chem.Chem.Phys. 18, 20486-20498 (2016).
[8] Y.Ma, C.Zagar, D.Klemme, D.Sikdar, L.Velleman, Y. Montelongo, S.-H.Oh, A.R.Kucernak, J.B.Edel, A.A.Kornyshev, "Tunable nanoplasmonic mirror at electrochemical interface", ACS Photonics 5, 4604-4616 (2018).
[9] H.Weir, J.B.Edel, A.A.Kornyshev, D.Sikdar, "Towards electrotunable Fabry-Perot Interferometer", Sci.Rep. 8, 2045-2322 (2018).
[10] D.Sikdar, A.Bucher, C.Zagar, A.A.Kornyshev, "Electrochemical plasmonic metamaterials: towards fast electro-tuneable reflecting nanoshutters", Faraday Discuss. 199, 585-602 (2017).

Atomically-thin tunable zone plate lens

Jorik van de Groep[1], Jung-Hwan Song[1], Umberto Celano[1,2], and Mark L. Brongersma[1]

[1]Geballe Laboratory for Advanced Materials, Stanford University, Stanford, USA
[2]IMEC, Leuven, Belgium
*corresponding author, E-mail: groep@stanford.edu

Abstract

Next-generation flat optics require dynamic control over optical functionalities. We demonstrate actively-tunable and atomically-thin optical lenses by carving them directly out of monolayer WS_2. Using ion-liquid gating to dynamically manipulate the material's exciton resonance we show actively modulation of the focal intensity.

1. Introduction

Since the development of diffractive optical elements in the 1970s research has focused on replacing bulky optical elements such as lenses and grating by thin counterparts. Over the last decade, nanophotonic metasurfaces rapidly advanced the development of flat optical elements based on the realization that resonant optical antenna elements enable local phase control. Present applications of metasurface flat optical elements include lenses, polarization control, and beam steering. Next-generation applications of flat optics require dynamic control over optical functionalities, e.g. the focal position or efficiency of optical elements. However, most nanophotonic structures are static after design and fabrication. Current approaches for dynamic control like electrical gating exhibit limited tunability due to the finite few-nm extend of the depletion and accumulation layers as result of Coulombic screening.

2. Results

Here, we demonstrate actively-tunable and atomically-thin optical lenses by carving them directly out of monolayer transition-metal dichalcogenides (TMDCs) like WS_2 with a strong excitonic resonance in the visible spectral range. This turns the 2D material into the antenna or metamaterial and incorporation of active materials into larger antenna structures will no longer be needed. Due to their sub-nm thickness, these materials are highly tunable through external control. We demonstrate dynamic electrical tuning of the focusing efficiency through manipulation of the excitonic material resonance properties as opposed to tuning of antenna resonances.

Large-area monolayer WS_2 on sapphire is obtained commercially and covered by a monolayer of graphene (Gr) through large-area manual wet-transfer. The graphene functions as a transparent conducting electrode to provide homogeneous gating of the WS_2. Next, Au electrodes and reference pads are fabricated using optical lithography, metal deposition and lift-off. The Gr/WS_2 bi-layer is then patterned into Fresnel zone plates through e-beam lithography and reactive-ion etching. The lens has a 1 mm diameter with a focal length $f = 2$ mm. Finally, an electro-chemical cell is fabricated on top of the sample and filled with ionic liquid (DEME-TFSI) to facilitate gating of the WS_2.

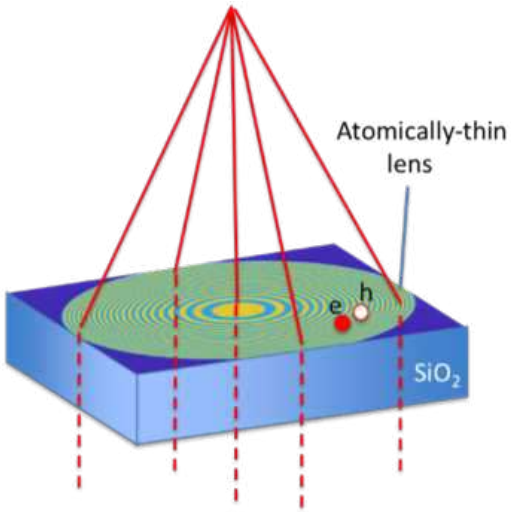


Figure 1: Atomically-thin zone plate carved into a 2D material with a strong excitonic response. Active tuning of the focusing intensity is demonstrated and quantified.

Using confocal microscopy, we characterize the focus that is formed above the surface in transmission (illuminated through substrate), and demonstrate active modulation of the focal intensity.

3. Summary

We demonstrate actively-tunable and atomically-thin optical lenses by carving them directly out of monolayer WS_2. Using confocal microscopy we characterize the focussing efficiency spectrum and identify the role of excitonic light scattering in the efficiency spectrum. Next, we employ ion-liquid gating to actively manipulate the excitonic materials resonance and use this to demonstrate active intensity modulation in the focus of the lens.

Beyond plasmonic functional materials: the challenge of magneto-plasmonics towards single molecule detection

Maria Grazia Manera, Adriano Colombelli, Maura Cesaria, Antonietta Taurino, Roberto Rella

[1]IMM-CNR, Institute for Microelectronics and Microsystems - Lecce section, Lecce, Italy
*corresponding author, E-mail: mariagrazia.manera@cnr.it

Abstract

The research activity developed by our group in the ambit of magneto plasmonic metal nanostructures and their functional characterization as chemical sensors with improved performances is here reviewed. Novel insights towards plasmon-molecule interactions studies are opened up.

1. Introduction

The resonant coupling of electromagnetic waves to collective oscillations of free electrons in metals, known as surface plasmon resonances (SPRs), has been exploited largely because of the possible control of light properties at the nanometer scale. Whether they are excited as guided modes propagating along flat planar or grating metal/dielectric interfaces (under the phase-matching with light) or as localized modes in metallic nanostructures with dimensions comparable to or smaller than the exciting light wavelength, high level of light confinement and of electromagnetic (EM) field enhancement can be achieved. New routes for integrated nanophotonics and miniaturized optoelectronic devices can be thus opened up [1].

Magneto-optical (MO) effects are also of prime interest to photonic control, as they allow fast modulation of light polarization and intensity via external magnetic fields [2]. They can be greatly affected by the huge EM enhancement occurring upon Surface Plasmon (SP) modes excitations in metal nanomaterials. Magnetic field induced modifications of the optical properties of materials were first observed by M. Faraday (1845) and J. Kerr (1877).

In the last decades, the possibility offered by the variety of nanofabrication tools, has started a race to develop even better nanomaterials where magnetic and plasmonic properties are intertwined, allowing for example plasmonic properties to become tunable upon the application of a magnetic field or the MO effects to be largely increased by plasmon resonance excitation [3]. Nanomaterials with large MO activity, low losses, and compatible with the fabrication processes are demanding in order to tailor optical and MO responses for improving the performance of components and devices such as isolators, modulators, or sensors.

The activity developed by our research group in this Active Plasmonics field is here reviewed and discussed. Our interest is the study on the effects that plasmon excitation (either localized or propagating) have on the MO activity of different kinds of nanostructures supported on glass substrates as a consequence of the EM field enhancement in the MO active component of the investigated structure. The final aim is the realization of novel transducers able to achieve higher sensing performances towards refractive index changes at the metal-dielectric interface with respect to traditional plasmonic passive transducing platforms.

2. Plasmonic and Magneto-Plasmonic Nanomaterials

First steps have been moved with metal multilayers supporting Propagating Surface Plasmon modes. Sustained by numerical simulation tools, a proper combination of noble metal and ferromagnetic thin films with suitable thickness has been proposed. When SPR conditions are satisfied, an enhancement of the MO activity due to the combined action of the intense decrease of the reflectivity of the system and the enhanced electromagnetic field inside the MO active layer can be observed. This amplification was highly dependent on the plasmon excitation, thus on the particular choice of the metals and on their optical properties as well as on the refractive index of the dielectric (in gas or liquid phase) in contact with them. These investigated multilayer structures can act as proper transducer components in a new SPR configuration, the so called magneto-optic surface plasmon resonance (MO-SPR) probe. MO activity is demonstrated by using metal heterostructures in Transversal MO Kerr geometry (T-MOKE) upon SPR excitation achieved by traditional prism coupling. These studies demonstrated in a fascinating way the possibility of modulating the optical response by means of an external agent, namely a magnetic field, and the exploitation of this phenomenon as a new probe for the development of innovative magneto-plasmonic sensing devices[4].

A great part of our recent research activity has been focused also on the realization and optical characterization of metal nanostructures on planar substrates. Metallic nanostructures supporting Localized Surface Plasmon Resonances (LSPR) are characterized by their unique ability to control and manipulate light at the nanoscale. Moreover, they have demonstrated to exhibit MO activity in the presence of modulated magnetic field of relatively low intensity in transversal configuration (T-MOKE). In these kinds of nanostructures where strong nanoantenna effects take place, the influence of the MO part become peculiar. Metal nanostructures of different diameters and thickness have been realized by proper combination of template-mediated nanofabrication tool and thermal evaporation techniques. Interparticles distanced in a long and short-range order have been taken into account as well. SPR excitations with spectral position tuned in the VIS-NIR range are thus obtained depending on the nanodisks size and distribution. Correlation between Kerr effects and the metal nanostructure polarizabilities allows a better understanding of MO response, thus tailoring the nanomaterials geometry to the functional needs [5].

Validation of experimental findings was achieved by numerical simulations based on Finite Element Method (FEM) techniques. The developed numerical models allowed studying the combination of the T-MOKE effect with the LSPR resonance of metal nanoparticles. Numerical optical and magneto-optical spectra provided a deep insight on the physical aspects behind the MO activity of metal nanostructures strictly related to the direction of oscillations electrical dipoles generated in resonance conditions.

3. Functional characterization in gas or liquid ambient

The ability of SP modes to sense even small refractive index changes occurring at the metal-dielectric interface where they are excited is well known. These properties make plasmonic platforms suitable for low-cost diagnostic devices, owing to their integration into microfluidic systems and sensitivity to changes of dielectric properties at the interface.
In spite of the extensive research efforts on SPR biosensing, detection of small analytes at very low concentrations remains still challenging. One of the strategies that can be used to amplify the SPR signal is using MO structures as active transducer elements. Through modulation of the intensity of reflected light, light localization associated with SPRs can be used for resonant enhancement of TMOKE. The enhanced EM field along the plasmonic surface is distributed inside the MO layer, thus increasing the MO activity. In contrast to the broad SPRs, TMOKE exhibits very sharp resonances, which are highly sensitive to the surrounding dielectric properties. This feature of TMOKE allows an increase of the device's resolution thus lowering the detection limits by up to 3 orders of magnitude. As a proof of concept, different sensing schemes have been tested by our research group. A proper choice of sensing layers deposited as thin film by physical and chemical methods on to the MO transducing platform allows the detection of chemical compounds in gas or liquid phase. Both organic and inorganic sensing layers have been investigated for application in food and environmental control. Research activity in this field is going with the aim of exploring also the effects of plasmon and molecular energy coupling with respect to the optical and MO behavior as well as on their functional aspects. A proper choice of organic sensing layers whose molecular resonances can be tuned across the plasmonic resonance energies allows for a deep investigation into the critical research field of plamon-molecule interactions. This would introduce magneto-optics to the so-called field of molecular plasmonics.

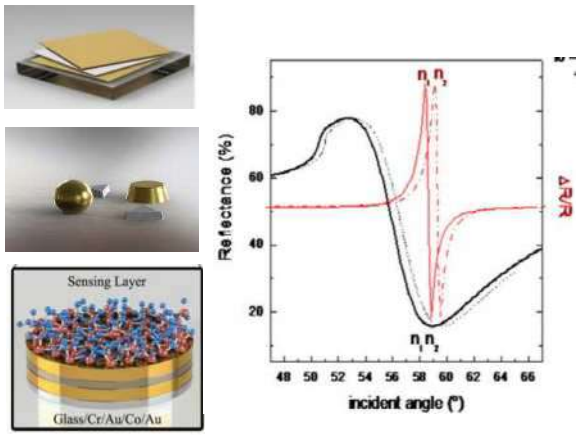


Figure 1: Schematic representation of the investigated plasmonic and magneto-plasmonic heterostructures and related optical and MO signals exploited as refractive index transducing probes.

References

[1] J. A. Jackman, A. Rahim Ferhan, N-J Cho, Nanoplasmonic sensors for biointerfacial science, *Chem Soc.Rev*. 46: 3615−3660, 2017.

[2] P.N. Prasad, *Photonic Crystals*. *In Nanophotonics*, P. N. Prasad (Ed.), 2004.

[3] G. Armelles et al., Magnetoplasmonics: Combining Magnetic and Plasmonic Functionalities *Adv*. *Opt*. *Mater*. 1: 10 – 35, 2013.

[4] M.G.Manera, R. Rella, Improved gas sensing performances in SPR sensors by transducers activation, *Sens.Actuators B* 179: 175-186, 2013.

[5] M.G. Manera et al., Magneto-Optical properties of noble-metal nanostructures: functional nanomaterials for bio sensing, *Sci*. *Rep*. 8: 12640, 2018.

Enhanced Magneto-Optical Activity of noble metal nanostructures

Adriano Colombelli[1], Maria Grazia Manera[1], Daniela Lospinoso[2], Antonietta Taurino[1], Roberto Rella[1]

[1]Institute for Microelectronics and Microsystems IMM-CNR, Campus Ecotekne, 73100 Lecce, Italy
[2]University of Salento, Campus Ecotekne, via Monteroni, 73100 Lecce, Italy;
*corresponding author, E-mail: adriano.colombelli@le.imm.cnr.it

Abstract

In this work, the magneto-optical activity of noble metal nanostructures in Kretschmann configuration has been investigated. The possible effect of an increasing order in their spatial distribution has been theoretically and experimentally investigated, by considering purely disordered, short-range and long-range ordered gold nanostructures. A sizable MO activity can be recognized by using an external magnetic field of low intensity. Modelling tools are used to predict and realize a proper design of the investigated materials tailored on the nanoscale.

1. Introduction

Plasmonic nanostructures provide new ways of manipulating the flow of light, with nanostructures and nanoparticles exhibiting optical properties never before seen in the macro-world. Therefore, researchers are constantly pushed towards the design and fabrication of innovative plasmonic systems characterized by novel functionalities and better performances. Recently, considerable activities have been performed for the development of new kinds of small, fast, and reliable plasmonic sensors, looking for the improvement of traditional Surface Plasmon Resonance (SPR) and Localized Surface Plasmon Resonance (LSPR) sensor performances. Various approaches have been proposed to enhance the sensitivity of traditional SPR based sensors. These include, for example, phase-sensitive detection schemes, use of highly ordered metallic nanostructures or hole arrays in metal films and several active modulation techniques that can be used to improve the signal to noise ratio (SNR) and enhance the limit of detection [1–3]. The design and implementation of configurations where an external agent, such as temperature4,5, electric6,7 or magnetic fields8, can control surface plasmons is actually known as Active Plasmonics9, and constitutes the basis for the development of innovative optoelectronic components.

Among different routes that have been proposed so far, the use of a magnetic field seems a very promising one. Taking advantage of the Magneto-Optical (MO) effect, the magnetic field provides an interesting way to actively control the resonant behavior of these structures, opening new perspectives in device applications. In order to ensure a sufficient plasmonic modulation inside metals nanoparticles, a promising approach is the incorporation of a ferromagnetic component into the plasmonic systems, thus forming innovative magneto-plasmonic (MP) nanostructures. However, as recently demonstrated [4], the MO effect might also be detected in Au nanostructures. The MO activity of bulk gold originates from the activation of the Lorentz force: light drives electrons to oscillate at the optical frequency, the presence of external magnetic field results in a rotation of the light polarization or in the intensity of the reflected light, depending on the relative position of the magnetic field with respect to the oscillating dipoles. This effect is normally smaller than that of ferromagnetic substitutes. However, when the LSPR conditions are satisfied, it is possible to observe an enhancement of the MO activity, which can be exploited as a new probe for the development of innovative magneto- plasmonic sensing devices [5,6]. Reflectance experiments in polar configuration can be found in literature as well as magnetic circular dichroism examples [7,8].

In this work, Au nanostructures characterized by different planar distribution on glass substrates are investigated in a Transverse MO configuration by prism coupling; a sizable MO activity can be recognized by using an external magnetic field of low intensity. The possible effect of an increasing order in their spatial distribution has been theoretically and experimentally investigated, by considering purely disordered, short-range and long-range ordered noble metal nanostructures. Modelling tools are used to predict and realize a proper design of the investigated materials tailored on the nanoscale. Optical and morphological properties will be correlated with functional properties of the realized Au nanostructures deposited on glass substrates showing that the recorded MO signal can be used as a novel transducer probe for refractive index sensing.

2. From disordered to periodic plasmonic nanostructures

In this work, three different fabrication technique have been implemented to fabricate planar distributions of metal nano-particles (NPs), characterized by an increasing order in their spatial distribution. Thermal de-wetting, Colloidal Lithography and Nano Sphere Lithography have been exploited to fabricate purely disordered, short-range ordered and long-range ordered Au NPs, respectively. In the case of thermal de-wetting, gold nanoparticles were prepared by a physical methodology consisting in electron beam

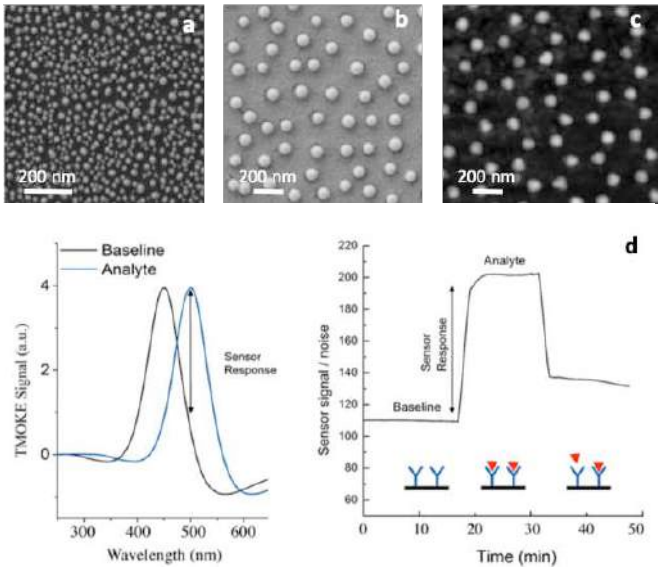


Figure 1. Morphology of the fabricated gold nanoparticles obtained by SEM analysis: a) disordered Au NPs obtained by thermal de-wetting; b) short-range ordered Au nano-disk obtained by CL; c) long-range ordered Au NPs obtained by NSL; d) Schematic representation of magneto-plasmonic sensing mechanism based on the dynamic measurement of TMOKE signal.

evaporation of a thin Au film onto corning glass substrates followed by a rapid thermal annealing treatment. This process allows the Au thin film to coarse into a dense and uniform array of metal nanoparticles characterized by disordered distribution as reported in Fig. 1a. In the case of CL, short-range ordered gold nano-disk arrays onto glass substrates were fabricated by electrostatically-driven self-assembly of negatively charged colloids onto a polydiallyldimethylammonium (PDDA) monolayer, as can be noticed in Fig. 1b. Finally, a modified NSL based technique was developed to fabricate highly ordered arrays of gold NPs distributed in hexagonal lattice onto glass substrates. These nano-structures were fabricated by a simple and reproducible approach based on the self-assembling of close-packed polystyrene particles at air/water interface. After the transfer onto a solid substrate, exploiting the interstitial geometry of the colloidal mask, periodic array of plasmonic nanostructures can be easily prepared. Also a simple but versatile approach for inducing shape modifications of metal nano-particles fabricated by NSL, while preserving their highly periodic distribution was developed. Based on the application of suitable thermal treatment, this approach enables to modify the size and morphology of nano-particles, from their original triangular geometry to more symmetric and spherical nano-structures, as reported in Fig. 1c.

3. Magneto-Optical Properties of Au NPs

The fabricated Au nanostructures have been investigated in Total internal Reflection configuration, in order to demonstrate a magneto-optical activity in TMOKE configuration, when their resonance conditions are satisfied. In order to optimize the structure of the plasmonic transducers and obtain further insight of the physical mechanism underlying these effects, numerical simulations have been performed for each kind of plasmonic transducer.
Unlike traditional LSPR sensors, based on optical measurements (Reflectivity, Transmission, Absorption, ECS, etc.), the magneto-plasmonic sensors are based on the measurement of the TMOKE signal when plasmonic events are excited. As can be noticed in Fig. 1d, this magnitude is also very sensitive to changes of the refractive index of the dielectric environment allowing the development of a new kind of chemical sensor.

References

[1] S. Y. Wu, H. P. Ho, W. C. Law, Chinlon Lin, and S. K. Kong, Highly sensitive differential phase-sensitive surface plasmon resonance biosensor based on the Mach–Zehnder configuration, Opt. Lett. 29, 2378 (2004).
[2] F. Romanato, K. H. Lee, H. K. Kang, G. Ruffato, and C. C. Wong, Sensitivity enhancement in grating coupled surface plasmon resonance by azimuthal control, Opt. Express 17, 12145 (2009).
[3] W. L. Barnes, W. A. Murray, J. Dintinger, E. Devaux, and T. W. Ebbesen, Surface Plasmon Polaritons and Their Role in the Enhanced Transmission of Light through Periodic Arrays of Subwavelength Holes in a Metal Film, Phys. Rev. Lett. 92, 107401 (2004).
[4] M.G. Manera, A. Colombelli, Antonietta Taurino, Antonio Garcia Martin & Roberto Rella, Magneto-Optical properties of noble-metal nanostructures: functional nanomaterials for bio sensing, Scientific Reports vol. 8, Article number: 12640 (2018)
[5] Sepúlveda, B., Calle, A., Lechuga, L. M. & Armelles, G. Highly sensitive detection of biomolecules with the magneto-optic surface-plasmon-resonance sensor. Opt. Lett. 31, 1085–1087 (2006).
[6] Manera, M. G. et al. Enhanced gas sensing performance of TiO2 functionalized magneto-optical SPR sensors. Journal of Materials Chemistry 21, 16049 (2011).
[7] B. Sepúlveda, J. B. González-Díaz, A. García-Martín, L. M. Lechuga, and G. Armelles, Plasmon-Induced Magneto-Optical Activity in Nanosized Gold Disks, Phys. Rev. Lett. 104, 147401
[8] F. Pineider, G. Campo, V. Bonanni, C. de Julián Fernández, G. Mattei, A. Caneschi, D. Gatteschi, and C. Sangregorio, Circular Magnetoplasmonic Modes in Gold Nanoparticles, Nano Lett. 2013, 13, 10, 4785-4789.

Designed electron temperature environments for the control of all-optical switching

Luke H. Nicholls[1], Tomasz Stefaniuk[2], Mazhar E. Nasir[1], Francisco J. Rodriguez-Fortuño[1], Gregory A. Wurtz[3] & Anatoly V. Zayats[1]

[1] Department of Physics and London Centre for Nanotechnology, King's College London, London, UK
[2] Department of Physics, University of Warsaw, Warsaw, Poland
[3] Department of Physics, University of North Florida, Jacksonville FL, USA
*corresponding author, E-mail: luke.nicholls@kcl.ac.uk

Abstract

By designing the electron temperature distribution in hyperbolic metamaterials, induced by control light illumination, we demonstrate the efficient control of the metamaterial's resultant optical dynamics, creating tuneable switching state durations of 200-500 fs. This is shown to be due to the overlap between the signal light mode and the evolving electron temperature distribution.

1. Introduction

Plasmonic metamaterials are known for their effectiveness at enhancing light matter interactions. This field enhancement has led to the investigation of plasmonic nanostructures to provide dynamic control of optical signals utilizing the free-electron nonlinearity of metals. While this Kerr-type nonlinearity responds to ultrafast excitation with changes to the refractive index on fs time scales, the typical relaxation mechanisms occur over several ps. The spatial distribution of the electron temperature, induced by a control light pulse and the source of permittivity changes in the metal, is often taken to be homogeneous to simplify the description of the system. However, this simplification can leave out important features in the optical dynamics at short timescales [1].

In this work, we demonstrate tailoring of the optical dynamics of a gold nanorod metamaterial through the spatial engineering of the electron temperature distribution. From pump-probe spectroscopy measurements, we find a sub-300 fs switching state dependent upon the induced hot electron distribution in the nanostructure, which can be modified by changing the control-signal mode overlap [2]. The design of electron temperature environments not only has consequences for switching rates, with the metamaterial proving to be an effective intensity and polarization modulator [3, 4], but also for efficient local control of hot carrier generation and extraction for use in photocatalytic processes [5].

2. Results

2.1. Sub-picosecond switching state

Pump-probe spectroscopy measurements were carried out on a nanorod metamaterial sample. The self-assembled nanorod metamaterial consists of an array of periodic gold rods oriented perpendicular to a glass substrate and embedded in an alumina matrix. The geometric parameters of the metamaterial are tuned to produce a resonance for TM polarized light at around 700 nm. On illumination with a control light pulse, this resonance red shifts due to induced electron temperature heating, which is probed by a signal light pulse delayed in time (fig. 1a).

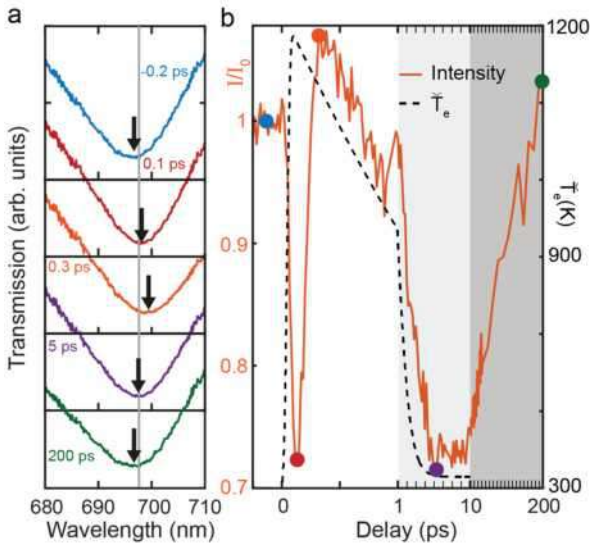


Figure 1. (a) Transmission of metamaterial sample at various delay times between signal and control light. (b) Change in intensity for the monitored wavelength indicated in (a) with corresponding average electron temperature dynamics.

If one monitors the transmitted intensity at the wavelength indicated by the grey line in fig. 1a, a ~300 fs switching state is observed as the resonance red-shifts across this wavelength (fig. 1b). The resonance then returns to its original position over 200 ps as the energy is dissipated in the system. One will note however that the point of maximum red-shift (orange dot in fig. 1) is not coincident with the maximum average electron temperature (indicated by the dashed line in fig. 1b). In fact, the maximum red shift is achieved 200 fs after the maximum average electron temperature $\check{T}_e$ is reached. This points to the importance of considering inhomogeneous electron dynamics (i.e. electron temperature diffusion) and the overlap between

the induced permittivity distribution and signal light mode in the nanorod.

2.2. Considering inhomogeneous electron temperature.

In the transient experiments, the absorbed control light induces an initial distribution of the electron temperature in the nanorods. This inhomogeneous distribution then diffuses across the structure, whilst energy is also coupled to phonons in the system. Therefore, at short times, the overlap between this electron temperature distribution and the spatial distribution of the signal light mode will be important for the optical dynamics. To show this, the weighted average electron temperature $WAv(T_e)$ was calculated for electron temperature distributions set up by different control light wavelengths. $WAv(T_e)$ is calculated as,

$$WAv(T_e, t = t_0) = \frac{\int |\boldsymbol{E}_S(x,y,z)|^2 T_e(x,y,z,t=t_0) dV}{\int |\boldsymbol{E}_S(x,y,z)|^2 dV} \quad (1)$$

Where, E_s is the electric field of the signal light mode. When we compare $WAv(T_e)$ with $\check{T}_e$, which is spatially averaged across the structure, we see large differences in the initial electron temperature dynamics.

The effect of changing the control mode on dynamics was experimentally investigated by transient optical measurements multiple control wavelengths. The fastest change in optical density is seen for the distribution with the greatest overlap with the signal mode. The control light distributions with less overlap have longer switching times, providing the ability to tune switching state times with proper design of electron temperature distributions.

3. Conclusion

In conclusion this work shows the ability to tune the optical dynamics of a system by designing initial electron temperature distributions and considering their overlap with signal light modes. The dynamic spatial control of permittivity in nanostructures has implications for direct tailoring of Kerr-type nonlinearities, allowing tuneable switching states for all-optical devices. Furthermore, this approach allows for the design of local electromagnetic environment affecting both spontaneous emission rates and second harmonic generation, useful in the design of nanoscale light sources and display technology.

Acknowledgements

This work has been supported, in part, by the EPSRC (UK) and the ERC iPLASMM project (321268). A.V.Z. acknowledges support from the Royal Society and the Wolfson Foundation. G.A.W. acknowledges support from the EC FP7 project 304179 (Marie Curie Actions). F.J.R.-F. acknowledges financial support from the ERC-2016-.0StG-714151 PSINFONI project.

References

[1] S. Peruch, et al., "Geometry Defines Ultrafast Hot-Carrier Dynamics and Kerr Nonlinearity in Plasmonic Metamaterial Waveguides and Cavities." Adv. Optical Mater., **5**, 1700299 (2017).

[2] L.H. Nicholls, et al., "Designer photonic dynamics: using non-uniform electron temperature distribution for on-demand all-optical switching times", *Submitted*.

[3] G.A. Wurtz, et al., "Designed ultrafast optical nonlinearity in a plasmonic nanorod metamaterial enhanced by nonlocality." Nat. Nano., **6**, 107-111, (2011).

[4] L.H. Nicholls, et al., "Ultrafast synthesis and switching of light polarization in nonlinear anisotropic metamaterials." Nat. Photon., **11,** 628-633, (2017).

[5] E. Cortés, et al., "Plasmonic hot electron transport drives nano-localized chemistry." Nat. Comm., **8**, 14880, (2017).

Playing with temperature at the nanoscale

Remo Proietti Zaccaria[1,2], Tianlong Guo[1], Joao Cunha[1], Alessandro Alabastri[3]

[1] Cixi Institute of Biomedical Engineering, Chinese Academy of Sciences, Ningbo, China
[2] Italian Institute of Technology, via Morego 30, 16163 Genova, Italy
[3] Department of Physics and Astronomy and Department of Electrical and Computer Engineering, Rice University, USA

*corresponding author, E-mail: remo.proietti@nimte.ac.cn

Abstract

The optical properties of any material are strongly related to the temperature of their surrounding environment as well as by any temperature-carrying-source, such as laser light, impinging on the material [1,2]. In this regard, it is well known that in bulky metals the reflectivity monotonically decreases upon increase of the temperature [3]. Here we will show that when the nano-patterning of a metallic substrate in form of nano-antennas is instead considered, the situation changes drastically with respect to the aforementioned bulk behavior. Indeed, upon temperature increase of the substrate, we can achieve either a reflectivity decrease (as for bulky metal) or the opposite behavior, namely a reflectivity increase. We will demonstrate that it is uniquely related to the aspect ratio of the antenna which determines a shift of the antenna absorption efficiency. The underneath mechanism is related to the possibility to increase or decrease the light-to-heat conversion rate depending on the temperature of the system. Furthermore, we shall demonstrate how the temperature sets a maximum value for the absorption efficiency and how this quantity can be geometrically tuned, thus leading to a temperature-controlled optical heat dissipation. In

This scenario can be related to the temperature-matched description of the classical antenna theory. Our results, experimentally demonstrated and numerically/analytically explained, open the route towards the design of nano-structures capable of providing temperature controlled optical heat dissipation [4].

Acknowledgements

R.P.Z. shall recognize the support from 3315 Innovative Team Project nr. Y70001DL01 of Ningbo/Cixi, Zhejiang province, China.

References

[1] A. Alabastri, S. Tuccio, A. Giugni, A. Toma, C. Liberale, G. Das, F. De Angelis, E. Di Fabrizio and R. Proietti Zaccaria, Molding of Plasmonic Resonances in Metallic Nanostructures: Dependence of the Non-Linear Electric Permittivity on System Size and Temperature, *Materials* 6, 4879, 2013.

[2] A. Alabastri, A. Toma, M. Malerba, F. De Angelis, and R. Proietti Zaccaria, High Temperature Nanoplasmonics: The Key Role of Nonlinear Effects, *ACS Photonics* 2, 115, 2015.

[3] J. R. Adleman, D. A. Boyd, D. G. Goodwin and D. Psaltis, Heterogenous Catalysis Mediated by Plasmon Heating, *Nano Letters* 9, 4417, 2009.

[4] A. Alabastri, M. Malerba, E. Calandrini, A. Manjavacas, F. De Angelis, A. Toma, and R. Proietti Zaccaria, Controlling the Heat Dissipation in Temperature-Matched Plasmonic Nanostructures, *Nano Letters* 17, 5472, 2017.

Active Terahertz Superconducting Metamaterial-Based Modulator

Jingbo Wu*, Chun Li, Caihong Zhang, Biaobing Jin

Research Institute of Superconductor Electronics (RISE), School of Electronic Science and Engineering,Nanjing University, Nanjing 210093, China
*corresponding author, E-mail: jbwu@nju.edu.cn

Abstract

At terahertz (THz) frequencies, superconducting metamaterials offers a promising avenue for low loss and tunable THz functional devices. Using superconducting (SC) NbN film, we realized the THz wave modulation by biasing different voltage. The modulation speed is up to 1 MHz and is mainly limited by the slow thermal diffusion in metamaterials. To improve the performance of modulators, we further proposed a type of NbN-Au hybrid metamaterials. The THz modulator shows good prospect in cryogenic THz systems.

1. Introduction

In the last decades, terahertz (THz) technology has experienced fast growth and is promising for applications such as wireless communication, radio astronomy and biomedical imaging *etc*.[1]. The THz modulators with high modulation speed and modulation depth is highly demanding for various THz application. The devices that combines artificial subwavelength resonant structures tunable materials in THz band provides a good way to develop high performance THz modulators.

For THz metamaterials, superconductor is not only used to deal with the loss issue, but also is widely used for tunable THz devices because the optical properties of superconductor can be altered by applying electric bias, laser illumination or magnetic field[2][3]. In this paper, we reviewed our work on the active modulation of THz wave based on superconducting niobium nitride (NbN) metamaterials. The applied voltage on the NbN resonators leads to the switching from superconducting state and normal state, so the THz transmission can be modulated dynamically[4][5]. The thermal effects of these modulators were investigated using low temperature scanning laser microscope(LTSLM) [6]. In order to improve the switching speed, we proposed a NbN-Au hybrid structure and the spectral response was studied by simulation. This study will be beneficial for developing high performance THz modulators.

2. Results and discussions

Figure 1 displays the diagram of the superconductor THz modulators. Each unit cell, made from 200 nm-thick NbN film, includes a split ring resonator and an outer square ring resonator. The NbN wire is connected to the gold electrode on the two sides of sample for voltage bias. The sample is fabricated onto a MgO substrate. We used low temperature THz time domain spectroscopy to characterize their spectral responses. When the NbN resonators are in superconducting state, we observed electromagnetic induced transparency-like spectral response in the measured THz transmission spectra. With the increase of applied bias voltage, the superconducting carriers are broken and THz transmission amplitude at transparency window gradually decreased. The highest modulation depth is nearly 80%. When the alternating voltage signal is applied, the THz transmission can be tuned dynamically. Using continuous wave measurement system, we found the modulation depth gradually falls down with the increase of frequency and the maximum modulation speed is 1 MHz.

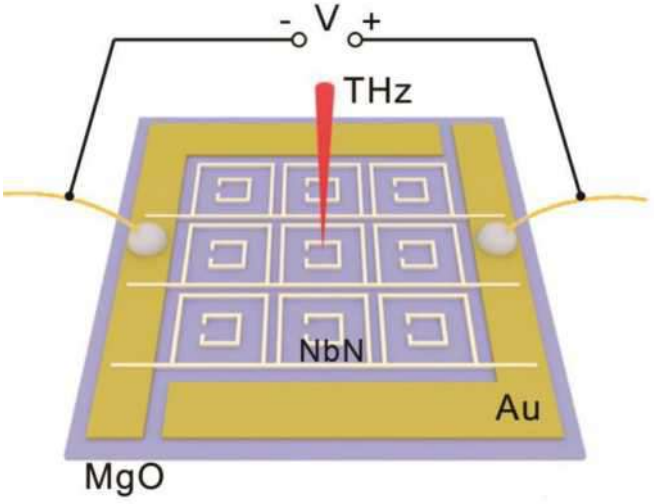


Figure 1 The diagram of THz superconducting NbN metamaterial-based modulator

In order to clarify the mechanism of devices, the LTSLM is used to study the Joule power distribution in cryogenic environment. The transition process from superconducting state to normal state at different voltage bias was recorded by the scanning images. We found that the state switching across the unit cell does not occur simultaneously. The hotspots first appear at the regions connecting the

neighboring unit cells and the transmission spectra experience obvious changes after the hotspots show up. Based on both experimental and theoretic study, we found that the thermal effects play an important role in THz wave modulation and the hotspots is of great help for increasing the modulation speed.

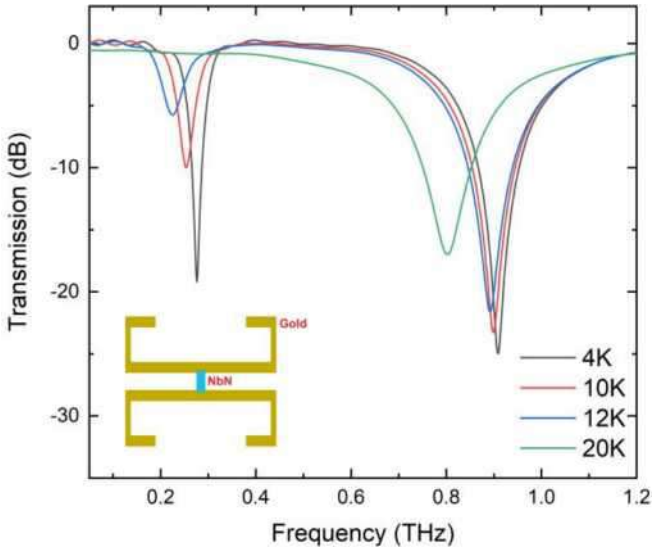


Figure 2 The simulated THz transmission spectra of proposed hybrid metamaterials at a variety of temperatures. The inset shows the unit cell structure of Au-NbN hybrid metamaterials.

In order to improve the performance of THz modulators, we proposed a new design in which the NbN-Au hybrid structure is used. As shown in the inset of Figure 2, the two gold split ring resonators are connected by a NbN microbridge. The thickness of NbN film is only 5 nm so as to speed up the thermal diffusion. The THz transmission spectra of this device was simulated using electromagnetic full wave simulation software and plotted in Figure 2. Though the simulation is done with the variation of temperature, the tuning behavior of the transmission spectra under electric bias is quite similar[4]. When the temperature exceeds the superconductor critical temperature of NbN (15 K), there is a remarkable change of the microbridge resistance. As a result, the two resonant modes merge into one mode after NbN goes into normal state. The resonant mode switching brings in a modulation depth as high as 98.7% around 0.27 THz. Compared with the design in Figure 1, the film thickness is decreased from 50 nm to 5 nm. In that case, the thermal capacitance can reduce at least one order. It is expected the modulation speed can reach to 10 MHz.

Besides that, the kinetic inductance of superconducting film is prominent and temperature-dependent, especially for the 5 nm-thick film. In our work, we found the resonance frequency red-shifts obviously as temperature increases. As shown in the Figure 2, the resonance frequency at low frequency regions decreases from 0.274 THz at 4 K to 0.227 THz at 12 K, the frequency shift is more than 17%. It suggests that we can use this hybrid metamaterials to realize the active control of resonance frequency shift.

3. Conclusions

Using the unique capability of metamaterials in manipulate electromagnetic wave and superconducting NbN film, we realized dynamic THz wave modulation with a modulation speed up to 1 MHz. By scanning the thermal distribution of superconducting modulators, we found that the thermal effects are essential for the THz wave modulation. We proposed a new type ofsuperconductor-metal hybrid metamaterials and they potentially have a higher modulation speed compared with the present superconducting modulator. These compact THz modulators will be of great benefit for THz systems working at cryogenic environment.

Acknowledgements

This work was supported by National Key Research and Development Program of China (2017YFA0700202), National Nature Science Foundation of China (NSFC) (61521001, 61701219, 61731010) and Jiangsu Provincial Natural Science Fund (BK20170649).

References

[1] T. Nagatsuma, G. Ducournau, and C. C. Renaud, “Advances in terahertz communications accelerated by photonics,” *Nat. Photonics*, vol. 10, no. 6, pp. 371–379, May 2016.

[2] B. Jin *et al.*, “Low loss and magnetic field-tunable superconducting terahertz metamaterial,” *Opt. Express*, vol. 18, no. 16, p. 17504, Aug. 2010.

[3] C. H. Zhang *et al.*, “Low-loss terahertz metamaterial from superconducting niobium nitride films,” *Opt. Express*, vol. 20, no. 1, p. 42, Jan. 2012.

[4] C. Li *et al.*, “Electrically tunable superconducting terahertz metamaterial with low insertion loss and high switchable ratios,” *Appl. Phys. Lett.*, vol. 109, no. 2, p. 022601, Jul. 2016.

[5] C. Li *et al.*, “Electrical dynamic modulation of THz radiation based on superconducting metamaterials,” *Appl. Phys. Lett.*, vol. 111, no. 9, p. 092601, Aug. 2017.

[6] C. Han *et al.*, “A study of thermal effects in superconducting terahertz modulator by low temperature scanning laser microscope,” *AIP Adv.*, vol. 8, no. 6, p. 065024, Jun. 2018.

Thermomechanical behavior of a multistable phase-change/dielectric bimaterial cantilever in response to radiative heat flux

Marta Reina*, Riccardo Messina, Philippe Ben-Abdallah

Laboratoire Charles Fabry, UMR 8501, Institut d'Optique, CNRS, Université Paris-Saclay,
2 Avenue Augustin Fresnel, 91127 Palaiseau Cedex, France
*corresponding author, E-mail: marta.reina@institutoptique.fr

Abstract

We study the thermomechanical behavior of a bimaterial cantilever made of a metal-insulator and a dielectric layer clamped on one of its ends to a wall at a fixed temperature and which interacts radiatively with two further reservoirs at two different temperatures. We show that with an appropriate choice of the three temperatures the cantilver has several stable stationary solutions, between which it can evolve by means of a local thermal excitation.

1. Introduction

The physics of cantilevers (i.e. beams fixed at one end and with no support at the other one) is relevant in many branches of physics, since they represent a key element in several experimental techniques. As a matter of fact, their deflection typically allows to infer the value of other physical quantites with a remarkable sensitivty. For example, this feature has been used in one of the very first measurements of radiative heat transfer at sub-micron distances [1]. A proper knowledge of their static and dynamical properties is thus relevant and interesting for numerous applications.

We discuss here the thermo-mechanical behavior of a cantilever in the presence of a radiative heat exchange with a structured environment. Radiative heat transfer is the photon-mediated energy exchange taking place between any couple of bodies kept at different temperatures, even when separated by vacuum. While it has been know for a long time that this energy flux is limited at large distances by Stefan-Boltzmann's law, the pioneering works of Polder, van Hove [2] and Rytov [3] showed more recenlty that it can overcome this limit even by several orders of magnitude when the two bodies are placed in the so-called near-field regime (i.e. at distances much closer than the thermal wavelength $\lambda_T = \hbar c/k_B T$, of the order of $10\,\mu$m at ambient temperature). This heat-flux amplification can be particularly pronounced when the two interacting bodies support resonant surface modes [4].

In this work, we exploit the properties of vanadium dioxide (VO_2), a material which undergoes a first-order transition [5, 6] from a low-temperature insulating phase to a high-temperature metallic phase close to room temperature ($T_c = 340\,$K). This peculiar optical response has allowed to highlight several effects in the domain of far- and near-field radiative heat transfer [7, 8, 9], ranging from bistability to the design of the thermal analogue of electrical components. By studying the mechanical and thermal properties of a cantilever induced by radiative heat transfer in the presence of VO_2, we highlight several interesting features, including a bi- and multistable behavior.

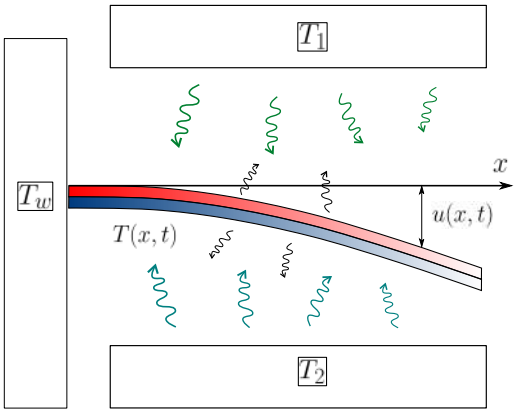


Figure 1: Geometry of our system. A cantilever is supported at its left end by a wall at temperature T_w, being kept free at the other end. It interacts through radiative heat transfer with two substrates at temperatures T_1 and T_2. Its displacement is described by $u(x,t)$, while $T(x,t)$ represents its temperature profile.

2. Physical system and theoretical approach

The system we consider is depicted in Fig. 1. A beam is attached to a wall mainteined at temperature T_w, whereas its right end is free. The beam is described in terms of its displacement $u(x,t)$ from the x axis, while $T(x,t)$ represents its temperature profile. Moreover, the beam exchanges heat radiatevely with two reservoirs at temperature T_1 (top in Fig. 1) and T_2 (bottom in Fig. 1), respectively. The beam has height h, length L, width δ and is made of two different materials having thicknesses h_1 and h_2, such that $h = h_1 + h_2$.

The radiative heat flux is described here by means of a fluctuational-electrodynamics approach, where the statistical properties of the charges flucuating inside each body are accounted for by means of the fluctuation-dissipation theorem [4], which correctly describes the heat exchange both

in the far and in the near field. In this framework, the heat flux per unit surface between two identical planar substrates at distance d and temperatures T_1 and T_2 can be written as a sum over all the frequencies ω, wavevectors $\mathbf{k}$ and polarizations p of the electromagnetic field as

$$\Phi = \int_0^\infty \frac{\mathrm{d}\omega}{2\pi}[\Theta(\omega,T_1)-\Theta(\omega,T_2)]\sum_j \int_0^\infty \frac{\mathrm{d}^2\mathbf{k}}{(2\pi)^2}\mathcal{T}_p(\omega,k,d), \tag{1}$$

where $\mathcal{T}_p(\omega,k,d)$ is the energy transmission coefficient and can be expressed in terms of the usual Fresnel coefficients as

$$\mathcal{T}_p(\omega,k,d) = \begin{cases} (1-|r_p|^2)^2/|D_p|^2, & k<\omega/c, \\ 4\,\mathrm{Im}(r_p)^2\mathrm{e}^{-2|k_z|d}/|D_p|^2, & k>\omega/c, \end{cases} \tag{2}$$

and $D_p = 1 - r_p^2 e^{2ik_z d}$ is a Fabry-Pérot denominator.

Concerning the x- and t-dependent temperature profile of the cantilever, it is solution of the following second-order differential equation

$$\rho C h \frac{\partial T(x,t)}{\partial t} = h\kappa \frac{\partial^2 T(x,t)}{\partial x^2} + \Phi\big(u(x,t),T(x,t)\big), \tag{3}$$

where ρ is the beam effective density, C its effective thermal capacity, while $\Phi\delta dx$ is the energy received per unit time by the infinitesimal element of the beam located between x and $x+dx$. Finally, the profile $u(x,t)$ of the beam is the solution of the fourth-order Euler-Bernoulli [10] differential equation

$$EI\frac{\partial^4 u(x,t)}{\partial x^4} = -\mu\frac{\partial^2 u(x,t)}{\partial t^2} + q(x,t), \tag{4}$$

where EI is the effective flexural rigidity of the beam, μ its effective linear mass density and $q(x,t)$ is a load term describing the presence of a radiative heat flux, which can be expressed explicitly as a function of the temperature profile $T(x,t)$.

3. Results

We study the coupled system of Eqs. (3) and (4) for different temperature configurations (T_w, T_1, T_2). By performing this investigation both statically and dynamically, we show that the first-order transition of VO_2 induces the appearance of a bistable or multistable behavior, i.e. two or more stationary solutions.

We discuss how this depends on the choice of the three external temperatures. Moreover, we prove that the injection of a controlled amount of power at the contact between the cantilever and the wall can be used to switch between the different stationary solutions. This can be exploited to produce, e.g., an oscillatory mechanical motion at the frequency of our externally-injected flux.

Our findings could be relevant for the modeling of the themo-mechanical coupling in micro- and nano-electromechanical systems, and could be promising for piezoelectric applications.

References

[1] E. Rousseau, A. Siria, G. Joudran, S. Volz, F. Comin, J. Chevrier, and J.-J. Greffet, *Radiative heat transfer at the nanoscale*, Nat. Photon. **3**, 514 (2009).

[2] D. Polder and M. van Hove, *Theory of Radiative Heat Transfer between Closely Spaced Bodies*, Phys. Rev. B **4**, 3303 (1971).

[3] S. M. Rytov, Y. A. Kravtsov, and V. I. Tatarskii, *Principles of Statistical Radiophysics*, Vol. 3 (Springer, New York, 1989).

[4] K. Joulain, J.-P. Mulet, F. Marquier, R. Carminati, and J.-J. Greffet, *Surface electromagnetic waves thermally excited: Radiative heat transfer, coherence properties and Casimir forces revisited in the near field*, Surf. Sci. Rep. **57**, 59 (2005).

[5] M. M. Qazilbash, M. Brehm, B. G. Chae, P.-C. Ho, G. O. Andreev, B. J. Kim, S. J. Yun, A. V. Balatsky, M. B. Maple, F. Keilmann, H. T. Kim, and D. N. Basov, *Mott Transition in VO_2 Revealed by Infrared Spectroscopy and Nano-Imaging*, Science **318**, 1750 (2007).

[6] A. S. Barker, H. W. Verleur, and H. J. Guggenheim, *Infrared Optical Properties of Vanadium Dioxide Above and Below the Transition Temperature*, Phys. Rev. Lett. **17**, 1286 (1966).

[7] P. Ben-Abdallah, H. Benisty, and M. Besbes, *Switchable thermal antenna by phase transition*, J. Appl. Phys. **116**, 034306 (2014).

[8] P. Ben-Abdallah and S.-A. Biehs, *Phase-change radiative thermal diode*, Appl. Phys. Lett. **103**, 191907 (2013).

[9] V. Kubytskyi, S.-A. Biehs, and P. Ben-Abdallah, *Radiative bistability and thermal memory*, Phys. Rev. Lett. **113**, 074301 (2014).

[10] R. J. Roark and W. C. Young, *Formulas for Stress and Strain*, 5th edn. (McGraw-Hill, New York, 1972).

Coupled resonances of Surface Plasmon Polaritons and Localized Surface Plasmons in Ferromagnetic Nanoparticle Arrays

Francisco Freire-Fernández[1], Mikko Kataja[2], and Sebastiaan van Dijken[1]

[1]Department of Applied Physics, Aalto University School of Science, FI-00076 Aalto, Finland
[2]Institut de Ciència de Materials de Barcelona (ICMAB-CSIC), Campus de la UAB, 08193 Bellaterra, Spain

Abstract

Surface lattice resonances are coupled resonances in periodic arrays of noble metal nanoparticles that circumvent optical losses and enable surface plasmons resonances with linewidths below 5 nm. However, he excitation of such ultra-narrow modes in magneto-optical systems remains elusive. We investigate coupled resonances in a Ni nanodisk array placed on top of a continuous SiO_2/Au bilayer where the near-field of surface plasmon polaritons in Au induces an intense and spectrally narrow localized surface plasmon resonance in the Ni nanodisks.

1. Introduction

Ordered ensembles of noble metal nanostructures can support ultra-narrow surface lattice resonances (SLRs). These modes circumvent optical losses in noble metals and are able to produce resonances with linewidths below 5 nm [1,2]. The locally enhanced electric field intensities near the plasmon resonances offer interesting prospects to enhance light-matter interactions. Therefore, it is appealing to integrate plasmonic antennas with materials that have externally controllable properties, such as magneto- or electro-optically active materials. Indeed, arrays of ferromagnetic Ni nanoparticles have been shown to support similar resonant modes, despite their larger intrinsic ohmic damping [3,4]. The magnetization of the particles combined with their plasmon resonances was shown to result in enhanced magneto-optical activity at resonant frequencies. However, the ohmic damping of nickel limits the linewidth of the SLR modes to ~ 100 nm and accordingly reduces the intensity of the resonant modes present in the optical and magneto-optical spectra. Here, we demonstrate that narrow linewidth and intense magneto-optical resonances can be attained by placing Ni nanodisk arrays within the optical near field of surface plasmon polaritons (SPPs) that propagate along a SiO_2/Au interface.

2. Results

Ni nanodisks with a diameter of 190 nm and a thickness of 40 nm were patterned on top of 5 – 60 nm SiO_2/150 nm Au bilayers by e-beam lithography. The nanodisks were ordered into square arrays with periodicities ranging from 350 nm to 500 nm. The geometry of the system is depicted in Figure 1(a). For comparison, identical Ni nanoparticle arrays without the SiO_2/Au bilayer were fabricated on glass substrates. A SEM image of a nanodisk array is shown in Figure 1(b). Due to the periodic corrugation provided by the Ni nanodisks, SPPs are excited at the SiO_2/Au interface if the SPP condition for normal incidence radiation is met;

$$\lambda = \frac{d}{m}\sqrt{\frac{\varepsilon_1\varepsilon_2}{(\varepsilon_1+\varepsilon_2)}}. \qquad (1)$$

Here, d is the periodicity of the nanoparticle array, m is an integer denoting the order of the diffracted order and ε_1 and ε_2 are the permittivities of the Au and SiO_2 layers. Due to their proximity to the Au film, the electric field of the SPPs extends to the Ni nanodisks where it induces a spectrally narrow localized surface plasmon resonance (LSPR). This resonance manifests as an extinction maximum indicated by the downward arrow in the extinction spectrum of Figure 1 (c). This intense SPP mode at λ_1 = 710 nm has a FWHM of ~30 nm. A broader and less intense resonance is measured at λ_2 > 1000 nm. This mode can be identified as the SLR of the Ni nanodisk array.

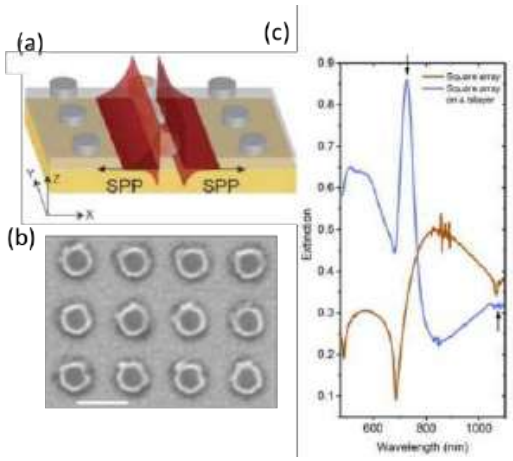


Figure 1: (a) Schematic of the hybrid magnetoplasmonic system. (b) SEM image of a Ni nanodisk array on a SiO_2/Au bilayer. (c) Extinction of the d = 450 nm Ni nanodisk array with and without the Au/(10 nm)SiO_2 underlayer. Due to the reflective underlayer, extinction for the bilayer sample was measured in reflection geometry and defined as inverse of reflection E = 1-R. The sample without the underlayer was measured in transmission where the extinction is given by E = 1-T.

The calculated wavelength for the SPP mode using equation 1 and d = 450 nm is 706 nm, which is in good agreement with our experimental observation. In Figure 1(c), we compare the

extinction spectrum of the Ni nanodisk array on the SiO_2/Au bilayer to the extinction spectrum of the same nanodisk array on glass. In the latter, a broad SLR with a maximum centered at λ = 850 nm is measured. Figure 2(a) shows the magneto-optical Kerr spectrum of the same two samples. In the Ni nanodisk array on glass, the relatively broad SLR mode produces a Kerr angle of about 5 mrad at 870 nm. For Ni nanodisks patterned onto the SiO_2/Au bilayer, we measure a narrow (FWHM = 30 nm) and three times more intense magneto-optical resonance at λ_1 = 710 nm that arises from the SPP-induced LSPR resonance. In addition, we observe a second peak in the magneto-optical spectrum that is associated with the SLR mode at λ_2 = 955 nm.

3. Discussion

As previously demonstrated for noble metal nanodisk arrays [5,6], a propagating SPP mode can induce intense electric dipoles on the nanodisks over a narrow wavelength range. In our Ni nanodisks, this effect produces a strong magneto-optical Kerr effect via the spin-orbit coupling [7]. To gain further insight into the character of plasmon modes in our hybrid magnetoplasmonic system, we performed finite-difference time-domain (FDTD) simulations of the electric field distributions at λ_1 and λ_2 using Lumerical software. The results are shown in Figures 2(b) and 2(c). The simulations clearly confirm that the narrow SPP mode at λ_1 induces much stronger LSPRs on the Ni nanodisks than the broader SLR mode at λ_2 and thus results in a much stronger resonant enhancement of the magneto-optical signal.

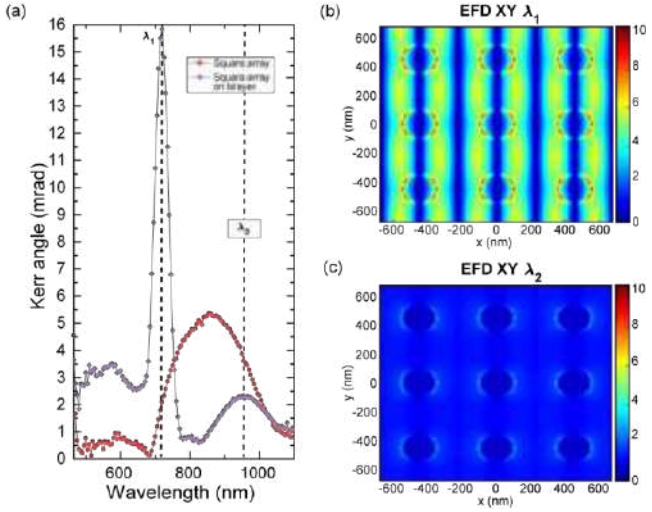


Figure 2 (a) Magneto-optical Kerr angle spectrum of a Ni nanodisk array with d = 450 nm on a glass substrate (red data) and on a 10 nm SiO_2/150 nm Au bilayer (violet data). (b,c) Electric field distribution (EFD) at λ_1 and λ_2 of the Ni nanodisk array on SiO_2/Au. The XY monitor in the simulations is located on top of the Ni nanodisks.

4. Conclusions

We have experimentally shown that propagating SPPs in combination with ferromagnetic plasmonic nanodisks produce narrow and intense resonances in optical and magneto-optical spectra. A control sample of an identical nanodisk array on glass enabled us to compare two distinct coupling mechanisms between the Ni nanodisks, i.e., far-field radiative (SLR) and near-field (SPP) coupling. The larger electric-field intensity of the SPP mode induces more intense electric dipoles in the Ni nanodisks, giving rise to a stronger magneto-optical response. Our results reveal a new configuration where plasmonics can be used to further enhance the magneto-optical activity of ferromagnetic nanostructures, which could find applications in biosensing, non-reciprocal optoelectronic devices, nonlinear optics, and localized all-optical magnetic switching [8].

Acknowledgements

We acknowledge financial support by the Academy of Finland (grant No. 316857) and by the Spanish Ministerio de Economía y Competitividad through projects MAT2017-85232-R (AEI/FEDER,UE) and by the European Comission (Marie Skłodowska-Curie IF EMPHASIS - DLV-748429).

References

[1] S. Zou, N. Janel, and G. Schatz, "Silver nanoparticle array structures that produce remarkably narrow plasmon lineshapes", J. Chem. Phys. 120, 10871 (2004).

[2] B. Auguié and W. L. Barnes, “Collective Resonances in Gold Nanoparticle Arrays”, Phys. Rev. Lett. 101, 143902 (2008).

[3] M. Kataja, T. Hakala, A. Julku, M. Huttunen, S. van Dijken, and P. Törmä, "Surface lattice resonances and magneto-optical response in magnetic nanoparticle arrays", Nat. Commun. 6, 7072 (2015).

[4] N. Maccaferri et al., “Anisotropic Nanoantenna-Based Magnetoplasmonic Crystals for Highly Enhanced and Tunable Magneto-Optical Activity”, Nano Lett. 16(4), pp. 2533-2544 (2016).

[5] Y. Chu and B. Crozier, "Experimental study of the interaction between localized and propagating surface plasmons", Opt. Lett. 34, 244 (2009).

[6] N. Papanikoloau, “Optical properties of metallic nanoparticle arrays on a thin metallic film”, Phys. Rev. B 75, 235426 (2007).

[7] N. Maccaferri et al., "Tuning the magneto-optical response of nanosize ferromagnetic Ni disks using the phase of localized plasmons", Phys. Rev. Lett. 111, 167401 (2013).

[8] M. Kataja, F. Freire-Fernández, J. Witteveen, T. Hakala, P. Törmä, and S. van Dijken, "Plasmon-induced demagnetization and magnetic switching in nickel nanoparticle arrays", Appl. Phys. Lett. 112, 072406 (2018).

Transformation optics concept and applications

Designing devices for sub-wavelength imaging using a transformation-optics approach

Mircea Giloan*, Robert Gutt and Gavril Saplacan

Company for Applied Informatics, Cluj-Napoca, Romania
*corresponding author, E-mail: mircea_giloan@cianet.ro

Abstract

Transformation-optics inspired flat lenses are used to build up optical systems capable to transpose a sub-wavelength sized area surrounding the object focal point of the system into a magnified area surrounding the image focal point of the system. The anisotropic and inhomogeneous media constituting the lenses enable the processing of the high spatial frequencies waves without converting them in evanescent waves. Numerical simulations show the capability of the proposed devices to perform magnified discernible images of the sub-wavelength details.

Projective imaging systems based on lenses are the best option for high-speed optical microscopy. The resolution of these optical devices is limited due to the fact that sub-wavelength information from an object is carried by high spatial frequency waves which become evanescent inside of conventional optical lenses. Transformation-optics approach opened a path for designing anisotropic and inhomogeneous media, capable to manipulate not only the wave paths but also the wave vectors [1]. Recently, a general method was proposed for designing both converging and diverging flat lenses made of media derived from specific coordinate transformations [2].

The concept of the proposed optical system is schematically represented in figure 1. The $(y-z)$-plane view of two identical converging flat lenses, object lens (left) and image lens (right), embedded in the free space (green rectangles) is depicted in figure 1(a). The lenses have a thickness (d) to focal distance (φ) ration equal to four $(\rho = 4)$. The permittivity and permeability tensors of a converging lens of thickness d and focal distance φ, embedded in an isotropic and homogeneous medium having $\varepsilon = \mu = m$, is generated by the following transformation function applied to z coordinate $(z' = z/h(x, y))$:

$$h(x, y) = m\left[\delta - \gamma(\varphi^2 + x^2 + y^2)^{1/2}\right], \qquad (1)$$

where $\delta = 1 + \varphi/d$ and $\gamma = 1/d$. When $m = 1$ the lens is embedded in the free space $\varepsilon = \mu = 1$. The cases when parameter m is supra-unitary $(m > 1)$ or sub-unitary $(m < 1)$ can be viewed as an additional transformation of the space like a compression or dilation, respectively. The object and image lenses are depicted by red and blue rectangles and

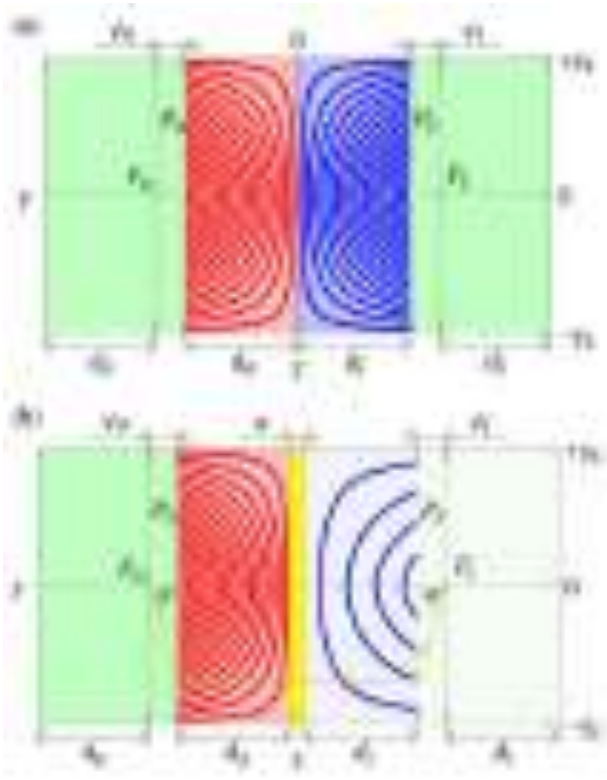


Figure 1: (a) $(y - z)$-plane view of two identical transformation-optics inspired flat lenses embedded in free space (green). The thickness, focal length and focal point of the object lens (red) are denoted by d_o, φ_o and F_o respectively, while for the image (blue) lens are denoted by d_i, φ_i and F_i respectively. (b) $(y - z)$-plane view of the proposed optical device. The focal points of the object (red) and image (light blue) lenses are placed in the free space (green) and a dilated space (light green), respectively. An absorption layer (yellow) of thickness a, is inserted between lenses.

correspond to negative and positive values of z-coordinate, respectively. The curves of constant transformed z coordinate are depicted by red and blue lines inside the area of the object and image lenses respectively.

Figure 1(b) depicts the setup of the studied optical devices. The object lens and its adjacent space are dilated by a factor of 4 ($m = 1/4$ in Eq. (1) and $\varepsilon = \mu = 1/4$ for the object area). The curves of constant transformed z

coordinate are depicted rarefied inside the area of the image lens in order to suggest the transformation by dilation of this lens area. Since the proposed device is confined to positive optical parameters of the constituent lenses the depicted area is limited on y-axis by the singularity point $y_S = \varphi(\rho(\rho+2))^{1/2}$ derived from Eq. (1). An optical ray leaving the object focal point under an angle α with the z-axis will arrive into the image focal point under the same angle α with the z-axis (see orange straight lines in Fig. 1(b)). The electromagnetic wave following this path, from F_o to F_i, will be affected by reflection/transmission at the input (P_o) and output (P_i) interfaces of the device (see Fig. 1(b)) In order to withdraw the dependence on α angle of the system transmission, an additional layer which introduce an absorption given by:

$$\tau(\alpha) = \frac{\rho+1}{(\rho+2)^2}\frac{(1+\cos\alpha)^2}{\cos\alpha}, \qquad (2)$$

is placed between the object and image lenses (yellow vertical strip in Fig. 1(b)).

The electromagnetic behavior of the proposed optical system is investigated using numerical simulations. For simplicity, the response of the designed optical device is analyzed in a two-dimensional simulation setup which reduces the computations to the field components $\{E_x, H_y, H_z\}$. The numerical simulations are performed using a two-dimensional finite-difference-time-domain (FDTD) algorithm. Two electric dipole sources generated by electric currents parallel to x-axis, are placed symmetrically with respect to z-axis and object focal point (F_o) at a distance equal to $3\lambda/4$, where λ is the free space wavelength of the sources. The sources are generated coherently, i.e. in phase. Figure 2(a) shows the intensity inside a square area of side length 8λ surrounding the object focal point. The dipole sources are clearly observed as the points with the highest intensity. They are placed symmetrically with respect to z-axis and the distance between them is $3\lambda/4$.

Figure 2(b) shows the intensity inside a square area of side length 8λ surrounding the image focal point (F_i). The image of the dipole sources are clearly observed as two areas of high intensity placed symmetrically with respect to z-axis. The increased distance between the image spots compered with the distance between the dipole sources shows the magnification ability of the proposed optical device for sub-wavelength features. Two additional spots of significantly high intensity can be observed along the z-axis without disturbing the image of the dipole sources [3].

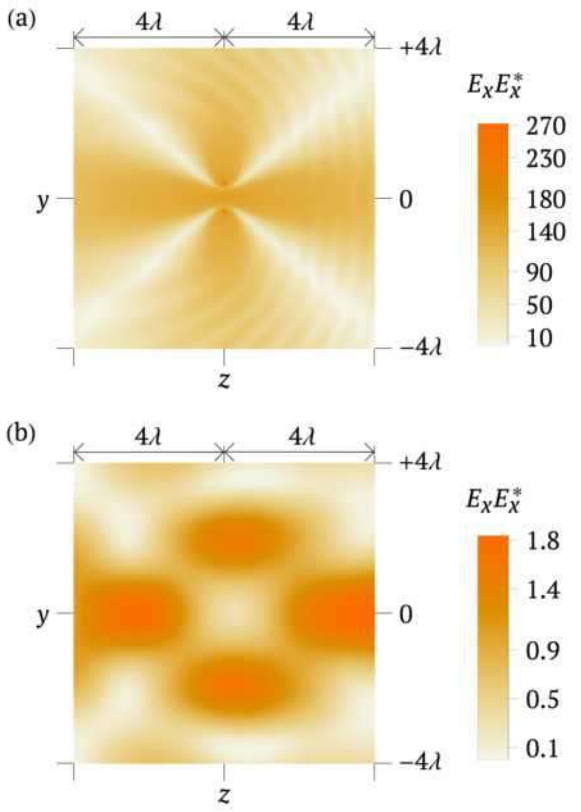


Figure 2: (a) Electric field intensity (E_xE_x*) inside a square of side length 8λ having in its center the object focal point (F_o). (b) Electric field intensity (E_xE_x*) inside a square of side length 8λ having in its center the image focal point (F_i).

Acknowledgement

This work was developed by the Company for Applied Informatics using infrastructure obtained through program POSCCE − A2/O2.3.2, project ID SMIS: 44023/2012, and it was partially supported by program POC − A2/221, project ID MySMIS:115641/2017.

References

[1] D. Schurig, J. B. Pendry, and D. R. Smith, Calculation of material properties and ray tracing in transformation media, *Opt. Express* 14, 9794–9804, 2006.

[2] M. Giloan, Designing Devices for Wave-Vector Manipulation Using a Transformation-Optics Approach, *Phys. Rev. Appl.* 8, 014005, 2017.

[3] M. Giloan and R. Gutt, Sub-wavelength imaging by space dilation, *arXiv:1808.03187* .

Extended two dimensional transformation optics for reflection suppression

Hossein Eskandari[1], Oscar Quevedo-Teruel[2], Amir Reza Attari[1], and Mohammad Saeed Majedi[1]

[1]Department of Electrical Engineering, Ferdowsi University of Mashhad, Mashhad, Iran
[2]Devision of Electromagnetic Engineering, KTH Royal Institute of Technology, Stockholm, Sweden
*corresponding author, E-mail: Hossein.skandari@gmail.com

Abstract

Here, we demonstrate that by extending the common two-dimensional (2D) transformation optics (TO) to the third dimension in an engineered fashion, it is possible to eliminate unwanted reflections from the device boundaries in cases where the compression or expansion of the space makes the ideal transmission of the power impossible in the common formulation. The feasibility of the proposed idea is demonstrated by an example simulated in COMSOL.

1. Introduction

Ever since the two pioneering papers by Pendry and Leaohardt got published in 2006 putting forward the idea of TO, researchers have adopted the method to propose various new devices [1, 2]. What makes TO interesting is the freedom to create marvelous practical devices just by proposing a mapping between two spaces. The most well-known device is the cloak of invisibility where an incoming wave is guided around a concealment area by a cylindrical or spherical metamaterial shell. The idea of cloak was soon followed by several new devices like polarization splitters [3, 4], flat and bespoke lenses [5, 6] and couplers [7, 8, 9].

TO relates the electromagnetic quantities between two spaces namely virtual and physical spaces. Based on TO, the physical space ((x', y', z') coordinates) medium is related to the virtual ((x, y, z) coordinates) medium through the well-known TO formula:

$$\varepsilon = \mu = \frac{JJ^T}{\det(J)}, \tag{1}$$

where $J = \partial(x', y', z')/\partial(x, y, z)$ is the Jacobian matrix which defines the coordinate transformation between two spaces. Equation 1 leads to two similar tensors for the permittivity and permeability tensors. It is shown by following Maxwell equations that TE (E_z, H_x, H_y) and TM (H_z, E_x, E_y) polarizations are affected by $(\mu_{xx}, \mu_{xy}, \mu_{yx}, \mu_{yy}, \varepsilon_{zz})$ and $(\varepsilon_{xx}, \varepsilon_{xy}, \varepsilon_{yx}, \varepsilon_{yy}, \mu_{zz})$ parameters, respectively. Here, we consider TE polarization and TM case can be treated similarly. The dispersion equation and the functionality of the device is maintained as long as the multiplication of $(\mu_{xx}, \mu_{xy}, \mu_{yx}, \mu_{yy})$ and ε_{zz} is not changed for TE polarization.

Since the reflection suppression is meant to be achieved, the Brewster angle β for an interface along y-axis between the vacuum and an anisotropic material is derived and presented as follows:

$$\cos^2\beta = \frac{(\mu_{xx}\varepsilon_{zz} - 1)}{(\mu_{xx}\mu_{yy} - \mu_{xy}\mu_{yx}) - 1}. \tag{2}$$

A 2D TO is defined in the most general form as $x' = f(x, y)$, $y' = g(x, y)$, $z' = z$, where $f(x, y)$ and $g(x, y)$ are the two functions that map the spaces to realize a desired functionality. In such definition, it is assumed that the medium and fields do not alter with respect to the z coordinate and the material defined in the $x - y$ plane is stretched along z axis to the infinity. Following Eq. 1, it is understood that for all 2D TO designs, the in-plane tensor elements of the permeability tensor $\mu_{x-y} = (\mu_{xx}, \mu_{xy}, \mu_{yx}, \mu_{yy})$ intrinsically satisfy $\mu_{xx}\mu_{yy} - \mu_{xy}^2 = 1$, meaning that the eigenvalues multiplication of μ_{x-y} is unity. This is a crucial property for the omnidirectional reflectionless feature which has been previously observed in the case of invisibility cloaks [10]. However, many TO based devices do not require the reflectionless property to be omnidirectional since the wave interact with a certain boundary of the device from a known angle. The unity eigenvalues multiplication causes unwanted reflections for devices where a boundary in the virtual space is expanded, squeezed or flattened.

2. Extended 2D Transformation

Now, consider the extended 2D TO described as $x' = f(x, y)$, $y' = g(x, y)$, $z' = h(x, y)z$ where $h(x, y)$ is added to eliminate the boundary reflections. Using Eq. 1, the transformation will lead to a three-dimensional (3D) medium which changes along the z coordinate. However, if we take the resulting medium at $z = 0$ plane and stretch it along z-axis, an intrusting property is achieved. Using Eq. 1, it is seen that for the resulting medium, the eigenvalues multiplication of μ_{x-y} is no longer unity and equals $\mu_{xx}\mu_{yy} - \mu_{xy}^2 = h^{-2}(x, y)$. Also, introducing $h(x, y)$ does not change the dispersion equation.

3. Simulation Results

Here, we apply the idea to the design of a cylindrical-to-plane-wave converter used inside a horn antenna. Inspired by the original idea of Jiang et al., such device has a trans-

formation formula as follows [5]:

$$r' = \frac{(c-a)r^2(x-a)}{x(bx-ar)} + \frac{ar}{x},\ \varphi' = \varphi,\ z' = z, \quad (3)$$

where $x = a$ is mapped to $x' = a$ and the transformation is continuous, leading to an omnidirectional reflectionless property. Also, $r = b$ is mapped to $x' = c$. Since a circular phase front $r = b$ in the virtual space is flattened to a planar one $x' = c$ in the physical space, reflections are produced at this boundary.

The waves at $x' = c$ boundary are perpendicular to it, hence if only one can satisfy the Brewster angle for normal incident at this boundary, the reflections will be suppressed. Considering Eq. 2, condition $\mu_{xx}\mu_{yy} - \mu_{xy}^2 = h^{-2}(x,y) = \mu_{xx}\varepsilon_{zz}$ should be met at the output boundary. Hence we define a smooth function for $h(x,y)$ to have a value of 1 at $x = a$ and the value of $(\mu_{xx}\varepsilon_{zz})^{-2}$ at $r = b$.

This technique is used to flatten the phase front of a horn with flare angle of $\pi/4$. Simulations were carried out at 9 GHz where design parameters in Eq. 3 are $a = 0.1\text{m}$, $b = 0.21\text{m}$ and $c = 0.15\text{m}$. Results for the common 2D and extended 2D TO cases are illustrated in Fig. 1. The reflections of the 2D TO are 13% and the extended TO suppressed reflections, being less than 1%.

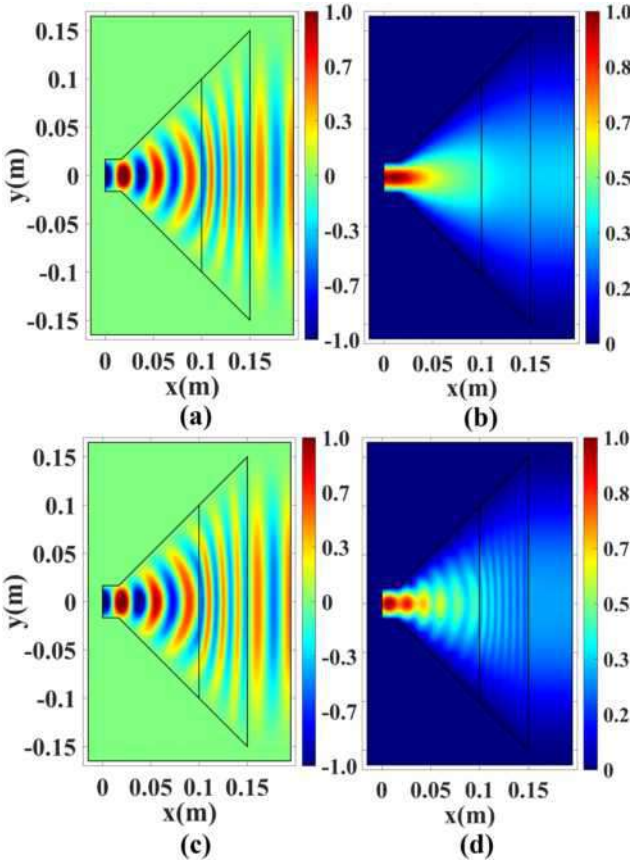


Figure 1: Simulated electric field for a cylindrical-to-plane wave converter used inside a horn antenna. (a) Real part and (b) magnitude of E_z for the extended 2D case. (c) Real part and (d) magnitude of E_z for the common 2D case.

4. Conclusions

A extended 2D transformation is proposed that suppresses the reflection from the boundary of TO-based devices. The formulation is specially useful for devices where one stretches, compresses or flattens a boundary of virtual space to achieve a certain functionality. The validity of the method is verified by an example from the literature.

References

[1] U. Leonhardt, "Optical conformal mapping," *Science*, vol. 312, no. 5781, pp. 1777–1780, Jun. 2006.

[2] J. B. Pendry, "Controlling electromagnetic fields," *Science*, vol. 312, no. 5781, pp. 1780–1782, Jun. 2006.

[3] H. Eskandari, M. S. Majedi, and A. R. Attari, "Design of reflectionless non-magnetic homogeneous polarization splitters with minimum anisotropy based on transformation electromagnetics," *Journal of the Optical Society of America B*, vol. 34, no. 6, p. 1191, May 2017.

[4] H. Eskandari, A. R. Attari, and M. S. Majedi, "Design of polarization splitting devices with ideal transmission and anisotropy considerations," *Journal of the Optical Society of America B*, vol. 35, no. 7, p. 1585, Jun. 2018.

[5] W. X. Jiang, T. J. Cui, H. F. Ma, X. Y. Zhou, and Q. Cheng, "Cylindrical-to-plane-wave conversion via embedded optical transformation," *Applied Physics Letters*, vol. 92, no. 26, p. 261903, jun 2008.

[6] M. Ebrahimpouri and O. Quevedo-Teruel, "Bespoke lenses based on quasi-conformal transformation optics technique," *IEEE Transactions on Antennas and Propagation*, vol. 65, no. 5, pp. 2256–2264, 2017.

[7] M. Rahm, D. A. Roberts, J. B. Pendry, and D. R. Smith, "Transformation-optical design of adaptive beam bends and beam expanders," *Optics Express*, vol. 16, no. 15, p. 11555, Jul. 2008.

[8] H. Eskandari, M. S. Majedi, and A. R. Attari, "Reflectionless compact nonmagnetic optical waveguide coupler design based on transformation optics," *Applied Optics*, vol. 56, no. 20, p. 5599, Jul. 2017.

[9] H. Eskandari, A. R. Attari, and M. S. Majedi, "Reflectionless design of a nonmagnetic homogeneous optical waveguide coupler based on transformation optics," *Journal of the Optical Society of America B*, vol. 35, no. 1, p. 54, Dec. 2017.

[10] G. Gok and A. Grbic, "A physical explanation for the all-angle reflectionless property of transformation optics designs," *Journal of Optics*, vol. 18, no. 4, p. 044020, apr 2016.

Space Transformation Based Recombinable Lens for Generating Multi-mode OAM Radio Beams

Jianjia Yi[1]*, Xueqi Cao[1], Zhihao Jiang[2], Rui Feng[1], Badreddine Ratni[3], André de Lustrac[4], and Shah Nawaz Burokur[3]

[1] Key Laboratory of Integrated Services Networks, Xidian University, Xi'an, China
[2]State Key Laboratory of Millimeter Waves, Southeast University, Nanjing, China
[3] LEME, UPL, Univ Paris Nanterre, 92410 Ville d'Avray, France
[4] Centre de Nanosciences et de Nanotechnologies, CNRS, Univ. Paris-Sud, Université Paris-Saclay, 91120 Palaiseau, France
*corresponding author, E-mail: jianjia.yi@xidian.edu.cn

Abstract

A novel generation method for OAM with different topological charges using the concept of space transformation is presented. The whole device is equally divided into 8 modules which represent the 2π phase range. Designed modules with different phase values can be judiciously arranged to generate beams carrying OAM with different modes. Three-dimensional full-wave simulations validate the spiral-shaped phase fronts of the emitted vortex wave. The proposed method illustrates the practicality of space transformation to achieve a new class of optical devices.

1. Introduction

An electromagnetic wave carrying OAM modes is referred to as a vortex electromagnetic wave, presenting a phase quantified by exp ($il\varphi$) (l = 0, ±1, ±2, ±3…) in its wave front, where l is the intrinsic value of orbital angular momentum and φ is the transverse azimuthal angle. OAM vortex waves with different topological modes are mutually orthogonal to each other. The main methods used to generate orbital angular momentum vortex beams include antenna arrays, metasurfaces, and spiral phase plates (SPPs) [1-2]. However, most of them can only generate OAM waves with single-mode. Therefore, it is necessary to put forward a technology able to generate multi-modes OAM beams.

Space transformation is well known in controlling electromagnetic fields in unprecedented ways through the use of judiciously engineered materials with parameters that vary spatially. This concept offers a technique to manipulate electromagnetic fields into desired spatial patterns, providing applications in engineering and applied sciences, such as invisibility cloaking, focusing devices, and so on [3]. In this paper, based on the concept of space transformation, we present a design methodology of an all-dielectric reflection lens, which can generate OAM waves with different modes. Eight sectors representing different phase variation are obtained, which can cover a total range of 2π. Each sector presents the same physical size but different relative permittivity distribution. Adjusting the arrangement of each sector allows OAM waves with modes l= ±1 and ±2 to be generated. The proposed all-dielectric lens is designed and simulated to validate the proposed design.

2. Design of the OAM generation device

A piece of metal parabolic with central angle of θ= π/4 is shown in Fig. 1(a). When a beam is incident on the surface, the different regions of the wave-front will produce relative phase delays due to the non-planar spiral structure of the metallic parabola, thus achieving the effect of wave-front twisting.

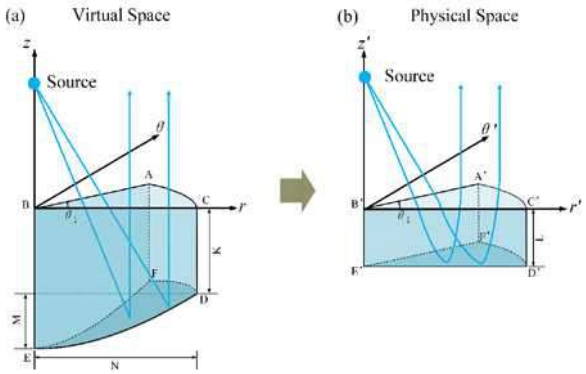


Figure 1: Representation of the space transformation from virtual space to physical space, the curved metal reflector is transformed into a sector of the proposed lens.

Based on the concept of space transformation, a flat shaped lens which has the same function as the reflector is designed, as shown in Fig. 1(b). The physical and virtual space coordinates are respectively denoted by (r, θ, z) and (r', θ', z'). Three-dimensional space *ABCDEF* represents the metallic parabola with air-filled virtual space and the desired physical space is formed by space *A'B'C'D'E'F'*. The curved surface *DEF* and plane *D'E'F'* are perfect electric conductor boundaries. Note that the thickness of physical space is a constant L. The Neumann-Dirichlet

sliding boundary condition is set at the edge of the microwave lens as follows:

$$\begin{cases} r\big|_{O'P',P'Q',O'Q',T'R',O'R',Q'T',P'S'} = r' \\ \hat{n}\cdot\nabla r\big|_{S'T',R'S'} = 0 \end{cases}, \quad (1)$$

$$\begin{cases} z\big|_{O'P',P'Q',O'Q'} = 0 \\ z\Big|_{S'T',R'S'} = \dfrac{M}{N^2}(r')^2 - (K+M) \\ \hat{n}\cdot\nabla z\big|_{P'S',O'R',Q'T',R'T'} = 0 \end{cases}, \quad (2)$$

where $\hat{n}$ is the vector normal to the boundaries of the surface. Through simulations and optimization of variable K, eight sectors with different permittivity distribution are utilized. The distribution of calculated permittivity of the physical domain is presented. The permittivity of each sector shares similar distribution but different range and the phase variation between two adjacent sectors is $\pi/4$. With different combinations of such sectors, the transformed media corresponding to different modes of OAM waves are shown in Fig. 2.

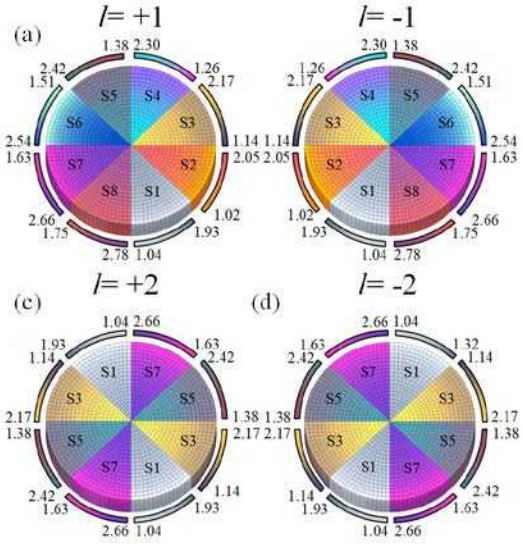


Figure 2: Permittivity distributions of (a) l= +1, (b) l= -1, (c) l= +2. (d) l= -2.

3. Simulation of all-dielectric lens

Three-dimensional simulations are performed to verify the functionalities of the OAM generation lenses at 12 GHz using the finite element method based software HFSS. A regular wave port emitting spherical waves located along the central axis of the microwave device is utilized as feeding source and is placed at 50 mm (2λ at 12 GHz, with λ being the wavelength) away from the upper surface of the transformed medium, which is backed by a circular reflecting metallic plate. From the phase profiles of the electric near-field distributions at 12 GHz (Fig. 3), it can be clearly observed that vortex waves with topological charge l= ±1, ±2 are indeed respectively generated by the different permittivity distribution configurations in the device. The helical transverse phase distribution of an electromagnetic wave carrying an OAM mode can be obviously observed from Fig. 3.

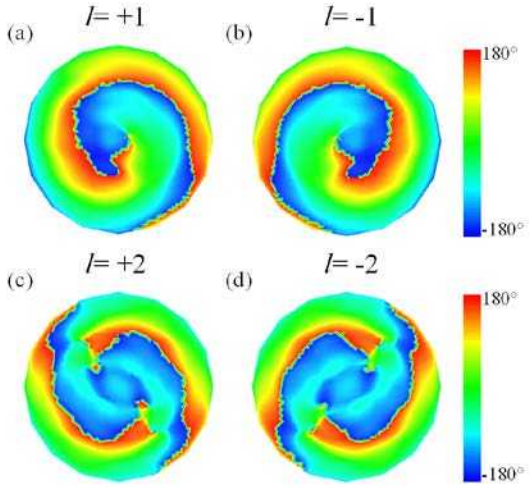


Figure 3: Numerical simulation results for four different generation lenses of mode l= ±1, ±2 at 12 GHz.

4. Conclusions

In summary, based on the concept of space transformation, we propose a universal method to generate electromagnetic waves carrying different OAM modes respectively in an effective manner. By arranging the sectors which represent different phase variations, the OAM vortex wave with different modes can be feasibly realized. In order to validate the OAM characteristics, different configurations of the device generating vortex waves with topological charge l = ±1, ±2 were simulated at 12 GHz. The phase profiles simulated from the vortex beam generators are consistent with the theoretical distributions. Such space transformation based design method is an efficient way to tailor electromagnetic waves with any desired property.

Acknowledgements

This work was supported by the National Natural Science Foundation of China (NSFC) (No. 61601345) and the Fundamental Research Funds for the Central Universities (No. JB190109).

References

[1] Z.H. Jiang, L. Kang, W. H, D.H. Werner, Highly Efficient Broadband Multiplexed Millimeter-Wave Vortices from Metasurface-Enabled Transmit-Arrays of Subwavelength Thickness, *Phys. Rev. A* 9: 064009, 2018.

[2] Q. Ma, C.B. Shi, G.D. Bai, T.Y Chen, A. Noor, and T.J. Cui, Beam-Editing Coding Metasurfaces Based on Polarization Bit and Orbital-Angular-Momentum-Mode Bit, *Adv Opt Mater* 5: 1700548, 2017.

[3] T. Liu, R. Feng, J.J. Yi, S.N. Burokur, C.X. Mao, H.L. Zhang, D.H. Werner, All-dielectric transformation medium mimicking a broadband converging lens, *Opt. Express* 26: 20331-20341, 2018.

Electromagnetic wave shaping, wire media, and transformation optics

Paul Kinsler, Jonathan Gratus, Taylor Boyd

Physics Department, Lancaster University, Lancaster LA1 4YB, UK;
Cockcroft Institute, Daresbury WA4 4AD, UK.
E-mail: dr.paul.kinsler@physics.org

Abstract

Using the tools of transformation optics, we show how spatially modulated wire media can be treated as if they (instead) had a spatially modulated plasma frequency, in agreement with intensive 3D numerical simulation results.

1. Introduction

Wire media [1] are a type of metamaterial which can be used to directly design the electromagnetic field profile within a structure. Analysis is usually [2, 3, 4, 5] based on a straightforward multi-step procedure where numerical results from uniform wires (see fig. 1) are combined to generate modulated wire designs with the desired properties. This process turns out to be unexpectedly simple, but why it works so well is less clear. Here I take a transformation optics (TO) approach to explain the mechanisms involved.

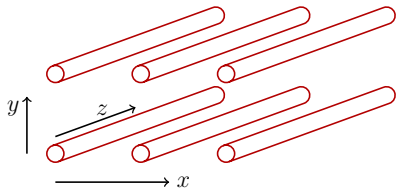


Figure 1: Part of a wire medium formed from a rectangular array of parallel dielectric rods.

2. Mathieu's equation

Mathieu's equation [6] is a well established differential equation with a set of known solutions, and is

$$\partial_\sigma^2 Y + [a - 2q\cos(2\sigma)]\, Y = 0. \tag{1}$$

where the free parameters q and a control the properties of the solution. For a given q there always exists a discrete spectrum of a values such that the solutions $Y(\sigma)$ are periodic over 2π. In the simplest case where $q = 0$, a has the set of possible values $\{0, 1, 4, 9, ...\}$. Mathieu solutions have a wide range of possible profiles, but for the purposes here we note only several possibilities, i.e. those that are quasi-sinusoidal, but have either flat-tops or that are strongly peaked. Our challenge here is to show how field profiles might be generated directly by a TO scheme, whether based on Mathieu functions or some other scheme.

If Mathieu's equation above were adapted with $\omega = \sqrt{a}$ and a Fourier transform into the time domain, giving us

$$\partial_t^2 Y - \partial_\sigma^2 Y + 2q\cos(2\sigma) Y = 0, \tag{2}$$

which is essentially the same as a scalar wave equation for a plasma-like system, but with a scaling $\sigma = z/L$, where L is the unit-cell length; and an extra oscillating potential-like term proportional to q. We will use this similarity below.

3. Wire Media

Wire media metamaterials consisting of a lattice of parallel wires of small radius. One of the useful features of these structures is that they support purely electric longitudinal modes which have a simple dispersion relation.

Of course, real wire media are complex, three-dimensional, and inhomogeneous, which makes them difficult to study in detail without recourse to numerics [2, 3, 4, 5]. Consequently, here we only investigate the longitudinal modes, which have a plasma-like dispersion relation, and which exhibit spatial dispersion. Leaving aside the detailed physics, the dispersion relation for these modes is

$$\omega^2 - \beta^2 c^2 k^2 + \left(\omega_0^2 - \omega_p^2\right) \quad = 0, \tag{3}$$

where βc is an effective wave speed (polariton velocity), ω_0 is the polariton resonance frequency, and ω_p is the plasma frequency parameter. We can immediately see that this is compatible with the Mathieu equation above, if we can match

$$[a - 2q\cos(2\sigma)] \quad \propto \left[\omega^2 + \omega_p^2 - \omega_p^2\right]. \tag{4}$$

The point to note here is that one or both of ω_0 or ω_p need to provide the spatial variation matching the $\cos(2\sigma)$ term.

In existing work [2, 3, 4] this variation has been shown numerically to be achievable by means of a modulation of the wire radius. This is because if a suitable set of full-wave 3D reference simulations are available, a modulation can be designed that gives the desired effective a and q parameters.

However the proposal for radius modulation is based largely on expected fabrication constraints, it should also be possible to achieve the necessary variations in $\omega_0^2 + \omega_p^2$ by means of a permittivity variation instead; this has been verified numerically. A familiarity with the machinery of TO then leads to the concept used in the next section, where the permittivity variation is designed by an appropriate stretching and contraction of the actual longitudinal coordinate z'

onto a reference one z, where the reference situation has a uniform wire radius and uniform permittivity.

In the transformation calculation below, we need a dynamic model that matches the dispersion relation. We get this with Fourier transforms in ω and k, so that

$$\partial_t^2 E - \partial_z c_E^2 \partial_z E + \omega_E^2 E = 0, \tag{5}$$

which, with $c_E^2 = 1/\epsilon\mu$, can be deconstructed [7] into

$$\partial_t D = \partial_t (\epsilon E) = (\partial_z + \kappa_E) H \tag{6}$$

$$\partial_t B = \partial_t (\mu H) = (\partial_z - \kappa_E) E. \tag{7}$$

In this form ω_0^2 and ω_p^2 have been combined into a single ω_E^2, which appears above as the κ_E terms; the polariton velocity βc has been merged into ϵ. We will focus on the non-magnetic case, with $\mu \equiv \mu_0$ in line with fabrication constraints and experimental proposals [5].

4. Transformation Design

The machinery of TO and other forms of transformation design is most simply – but not strictly accurately [8] – expressed as a coordinate transformation. In dielectric wire media, we can make a very good approximation that the net effect of that modulation in the wire radius is simply the effect on the resonance term κ_E.

Now, in the 1+1D case (i.e. only t and z) we allow both a $\kappa_E(z)$ and a transformation between standard space z and transformed space z' where $z = f(z')$ such that

$$\frac{dz'}{dz} = \left[\frac{df(z')}{dz'}\right]^{-1} = \Gamma(z') \tag{8}$$

After applying this transformation, we can define either speed $c_E^2 = 1/\epsilon\mu_0$, or speed $c_B^2 = \Gamma^2/\epsilon\mu_0 = \Gamma^2 c_E^2$, which then gives us two versions of (5) to choose from, namely

$$\partial_t^2 E = \Gamma^2 c_E^2 \partial_{z'}^2 E - c_E^2 \kappa^2 E \quad + \Gamma^2 c_E^2 X, \tag{9}$$

$$\text{or} \quad \partial_t^2 E = \quad c_B^2 \partial_{z'}^2 E - \frac{c_B^2 \kappa^2}{\Gamma^2} E \quad + \quad c_B^2 X. \tag{10}$$

Here X combines a range of z' derivative terms involving Γ, κ, and E. Whilst it is not obvious that X can always (or ever) be neglected, note that such approximations are relatively routine in TO, where the necessity for matched electric and magnetic responses is ignored in return for the simplicity of an dielectric-only design. In this summary, we simply assume these terms are negligible.

Examining (9), we see that if the transform f gives a Γ, which is matched to (and cancels) the variation in c_E^2 (i.e. ϵ), this in turn adds a compensating modulation to κ. Thus an oscillation in ϵ transformed by a suitable Γ can be converted into an effectively unvarying wire with a varying resonance parameter κ.

Likewise, examining (10), we see that if the transform f gives a Γ, which is matched to (and cancels) the variation in κ, this in turn (via c_B^2) adds a compensating modulation to ϵ. Hence although we might start with a modulated wire media with an (effective) oscillating resonance parameter κ; we can use an appropriate transformation Γ to cancel that oscillation in κ, whilst inducing an oscillation in ϵ.

5. Conclusions

The work summarized here shows how transformation design techniques explain why a spatially modulated wire medium can be treated as if it acted as a plasma-like medium with a modulated plasma frequency. This helps us understand why the numerical approach for modelling such wire media [4] works so well, making the design process for customized EM field profiles remarkably efficient.

In the conference presentation, more theoretical detail will be shown, along with numerical results.

Acknowledgement

We are grateful for the support of STFC (Cockcroft Institute, ST/P002056/1) and EPSRC (Alpha-X, EP/N028694/1). PK would like to acknowledge the hospitality of Imperial College London.

References

[1] P. A. Belov, R. Marqués, S. I. Maslovski, I. S. Nefedov, M. Silveirinha, C. R. Simovski, and S. A. Tretyakov, "Strong spatial dispersion in wire media in the very large wavelength limit," *Phys. Rev. B*, vol. 67, no. 11, p. 113103, March 2003. [Online]. Available: 10.1103/PhysRevB.67.113103

[2] J. Gratus, P. Kinsler, R. Letizia, and T. Boyd, "Electromagnetic mode profile shaping in waveguides," *Appl. Phys. A*, vol. 123, no. 1, p. 108, January 2017. [Online]. Available: 10.1007/s00339-016-0649-8

[3] ——, "Subwavelength mode profile customisation using functional materials," *J. Phys. Commun.*, vol. 1, no. 2, p. 025003, September 2017. [Online]. Available: 10.1088/2399-6528/aa81bb

[4] T. Boyd, J. Gratus, P. Kinsler, and R. Letizia, "Customized longitudinal electric field profiles using dielectric wires," *Opt. Express*, vol. 26, no. 3, pp. 2478–2494, February 2018. [Online]. Available: 10.1364/OE.26.002478

[5] T. Boyd, J. Gratus, P. Kinsler, R. Letizia, and R. Seviour, "Mode profile shaping in wire media: Towards an experimental verification," *Appl. Sci.*, vol. 8, no. 8, p. 1276, August 2018. [Online]. Available: 10.3390/app8081276

[6] MathWorld, "Mathieu functions." [Online]. Available: http://mathworld.wolfram.com/MathieuFunction.html

[7] P. Kinsler, "The deconstructed hydrodynamic model for plasmonics," *Arxiv*, 2018. [Online]. Available: http://arxiv.org/abs/1712.06321

[8] P. Kinsler and M. W. McCall, "Transformation design: metrics and speeds," *Wave Motion*, vol. 77, pp. 91–106, March 2018. [Online]. Available: 10.1016/j.wavemoti.2017.11.002

Applications of semiconductor-based and conformal Metasurfaces

P. Ni[1], A. De Luna Bugallo[2], Yi-Yang Xie[3], H. Ren[1], G. Brière[1], S. Chenot[1], S. Vézian[1], V. Brandli[1], B. Damilano[1], J.Y Duboz[1], M. Iwanaga[4] and P. Genevet[1]*

1. Université Côte d'Azur, CNRS, Centre de Recherche sur l'Hétéro-Epitaxie et ses Applications, 1 Rue Bernard Gregory, 06560, Sophia-Antipolis, France
2. Laboratorio de Materiales de Baja Dimensionalidad, Consejo Nacional de Ciencia y Tecnología (Conacyt), Querétaro, Cinvestav. Mexico.
3. Key Laboratory of Optoelectronics Technology (Beijing University of Technology) Ministry of Education, Beijing 100124, China
4. National Institute for Materials Science (NIMS), 1-1 Namiki, Tsukuba 305-0044, Japan

* email: pg@crhea.cnrs.fr

Abstract

During this presentation, we will review the recent developments realized at CRHEA on the fabrication and design of 2D metasurfaces in the passive and active regime. Passive GaN metasurfaces for beam steering and orbital angular momentum holography will be discussed. We will also present tunable gate-voltage controlled light emission at hybridized MoS2/Metasurface. The concluding remarks will be devoted to the works on conformal metasurfaces.

1. Introduction

A new class of planar, wavelength-thick optical components exhibiting exceptional optical properties have emerged in recent years[1-3]. These artificial interfaces, known as metasurfaces, rely on the scattering properties of the subwavelength structures patterned at interfaces to mold the wavefront of light in almost any desired manner. To further develop this technology towards dynamic tuning, broadband application and industrial production, new materials and new fabrication methods are required.

2. Presentation summary

In the first part we will discuss the realization of GaN based metasurfaces for visible applications. In particular, we demonstrate basic metalens fabrication and further utilize these GaN metasurface [4] for the demonstration of an entirely new concept of metasurface OAM holography [5]. The latter are capable of reconstructing a range of distinctive OAM-dependent holographic images from a single meta-hologram.

The remarkable control over the electromagnetic fields offered by the metasurface technology can be further extended to the active regime in order to manipulate the light characteristics in real-time. In this presentation we will begin by discussing the hybridization of atomic-thin MoS2 flakes material with gap-surface-plasmon(GSP) metasurfaces[6]. By doing this, the light emission polarization of the MoS2 flake can be effectively controlled. Furthermore, applying gate voltage directly on the metasurface could is performed to control the trapping charges density at interface, leading to gate-tunable polarized photoluminescence into GSP mode.

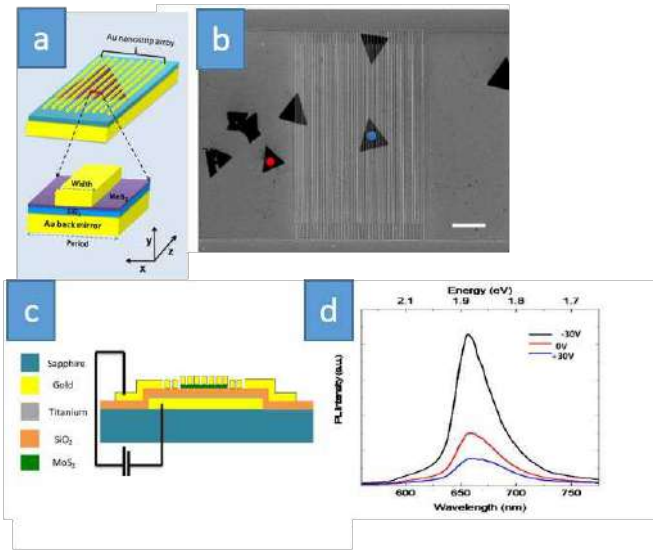


Figure 1: (a) The schematic of the gap plasmon metasurfaces which comprises an array of Au metallic stripe and Au substrate, separated by a 100nm thick insulating SiO2 dielectric layer and a monolayer MoS2 flakes (b) The SEM image of the fabricated hybrid MoS2 gap-mode metasurface. (c) Schematic representation of the fabricated tunable devices. (d) Photoluminescence spectra of gated MoS2-gap plasmon metasurfaces for different applied voltages, indicating strong voltage tunable light emissions. . This structure shows extraordinary advantages of controlling the light emitting characteristics such as polarization control, and selective enhancement of emission, benefitting from its unique resonant coupling between the excitonic resonance and the gap plasmon resonance.

In the second part of the discussion, we will address the problem of conformal metasurface design. The discontinuous variation of these electromagnetic fields across traditional planar metasurfaces can be modelled by considering specific boundary conditions called generalised sheet transition conditions (GSTCs). In this framework,

metasurfaces are described as a 2D interface with abrupt surface susceptibilities, corresponding to complex reflection and transmission coefficients. To go beyond planar metasurfaces, getting into the regime of metasurfaces with arbitrarily curved shapes, the design of free-form metasurface optical elements turns out to be remarkably complex and requires careful consideration of the substrate geometry. Recently, we have proposed a new theoretical framework called 'conformal boundary optics' to describe the electromagnetic boundary conditions at the boundaries of arbitrary geometries. Given input and output field distributions, conformal boundary optics addresses the inverse engineering problems of calculating the interface response at interfaces with arbitrarily curved shapes. This model applies the concept of transformation optics at the level of the boundary conditions, transforming the electromagnetic fields expressed in the laboratory coordinate to their expression in the coordinate system conformal to the interface. As a result, it is possible to obtain designer reflection or refraction of light from objects with unconventional shapes[7].

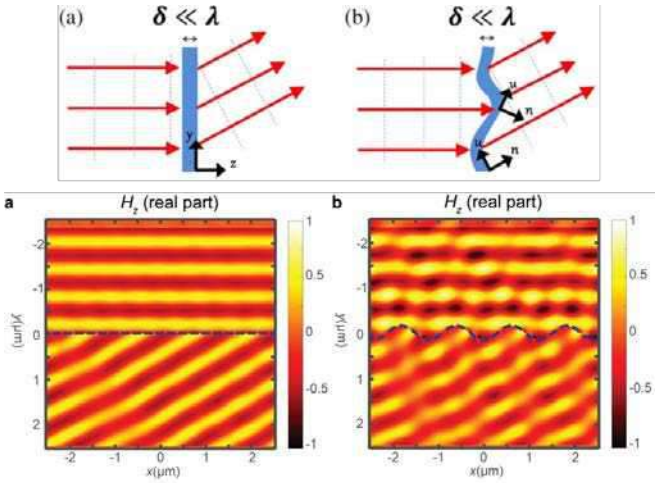


Figure 2: Top: 2D planar metasurface of subwavelength thickness. For planar interfaces, generalized sheet boundary conditions readily apply, and the surface susceptibility tensors can be calculated. (b) The local coordinate system of the surface follows its local curvature, changing with the position along the interface. Boundary conditions of the fields are obtained in the coordinate system of the interface and are therefore position dependent. To produce an effect equivalent to that in (a), the surface susceptibilities of the optical interface have to be engineered to account for the effect of the physical distortion. The dashed blue lines denote the equiphase fronts of the electromagnetic fields.
Bottom: Results of numerical simulation showing the magnetic field intensity distribution of beam deflector designed, according to the generalized Snell laws, to refract light to an angle of rad. In the calculations, the incident light is a TM polarized plane wave propagating along the direction. (a) and (b) Gray intensity distributions of planar and sinusoidal beam deflector.

3. Conclusions

The research on metasurface holds tremendous potential to discover some exotic new physical phenomena and could eventually lead to some unprecedented optical components, but there is still a long journey to implement these advanced concepts.
In this presentation, we report on some of our research efforts to achieve semiconductor-based metasurfaces in the passive (GaN based metasurfaces) and active regimes as well as free-form metasurfaces design for interfaces of arbitrary shapes and functionalities.

Acknowledgements

We acknowledge support from the European Research Council (ERC) under the European Union's Horizon 2020 research and innovation programme (Grant agreement no. 639109).

References

[1] P. Genevet, F. Capasso, F. Aieta, M. Khorasaninejad, R. Devlin. Optica. 4, 2017, Vol. 1, 139-152.
[2] H.T. Chen, A.J. Taylor, N. Yu. Reports on Progress in Physics. 79, 2016, Vol. 7, 076401.
[3] R. Sawant, P. Bhumkar, A. Y. Zhu, P. Ni, F. Capasso, and P. Genevet, Adv. Mater. 2019, 31, 1805555.
[4] G. Brière, P. Ni, S. Héron, S. Chenot, S. Vézian, V. Brandli, B. Damilano, J.Y Duboz, M. Iwanaga and P. Genevet, Advanced Optical Materials (2019)
[5] H. Ren, G. Briere, X. Fang, P. Ni, R. Sawant, S. Héron, S. Chenot, S. Vézian, B. Damilano, V. Brändli, S. A. Maier, and P. Genevet, submitted (2019).
[6] P. Ni, A. De Luna Bugallo, V. M. Arellano Arreola, M. Flores Salazar, B. Alloing, and P. Genevet, submitted (2019).
[7] K. Wu, Q.J. Wang, P. Coquet and P. Genevet, Nat. Comm. 9:3494 (2018).

Transformation optics with "invisible" loss and gain

Yun Lai[1] and Jie Luo[1]

[1]School of Physics, Nanjing University, Nanjing, China
*corresponding author, E-mail: laiyun@nju.edu.cn

Abstract

We introduce balanced loss and gain into a general class of non-Hermitian systems by using transformation optics. We demonstrate that loss and gain turn "invisible" in such systems, and provides a perfect way of energy transportation in open systems.

1. Introduction

Since the proposal of transformation optics [1, 2], this fascinating theory has led to numerous intriguing concepts and applications such as invisibility cloaks [1, 2] and illusion optics [3]. In this talk, I will discuss some interesting effects when loss and gain are introduced into transformation optics. We show that through transformation optics, loss and gain can be perfectly balanced, bestowing the non-Hermitian system with passive responses for arbitrary external waves. Therefore, loss and gain become "invisible" [5]. Energy is perfectly transported between loss and gain internally. We will also discuss the potential application and advantage of this system, such as wireless charging.

.

2. Main results

We demonstrate some examples of transformation optics involving balanced loss and gain. For instance, such a system can be realized by using space folding operation, which has led to intriguing effects such as cloaking at a distance [4] and illusion optics [3]. We find that when loss and gain are balanced, the response of the system is always passive despite that the system itself is inherently non-Hermitian. By designing practical metamaterials, we have demonstrated such an intriguing phenomenon. However, it should be noticed that much of the energy transportation is mediated by evanescent waves instead of propagating waves. Therefore, it also imposes a high requirement on metamaterials. We have analyzed the quality of such an effect by using different types of metamaterials and even photonics crystals [6]

3. Discussion

This non-Hermitian system designed by transformation optics is especially valuable for realizing perfect transportation of energy between loss and gain, e.g. wireless charging. Traditionally, energy transportation in opens systems has a low efficiency because of radiation loss. In this open system, we show that the radiation loss tends to zero. Therefore, it provides a perfect approach for the application of wireless charging [5].

4. Conclusions

We have demonstrated that transformation optics can be applied to establish non-Hermitian systems with perfectly balanced "invisible" loss and gain, with significant potential applications for energy transportation in open systems such as wireless charging.

References

[1] J. B. Pendry, D. Schurig, and D. R. Smith, Controlling electromagnetic fields, Science 312, 1780-1782 (2006).

[2] U. Leonhardt, Optical conformal mapping, Science 312, 1777-1780 (2006).

[3] Y. Lai, H. Chen, Z. Zhang, and C.T. Chan, Complementary Media Invisibility Cloak that Cloaks Objects at a Distance Outside the Cloaking Shell. Phys. Rev. Lett. **102**, 093901 (2009)..

[4] Y. Lai, J. Ng, H. Chen, D. Han, J. Xiao, Z. Zhang, and C.T. Chan, Illusion optics: The optical transformation of an object into another object, Phys. Rev. Lett. **102**, 253902 (2009).

[5] J. Luo and Y. Lai, submitted.

[6] J. Luo, Y. Yang, Z. Yao, W. Lu, B. Hou, Z. H. Hang, C. T. Chan, and Y. Lai, Ultratransparent media and transformation optics with shifted spatial dispersions, Phys. Rev. Lett. 117, 223901 (2016).

Biophotonics

Numerical Design of Bio-Resonator with Filtering Effect

N. Raeis-Hosseini[1*] and C.Papvassiliou[1]

[1]Department of Electrical and Electronic Engineering, Imperial College London

*corresponding author: n.raeishosseini@imperial.ac.uk

Abstract- A bioinspired resonator based on a polysaccharide material for biodegradable nano-optics is designed and simulated. The device has a simple structure with a sandwiched spacer between two metal layers, which represents resonating effect. Due to biodegradability of the utilized material and its natural abundancy it has potential to be fabricated in large area. Base on the simulation results, the proposed resonant optical device exhibits a narrow bandwidth absorber absorption and filtering effect.

Utilization of light at subwavelength with extraordinary optical properties is achieved by nanophotonic materials.[1, 2] Particularly, supernatural transmission and absorption filters based on localized/delocalized resonances have been triumphed by plasmonic metamaterials.[3] However, attainment of large area superior optical filters built on nanoplasmonics under visible wavelength is defying because of high-cost lithography techniques and deficiencies of nanofabrication.[4] We report a planar optical resonator built on a Fabry-Perot (FP) etalon with a lithography-less fabrication[5] process, which is extremely cost-effective.

Multi-layered optical devices have earned research attentions owing to their unique performance and lucrative fabrication in employing of light. The conventional planar resonators encounter deficiencies in sensing abilities due to the inconvenient impact of analytes on the physical variables of the insulator film.[5] We exploited the advantage of a natural biomaterial (NBM) as a bio-inspired material to fabricate an optical device with M-I-M structure, which is capable of being utilized in bio-sensing.

We employ NBM as insulator layer or spacer of the suggested device with biocompatibility, non-toxicity, and biodegradability. The utilized NBM offers exceptional features of the homogeneity, transparency, and hydrogel properties, which makes it a proper material for an absorber and color filter. Through reaction of the insulator thin film with humidified environment, it tunes the resonance wavelengths by swelling. The proposed NBM is sandwiched between two Ag layers, while the substrate is made of NBM (Figure 1a). The NBM, which serves as insulator layer or the spacer of the color filter reacts with the environmental liquids (water) and swells (Figure 1b, c). The resonance mode is altered due to a shift of refractive index (RI) causing an increase in the volume of the spacer.[5] The FP resonances can get tuned by liquid absorption of NBM spacer. During the experiment and measurement, the amount of swelling is governed by changing the liquid type and its pH.

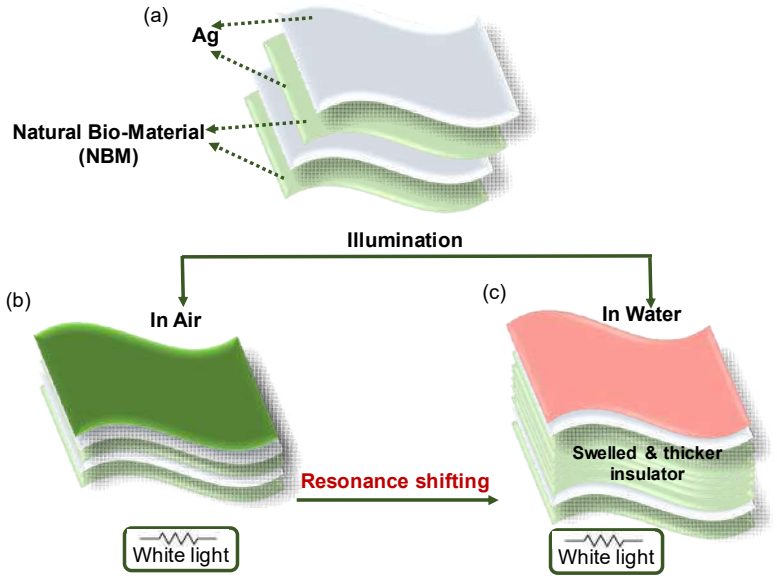


Figure 1. (a) Schematic illustration of a color filter with M-I-M structure; a natural biomaterial (NBM) is sandwiched between two metal layers. (b, c) Illumination of the device under white light in air and water, respectively.

In summary, we designed and simulated a an absorber and color filter based on NBMs. Our suggested super absorber shows similar properties of nanostructured plasmonic materials.

REFERENCES

1. Smith, D.R., J.B. Pendry, and M.C. Wiltshire, "Metamaterials and negative refractive index", *Science*, Vol. 305, No. 5685, 788-792, 2004.
2. Zhu, H., F. Yi, and E. Cubukcu, "Plasmonic metamaterial absorber for broadband manipulation of mechanical resonances", *Nature Photonics*, Vol. 10, 709–714, 2016.
3. Burgos, S.P., et al., "A single-layer wide-angle negative-index metamaterial at visible frequencies", *Nature Materials,* Vol. 9, No. 5, 407-412, 2010.
4. Li, Z., S. Butun, and K. Aydin, "Large-area, lithography-free super absorbers and color filters at visible frequencies using ultrathin metallic films", *ACS Photonics*, Vol. 2, No. 2, 183-188, 2015.
5. Kwon, H. and S. Kim, "Chemically tunable, biocompatible, and cost-effective metal–insulator–metal resonators using silk protein and ultrathin silver films", *ACS Photonics*, Vol. 2, No. 12, 1675-1680, 2015.

New materials for photonics (Graphene, MoS2, WS2, etc)

Synthesis and Plasmon Responses of Sodium Tungsten Bronze Nanoparticles

Levi Tegg[1], Dylan Cuskelly[2], and Vicki J. Keast[1]

[1]School of Mathematical and Physical Sciences, University of Newcastle, Callaghan 2308, NSW, Australia
[2]School of Engineering, University of Newcastle, Callaghan 2308, NSW, Australia
*corresponding author, E-mail: Levi.Tegg@uon.edu.au

Abstract

The sodium tungsten bronzes are sub-stoichiometric metal oxides with interesting electrical and optical properties which vary with the sodium content. We have developed a synthesis technique which makes high-purity sodium tungsten bronze nanoparticles across a wide composition range. Results from electron energy-loss spectroscopy reveal that these materials support high-quality localised surface plasmons, with resonance frequencies which are tunable across visible and near-infrared frequencies by varying the sodium content.

1. Introduction

To date, Au and Ag have been the materials-of-choice for most plasmonic applications. Au has high chemical stability, but plasmon resonances are damped due to interband transitions. In contrast, Ag supports very strong plasmon resonances, but corrosion in air is a significant issue. The ideal material for plasmonics should be an inexpensive metal with high chemical stability, simple nanofabrication techniques, and low intrinsic damping losses [1].

The sodium tungsten bronzes (Na_xWO_3, $0 \leq x \leq 1$) are sub-stoichiometric metal oxides with properties which vary with the Na content, x [2]. For $x > 0.4$, Na is inserted into a perovskite-like framework of corner-sharing WO_6 octahedra, forming a solid solution with a Na:W ratio of x. The inserted Na donates its 3s electron to the WO_3 conduction band. This gives Na_xWO_3 metallic optical properties, with a plasma frequency which approximately varies with $\omega_\mathrm{p} \propto \sqrt{x}$ [2]. In this presentation, we show that Na_xWO_3 is a promising new plasmonic material due to its simple nanoparticle synthesis and tunable, low-loss nanoparticle plasmon responses.

2. Methods

For a detailed description of the synthesis and characterisation techniques, see reference [3]. Briefly, Na_xWO_3 nanoparticles were synthesised using a modified furnace-assisted method [4]. Sample composition was determined using X-ray diffraction and Rietveld refinement. Particle morphology was investigated using scanning electron microscopy (SEM). To map localised surface plasmon resonances (LSPRs), electron energy-loss spectroscopy (EELS) in the scanning transmission electron microscope (STEM) was performed on nanoparticles deposited on Si_3N_4 membranes. The boundary element method (BEM), as implemented in the MNPBEM toolbox [5], was used to simulate the optical properties and EELS responses of Na_xWO_3 nanoparticles. Dielectric function data for Na_xWO_3 was calculated previously using density functional theory [2].

3. Results

Figure 1 shows SEM micrographs of (a) $Na_{0.61}WO_3$ and (b) $Na_{0.83}WO_3$ nanoparticles. This synthesis method produces nanocubes when $x > 0.5$, and quasispheres mixed with rods when $x \approx 0.2 - 0.6$, with particle sizes around $d \approx 150 - 300$ nm. We have found that the ratio of quasispheres to rods varies with the sintering temperature [3]. Although these nanoparticles are large compared to those typically used in plasmonics, Na_xWO_3 has a lower ω_p than typical plasmonic materials, so low-order modes still dominate the near-infrared and visible optical properties.

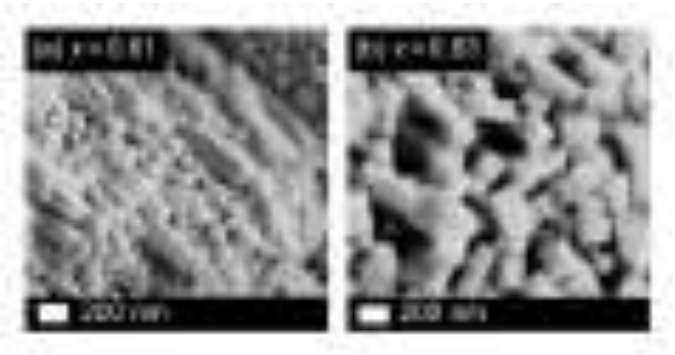


Figure 1: (a) SEM images of (a) $Na_{0.61}WO_3$ and (b) $Na_{0.83}WO_3$.

Fig. 2 (a) shows experimental EEL spectra from a prolate $Na_{0.61}WO_3$ nanoparticle. The three spectra shown are taken from the corresponding coloured points in (b), a high-angle annular dark-field (HAADF) image of the nanoparticle. After subtracting the Si_3N_4 spectrum and the zero-loss peak (ZLP), three Gaussians were fit to the spectra at the frequencies indicated by the vertical lines in (a). (c–e) map the magnitude of these Gaussians at each frequency. LSPR modes similar to those of spheroids are observed [6], with a longitudinal mode at $\hbar\omega_1 = 1.35$ eV and a transverse mode at $\hbar\omega_2 = 1.65$ eV. The bulk plasmon is observed at $\hbar\omega_\mathrm{BP} = 2.06$ eV, consistent with previous studies [2].

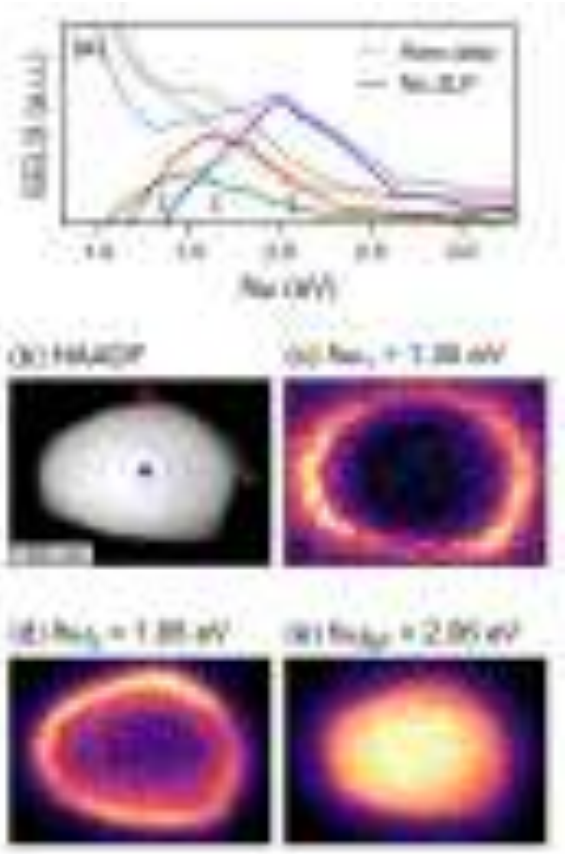


Figure 2: (a) Experimental EEL spectra from a $Na_{0.61}WO_3$ nanoparticle, taken from the three coloured points shown in (b), a HAADF image of the nanoparticle. (c–e) map of the magnitudes of Gaussians fit to the experimental EEL spectra at the frequencies indicated in (a).

As the particle morphology varies with x, quantitative comparison of the plasmon responses between different samples is challenging. Since BEM simulations accurately reproduce experimental results [3], they have been used to predict how resonance frequencies change as x is varied. Fig. 3 shows the calculated change in plasmon frequencies with x for nanospheres (low x) and nanocubes (high x). Similar to the variation in $\omega_{\mathrm{p}} \propto \sqrt{x}$, the LSPRs dramatically redshift with decreasing x from visible to near-infrared frequencies.

4. Discussion and conclusions

Our straightforward synthesis technique produces bulk quantities ($\approx$ 2.5 g) of plasmonic Na_xWO_3 nanoparticles using inexpensive reagents. Although work is continuing to reduce particle sizes further, we have started exploring applications in plasmonic photocatalysis and solar-control filtering. Over the course of this project ($\approx$ 2 years), we have observed little change in the composition or optical properties of our nanoparticle samples, suggesting a high corrosion resistance. EELS studies, supplemented with BEM simulations, show that Na_xWO_3 supports high-quality bulk

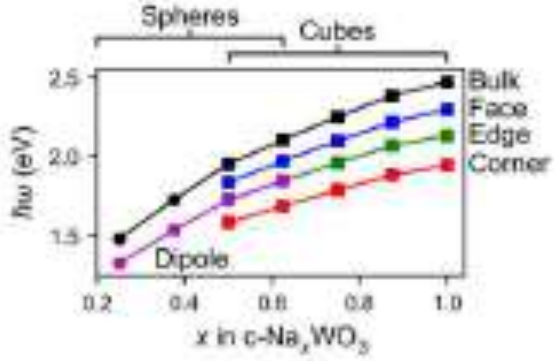


Figure 3: Calculated variation in plasmon frequencies with x for cubes and spheres of diameter $d = 10$ nm.

and nanoparticle plasmon resonances which blueshift from the near-infrared to the visible with increasing x. The variation in LSPR frequency with composition is additional to the standard tunability by particle size, shape and dielectric environment, and represents a great strength of Na_xWO_3 as a plasmonic material.

Acknowledgement

This research was supported by an Australian Government Research Training Program (RTP) scholarship. The technical support of the EMX unit at UON and the EMC at UOW are acknowledged.

References

[1] P.R. West, S. Ishii, G.V. Naik, N.K. Emani, V.M. Shalaev, A. Boltasseva, Searching for better plasmonic materials, *Laser & Photonics Reviews* 4: 795–808, 2010.

[2] L. Tegg, D. Cuskelly, V.J. Keast, The sodium tungsten bronzes as plasmonic materials: fabrication, calculation and characterization, *Mater. Res. Exp.* 6: 065703, 2017.

[3] L. Tegg, D. Cuskelly, V.J. Keast, Bulk scale fabrication of sodium tungsten bronze nanoparticles for applications in plasmonics, *Nanotechnology* 29: 40LT02, 2018.

[4] M.E. Straumanis, The Sodium Tungsten Bronzes. I. Chemical Properties and Structure, *J. Am. Chem. Soc.* 2: 679–683, 1949.

[5] U. Hohenester, A. Trügler. MNPBEM – A Matlab toolbox for the simulation of plasmonic nanoparticles, *Comput. Phys. Commun.* 182: 370–381, 2012.

[6] M. Pelton, G.W. Bryant, *Introduction to metal-nanoparticle plasmonics*, Wiley, New Jersey, 2013.

Optoelectronic Mixers Based on Graphene Photodetectors

Chuantong Cheng[1], Beiju Huang[1,2], Huan Zhang[1], Hengjie Zhang[1], Hongda Chen[1,2]

[1] State Key Laboratory on Integrated Optoelectronics, Institute of Semiconductors, Chinese Academy of Sciences, Beijing, China

[2] College of Materials Science and Opto-Electronic Technology, University of Chinese Academy of Sciences, Beijing, China

*corresponding author, E-mail: bjhuang@semi.ac.cn

Abstract

We demonstrated a novel optoelectronic mixer based on graphene photodetector in this work. Considering the ultrahigh carrier mobility and the CMOS compatible fabrication routing, graphene material is a potential candidate for the next generation radio frequency applications.

1. Introduction

Signal mixers are essential devices in radio frequency (RF) applications. The available mixers can only mix two electric signals and additional photodetectors are needed to convert the optical signals to electric signals. Hence, if both the photodetection and mixing functions can be achieved in a single device, a compact system can be obtained.

Graphene, the first discovered two-dimension monolayer material, is a potential candidate for future RF applications because of its ultrahigh carrier mobility and saturation velocity [1]. However, graphene field effect transistor (GFET) is hard to be turn off due to its zero band gap, which means it is suitable for analog circuit rather than digital application. Up to now, several promising RF devices such as voltage amplifier [2], frequency multiplier [3] and signal mixer [4] have been achieved with GFETs. Drain current saturation is essential for a high performance analog amplifier. However, a GFET with traditional structure just exhibits weak current saturation due to the absence of a band gap [5]. And some methods to obtain current saturation in GFET are at the cost of the performance or reliability degradation of the devices. On the other hand, signal mixers based on GFETs have attracted much interest because of the superior electrical properties of graphene. At the same time, graphene's linear output characteristic makes it particularly suitable for resistive mixer applications [6]. Lots of discrete RF mixers and wafer scale integrated circuits (ICs) operating as RF mixers have been reported successfully [6]- [8].

Therefore, to compete with tradition IC technologies based on silicon, requires that all high performance graphene based active and passive components be monolithically integrated onto single chip. In our case, to obtain signal mixer with high performances is extremely urgent. Here, we will show a novel work about graphene RF devices of our group. An optoelectronic mixer (OEM) based on graphene photodetectors (GPDs) have been achieved in our group and will be demonstrated in details here.

2. Results

Frequency upconversion is essential in high-speed communication systems nowadays. For example, before being radiated by antennas to the end customers, the base-band signal in radio-over fiber systems is upconverted to RF signal at first. The upconversion functions is commonly performed using mixers that modulate base-band to RF carriers by multiplying the base-band signal with a local oscillator (LO) signal. In traditional mixer, the mixing is performed through two electronic signals. However, a more compact alternative is based on OEMs, where both the photodetection and mixing functions are achieved in a single device. More clearly, OEMs are devices that mix two intensity-modulated optical signals and generate two electrical signals at frequencies $f_{up} = f_{opt1} + f_{opt2}$ (upconversion) and at $f_{down} = |f_{opt1} - f_{opt2}|$ (down-conversion). Here we report the first graphene based OEMs which can mix two RF optical signals.

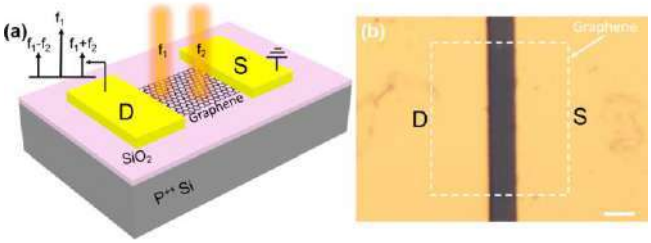


Fig. 1. (a) The three-dimensional schematic of the basic device structure and its operation principle are shown. Two optical signals with different frequency (f_1 and f_2) are absorbed by graphene and mixing electronic signals ($f_1 \pm f_2$) are obtained. (b) The optical micrograph of the fabricated GPD based OEM is displayed. The white dotted frame shows the location of the graphene and the scal bar is 3 μm.

Fig. 1(a) shows the three-dimensional schematic of the basic device structure and operation principle and Fig. 1(b) displays the optical micrograph of the fabricated GPD based OEM. The width and the length of the graphene channel is 20 μm and 3 μm, respectively. Fig. 2 shows the mixing

spectrum of a 3 GHz optical signal with wavelength of 1530 nm and 80 MHz optical signal with wavelength of 1570 nm. This GPD upconvertes the 80 MHz signal to 3000 ± 80 MHz. And the conversion loss is 23 dB.

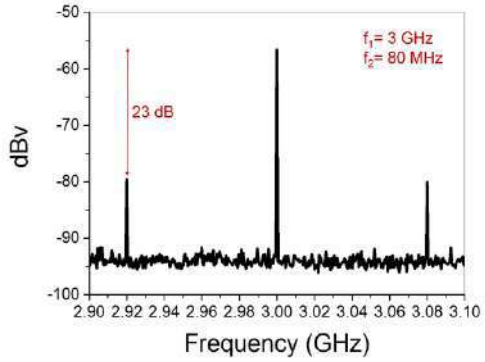


Fig. 6. The mixing spectrum of a 3 GHz optical signal with wavelength of 1530 nm and 80 MHz optical signal with wavelength of 1570 nm.

3. Discussion

As the channel length in all our GPD based RF devices are defined by photolithography processes, the operation bandwidths are limited by the device sizes. In consideration of graphene's potential ultrahigh carrier mobility and high saturation velocity, the bandwidth of graphene device is not limited by the carrier transit time, but mainly limited by the RC time constant of the device structure. With recent developments in GPDs, an intrinsic unity current gain frequencies higher than 400 GHz have been achieved [9], which makes graphene a promising material in future RF applications. Therefore, the reported novel RF devices here will see their importance in the graphene based RF optoelectronic applications in the near future.

4. Conclusions

In this paper, we have proposed a novel RF device based on GPDs. An OEM that can mix two optical signals effectively is also reported for the first time. The finished graphene based novel RF devices may have a far-reaching significance for the realization of graphene based IC for RF applications.

Acknowledgements

The authors are grateful for the financial support from the National Key Research and Development Program of China (Grant Nos. 2016YFB0402505, 2018YFA0209000, 2017YFB0403603, 2017YFA0205903, 2016YFB0700700), the China Postdoctoral Science Foundation (Grant Nos. 2018T110130, 2017M620874), the National Natural Science Foundation of China (Grant Nos. 61675191, 61634006, 61674146, 61335010, 61178051, 51673025).

References

[1] K.I. Bolotina, K.J. Sikesb, Z. Jianga,d, M. Klimac, G. Fudenberga, J. Honec, P. Kima, H.L. Stormer, "Ultrahigh electron mobility in suspended graphene", *Solid State Commun*., vol. 146, pp. 351–355, Mar 2008.

[2] S. J. Han, K. A. Jenkins, A. V. Garcia, A. D. Franklin, A. A. Bol, and W. Haensch, "High-Frequency Graphene Voltage Amplifier," Nano Lett., vol. 11, pp. 3690–3693, Aug. 2011.

[3] H. Wang, D. Nezich, J. Kong, and T. Palacios, "Graphene frequency multipliers," IEEE Electron Device Lett., vol. 30, no. 5, pp. 547–549, May 2009.

[4] O. Habibpour, S. Cherednichenko, J. Vukusic, K. Yhland, & J. Stake, "A subharmonic graphene FET mixer," IEEE Electron. Dev. Lett. vol. 33, no. 1, pp. 71–73, Jan. 2012.

[5] I. Meric, M. Y. Han, A. F. Young, B. Ozyilmaz, P. Kim, and K. L. Shepard, "Current saturation in zero-bandgap, top-gated graphene field-effect transistors," Nature Nanotechnol., vol. 3, pp. 654–659, Nov. 2008.

[6] H. M. Lyu, H. Q. Wu, J. B. Liu, Q. Lu, J. Y. Zhang, X. M. Wu, J. F. Li, T. Ma, J. B. Niu, W. C. Ren, H. M. Cheng, Z. P. Yu, and H. Qian, "Double-Balanced Graphene Integrated Mixer with Outstanding Linearity," Nano Lett., vol. 15, pp. 6677−6682, Sep. 2015.

[7] Y.-M. Lin et al., "Wafer-scale graphene integrated circuit," Science, vol. 332, no. 6035, pp. 1294–1297, Jun. 2011.

[8] S. J. Han, A. V. Garcia, S. Oida, K. A. Jenkins1 & W. Haensch, "Graphene radio frequency receiver integrated circuit", Nat Commun., vol. 7, pp. 8472, Oct. 2015.

[9] Cheng, R. et al., "High frequency self-aligned graphene transistors with transferred gate stack". Proc. Natl Acad. Sci. 109, pp.11588–11592, Jul. 2012.

Hybrid graphene-antenna structure for terahertz detection

Klaas-Jan Tielrooij[1*], Sebastián Castilla[2], Bernat Terrés[2], Marta Autore[3], Leonardo Viti[4], Alexey Nikitin[3], Miriam Vitiello[4], Rainer Hillenbrand[3], Frank Koppens[2]

[1]Catalan Institute of Nanoscience and Nanotechnology, Barcelona Institute of Science and Technology, Bellaterra (Barcelona), Spain
[2]ICFO – The Institute of Photonic Sciences, Barcelona Institute of Science and Technology, Castelldefels (Barcelona), Spain
[3]CIC nanoGUNE, E-20018 Donostia-San Sebastian, Spain
[4]NEST, CNR – Istituto Nanoscienze and Scuola Normale Superiore, Pisa, Italy
*corresponding author, E-mail: klaas.tielrooij@icn2.cat

Abstract

By combining high-quality graphene with a narrow-gap antenna structure, we demonstrate a very fast and highly sensitive terahertz (THz) detector. The detector is based on the efficient heating of graphene carriers induced by THz absorption and photocurrent generation through the photo-thermoelectric effect, where carrier heat leads to a photoresponse at a junction between two graphene regions with different carrier density, typically a *pn*-junction. Crucially, the metallic antenna structure leads to strong field enhancement exactly at the location of this junction.

1. Introduction

The detection of THz light is highly interesting for applications in fields such as sensing, security and quality control. However, currently there are no room-temperature THz detectors that are simultaneously sensitive, fast, and broadband. Since a few years, graphene has been suggested as a promising material that could overcome these limitations. However, there seems to be no consensus regarding the exact physical mechanisms that leads to a THz-induced photoresponse in graphene. Here [1], we have developed a THz detector based on high-quality graphene, where we optimize the response generated by the photo-thermoelectric (PTE) effect, where THz-induced carrier heating [2] at a *pn*-junction leads to a large photoresponse.

2. Detector design

A crucial challenge for our THz detectors based on the PTE effect is the large mismatch between the geometry that maximizes the PTE response, which is a graphene channel of typical size ~1 micron, and the THz wavelength of ~100 microns. To overcome this challenge, we used a dipolar antenna with a narrow gap (~100 nm), in order to funnel the incoming THz light into a very small volume around the antenna gap. In our design, the two branches of the antenna simultaneously serve as gates that create the *pn*-junction in the graphene channel situated just above the antenna, separated by hexagonal BN of ~15 nm thick. This junction is created by applying appropriate (opposite) voltages to the two antenna branches. Thus, the *pn*-junction coincides – by design – with the area where the incoming THz radiation is focused, optimizing the PTE response of the hybrid graphene-antenna structure.

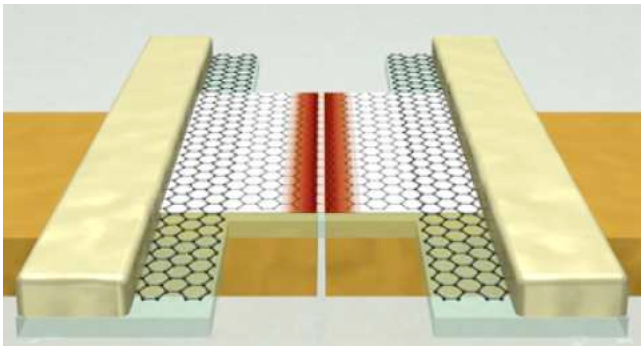


Figure 1: Schematic overview of the center part of the hybrid graphene-antenna structure, showing an H-shaped graphene channel above the antenna gap. The color scale indicates the intensity enhancement $|E/E_0|^2$ due to the antenna structure (in the plane of the graphene sheet), reaching a maximum of almost 10^5.

3. Results

We have characterized the sensitivity of our hybrid graphene-antenna THz detectors based on the PTE effect by measuring the photoresponse as a function of the voltages on the two split gates, *i.e.* the two antenna branches. We observe the characteristic sixfold pattern corresponding to a PTE photoresponse [3], with the maximum photoresponse for *pn* and *np* configurations. We also measured the noise of our device, which is given by Johnson noise, since the device is passive (no applied bias voltage), thus finding a noise-equivalent power of NEP <100 pW/Hz$^{1/2}$. This is a very good number for being a room-temperature detector.

The speed of the detector was determined by modulating in time the output of a THz quantum cascade laser, and measuring the photoresponse with an oscilloscope. We find that the response is faster than 30 ns, limited by our pre-amplifier with a bandwidth of 5 MHz. The intrinsic response is as fast as 10 ps, considering the RC-time of the device.

Finally, we measured the photoresponse over a large range of incident THz powers, finding a linear response over three orders of magnitude, and over a range of frequencies between 2 and 4 THz. Thus the detectors have a large dynamic range and are sensitive for a broad range of THz frequencies. The spectral sensitivity is determined by the antenna response and could therefore be extended by using more broadband antenna designs with a similar narrow gap.

4. Discussion

Since our hybrid graphene-antenna THz detectors show the characteristic sixfold pattern corresponding to a PTE response [3], we have developed a simple analytical model to describe the response. As input for this model we have used numerical simulations of the graphene-antenna structure to characterize how much of the incident THz radiation is absorbed in the graphene sheet. Based on this input, we find good agreement between our experimental results and the results of the analytical model. This agreement is highly valuable for understanding and optimizing PTE-based hybrid graphene-antenna THz photodetectors in particular, and PTE-based detectors in general.

5. Conclusions

In conclusion, we have developed [1] a hybrid graphene-antenna structure for THz detection, exploiting the strong field confinement around the gap of the narrow-gap antenna. The THz detector works at room temperature, is very sensitive (NEP <100 pW/Hz$^{1/2}$), fast (<30 ns, setup-limited), has a large dynamic range (3 orders of magnitude) and broad spectral sensitivity (2-4 THz, antenna-limited).

References

[1] S. Castilla et al., Fast and sensitive teraherz detection using an antenna-integrated graphene pn-junction, *under review*.

[2] Z. Mics et al., Thermodynamic picture of ultrafast charge transport in graphene. *Nat. Commun.* 5, 7655 (2015)

[3] N.M. Gabor et al., Hot carrier-assisted intrinsic photoresponse in graphene., *Science* 334, 648 (2011)

Plasmonic TiO_xN_y based micro-structured films obtained by ammonolysis photopatternable TiO_2 sol-gel film

Usuga Maria[1], Crespo-Monteiro Nicolas[1], Vocanson Francis[1], Koussi Erika[1], Jamon Damien[1], Verrier Isabelle, Langlet Michel[2], Jourlin Yves[1*]

[1] Univ Lyon, UJM-Saint-Etienne, CNRS, Institut d'Optique Graduate School, Laboratoire Hubert Curien UMR 5516, F-42023, SAINT-ETIENNE, France

[2]Universite Grenoble Alpes, LMGP, F-38000 Grenoble, France, CNRS, LMGP, F-38000 Grenoble, France

*corresponding author, E-mail: jourlin@univ-st-etienne.fr

Abstract.

This paper shows the obtention of thick titania sol-gel films and their technological processing to metallic films of TiO_xN_y by ammonolysis process. The aim of this process is the realization of subwavelength TiO_xN_y micro-structured surface for application in resonant plasmonic gratings in the Near - InfraRed range (NIR).

1. Introduction.

New metamaterials have been the subject of a lot of researches for plasmonic materials [1,2]. Among them, transition-metal nitrides, in particular titanium nitride (TiN), offer interesting properties for plasmonic applications in the Near-InfraRed (NIR) range [3,4]. Usually the TiN layer is deposited by means of expensive techniques such as PVD and CVD. Due to their intrinsic properties (hardness and chemical stability), their microstructuration such as gratings components is very difficult. Some technologies like lift-off lithography and/or physical or chemical etching process is used for this purpose [5] but their realization is time-consuming and expensive.

Another way to elaborate TiN layer is possible, using the ammonolysis process of TiO_2 films [6] and it allows to obtain a non-stoichiometric TiN_x or TiO_xN_y material. This technique is often used in a way to implement from low to a high level of nitrogen that it can be used to improve the photocatalytic activity [7].

Now, this technique deserves a new interest, because TiO_2 can support a high degree of nitridation and also it can be deposited by sol-gel method offering new interests and new fields of applications.

In this paper, the authors present an original approach and an experimental demonstration of a TiO_xN_y plasmonic grating fabrication using ammonolysis of titanium oxide from direct microstructuration of a photopatternable sol-gel layer, which acts like a negative photoresist [8]. The aim is the obtention of a TiO_2 grating by the direct photo-patterning of a sol-gel layer and their tranformation in a TiO_xN_y based grating, using the ammonolysis process.

2. Experimental procedure.

2.1 Sol-gel method.

The films used in this work were elaborated from a specific photo-patternable sol-gel prepared from titanium isopropoxyde orthotitanate (TIPT) complexed by benzoyl acetone (BzAc) in methanol and butanol using a previous procedure published [8–10]. After it was deposited by spin-coating on a silicon substrate, the sol-gel layer was first dried at room temperature and then heated at 110°C, leading at an inorganic polymer film constituted of Ti-O-Ti chains with organic chain-end groups arising from the sol formulation, mainly TIPT-BzAc complexed species. The main interest of this protocol relies on the properties of BzAc, which makes the film soluble in a solvent while being sensitive to UVA light. Indeed under UVA illumination, the TIPT-BzAc complex is partially degraded in insoluble species such as carbonates and/or carboxylates. Therefore, it will create a contrast of solubility between illuminated and non-illuminated areas.

2.2 Sol-gel films microstructuring.

The pattern to be printed on the samples is obtained by UV illumination through a chromium photomask of 1 μm period during 10 min under a 365 nm wavelength collimated light with an irradiance of 400 mW.cm-2. Then a short baking step of 8 min at 110°C is performed in order to increase solubility contrast between insolated and non-insolated areas. The photo-chemical or thermo-chemical effects of this three step process have been described in [8]. The development of samples was optimized by washing in ethanol that dissolves easily the non-insolated layer, leading to a grating whose period is the same as that of the photomask, i.e. a TiO_2 grating of 1μm period. Finally the sample was baked at 300°C for (15 min).

2.3 Nitridation process.

The Nitridation of TiO_2 sol-gel was realized by ammonolysis. The films were heat under Ar gas (100 sccm) in a SiO_2 glass tube furnace up to 800°C, 900°C or 1000°C.

Then, the temperature was keep constant and NH_3 flow (100 sccm) was applied during 30 min to achieve nitridation

3. Results and discussion.

In order to prove the ability of the fabricated TiO_xN_y grating to be used as a plasmonic component, measurements were performed with an experimental set-up. A collimated and linear polarized (TE or TM) polychromatic wave is incident onto the grating. This source is a halogen lamp, which emits on the desired bandwidth in the very near IR. A spectrometer measures the wavelength spectrum of the 0^{th} reflected order. The spectrometer is adapted to the NIR range and is able to detect the signal in the 900-2000 nm bandwidth. The angle of incidence α is fixed at three values: 25°, 30° or 35°. The figure 1 shows the 0^{th} reflected order of the TiO_xN_y grating in the 1300 - 1700 nm bandwidth and for the three chosen angles of incidence. One can observe in this figure a nice SPR depicted by a minimum of the 0^{th} reflected signal in TM polarization which appears at 1440 nm, 1515 nm and 1590 nm for incident angles of 25°, 30° and 35°, respectively. The TE mode exhibits a constant reflection close to 60% with no particular change whatever the incidence angle.

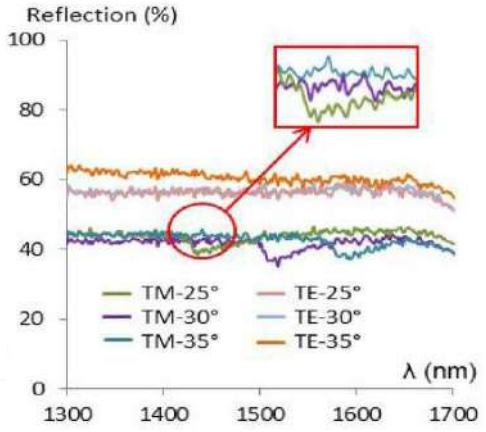


Figure 1 : Experimental measurement in 0^{th} reflected order of the TiOxNy grating for incidence angles of 25°, 30° and 35° and for TE or TM incidence

The structure of TiO_xN_y films was analysed by X-ray diffraction (XRD) and SEM images (figure 2). The results of XRD patterns indicate the presence of a single fcc crystallographic phase that may correspond to the TiN phase. Ammonolysis at 900°C leads to the crystallization of TiO_xN_y grains of around 30 nm in diameter. Even if so small grains cannot precisely be observed in the SEM image of Fig. 2(b) owing to resolution limitations, this image clearly depicts the granular morphology of the ammonolyzed grating. Thermo-mechanical stress occurring at the film-substrate interface during the pre-heating and post-cooling ammonolysis steps may also cause the formation of localized micro-cracks. Moreover, grain boundary and localized microcrack features are likely to induce the roughness depicted by AFM profiles after ammonolysis. These features can also reduce the conduction and optical performances of the fabricated grating, leading to losses for plasmonic applications. In other words, a same TiO_xN_y layer free of grain boundary and micro-crack features should exhibit better conduction and optical performances closer to that of stoichiometric TiN.

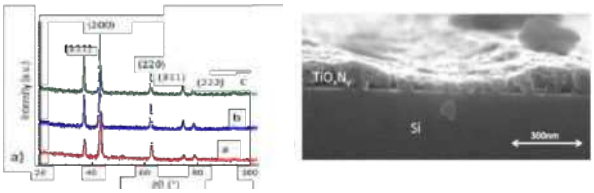


Figure 2: a) X-ray diffraction patterns for pre-treatment at 300°C and ammonolysis at a = 800°C, b = 900°C and c = 1000°C. b) SEM image of the TiO_xN_y grating in cross section view.

3 Conclusions.

A process for the ammonolysis of a TiO_2 grating involving a directly photopatternable sol-gel thin film layer has been demonstrated, with the aim to use the derived gating as a plasmonic component. The characteristics of the nitrided grating led to the experimental demonstration of the plasmonic resonance at the metal-air interface in the NIR range. The grating elaborated from the TiO_2 nitridation does not lead to a pure TiN and induces roughness due to the ammonolysis treatment but the derived plasmonic component is easy to realize and excitation of the plasmon is directly achieved by coupling the incident wave by a quasi-sinusoidal grating. From these promising results and despite the no perfect stoichiometry of the TiO_xN_y layer and its roughness, the authors are currently working on further understanding of the plasmon mode excitation on such TiO_xN_y and further developments to reduce losses to be used in different applications such as optical sensors [11], biosensors [12] and photovoltaics [13]

4 Acknowledgements.

The Authors would like to thank the French Region Auvergne Rhône-Alpes for its financial support, in the framework of Pack Ambition Recherche 2018, MICROSOLEN project.

References.

[1] G. V. Naik, J. Kim, and A. Boltasseva, Opt. Mater. Express **1**(6), (2011).
[2] R. Letizia and D. Pinto, J. Lightwave Technol. **32**(8), (2014).
[3] G. V. Naik, et al., Opt. Mater. Express **2**(4), (2012).
[4] N. C. Chen, et al. J. Appl. Phys. **109**(4), (2011).
[5] N. Kinsey et al., Opt. Express **22**(10), 12238–12247 (2014).
[6] K. Kamiya et al., J. Mater. Sci. **22**(3), 937–941 (1987).
[7] Y. Kuroda et al., Langmuir **21**(17), 8026–8034 (2005).
[8] S. Briche et al. J. Mater. Sci. **46**(5), 1474–1486 (2011).
[9] V. Gâté et al., Opt. Mater. **35**(9), 1706–1713 (2013).
[10] O. Shavdina et al., Langmuir **31**(28), 7877–7884 (2015).
[11] J. Homola et al., sensors and actuators B: chemical **54** (1-2), 3-15 (1999).
[12] E. Shkondin et al., optical materials express **7** (11), 4171-4172 (2017).
[13] H. Wang et al,. Photon pres **3** (6) 329-334 (2015)

Near-field nano-imaging of buried microcavity for enhancement of WS_2 monolayer exciton photoluminescence

Oliver Mey[1], Franziska Wall[1], Lorenz Maximilian Schneider[1], Darius Günder[1], Frederik Walla*[2], Amin Soltani[2], Hartmut G. Roskos[2], Ni Yao[3], Peng Qing[3], Wei Fang[3], and Arash Rahimi-Iman[1]

[1] Department of Physics and Materials Sciences Center, Philipps-Universität Marburg, Marburg, 35032, Germany

[2] Physikalisches Institut, Johann Wolfgang Goethe-Universität, 60438 Frankfurt am Main, Germany

[3] State Key Laboratory of Modern Optical Instrumentation, College of Optical Science and Engineering, Zhejiang University, Hangzhou 310027, China

*corresponding author, E-mail: walla@physik.uni-frankfurt.de

Abstract

Photoluminescence (PL) control in suspended 2D transition metal dichalcogenides (TMDC) monolayers is explored as a pathway for novel optoelectronic devices. By engineering the dielectric surrounding of TMDC layers one can significantly enhance both light absorption and PL emission. Nanostructured buried microcavities facilitate the enhancement of in- and out-coupled fields in both vertical and horizontal direction. Here, we demonstrate near-field nano-imaging as a tool for characterizing the in-coupled light on a WS_2 monolayer suspended above a circular Bragg microcavity designed for exciton PL enhancement.

1. Introduction

Transition metal dichalcogenide monolayers are 2D semiconductors that are studied due to their extraordinarily strong light-matter interaction. Thinning down TMDCs to 2D monolayers with sub-nanometer thickness leads to an indirect-to-direct energy gap transition and allows for increased photoluminescence [2]. Out of these materials, WS2 is particularly promising for nanophotonic applications due to comparatively easy exfoliation and a narrow and strong A-exciton photoluminescence peak [3] with high quantum yield [4].

Light interacting with the TMDC monolayers is subject to multiple reflection in the surrounding dielectrics and substrate. The arising interferences can be exploited to engineer enhancement and attenuation of the incident and emitted light by tuning the thickness and refractive indices of the surrounding media. It has been shown, that by taking into account multiple reflections in vertical and horizontal direction laser light in-coupling into and PL out-coupling from a TMDC monolayer flake can be optimized by structuring the substrate underneath the monolayer flake [5, 6].

Here, we examine a suspended WS_2 monolayer flake where the substrate underneath has been engineered and structured in vertical and horizontal direction with the aim of facilitating both in-coupling and out-coupling enhancement of light. Scattering-type near-field optical microscopy (s-SNOM) is applied as a tool to characterize the in-coupling engineering of incident light onto the WS_2 monolayer. We demonstrate that s-SNOM can resolve the near-field profile on a nanostructured microcavity, including the case where the cavity is covered by a suspended monolayer flake. In the scope of optimizing the PL enhancement, nano-resolved near-field mapping complements (multiple reflection) modelling to distinguish between the two effects of improved in-coupling and out-coupling enhancement.

2. Experiment and Results

We study here a hBN-buffered WS_2 monolayer flake on top of nanostructured GaP substrate using scattering-type near-field microscopy. The PL enhancement of the WS_2 flake is achieved through a buried circular Bragg microcavity which was embedded in the patterned substrate using FIB etching. The thin hBN buffer layer serves to avoid quenching effects. The trench height of 70 nm of the Bragg microcavity was optimized considering incident light at 532 nm and emitted light at the A-exciton wavelength of 615 nm using a multiple reflection model [6]. Figure 1(a) and

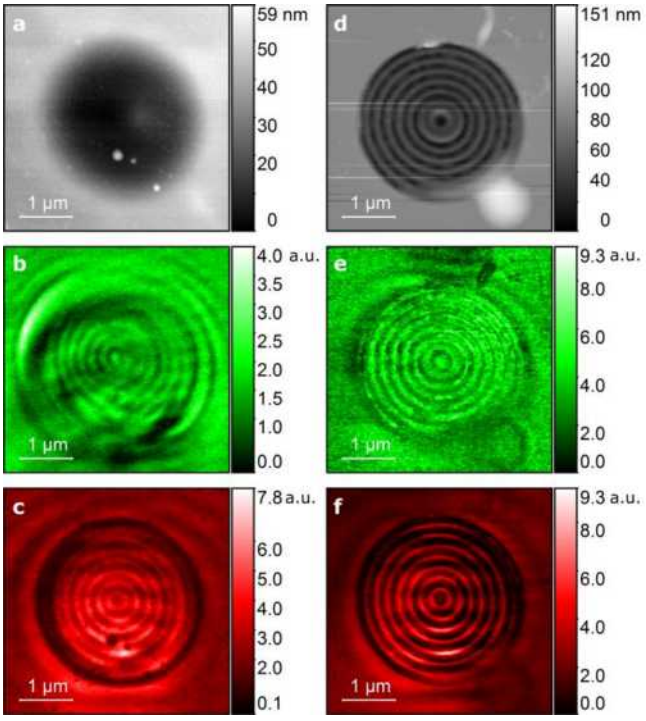


Figure 1: Topography and near-field measurements of monolayer-covered and open microcavity structure. (a-c) Topography and near-field maps at 532 nm and 850 nm, respectively, of covered cavity. (d-f) Topography and near-field maps at 532 nm and 850 nm, respectively, of open cavity.

1(b) show the AFM topography of the structure for two cases: covered with WS_2 monolayer flake and open microcavity.

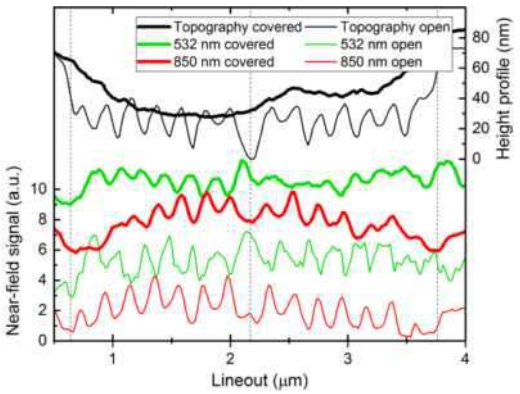


Figure 2: Horizontal line-outs taken from the AFM and s-SNOM measurement. a) Dashed vertical lines mark the edges and center of the microcavity structure. While the field maxima at 850 nm coincide with the topographical maxima of the Bragg cavity, the field distribution at 532 nm shows a different behavior. One can observe clear field maxima in the center of the cavity for both measurements taken at 532 nm.

To assess the effectiveness of the cavity, we investigate the local field distribution of the pump light using s-SNOM. The s-SNOM uses a metallized AFM tip oscillating at 260 kHz. Its apex is illuminated by a laser beam at the excitation wavelength 532 nm or at the off-resonant out-of-stopband wavelength 850 nm for reference. While the tip is kept at a constant time-averaged distance of 20 nm from the surface the sample is translated for raster-scanning. Meanwhile, the probe tip acts as a nano-antenna, scattering part of the near-field wave into the far-field revealing the near-field signature. The technique is sensitive to buried spectroscopic information and has a spatial resolution of 20-50 nm. It is thus feasible to resolve the wavelength-dependent in-coupling enhancement of the monolayer-covered Bragg microcavity. Figures 1(b-c) show the near-field map of the WS_2-covered cavity at the excitation wavelength of 532 nm and at 850 nm for reference, respectively. Figures 1(e-f) show the same near-field maps for the open microcavity at both wavelengths. For clarity, Figure 2 shows horizontal lineouts through the center for each panel presented in Figure 1. Vertical dashed lines indicate borders and center of the cavity.

3. Discussion

In both figures the in-coupling spatial enhancement of the in-coupled green light is prominent as a central peak in the cavity at 532 nm. On the other hand, the field distribution for excitation at the off-resonant out-of-stopband wavelength 850 nm shows opposite behavior and a minimum in the center. The same observation holds for the measurements on the open microcavity. This suggests that the spatial enhancement of in-coupling can be assigned to the lateral grating structure, while the vertical resonant behavior affects primarily the out-coupling enhancement of the WS_2 exciton PL. One may further note that while the near-field map at 850 nm matches the topographical profile, the signal at 532 nm shows field enhancement in the gaps of the microcavity for both the uncovered and covered sample. This may be attributed to the fact that s-SNOM measures two effects simultaneously: local electric fields and differences of material properties [38]. We follow that the signal at 532 nm resolves the strong field distribution with its maxima in the gaps. The signal at 850 nm, however, incorporates a rather strong spectroscopic material-dependent contribution.

4. Conclusions

We have demonstrated near-field maps of buried microcavities for PL enhancement of WS_2 monolayers. s-SNOM nano-imaging serves to assess the effectiveness of previously engineered substrate patterning and to distinguish between in- and out-coupling enhancement. Depending on the structure, material-dependent measurement artifacts must be taken into account. Finally, we confirm that the PL of the WS_2 is additionally locally enhanced by the Bragg microcavity through an increased resonant in-coupling efficiency of the exciting light.

Acknowledgements

The authors acknowledge financial support by the German Research Foundation (DFG: SFB1083, RA2841/5-1), the Philipps-Universität Marburg, the Federal Ministry of Education and Research (BMBF) in the frame of the German Academic Exchange Service's (DAAD) program Strategic Partnerships and Thematic Networks, the National Natural Science Foundation of China (No. 61635009), the Fundamental Research Funds for the Central Universities (No. 2018FZA5004) and the Friedrich-Ebert-Stiftung.

References

[1] K.F. Mak, C. Lee, J. Hone, J. Shan, T.F. Heinz. Atomically thin MoS_2: a new direct-gap semiconductor. *Phys. Rev. Lett.*, *105*, 136805, 2010.

[2] S. Jo, N. Ubrig, H. Berger, A.B. Kuzmenko, A.F. Morpurgo, Mono- and Bilayer WS_2 Light-Emitting Transistors. *Nano Lett.*, *14* (4), 2019.

[3] Y. Ye, Z.J. Wong, X. Lu, X. Ni, H. Zhu, X. Chen, Y. Wang, X. Zhang, Monolayer Excitonic Laser. *Nat. Photonics*, *9* (11), 733–737, 2015.

[4] D.H. Lien, et al.; Engineering Light Outcoupling in 2D Materials. *Nano Lett.*, *15* (2), 1356–1361, 2015.

[5] H. Zhang, Y. Wan, Y. Ma, W. Wang, Y. Wang, L. Dai, Interference Effect on Optical Signals of Monolayer MoS_2. *Appl. Phys. Lett.*, *107* (10), 1–5, 2015.

[6] O. Mey, F. Wall, L.M. Schneider, D. Günder, F. Walla, A. Soltani, H.G. Roskos, N. Yao, P. Qing, W. Fang, A. Rahimi-Iman, Enhancement of the Monolayer WS2 Exciton Photoluminescence with a 2D-Material/Air/GaP In-Plane Microcavity. arXiv:1812.10286, 2018.

Organic materials for plasmonics: nanoscale light-confinement using J-aggregates

Samuel Holder[1,2,*], Martin Lopez-Garcia[3], Ruth Oulton[2,4], and Sara Nunez-Sanchez[5]

[1]Quantum Engineering CDT, NSQI Building, University of Bristol, Bristol BS8 1FD, UK
[2]Quantum Engineering Technology Labs, School of Physics, University of Bristol, Bristol BS8 1TH, UK
[3]Department of Nanophotonics, INL-International Iberian Nanotechnology Laboratory, 4715-330 Braga, Portugal
[4]Department of Electrical and Electronic Engineering, University of Bristol, Bristol BS8 1TH, UK
[5]Departamento de Química Física and CINBIO, Universidade de Vigo, Vigo, Spain
*corresponding author, E-mail: samuel.holder@bristol.ac.uk

Abstract

In this work we demonstrate that a variety of J-aggregates can be used to make organic materials that confine light on the nanoscale. J-aggregate thin films were prepared by spin-coating a mixture of J-aggregate and a polymer matrix. A selection of J-aggregate thin films were chosen with metal-like optical properties from green to red wavelengths. The potential of these films for nanoscale light-confinement was then tested by coupling to the surface-exciton-polariton (SEP) mode of each film, using Fourier imaging spectroscopy.

1. Introduction

The field of plasmonics is primarily concerned with nanoscale light-confinement by metals. Metals are able to confine light due to their free electrons, which allow the bulk medium to become highly polarised in the presence of an electric field. However, free electrons are not the only possible origin of these optical properties. Large excitons, delocalised electron-hole pairs, can allow fundamentally different kinds of materials to reach similar values of electric permittivity, and hence such materials can confine light on the nanoscale [1]. Thin films of J-aggregate in a polymer matrix are observed to have metal-like properties in a narrow wavelength range, due to delocalised excitons in the constituent J-aggregates. Here we will demonstrate light-confinement using these organic materials based on J-aggregates, by coupling to the surface-exciton-polariton (SEP) mode of these materials.

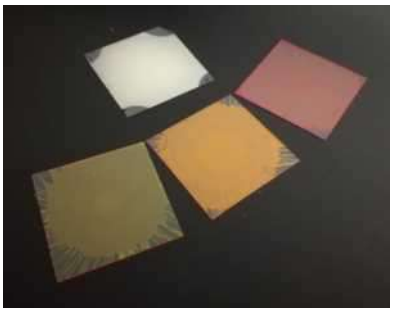


Figure 1: Thin films of three different J-aggregates (bottom), with a silver film (top) for comparison. Each film reflects in a narrow range of wavelengths close to the J-aggregate absorption, where the electric permittivity reaches metal-like values.

2. Preparation of films: making materials using J-aggregates

J-aggregates are large, organic dye molecules that self-assemble in solution under specific conditions. When monomers are assembled into J-aggregates, the electronic orbitals of individual monomers are coupled together, so that the aggregates support large excitons that are delocalised across many monomer units. These delocalised ex-

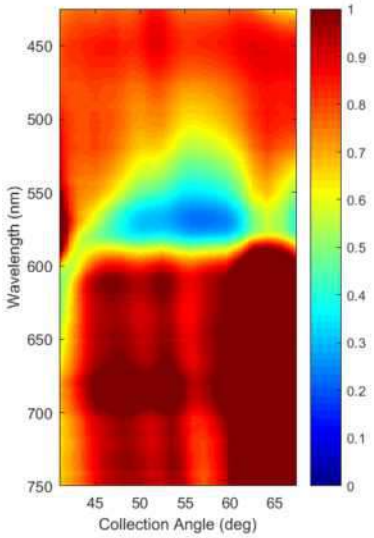


Figure 2: Reflectance of p-polarised light from a J-aggregate (TDBC) and PVA thin film. Notice the dip in reflectance below the J-aggregate absorption at 590nm: this is absorption into the SEP.

citons interact strongly with light [2].

In this work we produce polymer films doped with J-aggregates. Aqueous solutions of J-aggregate and poly(vinyl alcohol) (PVA) are mixed. The resulting solution can then be spin-coated onto hydrophillic substrates to yield films around 30nm thick. These films have metal-like electric permittivity in a narrow wavelength range due to the excitation of delocalised excitons close to the J-aggregate absorption. This gives these J-aggregate and polymer films a metal-like reflectance, coloured according to the wavelength of the absorption of the J-aggregate used to make the film (Fig. 1).

3. Optical measurement: exciting surface-exciton-polaritons in organic films

The aim of this work is to show that J-aggregates can be used as the building blocks for organic materials that confine light on the nanoscale. To do this we demonstrate coupling to the SEP mode of a J-aggregate thin film. The SEP mode is analogous to the surface-plasmon-polariton (SPP) mode in metals, and can be measured in a similar way. SPPs are traditionally observed in reflectance, using a metal film deposited on a prism, with light incident on the film from the glass side [3]. This is necessary to give the incoming light a large enough wavevector to match the dispersion of the SPP. By controlling the angle of incidence, the dispersion of the incoming light and the SPP are matched, and incoming light is coupled into the SPP resulting in a dip in reflectance. This only occurs for p-polarised light above the critical angle, which matches the polarisation of the SPP and exceeds the maximum possible wavevector in air.

The same measurement protocol as described above applies to SEPs. We implemented a prism-coupling configuration using an oil-immersion objective lense with a high numerical apperture. This was used to view J-aggregate and PVA films deposited on glass coverslips, with the objective lense contacting the glass side of the sample. This configuration was used to perform Fourier imaging spectroscopy, which measures the reflected spectrum at specific angles.

In a metal below the plasma frequency, SPPs can occur at a wide range of wavelengths and hence the dip in the reflectance of p-polarised light corresponding to an SPP is broad in wavelength. Contrastingly, a J-aggregate film only has metal-like optical properties for a narrow range of wavelengths, and hence, the measured dip in reflectance corresponding to an SEP is narrow in wavelength (Fig. 2). The metal-like region in which SEPs propagate is close to the J-aggregate absorption, on the short-wavelength side: therefore different J-aggregates yield SEP dips at different wavelengths. Surrounding these SEP dips, the reflectance is close to one: at these wavelengths, the J-aggregate film is a dielectric and we observe total internal reflection. Several J-aggregate and polymer films were tested and all supported SEPs, showing that J-aggregates can be used as the building blocks of an organic platform for plasmonics.

4. Conclusions

In this work we have demonstrated the 'plasmonic' capabilities of a new family of organic materials. This novel organic platform can exploit the fabrication tools of supramolecular chemistry, to control and design J-aggregates which give access to light-confinement at desirable new wavelengths across the visible and near infrared; extending plasmonics beyond the fixed properties of metals by a new means.

Acknowledgement

This work was supported by the UK EPSRC grant QuPIC (EP/N015126/1), and by the UK EPSRC Quantum Engineering Centre for Doctoral Training, University of Bristol.

References

[1] M.J. Gentile, S. Nunez-Sanchez, W.L. Barnes, Optical Field-Enhancement and Subwavelength Field-Confinement Using Excitonic Nanostructures, *Nano Lett.* 14 (5), 2339, 2014.

[2] J. Knoester, *Optical properties of molecular aggregates*, Proceedings of the International School of Physics 'Enrico Fermi', Volume 149, 2002.

[3] H. Raether, *Surface Plasmons on Smooth and Rough Surfaces and on Gratings*, Springer Tracts in Modern Physics, Vol. 111, Springer, Berlin, 1988.

Organic excitonic core-shell nanoparticles with plasmon-like response: Towards fully plastic metamaterials

S. Núñez-Sánchez*, C. Estevez-Varela, I. Pastoriza-Santos
Departamento de Química Física and CINBIO, Universidade de Vigo, 36310 Vigo, Pontevedra, Spain.
*corresponding author, E-mail: S.Nunez-Sanchez@uvigo.es

Abstract

Plasmonics and metamaterials have been a driven force for nanotechnology applications allowing concentrate the light right down to the nanoscale. Metals such as gold or silver have been the material platforms for the plasmonic revolution. In this work we show that organic materials can be the key to confine light at nanoscale and enhance light matter interactions with a plastic. Moreover, we will show that it is possible to define colloid chemistry routes to build up organic building blocks which can establish the fundamentals towards fully plastic metamaterials.

1. Introduction

Noble metals have been traditionally used as the materials palette for building blocks at nanoscale. However, some applications require crossing the visible range and obtaining plasmon-like response at infrared or ultraviolet wavelengths. A variety of alternative materials have been explored, including doped semiconductors, graphene or transparent conducting oxides. In 2014, Nunez-Sanchez and colleagues demonstrated that densely packed molecular thin films doped by J-aggregates can exhibit inherent metal-like properties being able to confine the field in at nanoscale as metals (see Figure 1).[1] More recently, in 2016, they shown that this metal-like behavior could be used in photonic design to define new types of optical modes.[2] Now, in this work, we will go further in the application of these molecular materials as building blocks at nanoscale exploring new chemistry routes for the preparation of molecular doped nanoparticles with plasmon-like response.

2. Excitonic materials with metal-like response

Decades ago, molecular crystals shown metallic reflection associated with strong interactions between neighbouring molecular excitons.[3] In these organic materials the individual molecules are spatially distributed in the crystal lattice and can be considered as small local dipoles that can be excited collectively under specific conditions. This behaviour is responsible for the optical properties of the material for which the real part of the permittivity can achieve negative values resembling metallic behavior in a restricted wavelength range (see Figure 1). This negative values of the permittivity can be also achieved by heavily J-aggregates doped polymers, where the polar molecules are randomly spatially distributed.[1] In this work we will study how we can control this metal-like band at nanoscale as a function of the loading of molecules in our excitonic core-shell nanoparticles establishing a relation with the optical properties of the bulk.

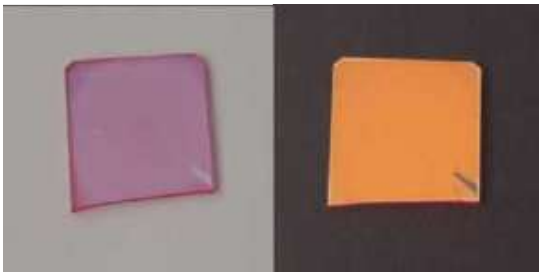


Figure 1.- Picture of a J-aggregate thin film deposited on top of a glass and located on top of a white (left) and black (right) paper. The reflected color shows a strong metal-like band in the orange.

3. Localized Surface Exciton Resonances (LSER) in Silica-J-aggregate core-shell nanoparticles

In this work, we have synthesized and studied stable colloidal dispersions of excitonic core-shell nanoparticles. These core-shell nanoparticles are formed by a core of silica and a shell of densely packed J-aggregates (see figure 2). The role of the silica nanoparticles is being the inorganic scaffold or template for molecular J-aggregates whom will provide the plasmon-like properties to the colloids.

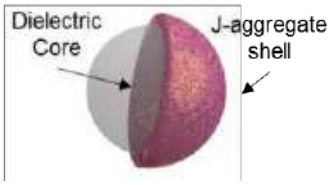


Figure 2.- Sketch with a graphical description of the core-shell nanoparticles with plasmon-like response synthetized by colloidal chemistry methods.

The first step was the synthesis of silica nanoparticles with

size control following the method proposed by Bogush et al.[4] In the next step, J-aggregates were deposited through electrostatics on the silica surface using the Layer-by-Layer technique. In order to stabilize the J-aggregates on the silica surface, polyelectrolytes were used after each J-aggregate layer. The deposition of the organic layer on the nanoparticle surface has been confirmed by Transmission Electron Microscopy (TEM), Zeta potential and UV-Vis spectroscopy.

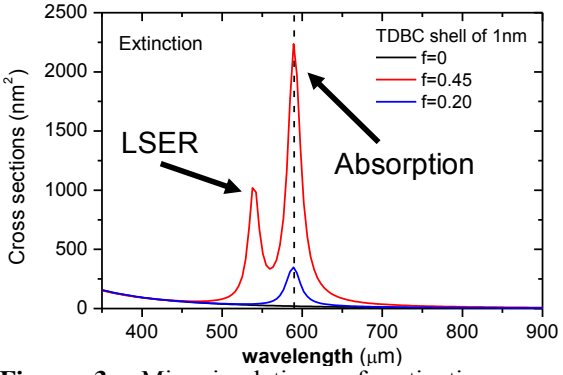


Figure 3.- Mie simulations of extinction cross sections of the excitonic core-shell nanoparticles. For low levels of molecular loading (f=0.20) a small peak associated to the absorption of the J-aggregates (TDBC) is observed on top of the silica core response. As the loading of molecules is increased (f=0.45) a second peak appears associated to the local surface exciton resonance.

The optical response of the hybrid nanoparticles was studied as a function of the number of J-aggregate layers deposited at the surface of the silica nanoparticles. For low molecular loaded samples, an absorption peak is observed on top of the silica core optical response due to the inherent absorption of J-aggregates. As the loading of J-aggregates increases a new excitonic resonance appears which can be only justified by a plasmon-like resonance (localized surface exciton resonance-LSER). These experimental results have been confirmed by numerical simulations revealing the potential use of J-aggregate materials as an excitonic alternative to plasmonics at nanoscale (see Figure 3) and corroborating their relation with the optical properties in the bulk.

4. Conclusions

In this work we have shown how J-aggregate doped polymers can establish a novel molecular route for plastic building blocks at nanoscale. Starting from excitonic thin films with metal-like optical response we have been build up core-shell nanoparticles by colloid chemistry methods. These Silica-J-aggregate core-shell nanoparticles shown LSER similar to localized surface plasmon resonances in metals corroborated by numerical simulations. In our knowledge this is the first experimental evidence than excitonic plastics can show plasmon-like response in nanostructures opening a new fully plastic era in metamaterials.

References

[1] M. J. Gentile, S. Núñez-Sánchez, and W. L. Barnes, "Optical field-enhancement and subwavelength field-confinement using excitonic nanostructures.," *Nano Lett.*, vol. 14, no. 5, pp. 2339–44, May 2014.

[2] S. Núñez-Sánchez *et al.*, "Excitonic Optical Tamm States: a step towards a full molecular-dielectric photonic integration," *ACS Photonics*, vol. 3, no. 5, pp. 743–748, 2016.

[3] M. R. Philpott, A. Brillante, I. R. Pockrand, and J. D. Swalen, "A New Optical Phenomenon: Exciton Surface Polaritons at Room Temperature," *Mol. Cryst. Liq. Cryst.*, vol. 50, no. 1, pp. 139–162, Jan. 1979.

[4] C. F. Bogush, G.H.; Tracy, M.A.; Zukoski IV, "Preparation of Monodisperse Silica Particles: control of size and mass fraction," *J. Non. Cryst. Solids*, vol. 104, pp. 95–106, 1988.

Hybrid plasmon-magnon polariton modes in graphene-antiferromagnet heterostructures

Yuliy V. Bludov[1], José N. Gomes[1], Gil A. Farias[3], Joaquin Fernández-Rossier[2,4], Mikhail I. Vasilevskiy[1,2], Nuno M. R. Peres[1,2]

[1]Department of Physics, Center of Physics, and QuantaLab, University of Minho, Campus of Gualtar, 4710-057, Braga, Portugal
[2]QuantaLab, International Iberian Nanotechnology Laboratory (INL), Av. Mestre José Veiga, 4715-330 Braga, Portugal
[3]Departamento de Física, Universidade Federal do Ceará, Caixa Postal 6030, Campus do Pici, 60455-900 Fortaleza, Ceará, Brazil
[4]Departamento de Física Aplicada, Universidad de Alicante,
Carretera de San Vicente del Raspeig 03690 San Vicente del Raspeig, Alicante, España
*corresponding author, E-mail: bludov@fisica.uminho.pt

Abstract

We consider a hybrid structure formed by graphene and an insulating antiferromagnet, separated by a dielectric of thickness up to $d \simeq 500\,nm$. When uncoupled, both graphene and the antiferromagneic surface host their own polariton modes coupling the electromagnetic field with plasmons in the case of graphene, and with magnons in the case of the antiferromagnet. We show that the hybrid structure can host two new types of hybrid polariton modes. First, a surface magnon-plasmon polariton whose dispersion is radically changed by the carrier density of the graphene layer, including a change of sign in the group velocity. Second, a surface plasmon-magnon polariton formed as a linear superposition of graphene surface plasmon and the antiferromagnetic bare magnon. This polariton has a dispersion with two branches, formed by the anticrossing between the dispersive surface plasmon and the magnon. We discuss the potential these new modes have for combining photons, magnons, and plasmons to reach new functionalities.

1. Introduction

It is known, that an uniaxial antiferromagnet (AF) can exhibit negative permeability in certain frequency range [1, 2]. As a consequence, surface of AF is able to support surface magnon-polaritons (SMPs) [3] – a special kind of electromagnetic waves coupled to the surface magnons of an antiferromagnet.

The fabrication of nanostructures offers a new arena to explore hybrid systems with collective modes in the spin and charge sectors, that could result in a new type of polariton, mixing spin and charge collective modes. In this paper we explore this possibility in a system that seems easy to fabricate with state of the art techniques. We consider the coupling of SMPs supported by AF to surface plasmon polaritons (SPPs) in graphene.

The main objective of this paper is to investigate how the presence of graphene in the vicinity of an AF influences the spectrum of SMPs, and *vice versa*, how the SPPs in graphene are affected by the AF. Thus, we consider the semi-infinite AF, and graphene monolayer, arranged at distance d parallel to the AF surface.

2. TE-polarized modes, propagating perpendicularly to the staggered magnetization

In this case the spectrum of SMPs is strongly modified owing to the influence of free charges in graphene on the electromagnetic field of the SMP, supported by the surface of the AF. As a result, hybrid surface magnon-plasmon-polariton (SMPP) mode is formed. The SMPP spectrum for relatively small distance $d = 500$ nm is depicted in Fig. 1(a) for different values of the Fermi energy. Thus, for finite doping of the graphene, SMPP spectrum has a starting-point with the frequency $\omega_i > \Omega_0$ (where Ω_0 is the frequency of the antiferromagnetic resonance), lying on the light line. An increase of the Fermi energy E_F results into the shift of the starting-point of the spectrum towards higher frequencies.

In the $k \to \infty$ limit, the spectrum tends to $\omega = \sqrt{\Omega_0^2 + \Omega_s^2}$ (horizontal dash-and-dotted line, where Ω_s stands for the saturation frequency). Therefore, as E_F is ramped up and the spectrum is pushed up in frequency at the smallest allowed values of k, so that the starting SMPP's frequency becomes larger than that limiting frequency ($\omega_i > \sqrt{\Omega_0^2 + \Omega_s^2}$), their group velocity $v_g = d\omega/dk$ has to be negative. This happens at experimentally attainable dopings of the graphene. For $E_F = 0.01$ eV and $E_F = 0.03$ eV, orange and green lines in Fig. 1(c), respectively, $v_g < 0$ in a range of high values of k. For higher values of E_F [$E_F = 0.4$ eV, red line in Fig. 1(c)] $v_g < 0$ for all values of k.

This result is distinct from the zero Fermi energy case, where SMPP's group velocity [slope of the dispersion curve, $\omega(k)$, depicted by solid blue line in Fig. 1(a)] is positive in all range of frequencies and wavevectors. It is possible to see, that the group velocity is much smaller than the speed of light in vacuum, c. Even more, in short-wavelength limit $ck/\Omega_0 \gtrsim 30$ the group velocity is less than $10^{-5}c$, i.e. SMPPs are slow waves.

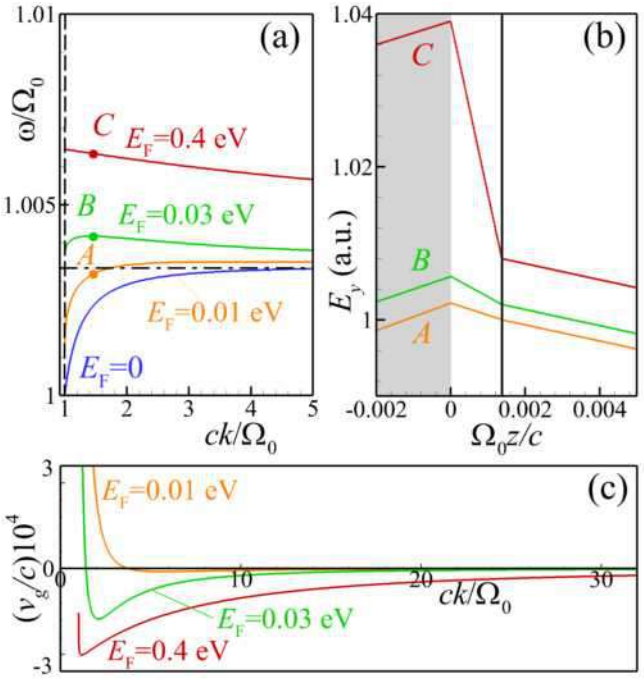


Figure 1: (a) Surface magnon–plasmon–polariton (SMPP) spectrum in the AF/graphene structure for Fermi energy values $E_F = 0$ (solid blue line), 0.01 eV (solid orange line), 0.03 eV (solid green line), and 0.4 eV (solid red line). Black dashed line stands for the light line in vacuum, $\omega = ck$; (b) Spatial distributions of the SMPP electric field for the modes with $ck/\Omega_0 = 1.46$ and 0.01 eV (orange line A), 0.03 eV (green line B), and 0.4 eV (red line C). These modes are indicated in panel (a) by the respective letters A, B and C. The region occupied by the AF is shadowed in panel (b) and the position of graphene is shown by vertical bold black solid line; (c) Group velocity, $v_g = d\omega/dk$ (in dimensionless units v_g/c) of the SMPP modes with $E_F = 0.01$ eV (orange line), 0.03 eV (green line), and 0.4 eV (red line). In all panels the fields and magnetization of AF are $\mu_0 H_a = 0.787$ T, $\mu_0 H_e = 55.3$ T, and $\mu_0 M_s = 0.756$ T, for the antiferromagnet MnF_2. The spacer between the AF and graphene has thickness $d = 500$ nm. The magnitude of the fields was chosen arbitrarily for convenient visualization of their profiles.

Examples of spatial profiles of SMPP modes are shown in Fig. 1(b). As can be seen from the figure, in the case of TE-polarized wave $E_y(0) > E_y(d)$, so the field is mainly concentrated nearby of the AF surface.

3. TM-polarized modes, propagating parallel to the staggered magnetization

We now consider the case of TM-polarization, for which the graphene layer is able to sustain SPPs. In the AF-graphene coupled structure, the graphene SPP is hybridized with the AF magnon, resulting in a polariton spectrum with 2 branches, that reflects the emergence of a hybrid collective mode that combines graphene plasmons with AF magnons. We shall call these hybrid excitations surface plasmon–magnon–polaritons (SPMPs). These two branches of SPMP are characterized by the anticrossing in the vicinity of AF resonance frequency. The electromagnetic field is, for all modes, predominantly concentrated nearby the graphene layer.

4. Conclusions

In this work we have investigated the electromagnetic properties of an antiferromagnetic insulator in the proximity of a graphene sheet. We have found two new types of hybrid polaritons (SMPP and SPMP) that combine the electromagnetic field with the magnetization in the magnetic material and the free carrier response of Dirac electrons in graphene. In both cases, a quantized theory of this new polaritons implies a new type of hybrid collective modes that combine of surface plasmons in graphene, magnons in the AF and the photon field. Their properties can be tuned by changing the carrier density in graphene.

Acknowledgement

Y. B., M. V. and N. M. R. P. acknowledge support from the European Commission through the project "Graphene- Driven Revolutions in ICT and Beyond" (Ref. No. 785219), and the Portuguese Foundation for Science and Technology (FCT) in the framework of the Strategic Financing UID/FIS/04650/2013. Additionally, N. M. R. P. acknowledges COMPETE2020, PORTUGAL2020, FEDER and the Portuguese Foundation for Science and Technology (FCT) through project PTDC/FIS-NAN/3668/2013 and FEDER and the portuguese Foundation for Science and Technology (FCT) through project POCI-01-0145-FEDER-028114. G. A. Farias acknowledge support from the Conselho Nacional de Desenvolvimento Científico e Tecnológico (CNPq) of Brazil. J. F.-R. acknowledge financial support from FCT for the P2020-PTDC/FIS-NAN/4662/2014, the P2020-PTDC/FIS-NAN/3668/2014 and the UTAPEXPL/NTec/0046/2017 projects, as well as Generalitat Valenciana funding Prometeo2017/139 and MINECO Spain (Grant No. MAT2016-78625-C2).

References

[1] M. Kaganov and V. Tsukernik, "The magnetic susceptibility of a uniaxial antiferromagnetic," *J. Exp. Theor. Phys.*, vol. 7, pp. 361–362, 1958.

[2] N. S. Almeida, G. A. Farias, N. T. Oliveira, and E. F. Vasconcelos, "Influence of a dc field on polaritons confined in magnetic wires," *Phys. Rev. B*, vol. 48, no. 13, pp. 9839–9842, 1993.

[3] R. E. Camley and D. L. Mills, "Surface polaritons on uniaxial antiferromagnets," *Phys. Rev. B*, vol. 26, pp. 1280–1287, 1982.

Electrically Controllable Directional Coupler Based on Dielectric Loaded Graphene Plasmon Waveguide

Wei Xu[1], Hanyu Wang[1], Chao Li[1], Jianfa Zhang[1], Chucai Guo[1], Ken Liu[1], Xiaodong Yuan[1], Zhihong Zhu[1], and Shiqiao Qin[1]

[1]National University of Defense Technology, Changsha, China
*corresponding author, E-mail: weixu08a@163.com

Abstract

We propose and numerically analyze a mid-infrared electrically controllable plasmonic waveguide directional coupler that is composed of two parallel identical straight dielectric loaded graphene plasmonic waveguide. By varying the Fermi energy level of the graphene sheet, the maximum power coupled from the input waveguide to the cross-waveguide and the corresponding coupling length could be effectively tuned. This directional coupler could serve as an electrically controlled optical switch or a 3-dB splitter around the wavelength of 10.5μm.

1. Introduction

Graphene is a promising candidate for mid-infrared to terahertz surface plasmons (SP) waveguide, due to its extraordinary properties. Here, we propose dielectric loaded graphene plasmon waveguide (DLGPW) [1], which is not influenced by the edge shape of graphene and could be produced in a straightforward way by, for example, standard processes of lithography. Moreover, the mode propagation characteristics of the DLGPW could be controlled by varying the Fermi energy level of graphene sheet through electrostatic gating. And the coupling between two DLGPW could be electrically controlled accordingly. Based on this study electrically controllable optical switch and 3-dB splitter is proposed.

2. Structure and results

Figure 1 shows the schematic of the directional coupler (DC) based on dielectric loaded graphene plasmon waveguide. Two parallel identical straight DLGPWs with edge-to-edge separation d constitute the coupling region. The coupling region with a length of L is connected to the output waveguides (Ps and Pc) by two S-shaped waveguide bends. SiO2 dielectric layer with a thickness of hs is used to separate the graphene sheet and the back-gated metal film. By applying a voltage between the graphene sheet and the back-gated metal film, the carrier concentration and thus the Fermi energy level of garaphene can be electrically tuned. Then the coupling between the two DLGPWs could be tuned. [2]

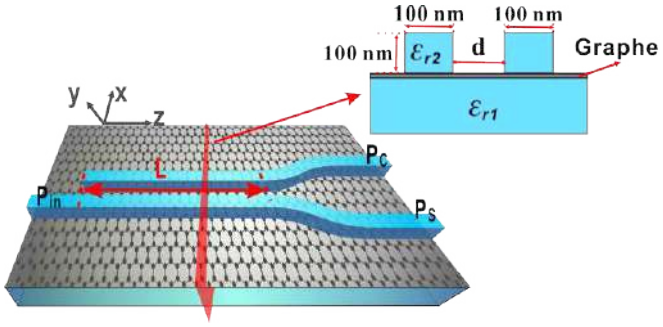


Figure 1: Schematic of the electrically tunable directional coupler based on dielectric loaded graphene plasmon waveguide.

Figure 2(a) shows the transmission of the proposed DC at different Fermi level energy of graphene, which indicates the output could be effectively tuned by varying the Fermi energy level. These results enable an electrically controllable optical switch, with E_F = 0.7 eV as switch on state and E_F = 0.5 eV as switch off state. The switch on-off extinction ratio is larger than 16 dB. Moreover, when E_F = 0.82eV, without changing the structure, the DC could serve as a 3-dB splitter. Figure 2(b) shows the power flow

distributions at different Fermi energy level for the wavelength of 10.5μm.

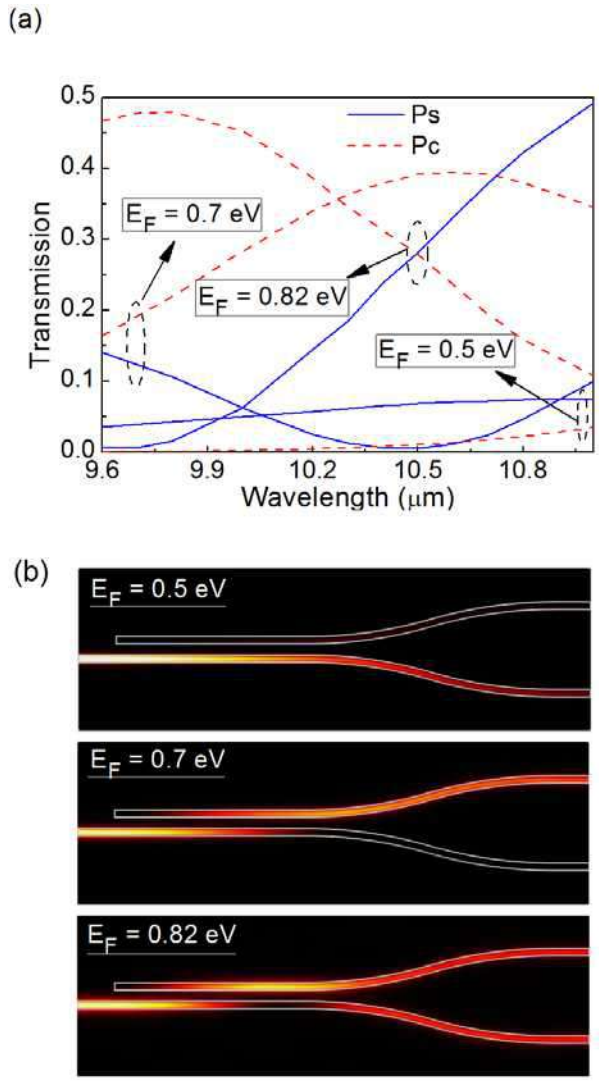


Figure 2: (a) Transmission rate of the proposed DC at different Fermi energy level with a coupling length of 2.6 μm. (b) power flow distributions at different Fermi energy level for the wavelength of 10.5 μm.

3. Conclusions

In summary, we have studied the coupling characters of a directional coupler (DC) consisting of two parallel identical straight DLGPWs in the mid-infrared regime. The maximal power coupled from the input waveguide to the cross-waveguide and the corresponding coupling length could be manipulated by changing the Fermi energy level of the graphene sheet, which enables electrically controlled functional devices. Based on this DC electrically controlled optical switch operating around the wavelength of 10.5 μ m is proposed and simulated. The switch on-off extinction ratio is larger than 16 dB. Moreover, without changing the structure, by varying the Fermi energy level, the function of the DC could be changed from an optical switch to a 3-dB splitter, making this DC a multifunction device. At the same time, the size of the entire device is only around 6 μ m × 3 μ m. This DC-based electrically controlled device may find potential applications in high-density integrated active plasmonic circuits.

Acknowledgements

This work is supported by the State Key Program for Basic Research of China (No. 2012CB933501) and the National Natural Science Foundation of China (Grant Nos. 61177051, 11304389, 61404174, and 61205087).

References

[1] W. Xu, Z. H. Zhu, K. Liu, J. F. Zhang, X. D. Yuan, Q. S. Lu, and S. Q. Qin, Opt. Express **23**, 5147 (2015).

[2] W. Xu, Z. H. Zhu, K. Liu, J. F. Zhang, X. D. Yuan, Q. S. Lu, and S. Q. Qin, Opt. Lett. **40**, 1603 (2015).

Electrically Tunable Graphene Polarization Controlling

Chao Li[1], Hanyu Wang [1], Wei Xu [1], Jianfa Zhang[1], Chucai Guo[1], Ken Liu[1], Xiaodong Yuan[1], Zhihong Zhu[1], and Shiqiao Qin[1]

[1]National University of Defense Technology, Changsha, China
*corresponding author, E-mail: zzhwcx@163.com

Abstract

We proposed a tunable terahertz half-wave plate composed of a periodic array of graphene nanodisk dimers supported on a dielectric spacer backed by a planar gold layer. The polarization conversion phenomena are attributed to the hybridization effect caused by coupling interactions between plasmonic resonances in the graphene nanodisk dimers. By varying the distance between graphene nanodisks, the polarization conversion performance can be controlled. Further, the polarization conversion can be dynamically tuned at different frequencies via electrostatic doping of graphene.

1. Introduction

Manipulating the polarization state of light is useful for practical applications. Conventional methods of manipulating the polarization include using natural anisotropic crystals or employing subwavelength gratings. Researchers have recently found that metamaterials and surface plasmon polariton structures can be used as alternative routes to controlling the polarization state of light at the nanoscale. Various polarization converters based on metamaterial structures have been achieved, such as metallic nanoparticles and metallic nanoslots. However, the operating frequencies of these reported polarization converters are fixed and cannot be electrically tuned, which limits their uses in practice. Graphene, a single-layer carbon atom arranged in a honeycomb lattice, appears to be a good candidate for designing tunable devices operating in the terahertz (THz) spectral range because of its tunable conductivity. In this paper, we focus on the polarization conversion properties of coupled graphene nanostructures. We confirm that using a periodic array of coupled isotropic graphene nanostructures is an alternative route to achieving polarization conversion. The proposed structure can convert linearly polarized light to its orthogonal polarization in the reflection mode simultaneously at two frequencies.

2. Structure and results

Figures 1(a) and 1(b) show a schematic illustration and the designed geometry of the proposed nanostructure. It consists of a periodic array of CGNs and a 150-nm-thick planar gold layer, separated by a 1250-nm-thick dielectric spacer. An ion gel layer is used to electrically dope the CGNs. Doped graphene nanostructures have been predicted to support strong plasmonic resonance.

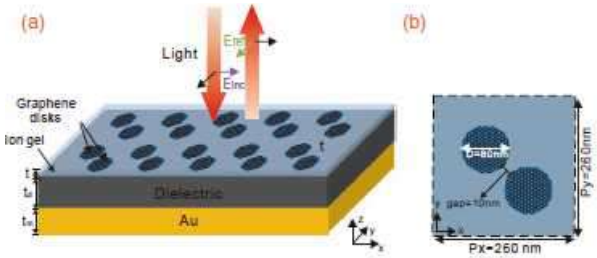


Figure 1: (a) Arrays of CGNs. (b) Unit cell of CGN

The polarized reflectances R_{xx} and R_{yx} (R_{lm} represent the complex amplitude of the reflected wave and denote the *l*-polarized reflectance from *m*-polarized excitation) as a function of frequency are shown in Figure 2(a). We can observe two reflection peaks in R_{yx} at about 47 and 51 THz, with corresponding dips in R_{xx}, indicating that the structure can realize energy transfer from x to y polarization after reflection. One key parameter of a wave plate is the polarization conversion rate (PCR), which is defined as $PCR = R_{yx}^2/(R_{xx}^2 + R_{yx}^2)$. As shown in Figure 2(b), the local maximum PCRs reach high values of 0.997 and 0.995 at about 47 and 51 THz, respectively, whereas the corresponding re flection phase differences approach 0 and 180°, indicating that a linear polarization state can be realized. The polarization conversion can be dynamically tuned on and off or tuned for activity at different frequencies via electrostatic doping of graphene. To demonstrate the tunability, we calculated the PCRs as a function of frequency when the Fermi energy of graphene varies from 0.7 to 1.0 eV, as shown in Figure 2(c). It can be seen that the local maximum of the PCR is still close to 1. The local PCR maximum is blue-shifted as E f increases, which can be interpreted as indicating the graphene resonance condition. The local maximum frequency of the PCR corresponds to the resonance frequency of graphene surface plasmons, which is proportional to square root of the Fermi energy level of

graphene. Hence, the proposed half-wave plate can be controlled by changing the Fermi energy of graphene in lieu of redesigning the structure.

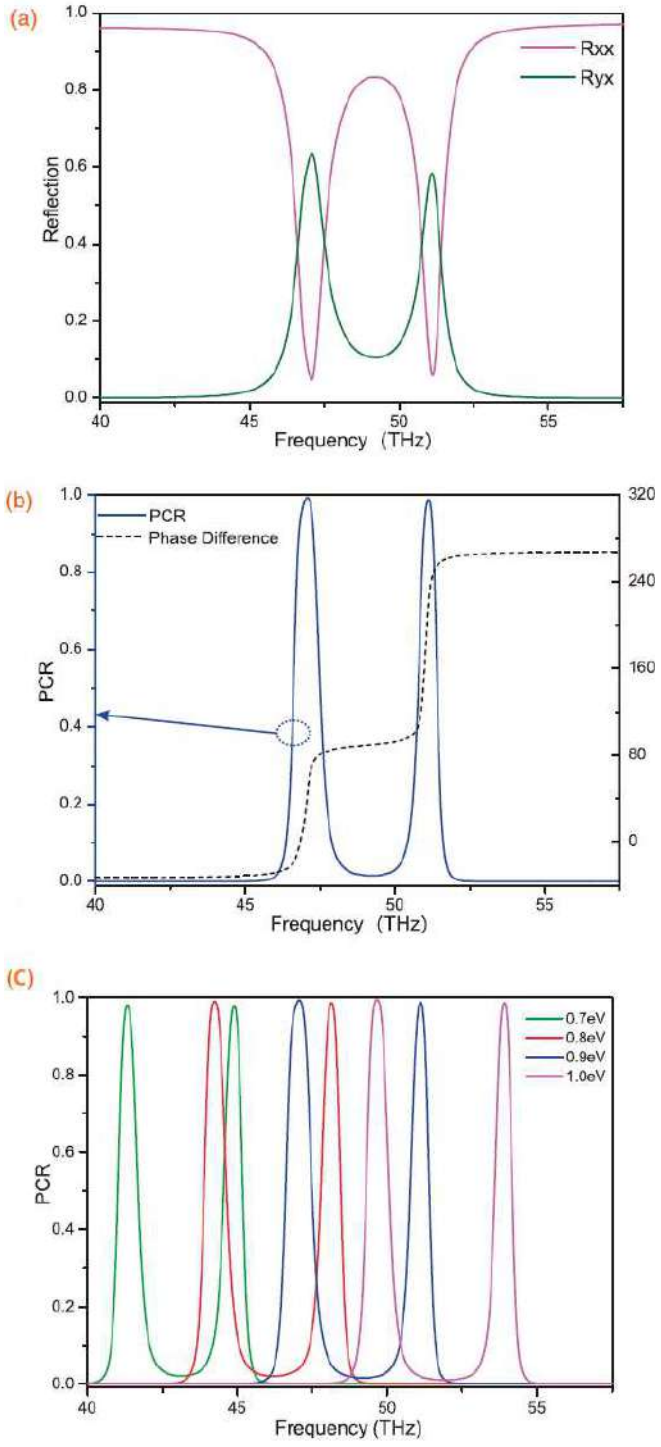


Figure 2: (a) Calculated reflectance R_{xx} and R_{xy}. (b) Polarization conversion rate (PCR) and the reflection phase difference. (c) PCRs of the CGN structure at different Fermi energy levels.

3. Conclusions

In conclusion, we proposed a tunable half-wave plate in the THz region based on a hybridization effect caused by coupling interactions between plasmonic resonances in graphene nanodisk dimers. We also demonstrated that using a periodic array of coupled isotropic graphene nanostructures instead of uncoupled anisotropic graphene nanostructures is another route to achieving polarization conversion. The polarization conversion properties hinge mainly on the distance between graphene nanostructures. The method of using coupled graphene nanostructures can be expanded to obtain other novel phenomena and interesting applications.

Acknowledgements

This work is supported by the National Natural Science Foundation of China (Grant Nos. 61177051 and 11304389).

References

[1] J. L. Peng, Z. H. Zhu, J. F. Zhang, X. D. Yuan, and S. Q. Qin, Applied Physics Express, 9(2016): 55102.

[2] Y. C. Tang, Z. H. Zhu, J. F. Zhang, C. C. Guo, X. D. Yuan, and S. Q. Qin, Journal of optics, 18(2016): 025002.

Graphene-based Perfect Absorption in the Near Infrared

Hanyu Wang [1], Wei Xu [1], Chao Li[1], Jianfa Zhang[1], Chucai Guo[1], Ken Liu[1], Xiaodong Yuan[1], Zhihong Zhu[1], and Shiqiao Qin[1]

[1]National University of Defense Technology, Changsha, China
*corresponding author, E-mail: zzhwcx@163.com

Abstract

In this work, we propose a kind of monolayer graphene based absorption structures which comprise dielectric materials with low refractive index contrast, and we directly verify the complete optical absorption in experiment for monolayer graphene based subwavelength structures in the near-infrared. Peak absorptions over 99% at wavelength around 1.5 μm with full-width at half maximum (FWHM) about 20 nm are demonstrated from monolayer graphene coupled with different subwavelength gratings on top of a back gold mirror.

1. Introduction

As a novel 2D material, graphene has been studied intensively due to its outstanding optical and electronic properties. However, the absorption efficiency of suspended monolayer graphene toward the normal incident light is only 2.3%, which limits its optoelectronic applications. In the visible and near-infrared, the absorption of graphene was normally enhanced by coupling graphene with dielectric or metallic resonant structures. And complete absorptions of monolayer graphene were numerically demonstrated by using critical coupling and guided mode resonance. However, the experimentally realization of complete absorption for monolayer graphene based structures in the optical range is still a great challenge.

2. Structure and results

The schematic image of the absorption structure under investigation in this work is demonstrated in Figure 1a. The structure comprises a monolayer graphene which is sandwiched between a 1D polymethy1-methacrylate (PMMA) grating and a silica layer, and a gold layer is coated in the back side of the silica layer. The absorption structure shown in Figure 1a supports several resonant modes which could be excited by outside incident waves under phase matching conditions. When the incident wave is coupled with a resonant mode, the absorption of the structure could be enhanced due to the field enhancement in the structure. And complete absorption can be obtained when the reflection wave is canceled by the emission wave of the resonant mode since the transmission of the structure is blocked by the gold layer.

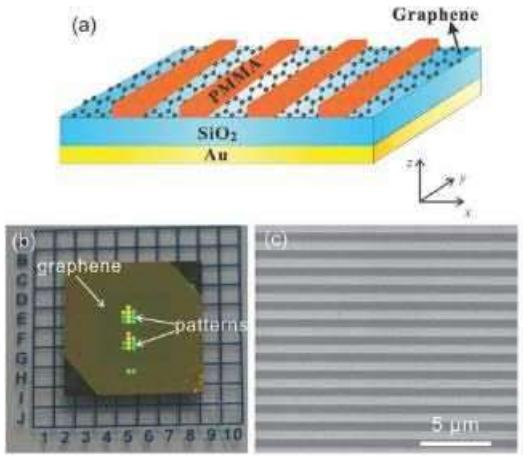


Figure 1: (a) Schematic image of the monolayer graphene based absorption structure. (b) Optical image of the fabricated sample. (c) Top SEM image of a fabricated pattern.

Figure 2(a) shows the reflection (R) and absorption (A) spectra of a fabricated structure with grating period d = 1254 nm for transverse-electric (TE) polarization, where the reflection spectrum was normalized by the reflected light of the 200 nm thick gold layer in the sample (assume the reflectivity of the gold layer R Au = 98.8% at the wavelength around 1500 nm according to the simulation result) and the absorption spectrum was derived based on the equation A = 1 − R since the transmission was blocked by the thick gold layer. As shown in Figure 2(a), peak absorption over 98% with absorption FWHM of 19 nm for TE polarization was measured. Figure 2(b) shows the measured absorption spectra of different fabricated monolayer graphene based absorption structures for TE polarization. Measurement results show that the peak absorptions of the structures with d = 1230 and 1254 nm are over 98% and the peak absorption of the structure with d = 1270 nm is over 97%.

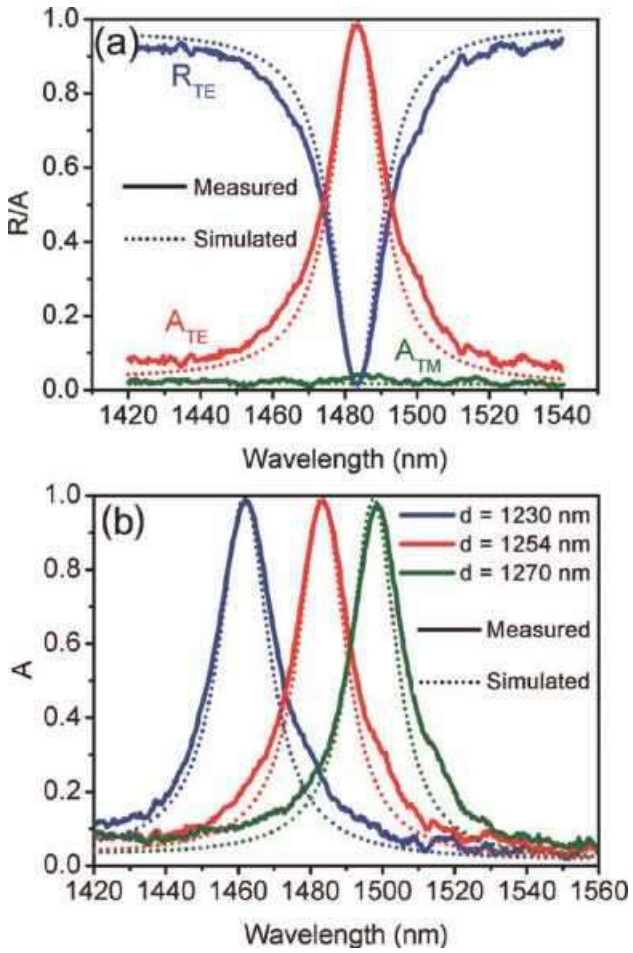


Figure 2: (a) Measured (solid line) and simulated (dot line) reflection and absorption spectra of a fabricated monolayer graphene based absorption structure with d = 1254 nm. (b) Measured (solid line) and simulated (dot line) reflection and absorption spectra of a fabricated monolayer graphene based absorption structure with different grating periods.

3. Conclusions

In conclusion, peak absorptions over 99% with FWHM about 20 nm in the near-infrared were measured for monolayer graphene coupled with subwavelength gratings on top of a back gold mirror. The demonstrated absorption structures with total thickness less than 1.0μm are very compact, and the absorption peak wavelength of the structure can be easily controlled by changing the geometric parameters of the structure. Because of their high absorption efficiency and loose fabrication requirements, the demonstrated structures may provide practical applications for graphene and other 2D material based optoelectronics devices, such as high efficiency photodetectors and high extinction ratio modulators.

Acknowledgements

This work is supported by the National Natural Science Foundation of China (Grant Nos. 61404174, and 11374367).

References

[1] C. C. Guo, Z. H. Zhu, X. D. Yuan, W. M. Ye, K. Liu, J. F. Zhang, W. Xu, and S. Q. Qin, Adv. Opt. Mater. 4(2016), 1955-1960.

Optical antennas and plasmonics-based devices

Multiband Antennas for Si-based Terahertz Detectors

Ke Wang, Fangfang Ren, Yi Yang, Ping Han, and Xiaoli Ji

School of Electronic Science and Engineering, Nanjing University, Nanjing, China
*corresponding author, E-mail: xji@nju.edu.cn

Abstract

The authors demonstrate a Si-based multiband terahertz antenna which can be fully integrated with MOSFET-based terahertz detectors in standard Si technologies. It consists of semicircular nesting rings and slots. For an optimized antenna structure with a size of 160μm×160μm, four separated bands can be achieved in the range of 0.1～1.2 THz with the central one located at 0.5THz with a bandwidth of 30GHz.

1. Introduction

MOSFET-based terahertz (THz) detectors are generally integrated with an on-chip antenna for collecting THz signals. Single-band RF antennas had already been widely designed with metals in standard CMOS process [1,2], possessing the advantages including low profile, light weight and easy fabrication. However, multiband and wideband antenna design remains challenges because of the mismatching of the input impedance of FET device with the multiband antennas. To overcome the difficulties, we propose a semicircular nesting ring antenna used for the application of silicon (Si)-based multiband THz detectors. It can be fabricated with standard CMOS technologies.

2. Semicircular nested antenna

When THz signal is incident upon a semiconductor material, surface plasmon resonances (SPRs) can be excited at the interface of metal/dielectric. Many semiconductor materials have been proposed to work as the plasmonic materials in THz because their free carrier concentrations can be steadily and easily controlled by doping, thermal, electrical or optical excitations. Through the employment of unique resonance structures, strong THz wave enhancement can be realized by poly-Si due to the plasmonic effect. The dielectric constant can be obtained by Drude model [3].

Figure 1 (a) shows the 3D schematic of the multiband antenna. It was designed based on the gate material of MOSFETs. Following the typical standard 0.18μm CMOS technology, the gate material is the poly-Si doping with density of 1×10^{20} cm^{-3} and thickness of 0.2μm. The structure of the multi-frequency antenna is completely symmetrical, consisting of two semicircular receiving faces and two rod mixing structures. The semicircle radius, inner ring radius, outer ring radius, rod length, rod width, slot width, gap width and the shortest distance of the end face from the rod are denoted as R_1, R_2, R_3, d, w, a, g, b, respectively. Figure1 (b) shows the cross-sectional view of antenna embedded Si FET detector. The MOSFET is located at the center of the antenna. We fabricate the antenna above the shallow trench isolation structure, below which is a Si substrate. The slots and surroundings of the antenna are filled with SiO_2, and the thickness of SiO_2 above the antenna is about 10.7μm.

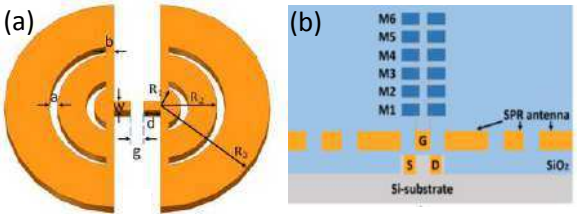


Figure 1: (a) 3D schematics of multi-frequency antennas; (b) A cross-sectional view of the detector based on 0.18μm CMOS technology.

3. Simulation results and analysis

During the simulation for the antenna design, the excitation THz source is located above the SPR antenna and a TM mode plane wave is radiated with frequencies in the range from 0.1 to 1.2 THz where the electric field direction is parallel to the rod and the electric field strength E_0 is set to 1V/m. The dielectric constants of Si and SiO_2 are roughly set to be 11.9 and 4, respectively. Figure 2 (a) shows the simulated frequency dependence of the center-position of the poly-Si antenna. It can be seen that the plasmon resonances of the antenna surface are effectively excited. When the geometric parameters of antenna are optimized as R_1=12μm, R_2 = 34μm, R_3 = 66μm, d = 13μm, w = 1μm, a = 2μm, g = 2μm, b = 1μm, the electric field gain E_X/E_0 is up to 150 times at the resonant frequencies of 0.4, 0.71 and 1.11THz, respectively, with a bandwidth above 30 GHz. The fourth resonance peak at 0.96 THz has a peak gain of about 100 times with more advantages in terms of narrower bandwidth. Figure 2 (b) shows the typical electric field distributions on the antenna surface at four response peaks with the optimized geometric parameters. It can be seen that the resonance modes I and IV around 0.4 and 1.11 THz might be induced along the semicircular slots with radius of R_2 and R_1, respectively. The modes II and III around 0.71 and 0.96 THz might be owing to the LC-type resonances based on electric dipoles. It also can be seen that the circular rings provide a discrete current path along the edges of the

ring. For the ring slot, the current path is well defined, similar to the operation of a circular disk antenna operating at its lowest or "fundamental" resonance.

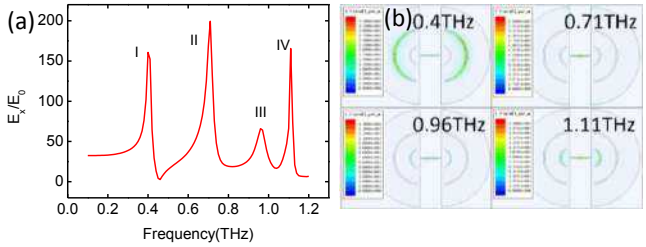


Figure 2: (a) The frequency dependence of the center-position response of the Si antenna; (b) The electric field distributions of the antenna surface at 0.4, 0.71, 0.96, and 1.11THz.

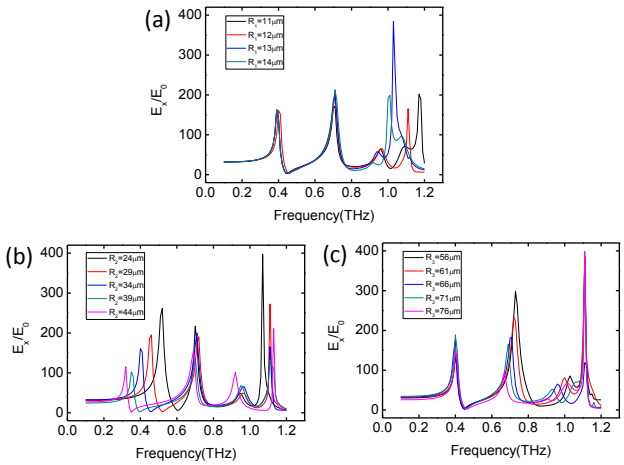


Figure 3: The frequency dependence of the center-position response of the Si antenna under different (a) R_1; (b) R_2; (c) R_3.

In order to accurately understand the mechanisms of the resonance modes, the frequency dependence of the center-position poly-Si antenna on the geometric parameters has been studied. As shown in Fig. 3(a), when R_1 is increased from 11 to 14μm, mode IV is redshifted from 1.17 to 1.01 THz, indicating that this resonance is strongly dependent on the length of the semicircular slot ($\approx \pi R_1$). Similarly, the size of the outer slot R_2 also has an important effect on the resonance modes of the multi-frequency antenna. As shown in Fig. 3(b), when the value of R_2 is modified from 24 to 44μm, the mode I is redshifted from 0.52 to 0.32 THz. As compared, the slight shift of mode IV can be negligible if considering the limited simulation accuracy. In summary, R_1 and R_2 have a decisive effect on the resonance modes of the antenna, and their values should be appropriate in order to reduce its effect on adjacent peaks, which is because the slot structure might change the current path on the antenna surface. On the basis of discussion in [4], the radius of R_1 or R_2 determines the length of inner or outer slot. When h = 200 nm and R_1=12μm, we can calculate the resonance frequency f = 1.12THz, which matches the simulation results very well. It also fits well for R_2. Figure 3(c) shows the frequency response of the center-position poly-Si antenna dependent on the varied value of R_3. As R_3 increases from 56 to 76μm, mode II is redshifted from 0.73 to 0.67THz and mode III is redshifted from 1.03 to 0.9THz. As discussed in Fig. 2(b), these two modes can be regarded as LC-type resonances occurring along the direction of rods by considering the fact that the strong near fields are concentrated at the center of antenna. It is therefore, the redshift of mode frequency can be attributed to the increase of capacitance with R_3 increasing, which is in consistent with the behavior of a traditional dipole SPR antenna.

4. Conclusions

In this work, we proposed a novel SPR antenna for multi-frequency THz detector. As compared to conventional one-frequency antenna, our design is demonstrated with a broader response frequency regime, and also promising for an improved performance with smaller area size and higher responsivity.

References

[1] E. Ojefors, U. R. Pfeiffer, A. Lisauskas and H. G. Roskos, "A 0.65 THz Focal-Plane Array in a Quarter-Micron CMOS Process Technology," in *IEEE Journal of Solid-State Circuits*, vol. 44, no. 7, pp. 1968-1976, July 2009.

[2] R. Al Hadi *et al.*, "A 1 k-Pixel Video Camera for 0.7–1.1 Terahertz Imaging Applications in 65-nm CMOS," in *IEEE Journal of Solid-State Circuits*, vol. 47, no. 12, pp. 2999-3012, Dec. 2012.

[3] Berrier, Audrey , et al. "Ultrafast active control of localized surface plasmon resonances in silicon bowtie antennas." *Opt. Express*., vol. 18, no. 22, pp. 23226-23235, May. 2007.

[4] C. T. P. Song, P. S. Hall and H. Ghafouri-Shiraz, "Multiband multiple ring monopole antennas," in *IEEE Transactions on Antennas and Propagation*, vol. 51, no. 4, pp. 722-729, April 2003.

Real-Time In-Situ Optical Tracking of Oxygen Vacancy Migration in Memristors

Giuliana Di Martino[1*], Dean Kos[1], Weiwei Li[2], Bonan Zhu[2], Xuejing Wang[3], Haiyan Wang[3], Angela Demetriadou[4], Judith Driscoll[2] and Jeremy Baumberg[1]

[1]NanoPhotonics Centre, Cavendish Laboratory, University of Cambridge, CB3 0HE, UK
[2] Department of Materials Science and Metallurgy, University of Cambridge, CB3 0FS, UK
[3]School of Materials Engineering, Purdue University, IN 47907-2045, USA
[4]School of Physics and Astronomy, University of Birmingham, B15 2TT, UK
*corresponding author, E-mail: gd392@cam.ac.uk

Abstract

The switching mechanism of valence change memories involves the migration, accumulation and rearrangement of oxygen vacancies within a dielectric medium to change the electrical conductivity, and is triggered by an external applied potential. Here, resistive switches are constructed to exploit the high sensitivity to morphology at tightly-confined plasmonic hotspots within the switching material. This gives a non-destructive technique to detect oxygen vacancy motion with nm-scale sensitivity using visible light.

1. Introduction

Resistive switches (RRAMs) are one of the most promising emerging devices for memory-in-logic operations, attracting great attention due to their high scalability, ultra-fast access times and ease of fabrication [1]. The ability to look deep inside materials to unveil how morphological changes characterize the functioning of active devices has triggered the interest of a wide scientific community. However, current technologies often result in destructive and invasive techniques. In this work, we adopt a new fully-optical non-destructive technique to observe the valence change mechanism (VCM), i.e. the motion of oxygen vacancies within a switching material, otherwise invisible to typical electron microscopy techniques.

2. Results

Resistive switches arranged in a nanoparticle-on-mirror geometry (Fig. 1a) are developed. Combining resistive switches and large field enhancements in nanoplasmonic systems has proven a powerful approach to understand the dynamics involved in the switching process of the closely related system of electrochemical metallization cells (ECM) [2]. In this previous pioneering study, we implemented optically-accessible ECM switches and monitored in real time the scattering signal coming from the plasmonic field which is tightly confined to the nanometer-sized switching gap.

In this talk we will show how it is possible to monitor in real time the scattering signal coming from VCM systems (Fig. 2b) enabling the observation of migration, accumulation and rearrangement of oxygen vacancies within a dielectric medium (Fig. 2c) [3].

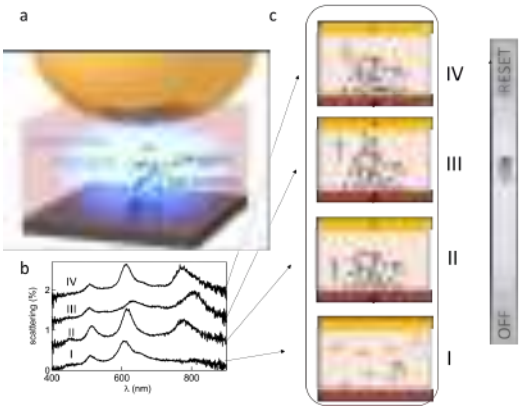


Figure 1: (a) Nanoparticle-on-mirror geometry in VCM cells and its (b) scattering signal correlated to (c) oxygen vacancies motion within the switching material.

3. Conclusions

We present an innovative technique able to follow in real time the drift (I) and accumulation (II) of oxygen vacancies and the subsequent creation (III) and dissolution (IV) of a conductive bridge triggered by an external applied field. This is a non-destructive and non-invasive technique able to detect oxygen vacancy migration in ambient conditions, leading to the investigation of the mechanism that underpins this new generation of ultra-low-energy memory nano-devices and their integration into fast, logic-in-memory architectures opening up new routes to sustainable future IT.

Acknowledgements

GD acknowledges support from the Winton Programme for the Physics of Sustainability and funding from ERC grant LINASS 320503 and EPSRC grant EP/L027151/1. W.L. and J.L.M.-D. acknowledge support from EPSRC grant EP/L011700/1, EP/N004272/1, EP/P007767/1 and the Isaac Newton Trust (Minute 13.38(k)).

References

[1] Siemon, A. et al., Realization of Boolean Logic Functionality Using Redox-Based Memristive Devices. *Adv. Funct. Mater.* **25**, 6414–6423 (2015).

[2] Di Martino, G., et al., Nanoscale Plasmon-Enhanced Spectroscopy in Memristive Switches. *Small* **12**, 1334–1341 (2016).

[3] Di Martino, G., et al., Real-Time In-Situ Optical Tracking of Oxygen Vacancy Migration in Memristors, In preparation (2019).

High Q-factor coupled Fabry-Perot plasmonic nanoresonator

Baptiste Fix [1*], *Julien Jaeck* [1], *Patrick Bouchon* [1], *Nathalie Bardou*[2], *Sébastien Héron* [1], *Benjamin Vest* [1] *and Riad Haïdar* [1,3]

[1] DOTA,ONERA,Université Paris Saclay F-91123 Palaiseau – France

[2]Center for Nanoscience and Nanotechnology (C2N)-CNRS, Univ. Paris-Sud,Université Paris-Saclay, 91128 Palaiseau, France

[3] Ecole Polytechnique, Département de Physique, 91128 Palaiseau, France,

*corresponding author, E-mail: baptiste.fix@onera.fr

Abstract

Fabry-Perot (FP) like resonances have been widely described in nanoantennas. In the original Fabry-Perot resonator, a third mirror can be added, resulting in a multimirror interferometer. However, in the case of combination of nanoantennas, it has been reported that each cavity behaves independently. Here, we evidence the interferences between two FP absorbing nanoantennas through a common mirror, which has a strong impact on the optical behavior. While the resonance wavelength is only slightly shifted, the level of absorption reaches nearly 100 \%. Moreover, the quality factor increases up to factor 7 and can be chosen by geometric design over a range from 11 to 75. We first demonstrate thanks to a simple analytical model that this coupling can be ascribed to a double FP cavity resonance, with the unique feature that each cavity is separately coupled to the outer medium. Based on this principle, we experimentally illustrate the existence of a high-Q factor resonance originating from the interference between two under-coupled ribbon-shaped nano Fabry-Perot.

1. Introduction

The Fabry-Perot (FP) interferometer was invented in 1899, and consisted of two parallel highly reflecting mirrors, the resonance behavior being characterized by peaks or dips in the transmission and reflection spectra [1]. It has been used in a variety of devices among which optical cavities for lasers or filters [2]. Since this seminal work, various evolutions of the FP interferometer have been introduced among which multi-mirror FP that give birth to a coherent superposition of all the beams [3]. Noteworthily, in most configurations, the mirrors are placed in series. In the past two decades, the development of nanophotonics has given birth to FP-like resonators [4]–[7], in which a guided mode in a metallic cavity has a behavior that is well described by the FP formalism. The advantages of these nanoresonators are their compactness, and the possibility to combine them to design broadband or multiband resonances. It is well accepted that, since these metallic cavities are the siege of localized resonances, they have negligible influences on each other when they are combined [8]–[12].

The two most common plasmonic nanostructures with a FP behavior are the metal-insulator-metal patch nanoantennas (horizontal resonance), and the high aspect ratio nanogrooves (vertical resonance). Both of these resonators are promising for applications ranging from thermal emission [12],[13], or infrared detection [14] to biosensing [15]. Yet, they suffer from their low quality factor.

In this letter, we introduce double cavity Fabry-Perot like nanoresonator in both vertical and horizontal configurations. It departs from previous works on multimirror FP resonators, as the mirrors are in an hybrid configuration between series and parallel. It gives birth to a spectacular effect where critical coupling, *i.e*. a zero of reflectivity, is obtained while, independently, each of the two cavities is loosely-coupled to free space. Moreover, the quality factor of the double cavity resonators is increased from 11 to 50, well beyond the limit for FP plasmonic nanoresonator [10]. We developed an analytical model that confirms the multimirror FP behavior. Last, but not least, we experimentally demonstrate the coupled Fabry-Perot resonance on a horizontal nanoresonator.

2. Analytical model of the coupled nano Fabry-Perot resonator

We study a periodic double-groove resonator whose period contains two grooves of different heights. While the reflectivity of the periodic single-groove resonators does not go below 85%, the resonance of the double-groove presents a zero of reflectivity and a quality factor of 50 (See Figure 1).

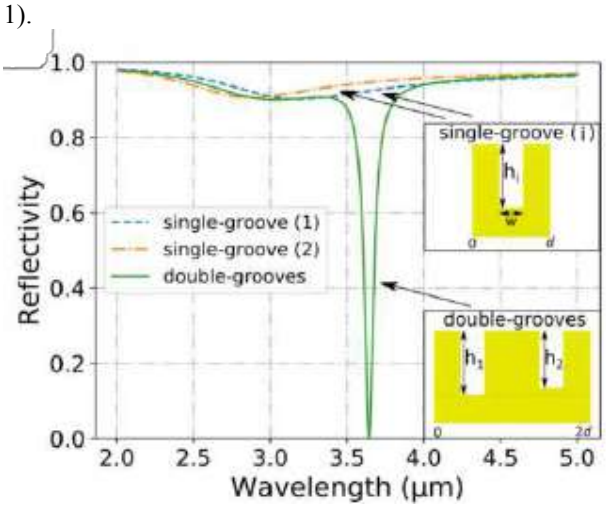


Figure 1 Comparison between the reflectivity of two loosely-coupled single-nanogroove resonators and the reflectivity of a critically coupled resonator composed of the two aforementioned cavities. The geometrical parameters of the cavities, described in the insets, are d=1 µm, w=0.3 µm, h_1=0.62 µm, h_2=0.55 µm.

We demonstrate thanks to an analytical model that this coupling can be ascribed to a double FP cavity resonance, with the unique feature that the cavities are coupled to one another through a common mirror.

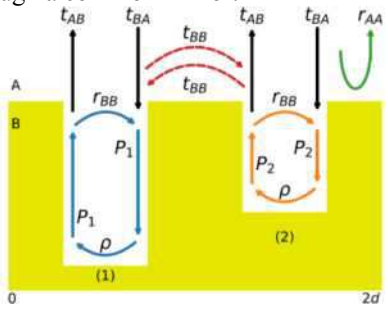


Figure 2: Scheme of the two-grooves structure and of the different coefficients used in the analytical model. All the coefficients are scalar element.

Using the reflection, transmition and propagations coefficients represented on the figure 2, we can write the reflectivity of the resonator as a sum of three terms :

$$RT = |r_{AA} + t_{AB}G_1 t_{BA} + t_{AB}G_2 t_{BA}|^2$$

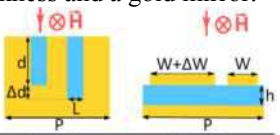
Where G_1 and G_2 represent the loop inside the first and second groove and can be written, in the steady state as :

$$\begin{cases} G_1 = \dfrac{\rho P_1^2 [t t' + \rho P_2^2 (t t' - r r_{BB})]}{(1 - \rho r_{BB} P_1^2)(1 - \rho r_{BB} P_2^2) - t' r_{BB} \rho^2 P_1^2 P_2^2} \\ G_2 = \dfrac{\rho P_2^2 [t t' + \rho P_1^2 (t t' - r r_{BB})]}{(1 - \rho r_{BB} P_1^2)(1 - \rho r_{BB} P_2^2) - t' r_{BB} \rho^2 P_1^2 P_2^2} \end{cases}$$

The critical coupling (zero of reflectivity) is then achieved through a three wave destructive interference dictate by the coupling parameter t_{BB}.

3. Experimental demonstration of the coupled nano Fabry-Perot resonance

For this experimental demonstration, we consider horizontal nano FP cavities. An analogy has been demonstrated between the vertical and horizontal nano FP cavities, providing a simple geometry transformation whose principal parameters are summarized in figure 3. The resulting horizontal coupled FP nanostructures studied in this letter are made of three layers as illustrated in the inset of the figure 4.b. A top periodic nanostructure composed of one or several gold ribbons of the same height (t=50 nm) but different width denoted by capital letters (W_A= 400 nm and W_B= 495 nm) is deposed on two continuous layers, a SiC insulating layer of 280 nm thickness and a gold mirror.



Coupled structures	bi-slit	bi-ribbon
resonance wavelength λ_0	d	W / 2
critical coupling (R=0)	Δ d	Δ W
Q-factor	L	h

Figure 3 Correspondence between the bi-slit and bi-ribbon coupled FP cavities.

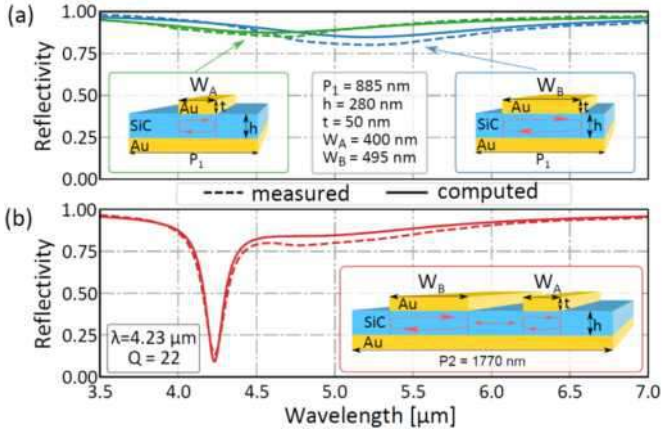


Figure 2: *Measured (dotted) and computed (plain) reflection spectra of (a) single-FP structures and (b) the coupled nano FP structure. Due to the thickness of the SiC layer, the two single FP resonators are under-coupled and their reflectivities do not go below 80%. Due to the coupling between the two FP, the new coupled FP resonance is visible at λ= 4.23 µm with a minimum of reflectivity of 14% and a high Q-factor of 22. The insets represent the different structures*

4. Conclusions

The description of the double-groove resonator paves the way to the manipulation and the engineering of the equivalent mirror coupling the two nanocavities, in order to reach multimirror interferences predictions. This structure is also very promising for many practical applications. For example, the wide dielectric layer is needed for nanostructured photodectors or a high Q-factor resonance is useful for gas detection.

Acknowledgements

The authors acknowledge the financial support from a DGA-MRIS scholarship.

References

[1] C. Fabry and A. Perot, *Ann Chim Phys*, 16,7, 1899.
[2] E. Schubert *et al.*, *Science*, vol. 265, no. 5174, 1994.
[3] H. Van de Stadt and J. M. Muller, *JOSA A*, 2, 8, 1985.
[4] J. A. Porto *et al.*,*Phys. Rev. Lett.*, vol. 83, 14, 1999.
[5] J. Dorfmüller *et al.*, *Nano Lett.*, vol. 9, no. 6, 2009.
[6] E. Cubukcu *et al.*, *Appl. Phys. Lett.*, vol. 95, 20, 2009.
[7] P. Bouchon *et al.*, *Appl. Phys. Lett.*, vol. 98, 2011.
[8] X. Liu *et al.*, *Phys. Rev. Lett.*, vol. 104, no. 20, 2010.
[9] P. Bouchon *et al.*, *Opt. Lett.*, vol. 37, no. 6, 2012.
[10] C. Koechlin *et al.*, *Opt. Express*, vol. 21, no. 6, 2013.
[11] Y. Cui *et al.*, *Laser Photonics Rev.*, vol. 8, 4, 2014.
[12] M. Makhsiyan *et al.*, *Appl. Phys. Lett.*, 107, 25, 2015.
[13] H. T. Miyazaki *et al.*, *Appl. Phys. Lett.*, vol. 92, 2008.
[14] M. W. Knight *et al.*, *Science*, 332, 6030, May 2011.
[15] A. Cattoni *et al.*, *Nano Lett.*, vol. 11, no. 9, 2011.

Antenna-Controlled Photon Antibunching from Individual Carbon Nanotubes as Quasi-1D systems

Lucas Lange[1,2], **Frank Schäfer**[1,2], **Alexander Biewald**[1,2]
Richard Ciesielski[1,2*], **Achim Hartschuh**[1,2]

[1]Department of Chemistry, Ludwig-Maximilians-University, Munich, Germany
[2]Center for NanoScience (CeNS), Munich, Germany
*corresponding author, E-mail: richard.ciesielski@cup.lmu.de

Abstract

We present a combined experimental and numerical study that utilizes optical antennas to convert a carbon nanotube as a model system for 1D emitters into a single photon source by localization and efficient exciton-exciton annihilation (EEA).

1. Introduction

Since its first report in 2008 [1], photon antibunching in the photoluminescence (PL) from semiconducting single-walled carbon nanotubes (SWCNTs) attracted considerable attention because of potential applications of SWCNTs as single-photon-sources. Known for single point-like quantum systems, the observed antibunching from a 1D nanomaterial also raised fundamental questions regarding the underlying mechanism. In general, antibunching is thought to require the efficient localization of the excited state energy at local minima in the exciton energy landscape or at chemical dopant sites and was reported for different nanotube materials and configurations upon optical as well as electrical excitation [2, 3, 4, 5].

2. Antenna-enhanced exciton-exciton annihilation for single photon emission

For SWCNTs it was found that high exciton mobility and EEA can lead to significant antibunching with reported values ranging from $g^{(2)}(0) \approx 0.3$ to 0.9 [2, 4]. In numerical simulations, the exciton density and the diffusion length of mobile excitons were found to be key parameters in controlling $g^{(2)}(0)$. Moreover, Ishii et al.[4] suggested that the former could be minimized using near-field optical techniques. To proof the feasibility of the approach, we used a Hanbury-Brown-Twiss interferometer and measured the second-order correlation function $g^{(2)}(\tau)$ of the PL emission from individual carbon nanotubes. The SWCNTs were deposited on a glass substrate and excited with a pulsed laser, either with or without a sharp gold tip acting as optical antenna, the principle of which is shown in Figure 1a. Starting at a low excitation rate with less than one absorbed photons per pulse on average, there is still a sizable chance to create two or more excitons at the same time since the number of photons in a laser pulse follows a Poisson distribution. The nearfield of a nanoantenna then acts as a funnel for the excitons, with the idea that by efficient exciton-exciton annihilation only one exciton per pulse will survive to later emit a photon. Figure 1b presents an optical nearfield image of an individual (6,5) SWCNT recorded with the setup at a resolution of around 20 nm. Figure 1c presents the normalized second order correlation function $g^{(2)}(\tau)$ of the PL emission of a (6,5) SWCNT, measured with and without an optical antenna. Antenna-controlled antibunching is seen as a reduction of $g^{(2)}(0)$ by around 0.2.We further employed a Monte-Carlo scheme to model and understand the physics of exciton diffusion, annihilation and decay at a nanotube [4, 6] in interaction with an optical antenna. Figure 1d presents the resulting magnitude of the three decay channels at an increasing field enhancement factor f for the situation of 4 initially created excitons. High field enhancement leads to a significantly amplified EEA channel, which in return controls and reduces the exciton number on the nanotube. From repeated simulation runs, the normalized second order correlation function can be calculated. The resulting values for $g^{(2)}(0)$ from numerous simulations are in good agreement with the findings from our measurements, if the typical parameters of an electrochemically etched gold tip antenna are estimated as $f \approx 2-5$ and $d \approx 20$ nm. Higher field enhancement factors, a longer diffusion length or lower quantum yield leads to even higher degrees of photon antibunching.

3. Conclusions

Nanoscale optical antennas can be used to control the photon emission statistics of one-dimensional emitters and turn them into single photon sources. Our Monte-Carlo simulations show that the degree of antibunching $g^{(2)}(0)$ can be reduced to below 0.3 for realistic parameter sets. Key for this behavior is the nearfield of the tip that leads to a locally enhanced exciton density, which increases EEA. Together with the enhanced radiative decay rate, single photon emission is favoured. Proof-of-concept experiments on SWCNTs show a reduction of $g^{(2)}(0)$ by about 0.2 in good agreement with the calculated results. Since the mechanism of antibunching does not rely on the used material here, the concept can be extended to other 1D materials that show EEA.

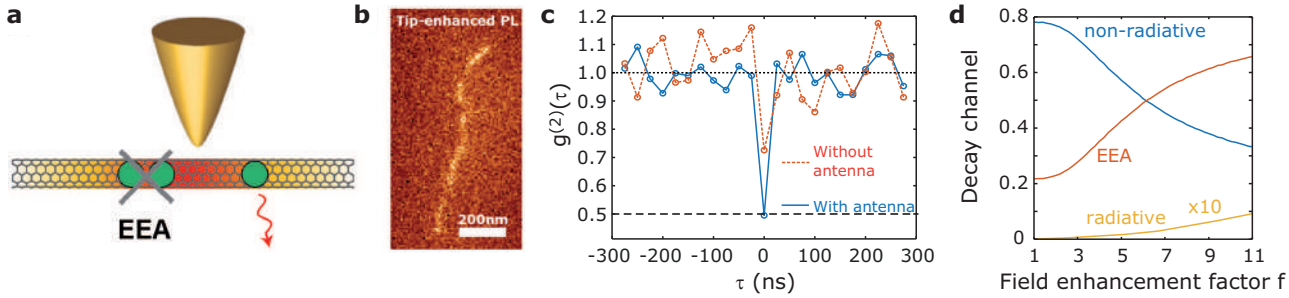


Figure 1: **a** Schematic of the approach for antenna-controlled photon antibunching. The presence of an optical antenna concentrates the excitons and leads to an increase in the exciton-exciton annihilation rate. **b** Antenna-enhanced near-field optical PL image of a (6,5) carbon nanotube. **c** Antenna-controlled antibunching: The normalized second order correlation function $g^{(2)}(\tau)$ of the PL of a (6,5) SWCNT with and without optical antenna, recorded after pulsed laser excitation. **d** Monte-Carlo simulations show the control of the relative decay rates by the local field enhancement factor f.

Acknowledgement

The authors acknowledge financial support from the the Deutsche Forschungsgemeinschaft through the Nanosystems Initiative Munich (NIM).

References

[1] A. Högele, C. Galland, M.Winger, A. Imamoglu, Photon Antibunching in the Photoluminescence Spectra of a Single Carbon Nanotube, *Phys. Rev. Lett.* 100: 217401, 2008.

[2] T. Endo, J. Ishi-Hayase, H. Maki, Photon antibunching in single-walled carbon nanotubes at telecommunication wavelengths and room temperature, *Appl. Phys. Lett.* 106:113106, 2015.

[3] S. Khasminskaya et al., Fully integrated quantum photonic circuit with an electrically driven light source, *Nat. Photonics* 10: 727, 2016.

[4] A. Ishii, T. Uda, Y. K. Kato, Room-temperature single-photon emission from micrometer-long air-suspended carbon nanotubes, *Phys. Rev. Appl.* 8: 054039, 2017.

[5] N. Mauser, A. Hartschuh, Tip-enhanced near-field optical microscopy, *Chem. Soc. Rev.* 42: 1248, 2014.

[6] C. Georgi, A. A. Green, M. C. Hersam, A. Hartschuh, Probing exciton localization in single-walled carbon nanotubes using high-resolution near-field microscopy, *ACS Nano* 4: 5914, 2010.

Self-Assembled Plasmonic DNA Origami Nanoantennas for Diagnostic Applications

Florian Steiner*[1], Carolin Vietz[2], Sarah Ochmann[1], Kateryna Trofymchuk[1], Viktorija Glembockyte[1], Cindy M. Close[1], Hakan Inan[1], Lennart Grabenhorst[1], Florian Selbach[1], Guillermo Acuna[3], Birka Lalkens[4], and Philip Tinnefeld[1]

[1]Department Chemie and Center of Nanoscience, Ludwig-Maximilians-Universität München, Butenandtstraße 5-13, 81377 München, Germany
[2]NanoBioSciences Group, Institute for Physical and Theoretical Chemistry, Technische Universität Braunschweig, Braunschweig Integrated Center of Systems Biology (BRICS), Rebenring 56, 38106 Braunschweig, Germany
[3]Department of Physics, University of Fribourg, Chemin du Museé 3, Fribourg CH-1700, Switzerland
[4]LENA, Institute of Semiconductor Technology, Langer Kamp 6a/b, 38106 Braunschweig, Germany
*corresponding author, E-mail: florian.steiner@cup.lmu.de

Abstract

By using DNA nanotechnology it is now possible to build complex nanostructures and hybrid materials. We used three dimensional DNA origami structures to design plasmonic nanoantennas containing a fluorescent dye or molecular assays that are placed in a controlled way into the hotspot of two metallic nanoparticles which are connected to the DNA origami. With these nanoantennas, we were able to optically detect Zika-virus related nucleic acids. The fluorescence enhancement enables detection of fluorescence signals of single dyes on low-tech devices such as smartphones.

1. DNA Origami Folding

To assemble DNA origamis [1], a long scaffold DNA strand of roughly 8000 nucleotides is folded into the desired shape by hybridizing about 200 short oligonucleotides. In this way, the short staple strands connect different parts of the scaffold strand and therefore predefine the structures. This can be programmed by choosing the right sequences of the staple strands. The principle of DNA origami is shown in Fig. 1 and has enabled several different structures in two and three dimensions. AFM images of a rectangular DNA origami with dimensions of 70 nm x 100 nm is exemplarily shown in Fig. 1b.

In addition to the structural control, it is possible to place functional groups at distinct positions on the origami during the folding process by using modified staple strands for certain positions. In a first example, DNA origamis were thus equipped with several fluorescent dyes to create dye patterns that could be resolved with a super-resolution fluorescence microscope [2, 3].

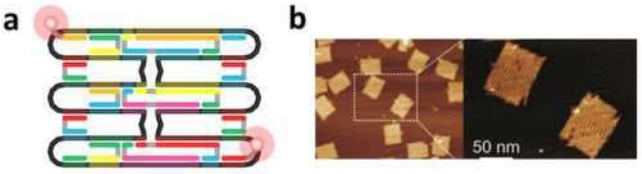


Figure 1: a) DNA origami nanostructures that are self-assembled from a single stranded circular DNA scaffold (black) by addition of multiple short staple strands (colored). Fluorescent dyes on staple strands are indicated as red shiny spheres in the upper left and lower right corner. The designed structure provides nanometer control for positioning e.g. fluorescent dyes, nanoparticles and proteins; b) AFM images of rectangular DNA origamis (edge lengths: 70 nm x 100 nm).

2. Single molecule diagnostics using DNA Origami Nanoantennas

Here, DNA origami nanostructures were used to arrange different components for nanophotonics applications [4]. One example is shown in Fig. 2 where two silver nanoparticles were arranged to build an antenna with a gap of 15-20 nm. These gold nanoparticles (diameter about 80-100 nm) create a plasmonic hotspot between the particles where the local electric field of the incident laser light is enhanced by hundred- to thousandfold [5]. It was already stated that the emitter or even larger biomolecular assays can be placed in the hotspot in a stoichometrically controlled manner. This is unique compared to optical antennas produced by nano-lithography.

To bind the nanoparticles to the DNA origami, they first have to be modified with thiolated DNA strands that are complementary to DNA strands protruding from the DNA origami. Additionally, the DNA origami structure is equipped with biotin modifications at the bottom for

selective immobilization on BSA-biotin-neutravidin passivated surfaces and a green fluorophore is placed near the bottom of the DNA origami pillar for visualization of bound nanostructures.
In the example shown in Fig. 2, a DNA hairpin assay is placed in the plasmonic hotspot created by two silver nanoparticles with a diameter of 80nm. The hairpin assay is modified by one ATTO647N dye and a Blackberry650 (BBQ-650) quencher. The fluorescence of the dye is therefore quenched when the hairpin is closed. Upon opening of the hairpin, the distance between quencher and dye is enlarged, and in turn the emerging weak fluorescence is enhanced in the hotspot and can be detected [6, 7].

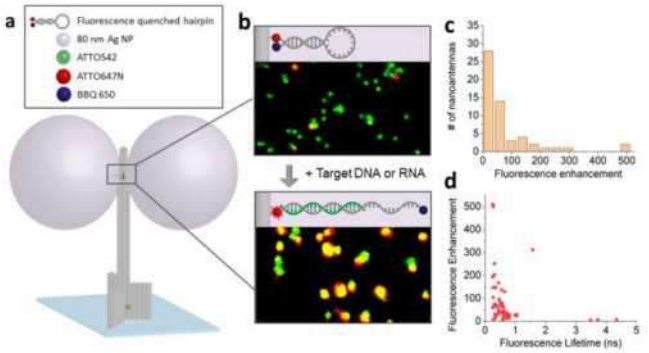


Figure 2: a) Sketch of three dimensional DNA origami with fluorescence quenching hairpin (ATTO647N, BBQ 650 quencher) and 80 nm silver nanoparticles; b) Illustration of the DNA detection assay. Upper panel: without target only green spots indicating the presence of the DNA origamis should be visible. Lower panel: After binding the target sequence, the dye is removed from the quencher and fluorescence is released indicated by the yellow spots in the false color images; c) Histogram of fluorescence enhancement factors of the opened hairpin relative to an ATTO647N dye bound to DNA; d) Fluorescence intensity versus fluorescence lifetime scatter plots. Three spots show a fluorescence lifetime of around 4 ns without fluorescence enhancement. This behavior is the expected for ATTO647N on DNA origami without silver nanoparticles in the vicinity. All remaining DNA origami structures carry the silver nanoparticles as visible by the shortened fluorescence lifetime and increased fluorescence intensity.

The idea of a single-molecule diagnostic assay is illustrated in Fig. 2b. In the original structure (without target), the hairpin is closed and the red fluorescence is quenched. Therefore, only green spots indicating the presence of the DNA origami structures are visible in false color fluorescence images (upper panel). After incubation with the target, the hairpin opens and the red fluorescence of ATTO647N is released. This leads to the appearance of yellow spots in the false color image (lower panel) indicating the co-localization of red and green fluorescence. The panels of Fig. 2c,d show the fluorescence enhancement and the fluorescence lifetime that was measured with such an assay. Fluorescence enhancements of up to several hundred fold were achieved while at the same time the fluorescence lifetimes were drastically shortened. This indicates that the presence of the nanoparticles not only increases the excitation intensity but also radiative and non-radiative decay rates are increased strongly.

The high fluorescence enhancement factors presented in this work encourage us to think that in the future it might be possible to detect the enhanced fluorescence intensity of single molecules on low-cost devices such as smartphone cameras. As a first approach to this vision it was already shown that a smartphone camera is able to image fluorescence beads with a low number of fluorophores [8]. Combining the smartphone-based microscope with DNA origami nanoantennas will be a breakthrough in future diagnostics procedures.

References

[1] P. W. Rothemund, "Folding DNA to create nanoscale shapes and patterns," Nature **440**, 297-302 (2006).

[2] J. J. Schmied, A. Gietl, P. Holzmeister, C. Forthmann, C. Steinhauer, T. Dammeyer, and P. Tinnefeld, "Fluorescence and super-resolution standards based on DNA origami," Nature Methods **9**, 1133-1134 (2012).

[3] J. J. Schmied, M. Raab, C. Forthmann, E. Pibiri, B. Wünsch, T. Dammeyer, and P. Tinnefeld, "DNA origami-based standards for quantitative fluorescence microscopy," Nature protocols **9**, 1367-1391 (2014).

[4] M. Pilo-Pais, G. P. Acuna, P. Tinnefeld, and T. Liedl, "Sculpting light by arranging optical components with DNA nanostructures," Mrs Bull **42**, 936-942 (2017).

[5] G. P. Acuna, F. M. Moller, P. Holzmeister, S. Beater, B. Lalkens, and P. Tinnefeld, "Fluorescence enhancement at docking sites of DNA-directed self-assembled nanoantennas," Science **338**, 506-510 (2012).

[6] C. Vietz, B. Lalkens, G. P. Acuna, and P. Tinnefeld, "Synergistic Combination of Unquenching and Plasmonic Fluorescence Enhancement in Fluorogenic Nucleic Acid Hybridization Probes," Nano Lett **17**, 6496-6500 (2017).

[7] S. E. Ochmann, C. Vietz, K. Trofymchuk, G. P. Acuna, B. Lalkens, and P. Tinnefeld, "Optical Nanoantenna for Single Molecule-Based Detection of Zika Virus Nucleic Acids without Molecular Multiplication," Anal Chem **89**, 13000-13007 (2017).

[8] C. Vietz, M. L. Schütte, Q. Wei, L. Richter, B. Lalkens, A. Ozcan, P. Tinnefeld, and G. P. Acuna, "Benchmarking Smartphone Fluorescence-Based Microscopy with DNA Origami Nanobeads: Reducing the Gap toward Single-Molecule Sensitivity," ACS Omega (2019)

Hexagonal Arrays of Gold Nanodot Dipole Nanoantennas Fabricated by Displacement Talbot Lithography

Jon R. Pugh[1], Pierre J. P. Chausse[3], Andrei Sarua[2], Philip A. Shields[3] and Martin. J. Cryan[1*]

[1]Department of Electronic & Electrical Engineering, University of Bristol, Clifton, Bristol, BS8 1UB, UK
[2]HH Wills Physics Laboratory, University of Bristol, Clifton, Bristol, BS8 1TL, UK
[3]Department of Electronic & Electrical Engineering, University of Bath, Claverton Down, Bath, BA2 7AY, UK
*corresponding author, E-mail: m.cryan@bristol.ac.uk

Abstract

This paper presents simulated fluorescence enhancement results for large area gold dipole nanoantenna arrays. The each array element consists of two circular gold nanodots with a small gap between their outer-edges. The hexagonal arrays can be formed by 'Double' Displacement Talbot Lithography via a lift-off process to pattern large area substrates. Intensity enhancement of ~2249 at λ=1371nm is simulated when an analyte of n=1.333 flows over the nanoantenna array.

1. Introduction

In-vitro fluorescence-based optical imaging of tissues and cells in the NIR-I (~700-900nm) spectral region is well established [1,2]. Simultaneous observation of several proteins in live cells via multicolor fluorescence has been achieved in this window, but imaging multiplicity is limited by the number of fluorescent channels with non-overlapping emission. Extending the spectral range into the second NIR optical window (NIR-II ; 1000-1700nm) has several advantages including increased image multiplexing capability. There has been much recent progress in this NIR-II window using Organic NIR fluorophores [3] and Carbon Nanotubes [4], and by coupling these emitters with an array of nanoantennas that can drastically enhance emission could yield a new era for biosensing applications.

These optical antennas, as with conventional RF antennas, can extract more energy from an electromagnetic source, an effect known as Purcell Enhancement, enabling increased sensitivity or reduced costs. Using conventional Electron-Beam Lithography (EBL) would prove expensive to write large area arrays into resist so an alternative, lower cost method using Displacement Talbot Lithography (DTL) [5,6] is explored in this work. In DTL a periodic mask produces a diffraction pattern that can expose an entire wafer in a single dose when moved vertically through one Talbot length.

The mechanisms for Purcell enhancement are described in our previous paper [7], where cross dipole nanoantennas were modelled and shown to enhance both absorption and emission in the antenna gap. Due to the proximity of the each nanoantenna, in an array it is important to consider array effects in terms of directional emission [8].

2. Fabrication

A Eulitha PhableR 100 DTL machine is used for exposing the resist. The technique has the advantage of a theoretically infinite depth of field but has the disadvantage of the low contrast between exposed and unexposed regions on the sample due to the mixing of the self-image and other secondary constructive interference features. Also, there is a restriction to simple periodic features. Nevertheless, the illumination process will not be sensitive to surface roughness, or imperfect parallelism between the mask and the sample, or the depth of field; all important parameters in conventional photolithography. By combining the system with a nano-positioning stage a new, high-throughput and rapid tool that allows the fabrication of complex periodic nano- to micron patterns over a large area is proposed – 'Double' Displacement Talbot Lithography (D2TL) [9]. By moving the wafer perpendicular to the axis of illumination, much more complex features are possible. One of which being a dual exposure, when combined with metal deposition and lift-off process, allows the fabrication of dual nanodots of metal separated by a small gap as shown in fig. 1, where dots of diameter ~300nm are separated by gaps of 30-50nm.

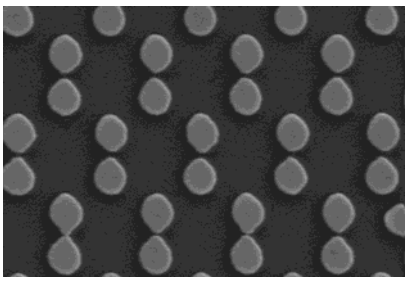


Figure 1: A scanning electron microscope image of a hexagonal array of gold nanodot antennas fabricated on a silicon substrate using D2TL.

3. Discussion

Intensity enhancement of a two-arm dipole nanoantenna is determined by several parameters. In this work, we have utilized Lumerical Finite-Difference Time-Domain simulation tools where a plane-wave source, polarized across the dipole gap, is incident onto an infinite hexagonal array of gold nanodot dipole nanoantennas. In this model, the individual nanodots have diameter 200nm and are 30nm thick, and the dipole gap is constant at 30nm. They are in a hexagonal array which is modelled as a unit cell with periodic boundary conditions. Fig. 2 shows the E_x intensity enhancement at the central position between the antenna nanodots normalized to the field for the free space simulation.

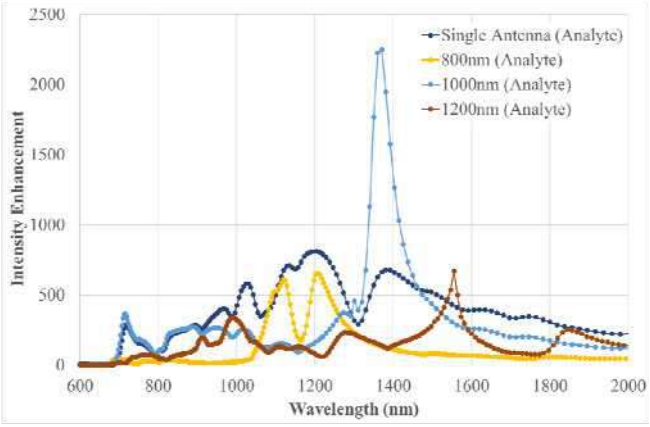


Figure 2: Intensity enhancement for various hexagonal array periods on a glass substrate with an analyte of n=1.333 flowing over the surface. The single antenna case is also shown.

The resonance is a result of localized surface plasmon resonance (LSPR). LSPR can be understood as a plasmonic standing wave on the surface of the antenna arms – Fig. 3 shows the |E|-field through the vertical centre of the arms. This wavelength is highly dependent on the characteristics of the antenna—such as size, shape, and material properties of both the antenna itself and analyte flowing above [10].

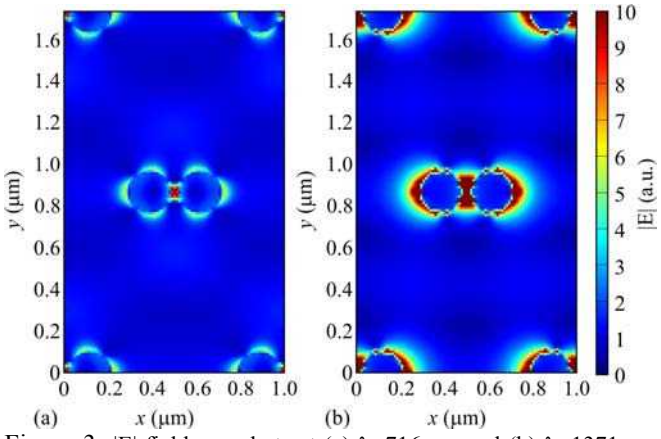


Figure 3: |E|-field snapshots at (a) λ=716nm, and (b) λ=1371nm for an 1μm spaced hexagonal array where intensity enhancement of ~366 and ~2249 was observed respectively.

The fundamental LSPR resonance shown in fig. 3(b) has an intensity enhancement of ~3.4x higher for the array as compared to the single antenna. In contrast the higher-order LSPR resonance shown in fig. 3(a) is only ~1.2x higher for the array. It is planned to place these arrays within a microfluidic channel, an example of one fabricated in Bristol is shown in fig 4.



Figure 4: A microfluidic channel formed in PDMS.

4. Conclusions

This paper shows the design and fabrication of gold nanodot dipole nanoantenna arrays for plasmonic, fluorescence-based sensing. Keeping the nanodot geometry constant, the array spacing has been explored showing an enhancement of up to ~2249 at the NIR λ=1371nm. In future, fluorescent nanoparticles will interact with these arrays within microfluidic channels in order to study their use in low cost biosensing applications.

References

[1] B. N. Giepmans, et al, The fluorescent toolbox for assessing protein location and function, *Science* 312: 217-224, 2006.

[2] G Hong, et al Carbon nanomaterials for biological imaging and nanomedicinal therapy, Chem Rev 115, 19: 10816-10906, 2015.

[3] S. Zhu et al, Molecular imaging of biological systems with a clickable dye in the broad 800- to 1700-nm near-infrared window, PNAS 114, 5: 962-967, 2017.

[4] G. Hong, et al, Metal-Enhanced Fluorescence of Carbon Nanotubes, J. Am. Chem. Soc., 132, 45 , 2010.

[5] H. H. Solak, et al, Phase shifting masks in DTL for printing nano-grids and periodic motifs, *Miroelectronic Eng.*, 143: 74-80, 2015.

[6] P. J. P. Chausse, E. D. Le Boulbar, S. D. Lis and P. A. Shields, Understanding resolution limit of DTL, *Opt. Exp.*, 27, 5:5918-5930, 2019.

[7] J. L. Stokes, Y. Yu, Z. H. Yuan, J. R. Pugh, M. Lopez-Garcia, N. Ahmad and M. J. Cryan, Analysis and design of a cross dipole nanoantenna for fluorescence-sensing applications, *J. Opt. Soc. Am. B*, 31, 2:302-310, 2014.

[8] N. Dorh, et al, Nanoantenna arrays combining enhancement and beam control for fluorescence-based sensing applications, App. Opt., 56, 29, 2017.

[9] P. J. P. Chausse and P. A. Shields, 'Double' DTL: a new approach for periodic nanostructure patterning, *Proc. SPIE 10587, Opt. Microlithography XXXI*, San Jose, USA, 2018.

[10] S. A. Maier, Plasmonics: Fundamentals and Applications (Springer, 2010).

Photoluminescence Enhancement by Hybrid plasmonic Nanodisks Arrays

Alireza R. Rashed[1,*], Mohsin Habib[1], Nekhel Das[1], and Humeyra Caglayan[1]

[1] Tampere University, Faculty of Engineering and Natural Sciences, Physics/Photonics, 33720 Tampere, Finland
*Alireza R. Rashed, E-mail: alireza.rashed@tuni.fi

Abstract

In this work, we have designed and fabricated an array of plasmonic nanodisks to investigate their interaction with different types of quantum emitters (QEs) in visible wavelength. We consider embedded fluorescent dye molecules in PMMA polymer as a potential QE for our investigation. The interaction between the strong subwavelength localized field at the edges of the gold nanodisks and QEs enhances the Purcell factor towards the modification of spontaneous emission and decay rate of QEs.

1. Introduction

Nano-scaled hybrid plasmonic−excitonic systems are offering promising features in light−matter interactions to achieve light amplification via enhancement in emission or absorption rates [1,2]. In addition, these hybrid nanostructures provide the opportunity of loss mitigation in plasmonic metamaterials through non-radiative energy transfer process from quantum emitters (QEs) to plasmonic absorber [3,4]. The Förster like dipole-dipole interaction between plasmonic and QEs modes is highly sensitive to donor-acceptor inter-distance, dipole-dipole orientation, donor and acceptor dipole moment strength, as well as, the spectral overlap between the emission band of the QE and the plasmon band of the nanostructure [5]. These are necessary conditions for both photoluminescence (PL) enhancement and quenching regimes. In the PL enhancement regime, due to the energy transfer from the QE to bright plasmonic modes, plasmonic structure operates as a transmitting nano-antenna and consequently, the quantum efficiency of the system enhances. While in quenching regime, this energy transfer is occurring to dark plasmonic modes, resulting in quenching of the emission and fluorescence lifetime of the QE [6].

In this regards, we have designed and fabricated an array of plasmonic nano-disks in order to study their interactions with different types of QEs in visible spectral range. The LDS 750 fluorescent dye molecules with three different concentrations are embedded in PMMA polymer as the host medium. The designed nano-antennas are fabricated with different periods and diameters in order to investigate how the spectral overlap between nanodisks absorption and QEs emission spectra affects the efficiency of the PL enhancement process. Alongside creating an efficient spectral overlap, a thin layer of the dielectric layer between the plasmonic structures and the gain medium layer provides an effective spatial overlap. The interaction between the strong subwavelength localized field at the edges of the gold nano-disks and QEs enhances Purcell factor towards the modification of the fluorescence and decay time of QEs.

The performed comprehensive study can lead the scientific community to understand deeper the details of the exciton-plasmon interactions in hybrid systems. Moreover, this study opens an avenue towards practical applications for novel light sources such as core-shell quantum dots (QDs), diamond nitrogen vacancy (NV) centers and 2D hexagonal boron nitrite (h-BN) [7], which are the vital components of future quantum technologies.

2. Discussion

We designed 3×3 matrices of gold plasmonic nanostructures with three different periods of 340 nm, 380 nm, 420 nm and three different diameters of 140nm 160 nm and 180 nm by using FDTD simulation method. Later we fabricated the designed nanodisks by applying standard EBL (electron beam lithography) method. As an example, a SEM image of one fabricated array of Au nano-disks is shown in Fig. 1.

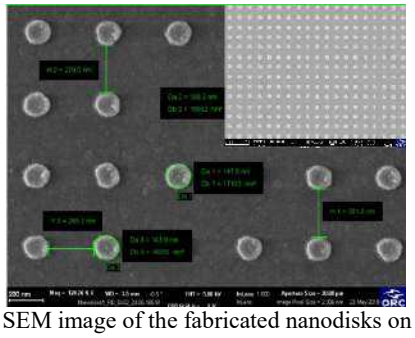


Figure 1: A SEM image of the fabricated nanodisks on fused silica substrate with period of 420 nm and diameter of 140 nm.

The applied alteration in period and diameter creates the opportunity of sweeping the nano-antennas reflection/absorption spectra (Fig. 2). This provides us the opportunity for achieving the spectral overlaps with different efficiencies between the fluorescent dye molecules emission and the plasmonic nanostructures reflectance spectra. As it is evident from Fig. 2, the increase in diameter of nano-disks

and decrease in their periodicity lead to the shift of reflectance spectrum to the longer wavelengths and the enhancement of the reflection intensity.

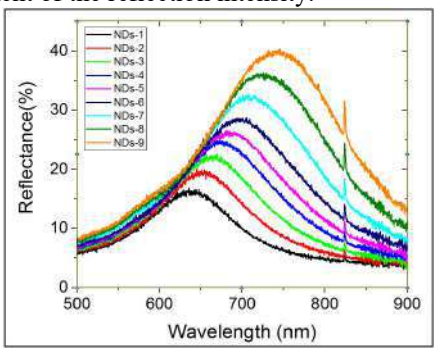


Figure 2: The measured reflectance spectra of 3×3 matrices of gold plasmonic nanostructures with different periods and diameters.

The PL spectrum of embedded LDS 750 QEs in PMMA A2 dielectric medium appears around 680 nm. The homogeneously dispersed dye molecules in PMMA polymer with three different concentrations are spin-coated over the nano-antennas, creating a thin gain layer of 60 nm. The emission spectrum of the gain medium overlaps with different percentages with the reflectance spectra of the fabricated nano-antennas. Such variated spectral overlaps change the efficiency of the RET (Resonance Energy Transfer) process from gain material to plasmonic nano-antennas and consequently, alters the Purcell factor enhancement. We observe an effective spontaneous emission enhancement for those better spectral overlap cases, because of a strong RET between gain medium and plasmonic nano-disks. Fig. 3 presents the maximum spontaneous emission intensity of the LDS 750 dye molecules with concentration of 0.005% in the presence and the absence of the nano-disks with a particular period and diameter. The slope modification of the curves is the signature of the non-radiative RET occurring in hybrid system.

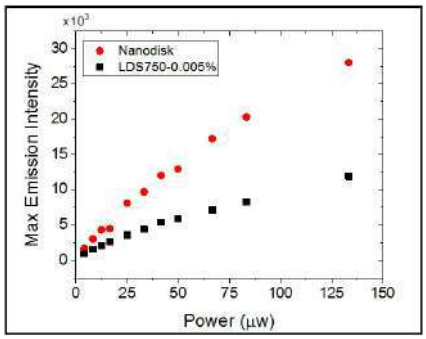


Figure 3: The maximum spontaneous emission intensity of the LDS 750 dye molecules with the concentration of 0.005% in the presence and the absence of the nano-disks with period and diameter of 420 nm and 140 nm, respectively.

The acquired decay time data, accompanied by the fluorescent lifetime imaging microscopy (FLIM) results are providing another evidences for the occurrence of the RET process among dye molecules and plasmonic nano-disks.

The existence of the emitter in close proximity of plasmonic nanostructure increases the optical density of states. According to Purcell effect, the radiative decay rate of the emitter increases because of the decrease in the modal volume, that is, the effective cavity where the mode is confined within [8]. The increase in radiative decay rate leads to a net increase in the emission intensity. Another definition for the observed PL enhancement is to consider metallic nano-disks as efficient antennas that out-couples the plasmons to the far field in a more efficient way, resulting in the boosting of the hybrid system emission.

3. Conclusions

Our experimental investigation proves the functionality of the designed nano-disks for spontaneous emission enhancement as a result of RET process between these nanostructures and fluorescent dye molecules. Such design has the potential for light boosting and lasing purposes by using other types of QEs such as QDs and 2D h-BNs layers and their flakes. Our comprehensive study assists us to design an efficient hybrid system towards PL enhancement applications in practical systems.

Acknowledgements

This work is supported by "COMPETITIVE FUNDING TO STRENGTHEN UNIVERSITY RESEARCH PROFILES funded by Academy of Finland, decision number 301820".

References

[1] T.T. Tran, D. Wang, Z. Xu, A. Yang, M. Toth, T.W. Odom, I. Aharonovich. Deterministic coupling of quantum emitters in 2D materials to plasmonic nanocavity arrays, *Nano lett.,* 4:2634- 2639, 2017.

[2] S. Tame, K. Mark, R. McEnery, Ş. K. Özdemir, J. Lee, S. A. Maier and M. S. Kim. Quantum plasmonics, *Nat. Phys.* 9:329-1499, 2013.

[3] A. F. Koenderink, A. Alu and A. Polman. Nanophotonics: Shrinking light-based technology, *Science* 348, (6234):516-521, 2015.

[4] A. R. Rashed, A. D. Luca, R. Dhama, A. Hosseinzadeh, M. Infusino, M. E. Kabbash, S. Ravaine, R. Bartolino and G. Strangi. Battling absorptive losses by plasmon–exciton coupling in multimeric nanostructures. *RSC Advances* 5:53245-53254, 2015.

[5] P. Viste, J. Plain, R. Jaffiol, A. Vial, P. M. Adam, and P. Royer, Enhancement and quenching regimes in metal-semiconductor hybrid optical nanosources, *ACS Nano*, 4:759–764, 2010.

[6] M. El Kabbash, R. A. Rashed, K. V. Sreekanth, A. De Luca, M. Infusino and G. Strangi, Plasmon-Exciton Resonant Energy Transfer: Across Scales Hybrid Systems, *J. Nanomater*., 2016:1-21, 2016.

[7] T.T. Tran, K. Bray, M.J. Ford, M. Toth and I. Aharonovich. Quantum emission from hexagonal boron nitride monolayers, *Nat. nanotechnol.* 11:37-41, 2016.

[8] K. J. Russell, T.-L. Liu, S. Cui, and E. L. Hu, Large spontaneous emission enhancement in plasmonic nanocavities, *Nature Photonics*, 6: 459–462, 2012.

A 10 μm $\times$ 10 μm Longwave Infrared Imaging Pixel Based on Split Ring Resonators

Mohammed R. AlShareef[1], Mohamed Ramy Abdel-Rahman[2]

[1]National Center for MEMS Technology, King Abdulaziz City for Science and Technology, Riyadh, Saudi Arabia
[2]Electrical Engineering Department, College of Engineering, King Saud University, Riyadh, Saudi Arabia
*corresponding author E-mail: alshareef@kacst.edu.sa

Abstract

In this work, a 10 μm $\times$ 10 μm infrared imaging pixel is proposed based on electrically small resonators. The novel pixel configuration is composed of eight split ring resonators electromagnetically coupled to two tapered transmission lines that are purposed to deliver the coupled electromagnetic power to a resistive sheet, representing a microbolometer. The proposed structure is simulated and the power absorption efficiency in the longwave infrared (8-12 μm) band is analyzed.

1. Introduction

An electrically small resonator-coupled detector configuration has been proposed for longwave infrared (8-12 μm) sensing in [1]. The proposed detector configuration advocated the possibility of using electrically small resonator-coupled sensors as alternatives to antenna-coupled detectors [2]-[4] for longwave infrared detection. Electrically small resonators are small-sized electromagnetic structures; they have achieved high absorption efficiencies in the microwave and terahertz bands [5, 6] when used in array configurations. Electrically small resonators, thus, can possibly achieve high absorption efficiencies in the infrared band; in addition, they can eventually be configured to be wavelength tunable and polarization agile, all of which supports their use as infrared imaging elements.

In this paper, a novel configuration of a 10 μm $\times$ 10 μm infrared imaging pixel is presented, based on electrically small resonator structures. The proposed pixel size is commensurate with current state of the art commercial infrared imaging pixel sizes. The pixel is made of eight metallic (gold, *Au*) split ring resonators (SRRs) suspended on a silicon dioxide (SiO_2) film having an underlying *Au* ground plane. The SRRs are purposed to absorb the incident infrared electromagnetic radiation and couple the absorbed power to two tapered transmission lines which in turn deliver the coupled power to a resistive sheet. The proposed configuration is simulated and optimized for maximum power absorption.

2. Geometrical Configuration

We propose a square shape arrangement composed of eight SRRs where they circulate two tapered transmission lines as seen in Fig. 1. The transmission lines have a very sharp tip directed inwardly to leaving a very narrow gap sets in the middle of the arrangement. Since the metallic materials in infrared frequency range are very lossy, choosing a proper metal is critical for device performance. We chose *Au* for the metallic structures and SiO_2 layer as a dielectric material. The gold layer has a conductivity $\sigma = 2.8\times10^6$ S/m, as measured in [7] and a thickness of 150 nm, while the silicon dioxide has a thickness h= 1.5 μm and dielectric constant ϵ_r= 4.84 + j0.097. We intentionally maintain a square-like shape with a square side length = 8 μm to have an accurate pixel configuration. The outer (l_1) and inner (l_2) arm lengths of the SRR are 2 μm and 1.45 μm, respectively. The gap opening dimension (g) is 0.6 μm while the spacing between two SRRs in y-direction (s) is 0.65 μm.

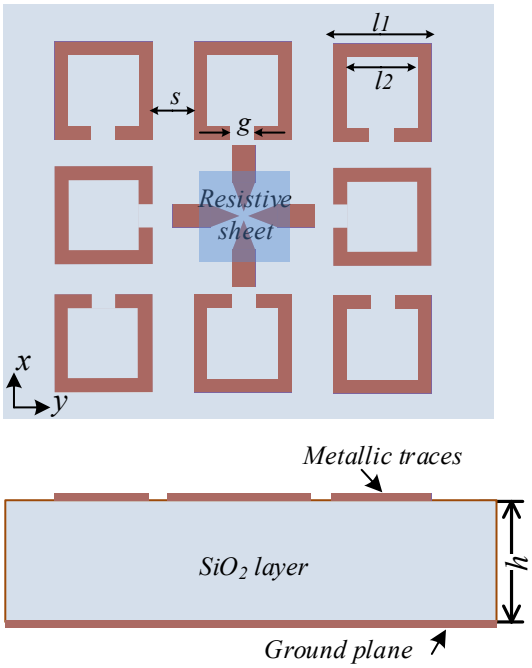


Figure 1: Layout of the infrared-wave collector structure, (a) top and (b) side view.

The resistance of the resistive sheet can be varied during the simulation to determine the optimum resistance where impedance matching between the structure and the resistive sheet is achieved.

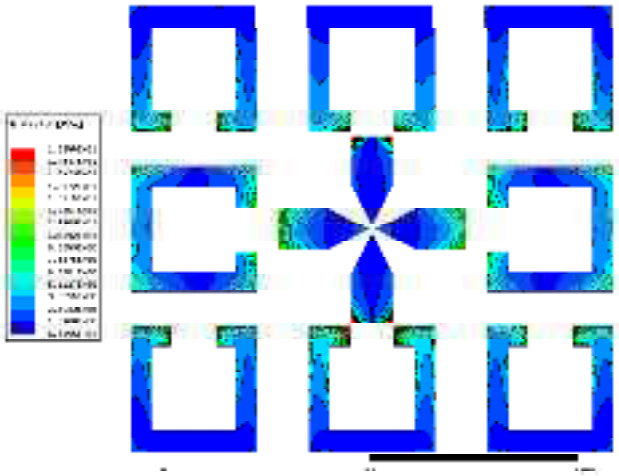


Figure 2: Simulated electric field distribution on the metallic elements in resonance state

3. Discussion and Results

The structure basic mechanism is to expose it to a perpendicular direct infrared wave allowing the eight SRRs to be in excitation mode with a high build up voltage across their gaps. Each gap can virtually be presented as a voltage source, while the TMS lines, set in the middle of the arrangement, couple and focus the collected energy from each SRR to a centric focal point. The structure is designed to operate from 20-25 THz. We simulate the proposed configuration using ANSYS® HFSS™ numerical full-wave simulation tool.

To gain more insights about the structure mechanism, we simulated the electric field distribution on the metallic inclusions in resonance state as depicted in Fig. 2. The image shows that the excited electric fields intensify around the SRRs gaps and at the edges of the TMS lines alike. The aforementioned comparatively high electric fields indicate to energy transition from the SRRs to the TMS lines without any physical connection. The less-connectivity feature will allow more pixel arrangements without compromising a metallic loss in the structure.

The next step then to examine the structure performance was to numerically calculate the structure reflection and transmission coefficients as seen in Fig. 3. The plots apparently indicate that both transmission and reflection power are suppressed within the structure. More precisely, 73% of power impinging the structure dwell in the structure, which results in reasonably good power confinement. Afterwards, Equation 1 in [5] was applied to calculate the power absorption efficiency:

$$\eta = \frac{P_{received}}{P_{incident}} \tag{1}$$

where $P_{incident}$ is defined as the available power at the surface of the structure and $P_{received}$ is the power absorbed across the resistive sheet. Fig. 4 shows that the proposed geometry can absorb approximately 36% of the incident power at such high and lossy frequency. Different resistive

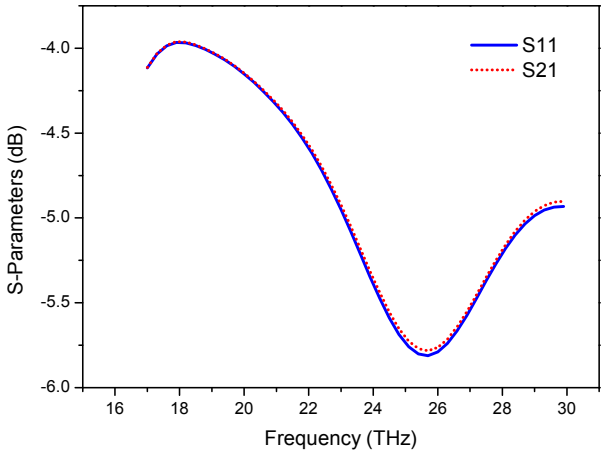


Figure 3: Simulated reflection coefficient of the proposed structure

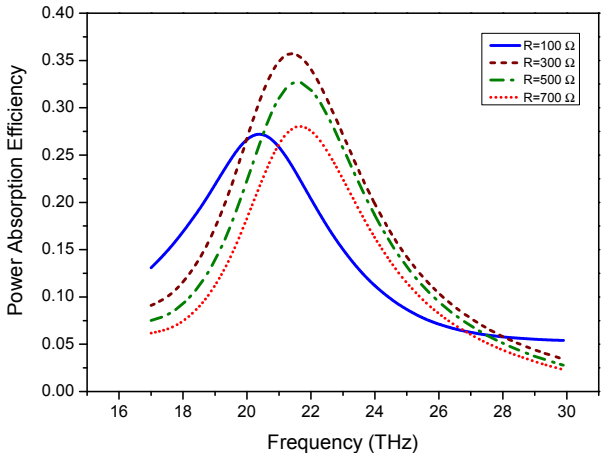


Figure 4: Calculated power absorption efficiency of the structure

load values were varied to check which resistance yields the highest absorption efficiency. One can say that the achieved efficiency is relatively small; however, better absorption efficiency can be realized by changing the structure's orientation and its topology. Improving efficiency will be further studied in future research.

4. Conclusion

Special arrangement of eight electrically small resonators and two tapered microstrip lines are placed together to function as energy collector. The structure is designed and numerically simulated to examine its ability of infrared detection. An initial power absorption efficiency of 36% is achieved utilizing the proposed structure. The relatively low efficiency is attributed to the metallic losses and the gold low conductivity at such high frequency. Dramatic absorption efficiency improvement will be presented during the conference.

Acknowledgement

This work was supported by King Abdulaziz City for Science and Technology.

References

[1] M. R. AlShareef and M. Abdel-Rahman, Electrically Small Resonators-Based Infrared Imaging Pixel Configuration, in *META 2018, the 9th International Conference on Metamaterials, Photonic Crystals and Plasmonics*, June 2018.

[2] S. Choi, Cross Bowtie Antenna-Coupled Detector for Circularly Polarized Infrared Wave Sensing, in *2018 International Symposium on Antennas and Propagation (ISAP)*, Busan, Korea (South), 2018.

[3] M. H. Mubarak, O. Sidek, M. Abdel-Rahman, M.T. Mustaffa, A. S. Mustapa Kamal, S. M. Mukras, Nano-Antenna Coupled Infrared Detector Design, *Sensors*, 18, 3714, 2018.

[4] M. Mubarak, O. Sidek, M. Abdel-Rahman, M. T. Mustaffa, A. S. Mustapa Kamal, S. Mukras, Fabrication of microparabolic reflector for infrared antenna coupled detectors, *Micro & Nano Letters*, 13(9), 1343, 2018.

[5] Mohammed R. AlShareef and O. Ramahi, Electrically small particles combining even- and odd-mode currents for microwave energy harvesting, *Applied Physics Letters* vol. 104, no. 25, pp. 253906-5, 2014

[6] M. R. AlShareef and O. Ramahi, Electrically small resonators for energy harvesting in the infrared regime, *J. Appl. Phys.* 114, 2013.

[7] D. Shelton, et al., Antenna-coupled microbolometers on a silicon nitride membrane, *J. Appl. Phys.* 104: 103514, 2008.

Photothermal and photoelectric nanophotonics

Thermal behavior and managament of thermophotovoltaic cells

Etienne Blandre[1], Rodolphe Vaillon[2], Jérémie Drevillon[1]

[1] Insitut PPrime, ENSIP, Poitiers, France
[2] IES, Univ. Montpellier, CNRS, F-34000 Montpellier, France
*corresponding author, E-mail: etienne.blandre@univ-poitiers.fr

Abstract

The thermal behavior of a thermophotovoltaic system composed of a metallodielectric spectrally selective radiator at 1500 K and a GaSb photovoltaic cell is investigated. Using a coupled radiative, electrical and thermal model, we highlight that without a large convective heat transfer coefficient applied to the cell, the raise in temperature of the PV cell induces dramatic efficiency losses. We then investigate radiative cooling as a potential passive cooling solution.

1. Introduction

Thermophotovoltaics (TPV) is a promising technology for converting heat into electricity using a radiator emitting thermal radiation toward a low-bandgap photovoltaic (PV) cell. During the past years, many studies focused on tailoring the spectral emission of the radiator such that the energy of the emitted photons matches with the bandgap of the PV cell [1], in order to maximize conversion of photons into electron-hole pairs. However, the point of view of the PV cell was often neglected. In particular, the raise in temperature of the PV cell due to thermalization of high energy photons, absorption of photons with subbangap energy and recombination losses inside the PV device can lead to dramatic losses in efficiency, as the performances of the junction decreases with the cell temperature. These thermal effects are a common issue in standard solar PV [2], where the incident solar radiative power is much lower than in thermophotovoltaics. This means that thermal losses in TPV can be expected to be extremely large. To highlight this, we simulate the behavior of a TPV system consisting of a 1D multilayer selective emitter made of W and HfO_2 and a p-on-n GaSb junction. Radiative heat transfer from the emitter to the cell, transport of electrical charges and recombinations inside the PV cell and variations of the cell temperature are accounted for. We also investigate radiative cooling as a potential cooling solution for TPV cells.

2. Modeling of the TPV system

Radiative heat transfer between the radiator and the PV cell is computed within the frame of fluctuational electrodynamics in conjunction with the S-matrix approach. The radiative power absorbed by the PV cell is then used to compute the local generation rate of electron-hole pairs, which is required to solve the minority carrier diffusion equation.The maximum electrical power output P_{max} and the efficiency η of the PV cell can then be calculated. The heat sources inside the PV cell Q_{PV} are then calculated as

$$Q_{\text{PV}} = Q_{\text{abs}} - P_{\text{max}}, \tag{1}$$

where Q_{abs} is the radiative power absorbed by the PV cell. Convective heat transfer is considered to cool the PV device, and its power Q_c is calculated as

$$Q_c = h_c(T_c - T_\infty). \tag{2}$$

Here, h_c is a convective heat transfer coefficient, T_c is the operating cell temperature and T_∞ is the temperature of the cooling fluid (set at 300 K in this study). As an addition to the cooling system, we also consider radiative cooling as a passive thermal management solution. To evaluate the limits of the impact of radiative cooling on the system performances, we consider that the thermal emission of the radiative cooler Q_{rad} is the one of a blackbody at the cell temperature, given by Stefan-Boltzmann law:

$$Q_{\text{rad}} = \sigma T_c^4. \tag{3}$$

By solving a thermal balance equation, the temperature of the PV cell can be calculated. The calculation is then performed again with updated temperature-dependent properties of the PV cell until convergence of the temperature of the PV device. The outputs of the calculations are the system efficiency, maximum power-output and operating cell temperature.

3. Thermal behavior of the TPV system

The system under consideration is depicted in Fig. 1(a). A 1D multilayer W-HfO2 spectrally selective radiator at 1500 K (similar to [3]) radiates thermal energy toward a GaSb pn-junction. At the rear of the junction, a gold layer is used as a backside reflector to recycle photons that have not been absorbed by the PV cell by reflecting them back to the radiator. A black surface is considered to act as a radiative cooler at the back of the cell, next to the gold layer. In Fig. 1(b), the spectral hemispherical emissivity and spectral emissive power of the selective radiator radiator are plotted. The designed radiator has high emissivity for photons with energy above the bandgap of the PV device, and low emissivity for subbangap photons.

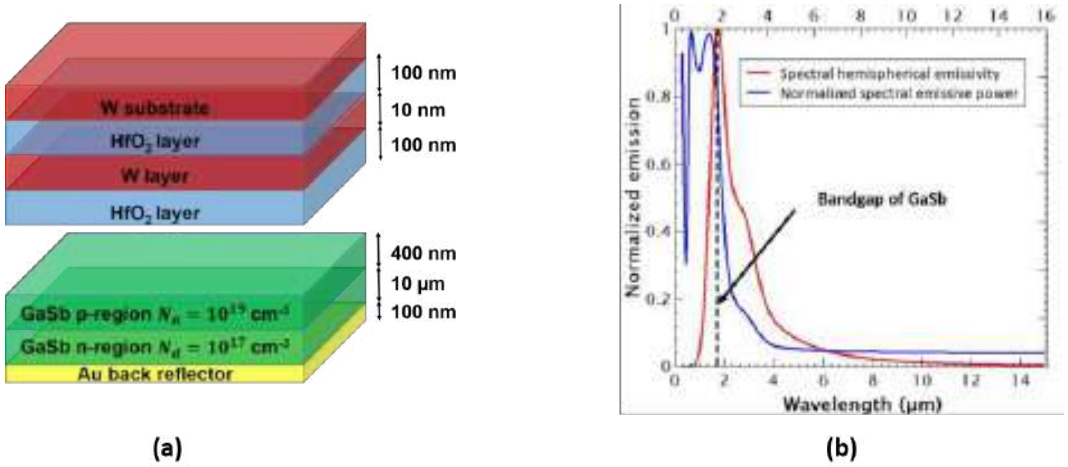


Figure 1: (a): Schematic representation of the TPV system under consideration. (b): Spectral hemispherical emissivity and normalized spectral emissive power of the selective radiator

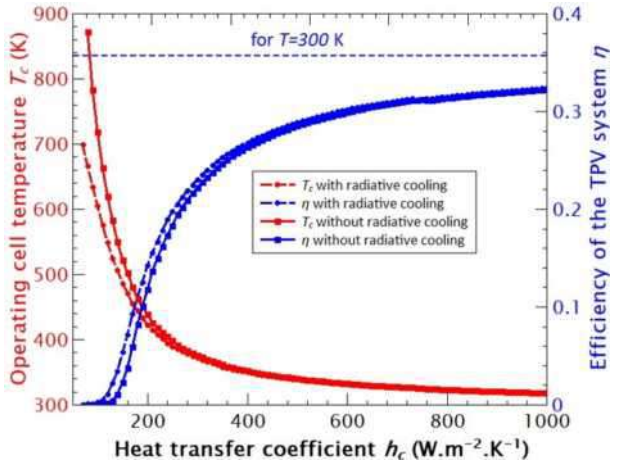


Figure 2: Efficiency loss of the TPV system as a function of the cell temperature.

Using the model discussed in the previous section, the efficiency of the system and the operating cell temperature are calculated as a function of the heat transfer coefficient applied to the PV cell. The results are displayed in Fig. 2, when considering radiative cooling or not.

It is observed that to maintain the cell temperature near the ambient, a large heat transfer coefficient must be applied to the PV cell. These values are much larger than what can be obtained with passive convection. For values of h_c below 100 W.m^{-2}.K^{-1}, due to the extremely large values of the cell temperature, the efficiency of the TPV system reaches values close to 0. As expected, due to the large heat flux emitted by the radiator at 1500 K, thermal effect arises as a major issue in TPV. The impact of radiative cooling can be observed by comparing the results for the two cases, with and without radiative cooling. At high values of h_c, radiative cooling has no significant impact on the system efficiency, because the convective heat power is much larger than the radiative one. However, when the values of h_c get lower, radiative cooling can decrease the cell temperature and therefore increase the system efficiency [4]. However, this occurs in the regime where the efficiency has already dropped significantly from its value at 300 K. Therefore, even if radiative cooling has a positive impact on the system performances, it is not a suitable solution to reach the optimal efficiency of the TPV system.

4. Conclusions

We have investigated the performances of a TPV system composed of a spectrally selective radiator and a GaSb PV cell. Results have highlighted that even a spectrally selectivity radiator has a large emissive power that induce high cell temperatures and low efficiencies if passive cooling system are considered. Radiative cooling is not a suitable solution to reach the optimal system efficiency. Therefore, thermal management of TPV devices should be issued in the design of TPV systems.

References

[1] R. Sakakibara, V. Stelmakh, W. R. Chan, M. Ghebrebrhan, J. D. Joannopoulos, M. Soljacic, I. elanovi, Practical emitters for thermophotovoltaics: a review, *J. of Photonics for Energy* 9(3), 032713, 2019.

[2] O. Dupré, R. Vaillon, M. A. Green, *Thermal Behavior of Photovoltaic Devices: Physics and Engineering*, Springer, 2017.

[3] E. Blandre, M. Shimizu, A. Kohiyama, H. Yugami, P.-O. Chapuis, R.Vaillon, Spectrally shaping high-temperature radiators for thermophotovoltaics using Mo-HfO_2 trilayer-on-substrate structures, *Opt. Express* 26(4):4346, 2018.

[4] R. Vaillon, O. Dupré, R. B. Cal, M. Calaf, Pathways for mitigating thermal losses in solar photovoltaics, *Sci. Rep.* 8(1), 2018.

Solar Thermal Characterisation of Micro Patterned Solar Absorbers

H. Cen[1], S. Nunez-Sanchez[3], N.A. Fox[2] and M.J.Cryan[1*]
[1]Department of Electrical and Electronic Engineering, University of Bristol
[2]School of Chemistry, University of Bristol
[3]University of Vigo, Spain
*corresponding author, E-mail: m.cryan@bristol.ac.uk

Abstract

This paper presents fabrication results showing large area laser patterning of molybdenum for use as a solar thermal absorber. Measured solar absorptance results show good performance and the temperature measurements of the samples show promise for solar thermal applications.

1. Introduction

Solar energy converters based on thermal processes require the maximum incident solar energy to be absorbed and converted into heat. Ideal solar absorbers therefore need to have excellent selective surface properties, absorbing all incident electromagnetic energy whilst minimising re-radiation[1]. It has been shown through electromagnetic modelling that surface nanopatterning can dramatically alter the optical response of an interface and that it can be tailored to enhance broadband absorption across the solar spectrum[2][3]. This paper looks at 2D Molybdenum microstructures that can be achieved over large areas using low cost laser processing and measure the reflectance and subsequent temperature rise achieved using a solar simulator both in air and simulated under vacuum conditions.

2. Fabrication and Optical characterization

As shown in Table 1, 10x10mm, 0.25mm thickness molybdenum samples have been produced by single pulse laser firing with different periods (10, 20 and 30μm) and at different laser energy (20%=28.6 μJ/pulse, 30%=38.3 μJ/pulse, 40%=48.1 μJ/pulse). Figure 1 shows an SEM of the surface the molybdenum sample laser milled at 28.6 μJ/pulse with a period of 30μm. Figure 2 shows the measured absorptivity for samples with the same period but produced at different laser powers.

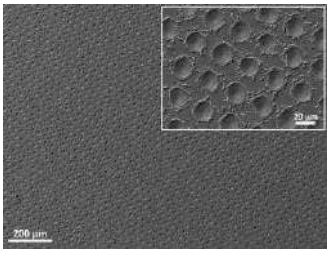


Figure 1: SEM laser patterned molybdenum produced at 20% laser power.

Table 1: Laser pulse period and laser energy used for 9 molybdenum samples

Sample Number	Pattern period [μm]	Laser energy [μJ/pulse]	Laser energy Percentage
1	10	28.6	20%
2	20	28.6	20%
3	30	28.6	20%
4	10	38.3	30%
5	20	38.3	30%
6	30	38.3	30%
7	10	48.1	40%
8	20	48.1	40%
9	30	48.1	40%

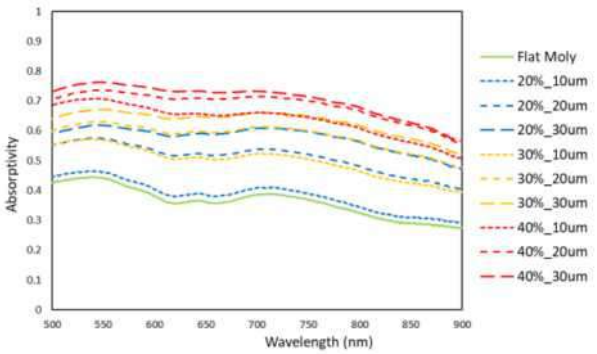


Figure 2: Experimental absorptivity of all samples

3. Thermal Measurements

Samples were illuminated using a focused solar simulator and temperature recorded over time using a thermocouple acting as the sample stage where samples were fixed on two glass slides. Figure 3 shows the temperature rise of both COMSOL modelled data and measurement for one of the samples. Figure 4 shows the measurement of the highest temperatures reached by ten different samples under 500s solar simulator illumination. The samples produced at higher laser energy (larger and deeper holes) show higher absorptivity in the visible and near IR range.

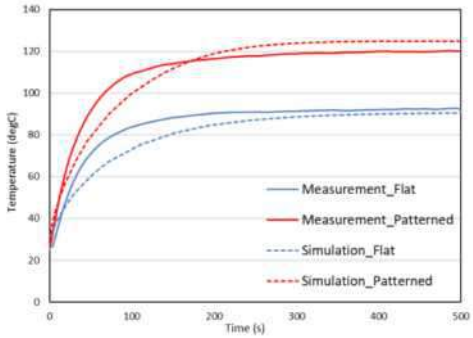


Figure 3: Simulated and measured temperature rise of 1x1cm, 0.25mm thick molybdenum square with patterning (30μm period and 40% laser energy) and without patterning under 500s solar illumination.

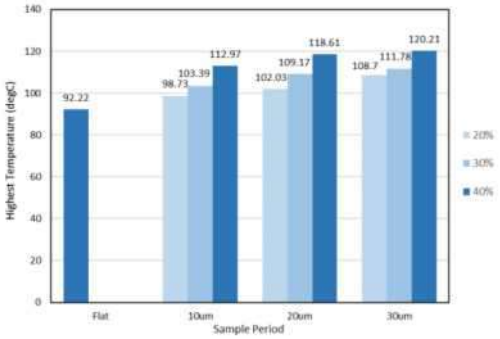


Figure 4: Measurement of the highest temperatures reached by ten different samples under 500s solar simulator illumination.

In order to minimise the thermal conduction and convection loss of the sample, we designed a vacuum device for mounting the sample as shown in Figure 5. The sample is fixed on a round quartz holder with a cut-out in the centre. The conduction loss is minimised since quartz glass is an excellent thermal insulator. A K-type bare wire thermocouple is attached to the back side of the sample and its two ends connect to two copper tube terminals. The device is pumped into vacuum through one copper tube. Figure 6 shows the comsol model for sample heating

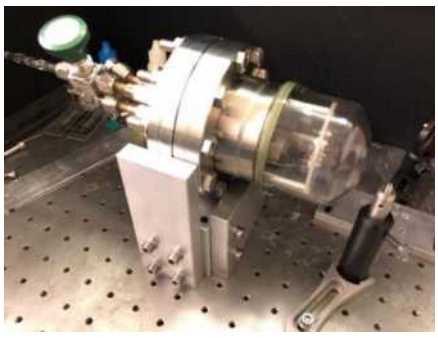


Figure 5: Vacuum device fixed on an aluminium base.

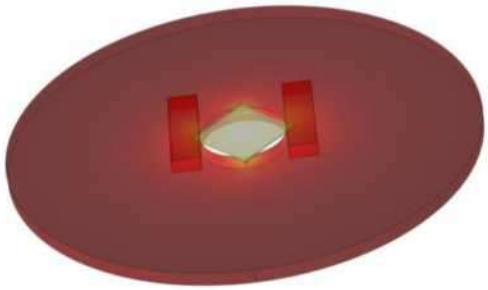


Figure 6: Quartz holder for mounting the sample.

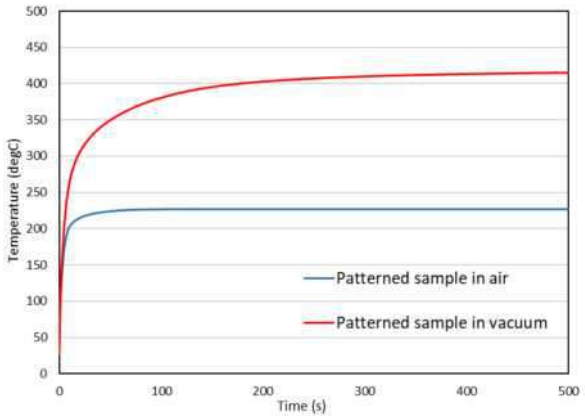


Figure 7: Simulated temperature rises of patterned molybdenum sample in air and vacuum.

Figure 7 shows the Comsol simulated temperature rises of patterned molybdenum sample in air and under vacuum conditions. It shows that the achieved temperature in vacuum is predicted to be nearly double to the temperature in air.

4. Conclusions

This paper has presented the optical absorption of micro-patterned molybdenum produced by laser etching. It is shown that this technique dramatically increases the absorptivity of molybdenum across 400-1000 nm which is ideal for solar thermal applications. Simulation results of the sample under vacuum condition shows that much higher temperatures can be achieved. We will verify these results with measurements and further increase the light intensity on the sample. This is very promising for solar thermal applications which operates at >500 degC.

5. References

[1] S. A. Kalogirou, Solar Energy Engineering Processes and Systems Second Edition. 2014.

[2] N. Ahmad, J. Stokes, and M. J. Cryan, “Solar absorbers using 1D and 2D periodic nanostructured nickel films,” J. Opt., vol. 16, no. 12, p. 125003, 2014.

[3] C.Wan, L.Chen, M.J.Cryan, “Broadband Metasurface Absorber for Solar Thermal Applications”, J. of Optics, 17, 125103, Nov 2015

Plasmon-enhanced photovoltaics, photocatalysis, and solar fuels

Optical properties of self-assembled, thin-walled nanotube TiO_2 arrays

Christin David

Madrid Institute for Advanced Studies in Nanoscience (IMDEA Nanoscience), Madrid, Spain
E-mail: christin.david@imdea.org

Abstract

Optical properties of two-dimensional arrays of hollow TiO_2 nanotubes are investigated. Their straightforward fabrication via electrochemical anodization allows precise tailoring of geometry and material properties. We calculate achievable field enhancement, including under additional charge doping occurring during fabrication, and the short circuit current for a range of configurations. For our simulations, we employ the Rigorous Coupled Wave Analysis to perform field enhancement studies of the optical response of arrays of thin-walled nanotubes relative to the bare Ti foil substrate.

1. Introduction

Two-dimensional arrays of hollow nanotubes (NTs) made of TiO_2 are a promising platform for sensing [1], spectroscopy [2, 3], nanosized test tubes in biomedicine [4] and light harvesting applications. The electrochemical growth TiO_2 nanotubes from a Ti foil allows studying self-assembled nanotube arrays [5, 6]. Annealed crystalline TiO_2 NTs show an increased doping level allowing to further improve electron transfer efficiency for bio-electrochemistry applications [3]. It was demonstrated that the additional charge carriers can yield high field enhancement in densely packed, thin-walled TiO_2 NT arrays, independent from the chemical environment [2].

We take a detailed look at the optical properties of regular TiO_2 NT arrays with an emphasis on achievable field enhancement and photocurrent gain in semiconductor substrates including additional charge carrier doping that occurs during fabrication. [2]. For our calculations, we employ the Rigorous Coupled Wave Analysis (RCWA) to perform field enhancement studies of the optical response of arrays of thin-walled nanotubes relative to the bare Ti foil substrate.

From an optical perspective, the nanotubular geometry adds directionality improving photon scattering towards a photo-active region [1]. Self-assembled nanostructures are favourable with view to their fabrication costs, in particular, in highly competitive industries such as solar cell technology. [7]

2. Discussion

The possible enhancement of reaction or transport rates due to a large surface area, see Fig. 1, strong electron confinement and short diffusion paths makes these structures highly interesting for (photo-) catalysis [8, 9, 10] and photovoltaics (PV) [11, 12, 1, 13, 14]. In addition, the high refractive index (RI) of TiO_2 makes this an interesting material for a broad range of further photonic and hybrid applications, i. e. exploiting plasmon-assisted enhancement effects by combining with metal nanoparticles [15]. These are typically used to enhance intrinsically low quantum efficiencies, e. g. in rare earth transition rates [14], and to sensitize the UV-active TiO_2 towards visible light [9]. The nanotubular geometry adds directionality to incoming light improving charge transfer towards an electrode or photon scattering towards a photo-active region [1, 13]. Self-assembled nanostructures are favourable with view to their fabrication costs, in particular, in a highly competitive industry such as solar cell technology. [7]

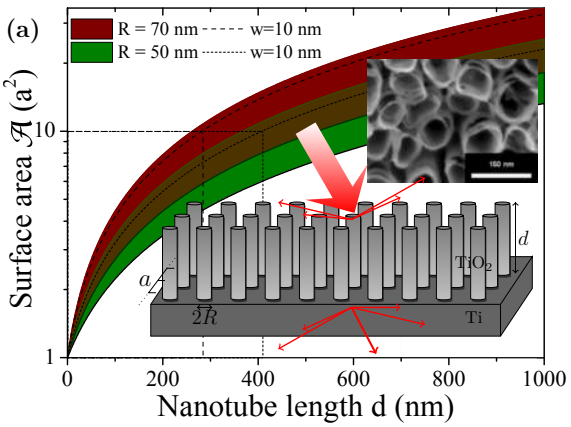


Figure 1: Increase in surface area as a function of nanotube length d for two different outer radii R and lattice period $a = 160$ nm. The shaded areas span the minimum to maximum achievable surface area from solid nanopillars (wall thickness $w = R$) to ultrathin walls $w \longrightarrow 0$, the dashed lines mark $w = 10$ nm. Insets: Illustration and SEM image of the geometry after self-assembly of hollow TiO_2 nanotubes on a Ti substrate.

3. Conclusions

Fabricated NT arrays can show a high degree of order and regularity which allows studying and optimizing their properties in direct comparison with available modeling tools which this work contributes to. While typically grown on Ti substrates or alloys, TiO_2 NTs can be produced as membranes through a lift-off process [6]. This technique allows em-

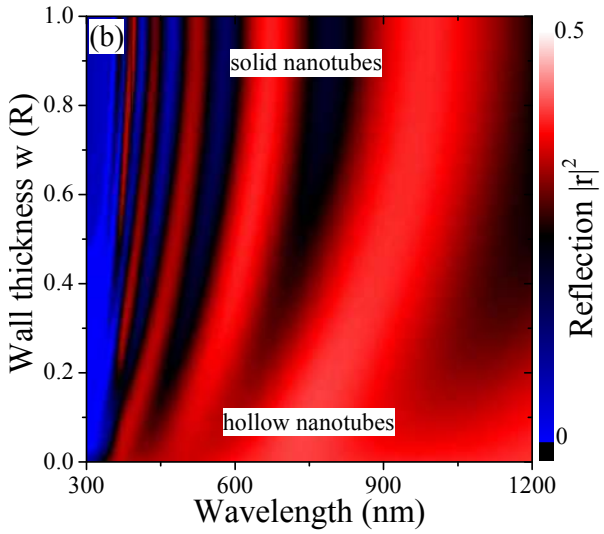


Figure 2: Studying the reduction in surface reflection of TiO_2 NT pillar arrays (with $d = 500$ nm, $a = 160$ nm, and $R = 70$ nm) as a function of the wall thickness w.

ploying them on different substrates such as Si or GaAs for solar cells. A further advantage for use in bionanotechnology, photocatalysis and related fields is the biocompatiblity of the material [3, 2], which makes an additional coating of the obtained oxide unnecessary.

References

[1] Y. Bai, I. Mora-Seró, F. De Angelis, J. Bisquert, and P. Wang, "Titanium dioxide nanomaterials for photovoltaic applications," *Chem. Rev.*, vol. 114, no. 19, pp. 10 095–10 130, 2014.

[2] I. H. Öner, C. J. Querebillo, **Christin David**, U. Gernert, C. Walter, M. Driess, S. Leimkühler, K. H. Ly, and I. M. Weidinger, "High electromagnetic field enhancement of TiO2 nanotube electrodes," *Angewandte Chemie International Edition*, vol. 57, no. 24, pp. 7225–7229, 2018.

[3] X. X. Han, C. Köhler, J. Kozuch, U. Kuhlmann, L. Paasche, A. Sivanesan, I. M. Weidinger, and P. Hildebrandt, "Potential-dependent surface-enhanced resonance raman spectroscopy at nanostructured TiO2: A case study on cytochrome b5," *Small*, vol. 9, no. 24, pp. 4175–4181, 2013.

[4] T. Rajh, N. M. Dimitrijevic, M. Bissonnette, T. Koritarov, and V. Konda, "Titanium dioxide in the service of the biomedical revolution," *Chem. Rev.*, vol. 114, no. 19, pp. 10 177–10 216, 2014.

[5] K. Lee, A. Mazare, and P. Schmuki, "One-dimensional titanium dioxide nanomaterials: Nanotubes," *Chem. Rev.*, vol. 114, no. 19, pp. 9385–9454, 2014.

[6] P. Roy, S. Berger, and P. Schmuki, "TiO2 nanotubes: Synthesis and applications," *Angewandte Chemie International Edition*, vol. 50, no. 13, pp. 2904–2939, 2011.

[7] T. A. Hamed, N. Adamovic, U. Aeberhard, D. Alonso-Alvarez, Z. Amin-Akhlaghi, M. A. der Maur, N. Beattie, N. Bednar, K. Berland, S. Birner, M. Califano, I. Capan, B. Cerne, I. Chilibon, J. P. Connolly, F. C. Juan, J. Coutinho, C. David et al., "Multiscale in modelling and validation for solar photovoltaics," *EPJ Photovoltaics*, vol. 9, p. 10, 2018.

[8] K. Awazu, M. Fujimaki, C. Rockstuhl, J. Tominaga, H. Murakami, Y. Ohki, N. Yoshida, and T. Watanabe, "A plasmonic photocatalyst consisting of silver nanoparticles embedded in titanium dioxide," *J. Am. Chem. Soc.*, vol. 130, no. 5, pp. 1676–1680, 2008.

[9] A. V. Akimov, A. J. Neukirch, and O. V. Prezhdo, "Theoretical insights into photoinduced charge transfer and catalysis at oxide interfaces," *Chem. Rev.*, vol. 113, no. 6, pp. 4496–4565, 2013.

[10] J. Schneider, M. Matsuoka, M. Takeuchi, J. Zhang, Y. Horiuchi, M. Anpo, and D. W. Bahnemann, "Understanding tio2 photocatalysis: Mechanisms and materials," *Chem. Rev.*, vol. 114, no. 19, pp. 9919–9986, 2014.

[11] E. Wang, T. P. White, and K. R. Catchpole, "Resonant enhancement of dielectric and metal nanoparticle arrays for light trapping in solar cells," *Opt. Express*, vol. 20, no. 12, pp. 13 226–13 237, 2012.

[12] S. Mubeen, J. Lee, W.-r. Lee, N. Singh, G. D. Stucky, and M. Moskovits, "On the plasmonic photovoltaic," *ACS Nano*, vol. 8, no. 6, pp. 6066–6073, 2014.

[13] M. Kapilashrami, Y. Zhang, Y.-S. Liu, A. Hagfeldt, and J. Guo, "Probing the optical property and electronic structure of tio2 nanomaterials for renewable energy applications," *Chem. Rev.*, vol. 114, no. 19, pp. 9662–9707, 2014.

[14] H. Lakhotiya, A. Nazir, S. P. Madsen, J. Christiansen, E. Eriksen, J. Vester-Petersen, S. R. Johannsen, B. R. Jeppesen, P. Balling, A. N. Larsen, and B. Julsgaard, "Plasmonically enhanced upconversion of 1500 nm light via trivalent er in a TiO2 matrix," *Applied Physics Letters*, vol. 109, no. 26, p. 263102, 2016.

[15] H. P. Paudel and M. N. Leuenberger, "Light-controlled plasmon switching using hybrid metal-semiconductor nanostructures," *Nano Lett.*, 2012.

Plasmon enhancement of energy transfer from single up-converting nanocrystals to P3HT

Justyna Grzelak[1,3], Aneta Prymaczek[1], Maciej Ćwierzona[1], Marcin Nyk[2], Dawid Piątkowski[1], Sebastian Maćkowski[1,3],

[1] Institute of Physics, Faculty of Physics, Astronomy and Informatics, Nicolaus Copernicus University, Torun, Poland
[2] Institute of Physical and Theoretical Chemistry, Wroclaw University of Technology, Wroclaw, Poland
[3] Baltic Institute of Technology, Gdynia, Poland

*corresponding author, E-mail: justynag@fizyka.umk.pl

Abstract

We report on the possibility of enhancing the energy transfer from colloidal single up-converting $NaYF_4$ nanocrystals doped with rare-earth ions to poly(3-hexylthiophene) (P3HT) polymer by plasmon excitation in a single silver nanowire. Based on such an approach we want to demonstrate how to sensitize organic solar cells to the infrared optical spectrum.

1. Introduction

Up-converting nanomaterials are promising candidates for sensitizing solar cells to infrared radiation [1]. Rare-earth doped materials, due to up-conversion process, absorb infrared radiation and convert into visible. It has been demonstrated that the presence of up-converting nanoparticles increases the efficiency of photovoltaic devices [2]. Additionally, relatively low efficiently of the up-conversion process can be improved by plasmonic excitation localized within metallic nanoparticles [3]. For enhancing the infrared optical response of organic polymer we use a single silver nanowire.

2. Materials & methods

Hybrid nanostructure studied in this work contains a single silver nanowire surrounded with Er and Yb doped 20-nm-large up-converting nanocrystals located in its vicinity. On top of such a structure a drop of P3HT polymer was applied in a controlled manner.

Up-converted emission of nanocrystals excited at 980 nm (Fig. 1, black line) spectrally overlaps with the absorption of P3HT (Fig. 1, blue line), and with the broad extinction spectrum of silver nanowires (Fig. 1, green line).

To examine the optical properties of the hybrid nanostructure, we used a confocal up-conversion fluorescence microscope with a sample mounted on a piezoelectric stage (P-517.3CL, Physik Instrumente). Sample was excited at 980 nm with asingle-mode continuous-wave/pulsed fiber laser (SpectraLaser) and illuminated through an oil-immersion objective (NA = 1.49), which was also used for collecting fluorescence signal. The special resolution of the microscope was 450 nm. Signal detection was carried out by a sensitive detector (SPCM-16, PerkinElmer) operating in accordance with the translation of the piezoelectric stage. Emission of the nanocrystals was extracted using appropriate bandpass filters (540/40 nm, 650/30 nm, Chroma), while the emergence of the P3HT fluorescence was probed with a 720/10 nm bandpass filter.

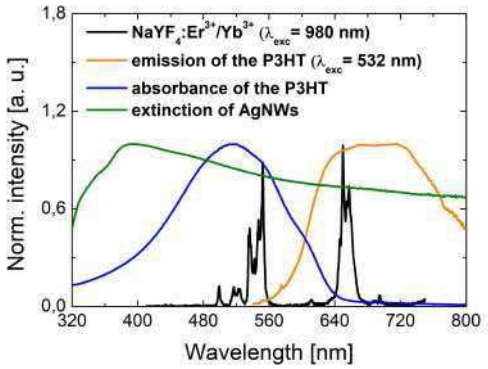


Fig. 1 Comparison of optical spectra of: $NaYF_4:Er^{3+}/Yb^{3+}$ nanocrystals (black line), emission of P3HT polymer for excitation 532 nm (orange line), absorbance of the P3HT polymer (blue line) and excitation of AgNWs (green line).

3. Results

A unique micro-deposition system allowed to place a glass capillary with P3HT polymer over the selected single nanowire, as shown in Fig. 2(a)-(b). To control the volume of P3HT polymer, the tip of capillary was elongated and had an outlet with a diameter of approximately 500 nm. Backscattered light intensity map of the selected single nanowire is shown in Fig. 2(c).

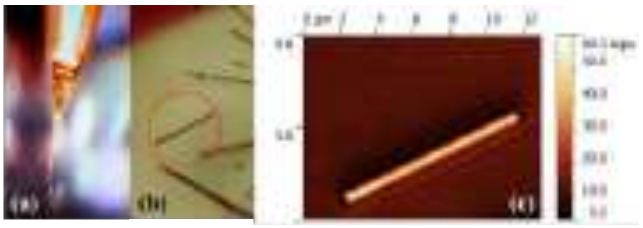


Fig. 2 P3HT polymer solution in a capillary (a), picture of the selected single nanowire (b), the silver nanowire imaged using backscattered laser light (c).

By probing both steady-state and time-resolved properties of individual up-converting nanocrystals excited with infra-red laser and located in vicinity of single nanowire, before (Fig. 3(a)) and after (Fig. 3(b)) drop-casting P3HT polymer, we demonstrated that upon up-conversion to the visible spectral range the energy is not only efficiently transferred from the nanocrystals to P3HT polymer, but this effect is also enhanced by the plasmon excitations in the single silver nanowire.

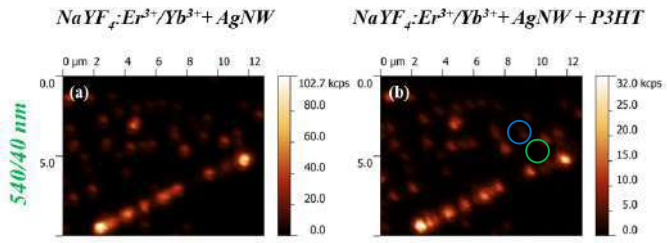


Fig. 3 Maps of luminescence intensities for the hybrid nanostructures: $NaYF_4:Er^{3+}/Yb^{3+}$ + AgNW and $NaYF_4:Er^{3+}/Yb^{3+}$ + AgNW + P3HT obtained for 980 nm excitation, (a)-(b) – green emission of nanocrystals (540/40 nm).

Time-resolved measurement shows significant shortening of the luminescence lifetime of selected nanocrystal (green circle, Fig. 3) in the vicinity of the single nanowire and far from nanowire (blue circle, Fig. 3) after drop-casting P3HT polymer, what is presented in Fig. 4.

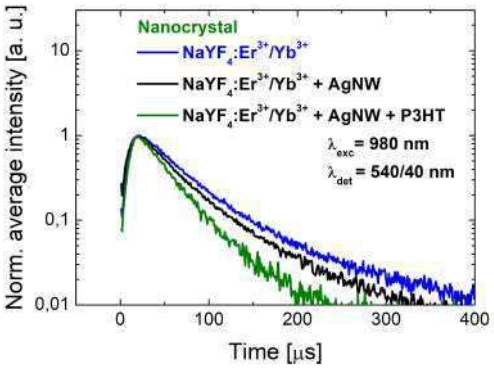


Fig. 4 Normalized luminescence decays for 540 nm emission for the single placed close to the nanowire (green) and for the reference (blue). Black line – emission transient measured for the same nanocrystals as green before covering the sample with a drop of P3HT polymer.

4. Conclusions

The obtained results prove that by proper fabrication of a hybrid nanostructure, where the interaction can be optimized, it is possible to sensitize the conductive polymers to the infrared radiation. These results are important for improving the spectral response of organic bulk heterojunction solar cells towards infrared region.

Acknowledgements

This work was supported by projects 2017/26/E/ST3/00209, 2017/27/B/ST3/02457 and 2016/21/B/ST3/02276 from the National Science Center and by the 3/DOT/2016 project from the City of Gdynia.

References

[1] N. Hartmann, D. Piatkowski, R. Ciesielski, S. Mackowski, A. Hartschuh, „Radiation Channels Close to a Plasmonic Nanowire Visualized by Back Focal Plane Imaging", *ACS Nano*, t. 7, nr 11, s. 10257–10262, 2013.

[2] V. Fthenakis, W.G.J.H. van Sark, A. Meijerink, R.E.I. Schropp, *Solar spectrum conversion for photovoltaics using nanoparticles. Third generation photovoltaics.* Intech, 2012.

[3] D. Piatkowski, N. Hartmann, T. Macabelli, M. Nyk, S. Mackowski, A. Hartschuh, „Silver nanowires as receiving-radiating nanoantennas in plasmon-enhanced up-conversion processes", *Nanoscale*, t. 7, nr 4, s. 1479–1484, 2015.

Designed Au-TiO_2 Nanoreactors for Photocatalytic Transformations in Living Cells

Ana Sousa-Castillo[1], Miguel Comesaña-Hermo[1,2], Moisés Pérez-Lorenzo[1], Miguel A. Correa-Duarte[1]

[1]Department of Physical Chemistry, Center for Biomedical Research (CINBIO), Southern Galicia Institute of Health Research (IISGS), and Biomedical Research Networking Center for Mental Health (CIBERSAM), Universidade de Vigo, 36310 Vigo, Spain

[2]Univ Paris Diderot, Sorbonne Paris Cité, ITODYS, UMR CNRS 7086, 15 rue J-A de Baïf, 75013, Paris, France

*corresponding author, E-mail: ana.sousa@uvigo.es

Abstract

We describe the fabrication of TiO_2-plasmonic hybrid nanocapsules with photocatalytic features. These hybrid structures hold a number of outstanding properties that make them valuable photocatalysts in biological media: (i) they can be excited with NIR radiation given the plasmon-induced activation of the semiconductor; (ii) the mesoporous nature of the silica shell surrounding the active species endows them with size selective capabilities and (iii) the production of ROS is limited to the inner space within the capsules, avoiding therefore any damage to the surrounding biological tissues.

1. Introduction

Titanium dioxide (TiO_2) stands out among the inorganic semiconductors due to its high abundance, low cost, chemical stability and unique photochemical and photoelectrochemical properties.1 Actually, the development of TiO_2-based photocatalysts has recently experienced an important growth, expanding the applicability of these materials in fields such as the production of renewable fuels [1], water remediation [2], or the formation of self-cleaning surfaces [3], among others. The major drawback limiting the applicability of TiO_2 in a biological context comes from its wide bandgap (3.2 eV), feature that restricts the impressive characteristics of this material to the ultraviolet (UV) segment of the solar radiation spectrum. Along these lines, the use of highly energetic photons is known to produce adverse effects to biological tissues due to the formation of reactive oxygen species (ROS) such as $O2^{\cdot-}$, H_2O_2 or $HO^{\cdot}$, small molecules that produce oxidative stress-related phenomena like lipid peroxidation, enzymatic deactivation or DNA damage that may disrupt important intracellular processes and eventually lead to cell apoptosis [4,5]. Thus, the development of TiO_2-based nanomaterials capable of holding a high photocatalytic activities in biological environments while presenting low cytotoxicity under irradiation remains a task of paramount importance. In that sense, near-infrared (NIR) light-responsive systems are especially attractive from a biological point of view, owing to their deep penetration capabilities. In this manner, the use of anisotropic plasmonic nanoparticles as photosensitizing agents would ensure that the main absorption contribution of the hybrid is kept in the first biological transparency window (650-950 nm) of the NIR range, where low scattering and energy absorption provide with optimal tissue transmission and maximum radiation penetration [6]. In this vein, the development of TiO_2/plasmonic hybrids that could provide controlled responses in real biological settings would represent a very significant scientific advance. Moreover, and in opposition to those studies in which TiO_2 is combined with upconverting (UC) materials [7,8], the aforementioned composites do not lead to the formation of UV photons throughout the photosensitization process, thus excluding any possible cytotoxicity issues.

2. Discussion

The work is focused in the development of a novel nanoreactor capable of overcoming the limitations that hamper the study and application of TiO_2-based photocatalysts in a biological context. In this manner, hollow mesoporous silica nanocapsules whose internal walls have been functionalized with TiO_2 nanoparticles and Au nanorods (Au-TiO_2NCs) have been synthesized (figure 1), creating a novel architecture that presents a number of characteristics that make it an ideal candidate for the applications mentioned above. The morphology of the hybrid nanostructure and the chemical composition of its outermost shell are two characteristics of major importance for the correct design of a final composite with the desired properties and functionalities. In a first set of experiments, it has been demonstrated the ability of these composites to selectively target specific molecules depending on their size. The different degradation obtained show that molecular diffusion through the mesoporous silica shell is essential for an efficient degradation of the chosen molecule.

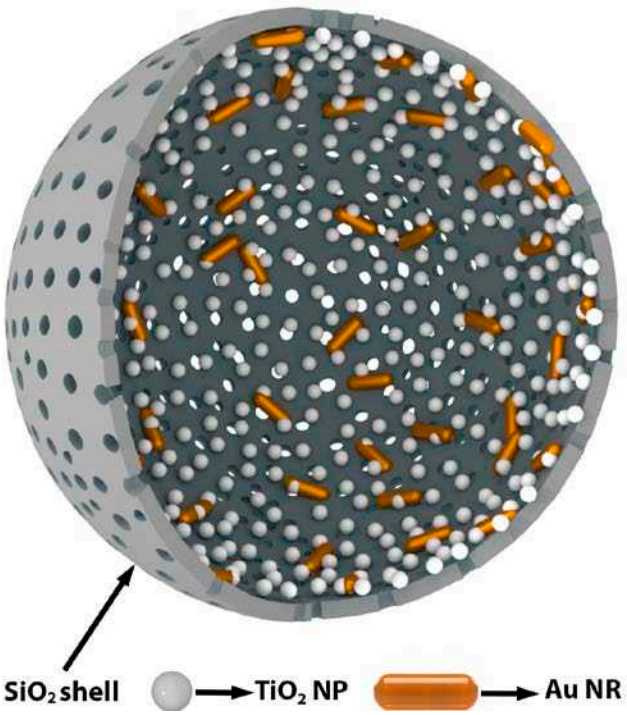


Figure 1. Illustration of Au-TiO_2NCs

On the other hand, it has been studied the photocatalytic activity of the Au-TiO_2NCs under NIR irradiation. This experiment also excludes the direct photosensitization of TiO_2 by RhB as a possible photodegradation mechanism under visible light that could interfere with the plasmon induced photosensitization of the semiconductor.

A preliminary study on the photocatalytic features of the Au-TiO_2NCs in a biological context has been performed. In order to do this the intracellular degradation of RhB in Vero cell culture and in the presence of the hybrid capsules has been studied under irradiation with a NIR laser (785 nm). In this manner, we have observed RhB molecules that had diffused within the internal cavity of the nanocapsules can be degraded given their interaction with the ROS created during the photoexcitation process.

3. Conclusions

In summary, we have successfully fabricated a novel TiO_2-plasmonic hybrid nanocapsule where the porosity of silica shell endows this nanoreactor with an unprecedented control over the reactivity of the photoactive components while providing them with an improved stability. Moreover, preliminary results show the ability of these nanohybrids to remain catalytically active in biological environments. Interestingly, no sign of cell degradation could be observed for short irradiation times, highlighting the possible suitability of this material as a valuable theranostic agent.

Acknowledgements

This work has received financial support from Spanish grants (SAF2016-76689-R, CTQ2017-84767-P, CTM2014-58481-R, CTM2017-84050-R and Orfeo-Cinqa network CTQ2016-81797-REDC), the Consellería de Cultura, Educación e Ordenación Universitaria (2015-CP082, ED431C/2017119 and Centro Singular de Investigación de Galicia accreditation 2016–2019, ED431G/09), the European Union (European Regional Development Fund-ERDF corresponding to the multiannual financial framework 2014–2020), and the European Research Council (Advanced Grant No. 340055).

References

[1] A. Fujishima, X. Zhang, D. A. Tryk, TiO_2 Photocatalysis and Related Surface, *Phenomena. Surf. Sci. Rep.*, 63, 515–582, 2008.

[2] C. Chen, W. Ma, J. Zhao, Semiconductor-Mediated Photodegradation of Pollutants under Visible-Light Irradiation. *Chem. Soc. Rev.*, *39*, 4206–4219 2010.

[3] S. Banerjee, D.D. Dionysiou, S. C. Pillai, Self-Cleaning Applications of TiO_2 by Photo-Induced Hydrophilicity and Photocatalysis. *Appl. Catal. B Environ., 176–177*, 396–428, 2015.

[4] C. M. Sayes, R. Wahi, P. A. Kurian, Y. Liu, J. L. West, K. D. Ausman, D. B. Warheit, V. L. Colvin, Correlating Nanoscale Titania Structure with Toxicity: A Cytotoxicity and Inflammatory Response Study with Human Dermal Fibroblasts and Human Lung Epithelial Cells. *Toxicol. Sci., 92*, 174–185. 2006.

[5] P. P. Fu, Q. Xia, H.-M. Hwang, P. C. Ray, H. Yu, Mechanisms of Nanotoxicity: Generation of Reactive Oxygen Species. *J. Food Drug Anal. 22*, 64–75, 2014.

[6] M.-F. Tsai, S-H. G Chang, F.-Y. Cheng, V. Shanmugam, Y.-S. Cheng, C.-H. Su, C.-S. Yeh, Au Nanorod Design as Light-Absorber in the First and Second Biological Near-Infrared Windows for in Vivo Photothermal Therapy. *ACS Nano*, 7, 5330–5342, 2013.

[7] S. S. Lucky, N. M. Idris, Z. Li, K. Huang, K. C. Soo, Y. Zhang, Titania Coated Upconversion Nanoparticles for Near-Infrared Light Triggered Photodynamic Therapy. *ACS Nano*, *9*, 191–205, 2015.

[8] S. Wu, J. P. Blinco, C. Barner-Kowollik, Near-Infrared Photoinduced Reactions Assisted by Upconverting Nanoparticles. *Chem. Eur. J., 23*, 1–9, 2017.

Plasmonics and nano-optics

Angle-Insensitive Mid-IR Spectrum Filter Using Slit Nanoresonator Structure

Evan M. Smith[1,2], Ivan Avrutsky[3], Shiva Vangala[2], Justin W. Cleary[2], Josh R. Hendrickson[2]

[1]KBRwyle, Beavercreek, Ohio 45440, USA
[2]Air Force Research Laboratory, Sensors Directorate, Wright-Patterson AFB, OH 45433, USA
[3]Wayne State University, Detroit, MI 48202, USA
*corresponding author, E-mail: evan.smith.31.ctr@us.af.mil

Abstract

Transmission characteristics of a mid-infrared spectral filter are presented for a device based on metal films with resonant nano-cavities filled with high-index dielectrics. These resonances resemble those in Fabry-Perot resonators and can yield high transmission with a narrow bandwidth. Importantly, the cavity slit resonance is decoupled from the plasmonic grating resonance, resulting in angular insensitivity for polarized light up to 60 degree incidence.

1. Introduction

Optical transmission filters operating in the mid-infrared are useful for hyperspectral imaging, remote chemical sensing, infrared countermeasures, and high sensitivity detectors. A desirable filter would be easy to integrate with existing photonic devices and offer a wide field of view, requiring angular insensitivity. Sharp resonances have been achieved through metal-dielectric layered coatings, as well as structures involving coupling to surface plasmon-polaritons [1]. While these structures provide great flexibility in designing the transmission characteristics, they can be difficult to integrate with photonic devices and are inherently angle-dependent. Metallic grating-based slit structures show Fabry-Perot resonances associated with modes propagating in the film voids in the direction orthogonal to the plane of the film [2], which can be angle-independent if no surface excitations are involved [3]. If these gratings are designed with a sufficiently small period, the angle-dependent grating resonance will be decoupled from the slit resonance, resulting in an angular independent transmission filter. Such a filter has been proposed for the visible spectrum which has transmission peaks narrow enough to act as a color filter for LCD displays [4].

Here we investigate a one-dimensional array of metallic nano-cavities optimized for mid-infrared transmission. The cavities are filled with a high-index medium to enhance light confinement and keep the thickness small. The cavities can be arranged periodically to cover a large area, although the periodicity is decoupled from the slit resonance; each individual cavity is a filter of its own. For TM polarized light, these filters have been configured to produce a sharp resonance around 8.6 μm and are angle independent up to 60°. The angular independence is desirable for display and imaging applications requiring a wide field of view.

2. Design and Fabrication

The structure consists of a metal grating whose cavities are filled with a high index material (see Figure 1). The substrate is low index and highly transparent in the mid-IR and long wave-IR. The cavities must be filled completely, and the surface must have a small roughness to achieve a high Q factor of the resonance. This structure is polarization-dependent; TM polarized light will resonate in the dielectric-filled cavity. This acts like a plasmonic gap resonance, with the system being the subwavelength dielectric core between metallic reflectors. The modal index, determined by the optical constants of the materials, will affect the resonance position. Optical losses in the metal will limit the resonant transmission. However, the origin of these resonances is not plasmonic in nature- in the case of a perfect conductor the plasmonic gap mode turns into a transmission line mode in a slit.

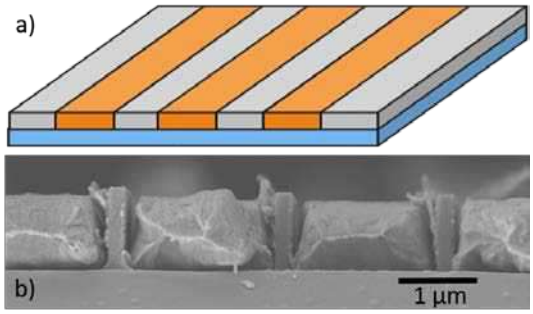


Figure 1. (a) Diagram of the device structure, (b) SEM cross sectional image taken after etch and metal evaporation.

The structure has been designed for mid-IR resonance and is 1 μm thick with a slit width of 0.5 μm and a periodicity of 2 μm. Barium fluoride is the chosen substrate, which is 90% transparent up to 12 μm and has an index of n=1.4. The metal chosen is silver and the dielectric is germanium, which has an index of about 4.

The sequence of processing is actually the opposite of the prior explanation; dielectric gratings are fabricated first and subsequently filled in with metal. Germanium is deposited onto a barium fluoride substrate, and is patterned with the grating structure via deep-UV photolithography. An anisotropic reactive ion etch (RIE) leaves only the germanium grating with nearly vertical sidewalls. Silver is deposited by e-beam evaporation in a tilted configuration to fill in the space between the dielectric gratings. Figure 1b shows a cross-sectional scanning electron microscope (SEM) image of the fabricated grating structure.

The transmission spectra for the filters were measured using a Bruker FTIR with a reflecting microscope objective to narrow the incident beam to a small section of the patterned material. Consequently, the incident light on the sample is not parallel but has a light cone of about 24° which excludes normal incidence. The sample is tilted with respect to normal incidence of this light cone, and for simplicity the sample tilt angles are reported. Transmittance is reported into the barium fluoride substrate; therefore a bare BaF_2 substrate is used as the reference material.

3. Results

Figure 2 shows results for the proposed design. Simulations locate the fundamental TM mode at 8.6μm, while the second harmonic is much smaller around 4.3 μm. Hence, the fundamental mode is largely isolated, providing a clean transmission line. There is little change in the transmitted intensity and resonant wavelength between light at normal incidence up to 60° incidence.

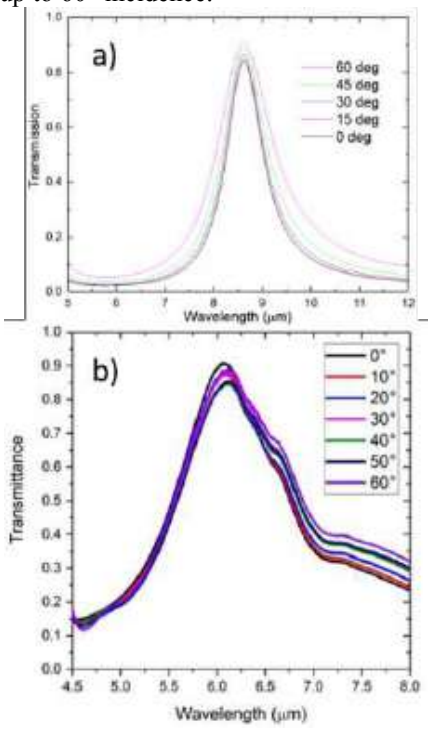


Figure 2: (a) Simulated and (b) measured transmission spectra for filters with TM polarized light incident at various angles.

Experimental data show a resonance with over 90% transmittance which is angle invariant up to 60° angle of incidence. The resonance deviates from the simulation in a large blue shift down to 6.1 μm. The full width half maximum of this resonance is extrapolated to be approximately 0.7 μm, similar to the simulation results; however the apparent transmission width is artificially higher due to overlapping resonances at 6.6 μm, which appears as a shoulder on the fundamental peak, and a broad feature around 7.3 μm. The change in resonant wavelength, as well as the additional resonant peaks, is likely caused by insufficient filling of the gaps between the germanium pillars by the deposited silver. The SEM image of the structure in Figure 1b shows that the metal is not completely rectangular but rather slightly trapezoidal, which produces small voids between the metal and dielectric. The dielectric therefore is no longer simply germanium but rather an effective medium of germanium and air, which has a reduced permittivity. Furthermore, the size of this air gap is inconsistent across multiple lines of the grating, producing an array of slightly different effective media. Altering the simulated structure to include an air gap of only 10 nm on either side of the metal produces a 1 μm blue-shift, while an air gap of 50 nm on either side produces a blue-shift of almost 3 μm from the fundamental 8.6 μm resonance. Refining the fabrication process to reduce the air gap and increase uniformity should result in transmission resonances closer to the design.

4. Conclusions

The experimental results show angular insensitive narrow band transmission similar to that suggested by the simulation. Multiple resonances were observed outside the reported spectral range for both TM and TE polarizations which also closely resembles the simulation results. Importantly, the location of the fundamental resonance does not shift with increased angle of incidence, and the resonance remains strong. Transmission characteristics should improve with a more consistent fabrication process that addresses the air gap between the metal and dielectric.

Acknowledgements

We wish to acknowledge support from the Air Force Office of Scientific Research (Program Manager Dr. Gernot Pomrenke) under award number FA9550-19RYCOR048.

References

[1] T.W. Ebbesen, H.J. Lezec, H.F. Ghaemi, T. Thio, P.A. Wolff, Extraordinary optical transmission through sub-wavelength hole arrays, *Nature* 391, 667-669 (1998).

[2] S. Astilean, Ph Lalanne, M. Palamaru, Light transmission through metallic channels much smaller than the wavelength, *Opt. Comm.* 175: 265-273 (2000).

[3] J. Bravo-Abad, L. Martin-Moreno, F.J. Garcia-Vidal, Transmission properties of a single metallic slit: From the subwavelength regime to the geometrical-optics limit, *Phys. Rev. E* 12: 1221-1227 (2006).

[4] J. Zhou and L.J. Guo, Achieving angle-insensitive spectrum filter with the slit nanoresonator array structure, *J. Nanophotonics* 9: 093795 (2014).

Coupling of Gap Plasmon and Lattice Plasmon Resonances in Metal-Dielectric-Metal Gratings

Ricky Gibson[1,2], Joshua R. Hendrickson[2], Shivashankar Vangala[2], Dennis E. Walker Jr.[2]

[1]University of Dayton Research Institute, Dayton, Ohio, United States
[2]Air Force Research Laboratory, Sensors Directorate, Wright-Patterson AFB, Ohio, United States
*corresponding author, E-mail: rgibson1@udayton.edu

Abstract

We investigate, both experimentally and with computational modeling, the coupling of gap plasmon modes and lattice plasmon modes in metal-dielectric-metal structures in the mid-wave infrared. Coupling between these modes is observed due to the asymmetric Fano-like lineshape at the resonant crossings both in finite-difference time-domain simulations and angle dependent spectra.

1. Introduction

Metal-dielectric-metal (MDM) structures have been developed for enhancement of single emitters [1,2] and for perfect absorbers for sensing [3] utilizing the gap plasmon mode. Recently, by integrating epsilon-near-zero (ENZ) films a flat-top, wideband perfect absorber has been demonstrated [4] as well as strong coupling between the gap plasmon mode and the ENZ mode [5]. The lattice plasmon resonance has been investigated in 1D nanogratings recently for the possibilities of light emission modification [6]. Lattice plasmon resonances have also been utilized in plasmonic all-optical modulation [7]. In this work the coupling between the lattice plasmon mode and the gap plasmon mode of a MDM structure is investigated in the mid-wave infrared (MWIR).

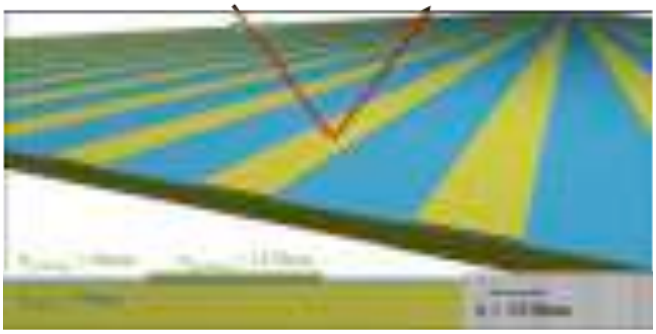


Figure 1: (Top) Diagram of TM poloarized light on MDM grating structure. (Bottom Left) Cross-section of MDM structure and (Bottom Right) plan-view SEM image of fabricated structure, 10,000X.

2. Modeling, Fabrication, and Measurement

The nominal design of the MDM structure consists of a gold ground plane, a 50nm SiO_2 dielectric spacer layer, and a gold grating with width (period) of 1270nm (3330nm) and a height of 60nm as depicted in Fig. 1.

2.1. Computational Modeling

The MDM structure is modeled using two-dimensional finite-difference time-domain (FDTD) technique implemented in a commercial software package (Lumerical FDTD). A mesh override in the dielectric region of the structure is used to achieve 5nm (10nm) meshing in directions parallel (orthogonal) to the surface normal of the structure. The broadband fixed angle source technique (BFAST) and corresponding boundary conditions are used requiring only a parameter sweep over the angle of incidence, θ, with transverse magnetic (TM) polarization. Permittivities built-in the software are used for the materials in the structure. The dispersion of the lattice plasmon and gap plasmon modes as modeled are shown in Fig. 2 with the gap plasmon displaying a small angle dependence while the lattice plasmon mode shifts from $\lambda \sim 3.3\mu m$ at $\theta = 0°$ to $\lambda \sim 5.9\mu m$ at $\theta = 60°$. The coupling between the modes occurs at $\lambda \sim 5.5\mu m$ at $\theta \sim 40°$.

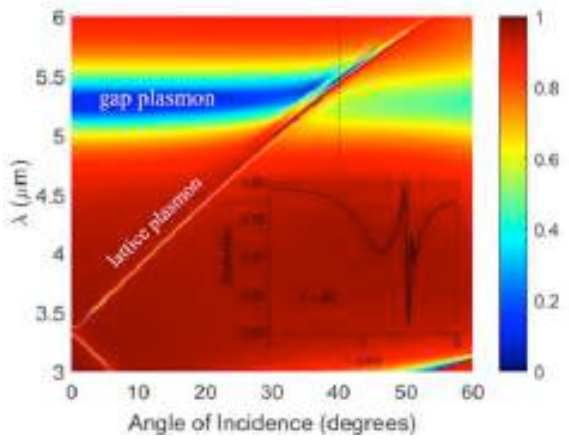


Figure 2: Simulated dispersion profile of the gap and lattice plasmon resonance of the MDM structure. (Inset) Spectral profile at the resonant crossing.

2.2. Sample Fabrication

The 380nm gold ground plane with 20nm titanium for adhesion is deposited by electron beam deposition on a silicon wafer. Subsequently PECVD is used to deposit the SiO_2 dielectric spacer layer. Using a standard lift-off technique, electron beam lithography (EBL), and electron beam deposition the 8x8mm metallic grating structure was fabricated. The EBL of a pattern this size required stitching of 500x500μm patterned regions. A scanning electron microscope (SEM) image in Fig. 1 bottom right shows a plan-view of a fabricated structure at 10kX magnification.

2.3. Experimental Measurements

Spectral scans at a constant angle of incidence as well as angle scans at a constant wavelength were done using a dual-angle goniometer and a tunable quantum cascade laser (QCL) module housing four QCLs (Daylight Solutions MIRCat). The wavelength range covered by this module is 3.96 to 5.96μm. The module is pulsed at a 100kHz frequency with 500ns pulses. Detection of the specular reflection from the sample is with a HgCdTe detector and a high-frequency lock-in amplifier (Zurich Instruments UHFLI). Sample spectra are normalized by a protected gold mirror. Normal incidence spectra are collected with a FTIR microscope (Bruker Vertex 80v and Hyperion microscope).

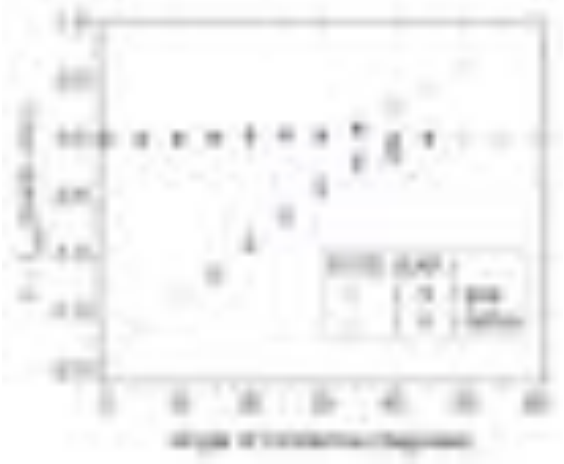


Figure 3: Simulated (solid) and experimental (open) spectral resonance locations of MDM structure relative to the gap plasmon resonance.

3. Discussion

Both computational modeling and experimental measurements display the resonant crossing of the lattice plasmon and gap plasmon modes. Due to fabrication imperfections the resonant wavelengths are about 0.4μm off. However, if we look at the spectral positions of the lattice plasmon relative to the gap plasmon mode, Fig. 3, the observed behavior is in good agreement for simulation and experiment. Both show resonant crossing between 35° and 40°, minimal gap plasmon angular dependence, comparable lattice plasmon dispersion, and exhibit Fano-like lineshapes at the resonant crossing. The role additional parameters play in controlling the coupling between these resonances will be discussed. This will include the dielectric complex permittivity, grating height, and role of a dielectric superstrate. The resonant coupling between the gap and lattice plasmon could have applications in emission enhancement and sensing techniques.

4. Conclusions

Resonant crossing and asymmetric Fano-like lineshapes due to the coupling of the gap plasmon and lattice plasmon resonances of the MDM structure are observed both in FDTD simulations and experimentally.

Acknowledgements

This work was supported by the Air Force Office of Scientific Research (Program Manager Dr. Gernot Pomrenke) under award number 15RYCOR159.

References

[1] Y. Luo, G. D. Shepard, J. V. Ardelean, D. A. Rhodes, B. Kim, K. Barmak, J. C. Hone, S. Strauf, Deterministic coupling of site-controlled quantum emitters in monolayer WSe_2 to plasmonic nanocavities, *Nature Nanotech.*, 13.12: 1137-1142, 2018.

[2] W. Wang, X. Yang, T. S. Luk, J. Gao, Enhanced Spontaneous Emission with metamaterial perfect absorbers, *Appl. Phys. Lett.*, 114.2: 021103, 2019.

[3] N. Liu, M. Mesch, T. Weiss, M. Hentschel, H. Giessen. Infrared perfect absorber and its application as plasmonic Sensor, *Nano Lett.,* 10.7: 2342-2348, 2010.

[4] J. R. Hendrickson, S. Vangala, C. K. Dass, R. Gibson, J. Goldsmith, K. Leedy, D. E. Walker, J. W. Cleary, W. Kim, J. Guo, Coupling of epsilon-near-zero mode to gap plasmon mode for flat-top wideband perfect light-absorption, *ACS Phot.*, 5.3: 776-781, 2018.

[5] J. R. Hendrickson, S. Vangala, C. K. Dass, R. Gibson, K. Leedy, D. E. Walker, J. W. Cleary, T. S. Luk, J. Guo, Experimental observation of strong coupling between an epsilon-near-zero mode in a deep subwavelength nanofilm and a gap plasmon mode, *arXiv*, 1801.03139: 2018.

[6] Y. Hua, A. K. Fumani, and T. W. Odom, Tunable lattice plasmon resonances in 1D nanogratings, *ACS Phot.*, Article ASAP 10.1021/acsphotonics.8b01541: 2019.

[7] M. Taghinejad, H. Taghinejad, Z. Xu, Y. Liu, S. P. Rodrigues, K.-T. Lee, T. Lian, A. Adibi, W. Cai, Hot-Electron-Assisted Femtosecond All-Optical Modulation in Plasmonics, *Adv. Mat.* 30.9: 1704915, 2018.

EIT-like Effect Induced by Hybrid State of Tamm and Localized Plasmon-Polaritons in the region of Infrared

Fusheng Deng [1,*], Lijuan Dong [1], Yanhong Liu [1], Lixiang Liu [1] and Yunlong Shi [1]

[1] Shanxi Provincial Key Laboratory of Electromagnetic Functional Materials for Microstructure, Shanxi Datong University, Datong, China

*corresponding author, E-mail:360476744@qq.com

Abstract

We investigate two kinds of electromagnetically-induced-transparency-like (EIT-like) effect induced by hybrid state of Tamm and localized Plasmon-Polaritons in the region of infrared. The EIT-like effects are corresponding to two mechanism, which induced by near-field coupling and standing-wave-field coupling, respectively.

Keywords—Plasmonics, Electromagnetically induced transparency, metamaterials

1. Introduction

Electromagnetically induced transparency (EIT) is a quantum coherence effect observed in three-level atomic systems in which a beam of light can find its way through the medium with almost no absorption [1]. Recently, some studies have shown that the EIT-like effect can be achieved using classical structures, such as waveguide system [2], multi-layer fish scales [3], coupled metal-stripe antennas [4], and planar metamaterials [5]. In those structures, EIT-like effect arises from the coupling effects in the near field interaction between "bright" and "dark" states. The EIT-like effect as a novel way of optical quantum control has a profound influence on the field of optics. More interestingly, in 2012, R¨ohlsberger et al. proposed a new mechanism to realize an EIT-like effect by using two ensembles of identical two-level nuclei embedded in a resonant cavity [6].

In this scheme, the EIT-like effect is induced by coupling between the bright and dark nuclei via standing wave field in a cavity. Above all, EIT-like effect can be generated based on the near-field coupling or standing-wave-field coupling. Theoretical and experimental studies on these two kinds of EIT-like phenomena have been done in microwave, terahertz, as well as infrared spectra. For example, very recently, the EIT-like effect induced by standing wave field in cavity has been experimentally demonstrated in microwave region [7].

In this work, two different EIT-like effects induced by hybrid state of Tamm Plasmon-Polaritons (TPPs) and LPPs in the region of infrared are investigated, simultaneously. Here, we use metal nanowire pairs that support Localized Plasmon-Polaritons(LPPs) as two levels "atoms", which can couple to TPPs field. Interestingly, the hybrid state of TPPs and LPPs can induce EIT-like effect, which strongly dependent on the sequence of the "dark atom" and "bright atom". In addition, we obtain the other EIT-like effect induced by near-field interaction.

2. Two kinds of EIT-like effect

2.1. EIT-like effect induced by standing -wave-field coupling

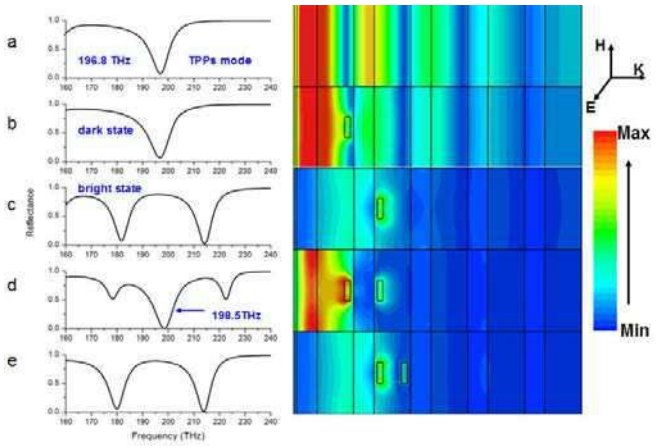


Fig. 1. Simulated reflectance spectra and electric field distribution for EIT-like effect induced by standing -wave-field coupling.

Figures 1 shows the simulated reflectance spectra and electric field distribution of different hybrid configurations. The result revealed the peculiar feature that EIT occurs only if the two "atoms" are arranged in a sequence in which the probing electromagnetic wave first reaches the "dark atom" and then the "bright atom". In contrast, the EIT can not occur if the "atoms" are placed in reverse order (bright, dark). In Figs. 1(b), the field distribution at the resonance frequency 196.8THz shows that the LPPs is not excited because of the very small amplitude of the standing wave at this site, and it can be described as a dark atom. Figures 1(c) present the spectra and field distribution for the situation where the nanowire is placed at an antinode where the E field reaches a maximum for the TPPs field. We find that the reflection spectrum splits into two dips. In Figs. 1(d), the

two anowires are arranged in the sequence node-antinode. In this case, an EIT-like reflection dip appears at the resonance frequency. The EIT-like effect disappears in the case of Figs.1 (e), where the two nanowires are arranged in the reverse sequence antinode-node. From the field distribution in Figs. 1(b)-(d), we can see that the electromagnetic energy transfers from “bright state” to “dark state”. That is, the "bright" and "dark" atoms can change energy through the standing-wave-field. This is a distinct feature of the EIT effect.

Interestingly, the simulation result revealed the peculiar feature that EIT occurs only when the two “atoms” are arranged in a sequence in which the electromagnetic wave first reaches the “dark atom” and then “bright atom”. In contrast, if the “atoms” are placed in reverse order (bright, dark), no EIT-effect is observed. That is, the hybrid state of TPPs and LPPs can induce EIT-like effect, which strongly dependent on the sequence of the “dark atom” and “bright atom”.

2.2. EIT-like effect induced by near-field coupling

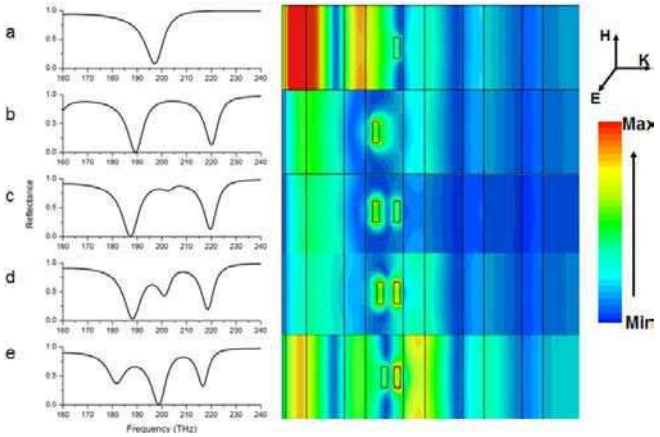


Fig. 2. Simulated reflectance spectra and electric field distribution for EIT-like effect induced by near-field coupling.

Figures 2 shows the simulated reflectance spectra and field distribution of different hybrid configurations, which demonstrate the EIT-like effect induced by near-field coupling. The configurations of EIT-like reflectance spectra vary gradually as the distance between “bright state” and “dark state” changed. In Figs. 2(a), the field distribution at the resonance frequency 196.8 THz shows that the LPPs is not excited at the node of the standing wave, and it can be described as a “dark atom”. Figures 2(b) present the spectra and field distribution for the situation where the nanowire is placed at a non-node for the TPPs field. We also find that the reflectance spectrum splits into two dips, and it can be described as a “bright atom”. As shown in Figs. 2(c)-(e), we can clearly see that coupling is strengthened and EIT-like effect is increasingly apparent as the distance reduces.

In this simulation, we obtain the other EIT-like effect induced by near-field interaction. Concretely, keeping the position of “dark atom” unchanged, we shorten the distance between bright atom” and “dark atom”. As the distance reduced, coupling is strengthened and EIT-like effect is increasingly apparent. In short, we have achieved two EIT-like effects based on the hybrid state of TPPs and LPPs in the region of infrared.

3. Conclusions

In summary, we numerically investigated the EIT-like effect induced by hybrid state of TPPs nd LPPs in the region of Infrared. The EIT-like effects are corresponding to two echanisms, which induced by near-field coupling and standing-wave-field coupling, respectively. The “bright” and “dark” states are excited by adjusting the position of the nanowire pair in the Bragg reflector.

Acknowledgements

The authors acknowledge acknowledge the financial support from the National Natural Science Foundation of China (Grant Nos. 11874245 and 11604186), the Natural Science Foundation of Shanxi Province, China (Grant Nos. 201601D202011) and the Science and Technology Project of Datong, Shanxi Province, China(Grant Nos.2016021).

References

[1] S. E. Harris, Electromagnetically induced transparency, Phys. Today 50, 36 1997.

[2] Y. Sun, H. T. Jiang, Y. P. Yang, Y. W. Zhang, H. Chen, and S. Y. Zhu, Electromagnetically inducedtransparency in metamaterials: influence of intrinsic loss and dynamic evolution, Phys. Rev. B 83, 195140, 2011.

[3] N. Papasimakis, V. A. Fedotov, N. I. Zheludev, and S. L. Prosvirnin, Metamaterial analog of electromagnetically induced transparenc, Phys. Rev. Lett. 101, 253903, 2008.

[4] R. D. Kekatpure, E. S. Barnard, W. Cai, and M. L. Brongersma, Phase-coupled plasmon-induced transparency, Phys. Rev. Lett. 104, 243902, 2010.

[5] J. Gu, R. Singh, X. Liu, X. Zhang, Xueqian Zhang, Y.F. Ma, S. Zhang, S. A. Maier, Z. Tian, A. K. Azad, H. T.Chen, A. J. Taylor, J. G. Han, and W. L. Zhang, Active control of electromagnetically induced transparency analogue in terahertz metamaterials, Nat. Commun. 3, 1151, 2012.

[6] R. R¨ohlsberger, H. C. Wille, K. Schlage, and Balaram Sahoo, Electromagnetically induced transparency with resonant nuclei in a cavity, Nature, 482, 199, 2012.

[7] Y. Y. Hu, W. X. Liu, Y. Sun, X. Shi, J. Jiang, Y. P. Yang, S. Y. Zhu, J. Evers, and H. Chen, Electromagnetically-induced-transparency–like phenomenon with resonant meta-atoms in a cavit, Phys Rev A 92, 053824, 2015.

Plasmon-assisted terahertz detection in graphene transistors

Dmitry Svintsov[1*], Denis Bandurin[2], Igor Gayduchenko[1,3], Maxim Moskotin[3], Andre Geim[2], and Georgy Fedorov[1,3]

1. Moscow Institute of Physics and Technology, Dolgoprudny 141700 Russia
2. School of Physics, University of Manchester, Oxford Road, Manchester M13 9PL, UK
3. Physics Department, Moscow State University of Education (MSPU), Moscow 119435, Russia

*corresponding author, E-mail: svintcov.da@mipt.ru

Abstract

Implementation of resonant plasmonic semiconductor-based detectors of terahertz (THz) radiation represents a major challenge due to high requirements on carrier mobility. We demonstrate the resonant plasmon-assisted THz detection in bilayer graphene/boron nitride heterstructures. Due to gate-voltage tuning of plasmon resonance, the reported devices can be used as on-chip THz spectrometers. We show that photovoltage spectroscopy offers a convenient tool to study plasmon spectra and damping in 2d channels, and use it to uncover novel plasmon modes in graphene Moiré superlattices.

1. Introduction

Graphene-based photodetectors offer ultrafast response but suffer from weak absorption of electromagnetic radiation by a single carbon sheet. This problem can be circumvented with excitation of graphene plasmons offering voltage tuning of resonance in a broad range of frequenies. Extending the graphene plasmonics down to terahertz (THz) range represents a significant challenge as the quality factor of plasma resonance scales linearly with frequency. For this reason, efficient excitation of THz plasmons requires ultra-long electron momentum relaxation time, and all previous attempts of plasmon-aided THz detection in graphene were unsuccessful [1-3].

2. Resonant terahertz detection in graphene transistor

In this paper, we demonstrate the long sought-for resonant plasmon assisted detection of terahertz radiation in graphene field-effect transistors (FETs) [4]. The FET channel was made of graphene bilayer encapsulated between boron nitride crystals, its source and gate terminals were connected to a broadband THz antenna, while the rectified photovoltage was read out between source and drain. In contrast to the previous studies where the photovoltage was proportional to the FET transconductance, our measurements reveal a strong oscillatory modulation of photovoltage vs. gate-controlled carrier density (Fig. 1a). We argue that the FET channel acts as a Fabry-Perot cavity for graphene plasmons, and the maxima of photoresponse occur once the cavity hosts an odd number of plasmon quarter-wavelengths [5].

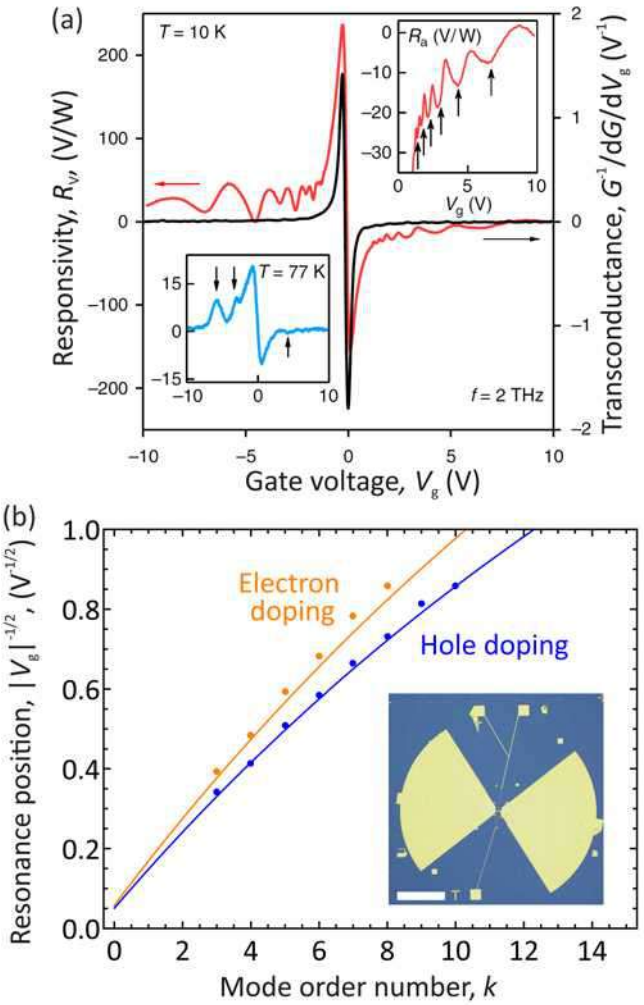


Figure 1: (a) Measured gate voltage dependence of detector responsivity at T=10 K anf f=2 THz. Top inset: magnified view of plasmon resonances for electron channel doping. Bottom inset: responsivity at 77 K (b) Positions of plasmon resonances on the voltage scale vs order number of plasmon modes (dots) compared with theory of gated 2d plasmons (lines). No fitting parameters are used. Inset: photograph of THz antenna with FET channel in its focus. Scale bar is10 mkm

We show that, independent of microscopic terahertz rectification mechanism, the responsivity R_V can be presented by the Fabry-Perot-type equation

$$R_V = \frac{R_0(\omega, V_G)}{\left|1 - r_s r_d e^{2iq(\omega,V_G)L}\right|^2}, \quad (1)$$

where $R_0(\omega, V_G)$ is a smooth (non-resonant) function of frequency ω and gate voltage V_G, while the resonant denominator is responsible for enhancement of responsivity under plasmonic resonance. Above, $q(\omega, V_G)$ is the plasmon wave vector, L is the source-to-drain distance, r_s and r_d are the reflection coefficients of plasma wave from source and drain terminals, respectively. For input signal fed at the source and output signal read at the drain, the reflection coefficients satisfy $r_s r_d \approx -1$, and the responsivity maxima occur at

$$L = \frac{\lambda_p}{4}(2k+1), \quad (2)$$

where λ_p is the plasmon wavelength and k is an integer.

The comparison of resonance positions with the theory of gated two-dimensional plasmons supports the plasmonic origin of enhanced responsivity (Fig. 1b). We find the fingerprints of plasmons in photoresponse up to liquid nitrogen temperature at 2 THz frequency, and down to 400 GHz frequency at T=10 K.

3. Photovoltage-based spectroscopy of 2d plasmons

Most previous studies of plasmons in 2d systems were performed using scanning near-field microscopy [6] and transmission spectroscopy of patterned 2d layers [7]. We show that spectroscopy of photovoltage in graphene-based FET offers an alternative and simpler tool to study the dispersion and damping of plasmons.

Indeed, known the 'quantization rule' for plasmons (2), one readily extracts the density-dependent plasmon wavelength. By performing the Lorentz fit to each individual resonant peak, one extracts the density-dependent plasmon lifetime. The extracted wavelength and lifetime are shown in Fig. 2. Analysis of resonance width indicates on extra plasmon damping channels, in addition to carrier scattering by impurities and phonons. We argue that the observed extra damping can be attributed to re-radiation of waves by antenna.

Finally, we managed to observe extra plasmon modes not described by conventional models in devices aligned with boron nitride substrates. These modes appear simultaneously with extra peaks in resistivity previously ascribed to cloning of Dirac fermions in graphene-boron nitride superlattices [8]. This fact allows us to interpret these modes as collective oscillations of second-generation Dirac electrons.

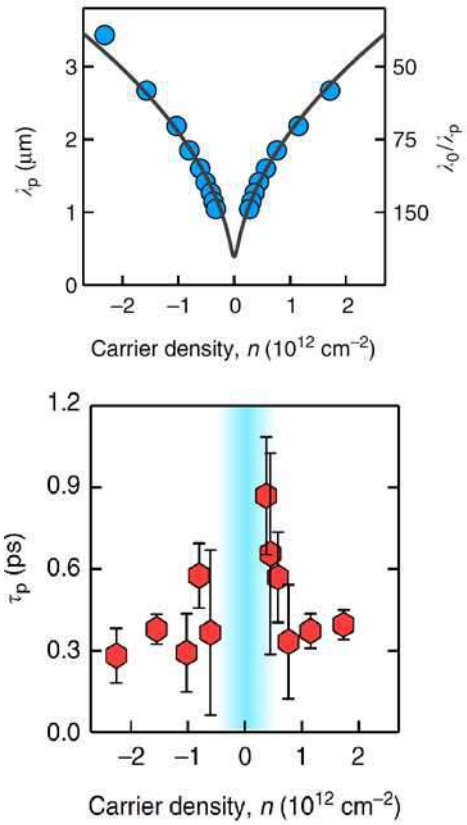


Figure 2: Extracted density dependence of plasmon wavelength (top) and lifetime (bottom). Right axis shows the ratio of free-space wavelength to plasmon wavelength. The transport relaxation time from mobility measurements is ~2 ps.

Acknowledgements

The work was supported by the grants 18-37-20058 and 18-29-20116 of the Russian Foundation for Basic Research.

References

[1] L. Vicarelli, M. S. Vitiello, D. Coquillat, A. Lombardo, A. C. Ferrari,W. Knap, M. Polini, V. Pellegrini and A. Tredicucci *Nat. Mater.* **11**: 865, 2012

[2] J. Tong, M. Muthee, S. Y. Chen, S. K. Yngvesson, J. Yan *Nano Lett.* **15**: 5295, 2015

[3] D.A. Bandurin, I. Gayduchencko, Y. Cao, M. Moskotin, A. Principi, I. Grigorieva, G. Goltsman, G. Fedorov, D. Svintsov *Appl. Phys. Lett.* **112**: 141101, 2018

[4] D. A. Bandurin, D. Svintsov, I. Gayduchenko, S.G. Xu, A. Principi, M. Moskotin, I. Tretyakov, D. Yagodkin, S. Zhukov, T. Taniguchi, K. Watanabe, I. V. Grigorieva, M. Polini, G. Goltsman, A. K. Geim, G. Fedorov *Nat. Commun.* **9**: art. number 5392, 2018

[5] M. Dyakonov, M. Shur *IEEE Trans. Electron. Devices:* **43**, 380, 1996

[6] A. Woessner et al. *Nat. Mater.* **14**: 421–425, 2015

[7] L. Ju et al., *Nat. Nanotechnol.* **6**: 630–634, 2011

[8] L. A. Ponomarenko et.al. *Nature* **497**: 594, 2013

Quantum Mechanical Analysis on Nanofocusing Limits of Metal-Insulator-Metal Plasmonic Waveguides

Daniel Assumpcao[1], Hyuck Choo[1,2]*

[1]Department of Electrical Engineering, California Institute of Technology, Pasadena, California
[2]Device Lab, Device & System Research Center, Samsung Advanced Institute of Technology (SAIT), Suwon, Republic of Korea
*corresponding author, E-mail: hyuck.choo@samsung.com

Abstract

We have numerically investigated the degradation of the nano-focusing/confinement performance of plasmonic metal-insulator-metal waveguides due to quantum effects at nanometer gap sizes. We demonstrate that Landau damping is the dominant effect for gaps larger than 0.5 nm but below ~5nm, decreasing the propagation length but not affecting the mode length. Below 0.5 nm, quantum tunneling significantly increases the losses, setting a practical limit of 0.5 nm for the minimum gap size.

1. Introduction

Waveguides based on surface plasmon polarition (SPP) are of significant interest for future integrated nanophotonic information processing technologies due to their ability to achieve confinement well below the diffraction limit [1]. The metal-insulator-metal (MIM) waveguide (Fig 1) is of interest due to its ability to achieve huge confinement through shrinking the inner dielectric gap [2, 3].

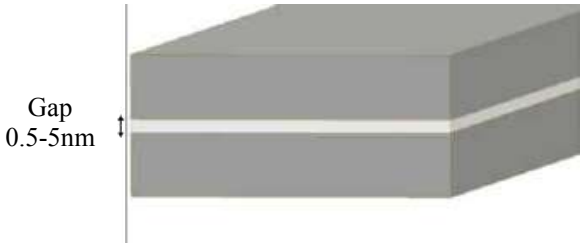


Figure 1. Diagram of MIM waveguide structure. The silver material is a metal (Ag) and the material in the gap is an insulator (air). Plasmon modes confine the energy in the gap.

Despite the interest in MIM waveguides, the limits to the achievable confinement and performance at small gap sizes are not well understood. Under the classical model, the MIM waveguide could achieve arbitrarily small confinement [2]. However, this model does not consider quantum effects that appear as the gap approaches atomic proportions [2].

Previous work has established two major effects in plasmonic structures with single and sub nanometer gaps, quantum tunneling and nonlocal effects. When plasmonic structures are separated by ~0.5 nm, electrons tunnel across the gap, changing the plasmonic modes [4-6]. For larger gap sizes below 5 nm, shifts in the modes are seen that have been phenomenologically modeled as nonlocal effects [7]. Recently, theoretical work has shown nonlocal effects can be attributed to Landau damping (LD), the absorption of high wavevector light leading to an effective increase in the damping constant of the metal [8, 9].

In this work, we numerically investigated the effect of Landau damping and quantum tunneling on the performance of MIM waveguides. The propagation length and mode length are analyzed to understand the losses and confinement respectively. It was found that in the 0.5 to 5 nm gap regime, quantum tunneling has negligible effects on the performance of the waveguide. Landau damping, however, significantly decreases the propagation length as the gap is shrunk but has a negligible effect on the mode length. Below 0.5 nm, quantum tunneling dominates and significantly increases the losses, thus providing a practical limit on the gap size. This will have significant ramifications for the future development of highly miniaturized MIM waveguides in integrated nanophotonic technologies.

2. Results

Simulations of the mode profile of Ag-air-Ag MIM waveguides (Fig 1a) were performed using FEM software. The effects of Landau damping on the waveguides were calculated using the approach in Ref. 9, whereby the LD induced damping rate is iteratively calculated.

The gap was varied from 0.5 to 5 nm with an excitation wavelength of 833 nm. Then the excitation wavelength was varied from 700 to 1500 nm with the gap fixed at 1nm. The magnitude of the LD induced damping rate increases with decreasing gap size and wavelength (Fig 2). However, even at ~2 nm the induced damping rate is already close in magnitude to the intrinsic damping rate of Ag.

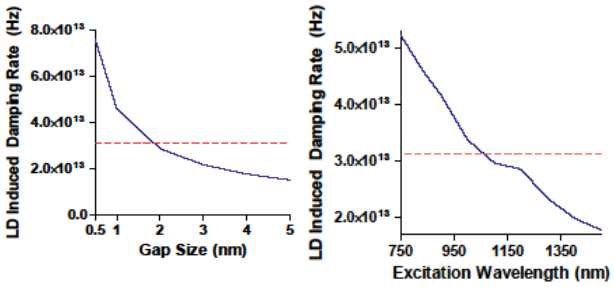


Figure 2. LD Induced Damping Rates. LD induced damping rate in the MIM structure for different gaps (left) and excitation wavelengths (right). For comparison, red dotted line indicates the intrinsic damping rate of Ag.

The propagation length of the waveguide was calculated (Figure 3A). A significant decrease in the propagation length due to Landau damping is observed. To understand the ramifications of this, an MIM waveguide made up of an ideal metal with no intrinsic loss was considered. Under classical models this lossless waveguide would have an infinite propagation length. However, with Landau damping considered, the propagation length is below a micron at a gap size of 1 nm. This indicates that Landau damping provides a limit on the maximum propagation length achievable with MIM waveguides that is not significantly better than what can be achieved using Ag.

To understanding Landau damping's effects on confinement, the mode length was calculated (Figure 3B). Landau damping does not significantly change the mode length. This indicates there is no limit to the confinement achievable with bulk metal MIM structures down to 0.5 nm.

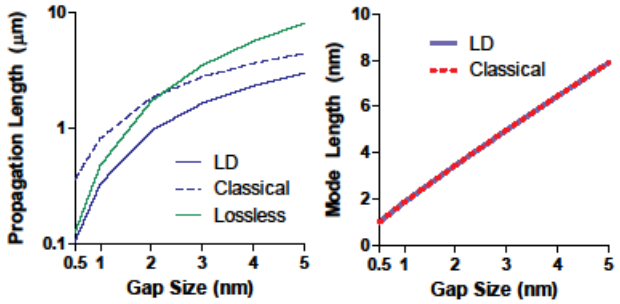


Figure 3. Effects of LD on MIM performance. (Left) Propagation length (PL) of the MIM waveguide mode versus gap size for LD and classical models. The PL of a lossless metal under the LD model is also present for comparison. (Right) Mode length versus gap size for LD and classical models. There is no significant difference between the two.

Finally, the effects of quantum tunneling were simulated through implementation of the Quantum-Corrected Model (QCM) [6]. The model changes the refractive index of the dielectric gap as a function of the gap size. The simulations showed no significant change for gaps down to 0.5 nm (Figure 4A), thus indicating that Landau damping is the dominant effect in that regime. Further calculations demonstrated that below ~0.5 nm, the tunneling induced loss tangent of the dielectric gap approaches that of Ag (Figure 4B), thus becoming dominantly lossy and practically limiting the minimum gap size for MIM waveguides [6].

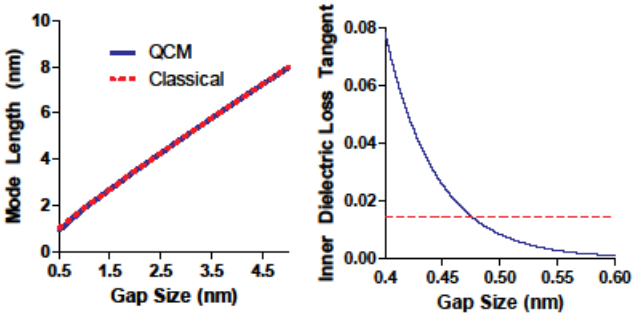


Figure 4. Effect of Tunneling on MIM Performance. (Left) Mode length of MIM structures under classical and tunneling (QCM) models. No significant change is seen. (Right) Calculated dielectric loss tangent of the inner dielectric from the QCM tunneling model. The red dashed line is the loss tangent for Ag.

3. Conclusion

From the above simulations, we have identified two regimes. The first is when the gap size is between 0.5 and 5 nm and Landau damping is the dominant effect. This is the more technologically relevant region, particularly for integrated nanophotonic applications. In this region, Landau damping caps the maximum achievable propagation length to below 1 μm for 1 nm gap sizes. This limits the potential applicability of highly compact MIM waveguides for data transfer in integrated photonic applications. This limitation can potentially be overcome through pursuing hybrid plasmonic-dielectric or plasmonic-electronic devices, or through using 2D materials [10]. In addition, the lack of effect on mode length ensures the ability of bulk MIM waveguides to confine energy to nanoscale lengths, allowing them to be packed tightly together for integrated nanophotonic technology and optically probe individual molecules.

Below 0.5 nm, quantum tunneling dominates and the induced loss becomes considerable, practically limiting the minimum MIM gap size to ~0.5 nm and thus limiting the maximum energy confinement (mode length) to ~1 nm.

Acknowledgements

This work was supported by the Caltech-Gist collaboration fund and the Heritage Medical Research Institute.

Referencess

[1] Fang, Y.; Sun, M., Nanoplasmonic waveguides: towards applications in integrated nanophotonic circuits. *Light: Science &Amp; Applications* **2015,** *4*, e294.

[2] Maier, S. A., *Plasmonics: Fundamentals and Applications*. Springer: New York, 2007.

[3] Choo, H. et al. , Nanofocusing in a metal–insulator–metal gap plasmon waveguide with a three-dimensional linear taper. *Nature Photonics* **2012,** *6*, 838.

[4] Savage, K. J. et al., Revealing the quantum regime in tunnelling plasmonics. *Nature* **2012,** *491*, 574.

[5] Zhu, W.; Crozier, K. B., Quantum mechanical limit to plasmonic enhancement as observed by surface-enhanced Raman scattering. Nature Communications 2014, 5, 5228.

[6] Esteban, R. et al., Bridging quantum and classical plasmonics with a quantum-corrected model. *Nature Communications* **2012,** *3*, 825.

[7] Zhu, W. et al., Quantum mechanical effects in plasmonic structures with subnanometre gaps. *Nature Communications* **2016,** *7*, 11495.

[8] Khurgin, J. B., Ultimate limit of field confinement by surface plasmon polaritons. *Faraday Discussions* **2015,** *178* (0), 109-122.

[9] 1. Khurgin, J. et al. Landau Damping and Limit to Field Confinement and Enhancement in Plasmonic Dimers. ACS Photonics 2017, 4 (11), 2871-2880.

[10] Alcaraz Iranzo, D. et al., Probing the ultimate plasmon confinement limits with a van der Waals heterostructure. *Science* **2018,** *360* (6386), 291-295.

Photon-plasmon coupling in microtubular optoplasmonic cavities

Yin Yin[1], Jiawei Wang[1,2], Libo Ma[1,*], and Oliver G. Schmidt[1,2]

[1]Institute for Integrative Nanosciences, IFW Dresden, Helmholtzstr. 20, 01069 Dresden, Germany
[2]Material Systems for Nanoelectronics, Technische Universität Chemnitz, Reichenhainer Str. 70, 09107 Chemnitz, Germany
*corresponding author, E-mail: l.ma@ifw-dresden.de

Abstract

Microtubular cavities, which are self-assembled from prestrained nanomembranes, can support optical whispering-gallery mode (WGM) resonances via light circulating in the tube wall. By coating plasmonic nanosturctures onto the microcavity surfaces, photon-plasmon coupling were investigated relying on the interaction of WGM resonant modes and surface plasmon resonances, which leads to many novel phenomena on optical tuning and potential applications. As a novel platform, our microtubular cavities imply promising applications for enhanced light-matter interactions, optical tuning, photonic integration and quantum optics.

1. Introduction

Plasmonic nanostructures integrated onto dielectric whispering-gallery mode (WGM) microcavities have been shown as a novel platform for the study of photon-plasmon coupling and enhanced light-matter interaction. [1,2] The combination of a dielectric WGM microcavity and plasmonic nanostructures leads to the benefits of maintaining relatively high Q factor, small modal volume, and the extremely enhanced electric field at a localized area (also called as “hotspot”), which are crucial for light-matter interactions and related applications. In recent years, novel phenomena of photon-plasmon coupling in a rolled-up microtube integrated with metal nanostructures have also been reported. [3-6] Microtubular cavities, which are self-assembled from prestrained nanomembranes, can support whispering-gallery mode (WGM) resonances in the rolled-up dielectric nanomembranes. Owing to the ultra-thin cavity wall, optical evanescent field greatly extend out of cavity surfaces, allowing for efficient interactions with the surrounding media. By designing the cavity structure and the gradient of refractive index, axial potential wells can be formed for the generation of higher order axial modes with promoted optical confinement. By combining metal nanosturctures onto the dielectric microcavity surfaces, the interaction between photonic modes and plasmonic modes were studied both theoretically and experimentally, showing a unique platform for the study of photon-plasmon coupling.

2. Results and discussion

Figure 1(a) shows photon-plasmon mode hybridization in a silver nanocap coated microtube cavity. The silver nanocap was fabricated by physical vapor deposition on top of a rolled-up microtube. In previous reports, uniformly distributed hybrid modes were explored, which in turn exhibit only monotonous fields with fixed polarization in the optoplasmonic WGM cavities. Here, we design and fabricate silver nanogaps coated on microtubular microcavities. In contrast to previous reports, angle-dependent non-uniform hybrid modes were realized in a single microcavity due to the varying coupling strength and shielding effect enabled by the metal nanocap. As such, not only the coupling strength but also the optical field polarizations can be tuned depending on the azimuthal angle. More interestingly, the intensity ratio of strongly hybridized transverse magnetic (TM) mode and transverse electric (TE) mode is extremely sensitive to nano-perturbations at the metal nanocap surface, thus providing a novel scheme for label-free sensing. This work reveals a metal nanocap capable of tuning the photon-plasmon coupling, and exhibits a novel scheme for manipulating light-mater interactions in a versatile nanotechnology platform.

For the study of light-matter interactions, the size mismatch between the optical wavelength and any interacting nano-objects is bridged by cavity quantum electrodynamics or plasmonic nanostructures integrated within the cavities. We designed a plasmonic nano-gap in microtubular cavities to demonstrate efficient coupling of localized surface plasmons (LSPs) and resonant light, as shown in Fig. 1(b). Moreover, selective coupling of LSPs and resonant modes are achieved, exhibiting spatial dependence of the plasmonic nanogap on the microcavities.

To combine metal nanoparticles onto optical microcavities, delicate nano-manipulations are required to transfer metal nanoparticles onto microcavities. However, in practical work it is of high interest to get mechanically more stable metal nanoparticles grown on dielectric microcavities in a reproducible and location-selective fashion which is limited in previous reports. To address this issue, we introduce an in-situ fabrication of silver nanoparticles on optical microtube cavities for the manipulation of photon-plasmon coupling, as schematically shown in Fig. 1(c). Moreover, by creating multiple plasmonic-nanoparticle spots on the

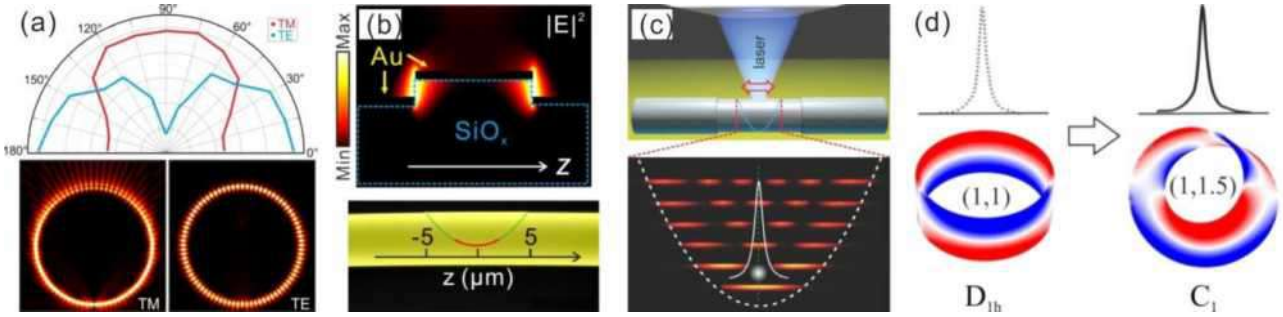


Figure 1: (a) Angle-dependent non-uniform hybrid modes induced by coupling with plasmonic nanocap. (b) Selective coupling between localized surface plasmon and resonance mode in a microtube cavity. (c) in-situ generation of plasmonic nanoparticles for photon-plasmon coupling. (d) Anomalous plasmon modes occurred in metallic Möbius nanorings due to the presence of Berry phase.

optical microcavity, optical modes are freely tuned due to multi-coupling between localized surface plasmon resonances supported by the metal nanoparticles and whispering-gallery-modes supported by the microtube cavity.

As a hot research field, the plasmonic resonances in metallic nanostructures mainly concern the structure size, geometry and symmetry, where the topology was excluded in the previous reports. In our group, we demonstrated topology induced anomalous plasmon modes in metallic Möbius nanorings, as shown in Fig. 1(d). Due to the occurrence of an extra phase (Berry phase) in the topological Möbius configuration, half-integer plasmon modes were observed which cannot exist in conventional plasmonic rings. Due to symmetry breaking, the higher-order plasmon modes turn into bright ones in the Möbius nanorings, which are supposed to be dark in conventional cylindrical rings. The feature of half-integer numbers of plasmon modes as well as the corresponding resonant frequencies is robust to the variation of the surface-charge distribution on the Möbius nanoring due to the non-trivial topology.

3. Conclusions

Self-assembled microtube cavities have been used to integrate plasmonic nanostructures for the study of photon-plasmon coupling. By tuning the coupling strength, site of localized surface plasmon resonances, and topology of the plasmonic structures, several phenomena have been revealed ranging from far-field directional emission, mode profile tuning, to anomalous plasmon modes, which show a versatile platform to manipulate photon-plasmon coupling for potential applications.

Acknowledgements

This work was supported by the German Research Foundation DFG (Grant No. FOR 1713 and SCHM 1298/22-1).

References

[1] B. Min, E. Ostby, V. Sorger, E. Ulin-Avila, L. Yang, X. Zhang, K. Vahala, High-Q surface-plasmon-polariton whispering-gallery microcavity *Nature* 457: 455-458, 2009.

[2] A. Rottler, M. Harland, M. Bröll, M. Klingbeil, J. Ehlermann, S. Mendach, A. High-Q Hybrid Plasmon-Photon Modes in a Bottle Resonator Realized with a Silver-Coated Glass Fiber with a Varying Diameter, *Phys. Rev. Lett.* 111: 253, 2013.

[3] Y. Yin, Y. Chen, E. S. G. Naz, X. Lu, S. Li, V. Engemaier, L. Ma, O. G. Schmidt, Silver nanocap enabled conversion and tuning of hybrid photon–plasmon modes in microtubular cavities, *ACS Photon.* 4: 736, 2017.

[4] Y. Yin, S. Li, S. Böttner, F. Yuan, S. Giudicatti, E. Saei Ghareh Naz, L. Ma and O. G. Schmidt, Localized Surface Plasmons Selectively Coupled to Resonant Light in Tubular Microcavities, *Phys. Rev. Lett.* 116: 253904, 2016.

[5] Y. Yin, J. Wang, X. Lu, Q. Hao, E. S. G. Naz, C. Cheng, L. Ma, O. G. Schmidt, In situ generation of plasmonic nanoparticles for manipulating photon–plasmon coupling in microtube cavities, *ACS Nano*. 12: 3726, 2018.

[6] Y. Yin, S. Li, V. Engemaier, E. S. G. Naz, S. Giudicatti, L. Ma, O. G. Schmidt, Topology induced anomalous plasmon modes in metallic Möbius nanorings, *Laser & Photon. Rev*. 11: 1600219, 2017.

Nonlocality and singular metasurfaces

Fan Yang[1*], Yao-Ting Wang[1], Paloma Arroyo Huidobro[1], and John B Pendry[1]

[1]The Blackett Laboratory, Department of Physics, Imperial College London, London SW7 2AZ, United Kingdom
*corresponding author, E-mail: f.yang16@imperial.ac.uk

Abstract

The far field spectrum of plasmonic metasurface with sharp features is very sensitive to nonlocality in the metal such that the microscopic nonlocal effects can be unveiled from far field measurements.

1. Introduction

Singular metasurfaces have a strong field enhancement, because of their ability to compress the wavelength of surface plasmons [1]. However, if the length scale of the singularity is smaller than the screening length of metal, nonlocal effects must be considered. In view of this, the hydrodynamic model is considered which takes into account the interaction between electrons. In this model, the longitudinal mode of plasmon becomes k-dependent and couples with transverse mode.

2. Results

Fig. 1(a) depicts our singular metasurface. In the presence of nonlocality, the surface charge becomes a volume charge, see the purple layer on top of the metasurface. The thickness of this layer is scaled by the nonlocal parameter β. To study this structure, a conformal mapping is employed to transform this singular metasurface into a slab array, shown in Fig. 1(b). As the longitudinal permittivity is k-dependent, the decay length in the transformed frame is not uniform such that the thickness of electron layer is thinner near the origin and increase when $x \to \pm\infty$ in the slab frame shown in Fig. 1(b). Then our analytical calculation is carried out in the slab frame, where the boundary matching is easier.

Using the method we have developed in a previous paper [2], the reflection spectrum is obtained and shown in Fig. 2(a). In this figure, the reflection spectrum with and without nonlocality are compared. From this comparison, we conclude that the introduction of nonlocality makes the spectrum discrete [3]. When the nonlocal parameter $\beta \to 0$, the discrete spectrum transits into a continuous one. Thus, nonlocality introduces a significant change in the spectrum and has to be considered for the real purpose. For the near field profile shown in Fig. 2(b), we see the electric field becomes continuous across the metal interface when the nonlocality is introduced. This is because of the absence of surface charge in the hydrodynamic description. Besides, the field in the nonlocal case oscillates much less rapidly

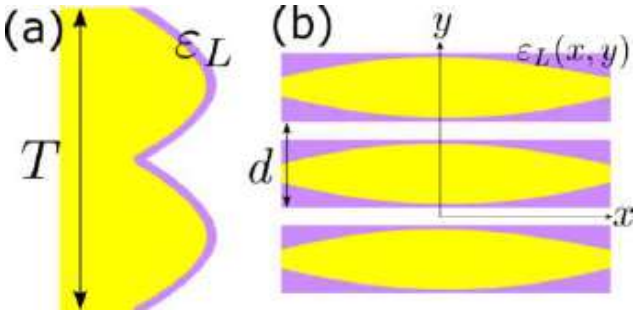


Figure 1: Panel (a) shows the nonlocal description of a singular metasurface where the purple layer stands for the decay length of longitudinal plasmon mode. Panel (b) shows the nonlocal description in the slab frame where the decay length varies along the slab.

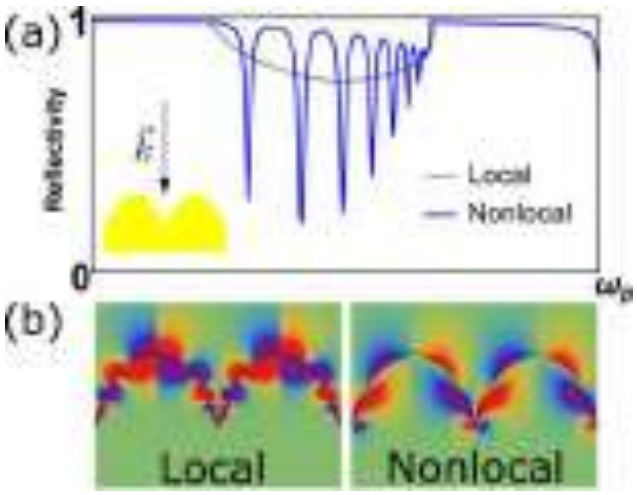


Figure 2: Panel (a) presents the reflection spectrum of a singular metasurface under normal incidence, in which the nonlocal calculation is compared with local one. Panel (b) presents the near field (electric field) profile with both local and nonlocal cases.

than the local case, which results in a weaker compression of the field.

We also studied the dependence of the spectrum on period of the metasurface, which is a length scale parameter that competes with nonlocal parameter. We show that increasing the period is equivalent to reducing β in the quasi-static limit. For large periods, the radiation loss comes into play which broadens the width of the peaks. However, we

show that this broadening is limited in our structure, especially for the high order peaks.

Acknowledgement

F.Y. acknowledges a Lee Family Scholarship for financial support. Y.T.W. acknowledges funding from the Leverhulme Trust. P.A.H and J.B.P. acknowledge funding from the Gordon and Betty Moore Foundation.

References

[1] J. Pendry, P. A. Huidobro, Y. Luo, and E. Galiffi, Compacted dimensions and singular plasmonic surfaces, *Science* 358: 915, 2017.

[2] F. Yang, P. A. Huidobro and J. B. Pendry, Transformation optics approach to singular metasurfaces *Phys. Rev. B*, 98: 125409, 2018.

[3] F. Yang, Y. T. Wang, P. A. Huidobro and J. B. Pendry, Nonlocal effects in singular plasmonic metasurfaces, under review.

Characterization of surface plasmon-polariton resonances at solvent-metal interfaces using Fano approximation

Dmitry V. Nesterenko[1,2,*], Roman Pavelkin[2], Shinji Hayashi[3,4], Victor Soifer[1,2]

[1]Image Processing Systems Institute RAS – Branch of the FSRC "Crystallography and Photonics" RAS, Samara, Russia
[2]Faculty of Informatics, Samara National Research University, Samara, Russia
[3]Optics and Photonics Center, Moroccan Foundation for Science, Innovation and Research (MAScIR), Rabat, Morocco
[4]Graduate School of Engineering, Kobe University, Kobe, Japan
*corresponding author, E-mail: dtnesteren@gmail.com

Abstract

Water, ethanol, and isopropyl alcohol are general solvents and dispersing media for different suspensions. We estimate the resonance properties of SPP modes excited at interfaces between silver and these solvents using Fano approximations in the ultraviolet, visible and infrared regions. The obtained results suggest potential applications of planar plasmonic structures in nanotechnology and biosensing in the near- and mid-infrared regions.

1. Introduction

Optical characterization of materials is important for a variety of applications in nanotechnology, sensing, spectroscopies. In such fields as biosensing and nanofabrication of nanoparticles, a liquid environment for the dispersed particles is generally employed [1]. Responses of optical resonant structures to changes in the optical characteristics of environment are widely used in optical sensing. It is well known that an interface between a metal and a dielectric supports propagation of surface plasmon-polaritons (SPP) modes [2]. The resonance characteristics of planar SPP structures in aqueous environment were obtained in the ultraviolet (UV), visible and near-IR regions using exact electromagnetic (EM) theory, which required heavy data processing [3, 4]. Recently, we analytically obtained Fano approximations for asymmetric resonance line shapes in spatial spectra of planar plasmonic structures [5]. In the present work, we analyze the resonance characteristics of SPP modes at solvent-metal interfaces for water, ethanol, and isopropyl alcohol (IPA) using our Fano approximations.

2. SPP resonances at dielectric-metal interfaces

Let us consider an interface between a dielectric and a metal with permittivities $\varepsilon_1 = \varepsilon_1' + \mathrm{i}\varepsilon_1''$ and $\varepsilon_2 = \varepsilon_2' + \mathrm{i}\varepsilon_2''$, respectively, where $\varepsilon_1' > 0$ and $\varepsilon_2' < 0$. SPP modes propagates along the interface provided that $\varepsilon_1' + \varepsilon_2' < 0$, $\varepsilon_1'\varepsilon_2' < 0$, $|\varepsilon_1''|, |\varepsilon_2''| \ll |\varepsilon_1'|, |\varepsilon_2'|$ [2]. The complex propagation constant $\gamma_{\mathrm{SPP}} = \gamma_{\mathrm{SPP}}' + \mathrm{i}\gamma_{\mathrm{SPP}}''$ of SPP mode is found as [2]

$$\gamma_{\mathrm{SPP}} = \sqrt{\varepsilon_1\varepsilon_2 / (\varepsilon_1 + \varepsilon_2)}\,. \qquad (1)$$

At the interface, the field of an external evanescent wave non-resonantly generates a secondary evanescent field and interacts with the SPP mode. If the in-plane wavevector of the external exciting wave approaches the wavevector of the SPP mode, the energy of the wave is partly transferred to the SPP mode that leads to the resonant increase of the SPP mode amplitude and near field enhancement. We demonstrated that interference of the secondary field and resonant response from the SPP mode results in asymmetric SPP resonances in spectra of near field enhancement that can be approximated by the Fano formula [5]:

$$|r(\alpha)|^2 = |r^c(\alpha)|^2 \frac{(\alpha - \gamma_z')^2 + \gamma_z''^2}{(\alpha - \gamma_p')^2 + \gamma_p''^2}, \qquad (2)$$

where α is the in-plane propagation constant of the external wave; $\gamma_z = \gamma_z' + \mathrm{i}\gamma_z'' = \gamma_{\mathrm{SPP}} + 2\gamma_{\mathrm{SPP}}^3 / [r_{12}^c(\varepsilon_2 - \varepsilon_1)]$ is the zero and $\gamma_p = \gamma_p' + \mathrm{i}\gamma_p'' = \gamma_{\mathrm{SPP}}$ is pole of function (2); $r^c(\alpha) = (\varepsilon_2 - \varepsilon_1)(\varepsilon_2 + \varepsilon_1)^{-1} + (\varepsilon_2 + \varepsilon_1)\gamma_{\mathrm{SPP}}^2(\varepsilon_2 - \varepsilon_1)^{-1}\alpha^{-2}$ is the non-resonant slowly changing near field enhancement component. The maximum near field enhancement can be estimated as $|r(\gamma_p')|^2_{\max} = |r^c(\gamma_p')|^2 [(\gamma_p' - \gamma_z')^2 + \gamma_z''^2] / \gamma_p''^2$. The resonance width in the spatial spectrum is determined as $\Gamma = 2\gamma_p'\gamma_p''$ [5].

3. Numerical results and discussion

The refractive indices for silver (Ag) [6, 7], ethanol and IPA [1], and water [8] were used for calculation of resonance characteristics of SPP modes, which are excited at interfaces between silver and the set of solvents. The propagation constant $\gamma_{\mathrm{SPP}}'(\lambda)$ calculated by Eq. (1) decrease with wavelength as demonstrated in Fig. 1. The difference in $\gamma_{\mathrm{SPP}}'(\lambda)$ between different solvents is maximal in the 1.0 – 2.8 μm region. The width Γ of the SPP resonance line shape takes its lowest values in the 1.0 – 2.4 μm region for all the considered solvents as shown in Fig. 2. The

maximum near field enhancement $|r|^2_{max}$ reaches its maximal values in the 0.5 – 1.6 μm region in all cases. The regions of SPP modes excitation are above 350 nm in all cases, respectively, and in the IR region up to 4.1 μm. In the case of ethanol and IPA, SPP mode can be excited also in the 3.6 – 6 μm region. The near field enhancement and resonance width degrade in the mid-IR region due to the increasing water absorption.

4. Conclusions

According to the data obtained by the Fano approximation, water can be used as a solvent for spectral measurements based on SPP resonances in the 0.4 - 2.65 μm and 3.55 - 4.05 μm regions, ethanol – in the 0.35 – 2.8 μm and 3.7 – 5.8 μm regions, and IPA – in the 0.35 – 2.8 μm, 3.2 – 3.3 μm, and 3.57 - 6.2 μm regions. The theoretical results can be used for engineering of the line shapes of SPP resonances in solutions and concentration measurements.

Acknowledgements

This work was supported by the Ministry of Science and Higher Education of the Russian Federation as part of the work on the State task of the FSRC "Crystallography and Photonics" of the Russian Academy of Sciences (Agreement No. 007-ГЗ/Ч3363/26) and the Russian Foundation for Basic Research (grant 18-29-20006).

References

[1] E. Sani and A. Dell'Oro, Spectral optical constants of ethanol and isopropanol from ultraviolet to far infrared, Opt. materials 60:137-141, 2016.

[2] M. Agranovich and D. L. Mills, Surface polaritons: electromagnetic waves at surfaces and interfaces, Amsterdam: North-Holland, 1982.

[3] D.V. Nesterenko and Z. Sekkat, Resolution Estimation of the Au, Ag, Cu, and Al Single- and Double-Layer Surface Plasmon Sensors in the Ultraviolet, Visible, and Infrared Regions, Plasmonics 8:1585-1595, 2013.

[4] D.V. Nesterenko, S.-U. Rehman, and Z. Sekkat, Surface plasmon sensing with different metals in single and double layer configurations, Appl. opt. 51:6673-82, 2012.

[5] D.V. Nesterenko, S. Hayashi, and Z. Sekkat, Asymmetric surface plasmon resonances revisited as Fano resonances, Phys. Rev. B 97:235437, 2018.

[6] H.J. Hagemann, W. Gudat, and C. Kunz, Optical-constants from far infrared to X-ray region - Mg, Al, Cu, Ag, Au, Bi, C, and Al_2O_3, JOSA 65:742-744, 1975.

[7] K.M. McPeak, S.V. Jayanti, S.J.P. Kress, S. Meyer, S. Iotti, A. Rossinelli, and D. J. Norris, Plasmonic films can easily be better: rules and recipes, ACS Photonics 2:326-333, 2015.

[8] D. J. Segelstein, The complex refractive index of water, M.S. thesis, Dept. of Physics, University of Missouri - Kansas City, Kansas City, Missouri, 1981.

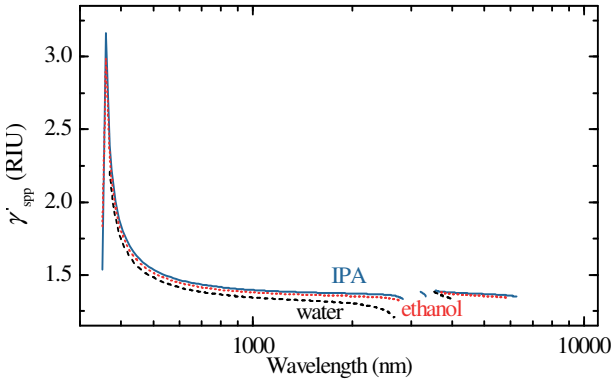


Figure 1: Dispersion relations of SPP modes at solvent-metal interfaces.

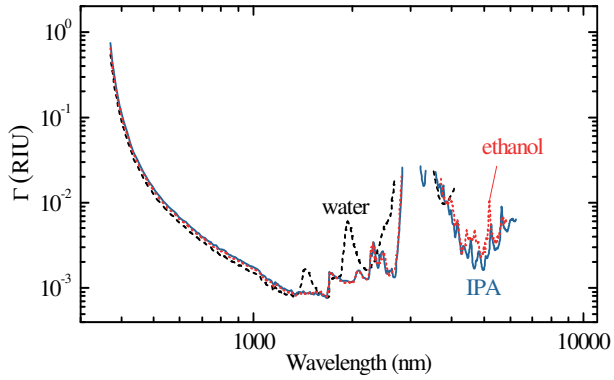


Figure 2: The width wavelength dependences of SPP resonances at the solvent-metal interfaces.

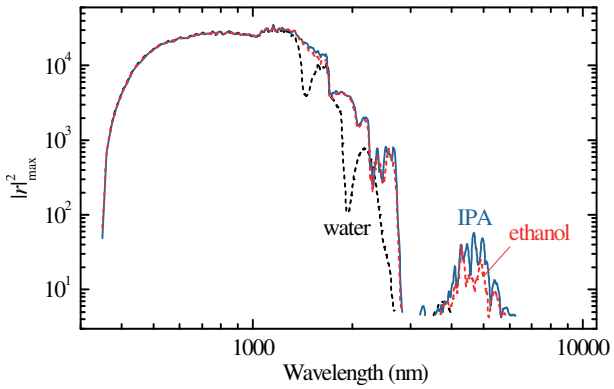


Figure 3: The wavelength dependences of maximum near field enhancement at the solvent-metal interfaces.

Generation of the Robust and Low Loss Diffration-free Bloch Surface Wave

R.X. Wang[1,2], D.G.Zhang[*3], A.M. Wu[*1,2]

[1]State Key Laboratory of Functional Materials for Informatics, Shanghai Institute of Microsystem and Information Technology, CAS, Shanghai, 200050, P.R. China
2Center of Materials Science and Optoelectronics Engineering, University of Chinese Academy of Sciences, Beijing, 100049, P.R. China
[3]Institute of Photonics, Department of Optics and Optical Engineering, University of Science and Technology of China, Hefei, Anhui, 230026, P.R. China
*corresponding author, E-mail: wuaimin@mail.sim.ac.cn & dgzhang@ustc.edu.cn

Abstract

In this article, we present a diffraction-free Bloch Surface Wave in an aqueous environment sustained on all-dielectric multilayers with two crossed gratings or silver nanowires. It can propagate in a straight line for distances longer than 110 μm at a wavelength of 633 nm and could be applied as an in-plane optical virtual probe. Its robustness and long diffraction-free distance to multiple obstacles make this wave ideal for certain applications in bio-photonics and chip-level optical interconnections.

1. Introduction

Recent development of photonic integrated circuits meet high demand for light confinement and manipulation at subwavelength scale [1]. Compared with the candidates such as Surface Plasmon Polaritons (SPPs) [2], the Bloch Surface Waves (BSWs) which are excited between a truncated periodic dielectric multilayer with a photonic band gap (PBG) and its surrounding medium is competitive for its lower loss as well as consequent longer propagation lengths. Both SPPs and BSWs undergo diffraction in the plane of the interface, which will induce coupling losses between the on-chip components as the wave packet spreads laterally during propagation. In recent years, many methods have been proposed to construct diffraction-free SPPs[3,4]. However, little effort had been devoted to constructing diffraction-free surface waves in an aqueous environment and in the visible light band, which is more favorable for biological applications. In the present report, we demonstrate both experimentally and theoretically that diffraction-free BSWs (DF-BSWs) can be generated on an all-dielectric multilayer with simple dielectric gratings or silver nanowires. Owing to the low loss of BSWs, it can propagate in a straight line for distances longer than 110 μm in an aqueous environment at a wavelength of 633 nm, which had not been demonstrated experimentally for any diffraction-free SPPs.

2. Results and Discussion

Figure 1b and 1c shows the experimental and numerical results of diffraction-free BSW with dielectric gratings. Both images have a significant main lobe and several parallel side lobes that appear and propagate toward the right side. The diffraction-free distance approaches 110μm, illustrating that the BSW can propagate much further than SPP. Another important advantage of this low-loss dielectric system is that the diffraction-free property can be preserved even after passing several obstacles. Figure 1e and 1f clearly show that the main lobe of the BSWs keep collimation after passing three separate obstacles. To the best of our knowledge, there is no previous report of diffraction-free SPPs that can pass through three obstacles.

Silver nanowires with crystalline structure can be synthesized with chemical approach, which is a convenient and low-cost method for practical applications. In figure 2, we demonstrate that two crossed silver nanowires instead of gratings can also be used for excitation of the diffraction-free BSW. Figure 2(a, c, e, g) show white light images of the two contacted Ag nanowires with different cross angles. The experimental results show that the non-diffracting distance and the full width at half maximum of the main lobe decreases as the cross angle of the two nanowires increases in Figure 2(b, d, f, h). Thus the DF-BSW can be regarded as an in-plane optical virtual probe since the width and the length can be tuned.

3. Conclusions

In summary, the crossed gratings and silver nanowires are used to generate the DF-BSW in water environment at visible light frequency, respectively. The low loss property of the dielectric multilayer configuration compared with a metal film, especially in the visible spectrum, makes BSWs more favorable than SPPs for the formation of diffraction-free surface waves. As it has longer diffraction-free propagation distance and robustness against disorder in the propagating path, DF-BSWs have potential prospect in areas such as on-chip optical interconnections, where the signal may encounter obstacles as the devices become more complex. Besides, the tunable capability by changing of the width and length of the DF-BSWs may also find applications in optical nano-manipulation of molecules in liquids.

Acknowledgements

This work was supported by International Collaboration Program of Chinese Ministry of Science and Technology (Grants 2016YFE0130000), and Science and Technology Commission of Shanghai Municipality (Grant 16ZR1442600).

References

[1] Li, M., Li, W., Huang, H., Wang, J., Li, Y., Wu, A., Sheng, Z., Wang, X., Zou, S., & Gan, F. All-Angle quasi-self-collimation effect in a rod-type silicon photonic crystal. IEEE Photonics J7, 1-8 (2015).

[2] Kumar, G., Li, S., Jadidi, M. M., Murphy, T. E. Terahertz surface plasmon waveguide based on a one-dimensional array of silicon pillars. New J Phys15, 085031 (2013).S.V. Patankar, *Numerical Heat Transfer and Fluid Flow*, Hemisphere Publishers, New York, 1980.

[3] Fornel, F., and Capasso, F., Cosine-Gauss Plasmon Beam: A Localized Long-Range Nondiffracting Surface Wave, Phys. Rev. Lett. 109, 093904-1/5(2012).

[4] 14. Li, L., Li, T., Wang, S. M., Zhang, C., and Zhu, S. N., Plasmonic Airy Beam Generated by In-Plane Diffraction, Phys. Rev. Lett. 107, 126804-1/4(2011).

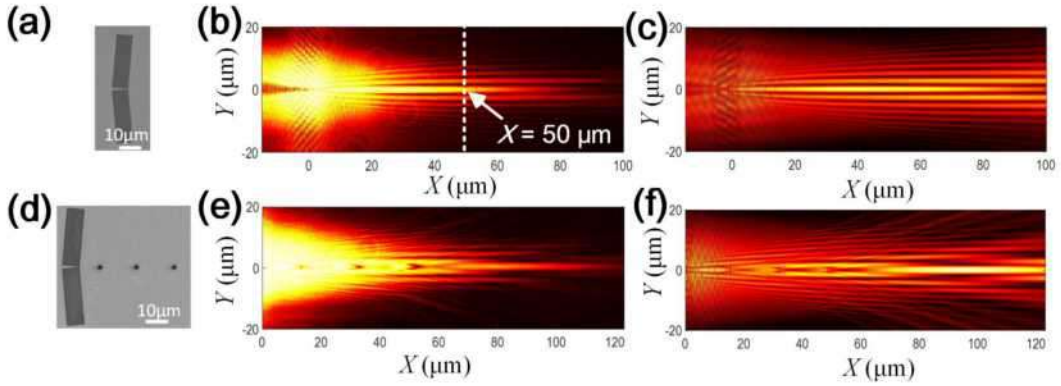


Figure1:(a,d) A scanning electron microscope (SEM) image of the grating in which the cross-angle of the two gratings is 170° and three square obstacles were inscribed on the axis between the two gratings as shown in (d). (b-c)Experimental and simulated results of the DF-BSW. The experimental image (e) and the simulated image (f) of the DF-BSW shows it propagating around the three obstacles.

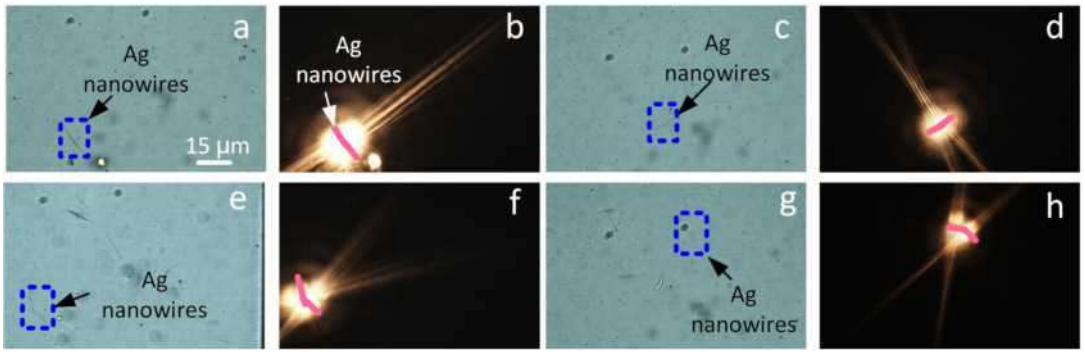


Figure2:(a, c, e, g)show white light images of the two contacted Ag nanowires with different cross angles. (b, d, f, h) present the corresponding images DF-BSWs by the crossed Ag nanowires.

Nonlocal optical processes mediated by surface plasmon polaritons

Dawid Piątkowski[1*], Aneta Prymaczek[1], Maciej Ćwierzona[1], Justyna Grzelak [1], Dorota Kowalska[1], Marcin Nyk[2], Sebastian Maćkowski[1]

[1] Institute of Physics, Faculty of Physics, Astronomy and Informatics, Nicolaus Copernicus University, Grudziadzka 5, 87-100 Torun, Poland
[2] Advanced Materials Engineering and Modelling Group, Faculty of Chemistry, Wroclaw University of Science and Technology, Wybrzeze Wyspianskiego 27, 50-370 Wroclaw, Poland
*corresponding author, E-mail: dapi@fizyka.umk.pl

Abstract

In this work we demonstrate that Surface Plasmon Polaritons (SPPs), propagating in a single silver nanowire, can be used for remote (bi-directional) communication with up-converting nanocrystals (UCNPs), which are anti-Stokes emitters. In particular, SPPs activated at one end of the nanowire induce emission of single UCNPs deposited at the opposite end of the nanowire. We show using spectrally- and time-resolved luminescence microscopy that range of this communication depends on light polarization, SPPs mode, and functionalization of the nanocrystals.

1. Introduction

Surface Plasmon Polaritons (SPPs) can be activated by light at the metal-dielectric interface. Apart from metallic layers, SPPs can propagate in silver nanowires, which behave like waveguides, routing the energy for quite long distances reaching many microns [1]. Due to small lateral dimensions of the nanowires (~100 nm), plasmonic waveguides allow construction and further miniaturization of optoelectronic circuits, far beyond diffraction limit for light. For this reason, metallic nanostructures attract great attention as promising candidates for new generation of on-chip optoelectronic devices.

It has been experimentally demonstrated that SPPs can transport the energy between spatially distant parts of the nanowire what can leads to activation of photoluminescence or Raman scattering [2]. As it has been shown, SPPs typically support only one-way (excitation/detection) communication channel, whereas complementary detection/excitation process requires far field optical microscope. For this reason, SPP-mediated processes have found rather limited number of applications despite their unique optical properties.

In this work we demonstrate that both excitation and detection processes, followed by spectrally- and time-resolved analysis, can by realized exclusively by SPPs propagating in a single silver nanowire. The results show that even ineffective two-photon up-conversion luminescence can be successfully activated and detected utilizing SPPs, propagating one way and back in a nanowire. The efficiency of such a “boomerang” effect strictly depends on the orientation of nanocrystals (dipoles) with respect to the nanowire, as well as particular configuration of the SPPs mode. Other non-local optical processes like polariton-mediated absorption are discussed and experimentally verified.

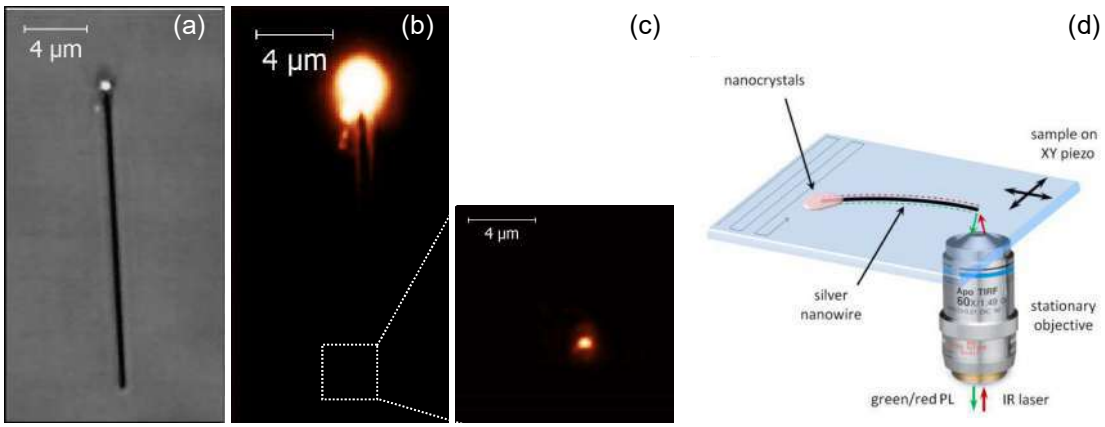


Fig. 1: Microscopic image of a single silver nanowire, decorated by small population of nanocrystals, visualized by (a) transmission and (b) photoluminescence microscopy (λ_{det}= 650 nm). (c) Photoluminescence map demonstrating emission of light from free (lower) end of the nanowire. (d) Experimental configuration used to investigate polariton-mediated excitation and emission processes.

2. Materials and methods

In the experiment we used single silver nanowires featuring diameters of about 100 nm and lengths about 10-20 μm. The nanowires were coupled with small population of anti-Stokes emitters, represented by α-$NaYF_4$:Er^{3+}/Yb^{3+} up-conversion nanocrystals. Small volume of the nanocrystals (~fL) was precisely deposited on one end of single silver nanowire using microinjection capillary tip. Such a sample was investigated using anti-Stokes confocal and wide-field photoluminescence (PL) microscopes, equipped with a high numerical aperture oil immersion objective (NA=1.49). For excitation we applied a single-mode infrared CW/pulsed laser operating at 980 nm. For detection we used a single photon counting unit, connected to the counter card (PL imaging) or to the multiscaler card (time-resolved imaging). Detailed topography of the sample, including arrangement of the nanocrystals near the nanowire tip were realized using Atomic Force Microscopy and Scanning Electron Microscopy techniques.

3. Results and discussion

The results of optical studies of the nanowire decorated with nanocrystals on one end are displayed in Fig. 1. The microscopic image of the nanowire, including a small disturbance at the top end of the nanowire, which we attribute to the nanocrystals, is presented in Fig. 1a. The luminescence (λ_{det}= 650 nm) intensity map obtained for the same nanowire (Fig. 1b) using confocal luminescence microscopy proves that the most of the emission originates from the top end of the nanowire, where the nanocrystals were deposited. However, one can see weak but a very well defined emission spot emerging at the lower end of the nanowire, where no nanocrystals were deposited (Fig. 1c). This observation means that when the nanowire is excited at this very end, as the result of interactions that are taking place at the interface between the nanowire and nanocrystals (at the other end), it itself becomes a light emitter [3].

To explain this effect it is required to consider and analyze the experimental conditions, in particular the locality and non-locality of both excitation and emission processes, what is illustrated in Fig. 1d. Excitation of the end of the nanowire where no nanocrystals are present must launch $SPPs^{exc}$, which propagate towards the second end of the nanowire, i.e. the one where the nanocrystals are present. It should be noted that the $SPPs^{exc}$ not only are capable of reaching the second end of the nanowire, but can also provide sufficient energy to activate the up-conversion process in these nanocrystals. In the final step, remotely excited nanocrystals convert the energy and launch $SPPs^{lum}$ corresponding to their emission lines. Eventually, they propagate back to the excitation spot, where radiation is released. The whole process has strong non-local character, since the excitation/detection spot is spatially distant from the optically active area of the nanocrystals.

Quite different functionality of the plasmonic nanostructure can be achieved through change of the sample geometry. For instance, when nanocrystals are positioned more in the middle of the nanowire, polaritons propagating through the wire can "probe" optical properties of surrounding nanocrystals. We will demonstrate that sensitivity of a such polariton-mediated process is high enough to map absorption lines, assigned to the optical transitions in the rare-earth doped nanocrystal. In addition, we will demonstrate that efficiency of polariton-nanocrystal interaction strongly depends on orientation of the dipole moments in the nanocrystals.

4. Conclusions

The central observation described in this work is the ability for a single silver nanowire to act (at the same time) as an energy transmitter and a remote activator of up-converted emission in nanocrystals. By developing a simple method of local deposition of nanocrystal solution on one of the nanowire ends and the ability to excite exclusively the second end of the nanowire, we demonstrate efficient remote activation and detection of the emission via surface plasmon polaritons. As the studied experimental configuration is diffraction-free in an optical manner, the results open rarely addressed facets of miniaturization of optoelectronic circuits further below the diffraction limit for light.

Acknowledgements

These research were supported by the projects no. 2017/26/E/ST3/00209 and 2017/27/B/ST3/02457 from the National Science Center of Poland.

References

[1] H. Ditlbacher et al., Phys. Rev. Lett. 95, 257403 (2005).
[2] Z. Zhang et al., Advance Science 3, 1500215 (2016).
[3] A. Prymaczek et al., Nanoscale 10, 12841 (2018).

Metal-enhanced up-conversion luminescence tuned by optically controlled orientation of dipoles

Maciej Ćwierzona[1], Aneta Prymaczek[1], Justyna Grzelak[1], Marcin Nyk[2], Sebastian Maćkowski[1], Dawid Piątkowski[1]*

[1] Institute of Physics, Faculty of Physics, Astronomy and Informatics, Nicolaus Copernicus University, Grudziadzka 5, 87-100 Torun, Poland
[2] Advanced Materials Engineering and Modelling Group, Faculty of Chemistry, Wroclaw University of Science and Technology, Wybrzeze Wyspianskiego 27, 50-370 Wroclaw, Poland
*corresponding author, E-mail: dapi@fizyka.umk.pl

Abstract

In this work we present the results regarding interaction between single emitters (nanocrystals) and metallic nanoparticles (silver nanowires). In the experiment we use Photoluminescence (PL) microscopy together with Fluorescence-Lifetime Imaging Microscopy (FLIM) to investigate radiative emission rates of the nanocrystals localized close to the nanowire. We use polarized laser beam to control orientation of the dipole moments of the nanocrystals to show that radiative rate enhancement strongly depends on orientation of the dipoles with respect to the nanowire, giving new insight into nature of the metal enhanced fluorescence process.

1. Introduction

Metal Enhanced Fluorescence (MEF) is one of the most interesting and widely investigated phenomenon in the last years. The most significant advantage regarding MEF is that quantum efficiency of a particular emitter can be controlled and frequently improved by positioning it close to a metallic nanoparticle.

There are several parameters that have to be optimized in order to activate MEF. Very important in this regard is the distance between the emitter and the metallic nanoparticle. It was showed that maximal enhancement can be observed for distances between 10 to 15 nm [1]. When the distance is too large, the metal-emitter interaction decreases and the enhancement disappears. On the other hand, when the distance is too small, the luminescence is strongly quenched by non-radiative transfer of the energy from the emitter to the metallic nanoparticle.

Additionally, optimal spectral matching between elements of the system has to be assured. To improve the efficiency of absorption, the plasmon resonance should overlap with the absorption of the emitter. This quite intuitive condition guarantees effective absorption of the excitation energy by the whole nanostructure. On the other hand, to increase spontaneous emission rates, a rather different spectral optimization is required. According to the experimental results, the largest enhancement of the radiative emission rates is usually observed for a system, where spectral position of the emission line is red-shifted with respect to the maximum of the extinction of metallic nanoparticles [2].

It should be noted that efficiency of interaction that takes place between the emitter and metallic nanoparticles depends also on mutual orientation of their dipolar moments. In this work we focus on understanding a microscopic image of the MEF processes. In the experiment we used a system, consisting of single silver nanowires and nanocrystals without permanent dipole moments. Instead, the nanocrystals feature induced dipole moments, which can be freely reoriented using external laser light with respect to the nanowire, giving new insights into nature of the MEF.

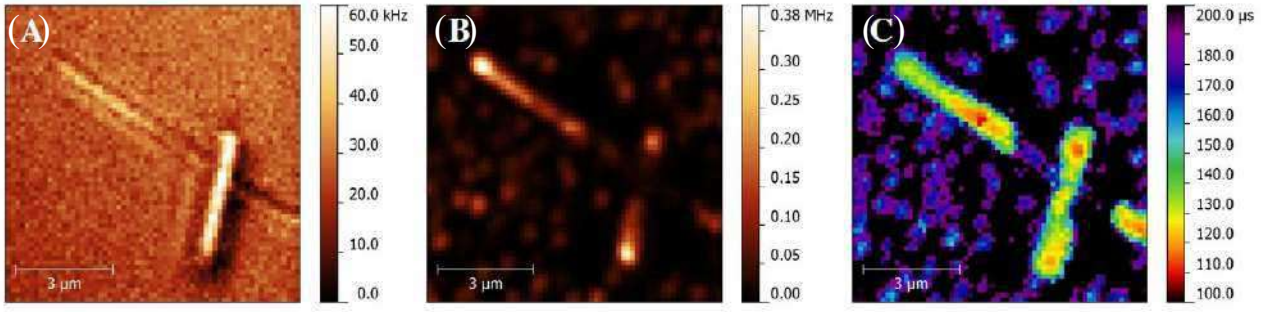


Figure. 1. Nanostructure consisting of single nanowires and nanocrystals, deposited on glass, imaged using: (a) elastically scattered laser light, (b) up-conversion photoluminescence microscopy and (c) fluorescence-lifetime imaging microscopy.

2. Materials and methods

The nanostructure studied in this work consists of silver nanowires (NWs) and dielectric $NaYF_4$ nanocrystals (NCs) doped with Er^{3+}/Yb^{3+} ions. Components were spin-coated on a glass substrate layer by layer. In contrast to organic dyes or semiconductor quantum dots, the emission of the NCs is very stable, it neither features blinking nor photobleaches under laser illumination. Furthermore, the infrared laser excitation generates no background in the visible spectral range, enabling straightforward observation of the emission of individual nanocrystals.

Samples were investigated using anti-Stokes confocal luminescence microscope, equipped with a high numerical aperture oil immersion objective (NA=1.49). For excitation we applied a single-mode infrared CW/pulsed laser operating at 980 nm. For detection we used a single photon counting unit, connected to the counter card (PL imaging) or to the multiscaler card for time-resolved imaging (FLIM). Luminescence transients were collected with 1 µs time resolution in a time window of 0-1 ms. Detailed topography of the sample was realized using AFM and SEM.

3. Results and discussion

The exemplary results of optical studies of the nanostructures are displayed in Fig. 1. All presented maps were measured over the same sample area, as evidenced by identical positions of the silver nanowires. The elastic scattering image (Fig. 1a) features two randomly oriented silver nanowires with lengths of about 4 and 10 µm. An up-conversion luminescence intensity map (Fig. 1b), acquired for the detection wavelength of 650 nm, corresponding to red emission of Er^{3+}, features two qualitatively different subsets of emitters. First, round and diffraction-limited spots attributed to the emission from individual or few close lying NCs (the reference), and the second – consisting of very bright stripes, whose positions correlate with the positions of the nanowires. These nanocrystals feature shorter lumine-scence decay times (~60 µs) than the reference ones (~100 µs), what can be seen on the FLIM map (Fig. 1c). We attribute this emission to the nanocrystals coupled with nanowires, and featuring the MEF effect [3].

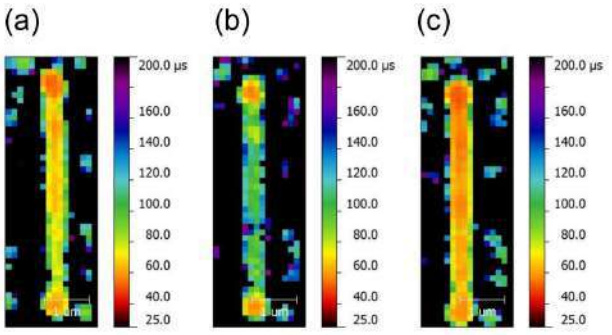


Figure 2. Single nanowire decorated by nanocrystals, visualized with FLIM at 660 nm. We used (a) unpolarized or polarized laser light oriented (b) parallel or (c) perpendicular to the nanowire.

Interestingly, efficiency of the luminescence enhancement strongly depends on the polarization of the excitation beam. We demonstrated previously that absorption of light by NCs coupled with NWs is the most efficient when the excitation beam is polarized parallel to the nanowire [3,4]. In this work, however, we demonstrate that NCs emission rates are also sensitive to the laser polarization [5]. We performed FLIM imaging using unpolarized (Fig. 2a) and polarized laser beam oriented parallel (Fig. 2b) and perpendicular (Fig. 2c) to the nanowire. We noticed that for the parallel polarization emission decays are significantly longer than for the perpendicular one. We attribute this effect to different orientation of dipole moments of the NCs, which can be controlled by the excitation laser. Our results will be discussed and confronted with theoretical simulations.

4. Conclusions

In this work we demonstrated very efficient coupling between up-converting nanocrystals and silver nanowires. In the vicinity of a single NW the up-conversion process is strongly enhanced. By using FLIM microscopy we proved the effect of plasmon excitations in silver nanowires on radiative transition rates of NCs placed in their vicinity. We noticed that the highest emission rates enhancement is observed for dipole moments oriented perpendicular to the nanowire. This observation gives a new insight into the MEF phenomenon.

Acknowledgements

These research were supported by the projects no. 2017/26/E/ST3/00209 and 2017/27/B/ST3/02457 from the National Science Center of Poland.

References

[1] P. Bharadwaj et al., Nanotechnology 18, 044017 (2007).
[2] P. Bharadwaj et al., Opt. Express. 15, 14266 (2007).
[3] D. Piatkowski et al., Nanoscale 7(4), 1479 (2015).
[4] A. Prymaczek et al., Nanoscale 10(26), 12841 (2018).
[5] D. Piatkowski et al., Materials 10, 905 (2017).

Propagation of surface plasmon polaritons in silver nanowires placed on graphene

Aneta Prymaczek[1], Maciej Ćwierzona[1], Justyna Grzelak[1], Dorota Kowalska[1], Marcin Nyk[2], Sebastian Maćkowski[1], Dawid Piątkowski[1*]

[1] Institute of Physics, Faculty of Physics, Astronomy and Informatics,
Nicolaus Copernicus University, Grudziadzka 5, 87-100 Torun, Poland
[2] Advanced Materials Engineering and Modelling Group, Faculty of Chemistry,
Wroclaw University of Science and Technology, Wybrzeze Wyspianskiego 27, 50-370 Wroclaw, Poland
*corresponding author, E-mail: dapi@fizyka.umk.pl

Abstract

We investigate a hybrid nanostructure consisting of a single silver nanowire placed on graphene, and with one end being locally decorated by a small amount of colloidal nanocrystals. We show how the propagation length of SPPs can be controlled by a graphene substrate and affects the up-conversion process in nanocrystals coupled with the metallic nanowire. Such structures are of particular interest because they can provide a platform for new applications in photovoltaic devices and various sensor architectures [1].

1. Introduction

Silver nanowires can effectively support surface plasmon polaritons (SPPs). They can operate as nanoscopic waveguides, capable of routing SPPs for quite long distances approaching tens of microns [2]. Recently, SPPs were used for remote activation of fluorescence, Raman scattering or catalysis of the chemical reactions [3]. Quite recently we have demonstrated that surface plasmon polaritons, propagating in a single silver nanowire, can remotely activate two-photon up-conversion luminescence [4].

In the last years, graphene has attracted much attention as an interesting component for new optoelectronic devices. Due to exceptional physicochemical and optical properties like flat absorption spectrum or perfect electrical conductivity, it became a platform for many sensoric applications. Despite this fact, there are some disadvantages associated with the use of graphene. In this work we present our results regarding the influence of the graphene substrates on SPPs. Of particular interest is potential graphene-induced SPPs quenching, which can translate to limited SPPs propagation range.

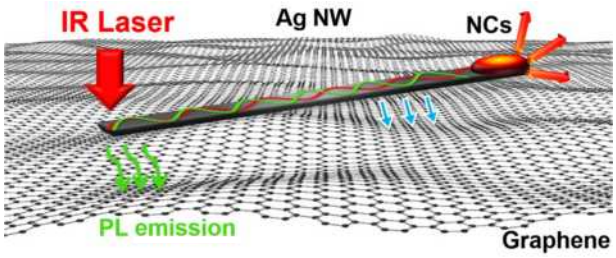


Figure 1: Schematic illustration of silver nanowire deposited on a graphene substrate with a droplet of nanocrystals at one end. Plasmon modes are induced by the infrared laser operating at 980 nm.

2. Materials and methods

In this work we investigate a nanostructure consisting of a long, single silver nanowire decorated with a small drop of nanocrystals (~fL), deposited precisely at one of its ends (Fig. 1). The nanowires feature lengths of about 10-15 microns. The extinction spectrum of colloidal nanowires ranges from about 400 nm to 1000 nm and is presented in Fig. 2.

$NaYF_4$ nanocrystals used in this work, are doped with erbium and ytterbium ions, and they have sizes of approximately 20 nm in diameter. Rare-earth ions are responsible for anti-Stokes luminescence (550 and 650 nm), which is activated by near-infrared radiation at 980 nm. Emission lines of nanocrystals are presented in Fig. 3. They overlap with the extinction of nanowires (Fig. 2), thus the interaction between them (under specific circumstances, such as optimal distance) can be very efficient and can lead to new effects.

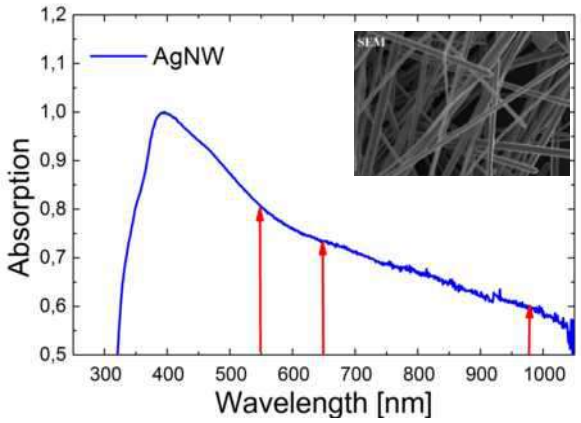


Figure 2: Extinction spectrum of colloidal nanowires. Arrows indicate the emission lines of nanocrystals and laser excitation used in the experiment.

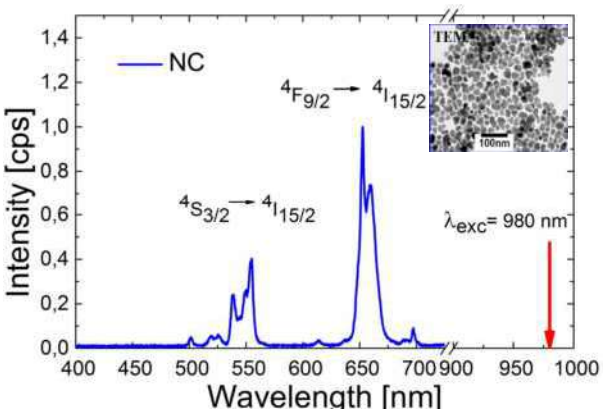


Figure 3: Emission spectrum of a single nanocrystal observed upon 980 nm laser excitation (red arrow).

Graphene is a monolayer of carbon atoms, tightly packed into two-dimensional hexagonal lattice. Monolayer graphene is a semimetal with a zero bandgap and can by considered also as plasmonic material. The most outstanding advantages of graphene are high electron mobility and high mechanical strength. From the optical point of view, single graphene layer shows about 2,3 % absorption of incident light, that occurs in a broad spectral range.

Our samples were investigated using anti-Stokes confocal photoluminescence microscope, equipped with a high numerical aperture oil immersion objective (NA=1.49). For excitation we applied a single-mode infrared CW/pulsed laser operating at 980 nm. For detection we used a single photon counting unit, connected to the counter card (PL imaging). Detailed topography of the sample, including arrangement of the nanocrystals near the nanowire end were realized using Atomic Force Microscopy and Scanning Electron Microscopy techniques.

3. Results and discussion

We used high numerical aperture objective to launch the SPPs by a laser beam focused at the free end of the nanowire (without nanocrystals). The SPPs propagate towards the other end, and activate luminescence of the nanocrystals deposited locally on the nanowire. Next, excited nanocrystals can induce polaritons, which propagate back to the starting excitation spot. This polaritons feature frequencies corresponding to the emission of nanocrystals, what is observed as a characteristic SPPs mode. The propagation of the energy in a silver nanowire is strongly substrate-dependent and is less efficient on graphene, mostly due to energy transfer from SPPs to graphene. Additionally, the efficiency of this process strongly depends on the polarization of the laser, diameter and length of the nanowire [5]. The key issue of our work was to introduce a spacer, limiting SPPs quenching, but conserving measurable coupling between nanocrystals, nanowires and graphene.

4. Conclusions

In this study, we proposed a complex hybrid nanostructure consists of up-conversion nanocrystals, silver nanowires and graphene, as an new interesting platform for optoelectronic application. We investigated and optimized efficiency of mutual interactions in order to obtain a structure featuring new functionality and best properties of its components.

Acknowledgements

These research were supported by the projects no. 2017/26/E/ST3/00209 and 2017/27/B/ST3/02457 from the National Science Center of Poland.

References

[1] B. Zhou et al., Nature nanotechnology 10, 924 (2015).
[2] H. Ditlbacher et al., Phys. Rev. Lett. 95, 257403 (2005).
[3] Z. Zhang et al., Advance Science 3, 1500215 (2016).
[4] A. Prymaczek et al., Nanoscale 10, 12841 (2018).
[5] M. Song et al., Opt. Express 25, 9138 (2017).

Rock-salt CdZnO for IR plasmonics

J. Tamayo-Arriola[1], E. Martínez Castellano[1], A. Huerta-Barberà[2], M. Montes Bajo[1], E. Muñoz[1], V. Muñoz-Sanjosé[2], and A. Hierro[1]

[1]ISOM, Universidad Politécnica de Madrid, Madrid, Spain
[2]Dept. Física aplicada i Electromagnetisme, Universitat de València, Burjassot, Spain
*corresponding author, E-mail: adrian.hierro@upm.es

Abstract

CdO is an n-type semiconductor with excellent transport properties, gaining attention in recent years for the study of strong light-matter interaction phenomena. Here we show the conductivity of the MOCVD-grown CdO can be improved by alloying it with ZnO, reducing the losses in the mid-IR and enhancing its performance as a plasmonic material. Here we combine infrared reflectance and ultraviolet-visible absorption spectroscopies together with Hall effect, to determine its optical and electrical transport characteristics for increasing Zn contents.

1. Introduction

The field of plasmonics was widely studied during the last decades, by using noble metals as Au and Ag, on which the plasma resonance falls in the visible region of the electromagnetic spectrum. Although metals have very high conductivities and behave as perfect reflectors at far infrared (IR) frequencies, in the mid-IR region they have very large optical losses due to the excitation of interband transitions. Thus, alternative compounds are needed for the mid-IR range and CdO fulfils the requirements for becoming a low-loss plasmonic material:[1] a high and tunable plasma frequency (ω_p) as well as a high electron mobility (μ) is attainable in as-grown material.

Some studies suggest the free electron concentration, and therefore ω_p, can be increased in CdO by alloying it with ZnO,[2,3] allowing to modulate the plasmonic resonance over a range of frequencies. However, in polycrystalline materials, grain boundary scattering limits the enhancement of electron mobility, a key parameter for reducing the optical losses.

Here we present the results[4] of the transport and optical properties of single-oriented CdZnO thin films grown on r-plane sapphire in rock-salt phase. Thanks to the high crystal quality achieved in the films, an enhancement in the electron mobility with Zn was found, which, combined with the rise in the free electron concentration, makes CdZnO an excellent candidate for IR plasmonics and leads to the lowest reported resistivity values for the rock-salt CdZnO ternary.

In addition, as a consequence of the bandstructure modification and the band filling, the incorporation of Zn to the rock-salt crystalline structure of CdO induces a blueshift of the optical bandgap, widening the transmission window of the material and therefore improving its performance as a transparent conductive oxide (TCO).

2. Samples and characterization techniques

The CdZnO films were grown by metal organic chemical vapor deposition (MOCVD) on r-plane sapphire substrates. Nominal Zn contents range from 0 to 25 % and the thickness is approximately 150 nm.

The optical properties of the films in the mid-IR were studied by means of infrared reflectance (R) spectroscopy with a Fourier Transform Infrared Spectrometer (FTIR). The R spectra were fitted using a dielectric function model, which accounts for the interaction between light and free electrons with a Drude term, as

$$\varepsilon(\omega) = \varepsilon_{\infty}^{CdZnO} - \frac{\omega_p^2}{\omega^2 + i\omega\gamma_p}, \quad (1)$$

where $\varepsilon_{\infty}^{CdZnO}$ is the background dielectric constant of the alloy, ω_p is the plasma frequency and γ_p its broadening. The plasma frequency is related to the optical electron concentration (n_{opt}) and the electron effective mass (m_e^*) by

$$\omega_p^2 = \frac{n_{opt}}{m_e^* \varepsilon_0}, \quad (2)$$

and the broadening of the plasma resonance is related to the optical mobility (μ_{opt}) by $\mu_{opt} = e/m_e^* c\gamma_p$, where c is the speed of light and e the electron charge.

The electrical properties of the CdZnO films were analyzed at room temperature with Hall effect in the Van der Pauw configuration. From Hall effect measurements, the Hall electron concentration (n_{Hall}), the Hall mobility (μ_{Hall}), and the electrical resistivity (ρ) was determined for each Zn content.

Finally, the optical bandgap, one of the fundamental parameters of TCOs, was determined from ultraviolet-visible transmission spectroscopy. Since CdO is a degenerate semiconductor, in order to derive the real bandgap of the material at the Γ point, band filling should be taken into account together with the conduction band (CB) nonparabolicity, as

$$E_{BM} = \left(\frac{\hbar^2}{2m_e^*}\right)(3\pi^2 n)^{2/3}, \quad (3)$$

where m_e^* of each film was derived from Eq. (2) considering $n_{opt} = n_{Hall}$.

3. Results and discussion

From the R measurements performed with the FTIR, the plasma frequency and its broadening are obtained and are shown in Figure 1.

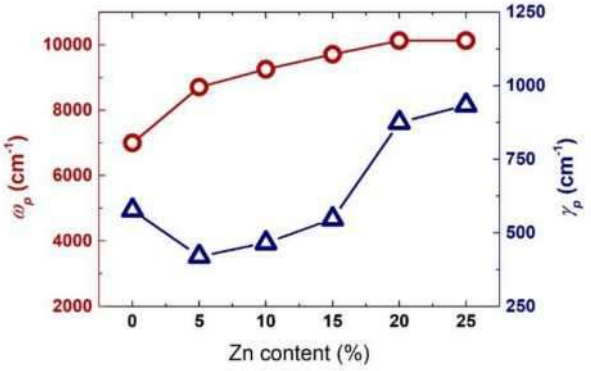


Figure 1. Plasma frequency and its broadening as a function of Zn content in the CdZnO films.

As the Zn content is increased, the plasma frequency shifts to higher energies, reaching a value of 10250 cm^{-1} for a Zn content of 25 %, indicating a rise of the optical electron concentration. On the other hand, the broadening is reduced from 577 cm^{-1} to 420 cm^{-1} as 5 % Zn is added to CdO, whereas for larger Zn contents it increases monotonically, although is maintained below 600 cm^{-1} for Zn contents up to 15 %. Only for the largest Zn contents a clear drop of γ_p is observed, indicating a degradation of the crystal quality of the alloy.

From the point of view of CdZnO as a plasmonic material, we want to highlight the plasma frequency can be tuned from 7000 cm^{-1} to 9000 cm^{-1} while maintaining or even reducing the optical losses.

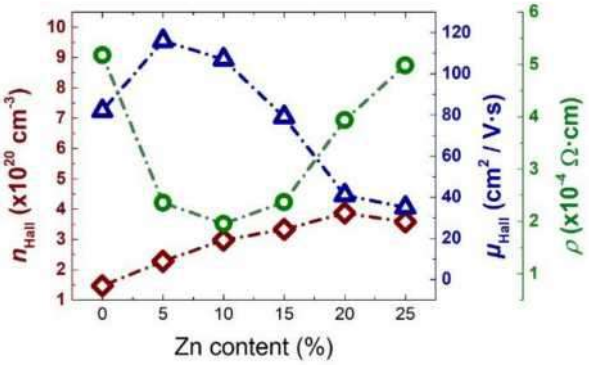


Figure 2. Dependence of the Hall electron concentration, Hall mobility and resistivity on the Zn content.

Regarding the Hall results showed in Figure 2, the trends observed of μ_{Hall} and n_{Hall} are similar than for the optical values. Free electron concentration values are above 10^{20} cm^{-3}, with a maximum value of 3.9x10^{20} cm^{-3} for 20 % Zn. The Hall mobility values are the highest for Zn contents of about 5 – 10 %. Combining both parameters, resistivity values are always below 6x10^{-4} cm^2/Vs, with a minimum value of 2x10^{-4} cm^2/Vs, which correspond to the lowest reported values for the CdZnO alloy.[2,3]

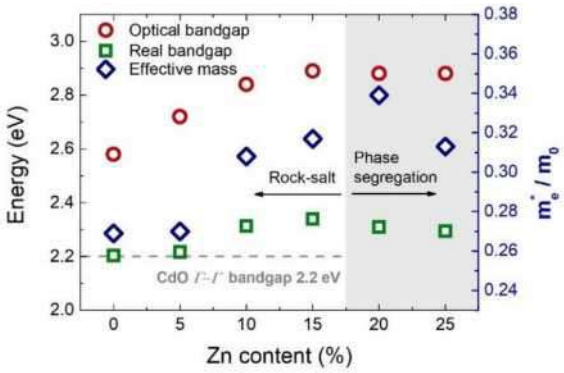


Figure 3. Dependence on the Zn content of the measured absorption band-edge energy, the calculated bandgap energy at the Γ point considering the Burstein-Moss shift from Eq. (3), and computed electron effective mass using Eq. (2).

The large blue-shit of the optical bandgap for increasing Zn contents is shown in Figure 3, together with the calculated bandgap with Eq. (3) and m_e^*. The rise of the optical bandgap widens the transmission window of the material from 2.58 eV to 2.9 eV, which, combined with the low resistivities, improves its perspectives as a TCO.

4. Conclusions

In summary, we have identified the rock-salt CdZnO ternary as an excellent candidate for IR plasmonics. The high crystal quality achieved in the CdZnO films reduces the plasma broadening and its frequency can be tuned with the Zn content. Indeed, the optical and electrical mobilities obtained correspond to the best reported values for the CdZnO alloy. Besides, the incorporation of Zn yields a simultaneous decrease of the electrical resistivity and a widening of the transmission window of the material, key parameters for TCOs.

Acknowledgements

This work was funded by the Spanish Ministry of Economy and Competitiveness (MINECO) through Projects TEC2014-60173-C2 and TEC2017-85912-C2, and by the EU (Feder) and Generalitat Valenciana, Project Prometeo II 2015/004. J.T.-A. holds a Predoctoral Contract from Universidad Politécnica de Madrid.

References

[1] E. Sachet, C.T. Shelton, J.S. Harris, B.E. Gaddy, D.L. Irving, S. Curtarolo, B.F. Donovan, P.E. Hopkins, P.A. Sharma, A.L. Sharma, J. Ihlefeld, S. Franzen, and J.P. Maria, Nat. Mater. **14**, 414 (2015).

[2] H. Tabet-derraz, N. Benramdane, D. Nacer, A. Bouzidi, and M. Medles, Sol. Energy Mater. **73**, 249 (2002).

[3] A.A. Ziabari and F.E. Ghodsi, J. Alloys Compd. **509**, 8748 (2011).

[4] J. Tamayo-Arriola, A. Huerta-Barberà, M. Montes Bajo, E. Muñoz, V. Muñoz-Sanjosé, and A. Hierro, Appl. Phys. Lett. **113**, 222101 (2018).

Double-interface surface plasmon modes in CdZnO thin films and their hybridization with phonons

E. Martínez Castellano[1], J. Tamayo-Arriola[1], M. Montes Bajo[1], A. Huerta-Barberà[2], E. Muñoz[1], V. Muñoz-Sanjosé[2], and A. Hierro[1*]

[1]ISOM, Universidad Politécnica de Madrid, Madrid, Spain
[2]Department Física Aplicada i Electromagnetisme, Universitat de València, Burjassot, Spain
*corresponding author, E-mail: adrian.hierro@upm.es

Abstract

CdZnO is a promising candidate to substitute metals in future IR plasmonic devices. As an approximation to these plasmonic phenomena, we have studied the plasmonic modes present in a double-interface asymmetric system. For this purpose, reflectance of thin CdZnO layers grown on r-sapphire substrate were measured in Otto configuration. In thick samples, modes appeared to be asymptotically pinned to the single-interface plasmon frequency. In contrast, the thinnest layers showed an important coupling between both interfaces, with a strongly confined ENZ mode at high energies and a hybrid Surface Plasmon-Phonon mode at lower frequencies.

1. Introduction

This study continues our previous work [1] about the electro-optical properties of CdZnO as a Transparent Conductive Oxide (TCO). We have previously shown that percentages of around 10 % Zn made the alloy a perfect candidate for plasmonic applications. This ternary showed a high plasma frequency (over 9000 cm^{-1}) with a relatively high mobility (110 $cm^2/V{\cdot}s$), values fully compatible with a plasmonic behavior in the IR.

In this work, we study the Surface Plasmon Resonance (SPR) in thin layers of CdZnO (10 % Zn) with an asymmetric air-TCO-sapphire system, and their coupling to surface phonons producing a hybrid Surface Phonon-Plasmon Resonance (SPhPR). TCO layers with different thicknesses were used, ranging from a thin 25 nm, close to the air-sapphire non-plasmonic limit, to 460 nm, where the air-CdZnO interaction domines.

According to theory [2], a thin metal layer (or TCO in our case) sandwiched between two dielectric semi-infinite media is able to stablish two different surface plasmon modes, a high energy one with symmetric distribution of the electric field across both interfaces, and a lower energy mode for an antisymmetric pattern. In our case, this symmetry will be broken by the use of different dielectric materials, but similar modes are expected.

For thin TCO layers, it has been theoretically [3] and experimentally [4] shown that the high amplification of the field across both interfaces can drive the higher energy mode to overpass its own single-interface frequency limit. The effect appears for layers thinner than $\lambda_p/5\pi$, with λ_p being the wavelength associated with the plasma frequency [4]. This is a low dispersive mode usually called epsilon near zero (ENZ), where the field is heavily amplified and confined in the TCO and the SPR almost reaches the plasma frequency of the material.

In the same range of small TCO thickness, the lower energy SPR is expected to reach frequencies small enough to interact with the substrate phononic modes. These Surface Phonon Resonances (SPhR) are surface modes, analogous to SPR, where light couples phonons as elementary oscillation instead of plasmons. While being formally similar to SPR, they have a much more restricted dispersion, with a range of frequencies limited to the reststrahlen band defined by transversal and longitudinal phononic modes [5].

2. Materials and methods

The CdZnO samples were grown by Chemical Vapor Deposition (CVD) on r-plane sapphire substrates at 330ºC. Their reflectance spectra were measured with a Fourier Transform Infrared (FTIR) spectrometer and fitted with a computational software based on the Transfer Matrix Method (TMM). Values of TCO thickness (d), high frequency dielectric constant (ε_∞), plasma frequency (ω_p), and damping (γ) were extracted from the fits.

For the study of the SPR, an Attenuated Total Reflection (ATR) configuration with a ZnSe prism was used in conjunction with the FTIR. P-reflectance of the samples was measured as a function of the angle of incidence and compared with theoretical reflectivity simulations where the previously fitted parameters were used.

Table 1: TCO parameters extracted from the reflectance fits.

d [nm]	ε_∞	ω_p [cm^{-1}]	γ [cm^{-1}]
25	5.1	8988	503
63	5.1	9254	550
150	5.1	9131	518
248	5.1	9307	518
460	5.1	9219	525

3. Results and discussion

As shown in Figure 1, the two expected SPR modes were find in each reflectance experiment as absorbing minima in reflectivity maps. Hence, they can be associated with the symmetric and antisymmetric distributions of the electric field we previously discussed.

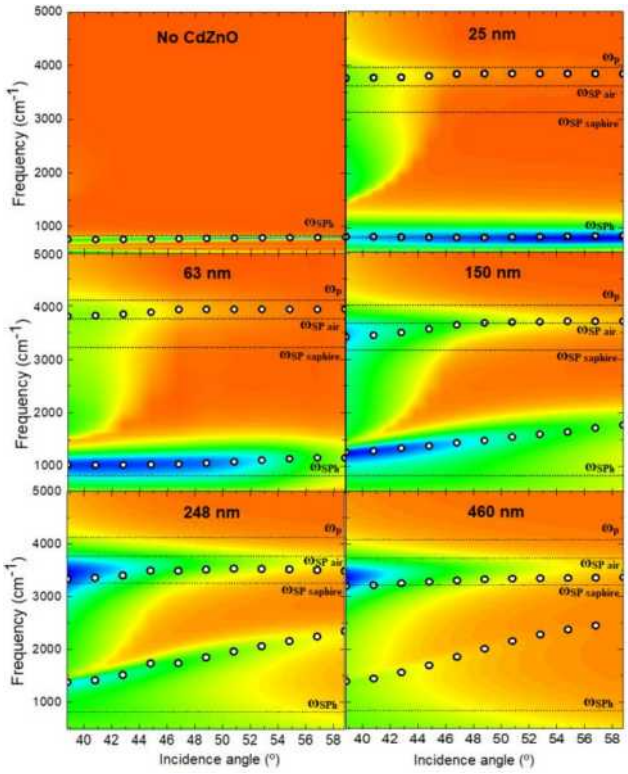


Figure 1: Theoretical ATR reflectance maps for different CdZnO thicknesses. The dots show minimums in the ATR experimental measurements. The dashed lines represent the SPh frequency of a sapphire-air interface (ω_{SPh}), the ZnCdO plasma frequency (ω_p), the single-interface ZnCdO-sapphire ($\omega_{sp\ sapphire}$) and the ZnCdO-air ($\omega_{sp\ air}$) SPR frequencies.

Regarding the upper branch, this is consistently under $\omega_{sp,Air}$, the single-interface air-CdZnO SP frequency in thick samples, acting as an asymptote. The case is indistinguishable from a simple air-CdZnO system, so this mode can be considered decoupled from the interface with sapphire. As the thickness decreases, this limit is clearly overpassed and the resonance almost reaches the plasma frequency of the TCO. Thus, we are clearly in the ENZ regime expected for such small thicknesses.

In contrast with the upper branch, the lower minima range is more intensely affected by changes in the TCO thickness. In thick samples, while the asymptotic decoupled limit ($\omega_{sp\ sapphire}$) is not reached in our experiment, the computational extension of the angle of incidence pins the minimum to the expected value. Thinner samples restrict the decrease in frequency to the SPhR limit measured in absence of plasmonic layer. Consequently, the lower branch in our system could be considered a hybrid Surface Phonon-Plasmon Resonance, preserving some of the desirable properties associated to both types of light interactions. From the SPR, it maintains the wide range of tunability via thickness control and doping. From the SPhR, the low widening of the absorption minima, especially at lower energies.

4. Conclusions

We show here that the CdZnO effectively supports surface plasmonic modes that can be conveniently tuned by a fine control of the thickness. For thin TCO layers, the strong interaction of the electric field across both interfaces leads to two strongly coupled modes that include a low dispersion ENZ mode and a highly tunable hybrid SPhPR. Thicker CdZnO layers decouple the interaction and those modes are expected to be indistinguishable from single-interface systems. Accordingly, a versatile plasmonic behavior of CdZnO has been proven, with the advantages associated to this ternary compound: high plasma frequency and mobility with a relatively low growth temperature.

Acknowledgements

This work was funded by the Spanish Ministry of Economy and Competitiveness (MINECO) through Project TEC2017-85912-C2, and by the EU (Feder) and Generalitat Valenciana, Project Prometeo II 2015/004. E.M.C. holds a Predoctoral Contract from Universidad Politécnica de Madrid.

References

[1] J. Tamayo-Arriola, A. Huerta-Barberà, M. Montes Bajo, E. Muñoz, V. Muñoz-Sanjosé, and A. Hierro, "Rock-salt CdZnO as a transparent conductive oxide," *Appl. Phys. Lett.*, vol. 113, no. 22, p. 222101, Nov. 2018.

[2] K. Y. Kim, *Plasmonics - Principles and Applications*. InTech, 2012.

[3] S. Campione, I. Brener, and F. Marquier, "Theory of epsilon-near-zero modes in ultrathin films," vol. 121408, pp. 1–5, 2015.

[4] E. L. Runnerstrom, K. P. Kelley, E. Sachet, C. T. Shelton, and J. P. Maria, "Epsilon-near-Zero Modes and Surface Plasmon Resonance in Fluorine-Doped Cadmium Oxide Thin Films," *ACS Photonics*, vol. 4, no. 8, pp. 1885–1892, 2017.

[5] M. Schubert, T. Hofmann, and J. Šik, "Long-wavelength interface modes in semiconductor layer structures," *Phys. Rev. B - Condens. Matter Mater. Phys.*, vol. 71, no. 3, pp. 1–9, 2005.

Direct Demonstration of Biexciton Quantum Yield Enhancement in an Individual Quantum Dot Coupled with Gold Nanoparticles in a Thin-film Hybrid Material

Victor Krivenkov[1,*], Pavel Samokhvalov[1], Ana Sanchez-Iglesias[2], Marek Grzelczak[3], Igor Nabiev[1,4], Yury Rakovich[1,3,5,6,*]

[1] National Research Nuclear University MEPhI (Moscow Engineering Physics Institute), 115409 Moscow, Russian Federation
[2] CIC biomaGUNE, Paseo de Miramon 182, 20014 Donostia-San Sebastian, Spain
[3] Donostia International Physics Center, Paseo Manuel Lardizabal 4, 20018 Donostia-San Sebastian, Spain
[4] Laboratoire de Recherche en Nanosciences, LRN-EA4682, Université de Reims Champagne-Ardenne, 51100 Reims, France
[3] Centro de Física de Materiales (MPC, CSIC-UPV/EHU) and Donostia International Physics Center, Paseo Manuel de Lardizabal 5, 20018 Donostia-San Sebastian, Spain
[4] IKERBASQUE, Basque Foundation for Science, Maria Diaz de Haro 3, 48013 Bilbao, Spain
*corresponding authors, E-mail: vkrivenkov@list.ru and Yury.Rakovich@ehu.eus

Abstract

Biexcitons, which can be excited in semiconductor quantum dots (QD), cause the multiphoton emission effect. However the photoluminescence quantum yield (QY) of biexcitons is low due to the Auger process. In this study we demonstrate the biexciton QY enhancement in single QDs due to their coupling with gold nanorods (GNRs). Measuring the photoluminescence properties of the same single QD before and after coupling with GNRs, we obtained a confirmation of the biexciton QY increase due to the Purcell effect.

1. Introduction

Semiconductor quantum dots (QDs) are known for their unique photophysical properties and, in particular, their ability to multiphoton emission caused by recombination of biexcitons that is practically simultaneous emission of two photons from single QD as a result of a biexciton / exciton cascade [1]. The latter phenomenon has an important implication for quantum technologies, since photons emitted by the biexciton and exciton can be entangled in polarization steaming from the spin of biexciton [2]. However, the luminescence quantum yield (QY) of biexciton states is relatively low due to the fast Auger non-radiative process, which limits the applicability of this effect in practice. Plasmonic nanoparticles (PNPs) can significantly modify the optical properties of nearby QDs [3, 4]. An important condition for plasmon-exciton coupling is the resonant overlapping of the plasmon modes and QD photoluminescence (PL) spectra. Particularly, PNP may acts as a near-field resonator, leading to an acceleration of the radiative recombination in QDs due to the change in the density of photon states, i.e. Purcell effect. If the rates of nonradiative processes remain unchanged, this should lead to the increase in PL QY. However in real systems, the change in the QY depends on the trade-off between the acceleration of the radiative process due to the Purcell effect and the acceleration of nonradiative losses due to resonant energy transfer. The purpose of our study was to create a composite thin-film material from QDs and gold PNPs with controlled distance between them, and during the fabrication of the material observe the same QD before and after deposition of PNPs to directly measure the changes in the PL properties of excitons and biexcitons [5].

2. Experimental

In this study we used the CdSe/ZnS/CdS/ZnS QDs in hexane solution with 90% QY and 5 nm diameter. The PL and extinction spectra of QDs are shown in Figure 1a. We used PNPs in the form of gold nanorods (GNRs) with 39.1±1.3 nm length and 20.5 ± 0.5 nm diameter. Their extinction spectrum is presented in Figure 1a. To prepare thin-film hybrid structure the hexane solution of QDs was spin-coated on the thin (~5 nm) film of PMMA on glass so that, as a result, there is no more than one QD per 1 μm^2. Then the one or two PMMA layers were spin-coated on the top of QDs to control the distance between QDs and GNRs. To study the emission properties of the same single QD before and after GNRs deposition, we used the following procedure. At first, the objective was fixed on the single QD and its time-resolved PL intensity, PL decay kinetics and second-order cross correlation function were measured. Then GNRs was dropped on the top of the structure and left to dry completely. After that the PL properties of the same QD were studied again (Figure 1b). To measure the PL properties a confocal time-resolved fluorescent microscope Micro Time 200 (PicoQuant) was used. For excitation, we used 485 nm diode laser working at a pulse regime with 5 MHz repetition rate and ~100 ps duration. The biexciton QY was estimated by comparison of central and side parts of cross-correlation function $g^{(2)}$ [1]:

$$\Phi_{XX} \approx \Phi_X \frac{\int_{-\Delta t}^{\Delta t} g^{(2)}(\tau)d\tau}{\int_{T-\Delta t}^{T+\Delta t} g^{(2)}(\tau)d\tau} = \Phi_X \frac{central\ peak}{average\ side\ peak}, (1)$$

where Φ_{XX} – biexciton QY, Φ_X – exciton QY, T – period between laser pulses, τ – time delay between detectors.

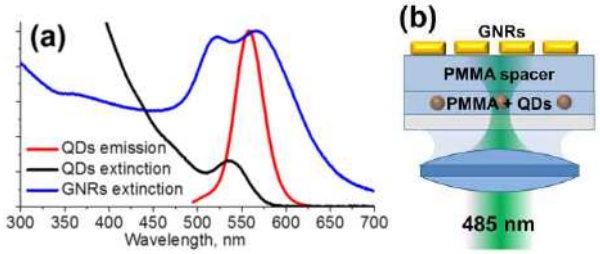


Figure 1. (a) PL (red line) and extinction (black line) spectra of QDs and also extinction spectra of GNRs (blue line). (b) Schematics of the hybrid QD-GNR structure during PL experiments on a single QD.

3. Results and discussion

We prepared a series of samples in which the QDs layer was separated from the GNRs by a PMMA spacer (from 5 to 170 nm). Then, time-resolved, time-correlated and photon correlation spectroscopy measurements was performed. In all samples the central part of $g^{(2)}$ did not exceed 30% of side parts (17.5% in Figure 2a). After the GNRs deposition in all samples the central part of $g^{(2)}$ increased to the values of 70÷120% of side parts (77% in Figure 2b) and the increase was the greater, the smaller the thickness of PMMA spacer. This situation may indicate an increase in the biexciton QY. Therefore, we measured the PL lifetime to prove the Purcell effect.

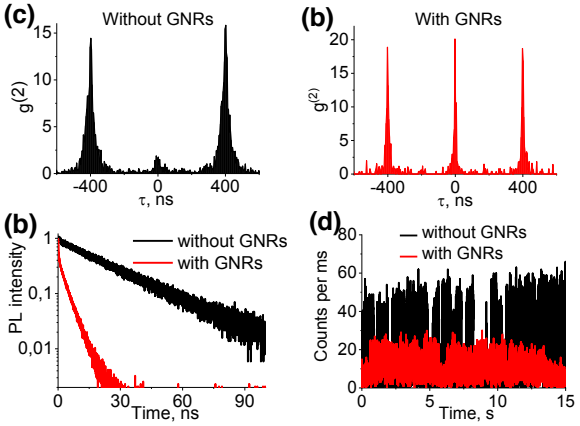


Figure 2. Changes in the PL properties of a single QD before and after deposition of the GNRs layer with 30 nm PMMA spacer. (a,b) – Cross-correlation function $g^{(2)}$ of single QD: (a) before GNRs deposition, and (b) after GNRs deposition. (c) – PL decay kinetics of single QD before GNRs deposition (black line) and after (red line). (d) – PL time trace from single QD before GNRs deposition (black line) and after (red line).

After GNRs deposition the PL lifetime shortened for all samples. For sample with 30 nm PMMA spacer this shortening was from 22.8 to 1.5 ns (Figure 2c). To show that this shortening is predominantly due to the Purcell effect, and not the plasmon-induced PL quenching, we measured the PL time trace before and after GNRs deposition. In all samples the average PL signal decreased in the presence of GNRs, but this decrease was much lower than PL lifetime shortening. For sample with 30 nm PMMA spacer this decrease was only 2.3 times (Figure 2d). This indicates an increase in the radiation rate due to the change in the density of the photon states, i.e. Purcell effect.

4. Conclusions

In this study we directly demonstrate the distance-controlled enhancement of the biexciton emission of single CdSe/ZnS/CdS/ZnS QDs due to their coupling with GNRs. Specifically, using photon correlation spectroscopy, accompanied by time-resolved luminescence studies of the same single QD before and after coupling with GNRs, we obtained an confirmation of the plasmon-mediated increase in the QY of biexciton states. By changing the separation between the QD and GNRs, we have demonstrated that the enhancement of the biexciton emission decreases monotonically with increasing distance. We explain this enhancement by the efficient coupling between the biexcitons in QDs and the GNRs plasmons, which leads to the predominant influence of the Purcell effect. Our findings constitute a reliable approach to managing the efficiency of multiphoton emission over a wide span of distances and can be used for the development of new materials, structures and devices with applications the fields of optoelectronics, optical computing and quantum technologies.

Acknowledgements

The authors acknowledge the financial support from the Ministry of Education and Science of the Russian Federation (Grant 14.Y26.31.0011).

References

[1] G. Nair, J. Zhao, M. G. Bawendi, Biexciton quantum yield of single semiconductor nanocrystals from photon statistics, *Nano Lett*. 11: 1136–1140, 2011.

[2] O. Benson, C. Santori, M. Pelton, Y. Yamamoto, Regulated and entangled photons from a single quantum dot, *Phys. Rev. Lett.*, 84: 2513, 2000.

[3] D. S. Dovzhenko, S. V. Ryabchuk, Y. P. Rakovich, I. R. Nabiev, Light–matter interaction in the strong coupling regime: configurations, conditions, and applications, *Nanoscale*, 10: 3589-3605, 2018.

[4] V. Krivenkov, S. Goncharov, I. Nabiev, Y. P. Rakovich, Induced transparency in plasmon–exciton nanostructures for sensing applications, *Laser Photonics Rev.*, 13: 1800176, 2019.

[5] V. Krivenkov, S. Goncharov, P. Samokhvalov, A. Sánchez-Iglesias, M. Grzelczak, I. Nabiev, Y. P. Rakovich, Enhancement of biexciton emission due to long-range interaction of single quantum dots and gold nanorods in a thin-film hybrid nanostructure, *J. Phys. Chem. Lett.*, 10: 481–486, 2019.

Ultrafast response of a plasmonic distributed feedback laser in large-signal modulation regime

Nikita E. Nefedkin[1,2,3*], Alexander A. Zyablovsky[1,2], Egveny S. Andrianov[1,2], Alexander A. Pukhov[1,2,3], and Alexey P. Vinogradov[1,2,3]

[1]Dukhov Research Institute of Automatics (VNIIA), Moscow, Russia
[2]Moscow Institute of Physics and Technology, Moscow, Russia
[3]Institute for Theoretical and Applied Electromagnetics, Moscow, Russia
*corresponding author, E-mail: nefedkin@phystech.edu

Abstract

The time response to an external signal is the main characteristic of optoelectronic devices which determines their maximum modulation speed. The use of plasmonic structures can significantly reduce the response time. In this paper, we show that the response time of a two-dimensional plasmonic DFB laser in the large-signal modulation regime strongly depends on the size of the pump beam. There is an optimal size of beam for which the modulation speed is a maximum, and can achieve 1 THz.

1. Introduction

For many optoelectronic applications, such as the modulation of optical signals and sensing, lasers with an ultrafast modulation response are required [1, 2]. Such devices often operate in a large-signal modulation scheme where a pumping pulse switches the laser between the subthreshold regime and the above-threshold regime. The maximal modulation frequency of surface emitting lasers based on dielectric structures is limited to several tens of GHz [3]. This frequency can be significantly increased if one use metallic plasmonic structures. In our paper, we study the dynamics in the large-signal modulation regime of a plasmonic distributed feedback (DFB) laser that consists of a gold film perforated by a periodic array of holes, and is coated with a layer of an active medium. We examine the behavior of the laser for different sizes of the pump beam. Combining numerical simulations of the laser dynamics within the framework developed in Ref. [4, 5] with an analytical evaluation, we show that the response time strongly depends on the size of the pump beam. We demonstrate that there is an optimal size of the pump beam, for which the response time reaches a minimum. For typical experimental parameters, the optimal size of the pump beam is $\sim 15\mu$m and the minimal response time is ~ 1 ps. The obtained value of the response time is in agreement with a recent experiment [1] where it has been shown that plasmonic lasers have a modulation frequency exceeding several hundred GHz in the large-signal modulation regime.

2. The time response of a plasmonic DFB laser

To describe the multimode dynamics of the plasmonic DFB laser we use an approach for considering ultrafast phenomena in dispersive dissipative media. This approach is based on the following equations:

$$\frac{dn_{jk}}{dt} = -\left(\gamma_j + \gamma_k\right) n_{jk} + i\left(\omega_j - \omega_k\right) n_{jk} + \\ + \sum_{m=1}^{N_{\text{atom}}} \left(\Omega_{km}\varphi_{jm} + \Omega_{jm}^{*}\varphi_{km}^{*}\right) \tag{1}$$

$$\frac{dD_m}{dt} = -\gamma_D\left(1 + D_m\right) - 2\sum_{j=1}^{N_{\text{mode}}} \left(\Omega_{jm}\varphi_{jm} + \Omega_{jm}^{*}\varphi_{jm}^{*}\right) \tag{2}$$

$$\frac{d\varphi_{jm}}{dt} = -\gamma_{jm}^{\varphi}\varphi_{jm} + i\left(\omega_j^a - \omega_\sigma\right)\varphi_{jm} + \\ + \frac{\Omega_{jm}^{*}}{2}\left(D_m + 1\right) + \sum_{l=1}^{N_{\text{mode}}} \Omega_{lm}^{*} n_{jl} D_m, \tag{3}$$

Here, n_{jj} is the photon number in the jth Bloch mode, n_{jk} is an interference term responsible for the flow of photons from the kth to the jth mode, when $j \neq k$. D_m is the population inversion of the mth atom and $\varphi_{jm} = -i\langle \hat{a}_j^{+}\hat{\sigma}_m\rangle$ describes the energy flow between the mth atom and jth mode. The parameters ω_j, γ_j correspond to the real and imaginary parts of the eigenfrequencies of the modes; ω_σ and γ_D are the atom transition frequency and the relaxation rate of the population inversion of the atoms, $\gamma_{jm}^{\varphi} = \gamma_\sigma + \gamma_j + \gamma_D/2$, γ_σ is the relaxation rate of the phase of the atom polarization. Ω_{jm} is the Rabi constant of coupling between the jth mode and the mth atom.

In Fig. 1 the dependence of the photon number on time is shown. There are three stages of the response of the system [6]. In the first stage, the response of the system is determined by the spontaneous emission in the active medium. The photon number in the plasmonic DFB laser is small. For the system under consideration, the duration of this stage, i.e., the delay time, turns out to be less than a picosecond.

$$t_{\text{delay}} = \gamma_\sigma \ln\left(N_{\text{at}}/2\right)/4N_{\text{at}}\Omega_R^2. \tag{4}$$

In the second stage, the photon number in the plasmonic laser rapidly increases due to stimulated emission in the active medium. This growth ceases with the saturation of the population inversion in the active medium. In the third stage, the photon number in the system decreases exponentially with time. We identify the total response time with the time when the number of photons in the system has decreased by a factor of ten from its maximum value. This time is about one picosecond.

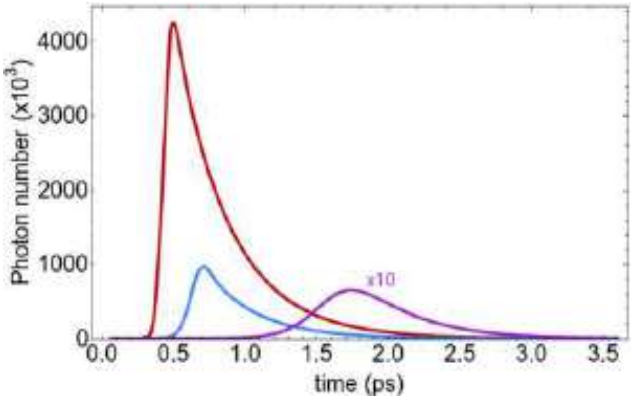


Figure 1: The dependence of the total photon number on the time at the different diameters of the pump beam. The diameters are equal to 20 μm (red line), 10 μm (blue line), and 5 μm (purple line).

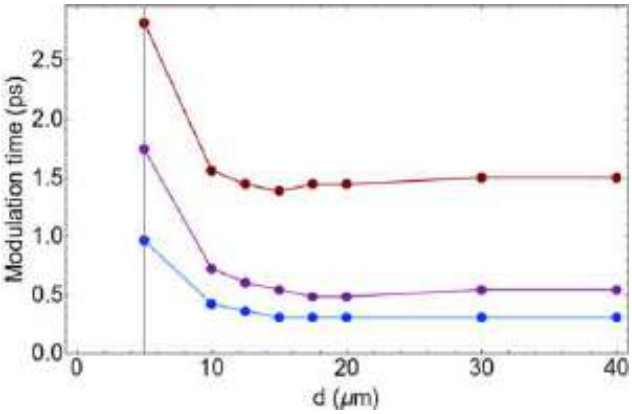


Figure 2: The dependence of the modulation times on the diameters of the pump beam. The blue line depicts the delay time; the purple line depicts the time of the end of the second stage; the red line depicts the total response time.

The dependence of the total photon number on time is qualitatively the same for different diameters of the pump beam. However, the response times manifest a non-monotonic dependence on the size of the pump beam, see Fig. 2. It can be seen that there is an optimal size of the pump beam at which the response time is a minimum. For the considered plasmonic DFB laser the optimal diameter of the pump beam is about 15 μm. As the pump beam diameter decreases, the response time increases rapidly. With an increase in the diameter of the pump beam, the response time changes slowly. This kind of behavior of the plasmonic DFB laser takes place at different initial values of the population inversion of the active atoms.

3. Conclusions

We have shown that the response time of such a laser for typical experimental parameters can be decreased to one picosecond, which corresponds to a modulation frequency of 1 THz. This value is close to the upper limit for plasmonic lasers (the total response time can not be shorter than the time of the third stage, which is determined by the losses in the cavity, and is ~ 1 ps).

It has been shown that the laser's response time can be shortened by optimizing the size of the pump beam, as a result of the consequent reduction of the delay time. The dependence of the response time on the size of the pump beam is for following reason. The interaction of the laser modes with the pumped active medium results in the emergence of a single collective mode. If the size of the pump beam exceeds the propagation length of the EM waves, this collective mode is located in the pumped area. The response time then grows logarithmically with increasing pump beam diameter. In contrast, when the mode is outside the pumped region, the response time is approximately inversely proportional to the square of the pump beam diameter, and so increases rapidly as this diameter decreases from its critical value. Thus, there is an optimal size of the pump beam, for which the response time is a minimum.

References

[1] K. S. Daskalakis, A I. Väkeväinen, J.-P. Martikainen, T.K. Hakala, P. Törmä, Ultrafast Pulse Generation in an Organic Nanoparticle-Array Laser, *Nano Letters* 18: 2658–2665, 2018.

[2] W. Zhou, M. Dridi, J. Y. Suh, C. H. Kim, D. T. Co, M. R. Wasielewski, G. C. Schatz, T. W. Odom, Lasing action in strongly coupled plasmonic nanocavity arrays *Nature Nanotechnology* 8: 506–511, 2013.

[3] J. W. Scott, B. J. Thibeault, C. J. Mahon, L. A. Coldren, F. H. Peters, High modulation efficiency of intracavity contacted vertical cavity lasers, *Applied physics letters* 65: 1483–1485, 1994.

[4] A. A. Zyablovsky, E. S. Andrianov, I. A. Nechepurenko, A. V. Dorofeenko, A. A. Pukhov,A. P. Vinogradov, Approach for describing spatial dynamics of quantum light-matter interaction in dispersive dissipative media, *Phys. Rev. A* 95: 053835, 2017.

[5] N. E. Nefedkin, A. A. Zyablovsky, E. S. Andrianov, A. A. Pukhov,A. P. Vinogradov, Mode Cooperation in a Two-Dimensional Plasmonic Distributed-Feedback Laser, *ACS Photonics* 5: 3031–3039, 2018.

[6] H. Altug, D. Englund, J. Vučković, Ultrafast photonic crystal nanocavity laser, *Nature physics* 2: 484, 2006.

Superradiant molecular aggregates on dielectric surfaces interacting with plasmonic structures

A. Eisfeld[1]

[1]Max Planck Institute for the Physics of Complex Systems, Nöthnitzer Strasse 38, 01187 Dresden, Germany

Abstract

Molecular aggregates formed on dielectric surfaces can show strong collective effects which can result in eigenstates which exhibit super- or sub-radiant emission. Here we discuss how nearby nano-structures influence these eigenstates of the aggregate and the resulting optical properties.

1. Introduction

Organic molecules can self-assemble on dielectric surfaces into regular structures, such as one-dimensional chains or two dimensional arrays. Because of strong resonant interaction between the transition dipoles of the individual molecules, collective eigenstates are formed where an electronic excitation is coherently shared by a large number of molecules. The optical properties of these states differ extremely from those of the individual molecules. In previous work on the organic semiconductor PTCDA on a potassium chloride surface we have created two-dimensional arrays consisting of hundreds of molecules [1]. As a result of the collective eigenstates we observed super-radiant and sub-radiant behavior [1, 2]. This formation of collective states also leads to coherent transfer of a localized excitation along the aggregate. One way of creating such localized excitation is via a metallic nanotip [3].

2. Coupling between tip and aggregate

Our basic setup is sketched in Fig. 1. A metallic tip is placed at nanometer distance above a molecular aggregate formed on a dielectric surface. In Ref. [4] we have shown that in this way one can create a localized excitation which can be used for near-field spectroscopy, circumventing the far-field selection rules. In the present contribution we focus on the interaction between the metallic nanotip and the aggregate, which can be quite strong depending on the size of the nanotip and its distance from the aggregate. One example is shown in the two panels at the bottom of Fig. 1. In the absorption the coupling to the nanotip leads to a broad background on which peaks stemming from the aggregate eigenstates are imprinted.

3. Conclusions

In conclusion, we have considered strong interaction of a metallic nano-tip with a molecular aggregate formed on a dielectric surface. This study is a further step in understanding and designing hybrid systems of molecular aggregates and metallic nanostructures for optical and energy transfer applications.

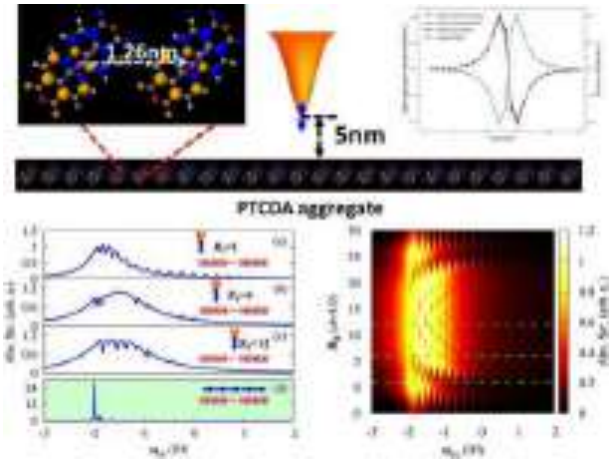


Figure 1: Top: Sketch of the basic setup. A metallic nanotip is placed above the molecular aggregate (here a linear chain of PTCDA molecules). To couple locally to the molecular aggregate the tip is irradiated by far-field radiation. It can be moved across the surface. Interaction between the tip and the aggregate can be probed via absorption spectroscopy. Bottom: left: linear absorption spectra at three different tip positions; as reference the far field spectrum is shown at the bottom. Right: Absorption spectra when scanning continuously over the sample. The green horizontal dashed lines indicate the tip position used in the left plot. In both cases there is strong exciton-plasmon coupling.

References

[1] M. Müller, A. Paulheim, A. Eisfeld, M. Sokolowski, "Finite size line broadening and superradiance of optical transitions in two dimensional long-range ordered molecular aggregates", J. Chem. Phys. **139**, 044302 (2013).

[2] A. Eisfeld, C. Marquardt, A. Paulheim, M. Sokolowski, "Superradiance from Two Dimensional Brick-Wall Aggregates of Dye Molecules: The Role of Size and Shape for the Temperature Dependence" Phys. Rev. Lett. **119** 097402 (2017).

[3] S. Berweger, J.M. Atkin, R.L. Olmon, M.B. Raschke, "Adiabatic Tip-Plasmon Focusing for Nano-Raman Spectroscopy", J. Phys. Chem. Lett. **1**, 3427 (2010).

[4] X. Gao, A. Eisfeld "Near-Field Spectroscopy of Nanoscale Molecular Aggregates", J. Phys. Chem. Lett. **9** 6003 (2018)

Propagation of Strongly Hybridized Plasmonic Modes: Theory and Applications

Ivan A. Pshenichnyuk[1*], Sergey S. Kosolobov[1], Andrei I. Maimistov[2], Vladimir P. Drachev[1,3]

[1]Skolkovo Institute of Science and Technology, ul. Nobelya 3, 121205 Moscow, Russia
[2]National Research Nuclear University 'MEPhI', Kashirskoe sh. 31, 115409 Moscow, Russia
[3]University of North Texas, USA, 76203 Texas, Denton, 1155 Union Circle
*corresponding author, E-mail: i.pshenichnyuk@skoltech.ru

Abstract

Propagation of a hybrid mode formed by mixing of a dielectric waveguide mode with several plasmonic modes, is studied numerically in 3D. Edge plasmons are used to maintain coupling between states with different polarisations. Proposed waveguide structures allow to reach a strong light-matter interaction regime and balance plasmonic losses, providing a convenient basis for various compact and efficient photonic devices, including electro-optical modulators and polarisation converters.

1. Introduction

Surface plasmon polariton (SPP) modes provide good optical confinement of light and play a significant role in nano-optics. One well-known drawback of these modes is connected with losses. On the other hand, dielectric nano-waveguides provide a loss-free way to transmit light, but the confinement is poor, to compare, for example, with the typical sizes of modern electronic components. The idea of hybrid plasmonic waveguides (HPWG) is to mix both concepts and obtain a compromise solution with a desired proportion between losses and confinement [1]. Strong optical confinement of SPP modes is accompanied by enhanced field intensity and strong light-matter interaction (via the oscillations of surface electrons plasma). This property is extremely useful in photonics and allows to construct small and efficient devices. For example, it is used in combination with epsilon-near-zero (ENZ) effect to produce compact waveguide based electro-optical modulators [2].

In classical hybrid waveguides [3] a layer of metal, separated by a thin dielectric, is placed on top of an ordinary waveguide. In this case at least two hybrid modes are formed (for a single mode waveguide) and participate in the evolution of the mixture. The strength of hybridisation can be controlled via the thickness of the insulating layer. There is at least one principle limitation of this structure connected with a polarisation of plasmons. They interacts only with waveguide modes polarised perpendicular to the metallic surface. Applications which assume a delicate polarisation processing require HPWG with more sophisticated structure.

Propagation of hybrid modes (even in the simplest case) is usually accompanied by a periodic oscillation of populations in different components of the mixture. There is a certain analogy between the behaviour of HPWG and directional couplers, where the optical signal travels back and forth between two waveguides, placed close to each other. Nevertheless, the theory of coupled waves, well developed for directional couplers is not efficient for HPWG, because of a strong interaction [1]. To study the propagation of strongly coupled plasmonic modes numerical calculations are necessary.

In our work we construct HPWG where the waveguide mode is hybridised with several SPP modes. Edge plasmons with a mixed polarisation state are used in our design to couple otherwise orthogonal states to each other. During the propagation of the mixture, polarisation oscillates between horizontal and vertical directions. It is discussed how to use the proposed principle for the construction of compact polarisation convertors [4] and expand the idea of a waveguide based plasmonic modulator to remove polarisation restrictions typical for this class of devices. Numerically heavy 3D calculations are performed to model the proposed HPWG.

2. Discussion

One of the proposed HPWG (see Fig. 1 (a) where the transverse cross-section is shown) consists of a single mode silicon waveguide with dimensions 600 nm $\times$ 200 nm. At the telecom wavelength of 1550 nm it supports one y-polarised propagating mode. On top of the waveguide there is a 10 nm layer of high quality dielectric HfO_2 and 15 nm layer of transparent conductive oxide ITO. In the absence of external fields the refractive indices of two materials (real parts) are close to each other and the boundary between them is almost optically homogeneous. The HfO_2/ITO junction is useful for applications, where the switching behaviour is required (like, for example, modulators). Applying the voltage one may initiate ENZ effect in ITO which leads to the strong attenuation of the signal. Above the ITO layer we place an additional block of ITO with dimensions 80 nm $\times$ 65 nm, which we call a geometrical defect or an impurity. The golden electrode placed at the top of the structure forms two golden edges at the Au/ITO boundary, which support edge plasmonic modes with mixed polarisation states. The existence of the geometrical defect thus allows to couple the y-polarised waveguide mode and two z-polarised plasmonic modes via edges. At the same time

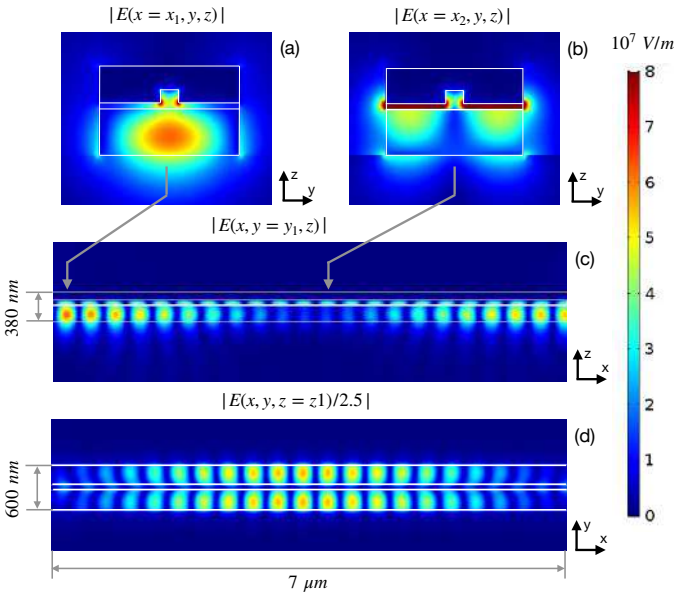


Figure 1: Distribution of an absolute value of the electric field in a hybrid waveguide. The mode propagates along x-axis. The transition of the field intensity from the waveguide into plasmonic modes and back is accompanied by double polarisation transformation. Edge plasmons provide coupling between states with orthogonal polarizations. Four cross-sections of a 3D model are shown: (a),(b) transverse cross-sections, (c) vertical cross-section at the center of the waveguide ('side view') (d) horizontal cross-section at the middle of the gap between the dielectric waveguide and the golden surface ('top view').

the defect brakes a symmetry in y-direction and makes 2D modelling of HPWG insufficient.

The propagation of light in the described structure is accompanied by the periodic oscillation of populations in the waveguide mode and plasmonic modes. The period depends significantly on coupling and thus the geometry of the defect. One period (which is close to 7 μm in our example) is shown in details in Fig. 1, where the absolute value of the electric field is plotted. To compute the field distribution, Maxwell equations are solved numerically in the frequency domain. Four different cross-sections of the 3D model are shown. In Fig. 1 (a) (b) cross-sections transverse to the direction of the propagation are plotted. In (a) the waveguide mode is maximally populated and in (b) most of the field is transmitted into plasmonic modes. In Fig. 1 (c) and (d) two other cross sections are shown: vertical (c) and horizontal (d) which can be considered as 'side view' and 'top view' respectively. In the first case the plane is fixed at the middle of the waveguide which allows to see mainly the waveguide mode. In the second case the plane passes through the center of the gap between the waveguide and the metal and allows to see the plasmon. In the last case the field is divided by 2.5 for the better visualisation.

3. Conclusion

In our work we analyse the propagation of hybrid modes with several plasmonic components (including edge plasmons) in different regimes. Influence of the geometry and materials properties on the mixed state evolution is studied. Numerically expensive 3D computations are employed in the analysis. Plasmonic losses are evaluated and structural advantages of the presented models for practical applications are studied. We discuss how to use proposed HPWG to produce efficient waveguide based electro-optical modulators, which work with y-polarised signals, and compact polarisation converters.

Acknowledgement

This work was partially supported by the Ministry of Education and Science of the Russian Federation, project RFMEFI58117X0026.

References

[1] M.Z. Alam, J.S. Aitchison, M. Mojahedi, A marriage of convenience: Hybridization of surface plasmon and dielectric waveguide modes, *Laser and Photonics Reviews* 8: 394–408, 2014.

[2] V.J. Sorger, N.D. Lanzillotti-Kimura, R.M. Ma, X. Zhang, Ultra-compact silicon nanophotonic modulator with broadband response, *Nanophotonics* 1: 17–22, 2012.

[3] D. Dai, S. He, A silicon-based hybrid plasmonic waveguide with a metal cap for a nano-scale light confinement, *Optics express*, 17, 16646–16653, 2009.

[4] I.A. Pshenichnyuk, S.S. Kosolobov, A. I. Maimistov, V. P. Drachev, Conversion of light polarisation in asymmetric plasmonic waveguides, *Quantum Electronics* 48: 1153–1156, 2018.

Near-field phase imaging using phase-shifting digital holography

Petr Dvořák[1,2], Michal Kvapil[1,2], Petr Bouchal[1,2], Zoltán Édes[1,2], Tomáš Šamořil[1,2], Michal Horák[1], Martin Hrtoň[1], Filip Ligmajer[1,2], Vlastimil Křápek[1,2], and Tomáš Šikola[1,2,*]

[1]Central European Institute of Technology, Brno University of Technology, Brno, Czech Republic
[2]Institute of Physical Engineering, Brno University of Technology, Brno, Czech Republic
*corresponding author, E-mail: sikola@fme.vutbr.cz

Abstract

We propose a novel method for the phase distribution measurement of the near electric field based on the principles of phase-shifting digital holography. The holographic interference occurs already in the near field and the phase distribution can be determined purely from the scanning near-field optical microscopy measurements. We demonstrate the capabilities of the proposed method by reconstruction of the phase difference between interfering surface plasmon waves and by imaging the phase of a single surface plasmon wave.

1. Introduction

The surface plasmon polaritons (SPPs) are evanescent electromagnetic surface waves coupled to the collective longitudinal oscillations of the free-electron gas in a metal propagating along a metal-dielectric interface. Spatial confinement of the electromagnetic field at the interface and smaller wavelength compared to the excitation light, corresponding enhancement of electromagnetic energy density at this interface, and the sensitivity of SPPs to dielectric functions of both material constituents forming the interface make SPPs attractive for many applications. Scanning near-field optical microscopy (SNOM) in combination with plasmonic interference structures is a powerful tool for imaging and analysis of SPPs [1].

2. Results and discussion

The correct interpretation of SNOM images requires profound understanding of principles behind their formation. To study fundamental principles of SNOM imaging in detail, we performed spectroscopic measurements by an aperture-type SNOM setup equipped with a supercontinuum laser and a polarizer, which gave us all the degrees of freedom necessary for our investigation. The series of wavelength- and polarization-resolved measurements, together with results of numerical simulations, then allowed us to identify the role of individual near-field components in formation of SNOM images, and to show that the out-of-plane component generally dominates within a broad range of parameters explored in our study [2]. Our results challenge the widespread notion that this component does not couple to the aperture-type SNOM probe and indicate that the issue of SNOM probe sensitivity towards the in-plane and out-of-plane near-field components — one of the most challenging tasks of near field interference SNOM measurements — is not yet fully resolved.

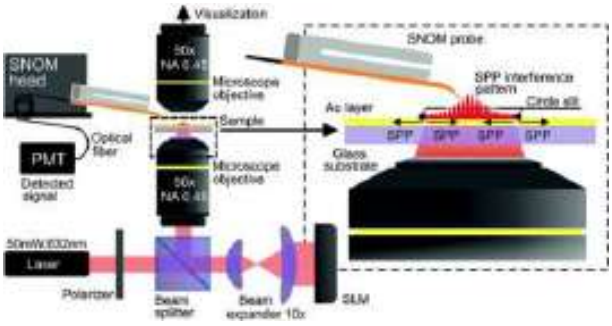


Figure 1: Scheme of the experimental setup for PPDH.

Moreover, we present a novel experimental method of plasmonic phase-shifting digital holography (PPDH) and demonstrate its potential for pure-near-field measurements of the surface plasmon polariton (SPP) phase distribution [3]. The experimental set-up for PPDH is shown in Fig. 1. The core of the proposed method is an on-chip interferometer which works with co-propagating or counter-propagating SPPs representing the analogy of signal and reference wave. The SPPs and consequently their interference patterns can be controlled by a Spatial Light Modulator (SLM) implemented in the far-field illumination path of an optical setup equipped with an aperture-type Scanning Near-Field Optical Microscope (a-SNOM) for SPP detection (collection mode) [1]. In this way, phase-controlled excitation of SPPs can be studied. By adopting the principles of the phase-shifting holography, we generate four slightly modified SPP interference patterns, allowing the numerical reconstruction of the SPP phase distribution in the pattern [4]. These four interference patterns differ in the mutual phase shifts between the individual SPPs (set by the SLM). An example of the measurement of the phase of plasmon standing wave created by a circular slit with the diameter of 0.01 mm is shown in Fig. 2. Since all information is collected in the near-field, our method provides a purely near-field measurement and it advantageously avoids the use of a far-field interferometer. Applying the SLM, this method can be directly used in a variety of techniques capa-

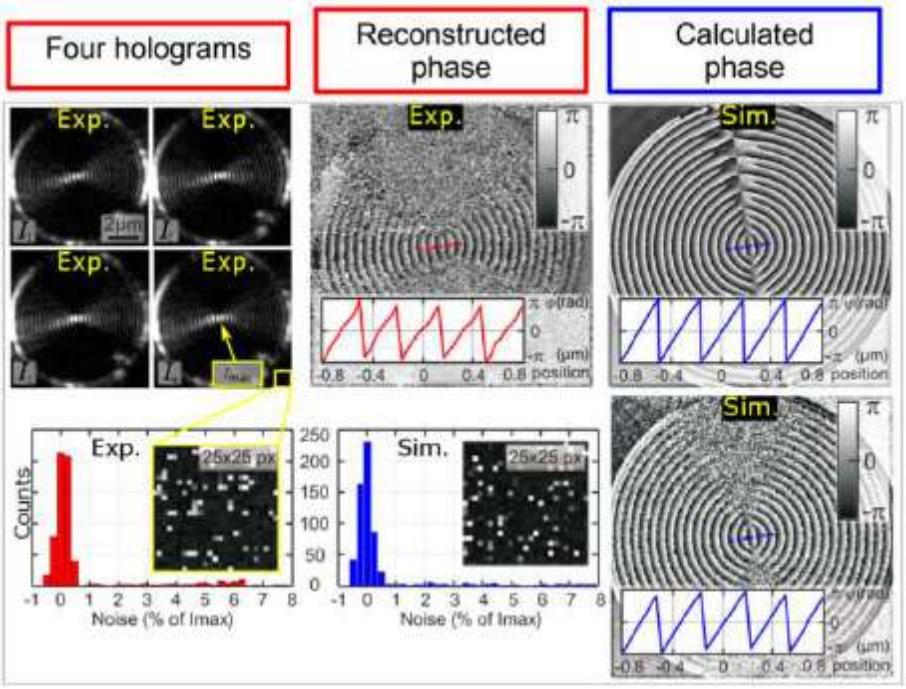


Figure 2: SPP phase reconstruction realized by numerical processing of the experimental and simulated interference patterns: Four measured interference patterns with the 4 distinct phase-shifts 0, $\pi/2$, π, and $3\pi/2$ introduced between the interfering SPPs by the SLM followed by the SPP phase difference reconstructed by numerical processing of the experimental data. To compare the experiment with the theory, the SPP phase difference image reconstructed by numerical processing of the FDTD simulated interference pattern is presented excluding and including the noise which disrupts the measured data. The profiles show cross-sections along the dashed lines in the central parts of the phase images.

ble of near-field imaging such as SNOM [2], PEEM (photon emission electron microscopy), PSTM (photon scanning tunneling microscopy), etc. The practical applicability of the method is demonstrated by phase-controlled excitation of SPPs that allows the shaping of interference patterns and the subsequent numerical reconstruction of phase differences between the interfering SPPs. Furthermore, we demonstrate the capability of our method by imaging the phase of a non-divergent SPP wave excited by a V-shaped slit structure, which interferes with the excitation light passing through the sample.

3. Conclusions

In summary, we have presented a new method for near-field phase imaging based on the principles of phase-shifting digital holography. We have demonstrated the capabilities of our method by reconstructing the phase difference between counter-propagating SPP waves excited inside a circular slit structure. The strength of this method lies in its compatibility with experimental techniques suitable for ultrafast SPP imaging, e.g. photoemission electron microscopy. This method presents an important step towards the development of 2D plasmonic holography for imaging of phase contrasts of objects (e.g. biological cells, plasmonic nanoantennas) bound to surfaces.

Acknowledgement

This research has been supported by the Czech Science Foundation (15-21581S and 18-01396S) and the MEYS CR under the projects CEITEC Nano RI (LM2015041, 2016-2019) and CEITEC 2020 (LQ1601).

References

[1] P. Dvořák, T. Neuman, L. Břínek, T. Šamořil, R. Kalousek, P. Dub, P. Varga, T. Šikola, Control and near-field detection of surface plasmon interference patterns, *Nano Lett.* 13: 2558–2563, 2013.

[2] P. Dvořák, Z. Édes, M. Kvapil, T. Šamořil, F. Ligmajer, M. Hrtoň, R. Kalousek, V. Křápek, P. Dub, J. Spousta, P. Varga, T. Šikola, Imaging of near-field interference patterns by aperture-type SNOM – influence of illumination wavelength and polarization state, *Opt. Express* 25: 16560–16573, 2017.

[3] P. Dvořák, M. Kvapil, P. Bouchal, Z. Édes, T. Šamořil, M. Hrtoň, F. Ligmajer, V. Křápek, T. Šikola, Near-field digital holography: a tool for plasmon phase imaging, *Nanoscale* 10: 21363–21368, 2018.

[4] I. Yamaguchi, T. Zhang, Phase-shifting digital holography, *Opt. Lett.* 22: 1268–1271, 1997.

Babinet's Principle for Solid and Hollow Plasmonic Antennas

Michal Horák[1], Vlastimil Křápek[1,2*], Martin Hrtoň[1], Andrea Konečná[3], Filip Ligmajer[1,2], Michael Stöger-Pollach[4], and Tomáš Šikola[1,2]

[1]Central European Institute of Technology, Brno University of Technology, Brno, Czech Republic
[2]Institute of Physical Engineering, Brno University of Technology, Brno, Czech Republic
[3]Materials Physics Center CSIC-UPV/EHU, San Sebastian, Spain
[4]University Service Centre for Transmission Electron Microscopy, TU Wien, Vienna, Austria
*corresponding author, E-mail: vlastimil.krapek@ceitec.vutbr.cz

Abstract

We present an experimental study of Babinet's principle of complementarity in plasmonics which relates the properties of solid plasmonic antennas and complemetary apertures in of the same size and shape. It allows, for example, studying the magnetic near field by measuring the electric near field by EELS in the complementary structure. We have focused on elementary disc-shaped plasmonic antennas followed by theoretical and experimental study of plasmonic antennas with electric and magnetic hot spots based on Babinet's principle.

1. Introduction

Localized surface plasmons (LSP) are self-sustained collective oscillations of free electrons in metal nano- and microstructures, often called plasmonic antennas, coupled to the local electromagnetic field. LSP resonances can be characterized by electron energy loss spectroscopy (EELS) and cathodoluminescence (CL). Both techniques utilize an electron beam that interacts with the metallic nanoparticle and excites the LSP resonances. EELS measures the energy transferred from electrons to the LSP. CL deals with the light which the LSP emit during their decay. Both techniques are sensitive to the electric near field of LSP.

Babinet's principle, originating in the wave theory of light and analysis of diffraction, relates the properties of a planar plasmonic antenna (particle) and a complemetary aperture in a thin metal film of the same size and shape [1]. In particular, the energies of LSP resonances in both antennas shall be identical and the corresponding near fields shall be complementary with the electric field distribution of the solid antenna corresponding to the magnetic field distribution of the complementary aperture. This link allows studying the magnetic near field, for example, by measuring the electric near field by EELS in the complementary structure.

We present a study of Babinet's principle of complementarity in plasmonics focused on elementary disc-shaped plasmonic antennas [2] followed by a theoretical and an experimental study of plasmonic antennas with electric and magnetic hot spots based on Babinet's principle [3, 4].

2. Results and discussion

We have studied a set of gold plasmonic antennas fabricated in the form of particles and apertures in a gold layer by focused ion beam lithography to investigate the basic properties of complementary structures and describe similarities and differences. Focused ion beam lithography is a suitable technique for fabrication of a small series of plasmonic antennas [5] allowing to fabricate easily both types of antennas (particles and apertures) on the same sample.

2.1. Disc-shaped plasmonic antennas

While the qualitative validity of Babinet's principle has been confirmed, quantitative differences have been found. As it is found by comparing the experimental data with a theoretical model, differences originate both from the limited theoretical validity of the Babinet's principle and from different operational conditions. In particular, apertures were found to exhibit stronger plasmonic response than solid antennas, which makes them a remarkable alternative of the usual plasmonic antennas design [2]. We have also examine magnetic near field imaging based on the Babinet's principle. Figure 1 shows dark field micrographs of a gold disc and aperture with the diameters of 100 nm together with intensity maps measured by EELS presenting the spatial distribution of the dipole LSP resonance at 1.75 eV for the particle and 1.5 eV for the aperture.

2.2. Bow-tie and diabolo antennas

We have studied plasmonic antennas featuring areas of extremely concentrated electric or magnetic field, known as hot spots. We combined two types of electric-magnetic complementarity to increase the degree of freedom for the design of the antennas: bow-tie and diabolo duality and Babinet's principle. The role of Babinet's principle in interchanging electric and magnetic field hot spots and its consequences for practical antenna design are discussed.

In particular, diabolo antennas exhibit slightly better performance than bow-ties in terms of larger field enhancement and larger Q factor. For specific resonance frequency, diabolo antennas are considerably smaller than bow-ties which makes them favourable for the integration into more

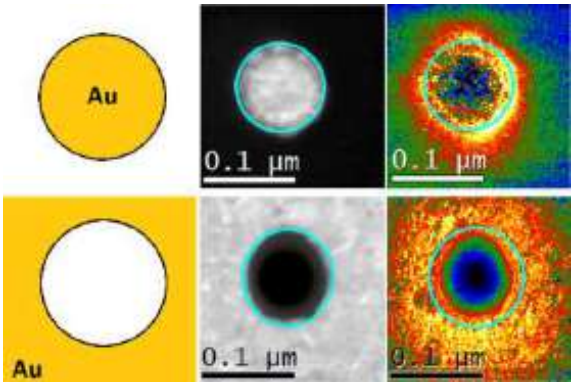


Figure 1: Schematic representation of a gold disc and aperture followed by dark field micrographs of the structures with the diameter of 100 nm together with EELS intensity maps corresponding to the dipole LSP resonance.

complex devices but also makes their fabrication more demanding in terms of spatial resolution [3].

Moreover, we have revisited plasmonic modes in nanoparticle dimers with conductive (diabolo or inverted bow-tie antennas) or insulating (bow-tie or inverted diabolo antennas) junction. In our study combining EELS, optical spectroscopy, and numerical simulations we show coexistence of strongly and weakly hybridized modes [4]. We show that Babinet's principle allows to engineer the near field of plasmonic modes independent of their energy. Finally, we show that combined EELS imaging of a plasmonic antenna and its Babinet-complementary counterpart allows to reconstruct the distribution of both electric and magnetic near fields of LSP resonances supported by the antenna as well as charge and current antinodes of related charge oscillations as shown in Figure 2 for the transversal dipole (TD) mode in the diabolo antenna.

3. Conclusions

We have studied a set of gold plasmonic antennas in the form of particles and apertures. By comparing the experimental data with a theoretical model we found differences originating both from the limited theoretical validity of the Babinet's principle and from different operational conditions for elementary disc-shaped plasmonic antennas. Further we have studied engineering of plasmonic antennas with electric and magnetic hot spots based on Babinet-complementary and revisit LSP modes in them showing a possibility to map the magnetic field by EELS by mapping the electric field of Babinet-complementary antenna.

Acknowledgement

This research has been supported by the Czech Science Foundation (17-25799S), the MEYS CR under the projects CEITEC Nano RI (LM2015041, 2016-2019) and CEITEC 2020 (LQ1601), and Brno University of Technology (FSI/STI-J-17-4623 and FSI/STI-J-18-5225).

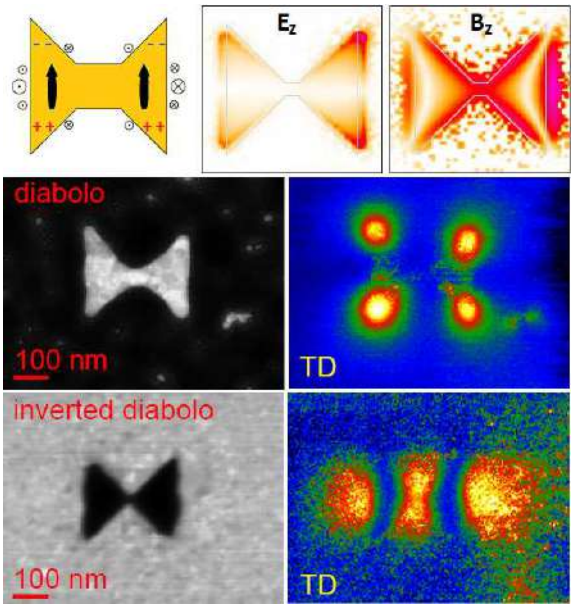


Figure 2: Schematic representation of TD mode in the diabolo antenna with calculated E_z and B_z field distribution followed by dark field micrographs of diabolo and inverted diabolo together with maeasured EELS intensity maps corresponding to TD mode.

References

[1] M. Hentschel, T. Weiss, S. Bagheri, H. Giessen, Babinet to the half: Coupling of solid and inverse plasmonic structures, *Nano Lett.* 13: 4428–4433, 2013.

[2] M. Horák, V. Křápek, M. Hrtoň, A. Konečná, F. Ligmajer, M. Stöger-Pollach, T. Šamořil, A. Paták, Z. Édes, O. Metelka, J. Babocký, T. Šikola, Limits of Babinet's principle for solid and hollow plasmonic antennas, *Sci. Rep.*, accepted, DOI: 10.1038/s41598-019-40500-1.

[3] M. Hrtoň, A. Konečná, M. Horák, T. Šikola, V. Křápek, Plasmonic antennas with electric, magnetic, and electromagnetic hot spots based on Babinets principle, *arXiv* 1901.*****.

[4] V. Křápek, A. Konečná, M. Horák, F. Ligmajer, M. Stöger-Pollach, M. Hrtoň, J. Babocký, T. Šikola Independent engineering of individual plasmon modes in plasmonic dimers with conductive and capacitive coupling, *in preparation*.

[5] M. Horák, K. Bukvišová, V. Švarc, J. Jaskowiec, V. Křápek, T. Šikola, Comparative study of plasmonic antennas fabricated by electron beam and focused ion beam lithography, *Sci. Rep.* 8: 9640, 2018.

An Atomistic Approach for Hybrid Plasmonic Systems

Giulia Giannone[1,2], **Fabio Della Sala**[1,3]
and Stefania D'Agostino[1]

[1]Center for Biomolecular Nanotechnologies @ UNILE-Istituto Italiano di Tecnologia, Arnesano, Italy
[2]Department of Mathematics and Physics "E. De Giorgi", University of Salento, Lecce, Italy
[3]CNR Institute for Microelectronics and Microsystems, Lecce, Italy
*corresponding author, E-mail: giulia.giannone@iit.it

Abstract

In the fully quantum mechanical framework of Time-Dependent Density Functional Theory (TD-DFT), we investigate the interactions between a localized surface plasmon excitable in a silver tetrahedral cluster and a molecular exciton optically active in the same energy range.

We show that the optical response of the system, for an ultra-near-field regime of interaction, is marked by the appearance of a two-peak structure.

We propose a plasmon-exciton electromagnetic interaction model as explanation of the spectra of this kind of hybrid systems of interest for molecular plasmonics.

1. State of the art

Fully atomistic approaches can offer important insights in the study of metal-molecule systems of interest in Nanophotonics and Plasmonics.

In fact, if on the experimental level, fabrication and characterization techniques can manage light-matter interaction at sub-nanometer scales, on the theoretical level application of computational methods from classical electrodynamics to these kind of systems breaks down [1]. In this context, TD-DFT [2] represents, nowadays, an established opportunity to study the electrodynamic coupling between molecules and metallic nanoantennas without neglecting intrinsic quantum effects and thus able to overcome the limits of the classical vision.

2. System and method

Using TD-DFT we studied the system depicted in the panel *a* of Fig. 1, which consists of a tetrahedral cluster of Ag_{20} and a molecule of *trans,trans*-1,4-diphenyl-1,3-butadiene (*t,t*-DPB) [3], a molecular emitter belonging to the class of photo-switches and for this reason interesting for promising applications in molecular plasmonics.

We computed the absorption spectra in an ultra-near-field regime of interaction with the aim to study how the optical response of the plasmonic cluster is influenced by the functionalization with the molecule. The physics underlying the absorption spectra has been well investigated in terms of transition densities, the results showing a plasmon-exciton electromagnetic interaction. All the calculations have been performed with the TURBOMOLE program [4].

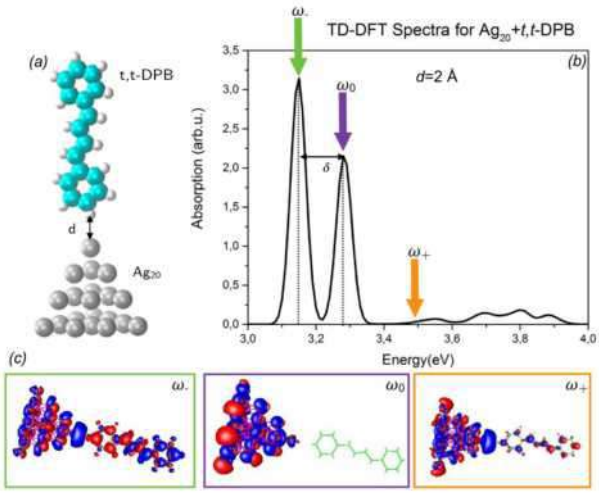


Figure 1: (a) Sketch of the system studied within TD-DFT: a single molecule of *t,t*-DPB positioned perpendicularly to the base of the tetrahedral Ag_{20} and put in front of its vertex. (b) TD-DFT absorption spectrum of the whole system for the metal-molecule distance of 2 Å.(c) In the insets are reported the transition densities corresponding to the excitations at different energies indicated by the three arrows.

3. Results and discussion

As the panel *b* of Fig. 1 illustrates, the absorption spectrum is marked by the presence of two well distinguishable peaks.

Reasoning in terms of two-coupled oscillators model, the absorption spectrum can be explained in the manner sketched in Fig. 2.

When the cluster and the molecule are close enough to allow a coupling between their transition dipole moments, the formation of two states becomes possible: B (bonding) at energy ω_- and A (anti-bonding) at energy ω_+.

The bonding state B originates from the aligning along the z axis of the two transition dipoles of the interacting components and, thus, it emits and absorbs far-field radiation and assumes an optically active or bright behavior. The anti-bonding state A originates from an anti-parallel align-

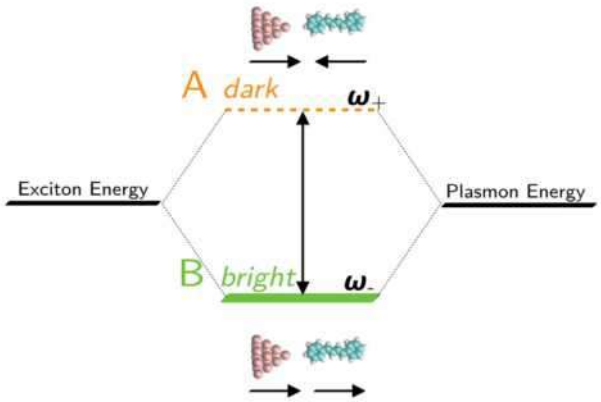


Figure 2: A pictorial scheme of the coupling between a plasmon and an exciton. The black thick lines indicate the excitation energies of the isolated molecule and cluster. When the counterparts are close enough to allow a coupling between their transition dipole moments, this interaction permits the formation of two states: the bright or *bonding* one *B* at energy ω_- represented by the green thick line and the dark or *anti-bonding* one *A* at energy ω_+ represented by the orange dashed line.

ment along the z axis of the transition dipole moments of the two components and, consequently, it is characterized by a small total transition dipole and it results to be optically inactive or dark. Between the bonding and anti-bonding excitations, there is the *plasmonic* peak of the cluster, due to the allowed states P_x and P_y which do not interact with the molecule.

This interaction scheme was confirmed by the results obtained from the transition densities analysis computed for the *bright*, *plasmonic* and *dark* peaks characterizing the absorption spectra in the distance range going from 2 to 4.5 Å. A scheme of this kind of analysis is reported in the panel *c* of Fig.1 for the distance of 2 Å, in which it clearly appears that both the excitations at energy ω_- and ω_+ are hybrid, while, the excitation at energy ω_0 is localized on the cluster.

Moreover, in order to investigate about the possible presence of charge transfer effects, we quantified the transition densities computing the integral over x-y plane of the three-dimensional transition densities for all the bright excitations in the distance range from 2 to 4.5 Å and we found that a small fraction of electronic charge (0.13 e for the distance of 2 Å) passes from the molecule to the cluster. Nevertheless, this contribution is so small that the coupling mechanism can be substantially explained in terms of a plasmon-exciton electromagnetic interaction model.

4. Conclusion

In conclusion, we have presented a TD-DFT analysis on the plasmon-exciton interactions characterizing a model system composed of a *t,t*-DPB molecule and a tetrahedral cluster of Ag_{20}, treating both the metallic and molecular counterparts atomistically. We have shown that, for ultra-near field regime of interaction, the optical response of the system is characterized by a double peak structure. We have analyzed the transition densities for the peaks energies and proposed a plasmon-exciton electromagnetic interaction model to explain the origin of the lower-energy resonance and the physics underlying the electrodynamic coupling in such hybrid systems.

This fully atomistic approach represents thus a complete theoretical scheme which, considering both the electronic and optical effects taking part to the interaction, can shed light on the mechanisms involving a plasmonic system interacting with a molecular switch.

Moreover, such hybrid configurations could result very appealing for applications in Nanophotonics, going from bio-sensing to quantum computing.

Acknowledgement

The authors thank E. Fabiano for useful discussions.

References

[1] R. Esteban, A. G. Borisov, P. Nordlander and J. Aizpurua, Bridging quantum and classical plasmonics with a quantum-corrected model, *Nat. Comm.* 3: 1–9, 2012.

[2] M. A. L. Marques and E. K. U. Gross, Time-dependent density functional theory, *Annu. Rev. Phys. Chem.* 55: 427–455, 2004.

[3] X. Zheng, G. Zhai, W. Gao, Y. Lei, L. Yu and C. Zhu, Photoisomerization mechanism from *trans,trans*-1,4-diphenyl-1,3-butadiene: CASSCF on-the-fly trajectory surface hopping dynamic simulations, *Phys. Chem. Chem. Phys.* 18: 8971–8979, 2016.

[4] Information available at www.turbomole.com.

Slender-body theory for localized-surface-plasmon resonance

Matias Ruiz[1*], **Ory Schnitzer**[1]

[1]Department of Mathematics, Imperial College London, London SW7 2AZ, UK
*corresponding author, E-mail: matias.ruiz@imperial.ac.uk

Abstract

We propose a slender-body theory for calculating the surface-plasmon eigenvalues and eigenmodes of smooth high-aspect-ratio metallic nanoparticles (of otherwise arbitrary shape) and their resonant excitation by incident electromagnetic radiation. Using matched asymptotic expansions, we develop an equivalent one-dimensional model which is straightforward to solve numerically and in special cases furnishes closed form solutions.

1. Introduction

Elongated metallic nanoparticles are frequently used in nanoplasmonics, as nano-antennas and bio-sensors, enabling wide tunability and strong field enhancements [1]. We are accordingly motivated to consider the problem of a *slender* metallic nanoparticle subjected to either incident radiation or a time-harmonic current density $\mathbf{J}(\mathbf{x})$ in its external vicinity. Assuming that the particle is deeply subwavelength, we adopt the quasi-static approximation of Maxwell's equations:

$$\boldsymbol{\nabla}\cdot(\epsilon(\mathbf{x})\mathbf{E}) = -\frac{i}{\epsilon_0\omega}\boldsymbol{\nabla}\cdot\mathbf{J}, \tag{1}$$

$$\mathbf{E}\to\mathbf{E}_\infty \quad \text{as} \quad |\mathbf{x}|\to\infty, \tag{2}$$

where $\mathbf{E}(\mathbf{x})$ is the electric field, $\mathbf{E}_\infty$ is a constant forcing term representing a possible incident plane wave and $\epsilon(\mathbf{x})$ is the electrical permittivity relative to its value ϵ_0 in free space; we adopt the usual convention for time-harmonic fields at angular frequencies ω. The relative permittivity $\epsilon(\mathbf{x})$ takes the constant positive value ϵ_m outside the particle and the complex-valued and frequency dependent constant $\epsilon_c(\omega)$ inside it.

The induced field $\mathbf{E}(\mathbf{x})$ can be expanded in terms of the solutions of the so-called *plasmonic eigenvalue problem*, which, in this context, consists of finding the values (eigenvalues) of the ratio between the inclusion permittivity and the medium permittivity, for which there exist non-trivial solutions to (1) and (2) when both $\mathbf{J}(\mathbf{x})$ and $\mathbf{E}_\infty$ are set to zero. In the case of a smooth inclusion, the eigenvalues are discrete, real, negative and accumulate at -1. We denote the n-th eigenvalue (counting multiplicities) and eigenmode as $\mathcal{E}^{(n)}$ and $\mathbf{E}^{(n)}$, respectively. Thus, assuming that the eigenvalue problem has been solved and that the eigenmodes have been properly normalised, we have [2]

$$\mathbf{E}(\mathbf{x}) = \mathbf{F}(\mathbf{x}) + \sum_{n=0}^{\infty}\frac{\epsilon_c/\epsilon_m - 1}{\epsilon_c/\epsilon_m - \mathcal{E}^{(n)}}\beta_n\mathbf{E}^{(n)}(\mathbf{x}), \tag{3}$$

where $\mathbf{F}(\mathbf{x})$ corresponds to the induced field in the absence of the particle and β_n represents an overlap integral depending solely on $\mathbf{F}(\mathbf{x})$ and $\mathbf{E}^{(n)}$ within the particle.

In the visible regime and when the metal is small compared to the operating wavelength, the real part of the inclusion's permittivity is negative while the imaginary part, which accounts for ohmic losses, is often relatively small. It follows that the n-th mode will be greatly enhanced if the frequency ω is such that $\Re(\epsilon_c(\omega)/\epsilon_m)/\mathcal{E}^{(n)} \approx 1$ and $\Im(\epsilon_c(\omega)/\epsilon_m)/\mathcal{E}^{(n)} \ll 1$, where $\Re$ and $\Im$ denote the real and imaginary parts respectively. Such resonant behaviour can therefore by captured by virtually a single term in the eigenfunction expansion (3).

In this work we use singular perturbation techniques, namely matched asymptotic expansions in the spirit of slender-body theory [3], to develop asymptotic solutions to the plasmonic eigenvalue problem in the limit where the slenderness of the particle vanishes. The asymptotic eigensolutions are subsequently used, in conjunction with (3), in order to obtain approximations for the induced field and optical cross sections in the case of plane-wave illumination.

Applications involving slender particles usually rely on lower-order modes that vary mainly in the longitudinal direction, as these efficiently couple with incident radiation and allow tuning the surface-plasmon frequencies down to the IR regime. Accordingly, it is convenient to focus here on axisymmetric particles, for which the longitudinal modes are easily identified with axisymmetry. We further assume that the particle is smooth, having locally paraboloidal tips, though otherwise its shape profile remains arbitrary.

2. Slender-body theory

2.1. Geometry

We introduce the cylindrical co-ordinates system (ar, az, θ), where $2a$ is the dimensional length of the major axis of the particle. The surface of the particle is described by the thickness profile $r = hf(z)$ $(-1\le z\le 1)$ where $h>0$ is a slenderness parameter and $f(z)$ is a positive real-valued smooth function such that $f = O(|z\mp 1|^{1/2})$ as $z\to\pm 1$. Given the axial symmetry of the geometry, the modes can be sought as functions of (r,z) times $\cos(m\theta)$ or $\sin(m\theta)$, where $m = 0, 1, 2, \ldots$.

2.2. Eigenvalue scaling

Let $\mathcal{E}$ denote some plasmonic eigenvalue. Using scaling arguments, it can be shown that for non-axisymmetric modes ($m \neq 0$) the limit $\mathcal{E} \to -1$ as $h \to 0$ holds, whereas for axisymmetric modes ($m = 0$):

$$\mathcal{E} \sim -\frac{\alpha}{h^2} \quad \text{as} \quad h \to 0, \tag{4}$$

where the pre-factor $0 < \alpha$ depends on the thickness profile and mode number; and as we shall see, the dependence of α upon h is strictly logarithmic.

2.3. Effective eigenvalue problem ($m = 0$)

Using the method of matched asymptotic expansions in the limit $h \ll 1$ we find the following effective eigenvalue problem for the reduced eigenvalue α and the corresponding leading-order voltage inside the inclusion $v(z)$ (coupled with the leading order surface charge per unit length $m(z)$),

$$m(z) + \pi\alpha \tfrac{d}{dz}\left(f^2 \tfrac{d}{dz} v(z)\right) = 0, \tag{5}$$

$$v(z) = \tfrac{m(z)}{2\pi} \log \tfrac{2\sqrt{1-z^2}}{h f(z)} + \tfrac{1}{4\pi} \int_{-1}^{1} \tfrac{m(\zeta)-m(z)}{|\zeta - z|} d\zeta. \tag{6}$$

2.4. Solutions to the effective eigenvalue problem

In the case of a *prolate spheroid*, for which $f(z) = (1 - z^2)^{1/2}$, analytical solutions to the effective eigenvalue problem can be found as

$$\alpha^{(n)} = \frac{1}{n(n+1)} \frac{2}{\log(2/h) - \sum_{k=1}^{n}(1/k)}, \tag{7}$$

where $n = 1, 2, \ldots$, with $v^{(n)}$ and $m^{(n)}$ proportional to the n'th Legendre polynomial. Fig. 1 shows excellent agreement between (7) and the exact eigenvalues of a prolate spheroid.

In the case of an *arbitrary* thickness profile, the eigenfunctions v and m can be expanded in terms of Legendre polynomials yielding, through controlled truncation, a generalised eigenvalue (matrix) problem whose solution can be found at a negligible computational cost. Fig. 2 compares the calculated first mode of a prolate spheroid and a deformed slender shape lacking fore-aft symmetry.

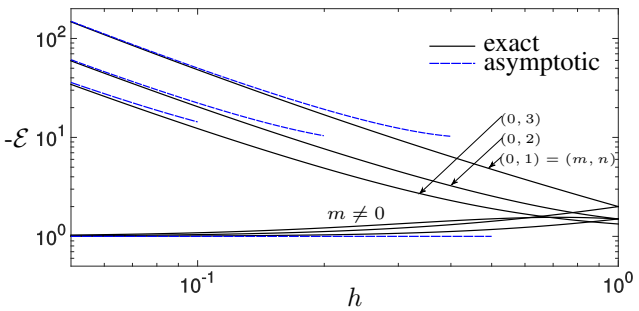


Figure 1: Analytical solutions and asymptotic approximations for the plasmonic eigenvalues of a prolate spheroid.

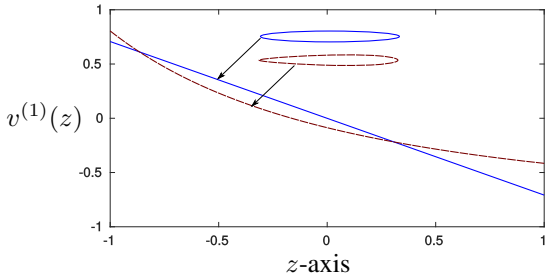


Figure 2: First eigenvoltage: prolate spheroid (blue) and an asymmetric slender shape (red); $h = 0.07$.

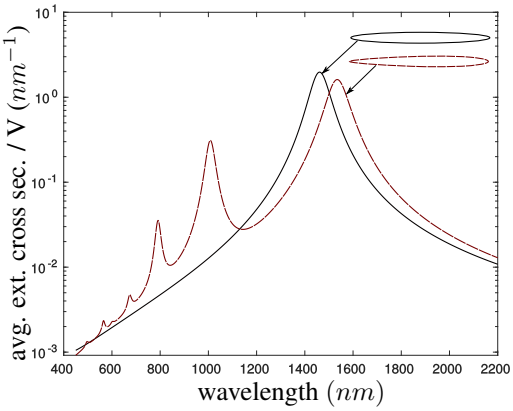


Figure 3: Angle-averaged extinction cross section per unit volume of a gold: prolate spheroid (black) and an asymmetric slender shape (red); $h = 0.07$.

3. Plane-wave illumination

In the scenario where the metallic nanoparticle is subjected to an incident plane wave, the above eigen-solutions together with (3) can be used to obtain asymptotic approximations to all quantities of interest. For example, Fig. 3 shows the angle-averaged extinction cross-section per unit volume in the case of a spheroid and a slender shape lacking fore-aft symmetry. We note the excitation of multiple resonances in the asymmetric case.

4. Acknowledgements

The authors acknowledge funding from EPSRC through New Investigator Award EP/R041458/1.

References

[1] J. Cao, T. Sun, K. T.V. Grattan. Gold nanorod-based localized surface plasmon resonance biosensors: A review. *Sensors and Actuators B: Chemical*, Volume 195, 2014, Pages 332-351, ISSN 0925-4005.

[2] D. J. Bergman and D. Stroud. Theory of resonances in the electromagnetic scattering by macro-scopic bodies. *Phys. Rev. B*, 22(8), 35273539 (1980).

[3] Batchelor, G. (1970). Slender-body theory for particles of arbitrary cross-section in Stokes flow. *Journal of Fluid Mechanics*, 44(3), 419-440.

From Classical to Quantum Interactions in Molecular Plasmonics

Giulia Giannone[1,2], Fabio Della Sala[1,3] and Stefania D'Agostino[1]

[1] Center for Biomolecular Nanotechnologies @ UNILE-Istituto Italiano di Tecnologia, Via Barsanti, Arnesano, Italy
[2] Department of Mathematics and Physics E. De Giorgi, University of Salento, Via Arnesano, Lecce, Italy
[3] CNR Institute for Microelectronics and Microsystems, SP Lecce-Monteroni, Lecce, Italy
*corresponding author, E-mail: stefania.dagostino@iit.it

Abstract

State-of-the-art fabrication and characterization techniques are to date able to experimentally control light-matter interaction at sub-nanometer scales where computational methods from classical electrodynamics fail. In this work we analyze the effects of the metal-molecule distance on the lower-energy peak appearing in the absorption spectra of hybrid plasmonic nanosystems underlying the importance of a fully quantum mechanical approach to take into account all the phenomena playing a role in such kind of electro-optical interactions.

1. Introduction

Classical electrodynamics has been until now largely applied to study the optical properties of many plasmonic systems. However, in the last few years, thanks to the development of fabrication and characterization techniques and to their capabilities to manage light-matter interaction at the sub-nanometer scale, a growing interest toward the quantum nature of matter is appearing in the scientific community dealing with plasmonics and above all molecular plasmonics. The goal is that to fully control the physics of interaction between plasmons and molecular emitters by considering at the same time electronic and optical effects. Differently from what happens in the regime of classical interactions, where extended systems far from each other are considered, non classical effects, such as the nonlocality or the spill-out of the electronic density, must be taken into account to manage the physics of multi-scale plasmonic systems - including subnanometers features - or sub-nanometer gaps configurations in which phenomena of resonant electron transfer of tunneling can emerge [1].

In this work we shed light on the role of these effects on the absorption response of hybrid metal-molecule nanosystems which could result very promising for applications in ultra-sensitive and selective biosensing as well to realize logic gates for quantum computing.

2. Method

In this work we focus on a system consisting of a molecular emitter, trans,trans-1,4-diphenyl-1,3-butadiene (t,t-DPB), and a tetrahedral cluster of Ag_{20}.

The molecule belongs to the important and vastly studied class of molecular photoswitches which can be converted from one configuration to one another via photoisomerization processes while the cluster is among the smallest ones having a plasmon-like excitation in the same spectral region of the above mentioned molecular emitter.

The system is treated at three different levels of approximation: (i) *Time-Dependent Density Functional Theory* (TD-DFT) [2], (ii) *Finite Element Method* (FEM) [5] and (iii) *dipole-dipole* model.

For what concerns the most rigorous approach (i), both the optical antenna and the quantum emitter are treated atomistically (see the sketch in Figure 1). All the DFT simulations on geometry relaxation, ground state and excited states have been performed with the TURBOMOLE program [3]. Regarding the structure relaxation, it was performed with a B3LYP functional for the exchange-correlation energy and a def2-SVP basis set for the molecular part and a PBE/def2-SVP prescription for the metallic nanocluster [4]. The DFT relaxed geometries of the isolated systems were, then, considered as a starting point for the TD-DFT analysis of the optical behavior of both the isolated components and the total system in which the photoswitch was rigidly shifted away from the silver nanoparticle in order to explore all the different distances (d_{DFT}). The distance considered for this approach was, thus, the difference between the z coordinates of the $H-$atom closest to the cluster and the top Ag atom of Ag_{20}, as indicated in Figure 1.

Regarding the FEM study, the absorption cross section spectra were simulated by using COMSOL Multiphysics [5]. In particular the tetrahedral cluster was modelled as an ideal tetrahedron of 1.8 nm side with rounded-cornes, i.e. curvature radius of 0.269 nm. The used dielectric function was the one tabulated by Palik for Ag [6]. The molecule was instead approximated as a small nanosphere (radius of 0.28 nm) with an *ad-hoc* dielectric function engineered in order to exactly give the TD-DFT absorption spectrum. The distance in this case was assumed as the $d_{DFT}+L_{mol}$, where L_{mol} is the distance between the outer H-atoms and the molecule center (0.66 nm). Finally, the system was studied within a classical dipole-dipole model in which the transition dipole moments of the two systems at the resonant energies were considered to extimate the

d_1 and d_2 values. The distance was, then, assumed to be $d_{DFT} + L_{mol} + L_{cluster}$, where $L_{cluster}$ was fixed to 0.3 nm (distance of a vertex from the Ag_{20} center).

3. Results

We analyzed the TD-DFT absorption spectra for several distances, going from 0.2 nm to 6 nm. We noted that, in the distance range going from 0.2 nm to 0.45 nm, each spectrum is characterized by the presence of two peaks, while, starting from the distance of 0.5 nm, the splitting gradually disappears, as long as, the single peak progressively becomes the sum of the absorption spectra of the two separated constituents, at 3.28 eV and 3.29 eV respectively for the cluster and the molecule.

In Figure 1 we report the effects of the metal-molecule distance, d_{DFT}, on the spectral position of the lower-energy peak. What is evident is that this state importantly depends on the cluster-molecule distance, as it is evident from the red-shift of the absorption peak reducing the metal-molecule distance and that also the TD-DFT trend seems to follow a dipole-dipole interaction law.

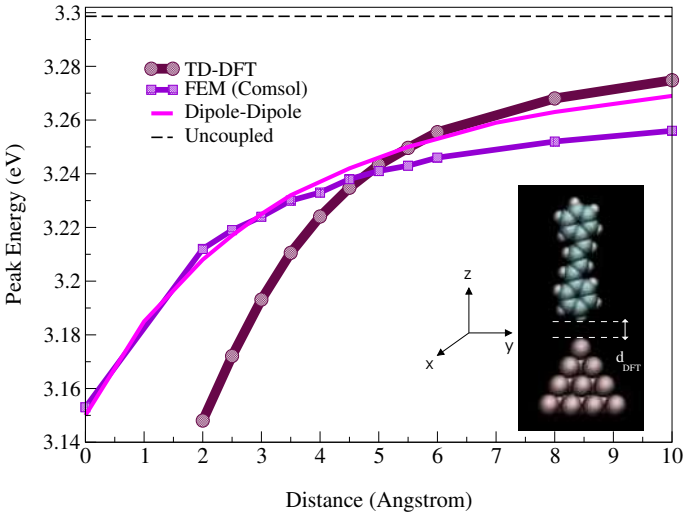
Reasoning in terms of two-coupled dipoles model, the two peaks in the absorption spectra found out for the distances range 0.2-0.45 nm, can be explained as the bonding dipole due to the hybridization of the z-components of the surface charge of the two oscillators (lower-energy distance-dependent resonant peak) and the uncoupled x- and y- modes of the three-fold degenerate plasmon excited inside the metallic cluster (fixed reference peak).

In more details, the molecule is characterized by a transition dipole moment oriented along the z-direction and this state interacts only with the z component of the cluster transition dipole. This creates two hybrid states: a bonding state at an energy lower with respect to the reference one and anti-bonding at an higher energy (with null oscillator strength and thus not visible or *dark*).

What is interesting is that, even if the dipole-dipole interaction model seems to work well in terms of trend for distance larger that 0.5 nm, the effects of the quantum electron density distribution appear to be crucial in order to faithfully describe the interaction among the two nanosystems. Even if effects as the charge transfer was proved to be negligible with respect to the electromagnetic contribution, the interaction among the two charge distributions at excitation results to be much larger in the quantum mechanical scheme, this attesting the necessity to take into account the real dislocation of the charge all over the systems and the atomistic nature of the quantum emitter. Classical models fail, thus, in reproducing TD-DFT results for the ultra-near-field regime of interaction, i.e. separation distance smaller that 0.5 nm.

4. Conclusion

In this work we use the TD-DFT framework to analyze the interactions in an ultra-near-field regime, between a localized surface plasmon excitable in a silver tetrahedral cluster and a molecular exciton with a resonant excitation energy. We report that, for metal-molecule distances below 0.5 nm, the optical response of the system presents the onset of a double peak structure which can be explained within a dipole-dipole interaction scheme.



However, the comparison among classical and quantum mechanical models shows that a pure classical description of the two nanosystems seems to be inappropriate to predict the right position of the hybrid peaks in the absorption spectra of suck kind of hybrid configurations which could result very promising for applications in bio-sensing as well as in quantum computing.

Acknowledgement

S.D. thanks C. Ciracì for technical insights on COMSOL.

References

[1] W. Zhu, R. Esteban, A. G. Borisov, J. J. Baumberg, P. Nordlander, H. J. Lezec, J. Aizpurua and K. B. Crozier, Quantum mechanical effects in plasmonic structures with subnanometre gaps, *Nat. Comm.* 7: 1–14, 2016.

[2] M. A. L. Marques and E. K. U. Gross, Time-dependent density functional theory, *Annu. Rev. Phys. Chem.* 55: 427–455, 2004.

[3] Information available at www.turbomole.com.

[4] Wolfram Koch and Max C. Holthausen, A Chemist's Guide to Density Functional Theory, WileyVCH Verlag GmbH, 2001.

[5] Comsol Multiphysics available at https://www.comsol.com/.

[6] Palik, E. D. Handbook of Optical Constants of Solids; Academic Press, 1998.

Angular momentum transfer from a swift electron to a small nanoparticle

José Ángel Castellanos-Reyes* **and Alejandro Reyes-Coronado**

Departamento de Física,
Facultad de Ciencias, Universidad Nacional Autónoma de México, Ciudad de México, México
*corresponding author, E-mail: castellanos_angel@ciencias.unam.mx

Abstract

In this work we present a study of the angular momentum transfer from a fast electron, like those typically used in Transmission Electron Microscopes, to a spherical nanoparticle using a classical electrodynamics approach within the small particle limit. We show preliminar results obtained for an aliminum-like nanoparticle modelled with a Drude dielectric function.

1. Introduction

Electron microscopy has been widely used to study physical and chemical properties of materials [1–3]. In particular, Transmission Electron Microscopes (TEMs) have reached, in recent times, unique capabilities such as a spatial resolution up to $0.5\,$Å, an energy resolution of $10\,$meV, the possibility to perform Electron Energy Loss Spectroscopy (EELS) in the low-energy regime $\sim 10\,$meV with a probe size less than $1\,$nm, and the possibility to inspect the momentum transfer dependence ($\hbar\mathbf{q}$) of vibrational modes with a momentum transfer resolution of $\Delta\mathbf{q} = \pm 0.5\text{Å}^{-1}$ and spatial resolution $< 2\,$nm [4, 5].

It has been shown that high-energy electron beams in TEMs, achieving energies up to $400\,$keV [3], may alter the samples under study. In particular, while operating in scanning mode (STEMs), it has been observed that the electron beam can induce movements on metallic nanoparticles [6], giving rise to the implementation of TEMs' electron beams to control and manipulate nanometric particles at will, a technology now called electronic tweezers [7].

Although important efforts have been made in the past to describe the linear momentum transfer from a swift electron to a spherical nanoparticle characterized by a dielectric function $\epsilon(\omega)$ [3,6,8–14], there is still a lot of work to do in order to fully understand the underlying physics. Precisely, for the angular momentum transfer study, there is still the need of a theoretical model that fully explains the dynamics of the nanoparticles induced by the swift electrons to completely understand the capabilities of electronic tweezers and exploit their technological potential.

In this work we present a model for the angular momentum transfer from a swift electron to a spherical nanoparticle, in the small particle limit approximation using the classical electrodynamics approach, as a function of the relevant parameters of the problem: radius of the nanoparticle, electron's speed and impact parameter. We show preliminar results for an aluminum-like spherical nanoparticle modelled with a Drude dielectric response.

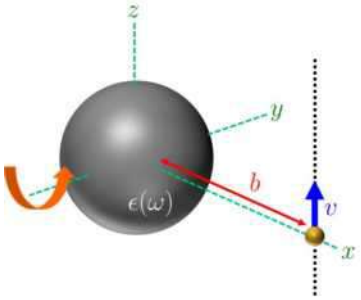


Figure 1: Sketch of the system under study: An electron (yellow spot) travels with constant speed v in a straight line at a distance b from the center of a spherical nanoparticle (grey sphere) with electromagnetic response $\epsilon(\omega)$. The electron transfers angular momentum to the nanoparticle inducing a rotation (orange arrow).

2. Theoretical model

For the calculation of the angular momentum transferred from a swift electron to a spherical nanoparticle, modelled with a Drude dielectric function and under the small particle limit, we consider that the electron is traveling with constant speed v in a straight line, at a distance b from the center of the nanoparticle, as illustrated in Fig. 1.

In the frame of classical electrodynamics and under the small particle limit, the response of a nanoparticle is mainly due to both the electric ($\mathbf{p}$) and a magnetic ($\mathbf{m}$) dipole moments induced by the external radiation [15]. For an isotropic nonmagnetic ($\mu = \mu_0$) sphere, immersed in vacuum, the electric and magnetic polarizabilities, α_E and α_M, respectively, can be obtained from Mie theory [16] (in S.I. units):

$$\alpha_E(\omega) = \frac{6\pi i}{k^3} a_1(\omega), \tag{1}$$

$$\alpha_M(\omega) = \frac{6\pi i}{k^3} b_1(\omega), \tag{2}$$

where $a_1(\omega)$ and $b_1(\omega)$ are the first Mie coefficients [16], k is the wavenumber and $i = \sqrt{-1}$. The dipole moments are given by $\mathbf{p}(\omega) = \epsilon_0 \alpha_E(\omega)\mathbf{E}^{ext}(\omega)$ and $\mathbf{m}(\omega) = \alpha_M(\omega)\mathbf{H}^{ext}(\omega)$ [17], where $\mathbf{E}^{ext}(\omega)$ and $\mathbf{H}^{ext}(\omega)$ are the electromagnetic fields produced by the bare electron [18]

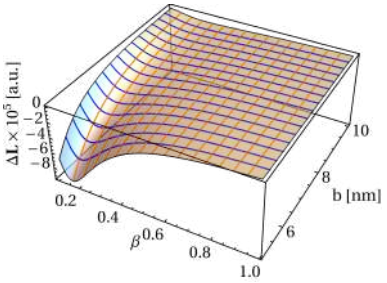


Figure 2: Angular momentum transfer from a fast electron, with speed v, to an aluminum-like spherical nanoparticle of radius 5 nm, with a Drude dielectric function, as a function of the impact parameter b and $\beta = v/c$.

evaluated at the center of the nanoparticle. The torque performed by the electromagnetic fields produced by the electron is

$$\boldsymbol{\tau} = \mathbf{p} \times \mathbf{E}^{ext} + \mathbf{m} \times \mathbf{H}^{ext}. \tag{3}$$

Expressing the electromagnetic fields by means of their Fourier transforms in Eq. (3), the total angular momentum transferred can be written as

$$\Delta\mathbf{L} = \int_0^\infty \boldsymbol{\mathcal{L}}(\omega)\, d\omega, \tag{4}$$

i.e., as the integral of a spectral contribution $\boldsymbol{\mathcal{L}}(\omega)$.

2.1. Aluminum-like nanoparticle

We consider the case of a spherical nanoparticle with a dielectric response given by the Drude model, with parameters mimicking the aluminum, and numerically study the angular momentum transfer from an electron traveling with different speeds and impact parameters. As a preliminar result, we show in Fig. 2 the angular momentum transfer $\Delta\mathbf{L}$ (in atomic units) for a nanoparticle with radius of 5 nm, as a function of both the impact parameter b and the electron's speed v, being $\beta = v/c$, where c is the speed of light, considering only the electric induced dipole moment $\mathbf{p}$.

References

[1] P. E. Batson, Damping of bulk plasmons in small aluminum spheres, *Solid State Commun.* 34: 477–480, 1980.

[2] P. E. Batson, A new surface plasmon resonance in clusters of small aluminum spheres, *Ultramicroscopy* 9: 277–282, 1982.

[3] F. J. García de Abajo, Optical excitations in electron microscopy, *Rev. Mod. Phys.* 82: 209–275, 2010.

[4] O. L. Krivanek, T. C. Lovejoy, N. Dellby, T. Aoki, R. W. Carpenter, P. Rez, E. Soignard, J. Zhu, P. E. Batson, M. J. Lagos, R. F. Egerton, P. A. Crozier, Vibrational spectroscopy in the electron microscope, *Nature* 514: 209–212, 2014.

[5] F. S. Hage, R. J. Nicholls, J. R. Yates, D. G. McCulloch, T. C. Lovejoy, N. Dellby, O. L. Krivanek, K. Refson, Q. M. Ramasse, Nanoscale momentum-resolved vibrational spectroscopy, *Sci. Adv.* 4: 7495, 2018.

[6] P. E. Batson, A. Reyes-Coronado, R. G. Barrera, A. Rivacoba, P. M. Echenique, J. Aizpurua, Plasmonic nanobilliards: Controlling nanoparticle movement using forces induced by swift electrons, *Nano Lett.*, 11: 3388–3393, 2011.

[7] V. P. Oleshko, J. M. Howe, Are electron tweezers possible?, *Ultramicroscopy* 111: 1599–1606, 2011.

[8] F. J. García de Abajo, Relativistic energy loss and induced photon emission in the interaction of a dielectric sphere with an external electron beam, *Phys. Rev. B* 59: 3095–3107, 1999.

[9] F. J. García de Abajo, Momentum transfer to small particles by passing electron beams, *Phys. Rev. B* 70: 115422, 2004.

[10] A. Reyes-Coronado, R. G. Barrera, P. E. Batson, P. M. Echenique, A. Rivacoba, J. Aizpurua, Electromagnetic forces on plasmonic nanoparticles induced by fast electron beams, *Phys. Rev. B* 82: 235429, 2010.

[11] P. E. Batson, A. Reyes-Coronado, R. G. Barrera, A. Rivacoba, P. M. Echenique, J. Aizpurua, Nanoparticle movement: Plasmonic forces and physical constraints, *Ultramicroscopy* 124: 50–58, 2012.

[12] E. J. R Vesseur, J. Aizpurua, T. Coenen, A. Reyes-Coronado, P. E. Batson, A. Polman, Plasmonic excitation and manipulation with an electron beam, *MRS Bulletin* 37: 752–760, 2012.

[13] M. J. Lagos, A. Reyes-Coronado, P. M. Echenique, J. Aizpurua, P. E. Batson, Attosecond forces imposed by swift electrons on nanometer-sized metal particles, *Microsc. and Microanal.* 20: 576–577, 2014.

[14] M. J Lagos, A. Reyes-Coronado, A. Konečná, P. M. Echenique, J. Aizpurua, P. E. Batson, Attosecond and femtosecond forces exerted on gold nanoparticles induced by swift electrons, *Phys. Rev. B* 93: 205440, 2016.

[15] H. C. van de Hulst, Light scattering by small particles, Dover Publications, New York, 1981.

[16] C. F. Bohren, D. R. Huffman, Absorption and Scattering of Light by Small Particles, John Wiley & Sons, New York, 1983.

[17] J. D. Jackson, Classical Electrodynamics, third ed., John Wiley & Sons, New York, 1999.

[18] C. Maciel-Escudero, A. Reyes-Coronado, Electromagnetic fields produced by a swift electron: A source of white light, *Wave Motion* 86: 137–149, 2019.

Fundamentals of linear momentum transfer from swift electrons to nanoparticles

Alejandro Reyes-Coronado[1*], Jesús Castrejón-Figueroa[1], and José Ángel Castellanos-Reyes[1]

[1] Departamento de Física, Facultad de Ciencias, Universidad Nacional Autónoma de México, Ciudad de México, México
*corresponding author, E-mail: coronado@ciencias.unam.mx

Abstract

Following a classical electrodynamics approach, we present an analysis of the linear momentum transfer from swift electrons to nanoparticles as a function of the relevant parameters: particle's radius, speed of the electron and its impact parameter. Since the momentum transfer is given in terms of the Maxwell stress tensor, we split the contribution to the momentum transfer in electric and magnetic components, and discuss their contribution to both attractive and repulsive regimes, previously found.

1. Introduction

Electrons have been widely used since many decades ago to gather information about electronic structure of materials. Nowadays, the use of scanning transmission electron microscope (STEM) machines is extensively spread in several areas besides physics, proving to be a fundamental tool, in particular for plasmonics. [1, 2] We have studied the interaction between swift electrons, likes those typically used in STEMs, and plasmonic nanoparticles (NPs), and we have shown that it is possible to induce forces on a small metallic NP (2-3 nanometers in radius). [3–7] Depending on the relevant parameters such as impact parameter and electron velocity, it is possible to move the NP towards the electron beam or away from it, opening the possibility of moving plasmonic NPs in a controllable way, technology named as *electronic tweezers*. [8]

For electrons traveling in the nearby of a neutral metallic NP, what is intuitively expected is an attractive interaction between the electron and the positive induced charge in the closest region of the NP respect to the electron trajectory. This is the case for large enough impact parameters, where the localised surface dipolar plasmon is mainly excited. However, for small enough impact parameters the higher-energy multipolar modes play a predominant role. [9, 10] Under this scenario, we showed that the interaction between the electron and the NP turns out to be repulsive, that is, the electron beam expels the NP away. [3] Thus, by controlling the impact parameter of the electron beam respect to the NPs, it is possible to induce attractive forces that triggers coalescence between pairs of particles, as it has been observed and studied experimentally, [11] or avoid that two NPs approach to each other.

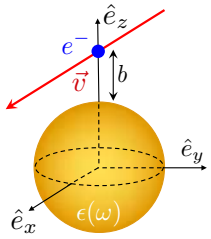


Figure 1: Sketch of the system: An electron (blue spot) travels with constant velocity $\vec{v}$ at a distance b from the center of a spherical nanoparticle (yellow sphere) with dielectric response function $\epsilon(\omega)$.

2. Theoretical model

The linear momentum transferred from a swift electron, traveling with constant speed in a straight line, to a nanoparticle characterized by a dielectric function $\epsilon(\omega)$ [see Fig. 1], can be calculated from the momentum conservation equation, [3] integrated along the whole electron trajectory

$$\Delta\vec{P}_{mec} = \int_{-\infty}^{\infty} \frac{d}{dt}\vec{P}_{mec}(t)\,dt = \int_{-\infty}^{\infty}\oint_S \overleftrightarrow{T}(\vec{r};t)\cdot\vec{da}\,dt,$$

where $\overleftrightarrow{T}$ is the Maxwell stress tensor, given by (cgs units system) [12]

$$\overleftrightarrow{T}(\vec{r};t) = \frac{1}{4\pi}\left[\vec{E}(\vec{r};t)\vec{E}(\vec{r};t) - \frac{1}{2}\overleftrightarrow{I}\,\vec{E}(\vec{r};t)\cdot\vec{E}(\vec{r};t) + \right.$$
$$\left. + \vec{B}(\vec{r};t)\vec{B}(\vec{r};t) - \frac{1}{2}\overleftrightarrow{I}\,\vec{B}(\vec{r};t)\cdot\vec{B}(\vec{r};t)\right].$$

By performing a Fourier transform of each electric and magnetic fields appearing in the Maxwell stress tensor, the total linear momentum transfer can be written as

$$\Delta\vec{P}_{mec} = \frac{1}{4\pi^2}\int_0^{\infty}\frac{d\mathcal{P}}{d\omega}d\omega$$

with

$$\frac{d\mathcal{P}}{d\omega} = \Re\left\{\oint_S\left[\vec{E}(\vec{r};\omega)\vec{E}^*(\vec{r};\omega) - \frac{1}{2}\overleftrightarrow{I}\,\vec{E}(\vec{r};\omega)\cdot\vec{E}^*(\vec{r};\omega) + \right.\right.$$
$$\left.\left. + \vec{B}(\vec{r};\omega)\vec{B}^*(\vec{r};\omega) - \frac{1}{2}\overleftrightarrow{I}\,\vec{B}(\vec{r};\omega)\cdot\vec{B}^*(\vec{r};\omega)\right]\cdot\vec{da}\right\},$$

and $\Re$ stands for the real part. The closed-surface integral is performed in a spherical grid concentric to the nanoparticle, with radius slightly larger than the particle's radius.

The electric $\vec{E}$ and magnetic $\vec{B}$ fields are the total fields: each of them is the sum of the electromagnetic fields produced by the bare electron, called external fields, and the fields produced by the nanoparticle (due to induced currents within the particle), called scattered field, that is

$$\vec{E} = \vec{E}_{ext} + \vec{E}_{scat} \quad \text{and} \quad \vec{B} = \vec{B}_{ext} + \vec{B}_{scat}.$$

The electromagnetic fields produced by the bare electron are closed expressions given in [13], while the ones generated by the nanoparticle are written in terms of a multipolar expansion. [3]

3. Results and remarks

The Maxwell stress tensor can be divided in two parts, electric and magnetic contributions. Even more, in each part of the Maxwell stress tensor, say the electric field part, appears the product of the electric field with itself, giving rise to three terms: one related to the product between the external electric field only, a second term related to the product of the scattered field only, and a third mixed term related to the product between the external and the scattered field. In this work we study the contribution of each of the six terms to the total linear momentum transfer. Actually, we already showed that the external-external term for both electric and magnetic contributions is zero. Additionally, since the scattered field is given as a multipolar expansion, we also present an analysis of the contribution of each multipole to each of the six terms.

For the detailed analysis, which is currently in process, we are considering different materials for the nanoparticle: the simplest dielectric function given by the Drude model (mimicking Al), more realistic metallic materiales such as Au and Ag, and also MgO and SiC as dielectric materials. It is worth to mention that in this work we are incorporating new numerical methods, such as Gauss-Kronrod and exp-sinh quadratures, [14, 15] to get good convergence in several integrations steps. It is also remarkable that this is the fisrt time we manage to consider nanoparticles with radius larger than 1 nm, and we are in position to study the linear momentum transfer as a function of the particle's radius.

As a preliminar result, we observed that the electric contribution to the linear momentum transfer is out of phase respect to the magnetic contribution, that is, whilst the electric contribution gives one sign, the magnetic counterpart gives the opposite sign. At the end, the attractive/repulsive regime for specific set of parameters depends on a delicate balance between both contributions.

Acknowledgement

This work was supported by UNAM-PAPIIT IN114919.

References

[1] P. E. Batson, A new surface plasmon resonance in clusters of small aluminum spheres, *Ultramicroscopy* 9: 277–282, 1982.

[2] F. J. García de Abajo, Optical excitations in electron microscopy, *Rev. Mod. Phys.* 82: 209–275, 2010.

[3] A. Reyes-Coronado, R. G. Barrera, P. E. Batson, P. M. Echenique, A. Rivacoba, and J. Aizpurua, Electromagnetic forces on plasmonic nanoparticles induced by fast electron beams, *Phys. Rev. B* 82: 235429, 2010.

[4] P. E. Batson, A. Reyes-Coronado, R. G. Barrera, A. Rivacoba, P. M. Echenique, and J. Aizpurua, Plasmonic nanobilliards: Controlling nanoparticle movement using forces induced by swift electrons, *Nano Lett.*, 11: 3388–3393, 2011.

[5] P. E. Batson, A. Reyes-Coronado, R. G. Barrera, A. Rivacoba, P. M. Echenique, and J. Aizpurua, Nanoparticle movement: Plasmonic forces and physical constraints, *Ultramicroscopy* 124: 50–58, 2012.

[6] E. J. R Vesseur, J. Aizpurua, T. Coenen, A. Reyes-Coronado, P. E. Batson, and A. Polman, Plasmonic excitation and manipulation with an electron beam, *MRS Bulletin* 37: 752–760, 2012.

[7] M. J Lagos, A. Reyes-Coronado, A. Konečná, P. M. Echenique, J. Aizpurua, and P. E. Batson, Attosecond and femtosecond forces exerted on gold nanoparticles induced by swift electrons, *Phys. Rev. B* 93: 205440, 2016.

[8] V. P. Oleshko, J. M. Howe, Are electron tweezers possible?, *Ultramicroscopy* 111: 1599–1606, 2011.

[9] T. L. Ferrel and P. M. Echenique, Generation of Surface Excitations on Dielectric Spheres by an External Electron Beam, *Phys. Rev. Lett.* 55:1526–1529, 1985.

[10] F. J. García de Abajo and A. Howie, Relativistic Electron Energy Loss and Electron-Induced Photon Emission in Inhomogeneous Dielectrics, *Phys. Rev. Lett.* 80:5180–5183, 1998.

[11] P. E. Batson, Motion of Gold Atoms on Carbon in the Aberration-Corrected STEM, *Microsc. Microanal.* 14:89–97, 2008.

[12] J. D. Jackson, *Classical Electrodynamics*, third ed., John Wiley & Sons, New York, 1999.

[13] C. Maciel-Escudero, A. Reyes-Coronado, Electromagnetic fields produced by a swift electron: A source of white light, *Wave Motion* 86: 137–149, 2019.

[14] A. Kronrod, *Nodes and weights of quadrature formulas. Sixteen-place tables*, New York: Consultants Bureau, 1965.

[15] M. Mori and M. Sugihara, The double-exponential transformation in numerical analysis, *J. Comput. Appl. Math.* 127:287-296, 2001.

Pure toroidal dipole excitation in dielectric nanoparticles

Reza Masoudian Saadabad[1], Marcus Cai[2], Lei Xu[1], Andrey E. Miroshnichenko[1]

[1]School of Engineering and Information Technology, University of New South Wales, Canberra, Australia
[2]Australian National University, Australia
*corresponding author, E-mail: andrey.miroshnichenko@unsw.edu.au

Abstract

A tightly focused, radially polarised cylindrical vector beam in conjunction with a plane wave has been applied to launches toroidal dipole moment while suppressing electric dipole moment in a silicon nanodisk. The nanodisk was illuminated in z-axis by the cylindrical vector beam while the plane wave exposed the disk in a 45° direction relative to the beam. In a given configuration we were able to achieve the strongest toroidal dipole moment excitation.

Introduction

Properties of electromagnetic media are traditionally described by electric and magnetic dipoles and a set of their combinations called multipoles. Although the typical set of multipoles consists of two families of electric and magnetic multipoles, there is another type of electromagnetic sources named as toroidal multipoles. Toroidal modes are complementary terms for standard multipole expansion and show the scattering contribution of poloidal currents. They can be used to describe unusual electromagnetic properties of metamaterials and subwavelength structures. Toroidal dipole, which is the lowest order of toroidal family, is associated with surface currents, **J**, that flow along the meridians of a virtual toroid. Toroidal dipole moment is along the torus axis and given by [1]:

$$\mathbf{T} = \frac{1}{10c}\int d^3\mathbf{r}[\mathbf{r}(\mathbf{r}.\mathbf{J}) - 2\mathbf{r}^2\mathbf{J}], \qquad (1)$$

where c is referred to as light speed. In spite of distinction between the electric and toroidal dipoles nature, their radiated fields have the same parity and angular momentum and therefore, they are indistinguishable in long distance. Consequently, a specific superposition of moments of toroidal and electric dipoles can lead to a destructive interference [2].

In this paper, a radially polarised cylindrical vector beam (CVB) in conjunction with a plane wave is used to illuminate a silicon nanodisk to excite toroidal dipole moment while suppressing electric dipole moment. An applied CVB excites both toroidal and electric dipole moments in nanodisk. Importantly, the electric dipole moment can be suppressed via appropriately following CVB with a plane wave. The proposed scheme of simulation is illustrated in Fig.1 where a tightly focused,

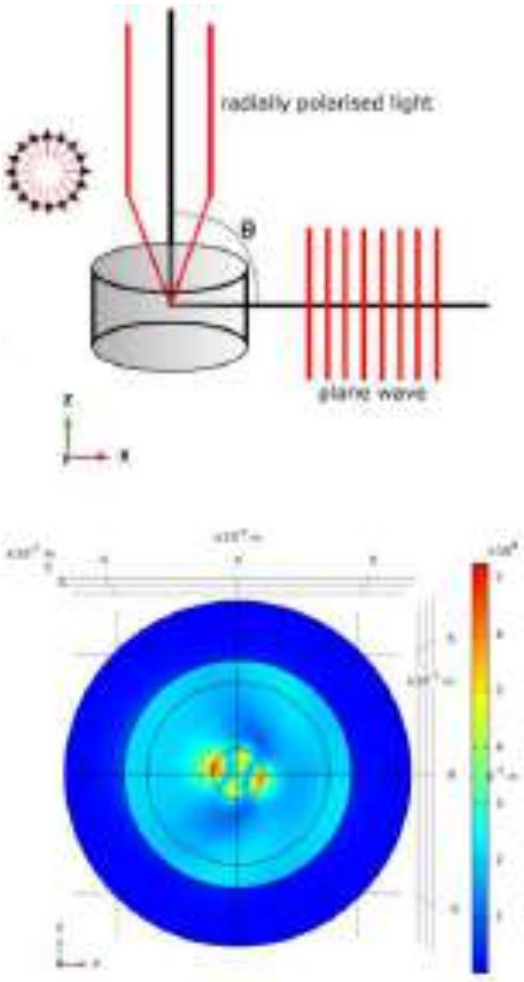


Figure 1: setup of simulation. A radially polarized cylindrical vector beam (CVB) in conjunction with a plane wave are used to illuminate a silicon nanodisk. Theta is the angle which plane wave makes with z axis. x-y plane electric field in focal point is also illustrated.

radially polarised CVB exposes nanodisk along the z-axis and a plane wave is applied at an angle relative to CVB. For a radially polarized CVB, electric field around focus is described by two components of longitudinal and radial as bellow while azimuthal component is zero [3]

$$e_{\rho}^{(s)}(\rho_s, z_s) = A\int_0^{\alpha} \cos^{1/2}\Theta \sin 2\theta\, l_0(\Theta) J_1(k\rho_s \sin\Theta) e^{(ikz_s \cos\Theta)} d\Theta \quad ,(2)$$

$$e_{z}^{(s)}(\rho_s, z_s) = 2iA\int_0^{\alpha} \cos^{1/2}\Theta \sin^2\Theta\, l_0(\Theta) J_1(k\rho_s \sin\Theta) e^{(ikz_s \cos\Theta)} d\Theta$$

where $\mathbf{r} = (\rho_s, \phi_s, z_s)$ represents cylindrical coordinates, l_0 shows relative amplitude of the filed, and J is Bessel function.

1. Results and discussion

Simulations have been conducted based on the setup illustrated in Fig.1. Both light sources have the same amplitude of 6032.7 Vcm-1. Silicon disk of 100 nm radius and 108 nm height is placed in a medium with a refractive index of 3.5. Furthermore, the numerical aperture of the lens and beam waist are considered to be 0.86 and 1 μm. While it is expected that efficient suppression of electric dipole moment is more effective at $\theta = 90^{o}$, the best outcome is achieved at $\theta = 45^{o}$. The electric and toroidal dipole moments of the nanodisk are indicated in Fig.2 as a function of light wavelength for two angles 45° and 90°. The ratio of the toroidal moment to the electric moment is also shown in the figure. As can be seen, the values of electric dipole moment at two angles are almost equal, although the angle of 45° shows smaller moments. The maximal value of toroidal moment/electric moment ratio is 27.042 and achieved at wavelength 463.5 nm.

2. Conclusions

Excitation of the electric and toroidal dipole moments in a silicon nanodisk using a plane wave and radially polarised cylindrically vector beam has been studied numerically. We found that when the angle between the cylindrical vector beam and the plane wave is 45°, the strength of the electric dipole moment is reduced while the toroidal dipole moment is increased. As a next step, we are planning to conduct experimental studies to verify these results. The outcomes of such research can be applied in various areas of optical communication.

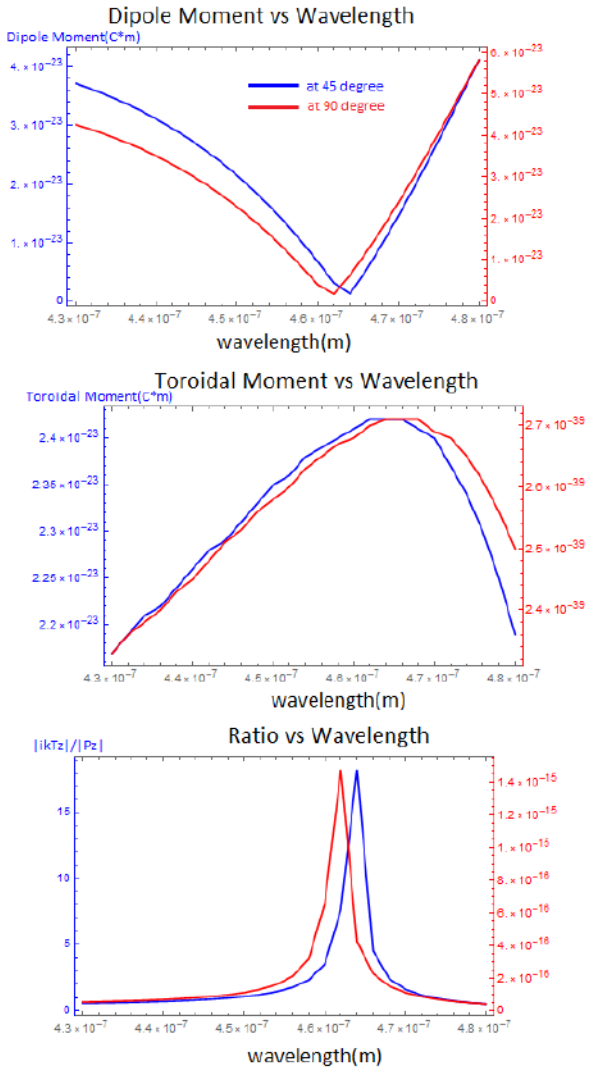


Figure 2: The electric and toroidal dipole moments of nanodisk is indicated as a function of light wavelength for two angles 45° and 90°. Ratio of toroidal moment to electric moment is also indicated.

References

[1] N. Papasimakis, V. A. Fedotov, V. Savinov, T. A. Raybould, N. I. Zheludev, Electromagnetic toroidal excitations in matter and free space, *Nature Materials* 15: 263–271, 2016.

[2] A. I. Kuznetsov, A. E. Miroshnichenko, M. L. Brongersma, Y. S. Kivshar, B. Luk'yanchuk, Optically resonant dielectric nanostructures, *Science* 354: aag2472-1– aag2472-8, 2016.

[3] K. S. Youngworth and T. G Brown, Focusing of high numerical aperture cylindrical-vector beams, *Optics Express* 7: 77–87, 2000.

[4] P. Woźniak, P. Banzer, and G. Leuchs, Selective switching of individual multipole resonances in single dielectric nanoparticles, *Laser&Photonics Reviews* 9, 231-240 (2015).

Synthesis and Plasmonic Properties of Au Double Nanorings Supported by Pd Cyclic Nanosheets

Yukie Yokota[1,2], Takumi Takatsuki[1], Tsuyoshi Tokita[1], Yushi Yabuki[1], Kazuo Watanabe[1*]

[1] Department of Chemistry, Faculty of Science, Tokyo University of Science, Tokyo, Japan
[2] Metamaterials Lab., RIKEN, Saitama, Japan
*Corresponding author, E-mail: kazuo@rs.tus.ac.jp

Abstract

Localized surface plasmon resonances (LSPR) of metal nanostructures exhibit peculiar resonance spectra depending on their size, shape and composition. We focus on Au nanorings supported by Pd nanosheets for possible applications in catalysts. In this study, we have prepared Au double nanorings by chemical synthesis in the liquid phase and investigated their optical properties.

1. Introduction

Ultrathin nanosheets of transition metal Pd have high catalytic activity because of their large surface areas. On the other hand, nanostructures of noble metals such as gold and silver are applied to surface-enhanced Raman spectroscopy and biosensing because of the enhanced electric field of LSPR. The fabrication of complicated nanostructures requires expensive equipment such as an electron beam lithography facility and complex processes. Therefore, it is desirable to establish a chemical synthesis method that can control the shapes of metal nanoparticles in large quantities at low cost. In this research, we synthesized chemically Au double nanorings supported by Pd cyclic nanosheets. We investigated the size control and optical properties of Au double nanorings.

2. Experimental Section

2.1. Synthesis of Au double nanorings supported by Pd cyclic nanosheets

Pd nanosheets were synthesized by reducing the Pd precursor in a DMF solution. By oxidatively etching the Pd nanosheets in the presence of halide ions, a central portion of the sheets were perforated to produce Pd cyclic nanosheets. By injecting chloroauric acid into the Pd cyclic nanosheet solution at a constant speed and selectively depositing Au along the inner and outer edges of the nanosheets, we synthesized Au double nanorings supported by Pd cyclic nanosheets. The outer diameter of the Au double nanorings were controlled by the diameter of the Pd nanosheet support. Pd nanosheets with large diameters were synthesized with varying amounts of citric acid and protective agent.

2.2. Structural and Optical properties

Transmission electron microscopy (TEM) images were obtained using a JEOL JEM-200EX II microscope at an acceleration voltage of 100 kV. The Au nanorings were dispersed in an ethanol solution, and the absorption spectra were measured with an ultraviolet-visible spectrophotometer.

3. Results and Discussion

3.1. Au double nanorings supported Pd cyclic nanosheets

Fig. 1 shows a TEM image of an Au double nanoring of 60 nm in diameter. It is seen that the ring structures were formed by growth and aggregation of the Au particles along the outer and the inner peripheries of the Pd cyclic nanosheet. The widths of the gold rings were less than about 10 nm.

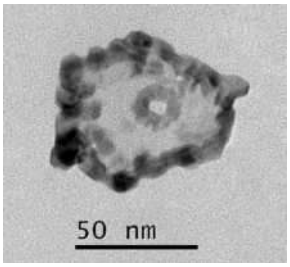


Figure 1: TEM image of an Au double nanoring supported by a Pd cyclic nanosheet.

3.2. Optical properties of the Au double nanorings

Fig. 2 shows the absorption spectra of the Au nanorings of 60 nm in diameter supported by Pd nanosheet without an opening in the center and the Au double nanorings with the same outer diameter supported by a cyclic Pd nanosheet.

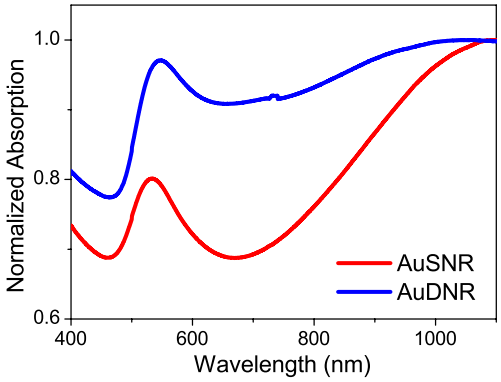


Figure 2: Absorption spectra of Au single nanorings (AuSNR) and Au double nanorings (AuDNR) of 40 nm in diameter dispersed in ethanol.

In both cases, two LSPR peaks derived from Au were observed. The broad peak at around 1100 nm is attributable to an in-plane resonance mode parallel to the ring plane, and the relatively sharp peak at around 550 nm to the out-of-plane resonance mode perpendicular to the ring plane [3]. It should be noted that, due to the influence of the inner Au nanoring, the out-of-plane mode peak of the Au double nanorings is relatively more pronounced and red-shifted compared to that of the Au single nanorings.

The absorption spectrum of Au double nanorings of 40 nm in diameter synthesized using smaller Pd cyclic nanosheets is compared with the Au nanoring 60 nm in diameter in Fig.3. The peak of the in-plane resonance mode is blue shifted by about 220 nm from 1050 nm to 835 nm. This suggests that the peak wavelength of the plasmon resonance in the near infrared region can be controlled by changing the outer diameter of the Pd cyclic nanosheet support.

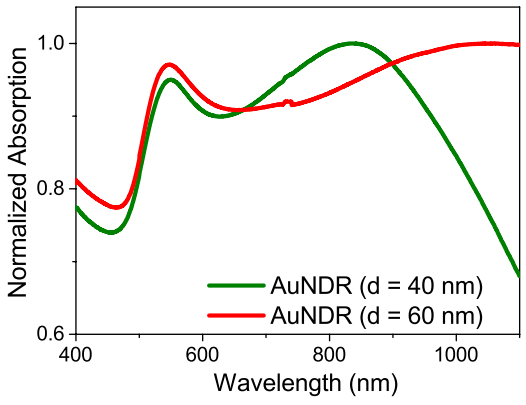


Figure 3: Absorption spectra of Au double nanorings with the diameters of 40 and 60 nm in ethanol.

4. Conclusions

We synthesized Au double nanorings supported by Pd cyclic nanosheets using a seed-mediated growth approach. The LSPR characteristics of the gold double nanorings can be adjusted by varying the diameter of the supporting Pd cyclic nanosheets.

Acknowledgements

We acknowledge financial support from the Futaba Research Grant Program of the Futaba Foundation.

References

[1] D. Li, and D. Yang, Seed-mediated growth of Au nanorings with size control on Pd ultrathin nanosheets and their tunable surface plasmonic properties, *Nanoscale*, **8**, 3704 (2016).

[2] C. Jin, Z. Zhang, and D. Yang, Ultrathin two-dimensional Pd-based nanorings as catalysts for hydrogenation with high activity and stability, *Small*, **36**, 4745 (2015).

[3] T. Ozel, M. Ashley, G. Bourret, M. Ross, G. Schatz and C. Mirkin, Solution-dispersible metal nanorings with deliberately controllable compositions and architectural parameters for tunable plasmonic response, *Nano. Lett*. **15**, 5273 (2015).

Efficient Resonance of Double Active Silicon Nanowires

Shengqiong Chen[1], Lina Shi[2], Jiebin Niu[3], and Changqing Xie[4]

[1]Institute of Microelectronics, Chinese Academy of Sciences, Beijing, China

*corresponding author, E-mail: chenshengqiong@ime.ac.cn

Abstract

The optical properties in active double SiO2-Si wire system have been investigated by using Four-Level Two-Electron model with the Finite-Difference Time-Domain(FDTD) solutions. The super resonance occurs with appropriate dimensions of the width of the Si wires and the gap between them. Furthermore, with increasing the separation between two Si wires, the peak value decreases in the beginning and then increases when the optical path difference is exactly equal to the emission wavelength of the gain material.

1. Introduction

In recent years, the active coated has drawn great attention of many researchers for the reason that the gain molecules embedded in nanostructures can provide large gain coefficients to compensate the loss of surface plasmons (SPs) of metallic nanostructures and amplify the desired SP response. Considering a series of inherent defects in metal, nanostructures consisted of semiconductor nanoparticle has been started to research.

In this paper, we adopted Four-Level Two-Electron model to calculate the spectra of silicon nanostructure combined with a specific gain material, an organic dye Oregon Green 488 (OG-488, Invitrogen, Thermo Fisher Scientific). This model is more practical because it presents parameters of material which can be found or maked in reality.

2. Calculation

We use FDTD solutions to calculate the double silicon wire systems with doped silica shells placed on the top of a SiO_2 layer.

2.1. Parameters of Four-Level Two-Electron model

According to absorption and emission spectra provided by the gain material provider and approximate life time measured in ref.6, we estimated the parameters of Four-Level Two-Electron model in FDTD solutions by fitting to the full set of rate equations for the four-level system. And the gain material of these parameters was considered in the later calculations.

2.2. Simulation

As showed in Figure 1, an active double Si wires system is comprised of two silicon nanowires, which are coated with dye-doped silica shell, supported on silica capped silicon substrate.

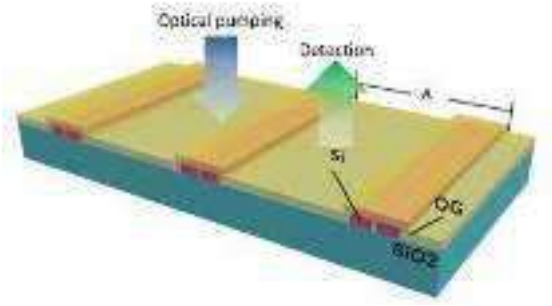


Figure 1: Schematic of double Si wires and experimental configuration with FDTD.

The width, height and the period of the double Si wires system are 306nm, 150nm and 3um respectively. The incident light (linearly polarized plane wave) was gradually increased until the inverted gain medium inside the silica shell reach a sufficient amount to observe a significant laser phenomenon.

3. Discussion

3.1. Results

We explored the relationship of simulated emission spectra and the gap between the two Si wires (Figure 2). The center frequency of the emission spectrum stayed almost the same with the gap below 200 nm. And the value of the peak point of emission spectrum reached maximum when the gap is 30 nm which means the coupling occurred between the two wires. The center frequency of the spectrum has a red shift phenomenon with the increase of the gap above 300 nm. Furthermore, the peak value is greatly enhanced again with the gap above 400 nm. Because these gaps are much larger than near-field on the surface of Si wires, the twice enhancement of the peak with gaps of these dimensions do not due to the coupling between the two wires. The optical path difference between the two Si wires is exactly at the emission wavelength of the gain material. So the interference of light between the two wires may be the reason for the twice enhancement of measured emission spectrum.

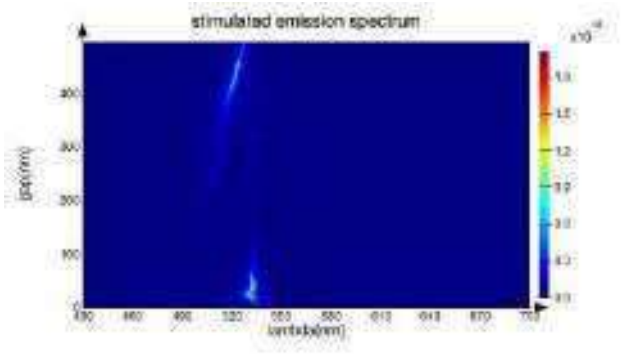


Figure 2: stimulated emission spectra of double Si/silica/dye systems.

Fig. 3 is the stimulated emission spectrum of double Si-SiO2 system with the gap of 30nm. The width of the spectrum is 2.1 nm and the Q-factor is 253 which calculated by the equation

$$Q = \frac{\lambda_0}{\Delta\lambda}, \quad (1)$$

where λ_0 is the center frequency of the emission spectra and $\Delta\lambda$ is the full width at half maxima of the spectrum.

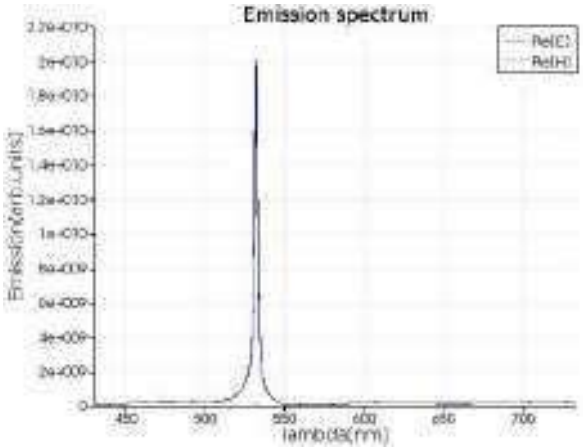


Figure 3: stimulated emission spectrum of double Si/silica/dye nanostructures with gap of 30 nm.

4. Conclusions

The super resonance properties of the active double Si wires system have been investigated by the use of Four-Level Two-Electron model and FDTD solutions. At the appropriate dimensions of Si wire and the gap, the width of emission spectrum can reach minimum value which means super resonance. At the peak of the emission spectrum, the peak value of active emission spectrum is enhanced compared to passive structures. And the peak value at 526nm extremely enhanced because of optical interference when the optical path difference between the two Si wires is exactly near the peak wavelength of the gain material emission spectrum when the gap is above 300nm.

Acknowledgements

This work is supported by National Natural Science Foundation of China (Grant No.61875225) and National Key research and Development Program of China (Grant No.2017YFA0206002).

References

[1] Wu, D. J.; Yu, H. Q.; Yao, J.; Ma, Q. Y.; Cheng, Y.; Liu, X. J., Efficient Magnetic Resonance Amplification and Near-Field Enhancement from Gain-Assisted Silicon Nanospheres and Nanoshells. *J. Phys. Chem. C* **2016,** *120* (24), 13227-13233.

[2] Hess, O.; Pendry, J. B.; Maier, S. A.; Oulton, R. F.; Hamm, J. M.; Tsakmakidis, K. L., Active nanoplasmonic metamaterials. *Nature Materials* **2012,** *11* (7), 573-584.

[3] Sadeghi, S. M.; Nejat, A.; Mao, C. B., Enhancement of emission efficiency of colloidal CdSe quantum dots on silicon substrate via an ultra-thin layer of aluminum oxide. *Nanotechnology* **2014,** *25* (15), 8.

[4] Kim, S.-H.; Han, W. S.; Jeong, T.-Y.; Lee, H.-R.; Jeong, H.; Lee, D.; Shim, S.-B.; Kim, D.-S.; Ahn, K. J.; Yee, K.-J., Broadband Surface Plasmon Lasing in One-dimensional Metallic Gratings on Semiconductor. *Scientific Reports* **2017,** *7* (1), 7907.

[5] Dadoenkova, Y. S.; Moiseev, S. G.; Zolotovskii, I. O.; Pavlov, D. A., Electrically pumped spaser based on semiconductor film / graphene / dielectric structure. *AIP Conference Proceedings* **2017,** *1874* (1), 040038.

[6] Noginov, M. A.; Zhu, G.; Belgrave, A. M.; Bakker, R.; Shalaev, V. M.; Narimanov, E. E.; Stout, S.; Herz, E.; Suteewong, T.; Wiesner, U., Demonstration of a spaser-based nanolaser. *Nature* **2009,** *460* (7259), 1110-U68.

Chemistry of remotely separated species hybridized by strong light-matter coupling

Matthew Du[1*], Raphael F. Ribeiro[1], Luis A. Martínez-Martínez[1], Zixuan Hu[2], Vinod M. Menon[3,4], Joel Yuen-Zhou[1]

[1]Department of Chemistry and Biochemistry, University of California San Diego, La Jolla, California, USA
[2]Departments of Chemistry, Department of Physics, and Birck Nanotechnology Center, Purdue University, West Lafayette, Indiana, USA
[3]Department of Physics, City College, City University of New York, New York, United States.
[4]Department of Physics, Graduate Center, City University of New York, New York, United States
*corresponding author, E-mail: madu@ucsd.edu

Abstract

Quantum states in different molecules can be hybridized by strong light-matter interaction. Here we present strategies that employ such coupling to enable photochemistry involving remotely separated species. First, we show how polariton-assisted remote energy transfer (PARET) across hundreds of nanometers occurs when surface plasmons strongly interact with both donor and acceptor chromophores. We then propose a remote control of chemistry whereby photoexcitation of molecules in one optical microcavity influences the photoinduced reactivity of molecules in another microcavity.

1. Introduction

In the limit where a molecular transition strongly interacts with light, the coupled species hybridize into quantum states called polaritons. Compared to the original (or bare) matter states, the polaritons are significantly photonic in character and shifted in energy. These properties themselves have important consequences for molecular processes [1]. However, polaritonic setups typically employ a macroscopic chemical sample. As a result, almost all superpositions of the coupled transition in each molecule are not coupled to light. These linear combinations are known as dark states, which remain in energy at the bare transition. Nevertheless, this dense reservoir of states also affects chemical dynamics under strong light-matter coupling [1], namely by acting as an energy sink for polaritons [2]. Given the above phenomena, it would be interesting to explore what novel chemical opportunities are available by strongly coupling transitions of several compounds to light. In this work, we theoretically demonstrate two intriguing examples of polariton photochemistry involving spatially separated compounds. We first discuss polariton-assisted remote energy transfer (PARET) between donor and acceptor chromophores both strongly coupled to surface plasmons [3]. Then, we introduce a polaritonic device that supports remote control of chemistry [4].

2. Results and discussion

2.1. Polariton-assisted remote energy transfer (PARET)

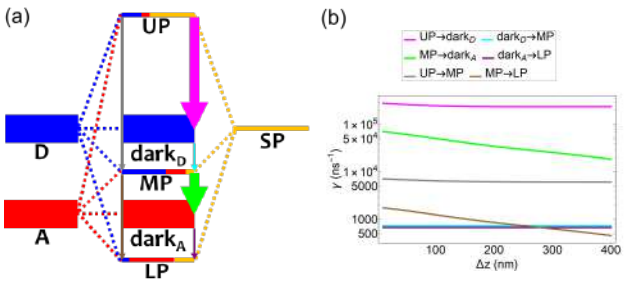


Figure 1: (a) Schematic energy-level diagram depicting polariton-assisted remote energy transfer (PARET) transitions among polariton (upper, UP; middle, MP; lower, LP) and dark states for both donor (D) and acceptor (A) chromophores strongly coupled to donor-resonant surface plasmon (SP). (b) Rates γ for selected energetically downhill transitions as a function of separation Δz between slabs of each chromophore. Adapted from [3].

In typical samples of donor and acceptor chromophores (without the presence of surface plasmons), electronic photoexcitation of the former species is followed by energy transfer, of the Förster type, to the latter. The second process is Coulombic in nature and occurs only when interchromophoric separation lies within $\sim 1 - 10$ nm. To extend the range of energy exchange, we consider strongly coupling a surface plasmon mode to the first electronic transition of each dye.

Specifically, we study PARET (Fig. 1) in a setup consisting of—from bottom to top—a metal film, a slab of donor molecules, and slab of acceptor molecules. Although resonant with the donor, the surface plasmon mode of interest has strong interaction with both types of chromophores. In particular, the three polaritons are delocalized across donors, acceptors, and surface plasmon (Fig. 1a).

Therefore, upon excitation of either of the higher-energy polaritons, vibrational relaxation to the lowest-energy polariton occurs through a series (Fig. 1a) of ultrafast (Fig. 1b) transitions to and from dark states. Such decay processes occur for interslab distances of up to ∼400 nm (Fig. 1b) and are induced by the vibronic coupling inherent to molecules in general. Notice that the higher-energy polaritons have molecular character of mostly donor while the lowest-energy polariton has that mostly of acceptor. It follows that PARET from donor-like state to acceptor-like state is achieved. In fact, our theory is in good agreement (Table 2 of [3]) with experiment [5].

2.2. Remote control of chemistry

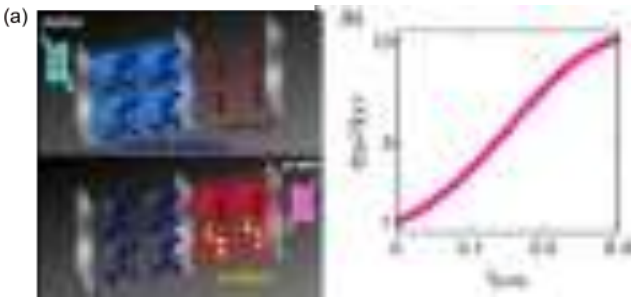


Figure 2: (a) Scheme illustrating remote control of chemistry using optical microcavities. 'Pump'-pulse excitation of a polariton whose character is mostly 'remote catalyst' glyoxylic acid (*trans-cis* conformer) and its cavity enables the 'probe' pulse to efficiently excite a polariton whose character is mostly reactant *cis*-HONO and its cavity; subsequently, the reactant isomerizes into product *trans*-HONO. (b) Enhancement $\eta_{\mathrm{ON}}/\eta_{\mathrm{OFF}}$ of reaction efficiency (compared to $f_{\mathrm{pump}} = 0$, probe excitation only) as a function of fraction f_{pump} of pump-excited remote catalyst. Adapted from [4].

Conventionally, a catalyst binds its reactant to accelerate the conversion to product. Given the ability for strong light-matter interaction to hybridize molecular species separated well beyond chemical length scales, we design a device where acting on a 'remote catalyst' (RC) affects the reaction of a spatially separated reactant. This device consists of *trans-cis* conformer of glyoxylic acid as RC in one optical microcavity and *cis*-nitrous acid (HONO) as reactant in another optical microcavity (Fig. 2a). Suppose that the OH stretch vibration of each compound interacts strongly with the corresponding host cavity. The cavities themselves also experience strong coupling. Thus, both molecular species and their respective cavities hybridize into four polaritons. Due to the anharmonicity of the RC OH stretch mode, exciting the highest, RC-like polariton modifies the energy and mixing fraction of each polariton [6]. Consequently, this 'pumping' of an RC-like polariton modifies the reactivity induced by exciting the lowest, reactant-like polariton with a near-resonant 'probe' pulse. Indeed, increasing the population of excited RC enhances the efficiency of *cis* → *trans* isomerization of HONO by an order of magnitude (Fig. 2b). Hence, we establish remote control of chemistry.

3. Conclusions

In summary, we first find that when both donor and acceptor dyes are strongly coupled to a surface plasmon mode, energy transfer from donor-like polariton to acceptor-like polariton occurs via vibrational relaxation for interchromophoric separations up to hundreds of nanometers. We next reveal remote control of chemistry: raising the excitation of a 'remote catalyst'-like polariton in one optical microcavity enhances the infrared-induced conformational isomerization of a *cis*-HONO-like polariton in another optical microcavity by an order of magnitude.

Acknowledgement

M.D., R.F.R., L.A.M.-M. are grateful for generous UCSD startup funds. M.D., R.F.R., and J.Y.-Z. acknowledge funding from the NSF CAREER Award CHE-164732. M.D. and J.Y.-Z. were supported by U.S. Department of Energy, Office of Science, Basic Energy Sciences, CPIMS program, Early Career Research Program under Award No. DE-SC0019188. R.F.R. acknowledges funding from a UCSD CRES postdoctoral award and AFOSR award FA9550-18-1-0289. L.A.M.-M. is grateful for the UC-Mexus CONACyT scholarship for doctoral studies. V.M.M. thanks DOE BES for Award DE-SC0017760.

References

[1] R.F. Ribeiro, L.A. Martínez-Martínez, M. Du, J. Campos-Gonzalez-Angulo and J. Yuen-Zhou, Polariton chemistry: controlling molecular dynamics with optical cavities, *Chem. Sci.* 9: 6325-6339, 2018.

[2] V.M. Agranovich, M. Litinskaia, M, D.G. Lidzey, Cavity polaritons in microcavities containing disordered organic semiconductors, *Phys. Rev. B* 67 (8): 085311, 2003.

[3] M. Du, L.A. Martínez-Martínez, R.F. Ribeiro, Z. Hu, V.M. Menon, J. Yuen-Zhou, Theory for polariton-assisted remote energy transfer, *Chem. Sci.* 9: 6659-6669, 2018.

[4] M. Du, R.F. Ribeiro, J. Yuen-Zhou, Remote control of chemistry in optical cavities, *Chem* Accepted, 2019.

[5] D.M. Coles, N. Somaschi, P. Michetti, C. Clark, P.G. Lagoudakis, P.G. Savvidis, D.G. Lidzey, Polariton-mediated energy transfer between organic dyes in a strongly coupled optical microcavity, *Nat. Mater.* 13: 712-719, 2014.

[6] R.F. Ribeiro, A.D. Dunkelberger, B. Xiang, W. Xiong, B.S. Simpkins, J.C. Owrutsky, J. Yuen-Zhou, Theory for Nonlinear Spectroscopy of Vibrational Polaritons, *J. Phys. Chem. Lett.* 9: 3766-3771, 2018.

Plasmonic Properties of Silver Amalgam Nano- and Microparticles

Lukáš Kejík[1,2*], Filip Ligmajer[1,2,3], Michal Horák[1], Aleš Daňhel[2], Miroslav Fojta[2,4], and Tomáš Šikola[1,3]

[1]Central European Institute of Technology, Brno University of Technology, Brno, Czech Republic
[2]Institute of Biophysics of the Czech Academy of Sciences, Brno, Czech Republic
[3]Institute of Physical Engineering, Brno University of Technology, Brno, Czech Republic
[4]Central European Institute of Technology, Masaryk University, Brno, Czech Republic
*corresponding author, E-mail: lukas.kejik@ceitec.vutbr.cz

Abstract

Silver amalgam represents the most suitable alternative electrode material to a metallic mercury in electroanalytical chemistry. Nanostructuring the amalgam promises improved electrochemical performance and brings along the prospect of plasmonic activity. Here, we present a detailed study of plasmonic properties of silver amalgam nano- and microparticles with plasmon resonance wavelengths spanning from ultraviolet to the mid-infrared region depending on the particle size. This combined electrochemical and plasmonic functionality renders the system as a very promising electrode material for spectroelectrochemical studies.

1. Introduction

Silver amalgam was found to be one of the most suitable solid electrode materials in electroanalysis of various reducible organic and inorganic compounds including heavy metals, agrochemicals, colorants, drugs, environmental pollutants, or biologically important compounds such as DNA and proteins [1, 2]. Recently, similarly to other research areas, electrochemistry has benefited from the emergence of nanomaterials such as gold nanoparticles and carbon nanotubes [3]. When such materials are applied to the conventional electrodes, they help to increase its active surface area, charge transfer efficiency and overall sensitivity, though it also introduces additional complexity to the system. Synthesizing the nanoparticles directly from the silver amalgam can, therefore, bring along the benefits of the nanostructured electrodes without complicating the system structure by the presence of additional materials. However, currently there is a lack of knowledge about the optical properties of nanostructured or even bulk silver amalgam which prevents its use in spectroelectrochemical and photochemical studies.

Here, we present a detailed study of optical properties of silver amalgam and we demonstrate the plasmonic nature of its nano- and microparticles using optical and electron beam spectroscopy.

2. Results and discussion

Silver amalgam nano- and microparticles were prepared by controlled electrodeposition on a conductive indium tin oxide (ITO) support from a mixed solution of silver and mercury ions [4]. Their optical response was obtained using Fourier-transform infrared spectrometer which confirmed the plasmon resonance of sufficient quality for spectroelectrochemistry ranging from ultraviolet to mid-infrared region depending on the particle size. To support our findings, numerical simulations were performed employing the dielectric function of a thick silver amalgam layer which was obtained by spectroscopic elipsometry.

To understand the nature of plasmonic modes in amalgam particles, focus was brought from the ensemble response down to a single-particle level utilizing the scanning transmission electron microscopy (STEM) combined with electron energy loss spectroscopy (EELS). In order to prepare the samples for EELS, amalgam nanoparticles were washed off the ITO into a demineralized water in an ultrasonic bath and the resulting solution was dropped and dried on a silicon nitride membrane. A typical rod-shaped nanoparticle with the length of 170 nm, width of 120 nm and the thickness of 80 nm is shown in Figure 1. The chemical composition of this amalgam nanoparticle measured by energy dispersive X-ray spectroscopy (EDS) in STEM is homogeneous and in weight percent corresponds to $(67 \pm 6)\%$ of Ag and $(33 \pm 6)\%$ of Hg. The rod-shaped amalgam nanoparticle exhibits three different resonant modes which were also complemented by the numerical simulations using boundary element method (BEM). The first peak that is at 1.77 eV in the experiment (1.60 eV in BEM simulation) corresponds to the longitudinal dipole mode, which has the maximum in the middle of nanoparticle's short edge. The second peak at around 2.8 eV in the experiment (2.84 eV in BEM simulation) indicates a transversal dipole mode, which has the maximum in the middle of nanoparticle's long edge. The third peak around 3.2 eV in the experiment (3.15 eV in BEM simulation) corresponds to a quadrupole mode. The results of the simulations show reasonable qualitative and quantitative agreement with the experiment giving us better understanding of experimentally observed plasmonic peaks.

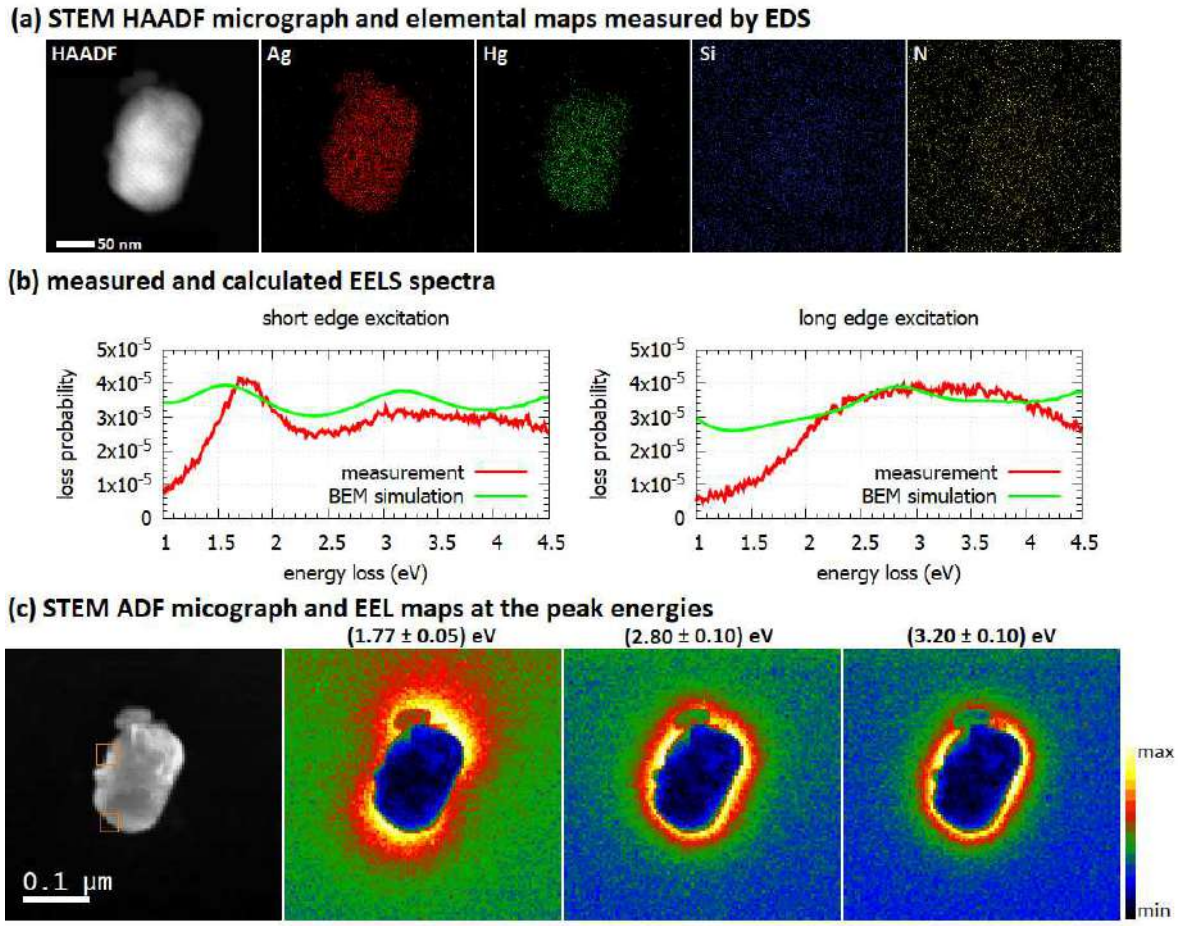


Figure 1: A rod-shaped silver amalgam nanoparticle - 170 nm long, 120 nm wide, and 80 nm thick laying on a SiN_x membrane: (a) STEM HAADF micrograph and chemical composition mapped by EDS, (b) EEL spectra after subtraction of zero-loss peak and background integrated over the orange squares in (c) complemented by the numerical simulations in BEM corresponding to the excitation in the middle of nanoparticle's short and long edges, respectively, (c) STEM ADF micrograph and measured EEL maps at the peak energies in (b).

3. Conclusions

To conclude, we have demonstrated that silver amalgam, apart from its proven usefulness in electroanalytic chemistry, can also be regarded as novel plasmonic material with promising optical properties. We have synthesized silver amalgam nano- and microparticles which exhibit strong plasmon resonances in ultraviolet to mid-infrared regions depending on the particle size, while in single nanoparticle studies we have also identified individual plasmonic modes. These findings will help in designing a unique spectroelectrochemical platform, where the synergy between its plasmonic and electrochemical qualities can be fully utilized.

Acknowledgement

This research was supported by the Czech Science Foundation (17-23634Y), ERDF under the SYMBIT project (CZ.02.1.01/0.0/0.0/15_003/0000477), and the MEYS CR under the projects CEITEC Nano RI (LM2015041, 2016-2019) and CEITEC 2020 (LQ1601).

References

[1] A. Daňhel, J. Barek, Amalgam Electrodes in Organic Electrochemistry, *Curr. Org. Chem.* 15: 2957–2969, 2011.

[2] A. Daňhel, B. Josypcuk, J. Barek, M. Fojta, Possibilities and Prospects of Silver Amalgam in Electroanalytical Chemistry, *Chem. List.* 110: 215–221, 2016.

[3] A. Walcarius, S. D. Minteer, J. Wang,Y. Lin, A. Merkoi, Nanomaterials for Bio-Functionalized Electrodes: Recent Trends, *J. Mater. Chem. B* 1: 4878–4908, 2013.

[4] A. Daňhel, F. Ligmajer, T. Šikola, A. Walcarius, M. Fojta, Electrodeposition of Silver Amalgam Particles on ITO Towards Novel Electrode Material, *J. Electroanal. Chem.* 821: 53–59, 2018.

Coupling a single carbon-nanotube to a plasmonic "hotpots-patch" antenna.

Clément Beaufils, Nicolas Izard, Didier Felbacq, Guillaume Cassabois and Emmanuel Rousseau*

Laboratoire Charles Coulomb (L2C) - UMR 5221 - Université de Montpellier - CNRS
*corresponding author, E-mail: emmanuel.rousseau@umontpellier.fr

Abstract

We report on the coupling of single carbon-nanotubes to plasmonic "hotspots-patch" antennas made by a random collection of metallic scatterers. Preliminarily to luminescence experiments, we have characterized the quenching of a single carbon-nanotube due to the metallic plane. We highlight that the experimental results fit well with the power radiated by a dipole parallel to the metallic plane. Finally we show that the hotspots lead to luminescence enhancement. Interestingly we report on plasmonic modes with quality factor of the order of $Q \sim 80$ up to $Q \sim 200$.

1. Introduction

With the adequate chirality, semiconducting carbon nanotubes can radiate in the near-infrared window range[900 nm,1600 nm], more specifically in the telecom window range. Despite this very interesting wavelengths range, carbon nanotubes surfer from very low quantum yields because of their unidimensional geometry. As a consequence they are poorly light emitting-sources. We investigate the possibility of luminescence enhancement thanks to plasmonic nanostructures.

Plasmonic nanostructures are known to enhancement luminescence due to an increase of energy extraction from the emitter to the far-field because of a high density of electromagnetic states as compared to the vacuum. Luminescence enhancement also arises because of radiation redirection due to antenna effects. A possible geometry for the plasmonic structure is a patch antenna made by a small metallic particle separated from a metallic plane by a dielectric layer (see Fig:2-a) for illustration). The metallic patch supports surface plasmon-polariton resonances and luminescence is enhanced as compared to its value in the vacuum[1]. This geometry is attractive because of its simplicity, because of its ease of implementation and because light emission is redirected in only one half-space. This geometry has shown quantum-dots luminescence enhancement[2]. Unfortunately luminescence enhancement in this geometry is highly dependent on the orientation of the emitter dipole[1]. Indeed, Purcell-factor on the order of 70 are predicted for dipoles perpendicular to the metallic plane whereas the Purcell-factor value saturated at 5 in the case of a parallel dipole[1]. Because of the unidimensional character of carbon nanotubes, their emitting dipole is parallel to the metallic plane. So the patch-antenna geometry is not really suitable to get a large enhancement of luminescence in the case of carbon nanotubes. We have tried to circumvent this difficulty by implementing a "patch" exhibiting electromagnetic hotspots. Electromagnetic hotspots result from lightning-rod effects leading to large values of the electric-field. Hotspots generally appears on semicontinuous metallic films. The ref.[3] have demonstrated luminescence enhancement for carbon nanotubes above a gold semicontinuous film. In our sample the "hotspots-patch" antennas are made by a random collection of metallic scatterers separated from metallic plane by a dielectric layer. The geometry under study is depicted on Fig:2-a). On a 200 nm thick gold mirror, the dielectric layer is deposited. The spacer thickness has been varied from d=0 nm up to d=200 nm. It is made on a PFO polymer except for the d=200 nm thickness for which the polymer is PMMA. Then a 5 nm thick layer of PFO enriched with carbon nanotubes is deposited on top of the dielectric spacer. Finally, the metallic scatterers are spread over the sample. They are gold nanorods with radius 10 nm and length 80 nm. Their resonant-wavelength is around $\lambda_s \simeq 1280nm$. Some nanorods aggregate to form a patch.

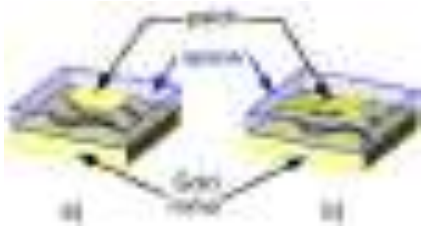


Figure 1: a) Typical patch-antenna geometry made by a disc separated from a metallic plane by a dielectric spacer. The dielectric spacer contains the emitters. b) The "hotspots-patch" antenna geometry. The "patch" is made by a random collection of metallic nanorods separated by a dielectric layer from the gold plane. Because of the randomness, electromagnetic hotspots occur along the patch.

2. Quenching of the luminescence of a carbon nanotube due to a gold mirror

First we measure the quenching of the carbon nanotubes luminescence as a function of the spacer thickness. Indeed, because gold films support surface plasmon-polariton, which are non-radiative electromagnetic modes, the luminescence intensity decreases when the distance between the

gold plane and the emitter decreases. In order to quantify this decrease, we have measured the intensity of carbon nanotubes luminescence as a function of the dielectric layer thickness (PFO polymer). The results are presented on Fig (2) where we have plotted the logarithm of spontaneous decay rate as a function of the carbon nanotubes height above the gold plane. The data have been normalized in reference to the luminescence intensity for the height $d = 200nm$ above the gold film.

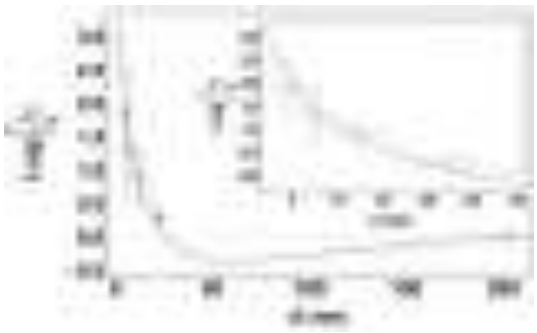


Figure 2: Logarithm of the normalized Decay rate for a single carbon-nanotube luminescence $\Gamma_{\|}$ as a function of the distance from the gold plane. The normalization is done with the decay-rate value at 200 nm, Γ_0, as a reference. The insert is a zoom on the distance range $[0, 30nm]$.

Our measurements (circles with error-bars in Fig 2) are well reproduced by the spontaneous decay of an electric dipole parallel to the gold film (red dashed curve in Fig 2). These measurements confirm that the dipole of the carbon nanotubes is parallel to gold mirror.

3. Luminescence enhancement thanks to electromagnetic hotspots

We now present the experimental results for the "hotspots-patch" antenna. Only results with spacer thickness $d = 0\ nm$ are presented on Fig 3. Figure 3-b is the spectrum for an ensemble of carbon nanotubes in PFO (no plasmonic antenna for this result). Our sample of carbon nanotubes contains 5 chiralities that can emit light in the experiment. Each chirality gives rise to one single peak in the spectrum. Inhomogeneous broadening being quite small, the width of the luminescence peak due to a single carbon nanotube is similar to the width of the peaks in Fig. 3-b. Coupling carbon nanotubes to a "hotspots-patch" antenna leads to spectra plotted on Fig. 3-c, Fig. 3-d and Fig. 3-e. In Fig. 3-c, the peak corresponding to the chirality emitting near $1.2\ eV$ is enhanced as compared to the other chirality. Moreover the luminescence peak is split in two narrow peaks. In Fig. 3-c, the luminescence of two chiralities is enhanced by the "hotspots-patch" antenna. The peak near $1\ eV$ is split in two narrow peaks. Finally, only the luminescence of one chirality is enhanced in Fig. (3-e) but the peak width is very small as compared to the peak of the corresponding chirality with the "hotspots-patch" antenna. We explain these features from the existence of electromagnetic hotspots on the patch. Some of them have a large quality factor leading to the narrow peaks in Fig. 3. The quality factor of these modes is larger than the quality factor of a single gold-nanorod as it can be seen on Fig. 3-a, which is the scattering spectrum of a single nanorod on a gold plane.

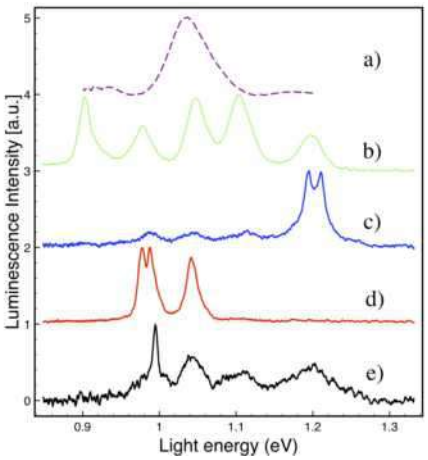


Figure 3: a) Scattering spectrum of a single gold-nanorod. b) Luminescence spectrum of an ensemble of carbon nanotubes in PFO exhibiting the five chiralities that emit light in the experiment. c,d,e) Spectra for the coupled systems: carbon nanotubes and "hotspots-patch" antenna. The maximum of all curves has been normalized to one. The curves have been shiftted for clarity.

4. Conclusions

To conclude, we have shown that a patch antenna exhibiting hotspots can enhance the luminescence of carbon nanotubes despite that their dipole is parallel to the metallic mirror. The orientation of the emitting-dipole has been confirmed from the evolution of the radiative rate with the distance from the gold plane. "Hotspots-patch" antenna has also the interesting feature of exhibiting high quality-factor modes. The quality factor of these modes ($Q \sim 80$) is larger than both the quality factor of a single gold nanorod ($Q \sim 15$) or the quality factor of the luminescence peak of a single carbon nanotube ($Q \sim 40$).

References

[1] R. Esteban, T. V. Teperik and J. J, Greffet, Optical Patch Antennas for Single Photon Emission Using Surface Plasmon Resonances *Phys. Rev. Lett.* 104:026802, 2010

[2] C. Belacel, *et al.*, Controlling Spontaneous Emission with Plasmonic Optical Patch Antennas *Nano Lett.* 13:1516–1521, 2013

[3] Guosong Hong,*et. al.* Metal-Enhanced Fluorescence of Carbon Nanotubes *J. Am. Chem. Soc.* 132:15920–15923, 2010

Unidirectional Optical Nanoantenna Design by Bayesian Optimization

F. F. Qin[1,2], D. S. Zhang[1,2], and J. J. Xiao[1,2,*]

[1]Shenzhen Engineering Laboratory of Aerospace Detection and Imaging, Harbin Institute of Technology (Shenzhen), Shenzhen, China
[2]College of Electronic and Information Engineering, Harbin Institute of Technology (Shenzhen), Shenzhen, China

*corresponding author, E-mail: eiexiao@hitsz.edu.cn

Abstract

Unidirectional light scattering by a nanoantenna, placed in homogeneous medium or on a substrate is studied in this paper. A fully intelligent method, combining Bayesian optimization algorithm and commercial electromagnetic solver, is utilized to optimize the parameters of the nanoantenna to realize unidirectional scattering. With the aid of the machine learning method, a strong forward or backward scattering by the designed nanoantenna at arbitrary wavelength can be effectively achieved.

1. Introduction

Due to its profound implications and vast applicability, scattering of light by nanoantenna has gained great attention in recent years. Generally, the unidirectional scattering can be achieved in two distinct ways: detuned electric dipoles approach and the excitation of electric and magnetic multipole (ED and MD) resonance simultaneously. While for the first approach, it is difficult to realize miniaturization and integration since the separation of the constitute nanoantenna is about a quarter-wavelength. And the later one is the physical theme of our design nanoantenna in this work. Often, numerical simulations are used for obtaining suitable structures. While due to the complexity of nanoantenna that can support ED and MD resonance simultaneously [1], the parameters spaces are mostly high-dimensional and naïve optimization strategy fail to provide fast and reliable result.

In this work, we describe a mechanism based on geometric parameter optimization to realize superior unidirectional scattering at one or two wavelengths. We show that by combining a computational electromagnetic solver and the Bayesian optimization method, a strong forward or backward scattering for nanoantenna, placed in homogeneous surroundings or on a substrate, can be automatically achieved, in aommonly affordable time and cost.

2. Design Method

Figure 1 depicts the flow of the unidirectional scattering nanoantenna design, which has four basic ingredients: candidate set, evaluator, calculator and optimization method. Firstly, we set the parameters to be optimized and then construct the candidate sets. It should be noted that all full wave electromagnetic calculations are performed using commercial simulation package COMSOL Multiphysics based on the finite element method (FEM). For the evaluator, the directivity $G_{FB} = 10\log_{10}(S_F / S_B)$ is chosen to quantitatively evaluate the performance of each configuration, where S_F and S_B are the radiated powers evaluated at the forward ($z = +\infty$) and the backward ($z = -\infty$) directions, respectively. After confirming the candidate set and evaluator, a bridge between the COMSOL and Bayesian optimization has been built up. Bayesian optimization, an experimental design algorithm is utilized to achieve the optimal size of the structure that has strong asymmetric scattering. And Gaussian processes [2] have been adopted as surrogate models for the Bayesian optimization due to their flexibility and tractability.

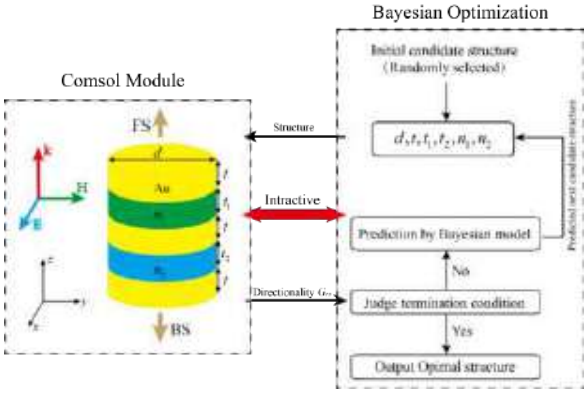


Figure 1 The flowchart for the optimal design of unidirectional scattering nanoantenna. In the Comsol module, schematic figure of the nanoantenna consisting of three gold nanodisk with diameter d and thickness t and they are

separated by two different layers of thickness t_1 and t_2 , respectively. The FS (forward scattering) are along the wave vector of the incident light $\mathbf{k}$, and it is opposite for the BS (backward scattering).

3. Nanoantenna placed in homogeneous medium or on a substrate

For the case of nanoanternna placed in an homogeneous surrounding (for example vacuum) The optimizatized result is shown in Fig. 2. we can clearly see that all optimizations process with different initial training set can be quickly converge to the same minimum or maximum within 900 iteractions (comparing with the total number of candidate set), as shown in Fig. 2(a). And the optimal parameters are given in Table 1 and the corresponding G_{FB} of the two

Table 1. The optimal parameters of the nanoantenna-IV and V (unit: nm)

	d	*t*	t_1	t_2	n_1	n_2
Ⅰ	90	10	100	90	5	1
Ⅱ	100	10	70	100	1.8	5

nanoantenna are plotted in figure 2(b). Figure 2(c) and 2(d) show the far-field radiation pattern of the two nanoantennas at $\lambda = 670$ nm, respectively. It is clearly seen that a nearly complete cancellation of BS or FS is present. Note that **I** respects the structure for BS and **II** corresponds to the structure for FS. Three-dimensional (3D) radiation patterns for nanoantenna-**I** (c) and nanoantenna-**II** (d) at $\lambda = 670$ nm.

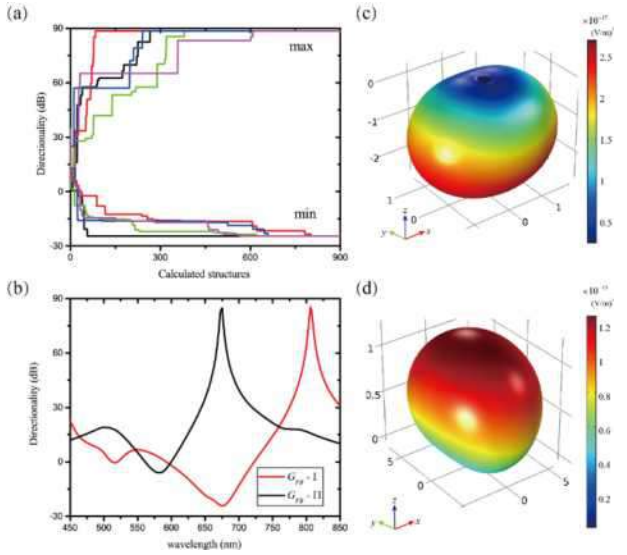


Figure 2. FS and BS structure optimization for wavelength $\lambda = 670$ nm. (a) 5 optimization runs with different initial choices of candidate sets for the case of forward and backward unidirectional scattering, respectively. (b) Far-field directivity G_{FB} of the two nanoantennas. Three-dimensional (3D) radiation patterns for nanoantenna-**I** (c) and nanoantenna-**II** (d) at $\lambda = 670$ nm.

This method is also adapted to design unidirectional scattering in opposite direction at different wavelengths for the case of the nanoantenna placed on a substrate. Figure 3 shows the optimized result of nanoantenna placed on a glass substrate. We can see that the strong FS and BS are separately occurred at the $\lambda = 650$ nm and $\lambda = 670$ nm, which is confirmed by the scattering patterns (see Fig. 3(b) and 3(c)).

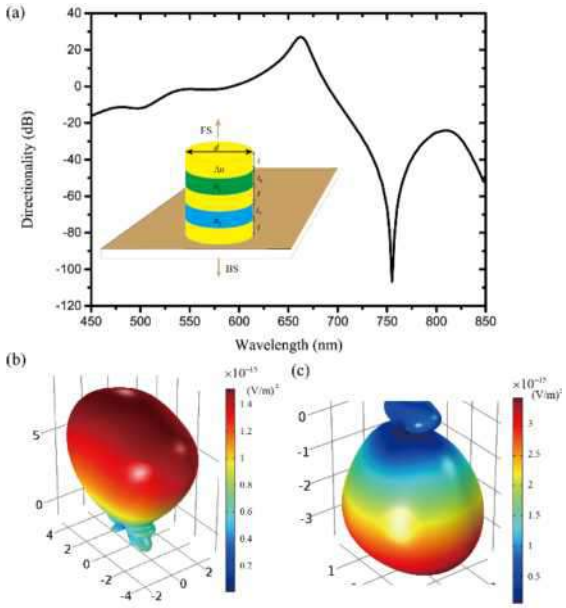


Figure 3 (a) Far-field directivity G_{FB} for nanoantenna placed on a glass substrate. The inset show the sketch of structure. (b) and (c) show the 3D radiation patterns at different wavelengths.

4. Conclusions

Combing a well established electromagnetic solver and a home-made Bayesian optimization implementation, we can quickly design nanoantennas placed in homogeneous surroundings or on a substrate (metal or dielectric), with unidirectional scattering at one wavelength or unidirectional scattering in opposite directions at different wavelengths.

Acknowledgements

This work was supported by the Shenzhen Municipal Science and Technology Plan (Grant No. JCYJ20170811154119292), NSF of Guangdong Province (Grant No. 2015A030313748).

References

[1] M. Kerker, D. S. Wang, and C. L. Giles, Electromagnetic scattering by magnetic spheres, *J. Opt. Soc. Am.* 73(6) 765-767, 1983.

[2] C. E. Rasmussen and C. K. I. Williams, Gaussian Processes for Machine Learning, *Cambridge, MA: MIT Press* 2006.

Wavelength-dependent surface plasmon polariton propagation in long silver nanowire waveguide

Dorota Buczyńska[1*], Michał Ćwik[1], Ewa Roźniecka[1], Sebastian Maćkowski[2], Joanna Niedziółka-Jönsson[1]

[1]Institute of Physical Chemistry, Polish Academy of Sciences, Warsaw, Poland
[2]Faculty of Physics, Astronomy and Informatics, Nicolaus Copernicus University, Torun, Poland
*corresponding author, E-mail: dbuczynska@ichf.edu.pl

Abstract

Using our fluorescence microscope setup, with confocal excitation and wide-field fluorescence detection, we were able to excite Surface Plasmon Polaritons (SPP) in a silver nanowire (AgNW) structure, which we demonstrate for several excitation wavelengths. We want to combine the capabilities of our optical setup and experience in chemical synthesis of long AgNWs [1] to achieve long distance SPP propagation. We intend to first determine experimentally the influence of different dimensions and surface functionality on SPP propagation.

1. Introduction

Silver nanowires have a dual functionality of an optical antenna, capable of capturing energy of incoming light and focusing electric field near the structure's surface [2], [3], and of plasmonic waveguides [4] able to deliver this excitation, through SPPs, to a distant location along the wire. The chemical methods of AgNWs synthesis [5] provide an advantage over lithographic methods by yielding single-crystalline structures and good control over morphology, they do not however give good control over dimensions of nanowires. Hydrothermal methods commonly produce AgNWs with lengths exceeding 100 μm [6], [7]. A high numerical aperture (NA) objective lens [8] enables light coupling into bound, rather than leaky SPP modes, which can deliver excitation to more distant locations. Millimeters long propagation lengths have been demonstrated for metal stripe waveguides, embedded in homogeneous dielectric medium when SPP modes were excited using end-fire technique [9], however use of nanowires in sensing applications will require less favorable conditions, close contact with probes and surface functionalization, that will influence refractive index of surrounding medium and disturb SPP propagation. Furthermore while longer wavelength can excite SPPs that propagate further, they may not couple with energy levels of the probes as well. In our work we used a fluorescent probe to study SPP propagation. We show how different excitation wavelengths influence SPP propagation and present results of hydrothermal synthesis of long AgNWs

2. Materials and Methods

2.1. Fluorescence microscopy

To effectively excite SPP modes in AgNWs we deliver laser light through single mode optical fibers, an achromatic collimating lens and a high NA objective. We can focus the excitation light to a <1μm in diameter spot for each of the excitation wavelengths used: 635, 532, 488 and, 405 nm. Detection in wide-field mode allows for observation of fluorescence excited at a distance from the excitation spot, along the entire nanowire length and at the distal end. Set of optical filters is used to prevent, as much as possible, laser radiation from reaching the camera detector. Water soluble, CdTe (QDs) were used as a fluorescent probe with maximum emission wavelength of 720 nm. AgNWs and QDs are embedded in PVA polymer to reduce scattering which would otherwise arise at the glass-air interface.

2.2. Long AgNWs

The silver nanowires we studied were synthesized using a hydrothermal method with peroxide used as a reducing agent [1]. We were able to achieve AgNWs nearly 800 μm long, with 10 % of the structures reaching at least 400 μm. Their diameter is in the range of 40-180 nm. Silver nanowires acquired in this method are covered by a PVP polymer cap, which stabilizes the wire in solution, but also likely influences SPP propagation, as its morphology can change over time.

3. Results and Discussion

For our experiments we have taken water dispersed AgNWs prepared using the hydrothermal synthesis method, mixed them with QDs and PVA polymer and spin-coated the solution on a glass coverslip. The resultant sample is a thin polymer layer that has QDs and AgNWs embedded in it. For a few of the AgNWs sequences of fluorescence images were taken when one of the nanowires ends was illuminated with a laser beam of wavelengths 635, 532, 488 and 405 nm, in this specific order, and power of around 10 μW. One

set of such measurements is shown in Fig. 1. It is worth noting that though the fluorophore is present in the entire polymer film, unless the beam is positioned at the nanowire's end, the fluorescence is only observed coming from the position of excitation spot. When beam points at one of the AgNW's ends, then the fluorescence is also visible along the AgNW and at its other end. The fluorescence intensity profiles differ as a function of excitation wavelength with excitation at 635 nm producing the slowest and excitation at 405 nm the fastest decrease in fluorescence intensity as the excitation travels along the wire. In all cases fluorescence is excited at the other end of the nanowire as well.

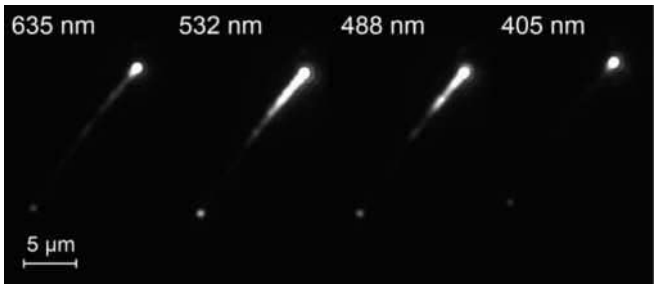


Figure 1: QDs fluorescence along a single AgNW excited at 635, 532, 488 and 405 nm.

We want to use this technique to study SPP propagation in AgNWs, specifically influence of structure diameter and surface functionality on SPP propagation, and eventually obtain long distance SPP propagation in surface modified structures. At the same time we work to obtain very long AgNW, like those shown in Fig. 2 with the intention of achieving SPP propagation that would span the entire structure length – few hundred micrometers. At such distances we would expect only bound modes to propagate efficiently, so surface functionality will likely have great impact on the process.

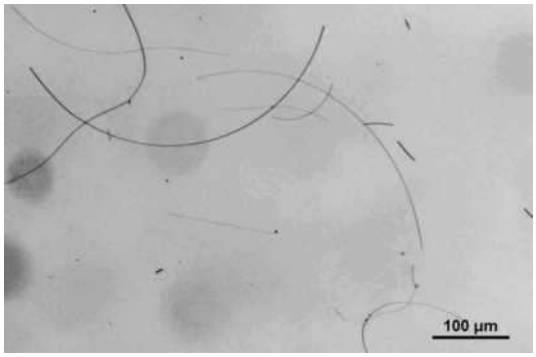


Figure 2: Bright-field reflection image of AgNWs dispersed on glass.

4. Conclusions

For a single silver nanowire surrounded with fluorescent CdTe QDs, we demonstrated wavelength-dependent SPP propagation. We want to further extend our research to correlate structure diameter or surface functionality and SPP propagation. In parallel we work on fabricating AgNWs that would enable long range SPP propagation.

Acknowledgements

We acknowledge financial support by projects 2017/27/B/ST3/02457, 2016/21/B/ST3/02276 and 2016/22/E/ST5/00531 from the National Science Centre (Poland).

References

[1] M. Ćwik, D. Buczyńska, K. Sulowska, E. Roźniecka, S. Mackowski, and J. Niedziółka-Jönsson, Optical Properties of Submillimeter Silver Nanowires Synthesized Using the Hydrothermal Method, *Materials* 12 , p. 721, 2019.

[2] P. Anger, P. Bharadwaj, and L. Novotny, Enhancement and quenching of single-molecule fluorescence, *Phys. Rev. Lett.* 96, p. 113002, 2006.

[3] D. Kowalska *et al.*, Metal-Enhanced Fluorescence of Chlorophylls in Light-Harvesting Complexes Coupled to Silver Nanowires, *Sci. World J.* 2013, pp. 1–12, 2013.

[4] A. Prymaczek *et al.*, Remote activation and detection of up-converted luminescence *via* surface plasmon polaritons propagating in a silver nanowire, *Nanoscale* 10, pp. 12841–12847, 2018.

[5] H. Wei *et al.*, Plasmon Waveguiding in Nanowires, *Chem. Rev.* 118, pp. 2882–2926, 2018.

[6] B. Bari *et al.*, Simple hydrothermal synthesis of very-long and thin silver nanowires and their application in high quality transparent electrodes, *J. Mater. Chem. A* 4, pp. 11365–11371, 2016.

[7] Y. Li, S. Guo, H. Yang, Y. Chao, S. Jiang, and C. Wang, One-step synthesis of ultra-long silver nanowires of over 100 µm and their application in flexible transparent conductive films, *RSC Adv.* 8, pp. 8057–8063, 2018.

[8] H. Ditlbacher *et al.*, Silver Nanowires as Surface Plasmon Resonators, *Phys. Rev. Lett.* 95, 2005.

[9] K. Leosson, T. Nikolajsen, A. Boltasseva, and S. I. Bozhevolnyi, Long-range surface plasmon polariton nanowire waveguides for device applications, *Opt. Express* 14, p. 314, 2006.

Metamaterial flat lens with properties independent of light polarization

A. V. Agashkov[1], N. A. Ivanova[2], N. S. Kazak[1], V. E. Agabekov[2*]

[1] B.I.Stepanov Institute of Physics, National Academy of Sciences of Belarus, Minsk, Belarus

[2] Institute of Chemistry of New Materials of National Academy of Sciences of Belarus, Minsk, Belarus

[*]corresponding author: ichnm@ichnm.basnet.by

Abstract-Experimental and theoretical investigations of promising metamaterial flat lens have been carried out. Unique optical properties are detected of the polymer film PVA/PVP with nanoparticles of gold displaying independence of polarization of incident radiation and low losses in absorption.

One of the most interesting applications of metamaterials is the light focusing by flat lenses with subwavelength resolution. The phase profile, which determines the possibility of focusing, transfer function and spatial resolution of lenses based on metal-dielectric (MD) structures have been calculated for the wavelengths of the visible and ultraviolet ranges.[1] Measurements with modified walk-off interferometer have shown that investigated MD-structure (Ag/SiO_2) possesses necessary phase characteristic of flat lens only for *p*-polarized light.[2] The generalization of this result to the variant of real three-dimensional beams allows one to assert that the flat MD-structure focuses radially polarized beams. The second disadvantage is high enough loss in wave propagation when there is no impedance matched to air. The aim of our paper is to propose and investigate a metamaterial flat lens with low losses in absorption and properties independent of polarization of incident light.

In order to form coatings based on gold nanoparticles (NPs) in a dielectric polymer complex matrix of polyvinylpyrrolidone (PVP) and polyvinyl alcohol (PVA) we used PVA "Mowiol 28-99" (Hoechst Akiengesllschaft, Germany) and PVP M = 1000000-1500000 g/mol (AppliChem, Germany). We prepared two aqueous polymer solution: 15 wt% PVA and 10 wt% PVP, which are then mixed in different proportions so that the total polymer content of the composition was 10 wt% Then, after thorough mixing, was introduced a sample of $HAuCl_4$, dissolved in water. The solution was dispersed in an ultrasonic bath for 1h at 60°C. Then film was deposited on a glass substrate using spin-coating and further drying at T = 65 ± 5°C for 1-3 hours. Samples were annealed at 250°C for 2 hours to decrease the thickness of PVA/PVP-Au films and removal of the polymer matrix. Investigations with SEM and AFM have shown that less than 20 nm gold NPs and almost smooth surface were observed after annealing of PVA/PVP-Au films.

In our investigation we used direct measurement of the phase shift produced by a film inclined to incident laser beam at specified angles. During the experiment in the modified walk-off interferometer there was used the radiation of single-mode He-Ne laser with the radiation wavelength of λ = 632.8 nm. According to the technique used in the walk-off interferometer the film under investigation has been deposited on the part of surface of plane-parallel glass substrate of high optical quality. When changing the beam incident angle θ_{in}, we measured the angular dependence of phase shift $\Delta\varphi(\theta_{in})$ passing through the sample radiation. Fig. 1 shows experimentally measured optical path difference Δp (phase shift $\Delta\varphi$ in arc degrees $\Delta\varphi = 360\Delta p/\lambda$) of light beam passed through the sample. Investigated film is characterized by high homogeneity. At the light wavelength of λ = 632.8 nm film possesses small losses in absorption and scattering less than 5%.

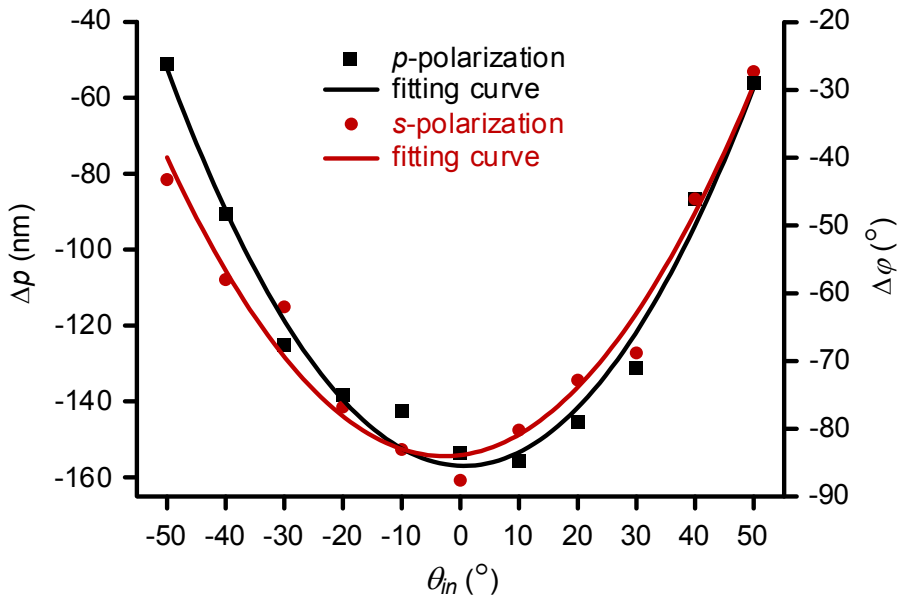


Figure 1. Optical path difference Δp and phase shift $\Delta\varphi$ versus angle of incidence θ_{in}.

The polymer film PVA/PVP with nanoparticles of gold possesses the necessary phase feature for creation on its base of flat lens with properties independent of polarization of incident radiation. The figure of merit of flat lens based on similar structure can achieve large values due to low losses on absorption.

Numerical simulation of propagation of plane wave through dielectric film with randomly distributed golden nanoparticles was performed. Phase of transmitted wave was calculated for different angles of incidence, film thicknesses and particle concentration. Increase of metal concentration up to 1,0% for film thickness about 100 nm and increase of film thickness for lower concentrations lead to similar angular phase dependences as ones observed in experiment.

REFERENCES

1. Belyi, V., M. Binhussain, N. Khilo and N. Kazak, "Far-field flat lens based on multilayered metal- dielectric structure," *Advance Electromagnetics*, Vol. 2, No. 2, 1–5, 2014.
2. Agashkov, A., V. Belyi, M. A. Binhussain, N. Kazak, V. Agabekov and N. Khilo, "Negative Phase Shift in a Layered Metal-Dielectric Structure: Theory and Experiment," in *Proceedings 9th International Congress – Metamaterials 2015*, Oxford, United Kingdom, September 2015, 592–594.

Spontaneous Formation of Cold-Welded Plasmonic Nanostructures at the Air-Water Interface for Intense Raman Scattering

Andrea Mariño-López[1], María Blanco-Formoso[1], Leonardo N. Furini[1], Ana Sousa-Castillo[1], Ecem Tiryaki[1], Moisés Pérez-Lorenzo[1], Martín Testa-Anta[2], Verónica Salgueiriño[2], and Miguel A. Correa-Duarte[1]

[1]Department of Physical Chemistry, Biomedical Research Center, Southern Galicia Institute of Health Research and Biomedical Research Networking Center for Mental Health, Universidade de Vigo, 36310 Vigo, Spain
[2]Departmento de Física Aplicada, Universidade de Vigo, 36310 Vigo, Spain
*corresponding author, E-mail: macorrea@uvigo.es

Abstract

Plasmonic films with concave shapes are known to enhance Raman scattering. Herein, we present monoparticulate films that are formed via self-assembly of gold nanoparticles (NPs) at the air-water interface, upon heating to 80 degrees C a solution containing the NPs. Molecular analytes present in the water can be adsorbed on the metal NPs and be concentrated at the surface, allowing a higher sensitivity for analysis of aliphatic molecules by surface-enhanced Raman Spectroscopy (SERS).

1. Introduction

Nanostructures with complex shapes can be used for many applications, such as (meta)optical devices [1], sensing [2] or catalysis [3], and they can be synthetized by different techniques, such as gas-phase methods [4] or colloidal approaches [5]. An example of these colloidal techniques are films directly formed in solution at the interface of two immiscible liquids. This process is driven by the decreased interfacial energy when NPs are trapped at the interface [6]. Although some of these processes have been shown to occur spontaneously, most of them require the covalent functionalization of the NPs [7], hindering the applications where close plasmonics, SERS and catalysis [8]. The synthesis of complex interconnected refracted nanoscale geometries presents many advantages for these applications due to the strong enhancement of electromagnetic field in concave nanostructures, although it is limited by their inherent thermodynamic instability. These nanostructures formed at the interfaces would be greatly beneficial for SERS measurements, since in this way the plasmonic films are more accessible to phonons and analytes alike [9].
Herein, plasmonic films presenting optical homogeneity and high reproducibility are prepared based on the self-organization of NPs at the air-water interface (Figure 1).

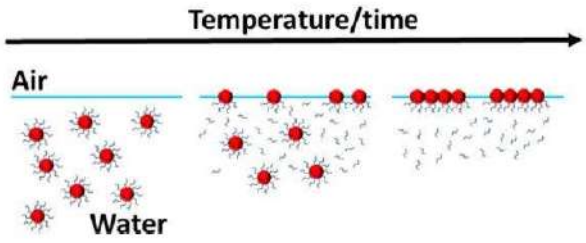


Figure 1: Accumulation and self-assembly of NPs at the air-water interface.

2. Discussion

The synthesis of the initial gold NPs (AuNPs) [10] consists on the reduction of gold(III) in the presence of tetrakis-(hydroxymethyl)phosphonium chloride (THPC) in an alkaline aqueous medium. AuNPs of about 3 nm diameter, weakly stabilized with THPC, are obtained. These NPs are stable at room temperature, but when they are placed in a closed reactor at 80 °C, a plasmonic monolayer at the air-water interface is obtained. Figure 2 shows TEM images of the cold-welded films transferred to TEM grids at different assembly times.
In most cases, the plasmonic NPs form discrete unconnected films at the interface [11,12]. However, in this case the preparation of dendritic structures with a homogeneous character is carried out. The formation of these chains is favored by the positive balance between repulsive and attractive forces [13], in addition to the low affinity of THPC for the gold surface. It was observed that the NP merger proceeds only to a certain point (24 h), without major changes when increasing the heating time. On the other hand, the obtained plasmonic films can be easily transferred to different substrates: glass, cellulose filters or silicon wafers, among others.

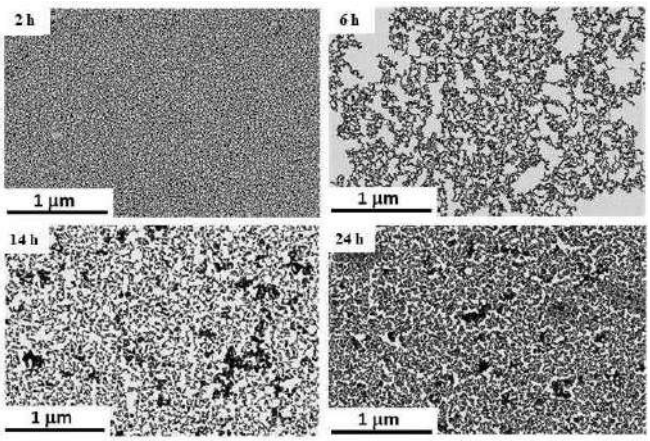


Figure 2: TEM images of the films at different heating times.

Different techniques for the characterization of these films have been carried out. In their optical characterization, it was observed that the films present a localized surface plasmon resonance (LSPR) band that slowly redshifts and increases in intensity as the incubation time increases. For the SERS characterization, 4-mercaptobenzoic acid (4-MBA) has been used as molecular probe. SERS intensities are considerably larger for the cold-welded films as compared with other conventional substrates. This is due to the fact that, in this case, the analyte is adsorbed and concentrated onto the AuNPs that subsequently migrate to the interface to form the films, which considerably increases the local concentration of the analyte at the point of measurement. Both SERS intensity and intensity homogeneity suggest that the cold-welded films can serve as optimal substrates for SERS quantification. This is tested using thiram, which is an aliphatic fungicide with a small SERS cross-section, and its vibrational pattern is clearly recognized for concentrations less than nM. Therefore, the applicability of the films for the ultraquantitative determination of aliphatic molecules in aqueous media was demonstrated.

3. Conclusions

The synthesis of gold nanostructures with metastabled concave geometries has been carried out through self-assembly of AuNPs at the air-water interface. The weakly-bonded THPC surface ligands facilitate the assembly and merging of the plasmonic NP into nanostructures with refracted geometries. The characterization of the films shows a homogeneous structure with a high density of hot spots. These properties allow the use of these films for the ultrasensitive quantification of aliphatic molecules in aqueous medium by SERS.

Acknowledgements

This work was funded by MINECO (CTQ2017-88648-R, CTM2014-58481-R, CTM2017-84050-R), Xunta de Galicia (Acc. 2016-2019 and EM2014/035), Generalitat de Cataluña (2017SGR883), URV (2018PFR-URV-B2-02 and 2017EXIT-08), the European Union (ERDF), and the National Science Foundation (NSF 1463474 and NSF 1566460).

References

[1] P. Cheben, R. Halir, J. H. Schmid, H. A. Atwater, D. R. Smith, Subwavelength integrated photonics, *Nature* 560: 565−572, 2018

[2] M. D. Scanlon, E. Smirnov, T. J. Stockmann, P. Peljo, Gold Nanofilms at Liquid−Liquid Interfaces: An Emerging Platform for Redox Electrocatalysis, Nanoplasmonic Sensors, and Electrovariable Optics. *Chem. Rev.* 118: 3722−3751, 2018

[3] X. Huang, S. Tang, X. Mu, Y. Dai, G. Chen, Z. Zhou, F. Ruan, Z. Yang, N. Zheng, Freestanding Palladium Nanosheets with Plasmonic and Catalytic Properties, *Nat. Nanotechnol.* 6: 28, 2011

[4] G. J. Leggett, Direct Writing of Metal Nanostructures: Lithographic Tools for Nanoplasmonics Research, *ACS Nano* 5: 1575−1579, 2011

[5] M. L. Personick, C. A. Mirkin, Making Sense of the Mayhem behind Shape Control in the Synthesis of Gold Nanoparticles, *J. Am. Chem. Soc.* 135: 18238−18247, 2013

[6] P. Pieranski, Two-Dimensional Interfacial Colloidal Crystals, *Phys. Rev. Lett.* 45: 569−572, 1980

[7] J. J. Armao, I. Nyrkova, G. Fuks, A. Osypenko, M. Maaloum, E. Moulin, R. Arenal, O. Gavat, A. Semenov, N. Giuseppone, Anisotropic Self-Assembly of Supramolecular Polymers and Plasmonic Nanoparticles at the Liquid−Liquid Interface. *J. Am. Chem. Soc.* 139: 2345−2350, 2017

[8] G. J. Kovacs, R.O. Loutfy, P. S. Vincett, C. Jennings, R. Aroca, Distance Dependence of SERS Enhancement Factor from Langmuir-Blodgett Monolayers on Metal Island Films: Evidence for the Electromagnetic Mechanism, *Langmuir* 2: 689−694, 1986

[9] F.J. García de Abajo, Colloquium: Light Scattering by Particle and Hole Arrays. *Rev. Mod. Phys*. 79: 1267−1290, 2007

[10] D. G. Duff, A. Baiker, P. P. Edwards, A New Hydrosol of Gold Clusters, *J. Chem. Soc., Chem. Commun.* 96−98, 1993

[11] N. A. Kotov, F. C. Meldrum, C. Wu, J. H. Fendler, Monoparticulate Layer and Langmuir-Blodgett-Type Multiparticulate Layers of Size-Quantized Cadmium Sulfide Clusters: A Colloid-Chemical Approach to Superlattice Construction, *J. Phys. Chem.* 98: 2735−2738, 1994

[12] K. E. Mueggenburg, X.-M. Lin, R. H. Goldsmith, H. M. Jaeger, Elastic Membranes of Close-Packed Nanoparticle Arrays, *Nat. Mater.* 6: 656, 2007

[13] Z. Tang, N.A. Kotov, M. Giersig, Spontaneous Organization of Single CdTe Nanoparticles into Luminescent Nanowires, *Science* 297: 237−240, 2002

Double-sided, omnidirectional and broadband absorber in visible regime using moth-eye nanostructures covered by non-noble metal

Su Shen[1], Yun Zhou[1], Yanhua Liu[1], Shaolong Wu[1]

[1] School of Optoelectronic Science and Technology & Collaborative Innovation Center of Suzhou Nano Science and Technology, Soochow University, Suzhou, China
[2] Key Lab of Advanced Optical Manufacturing Technologies of Jiangsu Province & Key Lab of Modern Optical Technologies of Education Ministry of China, Suzhou, China
*corresponding author, E-mail: sushen@suda.edu.cn

Abstract

Optical obsorber is achieved by employing moth-eye nanostructure covered by a single-layer of non-noble metallic film. The architecture provides uniform, broadband, omnidirectional absorption for both the front- and back-sided incidence by taking advantage of the strong photon manipulation capability of the structure to couple and trap electromagnetic wave. Experimental results show that the absorber yields an average absorption of 90.0% and 89.3% at normal incidence, 79.8% and 81.5% at tilt 60^o incidence in spectrum of 400–800 nm for front- and back-sided incidence, respectively.

1. Introduction

After millions years of evolution, biological systems exhibit many amazing functionalities due to their unique morphologies and physico-chemical properties, such as the adhesive performance of gecko foots, the self-cleaning ability of lotus leaves, and the anti-fogging property of fly-eye. Similarly, the optical architectures of the cellular structures in the biological surface have been refined to control and manipulate light and span diverse array of applications such as sensitivity improvement, temperature control and mate attraction by making use of a wealth of optical physics.

Here we demonstrate a double-sided, omnidirectional broadband absorber based on a bio-inspired moth-eye nanostructure covered by a single-layer non-noble metal. It shows the capability of absorbing incident light a low sensitivity to the angle of incidence, which exceeds the structured bulk metallic surfaces as black-body performance. [1-4] The value of the proposed device as excellent absorber needs more attention due to several facts: (i) It has much simple device configuration compared with other types of optical absorber, such as plane film stack relied on Fabry-Perot cavity, metamaterial-based surfaces, and metallic nanostructures employing surface plasmonic phenomenon. (ii) It is easy to be fabricated by a combination of soft-nanoimprinting and metal deposition techniques. Only one single layer of non-noble metal material is contained. There needs no complicated fabrication procedure, such as the time-consuming and costly fabrication technology of electron beam lithography or focused ion beam milling. (iii) Capable of absorbing and trapping light from both the front- and back-sided incidence, the proposed absorber can contribute to enhancing the efficiency of new exciting perspectives, especially for thermophotovoltaics, thermal emitters, and other light-trapping optoelectronic devices. (iv) For its nonresonant absorption in nature, the absorber is characterized by high absorption for a broad range of incident angles over broadband. In this paper, we demonstrate experimentally that two-dimensional arrays of tapered moth-eye nanstructure ensure efficient, broadband and wide-angle absorption of unpolarized light over a large range of incident angles. It has potential applications in a wide range of passive and active photonic devices, including inkless printing, harvesting solar energy, as well as thermal emitter and optical detectors.

2. Discussion

2.1. Design and simulations

Independently absorptive properties of the wavelength, angle, and polarization of the incident radiation are of primary interest for fullfilling the fundamental requirements of harvesting more photons. A number of device configurations based on different working principles have been reported to achieve such purpose, but they suffer from unlimited fabrication complexity or are only capable of absorbing light from one incident side, which inevitably involve high cost and limit their utility for energy harvesting. The model of the optical absorber composed of moth-eye nanostructure with one single-layer non-noble metal is constructed through schematic diagrams in Fig. 1a. Ellipsoid-shaped moth-eye nanostructure with parameters of a 400 nm separation and a 1 μm height is used for simulation. The base diameter of the motheye is 350 nm. The shape profile of the moth-eye is fitted with the equation and a 50nm-thick chromium is deposited on the surface. The refractive index of the substrate and the UV resin is assumed to be 1.5. The optical absorption (A) is calculated by 1−T−R, where T is transmission, R is refection and both can be obtained directly from the simulation. For the periodic boundary condition is applied in x-y plane, the absorptive property is independent of the polarization orientation of the incident light. Fig. 1c - 1d show the contour plots of

absorption variation as a function of wavelength and incident angle for the double-sided incidence. The simulation results indicate that the absorber functions very well in both cases, thus demonstrating excellent broadband absorption feature at very large incident angle (up to 70°) in the visible wavelength range.

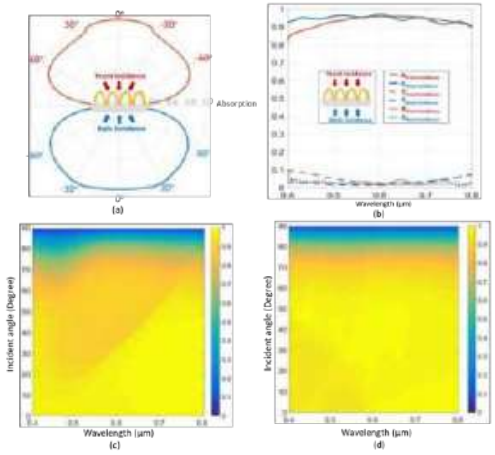


Figure 1. (a) Calculated incidence-angle dependence of absorption. (b) Simulated reflection (•••) and transmission (- -) and absorption (-) spectrum calculated by 1-R-T from both the front and back incidence. Contour plots of the absorpion as a function of wavelength from (c) front- and (d) back-sided incidence.

2.2. Experimental Results and Discussions

To experimentally verify and demonstrate the absorption property the process comprises the fabrication of an AAO template with high order pore array, replication of the nanostructure, and sputtering coating deposition (shown in Fig. 2a). There is no need for the fussy fabrication of discrete metallic gratings. In order to create high-order tapered nano-pore array, the aluminima anode oxide (AAO) template is fabricated by using a well-known two-step anodizaton process. Then, the AAO template is fluorosilane-treated to obtain an easier demolding condition, which is a critical issue in high aspect ratio nanostructure replication. Figure 2b shows the corresponding goniometer images for 1 μL droplets with apparent contact angles of before (top, 61°) and after (bottom, 117°) surface treatment, respectively. Larger contact angle means weaker adhesion of the treated AAO mold to the UV resin. After the soft lithgraphy process, a thin layer of metal (Cr, Al, etc.) is deposited on the moth-eye nanostructure by successive ion sputtering to obtain the omni-directional absorber. Figure 2c shows the top and side-view of the AAO template. The period of the nanopore array with high-filling factor is 400 nm. The height of the tapered hole is about 1 μm, and the diameter of the nanopores is 350 nm at the top and 40 nm at the bottom. Figure 2d - 2e show, respectively, the top and side-view of the replicated nanostructures. It can be clearly seen that, although the perfect ellipsoid-shape structure is difficult to fabricate, the tapered nanostructure in the mold has been well replicated to the UV resin with high fidility, high filling factor and high aspect ratio, which is useful for promoting optical performance.

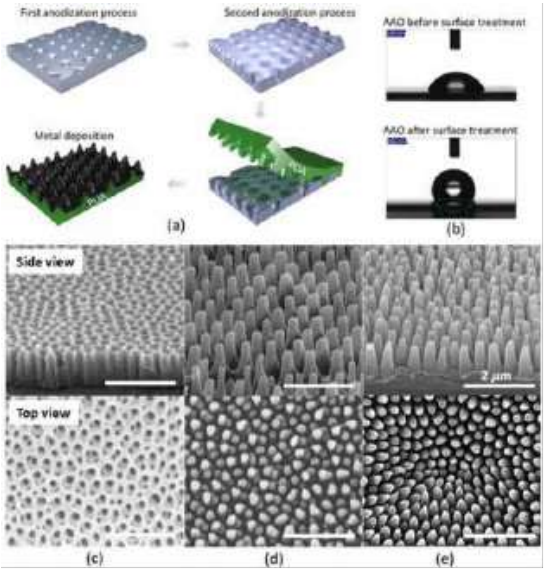


Figure 2. (a) Schematic of the steps involved in the fabrication of moth-eye nanostructure based absorber by using soft lithographic approach. The original AAO template is fabricated by a well-known two-step anodization process. Then the tapered nanonipple structure was obtained from the AAO template and metal Cr of 50 nm thickness is sputtered on the front surface. (b) Goniometer images for 1 μL droplets with apparent contact angles of PUA on the surface of the AAO template before surface treatment (top) and after surface treatment (bottom). SEM images in top and side views of the AAO template (c), the replicated moth-eye nanostructure before (d), and after Cr sputtering (e).

3. Conclusions

In conclusions, the proposed architecture provide great potential for manipulating light, because of the strong coupling between electromagnetic fields and surface charges. Theoretical and experimental characterizations clearly demonstrating that the biomimetic light absorber proposed here yields seductive double-sided omnidirectional absorption over the entire visible spectrum. It has potential applications in a wide range of passive and active photonic devices, including inkless printing, harvesting solar energy, as well as thermal emitter and optical detectors.

References

[1] S. Shu, Z. Li, and Y. Y. Li, Triple-layer Fabry-Perot absorber with near-perfect absorption in visible and near-infrared regime, *Opt. Express* 21, 25307, 2010.

[2] W. Wang, Y. Cui, Y. He, Y. Hao, Y. Lin, X. Tian, T. Ji, and S. He, Efficient multiband absorber based on 1D periodic metal-dielectric photonic crystal with a reflective substrate, *Opt. Lett.* 39, 331, 2014.

[3] C. M. Watts, X. Liu, and W. J. Padilla, Metamaterial electromagnetic wave absorbers, *Adv. Mater.* 24, OP98, 2012.

[4] D. Y. Shchegolkov, A. K. Azad, J. F. O'Hara, and E. I. Simakov, Perfect subwavelength fishnetlike metamaterial-based film terahertz absorbers, *Phys. Rev. B* 82, 205117, 2010.

Ultra-Narrowband and Wide-Angle Refractive Index Sensor Based on a Planar Multilayer Structure

Linling Qin, Shaolong Wu, Cheng Zhang, and Xiaofeng Li

School of Optoelectronic Science and Engineering & Collaborative Innovation Center of Suzhou Nano Science and Technology, Soochow University, Suzhou, China
*corresponding author, E-mail: qinll@suda.edu.cn

Abstract

This work reports a design of a narrowband and full-angle refractive index sensor based on Tamm plasmon resonance (TPR) by introducing a distributed Bragg reflector (DBR) integrated with a non-adjacent metal layer. The analyte flows into the cavity comprising of the DBR and the non-adjacent metal layer. Simulated results show that the incident light can be strongly confined in the specially designed cavity. The sharp reflection dip within the forbidden band of the isolated DBR indicates the excitation of Tamm mode, and the spectral characteristics were monitored upon exposure to various analytes with different refractive indices. The optimally designed system shows the sensitivity (*S*) and full width at half-maximum (FWHM) can be up to 860 nm/RIU (refractive index unit) and ~2.2 nm with a figure of merit (*FOM*) of 391. Furthermore, the highly-sensitive characteristic can be sustained in a wide angle range of 0° to almost 90°under both TM- and TE-polarized lights.

1. Introduction

Recently, optical sensors based on surface plasmon resonance (SPR) have experienced an unprecedented growth for chemical, biomedical and environment monitoring over the last two decades due to the possibility of high-sensitivity and label-free detection [1−3]. In terms of the SPR shift driven by the environment-plasmon interaction, SPR sensors based on various types of metal nanoparticles have attracted a great deal of attention [4−5]. Nevertheless, the trigger of SPR requires stringent injection conditions (e.g., polarization and incident angle) due to the momentum mismatch between light and SPR at the same frequency [9]. Besides, almost all of the existing SPR-based sensors employ metal/dielectric hybrid systems with delicately designed nanostructures, which normally have in-plane subwavelength (or deep-subwavelength) patterns and require complicated/costly fabrication. Therefore, part of the attention goes back to the planar scenarios for cost-effective strategies. Unfortunately, the poor optical performance in light trapping remains one of the major hurdles of the planar architectures. As a result, some carefully designed planar structures emerge. Studies on Tamm Plasmon resonance (TPR), proposed by A. V. Kavokin et al. in 2005, are flourishing [6-7]. In this work, we propose a refractive index sensor based on TPR, which is comprised of planar multilayer structure, with the advantages of easy-fabrication and cost-effectiveness relative to these devices using nanostructured films or periodical nanostructures. To explore the sensing potential of our proposed structure, we bound the Au layer to a flow cell sealed with the inverse DBR atop of a transparent superstrate. Through numerical simulation, we found that the sensor performance is highly dependent on the cavity height and the DBR parameters. By optimally tuning the TPR, the sensitivity of the proposed multilayer structure can be up to 860 nm/RIU (refractive index unit) and the full width at half-maximum (FWHM) can be 2.2 nm in the infrared range, therefore the figure of merit (*FOM*) can be up to 391.

2. Structure design and analysis

The proposed TPR sensor is based on a planar multilayer structure comprising of a DBR in the front side, a non-adjacent Au layer in the rear side, and a cavity consisting of the upper DBR and the lower Au layer, as shown in Fig. 1 (a). The analyte flows into the cavity with a width (*W*) far larger than the wavelength of incident light. The height of the cavity and the thickness of the Au layer are labelled as *H* and d_{Au}, respectively. When the wavelength of incident light coincides with the excitation of TPR, electromagnetic energy accumulates within the cavity closed to the Au interface and thus enables optical monitoring of the analytes' refractive index. Rigorous numerical simulations were conducted throughout the design to illustrate how the electromagnetic field is confined by TPR and tailor the structural parameters to the desired optical response.

For all the employed materials, the optical constants are from Palik. Rigorous coupled-wave analysis (RCWA) is firstly employed to calculate the optical dispersion characteristics to properly configure the device for the excitation of TPR. Fig. 1(b) plots the reflection spectra $R(\lambda)$ of the isolated DBR under normal incidence and the proposed device illustrated in Fig. 1(a), where the pair number of Al_2O_3/TiO_2 (N_{DBR}) is 7, H = 450 nm, and d_{Au} = 200 nm. It is clear that there exists a reflection dip for

different analytes with varying refractive indices (n) in the forbidden band of the isolated DBR, which indicates the excitation of TPR. Note that for most fluids, the refractive index is in the range of 1.32−1.45, while that of gas is around or a little larger than 1. In Fig. 1(b), the reflection dip for n = 1.0 is relatively gentle compared to those for the other two cases, which can be ascribed to the un-optimized height of the cavity, and the small and narrowband reflection for n around 1 can also be obtained by adjusting the sizes of the cavity. These results suggest the proposed structure may be used for sensing the refractive index for both the gas and the liquid.

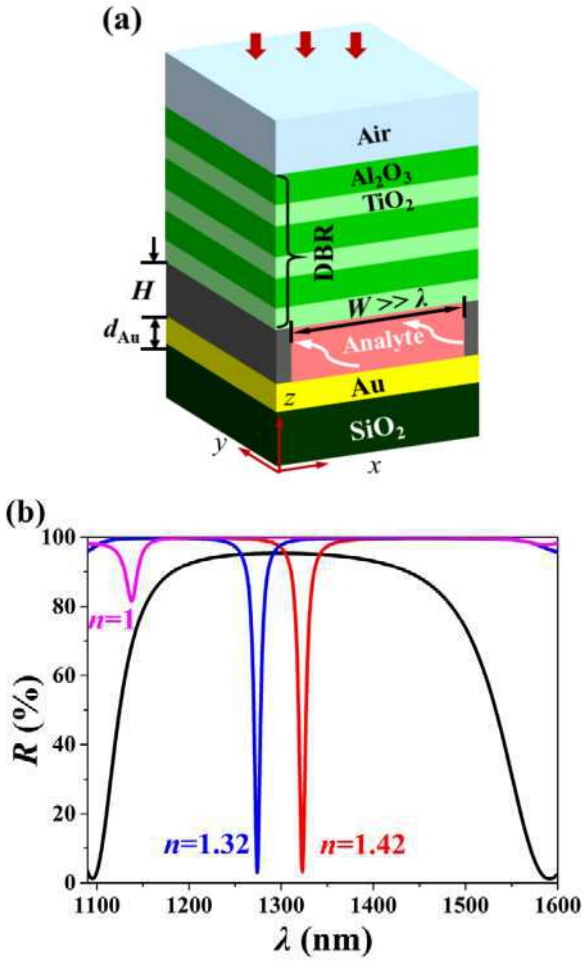


Figure 1: (a) Schematic diagram of the proposed planar multilayer structure comprising a distributed Bragg reflector (DBR), separating walls with various heights (H), and an Au layer atop of a SiO_2 substrate. (b) Reflection spectra of the isolated DBR (black line) and the proposed structure with various analytes (blue line for n=1.32, red line for n=1.42 and pink line for n=1).

3. Discussion

The optimally designed system shows the sensitivity (S) and full width at half-maximum (FWHM) can be up to 860 nm/RIU (refractive index unit) and ~2.2 nm with a figure of merit (*FOM*) of 391. Furthermore, the highly-sensitive characteristic can be sustained in a wide angle range of 0° to almost 90° under both TM- and TE-polarized lights.

4. Conclusions

In summary, we present a planar multilayer structure without the conventional highly nanostructured components for the refractive index sensing. The planar multilayer structure is designed to be composed of DBR, Au layer, and the formed cavity for analyte flowing. Such device structure can excite a very strong TPR, which confines the incident photon energy in the cavity. With varying the analyte index, the deep reflectance dip can be sustained with the sensitivity (*FOM*) close to 860 nm/RIU (391). The angular sensitivity is demonstrated to be sustained with the incident angle closed to 90°. This work sheds light on the achievement of the high-performance and low-cost refractive index sensing.

Acknowledgements

This work is supported by National Natural Science Foundation of China (61705151, 61675142, 61504088, 61875143), Natural Science Research of the Jiangsu Higher Education Institutions of China (17KJA480004), Natural Science Foundation of Jiangsu Province (BK20160327, BK20181169) and Priority Academic Program Development (PAPD) of Jiangsu Higher Education Institutions.

References

[1] J. N. Anker, W. P. Hall, O. Lyandres, N. C. Shah, J. Zhao, and R. P. Van Duyne, “Biosensing with plasmonic nanosensors,” Nat. Mater., vol. 7, no. 6, pp. 442–453, Jun. 2008.

[2] M. E. Stewart, C. R. Anderton, L. B. Thompson, J. Maria, S. K. Gray, J. A. Rogers, and R. G. Nuzzo, “Nanostructured Plasmonic Sensors,” Chem. Rev., vol. 108, no. 2, pp. 494−521, Jan. 2008.

[3] Y. Shen, J. Zhou, T. Liu, Y. Tao, R. Jiang, M. Liu, G. Xiao, J. Zhu, Z. Zhou, X. Wang, C. Jin, and J. Wang, “Plasmonic gold mushroom arrays with refractive index sensing figures of merit approaching the theoretical limit,” Nat. Commun., vol. 4, pp. 2381, Aug. 2013.

[4] A. Barik, L. M. Otto, D. Yoo, J. Jose, T. W. Johnson, and S. H. Oh, “Dielectrophoresis-enhanced plasmonic sensing with gold nanohole arrays,” Nano Lett., vol.14, no. 4, pp. 2006−2012, Apr. 2014.

[5] Q. R. Yang, L. L. Qin, G. Y. Cao, C. Zhang, and X. F. Li, “Refractive index sensor based on graphene-coated photonic surface wave resonance,” Opt. Lett., vol. 43, no. 4, pp. 639−642, Feb. 2018.

[6] W. L. Zhang and S. F. Yu, “Bistable switching using an optical Tamm cavity with a Kerr medium,” Opt. Commun., vol. 283, no. 12, pp. 2622–2626, Feb. 2010.

[7] W. L. Zhang, Y. Jiang, Y. Y. Zhu, F. Wang, and Y. J. Rao, “All-optical bistable logic control based on coupled Tamm plasmons,” Opt. Lett., vol. 38, no. 20, pp. 4092–4095, Oct. 2013.

Self-Similar Nanostructured Waveguides for Efficient and Direction Sensitive Plasmon Propagation

Mario Miscuglio[1#], Davide Spirito[1], Philip Schaefer[2], and Roman Krahne[1*]

[1] Optoelectronics Group, Istituto Italiano di Tecnologia, Genova, Italia
[2]Neaspec GmbH, München, Germany
[#]current address: George Washington University, Washington DC, USA
*corresponding author, E-mail: roman.krahne@iit.it

Abstract

We design chains of triangular and circular nanostructures and optimize their size, shape, and inter-distance for efficient plasmon propagation. Directional plasmon propagation is achieved by an elongated triangular shape, and by implementing a gradual change in size of the elements within a chain. The coupling between neighboring elements is optimized by carefully tuning the gap, or respectively the overlap, of the nanostructure elements. We analyze the optical nearfield of such self-similar chains by finite element simulations, and fabricate the waveguides from Au elements on Si substrates. The size and shape of the nanostructures is characterized by scanning electron microscopy (SEM), and the optical properties of the self-similar nanostructure chains are investigated by scattering near-field optical microscopy (SNOM).

1. Introduction

Plasmonics of metal nanostructures represent a highly versatile approach for the manipulation and localization of light in the visible and near-infrared spectral range.[1] Localized surface plasmon resonances (LSPRs) in metallic nanostructures are capable to confine light to a volume of nanoscale size that is much smaller than that given by the optical diffraction limit. The plasmon resonance depends on the size of the metallic elements, and the gap between neighboring elements can play a crucial role in the coupling.[2] However, the short decay length of plasmons in metallic waveguides remains an obstacle.[3] Tapered arrays of metallic nanostructures have demonstrated strong coupling and efficient plasmon propagation, and therefore represent an interesting alternative for plasmonic waveguiding. [4, 5]

2. Results and Discussion

Chains of Au nanostructure elements are fabricated by electron-beam lithography and metal evaporation. An example an isosceles triangle with an aspect ratio of around 2 is shown in Figure 1, together with an image of a chain of such triangles separated by a nanoscale gap. We systematically varied the distance of the neighboring elements in the chains from nanometer separation to a small overlap. Using finite element method simulations, we calculated the electrical nearfield distribution for excitation with a plane wave at different wavelength, and with parallel and perpendicular polarization to the long axis of the triangles.

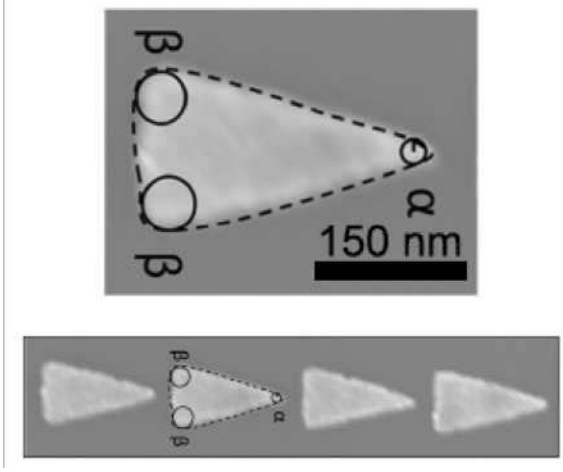


Figure 1: Scanning electron microscopy (SEM) images of the triangular elements in a chain. The curvature at the edges is evaluated by the radius of a circle.

Furthermore, we evaluated the coupling and the signal propagation along the chains. Figure 2 shows the field distribution (a) and the signal propagation (b) when the left end of the chain is illuminated with a Gaussian beam with a beam waist of 0.8 μm. Experimentally realized chains of triangles that manifest an overlap (top) or a gap (bottom) depicted in Figure 2c. Here also a gradual reduction in element size was introduced that increases the coupling of the larger element to the slightly smaller one on its right side, which enhances the unidirectional coupling and signal propagation in the chain. By comparing simulations of chains with gapped and overlapping elements, we find that the coupling and the signal propagation along the chain is enhanced when the triangular elements have a small overlap.

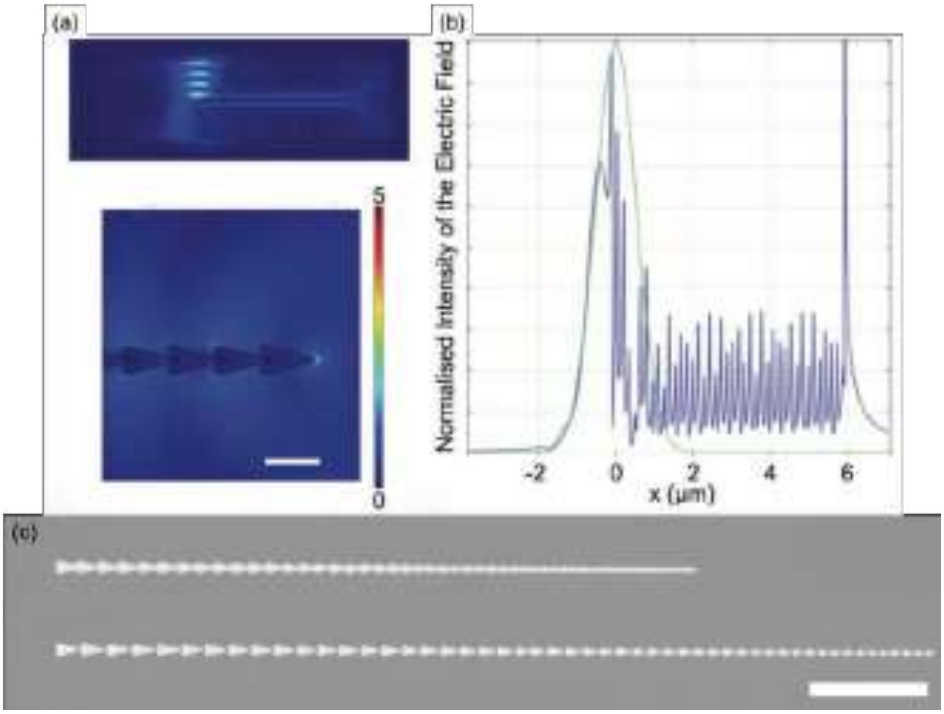


Figure 2: Calculated electric field distribution (a) and electric line profile (b) for a chain of truncated triangles with an overlap of 15 nm, under illumination with a Gaussian beam at the left side of the chain. The beam waist is 0.8 µm. Scale bar is 200 nm. (c) SEM images of chains with triangular elements that overlap (top), or are separated by a nanoscale gap (bottom).

We investigated the optical nearfield resonances in the chain-like waveguides by scattering scanning nearfield optical microscopy (s-SNOM) with a microscope from Neaspec. The samples were illuminated with a laser beam at 785 nm that was focused by a parabolic mirror, and the 3rd harmonic of the optical signal, together with its phase, was detected by a metal coated atomic force microscopy tip. Figure 3 shows the topography of a section of a tapered triangular chain, together with the optical nearfield signal and phase.

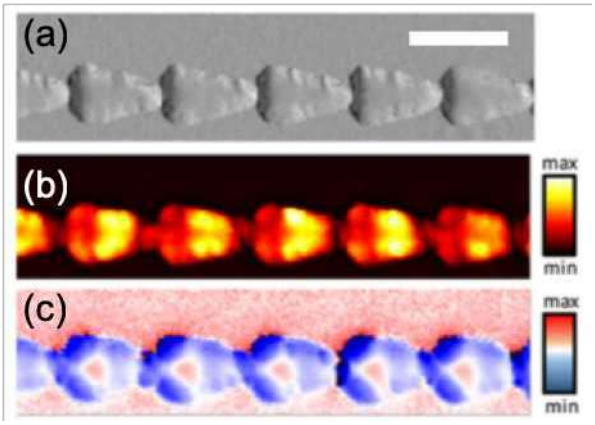


Figure 3: AFM topography (a), and intensity (b) and phase (c) of the 3rd harmonic of the optical nearfield signal. Scale bar is 300 nm.

3. Conclusions

Nanostructuring of plasmonic waveguides can be an efficient means to enhance the plasmon propagation length. The design of the shape and inter-distance of the elements in chain-type waveguides allows to optimize the nearfield coupling and thereby the propagation length. Unidirectional propagation can be obtained by asymmetric elements and by introducing a gradient in element size in the chains.

References

[1] Halas, N.J., et al., *Plasmons in Strongly Coupled Metallic Nanostructures.* Chemical Reviews, 2011. **111**(6): p. 3913-3961.

[2] Fromm, D.P., et al., *Gap-Dependent Optical Coupling of Single "Bowtie" Nanoantennas Resonant in the Visible.* Nano Letters, 2004. **4**(5): p. 957-961.

[3] Gür, F.N., et al., *DNA-Assembled Plasmonic Waveguides for Nanoscale Light Propagation to a Fluorescent Nanodiamond.* Nano Letters, 2018. **18**(11): p. 7323-7329.

[4] Hasan, S.B., F. Lederer, and C. Rockstuhl, *Nonlinear plasmonic antennas.* Materials Today, 2014. **17**(10): p. 478-485.

[5] Miscuglio, M., et al., *Shape Approaches for Enhancing Plasmon Propagation in Graphene.* ACS Photonics, 2016. **3**(11): p. 2170-2175.

Multi-polarized Nano-antenna for Surface Enhanced Raman Spectrescopy Applications

Monir Morshed[1,*], Ahasanul Haque[1], Lei Xu[1], Andrey Miroshnichenko [1], and Haroldo T. Hattori[1]

[1]School of Engineering and Information Technology, University of New South Wales Canberra, ACT 2610, Australia
*corresponding author, E-mail: Monir.Morshed@student.adfa.edu.au

Abstract

This article proposes a star gap quadrupole nano-antennas that can operate for both linear and circular polarizations. We have achieved the electric field enhancement of 27 and 37 for linear- and circular-polarized pump , respectively. The antenna is characterized using Raman spectroscopy which produce surface enhanced Raman scattering enhancement of 4.18×10^6 line for methanol.

1. Introduction

Plasmonic nano-antennas are capable of localizing light in a sub-wavelength region below the diffraction limit [1], leading to the generation of high electric fields by exploiting localized surface-plasmon resonance (LSPRs)[2]. Due to their large electric field enhancement, they have been used as probes in Surface Enhanced Raman Scattering (SERS)[3] to enhance the intensity of Raman signal, enabling single-molecule detection[4].
Many antennas reported in the literature (e.g. dipole antenna) work with linear polarization. A few antennas such as patch antennas[5] can work with circular polarized waves but they do not produce high electric field. Circularly polarized light is important, for example, in the study of chiral organic molecules. In this work, we design a star gap quadrupole antenna which has nearly 1.4 times stronger electric field enhancement factor for circular polarization than for linear polarization, has a larger footprint than bowtie antennas and a high electric field enhancement.

2. General description of the strutures and theoretical analysis

To obtain a high electric field intensity with strong resonance and multiple resonance responses, we have designed a star gap circular nano-antenna as shown in Figure 1.

The device is optimized with proper tuning of the parameters to get the maximum electric field enhancement factor in the star gap at the wavelength of 785 nm. The calculated electric field for the optimized parameters is presented in Figure 2 as a function of wavelength for both linear and circular polarization.The enhanced electric field in the gap of nano-antenna is calculated as,

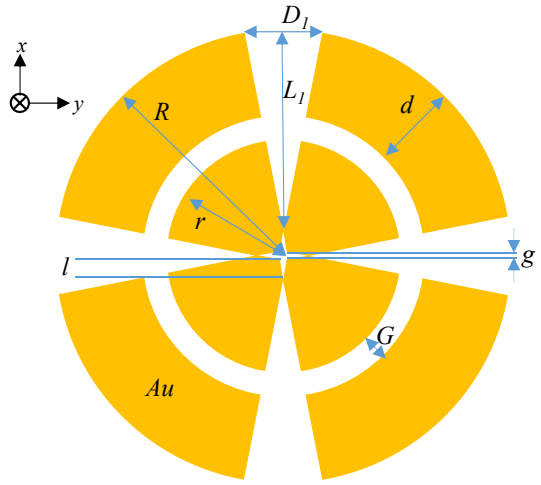


Figure 1: Schematic diagram of quadrupole nano-antenna with splitted circular ring.

$$F = \frac{\mid E_{gap,peak} \mid}{\mid E_{gap,peak} \mid} \tag{1}$$

where, $\mid E_{gap,peak} \mid$ is the magnitude of the electric field calculated in subwavelength gap of the nano-antenna, and $\mid E_{inc,peak} \mid$ is the magnitude of electric field of incoming light.

Figure 2 shows that the device has electric field enhancement factor of 27 for linear polarization and strongly resposne for circular polarization, giving electric filed enhancement factor of 37. Moreover, this device shows multiple resonaces over the spectral range with significant amount of electric field intensity.

3. Experimental Results

The device is fabricated with a FEI Helios 600 focused ion beam (FIB) system. A scanning electron microscopy (SEM) image of single structure is shown in Figure 3. Since the performance of nano-antennas are hard to measure directly; we can indirectly assess the theoretical results by using SERS . We have used a Renishaw in Via 2 spectrometer to analyze the spectrum of methanol with a concentra-

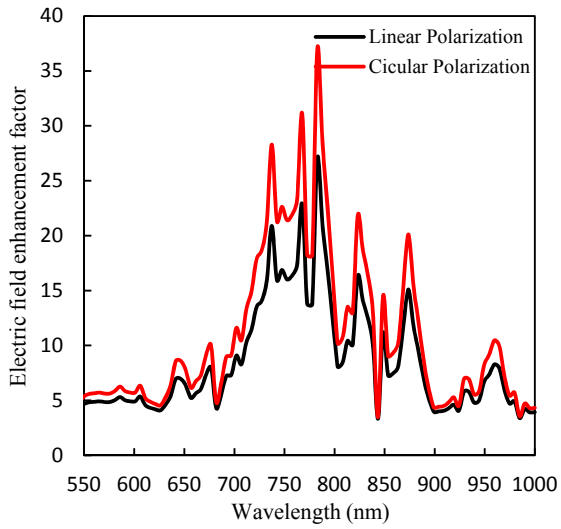


Figure 2: Spectral response of our designed device for both linear and circular polarization.

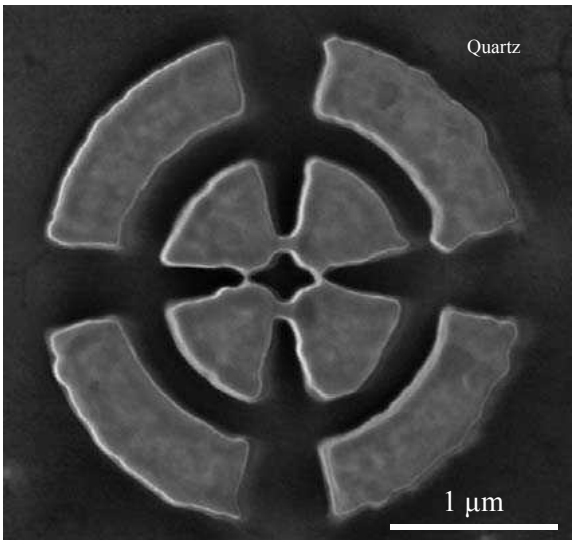


Figure 3: SEM image of single quadrupole nano-antenna with splitted circular ring.

tion of 17 mol/l in the presence of nano-antenna and only using glass slide. Firstly, we placed the methanol solution on the top of a quartz surface, which is used as a reference. Later, to get the intensity of methanol with structure, methanol is dropped from top using pipette on the sample and a glass plate is placed on the top of methanol drop to ensure methanol molecules attached well to the surface of the device. The Raman intensity of structure with methanol solution averaged over 20 spectra with an acquisition time of 32s and compared with the quartz surface. we got the intensity for methanol is 38279.50 counts and only quartz substrate is 3231 counts. The measured SERS EF of our periodic structure in the presence of methanol at 2943 cm^{-1} is 4.18×10^6, which is higher than the theoretical value 5.31×10^5 (considering the SERS enhancement is proportional to the fourth order of local electric field enhancement factor). Since, chemical factors for the total SERS EF is in the range between 10 and 100, therefore-the measured SERS enhancement factor is approximately 10 times higher than the theoretical value.

4. Conclusions

In summary, we have studied a star gap quadrupole nano-antenna that can boost the electric field by a factor of 27 for linearly-polarized pump and 37 for circularly-polarized pump, respectively. The performance of the fabricated nano-antenna is validated for linear polarization with Raman experiments, which shows that the SERS enhancement is 4.18×10^6 for the 2943 cm^{-1} line of methanol.

Acknowledgement

Authors appreciate financial supports from the Australian Research Council (ARC) and fabrication support from the Australian National Fabrication Facility (ANFF) ACT node.

References

[1] A. Javier, M. R.-G. José, M. L.-A. José, and G. Boreman, Optical antennas for nano-photonic applications, *Nanotechnology* 16: 230, 2005.

[2] L. Novotny and N. van Hulst, Antennas for light *Nat Photon* 5:83-90, 2011. Hemisphere Publishers, New York, 1980.

[3] J. Kneipp, H. Kneipp, and K. Kneipp, SERS—a single-molecule and nanoscale tool for bioanalytics, *Chemical Society Reviews*, 37: 1052-1060, 2008

[4] C. Zhao, Y. Liu, J. Yang, and J. Zhang, Single-molecule detection and radiation control in solutions at high concentrations via a heterogeneous optical slot antenna, *Nanoscale*, 6: 9103-9109,2014. Jeju, Korea, pp. 23–32, 2009.

[5] C. A. Balanis, *Antenna Theory: Analysis and Design* John Willey and Sons,Inc. Publication, 1997.

Self-beating during pulsed light transmitting through a plasmonic slit

Kuan-Ren Chen[1,*], Jian-Shiung Hong[1], and Alex E. Chen[2]

[1]Department of Physics, National Cheng Kung University, Tainan 70101, Taiwan
[2]Department of Electrical Engineering, The Pennsylvania State University, University Park, PA 16802, USA
*corresponding author, E-mail: chenkr@phys.ncku.edu.tw

Abstract

For explaining the physics puzzle, we discover a new physics of self-beating without nonlinearity, together with plasma effects. While a portion of the light pulse transmits through the slit as a sub-pulse, the rest is reflected at the exit, propagates a round-trip, and then reaches the exit again. These linear processes repeat. The superposition of sub-pulses with a phase delay in-between produces a periodic light that beats its original light frequency. Analytical models proposed agree well with simulations.

1. Introduction

Beating involves two waves of different frequencies and is a key mechanism of nonlinear science, besides the high order response of nonlinear materials to large wave amplitude.

When light pulses are transmitted through a subwavelength plasmonic aperture, a few phenomena [1, 2] have been observed experimentally. Besides extended second half pulse duration [1], the transmitted spectrum can become flatter [2]. Different theoretical explanations are proposed. In the Fabry-Perot like mechanism, the light spectrums transmitted through a perfect electric conductor (PEC) are calculated and the results show that the spectrums become slightly narrower [3] or that the pulse widths are broadened [4], while the shapes remain about the same. But, the physics proposed for PEC [3] cannot be applied to explain what observed for plasmonic metal film [5, 6]. Surface plasmon [5] and nonlinear beating [6] are phenomenologically proposed for complicated phenomena observed in FDTD simulations.

Considering only linear materials and processes, we discover a new physics of self-beating when a Gaussian light pulse transmits through a subwavelength plasmonic slit. Together with the plasma effects of non-uniform dispersion and sub-pulse spreading, self-beating can explain various phenomena observed. Analytical models are proposed and the modeling results agree well with simulations.

2. Gaussian pulse transmitting through a PEC slit

The magnetic field of Gaussian pulse light at the source is

$$\boldsymbol{H_i} = H_i e^{-\alpha(t-\tau_s)^2} \sin[\omega_0(t-\tau_s)], \quad (1)$$

where $\alpha=\ln 2/[2(\Delta/2)^2]$, Δ is the FWHM of the intensity, and τ_s is the time of the source peak. The magnetic field transmitted without reflection can be written as

$$\boldsymbol{H_0} = H_0 e^{-\alpha(t-\tau_0)^2} \sin[\omega_0(t-\tau_0)], \quad (2)$$

where τ_0 is the time of the peak to exit the slit. The roundtrip reflections produce sub-pulses as

$$\boldsymbol{H_j} = H_0 r^j e^{-\alpha(t-\tau_0-j\tau_{rt})^2} \sin[\omega_0(t-\tau_0)-j\phi], \quad (3)$$

where j is the roundtrip number and ϕ is the phase delay. The superposition principle gives the transmitted magnetic field up to n times of the roundtrip can be expressed as $\boldsymbol{H_{sn}} = \sum_{j=0}^{n} \boldsymbol{H_j}$ so that

$$\boldsymbol{H_{sn}} = \{\sum_{j=0}^{n} r^j \cos(j\phi)\, e^{-\alpha(t-\tau_0-j\tau_{rt})^2} \sin(\omega_0 t) - \sum_{j=0}^{n} r^j \sin(j\phi)\, e^{-\alpha(t-\tau_0-j\tau_{rt})^2} \cos(\omega_0 t)\}. \quad (4)$$

Figure 1 shows the transmitted wave functions. As shown in Fig. 1(a) for the case of $\phi = 2.5 \times 2\pi$, the off phase effect causes the cancellation of the field so that the resultant pulse width is significantly shortened. In contrast, for the $\phi = 6\pi$ case as shown in Fig. 1(b), the in phase effect enhances the pulse amplitude and significantly extends the pulse length so as to form a long tail. Note that a small change in the phase delay can be so critical to determine the resultant pulse. When the phase delay is twice the original pulse FWHM, the resultant wave function is modulated as shown in Fig. 1(c). For an even longer phase delay, as shown in Fig. 1(d), the sub-pulses do not overlap and a pulse train is observed. The resultant wave functions can be quite different with the original light pulse. All the FDTD simulation results agree well with their corresponding modeling results.

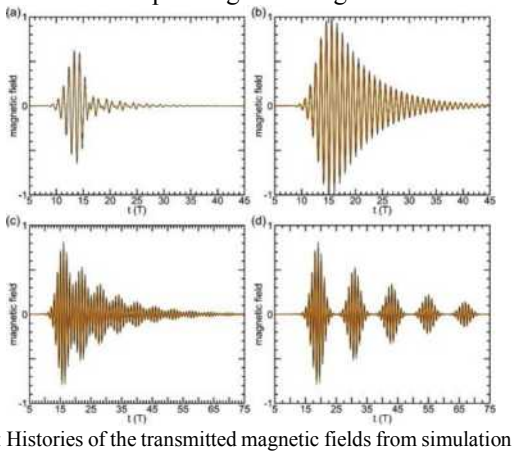


Figure 1: Histories of the transmitted magnetic fields from simulation (black) and modeling (orange) for (a) $\phi = 5\pi$, (b) $\phi = 6\pi$, (c) $\phi = 12\pi$ and (d) $\phi = 24\pi$.

Figure 2 shows the corresponding spectrums obtained by Fourier transform from t = 0 to t = 150T. While the phase delay is 3.5 periods that is out-of-phase, the spectrum becomes flat and the shape has dramatically changed, as shown in Fig. 2(a). When the phase delay is increased to 5.5 periods, two side bands arise while the central frequency band

becomes a flat valley. In contrast, for a slightly larger phase delay of 6 periods, the spectrum peaks at the central frequency as other in-phase cases while the spectral width decreases and two weak side bands appear. As the phase delay is doubled, these two side bands grow higher and move closer to the central frequency, and two more side bands appear, as shown in Fig. 2(b). The number of the spectral peaks for the out-of-phase and in-phase cases are even and odd, respectively. Again, all the simulation results agree well with their corresponding modeling results.

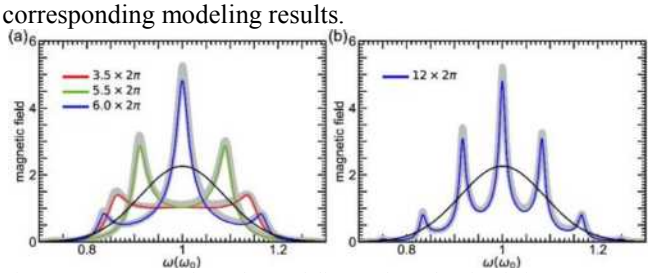


Figure 2: Spectrums from the modeling (color), the simulation (gray), and the incident pulse (black) (a) $\phi = 7\pi$, $\phi = 11\pi$, $\phi = 12\pi$, and (b) $\phi = 24\pi$.

3. Gaussian pulse transmitting through a plasmonic metallic slit

The dispersion relation of the wave in the slit is given as [7]

$$\tanh(a\sqrt{k^2 - k_0^2}) = -\sqrt{k^2 - \varepsilon_m k_0^2}/\varepsilon_m\sqrt{k^2 - k_0^2}, \quad (5)$$

where k is the wave number, $\varepsilon_m = 1 - \omega_p^2/\omega^2$, and ω_p is the plasma frequency. In the frequency domain, a component of the incident pulse at the entrance is expressed as

$$\boldsymbol{H_h}(\omega) = H_i \int_0^\infty e^{-\alpha(t-\tau_s-\tau_d)^2} \times \sin[\omega_0(t-\tau_s-\tau_d)]\exp(i\omega t)dt. \quad (6)$$

The magnetic field transmitted without reflection becomes

$$\boldsymbol{H_0}(\omega) = \boldsymbol{H_h}(\omega)\boldsymbol{t_c}(\omega)e^{ik(\omega)h}, \quad (7)$$

where $\boldsymbol{t_c}$ (and $\boldsymbol{r}$ later) is in the frequency domain. The magnetic field transmitted after the jth roundtrip is

$$\boldsymbol{H_j}(\omega) = \boldsymbol{H_0}(\omega)\boldsymbol{r}^j(\omega)e^{i2jk(\omega)h}. \quad (8)$$

In the time domain, the jth sub-pulse can be obtained by inverse Fourier transform.

Figure 3 shows the results of the pulse transmission through a slit in a plasmonic metal film. The transmitting pulse inside the slit of the plasmonic metal film of $\omega_p/\omega_0 = 4.0$ shows that the wavelength is shorter and the peak arrives to the center later because of the plasma dispersion. The peak amplitude is lower due to the excitation of surface plasmon and the field energy penetrating into the metal. For $\omega_p/\omega_0 = 2.0$, the wavelength reduces more at the peak and, in fact, even shorter (longer) at the rear (front) part, while the peak amplitude is further lower. The group velocity of the peak is $v_g = 0.14c$ while the front (rear) propagates faster (slower) and thus the pulse disperses during propagation. From the transmitted sub-pulses, we find the transmission and reflection coefficients depend on the wave frequency. For $\omega_p/\omega_0 = 4.0$, the transmitted field history is similar to that of Fig. 1(c), as shown on Fig. 3(a). As for the $\omega_p/\omega_0 = 2.0$ case, the sub-pulses are elongated as shown on Fig. 3(b). The more roundtrips, the longer elongation. For both cases, the simulation and modeling results agree well.

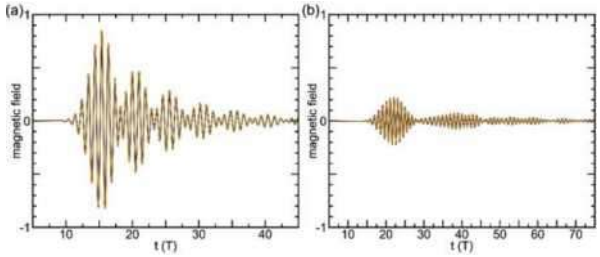


Figure 3: The histories of the magnetic field measured at the slit exit from the model (orange) and the simulation (black) for a h = 660 nm film of (a) $\omega_p/\omega_0 = 4.0$ and (b) $\omega_p/\omega_0 = 2.0$.

4. Discussion

From the viewpoint of cause, what we find is the new physics of self-beating without nonlinearity. From that of effect, the consequence is the same as nonlinear beating so that we may also consider it as meta-nonlinearity. It is a spectrum beating with the original frequency.

5. Conclusions

We have revealed the new physics of self-beating and, together with plasma effects, explained various phenomena occurs during pulsed lights transmit through a plasmonic metallic slit. Although our study is in the time domain, the concepts, mathematics, physics and results may be generalized to multi-dimensional spatial domain, including free space. Besides nonlinear sciences, physics, materials and photonics, this study may be applied to other areas of wave mechanics from classical to quantum.

Acknowledgements

Ministry of Science and Technology, Taiwan, and National Center for High-performance Computing.

References

[1] B. A. Nechay, U. Siegner, M. Achermann, H. Bielefeldt and U. Keller, Femtosecond pump-probe near-field optical microscopy, *Rev. Sci. Instrum.* 70: 2758, 1999.

[2] O. Mitrofanov, M. Lee, …*et. al*., Terahertz pulse propagation through small apertures, *Appl. Phys. Lett.* 79: 907−909, 2001.

[3] M. Mechler, O. Samek and S. V. Kukhlevsky, Enhanced transmission and reflection of few-cycle pulses by a single slit, *Phys. Rev. Lett.* 98: 163901, 2007.

[4] S. V. Kukhlevsky, M. Mechler, L. Csapó and K. Janssens, Near-field diffraction of fs and sub-fs pulses: Super resolution of nsom in space and time, *Phys. Lett. A* 319: 439−447, 2003.

[5] A. Dechant and A. Y. Elezzabi, Femtosecond optical pulse propagation in subwavelength metallic slits, *Appl. Phys. Lett.* 84:4678−4680, 2004.

[6] R. Müller and J. Bethge, Plasmonic decay in a metallic grating after femtosecond pulse excitation, *Phys. Rev. B* 82: 115408, 2010.

[7] R. Gordon, Light in a subwavelength slit in a metal: Propagation and reflection, *Phys. Rev. B* 73: 153405, 2006.

Bridging Classical and Quantum Plasmons via an FDTD-TDDFT Hybrid Model

Jian Wei You and Nicolae C. Panoiu

Department of Electronic and Electrical Engineering, University College London, London, United Kingdom
*corresponding author, E-mail: jvyou@ucl.ac.uk

Abstract

The interaction between classical plasmons of a gold bowtie nanoantenna and quantum plasmons of graphene nanoflakes (GNF) placed in the narrow gap of the nanoantenna is studied by a proposed FDTD-TDDFT hybrid numerical method. Our analysis shows that the quantum plasmon response of a molecular-scale GNF can be enhanced by more than two orders of magnitude in this hybrid system. This finding can be particularly useful for applications to molecular sensors and quantum optics.

1. Introduction

Recently, plasmons in two-dimensional (2D) materials, such as graphene, have attracted increasing research interest, primarily because of the new rich physics characterizing these materials. However, when the geometrical size of plasmonic nanoparticles is less than about 10 nm, the description of their optical properties becomes more challenging because quantum effects begin to play an important role. At this scale, plasmon resonances become more sensitive to the quantum nature of the conduction electrons [1], thus the theoretical predictions of classical approaches based entirely on the Maxwell equations are less successful in describing experimental results [2]. The shortcomings of the classical theory stem chiefly from neglecting three quantum effects: i) spill-out of electrons at medium boundaries, ii) surface-enabled electron-hole pair creation, and iii) nonlocal effects of electron wavefunction. These quantum effects can significantly change the features of plasmon spectra predicted by the classical theory [3]. To overcome these shortcomings of the classical theory, a new research area that combines plasmonics with quantum mechanics, known as quantum plasmonics, has recently emerged [4]. In this paper, we apply an FDTD-TDDFT hybrid numerical method [5] to study the classical-quantum plasmon interaction of a multiphysics system in the weak-coupling regime.

2. Physical System

The physical system used to illustrate the main features of our numerical method is shown in Fig. 1. It consists of a gold bowtie nanoantenna placed on a silica substrate and a molecular-scale GNF located in the narrow gap of the nanoantenna. The nanoantenna is made of two triangular gold plates with angle, α, length, L, and thickness, t, the separation distance between the tips of the gold plates being Δ. In all our simulations α=12°, Δ=10 nm, and t=30 nm, but L will be varied. Moreover, the GNF has a triangular shape, too, with side length, a=1.23 nm, namely there are six carbon atoms along each side of the triangle. It should be noted that triangular GNFs is one of the stable configurations in which they exist [6]. The GNF is positioned in such a way that its symmetry axis coincides with the longitudinal axis of the nanoantenna. The bowtie nanoantenna has plasmon resonances associated with the triangular plates and strongly localized (hot-spot) plasmons generated in the narrow gap of the nanoantenna.

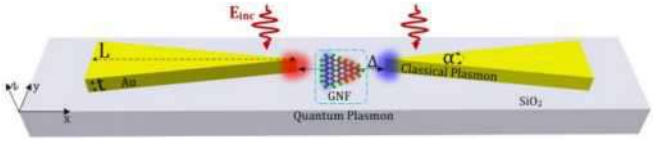


Figure 1: A classical and quantum plasmon multiphysical system, where the quantum plasmon of a graphene nanoflake interacts with the classical plasmon of a gold bowtie nanoantenna via the optical near-field.

3. Results and Discussion

3.1. Quantum plasmons of graphene nanoflakes

We considered first the GNFs described in the preceding section and used the TDDFT method to investigate their optical spectra. More specifically, we used the Octopus code package [7]. The GNF is freestanding and it only interacts with an external time-dependent and spatially constant electric field. We assumed that the time dependence of the field was described by a delta-function. In the right-side inset of Fig. 2, we have performed a calculation for a GNF with charge doping concentration of 15%. Here, the charge doping concentration is defined as the ratio of the number of excess charges to the number of carbon atoms in the GNF. The quantum response of the GNF is quantified by the dipole strength function $S(\omega)$. It can be seen in this figure that the main resonance peak of this GNF is located in the infra-red region. Moreover, we have also calculated the distribution of the net charge density at the resonance frequencies, as compared to that in the ground state. The blue and red colors correspond to the negative and positive net charge density, respectively. This net charge distribution does prove that this resonance peak corresponds to collective electron density oscillations, i.e. it can be viewed as a quantum plasmon.

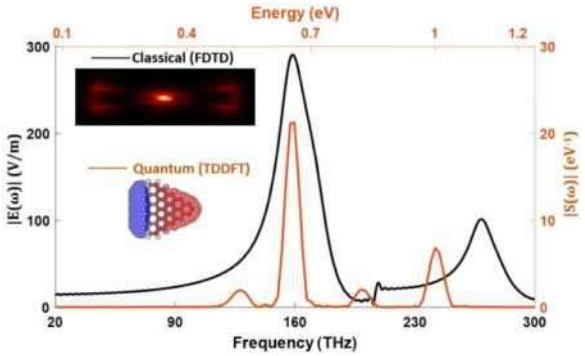


Figure 2: Spectra of the bowtie nanoantenna (black line) and GNF. In insets, the profile of the optical near-field of the hot-spot plasmon and the charge distribution of the quantum plasmon, calculated at the resonance frequency.

3.2. Classical plasmons of gold bowtie

The second part of our study consists of the calculation of the optical spectra of the bowtie nanoantenna. The nanoantenna is illuminated by a normally incident plane wave. Based on FDTD method, the electric field at center of the gap of a nanoantenna with L = 280 nm is given in Fig. 2, where the spectra $|E(\omega)|$ has been normalized to the amplitude of the incident electric field. The spectra reveal that the amplitude of the optical near-field could be enhanced by more than two orders of magnitude. To gain more physical insights, we have calculated the electric field profile corresponding to the frequency of the major spectral peak. The result, shown as left-side inset in Fig. 2, shows this main resonance corresponds to a strongly localized plasmon formed in the narrow gap of the nanoantenna (a so-called hot-spot plasmon). Moreover, particularly relevant to our study is the fact that the hot-spot plasmon is strongly confined in the gap of the bowtie nanoantenna, which would lead to a strong field overlap and implicitly enhanced interaction with the quantum plasmon of a GNF placed in the gap.

3.3. Interaction between classical and quantum plasmons

The interaction between the classical and quantum plasmons can be characterized quantitatively by analyzing the combined hybrid plasmonic system. In Fig. 2, we show the two plasmon resonances are located at the same frequency of 159 THz. To assess the influence of the field enhancement effect induced by the classical plasmon resonance of bowtie nanoantenna on the quantum plasmon of the GNF, we place such a GNF at the center of the gap of the optimized bowtie nanoantenna, as illustrated in Fig. 3(a). For reference, we also calculated the spectrum of the GNF without the nanoantenna but under the same pulsed plane wave excitation conditions, as depicted in Fig. 3(b). In Fig. 3(c), we show the spectra of the amplitude of the dipole moments, $|p_a|$ and $|p_b|$, corresponding to the two systems. For a better comparison, we plot in the inset of Fig. 3(c) the ratio $|p_a|/|p_b|$. The two spectra suggest that the frequency of the quantum plasmon of the GNF is not affected by the excitation of the hot-spot plasmon, which means that, as expected, the effects of the quantum plasmon on the classical one are negligible. More importantly, however, it can be seen that the response of the quantum plasmon of the GNF can be enhanced by more than two orders of magnitude upon interaction with the hot-spot plasmon of a specially designed gold bowtie nanoantenna.

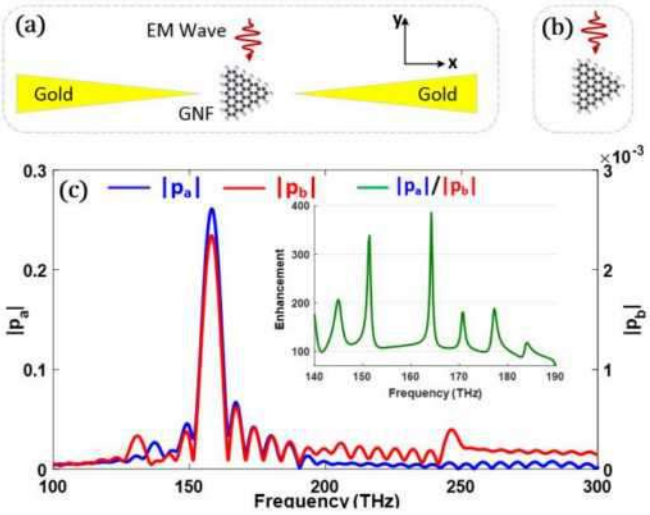


Figure 3: (a), (b) Schematics of a GNF placed in the gap of a bowtie nanoantenna and of an isolated GNF, respectively. (c) Spectra of the dipole moments $|p_a|$ and $|p_b|$ corresponding to the configurations shown in panels Fig.3(a) and 3(b), respectively.

Acknowledgements

The authors acknowledge the use of the UCL Legion High Performance Computing Facility (Legion@UCL), and associated support services, in the completion of this work. This work was supported by the European Research Council (ERC), Grant Agreement no. ERC-2014-CoG-648328.

References

[1] J. A. Scholl, A. L. Koh, and J. A. Dionne, Quantum plasmon resonances of individual metallic nanoparticles, *Nature*, 483 (7390):421, 2012.

[2] K. J. Savage, M. M. Hawkeye, R. Esteban, A. G. Borisov, J. Aizpurua, and J. J. Baumberg, Revealing the quantum regime in tunneling plasmonics, *Nature*, 491 (7425):574, 2012.

[3] W. Yan, M. Wubs, and N. A. Mortensen, Projected dipole model for quantum plasmonics, *Phys. Rev. Lett.*, 115(13):137403, 2015.

[4] M. S. Tame, K. R. McEnery, S. K. Ozdemir, J. Lee, S. A. Maier, and M. S. Kim, Quantum plasmonics, *Nat. Phys.*, 9(6):329, 2013.

[5] J. W. You and N. C. Panoiu, Analysis of the interaction between classical and quantum plasmons via FDTD-TDDFT method, *IEEE J. Multiscale Multiphys. Comput. Tech.*, 2019 (to be published).

[6] D. Z. Manrique, J. W. You, H. Deng, F. Ye, and N. C. Panoiu, Quantum Plasmon Engineering with Interacting Graphene Nanoflakes, *J. Phys. Chem. C*, 121(49):27597-27602, 2017.

[7] M. A. Marques, A. Castro, G .F. Bertsch, and A. Rubio, octopus: a first-principles tool for excited electron-ion dynamics, *Comput. Phys. Commun.*, 151(1):60-78, 2003.

Controlling the polarization of surface phonon polaritons

Michael A. Meeker[1*], Eric M. Jackson[1], Chase T. Ellis[1], Zhizhen Ma[2], Mario Miscuglio[2], Marko J. Tadjer[1], Sarah Brittman[1], Janice E. Boercker[1], Nii-Okaitey Tetteh[1], Volker J. Sorger[2], and Joseph G. Tischler[1]

[1] U.S. Naval Research Laboratory, Washington D.C, USA

[2] Department of Electrical and Computer Engineering, The George Washington University, Washington, DC, USA

*corresponding author, E-mail: michael.meeker.ctr@nrl.navy.mil

Abstract

We investigate the evolution of localized surface phonon polariton (SPhP) resonances supported by L-shaped nanoresonators for a range of geometries and incident polarizations. As indicated by polarized reflection spectroscopy, we observe three distinct resonances with in- and out-of-plane polarization selection rules that can be widely varied by changing the length of only a single resonator arm. Such polarization control is expected to play an important role in optimizing light-matter interactions.

1. Introduction

The ability of surface plasmon polaritons (SPPs) to enhance local fields provides major benefits for surface enhanced spectroscopy and sensing. Furthermore, since chemicals and molecules tend to have specific selection rules, controlling the polarization of SPPs can influence the coupling between light and matter. While research continues to investigate ways in which SPPs interact with and manipulate polarized light [1-2], the high losses of metals limit the ability to harness plasmonic effects in the infrared (IR) and explore new physical phenomena. In contrast, SPhPs support, low-loss, high-quality (Q)-factor resonances that allow us to directly observe physical phenomena otherwise obscured by the losses in traditional SPPs.

We observe the effects of symmetry breaking on SPhP resonances that are supported by SiC L-nanoresonators. As opposed to work previously performed on plasmonic L-shaped nanoresonators, where the spacing [2] or angle [3] between resonator arms was varied, we investigate how resonances are modified by changing the relative length between the two arms of the L-resonator. By controlling the relative arm length (characterized by an aspect ratio, AR), we find that we can control the relative orientation between the two fundamental modes of the L-resonator. In addition, we find that the degree to which modes are linearly polarized in-sample-plane is also affected by controlling the AR. Using polarized reflection spectroscopy, we are able to determine the polarization selection rules for three localized SPhP resonances that are supported by the L-geometry. Furthermore, the optical behavior of these modes is fully captured by full-wave electromagnetic modeling.

2. Experiment

2.1. Fabrication

Arrays of L-shaped pillars made up of 6H-SiC were fabricated on a bulk 6H-SiC substrate. Refer to reference 4 for fabrication details. Each L-resonator geometry is characterized by an aspect ratio, defined as the length ratio between the long and short arms. Here, we focus on resonators with nominal ARs of 1, 1.5, and 2. Fig. 1a shows an SEM of one of our structures for an AR of 1.5.

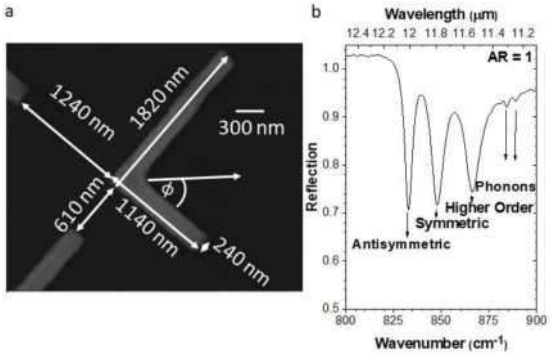


Figure 1: a) Scanning electron micrograph (SEM) image of a SiC L nanoresonator with nominal AR of 1.5, and incident polarization orientation denoted by ϕ. b) Typical unpolarized reflection spectra measured for an AR = 1 L structure.

2.2. SPhP Mode Assignment

The resonant energies, Q-factors, and polarization selection rules of SPhP modes supported by the L- resonators are investigated through polarized reflectivity measurements. To determine the polarization selection rules of these modes, we track the magnitude of resonances as a function of incident polarization angle. Three distinct modes are observed in the reflection spectra for all three L-resonator patterns (AR=1 shown in Fig. 1b). As indicated by the polarization orientation that yields maximal differential reflectance (see figure 2a), the three observed modes are optimally excited when the incident polarization is oriented at $\phi = 135^{o}$ for the mode at 832.6 cm^{-1} (where ϕ is defined in Fig. 1), $\phi = 60^{o}$ for the mode at 847.6 cm^{-1}, and $\phi = 90^{o}$ for the high-energy mode at 866.4

cm^{-1}. Based on full-wave electromagnetic modeling (COMSOL), we are able to identify these modes as antisymmetric, a symmetric and a higher order symmetric resonances, respectively (as indicated by resonant charge distributions). Unlike the low-energy symmetric mode, the higher order symmetric mode has a large polarization component oriented out-of-plane. The antisymmetric and symmetric resonances are similar to those found in previous reports of SPPs analogs [1,3].

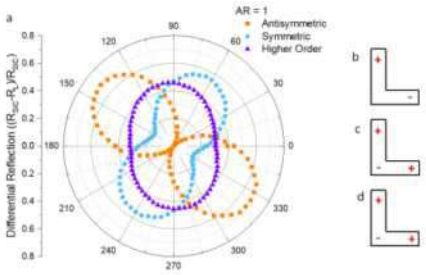


Figure 2: a) Experimental differential reflection between the SiC substrate (R_{SiC}), and L-resonators (R_L), showing the polarization orientation of the antisymmetric (orange squares), symmetric (light blue circles), and higher order mode (purple stars) for the AR = 1 resonator array. Illustration of the in-plane charge distribution for the b) the antisymmetric mode, c) the symmetric mode, and d) the higher order mode.

3. Discussion

As shown in Fig. 2a, the antisymmetric mode of the AR=1 L-resonators has a polarization dependence that is typically observed for a linearly polarized mode that lies fully within the sample-plane. In comparison, the symmetric mode has a noticeable waist that does not fully extinguish the resonance when the incident polarization is perpendicular ($\phi = 150^o$) to the main excitation axis of the mode ($\phi = 60^o$). This indicates that a portion of this mode is oriented out-of-plane. In contrast to the symmetric and antisymmetric modes, the polarization of the higher order mode, lies largely out of plane.

The polarization direction of the antisymmetric and symmetric modes is highly affected by the change in the relative leg lengths. As shown in Fig. 3a, the antisymmetric mode exhibits a rotation of the in-plane polarization orientation as the AR increases. We explain this behavior by noting that the antisymmetric mode is a dipole mode, with a dipole oriented along the hypotenuse of the structure. As the length of one arm increases, the angle between the legs and the L-hypotenuse is modified, which translates into an in-plane rotation of the polarization selection rule. On the other hand, the symmetric mode is only weakly dependent on AR, as shown in Fig. 3b. However, unlike the antisymmetric mode, the symmetric mode gains a significant out-of-plane polarization component as AR increases, which is indicated by the broadening of the polarization ellipse as AR is increased (Fig. 3b). In order to quantify the degree of out-of-plane polarization, we calculate the ratio of the minimum to maximum extinction (P) for each mode, where P=0 corresponds to a mode that is perfectly polarized in-plane, P=1 corresponds to a mode that is largely polarized out-of-plane. For the symmetric mode, the polarization ratio increases from 0.28 to 0.71 as AR increases, indicating a significant portion of the mode is polarized out-of-plane, which can be controlled by the carefully designing the resonator. However, for the antisymmetric mode, P varies from 0.007 to 0.067, as AR increases, indicating the antisymmetric mode remains largely polarized in-plane for this range of AR.

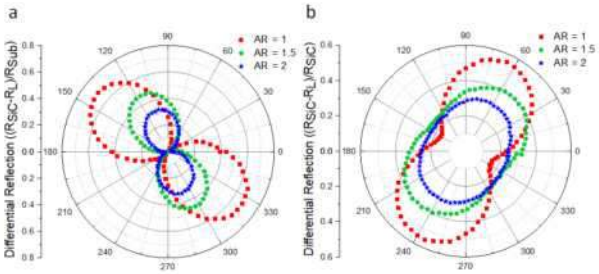


Figure 3: Experimental data showing the polarization orientation of the a) antisymmetric, and b) symmetric resonance for AR = 1 (red squares), 1.5 (green circles) and 2 (blue stars).

4. Conclusions

Overall, this work demonstrates that both the in-plane and out-of-plane selection rules of localized SPhP resonances that are supported by L-shaped nanoresonators can be manipulated by controlling the resonator geometry. The symmetric mode is especially interesting since our measurements indicated that its selection rules can be widely tuned from an in-plane to out-of-plane mode by simply elongating a single arm of the L-resonator.

Acknowledgements

MAM and SB acknowledge the support of the NRC Research Associate Programs. This work is supported by the Office of Naval Research.

References

[1] H. Husu, J. Mkitalo, J. Laukkan, et. al., "Particle plasmon resonances in L-Shaped gold nanoparticles", Opt. Express 18, 2010

[2] L-J. Black, Y. Wang, C. H. de Groot, et. al., "Optimal Polarization Conversion in Coupled Dimer Plasmonic Nanoantennas for Metasurfaces", ACS Nano 8, 6390 (2014)

[3] R. Blanchard, G. Aoust, P. Genevet, et. al., "Modeling nanoscale V-shaped antennas for the design of optical phased arrays", Phys. Rev. B. 85, 155457 (2012)

[4] C. T. Ellis, J. G. Tischler, O. J. Glembocki, et. al., "Aspect-ratio driven evolution of high-order resonant modes and near-field distributions in localized surface phonon polariton nanostructures" Sci. Reports 6, 32959 (2016)

Glass microspheres doped with Ag nanoparticles and CdTe quantum dots: towards a plasmonic microlaser

Piotr Piotrowski*[1], Rafał Nowaczyński[1,2], Barbara H. Surma[3], Dorota A. Pawlak[1,3]

[1]Faculty of Chemistry, University of Warsaw, Poland
[2]Faculty of Materials Science and Engineering, Warsaw University of Technology, Warsaw, Poland
[3]Institute of Electronic Materials Technology, Warsaw, Poland
*corresponding author, E-mail: p.piotrowski@chem.uw.edu.pl

Abstract

Plasmonic materials are utilized in plenty of areas like optoelectronics and photonics, due to their unique electromagnetic properties. Nanoparticles with plasmonic properties are added to the materials to greatly enhance their optical performance e.g. luminescence, Raman scattering or optical non-linearities.

The aim of our work is to develop an efficient microlaser based on the sodium borophospate glass (NBP) co-doped simultaneously with plasmonic silver nanoparticles (AgNPs) and cadmium telluride quantum dots (CdTe QDs). Introduction of NPs into the matrix is carried out by the NanoParticle Direct Doping method [1]. AgNPs greatly enhance the intensity of PL from the light emitters. Microspheres are obtained by the method described by Ward *et al*. [2]. Response of the system exhibits strong dependence on excitation power. What is more, PL spectra are different in various points in the microsphere, showing whispering gallery modes fine structure while the illumination is centered on the edge of the microbead (Figure 1).

Miniaturization of the laser opens possibilities of its integration into e.g. microfluidic system or can lead to new applications, such as biosensing *in vivo*. Observation of WGM gives promise to utilize the plasmonic microspheres in optical switches or as a narrow band laser.

Acknowledgements

The authors thank the TEAM Project (TEAM/2016-3/29) of the Foundation for Polish Science co-financed by the European Union under the European Regional Development Fund and the MAESTRO Project (2011/02/A/ST5/00471) from the National Science Centre for support of this work.

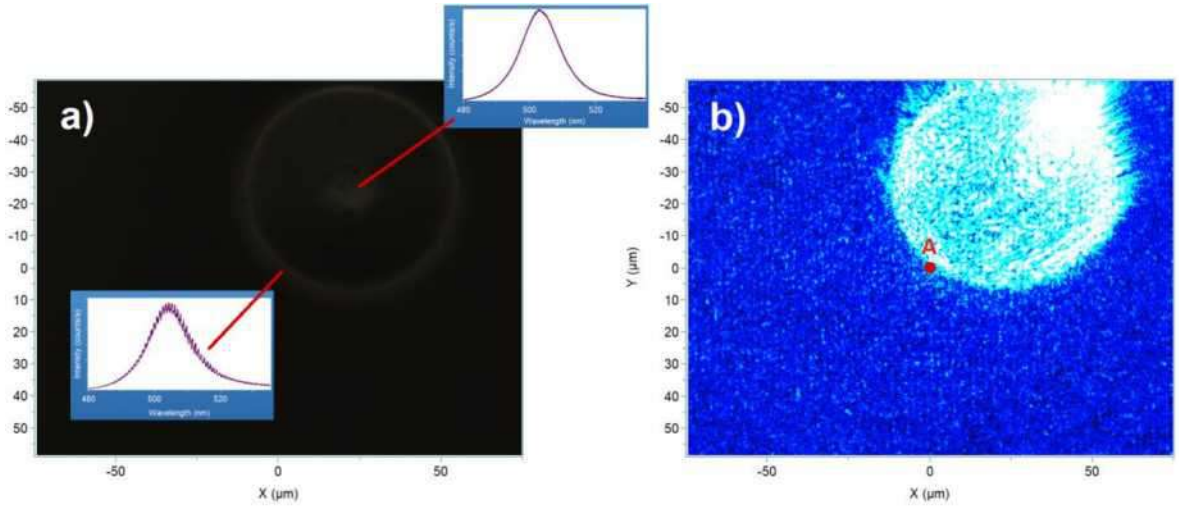


Figure 1: a) Optical image of the microsphere, objective 50x; insets: PL collected from the points indicated by red lines. Spectrum collected from the edge exhibits a periodic fine structure linked to WGM; λ_{exc} = 473 nm. b) Propagation of light on the surface of the microsphere illuminated by the laser focused on the microsphere edge (point A).

Off-axis digital holography for cathodoluminescence microscopy

Nick Schilder[1], Femius Koenderink[1], and Albert Polman[1]

[1]Center for Nanophotonics, AMOLF, Science Park 104, 1098 XG, Amsterdam, The Netherlands

*corresponding author, E-mail: schilder@amolf.nl

Abstract

We introduce off-axis digital holography for cathodoluminescence microscopy. We perform experiments on nanoholes in aluminium. The incident electron directly excites both surface plasmon polaritons and transition radiation simultaneously. The former scatter from the nanoholes and subsequently interfere in the farfield with (p-polarized) transition radiation, which serves as a reference field. By numerically isolating the interference terms of the farfield intensity, the complex-valued p-polarized electric field can be extracted.

1. Introduction

With cathodoluminescence microscopy fast electrons (1 – 100 keV) are used to characterize optical properties of nanostructures. The localized excitation of nanostructures allows deep-subwavelength imaging of modes. Each radiative mode has its own angular and wavelength dependent electric field amplitude, polarization and phase. Recent achievements in the field have enabled measuring both the angle-resolved amplitude and the polarization [1,2]. Access to the phase in cathodoluminescence microscopy has been elusive so far.

From other spectroscopy techniques such as near-field scanning optical microscopy (NSOM) or Fourier microscopy, we know that access to the wave front of light is important in for example the study of chiral light. This work shows the first steps towards phase-resolved cathodoluminescence microscopy. We use off-axis digital holography to retrieve the complex-valued electric field scattered by a nanostructure on a metallic film. It is the interference between scattered surface plasmon polaritons (SPPs) and transition radiation as the reference field that gives access to the phase.

2. Transition Radiation as Reference Field

For any interferometric technique, a (coherent) reference field is needed. Whenever a fast electron crosses an interface, broadband transition radiation is produced, which has a donut shape radiation pattern in the upper hemisphere and is perfectly p-polarized. This reference field serves to retrieve the complex p-polarized electric field scattered by an object that is positioned away from the excitation place of the electron.

3. Off-axis digital holography for cathodoluminescence

We use nanoholes in aluminium as scattering object. The incident fast electron excites both cylindrical SPPs and transition radiation. The SPPs induce multipoles in the structure that subsequently radiate. The p-polarized scattered light interferes with the spherical wave front of transition radiation in the farfield. This leads to interference fringes in the far field, where the interfringe distance depends on the spatial separation of the sources (see Fig. 1). The farfield intensity has four components: $I_{TR}+I_{scatterer}+E_{TR}E_{scatterer}^{*}+E_{TR}^{*}E_{scatterer}$. When calculating the Fourier transform of the farfield intensity, the last two interference terms show up as displaced patterns from the origin. By isolating these terms, the intensity and phase pattern are retrieved (see Fig. 2).

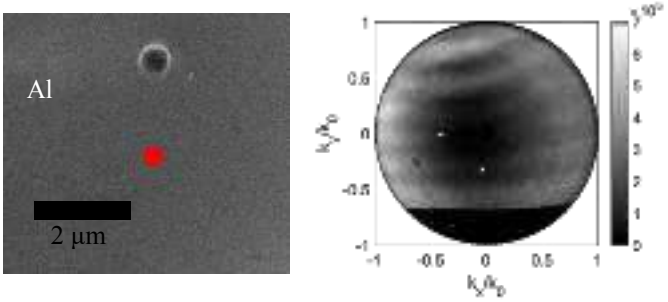


Figure 1: SEM image of a d = 500 nm hole in singlecrystalline aluminium, with the red dot indicating the excitation point with a 30-keV electron beam (left). Far field intensity pattern for 580 < λ (nm) < 620 showing an interference pattern (right).

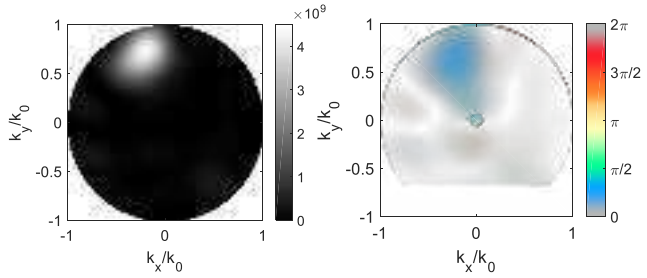


Figure 2: Retrieved farfield intensity (left) and phase distribution (right) of the p-polarized component of the scattered field.

References

[1] T. Coenen, E.J.R. Vesseur, and A. Polman, Angle-resolved cathodoluminescence spectroscopy, *Appl. Phys. Lett.* 99: 143103, 2011.

[2] C.I. Osorio, T. Coenen, B.J.M. Brenny, A. Polman, and A.F. Koenderink, Angle-resolved cathodoluminescence imaging polarimetry, *ACS Photonics* 3: 147-154, 2015.

Metamaterials-based probing weak quantum absorber in coupled three-resonator system with guided wave surface plasmons: sensing or all-optical switching?

Alina Karabchevsky[1,2*] and Adir Hazan[1]

[1]Electrooptics and Photonics Engineering Department, Beer-Sheva 8410501, Israel.
[2]Ilse Katz Institute for Nanoscale Science & Technology, Center for Quantum Information Science and Technology, Ben-Gurion University of the Negev, Beer-Sheva 8410501, Israel.
*corresponding author, E-mail: alinak@bgu.ac.il

Abstract

Optical switches selectively switch optical signal from switched-on to switched-off. Compared to the traditional electronic switches, optical switches are not limited by thermal effects or electromagnetic interferences. Here we show metamaterials-based probing of weak quantum absorber in coupled three-resonator system which reveals the signature of optical switching. The polarization dependent probing of molecular overtones excited in a hybrid system tune the state: when the system is illuminated by transverse magnetic polarized light the switch is on while for the transverse electric polarized light the switch is off.

1. Introduction

All-optical switching allows light controls light through unique optical effects. As the field of optical fiber technology has expanded [1], optical switches have been studied and progressed naturally [2,3] giving rise to new configurations such as optically switchable organic light-emitting transistors [4], sub-femtojoule switches [5], plasmonic bandpass filter thermal switches [6], optical control of antiferromagnetic domains [7], utilizing high-mobility of cadmium oxide for ultrafast polarization-controlled [8], multimodal switching of a redox-active macrocycle molecules state toggle [9] active control of anapole states by structuring the phase-change alloy [10] ultrafast optical switching of infrared plasmon polaritons in high-mobility graphene [11]. The efficiency of the switch is defined by its size which dictates the number of input and output ports; switching time of reconfiguration from one state to another; propagation delay time; switching energy to turn on the switch; power dissipation during the switching; crosstalk due to the power leakage to other ports; and physical dimensions [2]. Even though the optical fibers are considered as a pivot of conventional optic telecommunication system [1] their role in switching and processing of photonic signals is limited and fulfilled by electronics. Here we report on all-optical switch due to the excitation of molecular overtones in hybrid plasmonic-dielectric configuration. By coupling of photons with the conductive charges at the metal-dielectric interface, plasmonics gives rise to nanoscale optical devices operating at sub-wavelength regime [13]. Hybrid plasmonic-dielectric configuration possesses a unique property to controlling the switch with polarization state of light that allows two different plasmonic modes co-exist while exciting single molecular overtone absorption band. Due to the possibility of developing energy efficient, real-time analyzing, and ultra-compact components at an affordable cost, plasmonics may be the next arrangement in optical communications. Despite the fact that many plasmonics-based applications appeared, such as sensors [14], detectors, modulators, switches, and microwave components, no attempts were done so far to designing all-optical hybrid plasmonic-dielectric switching systems based on effect of excitation of forbidden molecular overtones transitions.

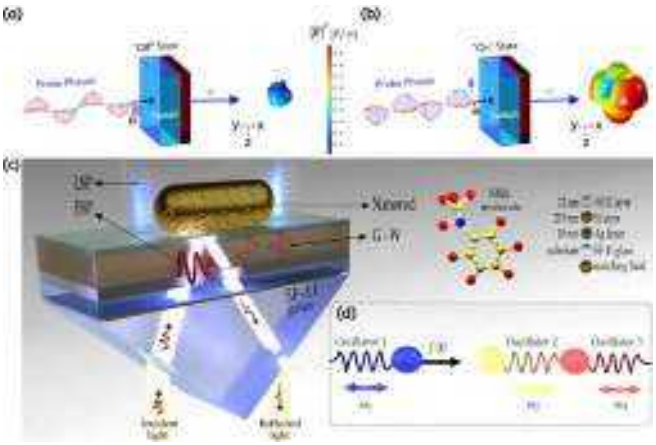


Figure 1: (a) Schematic illustration of polarized beam incident the switch. The state ‘off’ is activated when the TE polarized beam hits the switch, (b) the state ‘on’ is activated when the TM polarized light hits the switch. (c) Artistic representation of experimental setup. (d) Mechanism of coupled oscillators.

2. Results and Discussion

Here we study on all-optical switch due to the excitation of molecular overtones in hybrid plasmonic-dielectric configuration. Figure 1 illustrates the concept of the system based on molecular excitation under TE and TM polarized light. In the state 'off', Figure 1a, TE polarized light is being transmitted through the medium. Figure 1b illustrates state 'on' in which TM polarized light excites molecular overtone transition resulting in a well-defined resonance due to the strong light absorption. Calculated far-field radiation diagrams in subplots Figure 1a and Figure 1b show the directivities for each state. At lower wavelengths however, excited molecular signatures experience different response to the incident light under TE and TM polarizations.

Figure 1c shows the modeled and tested experimentally system in which polarized incident polychromatic light illuminates the facet of the prism. Thin film composed of silicon on silver is placed on the prism with matching oil. N-Mathylaniline molecule is dripped on the surface of the film together with gold nanorods. Light hits the base of the prism and penetrates through the thin film while exciting the guided modes. Guided modes in turn excite the molecular overtones. The energy transfer occurs between the molecular overtone vibrations to the localized surface plasmon excited in nanorod. We treat the coupling between the guided wave-to overtone-to localized surface plasmon as a system with three coupled oscillators having eigenfrequencies $\omega_{1,2,3} = \sqrt{\frac{k_{1,2,3}}{m_{1,2,3}}}$, ω_1, ω_2 and ω_3 coupled together with coupling spring constants k_1, k_2 and k_3 and masses m_1, m_2 and m_3. Figure 1d shows the oscillating mechanism of the system. Oscillator 1 is the guided mode surface plasmon, oscillator 2 is the molecular overtone vibration and oscillator 3 is the localized surface plasmon oscillator. The oscillators requirement is extremely demanding.

3. Conclusions

In summary, we explored the system in which three coupled oscillators are excited. Despite the relatively low oscillator strength of the corresponding forbidden dipole transition in harmonic oscillator approximation we constructed an optical switching system based on polarization depending properties of the plasmon-to-overtone coupled modes. This all-optical switching manifold is realized by excited localized surface plasmons (LSP) which couple to the molecular vibrations overtones. LSP in the system are excited by the extended surface plasmons (ESP) which in turn are excited by the guided modes of a waveguide structure.

References

1 Midwinter, J. E. Trends in optical fibre transmission research. Nature 261, 371-376 (1976).

2 Saleh, B. E. & Teich, M. C. Fundamentals of photonics. (john Wiley & sons, 2019).

3 Midwinter, J. E. Photonics in switching. (Academic Press, 2012).

4 Hou, L. et al. Optically switchable organic light-emitting transistors. Nature Nanotechnology, doi:10.1038/s41565-019-0370-9 (2019).

5 Nozaki, K. et al. Sub-femtojoule all-optical switching using a photonic-crystal nanocavity. Nature Photonics 4, 477, doi:10.1038/nphoton.2010.89 https://www.nature.com/articles/nphoton.2010.89#supplementary-information (2010).

6 Sun, M. et al. A Photonic Switch Based on a Hybrid Combination of Metallic Nanoholes and Phase-change Vanadium Dioxide. Scientific Reports 8, 11106, doi:10.1038/s41598-018-29476-6 (2018).

7 Manz, S. et al. Reversible optical switching of antiferromagnetism in TbMnO3. Nature Photonics 10, 653, doi:10.1038/nphoton.2016.146 https://www.nature.com/articles/nphoton.2016.146#supplementary-information (2016).

8 Yang, Y. et al. Femtosecond optical polarization switching using a cadmium oxide-based perfect absorber. Nature Photonics 11, 390, doi:10.1038/nphoton.2017.64 https://www.nature.com/articles/nphoton.2017.64#supplementary-information (2017).

9 Payne, D. T. et al. Multimodal switching of a redox-active macrocycle. Nature Communications 10, 1007, doi:10.1038/s41467-019-08978-5 (2019).

10 Tian, J. et al. Active control of anapole states by structuring the phase-change alloy Ge2Sb2Te5. Nature Communications 10, 396, doi:10.1038/s41467-018-08057-1 (2019).

11 Ni, G. X. et al. Ultrafast optical switching of infrared plasmon polaritons in high-mobility graphene. Nature Photonics 10, 244, doi:10.1038/nphoton.2016.45 https://www.nature.com/articles/nphoton.2016.45#supplementary-information (2016).

12 Barnes, W. L., Dereux, A. & Ebbesen, T. W. J. n. Surface plasmon subwavelength optics. 424, 824 (2003).

13 Karabchevsky, A., Mosayyebi, A. & Kavokin, A. V. Tuning the chemiluminescence of a luminol flow using plasmonic nanoparticles. Light: Science & Applications 5, doi:doi: 10.1038/lsa.2016.164 (2016).

Biomechanical sensor based on gold plasmonic nanorods for mechanotransduction investigation

M. Salbini[1,2], T. Stomeo[1], C. Ciracì[1], R. Fiammengo[1], V. Mangini[1], M. Leoncini[3], A. Toma[3] F. Pisano[1], F. Pisanello[1], T. Verri[2], D. R. Smith[4], M. De Vittorio[1,5].

[1] Center for Biomolecular Nanotechnologies, Istituto Italiano di Tecnologia, Arnesano (Lecce), Italy;
[2]Dipartimento di Scienze e Tecnologie Biologiche e Ambientali, Università del Salento, Lecce, Italy;
[3]Istituto Italiano di Tecnologia, Genova, Italy;
[4]Center for Metamaterials and Integrated Plasmonics, Duke University, Durham, NC, United States;
[5]Dipartimento di ingegneria dell'innovazione, Università Del Salento, Lecce, Italy.
*corresponding author, E-mail: maria.salbini@iit.it

Abstract

We discuss the possibility of implementing a novel bio-sensing platform based on surface plasmon resonances (SPRs) for investigating mechanotransduction and force generation by mechanosensory cells and organs. In particular, we present a study about the generation and analysis of optical resonances caused by gold nanorods (GNRs) adsorbed on films, separated by a polyelectrolyte (PE) thin layer assembled using a Layer-by-Layer (LbL) deposition technique. These devices with different PE layer/GNRs coupling were characterized and tested in phosphate buffer saline (PBS) in order to be able to control in a dynamic way the PE layer thickness swelling. Moreover, controlling the wettability of the surface, in particular after the deposition of GNRs, allows adjusting the hydrophilic/hydrophobic character of the surface, considering that the wetting property and wetting process are closely related to the surface morphology and roughness. We performed a deep study to confirm that this sensor, exploiting SPR, can be dynamic and compatible with biological environments.

1. Introduction

Sensing of force and movement in biological systems involves the conversion of an external mechanical stimulus into a biochemical signal, a process termed *mechanotransduction*. It plays important role in biology, from e.g. embryogenesis, to physiology and patho-physiology, from cancer to neurodegenerative disorders, and in a variety of sensory systems including those that respond to sound, acceleration, and touch [1, 2]. Analysis of cellular mechanotransduction has focused on identification of critical mechanosensitive molecules and cellular components. In this work, we present results on an innovative biomechanical sensor based on plasmonic nanostructures for sensing forces at the cellular level. When light impinges on a metallic structure, resonant oscillation of the conductive electrons, known as surface plasmons, are excited. Metallic nanoparticles smaller than the wavelength of the light can support localized surface plasmon resonance (LSPR) and confine light in a region beyond the diffraction limit with greatly increased local density of states enabling a variety of applications: from super resolution imaging [3] to biosensing [4] and photodetectors [5]. Systems in which GNRs are within a short distance from a gold film are optically very sensitive to any modification occurring in the gap and represent a promising platform for creating next-generation biosensors [6]. Here, we focus on the specific system where GNRs are coupled to a thin gold film in SPR configuration, in order to interrogate small, dynamic molecular conformational changes by measuring the actuation of molecular spacer layer in response to aqueous solution.

2. Experimental section

We performed numerical analysis and experimental spectroscopy of GNRs over a gold thin film with a precisely sized polyelectrolyte layer defining the gap between them. We studied this system as a function of gap size and determined modifications of its plasmon modes. GNRs were chemically synthesized using seed mediated growth technique. The final size were 35 ± 5 nm in length and 20 ± 4 nm in width. Substrates were prepared by evaporating 50 nm of Au film onto 5 nm of Ti adhesion layer covering a silicon wafer via electron beam evaporation. Dielectric spacer layers of varying thickness in the range 1÷ 9 nm, composed of alternating polyelectrolyte (PE) layers of poly (allylamine hydrochloride) (PAH-3mM) and polystyrene sulfonate (PSS-3mM) were deposited onto the gold film via Layer-by-Layer deposition. The sequential deposition of PAH and PSS was continued until the desired thickness was attained, with the terminating layer being cationic (PAH). Negatively charged GNRs were absorbed onto the terminal PE layer via short incubation with the colloidal solution. The films were rinsed with ultrapure water and dried with N2. The schematic arrangement of the GNRs over metal film system is presented in Fig. 1A. The GNRs as fabricated and after deposition on the gold film were observed, respectively, by a Transmission Electron Microscope (TEM) (Fig. 1B) and by Scanning Electron Microscopy (SEM). Reflectance spectra at normal incidence were measured with a custom made optical setup. Samples were positioned on an upright microscope, modified to accommodate for a reflectometry path. Broadband, incoherent light (Ocean Optics HL 2000) passing through a 100 μm pinhole was collimated with a lens (focal 250 mm), reflected by a beam splitter (50/50) and

focused on the sample with a low numerical aperture (NA), infinity-corrected objective (5x, 0.13 NA). The reflected light passing, through the beam splitter, was injected into a multimode optical fiber with an objective lens (20x, NA 0.5) and sent to a spectrometer (Horiba Scientific iHR320) equipped with an EMCCD camera (Horiba Scientific Synapse, 1600x200 pixels).

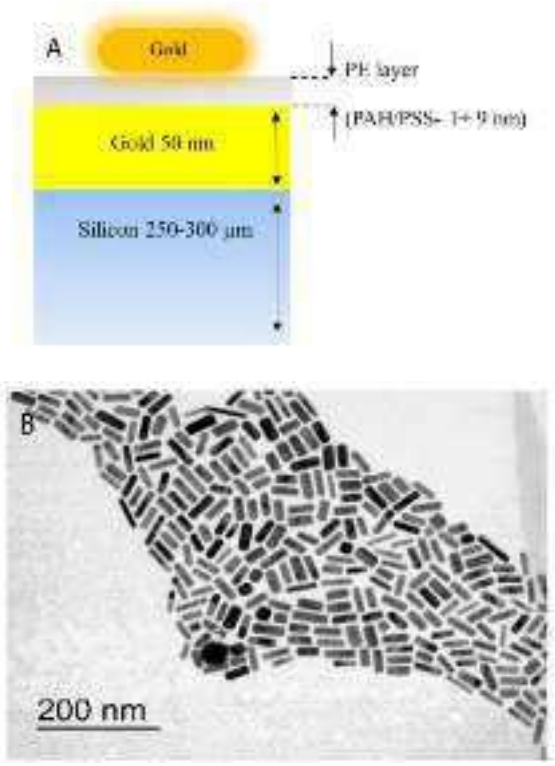
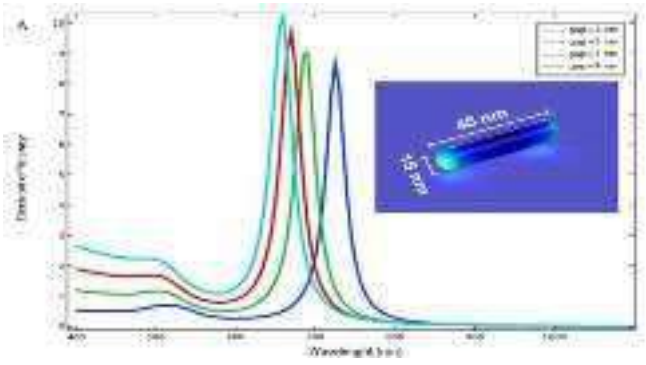


Figure 1. Au nanorods over a Au film (A). TEM image of GNRs as fabricated (B).

Since our biosensor will be in contact with the cells, it is desirable to be able to control both the swelling level of the PE layer by specific stimulus and the wettability of the surface. PE layers of different thickness were assembled with the dipping solution at pH 6- 6.5. We started studying the properties of the PE layer composed of PAH/PSS in PBS (pH 7.4). To compare PE layers swelling behavior, the films were examined as prepared and then a time course of 30 minutes was acquired during immersion in PBS. The films were dried to examine whether if swelling influences the dry-state thickness and to determine a "molecular memory" caused by previous treatment. Afterward, to understand the wettability of the surface a contact angle experiment in sessile drop mode was performed. The wetting state of surface can be controlled physically from the highly hydrophobic to hydrophilic states using GNRs by means of contact angle, because the wetting property is closely related to the surface morphology and roughness.

2. Results and Discussion

The plasmonic nanostructures are formed from colloidally synthesized metal nanorods deposited on top of a metal film and separated by a polymer spacer with nanometer accuracy. There are several appealing nanoscale properties of this plasmonic architecture. For example, the plasmon resonance between the metal nanorods and the film can be precisely controlled by varying the thickness of the polyelectrolyte spacer layer and the rods size. We created a GNRs-film sample with 50 nm gold film, a polyelectrolyte spacer layer of different thickness and gold nanorods, which produced a GNRs-film separation distance starting from 1 nm to 9 nm. The higher the separation, the higher the blue-shift of the coupled nanoparticles-film SPR. The spacer layer between the nanorods and the gold film is completely transparent at visible and near IR wavelengths. Fig. 2 shows the position of the measured resonance as a function of the overall thickness under the rods, assuming that the nanorods-film separation distance is the sum of the PE spacer layer thickness and the 5 nm thickness of the stabilizer coating that surrounds the rods. The position of the resonance can be accurately determined by 3D simulation (Fig. 2A). As typical with nano-plasmonic systems, their resonances are extremely sensitive to the thickness and the dielectric properties of the spacer layer, making the reflectance properties of the surface easily tunable by slightly changing the gap dimension. Based on our simulations, in which a single nanorod is coupled to a metallic film, we could expect a small reflectance even for low surface coverage. Changes in the refractive index (RI) near the nanoparticles induced a shift in the SPR peak position (Fig. 2B). Both simulation and experimental results showed that the plasmon resonance of the nanorods blue- shifts with increasing gap size. The agreement between our experiments and simulations confirms that our numerical model is adequately capturing the physics of the nanorods metal film coupling system.



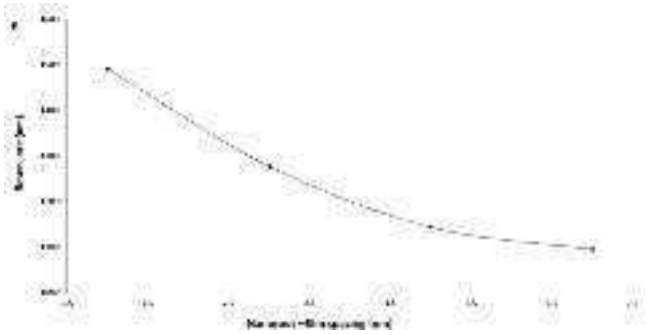


Figure 2. Tunability of the reflectance. Position of the resonance as a function of the spacer thickness. (A) Simulation results. (B) Experimental results.

Contact angle measurements were carried out on GNRs deposited on the PE film and on PE film with no nanoparticles, to study the wettability in presence (or absence) of the nanorods and at different thickness of the dielectric layer [7]. The nanorods deposition on the PE layer increased the surface roughness, leading to higher contact angles values.

We next used the GNRs-film coupling in the plasmonic configuration to interrogate small, dynamic molecular conformal changes by measuring the actuation of molecular spacer layers in response to aqueous solution like water or Phosphate Buffer Saline (pH-7.4). It is well known that multilayer films assembled from PAH/PSS under specific pH conditions exhibit unique time-dependent swelling behavior. Fig. 3 shows representative GNRs-film SPR data at different time during PBS immersion and after drying. The GNR-film coupled resonance, which is between 645 and 655 nm, blue shifts when immersed in PBS solution but during the immersion, we can notice a red shift. This implies that during immersion the GNRs on the top of the PE layer are further away from the film, because the spacer layer is swollen, but when we came back to the dry state, the nanorods are closer to the film because of the PE layer shrinking.

This particular behavior was verified in both 7 and 9 nm PE layer samples. Based on these observations, the tuning of the plasmon resonance observed in our experiment is mostly likely caused by the increasing and decreasing of the thickness of the PE layer. Immersion in PBS for 30' of a 7 nm thick PE layer leads to an SPR resonance corresponding to that of a 9 nm thick unswollen sample, demonstrating that the amount of thickness increase in the swelling process is about ~ 2 nm.

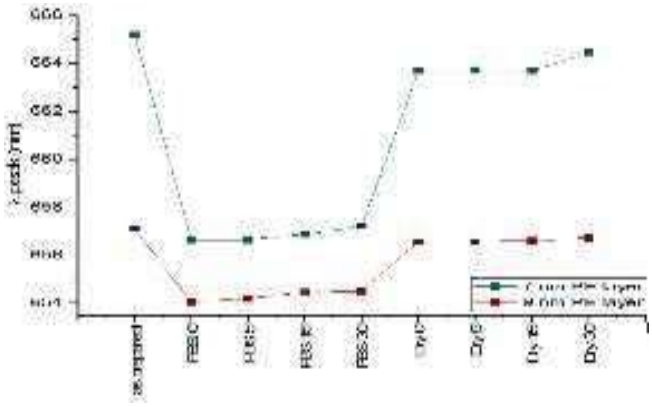


Figure 3. Time dependence of swelling level: during immersion and dry conditions.

3. Conclusions

In conclusion, we have fabricated and measured the spectra of GNRs coupled to a gold thin film. Using experimental and numerical analysis of this geometry, we found that the observed resonances can be understood as waveguide cavity modes, where the gap between the GNRs and the metal film defines a waveguide cavity where electromagnetic energy can resonantly reflect back and forth. These resonances are extremely sensitive to the gap size separating the GNRs from the gold film, a property that could potentially be exploited for novel biosensing platforms. The wetting state of surface can be controlled from highly hydrophobic to hydrophilic states by using nanorods. Indeed, contact angle measurements show that by increasing the surface coverage of the PE layers using nanoparticles the contact angle increases to high values, with a difference of ~20° between the non-covered surface and the one covered with nanorods. A nanorods-film coupling is used in SPR spectroscopy mode to characterize the induced swelling of a PE layer. Spectra show a shift of the coupled NR-film SPR by incubation in PBS, suggesting that the gold nanorods have been pushed away from the gold film because the PE layer is in a swollen state. The system goes back to its previous state when the sample is dried, suggesting PE layer deswelling, so the PE layer has not any significant "molecular memory" of previous swelling treatment. It is also shown that the immersion in PBS for 30' of a 7 nm thick PE layer leads to an SPR resonance corresponding to that of a 9 nm thick unswollen sample, demonstrating that the amount of thickness increase in the swelling process is of about ~ 2 nm. These results represent a step towards a fiber-embedded biomechanical sensor, where tiny cell pressures lead to shift of the SPR resonance wavelength because of the reduced thickness of the spacer layer.

References

[1] M. Chalfie, Neurosensory mechanotransduction, Nature Reviews Molecular Cell Biology 10 (2009) 44.

[2] C. Hahn, M.A. Schwartz, Mechanotransduction in vascular physiology and atherogenesis, Nature Reviews Molecular Cell Biology 10 (2009) 53.

[3] M. Rycenga, X. Xia, C.H. Moran, F. Zhou, D. Qin, Z.-Y. Li, Y. Xia, Generation of Hot Spots with Silver Nanocubes for Single-Molecule Detection by Surface-Enhanced Raman Scattering, Angewandte Chemie International Edition 50(24) (2011) 5473-5477.

[4] J.N. Anker, O. Hall Wp Fau - Lyandres, N.C. Lyandres O Fau - Shah, J. Shah Nc Fau - Zhao, R.P. Zhao J Fau - Van Duyne, R.P. Van Duyne, Biosensing with plasmonic nanosensors, (1476-1122 (Print)).

[5] G.M. Akselrod, J. Huang, T.B. Hoang, P.T. Bowen, L. Su, D.R. Smith, M.H. Mikkelsen, Large-Area Metasurface Perfect Absorbers from Visible to Near-Infrared, (1521-4095 (Electronic)).

[6] G. Jiang, A. Baba, H. Ikarashi, R. Xu, J. Locklin, K.R. Kashif, K. Shinbo, K. Kato, F. Kaneko, R. Advincula, Signal Enhancement and Tuning of Surface Plasmon Resonance in Au Nanoparticle/Polyelectrolyte Ultrathin Films, The Journal of Physical Chemistry C 111(50) (2007) 18687-18694.

[7] A.F. Stalder, T. Melchior, M. Müller, D. Sage, T. Blu, M. Unser, Low-bond axisymmetric drop shape analysis for surface tension and contact angle measurements of sessile drops, Colloids and Surfaces A: Physicochemical and Engineering Aspects 364(1) (2010) 72-81.

A Deep Sub-wavelength Scale Surface Plasmon Polariton Travel Wave Amplifier with Multiple Quantum Wells

Ruijian Rao[1*], Shuwen Chen[1], Bing Chen[2]

[1]National University of Defense Technology, Information and Communication College, Xi'an, P. R. China
[2]Xi'an Jiaotong University, Xi'an, P. R. China
*corresponding author, E-mail: rjrao@163.com

Abstract

We propose a deep sub-wavelength scale surface plasmon polariton(SPP) travel wave amplifier (TWA) with multiple quantum wells (MQW) working at 1310nm communication window. The InGaAlAs tensile MQW are adopted for the polarization-independent amplification. We analyze this TWA's electrical and optical characterizes by the finite element method. Simulation results suggest that the completely independent polarization gain appears at 1317nm in which the mode gain 110cm^{-1} and mode width 163nm are obtained at the 5×10^{24}/m^3 injected electron concentration and 260nm×10nm gap size.

1. Introduction

The SPP components are being developed for ultra compact photonic integrated circuits(PIC). But the high propagation loss of the SPP wave is the main obstacle in the progress. In order to solve this problem, various structures and active media are proposed to construct the SPP amplifiers, such as the SPP with MQW[1-4], the DLSPP with Schottky junction[5], the gap SPP with double heterostructure[6-11]and so on.

Specially compensating the SPP loss with MQW was proposed first in the Ref. [2]. Also in the Ref. [1, 4] the MQW SPP with insulator-metal-insulator structure was explored by experiments.

Theoretically the SPP wave is TM polarization in the infinite slab structure. But in the real finite-size-device the SPP wave is a hybrid one in which both TM and TE polarization field exist simultaneously.

In normal lattice matched MQW structures, the TE polarization field gain is higher than that of the TM's. For high fidelity amplification of the hybrid SPP wave, it is necessary to adopt the strain MQW which has the equal gain about the TE and TM field[12].

In this paper, we propose a deep sub-wavelength scale SPP TWA with the lateral current injection (LCI) MQW. There are two creative points in our works. First a tensile strain MQW is designed for high-fidelity amplification of the hybrid SPP wave. Second, by adjusting the gap layer height and width, both the little mode width and the high mode gain are obtained simultaneously. So far to our best knowledge, the polarization independent MQW SPP TWA has not been designed and researched before.

2. The SPP TWA Structure

The reason of using the LCI MQW in our SPP TWA is as following. The SPP wave reaches its peak at the metal-dielectric-interface and decays quickly from both sides of this interface. For effectively amplifying the SPP mode, it is necessary to push the amplification medium close to the interface enough. As the nanoscale-thickness-barrier and the LCI in MQW, the effective amplification area, i.e. the quantum well (QW) can reach the metal-dielectric-interface very closely and amplify the SPP wave effectively. Therefore the MQW with LCI is adopted in our SPP TWA. The SPP TWA cross section is shown in Fig. 1. From top to down there are air cladding, noble metal Ag, SiO_2 gap, MQW and substrate InP. On each lateral side of the MQW there are the p-InP and n-InP which guide current to MQW from both sides, i.e. the LCI. And the p-InP and n-InP doping concentration are $4\times10^{24}/m^3$.

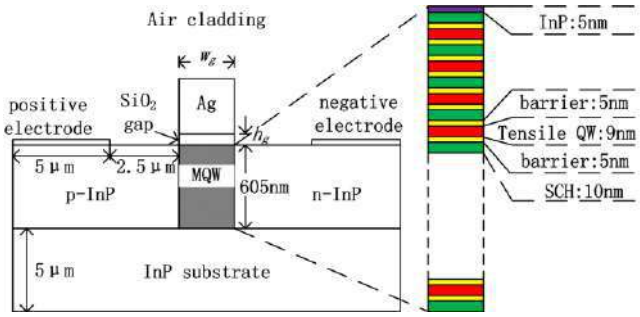


Fig. 1 The SPP TWA cross section

In Fig. 1 the MQW plays two roles. One is to amplify the SPP wave. The other is a part of the gap SPP waveguide which includes the high-index-MQW, low-index-gap(SiO_2)and metal Ag.

Also in Fig. 1 the SiO_2 is selected as the gap material for three reasons. First, SiO_2 is insulator, which isolates the metal Ag from current injection area. Second, the SiO_2 has low refractive index, which is necessary in the gap SPP waveguide. Third, it is transparent in 1310nm window

which is the SPP TWA working range.

And shown in Fig. 1 both the positive and negative electrodes are $5\mu m$ width and are apart from the MQW edges $2.5\mu m$. And the InP substrate is $5\mu m$ thickness.

By adjusting the low-index SiO_2 gap height h_g and width w_g , the SPP mode field size and propagation loss can be changed. In addition, the metal Ag and MQW width also are w_g .

3. The Design of the MQW

In QW structures the light generated by recombination of electron-heavy hole and electron-light hole is TE or TM polarization separately. In general QW structures, the transition probability between an electron and a heavy hole is higher than that between an electron and a light hole, so that the TE polarization is dominant in the optical gain[12]. This results in large optical gain polarization dependence in the general QW optical amplifier. So a number of designs have been developed to minimize the optical gain polarization difference in InP-based QWs[13-17].

In this paper, we design a tensile strain QW structure for SPP wave polarization-independent amplification. For a relevant material system, we adopted the $In_{1-x-y}Ga_xAl_yAs$ to realize the layers of the MQW since it is known to have superior characteristics in temperature performance.

In Fig.1 the MQW is consisted of 20 QW units, each of which includes the 5nm-barrier, 9nm-tensile-QW, 5nm-barrier from top to down. And these QWs are separated by the 10nm separate confinement heterostructure (SCH) layers. Also shown in Fig. 1 at the top of the MQW it is the 5nm-thickness-InP which is next to the gap area. Simulation indicates that the multi-mode will appear if the whole MQW thickness is larger than 620nm. Therefore we use 20 tensile strain QWs to compose the 605nm-thickness-MQW.

The Eq. (1) is the relationship between the energy gap E_g and the composition ratio x,y[18].

$$\mathrm{E_g}=\begin{cases} 0.75+1.548\mathrm{y} \text{ and } (1-\mathrm{x}-\mathrm{y}=0.53) \text{ as lattice matched} \\ 0.79+1.568\mathrm{y} \text{ and } (1-\mathrm{x}-\mathrm{y}=0.38) \text{ as 1\% tensile strain} \\ 0.81+1.578\mathrm{y} \text{ and } (1-\mathrm{x}-\mathrm{y}=0.307) \text{ as 1.5\% tensile strain} \\ 0.83+1.588\mathrm{y} \text{ and } (1-\mathrm{x}-\mathrm{y}=0.225) \text{ as 2\% tensile strain} \end{cases} \quad (1)$$

First the energy gap of the barrier, QW and SCH are decided on the principle of the gain peak being in the 1310nm window. Second, circularly carrying on these following three steps: adjusting the QW tensile strain coefficients, utilizing the Eq(1) to calculate the ratio x,y , estimating the TE and TM polarization gain by the software Crosslight PIC3D until these two gain coefficient curves are as close as possible in the 1310nm window. Finally we get the composition ratio $[x, y]$ of the barrier, QW and SCH layers to be $[0.203, 0.267]$,$[0.4198, 0.0625]$ and $[0.0646, 0.4054]$

In above process, the TE and TM polarization gain is calculated using the software Crosslight PIC3D from the Eq. (2) proposed in the Ref[19] in the condition of the MQW being infinite slab layer structure.

$$G(E') = \frac{q^2 |M_B|^2}{E' \varepsilon_0 m_0^2 c \hbar n_{eff} T} \cdot \sum_{i,j} \int_{E_g}^{E_{gb}} m_{r,ij} C_{ij} A_{ij} (f_c - f_v) L(E) dE \quad (2)$$

where

q is the electron charge.

$|M_B|^2$ is the bulk momentum transition matrix element.

E' is the photon energy.

ε_0 is the free space permittivity.

c is the vacuum speed of light.

n_{eff} is the effective refractive index of the laser structure.

T is the thickness of the quantum well.

i *and* j is the conduction and valence band quantum numbers.

$m_{r,ij}$ is the spatially weighted reduced mass for transition.

C_{ij} is the spatial overlap factor between the state i and j .

$A_{i,j}$ is the angular anisotropy factor.

f_c and f_v is the electron quasi-Fermi functions in the conduction and valence band, respectively.

$L(E)$ is the Lorentzian lineshape function, commonly used to include the spectral broadening of each transition.

The infinite slab MQW gain are shown in Fig. 2, from which it can be found that the TE and TM gain are equal at 1317nm wavelength from 3×10^{24} to 6×10^{24} (m^{-3}) injected electron concentration .

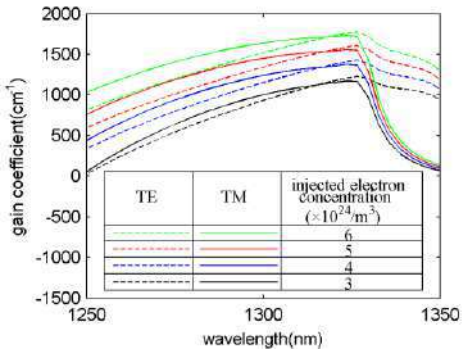


Fig. 2 The gain coefficient of the infinite slab MQW

4. The SPP TWA Characteristics

4.1. The electrical properties

By the Crosslight PIC3D simulation, as the applied voltage is 1.3v, the 500nm-width MQW electron concentration is obtained and shown in Fig.3(a). In Fig.3(b) it is the electron concentration along the middle white dashed line in Fig. 3(a). From Fig.3(a) (b), we can know that the electron

concentration can reach about $5\times10^{24}/m^3$. And in this condition the MQW local gain can reach about $2000cm^{-1}$ shown in Fig. 3(c)(d). The Fig. 3(d) is the gain along the white dotted line in Fig. 3(c).

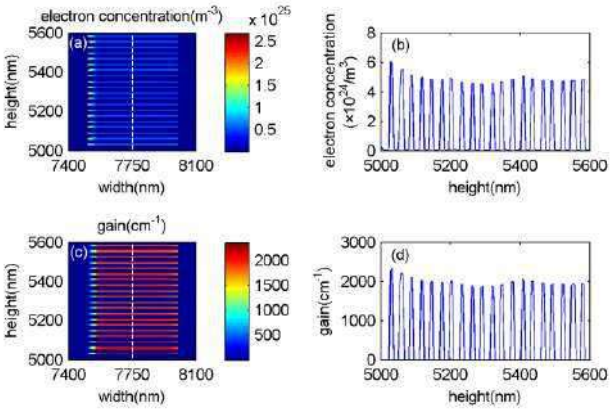


Fig. 3 As the applied voltage 1.3v (a)The MQW electron concentration.(b)The MQW electron concentration along the white dash line in the middle of the MQW. (c) The local gain in the MQW area. (d) The gain along the middle dash line in (c).

4.2. The optical properties

As mentioned above, at 1317nm the MQW have equal polarization local gain coefficient $2000cm^{-1}$. Therefore we simulate and analyze the SPP TWA characteristics at 1317nm with local gain coefficient $2000cm^{-1}$ in the QW area. And the dielectric constants of these media in the SPP TWA are gotten as the following. The $In_{1-x-y}Ga_xAl_yAs$ dielectric constants $\varepsilon_{InGaAlAs}$ are gotten from Eq. (3)[12].

$$\varepsilon_{InGaAlAs}=(1-x-y)\varepsilon_{InAs}+x\varepsilon_{GaAs}+y\varepsilon_{AlAs} \qquad (3)$$

where $\varepsilon_{InAs},\varepsilon_{GaAs},\varepsilon_{AlAs}$ are the InAs, GaAs and AlAs dielectric constant which can be gotten by interpolating the data from the Ref [20]. From the equation(2), the barrier, the SCH, the tensile QW dielectric constants are calculated to be 11.2181, 11.8544, 11.8398 respectively. The silver permittivity is -67.3544-6.3369i, the gap SiO_2 one is 2.3409 and the InP substrate, n-InP, p-InP are assumed to be the equal one 10.2674[20]. Additionally the metal Ag thickness is 100m. And the substrate InP is semi-infinite during simulation. We use the software COMSOL Multiphysics to get the relationship curves between the gap size and SPP wave characteristics including the mode effective refractive index n_{eff} , mode gain and mode width.

The definitions of the mode gain and mode width are explained as follows. If the mode power is amplified by $e^{\alpha z}$ after propagating distance z (cm), the mode gain is defined as $\alpha\left(cm^{-1}\right)$ [21]. Because the mode field lateral distribution size is important in realizing the high integration density PIC, we propose the mode width to describe the mode field lateral distribution. Assuming the horizontal and the vertical axis to be x and y separately, the TWA cross-section to be symmetric along y axis and the mode Poynting vector is $\vec{A}$.

$$\text{If} \quad \frac{\iint\limits_{\substack{-\frac{x_0}{2}<x<\frac{x_0}{2}\\-\infty<y<+\infty}} \vec{A}\bullet d\vec{s}}{\iint\limits_{\substack{-\infty<x<+\infty\\-\infty<y<+\infty}} \vec{A}\bullet d\vec{s}}=\eta$$

, the mode width is defined as x_0 in the x direction. Here η is the ratio of the mode power in $x\in\left[-\frac{x_0}{2},\frac{x_0}{2}\right]$. In this paper it is assumed $\eta=50\%$.

By simulation the mode characteristics curves are got and shown in Fig.4(a)(b)(c) respectively.

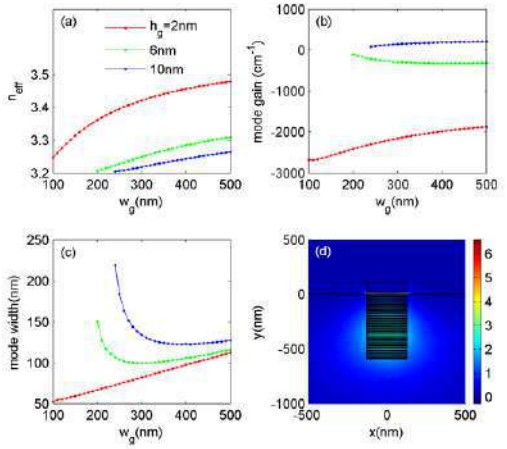


Fig. 4 The relationship between the SPP wave characteristics and gap width w_g , height h_g .(a) mode effective refractive index n_{eff} .(b) mode gain $\left(cm^{-1}\right)$. (c) mode width (nm). (d) mode normalized Poynting vector magnitude distribution as the gap size $\left[h_g,w_g\right]=[10,260]nm$.

First the guided mode has cut-off width illustrated in Fig.4(a). As w_g is less than this width, the guided mode will not exist. Shown in Fig.4(a), when h_g is fixed to be $6nm$ or $10nm$, the guided mode effective index n_{eff} falls down with w_g narrowed. Until n_{eff} drops lower than 3.20 which is the lateral p-InP and n-InP refractive index, the guided mode disappears. As a matter of fact the cut-off width of w_g is about 200nm as $h_g=6nm$.

Second illustrated in Fig. 4(b), as the $h_g=2nm$ or $6nm$, the mode gain is less than zero although the MQW local gain is $2000cm^{-1}$. However, as $h_g=10nm$ and

$w_g > 240nm$, the mode gain is larger than zero, which is necessary for SPP TWA.

Third shown in Fig. 4(c), at $h_g = 6nm$ or $10nm$ mode width have a minimum with w_g variation, which originates from the following illustrations. The guide mode is the hybrid one from the interaction between the general dielectric waveguide and SPP one. As the SPP one is dominant, the mode width and mode gain decrease with w_g diminished. However, as the general dielectric waveguide is superior, the mode width will rise with w_g falling down. Therefore the minimums of the mode width and mode gain appear at the junction point of these two actions.

In the Fig. 4(d)it is the mode field as the gap size $\left[h_g, w_g\right]$ is $\left[10, 260\right]nm$. And in this condition that the SPP mode gain is 110cm^{-1} and mode width is 163nm which is deep sub-wavelength scale.

5. Conclusion

We propose a LCI MQW SPP TWA with deep-sub-wavelength mode confinement size. In this SPP TWA the InGaAlAs tensile MQW is designed for the polarization-independent amplification. Simulation suggests that at 1317nm wavelength the MQW gain is completely polarization independent. And at this wavelength the mode width is 163nm, the mode gain is $110cm^{-1}$ in the condition of 260nm$\times$10nm gap size and $5\times10^{24}/m^3$ injected electron concentration.

6. Acknowledgements

This work was supported by National Natural Science Foundation of China (Grant No.61605247) and the National University of Defense Technology Foundation (Grant No.ZK17-03-26).

References

[1] Zhang, X., et al., *Gain-assisted propagation of surface plasmon polaritons via electrically pumped quantum wells*. Opt. Lett., 2010. **35**(18): p. 3075-3077.

[2] Alam, M.Z., et al., *Gain assisted surface plasmon polariton in quantum wells structures*. Opt. Express, 2007. **15**(1): p. 176-182.

[3] Li, Y., et al., *Effect of dielectric cladding on active plasmonic device based on InGaAsP multiple quantum wells*. Opt. Express, 2014. **22**(21): p. 25599-25607.

[4] Li, Y., et al., *Short-range surface plasmon propagation supported by stimulated amplification using electrical injection*. Opt. Express, 2011. **19**(22): p. 22107-22112.

[5] Fedyanin, D.Y., et al., *Surface Plasmon Polariton Amplification upon Electrical Injection in Highly Integrated Plasmonic Circuits*. Nano Lett., 2012. **12**: p. 2459-2463.

[6] Costantini, D., et al., *A hybrid plasmonic semiconductor laser*. Appl. Phys. Lett, 2013. **102**(10): p. 101106.

[7] Kéna-Cohen, S.p., et al., *Confined Surface Plasmon−Polariton Amplifiers.* Nano. Lett., 2013. **13**: p. 1323-1329.

[8] Nielsen, M. and A.Y. Elezzabi, *An ultrafast nanoplasmonic InGaAs amplifier*. Journal of Optics, 2013. **15**: p. 075202.

[9] Wijesinghe, T., M. Premaratne, and G.P. Agrawal, *Electrically pumped hybrid plasmonic waveguide*. Opt. Express, 2014. **22**(3): p. 2681-2694.

[10] Svintsov, D.A., A.V. Arsenin, and D.Y. Fedyanin, *Full loss compensation in hybrid plasmonic waveguides under electrical pumping*. Opt.Express, 2015. **23**(15): p. 19358-19375.

[11] Hill, M.T., et al., *Lasing in metal-insulator-metal sub-wavelength plasmonic waveguides*. Opt. Express, 2009. **17**(13): p. 11107-11112.

[12] Minch, J., et al., *Theory and Experiment of In[1-x]Ga[x] As[y]P[1-y] and In[1-x-y]Ga[x] Al[y] As Long-Wavelength Strained Quantum-Well Lasers*. IEEE JOURNAL OF QUANTUM ELECTRONICS, 1999. **35**(5): p. 771-782.

[13] Yamaguchi, Y., et al., *Tensile strained MQW semiconductor optical amplifier*, in *International Conference on Indium Phosphide and Related Materials*. 1995: Sapporo, Jpn. p. 500-503.

[14] Newkirk, M.A., et al., *1.5 mu m multiquantum-well semiconductor optical amplifier with tensile and compressively strained wells for polarization-independent gain* IEEE Photonics Technology Letters 1993. **5**(4): p. 406-408.

[15] Magari, K., et al., *Polarization-insensitive optical amplifier with tensile-strained-barrier MQW structure*. IEEE Journal of Quantum Electronics, 1994. **30**(3): p. 695-702.

[16] Godefroy, A., et al., *1.55-μm polarization-insensitive optical amplifier with strain-balanced superlattice active layer* IEEE Photonics Technology Letters 1995. **7**(5): p. 473 - 475.

[17] Bae, S.J., S.H. Park, and Y.T. Lee, *Design of polarization independent InGaAs/InGaAlAs coupled quantum well structure in 1.55 um wavelength region*. Optical and Quantum Electronics, 2003. **35**: p. 967-977.

[18] Selmic, S.R., et al., *Design and Characterization of 1.3um AlGaInAs–InP Multiple-Quantum-Well Lasers*. IEEE JOURNAL ON SELECTED TOPICS IN QUANTUM ELECTRONICS, 2001. **7**(2): p. 340-348.

[19] Chang, C.-S. and S.L. Chuang, *Modeling of strained quantum-well lasers with spin-orbit coupling* IEEE Journal of Selected Topics in Quantum Electronics, 1995. **1**(2): p. 218 - 229.

[20] Palik, E.D., *Handbook of Optical Constants of Solids*. 1985, Orlando San Diego NewYork: Academic Press Inc.

[21] Yariv, A., *Photonics: Optical Electronics in Modern Communications (Sixth Edition)*. 2007, London: Oxford University Press, Inc.

Scattering by Core-Shell Semiconductor Microinclusions for Plasmonically Enhanced Near-IR Applications

Fahime Seyedheydari[1], **Kevin Conley**[1], **Tapio Ala-Nissila**[1,2]

[1]Department of Applied Physics and QTF Center of Excellence, Aalto University, P.O. Box 13500, FI-00076, Aalto, Finland
[2]Interdisciplinary Centre for Mathematical Modelling, Department of Mathematical Sciences, Loughborough University, Loughborough, Leicestershire LE11 3TU, United Kingdom
*corresponding author, E-mail: Kevin.conley@aalto.fi

Abstract

We computationally design highly reflective, plasmonically enhanced coatings for more sensitive and versatile radiation detectors in the infrared regime. The large scattering cross-sections of microinclusions are exploited to design devices and spectrally sensitive coatings for sensors, high temperature insulators, and solar applications. We focus on core-shell microinclusions composed of silver or low-bandgap semiconductor which have plasmonic resonances with excellent and tunable scattering properties without suffering from losses at high temperatures. These particles display a rich spectral response dependent on the complex refractive index of the particles.

1. Introduction

Fires and explosions are a threat to life, property, and environment. About one-third of the thermal energy in fires is released as thermal radiation, i.e. electromagnetic radiation in the IR range [1]. Technologies based on gradient heat flux sensors allow small , non-intrusive detectors to directly and instantaneously measure the heat flux [2], unlike in detectors which measure the consequences of fire (heat convection or smoke). To distinguish between radiation from fire and other heat sources, it is necessary to extract spectral information from the detectors. A promising approach is to coat the sensors with a spectrally-sensitive film embedded with semiconductor microinclusions. The embedded particles reflect unwanted wavelengths using localized surface plasmons allowing the gradient heat flux sensors to distinguish between emission sources. Indeed, the enhanced scattering by the plasmonic resonances in low-bandgap semiconductor microinclusions can maximize reflectance of the incident infrared radiation even at small volume fractions in an insulating dielectric [3]. These properties can be exploited for preventing radiative thermal losses in high temperature applications. The localized surface plasmon resonances of the spherical semiconductors have been shown to reflect up to 90% of the incident light at specific wavelengths [4]. These applications will lead to improved work safety, reduced fire-induced losses, and better incident management capabilities. In addition to improving sensor technologies for fire safety, these microcomposite bandpass filters can be used as high temperature insulators and solar applications and can provide new understanding of radiation transport through films.

In general, the scattered field is a superposition of normal modes, each weighted by the appropriate coefficient a_n or b_n. The plasmon frequency and scattering efficiency of semiconductors are highly tunable by adjusting the size, geometry, and dielectric environment [3]. The plasmon resonance frequencies of doped semiconductors can be modified by changing the material's electronic structure, and is another method of controlling the resonances [5]. In core-shell particles, the interaction between the sphere and cavity yields a splitting of the plasmon resonance into a symmetric or bonding and an antisymmetric or antibonding plasmon which is controlled by the thickness of the shell layer [6].

In this paper, we solve the dielectric response of small particles in an external electromagnetic field using Mie theory and polarizability equations. In the following, we study the resonances in multilayered spherical microparticles. First we consider core-shell particles with Si as the core material which is coated with TiO_2, SiO_2, or ZrO_2. Next we focus on hollow Ag particles which can be treated with the Drude theory.

2. Methods

We consider the problem of scattering by a homogeneous sphere coated with a homogeneous layer of uniform thickness. This is one of the simplest examples of a particle with a spatially variable refractive index. We solve the dielectric response of an electromagnetic wave incident on a coated sphere with inner radius, r, and outer radius, R, as shown in Figure 1. Solving Maxwell's equations yields the electric and magnetic Mie coefficients a_n and b_n, respectively, which contain the Riccati-Bessel functions in spherical coordinates. If the permeability of the particle and the surrounding medium is considered to be the same, then the coefficients for a multilayered sphere are given by

$$a_n = \frac{\psi_n(y)\left[\psi\prime_n(m_2y) - A_n\chi\prime_n(m_2y)\right] - m_2\psi\prime_n(y)\left[\psi_n(m_2y) - A_n\chi_n(m_2y)\right]}{\xi_n(y)\left[\psi\prime_n(m_2y) - A_n\chi\prime_n(m_2y)\right] - m_2\xi\prime_n(y)\left[\psi_n(m_2y) - A_n\chi_n(m_2y)\right]}, \tag{1}$$

$$b_n = \frac{m_2\psi_n(y)\left[\psi\prime_n(m_2y) - B_n\chi\prime_n(m_2y)\right] - \psi\prime_n(y)\left[\psi_n(m_2y) - B_n\chi_n(m_2y)\right]}{m_2\xi_n(y)\left[\psi\prime_n(m_2y) - B_n\chi\prime_n(m_2y)\right] - \xi\prime_n(y)\left[\psi_n(m_2y) - B_n\chi_n(m_2y)\right]}, \quad (2)$$

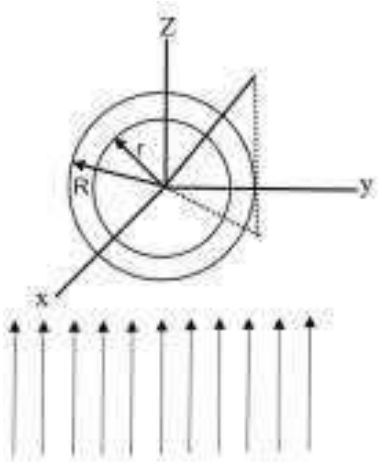


Figure 1: Coated sphere model adapted from Bohren and Huffman [7].

where

$$A_n = \frac{m_2\psi_n(m_2x)\psi\prime_n(m_1x) - m_1\psi\prime_n(m_2x)\psi_n(m_1x)}{m_2\chi_n(m_2x)\psi\prime_n(m_1x) - m_1\chi\prime_n(m_2x)\psi_n(m_1x)},$$

and

$$B_n = \frac{m_2\psi_n(m_1x)\psi\prime_n(m_2x) - m_1\psi_n(m_2x)\psi\prime_n(m_1x)}{m_2\chi\prime_n(m_2x)\psi_n(m_1x) - m_1\psi\prime_n(m_1x)\chi_n(m_2x)},$$

and $\psi_n(x)$ and $\xi_n(x)$ are Riccati-Bessel functions [7]. The size parameters are given by $x = kr$ and $y = kR$. The relative refractive indices, m_1 and m_2, are the refractive indices of the core and coating relative to the surrounding medium. The order of the resonance is represented by n, where the dipole is $n = 1$, the quadrupole is $n = 2$, the octupole $n = 3$, and so on [3]. The efficiency of scattering can be calculated as

$$Q_{\text{sca}} = \frac{2}{y^2}\sum_{n=1}^{N}(2n+1)(|a_n|^2 + |b_n|^2). \quad (3)$$

The spherical particles are surrounded by a non-absorbing insulating medium with constant refractive index of 1.5 and irradiated by Near Infrared (NIR) light, λ = 1 to 5 μm. Si has a bandgap of 1.11 eV (λ = 1.11 μm) and the oxide refractive indices vary from approximately 1.4 to 2.4. The bulk complex indices of refraction were obtained from Palik [8]. The bulk refractive indices of birefringent TiO_2 are averaged over the ordinary and the extraordinary directions. To represent IR grade fused silica, the extinction coefficient of silica is assumed to be zero below 3.5 μm. The extinction coefficient of ZrO_2 was assumed to be zero and the refractive index restricted to wavelengths less than 5.1 μm [9].

3. Results

Consider now a core-shell spherical particle with Si as the core material of $r = 0.6\mu$m and an oxide shell with thickness, t, varying from $t = 0$ to 0.5μm, in a host medium of refractive index $n_m = 1.5$. Figure 2 presents the scattering efficiency for these particles such that the blue lines are the maximum of the scattering efficiency and y axis shows the variable oxide shell thickness. According to Mie theory for gold nanoparticles [10] the average particle size is proportional to the displacement of the scattering wavelength peak. Figures 2.a) and 2.b) show red-shifting of Si−TiO_2 and Si−ZrO_2 with increasing size of the particles. Compared to Si−TiO_2 and Si−ZrO_2 it is observed that there is no red-shifting for Si−SiO_2 . This sequence illustrates the affect of a different shell material on the scattering efficiency. In the SiO_2 coated particles, the relative refractive index, m_2, is approximately ~ 1. When $m_2 = 1$, the Mie coefficients reduce to those for a sphere of radius r and relative refractive index m_1 [7]. Thus there is no shifting in the SiO_2 coated particles. For TiO_2 and ZrO_2 $m_2 > 1$ and the resonances redshift with increasing shell thickness. These different patterns show the role of the refractive index of the shell (m_2). For photon energies which are large compared with the band gap in semiconductors, electronic transitions are only slightly perturbed by the presence of the gap; the valence electrons in this instance act like free electrons. Thus, the high-energy optical properties of semiconductors are similar to those of free-electron metals. But there are marked differences in their low-energy optical properties [7]. In the following, we mostly focus on metals, especially for silver. Relatively small energies are required to excite electrons in metals, and metals tend to be highly absorbing and reflecting at visible and infrared wavelengths. The optical response of a collection of free electrons can be obtained from the Lorentz harmonic oscillator model.

Figure 3 shows the scattering efficiency of an air-silver particle with a total particle size of $R = 20$ nm and hollow core with an inner radius $r = 16$ nm. Additionally, it shows the absolute value of the first three Mie coefficients a_1, a_2 and b_1. The position of Mie coefficients on the scattering efficiency of a composite sphere indicated by vertical arrows.

3.1. Surface Modes in Small Spheres

3.1.1. The Lorentz-Drude Model

Silver and gold are commonly used metals for plasmonic experiments in visible and near-infrared experiments [11]. Here the dielectric function of silver is described well by the Drude theory. The dielectric function for a electron-

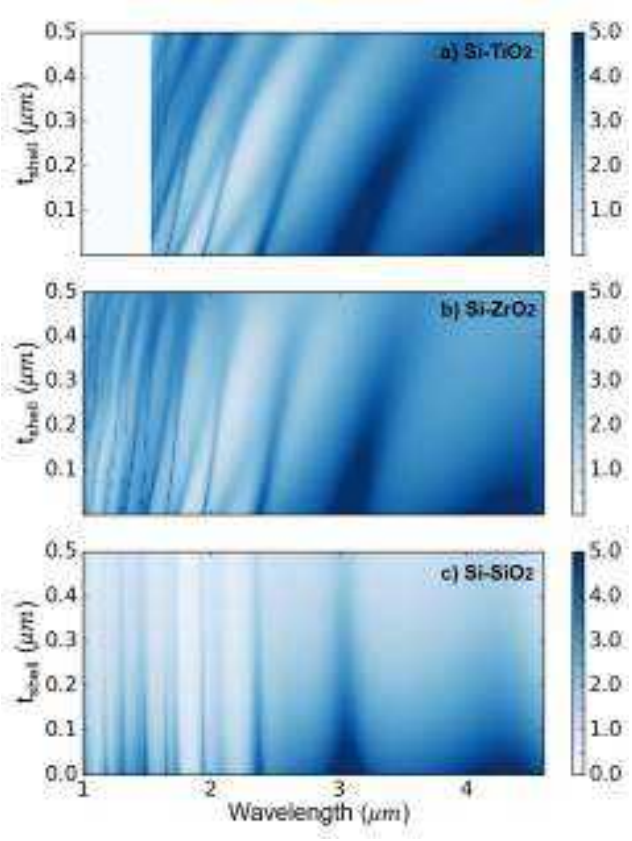


Figure 2: Q_{sca} of core-shell semiconductor particles a) Si−TiO_2 , b) Si−ZrO_2 and c) Si−SiO_2 . All particles are embedded in a medium with a refractive of 1.5 and $r = 0.6$ micron.

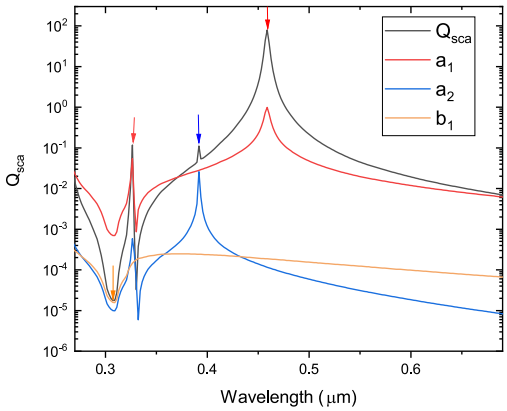


Figure 3: The scattering efficiency (black line) and additionally a_1 (red), a_2 (blue), and b_1 (orange) illustrate the first three Mie coefficients as function of the wavelength which the Mie coefficients are confined between $[0, 1]$, in logarithmic scale.

spring system can be treated as simple harmonic oscillator in the approach known as the Lorentz Model. Therefore, the dielectric function for the system of simple harmonic oscillators is

$$\varepsilon = 1 + \frac{\omega_{\text{p}}^2}{\omega_0^2 - \omega^2 - i\omega\gamma}. \tag{4}$$

For frequencies much less than the resonance frequency, the real and imaginary parts are given by

$$\varepsilon' \simeq 1 + \frac{\omega_{\text{p}}^2}{\omega_0^2};$$
$$\varepsilon'' \simeq \frac{\gamma\omega_{\text{p}}^2\omega}{\omega_0^4}.$$

The optical response of a collection of free electrons can be obtained from the Lorentz harmonic oscillator model, the dielectric function for free electrons follows from (4) with $\omega_0 = 0$. For metal with low interband absorption, the dielectric function can be described by the Drude model,

$$\varepsilon = 1 - \frac{\omega_{\text{p}}^2}{\omega^2 + i\omega\gamma} \tag{5}$$

where ω_{p} is bulk plasmon frequency [7].

3.1.2. Polarizability

In the electrostatics approximation the scattering and extinction efficiency of a small sphere is given by

$$Q_{\text{sca}} = \frac{8}{3}x^4\left|\frac{\varepsilon_1 - \varepsilon_m}{\varepsilon_1 + 2\varepsilon_m}\right|^2. \tag{6}$$

$$Q_{\text{ext}} = 4x\,\text{Im}\left|\frac{\varepsilon_1 - \varepsilon_m}{\varepsilon_1 + 2\varepsilon_m}\right|^2. \tag{7}$$

where ε_1 and ε_m are the permittivity of the sphere and the surrounding medium, respectively. In addition the polarizability of a small sphere in a uniform field (electrostatic approximation) is

$$\alpha = V\frac{(\varepsilon_1 - \varepsilon_m)}{(\varepsilon_1 + 2\varepsilon_m)}, \tag{8}$$

where V is particle volume [7].

The term $(\varepsilon_1 - \varepsilon_m)/(\varepsilon_1 + 2\varepsilon_m)$ that can be seen in equations (6) and (8), illustrates a connection between electrostatics and scattering by particles small compared with the wavelength. By minimizing the denominator of equation (8), the Fröhlich condition is satisfied, which for the case of small Im$[\varepsilon]$ around the resonance simplifies to

$$\text{Re}[\varepsilon(\omega)] = -2\varepsilon_m. \tag{9}$$

At $\varepsilon(\omega) = -2\varepsilon_m$ the polarizability will become very large, which is known as the surface plasmon resonance. Inserting equation (5) into equation (8) in free space leads to

$$\alpha = V\frac{\omega_P^2}{\omega_P^2 - 3\omega^2 - i\omega\gamma}. \tag{10}$$

The polarizability can be compared with the earlier calculation of the Mie coefficients. Figure 4 shows an agreement in the wavelength of the polarizability and a_1 maxima of a core-shell sphere at λ= 0.326 μm. We will examine the nature of the second a_1 peak below.

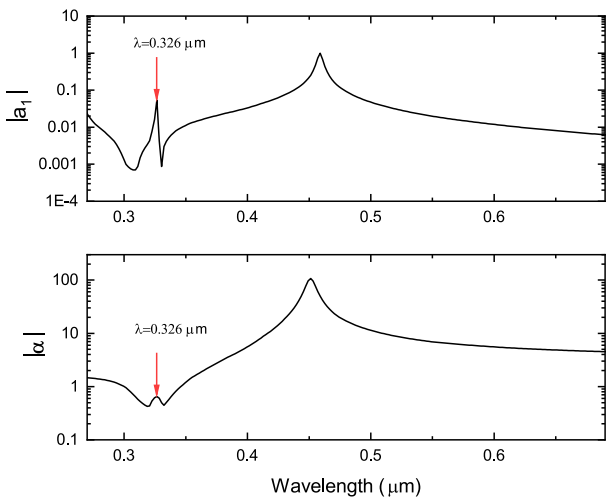


Figure 4: Similarities in positions of their resonant modes from Mie coefficient a_1 and the polarizability for a air-silver core-shell particle (in logarithmic scale) indicated by vertical red arrow-marks. The particle size is the same as in Figure 3.

3.2. Expansion

By expanding the Mie coefficients a_n and b_n as a power series and retain only the first few terms we have [7],

$$a_1 = -\frac{i2x^3}{3}\frac{\varepsilon-\varepsilon_m}{\varepsilon+2\varepsilon_m} - \frac{i2x^5}{5}\frac{(\varepsilon-2\varepsilon_m)(\varepsilon-\varepsilon_m)}{(\varepsilon+2\varepsilon_m)^2} + O(x^6); \tag{11}$$

$$b_1 = -\frac{ix^5}{45}(\varepsilon-\varepsilon_m) + O(x^7); \tag{12}$$

$$a_2 = -\frac{ix^5}{15}\frac{\varepsilon-\varepsilon_m}{2\varepsilon+3\varepsilon_m} + O(x^7). \tag{13}$$

The lowest term of equation (11) is directly proportional to the polarizability in equation (8) implying that the electric Mie coefficients contains the same polarization enhancing character as the electrostatic polarizability [12].

3.3. Core-Shell polarizability

Polarizability of the nanovoid can be obtained by the substitutions $\varepsilon_1 \to \varepsilon_m$ and $\varepsilon_m \to \varepsilon_1$ in equation (8),

$$\alpha = V\frac{(\varepsilon_m-\varepsilon_1)}{(\varepsilon_m+2\varepsilon_1)}, \tag{14}$$

then the dipole moment of the void can be obtained. The Fröhlich condition now takes the form [13],

$$\mathrm{Re}[\varepsilon(\omega)] = -\frac{1}{2}\varepsilon_m. \tag{15}$$

Because of the wide tunability of the plasmon resonance in core-shell particles with metallic shell, we want to focus on the polarizability of a coated sphere. The polarizability of a homogeneous core sphere (ε_1) coated with a shell (ε_2) is given by

$$\alpha = V\frac{(\varepsilon_2-\varepsilon_m)(\varepsilon_1+2\varepsilon_2)+f(\varepsilon_1-\varepsilon_2)(\varepsilon_m+2\varepsilon_2)}{(\varepsilon_2+2\varepsilon_m)(\varepsilon_1+2\varepsilon_2)+f(2\varepsilon_2-2\varepsilon_m)(\varepsilon_1-\varepsilon_2)}, \tag{16}$$

where f is the fraction of the total particle volume occupied by the core. The condition for excitation of the first order surface mode or the Fröhlich mode can be obtained by minimizing the denominator of equation (16),

$$(\varepsilon_2+2\varepsilon_m)(\varepsilon_1+2\varepsilon_2)+f(2\varepsilon_2-2\varepsilon_m)(\varepsilon_1-\varepsilon_2) = 0. \tag{17}$$

By considering a hollow sphere in air ($\varepsilon_m = 1$) we can find the resonance condition as

$$(\varepsilon+2)(1+2\varepsilon)+f(2\varepsilon-2)(1-\varepsilon) = 0, \tag{18}$$

where ε is the dielectric function of the shell. The roots of equation (18) are given by

$$\varepsilon_\pm = \frac{-(5+4f)\pm 3\sqrt{1+8f}}{4-4f}. \tag{19}$$

These roots are known as the symmetric (ε_-) and antisymmetric (ε_+) modes [7]. Figure 5 illustrates the absolute value of the polarizability for two different sizes of the core for a core-shell air-silver system. The symmetric mode has a red shift with increasing hollow core. The antibonding resonance is weaker and narrower than the bonding one [12]. There is a minimum at $\varepsilon = -1/2$ which is indicated by a dashed line that according equation (15) comes from the Fröhlich mode and is independent of the core size.

3.4. Void Plasmons and Hybridization Model

The polarizability of a particle consisting of a dielectric core (air) and a thin metallic shell (silver) can be described using the quasistatic Mie equation (16). These two fundamental dipolar modes of a core-shell nanoparticle can be explained by the hybridization of the dipolar modes of a metallic sphere and a dielectric void. In other words, two hybridized plasmon modes are the result of the interaction of the plasmons of a nanoparticle on the inner (metallic sphere) and outer (dielectric void) surfaces. The frequencies of these modes are given by

$$\omega^2_{l,\pm} = \frac{\omega_p^2}{2}\left[1 \pm \frac{1}{2l+1}\sqrt{1+4l(l+1)\left(\frac{r}{R}\right)^{2l+1}}\right], \tag{20}$$

where r and R are the inner and outer radius of the shell, respectively. The $|\omega_+\rangle$ and $|\omega_-\rangle$ modes correspond to the antisymmetric and symmetric modes, respectively [6].

4. Conclusions

We have simulated the scattering from surface coatings embedded with spherical microparticles using Mie theory. By adjusting the material, the size of the core or the shell, and

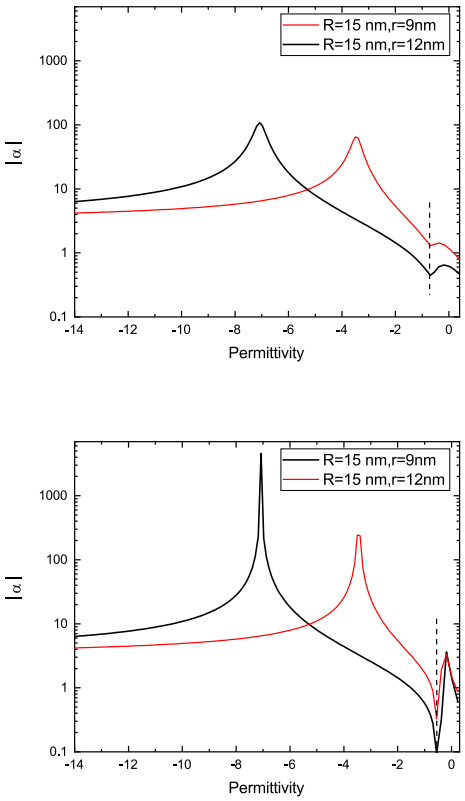


Figure 5: The absolute value of the polarizability in terms of permittivity for two different core sizes. The upper part of the figure shows the result for lossy material, ($\varepsilon_{\mathrm{i}} = \varepsilon_{\mathrm{i}}^{'} + i\varepsilon_{\mathrm{i}}^{''}$) and the lower part for lossless material ($\varepsilon_{\mathrm{i}}^{''} = 0$) in logarithmic scale.

refractive index of medium, the energy of the surface plasmon resonances can be tuned to match the incident spectrum.

In the scattering efficiency equation of a metallic nanoparticle in the quasi-static approximation, there is a polarizability term. Indeed for metal nanoparticles both absorption and scattering are resonantly enhanced at the dipole particle plasmon resonance. Further, it can be seen by expanding the Mie coefficients for a bare sphere the polarizability term exists in lowest term of a_1.

The hybridization model explains the polarizability of a dielectric void and a thin metallic shell which defines two dipolar modes of this system. We have been shown with increasing size of core symmetric mode has blue shift.

Acknowledgement

This work was performed as part of the Academy of Finland project 314488 and QTF Centre of Excellence program (project 312298). We acknowledge computational resources provided by CSC IT Center for Science (Finland) and by the Aalto Science-IT project (Aalto University School of Science).

References

[1] G. Association *et al.*, "World fire statistics bulletin no. 29," *The Geneva Association, Geneva*, 2014.

[2] A. V. Mityakov, S. Z. Sapozhnikov, V. Y. Mityakov, A. A. Snarskii, M. I. Zhenirovsky, and J. J. Pyrhönen, "Gradient heat flux sensors for high temperature environments," *Sens. Actuator A-Phys.*, vol. 176, pp. 1–9, 2012.

[3] J. Tang, V. Thakore, and T. Ala-Nissilä, "Plasmonically enhanced reflectance of heat radiation from low-bandgap semiconductor microinclusions," *Sci Rep.*, vol. 7, p. 5696, 2017.

[4] K. Conley, V. Thakore, and T. Ala-Nissila, "Plasmonically enhanced spectrally-sensitive coatings for gradient heat flux sensors," in *2018 Progress in Electromagnetics Research Symposium (PIERS-Toyama)*. IEEE, 2018, pp. 2435–2441.

[5] R. J. Mendelsberg, G. Garcia, H. Li, L. Manna, and D. J. Milliron, "Understanding the plasmon resonance in ensembles of degenerately doped semiconductor nanocrystals," *The Journal of Physical Chemistry C*, vol. 116, no. 22, pp. 12 226–12 231, 2012.

[6] E. Prodan, C. Radloff, N. J. Halas, and P. Nordlander, "A hybridization model for the plasmon response of complex nanostructures," *Science*, vol. 302, no. 5644, pp. 419–422, 2003.

[7] C. F. Bohren and D. R. Huffman, *Absorption and scattering of light by small particles*. John Wiley & Sons, 2008.

[8] E. D. Palik, *Handbook of optical constants of solids*. Academic press, 1998, vol. 3.

[9] D. L. Wood and K. Nassau, "Refractive index of cubic zirconia stabilized with yttria," *Appl. Opt.*, vol. 21, no. 16, pp. 2978–2981, 1982.

[10] G. Mie, "Contributions to the optics of turbid media, particularly of colloidal metal solutions," *Contributions to the optics of turbid media, particularly of colloidal metal solutions Transl. into ENGLISH from Ann. Phys.(Leipzig), v. 25, no. 3, 1908 p 377-445*, 1976.

[11] J. M. McMahon, G. C. Schatz, and S. K. Gray, "Plasmonics in the ultraviolet with the poor metals al, ga, in, sn, tl, pb, and bi," *Physical Chemistry Chemical Physics*, vol. 15, no. 15, pp. 5415–5423, 2013.

[12] A. Sihvola, D. C. Tzarouchis, P. Ylä-Oijala, and H. Wallén, "Properties of hybridized modes in core–shell scatterers," in *2018 2nd URSI Atlantic Radio Science Meeting (AT-RASC)*. IEEE, 2018, pp. 1–3.

[13] S. A. Maier, *Plasmonics: fundamentals and applications*. Springer Science & Business Media, 2007.

Gain Mediated Surface Plasmon Polariton Propagation in the Near-Infrared

Preksha Tiwari*[1], Svenja Mauthe[1], Noelia Vico Triviño[1], Markus Scherrer[1], Chang-Won Lee[2], and Kirsten Moselund[1]

[1]Science and Technology Department, IBM Research Zurich, Rüschlikon, Switzerland
[2]Institute of Advanced Optics and Photonics, Hanbat National University, Daejeon, South Korea
*corresponding author, E-mail: tiw@ibm.zurich.com

Abstract

We demonstrate gain mediated propagation of hybrid plasmonic-photonic modes in near-infrared at temperatures ranging from 95 K to 300 K. Hybrid modes are formed in an oxide layer sandwiched by a gold film and an InP substrate. Optical pumping at 750 nm results in photoluminescence from InP which couples to surface plasmon polaritons. In contrast to the photoluminescence efficiency, the propagation losses are only weakly temperature dependent. We attribute this weak dependence predominantly to scattering caused by the gold film's polycrystallinity.

1. Introduction

To leverage the interconnect bottleneck, the realization of directly integrated III-V infrared nanolasers is crucial, since it would enable high-speed optical on-chip communication [1, 2]. Hybrid plasmonic-photonic structures would offer a suitable solution to shrink optical components to dimensions closer to that of integrated electronic devices. Hybrid modes achieve longer propagation lengths compared to pure plasmonic modes, while allowing sub-diffraction confinement compared to pure dielectric modes [3]. Here we demonstrate the propagation of such hybrid plasmonic modes via the near-infrared (NIR) luminescence of optically pumped InP at different temperatures.

2. Results and Discussions

Figure 1 shows the layer stack of the waveguide. The oxide layer is deposited on indium phosphide (InP) via atomic layer deposition. Aluminum oxide (Al_2O_3) is chosen since it ensures a good interface at the substrate. A 1 nm thick germanium (Ge) adhesion layer and 100 nm gold (Au) are deposited by successive e-beam evaporation. Various shapes of plasmonic structures are fabricated by electron-beam lithography using HSQ as resist and patterns are transferred into the gold by argon-ion milling. The excitation of the hybrid modes and the imaging of the outcoupled light are performed by a 100× objective with a numerical aperture of 0.6. A laser beam at 750 nm is focused on one edge of a gold pattern to generate photoluminescence (PL) from the InP. The scattered light collected by the same objective is imaged by a camera after passing an analyzer and a long-pass filter with cutoff wavelength at 800 nm, to ensure that only the PL and the transversal magnetic polarized light is imaged. As illustrated in Figure 1 we expect a co-propagation of the pump- and emission wavelengths along the metal-dielectric interface. Here we investigate different geometries for hybrid plasmon propagation such as straight waveguides and slabs with slits for exciting the PL and staircased out coupling slots. Scanning electron micrographs (SEM) of those structures are shown in Figure 2. Figure 3 shows images of a 13 µm long waveguide where experiments were performed at temperatures ranging from 95 K to 300 K. The PL intensity decreases with increasing length, as expected. The brightness of the images is enhanced for better visibility. Figure 4 depicts typical images for different waveguide lengths. To evaluate the propagation loss, we normalize the outcoupled PL intensity to the value of the shortest waveguide at the given temperatures (see Figure 5). This normalization gives the possibility to correct for variations in emission efficiency as well as initial coupling loss to the waveguide. Interestingly, the plasmonic losses are only weakly temperature dependent. A possible explanation could be that the propagation in our films is mainly limited by the roughness and polycrystallinity rather than temperature-dependent electrical properties of our films, such as electron-electron or electron-phonon scattering [4]. Indeed, the atomic force microscope (AFM) image in Figure 6 shows that the film is smooth (surface roughness: 0.7 nm RMS) but grainy. The propagation loss coefficient α lies between 0.18 μm^{-1} (at 95 K) and 0.33 μm^{-1} (at 300 K) and is obtained by an exponential fit as shown in Figure 5. This value is much lower than the coefficient obtained from finite difference time domain simulations, where we obtain $\alpha = 1.9\ \mu m^{-1}$ for a mode propagating at 900 nm. This may indicate that the propagation losses are counterbalanced by the PL gain provided by the continuous optical pumping of the InP with a pulsed laser source and the resulting co-propagation of the pump light. Figure 7 summarizes the results shown in Figure 4 and 5: The incoupling and outcoupled PL intensity for different temperatures for a 13 µm long waveguide are compared. Since the incoupled PL is oversaturated in the camera, the oversaturation width in pixels is studied at the dashed blue line in the inset image. The outcoupled intensities are extracted by intensity integration in the region marked by the dashed orange rectangular in the inset image and corrected by background subtraction. The PL intensity from

the InP shows a decreasing trend with increasing temperature. This trend cannot be seen for the propagation losses, in the case where the PL intensity is normalized with the intensity of the shortest waveguide.

3. Conclusion

We showed PL mediated plasmon propagation on different Au structures on InP with a thin oxide layer sandwiched in between and investigated the temperature dependence of the propagation. While the PL emission is strongly temperature dependent, the losses in the plasmonic waveguides are dominated by scattering at grain boundaries of the Au film.

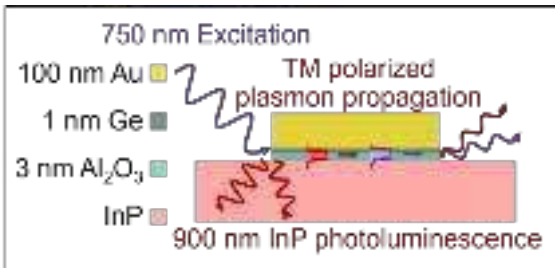


Figure 1: Layer stack of the studied waveguide. The InP wafer serves as a gain material, with a PL peak ranging from 880 to 905 nm, depending on the temperature. The gold film enables the presence of plasmons. The laser excites the InP which results in PL emission. Both the laser and the PL light can couple to plasmon modes.

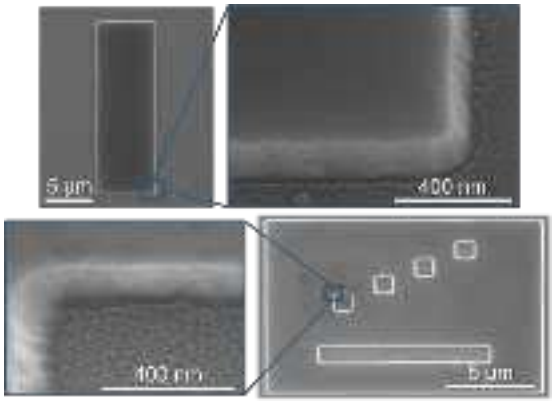


Figure 2: SEM images of the studied waveguides. The structures are formed via Argon ion milling after being written and developed in HSQ using electron beam lithography.

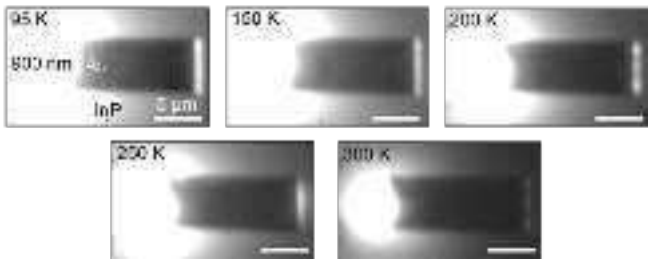


Figure 3: PL of incoupled and outcoupled light (contrast enhanced for visibility) for a 13 µm long waveguide at temperatures ranging from 95 K to 300 K. The PL intensity decreases with increasing temperature.

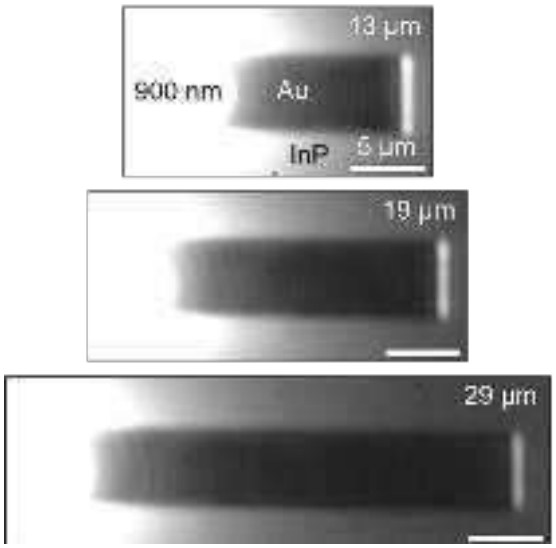


Figure 4: PL of incoupled and outcoupled light (contrast enhanced for visibility) for a 13 µm, 19 µm and 29 µm long waveguides at 95 K. The PL intensity decreases with increasing length.

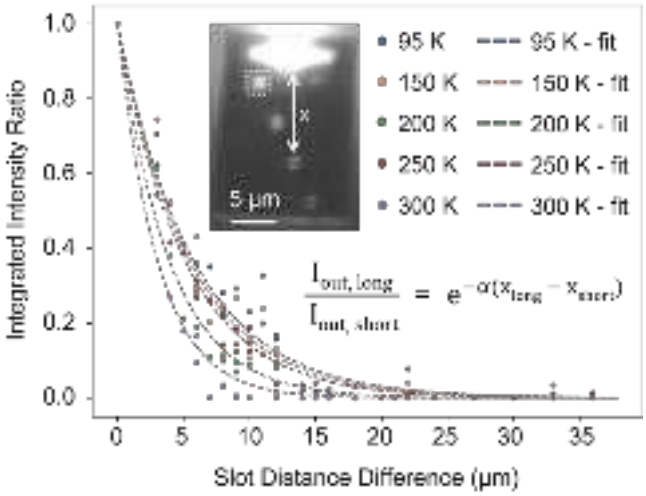


Figure 5: Outcoupled PL intensity for waveguides with different lengths, normalized to the outcoupled intensity of the shortest waveguide. This normalization is done to account for the impact of the stronger PL at lower temperatures. The propagation losses show only a weak temperature dependence. Propagation loss coefficients lie between 0.18 μm^{-1} (at 95 K) and 0.33 μm^{-1} (at 300 K) and are extracted by an exponential fit using the inset formula.

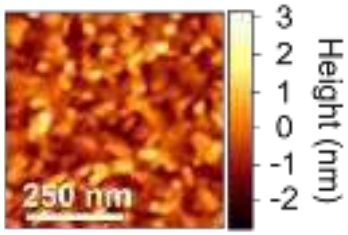


Figure 6: AFM image of the Au surface. The surface roughness is 0.7 nm RMS and the film is granular and polycrystalline.

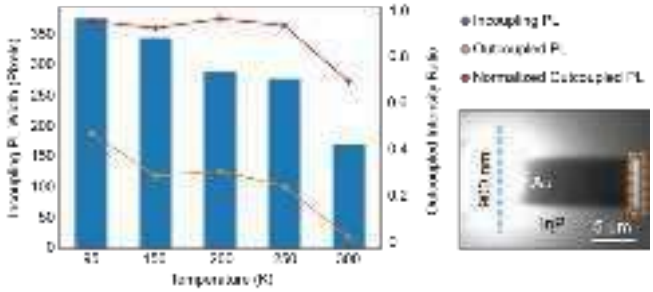


Figure 7: Width of the intensity oversaturation of incoupling PL in pixels (blue, extracted at the profile of the blue dashed line) and outcoupled intensity (orange, extracted by intensity integration in the region of the dashed orange rectangular and corrected by background subtraction) for a 13 µm long waveguide at different temperatures. The incoupled PL intensity and thus the outcoupled intensity too, show a decreasing trend with increasing temperature. Once the outcoupled PL intensity is normalized with respect to the shortest waveguide (red), there is only a weak temperature dependence for the propagation loss at transition to 300 K.

Acknowledgements

We received financial support from H2020 ERC StG PLASMIC, Grant #678567 and from NRF grant funded by the Korea MSIT (No. 2017R1A2B4007219). We acknowledge the BRNC staff, Antonis Olziersky, Philipp Staudinger, and Andreas Schenk for technical discussions and assistance.

References

[1] M.P. Nezhad, A. Simic, O. Bondarenko, B. Slutsky, A. Mizrahi, L. Feng, V. Lomakin, Y. Fainman, Room-temperature subwavelength metallo-dielectric lasers, *Nature Photonics* 4: pp. 395 – 399, 2010.

[2] E. Ozbay, Plasmonics: Merging Photonics and Electronics at Nanoscale Dimensions, *Science* 311: pp. 189 – 193, 2006.

[3] R.F. Oulton, V.J. Sorger, D.A. Genov, D.F.P Pile, X. Zhang, A hybrid plasmonic waveguide for subwavelength confinement and long-range propagation, Nature Photonics, 2: pp. 496 – 500, 2008.

[4] S.V. Jayanti, J.H. Park, A. Dejneka, D. Chvostova, K.M. McPeak, X. Chen, S.-H. Oh, D.J. Norris, Low-temperature enhancement of plasmonic performance in silver films, *Optical Materials Express* 5, pp. 1147 – 1155, 2015.

Ultimate Material Selection Methodology for Ultra-Broadband M-I-M Metamaterial Absorber

Imre Ozbay

Department of Electrical and Electronics Engineering, Middle East Technical University, Ankara Turkey 06810
Corresponding authors: ozbayimre@gmail.com

Abstract

We demonstrate an ultra-broadband metal-insulator-metal (MIM) metamaterial absorber of unrivaled bandwidth within the near-infrared (NIR) regime.

For any metal with a given n-k data, the maximum attainable absorption bandwidth for a MIM cavity is investigated. An ideal metal in such structures should have positive real permittivity part in the NIR regime. Through our novel analysis methodology based on transfer matrix method (TMM), we reveal and exploit the extraordinary optical response of Bismuth (Bi) metal. Contrary to noble and lossy metals utilized by most research groups within the field, this requirement is satisfied only by Bismuth, whose data greatly adheres to the ideal material properties predicted by our analysis. A Bi nano disc MIM resonator with an absorption above 0.9 in an ultra-broadband range of 800 nm- 2410 nm is designed, fabricated, and characterized. To the best of our knowledge, this is the broadest absorption bandwidth (BW) reported for a MIM cavity in the near infrared with its upper to lower absorption edge ratio of more than three.

Photogenerated Excitons of Cesium Lead Bromide Perovskite Quantum dots through ligand Passivation

Sunjoong Park, Hyunjin Cho, Wonseok Choi, Hongjoo Shin and Duk Young Jeon

Dept. of Materials Science and Engineering, Korea Advanced Institute of Science and Technology, 291 Daehak-ro, Yuseong-gu, Daejeon 305–338, Korea

Abstract

We investigated the mechanism of exciton decay dynamics of cesium lead bromide ($CsPbBr_3$) perovskite quantum dots (QDs) through the X-type ligand passivation process. 1-Dodecanethiol (DDT) ligand passivates the Br vacancy of $CsPbBr_3$ QDs and photoluminescence quantum yield (PLQY) is increased from 76.7 % to 99.76 %. To clarify this phenomenon, we observed exciton decay dynamics by varying the temperature (80k ~ 300k). Our results suggest that Br vacancy of $CsPbBr_3$ QDs affects the increased exciton lifetime;

Rapid and Highly efficient annealing process for photoluminescence efficiency improvement of quantum dots using intence pulse light

Chulhee Lee, Taeyoung Song, and Duk Young Jeon

Korea Advanced Institute of Science and Technology, Korea

Abstract

Typical quantum dots (QDs) have surface trap sites causing low photoluminescence efficiency. To solve this issue, we have introduced the intense pulse light (IPL) annealing that almost instantaneously supplies heat within very short time and brings enough energy to QDs. The IPL annealing technique is possible to remove the defect by applying optimum amount of heat to QDs using very short pulse, and we have observed considerable improvement from 20% to 40% of quantum efficiency of the QDs.

Tunable Infrared Energy Transfer through Surface Phonon Polaritons

Mohsen Janipour[1]*, Matthias Hensen[2], and Walter Pfeiffer[1]*

[1] Fakultät für Physik, Universität Bielefeld, Universitätsstr. 25, Bielefeld 33615, Germany
[2] Physikalische Chemie, Universität Würzburg, Am Hubland, Würzburg, Germany

*corresponding author, E-mail: mjanipour@physik.uni-bielefeld.de;
pfeiffer@physik.uni-bielefeld.de

Abstract

Realizing and designing switchable cavities in order to establish effective communication between two large distance separated points at the infrared frequencies is crucial for achieving novel integrated photonic circuits. In the infrared and terahertz regime, polar dielectrics can support propagation of surface phonon polaritons with the ability of tuning through carrier concentration. In this context, we investigate a tunable heterojunction elliptical cavity for efficient energy transfer through coupled surface phonon-plasmon polariton modes.

Quantum and topological photonics

Unidirectional edge states in two dimensional plasmonic arrays

Matthew Proctor[1,2,*], Stefan A. Maier[1], Richard V. Craster[2], Paloma Arroyo Huidobro[1]

[1]Department of Physics, Imperial College London, London, SW7 2AZ, United Kingdom
[2] Department of Mathematics, Imperial College London, London, SW7 2AZ, United Kingdom
[*] corresponding author E-mail: matthew.proctor12@imperial.ac.uk

Abstract

The combination of topologically protected states with plasmonic systems presents the opportunity to control electromagnetic waves reliably on the nanoscale. Motivated by these effects we investigate arrays of plasmonic nanoparticles with hallmarks of topological effects, including band inversion and unidirectional edge states. These states are a result of particular lattice symmetries. By treating the nanoparticles as point dipoles and applying the coupled dipole method, we model infinite arrays and semi-infinite ribbons.

1. Introduction

Topological insulators are materials which are insulating in the bulk and which possess conduction states protected against disorder along the surface [1]. The success of these systems has inspired research into photonic and other bosonic analogues. Topological states in electronic materials rely on specific properties of fermions and their behaviour under time-reversal symmetry operations. Alternative techniques are therefore required to design photonic topological insulators but there has been considerable success in this area [2].

Time reversal invariant systems are particularly appealing as they do not require complicated set ups such as background magnetic fields. A method of designing a quantum spin Hall like effect in a photonic crystal using the symmetry properties of the lattice itself was proposed [3] and has since been applied to a wide array of bosonic systems. Whilst not a strict topological effect, the hallmarks of topological systems such as band inversion and unidirectional edge states are demonstrated to exist in this scheme.

Plasmonic systems have attracted significant attention over the past decade, finding applications in sensing, subwavelength imaging and waveguiding. The coupling of plasmons with light offers unprecedented control of electromagnetic fields on the nanoscale. This is due to the enhancement and localisation of electric fields accompanying plasmon resonances [4]. Metallic and dielectric nanoparticles and graphene nanodisks can host localised surface plasmon resonances. When arranged in lattices, the resonances of individual nanoparticles can couple with each other becoming delocalised across the lattice [5]. The properties of these surface lattice plasmon resonances can be tuned by changing the lattice arrangement or the resonators themselves. In the regime where lattice constants are small compared to the resonant wavelength of the elements, collective excitations arise. Unlike three dimensional metamaterials, these plasmonic metasurfaces are easier to fabricate and realise experimentally and their two dimensional nature suggests on-chip applications [6].

In this work, we lay the foundation for designing topological states in plasmonic systems at optical frequencies by applying a method which ensures unidirectional, spin locked edge states at $\mathbf{\Gamma}$ [3]. By first taking a quasistatic approximation, we set up a semi-analytical model which allows us to quickly model the behaviour of the system. This model is built upon by considering radiative and retarded interactions in order to provide a realistic description of the plasmonic array.

2. Theory

The honeycomb lattice of plasmonic nanoparticles has been studied previously in the context of topological states [7]. It is shown that the out of plane and in plane polarised modes can be decoupled such that they can be studied independently. We go further by considering spheroids elongated along the z-axis, in order to separate the frequency ranges of the out of plane and in plane modes. By approximating the nanoparticles as point dipoles, electromagnetic interactions are modelled using Green's functions.

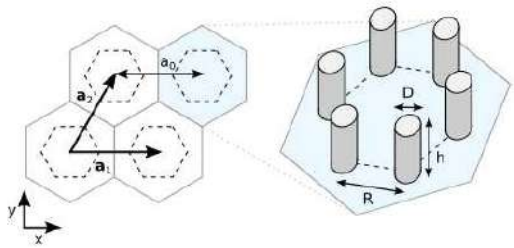


Figure 1: Layout for the lattice. Metallic rods are arranged in hexagons. The size of the hexagons within the unit cell determines the topological phase.

3. Results

3.1. Bulk systems

The honeycomb lattice has a Dirac degeneracy at the **K** point, which is folded onto $\mathbf{\Gamma}$ ($\mathbf{q} = 0$) when the unit cell is extended. By perturbing the system away from the honeycomb, the degeneracy is broken [3]. The phase transition from the trivial to the topological phase is associated with a band inversion, where the dipolar and quadropular bands switch at $\mathbf{\Gamma}$. A similar band inversion occurs in the in plane modes.

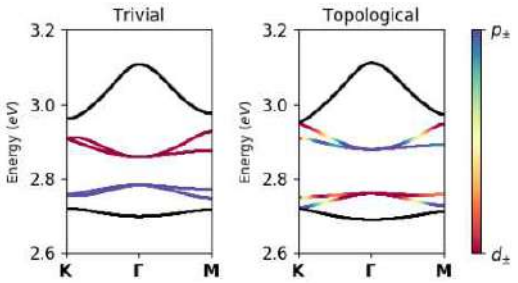


Figure 2: Demonstration of the band inversion in the out of plane modes associated with a topological phase transition in the system. Long range interactions in a quasistatic approximation are used.

3.2. Ribbon systems

Interfaces between regions of different topological phases allow edge states to be explored. The necessary breaking of the lattice symmetry at an interface results in a band gap always existing at $\mathbf{\Gamma}$ but despite this the edge states persist. The absence of linear Dirac dispersion at $\mathbf{\Gamma}$ is evidence of the these edge states not being strictly topologically protected.

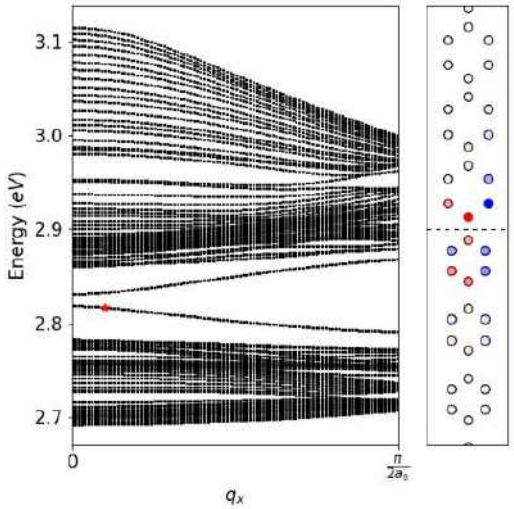


Figure 3: States localised at the interface between topological and trivial regions of the lattice.

4. Conclusions

In this work, we show that it is possible to design unidirectional edge modes in plasmonic systems. These modes are inspired by the quantum spin Hall effect but instead rely on lattice symmetries. They suggest a reliable way of controlling electromagnetic waves on the nanoscale.

We find that the out of plane modes in this system and the modes in photonic crystals previously studied possess similar properties. By perturbing the lattice away from a honeycomb lattice a band inversion occurs accompanied by unidirectional edge modes. These modes are localised along the interface between trivial and topological phases of the lattice.

Whilst not studied in detail here, the in plane modes also show topological properties. Unlike the out of plane modes they can not be trivially classified as dipolar or quadrupolar. A band inversion still occurs when the phase transition takes place but more bands are involved in the inversion.

The coupled dipole method is readily applicable to the study of topological effects which rely on other symmetries, such as valley topological effects associated with inversion symmetry.

Acknowledgement

M.P. acknowledges funding from the Leverhulme Trust.

References

[1] M. Z. Hasan and C. L. Kane, "Colloquium: Topological insulators," *Reviews of Modern Physics*, vol. 82, no. 4, p. 3045, 2010.

[2] M. S. Rider, S. J. Palmer, S. R. Pocock, X. Xiao, P. A. Huidobro, and V. Giannini, "A perspective on topological nanophotonics: current status and future challenges," *arXiv preprint arXiv:1812.08679*, 2018.

[3] L.-H. Wu and X. Hu, "Scheme for achieving a topological photonic crystal by using dielectric material," *Physical Review Letters*, vol. 114, no. 22, p. 223901, 2015.

[4] S. A. Maier, *Plasmonics: Fundamentals and Applications*. Springer Science & Business Media, 2007.

[5] V. Kravets, A. Kabashin, W. Barnes, and A. Grigorenko, "Plasmonic surface lattice resonances: A review of properties and applications," *Chemical reviews*, 2018.

[6] N. Meinzer, W. L. Barnes, and I. R. Hooper, "Plasmonic meta-atoms and metasurfaces," *Nature Photonics*, vol. 8, no. 12, p. 889, 2014.

[7] L. Wang, R.-Y. Zhang, M. Xiao, D. Han, C. T. Chan, and W. Wen, "The existence of topological edge states in honeycomb plasmonic lattices," *New Journal of Physics*, vol. 18, no. 10, p. 103029, 2016.

Dynamics of entanglement for quantum emitters near MoS_2 nanodisks

Nikolaos Iliopoulos[1], Vasilios Karanikolas[1], Dionisios Stefanatos[1], Emmanuel Paspalakis[1]

[1]Materials Science Department, School of Natural Sciences, University of Patras, Patras 265 04, Greece
*corresponding author, E-mail: paspalak@upatras.gr

Abstract

We study the dynamics of entanglement for a composite system that consists of a pair of two-level quantum emitters, with picosecond free-space decay time, each one close to a MoS_2 nanodisk. We take into consideration the counter-rotating terms and present the time evolution of the concurrence, our entanglement measure, for different initial states of this hybrid system, under strong coupling conditions.

1. Introduction

It is well known that the localized surface states emerging in photonic nanostructures dramatically change the local photonic environment. Thus, putting a quantum emitter (QE) close to such a nanostructure, strong light-matter coupling effects could be observed, which are really important for various applications, including quantum technology and nanotechnology. It has been recently realized that entanglement dynamics between two QEs is strongly influenced by strong coupling phenomena at the nanoscale by placing the QEs near plasmonic nanostructures, like plasmonic nanoshells, nanospheres and nanocavities, and phenomena such as non-Markovian dynamics and entanglement trapping are found [1, 2, 3, 4]. Here, we propose another photonic nanostructure that may induce strong coupling effects in the entanglement dynamics of two QEs, in significantly larger distances than the plasmonic nanostructures. To succeed this, we explore the localized exciton-polariton modes of a MoS_2 nanodisk.

2. Theoretical methodology

We consider a two-level QE located at $\mathbf{r} = (0, 0, z)$ of a coordinate system with origin at the center of a MoS_2 nanodisk, as shown in Fig. 1. The dynamics of the QE is described by the following integro-differential equation for the probability amplitude of the upper state $|1\rangle$, $c_1(t)$, which has been obtained without using the rotating wave approximation and taking into account the presence of the photonic nanostructure (here the MoS_2 nanodisk) [3]:

$$\dot{c}_1(t) = -\int_0^t dt' \int_0^\infty d\omega J(\omega, \mathbf{r}) e^{i(\omega_0' - \omega)(t-t')} c_1(t') \,, \quad (1)$$

$$J(\omega, \mathbf{r}) = \left(\frac{2\omega_0}{\omega_0 + \omega}\right)^2 \frac{\Gamma_0(\omega_0)}{2\pi} \lambda(\omega, \mathbf{r}) \left(\frac{\omega}{\omega_0}\right)^3 , \quad (2)$$

where $\omega_0' = \omega_0 + \Delta\omega_0$, with the relative frequency shifts being $\Delta\omega_0 = -\int_0^\infty d\omega \frac{2\omega_0}{(\omega_0+\omega)^2} \frac{\Gamma_0(\omega_0)}{2\pi} \lambda(\omega, \mathbf{r}) \left(\frac{\omega}{\omega_0}\right)^3$. Here,

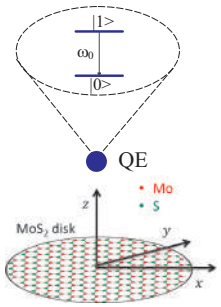


Figure 1: A two-level QE (the qubit) located at distance z from the center of a MoS_2 nanodisk.

$\Gamma_0(\omega_0)$ is the free-space decay rate of the QE with resonant frequency ω_0 and $\lambda(\omega, \mathbf{r})$ is the Purcell factor due to the positioning of the QE at distance $\mathbf{r}$ close to the nanodisk.

The presence of the MoS_2 nanodisk strongly modifies the density of modes around it. As a result, the Purcell factor for a QE in the vicinity of the nanodisk increases significantly and also have a rather narrow frequency distribution, due to the localized exciton-polariton modes that emerge in the nanodisk [5]. This leads to strong coupling effects.

We take that our composite system consists by two identical QEs. Each QE is near a two-dimensional MoS_2 nanodisk of radius R. The two QEs are far apart so they do not interact with each other and assume that our composite system is prepared in the Bell-like states

$$|\Phi\rangle = a|01\rangle + \sqrt{1-a^2}|10\rangle, \quad (3)$$

$$|\Psi\rangle = a|00\rangle + \sqrt{1-a^2}|11\rangle, \quad (4)$$

with $0 \leq a \leq 1$. In this work we use concurrence as a measure of entanglement [3]. The calculation of concurrence for these specific initial states gives [3]

$$C_\Phi(t) = 2a\sqrt{1-a^2}|c_1(t)|^2 \,, \quad (5)$$

$$C_\Psi(t) = 2\max[0, C(t)] \,, \quad (6)$$

correspondingly, with

$$C(t) = \sqrt{1-a^2}|c_1(t)|^2 \left[a - \sqrt{1-a^2}(1-|c_1(t)|^2)\right]. \quad (7)$$

We notice that for both cases concurrence depends on the time evolution of the upper state population $|c_1(t)|^2$.

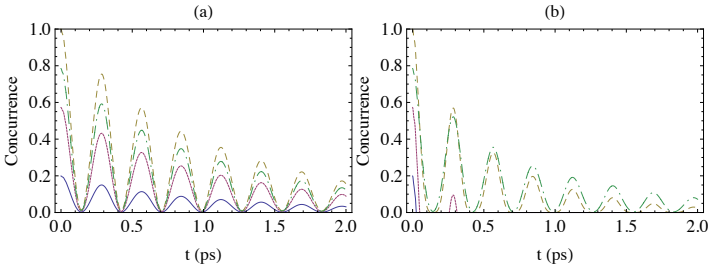


Figure 2: (a) Time evolution of concurrence in the presence of the nanodisk for the initial state $|\Phi\rangle$. The qubits have $\hbar\omega_0 = 1.949$ eV and free space decay rate is $1/\Gamma_0(\omega_0) = 82.7$ ps (corresponding to J-aggregates). For solid blue curve $a = 0.1$, for dotted red curve $a = 0.3$, for dashed yellow curve $a = 1/\sqrt{2}$ and for dot-dashed green curve $a = 0.9$. (b) The same as (a) but for the initial state $|\Psi\rangle$.

3. Numerical results

Figure 2 shows the time evolution of concurrence when the QEs have prepared in the initial state $|\Phi\rangle$ [Fig. 2(a)] and $|\Psi\rangle$ [Fig. 2(b)]. Each QE is at distance $\mathbf{r} = (0, 0, 15)$ nm from a MoS_2 nanodisk with radius $R = 30$ nm. For the computation of concurrence, we first find the Purcell factor, calculating the electromagnetic Green's tensor near the MoS_2 nanodisk using the method of Ref. [5] to determine $J(\omega, \mathbf{r})$ and $\Delta\omega_0$, then we solve numerically the integro-differential Eq. (1) using the effective mode differential equation methodology [6], and finally apply Eqs. (5) and (6).

We observe that for the initial state $|\Phi\rangle$, see Fig. 2(a), concurrence has the same decaying oscillatory behaviour for all values of the parameter a, as its value is proportional to $|c_1(t)|^2$, and its magnitude depends strongly on a, with the higher value for $a = 1/\sqrt{2}$ and the lower for $a = 0.1$. However, this is not true for the initial state $|\Psi\rangle$, see Fig. 2(b), where we find that for small values of a the phenomenon of entanglement sudden death (ESD) takes place [7]. Specifically, ESD emerges for $a < 1/\sqrt{2}$, as the term $C(t)$, takes negative values as the system evolves in time. Additionally, in Fig. 2(b) we note the manifestation of another interesting phenomenon, the revival of entanglement, for some values of a (e.g. see the dotted red curve for $a = 0.3$), which occur as the term $C(t)$ can take negative values for some initial time period and then for another small period of time can take again positive values. For $a > 1/\sqrt{2}$, concurrence has an oscillatory character which decays gradually to zero, similar to the initial state $|\Phi\rangle$, as the term $C(t)$ takes always positive values. We emphasize the fact that although at $t = 0$ we have the maximum entanglement for $a = 1/\sqrt{2}$ for both initial states, this does not happen during the whole time evolution for the initial state $|\Psi\rangle$, since after some time the dominant value of concurrence occurs for $a = 0.9$. Interestingly, in both cases, the non-Markovian dynamics happens in much larger distances (about five times larger) than in plasmonic nanostructures, such as for example, metallic nanospheres [3, 4].

4. Conclusions

In conclusion, we have analyzed the entanglement of two initially entangled qubits, each interacting locally with a MoS_2 nanodisk, and study how entanglement evolves with time. Using Bell-like states as initial states of our composite system, we observe some interesting phenomena induced by strong coupling, including clear non-Markovian dynamics, as well as, ESD and revival of entanglement for specific initial states. We also note, that besides changing the initial conditions, we can also control the non-Markovian character of entanglement dynamics simply by changing the distance of each QE from the corresponding nanodisk (not shown here).

Acknowledgement

The research is implemented through the Operational Program "Human Resources Development, Education and Lifelong Learning" and is co-financed by the European Union (European Social Fund) and Greek national funds (project EΔBM34, code MIS 5005825). We are grateful to Prof. Ioannis Thanopulos for useful discussions and invaluable help in the calculations.

References

[1] J. Hakami and M.S. Zubairy, Nanoshell-mediated robust entanglement between coupled quantum dots, *Phys. Rev. A* 93: 022320, 2016.

[2] M. Hensen, T. Heilpern, S. K. Gray, and W. Pfeiffer, Strong coupling and entanglement of quantum emitters embedded in a nanoantenna-enhanced plasmonic cavity, *ACS Photon.* 5: 240, 2018.

[3] N. Iliopoulos, I. Thanopulos, V. Yannopapas, and E. Paspalakis, Counter-rotating effects and entanglement dynamics in strongly coupled quantum-emitter-metallic-nanoparticle structures, *Phys. Rev. B* 97: 115402, 2018.

[4] N. Iliopoulos, I. Thanopulos, V. Yannopapas, and E. Paspalakis, Quantum correlations in quantum emitters strongly coupled with metallic nanoparticles, *Quant. Infor. Process.* 18: 110, 2019.

[5] V. D. Karanikolas, and E. Paspalakis, Localized exciton modes and high quantum efficiency of a quantum emitter close to a MoS_2 nanodisk, *Phys. Rev. B* 96: 041404(R), 2017.

[6] I. Thanopulos, V. Yannopapas, and E. Paspalakis, Non-Markovian dynamics in plasmon-induced spontaneous emission interference, *Phys. Rev. B* 95: 075412, 2017.

[7] T. Yu and J. H. Eberly, Finite-time disentanglement via spontaneous emission, *Phys. Rev. Lett.* 93: 140404, 2004.

Long-lived Event Horizon Created by Topological Phase Transition

Meng Kang[1,2], Huaqing Huang[2], Shunping Zhang[1], Hongxing Xu[1,3,*] and Feng Liu [2,4,†]

[1]School of Physics and Technology, Center for Nanoscience and Nanotechnology, and Key Laboratory of Artificial Micro- and Nano-structures of Ministry of Education, Wuhan University, Wuhan 430072, China
[2]Department of Materials Science and Engineering, University of Utah, Salt Lake City, Utah 84112, USA
[3]The Institute for Advanced Studies, Wuhan University, Wuhan 430072, China
[4]Collaborative Innovation Center of Quantum Matter, Beijing 100084, China
*corresponding author, E-mail: hxxu@whu.edu.cn, fliu@eng.utah.edu

Abstract

As a quantum field theory in curved spacetime, Hawking radiation has been extensively studied in various analogue systems. However there remains debate on its experimental verification. One challenge is that a long-lived event horizon is difficult to achieve experimentally. Here we theoretically propose a novel analog of Hawking effect based on topological phase transition from a type-II to type-I Dirac cone, where their interface (a type-III Dirac cone) acts as a stable event horizon.

1. Introduction

Hawking radiation [1] is a quantum field theory in curved spacetime. However it is difficult to be probed in gravitational black hole (BH) for its extremely low temperature. A sonic BH analog [2] proposed by Unruh opens a new avenue for studying Hawking effect. However, although extensive theoretical and experimental studies of various BH analogs have emerged [3], an undisputed confirmation of Hawking radiation remains elusive. One challenge is that a long-lived horizon is difficult to achieve experimentally because it is usually unstable [4].

Topological phase transition from a type-II to type-I Dirac cone (DC) in inhomogeneous systems shows corresponding features with the evolution of light cone in BH [5-7], providing a novel optical analogue platform. The transition interface (a type-III DC) between type-II and type-I DC simulates an event horizon. Trapped photons in the type-II region quantum mechanically tunnel through the horizon to emit as a analog of Hawking radiation. Here we design a long-lived horizon arising from a stationary "spacetime" configuration in an inhomogeneous waveguide array based on a tight-binding model.

2. Hawking radiation analog

The effective Hamiltonian around Dirac points (DPs) in two-dimension is:

$$H(k) = c_x \delta k_x \sigma_x + c_y \delta k_y \sigma_y + v_x \delta k_x \sigma_0, \quad (1)$$

where σ_x and σ_y are Pauli matrixes, σ_0 is the unitary matrix, c_x and c_y is the tilt angle along the k_x and k_y direction respectively, and v_x determines the tilt of DC relative to k_x . DC is tuned by v_x to be type-I for $|v_x| < |c_x|$, type-II for $|v_x| > |c_x|$ and type-III for $|v_x| = |c_x|$.

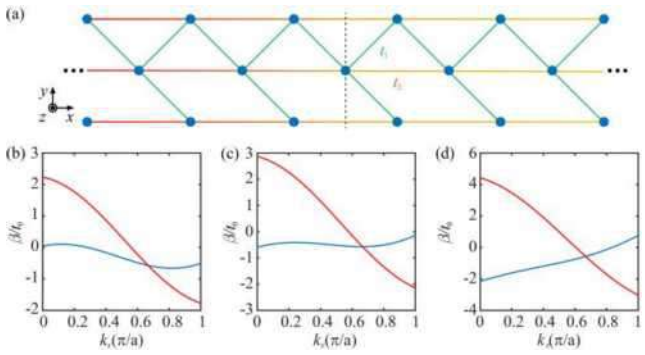


Figure 1. (a) Sketch of the inhomogeneous graphyne-like photonic lattice. It contains a centered-square lattice of waveguides (blue dots), whose inter- and intra-hopping (t_1, t_2) can be constructed by a chain of waveguides. The type-II DC gradually evolves into type-I DC with the decrease of intra-hopping t_2 along x direction. Their interface (dashed line) represents the event horizon. Calculated band diagram for (b) type-II DC with a conical-like Fermi surface (the intra-hopping t_1 = 0.63 t_0, the inter-hopping t_2 = 0.9 t_1), (c) type-III DC (t_1 = t_0, t_2 = 0.57 t_1) and (d) tilted type-I DC with a point-like Fermi surface (t_1 =1.9 t_0, t_2 = 0.3 t_1). The intra-hopping t_1 is tuned to maintain DP at the same level.

Next we demonstrate the three types DC in an inhomogeneous graphyne-like photonic lattice [8], as shown in Fig. 1(a). According to tight-binding model, the diffraction of light in waveguide arrays is determined by

$$i\partial_z \psi_{mn}(z) = \sum_{m',n'} t_{m'n'} \psi_{m'n'}(z), \quad (2)$$

where $t_{m'n'}$ is the hopping strength between two adjacent waveguides, and ψ_{mn} is the amplitude of the m, nth waveguide. The Hamiltonian $H = \begin{pmatrix} h'(\mathbf{k}) & h(\mathbf{k}) \\ h^*(\mathbf{k}) & h'(\mathbf{k}) \end{pmatrix}$ is

obtained, where $h(\mathbf{k}) = t_1[1+\cos k_y + \cos(k_y - k_x) + i\sin k_y + i\sin(k_y - k_x)]$, $h'(\mathbf{k}) = 2t_2 \cos k_x$. The position of DC is replaced by $|h(\mathbf{k})| = 0$. Light velocity $c_x = \partial \,\mathrm{Re}[h(\mathbf{k})]/\partial k_x$ and $c_y = \partial \,\mathrm{Im}[h(\mathbf{k})]/\partial k_y$ depend on intra-hopping t_1. Dragging velocity $v_x = \partial h'(\mathbf{k})/\partial k_x$ is only related to inter-hopping t_2. By gradually decreasing the inter-hopping t_2/t_1 along x direction, DC is tuned from type-II [Fig. 1(b)] to type-III [Fig. 1(c)] and then to type-I [Fig. 1(d)].

The inhomogeneous photonic lattice creates an effective fluid flow as an analog of optical BH spacetime. The outgoing mode [blue lines in Fig. 1(b-c)] is mainly related to Hawking effect. In type-I region, the dragging velocity is smaller than light velocity so that the outgoing photons can escape. The dragging velocity overtakes light velocity in type-II region, where outgoing photons are trapped. The outgoing mode is stationary at their interface, i.e. type-III region. Thus type-II region simulates an optical BH, type-III region plays the role of an event horizon, and type-I region is outside the BH. Photons in type-II region can quantum mechanically tunnel through the horizon from type-II to type-I region to emit a radiation. This analogous Hawking radiation has a temperature

$$T_H = \frac{\hbar}{2\pi k_B} \left. \frac{dv_x}{dx} \right|_{x_h}, \qquad (3)$$

which depends on surface gravity $E_{gh} = dv_x / c_x dx|_{x_h}$ at the horizon. Here k_B is Boltzmann constant.

3. Discussion

Waveguide arrays provide a stationary "spacetime" configuration and hence create a long-lived event horizon. They can be fabricated via the femtosecond laser direct-writing method [9]. Two adjacent waveguides couple with each other by a chain of waveguides. Hopping is tunable by modifying the refractive index of the waveguide chain. Hawking temperature can be improved by increasing the surface gravity at the horizon.

4. Conclusions

We theoretically propose a new optical BH analog by topological phase transition from type-II to type-I DC. Their interface simulates a long-lived event horizon. Photons tunnel through the horizon to emit as Hawking radiation. We demonstrate this analog in an inhomogeneous waveguide array.

Acknowledgements

Work at Wuhan was supported by the National Key Basic Research Program (Grant No. 2015CB932400) and the National Natural Science Foundation of China (Grant Nos. 11674255, 11674256). Work at Utah was supported by U.S. DOE-BES (Grant No. DE-FG02-04ER46148).

References

[1] S.W. Hawking, Black hole explosions?, Nature, 248 (1974) 30-31.

[2] W.G. Unruh, Experimental Black-Hole Evaporation?, Phys. Rev. Lett., 46 (1981) 1351-1353.

[3] D. Faccio, F. Belgiorno, S. Cacciatori, V. Gorini, S. Liberati, U. Moschella, Analogue gravity phenomenology: analogue spacetimes and horizons, from theory to experiment, Springer, 2013.

[4] C. Barceló, Analogue black-hole horizons, Nat. Phys., (2018) 1.

[5] G.E. Volovik, Black hole and hawking radiation by type-II Weyl fermions, JETP Lett., 104 (2016) 645-648.

[6] H. Huang, K.-H. Jin, F. Liu, Black-hole horizon in the Dirac semimetal Zn 2 In 2 S 5, Phys. Rev. B, 98 (2018) 121110.

[7] H. Liu, J.-T. Sun, H. Huang, F. Liu, S. Meng, Fermionic analogue of black hole radiation with a super high Hawking temperature, arXiv:1809.00479, (2018).

[8] G.G. Pyrialakos, N.S. Nye, N.V. Kantartzis, D.N. Christodoulides, Emergence of Type-II Dirac Points in Graphynelike Photonic Lattices, Phys. Rev. Lett., 119 (2017) 113901.

[9] A. Szameit, S. Nolte, Discrete optics in femtosecond-laser-written photonic structures, J. Phys. B, 43 (2010) 163001.

Bifurcations of topological edge states in non-linear quantum walks: originating from unique features to Floquet non-linear systems

Ken Mochizuki[1], Norio Kawakami[2], and Hideaki Obuse[1]

[1]Department of Applied Physics, Hokkaido University, Sapporo, Japan
[2]Department of Physics, Kyoto University, Kyoto, Japan

1. topological edge states in quantum walks

A quantum walk is a quantum version of the classical random walk and a kind of Floquet systems, since the quantum walk has discrete time-periodicity. Quantum walks describe dynamics of quantum particles and have several unique features. For example, probability distributions of particles in quantum walks are quite different from those in classical random walks due to quantum interference, Grover search algorithms can be implemented by using quantum walks, energy levels of quantum walks have 2π periodicity due to discrete time-periodicity, and so on. Among these unique features, it is peculiarly interesting that quantum walks can have nontrivial topological phases which result in emergence of edge states. Topological phases of quantum walks have been studied theoretically[1] and experimentally[2]. Quantum walks have been realized experimentally using single photons or laser beams passing through optical devices, and real space observations of edge states hove been done in quantum walks of single photons[2]. Quantum walks have been paid attention to, since such observations of edge states with high resolution are difficult in topological materials. Not only the real space observation of edge states, but also quantum walks have uniqueness in comparison to topological materials. For instance, in quantum walks, there exist not only 0 energy edge states but also π energy edge states, whose origin is time-periodicity[1]. Another example is that photon loss effect can be introduced in quantum walks and it drastically changes the behavior of edge states[3].

2. non-linear quantum walks

In addition to the above interesting features, non-linear effects in quantum walks have been considered theoretically[4]. The theoretical proposition is as follows. At some positions and time-steps in the dynamics, intensity of light is detected. By using results obtained from the detection, conditions of optical devices are changed, which the beam passes through in the next step. Such feed-forward controls generate non-linear effects in the dynamics of quantum walks. It is expected that, the non-linear effect can make dynamics of quantum walks richer.

3. stability of topological edge states in non-linear quantum walks

In 2016, it was clarified that, in a non-linear one-dimensional quamtum walk, topologically protected edge states become attacter or repeller, depending on its chirality[5]. This has been done by using a linear-stability analysis of edge states for an effective Hamiltonian which is derived from the time-evolution operator of the quantum walk by taking the continuum limit for space and time. On the other hand, time-evolution operators play a key role in qusntum walks, as it include the effect of the time-periodicity. Also, different from many other Floquet systems, time-evolution operators are explicitly defined in quantum walks, without approximation. Therefore, it can be said that the stability analysis in Ref. [5] does not fully make use of features that quantum walks possess, since the effective Hamiltonian in the continuous limit loses the effect of the discrete time-periodicity. In this work, we study stability of topologically protected edge states in non-linear quantum walks, without taking the continuous limit. As a result, we find bifurcations where edge states change from attracter to repeller, irrespective to chirality of edge states. The bifurcations we shall show are unique to Floquet non-linear systems, as it originates from the time-periodicity of quantum walks.

References

[1] T. Kitagawa, M. S. Rudner, E. Berg, and E. Demler, Phys. Rev. A **82**, 033429 (2010).

[2] T. Kitagawa, M. A. Broome, A. Fedrizzi, M. S. Rudner, E. Berg, I. Kassal, A. Aspuru-Guzik, E. Demler, and A. G. White, Nat. Commun. **3**, 882 (2012).

[3] L. Xiao, X. Zhan, Z. H. Bian, K. K. Wang, X. Zhang, X. P. Wang, J. Li, K. Mochizuki, D. Kim, N. Kawakami, W. Yi, H. Obuse, B. C. Sanders, and P. Xue, Nat. Phys. **13**, 1117 (2017).

[4] Y. Shikano, T. Wada, and J. Horikawa, Sci. Rep. **4**, 4427 (2014).

[5] Y. Gerasimenko, B. Tarasinski, and C.W. J. Beenakker, Phys. Rev. A **93**, 022329 (2016).

Correlation between bands structure and quantum magneto-transport in $In_{0.53}Ga_{0.47}As$/InP type I superlattice for short-infrared detection

Merieme Benaadad[1], Abdelhakim Nafidi*[1], Samir Melkoud[1], Nassima Benchtaber[1], Es-saïd Es-Salhi[1], Fatiha Chibane[1] and Mustapha Massaq[1]

[1]Laboratory of Condensed Matter Physics and Nanomaterials for Renewable energy, University Ibn Zohr, 80000 Agadir, Morocco

*corresponding author, E-mail: nafidi21@yahoo.fr

Abstract

In this paper, we investigated the band structures and quantum magneto transport properties of the $In_{0.53}Ga_{0.47}As$ (d_1=100Å)/InP(d_2=70Å) type I superlattice (SL) at low temperature. These studies were based on the envelope function formalism. We studied the effect of d_1, d_2, the band valence offset and temperature on the cut-off wavelength in the short infrared region and on the band gap of the present superlattice. The result of the computed density of states and the position of Fermi level indicates that this sample is n-type quasi two-dimensional system. Moreover, the cutoff wavelength predicts that this sample can be employed as a short-infrared detector. Furthermore, we interpreted theoretically the photoluminescence, the Shubnikov de Haas and quantum Hall effects observed by Pusep et al.

1. Introduction

The $In_xGa_{1-x}As$/InP heterostructures are considered as one of the most important semiconductor superlattices (SLs), due to their technological applications, especially in infrared optoelectronics, THz, superlattice-emitter resonant tunneling bipolar transistor (SE-RTBT) and photodetectors. Moreover, such materials can be used in spintronics and quantum information processing field. Their electronics properties can be tuned by varying layers thicknesses and indium composition x. Their application in infrared detectors have generated a lot of interest for low cost, low dark current, high speed and high temperature operation detectors in short wavelength infrared (SWIR) [1,2].

In general, the $In_xGa_{1-x}As$/InP structure is grown by molecular beam epitaxy (MBE) technique with different indium fraction x. This periodic SL is made from repeated layers of two materials which have nearly a similar structure but a different electrical properties, $In_xGa_{1-x}As$ (well) and InP (barrier) [3].

It is well know that the reduction of the dimensionality of a system under extreme conditions like low temperatures and high magnetic fields, conduct to the observation of quantum electronic transport effects like Shubnikov-de Haas effect (SdH) and quantum Hall effect (QHE).

In the literature the calculation of the energy band structure and the effect of basic parameters on the band gap of this SL are very rare or inexistent. So we are attempted to calculated the band structure of the $In_{0.53}Ga_{0.47}As$(d_1=100Å)/InP(d_2=70Å) type I SL in the envelope function formalism [4]. The aim of this work is to show the correlation between calculated bands structures and magneto-transport properties in $In_{0.53}Ga_{0.47}As$/InP nanostructure superlattice. We studied the effects of thickness d_1 of well (d_2 of barrier), the valence bands offset and temperature on the band gap. These results permit us the interpretation of the photoluminescence, the SDH and QHE Effects observed by Pusep et al. [5] in the same sample.

2. Theoretical formulations and computation of type I superlattices bands structure

2.1 Dispersion relations in $In_xGa_{1-x}As$/InP superlattice

In general the calculations of electronic band structure for semiconductors based on the k.p theory [6], it provides a detailed description of a material's energy [7]. For our calculations of the spectra of enrgy $E(k_z)$ in the direction of growth and $E(k_p)$ in plane of this superlattice, we adopted the envelope function formalism.

The expression of dispersion relation for $In_xGa_{1-x}As$/InP superlattice, within this formalism and effective mass approximation, is given by [8,9] :

$$\cos[k_z(d_1+d_2)] = \cos(k_1d_1)\cos(k_2d_2) - \frac{1}{2}\left[(\xi+\frac{1}{\xi}) + \frac{k_p}{4k_1k_2}(r+\frac{1}{r}-2)\times\sin(k_1d_1)\sin(k_2d_2)\right] \quad (1)$$

Where the subscripts 1 and 2 refer to $In_xGa_{1-x}As$ and InP layers, respectively. With k_z the wave vectors in the growth direction axis and $k_p(k_x,k_y)$ the superlattice wave vector in-plane. In this superlattice, the origin of energy E has been chosen at the top of InP valence band as shown in the Fig. 1. With k_1 and k_2 describe the movement perpendicular to the layer of bulk materials.

2.2 Electrons and light holes mini-bands:

The expression of ξ and r for light particles are:

$$\xi = \frac{k_1}{k_2}r, \text{ and } \quad r = \frac{E-\varepsilon_2}{E-\varepsilon_1-\Lambda}, \quad (2)$$

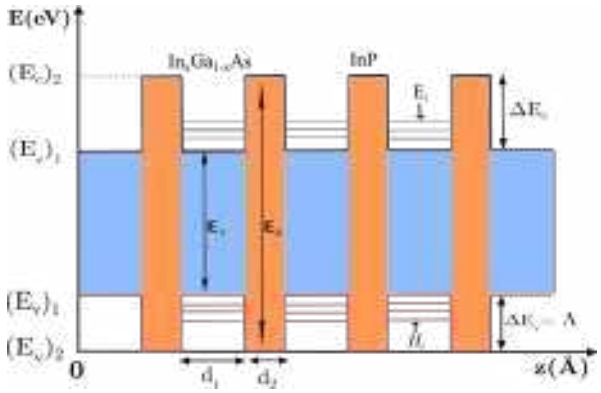


Figure 1: Schematic illustration of band lineup between $In_xGa_{1-x}As$ and InP along the growth direction with different parameters of electronic band structures. $(E_c)_i$, $(E_v)_i$ and ε_i where i= 1, 2 are the conduction and valence bands edges and band gap of bulks, respectively.

Here ε_i(i= 1, 2) the band gaps of bulk materials and Λ is the valence band offset (VBO). At a given energy, the two-band Kane model [10], gives the wave vector (k_i^2+k_p^2) in each host material (i=1 or 2) by:

$$\begin{cases} 2P_1^2\hbar^2(k_1^2+k_p^2) = 3(E-\varepsilon_1-\Lambda)\,(E-\Lambda) & for\ In_xGa_{1-x}As \\ 2P_2^2\hbar^2(k_2^2+k_p^2) = 3E\,(E-\varepsilon_2) & for\ InP \end{cases} \quad (3)$$

We calculated the Kane matrix element P_i using the formula of Kane energy E_{pi} [11]:

$$P_i^2 = \frac{E_{pi}}{2m_0} \quad (4)$$

For our calculations, we adopted the values of E_{pi} cited in [12].

2.3 Heavy holes mini-bands

The superlattice heavy holes mini-bands can be obtained from the Eq. (1) with the following relations:

$$\begin{cases} -\hbar^2(k_1^2+k_p^2) = 2\left(m^*_{hh}\right)_1(E-\Lambda) & for\ In_xGa_{1-x}As \\ -\hbar^2(k_2^2+k_p^2) = 2\left(m^*_{hh}\right)_2 E & for\ InP \end{cases} \quad (5)$$

With $\xi = \frac{k_1}{k_2}r$ and $r = \frac{\left(m^*_{hh}\right)_2}{\left(m^*_{hh}\right)_1}$

Here, $(m^*_{hh})_1$= 0.47m_0 and $(m^*_{hh})_2$= 0.6m_0 are the heavy holes effective masses of $In_{0.53}Ga0.47As$ and InP respectively as given in [13,14].

The band gaps parameters ε_i(i=1,2) used here, are obtained by the empirical expressions of $In_xGa_{1-x}As$ and InP respectively, as a function of alloy composition x and temperature T [15,16]:

$$\varepsilon_1^{\Gamma}(T,x) = 1.045 - 0.625x + 0.475\times(1-x)^2 - \left(\frac{4.19}{(T+271)} - \frac{5.8}{T+300}\right)10^{-4}T^2x - \frac{5.8\times10^{-4}T^2}{T+300} \quad (6)$$

$$\varepsilon_2^{\Gamma}(T) = 1.421 - \frac{4.9\times10^{-4}T^2}{(T+327)} \quad (7)$$

We use the experimental valence band offset (VBO) Λ= 346 meV determined by by admittance spectroscopy [17].
We solve the previous relations using the adopted parameters to compute the electronic structure and related properties for the investigated sample.

3. Theoretical results and discussions

3.1 Band structures, band gap and effective mass

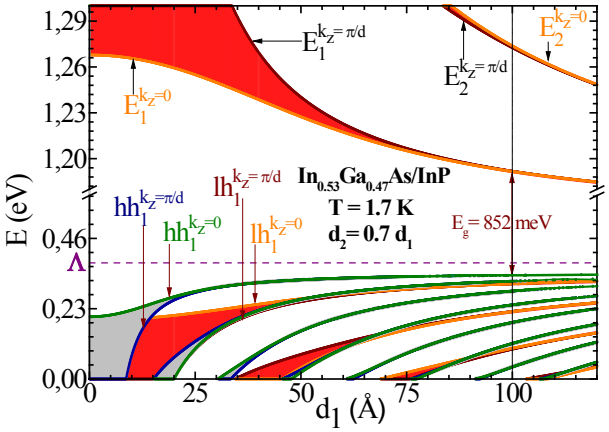


Figure 2: Energy of both conduction (upper part) and valence (lower part) sub-bands as function of well thickness d_1 at 1.7 K with d_1=1.43 d_2. The solid areas show the width of sub-bands in the first Brillouin zone.

The Fig. 2, shows the energy of conduction (E_i), light-hole (lh_i) and heavy-hole (hh_i) mini-bands at the center Γ(k_z= 0) and the limit (k_z= π/d) of the first Brillouin zone as a function of well thickness d_1 with the ratio d_2=0.7 d_1. The calculated band gap, from the bottom of the first conduction (E_1) to the top of the first valence sub-bands (hh_1) at T=1.7 K is $E_g(\Gamma)$= E_1 - hh_1= 852 meV, as indicated by a vertical dashed line. This value agree favorably with the direct gap of 820 meV measured by photoluminescence by Y.A. Pusep et al. [5]. The difference of 4% between two values obtained

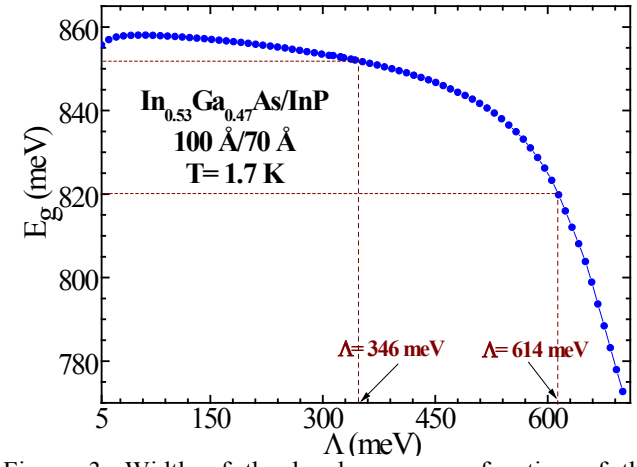


Figure 3: Width of the band gap as a function of the discontinuity Λ of the valence bands (VBO).

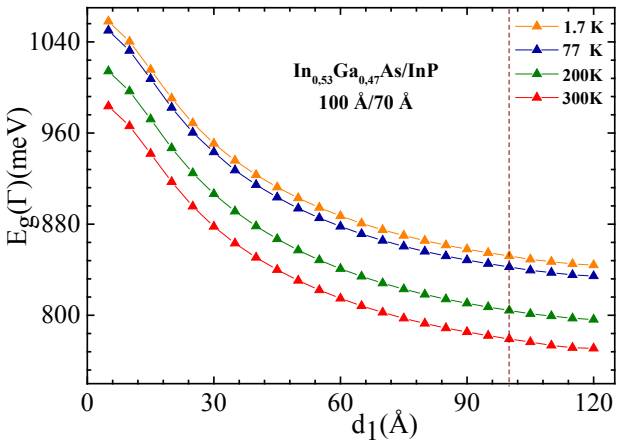


Figure 4: The band gap of the investigated superlattice as a function of well thickness in different temperatures.

can be due to the basic parameters adopted here, particularly, the valence band offset (VBO). In Fig. 3, we can see the effect of the VBO on the band gap of theinvestigated superlattice at 1.7K. The band gap increases to a maximum at 70 meV, then decreases prabolically when the valence band offset increases. As the figure shows the experimental gap is obtained for Λ near of 615 meV. Nevertheless, we used the measured experimental value Λ=346 meV by spectroscopy and Xray photoemission spectroscopy for x=0.53 [18]. The difference observed can be due also to the small incertitude on the measured thickness d_1 and d_2 and/or to the strain effects which create a large piezoelectric field in these structures, and modify the band structure due to a large change in their energy band edges [19]. When the well's thickness d_1 increases, the band gap and the sub-band width decreases to discrete energy levels of isolated quantum wells for $d_1 \geq 170A°$ (Fig. 2). So the electron gas is bidimentional.

We are interested to explain the effect of some basic parameters on the band gap like well thickness and temperature. We plotted the evolution of the band gap E_g, at the centre Γ of the first Brillouin zone, as a function of well width d_1 for various temperatures in Figure. 4. For a given T,

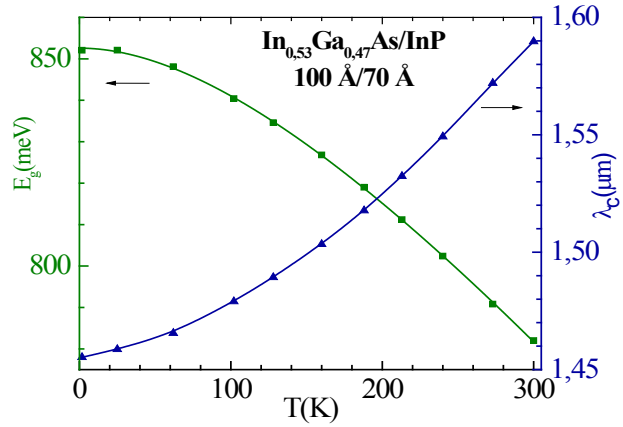


Figure 5: The band gap energy and the cut-off wavelength as function of temperature of the SL, at the center Γ of the first Brillouin zone.

E_g decreases significantly with the increasing d_1, which could be reflect the formation of the thin single quantum well between lattice-matched InP and InGaAs [20]. In addition, this phenomenon can be due to the creation of more allowed states in the forbidden bands. Such regions can be occupied by electrons; because of the number of overlapping orbitals between nearest atoms grows with thickness. Thus, the conduction and valence bands starts to get closer, leading to a reduction of the band gap [21]. Fig. 5 shows the variation of the band gap E_g and the cut-off wavelength λ_c, at the center Γ of the first Brillouin zone, as a function of the temperature in the range 1.7 to 300 K. When the temperature increases, E_g decreases from 852 at 1.7 K to 780 at 300 K, whereas λ_c increases. Our results agree well with those of Fernandes dos Santos et al measured by photoluminescence for T>50 K [22], with a small difference of 10 meV that can be attributed to the basic parameters of calculations used here. To explain such behavior of band gap as a function of temperature in semiconductors, many theoretical models were developed like the semi-empirical relation of Varshni [23].

$$E_g(T) = E_g(0) - \alpha\left(\frac{T^2}{T+\beta}\right) \tag{8}$$

In our case, the best fitting was obtained with α = 0.49 meV K^{-1}, β = 331 K and the gap at absolute zero $E_g(0)$ = 851 meV. These values are in agreement with those indicated in Ref. [23]. From other hand, there are novels theoretical models out of fitting parameters, one was proposed of Peiji Geng and al. [24].

We calculated the detection cut-off wave length in Fig. 5, using the formula:

$$\lambda_c(\mu m) = \frac{1240}{E_g(meV)} \tag{9}$$

The variation $1.46 \leq \lambda_c(\mu m) \leq 1.55$ indicated that this sample can be used as short-infrared detector.

Fig. 6 shows the band structure of $In_{0.53}Ga_{0.47}As/InP$ superlattice, at very low temperature (T=1.7 K) along the

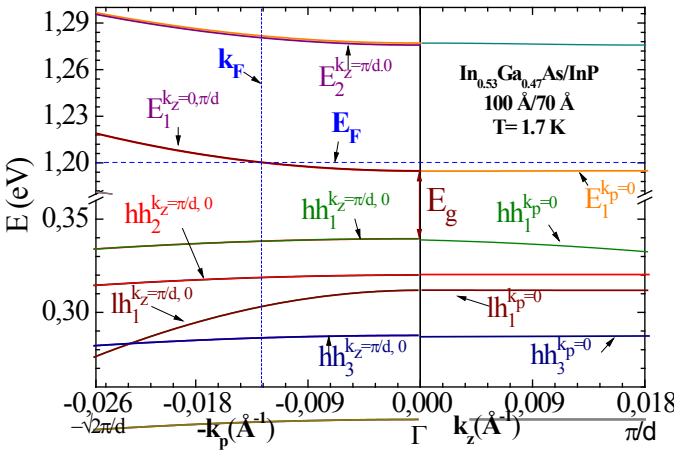


Figure 6: Calculated band structures of the investigated superlattice along the growth direction k_z and in-plane k_p.

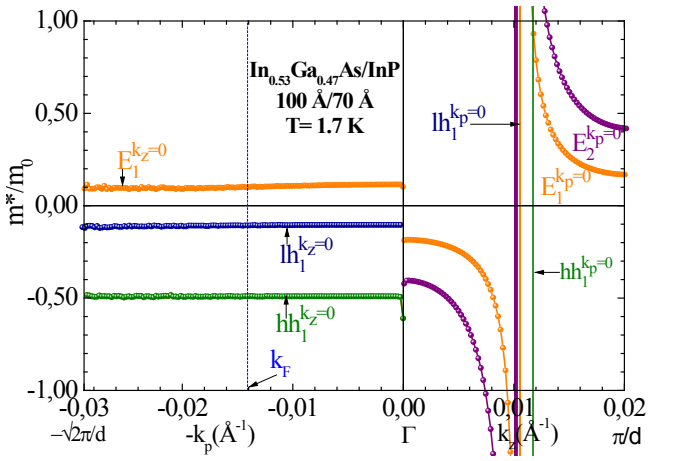


Figure 7: Carriers effective mass ratio of the first conduction and valence mini-bands with m_0 the rest mass of an electron

growth direction k_z, and in-plane $k_p(k_x,k_y)$, in the first Brillouin zone. Near the forbidden energy gap, two first conduction (E_1 and E_2), three heavy holes $hh_{1,2,3}$ and light holes lh_1 mini-bands are observed. The plot of $E(k_z^2, k_p^2)$ shows that all the mini-bands are parabolic in the first Brillouin zone. There is a weak variation following k_z, which can be due to the weak coupling between superlattice wells layers. We deduce that the electronic transport is dominated in-plane of this superlattice. We can see also that the top of valence band is dominated by the heavy holes hh_1.

The electrons and holes effective masse are giving in Figure 7, in the plane $k_p(k_x, k_y)$, and along the growth direction k_z of the reciprocal space. We extract the carriers effective mass from the dispersion of the curves in Figure 5, using the following relation given by Kittel [25]:

$$\left(\frac{1}{m^*}\right)_{ij} = \frac{1}{\hbar^2}\frac{\partial^2 E_{k_{ij}}}{\partial k_i \partial k_j} \qquad (10)$$

Where i and j are x,y or z-axis directions.

Along k_p direction, we remark that the heavy holes and electrons effective masses still almost constant. The corresponding values are: $m_{HH1}^* = -0.47\ m_0$ and $m_e^* = 0.109\ m_0$, respectively. Whereas, the light-holes decreases slightly from $m_{lh1}^* = -0.07\ m_0$ to $m_{lh1}^* = -0.06\ m_0$.

The figure 8 show the relation between the longitudinal $m^*_{E1}(k_F)$ along k_p and the well thickness d_1 at different temperatures. The carriers' effective mass marked an important decrease approaching 16 % when d_1 increases from 5 to 100. It is obvious that the thickness d_1(or d_2) have a strong impact on m^*_{E1}. Such result can be useful in varying the widths of materials superlattice to attain the carrier mobility requested, which can be applied technologically.

As seen in the Fig. 9, we have plotted the evolution of the calculated k_F-point energy of heavy-holes, light particles bands and the two-dimensional (2D) Fermi level, as a function of temperature. When the temperature increases from 1.7 K to 300 K, the energy of the hh_i(i=1,2) states remain almost constant, that of lh_1 decreases with a small variation and that of E_1 suddenly decreases by 100 meV. The later confirm the decrease of the band gap E_g= E.-hh_1.

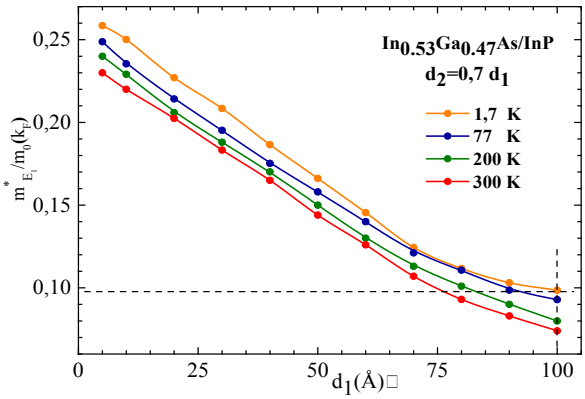


Figure 8: Evolution of the effective mass at the bottom of the conduction band at k_F as a function of d_1 and/or d_2 for $In_{0.53}Ga_{0.47}As(d_1)/InP(d_2)$ with d_1=1.43 d_2.

On the other hand, the Fermi level energy (E_F) does not depend on temperature which is the signature of a two-dimensional electrons gas.

3.2 Fermi level and density of states

In order to determine the Fermi level, we used the measurements of Pusep et al. [5] of the longitudinal magneto-resistance (ρ_{xx}) at 1.7 K. The oscillations of ρ_{xx}, at low temperature and under high magnetic fields, are periodic with respect to 1/B. The calculated period $\Delta_{1/B}$ allows us to determine the density of electrons n_{2D}, by the formula:

$$n_{2D} = \left| e/\left(\pi\hbar\Delta_{1/B}\right)\right| \qquad (11)$$

The relation between the inverse of the minima $1/B_{min}$ and the entire N, Landau level index is given by:

$$1/B_{min} = \Delta_{1/B}\left(N + 1/2\right) \qquad (12)$$

The oscillations period obtained by the straight line slope of (Eq. 12), $\Delta_{1/B}$= 0,11985 T^{-1} and the value of the electrons concentration, is $n_{2D} = 2.02\ 10^{11}\ cm^{-2}$.
The Fermi wave vector of two-dimensional electron gas

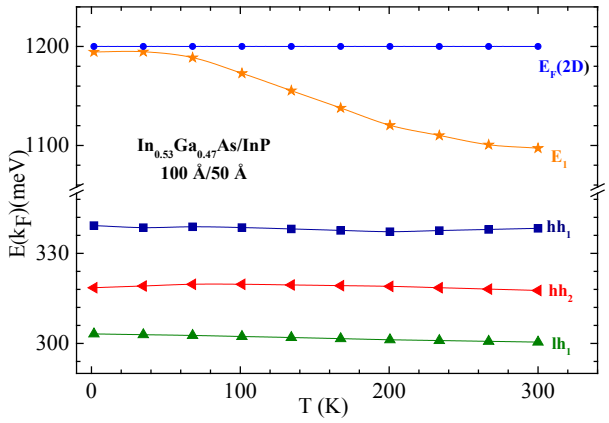


Figure 9: Evolution of band energy of light particles and heavy holes, calculated at the Fermi wave vector k_F, as a function of temperature of $In_{0.53}Ga_{0.47}As(d_1)/InP(d_2)$. $E_f(2D)$ represents the Fermi level energy.

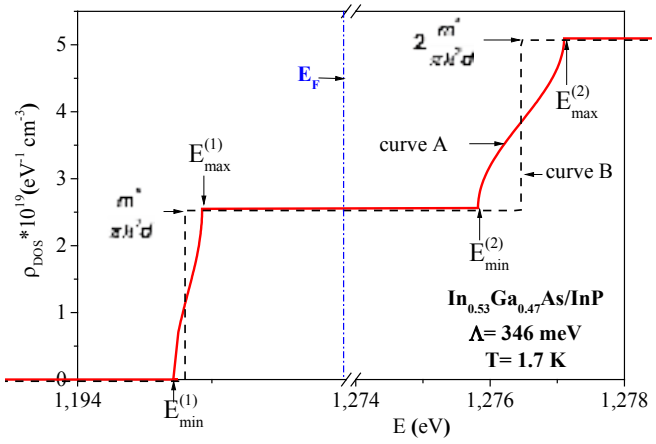


Figure 10: Density of states versus energy arising from the two lowest conduction mini-bands E_1 and E_2.

was calculated using the formula: $k_F^2 = 2\pi n_{2D}$, which give, k_F = 0.0127 $A^{\circ -1}$, as indicated in Fig. 6 and 7, by blue vertical dashed line. The corresponding electron effective masse is $(m^*_{E1})_{EF}=0.097\ m_0$ from Fig. 7.

The Fermi level energy is given by the following relation:

$$\left|E_F - E_c\right| = \left|\hbar^2 k_F^2 / \left(2m^*_{E_1}\right)_{E_F}\right| = \left|n_{2D}\pi\hbar^2 / \left(m^*_{E_1}\right)_{E_F}\right| \qquad (13)$$

Since E_c = 1.196 eV, so E_F = 1.200 eV and the half of the band $E_1(k_p)$ is full (Fig. 6). This shows that the studied sample has n-type conductivity at 1.7 K.

Moreover, we calculated the Fermi level energy using the Fermi–Dirac integral as a function of temperature [26, 27]. The resolution of such integrals give the exact value, E_F = 1.996 eV.

The density of states (DOS) of the i^{th} mini-band for a finite mini-band energy width $\Delta E^{(i)}=E^{(i)}_{max} - E^{(i)}_{min}$, is given by [28]:

$$\rho^{(i)}_{DOS}(E) = \begin{cases} \left(m^* / \pi^2\hbar^2\right)k_z(E) & for \quad E^{(i)}_{min} \le E \le E^{(i)}_{max} \\ 0 & otherwise \end{cases} \qquad (14)$$

The generalization of Eq.(14) required a sum over all mini-bands:

$$\rho_{DOS}(E) = \sum_{i=1}^{n} \rho^{(i)}_{DOS}(E) \qquad (15)$$

Fig.10, shows the density of states of the first two conduction subbands of this sample. We can see that only the first conduction subband $E_1(k_z)$ is occupied ($E_1 < E_F$ in Fig. 6) and the density of states is quantified in terms of $m^*/\pi\hbar^2 d$. The position of the Fermi level energy, indicated by dashed vertical line, show that E_1 and all the bands bellow are occupied and the sample had n-type conductivity at 1.7 K. A very weak dispersion of E_1 along k_z occurs indicating that the quantum wells are weakly coupled from each other and the system is quasi two-dimensional.

We calculated the Landau levels (LLs) for the conduction band E_1 as a function of magnetic field by

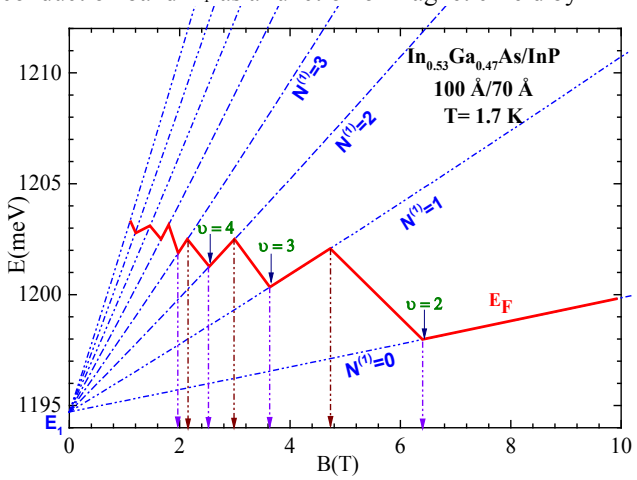


Figure 11: LLs of E_1 and the Fermi level energy for 20 periods as a function of magnetic field in this SL at 1.7 K.

transposing the quantification rule of the wave vector k_p in-plan of the SL in $E(k_p)$ as shown Fig. 11 :

$$k_p^2 = (2N+1)\frac{eB}{\hbar}, \qquad (16)$$

We have computed the Fermi level energy as a function of B, by using the following formula:

$$n_{2D} = \int_0^{+\infty} \rho^{2D}_{DOS}(E,B)\, f(E)\, dE \qquad (17)$$

$$\text{with } f(E) = 1/\left(1+\exp\left(E - E_F / k_B T\right)\right)$$

The expression of the DOS(B) is given in [29]:

$$\rho^{2D}_{DOS}(E,B) = \frac{|e|B}{\hbar}\sum_i \sum_{N^{(i)}} \delta\left(E - E^{(i)}\right) \qquad (18)$$

$n_{2D} = B / \rho_{xy}\, e$, with e the charge of electron, is obtained from the measured $\rho_{xy}(B)$ by [5].

When the magnetic field increases, crossovers between the calculated Landau levels (for N = 0–4) and Fermi level indicate the same minima of the transverse magnetoresistance $\rho_{xx}(B)$ oscillations (Shubnikov–de Haas effect), observed in Ref. [5] as shown in table 1, at B = 6, 3.87, 2.75, and 2.21 T. We calculated the filling factor using the formulate: $R_{xy}(\Omega)=h/\nu N_{SL}e^2$ [30]. At these values of magnetic field, the Hall resistance, R_{xy}, shows quantized

TABLE 1. Comparison between experimental observations (ref. 6) and the calculated magnetic field of R_{xx} minima and maxima, labeled here by B_{min} and B_{max}, respectively.

B_{min}(T)		B_{max}(T)	
Theoretical	Experimental (ref.[6])	Theoretical	Experimental (ref.[6])
4.70	4.70	6.38	6.40
2.97	2.70	3.63	3.21
2.10	1.70	2.50	2.51
1.70	1.1	1.96	1.80

plateaux. So we interpreted the Shubnikov de Haas oscillations and the Quantum Hall (QHE) plateaus observed by Pusep et al.

To observed such oscillations and the QHE, the separation $\hbar\,\omega_c$ ($\omega_c=eB/m^*_{E1}$ is the cyclotron pulsation) between LL must be superior to activation thermal energy k_BT. The magnetic field B must be greaten then 0.2 T ($B > k_B\,m^*_{EF}\,T/\hbar\,e$) with $m^*_{EF}=0.109m_0$.

We calculated also the transport scattering time $\tau_p=\mu_H\,m^*_{EF}/e$ =3.22 ps for the measured Hall mobility μ_H=5.2 10^3 cm^2/Vs at 1.7 K by [5] with our $m^*_{EF}=0.109m_0$. This value of τ_p is comparable to the quantum relaxation time τ_q= 0.5 ps and τ_p=2.34 ps measured in AlGaN/GaN two-dimensional electron gas [31]. The velocity of electrons on the Fermi surface is $v_F = \hbar k_F/ m^*_{EF}$ =1.35 10^{10} m/s. This is a clear demonstration of faster collision between electrons and phonon and high transport performances of this SL.

4. Conclusion

We have investigated the electronic transport properties of $In_{0.53}Ga_{0.47}As(d_1$=100Å)/InP(d_2=70 Å) SL at 1.7 K on the basis of the bands structure using the envelop function formalism. The optical band-gap E_g and the cut-off wavelength λ_c, were calculated as a function of d_1 and/or $d_2=0.7d_1$ and temperature. In the range of 1.7-300 K, $1.46\leq \lambda_c(\mu m) \leq 1.55$ shows that the investigated sample can be used for the active zone photodetector in short-infrared SWIR atmospheric windows. The position of the Fermi level, on the density of states showed n type conductivity and quasi-two-dimensional electrons gas. The calculated Fermi level energy and LLs as a function of magnetic field permit us the interpretation of the photoluminescence, the Shubnikov de Haas and quantum Hall Effects observed by Pusep et al. These transport parameters results are useful for the design of this nanostructure SL as short-infrared detector and other applications.

References

[1] D. Barkissy, A. Nafidi, et al, *Appl. Phys. A* 123: 54-60, 2017.

[2] A. Rogalski, Quantum Well Infrared Photodetectors, *Infrared Detect*, Second Ed, CRC Press: 542–600, 2010.

[3] Tarık Asar, Suleyman et al, *Appl. Phys*, 115, 2014.

[4] M. Peressi, S. Baroni, *Phys. Rev. B,* 41, 1990.

[5] Y.A. Pusep et al. J. *Phys. Condens. Matter*, 2, 2015.

[6] C. Persson, C. A. Draxl, Comp. *Phys. Communications* 177: 280–287, 2007.

[7] T. E. Ostromek. *Physical review.B, Condensed matter,* 54, 1996.

[8] G. Bastard, *Phys. Rev.* B 24, 5693, 5697, 1981.

[9] G. Bastard, *Phys. Rev*. B 25, 7584, 1982.

[10] E.O. Kane, J. Phys. Chem. Solids 1, 249, 1957.

[11] S.Z. Karazhanov, Semiconductors 39, 161, 2005.

[12] I. Vurgaftman, J.R. Meyer, L.R. Ram-Mohan, *Appl. Phys.* 89, 5815, 2001.

[13] Y.A. Goldberg, Gallium indium phosphide ($Ga_xIn_{1-x}P$), in: *Handb. Ser. Semicond. Parameters Vol. 2 Ternary Quat. III-V Compd*, pp. 62-88, 1996.

[14] K. Alavi, R. L. Aggarwal, and S. H. Groves, *Phys. Rev.* B 21, 1311,1980.

[15] S. Paul, J.B. Roy, P.K. Basu, J. *Appl. Phys*. 69: 827–829, 1991.

[16] Y.A. Goldberg, Gallium indium phosphide ($Ga_xIn_{1-x}P$), in: *Handb. Ser. Semicond. Parameters* Vol. 2 Ternary Quat. III-V Compd, pp. pp. 37-61, 1996.

[17] D. V. Lang, M.B. Panish, F. Capasso, J. Allam, R.A. Hamm, A.M. Sergent, et al., *Appl. Phys*. Lett. 50,736–738, 1987.

[18] R. Waldrop, E. A. Kraut, C. W. Farley, and R. W. Grant, J. *Appl. Phys*. 69, 372, 1990.

[19] W. Q. Chen and S. K. Hark, *Journal of Applied Physics* 77, 5747, 1995.

[20] Wisanu PECHARAPA et al. *Journal of Metals, Materials and Minerals,* 13: 1-5, 2003.

[21] S.V.Gaponenko, Optical Properties of Semiconductor Nanocrystals, *Cambridge University Press*, 27–54, 1998.

[22] L. Fernandes dos Santos, Y. Pusep, A. R. Zanatta, and R.R. LaPierre, J. Phys. D. *Appl. Phys*. 48, 2015.

[23] Y. P. Varshni, Temperature dependence of the energy gap in semiconductors, *Physica*, 34: 149–154, 1967.

[24] Peiji Geng et al. J. Phys. D, *Appl. Phys*. 50 40LT02 (5pp), 2017.

[25] C. Kittel, Introduction to Solid State Physics, Wiley, New York, 333, 2001.

[26] R. Kim and M. Lundstrom, Notes on Fermi-Dirac Integrals, 2, 2008.

[27] E.F. Schubert, Doping in III–V Semiconductors, *Cambridge University Press*, 1993.

[28] H.-S. Cho, Density of states of quasi-two, -one, and -zero dimensional superlattices, J. Vac. *Sci. Technol. B Microelectron. Nanom. Struct.* 71363.

[29] T. Ihn, Semiconductor Nanostructures Quantum states and electronic transport, *Oxford University Press* 7: 287–334, 2009.

[30] M. Dresselhaus, G. Dresselhaus, S. B. Cronin, A. Gomes Souza Filho, Solid State Properties: From Bulk to Nano, *Springer-Verlag GmbH Germany*, 308, 2018.

[31] A. Saxler, P. Debray, R. Perrin, et al, Electrical transport of an AlGaN/GaN two-dimensional electron gas, *Materials Research Society Internet Journal of Nitride Semiconductor Research* 5: 619-625, 2014.

Super-resolution imaging

Superresolution Stimulated Raman Microscopy

Sergey Kharintsev[1*], Anton Kharitonov[1], Alexander Alekseev[2,3], and Sergei Kazarian[4]

[1]Department of Optics and Nanophotonics, Institute of Physics, Kazan Federal University, Kazan, Russia
[2]National Laboratory Astana, Nazarbayev University, Astana, Kazakhstan
[3]STC NMST, Moscow Institute for Electronic Technology, Moscow, Russia
[4]Department of Chemical Engineering, Imperial College London, London, United Kingdom
*corresponding author, E-mail: skharint@gmail.com

Abstract

Titanium oxynitride (TiON), being metal-dielectric nano-composite ceramics, near the percolation threshold exhibits a double epsilon-near-zero (2-ENZ) behavior. It favours super-coupling of the incident laser light to surface plasmon resonances. In this work, we experimentally observe stimulated Raman gain emission from continuous and nano-structured TiON thin films exposed to low-power laser light. It is shown that super-resolution of <100 nm (better than λ/80) in the far-field is achieved due to both the enhanced third-order optical nonlinearity and the multiplicative nature of four-wave mixing.

1. Introduction

Titanium oxynitride (TiON) thin films, for the first time synthesized by Mihai and coworkers,[1] exhibit a tunable double epsilon-near-zero (2-ENZ) behavior in the visible and near-infrared regions. These refractory ceramics comprise a mixture of TiN, TiO_x, and TiO_xN_y compounds. Using the Maxwell-Garnett theory (MGT), the origin of this phenomenon can be understood by diluting nano-sized metallic inclusions of TiN within a TiO_2 host.[1] Near-field interactions between adjacent metallic inclusions can be further enhanced through excitation of delocalized surface plasmon-polaritons (SPPs) or leaky plasmon modes (LPMs). Interparticle junctions behave as hot spots that are able to enhance electric fields as strongly as interatomic fields, thus, higher-order optical nonlinearities become possible on the nanoscale.[2] If the metamaterial of interest is a Raman-active medium then inelastically scattered Raman photons, down-shifted by the phonon frequency Ω, are generated. Strong internal electrical fields allow a confined Raman-active medium to support the beating between a SPP/LPM pump and a localized Stokes signal. Thus, stimulated Raman scattering (SRS) occurs. It leads to the generation of a coherence wave of synchronized lattice vibrations that further exponentially enhances scattering into one of the overtones with frequencies $\omega_m = \omega_0 - m\Omega$ (ω_0 is a pump frequency, $m = 1, 2, \ldots$). The specific behavior of the 2-ENZ metamaterial in the vicinity of the zero points permits light to freely couple and/or decouple with the SPP/LPM, not using such couplers as a prism, a grating, etc.

In this paper, we report on LPM-assisted stimulated Raman scattering from continuous and nano-structured TiON thin films exposed to continuous-wave (cw) laser light with the power of a few mW's. We demonstrate the superlensing effect by showing a super-resolution of <100 nm in the far-field region, respectively. This effect is a recognition of the multiplicative nature of the SRS and the enhanced third-order optical nonlinearity. With the latter, we show that the sub-wavelength resolution is achieved through the strong localization of the internal electric fields at Stokes frequencies that sustains quasi-bound slow modes inside lossy media with the increased group refractive index.

2. Discussion

It is well-established that SPP-assisted stimulated Raman scattering may occur in confined Raman-active media.[3] The intensity of the localized Stokes wave, as a function of the distance L, experiences an exponential growth at the down-shifted frequency ω_m : $I_m(L) = I_m(0)\exp[\chi_R(\omega_m) I_0 L]$. Clearly, the strength of the optical amplification is provided by maximizing the product $\chi_R(\omega_m) I_0 L$. Since we deal with the confined medium, $L \to 0$, and the low-intensity pump I_0 (a few $\mathrm{mW/cm^2}$), the SRS performance is improved by enhancing the Raman factor $\chi_R(\omega_m)$. The energy exchange between the pump and the Stokes components can be greatly supported by surface plasmon resonances.

In the SRS regime all four waves ($\omega_m = \omega_0 + \omega_m - \omega_0$) become enhanced. Thus, the third-order Raman susceptibility changes as

$$\chi_R^{(3)}(\omega_m; \omega_0, -\omega_0, \omega_m) \to \\ \to g_0^2 g_m^2 \chi_R^{(3)}(\omega_m; \omega_0, -\omega_0, \omega_m), \quad (1)$$

where g_0 and g_m are the local field-enhancement factors for the pump and the Stokes signal, respectively. With that, the Raman gain factor $\chi_R(\omega_m)$ reads as:

$$\chi_R(\omega_m) = -\frac{3\omega_m}{n_m n_0 \varepsilon_0 c^2} g_0^2 g_m^2 \, \mathrm{Im}[\chi_R^{(3)}], \qquad (2)$$

where $n_0 = n(\omega_0)$ are $n_m = n(\omega_m)$ are the group refractive indexes for the pump and the Stokes wave, c is the speed of light in vacuum. Compared to the approach considered in

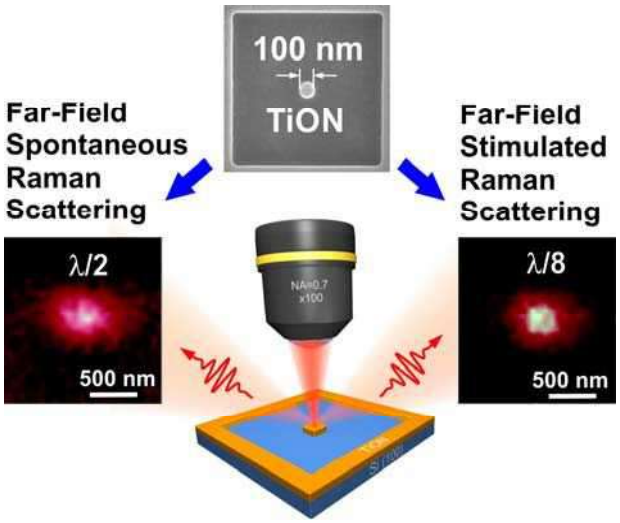


Figure 1: Far-field spontaneous and stimulated Raman scattering of a square TiON nanoantenna.

Ref.[3], both the field enhancements of the pump and the Stokes wave are taken into account in Eq. (2). The real part of $\chi_R^{(3)}$ contributes into the accumulated Raman phase shift $\Delta\phi_R$ for the Stokes wave and it corresponds to the Kerr optical nonlinearity. As follows from Eq. (2) a link between the group and effective refractive index, n_m and n_{eff}, at the Raman shift ω_m is expressed by the following relationship

$$g_m = \sqrt{\frac{n_m}{n_{\mathrm{eff}}}}. \qquad (3)$$

Most intriguing feature of the 2-ENZ metamaterial is its capability to far-field superlensing. We fabricated a 100x100 nm^2 square antenna on the TiON thin film with focused ion beam milling, as shown in Fig. 1. With that, it is demonstrated far-field spontaneous and stimulated Raman scattering of this antenna. In the latter case, we achieve the improvement of spatial resolution down to 80 nm (λ/8).

The physical origin of this phenomenon can be clarified by the increased group refractive index due to the local field enhancement factor, Eq. (3). The enhanced leaky slow-mode propagates along conducting nanoparticles chains within near-zero refractive index media. As a result, the Airy function $\mathrm{PSF}(\rho,\theta)$, inevitably becomes narrower

$$\mathrm{PSF}(\rho,\theta) = \left| J_1(k n_m \rho \sin(\theta)/2)/k n_m \rho \sin(\theta)/4 \right|^2, \qquad (4)$$

where $J_1(x)$ is a Bessel function of the first kind. Thus, as follows from Eq. (4), the spatial resolution is eventually determined by the local field-enhancement factor g_m. It is important to note that this result is valid for the Stokes components $\omega_m = \omega_0 - m\Omega$ only. It means that in the total scattered light we can observe the super-resolution effect at the anharmonicity-free overtones.

It may be realized that the whole antenna surface radiates more or less uniformly and this is not localized to the edges of the sample, as has been observed with the planar TiN antenna.[3] This follows the slight deviation of the dispersion curve of the 2-ENZ metamaterial from the light line and the presence of the intrinsic roughness of the antenna surface. Previously, the similar result was obtained through coherent anti-Stokes Raman scattering by using a Toraldo-style pupil phase filter.[4]

Another important contribution into the resolution improvement is the multiplicative nature of the SRS. It is well established that the third-order nonlinear effects are recognized by (1) the cubic behavior of the SRS intensity I_m vs the pump power I_0:

$$I_m = aI_0 + bI_0^3, \qquad (5)$$

where a and b are constants for spontaneous and coherent contributions, respectively, and (2) the decrease of the full width at half height with the pump power.

3. Conclusions

In conclusion, we have demonstrated the superlensing effect by showing a super-resolution of <100 nm in the far-field region using the SRS. We believe that our findings will provide a basis of diffraction-free far-field optical microscopy.

Acknowledgements

This work was supported by grant No. 19-12-00066 of the Russian Science Foundation. The authors are indebted to Dr. A. Mihai (Imperial College London, UK) for kindly providing a TiON sample.

References

[1] L. Braic, N. Vasilantonakis, A. Mihai, I. J. V. Garcia, S. Fearn, B. Zou, N. M. Alford, B. Dolron, R. F. Oulton, S. A. Maier, A. V. Zayats and P. K. Petrov, Titanium oxynitride thin films with tunable double epsilon-near-zero behavior for nanophotonic applications, *ACS Appl. Mater. Inter.*, 9: 29857–29862, 2017.

[2] W. Cai, V. Shalaev, *Optical Metamaterials*: Fundamentals and Applications, Springer, 2010.

[3] S.S. Kharintsev, A.V. Kharitonov, S.K. Saikin, A.M. Alekseev and S.G. Kazarian, Nonlinear Raman effects enhanced by surface plasmon excitation in planar refractory nano-Antennas, *Nano Lett.* 17: 5533–5539, 2017.

[4] H. Kim, G.W. Bryant and S. J. Stranick, Superresolution four-wave mixing microscopy, *Opt. Express* 20: 6042–6051, 2012.

Haze removal method based on decomposition

Xifang Zhu[1], Ruxi Xiang*[1; 2; 3], Feng Wu[1], Qingquan Xu[1] and Ye Lu[1]
[1]School of Photoelectronic Engineering, Changzhou Institute of Technology, 213032, China
[2]Changzhou Institute of Modern Optical Technology, 213032, China
[3]Changzhou Key Laboratory of Optoelectronic Materials and Devices, 213032，China
*corresponding author, E-mail: xiangrx@czu.cn

Abstract

To obtain a reflected image free of haze, a new haze-removing method is proposed based on decomposition, which effectively reconstructs a reflected image from the hazy image. The decomposition problem can be formulated as a constrained quadratic programming optimization problem which can be obtained by combining the Bregman method with the fast Fourier transform method. Compared with existing methods, our results show that our method can effectively remove the haze and improve image qualities such as contrast, sharpness and color.

1. Introduction

Image haze-removal technologies can effectively improve outdoor vision system performance (e.g., sharpness, color, and contrast). Particularly, single image haze-removal technology has become an important subject for computer vision. At present, many classical single image haze-removal methods have been propose. Tan estimated the optimized atmospheric light value by combining a Markov random field (MRF) with the theory of graph cuts to improve image quality. Fattal derived the shading and transmission by the statistical decomposition method based on the assumption that the shading and transmission functions are locally statistically uncorrelated . He, et al. performed a rough estimate of the transmission map by applying the darkness prior, and then used the soft matting method to improve it.

These single image haze-removal methods have a common disadvantage: the MASM physical model solution is an ill-posed inverse problem. The solution often results in great computational complexity resulting in the need for an optimized tool. To obtain an effective transmission map, we introduce a new optimized method based on the regularized total variance method. Compared with existing methods, experimental results show that the proposed method can effectively remove haze from poor weather conditions to improve image quality (e.g., sharpness, color and contrast.).

2. MASM model

. Using Narasimhan's9 scattering theory, we explain the classic MASM model, defined as:

$$\mathrm{I}(p) = J(p)t(p) + A(1 - t(p)) \tag{1}$$

where p is the pixel position of the image, I(p) is the observed image with haze, J(p) is the image without haze to be estimated, t(p) denotes atmosphere transmittance, and A is the atmospheric light. It was assumed that A's value (a global value) is unrelated to the pixel position. The first term of equation (1) is the direct attenuation, while the second term is the indirect attenuation. To use the classic Retinex model, we begin by rewriting equation (1) as

$$A - I(p) = (A - J(p))t(p) \tag{2}$$

which is like the classic Retinex model, which assumes the image can be represented as the product of reflectance and illumination. From equation (2), it can be observed that the observer image can also consist of two parts: similar reflectance and illumination. To make use of edge-preservation and scale-dependent decomposition capacity11 of the L2 model, we take the logarithm of equation (2) to obtain the additive impact of illumination:

$$i(p) = j(p) + b(p)$$

$$i(p) = \log(A - I(p)), j(p) = \log(A - J(p)), b(p) = \log(t(p)) \tag{3}$$

Since the illumination b is assumed to be a smooth variation, the reflectance j is assumed to have details, such as texture and edges. To decompose the image, we proposed a new decomposition method based on relative smoothness, which is like the classic Retinex method.

3. Proposed method

To obtain a clear image without haze from multiple models, we implement a new method by constructing an effective energy function to extract a clear image. The TV+L2 method can remove the reflection with defocus blur based on a single image. However, the edges and texture of the image obtained by the method remain blurred, and the step effect of the image is easily observed. Hence, we introduce a new variation regularized model to reduce these defects. The energy of the new variation regularized model is defined as

$$\begin{aligned} &\min \| \nabla r \|_2^2 + \frac{\alpha}{2} \| \Delta(i - r) \|_2^2 + \frac{\beta}{2} \| i - r \|_2^2 \\ &\text{s.t.} \quad e = \Delta(i - r) \end{aligned} \tag{4}$$

where is a p normal space, where p is selected as 1 or 2. β and α are constants that control the smoothness of the output image. The first two terms are regular and preserve the smoothness of the decomposition image. The third term is a residual term that preserves some main features of the observed image. That is, the

reflectance r is like that of the input image. We address the new constraint by introducing the following Lagrangian; equation (4) was modified to the unconstrained form

$$\min \frac{1}{2}\|\nabla r\|_2^2 + \frac{\alpha}{2}\|\Delta(i-r)\|_2^2 + \frac{\beta}{2}\|i-r\|_2^2 + \frac{\lambda}{2}\|e+\Delta r-\Delta i-be\|_2^2 \quad (5)$$

For the solutions of equation (5), we adopted a split Bregman iterative algorithm. To easily obtain a solution for *r*, we can apply a 2D FFT. The solution of equation (5) is defined as

$$F(r)=\frac{\lambda F_l \circ F_{b_e^k} + \lambda F_l \circ F_l^* \circ F_i - \lambda F_l \circ F_{e^k} + \alpha F_l \circ F_l^* \circ F_i + \beta F_i}{F_x \circ F_x^* + F_y \circ F_y^* + \alpha F_l \circ F_l^* + \lambda F_l \circ F_l^* + \beta} \quad (6)$$

where F_l, F_x, F_y, F_e, F_{b_e} and F_i are the fast Fourier transforms of the variables l, x, y, e^k, $b_e{}^k$ and i, respectively.

we obtained the approximate atmospheric transmittance map by analyzing the ALATM. First, the AATM t was subtracted from the constant cn, expressed as

$$t = k\left(exp\ \left(\max(ALATM)\right) - cn\right) \quad (7)$$

where the variables k and cn are two controlling transmission factors.

4. Experimental results and discussion

In this subsection, we verify the performance of our method using MATLAB 2010b in a computer with a 1.8 GHz Intel i5 Processor. We make several experiments to assess the performance of our method for different kinds of hazy images and compare our results with He's results and Fattal's results.

Figure 1 shows the dehazed results and the corresponding assessment values using different haze-removal methods using the swan image. As we can see in Figure 1, the proposed method can effectively remove haze from scenes by comparing other state-of-the–art methods, including He's, Tan's, Kratz's and Nishino's methods. In Figures 1(c), 1(d), and 1(e), the colors of the results are often over-saturated since their transmission maps may be underestimated. Our proposed method and He's method can both recover the color features. However, the proposed method can obtain improved sharpness, as shown in Figures 1(b) and 1(f). There are halo artifacts in all the results. Nevertheless, results from the proposed method and He's method have significantly smaller halo artifacts.

From the perspective of the assessment values, we can find that the effect of the haze-removal using the method proposed by Tan is the best. However,, the color of the dehazed image is over-saturated. The assessment values of the image produced using our proposed method is closer to Tan's value. However, the color of our result is better.

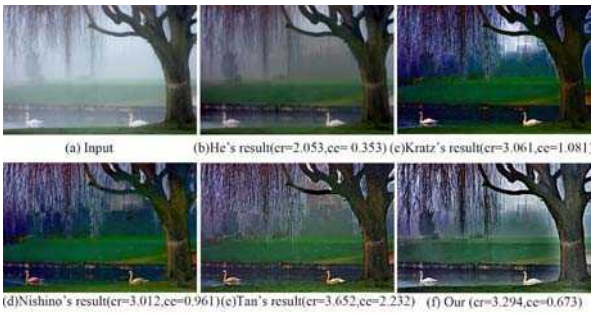


Fig. 1 Comparison of different haze-removal methods in the swan image

5. Conclusions

In this study, we modified the monochrome atmospheric scattering model to obtain the approximate Retinex model, and then the approximate atmospheric transmittance map was computed by decomposing the approximate Retinex model, based on the constrained regularized total variance method. To obtain a solution to the constrained regularized total variance model, we effectively combined the Bregman iteration method to obtain an optimum solution for the approximate logarithmic atmospheric transmittance map, and then the approximate atmospheric transmittance map was computed by taking the maximum channel out of the three channels of the decomposition transmittance map. Finally, the reflectance image was obtained using the MASM. Compared with other existing methods, our results show that the proposed method can effectively remove haze from bad weather conditions and improve image quality, including the contrast, sharpness, and color. .

Acknowledgements

This work was supported by the Natural Science Foundation of China (Grant Nos.61475027 and 61875022), Science and Technology Support Program (Social Development)(pre-funding) of Changzhou (CE20185029).

References

[1] R. T. Tan.Visibility in bad weather from a single image.*Proc. CVPR* 10139948, 1-8 ,2008.

[2] R. Fattal.Single image dehazing.*ACM Trans. Graphics,* 27(3), 72 ,2008.

[3] K. He, J. Sun and X. Tang.Single Image Haze Removal Using Dark Channel Prior," *IEEE PAMI*, 33(12), 2341-2353,2011.

[4] L. Kratz and K. Nishino,Factorizing scene albedo and depth from a single foggy image. *Proc. ICCV* 11367823 , 1701-1708 ,2009.

[5] K. Tang, J. Yang, and J. Wang. Investigating haze-relevant features in a learning framework for image dehazing,*Proc. CVPR* 14632059, 2995-3002,2014.

D. Berman, T. Treibitz, and S. Avidan,.Non-local image dehazing. *Proc. CVPR* 16526883 , 1674-1682,2016.

Haze Removal based on New Estimation of the Atmospheric Light

Ruxi Xiang[*1; 2; 3],Xifang Zhu[*1], Feng Wu[1], Qingquan Xu[1] and Ye Lu[1]
[1]School of Photoelectronic Engineering, Changzhou Institute of Technology, 213032, China
[2]Changzhou Institute of Modern Optical Technology, 213032, China
[3]Changzhou Key Laboratory of Optoelectronic Materials and Devices, 213032，China
*corresponding author, E-mail: zhuxfcz@yeah.net

Abstract

In order to obtain the accurate estimation of the atmospheric light, we present a new and effective method for computing the atmospheric light based on the salient region of the input haze image, which estimates the atmospheric light by combining the statistical characteristics of between the darkness channel and the region of the atmospheric light. Compared with existing methods, our results show that our method can accurately recover the atmospheric light and effectively remove the haze from the bad weather.

1. Introduction

Images captured from the haze weather is prone to suffering from some degradations including low visibility, poor contrast and color distortion because of the scattering of the air light by the larger particles in the air, which greatly affects the further analysis of images. In order to improve the image quality, some experts make a lot of efforts and propose some removal haze methods based on the single image. For instance, Tan et al enhance the contrast of the image for removing the haze by maximizing the local contrast[1]. Fattal improves the quality of the image by estimating the albedo of the radiance image[2], and He et al restore the radiance image relying on the dark channel prior[3].

Above mentioned methods can improve the colorless, visibility or contrast. However, each method has different estimation of the atmospheric light. Tan's method treats the brightest pixels in the input image as the estimation of the atmospheric light[1]. Fattal's method treats the sky regions as the estimation of the atmospheric light[2], and He's method treats the top 0.1 % brightest pixels in the dark channel as the estimation of the atmospheric light[3]. To improve the image quality, we propose a new estimation of the atmospheric light method for removing the haze, which effectively combines the salient region of the input. Compared with existing methods, experimental results show that the proposed method can effectively remove haze from poor weather conditions to improve image quality .

2. MASM model

The MASM [4]widely used in the bad weather condition is usually defined as

$$I(x)=J(x)t(x)+A(1-t(x)), \quad (1)$$

where I is the input image with haze, J is the scene radiance with free haze, x denotes the image position, A is the global atmospheric light, t is the transmission map describing the portion of scene reaching the camera.The first term is the direct attenuation of the scene and the second is the indirect attenuation by the atmosphere. The radiance image J based on the MASM theory can be rewritten as

$$J(x)=\frac{I(x)-A}{\max(t(x),th)}+A, \quad (2)$$

where the variable th is a threshold ,in this paper , th can automatically be adjusted.

3. Proposed method

The proposed removal haze method is illustrated in Fig.1.As one can see, the method consists of five parts: input, computing the atmospheric light, computing the transmission map, restoring the radiance image and color correction.

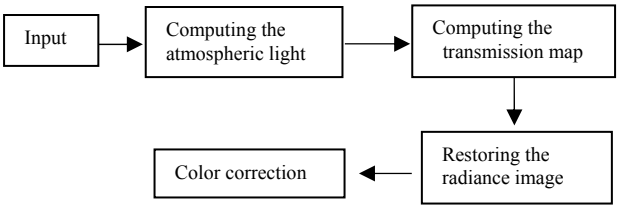


Fig.1 The architecture of the proposed method.

3.1. Estimation of the atmospheric light

The atmospheric light is a key factor for removing the haze based on the MASM model. The more precision its estimation is, the better the performance of haze removal will be. In order to further improve the precision, we effectively combine the salient region with the dark channel prior to estimate the atmospheric light because it is very small that the probability of the atmospheric light is located in the salient area of the image. The salient region is computed by analyzing the log-spectrum of an input image, and then adaptively extract the spectral residual of an image in spectral domain. After obtaining the salient region, we integrate with the dark channel prior to estimate the atmospheric light.

3.2. Computing transmission map

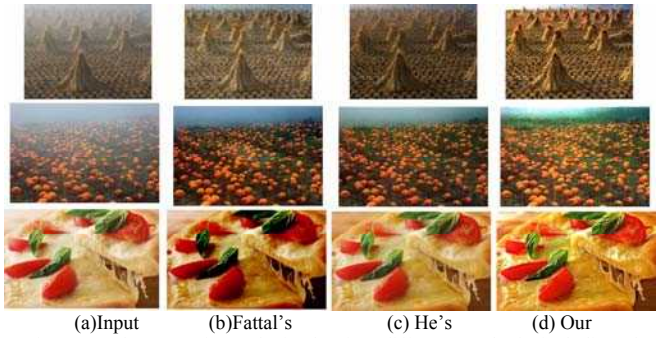
According to the equation (1), the transmission map t(x) is rewritten as :

$$t(x) = 1 - \min_{c}(\min_{q \in Q(x)}(\frac{I^c(q)}{A^c})) / \min_{c}(\min_{q \in Q(x)}(\frac{J^c(q)}{A^c}))$$

, posing a dilemma. To resolve this, He et al assume that the radiance image J is close to 0 based on statistics of the dark channel of outdoor images because the equation in which two variables are to be solved for. We also assume that the dark channel of the radiance image is close to zero and we combine the salient region to automatically adjust the threshold. On the contrary, the classical He's method computes it by fixed threshold. The transmission map t(x) is then computed with (2).After obtaining the rough transmission map, we observed that the transmission map contains some block effect and needed to be refined. Therefore, we refine it by the multi-kernel guided filter to enhance the image quantity. Finally, the radiance image is restored using the equation (2) and the refined transmission map. In order to further improve the image quality, we adopt a new white balance method to correct the color of the removal haze.

4. Experimental results and discussion

In this subsection, we verify the performance of our method using MATLAB 2010b in a computer with a 1.8 GHz Intel i5 Processor. We make several experiments to assess the performance of our method for different kinds of hazy images and compare our results with He's results and Fattal's results. Fig. 2 shows the results of Fattal's, He's method and our method for several different hazy images. The left column is the input images, the second shows the results of fattal's method ,the third shows the results of He's method, and the right shows the results of our method. As we can see in Fig.2, the proposed method can effectively remove haze from scenes by comparing other state-of-the–art methods, including He's and Fattal's methods. In Fig.2 (b), the colors of the results are often over-saturated since their transmission maps may be underestimated. Our method and He's method can both recover the color features. Fig.2(c), the sharpness obtained by He's method is weaker than that of our method because the estimation of the atmospheric light obtained by our method is precise than that of He's method. Consequently, the proposed method can obtain improved sharpness, as shown in Fig.2(d).



(a)Input (b)Fattal's (c) He's (d) Our

Fig.2. Result comparison obtained using different methods including (b) Fattal's ,(c) He's and (d)Our method.

To further evaluate the performance of the proposed method, we compare the assessment LSIA[5] of each method as shown in Table 1. In Table 1, we label the top LSIA in each by bold font, and we find that our method outperform He's method and Fattal's method. That is to say, our method not only can obtain better color, contrast, and visibility with respect to performance of the removal haze but obtain high image assessment value .

Table 1: Comparisons of Assessment values of different method

	input	Fattal	He	our
cones	0.8451	0.8550	0.8591	**0.8918**
pumpkins	0.8789	0.8761	0.8870	**0.8887**
pizza_	0.9023	0.9294	0.8919	**0.9316**

5. Conclusions

In this paper, we present a new and efficient method for removing haze, which is based on new estimation of the atmospheric light. We can effectively remove the haze from different scenes and obtain better color, contrast, and visibility, especially the precision of the atmospheric light. Compared with He's method and Fattal's method, the proposed method can obtain better performance. However, our method still will produce small halo artefacts at boundaries with abrupt depth changes for a lot of dense haze, which is left to future research .

Acknowledgements

This work was supported by the Natural Science Foundation of China (Grant Nos.61475027 and 61875022), Science and Technology Support Program (Social Development)(pre-funding) of Changzhou (CE20185029).

References

[1] R. T. Tan,"Visibility in bad weather from a single image," Proc. *CVPR* 10139948, 1-8 ,2008.

[2] R. Fattal,"Single image dehazing,"*ACM Trans.Graphics*, Papers 27(3), 72,2008.

[3] K. He, J. Sun and X. Tang, "Single Image Haze Removal Using Dark Channel Prior," *IEEE PAMI,* 33(12), 2341-2353,2011.

[4] Narasimhan S G, Nayar S K, "Contrast restoration of weather degraded images," *IEEE PAMI* ,25(6), 713-724 2003.

[5] Xiang Ruxi, Xu Qingquan, Zhu Xifang, et al. No-reference Blur Image Assessment based on Local Sharpness. *Microelectronics & Computer*, 34 (3),125-128,2017.

Ultrafast and nonlinear phenomena

Nonlinear Optical Bleaching of a Monolayer of Au Plasmonic Coupled Nanoparticles and Percolation-like Films with Nanoslits

Vladimir Kaydashev[1,2], Piero Ferrari[3], Pavel Timoshenko[2], Mikhail Shestakov[3], Ewald Janssens[3], Peter Lievens[3] and Evgeni Kaidashev[2]

[1]Moscow Institute of Physics and Technology , 2D materials` Optoelectronics Lab, Dolgoprudny, Russia
[2]Southern Federal University, Laboratory of Nanomaterials, Rostov-on-Don, Russia
[3]KULeuven, Laboratory of Solid State Physics and Magnetism, Leuven, Belgium

*corresponding author, E-mail: kaydashev@gmail.com

Abstract

The optical transmittance of a monolayer of Au plasmonic coupled nanoparticles and percolation-like films with nanoslits is controlled from 54% to 86% and from 13% to 54%, correspondingly, upon excitation by intense nanosecond laser pulses.

1. Introduction

Strongly coupled plasmonic nanosystems with nanometer scale gaps are an emerging generation of plasmonic systems in which the focusing of incident electromagnetic energy in the near field is highly efficient. These systems provide great opportunities for ultra-sensitive molecular sensing based on SERS and fluorescence enhancement, high harmonics generation, design of super-resolution tools. Moreover, coupled plasmonic nanostructures show new nonlinear optical properties that differ from those of isolated particles, opening promising opportunities in the modulation of light transmission by the use of intense laser pulses. We study the optical bleaching of a monolayer of Au plasmonic coupled nanoparticles and percolation-like films with nanoslits using Z-scan technique.

2. Array of plasmonic coupled nanoparticles

A macroscopic array of self-assembled plasmonic coupled Au nanoparticles with distribution maximum near 8 nm and separating gaps of 3-8 nm were prepared by pulsed laser deposition at high Ar pressure. The optical transmittance spectrum reveals two broad bands with local minima near 770 nm and 350 nm. The presence of those two absorption maxima is well understood and is attributed to the hybridization of dipolar plasmon excitations, which results in “bonding” and “anti-bonding” modes for nanoparticle pairs. Note that a plasmon band of isolated Au nanoparticles of comparable sizes is typically observed near 520 nm. We numerically modeled the arrays of hemispherical and semi-elliptical particles of different sizes, shapes and separating gaps and have found several important trends, which support the red shift and broadening of the particles absorption spectra. The nonlinear optical properties were studied using the z-scan technique in combination with nanosecond laser excitation. This was done as function of incident laser irradiance at wavelengths within the bonding and anti-bonding hybridized plasmonic bands as shown in Figure 1.

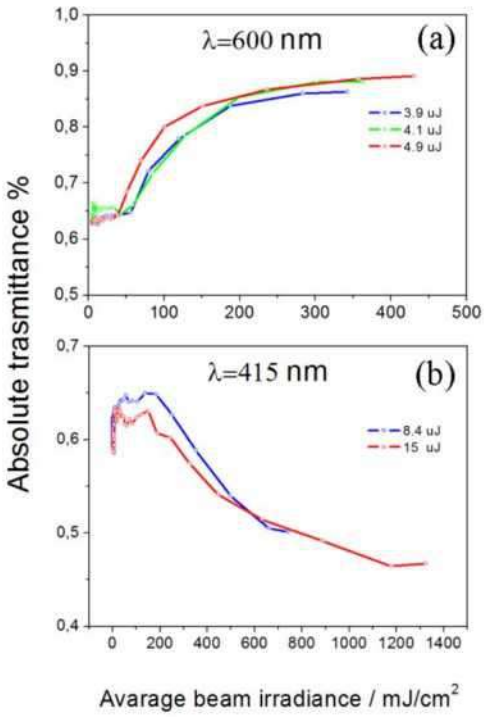


Figure 1: Irradiance dependent transmittance of plasmonic coupled Au nanoparticle array measured by the z-scan technique in the open aperture configuration for excitation within “bonding” (a) and “anti-bonding” (b) bands at 600 nm and 415 nm, correspondingly.

At 600 nm excitation by nanosecond pulses near the beam waist the absorption coefficient is effected by optical nonlinearities; once the fluence threshold is reached, transmission increases from ~63 to ~90%, i.e. nonlinear optical bleaching of the Au layer is observed. Interestingly,

the z-scan curve measured at 415 nm is fundamentally different from that measured at 600 nm, and has a similar shape as those typically observed for isolated Ag or Au particles in solutions, nano-composites, or glass hosts.

3. Discussion

The observed phenomenon can`t be explained by nonlinear plasmonic scattering effect but is caused by particles absorption only. Indeed, the Au nanoparticles larger than ~40 nm do effect also the scattering, which give input to detected extinction even in linear regime. In nonlinear regime the scattering of such objects normally evolves to strong defocussing of beam, i.e. results in the enlargement of a Gaussian beam in detector plane during z-scan measurement. Besides, "speckle-like" pattern of multiple bright spots is normally observed for scattering objects. The studied nanoparticles are too small to show some detectable scattering and the there was no any sign of beam profile change/speckle pattern observed in support to our argumentation. Moreover, if any nonlinear defocussing occurs, the z-scan would show the central dip similar to those reported for larger isolated particles. For our plasmonic coupled system we in contrast observed the significant optical bleaching which is opposite to transmission decrease for larger isolated nanoparticles where both nonlinear scattering and multi-photon absorption reduce the transmission.

The irradiance dependent transmittance of the plasmonic coupled nanoparticle arrays is also very different from that of isolated nanoparticles at this excitation wavelength. In particular, at moderate incident laser irradiances, isolated nanoparticles typically show a small transmittance increase induced by optical absorption saturation. At higher laser fluence, z-scan curves typically reveal a valley around z=0, corresponding to an "opening" of the two-photon absorption channel. In contrast, for the present case of plasmonic coupled nanoparticles, the two-photon absorption channel does not open by increasing the incident irradiance, instead the samples gradually becomes more transparent. When power density is below ~ 140 MW/cm^2 (irradiance on beam axis lower than 1 J/cm^2), the observed effect is well reproducible without degradation of the nanoparticles. The large change in transmission of 27%, from the lower to the higher irradiance regime, is comparable to that found in plasmonic coupled particle-cluster aggregates in solution. Thus, in contrast to studies on isolated particles, z-scan curves of the coupled nanoparticles, excited at 600 nm, do not show a crossover from saturable absorption to transmission decrease.

Remarkable, that similar and even more pronounced nonlinear effects were observed later for percolation-like Au films with nanoslits as shown in Figure 2.

4. Conclusions

We demonste the unusually large nonlinear optical transmission increase in a macroscopic quasi-homogeneous array of plasmonic coupled nanoparticles, which is controllable by the irradiance of nanosecond laser pulses. These plasmonic coupled structures show both linear and nonlinear wavelength and irradiance dependent optical properties very unlike to those of isolated nanoparticles.

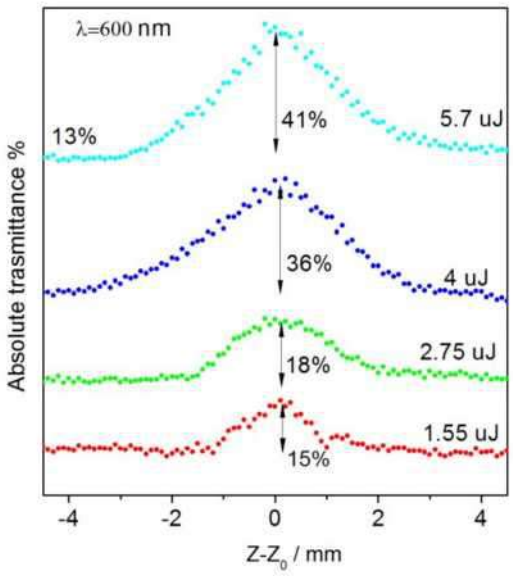


Figure 2: Nonlinear optical transmittance change of Au percolation-like film with nanosized slits

In contrast to single plasmonic nano-objects, the usual saturation absorption to transmission decrease turnover in z-scan curves is not observed, when exciting in the "bonding" plasmon band. However, for excitation within the "anti-bonding" band, z-scan curves resemble those characteristic for isolated particles. These phenomena are observed when coupled particles are excited by nanosecond laser pulses, which is very different from the previously reported nonlinear-induced transparency increase on femtosecond and picosecond timescales and can`t be explained in terms of electron-phonon relaxation dynamics only. For nonlinear optical bleaching in nanosecond timescales we provide an explanation based on light retardation effects and the destructive interference phenomenon known in literature as electromagnetically induced transparency.

Acknowledgements

This work was financially supported by Russian Federation President Grant № MK-8369.2016.2 "A study of an optical absorption and electromagnetic field concentration in strongly coupled plasmon nanosystems", by Russian Education and Science Ministry project No. 16.5405.2017/8.9 and by the Research Foundation-Flanders (FWO), grant G.0A18.17 "Second- and third-order nonlinear optical properties of noble metal clusters" P.F. acknowledges the FWO for a post-doctoral fellowship. The theoretical modeling was supported by RFBR research project №18-02-00151A "Study of photothermal effect in plasmonic coupled nanosystems".

Acoustic and seismic metamaterials

Multiple Weyl and Double-Weyl Points in Elastic Chiral Lattices

Yao-Ting Wang[1], Ya-Wen Tsai[2]

[1] *Department of Physics, Imperial College London, London, SW7 2AZ, United Kingdom*

[2] *Department of Materials Science and Engineering, National Tsing-Hua University, Hsinchu, 30068 Taiwan*

In the past decade, Weyl semimetals, which are categorised into solid state crystals and its Fermi energy is located precisely at Weyl points, have been widely investigated in condensed matter physics. Here we prove that multiple Weyl and double Weyl points exist in a chiral elastic system via stacking two-dimensional honeycomb elastic structures. On the distinct k_z plane, the band structures given by a p_x-p_y tight-binding model show the emergence of Weyl points at K point and double Weyl Points at Brillouin centre. Based on the theoretical prediction, a practical chiral mechanical structure can be constructed by current 3D printing technology. The numerical calculation presents several Weyl and double-Weyl points as expected in our analysis of the tight-binding model. To verify the topological feature, the topological charge of degeneracy and the band Chern number are both calculated. Due to the presence of the band Chern numbers marked in Fig. 1a, there are two topologically non-trivial bandgaps guaranteed by bulk-boundary correspondence. Fig. 1b depicts the projected band structures on the $k_z = \pi/2c$ plane and there are surface states within two bandgaps. To further verify its topological protection feature, at $k_z = \pi/2c$ and $f = 6.70$ kHz, the elastic waves present a one-way transport along the truncated surface and propagate robustly against the disorder, as shown in Fig. 1c.

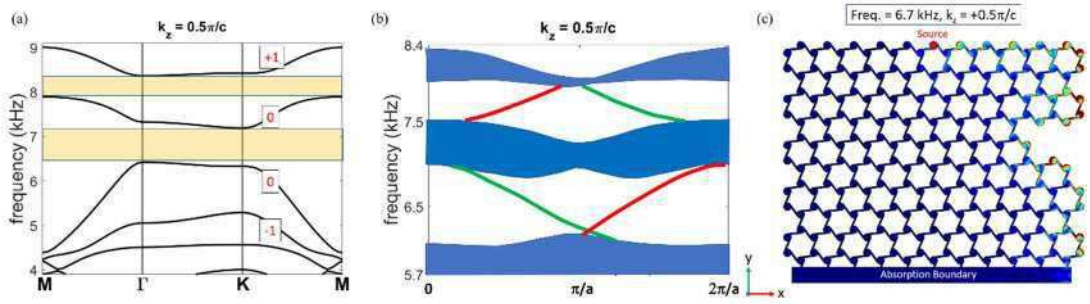


Fig. 1 (a) Fixing k_z values as the synthetic gauge field for the band structure in the 2D subdomain. Numbers attached to bands denote the corresponding Chern numbers. (b) Projected band structure with truncation along x axis. Topological surface modes are coloured in red and green to differ from the surface modes located at the upper and lower boundaries. On the different k_z planes, the surface modes with topological protection are demonstrated in (c).

Phononic Crystals with Archimedean-Like Tiling's: Transmission, Band Structure and Transformation of Sound

Zafer Ozer[1,*]

[1]Mersin Vocational High School Electronic and Automation Department, Mersin University, Mersin, Turkey
*zaferozer@hotmail.com

In this study we investigate acoustic wave propagation in 3D phononic crystal (PnC) slabs which scatterers having different cross sections by using finite element method (FEM). The PnC consists of scatterers embedded in the host material arranged in a square lattice and with Archimedean-like tiling's (bathroom and ladybug) as seen in fig.1 and 2. By determining the eigenmodes and band gaps complete and accurate band structures and transmission spectra are obtained. Compared to traditional square lattice PnC's, it has been observed that the bands obtained in Archimedean-like structures may have some advantages in terms of width and position. It was also shown that the low frequency response of two Archimedean-like structures was similar in with respect to the traditional square lattice.

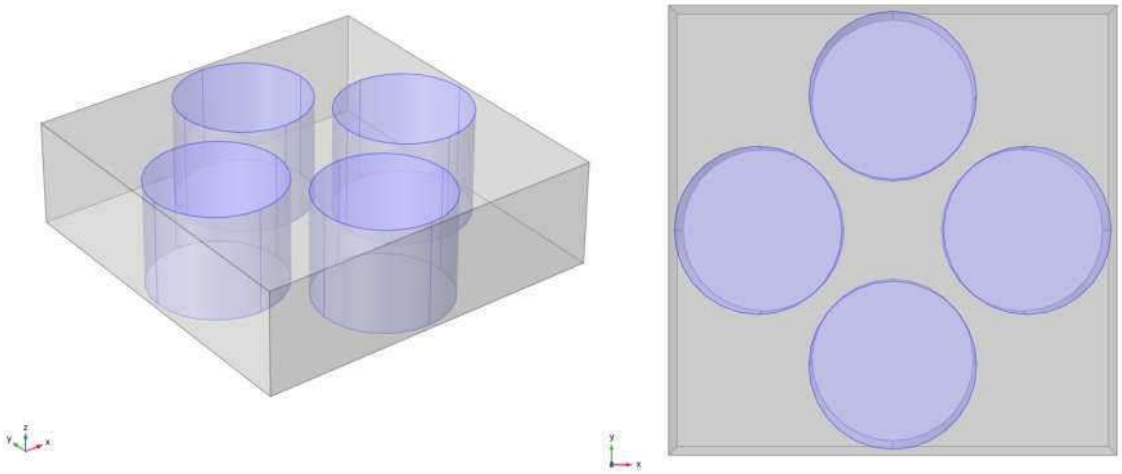


Fig. 1 3D primitive unit cell Archimedean-like (bathroom) lattice

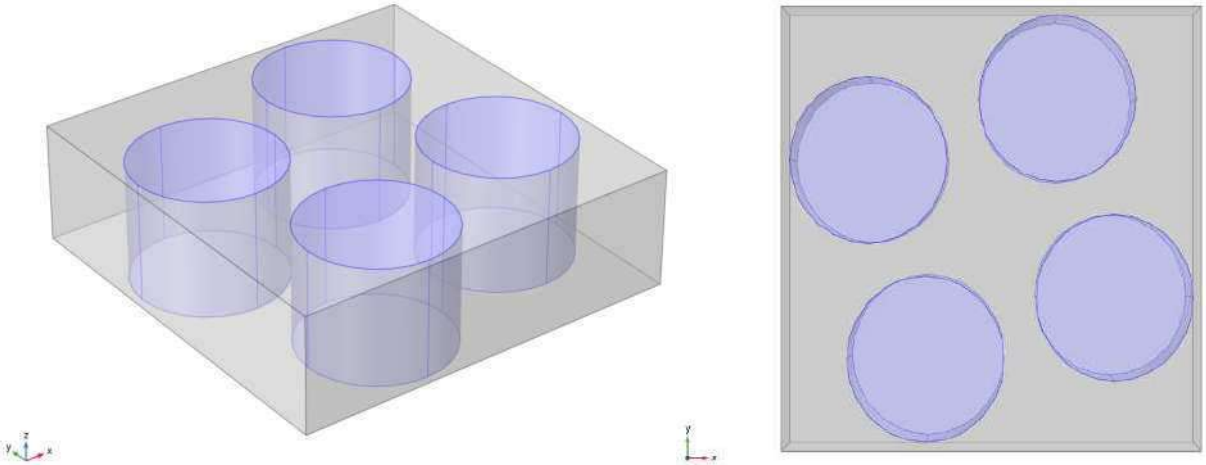


Fig. 2 3D primitive unit cell Archimedean-like (ladybug) lattice

Elastic Wave Control in Double-Zero-Index Elastic Metamaterials

Bing Li[1,2*], Zheng Li[3], Johan Christensen[4], K.T. Tan[2,†]

[1]School of Aeronautics, Northwestern Polytechnical University, Xi'an, Shaanxi, 710072, China
[2]Department of Mechanical Engineering, The University of Akron, Akron, OH 44325-3903, USA
[3]Department of Mechanics and Engineering Science, Peking University, Beijing 100871, China
[4]Instituto Gregorio Millan Barbany, Universidad Carlos III de Madrid, ES-28916 Legans (Madrid), Spain
Corresponding author, E-mail: *bingli@nwpu.edu.cn, †ktan@uakron.edu

Abstract

Double-zero-index properties in electromagnetic and acoustic waveguides have been recently realized, however, limited research has been reported on double-zero-index structural systems of elastic waveguides. Here, we report an elastic metamaterial consisting of non-perforated taper holes with a periodic array of Lieb-like lattice. Based on the proposed elastic medium, two separated elastic-wave Dirac-like cones are simultaneously observed at the Brillouin zone center, and double-zero-index properties at the neighborhood of Dirac-like points are theoretically, numerically and experimentally investigated.

1. Introduction

A rich variety of distinctive phenomena not typically found in nature have been revealed by both quantum and classical transports in crystals and metamaterials [1-3], depending on interparticle interactions, lattice topology, presence of disorders and external energy. As a topic of particular interest, flat-band systems with a Dirac cone, which can generate dispersionless and macroscopically degenerated energy bands, have attracted ever-increasing attention. The flat-band properties around the Dirac/Dirac-like cone was pioneeringly realized in electromagnetic waveguides. Recently, much effort has been devoted to Dirac/Dirac-like cones in phononic/acoustic counterparts.

The acoustic Dirac-like cones can be divided into three main types. The first type is a single Dirac cone composed of two linearly touching bands at the corner of the Brillouin zone (BZ). The second category comes from an accidental three-fold degeneracy of two linearly dispersing bands and an additional flat-band, and the Dirac point occurs at the center of BZ. The third type is an emerging double-Dirac cone with a four-fold degeneracy, where a pair of identical Dirac cones overlap at a single Dirac point at the BZ center. Most recently, the Dirac/Dirac-like cones at the center of BZ have been already demonstrated as an approach of enormous potential to realize double-zero-index properties in electromagnetic and acoustic waveguides, i.e., epsilon-and-mu-near-zero or simultaneously zero effective density and infinite bulk modulus. However, the extension of zero-index structural systems to elastic waveguides remains an open challenge since elastic waves in solid structures have more polarization degrees of freedom, various deformation modes and scattering complexity than electromagnetic and acoustic waves. Up to now, very limited research has been devoted to elastic wave Dirac-like cones , even much less attempt has been conducted regarding the double-zero-index elastic phononic waveguides [4].

In this research, we present the development of an elastic Lieb-like lattice metamaterial to realize two separated Dirac-like cones at the BZ center [5]. The double-zero-index effective properties for various elastic wave modes around both Dirac-like points are theoretically, numerically and experimentally investigated. The unique elastic wave control and manipulation in the proposed elastic phononic waveguide are explored.

2. Design and results

2.1. Elastic Lieb-like metamaterial

A schematic of the proposed elastic Lieb-like lattice metamaterial is illustrated in Fig. 1(a).

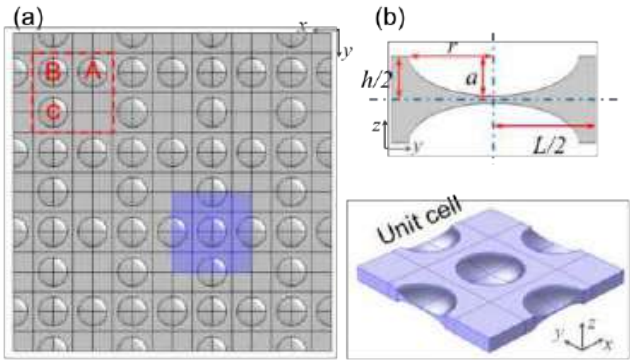


Figure 1: (a) Schematic of the proposed Lieb-like lattice elastic metamaterial. (b) Cross section and isometric view of a periodic unit cell.

Three geometric inhomogeneities with non-perforated taper holes, which are built symmetrically from both the upper and lower surfaces, are arranged as a Lieb-like periodic symmetry. The y-z cross section of each inhomogeneity is

exhibited in Fig. 1(b), two semi-elliptic holes are symmetric with respect to the mid-plane of plate. For this infinite structural waveguide, it can be further described by a unit cell, with a periodic array of square C4v symmetry.

2.2. Dispersion spectrum and dual Dirac-like cones

The material of aluminum is applied to the proposed elastic metamaterial. By carefully selecting the geometric parameters of a unit cell, we can obtain an exciting dispersion spectrum that exhibits two Dirac-like points at two different frequencies, as shown in Fig. 2.

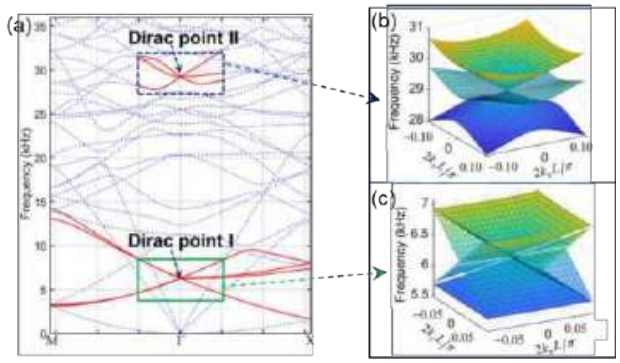


Figure 2: (a) Dispersion relations of an infinite Lieb-like lattice metamaterial. (b) Three-dimensional dispersion surfaces around Dirac-like point I and (c) Dirac-like point II.

2.3. Elastic wave control

According to the boundary effective medium theory, double-zero-index property is verified for A0 mode at Dirac point I, and for S0 mode at Dirac point II. On basis of the double-zero-index properties, we further investigate the elastic wave control by using the proposed metamaterial. We obtain the nearly full transmission without phase variation around the frequencies of Dirac points, and further capture the performance of wave-front shaping numerically and experimentally.

3. Conclusions

Two separated Dirac-like cones around different Dirac points have been simultaneously generated by an elastic Lieb-like metamaterial at the BZ center. Double-zero-index properties of the proposed elastic waveguide have been theoretically, numerically and experimentally investigated around the frequencies of both Dirac-like points. The unique transmission properties and the performance of wave-front shaping have been further observed for various wave modes.

Acknowledgements

K.T. Tan acknowledges the Faculty Start-Up Grant support from The University of Akron. J. C. gratefully acknowledges financial support from the MINECO through a Ramón y Cajal grant (RYC-2015-17156). Z. Li acknowledges financial support from the National Natural Science Foundation of China under grant No. 11672004.

References

[1] J. Christensen, M. Kadic, M. Wegener, O. Kraft, M. Wegener, Vibrant times for mechanical metamaterials. *Mrs Commun*. 5:453-462, 2015.

[2] G. Ma, P Sheng, Acoustic metamaterials: From local resonances to broad horizons. *Sci. Adv*. 2:16 2016.

[3] K. Bertoldi et al, Flexible mechanical metamaterials. *Nat Rev Mater* 2: 17066, 2017.

[4] H. Zhu, and F. Semperlotti. Double-zero-index structural phononic waveguides. *Phys. Rev. Appl.* 8: 064031 2017.

[5] B. Li, Z. Li, J. Christensen, K.T. Tan, Dual Dirac cones in elastic Lieb-like lattice metamaterials, *Appl. Phys. Lett.*, *Accepted* 2019.

Band Gap and Wave Propagation on Liquid Crystal Based Sonic Metamaterials

Selami Palaz

Faculty of Science and Letters, Department of Physics, Harran University, Sanlıurfa,Turkey
*spalaz@harran.edu.tr

Abstract

The propagation of acoustic waves in 2D sonic crystals (SC) is studied experimentally and theoretically by using plane-wave expansion (PWE) method. 2D SC with square and hexagonal lattices composed of cylindrical rods embedded in the different lyotropic liquid crystals matrices are studied to find the allowed and stop bands for the waves of certain energy. The calculated phonon dispersion results indicate the existence of full acoustic modes in the proposal structure along the high symmetry points.

Band Structure and Transmission in Multiferroic based Sierpinski Carpet Phononic Crystal

Selami Palaz[1*], Zafer Ozer[2], Amirullah M. Mamedov[3,4], Ekmel Ozbay[3]

[1]Faculty of Science and Letters, Department of Physics, Haran University, Sanlıurfa, Turkey
[1]Mersin Vocational High School Electronic and Automation Department, Mersin University, Mersin, Turkey
[3]Nanotechnology Research Center (NANOTAM), Bilkent University, Ankara, Turkey
[4]International Scientific Center, Baku State University, Baku, Azerbaijan
*spalaz@harran.edu.tr

Abstract

In this study, quasi Sierpinski-carpet phononic crystals (PnCs) were first identified as unit cells and the band structure obtained in the direction of the Γ-X-M-Γ. The Floquet periodicity conditions are applied to the supercells and the band structures are obtained by using the finite element method (FEM). The band gap structure, transmission spectra and displacement fields of eigenmodes of the proposed structures are calculated by using FEM.

Nonviscous damping effects on the wave dispersion and dissipation of locally resonant acoustic metamaterials

Taufeeq Ur Rehman Abbasi[1], Hui Zheng[1*]

[1]State Key Laboratory of Mechanical Systems and Vibration, Institute of Vibration, Shock and Noise, Shanghai Jiao Tong University, Shanghai 200240, China
*corresponding author, E-mail: huizheng@sjtu.edu.cn

Abstract

Periodic structures for various level of wave dispersion and dissipation use material damping, which may contribute to the performance enhancement of locally resonant acoustic metamaterials (AMMs). We investigate the wave dispersion and dissipation performance of AMM by considering the effects of nonviscous damping. A new state-space method in a symmetric form based on an anelastic displacement fields (ADF) model for the analysis of periodic structures is developed. It is demonstrated that the effect of nonviscous damping increases the wave dispersion and dissipation performance of AMM by suitable selection of material parameters.

1. Introduction

Engineering problems involving wave dispersion and dissipation are frequently encountered in the periodic structures. It is usually significant to control elastic and/or sound waves propagation by introducing material that contains unusual dynamic properties called acoustic metamaterial (AMMs). AMM is the engineered designed material, which forms frequency band gaps for stopping the wave propagation to provide superior vibration suppression performance. In AMM design, the inclusion of local resonance is the primary component, which makes the metamaterials applicable for novel applications including an acoustic waveguide, noise and sound treatment, and underwater acoustics [1, 2]. The local resonance mechanism-based design approach provides wave attenuation in the low-frequency and advantages over the traditional approaches that normally required large and/or heavy structures [2, 3]. Metadamping defined by the combination of locally resonant elements and damping material enhanced its importance for various practical applications that demand to control the wave propagation [4].

It is therefore important to consider the factor of damping modeled as viscous and/or nonviscous system for the dispersion and dissipation analysis of periodic systems. Viscous damping is used for the systems in which energy-dissipation by the viscosity is the dominant dissipative mechanism. Owing to modeling errors, the viscous model does not accurately calculate the damping behavior of vibrating systems. Nonviscous damping is more suitable for the materials, for example, polymers that exhibit material loss and/or perform micromechanical relaxation process [5]. The influence of nonviscous damping on the wave dispersion and dissipation behavior of AMM will be studied by developing the new method for wave propagation problems.

2. Bloch's theorem based state-space method for wave propagation problems

The state-space matrices based on Bloch's theorem for the nonviscously damped unit cell are represented by

$$\bar{\mathbf{A}} = \begin{bmatrix} 0 & \bar{\mathbf{M}} & 0 & \cdots & 0 \\ \bar{\mathbf{M}} & \bar{\mathbf{D}} & 0 & \cdots & 0 \\ 0 & 0 & \frac{\Delta_1}{\Omega_1}\bar{\mathbf{K}}_V & \cdots & 0 \\ \vdots & \vdots & \vdots & \ddots & \vdots \\ 0 & 0 & 0 & \cdots & \frac{\Delta_l}{\Omega_l}\bar{\mathbf{K}}_V \end{bmatrix} \tag{1}$$

$$\bar{\mathbf{B}} = \begin{bmatrix} -\bar{\mathbf{M}} & 0 & 0 & \cdots & 0 \\ 0 & \left(\bar{\mathbf{K}} + \mathbf{K}^{V0}\right) & -\Delta_1\bar{\mathbf{K}}_V & \cdots & -\Delta_l\bar{\mathbf{K}}_V \\ 0 & -\Delta_1\bar{\mathbf{K}}_V & \Delta_1\bar{\mathbf{K}}_V & \cdots & 0 \\ \vdots & \vdots & \vdots & \ddots & \vdots \\ 0 & -\Delta_l\bar{\mathbf{K}}_V & 0 & \cdots & \Delta_l\bar{\mathbf{K}}_V \end{bmatrix} \tag{2}$$

The damping ratio and frequency for calculating the wave dispersion and dissipation are dependent on the wavevector as defined by

$$\xi_s(\boldsymbol{\kappa}) = -\frac{\text{Re}\left[\lambda_s(\boldsymbol{\kappa})\right]}{\text{Abs}\left[\lambda_s(\boldsymbol{\kappa})\right]}, \omega_{d_s}(\boldsymbol{\kappa}) = \text{Im}\left[\lambda_s(\boldsymbol{\kappa})\right] \tag{3}$$

3. Numerical results and discussions

3.1. Effect of nonviscous damping on the performance of AMM

The performance of AMM in terms of nonviscous damping is studied by using Eqs. (1-3) and varying the damping intensity from $\alpha/\omega_0 = 0.1$ to $\alpha/\omega_0 = 0.4$ across the wavenumber axis. A unit cell is considered from the system shown in Fig. 1 and their values of the mass, stiffness and damping ratios are set as $\theta_2 = 9$, $\delta_2 = 1$ and $\tau_2 = 1/2$, while parametric value of resonant frequency $\omega_0 = 149.07$rad/s. Fig. 2a shows the increasing trend of optical curves of AMM with the increase of damping intensity across the wavenumber domain. The shifting of op-

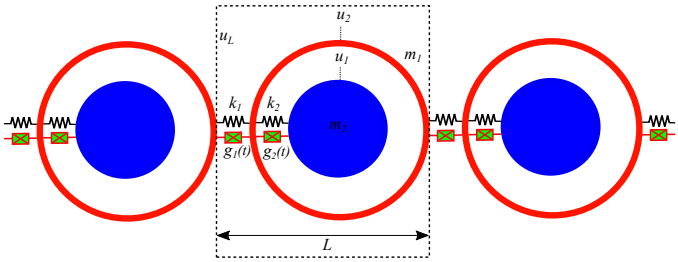
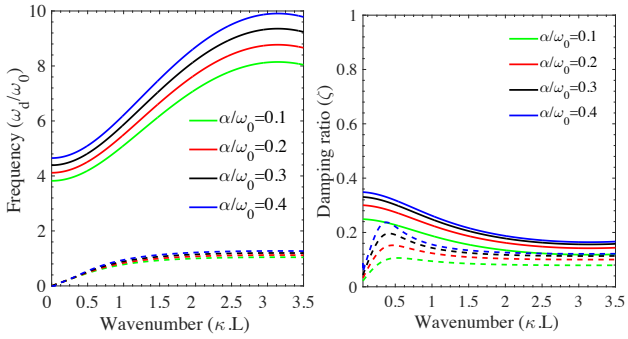


Figure 1: A 2-DOF system (mass-in-mass) with nonviscous damping; apply the boundary conditions by considering the unit cell represented in the center.

tical curves in the ascending order across the wavenumber domain manifests that the portion of mechanical energy associated with the nonviscous forces is conserved instead of energy-dissipation as in the case of viscous damping, which in turn leads to increase the wave dispersion performance of AMM. The dissipative diagram is shown in Fig. 2b in which the overall value of the damping ratio is much less and decreasing across the whole wavenumber domain. To improve the wave dissipation performance of AMM, a parametric study is performed in the next section.



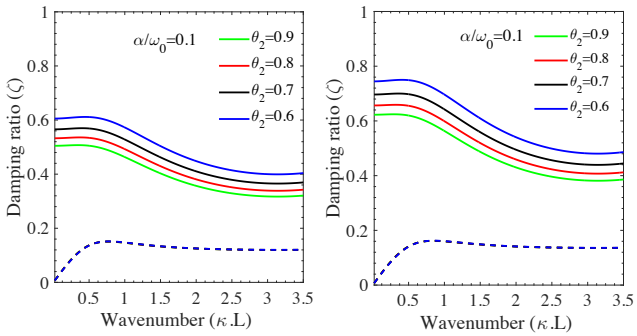
(a) Dispersion diagram (b) Dissipation diagram

Figure 2: Dispersion and dissipation of nonviscously damped mass-in-mass unit cell; Optical curves are represented by solid lines and acoustic curves are represented by dashed lines.

3.2. Effect of material parameters on the performance of AMM

The effect of materials parameters on the wave dissipation performance of AMM is studied by fixing the damping intensity of α/ω and varying the mass ratio of θ_2. The parametric value of $\omega_0 = 75.0$rad/s, while the values of δ_2 and τ_2 are kept the same. The dissipative diagram is shown in Fig. 3a, which indicate the increasing value of damping ratio with the decrease of mass ratio from $\theta_2 = 0.9$ to $\theta_2 = 0.6$ at $\alpha/\omega = 0.1$. The increasing of damping ratio at the lower α/ω, in turn, yields temporal wave attenuation at each point of wavenumber.

To further study the wave dissipation performance of AMM, the value of ω_0 is decreased to 65.0rad/s, while the values of θ_2 are kept the same. The dissipative diagram is shown in Fig. 3b. It is shown that the value of damping ratio increases further by decreasing the value of ω_0, which imply that the lower values of θ_2 and ω_0 are more suitable to enhance the wave dissipation performance of AMM.



(a) (b)

Figure 3: Dissipation of nonviscously damped unit cell at differerent values of θ_2 and ω_0.

4. Conclusions

In conclusions, the performance of acoustic metamaterials in terms of wave dispersion and dissipation is studied by introducing nonviscous damping. It is verified that the wave dispersion performance of AMM is higher in the nonviscous damping. The analysis also reveals that the nonviscous damping increases the wave dissipation performance of AMM by the selection of suitable material parameters. Further discussions on the performance of AMM in terms of the metadamping phenomenon will be presented.

Acknowledgements

This work is financially supported by the Basic Research Program of China (Grant no. 2014CB046302).

References

[1] J. H. Oh, S. Qi, Y. Y. Kim, B. Assouar, Elastic metamaterial insulator for broadband low-frequency flexural vibration shielding. *Phys. Rev. Appl.* 8(5), p. 054034, 2017.

[2] Y. Li, B. M. Assouar, Acoustic metasurface-based perfect absorber with deep subwavelength thickness. *Phys. Rev. Lett.* 108(6), p. 063502, 2016.

[3] B. Florijn, C. Coulais, M. van Hecke, Programmable mechanical metamaterials. *Phys. Rev. Lett.* 113(17), p. 175503, 2014.

[4] M. I. Hussein, M. J. Frazier, Metadamping: An emergent phenomenon in dissipative metamaterials. *J. Sound Vib.* 332(20), pp. 4767-4774, 2013.

[5] A. Raman, W. Shin, S. Fan, Upper bound on the modal material loss rate in plasmonic and metamaterial systems. *Phys. Rev. Lett.* 110(18), p. 183901, 2013.

Asymmetric Wave Transmission in Dissipative Acoustic Metamaterials

Sagr Alamri[1], Bing Li[2, †], K.T. Tan[3, *]

[1]Department of Mechanical Engineering, King Khalid University, Abha 62529, Saudi Arabia
[2]School of Aeronautics, Northwestern Polytechnical University, Xi'an, Shaanxi, 710072, China
[3]Department of Mechanical Engineering, The University of Akron, Akron, Ohio 44325-3903, USA
*corresponding authors E-mail: † *bingli@nwpu.edu.cn,* * *ktan@uakron.edu*

Abstract

We propose a dissipative triatomic elastic metamaterial to extend the range of the asymmetric elastic wave transmission and to control the elastic wave in two low-frequency bands. A triatomic metamaterial structure consisting of several small-sized unit cells is proposed and verified analytically. The analytical results are verified numerically by analytical lattice and continuum models. We further explore the asymmetric wave transmission experimentally, and the transient wave responses in the time and frequency domains are also investigated to verify the results.

1. Introduction

Elastic wave propagation is considered symmetric in regular materials and structures. As a matter of recent interest, asymmetric transmission of elastic waves has attracted more attention due to the difficulties to achieve one-way elastic wave transmission, as well as the potential of many practical applications [1]. Many methods have been proposed to obtain asymmetric elastic wave transmission. These methods can be classified, based on whether an external energy is needed, into two categories: active and passive designs. By utilizing a circulating fluid as an odd-vector bias, Fleury *et al.* proposed a linear ring cavity and split the structure's azimuthal resonant modes, which lead to giant acoustic nonreciprocity [2].

By means of nonlinear mechanisms, various passive designs have also been reported to break the acoustic reciprocity without depending on the external energy. Liang *et al.* suggested a pioneer nonlinear acoustic rectifier and observed the significant rectifying effect experimentally [3]. Also, to realize asymmetric elastic wave transmission in low-frequency bands, Li *et al.* proposed and designed linear diatomic metamaterial structure which can exhibit large asymmetric transmission in multiple low-frequency regions [4,5].

However, the frequency bandwidths for asymmetric transmission in these structures are normally limited to narrow frequency ranges, and to the number of internal resonators which are difficult to manufacture for practical applications, and the potential to realize asymmetric elastic wave transmission in multiple broadband frequency regions still needs more research. Moreover, less research has been done on the damping effects of asymmetric wave transmission in triatomic structures. In this work, we propose a dissipative triatomic metamaterial to obtain broadband asymmetric elastic wave propagation. The broadening effects of the asymmetric transmission band bandwidths induced by the dissipative oscillators are systematically analyzed and performed by analytical equations and numerical verification in both continuum model and lattice system. In addition, we perform experimental observation of asymmetric elastic wave transmission in the proposed structure. We further show the transient wave responses in time and frequency domains for the experimental results.

2. Design and equivalent models

The schematic design and the dimensions of the proposed triatomic structure are shown in Figure 1.

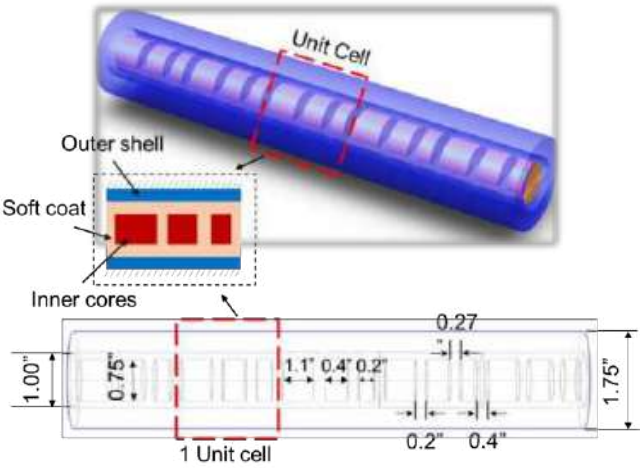


Figure 1: Schematic of the continuum model for the proposed dissipative triatomic elastic metamaterial.

One-unit cell of the triatomic metamaterial rod can be mathematically described by a mass-spring-dashpot model to investigate the unusual characteristics of elastic metamaterials. By utilizing the concept of equivalent mass in mass-spring model, this dissipative triatomic mass-spring-dashpot system can be further described by an equivalent dissipative mass-spring-dashpot model. The original triatomic chain can be symbolized by three effective masses: m_1^e, m_2^e and m_3^e.

2.1. Non-dissipative model

Asymmetric elastic wave transmission in the proposed dissipative triatomic metamaterial is investigated analytically and verified numerically without introducing damping effects for better comparison later. The results from the analytical dispersion relation along with the continuum model are compared in Figure 2(a). The transmission coefficients are compared in Figure 2(b).

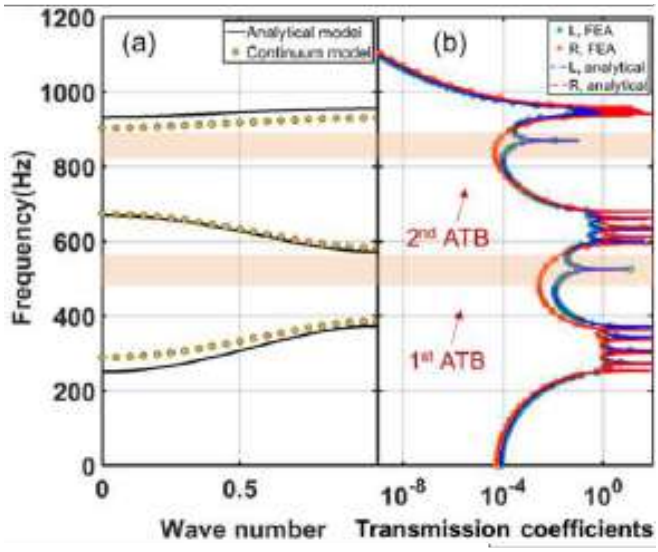


Figure 2: (a) Analytical and continuum dispersion relations of the infinite periodic rod. (b) Transmission coefficient-frequency profiles obtained by a finite continuum rod consisting of 6-unit cells along directions *L* and *R*.

2.2. Dissipative model

To quantitatively explore the damping effects on the ATB bandwidth, we calculate the asymmetric contrast ratio under various damping coefficients. The contrast ratio α is calculated by defining the total transmission coefficients along left direction *L* and right direction *R* as:

$$\alpha = \frac{\left|T^L - T^R\right|}{(T^L + T^R)}$$

The Rayleigh damping is applied to the soft material of the continuum model to represent the performance of damping on the lattice system.

2.3. Experimental verification

The experimental results for the two opposite directions are also verified. It is noticed that the transmission properties along both directions are very similar before 480 Hz, then clear separation starts to occur in the experimental data. The separation region between 484-1592 Hz represents the first asymmetric transmission band, while the second ATB band exist between 1650-3650 Hz.

3. Conclusion

By using the proposed dissipative triatomic metamaterial structure, asymmetric elastic wave transmission can be realized in two frequency bands compared with dual resonator system which is hard to be manufactured. The effect of damping on the ATB bandwidth is systematically investigated by 6-unit cells continuum model and verified systematically by a theoretical mass-spring-damper model. It is observed that ATB bandwidths can be enlarged by using the merging effects induced by using the proper damping design.

References

[1] X.F. Li, X. Ni, L.A. Feng, M.H. Lu, C. He, Y.F. Chen, Tunable unidirectional sound propagation through a sonic-crystal-based acoustic diode, Phys. Rev. Lett., 106 (2011) 084301.

[2] R. Fleury, D.L. Sounas, C.F. Sieck, M.R. Haberman, A. Alu, Sound isolation and giant linear nonreciprocity in a compact acoustic circulator, Science, 343 (2014) 516-519.

[3] B. Liang, B. Yuan, J.C. Cheng, Acoustic diode: rectification of acoustic energy flux in one-dimensional systems, Phys. Rev. Lett., 103 (2009) 104301.

[4] B. Li, K.T. Tan, Asymmetric wave transmission in a diatomic acoustic/elastic metamaterial, J. Appl. Phys., 120 (2016) 075103.

[5] B. Li, S. Alamri, K.T. Tan, A diatomic elastic metamaterial for tunable asymmetric wave transmission in multiple frequency bands, Sci. Rep., 7 (2017) 6226.

Acoustic Metamaterial Lenses for 40kHz Ultrasound Fabricated with Consumer 3D-printers

James Hardwick, Jordi Prat-Camps, Sriram Subramanian

Interact Lab, Department of Informatics, University of Sussex, Brighton, United Kingdom

Abstract

With the advent of high resolution 3D printing we can now fabricate complex and intricate structures with relative ease and low cost. In this project we design different acoustic lenses for ultrasonic waves of frequency 40kHz using a set of phase delaying unit cell bricks arranged into specific patterns. We use different consumer 3D printers to fabricate them and compare the results of these different printing techniques. Finally, we test the performance of each in terms of acoustic field control.

1. Unit Cells & Lens Construction

Acoustic metamaterials allow new methods for controlling ultrasound fields which were not available only a few short years ago. Previously the techniques available for focusing a given ultrasound field were limited to costly phased arrays of transducers or bulky static lenses [1, 2]. As demonstrated by Memoli et al. [3], it is possible to construct a transmissive metasurface lens from a series of unit cells, each providing a well-defined delay to the phase of any ultrasound wave which passes through them. These unit cells take the form of small maze-like structures which coil the space within them [4]. They each have a height of λ and a side-length of $\lambda/2$. The working frequency is a constant 40kHz and it is assumed the waves are travelling through air at 25°, corresponding to a wavelength of $\lambda \approx 8.66$mm. These unit cells, which we call "bricks", consist of a rectangular cuboid-shaped channel with four bars protruding inwards at a perpendicular angle to the wall. The mazes are increased in complexity by altering the length (l) and spacing between these bars (s). By carefully tuning these two parameters a set of bricks were designed which offers 16 different phase delays spread equally between 0 and 2π. A cross section of three bricks is shown in Fig 1. We performed 3D finite-element simulations with COMSOL Multiphysics to verify that the designed bricks imprint the desired phase delays.

As mentioned before, these bricks have a side-length of $\lambda/2$. In terms of acoustic pressure reconstruction, a better performance could be achieved by considering smaller bricks. However, it has been shown that the sampling of a continuous analog phase map at a spatial frequency of $\lambda/2$ makes it possible to achieve an excellent pressure reconstruction in the far field while still offering a good balance in the tradeoff between acoustic pressure control and ease of fabrication [5].

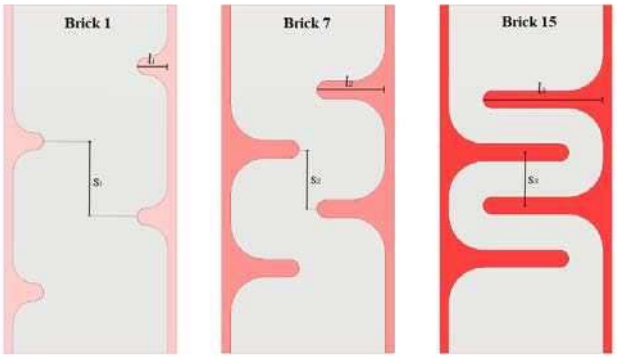


Fig.1 – Here we see a cross section of bricks 1, 7 and 15 corresponding to phase delays of 22.5°, 157.5° and 337.5° respectively. We also see how the two parameters, l and s, change in order to increase the phase delay provided by each.

The bricks are then assembled into lenses. So far, these take the form of convergent lenses with different focal lengths. The focal length is arbitrary and can be specified by the user during the construction process. A short algorithm was written which takes the desired brick array and focal lengths and uses simple Pythagorean geometry to determine the analog phase map for a lens which conforms to these parameters. The algorithm then discretizes this by finding the average phase value of each $\lambda/2$ by $\lambda/2$ (1 unit cell) area of the lens and reassigns it to the closest brick phase value out of the 16 available. This newly discretized phase map can then be translated directly into positions for the appropriate bricks in a number of 3D modelling programs and made into a printable lens.

The fabrication of the lenses is done using commercial 3D printers. In order to aid in the printing process the outer edges of the lens are made thicker. A buffer layer is added to raise the whole structure from the floor of the printer and a skirt is built around the bottom to help prevent the entire structure from curling upwards during the course of the printing. The prototypes were created using three different consumer-level 3D-printers. The Stratasys F370 & Flashforge Creator Pro are both Fused-Filament (FF) printers and used ASA and PLA as printing materials respectively. The stereolithographic Form2 used Formlabs resin (RS-F2-GPGR-04). The Flashforge is the cheapest of the three and does not use a support material to aid printing. The Stratasys is the most expensive of the three and uses a

water soluble material for support. The Form2 has a cost somewhere between the other two. It also requires an extensive scaffold-like support structure, made from the same Formlabs resin, to achieve a successful print. An image of one completed lens from each of the three printers is shown in Fig.2. The results of each of these printing methods were compared to see which gave the best balance between accuracy and cost. The low resolution of the Flashforge meant it struggled to print the thin bars properly. The Stratasys performed reasonably well in this regard but the low resolutions endemic to FF printers were still noticeable. The higher resolution and stereolithographic nature of the Form2 made it superior to both FF printers at producing the extremely thin unit cell bars accurately but it struggled to make it through a full print without an extensive network of supportive scaffolding, increasing the cost of the print significantly. New iterations are still being tried with all of the printers and until we can properly test the capabilities of each printed lens with our upcoming measurement system, we won't know for sure which gives us the best results.

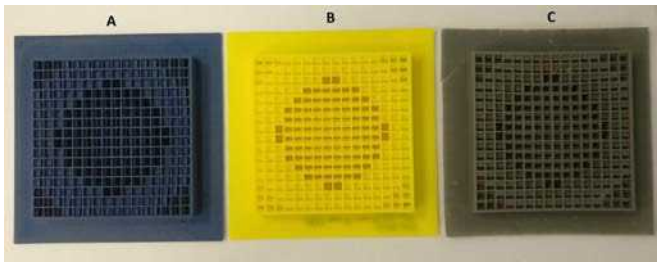


Fig.2 – Three 100mm focal length lenses each created in a different printer and with different materials. **A**: Stratasys F370 using ASA material. **B**: Flashforge Creator Pro using PLA. **C**: Form2 using Formlabs resin.

2. Measurements

In order to compare the performance of the different lenses, we intend to perform acoustic measurements of the pressure distribution on the far side of each of the lenses when an f_0=40kHz acoustic wave is sent through it. The source of waves is a single ultrasonic transducer (Murata MA40S4S) which is fed with a sinusoidal signal of frequency f_0 and is placed at a distance of 16 cm from the lens. The transmitted pressure is measured with a B&K microphone (model 4138-A-015), which is connected to a conditioning amplifier (Nexus Type 2692, final gain: -20dB) and this, in turn, to a PicoScope data acquisition unit (Pico Instruments, model: 5444b). The microphone is mounted on a 3D computer-controlled stage that allows it to scan the pressure distribution at multiple planes. At the time of the submission of this abstract we are in the process of completing the measuring setup and we expect to start acquiring experimental data in the coming weeks and months.

3. Future Perspectives

Currently the only lenses designed and built are convergent lenses which create a focal point above their center points. We plan to design, fabricate and measure other kinds of structures such as steering lenses that alter the direction of the incident field in a uniform way rather than focusing it. Multiple steering and focusing lenses can even be stacked on top of one another to create more complex field manipulation devices which allow both steering and focus and could be described as "acoustic tractor beams" [6].

Acknowledgements

This project has received funding from the EU's ERC advanced grant No. 787413.
JPC is funded by a Leverhulme Trust Early Career fellowship (ECF-2018-447).
SS is funded by the Royal Academy of Engineering grant CiET1718\14

References

[1] Ahmad, R., Kundu, T., & Placko, D. (2005). *Modeling of phased array transducers*. *The Journal of the Acoustical Society of America* (Vol. 117). https://doi.org/10.1121/1.1835506

[2] Spadoni, A., & Daraio, C. (2010). Generation and control of sound bullets with a nonlinear acoustic lens. *Proceedings of the National Academy of Sciences*, *107*(16), 7230 LP-7234. https://doi.org/10.1073/pnas.1001514107

[3] Memoli, G., Caleap, M., Asakawa, M., Sahoo, D. R., Drinkwater, B. W., & Subramanian, S. (2017). Metamaterial bricks and quantization of meta-surfaces. *Nature Communications*, *8*, 1–8. https://doi.org/10.1038/ncomms14608

[4] Liang, Z., & Li, J. (2012). Extreme Acoustic Metamaterial by Coiling Up Space. *Physical Review Letters*, *108*(11), 114301. https://doi.org/10.1103/PhysRevLett.108.114301

[5] J. Prat-Camps, G. Christopoulos, J. Hardwick, S. Subramanian, *Optimal sampling of acoustic metamaterials and metasurfaces*, in preparation.

[6] Marzo, A., Seah, S. A., Drinkwater, B. W., Sahoo, D. R., Long, B., & Subramanian, S. (2015). Holographic acoustic elements for manipulation of levitated objects. *Nature Communications*, *6*, 8661. Retrieved from https://doi.org/10.1038/ncomms9661

$Sn_2P_2X_2$ (X=S, Se) as novel materials for phononic crystals

Selami Palaz[1], Zafer Ozer[2], Sevket Simsek[3], Husnu Koc[4], Amirullah M. Mamedov[5,6,*], and Ekmel Ozbay[5]

[1]Department of Physics, Harran University, Sanliurfa, Turkey
[2]Mersin Vocational High School, Mersin University, Mersin, Turkey
[3]Department of Materials Science and Engineering, Hakkari University, Hakkari, Turkey
[4]Department of Department of Physics, Siirt University, Siirt, Turkey
[5]Nanotechnology Research Center (NANOTAM), Bilkent University, Ankara, Turkey
[6]International Scientific Center, Baku State University, Baku, Azerbaijan
*mamedov@bilkent.edu.tr

In this investigation the linear and nonlinear optical properties, band structures and electro-optic effects of $Sn_2P_2X_6$ (X=S,Se) ferroelectrics are studied by the density functional theory (DFT) in the local density approximation (LDA) expressions based on first principle calculations. We present calculations of the frequency-dependent complex dielectric function ($\varepsilon^*= \varepsilon 1-i\varepsilon 2$) and the second harmonic generation response coefficient $\chi(2)(-2\omega,\omega,\omega)$ over a large frequency range in different phases. The electronic linear electro-optic susceptibility $\chi(2)$ $(-\omega,\omega,0)$ is also evaluated below the band gap. These results are based on a series of the LDA calculation using DFT. Results for $\chi(2)$ $(-\omega,\omega,0)$ are in agreement with the experiment below the band gap and those for $\chi(2)(-2\omega,\omega,\omega)$ are compared with the experimental data where available. Also, in present work the acoustic band structure and acoustic wave propagations in a two-dimensional (2D) phononic crystals (PC) containing a $Sn_2P_2X_6$ ferroelectrics were investigated theoretically and numerically by the plane-wave-expansion (PWE) method. Two-dimensional PC with square lattices composed of semiconducting ferroelectric cylindrical rods embedded in the organic/inorganic matrix is studied to find the existence of stop bands for the waves of certain energy. This phononic bandgap–forbidden frequency range-allows sound to be controlled in many useful ways in structures that can act as sonic filters, waveguides or resonant cavities. Phononic band diagramы for a 2D PC wyку plotted versus the wavevector k along the Γ-X-M-Γ path in the square Brillouin zone (BZ) show four stop bands in the wide frequency range. The unusual properties of matrix and ferroelectric properties of $Sn_2P_2X_6$ give us ability to control the wave propagation through the PC in over a wide frequency range.

Negative phase velocity sound propagation in 1D hyperbolic phononic metamaterials

Yurii Zubov[1], **Arkadii Krokhin**[1], **Bahram Djafari-Rouhani**[2]

[1]Department of Physics, University of North Texas, P.O. Box 311427, Denton, TX 76203, USA
[2]Institut d'Electronique, de Microélectronique et de Nanotechnologie, Université de Lille 1 59655, France
*corresponding author, E-mail: yuriizubov@my.unt.edu

Abstract

Analytical formulas are obtained for the tensor of effective mass densities and for the effective elastic modulus of a binary superlattice in the long wavelength limit. They are valid for high frequencies and oblique propagation. Within the region of frequencies with anomalous dispersion, the equifrequency curves are hyperbolic and the effective masses exhibit strong anisotropy. It is demonstrated that hyperbolic dispersion in a 1D periodic system leads to negative refraction for phase velocity. The group velocity refraction remains positive.

1. Introduction

Homogenization procedures developed for elastic superlattices allow numerical calculation of the effective parameters (effective mass density and effective elastic modulus) for long wavelength sound [1, 2]. The obtained effective parameters reproduce well the exact dispersion curves [3] provided that sound propagates *along the superlattice axis.* Numerous applications of elastic superlattices require more general information about the effective parameters, in particular, the explicit dispersion relation for a sound wave propagating *in arbitrary direction*. Here we propose a homogenization procedure based on a simple and natural dynamical assumptions that lead to the analytical formulas for the effective parameters. We apply the obtained analytical results to detailed study of the process of refraction of sound waves through a finite-size slab of periodic water-steel layers. The effective parameters show the region of frequencies with hyperbolic dispersion of sound in the slab. This, however, does not lead to negative refraction, as it occurs for 2D layered phononic crystals: perforated plates [4] or membranes [5]. In 1D periodic structures, the refraction related to the directions of the phase velocities turns out to be negative, while the group velocity follows positive refraction. Thus, 1D periodic elastic structures cannot be used as the basic element of a superlens.

2. The effective parameters

The frequency dispersion relationship for the case of oblique propagation of acoustic waves through homogeneous media takes the form:

$$k_x^2/\rho_x + k_y^2/\rho_y = \omega^2/\lambda. \tag{1}$$

If $\rho_x\rho_y < 0$, then the equifrequency curves take a hyperbolic form. Since all the effective parameters are strongly frequency dependent in the higher bands, the formulas in the quasistatic limit are not applicable. Therefore, we developed a new homogenization method which is based on a natural requirement that the acceleration and displacement of the effective medium in an oscillating acoustic field must coincide with the corresponding quantities averaged over the unit cell. The proposed method leads to the following analytical expressions for the effective parameters:

$$\begin{aligned}
\rho_x &= \frac{\rho_a\left\{\rho_a k_b \sin\left(ak_a/2\right)\cos\left(bk_b/2\right) + k_a\rho_b\cos\left(ak_a/2\right)\sin\left(bk_b/2\right)\right\}}{\rho_a\left[k_a\sin\left(bk_b/2\right) + k_b\sin\left(ak_a/2\right)\cos\left(bk_b/2\right)\right] - 2k_a\rho_b\sin^2\left(a/k_a 4\right)\sin\left(bk_b/2\right)},\\
\rho_y &= -\frac{0.5(a+b)k_a\rho_a k_b\left[\rho_a k_b\sin\left(ak_a/2\right)\sin\left(bk_b/2\right) - k_a\rho_b\cos\left(ak_a/2\right)\cos\left(bk_b/2\right)\right]}{\rho_a\sin\left(bk_b/2\right)\left(k_b^2\cos\left(ak_a/2\right) + k_a^2 - k_b^2\right) + k_a k_b\rho_b\sin\left(ak_a/2\right)\cos\left(bk_b/2\right)},\\
\lambda &= -\frac{0.5(a+b)k_a\lambda_a k_b\lambda_b\left[\rho_a k_b\sin\left(ak_a/2\right)\sin\left(bk_b/2\right) - k_a\rho_b\cos\left(ak_a/2\right)\cos\left(bk_b/2\right)\right]}{\lambda_a k_a^2\rho_b\sin\left(bk_b/2\right) + k_b\lambda_b\left[k_a\rho_b\sin\left(ak_a/2\right)\cos\left(bk_b/2\right) - 2\rho_a k_b\sin^2\left(ak_a/4\right)\sin\left(bk_b/2\right)\right]}.
\end{aligned} \tag{2}$$

Here, the wavevectors in each layer are defined as $k_i = \sqrt{\omega^2/c_i^2 - k_y^2}$, where $i = a, b$. These formulas are valid near Γ-point, if $kd \ll 1$, where k is Bloch vector. The frequency ω is not necessarily small. In the limit $\omega \to 0$ the quasi-static results are recovered. Note that the effective parameters (2) take into account the effects of spatial dispersion. Therefore, the dispersion relation Eq. (1) in

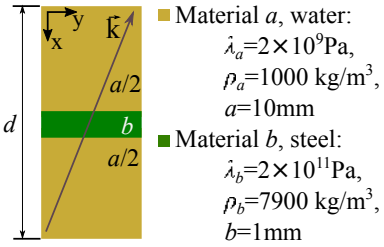


Figure 1: Symmetric unit cell of water-steel structure. Arrow shows oblique propagation with Bloch vector **k**.

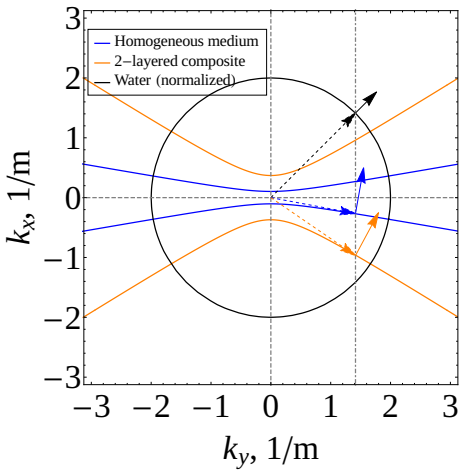


Figure 2: Equifrequency contour diagrams for water (black), water-steel composite (orange) and effective media (blue) for frequency 95.1 kHz.

general case defines a curve of order higher than two.

3. Structure of equifrequency curves

The equifrequency curves in Fig. (2) are plotted for 95.1 kHz that is very close to the top of the second allowed band $(95, 115)$ Hz, which exhibits anomalous dispersion. Both, the blue curve obtained from Eqs. (1, 2) and the orange curve obtained from the exact Rytov's equation exhibit hyperbolic dispersion. They coincide asymptotically at Γ-point. For the frequencies near the top of the second band these curves remain close to each other. The group velocities in Fig. (2) are directed toward the gradients $\nabla_{\mathbf{k}}\omega$. The directions of the phase and group velocities in Fig. (2) correspond to anomalous dispersion along the superlattice axis (axis x).

The refraction of sound waves at the interface between water and the superlattice is shown in Fig. (3). The angle of incidence is 8° and the angle of refraction is 36° for the group velocity. The direction of the group velocity in the superlattice (green arrow) with respect to the direction of incidence (yellow line) corresponds to positive refraction. However, the phase velocity in the superlattice is directed towards the interface. For the phase velocity, the angle of refraction is 130° which is the manifestation of strong anisotropy of the effective medium together with anomalous dispersion. Indeed, the effective masses not only have

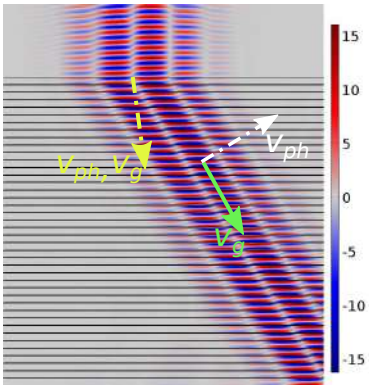


Figure 3: Pressure-field simulation of positive refraction of sound with frequency 95.1 kHz at water-superlattice interface.

opposite signs, but their absolute values are very different, $\rho_x/\rho_y \approx 10^{-2}$. Very light effective mass ρ_x is due to small curvature of the dispersion curve near Γ-point. Exactly at this point the effective mass vanishes and sound does not propagate since a standing wave is formed.

4. Conclusions

Our study demonstrates that a layered medium (without internal structure) in the long wavelength limit may behave as a hyperbolic metamaterial. However, unlike the layered media with internal structures, [4, 5] it does not exhibit negative refraction for the group velocity. The refraction for phase velocity remains anomalous – the vector of phase velocity rotates by an angle greater than 90°.

Acknowledgement

This work is supported by EFRI grant No. 1741677 from the National Science Foundation.

References

[1] S. Nemat-Nasser, J.R. Willis, A. Srivastava, and A.V. Amirkhizi, Homogenization of periodic elastic composites and locally resonant sonic materials, *Phys. Rev. B* **83**, 104103 (2011).

[2] I.S. Solís-Mora, M.A. Palomino-Ovando, and F. Pérez-Rodrguez, Elastic superlattices with simultaneously negative effective mass density and shear modulus, *J. Appl. Phys.* **113**, 093508 (2013).

[3] S.M. Rytov, Properties of laminated medium, *Sov. Phys. Acoust.* **2**, 68 (1956).

[4] J. Christensen and F. J. de Abajo, Anisotropic metamaterials for full control of acoustic waves, *Phys. Rev. Lett.* **108**, 124301 (2012).

[5] Ch. Shen, *et al.* Broadband acoustic hyperbolic metamaterial, *Phys. Rev. Lett.* **115**, 254301 (2015).

Negative In-plane Elastic Moduli of Metallic Lattices: Experimental Investigations

Sondipon Adhikari[1,*], **Alex Shaw**[1], **Tanmoy Mukhopadhyay**[2], **Nicholas P Lavery**[1]

[1]College of Engineering, Swansea University, Bay Campus, Fabian Way, Crymlyn Burrows, Swansea, SA1 8EN, UK
[2]Department of Engineering Science, University of Oxford, Oxford, UK
*corresponding author, E-mail: s.adhikari@swansea.ac.uk

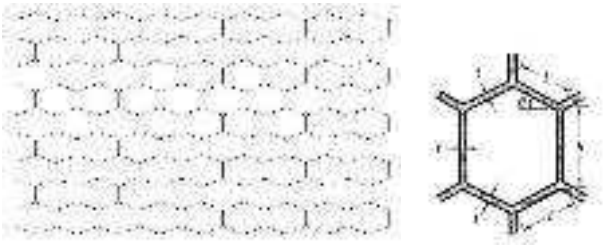
Abstract

In plane elastic moduli of lattice mechanical metamaterials include elastic moduli in the X and Y directions and a shear modulus. Historically, these moduli were described by positive real values considering the deformation of the material under a static stress field. When dynamic behaviour of lattice metamaterials are considered, it is possible to express elastic moduli as functions of frequency. In this case, it is first theoretically shown that there exist a critical frequency beyond which the elastic moduli become negative. The analysis is based on a dynamic equilibrium of a unit cell. Experimental investigations involve dynamic testing of a hexagonal lattice made of a titanium alloy. Theoretical predictions of equivalent elastic moduli and negative frequency values are validated with experimental results.

1. Introduction

A mechanics-based bottom-up framework, combined with experimental dynamic testings, is proposed for probing the frequency-dependence of metallic lattice material microstructures. Under a vibrating condition, effective elastic moduli of such microstructured materials can become negative for certain frequency values, leading to an unusual mechanical behaviour with multitude of potential applications. We first show the fundamental theoretical limits for the minimum frequency, beyond which the negative effective moduli of the materials could be obtained. An efficient dynamic stiffness matrix based approach is adopted to obtain the closed-form limits, which can capture the subwavelength scale dynamics. The limits turn out to be a fundamental property of the lattice materials and depend on certain material and geometric parameters of the lattice in a unique manner. An explicit characterization of the theoretical limits of negative elastic moduli along with adequate physical insights would accelerate the process of its potential exploitation in various engineered materials and structural systems under dynamic regime across the length-scales.

The global mechanical properties can be engineered in lattice materials by intelligently identifying the material microstructures as the properties in these materials are often defined by their structural configuration along with the intrinsic material properties of the constituent members. This novel class of materials with tailorable application-specific mechanical properties (like equivalent elastic moduli, buckling, vibration and wave propagation characteristics with modulation features) have tremendous potential applications for future aerospace, civil, mechanical, electronics and medical applications across the length-scales. Naturally occurring materials cannot exhibit unprecedented and fascinating properties such as extremely lightweight, negative elastic moduli, negative mass density, pentamode material characteristics (meta-fluid), which can be achieved by an intelligent microstructural design [1, 2]. For example, the conventional positive value of Poisson's ratio in a hexagonal lattice structure can be converted to a negative value [3] by making the cell angle θ in Figure 1(b) negative.



(a) The hexagonal lattice ($\theta = 30°$) (b) Unit cell

Figure 1: The hexagonal lattice and the corresponding unit cell

Lattice microstructures are often modelled as a continuous solid medium with a set of effective elastic moduli throughout the entire domain based on an unit cell approach [4]. The basic mechanics of deformation for the lattices being scale-independent, the formulations developed in this context are generally applicable for wide range of materials and structural forms. Two dimensional hexagonal lattices of natural and artificial nature can be identified across different length-scales (nano to macro) in auxetic and non-auxetic forms [5]. This has led to our focus on hexagonal lattices in this article while selecting a lattice configuration to demonstrate the concepts.

2. The dynamic stiffness approach

A bottom-up theoretical framework is developed here (refer to Figure 1) to investigate the limits of natural frequency that would cause negative axial or shear moduli. A lattice-like structure can be analysed by considering an unit cell as shown in figure 1(b), while the unit cell consists of beam elements. In a vibrating condition, the dy-

namic motion of the overall lattice corresponds to vibration of individual beams, which would exhibit a different frequency-dependent deformation behaviour compared to the conventional static analyses. Thus, we first form the frequency-dependent elastic stiffness matrix for a beam element ($\mathbf{D}(\omega) = [D_{ij}]$, where $i, j \in [1, 2, ...4]$ and ω is the frequency of vibration) and thereby, the frequency-dependent deformation characteristics of an unit cell are developed. Eventually, frequency-dependent equivalent elastic moduli of the overall lattice structure are derived based on the deformation behaviour of a unit cell. The theoretical limits of frequencies to obtain negative elastic moduli are obtained using their respective frequency-dependent expressions.

The equation of motion of free vibration of a damped beam depicting one element of the unit cell in Figure 1(b) can be expressed as

$$EI\frac{\partial^4 V(x,t)}{\partial x^4} + \widehat{c}_1\frac{\partial^5 V(x,t)}{\partial x^4 \partial t} + m\frac{\partial^2 V(x,t)}{\partial t^2} + \widehat{c}_2\frac{\partial V(x,t)}{\partial t} = 0 \quad (1)$$

It is assumed that the behaviour of the beam follows the Euler-Bernoulli hypotheses. In the above equation EI is the bending rigidity, m is mass per unit length, $\widehat{c}_1$ is the strain-rate-dependent viscous damping coefficient, $\widehat{c}_2$ is the velocity-dependent viscous damping coefficient and $V(x,t)$ is the transverse displacement. The length of the beam is assumed to be L. Considering a harmonic motion with frequency ω we have

$$V(x,t) = v(x)\exp[\mathrm{i}\omega t] \quad (2)$$

where $\mathrm{i} = \sqrt{-1}$. Substituting this in the beam equation (1) one obtains

$$\frac{\mathrm{d}^4 v}{\mathrm{d}x^4} - b^4 v = 0; \quad b^4 = \frac{m\omega^2 - \mathrm{i}\omega\widehat{c}_2}{EI + \mathrm{i}\omega\widehat{c}_1} \quad (3)$$

The constant b is in general a complex number for any physically realistic damping values.

The stiffness and mass matrices of the element can be obtained following the conventional variational formulation [6]. It can be shown that the dynamic stiffness matrix [7] is given by the following closed-form expression

$$\frac{\mathbf{D}(\omega)}{\alpha} = \begin{bmatrix} -b^2(cS+Cs) & -sbS & b^2(S+s) & -b(C-c) \\ -sbS & -Cs+cS & b(C-c) & -S+s \\ b^2(S+s) & b(C-c) & -b^2(cS+Cs) & sbS \\ -b(C-c) & -S+s & sbS & -Cs+cS \end{bmatrix} \quad (4)$$

where $\alpha = \frac{EIb}{(cC-1)}$, $C = \cosh(bL)$, $c = \cos(bL)$, $S = \sinh(bL)$ and $s = \sin(bL)$. The elements of this matrix are frequency dependent complex quantities because b is a function of ω and the damping factors.

3. Experimental approach

Following [8], it can be shown that the elastic moduli $E_1(\omega)$ and $E_2(\omega)$ can be expressed in terms of the element of the dynamic stiffness matrix as

$$E_1(\omega) = \frac{D_{33} l\cos\theta}{(h + l\sin\theta)\bar{b}\sin^2\theta}, E_2(\omega) = \frac{D_{33}(h + l\sin\theta)}{l\bar{b}\cos^3\theta} \quad (5)$$

For certain values of the frequency, the real part of the above elastic moduli will become negative. A hexagonal lattice made of Titanium alloy Ti-6Al-4V shown in Figure 2 will be used to experimentally investigate the negative elastic moduli.



Figure 2: The hexagonal lattice made of Titanium alloy Ti-6Al-4V (E=115GPa, ν=0.34)

4. Conclusions

It has been theoretically shown that in certain frequency ranges the effective elastic moduli of lattice materials can be negative. This paper explores this using experimental approaches using dynamic testing of metallic lattice metamaterials.

References

[1] A. A. Zadpoor, "Mechanical meta-materials," *Materials Horizons*, vol. 3, no. 5, pp. 371–381, 2016.

[2] N. A. Fleck, V. S. Deshpande, and M. F. Ashby, "Micro-architectured materials: past, present and future," *Proceedings of the Royal Society of London A: Mathematical, Physical and Engineering Sciences*, vol. 466, no. 2121, pp. 2495–2516, 2010.

[3] T. Mukhopadhyay and S. Adhikari, "Effective in-plane elastic properties of auxetic honeycombs with spatial irregularity," *Mechanics of Materials*, vol. 95, pp. 204 – 222, 2016.

[4] L. Gibson and M. F. Ashby, *Cellular Solids Structure and Properties*. Cambridge, UK: Cambridge University Press, 1999.

[5] T. Mukhopadhyay and S. Adhikari, "Equivalent in-plane elastic properties of irregular honeycombs: An analytical approach," *International Journal of Solids and Structures*, vol. 91, pp. 169 – 184, 2016.

[6] D. Dawe, *Matrix and Finite Element Displacement Analysis of Structures*. Oxford, UK: Oxford University Press, 1984.

[7] J. R. Banerjee, "Dynamic stiffness formulation for structural elements: A general approach," *Computer and Structures*, vol. 63, no. 1, pp. 101–103, 1997.

[8] T. Mukhopadhyay, S. Adhikari, and A. Alu, "Probing the frequency-dependent elastic moduli of lattice materials," *Acta Materialia*, vol. 165, no. 2, pp. 654–665, 2019.

Chiral and bianisotropic materials

High-efficiency asymmetric transmisson in terahertz metamaterials

Jinhui Shi[1*], Tingting Lv[1,2], Guohua Dong[1], Zheng Zhu[1], Yuxiang Li[1], Chunying Guan[1]

[1]Key Laboratory of In-Fiber Integrated Optics of Ministry of Education, College of Science, Harbin Engineering University, Harbin 150001, China
[2] School of Electronic Science, Northeast Petroleum University, Daqing 163318, China
*corresponding author, E-mail: shijinhui@hrbeu.edu.cn

Abstract

A chiral metamaterial with crossed-S resonators is proposed and demonstrated experimentally based on the broken symmetry along the propagation direction, which enables a high efficient, broadband and mutually independent dual-band asymmetric transmission (AT) in both x and y polarized directions. It is worth mentioning that the AT performance is robust against a wide range of oblique incidence and suitable different linearly polarization. The proposed multilayer chiral metamaterial in our work provides an alternative way to improve its response to the terahertz wave and will be a significant candidate in the applications of communications and ultrafast information processing.

1. Introduction

Metamaterials with periodic arrays of artificially designed subwavelength elements can achieve exotic electromagnetic properties that are inaccessible in naturally occurring materials [1]. Over the past decades, many attempts have be devoted to manipulating the polarization, phase, amplitude and propagation direction of electromagnetic wave [1]. Meanwhile, various intriguing phenomenahave been presented in metamaterial, including optical activity [2], anomalous refraction [1], asymmetric transmission (AT) [3]. The AT phenomenon was first discovered and investigated by Fedotov *et al* in an intrinsically 2D-chiral metamaterial for circularly polarized waves at normal incidence [3], which belongs to the asymmetric effect in a reciprocal system. It is well known that the AT response of linearly and circularly polarized waves have been extensively reported [3-8]. Terahertz (THz) technology highly demands high-quality terahertz devices. However, the asymmetric transmission of the terahertz metamaterials is still weak, therefore, it is of great significance that here we realize high-performance AT of THz waves for more flexible polarization manipulation.

2. Asymmetric transmission of the metamaterial

The proposed metamaterial configuration is schematically illustrated in Fig. 1(a). A free-standing polyimide film with the thickness of t=24 um is embedded in two layers of metallic crossed S-shaped resonators (CSR). The two CSRs are identical in their geometry except that the back layer is mirrored along the x axis and twisted by 90°along the z axis with respect to the front one. Furthermore, two layers polyimide coating with the thickness of tm=10 um are also added upon the outermost layer so as to protect the CSR metallic layer against external environment pollution. Each CSR layer is made from 200nm thick aluminum. Other dimensions are set as w = 10 μm and g1=g2=g3=g4=10 μm as shown in Fig. 1(b). Conventional photolithography was employed to fabricate the sample, which consists of 300 × 300 unit cells with a period of a=60 μm. Photograph of the sample is shown in Fig. 1(c).

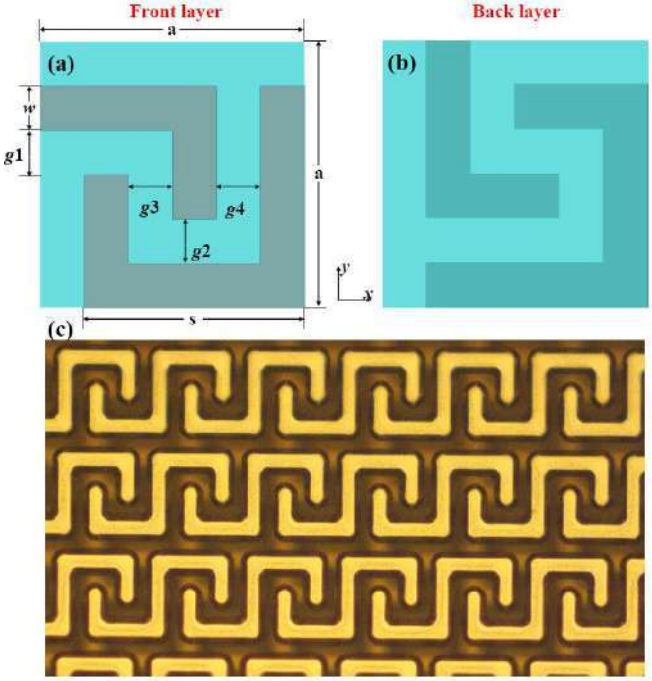


Figure 1: The schematic of the bilayer metamaterial. (a) The view of the front layer. (b) The view of the back layer. (c) The picture of the fabricated metamaterials.

Figure 2 illustrates the simulated transmission spectra in the CSRs chiral metamaterial. For a y-polarized wave propagating the forward (-z) direction at normal incidence, the simulated cross-polarization transmission coefficient t_{xy}

has two resonant peaks with a maximum of around 81.7% and 80% corresponding to the frequencies of 0.53 and 0.90 THz, which shows an FWHM of ~0.7 THz. Likewise, the coefficient t_{yx} exhibits a maximum of 71% with the FWHM of ~0.63 THz at around 1.42 THz for x-polarized incident wave. The two cross-polarization passbands interchange with each other along the two opposite propagations based on the reciprocity theorem. In addition, the two weak co-polarization coefficients of ~30% are exactly equal to each other regardless of the propagation directions.

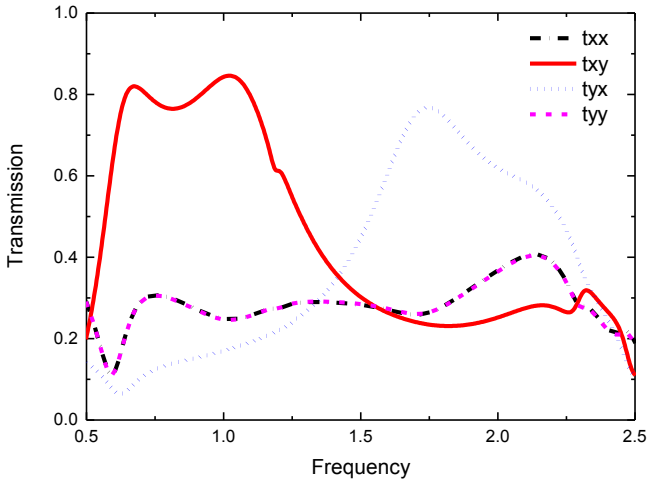


Figure 2: Simulated transmission of linearly polarized wave in metamaterial.

The calculated simulated and measured AT parameters Δ for the forward propagation are illustrated in Fig. 3. Obviously, Δx and Δy are exactly contrary to each other as expected. The Δy yields a maximum of 0.63/0.66 and 0.64/0.59 at around 0.53/0.50 THz and 0.90/0.83 THz as well as a minimum of -0.43/-0.34 at around 1.42/1.42 THz in the simulation and measurement, respectively. Despite of some shift in frequency and slight difference in amplitude between the simulation and experimental results steming from imperfections in sample preparation, they are in very good agreement. Therefore, the proposed CSRs chiral metamaterial can fulfill the strong and mutually dual-band AT effect in the THz spectral.

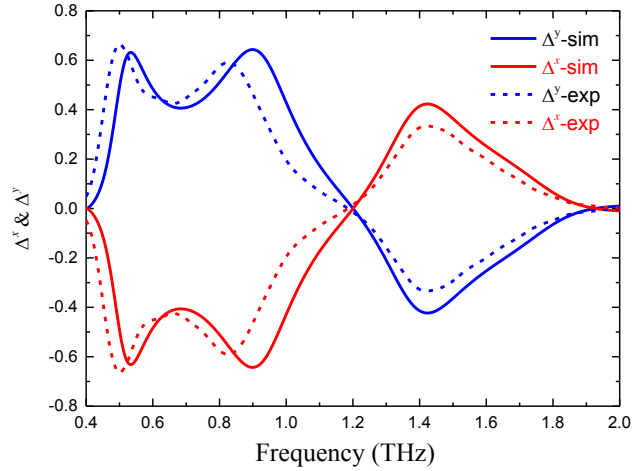


Figure 3: Simulated and measured asymmetric transmission of the metamaterial for linearly polarized wave.

3. Conclusions

In summary, we numerically and experimentally demonstrate a high-performance AT response for normally incident linear polarized waves in multilayer chiral metamaterial with crossed-S patterns. The results indicated that a mutually independent dual-band AT response can be implemented with a maximum of 0.64 and 0.53 for x- and y-polarized waves, respectively. The proposed multilayer chiral metamaterials are beneficial in designing polarization control devices and offer considerable opportunities and flexibility for practical applications.

Acknowledgements

The authors acknowledge financial supports from National Natural Science Foundation of China (NSFC) (61875044, 61675054 and 91750107), Natural Science Foundation of Heilongjiang Province (ZD2018015), Postdoctoral Scientific Research Developmental Fund of Heilongjiang Province (Grant No. LBH-Q15036), 111 project to the Harbin Engineering University (B13015), Fundamental Research Funds for Harbin Engineering University (HEU) of China.

References

[1] N. Yu, F. Capasso, Flat optics with designer metasurfaces, *Nat. Mater.* 13: 139-150, 2014.

[2] Y. Liu and X. Zhang, Metamaterials: a new frontier of science and technology, *Chem. Soc. Rev.* 40(5): 2494–2507, 2011.

[3] V. A. Fedotov, P. L. Mladyonov, S. L. Prosvirnin, A. V. Rogacheva, Y. Chen, N. I. Zheludev, Asymmetric propagation of electromagnetic waves through a planar chiral structure, *Phys. Rev. Lett.* 97: 167401, 2006.

[4] C. Huang, Y. J. Feng, J. M. Zhao, Z. B. Wang and T. Jiang, Asymmetric electromagnetic wave transmission of linear polarization via polarization conversion through chiral metamaterial structures, *Phys. Rev. B* 85: 195131, 2012.

[5] C. Pfeiffer, C. Zhang, V. Ray, L. J. Guo, and A. Grbic, High performance bianisotropic metasurfaces: asymmetric transmission of light, *Phys. Rev. Lett.* 113(2): 023902, 2014.

[6] T. T. Lv, Y. X. Li, H. F. Ma, Z. Zhu, Z. P. Li, C. Y. Guan, J. H. Shi, H. Zhang, T. J. Cui, Hybrid metamaterial switching for manipulating chirality based on VO2 phase transition*Sci. Rep.* 6: 23186, 2016.

[7] J. H. Shi, X. C. Liu, S. W. Yu, T. T. Lv, Z. Zhu, H. F. Ma, T. J. Cui, Dual-band asymmetric transmission of linear polarization in bilayered chiral metamaterial, *Appl. Phys. Lett.* 102: 191905, 2013.

[8] S. Y. Fang, K. Luan, H. F. Ma, W. J. Lv, Y. X. Li, Z. Zhu, C. Y. Guan, J. H. Shi, T. J. Cui, Asymmetric transmission of linearly polarized waves in terahertz chiral metamaterials, *J. Appl. Phys.* 121: 033103, 2017.

The roles of "superchirality", optical chirality dissipation and interference in biomolecular detection with chiral plasmonic structures

Cameron Gilroy[1], Shun Hashiyada[2], Kensaku Endo[3], Affar S. Karimullah[1], Laurence D. Barron[1], Horomi Okamoto[2], Yoshihiko Togawa[3] and Malcolm Kadodwala[1*]

[1]School of Chemistry, Joseph Black Building, University of Glasgow, Glasgow, G12 8QQ
[2]Institute for Molecular Science and The Graduate University for Advanced Studies (Sokendai), 38 Nishigonaka, Myodaiji, Okazaki, Aichi 444-8585, Japan
[3]Department of Physics and Electronics, Osaka Prefecture University, Sakai 599-8570, Japan
*Malcolm Kadodwala, E-mail: Malcolm.Kadodwala@glasgow.ac.uk

Abstract

Chiral plasmonic nanostructures enable the ≤ pg detection of biomaterials. Sensing capabilities are associated with the chiral asymmetry of generated near fields which can be greater than circularly polarized light, a property known as superchirality. We show that chiral sensing is correlated to the thickness of a nanostructure which we reconcile with a previously unconsidered mechanism for the phenomenon. It involves the "dissipation" of optical chirality into chiral material currents through the interference of fields generated by two spatially separated chiral modes.

1. Introduction

The detection and characterisation of inherently chiral biological materials is of both fundamental and practical interest, with applications in the life and analytical sciences. The presence of chiral dielectric materials, such as biomacromolecules, within the near field region of chiral nanostructures induces asymmetric changes in the optical properties (CD, ORD and reflectance spectra) of chiral plasmonic nanostructures [1] and hence can form the basis of biological sensing.

The origin of this asymmetry is undoubtedly the chiral asymmetry of the near fields which are generated around the nanostructure. This chiral asymmetry can be parameterized by an optical chirality factor [2]. If the optical chirality of near fields is greater than that of equivalent CPL then it is *"superchiral"*[2].

In this work, we present evidence to suggest that the sensing capability of a chiral structure is dependent upon a chiral dielectric inducing asymmetry in the capacity of left and right handed structures to convert the chirality of light into chiral surface charge distributions, a process which has been referred to as the dissipation of optical chirality [3], [4].

To account for this asymmetry we propose a previously unconsidered mechanism of optical chirality dissipation based on the interference between chiral fields generated by spatially separated sources. The far field photon (energy) fluxes, which are monitored to obtain extinction spectra, have contributions due to absorption and scattering. Thus by analogy we propose the hypothesis that optical chirality, a conserved quantity like energy, is dissipated through both absorption and scattering.

1.1. Modelling Procedure

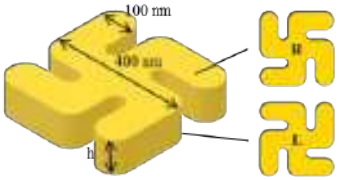


Figure 1: Simulated idealised gammadion belonging to the C_{4h} point group. The right (R) and left (L) handedness of the structure's two planar faces are identified.

Numerical electromagnetic (EM) simulations were performed using the finite element method implemented on the COMSOL Multiphysics platform. The structures studied are periodic (periodicity = 570 nm) gammadions of varying heights (*h = 5, 30, 100 nm)* with dimensions shown in

. Each planar face of the structure is either intrinsically left (L) or right (R) handed thus the surface plasmons associated with these interfaces are chiral. We embed each structure in achiral and chiral dielectrics of refractive index 1.523. The approach for modelling chiral dielectrics has been described previously [5].

2. Results & Discussion

Simulations were performed with left and right circularly polarised light (LCP/RCP) incident on L and R faces of the structure (i.e. four combinations). Circular dichroism spectra were derived from the differential transmission of LCP/RCP, *Figure 2* for the structures in achiral and chiral electrics.

In both the achiral and chiral media, a CD signal is observed for all gammadion thicknesses and the sign is dependent on the handedness of the planar surface light is incident upon. The 5 nm structure shows the smallest CD, an order of magnitude smaller than the 30 nm structure which in turn is 5 times smaller than the 100 nm structure. When surrounded by chiral media, the 100 nm thick structure shows the largest asymmetry, several orders of magnitude larger than in the thinner structures.

The chiral asymmetry of near fields is parameterized by the optical chirality parameter C. By analogy with Poynting's theorem the following expression is derived for the optical chirality flux (***F***):

$$\frac{\partial C}{\partial t} + \frac{1}{\mu}\nabla \cdot \boldsymbol{F} = -\frac{1}{2}(\boldsymbol{j} \cdot \nabla \times \boldsymbol{E} + \boldsymbol{E} \cdot \nabla \times \boldsymbol{j}) \qquad (1)$$

where $\boldsymbol{j}$ are material currents and E are time dependent electric fields. The implication of Equation (1) is that chiralities of electromagnetic fields and electronic motion can be interconverted.

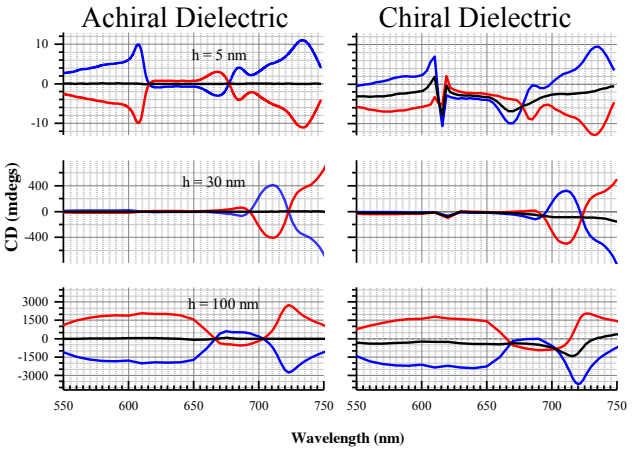


Figure 2: CD spectra for gammadions of h = 5 (30 and 100 nm when light is incident on the R (blue) and L (red) faces when surrounded by both achiral and chiral dielectrics Their mean is shown in black.

We calculate time-average optical chirality flux $\bar{F}$ for the two directions of light incidence and incident light polarization states for each of the structure thicknesses, *Figure 3*. It has previously been shown that $\bar{F}$ is proportional to the level of circular polarization measured in the far field [4].

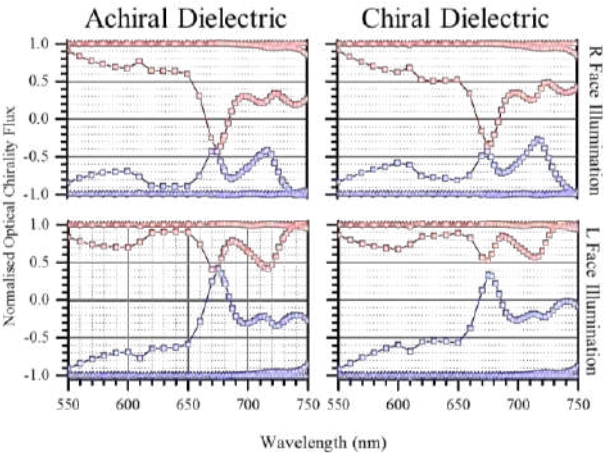


Figure 3: Normalised optical chirality flux plots for h = 5 (triangles) 30 (circles) and 100 nm (square) structures for LCP (blue) and RCP (red) light incident upon R and L faces of the gammadion.

In all cases, the 100 nm thick structure shows the largest dissipation of optical chirality. Equation (1) states that changes in $\bar{F}$ must be offset by a commensurate change in the chirality of the electron distributions which we have calculated for each of the thicknesses. Data is presented only for RCP incident on an R face for brevity; however other combinations show a similar pattern.

For h = 5 and 30 nm the top and bottom faces are identical and 180° out of phase respectively (which, when time averaged would show the same distribution). Their side profiles also show very little asymmetry. In the 100 nm thick case however, the two faces show distinct charge distributions and the side profile shows a large asymmetry. Consequently, for h = 100 nm the time averaged surface charge distribution acts as a significant chiral perturbation lifting the horizontal mirror plane of the gammadion.

For combinations which are related by symmetry (such as LCP incident upon a L face and RCP incident upon a R face) the $\bar{F}$ spectra show equal but opposite behaviour. However, when surrounded in the chiral dielectric this relationship no longer holds.

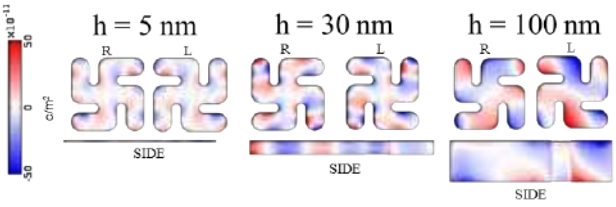


Figure 4: Surface charge density plots for h = 5, 30 and 100 nm thick structures on their L and R faces and side profiles.

We propose a model for the dissipation of optical chirality flux through an interference mechanism. The model assumes that the two oppositely handed faces of a gammadion act as spatially separated sources of chiral near fields which can interfere both which each other and light incident upon the structures. The result of which is that the optical chirality flux $\bar{F}$ is dependent on the phase differences between the two sources and incident light; a phase difference which can be modulated by changing the height of the nanostructure.

In achiral media, this phase difference is the same for combinations related by symmetry. In chiral media however, the presence of a chiral dielectric (molecules) has an asymmetric influence on the phase difference between the two sources of chiral fields, leading to an asymmetry in the level of conversion of optical chirality to chiral material currents. This leads to an asymmetric change in the (chir)optical properties of the plasmonic structures which manifests itself in an asymmetry in the resulting CD spectra. Thus our work provides the starting point for the development of a design framework to optimise the sensing capabilities of chiral plasmonic nanostructures.

3. References

[1] E. Hendry *et al.*, "Ultrasensitive detection and characterization of biomolecules using superchiral fields," *Nat. Nanotechnol.*, vol. 5, no. 11, pp. 783–787, 2010.

[2] Y. Tang and A. E. Cohen, "Enhanced Enantioselectivity in Excitation of Chiral Molecules by Superchiral Light," *Science (80-.).*, vol. 332, no. 6027, pp. 333–336, 2011.

[3] J. E. Vázquez-Lozano and A. Martínez, "Optical Chirality in Dispersive and Lossy Media," *Phys. Rev. Lett.*, vol. 121, no. 4, 2018.

[4] L. V. Poulikakos *et al.*, "Optical Chirality Flux as a Useful Far-Field Probe of Chiral Near Fields," *ACS Photonics*, vol. 3, no. 9, pp. 1619–1625, 2016.

[5] C. Kelly *et al.*, "Controlling Metamaterial Transparency with Superchiral Fields," *ACS Photonics*, vol. 5, no. 2, pp. 535–543, 2018.

Metamaterial-based devices

All dielectric frequency-division multiplexing wave plate metasurface

Shuo Du[1,2], Zhe Liu[1,3], Junjie Li [1,2,4], Changzhi Gu [1,2]

[1] Beijing National Laboratory for Condensed Matter Physics, Institute of Physics, Chinese Academy of Sciences, Beijing, China
[2] School of Physical Sciences, CAS Key Laboratory of Vacuum Physics, University of Chinese Academy of Sciences, Beijing, China
[3] Niels Bohr Institute, University of Copenhagen, Blegdamsvej, Copenhagen, Denmark
[4] Songshan Lake Materials Laboratory, Dongguan, Guangdong, China
*corresponding author, E-mail: czgu@iphy.ac.cn

Abstract

We report an all dielectric frequency-division multiplexing wave plate metasurface, which simultaneously possesses the function of broadband half/quarter-wave plates for transmission spectral in mid/near-infrared. The structure units of our metasurface are silicon cross-nanoblocks, which are easy to be fabricated by planar precesses. Besides, at wavelengths with the function of high working efficiency half-wave plate, the structure units can be used to design variety of wavefront optical devices, such as metalens and holographic imaging.

1. Introduction

It is of critical importance to control the polarization states of light in the field of coding, imaging and communication. Linear and circular polarization are two basic states, and the wave plates, including half/quarter-wave plate, are tools achieving the mutual conversion between them. In general, wave plate Metasurfaces can conquer the disadvantages of typical wave plates, such as bulky and complicated processing[1]. But it appears that most of them can only achieve a single function of wave pale either half-wave plate or quarter-wave plate, suffering from low working efficiency and narrow conversion band[2, 3]. Here we experimental demonstrate an all dielectric high efficiency and broadband frequency-division multiplexing half/quarter-wave plate metasurface. It has promising application in wavefront manipulation optical elements and is easy to be fabricated.

2. Structure design

The units of our design are cross silicon nanoblocks, and by tuning the parameter of central rectangular column, the elements of general complex Jones matrix can satisfy the magnitude and phase requirements of being half/quarter-wave plate in different wavelength band, respectively.

3. Results and dicussion

This metasurface, as shown in figure 1, is fabricated by simple planar processes (including lithography, deposition, and etching)[4]. The transmission spectral is simulated by commercial software CST Microwave Studio and characterized by Fourier transform infrared (FTIR) spectrometer. The results appear that our metamaterial implements the function of high efficiency and broadband frequency-division multiplexing half/quarter-wave plate in mid-infrared.

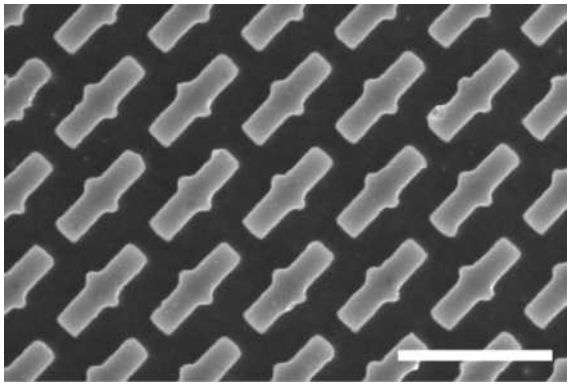


Figure 1: The SEM image of the top view of fabricated frequency-division multiplexing wave plate metasurface, and the scale bar is 2 μm.

4. Conclusions

We proposed a novel design for all dielectric frequency-division multiplexing wave plate metasurface, which is easy to be fabricated by planar processes. For its high working efficiency and broad working band, our metasufaces are highly promising for potential application in the field of communication, imaging and coding.

Acknowledgements

This work is supported by the National Key Research and Development Program of China under Grant Nos. 2016YFA0200400 and No. 2016YFA0200800; the National Natural Science Foundation of China under Grants Nos. 61888102, 91323304, 11674387, 11504414, 11574369, 11574385, 11574368 and 61390503; Strategic Priority Research Program and Key Research Program of Frontier Sciences, CAS, Grant Nos.XDB07020200 and QYZDJ-SSW-SLH042.

References

[1] C. Pfeiffer, C. Zhang, V. Ray, L.J. Guo, A. Grbic, High Performance Bianisotropic Metasurfaces: Asymmetric Transmission of Light, *Physical Review Letters* 113: 023902, 2014.

[2] N.K. Grady, J.E. Heyes, D.R. Chowdhury, Y. Zeng, M.T. Reiten, A.K. Azad, A.J. Taylor, D.A.R. Dalvit, H.-T. Chen, Terahertz Metamaterials for Linear Polarization Conversion and Anomalous Refraction, *Science* 340: 1304-1307, 2013.

[3] Y. Zhao, A. Alu, Tailoring the dispersion of plasmonic nanorods to realize broadband optical meta-waveplates, *Nano Lett* 13: 1086-91, 2013.

[4] Z. Liu, A. Cui, J. Li, C. Gu, Folding 2D Structures into 3D Configurations at the Micro/Nanoscale: Principles, Techniques, and Applications, *Adv Mater* e1802211, 2018.

Polarization-sensitive coherent absorption in metamaterials

Yuxiang Li[1*], Bowen Li[1], Jintong Shi[1], Wenjin Lv[1], Chunying Guan[1], Jinhui Shi[1,2]

[1]Key Laboratory of In-Fiber Integrated Optics of Ministry of Education, College of Science, Harbin Engineering University, Harbin 150001, China
[2]SZU-NUS Collaborative Innovation Centre for Optoelectronic Science & Technology, and Key Laboratory of Optoelectronic Devices and Systems of Ministry of Education and Guangdong Province, Shenzhen University, Shenzhen 518060, China
*corresponding author, E-mail: liyuxiang11@hrbeu.edu.cn

Abstract

We reported multi-band absorption in bilayered asymmetrically split ring metamaterials. The absorption can be coherently modulated by a second counterpropagating wave. The spectrally overlapped electric and magnetic resonances can be selectively observed based on the interaction of light with light on metamaterials. In particular, the scheme for realizing multi-band coherent perfect absorption operates from microwave to optical frequency.

1. Introduction

The field of metamaterials has been developing rapidly in recent years. Metamaterials with subwavelength elements can control properties of electromagnetic wave to realize desirable amplitude, phase-shift or polarization conversion in unconventional way that can be unachievable using traditional materials. Recently, it was demonstrated that in slabs of linear material of sub-wavelength thickness optical manifestations of birefringence and optical activity can be controlled in the coherent technique [1-9]. We will show that multi-band coherent perfect absorption (CPA) can be achieved in bilayered asymmetrically split ring metamaterials via coherently controlled technique. Such control can be applied at arbitrarily low intensities, thus arguably allowing for fast handling of electromagnetic signals without facing thermal management and energy challenges.

2. Coherent perfect absorptions

If a metamaterial of subwavelength thickness is placed at a node or antinode of the standing wave, it will lead to different results in controlling intensity and absorption of the output beams when two coherent beams named “Signal Beam ” and “Coherent Beam ” pass though it normally shown in Fig. 1(a). Generally, the nodes and antinodes of the standing wave are defined in the electric field. An electric antinode corresponds to the magnetic node, or vice versa. Firstly, if the ultrathin film is placed on electric nodes (corresponding to the phase difference of $\varphi = 180°$ between two input beams), the metamaterial is transparent to both counter-propagating incident beams. In this case, the ASRs experiences no electric excitation, however, strong magnetic excitation in ASRs is twice larger than the case of one beam illumination. Secondly, two output beams totally vanish when the film is placed at an antinode (corresponding to the phase difference of $\varphi = 180°$ between two input beams). In this case, twice electric excitation of the ASRs compared to one beam illumination and no magnetic excitation happen. When modulating phase of the coherent beam, the intensity of the output beam changes correspondingly. The structures of bilayered asymmetrically split rings (ASRs) are shown in Fig. 1(b). The ASRs are periodic along the x and y directions with a lattice constant of $d = 15$mm. The ASRs etched from the copper cladding can be fabricated on either side of the FR4 printed circuit board with a thickness $t = 1.5$mm. Each ASR consists of two copper wire arcs with open angles of $\alpha = 140°$and $\beta = 160°$. The inner radius of the ASRs is $r = 5.6$mm and the wire width is $w = 0.8$mm. Each stereo ASR dimer consists of two spatially separated ASRs, which are structurally identical.

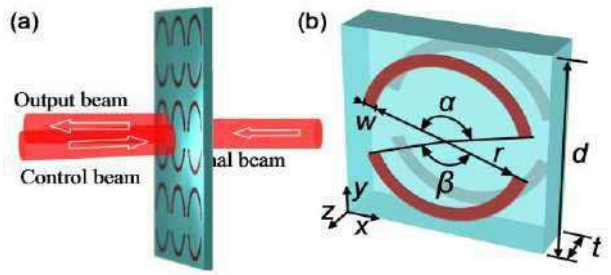


Figure 1: (a) The principle of coherent perfect absorption. (b) Snapshots of unit cells of bilayered metamaterials consisting of asymmetrically split rings (ASRs).

Based on full-wave simulations using a three-dimensional Maxwell finite element method solver (COMSOL Multiphysics), the absorption spectra are shown in Figure 2. In the simulations, the copper was treated as a perfect electric conductor and a permittivity $\varepsilon = 4.05\text{-}i0.05$ was assumed for the lossy dielectric substrate. The bilayered metamaterial exhibits triple-band absorption in the frequency range from 4 GHz to 8 GHz for an x-polarized input beams illumination while it exhibits double-band

absorption in the frequency range from 8 GHz to 12 GHz for a *y*-polarized input beams illumination along the *z* direction, respectively. The both input beams are x- or y-polarized in the coherent case. The intensity of the beam is defined as 1 in the case of one beam illumination while the intensities of two input beams are defined as 0.5 in the coherent case. Obviously, the bilayered metamaterial reveals distinct absorption peaks at electric nodes and anti-nodes of the standing wave. More importantly, three absorption bands can be selectively switched on/off at lower frequencies and other two absorption bands occur at higher frequencies, depending on the phase difference of two input beams. Figure 2 shows the absorption spectra surface current density of the bilayered metamaterial. In Figure 2 (a) and (b), electric and magnetic responses can be selectively enhanced or eliminated with the phase difference varies for same polarization of input beams. The experimental setup is shown in Fig. 2(c) and the measured coherent absorption spectra are given for x-polarized wave in Fig. 2(d).

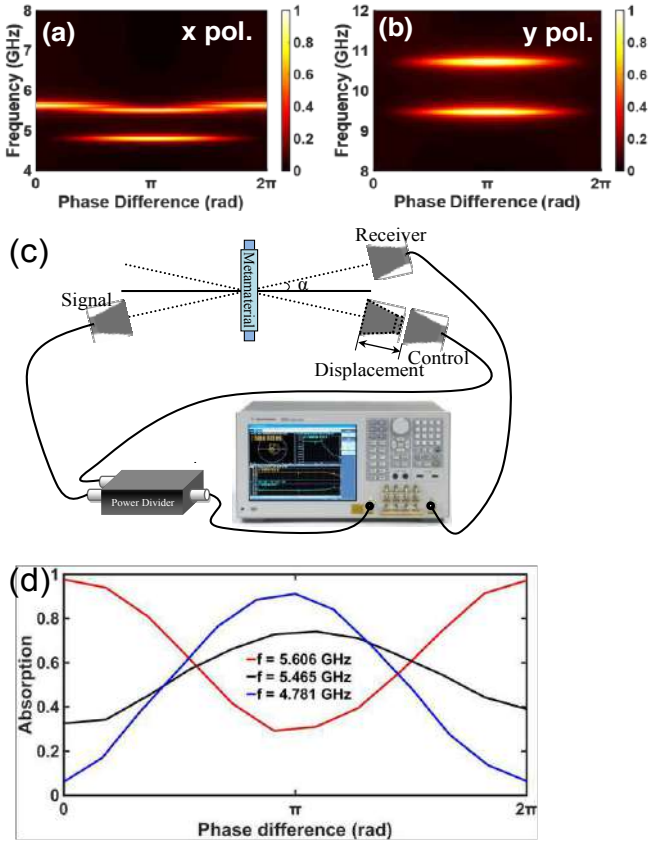


Figure 2: Simulated coherent perfect absorption of metamaterials as a function of frequency and phase difference in for (a) x- and (b) y-polarization. (c) Experimental setup. (d) The measured results for x-polarized wave.

3. Conclusions

In summary, we numerically and experimentally demonstrate polarization-sensitive coherent perfect absorbers in bilayered metamaterial based on the full wave simulations. The bilayered metamaterial are constructed by asymmetrically split rings. The polarization-sensitive coherent perfect absorption can be realized depending on electromagnetic mode switching effect, i.e., the in-phase electric resonances are only coherently excited at an electric antinode while the out-of-phase magnetic resonances only at a magnetic antinode. We also measured three selected frequencies when x-polarization waves incident. The coherently controlled metamaterials will be promising candidates for designing selective multiband absorbers and this technique offers considerable flexibility of operating at any frequencies from the microwave to optical range and provides an opportunity to realize coherent data processing network and recognize the nature of electromagnetic modes.

Acknowledgements

The authors acknowledge financial supports from National Natural Science Foundation of China (NSFC) (61875044, 61675054 and 91750107), Natural Science Foundation of Heilongjiang Province (ZD2018015), Postdoctoral Scientific Research Developmental Fund of Heilongjiang Province (Grant No. LBH-Q15036), 111 project to the Harbin Engineering University (B13015), Fundamental Research Funds for Harbin Engineering University (HEU) of China.

References

[1] J. F. Zhang, C. C. Guo, K. Liu, Z. L. Zhu, W. M. Ye, X. D. Yuan, S. Q. Qin, Coherent perfect absorption and transparency in a nanostructured graphene film, *Opt. Express* 22: 12524-12532, 2014.

[2] Z. Zhu, H. Liu, D. Wang, Y. X. Li, C. Y. Guan, H. Zhang and Shi J. H., Coherent control of double deflected anomalous modes in ultrathin trapezoid-shaped slit metasurface, *Sci. Rep.* 6, 37476, 2016.

[3] Kita, S., Takata, K., Ono, M., Nozaki, K., Kuramochi, E., Takeda, K., and Notomi, M., Coherent control of high efficiency metasurface beam deflectors with a back partial reflector, *APL Photonics* 2, 046104 ,2017.

[4] M. Kang, H. Wang and W. Zhu, Wavefront manipulation with a dipolar metasurface under coherent control, *J. Appli. Phys.* 122, 013105,2017.

[5] G.Y. Nie, Q.C. Shi, Z. Zhu and J. H. Shi, Selective coherent perfect absorption in metamaterials, *Appl. Phys. Lett.* 105, 201909 , 2014.

[6] W. Tan, C. H. Zhang, C. Li, X. Y. Zhou, X. Q. Jia, Z. Feng, J. Su and B.B. Jin, Selective coherent perfect absorption of subradiant mode in ultrathin bi-layer metamaterial via antisymmetric excitation, *Appl. Phys. Lett.*110, 181111,2017.

[7] Tseng, M. L., Fang, X., Savinov, V., Wu, P. C., Ou, J.-Y., Zheludev, N. I. and Tsai, D. P., Coherent selection of invisible high-order electromagnetic excitations, *Sci. Rep.* 7, 44488,2017.

[8] X. Zhang and Y. Wu, Scheme for achieving coherent perfect absorption by anisotropic metamaterials, *Opt. Express*. 25, 4860, 2017.

[9] J.H.Shi, X.Fang, Rogers, E. T. F., Plum, E., MacDonald, K. F. and Zheludev, N. I., Coherent control of Snell's law at metasurfaces, *Opt. Express*, 22, 21051-21060,2014.

Control of IR emissivity with metasurface structures

Roxana Tomescu*, Mihai Kusko*, Dana Cristea*, Laura Mihai, Ramona Calinoiu*, Cristian Kusko*, Catalin Parvulescu***

*National Institute for R&D in Microtechnologies – IMT Bucharest, Bucharest, Romania
**Center for Advanced Laser Technologies – CETAL, National Institute for Laser Plasma and Radiation Physics, Magurele, Romania
E-mail: roxana.tomescu@imt.ro

Abstract

We propose a compact photonic device that presents an improved and controlled emissivity on specific tight infrared wavelengths intervals, consisting in an infrared thermal source and a metasurface absorber. The source is composed of 200nm thick chromium layer in meander configuration, the line width is 100µm and the resistor area is 1mm^2. The metasurface is tailored to attain almost perfect absorption on infrared wavelengths intervals specific for gases that may be found in industrial infrastructures like methane or carbon dioxide.

1. Introduction

The most frequent toxically gas molecules present in industrial infrastructures are: methane (CH_4), carbon oxides (CO_2, CO), azote oxides (NO_2, NO), ozone (O_3), formaldehydes (H_2CO/CH_2O), etc. The absorption wavelengths of each one of these gases are close to one another, therefore, for work security and health purposes it is necessary to develop highly sensitive sensors for tight IR wavelength intervals [1]. Our objective is to develop IR sources with high emissivity control, in order to obtain sensors for each specific gas. The emission control is achieved by tailoring a metamaterial to attain approximatively total absorption for a wavelengths intervals with the peck at the maximum absorption of the specific gas.

Metamaterials have specific properties such as negative permittivity, permeability and refraction index, allowing them to be used for beam shaping or for realization of a perfect absorber for photonic and optoelectronic applications. With a specifically tailored metamaterial one can achieve an absorption value close to 1 in any frequency domain [2, 3]. Furthermore, Kirchhoff law states that the emissivity of a material is equal to the absorption at equilibrium [3] which makes this type of structures ideal for our designated application.

2. Model and discussion

We develop a highly emissivity control IR source consisting in an infrared thermal source and a metasurface absorber, which ca be integrated in gas detection systems for industrial infrastructures. In figure 1 one can observe the diagram of our proposed system with the IR source and two Fresnel lenses, one to collimate the source emission and one to focalize the radiation on the commercial detector.

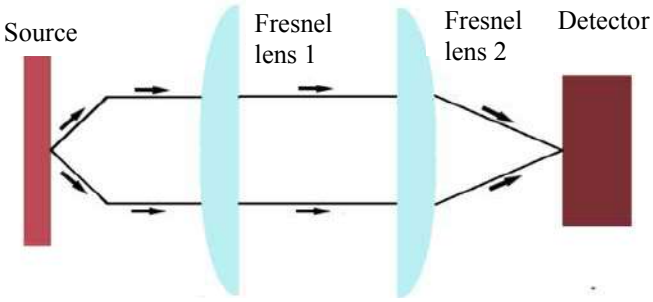


Fig.1 Diagram of the gas detection system

The IR thermal source consists in a resistor with a 200 nm thick chromium layer in meander configuration. The line width of the meander is 100 µm and the resistor area is 1 mm^2.

In figure 2 we represent the diagram of the proposed resistor and the black body emission distribution calculated for 550K temperature corresponding to a maximum emission in medium IR.

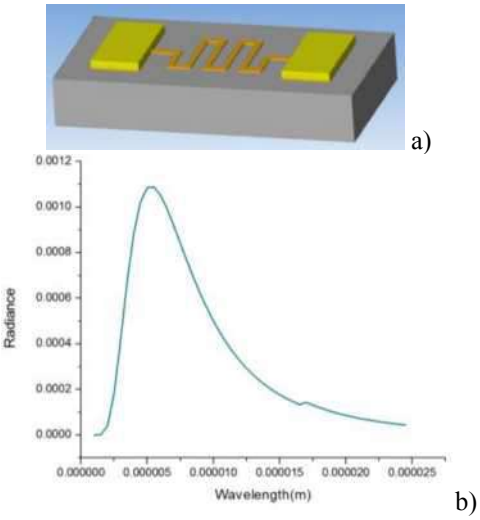


Fig 2. a) IR thermal source; b) Calculated blackbody radiation spectrum at 550K temperature

The fabrication of the meander source is realized by classical microfabrication technics such as: sputtering for metal deposition (chromium for the meander resistor and gold for the contact pads); photolithography to pattern the meander and contact pads, and lift-off to obtain the final metal structure. For the photolithography step we use three photolithographic masks designed with CleWin software: i) the first one is designed to pattern the meander resistor and the metallic contact pads; ii) the second one is used to remove the thin gold film from the meander area, this layer being utilised only on the contact pads; iii) the third one is employed in micro-patterning the gold pillars metasurface.
In order to achieve the selectivity of the IR source, we proposed an absorber metasurface place on top of the meander resistor. This metasurface is composed of gold pillars micro-patterned on an amorphous silicon thin layer. The aim of this pillars array is to filter a specific tight wavelengths interval. In figure 3 one can observe the configuration of the tailored metasurface pattern on top of the IR thermal source.

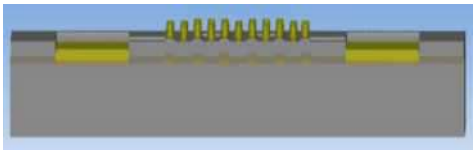


Fig. 3 Diagram of the developed source with controlled emissivity

3. Conclusions

We calculated, fabricated and measured a thermal IR source based on a meander chromium resistor. Also, an IR absorber metasurface was fabricated using photolithography and lift-off method.
In order to obtain an IR source with controlled emissivity we decided to place the absorbent metasurface on top of the meander resistor source. In the first instance we considered as insulator layer between the two structures a SiO_2 deposited by RF-Sputtering. After the deposition of the amorphous silicon substrate necessary for the absorption configuration we observed the exfoliation of the SiO_2 due to the fact that was deposited on a 3D profile of 1μm height. In order to resolve the insulator adherence problem we will replace the SiO_2 insulator with Al_2O_3 obtaine by Atomic Layer Deposition.
The radiance spectra were measured using an OL750 spectroradiometer system from Gooch&Housego in configuration for emittance measurements. The system is composed by double monochromator with IR diffraction gratings and 5 mm slits/apertures at the entrance, middle and exit ports, a collimation optical system, and a standard InSb detector with high sensitivity in the spectral range 1 - 5.5 microns.

Acknowledgements

This work was supported by a grant of the Romanian Ministery of Research and Innovation, CCCDI – UEFISCDI, project number PN-III-P1-1.2-PCCDI-2017-0419 / SENSIS – P3 – Infrared sensors for infrastructure security applications, within PNCDI III."

References

[1] Kumar, P., Morawska, L., Martani, C., Biskos, G., Neophytou, M., Di Sabatino, S., Bell, M., Norford, L. and Britter, R., 2015. The rise of low-cost sensing for managing air pollution in cities. Environment international, 75, pp.199-205.

[2] - Weiren Zhu, Xiaopeng Zhao, Boyi Gong, Longhai Liu, Bin Su, Optical metamaterial absorber based on leaf-shaped cells, Appl Phys A, 102: 147–151, 2011.

[3] - Xianliang Liu, Talmage Tyler, Tatiana Starr, Anthony F. Starr, Nan Marie Jokerst, and Willie J. Padilla, Taming the Blackbody with Infrared Metamaterials as Selective Thermal Emitters, PRL 107, 2011.

Detection of organic molecules using asymmetric plasmonic nanostructures

Ili F. Mohamad Ali Nasri[1,2], Graham J. Sharp[1], Richard M. De La Rue[1], Nigel P. Johnson[1], Marc Sorel[1], and Caroline Gauchotte-Lindsay[2*]

[1]Electronic and Nanoscale Engineering, School of Engineering, University of Glasgow, Glasgow, UK
[2]Infrastructure and Environment, School of Engineering, University of Glasgow, Glasgow, UK
*corresponding author, E-mail: Caroline.Gauchotte-Lindsay@glasgow.ac.uk

Abstract

We demonstrate the fabrication and characterization of an array of plasmonic metamaterial nanostructures based on asymmetric split H (ASH) resonators on a zinc selenide substrate that produce plasmonic resonances matched with the molecular vibrations of an organic material. Estrogenic hormones; 17β-Estradiol (E2) and Estrone (E1) were chosen as analytes for coupling with the plasmonic resonances. The experimental results show there is a good match with the molecular bond resonances of the C-H, C=O and C=C observed in estrogen and we have also shown that it is possible to differentiate the molecular bond resonance spectrum of E2 in a mixture with E1.

1. Introduction

Surface enhanced infrared absorption (SEIRA) spectroscopy is widely used in sensing applications for environmental monitoring and clinical diagnostics. By applying an organic analyte on the metal-air interface of the metamaterial structures, the characteristic molecular vibrations of the analyte material can be detected and enhanced if they coincide with the plasmonic resonant wavelengths. The resultant red-shift in the plasmonic resonance can be measured and used to calculate the sensitivity for use as an optical biosensor [1]–[3]. In this paper, we show that analytical techniques based on the plasmonic properties of gold nanostructures, to be eventually used for rapid environmental analysis. We present the plasmonic metamaterial nanostructure arrays of asymmetric split H (ASH) resonators that have been optimized to produce plasmonic resonances that match the resonant molecular vibrations of a biological material [4]. ASHs were designed for sensing organic molecules of two selected estrogens, 17β-Estradiol (E2) and Estrone (E1). Also, the target is to identify the common (O-H, C-H and C=C bonds) and different (C=O bonds) molecular bond resonances for the two estrogen molecules in the mid infrared (IR) wavelength range (2 to 8 μm).

Estrogen is one of the endocrine disruption compounds (EDC) that has been discovered regularly in various water sources. It has been found at concentrations as low as 1 to 10 ng/l due to its poor solubility. EDC contamination is potentially found in food, the water supply and consumer products and can lead to adverse health effects, particularly with regard to reproduction and the bodily development process. EU government has suggested monitoring the issues in the water source contamination because of the potential harm to the aquatic species, such as alterations of sexual development and inter-sex species (e.g feminization of male fish) [5]–[8]. E2 is a steroid hormone and a major sex hormone in females that functions in the development of reproductive systems and other physical features. E1 can be found after the menopause in the female body.

2. Plasmonic Metamaterial Nanostructures

We have fabricated ASH arrays using electron beam lithography on a zinc selenide (ZnSe) substrates. This transparent and high refractive index material allows detection in the longer wavelength range of 600 nm to 21 μm. The ASH nanostructures were formed with asymmetric vertical dipoles and cross bar dipoles. Scanning electron micrograph (SEM) images of ASHs are shown in Figure 1. The two different sizes of ASH labelled as ASH_1 and ASH_2, with ASH_1 arm length (L_1 and L_2) varying between 450 nm and 800 nm and ASH_2 arm lengths between 1.2 μm and 1.6 μm were chosen for the mid-IR region. When the incident wave is polarized along y-axis, parallel with the vertical asymmetric arms, the basic structure exhibits two plasmonic resonance peaks, due to the asymmetry of the arm-lengths.

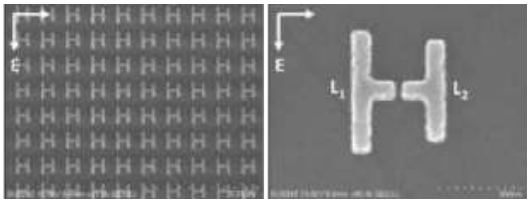


Figure 1: Scanning electron micrograph of (a) an array and (b) one-unit cell of asymmetric split H (ASH) resonators.

3. Optical Sensing of estrogenic hormones

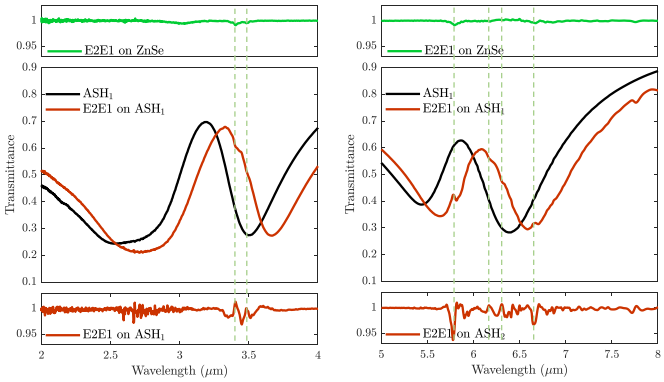
Table 1 shows that E2 and E1 exhibit a strong molecular vibration of the C-H bond at wavelengths between 3.40 μm and 3.49 μm. Carbon to carbon double bond stretching (C=C) also occurs in the wavelength range from 6.30 μm to 7.00 μm. The significant chemical difference between E1 and E2 lies in a single bond, which is a C-OH in E2 and the C=O bond in E1. Molecular vibrations for this C=O bond

occur at wavelengths of 5.79 µm and 5.85 µm. The plasmonic nanostructures were coated consecutively with a thin layer of E1 in absolute ethanol (1mg/ml), a thin layer of E2 (1mg/ml) and various mixtures of E2 and E1, all with a total estrogen concentration of 2mg/ml but different E2:E1 ratios. The samples were left to evaporate overnight before the measurements were performed - by which point the estrogen had crystallized on top the resonators. The ASH structures were tuned to resonate at the wavelength of the C-H bonds of interest and found good matches with ASH_1 resonant using the length sizes of L_1 = 800 nm, L_2 = 600 nm. While for ASH_2 the sizes of L_1 = 1.5 µm and L_2 = 1.2 µm demonstrated close matches to the two double bond resonances.

Table 1: Summary of molecular bonds features in 17β - Estradiol and Estrone in the mid-IR wavelength

Molecular Bonds	E1 (µm)	E2 (µm)
O-H	3.05	2.96
C-H	3.40	3.41
	3.49	3.48
C=O	5.79	x
	5.85	
C=C	6.30	6.30
	6.67	6.67
	6.80	6.80

A substantial resonance red-shift was produced between the positions for the uncoated ASHs and the corresponding positions when the ASHs were coated with estrogen. The resonance shifted 220 nm from the initial position of the uncoated ASHs. For instance, the resonant wavelength for ASH_2 were shifted from 5.46 µm to 5.68 µm and from 6.39 µm to 6.63 µm. When the mixture of E2 and E1 was deposited on the nanostructures, transmittance resonance (Figure 2 (a) and (b) in red lines) produced a small feature at a wavelength of around 5.79 µm as shown for ASH_2 in Figure 2(b), that matched the vibration of the C=O bond present in E1. The vibrational signal enhancement of estrogen deposited on nanostructure arrays could be quantified by comparison with the deposition of the estrogen mixtures on the bare ZnSe substrate (green line in Figure 2). Baseline corrections were used to extract the peak strengths of the various molecular vibrations. We found that the molecular bond resonances are typically five times larger, easily visible and differentiated the ASHs, as compared with those deposited on bare substrates. Additionally, we could quantitatively separate out the contribution of each type of estrogen.



(a) (b)

Figure 2: Plots transmittance resonances from the (a) ASH_1 and (b) ASH_2 with the mixture of E2 and E1 (50:50) show the vibrational resonances and the baseline corrected in the fingerprints of O-H, C-H, C=O and C=C bonds

4. Conclusions

In conclusion, we tuned the geometry of the asymmetric split H resonators which can be utilized to enhance the molecular C-H, C=O and C=C bond resonances of E2 and E1. The plasmonic resonance were red-shifted towards longer wavelengths through the deposition of organic materials on the nanostructures. This study will support the development of plasmonic biosensors that can be used to detect and differentiate the presence of small amounts of different organic molecules with lower detection limits.

Acknowledgements

IFMAN gratefully acknowledges funding by the Malaysian Government, through Majlis Amanah Rakyat (MARA) Malaysia. We also acknowledge the staff and facilities of the James Watt Nanofabrication Centre (JWNC) at the University of Glasgow for the provision of device fabrication facilities and the environmental biotechnology laboratory for the preparation of organic materials.

References

[1] F. Neubrech, *Chem. Rev.*, p. acs.chemrev.6b00743, Mar. 2017.

[2] A. John-Herpin, *ACS Photonics*, vol. 5, no. 10, pp. 4117–4124, Oct. 2018.

[3] T. H. H. Le, *ACS Nano*, p. acsnano.7b02743, Sep. 2017.

[4] I. G. Mbomson, *Appl. Phys. Lett.*, vol. 112, no. 7, p. 073105, Feb. 2018.

[5] H. Hamid, *Water Research*, vol. 46, no. 18. pp. 5813–5833, 2012.

[6] M. Adeel, *Environ. Int.*, vol. 99, pp. 107–119, Feb. 2017.

[7] M. Velicu, *Environ. Monit. Assess.*, vol. 154, no. 1–4, pp. 349–359, Jul. 2009.

[8] http://ec.europa.eu/environment/water/water-framework/info/intro_en.htm.

Wave Propagation in Mechanical Metamaterial Configurations with Piezoelectric Vibration Energy Harvestors

Jatin Patrick[1] **and Sondipon Adhikari**[1]

[1]College of Engineering, Swansea University, Bay Campus, Fabian Way, Crymlyn Burrows, Swansea, SA1 8EN, UK
E-mail: 642550@swansea.ac.uk and S.Adhikari@swansea.ac.uk

Abstract

The research work carried out sheds light on wave propagation in different configurations of mechanical metamaterials with vibration energy harvesters.

1. Introduction

Understanding the dynamics of periodic structures has been a key area of research for the past few decades due to its complexity and potential to be exploited efficiently. Periodic structures are artificial (man-made) structures which possess specific characteristics that are not found naturally and as the name suggests, they have an element of periodicity in them.

Periodic structures or periodicity can be found in many mechanical designs and this characteristic can be exploited to harvest vibration energy and power electronic devices. These structures or mechanical designs can be referred to as mechanical metamaterials.

The theoretical and experimental aspects of wave propagation and harnessing vibrational energy to efficiently generate power have received significant attention in terms of research as they carry an immense amount of scope.

One (1 degree of freedom) and two (2 degree of freedom) dimensional mechanical metamaterials with vibration energy harvesters were modelled in SOLIDWORKS. The various configurations addressed in the paper include 1D and 2D metamaterials with monoatomic and diatomic unit cells and the piezoelectric shunt circuit comprising of a resistor and inductor and just a resistor.

Mathematical models were formulated and dispersion relations (equations in terms of the natural frequency) for different configurations were obtained. Two different approaches to obtain the dispersion relations have been discussed. Both the approaches involve the implementation of the solution for propagating waves. One approach involves the utilization of non-dimensional parameters and the other involves the employment of the state space method. The two approaches discussed were used to compute wavenumber dependent natural frequencies as either complex and non-dimensional or dimensional values. The dispersion equations obtained were exploited to compute the phase velocities and group velocities.

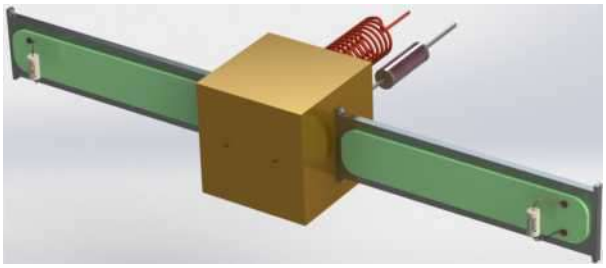


Figure 1: An image of one of the 1D monoatomic unit cells

2. Mechanical Designs

Figure 1 shows an image of one of the 1D (1 dof) monoatomic unit cells. As the unit cells are monoatomic, they consist of only 1 mass. The assembly of the square block, spring, dampener, two beams, green coloured piezoelectric patches and shunt circuits is designated as a unit cell and can be clearly seen in the figure. A combination of the unit cells forms the mechanical metastructure or metamaterial.

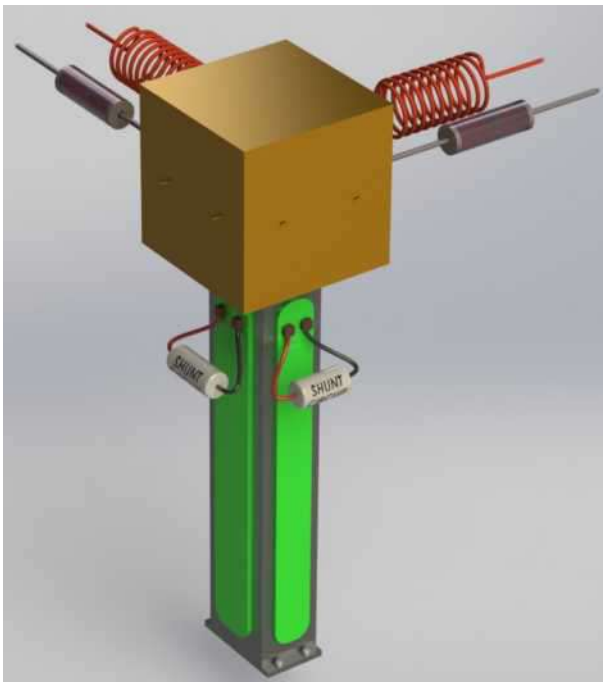


Figure 2: An image of one of the 2D monoatomic unit cells

Figure 2 shows an image of one of the 2D (2 dof) monoatomic unit cells. The assembly of the square block, two springs, two dampeners, beam, green coloured piezoelectric patches and shunt circuits is designated as a unit cell and can be clearly seen in the figure.

3. Mathematical Models

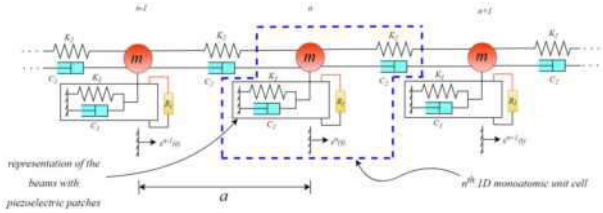


Figure 3: Mathematical model of a 1D monoatomic system under free vibration and with shunt circuits comprising of resistors only

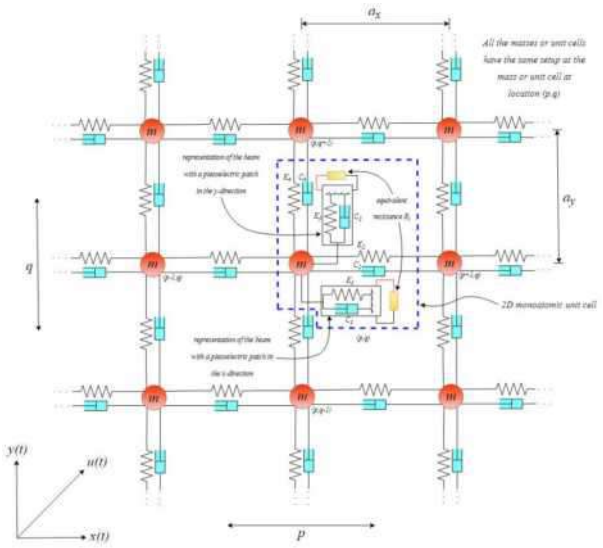


Figure 4: Mathematical model of a 2D monoatomic system under free vibration and with shunt circuits comprising of resistors only

Mathematical models for different configurations of the 1D and 2D cases shown in figures 3 and 4 have been presented and the wavenumber dependent natural frequencies have been obtained by implementing the solution for propagating waves in the governing equations.

4. Examples of Results

Dispersion curves have been plotted using MATLAB for each of the configurations presented. An example of a 1D and 2D dispersion curve is illustrated in figures 5 and 6 respectively. Study was also performed to understand the behaviour of the dispersion curve as the values of the constants involved in the dispersion relation are varied.

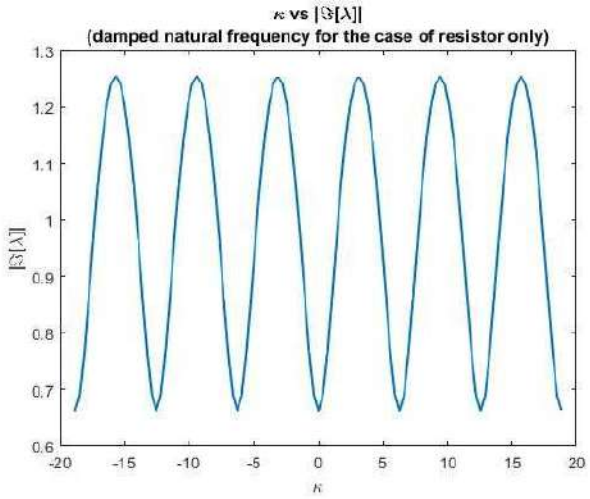


Figure 5: κ (wavenumber) vs. ω_d (damped natural frequency) for the case of 1D monoatomic system with resistor only

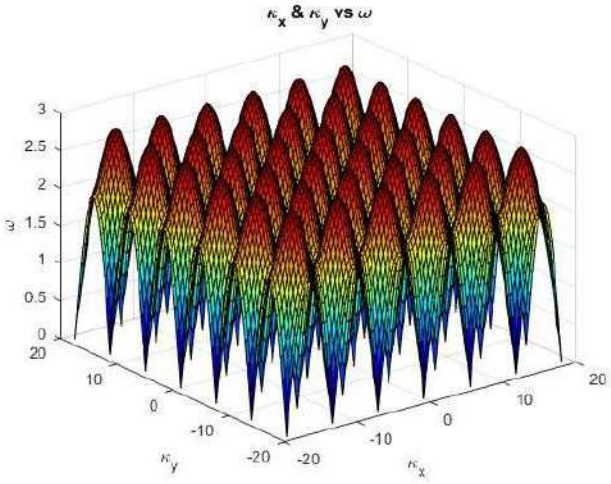


Figure 6: κ (wavenumber) vs. ω_d (damped natural frequency) for the case of 2D monoatomic system with resistor only

Plots of phase velocities and group velocities have also been generated by symbolically manipulating the dispersion relation in MATLAB.

Tunable high-birefringence metamaterial nanoparticles dispersed in water

Ying Tang[1], Seungkyu Ha[2], Thomas Begou[3], Julien Lumeau[3], Nynke Dekker[2], Aurèle Adam[1*] and Paul Urbach[1]

[1]Department of Imaging Physics, Faculty of Applied Sciences, Delft University of Technology, The Netherlands
[2]Department of Bionanoscience, Kavli Institute of Nanoscience, Faculty of Applied Sciences, Delft University of Technology, The Netherlands
[3]Aix Marseille Université, CNRS, Centrale Marseille, Institut Fresnel, Marseille, France
*corresponding author, E-mail: a.j.l.adam@tudelft.nl

Abstract

We present the design, fabrication, and characterization of birefringent multilayer metamaterial particles (MMP) at nanoscale, dispersed in aqueous solutions. We have designed MMP using the effective medium theory (EMT) and the finite element method (FEM). Our top-down fabricated MMP feature optical properties that are tunable through changes in the composite material filling ratio. The MMP are also chemically stable, highly uniform, and ready for volume production and wide range of applications such as optical torque wrench (OTW).

1. Introduction

Nanoparticles made of various materials have been widely used in diverse fields of science and engineering. However, their application have been fundamentally limited by the fixed material properties of the naturally given materials. For example, the OTW allows the direct application and measurement of both torque and angle on single molecules or rotary nanomotors. To maximize the applicable torque in an OTW, it is preferable to use probe material with large birefringence. However, naturally available highly-birefringent materials also tend to exhibit a large refractive index Fig. 1(a), which severely limits the trappable probe dimension due to the large scattering. To overcome this kind of conflicting requirements for material properties, tailored metamaterials can provide solutions. Here, we suggest dielectric multilayer metamaterial as a probe material for OTW. Unlike most of the conventional OTW probe materials, these MMP can have large birefringence at only moderate refractive index to expand the range of 3D-trappable particle dimensions. Moreover, by changing the filling ratio of the composed materials in fabrication, the optical properties of such OTW probe can be adapted to each specific application.

2. Birefringent metamaterial nano-particle

2.1. Design

An artificial material with optical birefringence is obtained using multilayers. With a succession of low and high index dielectric layers, with sub-wavelength thicknesses, one can mimic birefringence. To anticipate the optical response of the multilayer structure, the EMT is used. The effective optical permittivity of the structure can be approximated by a tensor:

$$\underline{\underline{\epsilon}} = \begin{bmatrix} \epsilon_{\parallel} & 0 & 0 \\ 0 & \epsilon_{\parallel} & 0 \\ 0 & 0 & \epsilon_{\perp} \end{bmatrix}, \quad (1)$$

where $\epsilon_{\parallel}$ and $\epsilon_{\perp}$ are the permittivity component parallel and perpendicular to the interface of the multilayer stack, respectively. The values of them are given by

$$\epsilon_{\parallel} = f\epsilon_1 + (1-f)\epsilon_2, \epsilon_{\perp} \quad = \frac{1}{f\epsilon_1^{-1} + (1-f)\epsilon_2^{-1}}, \quad (2)$$

where f is the material filling ratio in a unit cell and ϵ_1 and ϵ_2 are the permittivity values of the two consisting materials, respectively.

The consisting dielectrics chosen here are SiO_2 and Nb_2O_5. In Fig. 1(b) the effective refractive indices of SiO_2/Nb_2O_5 multilayer stack as functions of filling ratio are shown. It can be seen that the $n_{\parallel}$ is a straight line as a function of filling ratio f, while the $n_{\perp}$ is a concave curve, being always smaller than $n_{\parallel}$. Effectively the multilayer metamaterial behaves as a negative uniaxial birefringent material with $n_e = n_{\parallel} < n_o = n_{\perp}$.

The resulting optical properties of such birefringent material are tunable. The MM can achieve relatively low index of refraction from 1.5 to 2.2 and achieve a large birefringence topping above 0.15 (in comparison with the parameter of the conventional crystalline materials used as OTW probes see Fig. 1(a)).

2.2. Fabrication

The square cuboids nanoparticles (Fig. 1(c)) are fabricated with top-down fabrication process. First, a 100 nm sacrificial chromium (Cr) layer is deposited on the silicon wafer. Then in total 300 nm or 400 nm thick SiO_2/Nb_2O_5 multilayer films are deposited using plasma assisted reactive magnetron sputtering.

Resist is spin-coated, followed by electron-beam lithography for patterning the particle shape with aspect ratios

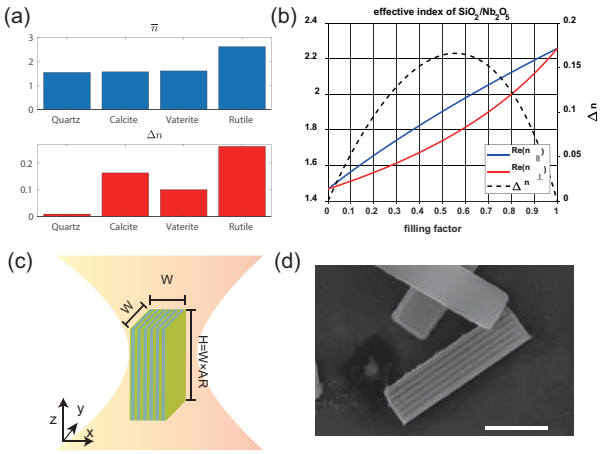


Figure 1: (a) The average refractive index of the most common birefringent crystals materials and their index difference; (b) The effective index and index difference of SiO_2 & Nb_2O_5 multilayer structure as a function of material filling factor. (c) MMP trapped in the focus of a beam. (d) Scanning electron microscopy (SEM) image of fabricated MMP.

(AR) of 3-5. After development, a Cr hard mask layer is deposited on top using sputtering. For the lift-off process, adhesive tape is used to remove most of the top Cr layer, and then the resist is removed in a resist stripper solution. The substrate is soaked in a chromium etchant to remove the remaining Cr etch masks and dissolve the underlying sacrificial Cr layer. Finally, the particles are released from the substrate (Fig. 1(d)) and become free-floating, by immersing the substrate into de-ionised water.

2.3. Modeling

The FEM is used to calculate the optical response of the free floating MMP in water. Each square cuboid particle is enclosed by water, and the water domain is terminated by a perfectly matched layer. The scattering of the particle is calculated under the background illumination of a highly focused Gaussian beam. The optical force and torque is retrieved by integrating Maxwell stress tensor on a virtual sphere surrounding the particle. [1]

The viscous drag coefficient in water is also obtained, using the computational fluid dynamics calculations. The solutions of Navier-Stokes equations result in force and torque as a function of the speed of medium flow, from which the linear (rotational) drag coefficients can be extracted.

3. Results

Several batches with different dimensions (W=300-4000 nm, AR=3-5) and filling ratios (0.3-0.5) were fabricated and measured. The OTW experiments were conducted with a home-built system.[2] It shows that the MMP are trappable and can be rotated. The particles within the same batch behave very consistently (within 10% relative standard deviation). This confirms that our particles are very uniform and with controllable optical properties.

The measured linear and angular stiffnesses agree well with the trend of the calculation outcomes, being 60% of the calculated values, probably due to the aberrations of the optical system that are not considered in the calculations.

The MMP exhibit almost the same optical properties as like calcite (Fig. 1(a)) but do not become dissolved in water unlike calcite. The well-defined high-birefringence of MMP is evidenced by the torque measurements. A typical trace of transferred torque as a function of polarisation rotation frequency is shown in Fig. 2. It can be clearly seen that as the polarisation rotation increases, the amount of transferred torque also increases linearly. After the maximum transferable torque takes place, the particle can no longer follow the rotation of the polarisation and hence the amount of transferred torque drops. These particles can achieve $>$ 10 nN·nm torques at the rotational frequencies of a few kHz (at 92 mW input laser beam power) in water.

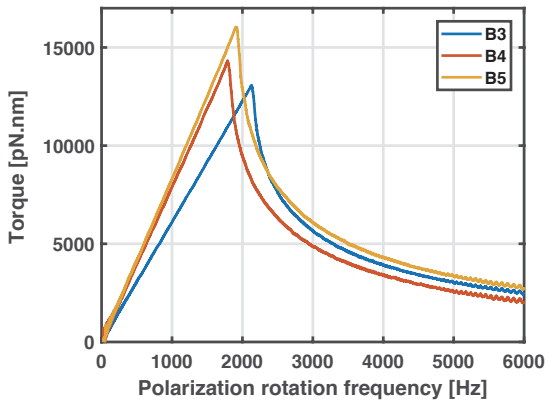


Figure 2: A typical frequency sweep trace measurement for the MMP. The MMP with W = 400 nm and filling ratio 0.3 is shown here The three traces (B3, B4, B5) are obtained from MMP with different aspect ratios (AR = 3, 4, 5).

4. Conclusions

We have designed, fabricated and characterised free-floating birefringent nanoscale metamaterials based on dielectric multilayers. These particles have been successfully demonstrated in an OTW set-up. Thanks to their adaptable optical properties and free-floating nanoparticle formation, they have a large potential of applications in diverse field of science and engineering in which nanoparticles are being used.

References

[1] J. Chen, J. Ng, Z. Lin, C.T. Chan, Optical pulling force, Nature Photonics 5: 531-534, 2011.

[2] F. Pedaci, Z. Huang, M. van Oene, S. Barland, N.H. Dekker, Excitable particles in an optical torque wrench, Nature Photonics 7: 259-264, 2011.

Monolithic high contrast gratings – highly reflective mirrors for VCSELs

Magdalena Marciniak[1,2*], Artur Broda[3], Marcin Gębski[1,2], Jan Muszalski[3], Maciej Dems[2], Michał Wasiak[2], James A. Lott[1], and Tomasz Czyszanowski[2]

[1]Center of Nanophotonics, Institute of Solid State Physics, Technische Universität Berlin, Germany
[2]Institute of Physics, Lodz University of Technology, Poland
[3]Institute of Electron Technology, Warsaw, Poland
*corresponding author, E-mail: magdalena.marciniak@p.lodz.pl

Abstract

High contrast gratings (HCGs) are an attractive alternative to Distributed Bragg Reflectors (DBRs) as highly reflective mirrors for Vertical-Cavity Surface-Emitting Lasers (VCSELs). In our group we investigate the use of monolithic HCGs (MHCGs) to reduce the vertical thickness and simplify the epitaxial structure of VCSELs. In this work we present power reflectance measurement for MHCGs and we discuss properties of these diffraction grating structures.

1. Introduction

Vertical-Cavity Surface-Emitting Lasers (VCSELs) have numerous adventages in comparision to commonly used Edge Emitting Lasers (EELs): single-longitudinal-mode operation, low threshold current, modulation at very high frequencies, and on-wafer testing which is allowed by the device's vertical geometry. Due to their small relative gain VCSELs require mirrors with very high power reflectance (close to unity). Usually, Distributted Bragg Reflectors (DBRs) are employed as mirrors. To fabricate proper DBRs we have to use two materials, which meet the following conditions: a high contrast of refractive indices; the lowest possible mismatch of the lattice constants and thermal expansion coefficients; and low thermal and electrical resistance. For now only GaAs-based VCSELs are commercialy available at large volumes. In other material systems (especially nitride and phosphide based) problems with materials for DBRs are the main obstacle to fabricate efficient and high performance VCSELs.

To overcome the limitations of semiconductor DBRs other than those based on AlGaAs for emission at 600-1100 nm, High refractive index Contrast Gratings (HCGs) can be employed. HCGs are diffraction gratings with subwavelength period and thickness made of materials of high, in comparison to the surroundings, refractive index [1]. HCGs can be realizad in different ways, for example as a membrane suspended in air [1], as a grating put on a cladding layer [], as a zero-contrast grating [2], or a monolithic HCG (MHCG) made of the same material as cladding layer [4].

In our group we investigate MHCGs as mirrors for VCSELs. As we schowed in [5], MHCGs can be made of any semiconductor material with a refractive index higher than 1.75. In [6] we showed a first MHCG VCSEL, which is based on GaAs and emits around $980\,\mathrm{nm}$. Recently S. Kim et al. reported also first MHCG-cavity polariton laser [**?**]. In this paper we discuss different designs of MHCGs, and their optimization and fabrication. We also present power reflectance measurements for GaAs MHCGs.

2. MHCG: optimization and fabrication

To investigate the properties of MHCG we employed a computer model developed by the Photonics Group from Lodz University of Technology. This is a three-dimensional fully-vectorial model, which is based on the Plane-Wave Admittance Method (PWAM) described in [8]. To find the optimal parameters of an MHCG we consider power reflectance as a three dimensional function of the grating's parameters: 1) period of the grating; 2) height of stripes; and 3) width of stripes (see figure 1).

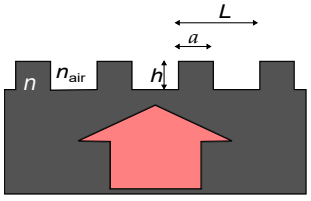


Figure 1: Schematic structure of a monolithic high contrast grating mirror, where L is the period of the structure, h is the height and a is the width of stripes. The arrow shows the direction of incident light.

As we showed in [6] numerous sets of MHCG spatial parameters which provide high power reflectance can be found for different materials. Also MHCGs can be designed for transverse electric (TE) and transverse magnetic (TM) polarization of incident light. For TE polarization the electric field is perpendicular to the grating stripes and for TM electric field is parallel to the grating stripes.

To fabricated an MHCG we employ electron-beam lithography (EBL) and Inductively Coupled Plasma Reactive Ion Etching (ICP-RIE). Example SEM photographs of an MHCG fabricated at the Technical University of Berlin is shown in Figure 2. EBL and ICP RIE enable us to fabri-

cate MHCG with a broad range of parameters with tens of nanometers of precission. However, the spatial parameters of a fabricated MHCG can be slightly different then then planned.

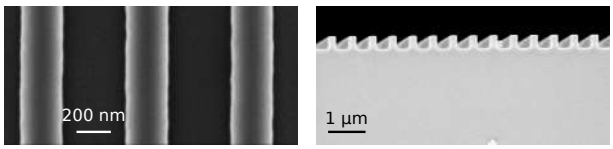


Figure 2: Example SEM photographs of a top view (left) and of a cross-sectional view (right) of an MHCG.

3. Power reflectance of MHCGs

We fabricated a set of GaAs MHCGs with different spatial parameters. All MHCGs are designed for TM polarization and have the same period $L = 605\,\mathrm{nm}$ and height of stripes $h = 400\,\mathrm{nm}$. We varied the fill factor F, which is the ratio of the grating stripe width divided by the grating period. We obtained different values of fill factor by changing the electron beam lithography (EBL) writing mask pattern or by varying the EBL exposure dose.

In Figure 3 one can see the setup, which we used to measure power reflectance of fabricated MHCGs. Measurements were taken for wavelengths between 900 and 1040 nm. In Figure 4 one can see measured power reflectance spectra in comparison with calculated spectra for three different MHCGs with fill factors of 0.37, 0.41 and 0.47.

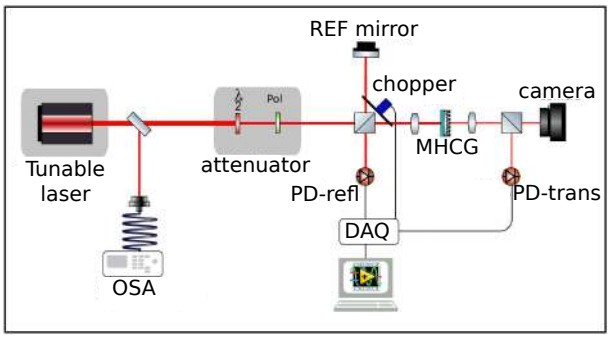


Figure 3: Experimental set up employed to to perform the power reflectance measurements of the MHCGs.

The agreement between theory and experiment is quite good. For both one can notice, that power reflectance spectra move in the direction of longer wavelength for larger fill factors. The difference between the simulated and the measured results is most likely due to processing imperfections.

4. Summary

MHCGs can have very high power reflectance and replace DBRs in VCSELs. For now we are able to fabricate MHCGs of power reflectance of about 80%. MHCGs with this power reflectance should be supported with around 7

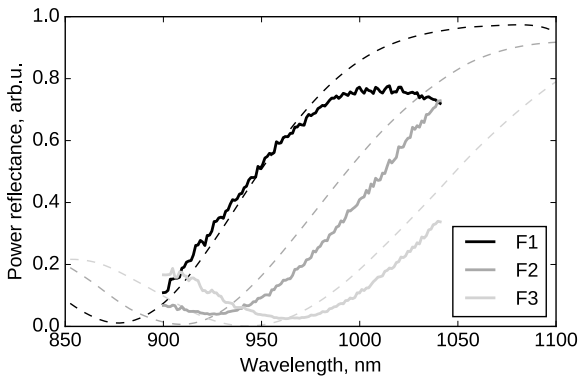


Figure 4: Measured (solid lines) and calculated (dotted lines) power reflectance spectra; the fill factors are $F_1 = 0.37$, $F_2 = 0.41$, and $F_3 = 0.47$.

pairs of DBRs to reach 99% power reflectance of the composite out coupling mirror of a VCSEL. This could reduce the vertical height of VCSELs by 30%. The ultimate goal is to eliminate the top DBR completely and fabricate VCSELs with MHCG-only top out coupling mirrors characterized by power reflectance exceeding 99%. This can be achieved by further optimization of the MHCG's design and processing.

Acknowledgement

The authors would like to acknowledge the support of the German Research Foundation (via the Collaborative Research Center 787) and the Polish National Science Center (via the project 2014/15/B/ST7/05258). Magdalena Marciniak would like to acknowledge the support of the Polish National Science Center (via the project 2018/29/N/ST7/02460).

References

[1] Y. Zhou et al., *Optics express* 16(18): 14221–14226, 2008.

[2] C. Mateus et al, *IEEE Photonics Technology Letters* 16(2): 518-–520, 2004.

[3] R. Magnusson, *Optics Letters* 39(15): 4337–4340, 2014.

[4] S. Goeman et al, *IEEE Photonics Technology Letters* 10(9): 1205—1207, 1998.

[5] M. Gębski et al, *Optics express* 23(9): 11674-–11686, 2015.

[6] M. Marciniak et al, *Optics Letters* 41(15): 3495-–3498, 2016.

[7] S. Kim et al, *ACS Photonics* 6(1): 18-22, 2018.

[8] M. Dems et al, *Optics Express* 13(9): 3196—3207, 2005.

Frequency Shift of Light in Highly Dispersive Time-Varying Metasurfaces

Jagang Park[1], Hyukjoon Cho[1], Hyun Sung Park[1], and Bumki Min[1*]

[1]Department of Mechanical Engineering, Korea Advanced Institute of Science and Technology, Daejeon, Republic of Korea
*corresponding author, E-mail: bmin@kaist.ac.kr

Abstract

This work suggests a new class of time-varying metasurface for efficient frequency shift of light. The proposed metasurface is properly designed to exhibit highly dispersive phase responses, so that a dynamic change in the spectral response gives a rapid phase sweep of transmitted light, which directly corresponds to a frequency shift. The frequency-converted waves through the metasurface are analysed based upon a temporal coupled-mode formalism. Furthermore, we compare our time-varying metasurfaces with the conventionally studied angular Doppler effect.

1. Introduction

Instead of the common usage of nonlinear materials for frequency conversion of light, time-varying media can be alternative candidates in the cases when the light intensity is weak or a suitable nonlinear material for the target frequency has been undiscovered. Since the first speculation by Morgenthaler [1], his concept of the velocity modulation has been implemented on a variety of platforms to observe frequency conversion of light, for example, by dynamically modulating the resonance frequency of an optical cavity or the effective refractive index of an optical waveguide [2-4]. Most of attempts exploited adiabatic evolution of the optical modes inside the media, therefore relatively high conversion efficiency and large frequency shift were achieved.

Recently, the idea of frequency conversion with time-varying media has been expanded to the field of metasurfaces, where the new spectral components were generated by sudden merging of meta-atoms [5]. However, the sudden change in the resonance mode breaks the adiabaticity, and provides only a much smaller conversion efficiency compared to adiabatic cases.

Here, we suggest an adiabatic version of time-varying metasurface that can promise high conversion efficiency within a deep subwavelength thickness, by dynamically sweeping the phase of light. We show that a continuous and rapid phase sweep can be realized by tailoring a particular transmission spectrum with multiple meta-atoms, and modulating their resonance frequencies in time. We analyse the dynamics of the time-varying metasurfaces based upon a temporal coupled-mode formalism, and calculate exact solutions for simple cases. Furthermore, we compare the similarities and differences between the proposed time-varying metasurface and the conventionally studied angular Doppler effect, which is a frequency shift induced by a mechanically rotating half-wave plate [6].

2. Result

First, we develop the highly dispersive metasurface, whose unit cell consists of multiple anisotropic resonators. The transmission is analysed with temporal coupled-mode formalism. Second, a temporal modulation of the resonance frequencies is assumed, and the frequency-shifted spectrum is presented. Lastly, the behaviour of the time-varying metasurface is compared with the conventional angular Doppler effect.

2.1. Design of the metasurface and its static response

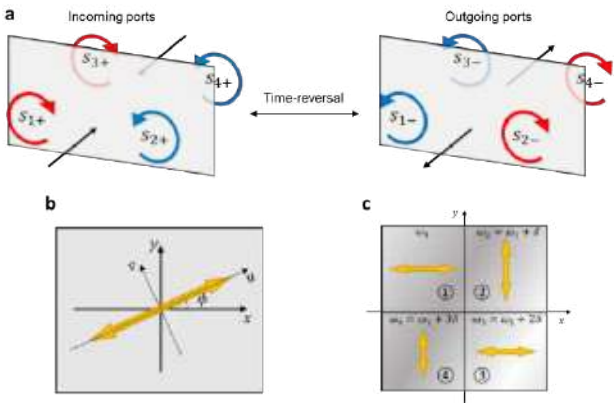


Figure 1: (a) Incoming and outgoing ports are depicted on both sides of the metasurface (gray rectangle). The ports are circular polarization-dependent. The schematic illustrations of the metasurfaces with (b) a single anisotropic resonator and (c) multiple anisotropic resonators.

Based on the configurations depicted in Fig 1, the temporal coupled-mode equations can be written as follows.

$$\frac{d\mathbf{a}}{dt} = (j\boldsymbol{\Omega}(t) - \boldsymbol{\Gamma})\mathbf{a} + \mathbf{K}^{\mathbf{T}}\boldsymbol{s}_{+} \quad (1)$$

$$\mathbf{s}_{-} = \mathbf{C}\mathbf{s}_{+} + \mathbf{D}\mathbf{a} \quad (2)$$

Because the resonators are linearly anisotropic while the ports are established with the circular polarization basis, the coupling coefficient between the ports and the q-th resonator.

$$d_q = j\sqrt{\frac{\gamma}{2}}\begin{pmatrix} e^{j\phi_q} \\ e^{-j\phi_q} \\ e^{j\phi_q} \\ e^{-j\phi_q} \end{pmatrix} \quad (3)$$

For the case of the proposed metasurface as shown in Fig. 1c, the angles of the resonators are set to be 0, π/2, π, 3π/2. Therefore the coupling matrix can be specified as below.

$$\mathbf{D} = j\sqrt{\frac{\gamma}{2}}\begin{pmatrix} 1 & j & -1 & -j \\ 1 & -j & -1 & j \\ 1 & j & -1 & -j \\ 1 & -j & -1 & j \end{pmatrix} \quad (3)$$

As clearly shown in Fig. 2, the metasurface exhibit high flat-top transmission window, in which the phase forms a steep gradient.

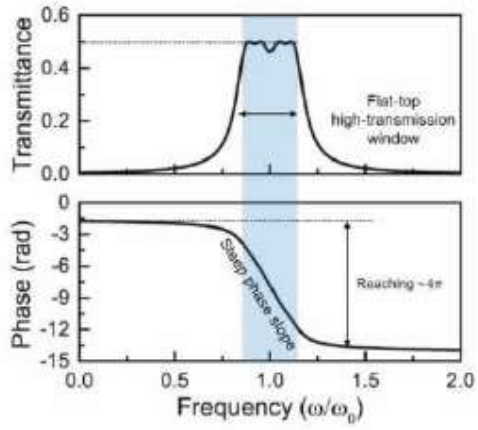


Figure 2: Static cross-polarization transmission response of the proposed metasurface

2.2. Time-varying responses

As a representative example, we assume that all the resonance frequencies of the meta-atoms are linearly varying in time.

$$\mathbf{\Omega}(t) = \mathbf{\Omega}_0 + at\mathbf{I} \quad (4)$$

For this case, the exact solution for the outgoing waves can be obtained, and the spectrum of the polarization-converted transmitted wave is shown in Fig 3.

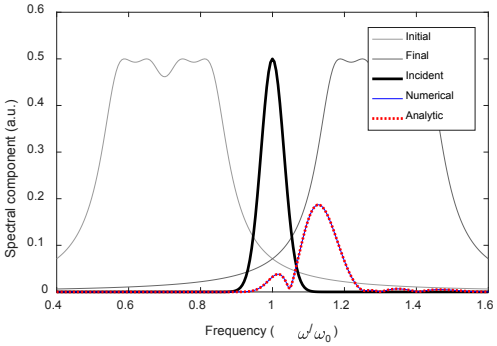


Figure 3: Transmission spectrum of the time-varying metasurface.

2.3. Comparison with angular Doppler effect

The amount frequency shift and the conversion efficiency depend of the rate of resonance shifting, similar as they depend on the angular velocity in the angular Doppler effect.

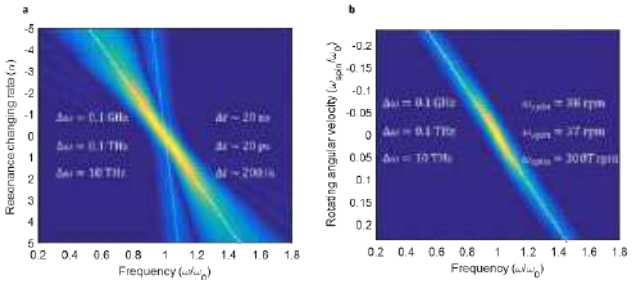


Figure 4: Transmission spectra of polarization-converted waved through (a) the time-varying metasurface and (b) the mechanically rotating metasurface

3. Discussion

The concept of resonators and metasurface can be applied over a broad frequency range from microwave to visible in principle. For a microwave at a target frequency of 10 GHz, the resonance frequency of the time-varying metasurface should be changed in a nanosecond scale to observe the frequency shift of 1 GHz. However, 1 GHz frequency shift corresponds to 30 billion rpm in the angular Doppler effect. If this metasurface is used in visible, the equivalent angular velocity becomes much higher.

4. Conclusions

We theoretically investigated a new way to shift the frequency of light with time-varying metasurfaces. The highly dispersive metasurface was suggested for efficient frequency shift and its response was analysed with temporal-coupled-mode equations. The amount of frequency shift and the conversion efficiency can be controlled with the rate of change in the resonance frequencies.

References

[1] F. R. Morgenthaler, Velocity modulation of electromagnetic waves, *IRE Trans. Microw. Theory Tech.* 6 (2): 167−172, 1958.

[2] M. Notomi, S. Mitsugi, Wavelength conversion via dynamic refractive index tuning of a cavity, *Phys. Rev. A* 73, 051803, 2006.

[3] S. F. Preble, Q. Xu, M. Lipson, Changing the colour of light in a silicon resonator, *Nat. Photon.* 1: 293-296, 2007.

[4] L. Fan, C.-L. Zou, M. Poot, R. Cheng, X. Guo, X. Han, H. X. Tang, Integrated optomechanical single-photon frequency shifter, *Nat. Photon.* 10: 766-770, 2016.

[5] K. Lee, J. Son, J. Park, B. Kang, W. Jeon, F. Rotermund, B. Min, Linear frequency conversion via sudden merging of meta-atoms in time-variant metasurfaces, *Nat. Photon.* 12: 765-773, 2018.

[6] B. A. Garetz, S. Arnold, Variable frequency shifting of circularly polarized laser radiation via a rotating half-wave retardation plate, *Optics Communications* 31 (1): 1-3, 1979.

[7] H. A. Haus, *Waves and fields in optoelectronics*, Prentis Hall, pp. 197-234, 1984.

Quantification of Resonance Scaling for Open Subwavelength-Resonator Based Structures

Andriy E Serebryannikov[1,2,*], Guy A E Vandenbosch[1], and Ekmel Ozbay[3,4]

[1]ESAT-TELEMIC, Katholieke Universiteit Leuven, 3000 Leuven, Belgium
[2]Faculty of Physics, Adam Mickiewicz University, 61-614 Poznan, Poland
[3]Nanotechnology Research Center (NANOTAM), Bilkent University, 06800 Ankara, Turkey
[4]Department of Physics, Department of Electrical Engineering, and National Nanotechnology Research Center (UNAM), Bilkent University, 06800 Ankara, Turkey
*corresponding author, E-mail: aserebry@esat.kuleuven.be

Abstract

Scaling of resonance structures and resonance frequencies therein has always been important for applications. We demonstrate that although the classical scaling rule does not work for open resonance structures, the effect of permittivity of substrate/spacer on resonance frequencies can be quantified. Examples of the scaling are presented for few-layer metasurfaces and miniature microwave antennas.

1. Introduction

The interest to the scaling problem has recently been stimulated by demand in subwavelength resonators for radiation and transformation of electromagnetic waves. The general approach to the scaling assumes that a proportional change of all geometrical parameters of a resonance structure leads to an inversely proportional change in resonance frequency, i.e., $f \propto a^{-1}$, where a is a geometrical size. The said above is true for both open resonance structures and closed resonance structures (cavities), assuming the used materials to be weakly dispersive and weakly lossy. In the microwave cavities, change in permittivity of the filling medium, ε, leads to the classical scaling rule for resonance frequencies, $f \propto \varepsilon^{-1/2}$, while all sizes are fixed. In open resonance structures, including the ones based on subwavelength resonators, results of changing ε of the substrate/spacer material cannot be quantified without a detailed numerical study. This occurs due to the fact that there is no definite boundary of the volume occupied by the resonance field. The main purpose of this work is to obtain examples of quantification of the scaling, which is possible due to variations in ε of the substrate/spacer material in open structures comprising subwavelength resonators.

2. Examples of Scaling

We consider two types of open microwave resonance structures, which are used (i) in polarization manipulation and (ii) in miniature microwave antennas. The first one represents few-layer metasurfaces based on two coupled arrays of U-shaped subwavelength resonators, one of which is rotated by 90°, see Fig. 1, inset. The second one represents the metamaterial inspired miniature antennas with split loop(s), as shown in Fig. 2, inset.

2.1. Coupled Arrays for Polarization Manipulation

The structure in Fig. 1(a) generally contains five layers: two outer arrays, two spacers, and a centered metallic grid. The physical mechanism of polarization conversion has been discussed in [1]. For a part of the studied performances, there are three layers, i.e., no grid and one spacer. Permittivity of the spacers is varied from 1 (vacuum) to 100 (ceramics, K-100).

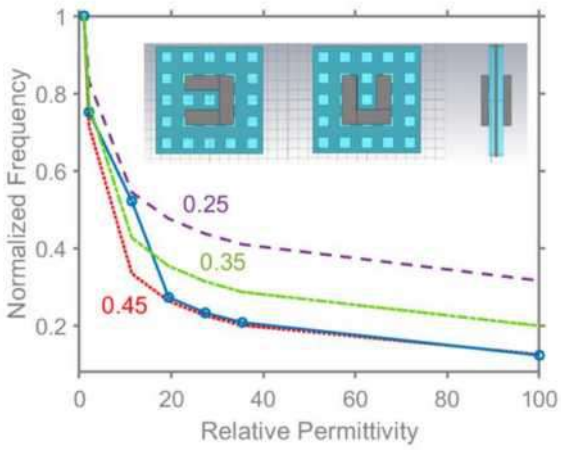


Figure 1: First normalized resonance frequency, f, vs. relative permittivity of spacers, ε, for a structure with a centered grid: blue solid line - numerical results (CST Microwave Studio); red dotted, green dash-dotted, and violet dashed lines - $f(\varepsilon)=\varepsilon^{-\alpha}$ with $\alpha = 0.45$, 0.35, and 0.25, respectively; $f(1) = 1$; inset – front, back, and side view of a unit cell of two coupled arrays of subwavelength resonators, which are separated by a centered grid and two spacers; PEC approximation is adopted here for the resonators and grid.

The incident linear polarization is converted to the orthogonal one at polarization-conversion resonances. The results in [2] show that the first resonance frequency can be approximated, for the two selected structures, by $f \propto \varepsilon^{-0.39}$ and $f \propto \varepsilon^{-0.45}$. However, these estimates do not take into account the specifics of the different parts of the entire ε-range. The main purpose here is to quantify the changes in the resonance frequencies in different parts of the ε-range.

According to the results shown in Fig. 1, $\alpha = 0.45$ is better suitable to approximate the effect of ε between 1 and 2.1 and then above 20. Smaller values of α (e.g., 0.25) can be more suitable for ε between 2.1 and 20. The observed difference between the results in Fig. 1 and the classical scaling rule is not dramatic because of the strong field confinement in the resonators of the studied structure. While polarization state of the incident wave, at which conversion may occur in transmission mode, depends on the presence of a centered metal grid, the scaling rule is not affected strongly. This indicates the dominant role of the properties of the resonator arrays for the value of α.

Note that polarization-conversion resonances appear in the entire ε-range, and conversion may be (nearly) perfect in the lossless approximation, starting from a certain value of $\varepsilon = \varepsilon_{\text{perf}} > 1$. Similar fitting of the obtained numerical data has been performed for metasurfaces with and without rotation of one of arrays and for complementary metasurfaces, with the use of a lossy-metal model in THz and microwave ranges.

2.2. Miniature Antennas Inspired by Metamaterials

For small antennas, the scaling rule aspect is directly connected with the extent of achievable miniaturization. Moreover, number of resonances observed in the subwavelength range depends on ε of the substrate.

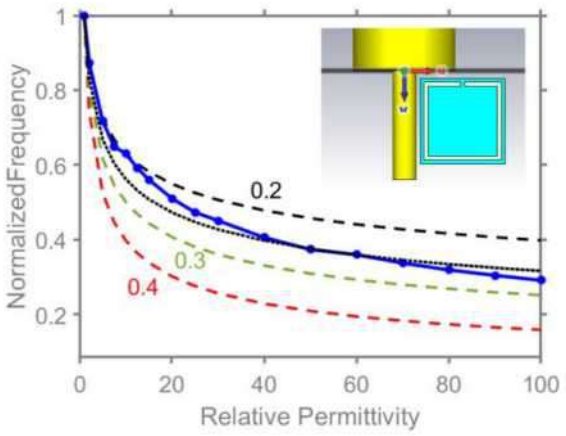


Figure 2: First normalized resonance frequency, f, vs. relative permittivity of substrate, ε: blue solid line – numerical results (CST Microwave Studio); red dashed, green dashed, black dotted, and black dashed lines - $f(\varepsilon) = \varepsilon^{-\alpha}$ with $\alpha = 0.4$, 0.3, 0.25, and 0.2; $f(1) = 1$; inset – top view of the studied coaxial-fed single-split-loop antenna; losses are taken into account via $\tan\delta$.

Figure 2 demonstrates how quantification of the scaling of resonances can be introduced for a near-field coupled single-split-loop antenna, while ε is varied in a wide range. The studied configuration is similar to but simpler than that in [3]. It is observed that at $1<\varepsilon<15$, $\alpha = 0.2$ provides the best approximation. On the other hand, at $25<\varepsilon<100$, $\alpha = 0.25$ might be more suitable, whereas α tends to grow with ε. Hence, deviation from the classical scaling rule is stronger here than for the above discussed arrays for polarization conversion. It is noteworthy that radiation occurs in the entire range of ε, and the lowest radiation frequency is just gradually shifted while varying ε. In the talk, the results will also be presented for the antennas with three split loops and different location of the loops with respect to each other.

3. Conclusion

The presented examples of quantification of the resonance scaling in open microwave resonance structures may serve a good starting point for development of approximate physical models, and for understanding limits and design of practical devices based on subwavelength resonators. For the studied structures, $0.25 \le \alpha \le 0.45$ in the general form of the scaling rule, i.e., $f \propto \varepsilon^{-\alpha}$. Presently, the scaling of resonances in plasmonic near-infrared structures is under study, and some examples will be presented in the talk.

Acknowledgements

This work has been supported by EU Horizon-2020 via Marie Skłodowska-Curie IF program (grant no. 708200 – ADVANTA) and NCN, Poland (DEC-2015/17/B/ST3/00118 – Metasel).

References

[1] M. Mutlu, A.E. Akosman, A.E. Serebryannikov, E. Ozbay, Diodelike asymmetric transmission of linearly polarized waves using magnetoelectric coupling and electromagnetic wave tunneling, *Phys Rev Lett* 108: 213905, 2012.

[2] A.E. Serebryannikov, M. Mutlu, E. Ozbay, Dielectric inspired scaling of polarization conversion subwavelength resonances in open ultrathin chiral structures, *Appl Phys Lett* 107: 221907, 2015.

[3] A.E. Serebryannikov, M. Gokkavas, F.T. Gundogdu, G.A.E. Vandenbosch, A. Vasylchenko, E. Ozbay, Ultra-miniature dual-band antenna based on subwavelength resonators on $LiNbO_3$ substrate, *Proc. EuCAP18*, London, UK, 2018.

Dual-Band Wireless Power Transmission Using Coupled Metamaterial Resonators for Wireless Sensor Networks

Safiullah Khan* **and Thomas F. Eibert**

Chair of High-Frequency Engineering, Department of Electrical and Computer Engineering,
Technical University of Munich, 80290 Munich, Germany
*corresponding author, E-mail: safiullah.khan@tum.de

Abstract

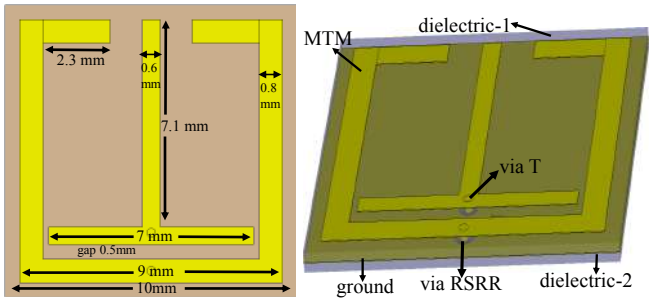
A metamaterial based dual-band microwave energy harvester is investigated. The miniaturized unit cell is composed of two distinct types of resonators, a rectangular split ring resonator coupled together with a T-type resonator, to achieve the desired resonances at 7.16 GHz and 9.25 GHz. The resonance frequencies can be controlled independently with very few parameters. The structure is backed by a metal film. A via on each of the resonating elements is used to divert the current to resistive loads. The power conversion efficiency and the power harvesting efficiency for the structure at 7.16 GHz (9.25 GHz) are 74.7% (65.6%) and 60.5% (51%), respectively.

1. Introduction

Metamaterial (MTM) based composite structures have been widely used in different applications, e.g., bio-medical devices, sensors for characterization of materials, frequency selective surfaces, and integrated circuits, etc. More recently, they have been explored as energy harvester for wireless power transmission systems. MTM based energy harvesters have advantages over conventional designs due to the extraordinary properties of MTMs, which allow resonance control, polarization stability, miniaturization, and impedance matching, etc. [1].

In wireless sensor networks, many sensor nodes are spatially distributed in large areas to gather information, such as temperature and humidity, and send it to a sink node (for example, a base station) for processing. The sensor nodes may be positioned arbitrarily at locations, which are inaccessible. In such situations, the sensor nodes must be highly efficient, consume low power, and work for a long period of time. One way of managing the power is that the nodes go into sleep mode on idle and periodically wake-up after a predefined duration of time [2]. This approach is not efficient because the node may well stay awake and consume power even if no information is requested. Therefore, a more dynamic power management method is required. As a solution, MTM based energy harvesters can be used to wake-up the nodes to send/receive information whenever it is required at the base station.

The design of an energy harvester can be broken down into a two-step process, firstly, designing an MTM structure, which absorbs the incident electromagnetic (EM) wave. This is achieved by matching the input impedance of the absorber to the impedance of the medium of the incident wave and by delivering the absorbed power to the load. Maximum power can be transferred when the load impedance is equal to the conjugate of the output impedance of the structure.



(a) Top view (b) Perspective view

Figure 1: MTM unit cell configuration where via = 0.3 mm Ø.

A recently proposed MTM design in [3] is investigated for a dual-band energy harvesting response and improved efficiencies. The efficiencies that determine the performance of the energy harvester are: absorption efficiency (A_e), it is the ratio of the power accepted (P_a) by the MTM unit cell to the incident power (P_{in}) over the unit cell; harvesting efficiency (H_e), it is the ratio of the power delivered to the load (P_l) to P_{in}; and conversion efficiency (C_e), it is the ratio of P_l to P_a.

2. Design

Two distinct types of resonating elements, a T-type resonator and a rectangular split ring resonator (RSRR), are combined together on a dielectric substrate RO5880 as shown in Fig. 1. The dielectric layer is backed by a copper film, which acts as ground, followed by another dielectric layer. The dielectric substrates have a thickness of 0.254 mm with a relative permittivity equal to 2.2 and a loss tangent of 0.0009. The vias of equal diameter are placed at the bottom of each resonator to connect the load to the ground. The structure has been simulated in CST Microwave Studio using the frequency domain solver.

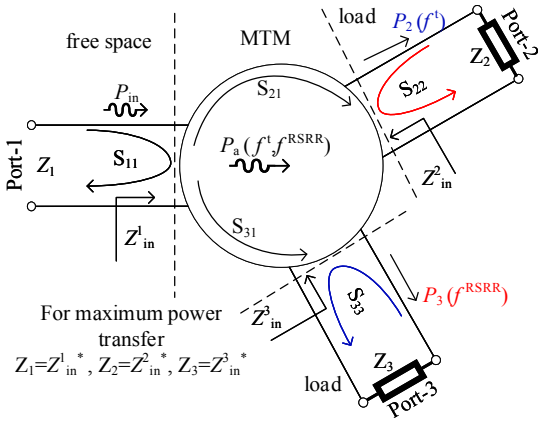


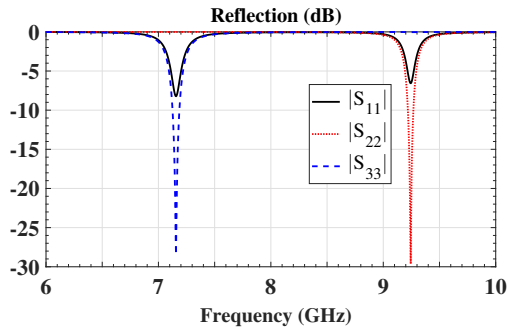
Figure 2: Equivalent three-port network layout for the proposed MTM energy harvesting system. Z_1 represents the free space impedance. $|S_{23}|$ and $|S_{32}|$ are below -25 dB and hence not shown.

3. Results and Discussion

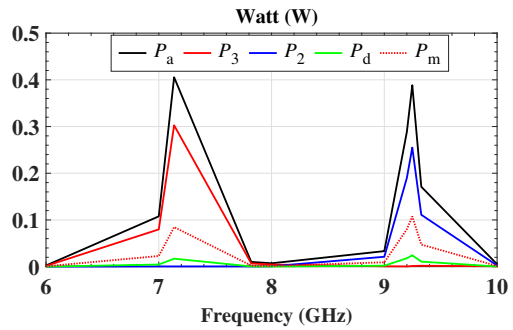
Consider an electromagnetic plane wave incident normally on the proposed MTM structure. The incident wave is y-polarized and it is travelling in the $-z$-direction. The wave is partly reflected and partly transmitted from the structure at the resonance frequencies. Since the structure has two resonating elements placed close together, the individual resonance frequencies of the RSRR and the T-type resonator will be affected by the mutual coupling between them. To design an energy harvester, the goal is to minimize the reflection of the incident wave so that the absorption can be maximized at the resonance frequencies. This is done by matching the impedance of the structure with the incident medium, which is free space and its value is $376.7\,\Omega$. An identical permittivity and permeability of the structure will result in achieving a matched condition. To deliver absorbed power to the load the power must be retained within the structure. Therefore, a metal film is used to minimize the transmission back into free space. The concept of harvesting energy at two different frequencies with two different loads, respectively, is illustrated through a three-port network shown in Fig. 2 where different ports (2 and 3) are used for two different loads. In order to achieve maximum power transfer to the loads, the output impedances of the structure must be equal to the complex conjugate impedances of the loads; otherwise, matching networks will be required. In this paper, resistive loads are modeled for simplicity. Vias are used to connect the loads to the structure. Fig. 3(a) shows the reflection coefficient for all the ports. The resonance frequencies (load resistance) for the RSRR and the T-type resonator are 7.16 GHz ($1040\,\Omega$) and 9.25 GHz ($750\,\Omega$), respectively. Fig. 3(b) shows the power absorbed, the power delivered to the loads, and the power dissipated in the dielectric (P_d) and the metal (P_m). Table 1

Table 1: Power Efficiencies

Resonance frequency	A_e	H_e	C_e
7.16 GHz	81%	60.5%	74.7%
9.25 GHz	77.6%	51%	65.6%



(a)



(b)

Figure 3: (a) Magnitude of the reflection coefficients at different ports as a function of frequency. (b) Power absorbed by materials and loads as a function of frequency.

shows the comparison of the efficiencies at the resonance frequencies. Increasing the load resistances increases A_e but H_e starts to decrease, if the load resistance exceeds a certain value. Decreasing the gap between the resonators improves the efficiencies at the lower resonance but reduces the efficiencies at the higher resonance (not shown here).

4. Conclusions

A highly efficient miniaturized microwave energy harvester was presented, which can absorb and deliver power to different loads at 7.16 GHz and 9.25 GHz simultaneously. The normal incidence case was discussed and an equivalent three-port network layout was demonstrated. The structure can be used in nodes in wireless sensor networks.

References

[1] G. Singh , Rajni , A. Marwaha, A review of metamaterials and its applications, *International Journal of Engineering Trends and Technology*, vol. 19, no. 6, 2015.

[2] E. Popovici, M. Magno and S. Marinkovic, Power management techniques for wireless sensor networks: a review, *IEEE International Workshop on Advances in Sensors and Interfaces* (IWASI), Bari, Italy, 2013, pp. 194-198.

[3] S. Khan and T. F. Eibert, A highly efficient miniaturized microwave collector for wireless power transmission, *Applied Computational Electromagnetics Society Symposium* (ACES), Denver, CO, 2018, pp. 1-2.

Broadband Metamaterial Absorbers: Gold and Tungsten Boride

Ahasanul Haque[1*], Monir Morshed[1], Ziyuan Li[2], Li Li[3], Kaushal Vora[3], Lei Xu[1], Lan Fu[2], Andrey Miroshnichenko[1], and Haroldo T. Hattori[1]

[1]School of Engineering and Information Technology, University of New South Wales Canberra, ACT 2610, Australia
[2]Department of Electronic Materials Engineering, Research School of Physics and Engineering, The Australian National University, Canberra, ACT 2601, Australia
[3]Australian National Fabrication Facility, The Australian National University, Canberra, ACT 2601,
*corresponding author, E-mail: ahasanul.haque@student.adfa.edu.au

Abstract

In this paper, we experimentally analyze the absorption of two metamaterial perfect absorbers made of different materials: gold (Au) and tungsten boride (WB, a refractory ceramic). We show that WB has wider absorption bandwidth than that of the gold counterpart. Moreover, WB reveals better performance with absorption more than 90% over the spectral range from 950 to 1400 nm.

1. Introduction

Metamaterials bring new opportunities for absorbers due to their designed electrodynamic properties: they provide versatile and strong control of their absorption, reflection, and propagation of electromagnetic waves [1, 2]. Metamaterials are used in different applications such as perfect lenses, black holes, plasmonic sensors and energy harvesting concepts [3, 4]. The performance of metamaterials absorbers [5, 6] depends on their constituent materials and geometry. Different types of metals have been used such as Au, Ag, Cu and Ni as metamaterials absorbers in the optical ranges due to their ability to considerably rise the optical cross section of the structure, leading to greatly improved absorption in certain spectral ranges caused by surface plasmon excitations [7]. However, due to the resonant nature of the plasmon excitation, the absorption bandwidth is limited. The key parameters for designing a perfect absorber is the efficient suppression of reflection of light and transmission. One of the recent technique for high absorption is to use single ultrathin film deposited on metals or polar materials. Such metamaterial devices have a large bandwidth and near zero reflectivity, which is attractive for energy harvesting application such as solar thermal photovoltaics (STPV) [8, 9]. On the other hand, tungsten boride (WB) is an inexpensive, super hard and lossy material [10]. By combing the plasmonic nature and large intrinsic loss of WB, we are able to design metamaterial structures toward high optical absorption over a broad range.

In this work, a WB metamaterial perfect absorber (MMPA) with efficient, broadband light absorption was designed and fabricated. The resulting 200 nm thick metamaterial absorber with square structure exhibits polarization-independent (patterns are symmetric) broad absorption over the near infrared range of 900–1400 nm at a large incident angle (up to 60°). Most importantly, the fabricated WB metamaterial absorber shows vastly improved high power absorption in comparison with Au counterpart, illustrating its potential for the high power applications such as STPV.

2. General description of the devices

The proposed metamaterials absorber was fabricated on a Si substrate consisting of three different material layers as shown in Figure 1: metallic structures made of Au (yellow) or WB (Maroon) as a top layer, a SiO_2 layer (light grey) of 140 nm in the middle, and the bottom Cr layer (deep gray) of 400 nm as a ground reflector for the absorber. The optimized geometrical parameters of the metallic structures are as follows: the length of each square L equals its width W as 322 and 400 nm, pitch of the device P is 900 and 1030 nm, and the thickness t is 100 and 200 nm for Au and WB, respectively.

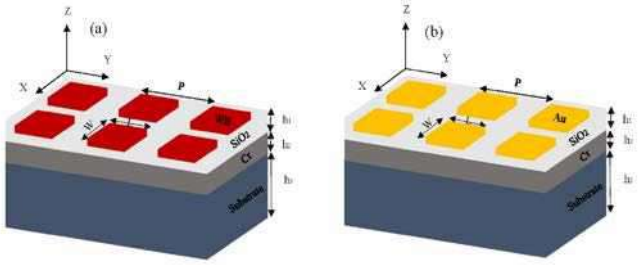


Figure 1: 3D-view schematic diagram of (a) Au and (b) WB metamaterial absorbers. W and L represent the width and length of each rectangular metallic structure along the x and y axis respectively, and h_1 and h_2 represent the thickness of dielectric spacer and bottom Cr layer respectively. P indicates the lattice constant.

3. Fabrication and characterization

To fabricate the WB metamaterial absorber, a sputter was first employed to deposit 400 nm Cr on a silicon substrate with a deposition rate of 2.58 nm/min. Then a SiO_2 layer of 140 nm was deposited by a plasma enhanced chemical vapor deposition (PECVD) system with a deposition rate of 48 nm/min. After that, 5 nm Cr as an adhesion layer and 200 nm WB were deposited on top (deposition rate of WB was 4.8 nm/min) by the sputter. Finally, we patterned square structure on the Cr layer by focused ion beam (FIB) milling. On the other hand, 100 nm Au metallic structures were obtained by electron-beam deposition followed by electron-beam lithography (EBL) and lift-off process as an experimental reference. Figure 2 shows the fabricated patterns and experimentally measured absorption as a function of wavelength in different incidence angles for Au and WB metamaterials respectively.

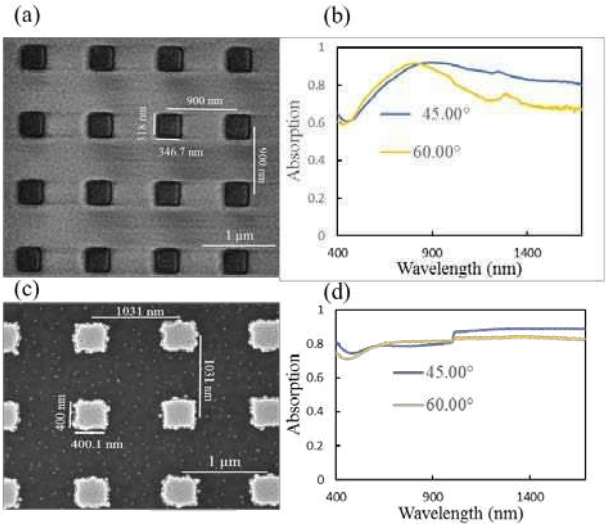


Figure 2: (a) SEM image and (b) measured absorption spectra of the fabricated Au metamaterial absorber. (c) SEM image and (d) measured absorption spectra of the fabricated WB metamaterial absorber.

We used a variable angle spectroscopic ellipsometer (V-VASE) for reflection measurement with optional focusing probes, which focuses the beam to a spot size diameter of around 300 μm. Therefore, we prepared the metallic particle arrays with a size of about 400 μm × 400 μm to make sure the whole measured area was covered. We also optimized the injected current by measuring several WB samples. Figures 2 (b) and (d) show the measured absorption spectra for Au and WB, respectively. The nature of the proposed metamaterial absorber is similar to the infrared absorber demonstrated in [9]: both are attributed to the excitation of the fundamental electromagnetic resonant modes. The mechanism may be explained as the localized electromagnetic fields which are strongly enhanced at a resonance. The incident light is trapped efficiently between metallic particle array and ground metallic layer and then the absorbed light is dissipated due to losses. The proposed device is independent of polarization of normally incident of light due to the symmetrical pattern (the length and width of the Au and WB particle are set to be equal in x and y axes) [25]. Moreover, the absorption is strong for inclined incident angle for such type of absorber. It can also be observed from Figure 2 that the WB metamaterial shows wider bandwidth as compared to the Au counterpart. It may be due to the placing of metallic resonators along the horizontal direction which allows broadband perfect absorption by mixing multiple resonances.

4. Conclusions

In summary, we have designed, fabricated and optically characterized a WB broadband absorber with an average absorption of 90% over the range of 950–1400 nm. In contrast with noble metal optical absorbers which utilize only plasmonic resonances to achieve high absorption, the WB absorber enables us to combine both the intrinsic loss of the material and the plasmonic resonances in the near infrared range for high power applications.

Acknowledgements

Authors appreciate financial support from the Australian Research Council (ARC) and fabrication support from the Australian National Fabrication Facility (ANFF) ACT node.

References

[1] X. Ni, N. K. Emani, A. V. Kildishev, A. Boltasseva, and V. M. Shalaev, Broadband light bending with plasmonic nanoantennas, *Science*, 335: 427-427, 2012.

[2] K. L. Tsakmakidis, A. D. Boardman, and O. Hess, 'Trapped rainbow' storage of light in metamaterials, *Nature*, 450: 397, 2007.

[3] H. A. Atwater and A. Polman, Plasmonics for improved photovoltaic devices, *Nat. Mater.*, 9: 205, 2010.

[4] X. Liu, T. Tyler, T. Starr, A. F. Starr, N. M. Jokerst, and W. J. Padilla, Taming the blackbody with infrared metamaterials as selective thermal emitters, *Phys. Rev. Lett.*, 107: 045901, 2011.

[5] N. I. Landy, S. Sajuyigbe, J. J. Mock, D. R. Smith, and W. J. Padilla, Perfect metamaterial absorber, *Phys. Rev. Lett.*, 100: 207402, 2008.

[6] J. Hao, J. Wang, X. Liu, W. J. Padilla, L. Zhou, and M. Qiu, High performance optical absorber based on a plasmonic metamaterial, *Phys. Rev. Lett.*, 96: 251104, 2010.

[7] W. Cai and V. M. Shalaev, *Optical metamaterials* (no. 6011), Springer, New York, 2010.

[8] Bermel, Peter, M. Ghebrebrhan, M. Harradon, Y. X. Yeng, I. Celanovic, John D. Joannopoulos, and M. Soljacic. "Tailoring photonic metamaterial resonances for thermal radiation, *Nanoscale Res. Lett.*, 6: 549, 2011.

[9] J. Hao, L. Zhou, and M. Qiu, Nearly total absorption of light and heat generation by plasmonic metamaterials, *Phys. Rev. B*, 83: 165107, 2011.

[10] N. G. Szwacki, The structure and hardness of the highest boride of tungsten, a borophene-based compound, *Sci. Rep.,* 7: 4082, 2017

Metasurfaces based coils for MRI

Alena V. Shchelokova[1], Alexey P. Slobozhanyuk[1], Stanislav B. Glybovski[1], Irina V. Melchakova[1], Pavel A. Belov[1*]

[1]ITMO University, St. Petersburg, Russia
*corresponding author, E-mail: belov@metalab.ifmo.ru

Abstract

Metasurfaces represent a new paradigm in artificial subwavelength structures due to their potential to overcome many challenges typically associated with bulk metamaterials. The ability to make very thin structures and change their properties dynamically makes metasurfaces an exceptional meta-optics platform for engineering advanced electromagnetic and photonic metadevices. Here, we suggest and demonstrate experimentally several metasurfaces capable of enhancing significantly the local image quality in magnetic resonance imaging (MRI).

1. Introduction

In order to boost the performance of MRI without increasing the static magnetic field, it is necessary to increase its intrinsic sensitivity [1]. This allows a reduction in the scanning time, increased spatial resolution, and can enable low-field strength systems (which are much cheaper and can be used to scan patients with metallic implants) to have a higher signal-to-noise ratio (SNR) so that they are comparable to more expensive higher field strength systems. In this contribution, we demonstrate a new generation of radiofrequency field enhancing and shaping devices based on metasurfaces. These structures can substantially enhance SNR, thus potentially increasing image resolution or allowing faster examinations.

2. Metasurface for improvement of transmit efficiency

The vast majority of clinical MRI scans use a body coil for transmission. While this allows homogeneous excitation over all body parts at a field strength of 1.5 T, it is naturally quite inefficient for imaging relatively small regions of the body such as the extremities. Although specific absorption rate (SAR) is not typically a limiting factor at 1.5 T, it does become an issue when patients with metallic implants have to be scanned. In this case the local SAR limits must be reduced significantly, even if the body part being imaged does not correspond spatially to a region of high SAR. Therefore, it would be highly advantageous to be able to increase the local transmit efficiency close to the imaging region-of-interest since the overall power, and therefore SAR delivered to the patient can be decreased while maintaining optimum image quality. We demonstrate proof-of-principle experiments in the form of in vivo scans using a metasurface, formed by an array of brass wires embedded in a high permittivity low loss medium, for local enhancement of the RF magnetic field in the region-of interest under clinical scanning conditions [2]. This metasurface can be considered as a wireless coil that redistributes electromagnetic fields and increases the local transmit efficiency in the area of interest. As such it operates in a very similar way to inductively coupled wireless local coils, and indeed the mode structure is related to that of a low-pass planar ‘‘ladder” coil, albeit with the advantage of more flexible and intrinsically symmetric tuning via the dielectric rather than a large number of lumped element capacitors.

3. Volumetric wireless coil based on split-loop resonators

Here, a new wireless coil design for wrist imaging on a 1.5 T clinical scanner was proposed and characterized numerically and experimentally [3]. The wireless coil was designed to provide high image homogeneity and to operate via inductive coupling with a birdcage coil, the latter being used for both transmit and receive. The proposed wireless coil based on a periodic array of coupled split-loop resonators (SLRs). The coil is self-resonant and uses structural capacitance of overlapping traces printed on dielectric substrates connected with telescopic brass tubes allowing to tune the first resonance of the structure to 63.8MHz. An experimental comparison in terms of SNR of the wireless coil to a standard cable connected receive coil of similar dimensions in combination with the same transmitting birdcage coil is presented. Moreover, the issues of the mutual coupling between the wireless coil and the birdcage coil, local SAR and B1 redistribution are discussed. The wireless coil placed into birdcage coil gave the measured B1 increase of the latter by 8.6 times for the same accepted power. The phantom and in vivo wrist imaging showed that the birdcage coil in receiving with the wireless coil inside reached equal or higher signal-to-noise ratio than the conventional clinical setup comprising the transmit-only birdcage coil and a commercial receive-only flex-coil and created no artifacts. Simulations and on-bench measurements proved safety in terms of SAR and reflected transmit power.

4. Conclusions

The results showed that the proposed metasurfaces based coils could be an alternative to standard cable-connected receive coils in clinical magnetic resonance imaging. As an example, with no cable connection, the metamaterials based coil allowed wrist imaging on a 1.5 T clinical machine using a full-body birdcage coil for transmitting and receive with the desired signal-to-noise ratio, image quality, and safety.

Acknowledgements

This work was supported by the Government of the Russian Federation (Grant No. 074-U01) and by the Ministry of Education and Science of the Russian Federation (Zadanie No. 3.2465.2017/4.6).

References

[1] E. M. Haacke, R.W. Brown, M. R. Thompson, and R. Venkatesan, *Magnetic Resonance Imaging: Principles and Sequence Design*, Wiley, New York 1999.

[2] A. V. Shchelokova, A. P. Slobozhanyuk, P. de Bruin, I. Zivkovic, E. Kallos, P. A. Belov, A. Webb, Experimental investigation of a metasurface resonator for in vivo imaging at 1.5 T, *Journal of Magnetic Resonance* 286, 78–81 2018.

[3] A. V. Shchelokova et al., Volumetric wireless coil based on periodically coupled split-loop resonators for clinical wrist imaging, *Magn Reson Med*. 80, 1726-1737, 2018.

Interference phenomena and pulse propagation in a plasmonic wide-ridge metal-dielectric waveguide

Georgiy Yankovskii[1], Vladimir Kornienko[1,2], Alexey Shaimanov[1,2], Anton Ignatov[1], Alexander Merzlikin[1,3], and Alexander Baryshev[1,*]

[1]Dukhov All-Russia Research Institute of Automatics, 127055 Moscow, Russia
[2]Faculty of Physics, Moscow State University, 119992 Moscow, Russia
[3]Institute for Theoretical and Applied Electromagnetics, Russian Academy of Sciences, Moscow 125412, Russia
*corresponding author, E-mail: baryshev@vniia.ru

Abstract

We demonstrate characteristics of plasmonic wide-ridge waveguides made from an Al_2O_3-Au-Al_2O_3 sandwich formed on a fused quartz substrate. Interference of travelling waves in the long-range plasmon propagation regime, their damping, throughput and cross-talk were studied when using pulsed laser source.

1. Introduction

Over the past decade plasmonic waveguides are extensively studied due to their great potential for miniaturizing optical circuits and for improving their functionalities [1-3]. The most intriguing are the plasmonic waveguides utilizing the idea of long-range plasmon (LRP) [4-8]. These LRP waves propagate at both interfaces of an ultra-thin noble metal film, and the best condition for them to exist–to propagate over long distances–is when the film faces (or sandwiched in) the same dielectric background. Another important feature of LRP waves is their spatial localization.

In the present work, we discuss properties of plasmonic wide-ridge waveguides made from an Al_2O_3-Au-Al_2O_3 sandwich formed on a fused quartz substrate. It was found that the waveguiding modes can travel along different paths and build an interference pattern. We also report on main characteristics of these waveguides of different length (attenuation constant, pulse propagation, bandwidth and cross talk).

2. Samples and experiment

Experimental samples were 70 μm-wide and 0.5-1 mm-long ridge waveguides formed by etching an Al_2O_3-Au-Al_2O_3 sandwich grown on a fused silica substrate. The sandwich was prepared by electron beam evaporation and had the next structural parameters: a 240 nm-thick top Al_2O_3 layer, a 10 nm-thick Au layer and the bottom 70 nm-thick Al_2O_3 layer.

Experiments were done by utilizing the following instruments: a tunable pulsed laser source Fianium (NTK Photonics) with a pulse width of 150 ps and a repetition rate of 40 MHz, an Ntegra system (NT-MDT), a Beamage CMOS camera (Gentec-EO) and a tunable delay line for resolving sequence of pulses.

To excite the LRP wave, light beams with Gaussian profiles were focused (FWHM = 2 μm). For the waveguides, working wavelengths were in the vicinity of λ =765 nm, and all the structural parameters were optimized so that to support a single LRP mode for only the **E**-field oscillating along the ridge.

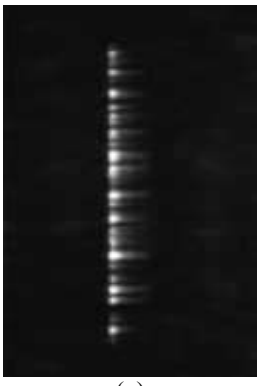
To couple/decouple light, input/output 1D gratings were etched through top Al_2O_3 layer and Au of the Al_2O_3-Au-Al_2O_3 sandwich. Incident light was focused onto the input grating by an objective (60×/0.7), and decoupled light was visualized by a system having a 100×/0.5 objective and the CMOS camera. Visualization of decoupled LRP waves was done by Beamage CMOS camera detecting over the full area (40×70 μm) of the output grating. Images were acquired with commercial software (PC-Beamage V1.03.04) and further processed. Figure 1 shows a typical captured image of the light intensity.

Pulse propagation was studied by a photon counting module of the Ntegra system, and the delay line was used to tune a time gap (150-300 ps) between the nearest pulses.

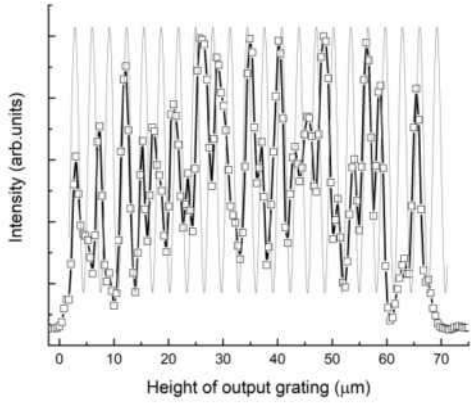
3. Results and discussion

Figure 1 illustrates the interference pattern, which appears upon the output grating for the LRP wave traveling from the left-hand side, and an intensity profile that is cut across the propagation direction. The observed amplitude was found to strongly depend on the excitation coordinate; the maximum was when only one half of the radiation spot was in the area of the input grating and the other half struck the Al_2O_3-Au-Al_2O_3 sandwich, i.e. when the spot was shifted towards the output grating.

Plot (b) shows a series of bright spots similar to the case of two-beam interference. It is obvious that the side walls of the ridge waveguide act as reflection mirrors, and the total interference pattern is likely built by the LRP wave propagating directly along the waveguide and reflected form the side walls. It is worth noting that image (a) has spots various in brightness and manifests presence of fabrication imperfections.



(a)



(b)

Figure 1: (a) Image of an interference pattern for a 700 μm-long waveguide visualized in the area of the output grating. (b) Intensity distribution along a section line in image (a); the gray sine curve is guide for the eye and demonstrates a periodicity of the pattern. Working λ = 765 nm.

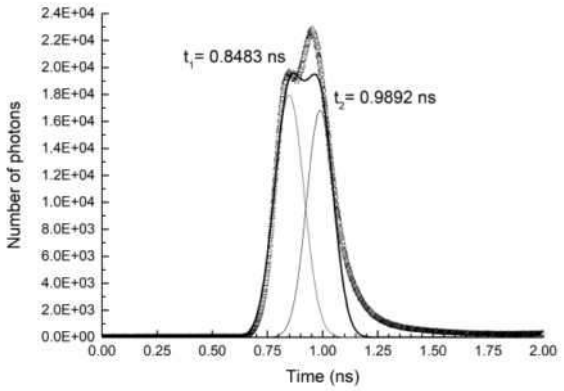


Figure 2: Time-resolved kinetics for two nearest pulses with a delay of 150 ps (triangles). Double-peak fitting Gaussian curve (black line). Working λ = 765 nm.

Figure 2 demonstrates a time-resolved kinetics detected for two nearest pulses with a delay of 150 ps (triangles); the delay time was set and measured for the single pulses. These two almost equal in intensity pulses propagate without any distortion. Demonstrated bandwidth in these experiments was 8 Gbit/s, which was limited by the used laser source. It should be mentioned that the fitting curve (black line) did not coincide with the experimental one because of the instrument function of the detecting Ntegra system.

4. Conclusions

Characteristics of plasmonic Al_2O_3-Au-Al_2O_3 wide-ridge waveguides have been studied. The 0.5-1 mm-long waveguides supported propagation and interference of the LRP waves from a pulsed laser. The studied plasmonic wide-ridge wave guides are proposed for the first time and are of interest from both fundamental and application points of view.

Acknowledgements

This work was funded by Advanced Research Foundation (Russia), research project No. 7/004/2013-2018. We thank the technology team at the BMSTU Nanofabrication Facility (Functional Micro/Nanosystems, FMNS REC, ID 74300) for waveguides fabrication.

References

[1] S.I. Bozhevolnyi (Ed.), *Plasmonic Nanoguides and Circuits*, Pan Stanford Publishing Pte. Ltd. Singapore, 2009.

[2] D.K. Gramotnev, S.I. Bozhevolnyi, Plasmonics beyond the diffraction limit, *Nature Photonics* 4: 83-91, 2010.

[3] A.I. Ignatov, A.M. Merzlikin, Holograms for power-efficient excitation of optical surface waves, *J. Opt. Soc. Am. B* 35: 308-316, 2018.

[4] P. Berini, Long-range surface plasmon polaritons, *Advances in Optics and Photonics* 1: 484–588, 2009.

[5] A. Kumar, J. Gosciniak, V.S. Volkov et al., Dielectric-loaded plasmonic waveguide components: Going practical, *Laser Photonics Rev*. 7: 938–951, 2013.

[6] S. Kharitonov, R. Kiselev, A. Kumar et al., Data transmission in long-range dielectric-loaded surface plasmon polariton waveguides, *Optics Express* 22: 26742-26751, 2014.

[7] V.S. Volkov, Zhanghua Han, M.G. Nielsen et al., Long-range dielectric-loaded surface plasmon polariton waveguides operating at telecommunication wavelengths, *Optics Letters* 36: 4278-4280, 2011.

[8] J.T. Kim, J.J. Ju, S. Park, M. Kim, S.K. Park et al., Chip-to-chip optical interconnect using gold long-range surface plasmon polariton waveguides, *Optics Express* 16: 13133, 2008.

Miniature Spectroscopes with Metasurfaced Transmitted Color Filters Integrated on a Photodiode Array

Yoshiaki Kanamori[1*], Daisuke Ema[1], and Kazuhiro Hane[1],

[1]Department of Finemechanics, Tohoku University, Sendai, Japan
*corresponding author, E-mail: kanamori@hane.mech.tohoku.ac.jp

Abstract

As an application of metamaterial, we fabricated meta-surfaced transmitted color filters integrated on a photodiode array for miniature spectroscopes. The color filters consisted of two-dimensional guided-mode resonant metal grating filters. Characteristics of the fabricated color filters and miniature spectroscopes were evaluated. Transmittance characteristics of the fabricated color filters showed that the peak wavelengths were proportional to grating periods as designed. From measurement of the fabricated spectroscopes using monochromatic lights, obtained spectra agreed with the center wavelengths of the monochromatic lights.

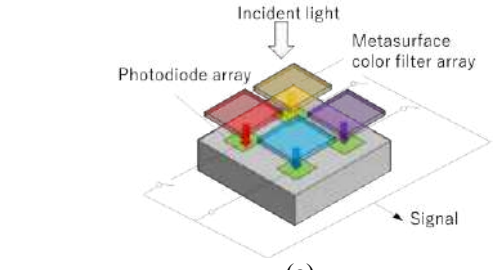
1. Introduction

Since Ebbesen *et al*. discovered extraordinary transmission phenomenon in 1998 [1], various metamaterial color filters have been studied [2,3]. In recent years, novel spectrometers that do not require diffraction gratings have been reported by combining plasmonic color filters and complementary metal-oxide semiconductor (CMOS) sensors [4,5]. The color filter is formed on each pixel of the CMOS sensor, and spectral information is obtained by post-processing using signals obtained from each pixel. Such filter array spectrometers are believed to have the potential to broaden the scope of use of spectroscopic devices because of the miniature size with low cost features. There are few studies on filter array spectrometers as far as we know. The spectral characteristics depend on the filter characteristics, and improvement of the filter characteristics is desired.

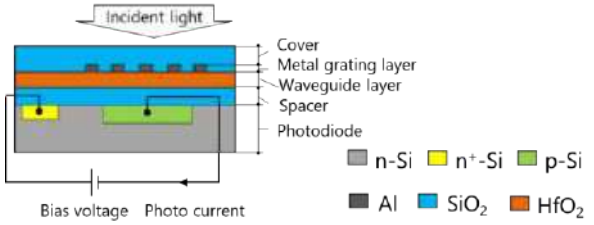
Recently, we designed novel metamaterial color filters, and fabricated miniature spectroscopes in which the color filters were integrated on a photodiode array [6]. It is the first demonstration of filter array spectroscopes combining two-dimensional guided-mode resonant metal grating filters and photodiodes. Here, we discuss about the characteristics of the fabricated color filters and miniature spectroscopes in detail.

2. Concept of device

Figure 1(a) shows a perspective view of proposed spectroscopes in the case of 2 by 2 pixels. Metasurfaced color filter array is integrally formed on the Si photodiode array, and the photocurrent signal from each photodiode is read out sequentially. Then, spectrum of incident light is reconstructed by post-processing. Figure 1(b) shows a cross-section of one pixel consisting of a metasurfaced color filter formed on a photodiode through an SiO_2 spacer. The color filter consists of a two-dimensional guided-mode resonant metal grating which is coated with an SiO_2 layer. The metal grating and waveguide layers consist of Al and HfO_2, respectively.



(a)



(b)

Figure 1: Schematics of proposed spectroscopes. (a) Perspective view in case of 2 by 2 pixels. (b) Cross-section of one pixel.

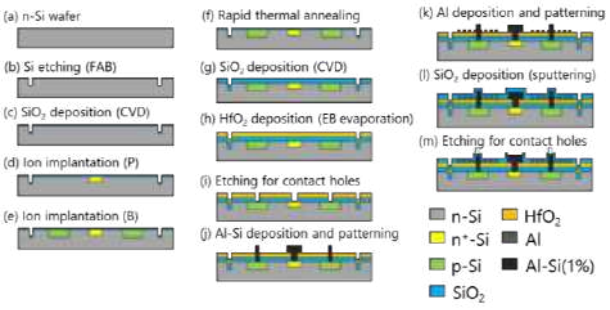


Figure 2: Fabrication steps.

3. Fabrication

Figure 2 shows fabrication steps. First, photodiode array is fabricated from n-Si wafer using etching, deposition, ion implantation, and rapid thermal annealing processes. Second, spacer layer is formed with SiO_2 deposition. Third, color filter structures are formed with deposition, etching, and patterning processes. At the last, SiO_2 deposition for a cover layer and etching for contact holes are carried out.

Figure 3 shows a reflection image of an optical microphotograph of fabricated device (left) and scanning electron microscope (SEM) image of one color filter with a period of 220 nm (right). The color filters are fabricated in 25 (5 by 5) patterns with grating periods between 220 nm and 460 nm at increments of 10 nm. It can be seen that electrical wirings are also formed.

4. Device characteristics and Discussion

Figure 4 shows reconstructed incident light spectra with solid lines. By way of comparison, spectra of incident light measured with a commercially available spectrometer (HR4000CG-UV-NIR, Ocean optics, Inc., Largo, FL, USA) are shown as original spectra with dotted lines.

Figure 5 shows peak wavelengths of reconstructed spectra as a function of center wavelengths of monochromatic lights extracted from the results of Figure 4. It is apparent that the peak wavelengths of the reconstructed spectra are in good agreement with the original spectra. From figures 4 and5, we believe that the spectroscopic measurement was successfully performed with the fabricated device.

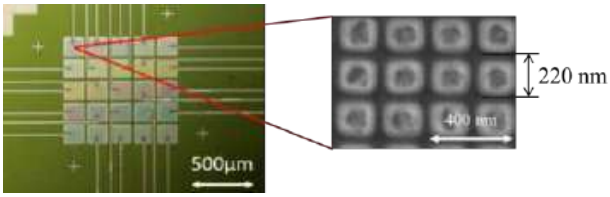


Figure 3: The optical microphotograph of fabricated device (left) and SEM image of one color filter (right).

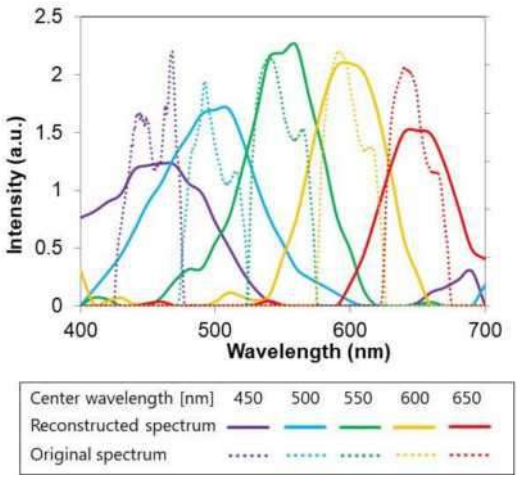


Figure 4: Reconstructed spectrum.

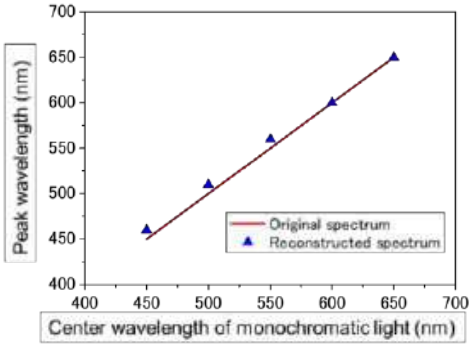


Figure 5: Peak wavelengths of reconstructed spectra as a function of center wavelengths of monochromatic lights.

5. Conclusions

We fabricated meta-surfaced transmitted color filters integrated on a photodiode array for miniature spectroscopes. The color filters consisted of two-dimensional guided-mode resonant metal grating filters. 25 color filters with grating periods between 220 nm and 460 nm at increments of 10 nm were fabricated on respective photo diodes with high accuracy. It was found that the peak wavelength could be reconstructed with high accuracy by using fabricated spectroscope device.

Acknowledgements

A part of this research was funded by the MEXT KAKENHI 16K13648 and 16H04342.

References

[1] T. W. Ebbesen, H. J. Lezec, H. F. Ghaemi, T. Thio, P. A. Wolff, Extraordinary optical transmission through sub-wavelength hole arrays, *Nature* 391: 667–669, 1998.

[2] C. Genet, T. W. Ebbesen, Light in tiny holes, *Nature* 445: 39–46, 2007.

[3] H. S. Lee, Y. T. Yoon, S. S. Lee, S. H. Kim, K. D. Lee, Color filter based on a subwavelength patterned metal grating, *Opt. Express*:15, 15457–15463, 2007.

[4] C. C. Chang, N. T. Lin, U. Kurokawa, B. I. Choi, Spectrum reconstruction for filter-array spectrum sensor from sparse template selection, *Opt. Eng.*: 50, 114402, 2011.

[5] U. Kurokawa, B. I. Choi, C. C. Chang, Filter-based miniature spectrometers: spectrum reconstruction using adaptive regularization, *IEEE Sens. J.*: 11, 1556–1563, 2011.

[6] Y. Kanamori, D. Ema, K. Hane, Miniature spectroscopes with two-dimensional guided-mode resonant metal grating filters integrated on a photodiode array, *Materials* 11: 1924, 2018.

Wideband Absorbing Nonlinear Optical Metamaterials Using Coupled Epsilon-Near-Zero Mode

Jinnan Chen[1], Evan M. Smith [2,3], Justin W. Cleary[2], Chandriker Dass [2,3], Amber Reed [2,3], Shiva Vangala[2], Joshua R. Hendrickson[2], and Junpeng Guo[*, 1]

[1]Department of Electrical and Computer Engineering, University of Alabama in Huntsville, Huntsville, AL 35899, USA
[2]Air Force Research Laboratory, Sensors Directorate, Wright-Patterson AFB, OH 45433, USA
[3]KBRwyle, Beavercreek, OH 45435, USA
*Corresponding author, e-mail: guoj@uah.edu

Abstract

Metamaterials made of epsilon-near-zero indium tin oxide and dielectric multiple layers were investigated for wideband perfect light absorption in the near wavelength range. The enhanced wideband absorption was used for nonlinear optical second harmonic generations.

1. Introduction

Materials with vanishing real part of the electric permittivity in certain wavelength regions are promising optical materials for many applications. This type of materials are called epsilon-near-zero (ENZ) materials because the real part of the electric permittivity crosses zero at certain wavelengths [1]. The most common ENZ materials are transparent conducting oxides and doped semiconductors. One such ENZ material is indium tin oxide (ITO) with an ENZ wavelength around 1550 nm. ITO material has been previously investigated for making tunable devices [2] and nonlinear optics [3]. In this work, multiple ENZ material and dielectric layer structures were investigated for wideband absorption and nonlinear optical applications.

2. Wideband perfect light absorbers using multiple dielectric and ENZ material layers

Previously, wideband perfect light absorbers made of multilayer metal and dielectric layers were reported for absorbing wideband solar light radiations [4,5]. In this work, we replace the metal layers with ITO ENZ layers for wide band absorption and nonlinear optical second harmonic generation applications. Figure 1(a) shows the multilayer ITO/SiO_2 structure. Starting from the top, there are alternative thin SiO_2 layer and ITO thin film layers that form optical cavities for trapping light and enhancing absorption. A 200 nm optically thick TiN layer is at the bottom to prohibit light transmission from the device. Fig. 1(b) shows the measured real part and imaginary parts of the electric permittivity, where the crossing-zero wavelength is around 1.45 micron [6].

The measured electric permittivity of 100 nm ITO film was used for calculating optical absorptance. The optical absorptance curves of devices of different number of SiO_2 /ITO pairs versus wavelength were calculated and shown in Figure 2 (a). It can be seen from this Figure 2(a) that ITO/ dielectric multilayer structures have high absorption in the near infrared region. By increasing number of pairs, multiple absorption resonance modes result in wide absorption band. Devices with different number of SiO_2/ITO pairs were fabricated and the absorbance curves were measured. Figure 2(b) shows the measured absorbance curves of fabricated devices with different number of SiO_2/Ti pairs. It shows that as the number of pairs increases, the absorption band increases. Second harmonic generation from fabricated

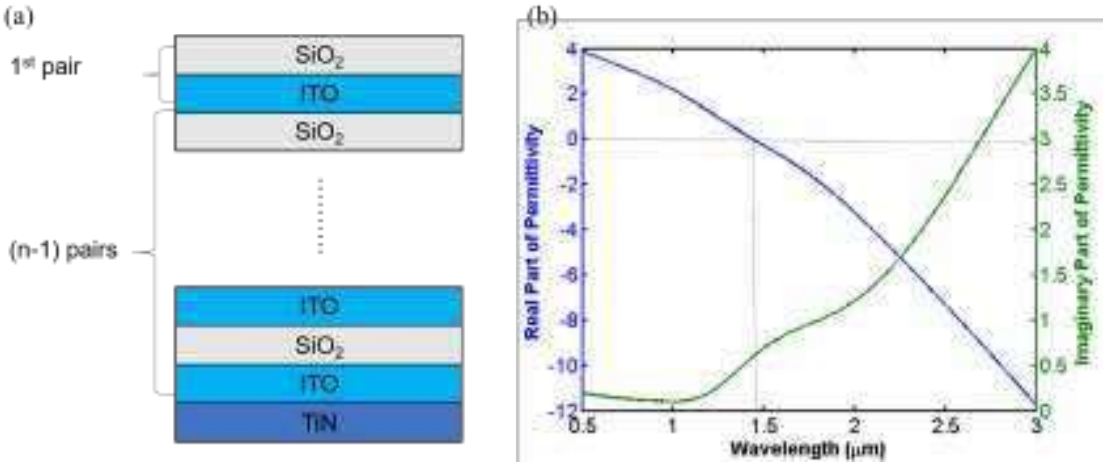


Figure 1: (a) Super absorbing metamaterial of multiple SiO_2 and ITO thin films. (b) Measured electric permittivity of a ITO thin film.

wideband absorber devices was measured. Strong enhancement of SHG was observed the when the devices were excited within the absorption band.

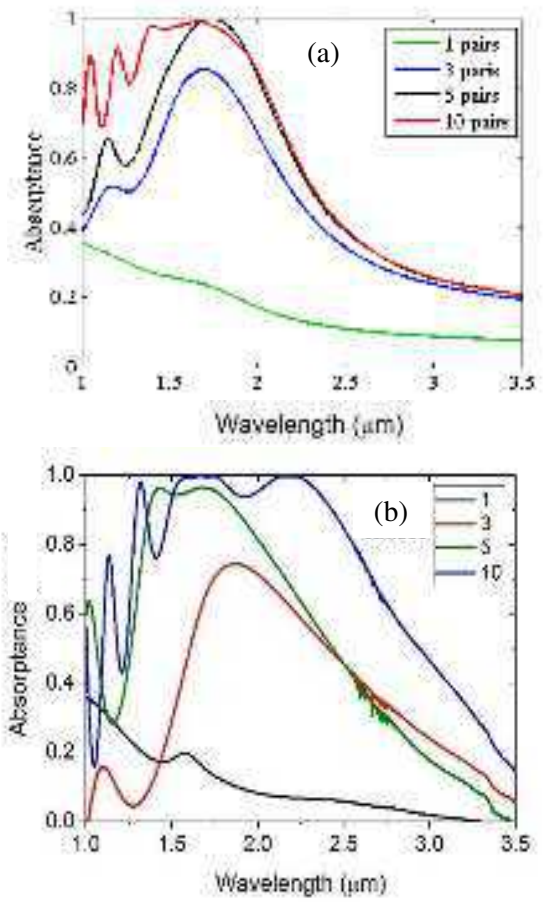


Figure 2: (a) Calculated absorptance versus wavelength for devices with different number of SiO_2/ITO pairs. (b) Measured absorptance versus wavelength for fabricated devices with different number of SiO_2 /ITO pairs.

3. Summary

Metamaterials made of epsilon near zero ITO and SiO_2 multiple layers can have wideband near perfect absorption in the near infrared wavelength rang near the ENZ wavelength. Optical absorptance with different number of ENZ- dielectric thin film pairs was calculated. Simulation results show that the periodic ENZ-dielectric thin film structures have near perfect light absorption over a wide spectral range. Increasing number of pairs results in more absorption resonance modes and wider absorption band. Devices were fabricated and characterized and the results agree well with simulation results. Second harmonic generations were measured and it has shown that enhanced nonlinear optical effect occurs near the ENZ wavelength within the near perfect absorption band.

References

[1] S. Vassant, J. P. Hugonin, F. Marquier, and J. J. Greffet, "Berreman mode and epsilon near zero mode," Optics express, 20(21), pp. 23971-23977, 2012.

[2] J. Park, J.-H. Kang, X. Liu, and M. L. Brongersma, "Electrically tunable epsilon-near-zero (ENZ) metafilm absorbers," Sci. Rep. 5, p. 15754, 2015.

[3] M. Alam, S.A. Schulz, J. Upham, I. De Leon, and R. Boyd, "Large optical nonlinearity of nanoantennas coupled to an epsilon-near-zero material," Nature Photonics, 12(2), p. 79 , 201).

[4] J. Chen, J. Guo, and L. Chen, "Super-wideband perfect solar light absorbers using titanium and silicon dioxide thin-film cascade optical nanocavities," Optical Materials Express, 6(12), pp. 3804-3813, 2016.

[5] E. Hu, Y. Yao, K. Zang, X. Liu, A. Jiang, J. Zheng, K. Yu, W. Wei, Y. Zheng, R. Zhang, S. Wang, H. Zhao, O. Yoshie, Y. Lee, C. Wang, D. W. Lynch, J. Guo and L. Chen, "High photon-to-heat conversion efficiency in the wavelength region of 250–1200 nm based on a thermoelectric Bi2Te3 film structure," Scientific Reports 7, p. 44614, 2017.

[6] J. R. Hendrickson, S. Vangala, C. Dass, R. Gibson, J. Goldsmith, K. Leedy, D. E. Walker, J. W. Cleary, W. Kim, and J. Guo, "Coupling of epsilon-near-zero mode to gap plasmon mode for flat-top wideband perfect light absorption," ACS Photonics, 5 (3), pp.776-781, 2018..

Metamaterials and negative index materials

Programmable Electromagnetic Properties of Microwire Metacomposites

Azim Uddin[1] and Faxiang Qin[1*]

[1]Institute for Composites Science Innovation（InCSI）, School of Materials Science and Engineering, Zhejiang University, Zheda Road, Hangzhou, 310027, PR. China

*corresponding author, E-mail: faxiangqin@zju.edu.cn

Abstract

The multifunctional structural composites have gained more attention due to their incorporation of electromagnetic (EM) features into light-weight host materials. In this work, we present a composite medium demonstrating strong microwave dispersion properties enabled by an array of short-cut microwires. They behave as radiative elements with different structural properties into polymer-based composite. The arrangement of wires plays a remarkable role in achieving the controllable EM response.

1. Introduction

A metamaterial is intended to be an engineered material having unusual physical properties beyond the natural materials[1]. Over the years a vast interest is seen in the development of engineered multifunctional composites containing micro or nanoscale fillers in terms of their electromagnetic properties for microwave applications phenomena such as reconfigurable and tunable microwave devices to non-destructive testing[2]. Glass-coated ferromagnetic microwires[3] gained more attention due to their fine size and properties like magnetoimpedance (MI) with enhanced soft magnetic characteristics which makes them distinguished from other materials. These wires act as radiative elements when incorporated into polymer matrix providing various EM properties[3].

The effective EM response of a wire filled composite is mainly controlled by the high frequency MI properties of wires, , distance between them, and by external stimuli such as magnetic field, stress, or temperature[4]. In order to expand the choice of microwave dispersion characteristics of the wire filled composites, we propose a new DC current annealing procedure for the wire inclusions together with their special structural ordering. Previously such work elsewhere [5] has not been fully exploited. In the approach developed in this work, modulation of the resonant response of wire media to an EM wave is achieved by incorporating differently annealed wires of same composition ordered in different arrangements. This permits one to improve significantly the design variety and helps programing the operation frequencies with the active use of an adjusting parameter of arrangement of wires.

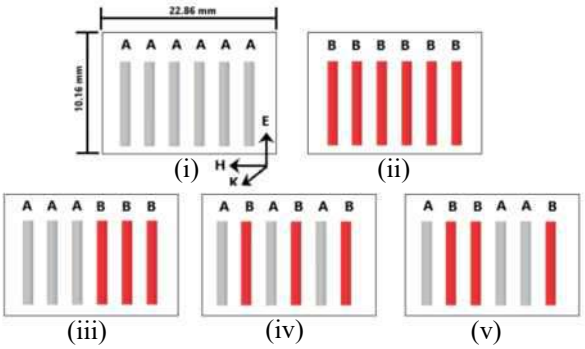


Fig. 1. Arrangement of wires; (i) & (ii) are the as-casted (labeled as A) and current annealed wires at 40 mA (labeled as B). Whereas, (iii), (iv) & (v) are the incorporated wires with different arrangements as AAABBB, ABABAB & ABBAAB respectively.

In our experiments, we used a CoFeSiB alloy composition of microwire. Six pieces of short-cut wires were arranged parallel to each other in an array with a spacing of 2mm in between them in a polymer-based composite, as shown in Fig. 1. The annealing of wires was done by applying DC 40 mA at specific duration.

2. Results and Discussion

Fig. 2 represents the X-Ray Diffraction (XRD) spectra for glass-coated microwire with the alloy composition of $Co_{60}Fe_{15}Si_{10}B_{15}$ having a diameter of metallic core 27.2 um and total diameter of wire is 35.4 um produced by Taylor Ulitovski technique. The spectra confirm that as-cast wires present amorphous structure (black spectrum) consisting of a halo originating from the glass shell and amorphous halo from the amorphous phase. After current annealing at 40 mA for 10 minutes, the XRD is almost the same as in as-cast state (red spectrum). This method of annealing helps to boosting the magnetic properties that could influence the EM properties as it will be elucidated later, revealing a novel way to program the EM responses in a composite.

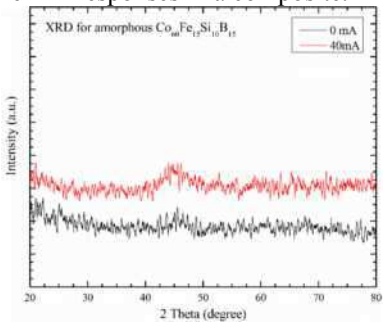


Fig. 2. XRD spectra for microwires with the alloy composition of $Co_{60}Fe_{15}Si_{10}B_{15}$ for as-cast wires (black spectrum) and current annealed wires at 40 mA (red spectrum).

Transmission co-efficient (S21/12) of the wire composites are measured by a vector network analyzer (VNA) in the rectangular waveguide (22.86 x 10.16 x 2 mm^3). Fig. 3 shows the measured transmission spectra of as-cast=A, current annealed at 40 mA=B wire array-composite and integrated wire array-composite with different arrangements. For A-wires, a transmission minimum occurs at 11.96 GHz corresponding to the Lorentz-type dielectric resonance or dipolar behavior of the short-cut microwires. Short-cut wire inclusions act as dielectric dipoles when interacting with the electrical component of waves[3] with the resonance frequency $f_{res} = \frac{c}{2l\sqrt{\varepsilon_m}}$, where c is the speed of light, ε_m is the relative permittivity of composite matrix, and l is the length of the wire.. Taking ε_m as 2 and l as 10.16 mm (fixed in our case) into above equation, we obtain $f_{res} = 10.44$ GHz, which fairly coincides with the identified minimum in Fig. 3.

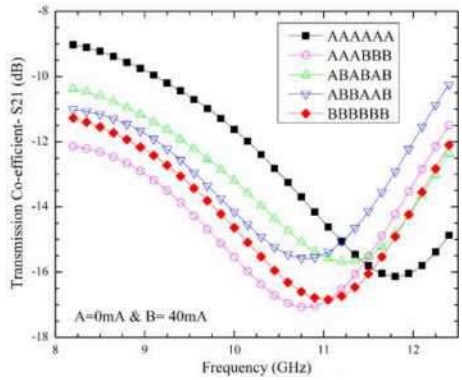


Fig. 3. Measured dispersion of the transmission coefficient for wires of the types A and B and differently arranged having spacing of 2mm in between them.

The visible change is seen in the current annealed wire which shifts the transmission spectra towards lower frequency, i.e. 11.06 GHz. This shift was caused by the change in the structural relaxation of the wire alloy produced by current annealing. The annealing at 40 mA current is high enough (but lower than the crystallization temperature, as evidenced in Fig. 2) for structural relaxation and partial relief of the internal residual stresses[6].

For the composites containing combination of the as-cast and annealed wires (Fig. 1), the wire arrangement has shown a profound impact on the transmission minimum and amplitude. When different types of wires are added in the same amount but in different order as shown in Fig. 1, the transmission minimum or dipolar resonance trends to the lower frequencies than to the as-cast wires. This trend coincides to that of the composites containing the same type of wires (AAAAAA and BBBBBB), the most pronounced red-shift is of the AAABBB sample i.e., 10.82 GHz beyond to that of individual wire frequency range for as-cast and current annealed wires. When the wires are arranged in an alternate manner i.e. ABABAB, the transmission minimum follows the trend with frequency, i.e. red-shifting with the incorporation of 40 mA-annealed wire B closer to as-cast wire, i.e. 11.26 GHz. Finally, when the two wires in the middle of array ABABAB are swapped, i.e. ABBAAB, the critical frequency once again shifts on the side of the 40 mA-annealed wires B, i.e. 10.795 GHz. In addition, the transmission amplitude of the composites also decreases as the wires B is incorporated in the array. Therefore, we can infer a dominant influence of the annealed wires over the as-cast wires on dictating the EM response of the composites.

From our experimental results, we can conclude that the current annealing of wires causes an effective improvement to its magnetic properties especially structural relaxation. These tailored wires can effectively mixed with cast wires, producing a composite with controllable behavior.

3. Conclusions

We have demonstrated that a small DC current can be used as a EM property control parameter. The proposed annealing procedure together with different wire arrangements allowed us to strongly modify microwave dispersion properties of the wire filled composites.

Acknowledgements

The work is supported under NSFC No. 51671171.

References

[1] J. B. Pendry, A. J. Holden, D. J. Robbins and WJS. Magnetism from Conductors and Enhanced Nonlinear Phenomena. *IEEE Trans Microw THEORY Tech*; VOL 17:525–40, 1999.

[2] Panina L V., Ipatov M, Zhukova V, Zhukov A, Gonzalez J. Microwave metamaterials with ferromagnetic microwires. *Appl Phys A Mater Sci Process*;103:653–7, 2011.

[3] Panina L V., Ipatov M, Zhukova V, Estevez J, Zhukov A. Microwave metamaterials containing magnetically soft microwires. *Mater Res Soc Symp Proc*;1312:313–8, 2011.

[4] Makhnovskiy D, Zhukov A, Zhukova V, Gonzalez J. Tunable and Self-Sensing Microwave Composite Materials Incorporating Ferromagnetic Microwires. *Adv Sci Technol*; 54:201–10, 2008.

[5] García-Miquel H, Carbonell J, Sánchez-Dehesa J. Left handed material based on amorphous ferromagnetic microwires tunable by dc current. *Appl Phys Lett*;97:2010–2, 2010.

[6] Dzhumazoda A, Panina L V., Nematov MG, Ukhasov AA, Yudanov NA, Morchenko AT, et al. Temperature-stable magnetoimpedance (MI) of current-annealed Co-based amorphous microwires. J *Magn Magn Mater*;474:374–80, 2019.

Dielectric metamaterials with epsilon-near-zero regime

Ekaterina E. Maslova[1,*] **and Mikhail V. Rybin**[1,2]

[1]Department of Physics and Engineering, ITMO University, St Petersburg 197101, Russia
[2]Ioffe Institute, St. Petersburg 194021, Russia
*corresponding author, E-mail: ekaterina.maslova@metalab.ifmo.ru

Abstract

We consider all-dielectric metamaterials with electric response allowing an epsilon-near zero regime. The metamaterials being a hexagonal lattice of dielectric rods are studied. We construct a photonic phase diagram by analyzing photonic band diagrams. A near-boundary phase with a strong spatial dispersion is found in the structures with a hexagonal lattice, which is not observed in the case of a square lattice.

1. Introduction

Near-zero refractive index provides many opportunities for studying light-matter interactions [1]. Related materials can be classified as epsilon-near-zero (ENZ), dielectric permittivity $\varepsilon \approx 0$, mu-near-zero (MNZ), magnetic permeability $\mu \approx 0$, and epsilon-and-mu-near-zero (EMNZ), $\varepsilon \approx 0$ and $\mu \approx 0$ media. The dispersion relation $\omega^2 = \varepsilon\mu|\mathbf{k}|^2$ leads to a wavelength 'stretching' effect for the case of near-zero regime, and thus a spatial (wavelength) and a temporal (frequency) field variations are decoupled. It allows an unconventional physics of structures with near-zero parameters, which has both an academic interest and a great application potential in unusual device designing, since the near-zero index regimes can be exploited to enhancement of the light-matter interactions.

Metamaterials are artificial structures described by effective indices, permittivity ε and permeability μ, as conventional materials. A special design of structure allows for these parameters to take a desired positive or negative value, which depends on properties of the structural elements. Since natural materials enable dielectric permittivity in a wide interval of values including ENZ, the main efforts were focused on the development of structures with artificial magnetic response. For a long time, material losses were the challenger problem, until low-losses dielectric systems with the structural elements supporting magnetic and electric Mie resonance was introduced [2]. The periodic dielectric structures are usually considered either as a photonic crystal, which properties are related to Bragg resonances, or metamaterials operating due to local Mie resonances sustained by each structural elements.

A phase diagram for a square lattice of dielectric rods was developed as a function of rod density and permittivity [3]. This phase diagram uncovers the range of parameters allowing the dielectric metamaterials with magnetic response. Although dielectric metamaterials were the subject of intensive studies, the structures with resonant electric response were reported in 2018 only [4].

Here we construct a phase diagram "photonic crystal – metamaterial" for a hexagonal lattice of dielectric cylinders in the case of TE (the magnetic field oscillates along the rod axis) and TM (the electric field oscillates along the axis) polarization. The phase diagram is constructed by analyzing the photonic band diagrams of the periodic structures. The first branch in the band diagram has minimum at the Γ point and increases to boundary of the Brillouin zone. In a photonic crystal structure related to a Bragg resonance the second branch of dispersion has a minimum on boundary of the Brillouin zone and a maximum at the Γ point. In the case of metamaterial the band diagram has a polaritonic feature [5]. Unlike the case of square lattice, we find a near-

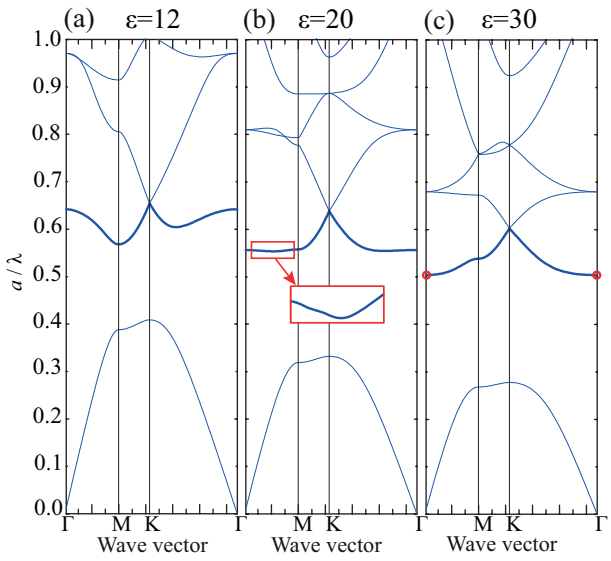


Figure 1: Photonic band diagrams of dielectric rods arranged in a hexagonal lattice for TM polarization. (a) A photonic crystal with ε=12 and r/a=0.1. (b) A near-boundary phase with $\varepsilon = 20$ an $r/a = 0.1$. (c) A metamaterial with ε=30 and r/a=0.1. The second branches in the diagrams are marked by thick lines. The red circles correspond to the bottom boundary of the second band at a/λ=0.504.

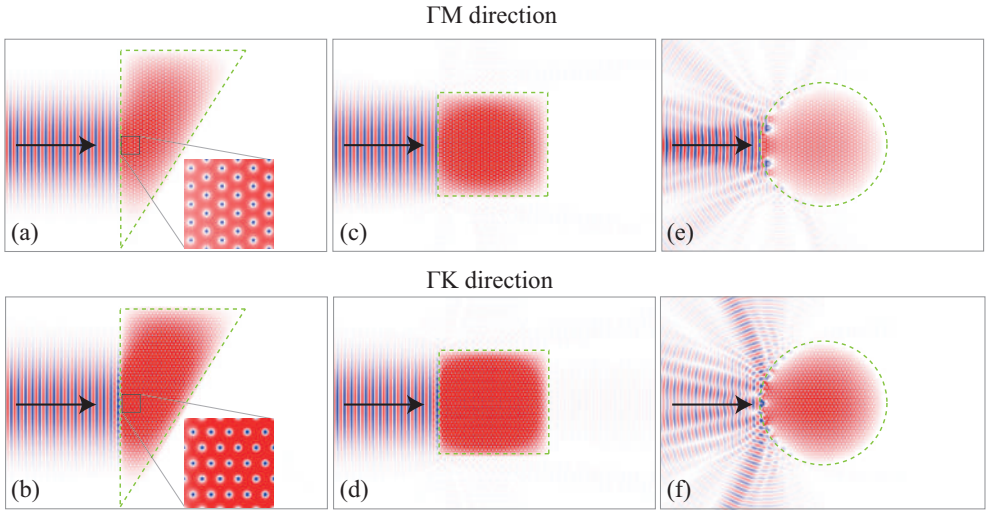


Figure 2: Distributions of the electric field for the ε-near zero modes in electric metamaterials with different shapes [triangle (a), (b), square (c), (d), and circle (e), (f)] and different lattice orientations [ΓM (a), (c), (e) and ΓK (b), (d), (f) directions]. Green dashed lines show metamaterial structure boundaries. Black arrows indicate the Gaussian beam incident direction. Insets in panels (a) and (b) show the electric field distribution on a larger scale. a/λ=0.504, ε=30, r/a=0.1, TM polarization.

boundary phase in structures with the hexagonal lattice [6].

2. Results

We consider a hexagonal lattice of dielectric rods in the case of TM polarization. Fig. 1 demonstrates a modification of the band diagram with the increase of the rod permittivity. Fig. 1a shows the band diagram of photonic crystal, which exhibits a typical Bragg gap (the second branch has the minimum at the M point).

We find a near-boundary phase existing for the structure with $\varepsilon \approx$20, r/a=0.1. Its dispersion is shown in Fig. 1b. In the near-boundary phase the second branch has a local minimum inside the Brillouin zone and there are a range of two states per a single frequency value indicating conditions of a strong spatial dispersion. Therefore, the structure in the near-boundary phase cannot be described by using effective material parameters ε and μ.

When we increase the dielectric permittivity the minimum of second branch moves to the Γ point (Fig. 1c) forming the polaritonic feature that is the signature of metamaterial phase. However, when the permittivity is relatively small the band diagram shows a weak polaritonic feature and we simulate a propagation of electromagnetic wave to verify that it is metamaterial regime indeed.

We study the wave propagation through confined structures [4, 6] with different shapes (prism, circle and square), which consist of about 1100 rods (the actual rod number depends on the shape and the lattice orientation). A Gaussian beam with a $10a$ waist impinges the metamaterial structures. Results illustrate that in the metamaterial regime it is possible to observe ENZ regime. A distribution of electric field is uniform throughout the structures and it does not depend on their shape, which confirms the metamaterial regime of these dielectric structures (Fig. 2).

To summarize, we have considered dielectric structures with the hexagonal lattice, in which the near-boundary phase having a strong spatial dispersion has been found. We have shown that the metamaterial in the ENZ regime does not undergo the lattice orientation and sample shape. Metamaterials with ENZ modes make it possible to enhance the light-matter interactions and pave the way for sensitive devices.

We acknowledge a support from the Ministry of Education and Science of the Russian Federation (3.1500.2017/4.6).

References

[1] I. Liberal, N. Engheta, Near-zero refractive index photonics, *Nature Phot.* 11: 149–158, 2017.

[2] S. Jahani, Z. Jacob, All-dielectric metamaterials, *Nature nanotechnology* 11: 23–36, 2016.

[3] M.V. Rybin et al., Phase diagram for the transition from photonic crystals to dielectric metamaterials, *Nature Commun.* 6: 2015.

[4] E.E. Maslova, M.F. Limonov, M.V. Rybin, Dielectric metamaterials with electric response, *Opt. Lett.* 43: 5516–5519, 2018.

[5] Kaina N., Lemoult F., Fink M., Lerosey G., Negative refractive index and acoustic superlens from multiple scattering in single negative metamaterials, *Nature* 77: 77–81, 2015.

[6] E.E. Maslova, M.F. Limonov, M.V. Rybin, Transition "photonic crystal–metamaterial with electric response" in dielectric structures, *JETP Letters* 109: 348–353, 2019.

Anti-crossing of counter propagating modes within the Brillouin Zone

Milo Baraclough, William L. Barnes, Ian R. Hooper

Department of Physics and Astronomy, University of Exeter, Exeter, United Kingdom, EX4 4QL
*corresponding author, E-mail: mb504@exeter.ac.uk

Abstract

Bandgaps resulting from anti-crossings between modes are a common feature of periodic media. Typically they occur at the Brillouin zone boundary, or result from interactions between forward propagating modes of different character. By breaking the symmetry of a metamaterial waveguide that supports both forward and backward propagating modes we demonstrate an anti-crossing within the Brillouin zone that exhibits band edges with zero group velocity.

1. Introduction

Chains of meta-atoms of various types have proved to be promising candidates for sub-wavelength guiding of electromagnetic energy [1, 2]. Recently it has been demonstrated that they can even support backward propagating waves; waves whose phase velocity is in the opposite direction to their group velocity [3, 4, 5].



Figure 1: Model of non-bianisotropic framed resonator as designed by Seetharaman et al where the orange areas are 30 μm of copper. The inner and outer rings have external radii of 16 and 13.6 mm respectively, thickness of 1.2 mm and a split size of 1.5 mm. The frame has an inner radius of 17.2 mm, a height of 37 mm and a width of 38.5 mm.

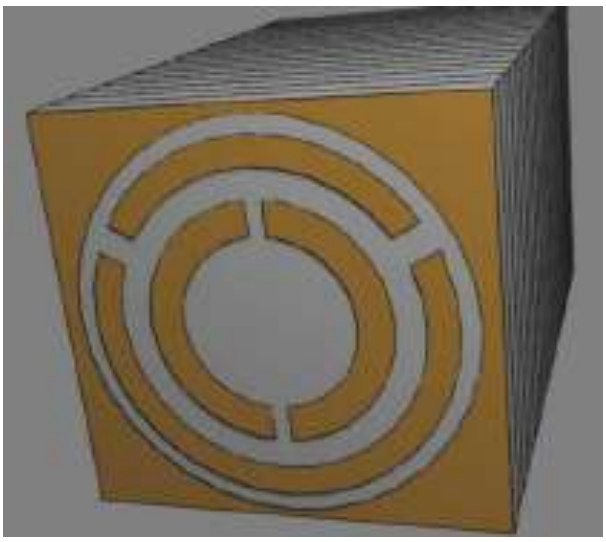


Figure 2: Chain of symmetry broken framed resonators.

Though chains of meta-atoms that support both forward and backward propagating waves are possible, to our knowledge these have previously always occurred within different frequency bands. Here we present a design that supports forward and backward going modes within the same frequency band, allowing us to probe their interactions.

2. Design & Methods

We use a variant of a meta-atom investigated by Seetharaman et. al. [5] that supports a backwards propagating wave over a wide bandwidth. By taking the negative of that structure we obtain the meta-atom design shown in Figure 1. The outer metallic frame of this meta atom supports a backward propagating wave, whilst the inner ring structure supports a forward propagating wave. Importantly, this structure can be designed so that the frequency bands of the different modes overlap.

This meta-atom design is non-bianisotopic, the fields of the forward and backward propagating modes are orthogonal (the forward has only longitudinal magnetic dipole moments, the backward has only transverse electric dipole moments) and thus do not interact with each other. However, by breaking the symmetry through a simple rotation of the splits of the outer ring, we can controllably introduce bianisotropy. This results in the modes coupling together to

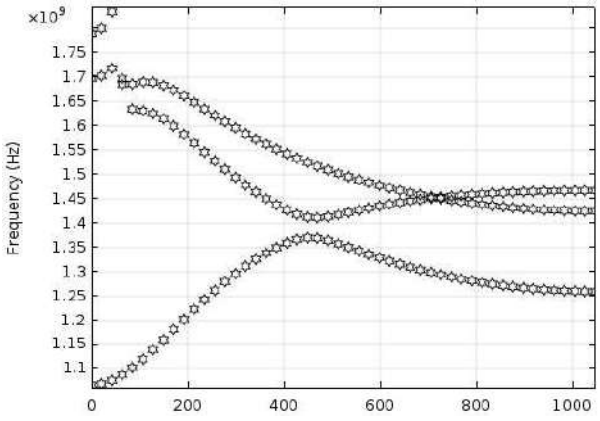


Figure 3: Modelled dispersion of a chain of broken symmetry framed split rings stacked with a period of 3 mm. Anti-crossing between backwards propagating mode and forwards propagating mode can be seen at a k value of 450 m^{-1}.

produce anti-crossing.

3. Results

Figure 3 shows the modelled band-structure of an infinite chain of our meta-atom design. A clear anti-crossing at a wavevector of approximately 450 m^{-1} is evident between two of the modes. The additional mode corresponds to a dipolar mode associated with the frame, oriented in the direction in which symmetry has been maintained; as a result it does not interact with the forward propagating mode and they cross at approximately 700 m^{-1}.

Intriguingly, since the anti-crossing is a result of an interaction between a forward and backward propagating mode (as opposed to the usual case where it is between two forward propagating modes, or a forward propagating mode and a stationary mode), the anti-crossing exhibits band edges with zero group velocity *within the Brillouin zone*. This character would usually be associated with bandgaps formed at Brillouin zone boundaries due to counter-propagating modes resulting from scattering due to the periodic nature of the structure. Achieving this behaviour within the Brillouin zone may be of significant interest to researchers interested in slow light, pulse-shaping, etc.

4. Summary

We have demonstrated a 1D waveguide formed of a periodic chain of meta-atoms that exhibits an anti-crossing between forward and backward propagating modes *within it's Brillouin zone*. The band edges of this anti-crossing have zero group velocity and resemble the bandgaps one usually finds at the Brillouin zone boundary of periodic systems. These results may be of significant interest to researchers working in the fields of slow light, pulse shaping, etc. However, more generally it is a highly unusual phenomenon that researchers in other areas of solid-state physics may also find intriguing. Further work to test the results of this numerical modelling through experiment are currently underway.

5. Acknowledgements

We acknowledge financial support from the Engineering and Physical Sciences Research Council (EPSRC) of the United Kingdom, via the EPSRC Centre for Doctoral Training in Metamaterials (Grant No. EP/L015331/1). W.L.B. acknowledges the support of the European Research Council through project Photmat (ERC-2016-AdG-742222). I.R.H. acknowledges support from the EPSRC via the TEAM-A prosperity partnership (Grant No. EP/R004781/1). We would also like to thank Sathya Sai Seetharaman for his help and advice.

References

[1] E. Shamonina, V. Kalinin, K. H. Ringhofer, and L. Solymar, "Magnetoinductive waves in one, two, and three dimensions," *Journal of Applied Physics*, vol. 92, 11 2002.

[2] E. Shamonina and L. Solymar, "Magneto-inductive waves supported by metamaterial elements: components for a one-dimensional waveguide," *J. Phys. D: Appl. Phys*, vol. 37, pp. 362–367, 02 2004.

[3] V. G. Veselago, "The electrodynamics of substances with simultaneously negative values of ϵ and μ," *Soviet Physics Uspekhi*, vol. **10**, p. 509, 1968.

[4] J. B. Pendry, A. J. Holden, D. J. Robbins, and W. J. Stewart, "Magnetism from conductors and enhanced nonlinear phenomena," *IEEE Transactions on Microwave Theory and Techniques*, vol. **47**, p. 2075, 1999.

[5] S. S. Seetharaman, B. Tremain, W. L. Barnes, and I. R. Hooper, "Realizing an ultra-wideband backward-wave metamaterial waveguide," *Phys. Rev. B*, vol. 98, p. 235408, Dec 2018. [Online]. Available: https://link.aps.org/doi/10.1103/PhysRevB.98.235408

Synthetic Biological Approaches for the Fabrication of Optical Metamaterials

***Simon Butler[1], Prof. Rebecca Seviour[1]**

[1]School of Computing and Engineering, University of Huddersfield, West Yorkshire, UK
*corresponding author, E-mail: simon.butler@hud.ac.uk

Abstract

Conventional nanofabrication techniques lack the throughput and fidelity to create large scale metamaterial structures capable of operating in the optical regime [1]. Synthetic biological approaches can create nanometer feature size [2] DNA based nanostructures with throughput in the region of over a million individual constructs, per reaction, with high fidelity [3]. We present a pathway for the design of arbitrary, via a modular DNA origami circuit/breadboard, and fabrication, of continuously metalised, 10 nanometer feature size structures by someone unfamiliar with the methodology.

Introduction

As described by Pendry [4] a metamaterial must have a period cell significantly smaller than any specific wavelength of interest. As the optical regime lies, roughly, between 400 and 800 nanometres in wavelength, any metamaterial operating in this range would need to be between 40 and 160 nanometres in size (Assuming a unit cell between 5 and 10 times smaller than the wavelength). This caveat of optical metamaterial creation means that their construction sits firmly within the boundaries of nanofabrication (Where we define nanofabrication as the creation of an artefact with at least 1 feature size of less than 100 nanometres).

Currently all conventional nanofabrication systems suffer from the same broad limitations, where throughput is limited by our ability to either create a completely defined system (Where nanofabrication approaches atomic definition), or wield external force in a manner capable of reproducibly modifying the system (Or accurately modifying enough systems within a time frame to make the approach viable).

Originally demonstrated by rothemund [5] scaffolded DNA origami, where a single, none repeating strand of DNA, typically created by biological systems, such as a harmless viral plasmid, can be annealed by smaller, chemically synthesised sequences, creating tension and causing a rigid super structure to be formed of both scaffold and staples.
However, DNA, while useful for construction/scaffolding, is electromagnetically inert and only exists stably in the, comparatively, mild environments dictated by physiological condition with few minor exceptions. For a material to be readily incorporated into DNA Origami based design, in a site specific manner, it must first be somehow complemented by its own unique DNA sequence. Mirkin first demonstrated that DNA sequences ended with sulphur containing thiol groups [6] could attach directly to the surface of a gold nanoparticle, once a gold nanoparticle, or any functional moiety stable in DNAs buffers solution or ultra purified water, has a DNA sequence attached it can be site specifically annealed to a DNA origami design [7].

1. Design – Metamaterial

As the rough size of individual unit cells is already stipulated by our metamaterial definition HFSS simulations were conducted on a split ring resonator design within our fabrication capabilities.

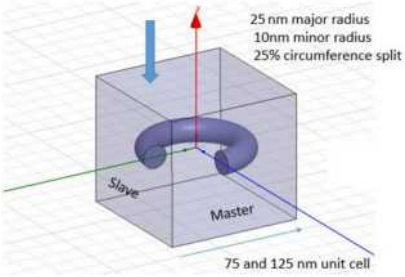


Figure 1 A single resonator in its unit cell

HFSS was used to simulate exposure of an infinite 2D sheet of these structures (Fig 1) to EM waves of interest. From these simulations scattering parameters (S11 and S21) were be recovered.

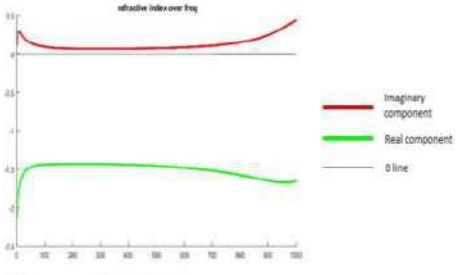


Figure 2 The real (Green) and imaginary (Red) components of the refractive index over the frequency range of 1 – 1000 terahertz

The components of the refractive index (Fig 2) were then recovered using a modified Nicholson-Ross-Weir approach described by Smith [8].

2. Design – Origami Board

We use the P7249 scaffold and ~200 smaller staples strands to create a 50 x 50 x 2 nanometer breadboard. Interhelical crossovers points, facilitated by staple strands, give structure to the longer scaffold sequence, while functional points, where components are attached, are created by simply extending the existing staples out into the area around an individual origami design.

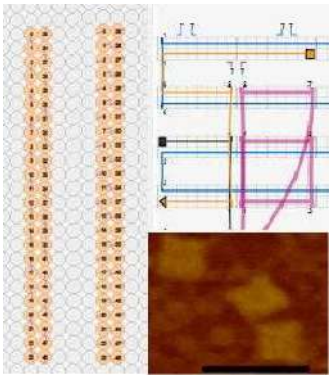


Figure 3 left - a caDNAno blueprint of the relative helical pitch of the 24 helices, which comprise the board, at 2 points. Top right – an example of how staples (colours) anneal the scaffold into shape by joining spatially distant region and giving the structure rigidity and can also leave the design to anchor artificial groups to the structure. Bottom right – AFM image (Black bar = 100 nanometers) of the naked DNA origami boards themselves

Both crossovers and functional points take advantage of the naturally occurring helical pitch of a DNA helix (Fig 3). As the antiparallel helix progresses base by base it will come into close proximity to its neighbouring strands, or conversely, be travelling parallel to the edge of the structure. It is at these points that crossovers and functional points can be placed effectively without disrupting the overall structure of the final design.

As individual DNA bases bind only via their 5' carbon to their neighbours 3' carbon a DNA sequence is effectively directional. Wherever a sequence is extended to 'leave' the origami its neighbour can also be extended in a similar manner to 'enter'. This method allows close proximity anchoring points to be created, and several sequences used to bind single nanoparticles, with high precision, and reliable attachment rates.

3. Fabrication

Fabrication can be divided into 3 stages: Fabrication of the DNA origami board, synthesis and functionalisation of gold nanoparticles, and then the purification of any created structures from their respective fabrication components, leaving a solution containing only correctly fabricated structures.

The origami board is fabricated by adding all required staples strands to a scaffold solution, under specific ionic conditions followed by a specific thermal ramp cycle. Thermal ramping begins at a temperature where all hydrogen bonding between strands breaks down, and is then lowered gradually to a specific molten globular folding point where, hydrogen bonding is restored, and most folding occurs.

Once the origami stuctures have been fabricated they must be separated from all remaining fabrication components. A common issue preventing correct fabrication is the presence of DNA strands with complementing sequences to functional groups still being present in solution but not attached to an origami structure. If this is the case, due to their relatively high mobility compared to their sisters anchored in boards, they will attach to complementing sequences must quicker, preventing correct attachment by competitive inhibition. Fig.2 shows a sample which has been purified from its fabrication components and is ready to go on to be functionalized with nanoparticles.

Synthesis of gold nanoparticles is conducted via an inverse Turkevich approach [9] which produces stable, polydisperse, 10 nanometer gold nanoparticles.

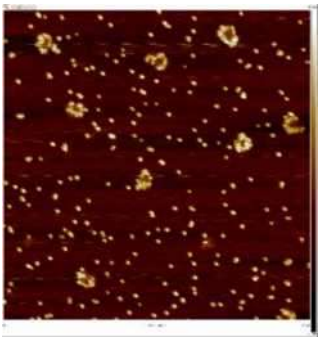


Figure 4 An AFM image (1 x 1 micrometer) of a sample of the gold nanoparticle and DNA origami fabrication solution. Gold nanoparticles are attached to DNA origami boards but excess gold nanoparticles still need to be purified from the sample

Once purified, functionalized, gold nanoparticles, and DNA origami boards are fabricated they are conjugated in solution by incubation at room temperature (Fig 4). This solution can be concentrated via centrifuge.

Conclusion

We present the principles and methodology, along with a detailed report/supplementary paper, which precisely details the protocols, and methods to identify protocols when deviation from our device is required, we use to fabricate continuously metalised origamis.

References

[1] X. Zhao, Bottom-up fabrication methods of optical metamaterials, *J*. *Mater*. *Chem* 22: 9439-9449, 2012.

[2] H. Li, J.-D. Carter, T.-H. LaBean, Nanofabrication by DNA self-assembly, *Materialstoday*, 12: 24-32, 2009.

[3] J. Sobczak, T. Martin, T. Gerling, H. Dietz, Rapid Folding of DNA into Nanoscale Shapes at Constant Temperature, *Science*, 338: 1458-1461, 2012.

[4] J. Pendry, Negative Refraction Makes a Perfect Lens, *Phys*. *Rev*. *Lett*, 85: 3966, 2000.

[5] P. Rothemund, Folding DNA to create nanoscale shapes and patterns, *Nature*, 440: 297-302, 2006.

[6] Z. Li, R. Jin, C.-A. Mirkin, R.-L, Letsinger, Multiple thiol-anchor capped DNA-gold nanoparticle conjugates, *Nucleic Acids Research*, 30: 1558-1562, 2002.

[7] A. Kuzyk, R. Schreiber, Z. Fan, G. Pardatscher, E. Roller, A. Hogele, F. Simmel, A. Govorov, T. Liedl, DNA-based self-assembly of chiral plasmonic nanostructures with tailored optical response, *Nature*, 483: 311-314, 2012.

[8] D. Smith, D. Vier, T. Koschny and C. Soukoulis, Electromagnetic parameter retrieval from inhomogeneous metamaterials, *Physical Review E*, 71, (2005)

[9] S.-K. Sivaraman, S. Kumar, V, Santhanam, Monodisperse sub-10nm gold nanoparticles by reversing the order of addition in Turkevich method—the role of chloroauric acid., *J Colloid Interface Sci*, 361:543-547, (2011)

Complex Band Structure and Dispersion Relation of Acoustic Waves in Piezoelectric Based Topological Phononic Crystals

Selami Palaz[1], Zafer Ozer[2], Sevket Simsek[3], Husnu Koc[4], Amirullah M. Mamedov[5,6,*], and Ekmel Ozbay[5]

[1]Department of Physics, Harran University, Sanliurfa, Turkey
[2]Mersin Vocational High School, Mersin University, Mersin, Turkey
[3]Department of Materials Science and Engineering, Hakkari University, Hakkari, Turkey
[4]Department of Department of Physics, Siirt University, Siirt, Turkey
[5]Nanotechnology Research Center (NANOTAM), Bilkent University, Ankara, Turkey
[6]International Scientific Center, Baku State University, Baku, Azerbaijan
*corresponding author, E-mail: mamedov@bilkent.edu.tr

Abstract

In present work, the acoustic band structure of a 2D phononic crystal (PC) containing piezoelectric materials ($Bi_{12}XO_{20}$, X=Si, Ge, Ti; $LiTaO_3$) were investigated by the finite element method. 2D PC with triangular and honeycomb lattices composed of piezoelectric cylindrical rods are in the air and liquid matrix. The existence of stop bands are investigated for the waves of certain frequency ranges. This phononic band - forbidden frequency range - allows sound to be controlled in many useful ways in structures. These structure can be used as sonic filters, waveguides or resonant cavities. The calculated phonon dispersion results indicate the existence of full acoustic modes in the proposed structure along the high symmetry points. We have also calculated the band structures of the different types of unit cells that are yielded by space group symmetry operations of the triangular resonators. The results show that these acoustic metamaterials with Helmholtz resonators can be used successfully to reduce the Dirac cone frequencies. Dirac cone frequency decreases gradually with increasing filling ratio, which indicates a possible way to control wave propagation on the subwavelength scale. Numerical simulation results show that acoustic metamaterials can behave like zero-refractive-index media and can be applied to acoustic tunneling.

In present work, the elastic and mechanical properties of piezoelectric materials have been investigated by means of first principles calculations, too. The elastic constants of these materials were calculated using the strain-stress method as implemented in the VASP. The bulk modules, shear modules, Young's modulus and Poisson ratios, anisotropy factors, sound velocities, and Debye temperatures of investigated piezoelectric compounds have been calculated using VASP.

Split Ring Resonator Loaded Double Opposite E-shaped Left-Handed Metamaterial for Modern Electronic Communications

Ahmed Mahfuz Tamim[1*], Mohammad Rashed Iqbal Faruque[1*], Mohammad Tariqul Islam[2]

[1] Space Science Centre (ANGKASA), Universiti Kebangsaan Malaysia, Bangi, Selangor, MALAYSIA.
[2] Centre of Advanced Electronic and Communication Engineering, Universiti Kebangsaan Malaysia, Bangi, Selangor, MALAYSIA.
*corresponding author, E-mail: tamim_mahfuz@yahoo.com, rashed@ukm.edu.my

Abstract

A compact double opposite E-structured metamaterial emerged on split ring resonator (SRR) is introduced and discussed for quad-frequency applications. CST Microwave Studio software has been utilized for the design and simulation perspectives. The unit cell is formed by etching copper on FR4 and its size is 11.12×11.12 mm^2. The unit cell shows both the characteristics of negative refractive index and double-negative characteristics. The metamaterial unit cell has SAR reduction about 84% and 78% for 1gm and about 91% and 90% for 10gm at 1768 MHz and 2164 MHz, respectively. These results proceed to a guideway of better SAR reduction of modern electronic communications.

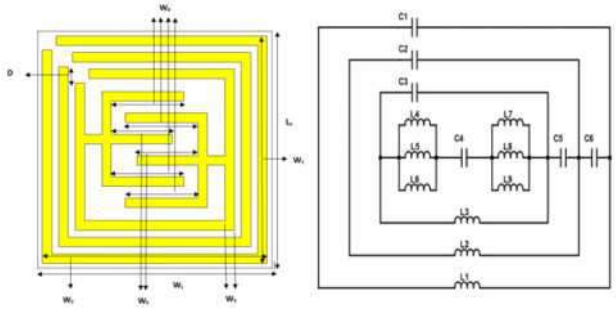
1. Introduction

Electromagnetic (EM) metamaterials, with their extraordinary properties which cannot be obtained in most naturally existing materials, have been shown tremendous potentials in many fields of science and technology [1]. These properties are negative permeability, negative permittivity, and negative refractive index [2]. Due to these properties, nowadays metamaterials have been using in different applications like super lenses [3], invisible cloaking [4], antenna performance enhancement, SAR reduction [5] etc.

SAR is the estimation of the electromagnetic field (EMF) of higher radio frequency (RF) consumed by the human body when utilizing an electronic or communication gadget. This rate is estimated in a standard estimation of watts per kilogram (W/Kg) as the power observed inside a characterized region of body tissue. SAR measures 100 KHz to 10000000 KHz frequency range exposure that includes electronic and communication devices such as laptops, smart mobile phones, and WiFi routers etc.

2. Design of Unit Cell

The structural design of the metamaterial unit cell has been shown in Figure 1 along with the parameters present in Table 1. Copper (Annealed) has been used as conducting element which is etched on the FR4 dielectric material. The following unit cell is developed by creating EF-structure surrounded by SRR which is added to create the negative permeability along with the negative permittivity.



(a) (b)

Figure 1: (a) Configuration of unit cell (b) Equivalent circuit of the unit cell.

Table 1: Parameters of the EF-structured meta-atom.

Parameters	Values (mm)	Parameters	Values (mm)
W_s	11.12	W_2	10.2
L_s	11.12	W_3	0.45
D	2.22	W_4	3.45
W_1	10.2	W_5	2.89

3. Methodology and Experimental Setup

High frequency electromagnetic simulation software has been used to design, simulation, and SAR evaluations of the metamaterial unit cell. Experimental set up has been done as like a simulation setup where the unit cell has been set on between the two waveguides of negative and positive sides of Z - axis. Limit states of perfect electrical field and perfect magnetic field has been set independently to the X – and Y - axis. Measurement has been done from 1 to 7 GHz.

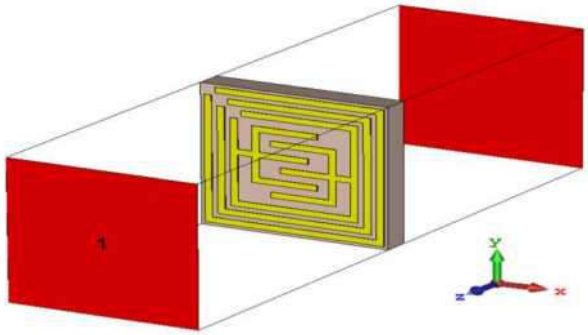


Figure 2: Simulation of unit cell between two waveguides.

While diverse sorts of strategies are accessible, the Nicolson-Ross-Weir (NRW) has been used to extract the permittivity and permittivity from the S_{11} and S_{21}.

4. Results and Discussions

Transmission coefficient (S_{21}) of the introduced metamaterial unit cell has been presented in Figure 3. The unit cell shows resonance at frequencies at 1768 MHz, 2164 MHz, 4780 MHz, and 5860 MHz having values of -23.62 dB, -19.24 dB, -24.76 dB, -22.41 dB, respectively.

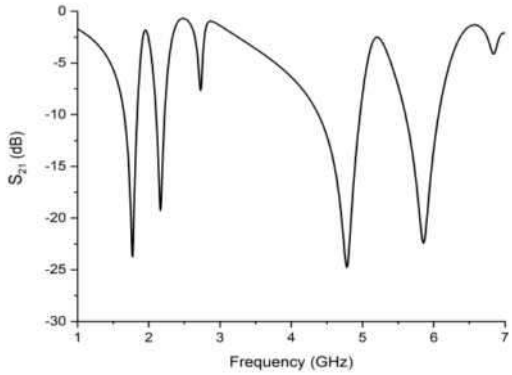


Figure 3: Transmission characteristics (S_{21}) of meta-atom in dB.

The unit cell metamaterial additionally displays double-negative properties over the frequency ranges from 3.934–4.576 GHz, 5.17–5.488 GHz, 6.286–6.784 GHz and negative refractive index from 3.142–7 GHz.

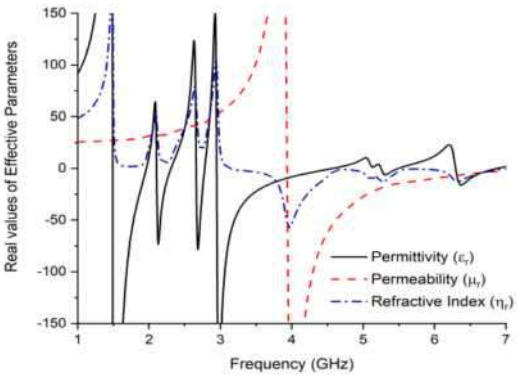
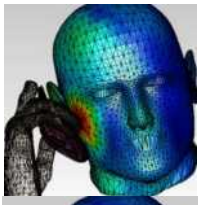
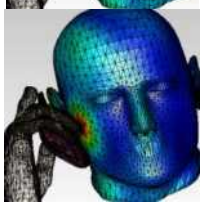


Figure 4: Real values of effective permittivity, permeability, and refractive index

4.1. SAR Evaluations

SAR performances has been investigated by placing the unit cell into the mobile phone phantom model to check compatibility of it for using it with the modern mobile phones. The metamaterial unit cell has electromagnetic absorption rate about 84% and 78% at 1768 MHz and 2164 MHz, respectively for 1gm whereas it has reduction rate about 91% and 90% at 1800 1768 MHz and 2164 MHz, respectively for 10gm.

Frequency (MHz)	Visual Model	Value of SAR (W/kg)	
1768		1gm	0.26
		10gm	0.173
2164		1gm	0.352
		10gm	0.21

5. Conclusions

In this article, a novel SRR loaded double opposite E-shaped metamaterial is presented which is applicable in quad-frequency applications. The metamaterial unit cell has a high effective medium ratio of about 14.82. The metamaterial also exhibits double-negative properties along with negative refractive index over the frequency ranges. The meta-atom has average SAR reduction about 85%. Overall, a novel unit cell metamaterial has been presented where the compactness of the size of the meta-atom and its performances makes it compatible to use for the applications of 1768 MHz, 2164 MHz, 4780 MHz, and 5860 MHz i.e. for digital cellular system (DCS), earth exploration-satellite communications (EESC), lower band 5G mobile communications, and WiMAX applications, respectively.

Acknowledgements

This work was supported by the Research Universiti Grant, Universiti Kebangsaan Malaysia, Geran Universiti Penyelidikan (GUP), code: 2018-133.

References

[1] Vendik, I. B., & Vendik, O. G. (2013). Metamaterials and their application in microwaves: A review. *Technical physics*, *58*(1), 1-24.

[2] Veselago, V. G. (1968). The electrodynamics of substances with simultaneously negative values of and μ. *Soviet physics uspekhi*, 10(4), 509.

[3] Park, J. J., Park, C. M., Lee, K. J. B., & Lee, S. H. (2015). Acoustic superlens using membrane-based metamaterials. *Applied Physics Letters*, 106(5), 051901.

[4] Islam, S. S., Faruque, M. R. I., & Islam, M. T. (2016). An object-independent ENZ metamaterial-based wideband electromagnetic cloak. *Scientific reports*, 6, 33624.

[5] Faruque, M. R. I., & Islam, M. T. (2014). Design of miniaturized double-negative material for specific absorption rate reduction in human head. *PloS one*, *9*(10), e109947.

Much Ado About Nothing: Applying a Metamaterial Model with Negative Energy to Address the Vacuum Catastrophe

Thomas P. Weldon and Kathryn L. Smith*

Department of Electrical and Computer Engineering, University of North Carolina at Charlotte, Charlotte, NC, USA
*corresponding author, E-mail: Kathryn.Smith@uncc.edu

Abstract

The vacuum catastrophe remains one of the great enigmas of physics, with more than 50 orders of magnitude separating the observed nanojoule per cubic meter vacuum energy from the theoretical electromagnetic quantum vacuum energy density. Toward bridging this wide gap, we consider an unconventional model for the vacuum using hypothetical metamaterial foam including pockets having negative parameters and negative energy density. The proposed metamaterial properties are selected to preserve normal vacuum behavior after homogenization.

1. Introduction

The vacuum catastrophe remains one of the great unsolved problems in physics, where astronomical observations provide a measured vacuum energy density of $\sim\ 6.4 \times 10^{-10}$ J/m^3 compared to the predicted theoretical electromagnetic quantum vacuum energy density of $\sim\ 10^{114}$ J/m^3, with a ratio of $\approx\ 1.6 \times 10^{123}$ [1, 2]. More recently, the discrepancy has been reduced to 54 orders of magnitude in Martin [3]. This huge disparity suggests that any resolution of this problem is likely to require a substantial deviation from existing theory, rather than some modest adjustment to existing theory. We therefore investigate an unorthodox metamaterial model of vacuum, where vacuum is comprised of a metamaterial foam including pockets that have negative parameters and negative energy density.

2. Metamaterial Model of Vacuum

Our proposed model is in part motivated by "space-time foam" notions in certain quantum gravity models, and by earlier investigation of the role of dispersive "foamy" vacuum models in resolving observation of the late arrival of high-energy gamma rays in short gamma bursts [4, 5]. For our vacuum-catastrophe model, we similarly propose a "foamy" structure for the vacuum, where the vacuum is a metamaterial comprised of a mixture of regions having positive and negative permeability and permittivity (and possibly gain or loss) and positive and negative energy densities. The resulting proposed "foamy-vacuum metamaterial" (FVM) must exhibit the normal properties of vacuum, but with the added feature of eliminating the vacuum catastrophe error factor of $\approx 10^{54}$.

In one possible embodiment of the proposed FVM, the metamaterial foam illustrated in Fig. 1 can be comprised of sub-wavelength regions with negative relative permittivity $\epsilon_{rn} \ll 0$ and permeability $\mu_{rn} \ll 0$ embedded in a medium with relative permittivity $\epsilon_{rp} = 1 - \epsilon_{rn}$ and permeability $\mu_{rp} = 1 - \mu_{rn}$. For this example, if the negative regions occupy 50% of the volume, the effective permittivity and permeability of the composite would be $\epsilon_r = 1$ and $\mu_r = 1$ and equivalent to vacuum [6]. Here, the primary motivation for the new model is to divide space into an embedding positive index that contains regions of negative index, where the positive-index regions have very large positive energy densities and very large negative energy densities respectively. Such negative energy densities have been proposed by a number of investigators [7, 8]. Importantly, the average energy density at large scales can be much smaller than the local energy densities when the positive and negative densities nearly cancel each other. The primary motivation is that this model may then simultaneously support the lower energy densities associated with astronomical observations of $\sim\ 6.4{\times}10^{-10}$ J/m^3 along with localized high energy densities that may be associated with the $\approx 10^{54}$ larger quantum vacuum energy densities.

In the foregoing example, the overall medium should not suffer from dispersion issues, since $\epsilon_r = 1$ and $\mu_r = 1$. Although the model includes large local field energies, the total average energy at large scale would equal the observed zero-point or vacuum energy. In essence, passivity and energy conservation are taken to be phenomena applicable at larger scale. Depending on the nature of the underlying metamaterial unit cells and quantum concentrations, it



Figure 1: Illustration of vacuum metamaterial model. The foamy vacuum metamaterial model consists of subwavelength regions (illustrated as spheres above) with different relative permittivity and permeability than the embedding medium, such that the overall medium exhibits the normal vacuum parameters $\epsilon_r = 1$ and $\mu_r = 1$.

seems possible that the distribution of energies could be similar to Boltzman, Bose-Einstein, or Fermi-Dirac statistics, but somehow recast in a manner to properly accommodate local negative energy densities.

3. Field Energy Considerations

The primary goal of the proposed model is to provide the large energy densities in line with electromagnetic quantum vacuum energy, while retaining the low vacuum energy density at large scale, consistent with astronomical observations. In a region with no sources, Poynting's theorem is

$$\oint \mathbf{E} \times \mathbf{H} \cdot \partial s = -\int \left(\mathbf{E} \cdot \frac{\partial \mathbf{D}}{\partial t} + \mathbf{H} \cdot \frac{\partial \mathbf{B}}{\partial t} \right) \partial v \, . \quad (1)$$

With $\mathbf{D} = \epsilon_{rp}\epsilon_\circ \mathbf{E}$ and $\mathbf{B} = \mu_{rp}\mu_\circ \mathbf{H}$, Poynting's theorem in the positive-index regions is then

$$\oint_p \mathbf{E} \times \mathbf{H} \cdot \partial s = \\ -\int \epsilon_{rp}\epsilon_\circ \mathbf{E} \cdot \frac{\partial \mathbf{E}}{\partial t} \partial v - \int \mu_{rp}\mu_\circ \mathbf{H} \cdot \frac{\partial \mathbf{H}}{\partial t} \partial v \, . \quad (2)$$

Similarly, Poynting's theorem in the in the negative-index regions with $\mathbf{D} = \epsilon_{rn}\epsilon_\circ \mathbf{E}$ and $\mathbf{B} = \mu_{rn}\mu_\circ \mathbf{H}$ is

$$\oint_n \mathbf{E} \times \mathbf{H} \cdot \partial s = \\ -\int \epsilon_{rn}\epsilon_\circ \mathbf{E} \cdot \frac{\partial \mathbf{E}}{\partial t} \partial v - \int \mu_{rn}\mu_\circ \mathbf{H} \cdot \frac{\partial \mathbf{H}}{\partial t} \partial v \, . \quad (3)$$

Finally, Poynting's theorem in a composite region (overlapping many spheres and their embedding regions in Fig. 1) with effective relative permittivitty and permeability $\epsilon_r = 1$ and $\mu_r = 1$ is simply given as in (1). As noted above, the proposed model is designed to support localized high energy densities within the spheres and within the embedding regions, as may be associated with the large quantum vacuum energy density. Furthermore, the model is also designed to simultaneously present the much lower average energy densities of astronomical observations within composite volumes comprised of both materials.

As a first approximation, suppose that the terms associated with the magnetic and electric field components are of similar proportion in (2) and (3). Next, let $\epsilon_{rn} \ll 1$, $\epsilon_{rp} = 1 - \epsilon_{rn}$, and $\mu_{rp}/\epsilon_{rp} = \mu_{rn}/\epsilon_{rn} = 1$. Then, to have the ratio of local energy density to large-scale energy density be $\approx 10^{54}$, would require $\epsilon_{rp} \approx -\epsilon_{rn} \approx 10^{54}$, and similarly $\mu_{rp} \approx -\mu_{rn} \approx 10^{54}$. The large-scale energy density over a large spatial volume would be $\approx 10^{54}$ times smaller, since $\epsilon_{rp} + \epsilon_{rn} = 1$ and $\mu_{rp} + \mu_{rn} = 1$ after homogenization over large regions.

Beyond the foregoing example, more complicated redistribution of local energies between electric and magnetic fields could be possible, but in even the most extreme redistribution of local electric and magnetic energy, at least one parameter would be of the order $\approx 10^{54}$. In addition, the results clearly do not depend on a 50% volume fraction. Lastly, retaining an average effective medium with $\epsilon_r = 1$ and $\mu_r = 1$ down to Planck scale may require the unit cells to be less than the Planck length of 1.5×10^{-35} m.

4. Conclusion

A metamaterial model for vacuum has been presented as a possible avenue to explain the $\approx 10^{54}$ ratio of theoretical and experimental energy densities known as the vacuum catastrophe. The model preserves the measured large-scale permittivity, permeability, and measured energy density of vacuum, while locally admitting energy densities $\approx 10^{54}$ larger than the large-scale average energy density.

Acknowledgement: This material is based upon work supported by the National Science Foundation under Grant No. 1731675.

References

[1] R. J. Adler, B. Casey, and O. C. Jacob, "Vacuum catastrophe: An elementary exposition of the cosmological constant problem," *American Journal of Physics*, vol. 63, no. 7, pp. 620–626, 1995.

[2] G. J. Maclay, H. Fearn, and P. W. Milonni, "Of some theoretical significance: implications of Casimir effects," *European Journal of Physics*, vol. 22, no. 4, p. 463, 2001.

[3] J. Martin, "Everything you always wanted to know about the cosmological constant problem (but were afraid to ask)," *Comptes Rendus Physique*, vol. 13, no. 6, pp. 566 – 665, 2012.

[4] J. Ellis, N. Mavromatos, and D. Nanopoulos, "Derivation of a vacuum refractive index in a stringy space–time foam model," *Physics Letters B*, vol. 665, no. 5, pp. 412 – 417, 2008.

[5] T. P. Weldon, R. S. Adams, K. Daneshvar, and R. K. Mulagada, "Metamaterials, gamma-ray bursts, quantum gravity, and the search for the missing half of the Maxwell equations," in *IEEE MTT-S Int. Microw. Symp. Dig.*, Jun. 2011.

[6] A. Alù, A. D. Yaghjian, R. A. Shore, and M. G. Silveirinha, "Causality relations in the homogenization of metamaterials," *Phys. Rev. B*, vol. 84, p. 054305, Aug. 2011.

[7] Shivanand and K. J. Webb, "Electromagnetic field energy density in homogeneous negative index materials," *Opt. Express*, vol. 20, no. 10, pp. 11 370–11 381, May 2012.

[8] R. W. Ziolkowski, "Superluminal transmission of information through an electromagnetic metamaterial," *Phys. Rev. E*, vol. 63, p. 046604, Mar. 2001.

Near Perfect Absorption in Epsilon Near Zero Thin Films

Stephen O'Brien[1,2], Frank Bello[1,2], Lisanne Peters[1,2], Niall McEvoy[2], David McCloskey[1,2], John Donegan[1,2]

[1]School of Physics, Trinity College Dublin, Dublin 2, Ireland
[2]AMBER, Trinity College Dublin, Pearse Street, Dublin 2, Ireland

Abstract

We report a study of ENZ behavior in thin-film ITO samples by exciting the Ferrell-Berreman mode. We excite this mode in ITO films on glass, and ITO films with a 10 nm Pt metal backing. We demonstrate that the presence of this 10 nm Pt backing significantly enhances the absorption from this mode from 52.6% without to 89.9% with the metal.

1. Introduction

Epsilon-near-zero metamaterials are materials that exhibit a zero or near-zero dielectric permittivity, ε in their dispersion. The novel physics of these materials have been studied theoretically and experimentally including effects such as infinite phase velocity[1], reduced group velocity[2], super-coupling[3], and a decoupling of electricity magnetism[4] have all been reported. Of particular interest is the ability to achieve perfect, or near perfect absorption[5] about the ENZ region, attributed to the excitation of a bulk plasmon polariton mode lying to the left of the light line known as the Ferrell-Berreman mode[6]. Initially it was believed that this mode could only be excited by an ENZ material with a metallic backing, however Campione et al. demonstrated the excitation of this mode on ITO on glass in 2016. We examine the excitation of this mode in thin films of ITO, a transparent conducting oxide with ENZ behavior in the near-infrared.

2. Drude model for ITO

ITO, being a transparent conducting oxide with free electrons can be modelled using the Drude Model.

$$\varepsilon(\omega) = \varepsilon_\infty - \frac{\omega_p^2}{\omega(\omega + i\gamma)} \qquad (1)$$

where ε_∞ is the high frequency permittivity, γ is the scattering rate, and ω_p^2 is the plasma frequency, given by

$$\omega_p = \sqrt{\frac{Ne^2}{m^* \varepsilon_0}} \qquad (2)$$

where N is the carrier concentration and e is the charge of an electron, and m^* is the effective mass of the charge carriers. The ENZ frequency can then be determined using

$$\omega_{ENZ} = \sqrt{\frac{\omega_p^2}{\varepsilon_\infty} - \gamma^2} \qquad (3)$$

The ITO films used in this research were purchased from Sigma Aldrich and the Drude parameters were determined by fitting data taken from NIR spectroscopic ellipsometry to a Drude model. The fitted parameters are listed in Table 1.

Table 1: Drude parameters of ITO thin films.

Sample	ε_∞	ω_p (rad fs^{-1})	γ (rad fs^{-1})
8 – 12 Ω sq^{-1}	3.6596	2.95757	0.189305
30 – 60 Ω sq^{-1}	3.15153	2.74525	0.278178
70 – 100 Ω sq^{-1}	2.82058	2.63297	0.325611

3. Transfer matrix method for multilayer structures

The structures studies in the research are composed of multiple thin films layers and due to this we use a technique known as the transfer matrix method to model the reflection and transmission from the multilayered ENZ structure. The transfer matrix method examines the reflected (E^+) and transmitted (E^-) components of the incident TM polarized electric field at the boundaries of the layer i and $i+1$ for the film of thickness d. The propagation of the electric field through successive layers can be described using a 2×2 transfer matrix, $M_{i,i+1}$, which is composed of the Fresnel reflection and transmission coefficients.

$$\begin{pmatrix} E_i^+ e^{ik_{z_i} d_i} \\ E_i^- e^{-ik_{z_i} d_i} \end{pmatrix} = \begin{pmatrix} 1/t_{i,i+1} & r_{i,i+1}/t_{i,i+1} \\ r_{i,i+1}/t_{i,i+1} & 1/t_{i,i+1} \end{pmatrix} \begin{pmatrix} E_{i+1}^+ e^{ik_{z_{i+1}} d_{i+1}} \\ E_{i+1}^- e^{-ik_{z_{i+1}} d_{i+1}} \end{pmatrix} \qquad (4)$$

Here k_{z_i} is the wavevector normal to the incident plane of the layer and is given by

$$k_{z_i} = \sqrt{\frac{\varepsilon_i \omega^2}{c^2} - k_0^2 \varepsilon_i \sin^2 \theta_i} \qquad (5)$$

where k_0 is the wavevector incident from free space. The transfer matrix of the overall structure then be obtained by taking the product of the successive transfer matrices for each layer, i.e.

$$T = \prod_i M_{i,i+1} \qquad (6)$$

From this, the reflection and transmission coefficients for the composite structure can be determined and the absorption can be determined by taking 1 – R – T.

4. Results & Discussion

Figure 1 compares experimental data (a) for ITO thin films of thicknesses 127 nm, 17, nm, and 11 nm for samples 8 – 12, 30 – 60, and 70 – 100 Ω sq^{-1} respectively. There is a region of particularly low reflection in the wavelength range 1000 – 1200 nm and between 30° – 70° incidence. The samples were excited from air from the ITO side and this region of low reflectivity is attributed to the excitation of the Ferrell-Berreman mode of ITO. Figure 1(b) shows the T-matrix simulations using the fitted Drude parameters from

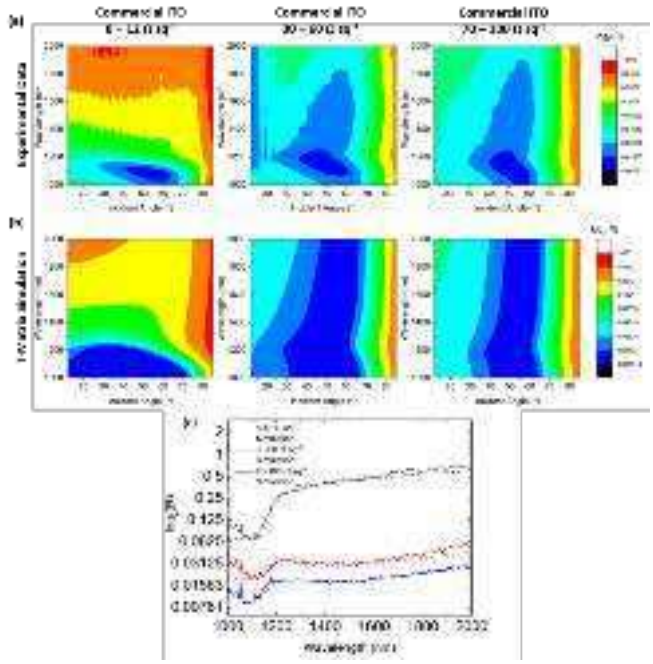


Figure 1 Experimental data for the angle-resolved reflectivity of ITO films purchased from Sigma Aldrich. The films are quoted in terms of their sheet resistance range, 8 – 12, 30 – 60, and 70 – 100 Ω sq^{-1} with thicknesses 127 nm, 17 nm, and 11 nm respectively. (b) The corresponding T-matrix simulations and (c) a comparison of experimental and simulated reflectivities at 53˚.

Table 1. There is high agreement between experiment and simulation, demonstrating that these simple models can be used in conjunction to model the ENZ behavior of ITO films. There is some minor disagreement in the relative values, however this is attributed to the limits of detection of the apparatus used. From this, the reflection and transmission coefficients for the composite structure can be determined and the absorption can be determined by taking 1 – R – T. Figure 1(c) compares simulation and experiment for the reflectivity at 53˚ incidence. The reflectivity data is presented on a log scale to aid visibility. Transmission measurements were also taken, and the absorption was determined. The 8 – 12 Ω sq^{-1} sample exhibited the largest absorption and this data is presented in Figure 2(a). The absorption in the ITO film alone was 52.6%. 10 nm of Pt metal was then deposited on the ITO side of the sample using argon ion sputtering with a Gatan PEC system. This sample was then given the same treatment as before. Figure 2(b) shows the absorption for this Pt-backed sample. The presence of the Pt metal causes a significant enhancement in the absorption of the Ferrell-Berreman mode, bringing the absorption from 52.6% without the metal to 89.9% with the metal.

5. Conclusions

We conclude that the relatively simple Drude free-electron model combined with the transfer matrix method can accurately model ENZ behavior in ITO thin films. We also conclude that the Ferrell-Berreman can indeed be excited without the need for a metal backing, but that the metal backing serves to enhance the absorption of light at the NPA wavelength.

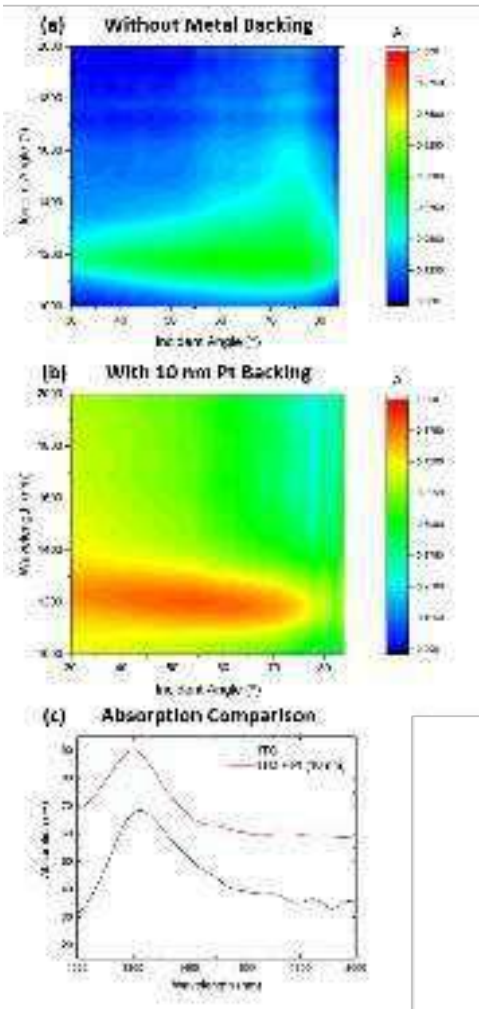


Figure 2(a) Absorption data for an ITO film of 127 nm thickness, (b) absorption data for the same film with 10 nm of PT deposited on the ITO side, and (c) comparison of absorption at 53˚. As shown, there is significant enhancement of the Ferrell-Berreman with the addition of 10 nm of Pt.

Acknowledgements

We would like to acknowledge the financial contribution of Science Foundation Ireland (12/RC/2278) in funding this research.

References

[1] Y. Li *et al.*, "On-chip zero-index metamaterials," *Nat Phot.*, vol. 9, no. 11, pp. 738–742, 2015.

[2] F. Bello, A. F. Page, A. Pusch, J. M. Hamm, J. F. Donegan, and O. Hess, "Combining ε-Near-Zero Behavior and Stopped Light Energy Bands for Ultra-Low Reflection and Reduced Dispersion of Slow Light," *Sci. Rep.*, vol. 7, no. 1, p. 8702, 2017.

[3] A. M. Mahmoud, I. Liberal, and N. Engheta, "Dipole-dipole interactions mediated by epsilon-and-mu-near-zero waveguide supercoupling [Invited]," *Opt. Mater. Express*, vol. 7, no. 2, p. 415, 2017.

[4] I. Liberal, A. M. Mahmoud, and N. Engheta, "Geometry-invariant resonant cavities," *Nat Commun*, vol. 7, 2016.

[5] S. Campione, I. Kim, D. De Ceglia, G. A. Keeler, and T. S. Luk, "Experimental verification of epsilon-near-zero plasmon polariton modes in degenerately doped semiconductor nanolayers," *Opt. Express*, vol. 24, no. 16, pp. 18782–18789, 2016.

[6] W. D. Newman, C. L. Cortes, J. Atkinson, S. Pramanik, R. G. DeCorby, and Z. Jacob, "Ferrell–Berreman Modes in Plasmonic Epsilon-near-Zero Media," *ACS Photonics*, vol. 2, no. 1, pp. 2–7, 2015.

Blueshift in graphene-based hyperbolic metamaterials as a tunable narrowband reflection modulators

Alessandro Pianelli*, Rafal Kowerdziej, Marek Olifierczuk, Karol Sielezin, Michal Dudek, Janusz Parka

Military University of Technology, Faculty of Advanced Technologies and Chemestry, Warsaw, Poland

*corresponding author, E-mail: alessandro.pianelli@wat.edu.pl

Abstract

Here, we examine numerically the hyperbolic metamaterials based on graphene(1D-GHMM) in mid-IR frequencies. Using the ability to tune the hyperbolic dispersion of graphene-based HMM by varying the chemical potential, we report a tunable narrowband blueshift in reflectance, especially for different incidence angle in TE/TM modes. Furthermore, a type II and type I hyperbolic dispersion and an effective metal behavior are presented.

1. Introduction

The hyperbolic metamaterial (HMM) is a new class of uniaxial anisotropic metamaterials that has drawn the attention of several engineers and scientists as one of the most influential media in optical and quasi-optical frequencies. HMMs are classified as Type I and type II. In the case of Type I ($\varepsilon_{\parallel} > 0$ and $\varepsilon_{\perp} < 0$) the materials behaves as a dielectric in the plane xy and as a metal in the z direction. Type II ($\varepsilon_{\parallel} < 0$ and $\varepsilon_{\perp} > 0$) instead has two components of the dielectric tensor negative (in-plane) whereby the HMM behave as a metal [1]. This anisotropic behaviour therefore causes an unusual hyperbolic dispersion for the medium and as a result, many interesting phenomena have been observed as light enhacement [2], sub-wavelength imaging [3] etc. Lately, graphene plasmonics and HMMs based on grapheme (1D-GHMM) have stirred great interest in the scientific community because of the ability of graphene to tune the conductivity by changing the chemical potential (μ) [4-6].

2. Model and theory

The anisotropy of hyperbolic metamaterials can be described by their effective dielectic tensor $\bar{\bar{\varepsilon}} = [\varepsilon_{xx}, \varepsilon_{yy}, \varepsilon_{zz}]$. The dielectric components direction in plane and out-plane to the interface of the 1D-GHMM are $\varepsilon_{xx} = \varepsilon_{yy} = \varepsilon_{\parallel}$ and $\varepsilon_{zz} = \varepsilon_{\perp}$ respectively. The graphene-based HMM consisting of a unit cell (N) of graphene/dielectric (SiO_2) stack. The inset image in the Fig. 1 (a) is possible to see one unit cell (N=1). The value of the tensor components are as follows [7]:

$$\varepsilon_{\parallel} = \frac{t_g\varepsilon_g + t_d\varepsilon_d}{t_g + t_d}, \qquad \varepsilon_{\perp} = \frac{\varepsilon_g\varepsilon_d(t_g + t_d)}{t_g\varepsilon_d + t_d\varepsilon_g} \tag{1}$$

Here, t_d and ε_d are the thickness and dielectric permittivity of dielectric layer which in our calculations have been set at 150 nm and 2.10, respectively. Since the graphene thickness is negligible compared with dielectric layer, the perpendicular dielectric tensor can be considered equal to the permittivity of the dielectric layer ($\varepsilon_{\perp} \cong \varepsilon_d$). The graphene's effective permittivity can be written as [7]:

$$\varepsilon_g = 1 + J\frac{\sigma(\omega,\Gamma,\mu_c,T)}{\omega\varepsilon_0 t_g} \tag{2}$$

where ε_0 is the vacuum permittivity and σ is the conductivity of a single layer of graphene. The surface conductivity for a single layer of graphene is given by Kubo formula [8]:

$$\sigma(\omega,\Gamma,\mu_c,T) = \sigma_{intra} + \sigma_{inter} \tag{3}$$

$$\sigma_{intra} = \frac{-ie^2}{\pi\hbar(\omega+i2\Gamma)}\int_0^{\infty}\xi\left(\frac{\partial f_d(\xi)}{\partial\xi} - \frac{\partial f_d(-\xi)}{\partial\xi}\right)d\xi \tag{4}$$

$$\sigma_{inter} = \frac{ie^2(\omega+i2\Gamma)}{\pi\hbar^2}\int_0^{\infty}\frac{f_d(-\xi)-f_d(\xi)}{(\omega+i2\Gamma)^2-4(\xi/\hbar)^2}d\xi \tag{5}$$

$$f_d(\xi) \equiv \frac{1}{\exp((\xi-\mu_c)/(k_BT))+1} \tag{6}$$

where ω is the angular frequency of the incident electromagnetic wave, Γ is the scattering rate which we set equal 0.1 meV, μ_c is the chemical potential , T the temperature, e is the electron charge, $\hbar$ is the reduced Plank constant and k_B is the Boltzmann constant. The equation (6) is the Fermi-Dirac distribution. The two conductivity terms in (4) and (5) are referred to as the intraband and interband terms, respectively.

3. Result and discussion

Figure 1. (a), show a blue-shift in reflectance (up to 2.7 μm) as well as narrow band edge for the 20 bilayers of graphene/dielectric stack structure with 6 monolayers of graphene (6MG) for different value of chemical pot ential. The permittivity tensor componets for different monolayer of graphene is depicted in the Fig. 1 (b), transition for elliptic regime to hyperbolic type II regime is observed for the case (6MG) and (3MG);

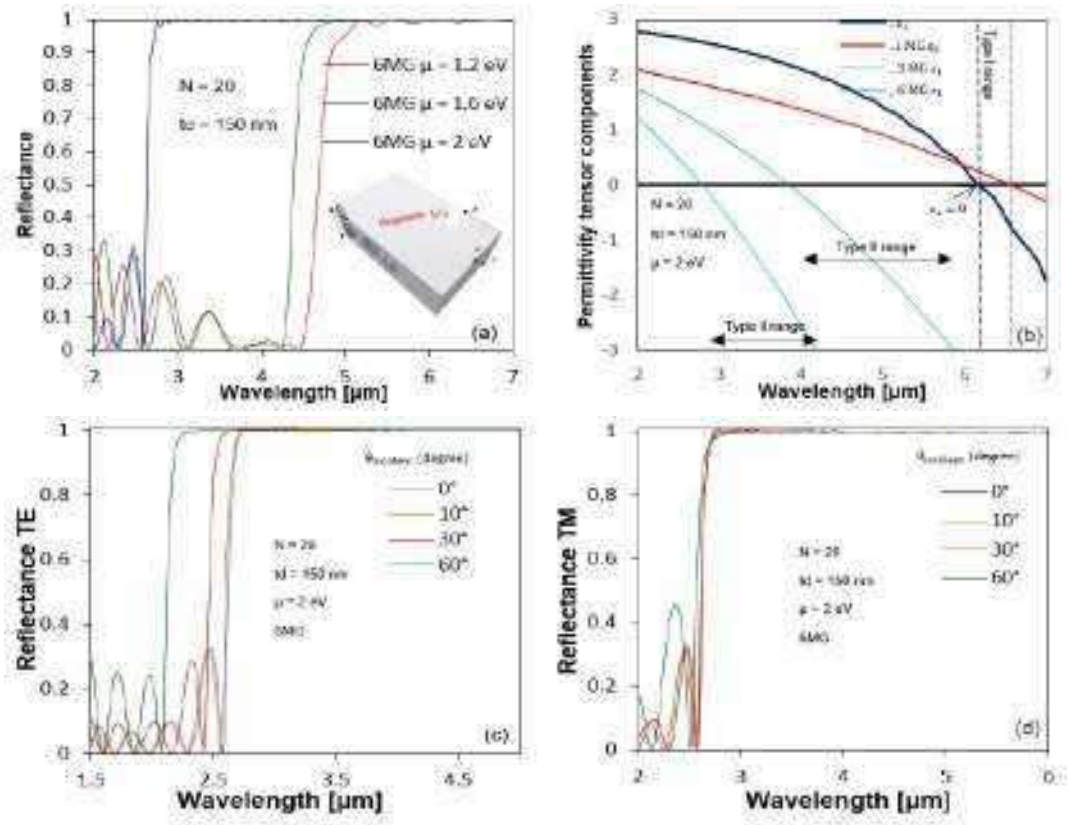


Fig. 1. (a) Reflectance spectrum as a function of the chemical potential, (b) permittivity tensor components for different monolayer of graphene, (c) and (d) reflectance spectra for TE and TM modes respectively.

stunning and fascinating behavior for the structure with 1MG; it is possible to observe different isofrequency dispersion: ($\varepsilon_{\parallel} \cdot \varepsilon_{\perp} > 0$) elliptic, isotropic ($\varepsilon_{\parallel} = \varepsilon_{\perp}$), Type I ($\varepsilon_{\parallel} > 0, \varepsilon_{\perp} < 0$) as well as effective metallic one ($\varepsilon_{\parallel} \cdot \varepsilon_{\perp} < 0$). Figures 1(c) and (d), illustrate the reflectivity spectra for the TE and TM modes for different angles of incidence theta θ; in here while the characterization angles dependency is less in the case of TM a more dependency of the incident angles is observed for the TE mode.

4. Conclusions

In this article, we investigate hyperbolic metamaterials based on graphene (1D-GHMM). The excellent advantage of using graphene instead of metal is the possibility to tune the optical properties in THz, infrared and in optical frequencies ranges as well by adjusting the chemical potential thus providing an active control of the hyperbolic dispersion. We have demonstrate how a tunable narrowband blueshit can be achieved in terms of reflectance in the mid-IR range. A type I and type II hyperbolic dispersion and an effective metal behaviour were obtained by modifying the number of graphene monolayers. The observed features make the 1D-GHMM as one of the most suitable candidates in terms of reflection modulator, tunable edge and narrowband spacial filter for novel optoelectronic applications.

Acknowledgements

The research leading to these results has received support by grant PPF N/34-186/2017 WAT, Tunable hyperbolic metamaterials for new generation photonic device.

References

[1] P. Shekhar, J. Atkinson, Z. Jacob, Hyperbolic metamaterials: fundamentals and applications, Nano Covergence 2014 1:14.

[2] Y. He, S. He, and X. Yang, Optical field enhancement in nanoscale slot waveguides of hyperbolic metamaterials, Opt. Lett. 37 (14), 2907-2909, 2012.

[3] Z. Liu, H. Lee, Y. Xiong, C. Sun, and X Zhang, Far-field optical hyperlens magnifying sub-diffraction-limited objects, Science 315 (5819), 1686, 2007.

[4] A.N Grigorenko, M. Polini, and K.S. Novoselov, Graphene plasmonics, Nature Photon. 6, 749, 2012.

[5] K.V. Sreekanth, A. De Luca, and G. Strangi, Negative refraction in graphene-based hyperbolic metamaterials, Appl. Phys. Lett. 103, 023107, 2013.

[6] M. Kieliszczyk, B. Janaszek, A. Tyszka-Zawadzka, and P. Szczepanski, Tunable spectral and spatial filters for the mid-infrared based on hyperbolic metamaterials, Appl. Opt. 57, 1182, 2018.

[7] R. Ning, S. Liu, H. Zhang, B. Bian and X. Kong, Tunable absorption in graphene-based hyperbolic metamaterials for mid-infrared range, Physica B 457, 144-148, 2015.

[8] G. W. Handon, Dyadic Green's functions and guided surface waves for a surface conductivity, J. Appl. Phys. Vol. 103, 064302, 2008.

Utilization of cross-metamaterial nano-antenna to expand the light absorption in the active layers of organic thin films

Yadgar I.Abdulkarim[1,2] **, Lianwen Deng** [1*]**, Fahmi F. Muhammad**[3]
Muharrem Karaaslan[4], **Shengxiang Huang** [1]

[1] School of Physics and Electronics, Central South University, Changsha, Hunan 410083, China
[2] Physics Department, College of Science, University of Sulaimani, 46001,Sulaimani Iraq
[3] Soft Materials and Devices Research Group, Department of Physics, Faculty of Science and Health, Koya University, 045 Koya,Iraq
[4] Department of Electrical and Electronics, Iskenderun Technical University, Hatay, 31100, Turkey
*corresponding author, E-mail: denglw@csu.edu.cn

Abstract

In this study, a new broadband metamaterial absorber based on cross-shaped nano-antenna was designed in order to improve the light absorption in organic active layers. The structure was composed of three layers, in which three split cross nano-antennas, made of metal aluminum, are encrusted on the top of different organic active layers, namely poly(3-hexylthiophene-2,5-diyl) (P3HT), [6,6]-Phenyl-C61-butyric acid methyl ester (PCBM) and bulk heterojunction of P3HT:PCBM. A numerical simulation has been performed by using high-frequency structure simulator (HFSS). According to the simulated results, our designed structure has significantly enhanced the light absorption in the organic thin films, whereby exhibited a broadband in the visible and infrared spectrum of light. When cross resonators are coated on the top of the active layers, an obvious redshift along the optical absorption edge was noticed. We believe that the proposed nano-antenna based metamaterial structure can be a promising approach for the application of organic and hybrid solar cells.

1. Introduction

Photovoltaics (PV) technology is the most dynamically developing area of today's renewable electricity production by means of using solar energy. PV devices are successfully utilized to convert sunlight energy into electricity by means of solar cells comprising various architectural designs and active materials [1–4]. However, conventional solar cells based on inorganic materials are suffering from the high cost and high-energy requirement during the production process. Alternatively, organic based PV devices have received considerable attention for their flexible, ambient solution-processed and lightweight properties [5–7]. In this way, various binary bulk heterojunction (BBHJ) and ternary bulk heterojunction (TBHJ) architectures have been proposed to achieve an improved absorption of light by the active layers [3, 8–12]. Upon having larger thickness of organic thin films, the increased light absorption comes at the expense of charge transport efficiency. This is because the larger thickness of the active layer can become a bottleneck in front of the soon arrival of free charge carriers (electrons and holes) to their respective electrodes, leading to the recombination of charges and hence a decreased charge mobility. The utilization of nanosized structures [13] or subwavelength sized materials, known as metamaterials [14, 15], is technically important [16, 17]. In the past decade, metamaterials have attracted increasing research attention in artificial engineering and synthetic composite material for their exhibiting properties unattainable in naturally occurring materials [18, 20]. These advanced metamaterials have been applied in cloaking [21], energy harvesting [22], solar cells [23] and super lens [24]. Furthermore, researches on perfect metamaterials absorber (MMA) in the microwave frequency [25], THz frequencies [26], infrared [27] and optical [28] ranges have been widely carried out. In the process of designing perfect metamaterial absorber structures, one of the most important steps is the selection of their size, shape and geometrical orientation (geometrical parameters) for any intended metamaterial absorber unit cell. Researchers have considered various metamaterial shapes, namely sawtooth, rectangular and circular shapes to improve the light absorption by organic and inorganic thin films for the application of solar cells [17, 29, 30], while little attention has been paid to the utilization of cross-shaped metamaterials for the light absorption enhancement in organic thin films. Hence, in the current research work, a new broadband metamaterial unit based on cross-shaped structure is designed and utilized to improve the light absorption in organic active layers.

2. Design and Simulation of the Proposed Structure

The architectural design of the proposed metamaterial structure is shown in Figure 1, which consists of three main layers deposited onto a glass substrate from bottom to top as follows: ITO, organic active layer and aluminum resonators (cross-shaped nano antenna). Hereafter, the whole proposed design is referred to as metal-absorber-metal (MAM), while the three active layers, namely P3HT, PCBM and P3HT:PCBM are investigated for their absorption profile in the visible and infrared spectral range with

and without coating the metamaterial nano-antenna onto their surfaces. Table1 presents the optical and magnetic related parameters of the three layers that were used in the simulation process. The nano-antenna was chosen to be a metal aluminum with an electric conductivity of about $3.56 * 10^7$ S/m.

The other geometric parameters that appear in Figure 1 are as follows: $p_x = p_x = 520$ nm, $W = 30$ nm, $l = 100$ nm, $h_1 = 20$ nm, $h_2 = 35$ nm, $h_3 = 70$ nm and $h_4 = 15$ nm. A full-wave electromagnetic simulation was performed by using finite-element analysis based on the High-Frequency Structure Simulator (HFSS). The periodic boundary conditions (PBCs) and floquet port are utilized to simulate the infinite periodic cells.

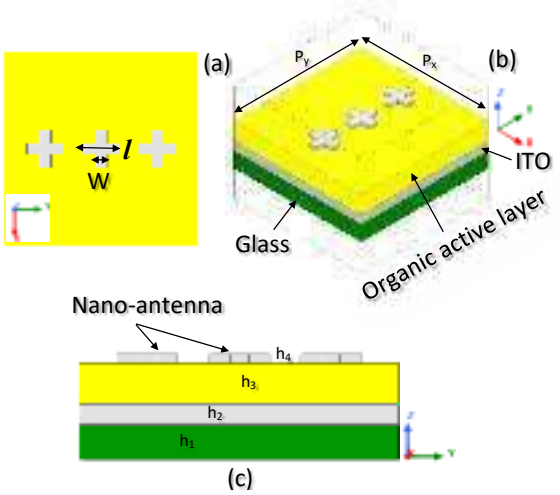


Figure 1: Schematic structure of the designed MAM (a) top view (b) oblique view (c) side view.

Table 1: The electrical and magnetic related parameters for the layers used in the simulation design in HFSS [31–33]

Parameters	P3HT	PCBM	P3HT:PCBM	ITO
ε_r	3.920	3.579	3.500	3.6150
μ_r	1.010	1.028	1.010	1.0001
σ (S/m)	0.300	0.320	0.310	106
ρ (Kg/m^3)	1300	1300	1300	6800

3. Results and Discussion

The overall absorptivity characteristic of the proposed structure can be calculated by using the well known equation;

$$A(w) = 1 - |S_{11}(w)|^2 - |S_{21}(w)|^2 \quad (1)$$

Where $S_{11}(w)$ and $S_{21}(w)$ represents reflection and transmission coefficients of the metamaterial unit cell, respectively. As it is expected, simulations indicate that the transmittance $T = |S_{21}(w)|^2$ is effectively zero across the entire frequency range due to the metallic ground plane. The reflectance $R = |S_{11}(w)|^2$ is relatively high except where the metamaterial has a strong impedance matching with the incident wave medium and it reaches its minimum value. Hence, the transmission value can be removed from the equation,

$$A(w) = 1 - |S_{11}(w)|^2 \quad (2)$$

Furthermore, the dispersive behavior of the extinction coefficient and refractive index of the organic active layers in the visible regime are shown in Figure 2.

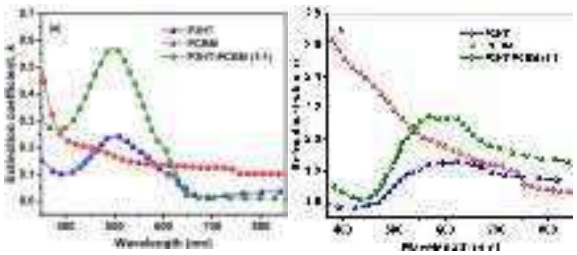


Figure 2: Dispersion spectra of the P3HT, PCBM and P3HT:PCBM thin films:(a) extinction coefficient(b) refractive index.

In the simulation process, the values of relative permittivity (ε_r) and relative permeability (μ_r) were considered around the characteristic absorption peaks of the films, whereas the simulation program compensated for the dispersive response of the active layer. The relative permittivity and relative permeability were calculated respectively from the following equations [34].

$$\varepsilon_r = n^2 - k^2 \quad (3)$$

$$n = \sqrt{\varepsilon_r + \mu_r} \quad (4)$$

Figure 3 shows the normalized absorption curves for P3HT active layer with and without cross rnano antenna. Noticeably, the absorption spectrum without resonator, resembling the experimentally observed spectrum, shows a single peak at 595 nm. This is ascribed to the electronic transitions from bonding (π) to antibonding (π^*) energy levels [35]. Comparatively, in the presence of nano antenna, there are two essential peaks at 525 nm and 710 nm observed corresponding to the absorptivity of 92% and 100%, respectively. The coating of three cross nano antena on the top of P3HT has led to a broadened absorption spectrum and redshift in the absorption peak (shifting towards higher wavelength), as shown in Figure 3. This is specifically important for solar cells application because a wider range of solar spectrum can be possible to be absorbed by the active layer, which in turn results in a larger charge carrier generation and hence higher efficiency is yielded [36].

Figure 4 shows the simulated absorption spectra generated for PCBM with and without the cross shaped nano-antenna. The active layer without nano-antenna (pristine

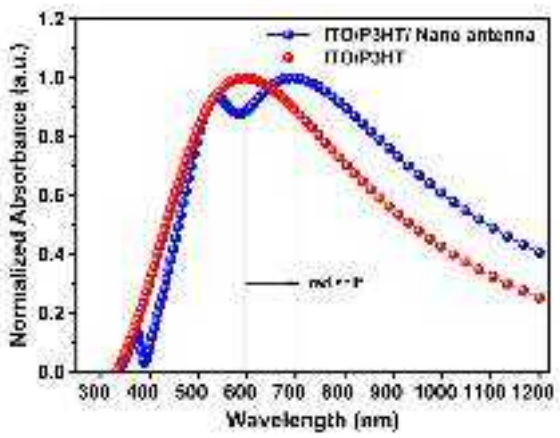


Figure 3: Absorption spectra of the P3HT thin film with and without the presence of cross nano-antenna.

PCBM) exhibits an absorption peak around 355 nm, which is close enough to that of the experimentally grown PCBM films [12, 32]. The shape consistency of the characteristic peak of PCBM with nano-antenna indicates the existence of a strong coupling between cross nano-antenna and PCBM film, whereby interesting electromagnetic scattering and constructive interference have been resulted.

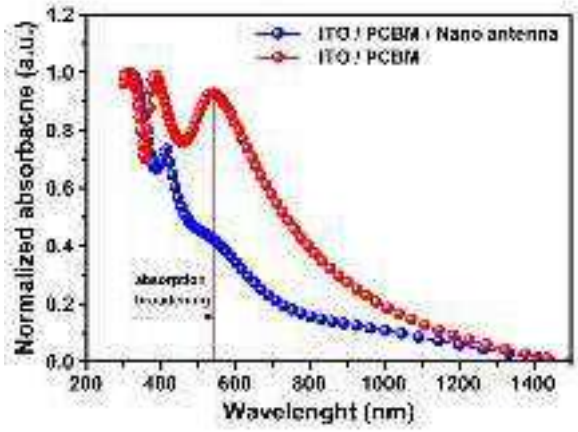


Figure 4: Absorption spectra of MAM structure, considering PCBM as the absorber active layer for the proposed MAM with and without nano-antenna coated onto PCBM thin film.

Figure 5 shows the simulated absorption spectra of the designed MAM structure for the P3HT:PCBM active layer with and without the coating of cross nano antenna. One can obviously see that the absorption spectrum with nano natenna is broadened compared to that of the pristine active layer. Consequently, the main characteristic peak of P3HT:PCBM is redshifted from about 565 nm to 725 nm with the presence of cross nano antenna. This peak is ascribed to band-to-band transitions inferred from $\pi - \pi^*$ transitions between the allowed highest occupied molecular orbital (HOMO) and the lowest unoccupied molecular orbital (LUMO) [35, 37].

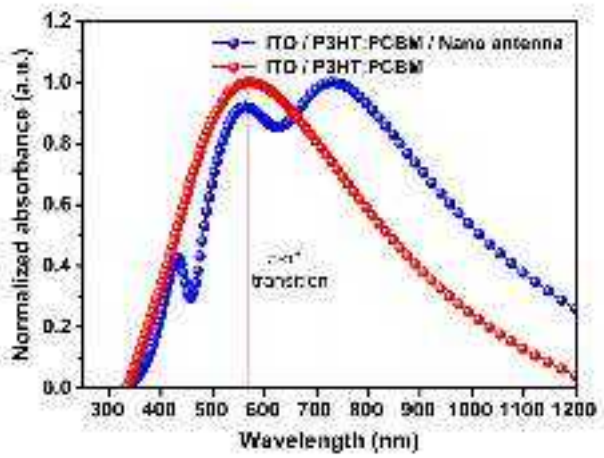


Figure 5: Absorption spectra for metamaterials absorber of P3HT: PCBM active layer with without coating the cross shaped nano-antenna onto P3HT:PCBM thin film.

In order to investigate the variations happen in the apparent optical energy gap of the proposed structures due to the coating of the nano-antenna resonators, Tauc's equation was applied to plot curves of $(\alpha h\nu)^2$ against the energy of photons thereby estimating the precise value of energy band gap (absorption edge position), as shown in Figure 6(a). Where, α is the absorption coefficient, h is Planck's constant and v is the photon frequency. Complete information regarding the use of this equation to determine the optical band gap is given in [31]. One can find the value of energy gap E_g directly from the intersection of x-axis at the point where $(\alpha h\nu)^2 = 0$. By using this technique, energy gap of the proposed metamaterial absorber for P3HT layer with nano-antenna and without nano-antenna were estimated to be 1.5 eV and 1.7 eV, respectively. In this way, the band gap of the active layers is interestingly reduced, meaning that the low energy photons of sunlight can also be involved in the process of photo-absorption. Concludingly, the wider range of photon absorption results in higher free electrons and holes generation, thereby improving the overall performance of organic solar cells.These energy gaps are corresponding to the wavelength of 824 nm and 727 nm, respectively, indicating the present of a useful redshift in the absorption spectra of the P3HT organic thin film

It is seen from Figure 6(b) that when the PCBM active layer is coupled with the nano-antennas, the active layer exhibited a broad absorption band comprising three absorption peaks. Consequently, the absorption edge of the spectrum is greatly redshifted, i.e. the apparent energy gap of the metamaterial unit is considerably reduced. The value of energy gap was measured to be 2.76 eV and 1.95 eV for the MAM structure without and with the nano-antenna coated onto the PCBM layer, corresponding to the absorption edge of 449 nm and 635 nm, respectively.

Noteworthy, the energy gap of P3HT:PCBM (see Figure 6(c)) was found to be higher than that of pristine P3HT film (see Figure 6(a)). This could be attributed to the influence of PCBM absorption which is mainly in the ultraviolet region [37]. It was noticed that the value of apparent energy gap is 2.49 eV before coating the nano-antenna resonators onto the P3HT:PCBM. However, by considering the nano-antenna into account, the absorption edge in terms of energy gap was significantly reduced to 1.61 eV. As such, the deposition of cross nano-antenna on top of organic thin films can greatly enhance their light absorption capability, suggesting the viable contribution of cross shaped resonators in the improvement of light absorption of organic thin films.

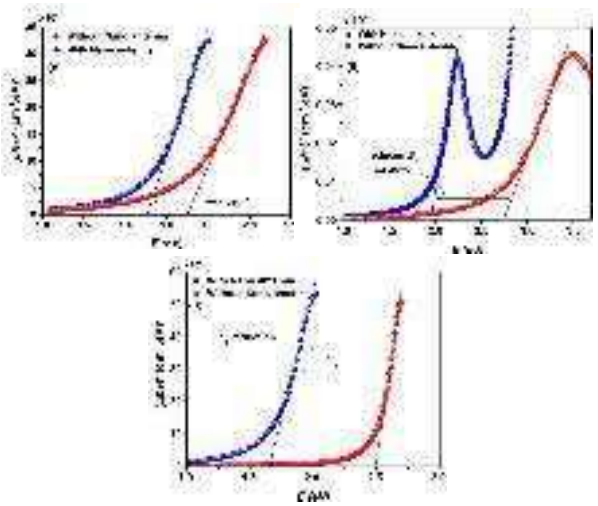


Figure 6: Plot of $(\alpha h\nu)^2$ versus photon energy (E),with nano-antenna and without nano-antenna for (A) P3HT (B) PCBM and (C) P3HT:PCBM organic active layers.

To investigate the photovoltaic performance of a representative OSC based on the proposed P3HT:PCBM/Al-resonator system, theoretical equations were utilized to estimate the short circuit current (J_{sc}), open circuit voltage (V_{oc}) and maximum power (P_m = V_m * I_m), thereby extracting the current-voltage (I-V) characteristic of the device. From the spectrally resolved absorption A (λ) in the active layer, short circuit current density (J_{sc}) was calculated as follows [38]:

$$J_{sc} = \int \frac{q\lambda}{hc} A(\lambda).AM1.5G(\lambda)d\lambda \qquad (5)$$

where q is the electron charge, h is Planck's constant, c is the speed of light and AM 1.5G defines the global spectral solar irradiance [14]. Interestingly, the value of V_{oc} was determined according to this formula [39]:

$$V_{oc} = \frac{nKT}{q} ln(\frac{J_{sc}}{J_o} + 1) \qquad (6)$$

where n is the ideality factor of the cell, T is the cell temperature in Kelvin, k is Boltzmann's constant and J_o is the saturation current which can be determined by:

$$J_o = N_v N_c \mu KT exp(\frac{-E_g}{KT}) \frac{1}{LN_A} \qquad (7)$$

Where N_v/C is the effective density of states in the valence/conduction band, L is the diffusion length, N_A is the acceptor density and μ is the mobility. We have previously noticed that for thiophene based OSC, the ratio of V_{oc}/V_m is about 1.60 [12]. Consequently, by assuming an ideality factor of n = 2 for the devices and considering the single-diode modelling [40], simulated I-V data for the proposed structure with and without the presence of corss shaped nano-antenna resonators have been extracted. Figure7 shows the I-V characteristic curves of the proposed design, while Table 2 tabulated the photovoltaic parameters and devices efficiency. Results showed that the deposition of cross shaped nano-antenna resonators onto the P3HT:PCBM active layer has led to improvement in the overall efficiency of the device from about 2.61 % to 2.66 %. It is worth mentioning that the addition of resonators acted to increase J_{sc} but a trivial decrease in V_{oc}, whereas the overall power was seen to be increased and hence a better device performance was achieved.

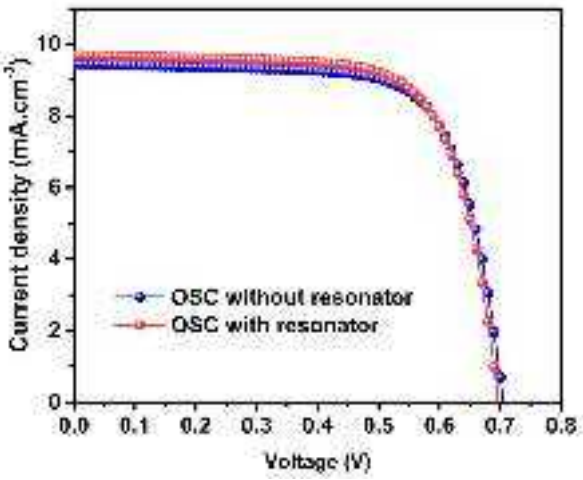


Figure 7: Current-voltage characteristic of the OSC based on P3HT: PCBM active layer with and without cross-shaped resonators.

Table 2: The simulated photovoltaic parameters of OSC based on P3HT: PCBM active layer with and without the presence of nano antenna resonator

Device structure	J_{sc}(mA.cm^{-2})	V_{oc}(V)	Efficiency (%)
ITO/P3HT:PCBM	9.460	0.707	2.61
ITO/P3HT:PCBM/Al Resonator	9.711	0.698	2.66

In order to understand the absorption mechanism of the proposed metamaterial structure and the resonance behaviour, the electric field and magnetic field distribution for the three different active layers were investigated at the

main characteristic absorption peak of the active layers.

Figure 8 shows the electric field distribution of the resonator-coated organic thin films at different resonant wavelengths for the different organic active layers. It is noticed that at resonant wavelength of 710 nm for the P3HT layer and 750 nm for the P3HT:PCBM the electric field is weakened.. When the structures are illuminated by the low energy incident light, localized surface plasmon is difficult to reach the excitation threshold due to the mismatched frequencies between the absorbed photons and the characteristic absorption peak of the active layer. While for the PCBM at incident wavelength of 560 nm, the electric field intensity is mostly concentrated around the edge of cross-shaped resonators. This is because the high energy/frequency electric field component of the incident wave produces surface current in the cross-shaped metamaterial [41], thereby oscillating the surface charges along the external electric field. This demonstrates effects of the localized surface plasmon in metamaterials [17].

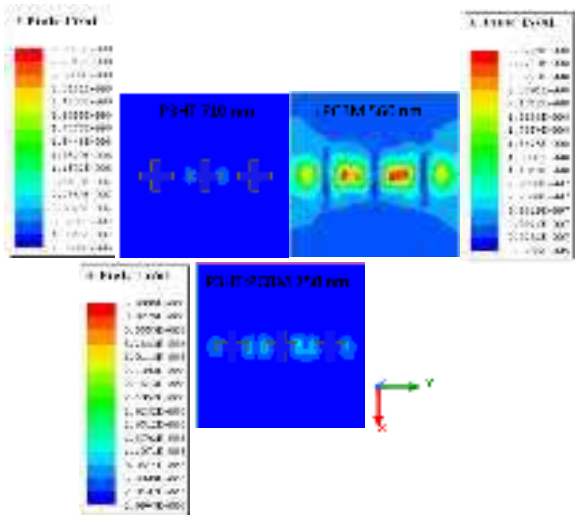


Figure 8: Electric field distribution of the proposed structures at the main characteristic peaks of the organic thin films.

Figure 9 shows the colour map representation of magnetic field distribution for the three organic active layers at main resonance wavelengths. For the P3HT active layer at resonance wavelength of 710 nm, a strong magnetic field in the centre of cross resonator was observed. This is in agreement with our previous observation, where the electric filed distribution is weak/strong at the certain resonant wavelength, instead, the magnetic field confinement spreads within the whole structure and is strong/weak at the corresponding resonant wavelength. Thus, strong magnetic field is observed at 710 nm [17]. At the incident wavelength of 560 for the PCBM, magnetic field distribution is weak compared to that of the P3HT layer. For the structure of ITO/P3HT: PCBM/resonator, the magnetic field distribution at 750 nm showed a strong localized field at the centre of cross resonator. According to the simulated results, both electric field and magnetic field resonances are capable of well improving the light distribution within the organic active layers.

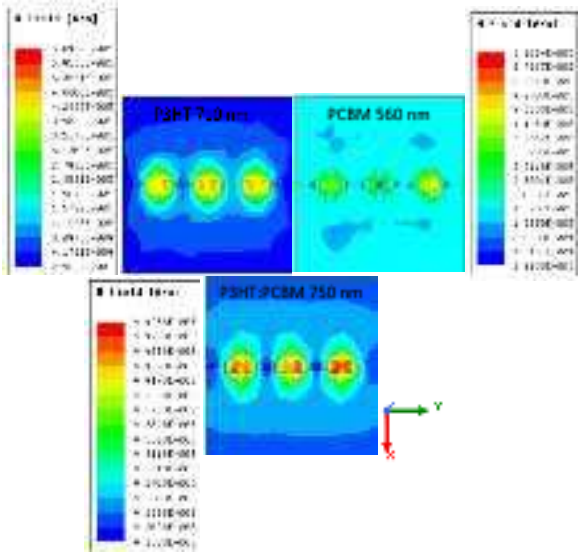


Figure 9: Magnetic field distribution for the metamaterial absorbers at 710 nm incident wavelengths for the PEHT, 560 nm for the PCBM and 750 for the P3HT:PCBM active layers, respectively.

4. Conclusions

A new metamaterial structure was designed by incorporating cross-shaped metamaterial resonators on the top of organic active layers of P3HT, PCBM and P3HT: PCBM. The main characteristic peak of P3HT: PCBM is redshifted from about 565 nm to 725 nm with the presence of resonators. The apparent energy gap can be reduced from 2.49 eV to 1.61 eV by incorporating aluminum resonators with the P3HT: PCBM system. The electromagnetic field distribution exhibited that red shifting in the absorption peaks is provided by the cross-shaped resonators. The designed structure has significantly enhanced light absorption ability in organic thin films and exhibited a broadband in the visible and infrared spectra. The proposed metamaterial structure was found to improve the overall performance of organic solar cells based on P3HT:PCBM active layer, suggesting a viable utilization of cross shaped resonators for enhancing organic and hybrid solar cells.

Acknowledgement

The authors are grateful to the National Key Research and Development Program of China (Grant No.2017YFA0204600),the National Natural Science Foundation of China (Grant No.51802352), and Central South University under grant No.2018zzts355.

References

[1] Li Z-S, Zhang G-Q, Li D-M, Zhou J, Li L-J, Li L-X, 'Application and development of solar energy in building industry and its prospects in China', *Energy Policy*, 35,4121-4127,2007.

[2] McEvoy AJ, Castaner L, Markvart T., 'Solar cells, materials, manufacture and operation', *Academic Press* second edition,2012.

[3] Muhammad FF, Yahya MY, Sulaiman K., 'Improving the performance of solution-processed organic solar cells by incorporating small molecule acceptors into a ternary bulk heterojunction based on DH6T: Mq3: PCBM (M= Ga, Al)', *Materials Chemistry and Physics*, 188,86-94,2017.

[4] Otte K, Makhova L, Braun A, Konovalov I., 'Flexible Cu (In, Ga) Se2 thin-film solar cells for space application', *Thin Solid Films*' ,511,613-622,2006.

[5] Dennler G, Sariciftci NS.,'Flexible Conjugated Polymer-Based Plastic Solar Cells: From Basics to Applications', *Proceedings of the IEEE* , 93,1429-39,2005.

[6] Yin B, Yang L, Liu Y, Chen Y, Qi Q, Zhang F., 'Solution-processed bulk heterojunction organic solar cells based on an oligothiophene derivative', *Applied Physics Letters* , 97,023303,2010.

[7] Muhammad FF, Sulaiman K., 'Thermal Stability and Reproducibility Enhancement of Organic Solar Cells by Tris (hydroxyquinoline) gallium Dopant Forming a Dual Acceptor Active Layer', *ARO-THE SCIENTIFIC JOURNAL OF KOYA UNIVERSITY* , 6,69-78,2018.

[8] Cha H, Chung DS, Bae SY, Lee M-J, An TK, Hwang J., 'Complementary Absorbing Star-Shaped Small Molecules for the Preparation of Ternary Cascade Energy Structures in Organic Photovoltaic Cells', *Advanced Functional Materials* , 23,1556-1565,2013.

[9] Lu L, Xu T, Chen W, Landry ES, Yu L.,'Ternary blend polymer solar cells with enhanced power conversion efficiency', *Nature Photonics* , 8,716-722,2014.

[10] Gebeyehu D, Maennig B, Drechsel J, Leo K, Pfeiffer M.,'Bulk-heterojunction photovoltaic devices based on donor–acceptor organic small molecule blends',*Solar Energy Materials and Solar Cells* , 79,81-92,2003.

[11] Muhammad FF, Ketuly KA, Yahya MY.,'Effect of Thermal Annealing on a Ternary Organic Solar Cell Incorporating Gaq3 Organometallic as a Boosting Acceptor',*Journal of Inorganic and Organometallic Polymers and Materials* , 28,102-109,2018.

[12] Muhammad FF, Sulaiman K.,' Photovoltaic performance of organic solar cells based on DH6T/PCBM thin film active layers', *Thin Solid Films* , 519,5230-5233,2011.

[13] Khodasevych IE, Wang L, Mitchell A, Rosengarten G.,' Micro-and nanostructured surfaces for selective solar absorption', *Advanced Optical Materials* , 3,852-881,2015.

[14] Jahani S., Jacob Z.,' All-dielectric metamaterials',*Nature Nanotechnology*, 11, 23–36,2016.

[15] Xu H, Li HJ, He ZH, Chen ZQ, Zheng MF, Zhao MZ.,'Theoretical analysis of optical properties and sensing in a dual-layer asymmetric metamaterial',*Optical Communications*, 407,250–254,2018.

[16] Atwater HA, Polman A.,'Plasmonics for improved photovoltaic devices', *Nature materials* ,9,205,2010.

[17] Zhang C, Zhou W, Sun S, Yi N, Song Q, Xiao S.,'Absorption enhancement in thin-film organic solar cells through electric and magnetic resonances in optical metamaterial', *Optical Materials Express* ,5,1954-1961,2015.

[18] Smith DR, Padilla WJ, Vier D, Nemat-Nasser SC, Schultz S.,'Composite medium with simultaneously negative permeability and permittivity', *Physical review letters* ,84,4184,2000.

[19] Shelby RA, Smith DR, Schultz S.,' Experimental verification of a negative index of refraction', *science*, 292,77-79,2001.

[20] Veselago VG.,' The electrodynamics of substances with simultaneously negative values of $Epsilon$ and Mu', *Soviet physics uspekhi* ,10,509,1968.

[21] Cai W, Chettiar UK, Kildishev AV, Shalaev VM.,' Optical cloaking with metamaterials', *Nature photonics* ,1,224,2007.

[22] Wang H, Sivan VP, Mitchell A, Rosengarten G, Phelan P, Wang L.,'Highly efficient selective metamaterial absorber for high-temperature solar thermal energy harvesting', *Solar Energy Materials and Solar Cells* ,137,235-242,2015.

[23] Liu Y, Chen Y, Li J, Hung T-c, Li J.,' Study of energy absorption on solar cell using metamaterials', *Solar energy* ,86,1586-1599,2012.

[24] Fang N, Zhang X.,' Imaging properties of a metamaterial superlens', *Applied Physics Letters* , 82,161,2002.

[25] Landy NI, Sajuyigbe S, Mock JJ, Smith DR, Padilla WJ.,'Perfect metamaterial absorber', *Physical review letters* , 100,207402,2008.

[26] Gao R, Xu Z, Ding C, Wu L, Yao J.,'Graphene metamaterial for multiband and broadband terahertz absorber', *Optics Communications*, 356,400-4004,2015.

[27] Feng R, Qiu J, Cao Y, Liu L, Ding W, Chen L.,'Omnidirectional and polarization insensitive nearly perfect absorber in one dimensional metastructure', *Applied Physics Letters*, 105,181102,2014.

[28] Wu J, Zhou C, Yu J, Cao H, Li S, Jia W.,'Polarization-Independent absorber based on a cascaded metal–dielectric grating structure', *IEEE Photonics Technology Letters* , 26,949-952,2014.

[29] Cui Y, Fung KH, Xu J, Ma H, Jin Y, He S.,'Ultrabroadband light absorption by a sawtooth anisotropic metamaterial slab', *Nano letters* , 12,1443-1447,2012.

[30] Huang H-L, Xia H, Guo Z-B, Xie D, Li H-J.,' Design of broadband metamaterial absorbers for permittivity sensitivity and solar cell application', *Chinese Physics Letters*, 34,117801,2017.

[31] Moerland RJ, Hoogenboom JP.,' Subnanometer-accuracy optical distance ruler based on fluorescence quenching by transparent conductors', *Optica* , 3,112-117,2016.

[32] Stelling C, Singh CR, Karg M, König TA, Thelakkat M, Retsch M.,' plasmonic nanomeshes: their ambivalent role as transparent electrodes in organic solar cells',*Scientific reports* , 7,42530,2017.

[33] Polyanskiy MN.,' Refractive index database', *Refractive index.info*, 2016.

[34] F.F. Muhammad, M.Y. Yahya, F. Aziz, M.A. Rasheed, K. Sulaiman,' Tuning the extinction coefficient, refractive index, dielectric constant and optical conductivity of Gaq3 films for the application of OLED displays technology',*Materials in Electronics* , 28(19),14777-14786,2017.

[35] Etxebarria I, Ajuria J, Pacios R.,' Solution-processable polymeric solar cells: a review on materials, strategies and cell architectures to overcome 10%', *Organic Electronics*, 19,34-60,2015.

[36] Reyes-Reyes M, Kim K, Carroll DL.,' High-efficiency photovoltaic devices based on annealed poly (3-hexylthiophene) and 1-(3-methoxycarbonyl)-propyl-1-phenyl-(6,6) C 61 blends', *Apply Physics Letter*, 87,083506,2015.

[37] Rahimi K, Botiz I, Agumba JO, Motamen S, Stingelin N, Reiter G.,' SLight absorption of poly (3-hexylthiophene) single crystals', *RSC Adv* , 4,11121-11123,2014.

[38] Chen CP, Chan SH, Chao TC, Ting C, Ko BT.,' Low-bandgap poly (thiophene-phenylene-thiophene) derivatives with broaden absorption spectra for use in high performance bulk-heterojunction polymer solar cells', *J Am Chem Soc*, 130,12828-128233,2008.

[39] Muhammad FF, Sulaiman K.,'Utilizing a simple and reliable method to investigate the optical functions of small molecular organic films–Alq3 and Gaq3 as examples', *Measurement* , 44,1468–1474,2011.

[40] Müllerová J, Kaiser M, Nádaždy V, Šiffalovič P, Majková E.,'Optical absorption study of P3HT:PCBM blend photo-oxidation for bulk heterojunction solar cells',*Solar Energy*, 134,294–301,2016.

[41] He LH, Deng LW, Li YH, Luo H, He J, Huang SX, et al.,' Wide-angle microwave absorption performance of polyurethane foams combined with cross-shaped metamaterial absorber',*Results Physics* , 11,769–776,2018.

Conception of Circular Microstrip Patch Antenna Based on SINRD Substrate for WI-FI Application

Narimane KORCHI[1], Rachid OUSSAID[2].

[1]Houari Boumediene University of Sciences and Technology, laboratory of Instrumentation, Bp 32 El Alia, Algiers, Algeria
[2]ENPEI-BAdji Mokhtar, Bp 05 Rouiba Alger, Algerie
*corresponding author: Korchi.narimane@hotmail.fr

Abstract

This paper demonstrates a study Circular Patch Antenna using SINRD substrate. The SINRD structure is the air holes used in the substrate. The proposed antenna is designed at an operating resonant frequency of 2.4 GHz to meet Wi-Fi 802.11applications. The designed microstrip patch antenna's gain, bandwidth and directivity are analyzed before and after introducing SINRD structure. From the comparison of three different configurations of SINRD substrate have been studied. The simulation has been performed using CST Microwave Studio.

I. INTRODUCTION

The microstrip patch antennas have been increasingly used in recent years in wide range of application in wireless communication systems and satellite communication systems due to their great advantages: light weight, low cost, low profile, and conformable. On the other hand, it suffers from some disadvantages as: narrow bandwidth, low gain, excitation of surface waves.

Among the most popular configuration is the circular patch, It also has received a lot of attention not only as a single element [1-3]. Some technique was used to increase the gain and directivity of microstrip antenna in microwave frequency regime, and topologies have been investigated in several researches [4-5].

A solution proposed in this work is the concept of substrate integrated circuits (SICs), which was used of a specific air hole pattern that can effectively lower the dielectric constant of a dielectric substrate region of interest, thus, creating a wave-guiding dielectric channel in the substrate. This synthesized channel becomes a substrate integrated NRD guide or SINRD [6].

The substrate integrated nonradiative dielectric (SINRD) waveguide belongs to the family of substrate integrated circuits [7], [8], a promising low-cost high-performance technology for millimeter-wave and terahertz applications. In this technology, the air region of a nonradiative dielectric (NRD) guide is replaced by air holes or a low-dielectric agent on the same substrate, which removes the problem of mechanical support and assembling of the planar substrate that arises in the case of hybrid planar/NRD schemes [9].

In this letter, we propose a new design of realizing high directivity of the patch antenna under CST software working at a frequency of 2.4 GHz, inspired by a work already done for rectangular microstrip patch antenna. We will carry out several simulations of patch antennas based on standard dielectric substrates and then based on SINRD substrates with different configurations of the air holes.

At the end a comparative study was made between the results of circular microstrip patch antenna and of the rectangular microstrip patch antenna.

II. DESIGN AND ANALYSIS

The microstrip patch antenna is a planar antenna whose radiating element is a generally square conductive surface, separated from a conductive reflector plane (ground plane) by a dielectric sheet called substrate as shown in Fig. 1(a).

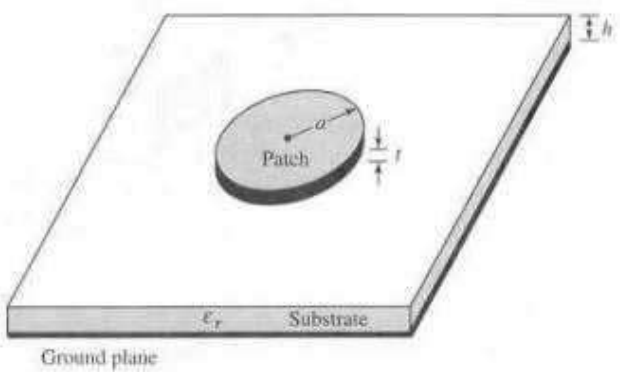


Figure 1a. Patch antenna with rectangular radiation.

In this configuration, upper conducting layer is the source of radiation where electromagnetic energy fringes off the edges of the patch and into the substrate. The lower conducting layer acts as a perfectly reflecting ground plane, bouncing energy back through the substrate and into the free-space. The antenna size mostly depends on the frequency band of operation.

Topology of the proposed SINRD guide is illustrated in Fig. 1(b). shows the pattern of air holes used to lower dielectric constant of the substrate with geometrical dimensions.

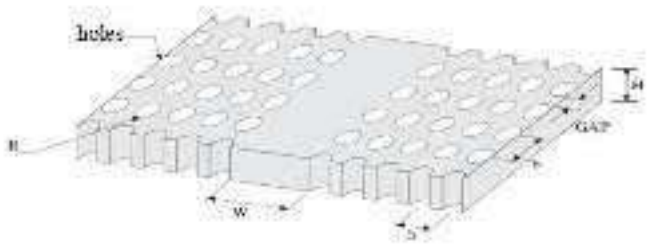


Figure 1(b): 3-D view of the hybrid planar/SINRD guide arrangement.

In this equivalent guide, εr equals to εeff of the air holes patterned region.

This equivalent NRD guide greatly simplifies the design of SINRD circuits. Note that the air hole pattern should not be subject to the generation of electromagnetic bandgap (EBG) phenomena.

A. Design Circulaire Microstrip Patch antenna

The parameters of the radiating microstrip patch antenna are calculated with following equations [10].

$$a = \frac{F}{\{1+\frac{2h}{\pi\varepsilon_r F}[\ln(\frac{\pi F}{2h})+1.7726]\}^{1/2}} \quad (1)$$

$$F = \frac{8.791\times10^9}{f_r\sqrt{\varepsilon_r}} \quad (2)$$

The dominant mode is the TM_{110}^z whose resonant frequency is:

$$(f_r)_{110} = \frac{1.8412v_0}{2\pi a\sqrt{\varepsilon_r}} \quad (3)$$

The resonant frequency of equation (3) does not take into account fringing. Fringing makes the patch look electrically larger and it was taken into account by introducing a length correction factor. Similarly for the circular patch a correction is introduced by using an effective radius a_e, to replace the actual radius a,

$$a_e = a\{1+\frac{2h}{\pi\varepsilon_r a}[\ln(\frac{\pi a}{2h})+1.7726]\}^{1/2} \quad (4)$$

Therefore the resonant frequency of equation(3) should be modified by using equation(4) and expressed as:

$$(f_r)_{110} = \frac{1.8412v_0}{2\pi a_e\sqrt{\varepsilon_r}} \quad (5)$$

Where v_0 is the speed of light infree-space.

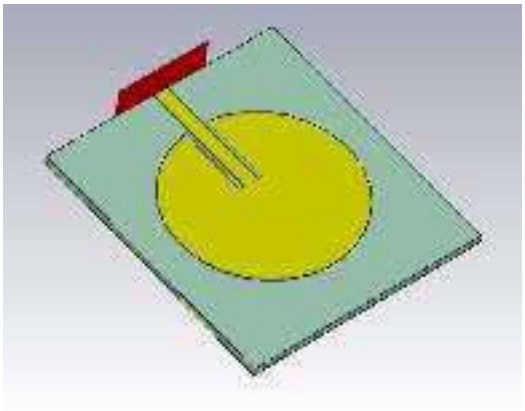


Figure 2: Geometry of circular microstrip patch antenna.

Figure 2 shows the geometrical configuration of the proposed circular microstrip patch antenna in CST Microwave Studio. The radiating circulair patch has the dimensions (F=1.7664mm, a=17.1405mm, a_e = 17.68mm). The circular patch was printed on one side of FR4 (loss free) substrate with relative permittivity εr = 4.3 and at height of 1.6mm from the ground plane.

B. Design air hole pattern

The first step in the design of an SINRD guide is to evaluate for a specific cell lattice with a specific dielectric material.

It is known [11-12] that an appropriate air hole arrangement in a planar dielectric substrate could reduce the effective dielectric constant of the structure. The choice depends on the dielectric profile needed, the layout of the circuit and the, mechanical strength of the substrate [7]. Three possible holes patterns, namely, a square lattice, an equilateral triangular lattice and a star lattice. In each case, the static effective dielectric constant of one cell can approximately be calculated by using [8].

$$\varepsilon_{eff} = \frac{\varepsilon_r(S_{CELL}-S_{AIR})+S_{AIR}}{S_{CELL}} \quad (6)$$

Where, S_{CELL} is the area of a unit cell of the pattern and S_{AIR} is the area of air holes in the unit cell.

Table I gives the value of ε_{eff} of each pattern (or lattice) for different holes diameters.

TABLE I. ε_{eff} EACH PATTERN

Diameter	**Topology**		
	Square	***Triangular***	***Star***
R=1.75 mm r=0.5mm Gap=0.25mm	2.0422	1.693	1.8579

C. Circular Microstrip Patch Antenna with SINRD substrate

The design of the circular patch antennas with SINRD substrate are based on the same model of the waveguide

(width of the non-perforated zone, radius of the air holes "R" and the distance between the holes "Gap") integrated in the substrate Dielectric FR-4 for the three arrangements of the SINRD holes.

The choice of the geometry of the SINRD substrate was made according to several criteria:

- R should be as large as possible to improve antenna performance and reduce the losses in the guide.
- Gap must also be as large as possible to allow the mechanical integrity of the guide.
- The diameter of the air holes must be limited to prevent the phenomena of Electromagnetic BandGap (EBG) in the desired frequency band.

The Fig. 3 and 4, 5 shows integration of SINRD structures for the circular patch antenna with air holes in dielectric square, triangular, star lattice respectively at 2.4 GHz frequency region.

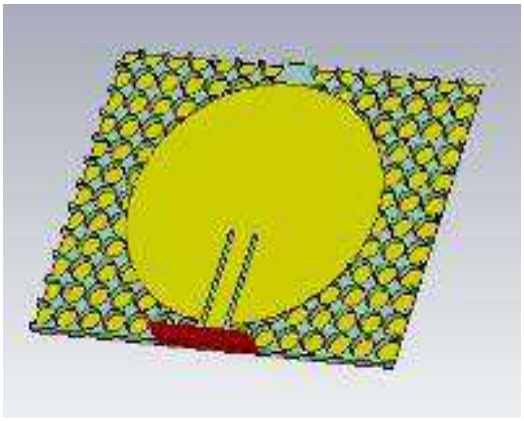


Figure3: Circular Patch Antenna with SINRD substrate square lattice.

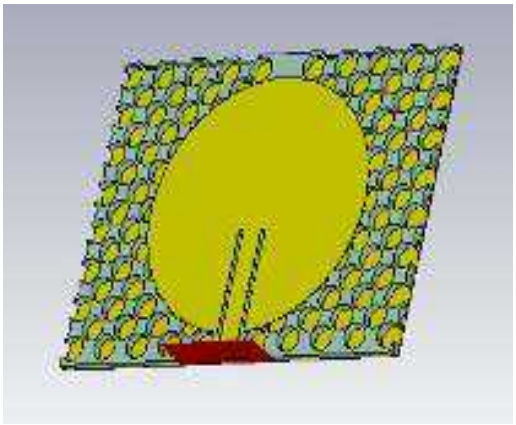


Figure 4: Circular Patch Antenna with SINRD substrate triangular lattice.

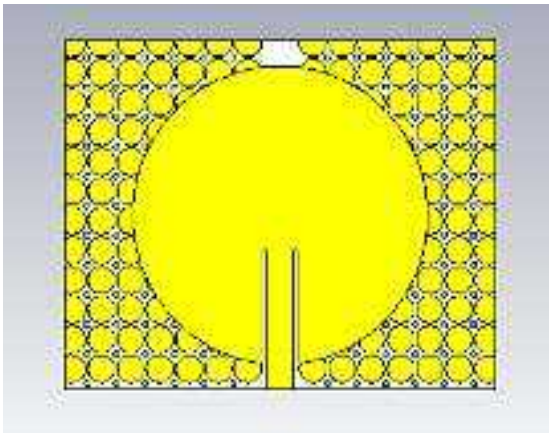


Figure 5: Circular Patch Antenna with SINRD substrate star lattice.

IV. RESULT SIMULATION AND DISCUSSION

The result simulation was obtained using TIME DOMAIN solver in CST Microwave Studio with accurancy -40dB.

A. Impedance bandwidth

The simulated return loss of circular microstrip patch antenna *S11* represents the reflection coefficient at the antenna input. This parameter also allows ensuring the adaptation of the antenna to the resonant frequency. The curve of the modulus of the coefficient of reflection of the antenna structure shows a good adaptation of about -31.56 dB at the resonant frequency of 2.4 GHz.

The impedance bandwidth for this antenna is 39.8 MHz calculated at -10dB return loss.

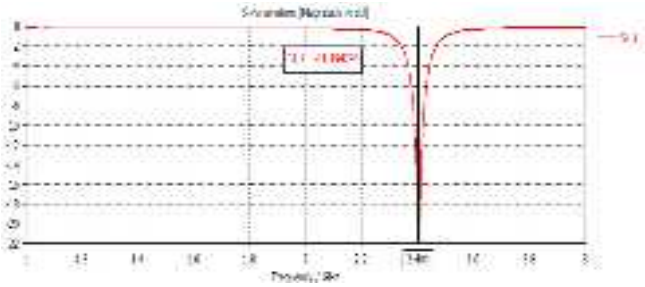


Figure 6: Simulation S11 for circular microstrip patch antenna with SINRD square lattice.

The adaptation of the patch antenna with SINRD substrate square lattice is very satisfactory with a reflection coefficient of less than -10 dB between 2.39and 2.42 GHz and a minimum of -21.19 dB at 2.4 GHz as shown in Fig. 6. The impedance bandwidth equal to 32.05 MHz is largely sufficient for our antenna.

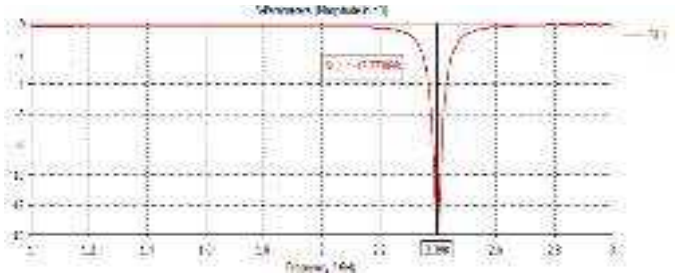


Figure 7: Simulation S11 for circular microstrip patch antenna with SINRD tringular lattice.

The Fig. 7 represent the reelection coefficient of the patch antenna with SINRD substrate triangular lattice, the impedance bandwidth is 21.20 MHz calculated at -10dB.

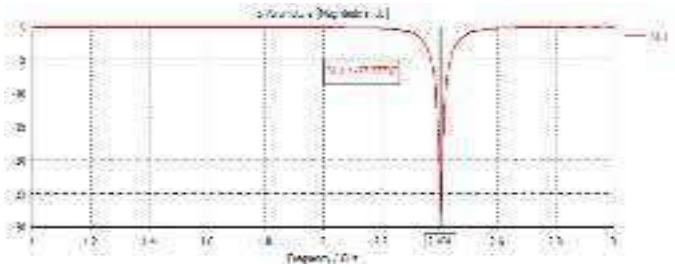


Figure 8: Simulation S11 for circular microstrip patch antenna with SINRD star lattice.

Adaptation of the circular microstrip patch antenna with SINRD substrate star lattice is done on a bandwidth of 32.98 MHz around 2.4 GHz, which is wider, compared to that found by the single microstrip patch antenna with a minimum of -27.78 dB as like represented in Fig. 8

B. Radiation pattern

The simulated radiation pattern for the gain and directivity of the circular microstrip patch antenna and the circular microstrip patch antenna with SINRD substrate with different structure (square, triangular, star) are indicated in Fig. 9, Fig. 10 and Fig. 11, Fig. 12, Fig. 13 , Fig. 14 respectively at 2.4 GHz frequency.

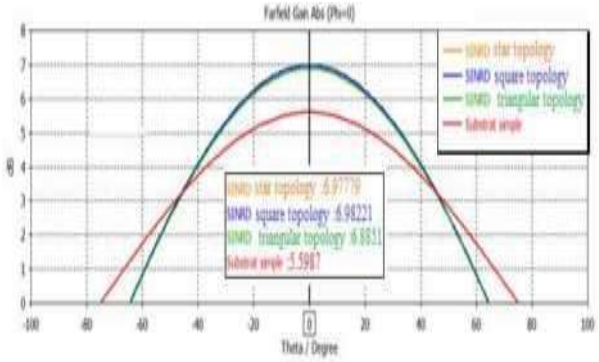


Figure 9: Diagrams of the gain of the four antennas in Cartesian coordinates.

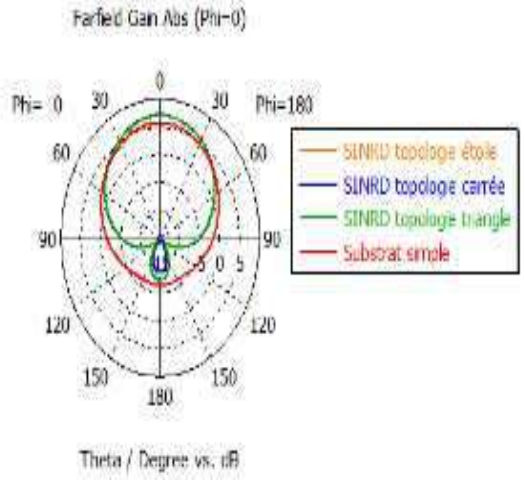


Figure 10: E plane far Radiation pattern of gain for Phi=0° for circular microstrip patch antenna with different substrate.

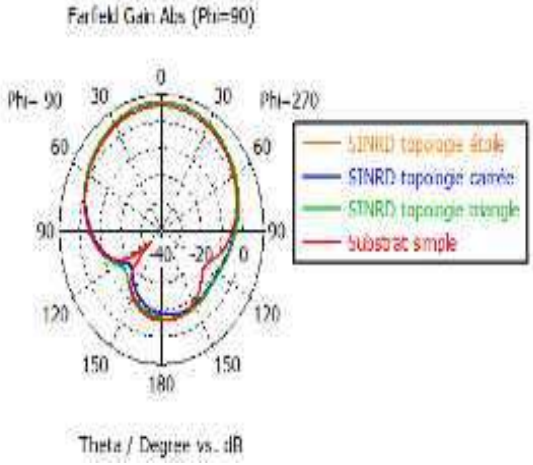


Figure 11: E plane far Radiation pattern of gain for Phi=90° for circular microstrip patch antenna with different substrate.

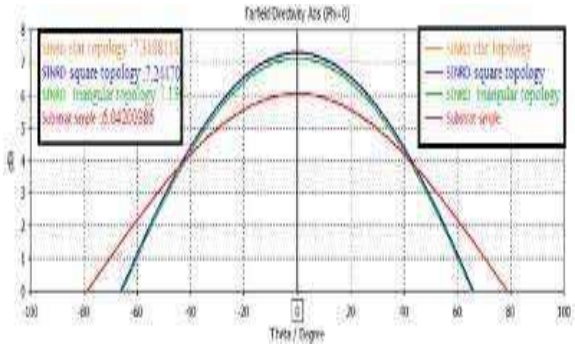


Figure 12: Diagrams of the directivities of the four antennas in Cartesian coordinates.

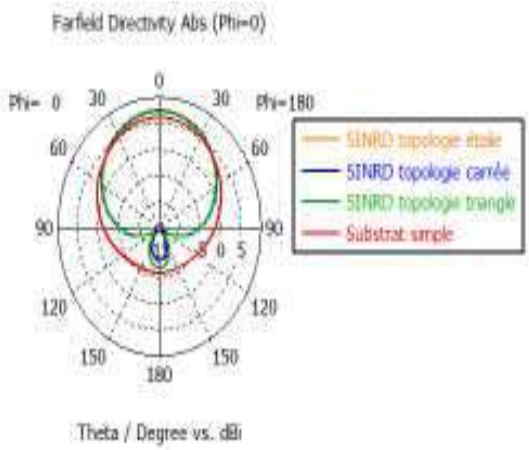


Figure 13: E plane far Radiation pattern of directivity for Phi=0° for circular microstrip patch antenna with different substrate.

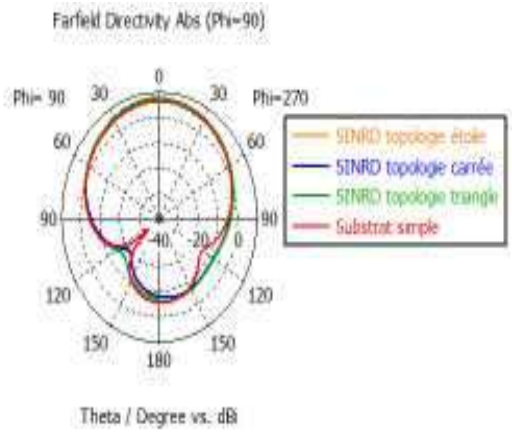


Figure 14: E plane far Radiation pattern of directivity for Phi=90° for circular microstrip patch antenna with different substrate.

The simulation results show that the main lobe direction for the gain reaches a maximum of 6.98 dB, and directivity 7.32 dBi of circular patch antenna with star lattice.

The Table II summarizes the simulated results obtained with different configurations of circular microstrip patch antenna.

The electromagnetic wave transmission properties of the circular patch antenna show that all of the improvements are due to the SINRD structure substrate.

TABLE II. COMPARAISON TABLE FOR DIFFERENT STRUCTURE OF PATCH ANTENNA

Antennes	**Parameter**		
	S_{11} (dB)	***Gain (dB)***	Directvity (dBi)
Simple patch Antenna	-31.5	5.599	6.042
Patch antenna with square lattice	-21.19	6.98	7.29
Patch antenna with tringular lattice	-13.77	6.89	7.14
Patch antenna with star lattice	-27.78	6.98	7.32

By comparing the results obtained, we can observe a good adaptation for the four types of antennas at the desired frequency 2.4 GHz.

The results obtained by simulation of the circular microstrip patch antenna with SINRD substrate are approximately similar for the three configurations are very satisfactory compared with the simple circular microstrip patch antenna.

The diameter of air gap has an effect on the radiation efficiency and gain of the proposed antenna. The maximum directivity is obtained for the circular patch antenna with substrate SINRD star holes which is 7.32 dBi.

We also find that the circular patch antenna SINRD substrate with star arrangement gives better performances compared to those of the square and triangular arrangement.

From the results obtained and from the comparative study of the different configurations with the literature, it seems that the circular patch antennas conceived based on substrates SINRD gives better results in particular in terms of directivity and gain.

V. CONCLUSION

In this paper, we have simulated four structures of circular microstirp patch antenna, conventional antenna, and circular microstirp patch antenna with SINRD substrate using different arrangement of the air holes, allowing a resonance in the operate frequency 2.4 GHz, in order to improve the electrical performance and radiation of the circular microstirp patch antenna.

The SINRD substrate is used to reduce the surface wave of the microstrip patch antenna. The gain and directivity was improved using SINRD substrate in the different configurations**.**

REFERENCES

[1] L. C. Shen, S. A. Long, M. R. Allerding, and M. D. Walton, “Resonant Frequency of a Circular Disc, Printed-Circuit Antenna,” *IEEE Trans. Antennas Propagat.*, Vol. AP-25, No. 4, pp. 595–596, July 1977.

[2] S. A. Long and M. D. Walton, “A Dual-Frequency Stacked Circular-Disc Antenna,” *IEEE Trans. Antennas Propagat.*, Vol. AP-27, No. 2, pp. 270–273, March 1979.

[3] J. T. Aberle and F. Zavosh, “Analysis of Probe-Fed Circular Microstrip Patches Backed by Circular Cavities,” *Electromagnetics*, Vol. 14, pp. 239–258, 1994.

[4] M.T. Islam, M.N. Shakin, High gain microstrip patch antenna , Eur.J.Sci.Res.32 (2)(2009) 187-193.

[5] T.A. Denidni, N. Hassaine, Q.Rao, Broadband and high gain E-shaped microstrip patch antennas for high-speed wirless networks, Prog. Electrom. Res. C1 (2008) 105-111.

[6] Priyanka Mondal and Ke Wu,‖A Leaky-Wave Antenna in Substrate Integrated Non-Radiative Dielectric (SINRD) Waveguide‖, IEEE TRANSACTIONS ON

ANTENNAS AND PROPAGATION, VOL. 61, NO. 4, APRIL 2013.

[7] Y. Cassivi and K. Wu, “Substrate integrated NRD (SINRD) guide on high dielectric constant substrate for millimeter wave circuits and systems,” *IMS Dig.*, vol. 3, pp. 1639–1642, 2004.

[8] Y. Cassivi and K. Wu, “Substrate integrated circuits concept applied to the nonradiative dielectric guide,” *IEE Proc.-Microw. Antennas Propag.*, vol. 152, pp. 424–433, Dec. 2005.

[9] Priyanka Mondal and Ke Wu,”A Leaky-Wave Antenna in Substrate Integrated Non-Radiative Dielectric (SINRD) Waveguide”, IEEE TRANSACTIONS ON ANTENNAS AND PROPAGATION, VOL. 61, NO. 4, APRIL 2013.

[10] Balanis C.A(1982) "Handbook of Microstrip Antennas". John Wiley and Sons New York.

[11] Wu, K.: ‘Integration and interconnect techniques of planar and nonplanar structures for microwave and millimeter-wave circuits – current status and future trend’. Asia-Pacific Microw. Conf., Taipei, Dec. 2001, pp. 411–416.

[12] Wu, K., and Boone, F.: ‘Guided-wave properties of synthesized nonradiative dielectric waveguide for substrate integrated circuits (SICs)’. IEEE Int. Microw. Symp., Phoenix, June 2001, Vol. 2, pp. 723–726.

Optical and Nonlinear-Optical Properties of Gold Nanorods' Based Hyperbolic Metamaterials

Irina A. Kolmychek*, Aleksander R. Pomozov, Vladimir B. Novikov, Aleksei P. Leontiev, Kirill S. Napolskii, and Tatiana V. Murzina

Moscow State University, 119991 GSP-1, Leninskie Gory, Moscow, Russia
*corresponding author, E-mail: irisha@shg.ru

Abstract

We present the experimental results on optical and nonlinear-optical effects in hyperbolic media based on gold nanorods arrays in porous anodic alumina, demonstrating pronounced effects attributed to epsilon-near-zero and epsilon-near-pole dispersion points. In the spectral vicinity of the epsilon-near-zero, an enhancement of the optical activity and of the second harmonic intensity are observed.

1. Introduction

Physics of hyperbolic metamaterials (HMM) that are artificial anisotropic uniaxial metal-dielectric nanostructured media [1, 2] attracts much attention nowadays. The main property of this type of material is the hyperbolic optical dispersion law. The two simplest designs of the HMM are (i) films of alternating conducting and non-conducting layers and (ii) arrays of metal (usually Au or Ag) nanorods in a dielectric matrix, which lead to the appearance of specific points in the ϵ components' spectra - epsilon-near-zero (ENZ) and epsilon-near-pole (ENP) [3], where a giant enhancement of optical effects is expected. Besides, new properties that are not observable in natural materials can appear close to these specific spectral points. Along with these spectral features, HMMs exhibit strong birefringence [4] and hyperbolic dispersion. It leads to the giant enhancement of well-known effects and appearance of novel optical phenomena that are not observable ordinary media. As an example negative refraction, enhancement of spontaneous emission, transformation of the evanescent field into propagating mode in the far field have been observed in HMM [1]. These effects are perspective for applications in nanophotonics, biosensing, high-resolution imaging, waveguiding. As well HMM are promising from the point of view of observing for the nonlinear optics [5, 6]. Although there are several works in this field, most of them are theoretical [5, 6]. It has been shown that the HMM dispersion law allows one to satisfy the phase-matching conditions for the sum- or difference-frequency nonlinear processes [7]. Spectral dispersion of HMM dielectric tensor components allows one to achieve various phase synchronisms involving different dispersion law regimes in frequency convertion process [7]. Numerical calculations predicted a strong enhancement of the third harmonic generation [8] and difference frequency generation [9] due to the phase-matching in hyperbolic multilayered films at definite spectral points. To the best of our knowledge the corresponding experiments have not been performed yet.

Nonlinear-optics is very sensitive to the resonant effects [10, 11] and electromagnetic field localization within an irradiated structure [12]. Particularly, the amplification of second harmonic generation (SHG) in a hyperbolic medium by the excitation of the Fabry-Perot modes in an effective film was observed [13]. It was shown that when the pump or second-harmonic wavelength lies in the region of hyperbolic dispersion, the value of effective second-order susceptibility is comparable with the susceptibilities of well-known nonlinear crystals such as lithium niobate ($LiNbO_3$) and potassium dihydrogenophosphate (KDP). The second-harmonic generation intensity can be enhanced in a wide spectral range due to the multiple waveguide modes in an anisotropic HMM film [14].

Nonlinear-optical effects in the spectral vicinity of the ENZ points have been analyzed in a number of papers. Due to the appearance of a singularity of the TM fundamental electric field E_ω for a material with the permittivity close to zero, nonlinear optical response should be enhanced manyfold. It takes place in an isotropic film with ENZ as well [15, 16], and quite recently was observed in the second harmonic generation (SHG) for arrays of nanorods in anodic aluminum oxide (AAO) [13] and ITO nanolayers in the visible range [17]. It should be noted here that third-order nonlinear effects are also enhanced near the ENZ point [18]. Nevertheless, listed works concern materials with poor plasmonic behaviour, where the ENZ point doestn't separate spectral regions with elliptical and hyperbolic dispersion.

One of the effective and convenient techniques for the HMMs fabrication is templated electrodeposition of gold or silver inside the cylindrical channels of anodic aluminum oxide (AAO) matrices. Such arrays of nanorods in dielectric matrix possess two plasmon resonances (along and perpendicular to the nanorods axes) that correspond to the electron gas oscilations [19].

In this paper the comparative experimental and numerical studies of the linear optical spectroscopic ellipsometry, SHG intensity and SHG phase spectroscopy of anisotropic gold-nanorods-based HMMs in the spectral vicinity of the ENZ and ENP points are presented.

2. Samples and experimental techniques

Arrays of gold nanorods in anodic aluminum oxide (AAO) matrices were made by templated electrodeposition as described in [20, 21]. Au nanorods of about 40 nm in diameter and 580 ± 40 nm in length are aligned perpendicular to the sample's surface, the volume fraction of metal being about 8%. Transmittance of the prepared films was studied using a halogen lamp as a broadband p-polarized light source. The polarization of the transmitted radiation was estimated using the commercial ellipsometer WVASE by J.A. Wollam Co., Inc. For the SHG experiments, we used the p-polarized output of a 80 fs pulsed Ti:Sapphire laser at tunable in the wavelength range, repetition rate of 80 MHz and the average power of 50 mW, focused on the sample into a spot of ≈50 μm in diameter. The sample was mounted on the rotation stage allowing changing of the angle of incidence. The transmitted SHG radiation was spectrally selected by a color filters and detected by a photomultiplier.

In order to reveal the variation of the second harmonic phase close to the ENZ point, the SHG phase spectroscopy was performed by means of the interferometry technique [22], when using a 50-nm-thick ITO film as a reference SHG source. The scheme of the experiment was similar to that described in [23]. During the measurements we changed the relative distance z between the reference ITO film and the sample varying the phase difference between the SHG waves generated in sample and reference due to the dispersion of air. The interferometry patterns were measured for all the accesible wavelengths of the pump radiations and were approximated by the function $I_{2\omega} \propto I_0 cos(2\pi z/d + \varphi_S) + const$, thus the spectrum $\varphi_S(\lambda)$ was obtained. Then the similar measurements were performed while the sample was replaced by another ITO film to obtain the spectrum $\varphi_R(\lambda)$ analogously. To normalize over the spectral changes of the period d of the interferometry pattern the phase φ_R was subtracted from the phase of the sample φ_S.

Simulations of nonlinear-optical spectra were performed for the effective slab, taking into account strong anisotropy of the medium, the distribution of the vectorial electric field within the structure and neglecting the spectral dependencies of the second-order susceptibility tensor components.

3. Experimental and simulation results

Transmission spectrum of the sample (Fig. 1 (a)), measured for the angle of incidence of θ =45° shows the two minima centered at about 540 nm and 820 nm, which correspond to the transverse and longitudinal local plasmon resonances of free electrons Au rods in the directions perpendicular and parallel to the nanorods' axis, respectively [19]. Longitudional resonance cannot be excited at normal incidence of pump radiation and the depth of the long-wavelength minimum increases with increasing θ as was discussed earlier [20]. It is worth noting that the minima are absent for bulky Au or AAO.

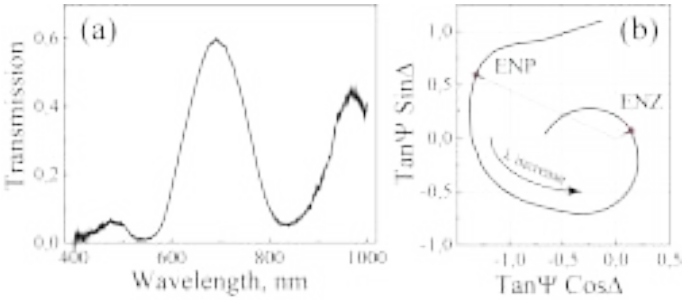


Figure 1: Linear-optical properties of the HMM sample: (a) transmission spectrum, (b) ellipsometry data. Both data were obtained for the angle of incidence of 45°.

The main ellipsometry parameter T_1 was estimated as the ratio of the complex field transmission coefficient, $T_1 = T_{pp}/T_{ss} = tan\Psi e^{i\Delta}$, with pp and ss subscripts denoting the polarization of the incident and transmitted light. Fig. 1 (b) shows the obtained T_1 spectrum with the indicated ENP and ENZ points. One can see that the smallest absolute value of T_1 corresponds to the ENZ point characterized by a strong absorption of p-polarized light in this spectral region.

Both experimental and simulation data indicate that the spectral behavior of the SHG spectra strongly depends on the angle of incidence (Fig. 2). For $\theta = 25°$ we observed about five times enhancement of the nonlinear signal in close vicinity of 820 nm fundamental wavelength, corresponding to the the long-wavelength minimum of linear transmission. At the same time for the normal incidence and for $\theta = 45°$ no SHG intensity enhancement was revealed in the spectral region under study which agreed qualitatively with the numerical results.

The interferometry mearurements were performed for the angle of incidence $\theta = 25°$, as it corresponds to the enhancement of the SHG intensity. A typical interferometry pattern (for pump wavelenth $\lambda = 840$ nm), i.e. the dependence of the SHG signal on the position of the reference sample, is shown in Fig.3 (a). The period of the pattern $d = 6.3$ mm corresponds to the value, predicted in [22] for this wavelength due to the air dispersion. Similar graphs were obtained for other accesible wavelengths and the spectrum of the SHG phase was calculated accordingly to the procedure described above. The spectrum of the SHG phase relative to that of the reference film is shown in Fig. 3 (b). One can see the phaseshift modulation of about 120-130° in the available spectral region, including the resonance at $\lambda = 820$ nm. This modulation should be attributed solely to the HMM, as the reference film does not possess specific features in the studied spectral range.

4. Discussion

As the studied HMM is an uniaxial anisotropic medium, its optical properties are defined by two components of the effective dielectric tensor $\epsilon_\perp$ and $\epsilon_\parallel$, which describe the optical response of the composite in the directions that are per-

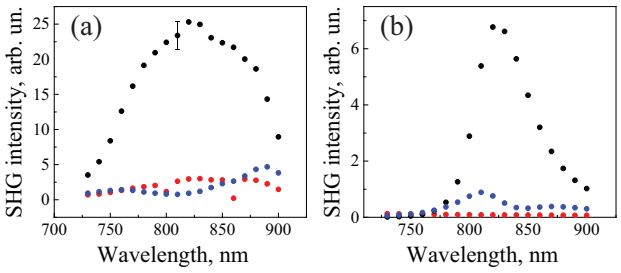


Figure 2: Experimental (a) and simulated (b) wavelength dependencies of the p-polarized SHG intensity obtained for the angles of incidence of 0° (red circles), 25° (black circles) and 45° (blue circles).

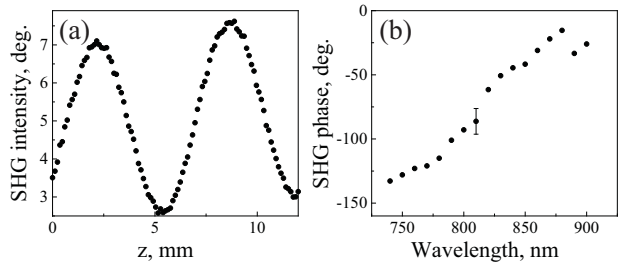


Figure 3: Interferometry data for the angle of incidence of 25°: (a) interferometry pattern $I_{2\omega}(z)$ for $\lambda = 840$ nm, (b) the spectrum of the SHG phase.

pendicular and parallel to the rods, respectively. The spectra of the permittivity components for analogous samples were calculated within the effective medium model and are presented in the paper [20]. We showed that two minima in the transmission spectrum correspond to the ENP and ENZ points. The hyperbolic dispersion regime is achieved in the spectral region at the wavelegths larger than the ENZ point, i.e. in our case $\lambda > 820$ nm.

The ellipsometry data manifest the strong polarization changing of light passed through the HMM. Due to large anisotropy of the HMM the transmitted light acquires elliptic polarization. It stems from the two properties of the composite medium: anisotropy of absorption and birefringence. Firstly, near the ENZ p-polarized light experiences stronger absorption as compared to the s-polarized one, resulting to the polarization plane rotation. It originates from the excitation of the longitudinal plasmon resonance corresponding to the minimum of the $|T_1| = Tan\Psi$ at $\lambda = 820$ nm that coincides with the ENZ point. Secondly, the phase difference $arg(T_1) = \Delta$ between the ordinary and extraordinary outgoing beams is aquired (Fig. 1(b)), resulting to the ellipticity of the polarization state of the transmitted light. The relevant spectrum shows that the HMM acts as a submicron thick birefringent crystal. Thus the HMM can work as an efficient polarization light converter due to the strong anisotropy-induced large differences in the optical properties (absorption coefficient and phase velocity) of the ordinary (TE) and extraordinary (TM) beams.

The SHG responce of the sample in the spectral vicinity of the ENZ point is attributed to three main factors. Firstly, due to the continuity of the transversal to the HMM interface component of the displacement field, the enhancement of the $(E_\omega)_z$ within the structure occurs (here and below we possess z-axis along the normal to the sample, xOz is the plane of incidence). Such enhancement can lead to the growth of the nonlinear-optical responce. Secondly, as the effective HMM slab can be considered as a medium with inversion symmetry, in the p-p combination of pump and second harmonic beam the SHG field is defined by the second-order susceptibility tensor components [24]: $\chi_{xxz} = \chi_{xzx}$, χ_{zzz} and χ_{zxx}. The first two of them involve resonant enhanced $(E_\omega)_z$ fundamental field component in the spectral region under study, the third one is double resonant in this sense and the last one is nonresonant. The contributions of these components to the SHG intensity can vary depending on θ. Finally, in the spectral vicinity of the ENZ point strong absorption of the TM radiation occurs that can lead to the decreasing of the nonlinear-optical responce.

For the normal incidence no longitudional resonance can be excited that is why no enhancement of the SHG intensity near the ENZ point was observed (Fig.2, red circles). For the case $\theta = 25°$ the resonant increase of the nonlinear-optical responce prevails over the strong absorption effects. It leads to the maximum of the SHG intensity near the ENZ point $\lambda = 820$ nm (Fig.2, black circles). At the same time, for $\theta = 45°$ absorption is high and prevails over other effects that results to the observed slight spectral dependence of the SHG intensity.

Simulation results are qulitatively similar to the experimental ones. Broadening of the resonant curve in the experimental data (Fig. 2 (a), black circles) compared with simulated curve (Fig. 2 (b), black circles) can be caused by the dispersion of the nanorods' length in the sample under study.

The spectrum of the SHG phase is the result of resonant, nonresonant and double-resonant contributions of the second-order susceptibility tensor components, indicated above. These contributions possess the phase modulations equal to π, zero, and 2π when passing through the ENZ point, respectively [23, 25]. The Fano-type interference between these components gives the value of the phaseshift about 120-130° in the available spectral region.

5. Conclusions

We studied optical and nonlinear-optical properties of an array of gold nanorods in porous anodic alumina matrix. Epsilon-near-pole and epsilon-near-zero spectral points appear as the minima in the linear transmission spectrum. We demosntrated considerable polarization state changes of light passed throught the HMM, which acts as the subwavelength polarization light converter. Contributions of the birefringence and the linear dichroism in polarization variations are discussed. Strong enhancement of the SHG response revealed in the spectral vicinity of the epsilon-near-zero point confirms the increase in the local field at

the fundamental wavelength within the structure.

Acknowledgement

The financial support of the RFBR grant 18-02-00830 and MK-5704.2018.2 is greatly acknowledged.

References

[1] A. Poddubny et al., Hyperbolic metamaterials, *Nature Photonics* 7: 948–957, 2013.

[2] M.G. Silveirinha, Nonlocal homogenization model for a periodic array of ϵ-negative rods, *Phys. Rev. E* 73: 046612, 2006.

[3] P. Shekhar et al., Hyperbolic metamaterials: fundamentals and applications, *Nanoconvergence* 1 (14): 1–17, 2014.

[4] P. Ginzburg et al., Manipulating polarization of light with ultrathin epsilon-near-zero metamaterials, *Opt. Express* 21 (12): 14907–14917, 2013.

[5] P. Segovia et al., Hyperbolic metamaterial antenna for second harmonic generation tomography, *Opt. Express* 23 (24): 30730, 2015.

[6] D. de Ceglia et al., Second harmonic double-resonance cones in dispersive hyperbolic metamaterials, *Phys. Rev. B* 89: 075123 (1–7), 2014.

[7] B. Duncan et al., New avenues for phase matching in nonlinear hyperbolic metamaterials, *Scien. rep.* 5: 8983 (1–6), 2015.

[8] S. Wicharn et al., A birefringent phase-matching method in multilayered hyperbolic metamaterials, *Proc. of SPIE* 10516: 105161M (1–11), 2018.

[9] P. Buranasiri et al., A numerical investigation of difference frequency generation in nonlinear multilayered metamaterials, *Proc. of SPIE* 10343: 103432W (1–8), 2017.

[10] A.Wokaun et al., Surface second-harmonic generation from metal island films and microlithographic structures, *Phys. Rev. B* 24: 849–856, 1981.

[11] I.A. Kolmychek et al., Plasmon-assisted enhancement of third-order nonlinear optical effects in core (shell) nanoparticles, *JOSA B* 29 (1): 138–143, 2012.

[12] E.A. Mamonov et al., Coherent and incoherent second harmonic generation in planar G-shaped nanostructures, *Optics Letters* 36 (18): 3681–3683, 2011.

[13] B. Wells et al., Structural second-order nonlinearity in plasmonic metamaterials, *Optica* 5 (12): 1502, 2018.

[14] G. Marino et al., Second-Harmonic Generation from Hyperbolic Plasmonic Nanorod Metamaterial Slab, *Laser Photonics Rev.* 1700189 (1–9), 2018.

[15] X. Wen et al., Doubly enhanced second harmonic generation through structural and epsilon-near-zero resonances in TiN nanostructures, *ACS Photonics* 5 (6): 2087–2093, 2018.

[16] M.A. Vincenti et al., Singularity-driven second- and third-harmonic generation at ϵ-near-zero crossing points, *Phys. Rev. A* 84: 063826, 2011.

[17] A. Capretti et al., Comparative Study of Second-Harmonic Generation from Epsilon-Near-Zero Indium Tin Oxide and Titanium Nitride Nanolayers Excited in the Near-Infrared Spectral Range, *ACS Photonics* 2: 1584–1591, 2015.

[18] M. Z. Alam et al., Large Optical Nonlinearity of Indium Tin Oxide in Its Epsilon-near-Zero Region, *Science* 352: 795–797, 2016.

[19] R. Atkinson et al., Anisotropic optical properties of arrays of gold nanorods embedded in alumina, *Phys. Rev. B* 73: 235402, 2006.

[20] I.A. Kolmychek et al., Magneto-optical effects in hyperbolic metamaterials, *Opt. Lett.* 43 (16): 3917-3920, 2018.

[21] A.P. Leontiev et al., Tuning the optical properties of hyperbolic metamaterials by controlling the volume fraction of metallic nanorods, *Nanomaterials* 9 (5): 739 (2019).

[22] R.Stolle et. al., Phase measurements in nonlinear optics, *Appl.Phys. B* 63: 491 (1996).

[23] I.A. Kolmychek et al., Second harmonic generation interferometry in magnetic-dipole nanostructures, *Opt. Lett.* 40 (16): 3758–3761, 2015.

[24] P. Guyot-Sionnest et al., General considerations on optical second harmonic generation from surfaces and interfaces, *Phys. Rev. B* 33 (12): 8254–8263, 1986.

[25] I.A. Kolmychek et al., Magnetization-induced effects in second harmonic generation under the lattice plasmon resonance excitation, *Opt. Lett.* 41 (23): 5446–5449, 2016.

Optical properties of planar metal-dieletric layered films: from coupled Fabry-Pérot resonators to hyperbolic metamaterials

Manuel Gonçalves[1*], Hayk Minassian[2], Armen Melikyan[3], Othmar Marti[1]

[1]Institute of Experimental Physics - Ulm University, Ulm, Germany
[2]Yerevan Institute of Physics, Yerevan, Armenia
[3]Russian-Armenian University, Yerevan, Armenia
*corresponding author, E-mail: manuel.goncalves@uni-ulm.de

Abstract

We present a theoretical and experimental study of coupled Fabry-Pérot resonators based on layered thin films of silver and a dielectric. Despite the optical losses of the metal we show how these resonators can achieve narrow bandwidths of less than 5 nm at optical wavelengths. By adding several pairs of silver-dielectric layers and reducing the film thickness we reach the regime of hyperbolic metamaterial. We present some advantages of employing these multilayered materials in plasmonic applications.

1. Introduction

Plasmonic resonances in isolated particles have in general small Q-factors ($Q < 10$) due to the optical losses of the metal. Planar resonators provide a better solution for achieving much larger Q-factors. One of the most simple examples is the IMIMI planar structure, a metal-insulator-metal (MIM) surrounded by two dielectric layers, supporting leaky and guided modes. When the thickness of the insulator is of the order of $\lambda/2$ the IMIMI operates as a Fabry-Pérot resonator (FP). Such resonators were used to investigate the fluorescence lifetime of dye molecules [1]. Theoretical calculations based on plane waves predict Q-factors surpassing 100 by using a coupled system of two or more resonators. In general, the full-width at half-maximum (FWHM) of the FP resonances measured in reflection, or in transmission can reach values between 5 nm and 20 nm, at optical wavelengths. Coupled FP cavities are not very sensitive to variations of the refractive index of the medium outside the cavity, but are very sensitive to a small variation of the refractive index of the cavity material. When one of the media of the coupled FPs is replaced by a polymer, or by a liquid where the refractive index changes sensing applications can be envisaged. On the other hand, these structures support non-radiating plasmonic guided modes and can be applied in radiative decay engineering [2].

When the thickness of the metal and dielectric layers decrease there is a blue shift and a broadening of the resonances. By stacking several MIM structures together, one obtains a highly anisotropic uniaxial metamaterial. The effective dielectric function becomes under certain conditions hyperbolic [3]. Hyperbolic metamaterials (HMM) have received an increasing attention in plasmonics due to their exceptional light propagation properties. HMMs are most advantageous because their dispersion contains modes of large k-vector arising for evanescent guided waves. If a nanometer sized radiation source is localized near the layered material it decays faster than near a single metal surface (Purcell effect) and its angular spectrum forms a cone (conical emission) [4]. We discuss the properties of FP resonators and their extention to hyperbolic metamaterials using simple multilayered materials based on silver and aluminum oxide (Al2O3).

2. Methods

The optical properties of layered structures of silver and a dielectric were investigated both experimentally and theoretically. The reflection, transmission spectra and the guided modes were calculated using the transfer matrix method (TMM) [5]. Near-fields across the structure were also investigated using a MATLAB based code relying on the scattering matrix [6, 7]. The dispersion relation for propagating and evanescent modes was obtained from the theory of Ford and Weber [8]. We assume a dipole located in the first semi-infinite medium, 10 nm away from the next interface. The theory predicts the dissipated power of the dipole as function of the k-vector (real and complex) and the wavelength. The dipole can be oriented vertically, horizontally, or isotropically comparing to the plane of first interface. For a fixed wavelength the dissipated power decays exponentially as the k-vector mismatches the guided modes. Therefore, the color scale appearing in the dispersion maps is logarithmic.

The fabrication of the samples consists on the successive deposition of silver and dielectric thin films, by electron-beam evaporation on glass cover slides, silica, or quartz substrates. The investigation of the optical reflection at quasi-vertical incidence was done using an optical microscope with confocal detection and a small numerical aperture objective for illumination, coupled with an optical spectrometer. An angle resolved spectroscopy system was used for other angles of incidence.

3. Discussion

The number of adjacent resonances appearing in the reflectance and transmittance spectra equals the number of Fabry-Pérot resonators formed in the multilayer (see Fig. 1). The spectral separation between the resonances depends on the thickness of the metal film, which is related to the coupling constant between two independent resonators. Surprisingly, by stacking several FP resonators the FWHM of the resonant bands decreases. A drawback in the experimental fabrication is the increasing surface roughness and policrystallinity associated with the number of layers deposited, which penalizes the FWHM (see Fig. 3 and 4). The spectral position of the narrow bands varies slowly with the angle of incidence of a plane wave. Thus, a slight tuning of the reflected, or transmitted band can be achieved by sample tilting (see Fig. 2). Moreover, if the last silver layer of the resonator is made thick enough to prevent transmission of light total absorption at the narrow bands can be achieved.

The stacking of several coupled FP resonators of lower metal film thickness (in the range of 10-50 nm) leads to resonance broadening and band overlapping (see Fig. 7). The transmittance for short wavelengths can reach values over 70%. This property in the reflectance can be exploited in the design of colored filters. Since 2012, the properties of colored thin films using absorbing layers have been investigated [9, 10]. But the resulting colored mirrors were only useful for reflection. Metamaterials based on multilayer metal-dielectric stacking can also be use in transmission.

Hyperbolic metamaterials have been proposed as good candidates for broadband Purcell effect, due to the band structure of the evanescent waves [3]. We also have investigated the band structure of some multilayered MIMs. Our calculations of the dispersion were neither based on the homogenization of the dielectric function used in the effective medium theory (EMT), nor on the Bloch equation for periodic multilayers.

In this article the materials used in the experiments and calculations were Ag and Al2O3, because of the low absorption loss of Ag and the hardness and relative high refractive index of Al2O3. However, Al, Au, TiO2, MF2 and other materials can be used as well. The optical constants of the materials used in the calculations were taken from the articles of Johnson and Christy for Ag [11] and the Refractive Index Database for Al2O3 using the Sellmeier equation [12].

3.1. Reflectance and transmittance of Fabry-Pérot coupled resonators

We have investigated theoretically and experimentally the reflectance spectra of a single IMIMI and longer stacked multilayer using for the Al2O3 dielectric layer a thickness around 150 nm. The FP resonators are optically coupled because of the transmission of the middle Ag layers. The outer Ag layers can be made slightly thicker to improve the reflected, or transmitted light at specific resonance wavelengths. The theoretical calculations predict a decrease of the FWHM of the first resonance (shortest wavelength) by attaching several FP resonators, comparing to the result for a single FP resonator. However, the experimental results cannot confirm this Q-factor increase. The main reason for that could be the roughness of the films surface and the polycrystallinity. Single crystal films could achieve that improvement in the VIS and NIR spectral regions. In Fig. 1 we compare the theoretical reflectances achieved for vertical incidence for single and double FP resonators. In Fig. 2 are presented the reflectance and transmittance for all angles of incidence between 0 and 90°. For small angles on incidence we observe a slight shift of the resonances with the angle of incidence. The experimental results are shown in Fig. 3 and Fig. 4. The differences in the spectra among the samples are due to different thickness of the films deposited.

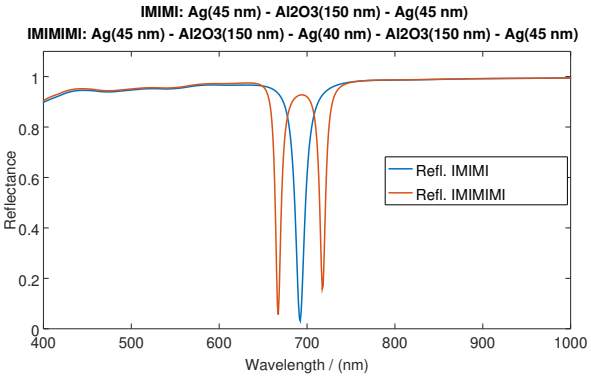


Figure 1: Theoretical reflection of a single and two coupled FP-resonators of Ag films separated by layers of Al2O3 with 150 nm thickness. The optical coupling arises if the middle Ag layer is 50 nm thick, or less. The number of resonances equals the number of coupled resonators. The Q-factor of the first resonance (shortest wavelength) increases with the number of coupled resonators.

3.2. Reflectance and transmittance of hyperbolic layered metamaterials

Already in 1955, Rytov dedicated an investigation on the optics of stratified materials [13]. Long after the theoretical developments and applications of planar dielectric waveguides in photonics a deeper interest on plasmonic multilayers emerged in the last decades of the 20th century. These materials have several properties that make them attractive for classical and quantum optics applications: they can strongly confine and guide light along the metal-dielectric interfaces and they can increase the local density of optical states leading to large Purcell effect [4, 14]. An emitter near a plasmonic multilayered material may decay faster than near a mirror.

The optical modes of IMIMIs and more complex planar structures can be calculated using the transfer matrix method, the scattering matrix method, or by numerical

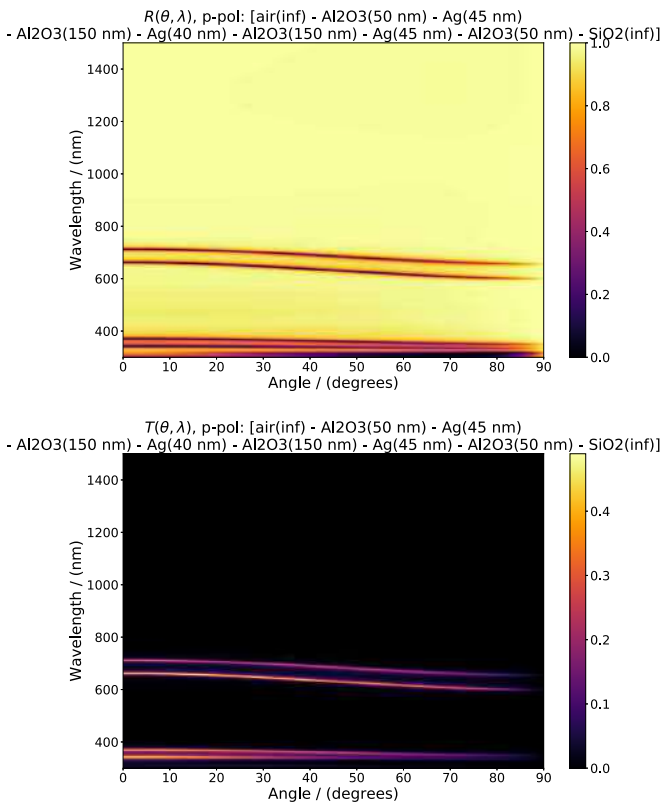


Figure 2: Reflection (top) and transmission (bottom) of a planar Ag-Al2O3 layered structure, based on two coupled Fabry-Pérot cavities. The Al2O3 cavities are 150 nm thick and they are separated by a 40 nm film of Ag. The spectral FWHM of the reflection notch filters, or transmitted bands is approximately 6 nm.

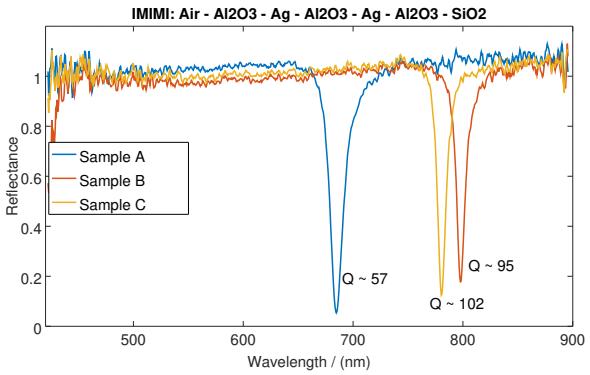


Figure 3: Experimental reflectance of a single FP-resonator of Ag films separated by a layer of Al2O3 with 150 nm thickness. Q-factors above 100 can be reached.

computation. The first two methods are semi-analytical and permit to obtain the dispersion relation and the near-fields. The dispersion can be obtained by a theory developed by Ford and Weber [8]. Barnes applied this calculation to investigate the spontaneous emission of an emitter embedded in a dielectric near a metal or a metal-dielectric multi-

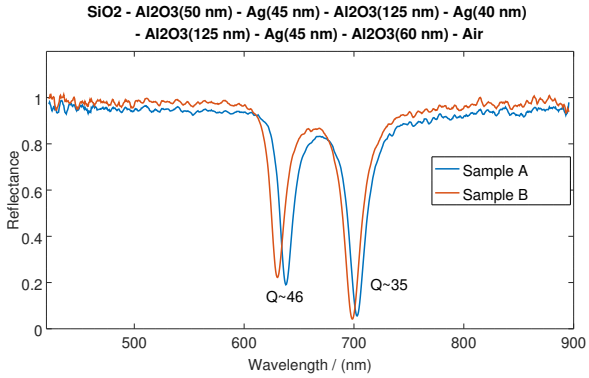


Figure 4: Experimental reflection of two coupled FP-resonator of Ag films separated by a layers of Al2O3 with 150 nm thickness. In contrast to the theoretical prediction, the experimental Q-factors of the resonances doe not increase comparing to a single resonator, mainly because of the increasing surface roughness with the number of layers and material polycrystallinity.

layer [2]. The same procedure can be applied for any planar multilayered structure.

When a metamaterial formed by a periodic array of metal-dielectric bilayers of thickness much smaller than the wavelength considered, the optical function can be approximated using the effective medium theory of Maxwell Garnett [15, 16]. This approach assumes that both the metal thickness (d_m) and the dielectric thickness (d_d) are very small comparing to the wavelength and thus, also the bilayer thickness is small, $d = d_m + d_d$. A material consisting of N bilayers is highly anisotropic and can be described by the effective dielectric functions for the propagation parallel and perpendicular to the layers plane,

$$\begin{cases} \epsilon_{\parallel} = \rho\epsilon_m + (1-\rho)\epsilon_d \\ \epsilon_{\perp} = \dfrac{\epsilon_m \epsilon_d}{(1-\rho)\epsilon_m + \rho\epsilon_d} \end{cases} \tag{1}$$

where $\rho = d_m/d$ is the filling fraction for the metal. Based on this homogenization it is easy to see that the effective dielectric function can be tuned and may achieve a certain range of values making the material more dielectric-like, or metallic-like. For layers parallel to the plane XY,

$$\frac{k_x^2 + k_y^2}{\epsilon_{\parallel}} + \frac{k_z^2}{\epsilon_{\perp}} = \frac{\omega^2}{c^2}. \tag{2}$$

Due to the negative real part of $\epsilon_m(\omega)$ for noble metals at optical frequencies the iso-frequencies of equation 2 corresponds to hyperboloids. By varying the value of ρ and the dielectric functions one can achieve a uni-axial type I hyperbolic metamaterial when $\epsilon_{xx} = \epsilon_{yy} = \epsilon_{\parallel} > 0$ and $\epsilon_{zz} = \epsilon_{\perp} < 0$, or the contrary (type II hyperbolic metamaterial). These conditions are reached when $\epsilon_{\parallel}\epsilon_{\perp} < 0$. When both $\epsilon_{\parallel}$ and $\epsilon_{\perp}$ are positive the material becomes effective anisotropic dielectric and when both $\epsilon_{\parallel} < 0$ and $\epsilon_{\perp} < 0$ the material becomes effective anisotropic metal.

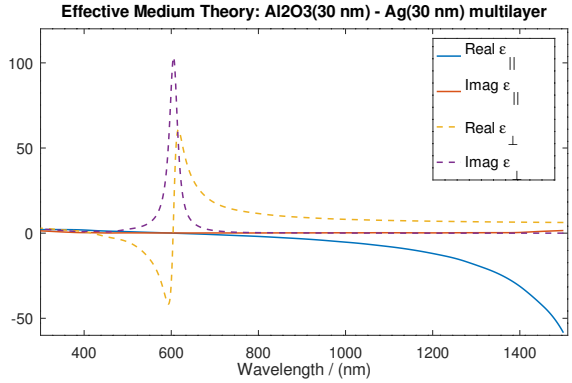


Figure 5: EMT real and imaginary parts of the dielectric functions $\epsilon_{\|}$ and $\epsilon_{\perp}$ for an undefined layered material of 30 nm Al2O3 and 30 nm Ag. For wavelengths above 600 nm the real part of the homogenized dielectric function component parallel to the layers becomes negative, like in plasmonic materials. Simultaneously, the corresponding imaginary part remains very small. The real part of the perpendicular component also becomes negative for shorter wavelengths, but the corresponding imaginary part becomes very large in that spectral region.

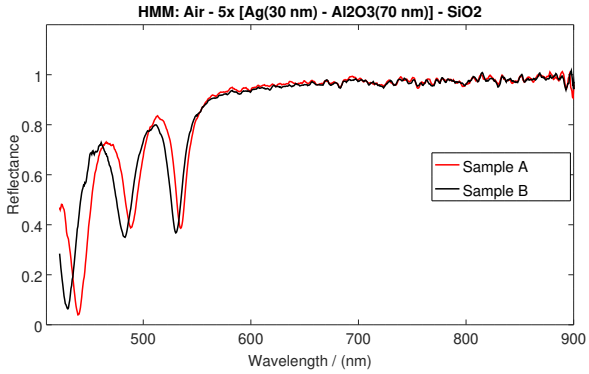


Figure 6: Experimental reflectance of samples prepared with 5 bilayers of Ag (30 nm) and Al2O3 (70 nm) on a cover slide substrate. All films were deposited by electron beam evaporation. The spectra of the reflected light were measured using an optical spectrometer and the illumination was done using an objective of small numerical aperture ($NA = 0.15$) mounted at normal incidence.

An example of effective dielectric functions $\epsilon_{\|}$ and $\epsilon_{\perp}$ obtained using the EMT calculation of an undefined medium based on 30 nm Ag and 30 nm Al2O3 layers is presented in Fig. 5.

However, this method is not adequate for a small number of layers, or if the layer thickness varies across the structure and has also other limitations [17, 18]. It should be only used as a first approach to calculate the dispersion. We used direct methods of the calculation of the dispersion avoiding approximations. Fig. 6 show the experimental reflectance for a HMM made of 5 bilayers of Ag (30 nm) and Al2O3 (70 nm). Fig. 7 shows the reflectance and transmittance for the 5 bilayers on top of a silica substrate, illuminated from the air side. These results are propagating waves using external far-field illumination. Guided modes present in the metamaterial require other mechanisms of coupling light with surface plasmons.

3.3. Guided modes

The experiments and theoretical results presented above are restricted for $k_x < k_0 = n_0(\omega/c)$, i.e. exclude evanescent waves. However, the most interesting properties exhibited by HMM materials are for large k-vectors ($k_x = k_{\|} > k_0$). We analyze in this section some results of the dispersion for a IMIMI resonator and for a HMM with 5 bilayers of Ag and Al2O3 and the near-field amplitude profiles of the modes for a fixed wavelength.

The dispersion for IMIMI resonator with a central dielectric layer of 150 nm has 4 modes (Fig. 8). The number of modes equals the number of metal-dielectric interfaces. The surface plasmon polaritons (SPP) supported in a IMI structure have a long ranged symmetric mode and a

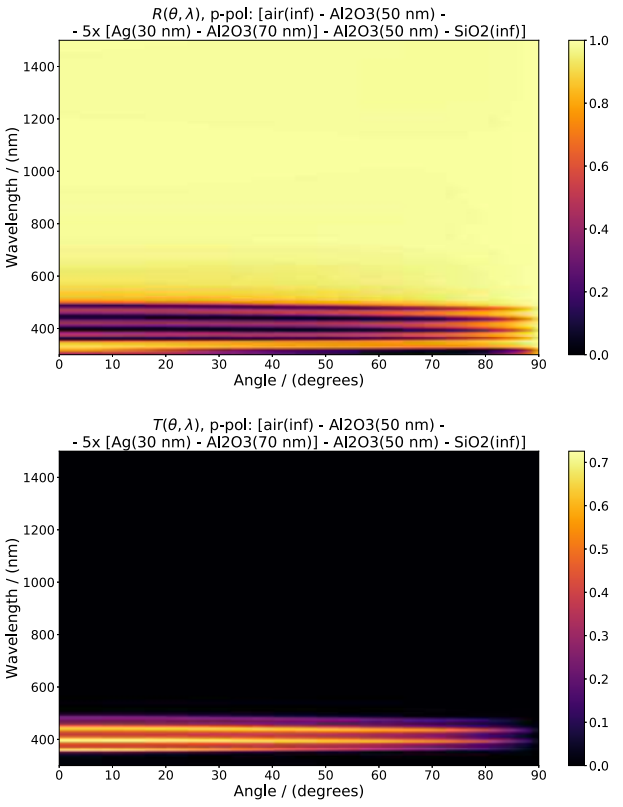


Figure 7: Reflection and transmission spectra of a hyperbolic metamaterial made of 5 bilayers of silver (30 nm) and aluminum oxide (70 nm). When the metal and dielectric thickness decreases the FP modes overlap in the short wavelength range. The transmission can reach values over 70%.

short ranged antisymmetric mode. For a fixed propagation constant the corresponding symmetric frequency $\omega_s > \omega_a$. Both modes degenerate to a single surface plasmon mode

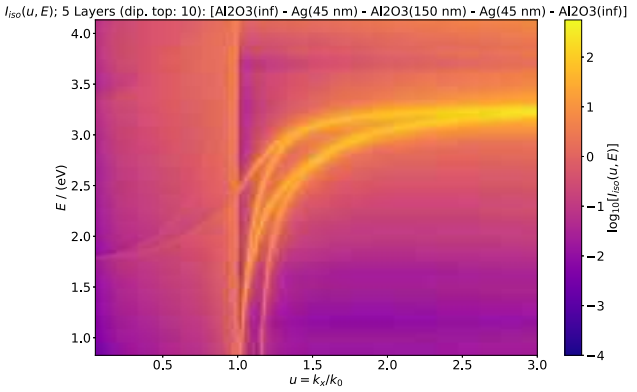


Figure 8: Dispersion of the guided modes for a single FP cavity. The k-vector was normalized to the propagation constant of the first medium. The dispersion was calculated based the power dissipated by a isotropic dipole localized 10 nm above the first silver layer. The left region ($k_{\|} < k_0$) corresponds to propagating modes through the stratified material. The TM-modes merges with the symmetric surface plasmon mode. Indeed, there is a mode hybridization between the symmetric and anti-symmetric plasmon modes and the leaky FP modes. The TE-mode at left in the propagating region has no contribution to the guided modes.

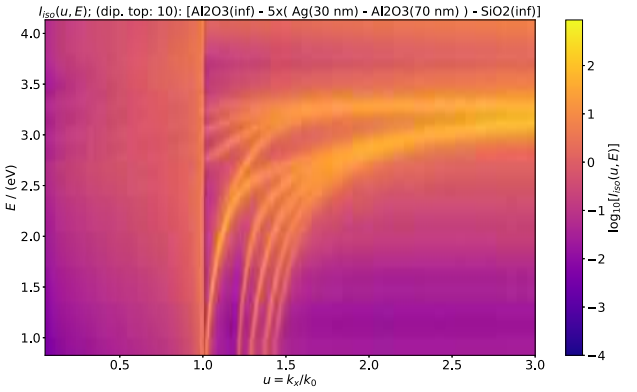


Figure 9: Dispersion of a hyperbolic metamaterial made of 5 double layers of Ag (30 nm) and aluminum oxide (70 nm) on top of a SiO2 substrate. The symmetric and antisymmetric surface plasmon modes do not converge to the light line for long wavelengths due to the mismatch of the refractive index of the substrate.

as the thickness of the metal layer increases. As we couple two IMI structures to form the IMIMI we end up with a hybridization between the FP mode and the SPP mode. However, the TE-mode of the FP resonator never crosses the light line. The same occurs for the HMM material. Here two aspects must be mentioned: for a fixed wavelength, the k-vector separation between modes increases as the thickness of the metal and dielectric layers decreases; the symmetric and antisymmetric plasmon modes, that separate the upper branch from the lower branch of the modes, do not necessarily converge to the light line for long wavelengths (see Fig. 9).

If the substrate and cover are of the same material of the dielectric layers, the symmetric and antisymmetric surface plasmon modes converge to the light line for long wavelength. If not they do not overlap as the wavelength increases (see Fig. 9). When the filling factor of metal reaches 0.5 the symmetric and antisymmetric surface plasmons modes merge. For a fixed wavelength, the reduction of the layers thickness leads to an increase of the k-vector of the modes and an large separation between them. In conclusion, a HMM with large number of guided modes, all of large k-vector requires a stack of many very thin layers of metal and dielectric (Fig. 10).

The near-field amplitude profile for each mode was calculated based on the scattering matrix. This method is more robust numerically, than the transfer matrix method and thus, preferred for thin metal-dielectric layers. For every fixed value of the wavelength, we can obtain the near-field amplitude profiles (H_y) for each mode of Fig. 8 and Fig. 9.

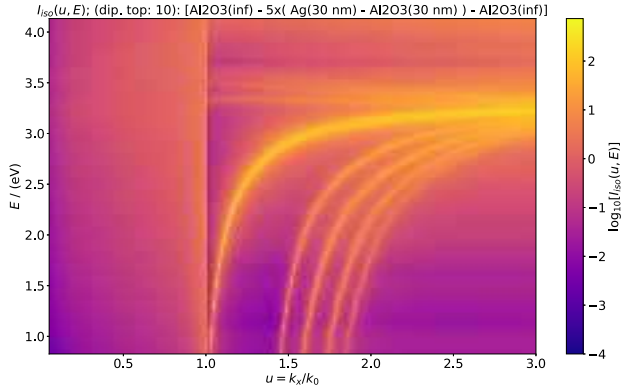


Figure 10: Dispersion of a hyperbolic metamaterial made of 5 double layers of Ag (30 nm) and aluminum oxide (30 nm) on top of a Al2O3 substrate. When the thickness of the layers becomes much smaller than the wavelength the symmetric and antisymmetric surface plasmon modes overlap. The effective index and k-vector of the guided modes and their relative separation also increases when the thickness of the layers decreases.

The results for $\lambda = 633$ nm ($E \simeq 1.96$ eV) are presented in Fig. 11 and Fig. 12. The order of the modes labeled k_i is set according to the increasing value of k_x. Due to the number of layers there is no pure symmetry, or antisymmetry of the field profile across the metal layer as in the simple IMI. Despite that, the full profile of the field has a mirror symmetry in the center of the structure. The modes labeled k_i have symmetric, or antisymmetric profile in a alternating way.

4. Conclusions

Multilayered metal-dielectric materials can either be used as narrow band optical filters for transmission of light, or

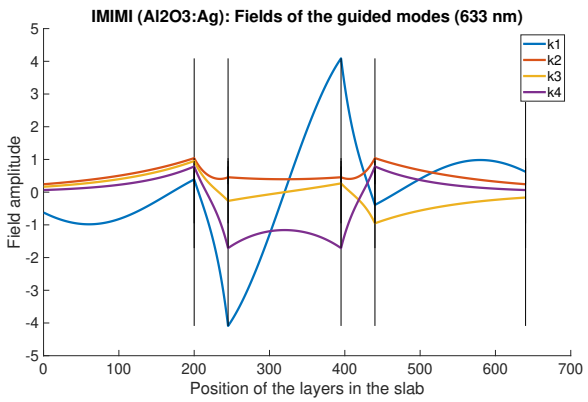


Figure 11: Field profiles of H_y for the guided modes of a single FP resonator. The mode labeled k_1 is smaller than k_0 and then is not a guided mode, rather a FP-mode for $\lambda = 633$ nm. Therefore, only two symmetric and one anti-symmetric mode exist for this wavelength.

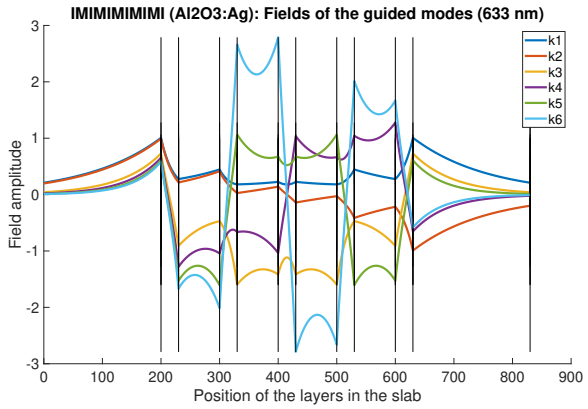


Figure 12: Field profiles of H_y for the guided modes of a layered material with 5 bilayers of Ag (30 nm) and aluminum oxide (70 nm). By increasing the number of layers the maximum amplitude of some guided modes also increases, e.g. k_6. The near-field profiles are almost never symmetric across the metal films, except in the central Ag layer, but all profiles have a mirror symmetry in the center of the structure.

as reflection notch filters. The stacking of several IMIMI resonators and a corresponding thickness reduction leads to hyperbolic metamaterials, with high impact in quantum plasmonics and radiative decay engineering. A large density of long very long k-vectors increases the density of optical states. The lifetime of emitters localized near the surface of the multilayers can be modified for a broadband of wavelengths. We have investigated the dispersion of metamaterials formed by a small number of metal-dielectric bilayers in order to understand how large k-vectors are obtained and give an intuitive description how HMMs can be achieved.

Acknowledgement

We acknowledge the Ministry of Education and Science of the Republic of Armenia (Grant 10/17) and the German Federal Ministry of Education and Research (BMBF Grant 01DK17040) for financial support. We also thank W. Barnes (University of Exeter, UK) and Antoine Moreau (Université Clermont-Auvergne, France) for discussions related to the guided modes in plasmonic multilayered materials.

References

[1] Mathias Steiner, Frank Schleifenbaum, Clemens Stupperich, Antonio V. Failla, Achim Hartschuh, Alfred J. Meixner, Microcavity-Controlled Single-Molecule Fluorescence, *Chem. Phys. Chem.* **6**(10) 2190 (2005). doi:10.1002/cphc.200500108

[2] W. L. Barnes, Fluorescence near interfaces: the role of photonic mode density, *J. Mod. Opt.* **45**, 661 (1998). doi:10.1080/09500349808230614

[3] Alexander Poddubny, Ivan Iorsh, Pavel Belov and Yuri Kivshar, Hyperbolic metamaterials, *Nature Photon.* **7**, 948 (2013). doi:10.1038/nphoton.2013.243

[4] C. L. Cortes, W. Newman, S. Molesky and Z. Jacob, Quantum nanophotonics using hyperbolic metamaterials, *J. Opt.* **16**, 129501 (2014). doi:10.1088/2040-8978/14/6/063001

[5] S. J. Byrnes, Multilayer optical calculations, arXiv:1603.02720 [physics.comp-ph]. https://arxiv.org/abs/1603.02720

[6] F. Krayzel, R. Pollès, A. Moreau, M. Mihailovic, G. Granet, Simulation and analysis of exotic non-specular phenomena, *J. Europ. Opt. Soc. - Rapid publications* **5** (2010). doi:10.2971/jeos.2010.10025

[7] J. Defrance, C. Lemaître, R. Ajib, J. Benedicto, E. Mallet, R. Pollès, J.-P. Plumey, M. Mihailovic, E. Centeno, C. Ciracì, D. R. Smith, and A. Moreau, Moosh: A Numerical Swiss Army Knife for the Optics of Multilayers in Octave/Matlab, *Journal of Open Research Software*, **4**, e13 (2016). doi:10.5334/jors.100

[8] G. W. Ford and W. H. Weber, Electromagnetic interactions of molecules with metal surfaces, *Physics Reports* **113**(4), 195–287 (1984). doi:10.1016/0370-1573(84)90098-X

[9] Mikhail A. Kats, Deepika Sharma, Jiao Lin, Patrice Genevet, Romain Blanchard, Zheng Yang, M. Mumtaz Qazilbash, D. N. Basov, Shriram Ramanathan, and Federico Capasso, Ultra-thin perfect absorber employing a tunable phase change material *Appl. Phys. Lett.* **101**, 221101 (2012). doi:10.1063/1.4767646

[10] Mikhail A. Kats, Romain Blanchard, Shriram Ramanathan and Federico Capasso, Thin-Film Interference in Lossy, Ultra-Thin Layers, *Opt. & Photon. News* **25**(1), 40 (2014). doi:10.1364/OPN.25.1.000040

[11] P. B. Johnson and R. W. Christy, Optical Constants of the Noble Metals, *Phys. Rev. B* **6**, 4370 (1972). doi:10.1103/PhysRevB.6.4370

[12] M. N. Polyanskiy, Refractive index database, (2019). https://refractiveindex.info

[13] S. M. Rytov, Electromagnetic Properties of a Finely Stratified Medium, *Soviet Physics JETP* **2**(3), 466 (1956).

[14] V. Popov, A. V. Lavrinenko, A. Novitsky, Surface waves on multilayer hyperbolic metamaterials: Operator approach to effective medium approximation, *Phys. Rev. B* **97**, 125428 (2018). doi:10.1103/PhysRevB.97.125428

[15] J. C. Maxwell Garnett, XII. Colours in metal glasses and in metallic films, *Phil. Trans. Royal Soc. A* **203**(359–371), (1904). doi:10.1098/rsta.1904.0024

[16] J. C. Maxwell Garnett, VII. Colours in metal glasses, in metallic films, and in metallic solutions.II, *Phil. Trans. Royal Soc. A* **205**(387–401), (1906). doi:10.1098/rsta.1906.0007

[17] O. Kidwai, S. V. Zhukovsky, and J. E. Sipe, Effective-medium approach to planar multilayer hyperbolic metamaterials: Strengths and limitations, *Phys. Rev. A* **85**, 053842 (2012). doi:10.1103/PhysRevA.85.053842

[18] T. Li and J. B. Khurgin, Hyperbolic metamaterials: beyond the effective medium theory, *Optica* **3**(12), 1388–1396 (2016). doi:10.1364/OPTICA.3.001388

Metasurfaces and flat optics, FSS, HIS,

Touching-dimer metagratings with high asymmetric diffraction in the full visible range

Tan Shi[1], Yujie Wang[2], Zi-Lan Deng[1,*], Shumin Xiao[2], Xiangping Li[1,*]

[1]Guangdong Provincial Key Laboratory of Optical Fiber Sensing and Communications, Institute of Photonics Technology, Jinan University, Guangzhou 510632, China.

[2]State Key Laboratory on Tunable Laser Technology, Ministry of Industry and Information Technology Key Lab of Micro-Nano Optoelectronic Information System, Shenzhen Graduate School, Harbin Institute of Technology, Shenzhen, Guangdong 518055, China.

[*]E-mail: zilandeng@jnu.edu.cn, xiangpingli@jnu.edu.cn

Abstract

We propose a kind of all-dielectric touching-dimer metagratings that can achieve flat-top broadband all-angle high asymmetric diffractions in visible light. High diffraction light deflection is obtained by proper design of two touching titanium dioxide pillars with various cross-section shapes in each unit-cell of the metagrating, without creating a discrete gradient phase profile as traditional metasurfaces always do. The touching-dimer architecture is superior to many previous multiple scatters metagrating designs that are typically optimized at single wavelength and inicident angle, and is promising for many high-performance angle-controllable wavefront shaping applications.

Introduction

In the past few years, advances in metasurfaces technology have enabled optical manipulation at wavelength or sub-wavelength scales[1]. Phase-gradient metasurfaces require spatially-varying building block structures to realize the discrete levels of a given phase profile, which suffer from the fundamental limits on the overall efficiency and fabrication challenge on spatial resolution, especially for extreme large angle wavefront shaping[2]. In this regard, high diffraction metagratings with identical structure in each unit cell are proposed [2-6]. To achieve the high diffraction efficiency in metagrating, one can either break the symmetry of the building block of the metagrating, or break the symmetry of the illumination condition of the metagrating (typically by oblique incidence). In previous asymmetric metagrating designs, separated multiple inclusions are typically employed to optimize the maximum diffraction efficiency at a given wavelength and incident angle. Here, we propose a kind of touching-dimer metagratings (Fig. 1(a)), which can achieve high asymmetric diffraction with all-incident angles in the full visible range. The building block of the metagrating is formed by touching two different shaped polygons, which supports the ultra-high directional scattering (Fig. 1(b)). Arranging such asymmetric building blocks as a periodical array to form a metagrating, maximum asymmetric diffraction up to 90% and bandwidth of nearly 200 nm in the visible range for normal incidence can be obtained (Fig. 1(c)). In addition, by changing the direction of incidence angle, broadband can be obtained in the range of 0 to nearly 90 degrees, covering almost the whole visible range (Fig. 1(d)). Our research can provide a feasible scheme for broadband large-angle arbitrary

wavefront shaping applications.

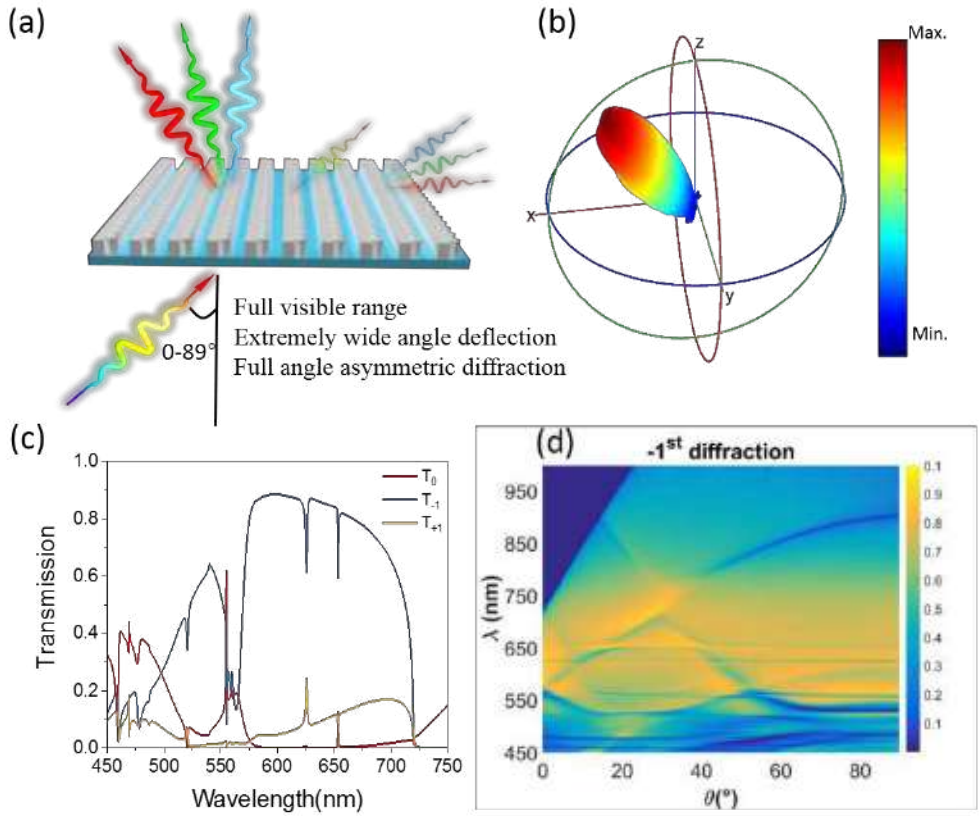


Fig. 1. (a) Schematic of the touching-dimer metagrating. (b) Far-field scattering pattern of the touching dimer at the wavelength of 598 nm. (c) Transmitted diffraction spectra of diffrent orders for TM-polarized normal incidence. (d) The calculated T_{-1} for varying incident angles from 0° to 90° and varying wavelengths from 450 nm to 1000 nm for TM-polarized incidence.

Acknowledgements

This research was supported by National Natural Science Foundation of China (NSFC) (Grant 11604217, 61522504, 61420106014, 11774145, 11734012, 11574218), Guangdong Provincial Innovation and Entrepreneurship Project (Grant 2016ZT06D081), Applied Science and Technology Project of Guangdong Science and Technology Department (2017B090918001).

References

[1] N. Yu, P. Genevet, M. A. Kats, F. Aieta, J. P. Tetienne, F. Capasso, and Z. Gaburro, Science **334**, 333 (2011).

[2] Y. Ra'di, D. L. Sounas, and A. Alù, Phys. Rev. Lett. **119**, 067404 (2017).

[3] Z.-L. Deng, S. Zhang, and G. P. Wang, Nanoscale **8**, 1588 (2016).

[4] Z.-L. Deng *et al.*, Light Sci. & Appl. **7**, 78 (2018).

[5] E. Khaidarov *et al.*, Nano Lett **17**, 6267 (2017).

[6] Z.-L. Deng, Y. Cao, X. Li, and G. P. Wang, Photon. Res. **6**, 443 (2018).

Focusing and Ultra-high Resolution by Integrated Metalens

Juntao Li[1*], Qian Sun[1], Yuhao Ren[1], and Haowen Liang[1*]

[1] State Key Laboratory of Optoelectronic Materials and Technologies, School of Physics, Sun Yat-sen University, No. 135 Xingang-Xi Rd., 510275, Guangzhou, China
*corresponding author, E-mail: lijt3@mail.sysu.edu.cn, lianghw26@mail.sysu.edu.cn

Abstract

We present a metalens composed of double layer crystalline silicon metasurfaces to achieve an optical needle focusing with ultra-high resolution of λ/5. This metalens is promising for non-intrusive, far-field super-resolution optical imaging.

1. Introduction

Metasurfaces are ultra-thin optical structures relying on the scattering properties of subwavelength scale optical resonators to control the polarization, phase, amplitude and dispersion of light [1]. Recent years have witnessed the fast development of metasurfaces in optical focusing and optical field manipulation, showing that metasurfaces is a versatile platform for photonic engineering [2-4]. Among the dielectric metasurfaces, the high index dielectric materials of crystalline silicon (c-Si) has been shown to be used in the high transmission metasurfaces at visible wavelength because of its low loss and low cost [5-7]. Furthermore, we have showed that c-Si allow metasurfaces to be embedded into other solid materials as the ultra-high NA meatlens, indicating that c-Si metasurfaces can be vertically integrated to build miniaturized systems [7].

The c-Si integrated metalens has the potential to be used in the super-resolution imaging system. The Traditional objective lenses in modern microscopy are restricted by the Rayleigh diffraction limit 0.61λ/NA (where NA is numerical aperture). Great efforts, such as near-field scanning optical microscopy (NSOM), stimulated emission depletion microscopy (STED), photo-activated localization microscopy (PALM) and stochastic optical reconstruction microscopy (STORM), have been devoted to overcome the limit in either near-field or far-field during the past decades. However, all of these approaches are either optically intrusive or physically intrusive that none of them is a truly non-intrusive universal imaging technique. On the contrary, the manipulation of cylindrical vector beams provides a promising method for the non-intrusive imaging. A sharper focusing needle beyond the diffraction limit can be generated in any medium with spatially modulated radially polarized (RP) and azimuthally polarized (AP) beams [8]. However, this technique requires precise alignment of optical alignments that it brings significant challenges to be experimentally set up [9].

In this work, we firstly showed our previous work of an oil front-immersion metalens with NA = 1.48, a bandwidth of 211 nm and a focusing efficiency of 48% at 532 nm wavelength, based on a 500 nm thick c-Si on sapphire [7]. Then we propose an integrated metalens to generate optical needle with ultra-small resolution in the far-field. The miniature system consists an ultra-high NA metalens and a vector beam controlling metasurface. With the evolutionary algorithm for inverse design, the first metasurface performs as a metalens enabling NA = 1.48 to realize sharp focusing; while the second metasurface is able to efficiently convert the linearly polarized (LP) beam into RP beam. An optical resolution of 0.22λ is achieved with the proposed integrated system. This integrated system can be fully fabricated by mature micro-electronic process with nano-level alignment accuracy, giving rise to achieve truly non-intrusive, far-field nano-imaging in an easy and cost-efficient way.

2. Results

The first metasurfaces behaves as a controller to generate pure RP beam with ellipsoid meta-atoms. For the second layer, the metasurfaces performs as a metalens that only contains the high spatial frequencies. The central part of the metalens (corresponding to low spatial frequencies) is covered by gold. The high spatial frequencies part consists of a series of large angle deflectors. The deflectors are inverse-designed by our hybrid optimization algorithm to ensure simultaneously high transmission and large angle deflection on x and y incident polarizations. Then two metasurfaces layers are bonded and aligned together.

The designate large angle deflector and RP controller are shown in Fig. 1, respectively. The focusing performance of the integrated metalens is also shown in Fig. 1. The high spatial frequencies design will naturally elongate the focal spot to an optical needle, while the lateral resolution of the optical needle is reduced beyond the diffraction limit. The inverse-design deflectors yield a deflection angle of 78.2412°, indicating a 1.48 numerical aperture of the metalens under immersion oil with the index of 1.515. The full width half maximum (FWHM) of the optical needle is

115 nm, showing an 0.22λ lateral resolution at the wavelength of 532 nm. The depth of focus (DOF) is about 10 μm (≈18λ) with the diameter of 50 μm of the metalens, ensuring high tolerance in axial positioning. All these benefits enable us to achieve a high-quality image for a large-area object at a high scanning speed under laser confocal microscope. Moreover, the precise alignment of the layered metasurfaces ensures high symmetrical vector beam focusing, which significantly simplifies the complexity of the system and increases the imaging robustness.

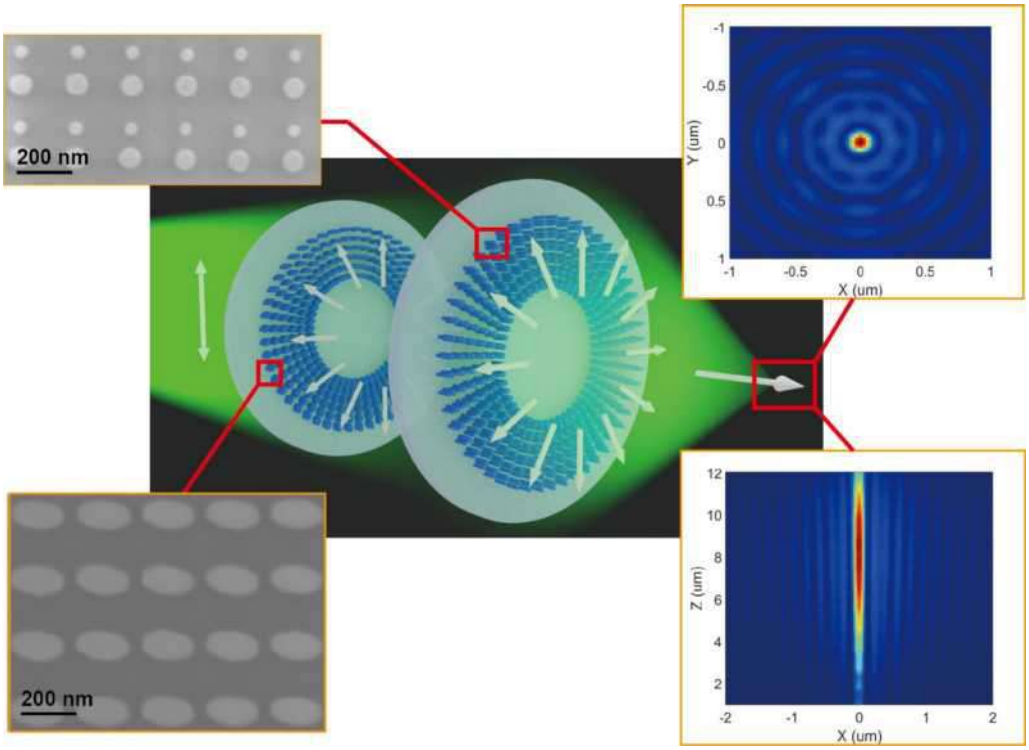


Figure 1: The schematic show of the integrated metalens. The large angle deflectors guarantee that the focal spot is mainly contributed by the light with high spatial frequencies. The focal spot then is elongated by the high spatial frequencies and is compressed at the lateral resolution by the modulation of RP beam.

3. Conclusion

Here we show an c-Si integrated metalens to generate an optical needle with ultra-high resolution. The structure composed of two metasurfaces with precise alignment. One metasurface is able to efficiently convert LP beam into RP beam, while the other one enable a large angle focusing of the RP beam. With the modulation of the two metasurfaces, an optical needle is achieved with a lateral resolution of 115 nm (0.22λ) and DOF of 10 μm (≈18λ) at the wavelength of 532 nm. The unique features of this integrated metalens shows various benefits in nano-scale imaging, including high tolerance in axial positioning, high quality imaging at a high scanning speed and a higher resolution. We envision that this integrated design will significantly reduce the complexity of the construction of super-resolution imaging system, giving rise to achieve truly non-intrusive, far-field nano-imaging in an easy and cost-efficient way.

References

[1] N. Yu, et al., Flat Optics with designer metasurfaces, *Nat. Mater.*, 11: 917-924, 2012.

[2] M. Khorasaninejad, et al., Metalenses at visible wavelengths: Diffraction-limited focusing and subwavelength resolution imaging, *Science*, 352: 1190-1194, 2016.

[3] A. Arbabi, et al., Dielectric metasurfaces for complete control of phase and polarization with subwavelength spatial resolution and high transmission, *Nat. Nanotechnol.*, 10: 937-943, 2015.

[4] S. Wang, et al., A broadband achromatic metalens in the visible, *Nat. Nanotechnol.*, 13: 227-232, 2018.

[5] Z. Zhou, et al. Efficient Silicon Metasurfaces for Visible Light, *ACS Photon.*, 4: 544-551, 2017.

[6] D. Sell, et al., Visible Light Metasurfaces Based on Single-Crystal Silicon, *ACS Photon.*, 3: 1919-1925, 2016.

[7] H. Liang, et al., Ultrahigh Numerical Aperture Metalens at Visible Wavelengths, *Nano Lett.*, 18: 4460-4466, 2018.

[8] H. Wang, et al., Creation of a needle of longitudinally polarized light in vacuum using binary optics, *Nat.Photon.*, 2: 501-505, 2008.

[9] X. Xie, et al., Harnessing the Point-Spread Function for High-Resolution Far-Field Optical Microscopy, *Phys. Rev. Lett.*, 113: 263901, 2014.

Comparison of the negative energy flow in linearly and circularly polarized beams focused with metalens

Victor Kotlyar[1], Anton Nalimov[2*], Sergey Stafeev[2]

[1]IPSI RAS – Branch of the FSRC "Crystallography and photonics" RAS, Samara, Russia
[2]Samara National Research University, Samara, Russia
*corresponding author, E-mail: anton@smr.ru

Abstract

Using the FDTD-aided numerical simulation, we show that uniform linearly or circularly polarized light passing through the proposed optical metasurface with m=2 and then tightly focused with a binary zone plate generates an on-axis near-focus energy backflow comparable in magnitude with the incident energy. Notably, the magnitude of the reverse energy flow is shown to be the same when focusing a circularly polarized optical vortex with topological charge m=2 and a light beam with the second-order polarization singularity.

1. Introduction

Optical vortex beams have been known for a long time [1]. Such beams have a spiral phase, which affects the propagation properties of these beams [2]. Interest in them results from a variety of possibilities for use. For example, vortex beams can be used in telescopes for detecting distant planets [3], controlling the movement of microparticles in optical tweezers [4, 5], etc. Another possibility of using optical vortices is to create beams with an area where the energy flows in the opposite direction for the propagation of the beam [6]. In this work a metalens containing binary zone plates with a numerical aperture close to one and a set of binary subwavelength diffraction gratings that work as half-wave plates and rotate the polarization vector of the incident field by the angle mφ is considered. It is theoretically and numerically shown that the metalens forms an m-th order converging polarization vortex (with linearly polarized incident light) or phase vortex with topological charge m and circular polarization (when circularly polarized incident light is used). In the sharp focus of such a converging light beam on the optical axis, there is a reverse flow of light energy, comparable to the direct flow.

2. Focusing a field with polarization singularity

Projections Ex and Ey of the electric vector in case of polarization singularity are shown in Fig. 1.

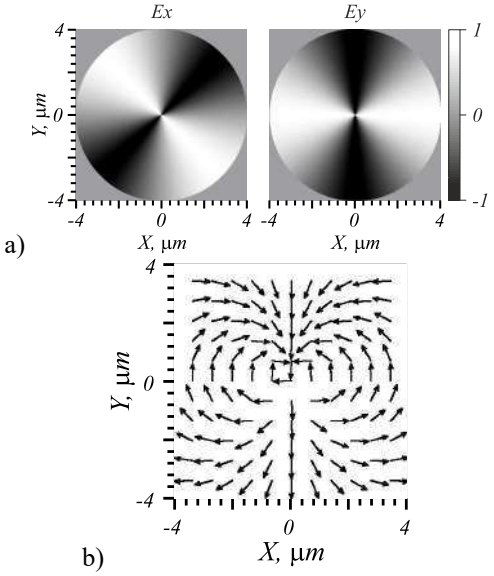


Fig. 1. Projections of the E-vector on the X- and Y-axes (a): the maximum value is marked with white color (+1), the minimal value - with black color (-1), and zero value marked as grey; Pattern of polarization states in the field (b)

The polarization pattern of the field is depicted in Fig. 2b, with the unit intensity assumed over the entire field.
Figure 3 depicts the result of focusing the beam from Fig. 2a using a binary zone plate. Shown in Fig. 3 a,b are two-dimensional patterns of intensity:

$$I = I_x + I_y + I_z = \left|E_x\right|^2 + \left|E_y\right|^2 + \left|E_z\right|^2 \quad (1)$$

and the longitudinal component Sz of the Poynting vector

$$\mathbf{S} = \frac{1}{2}\mathrm{Re}\left[\mathbf{E}\times\mathbf{H}^*\right] \quad (2)$$

in the focal plane (z=600 nm). Using an FDTD-aided approach, we numerically simulated the focusing of the beam with polarization singularity with a six-ring binary zone plate on the assumption of the incident wavelength λ=633 nm, focal length f=λ, and a λ/30 increment of the simulation grid on all three coordinates. The field and the zone plate were bounded by a 8-μm circular aperture.

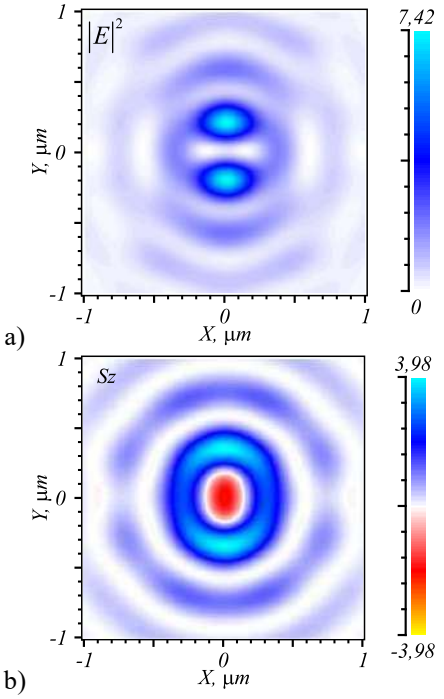
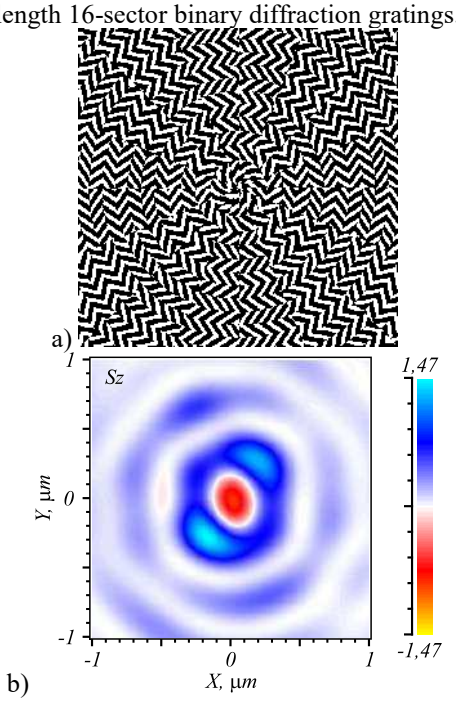


Fig. 3. Intensity I of the light field (a) and longitudinal component Sz of the Poynting vector (b) in the focal plane 0.6-μm behind the zone plate.

It is seen from Fig. 3d that when focusing the field of interest, an on-axis energy backflow occurs in the focal spot.

3. A metalens for simultaneous polarization conversion and focusing of light

The idea is that the metasurface-assisted polarization converter (MPC) and a focusing binary zone plate can be combined, resulting in a single metalens. Presented in Fig. 4a is the external appearance of a MPC composed of subwavelength 16-sector binary diffraction gratings.



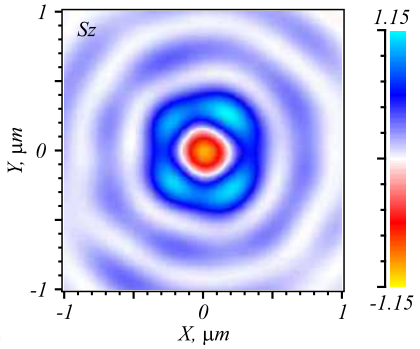


Fig. 4. A combined metalens (a) to simultaneously generate and focus the polarization vortex; longitudinal projection of Poynting vector Sz in the focal plane 0.6-μm away from the metalens for a linearly polarized incident wave (b) and left-circular polarized incident wave (c).

It is seen from fig. 4b,c that at m=2, for both the polarization and phase singularities, the on-axis near-focus reverse flow of light energy is comparable in magnitude with the incident energy.

Acknowledgements

The work was partly funded by the Russian Science Foundation under grant # 17-19-01186.

References

[1] Nye JF, Berry MV. Dislocations in wave trains. Proc. R. Soc. London Ser. A, 1974; 336: 165–90.

[2] Soskin MS, Vasnetsov MV. "Singular optics," in Progress in Optics, E. Wolf, ed. (Elsevier, 2001), Chap. 4, pp. 219–276.

[3] Grover AS, Jr. The optical vortex coronagraph. J. Opt. A, 2009; 11: 094022.

[4] Gahagan KT, Swartzlander GA. Optical vortex trapping of particles. Opt. Lett., 1996; 21: 827–9.

[5] Gecevičius M, Drevinskas R, Beresna M, Kazansky PG. Single beam optical vortex tweezers with tunable orbital angular momentum. Appl. Phys. Lett., 2014; 104: 231110.

[6] Stafeev SS, Nalimov AG. Longitudinal component of the Poynting vector of a tightly focused optical vortex with circular polarization. Computer Optics 2018; 42(2): 190-196. DOI: 10.18287/2412-6179-2018-42-2-190-196.

Spiral metalens for tight focusing of azimuthally polarized optical vortex

Anton G. Nalimov[1,2], Sergey S. Stafeev[1,2], Liam O'Faolain[3], Victor V. Kotlyar[1,2]

[1]Image Processing Systems Institute – Branch of the Federal Scientific Research Centre "Crystallography and Photonics" of the Russian Academy of Sciences, Samara, Russia
[2]Samara National Research University, Samara, Russia
[3]Centre for Advanced Photonics and Process Analysis, Cork Institute of Technology, Cork, Ireland
*corresponding author, E-mail: sergey.stafeev@gmail.com

Abstract

We investigated a spiral metalens fabricated on a thin film of amorphous silicon and consisting of a set of subwavelength binary diffractive gratings. The metalens converts linearly polarized incident light into an azimuthally polarized optical vortex, and focuses it at a distance approximately equal to the wavelength of the incident light 633 nm. Using a scanning near-field optical microscope, it is shown experimentally that the metalens forms an elliptical focal spot with diameters smaller than the diffraction limit: 0.32 and 0.51 of the wavelength. The experimental results are close to the those of a numerical simulation using the FDTD method, with 0.37 and 0.49 of the wavelength.

1. Introduction

A significant number of recent scientific papers have been devoted to the investigation of metasurfaces, thin optical elements that simultaneously control the amplitude, phase and polarization of propagated light [1]. Metasurface-based elements can focus light into a ring [2], a segment [3], or a spot [4]. A special case of a metasurface is a simple subwavelength grating. Subwavelength gratings are anisotropic, meaning that TE- and TM-polarized waves propagated through them have different phases. Based on this effect, it is possible to create analogues of the classical half-wave plates, which rotate the direction of polarization. In our work, we have investigated elements based on subwavelength gratings that are designed to produce cylindrical vector beams, that is, beams in which the direction of polarization has radial symmetry [5].

In this work, we investigate a 16-sector spiral metalens consisting of subwavelength gratings. This metalens converts linearly polarized light to an azimuthally polarized optical vortex and focuses it. Using a scanning near-field optical microscope, it is shown experimentally that the metalens forms a focal spot with a diameters smaller than the diffraction limit: FWHMx = 0.32λ and FWHMy = 0.51λ.

2. Design and manufacturing

The investigated spiral metalens (Fig. 1a) is a combination of a spiral zone plate with a topological charge $m = 1$ (Fig. 1b) and a sectorial subwavelength grating that acts as a halfwaveplate. The lens consists of 16 radial sectors, each of which rotates the polarization of the incident light to produce the azimuthal polarization (Fig. 1c). Each sector is divided into sub-areas in the shape of a circular arc. The angle of the relief in neighboring areas within one sector is chosen such that the polarization of the light passing through them differs by π (Fig. 1c). Linearly polarized incident light (the incident polarization in Fig. 1 is directed vertically) is transformed into a focused, azimuthally polarized optical vortex. The period of the grating is 220 nm, and the depth of the relief is 120 nm. The focal length of the zone plate (shown in Fig. 1b) is equal to the illumination wavelength, $f = \lambda = 633$ nm.

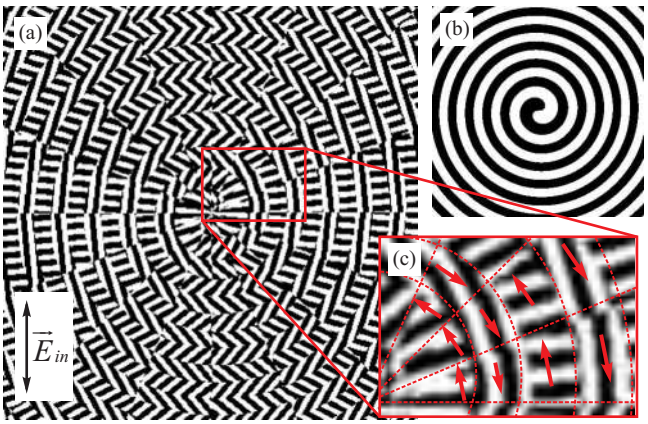


Figure 1: (a) Spiral metalens, (b) corresponding binary spiral zone plate with topological charge $m = 1$, (c) polarization of light transmitted through the metalens.

A metalens with the relief shown in Fig. 1a was fabricated using electron beam lithography. A 130-nm-thick amorphous silicon film (a-Si) (with refractive index $n = 4.35 + i0.486$) was deposited on a transparent pyrex substrate (with refractive index $n = 1.5$), coated with a 320-nm-thick PMMA resist, and baked at a temperature of 180C°. To prevent charging, the surface was sputtered with a gold layer 15 nm in thickness. A binary template was transferred onto the resist surface using a 30 kV electron beam. The specimen was developed in water blended with isopropanol in the ratio 3:7, and the template was then transferred from the resist into the a-Si film, using reactive

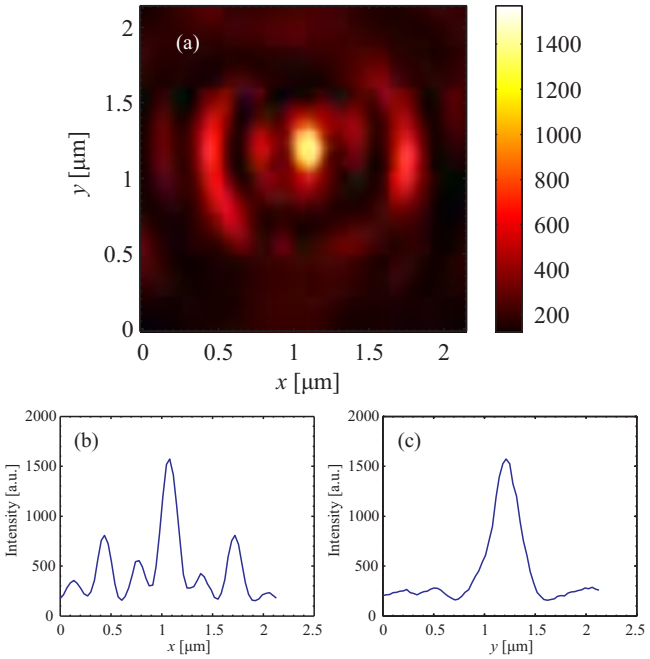


Figure 2: Measured intensity of the focal spot of the metalens: 2D intensity pattern (a) and intensity profiles along the (b) x- and (c) y- axes.

ion etching in a gaseous atmosphere of CHF_3 and SF_6. The aspect ratio of the etch rate of the material and the photomask was found to be 1:2.5. As a result of this process, the gold was completely washed out from the PMMA surface.

3. Experiment

The focusing by the fabricated spiral metalens was investigated experimentally using a scanning near-field optical microscope (Ntegra Spectra, NT-MDT). In this experiment, a light beam from an He-Ne laser (wavelength λ=633 nm) was used to illuminate the metalens. The full width of the incident beam was 30 μm. The intensity of the focal spot was measured using a hollow, metalized, pyramid-shaped probe with a 100 nm pinhole in the vertex. After passing through the pinhole, the light was collected by a 100x objective lens before travelling to the CCD camera (Andor, DV401-BV).

Fig. 2 shows the results of focusing. The intensity distribution is shown in Fig. 2a, and its sections along the x and y axes are shown in Fig. 2b and 2c, respectively. The focal spot diameters in Fig. 2 were FWHMx = 0.32λ (Fig. 2b) and FWHMy = 0.51λ (Fig. 2c). The maximum intensity of the focal spot was seven times larger than the maximum intensity of the input beam.

Next, we FDTD-simulated the propagation of light through the metalens with the manufactured relief. The focal length in this simulation was equal to 633 nm. Fig. 3 shows the intensity distribution of the focal spot.

The simulation shows that the manufactured metalens

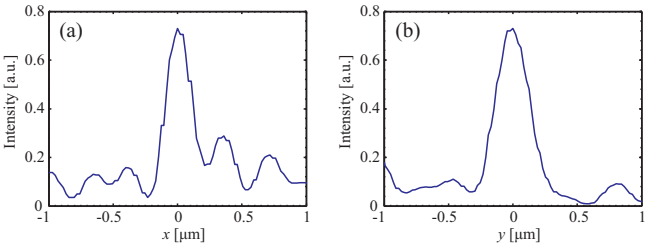


Figure 3: Calculated intensity of the focal spot: intensity profiles along the (a) x- and (b) y- axes.

forms an elliptical focal spot with half-maximum diameters that are smaller than the diffraction limit: FWHMx=0.37λ and FWHMy=0.49λ.

4. Conclusions

In this work, we investigate a spiral metalens based on subwavelength gratings. The metalens converts linearly polarized light to an azimuthally polarized optical vortex with topological charge $m = 1$ and focuses it. The metalens was fabricated using electron beam lithography applied to a amorphous silicon film deposited on a pyrex substrate. Using a scanning near-field optical microscope, it was shown experimentally that the metalens forms a focal spot with diameters that are smaller than the diffraction limit: FWHMx = 0.32λ and FWHMy = 0.51λ. The experimentally obtained values are close to the results of a numerical simulation of the manufactured metalens using the FDTD method, which are FWHMx = 0.37λ and FWHMy = 0.49λ.

Acknowledgement

Russian Foundation for Basic Research (18-29-20003).

References

[1] N. Yu, F. Capasso, Flat optics with designer metasurfaces, *Nat. Mater.* 13: 139–150, 2014.

[2] L. Lan, W. Jiang, Y. Ma, Three dimensional subwavelength focus by a near-field plate lens, *Appl. Phys. Lett.* 102: 231119, 2013.

[3] L. Verslegers, P.B. Catrysse, Z. Yu, J.S. White, E.S. Barnard, M.L. Brongersma, S. Fan, Planar lenses based on nanoscale slit arrays in a metallic film, *Nano Lett.* 9: 235-238, 2009.

[4] A. Arbabi, Y. Horie, A.J. Ball, M. Bagheri, A. Faraon, Subwavelength-thick lenses with high numerical apertures and large efficiency based on high-contrast transmitarrays, *Nat. Commun.* 6: 7069, 2015

[5] Q. Zhan, Cylindrical vector beams: From mathematical concepts to applications, *Adv. Opt. Photon.*, 1: 1–57, 2009.

Design and Manufacturing of Bitmap-type Microwave Absorber Metasurface

Ye-Pil Kwon[1], Eun-chae Jeon[1], Tae-Jin Je[2], Je-Ryung Lee[2], Seunghwan Moon[2], Myungjoon Kim[3], Joonkyo Jung[3], Jonghwa Shin[3], Doo-Sun Choi[2,*]

[1]School of Materials Science and Engineering, University of Ulsan, Ulsan, Korea
[2]Department of Nanomanufacturing Technology, Korea Institute of Machinery and Materials, Daejeon, Korea
[3]Department of Materials Science and Engineering, KAIST, Daejeon, Korea
*corresponding author, E-mail: choids@kimm.re.kr

Abstract

Metasurfaces having a large degree of freedom are highlighted in order to replace absorptive paints for microwave stealth function. We suggested new methods to design and to manufacture bitmap-type microwave absorber metasurfaces based on an inductive and a deductive design approaches and mechanical machining technologies in this study. A manufactured metasurface having 300mm in size showed less than -10dB reflectivity from 9GHz to 12GHz.

1. Introduction

Microwave stealth technology against radar detection is becoming ever more important in protecting soldiers and assets and in assuring the success of mission, with recent development of various counter-measures. So far, absorptive paints have been the dominant material technology for the microwave stealth function. However, the paint is expensive and requires frequent reapplications. Moreover, once applied, the paint has a fixed frequency band of effectivity. In order to address these problems, we propose bitmap-type microwave absorber metasurfaces in this study. The suggested metasurfaces are relatively easy to manufacture by mechanical machining technologies and have a large degree of freedom in terms of the choice of the target microwave frequency and the bandwidth.

2. Design of microwave absorber metasurface

We utilized two design approaches to optimize the bitmap structure: a genetic algorithm (an inductive method) and an equivalent circuit model (a deductive method). The target microwave band was selected as the X-band (8–12 GHz), but the design can be scaled to other bands as well. The whole structure is composed of a back reflector (optically thick metal layer), a dielectric spacer, and the top patterned conductive ink layer. The equivalent circuit model was first used to investigate the general performance boundaries achievable by a single or dual resonances near the target frequency, irrespective of the actual implementation of those resonances. Then, the genetic algorithm was used to obtain an optimized bitmap structure as shown in Fig. 1. By comparing the performance of the resulting design to the performance of a hypothetical design with optimal resonances, it was confirmed that the current design is very near to the global optimum. The conductive ink is filled in an dielectric substrate according to the optimized pattern (black squares in Fig. 1). The optimized bitmap structure in Fig. 1 is a unit cell and it can be periodically arranged along both the X-axis and Y-axis to meet the required size of microwave absorber. For example, the unit cell can be repeated by 20×20 to produce a absorptive surface of 300mm×300mm in size.

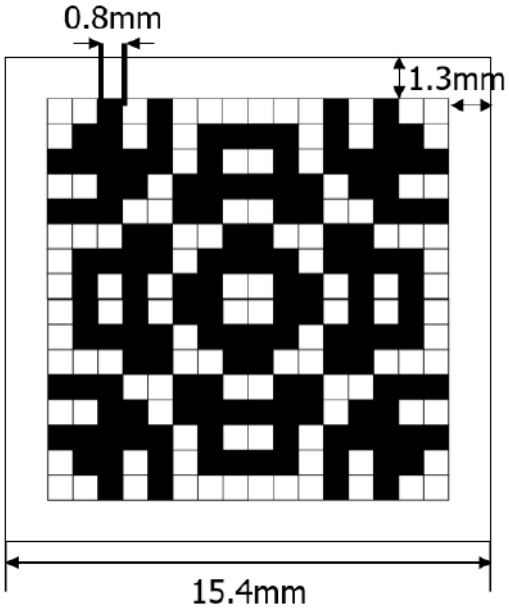


Figure 1: A designed unit cell of a bitmap-type microwave absorber metasurface.

3.

3. Manufacturing and characterization of microwave absorber metasurface

Materials of transparent acrylate plate as the dielectric spacer at the black squares in Fig. 1 were removed by micro end-milling technology in order to fill the commercial

conductive ink as the top patterned layer. The micro end-milling technology is proper to machine discrete squares, circles and et al. with high-speed. The shape error between the designed squares and the machined squares was generally below 1%. Then, the conductive ink was coated on whole top surface of the dielectric spacer, and only the conductive ink on the white squares was removed by ultra-fine planing technology. The ultra-fine planing technology is proper to machine precise flat surfaces having several tens of nanometers of roughness [1]. After ink removing, the conductive ink was filled only at the black squares. Fig. 2 and Fig. 3 show the processes from ink coating to final ink removing and the manufactured unit cell of microwave absorber metasurface, respectively. The unit cell was periodically repeated 20×20 for characterization at X-band, finally, a metasurface of 300mm×300mm in size was manufactured.

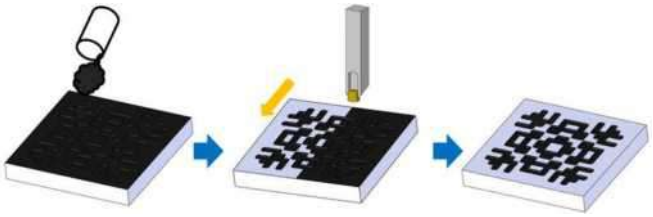


Figure 2: A schematic diagram of processes from ink coating to final ink removing.

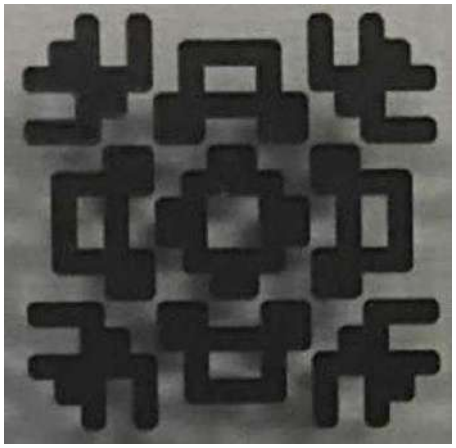


Figure 3: A manufactured unit cell of a bitmap-type microwave absorber metasurface.

The reflectivity at normal direction of the manufactured metasurface at X-band was measured. The measured reflectivity was continuously decreased from 8GHz to 9.5GHz and relatively stable from 9.5GHz to 12GHz. Especially, the reflectivity was less than -10dB from 9GHz to 12GHz. It was verified that bitmap-type microwave absorber metasurface which was newly designed by the two approaches and manufactured by the mechanical machining technology in this study had microwave stealth function at X-band.

4. Conclusions

We designed and manufactured a bitmap-type microwave absorber metasurface in this study. The details are below.

1) The shapes of a bitmap-type microwave absorber metasurface were optimized effectively by a genetic algorithm and an equivalent circuit model according to target microwave frequency and the bandwidth.
2) A bitmap-type microwave absorber metasurface was manufactured precisely by micro end-milling technology, ink-coating technology and an ultra-fine planing technology according to the optimized design.
3) The manufactured metasurface having periodically repeated 20×20 unit cells of 300mm×300mm in size showed less than -10dB reflectivity from 9GHz to 12GHz.
4) Based on the results, we suggest that a bitmap-type microwave absorber metasurface can be used as a microwave stealth panel without absorptive paints.

Acknowledgements

This research was supported by the ‘Center for Advanced Meta-Materials(CAMM)’ funded by the ‘Ministry of Science, ICT and Future Planning’ as ‘Global Frontier Project (CAMM-2014M3A6B3063707)’.

References

[1] C. Cho, S. Jeon, H.-J. Choi, N. Shin, B.S. Kim, E.-c. Jeon, J.-Y. Lee, Toward perfect light trapping in thin-film photovoltaic cells: full utilization of the dual characteristics of light, Adv. Opt. Mater. 3: 1697-1702, 2015.

Singular Polaritonic Metasurfaces: Graphene and Beyond

Emanuele Galiffi[1], Paloma A. Huidobro[1], John Pendry*[1],

[1]The Blackett Laboratory, Imperial College London, South Kensington Campus. London, UK
E-mail: emanuele.galiffi12@imperial.ac.uk

Abstract

We propose a new class of periodically modulated surfaces, which are able to couple light to surface polaritons over a continuum of frequencies by exploiting geometrical singularities in their subwavelength structure. We illuminate how this concept shares its roots with dimensional compactification in high-dimensional field theories, and demonstrate this effect on realistic platforms with plasmons in graphene and phonons in hexagonal boron nitride, paving a novel route towards broadband polaritonics.

1. Introduction

Surface polaritons are coupled light-matter modes confined near a surface, which can break the diffraction limit and achieve remarkable field enhancement. Periodic structuring of a surface can provide the necessary momentum to strongly couple far-field radiation to these surface waves over a discrete set of frequencies at a given angle of incidence. However, the periodicity of these subwavelength structures typically defines a length scale over which the bound modes quantise. This poses limitations on their bandwidth, so that typically only a few polaritonic modes can be excited within the frequency window over which they can exist.

Here, we report a novel class of subwavelength gratings which can be used to excite polaritons over remarkably broad bands, due to adiabatically vanishing thickness, or, equivalently, optical conductivity [1]. The analytical framework of transformation optics highlights a curious analogy between singular surfaces and the concept of compacted dimensions in theoretical physics, by demonstrating that these structures are spectrally equivalent to systems of higher dimensionality [2]. We demonstrate this exotic effect on a periodically doped graphene sheet, in the limit where the doping level periodically approaches the charge neutrality point, and show the resulting merging of the discrete surface plasmon spectra into a continuum. We report equivalent results with phonon polaritons in hBN, and highlight the robustness of this effect against imperfections.

2. Results and Discussion

In the subwavelength limit, the optical response of a polaritonic system is governed by the scalar potential $\phi(x,y)$, which obeys $\nabla^2\phi = 0$. The symmetry of the Laplace operator under a conformal transformation $\tilde{z} \to \tilde{z}'(\tilde{z}) = x'(x,y) + iy'(x,y)$ implies that $\phi(x,y) = \phi(x'(x,y), y'(x,y))$ is conserved across such a transformation, so that conformally related structures share the same spectral response [3].

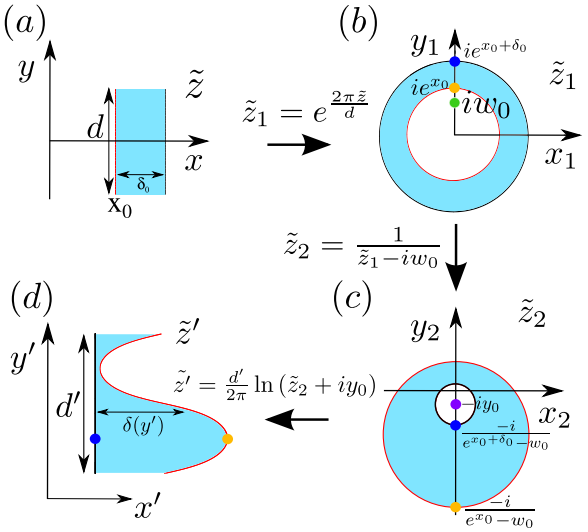


Figure 1: A series of conformal transformation maps a flat slab to a grating with the same resonance spectrum.

A translationally invariant slab may be transformed into a smooth grating via the transformation shown in Fig. 1: each length d of the slab is first wrapped into an annulus. Secondly, inverting the structure with respect to the shifted origin (green dot) returns a non-concentric annulus. Finally, after shifting the origin to the center of the smaller (black) circle (purple dot), the structure can be unwrapped via a logarithmic transformation, thus realising a smooth grating shape. Due to the aforementioned symmetry, all these structures share the same response, as long as their size is much smaller than the free-space wavelength.

The desired singular structure consists of the limit where the valley thickness of the grating is strongly suppressed. This can be achieved by a two-step limiting procedure: as the inversion point $\tilde{z}_1 = iw_0$ is let approach the inner circle in (b), the yellow dot is mapped to $\tilde{z}_2 \to -i\infty$, resulting in a grating of diverging thickness. However, since the length d of the original slab rescales both the real and imaginary part of $\tilde{z}$, letting $d \to \infty$ renormalises the final structure, while squeezing the valley-point thickness to an arbitrarily small extent.

We demonstrate the effect of such modulation by calcu-

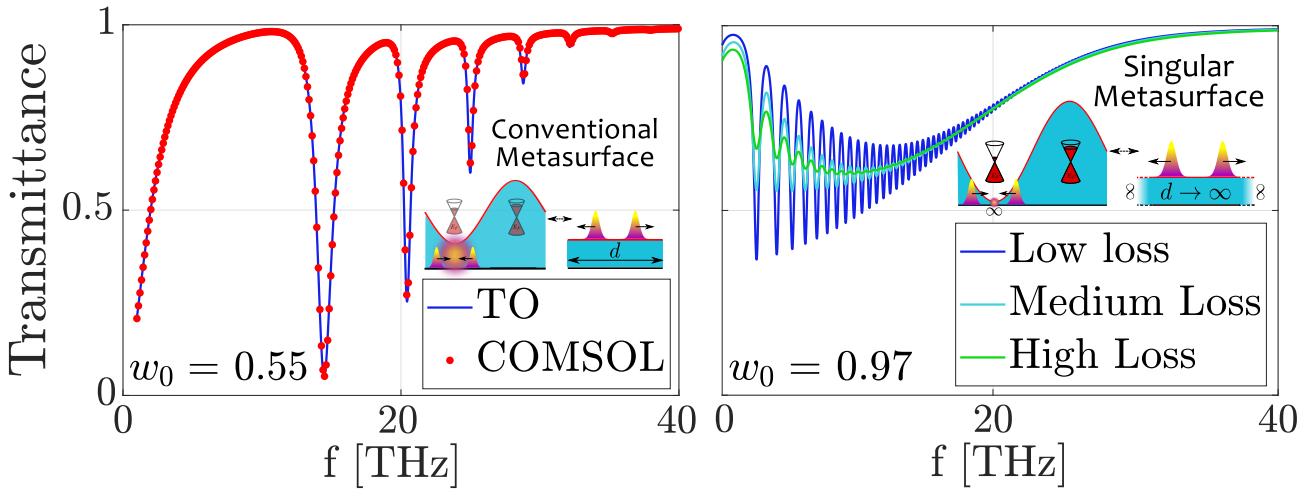


Figure 2: The transmittance spectrum of a conventional graphene metasurface features dips at the discrete frequencies at which surface plasmons are excited (left). This spectrum changes dramatically in a singular metasurface, where the Fermi level of the graphene sheet is strongly suppressed periodically, while keeping the same maximum doping. As the loss is increased, the finely spaced transmission dips merge in a broad band of plasmon modes extremely confined near the singular point.

lating transmittance through a graphene sheet, whose conductivity is spatially modulated (e.g. via an external gate voltage) according to the design above, as illustrated in Fig 2. When THz radiation impinges on a conventional graphene metasurface (left plot), surface plasmons can be excited at a discrete set of frequencies, which results in strong transmittance dips. By contrast, a singular metasurface (right plot), realised by periodically suppressing the doping level of graphene by a factor of the order of ~ 100, results in the merging of these transmission dips into a plethora of finely spaced resonances, which eventually become a continuum as a result of broadening.

The conformal map used to design this metasurface holds the key to understanding its behaviour: the length d of the slab in the $\tilde{z}$ frame must diverge, in order to realise the singular grating. This length encodes the quantisation box which accounts for the periodicity of the grating. Hence, as this length tends to infinity, the plasmons are effectively quantised over an infinite period, thus forming a continuum of modes, as can be witnessed by folding the dispersion relation over a first Brillouin zone which is renormalised according to the stretching of the periodicity in the slab frame [4]. However, quite remarkably, the physical period d' of the grating is unchanged.

In fact, as $d \to \infty$ a third dimension is intruded into the slab frame, which constitutes a periodic system, with an infinite period. In the grating frame, this extra dimension is hidden from sight in the singular point, which effectively acts like a sink for the plasmon, which travels towards this point, without, in a local model, ever reaching it. The hiding of an extra dimension is known as compactification, and it is customarily used in high-dimensional string theories in order to explain the fact that spacetime appears, to our measurements, only four-dimensional [5]. The practical consequence is the availability of an extra spatial degree of freedom, and its corresponding momentum component, which allows incoming radiation of any frequency and wavevector to satisfy the polaritonic dispersion relation.

Finally, far from a mere mathematical curiosity, this effect is extremely robust against limitations in the fabrication process: in fact we found that the merging of a polaritonic spectrum can be observed with a grating which consists of a sequence of only six linear segments, which is well within current lithographic capabilities.

Acknowledgement

EG was supported through a studentship in the Centre for Doctoral Training on Theory and Simulation of Materials at Imperial College London funded by the EPSRC (EP/L015579/1). JP and PAH acknowledge support from the Gordon and Betty Moore Foundation.

References

[1] Galiffi E, Pendry JB and Huidobro PA. Broadband tunable THz absorption with singular graphene metasurfaces. *ACS nano* 2018 Jan 23;12(2):1006-13.

[2] Pendry JB, Huidobro PA, Luo Y and Galiffi E "Compacted dimensions and singular plasmonic surfaces." *Science* 358, no. 6365 (2017): 915-917.

[3] Huidobro PA, Kraft M, Kun R, Maier SA, Pendry JB. Graphene, plasmons and transformation optics. *J. Opt.* 2016 1;18(4):044024

[4] Galiffi E, Pendry JB and Huidobro PA *EPJ Appl. Metamat.* Vol. 6, 2019, THz Metamat. 10, 9

[5] Klein O, Quantentheorie und fünfdimensionale Relativittstheorie. *Zeitschrift fr Physik A.* 37, 895906 (1926)

Ultrafast modulation in a THz graphene-based flat absorber through negative photoconductivity

Anna C. Tasolamprou[1], Anastasios D. Koulouklidis[1], Christina Daskalaki[1], Charalampos P. Mavidis[1,2],George Kenanakis[1], George Deligeorgis[1], Zacharias Viskadourakis[1], Polina Kuzhir[3,4], Stelios Tzortzakis[1,2,5], Eleftherios N. Economou[1,6], Maria Kafesaki [1,2] and Costas M. Soukoulis[1,7]

1. Institute of Electronic Structure and Laser, FORTH, 70013 Heraklion, Crete, Greece
2. Department of Materials Science and Technology, University of Crete, 70013, Heraklion, Crete, Greece
3. Institute for Nuclear Problems, Belarusian State University, Bobruiskaya 11, 220030 Minsk, Belarus
4. Tomsk State University, 36 Lenin Ave., Tomsk 634050, Russia
5. Science Program, Texas A&M University at Qatar, P.O. Box 23874 Doha, Qatar
6. Department of Physics, University of Crete, 70013, Heraklion, Crete, Greece
7. Ames Laboratory and Department of Physics and Astronomy, Iowa State University, Ames, Iowa 50011, United States
*corresponding author, E-mail: atasolam@iesl.forth.gr

Abstract

We present the experimental and theoretical study of an ultrafast graphene-based thin film absorption modulator for operation in the THz regime. The flat modulator is composed of a graphene-sheet placed on a dielectric layer backed by a metallic back-reflector. A near-IR pulse induces the generation of hot carriers in the graphene sheet reducing effectively its conductivity. The system provides a platform with ultrafast modulation capability for flat optics and graphene-based metasurfaces applications.

1. Introduction

Graphene is a two-dimensional material made of carbon atoms arranged in a honeycomb lattice with unique mechanical, thermal, electrical and optical properties. Particularly in the THz spectrum, graphene exhibits a Drude-like response due to its easily generated and controlled free carriers; therefore, it is considered a suitable platform for dynamically tunable metasurface components [1]. Such an example, are the so called thin film absorbers that are structures capable of absorbing all power of incident electromagnetic waves [2]. Within the concept of metasurfaces, thin film absorbers, are usually implemented by placing a lossy material, uniform or with features, on the top of a perfectly conducting metallic plate A simple but yet remarkable graphene component/metasurface is based on the coherent absorption principle. It consists of a single uniform sheet of graphene placed on top of a dielectric film which is placed on a metallic plate [3]. Here we demonstrate experimentally ultrafast (of the order of few ps) THz amplitude modulation of such a graphene based ultra-thin absorber induced by photoexcitation via an optical pump signal [4]. For the experimental characterization we use a broadband THz time-domain-spectroscopic system (THz-TDS) in an IR pump-THz probe configuration. Absorption modulation at 2.17 THz in the order of 40% is reported through a decrease in the conductivity upon photoexitation. Detailed analysis of the experimental observations reveals the negative dynamics of the THz photo-conductivity in the graphene sheet which is observed in highly doped samples [5]. Our study unveils the capability of such an ultrathin system to provide ultrafast modulation appropriate for the demanding future flat optics modulation applications and graphene-based metasurfaces.

2. Discussion

In Figure 1(a) we present the schematic of the component under investigation. It consits of an uniform graphene sheet placed on a backplated dielectric substrate. The stuctre is designed to provide enhanced absorption though the conherent intereference of the impinging and backreflected waves at the lossy graphene sheet. This is achieved when the equivelent metasurface is impedance matched with the free space. Impedance match is forced by properly enginnering the detail condition of the graphene and the thickness of the substrate. The modulation of the THz absorption spectrum upon photoexcitation is presented in Figure 1(a). For the characterization we use a powerful THz-TDS system that provides the ability of measurements in reflection mode. It is based on a pump-probe, coherent detection approach, and uses an amplified kHz Ti:Sapphire laser system delivering 35 fs pulses at 800 nm central wavelength and maximum energy of 2.3 mJ/pulse. The initial beam is focused in ambient air after partial frequency doubling in a beta-barium-borate (BBO) crystal (50 m thick) to produce a two-color filament and subsequently, THz radiation (>200 kV/cm). The inset in Figure 1(a) presents the optical pump induced THz relative reflectivity change (DR/R) as a function of pump delay. The measurement refers to the peak of the first pulse reflected by the graphene sheet, prior to cavity. The observed change in the reflectivity points to a reduction of the graphene conductivity in the regime under investigation. This counterintuitive result is connected with the detail conditions of the graphene sheet. In fact, it has been demonstrated that photoexcitation in a graphene sheet

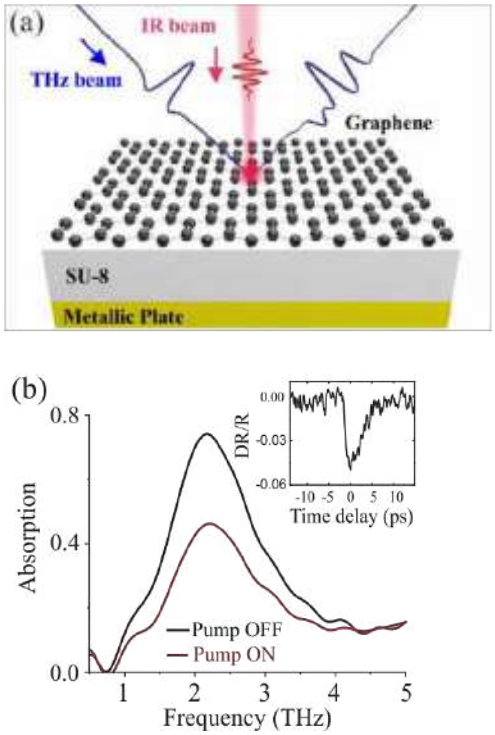


Figure 1: (a) Schematic of the component consisting of a single uniform sheet of graphene placed on top of a back-plated dielectric film and description of modulation operation. (b) THz absorption modulation upon photoexcitation that leads to absorption decrease, inset shows the ultrafast reflectivity modification of the graphene sheet. The decay time is equal to 2.79 ps.

of neutral charge point results in a rise of the carrier concentration and an increase of conductivity, whereas when the initial doping level is high, photoexcitation affects the scattering rate of the carriers that may lead to a conductivity decrease as we observe in our experiment. The feature is connected with the generation of hot carries, the increase of the electronic temperature and the overall increase of the scattering rate observed in highly doped samples. As seen in Figure 1(b), without the photoexcitation the graphene-based structure absorbs a maximum of 75% of the incoming wave at f = 2.17 THz. With photoexcitation the properties of the graphene sheet are modified and the maximum absorption drops; for maximum fluence equal to I = 0.69 mJ/cm^2 the absorption drops to 45% providing thus an ultrafast modulation of the absorption of the order of 40%.

3. Conclusions

We studied both experimentally and theoretically a graphene-based thin-film absorber exhibiting ultrafast tunable operation in the THz regime. The structure consists of a uniform graphene sheet grown by CVD on a grounded dielectric substrate; it is designed to provide enhanced absorption based on the coherent interference of the impinging and reflected waves when they are in phase at the lossy graphene sheet at the frequency of 2.17 THz. Our results provide evidence that in our highly doped sample photoexcitation leads to a reduction of the THz conductivity with a decay of 2.79 ps, resulting to an absorption intensity decrease of 40%. We have discussed the dynamics of the photoinduced reduction of the conductivity which is connected with the generation of hot carries, the increase of the electronic temperature and the overall increase of the scattering rate. Our system provides ultrathin, ultrafast modulation appropriate for the demanding future flat optics modulation applications.

Acknowledgements

This work was supported by the European Union's Horizon 2020 Project 696656 Graphene Flagship, the European Research Council under ERC Advanced Grant no. 320081 (project PHOTOMETA) and the European Union's Horizon 2020 Future Emerging Technologies call (FETOPEN-RIA) under grant agreement no. 736876 (project VISORSURF), the Hellenic Foundation for Research and Innovation (HFRI) and the General Secretariat for Research and Technology (GSRT), under the HFRI PhD Fellowship grant (GA. no. 4894), the National Priorities Research Program grant No. NPRP9 329-1-067 from the Qatar National Research Fund (member of The Qatar Foundation), the H2020 Laserlab-Europe (EC GA 654148) and H2020 MIR-BOSE (EC-GA 737017) projects, Tomsk State University competitive programme and H2020-MSCA RISE-2014 Project ID 644076 CoExAN.

References

[1] S. Mousavi, I. Kholmanov, K. Alici., D. Purtseladze, N. Arju, K. Tatar, D. Fozdar, J. Suk, Y. Hao, A. Khanikaev, R Ruo and G. Shvets, Inductive tuning of fano-resonant metasurfaces using plasmonic response of graphene in the mid-infrared, *Nano Letters*, 2013 13, 1111, 2013.

[2] Y. Radi, C. R. Simovski and S. A. Tretyakov, Thin Perfect Absorbers for Electromagnetic Waves: Theory, Design, and Realizations, *Phys. Rev. Appl.* 3, 037001, 2015.

[3] N. Kakenov, O. Balci, T. Takan, V. A. Ozkan, H. Altan and C. Kocabas, Observation of Gate-Tunable Coherent Perfect Absorption of Terahertz Radiation in Graphene, *ACS Photonics* 3, 1531, 2016.

[4] A. C. Tasolamprou, A. D. Koulouklidis, C. Daskalaki, C. P. Mavidis, G. Kenanakis, G. Deligeorgis, Z. Viskadourakis, P. Kuzhir, S. Tzortzakis, M. Kafesaki, E. N. Economou and C. M. Soukoulis, Experimental demonstration of ultrafast THz modulation in a graphene-based thin film absorber through negative photoinduced conductivity, *ACS Photonics*, doi: 10.1021/acsphotonics.8b01595, 2019.

[5] S. Kar, D. Mohapatra, E. Freysz, A. Sood, Tuning photoinduced terahertz conductivity in monolayer graphene: Optical-pump terahertz-probe spectroscopy, *Phys. Rev. B.*, 90, 165420, 2014.

Reconfigurable coding metamaterial

Eistiak Ahamed[1], Mohammad Rashed Iqbal Faruque[1], Mohd Fais Bin Mansor[2]

[1]Space Science Centre (ANGKASA), Universiti Kebangsaan Malaysia
[2] Centre of Advanced Electronic and Communication Engineering, Universiti Kebangsan Malaysia, 43600 UKM, Bangi, Selangor, Malaysia
E-mail: rashed@ukm.edu.my

Abstract

Reconfigurable coded metasurface is introduced inspired by electric split ring resonator (eSRR) that is working in the terahertz frequency range. The proposed metamaterial structures can be structurally reconfigured to determine its effect on scattering parameters and effective properties by bending its metal strip. Three different kinds of structures are investigated here for coded metasurface with 0, π and 2π phase response. The metamaterial structure shows polarized tunibility by reconfiguring its structure size. The tunibility dependent on the polarization and it is verified by electromagnetic simulation.

1. Introduction

Metamaterials are the new era of artificial material that shows abnormal electromagnetic properties of their geometry rather than their chemistry or band structure. Motivated by the perception of coding metasurface where two different unit cell is used to establish the programmable, coded and digital metamaterial concept using the different phase response [1]. Laser light illumination was used to vary effective properties in electromagnetic field in various methods in [2, 3]. External magneto static field's external bias voltages electrical or thermal effects in liquid crystals [4] and nonlinear effects of resonators or substrates were also used to demonstrate the effect on effective properties.

In this work, three different types of metamaterials structure are proposed to demonstrate reconfigurable coded metasurface and justify their ability to manipulate electromagnetic wave by using coding structure sequences. The proposed metamaterial structure shows two resonance frequencies and double negative properties in 25.40 THz. Three phase response is also analyzed to determine the coding sequence. It also shows large negative refractive index almost 1.50THz bandwidth. Geometrically reconfigurable two other design are compared with the proposed metamaterial structure. That two reconfigurable eSRR shows MNG (mu-negative) properties. Three eSRR structure are not only shows negative resonance frequency ,but also polarization based tunibility.

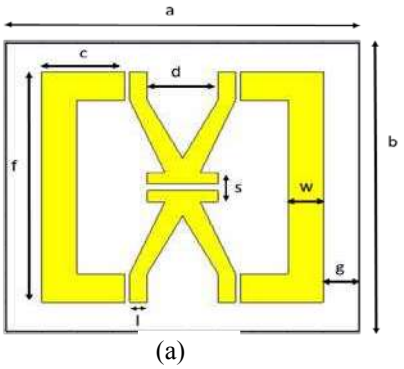
2. Design and Methodology

The proposed V shaped eSRR metamaterial design schematic view is presented in Figure 1. The parameter specification is presented in Table 1. The proposed metamaterial structure is designed on silicon substrate (10 × 10 μm^2) where its permittivity is 11.9 and dielectric constant 0.00025. The aluminum metal strip is used to design the structure on Si substrate. The thickness of the silicon substrate is 2 μm and the aluminium metal strip thickness is 0.035 μm.

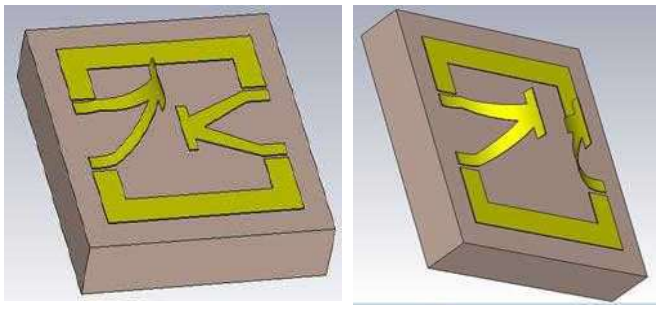
Table 1: Design parameters specification.

Parameters	Dimension [μm]	Parameters	Dimension [μm]
a	10.00	w	1.00
b	10.00	s	1.00
c	2.35	g	1.00
d	2.00	l	0.50
f	8.00		

A finite integration technique based electromagnetic simulator CST microwave studio was applied to determine the scattering parameters (transmission coefficient S_{21} and reflection coefficient S_{11}). Two types of polarization are investigated here extraordinary polarization and ordinary polarization. So boundary conditions are applied here in two times for ordinary polarization x and y axis are set as perfect electric and perfect magnetic boundary respectively.



(a)



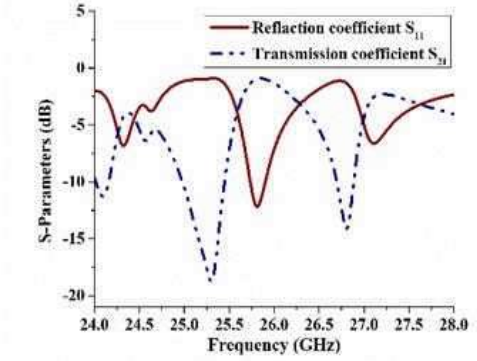
(b) (c)

Figure 1: (a) Schematic view of proposed metamaterial (b) bending one arm (c) bending two arms

The electromagnetic force is applied in the z direction and for extraordinary polarization the direction is opposite that are applied in ordinary polarization. The capacitance and inductive effect are created in split gap and metal strip respectively in metamaterial. Resonance frequencies are varied by increasing or decreasing the metal strip or split gap. There are two types of new modified proposed metamaterial structure are presented that are shown in Figure 1(b) and (c). These two structures are shown different types of transmission characteristics. Furthermore, establishing the coding sequence planner wave is used and it's RCS (radar cross section) is determined along with far field.

3. Analyzing Results

Proposed three structures are investigated in two important polarization position; normal polarization and extraordinary polarization position. In ordinary polarization effect on without bending metamaterial structure is resulted by its transmission coefficient in Figure 2 (a). By applying Nicolson rose wire method its abnormal effective parameters are determined in Figure 2 (b). Three structures combinations are exhibited 2-bit coding metasurface. It exhibits double negative properties in the 25.6 THz frequency range. To investigate its bending metal strip to reducing or increasing the capacitance or inductance effect on metamaterial other two bending structures is also applied ordinary polarization effect. They simultaneously showed MNG (mu-negative) properties in its two resonance frequencies for bending one V-arm. For two V-arm bending three resonance frequencies is found, but its dB is quite lower than other two designs. Three metamaterial structural results comparison is presented in Figure 2 (c).



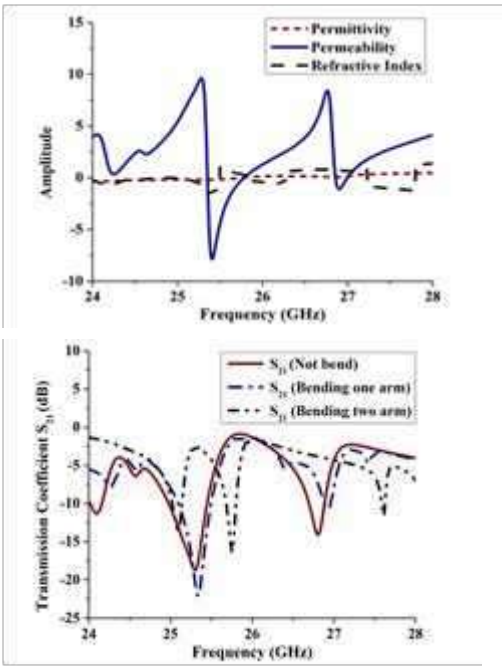


Figure 2: Proposed metamaterial (a) Transmission coefficient and (b) effective parameters. (c) Comparison among three metamaterial structures.

4. Conclusions

The proposed reconfigurable coding metamaterial concept is presented with the three electric split ring resonators (eSRR). The reconfigurable metamaterial bending design scattering parameters are investigated in the terahertz frequency region. The composite metamaterial represent 2-bit coding. The proposed structure shows large negative refractive index and double negative properties. The design metamaterial investigated polarized based variation in transmission characteristics by bending the metal strip.

Acknowledgements

This work was supported by the Research -Universiti Grant, Geran Universiti Penyelidikan (GUP), code: 2018-134.

References

[1] T.J. Cui, M.Q. Qi, X. Wan, J. Zhao, Q. Cheng, Coding metamaterils, digital metamatrils and programmable metamaterials, light: sci. & App. 3: e218, 2014.

[2] C. Wang, C. Yan, J. Tian, Y. Han, R. Zon, D. Li, D. Zhang, "Actively tunable metamaterial resonators based on colossal magnetoresistance in the infrared regime," *Chin. Opt. Lett. vol. 13*: 051601, 2015

[3] H.T. Chen, W.J. Padilla, J.M. Zide, A.C. Gossard, A.J. Taylor, Active terahertz metamaterial devices. *Nature 444*: 597–600, 2006.

[4] J. Zhu, J. Han, Z. Tian, J.Gu, Z.Chen, W. Zhang, Thermal broadband tunable Terahertz metamaterials, *optics communications 284*: 3129-3133, 2011.

Computational Spectral Imaging with Metasurface-based, Pixel-scale Color Splitters

Masashi Miyata[1,*], Mitsumasa Nakajima[1], Toshikazu Hashimoto[1]
[1]NTT Device Technology Laboratories, NTT Corporation, Japan
*corresponding author, E-mail: masashi.miyata.xu@hco.ntt.co.jp

Abstract

We present a single-shot multispectral imaging system using pixel-scale color splitters based on silicon nitride metasurfaces. We demonstrate that the system can computationally create multispectral images without the degradation of the signal levels and spatial resolution achievable in monochrome image sensors. These features are promising for developing high-sensitivity, high-spatial-resolution multispectral imaging system in an integrated device fashion.

1. Introduction

Multispectral imaging provides both spectral and spatial information about objects, which can be useful for machine-vision applications. So far, such imaging has extensively been explored by utilizing dispersive optics (e.g., a grating or prism) or tunable filters (e.g., liquid-crystal tunable filters) in imaging systems. However, these approaches often require bulky and heavy optics, and more importantly, they commonly need multiple shots to acquire multispectral images, which inherently limits the temporal resolution and thus induces motion artifacts. A recent approach introduced a multispectral filter array (e.g., plasmonic filters [1]) in front of an image sensor to realize multispectral imagers. Although this approach enables a single-shot operation with a cost-efficient, integrated imager system, it suffers from low signal sensitivity due to the absorption of light outside the passband of each filter. An imager employing transparent multi-level diffractive optics has also been proposed for single-shot multispectral imaging with increased signal levels [2]; however, crosstalk between neighboring sensor pixels due to the diffracted light inherently limits the achievable spatial resolution.

Here, we demonstrate an alternative imager system to achieve single-shot multispectral imaging without absorptive multispectral filters. This is accomplished by employing dielectric-metasurface-based, pixel-scale color splitters [3] in combination with computational imaging techniques. Since our system spectrally disperses incident visible light on a few sensor pixels using transparent splitters, multispectral images can be computationally created without significant optical losses while preserving the spatial resolution of state-of-art image sensors.

2. Results

Figure 1(a) schematically shows the proposed imager system. The system consists of metasurface color splitters arranged on a monochrome image sensor. The splitters are based on dielectric nanoposts that can be designed to provide the degrees of freedom for controlling optical phases while preserving high transmittance (i.e., impedance matching) [4, 5]. By utilizing a dispersion-managed metasurface concept [6], a dielectric metasurface pattern can be designed to achieve spatial splitting of incident light into the three primary colors even within a pixel-scale footprint. Therefore, the three pixels under the splitter yield completely different spectral responses without the use of absorptive filters, as schematically shown in Fig. 1(b). Since computational techniques [2, 7] can estimate an incident spectrum from three-pixel signals with such pre-defined spectral responses, our system can potentially reconstruct spectral information at each set of three pixels, thus leading to the creation of multispectral images in the visible wavelength range.

To experimentally verify the proposed system, we fabricated metasurface color splitters designed for a high-pixel-density image sensor with a 1.43×1.43 μm^2 pixel size. Figure 1(c) shows scanning electron microscopy (SEM) images of fabricated splitters. Each splitter consists of 615-nm-thick silicon nitride (SiN) nanoposts with widths of 125 and 295 nm [3]. The characterization of the system was performed with an optical-microscopy-based setup that virtually realizes the image sensor configuration by imaging the plane where the pixel array is assumed to be placed (3.2 μm away from the splitters). A shortpass filter (< wavelength λ_0 = 650 nm) was inserted into the setup to remove near-infrared light. We used an "N" character composed of known color filters as a target object. Once the monochrome image was measured with this setup, the pixel size in the image was resized to match 1.43×1.43 μm^2 in physical dimensions by averaging signals of multiple neighboring pixels. Computational spectrum estimation was then performed at any set of neighboring three pixels. This enables the spectrum estimation on each pixel. We here considered this estimation to be a typical inverse problem and solved it by using an iterative algorithm; however, other numerical methods can potentially be employed.

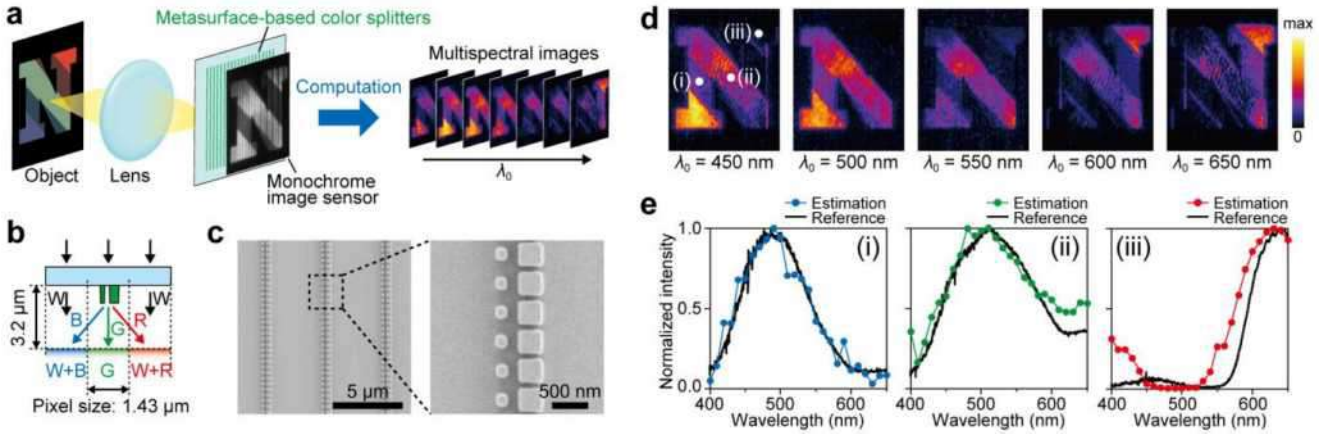


Figure 1: (a) Schematic of a single-shot multispectral imaging system with metasurface-based color splitters. (b) Schematic of the side view of the image sensor configuration. (c) SEM images of the fabricated splitters. (d) Computationally reconstructed multispectral images of a colored "N". (e) Estimated spectra at the three different points in the "N" image.

Figure 1(d) shows spectral images (ranging from 400 nm to 650 nm separated by a 10-nm wavelength step, 130×166 pixels) reconstructed from the measured single-shot monochrome image. They show different intensity distributions depending on the wavelength. The estimated spectra at the three points (i–iii) in the image are shown in Fig. 1(e). The intensity of each spectrum is normalized to its maximum. These spectra are in good agreement with the reference spectra measured with a conventional spectrometer (also plotted in the graphs). The spectral errors, defined as the root-mean-square errors between the estimated and reference spectra, were also calculated for each point. For this purpose, the reference spectra were down-sampled to match the spectral resolution of the estimated spectra. The errors are 7.20, 10.32, and 16.99% for the points (i), (ii), and (iii), respectively.

3. Discussion

The experimental results indicate that our single-shot imager system can provide spectral information at the spatial resolution of state-of-art image sensors. The light transmission averaged over the visible wavelengths was ~96% for the splitter array. Thus, it is clear that almost all the incident light is utilized for multispectral imaging. This feature is the great advantage our system has over filter-based counterparts, and it will significantly improve the sensitivity or temporal resolution. To quantify the spectral resolution $\Delta\lambda$, we calculated the spectral correlation function that quantifies the change in wavelength required to generate an uncorrelated intensity distribution on the pixels [7]. From this analysis, $\Delta\lambda$ was estimated to be ~40 nm. The simultaneously measurable spectral range was also estimated using the simple relation $2M\Delta\lambda$, where M is the pixel number used for the estimation on one pixel (i.e., M = 3 in our case) [7]. The spectral range was estimated to be ~240 nm, well matching the entire visible spectral range.

To further improve the spectral accuracy within the fixed spectral range (e.g., the visible spectral range), it is necessary to simultaneously decrease $\Delta\lambda$ and increase M. Decreasing $\Delta\lambda$ will require a highly dispersive metasurface to enhance the spectral decorrelation of the intensity distribution on the pixels. To create such a metasurface, the advanced optimization method in [8] may be promising. Increasing M is straightforward: it can be done by redesigning the sensor configuration to utilize more pixels with different spectral responses for the spectrum estimation, at the expense of spatial resolution. As such, there is a trade-off between the spectral accuracy and the spatial resolution, and which one is given priority will depend on the application. From this viewpoint, the system shown here can be regarded as a multispectral imaging system specialized for high spatial resolution.

4. Conclusions

We presented a filterless, single-shot multispectral imaging system based on metasurface-based color splitters and computational techniques. We demonstrated that our system can create multispectral images by utilizing almost all the incident light while preserving the spatial resolution of state-of-art image sensors. This configuration also enables high-sensitivity color imaging with color signal processing [3]. Therefore, our system can provide both color and multispectral images without the degradation of the signal levels and spatial resolution achievable in monochrome image sensors. Further, the CMOS-compatible feature of SiN metasurfaces opens a pathway to their monolithic integration into CMOS image sensors. These features will enable high-sensitivity, multi-information imaging in an integrated device fashion.

References

[1] S. Yokogawa *et al*., Nano Lett. **12**, 4349–4354 (2012).
[2] P. Wang *et al*., Optica **2**, 933–939 (2015).
[3] M. Miyata *et al*., in submission.
[4] A. Arbabi *et al*., Nat. Nanotechnol. **10**, 937–943 (2015).
[5] M. Miyata *et al*., J. Appl. Phys. in press.
[6] E. Arbabi *et al*., Optica **4**, 625–632 (2017).
[7] B. Redding *et al*., Nat. Photonics **7**, 746–751 (2013).
[8] D. Sell et al., Adv. Opt. Mater. **5**, 1700645 (2017).

High-efficiency anomalous refraction in terahertz metamaterial

Chunying Guan*, Ruiqiang Zhao, Rongyu Liu, Zheng Zhu, Yuxiang Li, Jinhui Shi

Key Laboratory of In-Fiber Integrated Optics of Ministry of Education, College of Science, Harbin Engineering University, Harbin 150001, China
*corresponding author, E-mail: cyguan@163.com

Abstract

A fair amount of theoretical work has showed that Huygens' metasurfaces modulate electromagnetic waves by designing electrical impedance and magnetic admittance. In this work, a transmission type Huygens' metasurfaces with a two-layer metal structure is studied, which achieves reflectless phase modulation at a specific frequency for linear polarization. Simulation results show that this metasurface can achieve 2π phase coverage in 0.83 THz, and phase change can be achieved by changing a single geometric parameter of the structure, with similar transmission effect. We design a beam deflector to realize an anomalous refraction angle with 19.8°.

1. Introduction

Metasurfaces, as 2D nanostructures, have attracted enormous attention since they provide unprecedented opportunities in controlling light-matter interaction as well as propagation of electromagnetic waves [1, 2]. In general, metasurfaces are able to modify phase, amplitude and polarization of electromagnetic waves. Novel phenomena and devices have been developed by properly engineering the geometries of nanostructures in metasurfaces [1-3], such as strong spin-orbit interaction, ultra-thin focusing or diverging lens, nonlinear phase control, anomalous refraction and reflection. Huygens' principle can be applied to design metasurfaces with well engineered electromagnetic responses [4]. In recent years, there have been many researches on Huygens' metasurfaces [4-12], involving from microwave to light wave. However, there is few reports on terahertz Huygens' metasurfaces that are desirable for practical terahertz applications.

Here, we introduce a kind of Huygens' metasurface with metal structure, which is used to control the linear polarization electromagnetic wave in terahertz band. Compared with the existing Huygens' metasurfaces, such as the wire/loop type metasurfaces working in microwave and the three-layer shunt-admittance unit cell, it has a simpler structural design.

2. The design of metamaterials

Huygens' metasurfaces are characterized by its surface impedance $\mathbf{Z}_{es}$ and surface admittance $\mathbf{Y}_{ms}$, inducing discontinuities in tangential magnetic and electric field components, respectively, given by the generalized sheet transition conditions(GSTC)

$$\begin{aligned}\frac{1}{2}\left(\mathbf{E}_2^+ + \mathbf{E}_1^-\right) &= \mathbf{Z}_{se}\cdot\left[\hat{\mathbf{n}}\times\left(\mathbf{H}_2^+ - \mathbf{H}_1^-\right)\right],\\ \frac{1}{2}\left(\mathbf{H}_2^+ + \mathbf{H}_1^-\right) &= \mathbf{Y}_{sm}\cdot\left[-\hat{\mathbf{n}}\times\left(\mathbf{E}_2^+ - \mathbf{E}_1^-\right)\right].\end{aligned} \tag{1}$$

The Huygens' metasurfaces designed in this paper focuses on the efficient transmission and control transmission direction of electromagnetic wave while maintaining the polarization. The following formula can be derived,

$$\begin{aligned}\frac{\eta}{2Z_{se}} &= \frac{E_{inc}-E_{trans}-E_{ref}}{E_{inc}+E_{trans}+E_{ref}},\\ \frac{1}{2\eta Y_{sm}} &= \frac{E_{inc}-E_{trans}+E_{ref}}{E_{inc}+E_{trans}-E_{ref}}.\end{aligned} \tag{2}$$

Eq.(2) is the same as the formula given in [5]. By directly connecting the surface impedance and surface admittance with the reflection and transmission characteristics of the structure, it is very convenient to carry out the metasurface design. Phase modulation in the 2π range and high transmission efficiency can be achieved by reasonably designing the surface impedance and surface admittance of the metasurfaces.

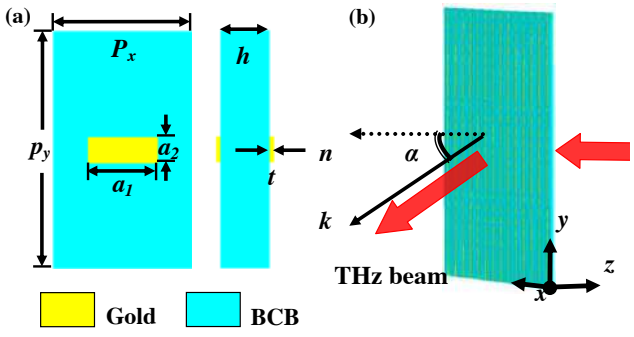


Figure 1: The schematic of cut-wire terahertz metasurface. (a) The front and lateral views. (b) The whole view. The light blue and yellow colors indicate gold and the dielectric material BCB.

Figure 1(a) shows the model diagram of one unit cell, and Figure 1(b) shows the whole design of the metasurfaces. A

group of metal wire pairs were designed on both sides of the dielectric layer with a thickness of h=44um and the 24-um-width metal pairs' thickness is 200nm, respectively. One unit cell has different period lengths in the x and y directions in order to reduce unnecessary coupling. The spacer is a benzocyclobutene (BCB) layer with a permittivity of ε=2.67 and a loss tangent of δ=0.012. The metal layers are made from gold with the conductivity of $\sigma=4.56\times10^7$ S/m. The spectral response of the unit cell was calculated using CST Microwave Studio TM simulations. The incident wave is a plane wave with the electric field polarization along the x-axis, as shown in Fig. 1(a). For the transmitted Huygens' metasurfaces, we expect that $\mathrm{Re}(h/Z_{se})=\mathrm{Re}(1/hY_{sm})=0$ and $\mathrm{Im}(\eta/Z_{se})=\mathrm{Im}(1/\eta Y_{sm})$ can be used to achieve perfect transmission. We choose eight resonators with different length as shown in Fig. 1(a), where the parameter a_1 is the only parameter related to the phase change of the transmitted wave. The amplitude and phase of the transmitted wave of this design are shown in Fig. 2. The transmission coefficient of this structure remains above 0.78, while the phase covers 0-2π range.

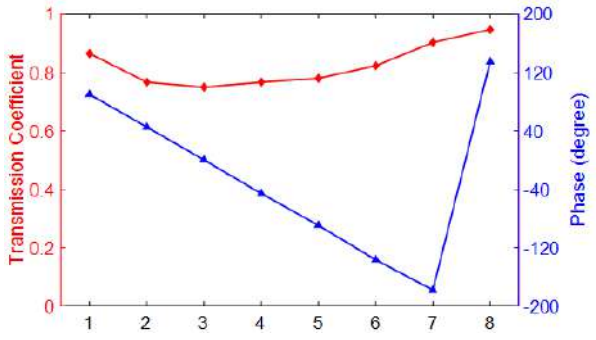


Figure 2: The amplitude and phase of eight cut-wire pairs in the Huygen metasurface. The lengths is from 62.5 to 127.5um.

Figure 3 shows the simulation results of energy distribution in the direction of diffraction, these results show that the main diffraction along 19.84° (not shown here) occupies about 66% of the incident energy at 0.83THz. Compared with the Huygens' metasurfaces of wire/loop structures realized in microwave, the superstructure surface we designed reduces the structural complexity and manufacturing difficulty, especially in terahertz range.

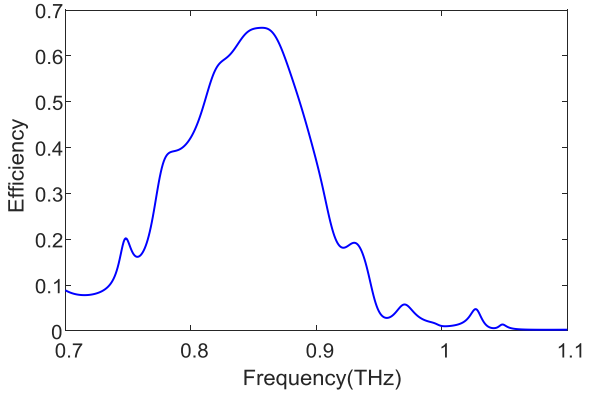


Figure 3: Simulated anomalous refraction of the Huygen metasurface. The metasurface is composed of eight cut-wire pairs with different lengths from 62.5 to 127.5um.

3. Conclusions

In conclusion, we designed a direct Huygens' metasurfaces with a two-layer metal structure. These metasurfaces use carefully designed structural elements to achieve both electric and magnetic dipole resonance at the desired frequency to form Huygens sources. This discontinuous field on the surface can interact with the incident electromagnetic wave and modulate the transmitted light's phase in 2π range while maintaining a low reflection. Compared with the equivalent Huygens surface with three-layer metal design, our design retains the view that huygens source is formed directly on the metasurface, and further research on this basis may realize the broadband Huygens' metasurfaces.

Acknowledgements

The authors acknowledge financial supports from National Natural Science Foundation of China (NSFC) (61875044, 61675054 and 91750107), Natural Science Foundation of Heilongjiang Province (ZD2018015), Postdoctoral Scientific Research Developmental Fund of Heilongjiang Province (Grant No. LBH-Q15036), 111 project to the Harbin Engineering University (B13015), Fundamental Research Funds for Harbin Engineering University (HEU) of China.

References

[1] A.V. Kildishev, A. Boltasseva, V.M. Shalaev, Planar photonics with metasurfaces, *Science* 339: 1232009, 2013.

[2] N. Yu, F. Capasso, Flat optics with designer metasurfaces, *Nat. Mater.* 13: 139-150, 2014.

[3] N. K. Grady, J. E. Heyes, D. R. Chowdhury, Y. Zeng, M. T. Reiten, A. K. Azad, A. J. Taylor, D. A. R. Dalvit, and H.-T. Chen, Terahertz metamaterials for linear polarization conversion and anomalous refraction, *Science* 340: 1304–1307, 2013.

[4] M. Selvanayagam and G. V. Eleftheriades, Discontinuous electromagnetic fields using orthogonal electric and magnetic currents for wavefront Manipulation, *Opt. Express* 21 (12): 14409-14429 2013.

[5] C. Pfeiffer and A. Grbic, Metamaterial Huygens' Surfaces: Tailoring Wave Fronts with Reflectionless Sheets, *Phys. Rev. Lett.* 110(19): 197401, 2013.

[6] C. Pfeiffer, N. K. Emani, A. M. Shaltout, A. Boltasseva, V. M. Shalaev, and A. Grbic, Efficient light bending with isotropic metamaterial Huygens' surfaces, *Nano Lett.* 14 (5): 2491-2497, 2014.

[7] M. Chen, E. Abdo-Sanchez, A. Epstein, and G. V. Eleftheriades, Theory, design, and experimental verification of a reflectionless bianisotropic Huygens' metasurface for wide-angle refraction, *Phys. Rev. B* 97 (12): 125433, 2018.

Efficiency improvement in wireless power transfer system using artificial magnetic conductors

Lijuan Dong*, Fusheng Deng, Yanhong Liu, Lixiang Liu and Yunlong Shi

Shanxi Provincial Key Laboratory of Electromagnetic Functional Materials for Microstructure, Shanxi Datong University, Datong, China

Abstract

In this paper, transfer performance improvement in wireless power transfer (WPT) system using a mushroom-type artificial magnetic conductors (AMC) is reported. Numerical simulations confirm that AMC possesses great power for enhancing the WPT efficiency between two non-resonant coils.

1. Introduction

Since the earliest imagination of wireless power transfer (WPT) by N. Tesla in 1914, the concept of wirelessly transmitting electric power from one place to another has gained enormous attention from researchers and engineers. Among several sorts of WPT methods, the magnetic induction is the most powerful scheme to achieve high efficiency in mid-range. Especially, the magnetically resonant version by A. Kurs and his colleagues from MIT invented an considerably efficient way to wirelessly convey the electric energy over short or mid distance by making the coils self-resonant[1]. In this case, the magnetic coupling strengthened by magnetic resonance eventually leads to fast energy exchange rate, realizing high overall efficiency. However, this technique is very sensitive to the transfer distance. Once the gap between two resonant coils becomes shorter than the perfect-coupling distance, the transfer efficiency will naturally decrease since the frequency splitting takes place, due to the over-coupling effect [2]. In order to modulate the transfer performance of WPT, much efforts have been devoted in the development of complexity of external matching circuits [2]. In addition to those traditional methods, feasible regulation functions from metamaterials are increasingly favored by both physicists and engineers.

Metamaterials (MMs) refers to a sort of periodic artificial electromagnetic micro-structures[3]. In the past decade, MM has captured great research interests. One of the most well-known finding is the artificial magnetic conductors (AMC)[4], which is characterized by high-impedance and in-phase reflections for incident waves over a specific frequency band[4]. They can modulate the propagation behavior of electromagnetic (EM) waves significantly. Major breakthroughs of AMC include reducing back-radiation[5], increasing gain[6], and broadening bandwidth when they are employed as the antenna ground plane. These works inspire people with great confidence for the practical applications of AMC in a wider region.

In this paper, we propose to utilize a mushroom-type AMC, positioned behind the source, to realize the improvement on transfer performance of WPT system and magnetic shielding for unexpected field. The AMC structure consists of an array of capacitive patches on the top of a grounded ferrite substrate, and shorting via-holes connecting the patches to the ground plane. Lumped capacitors are used between the patches for AMC miniaturization. By introducing the AMC slab into non-resonant coils, the overall efficiency is significant enhanced, due to the magnetostatic resonant modes within the slab. Further investigations on the spatial magnetic-field distributions demonstrate that a variety of magnetic-field patterns in a near range can be effectively realized, and also show the superior performance in magnetic shielding. Importantly, all these improvements are not at a cost of transfer distance, which increases the practical applications of this composite AMC-WPT structure.

2. Working principle and design of AMC

Now, we give a simple schematic shown in Fig. 1 to illustrate our AMC-based inductively non-radiative WPT system. The transmitter and receiver of WPT, sharing the same diameter of 15 cm, are set with a transfer distance l. They are extremely smaller than the wavelength, and can be treated as magnetic dipoles. A mushroom-type AMC structure, positioned behind the transmitter with a spacing h=1 mm, is used to realize the improvement on transfer performance of WPT system. The physical mechanism is electromagnetic power resonates of AMC driven by the current loop and in-phase reflection at air-AMC interface.

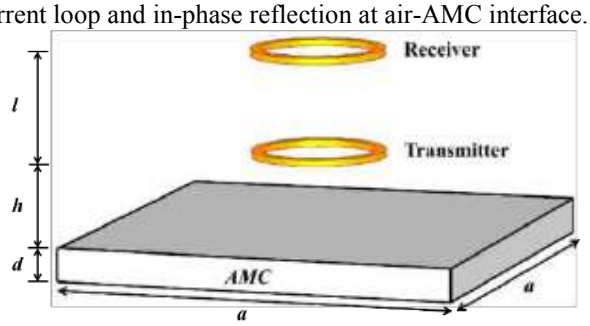


Figure 1: Schematic of our AMC-based inductively non-radiative WPT system.

The proposed mushroom-type AMC structure is shown in Fig. 2. It is made up of an array of capacitive patches on the top of a grounded dielectric substrate, and shorting via-holes connecting the patches to the ground plane. Lumped capacitors are used between the patches for AMC miniaturization. The detailed dimensions are as follows. The AMC slab consists of 20×20 unit square patches. The patches have a separation of 2 mm, with an edge length of m=50 mm, and the resulting period is p=52 mm. The patches are situated on a barium cobalt hexaferrite substrate, $Ba_3Co_2Fe_{24}O_{41}$ (Co_2Z), with a permeability of 150 and a thickness d=5 mm. The value of lumped capacitors used is C=0.72 nF.

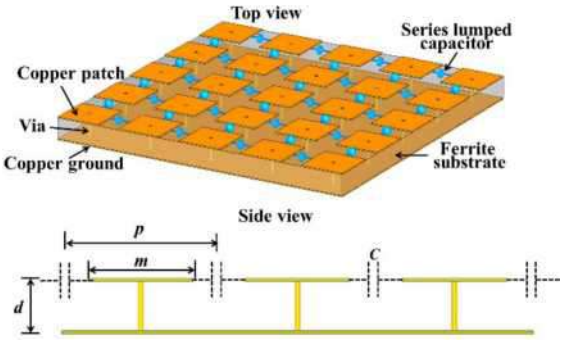


Figure 2: Geometry of the mushroom-like AMC structure.

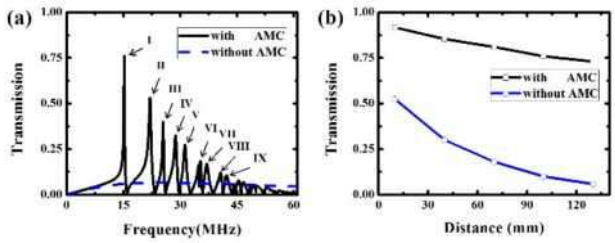


Figure 3: (a) Simulated transfer efficiencies at 10 cm for w/o AMC cases. (b) Simulated efficiencies at 15.2 MHz for w/o AMC cases as a function of transfer distance from 1 cm to 13 cm.

3. Simulation results and discussion

Numerical simulations are carried out by a commercial finite-integration-technique (FIT) EM solver from CST Microwave Studio. For comparison, the transmission spectrum of non-resonant wireless power transfer w/o AMC is figured out, shown as Figure 3(a). It is clear that the efficiency is increased from 5 % to 76% at 15.2 MHz after the AMC slab is introduced, with transfer distance l=10 cm. Also important phenomenon is that the appearance of many transmission peaks, as named from I to IX. The peaks indicate that the magnetic field at these corresponding frequencies receive great enhancement simultaneously. Note that, there is no material placed into the transfer path, which increases the practical applications of this method. Figure 3(b) shows that as the transfer distance becomes larger from 1 cm to 13 cm, the efficiency of composite AMC-WPT scheme at 15.2 MHz drops from 92% to 73%, larger and decreasing slower than that of the original not-resonant WPT system. It is worth mentioned that, this efficiency improvement is with an ideal AMC. As a real AMC implemented, the ohmic loss and resonant loss of AMC and the impedance mismatch will lead to a relatively low efficiency. Fortunately, the experience in previous works indicates that these losses in fabricated metamaterials can be controlled to be small compared to the efficiency gains.transfer distance from 1 cm to 13 cm.

4. Conclusions

To sum up, a mushroom-type artificial magnetic conductors (AMC) is proposed to regulate non-resonant wireless power transfer. Significant enhancement in the overall efficiency of the non-resonant wireless power transfer has been demonstrated by adding the AMC to non-resonant coils. Since the wireless power transfer system based on AMC has many benefits, we believe it can be widely used in medical research, electric vehicle charging, civilian industry, and so on.

Acknowledgements

The authors acknowledge the financial support from the National Natural Science Foundation of China (Grant Nos. 11874245 and 11604186), the Natural Science Foundation of Shanxi Province, China (Grant Nos. 201601D202011) and the Science and Technology Project of Datong, Shanxi Province, China (Grant Nos.2016021).

References

[1] A. Karalis, J.D. Joannopoulos and M. Soljacic, Efficient wireless non-radiative mid-range energy transfer, *Annals of Physics*. 323: 34-48. 2008.

[2] A.P. Sample, D.A. Meyer and J.R. Smith, Analysis, Experimental Results, and Range Adaptation of Magnetically Coupled Resonators for Wireless Power Transfer, *Ieee Transactions on Industrial Electronics*. 58: 544-554. 2011.

[3] R. Diaz: Magnetic loading of artificial magnetic conductors for bandwidth enhancement," IEEE Antennas and Propagation Society International Symposium. Digest. Held in conjunction with: USNC/CNC/URSI North American Radio Sci. Meeting (Cat. No.03CH37450) (2003), p. 431-434 vol.432.

[4] Y. Fan and Y. Rahmat-Samii, Reflection phase characterizations of the EBG ground plane for low profile wire antenna applications, *IEEE Trans. Antennas Propag.* 51: 2691-2703. 2003.

[5] H. Nakano, K. Hitosugi, N. Tatsuzawa, D. Togashi, H. Mimaki and J. Yamauchi, Effects on the radiation characteristics of using a corrugated reflector with a helical antenna and an electromagnetic band-gap reflector with a spiral antenna, *IEEE Trans. Antennas Propag.* 53: 191-199. 2005.

[6] H. Nakano, K. Kikkawa, N. Kondo, Y. Iitsuka and J. Yamauchi, Low-Profile Equiangular Spiral Antenna Backed by an EBG Reflector, *IEEE Trans. Antennas Propag.* 57: 1309-1318. 2009.

Coding Huygens' Metasurface for Microwave Holography

Chunsheng Guan[1], Xumin Ding[1], Kuang Zhang[1], Badreddine Ratni[2], Shah Nawaz Burokur[2], Ming Jin[1] and Qun Wu[1]

[1] Department of Microwave Engineering, Harbin Institute of Technology, Harbin 150001, China
[2] LEME, UPL, Univ Paris Nanterre, F92410 Ville d'Avray, France
*corresponding author, E-mail: xuminding@hit.edu.cn

Abstract

In this paper, coding Huygens' metasurface (CHM) is proposed for holographic imaging with enhanced quality. A weighted holographic algorithm is utilized to calculate the phase distribution at the interface and to design the CHM. Experimental demonstration performed in the microwave region validates holographic imaging with the ability to modulate energy distribution among focal points and improve the quality of the image. By judiciously engineering both electric and magnetic dipolar resonators, the proposed digital Huygens' meta-atom is able to provide a full transmission–phase covering the whole range of 2π together with a near-unity transmission efficiency. The proof-of-concept experiments show that the quality of holographic imaging can be indeed improved by utilizing digital meta-atoms with several bits. The proposed CHM hologram shows great potential in a variety of application fields, such as programmable high-resolution imaging lenses, microscopy, data storage, information processing and computer-generated holograms.

1. Introduction

Metasurfaces, the two-dimensional (2D) version of metamaterials, show great ability in manipulating wavefronts in arbitrary manner by introducing corresponding phase discontinuities at the interface. A metasurface is typically composed of an array of subwavelength artificial meta-atoms with specially designed geometries [1] and orientations [2, 3], and several devices have been implemented based on the construction of metasurfaces, including couplers [4], beam shapers [5], invisibility cloaks [6], imaging systems [7, 8], and other functional devices [9-11]. A main challenge for most metasurfaces operating in transmission mode is to fully control the transmission phase, while at the same time being able to guarantee high transmission efficiency. It can also be solved by using the so called Huygens' metasurface [12] that enables to fully control both the phase and the amplitude of co-polarized transmitted wave without polarization conversion losses. Due to the outstanding ability in manipulating electromagnetic waves, applications of the Huygens' metasurface have been reported in beam-refracting [13], focusing [14, 15], beam-shaping [16], and hologram imaging [17].

Recently, the concept of coding metasurfaces has been proposed [18] and applied in beam-editing [19], diffuse scattering [20] and energy radiations controlling [21]. Coding metasurface presenting the ability to describe information in a digital way is usually composed of digital meta-atoms with different out-of-phase responses, allowing to manipulate electromagnetic waves. The meta-atoms with different designed functions can be represented by binary codes, which are deemed to be coding elements. For example, based on the out-of-phase responses, binary coding elements for the simplest 1-bit coding metasurface are "0" and "1", which correspond to "0" and "π" phase response, respectively. Similarly, a 2-bits coding metasurface is composed of four coding elements "00", "01", "10" and "11", which have "0", "π/2", "π" and "3π/2" phase response, respectively. The generation of n-bit coding metasurface obeys the same rule. In this way, the information of the metasurface can be recorded in a digital way, which creates the connection between the physical meta-atom and digital codes. The digital description of metasurfaces has changed the way of describing, analyzing, and designing metasurface.

Here in this work, we propose the concept of coding Huygens' metasurface (CHM) for microwave holographic imaging. To construct the CHM, we use Huygens' meta-atoms as the basic coding elements. By correctly designing geometrical parameters of the electric and magnetic dipoles, meta-atoms able to cover full 2π-phase range with near-unity transmission amplitude can be obtained. A weighted holographic algorithm is proposed to calculate the phase distribution along the metasurface. Then, arbitrary n-bit CHMs can be realized by discretizing the calculated phase distribution by 2^n over 2π. For validation of the proposed concept, 1-, 2-, and 3-bits CHMs are designed, fabricated and measured to find the relationship between imaging quality of the CHM holograms and phase-quantization level. Moreover, we modulate the intensity distribution of focal points using the proposed 3-bits CHMs to verify the feasibility of our proposed weighted holographic algorithm. Experimental verifications performed at microwave frequencies agree qualitatively with theoretical calculations and numerical simulations, indicating the feasibility and

high imaging quality of the proposed CHM holograms.

2. CHM holograms

In order to achieve the desired holographic imaging, the phase profile at the interface of the metasurface is designed from the proposed holographic algorithm [22]. Different from algorithm for manipulating the radiation pattern of the antenna [23], we propose holographic algorithm to converge the incident wave to four specific focal points in the near field, at a distance about 3.3λ away from the metasurface. The schematic diagram for the theoretical analysis is illustrated in Fig. 1. One fundamental method is that we are able to select ideal point sources as virtual sources and place them at pre-designed focal points positions. We consider N focal points located at (x_i, y_i, z_i) (i = 1 to N). Then, by superposing the electromagnetic field generated by all the virtual sources, which can be described utilizing Green function, the phase delay at the position of each meta-atom $\varphi(x_j, y_j, 0)$ (j = 1 to M) can be retrieved. Accordingly, the reconstructed electric field is converged to the pre-designed focal points. However, the assumption of in-phase radiation can only ensure the convergence of the incident wave to the preset focal points, but is not sufficient to modulate the intensity distribution of the focal points. This problem is solved by introducing a weight factor w_n so as to modify the phase distribution on the metasurface and hence to modulate energy distribution. An iterative procedure is adopted to obtain the phase distribution φ_m on the CHM, as follows:

$$\phi_m^p = \arg\left(\sum_{n=1}^{N} \frac{e^{ikr_m^n}}{r_m^n} \frac{w_n^p E_n^{p-1}}{\left|E_n^{p-1}\right|}\right) \tag{1}$$

Where r_m^n is the distance between the m^{th} meta-atom and the n^{th} focal point, k is the phase constant, w_n presents the intensity ratio of nth focus to the first one, and the superscript p represents the pth iteration. denotes the electric field intensity of the nth focal point in the (p-1)th iterative step. Once the phase value of each meta-atom is obtained, the reconstructed field can be calculated by superposing the field component emitted by each meta-atom. Since the radiation of the meta-atom also obeys the Greens' function, the reconstructed electromagnetic field at the position of each focal point can be retrieved as:

$$E_n^p = \sum_{m=1}^{M} \frac{e^{-ikr_m^n + i\phi_m}}{r_m^n} \tag{2}$$

$$w_n^p = w_n^{p-1} \frac{s_n \sum_{n=1}^{N} \left|E_n^{p-1}\right|}{E_n^{p-1} \sum_{n=1}^{N} s_n} \tag{3}$$

where s_n is the preset intensity ratio of the n^{th} focal point. According to the above details about the algorithm, w_n is adjusted to eliminate the deviations of $|E_n|$ from the desired intensity. The initial condition is set as:

$$w_n^0 = 1, \quad \phi_m^0 = \frac{2\pi m}{M} \tag{4}$$

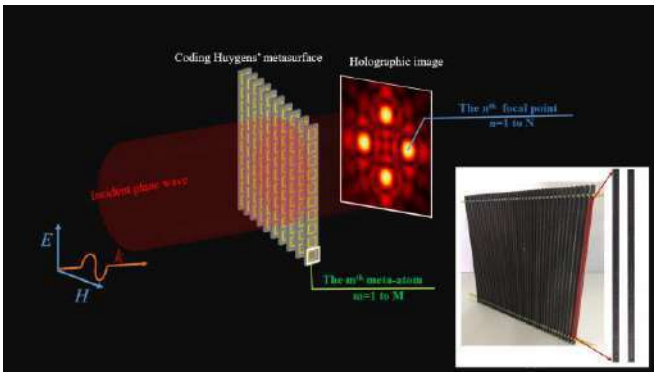


Figure 1: Schematic illustration of the holographic imaging process. A weighted Huygens' metasurface incorporating coding electric and magnetic dipolar resonators is illuminated by an incident plane wave to produce a hologram. Photography and structural details of a fabricated CHM sample (image lower right).

3. Design of the coding elements

The proposed CHMs consist of a two-dimensional square array of Huygens' meta-atoms as shown in Fig. 2(a). A split-ring resonator (SRR) is placed on one side of the substrate playing the role of the magnetic dipole and an electric-*LC* resonator acting as the electric dipole is arranged on the other side of the substrate. With the combination of magnetic and electric dipole sources, the meta-atom can be considered as a small Huygens' source. To reveal the mechanism of the proposed Huygens' meta-atom, the surface current flowing along the metallic patterns of the meta-atom is plotted in Fig. 2(b). A photography of a fabricated CHM sample is shown in the inset of Fig. 1. The proposed CHMs, which are fabricated using conventional PCB photolithography, consist of coding elements covering an area of 205 × 201.2 mm^2. A CHM is assembled by stacking 41 identical circuit board strips with 3.5 mm air gap between each strip, and each board strip consists of 57 meta-atoms. The top and the bottom sides of the strips provide the required electric and magnetic currents, respectively.

In our proposed Huygens' meta-atom, by changing the length l_e and l_m of the electric and magnetic resonators, electric and magnetic sheet impedances can be adjusted to achieve the desired amplitude and phase responses. Therefore, a flexible and efficient method to engineer electromagnetic wavefronts can be anticipated. The proposed meta-atom with fixed parameters (l_e=3.5 mm, l_m=2.7 mm) is simulated using the commercial software CST Microwave Studio by applying unit cell boundary conditions in x- and y-directions under y-polarized plane wave incidence. The simulation results are shown in Figs. 2(c) and 2(d). It can be observed that the resonance frequency of the meta-atom is around 10GHz, so the operating frequency of our proposed CHM is designed to be 10 GHz. By modulating the parameters l_e and l_m, the amplitude of the transmission coefficient ranges from 0 to 0.99, and the phase of the transmission coefficient covers

the whole 2π range at 10 GHz, as shown in Figs. 2(e) and 2(f). It is important to observe that the transmission phase can be freely manipulated by changing l_e and l_m, while keeping the transmission amplitude at a high level. The designs of 1-, 2-, and 3-bits coding elements with different phase shift of π, π/2 and π/4 are depicted in Fig. 3. The transmission amplitude of all the coding elements can be kept above 0.9 so as to achieve a high transmittance efficiency.

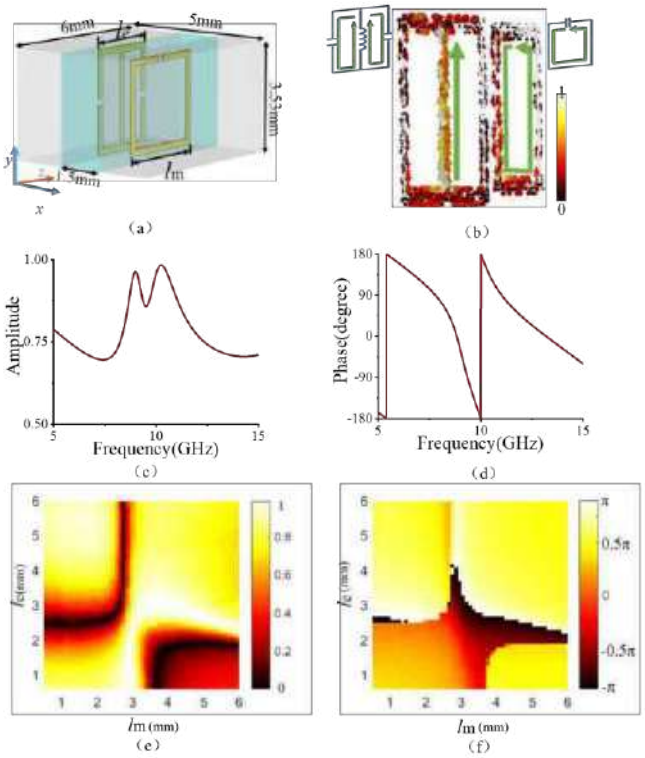


Figure 2: This is the figure caption. Color figures are acceptable. Design of the coding elements. (a) Schematic view of the Huygens' meta-atom composed of electric and magnetic dipoles. The thickness of the substrate ($\varepsilon_r = 3$ and $\tan\delta = 0.002$) is 1.5 mm and the periodicity of the elementary meta-atom is respectively 5 mm and 3.53 mm along x- and y-directions. (b) Simulated electric and magnetic currents along the metallic electric and magnetic dipolar resonators excited by a y-polarized incident wave. (c) Simulated amplitude of the transmission coefficient and (d) simulated phase of the transmission coefficient of the Huygens' meta-atom with fixed parameters l_e and l_m. (e) Simulated transmission amplitude and (f) transmission phase of the Huygens' meta-atom with different parameters l_e and l_m.

A series of CHMs is fabricated to generate holograms and to modulate focal intensity ratio of the focal points. For the uniform holograms, all the intensity ratio s_n are set to the same value and are equal to 1, such that the incident energy can be transformed equally into each focal point. To evaluate the imaging quality, two parameters are adopted here: the imaging efficiency and the root-mean-square error (RMSE). The imaging efficiency is defined as the ratio of the energy converged to designated points to the energy of the incident wave. The RMSE describing the deviations between the measured intensity ratios and the theoretical values, is used to evaluate the manipulation ability of energy allocation of focal points. Particularly, the RMSE can be calculated as:

$$\sigma = \sqrt{\frac{1}{N}\sum_{n=1}^{N}\left(\frac{|E_n|}{\sum_{n=1}^{N}|E_n|} - \frac{s_n}{\sum_{n=1}^{N}s_n}\right)^2} \tag{5}$$

phase	0	π/4	π/2	3π/4	π	5π/4	3π/2	7π/4
shape								
l_e(mm)	2.1	2.3	2.7	2.7	3.6	5.4	0.6	1.1
l_m(mm)	2.9	3.0	3.0	3.5	3.5	2.1	2.6	3.0
1-bit	0				1			
2-bit	00		01		10		11	
3-bit	000	001	010	011	100	101	110	111

Figure 3: Coding elements for 1-, 2-, and 3-bits CHMs extracted from the simulation results of the Huygens' meta-atom.

Based on the proposed weighted holographic algorithm, the phase profile at the interface of the CHM can be obtained. The focal distance is chosen to be 100 mm because of the convenience of measurement. To replace continuous phase distribution in proof-of-concept prototypes, approximated discrete phase values are used. Then arbitrary n-bit CHM can be built through discretization of the phase profile over 2π by 2^n. Taking for instance 1-bit CHM as example, the calculated phase profile at the interface can be divided into two intervals over 2π. The phases for the two intervals are quantified to be 0 and π, which are represented by code "0" and "1", respectively. In this way, the phase information can be described by codes distribution on CHM. Figure 4 shows the code distribution of the proposed 1-, 2-, and 3-bits CHMs for uniform holograms, and code distribution of the 3-bits CHMs for modulation of focal intensity distribution. Utilizing the calculated code distributions, the CHMs can be easily built up by arranging coding elements at corresponding positions.

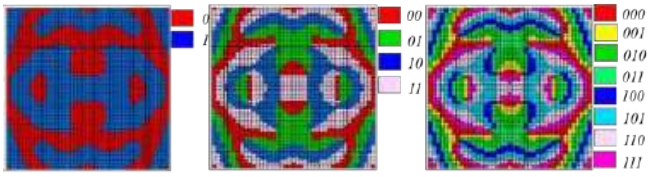


Figure 4:Code distribution of the proposed CHMs for (a) 1-bit, (b) 2-bits, (c) 3-bits uniform holograms, and code distribution for modulation of focal energy

4. Experimental results and discussion

The fabricated samples of the CHMs are experimentally validated using a near field scanning system. A feeding horn antenna is placed 65 cm away from the metasurface to ensure the incident quasi-plane wave at 10 GHz. A fibre

optic active antenna is used as field probe to measure the electric field distribution in the transmission region. The vector network analyzer (Agilent 8722ES) is connected to the feeding horn antenna and field receiving probe to measure the transmission coefficients. The holographic image of a rhombus is realized with uniform intensity distribution as shown in Fig. 5. Figure 5(a) shows the theoretical result obtained from the Huygens' metasurface with the calculated continuous phase profile. Figures 5(b)-5(d) show the measured images at the frequency of 10.2 GHz of the 1-, 2- and 3-bits CHMs at a distance of 100 mm above the CHMs. The parameters used to evaluate the imaging quality of the CHM holograms are listed in Table 1, where we can clearly observe that imaging efficiency is significantly improved from 27.1% for 1-bit hologram to 51.5% for 3-bits hologram, which is superior compared with previous metasurface holograms [14, 17]. It can also be noted that the total image efficiency is improved by 57.2% from 1-bit to 2-bits, and 20.9% from 2-bits to 3-bits hologram, meaning that the imaging quality improvement effect will be slight when the phase-quantization increases to a relatively high level. Therefore, we need to take both design complexity and imaging quality into consideration and choose coding elements with suitable bits for real-life practical applications. Table 1 also depicts the RMSE of the uniform holograms. For the 3-bits hologram, the measured RMSE can be as low as 0.77%, indicating a low deviation between calculation and measurement when the incident energy is transformed to the desired focus points equally. The signal to noise ratio (SNR), which is defined as the ratio of the peak intensity in the image to the standard deviation of the background noise [20], is found to be above 10 for all the measured CHM holograms as shown in Table 1. Figures 5(e)-5(g) show the measured images at 9GHz, 10GHz and 11GHz, respectively. The image quality will decrease when the operating frequency deviates from the designed one. Since the phase responses of the meta-atoms are extracted from the simulated results at 10 GHz, and the phase distribution at the interface is calculated using the operating wavelength at 10 GHz, which means the phase delay at the focal plane will be affected when the operating frequency deviates. The simulation results of 3-bits CHM at different focal distance of 90 mm, 100 mm and 110 mm are also given in Figs. 5(h)-5(j). When the focal distance deviates from the designed value, the image quality will decrease owing to the change of phase delay on the focal plane.

5. Conclusion

In conclusion, CHM holograms are realized using Huygens' meta-atoms as coding elements and are experimentally validated in microwave regime. By adjusting the geometrical parameters of the electric and magnetic dipoles, 1-, 2-, and 3-bits coding elements are built based on the transmission phase. A weighted holographic algorithm is proposed to achieve the phase profile along the metasurface, and 1-bit, 2-bits and 3-bits CHM holograms are designed, fabricated and measured. The imaging efficiency of the 3-bits CHM hologram is measured to be as high as 51.5%, showing outstanding imaging quality. Based on the measured results, the influence of the phase-quantization level to the imaging quality is discussed to improve imaging quality. Moreover, several 3-bits CHMs designed to modulate intensity distribution among focal points are experimentally demonstrated. The RMSE of the measured results verify the great intensity modulation ability of our proposed CHMs. The proposed CHM holograms provide more freedom to electromagnetic wave manipulation, which may have many practical applications in computer-generated holograms, imaging lenses and microscopy. Furthermore, the concept shows great potentials in constructing programmable CHMs by loading controllable elements to realize dynamic holograms and wave focusing.

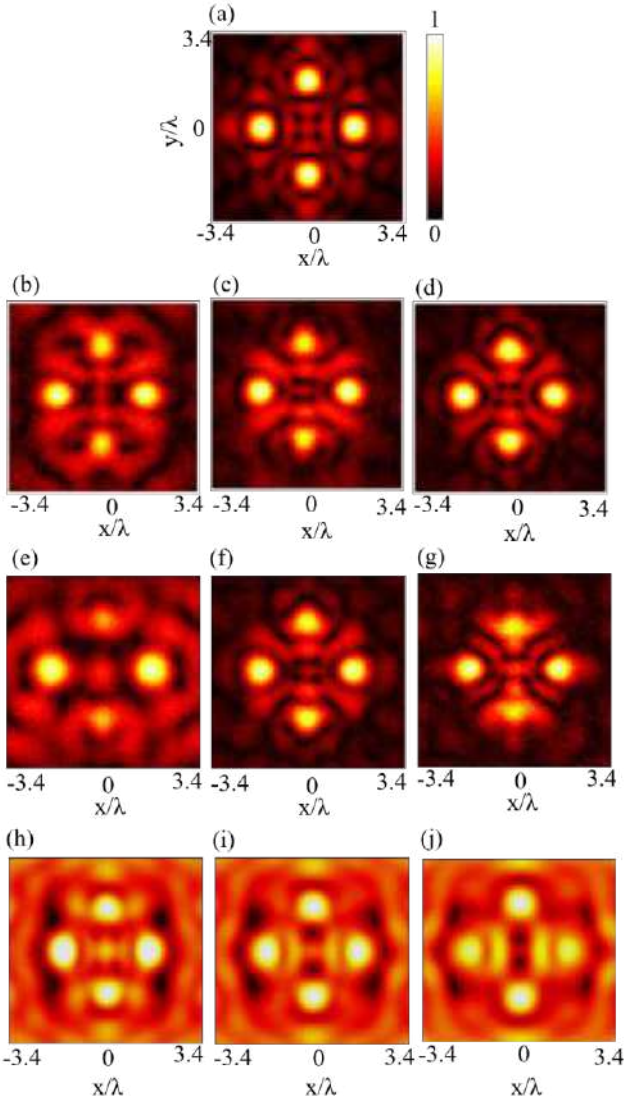


Figure 5: Holographic images of CHMs with different bits. (a) Theoretical results with calculated continuous phase profile. (b) Experimental image of 1-bit CHM at 10.2 GHz. (c) Experimental image of 2-bits CHM at 10.2 GHz. (d) Experimental image of 3-bits CHM at 10.2 GHz. (e), (f) and (g) Experimental images of 3-bits CHM at 9 GHz, 10 GHz and 11 GHz respectively. (h), (i) and (j) Simulation images

of 3-bits CHM at different focal distances of 90 mm, 100 mm and 110 mm respectively.

Acknowledgements

This paper is supported by the National Natural Science Foundation of China (Grant No. 61701141), and the Fundamental Research Funds for the Central Universities (Grant No.HIT.NSRIF.2019029).

References

[1] N. N. Yu, P. Genevet, M. A. Kats, F. Aieta, J. Tetienne, F. Capasso, and Z. Gaburro, Light propagation with phase discontinuities: generalized laws of reflection and refraction, Science, pp. 1210113, 2011.

[2] E. Hasman, V. Kleiner, G. Biener, and A. Niv, Polarization dependent focusing lens by use of quantized Pancharatnam–Berry phase diffractive optics, Appl. Phys. Lett, pp. 328–330, 2003.

[3] X. Ding, F. Monticone, K. Zhang, L. Zhang, D. Gao, S. N. Burokur, A. de Lustrac, Q. Wu, C. W. Qiu, and A. Alù, Ultrathin Pancharatnam-Berry Metasurface with Maximal Cross-Polarization Efficiency, Adv. Mater, pp. 1195–1200, 2015.

[4] Q. Xu, X. Zhang, M. Wei, G. Ren, Y. Xu, Y. Li, H. Wang, C. Ouyang, J. Han, and W. Zhang, Efficient Metacoupler for Complex Surface Plasmon Launching, Adv. Opt. Mater, pp. 1701117, 2018.

[5] H. Zhang, X. Zhang, Q. Xu, C. Tian, Q. Wang, Y. Xu, Y. Li, J. Gu, Z. Tian, C. Ouyang, X. Zhang, C. Hu, J. Han, and W. Zhang, High Efficiency Dielectric Metasurfaces for Polarization Dependent Terahertz Wavefront Manipulation, Adv. Opt. Mater, pp. 1700773, 2018.

[6] A. Epstein, J. P. S. Wong, and G. V. Eleftheriades, Cavity-excited Huygens' metasurface antennas for nearunity aperture illumination efficiency from arbitrarily large apertures, Nat. Commun, pp. 20510, 2016.

[7] M. Selvanayagam and G. V. Eleftheriades, Discontinuous electromagnetic fields using orthogonal electric and magnetic currents for wavefront manipulation, Opt. Express, pp. 14409–14429, 2013.

[8] Y. Yifat, M. Eitan, Z. Iluz, Y. Hanein, A. Boag, and J. Scheuer, Highly efficient and broadband wide-angle holography using patch-dipole nanoantenna reflectarrays, Nano Lett, pp. 2485–2490, 2014.

[9] Y. Yuan, X. Ding, K. Zhang, and Q. Wu, Planar efficient metasurface for vortex beam generating and converging in microwave region, IEEE Trans. Magn, pp. 1–4, 2017.

[10] K. Zhang, Y. Yuan, D. Zhang, X. Ding, B. Ratni, S. N. Burokur, M. Lu, K. Tang, and Q. Wu, Phase-engineered metalenses to generate converging and non-diffractive vortex beam carrying orbital angular momentum in microwave region, Opt. Express, pp. 1351–1360, 2018.

[11] Y. Yuan, K. Zhang, X. Ding, B. Ratni, S. N. Burokur, and Q. Wu, Complementary transmissive ultra-thin metadeflectors for broadband polarization-independent refractions in the microwave region, Photon. Res, pp.80– 88, 2019.

[12] C. Pfeiffer and A. Grbic, Metamaterial Huygens' surfaces: tailoring wave fronts with reflectionless sheets, Phys. Rev. Lett, pp. 197401, 2013.

[13] B. U. Zhu and Y. Feng, Passive metasurface for reflectionless and arbitary control of electromagnetic wave transmission, IEEE Trans. Antenn. Propag, 5500–5511, 2015.

[14] K. Chen, Y. Feng, F. Monticone, J. Zhao, B. Zhu, T. Jiang, L. Zhang, Y. Kim, X. Ding, S. Zhang, A. Alù, and C. W. Qiu, A Reconfigurable Active Huygens' Metalens, Adv. Mater, pp. 1606422, 2017.

[15] Z. Wang, X. Ding, K. Zhang, and Q. Wu, Spacial Energy Distribution Manipulation with Multi-focus Huygens Metamirror, Sci. Rep, pp. 9081, 2017.

[16] A. Epstein and G. V. Eleftheriades, Passive lossless Huygens' metasurfaces for conversion of arbitrary source field to directive radiation, IEEE Trans. Antenn. Propag, pp. 5680–5695, (2014).

[17] W. Zhao, H. Jiang, B. Liu, J. Song, Y. Jiang, C. Tang, and J. Li, Dielectric Huygens' metasurface for highefficiency hologram operating in transmission mode, Sci. Rep, pp. 30613, 2016.

[18] T. J. Cui, M. Q. Qi, X. Wan, J. Zhao, and Q. Cheng, Coding metamaterials, digital metamaterials and programmable metamaterials, Light Sci. Appl, pp. e218, 2014.

[19] L. H. Gao, Q. Cheng, J. Yang, S. J. Ma, J. Zhao, S. Liu, H. B. Chen, Q. He, W. X. Jiang, H. F. Ma, Q. Y. Wen, L. J. Liang, B. B. Jin, W. W. Liu, L. Zhou, J. Q. Yao, P. H. Wu, and T. J. Cui, Broadband diffusion of terahertz waves by multi-bit coding metasurfaces, Light Sci. Appl, pp. e324, 2015.

[20] D. S. Dong, J. Yang, Q. Cheng, J. Zhao, L. H. Gao, S. J. Ma, S. Liu, H. B. Chen, Q. He, W. W. Liu, Z. Fang, L. Zhou, and T. J. Cui, Terahertz broadband low-reflection metasurface by controlling phase distributions, Adv. Opt. Mater, pp. 1405–1410, 2015.

[21] L. Liang, M. Qi, J. Yang, X. Shen, J. Zhai, W. Xu, B. Jin, W. Liu, Y. Feng, C. Zhang, H. Lu, H. T. Chen, L. Kang, W. Xu, J. Chen, T. J. Cui, P. Wu, and S. Liu, Anomalous terahertz reflection and scattering by flexible and conformal coding metamaterials, Adv. Opt. Mater, pp. 1374–1380, 2015.

[22] Z. Wang, X. Ding, K. Zhang, B. Ratni, S. N. Burokur, X. Gu, and Q. Wu, Huygens Metasurface Holograms with the Modulation of Focal Energy Distribution, Adv. Opt. Mater, pp. 1800121, 2018.

[23] H.-X. Xu, T. Cai, Y.-Q. Zhuang, Q. Peng, G.-M. Wang, and J.-G. Liang, Dual-mode transmissive metasurface and its applications in multibeam transmitarray, IEEE Trans. Antenn. Propag, pp. 1797–1806, 2017.

Broadband flattened parabolic reflector antenna based on metasurface

Vivien Taverny[1], Badreddine Ratni[1], and Shah Nawaz Burokur[1]

[1]LEME, UPL, Univ Paris Nanterre, F92410 Ville d'Avray, France
*corresponding author, E-mail: badreddine.ratni@parisnanterre.fr

Abstract

A flattened parabolic reflector antenna is designed to operate under right-hand circular polarization (RHCP) by using a reflective metasurface composed of square patches printed on a grounded dielectric substrate. A circularly-polarized patch antenna placed at the focal point of the metasurface reflector is used as the primary feed. Numerical simulations are conducted and far-field simulation results show a highly directive beam with a realized gain of 20 dBic.

1. Introduction

Planar version of metamaterials called metasurfaces have been developed these last two decades. They are known for having reduced profile and reduced losses compared to the 3D bulky version of metamaterials [1]. Their characteristics allow their implementation in different types of antennas such partially reflecting surface (PRS) based Fabry-Perot cavity antennas [2-5], lens antennas [6] and reflector antennas [7-8].

2. Metasurface-based reflector

The use of metasurfaces makes it possible today to realize a very great variety of extraordinary structures. We have recently demonstrated that we can use metasurfaces to make different reflector antennas [8]. In this previous work, we have used a reconfigurable metasurface that allows frequency and angular reconfigurability. The proposed structure was composed of unit cells that incorporate varactor diodes. Nevertheless, although this structure was able to cover a wide frequency band spanning from 9 GHz to 12 GHz, the instantaneous bandwidth was narrow due to the resonant nature of the unit cells. In this work, we propose a new broadband passive metasurface that is used to design a flattened parabolic reflector antenna able to operate and cover the targeted frequency band from 10.7 GHz to 12.7 GHz. The unit cell composing the multi-layer metasurface is shown in Fig. 1 and is composed of three layers. The first layer consists of a continuous metallic ground plane while the second and third layers are each composed of square metallic patch with geometric dimensions a and $k*a$, respectively. At a fixed dimension of the parameter a, the factor k has been optimized in such a way to obtain the least variation of the phase on the entire frequency band (from 10.7 GHz to 12.7 GHz). In our case, the periodicity of the unit cell is fixed to p = 6 mm and the dimensions of the square patches is varied from a = 0.2 mm to 5.9 mm. The most optimum k factor is found to be 0.9. Two layers of F4BM dielectric substrate (relative permittivity ε_r = 2.2) with thickness t_1 = 1 mm and t_2 = 1.5 mm are chosen as spacers.

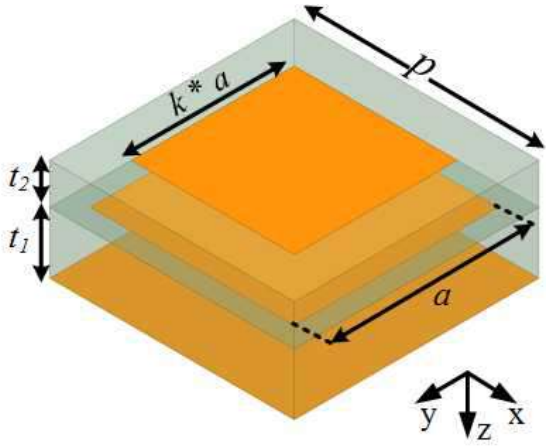


Figure 1: Schematic view of the designed unit cell with periodicity of p = 6 mm.

3. Results

In order to obtain the characteristics of a parabolic reflector, the phase profile is calculated as follows:

$$\varphi(x) = \frac{2\pi}{\lambda}\left(\frac{x^2 + y^2}{4f}\right) + \varphi_0$$

where λ is the operating wavelength, f = 30 mm is the focal distance and ϕ_0 is the reflection phase shift at (x = 0 mm, y = 0 mm). The calculated phase profile along the whole metasurface composed of 30 x 30 unit cells, is presented in Fig. 2. By varying the dimensions of the square patches the reflection phase response can be varied from -180° to 180°. The metasurface is then designed by optimizing each unit cell to obtain the required phase response. Once designed, the metasurface reflector is fed at the predefined focal point (f = 30 mm) by a wideband circularly polarized patch antenna. Full-wave simualtions are performed using a finite

element based commercial solver. A directive beam is obtained over the entire band spanning from 10.7 GHz to 12.7 GHz. The simulated radiation patterns at 10.7 GHz and 12.7 GHz are presented in Fig. 3. A right handed circular polarization (RHCP) is obtained with an axial ratio lower than 3 dB over the entire frequency band. The realized gain of the patch antenna is around 6 dBic while the metasurface-based flattened parabola allows to increase the gain to 20 dBic.

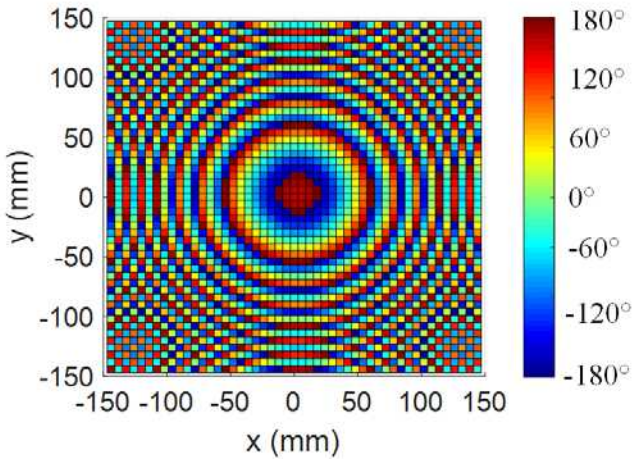


Figure 2: Applied phase distribution along the metasurface for a focal point fixed at f = 30 mm.

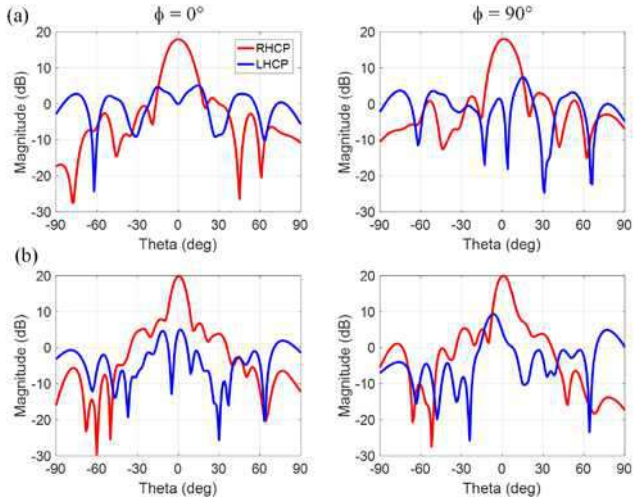


Figure 3: Simulated far-field radiation patterns showing RHCP directive beam with a gain of 20 dBic at the frequencies of (a) 10.7 GHz and (b) 12.7 GHz.

4. Conclusions

In summary, a broadband planar parabolic reflector antenna based on metasurface is proposed. The metasurface is composed of square patches printed on a grounded dielectric substrate. A broadband patch antenna placed on the focal point is used as a primary feed. Simulation of the proposed antenna structure is performed and the results shows a highly directive beam with a high realized gain of 20 dBic.

References

[1] C. L. Holloway, E. F. Kuester, J. A. Gordon, J. O'Hara, J. Booth, D. R. Smith, An overview of the theory and applications of metasurfaces: the two-dimensional equivalents of metamaterials, *IEEE Antennas Propag. Mag*. 54: 10-35, 2012.

[2] A. Ghasemi, S. N. Burokur, A. Dhouibi, and A. de Lustrac, High beam steering in Fabry-Pérot leaky-wave antennas, *IEEE Antennas Wireless Propag. Lett.*, Vol. 12, 261-264, 2013.

[3] S. N. Burokur, J.-P. Daniel, P. Ratajczak, and A. de Lustrac, Tunable bi-layered metasurface for frequency reconfigurable directive emissions, *Appl. Phys. Lett.*, vol. 97, no. 6, p. 064101, Aug 2010.

[4] B. Ratni, W. A. Merzouk, A. de Lustrac, S. Villers, G.-P. Piau, and S. N. Burokur, Design of phase-modulated metasurfaces for beam steering in Fabry-Perot cavity antennas, *IEEE Antennas Wireless Propag. Lett.*, vol. 16, pp. 1401-1404, 2017.

[5] B. Ratni, A. de Lustrac, G.-P. Piau, and S. N. Burokur, "Modeling and design of metasurfaces for beam scanning," *Appl. Phys. A: Materials Science & Processsing*, vol. 123, no. 1, p. 50, Jan. 2017.

[6] A. Dhouibi, Burokur, S. N., de Lustrac, A. and Priou, A., Metamaterial-based half Maxwell fish-eye lens for broadband directive emissions, *Appl. Phys. Lett.*, Vol. 102, No. 2, 024102, 2013.

[7] B. Ratni, A. de Lustrac, G.-P. Piau, S. N. Burokur, Active metasurface for reconfigurable reflectors, *Appl. Phys. A* 124: 104, 2018.

[8] B. Ratni, A. de Lustrac, G.-P. Piau, S. N. Burokur, Reconfigurable meta-mirror for wavefronts control: applications to microwave antenna, *Opt. Express* 26: 2613-2624, 2018.

Mitigating Chromatic Dispersion with Hybrid Optical Metasurfaces

Rajath Sawant[1], Purva Bhumkar[1], Alexander Y. Zhu[2], Peinan Ni[1], Federico Capasso[2], Patrice Genevet[1*]

[1]CNRS-CRHEA, Université Côte d'Azur, Sophia Antipolis, Valbonne, France

[2]John A. Paulson School of Engineering and Applied Sciences, Harvard University, Cambridge, MA 02138, USA

*corresponding author, E-mail: pg@crhea.cnrs.fr

Abstract

Metasurfaces, arrays of subwavelength spaced nanostructures, control various properties of light. The dispersion of outgoing light can also be controlled using the phase gradient of a metasurface . Exploiting this property, hybrid refractive-metasurface devices is designed to realize nondispersive refraction in the visible. The dispersion of hybrid component, characterized by using a Fourier plane imaging microscopy setup, is essentially achromatic over about 200nm in the visible. Broadband focusing with composite plano-convex metasurface lens is also proposed.

Introduction

Conventional optical components are macroscopic in size which is a hindrance for miniaturization of optical devices. Dispersive response from the material used is their major drawback leading to chromatic aberration. For example, to correct the chromatic aberration of a lens a popular technique in practice is to use series of cascading lenses, which results in bulky devices. Metasurfaces, an array of nanoantennas of sub-wavelength thickness can be employed to achieve this as they are compact and effective. Metasurfaces are known to cause abrupt phase and polarization shift in the outgoing light. Recently, the dispersion of metasurfaces has been shown to vary from positive to zero to negative in the infra-red region [1]. Also a general approach to design an achromatic metalens has been demonstrated in the visible region using the geometric phase property [2]. In this work, we demonstrate dispersion compensation of a prism and a plano convex lens by a simpler method using phase gradient metasurfaces [3].

For a desired functionality, one can fabricate the metasurface with corresponding phase profile using nanoantennas. For our study, we use constant phase gradient metasurface made of TiO_2 nanopillars (dielectric material) on SiO_2 substrate. Using FDTD technique, the phase and transmission map for nanopillars of different radius for different incident wavelength is computed. Phase gradient is obtained by placing 0 to 2π phase elements in the increasing order along one particular direction and periodically repeating the same arrangement. One can see that this mimics the conventional blazed gratings in design and also functionality. The generalized laws of refraction at the metasurface-air interface [4] are used for the calculations. The phase gradient is a parameter to design the metasurface given the angle of incidence (30°) and the design wavelength of light [Eqn 1]. The technique of Fourier plane imaging and spectroscopy is utilized to study minute angles of dispersion in the prism's case (Fig 2). The results obtained are for broadband visible region of 550-800 nm. Extending the same principle to a plano-convex lens, to mitigate its chromatic aberration phase gradient metasurface is placed on its planar side. Phase gradient of the device varies linearly as a function of distance from the center of the lens unlike in the case of prism [Eqn 2].

Figures

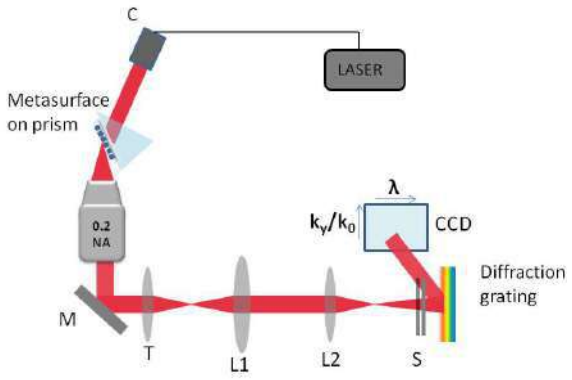
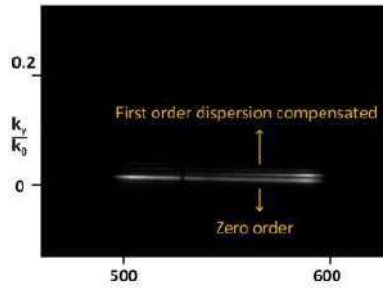


Figure 1: Optical setup for k-space imaging and spectroscopy. T, L1, L2 are achromatic convex lenses. C – Collimator, M – Mirror, S- slit.



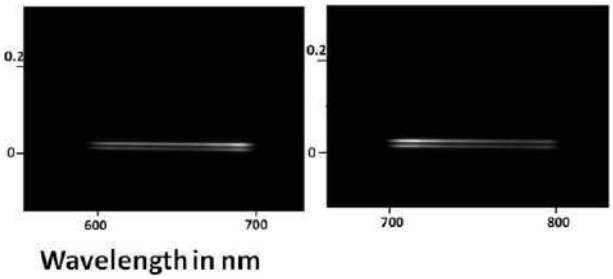


Figure 2: K-space spectra of prism-metasurface combination in the wavelength range of 500 nm – 800 nm.

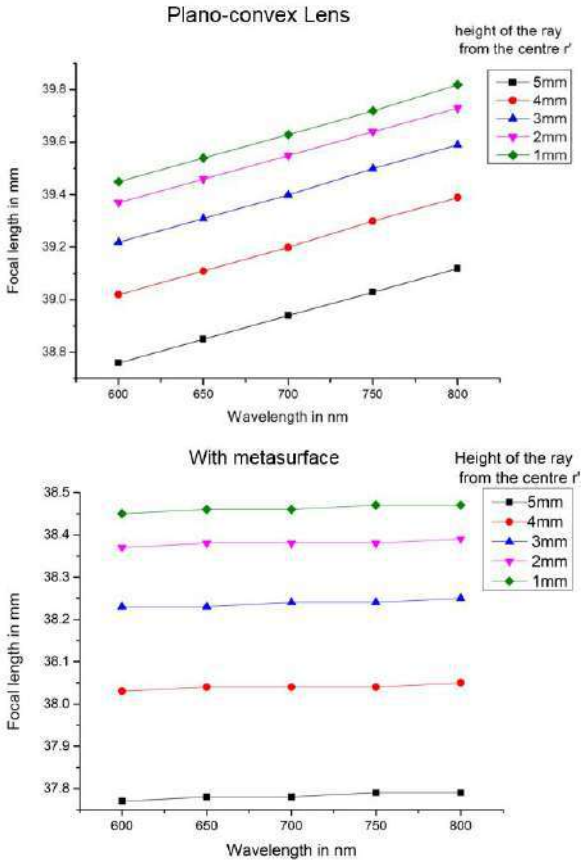


Figure 3 : Ray tracing results of chromatic aberration mitigation by metasurface. Top- Just with plano-convex lens, Bottom- Metasurface lens combination.

1.1. Tables

Comparison of dispersion slopes for prism without metasurface and with metasurface

Wavelength in nm	Prism ky/k0 per nm (e-5)	Prism+metasurface ky/k0 per nm (e-5)	% compensation [mean value]
540-600	-4.2 ± 0.1	-2.0 ± 0.5	52
600-700	-2.8 ± 0.1	-0.5 ± 0.9	82
700-800	-1.4 ± 0.1	0.2 ± 0.6	114

1.3 Equations

Phase gradient relation of metasurface for chromatic aberration mitigation of (1) Prism, (2) Plano convex lens

$$\frac{d\phi}{dx} = \frac{2\pi B}{\lambda_0^3} \qquad (1)$$

$$\frac{d\phi}{dr} = \frac{4\pi B}{\lambda_0^3}\frac{r}{R} \qquad (2)$$

Where B is the co-efficient of λ^{-2} in Cauchy's relation and λ_0 is the design wavelength of metasurface. 'R' is the radius of curvature of lens and 'r' is the height of incident ray from the centre of lens.

2. Discussion

The motivation behind this work is to combine refractive components with normal dispersion and metasurfaces with negative dispersion to design hybrid achromatic devices. Metalenses reported so far are constructed by engineering phase at each point, have low numerical aperture and efficiency. On the other hand, we have exploited phase gradient property of the metasurface which is a global parameter. They have an efficiency of atleast 60%.

3. Conclusions

All in all, we report mitigation of dispersion of prism to atleast 80% (experimental) and lens upto 94% (ray tracing results) using metasurfaces in broadband visible region of 600-800 nm. Other aberrations of lens can also be addressed using the same approach.

Acknowledgements

This project was funded by the European Research Council (ERC) under the European Union's Horizon 2020 research and innovation programme (Grant Agreement No. 639109) and by the Air Force Office of Scientific Research (Grants # FA9550-14-1-0389 and FA9550-16-1-0156).

References

1. E. Arbabi, A. Arbabi, S.M. Kamali, Y. Horie, and A. Faraon, **4**, (2017).

2. W.T. Chen, A.Y. Zhu, V. Sanjeev, M. Khorasaninejad, Z. Shi, E. Lee, and F. Capasso, Nat. Nanotechnol. **13**, 220 (2018).

3. R. Sawant, P. Bhumkar, A.Y. Zhu, P. Ni, F. Capasso, and P. Genevet, Adv. Mater. **31**, 1805555 (2019).

4. N. Yu, P. Genevet, M.A. Kats, F. Aieta, J.-P. Tetienne, F. Capasso, and Z. Gaburro, Science (80-.). **334**, 333 LP (2011).

Metasurface-based ultra-lightweight high-gain flat parabolic reflectarray for microwave beam collimation/focusing

Sinhara R Silva[1], Abdur Rahman[1,2], Wilton de Melo Kort-Kamp[3], Diego A. R. Dalvit[4], Hou-Tong Chen[1], and Abul K. Azad[1]*

[1] Center for Integrated Nanotechnologies, Los Alamos National Laboratory, MS K771, Los Alamos, NM, 87545, USA
[2] Physics and Technology Department, Edinboro University of Pennsylvania, Edinboro, PA 16444, USA
[3]Theoretical Division, Los Alamos National Laboratory, MS B262, Los Alamos, NM 87545, USA
[4]Theoretical Division, Los Alamos National Laboratory, MS B213, Los Alamos, NM 87545, USA
*corresponding author, E-mail: s_rishi_s@lanl.gov

Abstract:

We demonstrate a metasurface-based flat reflectarray antenna with the capability of beam collimation and focusing. The reflectarray is designed to operate at 12GHz with a focal distance of 50cm in a center-fed configuration. It consist of 32 metallic patch resonators of variable sizes to cover a full 2π phase range. The reflectarray exhibits a measured gain enhancement of 28dBi at the central operating frequency of 11.8GHz and focuses at 50cm with a depth of focusing of 8cm and has a 3dB directionality ±1.6°. The demonstrated reflectarrays may enable low-cost, lightweight, and high-gain deployable transceivers for small-satellite platforms

Introduction:

Small satellites (SmallSats) are emerging space research capabilities for many intriguing applications such as sensing, imaging, tracking, surveillance, and high-speed communications. The use of SmallSats has been rapidly growing in recent years due to multiple factors including miniaturization of electronics, high-speed data processing and high-density data storage, ride-share with other satellites, and reduced cost for their design, build, and operation. Antennas are the key component for satellites to transmit/receive electromagnetic signals for wireless communications. Conventional satellites employ parabolic dish antennas for wireless communication links. Due to the limited size, weight, and power (SWaP) requirements of SmallSats , they mostly rely on small, light-weight, and isotropic antennas such as dipole, monopole, or helix. Although SmallSats are capable of collecting huge amounts of data, they severely suffer from a bottleneck effect while transmitting/receiving data to the ground/command stations due to the inherit limited performances of these inefficient antennas. Therefore, it is very important to explore alternative approaches to enable lightweight high-gain antennas that occupy a considerably small fraction of the payload and volume of SmallSats. There have been a handful of initiatives in realizing high-performance lightweight antennas for small satellites[1] including Fabry-Pérot cavity antennas[2], deployable mesh reflectors[3], inflatable balloon reflectors[4], and deployable waveguide slot antennas[5]. Very recently, planar reflectarrays have been studied as a viable option for enabling high-gain antennas for SmallSat applications [5].

Our proposed flat parabolic reflectarray is based on a single layer metasurface which consist of patches separated from a metallic ground plane by a thin dielectric spacer as shown in inset of Fig 1(a). The metasurface is polarization-dependent, with the electric field of the incident/emitted microwave radiation along the longer axis of the patches. We use a square unit-cell of size 10 mm to operate at 12 GHz, which introduces ~2000 pixels in the reflectarray surface. To cover the required full 2π phase range, we vary the structural parameters length (L), width (W), and gap (g) of the resonators and obtain 32 phase values from 0 to 2π in increments of $\pi/16$ as shown in Fig 1(a) with their corresponding reflectance higher than 85%. The discrete values of the phase are derived using commercially available full-wave numerical simulation software (CST).

The polarization-dependent ultrathin flat reflectarray works similarly to parabolic dish antenna and its operational frequency, focal length of the designed metasurface can be tuned by scaling the resonator and redistributing the phase profile. In a center-fed reflector or a lens, where the phase distribution is radially symmetric as shown in Fig 1(b). The required phase distribution as a function of position (x,y) on the metasurface is given by

$$\psi(x,y) = \frac{2\pi}{\lambda}\left\{\sqrt{x^2+y^2} - z_f\right\}$$

Where λ is the operating wavelength and $f = z_f$ is the focal length. The size of our proposed reflectarray

is $440\,mm \times 440\,mm$ with a focal length of $500\,mm$.

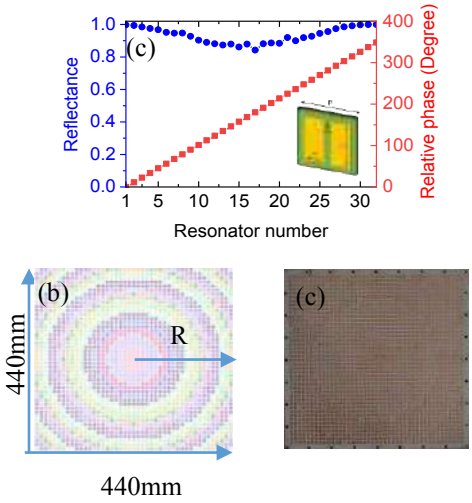


Figure 1: (a) Phase (red) and reflectance (blue) of meta-atoms. (b) Spatial phase profile of the metasurface (c) fabricated reflectarray antenna

Fig 1(b) shows the spatial phase profile of the metasurface, where the color coding represents the use of 32 discrete phase values. The metasurface reflectarray was fabricated on a double copper cladding printed circuit boards (PCBs) from Rogers Corporation (RO 4003C, thickness=0.508 mm) using chemical etching of copper. An image of the fabricated reflectarray is shown in Fig. 1(c) and it was characterized inside an anechoic chamber using a pair of broadband horn antennas and a vector network analyzer.

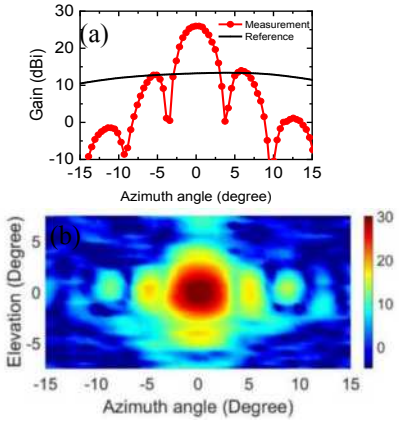


Figure 2 : Measured gain of the antenna as a function of the azimuth (horizontal) scan angle (c) 2D plot of the power density profile for 0° reflect angle

We investigate the far-field radiation pattern of the emitted microwave radiation from our off-axis parabolic reflectarray and measured the angle-dependent gain as a function of azimuth angle, varying from -15° to +15° for a fixed elevation angle as shown in Fig 2(a). A net gain of 27.5 dBi is observed for an azimuth angle of zero degree, confirming the validation of our reflectarray design for beam focusing/collimation. The measurement was repeated for each elevation angle from -15° to +15°. The measured 2D plot of the angle-dependent gain is shown in Fig 2(b). The radiation pattern shows a dominant Gaussian type main lobe, which is symmetrically bounded within ±3° for both azimuth and elevation angles. The angle of 3-dB gain enhancement is less than 2°, confirming good directionality and beam collimation. The circular field distribution is also a manifestation of good beam collimation, a pre-cursor for long-haul communication link.

In conclusion, we have designed, fabricated, and characterized a metasurface-based reflect array antenna at microwave frequencies consisting of an anisotropic resonator array with focusing/collimation. The fabricated reflect array demonstrates excellent focusing and collimation of the radiated microwaves from a feed-horn antenna. The measured results show a gain enhancement as high as 15.5 dBi, in addition to the 12 dBi gain from the feed horn antenna.

Acknowledgements

This work was performed, in part, at the Center for Integrated Nanotechnologies, Los Alamos National Laboratory. We acknowledge supports from the LDRD program, Los Alamos National Laboratory.

Reference

[1] Gao, S., et al., *Advanced Antennas for Small Satellites.* Proceedings of the Ieee, 2018. 106(3): p. 391-403.

[2] Qin, F., et al., *Wideband Circularly Polarized Fabry-Perot Antenna.* Ieee Antennas and Propagation Magazine, 2015. 57(5)

[3] Chahat, N., et al., *The Deep-Space Network Telecommunication CubeSat Antenna Using the deployable Ka-band mesh reflector antenna.* Ieee Antennas and Propagation Magazine, 2017. 59(2): p. 31-38.

[4] Babuscia, A., et al., *Inflatable Antenna for CubeSats: Development of the X-band Prototype.* Ieee Aerospace Conference, 2016.

[5] Arnieri, E., et al., *A compact high gain antenna for small satellite applications.* Ieee Transactions on Antennas and Propagation, 2007. 55(2): p. 277-282.

Incidence angle-dependence in image reconstruction crosstalk of broadband birefringent c-Si Metasurfaces

Augusto Martins[1], Juntao Li[2], Achiles F. Mota[1], Yin Wang[2], Luiz G. Neto[1], Ben-Hur V. Borges[1*] and Emiliano R. Martins[1]

[1]Metamaterials Group (GMeta), Department of Electrical Engineering, University of São Paulo, CEP 13566-590, São Carlos - SP, Brazil

[2]State Key Laboratory of Optoelectronic Materials and Technologies, School of Physics, Guangzhou 510275, China

*corresponding author, E-mail: benhur@sc.usp.br

Abstract

We investigate numerically and experimentally the image reconstruction crosstalk as function of the incidence angle for a broadband stereoscopic hologram metasurface operating in the visible range. To this end, we define a metasurface acceptance cone in which good performance can be achieved with reduced polarization crosstalk. The stereogram consists of a birefringent metasurface with elliptical crystalline silicon (c-Si) nanoposts. The optimum diffraction(transmission) efficiency calculated at normal incidence reach 52.3% (76.9%) at the design wavelength of 532 *nm*.

1. Introduction

Metasurfaces are planar subwavelength structures that allow local control of phase, amplitude and/or polarization of light [1]. Metasurfaces are fabricated either with metals (such as Au and Ag) or entirely with dielectrics. However, all-dielectric metasurfaces are the preferable choice because of their intrinsic lower losses [2]. Amorphous silicon (a-Si), for instance, has proven to be a suitable candidate due to its high refractive index in the visible range, resulting in structures with small aspect ratio (at the expense of high absorption losses). Crystalline silicon (c-Si), in contrast, is more adequate for holography applications than a-Si and poly-silicon (p-Si) due to its smaller absorption at these wavelengths [3]. In addition, c-Si based metasurface holograms have shown successfully broadband operation in the visible range [4, 5]. Most of the proposed metasurfaces, including those based on c-Si, rely on normal incidence. Nevertheless, it would be useful to assess the metasurface's performance under oblique incidence so that the degree-of-freedom allowed by this platform could be increased even further. In this sense, we suggest here an acceptance cone as a figure-of-merit to characterize the metasurface response in terms of the incidence angle for holography applications. To this end, we use a broadband birefringent c-Si metasurface capable of encoding holographic stereograms for imaging with depth perception [5]. The metasurface design is based on elliptical nanoposts capable of phase-shifting independently the transmitted light of two linear polarization states. The independent phase control allows the encoding of two different holograms in the same metasurface [5]. The metasurface acceptance cone (MAC) is defined in terms of the hologram's reconstruction quality (via signal to noise ratio), transmission and diffraction efficiencies, and cross-polarization crosstalk. The MAC performance is assessed numerically and verified experimentally.

2. Metasurface design

The metasurface's building blocks consist of c-Si elliptical nanoposts on top of a sapphire substrate, as illustrated in Fig. 1(a). The phase shift imparted on the transmitted light by this structure is different for light polarized along each of its semi-axes (x or y). Thus, independent phase control can be achieved with four phase levels for each polarization with high transmission for a 190 *nm* unit cell size [5]. The nanoposts are designed to operate at the wavelength of 532 *nm*. Nevertheless, this structure has demonstrated broadband operation with high quality experimental reconstructions even in the blue region of the spectrum [5]. The metasurface is fabricated on a 230 *nm* thick c-Si on sapphire (SOS) by electron beam lithography (EBL) and inductively coupled plasma (ICP) etching. The fabrication process is shown in Fig. 2. SEM images of the fabricated sample are shown in Figs. 1(b) and (c).

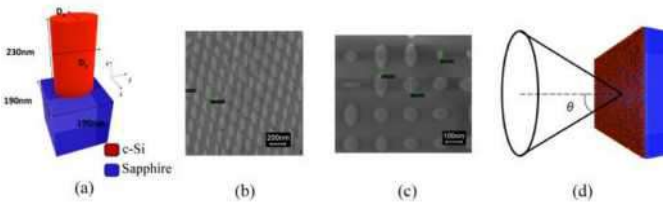


Figure 1: (a) Schematic representation of the birefringent c-Si based metasurface unit cell. (b) and (c) show SEMs of one of the fabricated metasurfaces. (d) Representation of the metasurface's acceptance cone (MAC) with openin angle 2θ. The maximum acceptable angle, θ, is measured relative to the metasurface's normal.

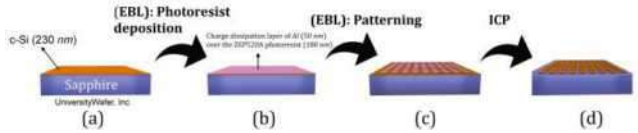


Figure 2: Fabrication steps of the fabricated metasurfaces. (a) UniversityWafer silicon on sapphire waver. (b)-(c) shows the steps involved on the fabrication. (EBL) Electron beam lithography. (ICP) Inductively coupled plasma.

3. Stereoscopic imaging

As described in [5], this design allows the encoding of two completely different phase distributions on the same metasurface, with each one accessible by either *x*- or *y*-polarized light. This allows us to encode the CGHs of both images of a stereogram in the same metasurface. The encoding process is repeated here for completeness. First, we generate two stereogram images, as illustrated in Figs. 3 (a) and (b). Then, we calculate a four-phase level CGH with 1024×1024 pixels for each image (Figs. 3 (c) and (d)) and encode them in a c-Si birefringent metasurface, as illustrated by each square in Fig. 3 (e). Note that the final metasurface is composed of a 2×2 hologram array. Thus, the size of the final metasurface is 389.12 μm × 389.12 μm.

We theoretically assess the metasurface's performance through a reconstruction analysis based on the Rayleigh-Sommerfeld (RS) integral [4]. Figs. 3 (f) and (g) show the resulting reconstructions for *x*- and *y*- polarizations, respectively, at 532 *nm* at normal incidence (the ideal case). The resulting diffraction (transmission) efficiencies for this case are 51.7% (76.9%) and 52.3% (76.7%) for *x*- and *y*-polarized light respectively, which are remarkable results for the visible range.

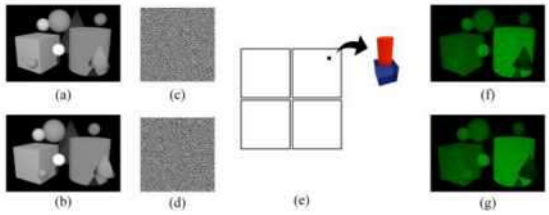


Figure 3: (a) and (b) show the two images that compose the stereogram. For each one, a four-phase level CGH with 1024×1024 pixels is calculated, as illustrated in (c) and (d). These CGHs are then encoded in a single birefringent c-Si based metasurface, represented by one square in (e). Note that the final metasurface is composed of a 2×2 hologram array. Thus, the size of the final metasurface is 389.12 μm × 389.12 μm. The inset highlights the pixel representation. (f) and (g) show the reconstruction of each stereogram image calculated through the Rayleigh-Sommerfeld integral at 532 *nm* [4].

The MAC, measured both experimentally and numerically, is defined in terms of the reconstructed image quality via signal-to-noise ratio, transmission and diffraction efficiencies, and cross-polarization crosstalk. The MAC cone is illustrated in Fig. 1 (d). This concept assumes that good quality image reconstruction can still be conveyed by he metasurface hologram if the incidence angle is within the MAC. Preliminary results indicate that the incidence condition for high contrast metasurfaces, such as (c-Si)-based metasurfaces, can be relaxed still maintaining good image reconstructions (low polarization crosstalk). A set of simulation and experimental results will be shown during the conference.

4. Conclusions

We have investigated, both numerically and experimentally, the angular dependence of the incidence beam on the performance of a broadband (c-Si)-based stereoscopic hologram metasurface in the visible range. Preliminary results suggest that high contrast metasurfaces, such as those based on c-Si, allow a certain degree-of-freedom for the incidence angle without sacrificing the 3D image reconstruction (low polarization crosstalk). This allowed us to define a new figure-of-merit, named metasurface acceptance cone, which is given in terms of the image reconstruction signal-to-noise-ratio, transmission and diffraction efficiencies, and cross-polarization crosstalk. We hope this investigation can pave the way for future metasurface designs with relaxed excitation conditions.

Acknowledgements

São Paulo Research Foundation (FAPESP) (2015/21455-1, 2013/07276-1, 2016/05809-0; National Natural Science Foundation of China (NSFC) (11674402, 11761131001, 91750207), National Council for Scientific and Technological Development (CNPq) (303562/2017-0), Coordenação de Aperfeiçoamento de Pessoal de Nível Superior - Brasil (CAPES) - Finance Code 001.

References

[1] N. Yu and F. Capasso, "Flat optics with designer metasurfaces," *Nature Materials,* vol. 13, pp. 139-150, January 2014.

[2] P. Genevet, F. Capasso, F. Aieta, M. Khorasaninejad, and R. Devlin, "Recent advances in planar optics: from plasmonic to dielectric metasurfaces," *Optica,* vol. 4, pp. 139-152, 2017.

[3] Z. Zhou, J. Li, R. Su, B. Yao, H. Fang, K. Li, L. Zhou, J. Liu, D. Stellinga, C. P. Reardon, T. F. Krauss, and X. Wang, "Efficient Silicon Metasurfaces for Visible Light," *ACS Photonics,* vol. 4, pp. 544–551, 2017/03/15 2017.

[4] A. Martins, J. Li, A. F. da Mota, Y. Wang, L. G. Neto, J. P. do Carmo, F. L. Teixeira, E. R. Martins, and B. V. Borges, "Highly efficient holograms based on c-Si metasurfaces in the visible range," *Opt Express,* vol. 26, pp. 9573-9583, Apr 16 2018.

[5] A. Martins, J. Li, A. F. da Mota, V. M. Pepino, Y. Wang, L. G. Neto, F. L. Teixeira, E. R. Martins, and B.-H. V. Borges, "Broadband c-Si metasurfaces with polarization control at visible wavelengths: applications to 3D stereoscopic holography," *Optics Express,* vol. 26, pp. 30740-30752, 2018/11/12 2018.

High-Resolution Quantitative Phase Imaging of Plasmonic Metasurfaces

Petr Bouchal[1,2], Petr Dvořák[1,2], Jiří Babocký[1,2], Zdeněk Bouchal[3], Filip Ligmajer[1,2], Lukáš Kejík[1,2], Martin Hrtoň[1,2], Vlastimil Křápek[1,2], Alexander Faßbender[4], Stefan Linden[4], Radim Chmelík[1,2], and Tomáš Šikola[1,2*]

[1]Institute of Physical Engineering, Brno University of Technology, Brno, Czech Republic
[2]Central European Institute of Technology, Brno University of Technology, Brno, Czech Republic
[3]Department of Optics, Palacký University, Olomouc, Czech Republic
[4]Physikalisches Institut, Universitat Bonn,Bonn, Germany
*corresponding author, E-mail: sikola@fme.vutbr.cz

Abstract

Optical metasurfaces have emerged as a new generation of building blocks for multifunctional optics. Design and realization of metasurface elements place ever-increasing demands on accurate assessment of phase alterations introduced by complex nanoantenna arrays. Here, we report on a new strategy in incoherent holographic imaging of metasurfaces, in which unprecedented spatial resolution and light sensitivity are achieved by taking full advantage of the polarization selective control of light through the geometric (Pancharatnam-Berry) phase.

1. Introduction

One of the fastest-growing areas of research in photonics is the field of metasurfaces, where nanoantennas and their ability to control light-matter interaction are utilized in light focusing, polarizing, and holography. In many of these metasurfaces, tailoring the near-field phase response among the individual building blocks is used to modify (e.g., to focus or to bend) the wavefront of light beam and thus modulate its far field projection. Compared to traditional refractive optics, metasurface-based components are physically thin and introduce abrupt phase changes observable in the far field. For the assessment of phase alterations introduced by a complex nanoantenna metasurfaces the high-resolution quantitative imaging of the phase directly in the metasurface plane is highly appreciated.

During the past years, this task has been addressed only in a few approaches including scanning near-field optical microscopy, which is inherently slow, and interference-based techniques, which require scanning to obtain widefield information. These drawbacks are partly solved in coherence-controlled holographic microscopy (CCHM) [1]. This technique allows widefield quantitative imaging of both the intensity and the phase in the metasurface plane and enables also 3D phase mapping of the wavefronts above the focusing metasurface [2]. Additionally, polarization-filtered CCHM has been used to map the phase of broadband Laguerre-Gaussian vortex beam converters based on Pancharatnam-Berry geometric phase [3]. Although the diffraction limit attainable in optical imaging is close to the size of nanoantennas, widefield imaging of metasurfaces with the resolution and the sensitivity sufficient for phase monitoring of a single nanoantenna has not yet been demonstrated and still remains a challenge.

Here, we present a new experimental strategy that overcomes the current state of the art by providing unprecedented spatial resolution and light sensitivity down to a single nanoantenna in the widefield quantitative phase mapping of plasmonic metasurfaces [4].

2. Results and discussion

The developed phase imaging technique, in this text referred to as quantitative 4G optics microscopy (Q4GOM), was implemented in Nikon Eclipse L150 microscope working with an add-on geometric-phase imaging module. This module benefits from the unique capabilities of a

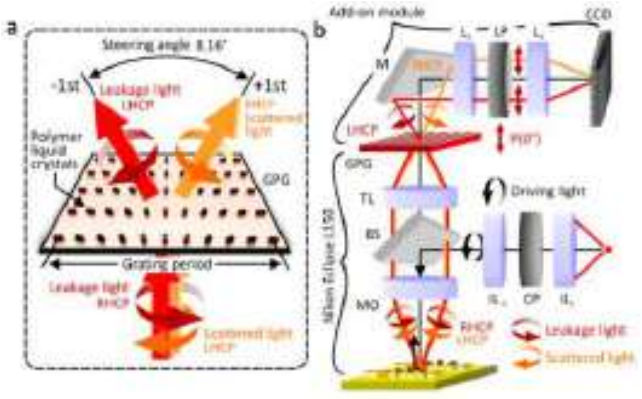


Figure 1: Experimental setup for high-resolution, widefield measurement of phase alterations introduced by plasmonic metasurfaces. (a) Geometric phase grating (GPG) for polarization-selective angular separation of leakage and scattered light coming from the metasurface. (b) Optical scheme of the imaging path: RHCP, right-handed circular polarization; LHCP, left-handed circular polarization; MO, microscope objective; BS, beam splitter; TL, tube lens; GPG, geometric phase grating; M, mirror; L1, L2, Fourier lenses; LP, linear polarizer; CCD, charged coupled device.

geometric-phase grating (GPG), providing polarization-selective angular separation of incident waves. The scheme of the setup used for the phase measurement of the metasurfaces is shown in Figure 1. The phase is quantitatively reconstructed from the mutual coherence function provided by off-axis holographic correlation records. The metasurfaces are excited by broadband spatially incoherent illumination and unlike other methods, the leakage light is not canceled, but its partial spatial correlation with the scattered light is used to capture the holographic records.

To demonstrate the capabilities of Q4GOM for the inspection of metasurfaces, we prepared a benchmark sample with a Pancharatnam-Berry type of metasurface. The sample is composed of identical nanoantennas schematically illustrated in Figure 2a, which were fabricated using electron beam lithography. The benchmark sample used in the measurement consists of 19 square areas with the size of (10×10) μm^2. In the areas numbered in ascending order, the angular rotation of the nanoantennas increases with a step of 10° as shown in Figure 2b, providing gradual variations of the geometric phase across the range $\langle 0, 2\pi \rangle$, and the resulting phase maps measured by Q4GOM are presented in Figure 2d.

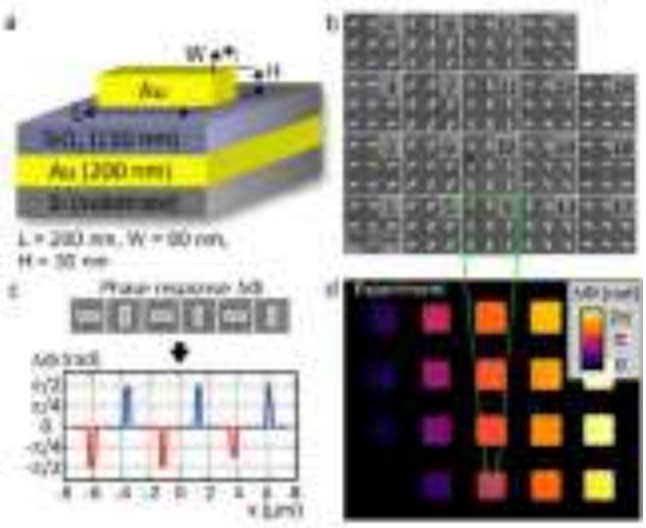


Figure 2: Phase imaging of the benchmark sample and single nanoantenna sensitivity verification. (a) Schematic illustration of a single nanoantenna. (b) Enlarged parts of SEM images showing the orientation of the nanoantennas in individual areas of the benchmark test. (d) Phase image of the benchmark test restored from correlation records acquired by Q4GOM. (c) Cross-section phase profile along the individual antennas shown above.

To convincingly demonstrate the unique capability of Q4GOM to capture and quantify the geometric phase altered by a single nanoantenna, we prepared a metasurface array composed of nanoantennas with the spacing of 2.5 μm and alternating angular orientation, which introduced the geometric phase with values $-\pi/2$ and $\pi/2$, respectively. The larger spacing of the nanoantennas was chosen to ensure an independent operation, in which restoration of the single nanoantenna phase remains unaffected by the signal from other nanoantennas. The cross-section phase profile of the restored phase image shown in Figure 2c demonstrates the high precision of the measurement and the ability to obtain the phase from individual nanoantennas which was achieved for the first time using widefield quantitative phase imaging methods.

3. Conclusions

In conclusion, we have presented a new concept of non-scanning imaging of plasmonic metasurfaces providing broadband achromatic operation, unprecedented spatial resolution and amplitude and phase sensitivity down to a single nanoantenna. The unique ability of Q4GOM to realize a complete mapping of alterations in amplitude and phase produced by individual nanoantennas represents a significant progress in the diagnostics of metasurfaces. Combination of high spatial resolution, measurement accuracy, and single shot operation might be of great importance also for studies of fundamental effects and dynamics of phase variations in active metasurfaces or plasmonic biosensors. We envision that the method can be used for real-time monitoring of active metasurfaces, possible identification of failing or lagging building blocks can also find its place in the study of plasmonic-enhanced chirality and chiral biomolecule sensing.

Acknowledgement

This work has been supported by the Grant Agency of the Czech Republic (GA17-33767L and GA18-01396S), Technological Agency of the Czech Republic (TE01020229 and TE01020233) and by MEYS CR (LM2015062 Czech-BioImaging, LM2015041 CEITEC Nano RI, 20162019). The research was partially carried out under the project H2020 Twinning project SINNCE (No. 810626) and CEITEC 2020 (LQ1601) with a support from the MEYS CR funder the National Sustainability Programme II.

References

[1] P. Kolman, Radim Chmelík, Coherence-controlled holographic microscope, *Opt. Express* 18: 21990–22004, 2010.

[2] J. Babocký, A. Křížová, L. Štrbková et al., Quantitative 3D Phase Imaging of Plasmonic Metasurfaces, *ACS Photonics* 4: 1389–1397, 2017.

[3] A. Faßbender, J. Babocký, P. Dvořák, V. Křápek, S. Linden, Direct phase mapping of broadband Laguerre-Gaussian metasurfaces, *APL Photonics* 3: 110803, 2018.

[4] P. Bouchal, P. Dvořák, J. Babocký et al., High-Resolution Quantitative Phase Imaging of Plasmonic Metasurfaces with Sensitivity down to a Single Nanoantenna, *Nano Letters* 19: 1242–1250, 2019.

Reflective metamirror grating for far field spatial filtering

Pei-Yu Wang[1*], Yu-Chieh Cheng[1], Ramon Herrero[2], Muriel Botey[2] and Kestutis Staliunas [2,3]

[1]National Taipei University of Technology, Department of Electro-Optical Engineering, No. 1, Sec. 3, Chung-Hsiao E. Rd, Taipei, 10608, Taiwan
[2]Universitat Politècnica de Catalunya, Departament de Física i Enginyeria Nuclear, Rambla Sant Nebridi 22, Terrassa 08222, Spain
[3]Institució Catalana de Recerca i Estudis Avançats (ICREA), Pg. Lluís Companys 23, Barcelona 08010, Spain
*corresponding author, E-mail: wpei941110@gmail.com

Abstract

We successfully demonstrate grating-based reflective spatial filtering devices. Modulation of the refraction index on the sub-micron scale exhibits optical beam shaping with transverse invariance. The paper presents a theoretical model for the proposed metamirrors based on multiple scattering theory. The theoretical results coincide with the numerical ones. The metamirror may serve as a versatile tool for narrowing beam with high efficiency and transverse invariance.

1. Introduction

Spatial filtering element is essential for many photonic applications. In recent years, scientists have started crafting tiny, thin diffraction optical devices during the photonic product became much smaller. However, spatial filtering devices based on external gratings are not capable for microlasers, semiconductor lasers [5] and vertical-cavity surface-emitting laser (VCSELs) because they are unavoidably low efficient and bulky. Moreover, conventional filtering methods require not only many curved lenses that filter along with an optical axis. Therefore, such external spatial filtering devices with an optical axis are barely used for many photonic applications.

Many novel researches based on photonic crystal (PhCs) have exposed numerous results for the spatial filtering such as one-dimensional (1D) [1] and two-dimensional (2D) photonic crystals [2] [4]. Our team have also presented a concentric ring to achieve the spatial filtering but the proposed ring was limited by its axisymmetric configuration that result in an optical axis [3]. Furthermore, all these arrangements are based on the beam transmitted structure. In this paper, we propose a reflective spatial filtering device without an optical axis. Our main purpose is to achieve a narrow and clean beam whose large angular components have been filtered out.

For the reason that we propose a compact reflective angular filtering device upon the reflection based on metamirros, they present the property of transverse invariance due to its periodic refraction index modulation. Moreover, device is sub-micron scale so the operating area of the spatial filtering is available for broad emissions from microlasers.

2. Reflective gratings for spatial filtering

2.1. Spatial filtering based on gratings

The main analyzing approach of the micro scale configuration combined by a flat metallic mirror and many of ellipse gratings by using Finite Difference Time Domain (FDTD) method to confirm this reflective metamirror grating. FDTD is a useful numerical simulation technique for solving the problems related to electromagnetism. The ideal arrangement of this structure is a metallic mirror with nearly 100% reflection and periodical ellipse-shaped gratings. Fig.1 shows the composed of metallic mirror and gratings can be regards as fold gratings. The parameter Dz is the distance between gratings and metallic mirror, which means the unfold gratings are separated by double Dz. The refractive index of the proposed ellipse-shaped gratings is 1.5. The longitudinal distance between each gratings Dx is 2μm.

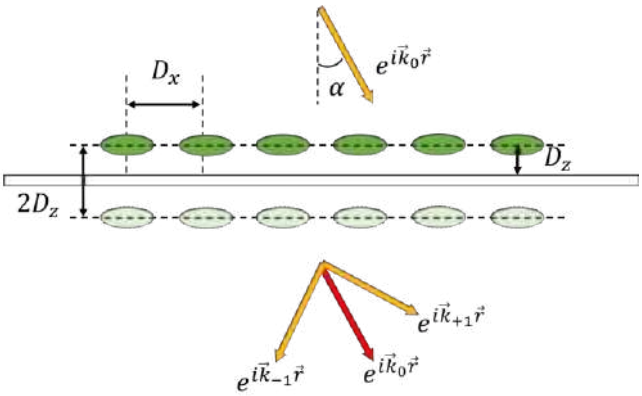


Figure 1: Illustration of the fold spatial filtering gratings which composed by one metallic mirror (white slim hollow rectangle) and the ellipse-shaped gratings (green ellipse) which distance between two components is Dz. The unfold gratings are combined by two lines ellipse-shaped gratings (green ellipse and light green ellipse) which distance between two lines gratings is 2Dz.

The analytical theory for this ideal model is based on paraxial approximation with a simple plane wave $U = e^{i\vec{k}_0\vec{r}}$ which has wavelength 1 μm. Focusing on the diffraction zero-order intensity $U = e^{i\vec{k}_0\vec{r}}$ in far-field area since the other order $U = e^{i\vec{k}_{+1}\vec{r}}$ or $U = e^{i\vec{k}_{-1}\vec{r}}$ diffraction in far-field area became negligible. Thus, employed the zero-order diffraction value to plot the 2D figure versus incident angle and Dz in Fig. 2(a). Fig. 2(a) it be apparently observed that diffraction pattern is periodically with respect to the incidence angle, and some regular feature with respect to Dz.

2.2. Simulation of gratings far-field filtering

A gaussian beam is incident into the periodical grating structure. The width and the operating wavelength of gaussian source is 4 μm and 1μm. The spatial filtering effect in the far field is obtained from the Fourier transformation of the electric field in the near field. The field distribution after reflecting from the gratings is calculate by using FDTD method. The comparison of far-field distributions of the gaussian beam between with and without the consideration of gratings are shown in Fig. 2. Fig. 2(b) and 2(d) both obviously show that the width of the gaussian beam become narrower through the grating structure. The imperfect spatial filtering result is shown in Fig. 2(c). Consequently, the filtering performance is dependent of the distance between the scatter and mirror, Dz.

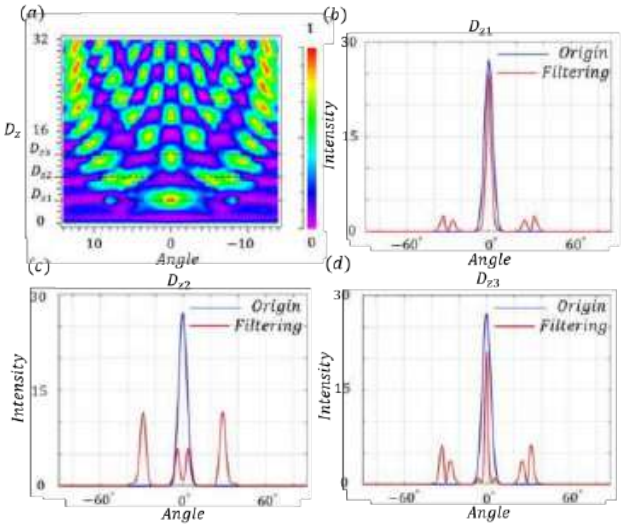


Figure 2: The spatial filtering performance in metamirror gratings. (a) The diffraction plot recorded the characteristic of diffraction zero-order intensity with variable incident angle and D_z. The vertical axis in (b), (c), (d) means the far-field intensity and horizontal axis indicates the angle from $-90^{\circ} \sim 90^{\circ}$. (b) D_{z1} = 4 μm (c) D_{z2} = 8 μm (d) D_{z3} = 12 μm

3. Discussion

Although Figure 2 uncovering the inspiring results for tiny PhCs devices which filter the gaussian beam effectively. However, the shaped of the gratings and refractive index of the material might also influence the ability of spatial filtering. Therefore, all these factors will be employed during the future optimization process of this gratings structure.

4. Conclusions

In this article, the simulation results have shown the metamirror for the spatial filtering in reflection. The narrow and clear spatial filtering effect is achievable in the micro-scale. Such tiny reflective grating is quite suitable for VCSELs or the other optical devices. The analytical model for the calculation of zero-order diffraction pattern is developing to compare with the FDTD results. The geometrical shape or the refractive index of these gratings results in varying performance of spatial filtering. We further optimize this metamirror for a cleanly and narrowly filtered beam.

Acknowledgements

We are grateful to co-authors of our papers: M. Peckus, M. Malinauskas, R. Herrero, M. Botey, J. Trull, R.Vilaseca, S.Kicas, R.Drazdyy, C. Cojocaru, H. Zeng, C.H. Ho and D.S. Wiersma who participated in the common research reviewed in this article. Additionally, we would like to acknowledge financial support by Spanish Ministerio de Educación y Ciencia and European FEDER (project FIS2015-65998-C2-1-P) and Ministry of Science and Technology in Taiwan, MOST (107-2636-M-027 -001).

References

[1] Z. Luo, Z. Tang, Y. Xiang, H. Luo, S. Wen, Polarization-independent low-pass spatial filters based on one-dimensional photonic crystals containing negative-index materials, S*pringer-Verlag*, 94, pp. 641–646, 2009.

[2] L. Maigyte, K. Staliunas, Spatial filtering with photonic crystals, *Appl. Phys. Rev.*, 2, 011102, 2015.

[3] V. Purlys, L. Maigyte, D. Gailevičius, M. Peckus, R. Gadonas, K. Staliunas, Super-collimation by axisymmetric photonic crystals, *Appl. Phys. Lett.* 104, 221108, 2014.

[4] L. Maigyte, T. Gertus, M. Peckus, J. Trull, C. Cojocaru, V. Sirutkaitis, and K. Staliunas, Signatures of light-beam spatial filtering in a three-dimensional photonic crystal, *Phys. Rev. A*, 82, 043819, 2010.

[5] R. Herrero, M. Botey, M. Radziunas, and K. Staliunas, Beam shaping in spatially modulated broad-area semiconductor amplifiers, *Opt. Lett*, 37, pp. 5253–5255, 2012.

Reaching the Abbe-Sine condition with curved conformal metasurfaces

Sandeep Yadav Golla[1], **Patrice Genevet**[1*]

[1]CNRS-CRHEA,Université Côte d'Azur, Sophia Antipolis, Valbonne, France
*corresponding author, E-mail: pg@crhea.cnrs.fr

Abstract

Metasurfaces have a variety of wide applications in the field of optics. We exploit the concept of conformal metasurface to account for the different types of aberration corrections analytically through wave optics approach and support the results with numerical simulations.

1. Introduction

Optical aberrations are the unavoidable phenomenon of the light which are not nullified even to date completely to all of its orders using conventional refractive optics. Recent developments in the field of metasurfaces have enabled new ultra-thin lenses capable of focusing light with diffraction limited performances[1]. The latter present serious aberrations which could significantly hamper their utilisation in imaging systems. This problem has been carefully studied already and several solutions exist, in particular in considering a metalens disposed on curved interfaces. Refraction across a curved metalens has been already considered by treating the problem using the ray optics approach [2]. Perfect imaging, related to the realization of the Abbe-Sine condition[3], is shown to be achieved when the radius of curvature of the substrate hosting the metalens is equal to the focal distance of the compound system. Going beyond the ray optics approach, we are considering the recently developed concept of conformal boundary optics to address refraction across interfaces of arbitrary geometries[4] and demonstrate that the Abbe-sine condition holds for proper interface curvature. The problem is solved in two steps, in the first section we introduce the general problem of conformal optics and it's application to the arbitrary geometries. In the second section we impose focusing condition of a normally incident plane wave passing across interfaces having different curvatures. Thus we extract the susceptibilities matching normal incident light with spherical wavefrotns. For imaging purpose, light is generally coming at various oblique angles, rather than normal incidence. The purpose of our calculation is to see the evolution of the aberrations as a function of the interface geometry. To do so, We calculate the transmitted fields for the case of oblique incidence considering previously obtained susceptibilities. The analytical expressions of the transmitted fields in the case of non normal incidence are decomposed using the wave aberration function through which we can identify the order of aberrations [2].

2. Electromagnetic fields at the interface of arbitrary geometries

Electromagnetic field boundary conditions at an arbitrary shaped metasurface separting two media, as shown in the fig. 1, are given

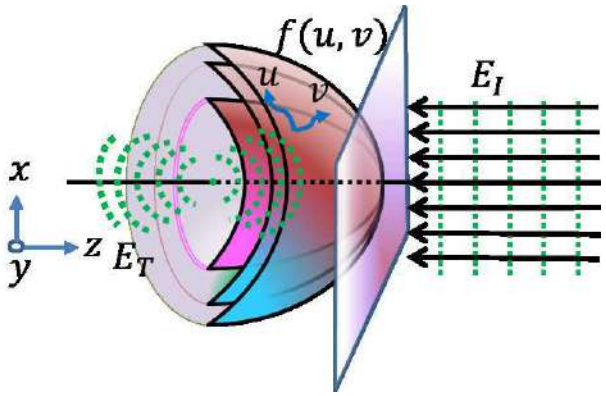


Figure 1: Schematic shows the perfect transmission of a normally incident plane wave on a conformal metasurface. The transmitted wavefront is modified by the metasurface and gives rise to focusing wave. In this analysis, we consider Cartesian coordinate system to describe the incident and transmitted fields denoted by x,y,z and a conformal coordinate system denoted u,v,n obtained by considering the tangent vectors to the interface.

by

$$\begin{pmatrix} 0 & 1 & \frac{\partial f}{\partial u} \\ -1 & 0 & -\frac{\partial f}{\partial v} \end{pmatrix} \begin{pmatrix} E_x|_-^+ \\ E_y|_-^+ \\ E_z|_-^+ \end{pmatrix} = \iota\omega\epsilon \begin{pmatrix} \chi_m^{ux} & \chi_m^{uy} & \chi_m^{uz} \\ \chi_m^{vx} & \chi_m^{vy} & \chi_m^{vz} \end{pmatrix} \begin{pmatrix} H_x^{\overline{av}} \\ H_y^{\overline{av}} \\ H_z^{\overline{av}} \end{pmatrix} \tag{1}$$

$$\begin{pmatrix} 0 & 1 & \frac{\partial f}{\partial u} \\ -1 & 0 & -\frac{\partial f}{\partial v} \end{pmatrix} \begin{pmatrix} H_x|_-^+ \\ H_y|_-^+ \\ H_z|_-^+ \end{pmatrix} = \iota\omega\mu \begin{pmatrix} \chi_e^{ux} & \chi_e^{uy} & \chi_e^{uz} \\ \chi_e^{vx} & \chi_e^{vy} & \chi_e^{vz} \end{pmatrix} \begin{pmatrix} E_x^{\overline{av}} \\ E_y^{\overline{av}} \\ E_z^{\overline{av}} \end{pmatrix} \tag{2}$$

In the equation$(1, 2)$ x,y,z are the ambient coordinate systems which describe the media on either side of the metasurface and u,v,n the coordinate system of the metasurface, which are mapped vice-versa through $x = u, y = v$ and $z = f(x, y)$ or $f(u, v)$. The quantities $E|_-^+$ and E^{av} are calculated using the fields on either side of the metasurface as mentioned in the paper[4].

2.1. Calculation of susceptibilities for the normal incidence

In this section we obtain the susceptibilities of the surface $f(x, y)$ by plugging the input normal plane wave and transmitted wave with spherical wave front directly in Eq.$(1, 2)$. After a rigorous

algebra it reduces to,

$$\begin{aligned}\chi_e^{ux} &= \frac{H_y|_-^+ + \frac{\partial f}{\partial v} H_z|_-^+}{\iota\omega\epsilon_0 E_x^{\overline{av}}} \\ \chi_m^{ux} &= \frac{E_y|_-^+ + \frac{\partial f}{\partial v} E_z|_-^+}{-\iota\omega\mu_0 H_x^{\overline{av}}} \\ \chi_m^{vy} &= \frac{E_x|_-^+ + \frac{\partial f}{\partial u} E_z|_-^+}{\iota\omega\mu_0 H_y^{\overline{av}}}\end{aligned} \tag{3}$$

and all the remaining susceptibilities are taken zero in order to make the system of equations consistent and solvable as discussed previously[6]. Note that our method require to calculate the susceptibilities for each different shape of the metasurface. The interface curvature $f(u, v)$ ranges from plane surface, parabolic surface, elliptic surface and spherical surface, decreasing the curvature. The different expressions obtained are similar to the one shown in equation (3), not shown here as they are simply obtained by substituting $f(u, v)$ in expression (3).

2.2. Calculation of the transmitted fields for oblique incidences

Given the susceptibilities as functions of the shape of metasurface from equation (3), we are considering incident oblique plane and transmitted wave given by:

$$E^- = \begin{pmatrix}0\\1\\0\end{pmatrix} \xi^{'-} H^- = \begin{pmatrix}\cos\theta^{'}\\0\\-\sin\theta^{'}\end{pmatrix} \frac{\xi^{'-}}{\eta} \tag{4}$$

and transmitted field as

$$E^+ = \begin{pmatrix}E_x\\E_y\\E_z\end{pmatrix} \xi^{'+} \tag{5}$$

$$H^+ = \begin{pmatrix}H_x\\H_y\\H_z\end{pmatrix} \frac{\xi^{'+}}{\eta} = \begin{pmatrix}k_y E_z - E_y k_Z\\k_z E_x - E_z k_x\\k_x E_y - E_x k_y\end{pmatrix} \frac{\xi^{'+}}{\omega\mu_o} \tag{6}$$

where

$$\begin{aligned}\xi^{'+} &= e^{-\iota(k_x x + k_y y + k_z z) + \omega t} \\ \xi^{'-} &= e^{-\iota k_o(\sin\theta^{'} x + \cos\theta^{'} x) + \omega t} \\ \eta &= \frac{k_0}{\omega\mu_0} = \sqrt{\frac{\mu_0}{\epsilon_0}}\end{aligned} \tag{7}$$

The former incident fields are known and the latter have to be determined after plugging the input oblique plane wave and calculated susceptibilities in the equation (1, 2) we obtain the following four equations

$$\begin{aligned}(E_y\xi^{'+} - \xi^{'+}) + E_z\xi^{'+}\frac{\partial f}{\partial v} &= -\iota\omega\mu_0\chi_m^{ux}(H_x + \cos\theta^{'}\frac{\xi^{'+}}{\eta}) \\ -E_x\xi^{'+} - \xi^{'+} + E_z\xi^{'+}\frac{\partial f}{\partial u} &= --\iota\omega\mu_0\chi_m^{vx}(H_x + \cos\theta^{'}\frac{\xi^{'+}}{\eta}) \\ H_y + \frac{\partial f}{\partial v}(H_y + \sin\theta^{'}\frac{\xi^{'+}}{\eta}) &= \iota\omega\epsilon_o\chi_e^{uz}E_z\xi^{'+} \\ -(H_x - \cos\theta^{'}\frac{\xi^{'+}}{\eta}) - \frac{\partial f}{\partial u}(H_y + \sin\theta^{'}\frac{\xi^{'+}}{\eta}) &= \iota\omega\epsilon_o\chi_e^{vz}E_z\xi^{'+}\end{aligned} \tag{8}$$

Considering total transmission conditions, we obtain two additional expressions,

$$\begin{aligned}K_x^2 + K_y^2 + K_z^2 &= 1 \\ E_x^2 + E_y^2 + E_z^2 &= 1\end{aligned} \tag{9}$$

Now using the set of equations from equation(8,9) we can analytically obtain the transmitted E-M fields and decompose into terms corresponding to the types of aberration and also can be solved numerically to support the analytical expressions.

3. Conclusion

In this presentation, we are utilizing the conformal boundary optics concept to analytically and numerically calculate the susceptibilities of arbitrary shaped metasurface and are further utilizing these quantity to study the impact of interface curvature on the focsuing properties of metalenses. We show that the aberrations are considerably affected by the curvature of interface hosting the metalens. This approach could help in designing spherical or non conventional metasurface that could achieve perfect focusing.

Acknowledgement

We acknowledge financial support from the European Union's Horizon 2020 under the European Research Council (ERC) grant agreement No. 639109 (project Flatlight).

References

[1] Wei Ting Chen, Alexander Y. Zhu, Jared Sisler, Yao-Wei Huang, Kerolos M. A. Yousef, Eric Lee, Cheng-Wei Qiu, and Federico Capasso, Broadband Achromatic Metasurface-Refractive Optics, *Nano Letters* 18 (12), 7801-7808, 2018. ASC Publishers

[2] F. Aieta, P. Genevet, M. Kats, and F. Capasso, Aberrations of flat lenses and aplanatic metasurfaces, *Opt. Express* 21, 31530-31539 , 2013.

[3] A. Small, Spherical aberration, coma, and the Abbe sine condition for physicists who don't design lenses, *American Journal of Physics* 86, 487–494 (2018). American Association of Physics Teachers.

[4] Teo, Jonathon Yi Han and Wong, Liang Jie and Molardi, Carlo and Genevet, Patrice, Controlling electromagnetic fields at boundaries of arbitrary geometries, *PhysRevA*,94.023820, 2016 American Physical Society.

[5] Francesco Aieta, Patrice Genevet, Mikhail A. Kats, Nanfang Yu, Romain Blanchard, Zeno Gaburro, and Federico Capasso, Aberration-Free Ultrathin Flat Lenses and Axicons at Telecom Wavelengths Based on Plasmonic Metasurfaces *Nano Letters* , 12 (9), 4932-4936, 2012 ASC Publishers.

[6] K. Achouri, M. A. Salem, and C. Caloz, General metasurface synthesis based on susceptibility tensors, *IEEE Trans. Antennas Propag.* , 63, 2977 (2015).

Simulation study of metasurfaces for hemp concrete hydration monitoring

Mehdi Ferhat[1], Badreddine Ratni[2], Fares Bennai[3,4], Franck Daout[1], Kamilia Abahri[3], and Eric Vourc'h[1]

[1] SATIE, UMR CNRS 8029, ENS Paris-Saclay, Université Paris-Saclay, 61 Avenue du président Wilson, 94230 Cachan, France
[2]LEME, UPL, Univ Paris Nanterre, 92410 ville d'Avray, France
[3]LMT, UMR CNRS 8535, ENS Paris-Saclay, Université Paris-Saclay 61 Avenue du président Wilson, 94230 Cachan, France
[4]LaSIE, UMR CNRS 7356, Université de La Rochelle, Avenue Michel Crépeau, 17042 La Rochelle Cedex, France
*corresponding author, E-mail: badreddine.ratni@parisnanterre.fr

Abstract

A metasurface is designed with a view to monitor the hemp concrete hydration. The metasurface is due to be implemented with a hemp concrete sample in an R-band waveguide. By measuring the variations of the resonance frequency of the obtained structure, the dielectric permittivity of the sample can be monitored during the sample hydration (i.e. during the first days or weeks following the material fabrication). In this paper, we optimize a metasurface and study he proposed monitoring method using finite elements simulations.

1. Introduction

Hemp concrete is an ecological building material used for hydric regulation and thermal insulation in buildings [1-2]. It consists of lime, chenevotte and water [3]. Monitoring the reaction between these elements during the first weeks of the manufacturing can be useful to understand hydration phenomena in hemp concrete. The variations of the volume fractions of each element during hydration implies a variation of the real dielectric permittivity $Re(\varepsilon^*_r)$ of the concrete. Recently, we have proposed to estimate the dielectric permittivity of a hemp concrete sample after hydration by measuring its S-parameters in a rectangular waveguide [4]. These parameters are then inverted to obtain the dielectric permittivity by means of the classical Nicolson-Ross-Weir method [5-6]. This first approach is suitable to observe permittivity variations. Nevertheless, the inversion of the parameters may feature some uncertainties due to the computation, which could make it difficult to monitor small variations. For this reason, a novel approach is proposed which should permit to monitor the hydration of hemp concrete by means of a resonant structure. The emergence of these thin periodic structures has enabled a considerable evolution in the control of electromagnetic (EM) waves [7]. Indeed, they enable to tailor effective local EM responses, whether in terms of magnitude, phase or polarizabilitiy. By measuring the variations of the resonance of the proposed structure, it is possible to follow the evolution of $Re(\varepsilon^*_r)$ and consequently that of the hydration of a hemp concrete, which can be useful with civil engineering applications in view.

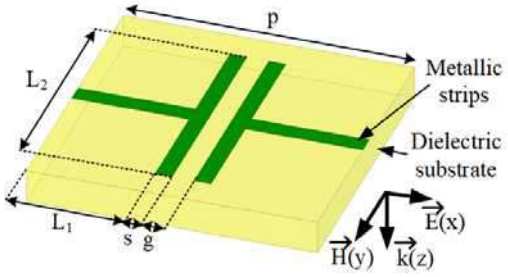


Figure 1 : Schematic view of the designed unit cell with a periodicity of p = 13.625 mm.

2. Metasurface-based resonator

The proposed metasurface is made up of (8 x 4) unit cells and it operates in the R waveguide frequency band [1.72 GHz – 2.61 GHz]. Each unit cell is made up of four metallic strips printed on an FR4 dielectric substrate (ε_r = 4.4, tan δ = 0.02). The first two strips which are separated by a g = 0.225 mm gap and are oriented perpendicularly to the electric field play the role of a capacitance. The two other strips which are parallel to the electric field play the role of an inductance. Thus, the whole structure makes it possible to obtain an LC resonator. The periodicity of each unit cell is fixed at p = 13.625 mm. This value is chosen so that the metasurface which is made up of 8 x 4 unit cells can be implemented into an R-band waveguide the dimensions of which are 109.22 mm x 54.61 mm. Starting from these dimensions, a structure was optimized with a finite elements (FE) modeling (HFSS software) in order to obtain a resonance in the targeted frequency band. The final geometrical dimensions are L_1 = 6.4 mm, L_2 = 10.5 mm, s = 0.3 mm and g = 0.225 mm.

3. Simulation results

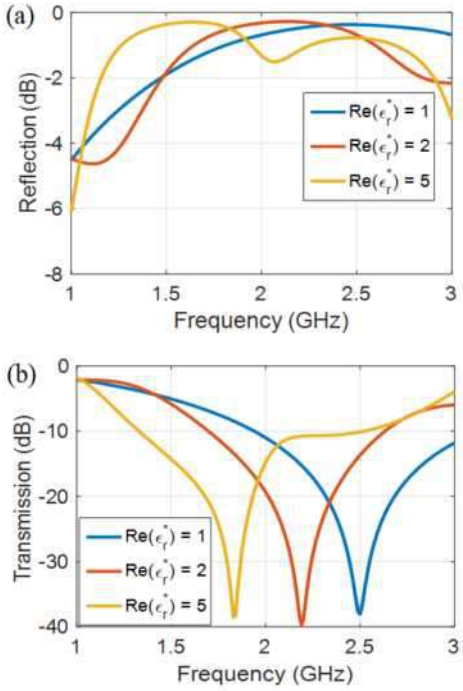


Figure 2 : (a) Reflection and (b) transmission coefficients for different values of the real part of the permittivity.

FE simulations using HFSS software were carried out considering a device consisting in the optimized metasurface (8 x 4 unit cells) placed in contact with a hemp concrete sample. The thickness of the sample is fixed at 50 mm. These simulations were carried out for a variety of values of the real part $Re(\varepsilon_r)$ of the dielectric permittivity of the material under test ranging from 1 to 5. Note that further developments could focus on designing astructure adapted to $Re(\varepsilon_r)$ higher than 5. Fig. 2 shows the simulated reflection and transmission coefficients corresponding to $Re(\varepsilon_r)$ values fixed at 1, 2 and 5 respectively. It is to be noted that the device resonance frequency shifts from 2.5 GHz to 1. 83 GHz. In addition, monitoring the imaginary part of ε_r is also an interesting approach in order to follow the evolution of the absorption of the electromagnetic signal in the material. For studying this point, $Re(\varepsilon_r)$ was fixed at a given value whereas the loss factor tanδ varied in the [0.01 to 0.1] range. Fig. 3 shows that the variation of tanδ leads to absorption variations. According to these results, the proposed structure allows the monitoring of the dielectric permittivity of a hemp concrete under hydration to be envisaged.

4. Conclusions

A metasurface based on LC resonance operating in the R band has been proposed and designed with a view to monitor the hydration of hemp concrete. The metasurface is due to be implemented with a material sample in a rectangular waveguide. The monitoring approach relies on the measurement of both the device resonance frequency and material absorption. The design of the metasurface has been optimized by simulations. The simulation results, either considering the use of the real or imaginary parts of the dielectric permittivity of the material, show a significant enough sensitivity for envisaging a device to be built and experimentally characterized.

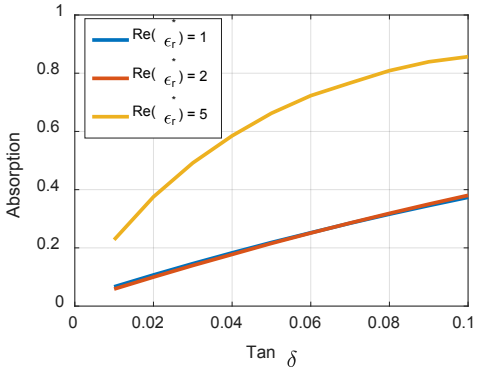


Figure 3: Evolution of the absorption of the material under test for different values of *tan δ.*

References

[1] S. Elfordy, F. Lucas, F. Tancret, Y. Schudeller, and L. Goudet, Mechanical and thermal properties of lime abd hemp concrete, *Constr. Build. Materials.*, vol. 22, no. 5, pp. 2116-2123, 2007.

[2] S. Pretot, F. Collet, and C. Garnier, Life cycle assessment of a hemp concrete wall: impact of thickness and coating, *Build. and Environ.*, vol. 72, pp.223-231, 2007

[3] F. Bennai, N. Issaadi, K. Abahri, R. Belarbi, A. Tahakourt, Experimental characterization of thermal and hygric properties of hemp concrete with consideration of the material age evolution, *Heat Mass Trans.*, Vol. 54, pp. 1189-1197, 2018.

[4] M. Ferhat, F. Bennai, B. Ratni, E. Vourc'h, K. Abahri, F. Daout, "Electromagnetic characterization of the hydric behavior of hemp concrete in the 2.4 GHz WiFi frequency band," presented at the *2nd Lat. Amer. Micro. Conf.*, Arequipa, Peru, Dec. 12-14, 2018.

[5] A. M. Nicolson and G. F. Ross, "Measurement of the intrinsic properties of materials by time domain techniques," *IEEE Trans. Instr. Meas.,* vol. 19, no. 4, pp. 377–382 , Nov. 1970.

[6] W. B. Weir, "Automatic measurement of complex dielectric constant and permeability at microwave frequencies," *Proceedings IEEE*, vol. 62, no. 1, pp. 33–36, Jan. 1974.

[7] C. L. Holloway, E. F. Kuester, J. A. Gordon, J. O'Hara, J. Booth, D. R. Smith, An overview of the theory and applications of metasurfaces: the two-dimensional equivalents of metamaterials, IEEE Antennas Propag. Mag. 54: 10-35, 2012.

Random interleaved meta-surface for controllable C-Points

Enliang Wang[1,2], Jiebin Niu[1], Lina Shi[1] , and Changqing Xie[1]

[1] Key Laboratory of Microelectronic Devices and Integrated Technology, Institute of Microelectronics, Chinese Academy of Sciences, Beijing 100029, China
[2] University of Chinese Academy of Sciences, Beijing 100049, China
*corresponding author, E-mail: xiechangqing@ime.ac.cn

Abstract

In this article, we introduced the random interleaved geometric meta-surface solution for the reconstruction of the controllable C-points in contrast to the kinoform operation. Lemon beams of the C-points are present. The ±1st order of the polarization-singular beams has same polarization singularity indices with the opposite handedness. Furthermore, spin-induced rotation of the Lemon beams are verified experimentally under different incident linear polarization states. Our work can be extended into other polarization singularity of C-points.

1. Introduction

Polarization singularities have attracted more attention in scientific community due to exotic space-varying polarization distributions. Polarization singularities can have undefined orientation and handedness [1,2], called C-point and V-Point[3,4]. The polarization-singular beams (PSB), also named full Poincaré-beam[5], are characterized by the polarization singularity indices [5,], $I_c = \frac{1}{2}\oint \nabla\gamma \cdot dl$ The well-known cylindrical vector beams (CVB) have a V-point singularity of index $+1$ and have been investigated in a plethora of practical application including metrology, optical manipulation and quantum communication. Recently, the lower order C-point singularities of index $\pm 1/2$ have proved the ability of the potential enhancement of chiral light-matter interaction [7], spin-orbit coupling [8] and surface structuring[9]. The current approaches to the beams carrying polarization singularities are the specific q-plate or the coherent superposition of structured left-and right-handed circularly polarized light spatial light modulator(SLM) , and interferometer[10,11]. Recently, dielectric metasurfaces, the monolayer of ultrathin a engineered artificial materials compared with conventional refractive optics, have been applied in the enormous interests in the control of an optical wavefront[12-16]. Especially, arbitrary orthogonal polarization states can be imparted with two independent phase profile [13, 14] for fascinating applications[15].

In this work, inspired by the interleaved geometric meta-surface [12], we introduce a random interleaved geometric meta-surface to realize the spin-controllable polarization state of C-point. The ±1st order of the polarization-singular beams has same polarization singularity indices with the opposite handedness. The C-Points orientation angle can be modulated by switching the axis-angle of the incident linear polarization.

2. Experimental and results and discussion

The geometric meta-surface consists of the rotated TiO_2 nano-fins that have proved high performance in visible range[13,15,16], which introduce opposite phase on the orthogonal circular polarization. Each nano-fins acts as a perfect half wave-plate with phase difference π between the long and short axis. The TiO_2 nano-fins are designed at the 532nm with designed length $L = 250\text{nm}$, width $w = 95\text{nm}$ and heigh $h = 600\text{nm}$, which is similar to the design in reference[16]. The cells are arranged with periods $P_x = P_y = 350\text{nm}$. The area of the sample is $\pi \times 50 \times 50\mu\text{m}^2$. The imparted Pancharatnam–Berry phase distribution Ψ are designed with spatially random-interleaved phase profile of the component of φ_1 and φ_2

$$\Psi = \text{Rand}[\varphi_1, \varphi_2]$$

Where

$$\begin{cases} \varphi_1 = angle(\exp(ik_x x)) \\ \varphi_2 = angle(\exp(-i(k_x x + m\theta))) \end{cases}$$

The function Rand is to randomly distribute the combination of φ_1 and φ_2, respectively. Figure 1 show the PB-phase profile RIGM of m=1. The ±1st order diffractions (Fig. 1 (b)) have same index and opposite handedness. As shown in Figure 2, the orthogonal polarization distribution of lemon beams are verified with the quarter wave-plate and analysis polarizer. As shown in Figure 3, spin-induced rotation of the lemon beams beam are verified experimentally under different incident polarization states.

3. Conclusions

In conclusion, we demonstrate a random-interleaved procedure of the geometric meta-surface for the spin-controllable C-Points. By switching the incident linear beam, we control the orientation of C-points. The procedure can be extend into q-plate, SLM for active design and other relevant frequencies using silicon meta-surface. We believe our work can promote the practical research involving C-points.

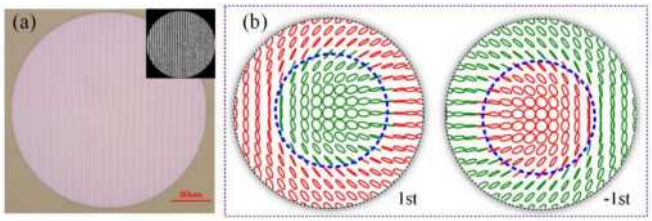


Figure 1: Random interleaved geometric metasurface. (a) The optical microscope image of the meta-surface. Inset: The design PB phase profile. (b) The polarization state of the orthogonal ± 1 st diffraction order (lemon beam) with $I_c = 1/2$.

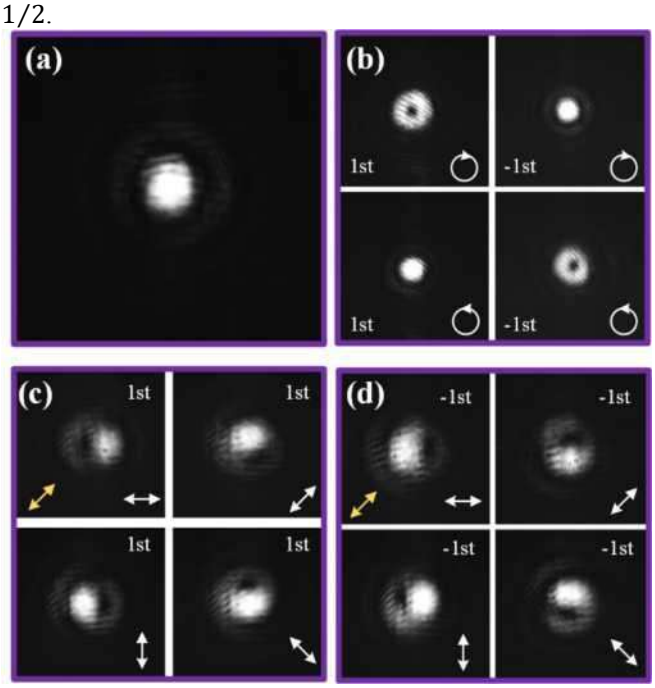


Figure 2: The captured intensity distribution of the ± 1 st diffraction order of the lemon beam. (b-d) The transmission intensity of the generated lemon beam of the ± 1 st diffraction order after the polarizer filter. The white polarization state denote the filter polarization state with the quarter wave-plate and polarizer. The yellow double-end arrow denote the linear polarization state of the incident beam.

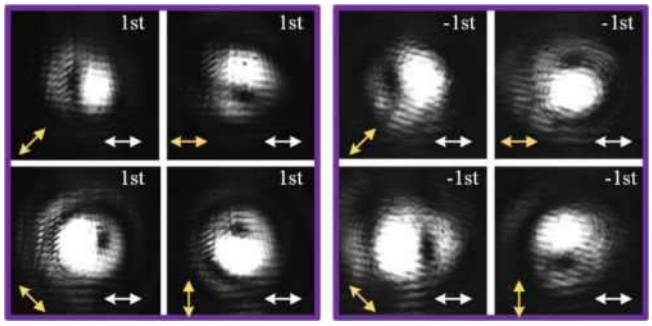


Figure 3: The transmission intensity of the orthogonal lemon beam of the ± 1 st diffraction order under different linear polarization state of the incident beam. The yellow double-end arrows denote the linear polarization state of the incident beam. The white arrows denote the analysis polarizer.

References

[1] Berry, M. V. & Dennis, M. R. Polarization singularities in isotropic random vector waves, Proc. *Math. Phys. Eng. Sci*. 141–155 , 2001.

[2] Dennis, M. R. Polarization singularities in paraxial vector fields: morphology and statistics, *Opt. Commun*. 213, 201–221, 2002.

[3] Freund, I. Polarization singularities in optical lattices, *Opt. Lett*. 29, 875–877, 2004.

[4] Dennis, M. R., O'Holleran, K. & Padgett, M. J, *Progress in Optics,* Elsevier 53, 293–363, 2009.

[5] Beckley, A. M., Brown, T. G. & Alonso, M. A. Full Poincaré beams, *Opt. Express* 18, 10777, 2010.

[6] Hasman, E., Biener, G., Niv, A. & Kleiner, V, *Progress in Optics* 47, 215–289, 2005.

[7] Lang, B., Oulton, R. & Beggs, D. M. Optimised photonic crystal waveguide for chiral light–matter interactions, *J. Opt*. 19, 045001, 2017.

[8] Wu, H.-J., Zhou, Z.-Y., Gao, W., Shi, B.-S. & Zhu, Z.-H. Dynamic tomography of the spin-orbit coupling in nonlinear optics, *Phys. Rev. A*, 99, 2019.

[9] Nivas, J. J. et al. Surface Structuring with Polarization-Singular Femtosecond Laser Beams Generated by a q-plate, *Sci. Rep*. 7, 2017.

[10] Galvez, E. J., Khadka, S., Schubert, W. H. & Nomoto, S. Poincaré-beam patterns produced by nonseparable superpositions of Laguerre–Gauss and polarization modes of light, *Appl. Opt*. 51, 2925, 2012.

[11] Cardano, F., Karimi, E., Marrucci, L., Lisio, C. de & Santamato, E. Generation and dynamics of optical beams with polarization singularities, *Opt. Express* 21, 8815–8820 , 2013.

[12] Maguid, E. et al. Multifunctional interleaved geometric-phase dielectric metasurfaces, *Light Sci. Appl*. 6, e17027 , 2017.

[13] Balthasar Mueller, J. P., Rubin, N. A., Devlin, R. C., Groever, B. & Capasso, F. Metasurface Polarization Optics: Independent Phase Control of Arbitrary Orthogonal States of Polarization, *Phys. Rev. Lett*. 118, 2017.

[14] Arbabi, A., Horie, Y., Bagheri, M. & Faraon, A. Dielectric metasurfaces for complete control of phase and polarization with subwavelength spatial resolution and high transmission, *Nat. Nanotechnol*. 10, 937–943 , 2015.

[15] Devlin, R. C., Ambrosio, A., Rubin, N. A., Mueller, J. P. B. & Capasso, F. Arbitrary spin-to-orbital angular momentum conversion of light, *Science*. 352, 1190 , 2017.

[16] Devlin, R. C., Khorasaninejad, M., Chen, W. T., Oh, J. & Capasso, F. Broadband high-efficiency dielectric metasurfaces for the visible spectrum, *Proc. Natl. Acad*. 113, 10473, 2016.

Resonant Lattice Kerker Effect in Metasurfaces of Titanium Dioxide Nanocubes

Longjie Li[1,2], Lina Shi[1,*] and Changqing Xie[1]

[1]Key Laboratory of Microelectronic Devices & Integrated Technology, Institute of Microelectronics, Chinese Academy of Sciences, Beijing, China
[2]University of Chinese Academy of Sciences, Beijing, China
*corresponding author, E-mail: shilina@ime.ac.cn

Abstract

We demonstrate the arrays of titanium dioxide nanocubes, which support electric dipole resonance, magnetic dipole resonance and lattice resonances. By choosing the lattice periods along the x and y directions, we achieve a full overlap between the electric dipole resonance and magnetic dipole resonance and realize the resonant lattice Kerker effect. Meanwhile, we present a new fabrication process to eliminate the influence of the substrate on the electric dipole resonance and magnetic dipole resonance.

Keywords: Resonance, Kerker effect, metasurface

1. Introduction

With the rapid development of the concept of light-induced artificial electromagnetics in the field of metamaterials, the Kerker effect (resonant suppression of the backward scattering or reflection) has been promoted as never before and quickly penetrated into nanophotonics [1]. Many optical phenomena such as perfect reflection and perfect transmission are linked directly to the multipolar interference mechanism of the generalized Kerker effects [2]. Nanostructures enabling Kerker effect have been demonstrated for example the periodic array of spherical and core-shell silicon nanparticles [3].

In this work, we numerically investigate the single cube-shaped titanium dioxide (TiO_2) particle which support electric dipole resonance (EDR) and magnetic dipole resonance (MDR) and the arrays of cube-shaped TiO_2 metasurfaces which support resonant lattice Kerker effect. Transparent TiO_2 is widely considered as a good candidate for fabricating all-dielectric metasurfaces in the visible range since it has lower loss than silicon and has larger refractive index than silica and polymer [4]. The resonant lattice Kerker effect of the TiO_2 metasurfaces and the scattering cross section of the single TiO_2 partilce are investigated by the finite difference time domain (FDTD) method.

2. Simulations and discussion

The structure in Fig. 1 we propose comprises the periodic arrays of TiO_2 nanocubes with the length of side D = 200nm. The periods of the arrays are P_x = 540nm and P_y = (480 to 680) nm in steps of 10nm. Normal incidence of light with electric field **E** along the x-direction.

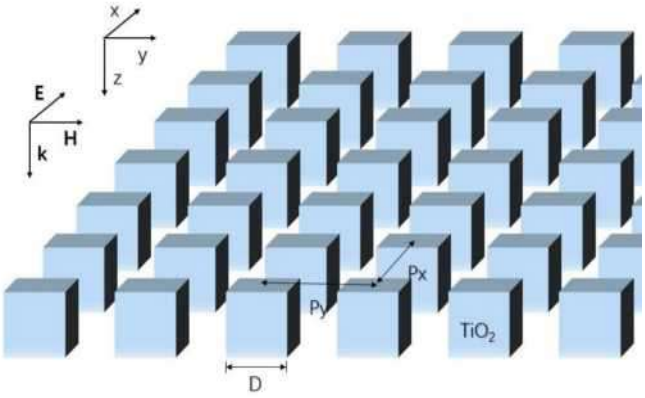


Figure 1: The tilt-view schematic of the arrays of TiO_2 nanocubes.

2.1. Resonance in single nanocube

We begin with the scattering cross section of the single TiO_2 nanocube in Fig. 2. We tried many individual cubes of different sizes so that we could find a cube that supports EDR and MDR. The scattering cross section assisted with the electric and magnetic field profiles for the EDR at λ = 437 nm and MDR at λ = 597 nm.

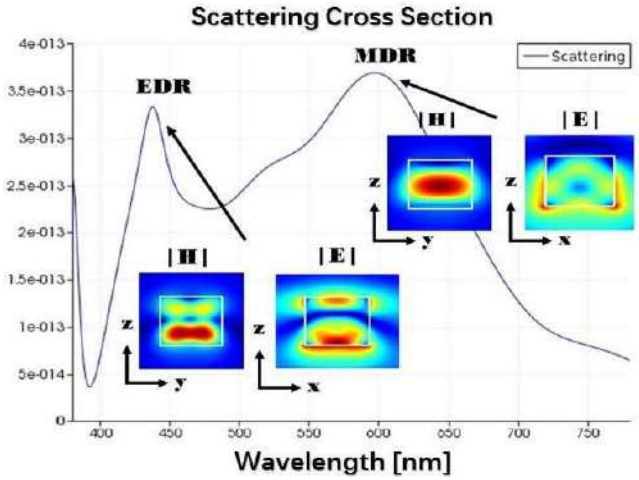


Figure 2: The scattering cross section of single cube with D = 200nm. The positons of EDR and MDR on the spectrum are pointed with arrows. Inset: The magnetic and electric field profiles of the EDR and MDR at peak wavelength respectively. White lines indicate the substrate and particle

position.

2.2. Resonance lattice Kerker effect in nanocubes

Then we investigate the arrays of TiO_2 nanocubes by varing periods P_y with fixed P_x and we excited lattice resonances (LR) at the wavelength close to Rayleigh anomalies (RA, from the side of long wavelengths). Resonant lattice Kerker effect can be observed when MDR and LR overlap at $\lambda = 610$ nm for the period of the array in y direction D_y = 580 nm. We can see that relectance is well suppressed at the overlap in Fig. 3.

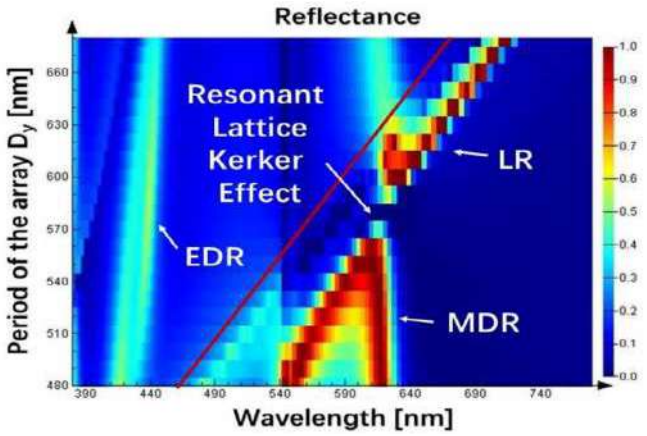


Figure 3: The reflectance of metasurface versus the array period P_y and wavelength for P_x = 540nm. It present that the peak resonance wavelength changes with the array period P_y. Red line shows wavelength of RA. White arrow points out the resonant lattice Kerker effect where the reflection is suppressed, EDR, MDR and LR respecticely.

2.3. Fabrication process

In practice, the substrate has a large influence on the array in order to fabricate it. To eliminate the influence of the substrate as much as possible, we present a new fabrication process. The fabrication process is as follows. First, 200 nm thick TiO2 film is deposited on the quartz substrate by magnetron sputtering. Second, 170 nm thick PMMA resist is spin-coated and then exposed by e-beam lithography. Third, 40 nm thick Cr film is deposited by electron beam evaporation. Finally, Cr etching mask is formed by lift-off and the pattern is transferred to TiO2 and the quartz substrate by dry etch.

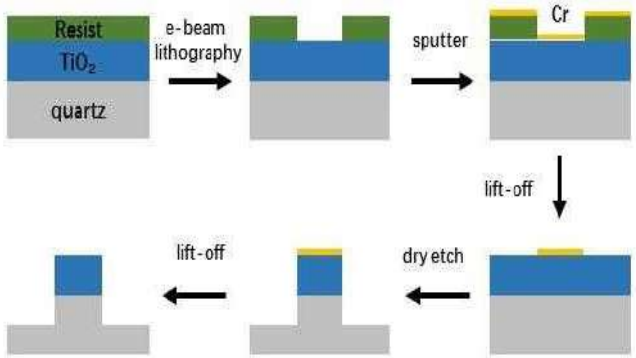


Figure 4: Fabrication process for the arrays of TiO_2 nanocubes in order to eliminate the influence of the substrate.

3. Conclusions

We have demonstrated the single TiO2 nanocube which support electric dipole resonance and magnetic dipole resonance and the arrays of TiO2 nanocubes which support resonant lattice Kerker effect. It is shown that the Kerker effect can be assisted by the lattice resonance and be inhibited by the substrate. After simulation verification and the proposed fabrication process, the metasurfaces with perfect transmission can be fabricated and provide a guidance to novel designs of optical metadevices for advanced applications.

Acknowledgements

This work is supported by the National Natural Science Foundation of China (grant 61875225).

References

[1] V. E. Babicheva, A. B. Evlyukhin, Resonant lattice Kerker effect in metasurfaces with electric and magnetic optical responses, *Laser & Photonics Reviews*, Vol. 11, 2017

[2] W. Liu, Y. S. Kivshar, Generalized Kerker effects in nanophotonics and meta-optics, *Opt Express* 26 (10), 13085, 2018

[3] I. Staude, A. E. Miroshnichenko, M. Decker, N. T. Fofang, S. Liu, E. Gonzales, J. Dominguez, T. S. Luk, D. N. Neshev, I. Brener, Y. Kivshar, *ACS NANO*, *STAUDE ET AL*. Vol. 7, No.9, 7824-7832, 2013

[4] S. Sun, Z. Zhou, C. Zhang, Y. Gao, Z. Duan, S. Xiao, Q. Song, All-dielectric full-color printing with TiO_2 metasurfaces, *ACS Publications*, 2017

Invisible metasurfaces based on high-order Kerker and anapole effects

Hadi K. Shamkhi[1], Kseniia V. Baryshnikova[1], Andrey Sayanskiy[1], Pavel D. Terekhov[1,2,3,4], Egor A. Gurvitz[1], Adria Canos Valero[1], Alina Karabchevsky[2,3,4], Polina Kapitanova[1], Andrey B. Evlyukhin[1,5], Pavel Belov[1], Yuri Kivshar[1,6], Alexander S. Shalin[1,*]

[1]ITMO University, 49 Kronverksky Ave., 197101, St. Petersburg, Russia
[2]Electrooptics and Photonics Engineering Department, Ben-Gurion University, Beer-Sheva 8410501, Israel
[3]Ilse Katz Institute for Nanoscale Science & Technology, Ben-Gurion University, Beer-Sheva 8410501, Israel
[4]Center for Quantum Information Science and Technology, Ben-Gurion University, Beer-Sheva 8410501, Israel
[5]Laser Zentrum Hannover e.V., Hollerithallee, D-30419, Hannover, Germany
[6]Nonlinear Physics Centre, Australian National University, Canberra, ACT 2601, Australia
*corresponding author, E-mail: alexandesh@gmail.com

Abstract

All-dielectric nanophotonics attracts more and more attention nowadays due to the possibility to control and configure light scattering on high-index semiconductor nanoparticles. It opens a room of opportunities for designing novel types of nanoscale elements and devices, paving the way to advanced technologies of light energy manipulation. One of the most pespective and interesting effects is directive light scattering provided by the so-called Kerker and anti-Kerker effects giving a possibility to realize Huygens light sources, fully transparent metasurfaces, different types of nanoantennae etc. Another one corresponds to the realization of so-called “anapole states” providing near-zero scattering accompanied with strong near-fields. Here we briefly review some new results on the induced invisibility regarding fully transparent metasurfaces based on the simultaneous cancellation of the forward and backward scattering via particular optical responses of multipoles (similar to Kerker effect), and invisible objects and structures governed by the novel type of anapoles – hybrid anapole states.

1. Introduction

Optical properties of high-refractive-index dielectric nanoparticles are attracting a great scientific interest nowadays [1,2,3]. These subwavelength scatterers can support the excitation of electric and magnetic multipolar resonances which allow the control over the electric and magnetic components of light by changing the nanoparticle size, geometry, and material [4,5]. Special interest is attracted by subwavelength structures - metamaterials and metasurfaces, allowing to manipulate light at the sub-wavelength regime [6-11]. Dielectric metasurfaces appeared as a counterpart of metallic plasmonic metasurfaces in the optical range. In contrast to plasmonic structures, dielectric metasurfaces can work effectively in transmitted-light regime. For fine tuning their optical properties, their size, shape, aspect ratio, material dispersion and surrounding medium properties should be controlled [12,13]. Their applications range from lossless waveguides [14] and nanoantennas, to cloaking devices and nonradiating configurations [15-17].

2. Results

Here we consider the transverse scattering by high-index nanoparticles with the simultaneous suppressing both forward and backward scattering. We consider silicon particles of the simplest forms (spheres and cubes) without any requirements on radial anisotropy, gain or non-symmetric form etc. For the first time we obtain essential conditions for the multipoles’ contributions, and reveal the step-by-step procedure of the lateral-only scattering pattern formation [18]. The appropriate conditions for multipoles are as following:

$$cp_x/m_y = 1; \quad cQ_{xz}/3M_{yz} = 1; \quad 2cp_x/ikM_{yz} = -1,$$

where *p, m, Q, M* – are electric and magnetic dipoles and quadrupoles respectively. We reveal and explain in details the strong suppression of the reflection from the metasurfaces taking place due to the aforementioned cancellation of forward and backward scattering. In this case light waves propagate through the metasurfaces almost without amplitude and phase changes (in spite the case of Huygens metasurface providing strong phase shifts) (Fig. 1 a,b) [19].

Secondly, we demonstrate another way to achieve a strong invisibility effect in the optical range induced by a hybrid anapole state, consisting of four overlapping anapoles originating from different terms in the Cartesian multipole expansion of the fields. The Fano-like shape of the hybrid anapole [17] has its local maxima close to its local minima, which may allow fast optical switching from invisibility to visibility states. Consequently, a metasurface consisting of such anapole particles becomes invisible, but the

mechanism is totally different from the previous one, Fig. 1 c,d.

Moreover, suppression of all dominant scattering channels in both the mentioned cases results in the field confinement inside the nanoparticle. Engineering of these energy hotspots could make them useful for nonlinear optics applications in the future.

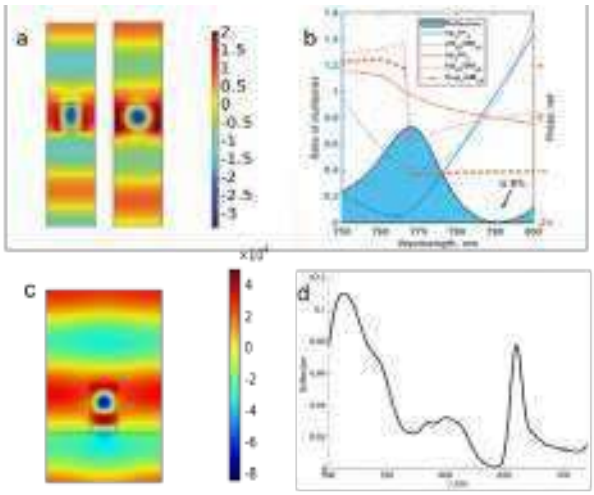


Figure 1. Two invisible metasurfaces based on either transverse scattering (a,b) or on hybrid anapole state (c,d); (a,c) – full fields in the metasurfaces. In (a) the metasurface consists of cubic Si nanoparticles with 250 nm edge, λ = 790 nm, spacing D = 400, (left), D = 300 nm, (right). (b) - amplitudes (blue) and phases (red) of the multipoles ratios providing transverse scattering for a cube with the edge of 250 nm and the period D = 400 nm, and the corresponding reflection coefficient (the black curve filled with blue). (c) – the metasurface consists of cylindrical Si particles with diameter 200 nm and height 300 nm, λ = 630 nm, D = 400 nm substrate - glass. (d) – scattering cross-section of a particle from the metasurface in Fig. 1c on glass substrate.

3. Conclusions

In summary, we have discussed the conditions for the formation of the transverse scattering pattern for high-index nanoparticles. This unusual behaviour takes place when the in-phase electric and magnetic dipoles are in anti-phase with the in-phase quadrupoles and all of them have comparable values. We considered regular metasurfaces consisting of the nanoparticles with the transverse scattering patterns and showed zero reflection spectral region corresponding to the similar conditions. Contradictory to “Huygens” structures the considered metasurface scattered neither forward, nor backward being almost invisible for an incident light. Moreover, we showed one more way to achieve a fully invisible metasurface based on utilizing high-order hybrid anapole states consisting of four overlapping anapoles of electric and magnetic types. This metasurface shows similar behaviour, but is governed by different physical mechanism and provides different near-fields. Dissimilar ways to achieve full transparency could be useful for designing novel coded metasurface architectures and holographic patterns

Acknowledgements

The authors acknowledge financial support from the Russian Foundation for Basic Research (grants 18-02-00414 and 18-52-00005); the Ministry of Education and Science of the Russian Federation (Goszadanie, grant 3.4982.2017/6.7); The calculations of multipole moments have been supported by the Russian Science Foundation Grant No. 16-12-10287.

References

[1] Kruk S and Kivshar Y 2017 *ACS Photonics* **4** 263849.
[2] Terekhov P D, Baryshnikova K V, Artemyev Y A, Karabchevsky A, Shalin A S and Evlyukhin A B 2017 *Phys. Rev. B* **96** 35443.
[3] Liu W and Kivshar Y S 2018 *Opt. Express* **26** 13085105.
[4] Kerker M, Wang D-S and Giles C L 1983 *J. Opt. Soc. Am.* **73** 7657.
[5] Nieto-Vesperinas M, Gomez-Medina R and Saenz J J 2011 *J. Opt. Soc. Am. A* **28** 5460.
[6] Betzig E and Trautman J K 1992 *Science* **257** 189-195.
[7] Gramotnev D K and Bozhevolnyi S I 2010 *Nature photonics* **4** 83.
[8] Shalin A S 2010 *JETP letters* **91** 636-642.
[9] Voroshilov P M, Simovski C R, Belov P A and Shalin A S 2015 *Journal of Applied Physics* **117** 203101.
[10] Milichko V A, Shalin A S, Mukhin I S, Kovrov A E, Krasilin A A, Vinogradov A V, Belov P A and Simovski C R 2016 *Physics-Uspekhi* **59** 727.
[11] Shalin A S, Ginzburg P, Orlov A A, Iorsh I, Belov P A, Kivshar Y S and Zayats A V 2015 *Physical Review B* **91** 125426.
[12] Kuznetsov A I, Miroshnichenko A E, Brongersma M L, Kivshar Y S and Lukyanchuk B 2016 *Science* **354.** aag2472-aag2472.
[13] Sukhov S, Shalin A, Haefner D, Dogariu A 2015 *Optics Express* **23**, 1, 247-252.
[14] Savelev R S, Filonov D S, Kapitanova P V., Krasnok A E, Miroshnichenko A E, Belov P A and Kivshar Y S 2014 *Appl. Phys. Lett.* **105.**
[15] Mirzaei A, Miroshnichenko A E, Shadrivov I V. and Kivshar Y S 2015 *Sci. Rep.* **5** 1–6.
[16] Miroshnichenko A E, Evlyukhin A B, Yu Y F, Bakker R M, Chipouline A, Kuznetsov A I, Luk’yanchuk B, Chichkov B N and Kivshar Y S 2015 *Nat. Comm.* **6** 1–8.
[17] Gurvitz E A, Ladutenko K S, Dergachev P A, Evlyukhin A B, Miroshnichenko A, Shalin A S and others 2018 *arXiv Prepr. arXiv1810.04945.*
[18] Shamkhi H K, Baryshnikova K V, Sayanskiy A, Kapitanova P, Terekhov P D, Karabchevsky A, Evlyukhin A B, Belov P, Kivshar Y and Shalin A S 2018 *Preprint arxiv:1808.10708 122*.
[19] Terekhov P D, Babicheva V E, Baryshnikova K V, Shalin A S, Karabchevsky A and Evlyukhin A B 2019 *Physical Review B* **99**(4) 045424.

A dual-to-single mode metasurface absorber using phase transition of vanadium dioxide

Ayman Negm[1], Mohamed Bakr[1], Matiar Howlader[1], Shirook Ali[2]

[1]Department of Electrical and Computer Engineering, McMaster University, Hamilton, Canada
[2]School of Mechanical and Electrical Engineering Technology, Sheridan College, Brampton, Canada
*corresponding author, E-mail: negma1@mcmaster.ca

Abstract

A tunable and polarization-insensitive absorber is proposed. The design employs a gold-based metasurface hybridized with vanadium dioxide. The phase-transition property of vanadium dioxide is used to control the operation of the metasurface absorber. In this paper, we study the behavior of the metasurface operating at mid-infrared frequencies in single or dual-band mode based on the operating temperature.

1. Introduction

The interest in using metasurfaces as electromagnetic absorbers significantly increased following the realization of the first perfect absorber metasurface by Landy et al. [1]. Metasurfaces can behave as perfect absorbers because they can satisfy impedance matching with air at the resonating wavelengths [2]. One of the most popular metasurface designs is the metal-insulator-metal (MIM) configuration. Examples of MIM metasurfaces include circular rings [3] and rectangular patches [4]. Metasurfaces can provide perfect multiband absorption using multiple elements of different sizes each resonating at different wavelength [5], or using a single patterned geometry [6].

A phase-change material is a material that can exist in metallic or semiconductor phase by applying external effect such as electric field [7], current [8], or temperature [9]. Vanadium dioxide (VO_2) is a popular material that experiences a change from semiconductor to metallic phase around a temperature of 67ºc [10]. This interesting property can be used to design metasurfaces with tunable properties by modifying the operating temperature.

In this work, we introduce a hybrid gold-VO_2 MIM metasurface with tunable resonance properties in the infrared range by employing the phase-transition property of VO_2. Fig. 1 shows the general geometry of the proposed MIM metasurface absorber. The top layer is a hybrid pattern of gold and VO_2 structures. The optical response of this layer changes with the change of the operating temperature. The thickness of the bottom gold layer of the MIM absorber is selected to be larger than the skin depth of gold at the operating wavelengths. This prevents the wave incident on the structure from being transmitted, and so can be confined within the structure for further absorption. Silicon dioxide is chosen as the dielectric material between the two metallic layers.

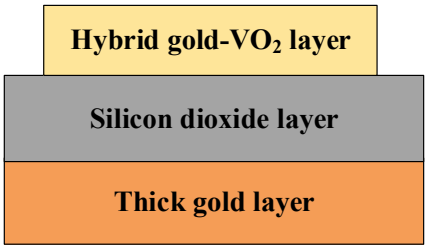


Figure 1: General configuration for the proposed hybrid MIM absorber.

To find the absorption characteristics of the structure, a normally incident transverse electric magnetic (TEM) plane wave is excited upon the metasurface. The absorptance A can be calculated using Equation (1):

$$A = 1 - R - T, \quad (1)$$

where R and T are the reflectance and transmittance respectively. The calculations were performed using finite-element modeling solver in COMSOL Multiphysics 5.3.

2. References

[1] N. I. Landy, S. Sajuyigbe, J. J. Mock, D. R. Smith and W. J. Padilla, "Perfect metamaterial absorber," Physical review letters, vol. 100, p. 207402, 2008.

[2] W. Tang and C. Ren, "Total transmission of airborne sound by impedance-matched ultra-thin metasurfaces," Journal of Physics D: Applied Physics, vol. 50, p. 105102, 2017.

[3] P. Yu, J. Wu, E. Ashalley, A. Govorov and Z. Wang, "Dual-band absorber for multispectral plasmon-enhanced infrared photodetection," Journal of Physics D: Applied Physics, vol. 49, p. 365101, 2016.

[4] Y. Liu, Y. Q. Zhang, X. R. Jin, S. Zhang and Y. P. Lee, "Dual-band infrared perfect absorber for plasmonic sensor based on the electromagnetically induced reflection-like effect," Optics Communications, vol. 371, pp. 173-177, 2016.

[5] S. Huang, Z. Xie, W. Chen, J. Lei, F. Wang, K. Liu and L. Li, "Metasurface with multi-sized structure for multi-band coherent perfect absorption," Optics express, vol. 26, pp. 7066-7078, 2018.

[6] T. Lu, D. Zhang, P. Qiu, J. Lian, M. Jing, B. Yu and J. Wen, "Ultrathin terahertz dual-band perfect metamaterial absorber using asymmetric double-split rings resonator," Symmetry, vol. 10, p. 293, 2018.

[7] B. Wu, A. Zimmers, H. Aubin, R. Ghosh, Y. Liu and R. Lopez, "Electric-field-driven phase transition in vanadium dioxide," Physical Review B, vol. 84, p. 241410, 2011.

[8] S. Zhang, M. A. Kats, Y. Cui, Y. Zhou, Y. Yao, S. Ramanathan and F. Capasso, "Current-modulated optical properties of vanadium dioxide thin films in the phase transition region," Applied Physics Letters, vol. 105, p. 211104, 2014.

[9] M. A. Kats, R. Blanchard, P. Genevet, Z. Yang, M. M. Qazilbash, D. N. Basov, S. Ramanathan and F. Capasso, "Thermal tuning of mid-infrared plasmonic antenna arrays using a phase change material," Optics letters, vol. 38, pp. 368-370, 2013.

[10] M. Liu, H. Y. Hwang, H. Tao, A. C. Strikwerda, K. Fan, G. R. Keiser, A. J. Sternbach, K. G. West, S. Kittiwatanakul, J. Lu and others, "Terahertz-field-induced insulator-to-metal transition in vanadium dioxide metamaterial," Nature, vol. 487, p. 345, 2012.

Hybrid achromats with metasurfaces for IR imaging

Philippe Lalanne

[1]LP2N, Institut d'Optique Graduate School, CNRS, Univ. Bordeaux, 33400 Talence, France
*corresponding author, E-mail: Philippe.lalanne@institutoptique.fr

Abstract

We report on the fabrication of hybrid achromats with metalenses for IR imaging.

1. Introduction

An achromatic lens or achromat is a lens that is designed to limit the effects of chromatic and spherical aberration. Achromatic lenses are corrected to bring two wavelengths (typically red and blue) into focus on the same plane.

The most common type of achromat is the achromatic doublet, which is composed of two individual lenses made from glasses with different amounts of dispersion. Typically, one element is a negative (concave) element with a relatively high dispersion, and the other is a positive (convex) element with a lower dispersion. The lens elements are often cemented together, and shaped so that the chromatic aberration of one is counterbalanced by that of the other. The drawback is that the association of a divergent and a convergent lens boost geometrical aberrations, and therefor one needs triplets …

An alternative solution is the hybrid diffractive-refractive achromat [1]. Its operation principle is simple. Longer wavelengths (red) are diffracted more with gratings, but refracted less than shorter wavelengths (violet) with prisms. Thus, by associating a prism and a grating, it is conceivable that blue and red light may be deviated identically. And since the diffractive dispersion in gratings is an order of magnitude larger than that of most refractive materials, the grating of the hybrid has a large periods and then is easily fabricated.

A hybrid diffractive-refractive achromat works the same. It is composed of a refractive lens and a diffractive one, the latter being composed of zones that are all much larger than the wavelength. It is easy to fabricate and offers large efficiencies, close to one at the central wavelength.

Hybrids lenses are studied for infrared imaging since 40 years or more [2]. The diffactive part can be fabricated either

- as a Fresnel lens with échelette continuous profile for instance with diamond turning tools,
- or as multivalued binary etched using multistep photolithography and several masks, typically 3 to 4.

None of these approaches is a panacea. Diamond turning is sequential and thus expensive, making replication techniques in high-index material highly desirable. Photolithography with multisteps need a precise alignment of the masks and a good control of resist redeposition.

Hereafter we report on our efforts to develop hybrids with metalenses [3] for IR imaging to lower the cost productions. Compared to visible light operation, much larger minimum feature sizes are required and the fabrication can be performed with standard photolithography. Additionally, one needs only a single photolithographic step.

2. AR coats of metagratings

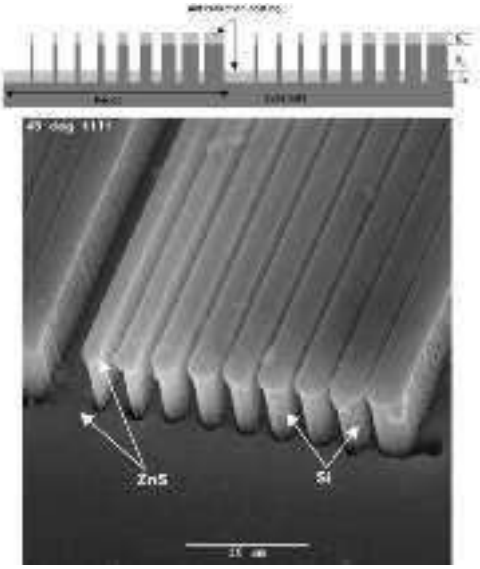


Figure 1. AR-coated metagrating fabricated at Thalès Angénieux.

In the IR, metalenses are rather fabricated in a high index semiconductor material. It is important to achieve an antireflection coating. Figure 1 shows an AR coated metagrating using zinc sulphide (ZnS), with a refractive index of 2.2, for operation at 10.6 µm. A fine tuning is carried out to maximize the transmitted first-order diffraction efficiency as a function of the grating depth and the zinc sulphide layer thickness. An efficiency of 93% in the transmitted first-order is obtained numerically while h_2=

4.9 μm and $h_1 = h_3 = 1.2$ μm. Experimentally, an efficiency of 80% at normal incidence is measured for TM polarization [4].

3. Hybrid metalens achromat

Our design takes into consideration the fact that the efficiency of most diffractive optical components varies with the wavelength, and blazing is achieved only at a specific nominal energy, the blaze wavelength. The existence of spurious light in undesirable orders represents a severe limitation that prevents using diffractive components in broadband systems, like for IR imaging.

We have experimentally demonstrated that broadband blazing over almost one octave can be achieved thanks to metalens dispersion chromatism. The design carefully exploits the highly chromatic behavior of semiconductor structures with mesoscopic dimensions only slightly smaller than the wavelength. Its peculiarity is the use of two different subwavelength patterns for achieving the 2π-phase variation across the grating periods. The combination relaxes the fabrication constraints on the etch depth and allows us to fully exploit the highly dispersive nature of artificial dielectrics with mesoscopic dimensions to render the 2π-phase variation almost achromatic.

The metalens is fabricated on 2-inch 300-μm-thick GaAs wafer. Figure 2 shows the diffraction efficiencies of the 0th, −1st and -2^{nd} orders for illumination at normal incidence. The efficiency is defined as the ratio between the energy funneled into a specific order normalized by the specular transmission of the GaAs wafer illuminated outside the patterned region. The salient result of Fig. 2 is evidenced by the blue rectangular window. The later shows that the incident energy is dominantly funneled into the -1^{st} order over almost one octave, from 8 μm to 15 μm. On spectral average, the relative efficiency of the -1^{st} order is 90%, whereas the relative efficiencies of the 0th and -2^{nd} orders are smaller than 6% and 3%, respectively. About 85% of the total transmitted light is funneled into the desired order.

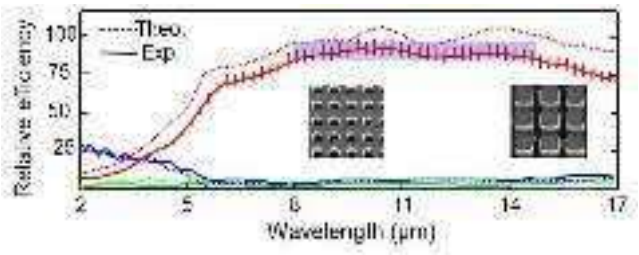


Figure 2. Metalens offering a broadband diffraction efficiency over almost one octave. The component is composed of both subwavelength holes and pillars.

The dotted curves represent theoretical predictions of the efficiencies. They are obtained with a semi-analytical method that combines scalar and vector-theory [6]. The method takes into consideration many fabrication imperfections, such as the actual measured size of the cylinders and pillars, which differs from the design values and the fact that the etching depth varies from 4.3 μm for tiny holes to 7 μm for large holes and pillars. The theoretical predictions confirm the realization of broadband blazing. We note however that the -1^{st} order experimental values are lower than the theoretical ones. The systematic offset may be explained by the rounded (not square) shape of the fabricated indentations that is not considered in the theoretical model and to an inevitable 2% scattering loss induced by the geometry rupture at the pillar-hole transition.

Acknowledgements

PL would like to thank Pierre Chavel, Jean-Pierre Huignard, Mane-Si Laure Lee (Thalès), Christophe Sauvan, Brigitte Loiseau (Thalès). He also acknowledges the support from the Direction Générale de l'Armement (DGA).

References

[1] T. Stone and N. George, *Hybrid diffractive-refractive lenses and achromats*, Appl. Opt. **27**, 2960 (1988).

[2] L. D'Auria, J.P. Huignard, A.M. Roy and E. Splitz, *Photolitographicfabrication of thin film lenses*, Opt. Comm. **5**, 232 (1972).

[3] P. Lalanne and P. Chavel, *Metalenses at visible wavelengths: past, present, perspectives*, Laser Photonics Rev. **11**, 1600295 (2017).

[4] M.S.L. Lee, P. Legagneux, P. Lalanne, J.C. Rodier, P. Gallais, C. Germain, J. Rollin, *Blazed-binary diffractive gratings with antireflection coating for improved operation at 10.6 μm*, Opt. Eng. (in press).

[5] C. Ribot, M.S.L. Lee, S. Collin, S. Bansropun, P. Plouhinec, D. Thenot, S. Cassette, B. Loiseaux, P. Lalanne, *Broadband and efficient diffraction*, Adv. Opt. Mat. (in press).

[6] C. Ribot, P. Lalanne, M.S.L. Lee, B. Loiseaux, J.P. Huignard, "Analysis of diffractive optical elements with slowly-varying phase functions", J. Opt. Soc. Am. A. **24**, 3819-3826 (2007).

Polarization and diffraction engineering of nonlinear dielectric metasurfaces

C. Gigli[1], G. Marino[1], S. Suffit [1], G. Patriarche[2], G. Beaudoin[2], K. Pantzas[2], I. Sagnes[2], I. Favero[2], and G. Leo[1,*]

[1] Laboratoire MPQ, Université Paris Diderot & CNRS, Paris, France
[2] C2N-CNRS - Université Paris-Sud-Paris-Saclay, Palaiseau, France
*corresponding author, E-mail: giuseppe.leo@univ-paris-diderot.fr

Abstract

We demonstrate the control of the polarization state in the second harmonic generated by periodic nanostructures. The knowledge of Mie-resonances in single dielectric nanoantennas enables to exploit their scattering features to design the polarization state of the harmonic field. We fabricate AlGaAs-on insulator nonlinear metasurfaces allowing to decouple polarization and diffraction features obtained by single resonators. This results in the possibility to collect a polarization-engineered second harmonic signal in a small angle around the normal to the surface.

1. Introduction

The efficient control of light-matter interaction through subwavelength resonating elements is a main interest issue in nanophotonics. Nanoresonators have recently attracted the interest of nonlinear optics community for the possibility to tightly confine the electromagnetic field in small volumes and enhance in turn nonlinear generation efficiency with respect to bulk materials. Furthermore, nanoresonator periodic arrays have shown to offer a large control for engineering polarization and phase of light in the nonlinear regime. Promising results in this sense have been obtained with plasmonic metamaterials, where the geometry and orientation of each meta-atom shapes the localized surface plasmon resonance responsible for the properties of scattered field. That approach led to the validation of polarization and phase control of nonlinear emitted beam [1] An alternative solution is represented by all-dielectric resonators offering both (1) a strong confinement inside the structure volume allowing to exploit the bulk nonlinearity of the material, and (2) negligible ohmic losses with respect to plasmonic counterparts. These features allowed to enhance by more than three orders of magnitude the nonlinear generation efficiency of single resonators compared to metallic structures [2]. As expected by Mie-theory, high-refractive-index subwavelength nanoparticles exhibit both electric and magnetic resonances which can be exploited to shape the phase and polarization of emitted field [3].

The possibility to engineer the polarization state of the harmonic beam around the normal direction to the surface is particularly interesting for practical applications. Here we demonstrate the control of second harmonic (SH) polarization state via a metasurface made of AlGaAs nanocylinders which exploit the properties of single resonators while partially redirecting the emitted beam.

2. Design procedure

The working principle of the devices prosed here is sketched in figure 1. The building block of our metasurfaces is an $Al_{0.18}Ga_{0.82}As$ nanocylinder about 350nm height laying on an AlOx substrate around 1μm thick. Resonators are designed to work at 1550nm and SH generated signal is collected in back-reflection.

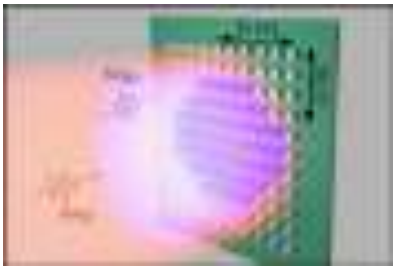


Figure 1 Artist's view of SHG by a metasurface, with the scattered signal collected in backward direction.

We propose two approaches for SH polarization control. In the first one we fix the fundamental frequency (FF) linear polarization along the [100] crystallographic direction and we exploit the orientation of elliptical base nanocylinders to break the symmetry of the system. In the latter we fix the geometry of circular base nanocylinders and rotate FF polarization from horizontal (aligned along [110]) to diagonal (along [100]). In both cases our polarization control mechanism relies on the properties of Mie-resonances in single resonators assuming the pillars far enough not to interfere in the near-field [4]. The directivity depends instead on far-field interference of independent emitters. For this reason, our design procedure starts from the study of resonant behavior of isolated structures. Pillar geometry has been optimized through finite element computations performed with COMSOL, using as figures of merit the contrast between orthogonal SHG polarizations and nonlinear generation efficiency.

Let us highlight that in the first approach the modes excited at SH when the ellipse is aligned along [110] or [1-10] near field distribution are identical except for a 90° rotation (see figure 2b), resulting in two mainly orthogonally polarized SH signals. In the second approach, the geometry is set and pump polarization is changed, which induces different dominating terms of nonlinear susceptibility tensor.

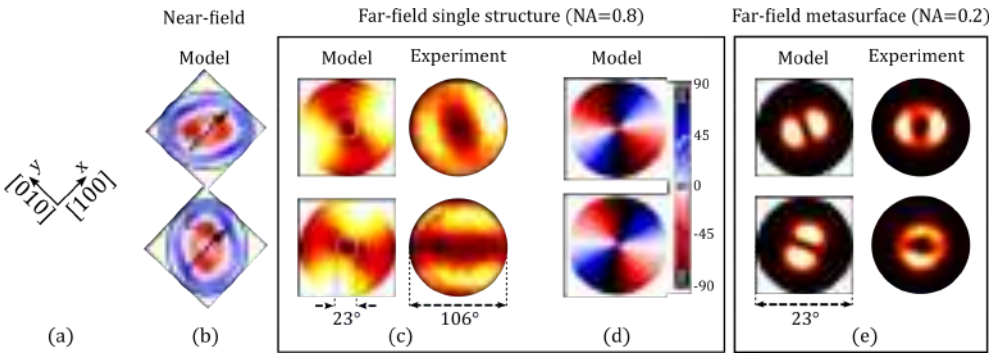


Figure 2. SH field distributions (simulations and experiments) for horizontally (top) and vertically (bottom) oriented nanocylinders with elliptical base. (a) Reference system, corresponding to AlGaAs crystal axes. (b) Near-field distribution of the mainly excited SH mode, with the indication of FF polarization. (c) SH radiation pattern of a single element within a solid angle set by the numerical aperture NA=0.8 (corresponding to 106° field of view) of the microscope objective. White dashes delimit a region with NA = 0.2 (corresponding to 23° field of view). (d) Inclination of SH linear polarization direction for the single element. (e) Back focal plane imaging of SH generated by a metasurface with the same constitutive elements as in c, period p=940nm, and collection restricted to NA=0.2.

In turn, different modes are excited at SH when the pump is along [100] or [110], resulting in SH mainly polarized along [010] and [1-10] respectively.

If this general idea proves the possibility to engineer emission features exploiting different resonating modes, it is also true that for isolated structures SH polarization and directivity properties are strictly related. This is shown in figure 2c,d which shows the computed far-field distribution and polarization state restricted to 0.8 numerical aperture.

When we move to periodic structures, in the assumption independent emitters the total radiation intensity can be expressed as the product between the far-field response of single emitter and the array factor of the metasurface. It is possible in this way to decouple polarization and directivity properties of SH signal and redirect the emission close to the normal direction, see figure 2e.

3. Measurements and discussion

Our measurements were carried out using a pulsed beam at 1550 nm, with SH collected in back-reflection. SHG is characterized in directivity by back focal plane imaging. The study is firstly performed for single structures and then for periodic array, moving from a numerical aperture NA=0.8 to NA=0.2 to ensure a collective excitation and a good angle resolution in the Fourier space. Good agreement between model and measurement found in both cases as reported in figure 2c,e. Successively, polarization is analyzed by mean of a wire grid polarizer to verify that polarization properties conferred by single structures are preserved when moving to metasurfaces. Results for the four analyzed configurations are reported in figure 3.

4. Conclusions

We showed how Mie-resonances of all-dielectric nanocylinders can be used to generate nonlinear emission with a well-defined polarization state. The extension of this concept to periodic structures, giving a further control on directionality, make us envisage the integration of this elements in photonic devices for quasi on-axis applications.

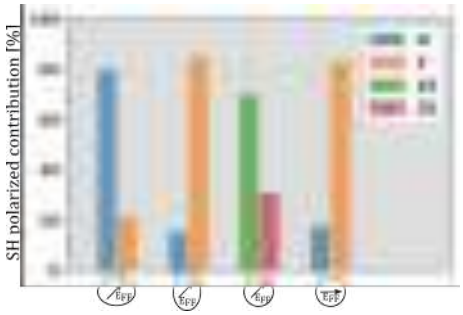


Figure 3 Experimental SH polarization analysis for the fabricated metasurfaces. SH signal was projected on two orthogonal polarization bases ([110]/[11-0] also called H/V and [010]/[100] also called D1/D2).

Acknowledgements

We thank C. De Angelis and T. Pertsch for fruitful discussions. G.L. acknowledges SEAM Labex (PANAMA Project) and NOMOS project (ANR-18-CE24-0026) for financial support. G.M.'s post-doc grant was funded by PANAMA Project and EU MULTIPLY program. G.P. thanks ANR for funding the TEMPOS project (10-EQPX-0050). I.S. acknowledges funding from RENATECH.

References

[1] E. Almeida et al, "Nonlinear metamaterials for holography," *Nat. Commun.* 7, p. 1, 2016.

[2] V. F. Gili *et al.*, "Monolithic AlGaAs second-harmonic nanoantennas," *Opt. Express* 24, p. 15965, 2016.

[3] A. Arbabi et al., "Dielectric metasurfaces for complete control of phase and polarization with subwavelength spatial resolution and high transmission," *Nat. Nanotechnol.* 10, p. 937, 2015.

[4] G. Marino *et al.*, "Zero-order second harmonic generation from AlGaAs-on-insulator metasurfaces," *ACS Photonics*, 10.1021/acsphotonics.9b00110 (2019).

Effect of Ballistic Electrons on the Optical Response of Hyperbolic Metamaterials

Guilherme M. Marega[1*], Achiles F. Mota[1], Ben-Hur V. Borges[1] and Euclydes Marega Jr.[2]

[1]São Carlos School of Engineering, University of São Paulo, São Carlos, Brazil
[2]São Carlos Institute of Physics, University of São Paulo, São Carlos, Brazil
*corresponding author, E-mail: marega.gui@gmail.com

Abstract

This paper presents a theoretical and experimental study of the effect of ballistic electrons on the optical response of a MIM (Metal-Insulator-Metal) like hyperbolic metamaterial structure. The simulated model using standard parameters and the experimental optical transmission shows a 20% peak difference due to the presence of ballistic transport in the metal. A semi-analytic approximation based in Drude's model is used for accurately predicting the optical response of the hyperbolic substrate and plasmon damping.

1. Introduction

In the past years, hyperbolic metamaterials have been widely studied due to the possibility of light confinement at the nanoscale. As hyperbolic metamaterials have its isofrequency surface given by a hyperbola, the wave propagation vector ($\vec{k}$) can by infinity in certain directions. Hence, the light wavelength for a direction in this material would be infinitely small, if the physical properties of its constituent material were perfect [1]. This exotic property permits optical confinement causing a spontaneous emission enhancement leading to a the large Purcell factor [2] of this class of metamaterial's. Emerging applications on lasing [5], LED's [3, 4] (quantum-)sensing [6, 7], imaging [8, 9] have been recently reported showing the interest of continue efforts in this area.

However, in the design of these devices, thin layers of metals with precise thickness are often used. As the metal thickness decreases, the effect of ballistic electrons is neglected as the models are usually fitted for a single thickness. Experimentally, this is seen by the increase of optical attenuation in the transmitted.

This paper presents a theoretical and experimental study of the effect of ballistic electrons on the optical response of a MIM (Metal-Insulator-Metal) like hyperbolic metamaterial structure consisting of silver and silicon oxide thin films. A semi-analytic model was construct based in the experimental data and the Drude's model with ballistic transport considerations. Finally, the effect of increased electron damping behavior was analyzed related to the plasmonic behavior of the structure.

2. Optical response of silver thin films

The Drude's model is the classical way of explaining the optical response of metals. However, when the mean free path of electrons in the material is comparable to its thickness, an extended description must be considered taking into account the effect of ballistic electrons on the material's complex permitivity.

2.1. Drude Model

The Drude's model considers that the electrons aren't bounded and move freely in a given metal. Hence, electrons excited by an exterior electromagnetic field move accordingly to the field, being only limited by the viscosity of the electrons in the metallic lattice. Mathematically, the movement is similar to a harmonic oscillator, Equation 1, where m represents the electron mass; Γ the damping factor; e the electron charge, $\vec{r}(t)$ the electron movement and $\vec{E}(t)$ the electromagnetic excitation.

$$m\frac{\partial^2\vec{r}(t)}{\partial t^2} + m\Gamma\frac{\partial\vec{r}(t)}{\partial t} = -e\vec{E}_0e^{-i\omega t} \tag{1}$$

The electronic movement induced by the exterior field defines the optical response of the material. The complex permittivity is given by the Equation 2 as a consequence of the Equation 1, where ω_p the plasma frequency; Γ the damping factor; ε_∞ the offset permittivity due to bounded electrons in the material [10].

$$\tilde{\varepsilon}(\omega) = \varepsilon_\infty - \frac{\omega_p^2}{\omega^2+\Gamma^2} + i\frac{\omega_p^2.\Gamma}{\omega(\omega^2+\Gamma^2)} \tag{2}$$

2.2. Optical Response of Silver Thin Films

Physically, the damping has a direct relation to the mean free path of the electron in the metal. Smaller the electron difficult of moving, bigger the mean free path. However, especially in silver which has a mean-free path of $53.3\ nm$ [11], films of the order of tenth's of nanometers imposes a new movement boundary for the electron. Therefore, increasing, the damping effect. These electrons have now a ballistic motion due to the interface limitation, as the thickness of the film is smaller than the mean-free path.

Equation 3 shows how the interface thickness (R) relates to the damping factor increase (Γ^*), where v_F : Fermi velocity and a : prefactor dependent of the geometry [10].

$$\Gamma^* = \Gamma + a\frac{v_F}{R} \tag{3}$$

Using equations 2 and 3, we construct the permittivity as a function of the wavelength for different thickness as shown in Figure 1. The numerical values of silver constants are taken from the data available for silver in Cai et al [10] where $\Gamma = 0.032 \times 10^{15}\ [s^{-1}]$, $\omega_p = 14.0 \times 10^{15}\ [rad/s]$ and $v_F = 1.4 \times 10^6\ [m/s]$ and $a = 1$ due to geometric symmetry of a continuous film.

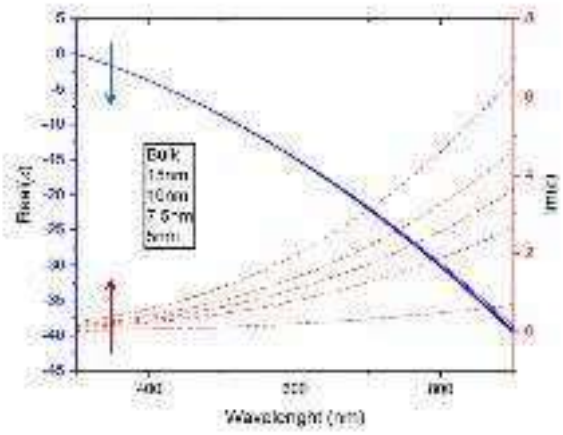


Figure 1: Drude's model of the Silver Permittivity in function of the thickness, real part ($Real(\varepsilon)$) in blue and imaginary part($Im(\varepsilon)$) in red.

2.3. Addition of ballistic effects in Experimental Data

Although the modelling of ballistic effect in thin films is expressed analytically in Drude's model, the real optical behaviour of materials takes into account external orbital interactions and atom bounded states. Nevertheless, the available experimental fit for materials usually is done for a single thickness and it doesn't consider the ballistic effect of electrons. For example, Palik's data for silver consider films of 30nm [12]. Hence, for verifying the validity of the standard silver models, the transmission of a 30 nm thermally evaporated silver is compared of Palik, CRC and Jonshon and Chirsty models in in Figure 2.

However, the experimental and simulated models are only valid for this thickness due to ballistic electrons effects in smaller thickness. Therefore, for improving simulations results for considering ballistic electrons effects, we use a semi-analytic method. This method consists in scaling experimental data in function of the proportionally seen between the optical response of silver films of different thickness in the Drude model. The coefficients $\alpha_{L(nm)}(\omega)$ and $\beta_{L(nm)}(\omega)$ describes the ratios in function of the thickness(L) and the film with 30nm for real and imaginary, respectively.

$$\alpha_{L(nm)}(\omega) = \frac{Real(\varepsilon_{Drude}(\omega))_{L(nm)}}{Real(\varepsilon_{Drude}(\omega))_{30nm}} \tag{4}$$

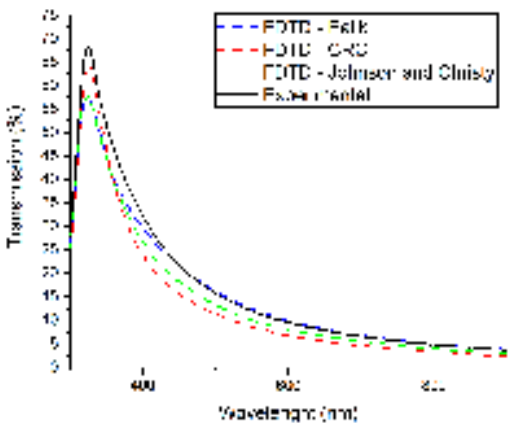


Figure 2: Experimental and Simulated transmission in a 30 nm silver film for CRC's, Palik's and Jonhson and Christy's model.

$$\beta_{L(nm)}(\omega) = \frac{Im(\varepsilon_{Drude}(\omega))_{L(nm)}}{Im(\varepsilon_{Drude}(\omega))_{30nm}} \tag{5}$$

Therefore, the silver experimental permittivity data can be scale in function of the thickness based in the analytic ratios $\alpha_{L(nm)}(\omega)$ and $\beta_{L(nm)}(\omega)$ extract from drude model.

$$\begin{aligned}\varepsilon^*(\omega, L) = \ & \alpha_{L(nm)}(\omega).Real(\varepsilon(\omega))_{30nm} + \\ & i.\beta_{L(nm)}(\omega).Im(\varepsilon(\omega))_{30nm}\end{aligned} \tag{6}$$

Figure 3 shows the correction realized in the experimental data available in CRC Handbook [13] for silver optical films.

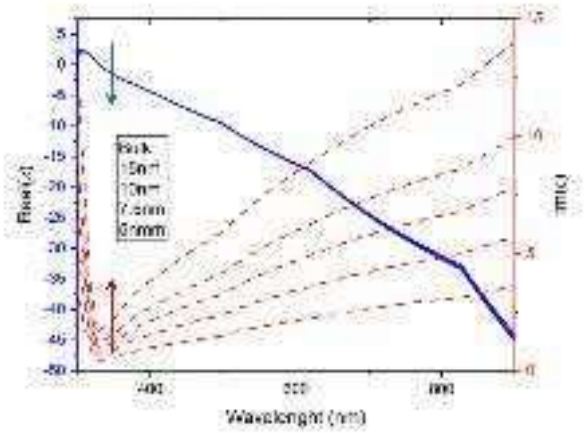


Figure 3: Interpolated Silver Permittivity Experimental Data and its correction in function of the thickness, real part in blue and imaginary part in red.

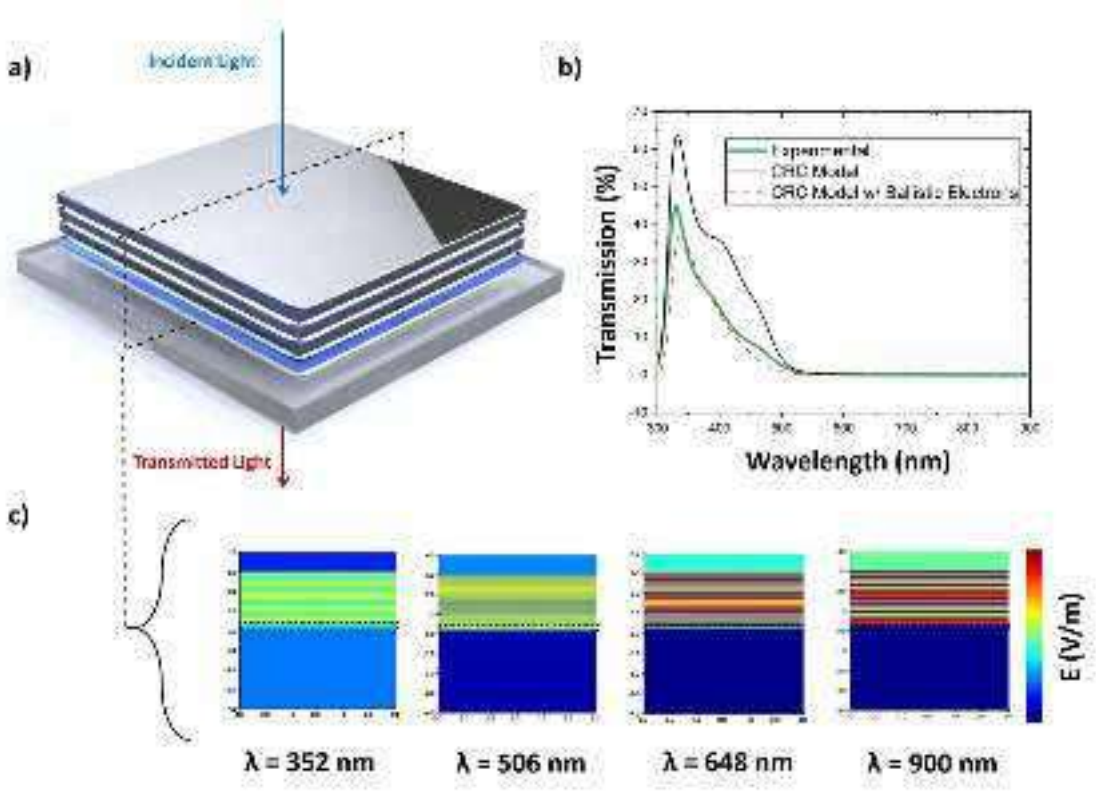


Figure 4: (a) 3D model of the MIM like substrate. (b) Experimental Simulated transmission spectrum of the substrate considering the model with and without ballistic electrons effects. (c) Electric Field maps in each wavelength.

2.4. Optical Response of Hyperbolic Substrate

The hyperbolic substrate considered in this paper is a multilayered MIM (Metal-Insulator-Metal) like structure (9 in total) film over a glass substrate. The top layer is a $7.5\ nm$ silver layer and the other layers are alternating from $15\ nm$ silver (Ag) and $60\ nm$ silicon oxide (SiO_2) [6]. Figure 4(a) is a three dimensional model of such structure.

The fabrication of this film is done by alternating cycles of thermal evaporation, for silver layers, and e-beam evaporation, for the silicon dioxide layers. The thickness was controlled by the standard oscillator frequency shift method embedded in both evaporators, and a posteriori, the total thickness was controlled by a Dektak XT Profilometer.

Figure 4(b) shows the film optical response for experimental and simulated substrate. The experimental optical response is obtained using a UV-Vis spectrometer. The optical transmission of the hyperbolic substrate is realized numerically with the sofware FDTD Lumerical© considering in a first time the standard CRC model, and next, the CRC with the proposed correction described in the precedent section. Figure 4(c) shows the simulated numerical electrical fields for different wavelengths.

2.5. Optical Response of Hyperbolic Metasurfaces

In this work, two metasurfaces were studied, a linear array of slits with $250\ nm$ period and $50\ nm$ width and a concentric array of circular rings with $50\ nm$ width separated by $350\ nm$. They were fabricated over a $20\mu m \times 20\mu m$ surface. Both structures were fabricated using a focused ion beam for milling the pattern over the previous substrate.

Figure 5(a) and 6(a) show the 3D modeling of the structures, and figure 5(b) and 6(b) the SEM images of the fabricated structure over the substrate.

The simulation of both structures was realized using the previous model with ballistic effects using symmetries for reducing memory need for mesh size while keeping a precise mesh within the structures. 128 Perfect Matched Layers were used for suppressing numerical oscillations. Figure 5(c) and 6(c) shows the optical transmission of the structure for both metasurfaces and the computed electric fields in the structure for different wavelengths. For the case of the periodic array of linear slits, two different polarization where used for exciting the TE (transverse electric), electric field parallel to the slits, and TM (transverse magnetic), electric field perpendicular to the slits, respectively. While for the array of concentric rings just one simulation was realized due to its invariant to polarization, but considering both standard and corrected models for the silver films.

Figure 5(d-e) present the optical image of the structures obtained by shining white light into the linear array using a Olympus transmission microscope. Each mode was excited by rotating a linear polarizer placed before the sample.

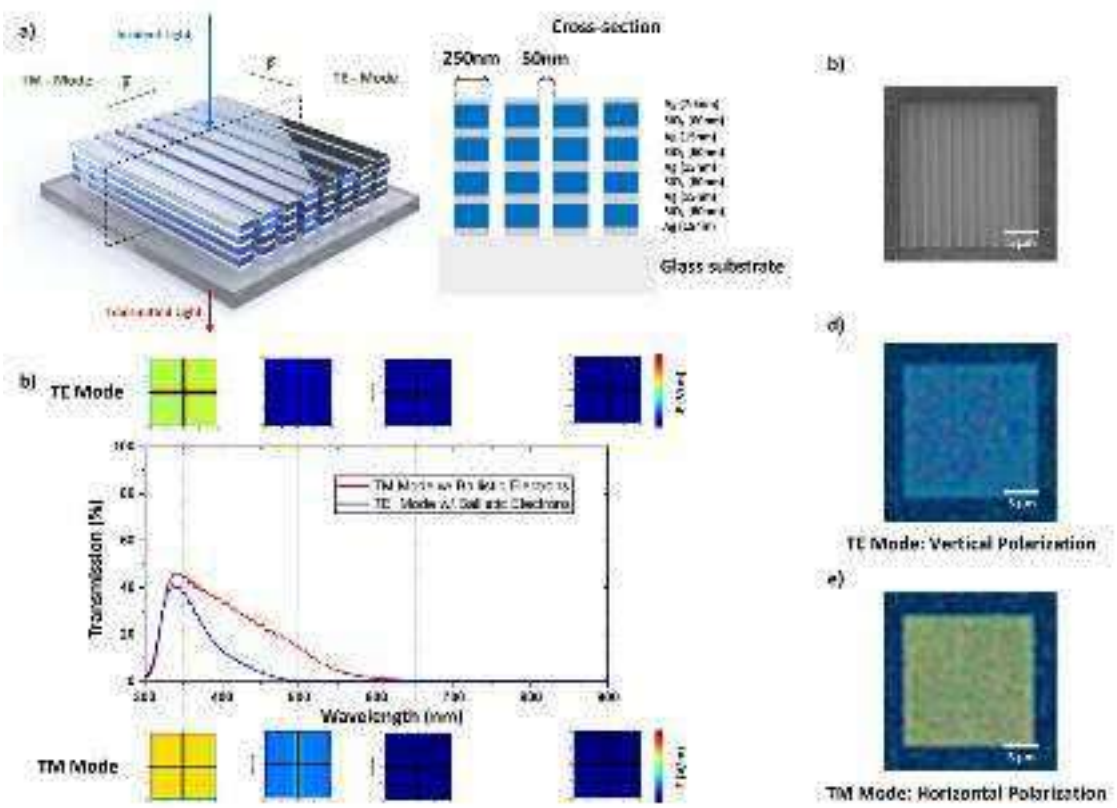


Figure 5: (a) 3D model of a linear array of slits metasurface. (b) SEM image of a linear array of slits with 250 nm period and 50 nm width. (c) Simulated normalized transmission spectrum of the metasurface for TE and TM modes and field maps. (d) and (e) are the far-field optical image of the transmitted through the film and the metasurface region as indicated in (b) with the incoming light polarized parallel (TE) to the slits and perpendicular (TM).

Finally, Figure 6(d) present the optical image of the structures obtained by shining white light into the rings array using a Olympus transmission microscope. Figure 6(e) presents the image from Figure 6(d) using a 594nm high-pass filter.

3. Discussions

Figure 4(b) shows the simulated with both models(standard and corrected) and experimental results of the substrate with almost the same behavior in the blue spectral range. However, the experimental data shows a peak transmission of about 20% lower than the one simulated using the bulk silver parameters. The model using the semi-analytic approximation reproduces more accurately the optical response including the 20% attenuation didn't see in the bulk silver constants. The mismatch observed near the pick happens due a interpolation inaccuracy in the simulation software.

This same effect must be considered in the treatment of the light transmitted in the metasurfaces region. As the electron mobility decreases, the plasmon quality may also decrease due to the greater material resistance. Using the semi-analytic approximation, a more thrust worth simulation of the proposed metastructures of the Figures 5(a) and 6(a) can be obtained.

The optical transmission of the linear array of slits presents in TE, 5(c), mode a blue spectra similar to what is optically observed in Figure 5(d). For TM mode a blue-green spectra similar to what is optically observed in Figure 5(e). Similarly, the same is observed for the array of concentric rings. The simulation predicts a weak red signal with emission in two principal lobes which is verified in the optical image using a red filter. The blue light transmission seen in the spectrum is due to the transmission mainly from the substrate without interacting with the structure. Also, Figure 6(c) shows the damping in the plasmonic response while considering the ballistic transport.

4. Conclusions

Therefore, this paper presented the effect of ballistic electrons of silver thin films in hyperbolic metasurfaces causing the underestimation of the attenuation factor in simulation compared to experiments. The ballistic transport also affects the plasmon quality in the structure due to increased resistance in its transport. A proposed semi-analytic approximation based on ballistic electrons effects in the Drude's model is used to accurate predict the optical response of the hyperbolic substrate and the metasurfaces.

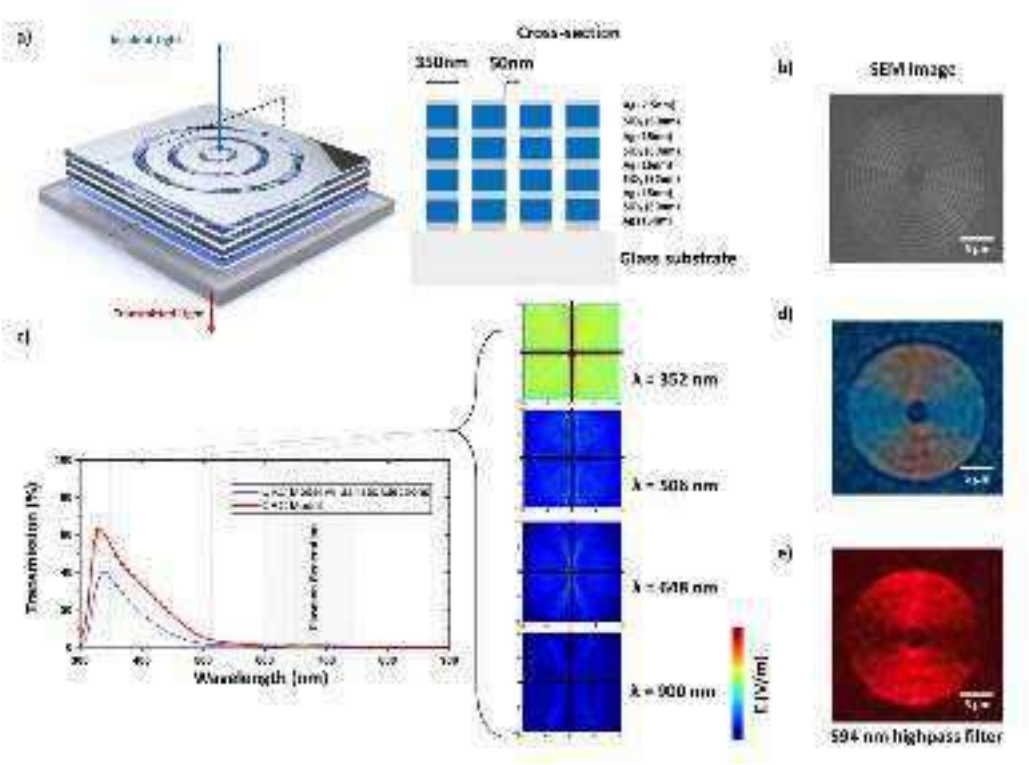


Figure 6: (a) 3D model of the concentric array of circular rings metasurface. (b) SEM image of a concentric array of circular rings with $50\ nm$ width separated by $400\ nm$. (c) Simulated normalized transmission spectrum of the metasurface and field maps. (d) far-field optical image of the transmitted through the film and the metasurface indicated in (b) with the light polarized in the horizontal axis. (e) is the (d) image with 594nm high pass filter (red filter).

Acknowledgement

Acknowledgements to The São Paulo Research (FAPESP) Foundation under the grant 2018/10011-3.

References

[1] A. Poddubny et al.,*Hyperbolic metamaterials,* Nature Photonics, vol. 7, no. 12, pp. 948957, Dec. 2013.

[2] Jacob, Z., Smolyaninov, I. Narimanov, E., *Broadband Purcell effect: radiative decay engineering with metamaterials.* Appl. Phys. Lett. 100, 181105 (2012).

[3] K. C. Shen et al., *Giant enhancement of emission efficiency and light directivity by using hyperbolic metacavity on deep-ultraviolet AlGaN emitter,* Nano Energy 45,353358 (2018).

[4] K. L. Tsakmakidis, R. W. Boyd, E. Yablonovitch, and X. Zhang, *Large spontaneous-emission enhancements in metallic nanostructures:towards LEDs faster than lasers,* Opt. Express 24, 1791617927 (2016).

[5] H. I. Lin et al., *Integration of Nanoscale Light Emitters and Hyperbolic Metamaterials: An Efficient Platform for the Enhancement of Random Laser Action.* ACS Photon. 5, 718727 (2018). ACS Photon. 5, 718727 (2018).

[6] A. F. Mota et al., *"2D semi-analytical model for optimizing the radiation emission of quantum emitters embedded in a bounded nano-patterned hyperbolic metamaterial,"* 2018 12th International Congress on Artificial Materials for Novel Wave Phenomena (Metamaterials), Espoo, 2018, pp. 128-130.

[7] C. L. Degen, F. Reinhard, and P. Cappellaro, *Quantum sensing,* Rev. Mod. Phys. 89, 139 (2017).

[8] Liu, Z., Lee, H., Xiong, Y., Sun, C. Zhang, X. *Far-field optical hyperlens magnifying sub-diffraction-limited objects.* Science 315, 1686 (2007).

[9] Ishii, S. et al., *Sub-wavelength interference pattern from volume plasmon polaritons in a hyperbolic medium*. Las. Photon. Rev. 7, 265271 (2013).

[10] W. Cai and V. Shalaev, *Optical Metamaterials*. Springer New York, 2010.

[11] GALL, D. *Electron mean free path in elemental metals.* Journal of Applied Physics,v. 119, n. 8, p. 085101, 2016.

[12] E.D. Palik (Editor), *Handbook of Optical Constants of Solids*, Academic Press, Orlando, 1985

[13] WEBER, M. J., *Handbook of Optical Materials*. [S.l.]: CRC Press, 2002.

Quantum metamaterials

Quantum electronic magneto-transport in GaAs/$Al_xGa_{1-x}As$ superlattice at high magnetic fields and low temperature for near-infrared detection

Rachid Ben Koujan[1], Abdelhakim Nafidi*[1], Merieme Benaadad[1], Samir Melkoud[1], Driss Barkissy[1], Nassima Benchtaber[1], and Abderrazak Boutramine[1]

[1]Laboratory of Condensed Matter Physics & Nano-Re, University Ibn Zohr, 80000 Agadir, Morocco
*corresponding author, E-mail: nafidi21@yahoo.fr

Abstract

The present work is a study of the band structure, the transport and magneto-transport properties of GaAs(d_1=183.95Å)/$Al_{0.18}Ga_{0.82}As$(d_2=42.45Å) superlattice at temperature of 0.3K. Our calculations have been made in the envelope function formalism and the approximation of the effective mass. We have gone down the effect of the discontinuity of the valence band and the temperature on the forbidden band. This superlattice has a band gap of 1.53 eV and can be used as a near infrared detector. The calculation of the density of states and the Fermi level shows that this SL is a quasi-two-dimensional system with n-type conductivity. We found correlation between the band structure, the quantum Hall effect and the shubnikov-de Haas effect observed by Pusep et al in this superlattice.

1. Introduction

The GaAs/$Al_xGa_{1-x}As$ superlattice type-I (SL) is a material of great interest for diverse technological applications, in the areas of optoelectronic [1] infrared devices and THz technologies [2, 3]. This SL is a periodic heterostructure made of repeated layers of two host materials which are structurally similar but possess different electrical properties, GaAs (well) and $Al_xGa_{1-x}As$ (barrier), the construction of this type of superlattice is a consequence of the development of molecular beam epitaxy (MBE) [4]. These materials are characterized by relatively wide band gap and high mobility of electrons, allowing these SL, to reach good performance and high temperature operations [5, 6].

The experimental studies of the GaAs/$Al_xGa_{1-x}As$ superlattice show that they have a band gap in the near-infrared range [6]. In particular, for GaAs/$Al_{0.18}Ga_{0.18}As$ SL, the measurements were made by Pusep et al. shows that it has a band gap of 0.52 eV at 1.6 K [7, 8]. In this work, we investigated the GaAs/$Al_{0.18}Ga_{0.18}As$ SL electronic band structure in the envelope function model, the approximation of the effective mass and the effect of different parameters such as the layers thickness of SL, temperature, valence band offset (VBO) on variation of band gap energy.

In order to characterize this superlattice, we studied the properties of magneto-transport, using the magnetoresistance experimental measurements of Pusep et al. [8]. At a sufficiently low temperature and under high magnetic field, the Shubnikov-de Haas (SdH) effect, which consists of oscillations in the magnetoresistance, allows us to deduce several transport parameters. For example, the periodicity of the oscillations of longitudinal magnetoresistance gives the carriers density and the Fermi level. We also showed some correlations between the band structures and the effect of SdH from the study of the density of states in the presence of magnetic field.

2. Dispersion relations in GaAs/$Al_xGa_{1-x}As$ superlattice

For semiconductors, the k.p theory makes it possible to describe the electronic bands with a relatively important accuracy [9]. We considered the k.p method to describe these states in the case of semi-conductor superlattice with the formalism of the envelope function and the approximation of the effective mass, in terms of some parameters noted by 1 and 2 for GaAs and $Al_{0.18}Ga_{0.82}As$ bulk materials, respectively.

The general expression of dispersion relation for GaAs/$Al_{0.18}Ga_{0.82}As$ superlattice, within the envelope function formalism and effective mass approximation, is given by [10, 11]:

$$cos[k_z(d_1+d_2)] = cos(k_1d_1)cos(k_2d_2) - \frac{1}{2}[(\xi+\frac{1}{\xi})+\frac{k_p}{4k_1k_2}(r+\frac{1}{r}-2)]\times sin(k_1d_1)sin(k_2d_2) \quad (1)$$

With k_z the wave vector in the direction of growth and $k_p(k_x,k_y)$ in the plane of the superlattice. k_1 and k_2 describe the movement perpendicular to the layer of bulk materials.

The SL light particles (electrons and light holes) subbands are obtained from the same Eq. (1) with:

- The expression of ξ and r in the Eq.(1) are:

$$\xi = \frac{k_1}{k_2}r \text{ and } r = \frac{E-\varepsilon_2}{E-\varepsilon_1-\Lambda}, \quad (2)$$

Where ε_i(i= 1, 2) the band gaps of bulk materials and Λ is the valence band offset (VBO).

At a given energy, the two-band Kane model [12] gives the wave vector (k_i^2+k_p^2) in each host material (i= 1 or 2) by:

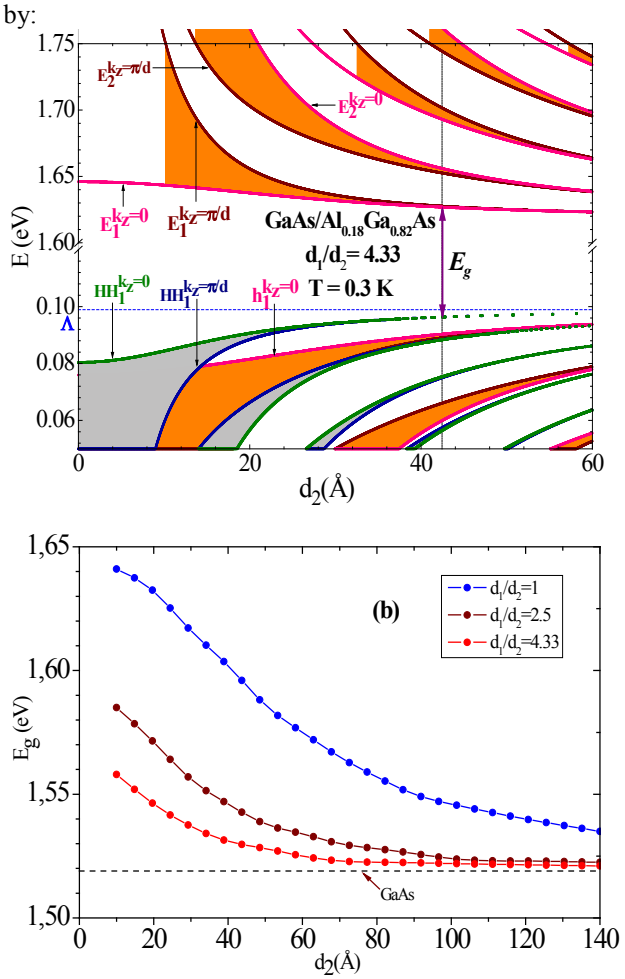


Figure 1: (a) Energy of conduction (upper part) and valence (lower part) mini-bands edges (The solid areas show the width of mini-bands) (b) band gap as a function of the barrier thickness d_2 of ($Al_{0.18}Ga_{0.82}As$).

$$\begin{cases} \frac{2}{3} P_1^2 \hbar^2 (k_1^2+k_p^2) = (E-\varepsilon_1-\Lambda)(E-\Lambda) & \text{for GaAs} \\ \frac{2}{3} P_2^2 \hbar^2 (k_2^2+k_p^2) = E(E-\varepsilon_2) & \text{for } Al_xGa_{1-x}As \end{cases}, \quad (3)$$

The Kane matrix element P_i was calculated by using the Kane energy E_{pi} formula [13]:

$$P_i^2 = \frac{E_{pi}}{2m_0}, \quad (4)$$

We used here, the empirical expressions of GaAs and $Al_xGa_{1-x}As$ band gaps ε_i(i= 1, 2), at Γ point, for x≤ 0.69 as a function of temperature [14, 15]:

$$\varepsilon_1(\Gamma) = 1.519 - \left(5.405\ 10^{-4}\ T^2\right)/(T+204), \quad (5)$$

$$\varepsilon_2(T,x) = (1.517+1.39x) - \frac{(5.5+3.35x)10^{-4}T^2}{T+(255+88x)}, \quad (6)$$

From the same equation (1), the superlattice heavy hole subbands can be calculated with the following relations:

$$\begin{cases} -\frac{\hbar^2}{2m^*_{HH_1}}(k_1^2+k_p^2) = (E-\Lambda) & \text{for GaAs} \\ -\frac{\hbar^2}{2m^*_{HH_2}}(k_2^2+k_p^2) = E & \text{for } Al_xGa_{1-x}As \end{cases}, \quad (7)$$

$$\text{With } \xi = \frac{k_1}{k_2} r \text{ and } r = \frac{m^*_{HH_2}}{m^*_{HH_1}}, \quad (8)$$

where m^*_{HH1}= 0.34m_0 and m^*_{HH2}= (0.33+0.18x)m_0 are the heavy hole effective masses of GaAs and $Al_xGa_{1-x}As$ bulks, respectively [15, 16].

The sample studied here consists of alternating d_1(GaAs)=183.93Å and d_2($Al_{0.18}Ga_{0.82}As$)=42.45Å. Consequently, d_1/d_2= 4.333Å and the superlattice period is d = d_1 + d_2 = 240 Å. We used the valence bands offset 105.66 meV from Λ(eV) = 0.587x calculated by Wang et al. [17, 18] in atomistic first principles approach.

3. Results and discussions

The results plotted in Figure 1 represent subbands energies and bandwidths of electrons (E_i), light holes (h_i) and heavy holes (HH_i), in the first Brillouin zone as a function of the barrier thickness (d_2) at 0.3 K for d_1 = 4.33 d_2. When the thickness d_2 increases the energy of electrons decreases and that of holes increases. Consequently, the forbidden band gap decreases. This can be attributed to the creation of authorized state levels in the band gap. As d_2 increases, the confinement of charge carriers in the GaAs (well) then augments. The superlattice acts as a set of isolated quantum wells and the band gap energy converges to that of GaAs.

The thickness of the barrier d_2 of the sample studied is indicated by a vertical dotted line. The gap energy is the difference between the first subband of electrons E_1 and heavy holes HH_1: E_g = E_1-HH_1. For the studied sample E_g =1.53 eV. This result is in good agreement with E_g = 1.523 eV obteined by PL measurements of Pusep et al. [8].

In figure 1b, we illustrated the band gap E_g as a function of well thickness d_2 for various ratio d_1/d_2. For each d_2, the calculated E_g increases as d_1/d_2 decreases. For a given ratio, when the thickness d_2 increases, the band

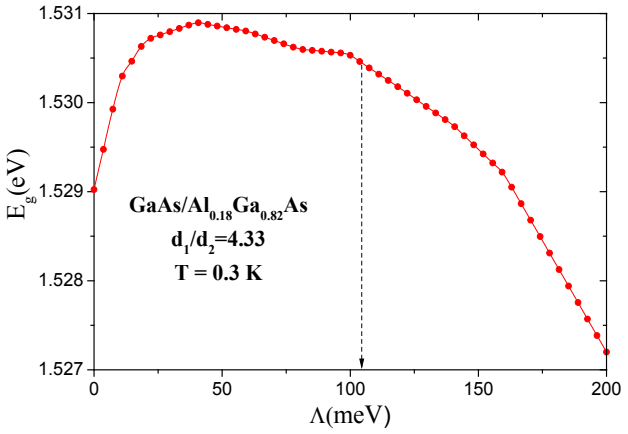


Figure 2: Band gap energy as function of VBO of GaAs/ $Al_{0.18}Ga_{0.82}As$ SL.

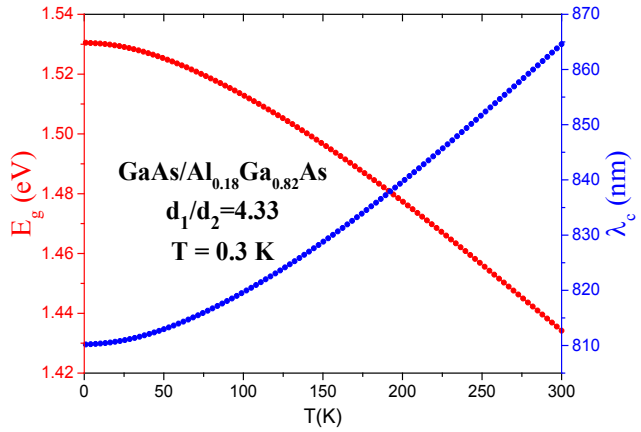


Figure 3: Band gap energy and the cutoff wavelength as function of temperature of GaAs/ $Al_{0.18}Ga_{0.82}As$ SL.

gap decreases. This phenomenon can be attributed to the creation of allowed states in the forbidden bands available to be occupied by electrons. Consequently, the valence and conduction bands separation starts to narrow, leading to a reduction of the band gap.

The effect of the VBO on the band structure was studied by varying the VBO and we set the other parameters. In figure 2, we show the SL band gap, for the temperature 0.3 K, as a function of Λ. The band gap increases to a maximum at Λ = 41 meV and then decreases. Our chosen offset is indicated by a vertical dashed line.

In figure 3, we illustrated the variation of the band gap SL and the cutoff wavelength in the range of 0.3 to 300 K. At low temperatures, the band gap changes weakly and then it decreases when the temperature increases. The cutoff wavelength in this range of temperature, $811\,nm \le \lambda_c \le 867\,nm$, situates this sample in the near-infrared region.

In figure 4, we have the dispersion curves of the first conduction and valence sub-bands in the first Brillouin

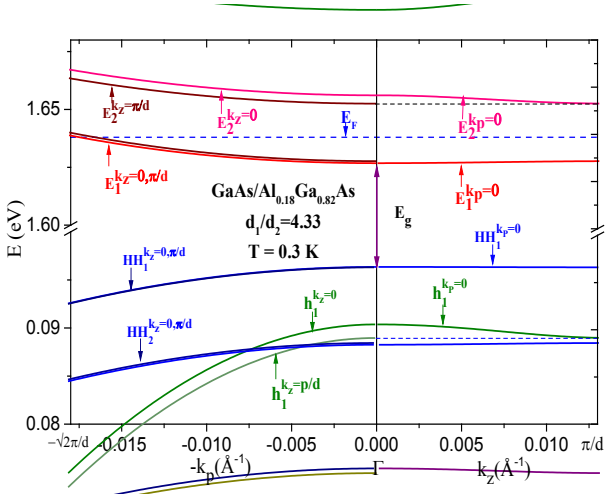


Figure 4: Band structures of GaAs/$Al_{0.18}Ga_{0.82}As$ superlattice along the growth direction (k_z) and in-plane (k_p).

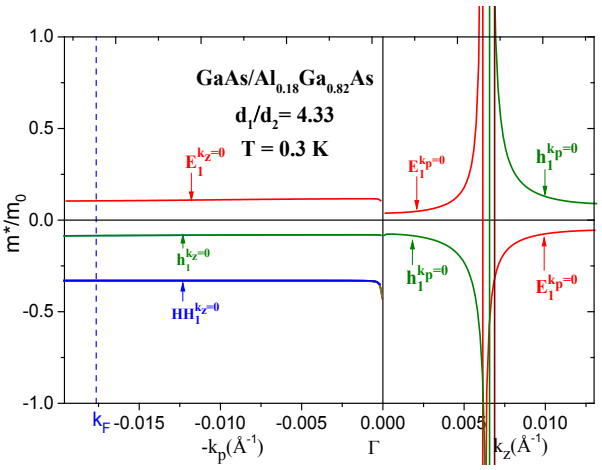


Figure 5: Carrier effective masse calculated along the growth direction and in the plane of GaAs/$Al_{0.18}Ga_{0.82}$ SL.

zone (in the direction of the wave vector k_z and in the planes k_p). The dispersion of energy subbands in the plane direction is larger compared to that along the growth direction. This indicates a weak interaction between adjacent wells. This result shows that the electronic transport is dominated in the plane of this superlattice (GaAs layers).

As the superlattice is anisotropic, the carrier's effective mass of the conduction and valence subbands is defined by the tensor whose elements in directions i and j are given by the following expression:

$$\left(\frac{1}{m^*}\right)_{ij} = \frac{1}{\hbar^2}\frac{\partial^2 E_{k_{ij}}}{\partial k_i \partial k_j} \qquad (9)$$

Figure 5 represents the effective mass of the first conduction and valence sub-band in the plane and along the growth direction $m^*(k_p, k_z)$. Along k_p, effective masses of heavy holes, light holes and electrons are almost constant and equal to $-0.33m_0$, $-0.08m_0$ and $0.11m_0$, respectively.

In order to determine the Fermi level, we used the experimental measurements of Pusep et al. [8] of longitudinal magneto-resistance (ρ_{xx}). The oscillations ofρ_{xx}, at low temperature and under high magnetic fields, are periodic with respect to 1/B. The determination of the period $\Delta_{1/B}$ allows us to determine the sheet density n_{2D} of electrons by the following relation:

$$n_{2D} = \left| e/\left(\pi\hbar\Delta_{1/B}\right)\right| \quad (10)$$

Once the n_{2D} is known, the Fermi wave vector k_F of two-dimensional electron gas can be calculated by the following expression: $k_F^2 = 2\pi\, n_{2D}$. Therefore, $n_{2D} = 4.95\ 10^{11}$ cm^{-2} and $k_F = 0.017$ Å^{-1}. The corresponding heavy hole $(m^*_{HH1})_{EF}$, light hole $(m^*_{h1})_{EF}$ and electron $(m^*_{E1})_{EF}$ effective masses are -0.33m_0, -0.084m_0 and -0.105m_0, respectively.

The Fermi level at low temperature is given by the following relation:

$$\left|E_F - E_c\right| = \left|\hbar^2 k_F^2 / \left(2m^*_{E_1}\right)_{E_F}\right| = \left|n_{2D}\pi\hbar^2 / \left(m^*_{E_1}\right)_{E_F}\right| \quad (11)$$

Since $E_c = 1.627$ eV, so $E_F = 1.637$ eV. This shows that the sample studied has n-type conductivity.

The VBO is one of the important design parameters for some device applications. Several theoretical approaches and experimental measurements on VBO of GaAs/$Al_xGa_{1-x}As$ SL. In this work, we have use the experimental measurements of T.E. Ostromek and P. Pfeffer et al. [19, 20] and the approach of Ref. 17.

The density of states of the ith mini-band of width $\Delta E^{(i)} = E^{(i)}_{max} - E^{(i)}_{min}$ of SL, is given by [21]:

$$\rho^{(i)}_{DOS}(E) = \begin{cases} \left(m^*/\pi^2\hbar^2\right)k_z(E) & for \quad E^{(i)}_{min} \le E \le E^{(i)}_{max} \\ 0 & otherwise \end{cases} \quad (12)$$

The term k_z (E) corresponds to the permissible states, which are solutions of the dispersion relations of the superlattice.

The general expression of the density of state is:

$$\rho_{DOS}(E) = \sum_{i=1}^{n} \rho^{(i)}_{DOS}(E) \quad (13)$$

Figure 6, shows the density of states of the first two conduction subbands of the studied sample. We found that only the first conduction subband is occupied ($E < E_F$) and the density of states is quantified in terms of $m^*/\pi\hbar^2 d$. We also found that the system is almost two-dimensional and a very weak dispersion following k_z occurs. Therefore, quantum wells are weakly coupled from each other.

In the presence of an intense external magnetic field applied, at low temperature, on a GaAs/$Al_{0.18}Ga_{0.82}As$ superlattice in the direction of growth, the quantization of DOS and the degeneration of each subband (i), in a series Landau subbands, takes place. Figure 7 shows the degeneration lift of the first conduction subband of Landau using the following total energy expression:

$$E^{(i)} = E^{(i)}(k_z) + \left(N^{(i)} + 1/2\right)\hbar\omega_c + E^{(i)}_{Zeeman} \quad (14)$$

where $E^{(i)}(k_z)$ is the energy associated with the movement of charge carriers along the z axis. While the energy associated with carrier motion in the plane is completely quantized in terms of $(N^{(i)} + 1/2)\hbar\omega_c$ with $N^{(i)} = 0, 1, 2, ..$ represent the index of Landau of the i^{th} sub-band. We can assume, here, that Zeeman spin splitting energy $E_{Zeeman} = \pm g^*\mu_B B/2$ is negligible compared to Landau mini-band splitting $\hbar\omega_c = \hbar eB/m^*$

The allowed states in the energy space, shown in Figure 7 (a), (c) and (e) for three values of magnetic fields, show that for a given $N^{(i)}$, charge carriers in the plane of the superlattice can have quasi-continuous values of $E^{(i)}$ between the center $E^{(i)}$ (k_z=0) and the limit $E^{(i)}$ ($k_z = \pi/d$) of the first Brillouin zone as we can see in figure 6.

For this quasi-two-dimensional SL, the presence of a strong perpendicular magnetic field leads to the quantization of the state density in terms of Dirac functions δ separated by cyclotron energy $\hbar\omega_c$, represented in figure 5b, d, and f for three values of magnetic fields, whose expression is written as [22]:

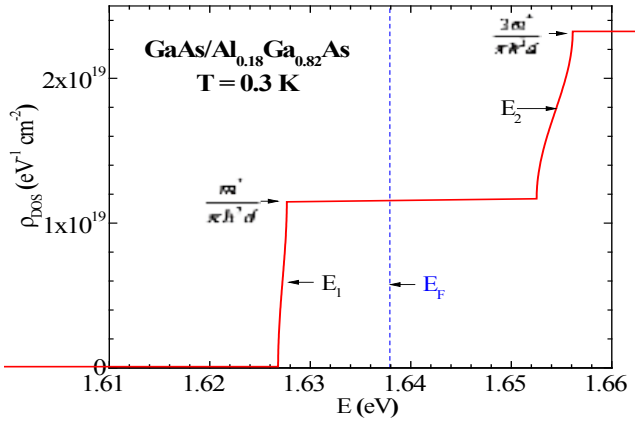


Figure 6: Density of states versus energy arising from the two lowest conduction mini-bands for the investigated superlattices.

$$\rho^{2D}_{DOS}(E,B) = \frac{|e|B}{\hbar}\sum_i\sum_{N^{(i)}}\delta\left(E - E^{(i)}\right) \quad (15)$$

In Figure 7, we made a comparison of the density of states for three values of magnetic fields. As the magnetic field decreases, cyclotron energy $\hbar\omega_c$ decreases and the gap between Landau levels decreases. When B becomes lower than 0.8T, the cyclotron energy becomes lower than $\Delta E^{(i)}$, so there is an interference between the levels of the density of states, it is the quantum limit.

The highest occupied level corresponds to the Fermi level, each time a subband of Landau crosses the Fermi level, and it depopulates the electrons that will contribute to the electronic transport, resulting in a minimum of longitudinal magnetoresistance R_{xx}. At very high magnetic fields, only the basic Landau subband ($N^{(1)} = 0$ or 1) is populated Figures 7 (a) and (b). Consequently, by varying the intensity of the magnetic field, the number of occupied Landau sub-bands varies with B, which leads to oscillations of magnetoresistance (Shubnikov-de Haas effect).

Such effects can be observed only if $\Delta E^{(i)} < \hbar\omega_c$. According to our calculations for B<0.8T, the two effects SdH and quantum Hall effect are no longer observed, since all the energies above $E^{(1)}_{center}+(N+1/2)\hbar\omega_c$ are allowed (continuous energy spectrum) as can be seen in figures 7 (e, f) These results are in good agreement with the experimental measurements of Pusep et al.

The application of an external magnetic field leads to the creation of Landau levels. Figure 8 represents calculated energies for E_1 and the variation of Fermi levels as a function of magnetic fields. These results are obtained by using the in-plane wave vectors quantification rule of superlattice given by the formula (16) and the expression (17) of the concentration of the n_{2D} electrons in the conduction band.

$$k_p^2 = \left(2N^{(i)} + \frac{1}{2}\right)\left(\frac{eB}{\hbar}\right) \tag{16}$$

Where $N^{(i)}$ de notes the Landau index of the i^{th} sub-band.

$$n_{2D} = \int_0^{+\infty} \rho_{DOS}^{2D}(E,B) f(E) dE \tag{17}$$

with $f(E) = 1/\left(1+\exp\left(E - E_F / k_B T\right)\right)$ the distribution of Fermi-Dirac

We can see that the energy of the Landau sub-bands increases linearly with the magnetic field B. The values of B, extrema indicate by the intersections between these sub-bands of Landau and the level of Fermi, are in good agreement with those of oscillations of the longitudinal magnetoresistance R_{xx} observed in Ref. 8, as shown in Table 1 and Figure 7.

However, it should be noted that under high magnetic fields, peaks of Shubnikov-de Haas oscillations (maxima of R_{xx}) occur at the jumps of the transverse magnetoresistance R_{xy} and each minima of R_{xx} corresponds to a plateau of R_{xy} (quantum Hall effect).

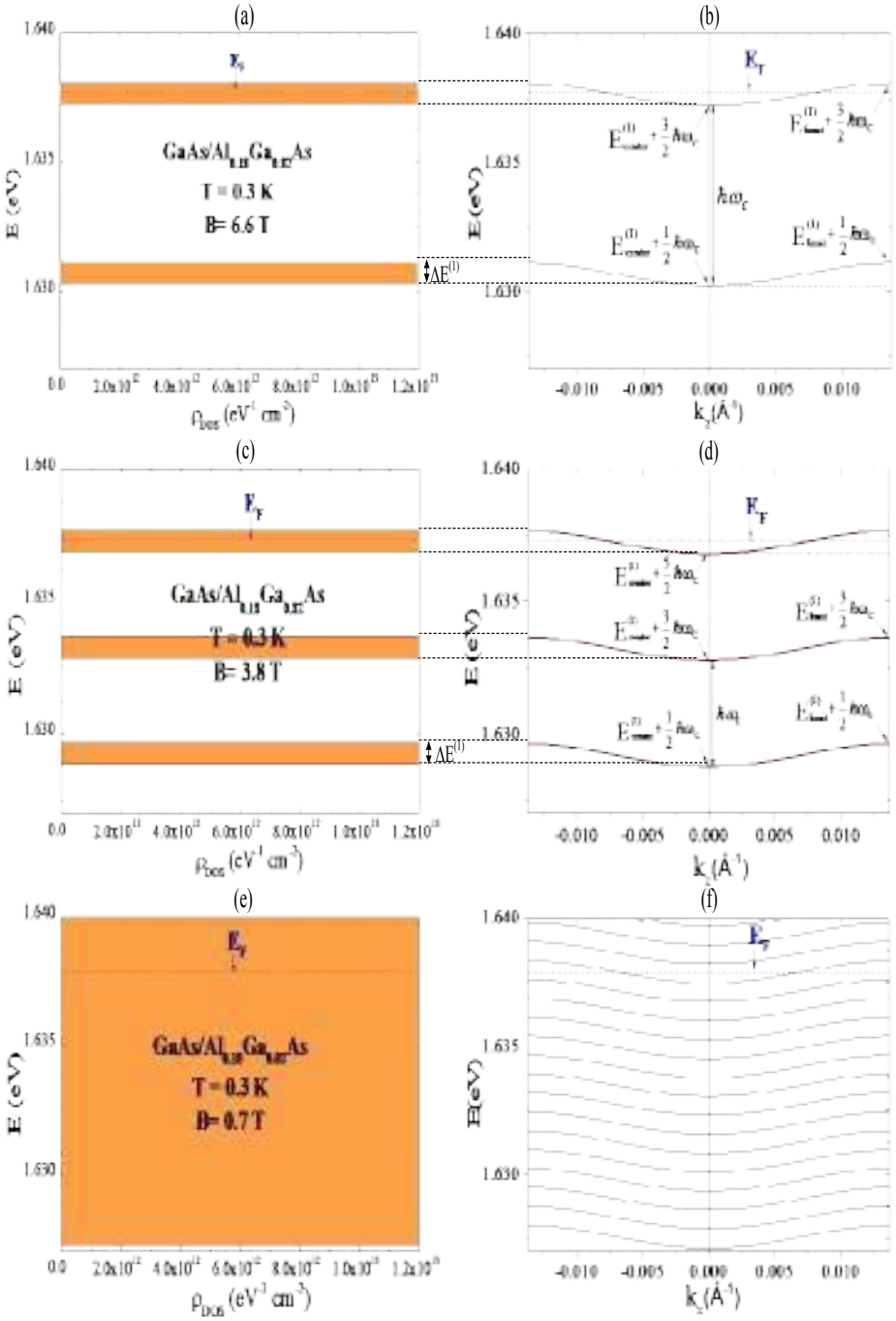


FIG. 7. (a), (c) and (e) Degeneracy lifting of the first conduction mini-band (E_1) into Landau mini-bands in the first Brillouin zone. (b), (d) and (f) total energy versus the electron density of states under different magnetic fields.

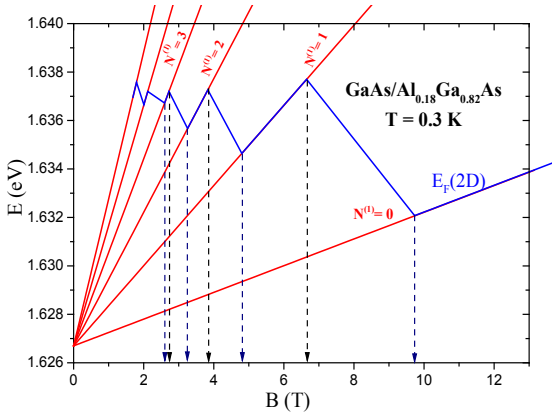


FIG. 8. Energy position of the calculated Landau levels of the first conduction E_1 sub-bands, and the Fermi level E_F, as a function of magnetic field

TABLE 1. Comparison between experimental observations (ref. 8) and the calculated magnetic field of R_{xx} minima and maxima, labeled here by B_{min} and B_{max}, respectively.

B_{min}(T)		B_{max}(T)	
Theoretical	Experimental (ref.[6])	Theoretical	Experimental (ref.[6])
2.6	2.5	2.2	2.4
3.2	3.4	2.7	2.9
4.8	5.1	3.8	4.0
9.7	10.1	6.6	6.9

On the other hand, the neighbor magnetoresistance minimus observed at the magnetic fields 9.7T, 4.8T, 3.2T and 2.5T correspond to the quantized Hall states with the filling factors $\nu = 2, 4, 6, 8$ respectively.

4. Conclusions

In this work, we have studied the GaAs/$Al_{0.18}Ga_{0.82}As$ superlattice, in the framework of the envelope function model and the effective mass approximation. The results obtained show that, when the thickness of the barriers d_2 increases, the separation of the conduction and valence bands, as well as the width of the forbidden band, decrease and tend to those of an isolated quantum wells (discrete levels). We showed the effect of VBO and the temperature on the band gap. The variation of the density of states of the system as a function of energy shows that this superlattice has an almost two-dimensional character with a small dispersion. The E(k_z, k_p) curves in the direction of growth and in the plane of the superlattice show that the first conduction and valence subbands are parabolic. The calculated Fermi level position E_F=1.637eV indicates that this sample has n-type conductivity. In the presence of an intense magnetic field, the separation of the Landau subbands increases with B, which shows the presence of Shubnikov-de Haas and quantum Hall effects. According to our calculations, these two effects can be observed only if B>0.8T for the temperature of 0.3K. We have interpreted the oscillations of longitudinal magnetism R_{xx} and transverse R_{xy} observed by Pusep et al.

References

[1] P. Martyniuk, M. Kopytko, A. Rogalski, Opto-Electronics Rev. 22, 127–146, 2014.

[2] C. Downs, TE. Vandervelde, Sensors 13, 5054–5098, 2013.

[3] E. Brundermann, H. W. Hubers, M.F. Kimmitt, Terahertz techniques 151, 51-101, 2012.

[4] L. Smrckaa, N.A. Goncharuka, P. Svobodaa, P. Vaseka, Yu. Krupkoa, W. Wegscheider, Microelectronics 39, 411–413, 2008.

[5] M. J. Manfra, Annu. Rev. Condens. Matter Phys. 5, 347, 2014.

[6] V. Umansky, M. Heiblum, Y. Levinson, J. Smet, J. Nübler, M. Dolev, J. Cryst. Growth. 311, 1658–1661, 2009.

[7] B. G. M. Tavares, M. A. Tito, Yu. A. Pusep, appl. Phys. 119, 234305, 2016.

[8] Y. A. Pusep, F.E.G. Guimaraes, H. Arakaki, C.A. de Souza, Physica E 40, 1439–1441, 2008.

[9] C. Persson, C. A. Draxl, Comp. Phys. Communications 177, 280–287, 2007.

[10] I. Vurgaftman, J.R. Meyer, L.R. Ram-Mohan, Appl. Phys. 89, 5815, 2001.

[11] G. Bastard, Phys. Rev. B 25, 7584, 1982.

[12] E.O. Kane, J. Phys. Chem. Solids 1, 249, 1957.

[13] S.Z. Karazhanov, Semiconductors 39, 161, 2005.

[14] Y. P. Varshni, Phys. Stat. sol. 19, 459, 1967.

[15] D. Barkissy, A. Nafidi, A. Boutramine, N. Benchtaber, A. Khalal, T. El Gouti, Appl. Phys. A 7, 123, 2017.

[16] K.E. Glukhov, A.I. Bercha, D.V. Korbutyak, V.G. Litovchenko, Semiconductors 38, 410, 2004.

[17] Y. Wang, F. Zahid, Y. Zhu, L. Liu, J. Wang, H. Guo, Appl. Phys. Lett. 102, 132109, 2013.

[18] O. Madelung, U. Rossler, "U. Rossler, M. Schulz, Group IV Elements, IV–IV and III–V Compounds. Part B-Electronic Transport, Optical and Other Properties", Springer Berlin 553, 1–11, 2002.

[19] T.E. Ostromek. Phys. Rev. B, 54, 14 467, 1996.

[20] P. Pfeffer, W. Zawadzki. Phys. Rev. B, 53, 12 813, 1996.

[21] H.-S. Cho, J. Vac. Sci. Technol. B Microelectron. Nanom. Struct. 6, 1363, 1989.

[22] T. Ihn, "Semiconductor Nanostructures Quantum states and electronic transport", Oxford University Press 7, 287–334, 2009.

Thermal metamaterials

Infrared metasurfaces for polarization control of thermal emission

Sergey A. Dyakov[1], Nikolay A. Gippius[1], Sergei G. Tikhodeev[2,3],

[1]Skolkovo Institute of Science and Technology, Moscow, Nobel Street 3, Moscow, Russia
[2]Faculty of Physics, Lomonosov Moscow State University, 119991 Moscow, Russia
[3]A. M. Prokhorov General Physics Institute, RAS, Vavilova 38, Moscow, Russia
*corresponding author, E-mail: s.dyakov@skoltech.ru

Abstract

Thermal radiation from bulk disorderly placed nonresonant emitters is incoherent, broadband and isotropic. However, the angular emission diagram and polarization of thermal radiation can be controlled by the emitter symmetry. In this work we study a chiral metasurface which has guided resonant modes in the middle infrared range. We demonstrate that due to the absence of a mirror symmetry of such metasurface, the thermally generated electromagnetic waves are circularly polarized with the circular polarization degree of 0.87. Using the Fourier modal method we study the structure eigenmodes and analyze the field distributions in them.

1. Introduction

In recent years, the study of thermal emission of periodic materials attracted a great deal of attention from researchers due to its high potential for important applications in near- and far-field thermal management [3, 1]. Usually, the thermal radiation from bulk emitters is incoherent, broadband and isotropic. By changing the emitter symmetry one can control the angular emission diagram and the polarization of thermal radiation. For instance, a structure which lacks a mirror symmetry emits circularly polarized thermal radiation. The mirror symmetry can be broken down by creating a structure with a chiral surface. Chiral metasurfaces can be used for obtaining circularly polarized photoluminescence of quantum dots [4]. The highest theoretically predicted circular polarization degree was as high as 99% while the corresponding experimental value was 81%. The degree of circular polarization depends on the surface geometry and can be optimized.

Here we use the concept of a chiral metasurface for generating circularly polarized thermal radiation. We demonstrate a structure with artificial rotational anisotropy which radiates the circularly polarized thermal emission and discuss this effect in detail.

2. Model structure and theory

In this paper, the thermal emitter consists of a ZnSe waveguide on KCl substrate. The waveguide has a two-dimensional array of etched rectangles (Fig. 1a). The bottom surface of rectangles is covered by 40-nm thick layer of Si_3N_4. In this work we study the guided resonance modes of this waveguide in the 7–15 μm wavelength range. ZnSe and KCl are transparent in the middle infrared range and therefore do not emit thermal emission. In contrast, Si_3N_4 has a wide absorption band and hence is the source of thermal radiation in the structure.

The emissivity spectra is calculated in accordance with the Kirhoff's law which states that the emissivity and absorptivity are equal. In turn, the absorptivity is calculated by the rigorous coupled wave analysis (RCWA) [5]. The scattering matrices were calculated using the Li's factorization rules with $13 \times 13 = 169$ spatial harmonics.

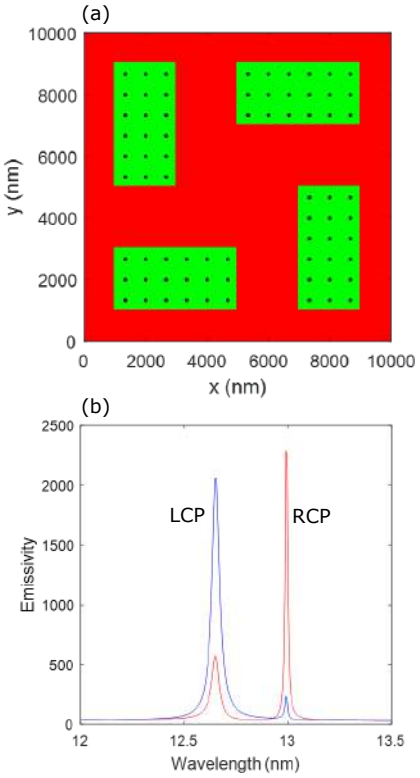


Figure 1: (a) Schematics of chiral metasurface. (b) LCP (blue) and RCP (red) emissivity spectra of the chiral metasurface.

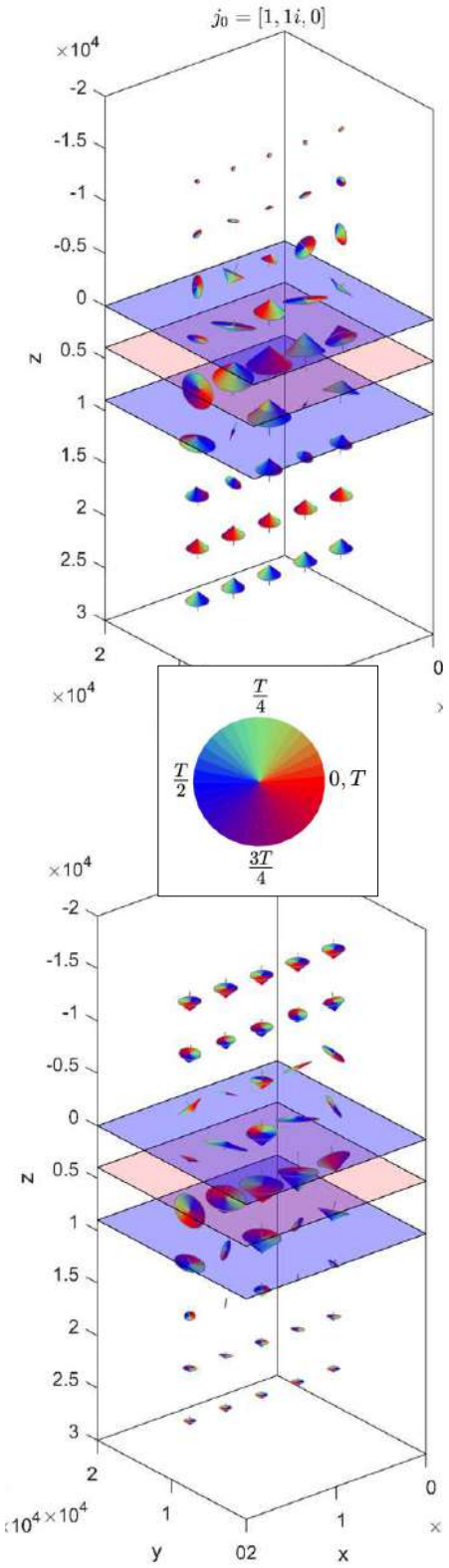


Figure 2: Cone plot representing electric field direction during the period of electromagnetic oscillations. Phase is shown by color as explained in the inset. See supplemental materials of Ref. [2] for details.

3. Results and discussions

To demonstrate the circularly polarized thermal emission, we calculate the emissivity spectra of chiral metasurface in left circular polarization (LCP) and right circular polarization (RCP) as well as the circular polarization degree (CPD). As shown in Fig. 1b, in the displayed spectral range, the emissivity spectra have two peaks at $\lambda \approx 12.7\,\mu$m and $13\,\mu$m which have different amplitudes in LCP and RCP. As a result, the degree of circular polarization is non-zero and reaches the values of 0.87. As shown in [2] for similar structure, the origin of the resonance behavior of emissivity is the guided resonance modes. Indeed, the periodic layer of ZnSe represents a waveguide since it's surrounded by the layers of smaller refractive index. Due to the metasurface periodicity, these eigenmodes are folded into the first Brillouin zone and, hence, are visible in the far field of thermal radiation.

Finally, our chiral metasurface can be considered as a beam router for clockwise and counterclockwise circularly polarized emitters (see Fig. 2).

4. Conclusion

In conclusion, we have demonstrated that the chiral metasurface can emit the circularly polarized thermal radiation with the circular polarization degree as high as 87%. We attribute this effect to the shape anisotropy of the photonic crystal part of the structure.

5. Acknowledgments

This work has been funded by Russian Science Foundation (Grant No. 16-12-10538).

References

[1] S. A. Dyakov, J. Dai, M. Yan, and M. Qiu. Near field thermal memory based on radiative phase bistability of VO_2. *Journal of Physics D: Applied Physics*, 48:305104, 2015.

[2] S. A. Dyakov, V. A. Semenenko, N. A. Gippius, and S. G. Tikhodeev. Magnetic field free circularly polarized thermal emission from a chiral metasurface. *Physical Review B*, 98(23):235416, 2018.

[3] J.-J. Greffet, Rémi Carminati, K. Joulain, J.-P. Mulet, S. Mainguy, and Y. Chen. Coherent emission of light by thermal sources. *Nature*, 416(6876):61–64, 2002.

[4] S. V. Lobanov, T. Weiss, N. A. Gippius, S. G. Tikhodeev, V. D. Kulakovskii, K. Konishi, and M. Kuwata-Gonokami. Polarization control of quantum dot emission by chiral photonic crystal slabs. *Optics letters*, 40(7):1528–1531, 2015.

[5] S. G. Tikhodeev, A. L. Yablonskii, E. A. Muljarov, N. A. Gippius, and T. Ishihara. Quasiguided modes and optical properties of photonic crystal slabs. *Phys. Rev. B*, 66:045102, 2002.

Background-independent thermal camouflage evolved from fin heat sink

Xiayao Peng, Jinlin Song, Run Hu*, and Xiaobing Luo

School of Energy and Power Engineering, Huazhong University of Science and Technology, Wuhan 430074, China
*Corresponding author, Email: hurun@hust.edu.cn

Abstract

By drawing inspiration from the fin heat sink, we propose a new kind of thermal camouflage device. The working principle lies in the high thermal conductivity of the folded fins, and the target objects will be concealed inside. The proposed device can work under dynamic background and moving anything inside will be thermal camouflaged adaptively and effectively. We also propose qualitative and quantitative index to evaluate the effect. Both steady and dynamic simulations were conducted to discuss and evaluate the thermal camouflage performance.

1. Introduction

Adaptive thermal camouflage refers to the function to conceal targets dynamically with adaption to the change of background temperature, which is more promising and powerful, compared with the conventional static camouflage, especially for movable targets like humans and animals. The current thermal camouflage reports mainly focus on the static one. Some work claims to move targets for thermal camouflage, but they just move the camouflage signature from one place to another while the real targets are still fixed and background temperature should be provided in advance. On the other hand, most the existing thermal camouflage devices are designed based on the theory of transformation thermotics or scattering cancellation, resulting in the critical requirement of anisotropic and inhomogeneous metamaterials. In this paper, we proposed background–independent adaptive thermal camouflage devices, which can realize good thermal camouflage performance and apply for the targets during the moving process. Both steady and dynamic simulation is conducted to verify the performance, with qualitative and quantitative analysis to evaluate the effect of thermal camouflage.

2. Background-independent

We the design the device as illustrated in Fig. 1. Comparing the temperature fields in Figs. 1(a) and 1(b), it is seen that when adding some fins, the temperature equivalence of T_1 (fin tip) and T_2 (fin root) could still be valid if the thermal conductivity of the fins is large and the fin height is small enough. It is perceived that the temperature in Fig. 1(b) will be the same as that in Fig. 1(a) in the IR camera projected downwardly. Keeping in mind with the goal of maintaining of T_d=T_b from point to point, we bend the fins towards to the center in both sides without moving the endpoints, resulting in an adjustable space in the center, as shown in Figs. 1(c) and 1(d). The actual structure is shown in Figs. 1(e). When some target object sit inside the adjustable space of folded fins, it will be concealed from the top IR camera, thus the thermal camouflage effect is achieved. It is seen that the thermal camouflage performance relies on the folded fins with high thermal conductivity, which is independent on the background plane no matter how the background temperature changes.

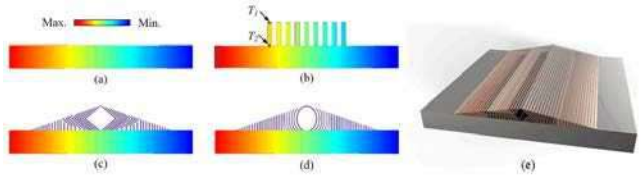


Figure. 1 Background-independent designs.

3. Simulation and Discussion

In the simulation, the plate with a length of 1000 mm, a width of 500 mm and a height of 50 mm is used as a background plate, and the material of the base plate is cast iron, κ_2=50 W/(m-K). The length of the base plate is lengthened to simulate the characteristics of the device moving on the base plate. Fifty copper fins of different lengths (κ_1=400 W/(m*K)) were mounted on the base plate to form an angular structure with a total length of 300 mm, and the maximum height of the fins is 32 mm. The angle between the angular structure and the horizontal plane is θ=12°. Part of the fins are bent at 90 degrees so that a square cavity is left in the middle. In order to ensure that the angular structure appears smooth and continuous from the side, the upper surface of the fin is machined to be inclined by 12° with respect to the horizontal plane. High temperature is set on the left side of the base plate and low temperature is on the right. The angular structure is moved from left to right on the plate. The steady-state temperature distribution map of the top view and the main view at different positions are shown in Fig. 2.

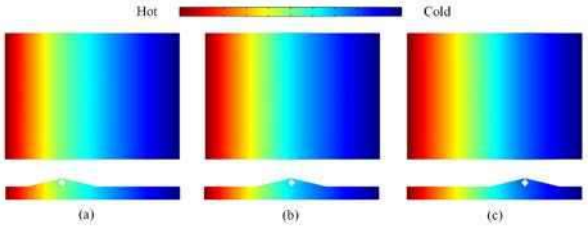


Figure. 2 Steady temperature field distribution with the camouflage device at three different locations: (a) left, (b) middle, and (c) right.

We define a parameter σ to denote the temperature variance between the top temperature from the device and the reference plate, as

$$\Delta T^2 = \frac{\sum_{i=1}^{k}(T_{id} - T_{ib})^2}{k} \quad (1)$$

where T_{id} is the temperature of point i on the device and T_{ib} is the temperature of point i from the corresponding positions on the background, k is the number of point taken. The larger the σ is, the larger the difference in temperature between device and background is, which means the effect of camouflage is worse.

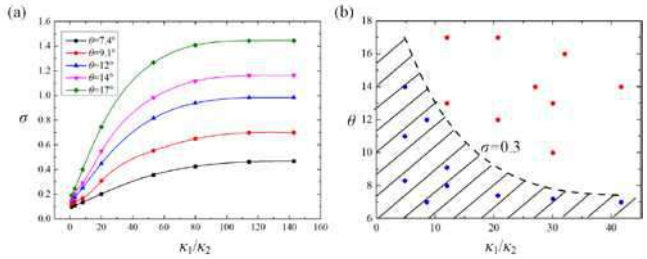


Figure. 3 (a) Dependence of temperature variance σ on thermal conductivity ratio κ_1/κ_2 and apparent inclination angle θ. (b) Dashed range of (κ_1/κ_2, θ) pair when the temperature variance σ is below 0.3.

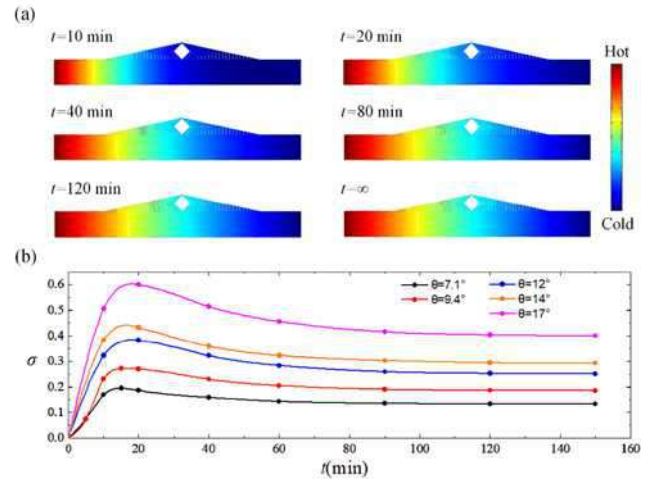


Figure. 4(a) Snapshots of the transient temperature field with time elapses until achieving steady state. (b) Corresponding temperature variance dependence on time at different θ.

Taking θ=12° and $\kappa 1/\kappa 2$ =8:1, we plot the temperature distribution of the front view and the top view at 10 min, 20 min, 40 min, 80 min, 120 min and steady state as Fig .5(a). It is found that the deviation coefficient σ first rises and then falls. The device undergoes an overshooting process, then it finally approaches the steady state. When $\kappa 1/\kappa 2$ is large which means the thermal conductivity of the fin is significantly higher than that of the base plate, the heat flow conducts further faster in the fin than the base plate, so that the temperature of the top of the blazing plate can be quickly adjusted to the base plate. The same, so that when the target and the device move, still achieve a good transient effect. In this way, the temperature at the top of the fin can be quickly adjusted to be the same as the base plate, so th at the target and the device can still achieve a good transient effect when moving.

4. Conclusions

To sum up, we design a thermal camouflage structure by drawing inspiration from the fin heat sink. Relying on the high thermal conductivity of the folded fins, the proposed thermal camouflage device can work well without knowing the background temperature in advanced. Both steady and dynamic simulations were conducted to discuss the thermal camouflage performance. We also propose a qualitative and quantitative index which is temperature variance to evaluate the camouflage effect. In this way we can analyze and compare camouflage levels visually. The temperature variance increases as the angle θ increases. This can also be used as a basis for structural design and material selection.

References

[1] T Han, X Bai, D Gao, J T L Thong, B W Li and C W Qiu, Experimental demonstration of a bilayer thermal cloak, *Phys. Rev. Lett.* 112 054302 2014

[2] R Hu, S L Zhou, X J Yu and X B Luo, Exploring the proper experimental conditions in 2D thermal cloaking demonstration, *J. Phys. D: Appl. Phys.* 49 415302 2016

[3] R Hu, X Wei, J Y Hu and X B Luo, Local heating realization by reverse thermal cloak, *Sci. Rep*. 4 3600 2014

[4] F Chen and D Y Lei, Experimental Realization of Extreme Heat Flux Concentration with Easy-to-Make Thermal Metamaterials, *Sci. Rep.* 5 11552 2015

[5] T C Han, X Bai, J T L Thong, B W Li and C W Qiu, Full Control and Manipulation of Heat Signatures: Cloaking, Camouflage and Thermal Metamaterials, *Adv. Mater.* 26 1731 2014

[6] X He and L Wu, Illusion thermodynamics: A camouflage technique changing an object into another one with arbitrary cross section, *Phys. Lett.* 105 221904 2014

[7] L J Xu, C R Jiang, J Shang, R Z Wang and J P Huang, Periodic composites: quasi-uniform heat conduction, Janus thermal illusion, and illusion thermal diodes, *Eur. Phys. J. B.* 90 221 2017

[8] R Hu, S L Zhou, W C Shu, B Xie, Y P Ma and X B Luo, Directional heat transport through thermal reflection meta-device, *AIP Adv.* 6 125111 2016

[9] R Hu, B Xie, J Y Hu, Q Chen and X B Luo, Carpet thermal cloak realization based on the refraction law of heat flux, *EPL* 111 54003 2015

[10] R Hu, S L Zhou, Y Li, D Y Lei, X B Luo and C W Qiu, Illusion Thermotics, *Adv. Mater.* 30 1707237 2018

[11] S L Zhou, R Hu and X B Luo, Thermal illusion with twinborn-like heat signatures, *International Journal of Heat and Mass Transfer* 127 607613 2017

Generalized Two-Temperature Fitting Algorithm for Ultrashort Laser Heating of Metal Films.

P. BRESSON[1,2] J-F. BRYCHE[2], J. MOREAU[1*], M. BESBES[1], P-L KARSENTI[2], D. MORRIS[2] P.G. CHARETTE[2] AND M. CANVA[2]

[1]Laboratoire Charles Fabry, Institut d'Optique Graduate School, Université Paris-Saclay, CNRS, Palaiseau 91127, France
[2]Laboratoire Nanotechnologies Nanosystèmes, CNRS UMI-3463, Université de Sherbrooke, Sherbrooke J1K 0A5, Canada
*corresponding author, E-mail: Julien.moreau@institutoptique.fr

Abstract

We have developed a numerical model and fitting algorithm which combined the classical two-temperature model, the thermal conduction phenomena and a 3D Finite-Element-Method to link the spatial and temporal distribution of temperature to the transient optical response of a metallic sample heated by ultrashort laser pulse. Using a pump-probe setup, the spectro-temporal optical response of different thin gold films were quantitatively compared to our model. Study of the dependency and importance of the different model's parameters was also realized.

1. Introduction

The ability to control electromagnetic energy in subwavelength volumes with surface plasmon polaritons has attracted much attention during the past decade in the field of nanosciences. To date, most of the work in plasmonics has been devoted to minimizing the heat dissipation process related to the oscillation of charges in nanostructures. Recently, work has focused on turning this problem into an opportunity: this emerging branch of plasmonics is called thermoplasmonics [1–3] and has potential for numerous applications in medicine, thermotronics, and energy conversion. To study quantitatively these photothermal phenomena in thin metallic films and nanoparticles, we have developed an ultra-fast pump-probe setup and a numerical model to retrieve the spatial and temporal distribution of electronic and lattice temperatures from the optical response of these samples heated by an ultrashort laser pulse.

2. Experimental Setup

A pump-probe based setup was built to acquire the spectro-temporal optical response of a sample with high temporal resolution. The laser source is a Ti:saphire oscillator coupled to an optical parametric amplifier. The sample is heated with short laser pump pulses (~70 fs) and small changes in the sample's reflectivity (or transmission) is observed with the time-delayed white probe pulses using lock-in detection. The pump and probe wavelengths can be adjusted in the range of 400 nm to 2000 nm. The ability to generate white pulses enables a full spectral characterization in the range of visible and near-infrared as depicted on Figure 1(left).

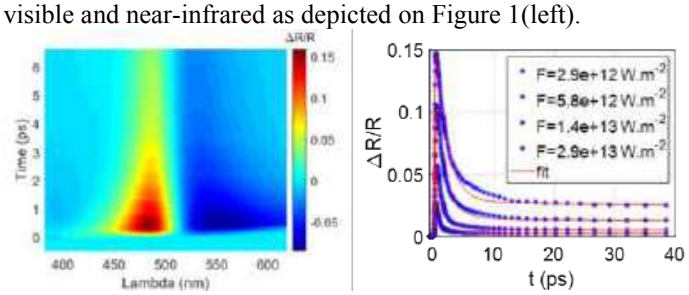


Figure 1.(left) Example of a transient transmittance map measured on a 50 nm gold film.(right) Temporal evolution extracted from the spectro-temporal maps, acquired at different pump powers, and fitting result.

3. Numerical modeling and results

The dynamic of photothermal phenomena is governed by a three-step mechanism involving electronic heating through photon absorption (~100 fs), thermalization via electron-phonon interaction (~ ps), and thermal diffusion outside the pump focal point (~ ns)). To model these processes a numerical model [4] was developed which is based on the two temperatures model, well-known in the field of ultrafast heating process, with a full 3D Finite Element Method electromagnetic (FEM EM) code considering the geometry of the sample. Electronic and lattice thermal conduction through the metal and substrate are also included in this model (Figure 2).

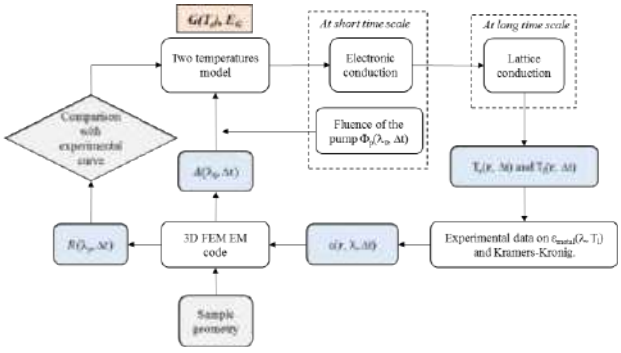


Figure 2. Schematic of the numerical model and fitting algorithm. The sample is described by FEM. The algorithm uses a two temperatures model combined with electronic (at short time scale) and lattice conduction (at long time scale) to estimate the electronic and lattice temperature spatial distribution.

Experimental transient optical responses can then be fitted with this model to retrieve the electronic and lattice temperatures spatial distribution and the different parameters involved in the photothermal phenomena. Figure 1 (right) shows an example of the fitting result on a 50 nm gold film for different pump fluences. An excellent agreement is obtained.

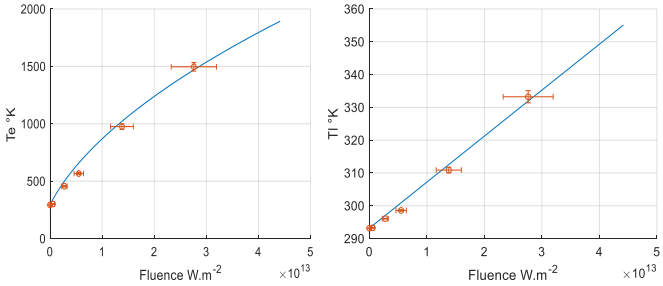


Figure 3. Maximum electronic (left) and lattice (right) temperature reach in a 50 nm gold film for different pump fluence.

Electronic and lattice temperature can then be extracted from the experimental data as can be seen in Figure 3 which shows the evolution of the maximum reach by these two temperatures after pump heating, as a function of pump fluence. A similar study was done for different film thickness. Preliminary results were also obtained on nanoparticles arrays.

References

[1] A. O. Govorov and H. H. Richardson, *Nano Today*, **2**, nº 1, p. 30 38 (2007).

[2] G. Baffou, R. Quidant, and C. Girard, *Applied Physics Letters*, **94**, nº 15, p. 153109, (2009).W.M. Kays, M.E. Crawford, *Heat transfer*, Wiley, New York, pp.256-258, 1990.

[3] P. Ben-Abdallah, S.-A. Biehs, and K. Joulain, *Physical Review Letters*, **107**, nº 11, (2011).

[4] P. Bresson, JF. Bryche, J. Moreau, P-L. Karsenti, D. Morris, P.G. Charette, M. Canva, to be submitted.

Laser and cavities

Monolithic Graphene single-mode Vertical-cavity Surface-emitting Lasers

Baolu Guan[1]*, Weiling Guo[1], Yiyang Xie[1], Chen Xu[1]

[1]Key Laboratory of Opto-electronics Technology, Ministry of Education,
Beijing University of Technology, Beijing, China
*corresponding author, E-mail: gbl@bjut.edu.cn

Abstract

An inter-cavity contact single mode 850 nm VCSEL was fabricated with a graphene assisted self-assembly curved dielectric bubble Bragg mirror for the first time. Taking the advantage of graphene's uniform low surface energy, the low cost dielectric bubble DBR (Si_3N_4/SiO_2) was deposited on top of the graphene/half-VCSEL structure via van der Waals Force (vdWF) without using any additional spacing elements and sacrificial layer release-etch process.

1. Introduction

Recent years have seen a burst of activity in VCSEL chips directed towards the development of functional integrated optical, which are based on single-mode optical fiber and high-speed VCSELs are developed. Such VCSELs have to be single transverse mode to enable efficient laser fiber coupling and to prevent excessive pulse broadening over longer transmission distances caused by chromatic dispersion in the fiber. Although VCSEL possess advantageous properties, however, VCSELs typically lase in multiple transverse modes as a result of strong index confinement from the oxide layers. High-power single mode operation is desired for a number of applications, including optical imaging and scanning, as well as data communication over single mode fiber. A fundamental issue to obtain a single mode VCSEL is that this usually requires reduction of the cavity cross section area to decrease the number of transverse modes that are supported. However, this produces reduced active volume, which can substantially limit the output power of the fundamental mode. Moreover, VCSEL structures, which increase the loss of higher order modes often also increase the loss of the fundamental mode, albeit to a lesser extent. Therefore, demonstrating high power fundamental mode emission from a VCSEL has to date been a challenge. We investigated graphene, a monolayer of carbon atoms with a regular sp^2-bonded atomic-scale hexagonal pattern. Its intriguing properties, like high carrier mobility, massless Dirac fermions, mechanical strength, thermal conductivity and stable chemical characteristics. Successful growth of high quality graphene has facilitated efforts to use it as a transparent electrode material in photodetector, nanolaserr, and solar cells. Mechanical characteristics and flexibility of graphene have been extensively investigated for numerous applications including flexible batteries, super capacitors, sensors, displays and flexible electronics. Particularly, graphene, as 2D materials buffered layer, can allow crystalline growth via van der Waals epitaxy, reducing defect density. These applications realize multi-use of graphene as transparent conducting electrodes in flexible optoelectronic devices and also for the growth of vertical high-performance optics composites that require formation of initial films with high optical function.

2. Fabrication and Design

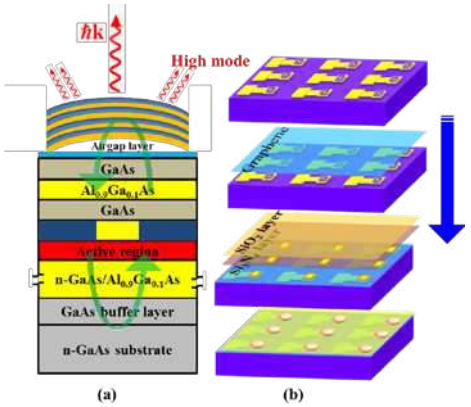


FIG. 1. (a) Schematic structure, (b) Schematic diagram of the transferring and device fabrication process. The Graphene films are synthesized by the CVD method on a copper foil with polishing in advance. The PMMA/CVD-G film was finally transferred to a Half-VCSEL substrate for device fabrication. And the dielectric Si_3N_4/SiO_2 layers were deposited at last.

The scheme of the graphene modulator-integrated VCSEL is shown in Fig. 1(a). The Half-VCSEL vertical structure is the same as that of conventional 850nm VCSELs. The bottom mirror consists of a 30-period Si-doped $Al_{0.9}Ga_{0.1}As/Al_{0.12}Ga_{0.88}As$ distributed Bragg-reflector (DBR). The active region has three $Al_{0.3}Ga_{0.7}As/\ Al_{0.12}In_{0.18}Ga_{0.7}As$ quantum wells sandwiched in one-λ cavity. The top mirror consists of a 2-period carbon-doped $Al_{0.9}Ga_{0.1}As/Al_{0.12}Ga_{0.88}As$ DBR. The second chip is 7-period dielectric Si_3N_4/SiO_2 bubbled DBR on the graphene via van der Waals regrow as a perfect mirror. A build-in strain gradient results in a concave curvature of this top DBR and allows an easy and tilt insensitive alignment of the two parts without any additional spacing elements, while regulating the waveguide routes with a curved shape guides a strong leaky travelling wave in the lateral direction from the VCSEL into an loss mode, which forms the single transverse mode in the VCSEL with larger oxide aperture. The device fabrication procedure is schematically shown in Figure 1(b).

The light absorption is directly associated with the graphene. This can be easily understood that the monolayer graphene absorbs about 2.3% of the impinging light in both

visible and near-infrared regions. However, on the graphene anchored surface the light gets transparent because of multiple internal reflections in the gaps of bubble DBR. Also, the graphene layer dimensions are very smaller than the wavelength. When the distances between the graphene and airgap interface are appropriate, light would interact differently on the graphene structures due to the equivalent gradient refractive index[1]. Electromagnetic simulations using FDTD (finite difference time domain) were carried out to simulate the light absorption in a cell section extracted from bubble DBR with graphene structure. The simulated absorption curves of DBR with graphene and without graphene reveal that the graphene have limited effect on the absorption which is less than 3%. Reflectance and transmittance of bubble DBR with graphene demonstrated a small reduce compared to without graphene film (Fig. 2b), the differential reflectivity is less than 2%.

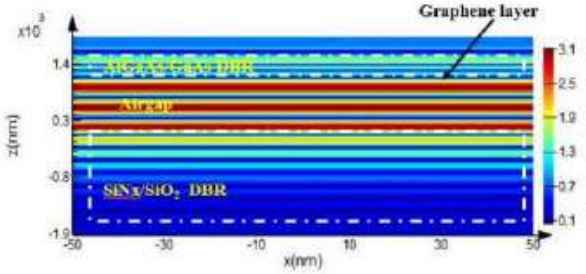


Fig 2a. Calculated cross-sectional electric field distributions of partial of bubble DBR with graphene at 850 nm.

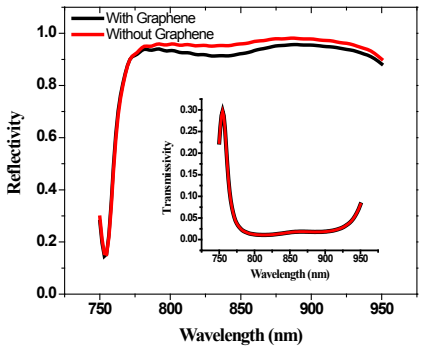


Fig 2b. Calculated reflectivity spectra of the bubble DBR with graphene layer (black) and without (red)

3. Discussion

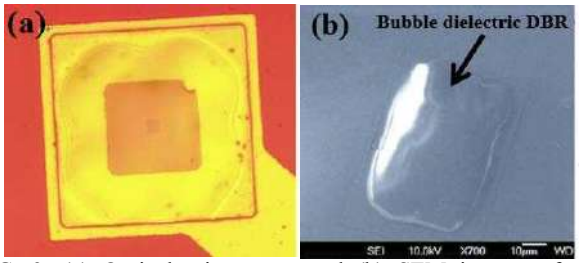


FIG. 3. (a) Optical microscope and (b) SEM images of the graphene transferred VCSEL with bubble dielectric DBR.

The concave-curve interference rings in Fig. 3 (a) are obvious and the reflectivity spectra are significantly broader. Larger fabrication tolerance in high contrast dielectric bubbled DBR was firstly experimentally demonstrated by our group in the context of VCSELs. In our method, the regrow of the dielectric Si_3N_4/SiO_2 layers on the graphene surface was induced by the accumulated internal strain of the build-in strained layer weak adhesion to graphene, as shown in Figure 3 (b). It was critical to select a proper strained material that satisfied the following conditions for uniform with a high yield: first, there is no chemical reaction to maintain the purity of the graphene; second, the adhesion energy to the graphene is weaker than between graphene and p-GaAs; and there is enough high build-in strain energy to separate from the graphene/GaAs interface. The adhesion energies between graphene and these substrate materials can be expected as $\Gamma=2(\gamma_{Gr}\times\gamma_{surface})^{1/2}$, where γ_{Gr} is the surface energy of graphene and $\gamma_{surface}$ is the surface energy of substrate material, respectively.[2] As reported, the values of adhesion energy derived from the measured monolayer grpahene/SiO_2 is 0.45 ± J m^{-2}, however to the GaAs (110) surface, the energy is about 0.86 J m^{-2}, so the values of adhesion energy of monolayer graphene/GaAs is $\Gamma=2(\gamma_{Gr}\times\gamma_{GaAs})^{1/2}$=0.829 J m^{-2}, which near more than two times of graphene/SiO_2 adhesion energy. In addition, the surface roughness also affects the adhesion between graphene and their substrates, making the adhesion energy of (0.275-0.4) J m^{-2}. The optical microscope images in Fig. 3 show that the transfer process of epitaxial graphene layer have been completely finished, including rectangular p-GaAs contact from the Half-VCSEL surface, and the Raman spectrum indicates that the quality of the graphene is maintained during the transfer (no D peak in the spectra). However, for obtaining perfect monolayer graphene and bubbled DBR in laser device, it is essential to selectively deposition by PECVD.

4. Conclusions

In summary, we have demonstrated fully functional Gr-VCSEL directed vdW grow of high-quality dielectric bubbled DBR structure on epitaxial graphene/Half-VCSEL substrates. An average single mode output power graphene-VCSELs were achieved, which are within the range to those of regular structure grown on the GaAs substrates by using MOCVD. In addition, the flexible, transparent, low resistance and resilient coating characteristics of the electrode technology also could be a powerful tool in improving high-frequency and polarization modulation of VCSEL.

References

[1] Raut HK, Ganesh VA, Nair AS, Ramakrishna S. Anti-reflective coatings: A critical, in-depth review. *Energy & Environmental Science* **4**, 3779-3804, 2011.

[2] Jonathan Proesel, Benjamin G. Lee, Christian W. Baks, and Clint Schow, Optical Fiber Communication Conference, OM2H.2, 2013.

Metasurface lasers based on resonant dark states

Sotiris Droulias[1*], Thomas Koschny[2], and Costas M. Soukoulis[1,2]

[1]Institute of Electronic Structure and Laser, FORTH, 71110 Heraklion, Crete, Greece
[2]Ames Laboratory and Department of Physics and Astronomy, Iowa State University, Ames, Iowa 50011, USA
*corresponding author, E-mail: sdroulias@iesl.forth.gr

Abstract

Recently our group proposed a metamaterial laser design, which enables the independent control of the stored energy and its outcoupling to radiation. The principle of operation is based on the excitation of a dark mode, i.e. a mode of zero net electric/magnetic moment that does not consequently radiate. With the aid of a small non-resonant scatterer, the dark mode is then coupled to radiation modes. Here we examine the proposed scheme in implementations that represent realistic experiments.

1. Introduction

In search of coherent light sources that can be integrated in small-scaled photonic systems, nanolasers have been the object of sustained research in latest years [1-3]. In order to scale the laser dimensions down, many diverse materials and techniques have been utilized so far. For example, all-dielectric systems have proven to offer high Q factors, but their size is limited to the order of magnitude of the operating wavelength [1]. With plasmon-based systems, on the other hand, the laser dimensions can become subwavelength but at the expense of very low Q factors, due to very high dissipative loss in the metal inclusions [2,3]. Our proposed laser system [4-6] overcomes this trade-off and offers radiation damping tunability, along with many other features, such as directionality, subwavelength integration and simple layer-by-layer fabrication.

2. Principle of operation

Our proposed laser consists of a very thin dielectric slab, in which silver of the same thickness is periodically inserted, as illustrated in Fig. 1(c) (a single unit cell is shown). This way, the continuous dark bound state of the dielectric slab (red line in Fig. 1(a)) is quantized and hence a discrete set of resonant dark states is achieved with wavevector at multiples of π/a. In fact, a band structure emerges, splitting the states into high Q (bottom of gap) and low Q modes (top of gap), as illustrated in Fig. 1(a) with the filled and open blue dots. Depending on the branch of the dispersion, an isolated mode with the desired operation frequency and spatial distribution can be then chosen for operation. Here we choose to work with the dark mode which is highlighted

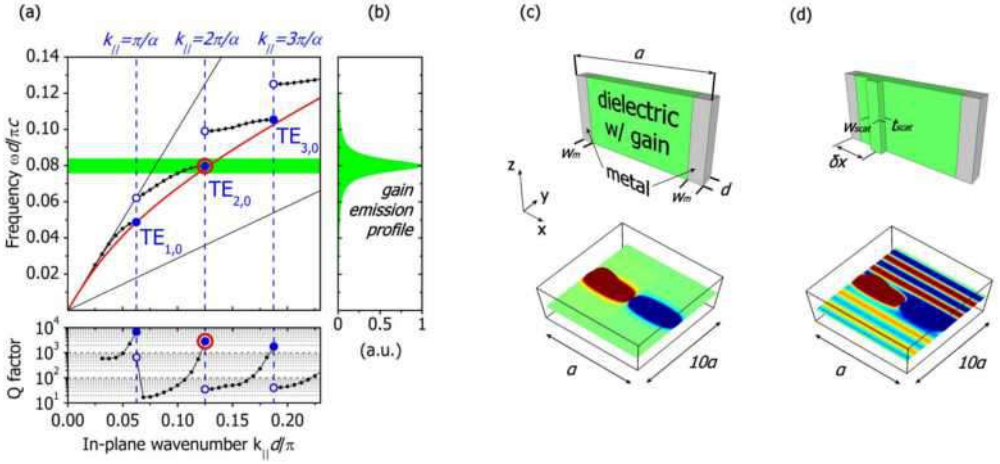


Figure 1: The dark-mode laser principle of operation. (a) Dispersion relation of the unpumped uniform dielectric slab of thickness d (red line) and band structure of the composite dielectric-metal system (connected dots). The shaded area depicts the linewidth of the gain material and the red circle marks the operation point. The Q factor of each mode is also shown below. (b) Spectral emission profile of gain material. (c) Perspective view of a single unit cell without the scatterer (top) and lasing snapshot (bottom). (d) Perspective view of the same unit cell with the scatterer incorporated (top) and lasing snapshot (bottom). The unit cell is periodically repeated along the x, z directions, forming an infinite radiating meta-surface.

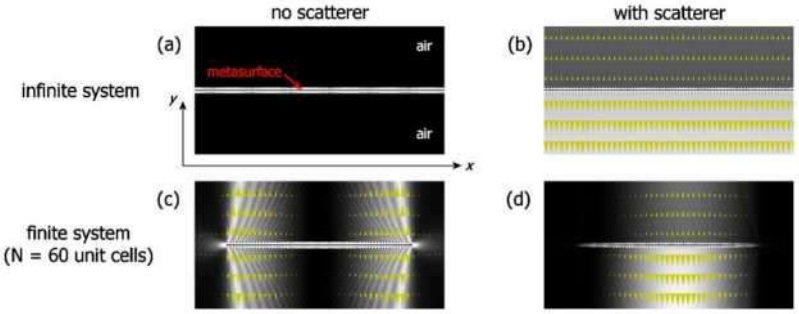


Figure 2: Intensity $|E_z|^2$ (grayscale density plot) and power flow (yellow arrows) for (a), (b) infinite system and (c), (d) a finite system of $N = 60$ unit cells. In (a), (c) no scatterer is present. In (b), (d) a scatterer with dimensions $w_{scat} = 60$ nm, $t_{scat} = 30$ nm has been placed at $\delta x/a \sim 0.31$ [see Fig. 1(d)]. The black line in the middle of each panel denotes the metasurface. Each double bright peak at the metasurface level corresponds to one unit cell, as it contains one sine-like dark mode [see Fig. 1(c), (d)].

in Fig. 1(a) with the red circle, and that has the simplest nonradiating distribution (see Fig. 1(c)). For operation at 1.5 μm with a slab of permittivity $\varepsilon_r = 12.1$, we use $d = 60$ nm (sub-wavelength thickness) and $a = 960$ nm. The silver width is $2w_m = 100$ nm, the gain material is embedded in the dielectric and the whole system is examined via self-consistent finite-difference time-domain (FDTD) calculations. When the gain material is pumped above the lasing threshold, the dark mode is excited as shown in Fig. 1(c), but the electromagnetic power remains stored in the mode and is not emitted. Then, a small scatterer of the same permittivity is placed on the surface [Fig. 1(d)] and the stored power can be outcoupled as E_z-polarized waves [4]. The stronger the scatterer, the more the outcoupling and the lower the Q factor due to radiation damping. For $\delta x/a = 0$, 0.5 or 1 emission can be completely suppressed, as the mirror symmetry (and hence the nonradiative character) of the dark mode is preserved.

3. Realistic systems of finite-size

The system of Fig.1 is an ideally infinite radiating metasurface. For realistic, finite-size implementations of N unit cells [total length $L = N \times a$], this picture is accurate, as long as N is sufficiently large. However, as the size of the system becomes smaller, leakage from the edges comes into play, qualitatively altering the physical behavior of the system. Leakage competes against two other loss channels to dissipate the modal energy, namely (undesired) dissipation due to material absorption and (intended) outcoupling due to the scatterers.

Our study reveals that the theoretical design rules that we established for infinitely large systems [1,2] are to be applied to realistic, finite-size experimental configurations in a nontrivial way; the overall performance now depends on the balanced competition between all existing loss channels. As it turns out, the size of the metasurface plays a crucial role, as it can qualitatively alter the physical behavior of the system, leading to distinct regimes of operation, which in some cases are counter-intuitive.

4. Conclusions

In this work we examine a new laser system that utilizes the concept of lasing into a dark mode. For sufficiently large systems the lasing power is not coupled to radiation unless some scatterer is incorporated and coupling can be therefore tuned independently of the energy storage mechanism. For smaller systems, leakage from the edge may alter the picture. We show how to obtain control on leakage and intended outcoupling for the realization of subwavelength coherent light sources in realistic finite-aperture designs.

Acknowledgements

This work was supported by the European Research Council under ERC Advanced Grant No. 320081 (PHOTOMETA). Work at Ames Laboratory was supported by the U.S. Department of Energy (Basic Energy Sciences, Division of Materials Sciences and Engineering) under Contract No. DE-AC02-07CH11358.

References

[1] O. Painter, R. K. Lee, A. Scherer, A. Yariv, J. D. O'Brien, P. D. Dapkus and I. Kim, Two-dimensional photonic band-gap defect mode laser, *Science* 284:1819, 1999.

[2] D. J. Bergman and M.I. Stockman, Surface Plasmon Amplification by Stimulated Emission of Radiation: Quantum Generation of Coherent Surface Plasmons in Nanosystems, *Phys. Rev. Lett.* 90:027402, 2003.

[3] N. I. Zheludev, S.L.Prosvirnin, N. Papasimakis and V. A.Fedotov, Lasing spaser, *Nature Photon.* 2:351, 2008.

[4] S. Droulias, A. Jain, T. Koschny and C. M. Soukoulis, Novel lasers based on resonant dark states, *Phys. Rev. Lett.* 118:073901, 2017.

[5] S. Droulias, A. Jain, T. Koschny and C. M. Soukoulis, Fundamentals of metasurface lasers based on resonant dark states, *Phys. Rev. B* 96:155143, 2017.

[6] S. Droulias, T. Koschny and C. M. Soukoulis, Finite-size effects in metasurface lasers based on resonant dark states, *ACS Photonics*, 5(9):3788, 2018.

Rabi splitting of broadband emission of strongly coupled organic dye excitons in tunable optical microcavity

Dmitriy Dovzhenko[1*], Konstantin Mochalov[2], Ivan Vaskan[1,2,3], Irina Kryukova[1], Yury Rakovich[1,4,5,6], and Igor Nabiev[1,7]

[1]National Research Nuclear University MEPhI (Moscow Engineering Physics Institute), Moscow, Russian Federation
[2]Shemyakin–Ovchinnikov Institute of Bioorganic Chemistry, Russian Academy of Sciences, Moscow, Russian Federation
[3]Moscow Institute of Physics and Technology, Moscow, Russian Federation
[4]Donostia International Physics Center, Donostia-San Sebastián, Spain
[5]Centro de Física de Materiales (MPC, CSIC-UPV/EHU) and Donostia International Physics Center, Donostia - San Sebastián, Spain
[6]IKERBASQUE, Basque Foundation for Science, Bilbao, Spain
[7]Laboratoire de Recherche en Nanosciences, LRN-EA4682, Université de Reims Champagne-Ardenne, Reims, France
*corresponding author, E-mail: dovzhenkods@gmail.com

Abstract

Resonance interaction between molecular excited states and localized electromagnetic field allows to control fundamental properties of a matter. In this study we have measured the emission spectra of Rhodamine 6G organic dye being placed in a precisely tunable Fabry-Perot microcavity. We have demonstrated emission from both upper and lower polaritonic states of strongly coupled organic dye excitons with relatively low and unoriented dipole moments. Rabi splitting estimated from emission spectra was as large as 225 meV.

1. Introduction

Light-matter interaction of dipole transition in ensembles of molecules is of special interest nowadays [1]. Hybridization of energy states of molecular excitons and electromagnetic modes in cavities or plasmonic nanostructures leads to the formation of new polaritonic states, which properties are significantly different from the properties of the original uncoupled states. Strong dependence of polaritonic state properties on electromagnetic mode characteristics leads to the ability to control them [2] using tunable microcavity modes. In previous studies [3] we have developed tunable microcavity cell (TMC) based on unstable Fabry-Perot resonator. Developed TMC provides an ability to precisely control cavity length at nanometer scale and hence mode volume, quality factor and spectral position of the mode. These properties of TMC provide an ability to directly measure the dispersion of polaritons in transmission as well as in emission of the light. In most studies, authors use ensembles of molecules with large dipole moments or highly oriented aggregates in order to increase the light-matter coupling strength [1]. It allows one to achieve strong coupling even with the use of optical microcavities with relatively large mode volumes. However, many organic dye molecules, which are widely used as the fluorophores due to the high quantum yields and large absorption cross-sections, have relatively low values of dipole moment and do not form oriented aggregates. Thereby, strong coupling regime has been previously reached mostly with the use of extremely localized plasmonic modes [4,5], which significantly limits the potential of practical applications for such coupled systems.

In reporting study, we have encapsulated the Rhodamine 6G (R6G) molecules in a polymer matrix, placed them in the developed TMC and investigated their emission and its dependence on the properties of microcavity modes [6]. Such an approach can be used to create novel tunable sources of coherent spontaneous emission.

2. Materials and methods

The design of developed TMC has been described in detail elsewhere [3]. Briefly, TMC consists of an unstable Fabry-Perot microcavity with flat bottom and top convex mirrors. Distance between mirrors could be finely tuned at few nanometer scale with Z-piezopositioner in range of up to 10 μm. Sample was deposited directly on the flat mirror surface. Such configuration leads to automatic fulfilment of plane-parallelism in one point of convex mirror, which is the nearest to the flat surface. On the other hand, curve surface leads to efficient mode selection and significantly lowers the mode volume [3,7]. A 488-nm line of Ar^+ laser was used in emission measurements. Transmission spectra were obtained with the use of white LED emission. R6G molecules were encapsulated in poly(methyl methacrylate) (PMMA) matrix and deposited on flat mirror surface using spin-coating [6]. The thickness of the R6G-PMMA film was measured using atomic force microscopy and estimated to be around 105 nm.

3. Results and discussion

In the previous study we have shown that the use of one convex mirror in developed TMC leads to significant

decrease of mode volumes down to few $(\lambda/n)^3$ what could help to achieve an order of magnitude higher coupling strength [7]. Although such values of the mode volumes are still few orders of magnitude larger than those of plasmonic modes, the optical TMC have much higher quality factors and could be precisely tuned thus allowing investigation of a wide range of materials with excitons transition in strong and weak coupling regimes.

In this study, we R6G-PMMA films with relatively low concentrations of dye molecules have been investigated. At the same time, weak transmission of microcavity and low signal-to-noise ratios leaded to the conditions in which number of exciting photons greatly overcomes the number of excited states in molecular ensemble thus avoiding the observation of coupling in transmission spectra (Figure 1). The results of emission measurements from R6G-PMMA film placed inside and outside of microcavity with presented transmission spectra are shown in Figure 1

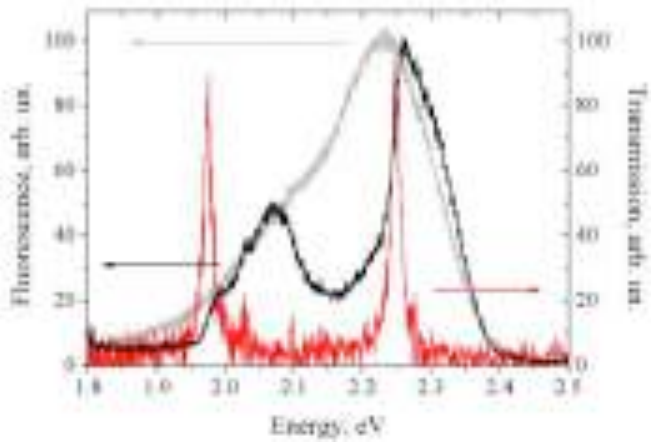


Figure 1: Normalized fluorescence spectrum of R6G-PMMA film in a tunable microcavity (black curve) in comparison with the normalized fluorescence spectrum of the same film on the substrate outside the microcavity (grey curve) and corresponding transmission spectrum of the microcavity (red curve).

Broadband emission spectrum of R6G splits into two distinct peaks corresponding to the lower and upper polariton emissions with peak energies of 2.07 and 2.28 eV, respectively. We speculate that the unusual appearance of both polaritonic branches is due to the low amount of uncoupled states in the ensemble. Otherwise, fast recombination of excitation from upper polaritonic state to the uncoupled state would prevail over the radiative relaxation to the ground state, and higher energy peak would not be observed [8]. In order to investigate the dispersion of polaritonic states and measure the anticrossing, the TMC was detuned using different mirror separations in a range from 1424 nm to 1552 nm, with the 25 nm step. Strong dependence of polariton state energy on the distance between mirrors has been measured. Resulting dependence of emission peak position on detuning has demonstrated clear anticrossing behavior. Rabi splitting was estimated to be around 225 meV, which is a rather large value for an ensemble of organic dye with exciton transitions coupled to the electromagnetic modes of the optical microcavity.

4. Conclusions

We have demonstrated controllable emission of strongly coupled organic dye excitons with relatively low unoriented dipole moments in tunable optical microcavity. Broadband emission spectrum of ensemble of R6G molecules has two distinct peaks related to the emission from the both, lower and upper polaritonic states. Dispersion of polaritonic branches has been measured while changing the cavity length and clear anticrossing behavior has been demonstrated. Estimated Rabi splitting energy was as large as 225 meV. Strong coupling regime being reached in optical microcavity with the few microns distance between the mirrors opens up great prospects for various practical applications, such as development of novel light sources, fabrication of flow cells for realization of dynamic strong coupling of the transitions of molecules in a microfluidic channel for biosensing and control of chemical reactions.

Acknowledgements

This work was supported by the Ministry of Education and Science of the Russian Federation under the Grant No. 14.Y26.31.0011.

References

[1] D.S. Dovzhenko, S.V. Ryabchuk, Y.P. Rakovich, and I.R. Nabiev, Light-matter interaction in the strong coupling regime: configurations, conditions, and applications, *Nanoscale* 10(8): 3589–3605, 2018.

[2] S. Noda, M. Fujita, and T. Asano, Spontaneous-emission control by photonic crystals and nanocavities, *Nat. Photonics* 1(8): 449–458, 2007.

[3] K.E. Mochalov, I.S. Vaskan, D.S. Dovzhenko, Y.P. Rakovich, and I. Nabiev, A versatile tunable microcavity for investigation of light-matter interaction, *Rev. Sci. Instrum*. 89(5): 053105, 2018.

[4] S.R.K. Rodriguez and J.G. Rivas, Surface lattice resonances strongly coupled to Rhodamine 6G excitons: tuning the plasmon-exciton-polariton mass and composition, *Opt. Express* 21(22): 27411–27421, 2013.

[5] N.I. Cade, T. Ritman-Meer, and D. Richards, Strong coupling of localized plasmons and molecular excitons in nanostructured silver films, *Phys. Rev. B Condens. Matter Mater. Phys.* 79(24): 241404, 2009.

[6] D.S. Dovzhenko, K.E. Mochalov, I.S. Vaskan, I.S. Kryukova, Y.P. Rakovich and I. Nabiev, Polariton-assisted splitting of broadband emission spectra of strongly coupled organic dye excitons in tunable optical microcavity, *Opt. Express* 27(4): 4077, 2019

[7] D.S. Dovzhenko, K.E. Mochalov, I.S. Vaskan, Y.P. Rakovich and I. Nabiev, Spectral and spatial characteristics of the electromagnetic modes in a tunable optical microcavity cell for studying hybrid light–matter states, *JETPH LETT* 109(1): 12-17, 2019.

[8] V. Agranovich, M. Litinskaia, and D. Lidzey, Cavity polaritons in microcavities containing disordered organic semiconductors, *Phys. Rev. B Condens. Matter Mater. Phys.* 67(8): 085311, 2003.

Electrically-injected vertical-cavity surface-emitting lasers incorporating monolithic high contrast gratings

M. Gębski[1,2], J. A. Lott[1], and T. Czyszanowski[2]

[1]Technische Universität Berlin, Institute of Solid-State Physics, Berlin, Germany
[2]Lodz University of Technology, Institute of Physics, Photonics Group, Łódź, Poland
*corresponding author, E-mail: marcin.gebski@p.lodz.pl

Abstract

We present the experimental realization of the first-of-its-kind vertical-cavity surface-emitting laser (VCSEL) incorporating a monolithic high-contrast grating (MHCG). The incorporation of an MHCG results in a 20% reduction of the epitaxial material usage, and enables stable linear polarization of the emitted light and single mode operation for more than a three times larger electrical oxide aperture diameter in comparison to a standard oxide-confined VCSEL. Our MHCG VCSELs are promising light sources for smartphones, optical communication systems, and sensing systems.

1. Introduction

A state-of-the-art vertical-cavity surface-emitting laser (VCSEL) is one of the most complicated optoelectronic devices. In a typical design, the $m{\cdot}\lambda/2$-optically thick cavity, where m is a positive integer, houses a multiple-quantum-well (QW) active region that is sandwiched between two distributed Bragg reflectors (DBRs) of very high ($R > 0.99$) power reflectance. In order to sufficiently decrease the device's electrical resistance, the whole structure or at least a large fraction of it should be doped using a rather deliberate doping scheme which results in diminishing the heterojunction electron and hole energy barriers at the DBR layer interfaces. Additionally, to decrease thermal resistance, improve heat spreading, increase reliability, and enable straight-forward planar processing the structure should be grown monolithically.

A DBR is a stack of alternating pairs of $\lambda/4$-optically thick layers chosen in such a way as to provide the largest possible refractive index contrast and at the same time the lowest possible lattice constants mismatch and lattice expansion coefficients mismatch between the DBR layers. Unfortunately, most pairs of semiconductor materials do not satisfy at least one of these requirements. As a result, high quality DBR mirrors made of GaAs, AlAs, and AlGaAs of various compositions can be monolithically grown with the rest of a VCSEL's cavity only in the arsenide material system, which allows for emission in the ~600 – 1100 nm range. In order to extend the emission range of VCSELs, phosphide- and nitride-based III-V devices must be realized. An attractive alternative for poor quality native or dielectric DBRs for those material systems is strongly required.

We proposed [1] a monolithic high-contrast grating (MHCG) mirror, which is a special case of a broad class of subwavelength high refractive index contrast gratings (HCGs) [2], as a mirror for a VCSEL. The MHCG is characterized by large polarization discrimination, an optical thickness comparable to λ, and can be designed to provide almost 100 % power reflectance (R~1.0) at normal incidence as required for a VCSEL.

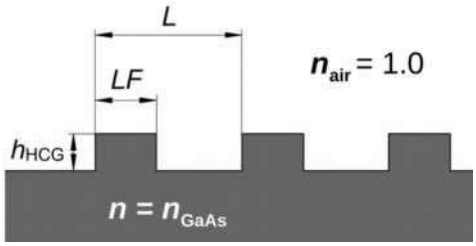


Figure 1. Schematic cross-section of an MHCG, were L is the period, F is the fill factor defined as the stripe width divided by the period, h_{HCG} is the grating height, and n is the refractive index.

In this paper we show experimental results of the first electrically-injected, 980 nm GaAs-based VCSEL incorporating an MHCG mirror. Our MHCG is combined with a 5.5-pair GaAs/AlGaAs DBR to stabilize the resonant wavelength.

2. Structure

The VCSEL structure is a $\lambda/2$-optically thick cavity with 5 InGaAs QWs sandwiched between a 37 pair bottom GaAs/AlGaAs n-doped DBR and a 5.5 pair top GaAs/AlGaAs p-doped DBR, on top of which a GaAs MHCG mirror is placed. Between the top DBR and the MHCG an ~400 nm-

thick GaAs layer for phase matching is grown. Two 20 nm-thick $Al_{0.98}Ga_{0.02}As$ layers for the formation of a current confinement aperture are placed in the Al-rich AlGaAs layers near the QWs. The devices are fabricated via our standard planar processing techniques and electron beam lithography (for the MHCG patterning). We used a high frequency layout for our VCSEL processing with ground-signal-ground metal contact pads (see Fig. 2).

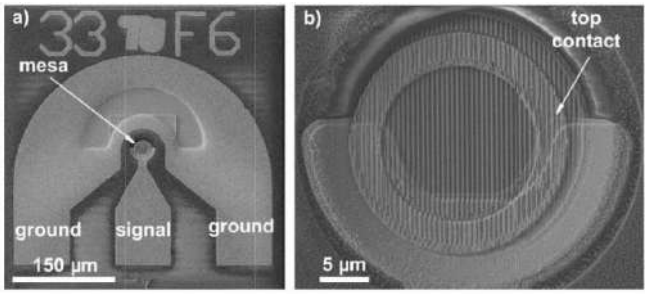


Figure 2. Example SEM images of the processed MHCG VCSEL. Top view of the entire structure a); and close-up view of the top mesa region and the MHCG b).

3. Results

We measured light-current-voltage (LIV) characteristics of our MHCG VCSELs at temperatures from 15 to 85 °C. The devices show lasing in a continuous wave regime up to 85 °C, with threshold currents as low as 2.5 mA and optical output powers (L) as high as ~1.0 mW. An example LIV curve for a VCSEL with L ~1.0 mW is shown in Fig. 3.

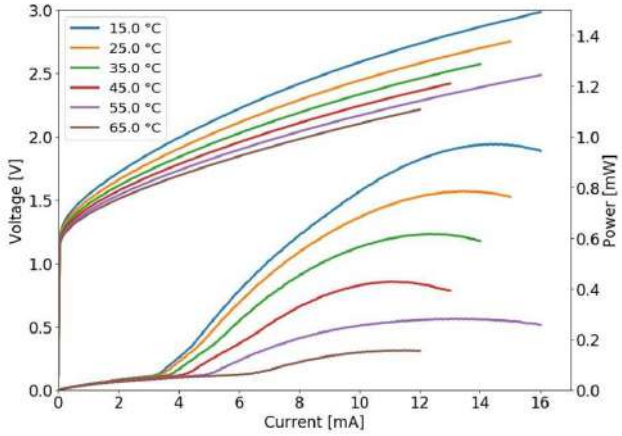


Figure 3. LIV measurements for device of 21 μm oxide aperture diameter taken at temperatures from 15 to 65 °C.

An exemplary emission spectrum of a ~13.5 μm oxide aperture diameter MHCG VCSEL is presented in Fig. 4. The device emits in a quasi-single transverse mode (the side-mode suppression ratio is ~36 dB) in a large range of bias currents from threshold to the LI rollover. A larger 16.5 μm device has a double peak emission mode (not shown here) at bias currents from threshold to LI rollover.

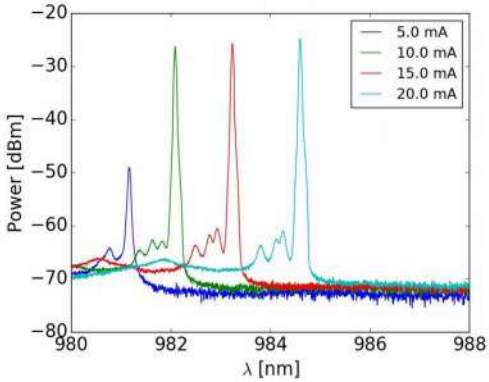


Figure 4. Emission spectrum of a quasi-single mode MHCG VCSEL with ϕ ~13.5 μm taken at 25 °C.

From spectral measurements at different temperatures we extract the thermal resistance of the VCSEL [3]. The 13.5 μm, single-mode device is characterized by a 0.59 ± 0.09 K/mW thermal resistance from a temperature of 15 to 75 °C. This result is comparable to the best result ever obtained for a single mode VCSEL [4].

4. Conclusions

We present the first VCSELs incorporating an MHGC mirror. The devices are electrically-injected and emit in a continuous wave regime up to 85 °C. Our static measurements show good performance and near-record low thermal resistance.

Acknowledgements

The authors acknowledge financial support from: 1) the German Research Foundation via the Collaborative Research Center (Sonderforschungsbereich) 787; 2) Project OPUS 2014/15/B/ST7/05258 of the Polish National Science Centre; and 3) the Polish National Science Centre ETIUDA scholarship 2015/16/T/ST7/00514.

References

[1] M. Gębski, *et al.*, *Monolithic high-index contrast grating: a material independent high-reflectance VCSEL mirror*, Opt. Exp., 23(9), pp. 11674–11686 (2015).

[2] M. C. Y. Huang, Y. Zhou, and C. J. Chang-Hasnain, *A surface-emitting laser incorporating a high-index-contrast subwavelength grating*, Nat. Phot. 1(5), 297 (2007).

[3] H. Li, *et al.*, *Thermal analysis of high-bandwidth and energy-efficient 980 nm VCSELs with optimized quantum well gain peak-to-cavity resonance wavelength offset*, APL 111, 243508 (2017).

[4] G. Zhao, *et al.*, *Record low thermal resistance of mode-confined VCSELs using AlAs/AlGaAs DBRs*, Proc. CLEO: 2013, OSA Technical Digest (online) (Optical Society of America, 2013), paper CF2F.7.

Optimal design of Quantum-Cascade Vertical-Cavity Surface-Emitting Laser

Sandra Grzempa[1], Włodzimierz Nakwaski[1] and Tomasz Czyszanowski[1*],

[1] Institute of Physics, Lodz University of Technology, Wólczańska 219, Łódź, Poland
*corresponding author, E-mail: tomasz.czyszanowski@p.lodz.pl

Abstract

Quantum-Cascade Vertical-Cavity Surface-Emitting Lasers (QC VCSELs) are anticipated to exhibit advantages of both the vertical-cavity surface-emitting lasers (VCSELs) and the unipolar quantum-cascade lasers (QCLs). In QC VCSELs vertical resonance and stimulated emission occurs due to positioning of QCs in the stripes of the monolithic high (refractive-index) contrast grating (MHCG).The performance of QC VCSELs relies on sophisticated design of MHCG and the active regions which takes into account distributions of the QC VCSEL modes.

1. Introduction

Quantum-Cascade Vertical-Cavity Surface-Emitting Laser (QC VCSEL) [1] combine the best features of two types of semiconductor lasers: Quantum-Cascade Lasers (QCLs) [2] with emission in broad range of infrared radiation up to 100 μm and Vertical-Cavity Surface-Emitting Lasers (VCSELs) [3]. The most common applications for QCLs are in spectroscopy and for free space optical communication. For each of these applications important operation properties include their high modulation speed, narrow emission spectrum, high coherence and low beam divergence. These properties can be provided by VCSELs. However when a quantum cascade is embedded into a conventional VCSEL structure stimulated emission is impossible because of the absence of the electrical field component which is perpendicular to the layers. In QC VCSELs stimulated emission of photons and vertical resonance is possible due to embedding QCs into the stripes of a monolithic high (refractive index) contrast grating (MHCG) [4].

2. Design of Quantum-Cascade Vertical-Cavity Surface-Emitting Laser (QC VCSEL)

Unipolarity of quantum cascades allows us to use more than one QC active region-each preferably at an anti-node of the z component of the electromagnetic field(E_z) distribution. Distribution of active regions is expected to increase the efficiency of stimulated emission by enhancing interaction between the optical modes and the active region and hence reduces the laser thereshold. The performance of QC VCSELs, is strongly dependent on MHCG design that must provide high power reflectance and efficient coupling between optical field and QCs embedded in MHCG. To meet those requirements finding an optimal values of three MHCG parameters: the width of the stripe *H,* the period of stripe *L* and the duty cycle *F* (fig. 1) is essential.

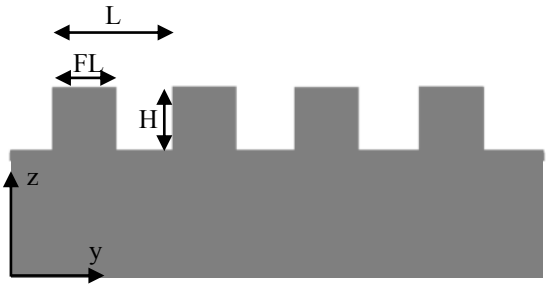


Figure 1. The structure of MHCG with three parameters: *L*-the period of grating, *F*-the duty cycle, *H*-the width of the stripe

Interactions between modes and the active regions is determined by the dimensions of the laser cavity and the positions of the active regions and provide the highest intensity of laser radiation. Spatial distributions of the modes are highly unintuitive and their numerical determination require the use of sophisticated, fully vectorial numerical methods solving Maxwell equations.

3. Conclusions

Taking into account technological limitations, QC VCSEL wafer should be possibly limited in vertical direction. In this paper, we present a designs with different numbers of the active regions and optimal parameters of the MHCG-the resonant cavities for a typical active-area thickness of 2 micrometers emitting wavelengths around 9 μm and compare their performance. We demonstrate a dependence between number of stripes in the MHCG and a threshold current.

Acknowledgements

This work was supported by the Polish National Science Center (NCN) through the project 2017/25/B/ST7/02380.

References

[1] T. Czyszanowski: Quantum-Cascade Vertical-Cavity Surface-Emitting Laser, IEEE Photon. Technol. Lett. vol. 29, pp. 351-354, 2018

[2] C. Gmachl, F. Capasso, D. L. Sivco, A. Y. Cho „Recent progres in quantum cascade lasers and applications" Reports on Progress in Physics, vol. 64, number 11 (2001)

[3] H. Soda, K. Iga, C. Kitahara and Y. Suematsu „GaInAsP/InP Surface emitting Injection Lasers" JPN. J. Appl. Phys. Vol. 18 (1979)

[4] M. Gębski, M. Dems, A. Szerling, M. Motyka, Ł. Marona, R. Kruszka, D. Urbańczyk, M. Walczakowski, N. Pałka, A. Wójcik-Jedlińska, Q. J. Wang, D. H. Zhang, M. Bugajski, M. Wasiak, T. Czyszanowski "Monolithic high-index contrast grating: a material independent high-reflectance VCSEL mirror" Opt. Exp., 23, pp. 11674-11686 (2015)

Mode cooperation in plasmonic lasers

Alexander Zyablovsky[1,2], Nikita Nefedkin[1-3], Evgeny Andrianov[1,2], Alexander Pukhov[1-3], Alexey Vinogradov[1-3]

[1]Dukhov Research Institute of Automatics, 127055, 22 Sushchevskaya, Moscow, Russia
[2]Moscow Institute Physics and Technology, 141700, 9 Institutskiy per., Moscow, Russia
[3]Institute for Theoretical and Applied Electromagnetics RAS, 125412, 13 Izhorskaya, Moscow, Russia
*corresponding author, E-mail: zyablovskiy@mail.ru

Abstract

We demonstrate that in a two-dimensional plasmonic distributed feedback laser where the pumping spot is smaller than the laser surface, the nonlinear interaction between the laser modes via the active medium can result in a new effect, namely, mode cooperation [1]. Mode cooperation arises due to non-orthogonality of the laser modes in the pumped area and leads to decrease their laser thresholds. In the plasmonic distributed feedback laser mode cooperation results in broadening of the radiation pattern, which has been observed in recent experiments [2].

1. Introduction

The two-dimensional plasmonic distributed feedback lasers are promising sources of the coherent radiation for optoelectronics and sensorics applications [3, 4]. Such lasers consist of a periodic plasmonic structure and an active medium [3, 4] is created by the external pumping. The interaction of the Bloch modes of the periodic plasmonic structure with the pumped active medium leads to the stimulated emission, and at a sufficiently high rate of pump to lasing.

In our work we study the multimode effects in the two-dimensional plasmonic distributed feedback lasers [1, 5]. We demonstrate that a new effect, named, mode cooperation takes place in two-dimensional plasmonic laser when the pumping spot is smaller than the laser surface [1]. In this system the Bloch modes of the plasmonic structure are no orthogonality within the pumping spot. For this reason, the electric field intensity in the pumped area of active medium depends on the difference phase between the modes. If the electric fields of the different modes add in phase then the electric field intensity increases and the effective coupling constant of the electric field with the active medium increases too. As a result, the lasing threshold for modes whose the electric fields add in phase decrease. The effect consists in decrease of the lasing threshold for the modes which interact with each other via the active medium we named as mode cooperation.

In the two-dimensional plasmonic distributed feedback laser the mode cooperation is manifested as the lasing of the bright modes with nonzero Bloch wavevectors instead of the dark modes with zero Bloch wavevectors. For this reason, above the threshold the radiation pattern of the two-dimensional plasmonic distributed feedback laser is wider than follows from Kogelnik's theory [6]. This result has been observed in recent experiments [2].

2. Laser equations

To describe the plasmonic distributed feedback laser we use multimode equations derived in Ref. [7]

$$\frac{dn_{jk}}{dt} = -\left(\gamma_j + \gamma_k\right) n_{jk} + i\left(\omega_j - \omega_k\right) n_{jk} + \sum_{m=1}^{N_{\text{atom}}} \left(\Omega_{km}\varphi_{jm} + \Omega_{jm}^{*}\varphi_{km}^{*}\right) \quad (1)$$

$$\frac{dD_m}{dt} = -\gamma_D\left(1 + D_m\right) - 2\sum_{j=1}^{N_{\text{mode}}} \left(\Omega_{jm}\varphi_{jm} + \Omega_{jm}^{*}\varphi_{jm}^{*}\right) \quad (2)$$

$$\frac{d\varphi_{jm}}{dt} = -\gamma_\sigma\varphi_{jm} + i\left(\omega_j - \omega_\sigma\right)\varphi_{jm} + \frac{\Omega_{jm}^{*}}{2}\left(D_m + 1\right) + \sum_{l=1}^{N_{\text{mode}}} \Omega_{lm}^{*} n_{jl} D_m \quad (3)$$

Here n_{jj} is the photon numbers in the jth Bloch mode; n_{jk} is an interference term responsible for the flow of photons from the kth to the jth mode, when $j \neq k$. D_m is the population inversion of the mth atom and φ_{jm} describes the energy flow between the mth atom and jth mode. The parameters ω_j and γ_j correspond to the real and imaginary parts of the eigenfrequencies of the modes; ω_σ and γ_D are the atom transition frequency and the relaxation rate of the population inversion of the atoms; γ_σ is the relaxation rate of the phase of the atom polarization. Ω_{jm} is the Rabi constant of coupling between the jth mode and the mth atom. These equations generalize the rate equations widely used in laser theory [8]. In addition to the dynamics of the photon number in each mode and the population inversion of each atom, they take into account the interference between the electric fields of the different modes, n_{jk}.

3. Results

Based on the Eqs. (1)-(3) we demonstrate that when the pumped area is smaller than the laser surface the nonlinear interaction between the Bloch modes of periodic plasmonic structure via the active medium can leads to a phase

synchronization of such modes [1]. Since, the pumped area occupies only part of the plasmonic structure the Bloch modes are no orthogonality within the pumped area. For this reason, the intensity of the electromagnetic field inside the pumped area depends on the phase difference between the modes. The electromagnetic fields of the sinchronized modes constructively interfere within the pump area that leads to increase of the coupling constant of such modes with the active medium. As a result, the lasing threshold of the synchronized modes decreases [1]. Thus, the interaction between the laser modes via the active medium can leads to decrease of the lasing threshold of such modes. This effect is opposite to mode competition and therefore, we name of it as a mode cooperation.

In the two-dimensional plasmonic distributed feedback the mode cooperation leads to lasing frequence shift in the allow band. Below the threshold the behavior of the laser is determined by the spontaneous emission which does not depend on the phase difference between the modes and so the maximum number of the photons is in the dark mode that has smallest radiation losses. Above the threshold the maximum number of the photons is in the bright modes lie in allow band which have greater radiation losses. That is the lasing takes place at the bright modes in the allow band instead of the dark mode at edge of the band gap. As a result the output power of the laser is greater than the than follows from conventional theory [8]. Since below the threshold the laser operates at the dark modes whereas above the threshold the one operates at the bright modes the transition to lasing is accompanied by the sharp increase of the output power, see Figure 1.

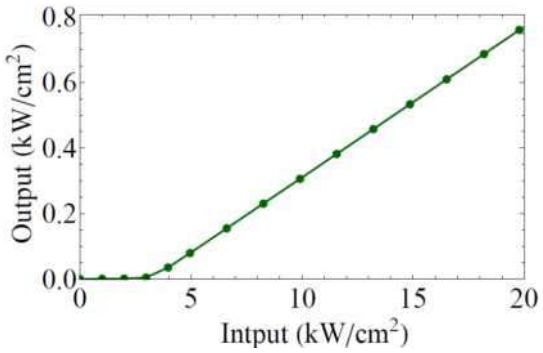


Figure 1: The dependence of output power on the input power.

Moreover, since the modes lie in allow band have non-zero Bloch wavevectors the radiation pattern of the two-dimensional plasmonic distributed feedback laser is wider than follows from Kogelnik's theory [6] which take not into account the mode ccoperation, see Figure 1. This distinction has been observed in recent experiment [2].

4. Conclusions

It is shown that in the two-dimensional plasmonic distributed feedback laser where the pumping spot is smaller than the laser surface effect mode cooperation takes place [1]. Mode cooperation consist in the decrease of laser thresholds for modes interacting with each other via the active medium. In the plasmonic distributed feedback laser mode cooperation results in broadening of the radiation pattern, which has been observed in recent experiments [2].

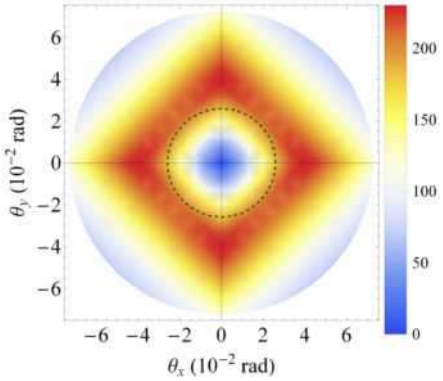


Figure 2: The radiation pattern of plasmonic DFB above the lasing threshold. The dashed lines correspond to the radiation pattern obtained by Kogelnik's theory [6].

Acknowledgements

The reported study was funded by RFBR according to the research project No. 18-32-00596.

References

[1] N. E. Nefedkin, A. A. Zyablovsky, E. S. Andrianov, A. A. Pukhov, and A. P. Vinogradov, Mode cooperation in a two-dimensional plasmonic distributed-feedback laser, *ACS Photonics*, 5: 3031, 2018.

[2] V. T. Tenner, M. J. A. de Dood, M. P. van Exter, Measurement of the phase and intensity profile of surface plasmon laser emission, *ACS Photonics* 3: 942, 2016.

[3] P. Melentiev, et al., Plasmonic nanolaser for intracavity spectroscopy and sensorics, *Appl. Phys. Lett.* 111: 213104, 2017.

[4] K. S. Daskalakis , A. I. Vakevainen, J.-P. Martikainen, T. K. Hakala, and P. Torma, Ultrafast pulse generation in an organic nanoparticle-array laser, *Nano Lett.* 18: 2658, 2018.

[5] A. A. Zyablovsky, I. A. Nechepurenko, E. S. Andrianov, A. V. Dorofeenko, A. A. Pukhov, A. P. Vinogradov, and A. A. Lisyansky, Optimum gain for plasmonic distributed feedback lasers, *Phys. Rev. B* 95: 205417, 2017.

[6] H. Kogelnik and C. V. Shank, Coupled‐wave theory of distributed feedback lasers, *Journal of Applied Physics* 43: 2327, 1972.

[7] A. A. Zyablovsky, E. S. Andrianov, I. A. Nechepurenko, A. V. Dorofeenko, A. A. Pukhov, and A. P. Vinogradov, Approach for describing spatial dynamics of quantum light-matter interaction in dispersive dissipative media, *Phys. Rev. A* 95: 053835, 2017.

[8] A. E. Siegman, Lasers, University Science Books Mill Valley, California, 1986.

Strong coupling and low, room temperature threshold in nanolasers using optical nanopatch antennas: an analytical and computational study

Patrick Bowen[1,2*], Xander Deputy[1], Roberto Zecca[1] and David R. Smith[1]

[1]Department of Electrical and Computer Engineering, Duke University, Durham, NC USA
[2]Metacept, Durham, NC, USA

*corresponding author, E-mail: patrick.bowen@duke.edu

Abstract

Despite major advances, nanolasers require either cryogenic temperatures or high thresholds. We demonstrate theoretically that optical nanopatch antenna lasers can yield thresholds orders of magnitude lower by enhancing the atom-cavity interaction into the strong coupling regime. This work presents the first analytic investigation of laser in film-coupled nanoparticles by expanding the optical field in a set of quasi-normal modes. Ohmic, radiative, surface plasmon, and spontaneous decay channels are included analytically, and which allows structures to be optimized to minimize threshold.

1. Introduction

One of the key devices for improving on-chip optical computing and communications is a fast, sub-diffractional laser with low threshold power, ideally operating at room temperature. While lasers with dielectric laser cavities are limited in size by the diffraction limit, plasmonic cavities can reduce the size of the laser cavity to dimensions much smaller than the wavelength. Reducing the cavity size creates large field enhancements, which can lead to giant Purcell enhancement, enhanced Raman scattering, and even strong coupling at room temperature. The disadvantage of plasmonic resonators, however, is that the Ohmic losses in the metal typically increase the cavity decay rate. In this paper, we demonstrate that a careful analytic approach can be used to design a plasmonic cavity with enhancements strong enough give a cavity interaction time that is sufficiently faster than the cavity decay rate to cause the system to be strongly coupled. This eventually yields designs for nanolasers with a threshold several order of magnitude lower than any other published optically pumped nanolaser at room temperature with a laser dye gain material.

2. Strong Coupling in Optical Nanopatch Cavities

The two key parameters for reducing threshold and increasing nonlinear and quantum effects in cavity quantum electrodynamics in general are the saturation photon number, $n_0 = \frac{2\gamma_\perp\gamma_\parallel}{g^2}$, and the critical atomic number, $N_0 = \frac{2\gamma_\perp\kappa}{g^2}$[1]. These are given in terms of $\gamma_\parallel$ and $\gamma_\perp$, which are the decay and dephasing rates, respectively. The decay rate of the cavity is κ, and the cavity coupling parameter $g = \boldsymbol{\mu}\cdot\mathbf{E}/\hbar$ is defined as the dot product of the atomic dipole moment $\boldsymbol{\mu}$ with the electric field when there is one photon with energy $\hbar\omega$ in the cavity. Most fundamentally, the field-enhancement that is observed in cavities with reduced mode volume increases the rate of the atom-cavity interaction given by g by concentrating the elecromagnetic field of the photon. The parameters n_0 and N_0, are therefore a comparison of two different timescales in the atom-cavity system: the rate of the atom-cavity interaction given by g, and the loss and dephasing mechanisms in both the gain material and the cavity. While reducing the saturation photon number and the critical atomic number to sub-unity values brings the atom-cavity system into the strong coupling regime, this work is focused on minimizing these parameters in order to minimize threshold for nanolasers.

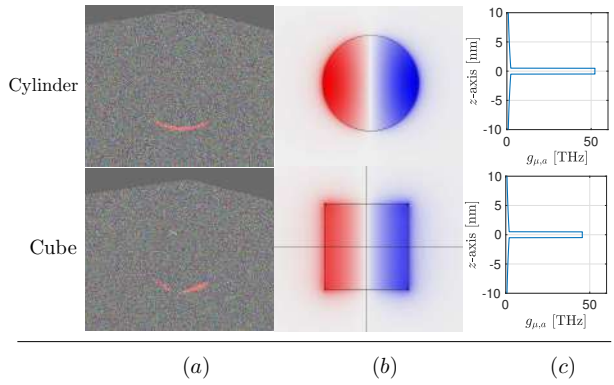


Figure 1: (a) Example cylindrical and cubic optical nanopatch antennas. (b) Top-down view of the fundamental QNM. (c) Enhanced cavity-coupling rate in the gap region of each nanopatch.

3. Quasinormal mode analysis of lasing in nanopatch antennas

In order to solve for the evolution of the electromagnetic field in the cavity due to the coupling with the gain material a Green's function for a cavity that has both radiative

and Ohmic losses needs to be developed. This is done by expanding the field in a set of optical modes using quasinormal mode (QNM) theory,[2] $\mathbf{E}(\mathbf{r},\omega) = \sum_\mu a_\mu(\omega)\mathbf{E}_\mu(\mathbf{r})$.

Each QNM is a solution to the source-free Maxwell's equations, but is distinct from normal modes by the requirement that the modes $\mathbf{E}_\nu(\mathbf{r})$ satisfy the Silver-Müller radiation condition as $r \to \infty$. This boundary condition yields Maxwell's equations non-Hermitian even in the presence of lossless materials, yielding complex eigenfrequencies for each QNM. Moreover, they are no longer orthogonal with respect to the standard conjugated Hermitian inner product, and instead the orthogonality relation is given by

$$\langle \mathbf{E}_\nu | \mathbf{E}_\mu \rangle = \frac{1}{2}\int_V \left.\frac{\partial\left[\omega\epsilon(\mathbf{r},\omega)\right]}{\partial\omega}\right|_{\omega_\nu} \mathbf{E}_\nu\cdot\mathbf{E}_\mu - \mu_0\mathbf{H}_\nu\cdot\mathbf{H}_\mu \mathrm{d}V. \tag{1}$$

The modes are then normalized such that $\langle \mathbf{E}_\nu|\mathbf{E}_\mu\rangle = \delta_{\mu\nu}\hbar\omega_\mu$. Once the eigenmodes are known, the cavity decay rate κ is given by the imaginary part of the eigenfrequency. The coupling to each mode by a polarization or magnetization in the cavity

$$a_\mu(\omega) = \frac{\omega^2}{2\hbar\omega_\mu^2(\omega_\mu-\omega)}\int(\mathbf{E}_\mu\cdot\mathbf{P} - \mu_0\mathbf{H}_\mu\cdot\mathbf{M})\,\mathrm{d}V. \tag{2}$$

can be used to model coupling with the gain material. Moreover, the mode expansion can be used to develop a Green's function, the imaginary part of which yields the Purcell-enhanced spontaneous emission rate $\gamma_{sp} = \sum_\nu \mathrm{Im}\left\{\omega^2 g_\nu(\mathbf{r})^2/\omega_\nu^2(\omega_\nu-\omega)\right\}$ in terms of the cavity coupling parameter, $g_\nu = \boldsymbol{\mu}\cdot\mathbf{E}_\nu/\hbar$.

4. Results

The field expansion is then used in a four-level optical Bloch quantum mechanical model of Rhodamine 600, including the spatially varying spontaneous emission rate. Evaluating these equations at a point yields eigenvalue equations for Rabi splitting and the strong coupling parameters shown in fig. 2.

Alternatively, integrating the rate equations over the volume of the cavity yields an eigenvalue equation for the lasing frequency, which is purely real when the population is sufficiently inverted. The model is continued to predict the required number of pump photons in the cavity and incident beam intensity using the same quasinormal coupled mode theory techniques.

Figure 3 gives a holistic picture of various physical processes in the cavity that are analytically predicted and compared with full-wave simulation, beyond the accurate prediction of the lasing threshold (vertical black line). The total population inversion in the simulated cavity N_2^t approaches the analytically predicted critical value $N_{2,c}^t$ as the intensity approaches threshold.

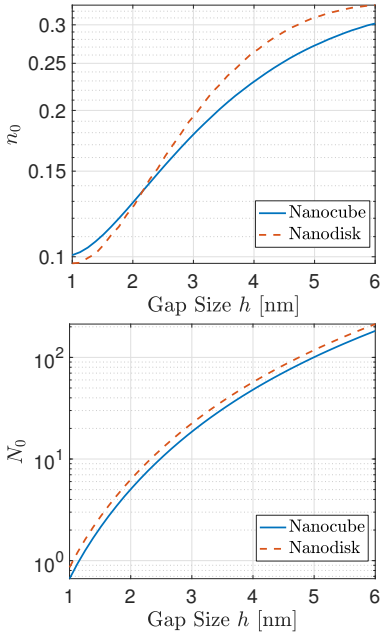


Figure 2: Saturation photon and critical atomic numbers for nanocube and nanodisk antennas.

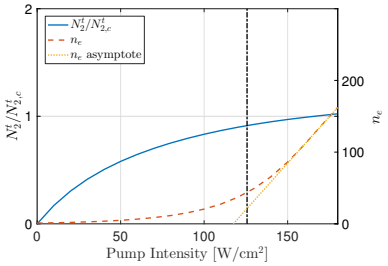


Figure 3: Comparison of analytically predicted threshold (vertical black line) with emission curve from nonlinear full-wave simulations of lasing.

5. Conclusions

The development of an accurate analytical model of lasing in plasmonic cavities gives two unique benefits. First, the fast modeling technique enables optimization of the geometry of the resonator for a particular gain material. Second, it uncovers the underlying physical mechanisms behind lowering the threshold in a low quality factor cavity, and allows direct comparison of all loss rates. This model leads to optical sources with ultralow threshold and fast switching times.

References

[1] Kimble, H Jeff, in Cavity Quantum Electrodynamics, edited by P. R. Berman, (Academic Press, San Diego, 1994.

[2] Leung, PT and Liu, SY and Young, K, Completeness and orthogonality of quasinormal modes in leaky optical cavities, *Physical Review A* 49:3057, 1994.

Spatio-temporal simulation of defect mode laser in 2D groove metal array inside MIM Structure

Seong-Han Kim[1]* and Chul-Sik Kee[1]

[1]Integrated Optics Laboratory,Advanced Photonics Research Institute, GIST, Gwangju 61005, South Korea
*corresponding author, E-mail: topofuni@gmail.com

Abstract

We numerically investigate the spatio-temporal dynamics of lasing action in a metallic resonant cavity with four-level gain media, based on defect modes on 2D groove metal array. By performing semiclassical time-domain simulations based on the finite-element method, we obtain dynamical distributions of populations and fields in gain medium and threshold behavior of the laser.

1. Introduction

Plasmonic nanolasers have attracted great interest for their fundamental and technological potential from spectroscopy, sensing, and integrated nanophotonic devices to quantum physics. Spoof surface plasmon polaritons (SPPs) on a structured metallic surface [1] have been widely applied for focusing[2], guiding[3], and localizing[4, 5] THz and GHz waves in a deep subwavelength scale. For development of coherent light sources at the nanoscale, the spoof SPPs would be a good candidate to localize infrared (IR) and visible waves at the nanoscale region because localization of the spoof SPPs allows confining and enhancing light fields at subwavelength scales. Furthermore, the increase of light-matter interaction can enhance the gain by an active medium close to a spoof SPP structures. Recently, spatio-temporal simulations have been exploited to investigate the nonlinear dynamics of active plasmonic system[6, 7, 8]. The spatio-temporal modeling of the spoof SPP modes at visible and IR frequencies could makes contribution toward development of plasmonic light sources in nanoscale.

In this work we report on a numerical study of the spatio-temporal dynamics in a small metallic resonant cavity array with four-level gain media for lasing light at IR frequency, based on guided spoof SPPs on 2D groove metal array(GMA). We investigate this problem by using three-dimensional semiclassical simulations based on a time-domain finite-element method[7, 8]. By performing these simulations, we are able to obtain the nonlinear spatio-temporal dynamics arising from the interaction of the gain medium with the nonuniform field distribution characterizing the system. The threshold behavior of the laser can be analyzed, as well.

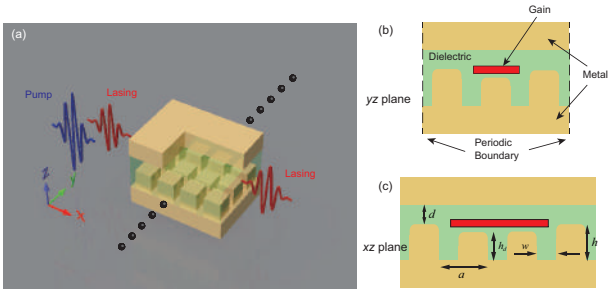


Figure 1: Schematic diagram of laser system in this study. Cross section in the yz plane (b) and the xz plane (c) with parameters of the cavity.

2. Results

Figure 1 shows a resonant cavity array in this study which is composed of defect structures in formed by introducing two defect structures with defect depth h_d = 85 nm on 2D GMA. The 2D GMA inside a MIM structure is composed of two overlapping 1D groove metal arrays perpendicular to each other with the lattice constant a = 150 nm, width w = 60 nm and depth h = 110 nm. The optical response in this resonant cavities is modeled by solving 3D Maxwell equations via the finite element method. The permittivity of metal ϵ_m is expressed by Drude model with the plasma frequency $\omega_p = 2\pi \times 2.175 \times 10^{15}$rad/s^{-1} and the damping constant $\gamma = 2\pi \times 6.5 \times 10^{12}$rad/s^{-1}. The refractive index n_d of the dielectric material is 1.49.

A four level gain medium with size of 150 nm $\times$ 300 nm $\times$ 25 nm is placed above the defect structures. The artificial gain medium is characterized by the lifetimes $\tau_{10} = \tau_{32}$ =50 fs, τ_{21} =5 ps, and τ_{30} =1 ps. The coupling constants are K_a = 10^{-6} C^2/kg and K_e = 10^{-4} C^2/kg, and the linewidths of their corresponding transitions are γ_a=1/100 fs and γ_e=1/100 fs. Finally, the initial population density parameter is $N_i = 5 \times 10^{23}$ m^{-3}. The population densities of the four level gain medium obeys the rate equations, and the gain medium interacts with the electromagnetic field through the gain polarization. Figure 2(a) shows simulated transmission, reflection, and absorption spectra for passive cavity. The spectra for the passive cavity show two resonances located at 231.8 and 250.6 THz, respectively. Also, from the electric field distributions as shown in insets of Fig. 2(a), we can verify that the cavities have resonances in the form of the Fabry-Perot resonance. Figure 2(b) shows

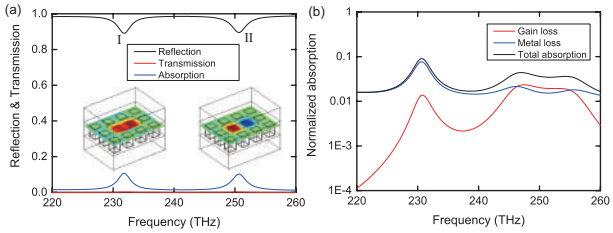


Figure 2: (a) For the passive cavity, simulated reflection, transmision, and absorption spectra for the passive cavity (without gain). The inset shows the z-component of electric fields, where I and II indicates the first and second resonant mode, respectively. (b) For the active cavity, total absorption as well as absorption in metal and absorption in the gain medium.

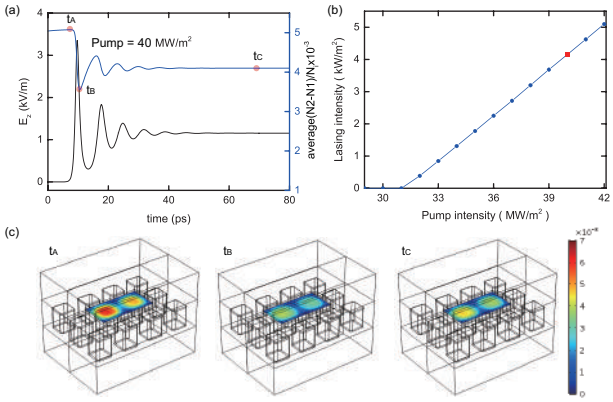


Figure 3: (a) Time evolution of electric field intensity (black line) at output plane and population inversion (blue line) averaged at the output plane for 40 MW/m^2 in pump power intensity. (b) Steady state lasing intensity vs. pump intensity. (c) Spatial distribution of the population inversion inside the active region computed at three representative times (labeled as t_A, t_B, and t_C in (a)).

simulated total absorption as well as absorption in metal and absorption in the gain medium for the active cavity. It is clear that the presence of the electronic transition in the gain medium strongly modifies the spectrum of the cavity array.

Figure 3 shows the spatio-temporal simulation results for this laser system. The intensity of the lasing field plotted in Fig. 3(a) spikes initially, but after about 40 ps, it becomes into steady state lasing. Also, population inversion is depicted in Fig. 3(a). Figure 3(b) plots the steady state lasing intensity vs. the pump intensity. A linear fit to the lasing data points indicates a threshold pump intensity of 31.2 MW/m^2. This threshold intensity depends on a number of variables, including all of the parameters of the gain medium, as well as defect mode resonances used to enhance both the pump and lasing transition(fig. 2 (b)). Figure 3(c) shows spatial distribution of the population inversion inside the active region at t_A, t_B, and t_C.

3. Conclusions

In summary, we have numerically studied the spatio-temporal dynamics of lasing action in a metallic resonant cavity with four-level gain media, based on defect modes on 2D groove metal array. By performing semiclassical time-domain simulations, based on the finite-element method, we obtained the nonlinear spatio-temporal dynamics arising from the interaction of the gain medium with the nonuniform field distribution characterizing the system. Also, the threshold behavior of the laser have been analyzed.

Acknowledgement

This research was supported by the Basic Science Research Program through the National Research Foundation of Korea (NRF-2015R1D1A1A01060180 and NRF-2018R1D1A1B07050116) and by GIST Research Institute (GRI) grant in 2019.

References

[1] J. B. Pendry, L. Martin-Moreno, F. J. Garcia-Vidal, Mimicking Surface Plasmons with Structured Surfaces, Science 305: 847–848 ,2004.

[2] S. A. Maier, *et al.*, Terahertz Surface Plasmon-Polariton Propagation and Focusing on Periodically Corrugated Metal Wires, *Phys. Rev. Lett.* 97: 176805, 2006.

[3] S.-H. Kim, *et al.*, Waveguiding of spoof surface plasmon polaritons, in *Proceedings of 2015 Conference on Lasers and Electro-Optics Pacific Rim,*, Busan, South Korea, 24-28 August 2015, 26P_78.

[4] S.-H. Kim ,*et al.* , Subwavelength localization and toroidal dipole moment of spoof surface plasmon polaritons, *Phys. Rev. B* 91: 035116, 2015.

[5] S.-H Kim, C.-S. Kee, Lasing Cavity based on Defect Modes in 2D Groove Metal Array inside MIM Structure, *Proc. meta 2018* Marseille, France, 2018.

[6] S. Wuestner, A. Pusch, K. L. Tsakmakidis, J. M. Hamm, and O. Hess, Overcoming Losses with Gain in a Negative Refractive Index Metamaterial,*Phys. Rev. Lett.* 105, 127401, 2010.

[7] C. Fietz, C. M. Soukoulis, Finite element simulation of microphotonic lasing system. *Opt. Express* 20, 11548 – 11560, 2012.

[8] J. Cuerda, F. J. Garcia-Vidal, J. Bravo-Abad, Spatio-temporal Modeling of Lasing Action in CoreShell Metallic Nanoparticles. *ACS Photonics* 3, 1952 – 1960, 2016.

Photonic crystals

Pseudo Jahn Teller effect: Application to Time Crystals

Zafer Ozer[1], Amirullah M. Mamedov[2,3,*], Ekmel Ozbay[2]

[1]Mersin Vocational High School Electronic and Automation Department, Mersin University, Mersin, Turkey
[2]Nanotechnology Research Center (NANOTAM), Bilkent University, Ankara, Turkey
[3]International Scientific Center, Baku State University, Baku, Azerbaijan
*mamedov@bilkent.edu.tr

It is well known that for the crystalline states, the interaction of local pseudo-Jahn-Teller distortions lead to structural transitions [1]. In the case when the local distortions are of the dipole type, the crystal in the ordered phase turns out to be spontaneously polarized. Relation are obtained between the parameters of the vibronic coupling we used in the spatially-periodic systems-time crystals (TC) [2].

TC are the temporal analogue of the photonic crystals (PCs) [2]. Usually, PCs are designed with a refractive index that changes periodically in space. However, due to the unique duality of time and space in waves equations, one can think of a photonic time crystal-PTC where the refractive index or dielectric permittivity (t), changes periodically in time, rather in space [2].

In present paper we analyzed a spatially homogeneous material with permittivity (t), which is modulated in time, such that $\varepsilon(t)$ changes periodically, with period T, in a step-like manner. This results in a binary PTC with two time segments. In the first time-segment $(t)=\varepsilon_1$ for a duration of t_1 seconds, followed by a second time-segment in which $\varepsilon(t)=\varepsilon_2$ for $t_2=T-t_1$ seconds. The field is polarized in the x direction, and propagates in the z direction. With every modulation of (t), a time reflection occurs, causing waves to partially reflect to their time reversed pair, while preserving the momentum k due to the homogeneity of space. The time reversed partner of a wave is a wave with the same momentum but with opposite spatial frequency. This is analogous to a wave conserving its energy, and scattering backwards in space in a PC. We proposed the concept of the PTC, and simulated electromagnetic wave propagation in 1D, and 2D PTC, the simulated results indicate that the scatter fields in PTC are more intensive than those in conventional PC, and the band gaps in PTC are larger than those in conventional PC.

References

[1] I.B. Bersuker, Modern aspects of the Jahn-Teller effect theory and applications to molecular problems, Chem. Rev., 101(4), 1067, 2001.

[2] L. Zeng, J. Xu, C. Wang, J. Zhang, Y. Zhao, J. Zeng, R. Song, Photonic time crystals, Scientific Reports, 7 :17165, 2017.

Angle-Independent Structural Colors for Personal Thermal Management

Zhijie Zhu, Xiang-Yun Du, Chang Liu, Qing Li, Su Chen*

State Key Laboratory of Materials-Oriented Chemical Engineering, College of Chemical Engineering Nanjing Tech University, Nanjing 210009 (P. R. China)
*corresponding author, E-mail: chensu@njtech.edu.cn

Abstract

Recently, bottom-up assembly of colloidal particles into structural colors represent a major research interest of optical devices for coating, sensing, and display. Despite much breakthroughs in the preparation of structural colors, the film forming strategy is still highly relied on conventional evaporation-induced processes. Herein, inspired from membrane separation processes, we develop a membrane separation-assisted assembly (MSAA) strategy for the preparation of angle-independent structural colors. The process is carried out by separating between water and solid particles in colloidal latex, allowing them to facilely form amorphous structures with robust functions.

Introduction

Angle-independent structural colors have received considerable attention on account of their abilities to control and manipulate light propagation.[1] These structures could be found in natural creatures such as elytra of longhorn beetles and the blue skin of the mandrill. Much efforts have been done for the construction of angle-independent structural colors, such as spray-coating of colloidal latex, fabrication of spherical colloidal crystal beads and improving refractive index of microspheres.[2] However, their practical applications are still limited. Also, it is desirable to develop new methods, or to extent current method which allow colloidal particles self-assemble into amorphous structures in a fast and low-cost way. Thus, this motivates us to develop new strategies for facilely producing amorphous structures with improved color saturation without sacrificing its brightness.[3] Herein, inspired by the graphene-based separation processes, we introduce a membrane separation-assisted assembly (MSAA) strategy to construct a new kind of amorphous photonic structure representation of angle-independent structural colors (Figure 1a, b).[4] Besides, we also propose an approach to use our structural color film in out-door thermal management applications, which is essential for personal cooling and energy saving.[5] By combining the synergetic effects of constructive scattering and slow photon, a maximal reduction of 6.9 ºC was achieved when exposed to sun radiation (Figure 1c). This finding opens a new pathway for fabrication of amorphous colloidal structures for personal thermal management applications.



Figure 1. a) Schematic illustration of the fabrication of rGO-SPM and assembly progress of the colloid film/graphene hybrid ordered membranes via MSAA method. b) Photograph of as-prepared colloidal film and its optical performance. c) Schematic illustration of the application of a rGO/poly(St-MMA-AA) membrane for out-door thermal management.

Disccusion

Figure 2a presents optical images of three different colloidal films, which are composed of poly(St-MMA-AA) microspheres with diameters of 195 nm, 218 nm and 256 nm, respectively. These colloidal films display virtually identical structural colors at the view angles changing from 90º to 30º. To visually characterize the angle dependence of the colloidal films, the angle-resolved reflection spectra and their corresponding contour maps were measured. As shown in Figure 2b, band positions of colloidal films prepared by MSAA barely shift (less than 5 nm) when the incident angle varies from 90º to 30º, indicating angle-independent property. Meanwhile, the corresponding contour maps with reflection wavelength (λ) on the x axis, view angle (θ) on the y axis and reflection intensity (I) being converted to colors in maps also prove their angle-independent behavior. The contour maps of colloidal films prepared by MSAA exhibit

consecutive and linear reflection bands that are vertical to x axises.

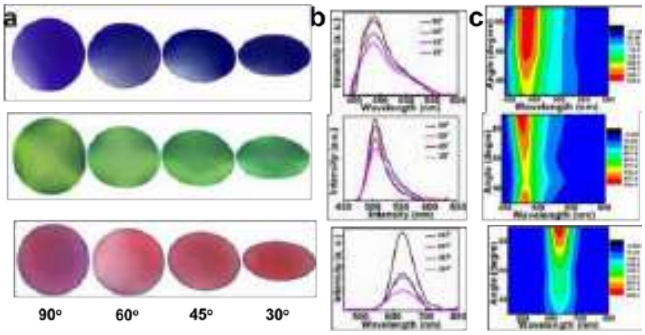


Figure 2. a) Photographs of three different photonic films observed at angles from 90° to approximately 30° and b) reflection spectra and c) corresponding contour maps.

The second set of experiments was focused on studying the passive cooling of structural color film (Figure 3). We studied the impact of stopband position on the efficiency of thermal insulation. To evaluate the influence of stopband positions on heat dissipation process, 8 individual structural colors that are composed of poly(St-MMA-AA) microspheres with different corresponding diameters are prepared. The obtained colors, covering the whole visible light regime are derived from MSAA method and are uniform and independent of viewing angles as demonstrated above. In a typical procedure, a colloidal film with a diameter of 50 mm was placed on top the shelf (obtained from a 3D printer). Under natural sun light radiation, the temperature of structural color film with stopband centered at 650 nm, increased from 24.6 °C to 34.3 °C within 360 s. In contrast, the bulk polystyrene film without a structural color showed a rapid temperature increase from 24.6 °C to 45.5 °C. The infrared photographs of sample films after 15 min of irradiation are shown in Figure 3a. The inserts are temperature differences (ΔT) between different sample surfaces (T_{sample}) and the cement floor background (T_{floor}). With the increase of stopband position, ΔT appears a downward trend. The stopband of a structural color film that inhibit certain wavelength propagation is the main reason for this result. The structural color films that possess red or near-infrared colors can prohibit more longer-wavelength light from absorption. For a more realistic case, we adopted structural color film to integrate on human skin, where the film was attached to a human hand. Figure 2d-f are human hands with structural color film (stopband centered at 650 nm), rGO-SPM film and bulk polystyrene film (without a color), respectively. Before measurement, all samples are in thermal equilibrium after solar radiation for at least 15 min. The temperature of bulk polystyrene film and rGO-SPM was 35 °C and 36 °C, respectively. On contrary, for structural color film, the temperature was maintained at 30.5 °C, lower than skin temperature 33 °C. This is consistent with the above results. It is worthwhile to note that our structural color film is composed of two sides: the structural color side and the black rGO-SPM side. It is expected that the color side can be processed to decrease solar radiation in summer, while the black rGO-SPM side been processed to absorb more in winter.

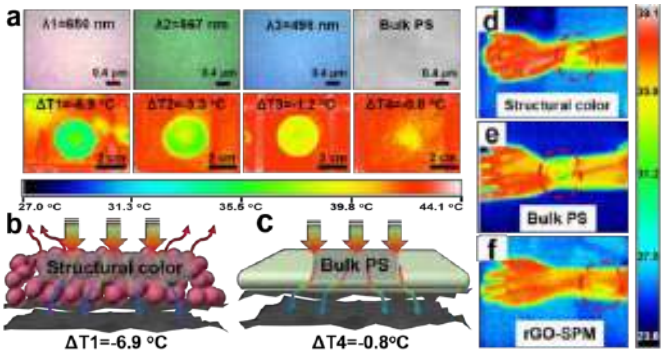


Figure 3. a) Structural colors prepared by MSAA by varying the diameters of poly(St-MMA-AA) and corresponding infrared photographs after 15 min of irradiation. Schematics of comparison between b) structural color film and c) bulk polystyrene film. Infrared images of d) structural color film, e) bulk polystyrene film and f) rGO-SPM (attached to human body) under radiation.

Conclusions

In summary, we report a strategy for the preparation of colloidal films with angle-independent structural colors based on membrane separation-assisted assembly (MSAA) method. By taking advantage of the water transport channels in sulfonated rGO, water and submicron particles could be separated easily, along with colloidal particles assembles into amorphous structures. We investigated the influence of structural colors on thermal insulation and applied it to personal thermal management. A maximal reduction of 6.9 °C can be achieved when the stopband of structural color is centered at 650 nm. Such colloidal films with angle-independent structural colors may provide new opptunity for out-door thermal management materials.

Acknowledgements

This work was supported by National Natural Science Foundation of China (21736006), National Key Research and Development Program of China (2016YFB0401700), Natural Science Foundation of Jiangsu Provice (BK20171013) and (PAPD). Fund of State Key Laboratry of Material-Oriented Chemical Engineering (ZK201704).

References

[1] Y. Zhang, B. Dong, A. Chen, X. Liu, L. Shi, J. Zi, Adv. Mater. 2015, 27, 4719-4724.

[2] Y. Takeoka, J. Mater. Chem. 2012, 22, 23299-23309.

[3] J. Zhang, Z. Zhu, Z. Yu, L. Ling, C.-F. Wang, S. Chen, Mater. Horiz. 2019, 6, 90-96.

[4] Z. Zhu, J. Zhang, Y.-L. Tong, G. Peng, T. Cui, C.-F. Wang, S. Chen, D. A. Weitz, ACS Photonics 2019, 6, 116-122.

[5] G. Smith, A. Gentle, M. Arnold, M. Cortie, Nanophotonics 2016, 5, 55-73.

Coalescence-controlled large-scale colloidal films towards robust structural colors

Su Chen*, Zhijie Zhu, Xiang-Yun Du, Chang Liu, Qing Li

State Key Laboratory of Materials-Oriented Chemical Engineering, College of Chemical Engineering Nanjing Tech University, Nanjing 210009 (P. R. China)
*corresponding author, E-mail: chensu@njtech.edu.cn

Abstract

Inspired by commonly-seen "milk skin" phenomena, a general and versatile scheme, namely the polymer colloid ensembles (named "colloid skin") -regulated assembly route, is demonstrated here for colloidal film deposition, which easily addressed the ubiquitous issues associated with the asymmetrical evaporation processes, implying a new broad-spectrum film-forming strategy.

Introduction

Colloidal photonic crystals (CPCs) with periodic micro/nanostructures, have attracted much attention because of their excellent iridescent structural colors.[1] However, they suffer from the ubiquitous "coffee ring" negative-effect phenomenon due to asymmetrical film-forming. Hence, it is still challenging for applications of the CPC coatings with a large scale in a variety of fields, such as advanced inks, printing, flexible display, packaging, textile printing and dyeing and chemical/biological sensors. Also, the development of a new broad-spectrum kind of film forming strategy is still a high concern, especially in frontiers of nanoimprinting, nanoink, etc.[2] In this work, we offer a novel and efficient concept for governing film forming and regulated assembly of CPCs for the first time. The strategy is mainly based on that fact, just as the commonly-seen "milk skin" phenomena of hot milk-containing liquids, the colloidal inks would also cause colloid coalescence on its top surface, forming a layer of "colloid skin" whilst evaporating (Figure 1A).[3] This "skin" would seal the drying liquid surfaces, break the outward capillary flow, and greatly vary the evaporative flux across the air-liquid surface. Hence, the coffee ring effect, the major obstacle for uniform colloid deposition, is completely suppressed, enabling the preparation of close-packed polymer colloids on diverse substrates over large scales (Figure 1B). Also, this "colloid skin" effect allows a variety of CPCs films to be facilely formed by either inkjet printing, bar coating or spray-painting technique (Figure 1C). This "colloid skin" concept also brings insight into the development of a new broad-spectrum kind of film forming strategy, and hence the issues associated with the asymmetrical evaporation process could be easily addressed. These findings undoubtedly present an unexpected adjustment and control strategy in coating and nanomaterial patterning areas

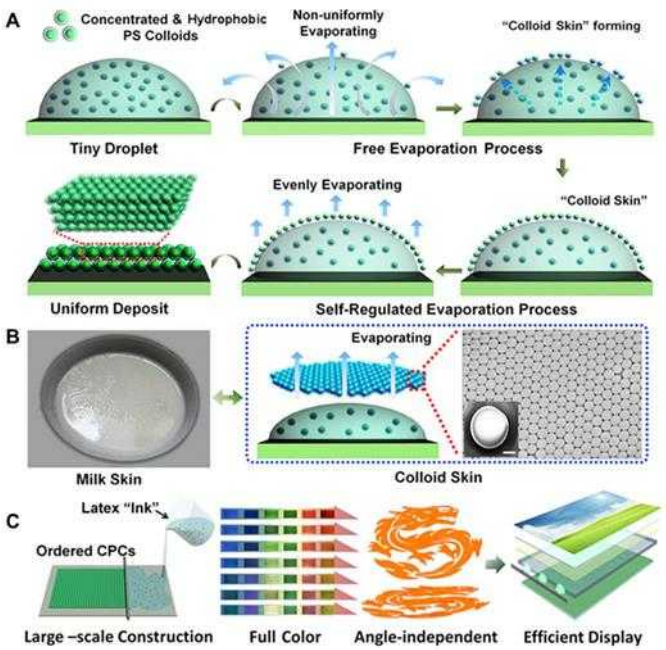


Figure 1. (A) Schematic illustration for the "colloid skin"-regulated self-assembly process. (B) Optical image of a bowl of hot milk with "milk skin" across its surface due to the denaturation of proteins. (C) Construction of large-scaled colloid crystal printings by either the spray or bar coating technique.

Disccusion

Specifically, aqueous mixtures containing 15 wt% of polystyrene (PS) colloids and 10 wt% of ethylene glycol (EG) were first prepared as the printing "ink", and a commercial printer (Jetlab 4, MicroFab Corp.) was used to generate tiny ink droplets with sizes ranging from 100 to 300 micrometer (Figure 2A and 2B). As Figure 2C shows, after the ejected droplets were deposited onto the substrate, a layer of colloid ensembles was noticed immediately on their top surfaces, forming the so-called "colloid skin". The possible mechanism could be attributed to that, similar to commonly-seen "milk skin" phenomena of hot milk-

containing liquids, herein, the hydrophobic PS colloids could also crystallize out from the ink droplets whilst evaporating and thus produce a layer of "colloid skin". More attractively, this preformed "skin" would give rise to totally different late-stage colloid assembly behavior, facilitating the formation of uniform CPC deposits. When the evaporating flux was ultralow due to the extremely high humidity of 80 % and low temperature of 20 ºC, the color of drying mirodroplets varied gradually from pale color to green and finally blue, giving plain-shaped deposits (Case III in Figure 2C, 2D). The phenomena could be explained by that the high humidity reduced the outward flow. Hence, the solvents in drying droplets were evaporated evenly and thus uniform colloid distribution was finally attained (Case III in Figure 2E).

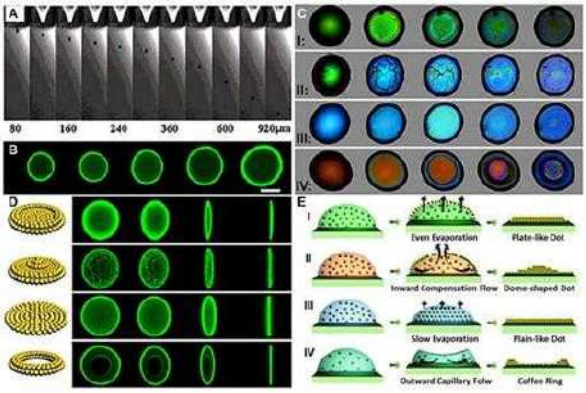


Figure 2. (A) Real-time droplet ejecting process ahead of the printer nozzle (Nozzle Orifice 70 μm) and (B) the confocal micrographs of printing dots. Scale bar = 100 μm. (C) Four typical colloid assembly processes correspond to the droplets drying at a temperature and humidity of (30 ºC, 40 %), (40 ºC, 50 %) and (20 ºC, 80 %), (20 ºC, 40 %) respectively. (D) Confocal micrographs of the final colloidal deposits. (E) Proposed mechanism for the colloidal deposition processes.

The "colloid skin"-regulated self-assembly strategy could also be applied to produce large-area colloidal crystal films through the spray-painting technology. Accordingly, a well-executed palette of structural colors was prepared by alternately spraying the inks containing PS colloids of 195, 215 and 272 nm onto the glass substrate (Figure 3A). The optical characteristics of multiple photonic bandgaps indicate that their colors originate from the overlay of different colloidal crystal deposits (Figure 3B). More attractively, the intermittently air-sprayed film displays identical colors rather than angle-dependent colors shown in conventional colloidal crystal film (Figure 3C). This feature can be attributed to the hemispherical symmetry of the dome-shaped deposits, resulting in identical photonic responses independent of the rotation of the axes. Accordingly, an orange-colored "Dragon" pattern was facilely prepared on a flexible polyethylene glycol terephthalate (PET) film (Figure 3D). This feature frees us from heavy synthesis burden and provides a simple but effective route to prepare full-spectrum structural colors with the synergy effects of colloid species.

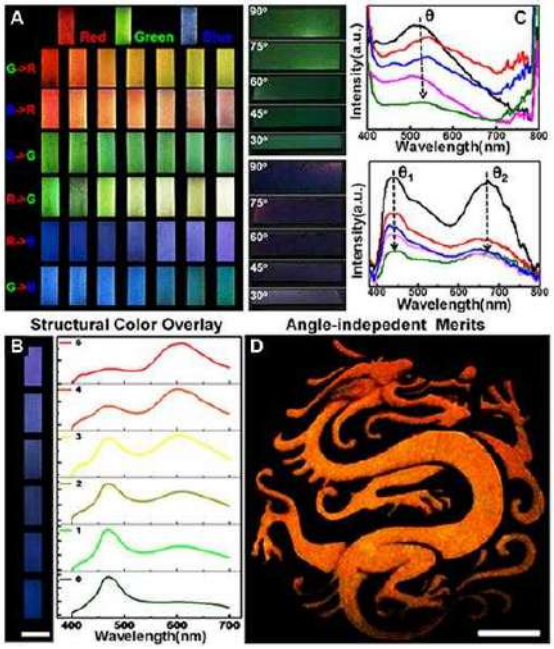


Figure 3. (A) Colloidal crystal films with diverse colors attained by alternately spraying the PS Colloids. (B) Optical photographs and corresponding reflectance spectra of the colloidal crystal films obtained by alternately spraying. (C) Optical images and reflectance spectra of the films at different viewing angles. (D) The angle-independent dragon pattern on PET films.

Conclusions

In conclusion, a "colloid skin"-regulated drying strategy was demonstrated in this work to achieve better control over the colloid deposition processes. Accordingly, the coffee-ring effect could be sufficiently suppressed. Perhaps, more importantly, this "colloid skin" concept suggests the development of a new broad-spectrum kind of film-forming strategy, and the issues associated with the asymmetrical evaporation process of latexes could be addressed. Also, this "colloid skin" concept could be applied in film forming of other water-borne resins, and thus a number of defects occurred during film forming for other waterborne films might be easily solved.

Acknowledgements

This work was supported by National Natural Science Foundation of China (21736006), National Key Research and Development Program of China (2016YFB0401700).

References

[1] Kuang, Minxuan, Jingxia Wang, and Lei Jiang. Chem. Soc. Rev. 2016, 45: 6833-6854.

[2] L. Bai, V. C. Mai, Y. Lim, S. Hou, H. Möhwald, H. Duan, Adv. Mater. 2018, 1705667

[3] J. Zhang, Z. Zhu, Z. Yu, L. Ling, C.-F. Wang, S. Chen, Mater. Horiz. 2019, 6, 90-96.

Versatile Functionalized Photonic Crystals and Their Self-Assembly Applications through Chip Microfluidic Technology

Chang Liu, Xiang-Yun Du, Zhijie Zhu, Qing Li, Su Chen*

State Key Laboratory of Materials-Oriented Chemical Engineering, College of Chemical Engineering
Nanjing Tech University, Nanjing 210009 (P. R. China)
*corresponding author, E-mail: chensu@njtech.edu.cn

Abstract

Through microfluidics and chips a variety of particles self-assembled more complex shapes, anisotropic nature, and diverse functionalities. We group develop an available magnetic-directed assembly strategy to construct a series of molecular-analogue photonic crystal cluster particles involving dot, line, triangle, tetrahedron, and triangular bipyramid configurations from solid−liquid Janus building blocks. These versatile multiplex molecular-analogue structural clusters can open a new promising access to a variety of robust hierarchical microstructural particle materials.

Introduction

Photonic crystal have received increasing attention due to their potential for applications such as remote manipulation, electrophoretic displays, self-assembly of multidimensional ordered structures, and sensors.[1,2] Herein, we developed a triphase microfluidic-directed self-assembly to construct supraparticles with controllable and predictable shape, and selectively introduced advanced functions to them.[2] The triphase microfluidic technique is a co-flowing system that produces continuous microdroplets comprising two immiscible phases. By adjusting the interfacial tension of each phase in the microfluidic system, supraparticles with tunable shape, varying from crescent, meniscus, and ellipsoid to spherical were prepare by the self-assembly of the monodisperse colloidal particles in these microdroplet templates.[3] In this work, we demonstrate an operable magnetic-directed assembly strategy to engineer PC particles into a series of molecular-analogue superstructural morphologies based on Janus building blocks. Herein, Janus building block composed of colloid PCs as the solid hemisphere and superparamagnetic nanoparticles confined in the other liquid part can be successfully designed via triphase microfluidics. Importantly, diverse functions can be integrated into the colloid PCs hemispheres of the Janus building block by loading fluorescent dyes or quantum dots (QDs), whereas the superparamagnetic liquid hemispheres allow the formation of hierarchical anisotropic structures via their coalescence upon collision under externally magnetic field, which confer the resulting materials on remote-controlled locomotion function.

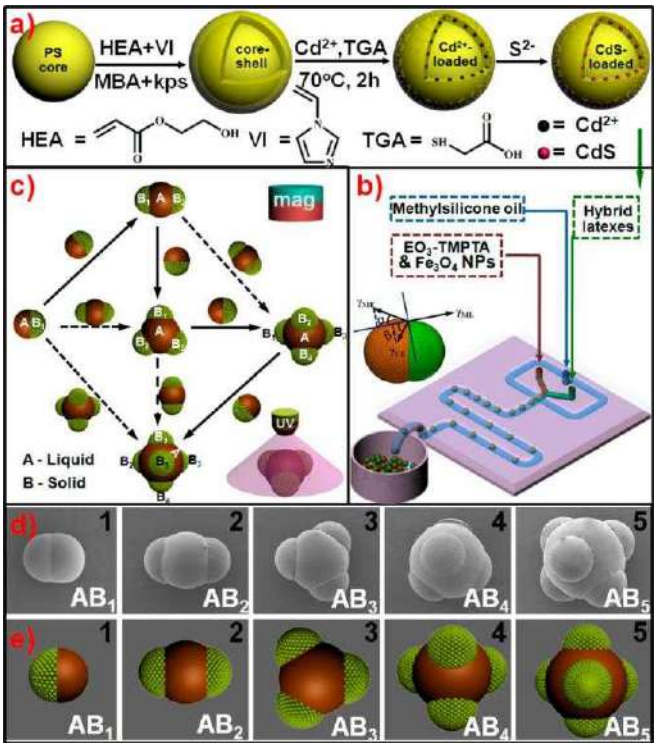


Figure 1. Anisotropic photonic crystal clusters constructed from solid−liquid Janus building blocks.

Discussion

Figure 1 presents the entire preparative strategy for producing magnetic-fluorescent PC clusters. Well-defined poly(styrene-co-2-hydroxyethyl acrylate) (PS-co-PHEA) cores and poly(Nvinylimidazole-co-2-hydroxyethyl acrylate) (PVI-co-PHEA) shells were designed as microreactors for the fundamental carrier to fabricate CdS QDs-loaded hybrid latexes, enabling PC to have both photonic bandgap and fluorescent properties. In the first step, we chose monodispersed PS-co-PHEA colloids as cores and poly(VI-co-HEA) hydrogels as shells to synthesize core−shell structural monodispersed colloids via seeded emulsion copolymerization. Taking advantage of the chelation of PVI within a shell to coordinate Cd^{2+}, CdS QDs with yellowish green fluorescence were in situ prepared within monodispersed microspheres after introducing a sulfur source (Na_2S). Next, a triphase microfluidic device

containing a parallel two-needle microchannel (providing channels for the discontinuous phases) and a tubular polydimethylsiloxane channel (providing channel for the continuous phase) was constructed, which allowed three liquid phases to flow simultaneously. One of the discontinuous flowing phases was the as-prepared CdS-loaded hybrid latexes, and the other one was the photopolymerizable monomer EO_3-TMPTA containing 2 wt% superparamagnetic ferroferric oxide (Fe_3O_4) nanoparticles. The two discontinuous streams were broken into a pair of droplets, and then immediately incorporated into a larger single biphasic one at the exits of the parallel two-needle microchannel by an outer continuous phase of methylsilicone oil. As advanced building blocks, a typical trait of Janus units is obvious double-faced geometry. Therefore, it is crucially important that the two immiscible phases in each droplet also show evident double-face structure in the creation of biphasic droplets.

The resulting Janus building block displayed restricted magnetic-responsive behavior under external magnetic field due to the presence of superparamagnetic Fe_3O_4 nanoparticles. As a small magnet was applied, the Janus building block moved to the external field and then rotated freely, facilitating the micromanipulation of liquid hemispheres direction and locomotion. Therefore, the liquid hemispheres of these Janus building blocks could collide and merge with each other into a larger hierarchical one with increased solid compartments via the pinpoint control of the center of the magnetic field (Figures1c). The simplified model can be expressed by eq 1:

$$A_1B_1 + A_1B_1 + ... + A_1B_1 = ABn \quad (1)$$

If the center of each PC compartment is regarded as a vertex of a polyhedron, the primer configurations can be denoted as AB_1 (dot, n =1), AB_2 (line, n=2), AB_3 (plane or triangle, n=3), AB_4 (tetrahedron, n=4), and AB_5 (triangular dipyramid, n=5). Once $n \geq 4$, these configurations consisting of the vertices are deemed to be polyhedra or deltahedra, whose faces are equilateral triangles. These special structures appear in many common molecules. Notably, the route involved in this process is fairly simple to execute, facilitating its use in the preparation of complex particle materials with elaborate structures.

To realize batch production of molecular-analogue photonic crystal structures, the magnet array was designed and applied for the organization of Janus building blocks. As described in Figure 2a, the magnetic needle array was immobilized on a flat substrate with the configuration of hexagonal modules. Because the Janus units can freely rotate under magnetic field, when the vessel containing solid−liquid Janus building blocks was placed on the magnet array (Figure 2b), the liquid hemispheres oriented toward the nearest magnet, driving the mobile of Janus units to the corresponding magnet needle. The Janus building blocks then met at the center of the magnetic field, and their liquid hemispheres collided and merged with each other into a larger hierarchical one (Figure 2c−e). After the magnet array was removed, the solid compartments on the surface of liquid always appeared as the colloidal molecules with spherically symmetric distribution (Figure 2f).

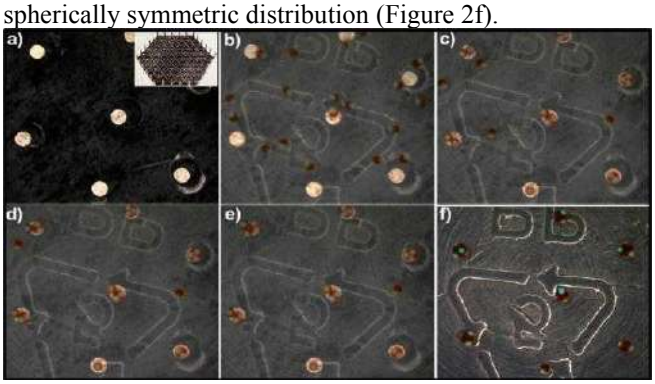


Figure 2. The assembly process of solid−liquid Janus building blocks into PC clusters under magnet arrays.

Conclusions

We have successfully established a robust strategy to fabricate a series of molecular-analogue photonic crystal structures with hierarchical microarchitectures based on solid−liquid Janus building blocks. The exceptional performance of these architectures presents a significant step toward construction of complex anisotropic particle materials with diverse geometries and versatile functions. The capability to precisely tune PC clusters into multiangular configurations (dot, line, triangle, and tetrahedron to triangular bipyramid) unlocks a vast potential for pipelined integration of photoelectricity material toward information communication. With this approach, we assert that various well-controlled molecular-analogue supraparticles can be designed and applied in anticounterfeiting, biolabeling, and information encoding.

Acknowledgements

This work was supported by the Natural Science Foundation of China (21076103, 21176122, 21474052, and 21506095), the Natural Science Foundation of Jiangsu Province (BK20140934 and BK20150940), Priority Academic Program Development of Jiangsu Higher Education Institutions (PAPD), and the Qing Lan Project.

References

[1] Pregibon, D. C.; Toner, M,; *Science.* 315: 1393−1396, 2007.

[2] Utada, A. S.; Lorenceau, E.; Link, D. R.; Kaplan, P. D.; Stone, H.A.; Weitz, D. A. *Science.* 308: 537−541, 2005.

[3] Norris D.J.; Arlinghaus G.; *Scriven. Adv. Mater.* 16:1393-1399, 2004.

[4] Maeda, K.; Onoe, H.; Takinoue, M.; Takeuchi, S. *Adv. Mater.* 24:1340−1346, 2012.

Photonic crystal bead 2D code patterns based on microfluidic 3D printing

Xiang-Yun Du, Zhijie Zhu, Chang Liu, Qing Li, Su Chen*

State Key Laboratory of Materials-Oriented Chemical Engineering, College of Chemical Engineering
Nanjing Tech University, Nanjing 210009 (P. R. China)
*corresponding author, E-mail: chensu@njtech.edu.cn

Abstract

A novel method for facile preparation of photonic crystal (PCs) bead two-dimensional (2D) code patterns through microfluidic 3D printing technology is developed. Poly(styrene-methyl methacrylate-acrylic acid)-CdTe/ZnS (P(St-MMA-AA)-CdTe/ZnS) hybrid microspheres with structure color and fluorescence are prepared by conjugating P(St-MMA-AA) and CdTe/ZnS quantum dots (QDs) using PAMAM dendrimers as bridges. This work open a promising way for the fabrication of multi-signal 2D code patterns with structural color and fluorescent properties, which has potential application in anti-counterfeiting and optoelectronic field.

1. Introduction

Photonic crystals (PC) have attracted intensive intersting due to their unique optical properties and extensive applications. Owing to their bright structure colors, PCs can be applied to construct multicolor patterns with bright, tunable and fadeless colors, which have potential applied in various fields of sensing[1], display[2], detection[3] and security areas[4]. Much effort has been carried out to manufacture the functional PCs patterns, such as inkjet printing[5], screen printing[6], 3D-printing[7] and microfluidic[8]. However, it is still a great challenge to improve their information capacity, color quality and functional performance, which are essential for practical applications. In this work, we exploit a facile method to precisely construct PCs 2D code patterns via microfluidic 3D printing technology, where PC beads were served as pixels. The as-prepared PCs patterns possessed both structural colors in daylight and fluorescence under UV light as well as it could be applied to facilely construct 2D robust codes. This novel microfluidic 3D printing technology developed in this work may pave a new way for the fabrication of multifunctional PC patterns.

Discussion

The synthesis process of P(St-MMA-AA)-CdTe/ZnS hybrid microspheres is exhibited in Fig.1 (a). Firstly, we prepared monodisperse core-shell P(St-MMA-AA) microspheres by taken polystyrene (PS) as a core using seed emulsion copolymerization. Then, the as-prepared colloid particles with abundant carboxyl groups were further grafted with generation 2 polyamindoamine (G2 PAMAM) dendrimers

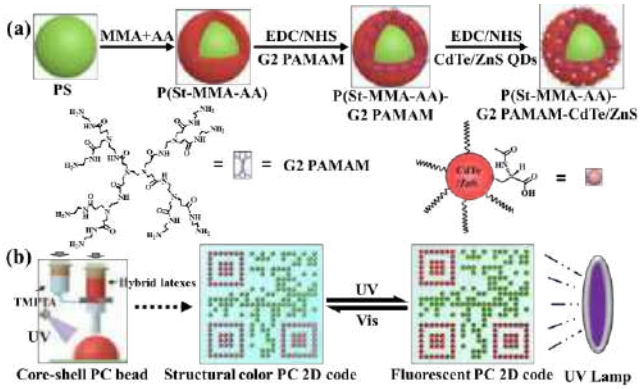


Figure 1. (a) Schematic illustration for the fabrication process of P(St-MMA-AA)-CdTe/ZnS hybrid microspheres. (b) Preparation of PCs bead 2D code with structural color and fluorescence via the microfluidic 3D printing equipment.

with rich terminal amino groups. Taking advantage of the interaction between the functional groups on the surface of CdTe/ZnS QDs and dendrimers, we successfully synthesized the P(St-MMA-AA)-CdTe/ZnS hybrid microspheres (Fig. 1a).

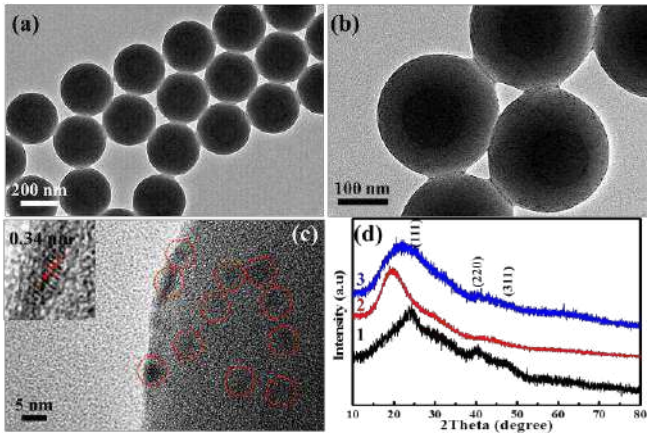


Fig. 2 TEM (a, b) and HRTEM (c) images of P(St-MMA-AA)-CdTe/ZnS hybrid microspheres. Inset: crystals lattices of CdTe/ZnS QDs. (d) XRD patterns of (1) CdTe/ZnS QDs, (2) P(St-MMA-AA)-G2 PAMAM microspheres and (3) P(St-MMA-AA)-CdTe/ZnS hybrid microspheres.

Transmission Electron Microscope (TEM) were employed to observe the morphological structure of the as-prepared P(St-MMA-AA)-CdTe/ZnS hybrid microspheres. As shown

in Fig. 2(a), the hybrid microspheres keep a well-defined spherical shape. The core-shell structure of microspheres can be clearly in sight in Fig. 2(b), which testifies that the hybrid microspheres are surrounded by CdTe/ZnS QDs. Fig. 2(c) shows the uniform dispersion of QDs with an average particle size of 3-4 nm on the surface of the microspheres. The high-resolution TEM (Inset in Fig. 2(c)) reveals the distinct lattice fringes of CdTe/ZnS QDs with the lattice spacing of about 0.34 nm, corresponding to the crystal plane of cubic CdTe/ZnS QDs (111). The lattice structures were further attested by XRD analysis. Three characteristic peaks at 2θ values of 24.3°, 40.4°, 47.7° are clearly observed in curve 1 of Fig. 2(d), corresponding to the (111), (220), (311) planes of cubic CdTe/ZnS QDs structure. The as-synthesized P(St-MMA-AA)-CdTe/ZnS hybrid microspheres (curve 3 of Fig. 2(d)) exhibit three characteristic peaks at the same values with CdTe/ZnS QDs, which is non-existence in P(St-MMA-AA)-G2 PAMAM microspheres (curve 2 of Fig. 2(d)). Above all, the results confirm this method realize the loading of QDs on the PCs.

For practical applications, we applied the as-fabricated PCs with fluorescence for 2D code patterns. Microfluidic 3D printing technology was adopted to fabricate PCs 2D code patterns using trimethylolpropane triacrylate (TMPTA) as external phase and hybrid microspheres as internal phase (Fig. 3(a)). Through precise control and arrangement of the PC beads, we successfully achieved 2D code pattern with two structural colors (red and green) (Fig. 3(b)), which also presents two fluorescence colors (red and green) under UV light (Fig. 3(c)). Compared with the traditional 2D code, the PCs bead 2D code was designed by endowing every pixel with special photonic bandgap and fluorescence features

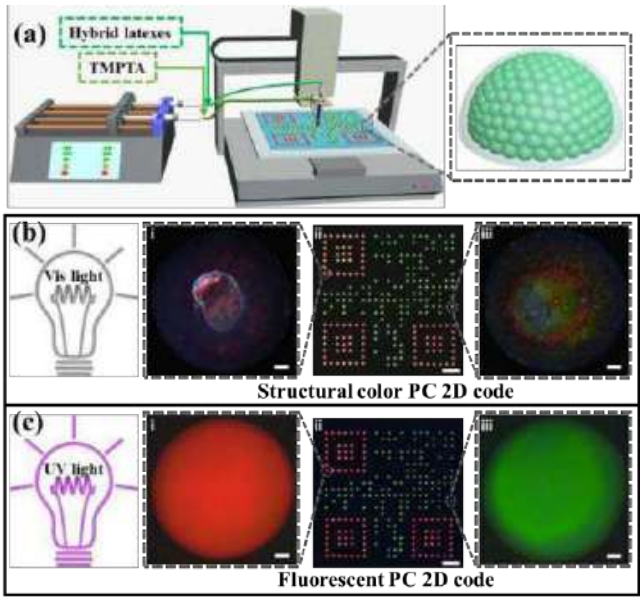


Fig. 3 (a) Schematic illustration of the preparation process of PC bead 2D code via microfluidic 3D printing equipment. (b) Optical images of PC bead 2D code. (The scale bars in i, ii and iii are 100 μm, 5 mm and 100 μm, respectively.) (c) Fluorescent images of PC bead 2D code. (The scale bars in i, ii and iii are 100 μm, 5 mm and 100 μm, respectively.)

thus giving the code with information transmission and anti-counterfeiting potentials. Despite immense progresses have been made, much efforts should be donated into improving information capacity of PC patterns. That motivates us to explore multifunctional PC patterns to satisfy the demand in practical applications.

Conclusions

In conclusion, we developed a new method for the rapid preparation of multi-signal PCs 2D code pattern through microfluidic 3D printing equipment. CdTe/ZnS QDs are loaded onto the surface of P(St-MMA-AA) microspheres by in situ reaction, endowing the hybrid microspheres with fluorescence properties. In virtue of a microfluidic 3D printing device developed in this work, we fabricated multi-signal PC 2D code pattern with different structural colors and fluorescent properties, which shows great potential in anti-counterfeiting and sensing applications.

Acknowledgements

This work was supported by National Natural Science Foundation of China (21736006, 21474052), the National Key Research and Development Program of China (2016YFB0401700), and Priority Academic Program Development of Jiangsu Higher Education Institutions (PAPD).

References

[1] Z. Cai, D. H. Kwak, D. Punihaole, Z. Hong, S. S. Velankar, X. Liu, S. A. Asher, *Angew. Chem. Int. Ed. Engl.* 54: 13036-13040, 2015.
[2] L. Nucara, V. Piazza, F. Greco, V. Robbiano, V. Cappello, M. Gemmi, F. Cacialli and V. Mattoli, *ACS Appl. Mater. Interfaces* 9: 4818-4827, 2017.
[3] Y. Fang, Y. Ni, S.-Y. Leo, C. Taylor, V. Basile, P. Jiang, *Nat. commun.* 6, 2015.
[4] M. Chen, Y. Tian, J. Zhang, R. Hong, L. Chen, S. Chen, D. Y. Son, *J. Mater. Chem. C* 4: 8765-8771, 2016.
[5] L. Shang, F. Fu, Y. Cheng, H. Wang, Y. Liu, Y. Zhao, Z. Gu, *J. Am. Chem. Soc.* 137: 15533-15539, 2015.
[6] J. Hou, H. Zhang, Q. Yang, M. Li, Y. Song, L. Jiang, *Angew. Chem. Int. Ed. Engl.* 53: 5791-5795, 2014.
[7] Y. Li, X. Zhou, Q. Yang, Y. Li, W. Li, H. Li, S. Chen, M. Li, Y. Song, *J. Mater. Chem. C* 5: 4621-4628, 2017.
[8] H. J. Bae, S. Bae, C. Park, S. Han, J. Kim, L. N. Kim, K. Kim, S.-H. Song, W. Park, S. Kwon, *Adv. Mater.*, 27: 2083-2089, 2015.

Near-field focusing devices

Yu-Chieh Cheng[1], and Kestutis Staliunas [2,3]

[1]National Taipei University of Technology, Department of Electro-Optical Engineering, No. 1, Sec. 3, Chung-Hsiao E. Rd, Taipei, 10608, Taiwan
[2]Universitat Politècnica de Catalunya, Departament de Física i Enginyeria Nuclear, Rambla Sant Nebridi 22, Terrassa 08222, Spain
[3]Institució Catalana de Recerca i Estudis Avançats (ICREA), Pg. Lluís Companys 23, Barcelona 08010, Spain
*corresponding author, E-mail: yu-chieh.cheng@ntut.edu.tw

Abstract

The paper shows the recent process towards the design of flat focusing optics in the near field and the far field. An important feature of the near-field flat focusing mirrors - the transverse invariant, i.e. they do not possess any optical axis, very different from the far-field flat optics. The paper also summarizes the near-field and far-field flat optics with a future outlook.

1. Introduction

Over the last few years, scientists have started crafting tiny, thin and flat lenses with a new methodology as shown in Fig. 1. Flat optics have been studied recently by with planar artificial nanostructures such as metasurface [1]. Such subwavelength-spaced phase shifters on the metal–dielectric interface can introduce abrupt phase variations in incident waves by either resonant phase retardation. However, to focus a light as a spherical lens, the nano-patterns on the flat optics must follow a radial distribution of phase discontinuities. Therefore, they unavoidably present optical axes due to symmetrically customized structures.

On the other hand, a new physical principal of flat focusing with a negative refractive index (NRI), also called a 'left-handed' medium, was proposed by the Russian scientific Victor Veselago theoretically[2]. The main advantages of such unprecedented flat lens are its transverse invariant and an arbitrary large NA, that traditional curved lenses/mirrors can never achieve.

Over the past decades, the implementations of these focusing features had generally been realized by the artificial materials in transmission but none of them were studied for focusing upon reflection. Until a few years ago, the authors demonstrated the first flat focusing mirror, which provided an adequately long focal length in the near field [3]–[7]. Such unprecedented features open new challenges for focusing and imaging arrangements.

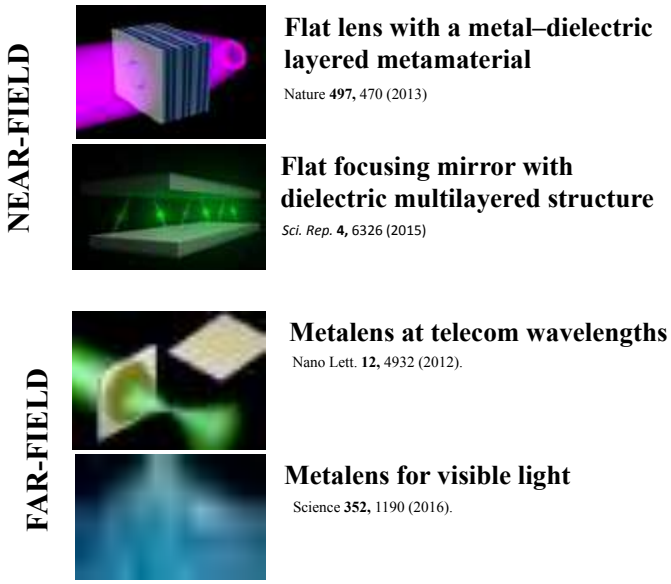


Figure 1: The highlighted near-field and far-field lenses/mirrors with flat surfaces.

2. Near-field and far-field focusing

2.1. Near-field focusing

The approach to making a near-field flat lens without an optical axis has been demonstrated by the near-field flat focusing mirror (FFM). These FFMs can focus a point source or a tightly-focused beam, regarded as a superposition of different plane waves propagating at different angles by manipulating the lateral displacement. The principle of the FFM relies on the anomalous dependence of the lateral shift *s* of the different light rays on the angle of incidence, as illustrated in Fig. 2. The condition is that the slope of the lateral displacement with respect to the angle of incidence should be negative. All the observations are compatible with the requirement of a negative slope of lateral shift with respect to angles and such a condition can also be applied to Pendry's flat lens as shown in Fig. 2a.

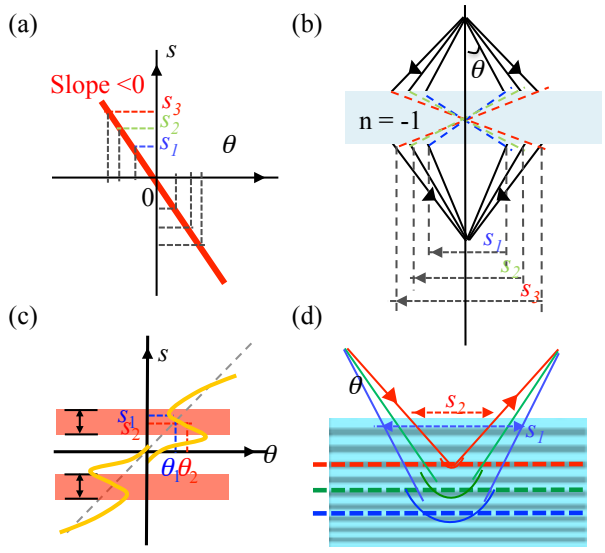


Figure 2: Focusing principle for near-field focusing optics. (a) The illustration of the flat lens with NIMs. (b) The flat lens follows the relation that the lateral displacement is inversely proportional to the angle of incidence. (c) The flat focusing mirror was achieved by the multilayered structures which also show (d) the slope of lateral displacement with respect to angles is negative.

2.2. Far-field focusing

Spatial manipulation of radiation in optical systems is conventionally performed by curved lenses/mirrors which represent a well-known type of far-field focusing. It should be noted that the focusing mechanism of carefully engineered high-contrast gratings (HCGs) and metallic optical antennas (metasurface) is based on far-field lensing. These planar focusing devices modulate the transmitted/reflected phase by tailoring spatial distribution symmetrically and it modifies the angles of refraction (far-field components) as shown in Fig. 3.

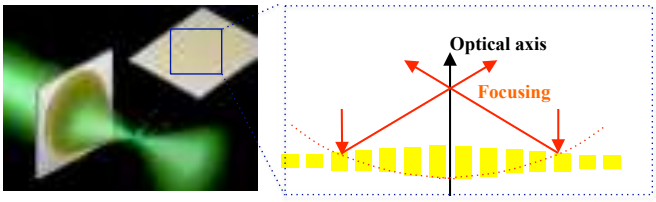


Figure 3: Focusing principle for far-field focusing optics. To focus a light, the metasurface is oriented with a radial symmetry, resulting in an optical axis.

3. Discussion

All the evidences show that the topic of flat focusing mirrors without any optical axis is relevant, innovative and groundbreaking. Such flat focusing mirror will be a major improvement towards widespread future application of flat optics that will certainly attract the interest of the industry. On the other hands, ultrathin flat lenses have undergone considerable development based on HCGs and metasurfaces, they all present optical axes like conventional lenses. It is not possible to eliminate the optical axis because the spatial modulation on a large spatial scale breaks the transverse invariance.

4. Conclusions

To conclude, this paper is devoted to the idea of flat focusing devices especially for focusing upon reflection with a prominent property: they do not have any optical axis. The review starts with the thoughtful discussion about different focusing mechanisms between far-field lens/mirrors and near-field lens/mirrors.

Acknowledgements

We are grateful to co-authors of our papers: M. Peckus, M. Malinauskas, R. Herrero, M. Botey, J. Trull, R.Vilaseca, S.Kicas, R.Drazdyy, C. Cojocaru, H. Zeng, C.H. Ho and D.S. Wiersma who participated in the common research reviewed in this article. Additionally, we would like to acknowledge financial support by Spanish Ministerio de Educación y Ciencia and European FEDER (project FIS2015-65998-C2-1-P) and Ministry of Science and Technology in Taiwan, MOST (106-2112-M-027-001-MY3).

References

[1] D. Lu and Z. Liu, “Hyperlenses and metalenses for far-field super-resolution imaging,” vol. 3, p. 1205, Nov. 2012.

[2] V. G. Veselago, “the Electrodynamics of Substances With Simultaneously Negative Values of and M,” *Sov. Phys. Uspekhi*, vol. 10, no. 4, pp. 509–514, 1968.

[3] Y. C. Cheng *et al.*, “Near-field Flat Focusing Mirror,” *Accepted by Applied Physics Review*.

[4] Y. C. Cheng *et al.*, “Flat Focusing Mirror,” *Sci. Rep.*, vol. 4, no. 1, p. 6326, May 2015.

[5] Y. C. Cheng *et al.*, “Beam focusing in reflection from flat chirped mirrors,” *Phys. Rev. A*, vol. 87, no. 4, p. 45802, 2013.

[6] Y. C. Cheng *et al.*, “Beam focalization in reflections from flat dielectric subwavelength gratings,” *Opt. Lett.*, vol. 39, no. 20, 2014.

[7] Y. C. Cheng, S. Kicas, and K. Staliunas, “Flat focusing in reflection from a chirped dielectric mirror with a defect layer,” *J. Nanophotonics*, vol. 9, no. 1, p. 93084, Mar. 2015.

Classification of deformed photonic Dirac cones

Jungmin Kim, Sunkyu Yu, and Namkyoo Park

Photonic Systems Laboratory, Department of Electrical and Computer Engineering,
Seoul National University, Seoul 08826, Korea
*corresponding author, E-mail: nkpark@snu.ac.kr

Abstract

We investigate the classification of photonic band structures in relation to the perturbed effective Hamiltonian for the Γ-point eigenmodes and their eigenfrequencies. As an example, by top-down engineering the relative spectral distribution of monopole and dipole modes, we classify the modification of the Dirac dispersion. The behavior of wave phenomena inside the designed structure, such as anisotropic Dirac dispersion, will also be discussed.

1. Introduction

The discovery of the massless Dirac fermion in graphene has opened a new horizon in condensed matter physics [1]. The photonic Dirac cone (PDC) for electromagnetic waves, as an optical analogue of the Dirac cone in electronics, has also attracted much attention due to various peculiar phenomena near the PDC, including the zero effective index of refraction [2], and a topological edge state [3].

Compared to the electronic Dirac cone in the graphene structure on the K and K' edges of the Brillouin zone, which originates from the parity symmetry of two basis atoms [4], in contrast, the accidentally induced triple degeneracy of the PDC at the Γ-point is not protected by such symmetries [2]. Therefore, the PDC is very sensitive to the on-site potential; a very small perturbation in elemental dielectric rods could result in to the collapse of the PDC.

This delicacy in PDC structure on the other hand, could provide a new degree of freedom for the manipulation of the band structure near the Dirac point. For example, the PDC spawns a ring of exceptional points under the broken time-reversal symmetry with complex optical potentials in the regime of non-Hermitian photonics [5]. There also exist several reports on the splitting of a Dirac cone into a pair of bulk Fermi arcs, carrying a nontrivial topological charge due to the broken rotational symmetry [6]. Connected with the topological properties, the manipulation of PDC band structures has recently become an emerging topic, covering broad areas of research: including topological photonics, metamaterials, and quantum-optical analogy.

Here, we apply the effective Hamiltonian theory for the systematic description and classification of the modulated PDC band structure. By examining the influence of each term on the variation of the band shape, we also discuss the modulation of the Γ-point eigenmode.

2. Results

We begin with a theoretical model to examine the band structure at the vicinity of the Γ-point. This model enables the prediction of the effect of the Γ-point eigenmode and eigen frequency on the band shape.

In a two-dimensional structure, the governing harmonic equation with frequency ω and TE-mode (E_z) wave is given by $\nabla^2 E_z + k_0^2 \epsilon(\mathbf{r}) E_z = 0$, where $k_0 = \omega/c$ and $\epsilon(\mathbf{r})$ is the periodic function of relative permittivity for a non-magnetic square-lattice photonic crystal. Due to the discrete translational symmetry, E_z is expressed by a Bloch wave $E_z(\mathbf{r}) = e^{i\mathbf{k}\cdot\mathbf{r}} u_{\mathbf{k}}(\mathbf{r})$. Using the $\mathbf{k}\cdot\mathbf{p}$ perturbation theory, this equation can be approximated as an eigenvalue equation: $\hat{H}(\mathbf{k})\,|u_{\mathbf{k}}\rangle = \omega_{\mathbf{k}}\,|u_{\mathbf{k}}\rangle$, where

$$\hat{H}(\mathbf{k}) = \begin{pmatrix} \omega_s & v_x k_x & v_y k_y \\ v_x^* k_x & \omega_{px} & 0 \\ v_y^* k_y & 0 & \omega_{py} \end{pmatrix} \tag{1}$$

and $|u_{\mathbf{k}}\rangle$ is a vector spanned by $\{|s\rangle, |p_x\rangle, |p_y\rangle\}$ basis [5]. Here ω_s (ω_{px}, ω_{py}) and $|s\rangle$ ($|p_x\rangle$, $|p_y\rangle$) denotes the monopole (dipole) eigenfrequency and corresponding mode profile at the Γ-point. v_x and v_y are overlap constants determined by the eigenmodes.

We emphasize that the relative values of the diagonal terms (ω_s, ω_{px}, and ω_{py}) significantly affect the topology

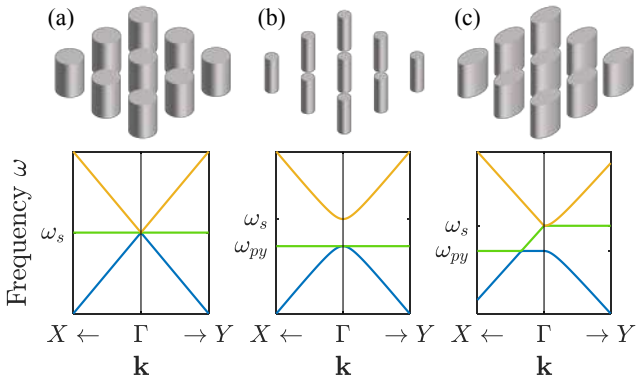


Figure 1: Lattice schematics (upper) and their band dispersions calculated by the effective Hamiltonian theory along k_x and k_y axes (lower) for (a) the photonic Dirac cone: $\omega_s = \omega_{px} = \omega_{py}$, (b) the parabolic–like dispersion: $\omega_s > \omega_{px} = \omega_{py}$, and (c) the anisotropic Dirac dispersion: $\omega_s = \omega_{px} > \omega_{py}$.

of the Hamiltonian on the k-space. For instance, we obtain the PDC characterized by linear dispersions as depicted in Fig. 1a, by setting $\omega_s = \omega_{px} = \omega_{py}$, while achieving a parabolic-like dispersion with flat band and bandgap in the case of $\omega_s \neq \omega_{px} = \omega_{py}$ (Fig. 1b) [7]. The dispersion shown in Fig. 1c, where the linearity of the band structure retains along x-directions but not for y-direction [8] is realized in the case of $\omega_s = \omega_{px} > \omega_{py}$.

3. Conclusions

We developed an effective Hamiltonian theory for the photonic band structure, especially for the classification of the deformation of the PDC. We expect an engineering of direction-selective linear dispersion based on our results. We will also discuss the design principle of the PDC photonic crystal structure based on our approach, for the realization of controlled band structure, and the wave flows.

Acknowledgement

We acknowledge financial supports from the National Research Foundation of Korea (NRF) through the Global Frontier Program (2014M3A6B3063708), the Basic Science Research Program (2016R1A6A3A04009723), and the Korea Research Fellowship Program (2016H1D3A1938069), all funded by the Korean government.

References

[1] K.S. Novoselov, A.K. Geim, S.V. Morozov, D. Jiang, M.I. Katsnelson, I.V. Grigorieva, S.V. Dubonos, and A.A. Firsov, Two-dimensional gas of massless Dirac fermions in graphene, *Nature* 438: 197-200, 2005.

[2] X. Huang, Y. Lai, Z.H. Hang, H. Zheng, and C.T. Chan, Dirac cones induced by accidental degeneracy in photonic crystals and zero-refractive-index materials, *Nat. Mater.* 10: 582-586, 2011.

[3] L.-H. Wu and X. Hu, Scheme to achive topological photonic crystal by dielectric material, *Phys. Rev. Lett.* 114: 223901, 2015.

[4] A.H.C. Neto, F. Guinea, N.M.R. Peres, K.S. Novoselov, and A.K. Geim, The electronic properties of graphene, *Rev. Mod. Phys.* 81: 109, 2009.

[5] B. Zhen, C.W. Hsu, Y. Igarashi, L. Lu, I. Kaminer, A. Pick, S.-L. Chua, J.D. Joannopoulos, and M. Soljačić, Spawning rings of exceptional points out of Dirac cones, *Nature* 525: 354-358, 2015.

[6] H. Zhou, C. Peng, Y. Yoon, C.W. Hsu, K.A. Nelson, L. Fu, J.D. Joannopoulos, M. Soljačić, and B. Zhen, Observation of the bulk Fermi arc and polarization half charge from paired exceptional points, *Science* 359: 1009-1012, 2018.

[7] J.D. Joannopoulos, S.G. Johnson, J.N. Winn, and R.D. Meade, *Photonic Crystals: Molding the Flow of Light (2nd edition)*, Princeton University Press, 2008.

[8] X.-T. He, Y.-N. Zhong, Y. Zhou, Z.-C. Zhong, and Z.-W. Dong, Dirac directional emission in anisotropic zero refractive index photonic crystals, *Sci. Rep.* 5: 13085, 2015.

Wavefront manipulation based of the excitation of bound states in dielectric photonic crystals and bilayer metasurfaces

Anna C. Tasolamprou[1], Maria Kafesaki[1,2], Thomas Koschny[3] and Costas M. Soukoulis[1,3]

1. Institute of Electronic Structure and Laser, FORTH, 70013 Heraklion, Crete, Greece
2. Department of Materials Science and Technology, University of Crete, 70013, Heraklion, Crete, Greece
3. Ames Laboratory and Department of Physics and Astronomy, Iowa State University, Ames, Iowa 50011, United States
*corresponding author, E-mail: atasolam@iesl.forth.gr

Abstract

We present the study of bound surface modes sustained at the termination of truncated bulk dielectric photonic crystals and isolated metasurfaces of dielectric meta-atoms. We discuss the origins of bound modes in the two systems and their relation. For both systems, we theoretically study and experimentally demonstrate wavefront manipulation, in particular directional emission, frequency splitting and beam collimation achieved by coupling of the bound states to radiation modes through leaky wave radiation mechanism using properly designed scattering gratings.

1. Introduction

Surface modes are non-radiating states that are found bound to the interface of different media. Traditionally bound states have been investigated at the interface of semi-infinite dielectric and metallic interfaces at the optical frequencies, the known, so-called surface plasmon polaritons (SPP). SPPs offered a very good platform for highly confining propagating waves and may enable the minimization of electromagnetic components. However, at the same time, dielectric/metallic SPPs suffer from high dissipation losses which pose various application restrictions. However, it was also known that bound states can also be supported in dielectric media. These bound states stem from the excitation of coupled Mie resonances in the dielectric system and lead to light confinement (Mie modes are generally more spatially extended than SPPs). The fact that dielectric media suffer no dissipation losses has brought the non-radiating bound states at the center of attention of composite, all-dielectric resonant structures and metamaterials [1]. In this work we present two type of structures that sustain surface modes, one consists of a metasurface of dielectric meta-atoms [2] and the other consists of truncated photonic crystals [3]. In the first case we demonstrate experimentally that beam collimation can be sustained at large distance via a system of cascading dielectric metasurfaces and in the other case we present the controlled directional emission engineered at the exit of photonic crystal line defect waveguide. For both cases we present the corresponding experimental demonstration which is conducted in the microwave regime and provides a proof of concept verification our analysis. The dielectric structures are be scaled down for the optical/NIR regime [4]. Additionally we will present a theoretical framework that analyses the nature and the origins of the bound surface states in the termination of truncated bulk photonic crystals and their relation to bound states sustained in isolated dielectric metasurfaces.

2. Discussion

The first structure under consideration consists of a system of dielectric metasurface bilayers; the first layer of each bilayer supports surface states and the rear, the grading layer

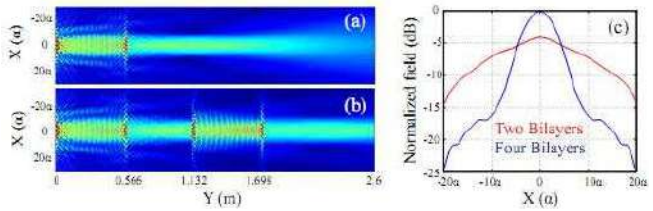


Figure 1: Simulation of the 2D field strength at the exit of a system of bilayer dielectric metasurfaces at the resonant frequency: case of (a) two metasurfaces and (b) four metasurfaces structure. (c) Normalized *x* cross section field distribution for the two cases at propagation distance 100λ.

couples the surface states to radiation modes. The first layer of each bilayer consists of 35 alumina circular rods with a lattice constant of α = 11 mm, while the second layer of square alumina rods with lattice constant $b = 2\alpha$. The experimental set-up consists of an HP E8364B network analyser, a horn antenna as the transmitter and a dipole antenna as the receiver. The horn antenna transmits a Gaussian beam with *E* polarization (the electric field parallel to the dielectric rods) and the dipole antenna scans the 2D experimental table, measuring the intensity of the local field close to the structure and the propagation, diffraction and interference of the outgoing waves. In Figure 1(a) and Figure 1(b) we present strength distribution in a multi-bilayer metasurface system and it has been experimentally verified. We also observe Fabry-Perot type standing wave oscillations that occur in the space that lies between the cascading metasurfaces. Nevertheless, beam collimation at large distances is observed. Figure 1(c) plots the normalized field distribution of the two structures at a propagation distance equal to 2.6 m (100λ). It is obvious that four cascading metasurfaces are capable of cancelling the divergence. The second type of the structure consists of a

photonic crystal terminate by a dielectric layer of the same periodicity and different size than the bulk photonic crystal. The dispersion diagram of the surface state in the bulk termination, shown in red, stands within the photonic crystal

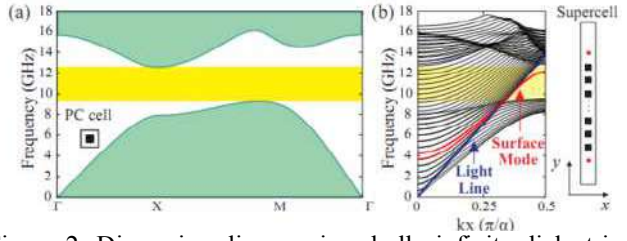


Figure 2: Dispersion diagram in a bulk, infinite dielectric photonic crystal of dielectric rods. The dispersion curves are calculated via the plane wave expansion method for the infinite periodic structure. (b) Dispersion curves for the finite PC along with the surface layer. They are calculated by applying the plane wave expansion in the supercell shown above. The surface mode dispersion is plotted in red; it lies within the badgap and below the light line (blue curve), and occurs at 10.1−12.2 GHz.

bandgap and below the light line which indicates that the mode is dark, bound between in the surface layer the bulk photonic crystal and the air as it is presented in Figure 2. It is in fact almost identical to that of the isolated metasurface of the dielectric of rods. This indicates that the origins of the surface states in the both system are similar. A line defect waveguide formed in the bulk photonic crystal feeds the dark mode that propagates to the exit sides of the structure. A grating layer with double periodicity placed after the surface layer undertakes the coupling of the surface modes into forward radiation. Forcing a small asymmetry in the grating layer leads to the frequency selective modification of the angle of the forward propagating waves. The angle of the emission obeys the surface mode dispersion and grating equation that describes the leaky wave radiation mechanism. In Figure 3 we present the experimentally measurement and numerical study of the near and intermediate field exciting the line defect waveguide. For the experimental study we use the same set-up as that described in the discussion of Figure 1. Oblique directionality at different frequencies is observed enabling the frequency splitting operation. Similar

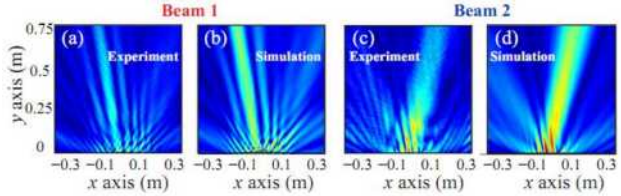


Figure 3: Experimental (a) and simulated (b) 2D plot of the strength of the outgoing near and intermediate field at the exit of a photonic crystal terminated by a surface layer and an asymmetric grating layer at frequency f^{exp1} = 11.70 GHz and f^{sim1} = 11.68 GHz. Axis x is parallel to the grating layer and axis y perpendicular to the grating layer. Experimental (c) and simulated (d) 2D plot of the intensity of the outgoing near and intermediate field at frequency f^{exp2} = 10.20 GHz and f^{sim2} = 10.18 GHz.

operation can be achieved in silicon based inverse photonic crystal for operation in the near infrared and optical regime. The corresponding structure and operation is thoroughly discussed in Ref. [4].

3. Conclusions

We studied theoretically and demonstrated experimentally the realization of wavefront manipulation functions based on the excitation and handling of dark bound surfaces states in dielectric resonant media such as photonic crystals and periodic metasurfaces made of dielectric meta-atoms. In particular, we have demonstrated the sustaining of the beam collimation is possible in a system of cascading dielectric metasurfaces. Additionally we showed that frequency selective, directional emission from a line defect photonic crystal waveguide can be attained if the bulk photonic crystal is properly terminated. The characteristics of the bound states are similar for the two systems indicative of their common origins. Experiments have been conducted in the microwave regime and the structures can be directly scaled in the near infrared and optical frequencies. Due to the absence of ohmic losses, the non-radiating bound states provide a promising platform for the manipulation of light attract the growing attention of the nanophotonic community

Acknowledgements

This work was supported by the European Research Council under ERC Advanced Grant no. 320081 (project PHOTOMETA) and the European Union's Horizon 2020 Future Emerging Technologies call (FETOPEN-RIA) under grant agreement no. 736876 (project VISORSURF). The work performed at Ames Laboratory was supported by the US Department of Energy (Basic Energy Science, Division of Materials Sciences and Engineering) under Contract No. DE-AC02-07CH11358.

References

[1] C .W. Hsu, B. Zhen, A.D. Stone, J.D. Joannopoulos, M. Soljacic, Bound states in the continuum, Nat. Rev. Mater.,1,16048, 2016.

[2] A. C. Tasolamprou, L. Zhang, M. Kafesaki, Th. Koschny, and C. M. Soukoulis, Experimentally excellent beaming in a two-layer dielectric structure, Opt. Express 22, 23147, 2014.

[3] A. C. Tasolamprou, L. Zhang, M. Kafesaki, Th. Koschny, and C. M. Soukoulis, Frequency splitter based on the directional emission from surface modes in dielectric photonic crystal structures, Opt. Express 23, 13972 , 2015.

[4] A. C. Tasolamprou, Th. Koschny,, M. Kafesaki, and C. M. Soukoulis, Near-Infrared and Optical Beam Steering and Frequency Splitting in Air-Holes-in-Silicon Inverse Photonic Crystals, ACS Photonics, 4, 2782, 2017.

Hybrid External Cavity Laser based on Silicon Nitride 1D Photonic Crystals Cavities for dWDM applications

S. Iadanza[1,2], A. Tedesco[3], G. Giannino[3], M. Grande[3] and L. O'Faolain[1,2]

[1]*Tyndall Institute of Technology, Lee Maltings, Dyke Parade, Cork, Ireland*
[2]*Cork Institute of Technology, Rossa Avenue, Bishopstown, Cork, Ireland*
[3]*Dipartimento di Ingegneria Elettrica e dell'Informazione (DEI) Politecnico di Bari, Via Amendola 126/b, Bari, Italy*

Abstract

In this paper we show a silicon nitride external cavity (SiN EC) laser based on a 250µm long AlInGaAs Reflective Semiconductor Optical Amplifier (rSOA) edge-coupled to a series of Si_3N_4 waveguides side-coupled to Si_3N_4 1D photonic crystals that acting as wavelength selective resonators mirror. The laser shows power outputs over 5 mW, lasing threshold of 25 mA with a characteristic Side-Mode Suppression Ratio in the range of 45 dB. This laser shows a mode-hop free lasing regime over a range of 50 mA (from 25 mA to 70 mA). Further on, the 1D photonic crystal resonators are 50um long and 2um wide, leading to reduction in footprint of this type of reflector by a factor of 30 compared to conventional gratings. All of this, combined with the very low thermo-optic coefficient of Si_3N_4 leads to neglectable wavelength drifts with temperature, paving the way to integrated SiN EC laser in Dense WDM and optical interconnect technologies, where transceivers have to operate over a wide temperature range without requiring active cooling.

1. Introduction

The ever-increasing demand higher data transmission bandwidths in long and short range telecommunications [1], leads to a critical need for new and energy efficient narrow linewidth laser sources which are compact and cost-effective in order to be integrated in dense Wavelength Division Multiplexing (dWDM) technology.
This kind of optical interconnects have to be employed in small spaces and in extreme environments that expose them to significant temperature variations, which fundamentally affects their wavelength of operation, hence complicating their utilization in application that require accurate wavelength control and stability, namely WDM [2]. Furthermore, Complementary Metal-Oxide Semiconductor (CMOS) processing is the only technology in which is possible to achieve fabrication of photonics in a cost-effective manner, due to the strict high yield and fabrication repeatability requirements.
The very inefficient light emission properties of silicon are greatly hindering the employment of the promising Silicon-On-Insulator (SOI) platform in optical applications. However, lattice mismatch and CMOS compatibility problems greatly reduce direct III-V materials growth and integration as active medium for WDM lasers.
Our solution to this problem consists in the deployment of hybrid external cavity lasers [2,3], whose cavity is composed by a commercially available Reflective Semiconductor Optical Amplifier (RSOA) edge-coupled to waveguides on a silicon nitride chip, which are side-coupled to 1D photonic crystals to function as narrow resonators.
This configuration allows separate fabrication of the active and the passive chips, unlocking the possibility of separate optimization of the chips and the independent modulation of the external cavity of the laser.
Currently, optical links for WDM applications in most datacenters and operating at telecomm wavelengths consist in DBR lasers and external modulators [4]. These devices are actively cooled [5] to counter the operating wavelength thermal drifts due to the high Thermo-Optic Coefficient (TOC) of the material subjected to the varying temperatures of the operation environment. This leads to a very high energy consumption and cost.
However, the very low TOC and free-carrier absorption of Si_3N_4 compared to silicon and its CMOS compatibility make it a valid material alternative for this of hybrid lasers, which have already shown a greatly reduced wavelength thermal stability [6].
In this paper we demonstrate a single-mode hybrid EC laser based on SiN 1D photonic crystal cavities, which operates in a mode-hop free regime over a broad range of driving currents, exhibiting low threshold, high power and 10 times narrower resonances compared to conventional Distributed Bragg Reflectors, to further improve laser stability. Furthermore, the 1D resonators are reducing footprint on the silicon chip by a factor of 30 compared to gratings, greatly enhancing integrability. Moreover, the wavelength thermal stability of the laser due to Si_3N_4 TOC could eliminate the need of active cooling of any kind, potentially making this type of lasers the devices of choice for WDM applications.

2. Laser Design

Figure 1a. shows schematics of one of the SiN 1D photonic crystal cavity side coupled to the waveguide. Figure 1b. shows the RSOA edge-coupled to the SiN chip. The waveguides on the silicon nitride chip have been designed to match the mode on the output of the RSOA, thus lowering coupling losses. The 1D photonic crystals are 50 µm long by 2 µm wide, greatly reducing the resonators footprint on chip, unlocking the route to high integration densities and high channel counts and allowing for short cleaving of the chip to improve packaging solutions. The 1D SiN resonators have been designed to operate in the S, C and L telecommunications bands. Intrinsic Q-Factors have been calculated in the range of $3*10^6$ and FWHM of the resonances have been measured to be approximately 0.09 nm.

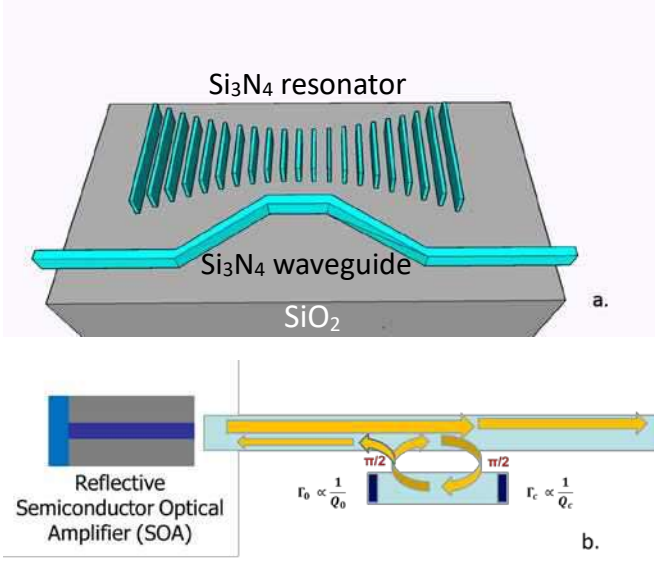


Figure 1 - a. Schematics of the 1D photonic crystal cavity side-coupled to the waveguide, b. schematics of the RSOA edge-coupled to the SiN chip

The RSOA consisted in a 250 µm long gain composed by AlInGaAs quaternary quantum wells, in which the prevention of carriers leakage provided by the Al^{+3} ions at temperature over 60°C [7], leading to an improvement of the RSOA emission at high temperatures. The end facet of the RSOA was AR coated to be used as one of the mirror of the laser, achieving a reflectivity of approximately 90%.

Each carrier injected in the RSOA recombine inside the quantum wells, generating a photon. The light emitted is then coupled to the SiN waveguide and is guided towards the end facet of the SiN chip. The portion of light not in resonance with the resonators is completely transmitted and dropped at the output of the SiN chip. The on resonance component of light on-resonance instead evanescently couples into the 1D photonic crystal cavity on the side of the waveguide and is partially coupled out in the waveguide towards the RSOA, leading to a wavelength-selective amplification loop between the resonator and the reflective edge of the RSOA, that constitutes the mirrors of the laser, whose characteristics are predicted by the overlapping of the gain curve and the longitudinal modes of the cavity.

3. Experimental Results and Discussion

The spectra of transmission of the 1D photonic crystal cavities have been collected through an end-fire setup, in which the light of a broadband source was propagating through an optical fiber, was collimated into the waveguides on the sample through a system of lenses and the light was collected on the output of the waveguides in an optical spectrum analyzer and a photodiode.

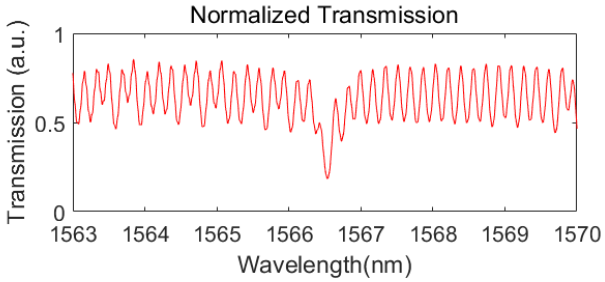


Figure 2 - Optical spectrum of the normalized transmission of one of the 1D photonic crystal cavities

After measuring the passive chips, the characteristics of the laser have been measured with increasing driving currents, with both the RSOA and SiN chips standing on temperature controlled stages. Figure 2 shows the hybrid EC laser time-averaged optical spectrum plotted in a false color map against increasing driving current. By accurately matching the longitudinal mode of the laser cavity with the resonance of the 1D photonic crystals, a mode-hop free single mode lasing regime has been achieved over a broad range of currents, from 21 mA to 70 mA. A low lasing threshold of 20 mA has been recorded.

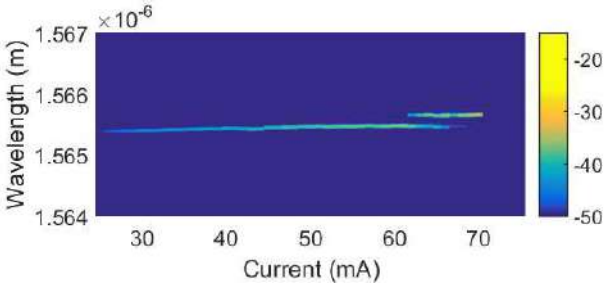


Figure 3 - Time-averaged optical spectrum of the EC laser against driving current

The light at the end facet of the SiN waveguide was collimated with a lens onto a power-meter sensor, and the hybrid EC lasers power have been measured to be all in the range of 3 to 5 mW.

4. Conclusions

To conclude, we have demonstrated a hybrid single mode EC laser based on SiN 1D photonic crystal cavities coupled

to a RSOA gain chip, characterized by low lasing threshold of 20 mA and high output power in the mW range, showing a mode-hop free regime over the driving current range from 21 mA to 70 mA, further improvable with AR coatings of the SiN chip. This associated with the very low TOC of SiN paves the way for future deployment of very compact photonic crystal cavities based SiN chips, with densely spaced resonances, coupled to arrays of RSOAs to build a network of low-cost, compact and potentially athermal transmitters, reducing their energy consumption, thus making these hybrid EC lasers the devices of choice for cost-effective dWDM technologies.

Acknowledgements

Science Foundation Ireland (SFI) (16/ERCS/3838, SFI12/RC/2276); (EP/L017008/1, EP/L505079/1); H2020 LEIT Information and Communication Technologies (ICT); COSMICC 688516; H2020-ICT27-2015); Research Council (EPSRC); H2020 European Research Council (ERC) (337508)

References

[1] R. A. Soref, “The Past, Present, and Future of Silicon Photonics”, IEEE Journal of Selected Topics in Quantum Electronics, Volume 12, No. 6 (2006).

[2] A. J. Zilkie, P. Seddighian, B. J. Bijlani, W. Qian, D. C. Lee, S. Fathololoumi, J. Fong, R. Shafiiha, D. Feng, B. J. Luff, X. Zheng, J. E. Cunningham, A. V. Krishnamoorthy, and M. Asghari “Power-efficient III-V/Silicon external cavity DBR lasers”, Opt. Express 20, Issue 21 (2012).

[3] A. A. Liles, K. Debnath, L. O’Faolain, “Lithographic wavelength control of an external cavity laser with a silicon photonic crystal cavity-based resonant reflector”, Optics Letters, Issue 41, 894-897 (2016)

[4] http://www.optomark.eu/products/cwdm-dwdm/dwdm-multiplexers.html

[5] H. Guan, A. Novack, T. Galfsky, Y. Ma, S. Fathololoumi, A. Horth, T. N. Huynh, J. Roman, R. Shi, M. Caverley, Y. Liu, T. Baehr-Jones, K. Bergman, and M. Hochberg, "Widely-tunable, narrow-linewidth III-V/silicon hybrid external-cavity laser for coherent communication," Opt. Express 26, 7920-7933 (2018)

[6] S. Iadanza, A. P. Bakoz, P. K. J. Singaravelu, D. Panettieri, S. A. Schulz, G. C. R. Devarapu, S. Guerber, C. Baudot, F. Boeuf, S. Hegarty, and L. O’Faolain, "Thermally stable hybrid cavity laser based on silicon nitride gratings," Appl. Opt. 57, E218-E223 (2018)

[7] E. Murphy, C. Michie, H. White, W. Johnstone, A. E. Kelly and I. Andonovic, “High Temperature Wavelength Division Network for Avionic Applications,” Journal of Lightwave Technology, Volume 31, No. 18, 3006-3013 (2013).

Emerging applications

Broadband photoacoustic microscopy based on surface plasmon resonance sensing

Changjun Min[1*]

[1] Nanophotonics Research Centre, Shenzhen University, 518060, China
*corresponding author, E-mail: cjmin@szu.edu.cn

Abstract

The ability to accurately detect pressure transients is critical for photoacoustic (PA) imaging of anatomic and functional information in biological tissues. Here, we propose a surface plasmon resonance (SPR) sensing approach for PA pressure detection, relying on the modulation of PA pressure to the refractive index. We realize a much broader PA bandwidth more than ~170 MHz and *in vivo* imaging of the microvasculature from mouse ears. This SPR sensing method has great potential in PA imaging for biomedical investigations.

1. Introduction

Relying on rich optical absorption contrasts within biological tissues, photoacoustic (PA) imaging technology contributes significantly in revealing physiological and pathological processes of biological tissue [1,2]. As a result of biomolecules' light absorption to laser pulses, pressure transients are produced thermo-elastically, which subsequently generate broadband ultrasounds (i.e., PA waves). Physiological information carried in PA waves allows for quantifying blood flow, oxygen metabolism, and cell micromorphology [3]. Among various PA imaging technologies, optical-resolution photoacoustic microscopy (OR-PAM) has attracted increasing attentions in biomedical researches, since its optical-diffraction-limited lateral resolution leads to better understanding to optical absorption-based molecular specificities at the cellular and even subcellular level.

OR-PAM usually employs piezoelectric transducer for ultrasonic detection, which is not sufficient for responding PA pressure transients due to the very limited bandwidth (centered at its resonance frequency) originated from inherent physical properties of the piezoelectric materials [4]. This degrades the resolution capability along the depth direction in OR-PAM, resulting in one order of magnitude worse compared to its lateral resolution.

Optical technologies of ultrasonic detection offer a promising alternative that potentially addresses the drawbacks in PA imaging, such as plano-concave optical microresonator, Fabry-Perot interferometer, and light interferometry. Unfortunately, inadequate frequency response (less than 70 MHz) can only give the PAM's depth resolution of more than 20 μm. Recently, optical surface wave (OSW) sensing approaches, such as surface plasmon resonance (SPR) sensor [5] and polarization-dependent reflection ultrasonic detection (PRUD) [6], have been developed for detecting PA pressure. However, low sensitivity in both SPRS and PRUD leads to very limited signal-to-noise ratio (SNR) in PA imaging.

2. Principle and Method

OSW sensing of ultrasonic waves offers opportunities to overcome the aforementioned difficulties from the traditional piezoelectric transducers. Here, we developed PAM system incorporating an OSW senser for PA detection. The sensor is configured at Kretschmann structure (Figure 1a), consisting of a gold layer deposited onto the surface of a quartz prism. A drop of deionized water serves as the coupling medium of laser-induced acoustic waves. In this work, we adopted the 50-nm thickness gold film as the sensing material, respectively. Figure 1b shows the light field distribution of the sensor with Au layer as a function of incident angle. Its angular-dependent reflectance spectra indicate that only the *p*-polarized electric field vector with the typical incident angle can excite the SPR. While SPR is independent on the *s*-polarization component.

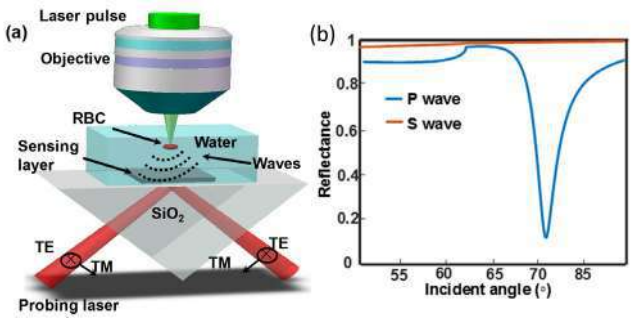


Figure 1: (a) Schematic diagram of optical surface wave (OSW) sensor for PA pressure detection. (b) Angle-dependent light reflection of p- and s-polarized light for SPR-based sensor.

During PAM imaging, a nanosecond laser pulse is focused onto the sample, generating ultrasonic pressure transients that sequentially impinge on the interface of the water (the coupling medium) and the sensing layer (Au film). Thus, a time-varying RI within the water is caused from

compressions and strains of the ultrasonic mechanical force, leading to temporal perturbations in the polarization-dependence OSW sensing. In consequence, we achieve a PA transient measurement by recording the time-varying light intensity difference between *s*- and *p*-polarization reflectance.

3. Results and discussion

We study the response of the OSW sensors to the PA pressure transient in Figure 2. A PA point source is created by coating a 30-nm graphene film onto a glass sheet. For the SPR sensor, Figure 2a shows the time-resolved PA impulse and its frequency spectrum with a 6-dB bandwidth. The frequency component up to ~170 MHz (Figure 2b) indicates an estimated axial resolution of ~7.8 μm.

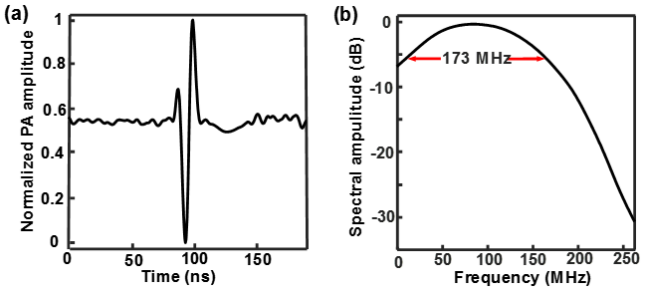


Figure 2: PA response of the SPR sensor. (a) and (b) Temporal and spectral profiles of the PA pressure transient.

Distinct from other optical technologies of ultrasonic detection, strongly-localized evanescent field forms nearby the interface, enabling a rapid temporal response. Thus, the PA pressure detection achieves an enhanced bandwidth of more than 100 MHz. Additionally, the sensors potentially quantify the optical absorption more accurately because the broadband detection effectively alleviates the saturation limitation.

In vivo images from mouse ears are acquired by the OSW-based PAM system. Based on strong optical absorption of hemoglobin at 532-nm illumination, PAM can noninvasively image the vasculature. With PAM equipping with the OSW sensor, both the major blood vessels and capillaries (with an estimated diameter of less than 10 μm) are visualized. During PA imaging, the excitation laser energy in the SPR-based sensor maintains equal values at 500 nJ per pulse. Both images of microvascular structures are observed at nearly identical SNR, suggesting the comparable ultrasonic detection sensitivity.

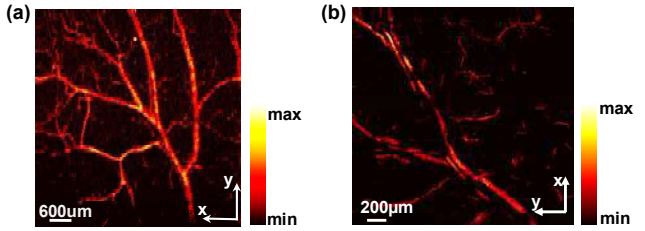


Figure 3: *In vivo* PAM microvascular imaging of mouse ears.

4. Conclusions

Based on the high detection sensitivity and broadband frequency response of the SPR sensor, we developed an OR-PAM system giving spatially isometric resolutions of a few micrometers. Label-free volumetric imaging was performed of the vascular microarchitecture in mouse ear *in vivo*. This photoacoustic microscopy may help in visualizing other anatomical sites, including the brain and the eye, and provide high-resolution information in biomedical research, including tumor microenvironments, neuroscience, and ophthalmology.

Acknowledgements

National Key Research and Development Program of China: 2016YFC0102401; National Natural Science Foundation of China (NSFC): 91750205.

References

[1] L. V. Wang, Multiscale photoacoustic microscopy and computed tomography, *Nature Photonics*, 3(9), 503-509, 2009.

[2] L. V. Wang and S. Hu, Photoacoustic tomography: in vivo imaging from organelles to organs, *Science*, 335 (6075), 1458-1462, 2012.

[3] J. Yao, L. Wang, J. M. Yang, K. I. Maslov, T. T. Wong, L. Li, C. H. Huang, J. Zou, and L. V. Wang, High-speed label-free functional photoacoustic microscopy of mouse brain in action. *Nat Methods*, 12(5), 407-410, 2015.

[4] Q. Zhou, S. Lau, D. Wu, and K. K. Shung, Piezoelectric films for high frequency ultrasonic transducers in biomedical applications, *Prog Mater Sci.*, 56, 139-174, 2011.

[5] T. Wang, R. Cao, B. Ning, A. J. Dixon, J. A. Hossack, A. L. Klibanov, Q. F. Zhou, A. Wang, and S. Hu, All-optical photoacoustic microscopy based on plasmonic detection of broadband ultrasound, *Appl. Phys. Lett.*, 107, 153702, 2015.

[6] X. Zhu, Z. Huang, G. Wang, W. Li, D. Zou, and C. Li, Ultrasonic detection based on polarization-dependent optical reflection, *Opt Lett*., 42(3), 439, 2017.

Bloch surface wave based sensor utilizing a multilayer interference filter

Michal Gryga*, Dalibor Ciprian, Petr Hlubina

Department of Physics, Technical University Ostrava, 17. listopadu 15, 708 00 Ostrava-Poruba, Czech Republic
*corresponding author, E-mail: michal.gryga.st@vsb.cz

Abstract

An experimental study of Bloch surface wave (BSW) based sensor which utilizes a one-dimensional photonic crystal (1DPhC) is presented. The 1DPhC is represented by a multilayer interference filter and we measure the response of a BK7 prism/multilayer/analyte system in the Kretschmann configuration. Dip in the reflectance spectrum for s-polarized wave represents the coupling of light wave to BSW and this is demonstrated for air and water. When the angle of incidence is decreased the dip depth is substantially enlarged due the conversion of the BSW to the radiation mode. We also model the response of the system and confirm agreement with the experiment.

1. Introduction

Bloch surface waves (BSWs) are waves that exist at the interface between a periodic system and homogeneous dielectric. In comparison to the surface plasmon wave propagating along the interface between a dielectric and thin metal film [1], BSWs are waves within the forbidden bandgap of a photonic crystal that can be excited at any wavelength by suitably changing the refractive indices and thicknesses of the dielectric materials in a multilayer structure. Consequently, sensors based on BSW are mechanically and chemically robust offering the possibility of operation in various environments and applications [2, 3, 4].

In this paper, an experimental study of BSW based sensor which utilizes a one-dimensional photonic crystal (1DPhC) is presented. The 1DPhC is represented by a multilayer interference filter comprising TiO_2 and SiO_2 layers of different thicknesses and we measure the response of a BK7 prism/multilayer/analyte system in the Kretschmann configuration. Dip in the reflectance spectrum for s-polarized wave is demonstrated for air and water, and when the angle of incidence is decreased the dip depth is substantially enlarged due the conversion of the BSW to the radiation mode. The theoretical model for the above system confirms good agreement between the experiment and theory.

2. Experimental method

The experimental setup used for measurement of s-polarized reflectance comprises a halogen lamp, a launching optical fiber terminated by collimating lens from which a light beam passes through the coupling equilateral prism made of glass BK7 to which a slide with a multilayer system, parameters of which are specified elsewhere [5], is attached. After the reflection from the structure, the light beam passes through analyzer oriented at 90° with respect to the plane of incidence, so that s-polarized component is propagating. The light is coupled into a read optical fiber which is connected to a spectrometer. In the experimental setup, the angle of incidence was varied [6, 7] to resolve the resonance.

3. Experimental results

First, we have used the setup to confirm experimentally that the resonance takes place for a suitable angle α between the incident beam and the normal to the entrance prism face. As an example, in Fig. 1 are shown the spectral dependencies of the response for s-polarized beam and two angles α, when the analyte is air. It is revealed that for angle $\alpha = 28°$ a resonance takes place due to excitation of the BSW and this is accompanied by a shallow dip in the signal at a wavelength of 813.18 nm. For angle $\alpha = 29°$ a resonance in the signal with the largest depth takes place due the conversion of the BSW to the radiation mode [5] at a wavelength of 818.12 nm.

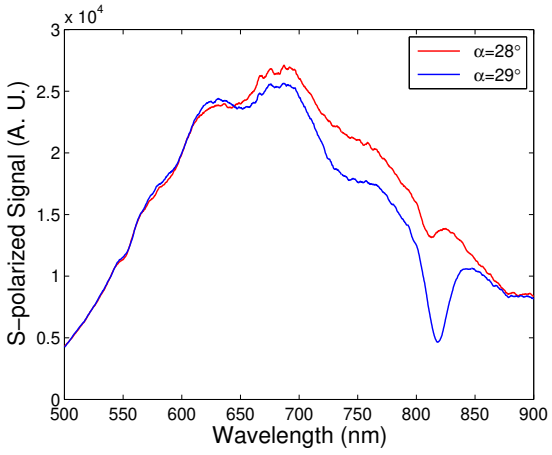


Figure 1: The spectral dependence of s-polarized signal for air and two angles of incidence α.

Contrary to the surface plasmon resonance, for which the resonance takes place for p-polarized component, in this case s-polarized component is responsible for the dip. In addition, the dip is substantially narrower compared to the SPR dip [6]. Similarly, in Fig. 2 are shown the spectral dependencies of the response for s-polarized beam and wa-

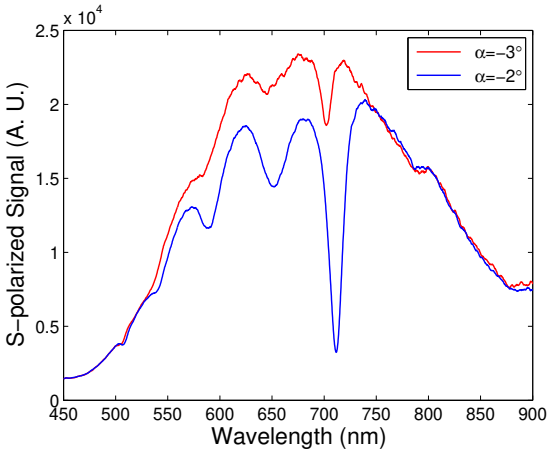


Figure 2: The spectral dependence of s-polarized signal for water and two angles of incidence α.

ter as analyte for two angles of incidence $\alpha = -3°$ and $\alpha = -2°$, respectively. It is revealed that for water the BSW resonance takes place for substantially different angle ($\alpha = -3°$) than for air ($\alpha = 28°$) and a shallow dip in the signal is at a wavelength of 702.26 nm. For angle $\alpha = -2°$, the BSW is converted to the radiation mode [5] and this is accompanied by a resonance dip with the largest depth at a wavelength of 711.89 nm.

4. Theoretical results

To model the response of the multilayer system represented by the interference filter, the sample was inspected by scanning electron microscopy and five layers of TiO_2 and four layers of SiO_2 were revealed. Material characterization of glass substrate and layers [5] was done employing a technique of the variable angle spectral ellipsometry (VASE, Woolam, Inc.). In addition, we assumed that the extinction coefficients for TiO_2 and SiO_2 layers are 1.6×10^{-3} and 3.4×10^{-4} [8], respectively. To express the response of the structure for s-polarized wave, a transfer matrix method [5, 7] was used.

Figure 3 shows the spectral dependencies of the theoretical response for s-polarized beam for air and two angles of incidence θ. It is clearly seen that for angle $\theta = 41.5°$ a resonance takes place due to excitation of the BSW and this is accompanied by a shallow dip in the signal at a wavelength of 810.6 nm. In this case, an exponential tail of the surface wave in the analyte is obtained from the intensity distribution $|E|^2$ in the structure at the resonance wavelength [5]. For angle $\theta = 41°$ a resonance with the largest depth takes place due the conversion of the BSW to the radiation mode at a wavelength of 813.2 nm. In this case, irradiation from the structure is obtained which is supported by the intensity distribution $|E|^2$ in the structure at the resonance wavelength [5]. Similarly, Fig. 4 shows the spectral dependencies of the theoretical response for s-polarized beam for water and two angles of incidence θ. For angle $\theta = 62°$ a resonance takes place due to excitation of the BSW and this is accompanied by a shallow dip in the signal at a wavelength of 696.8 nm, and for angle $\theta = 61.5°$ a resonance with the largest depth takes place due the conversion of the BSW to the radiation mode at a wavelength of 702.7 nm. The results obtained are in good agreement with the experimental ones.

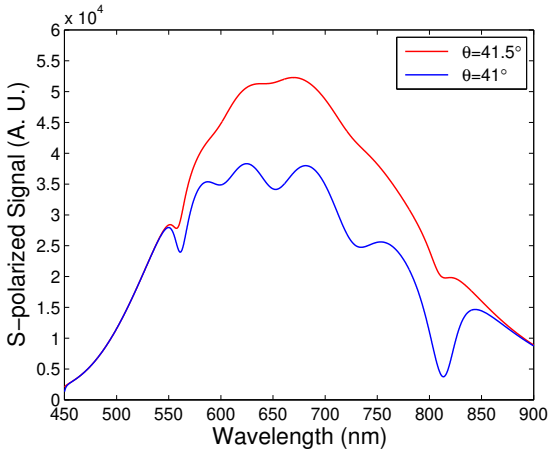


Figure 3: The theoretical spectral dependence of s-polarized signal for air and two angles of incidence θ.

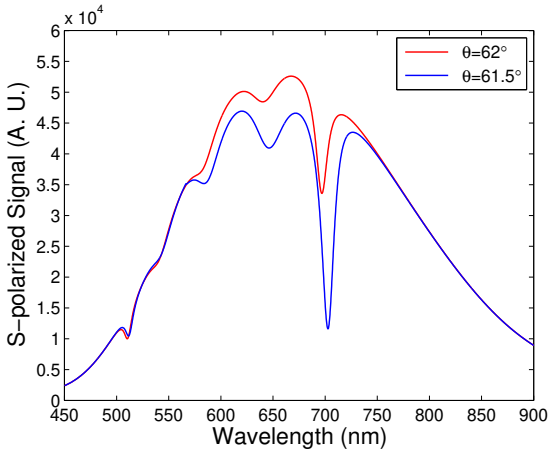


Figure 4: The theoretical spectral dependence of s-polarized signal for water and two angles of incidence θ.

5. Conclusions

In this paper, an experimental study of surface electromagnetic wave sensor utilizing a 1DPhC has been presented. The 1DPhC is represented by a multilayer interference filter, and the response of the system comprising a BK7 prism/multilayer/analyte in the Kretschmann configuration has been measured. We have revealed a shallow dip in the reflectance of s-polarized wave demonstrating a surface wave resonance. When the angle of incidence is decreased, the dip depth is substantially enlarged due the conversion of the BSW to the radiation mode, which is promising for sensing applications. Experimental results obtained for air

and water are supported by theoretical results. A transfer matrix method has been applied and good agreement between the results has been achieved.

In comparison to the surface plasmon resonance, the BSW or radiation mode resonance dip is narrower, but the sensitivity is approximately one order of magnitude lower. In any case, multilayer systems are mechanically and chemically robust so that the BSW based sensors are promising in various applications.

Acknowledgement

The work was supported by ERDF/ESF project New Composite Materials for Environmental Applications (No. CZ.02.1.01/0.0/0.0/17_048/0007399), and by the student grant system through project SP2019/26.

References

[1] J. Homola, *Surface Plasmon Resonance Based Sensors*. New York: Springer-Verlag, 2006.

[2] M. Shinn and W. Robertson, "Surface plasmon-like sensor based on surface electromagnetic waves in a photonic band-gap material," *Sens. Actuators B*, vol. 105, pp. 360–364, 2004.

[3] Y. Li, T. Yang, S. Song, Z. Pang, and G. Du, "Phase properties of Bloch surface waves and their sensing applications," *Appl. Phys. Lett.*, vol. 103, p. 041116, 2013.

[4] X. B. Kanga, L. Wen, and Z. G. Wang, "Design of guided Bloch surface wave resonance bio-sensors with high sensitivity," *Opt. Commun.*, vol. 383, pp. 531–536, 2017.

[5] M. Gryga, D. Vala, P. Kolejak, L. Gembalova, D. Ciprian, and P. Hlubina, "A new sensing concept based on Bloch surface waves and radiation modes," *Opt. Mater. Express*, vol. 9, pp. xxx–xxx, 2019.

[6] R. Chlebus, J. Chylek, D. Ciprian, and P. Hlubina, "Surface plasmon resonance based measurement of the dielectric function of a thin metal film," *Sensors*, vol. 18, p. 3693, 2018.

[7] P. Hlubina, M. Lunackova, and D. Ciprian, "Phase sensitive measurement of the wavelength dependence of the complex permittivity of a thin gold film using surface plasmon resonance," *Opt. Mater. Express*, vol. 9, pp. 992–1001, 2019.

[8] A. Sinibaldi, R. Rizzo, G. Figliozzi, E. Descrovi, N, Danz, P. Munzert, A. Anopchenko, and F. Michelotti, "A full ellipsometric approach to optical sensing with Bloch surface waves on photonic crystals," *Opt. Express*, vol. 21, pp. 23 331–23 344, 2013.

Micro/Nano fabrication and characterization techniques

Titanium nitride nanowires fabricated by oblique deposition for hyperbolic metamaterials

Kenichi Yatsugi*, and Kazutaka Nishikawa

Toyota Central R&D Labs., Inc., Aichi, Japan
*corresponding author, E-mail: yatsugi@mosk.tytlabs.co.jp

Abstract

We fabricated a nanowire array using titanium nitride, which has a high melting point, by dynamic oblique deposition of titanium and subsequent thermal treatment in ammonia. The opposite signs of in-plane and out-of-plane permittivity indicate that fabricated nanowire array behaves as a hyperbolic metamaterial. The nanowire array presented here is a promising candidate for hyperbolic metamaterials in high-temperature applications due to the high melting point of titanium nitride.

1. Introduction

Hyperbolic metamaterials (HMMs) are attracting attention due to the unique properties arising from their extreme optical anisotropies[1]. HMMs are characterized by the hyperbolic dispersion relation of the isofrequency surface $(k_x^2 + k_y^2) /\varepsilon_\perp + k_z^2/\varepsilon_{//} = (\omega/c)^2$, where k_x, k_y, and k_z are the x, y, and z components of the wave vector, respectively, ω is the angular frequency, and c is the speed of light). The hyperboloid shapes in the dispersion relation appear when the out-of-plane permittivity $\varepsilon_\perp$ and the in-plane permittivity $\varepsilon_{//}$ have opposite signs. This unique dispersion relationship offers potential for exotic applications such as subwavelength imaging[1] and broadband super-Planckian radiative heat transfer[2].

Metal nanowire arrays (NWAs) are promising candidates for HMMs because $\varepsilon_{//}$ shows dielectric behavior ($\varepsilon_{//} > 0$) while $\varepsilon_\perp$ shows metallic behavior ($\varepsilon_\perp < 0$)[1]. Unique applications of metal NWAs have been reported including negative refraction, near-field thermal transfer, and thermal waveguides. Conventional metal NWAs for HMMs have been fabricated by embedding noble metals with low melting points, such as Ag, in an anodic alumina membrane dielectric host[3]. However, the low melting temperature of noble metals limits the potential of these metal NWA HMMs for high-temperature applications such as thermophotovoltaics[4].

Titanium nitride (TiN) is attracting attention as an alternative to noble metals for metamaterials because of its similar optical properties to Au, high melting point (> 2900 °C), and chemical stability[5].TiN is being considered for high-temperature applications such as broadband absorbers and plasmonic heating.

In this study, we fabricated a TiN NWA by dynamic oblique deposition of Ti and subsequent thermal treatment in ammonia. The optical anisotropy of the TiN NWA was characterized by spectroscopic ellipsometry.

2. Method

2.1. Fabrication of the TiN NWA.

The titanium NWA was fabricated on a fused quartz substrate using electron beam deposition. For the deposition source material, a granular Ti metal (99.9%, Kojundo Chemical Lab.) with a diameter of 10 mm and thickness of 5 mm was used in a carbon crucible. The substrates were set at a parallel distance of 40 mm and a height of 250 mm from the metal source. The titanium NWA was annealed in ammonia using argon as the carrier gas. The crystal structure was characterized by X-ray diffraction measurement (XRD). The cross-section image of the sample was observed using a field emission scanning electron microscope (FE-SEM) after ion-beam polishing. The surface morphology was observed by a FE-SEM.

The observed peaks of XRD matched those of TiN well. Figures 1 (a) and (b) show the cross-sectional SEM image and the image observed from above, respectively. The TiN NWA was found to be densely fabricated on the SiO_2 substrate. The average height and diameter of the nanowires deduced from the cross-sectional SEM image were 1.7 μm and 110 nm, respectively.

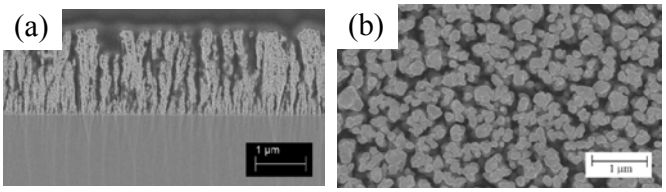


Figure 1: SEM images. (a) Cross-section image. (b) Image observed from above.

2.2. Evaluation of the optical anisotropy

The optical anisotropy of the fabricated TiN NWA was characterized by spectroscopic ellipsometry. Spectroscopic ellipsometry measures the amplitude ratio Ψ and phase difference Δ between *s*- and *p*- polarizations.

The measured spectra of ellipsometric paramters (Ψ, Δ) are fitted by a Fresnel reflection theoretical model considering the optical anisotropy and multiple reflections occurring in the nanowire layer.

The in-plane and out-of-plane permittivity were described by using Bruggeman effective medium theory.

$$\frac{(1-f)(\varepsilon_{air}-\varepsilon_{eff})}{\varepsilon_{eff,\parallel}+g(\varepsilon_{air}-\varepsilon_{eff})}+\frac{f(\varepsilon_{TiN}-\varepsilon_{eff})}{\varepsilon_{eff}+g(\varepsilon_{TiN}-\varepsilon_{eff})}=0 \qquad (1)$$

where ε_{air} and ε_{TiN} are the permittivities of air and TiN, respectively, f is the volume fraction of TiN, and g is a depolarizing factor that is set as 0.5 for the in-plane component of permittivity $\varepsilon_{eff,}$, g is 0 for the out-plane component of permittivity $\varepsilon_{eff,\perp}$. ε_{TiN} is expressed by the Drude–Lorentz model as $\varepsilon_{TiN} = \varepsilon_b - \omega_p^2/\{\omega(\omega+i\gamma_p)\} + f_1\omega_1^2/(\omega_1^2 - \omega^2 - i\gamma_1)$, where ε_b= 3.13, ω_p = 5.26 eV, γ_p = 1.12 eV, f_1 = 3.45, ω_1 = 1.50 eV, γ_1 = 1.50 eV, and f = 0.43. The literature values of SiO_2 permittivity are used for the substrate.

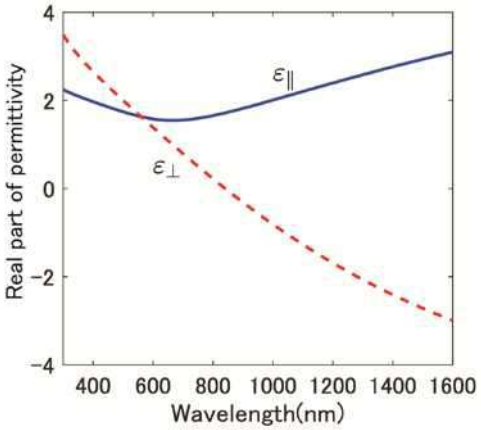


Figure 2: Real part of in-plane (solid line) and out-of-plane (dashed line) components of the permittivity.

The spectra of the real part of $\varepsilon_{eff,\parallel}$ and $\varepsilon_{eff,\perp}$ determined by fitting the experimental ellipsometric parameters are shown in Figure 2. The real part of $\varepsilon_{eff,\parallel}$ exhibits positive values. On the other hand, the real part of $\varepsilon_{eff,\perp}$ is negative for wavelengths longer than 850 nm.

3. Discussion

Opposite signs of $\varepsilon_{eff,\parallel}$ and $\varepsilon_{eff,\perp}$ shown in Figure 2 produce the hyperbolic dispersion of isofrequency surfaces. The TiN NWA was characterized as an HMM for wavelength longer than 850 nm. HMMs with positive $\varepsilon_{eff,\parallel}$ and negative $\varepsilon_{eff,\perp}$ are called type-I HMMs, and HMMs with negative $\varepsilon_{eff,\parallel}$ and positive $\varepsilon_{eff,\perp}$ are called type-II HMMs[1]. The TiN NWA presented here is classified as a type-I HMM, and type-I HMMs have more advantageous optical loss than type-II. Type-I HMMs in the near infrared and infrared ranges are desirable for thermal applications such as thermal waveguides[6]. The TiN NWA in this study is a particularly promising candidate for thermal waveguides because TiN has a high melting point, and the metal NWA maintains type-I hyperbolic dispersion in the infrared range[7]. Note that dynamic oblique deposition allows us to fabricate the TiN vertical nanostructure without nanofabrication techniques such as lithography. In addition, the fabrication technique shown here is suitable for large-scale production.

4. Conclusions

In conclusion, we fabricated a TiN NWA using the dynamic oblique deposition of Ti and subsequent thermal treatment in ammonia. Spectra of ellipsometric parameters were fitted by a Fresnel reflection theoretical model considering the optical anisotropy, in which the effective permittivity was described using effective medium theory and the Drude–Lorentz model. The vertical component of the effective permittivity was negative at $\lambda > 850$ nm, whereas the horizontal component was positive, which indicates that the fabricated nanowires have hyperbolic dispersion of isofrequency surfaces. The TiN NWA presented here has potential for high-temperature applications such as thermophotovoltaics.

Acknowledgements

We are grateful to Dr. Hideo Iizuka (Toyota Research Institute of North America, USA) for the fruitful discussions.

References

.

[1] A. Poddubny, I. Iorsh, P. Belov, and Y. Kivshar, Hyperbolic metamaterials, *Nat. Photon.* 7: 948, 2013.

[2] Y. Guo, C. L. Cortes, S. Molesky, and Z. Jacob, Broadband super-planckian thermal emission from hyperbolic metamaterials, *Appl. Phys. Lett.* 101: 131106, 2012.

[3] M. A. Noginov, Y. A. Barnakov, G. Zhu, T. Tumkur, H. Li, and E. E. Narimanov, Bulk photonic metamaterial with hyperbolic dispersion, *Appl. Phys. Lett.* 94: 151105, 2009.

[4] J. Chang, Y. Yang, and L. Wang, Tungsten nanowire based hyperbolic metamaterial emitters for near-field thermophotovoltaic applications, *Int. J. Heat Mass Transfer* 87: 237, 2015.

[5] G. V. Naik, V. M. Shalaev, and A. Boltasseva, Alternative plasmonic materials: beyond gold and silver, *Adv. Mater.* 25: 3264, 2013.

[6] J. Shi, B. Liu, P. Li, L. Y. Ng, and S. Shen, Near-field energy extraction with hyperbolic metamaterials, *Nano Lett.* 15: 1217, 2015

[7] B. Liu and S. Shen, Broadband near-field radiative thermal emitter/absorber based on hyperbolic metamaterials: direct numerical simulation by the Wiener chaos expansion method, Phys. Rev. B 87: 115403, 2013.

High Photoelectrochemical Activity of $CuInS_2$ Quantum Dots/In_2S_3/ZnO Nanowire Arrays Electrode

Yu-Kuei Hsu[1*] and Hao-Hsuan Chang[1]

[1] Department of Opto-Electronic Engineering, National Dong Hwa University, Hualien, 97401, Taiwan
*corresponding author, E-mail: ykhsu@gms.ndhu.edu.tw

Abstract

Deposition of $CuInS_2$ (CIS) quantum dots (QDs) on ZnO nanowires (NWs) with interlayer of In_2S_3 as photoelectrode has been successfully fabricated on FTO via the facile solution routes for photoelectrochemical application. The morphology and structure of the CIS QD/In_2S_3/ZnO NWs heterostructure are systematically analyzed with a SEM, TEM and XRD. In comparison with pristine ZnO NWs, the CIS QD/In_2S_3/ZnO photoelectrode illustrates efficient charge separation and charge transport path to achieve the highest photocurrent of 2.4 mA·cm^{-2} that is competitive with other Cd- and Pb-free QD-based materials.

1. Introduction

Because solar light is a clean, sustainable, and abundant renewable source of energy, the conversion of solar energy into a usable fuel has attracted substantial attention in the last decades. Among all techniques for the solar conversion, a photoelectrochemical (PEC) process via direct conversion of solar energy into hydrogen fuel through water splitting by semiconductors constitutes an attractive solution. Although the intense efforts of various morphologies and materials of semiconductor electrodes on the PEC performance carried out in the recent years, the satisfaction all of the stability, efficiency, and cost conditions required for industrial products of this technology haven't been achieved by single material [1]. The development of the hetero-structural photoelectrode for highly efficient PEC hydrogen generation is an important route. Recently, non-toxic I-III-VI_2 group QDs, especially $CuInS_2$ (CIS) QDs, with high absorption coefficient ($\sim 10^5$ cm^{-1}) and tunable band gap energy are attractive alternatives to the highly toxic cadmium and lead chalcogenide QDs [2]. In the concern on the green process and nontoxic materials, we propose the CIS QD/In_2S_3/ZnO NW array as efficient photoanode, because the In_2S_3 has similar band width to CdS. In this study, the colloidal CIS QDs was synthesized by chemical solution route, and then the deposition of CIS QDs on ZnO NWs was utilized the dip-coating process while the ZnO NW was decorated the In_2S_3 layer by successive ionic layer adsorption and reaction (SILAR) method before used. Finally the CIS QD/In_2S_3/ZnO NW was thermally treated to remove the capping ligands. Significantly, this novel CIS QD/In_2S_3/ZnO NW photoelectrode illustrates the excellent PEC activity in comparison with CIS QD/ZnO NW and other Cd- and Pb-free QDs photoelectrodes.

2. Experiments

2.1. Electrode preparation

In the synthesis of CIS QDs, 1 mM of copper iodide and 1 mM of indium acetate were employed as precursors, and 5 ml of DDT was used as solvent, S donor, and capping ligand. Under vacuum, the reaction was heated for 30 min at 100 °C, and then the temperature was raised to 230 °C. To complete QDs synthesis, the temperature was kept constant, and the time of the reaction was hold for 30 min. After synthesis, the temperature was naturally cool down 25 ^oC, and the as-synthesized CIS QDs were stored in N_2-purged toluene until further utilization. In the synthesis of ZnO NW, a 10-15 nm thin layer of ZnO nanopaeticles was deposited onto a FTO as seeded substrate by dip coating of 5 mM zinc acetate solution and heat treatment at 350 ^oC for 5 minutes in air. The seeded substrate was placed in an aqueous solution containing 5 mM zinc nitrate, 5 mM hexamethylenetetramine, 5 mM polyethyleneimine, and 0.25 M ammonium hydroxide at 90 ^oC for 5 h for the growth of the ZnO NW array. Subsequently, for the SILAR, 0.1 M $InCl_3$ and 75 mM Na_2S served as the precursor solutions of In and S ions. The ZnO template was immersed in the solution with order and time as $InCl_3$ 60 s, DI water 30 s, Na_2S 240 s, DI water 30 s, $InCl_3$ 60 s and DI 30 s in each cycle; this cycle was repeated and reproduced five times to fabricate the In_2S_3 nanostructure on the ZnO NW arrays. Then, the In_2S_3/ZnO NW was immersed into CIS QDs colloid for 3 s and rinsed with acetone. The as-prepared samples were then thermally treated at temperatures of 350 ^oC in vacuum for 1 h.

2.2. Characteristic analysis

The morphology of hierarchical CIS QD/In_2S_3/ZnO NW arrays was examined with a scanning electron microscope (SEM, JEM-4000EX); the structure of the samples was analyzed with a X-ray diffractometer (XRD, Bruker D8 Advance, Cu K_α radiation, λ=0.1506 nm). The chemical states of the elements were determined by X-ray photoelectron spectra (XPS, Perkin-Elmer model PHI 1600). The detailed microscopic structure and the chemical composition of the CIS QD/In_2S_3/ZnO NW were

investigated using high-resolution scanning transmission electron microscopes (HR-STEM, JEM2010F and JEM2200FS operating at 200 kV, JEOL).The PEC characteristic of the electrodes was measured in 0.1 M Na_2S and 0.35 M Na_2SO_3 solution with a potentiostat/galvanostat (CHI 6273D).

3. Discussion

The morphologic variation of CIS QD/In_2S_3/ZnO NWs was determined by SEM images. Figure 1a-c shows the surface morphologies of ZnO NW arrays synthesized via the hydrothermal method and decoration of CIS QD. After coating In_2S_3 and CIS QD layer on ZnO NW, their surface morphologies were displayed in Fig. 1c. The NW density is still remained, besides the slight aggregation of NWs owing to the evaporation of solvent during the SILAR process. To further analyze the heterostructural CIS QDs/In_2S_3/ZnO NWs, the HRTEM was performed. The Cu-, In-, S-, Zn- and O-compositions within single CIS QD/In_2S_3/ZnO multi-shell NW are also determined from EDXS line profiles, which are recorded along a line that passes through the NW and is perpendicular to its axis (Fig. 1d). SAED pattern of CIS QD/In_2S_3/ZnO NW (Fig. 1e) shows a few Deby-Scherrer rings with orange, green, and red colors, which can be attributed to the hexagonal ZnO, tetragonal CIS, and In_2S_3 crystallites, respectively.

To realize the PEC performance of the CIS QD/In_2S_3/ ZnO NW array electrode, 3-electrode PEC cell was adopted

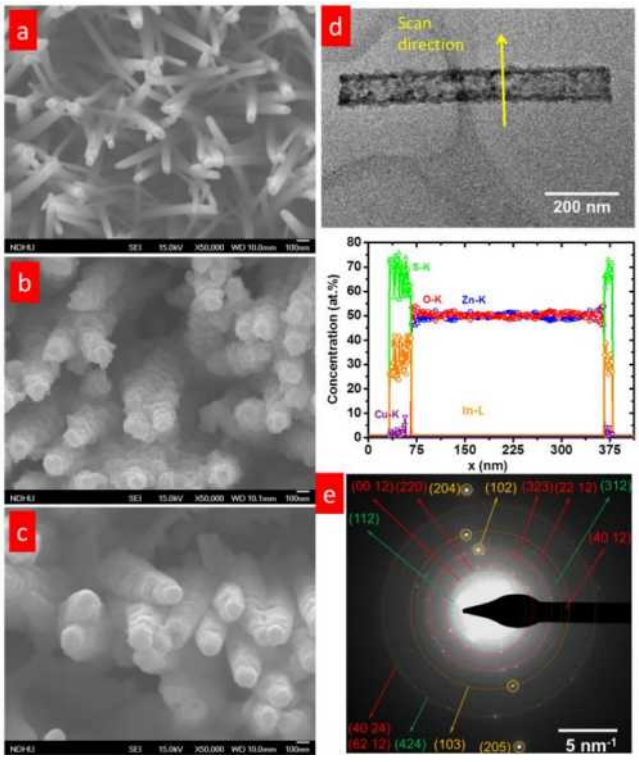


Figure 1: FESEM images of (a) pristine ZnO NWs, (b) In_2S_3/ZnO NWs, (c) CIS QDs/In_2S_3/ZnO NWs samples. (d) HAADF-STEM image of multi-shell NW and the quantification of the EDXS line scan. (e) SAED pattern of CIS QDs/In_2S_3/ZnO NW.

in an electrolyte of 0.1 M Na_2S and 0.35 M Na_2SO_3 solution for analysis. The photocurrent-potential curves of uncoated ZnO, and CIS QD/In_2S_3/ZnO NW arrays were recorded via linear sweep voltammetry (LSV) under continuous and chopped illumination, as shown in Fig. 2. The pristine ZnO NW shows low photocurrent of approximately 0.5 mA·cm^{-2} owing to the narrow absorption region of UV light. Remarkably, the photocurrents were significantly enhanced and the dark current decreased after the deposition of In_2S_3 layer in between the CIS QD and ZnO NWs. This indicates that the In_2S_3 inner layer could compensate the band mismatch and facilitate the photo-induced electron transport to ZnO. The high photocurrent of 2.4 mA·cm^{-2} can be achieved, which is two orders of magnitude greater than the CIS QD/ZnO NW sample and also higher than that of many other CIS-based photoelectrodes with Cd- and Pb-free.

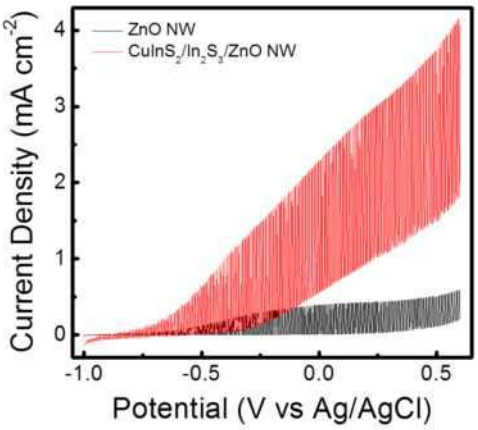


Figure 2: LSV of ZnO NW and CIS QDs/In_2S_3/ZnO NW samples under illumination.

4. Conclusions

Hierarchical heterojunction of CIS QD/In_2S_3/ZnO NWs arrays were successfully synthesized by a dip-coating process in CIS QD colloid while the ZnO NW was decorated the In_2S_3 layer by SILAR method. Significantly, the CIS QD/In_2S_3/ZnO NWs photoelectrode exhibits excellent photocurrent of 2.4 mA·cm^{-2}, which is two orders of magnitude higher than that of pristine ZnO NWs.

Acknowledgements

National Science Council and National Dong Hwa University supported this research under contracts MOST 105-2221-E-259-024-MY3 and MOST 107-2221-E-259 -029-MY3, respectively.

References

[1] O. Khaselev, J.A. Turner, A monolithic photovoltaic-photoelectrochemical device for hydrogen production via water splitting, *Science* 280: 425−427, 1998.

[2] D.H. Jara, S.J. Yoon, K.G. Stamplecoskie, P.V. Kamat, Size-Dependent Photovoltaic Performance of $CuInS_2$ Quantum Dot-Sensitized Solar Cells, *Chem. Mater*. 26: 7221−7228, 2014.

Scattering-type scanning near-field optical microscopy and spectroscopy for real space observation of various polaritons

Philip Schäfer[1*], Adrian Cernescu[1], Sergiu Amarie[1], Andreas Huber[1]

[1]neaspec GmbH, Haar (Munich), Germany
*Philip Schäfer, E-mail: philip.schaefer@neaspec.com

Abstract

Scattering-type Scanning Near-field Optical Microscopy and Spectroscopy is the ideal mean for the nano-scale analysis of sub-wavelength excitations in 2D-materials and meta-materials. Confining an incident light beam to the apex of a metallic AFM tip allows the local excitation as well as the local detection of phonon polaritons, exciton polaritons and surface plasmons. This enables a new routine analysis tool for quantum phenomena on the 10-nanometer length scale and sub-picosecond time scale.

1. Introduction

Two-dimensional materials like graphene, boron-nitride or transition-metal dichalcogenides are of rising interest for novel plasmonic and opto-electronic applications due to their unique characteristics and their broad application range. However, being highly sensitive to the local environment, their properties can strongly vary on the nanometer length scale, severely limiting the macroscopic performance of such novel devices. Scattering-type Scanning Near-field Optical Microscopy (s-SNOM) and nanoscale FTIR spectroscopy (nano-FTIR) systems have become the key technology to understand and resolve these limitations by measuring the optical and electronic properties of such nanostructures down to the 10-nanometer length scale.

2. s-SNOM on 2D-materials and metamaterials

Scattering-type Scanning Near-field Optical Microscopy (s-SNOM) is a scanning probe approach to optical microscopy and spectroscopy bypassing the ubiquitous diffraction limit of light to achieve a spatial resolution below 20 nanometers. s-SNOM employs the strong confinement of light at the apex of a sharp metallic AFM tip to create a nanoscale optical hot-spot. Analyzing the scattered light from the tip enables the extraction of the optical properties (dielectric function) of the sample directly below the tip and yields nanoscale resolved images simultaneous to topography [1]. In addition, the technology has been advanced to enable Fourier-Transform Infrared Spectroscopy on the nanoscale (nano-FTIR) [2] using broadband radiation from the visible spectral range to THz frequencies. Alternatively, interferometric s-SNOM can be used to map the nanoscale distribution of local optical fields.

2.1. Dirac plasmons in graphene

First visualization and analysis of Dirac plasmons propagating along graphene was realized using infrared light focused to the AFM tip in 2012. These studies demonstrated graphene plasmon interference mapping that allowed the direct extraction of local material properties such as conductivity, intrinsic doping and defects [3, 4]. Furthermore, relation with the control parameters: gate voltage, refractive index of the substrate and incident light were characterized. Direct control of propagating surface plasmons on graphene with resonant antennas and conductivity patterns could further be demonstrated [5, 6].

Additionally, the highly flexible design of our s-SNOM microscope enables a complete new level of correlation microscopy: near-field microscopy in ultrafast pump-probe configuration [7] could identify an increase in the effective electron temperature upon NIR pump and monitor its ps-scale relaxation dynamic.

s-SNOM could also be applied for the investigation of carrier relaxation in high-purity graphene in 2D-heterostructures [8] as well as for near-field photocurrent measurements on graphene device structures [6, 9].

Furthermore, a technological breakthrough in the field of near-field optics has been achieved with cryogenic near-

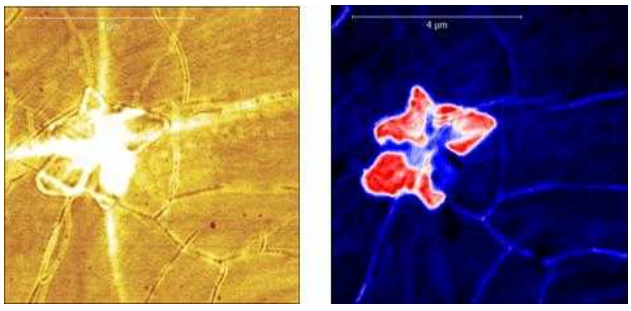


Figure 1: s-SNOM images of graphene at 8.5 K: a) optical amplitude; b) optical phase.

field imaging and spectroscopy, by the group of Dimitri Basov [10]. With the new cryo-neaSNOM we also extend our s-SNOM to the cryogenic temperature range (<10-300 Kelvin) and open a complete new world for nanoscale optical microscopy and spectroscopy [Figure 1]. This technology enables for example the direct mapping of phase-transitions in strongly correlated materials or the detection of low-energy elementary excitations at the surface of solid-state systems.

2.2. Exciton polaritons in molybdenum diselenide

Molybdenum diselenide is a known van der Waals semiconductor which can be used as medium for excitonic transfer in nanophotonic circuits. With s-SNOM it is for the first time possible to observe the propagation of exciton polariton modes in real space [11]. A phenomenal propagation length of up to 12 µm at room temperature was found. The exciton polariton wavelength was revealed to be controllable by the waveguide thickness.

2.3. Phonon polaritons in hexagonal boron nitride

Also phonon polaritons in van der Waals crystals of hexagonal boron nitride could be observed in real space using s-SNOM [12]. Reading out the phonon polariton wavelength directly from the interference pattern near the crystal edges led to a dispersion relation that turned out to be dependent from the number of atomic layers. By designing a hyperbolic meta-surface based on nanostructured hexagonal boron nitride, concave wavefronts could be demonstrated by using an Au-nanorod as the phonon polariton launcher and the AFM tip as the near-field probe [13].

3. Conclusions

s-SNOM proves itself inevitable for the characterization of fundamental excitations in 2D-materials and metamaterials. Only with this technology, waves like surface plasmons, exciton polaritons and phonon polaritons can be observed in real space with 10-20 nm spatial resolution. Moreover, s-SNOM allows ultrafast spectroscopy on the femtosecond time scale, and even measurements at cryogenic temperatures. Hence, s-SNOM will ultimately play a major role in future investigations of photonic nanostructures.

References

[1] F. Keilmann, R. Hillenbrand, Near-field microscopy by elastic light scattering from a tip, *Phil. Trans. R. Soc. Lond. A* 36: 787-805, 2004.

[2] F. Huth, A. Govyadinov, S. Amarie, W. Nuansing, F. Keilmann, R. Hillenbrand, Nano-FTIR absorption spectroscopy of molecular fingerprints at 20 nm spatial resolution, *Nano Lett*. 12: 3973-3978, 2012.

[3] J. Chen,, M. Badioli, P. Alonso-González, S. Thongrattanasiri, F. Huth, J. Osmond, M. Spasenovic, A. Centeno, A. Pesquera, P. Godignon, A. Zurutuza Elorza, N. Camara, F. J. García de Abajo, R. Hillenbrand, F. H. L. Koppens, Optical nano-imaging of gate-tunable graphene plasmons, *Nature* 487: 77-81, 2012.

[4] Z. Fei, A. S. Rodin, G. O. Andreev, W. Bao, A. S. McLeod, M. Wagner, L. M. Zhang, Z. Zhao, M. Thiemens, G. Dominguez, M. M. Fogler, A. H. Castro Neto, C. N. Lau, F. Keilmann, D. N. Basov, Gate-tuning of graphene plasmons revealed by infrared nano-imaging, *Nature* 487: 82-85, 2012.

[5] P. Alonso-González, A. Y. Nikitin, F. Golmar, A. Centeno, A. Pesquera, S. Vélez, J. Chen, G. Navickaite, F. Koppens, A. Zurutuza, F. Casanova, L. E. Hueso, R. Hillenbrand, Controlling graphene plasmons with resonant metal antennas and spatial conductivity patterns, *Science* 344: 1369-1373, 2014.

[6] M. B. Lundeberg, Y. Gao, A. Woessner, C. Tan, P. Alonso-González, K. Watanabe, T. Taniguchi, J. Hone, R. Hillenbrand, F. H. L. Koppens, Thermoelectric detection and imaging of propagating graphene plasmons, *Nature Mat*. 16: 204-207, 2017.

[7] M. Wagner, Z. Fei, A. S. McLeod, A. S. Rodin, W. Bao, E. G. Iwinski, Z. Zhao, M. Goldflam, M. Liu, G. Dominguez, M. Thiemens, M. M. Fogler, A. H. Castro Neto, C. N. Lau, S. Amarie, F. Keilmann, D. N. Basov, Ultrafast and nanoscale plasmonic phenomena in exfoliated graphene revealed by infrared pump−probe nanoscopy, *Nano Lett*. 14: 894-900, 2014.

[8] G. X. Ni, L. Wang, M. D. Goldflam, M. Wagner, Z. Fei, A. S. McLeod, M. K. Liu, F. Keilmann, B. Özyilmaz, A. H. Castro Neto, J. Hone, M. M. Fogler, D. N. Basov, Ultrafast optical switching of infrared plasmon polaritons in high-mobility graphene, *Nature Phot*. 10: 244-248, 2016.

[9] A. Woessner, P. Alonso-González, M. B. Lundeberg, Y. Gao, J. E. Barrios-Vargas, G. Navickaite, Q. Ma, D. Janner, K. Watanabe, A. W. Cummings, T. Taniguchi, V. Pruneri, S. Roche, P. Jarillo-Herrero, J. Hone, R. Hillenbrand, F. H.L. Koppens, Near-field photocurrent nanoscopy on bare and encapsulated graphene, *Nature Comm*. 7: 10783, 2016.

[10] H.T. Stinson, A. Sternbach, O. Najera, R. Jing, A.S. Mcleod, T.V. Slusar, A. Mueller, L. Anderegg, H.T. Kim, M. Rozenberg, D.N. Basov, Imaging the nanoscale phase separation in vanadium dioxide thin films at terahertz frequencies, *Nature Comm*. 9: 3604, 2018.

[11] F. Hu, Y. Luan, M. E. Scott, J. Yan, D. G. Mandrus, X. Xu, Z. Fei, Imaging exciton–polariton transport in MoSe2 waveguides, *Nature Photon*. 11: 356-360, 2017.

[12] S. Dai, Z. Fei, Q. Ma, A. S. Rodin, M. Wagner, A. S. McLeod, M. K. Liu, W. Gannett, W. Regan, K. Watanabe, T. Taniguchi, M. Thiemens, G. Dominguez, A. H. Castro Neto, A. Zettl, F. Keilmann, P. Jarillo-Herrero, M. M. Fogler, D. N. Basov, Tunable phonon polaritons in atomically thin van der Waals crystals of boron nitride, *Science* 343: 1126-1129, 2014.

[13] P. Li, I. Dolado, F. J. Alfaro-Mozaz, F. Casanova, L. E. Hueso, S. Liu, J. H. Edgar, A. Y. Nikitin, S. Vélez, R. Hillenbrand, Infrared hyperbolic metasurface based on nanostructured van der Waals materials, *Science* 359: 892-896, 2018.

Nanostructuring of Graphene Membranes with Focused Ion Beams: Towards 2D Metamaterials

Ivan Shorubalko[1]

[1]Empa – Swiss Federal Laboratories for Materials Science and Technology, Duebendorf, Switzerland
*corresponding author, E-mail: ivan.shorubalko@empa.ch

Abstract

Nanostructuring of two-dimensional membranes with focused ion beans is demonstrated to be a promising technique for creating metamaterials. Few-nanometer-small structures with a down to ten nanometer period are demonstrated in graphene. Understanding the interaction between focused ion beams and freestanding 2D materials is crucial for exploiting the method towards novel metamaterials.

1. Introduction

One of the important physical length-scales in electronic devices/materials is the charge carrier mean-free path (MFP). Fabricating devices with a characteristic feature size smaller than MFP leads to ballistic transport mechanisms dominating the conventional diffusive transport picture [1]. Consequently, these devices are called ballistic devices and exhibit various novel electronic properties that may survive to the THz regime due to their nature. Ballistic artificial nanomaterials – engineered to have novel properties that may not be found in nature and classified as a type of metamaterials, Fig.1(a) [2]. These materials can be envisioned as THz rectifiers. Electrical rectification in graphene based individual nanodevices has been demonstrated at room temperature [3, 4]. MFP in such typical graphene material is of sub-100nm. A large part of graphene research is devoted to its nanostructuring or modification on the nanometer scale. Except standard electron-beam lithography many other different techniques have been proposed and explored over the last decade. Most advanced method to controllably create true-nanoscale structures and even individual defects in suspended graphene is its irradiation by high energy electrons in transmission electron microscope (TEM). Nevertheless, the throughput and practicality of TEM method are limited. Sputtering by energetic focused ion beams (FIBs) has been envisioned and to a large extend demonstrated as a powerful method to create nanostructures in graphene [5-8]. Here we report on pushing the limits of this technique in several aspects: resolution, reproducibility, homogeneity, and throughput. Essential understanding of the graphene (or any other 2D material) sputtering by FIBs can be done by rather simple binary collision theory (BCT). Periodic arrays of a million of few-nm-small pores with narrow size distribution can be fabricated in free-standing graphene. Such perforated ultrathin membranes already find their applications in the field of quick and energy efficient filtration [9].

2. Experimental/Theoretical Study

He- and Ga- FIB tools are used to irradiate and pattern free-standing graphene. Scanning (transmission) electron microscopy and He-ion microscopy (HIM) are used for high resolution imaging. Raman focal spectroscopy is used for defect characterization.

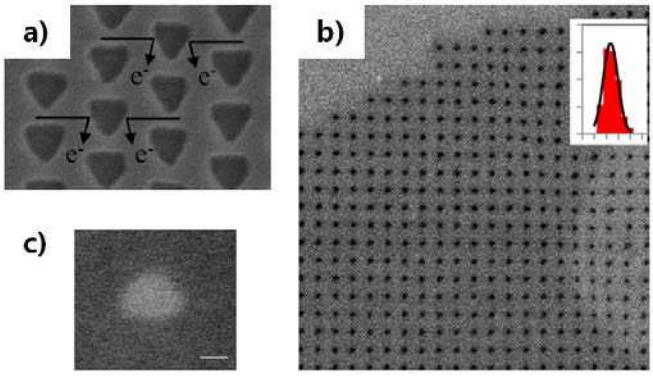


Figure 1: a) Scanning electron microscope image of an artificial functional material. The arrows indicate the typical electron trajectories. The devices operate similar to a bridge rectifier [2]. Triangles base is 200 nm large. b) Helium ion microscope image of perforated graphene membrane with He-FIB, period is 30 nm. Inset shows a typical pore diameter distribution in nm. c) Triangular pore in graphene by He-FIB. Scale is 10 nm.

3. Discussion

Exposing free-standing graphene to the controlled He- and Ga-ions irradiation allows precise determination of the sputtering yield. Graphene shows to be semi-transparent for 10-30keV energetic He-ions. 99-97% of He-ions pass graphene without crating lattice defects. In contrast, large Ga-ions spatter carbon atoms from graphene layer in 80-50% incidence cases, depending on kinetic energy 5-30keV.

Binary collision theory (BCT) explains well these experimental findings. Raman spectroscopy of damaged graphene reveals the defect formation mechanisms. He-ions create individual carbon vacancies until these defects overlap and amorphiszation occurs. Ga-ions can form mono and double vacancies as expected from BCT. Understanding the physics of the sputtering process allows to fabricate pores in graphene of only a few nm in diameter, ~2nm for He-beam and ~4nm for Ga. Eventually limited by ion beams diameters [8]. A million of nm-pore arrays are fabricated showing narrow pore diameter distribution, Fig.1(b). Pores as small as 10 nm and still resembling its triangular shape can be created in graphene, Fig.1(c).

4. Conclusions

Sputtering yields of free-standing graphene by He- and Ga-FIBs are experimentally determined. Defect density is measured by irradiation dose and compared to the extracted from Raman D to G peaks ratio. Binary collision theory is shown to be sufficient for explaining essential involved phenomena. Few-nm-small pores in graphene are demonstrated by He- and Ga-FIBs sputtering. Large-scale nanostructuring of graphene with small size-variation distributions is demonstrated. The method can be extended to other 2D membranes. Triangular (symmetry breaking) pores in graphene are be scaled down to 10 nm. These dimension length scales cross several physical length scales in typical 2D materials, such us: charge carriers and phonon mean free path. Presented study opens a way towards electrical rectifier metamaterials, frequency multipliers in THz range, phononic crystals and thermal rectifiers.

References

[1] I. Shorubalko, H.Q. Xu, I. Maximov, P. Omling, L. Samuelson, W. Seifert, *Appl. Phys. Lett.*, 79 (9), 1384-1386, 2001.

[2] A.M. Song, P. Omling, L. Samuelson, W. Seifert, I. Shorubalko, H. Zirath, *Appl. Phys. Lett.*, 79 (9), 1357-1359, 2001.

[3] A. Jacobsen, I. Shorubalko, L. Maag, U. Sennhauser, K. Ensslin, Appl. Phys. Lett., 97 (3), 032110, 2010.

[4] P. Butti, R. Brönnimann, K. Ensslin, I. Shorubalko, *Appl. Phys. Lett.*, 112 (13), 133501, 2018.

[5] I. Shorubalko, L. Pillatsch, I. Utke, *Book chapter in Helium Ion Microscopy*, Ch.15 doi:10.1007/978-3-319-41990-9_15, 2016

[6] O. Scholder, K. Jefimovs, I. Shorubalko, C. Hafner, U. Sennhauser, G.L. Bona, *Nanotechnology* 24 (39), 395301, 2013.

[7] J. Buchheim, R. M. Wyss, I. Shorubalko and H. G. Park, *Nanoscale*, 8, 8345-8354, 2016.

[8] I. Shorubalko, K. Choi, M. Stiefel and H. G. Park, *Beilstein J. Nanotechnol.*, 8, 682–687, 2017.

[9] K. Celebi, J. Buchheim, R. M. Wyss, A. Droudian, P. Gasser, I. Shorubalko, J. I. Kye, C. Lee and H. G. Park, *Science*, 344, 289-292, 2014.

Large area fabrication of complex periodic nanostructures by 'Double Displacement Talbot Lithography': Fundamentals and applications

Pierre Chausse[1*], Andrei Sarua[2], Jon Pugh[3], Pierre-Marie Coulon[1], Martin Cryan[3], Philip Shields[1]

[1]Departement of Electronic & Electrical Engineering, University of Bath, Claverton Down, Bath, BA2 7AY, UK
[2]HH Wills Physics Laboratory, University of Bristol, Clifton, Bristol, BS8 1TL, UK
[2]Departement of Electronic & Electrical Engineering, University of Bristol, Clifton, Bristol, BS8 1UB, UK
*corresponding author, E-mail: p.j.p.chausse@bath.ac.uk

Abstract

The fabrication of complex periodic metallic nanostructures has been performed at a wafer scale by combining 'Double' Displacement Talbot Lithography (D^2TL) and lift-off. Given the high flexibility and efficiency of D^2TL, a broad range of periodic configurations can be achieved from one mask, which could facilitate applications in numerous fields, including metamaterials, nanoplasomics or nanophotonics.

1. Introduction

Periodic patterning is essential for many technologies that use plasmonic [1-2], or photonic nanostructures [3-4]. Among the various lithography techniques employed in research, and to a certain extent in industry, none of them combines a fast, cheap and flexible approach to fabricate those patterns.

In this work, we present an upgrade of a new high-throughput and fast lithography tool called Displacement Talbot Lithography [5]. By introducing lateral displacements, the creation of a variety of complex periodic nano- to micron patterns can be achieved over a large area (up to 100-200 mm). [6] Combined with a lift-off process, a broad range of periodic metallic nanostructure arrays have been achieved for the creation of meta-material structures.

2. Methods

2.1. D^2TL patterning

Displacement Talbot Lithography (DTL) utilizes the periodic diffraction pattern on all space axes that results when a periodic mask is illuminated by a planar wave (Talbot effect). By displacing the wafer along the axis of illumination over integer spatial periods, the low depth of field is overcome [5]. In D^2TL, by additionally moving the wafer perpendicular to the axis of illumination, the range and complexity of features achieved from a single mask is dramatically extended. Furthermore, a single periodic mask can be used to create a large number of different patterns by using different lateral displacements (Fig. 1).

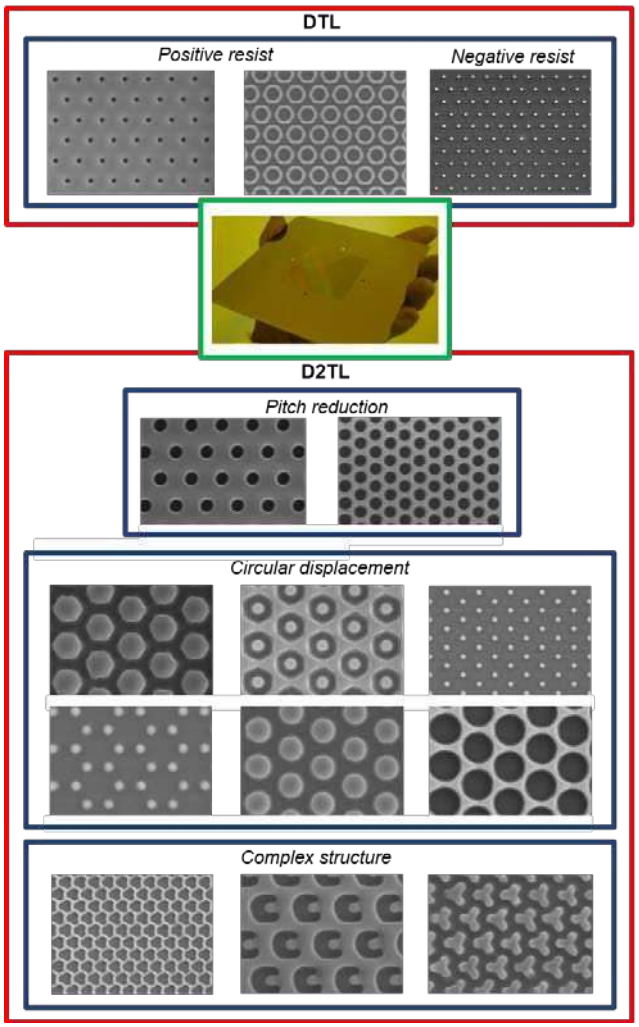


Figure 1: A selection of SEM images showing the variety of patterns that can be achieved from using a hexagonal mask with 800 nm features on a 1.5 um pitch (top) with classical DTL using positive and negative photoresist, and (bottom), the large numbers of structures that can be realized with D^2TL using the same mask and just positive resist.

2.2. Metallic structure lift-off

The transfer of the resist structures has been then performed thanks to a combination of Inductively Coupled Plasma etching (ICP) into a dielectric layer, and wet etching with low-dilution hydrofluoric acid (HF) to control the undercut profile. A metal deposition has then been realised via e-beam evaporation. The result of the patterns transferred in SiN and the one after the lift-off process are presented in Fig. 2.

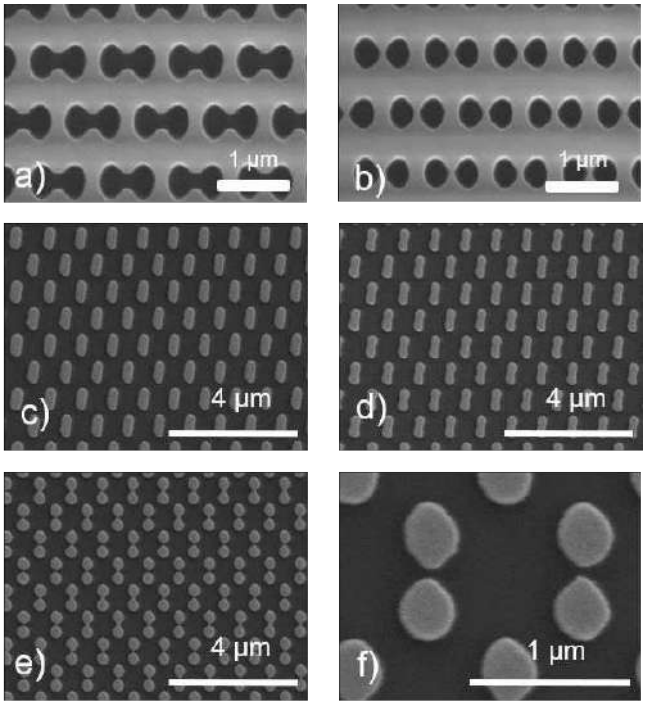


Figure 2: Dual DTL exposures with single lateral displacement for a 1 um hexagonal period amplitude mask. Secondary-electron SEM images of the etched SiN for two exposure doses of a) 275 and b) 250 mJ/cm2 and a constant displacement of 440 nm. (b-e) Metallic nanoparticle arrays after a lift-off process and displacements of approximately c) 200 nm, d) 300 nm and e) 400 nm. f) is a zoom of e) where the gaps were measured to be around 50nm.

Acknowledgements

Financial support is acknowledged from the EPSRC, UK via Grant No. EP/M015181/1, "Manufacturing nano-GaN".

References

[1] S. A. Maier, Plasmonics: Fundamentals and Applications (Springer, 2010).

[2] E. D. Le Boulbar, P. J. P Chausse, S. Lis, P. A. Shields, Displacement Talbot lithography: an alternative technique to fabricate nanostructured metamaterials, *Proc. SPIE 10248, Nanotechnology VIII*, 2017.

[3] P. M. Coulon, G. Kusch, E. D. Le Boulbar, P. Chausse, C. Bryce, R. W. Martin, and P. A. Shields, "Hybrid topdown/bottom-up fabrication of regular arrays of AlN nanorods for deep-UV core-Shell LEDs," Phys. Status Solidi, 1700445 (2017).

[4] P. M. Coulon, J. R. Pugh, M. Athanasiou, G. Kusch, E. D. Le Boulbar, A. Sarua, R. Smith, R. W. Martin, T. Wang, M. Cryan, D. W. E. Allsopp, and P. A. Shields, "Optical properties and resonant cavity modes in axial InGaN/GaN nanotube microcavities," Opt. Express 25(23), 28246–28257 (2017).

[5] H. H. Solak, C. Dais, F. Clube, L. Wang, Phase shifting masks in Displacement Talbot Lithography for printing nano-grids and periodic motifs, *Microelectronic Eng.*, 143: 74-80, 2015.

[6] P. J. P. Chausse and P. A. Shields, 'Double' displacement Talbot lithography: a new approach for periodic nanostructure patterning, *Proc. SPIE 10587, Optical Microlithography XXXI*, San Jose, USA, 2018.

Freestanding metallic mesh for transparent electromagnetic interference shielding

Yanhua Liu[1,2], Su Shen[1,2]

[1] School of Optoelectronic Science and Technology & Collaborative Innovation Center of Suzhou Nano Science and Technology, Soochow University, Suzhou, China
[2] Key Lab of Advanced Optical Manufacturing Technologies of Jiangsu Province & Key Lab of Modern Optical Technologies of Education Ministry of China, Suzhou, China
*corresponding author, E-mail: yhliu@suda.edu.cn

Abstract

A unique freestanding nickel (Ni) metallic mesh based electromagnetic interference shielding film has been fabricated though the direct-writing technique and a subsequent selective metal electrodeposited process. The structured freestanding Ni mesh film demonstrates a series of advantages, including ultrathin thickness (2.5-6.0 μm) and ultralight weight (0.23 mg cm^{-2}), extraordinary optoelectronic performance, and outstanding flexibility that it can withstand folded, rolled up and crumpled into various shapes while keeping the conductivity constant. Experimental results show that the film yields an average electromagnetic interference shielding effectiveness about 40 dB with transparency of 92%.

1. Introduction

Electromagnetic radiation pollution, severely exacerbated by the development of modern electronics packed with highly integrated circuits, leads to harmful effects on sensitive precision electronic equipment as well as the living environment for human beings, promoting the research focus on novel high-performance EMI shielding. Significantly, with the development of modern electronics toward being flexible and integratable, the EMI shielding film must simultaneously provide high optical transmittance, excellent EMI shielding effectiveness (EMI SE), and meanwhile bendability even twistability which is imperative to adapt to complex shaped or foldable applications. The fabrication of an ultrathin transparent freestanding metallic mesh EMI film, breaking off the tradeoff of the transmittance and EMI SE has never been reported. It remains a significant technological challenge to develop metallic materials that exhibit all the above-mentioned desirable features simultaneously.

Herein, we demonstrate the realization of a freestanding, ultrathin, lightweight, mechanically robust, and transparent Ni metallic mesh-based EMI shielding film**.** The ultrathin freestanding Ni mesh contributes to excellent flexibility, folding or even attaching to three-dimensional shapes with ignorable degradation of the EMI shielding efficiency. It also allows a free permeation of gas and liquid molecules, such as oxygen, moisture, etc., showing excellent air permeability. This Ni mesh films are characterized with extraordinary optoelectronic properties: a transparency about 92%-93%, a sheet resistance of 0.24-0.7 Ω sq^{-1}, and a high EMI about 40 dB shielding efficiency in 8.2-12.4 GHz frequency range (X-band) for plane and crooked Ni-mesh films. Above all, the high-performance Ni-mesh EMI film processing excellent electrical conductivity, high EMI SE, outstanding transmittance and mechanical properties are promising EMI materials for practical applications.

2. Discussion

2.1. Sample preparation and characterization

The fabrication process of the freestanding Ni-mesh mainly includes four steps, which are illustrated in Fig. 1(a). First, a photoresist layer with a thickness of 9.6 μm was obtained by spin-coating onto a pre-cleaned ITO glass. Then, the patterned micro-trenches on the photoresist layer was generated by the laser direct-writing technique. Following on, the Ni metal was electrodeposited inside the predefined micro mesh grooves though the selective electrodeposition, and the deposition time was carefully controlled to obtain the Ni metallic mesh layer with a desired thickness. Thanks to the space confinement of the micro-grooves, the Ni mesh only grow inside them without a broadening in the linewidth. Lastly, the Ni mesh conductive films were finally accomplished after being peeled off from the ITO glass substrate. For all the obtained samples, the width of the Ni line is fixed on 5 μm with the thickness ranging from 2.5 to 6.0 μm. Therefore, the sheet resistance can be adjusted in a wide range while keeping the transmittance of the Ni mesh film almost unchanged.

The metallic mesh fabrication method can be scaled up to the large area, and a 10×10 cm^2 Ni mesh film is obtained, as shown in Fig. 1(b). The freestanding Ni mesh film is competently completely transparent that the flower can be seen clearly through it. And meanwhile it exhibits excellent flexibility so that can be uniformly attached to complex shaped objects without any gap, such as the flower stem and the grape and even can stand upon the setaria viridis with sides dropping down naturally, which mainly attributes to its freestanding structure nature. Moreover, when the Ni mesh film was placed on the Albizia julibrissin, the flower filaments can even sustain their original state without any visible damage, delivering its ultralight features. For a 4.0 μm thickness Ni mesh film with an area of 10×10 cm^2, it only weighs 23.1 mg [Fig. 1(c)] showing a density of 0.23 mg cm^{-2}, while this lightweight Ni mesh still can sling a 100 g weight, more than 4000 times of the Ni mesh own weight.

When the weight was laid down, the Ni mesh film appears intact without any deformation, which was attributed to the firm texture of the Ni mesh.

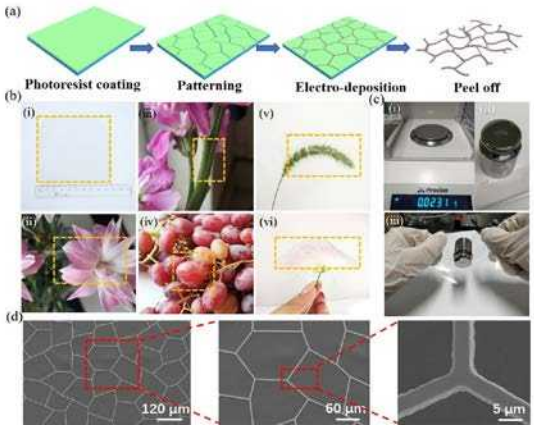


Figure 1. (a) The schematic illustration of the fabrication process of the freestanding Ni mesh conductive film. (b) The characterizations of freestanding Ni metallic mesh: (i) large-scaled, (ii) high optical transparency, (iii), (iv) flexible and (v), (vi) lightweight properties. (c) (i) The weight of a scaled 10×10 cm^2 Ni mesh film with 4.0 μm thickness, (ii) a 100 g weight and (iii) the mechanical property of the Ni mesh film. (d) SEM images with different scale bar.

2.2. Experimental Results and Discussions

To evaluate the EMI SE of those freestanding Ni mesh films, a vector network analyzer in the frequency of 8.2-12.4 GHz (X-band) is employed. Figure 2(a) shows the measured EMI SE spectra of transparent freestanding Ni mesh films with different thicknesses in the X-band frequency range. The EMI SE of the Ni mesh films exhibit similar tendency, whose values decrease gradually along with the increasing frequency. The EMI SE values of the 6-μm-thick Ni mesh film decrease from 41 to 38 dB with the frequency increases from 8.2 to 12.4 GHz, whereas the values of the 2.5-μm-thick Ni mesh film decline from 37 to 35 dB. We illustrate that the Ni mesh film with increased thickness performs better in EMI shielding, attributing to the gradually increased electric conductivity. The simulated data further confirms our experimental results, as shown in Fig. 2(b), in which the electric conductivity corresponds to calculated ones at different thicknesses. Furthermore, to adapt to complex 3D objects, such as nonplanar and irregular surfaces, the influence of bending curvatures of freestanding Ni mesh films on EMI SE has been investigated. According to Fig. 2(c), it is apparent that the EMI SE value trend of spherical Ni mesh films with a curvature of 0.3 cm^{-1} is in accordance with the complanate one. At the same frequency, SE is only 1 dB lower for the spherical Ni mesh film, in which the inappreciable gap can be ignored. In addition, as shown in Fig. 5(d), the EMI SE performance of the freestanding 4.0-μm-thick Ni mesh film with different curvatures of 0.45 cm^{-1}, 0.65 cm^{-1}, and 1 cm^{-1} was also tested, respectively. At the same frequency, EMI SE value decreases slightly with the decrease of the curvature radius, and the overall difference between them is within 1 dB. Compared with the flat Ni mesh film, the decrease in EMI SE of the curved Ni mesh films is within 3 dB, which can fully meet the requirements of the EMI shielding in complex topography. It is noteworthy that the freestanding Ni mesh here can maintain the high mechanical stability after being bended for thousands of cycles, and simultaneously hold high EMI SE values, as depicted in Fig. 2(e). To make a comparison with the metallic shielding materials in the recently reported works [1-3], as presented in Fig. 2(f), where the EMI SE and the transparency properties of our freestanding Ni mesh films are all superior to those reported.

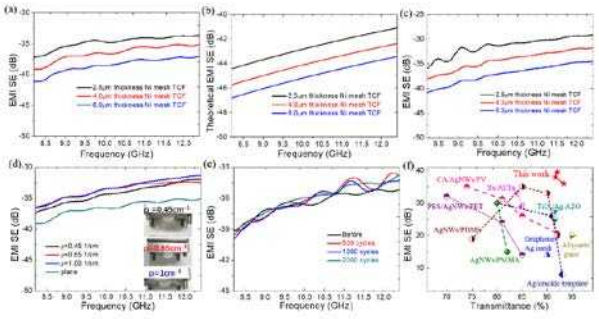


Figure 2. (a) EMI SE of fabricated Ni mesh films. (a) The measured EMI SE of plane Ni mesh films in X-band, (b) the theoretically calculated EMI SE of plane Ni mesh films, (c) the EMI SE of spherical Ni mesh films. (d) The EMI SE curves of the Ni mesh film with a thickness of 4 μm with different curvatures. (e) The EMI SE variation of a 4.0 μm thickness Ni mesh film with different bending cycles. (f) A comparison of the EMI SE *versus* transmittance characteristic of the measured sample with various flexible transparent EMI films in literature.

3. Conclusions

In conclusion, we demonstrate an ultrathin, lightweight, freestanding Ni mesh film that are fabricated by the direct-writing technique with a selective metal electrodeposited process, exhibiting EMI shielding efficiency ~40 dB in X-band and high mechanical flexibility (can be attached, folded, stretched, and crumpled into any shapes with almost no performance degradation). This freestanding metallic mesh structured electrode can be further explored or applied in various potential applications, such as conformal microwave antennas, transparent EMI windows, and wearable electronics.

References

[1] L. C. Jia, D. X. Yan, X. F. Liu, R. J. Ma, H. Y. Wu, and Z. M. Li, "Highly efficient and reliable transparent electromagnetic interference shielding film, *ACS Appl. Mater. Inter.* 10(14), 11941, 2018.

[2] M. J. Hu, J. F. Gao, Y. C. Dong, K. Li, G. C. Shan, S. L. Yang, and R. K. Y. Li, Flexible transparent PES/Silver nanowires/PET sandwich-structured film for high-efficiency electromagnetic interference shielding, *Langmuir* 28(18), 7101, 2012.

[3] X. Zhang, Y. L. Zhong, and Y. Yan, Electrical, mechanical, and electromagnetic shielding properties of silver nanowire-based transparent conductive films, *Phys. Status Solidi A* 215(14), 1800014, 2018.

FIB based Sketch & Peel for Fast and Precise Patterning of Large Plasmonic Arrays

Achim Nadzeyka[1], Michael Kahl[1], Huigao Duan[2], Yiqin Chen[2], and Kaixi Bi[2]

[1]Raith GmbH, Konrad-Adenauer-Allee 8, 44263 Dortmund, Germany
[2]College of Mechanical and Vehicle Engineering, Hunan University, Changsha 410082, People's Republic of China
*corresponding author, E-mail: achim.nadzeyka@raith.de

Abstract

FIB nanofabrication has proven unique strengths by numerous applications in R&D prototyping [1]. Moreover the slow patterning speed of direct FIB milling itself (as compared to resist-accelerated lithography) can be overcome by the method of sketch & peel. With the help of a scotch-tape method isolated metallic structures can be created by milling only the outline of the design elements. Here we further investigate sketch & peel as well as its applications employing various ion species.

1. Introduction

Focused ion beam (FIB) systems are valuable tools for nanofabrication and rapid prototyping tasks in R&D by providing direct, resistless, and three-dimensional patterning. Although FIB milling in many cases is slower than a resist based process, the relative simplification of the overall nanofabrication approach helps to achieve scientific results faster. To extend the capabilities of FIB nanofabrication, the method of sketch & peel has been recently proposed for direct patterning of thin gold films [2]. With this method, FIB milling is able to create isolated metallic structures that are difficult to fabricate by conventional subtractive milling process. Considering that isolated metallic structures [3] are more favorable for investigating some optical properties but usually lead to unacceptable time-consuming processes by removing most of the gold layer, the sketch & peel method is supposed to be substantially useful for FIB nanofabrication applications. In this work we further investigate FIB sketch & peel method for nanopatterning of thin gold layers using various ion species. The combination of sketch & peel with high resolution milling is shown for examples of plasmonic patterns. Furthermore, we have employed continuous writing strategies based on a laser interferometer controlled stage movement for creating a seamless groove across extended distances. This enables the fabrication of mm sized patterns within minutes and at the same time nm features, still showing clean removal.

2. Sketch & peel method

Sketch & peel was first proposed by Y. Chen et al. for fast ion beam patterning of plasmonic structures on gold layers with Ga and He ions [2]. Instead of removing the layer material completely between the elements of a structure or array, the ion beam mills only the element outlines. The metal between these elements and outside the array can then be removed from the substrate by pasting and stripping a tape (figure 1).

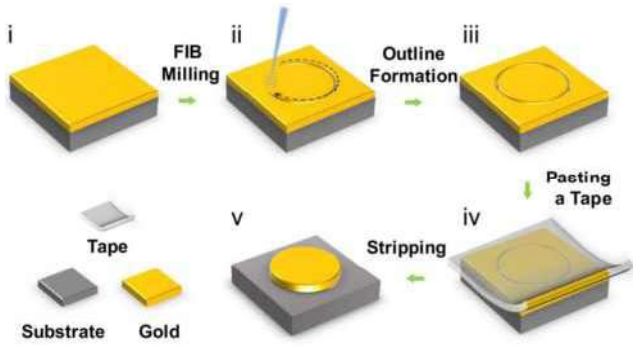


Figure 1: Principle of Sketch & Peel [2].

Use of a low-adhesion layer is important for process reliability. Hence, no adhesive layer should be used between gold and substrate. Furthermore, the outline cut should be deeper than the metal layer thickness, to form a link between metal and substrate. Obviously the throughput gain mainly depends on pattern density and element size, but can be orders of magnitude higher than usual FIB milling.

3. Fabrication of large plasmonic arrays

Due to the high throughput of this process, large plasmonic arrays can be created with low beam currents and high resolution in a reasonable time. Furthermore, the elements inside these arrays can be combined with conventional low-dose and high-resolution cuts within the same milling step.
Figure 2 shows an example of such a combined process, with a 100 µm x 100 µm array of 10,000 bowties prepared on a silicon sample with 50 nm gold layer. Each single 300 nm bowtie is created by a surrounding deep outline cut and a final low-dose cut in the center to separate it into two triangles with sub-10 nm gaps. Here we used a beam current of only 1.7 pA Ga+, resulting in 2 hours and 45 min process time. The gain in throughput is thus greater than a factor of 20 compared to conventional pure milling of the same array with the same beam current.
Another example of a plasmonic array is shown in figure 3. Here a 25 µm x 25 µm array of 625 gold nano-disks has been created by sketch & peel, including sinusoidal low-

dose cuts inside the disks. The complete pattern could be milled within a mere 25 min at 1.7 pA Ga+ beam current. This kind of nanoparticle arrays have been created earlier at Swinburne University using a mix and match process including EBL and FIB milling [4, 5].

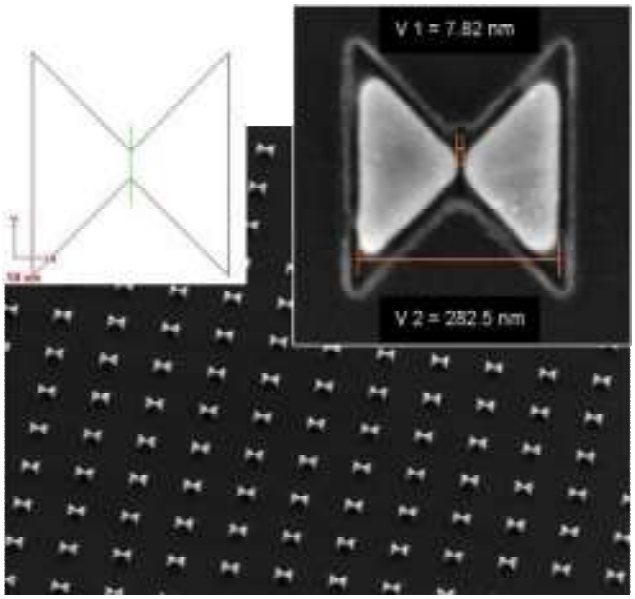


Figure 2: Tilted SEM view of the inner part of a 100 µm x 100 µm bowtie array after peeling. The inlets show the bowtie design including low dose cut in the center and a single 300 nm gold bowtie with sub-10 nm gap.

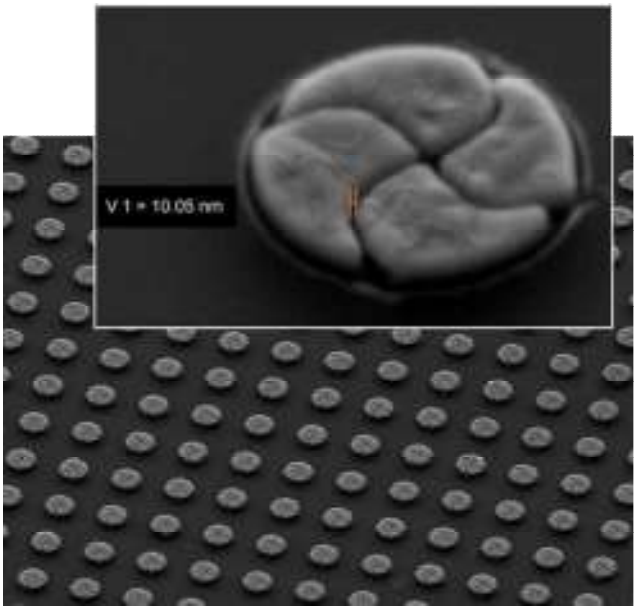


Figure 3: Tilted SEM view of a 25 µm x 25 µm gold nano-disk array with 1 µm period. The inlet shows a single disk with 500 nm diameter including a sinusoidal low dose cross cut with 10nm gap.

4. Ion Species

During this work we used a Raith VELION FIB-SEM Nanofabrication tool, which can be equipped with a Ga liquid metal ion source or with a liquid metal alloy ion source in combination with a mass separation filter to generate beams of different ion species. Hence, Ga contamination free FIB patterning is possible. Figure 4 shows close-up SEM views of circle arrays created with all our investigated ion species at doses where sketch & peel is reliably possible

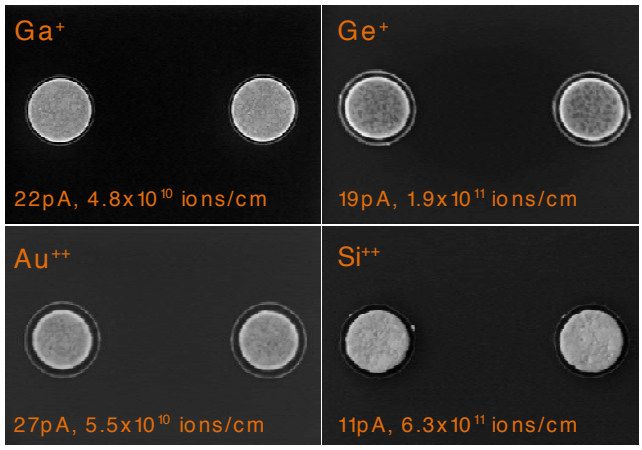


Figure 4: 800 nm circles created with 4 different ion species and corresponding optimum line doses for successful sketch & peel.

5. Conclusions

Sketch & peel is a reliable method of extremely fast FIB patterning for low-adhesion metal layers. Elements with <100 nm to >1 mm in size can be created, whereas combination with high-resolution conventional milling enables sub-10 nm features. Due to the high throughput, an accurate laser interferometer stage and fixed-beam moving-stage writing modes are highly effective at creating even cm size patterns. Other low-adhesion layers than gold might be investigated in the future.

References

[1] L. Bruchhaus et al., Appl. Phys. Rev. 4, 011302 (2017); doi: 10.1063/1.4972262.

[2] Y. Chen et al., ACS Nano 2016, 10, 11228-11236.

[3] M. . Hentschel et al., Nano Lett. 2010, 10, 2721-2726.

[4] G. Gervinskas et al., Adv. Optical Mater. 2013, 1, 456–459

[5] G. Seniutinas et al., Nanophotonics 2017; 6(5): 923–941

Direct-Write Electron-Beam Lithography

Soroosh Daqiqeh Rezaei[1,2], Jinfa Ho[2], Tao Wang[2], Seeram Ramakrishna[1], and Joel K.W. Yang[2,3]

[1]Department of Mechanical Engineering, Faculty of Engineering, National University of Singapore, 117575, Singapore
[2]Institute of Materials Research and Engineering (IMRE), A*STAR (Agency for Science, Technology and Research), 2 Fusionopolis Way, 138634, Singapore
[3]Pillar of Engineering Product Development, Singapore University of Technology and Design (SUTD), 8 Somapah Road, 487372, Singapore
*corresponding author, E-mail: joel_yang@sutd.edu.sg

Abstract

The capability to fabricate variable-height structures with nanometre resolution is an answer to the ever-increasing demand for metasurfaces shape complexity. Here, we demonstrate that the shrinkage arising from the direct exposure of polymethyl methacrylate (PMMA) to an electron beam can be used to conveniently create structures with nanometre spatial resolution and realize variable height structures. Since the electron-beam can directly shape the PMMA, no additional fabrication steps such as development or lift-off are required. We employ direct-write electron-beam lithography (DW-EBL) to create spatial variations in the height of a Fabry-Perot (FP) cavity, resulting in a direct colour print without the need for pre-patterning that is necessary for some direct laser writing methods. In addition, the resolution and pixel size of the colour prints are limited by the electron beam. We also demonstrate colorimetric height measurements through image analysis of a DW-EBL patterned FP cavity. Finally, we fabricated blazed gratings which cannot be fabricated by conventional EBL methods without using development processes.

1. Introduction

With its high resolution and throughput, electron-beam lithography (EBL) has enabled the realization of metasurfaces, which require high spatial resolution [1–10]. The increasing demand for metasurfaces shape complexity requires additional degrees of freedom in fabrication, specifically the ability to achieve varying heights, which is not possible by the conventional EBL and its resists without multiple fabrication steps [11–13]. Although there are alternative fabrication routes such as grey-scale lithography [14], additive nanofabrication [15], liquid phase-focused electron beam-induced deposition (LP-FEBID) [16], and ion beam etching redeposition [17] which can achieve varying height structres and even more complex 3D patterning, these methods either lack the EBL resolution advantage, which is crucial to some metasurfaces, or need particular precursors, equipment, and additional processing steps. Moreover, variable-height patterns can be achieved by EBL through some resists, however the fabrication still needs multiple fabrication steps [18,19].

Poly(methyl methacrylate) (PMMA) was the first resist used in advanced microlithography and is still one of the most widely-used resists in EBL [20]. Here we show that by directly exposing PMMA to an electron-beam (e-beam), it undergoes a dose-dependent shrinkage caused by the e-beam irradiation. This effect was employed to create patterns with nanometre height and spatial resolution in a single-step process without additional developing and lift-off. Our method circumvents the need for complex resists and fabrication processes and achieves complex topographies with the widely available PMMA.

Direct writing of structural colours offers numerous possibilities such as environmentally friendly and fadeless structural pigments, optical anti-counterfeiting, and camouflaging [21–25]. However, direct laser writing, which is the most common method, often needs a prepatterned area. As an alternative, we used PMMA as the dielectric layer in a FP cavity and employed DW-EBL to realize statured structural colours. Our approach does not need pre-pattering and benefits from the high EBL spatial resolution. The colours in a FP cavity are strongly dependent on the cavity length i.e., the PMMA layer's thickness. Therefore, the colours from an optical micrograph can be used to determine structures height as was done by our image analysis and confirmed by AFM. Our method can be employed to directly obtain structure height information while directly pattering a surface, eliminating the need to carry out AFM measurements. Finally, we fabricated blazed gratings by EBL-DW, which otherwise cannot be realized by conventional EBL resists in a single step [2,26].

2. Results

The single-step fabrication method is illustrated in Fig. 1a. A 500 nm thick PMMA layer is sandwiched between two metallic layers to form a FP cavity. The bottom 100 nm thick Al layer acts as the back-reflector and the top 6 nm thick Ni layer acts as the partial reflector. Exposing the FP cavity to an e-beam results in local shrinkage of the exposed region, which results in a change in the FP resonance and the reflected colour. Since the optical cavity reflection properties and colours heavily depend on the polymer thickness, various colours would appear depending on the exposure dose, as shown in Fig. 1b and 1c. Thicknesses are measured by fitting the experimental reflection spectra to the simulation data and is further confirmed by atomic force microscopy (AFM) measurements.

A higher e-beam exposure dose results in larger thickness change as plotted in Fig. 1c. The rate of thickness change decreases with the increase of the dosage, and the thickness change reaches about 35% of the initial thickness for a maximum dose of 100 μs. The shrinkage mechanism of PMMA is illustrated in Fig. 1d. When the structure is irradiated by an e-beam, the PMMA mainly undergoes a backbone chain scission and ester group removal. In addition, large quantities of gasses including CO, CO_2, CH_4, CH_3OH, and other gaseous products are released [28–30]. Since most of the residue are either gaseous or volatile in the low-pressure e-beam chamber, they evaporate and as a result, the polymer undergoes a thickness change.



Figure 1: Direct E-beam patterning of a FP cavity. (a) Schematic of the direct electron-beam writing fabrication method. (b) Computer generated layout of patterns with varying exposure dose (colour coded), height change (colour coded), and the experimentally observed colours. (c) Thickness change vs. exposure dose for experiments and a double exponential function fitted to the experimental data. (d) Schematic of PMMA decomposition showing two main pathways (left) main chain scission, and (right) ester group removal. Optical micrographs are captured by a 20× objective lens (NA: 0.45).

The controlled thickness change by varying the exposure dose spatially can be employed to realize various patterns as shown in Fig. 2a shows optical micrograph of the A*STAR, NUS, and SUTD logos, as well as colourful letters spelling "PMMA" realized by direct e-beam patterning. Square pixels with a 200 nm size were used to realize these patterns.

In addition to structural colour applications, direct e-beam writing can be used to fabricate nanopatterns with variable heights, as shown in Fig. 2b. Structural colour can be used to deduce the feature height, eliminating the need for AFM measurements, as illustrated in Fig. 2c. The height map in Fig. 2c is plotted through analysing the optical image in Fig. 2b and correlating the colours in each pixel to the calculated heights in Fig. 1b. As can be seen, the height map deduced from the structural colours is in a good agreement with the AFM measurements in Fig. 2d.

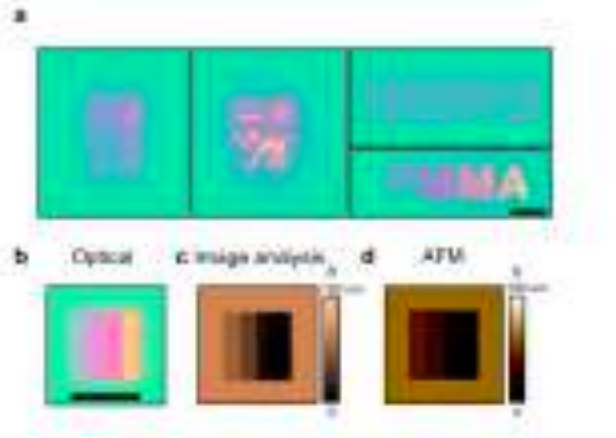


Figure 2: Direct e-beam writing of structural colours and patterns. (a) A*STAR, NUS, SUTD logos, and colourful letters spelling "PMMA," realized by direct patterning. (b) Optical micrographs of a multistep square. (c) A map of the height variation of the multistep square obtained by analysing the optical image in (b). (d) AFM micrograph of the multistep square. The scale bars in (a) and (b) are 25 μm and 10 μm respectively. Optical micrographs in (a) and (b) are captured by a 20× objective lens.

The method is not limited to patterning FP cavities but can be employed to realize any pattern with variable heights on PMMA. Here we fabricated blazed diffraction grating to disperse light. Since the blazed grating has a variable-height profile, it cannot be fabricated by conventional e-beam resists in a single step i.e., resist developing step is still necessary. The blazed grating with sawtooth grooves is illustrated in Fig. 3a. The Optical and AFM micrograph along with gratings grooves profiles are shown in Fig. 3b-d. As can be seen from the AFM profile in Fig. 3c, the sawtooth profile can be achieved in a single step.

Figure 3a shows reflection spectra for x and y-polarized lights at the normal incident for a blazed grating. The diffraction efficiency eta is shown for an x-polarized light at 20˚ tilted angle for blazed grating. As can be seen, the x-polarized and y-polarized lights are considerably different, which is expected. The maximum efficiency for the blazed gratings, has a maximum around the blue region.

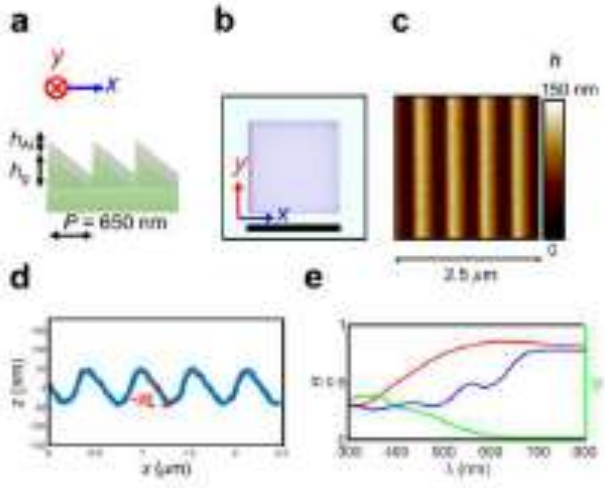


Figure 3: (a) Schematics of the blazed gratings (b) Optical micrograph of the blazed gratings for a *x*-polarized light source (c) The sawtooth AFM micrograph (d) The sawtooth profile (e) Reflection spectra for *x* and *y*-polarized lights at the normal incident for blazed grating. The diffraction efficiency η is shown for an *x*-polarized light at 20˚ tilted angle for blazed grating.

3. Conclusions

Direct patterning of surfaces was demonstrated by direct write electron-beam lithography direct (DW-EBL). We showed through AFM and reflectance measurements that PMMA height can be tuned with nanometer precision by controlling the e-beam dose through AFM and reflectance measurements. Colour prints were fabricated by directly patterning a FP cavity. Our pixel size can be reduced to the sub-diffraction limit of visible light without significantly affecting the colours. DW-EBL for colour printing does not require surface pre-patterning, which is necessary for some of the direct laser printing methods. Since the colour reflected by the FP cavity depends on its height, we were able to

infer the height map of an observed region by matching the reflected colour to its calculated height, which is in good agreement with AFM measurements. To further demonstrate the method's viability to realize structures that require variable heights, blazed gratings were fabricated without any resist developing process. The proposed method minimizes the fabrication steps and complexity while offering variable height as a new degree of freedom for realizing metasurfaces.

Acknowledgements

S.D.R acknowledges the financial support provided by Agency for Science, Technology and Research (A*STAR) through Singapore International Graduate Award (SINGA) program. We would like to acknowledge the funding support from Agency for Science, Technology and Research (A*STAR) SERC Pharos project (Grant Number 1527300025), A*STAR Young Investigatorship (Grant Number 0926030138), SERC (Grant Number 092154099), National Research Foundation Grant Award No. NRF-CRP001-021, NRF-CRP 8-2011-07, and A*STAR-JCO under Project Number 1437C00135.

.

References

[1] P. Cheben, R. Halir, J.H. Schmid, H.A. Atwater, D.R. Smith, Subwavelength integrated photonics, Nature. 560 (2018) 565–572. doi:10.1038/s41586-018-0421-7.

[2] Y. Chen, Nanofabrication by electron beam lithography and its applications: A review, Microelectron. Eng. 135 (2015) 57–72. doi:10.1016/j.mee.2015.02.042.

[3] K. Kumar, H. Duan, R.S. Hegde, S.C.W. Koh, J.N. Wei, Printing Colour at the Optical Diffraction Limit SUPPLEMENTARY INFORMATION, Nat. Nanotechnol. 7 (2012) 1–15. doi:10.1038/NNANO.2012.128.

[4] L. Jin, Z. Dong, S. Mei, Y.F. Yu, Z. Wei, Z. Pan, S.D. Rezaei, X. Li, A.I. Kuznetsov, Y.S. Kivshar, J.K.W. Yang, C.W. Qiu, Noninterleaved Metasurface for (2 6 -1) Spin- and Wavelength-Encoded Holograms, Nano Lett. 18 (2018) 8016–8024. doi:10.1021/acs.nanolett.8b04246.

[5] H. Harutyunyan, A.B.F. Martinson, D. Rosenmann, L.K. Khorashad, L. V. Besteiro, A.O. Govorov, G.P. Wiederrecht, Anomalous ultrafast dynamics of hot plasmonic electrons in nanostructures with hot spots, Nat. Nanotechnol. 10 (2015) 770–774. doi:10.1038/nnano.2015.165.

[6] N. Yu, F. Capasso, Flat optics with designer metasurfaces., Nat. Mater. 13 (2014) 139–50. doi:10.1038/nmat3839.

[7] M. Jang, Y. Horie, A. Shibukawa, J. Brake, Y. Liu, S.M. Kamali, A. Arbabi, H. Ruan, A. Faraon, C. Yang, Wavefront shaping with disorder-engineered metasurfaces, Nat. Photonics. 12 (2018) 84–90. doi:10.1038/s41566-017-0078-z.

[8] A. Arbabi, E. Arbabi, Y. Horie, S.M. Kamali, A. Faraon, Planar metasurface retroreflector, Nat. Photonics. (2017). doi:10.1038/nphoton.2017.96.

[9] F. Yesilkoy, E.R. Arvelo, Y. Jahani, M. Liu, A. Tittl, V. Cevher, Y. Kivshar, H. Altug, Ultrasensitive hyperspectral imaging and biodetection enabled by dielectric metasurfaces, Nat. Photonics. (2019). doi:10.1038/s41566-019-0394-6.

[10] G. Zheng, H. Mühlenbernd, M. Kenney, G. Li, T. Zentgraf, S. Zhang, Metasurface holograms reaching 80% efficiency, Nat. Nanotechnol. 10 (2015) 308–312. doi:10.1038/nnano.2015.2.

[11] D. Oran, S.G. Rodriques, R. Gao, S. Asano, M.A. Skylar-Scott, F. Chen, P.W. Tillberg, A.H. Marblestone, E.S. Boyden, 3D nanofabrication by volumetric deposition and controlled shrinkage of patterned scaffolds, Science (80-.). 362 (2018). doi:10.1126/science.aau5119.

[12] D. Chanda, K. Shigeta, S. Gupta, T. Cain, A. Carlson, A. Mihi, A.J. Baca, G.R. Bogart, P. Braun, J.A. Rogers, Large-area flexible 3D optical negative index metamaterial formed by nanotransfer printing, Nat. Nanotechnol. 6 (2011) 402–407. doi:10.1038/nnano.2011.82.

[13] Y. Chen, X. Yang, J. Gao, 3D Janus plasmonic helical nanoapertures for polarization-encrypted data storage, Light Sci. Appl. 8 (2019) 45. doi:10.1038/s41377-019-0156-8.

[14] J. Loomis, D. Ratnayake, C. McKenna, K.M. Walsh, Grayscale lithography—automated mask generation for complex three-dimensional topography, J. Micro/Nanolithography, MEMS, MOEMS. 15 (2016) 013511. doi:10.1117/1.jmm.15.1.013511.

[15] R.D. Piner, J. Zhu, F. Xu, S. Hong, C.A. Mirkin, "Dip-pen" nanolithography, Science (80-.). 283 (1999) 661–663. doi:10.1126/science.283.5402.661.

[16] J.S. Fisher, P.A. Kottke, S. Kim, A.G. Fedorov, Rapid Electron Beam Writing of Topologically Complex 3D Nanostructures Using Liquid Phase Precursor, Nano Lett. 15 (2015) 8385–8391. doi:10.1021/acs.nanolett.5b04225.

[17] B.X.E. Desbiolles, A. Bertsch, P. Renaud, Ion beam etching redeposition for 3D multimaterial nanostructure manufacturing, Microsystems Nanoeng. 5 (2019) 11. doi:10.1038/s41378-019-0052-7.

[18] Y. Matsubara, J. Taniguchi, I. Miyamoto, Fabrication of three-dimensional hydrogen silsesquioxane resist structure using electron beam lithography, Jpn. J. Appl. Phys. 45 (2006) 5538.

[19] R. Kirchner, V.A. Guzenko, I. Vartiainen, N. Chidambaram, H. Schift, ZEP520A - A resist for electron-beam grayscale lithography and thermal reflow, Microelectron. Eng. 153 (2016) 71–76. doi:10.1016/j.mee.2016.01.017.

[20] L.F. Thompson, C.G. Willson, M.J. Bowden,

Introduction to Microlithography, 1983. doi:10.1021/bk-1983-0219.

[21] X. Zhu, C. Vannahme, E. Højlund-Nielsen, N.A. Mortensen, A. Kristensen, Plasmonic colour laser printing, Nat. Nanotechnol. (2016). doi:10.1038/nnano.2015.285.

[22] S.D. Rezaei, R.J. Hong Ng, Z. Dong, J. Ho, E.H.H. Koay, S. Ramakrishna, J.K.W. Yang, Wide-Gamut Plasmonic Color Palettes with Constant Subwavelength Resolution, ACS Nano. 13 (2019) 3580–3588. doi:10.1021/acsnano.9b00139.

[23] X. Zhu, W. Yan, U. Levy, N.A. Mortensen, A. Kristensen, Resonant laser printing of structural colors on high-index dielectric metasurfaces, Sci. Adv. 3 (2017). doi:10.1126/sciadv.1602487.

[24] S.D. Rezaei, J. Ho, R.J.H. Ng, S. Ramakrishna, J.K.W. Yang, On the correlation of absorption cross-section with plasmonic color generation, Opt. Express. 25 (2017) 27652. doi:10.1364/OE.25.027652.

[25] A. Kristensen, J.K.W. Yang, S.I. Bozhevolnyi, S. Link, P. Nordlander, N.J. Halas, N.A. Mortensen, Plasmonic colour generation, Nat. Rev. Mater. 2 (2016) 16088. doi:10.1038/natrevmats.2016.88.

[26] U.D. Zeitner, M. Oliva, F. Fuchs, D. Michaelis, T. Benkenstein, T. Harzendorf, E.B. Kley, High performance diffraction gratings made by e-beam lithography, Appl. Phys. A Mater. Sci. Process. 109 (2012) 789–796. doi:10.1007/s00339-012-7346-z.

[27] T. Smith, J. Guild, The C.I.E. colorimetric standards and their use, Trans. Opt. Soc. 33 (1931) 73–134. doi:10.1088/1475-4878/33/3/301.

[28] J.O. Choi, Degradation of poly(methylmethacrylate) by deep ultraviolet, x-ray, electron beam, and proton beam irradiations, J. Vac. Sci. Technol. B Microelectron. Nanom. Struct. 6 (1988) 2286. doi:10.1116/1.584071.

[29] N. Grassie, Developments in Polymer Degradation—7, Springer Science & Business Media, 2012.

[30] E.H. Lee, G.R. Rao, L.K. Mansur, LET effect on cross-linking and scission mechanisms of PMMA during irradiation, Radiat. Phys. Chem. 55 (1999) 293–305. doi:10.1016/S0969-806X(99)00184-X.

Modeling and computational techniques

Invariant-Based Dynamics Towards Optimal Adiabatic Qubit-Information Detection with Superconducting Qubit Resonators

Jeong Ryeol Choi*

Department of Physics, Kyonggi University, Yeongtong-gu, Suwon, Gyeonggi-do 16227, Republic of Korea
*corresponding author, E-mail: choiardor@hanmail.net

Abstract

Time behavior of the Rayleigh-Lorentz invariant for a flux qubit resonator has been investigated in order to achieve better understanding of the resonator in quantum computing systems. We have analyzed the time variation of the Rayleigh-Lorentz invariant of the system and confirmed that such a variation is non-negligible especially when the parameters vary significantly. Through this analysis, we have studied the optimal evolution of the invariant that is necessary for adiabatic qubit-information detection with the qubit resonator.

1. Introduction

Adiabatic invariants of time-varying systems have attracted considerable interest from the early days of modern physics. A typical definition of an invariant is given by $I(t) = E(t)/\omega(t)$ where $E(t)$ and $\omega(t)$ are time-varying energy and angular frequency of the system, respectively. In 1895, Rayleigh [1] showed that $I(t)$ for a pendulum with a slowly varying length almost does not vary over time. Afterwards, Lorentz have rediscovered this consequence in the semiclassical regime and he have pronounced his discovery at the first Solvay Conference held in 1911. It is noticeable that such Rayleigh-Lorentz invariants are not exactly constants but approximately constants under the assumption that the change of parameters are very slow.

The study for the variance of Rayleigh-Lorentz invariants for specific systems may be interesting and provides insights for understanding the underlying mechanism associated with the invariants. The concept of such adiabatic invariants can be applied to analyzing various properties of mechanical and photonic systems, such as superconducting flux qubits, quantum control for adiabatic passage in atomic energy levels, and adiabatic quantum computation.

In this work, we will investigate the variance of the Rayleigh-Lorentz adiabatic invariant for a flux qubit resonator [2]. Flux qubit resonators are potential candidate for implementing quantum computation systems which are important in the field of quantum information science. If the adiabatic hypothesis relevant to Rayleigh-Lorentz adiabatic invariants holds, the initial eigenstate in the discrete spectrum of the Hamiltonian does not change over time. In order to process quantum information such as computing algorithms and the readout of the qubit state signals, a high-fidelity resonator is necessary. As an implementation of devices for such a purpose, flux qubit is an artificial two-level system that is a basic unit that stores quantum information. Typically, flux qubits are fabricated by superconducting circuits using nanotechnology facilities. The entanglement between flux qubit and a SQUID (superconducting quantum interference device) provides a protocol for measuring the quantum states [3]. By developing time variation of the Rayleigh-Lorentz invariant of the system, we study optimal evolution of the resonator needed for detecting qubit-informations with the resonator.

2. Dynamics for the time behavior of the invariant

We consider an extended Duffing equation [2, 4] that describes flux qubit resonators in quantum computation systems. We focus on the situation of weak Duffing-nonlinearity throughout this research. We have investigated the time evolution of $I(t)$ for several different values of the pumping angular frequency ω_p. While $I(t)$ almost does not vary for the case of small values of ω_p, it oscillates as ω_p becomes large. Sánchez-Soto and Zoido discovered similar oscillation of $I(t)$ for the system of lengthening pendulum [5]. We have also confirmed that $I(t)$ increases more or less as time goes by depending on the amplitude of the driving force. For large values of ξ_0, the increase of $I(t)$ over time is more rapid. From these analyses, we can confirm that, if the process of the change of the system parameters were too fast, $I(t)$ would not remain constant.

If the variance of the invariant has been minimized, the variation of the invariant would be very small enough that it can be negligible. Then, it is possible to achieve a reliable detection of states with high efficiency in quantum-limited metrology for quantum computing systems. One should bear this in mind when designing a flux qubit resonator.

3. Conclusions

Detailed analysis of quantum features of the flux qubit resonator can be fulfilled by means of the invariant quantity [6]. It has been confirmed that the Rayleigh-Lorentz invariant varies more or less over time. From the investigation of the time variance of the Rayleigh-Lorentz invariant for a flux qubit resonator, we have studied an optimal adiabatic evolution of the resonator which is necessary for efficient

detection of qubit-informations.

From the investigation performed in this work, our understanding for the characteristics of the Rayleigh-Lorentz invariant of the system has been deepen. As Einstein pointed out, the slow variation of the potential strength in a time-varying oscillator is directly related to quantum mechanics. In a case that the potential varies sufficiently slowly over a cycle of oscillation, the state of the oscillator at a later time remains the same as the initial one.

Acknowledgement

This research was supported by the Basic Science Research Program of the year 2018 through the National Research Foundation of Korea (NRF) funded by the Ministry of Education (Grant No.: NRF-2016R1D1A1A09919503).

References

[1] J.W.S. Rayleigh, On the pressure of vibrations, *Phil. Mag.* 3: 338-346, 1902.

[2] J.R. Choi, Time behavior of superconducting resonators in quantum circuits for quantum information processing, *Discovery* 38: 29-35, 2015.

[3] I. Chiorescu, P. Bertet, K. Semba, Y. Nakamura, C.J.P.M. Harmans, J.E. Mooij, Coherent dynamics of a flux qubit coupled to a harmonic oscillator, *Nature* 431: 159-162, 2004.

[4] P. Krantz, Parametrically pumped superconducting circuits, Thesis for the Degree of Licentiate of Engineering, Chalmbers University of Technology, Sweden, 2013.

[5] L.L. Sánchez-Soto, J. Zoido, Variations on the adiabatic invariance: the Lorentz pendulum, *Am. J. Phys.* 81: 57-62, 2013.

[6] J.R. Choi, Hamiltonian dynamics and adiabatic invariants for time-dependent superconducting qubit-oscillators and resonators in quantum computing systems, *Adv. Math. Phys.* 2015: 120573, 2015.

Inverse Design of THz Filter based on Self-Complementary Metasurfaces and Deep Neural Network

Celso M. Leite[1], Kyung-Bin Lee[1], Hyo-Jeong Kim[1], Pyeung-Hwi Choi[1], Muhammad T. Nouman[1], and Jae-Hyung Jang[1*]

[1]School of Electrical Engineering and Computer Science, Gwangju Institute of Science and Technology, Gwangju, Korea
*corresponding author, E-mail: jjang@gist.ac.kr

Abstract

We demonstrate the inverse design, where the geometry of the structure is obtained for an on-demand response, of terahertz (THz) filters using Deep Learning. The filter response is achieved by using self-complementary metasurfaces. Our Deep Neural Network is first trained with thousands of synthetic data results obtained from electromagnetic (EM) simulations and tested on its ability to predict the geometry of the metasurface. The presented results allow the on-demand design of THz filters in a rapid and systematic manner.

1. Introduction

In recent years, terahertz technology has attracted considerable attention due to its potential applications. THz waves have the benefit of being able to penetrate visually opaque materials while being harmless to human body, having applications such as bio-sensing [1] and material characterization [2]. However, its further development is still hindered by the lack of devices that can effectively control and manipulate THz waves, such as modulators, filters and polarizers. In the THz frequency band, compared to other frequency bands, more active and passive components are still required for THz devices to become a mature technology used in industrial applications [3]. Currently, the design and optimization of THz filters have remained a time-consuming task where the Maxwell's equations are solved iteratively until the desired response is achieved. For the case of inverse design, where the geometry of the structure is obtained for an on-demand response, common approaches are the use of evolution algorithms [4] and topology optimization [5]. However, those methods still remain time consuming and computationally demanding due to its random geometry approach [6].

In this work we demonstrate the inverse design of THz filters using Deep Learning. The filter response is achieved by using a self-complementary metasurface, two-dimensional arrays of artificial resonators and its complementary counterpart. Our Deep Neural Network is first trained with thousands of synthetic data results obtained from EM simulations and then tested on its ability to predict the geometry of the metasurface based solely on given filter responses.

2. Results and discussion

The metasurface chosen to realize the THz filter in this work was a self-complementary Jerusalem cross structure. The unit cell consists of a metallic Jerusalem cross and its complementary counterpart, as shown in Fig. 1. Self-complementary metamaterials are known for working as band-stop filters (BSF) for one linear polarization of the incident wave, while showing band-pass filter (BPF) response for the orthogonal polarization [7]. Also, due to Babinet's principle, the resonance frequency for both polarization states should be at the same frequency [8]. Those characteristics of self-complementary metamaterials enables the design of a 2-in-1 filter, whose response can be easily switched between BSF and BPF by mechanically rotating the device by 90°, making this type of metamaterials a good option for designing filters in the THz frequency band.

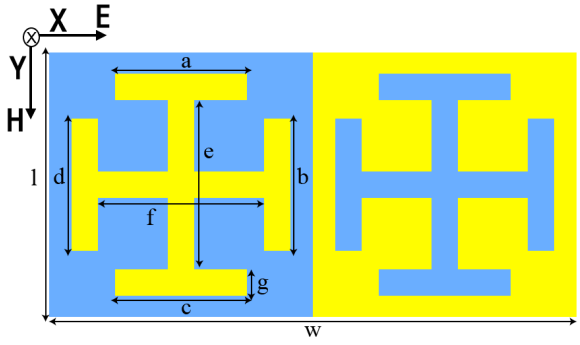


Figure 1: Self-complementary metasurface unit cell using Jerusalem cross design. The length of the loading ends a, b, c and d were varied during the simulations, while the other parameters were fixed at l = 50 μm, w = 100 μm, e = 42 μm, f = 40 μm, g = 5 μm. The metal thickness and substrate thickness were 200 nm and 700 μm, respectively.

The deep neural network approach for designing THz filters proposed here is shown in Fig. 2. The input consists of the transmission spectrum data of the desired filter and the output consists of the geometry parameters. The labeled data used to train the network was generated using ANSYS

HFSS, a simulation software. The frequency range of interest in the simulations was from 0.01 to 2 THz and the transmission response was discretized into 400 data points. The set of synthetic data contains 20000 results obtained by varying the length of the loading ends a, b, c and d between 5 μm and 53 μm, in a way so that the loading ends do not cross each other. In the simulations, the substrate used was lossless Zeonor modeled with a relative permittivity of 2.56, while the metallic parts of the metasurface used gold modeled with a conductivity of 4.561×10^7 S/m.

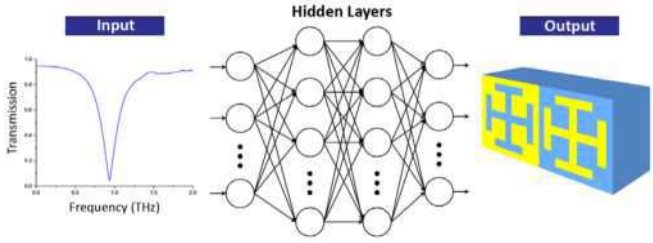


Figure 2: Inverse design network diagram. The model was constructed and tested using the open-source framework of TensorFlow in python language.

The neural network has three hidden layers of 600, 2000 and 400 units, respectively. The number of units in the input layer was defined as 400 to match the number of discretization points of the synthetic data. The output layer, in a similar way, has 4 units representing the length of the four loading ends in the Jerusalem cross. The generated data was shuffled and split into training and test sets having 16,000 and 4,000 instances, respectively. The learning rate, which defines how quickly a network updates its parameters, utilized was 0.0005 and the dropout rate, a regularization technique to avoid overfitting, was fixed at 30%. The optimization algorithm and activation function chosen were Adam and Swish, respectively.

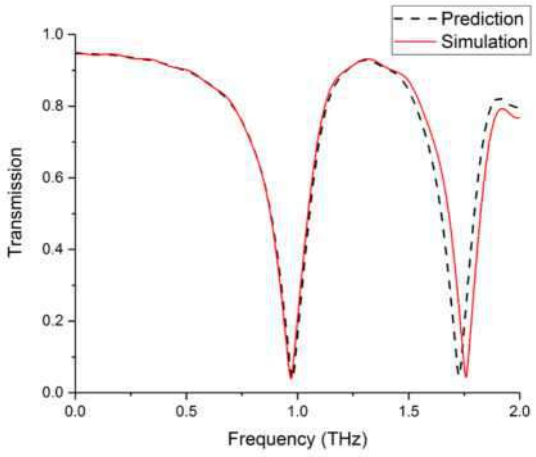


Figure 3: Comparison result for a randomly picked design. The black line represents the transmission spectrum for the geometry parameters obtained as output of the neural network. The red line represents the target spectrum utilized for this example.

During the training process, the network weights are updated to minimize the error by comparing the network prediction with the labeled data in the training set. After the training process, the performance of the network is tested on a set of unseen data. In Fig. 3 we show an example design by the neural network developed in this work. By comparing the predicted and simulated spectra, we notice that it reasonably satisfies the target response, although with still some mismatch in the second resonance peak around 1.75 THz. Our proposed network can produce suitable geometric parameters to achieve the desired response, and we expect that, with increasing the training data, we can further improve its performance.

3. Conclusions

We propose a method for the inverse design of THz filters using Deep Neural Network. The filter response was obtained by using a Jerusalem cross-shaped self-complementary metamaterial. In this approach, the training process is a one-time cost and the design itself takes only a fraction of second, where it can be used as a fast prototyping tool. This work may be further expanded by varying more geometry parameters, increasing the number of feasible filter responses for the same basic structure.

Acknowledgements

This research was supported by the National Research Foundation of Korea (NRF) grant funded by the Korea government (Ministry of Science, ICT and Future Planning) (No. 2017R1A2B3004049), and supported by Korea Electric Power Corporation. (Grant number: R18XA0679).

References

[1] P.H. Siegel, Terahertz in biology and medicine, IEEE TMTT 52.10:2438-2447, 2004.

[2] N. Nagai, T. Imai, R. Fukasawa, K. Kato, K. Yamauchi, Analysis of the intermolecular interaction of nanocomposites by THz spectroscopy, APL, 85.18:4010-4012, 2004.

[3] P. U. Jepsen, D. G. Cooke, M. Koch, Terahertz spectroscopy – Modern techniques and applications. Laser & Photonics reviews, 5.1:124-166, 2011.

[4] Z. Yu, H. Cui, X. Sun, Genetic-algorithm-optimized wideband on-chip polarization rotator with an ultrasmall footprint, Optics letters, 42.16:3093-3096, 2017.

[5] J. Yang, J. A. Fan, Topology-optimized metasurfaces: impact of initial geometric layout, Optics letters, 42.16:3161-3164, 2017.

[6] W. Ma, F. Cheng, Y. Liu, Deep-learning-enabled on-demand design of chiral metamaterials, ACS nano, 12.6:6326-6334, 2018.

[7] J. Ortiz, J. Baena, R. Marques, F. Medina, A band-pass/stop filter made of SRRs and C-SRRs, IEEE APSURSI, 2669-2672, 2011.

[8] J. Baena, J. P. d. Risco, A. P. Slobozhanyuk, S. B. Glybovski, P. A. Belov, Self-complementary metasurfaces for linear-to-circular polarization conversion, Physical review B, 92.24:245413, 2015.

Multiobjective Optimization-aided Metamaterial Synthesis

Ronald P. Jenkins*, Sawyer D. Campbell, Pingjuan L. Werner, and Douglas H. Werner

Department of Electrical Engineering, Penn State University, University Park, PA
*corresponding author, E-mail: rpj1@psu.edu

Abstract

Metamaterial design, from RF to optical frequencies, can present a significant challenge to engineers. In this paper, several recent tools that can aid in the process of metamaterial synthesis are presented, and their relative advantages are discussed for various kinds of design goals.

1. Introduction

Over the past few years, research into metamaterials has expanded the Electromagnetics (EM) community's understanding of their capabilities and led to the development of a tremendous range of unit cell designs with a host of properties and applications. Today's designers have a wide range of metamaterial designs which can produce many different bulk properties, and which through minor modifications can be altered to meet their particular needs. However, designing metamaterials to achieve novel properties is still a great challenge, and has in some cases necessitated breaking away from the familiar canonical metamaterial shapes which are commonly employed [1]. In such cases, synthesizing new metamaterial designs can be assisted greatly by developing an automated inverse-design process which loops unit cell generation, evaluation, and analysis with powerful optimization techniques. In this paper, the impact that the choice of performance goals and optimizer have on the synthesized metamaterial unit cell topology are discussed.

2. Metamaterial Synthesis

While there is no exclusive form for metamterial synthesis, the flowchart mapped out in Figure 1 presents a general inverse-deign process which combines optimization with unit cell generation, full wave evaluation, and effective parameter retrieval. The first stage in metamaterial synthesis is the design generator. This stage may take many forms depending on the evaluation tool used. However, one commonly used approach that is favored for its relative computational efficiency is that of a pixelated design [2, 3]. The choice of generator is further affected by fabrication considerations. For instance, in order for 3D metamaterials to be realized, it is either advantageous or necessary for the design to be contiguous.

Given an appropriate generator selection, the next stage of the synthesis pipeline is evaluation and analysis. While many different competing goals may affect which analysis tool is best suited for a given problem, EM simulators which, at a minimum, allow for periodic boundary conditions and S-parameter retrieval are sufficient to fulfill most needs. Depending on the intended behavior of the synthesized metamaterial, there are several possible values of interest that may be recovered from a doubly-periodic unit cell simulation. This process starts with the recovery of a design's complex reflection and transmission coefficients. From these fundamentals, bulk effective parameters such as ϵ or μ may be recovered and fed back to the optimizer in order to achieve a specific set of desired constituent material tensors. Secondary objectives like minimizing field enhancement or limiting the amount of a constituent material used may also be determined for the next stage, optimization, which can close the synthesis loop.

Optimization is the final stage of the synthesis procedure. At this stage, the various qualities of the generated designs may be considered together in order to guide the generator toward more optimal designs. While some design requirements may be captured by a single objective, others may be better understood by several, possibly competing objectives. Metamaterial synthesis, therefore, is a natural

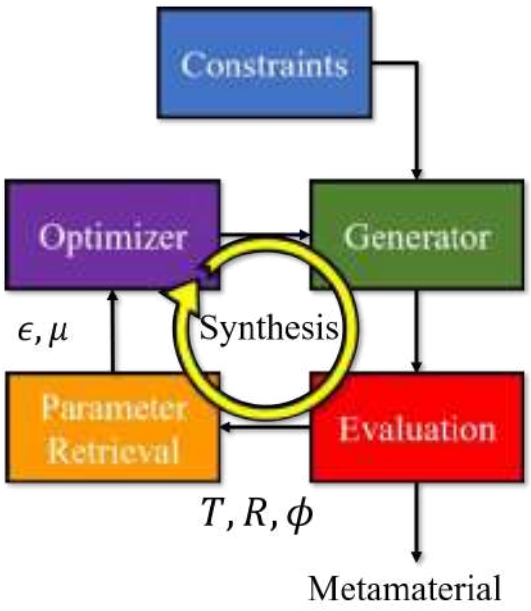


Figure 1: Flowchart showing the metamaterial synthesis feedback loop. This automated process allows the rapid generation of metamaterials which fulfill certain design constraints while maximizing performance in desired goals.

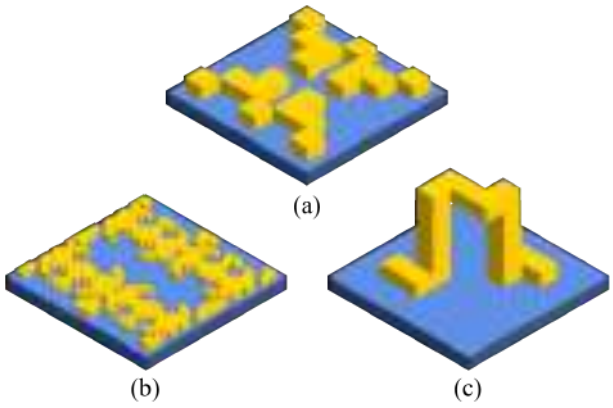


Figure 2: Examples of synthesized metamaterials. Optimizers and generators may be integrated to produce various usefully constrained metamaterials like (a) discontinuous metamaterials formed using GA, (b) high resolution metamaterial structures possible through a Bezier surface technique, and (c) 3D metamaterials which may still be fabricated due to being contiguous.

application of Multiobjective Optimization (MOO), from which there are many powerful options to choose [4]. Each optimizer integrates with the generator in a different way to produce dissimilar metamaterial shapes as shown in Figure 2. Therefore, the choice of optimizer should be selected based on the problem constraints and fabrication methods available. The Genetic Algorithm (GA) is a good choice for designs based on pixelated planar structures on a substrate like those in Figure 2(a). Since this optimizer may be used in either single objective or multiobjective fashion, it covers the most general design formulation [5]. For cases where a higher degree of granularity is needed for proper evaluation, metamaterials may also be parameterized in 2D or 3D by Bezier surfaces [6]. These allow the indexing of complex structures for which a fully pixelated version like that shown in Figure 2(b) would overwhelm the capabilities of a GA. Being continuous in nature, Bezier surfaces are best optimized by a continuous single objective or multiobjective optimizer like the Covariance Matrix Adaptation Evolutionary Strategy (CMAES) or the Auto-adaptive BORG optimizer respectively [7, 8, 9]. Bezier surfaces may also be used in conjunction with the Multiobjective Optimization with Tolerance Analysis (MOTOL) which is a more recent optimizer that uses surrogate models to actively optimize fabrication tolerances [10]. MOTOL can be used to accommodate the inherent manufacturing inaccuracies of real system fabrication and improve the robustness of metamaterial designs. Finally, some designs may even demand extension into 3D and require that all features of the structure be contiguous. For such a need, the recent Multiobjective Lazy Ant Colony Optimization algorithm (MOLACO) is opportune [1]. MOLACO actually acts as both optimizer and generator, constraining designs to maintain continuous feature connection which makes it well suited for designing structures for additive manufacturing like in Figure 2(c).

3. Conclusions

Metamaterial synthesis is a general automated design methodology that can be used to generate unique metamaterials which fulfill numerous different or even competing design criteria. The tools outlined above offer powerful options for achieve a number of different structural or fabrication goals for the creation of innovative metamaterials.

References

[1] D. Z. Zhu, P. L. Werner, and D. H. Werner, Design and Optimization of 3D Frequency Selective Surfaces Based on a Multi-Objective Lazy Ant Colony Optimization Algorithm, *IEEE Trans. Antennas Propag.* 65: 7137–7149, 2017.

[2] P. Y. Chen, C. H. Chen, H. Wang, J. H. Tsai, and W. X. Ni, Synthesis Design Of Artificial Magnetic Metamaterials Using A Genetic Algorithm, *Opt. Express* 16: 12806–12818, 2008.

[3] R. O. Ouedraogo, E. J. Rothwell, A. Diaz, S. Chen, A. Temme, and K. Fuchi, In Situ Optimization of Metamaterial-Inspired Loop Antennas, *IEEE Antennas Wirel. Propag. Lett.* 9: 75–78, 2010.

[4] J. Nagar, S. D. Campbell, Q. Ren, J. A. Easum, R. P. Jenkins, and D. H. Werner, Multi-objective Optimization Aided Metamaterials-by-Design with Application to Highly Directive Nano-Devices, *IEEE Journal on Multiscale and Multiphysics Computational Techniques* 2: 147–158, 2017. (Invited Paper).

[5] R. L. Haupt and D. H. Werner, *Genetic Algorithms in Electromagnetics*. John Wiley & Sons, 2007.

[6] P. E. Sieber and D. H. Werner, Reconfigurable Broadband Infrared Circularly Polarizing Reflectors Based On Phase Changing Birefringent Metasurfaces, *Opt. Express* 21: 1087–1100, 2013.

[7] M. D. Gregory, Z. Bayraktar, and D. H. Werner, Fast Optimization of Electromagnetic Design Problems Using the Covariance Matrix Adaptation Evolutionary Strategy, *IEEE Trans. Antennas Propag.* 59: 1275–1285, 2011.

[8] N. Hansen and A. Ostermeier, Adapting Arbitrary Normal Mutation Distributions In Evolution Strategies: The Covariance Matrix Adaptation, in *Proceedings of IEEE International Conference on Evolutionary Computation* 312–317, 1996.

[9] D. Hadka and P. Reed, Borg: An Auto-Adaptive Many-Objective Evolutionary Computing Framework, *Evol. Comput.* 21: 231–259, 2013.

[10] J. A. Easum, J. Nagar, P. L. Werner, and D. H. Werner, Efficient Multi-Objective Antenna Optimization with Tolerance Analysis Through the Use of Surrogate Models, *IEEE Trans. Antennas Propag.* 66: 6706–6715, 2018.

A Circuit Model for the Spoof Surface Plasmon Polariton Waveguides for the Terahertz Band

Gulay Ozsahin[1], M. Abdullah Unutmaz[1] and Mehmet Unlu[2]

[1]Ankara Yildirim Beyazit University, Department of Electrical and Electronics Engineering, Ankara
[2]TOBB University of Economics and Technology, Department of Electrical and Electronics Engineering, Ankara
165105109@ybu.edu.tr, maunutmaz@ybu.edu.tr, munlu@etu.tr

Abstract

We present a circuit model for the spoof Surface Plasmon Polaritons (sSPP) waveguides for the terahertz band. The circuit model uses the theorical calculation and optimization of the circuit elements in terms of the groove parameters. Here, we first simulate the sSPP waveguide by changing the groove dimensions that are the depth, aperture, and periodicity and extract the values of the circuit model parameters. Finally, we present the comparison of the proposed circuit model with the measurements.

1. Introduction

The surface plasmon polaritons (SPP) are electromagnetic waves that propagate along the metal and dielectric interfaces. These waves are strongly confined to the surfaces in the spectrum of ultraviolet and visible bands. However, as the spectrum shifts towards the terahertz and microwave bands, the metal surface behaves like a perfect electric conductor. However, surface waves that are named as the "spoof" surface plasmon polaritons are formed at the metal-dielectric interface that maintain high localization, showing a similar behavior to the SPP waves. In the literature, there are different examples of spoof surface plasmon polaritons. In [1], the sSPP structure is employed as an ultra-wideband filter. In other studies, it has been employed to form a frequency splitter and power divider [2, 3]. In addition to design and investigation of the sSPP devices, the circuit-modeling of the sSPP structure is also presented [4, 5].

In this paper, we present a circuit model for the spoof surface plasmon polariton waveguides at the terahertz regime. Here, the basic theorical formulations given in [4] and [6] are used for finding the values of some of the circuit elements, where the values of the rest are found using optimization. Finally, the results of the proposed model are compared with the measurement results.

2. The Proposed sSPP Circuit Model

We first describe the design of sSPP waveguides in this section. The sSPP waveguides are composed of a coplanar waveguide (CPW) section, transition section, and delay line section as in shown in Fig. 1. The sSPP parameters are selected considering the insertion loss, return loss, and insertion phase response of the sSPP delay line section. We simulate different sSPP structures using ANSYS HFSS for understanding effects of the groove parameters on the behavior of the insertion loss, return loss, and the insertion phase sSPP delay line. Using these simulations, the parameters with the best insertion loss/insertion phase behavior are selected, where the groove depth, h, is 30 μm, aperture, a, is 10 μm, and periodicity, d, is 25 μm.

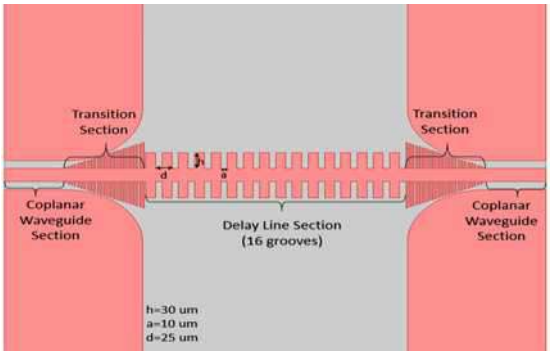


Figure 1: The schematic of the sSPP waveguide.

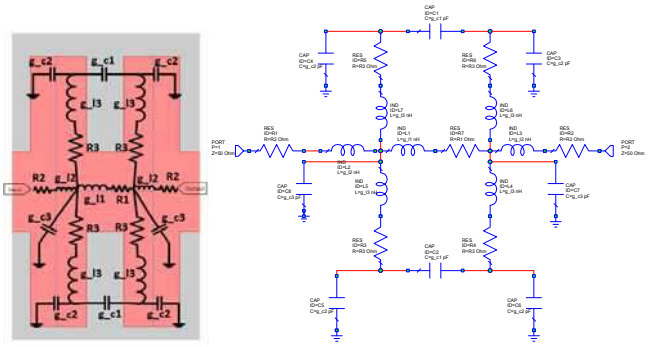


Figure 2: The proposed sSPP circuit model

After deciding on the structure to be modeled, we examine the circuit model of the spoof surface plasmon polariton structure. This study is carried out using AWR Microwave Office, and the operating frequency range is selected between 0.26 THz and 0.3 THz. The effects of the coplanar waveguide, transition, and delay line sections are all considered in the proposed circuit model, as they have been included in the ANSYS HFSS simulations.

For the circuit modeling of the sSPP waveguide, a 16-period delay line section is designed, and the element values of each groove period, indicated by Fig. 2, are calculated using the formulas given in [4, 6]. For the circuit elements' calculation, the other important parameter is the effective dielectric constant, which is given [7].

The calculations of gc_2, g_c3, g_l1, g_l2, and g_l3 are made by adapting the formulation in [4, 6] to the proposed circuit model for the terahertz band. The other element values, g_c1, R1, R2, and R3, are found using optimization, where the measurement results are used for comparison. The values of the circuit elements are given in Table 1.

Table 1: The values of the parameters for the proposed circuit model

Elements	Values
g_c1	3.79985 pF
g_c2	0.39513 pF
g_c3	18.07244 pF
g_l1	59.986 nH
g_l2	7.3825 nH
g_l3	6.1491 nH
R1	-55.34483 Ohm
R2	38.2906 Ohm
R3	-7.473573 Ohm

In addition to the delay line section modeling, the transition and coplanar waveguide sections are also modelled. For CPW, the closed form coplanar waveguide formulation is used. The model of the transition is also designed using the same approach, however, the element values are found by optimization, where the measurement results are taken as the optimization reference.

The results obtained by the proposed model are given in Fig. 3. The insertion loss and phase responses of the proposed model and measurement results exhibit similar behavior as shown in the graphs. The maximum least square error between the S-parameters of the circuit model and measurement results is found to be 0.01.

3. Conclusions

We presented a circuit model for the sSPP waveguide structures for the terahertz band, which targeted obtaining a minimum loss/maximum delay response. The proposed circuit model for a 16-section delay line showed good agreement with the measurement results between 0.26 and 0.3 THz. We believe that this model can be useful for the initial design of the sSPP waveguides, which will reduce the number of iterations and design time significantly compared to the full-wave electromagnetic simulations.

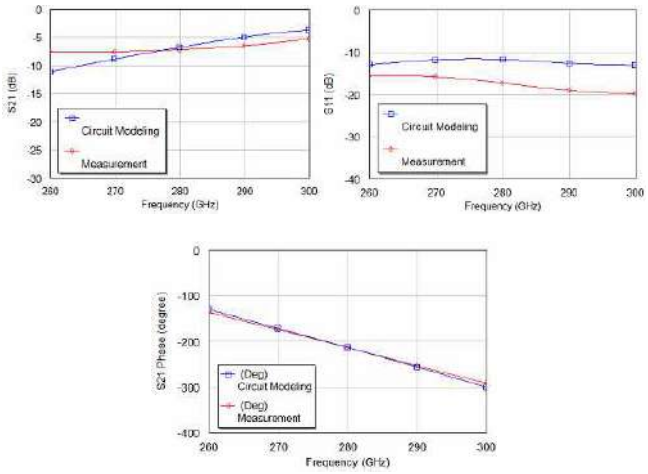


Figure 3: The comparison of the proposed circuit model and measurement results.

Acknowledgements

This work was supported by TUBITAK under grant 115E219 and TUBA under grant GEBIP 2015.

References

[1] X. Gao *et al.*, Ultra-wideband surface plasmonic Y-splitter, *Opt. Express*, 23: 23270-23277, 2014.

[2] C. Qi, S. Liao, and Q. Xue, Frequency splitter based on spoof surface plasmon polariton transmission lines, *Appl. Phys. Lett.*, 113: 161902, 2018.

[3] S. Zhou *et al.*, Spoof Surface Plasmon Polaritons Power Divider with large Isolation, *Sci. Rep.* 8: 5947, 2018.

[4] A. Kianinejad, Z. N. Chen, and C. W. Qiu, Design and modeling of spoof surface plasmon modes-based microwave slow-wave transmission line, *IEEE Trans. Microw. Theory Tech.*, 63: 1817–1825, 2015.

[5] A. Kianinejad, Z. N. Chen, C. W. Qiu, Full Modeling, Loss Reduction, and Mutual Coupling Control of Spoof Surface Plasmon-Based Meander Slow Wave Transmission Lines, *IEEE Trans. Microw. Theory Tech.*, 66: 3764-3772, 2018.

[6] C. R. Paul, *Analysis of Multiconductor Transmission Lines*, 2nd Ed., 2008.

[7] M. A. Unutmaz and M. Unlu, Modelling of the effective dielectric constant of planar spoof surface plasmon polariton waveguides, *Electron. Lett.* 53: 1418–1420 2017.

Effective Approach for Design and Simulation of Metalens Structures

Chenglin Xu[1], Matt Novak[2], Dan Herrmann[1], Li-Ce Hu[3], Evan Heller[1], and Mayank Bahl[1]

[1]RSoft Design Group, Optical Solutions Group, Synopsys, Ossining, NY, USA
[2]CODE V Team, Optical Solutions Group, Synopsys, Tucson, AZ, USA
[3]Cybernet System Taiwan, Hsinchu, Taiwan
*corresponding author, E-mail: chenglin@synopsys.com

Abstract

An effective simulation approach for metalens design is demonstrated by combining multiple algorithms. Finite-Difference Time-Domain (FDTD) or Rigorous Coupled Wave Analysis (RCWA) algorithms are used to calculate the phase delay of various nano-cells, and then efficient beam propagation methods are used to trace the beam through the metalens or its phase mask. The test example shows that this multi-algorithm combined approach is accurate and efficient with reduced demand on computational memory and time.

1. Introduction

A metalens is a difficult structure to design and simulate, since its overall size is large with many nano-structures. To simulate the nano-structures, a rigorous algorithm such as FDTD must be used. However, FDTD is computationally expensive, requiring substantial computer resources. The largest metalens that can be directly simulated in most labs through FDTD is only tens of micrometers in diameter, much smaller than what is needed [1].

In practice, FDTD is not required for the entire structure. Simulations can be decomposed into simpler elements solved individually by different methods. In this paper, we propose an approach using a rigorous algorithm to calculate the phase shift of a single unit nano-cell, from which a phase mask is constructed. More efficient methods then simulate propagation. In addition to FDTD, RCWA is an alternative algorithm for simulating the nano-cell. For the propagation, two separate, efficient methods with respect to computational resources are used in cross validation.

2. Simulation flow

2.1. Simulation of the unit nano-cell

The phase of each unit nano-cell is critical to metalens performance. Approximate estimation based on the phase shift of the mode guided in an isolated nano-cell is not accurate [1] because it ignores resonances inside the nano-cell and interference from neighboring nano-cells. In our study, we used the FullWAVE (FDTD) and DiffractMOD (RCWA) tools from RSoft [2] to calculate the phase delay for nano-cells with certain lattice patterns. Shown in Figure 1 are the calculated phase shifts as functions of normalized diameter for the nano-pillar and nano-hole (left), and for rectangular and hexagonal lattices of nano-pillars (right).

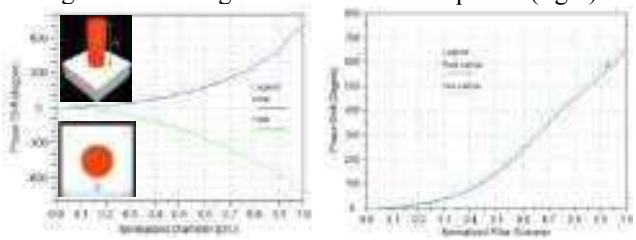


Figure 1: Phase shift of nano-pillar and nano-hole (left); for different lattices (right)

It is obvious that nano-pillar creates positive phase shift while nano-hole gives negative phase shift. It is also shown that the lattice pattern makes little difference and what matters is the normalized diameter that is associated with the fill factor.

2.2. Layout of the metalens

Based on the phase delay curves shown in Figure 1, the diameter of each cell in a metalens can be determined according the designed phase shift at that particular point. Shown in Figure 2 is the layout of an ideal metalens.

The phase profile of this metalens is shown in Equation 1.

$$\psi(x,y,\lambda_0) = -\frac{2\pi}{\lambda}\left(\sqrt{x^2+y^2+F^2}-F\right), \qquad (1)$$

where λ is the wavelength and F is the focal length. The lens is designed with a focal length of F=200μm, and a diamater of D=100μm, for green light (λ=532nm).

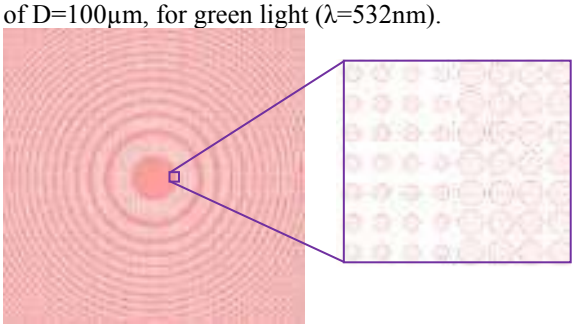


Figure 2: Layout of an ideal metalens built from nano-pillars

To make the metalens manufacturable, the normalized diameters are chosen in the range of [0.45,0.85], which can

provide 360° phase shift. The phase mask of the above metalens was generated and is shown in Figure 3.

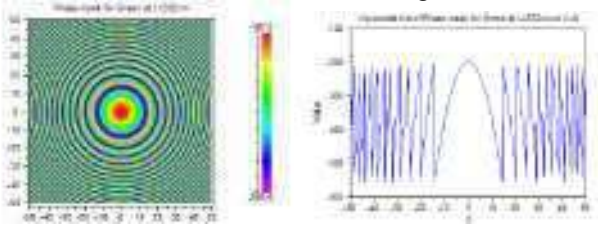


Figure 3: Phase mask of the metalens

2.3. Validation of BPM algorithm on a small structure

BPM is an efficient method to simulate forward propagation without accounting for backward reflection. We first validated BPM against the more rigorous FDTD on a small metalens 20μm in diameter and NA=0.25. The theoretical focal length is F=17.3μm. Shown in Figure 4 on the left is the BPM simulation result with F=16.96μm, and on the right is the FDTD result with F=17.14μm. The comparison shows that BPM agrees very well with FDTD for this application.

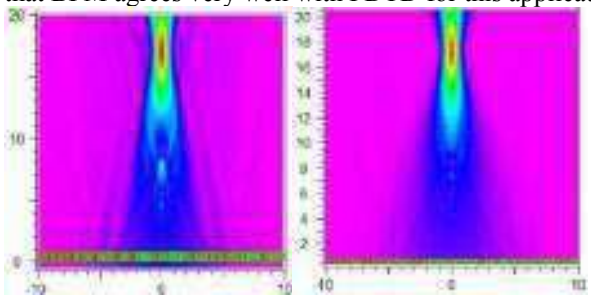


Figure 4: BPM result (left) and FDTD result (right)

For comparison the memory requirements for BPM were 0.19G and FDTD was 55G, and the respective simulation times were 1.5mins and 130 minutes.

2.4. Validation of BPM algorithm on a larger scale structure

A larger test structure is shown in Figure 2 with 100μm diameter and F=200μm. Shown in Figure 5 on the left is the BPM result with Gaussian input. The calculated focal length is F=200.1μm. The memory and time required were 3.3GB RAM and 4 minutes on a desktop computer.

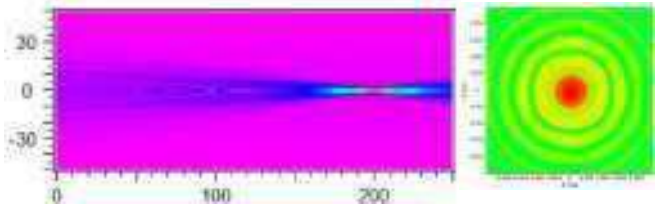


Figure 5: BPM result (left) and BSP result at L=200μm (right)

Because of memory requirements for FDTD, we validate BPM against another propagation algorithm, Beam Synthesis Propagation (BSP). BSP, due to its implementation, does not handle physical optics simulation of the nano-structures directly. Instead, it treats the metalens as a phase mask, as shown in Figure 3. The BSP result is shown in Figure 5 on the right. It confirms the smallest spot size obtained occurs at L=200μm, in agreement with the BPM result. For this simulation, BSP takes approximately 3 minutes with 4 GB RAM on a laptop.

3. Dispersion of the metalens

Chromatic dispersion of the metalens is a well-known problem. Accurate modeling of the dispersion is the key step to design of an achromatic metalens. As shown in Figure 6, the nano-pillar under study behaves very differently for each RGB wavelength, even with some phase jumps for blue and green light caused by resonances in the nano-pillar.

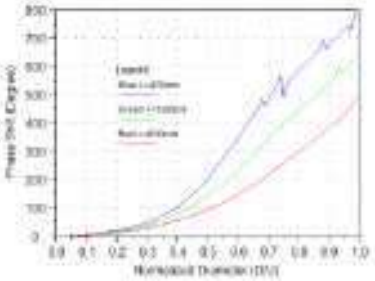


Figure 6: Dispersion of the nano-pillar

Based on the above curves, we can generate phase masks for blue and red light. We then performed BPM simulation. The focal lengths predicted via BPM are 223 μm and 161 μm for blue and red light, respectively. We also did a separate simulation using the phase masks and Synopsys' CODE V® optical design software [3]. BSP was used to verify the focus postions of 223 μm and 161 μm. The RMS fit of the beam profile was approximately λ/100 in each case. Transverse field profiles at focus are shown in Figure 7.

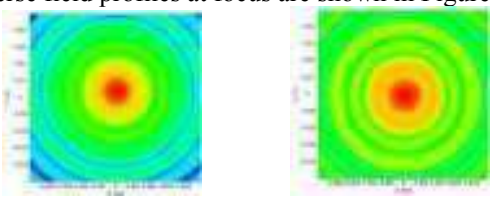


Figure 7: Transverse field obtained via BSP for blue (left) and red (right) light

4. Conclusions

We demonstrated an effective approach to design and simulate practical metalenses with rigorous FDTD or RCWA for nano-cell phase, and BPM or BSP for propagation through the metalens. The test examples shown demonstrate this is a viable approach, both accurate and efficient for computational resource requirements.

References

[1] Khorasaninejad, Mohammadreza, et al. "Polarization-insensitive metalenses at visible wavelengths." *Nano letters* 16.11 (2016): 7229-7234.

[2] https://www.synopsys.com/optical-solutions/rsoft.html

[3] https://www.synopsys.com/optical-solutions/codev.html